

# On the role of lysine in the active site Ser-X-X-Lys region of penicillin-recognizing enzymes

Saul Wolfe and Kiyull Yang

**Abstract:** Using Autodock, docking of penicillin G to the crystal structures of penicillin-recognizing enzymes leads to an alignment in the active site Ser-X-X-Lys region consisting of the serine hydroxyl group, the terminal amino group of lysine, a second hydroxyl group, and the N-C=O of the  $\beta$ -lactam. This alignment is consistent with the notion that acylation of the serine hydroxyl group proceeds by a one-step cooperative mechanism in which C-O bond formation and proton transfer to the  $\beta$ -lactam nitrogen take place through a heteroatom bridge. For the cooperative ring opening of penam by two molecules of methanol and one molecule of methylamine or one molecule of water, density functional theory with the B3LYP DFT gradient-corrected functional and the 6-31G(d) basis set reproduces the alignment seen in the docked structures. Methylamine lowers the barrier calculated at MP2/6-31G(d) from the DFT-optimized geometries by 3 kcal/mol; water increases the barrier by 4 kcal/mol. The function of the conserved lysine in the active sites of penicillin-recognizing enzymes is therefore to catalyze the formation of an acyl enzyme by a cooperative mechanism.

**Key words:** Autodock, cooperative mechanism, density functional theory (DFT), acyl enzyme.

**Résumé :** Les simulations à l'aide du programme Autodock montrent que l'arrimage de la pénicilline G aux structures cristallines des enzymes reconnaissant la pénicilline conduit à un alignement dans la région du site actif Ser-X-X-Lys formé du groupe hydroxyle de la lysine, du groupe aminé terminal de la lysine, du second groupe hydroxyle et du N-C=O du  $\beta$ -lactame. Cet arrangement est en accord avec la notion selon laquelle l'acylation du groupe hydroxyle de la lysine se produit par un mécanisme coopératif en une étape dans lequel la formation de la liaison C-O et le transfert de proton à partir de l'azote du  $\beta$ -lactame se produit par un pont hétéroatomique. Pour l'ouverture de cycle coopérative du pénam par deux molécules de méthanol et une molécule de méthylamine ou une molécule d'eau, l'utilisation de la théorie de la fonctionnelle de la densité, TFD, avec une fonctionnelle corrigée pour le gradient, B3LYP, et un ensemble de base 6-31G(d) permet de reproduire l'alignement observé dans les arrimages de structures. Pour la méthylamine la barrière calculée au niveau MP2/6-31G(d) est abaissée de 3 kcal/mol par rapport à la valeur obtenue par la TFD avec des géométries optimisées.

**Mots-clés :** Autodock, mécanisme coopératif, théorie de la fonctionnelle de la densité (TFD), enzyme acyle.

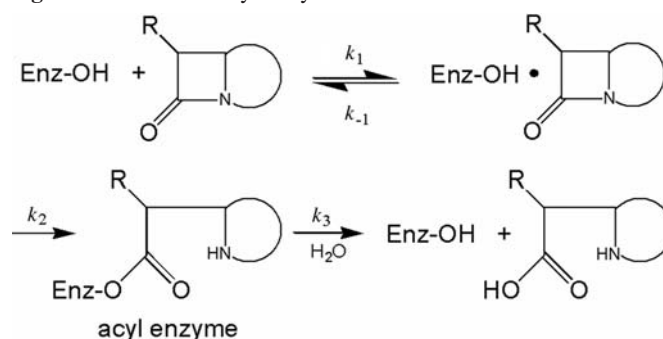
[Traduit par la Rédaction]

Penicillin-binding proteins (PBPs), the targets of  $\beta$ -lactam antibiotics,<sup>1</sup> and  $\beta$ -lactamases, which defend bacteria from the action of  $\beta$ -lactam antibiotics,<sup>2</sup> are related to each other structurally,<sup>3</sup> kinetically,<sup>4</sup> and in their evolution from a common ancestor.<sup>5</sup>

Structurally, PBPs and  $\beta$ -lactamases are serine peptidases whose catalytic serine is followed by lysine three residues towards the carboxyl terminus (Ser-X-X-Lys). PBPs and  $\beta$ -lactamases exhibit the same kinetics (Fig. 1), but with different rate constants:  $k_2 \gg k_3$  in a PBP and  $k_2 \approx k_3$  in a  $\beta$ -lactamase, and this difference is responsible for their different functions.

In the case of a PBP, the acyl enzyme cannot catalyze the final step of the synthesis of the peptidoglycan component

**Fig. 1.** Formation of acyl enzymes.



of the bacterial cell wall, which is weakened, and the internal osmotic pressure causes the cell to burst. In the case of a  $\beta$ -lactamase, hydrolysis of the acyl enzyme regenerates the enzyme and the antibiotic is inactivated as a result of the net hydrolysis of the  $\beta$ -lactam bond. This is an important mechanism of bacterial resistance to  $\beta$ -lactam antibiotics.

All of these reactions involve addition to a carbonyl group, the  $\beta$ -lactam carbonyl group in the formation of the acyl enzyme, and the carbonyl group of an ester in the hydrolysis of the acyl enzyme. There are many publications dealing with the mechanisms of these reactions, especially the roles of Lys73, Glu166 of  $\beta$ -lactamases, and a water

Received 20 May 2009. Accepted 31 August 2009. Published on the NRC Research Press Web site at canjchem.nrc.ca on 30 November 2009.

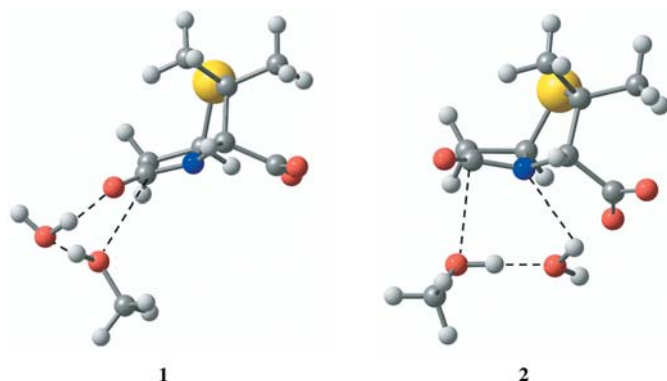
**S. Wolfe.**<sup>1</sup> Department of Chemistry, Simon Fraser University, Burnaby, BC V5A 1S6, Canada.

**K. Yang.** Department of Chemistry, Simon Fraser University, Burnaby, BC V5A 1S6, Canada; On leave from Department of Chemistry Education, Gyeongsang National University, Jinju 660-701, Korea.

<sup>1</sup>Corresponding author (e-mail: swolfe@sfu.ca).

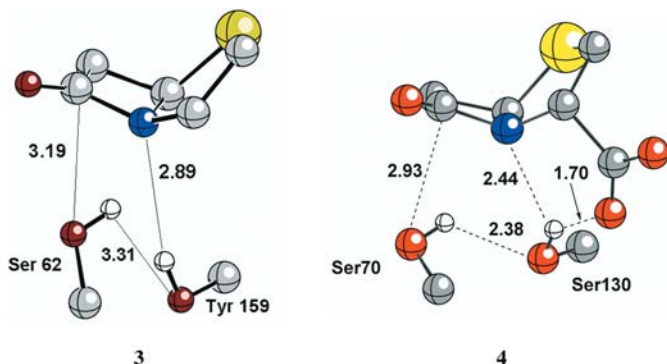
molecule.<sup>6</sup> Most of these publications propose stepwise ionic processes for these reactions. Our contrarian view regarding such mechanisms follows from the demonstration<sup>7</sup> that the aqueous hydration of an aldehyde or ketone does not proceed in a stepwise ionic manner but, rather, by a cyclic (cooperative) mechanism, with concurrent C–O bond formation and proton transfer to oxygen taking place through a solvent and (or) catalyst bridge. *The neutral hydrolysis of an ester also proceeds by a one-step cooperative mechanism.*<sup>8</sup>

Our interest in the cooperative mechanism evolved from a computational examination of the methanolysis of azetidinones,<sup>9</sup> which led to the conclusions that in the low-dielectric gas phase, an O-protonation pathway **1**, leading to a tetrahedral intermediate, is disfavoured relative to an N-protonation pathway **2**, that one water molecule provides over 10 kcal/mol of catalysis, that penam provides 5 kcal/mole of catalysis over *N*-methylazetidinone, and the 3 $\alpha$ -carboxyl group of the penicillin nucleus also provides 5 kcal/mol of catalysis.



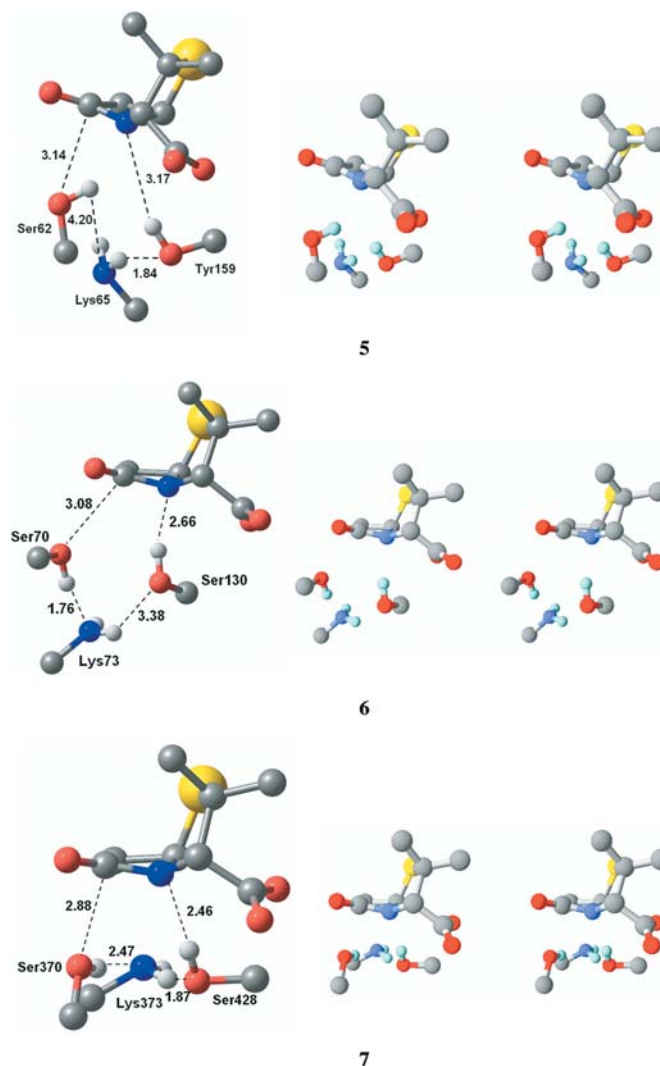
The data of ref. 9 were obtained by geometry optimization at the 3–21G(d) level followed by single-point calculation of energies at the MP2/6–31G(d) level.<sup>10</sup> We have now repeated these calculations using density functional theory with the B3LYP DFT gradient-corrected functional and the 6–31G(d) basis set,<sup>11</sup> and have confirmed the earlier trends.

Very significantly, in our view, structure **2** is now seen to resemble **3** and **4**, in which penicillin G has been docked<sup>12</sup> to the crystal structures of an exocellular PBP from *Streptomyces* R61,<sup>13</sup> and the RTEM Class A  $\beta$ -lactamase from *Escherichia coli*.<sup>14</sup> When the unprotonated terminus of the lysine residue of the Ser-X-X-Lys motif is included in these structures, the function of this conserved amino acid becomes clear.



Structures **5–7** are mono and stereo views of the active site regions of penicillin G docked to the crystal structures of *Streptomyces* R61 (**5**), the RTEM  $\beta$ -lactamase (**6**), and PBP1a from *Streptococcus pneumoniae* **7**.<sup>15</sup>

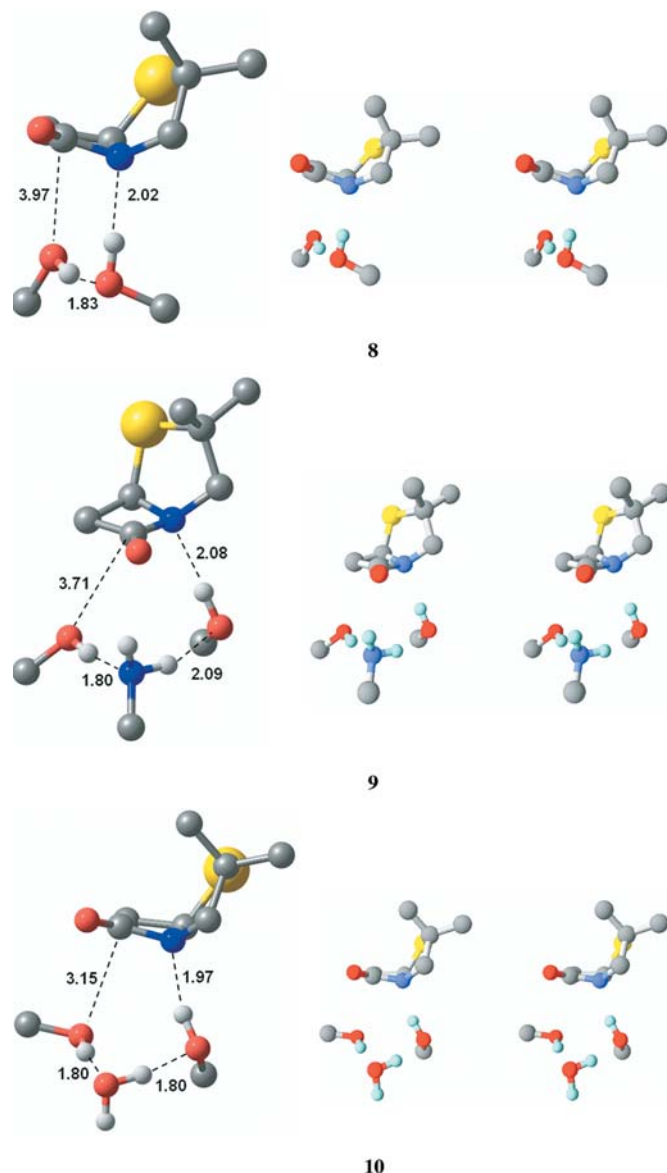
Each of these structures resembles the reactant complex of a cooperative process in which proton transfer from the hydroxyl groups of Ser62, Ser70, or Ser370 to the unprotonated<sup>16</sup> amino groups of Lys65, Lys73, or Lys373, proton transfer from these amino groups to the hydroxyl oxygens of Tyr159, Ser130, or Ser428, and proton transfer from these hydroxyl oxygens to the  $\beta$ -lactam nitrogen are accompanied by attack of the hydroxyl oxygens of Ser62, Ser70, or Ser370 on the carbon of the  $\beta$ -lactam carbonyl group.



On the basis of these observations, structures **8–10** are mono and stereo views of the reactant complexes, calculated using density functional theory with the B3LYP DFT gradient-corrected functional and the 6–31G(d) basis set, of the cooperative methanolysis of penam by two methanol molecules (**8**), two methanol molecules and one molecule of methylamine (**9**), and two methanol molecules and one molecule of water (**10**). The MP2/6–31G(d) barriers, calculated using the DFT-optimized geometries,<sup>17</sup> are the following: **8**, 28.64 kcal/mol, **9**, 25.77 kcal/mol, and **10**, 32.49 kcal/mol. Thus, methylamine catalyzes the cooperative reaction by



nearly 3 kcal/mol, but water inhibits the reaction by nearly 4 kcal/mol.



We conclude that the acyl enzymes formed in the reaction of penicillin G with penicillin-recognizing enzymes are produced by a cooperative mechanism, and that the uncharged amino group of the conserved lysine of the ubiquitous Ser-X-X-Lys motif catalyzes this process.

## Supplementary data

Supplementary data for this article (the coordinates of the docked structures, calculated reactant complexes, and calculated transition structures) are available on the journal Web site ([canjchem.nrc.ca](http://canjchem.nrc.ca)) or may be purchased from the Depository of Unpublished Data, Document Delivery, CISTI, National Research Council Canada, Ottawa, ON K1A 0R6, Canada. DUD 5299.

## Acknowledgements

This research was supported by a discovery grant from the Natural Sciences and Engineering Research Council of Canada (NSERC). We thank Drs. Zheng Shi and Yih-Huang Hsieh for preliminary docking experiments using Autodock.

## References

- (1) Waxman, D. J.; Strominger, J. L. *Annu. Rev. Biochem.* **1983**, 52 (1), 825. doi:10.1146/annurev.bi.52.070183.004141. PMID:6351730.
- (2) Frère, J.-M.; Joris, B.; Shockman, G. D. *Crit. Rev. Microbiol.* **1985**, 11 (4), 299. doi:10.3109/10408418409105906. PMID:3888533.
- (3) (a) Matagne, A.; Dubus, A.; Galleni, M.; Frère, J.-M. *Nat. Prod. Rep.* **1999**, 16 (1), 1. doi:10.1039/a705983c. PMID:10101880.; (b) Joris, B.; Ghuyssen, J.-M.; Dive, G.; Renard, A.; Dideberg, O.; Charlier, P.; Frère, J.-M.; Kelly, J. A.; Boyington, J. C.; Moews, P. C.; Knox, J. R. *Biochem. J.* **1988**, 250 (2), 313. PMID:3128280.; (c) Urbach, C.; Evrard, C.; Pudzaitis, V.; Fastrez, J.; Soumillon, P.; Declercq, J.-P. *J. Mol. Biol.* **2009**, 386 (1), 109. doi:10.1016/j.jmb.2008.12.001. PMID:19100272.; (d) Joris, B.; Ledent, P.; Dideberg, O.; Fonze, E.; Lamotte-Brasseur, J.; Kelly, J. A.; Ghuyssen, J.-M.; Frère, J.-M. *Antimicrob. Agents Chemother.* **1991**, 35 (11), 2294; and references cited therein. PMID:1804001.
- (4) Christensen, H.; Martin, M. T.; Waley, S. G. *Biochem. J.* **1990**, 266 (3), 853. PMID:2158301.
- (5) (a) Massova, I.; Mobashery, S. *Curr. Pharm. Des.* **1999**, 5 (11), 929. PMID:10539997.; (b) Massova, I.; Mobashery, S. *Antimicrob. Agents Chemother.* **1998**, 42 (1), 1. PMID:9449253.; (c) Massova, I.; Mobashery, S. *Acc. Chem. Res.* **1997**, 30 (4), 162. doi:10.1021/ar960007e.; (d) Meroueh, S. O.; Minasov, G.; Lee, W.; Shoichet, B. K.; Mobashery, S. *J. Am. Chem. Soc.* **2003**, 125 (32), 9612. doi:10.1021/ja034861u. PMID:12904027.
- (6) (a) Damblon, C.; Raquet, X.; Lian, L.-Y.; Lamotte-Brasseur, J.; Fonze, E.; Charlier, P.; Roberts, G. C. K.; Frère, J.-M. *Proc. Natl. Acad. Sci. U.S.A.* **1996**, 93 (5), 1747. doi:10.1073/pnas.93.5.1747. PMID:8700829.; (b) Lietz, E. J.; Truher, H.; Kahn, D.; Hokenson, M. J.; Fink, A. L. *Biochemistry* **2000**, 39 (17), 4971. doi:10.1021/bi992681k. PMID:10819961.; (c) Alvarez-Idaboy, J. R.; González-Jonte, R.; Hernández-Laguna, A.; Smeyers, Y. G. *J. Mol. Struct. THEOCHEM* **2000**, 504 (1-3), 13. doi:10.1016/S0166-1280(00)00351-1.; (d) Nukaga, M.; Mayama, K.; Hujer, A. M.; Bonomo, R. A.; Knox, J. R. *J. Mol. Biol.* **2003**, 328 (1), 289. doi:10.1016/S0022-2836(03)00210-9. PMID:12684014.; (e) Ishiguro, M.; Imajo, S. *J. Med. Chem.* **1996**, 39 (11), 2207. doi:10.1021/jm9506027. PMID:8667364.; (f) Díaz, N.; Suárez, D.; Sordo, T. L.; Merz, K. M., Jr. *J. Phys. Chem. B* **2001**, 105 (45), 11302. doi:10.1021/jp012881h.; (g) Gibson, R. M.; Christensen, H.; Waley, S. G. *Biochem. J.* **1990**, 272 (3), 613. PMID:1980064.; (h) Lamotte-Brasseur, J.; Dive, G.; Dideberg, O.; Charlier, P.; Frère, J.-M.; Ghuyssen, J. M. *Biochem. J.* **1991**, 279 (Pt 1), 213. PMID:1930139.; (i) Massova, I.; Kollman, P. A. *J. Comput. Chem.* **2002**, 23 (16), 1559. doi:10.1002/jcc.10129. PMID:12395425.; (j) Strynadka, N. C. J.; Adachi, H.; Jensen, S. E.; Johns, K.; Sielecki, A.; Betzel, C.; Sutouh, K.; James, M. N. G. *Nature* **1992**, 359 (6397), 700. doi:10.1038/359700a0. PMID:1436034.; (k) Strynadka, N. C. J.; Martin, R.; Jensen, S. E.; Gold, M.; Jones, J. B. *Nat. Struct. Biol.* **1996**, 3 (8), 688. doi:10.1038/nsb0896-688. PMID:8756327.

- (7) (a) Wolfe, S.; Kim, C.-K.; Yang, K.; Weinberg, N.; Shi, Z. *J. Am. Chem. Soc.* **1995**, *117* (15), 4240. doi:10.1021/ja00120a005.; (b) Wolfe, S.; Shi, Z.; Yang, K.; Ro, S.; Weinberg, N.; Kim, C.-K. *Can. J. Chem.* **1998**, *76* (1), 114. doi:10.1139/cjc-76-1-114.; (c) Hsieh, Y.-H.; Weinberg, N.; Yang, K.; Kim, C.-K.; Shi, Z.; Wolfe, S. *Can. J. Chem.* **2005**, *83* (6-7), 769. doi:10.1139/v05-027.; (d) Hsieh, Y.-H.; Weinberg, N.; Wolfe, S. *Can. J. Chem.* **2008**, *86* (2), 81. doi:10.1139/V07-074.
- (8) Shi, Z.; Hsieh, Y.-H.; Weinberg, N.; Wolfe, S. *Can. J. Chem.* **2009**, *87* (4), 544. doi:10.1139/V09-011.
- (9) Wolfe, S.; Kim, C. K.; Yang, K. *Can. J. Chem.* **1994**, *72* (4), 1033. doi:10.1139/v94-131.
- (10) Hehre, W. J.; Radom, L.; Schleyer, P. V. R.; Pople, J. A. *Ab initio Molecular Orbital Theory*; Wiley: New York, 1986.
- (11) (a) Kohn, W.; Sham, L. J. *Phys. Rev.* **1965**, *140* (4A), A1133. doi:10.1103/PhysRev.140.A1133.; (b) Kohn, W.; Becke, A. D.; Parr, R. G. *J. Phys. Chem.* **1996**, *100* (31), 12974. doi:10.1021/jp960669l.
- (12) Morris, G. M.; Goodsell, D. S.; Halliday, R. S.; Huey, R.; Hart, W. E.; Belew, R. K.; Olson, A. J. *J. Comput. Chem.* **1998**, *19* (14), 1639. doi:10.1002/(SICI)1096-987X(19981115)19:14<1639::AID-JCC10>3.0.CO;2-B.
- (13) Kelly, J. A.; Kuzin, A. P. *J. Mol. Biol.* **1995**, *254* (2), 223. doi:10.1006/jmbi.1995.0613. PMID:7490745.
- (14) Lim, D.; Park, H. U.; De Castro, L.; Kang, S. G.; Lee, H. S.; Jensen, S. E.; Lee, K. J.; Strynadka, N. C. *Nat. Struct. Biol.* **2001**, *8* (10), 848. doi:10.1038/nsb1001-848. PMID:11573088.
- (15) Contreras-Martel, C.; Job, V.; Di Guilmi, A. M.; Vernet, T.; Dideberg, O.; Dessen, A. *J. Mol. Biol.* **2006**, *355* (4), 684. doi:10.1016/j.jmb.2005.10.030. PMID:16316661.
- (16) Golemi-Kotra, D.; Meroueh, S. O.; Kim, C.; Vakulenko, S. B.; Bulychev, A.; Stemmler, A. J.; Stemmler, T. L.; Mobashery, S. *J. Biol. Chem.* **2004**, *279* (33), 34665. doi:10.1074/jbc.M313143200. PMID:15152012.
- (17) Yang, K.; Hsieh, Y.-H.; Kim, C.-K.; Zhang, H.; Wolfe, S. *Can. J. Chem.* **2010**, *88* (this issue).

# The effect of substituent rotation on aromatic quadrupole moments

Michael Lewis, Shana Beg, Aimee Clements, Dianne Tran, and Kristine Waggoner

**Abstract:** We recently reported substituent constants for the accurate prediction of molecular quadrupole moments of mono-, di-, tri- and tetra-substituted aromatics. Four of the substituents in the study,  $-\text{OH}$ ,  $-\text{NO}_2$ ,  $-\text{NH}_2$ , and  $-\text{CH}_3$ , were polyatomic and for these groups the substituent constants only hold for the lowest energy, or near-lowest energy, geometries. Herein, we report a computational investigation of the effect of rotation of  $-\text{OH}$ ,  $-\text{NO}_2$ ,  $-\text{NH}_2$ , and  $-\text{CH}_3$  groups on the aromatic quadrupole moment,  $\Theta_{zz}$ . As expected, rotation of these substituents significantly affects the aromatic  $\Theta_{zz}$  value; however, the effects are clearly periodic. Additionally, we have modified the methods to best employ our substituent constants.

**Key words:** aromatic quadrupole moment, substituent constants, substituent rotation, cation–arene complexes.

**Résumé :** On a récemment rapporté des constantes de substituant permettant de faire des prédictions précises de moments quadripolaires moléculaires de produits aromatiques mono-, di-, tri- et tétrasubstitués. Quatre des substituants examinés dans cette étude,  $-\text{OH}$ ,  $-\text{NO}_2$ ,  $-\text{NH}_2$  et  $-\text{CH}_3$ , sont polyatomiques et pour ces groupes les constantes de substituant ne sont valables que pour les géométries de plus basse énergie ou près de la plus basse énergie. Dans ce travail, on rapporte une étude théorique de l'effet de rotation des groupes  $-\text{OH}$ ,  $-\text{NO}_2$ ,  $-\text{NH}_2$  et  $-\text{CH}_3$  sur le moment quadripolaire aromatique,  $\Theta_{zz}$ . Tel qu'on s'y attendait, la rotation de ces substituants affecte d'une façon significative la valeur aromatique  $\Theta_{zz}$ , toutefois les effets sont clairement périodiques. De plus, on a modifié les méthodes qui permettent d'utiliser au mieux nos constantes de substituant.

**Mots-clés :** moment aromatique quadripolaire, constantes de substituant, rotation des substituants, complexes cation–arène.

[Traduit par la Rédaction]

## Introduction

Noncovalent interactions involving aromatic  $\pi$ -electron density<sup>1</sup> are ubiquitous in chemistry and biology with demonstrated importance in organic reaction development,<sup>2</sup> protein folding,<sup>3</sup> enzyme-substrate recognition,<sup>4</sup> solid-state organization,<sup>5</sup> the function of ion channels,<sup>6</sup> and in the design of organic semiconductors.<sup>7</sup> The aromatic molecular quadrupole moment,  $\Theta_{zz}$ , is widely used to explain the nature of the cation–arene complex (cation– $\pi$  interaction), the anion–arene complex (anion– $\pi$  interaction), and the arene–arene complex.<sup>1</sup> Dougherty and co-workers<sup>8</sup> showed that the aromatic electrostatic potential is all that need be considered when predicting the cation-binding energy of substituted aromatics, and we recently showed that the cation binding of substituted aromatics is directly related to the aromatic quadrupole moment,  $\Theta_{zz}$ .<sup>9</sup>

The relationship between the aromatic  $\Theta_{zz}$  value and cation–arene binding led our group to develop substituent constants for the accurate prediction of molecular quadrupole moments of mono-, di-, tri-, and tetra-substituted aromatics, which in turn allows for the prediction of cation–

arene binding energies based solely on the aromatic substitution pattern.<sup>10</sup> For polyatomic groups ( $-\text{OH}$ ,  $-\text{NO}_2$ ,  $-\text{NH}_2$ , and  $-\text{CH}_3$ ) the substituent constants only predict the aromatic quadrupole moment,  $\Theta_{zz}$ , if the substituents are at, or near, the lowest energy geometry. Of course, in highly anisotropic environments it is common for polyatomic substituents to assume geometries significantly distorted from gas-phase or solution-phase lowest energy geometries. For instance, solid-state structures of the electronic materials perylene diimides show significant rotation about the imide C–N bond.<sup>11</sup> In substituted nitrobenzenes, having a methyl or methoxy substituent at the ortho position,<sup>12</sup> or even a formyl group,<sup>13</sup> causes nitro group rotation in the solid state, and this area has been reviewed.<sup>14,15</sup> Aromatic substituent rotation also affects reactivity. Aromatic amines with large ortho groups undergo deamination or substitution more readily than nonsterically hindered amines and this is thought to be due to the rotation of the amino group.<sup>16–18</sup> 2,4-Dinitrochlorobenzenes partake in  $\text{S}_{\text{N}}\text{Ar}$  reactions less effectively when there is an alkyl group between the nitro substituents causing the nitro groups to rotate out of the plane of the aromatic.<sup>19,20</sup> Similarly, substituted bromothiophenes have been shown to undergo piperidinobromination significantly slower when a carboxamido group is adjacent to the bromo substituent, and this has been attributed to rotation of the carboxamido group.<sup>21</sup>

In an effort to begin understanding the effects of substituent rotation on the aromatic  $\Theta_{zz}$  value, herein, we report the effect of  $-\text{OH}$ ,  $-\text{NO}_2$ ,  $-\text{NH}_2$ , and  $-\text{CH}_3$  group rotation on the

Received 9 July 2009. Accepted 28 September 2009. Published on the NRC Research Press Web site at canjchem.nrc.ca on 9 December 2009.

M. Lewis,<sup>1</sup> S. Beg, A. Clements, D. Tran, and K. Waggoner. Department of Chemistry, Saint Louis University, 3501 Laclede Avenue, Saint Louis, MO 63103, USA.

<sup>1</sup>Corresponding author (e-mail: LewisM5@slu.edu).



aromatic quadrupole moment tensor component values. In the course of performing this study we have re-evaluated the initial approach we employed to determine aromatic quadrupole moments using our substituent constants, and here we present a modified approach.

## Theoretical background

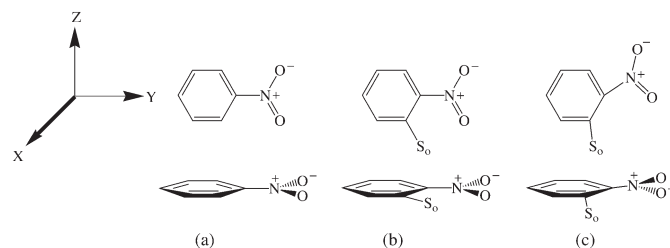
The aromatic quadrupole moment,  $\Theta_{zz}$ , is a  $3 \times 3$  tensor (eq. [1]) and for planar aromatics the off-diagonal elements are zero and eq. [2] determines  $\Theta_{zz}$ . Therefore, any effort to understand the affect of aromatic substitution on the overall aromatic  $\Theta_{zz}$  value is inherently an effort to understand the effect of substituents on the aromatic quadrupole moment diagonal tensor components. By considering the effects of aromatic substitution on the aromatic quadrupole moment diagonal tensor components we were able to develop substituent constants for the accurate prediction of the aromatic  $\Theta_{zz}$  value of mono-, di-, tri-, and tetra-substituted aromatics.<sup>10</sup>

$$[1] \quad \Theta_{zz} = \begin{bmatrix} Q_{xx} & Q_{yx} & Q_{zx} \\ Q_{xy} & Q_{yy} & Q_{zy} \\ Q_{xz} & Q_{yz} & Q_{zz} \end{bmatrix}$$

$$[2] \quad \Theta_{zz} = Q_{zz} - 0.5(Q_{xx} + Q_{yy})$$

A central assumption in the development of these substituent constants was that the aromatic substituents assume the lowest energy geometry of the relevant monosubstituted aromatic. For example, a nitro-substituted benzene with a substituent ortho to the nitro group may have a geometry where the  $-\text{NO}_2$  is in the same relative position as in the monosubstituted nitrobenzene (Fig. 1b compared to Fig. 1a). Conversely, the ortho substituent may affect the position of the nitro group by electrostatic repulsion, as seen by contrasting (c) and (a) in Fig. 1. In determining aromatic quadrupole moment substituent constants for F, Cl, Br, I, CN, OH,  $\text{CH}_3$ ,  $\text{NO}_2$ , and  $\text{NH}_2$ , the assumption that substituent positions in di-, tri- and tetra-substituted aromatics were approximately the same as they would be in the relevant monosubstituted aromatics proved to be quite reasonable.<sup>10</sup> The only cases where the assumption failed was when a highly electronegative group (F, Cl, and  $\text{NO}_2$ ) was ortho to a nitro group and electrostatic repulsion resulted in the substituent positions differing from the relevant monosubstituted aromatic, as depicted in Fig. 1c, or when OH and  $\text{NH}_2$  groups were ortho to an amino group and hydrogen-bonding resulted in the substituent positions differing from the relevant monosubstituted aromatic. While the affect illustrated in Fig. 1c was rarely observed for F, Cl, Br, I, CN, OH,  $\text{CH}_3$ ,  $\text{NO}_2$ , and  $\text{NH}_2$  substituents in di-, tri-, and tetra-substituted aromatics, it is important to note these were gas-phase calculations in a vacuum. As noted above, in highly anisotropic environments such as the solid-state, enzymes, proteins and nucleic acids the substituent positions of polysubstituted aromatics may vary greatly from the gas-phase, vacuum lowest energy geometry of the relevant monosubstituted aromatic. Of course, the most likely variation would be expected for the polyatomic substituents  $-\text{OH}$ ,  $-\text{NO}_2$ ,  $-\text{NH}_2$ , and  $-\text{CH}_3$  since these groups all have

**Fig. 1.** (a) Nitrobenzene. (b) Ortho-substituted nitrobenzene with the nitro group position unaffected by the ortho substituent, and in the same relative position as in nitrobenzene (a). (c) Ortho-substituted nitrobenzene with the nitro group position affected by the ortho substituent, and not in the same relative position as in nitrobenzene (a).



low energy rotations that could easily be initiated by the environment.

## Computational methods

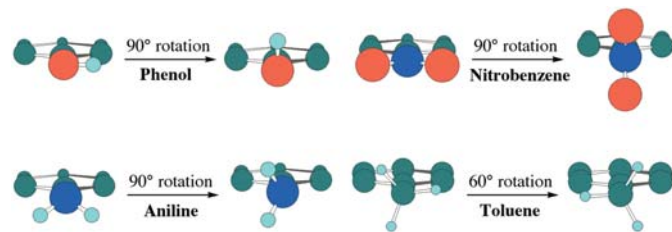
All calculations, including structure optimizations, frequency calculations, and quadrupole moment tensor component calculations were performed at the RHF/6-311G\*\* level of theory. In comparison to more rigorous theoretical methods, such as the correlated MP2 and QCISD(T) methods, and more flexible basis sets that included diffuse functions and increased polarization functions, the RHF/6-311G\*\* level of theory was shown to give the best agreement with experiment for calculating aromatic quadrupole moments.<sup>22</sup> The experimental  $\Theta_{zz}$  value for benzene is  $-8.7 \pm 0.5$  DÅ and for hexafluorobenzene it is  $+9.5 \pm 0.5$  DÅ;<sup>23</sup> the RHF/6-311G\*\* calculated values are  $-8.76$  DÅ and  $+10.06$  DÅ.<sup>10</sup> All calculations were performed using the Gaussian03 suite of programs.<sup>24</sup>

## Results and discussion

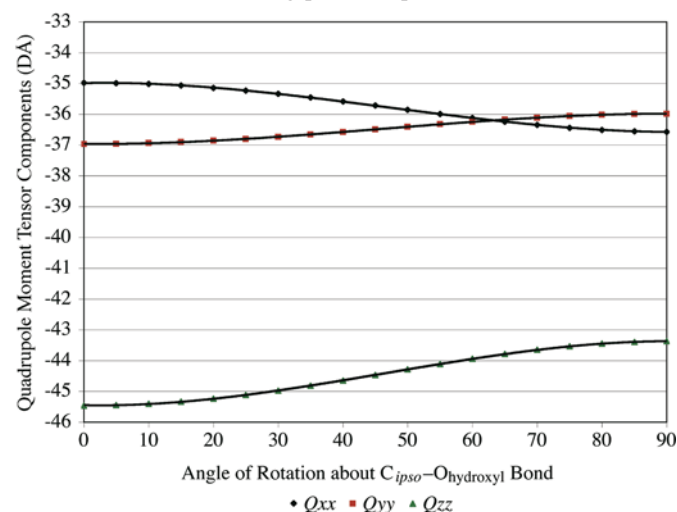
### Effects of aromatic substituent rotation on the quadrupole moment

The  $\text{C}_{\text{ipso}}$ -substituent bonds in phenol ( $-\text{OH}$ ), nitrobenzene ( $-\text{NO}_2$ ), aniline ( $-\text{NH}_2$ ), and toluene ( $-\text{CH}_3$ ) were rotated about the plane of the aromatic ring as shown in Fig. 2. For phenol, nitrobenzene, and aniline the substituents were rotated by  $90^\circ$  since this covers the unique, nonrepeating portion of the rotation. For toluene, the unique portion of the rotation is covered by a  $60^\circ$  rotation of the methyl carbon atom about the plane of the aromatic ring. In all cases, the rotations were performed in  $5^\circ$  increments and the quadrupole moment tensor components,  $Q_{xx}$ ,  $Q_{yy}$ , and  $Q_{zz}$ , were determined for each point. Importantly, the calculations were performed such that the dihedral angle corresponding to the substituent rotation was held constant, but all other geometric variables were optimized. Figures 3–6 show the plots for phenol, nitrobenzene, aniline, and toluene. Tables containing the numerical results are in the Supplementary data. The  $0^\circ$  dihedral angles in Figs. 3–6 represent the optimized geometries. For phenol (Fig. 3) this means the  $\text{H}_{\text{hydroxyl}}-\text{O}_{\text{hydroxyl}}-\text{C}_{\text{ipso}}-\text{C}_{\text{ortho}}$  dihedral angle is  $0^\circ$ , for nitrobenzene (Fig. 4) the  $\text{O}_{\text{nitro}}-\text{N}_{\text{nitro}}-\text{C}_{\text{ipso}}-\text{C}_{\text{ortho}}$  dihedral angle is  $0^\circ$ , and for toluene (Fig. 6) one of the  $\text{H}_{\text{methyl}}-\text{C}_{\text{methyl}}-\text{C}_{\text{ipso}}-\text{C}_{\text{ortho}}$  dihedral angles is  $0^\circ$ . For aniline, the optimized structure is pyrami-

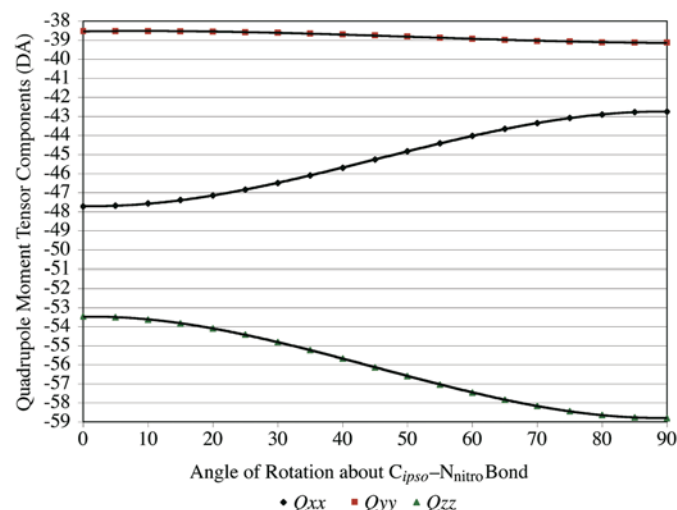
**Fig. 2.** The effect of aromatic  $-\text{OH}$ ,  $-\text{NO}_2$ ,  $-\text{NH}_2$ , and  $-\text{CH}_3$  substituent rotation was investigated by rotating about the aromatic ring plane the  $\text{C}_{\text{ipso}}-\text{O}_{\text{hydroxyl}}$  bond of phenol by  $90^\circ$ , the  $\text{C}_{\text{ipso}}-\text{N}_{\text{nitro}}$  bond of nitrobenzene by  $90^\circ$ , the  $\text{C}_{\text{ipso}}-\text{N}_{\text{amino}}$  bond of aniline by  $90^\circ$ , and the  $\text{C}_{\text{ipso}}-\text{C}_{\text{methyl}}$  bond of toluene by  $60^\circ$ .



**Fig. 3.** Plot of the aromatic quadrupole moment tensor components ( $Q_{xx}$ ,  $Q_{yy}$ , and  $Q_{zz}$ ) vs. the angle of rotation of the  $\text{C}_{\text{ipso}}-\text{O}_{\text{hydroxyl}}$  bond about the aromatic ring plane for phenol.



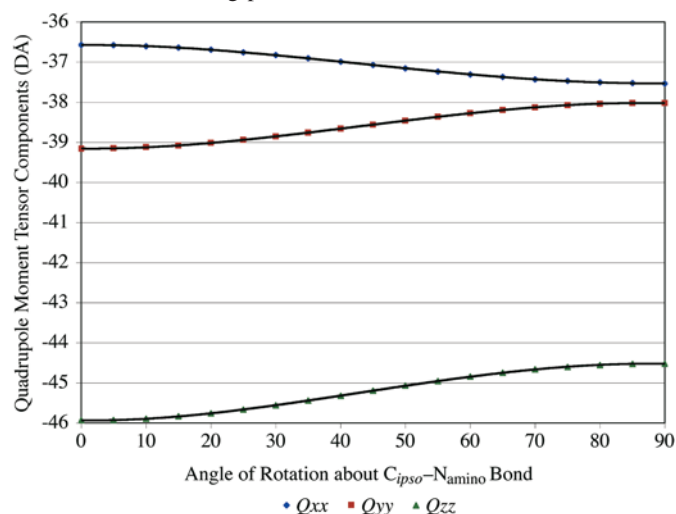
**Fig. 4.** Plot of the aromatic quadrupole moment tensor components ( $Q_{xx}$ ,  $Q_{yy}$ , and  $Q_{zz}$ ) vs. the angle of rotation of the  $\text{C}_{\text{ipso}}-\text{N}_{\text{nitro}}$  bond about the aromatic ring plane for nitrobenzene.



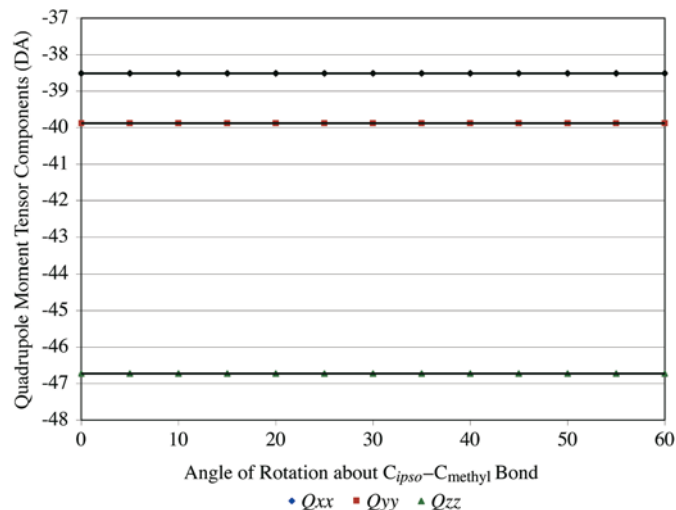
dal about the aniline nitrogen atom and thus the dihedral angle of  $0^\circ$  in Fig. 5 represents a  $\text{H}_{\text{amino}}-\text{N}_{\text{amino}}-\text{C}_{\text{ipso}}-\text{C}_{\text{ortho}}$  dihedral angles of  $45^\circ$ .

For phenol, nitrobenzene, and aniline, rotation about the

**Fig. 5.** Plot of the aromatic quadrupole moment tensor components ( $Q_{xx}$ ,  $Q_{yy}$ , and  $Q_{zz}$ ) vs. the angle of rotation of the  $\text{C}_{\text{ipso}}-\text{N}_{\text{amino}}$  bond about the aromatic ring plane for aniline.



**Fig. 6.** Plot of the aromatic quadrupole moment tensor components ( $Q_{xx}$ ,  $Q_{yy}$ , and  $Q_{zz}$ ) vs. the angle of rotation of the  $\text{C}_{\text{ipso}}-\text{C}_{\text{methyl}}$  bond about the aromatic ring plane for toluene.



$\text{C}_{\text{ipso}}$ -substituent bond results in the quadrupole moment tensor components varying by approximately 1–6 DA. However, for toluene this is not the case; rotation about the  $\text{C}_{\text{ipso}}-\text{C}_{\text{methyl}}$  bond results in essentially no change in the quadrupole moment tensor components, with variations between 0.001 and 0.004 DA (Fig. 6). The lack of variation of the quadrupole moment tensor components for toluene upon rotation of the  $\text{C}_{\text{ipso}}-\text{C}_{\text{methyl}}$  bond is easily explained by recognizing that the quadrupole moment tensor components,  $Q_{xx}$ ,  $Q_{yy}$ , and  $Q_{zz}$ , describe the distance electron density extends from the molecular center of mass in the  $x$ ,  $y$ , and  $z$  directions, respectively. Rotation of the methyl group does not significantly change the electron density distribution in any of the three Cartesian directions because there is always a hydrogen atom above or below the plane of the aromatic regardless of the methyl group geometry. Furthermore, there is little electron density about a hydrogen atom,

so the minor deviations in the H-atom positions as a result of methyl-group rotation are rendered even less significant.

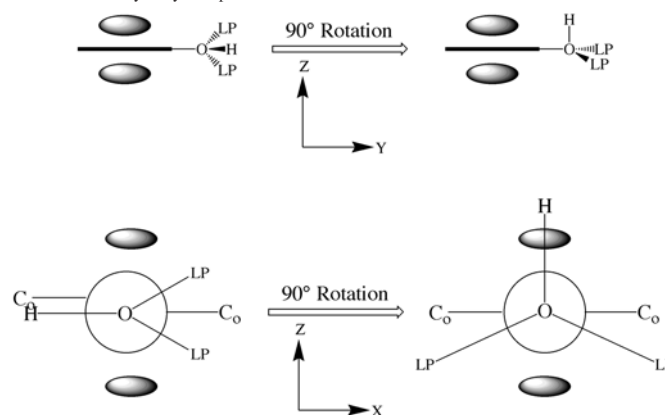
The variations in the quadrupole moment substituent constants for phenol, nitrobenzene, and aniline upon substituent rotation can also be explained by considering the effects on the electron density distribution; however, there are notable differences between the three substituted aromatics and toluene. First, as evidenced by Figs. 3–5, rotation of the substituent does significantly affect the quadrupole moment tensor components. Second, it is not only the orientation of the hydrogen atoms that is important, but additionally the position of the heteroatom lone pairs upon substituent rotation must also be considered to give the best rationale for the variations in the quadrupole moment tensor components. Figure 7 helps explain the quadrupole moment tensor component variations for phenol (Fig. 3). The tensor component  $Q_{xx}$  becomes more negative upon  $90^\circ$  rotation of the  $-\text{OH}$  group with respect to the plane of the aromatic. Thus, electron density extends further in the  $x$  direction upon rotation of the substituent. One explanation for  $Q_{xx}$  being more negative upon  $-\text{OH}$  group rotation is that in the optimized structure the oxygen lone pairs of phenol are largely orthogonal to the arene  $\pi$ -electron density; this is best viewed via the Newman projections at the bottom of Fig. 7. After a  $90^\circ$  rotation of the  $-\text{OH}$  group, the lone pairs should overlap with the arene  $\pi$ -cloud; however, this would obviously be quite repulsive. The result is that the aromatic  $\pi$ -electron density repels the lone pairs into the  $x$  direction, making  $Q_{xx}$  more negative.

The tensor component  $Q_{yy}$  is more positive upon rotation of the  $-\text{OH}$  group in phenol (Fig. 3) and thus the electron density in the  $y$  direction becomes more contracted. This can be explained using the top view of Fig. 7. As the  $-\text{OH}$  hydrogen atom becomes parallel with the arene  $\pi$ -electron density it can partake in hydrogen bonding and move closer to the aromatic. Thus, electron density moves closer to the molecular center of mass, making  $Q_{yy}$  more positive.

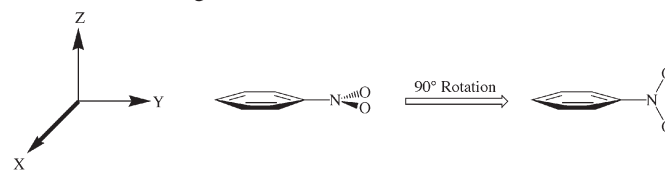
The quadrupole moment tensor component  $Q_{zz}$  is more positive upon rotation of the  $-\text{OH}$  group in phenol (Fig. 3), signifying the electron density extends less in the  $z$  direction. The Newman projections at the bottom of Fig. 7 clearly show that the hydrogen atom electron density extends more in the  $z$  direction upon rotation of the  $-\text{OH}$  group and this would make  $Q_{zz}$  more negative. However, as we noted in our explanation of the variation of the  $Q_{xx}$  tensor component, the oxygen atom lone pairs are repelled towards the  $x$  direction and away from the  $z$  direction by the aromatic  $\pi$ -electron density. Since  $Q_{zz}$  is less negative upon rotation of the  $-\text{OH}$  group, the repulsion of the oxygen atom lone pairs in the  $x$  direction must be greater than the electron density of the hydrogen atom.

The explanation for the variation of the quadrupole moment tensor components of nitrobenzene upon  $90^\circ$  rotation of the nitro group is simpler than the above explanation for phenol. The change in the  $Q_{yy}$  tensor component upon rotation of the nitro group about the plane of the aromatic ring in nitrobenzene is negligible (Fig. 4). This can be explained using Fig. 8 where it is evident that there is little change in the extension of the electron density in the  $y$  direction upon nitro group rotation; the lone pairs of the oxygen atoms extend in the  $y$  direction to approximately the same extent re-

**Fig. 7.** View of phenol, with lone pairs, down the  $x$  plane (top) and down the  $y$  plane (bottom). In the top view the solid line is the aromatic ring. The bottom view is a Newman projection viewed down the  $\text{O}_{\text{hydroxyl}}-\text{C}_{\text{ipso}}$  bond.



**Fig. 8.** Rotation of the nitro group in nitrobenzene about the plane of the aromatic ring.

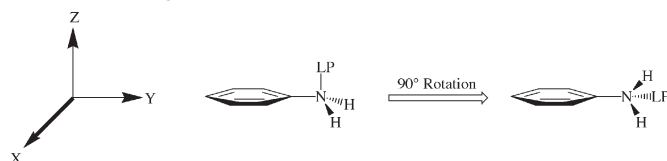


gardless of the nitro group orientation. The  $Q_{xx}$  quadrupole moment tensor component becomes more positive by approximately 5 DA upon rotation of the nitro group by  $90^\circ$  and Fig. 8 clearly shows why this is the case; as the nitro group is rotated the lone pairs of the oxygen atoms extend less in the  $x$  direction. Conversely, nitro group rotation results in the lone pairs of the oxygen atoms extending more in the  $z$  direction and this explains why the  $Q_{zz}$  tensor component becomes more negative by about 5 DA as the nitro group is rotated  $90^\circ$  about the plane of the aromatic ring.

The variation in the quadrupole moment tensor components of aniline upon  $90^\circ$  rotation of the  $-\text{NH}_2$  group about the plane of the aromatic ring (Fig. 5), much like for rotation of the nitro group in nitrobenzene, is relatively easily explained. The  $Q_{xx}$  tensor component becomes more negative upon rotation of the amino group and, as is evidenced by Fig. 9, this is because the nitrogen atom lone pair extends more in the  $x$  direction upon rotation. The  $Q_{yy}$  tensor component becomes more positive with amino group rotation (Fig. 5) and this too can be attributed to the orientation of the nitrogen atom lone pair. In the optimized geometry of aniline the aromatic ring  $\pi$ -electron density repels the nitrogen atom lone pair in the  $y$ -direction. In the structure where the amino group is rotated  $90^\circ$  the lone pair is orthogonal to the aromatic ring  $\pi$ -electron density and is therefore not repelled in the  $y$  direction. Thus, electron density extends less in the  $y$  direction upon amino group rotation and, consequently,  $Q_{yy}$  becomes more positive. The rotation of the amino group lone pair also results in electron density extending less in the  $z$  direction, as is obvious from Fig. 9, and this results in a more positive  $Q_{zz}$  quadrupole moment tensor component (Fig. 5).



**Fig. 9.** Rotation of the amino group in aniline about the plane of the aromatic ring.

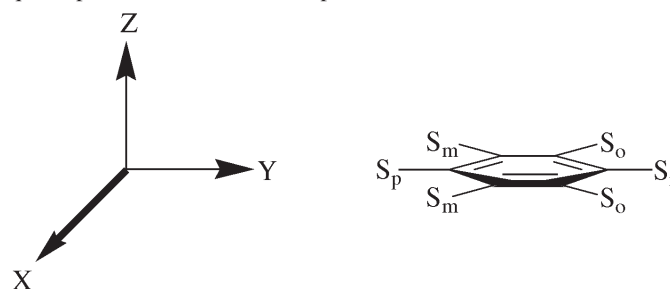


### Modified approach to employing quadrupole moment tensor component substituent constants

In our initial report detailing the development of quadrupole moment tensor component substituent constants for the prediction of aromatic quadrupole moments, we provided  $Q_{xx}$ ,  $Q_{yy}$ , and  $Q_{zz}$  substituent constants for substituents in the ipso, ortho, meta, and para positions and this amounted to 12 sets of substituent constants.<sup>10</sup> Upon reconsideration, this can be significantly simplified to seven sets of substituent constants. The  $Q_{zz}$  tensor component describes the electron density distribution in the  $z$  direction, and Fig. 10 shows that the effect on  $Q_{zz}$  should not be related to the position the substituent occupies. Thus, there is no need for  $Q_{zz,i}$ ,  $Q_{zz,o}$ ,  $Q_{zz,m}$ , and  $Q_{zz,p}$  substituent constants, as we initially reported, and one average value,  $Q_{zz}$ , would suffice. Table 1 lists the average  $Q_{zz}$  values for each substituent. There is a very small standard deviation for these values, generally on the order of a hundredth to a tenth DA, supporting the notion that the position of the substituent is inconsequential. To a lesser extent, simplification is also in order for the  $Q_{xx}$  quadrupole moment tensor component substituent constants. It is apparent from Fig. 10 that the electron density distribution in the  $x$  direction should be affected equally by ipso and para substitution and equally by ortho and meta substitution. Thus, instead of the four  $Q_{xx,i}$ ,  $Q_{xx,o}$ ,  $Q_{xx,m}$ , and  $Q_{xx,p}$  substituent constants,  $Q_{xx,ip}$  and  $Q_{xx,om}$  are all that is needed. The  $Q_{xx,ip}$  and  $Q_{xx,om}$  tensor component substituent constants, obtained by averaging the  $Q_{xx,i}$  and  $Q_{xx,p}$  values and the  $Q_{xx,o}$  and  $Q_{xx,m}$  values, respectively, are given in Table 1, and again, small standard deviations for these values support this approach. Finally, Fig. 10 shows that substituent position is important in determining electron density distribution in the  $y$  direction, and thus,  $Q_{yy}$  substituent constants are required for the four unique aromatic positions, ipso ( $Q_{yy,i}$ ), ortho ( $Q_{yy,o}$ ), meta ( $Q_{yy,m}$ ), and para ( $Q_{yy,p}$ ). These were reported in our initial study<sup>10</sup> and are shown in Table 1.

As we noted above, a central assumption in the development of these substituent constants was that the aromatic substituents assume the lowest energy geometry of the relevant monosubstituted aromatic, and that interactions with neighboring substituents are minimal.<sup>10</sup> This assumption broke down for penta- and hexa-substituted aromatics; however, it worked very well for mono-, di-, tri-, and tetra-substituted arenes. In the course of the present study, we recognized another important assumption that was unintentionally made in our initial study:<sup>10</sup> the center of mass of a substituted aromatic is the same as the average center of mass of the relevant monosubstituted aromatics. For instance, our approach assumed that the center of mass of 1-bromo-3-chloro-5-fluorobenzene is equal to the average of the center of masses of bromobenzene, chlorobenzene, and fluorobenzene; this assumption is obviously not true.

**Fig. 10.** Substituent positions used to determine effects on aromatic quadrupole moment tensor component substituent constants.



Further underlying the error of this assumption, constitutional substituted-benzene isomers would have the same center of mass; 1-bromo-3-chloro-5-fluorobenzene would have the same center of mass as 1-bromo-2-chloro-5-fluorobenzene. Again, this is obviously not true. Since our initial aim was to develop substituent constants that could be used to predict, with relative ease, the quadrupole moment of substituted aromatics, rather than complicate the approach by adding a center-of-mass component, we offer the set of rules in Table 2 on how to orient the substituted aromatics before employing the substituent constants in Table 1. The rules in Table 2 minimize our erroneous center of mass assumption by making sure the substituent with the greater number of atoms or, if the substituents have the same number of atoms, the heavier substituent is placed at the ipso position. The ipso position discussed in Table 2 represents the position shown in Fig. 10 ( $S_i$ ).

Going back to our initial assumption, that the aromatic substituents assume the lowest energy geometry of the relevant monosubstituted aromatic,<sup>10</sup> we now realize this affects more than just the  $\Theta_{zz}$  prediction of penta- and hexa-substituted aromatics. It also precludes predicting the  $\Theta_{zz}$  values of aromatics where three nonhydrogen atoms are adjacent to each other, as in a 1,2,3-trisubstituted aromatic or a 1,2,3,5-tetrasubstituted aromatic. For instance, using the substituent constants in Table 1 and placing either the heaviest atom or the polyatomic group with the most atoms in the ipso position, the predicted  $\Theta_{zz}$  values of 1,3-dichloro-2-nitrobenzene and 1-bromo-2-chloro-3-cyanobenzene are  $-10.59$  and  $-5.45$  DA, respectively. The calculated values are  $-0.82$  and  $+12.49$  DA, respectively. Given that we can predict the  $\Theta_{zz}$  values of 1,3,5-trisubstituted aromatics quite well, *vide infra*, the only explanation for this result is steric crowding, the same explanation we gave for the inability to predict penta- and hexa-substituted aromatics using our approach. The one caveat here is that if three substituents are adjacent to one another, and one of them is a fluorine atom, then the substituent constants (Table 1) and the orientation rules (Table 2) still work. Given the very small size of a fluorine atom this supports the notion that sterics are the primary factor in precluding  $\Theta_{zz}$  prediction of congested aromatics, where a congested aromatic can be defined as having three nonhydrogen atoms adjacent to each other, at least for the purpose of predicting aromatic  $\Theta_{zz}$  values. These insights about congested aromatics and the special consideration of fluorine atoms are accounted for in Table 2.

Using the simplified quadrupole moment substituent constants (Table 1) and the orientation rules (Table 2), we pre-

**Table 1.** Simplified quadrupole moment tensor component substituent constants for aromatic substituents (S). All values in DÅ.

S	$Q_{zz}$	$Q_{xx,ip}$	$Q_{xx,om}$	$Q_{yy,i}$	$Q_{yy,o}$	$Q_{yy,m}$	$Q_{yy,p}$
F	-3.23	-2.50	-8.55	-1.16	0.28	-9.80	-20.97
Cl	-11.82	-10.55	-16.59	-5.36	-7.22	-18.87	-31.41
Br	-17.68	-16.40	-21.42	-9.80	-13.17	-24.15	-35.57
I	-28.51	-27.40	-29.59	-19.60	-24.66	-33.90	-40.30
CN	-9.32	-7.65	-26.48	-5.42	-0.58	-28.35	-61.94
NO <sub>2</sub>	-13.48	-16.10	-30.61	-6.85	-6.77	-35.89	-65.78
NH <sub>2</sub>	-6.52	-4.64	-2.83	-8.34	-7.17	-0.98	3.61
CH <sub>3</sub>	-5.54	-6.83	-6.18	-8.20	-7.96	-5.36	-3.74
OH	-5.02	-3.46	-5.32	-5.29	-1.16	7.17	-6.61

**Table 2.** Orientation rules for how to orient di-, tri-, and tetra-substituted aromatics when predicting  $\Theta_{zz}$  values using the substituent constants in Table 1.

Substituted aromatic	Orientation rules <sup>a</sup>
Disubstituted, 1,3,5-trisubstituted, and 1,2,4,5-tetrasubstituted aromatics	The substituent with the greater number of atoms should be in the ipso position. If the substituents have the same number of atoms, the heavier one should be in the ipso position.
1,2,3-Trisubstituted aromatics	Only works if at least one substituent is F (sterics). Otherwise, see above rules for disubstituted and 1,3,5-trisubstituted aromatics.
1,2,4-Trisubstituted aromatics	One of the substituents in the 1- or 2-position must be ipso. Otherwise, see above rules for disubstituted and 1,3,5-trisubstituted aromatics.
1,2,3,4-Tetrasubstituted aromatics	Only works if F is in the 2- or 3-position (sterics). For the two nonfluorine substituents that are vicinal to each other, see above rules for disubstituted and 1,3,5-trisubstituted aromatics.
1,2,3,5-Tetrasubstituted aromatics	Only works if F is in either 1-, 2-, or 3-position (sterics). For the two nonfluorine substituents in the 1-, 2-, or 3-position, see above rules for disubstituted and 1,3,5-trisubstituted aromatics.

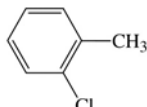
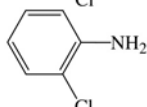
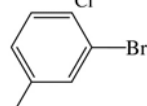
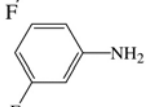
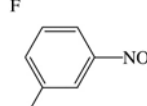
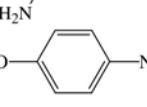
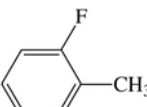
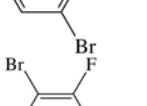
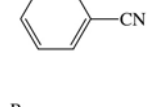
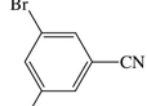
<sup>a</sup>The ipso position is defined by Fig. 10.

dicted the quadrupole moments for randomly substituted di-, tri-, and tetra-substituted aromatics, six examples of each (A–R), and these are compared to the calculated  $\Theta_{zz}$  values in Table 3. Our previous work illustrates exactly how the substituent constants are employed for predicting aromatic  $\Theta_{zz}$  values. For the disubstituted aromatics the predicted  $\Theta_{zz}$  values are almost identical to the calculated values. The only instances where caution should be taken in predicting aromatic quadrupole moments of disubstituted aromatics using the substituent constants in Table 1 is when the nature of atoms ortho to each other is such that they will cause their positions to change relative to the relevant monosubstituted aromatics. For instance, 1-fluoro-2-nitrobenzene has two highly electronegative groups ortho to each other and electrostatic repulsion would cause the position of the fluorine to not be the same as in fluorobenzene, and the position of the nitro group to not be the same as in nitrobenzene. This is exemplified by comparing the calculated quadrupole moment of 1-fluoro-2-nitrobenzene,  $\Theta_{zz} = -1.35$  DÅ, to the value predicted using the substituent constants in Table 1 and the orientation rules in Table 2,  $\Theta_{zz} = -9.85$  DÅ. This has nothing to do with the center of mass assumption and the resulting orientation rules, and instead is a result of the assumption from our original paper<sup>10</sup> that the aromatic substituents assume the lowest energy geometry of the relevant monosubstituted

tuted aromatic, and that interactions with neighboring substituents are minimal. As we noted in our original paper, the neighboring group interactions that would lead to this assumption failing include electronic repulsion by highly electronegative atoms being ortho to each other and hydrogen bonding from groups such as amino and hydroxyl being ortho to each other. As can be seen with ortho-chlorotoluene, A, and ortho-chloroaniline, B, in Table 3, the approach outlined in Tables 1 and 2 for predicting the  $\Theta_{zz}$  values of ortho-substituted aromatics where the groups are not highly electronegative, and not involved in hydrogen bonding, is excellent. Likewise, this approach also gives excellent results predicting the  $\Theta_{zz}$  values of meta (C–E) and para disubstituted aromatics (F), as shown in Table 3.

The 1,2,3-, 1,2,4-, and 1,3,5-substitution patterns are the three general possibilities for trisubstituted aromatics. As discussed above, and specified in Table 2, for 1,2,3-trisubstituted aromatics, one of the three substituents must be a fluorine atom, and when this is the case the  $\Theta_{zz}$  value can be predicted using Tables 1 and 2, as shown in Table 3 for aromatics G and H. For 1,3,5- (I) and 1,2,4-trisubstituted aromatics (J–L) the steric concern of having three adjacent substituents is moot and we see decent agreement between the calculated and predicted  $\Theta_{zz}$  values (Table 3). For the tetrasubstituted aromatics, both the 1,2,3,4- (M and N) and 1,2,3,5-substitu-

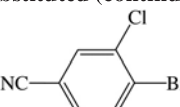
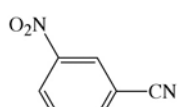
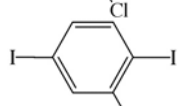
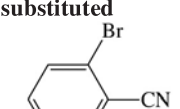
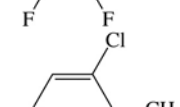
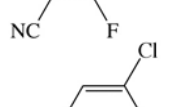
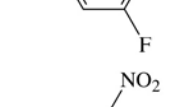
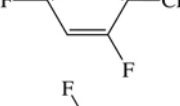
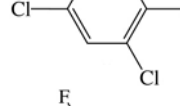
**Table 3.** Predicted and calculated  $\Theta_{zz}$  values for di-, tri-, and tetra-substituted aromatics.

		$\Theta_{zz}(\text{D}\text{\AA})$	
Aromatic		Calculated	Predicted
Di-substituted			
A		-6.45	-6.69
		-8.45	-8.70
B		-5.64	-7.39
		-2.98	-2.84
C		-15.10	-15.37
		-8.05	-8.77
Tri-substituted			
D		-5.20	-6.29
		-6.59	-5.53
E		+14.76	+11.48
			

tion patterns (**O** and **P**) have the possibility for steric crowding: however, so long as one of the substituents is a fluorine atom, the constants in Table 1 and the rules in Table 2 give predicted  $\Theta_{zz}$  values in good agreement with the calculated values (Table 3). Finally, the 1,2,4,5-tetrasubstituted aromatics (**Q** and **R**) do not have the problem of steric crowding and the predicted and calculated values are in good agreement.

Throughout the discussion of the results in Table 3, we have stated that the agreement between the calculated and predicted  $\Theta_{zz}$  values is good. Ultimately, the greatest value of the substituent constants in Table 1 and the orientation rules in Table 2 lie in being able to predict relative  $\Theta_{zz}$  values, although in many cases in Table 3 the agreement in absolute terms is quite good. Still, since the aromatic  $\Theta_{zz}$  value is an excellent predictor of how well an aromatic will

**Table 3.** Continued.

		$\Theta_{zz}(\text{D}\text{\AA})$	
Aromatic		Calculated	Predicted
Tri-substituted (continued)			
J		+11.72	+12.23
K		+11.01	+8.32
L		-3.47	-7.52
Tetra-substituted			
M		-2.86	-5.07
N		+6.59	+12.31
O		-3.75	-4.47
P		+5.35	+7.85
Q		-1.33	+1.43
R		+13.97	+18.50

**Note:** The quadrupole moment tensor components used to determine the calculated  $\Theta_{zz}$  values are provided in the Supplementary data.

bind a cation,<sup>9</sup> the ability to predict relative  $\Theta_{zz}$  values would allow one to say that a certain substitution pattern will allow for greater, or poorer, cation binding. As a means of quantifying how well the relative  $\Theta_{zz}$  value is predicted using the constants in Table 1 and the rules in Table 2, we



**Table 4.** Ranking of the calculated ( $\Theta_{zz,calc}$ ) and predicted ( $\Theta_{zz,pred}$ )  $\Theta_{zz}$  values for aromatics **A–R** and the absolute value of the difference between the rankings.

Aromatic	$\Theta_{zz,calc}$ rank	$\Theta_{zz,pred}$ rank	$ \Delta(Rank) $
<b>A</b>	5	6	1
<b>B</b>	2	3	1
<b>C</b>	6	5	1
<b>D</b>	10	11	1
<b>E</b>	1	1	0
<b>F</b>	3	2	1
<b>G</b>	7	7	0
<b>H</b>	4	8	4
<b>I</b>	18	15	3
<b>J</b>	16	16	0
<b>K</b>	15	14	1
<b>L</b>	9	4	5
<b>M</b>	11	9	2
<b>N</b>	14	17	3
<b>O</b>	8	10	2
<b>P</b>	13	13	0
<b>Q</b>	12	12	0
<b>R</b>	17	18	1

ranked the aromatics in Table 3 based on the calculated ( $\Theta_{zz,calc}$ ) and predicted ( $\Theta_{zz,pred}$ )  $\Theta_{zz}$  values and the results are collected in Table 4. The rankings give the aromatic with the most negative  $\Theta_{zz}$  value the number 1 and the most positive  $\Theta_{zz}$  aromatic is ranked 18. By calculating the absolute value of the difference between the two sets of rankings,  $|\Delta(rank)|$  (Table 4), we can quantify how well the predicted values perform in determining relative  $\Theta_{zz}$  values. As shown in Table 4, for two-thirds of the 18 aromatics in Table 3 the  $\Theta_{zz,calc}$  and  $\Theta_{zz,pred}$  rankings are exactly the same ( $|\Delta(rank)| = 0$ ), or they differ by one ( $|\Delta(rank)| = 1$ ). The average  $|\Delta(rank)|$  value for the 18 aromatics is 1.4. Thus, for the purposes of predicting relative  $\Theta_{zz}$  values and, subsequently, relative cation binding affinities, the predictive scheme outlined in Tables 1 and 2 performs quite well.

One final caveat should be noted. The amino group quadrupole moment substituent constants were developed from aniline and disubstituted anilines. Aniline, of course, is  $sp^3$  hybridized and pyramidal at the nitrogen atom; however many substituted anilines, such as para-nitro-aniline, have the amino nitrogen atom  $sp^2$  hybridized and conjugated with the aromatic ring such that the geometry about the nitrogen atom is planar. Thus, care should be taken when applying the approach outlined here for the prediction of the  $\Theta_{zz}$  values of substituted anilines that are planar about the amino nitrogen atom. Furthermore, a similar point can be made for substituted phenols. The H–O–C bond angle in phenol is  $111.1^\circ$  at the RHF/6-311G\*\* level of theory, and thus, the oxygen atom is  $sp^3$  hybridized. However, it is not difficult to envision substituents causing one of the phenol oxygen atom lone pairs to become conjugated with the aromatic ring, making the oxygen atom  $sp^2$  hybridized. This, of course, would have repercussions for the prediction of aromatic  $\Theta_{zz}$  values of substituted phenols. The issue of OH and  $NH_2$  conjugation with the aromatic, and how this conjugation is increased or decreased with substitution, will certainly make it a challenge to translate the success we have demonstrated in

predicting aromatic  $\Theta_{zz}$  values into successfully using the predicted  $\Theta_{zz}$  values to predict cation-substituted arene binding energies where one of the substituents is rotated. We are currently addressing this issue, and the preliminary results are encouraging. We look forward to reporting this work when it is complete.

## Conclusion

The rotation of an aromatic methyl group does not significantly affect the quadrupole moment tensor components; however, there is a noticeable change in these values when a hydroxyl, nitro, or amino group is rotated. These changes would ultimately change the molecular quadrupole moment in aromatics with rotated groups; however, since the change in quadrupole moment tensor components upon substituent rotation is periodic, it seems reasonable that the  $\Theta_{zz}$  value of aromatics with substituents at non-lowest energy geometries could possibly be predicted. Such prediction could be an extension of the substituent constants and orientation rules we present here, a modification of our previous work,<sup>10</sup> and current work in our group is directed at this problem. Certainly, the modified approach we present here for predicting aromatic  $\Theta_{zz}$  values works very well in predicting relative  $\Theta_{zz}$  values, and would therefore be useful in predicting cation–arene binding energies via simple inspection of the aromatic substitution pattern.

## Supplementary data

Supplementary data for this article are available on the journal Web site (<http://canjchem.nrc.ca>) or may be purchased from the Depository of Unpublished Data, Document Delivery, CISTI, National Research Council Canada, Ottawa, ON K1A 0R6, Canada. DUD 5300. For more information on obtaining material, refer to <http://cisti-icist.nrc-cnrc.gc.ca/eng/ibp/cisti/collection/unpublished-data.html>.

## Acknowledgement

This work was supported by the Research Corporation (7804) and the National Center for Supercomputing Applications (CHE050039N) through an allocation on the SGI Altix system.

## References

- (1) (a) Meyer, E. A.; Castellano, R. K.; Diederich, F. *Angew. Chem. Int. Ed.* **2003**, 42 (11), 1210. doi:10.1002/anie.200390319.; (b) Ma, J. C.; Dougherty, D. A. *Chem. Rev.* **1997**, 97 (5), 1303. doi:10.1021/cr9603744. PMID: 11851453.
- (2) (a) Gowrisankar, S.; Lee, K. Y.; Kim, S. C.; Kim, J. N. *Bull. Korean Chem. Soc.* **2005**, 26, 1443; (b) Jones, G. B. *Tetrahedron* **2001**, 57 (38), 7999. doi:10.1016/S0040-4020(01)00753-0.
- (3) (a) Guvench, O.; Brooks, C. L., III. *J. Am. Chem. Soc.* **2005**, 127 (13), 4668. doi:10.1021/ja043492e. PMID:15796532.; (b) Neelamkavil, S.; Arison, B.; Birzin, E.; Feng, J.-J.; Chen, K.-H.; Lin, A.; Cheng, F.-C.; Taylor, L.; Thornton, E. R.; Smith, A. B., III; Hirschmann, R. *J. Med. Chem.* **2005**, 48 (12), 4025. doi:10.1021/jm058184l. PMID:15943475.; (c) Gromiha, M. M.; Suwa, M. *Int. J. Biol. Macromol.* **2005**, 35 (1–2), 55. doi:10.1016/j.ijbiomac.2004.12.001. PMID:

- 15769516.; (d) Burley, S. K.; Petsko, G. A. *Science* **1985**, 229 (4708), 23. doi:10.1126/science.3892686. PMID: 3892686.
- (4) (a) Cashin, A. L.; Petersson, E. J.; Lester, H. A.; Dougherty, D. A. *J. Am. Chem. Soc.* **2005**, 127 (1), 350. doi:10.1021/ja0461771. PMID:15631485.; (b) Branduardi, D.; Gervasio, F. L.; Cavalli, A.; Recanatini, M.; Parrinello, M. *J. Am. Chem. Soc.* **2005**, 127 (25), 9147. doi:10.1021/ja0512780. PMID:15969593.
- (5) Miao, Q.; Chi, X.; Xiao, S.; Zeis, R.; Lefenfeld, M.; Siegrist, T.; Steigerwald, M. L.; Nuckolls, C. *J. Am. Chem. Soc.* **2006**, 128 (4), 1340. doi:10.1021/ja0570786. PMID: 16433553.
- (6) Weber, M. E.; Elliott, E. K.; Gokel, G. W. *Org. Biomol. Chem.* **2006**, 4 (1), 83. doi:10.1039/b513179k. PMID: 16358000.
- (7) Sokolov, A. N.; Frisci, T.; MacGillivray, L. R. *J. Am. Chem. Soc.* **2006**, 128 (9), 2806. doi:10.1021/ja057939a. PMID:16506752.
- (8) Mecozzi, S.; West, A. P.; Dougherty, D. A. *J. Am. Chem. Soc.* **1996**, 118 (9), 2307. doi:10.1021/ja9539608.
- (9) Clements, A.; Lewis, M. *J. Phys. Chem. A* **2006**, 110 (46), 12705. doi:10.1021/jp065175v. PMID:17107123.
- (10) Tran, D.; Beg, S.; Clements, A.; Lewis, M. *Chem. Phys. Lett.* **2006**, 425 (4–6), 347. doi:10.1016/j.cplett.2006.05.011.
- (11) Rajasingh, P.; Cohen, R.; Shirman, E.; Shimon, L. J. W.; Rybtchinski, B. *J. Org. Chem.* **2007**, 72 (16), 5973. doi:10.1021/jo070367n. PMID:17604397.
- (12) Hanson, J. R.; Hitchcock, P. B. *J. Chem. Res.* **2004**, 670. doi:10.3184/0308234043431726.
- (13) Hanson, J. R.; Hitchcock, P. B.; Toche, F. *J. Chem. Res.* **2008**, 476. doi:10.3184/030823408X338738.
- (14) Holden, J. R.; Dickinson, C. *J. Phys. Chem.* **1977**, 81 (15), 1505. doi:10.1021/j100530a018.
- (15) De Ridder, D. J. A.; Schenk, H. *Acta Crystallogr.* **1995**, B51, 221. doi:10.1107/S0108768194009213.
- (16) Remedi, M. V.; Buján, E. I.; Baggio, R.; Garland, M. T. *J. Phys. Org. Chem.* **1998**, 11, 895. doi:10.1002/(SICI)1099-1395(199812)11:12<895::AID-POC79>3.0.CO;2-5.
- (17) Baggio, R.; Remedi, M. V.; Garland, M. T.; Buján, E. I. *J. Chem. Crystallogr.* **1997**, 27 (9), 499. doi:10.1007/BF02576440.
- (18) De Vargas, E. B.; De Rossi, R. H.; Veglia, A. V. *J. Org. Chem.* **1986**, 51 (11), 1976. doi:10.1021/jo00361a007.
- (19) Consiglio, G.; Frenna, V.; Mugnoli, A.; Noto, R.; Pani, M.; Spinelli, D. *J. Chem. Soc., Perkin Trans. 2* **1997**, 309. doi:10.1039/a604516b.
- (20) Capon, B.; Chapman, N. B. *J. Chem. Soc.* **1957**, 600. doi:10.1039/jr9570000600.
- (21) Consiglio, G.; Arnone, C.; Spinelli, D.; Noto, R.; Frenna, V.; Fisichella, S.; Bottino, F. A. *J. Chem. Soc., Perkin Trans. 2* **1985**, 523. doi:10.1039/p29850000523.
- (22) Lewis, M.; Wu, Z.; Glaser, R. *Anisotropic Organic Materials: Approaches to Polar Order, ACS Symposium Series, Volume 798*; Glaser, R., Kaszynski, P., Eds.; American Chemical Society: Washington, D.C., 2001; p 97.
- (23) Battaglia, M. R.; Buckingham, A. D.; Williams, J. H. *Chem. Phys. Lett.* **1981**, 78 (3), 421. doi:10.1016/0009-2614(81)85228-1.
- (24) Frisch, M. J.; Trucks, G. W.; Schlegel, H. B.; Scuseria, G. E.; Robb, M. A.; Cheeseman, J. R.; Montgomery, J. A., Jr.; Vreven, T.; Kudin, K. N.; Burant, J. C.; Millam, J. M.; Iyengar, S. S.; Tomasi, J.; Barone, V.; Mennucci, B.; Cossi, M.; Scalmani, G.; Rega, N.; Petersson, G. A.; Nakatsuji, H.; Hada, M.; Ehara, M.; Toyota, K.; Fukuda, R.; Hasegawa, J.; Ishida, M.; Nakajima, T.; Honda, Y.; Kitao, O.; Nakai, H.; Klene, M.; Li, X.; Knox, J. E.; Hratchian, H. P.; Cross, J. B.; Bakken, V.; Adamo, C.; Jaramillo, J.; Gomperts, R.; Stratmann, R. E.; Yazyev, O.; Austin, A. J.; Cammi, R.; Pomelli, C.; Ochterski, J. W.; Ayala, P. Y.; Morokuma, K.; Voth, G. A.; Salvador, P.; Dannenberg, J. J.; Zakrzewski, V. G.; Dapprich, S.; Daniels, A. D.; Strain, M. C.; Farkas, O.; Malick, D. K.; Rabuck, A. D.; Raghavachari, K.; Foresman, J. B.; Ortiz, J. V.; Cui, Q.; Baboul, A. G.; Clifford, S.; Cio-slawski, J.; Stefanov, B. B.; Liu, G.; Liashenko, A.; Piskorz, P.; Komaromi, I.; Martin, R. L.; Fox, D. J.; Keith, T.; Al-Laham, M. A.; Peng, C. Y.; Nanayakkara, A.; Challacombe, M.; Gill, P. M. W.; Johnson, B.; Chen, W.; Wong, M. W.; Gonzalez, C.; Pople, J. A. *Gaussian 03*, Revision C.02. Gaussian, Inc.: Wallingford, CT, 2004.

# Highly stereoselective facile synthesis of $\beta$ -amino carbonyl compounds via a Mannich-type reaction catalyzed by $\gamma$ -Al<sub>2</sub>O<sub>3</sub>/MeSO<sub>3</sub>H (alumina/methanesulfonic acid: AMA) as a recyclable, efficient, and versatile heterogeneous catalyst

Hashem Sharghi and Mahboubeh Jokar

**Abstract:** Mannich reaction of ketones, aromatic aldehydes, and aromatic amines catalyzed efficiently by  $\gamma$ -Al<sub>2</sub>O<sub>3</sub>/MeSO<sub>3</sub>H (alumina/methanesulfonic acid: AMA) as a heterogeneous catalyst, which were carried out in EtOH at ambient temperature to afford the corresponding  $\beta$ -amino ketones in good yields and high stereoselectivities in favor of the anti isomer, was described for the first time. It was found that this catalyst could be completely recovered and reused without loss of its catalytic activities and is thus environmentally conscious. Furthermore, the use of  $\gamma$ -Al<sub>2</sub>O<sub>3</sub>/CH<sub>3</sub>SO<sub>3</sub>H (AMA) catalyst is feasible because of its easy preparation, easy handling, stability, easy recovery, reusability, good activity, stereoselectivity, and eco-friendliness. The use of this method provides a novel and improved modification of the three-component Mannich reaction in terms of mild reaction conditions and clean reaction profiles, using a very small quantity of catalyst and a simple workup procedure.

**Key words:** Mannich reaction,  $\beta$ -amino ketones, methanesulfonic acid,  $\gamma$ -Al<sub>2</sub>O<sub>3</sub>/MeSO<sub>3</sub>H (alumina/methanesulfonic acid: AMA), stereoselectivity, recyclable catalysis

**Résumé :** Opérant à la température ambiante, en solution dans l'éthanol, on a effectué des réactions de Mannich de cétones, d'aldéhydes aromatiques et d'amines aromatiques catalysées efficacement par un catalyseur hétérogène formé de  $\gamma$ -Al<sub>2</sub>O<sub>3</sub>/MeSO<sub>3</sub>H (alumine/acide méthanesulfonique: AAM) qui conduisent à la formation des  $\beta$ -aminocétone correspondantes, avec de bons rendements et par la première fois à des stéréosélectivités élevées en faveur de l'isomère anti. On a observé que le catalyseur peut être récupéré complètement sans perte de son activité catalytique et qu'il est écologique. De plus, l'utilisation du catalyseur  $\gamma$ -Al<sub>2</sub>O<sub>3</sub>/MeSO<sub>3</sub>H (alumine/acide méthanesulfonique) est possible en raison de sa facilité de préparation, de manutention, de récupération et de réutilisation ainsi que de sa bonne activité, de sa stéréosélectivité et de son caractère écologique. L'utilisation de cette méthode donne accès à une modification nouvelle et améliorée de la réaction de Mannich à trois composants en termes de conditions réactionnelles douces, avec des profils réactionnels propres, qui n'utilisent que de très faibles quantités de catalyseur et une méthode simple de récupération des produits.

**Mots-clés :** réaction de Mannich,  $\beta$ -aminocétone, acide méthanesulfonique,  $\gamma$ -Al<sub>2</sub>O<sub>3</sub>/MeSO<sub>3</sub>H (alumine/acide méthanesulfonique: AAM), stéréosélectivité, catalyseur recyclable

[Traduit par la Rédaction]

## Introduction

Mannich-type reactions are very important C–C bond-forming reactions in organic synthesis and one of the most widely utilized chemical transformations for the formation of  $\beta$ -amino ketones and other  $\beta$ -amino carbonyl compounds, which in turn are important synthetic intermediates for various pharmaceuticals and natural products, such as alkaloids

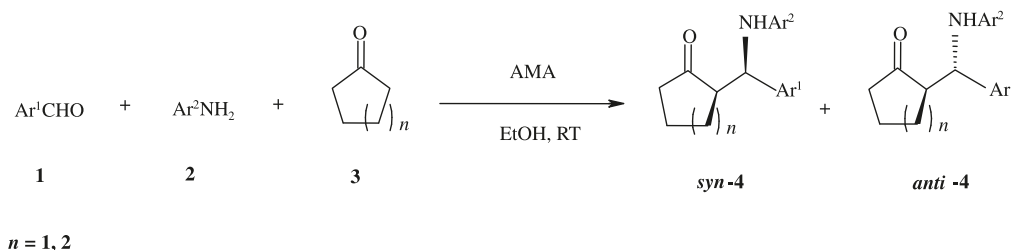
and polyketides.<sup>1,2</sup>  $\beta$ -Amino carbonyl compounds and their derivatives are used for the synthesis of amino alcohols, peptides, and lactams, and as precursors for optically active amino acids. Therefore, the development of new synthetic methods leading to  $\beta$ -amino carbonyl compounds or their derivatives has attracted much attention. However, the classic Mannich reaction has limited applications. To overcome the drawbacks of the classic method, numerous modern versions of the Mannich reaction using electrophiles, such as imines and stable nucleophiles, such as enolates, enol ethers, and enamines,<sup>3</sup> have been developed. But the preferred route is to use a one-pot, three-component strategy that opens a wide range of structural variations. Furthermore, only a few one-pot procedures on the use of unmodified aldehydes or ketones have been reported in the literature and a variety of

Received 15 March 2009. Accepted 16 September 2009.  
Published on the NRC Research Press Web site at  
canjchem.nrc.ca on 11 December 2009.

**H. Sharghi<sup>1</sup> and M. Jokar.** Department of Chemistry, College of Sciences, Shiraz University, Shiraz, 71454, Iran.

<sup>1</sup>Corresponding author (e-mail: shashem@chem.susc.ac.ir).



**Scheme 1.** One-pot, three-component Mannich reaction with cyclohexanone or cyclopentanone.

catalysts, such as  $\text{Zn}(\text{OTf})_2$ ,<sup>4</sup>  $\text{H}_3\text{PW}_{12}\text{O}_{40}$ ,<sup>5</sup>  $\text{ZrOCl}_2 \cdot 8\text{H}_2\text{O}$ ,<sup>6</sup> (*S*)-serine,<sup>7</sup> DBSA,<sup>8</sup>  $\text{SDS-HCl}$ ,<sup>9–11</sup>  $\text{Bi}(\text{OTf})_3 \cdot 4\text{H}_2\text{O}$ ,<sup>12</sup> sodium tetrakis(3,5-trifluoromethylphenyl) borate,<sup>13</sup>  $\text{PS-SO}_3\text{H}$ ,<sup>14</sup> L-proline,<sup>3h</sup>  $\text{NbCl}_5$ ,<sup>15</sup>  $\text{HClO}_4\text{-SiO}_2$ ,<sup>16a</sup> and silica sulfuric acid,<sup>16b</sup> have been investigated.

However, most Lewis acids cannot be used in this one-pot reaction because of the presence of free amines and  $\text{H}_2\text{O}$  produced in the imine formation.

Within recent years, the use of reusable heterogeneous catalysts has received considerable importance in organic synthesis because of their environmental, economical, and industrial aspects.<sup>6b,17</sup> Up to now several reusable and heterogeneous catalysts have been designed and used in various reactions. Metal colloids,<sup>18a</sup> mineral clays,<sup>18b</sup> and supported reagent on silica gel,<sup>18c,18d</sup> alumina,<sup>19</sup> and other solid supports are some common examples of heterogeneous catalysts that have extensive applications in organic transformations.

Aluminum oxides constitute an important technological material that can be widely used in catalytic processes. In particular,  $\gamma\text{-Al}_2\text{O}_3$  is used as both a catalyst and support because of its acid-base properties and mechanical and high-temperature resistance.<sup>6b</sup> This study is part of our ongoing interest in a mixture of the  $\gamma\text{-Al}_2\text{O}_3/\text{MeSO}_3\text{H}$  (alumina/methanesulfonic acid: AMA) catalyst in the Fries rearrangement,<sup>19</sup> Beckmann rearrangement,<sup>20</sup> direct conversions of aromatic aldehydes to the corresponding glycol monoesters,<sup>21</sup> hydration of nitriles into amides,<sup>22</sup> syntheses of macrocyclic polyether-diester,<sup>23</sup> syntheses of new hydroxythioxanthone derivatives,<sup>24</sup> direct sulfonylation of phenols with *p*-toluenesulfonic acid,<sup>25a</sup> and synthesis of coumarin derivatives.<sup>25b</sup> We report herein our results in the three-component  $\gamma\text{-Al}_2\text{O}_3/\text{MeSO}_3\text{H}$  (AMA) catalysed Mannich-type reaction.

## Results and discussion

In this research, we report a new, simple, mild, and effective procedure for the one-pot synthesis of  $\beta$ -amino carbonyl compounds via a multicomponent reaction between aryl aldehydes, anilines, and cyclohexanone or cyclopentanone in the presence of  $\gamma\text{-Al}_2\text{O}_3/\text{MeSO}_3\text{H}$  (AMA) as catalyst (Scheme 1).

To establish the optimum conditions for this reaction, initially, the three-component Mannich reaction of benzaldehyde (2.0 mmol), aniline (2.0 mmol), and cyclohexanone (2.2 mmol) was examined. To find out the optimum quantity of  $\gamma\text{-Al}_2\text{O}_3$ -supported methanesulfonic acid (AMA), the Mannich reaction was carried out at room temperature using different quantities of the catalyst (Table 1 and Fig. 1).

The reaction does not proceed if no catalyst is employed, despite prolonged reaction times (Table 1, entry 1). It should

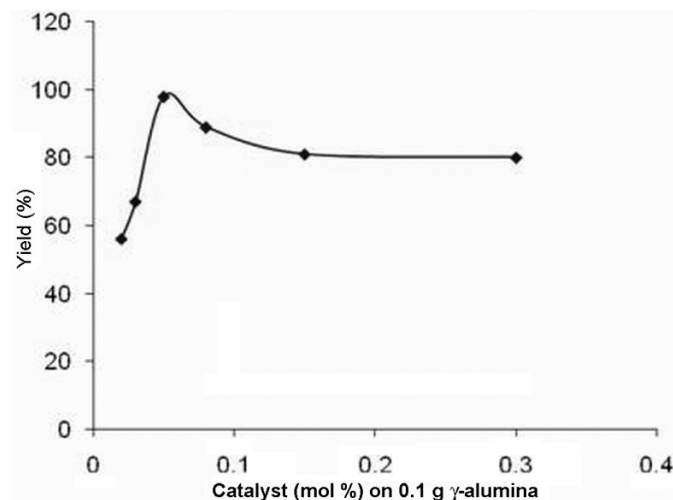
**Table 1.** Catalyzed Mannich reaction of benzaldehyde (2.0 mmol), aniline (2.0 mmol), and cyclohexanone (2.2 mmol) in EtOH at room temperature.

Entry	AMA (mol% $\text{MeSO}_3\text{H}$ on 0.1 g $\gamma\text{-Al}_2\text{O}_3$ )	Yields (%) <sup>a</sup>	Time (h)	Anti/syn <sup>b</sup>
1	None	0	10	—
2	0.02	56	10	90/10
3	0.03	67	6	89/11
4	0.05	98, 97, 97, 96 <sup>c</sup>	4	97/3
5	0.08	89	6	85/15
6	0.15	81	1.5	85/15
7	0.30	80	1	88/12

<sup>a</sup>Yield of isolated products.

<sup>b</sup>Anti/syn ratio was determined by  $^1\text{H}$  NMR.

<sup>c</sup>The same catalyst was used for each of the four runs.

**Fig. 1.** A plot of the yield of 2-[anilino(phenyl)methyl]cyclohexanone (**4a**) versus the amount of  $\gamma\text{-Al}_2\text{O}_3$ /methanesulfonic acid (AMA) as catalyst using benzaldehyde (2.0 mmol), aniline (2.0 mmol), and cyclohexanone (2.2 mmol) in ethanol at room temperature.

be noted that the optimal catalyst loading effect obtained from towards the  $\beta$ -amino carbonyl compounds peaked at a concentration of 0.05 mol% (Table 1, entry 4). A lower catalyst loading gave decreased yields (Table 1, entries 2 and 3), and increasing the catalyst loading also led to decreased yields (Table 1, entries 5–7). Thereafter, the reaction was carried out by varying the amount of cyclohexanone and aniline. The optimum ratio of benzaldehyde, cyclohexanone, and aniline was found to be 2:2.2:2, respectively, and 0.1 g AMA (equal to 0.05 mol%  $\text{H}^+$ ). Entry 4 of Table 1 described the yields of four consecutive reactions leading to

2-[anilino(phenyl)methyl]cyclohexanone (**4a**). In these experiments, the reaction mixture was diluted with AcOEt, and the catalyst was removed by filtration and washed with hot EtOH. The filtrate was dried at 120 °C for 24 h to give recycled AMA. Thus, the recovered catalyst, which always works the same, begins reloading with fresh reagents for further runs. No significant decrease in the yield was observed demonstrating the efficiency of AMA as a catalyst in the synthesis of  $\beta$ -amino carbonyl compounds.

With AMA as an effective catalyst for the Mannich-type reaction, conditions using various solvents such as MeCN, 1,4-dioxane, Et<sub>2</sub>O, THF, toluene, CHCl<sub>3</sub>, and EtOH were examined (Table 2). Benzaldehyde, aniline, and cyclohexanone were chosen as representative substrates. Interestingly, the Mannich reaction showed an intriguing solvent effect, and it was found that the solvent has an important role in terms of reaction rate, yields, and stereoselectivity. Among various solvents tested, toluene, MeCN, Et<sub>2</sub>O, CH<sub>2</sub>Cl<sub>2</sub>, and MeOH gave moderate yields of the expected product (Table 2, entries 1–5) and the reaction in 1,4-dioxane afforded a very poor yield (Table 2, entry 7, 27%). Excellent anti selectivity was observed in MeCN whereas the yield of the reaction exhibited was low (Table 2, entry 1, 55%) compared to EtOH that showed a high yield and excellent stereoselectivity. Obviously, EtOH is the solvent of choice with its fast reaction rate, high yield, excellent anti selectivity, cheapness, and environmental acceptability. According to step II of the mechanism for this reaction, which involves the formation of a Schiff base, we expected EtOH to stand out as the favorite solvent, since EtOH has proved to be one of the suitable solvents for the synthesis of Schiff bases.<sup>26</sup>

To optimize the temperature we carried out a model study with benzaldehyde (2 mmol), aniline (2 mmol), and cyclohexanone (2.2 mmol) using a catalyst (0.1 g, equal to 0.05 mol % H<sup>+</sup>) in EtOH at various temperatures (Table 3). Increasing the temperature to 80 °C favored side reactions and the formation of deeply colored products. If the reaction runs at refluxing temperature, no Mannich-reaction bases (**4**) can be isolated. Decreasing the temperature decreases the rates of the reaction, and also the rates of the side reactions. Table 3 clearly demonstrates that room temperature is an effective temperature in terms of reaction time and yield obtained.

Encouraged by the remarkable results obtained with the above reaction conditions, and to show the generality and scope of this new protocol, we used various aldehydes and amines (Table 4). A variety of aromatic aldehydes, including electron-withdrawing and electron-donating groups, were tested using our new method in EtOH in the presence of AMA. It was found that the electronic effect of substitutes had an influence on the yields. In this case, both the electron-rich and the electron-deficient benzaldehydes gave good to excellent anti selectivity at room temperature (Table 4, entries 1–14). However, when aryl aldehyde bearing an electron-withdrawing substituent was subjected to the reaction under standard conditions, there was a lower yield of desired adducts formed (Table 4, entry 9). An important feature of this procedure was the survival of a variety of functional groups, such as ethers, nitro, hydroxyl, halides, cyanide, etc., under the reaction conditions. Acid-sensitive

**Table 2.** Investigation of various solvent effects on the synthesis of  $\beta$ -amino carbonyl compounds via Mannich reaction of benzaldehyde (2.0 mmol), aniline (2.0 mmol), and cyclohexanone (2.2 mmol) and  $\gamma$ -Al<sub>2</sub>O<sub>3</sub>/CH<sub>3</sub>SO<sub>3</sub>H (AMA) (0.05 mol% H<sup>+</sup>) at room temperature.

Entry	Solvent	Yields (%) <sup>a</sup>	Time (h)	Anti/syn <sup>b</sup>
1	MeCN	55	5	93/7
2	CH <sub>2</sub> Cl <sub>2</sub>	58	5	85/15
3	Et <sub>2</sub> O	68	5	74/26
4	MeOH	75	5	69/31
5	Toluene	53	5	63/37
6	CHCl <sub>3</sub>	45	5	83/17
7	1,4-Dioxane	27	5	65/35
8	THF	48	5	70/30
9	H <sub>2</sub> O	— <sup>c</sup>	5	—
10	EtOH	98	4	98/2

<sup>a</sup>Yield of isolated products.

<sup>b</sup>Anti/syn ratio was determined by <sup>1</sup>H NMR.

<sup>c</sup>Main product was imine.

**Table 3.** Investigation of various temperature effects on the synthesis of  $\beta$ -amino carbonyl compounds via Mannich reaction of benzaldehyde (2.0 mmol), aniline (2.0 mmol), and cyclohexanone (2.2 mmol) and  $\gamma$ -Al<sub>2</sub>O<sub>3</sub>/CH<sub>3</sub>SO<sub>3</sub>H (AMA) (0.05 mol% H<sup>+</sup>) in EtOH.

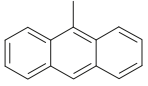
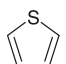
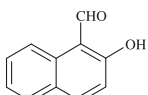
Entry	Temperature (°C)	Time (min)	Yield (%) <sup>a</sup>
1	10	900	63
2	RT	480	98
3	40	240	91
4	50	110	88
5	60	105	85
6	70	90	81
7	80	80	74
8	Reflux	120	0

<sup>a</sup>Yields refer to the pure isolated products.

substrates like 4-cyanobenzaldehyde also reacted in high yields without the formation of any side products (Table 4, entry 13). Heteroaryl aldehydes, such as 2-thiophenecarboxaldehyde (Table 4, entry 10), was well-tolerated in these mild conditions. The highly electron-deficient 4-nitroaniline almost did not work (Table 4, entry 15). By using <sup>1</sup>H NMR to monitor the reaction, we realized that the imine intermediate, 4-nitrobenzylidenephénylamine, was not formed during the reaction. Furthermore, the use of alkyl aldehydes (such as butylaldehyde) also failed to give the desired product, which implies that this reaction is limited to nonenolizable imines (Table 4, entry 16). A three-component reaction of benzaldehyde, aniline, and cyclopentanone did not produce the desired adduct, probably because of the polyaminoalkylation of cyclopentanone,<sup>27</sup> and in this case, another procedure was adopted in which benzaldehyde and aniline were first mixed to produce imine in situ before ketone was added. As is shown in Table 4, the desired adduct was generated with very good yields and excellent diastereoselectivities.

With the help of different probe molecules, surface properties of  $\gamma$ -Al<sub>2</sub>O<sub>3</sub> have been the object of many experimental works.<sup>28a</sup> Under atmospheric conditions, the surfaces adsorb

**Table 4.** Catalyzed Mannich reaction of aromatic aldehyde (2.0 mmol), aniline (2.0 mmol), and cyclohexanone or cyclopentanone (2.2 mmol) and AMA (0.1 g equal to 0.05 mol% H<sup>+</sup>) in EtOH (4–6 mL) at room temperature.

Entry	$\beta$ -Amino ketones	Ar <sup>1</sup>	Ar <sup>2</sup>	Cycloalkanone	Yield <sup>a</sup> (%)	Time (h)	Anti/syn <sup>b</sup>
1	<b>4a</b>	Ph	Ph	Cyclohexanone	98	1.40	98/2
2	<b>4b</b>	4-Me-C <sub>6</sub> H <sub>4</sub>	Ph	Cyclohexanone	90	1.30	98/2
3	<b>4c</b>	4-Cl-C <sub>6</sub> H <sub>4</sub>	Ph	Cyclohexanone	90	3	92/ 8
4	<b>4d</b>	Ph	Ph	Cyclopentanone	95	1	73/26
5	<b>4e</b>	Ph	4-Br-C <sub>6</sub> H <sub>4</sub>	Cyclopentanone	92	2.50	99/1
6	<b>4f</b>	4-Me-C <sub>6</sub> H <sub>4</sub>	Ph	Cyclopentanone	94	1.40	98/2
7	<b>4g</b>	4-Cl-C <sub>6</sub> H <sub>4</sub>	Ph	Cyclopentanone	94	3.30	97/3
8	<b>4h</b>		Ph	Cyclopentanone	92	1.45	100/0
9	<b>4i</b>	4-NO <sub>2</sub> -C <sub>6</sub> H <sub>4</sub>	Ph	Cyclopentanone	80	4	85/15
10	<b>4j</b>		Ph	Cyclopentanone	86	1.50	100/0
11	<b>4k</b>	4- <i>i</i> Pr-C <sub>6</sub> H <sub>4</sub>	4-Br-C <sub>6</sub> H <sub>4</sub>	Cyclopentanone	91	3.20	96/4
12	<b>4l</b>		Ph	Cyclopentanone	90	8	100/1
13	<b>4m</b>	4-CN-C <sub>6</sub> H <sub>4</sub>	Ph	Cyclopentanone	84	7	94/6
14	<b>4n</b>	3-HO-C <sub>6</sub> H <sub>4</sub>	Ph	Cyclopentanone	89	5	100/1
15	<b>4o</b>	Ph	4-NO <sub>2</sub> -C <sub>6</sub> H <sub>4</sub>	Cyclohexanone	—	10	—
16	<b>4p</b>	CH <sub>3</sub> (CH <sub>2</sub> ) <sub>2</sub>	Ph	Cyclohexanone	—	10	—
17	<b>4a</b>	Ph	Ph	Cyclohexanone	98 <sup>c</sup>	1.40	98

<sup>a</sup> Yield of isolated products.<sup>b</sup> Anti/syn ratio was determined by <sup>1</sup>H NMR.<sup>c</sup> The reaction was carried out on a 100 mmol scale.

water both molecularly<sup>28b,28c</sup> and dissociatively, giving rise to surface hydroxyls that persist even at temperatures higher than 1000 °C.<sup>28d,28e</sup> Surface characterization experiments have been monitored by IR<sup>28f</sup> and DRIFTS<sup>28g</sup> spectroscopies that show the presence of different hydroxyl groups, which are assigned primarily to the different possibilities for coordination of surface aluminum cations and, for a given coordination number, to the different environments of the site (Fig. 2).<sup>6b,28h,28i</sup>

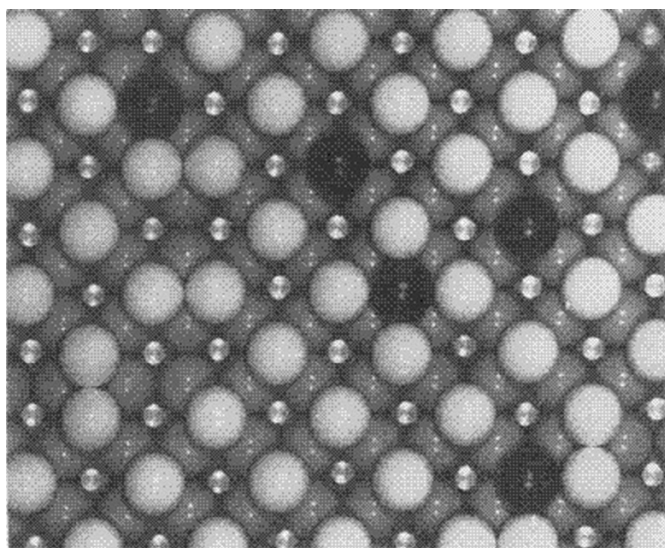
With regard to the latest articles about adsorption of some alcohols such as methanol, ethanol, propanol, and isopropanol on the  $\gamma$ -alumina surface,<sup>28j,28k</sup> we assume that methanesulfonic acid (MeSO<sub>3</sub>H) chemisorbs to the alumina surface with hydrogen bonding when they come close to the surface with suitable orientation between the OH hydrogen of

MeSO<sub>3</sub>H with a surface oxygen atom of  $\gamma$ -alumina, which is in turn close to a cation vacancy.

To explore the mechanism of the reaction, we monitored aldehyde consumption by GC analysis and found that the Schiff base is formed (within the first 20 min of the beginning of the reaction) and the rate determining step (RDS) was found to be the attack of in situ generated enolate I on the in situ generated aldimine II as shown in Scheme 2.<sup>6a,6b</sup> AMA, used in catalytic amounts, is recycled in the reaction and can be reused for subsequent reactions.

High anti selectivity was obtained with various substituted benzaldehydes (Table 4, entries 1–14). The two most stable possible transition states are shown in Scheme 2. Transition state III (Scheme 2) provides the anti isomer, whereas the syn isomer forms via V (Scheme 2). In V (Scheme 2), the

**Fig. 2.** Dry  $\gamma$ - $\text{Al}_2\text{O}_3$  where small circles:  $\text{Al}^{+3}$ , gray and white circles:  $\text{O}^{2-}$ , and black circles:  $\text{OH}^{2-}$  (**8i**).



two phenyl groups of aldimine are syn to each other, so they are unfavorable. Also in V (Scheme 2), steric repulsion exists between the hydrogen atoms of cyclohexanone's methylene and phenyl groups. The phenyl groups of aldimine in III (Scheme 2) are anti to each other; therefore, III (Scheme 2) should be more stable than V (Scheme 2) and is the most stable transition state that produces the anti isomer.<sup>16,17,29</sup>

The anti/syn ratio was determined by  $^1\text{H}$  NMR, using the intensity of the  $H_a$  (Scheme 3). The  $J_{H_a,H_b}$  signal of the anti isomer is higher than that of the syn isomer. According to the  $^1\text{H}$  NMR spectrum, the  $H_a$  signal for the anti isomer has a lower  $\delta$  value than that for the syn isomer. For instance, in the  $^1\text{H}$  NMR spectra of 2-[anilino(phenyl)methyl]cyclohexanone (**4a**), the signal at  $\delta = 4.63$  ppm ( $J = 7.1$  Hz) is contributed by the anti isomer, while the one at  $5.4$  ppm ( $J = 3.6$  Hz) is contributed by the syn isomer.<sup>6,16,17</sup>

To access the feasibility of applying this method in a preparative scale, we carried out the one-pot, three-component Mannich reaction of benzaldehyde with aniline and cyclohexanone on a 100 mmol scale (Table 4, entry 17). As expected, the reaction proceeded similarly to the case in Table 4 (entry 1) in a smaller scale, and the desired  $\beta$ -amino ketone was obtained in 98% isolated yield in 100 min.

The reaction proceeded not only for cycloalkanones but also for acyclic ketones such as acetophenones. As illustrated in Scheme 4, AMA did catalyze the Mannich reaction of acetophenones, substituted benzaldehydes, and anilines to yield the desired  $\beta$ -amino ketone products.

The optimum ratio of benzaldehyde, acetophenone, and aniline was found to be 2:2.2:2, respectively, and 0.2 g AMA (equal to 0.1 mol%  $\text{H}^+$ ). The expected products were obtained in good-to-high yields under these conditions. Acyclic ketones were less reactive than cyclohexanone and needed much more catalyst and a longer reaction time to afford the desired products (Table 5).

The reaction worked well with a variety of aldehydes including those bearing electron-withdrawing groups, and the corresponding  $\beta$ -amino ketones (**6**) were obtained in good yields (Table 5, entries 2, 3, and 7). Several electron-rich aromatic aldehydes led to the desired products in very good yields (Table 5, entries 4, 5, 8, 9, and 15).

The presented method has the ability to tolerate other functional groups such as methoxy, halides, and nitro on aryl aldehyde (Table 5).

The scope of our method could be extended to substituted anilines. Although para-substituent aromatic amines gave good results, ortho-substituent aromatic amines such as 2-methylaniline (Table 5, entry 12) failed to yield any product because of the steric effects. Furthermore, amines with electron-withdrawing groups, such as 4-chloroaniline, 4-fluoroaniline, and 4-bromoaniline, gave the desired product in good yields (Table 5, entries 10, 11, and 14).

To show the simplicity and efficiency of the over presented catalyzed Mannich reaction of benzaldehydes, anilines, and ketones, including acetophenones and cycloalkanones, they are compared with the reported works in Table 6.

## Conclusion

In conclusion, the present procedure provides an efficient and improved modification of Mannich type reactions. This new catalytic method provides a protocol that enables the synthesis of  $\beta$ -amino carbonyl compounds in a highly stereoselectivity pure form, while displaying good functional group tolerance. No toxic reagent(s) or byproduct(s) were involved. This procedure is ideally suited for automated application since the entire synthetic sequence can be carried out at room temperature in the presence of a reusable and heterogeneous catalyst. Mild reaction condition, low loading of catalyst, ease of workup, high yields, stability and recyclability of the catalyst, general applicability of both acyclic and cyclic ketones and aldehydes, large-scale synthesis, and simple procedure are features of this new protocol. Quite a number of products are insoluble in EtOH, which can be obtained by filtration and recrystallization. This simple work-up procedure is also beneficial in this method. These conditions are also environmentally friendly, cost effective, and possess high generality, making our methodology a valid contribution to the existing processes in the field of  $\beta$ -amino ketone synthesis. Further applications of this catalyst to other transformations are currently under investigation.

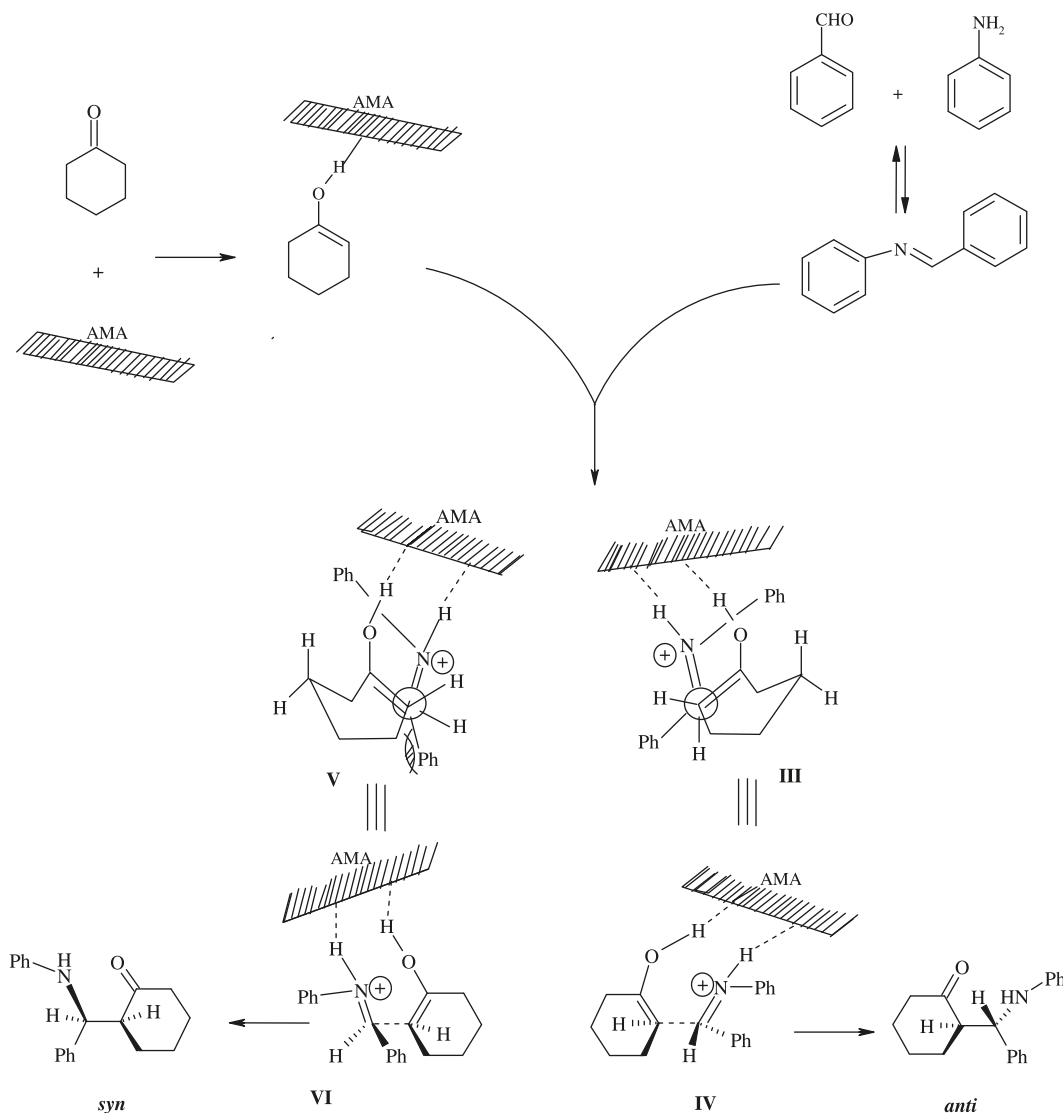
## Experimental

### Instrumentation, analysis, and starting material

NMR spectra were recorded on a Bruker Avance DPX-250 ( $^1\text{H}$  NMR 250 MHz and  $^{13}\text{C}$  NMR 62.9 MHz) spectrometer in pure deuterated solvents with tetramethylsilane as an internal standard. IR spectra were obtained using a Shimadzu FTIR 8300 spectrophotometer. Mass spectra were determined on a Shimadzu GCMS-QP 1000 EX instruments at 70 or 20 eV. Melting points were determined in open capillary tubes in a Büchi-535 circulating oil melting point apparatus. Elemental analyses were performed by Thermo Finnigan CHNS-O analyzer, 1112 series. The purity deter-



**Scheme 2.** Proposed reaction mechanism for the Mannich reaction of benzaldehyde, aniline, and cyclohexanone and the possible transition states leading to the anti isomer.

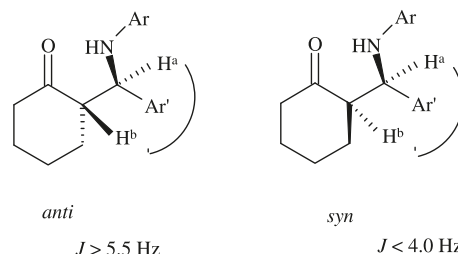


mination of the substrates and reaction monitoring were accomplished by TLC on silica gel PolyGram SILG/UV 254 plates. Column chromatography was carried out on short columns of silica gel 60 (70–230 mesh) in glass columns (2–3 cm diameter) using 15–30 g of silica gel per one gram of crude mixture. Chemical materials were either prepared in our laboratories or purchased from Fluka, Sigma-Aldrich, and Merck Companies. Acidic  $\gamma$ -alumina ( $\gamma$ - $\text{Al}_2\text{O}_3$ ) type 540 C was purchased from the Fluka Company.

#### Preparation of AMA (0.1 g, equal to 0.05 mol% $\text{H}^+$ )

Methanesulfonic acid (1.62 mL, 25 mmol) was added dropwise over a period of 90 min at 40 °C to a mixture of  $\gamma$ -alumina (50 g, 500 mmol) in dichloromethane (30 mL). After the addition was complete, the mixture was stirred for 2 h and then the solvent was evaporated under reduced pressure. After removal of  $\text{CH}_2\text{Cl}_2$  in a rotary evaporator, the solid powder was kept at 120 °C for 72 h. A white solid of 65.0 g was obtained.

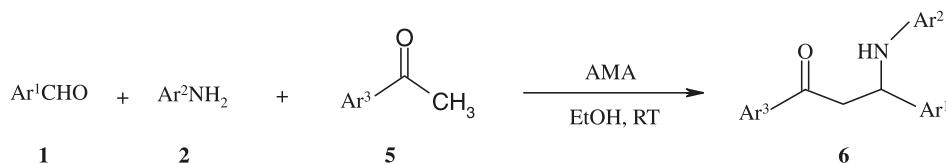
**Scheme 3.** Identification of anti and syn isomers by  $^1\text{H}$  NMR spectroscopy.



#### General procedure for synthesis of $\beta$ -amino carbonyl compounds 4

A mixture of the aldehyde (2 mmol), amine (2 mmol), and a solution of the catalyst (0.1 g, equal to 0.05 mol%  $\text{H}^+$ ) in EtOH (4–6 mL) was placed in a test tube and the reaction mixture was vigorously stirred at room temperature. Cyclohexanone or cyclopentanone (2.2 mmol) was then added to the mixture and after completion of the reaction as

**Scheme 4.** One-pot, three-component Mannich reaction of aromatic aldehydes (2 mmol) and anilines (2.0 mmol) with acetophenones (2.2 mmol).



indicated by TLC (Table 4), the reaction mixture was diluted with ethyl acetate, and the catalyst was removed by filtration. The organic phases were combined and dried over  $\text{Na}_2\text{SO}_4$ . The solvent was removed under reduced pressure to give the desired products. The residual crude product was purified by column chromatography on neutral silica gel (ethyl acetate/petroleum ether 1:5) or by recrystallization with  $\text{CH}_2\text{Cl}_2$ /petroleum ether or hexane to give the pure  $\beta$ -aminoketone as a mixture of diastereoisomers. The syn/anti ratio was determined by  $^1\text{H}$  NMR and  $^{13}\text{C}$  NMR analysis.

#### General procedure for synthesis of $\beta$ -amino carbonyl compounds 6

A mixture of the aldehyde (2 mmol), amine (2 mmol), and acetophenone (2.2 mmol) was added to a solution of the catalyst (0.2 g, equal to 0.1 mol%  $\text{H}^+$ ) in EtOH (4–6 mL) was placed in a test tube and the reaction mixture was vigorously stirred at room temperature for the appropriate time (Table 5). The reaction was monitored by TLC. The products precipitated from the reaction mixture. The precipitate was filtered off, dissolved in hot EtOH, and the catalyst was removed by hot filtration. The filtrate was kept at room temperature, was triturated with hexane (10 mL) and then filtered and was crystallized with EtOH/ $\text{H}_2\text{O}$  (2:1).

#### Recycling of $\gamma\text{-Al}_2\text{O}_3/\text{CH}_3\text{SO}_3\text{H}$ (AMA)

$\gamma\text{-Al}_2\text{O}_3/\text{CH}_3\text{SO}_3\text{H}$  (AMA) was prepared according to the abovementioned procedure. The catalyst was separated from the reaction mixture and washed with EtOH and dried at  $120^\circ\text{C}$  for 24 h to give recycled  $\gamma\text{-Al}_2\text{O}_3/\text{CH}_3\text{SO}_3\text{H}$  (AMA). The remaining catalyst begins reloading with fresh reagents for further runs. The reaction of benzaldehyde, aniline, and cyclohexanone was repeated with recycled catalyst and the yields were found to remain in the range of 96%–97% for four recycles.

All runs produced  $\beta$ -amino ketones characterized by detailed structural data using IR,  $^1\text{H}$  NMR,  $^{13}\text{C}$  NMR, and elemental analysis as given below.

#### 2-[Anilino(phenyl)methyl]cyclohexanone (4a)<sup>5</sup>

Purification by column chromatography on neutral silica gel, eluted with ethyl acetate/petroleum ether (1:5) or by recrystallization with  $\text{CH}_2\text{Cl}_2$ /petroleum ether gave compound **4a** as a colorless powder in a 98% yield; anti/syn 97/3; mp  $130\text{--}132^\circ\text{C}$ .  $^1\text{H}$  NMR (250 MHz,  $\text{CDCl}_3$ )  $\delta$ : 7.05–7.41 (6H, m), 6.55–6.68 (3H, m), 5.4 (0.02H, d,  $J = 3.6$  Hz), 4.8 (1H, br, s), 4.63 (0.98H, d,  $J = 7.1$  Hz), 2.78–2.80 (1H, m), 2.34–2.45 (2H, m), 1.66–1.92 (6H, m).  $^{13}\text{C}$  NMR (62.9 MHz,  $\text{CDCl}_3$ )  $\delta$ : 23.6, 27.1, 31.3, 41.7, 57.3, 58.2, 112.6, 113.8, 117.7, 126.2, 126.5, 127.2, 127.3, 128.4, 128.6, 141.4, 146.8, 191, 212.9. Anal. calcd. for  $\text{C}_{19}\text{H}_{21}\text{NO}$

(279.376; %): C 81.68, H 7.58, N 5.01; found: C 81.60, H 7.64, N 5.08.

#### 2-[Anilino(4-methylphenyl)methyl]cyclohexanone (4b)<sup>16a</sup>

Purification by column chromatography on neutral silica gel, eluted with ethyl acetate/petroleum ether (1:5) or by recrystallization with  $\text{CH}_2\text{Cl}_2$ /petroleum ether gave compound **4b** as a colorless powder in a 90% yield; anti/syn 97/3; mp  $115\text{--}118^\circ\text{C}$ .  $^1\text{H}$  NMR (250 MHz,  $\text{CDCl}_3$ )  $\delta$ : 7.26 (2H, d,  $J = 7.8$  Hz), 7.03–7.15 (4H, m), 6.63 (1H, t,  $J = 7.3$  Hz), 6.54 (2H, d,  $J = 7.8$  Hz), 5.4 (0.02H, d,  $J = 3.6$  Hz), 4.58 (0.98H, d,  $J = 7.3$  Hz), 2.74–2.76 (1H, m), 2.32–2.47 (2H, m), 2.29 (3H, s), 1.68–1.89 (6H, m).  $^{13}\text{C}$  NMR (62.9 MHz,  $\text{CDCl}_3$ )  $\delta$ : 21.1, 23.5, 27.8, 31.2, 41.6, 57.4, 113.6, 114.1, 117.4, 127.0, 127.1, 127.3, 129.0, 129.1, 136.7, 138.5, 147.2, 149.2, 190, 212. Anal. calcd. for  $\text{C}_{20}\text{H}_{23}\text{NO}$  (293.407; %): C 81.87, H 7.90, N 4.77; found: C 81.91, H 7.89, N 4.82.

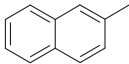
#### 2-[Anilino(4-chlorophenyl)methyl]cyclohexanone (4c)<sup>16a</sup>

Purification by column chromatography on neutral silica gel, eluted with ethyl acetate/petroleum ether (1:5) or by recrystallization with  $\text{CH}_2\text{Cl}_2$ /petroleum ether gave compound **4c** as a colorless powder in a 90% yield; anti/syn 92/8; mp  $268\text{--}270^\circ\text{C}$ .  $^1\text{H}$  NMR (250 MHz,  $\text{CDCl}_3$ )  $\delta$ : 7.2–7.37 (4H, m), 7.06 (2H, d,  $J = 7.9$  Hz), 6.67 (1H, t,  $J = 7.5$  Hz), 6.52 (2H, d,  $J = 7.5$  Hz), 5.09 (1H, br, s), 4.71 (0.08H, d,  $J = 4.2$  Hz), 4.54 (0.92H, d,  $J = 7.3$  Hz), 2.28–2.52 (2H, m), 1.87–2.28 (3H, m), 1.5–1.73 (4H, m).  $^{13}\text{C}$  NMR (62.9 MHz,  $\text{CDCl}_3$ )  $\delta$ : 20.4, 25.9, 39.1, 41.1, 54.0, 58.4, 113.6, 114.1, 118.1, 118.5, 128.7, 128.9, 129.0, 133.0, 140.2, 147.2, 191.0, 202.1, 218.9. Anal. calcd. for  $\text{C}_{19}\text{H}_{20}\text{ClNO}$  (313.821; %): C 72.72, H 6.42, N 4.46; found: C 72.80, H 6.35, N 4.40.

#### 2-[Anilino(phenyl)methyl]cyclopentanone (4d)<sup>31</sup>

Purification by column chromatography on neutral silica gel, eluted with ethyl acetate/petroleum ether (1:5) or by recrystallization with  $\text{CH}_2\text{Cl}_2$ /petroleum ether gave compound **4d** as a colorless powder in a 90% yield; anti/syn 73/26; mp  $166\text{--}168^\circ\text{C}$ .  $^1\text{H}$  NMR (250 MHz,  $\text{CDCl}_3$ )  $\delta$ : 7.2–7.4 (5H, m), 7.0–7.1 (2H, m), 6.65 (1H, t,  $J = 7.5$  Hz), 6.56 (2H, d,  $J = 7.8$  Hz), 4.9 (1H, br, s), 4.76 (0.17H, d,  $J = 4.4$  Hz), 4.55 (0.73H, d,  $J = 7.3$  Hz), 1.91–2.49 (2H, m), 1.18–1.19 (1H, m), 1.25–1.77 (4H, m).  $^{13}\text{C}$  NMR (62.9 MHz,  $\text{CDCl}_3$ , mixture of diastereoisomers)  $\delta$ : 20.5, 20.6, 25.8, 26.7, 39.2, 39.8, 53.3, 54.0, 57.7, 59.0, 113.6, 114.2, 117.4, 117.8, 127.1, 127.3, 127.4, 128.5, 128.6, 128.9, 129, 129.6, 141.0, 147.0, 219.0. Anal. calcd. for  $\text{C}_{18}\text{H}_{19}\text{NO}$  (265.350; %): C 81.47, H 7.22, N 5.28; found: C 81.55, H 7.30, N 5.20.

**Table 5.** Catalyzed Mannich reaction of aromatic aldehyde (2.0 mmol), aniline (2.0 mmol), and acetophenone (2.2 mmol) and AMA (0.2 g equal to 0.1 mol% H<sup>+</sup>) in EtOH (4–6 mL) at room temperature.

Entry	$\beta$ -Amino ketones	Ar <sup>1</sup>	Ar <sup>2</sup>	Ar <sup>3</sup>	Time (h)	Yield <sup>a</sup> (%)
1	<b>6a</b>	Ph	Ph	Ph	8	98
2	<b>6b</b>	3-Cl-C <sub>6</sub> H <sub>4</sub>	Ph	Ph	10	86
3	<b>6c</b>	4-Cl-C <sub>6</sub> H <sub>4</sub>	Ph	Ph	10	89
4	<b>6d</b>	4- <i>i</i> Pr-C <sub>6</sub> H <sub>4</sub>	Ph	Ph	6	96
5	<b>6e</b>	2,5-(CH <sub>3</sub> O) <sub>2</sub> -C <sub>6</sub> H <sub>3</sub>	Ph	Ph	9	90
6	<b>6f</b>		Ph	Ph	7	91
7	<b>6g</b>	4-NO <sub>2</sub> -C <sub>6</sub> H <sub>4</sub>	Ph	Ph	15	80
8	<b>6h</b>	4-CH <sub>3</sub> O-C <sub>6</sub> H <sub>4</sub>	Ph	Ph	7	91
9	<b>6i</b>	4-CH <sub>3</sub> -C <sub>6</sub> H <sub>4</sub>	Ph	Ph	6	92
10	<b>6j</b>	Ph	4-Br-C <sub>6</sub> H <sub>4</sub>	Ph	11	90
11	<b>6k</b>	Ph	4-F-C <sub>6</sub> H <sub>4</sub>	Ph	12	89
12	<b>6l</b>	Ph	2-CH <sub>3</sub> -C <sub>6</sub> H <sub>4</sub>	Ph	10	0
13	<b>6m</b>	Ph	Ph	4-Cl-C <sub>6</sub> H <sub>4</sub>	10	90
14	<b>6n</b>	Ph	4-Br-C <sub>6</sub> H <sub>4</sub>	4-Cl-C <sub>6</sub> H <sub>4</sub>	15	85
15	<b>6o</b>	2-CH <sub>3</sub> O-C <sub>6</sub> H <sub>4</sub>	Ph	Ph	10	89

<sup>a</sup> Yield of isolated products.**Table 6.** Catalyzed Mannich reaction of benzaldehydes, anilines, and ketones, including cyclohexanones and acetophenones, under various conditions.

Entry	Ketone	Conditions	Time (h)	Yield (%) <sup>a</sup>	Anti/syn
1	Acetophenone	H <sub>3</sub> Pmo <sub>12</sub> O <sub>40</sub> /H <sub>2</sub> O/RT <sup>5</sup>	18	76	—
2	Acetophenone	DBSA/H <sub>2</sub> O/23 °C <sup>8</sup>	12	69	—
3	Acetophenone	NaBAr <sub>4</sub> /H <sub>2</sub> O/30 °C <sup>13</sup>	48	81	—
4	Acetophenone	0.05 mol% MeSO <sub>3</sub> H on 0.1 g $\gamma$ -alumina/EtOH/RT	8	98	—
5	Cyclohexanone	Bi(OTf) <sub>3</sub> ·H <sub>2</sub> O/H <sub>2</sub> O/RT <sup>12</sup>	7	84	86/14
6	Cyclohexanone	NbCl <sub>5</sub> /RT <sup>15</sup>	12	95	85/15
7	Cyclohexanone	10 mol% Cu- <i>np</i> (18±2) nm methanol, RT, N <sub>2</sub> <sup>30</sup>	9	88	—
8	Cyclohexanone	HClO <sub>4</sub> -SiO <sub>2</sub> /EtOH/RT <sup>16a</sup>	2	98	99/1
9	Cyclohexanone	H <sub>3</sub> Pmo <sub>12</sub> O <sub>40</sub> /H <sub>2</sub> O/RT <sup>5</sup>	3–16	84	63/37
10	Cyclohexanone	0.05 mol% MeSO <sub>3</sub> H on 0.1 g $\gamma$ -alumina/EtOH/RT	4	98	97/3

<sup>a</sup>Yields refer to the pure isolated products.**2-[(4-Bromoanilino)(phenyl)methyl]cyclopentanone (4e)**

Purification by column chromatography on neutral silica gel, eluted with ethyl acetate/petroleum ether (1:5) or by recrystallization with CH<sub>2</sub>Cl<sub>2</sub>/petroleum ether gave compound **4e** as a colorless powder in a 92% yield; anti/syn 98/2; mp 142–144 °C. IR (KBr, cm<sup>-1</sup>): 3375, 2877, 1728, 1598, 1504, 1450, 1315, 817, 702. <sup>1</sup>H NMR (250 MHz, CDCl<sub>3</sub>)  $\delta$ : 7.2–7.4 (5H, m), 7.14 (2H, d, *J* = 6.9 Hz), 6.3 (2H, d, *J* = 7.0 Hz), 5.2 (1H, br, s), 4.67 (0.01H, d, *J* = 3.7 Hz), 4.45

(0.99H, d, *J* = 7.5 Hz), 2.1–2.4 (m, 2H), 1.18–1.19 (1H, m), 1.5–1.8 (4H, m). <sup>13</sup>C NMR (62.9 MHz, CDCl<sub>3</sub>)  $\delta$ : 20.4, 26.8, 39.3, 53.8, 59.2, 66.8, 109.6, 115.8, 117.0, 118.1, 127.0, 127.6, 128.7, 131.6, 140.0, 141.0, 146.1, 219.0. MS *m/z* (%): 346 (M<sup>+</sup> + 2, 0.7), 345 (M<sup>+</sup> + 1, 3.6), 344 (M<sup>+</sup>, 4.0), 279 (7.3), 260 (56.1), 171 (39.5), 149 (79.5), 115 (24.9), 83 (33.1), 57 (100.0). Anal. calcd. for C<sub>18</sub>H<sub>18</sub>BrNO (344.246; %): C 62.80, H 5.27, N 4.07; found: C 62.71, H 5.32, N 4.01.

**2-[Anilino(4-methylphenyl)methyl]cyclopentanone (4f)<sup>6b</sup>**

Purification by column chromatography on neutral silica gel, eluted with ethyl acetate/petroleum ether (1:5) or by recrystallization with CH<sub>2</sub>Cl<sub>2</sub>/petroleum ether gave compound **4f** as a colorless powder in a 94% yield; anti/syn 97/3; mp 127–129 °C. <sup>1</sup>H NMR (250 MHz, CDCl<sub>3</sub>) δ: 7.24–7.27 (3H, m), 7.12 (2H, d, *J* = 8.5 Hz), 7.05 (2H, d, *J* = 7.5), 6.68 (1H, t, *J* = 7.3 Hz), 6.5 (1H, d, *J* = 7.8 Hz), 5.0 (1H, br, s), 4.71 (0.02H, d, *J* = 4.5 Hz), 4.61 (0.98H, d, *J* = 7.3 Hz), 2.51–2.55 (1H, m), 2.129–2.48 (4H, m), 2.124–2.129 (1H, m), 1.85–1.91 (2H, m), 1.67–1.77 (2H, m). <sup>13</sup>C NMR (62.9 MHz, CDCl<sub>3</sub>) δ: 20.5, 21.1, 26.6, 39.2, 54.1, 58.7, 114.2, 117.8, 127.0, 127.9, 128.9, 129.0, 129.1, 129.3, 136.9, 138.5, 147.4, 149.2, 161.1, 193.1, 219.4. Anal. calcd. for C<sub>19</sub>H<sub>21</sub>NO (279.376; %): C 81.68, H 7.58, N 5.01; found: C 81.69, H 7.51, N 5.04.

**2-[Anilino(4-chlorophenyl)methyl]cyclopentanone (4g)<sup>6b</sup>**

Purification by column chromatography on neutral silica gel, eluted with ethyl acetate/petroleum ether (1:5) or by recrystallization with CH<sub>2</sub>Cl<sub>2</sub>/petroleum ether gave compound **4g** as a colorless powder in a 94% yield; anti/syn 97/3; mp 162–164 °C. <sup>1</sup>H NMR (250 MHz, CDCl<sub>3</sub>) δ: 7.24–7.37 (4H, m), 7.07 (2H, d, *J* = 7.5), 6.67 (1H, t, *J* = 7.3 Hz), 6.49 (2H, d, *J* = 7.8 Hz), 5.10 (1H, br, s), 4.7 (0.03H, d, *J* = 4.3 Hz), 4.52 (0.097H, d, *J* = 7.3 Hz), 1.87–2.08 (2H, m), 1.65–1.70 (5H, m). <sup>13</sup>C NMR (62.9 MHz, CDCl<sub>3</sub>) δ: 20.4, 26.6, 39.2, 54.0, 58.4, 114.1, 118.1, 127.9, 128.0, 128.3, 128.5, 128.8, 129.0, 133.0, 140.3, 147.2, 190.1, 218.93. Anal. calcd. for C<sub>18</sub>H<sub>18</sub>ClNO (299.794; %): C 72.11, H 6.05, N 4.67; found: C 72.20, H 5.98, N 4.74.

**2-[Anilino(9-anthryl)methyl]cyclopentanone (4h)**

Purification by column chromatography on neutral silica gel, eluted with ethyl acetate/petroleum ether (1:5) or by recrystallization with hexane gave compound **4h** as a pale yellow powder in a 92% yield; anti/syn 100/0; mp 206–208 °C. IR (KBr, cm<sup>-1</sup>) ν: 3328, 2873, 1720, 1596, 1492, 1253, 1068, 732, 486. <sup>1</sup>H NMR (250 MHz, CDCl<sub>3</sub>) δ: 9.41 (1H, d, *J* = 6 Hz), 8.63 (1H, d, *J* = 8.3 Hz), 8.45 (1H, s), 8.05 (2H, t, *J* = 8.0 Hz), 7.47–7.058 (4H, m), 6.92 (2H, t, *J* = 7.5 Hz), 6.55 (m, 3H), 5.97 (1H, d, *J* = 10.0 Hz), 3.26 (1H, q, *J* = 9.5 Hz), 2.36–2.43 (2H, m), 1.59–1.89 (1H, m), 1.29–1.46 (3H, m). <sup>13</sup>C NMR (62.9 MHz, CDCl<sub>3</sub>) δ: 20.5, 25.1, 39.4, 52.3, 55.4, 114.5, 117.8, 118.2, 123.1, 124.6, 125.0, 125.3, 125.9, 126.2, 126.4, 127.1, 128.6, 128.9, 129.5, 130.0, 131.3, 132.0, 137.9, 148.6, 166.2, 221.2. MS *m/z* (%): 367 (M<sup>+</sup> + 2, 1.3), 366 (M<sup>+</sup> + 1, 4.7), 365 (M<sup>+</sup>, 5.5), 282 (100.0), 255 (18.8), 215 (44.3), 177 (27.8), 104 (20.6), 77 (23.9), 55 (41.7). Anal. calcd. for C<sub>26</sub>H<sub>23</sub>NO (365.467; %): C 85.45, H 6.34, N 3.83; found: C 85.48, H 6.30, N 3.89.

**2-[Anilino(4-nitrophenyl)methyl]cyclopentanone (4i)**

Purification by column chromatography on neutral silica gel, eluted with ethyl acetate/petroleum ether (1:5) or by recrystallization with hexane gave compound **4i** as a colorless yellow powder in an 80% yield; anti/syn 85/15; mp 150–152 °C. IR (KBr, cm<sup>-1</sup>) ν: 3355, 2989, 1720, 1600, 1523, 1350, 1284, 856, 756, 698. <sup>1</sup>H NMR (250 MHz, DMSO) δ: 8.11–8.15 (2H, m), 7.5–7.63 (2H, m), 6.93–6.95 (2H, m), 6.47–6.5 (3H, m), 6.30 (0.15H, d, *J* = 4.6 Hz),

6.02 (0.85H, d, *J* = 7.5 Hz), 4.94 (1H, br, s), 2.6–2.7 (1H, m), 2.17–2.21 (1H, m), 1.32–2.02 (5H, m). <sup>13</sup>C NMR (62.9 MHz, DMSO mixture of diastereoisomers) δ: 20.3, 24.1, 25.6, 54.4, 54.9, 55.2, 113.3, 113.6, 116.9, 123.8, 123.8, 128.4, 129.0, 129.1, 129.2, 147.7, 147.8, 150.3, 152.0, 217.2, 217.9. MS *m/z* (%): 311 (M<sup>+</sup> + 1, 0.9), 310 (M<sup>+</sup>, 2.1), 279 (3.0), 256 (4.4), 227 (59.3), 181 (25.1), 149 (27.1), 129 (14.4), 111 (22.1), 83 (54.1), 57 (100.0). Anal. calcd. for C<sub>18</sub>H<sub>18</sub>N<sub>2</sub>O<sub>3</sub> (310.374; %): C 69.66, H 5.85, N 9.03; found: C 69.70, H 5.91, N 9.07.

**2-[Anilino(2-thienyl)methyl]cyclopentanone (4j)**

Purification by column chromatography on neutral silica gel, eluted with ethyl acetate/petroleum ether (1:5) or by recrystallization with CH<sub>2</sub>Cl<sub>2</sub>/petroleum ether gave compound **4j** as a colorless powder in an 86% yield; anti/syn 100/0; mp 175–177 °C. IR (KBr, cm<sup>-1</sup>) ν: 3394, 1689, 1508, 1141, 752, 717, 694, 516. <sup>1</sup>H NMR (250 MHz, CDCl<sub>3</sub>) δ: 7.61 (1H, t, *J* = 5.5 Hz), 7.49 (1H, d, *J* = 9 Hz), 7.01–7.11 (3H, m), 6.85–6.87 (1H, m), 6.58–6.63 (2H, m), 5.01 (1H, br, s), 4.89 (1H, d, *J* = 7.5 Hz), 2.66–2.97 (3H, m), 1.185–1.90 (2H, m), 1.18–1.48 (2H, m). <sup>13</sup>C NMR (62.9 MHz, CDCl<sub>3</sub>) δ: 23.3, 26.9, 54.2, 55.5, 68.1, 114.3, 118.4, 124.5, 126.5, 128.1, 129.0, 130.6, 133.3, 152.7, 199.0, 226.5. MS *m/z* (%): 273 (M<sup>+</sup> + 2, 6.1), 272 (M<sup>+</sup> + 1, 13.4), 271 (M<sup>+</sup>, 11.6), 236 (10.9), 186 (43.4), 152 (10.9), 135 (24.9), 111 (23.6), 83 (53.1), 57 (100.0). Anal. calcd. for C<sub>16</sub>H<sub>17</sub>NOS (271.378; %): C 70.81, H 6.31, N 5.16, S 11.82; found: C 70.75, H 6.36, N 5.14, S 11.90.

**2-[(4-Bromoanilino)(4-isopropylphenyl)methyl]cyclopentanone (4k)**

Purification by column chromatography on neutral silica gel, eluted with ethyl acetate/petroleum ether (1:5) or by recrystallization with CH<sub>2</sub>Cl<sub>2</sub>/petroleum ether gave compound **4k** as a colorless powder in a 91% yield; anti/syn 96/4; mp 142–144 °C. IR (KBr, cm<sup>-1</sup>) ν: 3379, 2962, 2873, 1732, 1596, 1508, 1485, 1269, 1249, 1126, 1072, 917, 486. <sup>1</sup>H NMR (250 MHz, CDCl<sub>3</sub>) δ: 7.06–7.53 (5H, m), 6.35–6.46 (2H, m), 5.2 (1H, br, s), 4.64 (0.04H, d, *J* = 4.0 Hz), 4.42 (0.96H, d, *J* = 7.8 Hz), 2.8–3.1 (1H, m), 1.86–1.91 (3H, m), 1.68–1.72 (4H, m), 1.21–1.24 (6H, m). <sup>13</sup>C NMR (62.9 MHz, CDCl<sub>3</sub>) δ: 20.4, 23.9, 26.9, 33.7, 39.2, 53.8, 58.9, 59.1, 109.4, 110, 115.0, 126.7, 126.9, 130, 131.6, 133, 138.4, 145.3, 146.6, 148.1, 219.5. MS *m/z* (%): 388 (M<sup>+</sup> + 2, 2.9), 387 (M<sup>+</sup> + 1, 6.2), 386 (M<sup>+</sup>, 5.4), 302 (74.8), 288 (13.9), 171 (29.6), 149 (13.6), 129 (18.0), 95 (17.0), 69 (100.0). Anal. calcd. for C<sub>21</sub>H<sub>24</sub>BrNO (386.325; %): C 65.29, H 6.26, N 3.63; found: C 65.20, H 6.31, N 3.70.

**2-[Anilino(2-hydroxy-1-naphthyl)methyl]cyclopentanone (4l)**

Purification by column chromatography on neutral silica gel, eluted with ethyl acetate/petroleum ether (1:5) or by recrystallization with hexane gave compound **4l** as a pale brown powder in a 90% yield; anti/syn 100/0; mp 208–210 °C. IR (KBr, cm<sup>-1</sup>) ν: 3367, 2980, 1735, 1596, 1496, 1430, 1400, 1226, 1149, 1038, 1014, 933, 817, 748, 694. <sup>1</sup>H NMR (250 MHz, CDCl<sub>3</sub>) δ: 8.0 (1H, d, *J* = 8.3 Hz), 7.92 (1H, d, *J* = 8.3 Hz), 7.5–7.72 (3H, m), 7.17–7.3 (2H, m), 7.03 (1H, d, *J* = 8.8 Hz), 6.69–6.88 (3H, m), 5.18 (1H, br, s), 4.42 (1H, d, *J* =



6.5 Hz), 3.01–3.17 (1H, m), 2.71–2.79 (2H, m), 1.54–1.64 (1H, m), 1.18–1.64 (3H, m).  $^{13}\text{C}$  NMR (62.9 MHz,  $\text{CDCl}_3$ )  $\delta$ : 23.0, 25.1, 26.1, 43.8, 45.7, 113.7, 115.1, 118.0, 119.1, 121.8, 122.9, 123.2, 124.0, 126.5, 127.6, 128.4, 129.6, 130.4, 130.9, 135.3, 199.0, 226.5. MS  $m/z$  (%): 333 ( $\text{M}^+ + 2$ , 0.3), 332 ( $\text{M}^+ + 1$ , 1.3), 331 ( $\text{M}^+$ , 4.3), 284 (2.7), 256 (3.1), 219 (20.5), 152 (11.0), 125 (16.3), 97 (38.6), 71 (60.4), 55 (100.0). Anal. calcd. for  $\text{C}_{22}\text{H}_{21}\text{NO}_2$  (331.408; %): C 79.73, H 6.39, N 4.23; found: C 79.80, H 6.31, N 4.30.

#### 4-[Anilino(2-oxocyclopentyl)methyl]benzonitrile (4m)

Purification by column chromatography on neutral silica gel, eluted with ethyl acetate/petroleum ether (1:5) or by recrystallization with  $\text{CH}_2\text{Cl}_2$ /petroleum ether gave compound **4m** as a brown powder in an 84% yield; anti/syn 94/6; mp 126–128 °C. IR (KBr,  $\text{cm}^{-1}$ )  $\nu$ : 3340, 2225, 1720, 1600, 1500, 844, 756, 698, 551.  $^1\text{H}$  NMR (250 MHz,  $\text{CDCl}_3$ )  $\delta$ : 7.63 (2H, d,  $J = 8.3$  Hz), 7.52 (2H, d,  $J = 8.3$  Hz), 7.09 (2H, t,  $J = 8.3$  Hz), 6.66 (1H, t,  $J = 7.3$  Hz), 6.42 (2H, d,  $J = 7.8$  Hz), 5 (1H, br, s), 4.8 (0.06H, d,  $J = 4.4$  Hz), 4.4 (0.94H, d,  $J = 7.3$  Hz), 1.89–1.97 (2H, m), 1.24–1.67 (5H, m).  $^{13}\text{C}$  NMR (62.9 MHz,  $\text{CDCl}_3$ )  $\delta$ : 20.4, 26.7, 39.1, 53.7, 58.7, 111.4, 114.1, 118.5, 118.7, 127.1, 127.8, 128.0, 129.1, 132.5, 133.1, 146.7, 147.4, 197.2, 218.4. MS  $m/z$  (%): 292 ( $\text{M}^+ + 2$ , 0.3), 291 ( $\text{M}^+ + 1$ , 1.9), 290 ( $\text{M}^+$ , 4.5), 207 (100.0), 149 (11.9), 77 (26.9), 55 (23.2). Anal. calcd. for  $\text{C}_{19}\text{H}_{18}\text{N}_2\text{O}$  (290.359; %): C 78.59, H 6.25, N 9.65; found: C 78.66, H 6.31, N 9.71.

#### 2-[Anilino(3-hydroxyphenyl)methyl]cyclopentanone (4n)

Purification by column chromatography on neutral silica gel, eluted with ethyl acetate/petroleum ether (1:5) or by recrystallization with hexane gave compound **4n** as a colorless powder in an 84% yield; anti/syn 100/0; mp 176–178 °C. IR (KBr,  $\text{cm}^{-1}$ )  $\nu$ : 3309, 3163, 2977, 1724, 1585, 1492, 1230, 752, 694.  $^1\text{H}$  NMR (250 MHz, DMSO)  $\delta$ : 9.1 (1H, s), 6.70–6.84 (3H, m), 6.26–6.44 (5H, m), 5.86 (1H, d,  $J = 5.8$  Hz), 4.36 (1H, s) 2.26–2.36 (1H, m), 1.18–1.64 (6H, m).  $^{13}\text{C}$  NMR (62.9 MHz, DMSO)  $\delta$ : 19.8, 24.9, 54.1, 56.0, 112.8, 113.8, 113.9, 116.0, 117.9, 118.2, 128.6, 129.1, 142.8, 146.2, 147.6, 157.1, 184.7, 218.2. MS  $m/z$  (%): 283 ( $\text{M}^+ + 2$ , 0.5), 282 ( $\text{M}^+ + 1$ , 1.9), 281 ( $\text{M}^+$ , 4.6), 198 (100.0), 104 (19.6), 77 (35.5), 55 (17.9). Anal. calcd. for  $\text{C}_{19}\text{H}_{18}\text{N}_2\text{O}$  (281.349; %): C 76.84, H 6.81, N 4.98; found: C 76.82, H 6.88, N 4.94.

#### 3-Anilino-1,3-diphenyl-1-propanone (6a)

The filtrate was triturated with hexane (10 mL), filtered, and then recrystallization with EtOH/ $\text{H}_2\text{O}$  (2:1) gave compound **6a** as a colorless powder in a 98% yield; mp 169–170 °C (lit. value<sup>32</sup> mp 170–171 °C).  $^1\text{H}$  NMR (250 MHz,  $\text{CDCl}_3$ )  $\delta$ : 7.90 (2H, d,  $J = 8.5$  Hz), 7.55 (2H, t,  $J = 7.3$  Hz), 7.23–7.47 (6H, m), 7.11 (2H, t,  $J = 7.5$  Hz), 6.76 (1H, t,  $J = 7.3$  Hz), 6.69 (2H, d,  $J = 7.8$  Hz), 5.01 (1H, t,  $J = 6.5$  Hz), 3.60 (2H, d,  $J = 5.8$  Hz).  $^{13}\text{C}$  NMR (62.9 MHz,  $\text{CDCl}_3$ )  $\delta$ : 46.2, 55.0, 95.2, 114.0, 117.8, 118.1, 126.4, 125.2, 127.4, 128.2, 128.7, 128.8, 129.1, 129.3, 133.4, 136.6, 142.7, 146.7, 159.2, 179.2, 198.2. Anal. calcd. for  $\text{C}_{21}\text{H}_{19}\text{NO}$  (301.382; %): C 83.69, H 6.35, N 4.65; found: C 83.75, H 6.42, N 4.59.

#### 3-Anilino-3-(3-chlorophenyl)-1-phenyl-1-propanone (6b)<sup>33</sup>

The filtrate was triturated with hexane (10 mL), filtered, and then recrystallization with EtOH/ $\text{H}_2\text{O}$  (2:1) gave compound **6b** as a colorless powder in an 86% yield; mp 120–122 °C.  $^1\text{H}$  NMR (250 MHz,  $\text{CDCl}_3$ )  $\delta$ : 7.93 (2H, d,  $J = 8.5$  Hz), 7.58 (1H, t,  $J = 8.3$  Hz), 7.43 (2H, t,  $J = 7.0$  Hz), 7.21–7.34 (4H, m), 7.08 (2H, t,  $J = 7.5$  Hz), 6.72 (1H, t,  $J = 7.5$  Hz), 6.54 (2H, d,  $J = 7.8$  Hz), 4.97 (1H, t,  $J = 6.0$  Hz), 4.20 (1H, s), 3.46 (2H, d,  $J = 5.5$  Hz).  $^{13}\text{C}$  NMR (62.9 MHz,  $\text{CDCl}_3$ )  $\delta$ : 46.1, 54.5, 113.9, 118.2, 119.0, 124.7, 126.6, 127.6, 128.2, 128.5, 128.8, 129.2, 130.1, 131.3, 133.6, 134.7, 136.5, 139.1, 145.3, 146.6, 197.7. Anal. calcd. for  $\text{C}_{21}\text{H}_{18}\text{ClNO}$  (335.826; %): C 75.11, H 5.40, N 4.17; found: C 75.19, H 5.48, N 4.21.

#### 3-Anilino-3-(4-chlorophenyl)-1-phenyl-1-propanone (6c)

The filtrate was triturated with hexane (10 mL), filtered, and then recrystallization with EtOH/ $\text{H}_2\text{O}$  (2:1) gave compound **6c** as a colorless powder in an 89% yield; mp 128–130 °C (lit. value<sup>16a</sup> mp 131–132 °C).  $^1\text{H}$  NMR (250 MHz,  $\text{CDCl}_3$ )  $\delta$ : 7.89 (2H, d,  $J = 7$  Hz), 7.55–7.64 (2H, m), 7.49 (2H, d,  $J = 8.8$  Hz), 7.43 (2H, d,  $J = 9$  Hz), 7.29 (1H, d,  $J = 8.5$  Hz), 7.11 (2H, t,  $J = 8.3$  Hz), 6.70 (1H, t,  $J = 8.0$  Hz), 6.54 (2H, d,  $J = 7.8$  Hz), 4.99 (1H, t,  $J = 6.5$  Hz), 4.59 (1H, s), 3.47 (2H, d,  $J = 5.8$  Hz).  $^{13}\text{C}$  NMR (62.9 MHz,  $\text{CDCl}_3$ )  $\delta$ : 46.1, 54.2, 113.9, 118.1, 122.5, 127.9, 128.2, 128.5, 128.6, 128.8, 128.9, 129.2, 129.6, 132.9, 133.4, 133.5, 136.6, 141.5, 143.2, 146.6, 197.9. Anal. calcd. for  $\text{C}_{21}\text{H}_{18}\text{ClNO}$  (335.826; %): C 75.11, H 5.40, N 4.17; found: C 75.15, H 5.34, N 4.24.

#### 3-Anilino-3-(4-isopropylphenyl)-1-phenyl-1-propanone (6d)<sup>13</sup>

The filtrate was triturated with hexane (10 mL), filtered, and then recrystallization with EtOH/ $\text{H}_2\text{O}$  (2:1) gave compound **6d** as a colorless powder in a 96% yield; mp 154–156 °C.  $^1\text{H}$  NMR (250 MHz,  $\text{CDCl}_3$ )  $\delta$ : 7.80 (2H, d,  $J = 8.3$  Hz), 7.47 (1H, t,  $J = 8.5$  Hz), 7.36 (2H, t,  $J = 7.8$  Hz), 7.27 (2H, d,  $J = 8.3$  Hz), 7.09 (2H, d,  $J = 8.3$  Hz), 7.0 (2H, t,  $J = 8.3$  Hz), 6.58 (1H, t,  $J = 7.5$  Hz), 6.51 (2H, d,  $J = 8.5$  Hz), 4.91 (1H, t,  $J = 5.8$  Hz), 3.41 (2H, d,  $J = 5.5$  Hz), 2.87 (1H, m), 1.19 (6H, d,  $J = 6.8$  Hz).  $^{13}\text{C}$  NMR (62.9 MHz,  $\text{CDCl}_3$ )  $\delta$ : 23.9, 24.0, 33.7, 46.2, 45.5, 113.8, 114.0, 117.7, 126.3, 126.8, 128.2, 128.6, 129.1, 130.1, 133.3, 134.2, 136.7, 140.1, 145.9, 146.9, 147.9, 149.4, 169.1, 198.4. Anal. calcd. for  $\text{C}_{24}\text{H}_{25}\text{NO}$  (343.461; %): C 83.93, H 7.34, N 4.08; found: C 83.89, H 7.30, N 4.12.

#### 3-Anilino-3-(2,5-dimethoxyphenyl)-1-phenyl-1-propanone (6e)

The filtrate was triturated with hexane (10 mL), filtered, and then recrystallization with EtOH/ $\text{H}_2\text{O}$  (2:1) gave compound **6e** as a pale yellow powder in a 90% yield; mp 148–150 °C. IR (KBr,  $\text{cm}^{-1}$ )  $\nu$ : 3344, 2831, 1670, 1600, 1492, 1288, 1041, 722, 694, 590, 470.  $^1\text{H}$  NMR (250 MHz,  $\text{CDCl}_3$ )  $\delta$ : 7.97 (2H, d,  $J = 8.3$  Hz), 7.56 (1H, t,  $J = 8.5$  Hz), 7.46 (2H, t,  $J = 9.0$  Hz), 7.11 (2H, t,  $J = 7.5$  Hz), 6.8 (1H, d,  $J = 9.0$  Hz), 6.6 (4H, d,  $J = 8.8$  Hz), 6.64 (1H, t,  $J = 8.0$  Hz), 5.26 (1H, t,  $J = 5.0$  Hz), 3.89 (3H, s), 3.82 (1H, d,  $J = 4.8$  Hz), 3.69 (3H, s), 3.36 (1H, m).  $^{13}\text{C}$  NMR (62.9 MHz,  $\text{CDCl}_3$ )  $\delta$ : 44.4, 51.0, 55.6, 55.8, 111.4, 112.4,

113.9, 114.0, 117.9, 123.1, 127.3, 128.4, 128.6, 129.0, 129.2, 131.1, 133.3, 136.6, 146.6, 150.7, 153.9, 155.4, 198.9. MS  $m/z$  (%): 363 ( $M^+ + 2$ , 2.6), 362 ( $M^+ + 1$ , 3.0), 361 ( $M^+$ , 4.7), 242 (38.4), 212 (10.9), 149 (27.8), 123 (15.1), 105 (39.8), 69 (100.0). Anal. calcd. for  $C_{23}H_{23}NO_3$  (361.434; %): C 76.43, H 6.41, N 3.88; found: C 76.39, H 6.88, N 3.92.

### 3-Anilino-3-(2-naphthyl)-1-phenyl-1-propanone (6f)

The filtrate was triturated with hexane (10 mL), filtered, and then recrystallization with EtOH/H<sub>2</sub>O (2:1) gave compound **6f** as a colorless powder in a 91% yield; mp 133–135 °C. IR (KBr, cm<sup>-1</sup>)  $\nu$ : 3363, 2893, 1670, 1600, 1508, 1288, 744, 686, 742. <sup>1</sup>H NMR (250 MHz, CDCl<sub>3</sub>)  $\delta$ : 7.89 (2H, t,  $J$  = 7 Hz), 7.78–8.0 (4H, m), 7.6 (1H, d,  $J$  = 8.0 Hz), 7.53 (4H, d,  $J$  = 7.5 Hz), 7.45 (2H, t,  $J$  = 8.5 Hz), 7.08 (2H, t,  $J$  = 7.3 Hz), 6.64 (3H, t,  $J$  = 7.8 Hz), 5.17 (1H, t,  $J$  = 5 Hz), 3.57 (2H, d,  $J$  = 5.3 Hz). <sup>13</sup>C NMR (62.9 MHz, CDCl<sub>3</sub>)  $\delta$ : 46.3, 55.1, 114.1, 118.0, 123.7, 124.6, 125.2, 125.8, 126.1, 127.4, 127.6, 127.8, 127.9, 128.2, 128.5, 128.6, 128.7, 129.1, 131.2, 133.0, 133.5, 140.4, 144.9, 146.9, 198.1. MS  $m/z$  (%): 353 ( $M^+ + 2$ , 0.4), 352 ( $M^+ + 1$ , 1.6), 351 ( $M^+$ , 3.6), 236 (25.4), 182 (31.7), 128 (38.1), 105 (36.5), 83 (61.9), 55 (100.0). Anal. calcd. for  $C_{25}H_{21}NO$  (351.440; %): C 85.44, H 6.02, N 3.99; found: C 85.49, H 6.08, N 3.94.

### 3-Anilino-3-(4-nitrophenyl)-1-phenyl-1-propanone (6g)

The filtrate was triturated with hexane (10 mL), filtered, and then recrystallization with EtOH/H<sub>2</sub>O (2:1) gave compound **6g** as a pale green powder in an 80% yield; mp 108–110 °C (lit. value<sup>34</sup> mp 108–109 °C). <sup>1</sup>H NMR (250 MHz, CDCl<sub>3</sub>)  $\delta$ : 8.1 (2H, d,  $J$  = 8.8 Hz), 7.89 (1H, d,  $J$  = 8 Hz), 7.6 (2H, d,  $J$  = 8.5 Hz), 7.57 (2H, t,  $J$  = 7.3 Hz), 7.44 (2H, t,  $J$  = 7.8 Hz), 7.11 (2H, t,  $J$  = 7.5 Hz), 6.70 (1H, d,  $J$  = 7.3 Hz), 6.55 (2H, d,  $J$  = 7.8 Hz), 5.1 (1H, t,  $J$  = 6.0 Hz), 3.5 (2H, d,  $J$  = 6.0 Hz). <sup>13</sup>C NMR (62.9 MHz, CDCl<sub>3</sub>)  $\delta$ : 45.5, 54.4, 114.1, 118.8, 123.6, 124.1, 124.2, 125.7, 127.5, 128.6, 128.8, 129.3, 129.6, 133.4, 133.8, 136.3, 141.5, 145.9, 147.2, 150.5, 197.1. Anal. calcd. for  $C_{21}H_{18}N_2O_3$  (346.379; %): C 72.82, H 5.24, N 8.09; found: C 72.78, H 5.29, N 8.15.

### 3-Anilino-3-(4-methoxyphenyl)-1-phenyl-1-propanone (6h)

The filtrate was triturated with hexane (10 mL), filtered, and then recrystallization with EtOH/H<sub>2</sub>O (2:1) gave compound **6h** as a colorless powder in a 91% yield; mp 148–150 °C (lit. value<sup>34</sup> mp 150–152 °C). <sup>1</sup>H NMR (250 MHz, CDCl<sub>3</sub>)  $\delta$ : 7.92 (2H, d,  $J$  = 8.3 Hz), 7.88 (1H, t,  $J$  = 8.5 Hz), 7.45 (2H, t,  $J$  = 7.8 Hz), 7.34 (2H, d,  $J$  = 8.8 Hz), 7.10 (2H, t,  $J$  = 7.5 Hz), 6.8 (2H, d,  $J$  = 8.8 Hz), 6.68 (1H, t,  $J$  = 8.0 Hz), 6.60 (2H, d,  $J$  = 7.5 Hz), 4.97 (1H, t,  $J$  = 6.5 Hz), 3.80 (3H, s), 3.47 (2H, d,  $J$  = 5.8 Hz). <sup>13</sup>C NMR (62.9 MHz, CDCl<sub>3</sub>)  $\delta$ : 46.2, 54.5, 55.2, 114.1, 114.2, 118.0, 123.2, 124.3, 124.9, 127.1, 127.5, 128.2, 128.7, 129.1, 133.3, 134.6, 136.1, 141.2, 145.8, 148.0, 158.8, 198.4. Anal. calcd. for  $C_{22}H_{21}NO_2$  (331.408; %): C 79.73, H 6.39, N 4.23; found: C 79.70, H 6.43, N 4.20.

### 3-Anilino-3-(4-methylphenyl)-1-phenyl-1-propanone (6i)

The filtrate was triturated with hexane (10 mL), filtered, and then recrystallization with EtOH/H<sub>2</sub>O (2:1) gave compound **6i** as a colorless powder in a 92% yield; mp 134–135 °C (lit. value<sup>34</sup> mp 131–132 °C). <sup>1</sup>H NMR (250 MHz, CDCl<sub>3</sub>)  $\delta$ : 7.92 (2H, d,  $J$  = 7.3 Hz), 7.56 (1H, t,  $J$  = 8.8 Hz), 7.44 (2H, t,  $J$  = 7.8 Hz), 7.32 (2H, d,  $J$  = 8.0 Hz), 7.06–7.14 (4H, m), 6.64 (1H, t,  $J$  = 7.3 Hz), 6.58 (2H, d,  $J$  = 8.8 Hz), 4.98 (1H, t,  $J$  = 6.0 Hz), 3.50 (2H, d,  $J$  = 5.5 Hz), 2.23 (3H, s, 3H). <sup>13</sup>C NMR (62.9 MHz, CDCl<sub>3</sub>)  $\delta$ : 21.1, 46.2, 54.7, 114.0, 114.9, 118.0, 124.4, 126.3, 127.3, 127.9, 128.2, 128.6, 129.1, 129.4, 133.2, 136.3, 139.0, 141.7, 145.5, 147.9, 159.0, 199.1. Anal. calcd. for  $C_{22}H_{21}NO$  (315.408; %): C 83.78, H 6.71, N 4.44; found: C 83.81, H 6.75, N 4.40.

### 3-(4-Bromoanilino)-1,3-diphenyl-1-propanone (6j)

The filtrate was triturated with hexane (10 mL), filtered, and then recrystallization with EtOH/H<sub>2</sub>O (2:1) gave compound **6j** as a colorless powder in a 90% yield; mp 182–184 °C (lit. value<sup>32</sup> mp 182–184 °C). <sup>1</sup>H NMR (250 MHz, CDCl<sub>3</sub>)  $\delta$ : 7.86 (2H, d,  $J$  = 8.3 Hz), 7.51 (2H, t,  $J$  = 7.3 Hz), 7.39 (2H, t,  $J$  = 7.5 Hz), 7.35 (2H, d,  $J$  = 7.5 Hz), 7.20–7.28 (4H, m), 6.77 (2H, d,  $J$  = 8.8 Hz), 4.99 (1H, t,  $J$  = 6.5 Hz), 3.85 (2H, d,  $J$  = 6.5 Hz). <sup>13</sup>C NMR (62.9 MHz, CDCl<sub>3</sub>)  $\delta$ : 43.7, 59.1, 114.0, 114.9, 120.7, 121.2, 124.1, 127.9, 128.1, 128.6, 128.7, 128.9, 132.2, 133.6, 136.2, 137.6, 138.0, 139.3, 144.9, 162.9, 196.6. Anal. calcd. for  $C_{21}H_{18}BrNO$  (380.278; %): C 66.33, H 4.77, N 3.68; found: C 66.29, H 4.70, N 3.71.

### 3-(4-Fluoroanilino)-1,3-diphenyl-1-propanone (6k)<sup>35</sup>

The filtrate was triturated with hexane (10 mL), filtered, and then recrystallization with EtOH/H<sub>2</sub>O (2:1) gave compound **6k** as a colorless powder in an 89% yield; mp 158–160 °C. <sup>1</sup>H NMR (250 MHz, CDCl<sub>3</sub>)  $\delta$ : 7.89 (2H, d,  $J$  = 7.3 Hz), 7.23–7.56 (8H, m), 6.78 (2H, t,  $J$  = 8.8 Hz), 6.49 (2H, d,  $J$  = 9.0 Hz), 4.91 (1H, t,  $J$  = 7.0 Hz), 3.45 (2H, d,  $J$  = 5.3 Hz). <sup>13</sup>C NMR (62.9 MHz, CDCl<sub>3</sub>)  $\delta$ : 46.3, 55.6, 114.9, 115.1, 115.3, 115.7, 116.0, 126.4, 127.5, 128.2, 128.5, 128.7, 128.9, 133.5, 136.6, 142.6, 143.1, 145.1, 154.1, 158.0, 198.2. Anal. calcd. for  $C_{21}H_{18}FNO$  (319.372; %): C 78.98, H 5.68, N 4.39; found: C 78.94, H 6.61, N 4.35.

### 3-Anilino-1-(4-chlorophenyl)-3-phenyl-1-propanone (6m)

The filtrate was triturated with hexane (10 mL), filtered, and then recrystallization with EtOH/H<sub>2</sub>O (2:1) gave compound **6m** as a colorless powder in a 90% yield; mp 119–120 °C (lit. value<sup>32</sup> mp 119–120 °C). <sup>1</sup>H NMR (250 MHz, CDCl<sub>3</sub>)  $\delta$ : 7.74 (2H, d,  $J$  = 8.5 Hz), 7.45 (3H, d,  $J$  = 8.3 Hz), 7.1–7.37 (4 H, m), 6.90 (2H, t,  $J$  = 8.0 Hz), 6.55 (3H, d,  $J$  = 8.3 Hz), 5.02 (1H, t,  $J$  = 6.8 Hz), 3.80 (2H, d,  $J$  = 6.3 Hz). <sup>13</sup>C NMR (62.9 MHz, CDCl<sub>3</sub>)  $\delta$ : 44.2, 59.0, 111.3, 118.35, 121.5, 122.7, 127.6, 128.3, 128.5, 128.8, 128.9, 129.0, 129.7, 129.9, 130.7, 134.7, 138.6, 139.9, 145.4, 178.9, 195.7. Anal. calcd. for  $C_{21}H_{18}ClNO$  (335.826; %): C 75.11, H 5.40, N 4.17; found: C 75.05, H 5.44, N 4.21.

### 3-(4-Bromoanilino)-1-(4-chlorophenyl)-3-phenyl-1-propanone (6n)

The filtrate was triturated with hexane (10 mL), filtered, and then recrystallization with EtOH/H<sub>2</sub>O (2:1) gave compound **6n** as a pale yellow powder in an 85% yield; mp 139–140 °C (lit value<sup>32</sup> mp 139–141 °C). <sup>1</sup>H NMR (250 MHz, CDCl<sub>3</sub>) δ: 7.80 (2H, d, *J* = 8.5 Hz), 7.32–7.42 (4H, m), 7.27 (3H, t, *J* = 8.0 Hz), 7.12 (2H, d, *J* = 8.8 Hz), 6.43 (2H, d, *J* = 8.8 Hz), 4.92 (1H, t, *J* = 5.8 Hz), 3.42 (2H, d, *J* = 7.3 Hz). <sup>13</sup>C NMR (62.9 MHz, CDCl<sub>3</sub>) δ: 46.0, 54.8, 109.7, 111.0, 113.2, 114.5, 115.5, 122.1, 126.3, 127.6, 128.9, 129.0, 129.6, 129.1, 130.4, 131.8, 134.9, 140.1, 142.1, 145.7, 196.9. Anal. calcd. for C<sub>21</sub>H<sub>17</sub>BrClNO (414.723; %): C 60.82, H 4.13, N 3.38; found: C 60.89, H 4.07, N 3.41.

### 3-Anilino-3-(2-methoxyphenyl)-1-phenyl-1-propanone (6o)

The filtrate was triturated with hexane (10 mL), filtered, and then recrystallization with EtOH/H<sub>2</sub>O (2:1) gave compound **6o** as a pale green powder in an 85% yield; mp 122–124 °C. IR (KBr, cm<sup>-1</sup>) ν: 3375, 1681, 1600, 1519, 1234, 748, 690, 574. <sup>1</sup>H NMR (250 MHz, CDCl<sub>3</sub>) δ: 7.91 (2H, d, *J* = 8.5 Hz), 7.39 (3H, t, *J* = 9.0 Hz), 7.21 (2H, t, *J* = 9.0 Hz), 7.05 (2H, t, *J* = 7.5 Hz), 6.84–6.92 (2H, m), 6.63 (1H t, *J* = 7.5 Hz), 6.53 (2H, d, *J* = 8.5 Hz), 5.22 (1H, dd, *J*<sub>1</sub> = 8.5 Hz, *J*<sub>2</sub> = 4.5 Hz), 3.92 (3H, s), 3.64 (1H, dd, *J*<sub>1</sub> = 15.0 Hz, *J*<sub>2</sub> = 4.8 Hz), 3.20 (1H, dd, *J*<sub>1</sub> = 15.0 Hz, *J*<sub>2</sub> = 8.3 Hz). <sup>13</sup>C NMR (62.9 MHz, CDCl<sub>3</sub>) δ: 44.5, 50.7, 55.4, 110.5, 113.5, 113.9, 117.7, 118.0, 121.0, 127.5, 128.33, 128.9, 129.1, 129.7, 129.8, 134.9, 135.0, 139.7, 140.1, 146.9, 156.5, 197.9. MS *m/z* (%): 333 (M<sup>+</sup> + 2, 1.0), 331 (M<sup>+</sup> + 1, 3.5), 330 (M<sup>+</sup>, 1.9), 279 (3.4), 257 (1.8), 241 (2.0), 212 (47.0), 167 (11.3), 149 (37.9), 119, 93 (17.6), 69 (100.0). Anal. calcd. for C<sub>22</sub>H<sub>21</sub>NO<sub>2</sub> (331.408; %): C 79.73, H 6.39, N 4.23; found: C 79.70, H 6.35, N 4.29.

### Acknowledgements

We gratefully acknowledge the support of this work by the Shiraz University Research Council. We are also grateful to Mr. H. Sajedian Fard for helpful cooperation.

### References

- (1) (a) Davis, F. A.; Zhang, Y.; Anilkumar, G. *J. Org. Chem.* **2003**, 68 (21), 8061. doi:10.1021/jo030208d. PMID: 14535782.; (b) Evans, G. B.; Furneaux, R. H.; Tyler, P. C.; Schramm, V. L. *Org. Lett.* **2003**, 5 (20), 3639. doi:10.1021/ol035293q. PMID:14507192.; (c) Martin, S. F. *Acc. Chem. Res.* **2002**, 35 (10), 895. doi:10.1021/ar950230w. PMID: 12379142.; (d) Fujita, T.; Nagasawa, H.; Uto, Y.; Hashimoto, T.; Asakawa, Y.; Hori, H. *Org. Lett.* **2004**, 6 (5), 827. doi:10.1021/ol049947m. PMID:14986985.; (e) Joshi, N. S.; Whitaker, L. R.; Francis, M. B. *J. Am. Chem. Soc.* **2004**, 126 (49), 15942. doi:10.1021/ja0439017. PMID:15584710.; (f) Wenzel, A. G.; Jacobsen, E. N. *J. Am. Chem. Soc.* **2002**, 124 (44), 12964. doi:10.1021/ja028353g. PMID:12405820.; (g) Ishimaru, K.; Kojima, T. *Tetrahedron Lett.* **2003**, 44 (29), 5441. doi:10.1016/S0040-4039(03)01314-5.; (h) Córdova, A. *Acc. Chem. Res.* **2004**, 37 (2), 102. doi:10.1021/ar030231l. PMID:14967057.; (i) Córdova, A. *Chem. Eur. J.* **2004**, 10 (8), 1987. doi:10.1002/chem.200305646.
- (2) (a) Blicke, F. F. *Org. React.* **1942**, 1, 303; (b) Leinmann, E. F. In *Comprehensive Organic Synthesis*; Trost, B. M., Ed.; Pergamon Press: New York, 1991; Vol. 2, Chapter 4.1; (c) Arend, M.; Westermann, B.; Risch, N. *Angew. Chem. Int. Ed. Engl.* **1998**, 37 (8), 1044. doi:10.1002/(SICI)1521-3773(19980504)37:8<1044::AID-ANIE1044>3.0.CO;2-E.; (d) Kobayashi, S.; Ishitani, H. *Chem. Rev.* **1999**, 99 (5), 1069. doi:10.1021/cr980414z. PMID:11749440.
- (3) (a) Trost, B. M.; Terrell, L. R. *J. Am. Chem. Soc.* **2003**, 125 (2), 338. doi:10.1021/ja028782e. PMID:12517138.; (b) Matsunaga, S.; Kumagai, N.; Harada, S.; Shibasaki, M. *J. Am. Chem. Soc.* **2003**, 125 (16), 4712. doi:10.1021/ja034787f. PMID:12696881.; (c) Juhl, K.; Gathergood, N.; Jørgensen, K. A. *Angew. Chem.* **2001**, 113 (16), 3083. doi:10.1002/1521-3757(20010817)113:16<3083::AID-ANGE3083>3.0.CO;2-C.; (d) List, B. *J. Am. Chem. Soc.* **2000**, 122 (38), 9336. doi:10.1021/ja001923x.; (e) List, B.; Pojarliev, P.; Biller, W. T.; Martin, H. J. *J. Am. Chem. Soc.* **2002**, 124 (5), 827. doi:10.1021/ja0174231. PMID: 11817958.; (f) Córdova, A.; Notz, W.; Zhong, G.; Betancort, J. M.; Barbas, C. F., III. *J. Am. Chem. Soc.* **2002**, 124 (9), 1842. doi:10.1021/ja017270h. PMID:11866583.; (g) Kobayashi, S.; Hamada, T.; Manabe, K. *J. Am. Chem. Soc.* **2002**, 124 (20), 5640. doi:10.1021/ja026094p. PMID:12010028.; (h) Hayashi, Y.; Tsuboi, W.; Ashimine, I.; Urushima, T.; Shoji, M.; Sakai, K. *Angew. Chem. Int. Ed.* **2003**, 42 (31), 3677. doi:10.1002/anie.200351813.
- (4) (a) Yang, Y.-Y.; Shou, W.-G.; Wang, Y.-G. *Tetrahedron* **2006**, 62 (43), 10079. doi:10.1016/j.tet.2006.08.063.; (b) Shou, W.-G.; Yang, Y.-Y.; Wang, Y.-G. *Tetrahedron Lett.* **2006**, 47 (11), 1845. doi:10.1016/j.tetlet.2005.12.136.
- (5) Azizi, N.; Torkiyan, L.; Saidi, M. R. *Org. Lett.* **2006**, 8 (10), 2079. doi:10.1021/ol060498v. PMID:16671786.
- (6) (a) Eftekhari-Sis, B.; Abdollahifar, A.; Hashemi, M. M.; Zirak, M. *Eur. J. Org. Chem.* **2006**, 5152. doi:10.1002/ejoc.200600493.; (b) Fernández Sanz, J.; Rabaã, H.; Poveda, F. M.; Márquez, A. M.; Calzado, C. J. *Int. J. Quantum Chem.* **1998**, 70, 359. doi:10.1002/(SICI)1097-461X(1998)70:2<359::AID-QUA12>3.0.CO;2-7.
- (7) Ibrahim, I.; Zou, W.; Engqvist, M.; Xu, Y.; Córdova, A. *Chem. Eur. J.* **2005**, 11 (23), 7024. doi:10.1002/chem.200500746.
- (8) Manabe, K.; Kobayashi, S. *Org. Lett.* **1999**, 1 (12), 1965. doi:10.1021/ol991113u.
- (9) Akiyama, T.; Matsuda, K.; Fuchibe, K. *Synlett* **2005**, 322. doi:10.1055/s-2004-836062.
- (10) Matsuda, K.; Mori, Y.; Kobayashi, S. *Tetrahedron* **2001**, 57 (40), 8443. doi:10.1016/S0040-4020(01)00828-6.
- (11) Akiyama, T.; Takaya, J.; Kagoshima, H. *Synlett* **1999**, 1045. doi:10.1055/s-1999-2789.
- (12) Ollevier, T.; Nadeau, E.; Guay-Begin, A. A. *Tetrahedron Lett.* **2006**, 47 (47), 8351. doi:10.1016/j.tetlet.2006.09.082.
- (13) Chang, C. T.; Liao, B. S.; Liu, S. T. *Tetrahedron Lett.* **2006**, 47 (52), 9257. doi:10.1016/j.tetlet.2006.10.125.
- (14) Iimura, S.; Nobutou, D.; Manabe, K.; Kobayashi, S. *Chem. Commun. (Camb.)* **2003**, 1644. doi:10.1039/b304343f.
- (15) Wang, R.; Li, B. G.; Huang, T. K.; Shi, L.; Lu, X. X. *Tetrahedron Lett.* **2007**, 48 (12), 2071. doi:10.1016/j.tetlet.2007.01.142.
- (16) (a) Bigdeli, M. A.; Nemati, F.; Mahdavinia, G. H. *Tetrahedron Lett.* **2007**, 48 (38), 6801. doi:10.1016/j.tetlet.2007.07.088.; (b) Wu, H.; Shen, Y.; Fan, L. y.; Wan, Y.; Zhang, P.; Chen, C.; Wang, W. *Tetrahedron* **2007**, 63 (11), 2404. doi:10.1016/j.tet.2007.01.015.



- (17) (a) Tamagaki, S.; Card, R. J.; Neckers, D. C. *J. Am. Chem. Soc.* **1978**, *100* (21), 6635. doi:10.1021/ja00489a013.; (b) Sharghi, H.; Hosseini Sarvari, M.; Moeini, F. *Can. J. Chem.* **2008**, *86* (11), 1044. doi:10.1139/V08-153.; (c) Sharghi, H.; Khalifeh, R.; Doroodmand, M. M. *Adv. Synth. Catal.* **2009**, *351*, 207. doi:10.1002/adsc.200800612.; (d) Sharghi, H.; Beyzavi, M. H.; Safavi, A.; Doroodmand, M. M.; Khalifeh, R. *Adv. Synth. Catal.* **2009**, *351*, 2391. doi:10.1002/adsc.200900353.; (e) Sharghi, H.; Hosseini Sarvari, M. *Synthesis* **2003**, 243. doi:10.1055/s-2003-36830.
- (18) (a) Yu, W.; Liu, M.; Liu, H.; An, X.; Liu, Z.; Ma, X. *J. Mol. Catal. Chem.* **1999**, *142* (2), 201. doi:10.1016/S1381-1169(98)00282-9.; (b) Varma, R. S. *Tetrahedron* **2002**, *58* (7), 1235. doi:10.1016/S0040-4020(01)01216-9.; (c) Mohammadpoor-Baltork, I.; Mirkhani, V.; Moghadam, M.; Tangestaninejad, S.; Zolfigol, M. A.; Abdollahi-Alibeik, M.; Khosropour, A. R.; Kargar, H.; Hojati, S. F. *Catal. Commun.* **2008**, *9* (5), 894. doi:10.1016/j.catcom.2007.09.017.; (d) Zolfigol, M. A. *Tetrahedron* **2001**, *57* (46), 9509. doi:10.1016/S0040-4020(01)00960-7.
- (19) Sharghi, H.; Kaboudin, B. *J. Chem. Res. (S)* **1998**, 628. doi:10.1039/a800158h.
- (20) Sharghi, H.; Hosseini Sarvari, M. *J. Chem. Res. (S)* **2001**, 446. doi:10.3184/030823401103168424.
- (21) Sharghi, H.; Hosseini Sarvari, M. *J. Org. Chem.* **2003**, *68* (10), 4096. doi:10.1021/jo020724o. PMID:12737600.
- (22) Sharghi, H.; Hosseini Sarvari, M. *Synth. Commun.* **2003**, *33* (2), 207. doi:10.1081/SCC-120015702.
- (23) Sharghi, H.; Hosseini Sarvari, M. *Tetrahedron* **2003**, *59* (20), 3627. doi:10.1016/S0040-4020(03)00518-0.
- (24) Sharghi, H.; Beni, A. R. S. *Synthesis* **2004**, *17* (17), 2900. doi:10.1055/s-2004-831253.
- (25) (a) Sharghi, H.; Shahsavari-Fard, Z. *J. Iran. Chem. Soc.* **2005**, *2*, (2), 47; (b) Sharghi, H.; Jokar, M. *Heterocycles* **2007**, *71* (12), 2721. doi:10.3987/COM-07-11175.
- (26) (a) Sharghi, H.; Aberi, M.; Doroodmand, M. M. *Adv. Synth. Catal.* **2008**, *350* (14–15), 2380. doi:10.1002/adsc.200800317.; (b) Sharghi, H.; Beyzavi, M. H.; Doroodmand, M. M. *Eur. J. Org. Chem.* **2008**, 4126. doi:10.1002/ejoc.200800351.
- (27) Wu, Y. S.; Cai, J.; Hu, Z. Y.; Lin, G. X. *Tetrahedron Lett.* **2004**, *45* (48), 8949. doi:10.1016/j.tetlet.2004.09.174.
- (28) (a) Zecchina, A.; Coluccia, S.; Morterra, C. *Appl. Spectrosc. Rev.* **1985**, *21* (3), 259. doi:10.1080/05704928508060432.; (b) De Boer, J. H.; Fortuin, J. H.; Lippens, B. C.; Meijs, W. H. *J. Catal.* **1963**, *2* (1), 1. doi:10.1016/0021-9517(63)90131-3.; (c) Maciver, D. S.; Tobin, H. H.; Barth, R. T. *J. Catal.* **1963**, *2* (6), 485. doi:10.1016/0021-9517(63)90004-6.; (d) Peri, J. B.; Hannan, R. B. *J. Phys. Chem.* **1960**, *64* (10), 1526. doi:10.1021/j100839a044.; (e) Peri, J. B. *J. Phys. Chem.* **1965**, *69* (1), 211. doi:10.1021/j100885a032.; (f) Knozinger, H. In *Adsorption on Ordered Surfaces of Ionic Solids and Thin Films*; Freund, H. J., Umbach, E. Eds. Springer Series in Surface Sciences 33, Springer-Verlag: Berlin, 1993; (g) Alvarez, L. J.; Fernández Sanz, J.; Capitán, M. J.; Centeno, M. A.; Odriozola, J. A. *J. Chem. Soc., Faraday Trans.* **1989**, *89*, 3623. doi:10.1039/ft9938903623.; (h) Abbattista, F.; Delmastro, S.; Gozzelino, G.; Mazza, D.; Vallino, M.; Busca, G.; Lorenzelli, V.; Ramis, G. *J. Catal.* **1989**, *117* (1), 42. doi:10.1016/0021-9517(89)90219-4.; (i) Peri, J. B. *J. Phys. Chem.* **1965**, *69* (1), 220. doi:10.1021/j100885a033.; (j) Cai, S.; Sohlberg, K. *J. Mol. Catal. Chem.* **2003**, *193* (1–2), 157. doi:10.1016/S1381-1169(02)00457-0.; (k) Feng, G.; Huo, C. F.; Deng, C. M.; Huang, L.; Li, Y. W.; Wang, J.; Jiao, H. *J. Mol. Catal. Chem.* **2009**, *304* (1–2), 58. doi:10.1016/j.molcata.2009.01.024.
- (29) (a) Loh, T. P.; Liung, S. B. K. W.; Tan, K.-L.; Wei, K. L. *Tetrahedron* **2000**, *56* (20), 3227. doi:10.1016/S0040-4020(00)00221-0.; (b) Gennari, C.; Venturini, I.; Gislón, F.; Schimperma, G. *Tetrahedron Lett.* **1987**, *28* (29), 227. doi:10.1016/S0040-4039(00)95693-4.; (c) Guanti, G.; Nari-sano, E.; Banfi, L. *Tetrahedron Lett.* **1987**, *28* (37), 4331. doi:10.1016/S0040-4039(00)96501-8.; (d) Ollevier, T.; Na-deau, E. *J. Org. Chem.* **2004**, *69* (26), 9292. doi:10.1021/jo048617c. PMID:15609969.; (e) Wu, H.; Chen, X. M.; Wan, Y.; Ye, L.; Xin, H. Q.; Xu, H. H.; Yue, C. H.; Pang, L. L.; Ma, R.; Shi, D. Q. *Tetrahedron Lett.* **2009**, *50* (9), 1062. doi:10.1016/j.tetlet.2008.12.067.
- (30) Kidwai, M.; Mishra, N. K.; Bansal, V.; Kumar, A.; Mozum-dar, S. *Tetrahedron Lett.* **2009**, *50* (12), 1355. doi:10.1016/j.tetlet.2009.01.031.
- (31) Ranu, B. C.; Samanta, S.; Guchhait, S. K. *Tetrahedron* **2002**, *58* (5), 983. doi:10.1016/S0040-4020(01)01177-2.
- (32) Lin, Y.; Huangshu, L.; Junhua, Z.; Xiujuan, X. *Synthesis* **1991**, 717. doi:10.1055/s-1991-26554.
- (33) Sawant, D. P.; Justus, J.; Balasubramanian, V. V.; Ariga, K.; Srinivasu, P.; Velmathi, S.; Halligudi, S. B.; Vinu, A. *Chem. Eur. J.* **2008**, *14* (10), 3200. doi:10.1002/chem.200701562.
- (34) Wang, L.; Han, J.; Sheng, J.; Tian, H.; Fan, Z. *Catal. Commun.* **2005**, *6* (3), 201. doi:10.1016/j.catcom.2004.12.009.
- (35) Rueping, M.; Sugiono, E.; Schoepke, F. R. *Synlett* **2007**, *9*, 1441. doi:10.1055/s-2007-980369.



# Ionophilic phosphonium-appended carbopalladacycle catalyst for Suzuki–Miyaura and Heck cross-coupling catalysis

Jocelyn J. Tindale and Paul J. Ragogna

**Abstract:** An ionic liquid, covalently tethered to an efficient transition-metal catalyst in the presence of an ionic liquid reaction medium, can utilize ionophilic interactions to improve catalyst activity, recyclability, and product isolation while decreasing catalyst leaching. Given the greater stability of phosphonium salts in comparison to imidazolium ionic liquids under basic conditions, phosphonium-tagged oxime carbopalladacycle salts were prepared and employed in both Heck and Suzuki–Miyaura reactions. The desired product was obtained in good yields for up to four catalyst cycles in the case of the Suzuki–Miyaura reaction. While taking advantage of the non-volatile nature of ionic liquids, the product was isolated through simple sublimation from the reaction mixture, eliminating issues associated with catalyst leaching, and the remaining ionic liquid solvent–catalyst mixture was ready for further catalysis.

**Key words:** phosphonium, ionic liquids, ionophilic catalysis, carbopalladacycle, ionic tag.

**Résumé :** Un liquide ionique lié d'une façon covalente à un catalyseur efficace à base d'un métal de transition, en présence d'un milieu réactionnel formé d'un liquide ionique, peut utiliser les interactions ionophiles pour améliorer l'activité du catalyseur, sa capacité à être recyclé et la facilité d'isoler le produit tout en diminuant la lixiviation du catalyseur. Se basant sur la plus grande stabilité des sels de phosphonium par comparaison aux liquides ioniques à base d'imidazolium dans des conditions basiques, on a préparé des sels à base carbocycles contenant du palladium sels et portant des phosphonium d'oximes comme étiquette ionique et on les a utilisés dans des réactions de Heck et de Suzuki–Miyaura. Le produit désiré a été obtenu avec de bons rendements pour au moins quatre cycles catalytiques dans le cas de la réaction de Suzuki–Miyaura. En tirant avantage de la nature non volatile des liquides ioniques, on a pu isoler le produit par simple sublimation à partir du milieu réactionnel, éliminant ainsi les problèmes associés avec la lixiviation du catalyseur et alors que le mélange solvant liquide ionique/catalyseur est prêt à être réutilisé pour d'autres réactions catalytiques.

**Mots-clés :** phosphonium, liquides ioniques, catalyse ionophile, carbocycles contenant du palladium, marquage ionique.

[Traduit par la Rédaction]

## Introduction

The use of ionic liquids (ILs) as an alternative solvent in catalysis has become popular over the last ten years as a means of rendering the reaction “green”.<sup>1</sup> This notion predominantly stems from the ionic nature of the salts, which give rise to a negligible vapor pressure. However, given recent reports on the toxicity of some ILs, their potential application as “green” solvents has faltered.<sup>2,3</sup> Nevertheless, many of their properties beyond non-volatility do render these materials highly amenable to many chemical reactions and applications. High thermal stabilities, wide liquid temperature ranges, and unique solubility parameters give rise to ionic liquids as good alternative solvents. Ionic liquids generally have the ability to dissolve many organic and organometallic compounds and are often immiscible with non-polar organic solvents.<sup>4</sup> The breadth of potential appli-

cations is further amplified given the general framework of common ionic liquids, such as imidazolium or pyridinium salts, is susceptible to chemical modification to attain a desired function while concomitantly maintaining the intrinsic properties of the low melting salts.

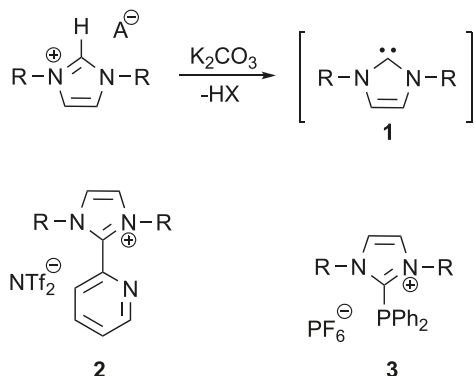
The ease of dissolution of transition metals in ionic liquids and the immiscibility observed with some organic solvents are both phenomena associated with ionic liquids that are often exploited in catalysis. These properties enable an improvement in the isolation of the organic product from the catalyst during simple extraction procedures.<sup>5,6</sup> Unfortunately, in some cases, the catalyst activity quickly decreases after several runs.<sup>7</sup> This is often a result of catalyst leaching during the extraction of the product from the reaction mixture or in the purification of the ionic liquid before the initiation of the next reaction cycle. To ensure retention of the catalyst within the ionic liquid phase and consequently improve the recyclability of the system and the isolation of products, modifications to the catalyst are required. A current methodology includes preparing a catalyst that mimics the physico-chemical properties of the ionic medium, thus increasing the ionophilicity of the catalyst. Shreeve et al. have synthesized a (carbene)palladium(II) catalyst that resembles the skeletal structure of the imidazolium ionic liquid reaction medium and was used successfully to facili-

Received 21 August 2009. Accepted 5 October 2009. Published on the NRC Research Press Web site at canjchem.nrc.ca on 17 December 2009.

**J.J. Tindale and P.J. Ragogna.**<sup>1</sup> Department of Chemistry, The University of Western Ontario, 1151 Richmond St, London, ON, N6A 5B7, Canada.

<sup>1</sup>Corresponding author (e-mail: pragogna@uwo.ca).

**Chart 1.** Illustration of the decomposition of an imidazolium cation in the presence of base resulting in the formation of a carbene, **1**, and alternative imidazolium cations protected at the C-2 position, **2** and **3**.



tate C–C bond forming reactions.<sup>8,9</sup> A more prevalent strategy to increase a catalyst's ionophilicity is to covalently integrate an ionic fragment into the catalyst framework. A critical review highlighting various successes employing ionic liquid ligands for the preparation of ionophilic catalysts has recently been published.<sup>10,11</sup>

Carbon–carbon bond forming reactions, such as Heck and Suzuki–Miyaura, are some of the most important reactions in organic synthesis. Substantial effort has been put forth to convert the successful homogeneous methodology into a heterogeneous system with enhanced catalyst recyclability. Recently, ionophilic ionic-liquid-tagged catalysts have been reported as a means of achieving this goal.<sup>12,13</sup> The ubiquitous imidazolium cation has been employed as an ion tag; however, it is susceptible to degradation under basic conditions, a requirement for the Heck and Suzuki–Miyaura reactions. The subsequent formation of a carbene, **1**, leads to poor yields, unwanted side-products, and inactive catalysts.<sup>14–16</sup> One approach to avoid this problem is the substitution of a metal-binding ligand such as a pyridine, **2**, or phosphine, **3**, at the C-2 position on the imidazolium cation (Chart 1).<sup>17,18</sup>

Our methodology, inspired by the work of Corma et al.,<sup>19</sup> also evades the susceptibility of imidazolium salts towards decomposition in the presence of base. Utilizing the ionophilic ionic-liquid-appended catalyst concept, a phosphonium salt was tethered to an oxime carbopalladacycle moiety, which was previously noted as an exceptional catalyst for Suzuki–Miyaura cross-coupling of aryl halides and arylboronic acids.<sup>20,21</sup> Phosphonium salts do not share the same vulnerability to basic conditions as observed for imidazolium cations and have been successfully used as alternative solvent media in Suzuki and Heck reactions without any signs of decomposition products such as Wittig-type reagents.<sup>22–26</sup> In this context, a phosphonium-tagged oxime carbopalladacycle catalyst precursor **8** has been synthesized and comprehensively characterized. It is important to note here that Singer et al. have prepared similar ionophilic ligands derived from oximes with pendant imidazolium salts. The salts were designed as capturing devices for sequestering metals from aqueous solutions, and their use as cross-coupling pre-catalysts was not investigated.<sup>27</sup> Herein, cross-coupling reactions catalyzed by the ionophilic catalyst,

**8**, were conducted using trihexyltetradecylphosphonium chloride, [P<sub>66614</sub>][Cl], as the reaction medium. Increased isolated yields and catalyst recyclability were noted as significant improvements to previous reports of ionophilic oxime carbopalladacycle cross-coupling catalysis.

## Experimental section

### Materials

The solvents were obtained from Caledon Laboratories. Dichloromethane, *N,N*-dimethylformamide, and toluene were dried using an Innovative Technologies Inc. Solvent Purification System, which utilizes dual-alumina columns, and were stored under a nitrogen or argon atmosphere in Strauss flasks or stored in the glovebox over 4 Å molecular sieves. Methanol was dried by storing over 3 Å molecular sieves. The trihexyltetradecylphosphonium chloride (Strem), styrene (Aldrich), *p*-methoxyphenyl boronic acid (Aldrich), and iodobenzene (Aldrich) were used as received and stored in a nitrogen-filled MBraun Labmaster 130 glovebox. The palladium dichloride (Pressure Chemicals), K<sub>3</sub>PO<sub>4</sub> (Riedel-deHaën), and LiCl (Caledon) were used as received and stored in a desiccator. Deuterated NMR solvents (CDCl<sub>3</sub>, DMSO) were purchased from Cambridge Isotope Laboratories and were stored over 4 Å molecular sieves. Tri-*n*-butyl phosphine was generously donated by Cytec Industries and was distilled prior to use. Manipulations involving the use of <sup>n</sup>Bu<sub>3</sub>P and the catalysis experiments were performed either in the glovebox or by using standard Schlenk techniques. The precursors 4-hydroxyacetophenone oxime and 4-(5-bromopentoxo)acetophenone oxime were synthesized using literature methods.<sup>19</sup>

### Measurements

Solution <sup>1</sup>H, <sup>31</sup>P{<sup>1</sup>H} and <sup>13</sup>C{<sup>1</sup>H}, gHMBC, and gHSQC NMR spectra were recorded on a Varian INOVA 400 MHz, Varian INOVA 600 MHz, or Mercury 400 MHz spectrometer. All samples for <sup>1</sup>H NMR, <sup>13</sup>C{<sup>1</sup>H}, gHMBC, and gHSQC spectroscopy were referenced to the residual protons in the solvent relative to (CH<sub>3</sub>)<sub>4</sub>Si (δ (ppm): <sup>1</sup>H: CDCl<sub>3</sub> 7.26, DMSO 2.50; <sup>13</sup>C{<sup>1</sup>H}: CDCl<sub>3</sub> 77.0, DMSO 39.52). Phosphorus-31 NMR chemical shifts were reported relative to an external standard (85% H<sub>3</sub>PO<sub>4</sub> δ = 0.00 ppm). Mass spectrometry measurements were recorded in positive and negative ion modes using an electrospray ionization Micro-mass LCT spectrometer. Elemental analyses were performed by Guelph Chemical Laboratories Ltd., Guelph, Ontario, Canada.

The decomposition temperatures were determined using thermogravimetric analysis (TGA) on a Q600 SDT TA Instrument for **7** or on a TGA/SDTA 851e Mettler Toledo instrument for **8**. A 0.005–0.010 g sample was heated in a 40 µL alumina crucible at a rate of 10 °C/min over a temperature range of 100–600 °C. Melting and glass transition points were determined using differential scanning calorimetry (DSC) on a Q20 DSC TA instrument for **7** or on a DSC 822e Mettler Toledo instrument for **8** using aluminum sample pans. For **7**, a 0.005–0.010 g sample was cooled to –90 °C and then heated to 200 °C at 10 °C/min, cooled to –90 °C at 10 °C/min, and finally reheated to 200 °C at 10 °C/min. The glass-transition temperatures were taken

from the final heat cycle. For **8**, a 0.005–0.010 g sample was cooled to  $-70\text{ }^{\circ}\text{C}$  where the temperature was sustained for 15 min, followed by heating to  $500\text{ }^{\circ}\text{C}$  at  $10\text{ }^{\circ}\text{C}/\text{min}$ . All thermal analysis experiments were conducted in a  $\text{N}_2(\text{g})$  atmosphere.

## Synthesis

### Preparation of **7**

To a solution of 4-(5-bromopentoxo)acetophenone oxime (0.970 g, 3.220 mmol) in DMF (17 mL)  $n\text{Bu}_3\text{P}$  (0.716 g, 3.542 mmol) was added, and the mixture was heated at  $70\text{ }^{\circ}\text{C}$  for 48 h under a flow of nitrogen. DMF was removed in vacuo, and the resulting viscous yellow liquid was dissolved in a minimal amount of  $\text{CH}_2\text{Cl}_2$ , which was extracted first with hexanes ( $2 \times 15\text{ mL}$ ) and then with THF ( $1 \times 15\text{ mL}$ ). The residual solvent was removed in vacuo yielding **7** as a viscous clear yellow liquid (1.083 g, 2.155 mmol, 67%).  $T_d = 343\text{ }^{\circ}\text{C}$ ;  $T_g = -2\text{ }^{\circ}\text{C}$ .  $^{31}\text{P}\{^1\text{H}\}$  NMR (161.96 MHz,  $\text{CDCl}_3$ )  $\delta$  (ppm): 30 (s).  $^1\text{H}$  NMR (599.69 MHz,  $\text{CDCl}_3$ )  $\delta$  (ppm): 7.57 (d, 2H,  $^3J = 9.0\text{ Hz}$ ), 7.42 (s, br, 1H), 6.86 (d, 2H,  $^3J = 8.4\text{ Hz}$ ), 4.00 (t, 2H,  $^3J = 6.0\text{ Hz}$ ), 2.60–2.55 (m, 2H), 2.48–2.43 (m, 6H), 2.25 (s, 3H), 1.87 (quintet, 2H,  $^3J = 6.6\text{ Hz}$ ), 1.74–1.64 (m, 4H), 1.56–1.51 (m, 12H), 0.97 (s, 9H).  $^{13}\text{C}\{^1\text{H}\}$  NMR (100.60 MHz,  $\text{CDCl}_3$ )  $\delta$  (ppm): 159.2, 153.6, 129.1, 126.8, 113.9, 67.2, 28.2, 27.1 (d,  $^3J_{\text{P-C}} = 13\text{ Hz}$ ), 23.5 (d,  $^3J_{\text{P-C}} = 12\text{ Hz}$ ), 23.4 (d,  $^2J_{\text{P-C}} = 3\text{ Hz}$ ), 21.3 (d,  $^2J_{\text{P-C}} = 4.6\text{ Hz}$ ), 19.1 (d,  $^1J_{\text{P-C}} = 47.5\text{ Hz}$ ), 18.7 (d,  $^1J_{\text{P-C}} = 47.0\text{ Hz}$ ), 13.2, 11.6. FTIR (drop-cast on KBr;  $\text{cm}^{-1}$ (ranked intensity)): 510(20), 561(14), 634(12), 725(11), 838(3), 924(4), 1006(7), 1094(16), 1182(9), 1250(1), 1304(10), 1376(15), 1464(8), 1515(6), 1610(5), 1673(21), 2870(17), 2959(2), 3169(13), 3207(19), 3263(18). MS (ESI)  $m/z^{+/-}$  (%): 422.3 (100) [ $\text{M}^+ - \text{Br}$ ], 923.6<sup>5</sup> [ $\text{M}_2\text{Br}^+$ ], 582.2 (35) [ $\text{MBr}_2$ ].

### Preparation of **8**

The  $\text{Li}_2\text{PdCl}_4$  was first prepared by the addition of  $\text{PdCl}_2$  (0.212 g, 1.193 mmol) to a solution of  $\text{LiCl}$  (0.101 g, 2.387 mmol) in  $\text{MeOH}$  (0.6 mL), which was then heated at  $60\text{ }^{\circ}\text{C}$  for 30 min until all the reagents dissolved. Sodium acetate (0.049 g, 0.597 mmol) and **7** (0.300 g, 0.597 mmol) in  $\text{MeOH}$  (0.65 mL) were then added dropwise to the resulting red methanolic  $\text{Li}_2\text{PdCl}_4$  solution, and the mixture was stirred at room temperature for 36 h. Methanol was then added (2 mL), and the heterogeneous mixture was centrifuged and the supernatant was decanted. The solids were washed with  $\text{MeOH}$  ( $4 \times 4\text{ mL}$ ) followed by acetone ( $4 \times 4\text{ mL}$ ) to selectively remove the red-brown solid. The acetone fractions were combined and cooled to  $-30\text{ }^{\circ}\text{C}$ . Upon precipitation of a beige solid, the mixture was centrifuged, the supernatant was removed, and the solid was dried in vacuo giving **8** as a beige powder (0.144 g, 0.112 mmol, 19%).  $T_d = 290\text{ }^{\circ}\text{C}$ ;  $T_m = 160\text{ }^{\circ}\text{C}$ .  $^{31}\text{P}\{^1\text{H}\}$  NMR (161.96 MHz,  $\text{CDCl}_3$ )  $\delta$  (ppm): 30 (s).  $^1\text{H}$  NMR (400.09 MHz,  $\text{DMSO}$ )  $\delta$  (ppm): 10.5 (s, br, 1H), 7.17 (s, br, 1H), 7.06 (d, 2H,  $^3J = 8.4\text{ Hz}$ ), 6.54 (d, 2H,  $^3J = 8.4\text{ Hz}$ ), 3.93 (t, 2H,  $^3J = 6.4\text{ Hz}$ ), 2.22–2.15 (m, 11H), 1.73 (quintet, 2H,  $^3J = 6.0\text{ Hz}$ ), 1.53–1.35 (m, 16H), 0.90 (t, 9H,  $^3J = 6.8\text{ Hz}$ ).  $^{13}\text{C}\{^1\text{H}\}/\text{gHSQC}/\text{gHMBC}$  (599.44 MHz,  $\text{DMSO}$ )  $\delta$  (ppm): 163.4, 157.5, 153.6, 138, 129, 120.8, 109.5, 66.8, 27.8, 26.7

(d,  $^3J_{\text{P-C}} = 14.9\text{ Hz}$ ), 23.3 (d,  $^3J_{\text{P-C}} = 17\text{ Hz}$ ), 22.6 (d,  $^2J_{\text{P-C}} = 3.9\text{ Hz}$ ), 20.4 (d,  $^2J_{\text{P-C}} = 3.8\text{ Hz}$ ), 17.5 (d,  $^1J_{\text{P-C}} = 46.1\text{ Hz}$ ), 17.3 (d,  $^1J_{\text{P-C}} = 47.7\text{ Hz}$ ), 13.2, 10.9. FTIR (CsI pellet;  $\text{cm}^{-1}$ (ranked intensity)): 227(21), 248(19), 280(26), 304(25), 440(24), 639(9), 722(20), 807(12), 917(17), 959(14), 1043(6), 1100(8), 1209(2), 1227(18), 1266(7), 1308(13), 1339(5), 1378(10), 1459(3), 1560(11), 1582(1), 1629(16), 1648(27), 2872(15), 2934(23), 3446(22). MS (ESI)  $m/z^{+/-}$  (%): 562.1 (55) [monomer], 1124<sup>2</sup> [dimer]. Anal. calcd. (found): C: 46.79 (48.21), H: 6.92 (7.37).

### Preparation of 4-methoxy-biphenyl via Suzuki–Miyaura cross-coupling reaction

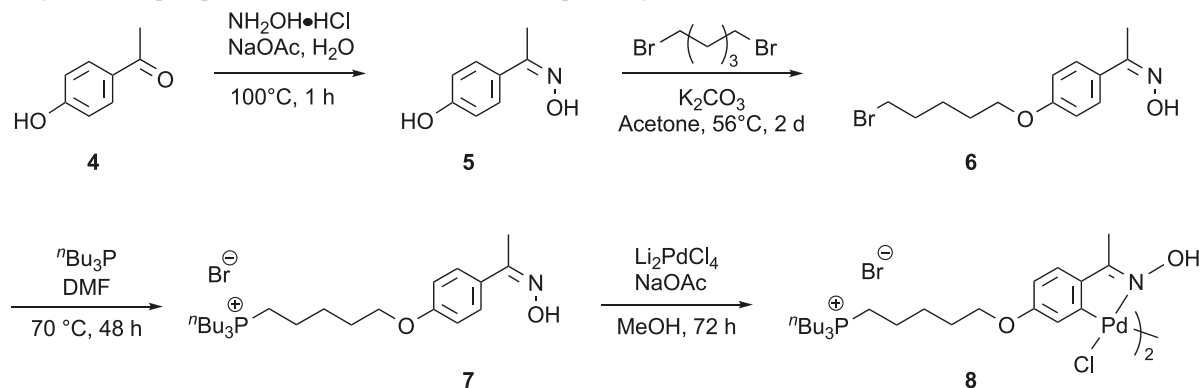
A 5 mol% mixture of the catalyst **8** (0.025 g, 0.019 mmol) in trihexyltetradecylphosphonium chloride (0.700 g, 1.348 mmol) was dissolved in  $\text{CH}_2\text{Cl}_2$  (1.5 mL) to facilitate the transfer of the mixture to a small, narrow Schlenk tube. The bulk of the solvent was removed in vacuo at room temperature, and the remaining residual solvent was removed at  $70\text{ }^{\circ}\text{C}$ . The mixture was cooled to room temperature, and neat  $\text{K}_3\text{PO}_4$  (0.275 g, 1.294 mmol), *p*-methoxyphenyl boronic acid (0.066 g, 0.431 mmol), and iodobenzene (0.080 g, 0.392 mmol) were added followed by the addition of toluene (0.1 mL) and distilled and  $\text{N}_2$ -purged  $\text{H}_2\text{O}$  (0.2 mL). The reaction mixture was stirred and heated at  $70\text{ }^{\circ}\text{C}$  for 5 h, and then the volatile solvents were removed in vacuo at room temperature. A cold finger was fitted to the Schlenk tube and the product was isolated from the ionic liquid mixture by sublimation at  $80\text{ }^{\circ}\text{C}$  for 14 h, yielding 4-methoxy-biphenyl as a white solid (0.057 g, 0.309 mmol, 99%).  $^1\text{H}$  NMR (400.09 MHz,  $\text{CDCl}_3$ )  $\delta$  (ppm): 7.56 (m, 4H), 7.42 (t, 2H,  $^3J = 7.6\text{ Hz}$ ), 7.30 (t, 1H,  $^3J = 7.6\text{ Hz}$ ), 6.98 (d, 2H,  $^3J = 8.8\text{ Hz}$ ), 3.86 (s, 3H).

### Preparation of trans-stilbene via Heck cross-coupling reaction

A 2 mol% mixture of the catalyst **8** (0.015 g, 0.012 mmol) in trihexyltetradecylphosphonium chloride (0.300 g, 0.578 mmol) was dissolved in  $\text{CH}_2\text{Cl}_2$  (1.5 mL) to more easily facilitate the transfer of the mixture to a small, narrow Schlenk tube and to assist in the dispersion and solvation of **8** in the ionic liquid solvent. The bulk of the solvent was removed in vacuo at room temperature, and the remaining residual solvent was removed at  $70\text{ }^{\circ}\text{C}$ . The mixture was cooled to room temperature, and neat styrene (0.094 g, 0.900 mmol), iodobenzene (0.122 g, 0.600 mmol), and  $\text{K}_3\text{PO}_4$  (0.255 g, 1.200 mmol) were added, followed by the addition of toluene (0.1 mL) and distilled,  $\text{N}_2$ -purged,  $\text{H}_2\text{O}$  (0.2 mL). The reaction mixture was stirred and heated at  $90\text{ }^{\circ}\text{C}$  for 5 h, and then the volatile solvents were removed in vacuo at room temperature. A cold finger was fitted to the Schlenk tube and the product was isolated from the ionic liquid mixture by sublimation at  $80\text{ }^{\circ}\text{C}$  for 14 h, yielding 4-methoxy-biphenyl as a white solid (0.106 g, 0.588 mmol, 98%).  $^1\text{H}$  NMR (400.09 MHz,  $\text{CDCl}_3$ )  $\delta$  (ppm): 7.52 (d, 4H,  $^3J = 8.4\text{ Hz}$ ), 7.36 (t, 4H,  $^3J = 7.6\text{ Hz}$ ), 7.26 (t, 2H,  $^3J = 7.6\text{ Hz}$ ), 7.12 (s, 2H).

### Procedure for recycling the catalyst and the ionic liquid

Upon completion of the catalysis, the product was isolated following the same procedure as noted. Proton NMR spec-

**Scheme 1.** Synthesis of phosphonium-functionalized oxime carbopalladacycle **8**.

troscopy of the resulting IL mixture confirmed the complete removal of the product. The reagents were then added in the same amounts, following the initial reaction conditions, and the catalysis was repeated.

## Results and discussion

### Synthesis

The synthetic route towards the preparation of the phosphonium salt catalyst **8** is summarized in Scheme 1. Compounds **4** through **6** were prepared according to literature procedures.<sup>19</sup> Given the likely reactivity of  $n\text{-Bu}_3\text{P}$  with palladium, the generation of the phosphonium salt **7** was completed first, followed by formation of the carbopalladacycle phosphonium salt **8**. The quaternization of tri-*n*-butylphosphine with **6** was monitored by  $^{31}\text{P}\{^1\text{H}\}$  NMR spectroscopy until the full consumption of  $n\text{-Bu}_3\text{P}$  ( $\delta = -32$  ppm) was observed.<sup>28</sup> The complete formation of the phosphonium salt ( $\delta = 35$  ppm) was detected within 48 h at 70 °C. The DMF was removed in vacuo, and the product was purified by extractions with hexanes and THF, respectively. Comprehensive characterization ascertained the formation of the phosphonium ionic liquid **7** as a yellow, clear, viscous liquid. Thermal analysis of **7** revealed a glass transition temperature of  $-2$  °C and a thermal decomposition temperature of 343 °C. The addition of **7** and NaOAc to methanolic  $\text{Li}_2\text{PdCl}_4$  resulted in immediate precipitation of a red-brown solid. Upon stirring for 3 days, a beige precipitate also formed. The solids were isolated and washed with MeOH followed by acetone and were finally recrystallized in acetone. The beige powder was fully characterized to confirm the formation of the carbopalladacycle using the following analytical and spectroscopic methods: 1D and 2D NMR spectroscopy, FTIR spectroscopy, UV-vis spectroscopy, electrospray ionization mass spectrometry, differential scanning calorimetry, thermogravimetric analysis, and elemental analysis. The most salient feature in the  $^1\text{H}$  NMR spectrum was the change in the pattern of the aromatic protons from AA'BB' to ABC, which was indicative of the formation of the aryl carbopalladacycle environment (Fig. 1).<sup>19,29</sup> The phosphonium carbopalladacycle **8** was isolated as a white powder in a modest yield (19%). Compound **8** was soluble in DCM, DMSO, acetone, and trihexyltetradecylphosphonium chloride,  $[\text{P}_{66614}][\text{Cl}]$ , and was insoluble in  $\text{CHCl}_3$  and apolar solvents, such as alkanes and ethers.

The FTIR spectrum for **7** displayed a characteristic C=N

stretching vibration of  $1673\text{ cm}^{-1}$ , and the corresponding C=N vibration in **8** was shifted by  $26\text{ cm}^{-1}$  (observed at  $1648\text{ cm}^{-1}$ ), which suggested N-Pd coordination (Fig. 2).<sup>30</sup> Analysis by UV-vis spectroscopy provided further evidence of the presence of the carbopalladacycle in **8**. An absorption at  $\lambda_{\text{max}}$  262 nm and an absorption band at  $\lambda_{\text{max}}$  307 nm with a broad shoulder peak corresponded to ligand centered absorptions on the phosphonium salt. Ionic liquid **7** displayed only one absorption band at  $\lambda_{\text{max}}$  260 nm. The absorption band at  $\lambda_{\text{max}}$  307 nm symbolized charge-transfer transitions, which were specific to metal-ligand orbital interactions, and was in accordance with literature results (Fig. 3).<sup>19</sup>

A typical oxime carbopalladacycle is often a chloro-bridged dimer, which occurs to fulfill the favorable four-coordinate geometry about the palladium centre. However, the imidazolium-tagged oxime carbopalladacycle was found to be monomeric. The last coordination site was filled by the imidazolium, preventing the formation of a dimer.<sup>19</sup> Evidence for both the monomer and dimer phosphonium analogues, **8**, were observed in ESI-MS with the most intense peak attributed to the monomer. The dimer was the most likely conformation, since there was no donor capability at the phosphonium centre in contrast to the imidazolium example. Attempts to grow crystals of suitable quality for X-ray diffraction studies resulted in microcrystalline powders or clusters; thus, solid-state characterization was not possible. No conclusive statement could be made from these results to declare the coordination environment about the palladium.

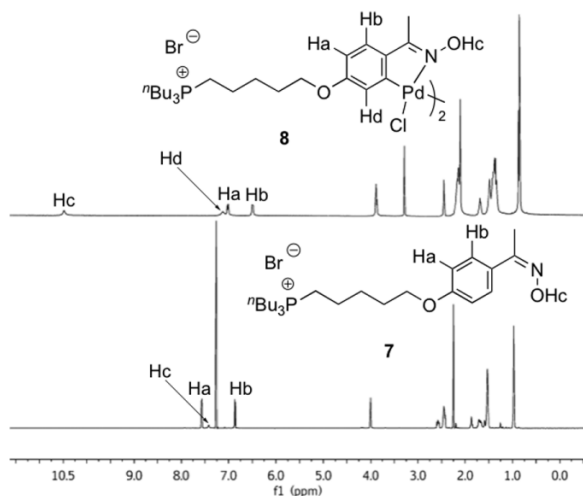
### Catalysis studies

To examine the catalytic ability of the phosphonium carbopalladacycle, two C-C bond forming cross-coupling reactions, Heck and Suzuki-Miyaura, were carried out. The evaluation of the Heck reaction was accomplished using styrene and iodobenzene with  $\text{K}_3\text{PO}_4$  and, the Suzuki-type reaction was carried out using *p*-methoxyphenylboronic acid and iodobenzene with  $\text{K}_3\text{PO}_4$  as the base. The reaction conditions including solvents, bases, reaction times, temperature, catalyst loading, and isolation techniques were varied, and the results are summarized in Table 1.

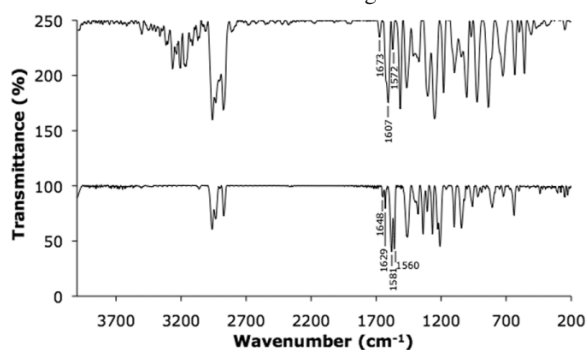
Oxygen-free conditions were required, as reactions carried out in the absence of an inert atmosphere resulted in low yields (Table 1, entries 1, 2, and 14). It was observed that a small amount of toluene and water were required to assist the dissolution of the reagents in the ionic liquid medium,



**Fig. 1.** Stacked  $^1\text{H}$  NMR spectra for **7** (bottom) and **8** (top), which clearly display the change in the environment about the phenyl protons, indicative of the incorporation of the palladium metal.



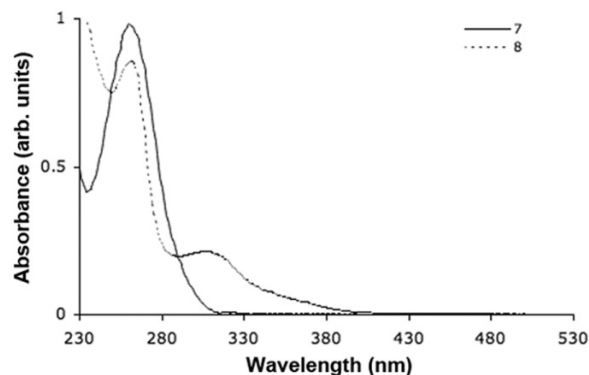
**Fig. 2.** FTIR spectrum of **7** (top) displays a C=N vibration at  $1673\text{ cm}^{-1}$ , and the FTIR spectrum of **8** (bottom) shows the shift of the C=N vibration to  $1648\text{ cm}^{-1}$  revealing N–Pd coordination.



as the reaction performed using solely  $[\text{P}_{66614}][\text{Cl}]$  yielded only trace amounts of the desired product (Table 1, entry 14). To attain a minimal reaction time under mild temperatures, the ideal catalyst loading was found to be 5 mol% (Table 1, entry 13) for the Suzuki reaction and 2 mol% for the Heck reaction (Table 1, entry 19).

With the use of viscous, non-volatile ionic liquids as solvents in chemical transformations, modifications to the conventional approaches to synthesis and product isolation are necessary. Previously reported product isolation techniques for Suzuki reactions performed in phosphonium ionic liquids were assessed, including aqueous and organic solvent extractions, followed by filtration through silica (Table 1, entries 2, 15, and 16) or alternatively, direct filtration of the reaction mixture through a silica plug (Table 1, entries 1 and 14); all of which proved unsatisfactory for various reasons. Separation of the product by extraction into organic solvent increased volatile solvent use, which is to be avoided if possible. Subsequent filtration through silica increased the steps required to obtain a pure product, which can reduce the final yield. The filtration of the ionic liquid mixture was formerly deemed necessary, since extracting

**Fig. 3.** UV–vis spectra of **7** (solid line) and **8** (dotted line). The emergence of a second band for **8** is indicative of a metal–ligand interaction.



the reaction mixture with hexanes does not always completely remove all of the biaryl product, given some of the biaryl species remains in the ionic liquid phase.<sup>22</sup> This filtration strategy is limited by the inability to reuse the catalyst and solvent because the phosphonium salts predominantly remain coordinated to the silica. However, it is important to note, that herein, no evidence of the phosphonium catalyst **8** was present in the hexanes extractions.

In this context, it was ascertained that the best way to isolate the products was through sublimation. One can take advantage of the non-volatility of the reaction medium and catalyst and simply remove the volatile product by sublimation. Initial experiments were carried out in a small vial ( $15 \times 48\text{ mm}$ ) with a septum cap for the delivery of  $\text{N}_{2(g)}$  by a needle, given the volume of the reaction mixture was small. Upon completion of the reaction, the mixture was dissolved in  $\text{CH}_2\text{Cl}_2$  and transferred to a Schlenk flask. The volatile solvent was removed under reduced pressure, the flask was then fitted with a cold finger, and the product was sublimed at  $0.5\text{ mm Hg}$  and  $80\text{ }^\circ\text{C}$ . To further optimize the isolation procedure, an unconventionally shaped Schlenk tube was designed not only to accommodate the small reaction volume, but also to include the capacity to fit a cold finger to the flask (Fig. 4). Under the optimized reaction conditions and with the appropriate glassware, high-yielding Suzuki and Heck cross-coupling reactions were achieved (Table 1, entries 13 and 19).

### Catalyst recyclability studies

While employing the optimized conditions, the recyclability of the ionophilic catalyst was demonstrated. For both the Heck and Suzuki reactions, upon completion of the reactions, the residual toluene and water were removed in vacuo at room temperature, and subsequently, a cold finger was inserted into the flask and the product was sublimed at  $0.5\text{ mm Hg}$  at  $80\text{ }^\circ\text{C}$  overnight.  $^1\text{H}$  NMR spectroscopy of the remaining IL mixture confirmed the absence of any product or starting reagents. If residual product was observed in the IL, then a second sublimation was performed. Without removal of any residual borates or phosphates, the starting reagents, not including fresh catalyst, were again added to the ionic liquid mixture and the catalysis was repeated at the optimized conditions, and the results are summarized in Table 2.

**Table 1.** Reaction conditions studies for the Suzuki- and Heck-type cross-coupling.

Entry	Reaction	<i>T</i> (°C)	Time (h)	Catalyst <b>8</b> (mol%)	Yield (%)
1	Suzuki <sup>a</sup>	55	1	1	Trace <sup>c,d</sup>
2		70	16	1	29 <sup>c,e</sup>
3		70	16	1	76 <sup>f</sup>
4		70	16	1	18 <sup>g</sup>
5		70	2	1	42 <sup>g</sup>
6		70	4	1	76 <sup>g</sup>
7		70	6	1	82 <sup>g</sup>
8		70	8	1	88 <sup>g</sup>
9		70	4	5	83 <sup>h</sup>
10		80	7	1	78 <sup>h</sup>
12		95	4	1	66 <sup>h</sup>
13		70	5	5	98 <sup>j</sup>
14	Heck <sup>b</sup>	130	24	2	Trace <sup>c,d,i</sup>
15		90	16	2	75 <sup>e</sup>
16		90	16	2	Trace <sup>e</sup>
17		90	4.5	2	73 <sup>h</sup>
18		90	6.5	2	74 <sup>h</sup>
19		90	5	2	98 <sup>j</sup>

<sup>a</sup>Iodobenzene (1 equiv.), *p*-methoxyphenylboronic acid (1.1 equiv.), K<sub>3</sub>PO<sub>4</sub> (3.3 equiv.), 0.7 g [P<sub>66614</sub>][Cl], 0.2 mL H<sub>2</sub>O, and 0.1 mL toluene.

<sup>b</sup>Iodobenzene (1 equiv.), styrene (1.5 equiv.), K<sub>3</sub>PO<sub>4</sub> (2 equiv.), 0.3 g [P<sub>66614</sub>][Cl], 0.2 mL H<sub>2</sub>O, and 0.1 mL toluene.

<sup>c</sup>Under atmospheric conditions.

<sup>d</sup>Product isolation by silica column filter.

<sup>e</sup>Product isolation by extraction with hexanes followed by silica column filter.

<sup>f</sup>Product isolation by extraction with hexanes, removal of solvent under reduced pressure followed by sublimation.

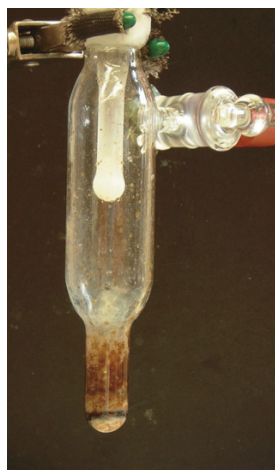
<sup>g</sup>Product isolation by aqueous extraction and sublimation of the remaining reaction mixture.

<sup>h</sup>Product isolation by sublimation from reaction mixture.

<sup>i</sup>No toluene or water added; NaOAc as base.

<sup>j</sup>Product isolation by sublimation in reaction flask.

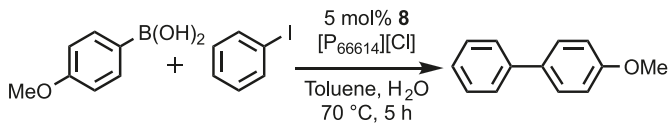
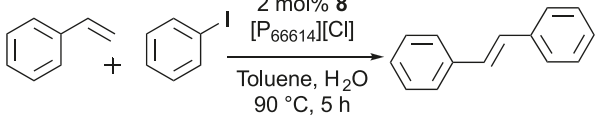
**Fig. 4.** Sublimation of *trans*-stilbene from the ionophilic catalyst **8** – [P<sub>66614</sub>][Cl] reaction mixture using the specially designed reaction tube.



The ionophilic catalyst **8** – [P<sub>66614</sub>][Cl] mixture was recycled three times before any decrease in activity was observed for the Suzuki reaction. After the third reuse of the catalyst, the IL mixture changed from yellow to black. This

is likely due to the formation of Pd black and is probably associated with the decrease in conversion. The phosphonium catalyst **8** exhibited good catalytic activity in Heck reaction as well; however, the recyclability of the catalyst was poor. The yields decreased by 20% on the second cycle and continued to diminish rapidly over the subsequent cycles. Again, the colour of the reaction mixture changed from yellow to a red-black on the first cycle, indicative of the initiation of catalyst decomposition. However, it is important to note that while **8** exhibits moderate recyclability, the imidazolium carbopalladacycle ionophilic catalyst by Corma et al. displayed quite low reactivity. The Heck and Suzuki coupling reactions exhibited yields ranging from 3%–25% on the first run, and therefore, the catalyst was not recyclable.<sup>19</sup> They proposed that the imidazolium tag was unstable under the basic conditions required, and the formation of carbene by deprotonation at C-2 on the imidazolium prevailed. The resulting carbene would then coordinate to the palladium and ultimately result in the decomposition of the catalyst, the formation of Pd black, and poor catalytic activity. Therefore, the substitution of a phosphonium salt for an imidazolium cation proves to be a more effective route towards the generation of an ionophilic tag for oxime carbopalladacycle cross-coupling reaction catalysts, given basic conditions are required for these types of reactions.

**Table 2.** Recyclability of **8** in Suzuki and Heck cross-coupling reactions.

Reaction	Cycle	Isolated yield (%)
<b>Suzuki</b>		
	1	92
	2	95
	3	99
	4	93
	5	66
<b>Heck</b>		
	1	87
	2	67
	3	37
	4	18
	5	—

## Conclusions

A phosphonium-tagged oxime carbopalladacycle catalyst **8** has been synthesized and comprehensively characterized. The catalyst displayed ionophilic properties in the C–C bond forming cross-coupling Heck and Suzuki reactions conducted in an ionic liquid medium. Based on the ionic nature of **8**, the catalyst selectively partitioned into the ionic liquid reaction phase, and furthermore, the ionic catalyst – solvent media allowed the isolation of the reaction products simply by sublimation without the need to use volatile organic solvents for extraction/separation techniques. This straightforward product-isolation methodology enabled and simplified the recycling of the catalyst and the reaction solvent. The substitution of a phosphonium appendage on an oxime carbopalladacycle as opposed to an imidazolium functionality resulted in increased tolerance towards the basic conditions required in Heck and Suzuki reactions and therefore increased catalytic activity.

## Acknowledgements

We thank the Natural Sciences and Engineering Research Council of Canada (NSERC), the Canada Foundation for Innovation (CFI), the Ontario Ministry of Research and Innovation, and The University of Western Ontario for funding. We also thank Professor K. M. Baines for the use of TGA and DSC instrumentation, D. Hairsine for the acquisition of mass spectrometry data, and Y. Rambour for glassware fabrication.

## References

- (1) Rogers, R. D.; Seddon, K. R. *Ionic Liquids as Green Solvents: Progress and Prospects*; American Chemical Society: WA, 2003.
- (2) Ranke, J.; Stolte, S.; Störmann, R.; Arning, J.; Jastorff, B. *Chem. Rev.* **2007**, *107* (6), 2183. doi:10.1021/cr050942s. PMID:17564479.
- (3) Welton, T. *Green Chem.* **2008**, *10* (5), 483. doi:10.1039/b805586f.
- (4) Wasserscheid, P.; Welton, T. *Ionic Liquids in Synthesis*, 2nd ed.; WILEY-VCH: Weinheim, 2008; Vol. 1.
- (5) Părvulescu, V. I.; Hardacre, C. *Chem. Rev.* **2007**, *107* (6), 2615. doi:10.1021/cr050948h. PMID:17518502.
- (6) Welton, T. *Coord. Chem. Rev.* **2004**, *248* (21–24), 2459. doi:10.1016/j.ccr.2004.04.015.
- (7) Buijsman, R. C.; van Vuuren, E.; Sterrenburg, J. G. *Org. Lett.* **2001**, *3* (23), 3785. doi:10.1021/ol016769d. PMID:11700138.
- (8) Wang, R.; Twamley, B.; Shreeve, J. M. *J. Org. Chem.* **2006**, *71* (1), 426. doi:10.1021/jo052098b. PMID:16388677.
- (9) Wang, B.; Zeng, Z.; Twamley, B.; Piekarski, M.; Shreeve, J. M. *Eur. J. Org. Chem.* **2007**, *2007* (4), 655. doi:10.1002/ejoc.200600828.
- (10) Šebesta, R.; Kmentová, I.; Toma, Š. *Green Chem.* **2008**, *10* (5), 484. doi:10.1039/b801456f.
- (11) Lin, I. J. B.; Vasam, C. S. *J. Organomet. Chem.* **2005**, *690* (15), 3498. doi:10.1016/j.jorganchem.2005.03.007.
- (12) Zhao, D.; Fei, Z.; Geldbach, T. J.; Scopelliti, R.; Dyson, P. J. *J. Am. Chem. Soc.* **2004**, *126* (48), 15876. doi:10.1021/ja0463482. PMID:15571412.
- (13) Alonso, F.; Beletskaya, I. P.; Yus, M. *Tetrahedron* **2008**, *64* (14), 3047. doi:10.1016/j.tet.2007.12.036.
- (14) Aggarwal, V. K.; Emme, I.; Mereu, A. *Chem. Commun. (Camb.)* **2002**, (15), 1612. doi:10.1039/b203079a. PMID:12170807.
- (15) Magna, L.; Chauvin, Y.; Niccolai, G. P.; Basset, J.-M. *Organometallics* **2003**, *22* (22), 4418. doi:10.1021/om021057s.
- (16) Mathews, C. J.; Smith, P. J.; Welton, T. *J. Mol. Catal. Chem.* **2004**, *214* (1), 27. doi:10.1016/j.molcata.2003.11.030.
- (17) Wang, R.; Xiao, J. C.; Twamley, B.; Shreeve, J. M. *Org. Biomol. Chem.* **2007**, *5* (4), 671. doi:10.1039/b616529j. PMID:17285176.
- (18) Wan, Q.-X.; Liu, Y.; Cai, Y.-Q. *Catal. Lett.* **2009**, *127* (3–4), 386. doi:10.1007/s10562-008-9700-5.
- (19) Corma, A.; García, H.; Leyva, A. *Tetrahedron* **2004**, *60* (38), 8553. doi:10.1016/j.tet.2004.06.121.
- (20) Alacid, E.; Alonso, D. A.; Botella, L.; Nájera, C.; Pacheco, M. C. *Chem. Rec.* **2006**, *6* (3), 117. doi:10.1002/tcr.20077. PMID:16795006.
- (21) Alonso, D. A.; Botella, L.; Nájera, C.; Pacheco, M. C. *Synthesis* **2004**, (10), 1713.
- (22) McNulty, J.; Capretta, A.; Wilson, J.; Dyck, J.; Adjabeng, G.; Robertson, A. J. *Chem. Commun. (Camb.)* **2002**, (17), 1986. doi:10.1039/b204699g. PMID:12271707.
- (23) Kaufmann, D. E.; Nouroozian, M.; Henze, H. *Synlett* **1996**, *1996* (11), 1091. doi:10.1055/s-1996-5658.
- (24) Gerritsma, D. A.; Robertson, A.; McNulty, J.; Capretta, A. *Tetrahedron Lett.* **2004**, *45* (41), 7629. doi:10.1016/j.tetlet.2004.08.103.

- (25) Fraser, K. J.; MacFarlane, D. R. *Aust. J. Chem.* **2009**, 62 (4), 309. doi:10.1071/CH08558.
- (26) Wong, H.-t.; Pink, C. J.; Ferreira, F. C.; Livingston, A. G. *Green Chem.* **2006**, 8 (4), 373. doi:10.1039/b516778g.
- (27) Naik, P. U.; McManus, G. J.; Zaworotko, M. J.; Singer, R. D. *Dalton Trans.* **2008**, (36): 4834. doi:10.1039/b811232k. PMID:18766212.
- (28) Kosolapoff, G. M.; Maier, L. *Organic Phosphorus Compounds*; John Wiley & Sons, Inc.: Toronto, ON, 1972; Vol. 2.
- (29) Botella, L.; Nájera, C. *J. Organomet. Chem.* **2002**, 663 (1-2), 46. doi:10.1016/S0022-328X(02)01727-8.
- (30) Nielson, A. J. *J. Chem. Soc., Dalton Trans.* **1981**, (1): 205. doi:10.1039/dt9810000205.



# Synthesis and electrochemical behavior of triazole-containing nicotinamide adenine dinucleotide analogs

Wujun Liu, Shuhua Hou, and Zongbao Kent Zhao

**Abstract:** The coupling of 2',3'-di-*O*-acetyl nicotinamide mononucleotide with 3-butyne-1-ol in the presence of 2,4,6-triisopropylbenzenesulfonyl chloride quantitatively afforded a terminal alkyne-containing intermediate. Furthermore, copper(I)-mediated Huisgen [3 + 2] cycloaddition with a series of azido compounds in a two-phase solvent system gave eight triazole-containing nicotinamide adenine dinucleotide analogs with yields over 88%. The cyclic voltammetric behaviors of these novel analogs were investigated with a glassy carbon electrode, and structural features of these analogs on their electrochemical properties were briefly discussed.

**Key words:** nicotinamide adenine dinucleotide, analog, click chemistry, cyclic voltammetry.

**Résumé :** Le couplage du mononucléotide du 2',3'-di-*O*-acétylnicotinamide avec le but-3-yn-1-ol, en présence de chlorure de 2,4,6-triisopropylbenzènesulfonyle conduit à la formation pratiquement quantitative d'un intermédiaire comportant un alcyne terminal. Une cycloaddition ultérieure [3 + 2] de Huisgen, catalysée par le cuivre(I), avec une série de composés azide, dans un système liquide à deux phases, conduit à la formation, avec des rendements globaux supérieurs à 88 %, d'analogues dinucléotides d'adénine nicotinamide contenant un triazole en position 8. On a étudié les comportements en voltampérométrie cyclique de ces nouveaux analogues à l'aide d'une électrode de carbone vitreux et on discute brièvement des caractéristiques structurales de ces analogues sur leurs propriétés électrochimiques.

**Mots-clés :** dinucléotide de l'adénine nicotinamide, analogue, chimie par clic, voltampérométrie cyclique.

[Traduit par la Rédaction]

## Introduction

Nicotinamide adenine dinucleotide (NAD<sup>+</sup>) and its reduced form, NADH, are involved in numerous biological systems, especially as cofactors for enzymes mediating oxidoreductive reactions.<sup>1</sup> In those oxidoreductive reactions, NAD(H) transfers hydrogen and electron shuttles, along with chemical potential change. The chemical potential of NAD<sup>+</sup> or its derivatives play critical roles in calcium homeostasis,<sup>2</sup> cross-membrane transportation,<sup>3</sup> oxidative stress resistance,<sup>4,5</sup> and reactive oxygen species clearance.<sup>6</sup> Although electrochemical studies have been done on a few model compounds,<sup>7</sup> and on applying a novel method<sup>8</sup> or materials<sup>9</sup> for modification of the surface of the electrode to improve the sensitivity of electrode response to NAD(H), there are few reports on testing the electrocatalytic reduction of synthetic NAD<sup>+</sup> analogs.

NAD<sup>+</sup> is a coupled product of the nicotinamide mononucleotide (NMN) part and the adenosine monophosphate (AMP) moiety (Fig. 1). The NMN part bestows its oxidoreductive property, whereas the AMP moiety is largely involved in binding in the biological environment. Early

study showed that a simple phosphodiester-type NAD<sup>+</sup> analog could be recognized by horse liver alcohol dehydrogenase, and that the system could be applied for reduction of prochiral ketones in moderate yields.<sup>10,11</sup> Thus, it is essential to have the NMN part in NAD<sup>+</sup> analogs so that their prospects as a redox chemistry mediator can be further explored. In these reactions, a synthetic cofactor was regenerated with valuable rhodium complexes, but low-cost electrochemical or photo driven regeneration of the NAD<sup>+</sup> cofactor led to a complex reaction.<sup>12,13</sup> One strategy to overcome these deficiencies is to modify the structure of the cofactor to improve electrode reaction activity.

We were recently interested in the preparation of NAD<sup>+</sup> analogs in which one phosphorus atom is removed from the original skeleton to meliorate electrode reaction activity of the natural coenzyme. In this work, we wish to report our efforts on the construction of 1,2,3-triazole-containing NAD<sup>+</sup> analogs (Fig. 1) and their electrochemical properties. We developed an efficient synthetic strategy for synthesis of these analogs based on CuSO<sub>4</sub>/sodium ascorbate-mediated Huisgen's 1,3-dipolar cycloaddition, or click reaction.<sup>14</sup>

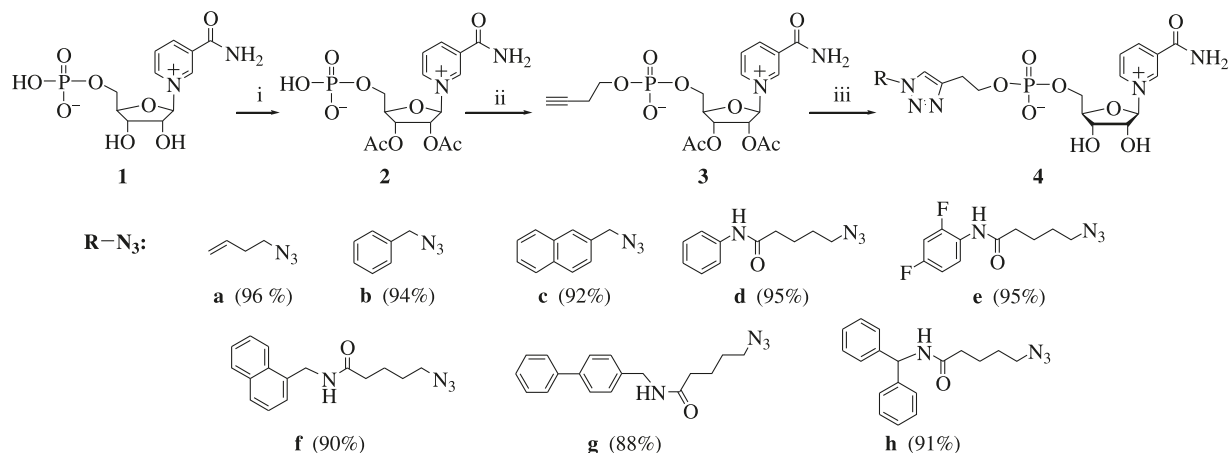
Received 10 July 2009. Accepted 14 September 2009. Published on the NRC Research Press Web site at canjchem.nrc.ca on 16 December 2009.

**W. Liu and S. Hou.** Dalian Institute of Chemical Physics, CAS, Dalian 116023, P. R. China; Graduate School of the Chinese Academy of Sciences, Beijing 100039, P. R. China.

**Z.K. Zhao.**<sup>1</sup> Dalian Institute of Chemical Physics, CAS, Dalian 116023, P. R. China; Dalian National Laboratory of Clean Energy, Dalian 116023, P. R. China.

<sup>1</sup>Corresponding author (e-mail: zhaozb@dicp.ac.cn).

**Scheme 1.** Synthesis of triazole-containing NAD<sup>+</sup> analogs. Reagents and conditions: (i) Ac<sub>2</sub>O/Py (1:1), 0–5 °C, 24 h, 98%; (ii) 3-butyn-1-ol (3 equiv.), TIPS-Cl (3 equiv.), DMF/Py (1:1), RT, 3 h, 99%; (iii) (a) R–N<sub>3</sub>, CuSO<sub>4</sub>/sodium ascorbate, H<sub>2</sub>O/DCM (1:1), RT, 0.5–6 h, 90%–98%, (b) NH<sub>4</sub>HCO<sub>3</sub> (1 mol/L), in H<sub>2</sub>O/MeOH (1:10), 98%. Data in the parentheses indicate the total isolated yield of each compound on Ac<sub>2</sub>NMN.



Compared to NAD<sup>+</sup>, these analogs showed relatively low reductive peak potentials ( $E_p$ ) and a distinct improvement of the electrode reaction rate constant ( $K_s$ ).

## Results and discussion

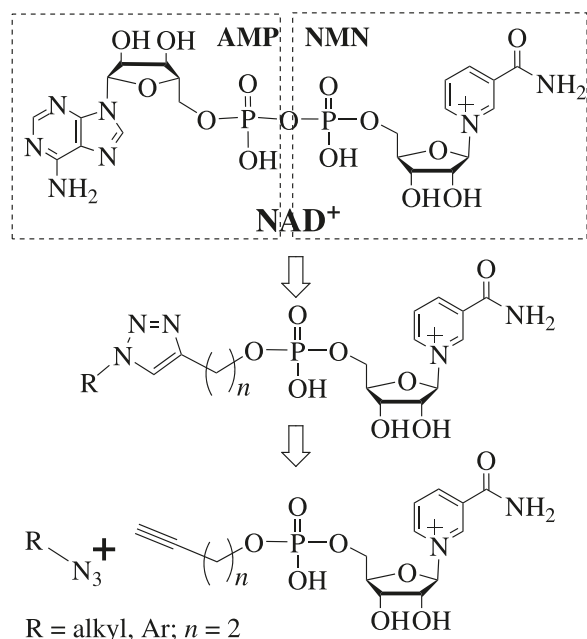
### Synthesis of triazole-containing NAD<sup>+</sup> analogs

Our in-house preparation of NMN was realized via selective hydrolysis of NAD<sup>+</sup> using ZrCl<sub>4</sub> as catalyst.<sup>15</sup> To synthesize the triazole-containing NAD<sup>+</sup> analogs, we originally tried to couple NMN with the corresponding alkynyl alcohol followed by click reaction with azides (Fig. 1). Because NMN is liable to form an inactive inner salt and has notoriously low solubility in most organic solvents (i.e., DMF (dimethylformamide), pyridine, MeCN), it was difficult to find an appropriate solvent system to realize the coupling reaction. Moreover, C–N bond breakage of the NMN molecule was substantial in many experiments. We then treated NMN with a mixture of Ac<sub>2</sub>O and pyridine at 0–5 °C, leading to the acetylated product of NMN, 2',3'-di-*O*-acetyl nicotinamide mononucleotide (Ac<sub>2</sub>NMN). It turned out that Ac<sub>2</sub>NMN had much better solubility and higher activity. Thus, the coupling of Ac<sub>2</sub>NMN with excess 3-butyn-1-ol in DMF/Py (1:1, *v/v*) in the presence of 2,4,6-triisopropylbenzenesulfonyl chloride (TIPS-Cl) at room temperature for 3 h afforded the key intermediate of 2',3'-di-*O*-acetyl β-nicotinamide ribose-5'-3-butynyl phosphate, **3**, in a 99% yield based on <sup>31</sup>P NMR analysis (Scheme 1).

To convert compound **3** into triazole-containing NAD<sup>+</sup> analogs, we prepared eight azides (Scheme 1). These compounds were selected to mimic the adenine moiety of the NAD<sup>+</sup> structure, mainly depending on their accessibility and aromatic ring structures. Azides **a–c** were obtained from the corresponding halides via a nucleophilic substitution using sodium azide, whereas azides **d–h** were made via acylation of the corresponding amines with 5-chloropentanoyl chloride followed by a nucleophilic substitution reaction using sodium azide.<sup>16</sup>

With intermediate **3** and azide compounds in hand, we

**Fig. 1.** Structures of NAD<sup>+</sup> and its triazole-containing analogs.



carried out cycloaddition experiments in the presence of copper sulfate and sodium ascorbate according to the strategy described by Sharpless and co-workers.<sup>17</sup> Upon testing a couple of solvent systems, i.e., water mixed with DMSO, DMF, DCM, THF, MeCN, or *t*-BuOH, we found that there was no significant difference whether the organic solvent was soluble or insoluble in water. This was likely because compound **3** and the coupled products had excellent solubility in water. To facilitate an easier recycling of azides, our synthesis was carried out in a two-phased system made of DCM and H<sub>2</sub>O. Using this strategy, we were successful in coupling azides **a–h** with **3** at room temperature in over 90% yields within 6 h. For most reactions, 5 mol% Cu(I) catalyst was enough to convert **3** within 2 h. The bulky azides **f** and **h** required 4 h for better yields. Because azide **g** had a poor solubility, up to 6 h was necessary to achieve

excellent conversion. We also tried the combination  $\text{CuSO}_4/\text{Cu}$  to mediate the coupling reaction. However, the products seemed liable to coordinate with copper, leading to a tedious purification process and low isolated yields.

It was interesting to note that those triazole-containing intermediates could be easily deacetylated by 1 mol/L  $\text{NH}_4\text{HCO}_3$  solution in  $\text{H}_2\text{O}/\text{MeOH}$  (1:10, v/v). Thus, crude compound **4** was achieved during the reverse phase silica gel chromatography purification.

Because  $\text{NAD}^+$  analogs are amphiphilic molecules containing both positive and negative charges, purification usually presents a major barrier to achieve an appreciable quantity of target compounds in the lab. Thus, successful procedures varied from case to case for the isolation of analogs **4a–4h**. Chromatography with various supporting materials, including activated charcoal, silica gel, octyl-functionalized silica gel, ion exchange resins, and Bio-Gel P-2 resin has been applied in different combinations to fulfill valid purification. Compound **4a** was purified with octyl-functionalized silica gel and  $201 \times 2 \text{ HCO}_2^-$  form of the anion resin followed by Bio-Gel P-2 resin. For compounds **4b**, **4d**, and **4e**, chromatography on octyl-functionalized silica gel and anion resin, at different elution conditions, gave the best results. For compounds **4c** and **4f–4h**, chromatography on octyl-functionalized silica gel and Bio-Gel P-2 resin gave our target molecules.

### Electrochemical behavior of triazole-containing $\text{NAD}^+$ analogs

With novel analogs in hand, we investigated their electrochemical performance on a glassy carbon (GC) electrode in aqueous solution. Oxido-reductive behaviors of these triazole-containing  $\text{NAD}^+$  analogs were estimated by cyclic voltammetry. The redox curves were also a two electron mechanism according to the Angulo et. al method.<sup>18</sup> Upon a reversal scan of the  $\text{NAD}^+$  analogs, both the reduction peak and reoxidation peak were observed, albeit the latter was much weaker than the former. The corresponding reoxidation peaks were stronger than that of  $\text{NAD}^+$  under the same conditions. Thus, the overall processes are not reversible.

The reductive potential ( $E_p$ ) of the triazole-containing analog (−1.141 V) was much lower than that of natural  $\text{NAD}^+$  (−1.269 V; Table 1). Upon four cyclic reversal scans, marginal decreases in the reductive peak currents of  $\text{NAD}^+$  analogs were observed, and the decrease range of **4h** was much smaller than that of  $\text{NAD}^+$  under the same conditions (Fig. 2). This indicated that triazole-containing analogs had relatively weak absorption on GC than natural  $\text{NAD}^+$ .

The cathodic peak currents ( $i_p$ ) of triazole-containing analogs increased curvilinearly with the square root of the scan rate ( $v$ ), an upper warp curve in the range of 20–200  $\text{mV s}^{-1}$ . All the upper data resulted in the reduction of triazole-containing  $\text{NAD}^+$ , which was an absorption-controlled irreversible process under our conditions.

According to Laviron theory,<sup>19</sup> absorption-controlled irreversible process potential ( $E_p$ ) is determined based on the following equation:

$$[1] \quad E_p = E^\circ - (RT/\alpha nF) \ln(\alpha nF/RTK_s) - (RT/\alpha nF) \ln v$$

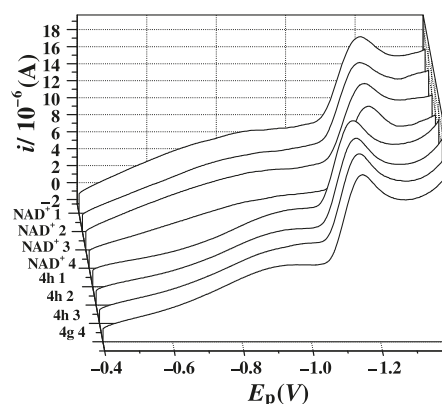
where  $E^\circ$ ,  $\ln v$ ,  $R$ ,  $T$ ,  $F$ ,  $n$ ,  $K_s$ , and  $\alpha$ , represent the standard

**Table 1.** Electrochemical dynamic constants of triazole-containing  $\text{NAD}^+$  analogs (**4a–4h**) and related compounds.

Compound	$E_p$ (V)	$K_s$ ( $\text{s}^{-1}$ )	$\alpha$
<b>4a</b>	−1.157	0.24	0.39
<b>4b</b>	−1.145	0.23	0.38
<b>4c</b>	−1.148	0.23	0.36
<b>4d</b>	−1.154	0.23	0.35
<b>4e</b>	−1.159	0.20	0.34
<b>4f</b>	−1.142	0.23	0.36
<b>4g</b>	−1.145	0.23	0.36
<b>4h</b>	−1.141	0.24	0.40
$\text{NAD}^+$	−1.269	0.11	0.22
NMN	−1.183	0.12	0.28
NAR	−1.211	0.12	0.21

**Note:** All data were the average value of three replicates.

**Fig. 2.** Overlay of the continuous reductive curves of  $\text{NAD}^+$  and **4h** under the same conditions.

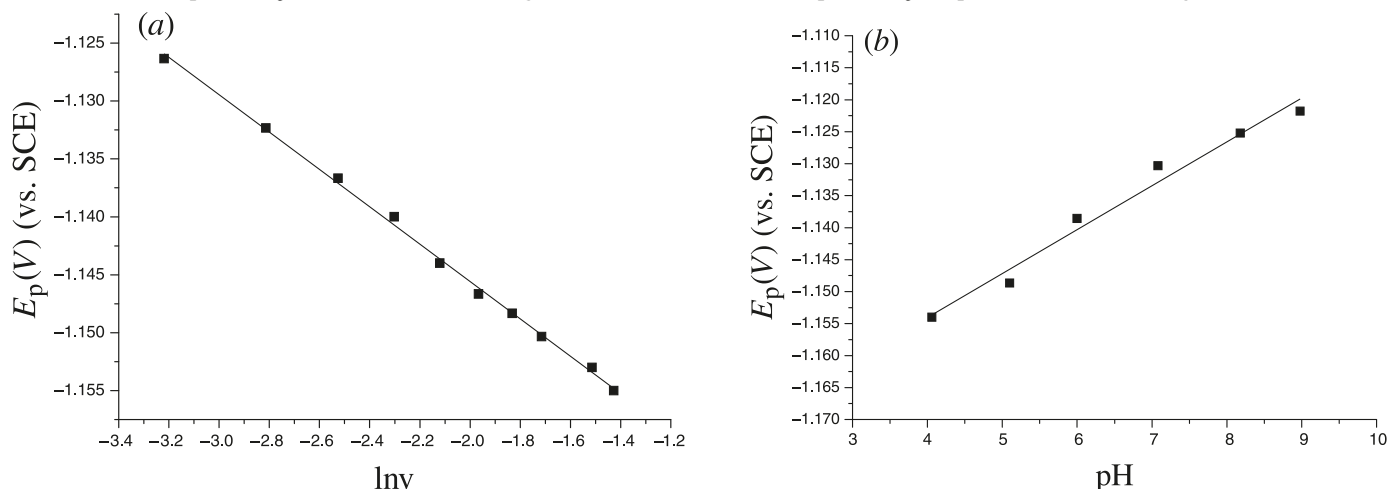


potential, logarithm of the scan rate ( $v$ ), gas constant, absolute temperature, Faraday constant, the transfer electron number ( $n = 2$  for  $\text{NAD}^+$  or its derivatives), electrode reaction rate constant, and electron transfer coefficient, respectively. The value of  $E^\circ$  of all compounds (vs the standard calomel electrode (SCE)) was obtained from the intercept of the plot of  $E_p$  vs.  $v$  (data not shown). The electrode reaction rate constant ( $K_s$ ) and the electron transfer coefficient ( $\alpha$ ) were calculated from the slope and intercept of  $E_p$  vs.  $\ln v$  according to the above equation (Fig. 3a). Accordingly, all triazole-containing  $\text{NAD}^+$  analogs and related compounds were tested and results were listed in Table 1.

It was obvious that analogs with bulky aromatic rings and **4b** have relatively low reductive peak potentials. Compound **4a** and **4h** have the largest  $K_s$  and  $\alpha$ . Compound **4e** shows the lowest  $K_s$  and  $\alpha$  in tris(hydroxymethyl)aminomethane (Tris)/NaCl buffer, which may be due to the presence of aromatic fluorine atoms in the molecule. To investigate the electrochemical property in more detail, we carried out additional experiments on **4h**.

To make a comparison, we also obtained the correlative constants of  $\text{NAD}^+$ , NMN, and nicotinamide ribose (NAR) under identical conditions. It was clear that  $\text{NAD}^+$  and NAR had similar reduction peak potentials ( $E_p$ ) and NMN had a more positive  $E_p$  value. However, all  $\text{NAD}^+$  analogs had even more positive  $E_p$  values. Thus, substitution of

**Fig. 3.** (a) Linear plot of  $E_p$  vs.  $\ln v$  of NAD<sup>+</sup> analog **4h** ( $r = 0.9986$ ). (b) Linear plot of  $E_p$  vs. pH of the NAD<sup>+</sup> analog **4h**.



AMP moiety of the NAD<sup>+</sup> skeleton with a triazole-containing structure could increase the  $E_p$  of the corresponding product.

$K_s$  and  $\alpha$  of **4h** were more than twofold larger than that of other compounds, especially to natural NAD<sup>+</sup>. That indicated that the reduction of NAD<sup>+</sup> analog **4h** on a GC electrode was faster than natural NAD<sup>+</sup> and related compounds. Thus, modification of pyrophosphate made NAD<sup>+</sup> reduce at a relatively lower potential and the triazole ring in the analog molecule made it reduce faster than natural NAD<sup>+</sup>. The triazole ring increased the charge transfer efficiency, which is similar to Zhou et al.'s<sup>20</sup> results. Thus, we concluded that triazole-containing NAD<sup>+</sup> analogs were more liable to be reduced than other compounds on a GC electrode.

To investigate the reoxide stability of **4h** at different pHs, the peak reductive potential of the NAD<sup>+</sup> analog was measured in 1 mol/L phosphate buffer containing  $10^{-3}$  mol/L **4h** at different pHs (pH = 4–9). It was found that the  $E_p$  increased linearly with pH and that reduction of **4h** would be much easier at a higher pH (Fig. 3b). It should be noted that **4h** was stable at these selected pHs and could be recovered by reverse-phase column chromatography in a 96% yield. However, no such correlations were observed for NAD<sup>+</sup>, NMN, or NAR at identical conditions (data not shown).

Based on the  $pK_a$  of nicotinamide and triazole, the amino group of nicotinamide and nitrogen atom of the triazole ring was protonated below pH 6. Thus, the NAD<sup>+</sup> analogs existed as an inner salt in solution at a wide range of pHs. The triazole ring had an interaction with H<sup>+</sup> and promoted conductance of the charge at a relatively high concentration of H<sup>+</sup>, so a higher  $E_p$  was needed to reduce analogs. When the pH was higher than 7, interaction between the triazole ring and proton on the NAD<sup>+</sup> analog gradually disappeared. The repulsion of the triazole ring with the hydroxide anion made analog **4h** reduce at a relatively lower potential.

## Conclusion

An efficient strategy to prepare novel triazole-containing NAD<sup>+</sup> analogs was developed. These compounds had a triazole ring and phosphatediester linkage as mimics of the adenosine heterocyclic ring and pyrophosphate, respectively.

These analogs were more liable to reduce than NAD<sup>+</sup> on a GC electrode in Tris/NaCl buffer. Triazole analogs showed a stable redoxide property at different pHs. The reductive peak potential of **4h** increased linearly with the solution pH. The triazole-containing analogs could be broadly applied in cofactor regeneration or biosensor. We are now exploring other special biological functions with these compounds in a wide variety of chemical and biological areas, and results will be reported in due course.

## Experimental section

### General

All reagents were analytical grade, obtained from commercial suppliers (ABCR, ACROS, or Sigma-Aldrich), and used without further purification. NMR spectra were measured with a Bruker DRX-400 spectrometer (400.3 MHz for <sup>1</sup>H NMR, 100.6 MHz for <sup>13</sup>C NMR, 160.1 MHz for <sup>31</sup>P NMR, and 376 MHz for <sup>19</sup>F NMR) at 298 K. High resolution mass spectroscopy was obtained on a LC/Q-TOF-MS and operated with an electrospray source in positive ion mode. F254 thin-layer and silica gel (400 mesh) were purchased from Yantai Jiangyou Silica Co., Ltd., China. Octyl-functionalized silica gel was purchased from Sigma-Aldrich. Ion exchange resin (100–200 mesh) was purchased from the Chemical Plant of Nankai University, Tianjin, China. Bio-Gel P-2 resin (45  $\mu$ m) was obtained from Bio-Rad Laboratories, Inc. All reactions were carried out under a nitrogen atmosphere. UV-vis spectra were obtained at room temperature on a JASCO V-530 UV-vis spectrophotometer. The electrochemical measurements were performed with a CHI 600C electrochemical analyzer (CH Instruments, USA) connected to a personal computer. All experiments were performed using a conventional three-electrode system with a glassy carbon (GC) disc (CHI 104, 3 mm diameter) working electrode, a saturated calomel reference electrode (CHI 150), and a platinum wire as the counter electrode (CHI 115).

### Preparation of Ac<sub>2</sub>NMN (2)

To a mixture of pyridine (7.5 mL) and Ac<sub>2</sub>O (7.5 mL) was added NMN (275 mg, 0.82 mmol) in H<sub>2</sub>O (160  $\mu$ L)



at  $-5\text{ }^{\circ}\text{C}$ . The suspension was kept at  $0\text{ }^{\circ}\text{C}$  until all solids dissolved. The solvents were removed and the residue was dissolved in a mixture of  $\text{H}_2\text{O}$  (2 mL) and pyridine (2 mL). The yellow solution was stirred at room temperature for 2 h and the solvents were evaporated at reduced pressure. The residue was lyophilized to give  $\text{Ac}_2\text{NMN}$  as an amorphous solid, which was used directly in the next reaction without additional purification.<sup>21</sup>

### Preparation of alkynyl ester (3)

$\text{Ac}_2\text{NMN}$  (344 mg, 0.82 mmol) and 3-butyn-1-ol (3 equiv. to  $\text{Ac}_2\text{NMN}$ ) were dissolved in  $\text{Py}/\text{DMF}$  (1:1,  $v/v$ ) under a nitrogen atmosphere.  $\text{TIPS-Cl}$  (3 equiv. to  $\text{Ac}_2\text{NMN}$ ) was added and the mixture was stirred at room temperature for 3 h in a 99% yield based on  $^{31}\text{P}$  NMR. The solvent was removed, and the residue was added to 10 mL of  $\text{H}_2\text{O}$  and extracted with  $\text{DCM}$  (15 mL  $\times$  3). The aqueous solution was concentrated, purified via ion exchange column chromatography on anion resin ( $201 \times 2$ ,  $\text{HCO}_2^-$  form) eluted with  $\text{H}_2\text{O}$ . Fractions were concentrated and lyophilized to give crude **3**, and it was used in the next reaction without further purification.

### General method for the preparation of azide compounds (a–h)

Azides (**a–c**) in Scheme 1 were synthesized via a nucleophilic substitution using sodium azide, whereas azides **d–h** were made via acylation of the corresponding amines with 5-chloropentanoyl chloride followed by a nucleophilic substitution reaction using sodium azide.<sup>16</sup>

### General method for the preparation of $\text{NAD}^+$ analogs (4a–4h)

A solution of compound **3** in  $\text{H}_2\text{O}$  and azide in  $\text{DCM}$  (or other solvent) was mixed. To the mixture was added an appropriate amount of  $\text{CuSO}_4/\text{sodium ascorbate}$  (5 mol%) in one portion. After the reaction was stirred at room temperature for 0.5–6 h, the organic layer was removed, and the aqueous phase was purified by octyl-functionalized silica gel eluted with water and 1 mol/L  $\text{NH}_4\text{HCO}_3$  solution in  $\text{CH}_3\text{OH}/\text{H}_2\text{O}$  (1:10,  $v/v$ ) to give the crude product. The product was further purified via anion resin ( $201 \times 2$ ,  $\text{HCO}_2^-$  form) or size-exclusion chromatography Bio-Gel® P-2 Gel polyacrylamide gel. The corresponding fractions were pooled and freeze dried to give the triazole-containing analogs.

#### Compound 4a

Compound **4a** was purified by anion resin ( $\text{HCO}_2^-$  form) column chromatography eluted with  $\text{H}_2\text{O}$  and the fraction was concentrated, followed by size-exclusion chromatography Bio-Gel® P-2 Gel polyacrylamide gel, eluted with a 25 mmol/L  $\text{NH}_4\text{HCO}_3$  water solution, to give **4a** as a colorless syrupy solid in a 96% yield.  $^1\text{H}$  NMR (400 MHz,  $\text{D}_2\text{O}$ , ppm)  $\delta$ : 2.46 (q, 2H), 2.85 (t,  $J = 6.16$  Hz, 2H), 3.83 (ddd,  $J = 11.96, 5.00, 2.2$  Hz, 1H), 3.94 (q, 2H), 3.96 (ddd,  $J = 11.96, 4.56, 2.4$  Hz, 1H), 4.22 (dd,  $J = 4.96, 2.72$  Hz, 1H), 4.29 (t,  $J = 6.68$  Hz, 2H), 4.34 (t,  $J = 5.2$  Hz, 1H), 4.41 (t,  $J = 2.44$  Hz, 1H), 4.82 (dd,  $J = 8.84, 1.48$  Hz, 1H), 4.87 (d,  $J = 1.52$  Hz, 1H), 5.62 (ddd,  $J = 23.96, 17.28, 10.44$  Hz, 1H), 6.06 (d,  $J = 5.44$  Hz, 1H), 7.72 (s, 1H), 8.12 (t,  $J = 6.48$  Hz,

1H), 8.84 (d,  $J = 8.12$  Hz, 1H), 9.09 (d,  $J = 6.28$  Hz, 1H), 9.28 (s, 1H).  $^{13}\text{C}$  NMR (100 MHz,  $\text{D}_2\text{O}$ , ppm)  $\delta$ : 168.05, 162.82, 148.47, 147.04, 144.86, 142.22, 136.41, 136.28, 130.95, 126.58, 120.34, 102.28, 89.59, 89.51, 80.13, 73.30, 67.21, 66.76, 52.03, 36.21, 28.83, 28.75, 22.56.  $^{31}\text{P}$  NMR (160 MHz,  $\text{D}_2\text{O}$ , ppm)  $\delta$ : 0.067. HR-MS (ESI) calcd. for  $\text{C}_{19}\text{H}_{26}\text{N}_5\text{O}_8\text{P}$  [ $\text{M} + \text{H}$ ] $^+$ : 484.1597; found: 484.1588.

#### Compound 4b

Compound **4b** was purified by anion resin ( $\text{HCO}_2^-$  form) column chromatography eluted with water to give **4b** as a colorless solid syrup in a 94% yield.  $^1\text{H}$  NMR (400 MHz,  $\text{D}_2\text{O}$ , ppm)  $\delta$ : 2.84 (t,  $J = 5.92$  Hz, 2H), 3.52 (ddd,  $J = 1.84, 4.64, 11.88$  Hz, 1H), 3.70 (ddd,  $J = 2.24, 4.40, 12$  Hz, 1H), 3.91 (dd,  $J = 5.92, 11.84$  Hz, 2H), 4.10 (dd,  $J = 2.48, 4.76$  Hz, 1H), 4.15 (t,  $J = 2.16$  Hz, 1H), 4.25 (t,  $J = 5.16$  Hz, 1H), 5.35 (s, 2H), 5.93 (d,  $J = 5.48$  Hz, 1H), 7.2 (m, 5H), 7.76 (s, 1H), 7.98 (dd,  $J = 6.48, 7.76$  Hz, 1H), 8.73 (d,  $J = 8.12$  Hz, 1H), 8.94 (d,  $J = 7.88$  Hz, 1H), 9.16 (s, 1H).  $^{13}\text{C}$  NMR (100 MHz,  $\text{D}_2\text{O}$ , ppm)  $\delta$ : 168.0, 148.42, 147.53, 144.70, 142.22, 142.22, 137.50, 136.43, 131.64, 131.26, 130.95, 130.72, 126.67, 102.29, 89.52, 80.15, 73.33, 67.20, 66.71, 56.33, 28.82.  $^{31}\text{P}$  NMR (160 MHz,  $\text{D}_2\text{O}$ , ppm)  $\delta$ : 0.01. HR-MS (ESI) calcd. for  $\text{C}_{22}\text{H}_{27}\text{N}_5\text{O}_8\text{P}$  [ $\text{M} + \text{H}$ ] $^+$ : 520.1597; found: 520.1617.

#### Compound 4c

Compound **4c** was purified by size-exclusion chromatography Bio-Gel® P-2 Gel polyacrylamide gel, eluted with 25 mmol/L  $\text{NH}_4\text{HCO}_3$  water solution, to give **4c** as a colorless solid syrup in a 92% yield.  $^1\text{H}$  NMR (400 MHz,  $\text{D}_2\text{O}$ , ppm)  $\delta$ : 2.91 (t, 2H), 3.61 (t, 2H), 3.94 (dd,  $J = 10.64, 5.16$  Hz, 1H), 3.99 (dd,  $J = 2.76$  Hz, 1H), 4.02 (t, 2H), 4.07 (t, 1H), 5.51 (d,  $J = 2.76$  Hz, 1H), 5.56 (d,  $J = 4.36$  Hz, 1H), 7.31 (d,  $J = 8.6$  Hz, 1H), 7.35 (dd,  $J = 6.16, 3.0$  Hz, 2H), 7.47 (t,  $J = 7.52$  Hz, 1H), 7.62 (m, 4H), 7.90 (s, 1H), 8.39 (d,  $J = 6.16$  Hz, 1H), 8.44 (d,  $J = 8.04$  Hz, 1H), 8.61 (s, 1H).  $^{13}\text{C}$  NMR (100 MHz,  $\text{D}_2\text{O}$ , ppm)  $\delta$ : 167.32, 147.92, 147.49, 143.43, 141.31, 135.46, 134.98, 134.84, 131.22, 130.33, 130.14, 130.02, 129.94, 129.43, 128.38, 126.41, 101.91, 89.46, 79.93, 73.32, 67.04, 66.83, 56.36, 28.83.  $^{31}\text{P}$  NMR (160 MHz,  $\text{D}_2\text{O}$ , ppm)  $\delta$ : 0.14. HR-MS (ESI) calcd. for  $\text{C}_{26}\text{H}_{28}\text{N}_5\text{O}_8\text{P}$  [ $\text{M} + \text{H}$ ] $^+$ : 570.1754; found: 570.1735.

#### Compound 4d

Compound **4d** was purified by anion resin ( $\text{HCO}_2^-$  form) column chromatography eluted with water to give **4d** as a colorless solid syrup in a 95% yield.  $^1\text{H}$  NMR (400 MHz,  $\text{D}_2\text{O}$ , ppm)  $\delta$ : 1.35 (m, 2H), 1.68 (m, 2H), 2.15 (t, 2H), 2.77 (t, 2H), 3.70 (ddd,  $J = 2.08, 5.08, 11.96$  Hz, 1H), 3.78–3.86 (m, 3H), 4.13–4.18 (m, 3H), 4.26 (t, 1H), 5.87 (d,  $J = 5.24$  Hz, 1H), 6.92 (m, 1H), 7.10 (d, 5H), 7.64 (s, 1H), 7.94 (t,  $J = 6.6$  Hz, 1H), 8.67 (d,  $J = 8.12$  Hz, 1H), 8.89 (d,  $J = 6.24$  Hz, 1H), 9.08 (s, 1H).  $^{13}\text{C}$  NMR (100 MHz,  $\text{D}_2\text{O}$ , ppm)  $\delta$ : 177.13, 173.46, 168.11, 167.85, 162.90, 148.26, 147.17, 144.61, 142.04, 139.20, 136.22, 131.55, 130.84, 127.82, 126.42, 124.07, 102.17, 89.34, 80.01, 73.10, 67.21, 66.68, 52.33, 37.96, 31.24, 28.70, 24.51.  $^{31}\text{P}$  NMR (160 MHz,  $\text{D}_2\text{O}$ , ppm)  $\delta$ : 0.01. HR-MS (ESI) calcd. for  $\text{C}_{26}\text{H}_{33}\text{N}_6\text{O}_9\text{P}$  [ $\text{M} + \text{H}$ ] $^+$ : 605.2125; found: 605.2103.

**Compound 4e**

Compound **4e** was purified by anion resin ( $\text{HCO}_2^-$  form) column chromatography, eluted with 5%  $\text{HCO}_2\text{NH}_4$  solution, followed by octyl-functionalized silica gel eluted with water, to give **4e** as a colorless solid syrup in a 95% yield.  $^1\text{H}$  NMR (400 MHz,  $\text{D}_2\text{O}$ , ppm)  $\delta$ : 1.48 (m, 2H), 1.80 (m, 2H), 2.31 (t, 2H), 2.86 (t, 2H), 3.80 (dd,  $J = 3.72$ , 10.6 Hz, 1H), 3.91–3.96 (m, 3H), 4.13–4.18 (m, 3H), 4.20 (s, 1H), 4.26–4.32 (m, 3H), 4.38 (s, 1H), 6.02 (d,  $J = 5.24$  Hz, 1H), 6.84–6.91 (m, 2H), 7.28 (dd,  $J = 2.72$ , 8.76 Hz, 1H), 7.31 (s, 1H), 8.09 (t,  $J = 6.72$  Hz, 1H), 8.81 (d,  $J = 8.12$  Hz, 1H), 9.05 (d,  $J = 6.28$  Hz, 1H), 9.24 (s, 1H).  $^{13}\text{C}$  NMR (100 MHz,  $\text{D}_2\text{O}$ , ppm)  $\delta$ : 178.13, 168.01, 148.45, 144.82, 142.19, 136.40, 130.94, 130.05, 126.52, 114.00, 113.78, 107.08, 106.83, 106.58, 102.30, 89.56, 80.13, 73.30, 67.26, 66.81, 52.38, 37.43, 31.26, 28.78, 24.60.  $^{31}\text{P}$  NMR (160 MHz,  $\text{D}_2\text{O}$ , ppm)  $\delta$ : 0.08.  $^{19}\text{F}$  NMR (376 MHz,  $\text{D}_2\text{O}$ , ppm)  $\delta$ : -111.8, -118.9. HR-MS (ESI) calcd. for  $\text{C}_{26}\text{H}_{31}\text{F}_2\text{N}_6\text{O}_9\text{P}$  [ $\text{M} + \text{H}$ ] $^+$ : 641.1936; found: 641.1960.

**Compound 4f**

Compound **4f** was purified by size-exclusion chromatography Bio-Gel<sup>®</sup> P-2 Gel polyacrylamide gel, eluted with 25 mmol/L  $\text{NH}_4\text{HCO}_3$  water solution, to give **4f** as a colorless solid syrup in a 90% yield.  $^1\text{H}$  NMR (400 MHz,  $\text{D}_2\text{O}$ )  $\delta$ : 1.36 (m, 2H), 1.54 (m, 2H), 2.10 (t, 2H), 2.82 (t, 2H), 3.80 (ddd,  $J = 11.96$ , 5.16, 1.92 Hz, 1H), 3.94 (m, 3H), 4.05 (t, 2H), 4.17 (dd,  $J = 4.52$ , 2.64 Hz, 1H), 4.22 (t, 1H), 4.34 (s, 1H), 4.52 (s, 2H), 5.88 (d,  $J = 5.32$  Hz, 1H), 7.32–7.17 (m, 4H), 7.44 (s, 1H), 7.64 (d,  $J = 2.44$  Hz, 1H), 7.66 (dd,  $J = 3.6$  Hz, 1H), 7.87 (t,  $J = 7.64$  Hz, 1H), 8.58 (d,  $J = 8.08$  Hz, 1H), 8.87 (d,  $J = 6.24$  Hz, 1H), 9.04 (s, 1H).  $^{13}\text{C}$  NMR (100 MHz,  $\text{D}_2\text{O}$ )  $\delta$ : 178.03, 167.54, 162.80, 148.02, 146.99, 144.49, 141.87, 135.85, 135.46, 132.88, 131.16, 130.64, 129.01, 128.66, 128.40, 128.12, 126.13, 125.48, 102.21, 89.37, 80.05, 73.11, 67.21, 66.74, 52.18, 43.43, 37.40, 31.21, 28.81, 24.82.  $^{31}\text{P}$  NMR (160 MHz,  $\text{D}_2\text{O}$ , ppm)  $\delta$ : 0.11. HR-MS (ESI) calcd. for  $\text{C}_{31}\text{H}_{37}\text{O}_9\text{N}_6\text{P}$  [ $\text{M} + \text{H}$ ] $^+$ : 669.2438; found: 669.2444.

**Compound 4g**

Compound **4g** was purified by size-exclusion chromatography Bio-Gel<sup>®</sup> P-2 Gel polyacrylamide gel, eluted with 25 mmol/L  $\text{NH}_4\text{HCO}_3$  water solution, to give **4g** as a colorless solid syrup in an 88% yield.  $^1\text{H}$  NMR (400 MHz,  $\text{D}_2\text{O}$ , ppm)  $\delta$ : 1.46 (m, 2H), 1.70 (m, 2H), 2.18 (t,  $J = 6.96$  Hz, 2H), 2.80 (t,  $J = 6.62$  Hz, 2H), 3.77 (dd,  $J = 11.36$ , 4.04 Hz, 1H), 3.88–3.93 (m, 3H), 4.17–4.22 (m, 5H), 4.27 (t,  $J = 5.16$  Hz, 1H), 4.32 (s, 1H), 5.90 (d,  $J = 5.48$  Hz, 1H), 7.16 (d,  $J = 7.96$  Hz, 2H), 7.21 (d,  $J = 7.12$  Hz, 1H), 7.27 (t,  $J = 7.24$  Hz, 2H), 7.41 (m, 5H), 7.64 (s, 1H), 8.01 (t,  $J = 6.88$  Hz, 1H), 8.72 (d,  $J = 8.08$ , 1H), 8.98 (d,  $J = 6.2$  Hz, 1H), 9.16 (s, 1H).  $^{13}\text{C}$  NMR (100 MHz,  $\text{D}_2\text{O}$ , ppm)  $\delta$ : 177.21, 167.63, 148.39, 144.79, 142.09, 141.24, 140.09, 136.32, 131.16, 130.97, 130.33, 129.61, 129.02, 128.81, 102.36, 89.63, 80.17, 73.23, 67.15, 66.76, 52.15, 44.87, 37.43, 31.51, 28.98, 24.88.  $^{31}\text{P}$  NMR (160 MHz,  $\text{D}_2\text{O}$ , ppm)  $\delta$ : 0.01. HR-MS (ESI) calcd. for  $\text{C}_{33}\text{H}_{39}\text{N}_6\text{O}_9\text{P}$  [ $\text{M} + \text{H}$ ] $^+$ : 695.2594; found: 695.2569.

**Compound 4h**

Compound **4h** was purified by size-exclusion chromatography Bio-Gel<sup>®</sup> P-2 Gel polyacrylamide gel, eluted with 25 mmol/L  $\text{NH}_4\text{HCO}_3$  water solution, to give **4h** as a colorless solid syrup in a 91% yield.  $^1\text{H}$  NMR (400 MHz,  $\text{D}_2\text{O}$ , ppm)  $\delta$ : 1.45 (m, 2H), 1.62 (m, 2H), 2.17 (t,  $J = 7$  Hz, 2H), 2.86 (t,  $J = 6$  Hz, 2H), 3.75 (dd,  $J = 11.4$ , 4.15 Hz, 1H), 3.92–4.11 (m, 3H), 4.14 (t,  $J = 6.8$  Hz, 2H), 4.18 (t,  $J = 2.4$  Hz, 1H), 4.24 (t,  $J = 5.4$  Hz, 1H), 4.35 (s, 1H), 5.91 (d,  $J = 5.2$  Hz, 1H), 7.28–7.39 (m, 5H), 7.5 (s, 3H), 7.68 (d,  $J = 7.8$  Hz, 2H), 7.75 (t,  $J = 8.2$  Hz, 2H), 7.91 (t,  $J = 6.8$  Hz, 2H), 8.63 (d,  $J = 8.08$  Hz, 1H), 8.92 (d,  $J = 6.16$  Hz, 1H), 9.08 (s, 1H).  $^{13}\text{C}$  NMR (100 MHz,  $\text{D}_2\text{O}$ , ppm)  $\delta$ : 176.29, 167.64, 148.39, 146.84, 144.82, 143.86, 142.1, 136.33, 130.95, 129.60, 126.01, 102.35, 89.66, 80.16, 73.22, 67.16, 66.76, 59.23, 52.04, 37.19, 31.47, 28.94, 24.83.  $^{31}\text{P}$  NMR (160 MHz,  $\text{D}_2\text{O}$ , ppm)  $\delta$ : 0.15. HR-MS (ESI) calcd. for  $\text{C}_{33}\text{H}_{39}\text{N}_6\text{O}_9\text{P}$  [ $\text{M} + \text{H}$ ] $^+$ : 695.2594; found: 695.2615.

**Electrochemical experiment**

All data were recorded on a CHI 600C electrochemical analyzer, and further processed using the software Origin 8.0 when necessary.<sup>22</sup> The working concentration of analytes was  $2 \times 10^{-3}$  mol/L. Solutions of either 0.01 mol/L Tris/NaCl (0.005 mol/L) or phosphate (1 mol/L) buffer were used as supporting electrolytes. The pH was adjusted with NaOH or  $\text{H}_3\text{PO}_4$ . Stock solutions of all compounds were stored at 4 °C to avoid decomposition. Solutions were sonicated and purged with purified nitrogen and the temperature was kept at  $25 \pm 0.2$  °C.

To use this electrode it was necessary to activate its surface. For this purpose, several methods were tried, namely, polishing with alumina powder, sonication, activation with sulfochromic mixture, etc. The treatment selected for the electrode, made before each measurement, was the following: washing with distilled water, putting the electrode into a sulfochromic mixture for 30 s, washing with distilled water, polishing with 0.3  $\mu\text{m}$  alumina powder and 0.05  $\mu\text{m}$  alumina powder, sonication for 2 min in distilled water, washing with distilled water, and drying with soft paper. Under such conditions measurements were highly reproducible.

To maintain the activity of  $\text{NAD}^+$ , all buffer pHs must be in the range of 5–7. Tris/NaCl (pH 7) was a better choice than the same pH phosphate for a sensitive GC electrode response. In NaCl (0.01 mol/L) / Tris (0.005 mol/L) buffer at pH 7, peak currents was invariable. The potential range used for  $\text{NAD}^+$  analog detection was -0.4 to -1.4 V, which was the most suitable (small peak current changes). The scan rate was 0.1 V/s.

Cyclic voltammogram for determination of dynamic constants was performed with a glassy carbon electrode vs. SCE in supporting electrolyte (0.01 mol/L NaCl / 0.005 mol/L Tris, pH 7). The response to  $2 \times 10^{-3}$  mol/L  $\text{NAD}^+$  analogs and corresponding compounds were measured in 10 mL of supporting electrolyte at  $298 \pm 0.2$  °C under a nitrogen atmosphere.

The cyclic voltammogram for pH dependence of **4h** was performed in 1 mol/L phosphate buffer at different pHs (pH 4–9) containing  $2 \times 10^{-3}$  mol/L **4h**.

## Acknowledgement

We are grateful for the support of the National Natural Science Foundation of China (No. 20472084).

## References

- (1) Haigis, M. C.; Mostoslavsky, R.; Haigis, K. M.; Fahie, K.; Christodoulou, D. C.; Murphy, A. J.; Valenzuela, D. M.; Yancopoulos, G. D.; Karow, M.; Blander, G.; Wolberger, C.; Prolla, T. A.; Weindrich, R.; Alt, F. W.; Guarente, L. *Cell* **2006**, *126* (5), 941. doi:10.1016/j.cell.2006.06.057. PMID:16959573.
- (2) Liu, Q.; Kriksunov, I. A.; Graeff, R.; Lee, H. C.; Hao, Q. *J. Biol. Chem.* **2007**, *282* (8), 5853. doi:10.1074/jbc.M609093200. PMID:17182614.
- (3) Alano, C. C.; Ying, W. H.; Swanson, R. A. *J. Biol. Chem.* **2004**, *279* (18), 18895. doi:10.1074/jbc.M313329200. PMID:14960594.
- (4) Olek, R. A.; Ziolkowski, W.; Kaczor, J. J.; Greci, L.; Popinigis, J.; Antosiewicz, J. *J. Biochem. Mol. Biol.* **2004**, *37* (4), 416. PMID:15469728.
- (5) Waypa, G. B.; Schumacker, P. T. *J. Appl. Physiol.* **2005**, *98* (1), 404. doi:10.1152/jappphysiol.00722.2004. PMID:15591310.
- (6) (a) Barker, C. D.; Reda, T.; Hirst, J. *Biochemistry (Mosc.)* **2007**, *46* (11), 3454. doi:10.1021/bi061988y.; (b) Zhang, Z.; Blake, D. R.; Stevens, C. R.; Kanczler, J. M.; Winyard, P. G.; Symons, M. C.; Benboubetra, M.; Harrison, R. *Free Radic. Res.* **1998**, *28* (2), 151. doi:10.3109/10715769809065801. PMID:9645392.
- (7) Damian, A.; Omanovic, S. *J. Mol. Catal. Chem.* **2006**, *253* (1–2), 222. doi:10.1016/j.molcata.2006.03.020.
- (8) Xu, X. H.; Chen, J. H.; Li, W.; Nie, Z.; Yao, S. Z. *Electrochem. Commun.* **2008**, *10* (10), 1459. doi:10.1016/j.elecom.2008.07.033.
- (9) Salimi, A.; Izadi, M.; Hallaj, R.; Soltanian, S.; Hadadzadeh, H. *J. Solid State Electrochem.* **2009**, *13* (3), 485. doi:10.1007/s10008-008-0583-6.
- (10) Lo, H. C.; Leiva, C.; Buriez, O.; Kerr, J. B.; Olmstead, M. M.; Fish, R. H. *Inorg. Chem.* **2001**, *40* (26), 6705. doi:10.1021/ic010562z. PMID:11735482.
- (11) Lo, H. C.; Fish, R. H. *Angew. Chem. Int. Ed.* **2002**, *41* (3), 478. doi:10.1002/1521-3773(20020201)41:3<478::AID-ANIE478>3.0.CO;2-K.
- (12) Song, H. K.; Lee, S. H.; Won, K.; Park, J. H.; Kim, J. K.; Lee, H.; Moon, S. J.; Kim, D. K.; Park, C. B. *Angew. Chem. Int. Ed.* **2008**, *47* (9), 1749. doi:10.1002/anie.200703632.
- (13) Lee, S. H.; Nam, D. H.; Kim, J. H.; Baeg, J. O.; Park, C. B. *ChemBioChem* **2009**, *10* (10), 1621. doi:10.1002/cbic.200900156. PMID:19551795.
- (14) Kolb, H. C.; Finn, M. G.; Sharpless, K. B. *Angew. Chem. Int. Ed.* **2001**, *40* (11), 2004. doi:10.1002/1521-3773(20010601)40:11<2004::AID-ANIE2004>3.0.CO;2-5.
- (15) Liu, R. H.; Visscher, J. *Nucleosides Nucleotides* **1994**, *13* (5), 1215. doi:10.1080/15257779408011891. PMID:11539878.
- (16) (a) Theocharis, A. B.; Alexandrou, N. E.; Terzis, A. *J. Heterocycl. Chem.* **1990**, *27* (6), 1741. doi:10.1002/jhet.5570270643.; (b) van der Peet, P.; Gannon, C. T.; Walker, I.; Dinev, Z.; Angelin, M.; Tam, S.; Ralton, J. E.; McConville, M. J.; Williams, S. J. *ChemBioChem* **2006**, *7* (9), 1384. doi:10.1002/cbic.200600159. PMID:16841351.; (c) Gunter, M. J.; Farquhar, S. M.; Mullen, K. M. *N. J. Chem.* **2004**, *28* (12), 1443. doi:10.1039/b411583j.
- (17) Rostovtsev, V. V.; Green, L. G.; Fokin, V. V.; Sharpless, K. B. *Angew. Chem. Int. Ed.* **2002**, *41* (14), 2596. doi:10.1002/1521-3773(20020715)41:14<2596::AID-ANIE2596>3.0.CO;2-4.
- (18) Angulo, M.; Ruiz Montoya, M.; Marin Galvin, R.; Rodriguez Mellado, J. *Electroanalysis* **1997**, *9* (4), 345. doi:10.1002/elan.1140090417.
- (19) Laviron, E. *J. Electroanal. Chem.* **1974**, *52* (3), 355. doi:10.1016/S0022-0728(74)80448-1.
- (20) Zhou, Z.; Li, S. W.; Zhang, Y. L.; Liu, M. L.; Li, W. *J. Am. Chem. Soc.* **2005**, *127* (31), 10824. doi:10.1021/ja052280u. PMID:16076176.
- (21) Graham, S. M.; Macaya, D. J.; Sengupta, R. N.; Turner, K. B. *Org. Lett.* **2004**, *6* (2), 233. doi:10.1021/ol036152r. PMID:14723536.
- (22) OriginLab Corporation. *Origin 8.0*; MicroCal, Inc.: Northampton, MA, USA, 2007.

# On the microwave-assisted synthesis of acylphenothiazine derivatives — Experiment versus theory synergism

**Luiza Gaina, Dan Porumb, Ioan Silaghi-Dumitrescu, Castelia Cristea, and Luminita Silaghi-Dumitrescu**

**Abstract:** The microwave-assisted synthesis of a series of acylphenothiazine derivatives is described. 10*H*-Phenothiazine-3-carbaldehyde derivatives were obtained in moderate yields by the Duff formylation reaction, and 10-acetyl-phenothiazine derivatives were obtained in excellent yields by acetylating phenothiazine derivatives with acetic anhydride. A theoretical explanation for the chemoselectivity and regioselectivity of these acylation reactions applied to phenothiazine substrates was attempted by molecular-modeling analyses based on molecular mechanics, and semi-empirical and DFT calculations.

**Key words:** phenothiazine, microwave-assisted organic synthesis (MAOS), Duff formylation, acetylation, DFT calculations, electrostatic potential.

**Résumé :** On décrit la synthèse assistée par des microondes d'une série de dérivés de l'acylphénothiazine. On a obtenu le 10*H*-phénothiazine-3-carbaldéhyde avec des rendements modérés en faisant appel à une réaction de formylation de Duff alors que les dérivés de la 10-acétylphénothiazine ont été obtenus avec d'excellents rendements par acétylation des dérivés de la phénothiazine à l'aide d'anhydride acétique. On a essayé de trouver une explication théorique de la chimiosélectivité et de la régiosélectivité de ces réactions d'acylation appliquées à des substrats phénothiazines en faisant appel à des analyses de modelages moléculaires basés sur des calculs de mécanique moléculaire, semi-empiriques ou des calculs basés sur la théorie de la fonctionnelle de densité.

**Mots-clés :** phénothiazine, synthèses organiques assistées par des microondes (SOAM), formylation de Duff, acétylation, calculs basés sur la théorie de la fonctionnelle de densité (TFD), potentiel électrostatique.

[Traduit par la Rédaction]

## Introduction

The increased popularity of the microwave-assisted organic synthesis (MAOS) technique in chemical synthesis on a laboratory scale is based on particularly efficient heating processes which afford shorter reaction times and offer the possibility of rapid optimization of the reaction conditions. An increasing number of published papers, several books,<sup>1,2</sup> and review articles show that almost all conventionally heated reactions, including synthesis and functionalization of heterocyclic compounds, were performed using this technique.<sup>3,4,5</sup> Since 1986, when Gedye<sup>6</sup> and Giguere<sup>7</sup> carried out the first reported organic syntheses using sealed vessels heated in domestic microwave ovens, several methods have been developed for the preparation of samples (with or without solvent) in both pressurized or open vessel systems; meanwhile dedicated multimode or monomode microwave reactors have been designed. Phenothiazine de-

rivatives were obtained by microwave-assisted thiation of diarylamines in reactions of neat reactants or adsorbed onto inorganic supports such as alumina and bentonite,<sup>8,9</sup> and in water as a solvent.<sup>10</sup> Chalcones containing phenothiazine units were successfully synthesized by microwave-assisted condensation of (hetero)aromatic carbonyl derivatives.<sup>11</sup>

One aim of this work was to optimize the microwave-assisted reaction conditions, as an eco-friendly approach for the synthesis of acyl-phenothiazine derivatives. These derivatives might prove to be useful substrates in the formation of coupled heterocyclic systems, by forming new C=C bonds in condensation reactions. Suitable substituted phenothiazine derivatives are candidates for developing potentially interesting organic solid-state properties (such as unconventional physical, nonlinear optical, magnetic, and (or) electrical properties), based on the well-known electron donor effect of the phenothiazine nucleus characterized by low and highly reversible first oxidation potential and a pronounced tendency to form stable cation-radicals.<sup>12</sup> Furthermore, when the 10*H*-phenothiazine unit appears unsubstituted at the heterocyclic nitrogen atom, the cation-radical formed by single-electron oxidation may be involved in protolytic equilibria as well, thus generating the isoelectronic conjugate base, the neutral radical.<sup>13–15</sup> Potential new materials may be obtained using such redox-active and pH-sensitive heterocyclic building blocks.

Received 13 March 2009. Accepted 16 October 2009. Published on the NRC Research Press Web site at canjchem.nrc.ca on 18 December 2009.

**L. Gaina, D. Porumb,<sup>1</sup> I. Silaghi-Dumitrescu, C. Cristea, and L. Silaghi-Dumitrescu.** Babeş-Bolyai University, Faculty of Chemistry and Chemical Engineering, 11, Arany Janos Street, 400028 Cluj-Napoca, Romania.

<sup>1</sup>Corresponding author (e-mail: pdan@chem.ubbcluj.ro).



## Experimental techniques

To ensure highly reproducible reaction conditions, the experimental technique employed for the microwave-assisted syntheses of acylphenothiazine derivatives described below is based on microwave power processing of materials using a microwave instrument Synthos 3000; this system provides multi-mode heating in sealed vessels equipped with built-in magnetic stirrer, pressure sensors, and internal temperature measurement. The instrument ensures cooling mechanisms, online power, and temperature control using the feedback from IR thermography. Software operation provides high-precision reaction control.

## Results and discussion

The chemical reactivity of phenothiazine towards electrophilic substitution was demonstrated in the preparation of numerous examples of N- or C-substituted derivatives. Chemical syntheses of acylphenothiazine derivatives were previously performed under conventional heating techniques which required long reaction times and usually generated mixtures of constitutional isomers. Although phenothiazine carbaldehydes were obtained by Vilsmeier formylation<sup>16</sup> and Bergman formylation<sup>17</sup> of *N*-alkyl-phenothiazine derivatives, this method is inappropriate for the C-formylation of 10*H*-phenothiazine because of the formation of *N*-formyl-phenothiazine derivatives in competitive reactions. We wish to report here a direct and C-regioselective formylation of 10*H*-phenothiazine substrates, based on the Duff reaction,<sup>18</sup> as the only reaction strategy generating good yields of 10*H*-phenothiazin-3-yl-carbaldehydes. Our promising results obtained by the microwave-assisted Duff formylation of unsubstituted 10*H*-phenothiazine<sup>11</sup> encouraged us to continue to apply this mild formylation reaction to several other substrates such as methyl-, halogeno-, and trifluoromethyl-10*H*-phenothiazine.

### Microwave-assisted synthesis of 10*H*-phenothiazine-3-carbaldehyde derivatives

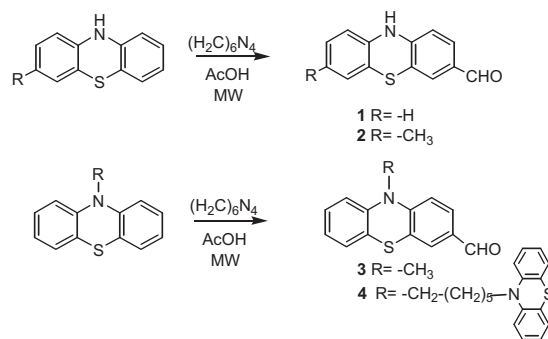
The microwave-assisted synthesis of 3-formyl-10*H*-phenothiazine derivatives was performed in the resonance cavity of a Synthos 3000 instrument by multimode microwave irradiation in pressurized systems (sealed quartz vessels) using acetic acid, a polar solvent which ensures a medium absorption efficiency and heating rate ( $\tan\delta = 0.174$ , dielectric loss  $\epsilon'' = 1.079$ ).<sup>19</sup>

3-Formyl-10*H*-phenothiazine (**1**) was synthesized in moderate yields by the microwave-assisted reaction of 10*H*-phenothiazine with urotropine in acetic acid solution. The same regioselectivity for substitution in position 3 of the heterocyclic substrate was observed in the microwave-assisted Duff formylation of some alkyl-substituted 10*H*-phenothiazine derivatives such as 3-methyl-phenothiazine, 10-methyl-phenothiazine, and 1,6-bis-(phenothiazin-10-yl)-hexane (Scheme 1).

The microwave-assisted Duff formylation reactions of some 2-substituted phenothiazine derivatives were also performed. As shown in Scheme 2, different carbaldehyde regioisomers may be formed according to the influence exerted by the substituent.

Electron-withdrawing substituents such as chlorine or tri-

Scheme 1.



fluoromethyl group attached in position 2 of the phenothiazine substrate does not reduce the reactivity for electrophilic aromatic substitution in position 3, so that 3-formyl- and 7-formyl-phenothiazine derivatives were obtained. When 2-chlorophenothiazine was subjected to the Duff formylation reaction, the two monoformyl derivatives 2-chloro-7-formyl-phenothiazine (**5a**) and 2-chloro-3-formylphenothiazine (**5b**) were obtained in 1.5:1 ratio.

2-Trifluoromethyl-phenothiazine generated the 3,7-di-formyl-2-trifluoromethylphenothiazine (**6**) as the main reaction product, in moderate yields.

The reaction conditions employed for these microwave-assisted syntheses (reaction temperature, reaction time, and ramp time to achieve the prescribed temperature) are shown in Table 1. Temperature-controlled experiments in the temperature range 150–190 °C show enhanced reactivity of unsubstituted phenothiazine as compared to substituted derivatives. Similar reaction conditions (time, temperature) were required for the formylation of alkyl-, 2-chloro-, and 2-trifluoromethyl-phenothiazine derivatives. Despite the alkyl chain length or its position in the substrate, mono formyl-derivatives were isolated, even in the case of 1,6-bis-(phenothiazin-10yl)-hexane which contains two equivalent phenothiazine units. Good yields of diformyl-phenothiazine derivative were obtained in the formylation of 2-trifluoromethyl-phenothiazine.

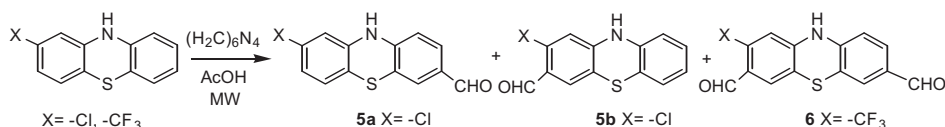
The regioselectivity of this reaction was experimentally proved by the failure of the formylation reaction when 3,7-dibromo-10-methylphenothiazine was subjected to a microwave-assisted Duff formylation reaction.

The structure assignments of compounds **1–6** are supported by spectroscopic data. FTIR spectroscopy indicates the stretching vibration of N–H bond in compounds **1**, **2**, **5**, and **6**, by the absorption band situated near 3300 cm<sup>–1</sup>. The substitution in position 3 of the phenothiazine units was unambiguously assigned according to the NMR spectra. The coupling patterns of the aromatic protons observed for the <sup>1</sup>H NMR signals were assigned using the 2D homocorrelation COSY–45 spectra for each of products **1–6**. <sup>13</sup>C NMR spectra together with 2D NMR heterocorrelation spectra HMQC and HMBC afforded the complete structural assignments.

### Microwave-assisted synthesis of acetyl-10*H*-phenothiazine derivatives

Acetylation of 10*H*-phenothiazine derivatives using acetic anhydride generates different *N*-acetyl-10*H*-phenothiazine

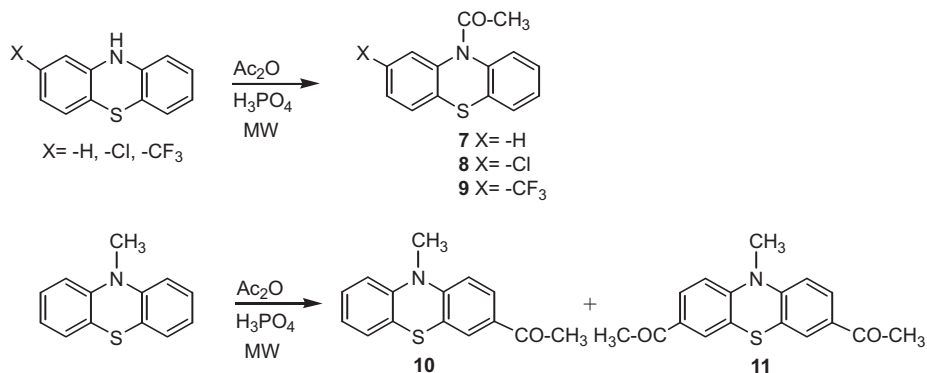
Scheme 2.



**Table 1.** Experimental conditions for the microwave-assisted Duff formylation reaction of phenothiazine derivatives using a Synthos 3000 microwave installation (reaction temperature, reaction time, and ramp time to achieve the prescribed temperature).

Product	Substrate	$T$ ( $^{\circ}\text{C}$ )	Time/ramp (min)	Yield (%)
<b>1</b>	10 <i>H</i> -Phenothiazine	120	30/10	50
		150	80	
		120	30	
<b>2</b>	3-Methyl-10 <i>H</i> -phenothiazine	150	5/4	50
		170	60	
		190	20	
<b>3</b>	10-Methyl-phenothiazine	140	20/4	50
		170	60	
		180	10	
<b>4</b>	1,6-Bis-(phenothiazin-10yl)-hexane	170	60/2	45
		200	10	
<b>5a</b>	2-Chloro-10 <i>H</i> -phenothiazine	150	20/10	65
<b>5b</b>		170	80	<b>5a/5b</b> = 1.5:1
<b>6</b>	2-Trifluoromethyl-10 <i>H</i> -phenothiazine	150	5/4	
		170	99	65
		180	30	
—	3,7-Dibromo-10 <i>H</i> -phenothiazine	100	10/5	—
		170	30	

Scheme 3.



and *C*-acetyl-10*H*-phenothiazine regioisomers according to the reaction conditions applied.<sup>20,21</sup>

The microwave-assisted acetylation of phenothiazine substrates was found to be highly chemoselective; *N*-acetylphenothiazine derivatives were obtained in almost quantitative yields. Scheme 3 presents the reactions of phenothiazine derivatives with acetic anhydride in the presence of catalytic amounts of phosphoric acid.

In the microwave-assisted acetylation of 10-methylphenothiazine, 3-acetyl-10-methylphenothiazine (**10**) was obtained in excellent yields. Table 2 summarizes the experimental conditions employed for the microwave-assisted acetylation of phenothiazine derivatives.

As expected, the less-reactive substrate in the acetylation reaction was *N*-methylphenothiazine. When longer reaction

time was allowed, 3,7-diacetyl-10-methylphenothiazine (**11**) was obtained in good yields.

Spectroscopic data support the structure assignment of acetyl-derivatives **7–11**. The recorded 300 MHz  $^1\text{H}$  NMR spectra show the diagnostic appearance of a singlet signal for the acetyl group protons situated at 2.5. Complete structural assignment for the aromatic protons and carbon atoms was performed by 2D NMR correlation spectra (COSY-45, HMQC and HMBC).

## Molecular modeling

The chemoselectivity and regioselectivity of these acylation reactions of the phenothiazine nucleus observed by experimental results were compared with theoretical data generated by DFT calculations.

**Table 2.** Experimental conditions for the microwave-assisted acetylation reaction of phenothiazine derivatives using a Synthos 3000 microwave installation (reaction temperature, reaction time, and ramp time to achieve the prescribed temperature).

Product	Substrate	<i>T</i> (°C)	Time/ramp (min)	Yield (%)
<b>7</b>	10 <i>H</i> -Phenothiazine	60	10/2	98
		70	30	
<b>8</b>	2-Chloro-10 <i>H</i> -phenothiazine	60	10/2	96
		70	30	
<b>9</b>	2-Trifluoromethyl-10 <i>H</i> -phenothiazine	60	10/2	97
		70	30	
<b>10</b>	10-Methyl-phenothiazine	60	5/3	45
		80	10	
<b>11</b>	10-Methyl-phenothiazine	60	5/3	55
		80	30	

**Table 3.** Electrostatic atomic charges calculated in phenothiazine substrates and intermediates, candidates for aromatic electrophilic substitution.

Compound	Electrostatic atomic charge in positions:				
	2	3	7	8	10
10 <i>H</i> -Phenothiazine	−0.038	−0.226	−0.226	−0.038	−0.661
10-Methylphenothiazine	−0.131	−0.175	−0.175	−0.131	−0.213
1,6-Bis(phenothiazin-10-yl)-hexane	−0.111	−0.189	−0.156	−0.150	−0.512
3-Methyl-10 <i>H</i> -phenothiazine	−0.257	0.365	−0.121	−0.059	−0.616
2-Chloro-10 <i>H</i> -phenothiazine	0.109	−0.201	−0.213	−0.051	−0.638
2-Trifluoromethyl-10 <i>H</i> -phenothiazine	0.175	−0.299	−0.193	−0.055	−0.629
2-Chloro-3-formyl-10 <i>H</i> -phenothiazine	0.173	−0.027	−0.236	−0.031	−0.618
2-Chloro-7-formyl-10 <i>H</i> -phenothiazine	0.234	−0.297	−0.013	−0.044	−0.607
3-formyl-2-trifluoromethyl-10 <i>H</i> -phenothiazine	0.005	−0.097	−0.183	−0.056	−0.596
7-Formyl-2-trifluoromethyl-10 <i>H</i> -phenothiazine	0.175	−0.358	0.044	−0.079	−0.615

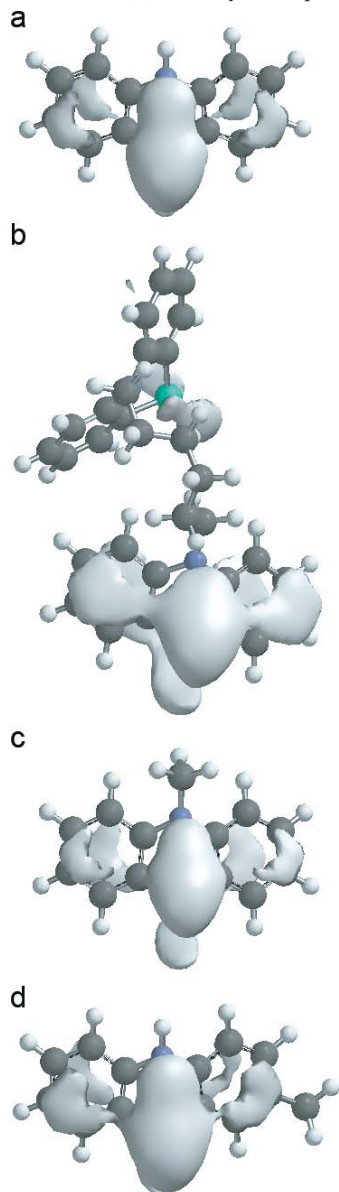
The minimum energy geometry of each phenothiazine derivative employed as a substrate in acylation reactions was obtained starting with molecular mechanics optimization of the conformers generated within the Confanal module of Spartan'06,<sup>22</sup> followed by semi-empirical (PM3) and 6–31G(d) B3LYP DFT<sup>23–25</sup> calculations on all such obtained conformers. The following discussion applies to the lowest energy conformers.

Theoretical explanations for the regioselectivity of the Duff formylation reaction and the chemoselectivity of the acetylation reaction, respectively, applied to substituted phenothiazine substrates may be formulated on the basis of the electrophilic aromatic substitution reaction mechanism. The soft electrophile  $\text{H}_2\text{C}=\text{N}^+ \leftrightarrow \text{H}_2\text{C}^+-\text{N}^-$  generated by urotropine during the Duff formylation reaction may selectively attack heterocyclic carbon atoms in positions characterized by high electron density, whereas the acylium ion  $\text{H}_3\text{C}-\text{CO}^+$  generated by the acetic anhydride in acidic media is a hard electrophile and it is preferentially attached to the heterocyclic nitrogen atom. Here, we adopt the electrostatic charges derived from the electrostatic potential as an indicator of the preferred reaction site on the ring. These atomic charges given in Table 3 show the highest (negative) value on the nitrogen atom (position 10 of the heterocyclic substrate), followed by the values assigned to the carbon atoms in positions 3 and 7, for each phenothiazine substrate employed in experimental acylation reactions.

The electrostatic potential surfaces (−18 kcal/mol isovalues) for relevant alkylphenothiazine substrates are also shown in Fig. 1. In each case, it can be noticed that the region around position 3 of the substrate exhibits a relatively high area of negative electrostatic potential, thus supporting the availability of this atom to electrophilic attack, in agreement with experimental data regarding the regioselective aromatic electrophilic substitution performed by the soft electrophile (see Schemes 1 and 2). Notable is the shape of the −18 kcal/mol electrostatic potential surface for 1,6-bis(phenothiazin-10-yl)-hexane (Fig. 1b) located only on one of the phenothiazine rings suggesting that only one of the rings is subjected to a possible electrophilic attack. Indeed, experimental data show that only a monocarbaldehyde **4** is formed under the experimental conditions within this work.

The formation of a mixture of carbaldehydes **5a** and **5b** in a 1.5:1 ratio (Table 1) during the formylation of 2-chlorophenothiazine is understandable in view of the electrostatic charges (Table 3) in positions 7 (−0.213) and 3 (−0.201). The generated electrostatic potential surface (isovalue −15 kcal/mol) for 2-chloro-10*H*-phenothiazine is shown in Fig. 2b and may also suggest the slightly higher preference for the formation of **5a**. Moreover, once position 3 (or 7) is substituted, no significant negative electrostatic potential is noticed in position 7 or 3 (Fig. 2a or 2c). According to Figs. 2a and 2c further electrophilic attack is suppressed since no negative electrostatic potential in position 7 of **5a**

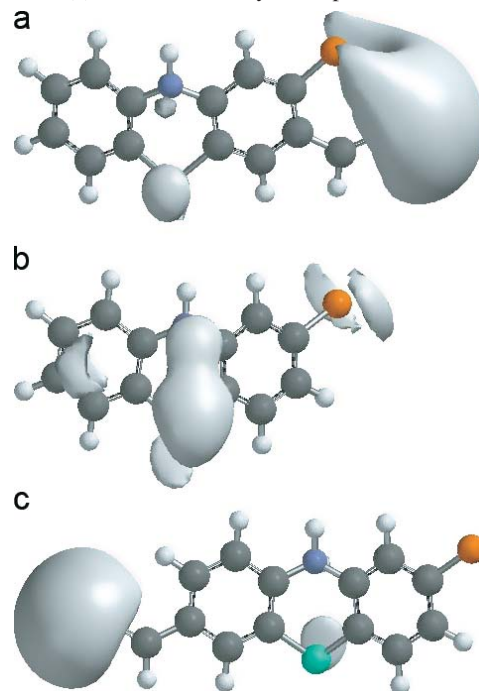
**Fig. 1.** Generated electrostatic potential (grayish envelope denotes negative electrostatic potential at isovalue  $-18$  kcal/mol) for (a) 10*H*-phenothiazine, (b) 1,6-bis(phenothiazin-10-yl)-hexane, (c) 10-methylphenothiazine, (d) 3-methyl-10*H*-phenothiazine.



(Fig. 2a), or in position 3 of **5b** (Fig. 2c) is displayed. Thus, the formation of a 3,7-dicarbaldehyde derivative of 2-chloro-10*H*-phenothiazine is not expected and the experimental procedures applied to the formylation of 2-chlorophenothiazine confirmed the theoretical hypothesis by leading only to monocarbaldehydes **5a** and **5b**.

In contrast, the experimental formation of 3,7-dicarbaldehyde (**6**) is supported by possible formylation of 2-trifluoromethyl-10*H*-phenothiazine-monocarbaldehyde intermediates. Note in Fig. 3 that negative electrostatic potential surfaces appear around the carbon atoms in position 7 of the 3-carbaldehyde intermediate (Fig. 3c) and in position 7 of the 7-carbaldehyde intermediate, respectively (Fig. 3b).

**Fig. 2.** Generated electrostatic potential (grayish envelope denotes negative electrostatic potential at isovalue  $-15$  kcal/mol); (a) 2-chloro-3-formyl-10*H*-phenothiazine (**5b**), (b) 2-chloro-10*H*-phenothiazine, (c) 2-chloro-7-formyl-10*H*-phenothiazine (**5a**).



## Conclusions

The Duff formylation reaction of phenothiazine derivatives appears for the moment as the only efficient alternative for obtaining new 10*H*-phenothiazine-3-carbaldehyde derivatives containing a free amino group able to participate in protolytic equilibria, as well as in redox processes characteristic for this heterocycle. The microwave-assisted Duff formylation reaction of phenothiazine derivatives is a technique which gives satisfactory experimental results affording good yields of 10*H*-phenothiazine-3-carbaldehyde derivatives.

The microwave-assisted acetylation reaction produced good to almost quantitative yields, in most of the experiments performed using phenothiazine substrates. Comparison of microwave-assisted synthesis with the conventional synthetic methods demonstrates advantages related to shorter reaction times and higher regioselectivity.

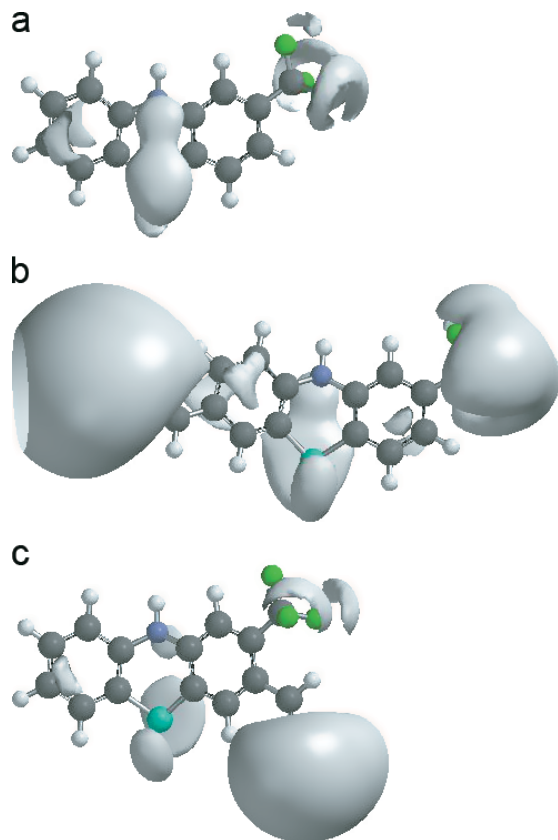
The electrostatic potential surfaces generated on the basis of 6-31G(d) B3LYP calculations support the preference for electrophilic attack and explain the regioselectivity of formylation reactions.

## Experimental section

The reactions were performed using a microwave installation Synthos 3000. Reagents from Merck were used. TLC was used to monitor the reaction progress (Merck silica gel F 254 plates). NMR spectra were recorded using a 300 MHz Bruker Avance NMR spectrometer. FTIR spectra were recorded using a Bruker Vector 22 FTIR spectrometer. Elemental analysis was carried out on a Thermo FlashEA 1112 Series instrument. The lowest-energy conformers generated



**Fig. 3.** The electrostatic potential surface (grayish envelope denotes negative electrostatic potential at isovalue  $-10$  kcal/mol); (a) 2-trifluoromethyl-10H-phenothiazine, (b) 7-formyl-2-trifluoromethyl-10H-phenothiazine, (c) 3-formyl-2-trifluoromethyl-10H-phenothiazine.



by using the MMFF force field implemented in Spartan'04 have been further fully optimized using the 6-31G(d) B3LYP hybrid DFT method.<sup>23–25</sup>

#### General procedure for microwave-assisted Duff formylation reaction of phenothiazine derivatives

The reaction mixture (5 mmol phenothiazine derivative and 7.5 mmol urotropine) dissolved in 20 mL acetic acid was introduced into the quartz reaction vessel, which was then sealed and subjected to microwave irradiation in the resonance cavity of the microwave power system. Prescribed sample temperatures were automatically monitored during the irradiation (Table 1). TLC was used to monitor the reaction progress. After irradiation, the reaction mixture was poured into water and neutralized with  $\text{Na}_2\text{CO}_3$ . Organic products were extracted in dichloromethane ( $3 \times 20$  mL). The combined organic layers were dried on anhydrous  $\text{Na}_2\text{SO}_4$  and concentrated to dryness. The product was purified by column chromatography (silica gel, toluene).

#### 10H-Phenothiazine-3-carbaldehyde (1)

Yellow precipitate recrystallized from toluene, mp  $192^\circ\text{C}$ .<sup>11,26</sup>  $^1\text{H}$  NMR (300 MHz,  $\text{CDCl}_3$ , ppm)  $\delta$ : 9.24 (s, 1H, NH), 9.64 (s, 1H, CHO), 7.50 (dd,  $^4J = 1.2$  Hz,  $^3J = 7.6$  Hz, 1H,  $\text{H}_2$ ), 7.35 (s, 1H,  $\text{H}_4$ ), 7.00 (t,  $^3J = 7.6$  Hz,  $^3J = 8$  Hz, 1H,  $\text{H}_8$ ),  $\delta$  7.90 (d,  $^3J = 8$  Hz, 1H,  $\text{H}_6$ ), 6.80 (t,  $^3J =$

8 Hz,  $^3J = 7.6$  Hz, 1H,  $\text{H}_7$ ), 6.70 (d,  $^3J = 7.6$  Hz, 1H,  $\text{H}_1$ ), 6.75 (dd,  $^3J = 8$  Hz,  $^4J = 2$  Hz, 1H,  $\text{H}_9$ ).  $^{13}\text{C}$  NMR (75.4 MHz,  $\text{CDCl}_3$ , ppm)  $\delta$ : 113.88 (CH,  $\text{C}_1$ ), 113.93 (CH,  $\text{C}_9$ ), 116.69 ( $\text{C}_{\text{quat}}$ ,  $\text{C}_{4a}$ ), 115.77 ( $\text{C}_{\text{quat}}$ ,  $\text{C}_{5a}$ ), 130.43 (CH,  $\text{C}_2$ ), 127.36 (CH,  $\text{C}_4$ ), 123.07 (CH,  $\text{C}_7$ ), 126.24 (CH,  $\text{C}_6$ ), 127.83 (CH,  $\text{C}_8$ ), 130.9 ( $\text{C}_{\text{quat}}$ ,  $\text{C}_3$ ), 139.57 ( $\text{C}_{\text{quat}}$ ,  $\text{C}_{9a}$ ), 147.12 ( $\text{C}_{\text{quat}}$ ,  $\text{C}_{10a}$ ). Anal. calcd. for  $\text{C}_{13}\text{H}_9\text{NOS}$  (227.2): C 68.70, H 3.99, N 6.16; found: C 68.62, H 3.99, N 6.09.

#### 7-Methyl-10H-phenothiazine-3-carbaldehyde (2)

$^1\text{H}$  NMR (300 MHz,  $\text{CDCl}_3$ , ppm)  $\delta$ : 2.22 (s, 3H), 6.54 (d,  $^3J = 7.5$  Hz, 1H,  $\text{H}_1$ ), 7.48 (d,  $^3J = 7.5$  Hz, 1H,  $\text{H}_2$ ), 7.44 (s, 1H,  $\text{H}_4$ ), 6.78 (s, 1H,  $\text{H}_6$ ), 9.72 (s, 1H, CHO), 6.81 (d,  $^3J = 7.7$  Hz, 1H,  $\text{H}_8$ ), 6.44 (d,  $^3J = 7.7$  Hz, 1H,  $\text{H}_9$ ), 6.04 (s, 1H, NH). Anal. calcd. for  $\text{C}_{14}\text{H}_{11}\text{NOS}$  (241.3): C 69.68, H 4.59, N 5.80; found: C 69.60, H 4.58, N 5.85.

#### 10-Methyl-10H-phenothiazine-3-carbaldehyde (3)

Yellow precipitate recrystallized from toluene, mp  $88^\circ\text{C}$ .<sup>16,27</sup>  $^1\text{H}$  NMR (300 MHz,  $\text{CDCl}_3$ , ppm)  $\delta$ : 9.80 (s, 1H, CHO), 7.65 (dd,  $^4J = 2$  Hz,  $^3J = 8.4$  Hz, 1H,  $\text{H}_2$ ), 7.59 (d,  $^4J = 2$  Hz, 1H,  $\text{H}_4$ ), 7.18 (td,  $^4J = 1.4$  Hz,  $^3J = 8.4$  Hz, 1H,  $\text{H}_8$ ), 7.12 (dd,  $^4J = 1.4$  Hz,  $^3J = 7.6$  Hz, 1H,  $\text{H}_6$ ), 6.98 (t,  $^3J = 7.6$  Hz,  $^3J = 8.4$  Hz, 1H,  $\text{H}_7$ ), 6.85 (d,  $^3J = 8.4$  Hz, 1H,  $\text{H}_1$ ), 6.84 (d,  $^3J = 8$  Hz, 1H,  $\text{H}_9$ ), 3.42 (s, 3H).  $^{13}\text{C}$  NMR (75.4 MHz,  $\text{CDCl}_3$ , ppm)  $\delta$ : 35.84 ( $\text{CH}_3$ ), 113.72 (CH,  $\text{C}_1$ ), 114.78 (CH,  $\text{C}_9$ ), 131.16 (CH,  $\text{C}_3$ ), 123.98 ( $\text{C}_{\text{quat}}$ ,  $\text{C}_{4a}$ ), 122.53 ( $\text{C}_{\text{quat}}$ ,  $\text{C}_{5a}$ ), 130.48 (CH,  $\text{C}_2$ ), 127.96 (CH,  $\text{C}_4$ ), 123.64 (CH,  $\text{C}_7$ ), 127.31 (CH,  $\text{C}_6$ ), 127.78 (CH,  $\text{C}_8$ ), 144.09 ( $\text{C}_{\text{quat}}$ ,  $\text{C}_{9a}$ ), 151.10 ( $\text{C}_{\text{quat}}$ ,  $\text{C}_{10a}$ ). Anal. calcd. for  $\text{C}_{14}\text{H}_{11}\text{NOS}$  (241.3): C 69.68, H 4.59, N 5.80; found: C 69.59, H 4.58, N 5.87.

#### 10-(6-(10H-Phenothiazin-10-yl)hexyl)-10H-phenothiazine-3-carbaldehyde (4)

Yellow precipitate recrystallized from toluene, mp  $98^\circ\text{C}$ .<sup>28</sup>  $^1\text{H}$  NMR (300 MHz,  $\text{CDCl}_3$ , ppm)  $\delta$ : 3.85 (t, 4H), 1.79 (m, 4H), 1.46 (m, 4H), 9.80 (s, 1H), 6.86 (m, 4H,  $\text{H}_{1,9}$ ), 6.92 (td, 2H,  $\text{H}_7$ ), 6.97 (td, 1H,  $\text{H}_7$ ), 7.11 (dd, 1H,  $\text{H}_6$ ), 7.15 (m, 5H,  $\text{H}_{6',8,8'}$ ), 7.58 (dd, 1H,  $\text{H}_4$ ), 7.62 (dd, 1H,  $\text{H}_2$ ).  $^{13}\text{C}$  NMR (75.4 MHz,  $\text{CDCl}_3$ )  $\delta$ : 26.73 ( $\text{CH}_2$ ), 26.77 ( $\text{CH}_2$ ), 26.99 ( $\text{CH}_2$ ), 27.07 ( $\text{CH}_2$ ), 47.41 ( $\text{CH}_2$ ), 48.10 ( $\text{CH}_2$ ), 115.29 (CH,  $\text{C}_1$ ), 115.90 (2CH,  $\text{C}_{1',9'}$ ), 116.44 (CH,  $\text{C}_9$ ), 122.83 (2 $\text{C}_{\text{quat}}$ ,  $\text{C}_{4a}$ ), 124.01 ( $\text{C}_{\text{quat}}$ ,  $\text{C}_{5a}$ ), 124.38 (CH,  $\text{C}_7$ ), 125.60 ( $\text{C}_{\text{quat}}$ ,  $\text{C}_{4a}$ ), 127.60 (2CH,  $\text{C}_{2',8'}$ ), 127.91 (2CH,  $\text{C}_{4',6'}$ ), 127.98 (CH,  $\text{C}_6$ ), 128.00 (CH,  $\text{C}_4$ ), 128.82 (CH,  $\text{C}_8$ ), 130.0 (CH,  $\text{C}_2$ ), 131.50 (CH,  $\text{C}_3$ ), 143.84 (2 $\text{C}_{\text{quat}}$ ,  $\text{C}_{9a}$ ), 145.70 ( $\text{C}_{\text{quat}}$ ,  $\text{C}_{9a}$ ), 151.14 ( $\text{C}_{\text{quat}}$ ,  $\text{C}_{10a}$ ), 190.40 (CH, CHO). Anal. calcd. for  $\text{C}_{31}\text{H}_{28}\text{N}_2\text{OS}_2$  (508.6) C 73.20, H 5.55, N 5.51, found: C 73.18, H 5.55, N 5.61.

#### 8-Chloro-10H-phenothiazine-3-carbaldehyde (5a)

Yellow precipitate recrystallized from toluene, mp  $195^\circ\text{C}$ .  $^1\text{H}$  NMR (300 MHz,  $\text{CDCl}_3$ , ppm)  $\delta$ : 9.65 (s, 1H, CHO), 7.51 (dd,  $^3J = 8.4$  Hz,  $^4J = 1.6$  Hz, 1H,  $\text{H}_2$ ), 7.37 (d,  $^4J = 1.6$  Hz, 1H,  $\text{H}_4$ ), 6.92 (d,  $^3J = 8.4$  Hz, 1H,  $\text{H}_6$ ), 6.84 (dd,  $^3J = 8.4$  Hz,  $^4J = 2$  Hz, 1H,  $\text{H}_7$ ), 6.73 (d,  $^3J = 8.4$  Hz, 1H,  $\text{H}_1$ ), 6.71 (d,  $^4J = 2$  Hz, 1H,  $\text{H}_9$ ).  $^{13}\text{C}$  NMR (75.4 MHz,  $\text{CDCl}_3$ , ppm)  $\delta$ : 114.59 (CH,  $\text{C}_1$ ), 114.49 (CH,  $\text{C}_9$ ), 122.76 (CH,  $\text{C}_7$ ), 127.63 (CH,  $\text{C}_6$ ), 124.74 (CH,  $\text{C}_2$ ), 130.78 (CH,  $\text{C}_4$ ), 190.39 (CH, CHO), 115.19 ( $\text{C}_{\text{quat}}$ ,  $\text{C}_{5a}$ ), 116.82 ( $\text{C}_{\text{quat}}$ ,  $\text{C}_{5a}$ ), 132.28 ( $\text{C}_{\text{quat}}$ ,  $\text{C}_8$ ), 131.15 ( $\text{C}_{\text{quat}}$ ,  $\text{C}_3$ ),

141.24 (C<sub>quat</sub>, C<sub>9a</sub>), 146.35 (C<sub>quat</sub>, C<sub>10a</sub>). Anal. calcd. for C<sub>13</sub>H<sub>8</sub>CINOS (261.7): C 59.66, H 3.08, N 5.35; found: C 59.59, H 3.08, N 5.38.

### 2-Chloro-10H-phenothiazine-3-carbaldehyde (5b)

Brown precipitate recrystallized from toluene, mp 224 °C. <sup>1</sup>H NMR (300 MHz, CDCl<sub>3</sub>, ppm) δ: 9.42 (s, 1H, NH), 9.96 (s, 1H, CHO), 7.27 (s, 1H, H<sub>4</sub>), 7.01 (t, <sup>3</sup>J = 7.2 Hz, <sup>3</sup>J = 8 Hz, 1H, H<sub>8</sub>), 6.91 (d, <sup>3</sup>J = 7.6 Hz, 1H, H<sub>6</sub>), 6.83 (t, <sup>3</sup>J = 7.6 Hz, <sup>3</sup>J = 7.2 Hz, 1H, H<sub>7</sub>), 6.66 (m, 2H, H<sub>1,9</sub>). <sup>13</sup>C NMR (75.4 MHz, CDCl<sub>3</sub>, ppm) δ: 113.64 (CH, C<sub>9</sub>), 115.09 (C<sub>quat</sub>, C<sub>5a</sub>), 115.93 (CH, C<sub>1</sub>), 115.26 (C<sub>quat</sub>, C<sub>4a</sub>), 123.29 (CH, C<sub>7</sub>), 125.18 (CH, C<sub>6</sub>), 126.03 (CH, C<sub>8</sub>), 126.28 (CH, C<sub>4</sub>), 127.69 (C<sub>quat</sub>, C<sub>3</sub>), 136.35 (C<sub>quat</sub>, C<sub>2</sub>), 138.01 (C<sub>quat</sub>, C<sub>9a</sub>), 147.16 (C<sub>quat</sub>, C<sub>10a</sub>), 186.27 (CH, CHO). Anal. calcd. for C<sub>13</sub>H<sub>8</sub>CINOS (261.7): C 59.66, H 3.08, N 5.35; found: C 59.59, H 3.08, N 5.38.

### 2-(Trifluoromethyl)-10H-phenothiazine-3,7-dicarbaldehyde (6)

<sup>1</sup>H NMR (300MHz, CDCl<sub>3</sub>, ppm) δ: 9.42 (s, 1H, NH), 9.96 (s, 1H, CHO), 10.35 (s, 1H, CHO), 7.39 (s, 1H, H<sub>4</sub>), 7.54 (dd, <sup>3</sup>J = 7.2 Hz, <sup>4</sup>J = 1.2 Hz 1H, H<sub>8</sub>), 7.46 (d, <sup>2</sup>J = 1.2 Hz, 1H, H<sub>6</sub>), 7.06 (s, 1H, H<sub>1</sub>), 7.39 (d, <sup>3</sup>J = 7.2 Hz, 1H, H<sub>9</sub>). <sup>13</sup>C NMR (75.4 MHz, CDCl<sub>3</sub>, ppm) δ: 115.95 (CH, C<sub>1</sub>), 120.64 (CH, C<sub>9</sub>), 118.09 (C<sub>quat</sub>, C<sub>5a</sub>), 122.26 (C<sub>quat</sub>, C<sub>4a</sub>), 131.29 (C<sub>quat</sub>, C<sub>7</sub>), 130.18 (CH, C<sub>6</sub>), 129.03 (CH, C<sub>8</sub>), 131.28 (CH, C<sub>4</sub>), 121.69 (C<sub>quat</sub>, C<sub>3</sub>), 128.35 (C<sub>quat</sub>, C<sub>2</sub>), 148.01 (C<sub>quat</sub>, C<sub>9a</sub>), 148.16 (C<sub>quat</sub>, C<sub>10a</sub>), 190.27 (CH, CHO), 191.34 (CH, CHO). Anal. calcd. for C<sub>15</sub>H<sub>8</sub>F<sub>3</sub>NO<sub>2</sub>S (323.2): C 55.73, H 2.49, N 4.33; found: C 55.69, H 2.49, N 4.42.

### General procedure for microwave-assisted acetylation reaction of phenothiazine derivatives

The reaction mixture (phenothiazine derivative – acetic anhydride ratio 1:10 and phosphoric acid in catalytic amounts) was introduced into the quartz reaction vessel, which was then sealed and subjected to microwave irradiation in the resonance cavity of the microwave power system. Prescribed sample temperatures were automatically monitored during the irradiation (Table 2). TLC was used to monitor the reaction progress. After irradiation, the reaction mixture was poured on ice and neutralized. The precipitate formed was filtered and thoroughly washed with water. The product was purified by recrystallization in toluene.

### 1-(10H-Phenothiazine-10-yl)ethanone (10-acetyl-10Hphenothiazine) (7)

White crystals recrystallized from toluene, mp 199 °C.<sup>29</sup> <sup>1</sup>H NMR (300 MHz, CDCl<sub>3</sub>, ppm) δ: 2.13 (s, 3H, CH<sub>3</sub>), 7.62 (d, <sup>3</sup>J = 8 Hz, 2H, H<sub>1,9</sub>), 7.40 (t, <sup>3</sup>J = 8 Hz, 2H, H<sub>2,8</sub>), 7.31 (t, <sup>3</sup>J = 7.2 Hz, <sup>3</sup>J = 7.6 Hz, 2H, H<sub>3,7</sub>), 7.56 (d, <sup>3</sup>J = 7.6 Hz, 2H, H<sub>4,6</sub>). <sup>13</sup>C NMR (CDCl<sub>3</sub>, ppm) δ: 127.93 (CH, C<sub>1</sub>), 126.95 (CH, C<sub>2</sub>), 126.67 (CH, C<sub>3</sub>), 127.17 (C<sub>quat</sub>, C<sub>5a</sub>), 22.39 (CH<sub>3</sub>), 169.27 (C<sub>quat</sub>, CO), 138.94 (C<sub>quat</sub>, C<sub>10a</sub>). Anal. calcd. for C<sub>14</sub>H<sub>11</sub>NOS (241.3): C 69.68, H 4.59, N 5.80; found: C 69.56, H 4.59, N 5.85.

### 1-(2-Chloro-10H-phenothiazine-10-yl)ethanone (10-acetyl-2-chloro-10Hphenothiazine) (8)

White precipitate recrystallized from toluene, mp 104 °C.<sup>30</sup> <sup>1</sup>H NMR (300 MHz, CDCl<sub>3</sub>, ppm) δ: 2.13 (s, 3H,

CH<sub>3</sub>), 7.47 (d, 1H, H<sub>1</sub>, <sup>4</sup>J = 1.6 Hz), 7.36 (t, 1H, H<sub>8</sub>, <sup>3</sup>J = 7.6 Hz), 7.35 (dd, 1H, H<sub>4</sub>, <sup>3</sup>J = 7.6 Hz), 7.26 (m, 2H, H<sub>3,6</sub>), 7.17 (td, 1H, H<sub>7</sub>, <sup>4</sup>J = 1.6 Hz, <sup>3</sup>J = 7.6 Hz), 7.13 (dd, 1H, H<sub>9</sub>, <sup>4</sup>J = 2 Hz, <sup>3</sup>J = 8.4 Hz). <sup>13</sup>C NMR (CDCl<sub>3</sub>, ppm) δ: 22.98 (CH<sub>3</sub>), 169.07 (C=O), 132.57 (CH, C<sub>2</sub>), 139.87 (C<sub>quat</sub>, C<sub>10a</sub>), 138.60 (C<sub>quat</sub>, C<sub>9a</sub>), 127.54 (C<sub>quat</sub>), 127.09 (2CH), 128.45 (CH), 128.06 (CH), 127.27 (CH, C), 127.96 (CH, C). Anal. calcd. for C<sub>14</sub>H<sub>10</sub>CINOS (275.7): C 69.98, H 3.66, N 5.08; found: C 69.89, H 3.66, N 5.19.

### 1-(2-(Trifluoromethyl)-10H-phenothiazine-10-yl)ethanone (9)

<sup>1</sup>H NMR (300 MHz, CDCl<sub>3</sub>, ppm) δ: 2.21 (s, 3H, CH<sub>3</sub>), 7.81 (s, 1H, H<sub>1</sub>), 7.25 (td, 1H, H<sub>7</sub>, <sup>3</sup>J = 7.6 Hz, <sup>3</sup>J = 7.7 Hz, <sup>4</sup>J = 1.6 Hz), 7.34 (td, 1H, H<sub>8</sub>, <sup>3</sup>J = 8 Hz, <sup>3</sup>J = 7.7 Hz, <sup>4</sup>J = 1.6 Hz), 7.51 (d, 1H, H<sub>4</sub>, <sup>3</sup>J = 8.4 Hz), 7.46 (m, 2H, H<sub>4,9</sub>). <sup>13</sup>C NMR (CDCl<sub>3</sub>, ppm) δ: 22.88 (CH<sub>3</sub>), 169.13 (C=O), 129.49 (CH, C<sub>2</sub>), 123.45 (C<sub>quat</sub>, CF<sub>3</sub>), 124.46 (C<sub>quat</sub>), 125.10 (C<sub>quat</sub>), 139.05 (C<sub>quat</sub>, C<sub>10a</sub>), 138.42 (C<sub>quat</sub>, C<sub>9a</sub>), 127.09 (CH), 127.31 (2 CH), 127.57 (2 CH), 128.12 (CH), 128.17 (CH). Anal. calcd. for C<sub>15</sub>H<sub>10</sub>F<sub>3</sub>NOS (309.3): C 58.25, H 3.26, N 4.53; found: C 58.14, H 3.26, N 4.61.

### 1-(10-Methyl-10H-phenothiazine-3yl)ethanone (10)

Recrystallized from toluene, mp 101 °C.<sup>21</sup> <sup>1</sup>H NMR (300 MHz, CDCl<sub>3</sub>, ppm) δ: 2.51 (s, 3H, CH<sub>3</sub>), 3.39 (s, 3H, H<sub>3</sub>C), 6.7 (d, 1H, H<sub>1</sub>), 7.76 (d, <sup>3</sup>J = 8.4 Hz, 1H, H<sub>2</sub>), 7.69 (s, 1H, H<sub>4</sub>), 7.12 (d, <sup>3</sup>J = 6.7 Hz, 1H, H<sub>6</sub>), 6.97 (t, <sup>3</sup>J = 7.2 Hz, <sup>3</sup>J = 7.6 Hz, 1H, H<sub>7</sub>), 7.17 (t, <sup>3</sup>J = 7.6 Hz, 1H, H<sub>8</sub>), 6.82 (d, <sup>3</sup>J = 7.6 Hz, 1H, H<sub>9</sub>). <sup>13</sup>C NMR (CDCl<sub>3</sub>, ppm) δ: 35.62 (CH<sub>3</sub>), 26.22 (CH<sub>3</sub>), 113.31 (CH, C<sub>1</sub>), 128.77 (CH, C<sub>2</sub>), 131.58 (CH, C<sub>3</sub>), 123.19 (C<sub>quat</sub>, C<sub>4a</sub>), 122.63 (C<sub>quat</sub>, C<sub>5a</sub>), 127.23 (CH, C<sub>6</sub>), 123.33 (CH, C<sub>7</sub>), 127.30 (CH, C<sub>8</sub>), 114.53 (CH, C<sub>9</sub>), 127.66 (CH, C<sub>4</sub>), 144.46 (C<sub>quat</sub>, C<sub>9a</sub>), 149.85 (C<sub>quat</sub>, C<sub>10a</sub>). Anal. calcd. for C<sub>15</sub>H<sub>13</sub>NOS (255.3): C 70.56, H 5.13, N 5.49; found: C 70.46, H 5.13, N 5.55.

### 1,1'-(10-Methyl-10H-phenothiazine-3,7-diyl)diethanone (11)

Yellow-green precipitate recrystallized from toluene (64 % yield), mp 202 °C.<sup>31</sup> <sup>1</sup>H NMR (300 MHz, CDCl<sub>3</sub>, ppm) δ: 2.54 (s, 6H, CH<sub>3</sub>), 3.46 (s, 3H, CH<sub>3</sub>), 6.84 (d, <sup>2</sup>J = 10 Hz, 2H, H<sub>1,9</sub>), 7.70 (s, 2H, H<sub>4,6</sub>), 7.79 (d, <sup>2</sup>J = 10 Hz, 2H, H<sub>2,8</sub>). <sup>13</sup>C NMR (CDCl<sub>3</sub>, ppm) δ: 26.7 (CH<sub>3</sub>), 36.4 (CH<sub>3</sub>), 114.4 (CH, C<sub>1,9</sub>), 123.3 (C<sub>quat</sub>, C<sub>4a</sub>), 127.8 (CH, C<sub>4,6</sub>), 129.1 (CH, C<sub>2,8</sub>), 132.9 (C<sub>quat</sub>, C<sub>3,7</sub>), 148.9 (C<sub>quat</sub>, C<sub>9a</sub>), 196.4 (C<sub>quat</sub>, CO). Anal. calcd. for C<sub>17</sub>H<sub>15</sub>NO<sub>2</sub>S (297.3): C 68.66, H 5.08, N 4.71; found: C 68.59, H 5.08, N 4.78.

### Acknowledgments

The authors thank the Romanian Government for financial support (grant ID\_564).

### References

- (1) *Microwaves in Organic Chemistry*; Loupy, A., Ed.; Wiley-VCH: Weinheim, 2002.
- (2) *Microwave-assisted Organic Synthesis*; Lidstrom, P.; Tierney, J. P., Eds.; Blackwell: Oxford, 2004.
- (3) Lidstrom, P.; Tierney, J.; Wathey, B.; Westman, J. *Tetrahedron* **2001**, 57 (45), 9225. doi:10.1016/S0040-4020(01)00906-1.

- (4) Kappe, C. O. *Angew. Chem.* **2004**, *43* (46), 6250. doi:10.1002/anie.200400655.
- (5) Dallinger, D.; Kappe, C. O. *Chem. Rev.* **2007**, *107* (6), 2653.
- (6) Gedye, R.; Smith, F.; Westaway, K.; Ali, H.; Baldisera, L.; Laberge, L.; Roussel, J. *Tetrahedron Lett.* **1986**, *27* (38), 279. doi:10.1016/S0040-4039(00)83996-9.
- (7) Giguere, R. J.; Bray, T. L.; Duncan, S. M.; Majetich, G. *Tetrahedron Lett.* **1986**, *27* (41), 4945. doi:10.1016/S0040-4039(00)85103-5.
- (8) Filip, S. V.; Silberg, I. A.; Surducian, E.; Vlassa, M.; Surducian, V. *Synth. Commun.* **1998**, *28* (2), 337. doi:10.1080/00397919808005727.
- (9) Porumb, D.; Cristea, C.; Silberg, I. A. *Studia UBB Ser. Chem. XLVII* **2002**, 1–2, 45.
- (10) Mayer, M.; Lang, P. T.; Gerber, S.; Madrid, P. B.; Pinto, I. G.; Guy, R. K.; James, T. L. *Chem. Biol.* **2006**, *13* (9), 993. doi:10.1016/j.chembiol.2006.07.009. PMID:16984889.
- (11) Găină, L.; Cristea, C.; Moldovan, C.; Porumb, D.; Surducian, E.; Deleanu, C.; Mahamoud, A.; Barbe, J.; Silberg, I. A. *Int. J. Mol. Sci.* **2007**, *8* (2), 70. doi:10.3390/i8020070.
- (12) Bodea, C.; Silberg, I. A. *Adv. Heterocycl. Chem.* **1968**, *9*, 321. doi:10.1016/S0065-2725(08)60375-X. PMID:4872979.
- (13) Gilbert, B. C.; Hanson, P.; Norman, R. O. C.; Sutcliffe, B. T. *Chem. Commun.* (London), **1966**, 161. doi:10.1039/C19660000161.
- (14) Clarke, D.; Gilbert, B. C.; Hanson, P. J. *Chem. Soc. Perkin 2* **1977**, (4), 517. doi:10.1039/p29770000517.
- (15) Hanson, P.; Norman, R. O. C. *J. Chem. Soc. Perkin 2* **1973**, (3), 264. doi:10.1039/p29730000264.
- (16) Buu-Hoi, N. P.; Hoán, N. *J. Chem. Soc.* **1951**, 1834. doi:10.1039/jr9510001834.
- (17) Bergman, J.; Renström, L.; Sjöberg, B. *Tetrahedron* **1980**, *36* (17), 2505. doi:10.1016/0040-4020(80)80230-4.
- (18) (a) Duff, J. C. *J. Chem. Soc.* **1941**, 547. doi:10.1039/jr9410000547.; (b) Larrow, J. F.; Jacobsen, E. N.; Gao, Y.; Hong, Y.; Nie, X.; Zepp, C. M. *J. Org. Chem.* **1994**, *59* (7), 1939. doi:10.1021/jo00086a062.; (c) Petrov, O. I.; Kalcheva, V. B.; Antonova, A. T. *Collect. Czech. Chem. Commun.* **1997**, *62* (3), 494. doi:10.1135/cccc19970494.; (d) Crozet, M. P.; Sabuco, J.-F.; Tamburlin, I.; Barreau, M.; Giraud, L.; Vanelle, P. *Heterocycles* **1993**, *36*, 45. doi:10.3987/COM-92-6028.; (e) Ubeda, J. I.; Avendaño, C.; Menéndez, J. C.; Villacampa, M. *Heterocycles* **1994**, *38*, 2677. doi:10.3987/COM-01-6886.; (f) Weidner-Wells, M. A.; Fraga-Spano, S. A. *Synth. Commun.* **1996**, *26* (14), 2775. doi:10.1080/00397919608004595.; (g) Sukuzi, Y.; Takahashi, H. *Chem. Pharm. Bull. (Tokyo)* **1983**, *31*, 1751.
- (19) Hayes, B. L. *Microwave synthesis: Chemistry at the speed of light*; CEM Publishing: Matthews NC, 2002; p. 35.
- (20) (a) Bernthsen, A. *Liebigs Ann. Chem.* **1885**, *230*, 73; doi:10.1002/jlac.18852300106.; (b) Bernthsen, A. *Chem. Ber.* **1906**, *39*, 1808; (c) Asinger, J.; Thiel, M.; Kaltwasser, H. *Liebigs Ann. Chem.* **1957**, *606* (1), 67. doi:10.1002/jlac.19576060107.; (d) Asinger, J.; Thiel, M.; Usbeck, H.; Gröbe, K.-H.; Grundmann, H.; Tränkner, S. *Liebigs Ann. Chem.* **1960**, *634* (1), 144. doi:10.1002/jlac.19606340115.; (e) Stoss, P.; Satzinger, G. *Chem. Ber.* **1978**, *111* (4), 1453. doi:10.1002/cber.19781110423.
- (21) Cauquil, G.; Casadevall, A. *Bull. Soc. Chim. Fr.* **1955**, *50*, 768.
- (22) SPARTAN'06 [computer program]; Wavefunction, Inc.: Irvine, CA, 2006.
- (23) Becke, A. D. *J. Chem. Phys.* **1993**, *98* (7), 5648. doi:10.1063/1.464913.
- (24) Stephens, P. J.; Devlin, F. J.; Chabalowski, C. F.; Frisch, M. J. *J. Phys. Chem.* **1994**, *98* (45), 11623. doi:10.1021/j100096a001.
- (25) Lee, C.; Yang, W.; Parr, R. G. *Phys. Rev. B* **1988**, *37* (2), 785. doi:10.1103/PhysRevB.37.785.
- (26) (a) Shindo, K.; Ishikawa, S.; Nozoe, T. *Bull. Chem. Soc. Jpn.* **1985**, *58* (1), 165. doi:10.1246/bcsj.58.165.; (b) Costa, S. P. G.; Oliviera-Campos, A. M. F.; Ferreira, J. A.; Kirsch, G. *J. Chem. Res. (S)* **1997**, 314. doi:10.1039/a702605f.
- (27) (a) Bodea, C.; Farcasan, V.; Oprean, I. *Rev. Roum. Chim.* **1965**, *10*, 1100; (b) Akgün, E.; Tunalı, M.; Pindur, U. *Arch. Pharm. (Weinheim)* **1987**, *320* (5), 397. doi:10.1002/ardp.19873200504.; (c) Ebdrup, S. *J. Chem. Soc. Perkin Trans. I* **1998**, (6), 1147. doi:10.1039/a705813f.
- (28) Lovász, T.; Túrós, G.; Găină, L.; Csámpai, A.; Frigyes, D.; Fábıán, B.; Silberg, I. A.; Sohár, P. *J. Mol. Struct.* **2005**, *751* (1–3), 100. doi:10.1016/j.molstruc.2005.04.037.
- (29) (a) Raileanu, M. *Rev. Chim. (Bucharest)* **1983**, *34*, 113; (b) Hirata, T.; Driscoll, J. S. *J. Pharm. Sci.* **1976**, *65* (11), 1699. doi:10.1002/jps.2600651136.
- (30) (a) Kano, H.; Fujimoto, M. *Pharm. Bull.* **1957**, *5* (5), 393. PMID:13505055.; (b) Kadaba, P. K. *J. Heterocycl. Chem.* **1966**, *3* (3), 345. doi:10.1002/jhet.5570030322.; (c) Siska, M.; Clauder, O.; Ruff, F.; Magda, K.; Szegi, J. *Acta Pharm. Hung.* **1965**, *35* (6), 272. PMID:5850155.
- (31) Lai, R. Y.; Fabrizio, E. F.; Lu, L.; Jenekhe, S. A.; Bard, A. J. *J. Am. Chem. Soc.* **2001**, *123* (37), 9112. doi:10.1021/ja0102235. PMID:11552819.



# Phytochemical constituents of *Cardamine diphylla*

Sabine Montaut, René S. Bleeker, and Carine Jacques

**Abstract:** From the methanol extract of the *Cardamine diphylla* rhizome, methylethyl- (1), 2-methylbutyl- (2), 3-methylpentyl- (4), 3-indolylmethyl- (5), 1-methoxy-3-indolylmethyl- (6), 4-methoxy-3-indolylmethyl- (7) glucosinolates, and desulfo-2-methylbutylglucosinolate (3) were isolated. The structure elucidation of the compounds was performed by spectroscopic methods. The toxicity on brine shrimp larvae of the methanol extract of the *C. diphylla* rhizome was evaluated. In addition, the free-radical-scavenging activity of the crude extract was carried out by the 1,1-diphenyl-2-picrylhydrazyl (DPPH) assay.

**Key words:** Brassicaceae, *Cardamine diphylla*, aliphatic glucosinolates, indole glucosinolates, desulfoglucosinolate, *Artemia salina*, toxicity, free-radical-scavenging activity, 1,1-diphenyl-2-picrylhydrazyl (DPPH).

**Résumé :** À partir de l'extrait méthanolique du rhizome de *Cardamine diphylla*, le méthyléthyl- (1), le 2-méthylbutyl- (2), le 3-méthylpentyl- (4), le 3-indolylméthyl- (5), le 1-méthoxy-3-indolylméthyl- (6), le 4-méthoxy-3-indolylméthyl- (7) glucosinolates et le désulfo-2-méthylbutylglucosinolate (3) ont été isolés. L'élucidation de la structure des composés a été réalisée au moyen de méthodes spectroscopiques. La toxicité sur les larves de crevettes *Artémia*, de l'extrait méthanolique du rhizome de *C. diphylla*, a été évaluée. De plus, l'activité de piégeage de radicaux libres sur l'extrait brut a été réalisée avec le test au 1,1-diphényl-2-picrylhydrazyl (DPPH).

**Mots-clés :** Brassicaceae, *Cardamine diphylla*, glucosinolates aliphatiques, glucosinolates indoliques, désulfoglucosinolate, *Artemia salina*, toxicité, activité de piégeur de radicaux libres, 1,1-diphényl-2-picrylhydrazyl (DPPH).

## Introduction

*Cardamine diphylla* (Michx.) A. Wood (Brassicaceae) (syn. *Dentaria diphylla* Michx.) is a wild endemic perennial plant found in Canada (New Brunswick, Nova Scotia, Quebec, and Ontario) and in the United States of America (from Michigan to Kentucky, South Carolina to Wisconsin, Tennessee, and Pennsylvania).<sup>1</sup> This uncommon species grows in fresh to dry and sandy to loamy tolerant hardwood stands. It can also be found in moist, clayey, intolerant, mixed wood stands.<sup>2</sup> *C. diphylla* has a long root that is all in one piece and often branched. A stem with two stalked and opposite leaves grows from the root. The white flowers are followed by long upright seed pods.<sup>2</sup> This plant is commonly referred to as toothwort, crinkleroot, and pepper-root, due to the pleasant, pungent taste of the rhizome.<sup>2</sup> The North American aboriginal people ate the roots raw or cooked. The roots were used for food and medicine, and in spring, the whole plant was used for medicine.<sup>3</sup> *C. diphylla* was of great medicinal importance for several North American First Nations. For example, the Algonquin gave an infusion of the plant to children with fevers, the Cherokee gargled an infusion of the root to aid sore throats, the Delaware used an infusion of the root as a stomach remedy and as a venereal aid when combined with other plants, and the Iroquois used an infusion of

the plant as a pulmonary aid for chest pains and also as a remedy for the first stages of tuberculosis.<sup>3</sup>

Only one previous phytochemical study has been conducted on *C. diphylla*.<sup>4</sup> During this investigation, the gas chromatography (GC) analysis of the hydrolyzed products of the compounds extracted from the rhizome, shoot, and leaf showed the presence of methylethyl-, 2-butyl-, and 2-methylbutyl isothiocyanates. These assignments were confirmed by comparison with authentic standards. This information suggested that the plant contained methylethyl- (1), 2-butyl-, and 2-methylbutyl glucosinolates (GLs) (2) (Fig. 1).

GLs are plant secondary metabolites, whose general structure consists of a  $\beta$ -D-thioglucose group with a sulfonated oxime moiety and a variable side chain derived from amino acids.<sup>5</sup> Aliphatic GLs are mainly derived from methionine, alanine, leucine, or valine. Indolic GLs are derived from tryptophan.<sup>6</sup> GLs can be hydrolyzed, by the plant enzyme myrosinase (thioglucoside glucohydrolase, EC 3.2.3.147), during cell damage, to produce isothiocyanates, nitriles, epithionitriles, oxazolidine-2-thiones, and thiocyanates.<sup>7</sup> The hydrolyzed products possess several different biological activities and in particular health-promoting effects.<sup>8</sup>

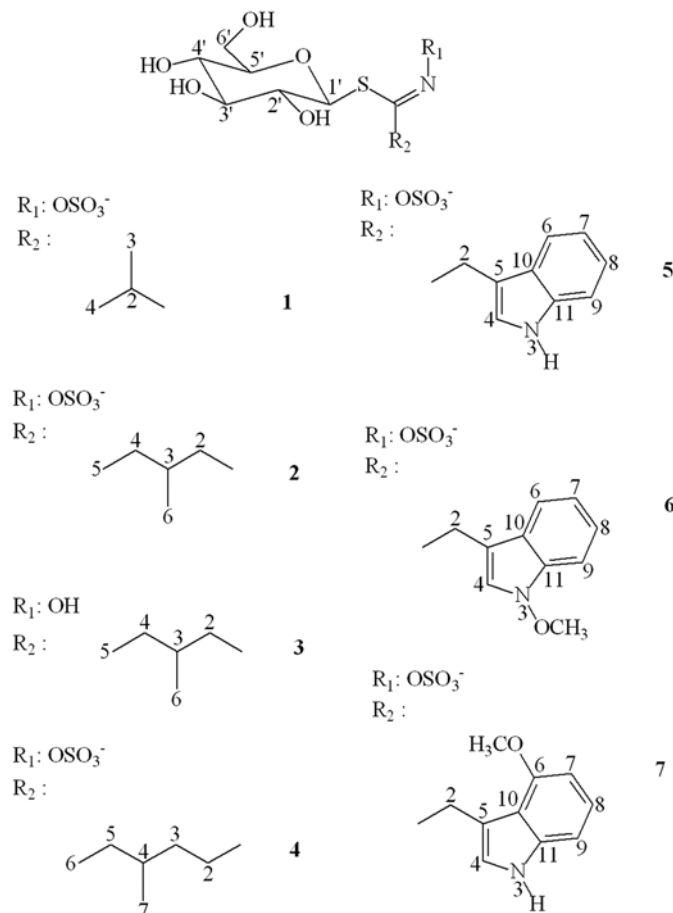
As part of our continued interest in the chemistry of the Brassicaceae, we initiated an investigation on the phytochemical content of the *C. diphylla* rhizome, probing the plant crude extract for some biological activities. This work describes the isolation and elucidation of the structure of two new intact GLs and one new desulfoGL together with four known GLs from the methanol extract of the *C. diphylla* rhizome. Furthermore, we present the results of the toxicity of the methanol extract on brine shrimp larvae and the free-radical-scavenging activity on 1,1-diphenyl-2-picrylhydrazyl (DPPH).

Received 27 July 2009. Accepted 2 October 2009. Published on the NRC Research Press Web site at canjchem.nrc.ca on 18 December 2009.

S. Montaut,<sup>1</sup> R.S. Bleeker, and C. Jacques. Department of Chemistry and Biochemistry, Laurentian University, 935 Ramsey Lake Road, Sudbury, ON P3E 2C6, Canada.

<sup>1</sup>Corresponding author (e-mail: smontaut@laurentian.ca).



**Fig. 1.** Molecular structures of compounds **1** to **7** from *C. diphylla*.

## Results and discussion

The investigation of the methanol extract of the rhizome of *C. diphylla* led to the isolation and identification of seven compounds (See the Materials and methods section).

Compound **1** was attributed to methylethylGL or isopropylGL or glucoputranjivin (**1**) (Fig. 1) by comparison of spectroscopic data (Tables 1 and 2) with published data.<sup>9</sup> The presence of compound **1** was expected because the methylthylisothiocyanate has already been detected, in this plant by GC, by Feeny and Rosenberry.<sup>4</sup> In our study, we have shown for the first time the presence of the intact GL.

Compound **2** displayed a UV spectrum characteristic of a nonaromatic compound with a  $\lambda_{\max}$  at 225 nm. From the high-resolution mass spectrum, the molecular formula C<sub>12</sub>H<sub>22</sub>NO<sub>9</sub>S<sub>2</sub> was established. FTIR absorption bands were found at 3391 (OH), 2964 (CH), 1652 (CN), 1054 (CO), 877 (sulfonic acid), and 617 (CS) cm<sup>-1</sup>. The <sup>1</sup>H NMR spectral data were indicative of the presence of two methyl groups ( $\delta_{\text{H}}$  0.85 and 0.91 ppm), two CH<sub>2</sub> groups  $\alpha$  to a stereocenter, each giving an AB coupling system ( $\delta_{\text{H}}$  A 2.47, B 2.18 and A 1.35, B 1.24 ppm) and one CH group ( $\delta_{\text{H}}$  1.86 ppm). These signals indicated that **2** possessed a branched aliphatic chain. In addition, signals attributable to a glucose unit were observed (Table 1). The doublet of the anomeric proton, H-1', at 4.57 ppm, with a coupling constant of 10.2 Hz, was assigned to a  $\beta$ -linked glucopyranosyl moiety.<sup>10</sup> The assignment of carbons and protons, achieved

by HMBC and HMQC 2D shift correlations, led us to propose that compound **2** was 2-methylbutylGL (Fig. 1). The presence of this GL was also expected because Feeny and Rosenberry<sup>4</sup> had already detected 2-methylbutylisothiocyanate, by GC, in this plant. This is the first time that the intact GL has been isolated from *C. diphylla*. In addition, we report for the first time the spectroscopic data of this intact GL.

The UV and FTIR spectroscopic data obtained for compound **3** were similar to that observed for compound **2**, which indicated that they had similar structures. The high-resolution mass spectrum suggested that the molecular formula was C<sub>12</sub>H<sub>22</sub>NO<sub>6</sub>S. The difference between the masses of **2** and **3** was 80 amu, which was consistent with **3** being the desulfo-2-methylbutylGL. As in the case of **2**, the <sup>1</sup>H NMR spectrum exhibited the presence of two methyl groups ( $\delta_{\text{H}}$  0.92 and 0.95 ppm), two CH<sub>2</sub> groups  $\alpha$  to a stereocenter, each giving an AB coupling system ( $\delta_{\text{H}}$  A 2.59, B 2.41 and A 1.46, B 1.21 ppm), and one CH group ( $\delta_{\text{H}}$  1.87 ppm). These signals indicated that **3** possessed a branched aliphatic chain. In addition, signals attributable to a glucose unit were observed (Table 1).<sup>10</sup> The coupling constant of 9.8 Hz determined from the doublet of the anomeric proton, H-1', at 4.98 ppm, was indicative of a  $\beta$ -linked glucopyranosyl moiety.<sup>10</sup> Support for **3** being a desulfoGL came from the <sup>13</sup>C NMR spectrum. The chemical shifts for the C-1 of desulfoGLs reported in the literature have been found between 155.3 to 156.3 ppm.<sup>11</sup> We observed a  $\delta_{\text{C}}$  at 156.0 ppm (Table 2), which was in this range. The assignment of carbons and protons, using HMBC and HMQC 2D shift correlations confirmed that compound **3** was desulfo-2-methylbutylGL (Fig. 1). It is the first time that this compound has been isolated from *C. diphylla* and we report for the first time the spectroscopic data of this desulfoGL. Moreover, it is worth noting that desulfoGLs are not common naturally occurring products in plants.<sup>12</sup> In addition, this metabolite seems to be the biosynthetic precursor of 2-methylbutylGL (**2**).<sup>6</sup>

The UV spectrum and IR data of **4** indicated that the metabolite was also an aliphatic GL. From the high-resolution mass spectrum, the molecular formula C<sub>13</sub>H<sub>24</sub>NO<sub>9</sub>S<sub>2</sub> was established. The difference between the masses of **2** and **4** was 14 amu, which corresponded to one CH<sub>2</sub> group. The <sup>1</sup>H NMR spectrum exhibited the presence of two methyl groups ( $\delta_{\text{H}}$  0.78 and 0.82 ppm), three CH<sub>2</sub> groups, two of them each giving an AB coupling system because they were  $\alpha$  to a stereocenter ( $\delta_{\text{H}}$  A 1.61, B 1.46 and A 1.29, B 1.10 ppm), and one CH group ( $\delta_{\text{H}}$  1.36 ppm). These signals indicated that **4** possessed a branched aliphatic chain. In addition, signals attributable to a  $\beta$ -linked glucopyranosyl moiety (Table 1) were observed.<sup>10</sup> The assignment of carbons and protons, using HMBC and HMQC 2D shift correlations, suggested that compound **4** was 3-methylpentylGL (Fig. 1). It is the first time that this intact GL has been isolated from a plant in the *Cardamine* genus. The structure of this branched-chain GL, previously found in *Coiccyia*, *Erucas-trum*, and *Hirshfeldia* genera, was inferred from the mass and partial <sup>1</sup>H NMR spectroscopic data of the desulfo-3-methylpentylGL obtained by sulfatase treatment of native GLs in extracts.<sup>11</sup> We report for the first time all the spectroscopic data of this intact GL.

**Table 1.** <sup>1</sup>H NMR spectroscopic data of compounds **1** to **7** from the rhizome of *C. diphylla* in D<sub>2</sub>O.

	<b>1<sup>a</sup></b>	<b>2<sup>a</sup></b>	<b>3<sup>b</sup></b>	<b>4<sup>a</sup></b>	<b>5<sup>a</sup></b>	<b>6<sup>b</sup></b>	<b>7<sup>b</sup></b>
<b>Glucose</b>							
1'	4.95 d (9.9)	4.57 d (10.2)	4.98 d (9.8)	4.90 d (9.5)	4.49 d (10.0)	4.76 <sup>c</sup>	4.83 <sup>c</sup>
2'	3.35 t (9.3)	3.58 m	3.46 m	3.36 m	3.19 m	3.33 t (9.5)	3.37 m
3'	3.47 m	3.49 m	3.56 m	3.45 m	3.10 m	3.23 t (9.4)	3.18 t (8.8)
4'	3.38 t (9.3)	3.38 m	3.49 m	3.38 m	3.25 m	3.38 t (9.1)	3.40 m
5'	3.45 m	3.52 m	3.57 m	3.44 m	2.87 m	3.02 m	2.98 m
6'	3.79 d (12.8)	3.90 d (12.6)	3.91 dd (12.7, 1.5)	3.80 d (13.3)	3.47 d (3.4)	3.58 d (3.8)	3.47 d (12.4)
	3.63 dd (12.8, 5.5)	3.72 dd (12.6, 5.7)	3.74 dd (12.7, 5.2)	3.62 dd (13.3, 5.5)			
<b>Aliphatic</b>							
2	2.91 sept (6.9)	2.47 m	2.59 dd (14.9, 7.1)	2.62 m	—	—	—
		2.18 dd (14.0, 6.3)	2.41 dd (14.9, 7.5)				
3	1.20 d (6.6)	1.86 m	1.87 m	1.61 m	—	—	—
				1.46 m			
4	1.19 d (6.4)	1.35 m	1.46 m	1.36 m	—	—	—
		1.24 m	1.21 m				
5	—	0.85 t (6.9)	0.92 t (7.4)	1.29 m	—	—	—
				1.10 m			
6	—	0.91 d (6.8)	0.95 d (6.7)	0.78 t (7.9)	—	—	—
7	—	—	—	0.82 d (8.5)	—	—	—
<b>Indolic</b>							
2	—	—	—	—	4.17 d (16.2)	4.27 d (16.7)	4.47 d (16.4)
					4.08 d (16.2)	4.19 d (16.7)	4.40 d (16.4)
4	—	—	—	—	7.25 s	7.56 s	7.19 s
6	—	—	—	—	7.66 d (8.3)	7.79 d (8.2)	—
7	—	—	—	—	7.11 t (7.7)	7.26 t (7.4)	6.69 d (7.3)
8	—	—	—	—	7.18 t (7.7)	7.39 t (7.6)	7.25 t (7.3)
9	—	—	—	—	7.44 d (8.4)	7.60 d (8.2)	7.21 m
CH <sub>3</sub> O—	—	—	—	—	—	4.13 s	3.98 s

<sup>a</sup>600 MHz. Coupling constant (*J* in Hz) in parentheses. s = singlet; d = doublet; t = triplet, sept = septet, dd = doublet of doublets; m = multiplet.<sup>b</sup>500 MHz. Coupling constant (*J* in Hz) in parentheses. s = singlet; d = doublet; t = triplet, sept = septet, dd = doublet of doublets; m = multiplet.<sup>c</sup>Partially under solvent peak.

Despite the fact that Feeny and Rosenberry<sup>4</sup> detected 2-butylisothiocyanate in *C. diphylla*, which would indicate that 2-butylGL was present in the plant, we were not able to detect this GL in our extract. This may be attributed to genetic, climatic, and soil differences.

Compounds **5–7** were identified as 3-indolylmethylGL or glucobrassicin (**5**), 1-methoxy-3-indolylmethylGL or neoglucobrassicin (**6**), and 4-methoxy-3-indolylmethylGL or 4-methoxyglucobrassicin (**7**) (Fig. 1), respectively, by comparison of spectroscopic data (Tables 1 and 2) with published data for intact GLs<sup>13,14</sup> and desulfoGLs.<sup>15</sup> Desulfo **5** and **7** have been detected previously in 10–15 day-old seedlings of *C. chenopodiifolia* Pers. by HPLC analysis of desulfoGLs.<sup>16</sup> In addition, desulfo **7** has been detected in leaves of *C. amara* L. by HPLC and LC–MS analysis of desulfoGLs.<sup>17</sup> Nevertheless, it is the first time that the intact GLs **5–7** were isolated from the *Cardamine* genus. We report for the first time the <sup>13</sup>C NMR, IR, and optical rotation data of intact **6** and the <sup>13</sup>C NMR and IR data of intact **7**. The occurrence of **5–7** in *C. diphylla* is very significant because **5** and the mixture of **5–7** have been shown to induce an increase in the CYP1A protein (phase I enzyme involved in detoxification of chemical carcinogens) levels and activities in rats.<sup>18</sup> However, no study has probed the potential of aliphatic GLs for health benefits.

The brine shrimp lethality test showed that the crude ex-

tract of *C. diphylla* was inactive against *Artemia salina* larvae at the tested concentrations (10, 100, and 1000 ppm).

The half-maximal scavenging concentration, SC<sub>50</sub>, of the methanolic crude extract of *C. diphylla*, in the DPPH assay, was 766 µg/mL (±3 µg/mL). The extract did not seem to exhibit strong free-radical-scavenging capabilities compared to ascorbic acid that showed a half-maximal scavenging concentration, SC<sub>50</sub>, of 7 µg/mL (±2 µg/mL) under our experimental conditions.

Bioassays on the effects of *C. diphylla* crude extract on phase I and phase II enzymes should be investigated to evaluate the potential effect of this wild crucifer in cancer chemoprevention.

## Materials and methods

### General experimental procedures

All solvents were ACS (American Chemical Society) grade and used as such, except for CHCl<sub>3</sub>, which was redistilled. All deuterated solvents were purchased from Cambridge Isotopes Laboratories, Inc. (Andover, MA). DMSO (dimethyl sulfoxide), ascorbic acid (reagent grade), and DPPH were purchased from Sigma-Aldrich (Oakville, ON). Formic acid was purchased from BDH (Toronto, ON). HPLC-grade MeOH, Et<sub>3</sub>N (reagent grade), and thymol were purchased from Fisher Scientific (Whitby, ON). HPLC-

**Table 2.**  $^{13}\text{C}$  NMR spectroscopic data of compounds **1** to **7** from the rhizome of *C. diphylla* in  $\text{D}_2\text{O}$ .

	<b>1<sup>a</sup></b>	<b>2<sup>a</sup></b>	<b>3<sup>b</sup></b>	<b>4<sup>a</sup></b>	<b>5<sup>a</sup></b>	<b>6<sup>b</sup></b>	<b>7<sup>b</sup></b>
<b>Glucose</b>							
1'	81.9	89.3	81.8	81.9	81.4	81.5	81.9
2'	72.0	69.5	72.2	71.8	71.7	71.8	74.3
3'	77.0	76.9	77.1	77.1	76.9	76.9	75.8
4'	69.1	69.1	69.1	69.0	68.6	68.6	68.3
5'	80.0	80.2	80.2	80.2	80.2	79.9	79.9
6'	60.4	60.7	60.6	60.5	60.1	60.2	60.8
1	168.6	173.0	156.0	165.3	163.1	162.6	164.0
<b>Aliphatic</b>							
2	32.6	41.1	38.9	30.1	—	—	—
3	19.9	31.9	32.6	33.6 <sup>c</sup>	—	—	—
4	21.2	28.7	28.4	33.5 <sup>c</sup>	—	—	—
5	—	10.5	10.5	28.3	—	—	—
6	—	18.2	18.1	10.6	—	—	—
7	—	—	—	18.3	—	—	—
<b>Indolic</b>							
2	—	—	—	—	29.3	29.0	30.1
4	—	—	—	—	124.1	122.8	122.9
5	—	—	—	—	108.1	105.3	108.9
6	—	—	—	—	118.4	119.0	153.8
7	—	—	—	—	119.6	120.4	100.0
8	—	—	—	—	122.2	123.1	123.1
9	—	—	—	—	112.0	108.8	105.5
10	—	—	—	—	126.1	122.7	118.7
11	—	—	—	—	136.2	132.3	137.8
CH <sub>3</sub> O—	—	—	—	—	—	66.0	55.2

<sup>a</sup>150 MHz.<sup>b</sup>125 MHz.<sup>c</sup>Superimposable.

grade  $\text{H}_2\text{O}$  was generated in the laboratory through a Nanopure Diamond Ultrapure water system by Barnstead (Dubuque, IA). Kieselgel 60 F254 analytical TLC aluminum sheets were purchased from EM Science (Gibbstown, NJ); compounds were visualized under UV light and by dipping the plates in sulfuric acid thymol solution containing 1% (w/v) thymol, 10% (v/v)  $\text{H}_2\text{SO}_4$ , and EtOH (95%), followed by heating. Preparative TLC was performed on precoated 20 cm  $\times$  20 cm silica gel 60 (0.5 mm thickness, Merck) plates. Flash column chromatography (FCC) was carried out using 70–230 mesh 60 Å normal phase silica gel (Sigma-Aldrich). Sephadex<sup>®</sup> LH-20 was purchased from Pharmacia Fine Chemicals (Uppsala, Sweden). C-18 silica gel cartridges (Mega Bond Elut<sup>®</sup> Flash, 10 g sorbent mass, 60 mL volume) were obtained from Varian, Inc. (Mississauga, ON). LC-MS analysis was performed by injecting a 20  $\mu\text{L}$  aliquot of the solution of crude extract or fraction into an Agilent Technologies HP 1100 (New Castle, DE) high-performance liquid chromatograph equipped with a quaternary pump, automatic injector, diode-array detector (wavelength range 190–600 nm), degasser, and a Hypersil ODS column (5  $\mu\text{m}$ , 4.6 mm  $\times$  200 mm). The two mobile phase solvents, MeOH and  $\text{H}_2\text{O}$ , were prepared with 0.15%  $\text{Et}_3\text{N}$  and 0.18%  $\text{HCO}_2\text{H}$ , added as ion-pairing reagents. Both solutions were filtered using 0.45  $\mu\text{m}$  nylon membranes. The initial mobile phase was 100% HPLC-grade  $\text{H}_2\text{O}$ . At 10 min, the mobile

phase was switched to a linear gradient of 100%  $\text{H}_2\text{O}$  to 100% MeOH over 60 min. After each run, the initial mobile phase conditions were set and the system was allowed to equilibrate. The flow rate was kept constant at 1 mL/min. The column temperature was held at room temperature.<sup>19</sup> The HPLC was interfaced to an Agilent model 6120 mass spectrometer (Toronto, ON) with a Chemstation data system LC-MSD B.03.01. The electrospray interface was a standard ES source operating with a capillary voltage of 4 kV and temperature of 350 °C. The system was operated in the negative and positive ion electrospray modes. Nitrogen was used as nebulizing and drying gas at a flow rate of 10 L/min (35 psig). The mass spectrometer was programmed to perform full scans between  $m/z$  100 and 1000 amu. Lyophilization was done in a Labconco Freezone 12 freeze dryer system. UV spectra were determined on a Biochrom Ultraspec 2100 pro UV–visible spectrophotometer (Cambridge, England). The specific rotation  $[\alpha]_D$  was measured with a Rudolph Research Corporation Autopol<sup>®</sup> II automatic polarimeter (Flanders, NJ), at ambient temperature, using a 20 cm path length cell. The specific rotation is expressed in units of  $10^{-1}$  deg  $\text{cm}^2 \text{g}^{-1}$  and the concentration ( $c$ ) in g/100 mL. Infrared spectra were recorded with a PerkinElmer Paragon 1000PC IR spectrometer (Waltham, Massachusetts, USA) using KBr (VWR, Mississauga, ON) disks. NMR spectra were recorded on a Bruker Avance

spectrometer at 600 MHz ( $^1\text{H}$ ) and 150 MHz ( $^{13}\text{C}$ ) at the Saskatchewan Structural Science Centre (Saskatoon, Canada) or on a Bruker DRX 500 spectrometer at 500 MHz ( $^1\text{H}$ ) and 125 MHz ( $^{13}\text{C}$ ) at Laurentian University (Sudbury, Canada);  $\delta$  values were referenced to  $\text{D}_2\text{O}$  at 4.80 ppm. HR-ESI-MS measurements were recorded using an API Qstar XL mass spectrometer at the Saskatchewan Structural Science Centre (Saskatoon, Canada). The measurements of free-radical-scavenging ability were done on a Biotek Powerwave XS and the data was interpreted using KC (Keneticalc. for Windows) 3.4 Rev. 21.

### Plant material

Fresh rhizome of *C. diphylla* was obtained from Semences et plantes internationales (Cantley, QC). A voucher specimen (number 21024) was deposited at the Department of Biology Herbarium at Laurentian University (Sudbury, Canada).

### Extraction and isolation

Freeze-dried rhizomes (431 g) were frozen in liquid  $\text{N}_2$ , ground in a mortar, and immediately extracted three times with MeOH (1.2 L for the first extraction, 0.8 L for the other extractions) for 30 min. The methanolic solution was filtered and concentrated to dryness (49.4 g). This extract was dissolved in  $\text{H}_2\text{O}$  (600 mL) and submitted to liquid-liquid extractions with solvents of increasing polarity, i.e.,  $\text{CHCl}_3$ , EtOAc, and BuOH. Each organic layer was concentrated ( $\text{CHCl}_3$  fraction 2.3 g, EtOAc fraction 1.1 g, and BuOH fraction 6.4 g), and the aqueous layer was lyophilized (37.5 g). The BuOH was separated by FCC column 1 (normal phase, gradient  $\text{CHCl}_3$ -MeOH, 8:2 and 7:3 v/v, 20 mL fractions). Fractions 27 to 130, obtained from the FCC column 1, were combined (2.3 g) and fractionated on a Sephadex LH-20 column 1 ( $\text{H}_2\text{O}$ -MeOH, 100:0 and 0:100 v/v, 5 mL fractions). Fractions 3 to 5, obtained from the Sephadex LH-20 column 1, were combined (2.1 g) and submitted to a FCC column 2 (normal phase, gradient acetone-MeOH, 95:5 and 90:10, v/v, 15 mL fractions). Fractions 1 to 12, from the FCC column 2, were combined (80 mg) and submitted to solid-phase separation 1 (C18 cartridge,  $\text{H}_2\text{O}$ -MeOH, 100:0 and 0:100 v/v, 3 mL fractions) yielding compound **1** (3.7 mg,  $8.6 \times 10^{-4}$  % of dry weight) in fractions 6 and 7. The combined fractions 11 to 54 (30 mg) were submitted to preparative TLC ( $\text{CHCl}_3$ -MeOH- $\text{H}_2\text{O}$ , 65:45:10, two successive migrations) yielding compound **3** (3.7 mg,  $8.6 \times 10^{-4}$  % of dry weight). The combined fractions 25 to 102, obtained from FCC column 2, submitted to solid-phase separation 2 (C18 cartridge,  $\text{H}_2\text{O}$ -MeOH, 100:0 and 0:100 v/v, 3 mL fractions) yielded compound **2** (26.1 mg,  $6.0 \times 10^{-3}$  % of dry weight) in fractions 12 to 15. Fractions 6 and 7, obtained from the Sephadex LH-20 column 1, were combined (110 mg) and submitted to solid-phase separation 3 (C18 cartridge,  $\text{H}_2\text{O}$ -MeOH, 100:0 and 0:100 v/v, 5 mL fractions). Fractions 33 to 58, obtained from the solid-phase separation 3, were combined (48 mg) and submitted to preparative TLC ( $\text{CHCl}_3$ -MeOH- $\text{H}_2\text{O}$ , 65:45:10) yielding **5** (20.4 mg,  $4.7 \times 10^{-3}$  % of dry weight) after filtration. The combined fractions 59 to 73, obtained from the solid-phase separation 3, yielded compound **4** (5.5 mg,  $1.3 \times 10^{-3}$  % of dry weight). The combined fractions 74 to 78 (28.1 mg), ob-

tained from the solid-phase separation 3, were submitted to preparative TLC ( $\text{CHCl}_3$ -MeOH- $\text{H}_2\text{O}$ , 65:45:10) and yielded compound **6** (3.2 mg,  $7.4 \times 10^{-4}$  % of dry weight) and compound **7** (5.3 mg,  $1.2 \times 10^{-3}$  % of dry weight).

#### 1-Methylethylglucosinolate (1)

White, amorphous powder. HPLC  $t_R$  = 17.5 min.  $[\alpha]_D^{22}$  -115.4 (c 0.052, MeOH). UV (MeOH)  $\lambda_{\text{max}}$  (nm, log  $\epsilon$ ): 225 (3.6). FTIR (KBr,  $\text{cm}^{-1}$ )  $\nu_{\text{max}}$ : 3412, 2923, 1738, 1628, 1448, 1276, 1089, 1059, 869, 790, 630. For  $^1\text{H}$  NMR ( $\text{D}_2\text{O}$ , 600 MHz) data see Table 1. For  $^{13}\text{C}$  NMR ( $\text{D}_2\text{O}$ , 150 MHz) data see Table 2. HR-ESI-MS  $m/z$  calcd. for  $\text{C}_{10}\text{H}_{18}\text{NO}_9\text{S}_2$ : 360.0423; found: 360.0427  $[\text{M}]^-$ .

#### 2-Methylbutylglucosinolate (2)

Yellowish, amorphous powder. HPLC  $t_R$  = 25.2 min.  $[\alpha]_D^{22}$  -20.1 (c 0.324, MeOH). UV (MeOH)  $\lambda_{\text{max}}$  (nm, log  $\epsilon$ ): 225 (3.7). FTIR (KBr,  $\text{cm}^{-1}$ )  $\nu_{\text{max}}$ : 3391, 2964, 1732, 1652, 1558, 1540, 1507, 1457, 1400, 1223, 1054, 877, 777, 617, 591. For  $^1\text{H}$  NMR ( $\text{D}_2\text{O}$ , 600 MHz) data see Table 1. For  $^{13}\text{C}$  NMR ( $\text{D}_2\text{O}$ , 150 MHz) data see Table 2. HR-ESI-MS  $m/z$  calcd. for  $\text{C}_{12}\text{H}_{22}\text{NO}_9\text{S}_2$ : 388.0741; found: 388.0732  $[\text{M}]^-$ .

#### Desulfo-2-methylbutylglucosinolate (3)

Yellowish, amorphous powder. HPLC  $t_R$  = 28.8 min.  $[\alpha]_D^{22}$  -19.2 (c 0.078, MeOH). UV (MeOH)  $\lambda_{\text{max}}$  (nm, log  $\epsilon$ ): 223 (3.6). FTIR (KBr,  $\text{cm}^{-1}$ )  $\nu_{\text{max}}$ : 3378, 3008, 2932, 1572, 1458, 1416, 1046, 1016, 926, 658, 616. For  $^1\text{H}$  NMR ( $\text{D}_2\text{O}$ , 500 MHz) data see Table 1. For  $^{13}\text{C}$  NMR ( $\text{D}_2\text{O}$ , 125 MHz) data see Table 2. HR-ESI-MS  $m/z$  calcd. for  $\text{C}_{12}\text{H}_{22}\text{NO}_6\text{S}$ : 308.1173; found: 308.1174  $[\text{M}]^-$ .

#### 3-Methylpentylglucosinolate (4)

Yellowish, amorphous powder. HPLC  $t_R$  = 30.2 min.  $[\alpha]_D^{22}$  -67.3 (c 0.052, MeOH). UV (MeOH)  $\lambda_{\text{max}}$  (nm, log  $\epsilon$ ): 219 (3.3). FTIR (KBr,  $\text{cm}^{-1}$ )  $\nu_{\text{max}}$ : 3393, 2929, 2858, 1725, 1648, 1467, 1089, 1042. For  $^1\text{H}$  NMR ( $\text{D}_2\text{O}$ , 600 MHz) data see Table 1. For  $^{13}\text{C}$  NMR ( $\text{D}_2\text{O}$ , 150 MHz) data see Table 2. HR-ESI-MS  $m/z$  calcd. for  $\text{C}_{13}\text{H}_{24}\text{NO}_9\text{S}_2$ : 402.0898; found: 402.0890  $[\text{M}]^-$ .

#### 3-Indolylmethylglucosinolate (5)

Yellowish, amorphous powder. HPLC  $t_R$  = 26.0 min.  $[\alpha]_D^{22}$  -36.8 (c 0.204, MeOH). UV (MeOH)  $\lambda_{\text{max}}$  (nm, log  $\epsilon$ ): 221 (4.4), 274 (3.6). FTIR (KBr,  $\text{cm}^{-1}$ )  $\nu_{\text{max}}$ : 3381, 2964, 2922, 1671, 1614, 1459, 1282, 1233, 1099, 1056, 802, 731, 604. For  $^1\text{H}$  NMR ( $\text{D}_2\text{O}$ , 600 MHz) data see Table 1. For  $^{13}\text{C}$  NMR ( $\text{D}_2\text{O}$ , 150 MHz) data see Table 2. HR-ESI-MS  $m/z$  calcd. for  $\text{C}_{16}\text{H}_{19}\text{N}_2\text{O}_9\text{S}_2$ : 447.0537; found: 447.0534  $[\text{M}]^-$ .

#### 1-Methoxy-3-indolylmethylglucosinolate (6)

Yellowish, amorphous powder. HPLC  $t_R$  = 32.6 min.  $[\alpha]_D^{22}$  -33.0 (c 0.106, MeOH). UV (MeOH)  $\lambda_{\text{max}}$  (nm, log  $\epsilon$ ): 221 (4.4), 275 (3.6). FTIR (KBr,  $\text{cm}^{-1}$ )  $\nu_{\text{max}}$ : 3369, 2952, 2927, 1710, 1509, 1456, 1270, 1058, 953, 876, 797, 743, 693, 633. For  $^1\text{H}$  NMR ( $\text{D}_2\text{O}$ , 500 MHz) data see Table 1. For  $^{13}\text{C}$  NMR ( $\text{D}_2\text{O}$ , 125 MHz) data see Table 2. HR-ESI-MS  $m/z$  calcd. for  $\text{C}_{12}\text{H}_{22}\text{NO}_9\text{S}_2$ : 477.0643; found: 477.0629  $[\text{M}]^-$ .

#### 4-Methoxy-3-indolylglucosinolate (7)

Yellowish, amorphous powder. HPLC  $t_R$  = 30.0 min. UV



(MeOH)  $\lambda_{\max}$  (nm): 221, 271. For  $^1\text{H}$  NMR ( $\text{D}_2\text{O}$ , 500 MHz) data see Table 1. For  $^{13}\text{C}$  NMR ( $\text{D}_2\text{O}$ , 125 MHz) data see Table 2. HR-ESI-MS  $m/z$  (calcd. for  $\text{C}_{17}\text{H}_{21}\text{N}_2\text{O}_{10}\text{S}_2$ : 477.0643; found: 477.0663  $[\text{M}]^-$ ).

### Brine shrimp lethality assay

Brine shrimp eggs were hatched, harvested, and the nauplii dispensed in a manner similar to that described by McLaughlin et al.<sup>20</sup> Several concentrations (10, 100, and 1000 ppm) of *C. diphylla* crude extract were prepared in triplicate by serial dilution using artificial seawater containing 1% DMSO. These solutions were added to live nauplii and following 24 h of drug treatment, at 22 °C, the brine shrimp lethality was measured by counting the number of dead (nonmotile) nauplii per vial. The results were obtained from three independent experiments. Seawater with 1% DMSO was used as the negative control. A positive assay was the death of all brine shrimp with 100  $\mu\text{mol/L}$  thymol.

### DPPH assay

Radical-scavenging activity was determined spectrophotometrically by reaction with DPPH radicals, as described by Gerhäuser et al.<sup>21</sup> Several concentrations (187.5, 375, 750, and 1000  $\mu\text{g/mL}$ ) of *C. diphylla* crude extract in 100% DMSO were treated with a solution of 100  $\mu\text{mol/L}$  DPPH in ethanol for 30 min at 37 °C. Scavenging activity was compared with a solvent control (0% radical-scavenging activity) and ascorbic acid (250  $\mu\text{mol/L}$  final concentration, 100% radical-scavenging activity, used as a positive control). The results were obtained from experiments run in triplicate and from three independent experiments. The half-maximal scavenging concentration,  $\text{SC}_{50}$ , was determined using the following formula:

$$[1] \quad \% \text{ scavenging activity} = \frac{(\text{negative control endpoint absorption} - \text{trial endpoint absorption}) / (\text{negative control endpoint absorption} - \text{positive control endpoint absorption})}{1}$$

### Acknowledgements

Financial support from the Natural Sciences and Engineering Research Council of Canada (Discovery grant), Laurentian University (Start-up funds, Placement Centre, Laurentian University Research Funds, and teaching assistantship and scholarship to R.B.), the Ontario Ministry of Northern Development and Mines (Summer Jobs Service Program), Canadian Foundation for Innovation (Leaders Opportunity Fund) – Ontario Research Fund is gratefully acknowledged by S.M. We also thank Dr. T.C. Tai for allowing us to use his multiplate reader, and Prof. H. Joly for her comments on the manuscript.

### References

- (1) Erichsen-Brown, C. *Use of Plants For the Past 500 Years*; Breezy Creeks Press: Aurora, ON, 1979; p 373.
- (2) Chambers, B.; Legasy, K.; Bentley, C. V. *Forest Plants of Central Ontario*; Lone Pine Publishing: Edmonton, AB, 1996; pp 225.
- (3) Moermann, D. E. *Native America Ethnobotany*; Timber Press: Portland, OR, 1998; pp 137.
- (4) Feeny, P.; Rosenberry, L. *Biochem. Syst. Ecol.* **1982**, *10* (1), 23. doi:10.1016/0305-1978(82)90047-3.
- (5) Fahey, J. W.; Zalcman, A. T.; Talalay, P. *Phytochemistry* **2001**, *56* (1), 5. doi:10.1016/S0031-9422(00)00316-2. PMID:11198818.
- (6) Halkier, B. A.; Gershenzon, J. *Annu. Rev. Plant Biol.* **2006**, *57* (1), 303. doi:10.1146/annurev.arplant.57.032905.105228. PMID:16669764.
- (7) Bones, A. M.; Rossiter, J. T. *Phytochemistry* **2006**, *67* (11), 1053. doi:10.1016/j.phytochem.2006.02.024. PMID:16624350.
- (8) Traka, M.; Mithen, R. *Phytochem. Rev.* **2009**, *8* (1), 269. doi:10.1007/s11101-008-9103-7.
- (9) Fabre, N. *Contribution à l'Étude des Glucosinolates de Brassicaceae*. Ph.D. thesis, Institut National Polytechnique de Toulouse, Toulouse, France. 1997. p 193.
- (10) Montaut, S.; Grandbois, J.; Righetti, L.; Barillari, J.; Iori, R.; Rollin, P. *J. Nat. Prod.* **2009**, *72* (5), 889. doi:10.1021/np800738w.
- (11) Agerbirk, N.; Warwick, S. I.; Hansen, P. R.; Olsen, C. E. *Phytochemistry* **2008**, *69* (17), 2937. doi:10.1016/j.phytochem.2008.08.014.
- (12) Weil, M. J.; Zhang, Y.; Nair, M. G. *Nutr. Cancer* **2004**, *48* (2), 207. doi:10.1207/s15327914nc4802\_11. PMID:15231456.
- (13) Iori, R.; Barillari, J.; Galletti, S.; Venturi, G.; Marotti, M.; Rollin, P. *Agroindustria* **2003**, *2*, 69.
- (14) Pedras, M. S. C.; Zheng, Q.-A.; Gadagi, R. S.; Rimmer, S. R. *Phytochemistry* **2008**, *69* (4), 894. doi:10.1016/j.phytochem.2007.10.019. PMID:18039546.
- (15) Agerbirk, N.; Petersen, B. L.; Olsen, C. E.; Halkier, B. A.; Nielsen, J. K. *J. Agric. Food Chem.* **2001**, *49* (3), 1502. doi:10.1021/jf001256r. PMID:11312886.
- (16) Bäuerle, R.; Wagner, H.; Schraudolph, H. *Experientia* **1986**, *42* (1), 86. doi:10.1007/BF01975909.
- (17) Windsor, A. J.; Reichelt, M.; Figuth, A.; Svato?, A.; Kroymann, J.; Kliebenstein, D. J.; Gershenzon, J.; Mitchell-Olds, T. *Phytochemistry* **2005**, *66*, 1321.
- (18) Bonnesen, C.; Stephensen, P. U.; Andersen, O.; Sørensen, H.; Vang, O. *Nutr. Cancer* **1999**, *33* (2), 178. doi:10.1207/S15327914NC330210. PMID:10368814.
- (19) Zrybko, C. L.; Fukuda, E. K.; Rosen, R. T. *J. Chromatogr. A* **1997**, *767* (1–2), 43. doi:10.1016/S0021-9673(96)01068-0.
- (20) McLaughlin, J. L.; Rogers, L. L.; Anderson, J. E. *Drug Inf. J.* **1998**, *32*, 513. doi:0092-8615/98 botanicals.
- (21) Gerhäuser, C.; Klimo, K.; Heiss, E.; Neumann, I.; Gamal-Eldeen, A.; Knauf, J.; Liu, G.; Sitthimonchai, S.; Frank, N. *Mutat. Res.* **2003**, *523–524*, 163. doi:10.1016/S00275107(02)00332-9.

# Hydration of acetone in the gas phase and in water solvent

Kiyull Yang, Yih-Huang Hsieh, Chan-Kyung Kim, Hui Zhang, and Saul Wolfe

**Abstract:** In water solvent, the hydration of acetone proceeds by a cyclic (cooperative) process in which concurrent C–O bond formation and proton transfer to oxygen take place through a solvent and (or) catalyst bridge. Reactivity is determined primarily by the concentration of a reactant complex and not the barrier from this complex. This situation is reversed in the gas phase; although the concentrations of reactive complexes are much higher than in solution, the barriers are also higher and dominant in determining reactivity. Calculations of isotope effects suggest that multiple hydron transfers are synchronous in the gas phase to avoid zwitterionic transition states. In solution, such transition states are stabilized by solvation and hydron transfers can be asynchronous.

**Key words:** hydration of acetone, isotope effects, MP2/6-31+G(d)//B3LYP/6-31G(d).

**Résumé :** En solution dans l'eau, l'hydratation de l'acétone se produit par un processus cyclique (coopératif) dans lequel la formation concurrente d'une liaison C–O et d'un transfert de proton vers l'oxygène se produit avec l'aide d'un pont avec un solvant ou un catalyseur. La réactivité est déterminée principalement par la concentration d'un complexe du réactant et non par une barrière à partir de ce complexe. Cette situation est inversée en phase gazeuse; même si les concentrations des complexes réactifs sont beaucoup plus élevées que celles en solution, les barrières sont aussi plus élevées et elles sont dominantes dans la détermination de la réactivité. Des calculs d'effets isotopiques suggèrent que de multiples transferts d'hydrons sont synchrones en phase gazeuse dans le but d'éviter les états de transitions zwitterioniques. En solution, de tels états de transition sont stabilisés par la solvation et les transferts d'hydrons peuvent être asynchrones.

**Mots-clés :** hydratation de l'acétone, effets isotopiques, MP2/6-31+G(d)//B3LYP/6-31G(d).

[Traduit par la Rédaction]

We have recently reported that the neutral,<sup>1</sup> acetic acid catalyzed,<sup>2</sup> and 2-hydroxypyridine (2-pyridone)-catalyzed<sup>3</sup> hydrations of acetone in water solvent do not proceed via ionic intermediates. Instead, as seen in Fig. 1, the reactant complexes of the principal channels of these aqueous reactions, there is in each case a cyclic (cooperative) process<sup>4</sup> in which concurrent C–O bond formation and proton transfer to oxygen take place through a solvent and (or) catalyst bridge. As originally suggested by Eigen,<sup>4a</sup> this mechanism overcomes the requirement that charged species undergo continuous solvation and desolvation as they appear and disappear.

The realization that an ionic mechanism is not obligatory in water solvent seems to have consequences. For example,<sup>2</sup> “it is necessary to reexamine the dogma<sup>5–10</sup> that multistep ionic mechanisms are operative in the *low* dielectric media that exist at the active sites of hydrolytic enzymes.” It is

also necessary to reexamine the notion<sup>11</sup> that hydrolytic enzymes manifest their catalytic effect via cooperative multiple-proton-transfer reactions coupled to tautomerism<sup>12</sup> at nonpolar active sites.<sup>13</sup> In water solvent, the availability of a multiple-proton-transfer pathway and (or) the existence of a low barrier do not seem to be necessary to catalyze the hydration of acetone.

Although four protons are in flight in the neutral reaction and three in the catalyzed reactions, the aqueous barrier of the 2-pyridone-catalyzed reaction (11.97 kcal/mol) is calculated<sup>3</sup> to be only slightly higher than that of the neutral reaction (11.34 kcal/mol) and significantly higher than that of the acetic acid catalyzed reaction (8.14 kcal/mol). Nonetheless, 2-hydroxypyridine, as its tautomer 2-pyridone dihydrate, exhibits a catalytic effect ( $k_{\text{cat}}/k_{\text{neut}}$ ) of  $4 \times 10^7$ , and acetic acid exhibits a catalytic effect of  $2 \times 10^6$ .

Received 20 May 2009. Accepted 31 July 2009. Published on the NRC Research Press Web site at canjchem.nrc.ca on 18 December 2009.

*This paper is dedicated to Russell J. Boyd of Dalhousie University in recognition of his many contributions to his university and his profession.*

**K. Yang.** Department of Chemistry, Simon Fraser University, Burnaby, BC V5A 1S6, Canada; On leave from Department of Chemistry Education, Gyeongsang National University, Jinju 660-701, Korea.

**Y.-H. Hsieh,<sup>1</sup> H. Zhang,<sup>2</sup> and S. Wolfe.<sup>3</sup>** Department of Chemistry, Simon Fraser University, Burnaby, BC V5A 1S6, Canada.

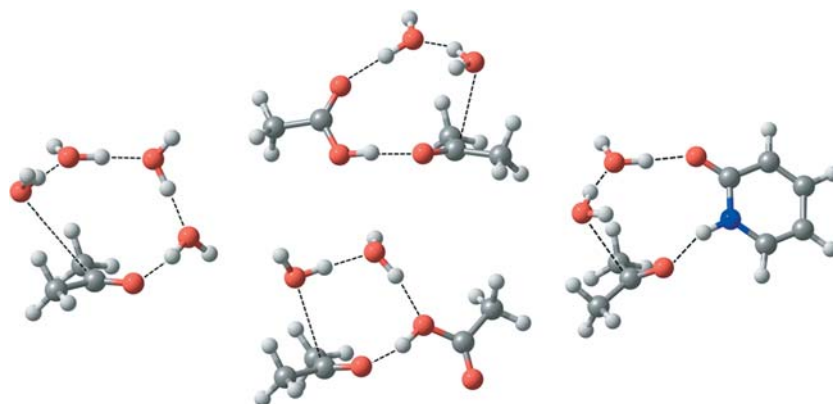
**C.-K. Kim.** Department of Chemistry, Simon Fraser University, Burnaby, BC V5A 1S6, Canada; On leave from Department of Chemistry, Inha University, Incheon 402-751, Korea.

<sup>1</sup>Present address: Smart Pharmaceutical Company Ningbo, China.

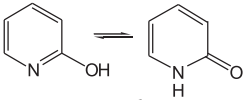
<sup>2</sup>Present address: Department of Chemistry, The University of Western Ontario, London ON N6A 5B7, Canada.

<sup>3</sup>Corresponding author (e-mail: swolfe@sfu.ca).

**Fig. 1.** Reactant complexes of the principal channels of neutral (left), acetic acid catalyzed (centre), and 2-hydroxypyridine-catalyzed hydration of acetone in water solvent.



**Table 1.** Thermochemistry of gas-phase dimerization and tautomerization (theoretical and experimental).

	$\Delta H$ (kcal mol <sup>-1</sup> )	$\Delta S$ (cal mol <sup>-1</sup> K <sup>-1</sup> )	$\Delta G^a$ (kcal mol <sup>-1</sup> )	$K_{eq}^a$
$H_2O + H_2O \rightleftharpoons (H_2O)_2$				
Experimental <sup>b</sup>	-3.59	-18.59	3.34	$1.10 \times 10^{-2}$ ( $T = 373$ K)
B3LYP/6-31G(d)	-5.85	-18.87	-0.22	1.45
B3LYP/6-31G(d) + BSSE	-1.99	-18.87	3.64	$2.14 \times 10^{-3}$
MP2/6-31+G(d)//B3LYP/6-31G(d)	-2.62	-18.87	3.00	$6.31 \times 10^{-3}$
MP2/6-31+G(d)//B3LYP/6-31G(d) + BSSE	-1.02	-18.87	4.61	$4.16 \times 10^{-4}$
$HOAc + HOAc \rightleftharpoons (HOAc)_2$				
Experimental <sup>c</sup>	-15.00	-36.00	-4.00	$8.58 \times 10^2$ ( $T = 298$ K)
B3LYP/6-31G(d)	-18.38	-37.47	-7.21	$1.94 \times 10^5$
B3LYP/6-31G(d) + BSSE	-14.11	-37.47	-2.94	$1.43 \times 10^2$
MP2/6-31+G(d)//B3LYP/6-31G(d)	-15.30	-37.47	-4.12	$1.05 \times 10^3$
MP2/6-31+G(d)//B3LYP/6-31G(d) + BSSE	-11.54	-37.47	-0.37	1.87
				
Experimental <sup>d</sup>			0.65	0.33 ( $T = 298$ K)
B3LYP/6-31G(d)	-1.09	0.45	-1.11	6.52
MP2/6-31+G(d)//B3LYP/6-31G(d)	1.89	0.45	0.75	0.28

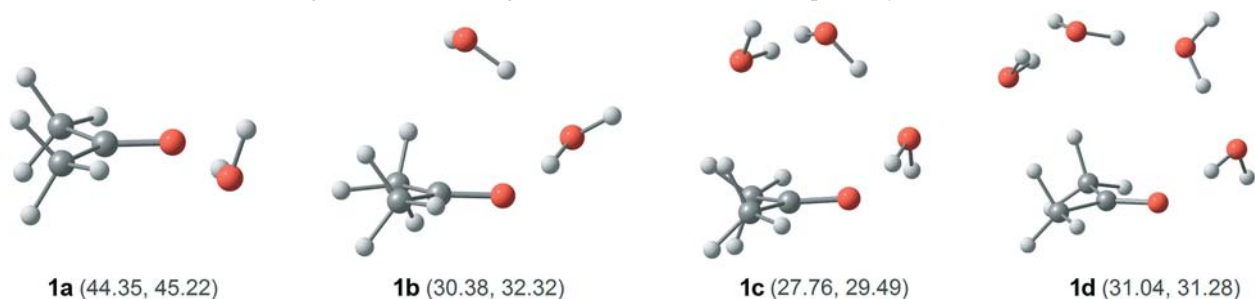
<sup>a</sup>Theoretical values are calculated at 298 K.

<sup>b</sup>Reference 19.

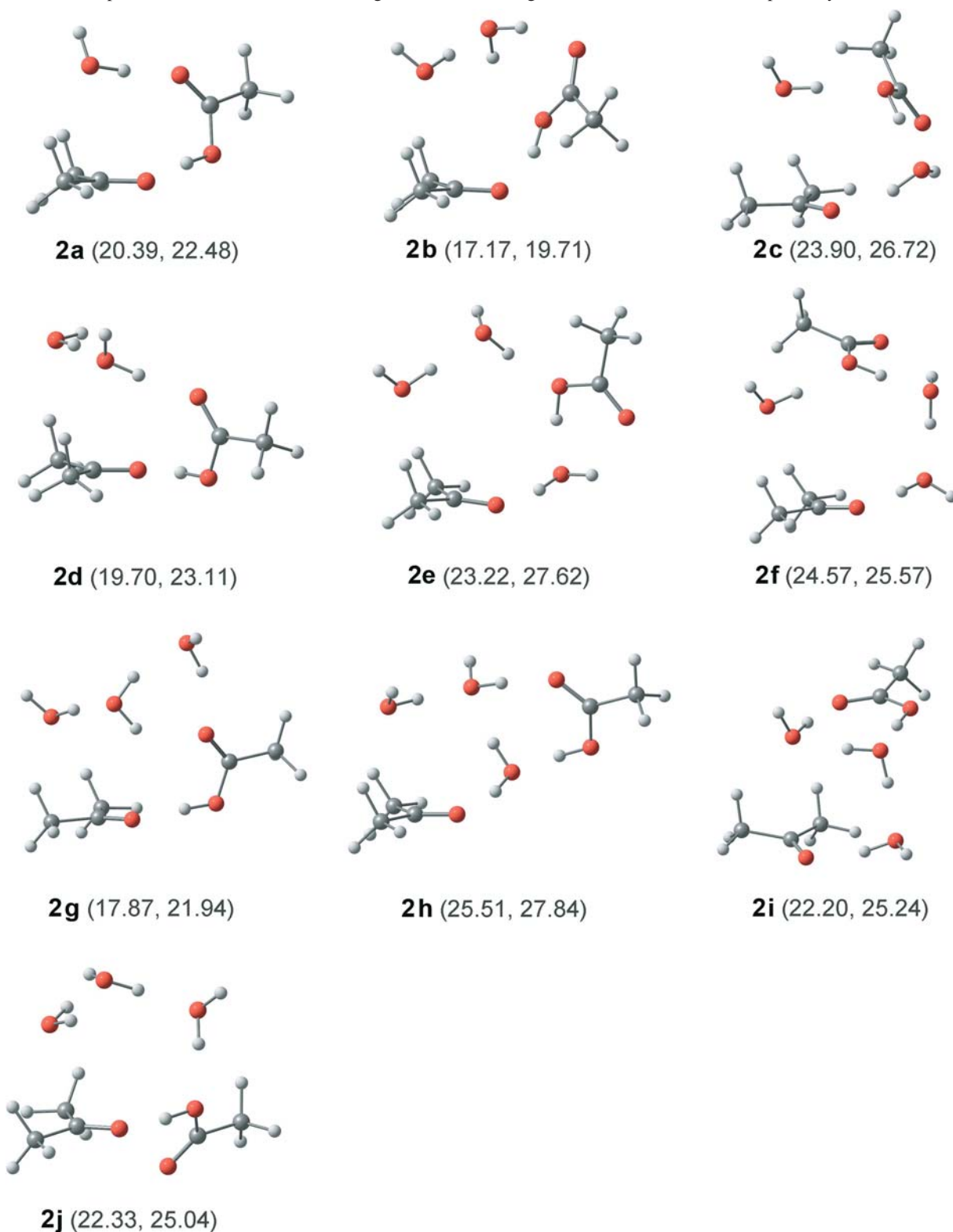
<sup>c</sup>Reference 20.

<sup>d</sup>Reference 21.

**Fig. 2.** Structures **1a–1d**, the reactant complexes of the gas-phase hydration of acetone by one, two, three, or four water molecules. Values in parentheses are the activation energies and Gibbs energies of activation at 298 K, respectively.



**Fig. 3.** Structures **2a–2j**, the reactant complexes of the acetic acid catalyzed gas-phase hydration of acetone by one, two, or three water molecules. Values in parentheses are the activation energies and Gibbs energies of activation at 298 K, respectively.



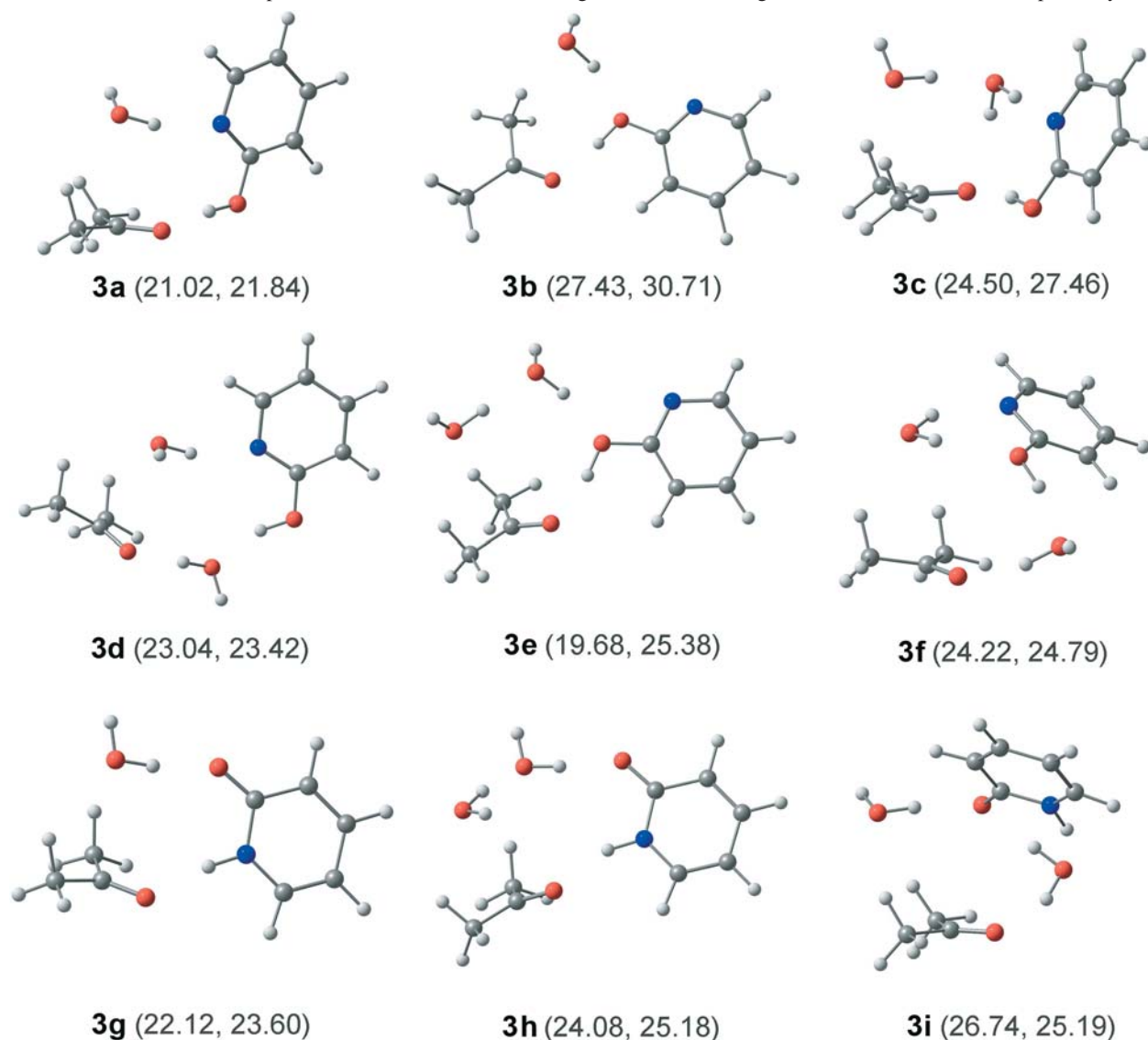
The reason is that, in contrast to the conventional view of the origin of *enzymatic* catalysis,<sup>14</sup> reactivity in water solvent is determined primarily by the concentration of the reactant complex not the reaction barrier.

These findings raise a number of questions, including the following:

- (i) Is the action of two or more functional groups an important factor in catalysis?<sup>15</sup>



**Fig. 4.** Structures **3a–3i**, the reactant complexes of the 2-hydroxypyridine- and 2-pyridone-catalyzed gas-phase hydration of acetone by one or two water molecules. Values in parentheses are the activation energies and Gibbs energies of activation at 298 K, respectively.



**Table 2.** Kinetic analysis for the neutral hydration of acetone at MP2/6–31+G(d)//B3LYP/6–31G(d).

Species	Concentration (mol/L)	Rate constant ( $\text{s}^{-1}$ )	Contribution (%)
$\text{H}_2\text{O}$	$4.058 \times 10^{-1}$		
$(\text{H}_2\text{O})_2$	$1.042 \times 10^{-3}$		
$(\text{H}_2\text{O})_3$	$5.132 \times 10^{-5}$		
$(\text{H}_2\text{O})_4$	$8.260 \times 10^{-2}$		
$(\text{H}_2\text{O})_8$	6.783		
$(\text{CH}_3)_2\text{CO}$	$9.995 \times 10^{-1}$		
<b>1a</b>	$4.292 \times 10^{-4}$	$1.799 \times 10^{-20}$	0.00
<b>1b</b>	$1.360 \times 10^{-7}$	$5.116 \times 10^{-11}$	0.10
<b>1c</b>	$2.907 \times 10^{-8}$	$6.067 \times 10^{-9}$	2.44
<b>1d</b>	$2.383 \times 10^{-5}$	$2.959 \times 10^{-10}$	97.47

**Note:** Calculated rate ( $\text{M s}^{-1}$ ) =  $7.23 \times 10^{-15}$  ( $\Delta G^\ddagger = 36.75 \text{ kcal/mol}$ ).

**Table 3.** Kinetic analysis for the acetic acid catalyzed hydration of acetone at MP2/6–31+G(d)//B3LYP/6–31G(d).

Species	Concentration (mol/L)	Rate constant (s <sup>-1</sup> )	Contribution (%)
H <sub>2</sub> O	0.407		
(H <sub>2</sub> O) <sub>2</sub>	1.047 × 10 <sup>-3</sup>		
(H <sub>2</sub> O) <sub>3</sub>	5.078 × 10 <sup>-5</sup>		
(H <sub>2</sub> O) <sub>4</sub>	8.192 × 10 <sup>-2</sup>		
(H <sub>2</sub> O) <sub>8</sub>	6.783		
(CH <sub>3</sub> ) <sub>2</sub> CO	0.999		
<b>1a</b>	4.375 × 10 <sup>-4</sup>	4.497 × 10 <sup>-21</sup>	0.00
<b>1b</b>	1.389 × 10 <sup>-7</sup>	1.279 × 10 <sup>-11</sup>	0.00
<b>1c</b>	2.926 × 10 <sup>-8</sup>	1.517 × 10 <sup>-9</sup>	0.00
<b>1d</b>	2.363 × 10 <sup>-5</sup>	7.397 × 10 <sup>-11</sup>	0.00
HOAc	4.111 × 10 <sup>-4</sup>		
(HOAc) <sub>2</sub>	2.537 × 10 <sup>-4</sup>		
<b>2a</b>	4.749 × 10 <sup>-6</sup>	2.081 × 10 <sup>-4</sup>	99.99
<b>2b</b>	7.596 × 10 <sup>-13</sup>	2.230 × 10 <sup>-2</sup>	0.00
<b>2c</b>	3.164 × 10 <sup>-11</sup>	1.625 × 10 <sup>-7</sup>	0.00
<b>2d</b>	1.386 × 10 <sup>-9</sup>	7.188 × 10 <sup>-5</sup>	0.01
<b>2e</b>	2.380 × 10 <sup>-12</sup>	3.559 × 10 <sup>-8</sup>	0.00
<b>2f</b>	1.152 × 10 <sup>-12</sup>	1.132 × 10 <sup>-6</sup>	0.00
<b>2g</b>	2.246 × 10 <sup>-11</sup>	5.177 × 10 <sup>-4</sup>	0.00
<b>2h</b>	2.406 × 10 <sup>-9</sup>	2.455 × 10 <sup>-8</sup>	0.00
<b>2i</b>	4.972 × 10 <sup>-9</sup>	1.975 × 10 <sup>-6</sup>	0.00
<b>2j</b>	9.251 × 10 <sup>-13</sup>	2.768 × 10 <sup>-6</sup>	0.00

**Note:** Calculated rate (M s<sup>-1</sup>) = 9.887 × 10<sup>-10</sup> ( $\Delta G^\ddagger$  = 28.92 kcal/mol). Calculated  $k_{\text{HA}}$  (M<sup>-1</sup>s<sup>-1</sup>) = 9.887 × 10<sup>-7</sup>. Calculated  $k_0$  (s<sup>-1</sup>) = 1.794 × 10<sup>-15</sup>.

(ii) Does the hydration of a carbonyl group in water differ mechanistically from that in the gas phase?<sup>16</sup>

(iii) Does the enzymatic catalysis require a medium of low dielectric constant?<sup>17</sup>

(iv) Do acetic acid and 2-hydroxypyridine catalyze the hydration of acetone in the gas phase?

These questions have led to the present work, a Gaussian 03 examination<sup>18</sup> of the gas-phase neutral, acetic acid catalyzed, and 2-hydroxypyridine/2-pyridone-catalyzed hydration of acetone. A necessary first objective was the selection of a computational strategy that would reproduce experimental gas-phase data such as the dimerization energy of water,<sup>19</sup> the dimerization energy of acetic acid,<sup>20</sup> and the tautomerization energy of 2-hydroxypyridine<sup>21</sup> (Table 1). As summarized in Table 1, this has been achieved by B3LYP/6–31G(d) optimization of geometries,<sup>22,23</sup> followed by single-point MP2/6–31+G(d) calculation of energies, which are converted to Gibbs energies at 298 K using eq. [1],

$$[1] \quad G = H - TS_{\text{vib}}$$

where  $H$  is the sum of the MP2 single-point energy and the zero-point and thermal correction energies obtained from the B3LYP/6–31G(d) frequency calculations, and  $S_{\text{vib}}$  is the vibrational entropy calculated at B3LYP/6–31G(d). With all calculations carried out at MP2/6–31+G(d)//B3LYP/6–31G(d), Fig. 2 shows the reactant complexes **1a–1d** for the neutral cooperative hydration of acetone by one, two, three or four water molecules, Fig. 3 shows the reactant complexes **2a–2j** for the acetic acid catalyzed cooperative hydration of acetone by one (**2a**), two (**2b–2d**), or three (**2e–2j**) water molecules, and Fig. 4 shows the reactant com-

**Table 4.** Kinetic analysis for the 2-hydroxypyridine(2-pyridone)-catalyzed hydration of acetone at MP2/6–31+G(d)// B3LYP/6–31G(d).

Species	Concentration (mol/L)	Rate constant (s <sup>-1</sup> )	Contribution (%)
H <sub>2</sub> O	0.407		
(H <sub>2</sub> O) <sub>2</sub>	1.049 × 10 <sup>-3</sup>		
(H <sub>2</sub> O) <sub>3</sub>	5.096 × 10 <sup>-5</sup>		
(H <sub>2</sub> O) <sub>4</sub>	8.228 × 10 <sup>-2</sup>		
(H <sub>2</sub> O) <sub>8</sub>	6.845		
(CH <sub>3</sub> ) <sub>2</sub> CO	0.999		
<b>1a</b>	4.379 × 10 <sup>-4</sup>	1.799 × 10 <sup>-20</sup>	0.00
<b>1b</b>	1.392 × 10 <sup>-7</sup>	5.116 × 10 <sup>-11</sup>	0.00
<b>1c</b>	2.936 × 10 <sup>-8</sup>	6.067 × 10 <sup>-9</sup>	0.00
<b>1d</b>	2.373 × 10 <sup>-5</sup>	2.959 × 10 <sup>-10</sup>	0.00
<b>3a</b>	6.527 × 10 <sup>-9</sup>	2.451 × 10 <sup>-3</sup>	5.56
<b>3b</b>	1.661 × 10 <sup>-11</sup>	7.742 × 10 <sup>-10</sup>	0.00
<b>3c</b>	1.363 × 10 <sup>-10</sup>	1.865 × 10 <sup>-7</sup>	0.00
<b>3d</b>	2.111 × 10 <sup>-12</sup>	1.704 × 10 <sup>-4</sup>	0.00
<b>3e</b>	1.093 × 10 <sup>-12</sup>	6.238 × 10 <sup>-6</sup>	0.00
<b>3f</b>	4.107 × 10 <sup>-13</sup>	1.688 × 10 <sup>-5</sup>	0.00
<b>3g</b>	2.160 × 10 <sup>-6</sup>	1.258 × 10 <sup>-4</sup>	94.43
<b>3h</b>	2.695 × 10 <sup>-9</sup>	8.742 × 10 <sup>-6</sup>	0.00
<b>3i</b>	5.946 × 10 <sup>-11</sup>	8.596 × 10 <sup>-6</sup>	0.00

**Note:** Calculated rate (M s<sup>-1</sup>) = 2.876 × 10<sup>-10</sup> ( $\Delta G^\ddagger$  = 30.48 kcal/mol). Calculated  $k_{\text{HA}}$  (M<sup>-1</sup>s<sup>-1</sup>) = 1.438 × 10<sup>-6</sup>. Calculated  $k_0$  (s<sup>-1</sup>) = 7.204 × 10<sup>-15</sup>.

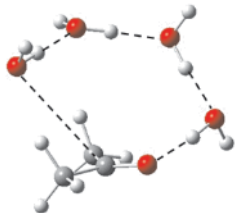
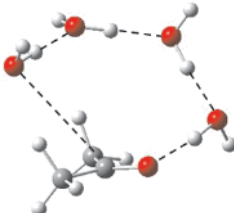
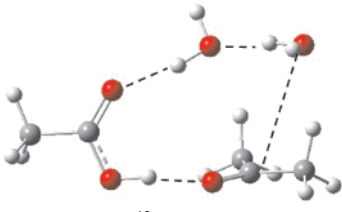
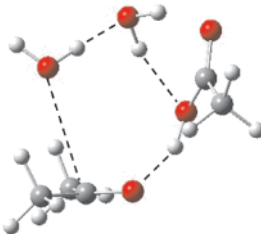
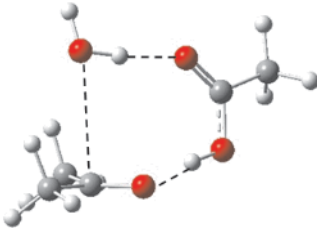
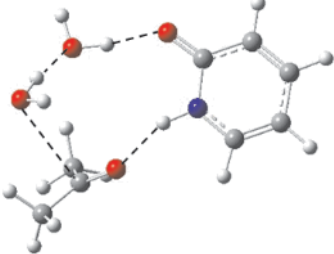
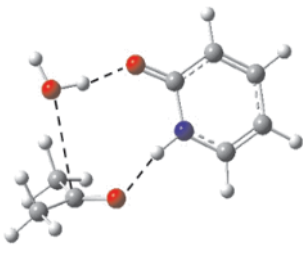
plexes **3a–3i** for the 2-hydroxypyridine (**3a–3f**) and 2-pyridone (**3g–3i**) catalyzed cooperative hydration of acetone by one (**3a, 3g**) or two (**3b–3f, 3h, and 3i**) water molecules.

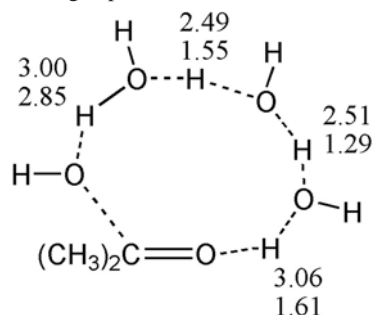
On the basis of these data, Table 2 provides the kinetic analysis of the gas-phase cooperative hydration of a 1 mol/L acetone solution, and Tables 3 and 4 summarize the catalytic effects of 1 mmol/L acetic acid or 0.2 mmol/L 2-hydroxypyridine/2-pyridone on the gas-phase hydration of a 1 mol/L acetone solution.<sup>24</sup> Table 5 summarizes what we have found for the hydration of acetone in water solvent and in the gas phase at the concentrations listed above. The second column of the table lists the experimental Gibbs energies of activation in solution at 298 K. The third column shows the structures of the principal calculated reactant complex(es) in solution, the concentrations of these complexes, and the barriers from these complexes. The fourth column provides the calculated gas-phase Gibbs energies of activation (from Tables 2–4), and the fifth column shows the structures of the principal reactant complexes, the concentrations of these complexes, and the barriers from these complexes.

The principal findings of Table 5 are that *all Gibbs energies of activation are much higher in the gas phase despite the much higher gas-phase concentrations of the principal reaction channels*. In contrast to the situation in solution, the gas-phase rates are determined by the barriers, not the concentrations of the reactant complexes. The specific answers to questions (i)–(iv) are therefore as follows:

(i) In the gas-phase, as well as in solution, the presence of two or more functional groups contributes to catalysis, but only one molecule of water is required for such catalysis.

**Table 5.** Gibbs energies of activation (kcal/mol) in the gas phase and in solution.

Reaction	In solution		In the gas phase	
	$\Delta G^\ddagger^a$	Principal channel <sup>b</sup>	$\Delta G^\ddagger^b$	Principal channel <sup>b</sup>
Neutral	24.34	 1.629 × 10 <sup>-10</sup> mol/L, 11.34 kcal/mol	36.75	 2.383 × 10 <sup>-5</sup> mol/L, 31.28 kcal/mol
Acetic acid catalyzed	20.89	 3.93 × 10 <sup>-12</sup> mol/L, 7.74 kcal/mol  9.76 × 10 <sup>-12</sup> mol/L, 8.14 kcal/mol	28.92	 4.749 × 10 <sup>-6</sup> mol/L, 22.48 kcal/mol
2-HP (2-PD)-catalyzed	21.39	 4.78 × 10 <sup>-8</sup> mol/L, 11.97 kcal/mol	30.48	 2.160 × 10 <sup>-6</sup> mol/L, 23.60 kcal/mol

<sup>a</sup> Experimental result.<sup>b</sup> Calculated result.**Fig. 5.** Calculated isotope effects in the gas phase (upper numbers) and in water solvent (lower numbers). The imaginary frequencies are 1328i cm<sup>-1</sup> in the gas phase and 504i cm<sup>-1</sup> in water.

(ii) The neutral reaction is the same in the gas phase and in solution, but the catalyzed reactions require less water.

(iii) There is no evidence that enzymatic catalysis requires a medium of low dielectric constant.

(iv) When compared to the neutral reaction, acetic acid and 2-pyridone catalyze the hydration of acetone in the gas phase.

Why are the gas-phase barriers so much higher? Fig. 5, which examines the solvent isotope effects in the neutral reactions, suggests the explanation. Hydron movement is synchronous in the gas-phase reaction to avoid a high-energy zwitterionic transition state.

Such structures are stabilized in solution and the hydron of the attacking water molecule makes the dominant contribution to the transition state.

## Supplementary data

Supplementary data (the coordinates of the calculated reactant complexes and transition structures) for this article are available on the journal Web site (canjchem.nrc.ca) or may be purchased from the Depository of Unpublished Data, Document Delivery, CISTI, National Research Council Canada, Ottawa, ON K1A 0R6, Canada. DUD 5298. For more information on obtaining material, refer to cisti-icist.nrc-cnrc.gc.ca/cms/unpub\_e.shtml.

## Acknowledgement

This research was supported financially by a discovery grant from the Natural Sciences and Engineering Research Council of Canada (NSERC).

## References

- (1) (a) Wolfe, S.; Kim, C.-K.; Yang, K.; Weinberg, N.; Shi, Z. *J. Am. Chem. Soc.* **1995**, *117* (15), 4240. doi:10.1021/ja00120a005.; (b) Wolfe, S.; Shi, Z.; Yang, K.; Ro, S.; Weinberg, N.; Kim, C.-K. *Can. J. Chem.* **1998**, *76* (1), 114. doi:10.1139/cjc-76-1-114.
- (2) Hsieh, Y.-H.; Weinberg, N.; Yang, K.; Kim, C.-K.; Shi, Z.; Wolfe, S. *Can. J. Chem.* **2005**, *83* (6-7), 769. doi:10.1139/v05-027.
- (3) Hsieh, Y.-H.; Weinberg, N.; Wolfe, S. *Can. J. Chem.* **2008**, *86* (2), 81. doi:10.1139/V07-074.
- (4) (a) Eigen, M. *Discuss. Faraday Soc.* **1965**, *39*, 7. doi:10.1039/df9653900007.; (b) Huang, H. H.; Robinson, R. R.; Long, F. A. *J. Am. Chem. Soc.* **1966**, *88* (9), 1866. doi:10.1021/ja00961a003.
- (5) (a) Swindells, M. B. *Protein Sci.* **1995**, *4* (1), 93. PMID: 7773181.; (b) Munson, M.; Balasubramanian, S.; Fleming, K. G.; Nagi, A. D.; O'Brien, R.; Sturtevant, J. M.; Regan, L. *Protein Sci.* **1996**, *5* (8), 1584. doi:10.1002/pro.5560050813. PMID:8844848.; (c) García-Moreno, B.; Dwyer, J. J.; Gittis, A. G.; Lattman, E. E.; Spencer, D. S.; Stites, W. E. *Biophys. Chem.* **1997**, *64* (1-3), 211. doi:10.1016/S0301-4622(96)02238-7. PMID:9127946.; (d) Lazar, G. A.; Handel, T. M. *Curr. Opin. Chem. Biol.* **1998**, *2* (6), 675. doi:10.1016/S1367-5931(98)80102-6. PMID:9914192.; (e) Hummer, G. *J. Am. Chem. Soc.* **1999**, *121* (26), 6299. doi:10.1021/ja984414s.; (f) Kim, Y.; Kim, H. D.; Lee, Y. *J. Chem. Soc., Faraday Trans.* **1997**, *93* (1), 99. doi:10.1039/a604844g.; (g) Callender, R.; Chen, D.; Lugtenburg, J.; Martin, C.; Rhee, K. W.; Sloan, D.; Vandersteen, R.; Yue, K. T. *Biochemistry* **1988**, *27* (10), 3672. doi:10.1021/bi00410a023. PMID:3408720.; (h) Kanski, R.; Murray, C. J. *Tetrahedron Lett.* **1993**, *34* (14), 2263. doi:10.1016/S0040-4039(00)77589-7.; (i) Silva, A. M.; Cachau, R. E.; Sham, H. L.; Erickson, J. W. *J. Mol. Biol.* **1996**, *255* (2), 321. doi:10.1006/jmbi.1996.0026. PMID:8551523.; (j) Schutz, C. N.; Warshel, A. *Proteins* **2001**, *44* (4), 400. doi:10.1002/prot.1106. PMID:11484218.; (k) Cui, Q.; Karplus, M. *J. Phys. Chem. B* **2002**, *106* (7), 1768. doi:10.1021/jp012659c.
- (6) (a) Thomas, B.; Wang, Y.; Stein, R. L. *Biochemistry* **2001**, *40* (51), 15811. doi:10.1021/bi011368r. PMID:11747459.; (b) Asbóth, B.; Polgár, L. *Biochemistry* **1983**, *22* (1), 117. doi:10.1021/bi00270a017. PMID:6338911.; (c) Tonge, P. J.; Carey, P. R. *Biochemistry* **1990**, *29* (48), 10723. doi:10.1021/bi00500a002. PMID:2271679.; (d) Daggett, V.; Schroeder, S.; Kollman, P. J. *Am. Chem. Soc.* **1991**, *113* (23), 8926. doi:10.1021/ja00023a047.; (e) Tonge, P. J.; Carey, P. R. *Biochemistry* **1992**, *31* (38), 9122. doi:10.1021/bi00153a002. PMID:1390699.; (f) Whiting, A. K.; Peticolas, W. L. *Biochemistry* **1994**, *33* (2), 552. doi:10.1021/bi00168a021. PMID:8286385.; (g) Chang, T. K.; Chiang, Y.; Guo, H.-X.; Kresge, A. J.; Mathew, L.; Powell, M. F.; Wells, J. A. *J. Am. Chem. Soc.* **1996**, *118* (37), 8802. doi:10.1021/ja9614326.; (h) Curley, K.; Pratt, R. F. *J. Am. Chem. Soc.* **1997**, *119* (7), 1529. doi:10.1021/ja9634942.; (i) Wladkowski, B. D.; Chenoweth, S. A.; Sanders, J. N.; Krauss, M.; Stevens, W. J. *J. Am. Chem. Soc.* **1997**, *119* (27), 6423. doi:10.1021/ja963678g.; (j) O'connell, T. P.; Day, R. M.; Torchilin, E. V.; Bachovchin, W. W.; Malthouse, J. G. *Biochem. J.* **1997**, *326* (Pt 3), 861. PMID:9307038.;
- (7) (a) Ordentlich, A.; Barak, D.; Kronman, C.; Ariel, N.; Segall, Y.; Velan, B.; Shafferman, A. *J. Biol. Chem.* **1998**, *273* (31), 19509. doi:10.1074/jbc.273.31.19509. PMID:9677373.; (b) Hu, C.-H.; Brinck, T.; Hult, K. *Int. J. Quantum Chem.* **1998**, *69* (1), 89. doi:10.1002/(SICI)1097-461X(1998)69:1<89::AID-QUA11>3.0.CO;2-0.; (c) Maveyraud, L.; Pratt, R. F.; Samama, J.-P. *Biochemistry* **1998**, *37* (8), 2622. doi:10.1021/bi972501b. PMID:9485412.; (d) Presnell, S. R.; Patil, G. S.; Mura, C.; Jude, K. M.; Conley, J. M.; Bertrand, J. A.; Kam, C.-M.; Powers, J. C.; Williams, L. D. *Biochemistry* **1998**, *37* (48), 17068. doi:10.1021/bi981636u. PMID: 9836602.; (e) Chittock, R. S.; Ward, S.; Wilkinson, A.-S.; Caspers, P.; Mensch, B.; Page, M. G. P.; Wharton, C. W. *Biochem. J.* **1999**, *338* (Pt 1), 153. doi:10.1042/0264-6021:3380153. PMID:9931311.; (f) Hokenson, M. J.; Cope, G. A.; Lewis, E. R.; Oberg, K. A.; Fink, A. L. *Biochemistry* **2000**, *39* (21), 6538. doi:10.1021/bi9928041. PMID: 10828970.; (g) Shokhen, M.; Albeck, A. *Proteins* **2000**, *40* (1), 154. doi:10.1002/(SICI)1097-0134(20000701)40:1<154::AID-PROT170>3.0.CO;2-V. PMID:10813840.; (h) Chen, C. C. H.; Herzberg, O. *Biochemistry* **2001**, *40* (8), 2351. doi:10.1021/bi002277h. PMID:11327855.; (i) Kursula, P.; Ojala, J.; Lambeir, A.-M.; Wierenga, R. K. *Biochemistry* **2002**, *41* (52), 15543. doi:10.1021/bi0266232. PMID: 12501183.; (j) Zhang, Y.; Kua, J.; McCammon, J. A. *J. Am. Chem. Soc.* **2002**, *124* (35), 10572. doi:10.1021/ja020243m. PMID:12197759.;
- (8) (a) Topf, M.; Várnai, P.; Richards, W. G. *J. Am. Chem. Soc.* **2002**, *124* (49), 14780. doi:10.1021/ja026219q. PMID: 12465991.; (b) Ishida, T.; Kato, S. *J. Am. Chem. Soc.* **2003**, *125* (39), 12035. doi:10.1021/ja021369m. PMID:14505425.; (c) Nemukhin, A. V.; Topol, I. A.; Burt, S. K. *Int. J. Quantum Chem.* **2002**, *88* (1), 34. doi:10.1002/qua.10076.; (d) Shimamura, T.; Ibuka, A.; Fushinobu, S.; Wakagi, T.; Ishiguro, M.; Ishii, Y.; Matsuzawa, H. *J. Biol. Chem.* **2002**, *277* (48), 46601. doi:10.1074/jbc.M207884200.; (e) Zhang, Y.; Kua, J.; McCammon, J. A. *J. Phys. Chem. B* **2003**, *107* (18), 4459. doi:10.1021/jp022525e.; (f) Fujii, Y.; Okimoto, N.; Hata, M.; Narumi, T.; Yasuoka, K.; Susukita, R.; Sue-naga, A.; Futatsugi, N.; Koishi, T.; Furusawa, H.; Kawai, A.; Ebisuzaki, T.; Neya, S.; Hoshino, T. *J. Phys. Chem. B* **2003**, *107* (37), 10274. doi:10.1021/jp034536t.; (g) Silvaggi, N. R.; Anderson, J. W.; Brinsmade, S. R.; Pratt, R. F.; Kelly, J. A. *Biochemistry* **2003**, *42* (5), 1199. doi:10.1021/bi0268955. PMID:12564922.; (h) Fisher, J.; Belasco, J. G.; Khosla, S.; Knowles, J. R. *Biochemistry* **1980**, *19* (13), 2895. doi:10.1021/bi00554a012. PMID:6994800.; (i) Chris-



- tensen, H.; Martin, M. T.; Waley, S. G. *Biochem. J.* **1990**, 266 (3), 853. PMID:2158301.; (j) Page, M. I.; Vilanova, B.; Layland, N. J. *J. Am. Chem. Soc.* **1995**, 117 (49), 12092. doi:10.1021/ja00154a009.;
- (9) (a) Brown, R. P. A.; Aplin, R. T.; Schofield, C. J. *Biochemistry* **1996**, 35 (38), 12421. doi:10.1021/bi961044g. PMID: 8823177.; (b) Coll, M.; Frau, J.; Vilanova, B.; Donoso, J.; Muñoz, F.; Blanco, F. G. *J. Phys. Chem. A* **1999**, 103 (44), 8879. doi:10.1021/jp991958n.; (c) Coll, M.; Frau, J.; Vilanova, B.; Donoso, J.; Muñoz, F.; Blanco, F. G. *J. Phys. Chem. B* **2000**, 104 (47), 11389. doi:10.1021/jp001989e.; (d) Díaz, N.; Suárez, D.; Sordo, T. L. *J. Am. Chem. Soc.* **2000**, 122 (28), 6710. doi:10.1021/ja993547q.; (e) Fujii, Y.; Hata, M.; Hoshino, T.; Tsuda, M. *J. Phys. Chem. B* **2002**, 106 (37), 9687. doi:10.1021/jp021414c.; (f) Fonze, E.; Vanhove, M.; Dive, G.; Sauvage, E.; Frère, J.-M.; Charlier, P. *Biochemistry* **2002**, 41 (6), 1877. doi:10.1021/bi015789k. PMID:11827533.; (g) Silvaggi, N. R.; Anderson, J. W.; Brinsmade, S. R.; Pratt, R. F.; Kelly, J. A. *Biochemistry* **2003**, 42 (5), 1199. doi:10.1021/bi0268955. PMID: 12564922.; (h) Page, M. I.; Laws, A. P. *Chem. Comm.* **1998**, 1609; (i) Morris, J. J.; Page, M. I. *J. Chem. Soc., Perkin Trans. 2* **1980**, (1), 212. doi:10.1039/p29800000212.; (j) Damblon, C.; Raquet, X.; Lian, L.-Y.; Lamotte-Brasseur, J.; Fonze, E.; Charlier, P.; Roberts, G. C. K.; Frère, J.-M. *Proc. Natl. Acad. Sci. U.S.A.* **1996**, 93 (5), 1747. doi:10.1073/pnas.93.5.1747. PMID:8700829.;
- (10) (a) Lietz, E. J.; Truher, H.; Kahn, D.; Hokenson, M. J.; Fink, A. L. *Biochemistry* **2000**, 39 (17), 4971. doi:10.1021/bi992681k. PMID:10819961.; (b) Alvarez-Idaboy, J. R.; González-Jonte, R.; Hernández-Laguna, A.; Smeyers, Y. G. *J. Mol. Struct. THEOCHEM* **2000**, 504 (1-3), 13. doi:10.1016/S0166-1280(00)00351-1.; (c) Nukaga, M.; Mayama, K.; Hujer, A. M.; Bonomo, R. A.; Knox, J. R. *J. Mol. Biol.* **2003**, 328 (1), 289. doi:10.1016/S0022-2836(03)00210-9. PMID:12684014.; (d) Ishiguro, M.; Imajo, S. *J. Med. Chem.* **1996**, 39 (11), 2207. doi:10.1021/jm9506027. PMID: 8667364.; (e) Díaz, N.; Suárez, D.; Sordo, T. L.; Merz, K. M., Jr. *J. Phys. Chem. B* **2001**, 105 (45), 11302. doi:10.1021/jp012881h.; (f) Gibson, R. M.; Christensen, H.; Waley, S. G. *Biochem. J.* **1990**, 272 (3), 613. PMID:1980064.; (g) Lamotte-Brasseur, J.; Dive, G.; Dideberg, O.; Charlier, P.; Frère, J.-M.; Ghuyssen, J. M. *Biochem. J.* **1991**, 279 (Pt 1), 213. PMID:1930139.; (h) Massova, I.; Kollman, P. A. *J. Comput. Chem.* **2002**, 23 (16), 1559. doi:10.1002/jcc.10129. PMID:12395425.; (i) Strynadka, N. C. J.; Martin, R.; Jensen, S. E.; Gold, M.; Jones, J. B. *Nat. Struct. Biol.* **1996**, 3 (8), 688. doi:10.1038/nsb0896-688. PMID:8756327.; (j) Hata, M.; Fujii, Y.; Ishii, M.; Hoshino, T.; Tsuda, M. *Chem. Pharm. Bull. (Tokyo)* **2000**, 48 (4), 447. PMID:10783059.
- (11) (a) Swain, C. G.; Brown, J. F., Jr. *J. Am. Chem. Soc.* **1952**, 74 (10), 2538. doi:10.1021/ja01130a024.; (b) Rony, P. R.; McCormack, W. E.; Wunderly, S. W. *J. Am. Chem. Soc.* **1969**, 91 (15), 4244. doi:10.1021/ja01043a037.; (c) Rony, P. R. *J. Am. Chem. Soc.* **1969**, 91 (22), 6090. doi:10.1021/ja01050a027.; (d) Rony, P. R.; Neff, R. O. *J. Am. Chem. Soc.* **1973**, 95 (9), 2896. doi:10.1021/ja00790a028.; (e) Engdahl, K.-A.; Bivehed, H.; Ahlberg, P.; Saunders, W. H., Jr. *J. Am. Chem. Soc.* **1983**, 105 (14), 4767. doi:10.1021/ja00352a040.; (f) Morpurgo, S.; Bossa, M. *Phys. Chem. Chem. Phys.* **2003**, 5 (6), 1181. doi:10.1039/b210328c.
- (12) Lee, Y.-N.; Schmir, G. L. *J. Am. Chem. Soc.* **1979**, 101 (11), 3026; and references cited therein. doi:10.1021/ja00505a033.
- (13) Sharon, N. *Sci. J. (London)* **1966**, 2 (4), 81.
- (14) (a) Pauling, L. *Chem. Eng. News* **1946**, 24, 1375; (b) Pauling, L. *Am. Sci.* **1948**, 36 (1), 51. PMID:18920436.; (c) Schowen, R. L. In *Transition States of Biochemical Processes*; Gandour, R. D. and Schowen, R. L., Eds.; Plenum Press: New York, 1978; p. 77.
- (15) Gold, H. J. *J. Am. Chem. Soc.* **1971**, 93 (24), 6387. doi:10.1021/ja00753a008.
- (16) (a) Warshel, A.; Åqvist, J.; Creighton, S. *Proc. Natl. Acad. Sci. U.S.A.* **1989**, 86 (15), 5820. doi:10.1073/pnas.86.15.5820. PMID:2762299.; (b) Cannon, W. R.; Benkovic, S. J. *J. Biol. Chem.* **1998**, 273 (41), 26257. doi:10.1074/jbc.273.41.26257. PMID:9756847.; (c) Warshel, A. *J. Biol. Chem.* **1998**, 273 (42), 27035. doi:10.1074/jbc.273.42.27035. PMID:9765214.; (d) Warshel, A. *J. Biol. Chem.* **1998**, 273 (42), 27035. doi:10.1074/jbc.273.42.27035. PMID:9765214.; (e) Warshel, A.; Strajbl, M.; Villà, J.; Florián, J. *Biochemistry* **2000**, 39 (48), 14728. doi:10.1021/bi000987h. PMID: 11101287.; (f) Villà, J.; Warshel, A. *J. Phys. Chem. B* **2001**, 105 (33), 7887. doi:10.1021/jp011048h.; (g) Hollfelder, F.; Kirby, A. J.; Tawfik, D. S. *J. Org. Chem.* **2001**, 66 (17), 5866. doi:10.1021/jo015723v. PMID:11511264.; (h) Warshel, A. *Annu. Rev. Biophys. Biomol. Struct.* **2003**, 32 (1), 425. doi:10.1146/annurev.biophys.32.110601.141807. PMID: 12574064.
- (17) Perutz, M. *Proc. R. Soc. Lond. B. Biol. Sci.* **1967**, 167 (1009), 448. doi:10.1098/rspb.1967.0046.
- (18) Frisch, M. J.; Trucks, G. W.; Schlegel, H. B.; Scuseria, G. E.; Robb, M. A.; Cheeseman, J. R.; Montgomery, J. A., Jr.; Vreven, T.; Kudin, K. N.; Burant, J. C.; Millam, J. M.; Iyengar, S. S.; Tomasi, J.; Barone, V.; Mennucci, B.; Cossi, M.; Scalmani, G.; Rega, N.; Petersson, G. A.; Nakatsuji, H.; Hada, M.; Ehara, M.; Toyota, K.; Fukuda, R.; Hasegawa, J.; Ishida, M.; Nakajima, T.; Honda, Y.; Kitao, O.; Nakai, H.; Klene, M.; Li, X.; Knox, J. E.; Hratchian, H. P.; Cross, J. B.; Adamo, C.; Jaramillo, J.; Gomperts, R.; Stratmann, R. E.; Yazyev, O.; Austin, A. J.; Cammi, R.; Pomelli, C.; Ochterski, J. W.; Ayala, P. Y.; Morokuma, K.; Voth, G. A.; Salvador, P.; Dannenberg, J. J.; Zakrzewski, V. G.; Dapprich, S.; Daniels, A. D.; Strain, M. C.; Farkas, O.; Malick, D. K.; Rabuck, A. D.; Raghavachari, K.; Foresman, J. B.; Ortiz, J. V.; Cui, Q.; Baboul, A. G.; Clifford, S.; Cioslowski, J.; Stefanov, B. B.; Liu, G.; Liashenko, A.; Piskorz, P.; Komaromi, I.; Martin, R. L.; Fox, D. J.; Keith, T.; Al-Laham, M. A.; Peng, C. Y.; Nanayakkara, A.; Challacombe, M.; Gill, P. M. W.; Johnson, B.; Chen, W.; Wong, M. W.; Gonzalez, C.; Pople, J. A. *Gaussian 03*, Revision B03; Gaussian, Inc.: Pittsburgh, PA, 2003.
- (19) (a) Curtiss, L. A.; Frurip, D. J.; Blander, M. *J. Chem. Phys.* **1979**, 71 (6), 2703. doi:10.1063/1.438628.; (b) Curtiss, L. A.; Blander, M. *Chem. Rev.* **1988**, 88 (6), 827. doi:10.1021/cr00088a002.
- (20) (a) Chocholoušová, J.; Vacek, J.; Hobza, P. *J. Phys. Chem. A* **2003**, 107 (17), 3086. doi:10.1021/jp027637k.; (b) Colominas, C.; Teixido, J.; Cemeli, J.; Luque, F. J.; Orozco, M. *J. Phys. Chem. B* **1998**, 102 (12), 2269. doi:10.1021/jp973414w.
- (21) Hatherley, L. D.; Brown, R. D.; Godfrey, P. D.; Pierlot, A. P.; Caminati, W.; Damiani, D.; Melandri, S.; Favero, L. B. *J. Phys. Chem.* **1993**, 97 (1), 46. doi:10.1021/j100103a011.
- (22) (a) Lee, C.; Yang, W.; Parr, R. G. *Phys. Rev. B* **1988**, 37 (2), 785. doi:10.1103/PhysRevB.37.785.; (b) Becke, A. D. *J. Chem. Phys.* **1993**, 98 (7), 5648. doi:10.1063/1.464913.
- (23) Hehre, W. J.; Radom, L.; v Schleyer, P. R.; Pople, J. A. *Ab initio Molecular Orbital Theory*; Wiley: New York, 1986.

(24) Kinetic analyses for the neutral and 2HP/2PD-catalyzed hydration reactions were performed using the strategies of refs. 1b and 3. For acetic-acid catalysis, the kinetic analysis was

performed using the strategy of ref. 2, including consideration of the dimerization of acetic acid.

# Trends in the frequencies of $\nu(\text{AsO}_x\text{H}_{x-1})$ [ $x = 2-4$ ] in selected As(V)-containing compounds investigated using quantum chemical calculations

Adrian Adamescu, Holly Gray, Katherine M.E. Stewart, I.P. Hamilton, and Hind A. Al-Abadleh

**Abstract:** The application of computational chemistry to studies in geochemistry is increasingly becoming invaluable in explaining experimentally observed trends for surface interactions of pollutants with sorbents ubiquitous in the environment. We report computational results on factors that affect the force constant of  $\text{AsO}_x$  bonds in As(V)-containing compounds relevant to geochemical environments. Geometries, atomic charges, and stretching frequencies of  $-\text{AsO}_x\text{H}_{x-1}$  ( $x = 2-4$ ) moieties in these molecules were calculated using semi-empirical methods (PM3) and density functional theory (B3LYP) for both isolated (gas phase) molecules and hydrated complexes in which the molecules are surrounded by four water molecules. We found that the number of organic substituents has a relatively smaller effect on the force constant of  $\text{AsO}_x$  bonds than protonation. The increase in resonance effect with deprotonation causes As–O bond lengths to increase, and the decrease in resonance in fully deprotonated species with increasing organic substitution causes As–O bond lengths to decrease. In the absence of the resonance effect in fully protonated species, As–O bond lengths increase with more organic substituents. Also, increasing organic substitution causes the charge on the central arsenic atom to decrease. Charges on oxygen atoms in As–OH bonds are more sensitive to deprotonation than to resonance relative to other oxygen atoms in As–O bonds. As expected, frequencies of  $\nu(\text{AsO}_x)$  show an inverse relationship with As–O bond lengths upon deprotonation and organic substitution. Our results have implication for the interpretation of infrared and X-ray absorption spectra of adsorbed As(V)-containing compounds.

**Key words:** organoarsenicals, arsenate, organic oxyanions, computational chemistry, optimized geometries, infrared frequencies, AsO stretching vibration, DFT/B3LYP

**Résumé :** L'application de la chimie théorique aux études de la géochimie devient de plus en plus indispensable pour expliquer les tendances observées expérimentalement les interactions superficielles de polluants avec des sorbants omniprésents de l'environnement. Dans ce travail, on rapporte les résultats de calculs sur les facteurs qui affectent la constante de force des liaisons  $\text{AsO}_x$  dans des composés contenant de l'arsenic pentavalent, As(V), intéressant pour les environnements géochimiques. On a calculé les géométries, les charges atomiques et les fréquences d'élongation des portions  $-\text{AsO}_x\text{H}_{x-1}$  ( $x = 2-4$ ) de ces molécules en faisant appel à des méthodes semi-empiriques (PM3) et à la théorie de la fonctionnelle de la densité (B3LYP) tant pour des molécules isolées (phase gazeuse) que pour des complexes hydratés dans lesquels les molécules sont entourées de quatre molécules d'eau. On a trouvé que, comparativement à la protonation, le nombre de substituants organiques n'a que peu d'effet sur la constante de force des liaisons  $\text{AsO}_x$ . L'augmentation de l'effet de résonance avec la déprotonation provoque une augmentation de la longueur de la liaison As–O alors que la diminution de résonance dans les espèces totalement déprotonées par une augmentation de la substitution organique cause une diminution dans les longueurs des liaisons As–O. En l'absence d'effet de résonance dans les espèces totalement protonées, les longueurs des liaisons As–O augmentent avec une augmentation du nombre de substituants organiques. De plus, une augmentation de la substitution organique provoque une diminution de la charge sur l'atome d'arsenic central. Par comparaison aux autres atomes d'oxygène dans les liaisons As–O, les charges sur les atomes d'oxygène des liaisons As–OH sont plus sensibles à la déprotonation qu'à la résonance. Tel que prévu, les fréquences  $\nu(\text{AsO}_x)$  présentent une relation inverse avec les longueurs des liaisons As–O lors d'une déprotonation ou une substitution organique. Les résultats obtenus dans ce travail ont des implications pour l'interprétation des spectres d'absorption infrarouge ou de rayons-X des composés adsorbés contenant du As(V).

**Mots-clés :** composés organoarséniés, arséniate, oxyanions organiques, chimie théorique, géométries optimisées, fréquences infrarouges, vibration d'élongation AsO, théorie de la fonctionnelle de la densité (TFD/B3LYP)

[Traduit par la Rédaction]

Received 22 July 2009. Accepted 5 October 2009. Published on the NRC Research Press Web site at canjchem.nrc.ca on 18 December 2009.

A. Adamescu, H. Gray, K.M.E. Stewart,<sup>1</sup> I.P. Hamilton, and H.A. Al-Abadleh.<sup>2</sup> Department of Chemistry, Wilfrid Laurier University, Waterloo, ON N2L 3C5, Canada.

<sup>1</sup>Present address: Department of Chemical Engineering, University of Waterloo, Waterloo, Ontario N2L 3G1, Canada.

<sup>2</sup>Corresponding author (e-mail: halabadleh@wlu.ca).

## Introduction

The application of computational chemistry to studies in geochemistry has been the subject of a number of excellent reviews,<sup>1–3</sup> which highlight the usefulness of quantum chemical calculations in explaining trends observed experimentally. In general, studies in geochemistry focus on pollutant origins and impacts, and are motivated by regulations designed to lower levels of contaminants in water and soil. Hence, the fate of contaminants, whether introduced to the environment naturally or anthropomorphically, needs to be quantified through properties such as transport and bioavailability. It is well-established that the interaction of pollutants with soil particles controls these properties.<sup>4</sup> This interaction is a surface phenomenon occurring at the water/solid interface, which necessitates the utilization of surface-sensitive techniques for quantifying thermodynamics and kinetics of binding, and for obtaining structural data on geometries of surface complexes. The most commonly used techniques are attenuated total internal reflectance Fourier transform infrared (ATR-FTIR)<sup>5</sup> and extended X-ray absorption fine structure (EXAFS)<sup>6</sup> spectroscopies, which have proven to be powerful in studying surface complexes under environmentally relevant conditions. For spectroscopic results to be useful in building models for predicting transport and bioavailability of pollutants in the environment, experimental data need to be complemented with computational results. Computational results can verify the interpretation of experimental data and minimize the parameterization of fits used to extract structural information. As an example, Kubicki et al. calculated frequencies, structures, and Gibbs free energy of adsorption ( $\Delta G_{\text{ads}}$ ) of oxyanion complexes of carbon, phosphorus, sulfur, and arsenic on iron and aluminum oxide clusters.<sup>7</sup> Computational results agreed with spectral data from infrared, X-ray absorption, and binding thermodynamics experiments, suggesting that model clusters of surface complexes are useful theoretical models of real systems.

There are, however, fewer theoretical studies on the surface chemistry of organic oxyanions in general, and organoarsenicals in particular. Kubicki and co-workers pioneered the use of hybrid molecular orbital/density functional theory (MO/DFT) for calculating the surface structure of glyphosate (an organophosphorus compound) on FeOOH.<sup>8</sup> For methylated organoarsenicals, the effect of methyl substituents on the AsO force constant (and bond order) was calculated by Gründler et al.,<sup>9</sup> who found that, for the fully deprotonated anions, the force constant (as well as the bond order) increases in this order:  $\text{AsO}_4^{3-} < \text{CH}_3\text{AsO}_3^{2-} < (\text{CH}_3)_2\text{AsO}_2^-$ . They attributed the increase in force constant to increasing As–O bond polarity and decreasing degree of multiple bonding upon oxygen substitution with carbon. Vansant et al.<sup>10</sup> calculated the As–O bond lengths for  $\text{CH}_3\text{AsO}_3\text{H}^-$  and  $\text{CH}_3\text{AsO}_3^{2-}$  species to be 1.65 and 1.69 Å, respectively, and 1.71 Å for As–OH in the former species. It is important to note here that these calculations were done for isolated molecules, which do not accurately reflect the geometry of solvated molecules. Myneni et al.<sup>11</sup> have shown, using quantum chemical calculations, that increasing the number of water molecules from one to four, to simulate solvated arsenate ions, results in decreasing the As–O bond lengths. Similar results were obtained from ab initio calculations by Pye and Rudolph on the geometries of hydrated phosphate ions,

where it was observed that increasing water molecules from one to six to simulate hydration causes an overall decrease in the P–O distances.<sup>12</sup> Such changes to bond distances have consequences for the stretching frequency of the As–O and P–O bonds,  $\nu(\text{AsO}_4)$  and  $\nu(\text{PO}_4)$ .

To accurately interpret the ATR-FTIR spectra of organoarsenicals surface complexes, factors that affect the IR-active vibrational modes of the  $\text{AsO}_x$  moiety in the bulk aqueous phases of these molecules must be understood. This is because binding of organoarsenicals to metal (oxyhydr)oxides occurs via a ligand-exchange mechanism between the  $\text{AsO}_x$  moiety in these molecules and metal cations, and factors such as protonation, hydrogen bonding, and the presence of organic substituents impact the number of infrared bands observed experimentally. We recently reported the ATR-FTIR and Raman spectra of a number of As(V)-containing organoarsenicals of importance in geochemical environments in bulk solid and aqueous phases, and compared these results with those for arsenic acid ( $\text{iAs(V)}$ ,  $\text{H}_3\text{AsO}_4$ ).<sup>13</sup> These compounds include monomethylarsonic acid ( $\text{MMA(V)}$ ,  $\text{CH}_3\text{AsO}_3\text{H}_2$ ), *p*-arsanilic acid ( $\text{p-AsA(V)}$ ,  $\text{H}_2\text{NC}_6\text{H}_4\text{AsO}_3\text{H}_2$ ), and dimethylarsinic acid ( $\text{DMA(V)}$ ,  $(\text{CH}_3)_2\text{AsO}_2\text{H}$ ). We observed, from the analysis of the aqueous phase infrared spectra that increasing the number of organic substituents on the  $\text{AsO}_x$  moiety (where  $x = 2\text{--}3$ ) results in increasing the frequency of  $\nu(\text{AsO}_x)$  for completely deprotonated anions, whereas the opposite trend is observed for completely protonated molecules. We also observed that for a given As(V)-containing compound, the decrease in the protonation state with increasing pH results in red shifting the frequency of  $\nu(\text{AsO}_x)$ . These observations were explained in light of the aforementioned studies<sup>9–11</sup> on the extent of the resonance effect as a result of replacing oxygen with carbon and the decrease in the number of hydrogen atoms bonded to oxygen.

In the present study, we report results from semi-empirical PM3 and DFT calculations on the equilibrium geometries, atomic charges, and vibrational frequencies of hydrated  $\text{iAs(V)}$ ,  $\text{MMA(V)}$ ,  $\text{p-AsA(V)}$ , and  $\text{DMA(V)}$  in order of increasing organic substitution. Due to the acidic nature of the  $-\text{AsO}_x\text{H}_{x-1}$  ( $x = 2\text{--}4$ ) moiety, each of these compounds can exist in multiple protonation states governed by their  $\text{pK}_a$  values.<sup>13,14</sup> Calculations were performed for these compounds in the isolated (gas phase) and hydrated (surrounded with four water molecules to simulate the first hydration sphere) clusters. The results are discussed in light of the resonance effect on calculated As–O bond lengths, atomic charges on arsenic and oxygen atoms, and frequencies of vibrations assigned to  $\nu(\text{AsO}_x)$ .

## Computational methods

Quantum chemical calculations were performed using Spartan 04 (v. 1.0.3)<sup>15</sup> for As(V)-containing compounds that include  $\text{iAs(V)}$ ,  $\text{MMA(V)}$ ,  $\text{p-AsA(V)}$ , and  $\text{DMA(V)}$ . These calculations were done on isolated and hydrated clusters. Hydration of As(V)-containing compounds was modeled by explicitly adding four water molecules. Calculations were also performed using Spartan 08 on fully protonated and deprotonated clusters to implicitly solvate them through a polarizable continuum model that simulates an aqueous environment. The water molecules were added one at a time,



**Table 1.** Bond lengths (Å) in isolated As(V)-containing compounds calculated using DFT (B3LYP).

Isolated species	6-31G*				6-311+G**				Previous theoretical studies		
	As=O <sub>1</sub>	As–O <sub>2</sub>	As–O <sub>3</sub>	As–O <sub>4</sub>	As=O <sub>1</sub>	As–O <sub>2</sub>	As–O <sub>3</sub>	As–O <sub>4</sub>	As–O	As–OH	References
HO–AsO <sub>3</sub> H <sub>2</sub>	1.61	1.74	1.75	1.76	1.62	1.75	1.76	1.77			
HO–AsO <sub>3</sub> H <sup>–</sup>	1.66	1.64	1.83	1.83	1.66	1.64	1.83	1.83	1.64	1.81	11
HO–AsO <sub>3</sub> <sup>2–</sup>	1.69	1.67	1.67	1.92	1.71	1.69	1.69	1.94	1.68	1.88	11
AsO <sub>4</sub> <sup>3–</sup>	1.74	1.74	1.74	1.74	1.76	1.76	1.76	1.76	1.74	—	11
CH <sub>3</sub> –AsO <sub>3</sub> H <sub>2</sub>	1.63	1.78	1.78	—	1.63	1.78	1.78	—			
CH <sub>3</sub> –AsO <sub>3</sub> H <sup>–</sup>	1.66	1.65	1.85	—	1.67	1.66	1.86	—	1.65	1.71	10
CH <sub>3</sub> –AsO <sub>3</sub> <sup>2–</sup>	1.69	1.69	1.69	—	1.71	1.71	1.71	—	1.69	—	10
H <sub>2</sub> NC <sub>6</sub> H <sub>4</sub> –AsO <sub>3</sub> H <sub>2</sub>	1.63	1.78	1.79	—	1.63	1.79	1.79	—			
H <sub>2</sub> NC <sub>6</sub> H <sub>4</sub> –AsO <sub>3</sub> H <sup>–</sup>	1.66	1.65	1.84	—	1.67	1.66	1.85	—			
H <sub>2</sub> NC <sub>6</sub> H <sub>4</sub> –AsO <sub>3</sub> <sup>2–</sup>	1.69	1.69	1.69	—	1.70	1.70	1.70	—			
(CH <sub>3</sub> ) <sub>2</sub> AsO <sub>2</sub> H	1.64	1.80	—	—	1.64	1.81	—	—			
(CH <sub>3</sub> ) <sub>2</sub> AsO <sub>2</sub> <sup>–</sup>	1.67	1.67	—	—	1.68	1.68	—	—			

and the geometry of the complex was optimized at each addition. All nuclear coordinates in the complex were relaxed to minimum potential-energy positions with no constraints on symmetry or structural parameters. Semi-empirical calculations using the PM3 method<sup>16</sup> were performed first to calculate the equilibrium geometry and vibrational frequencies. This method was used by Myneni et al.<sup>11</sup> for modeling iAs(V) clusters. We show below that this method overestimates vibrational frequencies when compared with experimental values. Hence, coordinates from these calculations were used as input for DFT calculations, which (as noted earlier) produced accurate results for oxyanion surface complexes. These calculations were performed with the B3LYP functional<sup>17,18</sup> using the 6-31G\* basis set,<sup>19</sup> and were followed by calculations using the larger 6-311+G\*\* basis set.<sup>20</sup> The latter basis set has diffuse functions on heavy atoms but not hydrogen. Throughout this paper, results reported are those for the larger basis set unless noted otherwise. After ensuring that all vibrational frequencies were real, adjustments to the optimized structure were made (typically by rotating one or more water molecules), and the resulting structure was re-optimized. This process was repeated until we were reasonably sure that we had found the minimum-energy equilibrium geometry.

Many methods have been proposed for calculating atomic charges, of which the best known is probably Mulliken population analysis.<sup>19</sup> However, it is well-known that Mulliken atomic charges are strongly basis-set-dependent. For greater consistency between the 6-31G\* and 6-311+G\*\* basis sets, we therefore use natural population analysis ( $Q_{\text{NPA}}$ ),<sup>21</sup> which has been shown to resolve largely the basis-set-dependence problem. As expected, results for  $Q_{\text{NPA}}$  from DFT calculations are similar with the two basis sets, 6-31G\* and 6-311+G\*\*, and values reported are those for the larger basis set.

Calculated vibrational frequencies are usually scaled by a factor,  $F$ , to correct for anharmonicity.<sup>21</sup> While a single scaling factor can typically be used for hydrocarbon vibrations, several authors have concluded that for metal systems, independent scaling factors should be used for each vibration involving the metal atom.<sup>22–24</sup> Scaling factors used here to correct harmonic frequencies corresponding to  $\nu(\text{AsO}_x)$  are  $F = 1.0199$  in iAs(V), and  $F = 0.9787$  in organoarsenicals MMA(V),  $p$ -AsA(V), and DMA(V). The former factor was used by Jensen et al.<sup>23</sup> to correct  $\nu(\text{As–O–As})$  in tetraarsenic

hexoxide ( $\text{As}_4\text{O}_6$ ), and the latter factor was used to correct  $\nu(\text{As=O})$  in trimethylarsine oxide  $[(\text{CH}_3)_3\text{AsO}]$ .<sup>24</sup> Kubicki et al.<sup>7</sup> used a factor of 0.96 to scale calculated frequencies for hydrated iAs(V) and iAs(III) and their surface complexes on iron and aluminum oxide clusters. These scaling factors for As(V)-containing compounds change frequency values by  $\pm 2\%$ – $4\%$ . According to Stewart and Seiler,<sup>16,25</sup> vibrational frequencies were not used in developing the PM3 method, and hence no scaling factors were used to correct frequencies from PM3 calculations.

## Results and discussion

### Equilibrium geometries of isolated and hydrated As(V)-containing compounds

Table 1 summarizes the As–O bond lengths from DFT(B3LYP) calculations on isolated As(V)-containing compounds along with values reported previously for iAs(V).<sup>10,11</sup> Analyzing trends in structural parameters for isolated species is important when discussing the effect of hydration and hydrogen bonding on these parameters for the same compounds (vide infra). Minimum-energy geometries of all protonation states of the  $-\text{AsO}_x\text{H}_{x-1}$  ( $x = 2-4$ ) moiety in each compound were calculated so that correlations could be drawn between the extent of charge delocalization (i.e., resonance) and As–O bond lengths. Bond lengths calculated for fully protonated and deprotonated species using DFT(B3LYP/6-31G\*) and a polarizable continuum model are within 0% to  $\pm 2\%$  of those calculated for the gas-phase species. Fully protonated As(V)-containing compounds have no resonance effect among the As–O bonds. For these molecules, increasing the number of organic substituents on the  $-\text{AsO}_x\text{H}_{x-1}$  ( $x = 2-4$ ) moiety slightly increased the length of the As=O<sub>1</sub> bond from 1.62 Å in  $\text{H}_3\text{AsO}_4$  to 1.64 Å in  $(\text{CH}_3)_2\text{AsO}_2\text{H}$ , and caused a more dramatic increase in the As–OH bond length from 1.76 Å in  $\text{H}_3\text{AsO}_4$  to 1.81 Å in  $(\text{CH}_3)_2\text{AsO}_2\text{H}$ . This trend may be attributed to the electron-donating abilities (to the central As atom) from methyl (in MMA and DMA) and phenyl groups (in  $p$ -AsA) causing a relative increase in electrostatic repulsion with the –OH group, hence increasing its distance from the central As atom.

Moreover, for a given isolated As(V)-containing compound, the increase in charge delocalization upon deprotona-

tion has a pronounced effect on the As–O bond lengths, i.e., As=O1 and As–OH bonds increase in length until all bond lengths become equal for the fully deprotonated species. For example, the lengths of the As=O1 and As–OH bonds in  $\text{CH}_3\text{AsO}_3\text{H}_2$  are 1.63 and 1.78 Å, which increase to 1.67 and 1.86 Å in  $\text{CH}_3\text{AsO}_3\text{H}^-$ . For  $\text{CH}_3\text{AsO}_3^{2-}$ , all As–O bonds are 1.71 Å in length. Also, bond lengths of the fully deprotonated species in each of the As(V)-containing compounds studied decrease in the following order:  $\text{AsO}_4^{3-} > \text{CH}_3\text{AsO}_3^{2-} \approx \text{H}_2\text{NC}_6\text{H}_4\text{AsO}_3^{2-} > (\text{CH}_3)_2\text{AsO}_2^-$ . This trend can be explained by the fact that charge delocalization occurs over four bonds in  $\text{AsO}_4^{3-}$  compared with three and two in  $\text{CH}_3\text{AsO}_3^{2-}$ ,  $\text{H}_2\text{NC}_6\text{H}_4\text{AsO}_3^{2-}$ , and  $(\text{CH}_3)_2\text{AsO}_2^-$ , respectively. Hence, lower degree of resonance shortens the As–O bonds with increasing organic substitution.

Since the goal of this study is to model the experimental infrared spectra of aqueous As(V)-containing compounds, explicit addition of water molecules to the isolated compounds is necessary to simulate an aqueous environment. Semi-empirical (PM3) and DFT(B3LYP) calculations were completed for all possible protonation states of the  $-\text{AsO}_x\text{H}_{x-1}$  ( $x = 2-4$ ) moiety in each As(V)-containing compound surrounded by four water molecules. Figure 1 shows energy-minimized geometries of these hydrated As(V)-containing clusters using DFT(B3LYP/6-311+G\*\*) from fully protonated (left side) to fully deprotonated (right side), and in order of increasing the number of organic substituents (top to bottom). Calculated values of the As–O bond lengths are summarized in Table 2, and also plotted as a function of the protonation state for each As(V)-containing compound in Fig. 2. Semi-empirical PM3 calculations were performed with eight water molecules for fully protonated and fully deprotonated species of each As(V)-containing compound, and results are listed in Table 2 and shown as empty circles in the left panel of Fig. 2. Bond-length values from our calculations on clusters of four  $\text{H}_2\text{O}$  molecules are close to those reported previously.<sup>11</sup> Kubicki et al.<sup>7</sup> calculated the optimized geometries of  $\text{H}_2\text{AsO}_4^-$  and  $\text{HAsO}_4^{2-}$  molecules surrounded by eight water molecules using a hybrid molecular orbital (MO/DFT) method and basis sets similar to those in our study, but the results of their calculations were not shown in the paper for comparison. Trends observed for these arsenic molecules are similar to those observed by Pye and Michels for the corresponding phosphorus molecules.<sup>26,27</sup>

Our results indicate that the four water molecules can be regarded as the first “hydration shell” through forming direct hydrogen bonds with the  $-\text{AsO}_x\text{H}_{x-1}$  ( $x = 2-4$ ) moiety in each As(V)-containing compound with  $\text{OH}\cdots\text{O}$  distances varying from 1.67 to 2.09 Å as in clusters XI and IV (Fig. 1), respectively. These hydrogen-bonding values are indicative of moderate-strength hydrogen bonds.<sup>28</sup> Table 3 lists the calculated hydrogen-bond distances in hydrated As(V)-containing clusters. Additional water molecules interact more strongly with each other and with the first “hydration shell”, with no direct interaction with the  $-\text{AsO}_x\text{H}_{x-1}$  ( $x = 2-4$ ) moiety. This might explain the insignificant change in the As–O bond lengths for clusters containing eight relative to four waters. Solid lines are shown in Fig. 2 to highlight trends in the As–O bond lengths in hydrated As(V)-containing clusters as a function of protonation

state and organic substitution, and their slopes are nearly similar using PM3 and DFT methods. These trends are also similar to those observed for isolated As(V)-containing compounds listed in Table 1 and explained earlier, namely, the increase in resonance effect with deprotonation causing As–O bonds to increase in length, and the decrease in resonance in fully deprotonated species with increasing the number of organic substituents causing As–O bonds to be shorter. The most obvious difference among As–O bond lengths for isolated and hydrated As(V)-containing compounds is the inequality observed for fully deprotonated and hydrated species. This is clearly due to the influence of hydrogen bonding between water molecules in the first hydration shell and the  $-\text{AsO}_x^{x-1}$  ( $x = 2-4$ ) moieties on charge delocalization among As–O bonds. The section below analyzes in detail the effect of protonation state and organic substitution on atomic charges in hydrated As(V)-containing compounds.

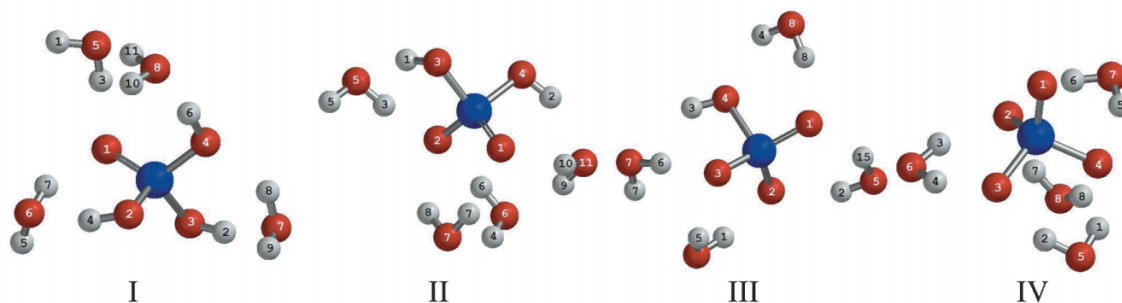
### Charge distribution in hydrated As(V)-containing compounds

To quantify the charge distribution as a function of protonation state and organic substitution, calculated charges derived from natural population analysis ( $Q_{\text{NPA}}$ ) on central arsenic atoms, oxygen atoms in As=O, and As–OH bonds, respectively, are shown in Fig. 3 for each hydrated As(V)-containing compound. The values of atomic  $Q_{\text{NPA}}$  were obtained from semi-empirical PM3 and DFT calculations, and the results are summarized in Table 4. It may be seen that, as expected, the PM3 calculations underestimate the magnitude of the charges on the arsenic and oxygen atoms relative to the DFT calculations. We note that, at least for oxygen atoms, an accurate procedure for correcting PM3 charges has been developed,<sup>29</sup> but for our systems, it was unnecessary to consider this procedure because DFT calculations are feasible and more accurate.

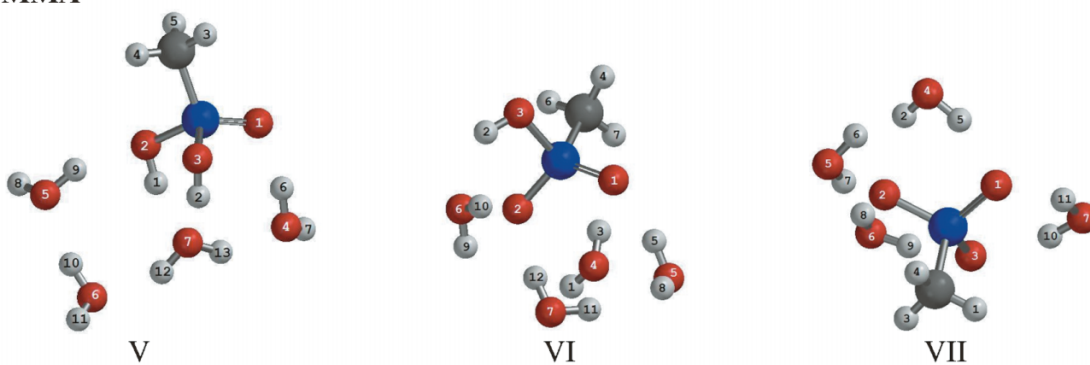
Values of atomic  $Q_{\text{NPA}}$  reveal that, for a given hydrated As(V)-containing compound, the partial positive charge on As changes little with decreasing protonation. The strongest effect on  $Q(\text{As})_{\text{NPA}}$  is the number of organic substituents, which as noted earlier, are electron-donating groups. For a given protonation state of the hydrated As(V)-containing compound, positive values of  $Q(\text{As})_{\text{NPA}}$  decrease in this order:  $\text{iAs(V)} > \text{MMA(V)} \approx \text{p-AsA(V)} > \text{DMA(V)}$ , consistent with the increase in electron donation from organic substituents to the central As atom, which is proportional to the number of substituents. In addition, Fig. 3b shows that the negative charge on O1, which is double bonded to the central As atom, becomes more negative with decreasing protonation, suggesting relatively more electron density on O1 in fully deprotonated species compared with the fully protonated species. This trend can be explained by the fact that the loss of protons from neighboring As–OH pumps electron density into As–O bonds. Oxygen atoms involved in resonance will experience additional negative charge on top of their own non-bonding lone pairs of electrons. It is interesting to note that the degree of organic substitution has minimal effect on  $Q(\text{O1})_{\text{NPA}}$ , compared with that on  $Q(\text{As})_{\text{NPA}}$ , which is likely due to the minimum orbital overlap between O1 and carbon atoms. The above interpretation explains why the value of  $Q(\text{O1})_{\text{NPA}}$  is the same for the first deprotonation state of all the hydrated As(V)-containing compound:

**Fig. 1.** Minimum-energy equilibrium geometries of hydrated As(V)-containing clusters using DFT(B3LYP/6-311+G\*\*) from fully protonated (left side) to fully deprotonated (right side). Atoms of different elements are shown in different colors: arsenic, blue; oxygen, red; hydrogen, light gray; carbon, dark gray; and nitrogen, light purple. The chemical formula of each cluster is listed in Table 2.

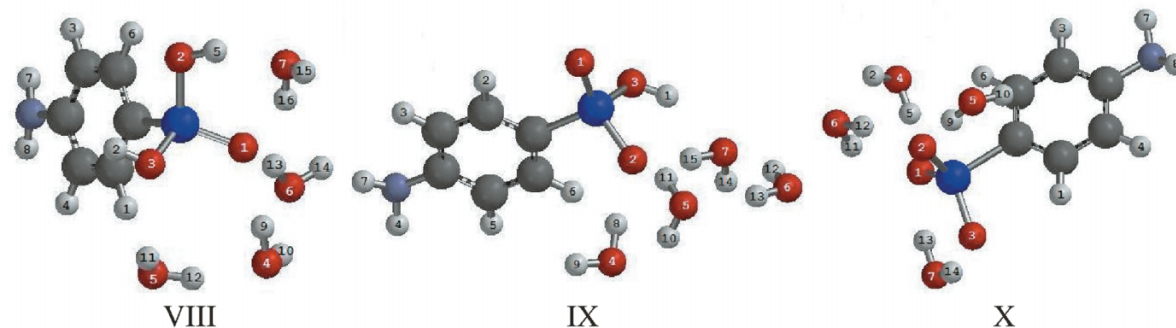
### iAs (V)



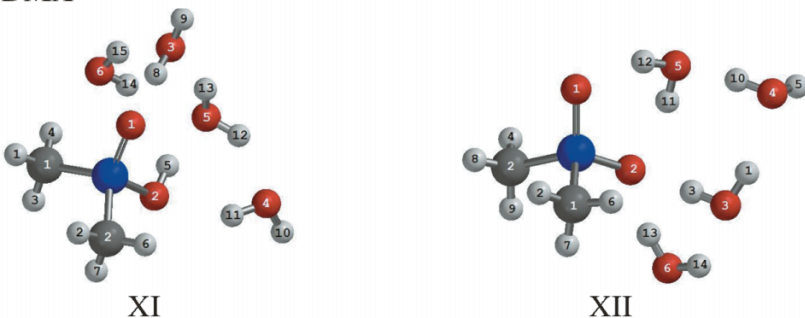
### MMA



### *p*-AsA



### DMA



$\text{H}_2\text{AsO}_4^-$ ,  $\text{CH}_3\text{-AsO}_3\text{H}^-$ ,  $\text{Ar-AsO}_3\text{H}^-$ , and  $(\text{CH}_3)_2\text{AsO}_2^-$ . The degree of resonance and charge delocalization between  $\text{As=O1}$  and  $\text{As-O}^-$  are relatively similar and independent of

the number of organic substituents. For the second protonation state of iAs(V), MMA(V), and *p*-AsA(V) ( $\text{HAsO}_4^{2-}$ ,  $\text{CH}_3\text{-AsO}_3^{2-}$ ,  $\text{Ar-AsO}_3^{2-}$ ), values of  $Q(\text{O1})_{\text{NPA}}$  in  $\text{CH}_3\text{-}$

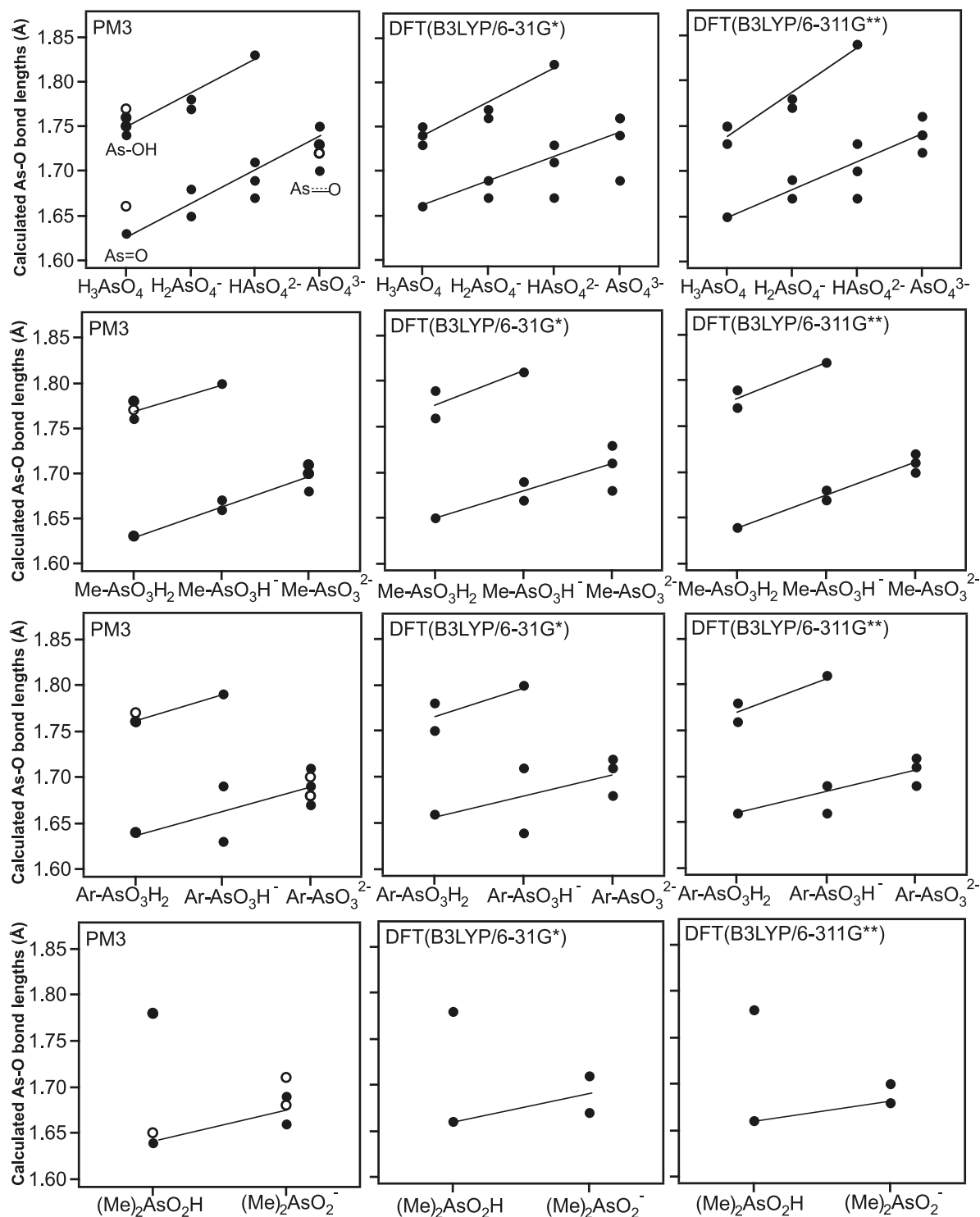
**Table 2.** Calculated As–O bond lengths (Å) in hydrated As(V)-containing compounds.

No. <sup>a</sup>	Hydrated species: M(H <sub>2</sub> O) <sub>4</sub> ; M =	PM3				DFT(B3LYP/6–31G*)				DFT(B3LYP/6–311+G**)				Previous theoretical studies		
		As=O <sub>1</sub>	As–O <sub>2</sub>	As–O <sub>3</sub>	As–O <sub>4</sub>	As=O <sub>1</sub>	As–O <sub>2</sub>	As–O <sub>3</sub>	As–O <sub>4</sub>	As=O <sub>1</sub>	As–O <sub>2</sub>	As–O <sub>3</sub>	As–O <sub>4</sub>	As–O	As–OH	References
I	HO–AsO <sub>3</sub> H <sub>2</sub>	1.63	1.75	1.74	1.76	1.66	1.75	1.73	1.74	1.65	1.75	1.73	1.75	1.60	1.76	11
	·····(H <sub>2</sub> O) <sub>8</sub>	1.66	1.77	1.75	1.76											
II	HO–AsO <sub>3</sub> H <sup>–</sup>	1.65	1.68	1.77	1.78	1.67	1.69	1.76	1.77	1.67	1.69	1.77	1.78	1.63	1.81	11
III	HO–AsO <sub>3</sub> <sup>2–</sup>	1.67	1.71	1.69	1.83	1.67	1.73	1.71	1.82	1.67	1.73	1.70	1.84	1.68	1.87	11
IV	AsO <sub>4</sub> <sup>3–</sup>	1.70	1.75	1.73	1.75	1.69	1.76	1.74	1.76	1.72	1.76	1.74	1.74	1.73	—	11
	···(H <sub>2</sub> O) <sub>8</sub>	1.72	1.73	1.72	1.72											
V	CH <sub>3</sub> –AsO <sub>3</sub> H <sub>2</sub>	1.63	1.78	1.76	—	1.65	1.76	1.79	—	1.64	1.79	1.77	—			
	···(H <sub>2</sub> O) <sub>8</sub>	1.63	1.78	1.77	—											
VI	CH <sub>3</sub> –AsO <sub>3</sub> H <sup>–</sup>	1.67	1.66	1.80	—	1.69	1.67	1.81	—	1.67	1.68	1.82	—			
VII	CH <sub>3</sub> –AsO <sub>3</sub> <sup>2–</sup>	1.70	1.71	1.68	—	1.71	1.68	1.73	—	1.71	1.72	1.70	—			
	···(H <sub>2</sub> O) <sub>8</sub>	1.70	1.70	1.71												
VIII	H <sub>2</sub> NC <sub>6</sub> H <sub>4</sub> –AsO <sub>3</sub> H <sub>2</sub>	1.64	1.76	1.76	—	1.66	1.75	1.78	—	1.66	1.76	1.78	—			
	···(H <sub>2</sub> O) <sub>8</sub>	1.64	1.76	1.77	—											
IX	H <sub>2</sub> NC <sub>6</sub> H <sub>4</sub> –AsO <sub>3</sub> H <sup>–</sup>	1.63	1.69	1.79	—	1.64	1.71	1.80	—	1.66	1.69	1.81	—			
X	H <sub>2</sub> NC <sub>6</sub> H <sub>4</sub> –As <sub>3</sub> <sup>2–</sup>	1.71	1.69	1.67	—	1.72	1.71	1.68	—	1.72	1.71	1.69	—			
	···(H <sub>2</sub> O) <sub>8</sub>	1.70	1.68	1.68												
XI	(CH <sub>3</sub> ) <sub>2</sub> AsO <sub>2</sub> H	1.64	1.78	—	—	1.66	1.78	—	—	1.66	1.78	—	—			
	···(H <sub>2</sub> O) <sub>8</sub>	1.65	1.78	—	—											
XII	(CH <sub>3</sub> ) <sub>2</sub> AsO <sub>2</sub> <sup>–</sup>	1.66	1.69	—	—	1.67	1.71	—	—	1.68	1.70	—	—			
	···(H <sub>2</sub> O) <sub>8</sub>	1.68	1.71	—	—											

<sup>a</sup>These numbers match those in Fig. 1. The reader is referred to Fig. 1 for numbers of oxygen atoms.



**Fig. 2.** Calculated As–O bond lengths in hydrated As(V)-containing clusters surrounded by four H<sub>2</sub>O molecules (filled circles) using PM3 (left), DFT(B3LYP/6–31G\*) (centre), and DFT(B3LYP/6–311G\*\*) (right), respectively. The *x*-axis represents the possible protonation states of the –AsO<sub>*x*</sub>H<sub>*x*–1</sub> (*x* = 2–4) moiety in iAs(V), MMA(V), *p*-AsA(V), and DMA(V) (from top). Me = CH<sub>3</sub> and Ar = H<sub>2</sub>NC<sub>6</sub>H<sub>4</sub>. The empty circles in the left panel are the As–O bond lengths in hydrated As(V)-containing clusters surrounded by eight H<sub>2</sub>O molecules. Trend lines are shown to guide the eye.



$AsO_3^{2-} \approx Ar-AsO_3^{2-}$  and are more negative than that in  $HAsO_4^{2-}$ . While the degree of resonance among As–O bonds is the same in these species, it is likely that this trend in  $Q(O1)_{NPA}$  is due to the electron-donating abilities of

methyl and aromatic substituents compared with the electron-withdrawing abilities of the OH group in  $HAsO_4^{2-}$ . It is interesting to note that  $Q(O1)_{NPA}$  in fully deprotonated iAs(V),  $AsO_4^{3-}$ , is the same as that in  $CH_3-AsO_3^{2-}$  and  $Ar-$

**Table 3.** Calculated hydrogen-bond lengths in hydrated As(V)-containing compounds between water molecules and  $-\text{AsO}_x\text{H}_{x-1}$  ( $x = 2-4$ ) moiety.

Hydrated species $\text{M}(\text{H}_2\text{O})_4$ ; $\text{M} =$	H-bond lengths (Å) – PM3 level	H-bond lengths (Å) – 6-31G* level	H-bond lengths (Å) – 6-311+G** level
$\text{HO}-\text{AsO}_3\text{H}_2$	O1H7: 1.80 O4H8: 1.83	O1H7: 1.86 O4H8: 2.01	O1H7: 1.93 O4H8: 2.03
$\text{HO}-\text{AsO}_3\text{H}^-$	O1H10: 1.81 O2H6: 1.78, O2H8: 1.84 H1O5: 1.86	O1H10: 1.93 O2H6: 1.88, O2H8: 1.95 H1O5: 1.95	O1H10: 2.03 O2H6: 1.95 H1O5: 1.98
$\text{HO}-\text{AsO}_3^{2-}$	O2H4: 1.77 O3H5: 1.80	O2H4: 1.76 O3H5: 1.87	O2H4: 1.77 O3H5: 1.99
$\text{AsO}_4^{3-}$	O2H6: 1.79, O2H7: 1.79 O3H2: 1.76, O3H4: 1.76 O4H1: 1.77, O4H8: 1.79	O2H6: 1.89, O2H7: 1.90 O3H2: 1.82, O3H4: 1.82 O4H1: 1.87, O4H8: 1.90	O2H5: 1.68, O2H7: 1.84 O3H4: 2.09, O3H9: 1.94 O4H6: 1.84, O4H8: 1.76
$\text{CH}_3-\text{AsO}_3\text{H}_2$	O1H6: 1.79 O2H9: 1.82 H1O7: 1.82 H2O7: 1.84	O1H6: 1.80 O2H9: 1.90 H1O7: 1.70 H2O7: 1.89	O1H6: 1.81 O2H9: 1.93 H1O7: 1.81 H2O7: 2.04
$\text{CH}_3-\text{AsO}_3\text{H}^-$	O1H3: 1.78, O1H5: 1.78 O2H10: 1.83, O2H12: 1.84	O1H3: 1.81, O1H5: 1.94 O2H10: 1.98, O2H12: 2.09	O1H3: 1.98, O1H5: 1.86 O2H10: 1.75, O2H12: 1.84
$\text{CH}_3-\text{AsO}_3^{2-}$	O1H5: 1.79, O1H11: 1.73 O2H7: 1.78, O2H8: 1.80 O3H9: 1.80	O1H5: 1.80, O1H11: 1.84 O2H7: 1.81, O2H8: 1.97 O3H9: 1.89	O1H5: 1.85, O1H11: 1.96 O2H7: 1.76, O2H8: 1.99 O3H9: 1.93, O3H10: 1.96
$\text{H}_2\text{NC}_6\text{H}_4-\text{AsO}_3\text{H}_2$	O1H13: 1.78, O1H16: 1.80 H5O7: 1.82	O1H9: 2.05, O1H13: 1.87 H5O7: 1.74	O1H9: 2.03, O1H13: 1.88 H5O7: 1.82
$\text{H}_2\text{NC}_6\text{H}_4-\text{AsO}_3\text{H}^-$	O2H8: 1.76, O2H11: 1.80 H1O7: 1.88	O2H8: 1.69, O2H11: 1.95, H1O7: 1.95	O1H5: 1.94, O1H13: 1.95 O2H9: 1.68, O2H12: 1.73, H1O5: 1.99
$\text{H}_2\text{NC}_6\text{H}_4-\text{AsO}_3^{2-}$	O1H5: 1.79, O1H11: 1.80 O2H9: 1.74, O2H12: 1.79 O3H14: 1.81	O1H5: 1.83, O1H11: 1.95 O2H9: 1.72, O2H12: 1.81 O3H14: 1.90	O1H5: 1.75, O1H11: 2.08 O2H9: 1.67, O2H12: 1.84 O3H14: 1.93
$(\text{CH}_3)_2\text{AsO}_2\text{H}$	O1H8: 1.77 O2H11: 1.83 H5O5: 1.78	O1H8: 1.67 O2H11: 1.99 H5O5: 1.68	O1H8: 1.67 O2H11: 2.08 H5O5: 1.73
$(\text{CH}_3)_2\text{AsO}_2^-$	O1H12: 1.81 O2H3: 1.79, O2H11: 1.80	O1H12: 1.85 O2H3: 1.81, O2H11: 1.89	O1H12: 1.92 O2H3: 1.84, O2H11: 1.94

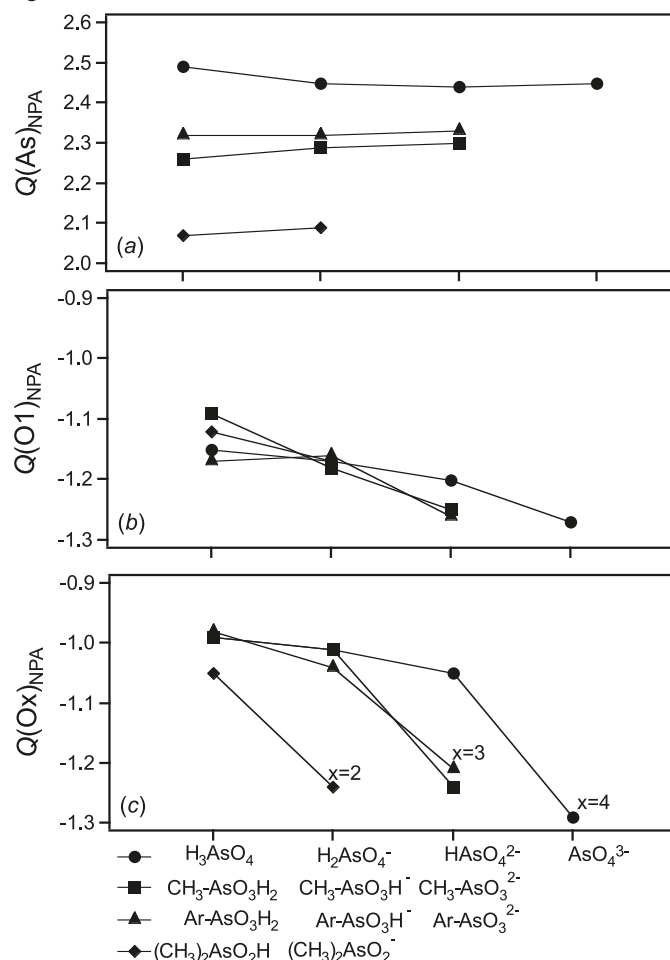
**Note:** The reader is referred to Fig. 1 for numbers of oxygen atoms.

$\text{AsO}_3^{2-}$ , suggesting that the loss of the last proton caused a relative increase in electron density in a manner similar to electron donation by organic substituents.

Moreover, Fig. 3c shows trends in the atomic  $Q(\text{Ox})_{\text{NPA}}$  ( $x = 2-4$ ) in hydrated disubstituted ( $x = 2$ ), monosubstituted ( $x = 3$ ), and unsubstituted ( $x = 4$ ) As(V)-containing compounds, respectively. These oxygen atoms are bonded to hydrogen (i.e., As–OH) and are the last ones to deprotonate. Values of  $Q(\text{Ox})_{\text{NPA}}$  ( $x = 2-4$ ) are clearly sensitive to deprotonation, and relatively insensitive to resonance among other As–O bonds. These atomic charge values become ~25% higher (i.e., more negative) in fully deprotonated and hydrated As(V)-containing compounds relative to the fully protonated species, compared with ~6% increase due to deprotonation of other As–OH bonds and the enhancement in resonance as a result. Judging from the relative values of  $Q(\text{Ox})_{\text{NPA}}$  ( $x = 2-4$ ) in fully protonated and deprotonated species, we conclude that the effect of the degree of organic substitution on these atomic charges is insignificant. It is interesting to note that when comparing values of  $Q(\text{O1})_{\text{NPA}}$  and  $Q(\text{Ox})_{\text{NPA}}$  ( $x = 2-4$ ) for fully deprotonated species, one would expect relative agreement due to resonance (i.e., same

charge values on O1 and Ox). This is indeed the case for  $\text{AsO}_4^{3-}$ ,  $\text{CH}_3-\text{AsO}_3^{2-}$ , and  $\text{Ar}-\text{AsO}_3^{2-}$ . For  $(\text{CH}_3)_2\text{AsO}_2^-$ ,  $Q(\text{O2})_{\text{NPA}}$  is larger (i.e., more negative) than  $Q(\text{O1})_{\text{NPA}}$  by a factor of 1.2, suggesting that the charge gained due to deprotonation is more localized. This observation might be explained by the lesser degree of resonance among the two As–O bonds in  $(\text{CH}_3)_2\text{AsO}_2^-$  compared with other fully deprotonated species, and also by the fact that O2 is involved in two hydrogen bonds with water in the first hydration shell compared with one hydrogen bond by O1 (Table 3). The involvement of oxygen atoms in hydrogen bonding makes their electron density less available for delocalization among other bonds. This interpretation can also explain the relatively small decrease in  $Q(\text{O1})_{\text{NPA}}$  for  $(\text{CH}_3)_2\text{AsO}_2^-$  compared with  $(\text{CH}_3)_2\text{AsO}_2\text{H}$  (Fig. 3b). Calculations performed using a polarizable continuum model on hydrated fully protonated and deprotonated clusters resulted in  $Q_{\text{NPA}}$  values that are in close agreement with those shown in Fig. 3. As illustrated in the next section, these trends in charge delocalization with its impact on bond lengths (and order) change the force constant of As–O bonds and consequently frequencies of  $\nu(\text{AsO}_x)$ .

**Fig. 3.** Calculated atomic charges,  $Q_{\text{NPA}}$ , for (a) As, (b) O1, and (c) O $_x$  ( $x = 2-4$ ), in hydrated As(V)-containing compounds. The  $x$ -axis shows the chemical formula of the clusters with increasing organic substitution (top to bottom) and deprotonation state (left to right); Ar =  $\text{H}_2\text{NC}_6\text{H}_4$ .



### Effect of protonation state and organic substitution on $\nu(\text{AsO}_x)$ in hydrated As(V)-containing compounds

Frequency calculations were performed on the optimized geometries of each hydrated As(V)-containing compound shown in Fig. 1 to identify vibrations in the spectral range 600–1100  $\text{cm}^{-1}$  containing  $\nu(\text{AsO}_x)$ . These frequencies were calculated using semi-empirical (PM3) and DFT(B3LYP), and the results are presented in Table 5. Filled circles in Fig. 4 show trends in the calculated and scaled frequencies of  $\nu(\text{AsO}_x)$  as a function of the protonation state of a given As(V)-containing compound and degree of organic substitution. Scaling factors,  $F$ , were used to correct calculated frequencies for anharmonicity as described in the Computational methods section. The most-intense spectral component assigned to  $\nu(\text{AsO}_x)$  in a given cluster is labeled by a superscript and was used to normalize the intensities of all spectral components assigned to the same vibration. Only spectral components with intensities greater than 11% of the most-intense  $\nu(\text{AsO}_x)$  component are reported in Table 5. Some of these components are found to be coupled to other vibrational modes such as frustrated rotation (i.e., librational mode) of water molecules in the first hydration shell;<sup>30</sup>

**Table 4.** Calculated atomic charge distribution on As and O in hydrated As(V)-containing compounds using the natural population analysis scheme ( $Q_{\text{NPA}}$ ).

No. <sup>a</sup>	Hydrated species M(H <sub>2</sub> O) <sub>4</sub> ; M =	PM3 level				DFT(B3LYP/6-31G*) level				DFT(B3LYP/6-311+G**) level						
		As	O1	O2	O3	O4	As	O1	O2	O3	O4	As	O1	O2	O3	O4
I	HO-AsO <sub>3</sub> H <sub>2</sub>	+2.12	-0.92	-0.68	-0.66	-0.74	+2.48	-1.10	-1.03	-1.01	-1.05	+2.49	-1.15	-1.04	-0.98	-0.99
II	HO-AsO <sub>3</sub> H <sup>-</sup>	+2.01	-0.94	-1.01	-0.71	-0.71	+2.42	-1.14	-1.16	-1.03	-1.02	+2.45	-1.17	-1.22	-1.01	-1.01
III	HO-AsO <sub>3</sub> <sup>2-</sup>	+1.91	-0.98	-1.05	-1.03	-0.74	+2.39	-1.15	-1.20	-1.17	-1.07	+2.44	-1.20	-1.27	-1.24	-1.05
IV	AsO <sub>3</sub> <sup>3-</sup>	+1.83	-1.09	-1.09	-1.09	-1.09	+2.35	-1.20	-1.23	-1.22	-1.23	+2.45	-1.27	-1.32	-1.29	-1.29
V	CH <sub>3</sub> -AsO <sub>3</sub> H <sub>2</sub>	+1.97	-0.86	-0.72	-0.68	—	+2.29	-1.06	-1.01	-1.06	—	+2.26	-1.09	-1.03	-0.99	—
VI	CH <sub>3</sub> -AsO <sub>3</sub> H <sup>-</sup>	+1.91	-0.98	-0.94	-0.70	—	+2.28	-1.16	-1.13	-1.02	—	+2.29	-1.18	-1.21	-1.01	—
VII	CH <sub>3</sub> -AsO <sub>3</sub> <sup>2-</sup>	+1.83	-1.04	-1.03	-1.00	—	+2.28	-1.18	-1.16	-1.20	—	+2.30	-1.25	-1.27	-1.24	—
VIII	H <sub>2</sub> NC <sub>6</sub> H <sub>4</sub> -AsO <sub>3</sub> H <sub>2</sub>	+2.06	-0.90	-0.72	-0.65	—	+2.33	-1.12	-1.03	-1.00	—	+2.32	-1.17	-1.00	-0.98	—
IX	H <sub>2</sub> NC <sub>6</sub> H <sub>4</sub> -AsO <sub>3</sub> H <sup>-</sup>	+1.95	-0.87	-1.02	-0.72	—	+2.30	-1.08	-1.08	-1.04	—	+2.32	-1.16	-1.20	-1.04	—
X	H <sub>2</sub> NC <sub>6</sub> H <sub>4</sub> -AsO <sub>3</sub> <sup>2-</sup>	+1.87	-1.01	-1.02	-0.98	—	+2.30	-1.19	-1.17	-1.16	—	+2.33	-1.26	-1.24	-1.21	—
XI	(CH <sub>3</sub> ) <sub>2</sub> AsO <sub>2</sub> H	+1.84	-0.85	-0.72	—	—	+2.13	-1.08	-1.06	—	—	+2.07	-1.12	-1.05	—	—
XII	(CH <sub>3</sub> ) <sub>2</sub> AsO <sub>2</sub> <sup>-</sup>	+1.78	-0.90	-0.96	—	—	+2.13	-1.12	-1.16	—	—	+2.09	-1.17	-1.24	—	—

<sup>a</sup>These numbers match those in Fig. 1. The reader is referred to Fig. 1 for numbers of oxygen atoms.

**Table 5.** Calculated frequencies (cm<sup>-1</sup>) of  $\nu(\text{AsO}_x)$  for hydrated As(V)-containing compounds.

Hydrated species: $\text{M}(\text{H}_2\text{O})_4$ ; M =	PM3 level					6-31G* level					6-311+G** level				
$\text{HO-AsO}_3\text{H}_2$	969		841 <sup>a</sup>	830		937		790	769 <sup>a,b</sup>	729	919 <sup>a</sup>				710
$\cdots(\text{H}_2\text{O})_8$		938	837 <sup>a</sup>	830	819										
Reference 11	998				812	805									
$\text{HO-AsO}_3\text{H}^-$		932 <sup>a</sup>			788 <sup>b</sup>	755 <sup>b</sup>	909	889 <sup>a,b</sup>	870	837	726 <sup>b</sup>	887	826 <sup>b</sup>	681 <sup>a</sup>	
Reference 11	1041	937			781	758									
$\text{HO-AsO}_3^{2-}$	929 <sup>a</sup>	910 <sup>b</sup>	860 <sup>b</sup>	851			904	831 <sup>a</sup>	814	764		865 <sup>a</sup>	797 <sup>b</sup>	782	739
Reference 11	944	895			697	684									
$\text{AsO}_4^{3-}$				877 <sup>a,b</sup>	822	796		864		752 <sup>a</sup>				750 <sup>a</sup>	709
$\cdots(\text{H}_2\text{O})_8$	958 <sup>a,b</sup>	905 <sup>b</sup>	898 <sup>b</sup>	885 <sup>b</sup>											702
Reference 11				878	849										
$\text{CH}_3\text{-AsO}_3\text{H}_2$	964 <sup>a</sup>		869 <sup>c</sup>		804	773 <sup>b</sup>	925 <sup>a</sup>				702	917	888		768 <sup>a,b,g</sup>
$\cdots(\text{H}_2\text{O})_8$	982 <sup>a</sup>	876		841	801	773									
$\text{CH}_3\text{-AsO}_3\text{H}^-$	977 <sup>a</sup>	941	905				869 <sup>c</sup>	852 <sup>a,b</sup>	833 <sup>b</sup>		628 <sup>b</sup>	880 <sup>c</sup>	851 <sup>c</sup>	845 <sup>c</sup>	594 <sup>b</sup>
$\text{CH}_3\text{-AsO}_3^{2-}$	944	888 <sup>a,b</sup>	855 <sup>b</sup>					857 <sup>a,b,c</sup>	828 <sup>c</sup>	801 <sup>c</sup>	772 <sup>c</sup>	731 <sup>b</sup>		832	730
$\cdots(\text{H}_2\text{O})_8$	952 <sup>a</sup>	919 <sup>b</sup>	882												
$\text{H}_2\text{NC}_6\text{H}_4\text{-AsO}_3\text{H}_2$	969 <sup>c</sup>				808	791 <sup>a</sup>	893 <sup>b</sup>	882 <sup>a,b</sup>		722 <sup>b</sup>	711 <sup>b</sup>		871 <sup>a</sup>		680
$\cdots(\text{H}_2\text{O})_8$	974				811	790 <sup>a</sup>									
$\text{H}_2\text{NC}_6\text{H}_4\text{-AsO}_3\text{H}^-$	924					767 <sup>a</sup>	951	935 <sup>d</sup>	929	807	784 <sup>a,d</sup>	910		774	716 <sup>a,b</sup>
$\text{H}_2\text{NC}_6\text{H}_4\text{-AsO}_3^{2-}$		902 <sup>a</sup>	888 <sup>f</sup>	882 <sup>b</sup>	852 <sup>f</sup>			861 <sup>a,e</sup>	856 <sup>c</sup>	829 <sup>b</sup>	787 <sup>b</sup>	778 <sup>b</sup>	756 <sup>b</sup>	825 <sup>d</sup>	733
$\cdots(\text{H}_2\text{O})_8$	993 <sup>b</sup>	922 <sup>b</sup>	904 <sup>b</sup>	891b <sup>b,f</sup>	871 <sup>b</sup>	843 <sup>b,d</sup>									
$(\text{CH}_3)_2\text{AsO}_2\text{H}$	958 <sup>a</sup>		863 <sup>c</sup>	860 <sup>c</sup>		733 <sup>b</sup>	912	892 <sup>c</sup>			693 <sup>a,b</sup>		892 <sup>a,c</sup>	873	668 <sup>a,c</sup>
$\cdots(\text{H}_2\text{O})_8$	957 <sup>a</sup>	940	847		820	805 <sup>b</sup>	737								
$(\text{CH}_3)_2\text{AsO}_2^-$	948 <sup>a</sup>	889					913 <sup>c</sup>	881 <sup>a,b,c</sup>						830 <sup>a</sup>	762 <sup>b,c</sup>
$\cdots(\text{H}_2\text{O})_8$	952 <sup>b</sup>	940 <sup>a,b</sup>	892 <sup>b</sup>	800 <sup>b</sup>											

**Note:** Scaling factors,  $F$ , are as following: for organoarsenicals,  $F = 0.9787$  for  $\nu(\text{As}=\text{O})$ , which was used to correct calculated frequencies of trimethylarsine oxide using DFT-B3LYP.<sup>24</sup> For inorganic As(V),  $F = 1.0199$  for  $\nu(\text{As}-\text{O})$ , which was used to correct calculated frequencies of tetraarsenic hexoxide.<sup>23</sup>

<sup>a</sup>Most intense spectral component. Intensities of other components are >11% of most intense component.

<sup>b</sup>Coupled with librational mode (i.e., frustrated rotation) of water molecules.<sup>30</sup>

<sup>c</sup>Coupled with  $\rho(\text{CH}_3)$ .

<sup>d</sup>Coupled with aromatic  $\delta(\text{CH})$ .

<sup>e</sup>Coupled with aromatic  $\delta(\text{NH}_2)$ .

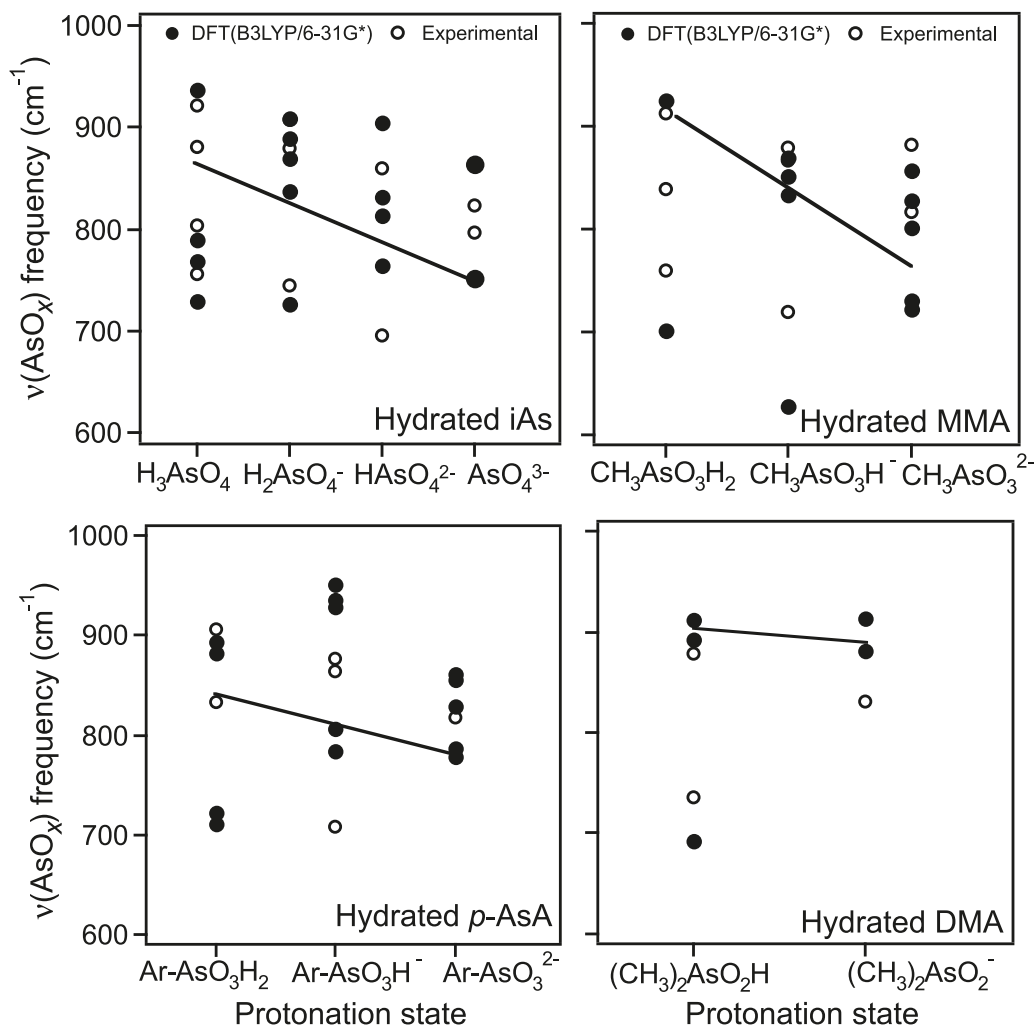
<sup>f</sup>Coupled with aromatic  $\nu(\text{C}-\text{C})$ .

<sup>g</sup>Coupled with  $\delta(\text{AsOH})$ .

<sup>h</sup>Coupled with  $\nu(\text{As}-\text{C})$ .



**Fig. 4.** Calculated vibrational frequencies of As–O bonds in hydrated As(V)-containing clusters calculated using DFT(B3LYP/6–31G\*) (filled circles) compared with the experimental values (empty circles) taken from ref. 13. The *x*-axis represents the possible protonation states of the AsO<sub>*x*</sub> group in iAs(V), MMA(V), *p*-AsA(V), and DMA(V) (from left). Trend lines are shown to guide the eye.

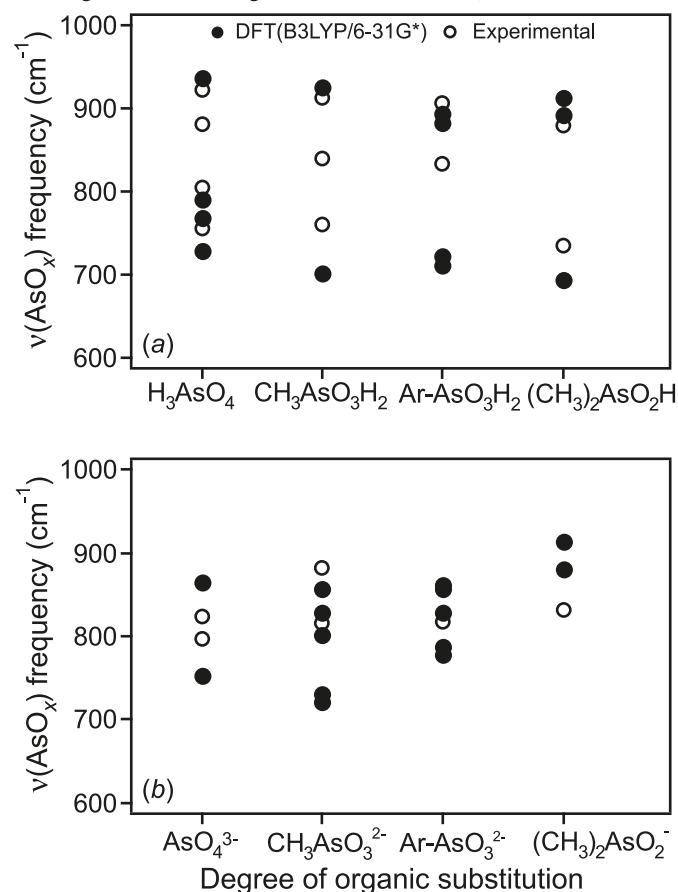


bending vibration of AsOH,  $\delta(\text{AsOH})$ ; rocking vibration of methyl group,  $\rho(\text{CH}_3)$ ; bending vibration of aromatic –CH groups,  $\delta(\text{CH})$ ; bending vibration of aromatic amine substituent,  $\delta(\text{NH}_2)$ ; and stretching vibration of aromatic C–C bonds,  $\nu(\text{C–C})$ . Vibrations coupled to  $\nu(\text{AsO}_x)$  were identified using the visualization tool in Spartan, and only those having similar intensities to that of  $\nu(\text{AsO}_x)$  were labeled in Table 5.

For a given hydrated As(V)-containing compound, calculated frequencies in Table 5 were compared with the experimental frequencies (empty circles in Fig. 4) of aqueous phase As(V)-containing compounds reported as a function of pH using ATR-FTIR.<sup>13</sup> The differences between the scaled frequencies from DFT(B3LYP/6–31G\*) calculations (filled circles) and the spectral components identified experimentally are within 10–80  $\text{cm}^{-1}$ , depending on the cluster. These differences between experimental and calculated frequencies are mainly due to the limitations and assumptions inherent in any computational method including DFT.<sup>31</sup> For hydrated iAs(V) compounds, Table 5 also shows that the frequencies of  $\nu(\text{AsO}_x)$  from our PM3 calculations are in close agreement with those reported by Myneni et al.<sup>11</sup> for

these systems. However, it is clear from Table 5 and Fig. 4 that the PM3 method overestimated the frequencies of  $\nu(\text{AsO}_x)$  when compared with the experimental values. Overall, the calculated frequencies show trends similar to those observed experimentally,<sup>13</sup> namely, inverse relationships of  $\nu(\text{AsO}_x)$  with deprotonation. These results are consistent with the explanation provided above on the effect of deprotonation on the degree of resonance among As–O bonds, i.e., increasing resonance among As–O bonds causes an overall increase in As–O bond lengths (Fig. 2) and a decrease in the force constant of these bonds with deprotonation. For PM3 frequency calculations completed on As(V)-containing compounds surrounded by eight water molecules, results shown in Table 5 agree fairly well with calculations on compounds surrounded by four water molecules. For some clusters with eight water molecules, there are extra spectral components with appreciable intensity compared with the four-water case, which most likely arise from a reduction in the symmetry of the cluster with additional water molecules. The number of spectral components becomes important when spectral fitting is done on the experimental spectra of a given As(V)-containing compound.<sup>32</sup> An in-

**Fig. 5.** Calculated vibrational frequencies of AsO bonds in hydrated As(V)-containing clusters calculated using DFT(B3LYP/6-31G\*) compared with the experimental values (empty circles) taken from ref.13 for (a) fully protonated and (b) fully deprotonated states showing the effect of organic substitution on  $\nu(\text{AsO}_x)$ .



creased number of spectral components assigned to  $\nu(\text{AsO}_x)$  was also observed for hydrated fully protonated and deprotonated As(V)-containing compounds when calculated using DFT(B3LYP/6-31G\*) and a polarizable continuum model. Frequency values are in very close proximity to those shown in Fig. 4. Hence, we conclude that the number of components shown in the filled circles in Fig. 4 is the minimum number needed to fit the experimentally observed data.

Figure 5 also shows frequencies of  $\nu(\text{AsO}_x)$  in hydrated As(V)-containing compounds calculated using DFT(B3LYP/6-31G\*) and compared with the experimental values (empty circles) taken from ref.13 for fully protonated (a) and fully deprotonated (b) states. The data in Fig. 5 are the same as those in Fig. 4, but plotted so as to show the effect of organic substitution on calculated  $\nu(\text{AsO}_x)$ . For fully protonated clusters, the resonance effect does not play a role in explaining trends in  $\nu(\text{AsO}_x)$ , and arsenic-oxygen interactions exist as well-defined As=O and As-OH bonds, giving rise to high frequency ( $>850\text{ cm}^{-1}$ ) and low frequency ( $<800\text{ cm}^{-1}$ ) spectral components. The slight decrease in calculated  $\nu(\text{AsO}_x)$  among fully protonated compounds with increasing number of organic substituents might be due to the increase in electrostatic repulsion with -OH groups that causes an increase in As=O and As-OH bond lengths (vide supra). Frequency trends shown in Fig. 3b for fully de-

protonated species can be explained by the relative degree of resonance among As-O bonds with increasing number of organic substituents. In this case, As-O<sup>-</sup> bonds in  $\text{AsO}_4^{3-}$  are replaced by one As-C bond in  $\text{CH}_3\text{AsO}_3^{2-}$  and  $\text{ArAsO}_3^{2-}$ , and two As-C bonds in  $(\text{CH}_3)_2\text{AsO}_2^-$ . The experimental and calculated frequencies show relatively higher  $\nu(\text{AsO}_x)$  for the latter hydrated compound, which is indicative of more charge localization and minimum resonance in this case. Overall, these results suggest that the number of organic substituents has a lesser effect on the values of  $\nu(\text{AsO}_x)$  compared with the number of -OH groups. This conclusion is consistent with that from the analysis of atomic charges on oxygens of the  $\text{AsO}_x\text{H}_{x-1}$  moiety in hydrated As(V)-containing compounds (Fig. 3). The implications of these results are presented in the following section.

## Conclusions and geochemical implications

In this paper, we reported results from theoretical calculations on the geometries, atomic charges, and vibrational frequencies of a number of As(V)-containing compounds relevant to geochemical environments. Results from quantum chemical calculations aid in the interpretation of the experimental data obtained using ATR-FTIR for characterization of surface complexes. As noted earlier, surface-sensitive measurements from infrared experiments are important for a molecular-level understanding of surface complexation of these compounds, which affects their transport and bioavailability properties. The compounds studied herein were surrounded by four water molecules, which we found to be reasonable for simulating an aqueous environment. These results have important implications for understanding the factors that affect the force constant of  $\text{AsO}_x$  bonds in these compounds, which include bonding to protons and carbon atoms. Protonation (i.e., binding to  $\text{H}^+$ ) of  $\text{AsO}_x$  bonds occurs in neutral and acidic environments and has a strong effect on charge distribution for O<sup>-</sup> atoms in the  $\text{AsO}_x$  moiety, and the overall symmetry of compounds containing this group. This results in increasing the number of IR-active spectral components. We found that the number of organic substituents has a relatively smaller effect on the force constant of  $\text{AsO}_x$  bonds than protonation. Additionally, binding of the  $\text{AsO}_x$  moiety to metal centres in minerals such as  $\text{Fe}^{3+}$  and  $\text{Mg}^{2+}$  instead of protons will also impact the force constant of AsO bonds depending on the nature of the metal cation. Myneni et al.<sup>11</sup> calculated (using the PM3 method)  $\nu(\text{AsO}_x)$  to be  $750\text{--}830\text{ cm}^{-1}$  for As-OM (M = complexing cation), which is blue-shifted relative to that in  $\text{AsO}_4^{3-}$ . We recently reported similar results from the adsorption of *p*-AsA(V) on iron (oxyhydr)oxides.<sup>33,34</sup>

We found, from the comparison of bond lengths and vibrational frequencies, using PM3 and DFT(B3LYP/6-31G\*) methods, that the latter method produces results that agree reasonably better with experimental data and trends expected from chemical intuition. Hence, the number of spectral components assigned to  $\nu(\text{AsO}_x)$  obtained from DFT(B3LYP/6-31G\*) calculations on hydrated As(V)-containing compounds can be used in spectral fitting routines of experimental infrared spectra of aqueous-phase As(V)-containing compounds. This way, the choice of the number of components has a physical basis and is not arbitrarily

chosen. Fitting experimental data is also done routinely when analyzing EXAFS spectra of adsorbed oxyanions on metal cations.<sup>6,35</sup> Spectra collected from standard compounds containing the element of interest in a given oxidation state are needed to obtain a good fit, so that information on the bond lengths in surface complexes and the number of nearest neighbors can be extracted. In the absence of spectra from standards (compounds in bulk aqueous and solid phases), it becomes challenging to fit EXAFS spectra of adsorbed complexes. Results from quantum chemical calculations are invaluable in these cases because they yield structural information on model adsorbed clusters. DFT calculations on the binding of organoarsenicals to metal oxide complexes are currently ongoing in our laboratory to simulate inner-sphere binding configurations similar to those used as model clusters for inorganic oxyanions.<sup>7</sup>

## Acknowledgements

The authors would like to acknowledge funding from Petro-Canada Young Innovator Award and Research Corporation Cottrell College Award for H.A.A., the Discovery Grant of the Natural Sciences and Engineering Research Council of Canada (NSERC) for I.P.H., and the Science and Technology Endowment Program at Wilfrid Laurier University.

## References

- (1) Kubicki, J. D. Comparison of As(III) and As(V) Complexation onto Al- and Fe-hydroxides. In *Advances in Arsenic Research: Integration of Experimental and Observational Studies and Implications for Mitigation*; O'Day, P. A., Vlasopoulos, D., Ming, X., and Benning, L. G., Eds.; ACS Symposium Series: WA, 2005; Vol. 915, pp 104–117.
- (2) Cygan, R. T. Molecular Modeling in Mineralogy and Geochemistry. In *Reviews in Mineralogy and Geochemistry*; Mineralogical Society of America: WA, 2001; Vol. 42, pp 1–35.
- (3) Kubicki, J. D. *Am. J. Sci.* **2005**, *305* (6–8), 621. doi:10.2475/ajls.305.6-8.621.
- (4) Sparks, D. L. *Environmental Soil Chemistry*, 1st ed.; Academic Press: SD, 1995.
- (5) Hind, A. R.; Bhargava, S. K.; McKinnon, A. *Adv. Colloid Interface Sci.* **2001**, *93* (1–3), 91. doi:10.1016/S0001-8686(00)00079-8. PMID:11591110.
- (6) Brown, G. E., Jr.; Parks, G. A.; O'Day, P. A. In *Mineral Surfaces*; Vaughan, D. J. and Patrick, R. A. D., Eds.; Chapman & Hall: New York, 1995; pp 129–183.
- (7) Kubicki, J. D.; Kwon, K. D.; Paul, K. W.; Sparks, D. L. *Eur. J. Soil Sci.* **2007**, *58* (4), 932. doi:10.1111/j.1365-2389.2007.00931.x.
- (8) Tribe, L.; Kwon, K. D.; Trout, C. C.; Kubicki, J. D. *Environ. Sci. Technol.* **2006**, *40* (12), 3836. doi:10.1021/es052363a. PMID:16830550.
- (9) Grundler, H.-V.; Schumann, H.-D.; Steger, E. *J. Mol. Struct.* **1974**, *21* (1), 149. doi:10.1016/0022-2860(74)80038-4.
- (10) Vansant, F. K.; Van der Veken, B. J.; Herman, M. A. *J. Mol. Struct.* **1976**, *35* (2), 191. doi:10.1016/0022-2860(76)82039-X.
- (11) Myneni, S. C. B.; Traina, S. J.; Waychunas, G. A.; Logan, T. J. *Geochim. Cosmochim. Acta* **1998**, *62* (19–20), 3285. [and references therein]. doi:10.1016/S0016-7037(98)00222-1.
- (12) Pye, C. C.; Rudolph, W. W. *J. Phys. Chem. A* **2003**, *107* (41), 8746. doi:10.1021/jp035594h.
- (13) Cowen, S.; Duggal, M.; Hoang, T. N.; Al-Abadleh, H. A. *Can. J. Chem.* **2008**, *86*, 942. doi:10.1139/V08-102.
- (14) Lide, D. R., Ed. In *CRC Handbook of Chemistry and Physics*; Taylor & Francis: Boca Raton, FL, 2006; Vol. 87.
- (15) Wavefunction. *Spartan 4.0*; Wavefunction Inc.: Irvine, CA; 2008.
- (16) Stewart, J. J. P.; Seiler, F. J. *J. Comput. Chem.* **1989**, *10* (2), 209. doi:10.1002/jcc.540100208.
- (17) Becke, A. D. *J. Chem. Phys.* **1993**, *98* (7), 5648. doi:10.1063/1.464913.
- (18) Lee, C. T.; Yang, W. T.; Parr, R. G. *Phys. Rev. B* **1988**, *37* (2), 785. doi:10.1103/PhysRevB.37.785.
- (19) Mulliken, R. S. *J. Chem. Phys.* **1955**, *23* (10), 1833. doi:10.1063/1.1740588.
- (20) Csonka, G. I. *J. Mol. Struct.* **2002**, *584*, 1.
- (21) Reed, R. E.; Weinstock, R. B.; Weinhold, F. *J. Chem. Phys.* **1985**, *83* (2), 735. doi:10.1063/1.449486.
- (22) Scott, A. P.; Radom, L. *J. Phys. Chem.* **1996**, *100* (41), 16502. doi:10.1021/jp960976r.
- (23) Jensen, J. O.; Gilliam, S. J.; Banerjee, A.; Zeroka, D.; Kirkby, S. J.; Merrow, C. N. *J. Mol. Struct. THEOCHEM* **2003**, *664–665*, 145. doi:10.1016/j.theochem.2003.08.109.
- (24) Jensen, J. O.; Jensen, J. L. *Spectrochim. Acta A Mol. Spec.* **2004**, *60* (13), 3065. doi:10.1016/j.saa.2004.01.028.
- (25) Stewart, J. J. P.; Seiler, F. J. *J. Comput. Chem.* **1989**, *10* (2), 221. doi:10.1002/jcc.540100209.
- (26) Pye, C. C.; Michels, M. R. *Can. J. Anal. Sci. Spectrosc.* **2005**, *50*, 70.
- (27) Pye, C. C.; Michels, M. R. *Can. J. Anal. Sci. Spectrosc.* **2004**, *49*, 175.
- (28) Parthasarathi, R.; Subramanian, V. Characterization of Hydrogen Bonding: From van der Waals Interactions to Covallency. In *Hydrogen Bonding — New Insights*; Grabowski, S., Ed.; Springer: Dordrecht, 2006; pp 1–50.
- (29) Storer, J. W.; Giesen, D. J.; Cramer, C. J.; Truhlar, D. G. *J. Comput. Aided Mol. Des.* **1995**, *9* (1), 87. doi:10.1007/BF00117280.
- (30) Oder, R.; Goring, D. A. *Spectrochim. Acta [A]* **1971**, *27A*, 2285.
- (31) Wong, M. W. *Chem. Phys. Lett.* **1996**, *256* (4–5), 391. doi:10.1016/0009-2614(96)00483-6.
- (32) Meier, R. J. *Vib. Spectrosc.* **2005**, *39* (2), 266. doi:10.1016/j.vibspec.2005.03.003.
- (33) Depalma, S.; Cowen, S.; Hoang, T. N.; Al-Abadleh, H. A. *Environ. Sci. Technol.* **2008**, *42* (6), 1922. doi:10.1021/es071752x. PMID:18409614.
- (34) Chabot, M.; Hoang, T. N.; Al-Abadleh, H. A. *Environ. Sci. Technol.* **2009**, *43* (9), 3142. doi:10.1021/es803178f. PMID:19534126.
- (35) Sparks, D. L. Metal and Oxyanion Sorption on Naturally Occurring Oxide and Clay Mineral Surfaces. In *Environmental Catalysis*; Grassian, V. H., Ed.; Taylor & Francis Group: Boca Raton, FL, 2005; pp 3–36.

## AWARD LECTURE / CONFÉRENCE D'HONNEUR

# Rate constants for decarboxylation reactions calculated using no barrier theory

J. Peter Guthrie, Sriyawathie Peiris, Margaret Simkin, and Yun Wang

**Abstract:** No barrier theory (NBT) provides both a qualitative way of thinking about what makes a reaction fast or slow and a quantitative way of calculating the rate constant (free energy of activation) corresponding to a particular mechanism. The origin and development of this idea are reviewed and examples of its use for qualitative understanding are presented before applying it to a set of decarboxylations. From the literature, a set of best values for rate constants for decarboxylation was picked. Detailed mechanistic models were developed for reactions leading to delocalized “anions” or to localized anions. It was necessary to have  $pK_a$  values for ionization of the carbon acids corresponding to all of these species and these were selected from the literature or estimated by linear free energy relations (or occasionally calculated from proton exchange data). Over the entire range of measured decarboxylation rate constants, a range of  $10^{25}$  in rate constant, the calculated values were in good agreement with experiment, with two exceptions: malonate dianion, which has been reported but probably not measured, and glycine, where it is possible that a different mechanism is being followed, unfortunately, one which we do not yet know how to treat by NBT. NBT is both a qualitatively and quantitatively useful tool for understanding chemistry.

**Key words:** decarboxylation, no barrier theory, reaction mechanism, intrinsic barrier.

**Résumé :** La théorie sans barrière fournit d'une part une façon qualitative de réfléchir sur ce qui fait qu'une réaction est rapide ou lente et d'autre part une façon quantitative de calculer la constante de vitesse (énergie libre d'activation) correspondant à un mécanisme particulier. On passe en revue l'origine et le développement de cette idée et on présente des exemples de son utilisation dans la compréhension qualitative avant de l'appliquer à un ensemble de décarboxylations. On a tiré de la littérature un ensemble des meilleures valeurs pour les constantes de vitesse de décarboxylation. Des modèles de mécanismes réactionnels détaillés ont été développés pour des réactions conduisant à des anions délocalisés ou localisés. Il était nécessaire d'avoir les valeurs de  $pK_a$  pour l'ionisation des acides carboniques correspondants à chacune des espèces et celles-ci ont été sélectionnées à partir de la littérature ou elles ont été évaluées par des relations d'énergie linéaires ou elles ont été occasionnellement calculées à partir de données d'échange de proton. Sur l'ensemble complet des constantes de vitesse de décarboxylation, une plage de constantes de vitesse relatives s'étalant de 1 à  $10^{25}$ , les valeurs calculées ont en bon accord avec les valeurs expérimentales, à deux exceptions près: le dianion de l'acide malonique a été rapporté, mais qui n'a probablement pas été mesuré et la glycine pour laquelle il est possible qu'un mécanisme différent soit impliqué, un mécanisme qu'on ne peut malheureusement pas encore traiter par la théorie sans barrière. La théorie sans barrière (TSB) est un outil qualitativement et quantitativement utile pour la compréhension de la chimie.

**Mots-clés :** décarboxylation, théorie sans barrière, mécanisme réactionnel, barrière intrinsèque.

[Traduit par la Rédaction]

## Introduction

Over the past ten years, we have been developing an approach to calculating rate constants for chemical reactions, which also provides a useful way to think about why

a particular reaction is inherently fast or slow. Because the essential idea is that for any process in which only one thing happens there is no barrier, the approach is called “no barrier theory”, NBT. We will first review how this idea arose, and then look at how it can be applied to a well-known, but inherently difficult reaction, decarboxylation.

Our approach to thinking about reactions developed from Marcus theory<sup>1-7</sup> and uses the same model, focusing on the actual transformation, which begins with an encounter complex of starting materials, with all atoms in position for the bond transformation to come, but with none of this transformation yet occurred, and ends with an encounter complex of products, with all atoms in the positions corresponding to the just completed bond transformation; this is illustrated in

Received 13 August 2009. Accepted 28 September 2009.

Published on the NRC Research Press Web site at [canjchem.nrc.ca](http://canjchem.nrc.ca) on 24 December 2009.

*Lemieux Award Lecture, 2008.*

J.P. Guthrie,<sup>1</sup> S. Peiris, M. Simkin, and Y. Wang, Department of Chemistry, University of Western Ontario, London, ON N6A 5B7, Canada.

<sup>1</sup>Corresponding author (e-mail: [peter.guthrie@uwo.ca](mailto:peter.guthrie@uwo.ca)).



**Fig. 1.** General model of a reaction used for Marcus theory and no barrier theory. The reactants, A and B, must come together to form an encounter complex, (A, B), with all atoms in position and ready to begin the bond transformation, which constitutes the chemical reaction. The cost in free energy of bringing A and B together is the work term,  $w_R$ . The reaction passes over a barrier with height  $\Delta G_{\text{corr}}^\ddagger$  and leads to the encounter complex of the products, (C, D). These then dissociate to give the products in their standard state. The cost in free energy of bringing C and D together in this complex is another work term,  $w_P$ . The free energy change for the reaction, beginning and ending with all species in their standard states,  $\Delta G^\circ$ , is generally different from the free energy change for reaction within the encounter complex,  $\Delta G_{\text{corr}}^\circ$ , just as the directly measurable free energy of activation,  $\Delta G_{\text{obs}}^\ddagger$ , is generally different from the free energy of activation within the encounter complex,  $\Delta G_{\text{corr}}^\ddagger$ .

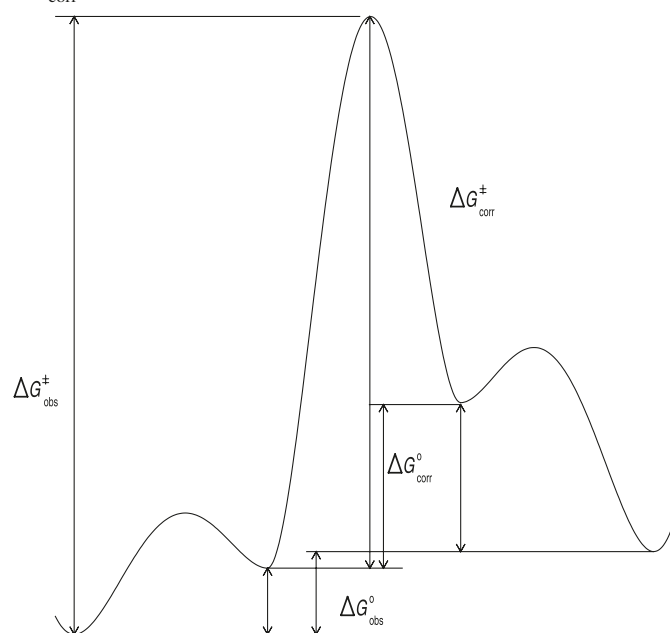


Fig. 1. The Marcus “work terms”,  $w_R$  and  $w_P$  represent all the costs in free energy to bring the starting materials and products from their equilibrium state in dilute solution to the encounter complexes. These work terms may include the entropic cost of bringing species together: conformational changes if the reactive conformation of starting material or product is not the equilibrium conformation, partial desolvation if one reactant must lose a solvent molecule to come into contact, proton transfer if the reactive species is not the tautomer favored at equilibrium, and so on. The Marcus equation, eq. [2],<sup>8</sup> allows prediction of rate from equilibrium if one knows the “intrinsic barrier”,  $\tilde{G}$ . One way of achieving this is the assumption of transferable intrinsic barriers, approximately the same for a set of similar reactions. This approach proved quite useful<sup>5,9–39</sup> but did require an empirical intrinsic barrier for each family of reactions. Furthermore, it is known that this approximation breaks down for wide enough ranges of equilibrium constants.<sup>31,32,40,41</sup>

$$[1] \quad \Delta G^\ddagger = w_r + \tilde{G} \left( 1 + \frac{\Delta G^\circ - w_r + w_p}{4\tilde{G}} \right)^2$$

$$[2] \quad \Delta G_{\text{corr}}^\ddagger = \tilde{G} \left( \frac{1 + \Delta G_{\text{corr}}^\circ}{4\tilde{G}} \right)^2$$

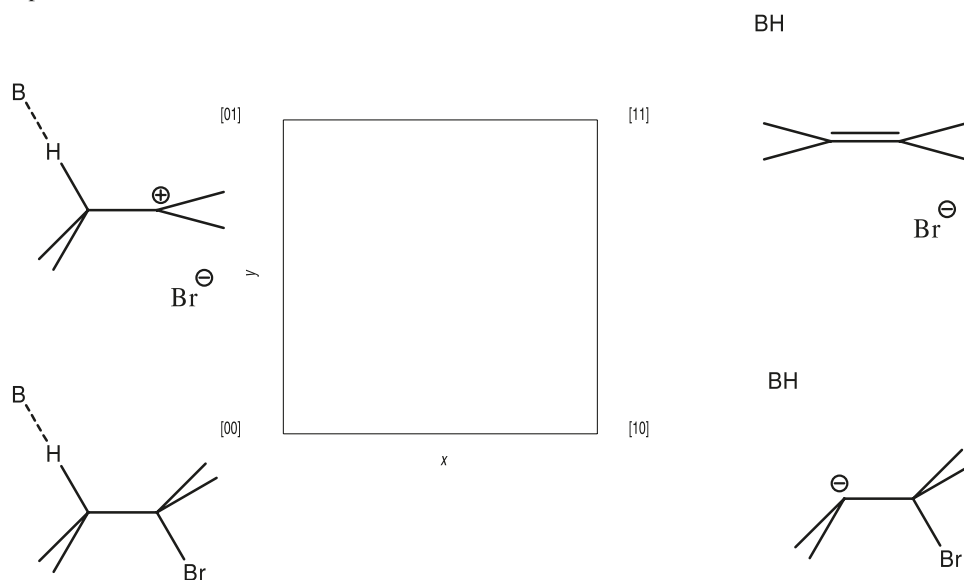
As a first step towards lessening the number of empirical values that had to be evaluated to extend this approach to more complicated reactions, multidimensional Marcus theory was developed.<sup>42</sup> In this approach a concerted reaction was regarded as the resultant of two simpler reactions each with its own intrinsic barrier, and the postulate that each section through the multidimensional reaction energy surface would obey the Marcus equation (eq. [2]). This approach was applied to the E2 elimination<sup>43</sup> (with the simpler reactions being the E1/S<sub>N</sub>1 ionization to an ion triple, and the E1cb deprotonation to a carbanion; see Fig. 2), and concerted acyl transfer<sup>44</sup> (with the simpler reactions being nucleophilic addition to give a tetrahedral intermediate and ionization to give an acylium ion; see Fig. 3).

An interesting conjecture arising from the multidimensional Marcus theory approach is that other things being equal, the more reaction dimensions required to describe a chemical transformation the higher will be the kinetic barrier for that transformation.<sup>42</sup> This can be proven in a very simple case<sup>42</sup> but a more general proof is more difficult and has not yet been achieved. This idea leads to the general proposition (with apologies to William Lyon McKenzie King) that reactions are “Concerted if necessary, but not necessarily concerted”. A reaction will be concerted if necessary to avoid high energy intermediates, but will not be concerted without necessity because the more elaborate path for the concerted reaction is inherently more difficult than a simpler reaction path where fewer things must happen in a concerted fashion.

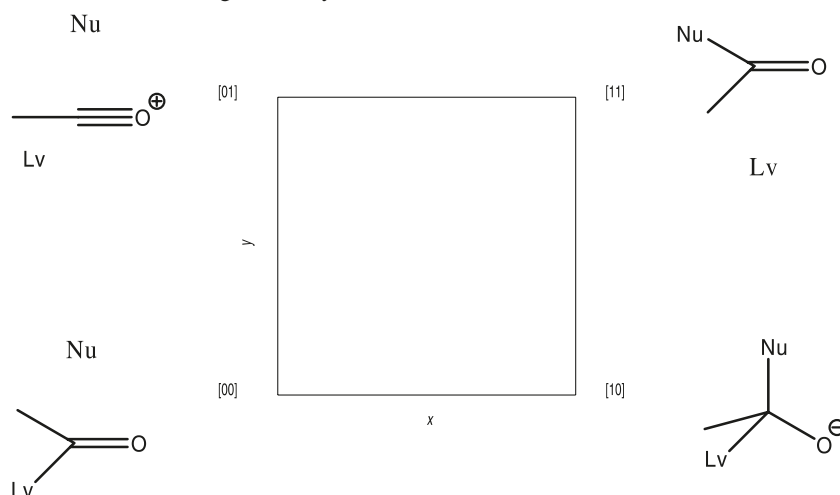
A reaction is concerted if all the stepwise intermediates are bad, but comparably bad, so that the only way to avoid any bad intermediate is to avoid all. If one intermediate is very bad the reaction will be stepwise or a lower dimensional concerted process, avoiding the bad intermediate, but not constrained to be fully concerted. If one intermediate is relatively unbad, then reaction will be stepwise by way of that intermediate. This principle is a generalization of ideas that have been around for some time, such as the Libido Rule of Jencks:<sup>45</sup> Concerted general acid base catalysis of a reaction occurs when the reaction converts a proton transfer from unfavorable to favorable with respect to the catalyst. If a stepwise process, involving either preliminary proton transfer or proton transfer only after the heavy atom bond formation, would require having an unstable intermediate on the reaction path, then the reaction will proceed with concerted proton transfer.

In Figs. 2 and 3, the behavior of energy along the diagonal linking the two stepwise intermediates controls what will happen. If the energy at some point along the diagonal is lower than either stepwise intermediate then the reaction will be concerted; if the reaction is concerted then the energy at some point along the diagonal must be lower than either intermediate. Things are a bit more complicated because of the intrinsic barriers for the edge reactions, but if the corner species are high energy intermediates, then the kinetic barrier to break down to starting materials or products must be small and the above must be approximately correct. The idea is that if a corner intermediate is bad then moving

**Fig. 2.** E2 elimination as an example of a potentially concerted reaction. The two stepwise alternatives are the E1/S<sub>N</sub>1 ionization to an ion triple, and the E1c<sub>b</sub> deprotonation to a carbanion.



**Fig. 3.** Concerted acyl transfer as an example of a potentially concerted reaction. The two stepwise alternatives are nucleophilic addition to give a tetrahedral intermediate and ionization to give an acylium ion.



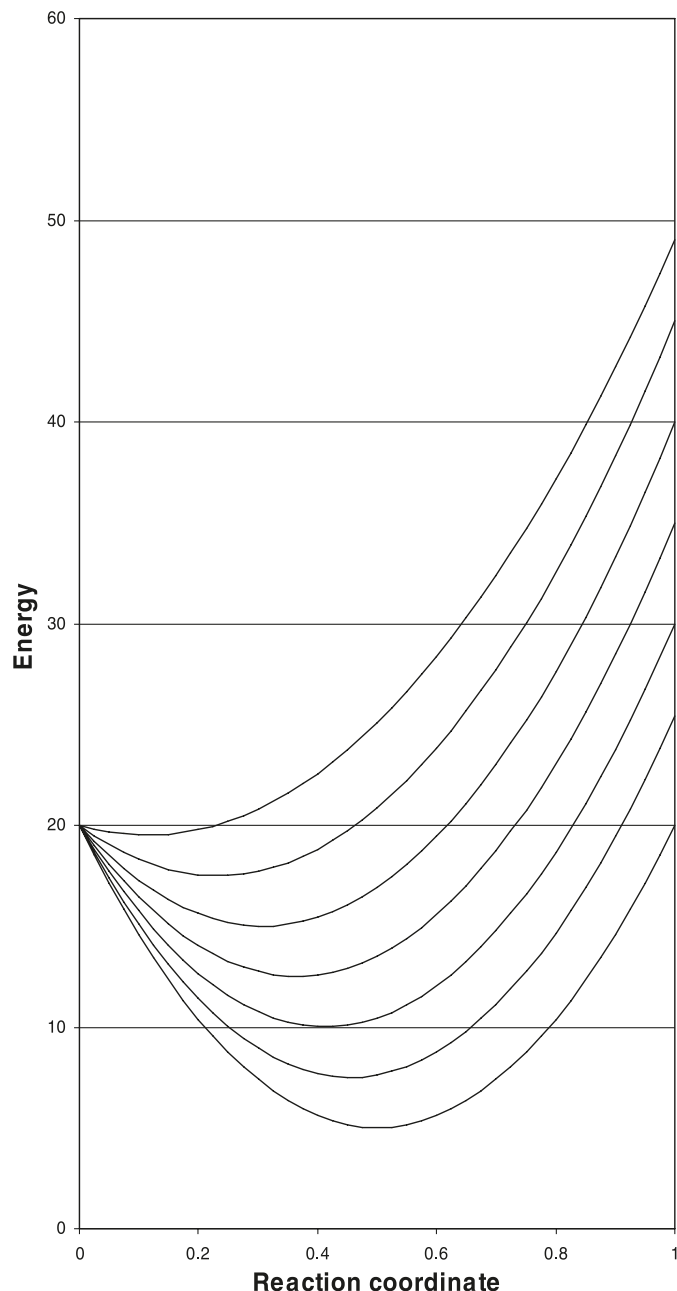
away from it towards the center of the diagram will make things better but proceeding too far along the diagonal leads to the other bad corner and raises the energy again. If one corner intermediate becomes increasingly worse than the other then a point will be reached where any motion away from the less bad intermediate towards the more bad intermediate leads to an increase in energy. In such a case, the reaction is constrained to be stepwise by way of the less bad intermediate. These ideas are illustrated in Fig. 4. This argument implies that anyone proposing a concerted reaction mechanism needs to present arguments that the stepwise intermediates being avoided are comparably bad; this is not always done. Arguments of this sort have been applied to potentially concerted phosphoryl and sulfonyl transfers.<sup>46</sup>

The next step was to do away with the need for an empirical intrinsic barrier by extending the approach of multidimensional Marcus theory and considering all reactions as the resultant of a set of “simple” reaction dimensions, where a simple reaction dimension is one for which with a

suitable progress variable the energy is a quadratic function of that progress variable. Thus, for such a simple process, “if only one thing happens then there is no barrier to that process” and the energy simply rises following a quadratic law for some suitable progress variable. This can be illustrated for the ionization of *tert*-butyl chloride, a two dimensional process, as shown in Fig. 5. The reaction dimensions are bond breaking and geometry change. The assumptions that all one dimensional processes follow quadratic laws allows us to draw in the four edges of the energy surface for a two dimensional reaction, as shown in Fig. 6. The additional assumption that all such parabolas have their minimum at the low energy end, allows us to fill in the entire energy surface. One needs then to find the minimum energy saddle point connecting the initial and final corners and this will be the transition state.

This new approach, no barrier theory, avoids the need for empirical intrinsic barriers, which constrained the application of Marcus theory or multidimensional Marcus theory to

**Fig. 4.** A series of parabolas of constant length passing through two points with different relative heights. This illustrates the behavior expected when there are two alternative, relatively high energy, intermediates through which a reaction could pass. If both are comparably high then the preferred path is a concerted avoidance of both. If one is much higher than the other then the reaction proceeds by way of the lower energy intermediate. This can also be illustrated by holding a short piece of rope and changing the relative heights of the ends.



organic reactions, and also, in effect, provides a procedure to calculate the intrinsic barrier for any reaction. This also provides an interpretation of the intrinsic barrier, and allows a useful qualitative analysis since a reaction that requires more reaction dimensions will be inherently slow, and can only be fast with a large thermodynamic driving force.

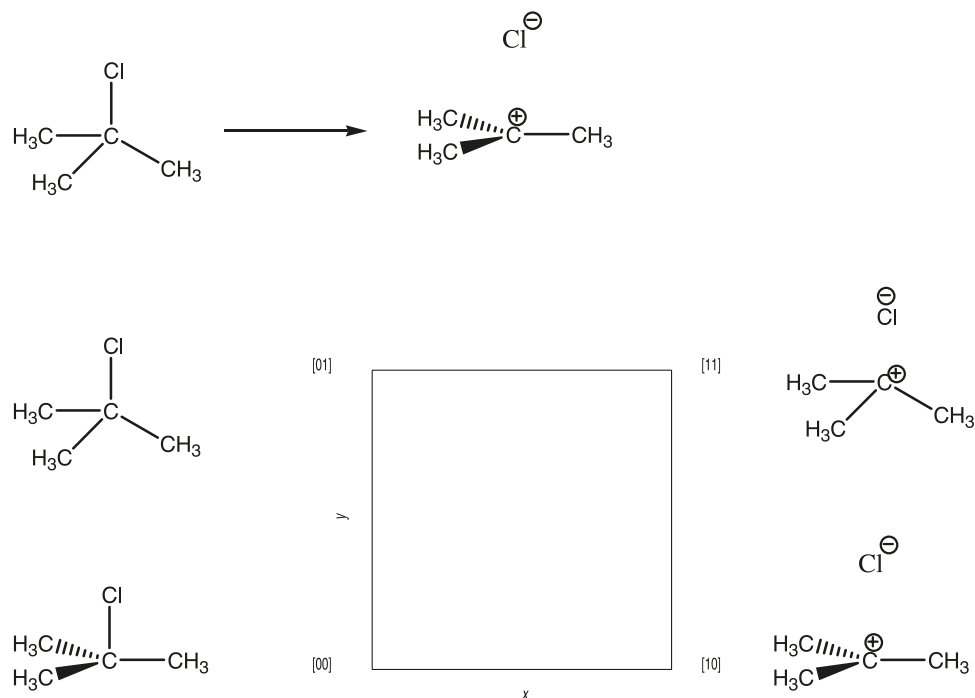
This can be illustrated for a set of reactions using data from the literature. In each case the qualitative facts are surprising based on usual ways of thinking but seem quite predictable using no barrier theory. The reactions to be compared are shown in Table 1. The naïve expectation (if intrinsic barriers were similar for both reactions in each pair) is that for  $K \approx 1$ ,  $\Delta \log(k) \approx 0.5 \Delta \log(K)$ ; if  $K \gg 1$ , then  $\Delta \log(k) \ll 0.5 \Delta \log(K)$ ; if  $K \ll 1$ , then  $\Delta \log(k) \approx \Delta \log(K) \gg 0.5 \Delta \log(K)$ . These expectations are not met for any of the examples. Clearly the intrinsic barriers are not comparable, and the challenge is to explain why this is so.

Hydrogen atom transfer is inherently faster (for similar equilibrium constants) from phenol than from ethyl benzene. The difference is that there is an additional reaction dimension needed for ethyl benzene: the geometry change at carbon. Other reaction dimensions should be comparable: the actual hydrogen atom transfer and the bond length changes accompanying delocalization.

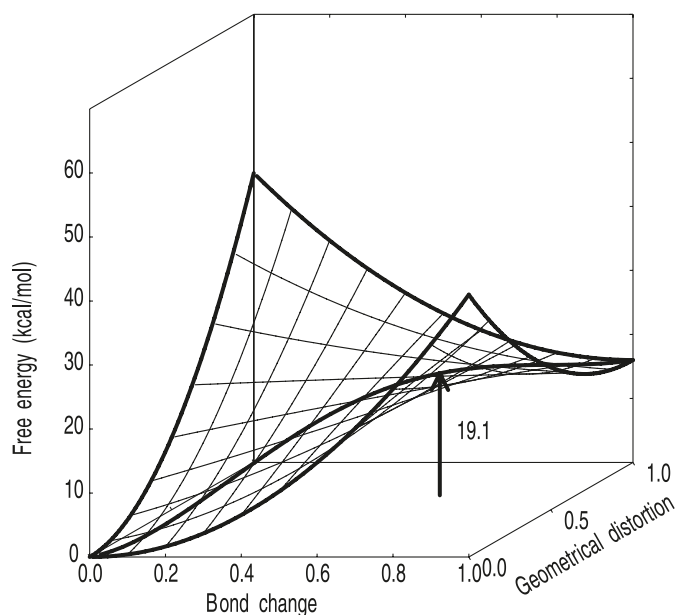
The addition of hydroxide to a carboxylate ester (to form an anionic tetrahedral intermediate) is inherently faster than the addition of hydroxide to a phosphate ester (to form an anionic trigonal bipyramidal intermediate). The reason can be seen by examining the angular distortions involved in the NBT analysis of this reaction; see Fig. 7. For the carboxylate ester, the distorted ester has three angles that would like to be  $120^\circ$  but are forced to be  $109^\circ$ , for  $11^\circ$  of distortion for each. For the phosphate ester, there are three angles that would like to be  $109^\circ$  but are forced to be  $120^\circ$ , for  $11^\circ$  of distortion for each, and three that would like to be  $109^\circ$  but are forced to be  $90^\circ$ , for  $19^\circ$  of distortion for each. For the carboxylate adduct, there are three angles that would like to be  $109^\circ$  but are forced to be  $120^\circ$  for  $11^\circ$  of distortion for each, and three that would like to be  $109^\circ$  but are forced to be  $90^\circ$ , for  $19^\circ$  of distortion for each. For the phosphate adduct, there are three angles that would like to be  $120^\circ$  but are forced to be  $109^\circ$ , for  $11^\circ$  of distortion for each, three that would like to be  $90^\circ$  but are forced to be  $109^\circ$ , for  $19^\circ$  of distortion for each, and three that would like to be  $90^\circ$  but are forced to be  $71^\circ$ , for  $19^\circ$  of distortion for each. For both the distorted ester and distorted adduct, the angular distortion is greater for the phosphate than for the carboxylate. Using the approximation that all bending force constants are the same (the basis for the principle of least motion), the pure distortion corners must be higher in energy for the phosphate reaction and thus the intrinsic barrier must be higher.

Acid-catalyzed addition of water to an amide, though itself a slow reaction, is inherently faster than acid-catalyzed addition of water to a nitrile, even though the equilibrium constant for the latter reaction is much less unfavorable. This is again a result of the difference in angular distortion; see Fig. 8. For the amide reaction, the distortions are the same as for the ester example above: three times  $11^\circ$  for each angle for the amide itself, and three times  $11^\circ$  plus three times  $19^\circ$  for each angle for the adduct. For the nitrile, the distorted form has an angle that would like to be  $180^\circ$  but is forced to be  $120^\circ$  for a distortion of  $60^\circ$ ; for the adduct there is one angle that wants to be  $120^\circ$  and is forced to be  $180^\circ$  and two that want to be  $120^\circ$  and are forced to be  $90^\circ$ , leading to one distortion of  $60^\circ$  and two of  $30^\circ$ . Since the energetic cost of an angular distortion depends on

**Fig. 5.** Ionization of *tert*-butyl chloride in water, a two dimensional process. The reaction dimensions are bond formation (with no geometry change) and geometry change (with no bond formation).



**Fig. 6.** Energy surface for the ionization of *tert*-butyl chloride, based on the assumption that at the edges (where one coordinate varies and the other is zero or one) the energy has a parabolic dependence on reaction coordinate (—) and further, for every section through the diagram where only one coordinate changes the energy is a parabola with its minimum at the lower energy end (—). This defines the energy surface, and the energy of the saddle point relative to the starting point is the free energy of activation. The curve from starting material to product traces a reaction path through the transition state



the square of the distortion, the distortion energies for the nitrile reaction are quite large and thus the intrinsic barrier is high.

The preceding discussion emphasized the qualitative utility of the ideas behind no barrier theory, but even more important is its ability to predict free energies of activation (rate constants) for a wide range of reactions.<sup>47-53</sup>

The goal of our research program is to develop a set of detailed mechanistic models for reactions that permit the rates of these reactions to be calculated from the equilibrium constants. These models must be internally consistent for a particular family of reactions, and consistent over the whole range of chemistry, which can be treated by the no barrier theory approach.

This paper will examine decarboxylation reactions over a wide range of reactivity as an illustration of the application of no barrier theory. This reaction is inherently slow, as shown by the experimental rate constants from the literature gathered in Table 2. Decarboxylation can be compared with an analogous retroaldol reaction<sup>11,70</sup> using two reactions of fairly similar thermodynamic driving force; the decarboxylation is much slower; see Table 1. Qualitatively, the difference lies in the much greater angular distortion for a change from  $sp^2$  to  $sp$  geometry than for a change from  $sp^3$  to  $sp^2$  geometry; see Fig. 9. For the retroaldol reaction, distortion of the starting material at the carbon, which is to become a carbonyl, forces three angles that want to be  $109^\circ$  to be  $120^\circ$ , for a distortion of  $11^\circ$ . In the product, three angles wanting to be  $120^\circ$  would be forced to be  $109^\circ$ , again for a distortion of  $11^\circ$ . In the decarboxylation reaction, distortion of the starting material at the carbon, which is to leave as  $CO_2$ , forces one angle that wants to be  $120^\circ$  to be  $180^\circ$  and two that want to be  $120^\circ$  to be  $90^\circ$ , giving one distortion of  $60^\circ$  and two of  $30^\circ$ . The energy cost of the distortions re-



**Table 1.** Reactions where the relation between equilibrium and rate is puzzling by traditional viewpoints but is readily given a qualitative explanation by no barrier theory.

Reaction	log <i>K</i>	log <i>k</i>
$(\text{CH}_3)_3\text{C}-\text{O}-\text{O}^\bullet + \text{C}_6\text{H}_5\text{OH}$	-1.7	3.5
$(\text{CH}_3)_3\text{C}-\text{O}-\text{O}^\bullet + \text{C}_6\text{H}_5\text{CH}_2\text{CH}_3$	-1.9	-1.0
$\text{CH}_3\text{COOCH}_3 + \text{HO}^\ominus \rightleftharpoons \text{CH}_3-\text{C}(\text{OH})(\text{OCH}_3)\text{O}^\ominus$	-6.0	-0.8
$(\text{CH}_3\text{O})_3\text{PO} + \text{HO}^\ominus \rightleftharpoons \text{CH}_3\text{O}-\text{P}(\text{O}^\ominus)(\text{OCH}_3)_2$	-2.8	-3.8
$\text{CH}_3-\text{C}\equiv\text{N} + \text{H}_2\text{O} + \text{H}^\oplus \rightleftharpoons \text{CH}_3-\text{C}(\text{OH})(\text{NH}) + \text{H}^\oplus$	-1.3	-9.1
$\text{CH}_3-\text{C}(=\text{O})\text{N}(\text{CH}_3)_2 + \text{H}_2\text{O} + \text{H}^\oplus \rightleftharpoons \text{CH}_3-\text{C}(\text{OH})(\text{N}(\text{CH}_3)_2) + \text{H}^\oplus$	-14.2	-6.0
$\text{H}_3\text{C}-\text{C}(=\text{O})\text{CH}_2\text{CH}_2\text{COO}^\ominus \rightleftharpoons \text{H}_3\text{C}-\text{C}(\text{O}^\ominus)=\text{CH}_2 + \text{HC}(\text{O})\text{CH}_3$	-5.2	-1.9
$\text{H}_3\text{C}-\text{C}(=\text{O})\text{CH}_2\text{COO}^\ominus \rightleftharpoons \text{H}_3\text{C}-\text{C}(\text{O}^\ominus)=\text{CH}_2 + \text{C}(\text{O})=\text{O}$	-7.9	-6.3

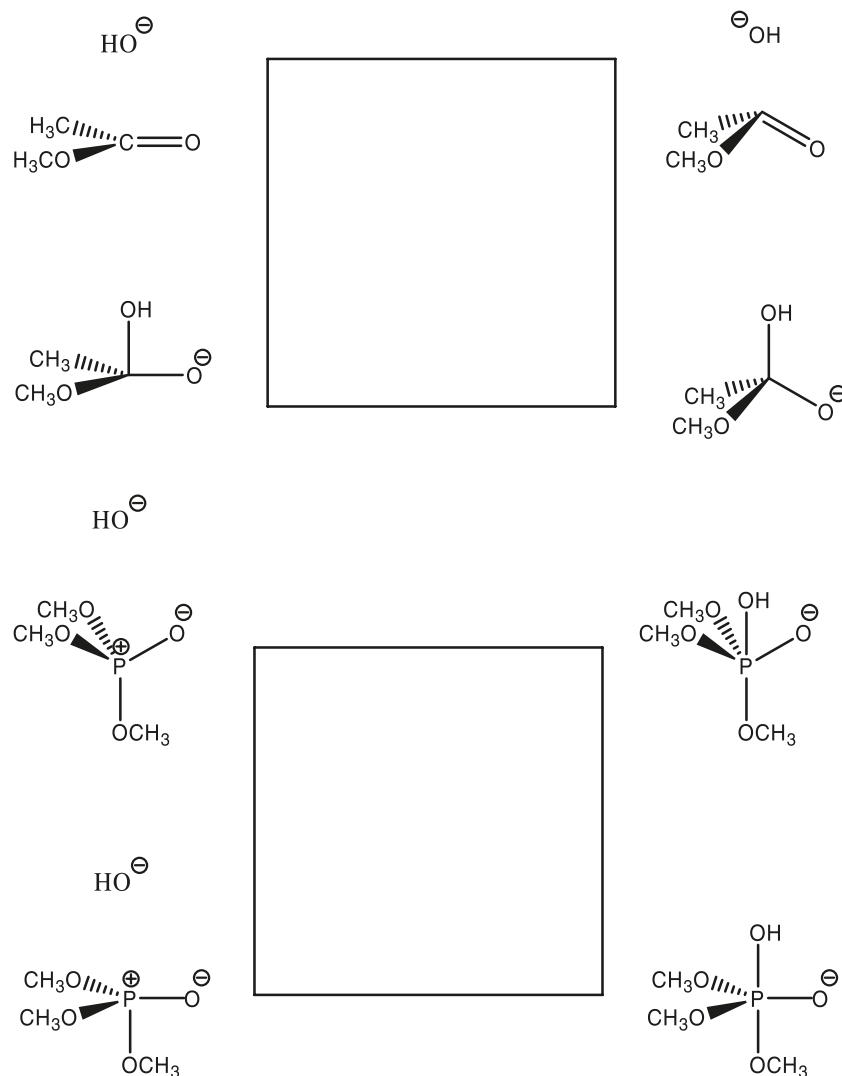
quired for the decarboxylation is higher and thus the intrinsic barrier is higher than for the retroaldol.

## Results and discussion

The no barrier theory approach calculates the rate corresponding to a particular model for the mechanism of the reaction. This model includes not only the detailed reaction path as specified in the “curly arrow mechanism” but also issues of whether partial desolvation is postulated for certain corners, and how one deals with the structure of ionic intermediates, which are often unstable in the gas phase, even though they have a lifetime (perhaps short) in solution. This latter problem is a consequence of the current not fully satisfactory state of computational chemistry. We have attempted to find ways of dealing with this problem with manageably small computational demands. In particular, for anions which decarboxylate readily, we add water molecules (one per lone pair) and minimize this structure. For zwitterions we also add a water solvating the acidic hydrogen, and,

where possible, arrange to have this water also form a hydrogen bond to one of the waters solvating an anionic oxygen. Then we remove the waters from the structure, and carry out a single point calculation to serve as the reference energy for distortion calculations, in all of which the geometrical features defining the reaction centers will be locked at either the initial or final values. Where the equilibrium structure with explicit waters did not correspond to one where the C–CO<sub>2</sub><sup>−</sup> bond was orthogonal to the plane of the delocalized “carbanion” (for those reactions where the loss of CO<sub>2</sub> left a delocalized lone pair) we carried out calculations with explicit waters and with this orthogonality enforced. To avoid needless crowding in some of the distortion structures, we also locked the conformation of the CO<sub>2</sub><sup>−</sup> so that this group was orthogonal to the electron withdrawing group in compounds where there was a delocalized carbanion product. These two constraints gave the “reactive conformation” and the unconstrained calculation gave the “equilibrium conformation”. The carbanions left behind when CO<sub>2</sub> departed differed in whether solvation might oc-

**Fig. 7.** Why phosphate esters are inherently slower to add hydroxide than carboxylate esters despite a smaller thermodynamic barrier. The distortions in starting material and product are compared for methyl acetate and trimethyl phosphate. There are more angles distorted in the phosphate case, and the total angular distortion is greater for addition to phosphate.

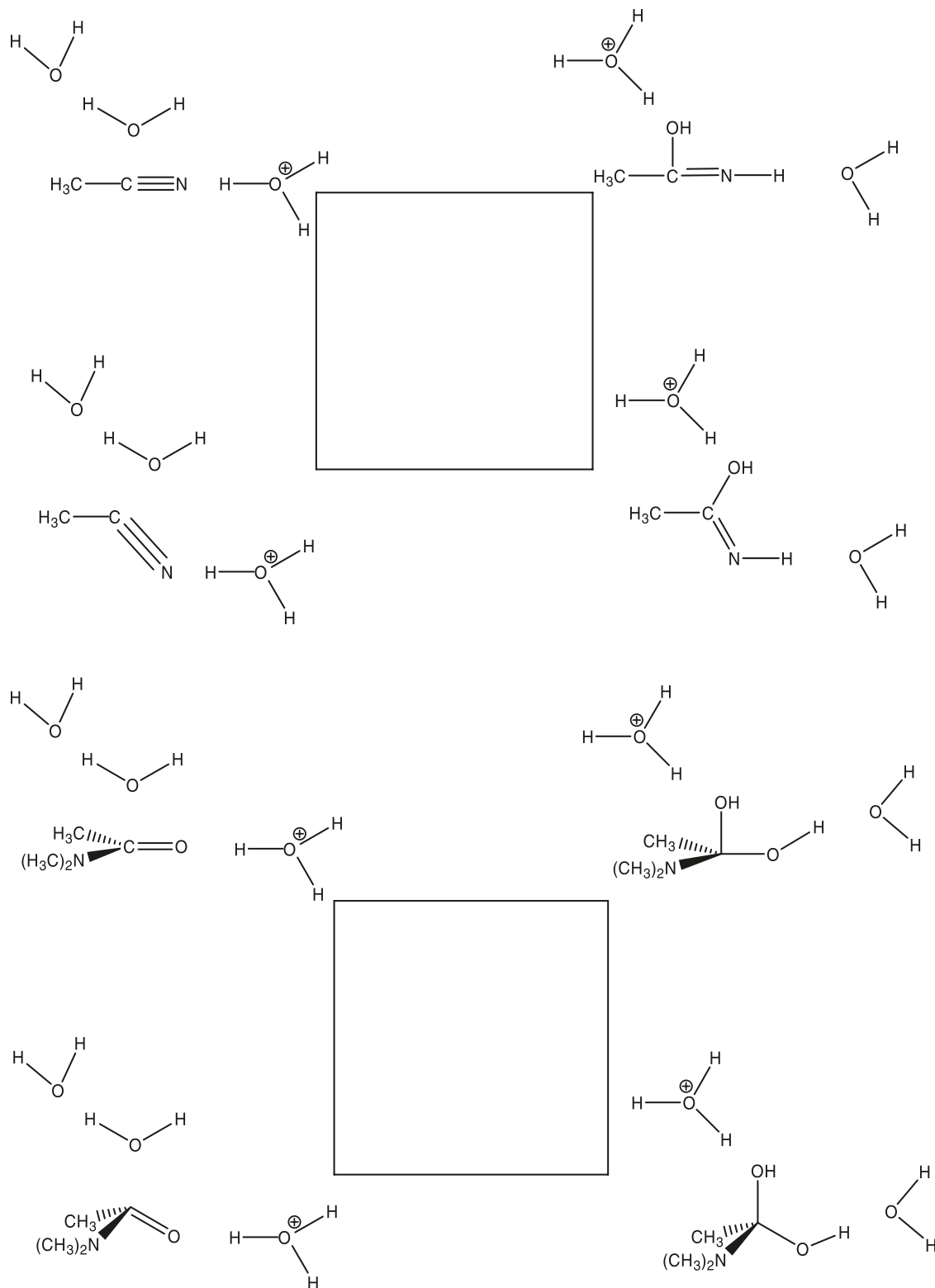


cur at the carbon from which  $\text{CO}_2$  departed (phenyl anion, uracil anion, methide, trichloromethide, trifluoromethide, ammoniomethide, water) or not (acetone enol or its enolate, acetic acid enol or its mono- or di-anionic forms, nitromethide ion, cyanomethide ion, 1-*H*-2-methylenedihydropyridine, 1-*H*-4-methylenedihydropyridine). The carbanions of the second class are extensively delocalized and solvation is expected to take place predominantly at the heteroatoms, which bear the charge or lone pair. (The carbanion may be an enolate or an enol or an enamine, for all of which carbanion resonance forms can be written.) For carbanions of the first class, if the measured or estimated  $\text{p}K_{\text{a}}$  refers to aqueous solution then it presumably refers to the species with hydrogen bonding solvation to the carbanion center, and in the immediate product of decarboxylation this solvation will be missing. In these cases, a correction for the cost of desolvation must be included. This is done following a model previously described,<sup>43</sup> and is summarized in Appendix A. If the measured or estimated  $\text{p}K_{\text{a}}$  refers to a nonaqueous,

nonhydrogen bonding solvent such as DMSO then the immediate product of decarboxylation in water corresponds to the conjugate base used in the definition of  $\text{p}K_{\text{a}}$  used and no correction for desolvation is needed. The  $\text{p}K_{\text{a}}$  values used here, which refer to DMSO as solvent, are for benzene and methane.

We have already reported two studies of decarboxylation reactions, of acetoacetic acid<sup>49</sup> and carbonic acid.<sup>51</sup> For the reaction of acetoacetic acid no barrier theory could be used as a mechanistic criterion: reaction by the textbook mechanism, eq. [3], did not lead to a free energy of activation consistent with experiment, but to a much higher value, and reaction by way of the zwitterion led to a free energy of activation that was consistent with experiment. The same result was obtained either for a cyclic model with two bridging waters or with the zwitterion; for the cyclic mechanism the proton transfers were complete at the transition state, and the mechanism was actually the zwitterion mechanism. For the decarboxylation of bicarbonate the opposite

**Fig. 8.** Why acid hydrolyses of nitriles are inherently slower than for analogous amides despite a smaller thermodynamic barrier. The distortions in starting material and product are compared for acetonitrile and *N,N*-dimethylacetamide. The total angular distortion is greater for the nitrile.



situation was obtained; the zwitterion mechanism gave a free energy of activation higher than experiment, while the cyclic mechanism led to good agreement, and corresponded to a concerted mechanism with only partial proton transfer

at the transition state. This difference in behavior is presumably the result of the relative stabilities of zwitterionic and neutral forms of the starting materials:  $\text{p}K_z = 9.57$  (from values in Table 3) for acetoacetic acid and 13.09 (from values

**Table 2.** Rate constants for decarboxylation reactions.

Starting material	Rate constant at 25 °C	Selected rate constant
Nitroacetate anion	$2.02 \times 10^{-3}{}^a$ $2.50 \times 10^{-3}{}^c$	$2.50 \times 10^{-3}{}^b$
Acetoacetic acid		$2.88 \times 10^{-5}{}^d$
Acetoacetate anion		$4.47 \times 10^{-7}{}^d$
Pyridine-2-acetic acid	$1.58 \times 10^{-8}{}^e$	$1.58 \times 10^{-8}$
Pyridine-4-acetic acid	$1.58 \times 10^{-8}{}^e$	$1.58 \times 10^{-8}$
Trichloroacetate anion	$5.53 \times 10^{-9}{}^f$ $2 \times 10^{-5}{}^g$	$5.53 \times 10^{-9}$
Malonic acid	$6.39 \times 10^{-10}{}^h$ $1.3 \times 10^{-8}{}^i$ $2 \times 10^{-7}{}^j$ $3.9 \times 10^{-9}{}^k$	$6.39 \times 10^{-10}$
Malonate monoanion	$1.68 \times 10^{-10}{}^h$ $4.4 \times 10^{-9}{}^i$ $1 \times 10^{-8}{}^l$ $6.0 \times 10^{-9}{}^m$	$1.68 \times 10^{-10}$
Malonate dianion	$6.7 \times 10^{-11}{}^i$	
Cyanoacetate anion	$5.62 \times 10^{-12}{}^n$ $1 \times 10^{-9}{}^o$	$5.62 \times 10^{-12}$
Trifluoroacetate anion	$1.04 \times 10^{-17}{}^p$ $4.77 \times 10^{-13}{}^q$ $1 \times 10^{-11}{}^r$	$1.04 \times 10^{-17}$
1-Methylorotate anion	$2.8 \times 10^{-16}{}^s$	$2.8 \times 10^{-16}$
Glycine zwitterion	$2 \times 10^{-17}{}^t$ $5.7 \times 10^{-14}{}^u$	$2 \times 10^{-17}$
$\text{C}_6\text{H}_5\text{-COO}^-$	$1.36 \times 10^{-28}{}^v$	$1.36 \times 10^{-28}$
$\text{CH}_3\text{-COO}^-$	$<4 \times 10^{-32}{}^w$	$<4 \times 10^{-32}$

**Note:** All in aqueous solution, at 25 °C unless otherwise noted. Dimension for rate constants is  $\text{s}^{-1}$ . Arranged in order of decreasing rate except that different protonation states of a compound are kept together.

<sup>a</sup>At 23.5 °C; ref. 54.

<sup>b</sup>Based on extrapolation of data from Finkbeiner<sup>54</sup> and Pedersen.<sup>55</sup>

<sup>c</sup>At 25 °C, extrapolated from data at 17.8 and 9.8 °C from ref. 55.

<sup>d</sup>Reference 56.

<sup>e</sup>Extrapolated to water from rate data for 4-pyridylacetic acid in 75%, 50%, and 25% dioxane; empirically a plot of  $\ln(k)$  vs. %dioxane is linear. Data from ref. 57. In water at 90 °C 2- and 4-pyridylacetic acids have very similar rates: 55.

<sup>f</sup>Extrapolated from data at 90, 80, 70, 60, and 50 °C; ref. 58.

<sup>g</sup>Calculated from activation parameters; ref. 59; the uncertainties are substantial: trichloroacetate,  $\ln k = -10 \pm 5$ .

<sup>h</sup>Extrapolated from data at 90 and 80 °C; ref. 60.

<sup>i</sup>Calculated from activation parameters; ref. 61; the uncertainties are substantial: malonic acid,  $\ln k = -18.14 \pm 1.37$ ; malonate monoanion,  $\ln k = -19.23 \pm 5.16$ ; malonate dianion,  $\ln k = -23.43 \pm 1.78$ .

<sup>j</sup>Calculated from activation parameters; ref. 59; the uncertainties are substantial: malonic acid,  $\ln k = -15.4 \pm 3.4$ .

<sup>k</sup>Calculated from activation parameters; ref. 62; the uncertainties are substantial: malonic acid,  $\ln k = -19.4 \pm 1.3$ .

<sup>l</sup>Calculated from activation parameters; ref. 59; the uncertainties are substantial: malonate monoanion,  $\ln k = -18.4 \pm 1.3$ .

<sup>m</sup>Calculated from activation parameters; ref. 62; the uncertainties are substantial: malonate monoanion,  $\ln k = -18.9 \pm 1.3$ .

<sup>n</sup>Extrapolated from data at 210, 200, 190, 180, 170, and 160 °C; ref. 63.

<sup>o</sup>Calculated from activation parameters; ref. 59; the uncertainties are substantial: cyanoacetate,  $\ln k = -19.0 \pm 2.1$ .

<sup>p</sup>Calculated as described in the text from data in refs. 64, 65, and 58.

<sup>q</sup>Extrapolated from data at 270, 260, 250, 240, 230, and 220 °C; ref. 63.

<sup>r</sup>Calculated from activation parameters; ref. 59; the uncertainties are substantial: trifluoroacetate,  $\ln k = -25.3 \pm 7.3$ .

<sup>s</sup>Reference 66.

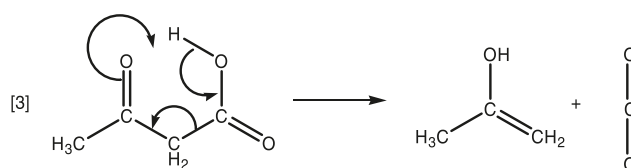
<sup>t</sup>Reference 67.

<sup>u</sup>Calculated from activation parameters; ref. 68; the uncertainties are substantial:  $\ln k = -30.50 \pm 2.57$

<sup>v</sup>Calculated from a rate constant at 344 °C and an estimated entropy of activation, both from ref. 69.

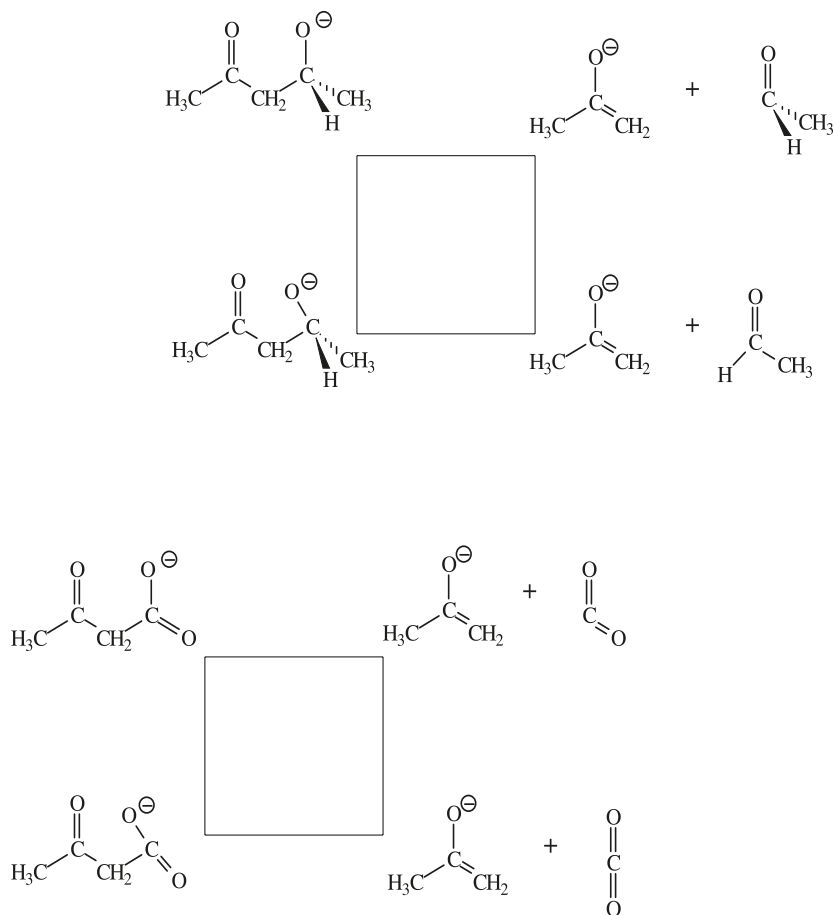
<sup>w</sup>Estimated, assuming 10% reaction could have been observed, from the absence of detectable reaction for 15 d at 344 °C; ref. 69.

in ref. 51) for carbonic acid. For a not too bad intermediate (acetoacetic acid case), the lowest energy path can go by this species and avoid the high intrinsic barrier concerted path. When the intermediate becomes less stable, the concerted path becomes preferable despite its higher intrinsic barrier and the bad intermediate can be avoided.





**Fig. 9.** Why decarboxylation is inherently slower than an analogous retroaldol reaction (itself a slow reaction). The angular distortion for  $sp^2$  to  $sp$  geometry is much larger than for  $sp^3$  to  $sp^2$  geometry, and the energy cost is proportional to the square of the angular distortion.



Rate constants for the decarboxylation reactions considered are collected in Table 2. Where there were multiple values we either averaged the values (taking account of the uncertainty in the reported values) or selected the value based on the shortest extrapolation from higher temperature.

Although decarboxylation of the pyridyl acetic acids has been studied several times, there seem to be no rate constants at 25 °C in water, nor rate constants at a set of higher temperatures allowing extrapolation to 25 °C. Values have been reported for decarboxylation of both acids at 90 °C in water; the two were very similar at each of three pH values.<sup>82</sup> From kinetics data in aqueous dioxane at 25 °C we can extrapolate to aqueous solution by plotting  $\ln(k)$  versus %dioxane. Empirically, this gives a reasonable line ( $r^2 = 0.976$ ); there is slight curvature, which suggests that the true value in water may be somewhat slower than the value given by linear interpolation. We will take the rate for both 2- and 4-pyridylacetic acids to be the same.

For trifluoroacetate decarboxylation, the rate constant at 25 °C was obtained (following an approach used by Zhang and Minear<sup>64</sup>) by extrapolation of an Arrhenius plot of data at elevated temperatures in ethylene glycol.<sup>65</sup> A small correction for the solvent effect was taken from the corresponding extrapolation of data for decarboxylation of trichloroacetate in ethylene glycol<sup>65</sup> and the value for water from Table 2.<sup>58</sup>

Where possible, we used experimental thermodynamic quantities to calculate equilibrium free energy changes. Table 4 gives the thermodynamic quantities, experimental and computational, for all compounds involved in the reactions considered. For each reaction (except for glycine where the problem of calculating solvation energies is extreme), we calculated heats of formation of carboxylic acids and neutral decarboxylation products using the G3MP2B3 method, entropies at the B3LYP/6-31+G\*\* level with the hindered-rotor option where possible (this does not always succeed) and solvation energies by our parameterized IPCM method.<sup>100</sup> There were problems with computed solvation energies of ketoacids and ketoesters. The values calculated were very sensitive to conformation, and there was very little barrier to rotation about the C–CO bonds. In one case, the IPCM calculation failed to converge with the normal isodensity parameter. For the keto tautomer of ethyl acetoacetate and for dimethyl malonate the computational solvation energies are much more negative than values derived from experiment (by correcting to the keto tautomer for ethyl acetoacetate, and from diethyl to dimethyl malonate). The previously reported value for acetoacetic acid is given in Table 4. For malonic acid we used the enthalpy of formation and standard entropy of the solid acid, and activity coefficients calculated from an equation reported by Clegg and Seinfeld.<sup>94</sup> From the activity coefficient we calculated the free energy change for

**Table 3.**  $pK_a$  values used in this work.

Acid	$pK_a$
$\text{CHCl}_3$	24.1 <sup>a</sup>
$\text{CHF}_3$	31.3 <sup>b</sup>
$\text{CH}_3\text{NO}_2$	10.21 <sup>c</sup>
$\text{CH}_4$	49.0 <sup>d</sup>
$\text{CH}_3\text{NH}_3^+$ , cation to neutral	10.62 <sup>c</sup>
$\text{CH}_3\text{NH}_3^+$ , cation to zwitterion	42.9 <sup>e</sup>
$\text{CCl}_3\text{COOH}$	0.26 <sup>f</sup>
$\text{CF}_3\text{COOH}$	0.47 <sup>g</sup>
$\text{CH}_3\text{CN}$	28.9 <sup>d</sup>
$\text{O}_2\text{NCH}_2\text{COOH}$	1.68 <sup>c</sup>
$\text{CH}_3\text{COOH}$	4.76 <sup>c</sup>
$\text{CH}_2=\text{C}(\text{OH})_2$ , neutral to anion	6.65 <sup>h</sup>
$\text{CH}_2=\text{C}(\text{OH})_2$ , anion to dianion	12.6 <sup>h</sup>
$\text{NCCH}_2\text{COOH}$	2.43 <sup>c</sup>
$\text{CH}_2(\text{COOH})_2$ , cation to neutral	-8.84 <sup>h</sup>
$\text{CH}_2(\text{COOH})_2$ , cation to zwitterion	0.90 <sup>h</sup>
$\text{CH}_2(\text{COOH})_2$ , neutral to anion	2.83 <sup>c</sup>
$\text{CH}_2(\text{COOH})_2$ , zwitterion to anion	-6.91 <sup>h</sup>
$\text{CH}_2(\text{COOH})_2$ , anion to dianion	5.69 <sup>c</sup>
$\text{CH}_2=\text{C}(\text{OH})(\text{CH}_3)$	10.94 <sup>i</sup>
1-Methyluracil	34±2 <sup>j</sup>
$\text{CH}_3\text{COCH}_2\text{COOH}$ , cation to neutral	-7.65 <sup>k</sup>
$\text{CH}_3\text{COCH}_2\text{COOH}$ , cation to zwitterion	1.95 <sup>k</sup>
$\text{CH}_3\text{COCH}_2\text{COOH}$ , neutral to anion	3.58 <sup>c</sup>
$\text{CH}_3\text{COCH}_2\text{COOH}$ , zwitterion to anion	-6.02 <sup>h</sup>
1-Methylorotic acid	2.07 <sup>l</sup>
$\text{C}_6\text{H}_6$	43 <sup>m</sup>
$\text{C}_6\text{H}_5\text{COOH}$	4.20 <sup>c</sup>
1- <i>H</i> -2-methylene-dihydropyridine, N-protonated to neutral	5 <sup>h</sup>
1- <i>H</i> -4-methylene-dihydropyridine, N-protonated to neutral	5 <sup>h</sup>
Pyridine-2-acetic acid, cation to neutral	4.15 <sup>n</sup>
Pyridine-2-acetic acid, cation to zwitterion	2.63 <sup>n</sup>
Pyridine-2-acetic acid, neutral to anion	4.26 <sup>n</sup>
Pyridine-2-acetic acid, zwitterion to anion	5.78 <sup>n</sup>
Pyridine-4-acetic acid, cation to neutral	5.00 <sup>n</sup>
Pyridine-4-acetic acid, cation to zwitterion	3.00 <sup>n</sup>
Pyridine-4-acetic acid, neutral to anion	3.87 <sup>n</sup>
Pyridine-4-acetic acid, zwitterion to anion	5.87 <sup>n</sup>

<sup>a</sup>Reference 71.<sup>b</sup>Reference 72.<sup>c</sup>Reference 73.<sup>d</sup>Reference 74a.<sup>e</sup>Estimated from linear free energy relations and the  $pK_a$  of methane, as described in the text.<sup>f</sup>Reference 75.<sup>g</sup>Reference 76.<sup>h</sup>Calculated as described in the text.<sup>i</sup>Reference 77.<sup>j</sup>Actually for 1,3-dimethyluracil, but the effect of the extra methyl is expected to be very small; ref. 78.<sup>k</sup>Reference 49.<sup>l</sup>Actually for orotic acid, but the effect of a methyl should be very small; ref. 79.<sup>m</sup>Reference 80.<sup>n</sup>Reference 81.

diluting a saturated solution (which by definition has the same free energy as the solid) to 0.01 mol/L solution, which was taken as dilute enough to be treated as ideal. We then calculated the free energy change for increasing the concentration from 0.01 mol/L to 1 mol/L ideal solution. These two combined gave the desired free energy change for the transformation from solid to 1 mol/L aqueous solution.

For the four cases where computational and experimental free energies of decarboxylation can both be calculated, the values agreed with an rms error of 1.92 kcal/mol, and a maximum absolute error of 2.87 kcal/mol for  $\text{CF}_3\text{COOH}$ ; see Table 5. In these calculations the experimental value for  $\text{CO}_2$  was used in all cases. Based on this agreement, we conclude that the computational values are adequate for the present purposes. To assume, as was implicitly done above, that all the error is in the computed values, is of course unrealistic; the experimental values are also subject to significant uncertainty.

$pK_a$  values used in this work are collected in Table 3. Various  $pK_a$  values, for which there are not experimental values, had to be estimated as described in what follows.

### $pK_a$ for $\text{CH}_3\text{NH}_3^+$ as a carbon acid

We can estimate this  $pK_a$  using a linear free energy relation. For fluoroform<sup>72</sup> and chloroform,<sup>71</sup> rate constants for exchange have been measured and thus a  $pK_a$  can be calculated; a  $pK_a$  value for methane has been estimated.<sup>74a</sup> For methylammonium ion acting as a carbon acid, there is no direct evidence. Richard et al.<sup>74a</sup> reported an upper limit on the rate constant for exchange of  $(\text{CH}_3)_4\text{N}^+$ ,  $4 \times 10^{-8} (\text{mol/L})^{-1} \text{s}^{-1}$ . Doering,<sup>74b</sup> working at higher temperatures, reported rate constants from which a value, extrapolated to 25 °C, of  $1 \times 10^{-14} (\text{mol/L})^{-1} \text{s}^{-1}$  can be derived. For ethane, a  $pK_a$  based on a computational approach has been reported. Taking the available data for  $pK_a$  values and  $\sigma^*$  values for the substituents (see Table 6) we get the plot shown in Fig. 10. Not surprisingly,  $\text{CHCl}_3$  deviates: heavy atoms are known to have special carbanion stabilizing power when directly attached.<sup>102</sup> From the line defined by three points we can estimate a  $pK_a$  for methylammonium of 43. The slope of the line is in reasonable agreement with expectation based on the generalization proposed by Perrin et al.;<sup>101</sup> predicted 3.2, observed 2.52.

### $pK_a$ values for malonic acid

For protonated malonic acid to neutral, we start with acetic acid for which  $pK_{\text{BH}^+} = -6.56^{103}$  and correct for the effect of the neighboring  $\text{COOH}$  as was done for acetoacetic acid.<sup>49</sup> This leads to a  $pK_{\text{BH}^+} = -8.84$  for protonated malonic acid. For protonated malonic acid to zwitterion, start with the first  $pK_a$  of malonic acid = 2.83,<sup>73</sup> which after correcting for the number of ionizable protons, gives the per proton value, 2.53. The effect of a neighboring positive charge was estimated as was done for acetoacetic acid.<sup>49</sup> This leads to a  $pK_a = 0.90$  for ionization of protonated malonic acid to the zwitterion, and consequently to a  $pK_Z$  (neutral to zwitterion) = 9.74. The  $pK_a$  for zwitterion to anion is easily calculated to be -6.91.

### $pK_a$ values for acetoacetic acid

$pK_a$  values for acetoacetic acid were taken from previous work,<sup>49</sup> except for the  $pK_a$  for zwitterion to anion, which can be calculated from the other  $pK_a$  values.

### $pK_a$ values for acetic acid enol

We have previously reported a value estimated from that for mandelic acid enol by an argument based on substituent effects; the value was 6.6.<sup>104</sup> An alternative estimation starts

**Table 4.** Thermodynamic quantities for compounds discussed in this paper, plus a few included to test the quality of computed  $\Delta G_{\text{equil}}$ .

Compound	$\Delta H_f(\text{g})$	$S^\circ(\text{g})$	$\Delta G_f(\text{g})^a$	$\Delta G_t$	$\Delta G_f(\text{aq})$
<b>(a) Compounds for which <math>\Delta G_f(\text{aq})</math> has not previously been reported, and computed values for some of these</b>					
Chloroform	-24.65 <sup>b</sup>	70.68 <sup>b</sup>	-16.83 <sup>b</sup>	0.83 <sup>c</sup>	-16.00 <sup>d</sup>
	-24.63 <sup>e</sup>	72.93 <sup>f</sup>	-17.49 <sup>g</sup>	0.56 <sup>h</sup>	-16.93 <sup>d</sup>
Fluoroform	-166.60 <sup>i,j</sup>	62.06 <sup>i,j</sup>	-158.31 <sup>d</sup>	2.71 <sup>c</sup>	-155.60 <sup>d</sup>
	-166.67 <sup>e</sup>	62.11 <sup>f</sup>	-158.40 <sup>d</sup>	2.38	-156.02 <sup>d</sup>
Nitromethane	-17.86±0.10 <sup>b</sup>	65.72 <sup>b</sup>	-1.63±0.10 <sup>b</sup>	-2.30 <sup>k</sup>	-3.93 <sup>d</sup>
	-16.78 <sup>e</sup>	70.42 <sup>l</sup>	-1.98 <sup>b</sup>	-2.36 <sup>h</sup>	-4.34 <sup>b</sup>
Methylamine	-5.49±0.10 <sup>b</sup>	58.18 <sup>b</sup>	7.69±0.10 <sup>b</sup>	-2.73 <sup>m</sup>	4.96±0.10 <sup>b</sup>
	-4.22 <sup>e</sup>	57.84 <sup>l</sup>	9.03 <sup>b</sup>	-4.54 <sup>h</sup>	4.49 <sup>b</sup>
Trichloroacetic acid	-103.65 <sup>j,n</sup>	88.42 <sup>f</sup>	-86.11 <sup>d</sup>	-3.65 <sup>o</sup>	-89.76 <sup>d</sup>
	-104.62 <sup>e</sup>		-87.24 <sup>d</sup>	-4.54 <sup>h</sup>	-91.78 <sup>d</sup>
Trifluoroacetic acid	-246.52 <sup>j,p</sup>	81.27 <sup>f</sup>	-229.02 <sup>d</sup>	-5.40 <sup>q</sup>	-234.42 <sup>d</sup>
	-245.76 <sup>e</sup>		-228.33 <sup>d</sup>	-4.10 <sup>h</sup>	-237.96 <sup>d</sup>
Nitroacetic acid	-98.96 <sup>e</sup>	84.51 <sup>f</sup>	-73.34 <sup>d</sup>	-12.51 <sup>h</sup>	-85.85 <sup>d</sup>
Cyanoacetic acid	-63.86 <sup>e</sup>	78.18 <sup>f</sup>	-50.57 <sup>d</sup>	-7.98 <sup>h</sup>	-58.55 <sup>d</sup>
Malonic acid	-212.97 <sup>r,s</sup>	35.61 <sup>s,t</sup>	-174.54 <sup>d,s</sup>	-1.60 <sup>u</sup>	-176.14 <sup>d</sup>
1- <i>H</i> -2-methylene-dihydropyridine	45.77 <sup>e</sup>	76.26 <sup>f</sup>	64.86 <sup>d</sup>	-3.50 <sup>h</sup>	61.36 <sup>d</sup>
1- <i>H</i> -4-methylene-dihydropyridine	45.37 <sup>e</sup>	77.15 <sup>f</sup>	64.19 <sup>d</sup>	-4.77 <sup>h</sup>	59.42 <sup>d</sup>
1-Methyluracil	-72.40 <sup>e</sup>	88.49 <sup>f</sup>	-40.59 <sup>d</sup>	-16.56 <sup>h</sup>	-57.15 <sup>d</sup>
Pyridine-2-acetic acid	-63.06 <sup>e</sup>	95.93 <sup>f</sup>	-34.42 <sup>d</sup>	-7.57 <sup>h</sup>	-41.99 <sup>d</sup>
Pyridine-4-acetic acid	-61.35 <sup>e</sup>	96.37 <sup>f</sup>	-32.84 <sup>d</sup>	-10.43 <sup>h</sup>	-43.27 <sup>d</sup>
1-Methylorotic acid	-154.19 <sup>e</sup>	102.10 <sup>f</sup>	-111.41 <sup>d</sup>	-18.50 <sup>h</sup>	-129.91 <sup>d</sup>
<b>(b) Computational values for compounds for which <math>\Delta G_f(\text{aq})</math> has previously been reported</b>					
Methane	-17.55 <sup>e</sup>	44.48 <sup>f</sup>	-11.79 <sup>d</sup>	3.08 <sup>h</sup>	-8.71 <sup>d</sup>
Acetic acid	-102.52 <sup>e</sup>	69.19 <sup>l</sup>	-89.12 <sup>d</sup>	-4.79 <sup>h</sup>	-93.91 <sup>d</sup>
Benzene	18.85 <sup>e</sup>	64.07 <sup>f</sup>	30.09 <sup>d</sup>	1.73 <sup>h</sup>	31.82 <sup>d</sup>
Benzoic acid	-71.84 <sup>e</sup>	84.01 <sup>f</sup>	-51.53 <sup>d</sup>	-7.83 <sup>h</sup>	-59.36 <sup>d</sup>
<b>(c) Compounds for which <math>\Delta G_f(\text{aq})</math> has previously been reported</b>					
Carbon dioxide					-92.25±0.06 <sup>v</sup>
Methane					-8.14±0.16 <sup>w</sup>
Acetonitrile					17.61±1.73 <sup>x</sup>
Acetic acid					-94.35±0.38 <sup>w</sup>
Acetic acid enol					-67.90±1.67 <sup>y</sup>
Glycine					-88.59±0.01 <sup>b</sup>
Benzene					31.94±0.21 <sup>w</sup>
Benzoic acid					-57.02±0.55 <sup>w</sup>
Acetoacetic acid					-120.04 <sup>v</sup>
Acetone					-38.48±0.21 <sup>w</sup>
Acetone enol					-27.02±0.22 <sup>v</sup>
<b>(d) Compounds for which only <math>\Delta G_f(\text{aq})</math> has been calculated in this work<sup>z</sup></b>					
Trichloromethide					16.91
Trifluoromethide					-112.80
Nitromethide					10.02
Methide					58.79
Ammonium methide					49.07
Trichloroacetate					-88.87
Trifluoroacetate					-234.11
Cyanomethide					57.09
Nitroacetate					-84.29
Acetic acid dienolate					-41.60
Acetic acid enolate					-58.82
Cyanoacetate					-55.23
Malonate dianion					-164.50
Malonate monoanion					-172.28
Malonic acid zwitterion					-162.84

**Table 4** (concluded).

Compound	$\Delta H_f(g)$	$S^\circ(g)$	$\Delta G_f(g)^a$	$\Delta G_t$	$\Delta G_f(aq)$
Malonic acid					-176.14
Phenyl anion					90.68
Benzoate					-51.28
1-Methyluracil-6-anion					-10.61
Pyridine-2-acetic acid zwitterion					-44.06
Pyridine-4-acetic acid zwitterion					-45.99
1-Methylorotate anion					-127.06

**Note:** All at 25 °C; enthalpies and free energies are in kcal/mol, entropies are in cal/°/mol, standard states are the ideal gas at 1 atm and 1 mol/L aqueous solution with an infinitely dilute reference state. Unless otherwise noted, enthalpies of formation are from ref. 98, entropies are from ref. 99, free energies of formation in the gas phase are calculated from the corresponding enthalpies of formation and the standard entropies, and free energies of formation in aqueous solution are calculated from the corresponding free energies of formation in the gas and free energies of transfer.

<sup>a</sup>Free energy of transfer from the gas at 1 atm to 1 mol/L aqueous solution.

<sup>b</sup>Reference 83.

<sup>c</sup>Reference 84.

<sup>d</sup>Calculated from other values in this table.

<sup>e</sup>Calculated, G3MP2B3.

<sup>f</sup>Calculated using the rigid rotor harmonic oscillator approximation as justified in ref. 85.

<sup>g</sup>Calculated from other values in this table.

<sup>h</sup>Calculated using IPCM/B3LYP/6-31+G\*\*//B3LYP/6-31+G\*\*, corrected by parameterization as described in ref. 86.

<sup>i</sup>Reference 87.

<sup>j</sup>From the NIST WebBook, <http://webbook.nist.gov/chemistry/form-ser.html>.

<sup>k</sup>Reference 88.

<sup>l</sup>Using the hindered rotor procedure in Gaussian03.

<sup>m</sup>Calculated from  $\Delta G_f(g)$  and  $\Delta G_f(aq)$  taken from ref. 83.

<sup>n</sup>Reference 89.

<sup>o</sup>Reference 90.

<sup>p</sup>Reference 91.

<sup>q</sup>Reference 76.

<sup>r</sup>Reference 92.

<sup>s</sup>Properties of the solid acid.

<sup>t</sup>Reference 93.

<sup>u</sup>Calculated using activity coefficient data from ref. 94, as described in the text.

<sup>v</sup>Reference 49.

<sup>w</sup>Reference 95.

<sup>x</sup>Reference 96.

<sup>y</sup>Reference 97.

<sup>z</sup>Calculated from free energies of formation from parts (a) or (b) of this table and  $pK_a$  values from Table 2.

from the  $pK_a$  for acetone enol, 10.94.<sup>77</sup> Using the general estimation procedure for  $\rho^*$  proposed by Perrin et al.,<sup>101</sup> we take  $\rho^* = 3.2$ ;  $\sigma^*$  for  $\text{CH}_3$  is 0.0 and  $\sigma^*$  for OH is 1.34. With these values the estimated  $pK_a$  for acetic acid enol is  $10.94 - 3.2 \times 1.34 = 6.65$ . The second  $pK_a$  can be approximately estimated by invoking Pauling's rule,<sup>105</sup> that successive  $pK_a$  values for  $\text{Z}(\text{OH})_n$  increase by 5  $pK_a$  units; this leads to a value of 12.

### $pK_a$ value for $\text{CHF}_3$

We used the rate constant for hydroxide-catalyzed hydrogen exchange reported by Symons and Clermont;<sup>72</sup> they measured the rate of reaction at higher temperatures and determined  $E_a = 32.0 \pm 1.6$  kcal/mol,  $\Delta H^\ddagger = 31.4 \pm 1.6$  kcal/mol, and  $\Delta S^\ddagger = 18 \pm 5$  cal/mol/K. From these values  $\Delta G^\ddagger = 26.04 \pm 2.19$  kcal/mol at 25 °C, or  $k = 5.15 \times 10^{-7}$  (mol/L<sup>-1</sup>) s<sup>-1</sup>. For the reverse reaction, expected to be very fast, we use the rate constant for the relaxation of water,  $1 \times 10^{11}$  s<sup>-1</sup>.<sup>106,107</sup> These two rate constants lead to a  $pK_a$  of 31.3.

### $pK_a$ values for benzene

Streitwieser et al.<sup>80</sup> have made various attempts to determine the  $pK_a$  of benzene, generally by extrapolation techniques. In 1972,<sup>80</sup> a value based on cesium cyclohexylamide in cyclohexylamine and referenced to 9-phenylfluorene of  $43.0 \pm 0.2$  was reported. The use of 9-phenylfluorene is significant because the conjugate base of this acid is highly delocalized and thus unlikely to be hydrogen bonded even in a protic solvent. In 1996,<sup>108</sup> values based on ion pair equilibration in THF were reported. The values were cesium ion pairs, benzene  $pK_a = 44.8$  at 25 °C; lithium ion pairs, benzene  $pK_a = 39.5$ . These experiments used highly delocalized indicator acids of known  $pK_a$ . Thus, experimental values lead to values of  $44 \pm 1$  as the  $pK_a$  of benzene in aprotic solvents. Shen et al.,<sup>109</sup> in a careful computational study of hydrocarbon and heterocycle  $pK_a$  values in DMSO reported the  $pK_a$  of benzene as 44.7.

### $pK_a$ values for methane

Bordwell<sup>110</sup> estimated a value for methane in DMSO by



**Table 5.** Comparison of experimental and equilibrium free energies of decarboxylation.

Reaction	Computational	Experimental	Difference
$\text{CCl}_3\text{COOH} \rightleftharpoons \text{CCl}_3\text{H} + \text{CO}_2$	-17.21	-18.49	-1.28
$\text{CF}_3\text{COOH} \rightleftharpoons \text{CF}_3\text{H} + \text{CO}_2$	-16.31	-13.43	2.87
$\text{C}_6\text{H}_5\text{COOH} \rightleftharpoons \text{C}_6\text{H}_6 + \text{CO}_2$	-1.06	-3.29	-2.23
$\text{CH}_3\text{COOH} \rightleftharpoons \text{CH}_4 + \text{CO}_2$	-7.05	-6.04	1.01
rms error			1.92

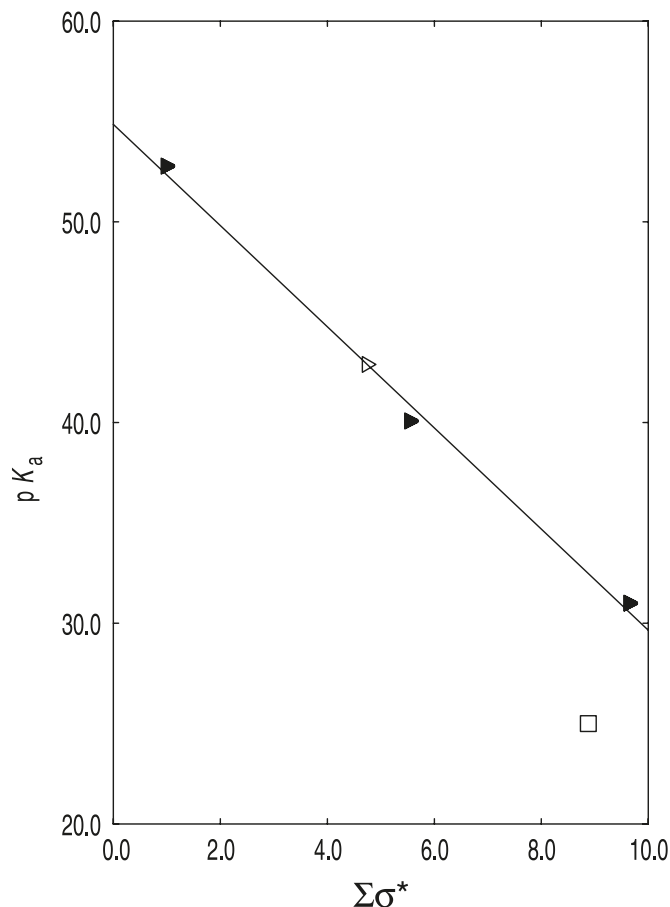
**Note:** In aqueous solution at 25 °C. For the computational values, the experimental  $\Delta G_f(\text{aq})$  for  $\text{CO}_2$  was used.

**Table 6.**  $\text{p}K_a$  values for weak carbon acids.

Compound	$\Sigma\sigma^*$ (for X, Y, Z in CH-XYZ)	$\text{p}K_a$ per H	$\text{p}K_a$ calcd.
$\text{CH}_3\text{CH}_3$	0.98	52.78	52.39
$(\text{CH}_3)_4\text{N}^+$	5.53	40.08	40.91
$\text{F}_3\text{CH}$	9.63	31	30.56
$\text{Cl}_3\text{CH}$	8.88	25	32.46
$\text{CH}_3\text{NH}_3^+$	4.74		42.90

**Note:** At 25 °C in water;  $\sigma^*$  values from ref. 101, and  $\text{p}K_a$  values from Table 3.

**Fig. 10.** Estimation of a  $\text{p}K_a$  for CH in methylammonium ion. Known  $\text{p}K_a$  values (see text) for ethane, tetramethylammonium, fluoroform, and chloroform are plotted against  $\sigma^*$  values (Table 6). The line was fitted by least squares with the point for chloroform ( $\square$ ) omitted: chlorine is expected to stabilize an anion by mechanisms not captured by  $\sigma^*$ . ( $\blacktriangle$ ) Experimental  $\text{p}K_a$  values; ( $\triangle$ )  $\text{p}K_a$  for  $\text{H-CH}_2\text{-NH}_3^+$  estimated using this correlation.



an extrapolation procedure and obtained a  $\text{p}K_a$  of 56. Richard et al.<sup>74a</sup> estimated a value in water of  $\text{p}K_a = 49$  based on a computational value for ethane<sup>74a,111</sup> corrected for the number of hydrogens. These values are roughly consistent: the expected desolvation energy for the anion (see below) is 13 pK units, leading to a  $\text{p}K_a$  in DMSO of 62. Bearing in mind that the independent  $\text{p}K_a$  estimates in water and DMSO have uncertainties of at least 2 kcal, and that the desolvation energy represents a considerable extrapolation and must also have a substantial uncertainty, this is about as good as one is entitled to hope for.

#### $\text{p}K_a$ values for N-protonation of 1-*H*-2-methylene-dihydropyridine and 1-*H*-4-methylene-dihydropyridine

Given the absence of any other information, we assume that an enol (e.g.,  $\text{p}K_a$  for  $\text{CH}_2=\text{CH}(\text{OH}) = 10.50$ ,<sup>77</sup>  $\text{p}K_a$  for  $\text{CH}_2=\text{C}(\text{CH}_3)(\text{OH}) = 10.94$ <sup>77</sup>) is similar in  $\text{p}K_a$  to a phenol ( $\text{p}K_a$  for  $\text{C}_6\text{H}_5(\text{OH}) = 9.95$ <sup>73</sup>), so an N-protonated enamine should be similar to a protonated aniline ( $\text{p}K_a$  for  $\text{C}_6\text{H}_5(\text{NH}_3^+) = 4.58$ <sup>73</sup>), and use  $\text{p}K_a$  values of 5 for N-protonated forms of both 1-*H*-2-methylene-dihydropyridine and 1-*H*-4-methylene-dihydropyridine.

The set of decarboxylation reactions to be considered involves several different types of compounds, which will be treated separately. The first set of reactions involves compounds where decarboxylation produces a delocalized carbanion, which may in fact be neutral if the starting material was a zwitterion. The reactions are the decarboxylations of acetoacetic acid (as the zwitterion), acetoacetate anion, malonic acid (as the zwitterion), malonate monoanion, malonate dianion, nitroacetate anion, cyanoacetate anion, pyridine-2-acetic acid, and pyridine-4-acetic acid, both of the last two as the zwitterions. The model for these reactions is discussed below. The results, Table 7 and Fig. 11, show that agreement is quite good except for malonate dianion. Examination of the origins of this number<sup>61</sup> shows that although it has been reported it has probably not been measured. It was assumed<sup>61</sup> that for a solution in which the dianion was the major species it was also the kinetically significant species. Since the monoanion can reasonably be expected to be much more reactive, this is not a safe assumption and only a demonstration that the rate is pH independent for a pH range where the dianion is the major species would allow the assignment of the observed rate to the dianion reaction.

The detailed model of the reaction is that the overall transformation involves two or three dimensions: geometry change at the carboxylate, geometry change at the carbanion carbon if there is a delocalized carbanion, and bond breaking. For some classes of reaction, bond length is a dimension but for other reactions it leads to excessively high

**Table 7.** Observed and calculated free energies of activation.

Reactant	$\Delta G_{\text{obs}}^{\circ}$	$\Delta G_{\text{desolv}}^{\text{pre or}}$	$\Delta G_{\text{rds}}$	$\Delta G_{\text{obs}}^{\ddagger}$	$\Delta G_{\text{rds}}^{\ddagger}$	$\tilde{G}^a$	$\Delta G_{\text{calc}}^{\ddagger}$
Acetate anion	54.39	13.40 <sup>b</sup>	67.79	$\geq 60.30$	$\geq 60.30$	$\geq 25.99$ 38.97 <sup>c</sup>	70.91
Acetoacetic zwitterion	0.77	13.07 <sup>d</sup>	-12.30	23.65	11.31	16.91	9.90
Acetoacetate anion	10.82		10.82	26.11	26.11	20.34	26.13
Benzoate anion	49.71		49.71	55.51	55.51	24.31	55.20
Cyanoacetate anion	20.06		20.06	30.80	30.80	15.92	31.55
Glycine zwitterion	45.41	11.80 <sup>b</sup>	57.21	40.26	40.26	— <sup>e</sup> 22.09 <sup>c</sup>	60.06
Glycine cyclic mechanism	1.30		1.30	40.26	40.26	39.60	
Malonate dianion	29.33		29.33	31.35	31.35	12.32 <sup>f</sup> 22.99 <sup>c</sup>	40.00
Malonate monoanion	21.26		21.26	30.80	30.80	18.66	32.67
Malonate zwitterion	15.99	13.30 <sup>d</sup>	2.68	30.00	16.70	15.33	18.13
1-Methylorotate anion	24.20	9.21 <sup>b</sup>	33.91	38.36	38.36	19.05	39.18
Nitroacetate	-2.25		-2.25	21.13	21.13	23.80	21.36
Pyridine-2-acetic acid	13.17		13.17		28.11	21.03	26.37
Pyridine-4-acetic acid	13.16		13.16		28.11	21.01	27.52
Trichloroacetate anion	13.54	7.00 <sup>c</sup>	20.54	28.44	28.44	16.57	29.03
Trifluoroacetate anion	29.01	8.60 <sup>c</sup>	37.61	40.65	40.65	19.55	42.88

**Note:** In aqueous solution at 25 °C.

<sup>a</sup>Intrinsic barrier calculated from  $\Delta G_{\text{rds}}$  and  $\Delta G_{\text{rds}}^{\ddagger}$ .

<sup>b</sup> $\Delta G_{\text{desolv}}$ ; see text.

<sup>c</sup>Calculated from  $\Delta G_{\text{rds}}$  and  $\Delta G_{\text{calc}}^{\ddagger}$ .

<sup>d</sup> $\Delta G_{\text{pre}}$  for zwitterion formation.

<sup>e</sup>These data are impossible; the free energy of activation is less than the free energy change for product formation. This suggests that the mechanism is different and leads to a different product than is assumed here.

<sup>f</sup>As discussed in the text, it seems likely that the rate of this reaction has not yet been measured.

intrinsic barriers. The key feature seems to be whether both ends of a bond are tied to the solvent structure by hydrogen bonding. Thus, simple carbonyl additions require bond length as a coordinate but decarboxylations or aldol additions do not. In a simple carbonyl addition both the nucleophile and the carbonyl oxygen are hydrogen bonded and linked to the solvent structure. In decarboxylation, both the C–O bonds of the carboxylate and (for delocalized carbanions) the bond to the electron withdrawing group change length, but only the termini of the entire reacting system are hydrogen bonded, and the carbons of the scissile bond (which are also the termini of the bonds that change length) are not tied to solvent. Desolvation must be allowed for when a localized carbanion is formed and is missing hydrogen bonding assumed to be present in the definition of the  $pK_a$  used to calculate the corner energy.

Normally, we would try for an equilibrium conformation as contrasted with the reactive conformation defined by the stereoelectronic demands of the mechanism. However, in the case of zwitterions there are additional problems. There is a strong anomeric effect, which favors the reactive conformation, tending to alter the geometry in the direction of product and lengthen the scissile bond. In the absence of explicit solvation or constraints this goes to completion. Conversely, there is a tendency, in the absence of explicit waters, for the conformation to change to one with an intramolecular hydrogen bond, or even to undergo a proton transfer. Such an intramolecular hydrogen bond is strongly stabilizing in the gas phase but this is spurious, because the estimated  $pK_a$

values on which the zwitterion content was based do not include this hydrogen bond even in its much weaker solution form. Such hydrogen bonds are much weaker in solution and are not even present in the reactive conformation. In most cases, there will not be a meaningful alternative conformation, nor should there be much difference in conformational energy (less electrostatic interactions, which are difficult to account for computationally).

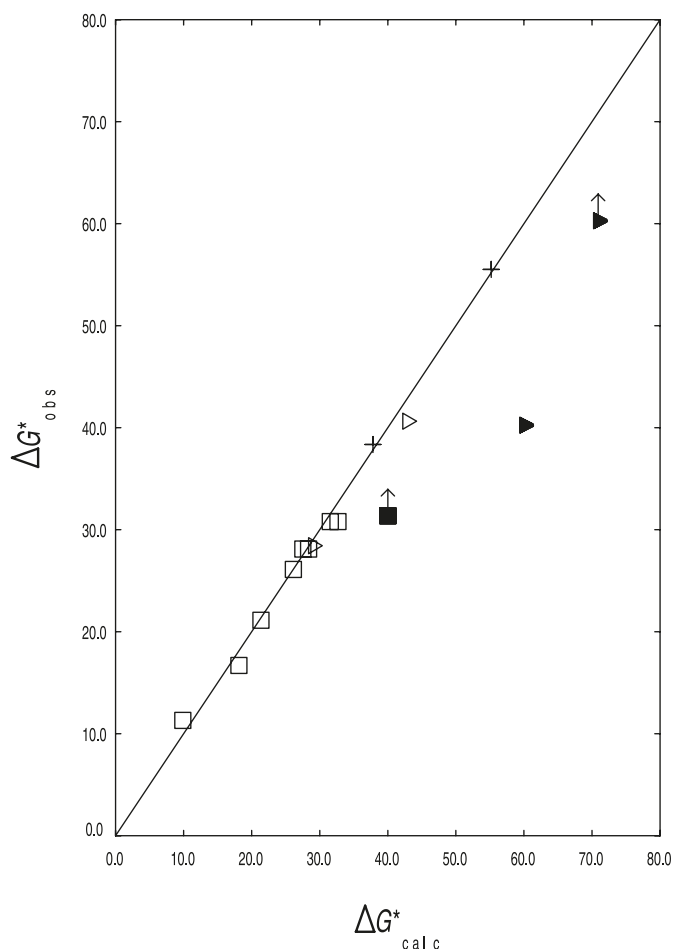
As an attempt to resolve these difficulties, the fully hydrated zwitterion was allowed to optimize without constraints and the result of these calculations was taken as the equilibrium form. These optimizations with multiple waters are very slow, so we normally stopped when the length of the scissile bond stabilized. The waters were then removed and a single point calculation was carried out to give the equilibrium energy.

Geometries and bond lengths for zwitterionic species were determined by optimization with enough waters to form hydrogen bonds to each acidic hydrogen and basic lone pair, with cyclic chains of hydrogen bonds wherever possible. This amount of explicit solvation allowed the zwitterions to stay together with modest C–C bond lengthening.

Desolvation energies for anions were estimated based on the change in  $pK_a$  from DMSO to water per hydrogen bond in the conjugate base for a series of alcohols with increasing numbers of fluorines, as described in Appendix A.

The next set of decarboxylation reactions to be considered involves arenecarboxylates, specifically benzoate and 1-methylorotate; see Fig. 12. For these reactions, the product

**Fig. 11.** Comparison of observed and calculated values of  $\Delta G^\ddagger$  for decarboxylation reactions. ( $\square$ ) Reactions that generate a delocalized "anion". (+) Reactions of arenecarboxylates. ( $\triangle$ ) Reactions that generate a localized  $sp^3$  anion. Filled symbols represent points that deviate significantly; arrows indicate points where the experimental value is a lower limit.



is a localized arenecarboxylate. The  $pK_a$  values of such ions can be determined, albeit indirectly, by measuring rates of exchange. Data are available for two reactions, the decarboxylations of benzoate and 1-methylorotate. In the case of 1-methylorotate, the  $pK_a$  for the product is actually available for 1,3-dimethyluridine but the extra methyl should make only a small difference to the  $pK_a$ . The calculated rate constants are in good agreement with experiment; benzoate is in fact the lower limit of reactivity for which the rate has been experimentally measurable to date.

Finally, we examined a number of cases where decarboxylation leads to an  $sp^3$  hybridized carbanion with a localized charge. There are experimental data for trifluoro- and trichloroacetate, and for glycine, and an upper limit for the rate constant for acetate.

The calculated free energies of activation are in good agreement with experiment for trifluoro- and trichloroacetate, and consistent with the reported upper limit for acetate. For glycine, the predicted free energy of activation is significantly too high; this may mean that the mechanism is not the simple decarboxylation assumed. It may be possible for

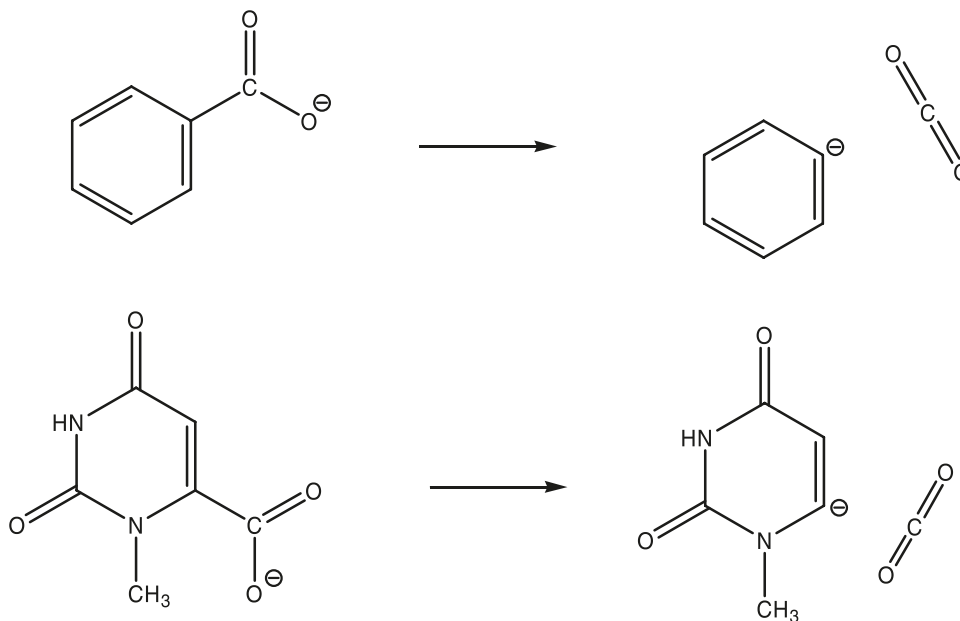
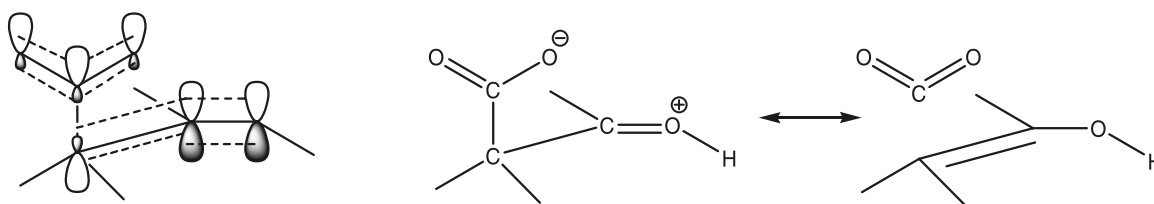
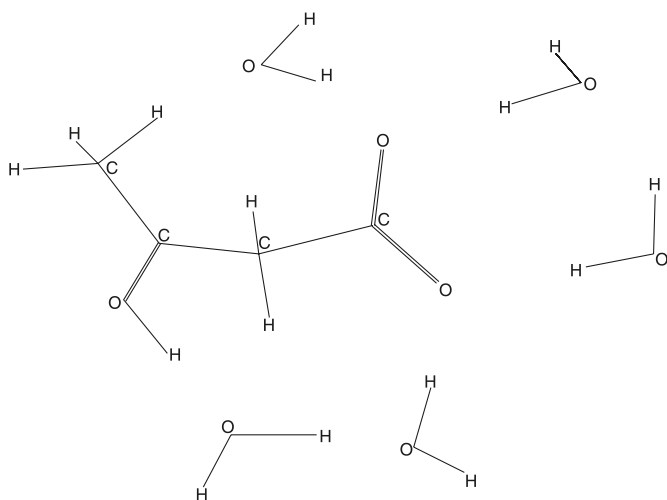
decarboxylation to be accompanied by a water mediated proton switch from nitrogen to carbon, leading directly to neutral methylamine as product. The intrinsic barrier calculated, assuming this is the process (zwitterion of glycine going directly to neutral methylamine), is much higher than that calculated assuming that the zwitterion of glycine leads to the zwitterion of methylamine. At present, we do not know how to treat the concerted electrophilic substitution at  $sp^3$  carbon, which would be involved in such a process, so this can only be a speculation.

Equilibrium free energy changes and free energies of activation for the reactions to be considered are gathered in Table 7. The corresponding empirical intrinsic barriers implied by the Marcus equation (eq. [2]) are also given in Table 7. Comparison of related reactions show that acetoacetate zwitterion has a lower intrinsic barrier than acetoacetate anion, and malonate zwitterion has a lower barrier than malonate monoanion. This can be explained in terms of an enhanced anomeric effect in the zwitterion, with lone pair electrons from the carboxylate ion feeding into the antibonding  $\sigma^*$  orbital for the C–C bond which is to break and from this to the  $\pi^*$  antibonding orbital for the protonated carbonyl, leading to a shift in bond lengths and geometry closer to those of the product. In the corresponding anion there is a poorer electron sink and consequently less hyperconjugation and less shift in bond lengths and geometry; see Fig. 13. To the extent that the geometry shifts towards the product, the distortion energies for the one thing at a time corners will be smaller and consequently the intrinsic barrier will be lower. To calculate these hyperconjugation induced geometry changes by molecular orbital (MO) theory requires explicit solvation because zwitterions are so unstable in gas that they would inevitably fall apart. The addition of five water molecules proved sufficient, with four solvating the carboxylate and one solvating the protonated carbonyl and also forming a bridging hydrogen bond to a water solvating the carboxylate; see Fig. 14.

The estimated values of  $\Delta G^\circ$  and the NBT values of  $\Delta G^\ddagger$  for acetate and glycine lead to intrinsic barriers of 24.15 and 24.79 kcal/mol, respectively, which is in good agreement with the values observed for other decarboxylations leading to localized carbanions (benzoate, orotate, trichloroacetate), though the value for trifluoroacetate is surprisingly low. This supports the idea that glycine reacts by a different mechanism, leading to a faster reaction than the one assumed for the NBT calculation. This cyclic path has a much lower thermodynamic barrier so it is faster despite the very high intrinsic barrier.

In summary, the NBT method has successfully predicted rate constants over the entire range reported to date, and can call attention to places (malonate dianion) where the literature may be incorrect. It also allows a choice to be made when literature values lead to strikingly different rate constants at 25 °C, as for trichloroacetate and trifluoroacetate where values based on the literature differ by four orders of magnitude. The faster rate constants are based on high temperature studies in metal cells (stainless steel or titanium),<sup>59,63</sup> and may be subject to transition metal catalysis.

NBT represents both a useful qualitative way to think about why some reactions are fast and some are slow, but also a quantitative way of calculating rates of reactions,

**Fig. 12.** Decarboxylation of aromatic carboxylic acids: benzoic acid and 1-methylorotic acid.**Fig. 13.** Hyperconjugation as an explanation for the lower intrinsic barrier in zwitterions of  $\beta$ -keto acids. This is illustrated using both hyperconjugation and bond–no-bond resonance.**Fig. 14.** Explicit solvation of the zwitterion of acetoacetic acid by five water molecules, four solvating the carboxylate and one the protonated carbonyl. The optimized structure (b3lyp/6-31+G\*\*) is shown.

which is much less computationally demanding than the traditional “brute force” approach of calculating the energy of the solvated transition state directly. We are now engaged in extending the range of reactions to which the method can be applied and also improving the computer programs used to

carry out the calculations in hopes of making the whole process easier and more accessible.

## Computational methods

All molecular orbital calculations were carried out using Gaussian03.<sup>112</sup> Heats of formation were calculated using the G3MP2B3 keyword, and the G3MP2 enthalpy was converted to heat of formation by way of the heat of atomization, using calculated G3MP2 enthalpies for the atoms and experimental heats of formation of the atoms. Entropies were calculated using B3LYP/6-31+G\*\*/freq// B3LYP/6-31+G\*\* or where possible B3LYP/6-31+G\*\*/freq=hindrot// B3LYP/6-31+G\*\*. Solvation energies were calculated using B3LYP/6-31+G\*\*/scrf=ipcm// B3LYP/6-31+G\*\* and then corrected using the set of parameters we have reported.<sup>100</sup>

The Supplementary data contains optimized geometries for all G3MP2B3 calculations, optimized geometries for all entropy calculations (the same geometries were used for solvation calculations), initial and final corner structures used for NBT calculations, and tables containing all the energy contributions to the final corner energies used to find the free energy of activation.

## Supplementary data

Supplementary data for this article are available on the journal Web site ([canjchem.nrc.ca](http://canjchem.nrc.ca)) or may be purchased



from the Depository of Unpublished Data, Document Delivery, CISTI, National Research Council Canada, Ottawa, ON K1A 0R6, Canada. DUD 5326. For more information on obtaining material, refer to [cisti-icist.nrc-cnrc.gc.ca/cms/unpub\\_e.shtml](http://cisti-icist.nrc-cnrc.gc.ca/cms/unpub_e.shtml).

## Acknowledgments

We thank the Natural Sciences and Engineering Research Council of Canada (NSERC) for financial support of this work and the Shared Hierarchical Academic Research Computing Network (SHARCNET) for computing resources.

## References

- (1) Marcus, R. A. *J. Chem. Phys.* **1956**, 24 (5), 966. doi:10.1063/1.1742723.
- (2) Marcus, R. A. *Discuss. Faraday Soc.* **1960**, 29, 21. doi:10.1039/df9602900021.
- (3) Marcus, R. A. *Annu. Rev. Phys. Chem.* **1964**, 15 (1), 155. doi:10.1146/annurev.pc.15.100164.001103.
- (4) Marcus, R. A. *J. Chem. Phys.* **1965**, 43 (2), 679. doi:10.1063/1.1696792.
- (5) Cohen, A. O.; Marcus, R. A. *J. Phys. Chem.* **1968**, 72 (12), 4249. doi:10.1021/j100858a052.
- (6) Marcus, R. A. *J. Phys. Chem.* **1968**, 72 (3), 891. doi:10.1021/j100849a019.
- (7) Marcus, R. A. *J. Am. Chem. Soc.* **1969**, 91 (26), 7224. doi:10.1021/ja01054a003.
- (8) Lewis, E.; Douglas, T.; McLaughlin, M. A. Quantitative Measure of Nucleophilic Character. In *Nucleophilicity*; Harris, J., McManus, S., Eds.; ACS Symposium Series 215, Advances in Chemistry; American Chemical Society: Washington, DC, 1987.
- (9) Hine, J. J. *Am. Chem. Soc.* **1971**, 93 (15), 3701. doi:10.1021/ja00744a025.
- (10) Guthrie, J. P. *J. Am. Chem. Soc.* **1978**, 100 (18), 5892. doi:10.1021/ja00486a048.
- (11) Guthrie, J. P. *J. Am. Chem. Soc.* **1991**, 113 (19), 7249. doi:10.1021/ja00019a024.
- (12) Guthrie, J. P.; Guo, J. J. *Am. Chem. Soc.* **1996**, 118 (46), 11472. doi:10.1021/ja9542471.
- (13) Kreevoy, M. M.; Konasewich, D. E. *Adv. Chem. Phys.* **1972**, 21, 243. doi:10.1002/9780470143698.ch17.
- (14) Alberty, W. J.; Campbell-Crawford, A. N.; Curran, J. S. *J. Chem. Soc. Perkin Trans. 2* **1972**, 2206. doi:10.1039/P29720002180.
- (15) Koeppl, G. W.; Kresge, A. J. *J. Chem. Soc. Chem. Commun.* **1973**, 371. doi:10.1039/c39730000371.
- (16) Kresge, A. J. *Chem. Soc. Rev.* **1973**, 2 (4), 475. doi:10.1039/cs9730200475.
- (17) Kresge, A. J. *Acc. Chem. Res.* **1975**, 8 (10), 354. doi:10.1021/ar50094a006.
- (18) Alberty, W. J. *Annu. Rev. Phys. Chem.* **1980**, 31 (1), 227. doi:10.1146/annurev.pc.31.100180.001303.
- (19) Pellerite, M. J.; Brauman, J. I. *J. Am. Chem. Soc.* **1983**, 105 (9), 2672. doi:10.1021/ja00347a026.
- (20) Murdoch, J. R. *J. Am. Chem. Soc.* **1983**, 105 (8), 2159. doi:10.1021/ja00346a010.
- (21) Murdoch, J. R. *J. Am. Chem. Soc.* **1983**, 105 (9), 2660. doi:10.1021/ja00347a024.
- (22) Kreevoy, M. M.; Lee, I.-S. H. *J. Am. Chem. Soc.* **1984**, 106 (9), 2550. doi:10.1021/ja00321a011.
- (23) Schlesener, C. J.; Amatore, C.; Kochi, J. K. *J. Am. Chem. Soc.* **1984**, 106 (12), 3567. doi:10.1021/ja00324a027.
- (24) Leussing, D. L.; Emly, M. *J. Am. Chem. Soc.* **1984**, 106 (2), 443. doi:10.1021/ja00314a043.
- (25) Chen, M. Y.; Murdoch, J. R. *J. Am. Chem. Soc.* **1984**, 106 (17), 4735. doi:10.1021/ja00329a016.
- (26) Ebersson, L.; Carlson, R.; Undheim, K.; Mörch, L.; Norin, T. *Acta Chem. Scand. A* **1984**, 38b, 439. doi:10.3891/acta.chem.scand.38b-0439.
- (27) Miller, B. A.; Leussing, D. L. *J. Am. Chem. Soc.* **1985**, 107 (24), 7146. doi:10.1021/ja00310a064.
- (28) Schlesener, C. J.; Amatore, C.; Kochi, J. K. *J. Phys. Chem.* **1986**, 90 (16), 3747. doi:10.1021/j100407a049.
- (29) Alberty, W. J. *J. Chem. Soc. Faraday Trans.* **1982**, 78 (5), 1579. doi:10.1039/f19827801579.
- (30) Bernasconi, C. F. *Acc. Chem. Res.* **1987**, 20 (8), 301. doi:10.1021/ar00140a006.
- (31) Kreevoy, M. M.; Ostovic, D.; Lee, I.-S. H.; Binder, D. A.; King, G. W. *J. Am. Chem. Soc.* **1988**, 110 (2), 524. doi:10.1021/ja00210a036.
- (32) Bunting, J. W.; Stefanidis, D. *J. Am. Chem. Soc.* **1989**, 111 (15), 5834. doi:10.1021/ja00197a051.
- (33) Lewis, E. S. *Bull. Soc. Chim. Fr.* **1988**, 259.
- (34) Yates, K. *J. Phys. Org. Chem.* **1989**, 2 (4), 300. doi:10.1002/poc.610020403.
- (35) Kurz, J. *J. Am. Chem. Soc.* **1989**, 111 (23), 8631. doi:10.1021/ja00205a012.
- (36) Kim, D.; Lee, I. H.; Kreevoy, M. M. *J. Am. Chem. Soc.* **1990**, 112 (5), 1889. doi:10.1021/ja00161a037.
- (37) Leussing, D. L. *J. Org. Chem.* **1990**, 55 (2), 666. doi:10.1021/jo00289a049.
- (38) Kristjansdottir, S. S.; Norton, J. R. *J. Am. Chem. Soc.* **1991**, 113 (11), 4366. doi:10.1021/ja00011a070.
- (39) Ebersson, L. *Adv. Phys. Org. Chem.* **1982**, 18, 79. doi:10.1016/S0065-3160(08)60139-2.
- (40) Richard, J. P.; Amyes, T. L.; Williams, K. B. *Pure Appl. Chem.* **1998**, 70 (10), 2007. doi:10.1351/pac199870102007.
- (41) Guthrie, J. P. *J. Am. Chem. Soc.* **2000**, 122 (23), 5529. doi:10.1021/ja992992i.
- (42) Guthrie, J. P. *J. Am. Chem. Soc.* **1996**, 118 (51), 12878. doi:10.1021/ja961860b.
- (43) Guthrie, J. P. *Can. J. Chem.* **1990**, 68 (10), 1643. doi:10.1139/v90-256.
- (44) Guthrie, J. P. *J. Am. Chem. Soc.* **1991**, 113 (10), 3941. doi:10.1021/ja00010a040.
- (45) Jencks, W. P. *Chem. Rev.* **1972**, 72 (6), 705. doi:10.1021/cr60280a004.
- (46) Guthrie, J. P. Tetrahedral Intermediates Derived From Carbonyl Compounds, Pentacoordinate Intermediates Derived From Phosphoryl and Sulfonyl Compounds, and Concerted Paths Which Avoid Them. In *Reviews of Reactive Intermediate Chemistry*; Platz, M. S., Moss, R. A., Jones, M., Eds.; John Wiley and Sons: Hoboken, NJ, 2007; pp. 3–46.
- (47) Guthrie, J. P.; Leandro, L.; Pitchko, V. *Can. J. Chem.* **2005**, 83 (9), 1654. doi:10.1139/v05-160.
- (48) Guthrie, J. P.; Pitchko, V. *J. Phys. Org. Chem.* **2004**, 17 (6–7), 548. doi:10.1002/poc.763.
- (49) Guthrie, J. P. *Bioorg. Chem.* **2002**, 30 (1), 32. doi:10.1006/bioo.2001.1231. PMID:11955001.
- (50) Guthrie, J. P.; Pitchko, V. *J. Am. Chem. Soc.* **2000**, 122 (23), 5520. doi:10.1021/ja992991q.
- (51) Guthrie, J. P. *Can. J. Chem.* **1999**, 77 (5–6), 934. doi:10.1139/cjc-77-5-6-934.
- (52) Guthrie, J. P. *J. Phys. Org. Chem.* **1998**, 11 (8–9), 632. doi:10.1002/(SICI)1099-1395(199808/09)11:8/9<632::AID-POC47>3.0.CO;2-1.

- (53) Guthrie, J. P. *J. Am. Chem. Soc.* **1998**, *120* (8), 1688. doi:10.1021/ja970506q.
- (54) Finkbeiner, H. L.; Stiles, M. *J. Am. Chem. Soc.* **1963**, *85* (5), 616. doi:10.1021/ja00888a031.
- (55) Pedersen, K. J. *J. Phys. Chem.* **1934**, *38* (5), 559. doi:10.1021/j150356a001.
- (56) Guthrie, J. P.; Jordan, F. *J. Am. Chem. Soc.* **1972**, *94* (26), 9136. doi:10.1021/ja00781a025.
- (57) Headley, G.; O'Leary, M. *J. Am. Chem. Soc.* **1990**, *112* (5), 1894. doi:10.1021/ja00161a038.
- (58) Verhoeck, F. H. *J. Am. Chem. Soc.* **1934**, *56* (3), 571. doi:10.1021/ja01318a014.
- (59) Belsky, A. J.; Maiella, P. G.; Brill, T. B. *J. Phys. Chem. A* **1999**, *103* (21), 4253. doi:10.1021/jp984122d.
- (60) Hall, G. A. *J. Am. Chem. Soc.* **1949**, *71* (8), 2691. doi:10.1021/ja01176a027.
- (61) Gunawardena, N. R.; Brill, T. B. *J. Phys. Chem. A* **2001**, *105* (10), 1876. doi:10.1021/jp003612e.
- (62) Maiella, P. G.; Brill, T. B. *J. Phys. Chem.* **1996**, *100* (34), 14352. doi:10.1021/jp960397m.
- (63) Miksa, D.; Li, J.; Brill, T. B. *J. Phys. Chem. A* **2002**, *106* (46), 11107. doi:10.1021/jp020941t.
- (64) (a) Zhang, X.; Minear, R. A. *Water Res.* **1997**, *31* (9), 1471. doi:10.1016/S0043-1354(97)00072-9.; (b) Zhang, X.; Minear, R. A. *Water Res.* **2002**, *36* (14), 3665. doi:10.1016/S0043-1354(02)00072-6. PMID:12230213.
- (65) Auerbach, I.; Verhoeck, F. H.; Henne, A. L. *J. Am. Chem. Soc.* **1950**, *72* (1), 299. doi:10.1021/ja01157a079.
- (66) Radzicka, A.; Wolfenden, R. *Science* **1995**, *267* (5194), 90. doi:10.1126/science.7809611. PMID:7809611.
- (67) Snider, M.; Wolfenden, R. *J. Am. Chem. Soc.* **2000**, *122* (46), 11507. doi:10.1021/ja002851c.
- (68) Li, J.; Brill, T. B. *Int. J. Chem. Kinet.* **2003**, *35* (11), 602. doi:10.1002/kin.10160.
- (69) Callahan, B. P.; Wolfenden, R. *J. Am. Chem. Soc.* **2004**, *126* (14), 4514. doi:10.1021/ja031720j. PMID:15070358.
- (70) Guthrie, J. P. *Can. J. Chem.* **1981**, *59* (1), 45. doi:10.1139/v81-008.
- (71) Lin, A. C.; Chiang, Y.; Dahlberg, D. B.; Kresge, A. J. *J. Am. Chem. Soc.* **1983**, *105* (16), 5380. doi:10.1021/ja00354a032.
- (72) Symons, E.; Clermont, M. *J. Am. Chem. Soc.* **1981**, *103* (11), 3127. doi:10.1021/ja00401a034.
- (73) Jencks, W. P.; Regenstein, J. Physical and Chemical Data. In *Handbook of Biochemistry and Molecular Biology*, 3rd ed.; Fassman, G., Ed.; Chemical Rubber Company: Cleveland, 1976; Vol. 1; pp 305–451.
- (74) (a) Richard, J.; Williams, G.; Gao, J. *J. Am. Chem. Soc.* **1999**, *121* (4), 715. doi:10.1021/ja982692l.; (b) Doering, W. V.; Hoffmann, A. K. *J. Am. Chem. Soc.* **1955**, *77*, 521.
- (75) Bowden, D.; Clegg, S.; Brimblecombe, P. *Water Air Soil Pollut.* **1998**, *101* (1/4), 197. doi:10.1023/A:1004966126770.
- (76) Bowden, D.; Clegg, S.; Brimblecombe, P. *Chemosphere* **1996**, *32* (2), 405. doi:10.1016/0045-6535(95)00330-4.
- (77) Keefe, J. R.; Kresge, A. J. Kinetics and Mechanism of Enolization and Ketoneization. In *The Chemistry of Enols*; Rappoport, Z., Ed.; Wiley: Chichester, 1990; pp 399–480.
- (78) Sievers, A.; Wolfenden, R. *J. Am. Chem. Soc.* **2002**, *124* (47), 13986. doi:10.1021/ja021073g. PMID:12440884.
- (79) Tucci, E. R.; Doody, E.; Li, N. C. *J. Phys. Chem.* **1961**, *65*, 1570. doi:10.1021/j100905a024.
- (80) Streitwieser, A., Jr.; Scannon, P. J.; Niemeyer, H. M. *J. Am. Chem. Soc.* **1972**, *94* (22), 7936. doi:10.1021/ja00777a053.
- (81) Button, R. G.; Taylor, P. J. *J. Chem. Soc. Perkin Trans.* **1973**, 557. doi:10.1039/P29730000557.
- (82) Stermitz, F. R.; Huang, W. H. *J. Am. Chem. Soc.* **1971**, *93* (14), 3427. doi:10.1021/ja00743a021.
- (83) Wagman, D. D.; Evans, W. H.; Parker, V. B.; Schumm, R. H.; Halow, I.; Bailey, S. M.; Churney, K. L.; Nuttall, R. L. *J. Phys. Chem. Ref. Data* **1982**, *11* (Suppl. 2), 100.
- (84) Guthrie, J. P. *Can. J. Chem.* **1991**, *69* (12), 1893. doi:10.1139/v91-274.
- (85) Guthrie, J. P. *J. Phys. Chem. A* **2001**, *105* (37), 8495. doi:10.1021/jp010321c.
- (86) Guthrie, J. P.; Povar, I. *Can. J. Chem.* **2009**, *87* (8), 1154. doi:10.1139/V09-071.
- (87) Chase, M. W. *NIST-JANAF Thermochemical Tables*, 4th ed. American Chemical Society: Washington, DC, 1998.
- (88) Rohrschneider, L. *Anal. Chem.* **1973**, *45* (7), 1241. doi:10.1021/ac60329a023.
- (89) Trifel, B. Y.; Smirnov, V. V.; Gloriov, I. P.; Kurbanov, N. I.; Mamedov, F. V. *Vestn. Mosk. Univ. Ser. 2. Khim.* **1992**, *33*, 547.
- (90) Bowden, D. J.; Clegg, S. L.; Brimblecombe, P. *J. Atmos. Chem.* **1998**, *29* (1), 85. doi:10.1023/A:1005899813756.
- (91) Kolesov, V. P.; Slavutskaya, G. M.; Papina, T. S. *Russ. J. Phys. Chem.* **1972**, *46*, 474.
- (92) Wilhoit, R. C.; Shiao, D. *J. Chem. Eng. Data* **1964**, *9* (4), 595. doi:10.1021/je60023a038.
- (93) Fukai, M.; Matsuo, T.; Suga, H. *Therm. Acta* **1991**, *183*, 215. doi:10.1016/0040-6031(91)80461-Q.
- (94) Clegg, S. L.; Seinfeld, J. H. *J. Phys. Chem. A* **2006**, *110* (17), 5692. doi:10.1021/jp056149k. PMID:16640364.
- (95) Guthrie, J. P. *Can. J. Chem.* **1992**, *70* (4), 1042. doi:10.1139/v92-139.
- (96) Guthrie, J. P.; Stein, A. R.; Huntington, A. P. *Can. J. Chem.* **1998**, *76* (6), 929. doi:10.1139/cjc-76-6-929.
- (97) Guthrie, J. P.; Liu, Z. *Can. J. Chem.* **1995**, *73* (9), 1395. doi:10.1139/v95-173.
- (98) Pedley, J. B.; Naylor, R. D.; Kirby, S. P. *Thermochemical Data of Organic Compounds*, 2nd ed.; Chapman and Hall: London, 1986.
- (99) Stull, D. R.; Westrum, E. F.; Sinke, G. C. *The Chemical Thermodynamics of Organic Compounds*; Wiley: New York, 1967.
- (100) Guthrie, J. P.; Povar, I. *Can. J. Chem.* **2009**, *87* (8), 1154. doi:10.1139/V09-071.
- (101) Perrin, D. D.; Dempsey, B.; Serjeant, E. P. *pK<sub>a</sub> Prediction For Organic Acids and Bases*; Chapman and Hall: London, 1981.
- (102) Bernasconi, C. F.; Kittredge, K. W. *J. Org. Chem.* **1998**, *63* (6), 1944. doi:10.1021/jo9719463.
- (103) Guthrie, J. P.; Pike, D. C. *Can. J. Chem.* **1987**, *65* (8), 1951. doi:10.1139/v87-326.
- (104) Guthrie, J. P. *Can. J. Chem.* **1993**, *71* (12), 2123. doi:10.1139/v93-263.
- (105) Pauling, L. *General Chemistry*; W.H. Freeman: San Francisco, CA, 1947.
- (106) Giese, K.; Kaatz, U.; Pottel, R. *J. Phys. Chem.* **1970**, *74* (21), 3718. doi:10.1021/j100715a005.
- (107) Fishbein, J.; Jencks, W. *J. Am. Chem. Soc.* **1988**, *110* (15), 5087. doi:10.1021/ja00223a029.
- (108) Stratakis, M.; Wang, P. G.; Streitwieser, A. *J. Org. Chem.* **1996**, *61* (9), 3145. doi:10.1021/jo9516401. PMID:11667177.
- (109) Shen, K.; Fu, Y.; Li, J.-N.; Liu, L.; Gui, Q.-X. *Tetrahedron* **2007**, *63* (7), 1568. doi:10.1016/j.tet.2006.12.032.

- (110) Bordwell, F. G. *Acc. Chem. Res.* **1988**, *21* (12), 456. doi:10.1021/ar00156a004.
- (111) Jorgensen, W. L.; Briggs, J. M. *J. Am. Chem. Soc.* **1989**, *111* (12), 4190. doi:10.1021/ja00194a007.
- (112) Frisch, M. J.; Trucks, G. W.; Schlegel, H. B.; Scuseria, G. E.; Robb, M. A.; Cheeseman, J. R.; Montgomery, J. J. A.; Vreven, T.; Kudin, K. N.; Burant, J. C.; Millam, S. S.; Iyengar, J. M.; Tomasi, J.; Barone, V.; Mennucci, B.; Cossi, M.; Scalmani, G.; Rega, N.; Petersson, G. A.; Nakatsuji, H.; Hada, M.; Ehara, M.; Toyota, K.; Fukuda, R.; Hasegawa, J.; Ishida, M.; Nakajima, T.; Honda, Y.; Kitao, O.; Nakai, H.; Klene, M.; Li, X.; Knox, J. E.; Hratchian, H. P.; Cross, J. B.; Adamo, C.; Jaramillo, J.; Gomperts, R.; Stratmann, R. E.; Yazyev, O.; Austin, A. J.; Cammi, R.; Pomelli, C.; Ochterski, J. W.; Ayala, P. Y.; Morokuma, K.; Voth, G. A.; Salvador, P.; Dannenberg, J. J.; Zakrzewski, V. G.; Dapprich, S.; Daniels, A. D.; Strain, M. C.; Farkas, O.; Malick, D. K.; Rabuck, A. D.; Raghavachari, K.; Foresman, J. B.; Ortiz, J. V.; Cui, Q.; Baboul, A. G.; Clifford, S.; Cioslowski, J.; Stefanov, B. B.; Liu, G.; Liashenko, A.; Piskorz, P.; Komaromi, I.; Martin, R. L.; Fox, D. J.; Keith, T.; Al-Laham, M. A.; Peng, C. Y.; Nanayakkara, A.; Challacombe, M.; Gill, P. M. W.; Johnson, B.; Chen, W.; Wong, M. W.; Gonzalez, C.; Pople, J. A. *Gaussian 03*, revision B.04; Gaussian, Inc.: Pittsburgh, PA, 2003.

## Appendix A Calculation of desolvation energies for anions

The desolvation cost of an anion was taken as the difference in  $pK_a$  per hydrogen bond between water, where it is assumed that there are three hydrogen bonds per lone pair of an alkoxide, and DMSO, where there are no hydrogen bonds. The pH dependence of the desolvation energy was estimated based on the pH dependence of the desolvation energy, using a set of alcohols, which should have no confounding interactions. The data used are summarized in Table A1. These data

lead to a linear relationship,  $\Delta pK_a/nHB = 0.333 \pm 0.099 + 0.266 \pm 0.008 pK_a^{H_2O}$ .

This relation can then be used to estimate the desolvation cost for loss of a hydrogen bond from any localized anion. This has been done for the anions of interest in this work.

**Table A1.** Correlation of  $\Delta pK_a$  per hydrogen bond (HB) with the  $pK_a$  of the conjugate acid.

Acid	$pK_a^{H_2O}$	$pK_a^{DMSO}$	$\Delta pK_a/nHB$
H <sub>2</sub> O	15.7	31.4	5.22 <sup>a</sup>
CH <sub>3</sub> OH	15.5 <sup>b</sup>	29.0	4.50 <sup>a</sup>
CH <sub>3</sub> CH <sub>2</sub> OH	16.0 <sup>b</sup>	29.8	4.60 <sup>a</sup>
CF <sub>3</sub> CH <sub>2</sub> OH	12.4 <sup>b</sup>	23.0	3.53 <sup>c</sup>
(CF <sub>3</sub> ) <sub>2</sub> CHOH	9.3 <sup>b</sup>	17.9	2.87 <sup>c</sup>
(CF <sub>3</sub> ) <sub>3</sub> COH	5.4 <sup>b</sup>	10.7	1.77 <sup>c</sup>
Cl <sub>3</sub> C-H	25		(7.0)
F <sub>3</sub> C-H	31		(8.6)
H <sub>3</sub> N <sup>+</sup> -CH <sub>2</sub> -H	43		(11.8)
CH <sub>3</sub> -H	49		(13.4)

**Note:** At 25 °C.

<sup>a</sup>Reference A1.

<sup>b</sup>Reference A2.

<sup>c</sup>Reference A3.

## References

- (A1) Olmstead, W. N.; Margolin, Z.; Bordwell, F. G. *J. Org. Chem.* **1980**, *45* (16), 3295. doi:10.1021/jo01304a032.
- (A2) Jencks, W. P.; Regenstein, J. Physical and Chemical Data. In *Handbook of Biochemistry and Molecular Biology*, 3rd ed.; Fassman, G., Ed.; Chemical Rubber Company: Cleveland, 1976; Vol. 1; pp 305–451.
- (A3) Bordwell, F. G. *Acc. Chem. Res.* **1988**, *21* (12), 456. doi:10.1021/ar00156a004.

# Synthesis, characterization, and application of palladium complexes containing 8-quinolyphosphinite ligands

Earl Cook, Jason D. Masuda, and Aibing Xia

**Abstract:** Palladium complexes containing 8-quinolyphosphinite ligands have been synthesized and characterized. Their solid state structures were determined by single-crystal X-ray diffraction. They were found to be active catalysts for Suzuki coupling reactions of phenylboronic acid and various aryl halides.

**Key words:** palladium complexes, unsymmetrical ligands, quinoline, the Suzuki reaction.

**Résumé :** On a effectué la synthèse et caractérisé des complexes du palladium avec des ligands 8-quinolyphosphiniques. On a déterminé leur structures à l'état solide par diffraction des rayons X par un cristal unique. On a trouvé qu'ils sont actifs comme catalyseurs dans les réactions de couplage de Suzuki entre l'acide phénylboronique et divers halogénures d'aryle.

**Mots-clés :** complexes du palladium, ligands non symétriques, réaction de Suzuki.

[Traduit par la Rédaction]

## Introduction

Unsymmetrical ligands with two or more different donors have attracted increasing attention due to their bonding versatility and catalytic applications. The combination of a soft donor and a hard donor induces different interactions between the metal centers and the unsymmetrical donors, which may lead to hemilabile properties.<sup>1–3</sup> The weak donors in the hemilabile ligands can dissociate from the metal center to facilitate substrate interaction, and rebind to the metal center to stabilize the reactive intermediates during catalytic cycles.

P,N-type ligands, containing strong donors such as phosphines and weak donors such as amines,<sup>4–9</sup> pyrazoles,<sup>10,11</sup> and pyridines<sup>12–19</sup> have been investigated in a variety of catalytic transformations. Recently Walther and co-workers<sup>20</sup> reported nickel complexes containing phosphinite ligands based on 8-hydroxyquinoline (Fig. 1, R = Ph, <sup>i</sup>Pr). The nickel diisopropylphosphinite complex was isolated, yet the diphenyl analogue was unstable and a tetrameric nickel complex was obtained instead. Very recently Crociani et al.<sup>21</sup> reported the synthesis of quinolyphosphinite palladium complexes containing di-*tert*-butyl groups (R = <sup>t</sup>Bu) and their catalytic applications. Here, we wish to report the synthesis, characterization, and catalytic applications of three new palladium complexes containing 8-quinolyphosphinites (R = Ph, <sup>i</sup>Pr, Cy).

## Experimental

### General

All experiments were performed under an argon atmosphere unless otherwise specified. All anhydrous solvents were purchased from Sigma-Aldrich Canada Ltd. and stored over 4 Å molecular sieves prior to use. 8-Hydroxyquinoline, chlorodiphenylphosphine, chlorodiisopropylphosphine, potassium hydride, and 4-*N,N*-dimethylaminopyridine (DMAP) were purchased from Sigma-Aldrich Canada Ltd. Bis(benzonitrile)dichloropalladium(II) and chlorodicyclohexylphosphine were purchased from Strem Chemicals, Inc. <sup>1</sup>H and <sup>31</sup>P NMR spectra were recorded on a Bruker Avance 500 spectrometer and referenced to SiMe<sub>4</sub> and 85% H<sub>3</sub>PO<sub>4</sub>, respectively. Infrared spectra were collected on a Nicolet Avatar 330 FT-IR spectrometer. Elemental analyses were carried out by Guelph Chemical Laboratories in Guelph, Ontario. Melting points were recorded on a Mel-Temp (Electrothermal) Apparatus and were uncorrected.

### Complex 1

8-Hydroxyquinoline (0.145 g, 1.00 mmol) and DMAP (0.122 g, 1.00 mmol) were dissolved in THF (10 mL). Chlorodiphenylphosphine (0.221 g, 1.00 mmol) in THF (5 mL) was added dropwise. The mixture was stirred overnight and filtered. A solution of bis(benzonitrile)dichloropalladium(II) (0.384 g, 1.00 mmol) in CH<sub>2</sub>Cl<sub>2</sub> (5 mL) was added to the filtrate. Yellow solids were formed after completion of the addition. The mixture was stirred overnight and filtered. The yellow solids were washed with hexane (2 × 5 mL). Yield 0.470 g (93%), mp 209 °C (dec). IR (KBr, cm<sup>-1</sup>) ν: 2924 (m), 1655 (w), 1560 (w), 1508 (s), 1464 (m), 1437 (m), 1310 (m), 1253 (m), 1105 (s), 927 (w), 828 (m), 762 (w), 694 (w), 539 (w), 492 (w). <sup>1</sup>H NMR (500.13 MHz, CDCl<sub>3</sub>, ppm) δ: 10.59 (dd, *J* = 1.5, 5.4 Hz, 1H, quinoly1), 8.44 (dd, *J* = 1.6, 8.3 Hz, 1H, quinoly1),

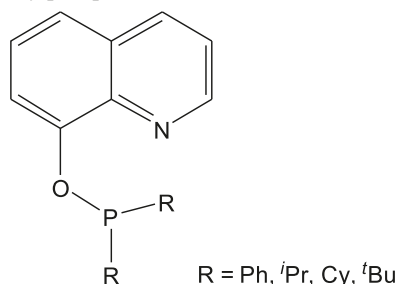
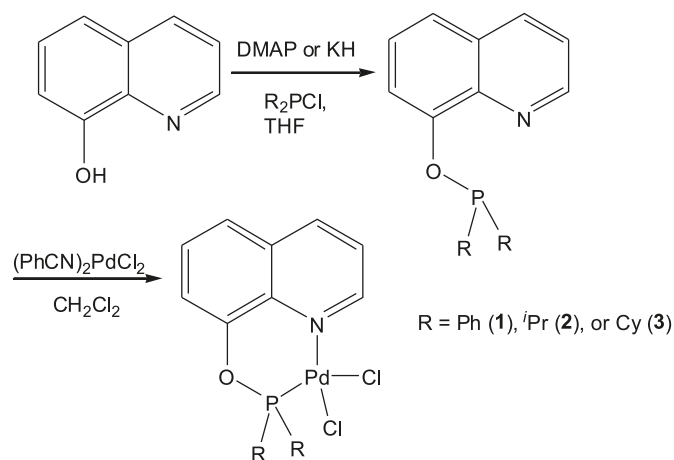
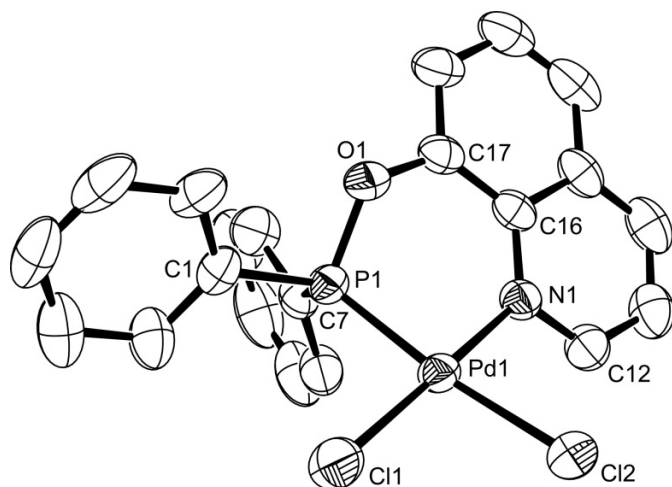
Received 18 August 2009. Accepted 6 October 2009. Published on the NRC Research Press Web site at canjchem.nrc.ca on 24 December 2009.

**E. Cook and A. Xia.**<sup>1</sup> Department of Chemistry, Mount Saint Vincent University, Halifax, NS B3M 2J6, Canada.

**J.D. Masuda.** Department of Chemistry, Saint Mary's University, Halifax, NS B3H 3C3, Canada.

<sup>1</sup>Corresponding author (e-mail: aibing.xia@msvu.ca).



**Fig. 1.** 8-Quinolylphosphinites.**Scheme 1.** Synthesis of palladium 8-quinolylphosphinite complexes.**Fig. 2.** Molecular structure of **1**.

7.97–7.93 (m, 4H, Ph), 7.74 (dd,  $J = 2.2, 7.6$  Hz, 1H, quinolyl), 7.62–7.56 (m, 5H, overlapping quinolyl and Ph), 7.51–7.47 (m, 4H, overlapping quinolyl and Ph).  $^{31}\text{P}$  NMR (202.47 MHz,  $\text{CDCl}_3$ , ppm)  $\delta$ : 115.24. Anal. Calcd. for  $\text{C}_{21}\text{H}_{16}\text{Cl}_2\text{NOPPd}$ : C 49.78, H 3.18, N 2.76; found: C 50.16, H 3.38, N 2.77.

### Complex 2

8-Hydroxyquinoline (0.145 g, 1.00 mmol) was dissolved in THF (10 mL). Potassium hydride (KH, 0.080 g, 2.00 mmol)

**Table 1.** Crystal data and structure refinement data for **1**.

Formula	$\text{C}_{21}\text{H}_{16}\text{Cl}_2\text{NOPPd}$
Formula weight	506.62
Crystal size ( $\text{mm}^3$ )	$0.368 \times 0.242 \times 0.216$
Space group	$P2(1)/n$
$a$ ( $\text{\AA}$ )	10.5513(4)
$b$ ( $\text{\AA}$ )	11.3256(4)
$c$ ( $\text{\AA}$ )	17.0524(6)
$\beta$ ( $^\circ$ )	99.2349(4)
$V$ ( $\text{\AA}^3$ )	2011.35(13)
$Z$	4
$D_{\text{calcd.}}$ ( $\text{g/cm}^3$ )	1.673
$\mu$ ( $\text{mm}^{-1}$ )	1.279
$F(000)$	1008
$\theta$ for data collection ( $^\circ$ )	2.17–25.50
No. of total reflns.	13594
No. of unique reflns.	3731
$R_1$ ( $I > 2\sigma(I)$ ) <sup>a</sup>	0.0234
$R_w$ (all data) <sup>b</sup>	0.0636

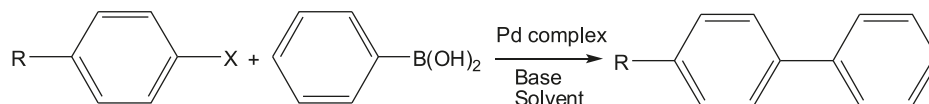
<sup>a</sup> $R = \Sigma(|F_o| - |F_c|) / \Sigma|F_o|$ .

<sup>b</sup> $R_w = [\Sigma w(F_o^2 - F_c^2)^2 / \Sigma (F_o^2)^4]^{1/2}$  where  $w = 1/[\sigma^2(F_o^2) + (0.0324 \times P)^2 + (0.6790 \times P)]$  where  $P = (F_o^2 + 2F_c^2)/3$ .

**Table 2.** Selected bond lengths ( $\text{\AA}$ ) and angles ( $^\circ$ ) for **1**.

Bond lengths ( $\text{\AA}$ )	
Pd(1)—N(1)	2.0803(18)
Pd(1)—P(1)	2.1765(6)
Pd(1)—Cl(1)	2.2880(7)
Pd(1)—Cl(2)	2.3809(6)
Pd(1)—N(1)	2.0803(18)
Bond angles ( $^\circ$ )	
N(1)—Pd(1)—P(1)	86.28(5)
N(1)—Pd(1)—Cl(1)	175.48(5)
P(1)—Pd(1)—Cl(1)	91.65(2)
N(1)—Pd(1)—Cl(2)	93.00(5)
P(1)—Pd(1)—Cl(2)	170.84(2)
Cl(1)—Pd(1)—Cl(2)	89.68(2)
N(1)—Pd(1)—P(1)	86.28(5)
N(1)—Pd(1)—Cl(1)	175.48(5)
P(1)—Pd(1)—Cl(1)	91.65(2)

was added slowly. The mixture was stirred for 10 min and filtered to afford a fluorescent green solution. Chlorodiisopropylphosphine (0.155 g, 1.00 mmol) in THF (5 mL) was added dropwise. The mixture was stirred for 1 h. Bis(benzonitrile)dichloropalladium(II) (0.384 g, 1.00 mmol) in  $\text{CH}_2\text{Cl}_2$  (5 mL) was added. The mixture was stirred overnight and filtered through celite. The volatiles were removed under vacuum to afford yellow solids. Yield 0.400 g (91%), mp 204–206  $^\circ\text{C}$ . IR (KBr,  $\text{cm}^{-1}$ )  $\nu$ : 3448 (w), 2921 (m), 1590 (w), 1508 (s), 1465 (s), 1385 (m), 1310 (w), 1252 (m), 1104 (s), 932 (m), 842 (s), 825 (s), 758 (m), 667 (m).  $^1\text{H}$  NMR (500.13 MHz,  $\text{CDCl}_3$ , ppm)  $\delta$ : 10.49 (dd,  $J = 1.5, 5.4$  Hz, 1H, quinolyl), 8.45 (dd,  $J = 1.4, 8.2$  Hz, 1H, quinolyl), 7.75–7.72 (dd,  $J = 1.4, 8.2$  Hz, 1H, quinolyl), 7.64 (t,  $J = 7.9$  Hz, 1H, quinolyl), 7.58–7.55 (m, 2H, quinolyl), 2.87 (sept,  $J = 6.7$  Hz, 2H,  $\text{CH}(\text{CH}_3)_2$ ), 1.56 (d,  $J = 6.7$  Hz, 6H,  $\text{CH}(\text{CH}_3)(\text{CH}_3)''$ ), 1.33 (d,  $J = 6.7$  Hz, 6H,  $\text{CH}(\text{CH}_3)(\text{CH}_3)''$ ).

**Table 3.** Suzuki–Miyaura couplings using palladium complexes **1–3**.

Entry	Pd complex	Solvent	Base	R	X	Yield (%) <sup>a</sup>
1	<b>1</b>	1,4-Dioxane	K <sub>3</sub> PO <sub>4</sub>	CH <sub>3</sub> O	Br	77
2	<b>1</b>	1,4-Dioxane	K <sub>2</sub> CO <sub>3</sub>	CH <sub>3</sub> O	Br	57
3	<b>1</b>	1,4-Dioxane	Cs <sub>2</sub> CO <sub>3</sub>	CH <sub>3</sub> O	Br	88
4	<b>1</b>	Toluene	Cs <sub>2</sub> CO <sub>3</sub>	CH <sub>3</sub> O	Br	65
5	<b>1</b>	THF	Cs <sub>2</sub> CO <sub>3</sub>	CH <sub>3</sub> O	Br	50
6	<b>1</b>	DMF	Cs <sub>2</sub> CO <sub>3</sub>	CH <sub>3</sub> O	Br	96
7	<b>1</b>	DMF	Cs <sub>2</sub> CO <sub>3</sub>	NO <sub>2</sub>	Cl	47
8	<b>3</b>	DMF	Cs <sub>2</sub> CO <sub>3</sub>	NO <sub>2</sub>	Cl	44
9	<b>1</b>	DMF	Cs <sub>2</sub> CO <sub>3</sub>	NO <sub>2</sub>	Cl	97 <sup>b</sup>
10	<b>2</b>	DMF	Cs <sub>2</sub> CO <sub>3</sub>	NO <sub>2</sub>	Cl	92 <sup>b</sup>
11	<b>3</b>	DMF	Cs <sub>2</sub> CO <sub>3</sub>	NO <sub>2</sub>	Cl	88 <sup>b</sup>
12	<b>1</b>	DMF	Cs <sub>2</sub> CO <sub>3</sub>	CH <sub>3</sub>	Cl	Trace
13	<b>2</b>	DMF	Cs <sub>2</sub> CO <sub>3</sub>	CH <sub>3</sub>	Cl	Trace
14	<b>3</b>	DMF	Cs <sub>2</sub> CO <sub>3</sub>	CH <sub>3</sub>	Cl	Trace
15	<b>1</b>	Toluene	K <sub>2</sub> CO <sub>3</sub>	COCH <sub>3</sub>	Cl	5 <sup>c</sup>
16	<b>2</b>	Toluene	K <sub>2</sub> CO <sub>3</sub>	COCH <sub>3</sub>	Cl	61 <sup>c</sup>
17	<b>3</b>	Toluene	K <sub>2</sub> CO <sub>3</sub>	COCH <sub>3</sub>	Cl	60 <sup>c</sup>

**Note:** Reaction conditions: 1.0 mmol aryl halide, 1.5 mmol phenyl boronic acid, 2.0 mmol base, 1 mol% palladium complex, 3 mL solvent, 100 °C, 18 h.

<sup>a</sup>GC yields based on aryl halides.

<sup>b</sup>2 mol% palladium complex used.

<sup>c</sup>110 °C, 2 h.

<sup>31</sup>P NMR (202.47 MHz, CDCl<sub>3</sub>, ppm)  $\delta$ : 162.13. Anal. Calcd. for C<sub>15</sub>H<sub>20</sub>Cl<sub>2</sub>NOPPd: C 41.07, H 4.60 N 3.19; found: C 41.16, H 4.88, N 3.13.

### Complex 3

In a procedure similar to the preparation of **2**, complex **3** was obtained as yellow solids. Yield 0.490 g (94%), mp 235 °C (dec). IR (KBr, cm<sup>-1</sup>)  $\nu$ : 2931 (s), 2850 (m), 1593 (w), 1510 (m), 1465 (w), 1448 (w), 1388 (w), 1311 (w), 1258 (m), 1170 (w), 1101 (m), 1043 (w), 1002 (w), 933 (w), 886 (w), 856 (w), 831 (m), 762 (w), 726 (w), 696 (w), 571 (w), 560 (w), 531 (w). <sup>1</sup>H NMR (500.13 MHz, CDCl<sub>3</sub>, ppm)  $\delta$ : 10.48 (dd, *J* = 1.5, 5.4 Hz, 1H, quinolyl), 8.44 (dd, *J* = 1.4, 8.3 Hz, 1H, quinolyl), 7.72 (dd, *J* = 1.4, 8.2 Hz, 1H, quinolyl), 7.64 (t, *J* = 7.9 Hz, 1H, quinolyl), 7.58–7.55 (m, 2H, quinolyl), 2.69–2.61 (m, 2H, Cy), 1.91–1.72 (m, 12H, Cy), 1.41–1.25 (m, 6H, Cy). <sup>31</sup>P NMR (202.47 MHz, CDCl<sub>3</sub>, ppm)  $\delta$ : 155.82. Anal. Calcd. for C<sub>21</sub>H<sub>28</sub>Cl<sub>2</sub>NOPPd: C 48.62, H 5.44, N 2.70; found: C 48.35, H 5.22, N 2.35.

### X-ray crystallography

Crystals of **1–3** were grown by slow evaporation of solutions in CH<sub>2</sub>Cl<sub>2</sub>/hexane at room temperature. Single crystals were mounted in thin-walled capillaries. The data were collected using the Bruker APEX2 software package<sup>22</sup> on a Siemens diffractometer equipped with an APEXII CCD detector, a graphite monochromator, and MoK $\alpha$  radiation ( $\lambda$  = 0.71073 Å). A hemisphere of data was collected in 1664 frames with 10 s exposure times. Data processing and absorption corrections were applied using the APEX2 software package.<sup>22</sup> The structure was solved (direct methods) and all

nonhydrogen atoms were refined anisotropically. Hydrogen atoms were placed in calculated positions using an appropriate riding model and coupled isotropic temperature factors. Thermal ellipsoid diagrams (50% probability level) were produced using Ortep-3 for Windows.<sup>23</sup>

### Suzuki coupling reaction

General procedures for Suzuki reactions: a 20 mL reaction tube was charged with an aryl halide, phenylboronic acid, the palladium complex, and a base in 3 mL of solvent under argon and heated to 100 °C for 18 h. The mixture was then cooled to room temperature. The volatiles were removed under a reduced pressure. The organic product was extracted with ether and analyzed on an Agilent 6890 GC-FID instrument. The GC yield was calculated based on unreacted aryl halide and calibrated relative to standards containing aryl halide starting material and biphenyl product.

## Results and discussion

### Synthesis

The syntheses of 8-quinolylphosphinite ligands and their palladium complexes were outlined in Scheme 1. Deprotonation of 8-hydroxyquinoline with DMAP or potassium hydride, followed by reactions with chlorophosphines, gave the phosphinites. Due to their air-sensitive nature,<sup>21</sup> the phosphinites were used directly without further purification to react with bis(benzonitrile)dichloropalladium(II) to afford the corresponding palladium quinolylphosphinite complexes (**1–3**). All the complexes are air stable and can be stored and handled in air. They were also thermally robust, showing no

sign of decomposition under 200 °C in air. They were characterized by  $^1\text{H}$  and  $^{31}\text{P}$  NMR spectroscopy and infrared (IR) spectroscopy. The solid state structures of the palladium complexes (**1–3**) were determined through X-ray diffraction studies. The elemental analysis results matched well with the expected values.

### Characterization

The  $^1\text{H}$  NMR spectra of the three palladium complexes contained chemical shifts for the quinolyl hydrogen around 10.5 ppm. This reflected a downfield shift of 1.5 ppm from the signal in the reported free ligands.<sup>20,21</sup> Other quinolyl hydrogens showed smaller shifts. The methyl groups in the isopropyl moieties in complex **2** became nonequivalent, reflecting the restriction of rotation of the isopropyl in the palladium complexes. The  $^{31}\text{P}$  signals ranged from 115 to 162 ppm.

Suitable crystals of **1–3** for X-ray analysis were grown from slow evaporation of solutions of dichloromethane and hexane. The molecular structures of the complexes were almost identical. A representative structure of **1** is shown in Fig. 2. The structural data of **2** and **3** were included in the Supplementary data. Selected bond lengths and angles are listed in Table 1. Crystal data and structure refinement data are listed in Table 2. The structure of **1** showed a distorted square-planar geometry around the palladium ion, which bonded to the quinolylphosphinite P and N atoms as well as two Cl atoms. The bond angles of N–Pd–Cl(1) and P–Pd–Cl(2) are 175.5° and 170.8°, respectively. The bond lengths for Pd–P (2.177 Å), Pd–N (2.080 Å), and Pd–Cl (2.288 and 2.381 Å) are comparable to the reported values in related *tert*-butyl quinolylphosphinite palladium complexes.<sup>21</sup> The Pd–Cl(2) distance trans to the phosphorus is slightly longer than the Pd–Cl(1) distance trans to the nitrogen atom, suggesting a stronger trans effect of the phosphinite donor.

### Catalytic studies

We evaluated the efficiency of the palladium phosphinite complexes in the Suzuki coupling reaction, one of the most important palladium-catalyzed cross-coupling carbon–carbon bond forming reactions in organic synthesis.<sup>24–26</sup> The results are listed in Table 3. For screening purposes, we used **1** as the palladium catalyst and chose 4-bromoanisole, a rather inert aryl bromide, as the organic substrate. We screened a few commonly used solvents and bases and found that  $\text{Cs}_2\text{CO}_3$  and DMF led to the best yield (96%, Table 3, entry 6).

Under similar conditions, the palladium complexes gave moderate yields for the coupling of 4-chloronitrobenzene, an activated aryl chloride (Table 3, entries 7 and 8). When the palladium loading was increased to 2 mol%, excellent yields were obtained with all three complexes (Table 3, entries 9–11). However, the complexes were ineffective toward 4-chlorotoluene, a neutral aryl chloride (Table 3, entries 12–14). In comparison, the recently reported *tert*-butyl analogue gave complete conversion of both activated and nonactivated aryl chlorides in toluene.<sup>21</sup> When toluene was used as the solvent and  $\text{K}_2\text{CO}_3$  as the base, **1–3** gave only low to modest yields for the coupling of 4'-chloroacetophenone (Table 3, entries 15–17). The higher efficiency of the *tert*-butyl analogue is likely due to its stronger donating ability

and larger steric hindrance, which are beneficial factors for the Suzuki reactions of more challenging aryl chlorides.<sup>25,26</sup>

### Conclusion

In summary, we have synthesized and characterized three palladium complexes containing 8-quinolylphosphinite ligands. The palladium complexes were easy to synthesize and stable in air. They were investigated in the Suzuki coupling reaction and showed excellent activity towards a deactivated aryl bromide but lower activity towards aryl chlorides.

### Supplementary data

Supplementary data for this article are available on the journal Web site ([canjchem.nrc.ca](http://canjchem.nrc.ca)) or may be purchased from the Depository of Unpublished Data, Document Delivery, CISTI, National Research Council Canada, Ottawa, ON K1A 0R6, Canada. DUD 5317. For more information on obtaining material, refer to [cisti-icist.nrc-cnrc.gc.ca/cms/unpub\\_e.shtml](http://cisti-icist.nrc-cnrc.gc.ca/cms/unpub_e.shtml). CCDC 743458–743460 contain the X-ray data in CIF format for seven complexes for this manuscript. These data can be obtained, free of charge, via [www.ccdc.cam.ac.uk/conts/retrieving.html](http://www.ccdc.cam.ac.uk/conts/retrieving.html) (or from the Cambridge Crystallographic Data Centre, 12 Union Road, Cambridge CB2 1EZ, UK; fax +44 1223 336033; or [deposit@ccdc.cam.ac.uk](mailto:deposit@ccdc.cam.ac.uk)).

### Acknowledgements

We thank the Natural Sciences and Engineering Research Council of Canada (NSERC) and the Canada Foundation for Innovation (CFI) for financial support.

### References

- (1) Angell, S. E.; Rogers, C. W.; Zhang, Y.; Wolf, M. O.; Jones, W. E., Jr. *Coord. Chem. Rev.* **2006**, 250 (13–14), 1829. doi:10.1016/j.ccr.2006.03.023.
- (2) Braunstein, P.; Naud, F. *Angew. Chem. Int. Ed.* **2001**, 40 (4), 680. doi:10.1002/1521-3773(20010216)40:4<680::AID-ANIE6800>3.0.CO;2-0.
- (3) Slone, C. S.; Weinberger, D. A.; Mirkin, C. A. *Prog. Inorg. Chem.* **2007**, 48, 233. doi:10.1002/9780470166499.ch3.
- (4) Ares, R.; Vázquez-García, D.; López-Torres, M.; Fernández, A.; Gómez-Blanco, N.; Vila, J. M.; Fernández, J. J. *J. Organomet. Chem.* **2008**, 693 (24), 3655. doi:10.1016/j.jorganchem.2008.08.023.
- (5) Puchta, R.; Dahlenburg, L.; Clark, T. *Chem. Eur. J.* **2008**, 14 (29), 8898. doi:10.1002/chem.200701921.
- (6) Wang, C. J.; Gao, F.; Liang, G. *Org. Lett.* **2008**, 10 (21), 4711. doi:10.1021/ol8018677. PMID:18817406.
- (7) Biricik, N.; Durap, F.; Kayan, C.; Gümgüm, B.; Gürbüz, N.; Özdemir, I.; Ang, W. H.; Fei, Z.; Scopelliti, R. *J. Organomet. Chem.* **2008**, 693 (16), 2693. doi:10.1016/j.jorganchem.2008.05.010.
- (8) Gopalakrishnan, J. *Appl. Organomet. Chem.* **2009**, 23 (8), 291. doi:10.1002/aoc.1515.
- (9) Bolliger, J. L.; Frech, C. M. *Adv. Synth. Catal.* **2009**, 351 (6), 891. doi:10.1002/adsc.200900112.
- (10) Mukherjee, A.; Subramanyam, U.; Puranik, V. G.; Mohandas, T. P.; Sarkar, A. *Eur. J. Inorg. Chem.* **2005**, 2005 (7), 1254. doi:10.1002/ejic.200400818.

- (11) Mukherjee, A.; Sarkar, A. *Tetrahedron Lett.* **2004**, *45* (52), 9525. doi:10.1016/j.tetlet.2004.11.016.
- (12) Takahashi, Y.; Murakami, N.; Fujita, K.; Yamaguchi, R. *Dalton Trans.* **2009**, 2029. doi:10.1039/b815890h. PMID: 19259574.
- (13) Li, P.; Wang, M.; Chen, L.; Liu, J.; Zhao, Z.; Sun, L. *Dalton Trans.* **2009**, 1919. doi:10.1039/b814336f. PMID:19259561.
- (14) Scrivanti, A.; Bertoldini, M.; Beghetto, V.; Matteoli, U.; Venzo, A. *J. Organomet. Chem.* **2009**, *694* (1), 131. doi:10.1016/j.jorganchem.2008.09.063.
- (15) Yoshida, H.; Nakano, S.; Mukae, M.; Ohshita, J. *Org. Lett.* **2008**, *10* (19), 4319. doi:10.1021/ol801788t. PMID: 18771266.
- (16) Usha Rani, P.; Muralidhar Reddy, P.; Shanker, K.; Ravinder, V. *Transition Met. Chem.* **2008**, *33* (2), 153. doi:10.1007/s11243-007-9030-2.
- (17) Yen, S. K.; Koh, L. L.; Huynh, H. V.; Hor, T. S. A. *Dalton Trans.* **2008**, 699. doi:10.1039/b713152f. PMID:18217127.
- (18) Scrivanti, A.; Benetollo, F.; Venzo, A.; Bertoldini, M.; Beghetto, V.; Matteoli, U. *J. Organomet. Chem.* **2007**, *692* (16), 3577. doi:10.1016/j.jorganchem.2007.04.021.
- (19) Reetz, M. T.; Bondarev, O. *Angew. Chem. Int. Ed.* **2007**, *46* (24), 4523. doi:10.1002/anie.200700533.
- (20) Langer, J.; Görls, H.; Gillies, G.; Walther, D. Z. *Anorg. Allg. Chem.* **2005**, *631* (13–14), 2719. doi:10.1002/zaac.200500114.
- (21) Crociani, B.; Antonaroli, S.; Burattini, M.; Benetollo, F.; Scrivanti, A.; Bertoldini, M. *J. Organomet. Chem.* **2008**, *693* (26), 3932. doi:10.1016/j.jorganchem.2008.10.001.
- (22) APEX2, version 2008.5; Bruker AXS, Inc.: Madison, WI, 2008.
- (23) Farrugia, L. J. *J. Appl. Cryst.* **1997**, *30* (5-1), 565. doi:10.1107/S0021889897003117.
- (24) Suzuki, A. *Chem. Commun. (Camb.)* **2005**, 4759. doi:10.1039/b507375h. PMID:16193109.
- (25) Bedford, R. B.; Cazin, C. S. J.; Holder, D. *Coord. Chem. Rev.* **2004**, *248* (21–24), 2283. doi:10.1016/j.ccr.2004.06.012.
- (26) Littke, A. F.; Fu, G. C. *Angew. Chem. Int. Ed.* **2002**, *41* (22), 4176. doi:10.1002/1521-3773(20021115)41:22<4176::AID-ANIE4176>3.0.CO;2-U.



# Cytotoxic phenolic compounds in leaf buds of *Populus tremuloides*

André Pichette, Azadeh Eftekhari, Patricia Georges, Serge Lavoie, Vakhtang Mshvildadze, and Jean Legault

**Abstract:** Phytochemical investigations of the EtOH extract of *Populus tremuloides* leaf buds led to the isolation of 19 phenolic compounds. Among them, (1*S*,2*S*)-1-[4-*O-E*-coumaroyl- $\beta$ -D-glucopyranosyloxy]cyclohexanediol was reported for the first time, and its structure was determined by spectroscopic (NMR and MS) and chemical methods. Seventeen of the isolated compounds were tested for their cytotoxicity against lung carcinoma (A549) and colorectal adenocarcinoma (DLD-1) human cell lines. Antibacterial activity was also evaluated against *Escherichia coli* and *Staphylococcus aureus*.

**Key words:** quaking aspen, coumarate, flavonoids, NMR.

**Résumé :** Une étude phytochimique d'un extrait éthanolique des bourgeons de feuilles du *Populus tremuloides* a permis d'isoler 19 composés phénoliques, dont le (1*S*,2*S*)-1-[4-*O-E*-coumaroyl- $\beta$ -D-glucopyranosyloxy]cyclohexanediol, un produit qui n'a jamais été rapporté antérieurement et dont la structure a été déterminée par des méthodes chimiques et spectroscopiques (RMN et spectrométrie de masse). Les propriétés cytotoxiques de 17 de ces produits ont été évalué contre des lignées de cellules humaines de carcinome du poumon (A549) et d'adénocarcinome (DLD-1). Leur activité antibactérienne a aussi été évalué contre l'*Escherichia coli* et le *Staphylococcus aureus*.

**Mots-clés :** peuplier faux-tremble, coumarate, flavonoïdes, RMN.

## Introduction

The buds exudates of many plant species of *Populus* genus are known as raw material processed by bees into propolis.<sup>1</sup> The latter product has been widely used in popular medicine as antibacterial,<sup>2–4</sup> anti-inflammatory,<sup>5</sup> antioxidant,<sup>6,7</sup> and cytostatic treatments.<sup>8</sup> The biological activity of propolis samples is mainly due to phenolic compounds like flavonoids, aromatic acids, and diterpenic acids,<sup>9,10</sup> which are the principal constituents of the buds of *Populus* species.<sup>11–13</sup> Recently, studies in the northern-type propolis showed a potential source of biologically active substances in *Populus tremuloides*,<sup>14</sup> which are widely spread across North America.<sup>15</sup> In spite of its use as ointment by Amerindian traditional medicine to treat numerous diseases, such as coughs, colds, and irritated nostrils,<sup>16</sup> few studies were carried out on the medicinal applications of *P. tremuloides*. In the present study, the isolation and structure elucidation of a new phenolic compound from *P. tremuloides* Michaux, along with 18 known products are described.

## Results and discussion

The leaf buds of *Populus tremuloides* were extracted with

EtOH and EtOH/H<sub>2</sub>O under reflux. After evaporation of EtOH in vacuo, the aqueous phase was successively partitioned with hexane and *n*-BuOH. The *n*-BuOH soluble extract was purified on an open Diaion® column with a gradient of decreasing polarity, and three fractions were obtained. Each fraction was investigated for in vitro cytotoxic and antibacterial biological activities. Cytotoxic activity evaluations were carried out on human lung cancer (A549), human colorectal cancer (DLD-1), and normal skin fibroblasts (WS1) using the resazurin reduction test as previously described in the literature.<sup>17</sup> Antibacterial activity was evaluated against *Escherichia coli* and *Staphylococcus aureus*. The results (Table 1) show that the last fraction C was found to exert a weak cytotoxic activity against A549 (IC<sub>50</sub>, 96 ± 7 µg mL<sup>-1</sup>) and DLD-1 (IC<sub>50</sub>, 89 ± 6 µg mL<sup>-1</sup>), but was inactive toward bacterial cell lines. Thus, bioassay-guided fractionation of fraction C was undertaken with a combination of different chromatographic techniques leading to the isolation of a new compound **1** together with 18 known compounds: chaenomeloidin (**2**),<sup>18</sup> prunin (**3**),<sup>19</sup> echinacin (**4**),<sup>20</sup> echinacin (**5**),<sup>21</sup> tremulacin (**6**),<sup>22</sup> salicine (**7**),<sup>23</sup> tremuloidin (**8**),<sup>24</sup> genkwanin (**9**),<sup>25</sup> rhamnocitrin (**10**),<sup>26</sup> sakuranetin (**11**),<sup>27</sup> acacetin (**12**),<sup>28</sup> kaempferide (**13**),<sup>29</sup> aromadendrin (**14**),<sup>30</sup> phenylmethyl coumarate (**15**),<sup>31</sup> phenethyl *p*-coumarate (**16**),<sup>32</sup> cinnamyl coumarate (**17**),<sup>33</sup> phenylmethyl caffeine (**18**),<sup>34</sup> and *trans*-ferulic acid (**19**)<sup>35</sup> (Fig. 1). Known compounds were identified by comparison of their spectroscopic data with the values found in the literature. NMR spectroscopic data for phenethyl *p*-coumarate (**16**), which was also isolated from buds of *P. tremuloides*, were not available. Therefore, complete <sup>1</sup>H and <sup>13</sup>C NMR spectroscopic data for **16** are also reported.

The molecular formula (C<sub>21</sub>H<sub>28</sub>O<sub>9</sub>) of **1**, a white amorphous powder, was determined from its HR-ESI-MS spec-

Received 16 July 2009. Accepted 28 September 2009. Published on the NRC Research Press Web site at canjchem.nrc.ca on 15 January 2010.

A. Pichette,<sup>1</sup> A. Eftekhari, P. Georges, S. Lavoie, V. Mshvildadze, and J. Legault. Chaire de recherche sur les agents anticancéreux d'origine naturelle, Département des sciences fondamentales, Université du Québec à Chicoutimi, QC G7H 2B1, Canada.

<sup>1</sup>Corresponding author (e-mail: andre\_pichette@uqac.ca).

**Table 1.** In vitro cytotoxicity and antibiotic results of the Diaion® column's fractions.

Samples	IC <sub>50</sub> (μg mL <sup>-1</sup> ) <sup>a</sup>			MIC <sup>b</sup>	
	A549	DLD-1	WS1	<i>S. aureus</i>	<i>E. coli</i>
Fraction A	>100	>100	>100	>100	>100
Fraction B	>100	>100	>100	>100	>100
Fraction C	96±7	89±6	80±10	>100	>100
Etoposide <sup>c</sup>	2.8±0.5	2±1	>50	NT <sup>d</sup>	NT <sup>d</sup>
Chloramphenicol <sup>c</sup>	NT <sup>d</sup>	NT <sup>d</sup>	NT <sup>d</sup>	>5	0.37±0.06

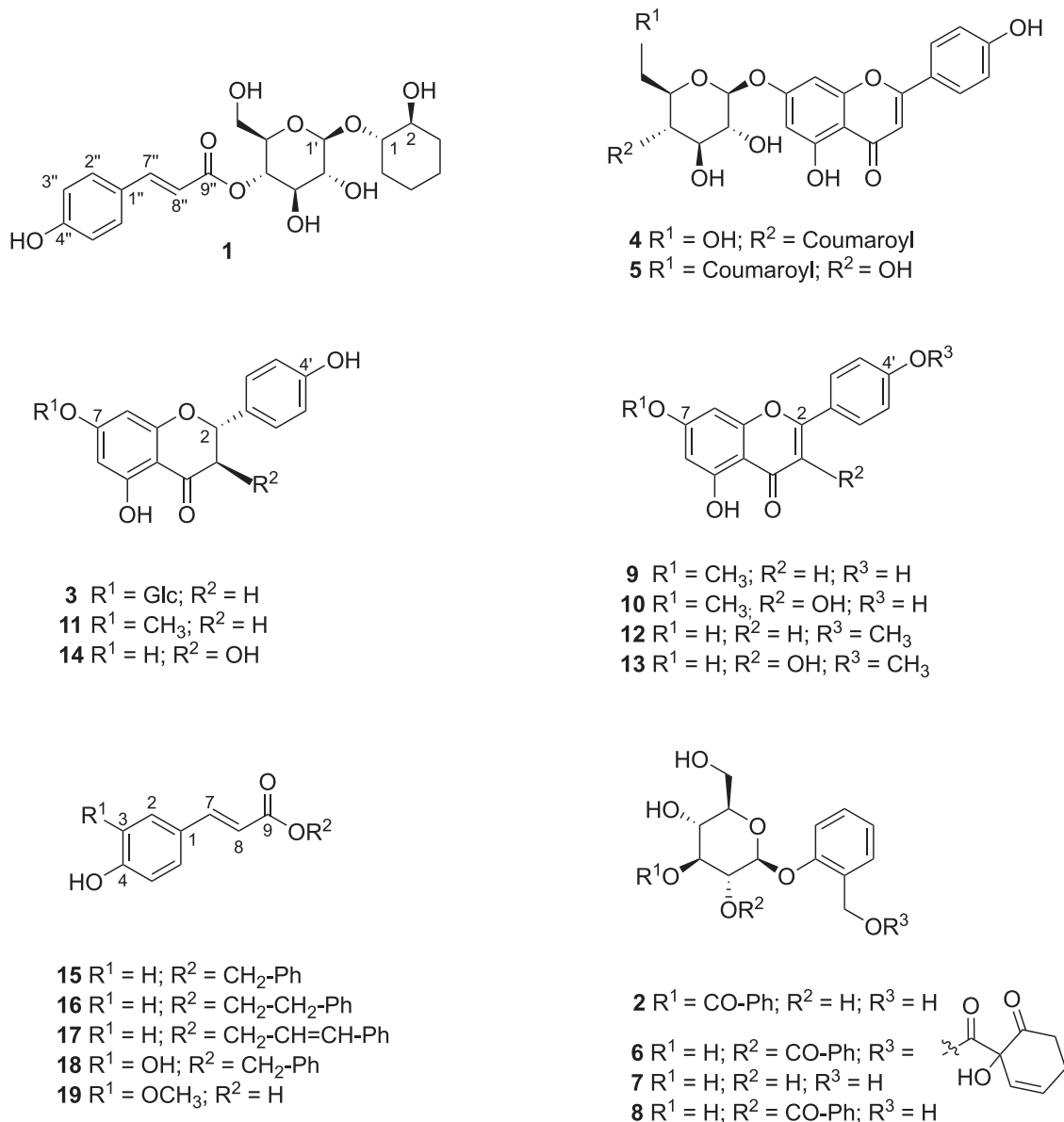
**Note:** Mean values (± standard deviation) for triplicate assays.

<sup>a</sup>Concentration of extract that caused 50% inhibition of cell proliferation.

<sup>b</sup>Minimum concentration of extract that resulted in inhibition of visible growth.

<sup>c</sup>Positive control.

<sup>d</sup>Not tested.

**Fig. 1.** Polyphenols from *Populus tremuloides*.

trum (positive-ion mode) on the basis of a quasimolecular ion peak at  $m/z$  447.1623  $[M + Na]^+$  (calcd. 447.1631). Infrared absorption bands at 3328, 1602, 1160, 982, and 833  $\text{cm}^{-1}$  suggested the presence of hydroxyl groups, aromatic system, and an ester carbonyl groups.  $^{13}\text{C}$  NMR spectrum displayed 19 carbon signals (Table 2) separated by DEPT spectrum into five methylenes, seven aliphatic oxy-methines, four unsaturated methines, and three quaternary carbons (one for an ester carbonyl). Among them, six resonances could be assigned to a sugar moiety.  $^1\text{H}$  NMR spectrum confirmed the presence of a hexose moiety with anomeric proton at  $\delta_{\text{H}}$  4.45 (1H, d,  $J = 7.8$  Hz).  $^1\text{H}$  NMR spectrum also shows the presence of two *trans*-olefinic protons at  $\delta_{\text{H}}$  7.66 (1H, d,  $J = 15.9$  Hz) and  $\delta_{\text{H}}$  6.37 (1H, d,  $J = 15.9$  Hz) and a 1,4-disubstituted aromatic ring with four protons at  $\delta_{\text{H}}$  7.47 (2H, d,  $J = 8.6$  Hz) and 6.81 (2H, d,  $J = 8.6$  Hz). HMBC correlations at  $\delta_{\text{H}}$  7.47 (H-2'', H-6'') and  $\delta_{\text{C}}$  147.3 (H-7''),  $\delta_{\text{H}}$  6.81 (H-3'', H-5'') and  $\delta_{\text{C}}$  161.5 (C-4''), and  $\delta_{\text{H}}$  7.66 (H-7'') and  $\delta_{\text{C}}$  168.6 (C-9'') suggested the presence of a coumaroyl moiety. Analysis of the COSY, HSQC, and HMBC spectra led to the identification of a third aglycone system: the cyclohexane-1,2-diol. HMBC correlation between the methine proton at  $\delta_{\text{H}}$  4.87 (H-4') and the carbonyl group at  $\delta_{\text{C}}$  168.6 (C-9'') suggested the linkage between the glucose and the coumaroyl moiety. Finally, the correlation between  $\delta_{\text{H}}$  4.45 (H-1') and  $\delta_{\text{C}}$  79.4 (C-1) indicated the linkage site of the glucose moiety to the aglycone.

Acidic hydrolysis of **1** and TLC analysis of the aqueous phase afforded identification of glucose as the sugar component. Absolute configuration of the glucose as D was determined by optical rotations in comparison with authentic standard. The presence of *p*-coumaric acid in the organic phase was confirmed by TLC in comparison with authentic standard. Cyclohexane-1,2-diol was also detected in the organic phase using GC-MS and NMR analysis.<sup>36</sup> The absolute configuration of cyclohexane-1,2-diol could be determined directly from the organic phase, since the other aglycon part, namely, *p*-coumaric acid, is optically inactive. The organic phase showed positive value in optical activity measurement meaning that (1*S*,2*S*)-cyclohexane-1,2-diol has been isolated.<sup>37</sup> The structure of **1** was thus confirmed as (1*S*,2*S*)-1-[4-*O*-*E*-coumaroyl- $\beta$ -D-glucopyranosyloxy]cyclohexanediol.

Compound **16** has been identified by many authors, but surprisingly, no complete NMR assignment was given.<sup>38</sup> Therefore, complete  $^1\text{H}$  and  $^{13}\text{C}$  characterization was accomplished using  $^1\text{H}$ ,  $^{13}\text{C}$ , and 2D spectra (Table 3). First, the same *p*-coumaroyl moieties as in **1** were identified with  $\delta_{\text{H}}$  at 6.29 (1H, d,  $J = 15.9$  Hz, H-8), 6.85 (2H, d,  $J = 8.1$  Hz, H-3 and H-5), 7.42 (2H, d,  $J = 8.1$  Hz, H-2 and H-6), and 7.62 (1H, d,  $J = 15.9$  Hz, H-7) and  $\delta_{\text{C}}$  at 115.5 (C-8), 115.9 (C-3 and C-5), 127.3 (C-1), 130.0 (C-2 and C-6), 144.6 (C-7), 157.7 (C-4), and 167.4 (C-9). Additionally, five overlapped  $^1\text{H}$  NMR signals between  $\delta_{\text{H}}$  7.20–7.30 along with two methylene triplets at 3.02 (2H, t,  $J = 6.9$  Hz, H-7') and 4.42 (2H, t,  $J = 6.9$  Hz, H-8') were attributed to a phenethyl moiety. The HMBC correlation between H-8' and C-9 confirmed the link between the phenethyl and the *p*-coumaroyl groups.

Compounds **10** and **13** were isolated as a mixture. Separation of each constituent was not performed due to their small amounts. Therefore, careful examination of NMR

**Table 2.**  $^1\text{H}$  (400 MHz) and  $^{13}\text{C}$  (100 MHz) NMR spectroscopic data for compound **1** in methanol- $d_4$ .

Position	$\delta_{\text{C}}$ (multiplicity) <sup>a</sup>	$\delta_{\text{H}}$ (multiplicity, $J$ in Hz)
1	79.4 ( <i>d</i> )	3.87 ( <i>m</i> )
2	71.0 ( <i>d</i> )	3.85 ( <i>m</i> )
3	31.5 ( <i>t</i> )	1.79 ( <i>m</i> )
		1.55 ( <i>m</i> )
4	22.4 ( <i>t</i> )	1.65 ( <i>m</i> )
		1.34 ( <i>m</i> )
5	23.1 ( <i>t</i> )	1.71 ( <i>m</i> )
		1.31 ( <i>m</i> )
6	27.6 ( <i>t</i> )	1.82 ( <i>m</i> )
		1.63 ( <i>m</i> )
1'	102.2 ( <i>d</i> )	4.45, ( <i>d</i> , 7.8)
2'	75.1 ( <i>d</i> )	3.35 ( <i>dd</i> , 9.3, 7.8)
3'	75.6 ( <i>d</i> )	3.65 ( <i>t</i> , 9.3)
4'	72.5 ( <i>d</i> )	4.87 ( <i>m</i> )
5'	76.1 ( <i>d</i> )	3.53 ( <i>m</i> )
6'	62.4 ( <i>t</i> )	3.62 ( <i>dd</i> , 15.0, 5.4)
		3.54 ( <i>m</i> )
1''	127.2 ( <i>s</i> )	
2'', 6''	131.3 ( <i>d</i> )	7.47 ( <i>d</i> , 8.6)
3'', 5''	116.9 ( <i>d</i> )	6.81 ( <i>d</i> , 8.6)
4''	161.5 ( <i>s</i> )	
7''	147.3 ( <i>d</i> )	7.66 ( <i>d</i> , 15.9)
8''	114.8 ( <i>d</i> )	6.37 ( <i>d</i> , 15.9)
9''	168.6 ( <i>s</i> )	

<sup>a</sup>Multiplicities were deduced from DEPT experiments.

**Table 3.**  $^1\text{H}$  (400 MHz) and  $^{13}\text{C}$  (100 MHz) NMR spectroscopic data for compound **16** in methanol- $d_4$ .

Position	$\delta_{\text{C}}$ (multiplicity) <sup>a</sup>	$\delta_{\text{H}}$ (multiplicity, $J$ in Hz)
1	127.3 ( <i>s</i> )	
2, 6	130.0 ( <i>d</i> )	7.42 ( <i>d</i> , 8.1)
3, 5	115.9 ( <i>d</i> )	6.85 ( <i>d</i> , 8.1)
4	157.7 ( <i>s</i> )	
7	144.6 ( <i>d</i> )	7.62 ( <i>d</i> , 15.9)
8	115.5 ( <i>d</i> )	6.29 ( <i>d</i> , 15.9)
9	167.4 ( <i>s</i> )	
1'	137.9 ( <i>s</i> )	
2', 6'	128.9 ( <i>d</i> )	7.26 ( <i>m</i> )
3', 5'	128.5 ( <i>d</i> )	7.32 ( <i>m</i> )
4'	126.6 ( <i>d</i> )	7.25 ( <i>m</i> )
7'	35.2 ( <i>t</i> )	3.02 ( <i>t</i> , 6.9)
8'	65.0 ( <i>t</i> )	4.42 ( <i>t</i> , 6.9)

<sup>a</sup>Multiplicities were deduced from DEPT experiments.

spectra ( $^1\text{H}$ ,  $^{13}\text{C}$ , DEPT, and HSQC) and comparison with literature allowed the identification of these components as rhamnocitrin (**10**)<sup>29</sup> and kaempferide (**13**).<sup>26</sup> Moreover, the biological results were obtained using commercial pure products. Because of the low isolated yields of compounds **3** and **19**, those compounds were also tested from commercial materials.

All isolated compounds, except compounds **2** and **4**, were evaluated using resazurin reduction test for their cytotoxicity against human lung cancer (A549), human colorectal cancer

(DLD-1), and normal skin fibroblasts (WS1).<sup>17</sup> Results presented in Table 4 are expressed as the concentration of product inhibiting cell growth by 50% (IC<sub>50</sub>). Etoposide was used as positive control with IC<sub>50</sub> of 2.8 and 2.0 µmol/L against A549 and DLD-1 cell lines, respectively. The phenolic compounds were regarded as active when the IC<sub>50</sub> was smaller than 100 µmol/L.<sup>39</sup> The compound **9** was found to be the most active with IC<sub>50</sub> ranging from 5.8 to 9.2 µmol/L. Moreover, compounds **10**, **12**, and **15** were moderately active against cancer cells with IC<sub>50</sub> ranging from 19 to 37 µmol/L. In contrast to compounds **9**, **12**, and **15**, compound **10** was significantly selective toward cancer cells with IC<sub>50</sub> of 31 µmol/L for A549 and 37 µmol/L for DLD-1 in comparison with 87 µmol/L for normal cells, WS1. Although the cytotoxicity of compounds **9** and **12** were known on A549 cells,<sup>40,41</sup> the activity on human colorectal adenocarcinoma DLD-1 was never reported. Finally, compounds **13** and **18** were found weakly cytotoxic, and all the other compounds tested were inactive. As far as structure–activity relationships are concerned, these in vitro results suggest that the addition of a double bond in C-2 position in molecule **9**, with regard to compound **11**, increases the cytotoxic activity. Similarly, the presence of a methoxy group in C-7 position and a hydroxyl in C-4' position in the flavone **9** seem to have a beneficial effect on the cytotoxic activity in comparison with the acacetin (**12**), where the inversion of these groups reduces the activity. On the other hand, the presence of hydroxyl group in R<sup>2</sup> of compounds **10** and **13** is detrimental for the activity in comparison with compounds **9** and **12**, respectively. In the case of compounds **15–19**, only molecules bearing a benzyl group exhibited cytotoxicities (**15** and **18**). Moreover, the hydroxyl group in R<sup>1</sup> of compound **18** reduces significantly the cytotoxicity in comparison with **15**. All compounds were also evaluated for their antibacterial activities against *S. aureus* and *E. coli*, but no significant activity was observed.

## Concluding remarks

In conclusion, the structure of a new compound **1** was described and 19 compounds were identified from *P. tremuloides*. Among them, compounds **2** and **5** were reported for the first time in *Populus* genus and compounds **3**, **4**, **9**, **10**, **12**, **16**, and **17** for the first time in *P. tremuloides*. Compound **9** was found to be the most cytotoxic against lung carcinoma cell (A549) and colorectal adenocarcinoma (DLD-1) human cell lines. Interestingly, compound **10** was selective toward both cancer cell lines in comparison with normal cells. Finally, all compounds tested do not possess antibacterial activity.

## Experimental

### General

Optical rotations were measured with an automatic polarimeter Rudolph Research Analytical Autopol IV. FTIR spectra were recorded with a PerkinElmer SpectrumOne. High resolution electrospray ionization mass spectrum was conducted in positive mode with an Applied Biosystems/MDS Sciex QSTARXL QqTOF MS system. 1D and 2D NMR spectra (<sup>1</sup>H–<sup>1</sup>H COSY, HSQC, and HMBC) were performed using an Avance 400 Bruker spectrometer equipped with a 5 mm QNP-probe. Chemical shifts were expressed in δ

(ppm) units relative to TMS as an internal standard, and coupling constants were given in Hz. Preparative HPLC was performed on an Agilent 1100 liquid chromatography system, equipped with a solvent delivery system, an auto-sampler and a UV-MWD detector. Samples were eluted in an Intertsil prep-ODS column C18 (20 × 250 mm; 10 µm) at room temperature with a flow rate of 10 mL min<sup>-1</sup>. GC–MS analyses were performed with an instrument (Agilent Technologies 6890N) fitted with a mass-selective detector (Agilent Technologies 5973), a split–splitless injection port, and an apolar capillary column DB-5MS (30 m × 0.25 mm × 0.25 µm).

Analytical thin-layer chromatography (TLC) was performed with silica gel 60 F<sub>254</sub>, 0.25 mm pre-coated TLC plates (Silicycle, Québec, Canada). Flash column chromatographies (CC) were performed on silica gel (40–63 µm with indicator F<sub>254</sub>, Silicycle, Québec, Canada) and on C<sub>18</sub> reversed-phase silica gel (carbon 11%, 40–69 µm, Silicycle, Québec, Canada). Polyamide CC-6 was purchased from Macherey-Nagel (Germany) and Diaion HP-20 from Supelco. Detection of the phenolic compounds was carried out by spraying TLC plates with polyethylene glycol (NP/PEG) reagent followed by heating at 110 °C and detected by UV absorption at 254 and 365 nm. TLC identification of monosaccharides was performed with CH<sub>2</sub>Cl<sub>2</sub>/MeOH/H<sub>2</sub>O (50:25:5) solvent system. The compounds were visualized by spraying an orthophosphoric acid solution of naphtorescinal 5% in EtOH, followed by heating at 110 °C.

The commercial samples used for biological tests, namely, prunin (**3**), kaempferide (**13**), and *trans*-ferulic acid (**19**), were purchased from Indofine Chemical Company (USA). Rhamnocitrin (**10**) was purchased from Apin Chemicals Ltd. (UK).

### Plant material

Leaf buds of *P. tremuloides* Michaux were collected in the boreal forest to the south of Chicoutimi, Québec, Canada, in April 2006. Samples were identified by Patrick Nadeau (Département des sciences fondamentales, Université du Québec à Chicoutimi). A voucher specimen (QFA-A540466) was deposited at the Herbarium Louis-Marie of Université Laval, Québec, Canada.

### Extraction and isolation

The buds of *P. tremuloides* (1 kg) were exhaustively extracted with EtOH (3 L, 60 °C, three times, 2 h each time) followed by EtOH/H<sub>2</sub>O (7:2). The extracts were filtered and pooled. After evaporation of EtOH in vacuo, the aqueous phase was extracted successively with hexane (500 mL × 5) and saturated *n*-BuOH with H<sub>2</sub>O (500 mL × 5). The *n*-BuOH phase was decanted and evaporated in vacuo. The residue (80 g) was fractionated using an open Diaion® column eluted with H<sub>2</sub>O/MeOH with 30%, 50%, and 80% of MeOH. Three fractions were obtained: A (6.46 g), B (7.24 g), and C (58.96 g).

Fraction C was purified on silica gel CC, eluted with CHCl<sub>3</sub>/MeOH gradient (60:1 → 5:1, v/v), and three fractions were obtained: C1, C2, and C3.

Fraction C1 (16.73 g) was subjected to silica gel using a gradient of CHCl<sub>3</sub>/MeOH (90:1 → 60:1, v/v) as eluent. Subfraction C1.1 (384 mg), obtained from CHCl<sub>3</sub>/MeOH



**Table 4.** In vitro cytotoxicity results of isolated compounds (1–19).

Compounds	IC <sub>50</sub> (μmol/L ± SD) <sup>a</sup>		
	A549	DLD-1	WS1
<b>1</b>	>100	>100	>100
<b>2</b>	NT <sup>b</sup>	NT <sup>b</sup>	NT <sup>b</sup>
<b>3</b>	>100	>100	>100
<b>4</b>	NT <sup>b</sup>	NT <sup>b</sup>	NT <sup>b</sup>
<b>5</b>	>100	>100	42±4
<b>6</b>	>100	>100	>100
<b>7</b>	>100	>100	>100
<b>8</b>	81±3	>100	>100
<b>9</b>	9±3	9.2±0.9	5.8±0.3
<b>10</b>	31±2	37±3	87±3
<b>11</b>	>100	>100	>100
<b>12</b>	27±3	23±6	20±2
<b>13</b>	60±10	>100	42±5
<b>14</b>	>100	>100	>100
<b>15</b>	19±2	19.2±0.9	26±3
<b>16</b>	>100	>100	>100
<b>17</b>	>100	>100	>100
<b>18</b>	45.8±0.9	39±3	51±7
<b>19</b>	>100	>100	>100
Etoposide <sup>c</sup>	2.8±0.5	2±1	>50

**Note:** Mean values (± standard deviation) for triplicate assays.

<sup>a</sup>Concentration that caused 50% inhibition of cell proliferation.

<sup>b</sup>Not tested.

<sup>c</sup>Positive control.

(90:1), was separated on silica gel CC with CHCl<sub>3</sub>/MeOH (80:1) as eluent, to give three fractions: C1.1A, C1.1B, and C1.1C. Subfraction C1.1A was purified by preparative HPLC with a gradient elution of MeOH/H<sub>2</sub>O (50:50 → 85:15, v/v) yielding compounds **15** (249 mg), **16** (5 mg), and **17** (41 mg). Subfraction C1.1B (2.36 g) was applied successively on a silica gel CC and a reversed-phase CC using MeOH/H<sub>2</sub>O gradient (50:50 → 70:30, v/v) as eluent to give **11** (160 mg). Compound **9** (3 mg), **12** (18 mg), and a mixture of **10** and **13** (27 mg) were isolated after a silica gel CC eluted with CHCl<sub>3</sub>/MeOH (90:1) and a preparative HPLC (isocratic CH<sub>3</sub>CN/H<sub>2</sub>O 40:60) of fraction C1.2. Compound **18** (50 mg) was obtained from fraction C1.3 (294 mg) after repeated silica gel CC (CHCl<sub>3</sub>/MeOH, 75:1) and polyamide flash column (MeOH/H<sub>2</sub>O, 50:50 → 75:25).

Fraction C2 was chromatographed on silica gel CC with a gradient elution of CHCl<sub>3</sub>/MeOH (75:1 → 15:1, v/v) to give eight fractions: C2.1–C2.8. Subfraction C2.7 (558 mg) was separated by preparative HPLC using an isocratic mobile phase of CH<sub>3</sub>CN/H<sub>2</sub>O/HCOOH (40:60:1) to afford **2** (19 mg) and **14** (3 mg).

Fraction C3 (5.4 g) was purified on silica gel using a gradient of CHCl<sub>3</sub>/MeOH (25:1 → 7:1) for elution to give five subfractions: C3.1–C3.5. C3.2 was separated on silica gel CC with CHCl<sub>3</sub>/MeOH (20:1) giving **6** (289 mg). Some purifications on different silica gel CC of subfraction C3.2.1 permitted to obtain **19** (2 mg). Subfraction C3.4 (418 mg) was separated by preparative HPLC using an isocratic mobile phase of CH<sub>3</sub>CN/H<sub>2</sub>O (30:70) to afford compounds **1** (20 mg), **3** (8 mg), **4** (14 mg), and **8** (37 mg). Subfraction

C3.5 (482 mg) was separated by HPLC using a gradient of MeOH/H<sub>2</sub>O (10:90 → 100:0) to give **5** (21 mg) and **7** (35 mg).

#### (1S,2S)-1-[4-O-E-coumaroyl-β-D-glucopyranosyloxy]cyclohexanediol (**1**)

White amorphous powder. [α]<sub>D</sub><sup>25</sup> −35.3° (c 1.0, MeOH). IR (neat) ν<sub>max</sub>: 3328, 2935, 1696, 1602, 1160, 1080, 1024, 982, and 833 cm<sup>−1</sup>. <sup>1</sup>H and <sup>13</sup>C NMR spectroscopic data: see Table 2. HR-ESI-MS *m/z*: 447.16225 [M + Na]<sup>+</sup> (calcd. for C<sub>21</sub>H<sub>28</sub>O<sub>9</sub>Na: 447.16310).

#### Acid hydrolysis of **1**

Compound **1** was dissolved in HCl 10% and heated at 110 °C for 4 h. The resulting hydrolysate was extracted with CHCl<sub>3</sub>. The organic phase was dried (MgSO<sub>4</sub>) and the solvent evaporated under reduced pressure. The presence of *p*-coumaric acid was confirmed with standard sample on TLC (CHCl<sub>3</sub>/MeOH 10:1 as eluent and developing with NP/PEG reagent). The presence of cyclohexane-1,2-diol in the organic phase ([α]<sub>D</sub> + 3.4) was confirmed with a GC-MS analysis: Injector temperature, 250 °C; ionization voltage, 70 eV (EI-MS); column temperature, 40 °C for the initial 2 min followed by an increase of 15 °C min<sup>−1</sup> up to 350 °C; carrier gas, He; column flow rate, 1 mL min<sup>−1</sup>. Cyclohexane-1,2-diol was detected at *R*<sub>t</sub> 7.55 min. The aqueous phase was neutralized with *N,N*-diethylmethylamine (10% in CHCl<sub>3</sub>), and the solvents were evaporated under reduced pressure. The residue contained the monosaccharide D-glucose ([α]<sub>D</sub> + 24.8).

#### Cell lines and culture conditions

Lung carcinoma (A549), colorectal adenocarcinoma (DLD-1), and normal skin fibroblast (WS1) human cell lines were obtained from the American Type Culture Collection (ATCC). All cell lines were cultured in minimum essential medium containing Earle's salts and L-glutamine (Mediatech Cellgro, VA) to which were added 10% fetal bovine serum (Hyclone), vitamins (1X), penicillin (100 IU mL<sup>−1</sup>) and streptomycin (100 μg mL<sup>−1</sup>), essential amino acids (1X), and sodium pyruvate (1X) (Mediatech Cellgro, VA). Cells were kept at 37 °C in a humidified environment containing 5% CO<sub>2</sub>.

#### Cytotoxicity assay

Exponentially growing cells were plated in 96-well microplates (BD Falcon) at a density of 5 × 10<sup>3</sup> cells per well in 100 μL of culture medium (DMEM with 10% SVF) and were allowed to adhere for 24 h before treatment. Increasing concentrations of each compound in MeOH or DMSO were then added (100 μL per well), and the cells were incubated for 48 h. The final concentration of MeOH or DMSO in the culture medium was maintained at 0.25% (v/v) to avoid solvent toxicity. Cytotoxicity was assessed using resazurin<sup>17</sup> on an automated 96-well Fluoroskan Ascent F1™ plate reader (Labsystems) using excitation and emission wavelengths of 530 and 590 nm, respectively. Fluorescence was proportional to the cellular metabolic activity in each well. Survival percentage was defined as the fluorescence in experimental wells compared to that in control wells after subtraction of blank values. Each experiment was carried

out three times in triplicate. IC<sub>50</sub> results were expressed as means  $\pm$  standard deviation.

### Antibacterial assays

Antibacterial activity was evaluated using the microdilution method<sup>42</sup> but with some modifications: exponentially growing bacteria were plated in 96-well flat bottom microplates (BD Flacon) at a density of  $5 \times 10^3$  Gram-negative *E. coli* (ATCC 25922) or  $40 \times 10^3$  Gram-positive *S. aureus* (ATCC 25923) per well in 100  $\mu$ L nutrient broth (Difco). The concentration of ethanol in the culture medium was maintained at 0.25% (v/v) to avoid solvent toxicity. Fifty microliters of 4% resazurin was added to each well, and the microplates were incubated for 6 h at 37 °C. Fluorescence was measured after 6 h on an automated 96-well Fluoroskan Ascent Fl<sup>TM</sup> plate reader (Labsystems) using excitation and emission wavelengths of 530 nm and 590 nm, respectively.

### Acknowledgement

The financial support of Fonds Québécois de la Recherche sur la Nature et les Technologies (FQRNT, fonds forestiers 02) is gratefully acknowledged. The authors wish to thank Carole Grenon for the HPLC separations, Catherine Dussault and Maxime Lebrun for biological assays. Finally, the authors also thank Dr Richard Menini for his corrections and helpful comments on this manuscript

### References

- (1) Marcucci, M. C. *Apidologie (Celle)* **1995**, 26 (2), 83. doi:10.1051/apido:19950202.
- (2) Kujumgiev, A.; Tsvetkova, I.; Serkedjieva, Y.; Bankova, V.; Christov, R.; Popov, S. *J. Ethnopharmacol.* **1999**, 64 (3), 235. doi:10.1016/S0378-8741(98)00131-7. PMID:10363838.
- (3) Nieva Moreno, M. I.; Isla, M. I.; Cudmani, N. G.; Vattuone, M. A.; Sampietro, A. R. *J. Ethnopharmacol.* **1999**, 68 (1-3), 97. doi:10.1016/S0378-8741(99)00051-3. PMID:10624867.
- (4) Sforzin, J. M.; Fernandes, A., Jr.; Lopes, C. A. M.; Bankova, V.; Funari, S. R. C. *J. Ethnopharmacol.* **2000**, 73 (1-2), 243. doi:10.1016/S0378-8741(00)00320-2. PMID:11025162.
- (5) Miyataka, H.; Nishiki, M.; Matsumoto, H.; Fujimoto, T.; Matsuka, M.; Satoh, T. *Biol. Pharm. Bull.* **1997**, 20 (5), 496. PMID:9178928.
- (6) Orhan, H.; Marol, S.; Hepşen, I. F.; Sahin, G. *Toxicology* **1999**, 139 (3), 219. doi:10.1016/S0300-483X(99)00128-6. PMID:10647922.
- (7) Volpert, R.; Elstner, E. F. *Z. Naturforsch. [C]* **1993**, 48 (11-12), 851. PMID:8297422.
- (8) Banskota, A. H.; Tezuka, Y.; Prasain, J. K.; Matsushige, K.; Saiki, I.; Kadota, S. *J. Nat. Prod.* **1998**, 61 (7), 896. doi:10.1021/np980028c. PMID:9677271.
- (9) Popova, M.; Bankova, V.; Butovska, D.; Petkov, V.; Nikolaeva-Damyanova, B.; Sabatini, A. G.; Marcuzzan, G. L.; Bogdanov, S. *Phytochem. Anal.* **2004**, 15 (4), 235. doi:10.1002/pca.777. PMID:15311843.
- (10) Silici, S.; Kutluca, S. *J. Ethnopharmacol.* **2005**, 99 (1), 69. doi:10.1016/j.jep.2005.01.046. PMID:15848022.
- (11) English, S.; Greenaway, W.; Whatley, F. R. *Can. J. Bot.* **1991**, 69 (10), 2291. doi:10.1139/b91-288.
- (12) Greenaway, W.; May, J.; Whatley, F. R. *J. Chromatogr. A* **1989**, 472, 393. doi:10.1016/S0021-9673(00)94139-6.
- (13) Hashimoto, T.; Tori, M.; Asakawa, Y.; Wollenweber, E. *Z. Naturforsch. [C]* **1988**, 43 (5-6), 470. PMID:2458657.
- (14) Christov, R.; Trusheva, B.; Popova, M.; Bankova, V.; Bertrand, M. *Nat. Prod. Res.* **2005**, 19 (7), 673. doi:10.1080/14786410512331328159. PMID:16076637.
- (15) Burns, R. M.; Honkala, B. H. *Silvics of North America*; United States Department of Agriculture, Forest Service: Washington, DC, 1990. www.na.fs.fed.us/spfo/pubs/silvics\_manual/volume\_2/populus/tremuloides.htm (accessed Feb 21, 2008).
- (16) Moerman, D. E. *Native American Ethnobotany*; Timber Press Inc.: OR, USA, 1998.
- (17) O'Brien, J.; Wilson, I.; Orton, T.; Pognan, F. *Eur. J. Biochem.* **2000**, 267 (17), 5421. doi:10.1046/j.1432-1327.2000.01606.x. PMID:10951200.
- (18) Mizuno, M.; Kato, M.; Misu, C.; Iinuma, M.; Tanaka, T. *J. Nat. Prod.* **1991**, 54 (5), 1447. doi:10.1021/np50077a042.
- (19) Lewinsohn, E.; Berman, E.; Mazur, Y.; Gressel, J. *Phytochemistry* **1986**, 25 (11), 2531. doi:10.1016/S0031-9422(00)84502-1.
- (20) Singh, K. N.; Pandey, V. B.; Banerjee, S.; Bohlmann, F.; Keinan, E. *Chem. Ind.* **1986**, 713.
- (21) Güvenalp, Z.; Özbek, H.; Ünsalar, T.; Kazaz, C.; Demirezer, L. Ö. *Turk. J. Chem.* **2006**, 30, 391.
- (22) Rasmussen, B.; Nkurunziza, A. J.; Witt, M.; Oketch-Rabah, H. A.; Jaroszewski, J. W.; Staerk, D. *J. Nat. Prod.* **2006**, 69 (9), 1300. doi:10.1021/np060204e. PMID:16989523.
- (23) Otsuka, H.; Yamasaki, K.; Yamauchi, T. *Phytochemistry* **1989**, 28 (11), 3197. doi:10.1016/0031-9422(89)80306-1.
- (24) Ishikawa, T.; Nishigaya, K.; Takami, K.; Uchikoshi, H.; Chen, I.-S.; Tsai, I.-L. *J. Nat. Prod.* **2004**, 67 (4), 659. doi:10.1021/np034052o. PMID:15104498.
- (25) Zahir, A.; Jossang, A.; Bodo, B.; Provost, J.; Cosson, J.-P.; Sévenet, T. *J. Nat. Prod.* **1996**, 59 (7), 701. doi:10.1021/np960336f. PMID:8759170.
- (26) Sakakibara, M.; Difeo, D., Jr.; Nakatani, N.; Timmermann, B.; Mabry, T. J. *Phytochemistry* **1976**, 15 (5), 727. doi:10.1016/S0031-9422(00)94430-3.
- (27) Perry, N. B.; Foster, L. M. *Planta Med.* **1994**, 60 (5), 491. doi:10.1055/s-2006-959549. PMID:7997487.
- (28) Tian, F.; McLaughlin, J. L. *Pharm. Biol.* **2000**, 38 (3), 229. doi:10.1076/1388-0209(200007)38:3;1-S;FT229.
- (29) Majumder, P. L.; Chattopadhyay, A. *J. Indian Chem. Soc.* **1985**, 62, 616.
- (30) Máñez, S.; Payá, M.; Terencio, C.; Villar, A. *Planta Med.* **1988**, 54 (2), 187. doi:10.1055/s-2006-962396. PMID:17265246.
- (31) El-Batta, A.; Jiang, C.; Zhao, W.; Anness, R.; Cooksy, A. L.; Bergdahl, M. *J. Org. Chem.* **2007**, 72 (14), 5244. doi:10.1021/jo070665k. PMID:17559278.
- (32) English, S.; Greenaway, W.; Whatley, F. R. *Phytochemistry* **1992**, 31 (4), 1255. doi:10.1016/0031-9422(92)80272-G.
- (33) Mali, R. S.; Papalkar, A. S. *J. Chem. Res.* **2001**, S433.
- (34) Yamauchi, R.; Kato, K.; Oida, S.; Kanaeda, J.; Ueno, Y. *Biosci. Biotechnol. Biochem.* **1992**, 56 (8), 1321. doi:10.1271/bbb.56.1321.
- (35) Kelley, C. J.; Harruff, R. C.; Carmack, M. *J. Org. Chem.* **1976**, 41 (3), 449. doi:10.1021/jo00865a007.
- (36) Pouchert, C. J. *Aldrich<sup>®</sup> Library of NMR Spectra*, 2nd ed.; 1983.
- (37) Porwoll, J. *Handbook of Fine Chemicals*; Aldrich Chemical Co.: Milwaukee, MI, 2007. Available from: [http://www.sigmaaldrich.com/catalog/ProductDetail.do?lang=en&N4=421804|ALDRICH&N5=SEARCH\\_CONCAT\\_PNO|BRAND\\_KEY&F=SPEC](http://www.sigmaaldrich.com/catalog/ProductDetail.do?lang=en&N4=421804|ALDRICH&N5=SEARCH_CONCAT_PNO|BRAND_KEY&F=SPEC) (accessed Oct 15, 2007).
- (38) Lee, Y.-T.; Don, M.-J.; Hung, P.-S.; Shen, Y.-C.; Lo, Y.-S.;

- Chang, K.-W.; Chen, C.-F.; Ho, L.-K. *Cancer Lett.* **2005**, 223 (1), 19. doi:10.1016/j.canlet.2004.09.048. PMID:15890233.
- (39) Boyd, M. R. In *Anticancer Drug Development Guide: Pre-clinical Screening, Clinical Trials, and Approval*; Teicher, B. A., Ed.; Humana Press: Totowa, NJ, 2004; pp 41–62.
- (40) Nagaoka, T.; Banskota, A. H.; Tezuka, Y.; Saiki, I.; Kadota, S. *Bioorg. Med. Chem.* **2002**, 10 (10), 3351. doi:10.1016/S0968-0896(02)00138-4. PMID:12150882.
- (41) Ryu, S. Y.; Kim, J. O.; Choi, S. U. *Planta Med.* **1997**, 63 (4), 384. doi:10.1055/s-2006-957714. PMID:9270388.
- (42) Banfi, E.; Scialino, G.; Monti-Bragadin, C. *J. Antimicrob. Chemother.* **2003**, 52 (5), 796. doi:10.1093/jac/dkg439. PMID:14519676.

# Solid-state $^{27}\text{Al}$ nuclear magnetic resonance investigation of three aluminum-centered dyes

Kamal H. Mroué, Abdul-Hamid M. Emwas, and William P. Power

**Abstract:** We report the first solid-state  $^{27}\text{Al}$  NMR study of three aluminum phthalocyanine dyes: aluminum phthalocyanine chloride,  $\text{AlPcCl}$  (**1**); aluminum-1,8,15,22-tetrakis(phenylthio)-29*H*,31*H*-phthalocyanine chloride,  $\text{AlPc}(\text{SPh})_4\text{Cl}$  (**2**); and aluminum-2,3-naphthalocyanine chloride,  $\text{AlNcCl}$  (**3**). Each of these compounds contains  $\text{Al}^{3+}$  ions coordinating to four nitrogen atoms and a chlorine atom. Solid-state  $^{27}\text{Al}$  NMR spectra, including multiple-quantum magic-angle spinning (MQMAS) spectra and quadrupolar Carr–Purcell–Meiboom–Gill (QCPMG) spectra of stationary powdered samples have been acquired at multiple high magnetic field strengths (11.7, 14.1, and 21.1 T) to determine their composition and number of aluminum sites, which were analyzed to extract detailed information on the aluminum electric field gradient (EFG) and nuclear magnetic shielding tensors. The quadrupolar parameters for each  $^{27}\text{Al}$  site were determined from spectral simulations, with quadrupolar coupling constants ( $C_Q$ ) ranging from 5.40 to 10.0 MHz and asymmetry parameters ( $\eta$ ) ranging from 0.10 to 0.50, and compared well with the results of quantum chemical calculations of these tensors. We also report the largest  $^{27}\text{Al}$  chemical shielding anisotropy (CSA), with a span of  $120 \pm 10$  ppm, observed directly in a solid material. The combination of MQMAS and computational predictions are used to interpret the presence of multiple aluminum sites in two of the three samples.

**Key words:** aluminum phthalocyanine dyes, solid-state  $^{27}\text{Al}$  NMR, electric field gradient tensor, aluminum chemical shift anisotropy, quantum chemical calculations.

**Résumé :** On a réalisé la première étude RMN du  $^{27}\text{Al}$  en phase solide de trois colorants à base de phthalocyanine d'aluminium, soit le chlorure de phthalocyanine d'aluminium,  $\text{AlPcCl}$  (**1**), le chlorure de la 1,8,15,22-tétrakis(phénylthio)-29*H*,31*H*-phthalocyanine d'aluminium,  $\text{AlPc}(\text{SPh})_4\text{Cl}$  (**2**) et le chlorure de la 2,3-dinaphthalocyanine d'aluminium,  $\text{AlNcCl}$  (**3**). Chacun de ces composés contient des ions de  $\text{Al}^{3+}$  coordonnés à quatre atomes d'azote et un atome de chlore. Les spectres RMN de l'aluminium-27 en phase solide, y compris les spectres multiquantiques à l'angle magique de rotation (« MQMAS ») et les spectres quadripolaires de Carr–Purcell–Meiboom–Gill (« QCPMG ») d'échantillons de poudres solides, ont été obtenus à des forces de champs magnétiques élevés diverses (11,7, 14,1 et 21,1 T) dans le but de déterminer leur composition et le nombre de sites d'aluminium et on les a analysés pour en extraire de l'information détaillée relative au gradient du champ électrique (GCE) de l'aluminium ainsi que les tenseurs de blindage du champ magnétique. On a déterminé les paramètres quadripolaires de chacun des sites d'aluminium-27 par simulations spectrales; les constantes de couplage quadripolaires ( $C_Q$ ) qui varient de 5,40 à 10,0 MHz et les paramètres d'asymétrie ( $\eta$ ) qui s'étalent de 0,10 à 0,50 se comparent bien avec les résultats obtenus pour ces tenseurs par le biais de calculs théoriques. On a aussi observé une anisotropie de blindage chimique (ABC) de l'aluminium-27 de  $120 \pm 10$  ppm qui correspond à la valeur la plus élevée jamais observée dans un matériel solide. On a utilisé une combinaison des valeurs expérimentales observées dans les spectres multiquantiques à l'angle magique de rotation avec les prédictions théoriques pour interpréter la présence de multiples sites d'aluminium dans deux des trois échantillons.

**Mots-clés :** colorants à base de phthalocyanine d'aluminium, RMN du  $^{27}\text{Al}$  en phase solide, tenseur du gradient du champ électrique, anisotropie du déplacement chimique de l'aluminium, calculs théoriques à base de chimie quantique.

[Traduit par la Rédaction]

## Introduction

Phthalocyanine complexes (Pcs), and the structurally related naphthalocyanines (Ncs), together with their metal-

centered derivatives, constitute an important class of macrocyclic compounds, which play a vital role in many modern practical and technological applications.<sup>1</sup> These materials have been intensively used in dyes, pigments, fuel and solar cells, electrophotography, semiconductors, liquid crystals, data-storage devices, photosensitizers for photodynamic therapy, and nonlinear optical materials, among others. This wide variety of applications is due mainly to their intense green-blue color, combined with their exceptional stability to acids, alkalis, heat, light, and common solvents. These properties and applications, among others as well, are discussed in several excellent monographs about phthalocyanines and their derivatives.<sup>2–8</sup>

Numerous techniques have been used to study these mate-

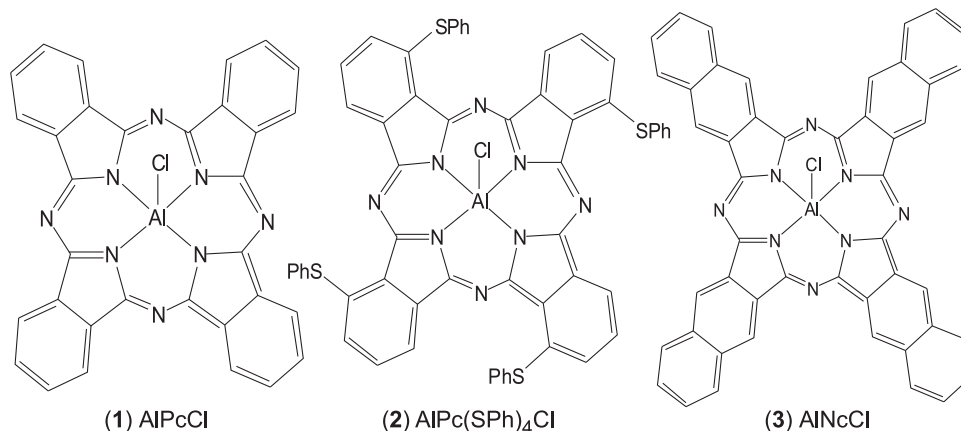
Received 16 June 2009. Accepted 5 October 2009. Published on the NRC Research Press Web site at [canjchem.nrc.ca](http://canjchem.nrc.ca) on 19 January 2010.

**K.H. Mroué, A.M. Emwas,<sup>1</sup> and W.P. Power,<sup>2</sup>** Department of Chemistry, University of Waterloo, 200 University Ave. West, Waterloo, ON N2L 3G1, Canada.

<sup>1</sup>Present address: King Abdullah University of Science and Technology, Jeddah 21534, Saudi Arabia.

<sup>2</sup>Corresponding author (e-mail: [wppower@uwaterloo.ca](mailto:wppower@uwaterloo.ca)).



**Fig. 1.** Molecular structures of the studied compounds.

rials, such as X-ray diffraction, mass spectrometry, Raman, IR, UV-vis, electronic absorption/emission, Mössbauer, electron paramagnetic, and nuclear magnetic resonance (NMR) spectroscopies, among others. Studies of these materials by liquid-state NMR have involved mainly the use of  $^1\text{H}$  and  $^{13}\text{C}$  NMR as identification tools.<sup>9,10</sup> Direct NMR observation of the metal nuclei in solid metal-centered phthalocyanines has been limited to few studies, including a  $^{59}\text{Co}$  NMR study of four hexacoordinated cobalt(III) phthalocyanines,<sup>11</sup> a  $^{25}\text{Mg}$  NMR study of monopyridinated aqua(magnesium) phthalocyanine,<sup>12</sup> and a recent  $^{71}\text{Ga}$  NMR study of gallium phthalocyanine chloride,  $\text{GaPcCl}$ .<sup>13,14</sup>

From a spectroscopic perspective, solid-state nuclear magnetic resonance (SSNMR) represents an ideal and powerful tool to probe the metal centre in a metalophthalocyanine. The advantages of NMR over other techniques, such as X-ray and neutron diffraction, is that while the latter techniques rely on the long-range order in the crystal lattice and require the availability of high-quality single crystals suitable for analysis, SSNMR focuses on the local electronic environment around the nucleus of interest without the necessity of single crystals. Given the limited solubility of metalophthalocyanines in both inorganic and organic solvents, and their large molecular weights, their analysis by single-crystal X-ray diffraction can be quite cumbersome, if at all possible. Moreover, the ability of SSNMR to characterize disordered and amorphous solid materials has been well-established and demonstrated in numerous instances (vide infra). Recently, the increasing availability of ultra-high-magnetic-field NMR spectrometers, together with the advances in instrumental hardware, and the introduction of new pulse sequences have also facilitated the application of SSNMR to study such poorly crystalline materials.<sup>15,16</sup>

Among the various metalophthalocyanines, aluminum-centered ones are well-suited for SSNMR experiments. This is due to the very favorable NMR properties that  $^{27}\text{Al}$  enjoys, including its high natural abundance (100%), large magnetogyric ratio ( $\gamma = 6.9762 \times 10^7 \text{ rad T}^{-1} \text{ s}^{-1}$ , close to  $^{13}\text{C}$ ), and a sizable chemical shift range of about 300 ppm.<sup>17</sup> However, the quadrupolar nature of  $^{27}\text{Al}$  (spin  $I = 5/2$ ) introduces various challenges in SSNMR studies of this nucleus. The most distinctive challenge arises from the nonzero nuclear quadrupole moment [ $Q(^{27}\text{Al}) = 14.66 \times 10^{-30} \text{ m}^2$ ],<sup>18</sup> which couples strongly with any electric field

gradient (EFG) arising naturally from lack of spherical symmetry in charge distribution around the aluminum nucleus. Such quadrupolar interactions have considerable effects on  $^{27}\text{Al}$  NMR spectra, often beyond those described under first-order perturbation theory. Usually, only the central transition (CT,  $+1/2 \leftrightarrow -1/2$ ) is observed in a SSNMR experiment of a polycrystalline powdered sample, and it is unaffected to first-order but is substantially broadened by second-order quadrupolar effects.<sup>19,20</sup> In addition to the quadrupolar interaction,  $^{27}\text{Al}$  is also sensitive to the chemical shift/shielding interaction. The EFG and chemical shift (CS) are both orientation-dependent NMR interactions that can provide reliable information about the local electronic environment of the nucleus of interest, and can potentially yield structural details not typically available from other techniques.<sup>21,22</sup>

Despite the complications caused by second-order quadrupolar broadening, solid-state  $^{27}\text{Al}$  NMR has been used frequently to study a wide variety of materials, most of which are inorganic and disordered solids such as glasses, zeolites, aluminosilicates, molecular sieves, cements, ceramics, as well as natural and synthetic minerals.<sup>23–38</sup> In these studies,  $^{27}\text{Al}$  magic-angle-spinning (MAS) NMR has been used primarily to narrow the central transition line shapes, and to enhance the spectral resolution to differentiate among tetrahedral, penta-coordinate, and octahedral local aluminum coordination environments (mainly in aluminum-(oxygen)<sub>n</sub> coordination,  $n = 4, 5, 6$ ) based on the different  $^{27}\text{Al}$  chemical shift ranges of each environment.<sup>15,39</sup> In the case of disordered and (or) amorphous solids, the conventional one-dimensional MAS spectrum does not give well-defined second-order quadrupolar line shapes. These lines are rather featureless and asymmetric, from which it is quite challenging to extract any information related to the chemical shift and quadrupolar interactions arising from overlapping signals.<sup>40–42</sup> For such materials, the two dimensional multiple-quantum magic-angle-spinning (MQMAS) experiment<sup>43,44</sup> is used to resolve overlapping resonances in multi-site systems, based on the difference in the chemical shift and quadrupolar parameters experienced by each site. In many instances, MQMAS makes it possible to not only resolve the different sites present in the system, but also allows extraction of sufficient information about the  $^{27}\text{Al}$  NMR parameters associated with each unique site.

In contrast to the plethora of inorganic and glassy materials investigated by solid-state  $^{27}\text{Al}$  NMR, it is surprising that only a handful of aluminum-containing organic compounds have been studied by this technique. Wasylishen and co-workers reported solid-state  $^{27}\text{Al}$  NMR spectra of tris(acetylacetonato)aluminum(III), tris(tropolonato)aluminum(III), and tris(2,2,6,6-tetramethyl-3,5-heptanedionato)aluminum(III).<sup>45</sup> The aluminum atoms in these compounds are each coordinated to six oxygen atoms in a distorted octahedral geometry, where small  $^{27}\text{Al}$  chemical shift anisotropy (CSA) values were observed for the three complexes. Gang Wu and co-workers also recorded solid-state  $^{27}\text{Al}$  NMR spectra of three blue-luminescent aluminum compounds containing terminal 7-azaindole ligands, in which the aluminum ions are in distorted tetrahedral coordination environments.<sup>46</sup> The same group successfully applied  $^{27}\text{Al}$  3QMAS spectroscopy to the identification of disorder and isomerism in two blue-luminescent aluminum compounds, in which the Al centres exhibit five-coordinated geometries.<sup>47</sup> Utz et al. studied the  $^{27}\text{Al}$  spectra of three different polymorphs of solid tris(8-hydroxyquinoline)aluminum(III) under MAS conditions.<sup>48</sup> These same systems were reinvestigated recently by Nishiyama et al. using  $^{27}\text{Al}$  1D MAS and 2D MQMAS NMR experiments.<sup>49</sup> Schurko et al. reported a very small  $^{27}\text{Al}$  quadrupolar interaction but a large aluminum chemical shielding anisotropy, with a span of 83 ppm, in the bis(pentamethylcyclopentadienyl)aluminum cation.<sup>50</sup> Schurko and co-workers applied the frequency-stepped technique in Hahn-echo and QCPMG pulse sequences to acquire ultrawide-line  $^{27}\text{Al}$  NMR spectra of stationary samples of three- and five-coordinate organoaluminum complexes.<sup>51</sup>

In this work, we investigate the solid-state  $^{27}\text{Al}$  NMR spectra of three aluminum-centered organic dyes: aluminum phthalocyanine chloride,  $\text{AlPcCl}$  (**1**); aluminum-1,8,15,22-tetrakis(phenylthio)-29*H*,31*H*-phthalocyanine chloride,  $\text{AlPc}(\text{SPh})_4\text{Cl}$  (**2**); and aluminum-2,3-naphthalocyanine chloride,  $\text{AlNcCl}$  (**3**) (Fig. 1). In addition to our main interest in the SSNMR of phthalocyanines (for the reasons mentioned above), these compounds have been chosen because they exhibit aluminum in penta-coordinate geometries, which is much less common than the four- and six-coordinate motifs. In all three systems, the  $\text{Al}^{3+}$  ions are coordinated to four isoindole nitrogen atoms and one chlorine atom in a square-pyramidal geometry. Such coordination geometry is relatively rare in solid-state  $^{27}\text{Al}$  NMR studies, both in inorganic and organic systems. We also report extensive density functional theory (DFT) and restricted Hartree–Fock (RHF) quantum chemical calculations of aluminum NMR interactions in molecular models of these complexes in an attempt to examine the orientation of NMR tensors within molecular frames and to help rationalize the origin of experimentally measured aluminum NMR parameters.

## Experimental

### Sample preparation

The three complexes were purchased from Aldrich Chemical Company. The dye contents are ~ 85%, 90%, and 80% for compounds **1**, **2**, and **3**, respectively. Attempts to obtain the pure compounds by recrystallization from a variety of

organic solvents or by vacuum sublimation were unfruitful. Hence, they were used as purchased. Samples of each complex were ground into fine powders with a mortar and pestle for X-ray powder diffraction experiments, and subsequently packed into 2.5 and 4.0 mm o.d. zirconia rotors for SSNMR experiments. Powder X-ray diffraction data were collected using an INEL powder diffractometer with a position-sensitive detector and Cu  $\text{K}\alpha_1$  radiation ( $\lambda = 1.54056 \text{ \AA}$ ). The operating conditions were 30 kV and 30 mA, with an exposure time of 5–10 min over the  $2\theta$  range from 0.0 to  $120^\circ$ .

### Solid-state $^{27}\text{Al}$ NMR spectroscopy

$^{27}\text{Al}$  solid-state NMR experiments were performed at Larmor frequencies of 130.3 MHz (11.75 T), 156.4 MHz (14.1 T), and 234.5 MHz (21.1 T) using Bruker Avance (11.75 and 14.1 T) and Avance II (21.1 T) consoles. The experiments at 11.75 and 14.1 T were performed at the University of Waterloo; experiments at 21.1 T were performed at the National Ultrahigh-Field NMR Facility for Solids at the National Research Council (NRC) in Ottawa, Ontario, Canada. Standard Bruker 2.5 mm double-resonance MAS probes were used at 14.1 and 21.1 T, whereas a Bruker 4 mm double-resonance MAS probe was used at 11.75 T. Pulse calibration and chemical shift referencing were performed using a 1.0 mol/L  $\text{Al}[(\text{H}_2\text{O})_6]^{3+}$  aqueous solution set at 0.0 ppm. A solid echo ( $\pi/2 - \tau_1 - \pi/2 - \tau_2 - \text{ACQ}$ ) and quadrupolar Carr–Purcell–Meiboom–Gill (QCPMG)<sup>52,53</sup> pulse sequences were used to acquire spectra of non-spinning samples. For experiments performed under MAS conditions, the sample spinning speed was 20.0 kHz at 14.1 T and 21.1 T, and 15.0 kHz at 11.75 T. A very short pulse ( $\pi/12$ ) was used in the one-dimensional MAS spectra to ensure quantification of all species. For the solid-echo and QCPMG experiments, a selective  $\pi/2$  pulse of 1.20–1.40  $\mu\text{s}$  was used.

Two-dimensional  $^{27}\text{Al}$  triple-quantum MAS (3QMAS) spectra of the three complexes were obtained at 21.1 T using a spinning rate of 20.0 kHz. The  $z$ -filtered 3QMAS pulse sequence was used,<sup>54</sup> consisting of excitation (1.90  $\mu\text{s}$ ) followed by evolution of the triple-quantum coherence during  $t_1$  followed by a conversion pulse (0.80  $\mu\text{s}$ ), a 20  $\mu\text{s}$   $z$ -filter, and a selective  $\pi/2$  pulse (7.50  $\mu\text{s}$ ) followed by acquisition during  $t_2$ . A total of 240 transients were obtained for each  $t_1$  increment; 64 complex points were acquired in  $t_1$ , with a  $t_1$  increment of 25  $\mu\text{s}$ , which corresponds to half the rotor period. Exponential apodization of 300 Hz was applied in both dimensions prior to zero-filling and Fourier transformation. A shearing transformation was performed during data processing to obtain the isotropic dimension along F1 and the anisotropic MAS dimension along F2. Recycle delays of 2.0 s, 3.0 s, and 5.0 s were sufficient at 11.75, 14.1, and 21.1 T, respectively. The 1D NMR spectra used for line-shape analysis were simulated with SIMPSON.<sup>55</sup> Spectral simulations were carried out iteratively and simultaneously at multiple fields, and the errors in the extracted parameters were determined by visual comparison of the resulting fit at each field with the corresponding experimental spectrum. Each parameter was optimized independently by varying it in both directions away from its best-fit value, while all other parameters were held fixed, until a visible difference

between experimental and simulated spectra was observed. Stack plots were generated with DMFit.<sup>56</sup>

### Quantum chemical calculations

All quantum chemical calculations were performed using Gaussian 03<sup>57</sup> running on the SHARCNET facility for high performance computing.<sup>58</sup> In an attempt to understand the experimentally observed <sup>27</sup>Al NMR parameters, three models for calculations of NMR interaction tensors were constructed for compound **1**: The first model was built using atomic coordinates obtained from the X-ray single-crystal study of Hasegawa and Sato,<sup>59,60</sup> and used directly for NMR calculations. Two additional models were constructed by the addition of either a chlorine atom or a water molecule below the phthalocyanine ring in an axial position to complete the octahedral coordination around the aluminum atom. The geometries of both models were then fully optimized at the RHF/6–311G\*\* method. Since there are no crystal structures reported for compounds **2** and **3**, the structures used in NMR calculations were derived from the reported structure of molecule **1** of compound **1**<sup>59,60</sup> by adding either four thiophenyl groups (**2**) or four naphthalo groups (**3**) in their respective peripheral positions, as depicted in Fig. 1. The two structures were then fully optimized at the RHF/6–311G\*\* method. Aluminum electric field gradient and nuclear magnetic shielding tensors were subsequently calculated for the resulting structures using both the restricted Hartree–Fock (RHF) and density functional theory (DFT) methods. The B3LYP exchange functional<sup>61,62</sup> was employed in the DFT calculations. The following standard Pople-type basis sets were employed on all atoms: 6–31G\*\*, 6–31++G\*\*, 6–311G\*\*, 6–311++G\*\*, and 6–311+G (2d, p). The nuclear magnetic shielding tensors were calculated using the gauge-including atomic orbitals (GIAO) method.<sup>63,64</sup> Because there is no established absolute magnetic shielding scale for <sup>27</sup>Al, the calculated <sup>27</sup>Al isotropic chemical shieldings ( $\sigma_{\text{iso}}$ ) were converted into the corresponding isotropic chemical shifts ( $\delta_{\text{iso}}$ ) using the formula  $\delta_{\text{iso}} = \sigma_{\text{ref}} - \sigma_{\text{iso}}$ , where  $\sigma_{\text{ref}}$  is the calculated isotropic shielding constant of  $[\text{Al}(\text{H}_2\text{O})_6]^{3+}$  cation, the reference species.<sup>17</sup> The geometry of this cation was fully optimized at the RHF/6–311G\*\* level. To avoid basis-set dependence of the calculated <sup>27</sup>Al chemical shifts, the reference chemical shielding  $\sigma_{\text{ref}}$  was computed for each basis set used. The calculated <sup>27</sup>Al EFG and CS parameters were extracted from the Gaussian output files using the EFGShield program (version 2.3) developed in the laboratory of D.L. Bryce.<sup>65</sup>

### Solid-state <sup>27</sup>Al NMR conventions

Prior to commencing the discussion of the <sup>27</sup>Al NMR results of this study, it is convenient to recall some NMR concepts and definitions relevant to the systems currently investigated, keeping in mind that the SSNMR theory for half-integer quadrupolar spins is detailed more elegantly elsewhere.<sup>19–22</sup> Aside from the Zeeman interaction, the spectrum of a half-integer quadrupolar spin (such as <sup>27</sup>Al,  $I = 5/2$ ) is dominated by the nuclear quadrupole interaction and the nuclear magnetic shielding interaction. The high-field approximation, in which the Zeeman interaction is assumed

to be at least ten times stronger than both interactions, is always applied in the interpretation of SSNMR spectra of these nuclei.

Nuclear magnetic shielding is the interaction between the nuclear spins and the local magnetic field induced by surrounding electrons, and depends on the orientation of the molecule with respect to the external applied magnetic field,  $\mathbf{B}_0$ ; in other words, it is anisotropic. Thus, it can be described by a second-rank tensor, denoted by  $\sigma$ . In its principal axis system (PAS), the symmetric component of  $\sigma$  is diagonal, and has three eigenvalues labeled and ordered such that:  $\sigma_{33} \geq \sigma_{22} \geq \sigma_{11}$ . Experimentally, the magnetic shielding at a nucleus is measured in terms of the chemical shift,  $\delta_{ii}$ , which gives the difference in ppm between the sample signal and that of a reference compound. Since chemical shielding and chemical shift vary conversely with frequency, the three principal components of the CS tensor are ordered as:  $\delta_{11} \geq \delta_{22} \geq \delta_{33}$ . Although the magnitude of the shielding (or shift) tensor can be fully described by its three eigenvalues, an alternative convention is used in which the magnitude of the tensor is fully described by: its isotropic chemical shift  $\delta_{\text{iso}} = (\delta_{11} + \delta_{22} + \delta_{33})/3$ ; its span  $\Omega = \sigma_{33} - \sigma_{11} \approx \delta_{11} - \delta_{33}$ ; and its skew  $\kappa = 3(\sigma_{\text{iso}} - \sigma_{22})/\Omega = 3(\delta_{\text{iso}} - \delta_{22})/\Omega$ , where  $-1.0 \leq \kappa \leq +1.0$ .<sup>66,67</sup> The span reflects the breadth of the powder pattern due to shielding anisotropy, while the skew describes the shape of the shielding tensor, with  $\kappa = \pm 1.0$  indicating an axially symmetrical CS tensor. It is very important to mention that the span of the CS tensor, represented by  $\Omega$ , scales linearly (when measured in Hz) with  $\mathbf{B}_0$ . This means that the effects of CSA are observed more clearly at high magnetic fields than at lower ones.

The quadrupolar interaction results from the coupling of the quadrupole moment of a nucleus with any electric field gradient (EFG) at that nucleus. The EFG is represented by a second-rank traceless and symmetric tensor. In its PAS, it has three components ordered as:  $|V_{33}| \geq |V_{22}| \geq |V_{11}|$ , with  $V_{11} + V_{22} + V_{33} = 0$ . Two parameters are sufficient to quantify the magnitude of the quadrupolar interaction: the quadrupolar coupling constant ( $C_Q$ ) to measure its size (strength), and the asymmetry parameter ( $\eta$ ) to measure the degree of axial asymmetry of the EFG tensor. They are given by  $C_Q = (eQV_{33})/h$  and  $\eta = (V_{11} - V_{22})/V_{33}$ . Here,  $e$  is the charge of an electron,  $Q$  is the nuclear quadrupole moment, and  $h$  is Planck's constant.  $C_Q$  is measured in Hz, while  $\eta$  is unitless and can take any value between 0 and 1 ( $\eta = 0$  corresponds to axial symmetry of the EFG tensor). The quadrupolar interaction can be treated as a second-order perturbation of the Zeeman interaction when the quadrupolar frequency,  $\nu_Q = 3C_Q/(2I(2I - 1)) = 0.15 C_Q$  for <sup>27</sup>Al, is less than 10% of the Larmor frequency,  $\nu_L$ .<sup>68</sup> This has two direct consequences for solid-state <sup>27</sup>Al NMR spectroscopy. First, the satellite transitions,  $(\pm 5/2 \leftrightarrow \pm 3/2)$  and  $(\pm 3/2 \leftrightarrow \pm 1/2)$ , often extend over a large spectral range so that they are difficult to both excite and detect; hence, experimentally only the central transition is typically observed. Second, the second-order quadrupolar breadth of the central transition line shape is directly proportional to  $C_Q^2/\nu_L$ .<sup>68,69</sup> This means that the second-order quadrupolar broadening (in Hz) scales inversely with  $\mathbf{B}_0$ , making it advantageous to acquire NMR spectra of half-integer quadrupolar nuclei at the highest pos-



sible magnetic field strengths to minimize such broadening. Another very important consequence of second-order quadrupolar effects is that the centre of gravity of the central transition ( $\delta_{cg}$ ) does not coincide with the true isotropic chemical shift ( $\delta_{iso}$ ). Rather, it is shifted away by the so-called isotropic second-order quadrupole induced shift ( $\delta_{qis}$ ). For a spin-5/2 nucleus such as  $^{27}\text{Al}$ ,  $\delta_{qis}$  of the central transition is given, in ppm, by<sup>15,70</sup>

$$[1] \quad \delta_{qis} = \delta_{cg} - \delta_{iso} = -6000 \frac{P_Q^2}{\nu_L^2}$$

where  $P_Q = C_Q(1+\eta^2/3)^{1/2}$  is the second-order quadrupole effect (SOQE) parameter, and sometimes is simply termed the quadrupolar product.

Of equal importance to the magnitudes of the CS and quadrupolar interactions is the information pertaining to the relative orientation of these two tensor quantities. This unique information is contained in three fixed Euler angles ( $\alpha$ ,  $\beta$ , and  $\gamma$ ) that describe the counter-clockwise rotations needed to bring the EFG PAS into coincidence with the CS PAS. The so-called “zyz” convention is usually used, where  $\alpha$  describes the counter-clockwise rotation about the initial  $z$  axis ( $V_{33}$ ) of the coordinate system, followed by a rotation about the new  $y'$  axis ( $V_{22}$ ) by  $\beta$ , followed by a rotation about the final  $z''$  axis ( $V_{33}$ ).<sup>71</sup>

## Results and discussion

Preliminary studies of compounds **1–3** using MQMAS at 21.1 T indicated that both compounds **1** and **2** were composed of multiple components, while compound **3** was composed largely of a single component (Fig. 2). All three spectra indicate one component with a signal near  $30 \pm 5$  ppm in each dimension, which can be described by an aluminum site with a quadrupolar coupling constant near 10 MHz and an isotropic chemical shift near 27 ppm, as well as a common minor impurity with a narrow peak near 10 ppm (vide infra). Therefore, for clarity, compound **3** will be described first, and those results will be used to help illustrate the situation for compounds **1** and **2**. This is completely consistent with the results of powder X-ray diffraction (provided in the Supplementary data), in which compound **1** displayed a multi-component nature with a number of overlapping reflections, **2** displayed no crystalline reflections (indicating an amorphous nature), while compound **3** displayed a clear diffraction pattern consistent with a single-phase crystalline sample.

The sheared 3QMAS spectrum of  $\text{AlNcCl}$  (**3**) at 21.1 T (Fig. 2c) clearly shows a unique Al site flanked with spinning sidebands. This ridge lies in a direction parallel to the F2 axis, a consequence of the strong quadrupolar interaction experienced by  $^{27}\text{Al}$  nuclei in this site. Another small ridge lies at the diagonal CS axis, with a very small intensity relative to the main peak, indicating that it corresponds to an aluminum-containing impurity. This impurity also appears as a low-frequency “shoulder” in the 1D MAS line shape, shown on top of the 2D spectrum. The 1D MAS spectra of  $\text{AlNcCl}$  at the three magnetic fields are all shown in Fig. 3, along with their corresponding simulations. Unlike the two other complexes, the MAS spectra of compound **3** reveal a polycrystalline and non-disordered powdered sample, despite

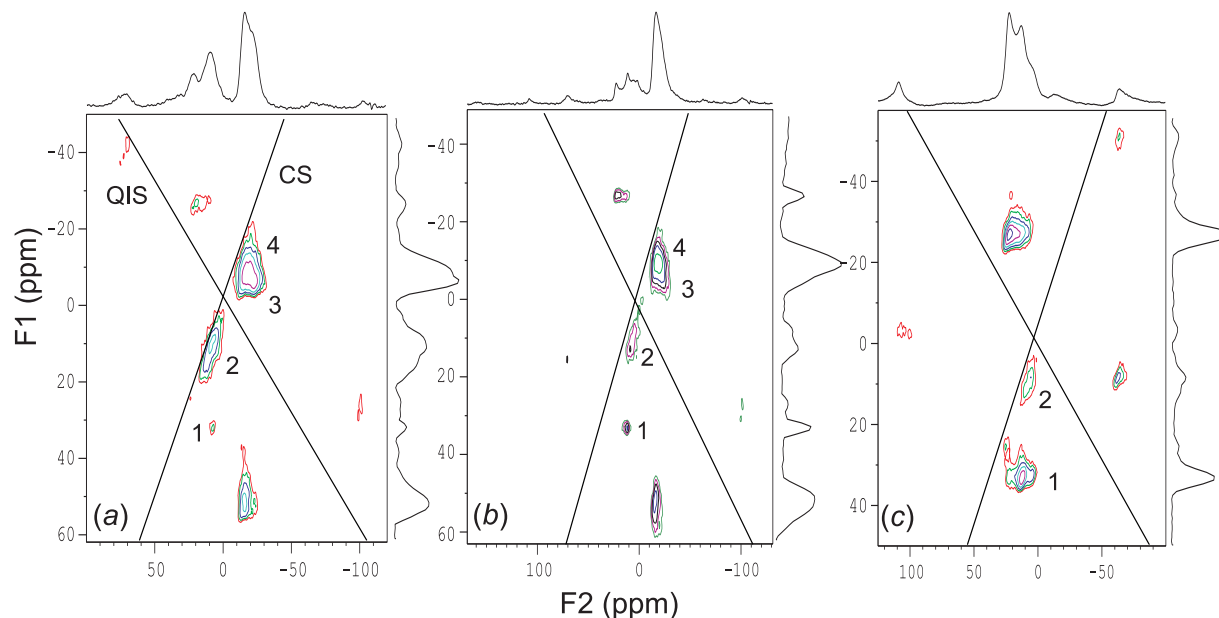
the presence of an impurity. It is obvious that the presence of this impurity hinders the exact agreement between the experimental line shapes and the simulated ones, notably at 21.1 T (Fig. 3a) due to the inherent higher sensitivity at this ultrahigh field. Simultaneous simulation of the three MAS spectra yields the best-fit values of 27.0 ppm, 9.80 MHz, and 0.10 for  $\delta_{iso}$ ,  $C_Q$ , and  $\eta$ , respectively, for the dominant component (Table 1).

In addition to the MAS spectra,  $^{27}\text{Al}$  QCPMG and solid-echo NMR spectra of a stationary powder sample of  $\text{AlNcCl}$  were acquired at 14.1 and 21.1 T, the results of which are shown in Fig. 4. Comparing the line widths of the static spectra at both fields, it can be readily observed that these line widths are almost equal when measured in Hz. This indicates that CSA has a significant contribution to the powder line shape, and is comparable to the second-order quadrupolar broadening. Had the spectra been dominated by the latter interaction only, then the line width at 21.1 T would have been equal to two thirds of that at 14.1 T. Clearly, this is not the case. To determine the contribution of the CSA to the line shape, the  $\delta_{iso}$ ,  $C_Q$ , and  $\eta$  values determined from the MAS experiments were used in the simultaneous simulation of the static spectra at both fields, and the experimental spectra could be reproduced fairly well with the inclusion of a span of  $120 \pm 10$  ppm and a skew of  $0.85 \pm 0.10$ . It is also important to mention that the line shape is very sensitive to the Euler angle  $\beta$ , which is the angle between  $V_{33}$  (the largest component of the EFG tensor) and  $\delta_{33}$  (the most shielded component of the CS tensor). The small experimental value of  $5^\circ$  for this angle indicates that these two components lie almost in the same direction, nearly perpendicular to the plane of the phthalocyanine ring.

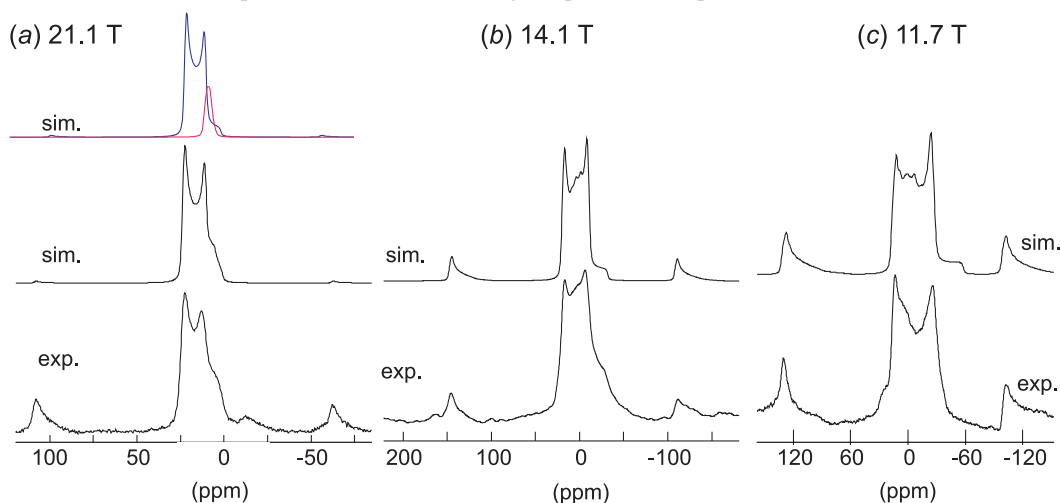
A number of studies have noted the presence and characteristics of penta-coordinated Al sites in aluminum oxide derived materials.<sup>72–76</sup> In accord with the results of those studies, isotropic  $^{27}\text{Al}$  chemical shifts of 30–40 ppm are observed, falling midway between the common shift ranges of tetrahedral and octahedral aluminum sites encountered in such materials. Quadrupolar coupling constants vary greatly but are generally smaller than what has been observed with these materials, and chemical shift anisotropies in oxide materials are expected to be small.<sup>45</sup> The most relevant comparisons to be made to the results reported here are from other metal-centered complexes involving heterocyclic ligands. Both reports of solid-state  $^{27}\text{Al}$  NMR characterizations of penta-coordinated Al sites, in 7-azaindolyl complexes by Aschenhurst et al.<sup>47</sup> and in bis-tetrahydrofurfuryloxide complexes by Tang et al.,<sup>51</sup> correspond to square-pyramidal geometries about the aluminum centre, similar to the compounds investigated here. However, due to structural distortions in these other compounds, there are some clear differences in the results, particularly with respect to quadrupolar coupling; these were smaller in the azaindolyl complexes, 5.5–6.8 MHz, while much larger in tetrahydrofurfuryloxide complexes, 19.6–19.9 MHz. Chemical shift data were unreported in ref. 51 as such influences on the acquired NMR spectra were no doubt negligible compared with the very large quadrupolar coupling; however, Aschenhurst et al. reported slightly higher  $^{27}\text{Al}$  chemical shifts of 43–56 ppm in azaindolyl complexes, compared with what has been found here. Of interest in the azaindolyl



**Fig. 2.** Triple-quantum MAS  $^{27}\text{Al}$  NMR spectra of the studied compounds acquired at 21.1 T with a spinning speed of 20.0 kHz. (a) compound **1**,  $\text{AlPcCl}$ ; (b) compound **2**,  $\text{AlPc}(\text{SPh})_4\text{Cl}$ ; and (c) compound **3**,  $\text{AlNcCl}$ . The unique Al sites are marked with numbers. The other peaks are spinning sidebands. To facilitate the interpretation of the spectrum, the chemical shift (CS) axis of gradient +1, and the quadrupole induced shift (QIS) axis with a gradient of  $-10/17$  are also drawn to scale.



**Fig. 3.** Experimental and simulated  $^{27}\text{Al}$  MAS NMR spectra of a powder sample of compound **3** acquired at three magnetic fields. Spinning rates are 20.0 kHz in (a) and (b), and 15.0 kHz in (c). The upper trace in (a) shows the simulation for each individual site, where site 1 is in blue and site 2 is in red. All simulated spectra were calculated using the parameters reported in Table 1.



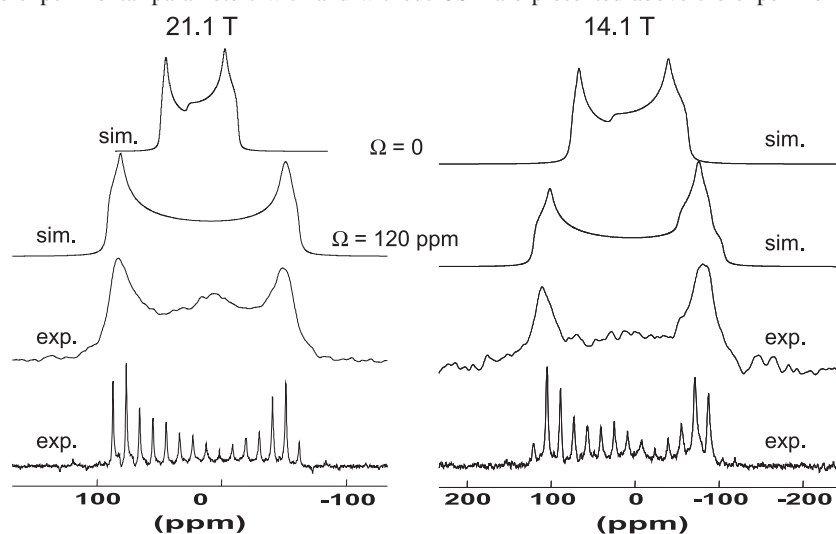
complexes is the apparent absence of any chemical shift anisotropy;  $^{27}\text{Al}$  NMR spectra obtained at 11.7 T could be simulated well without any inclusion of its effects. Clearly, in the square-pyramidal geometry encountered in the phthalocyanine complexes, chemical shift anisotropy has a much greater influence, a fact confirmed by both multiple-field NMR spectra and the computational chemistry results. This may be a reflection of the electron-rich nature of the macrocyclic ring or its rigid steric influence. Indeed, the  $^{27}\text{Al}$  chemical shift anisotropy measured for compound **3** and predicted for all compounds from calculations are the largest reported directly from  $^{27}\text{Al}$  NMR data of a solid material. The only anisotropies available in the literature that are

larger have been derived from gas-phase spin-rotation data for  $\text{AlNC}$  and  $\text{AlCl}$ , at 405.6 and 477.4 ppm, respectively.<sup>45</sup>

To gain more insight into the structure of compound **3** and to relate the experimental data to that structure, a series of quantum chemical calculations of the  $^{27}\text{Al}$  chemical shielding and EFG tensors were performed using a geometry-optimized model of this compound. The results of these calculations, using various basis sets at the RHF and B3LYP levels, are listed in Table 2. Also shown for comparison are the experimentally measured parameters for the major component (site 1) of this compound determined in the present solid-state study. A striking observation of the calculations is the lack of quantitative agreement between the experi-

**Table 1.** Experimental  $^{27}\text{Al}$  solid-state NMR data obtained from the MAS spectra of the three compounds studied.

Compound		Relative abundance (%)	$C_Q$ (MHz)	$\eta$	$\delta_{\text{iso}}$ (ppm)
<b>(1) AlPcCl</b>					
	Site 1	29.4±1.5	9.80±0.40	0.10±0.10	30.0±3.0
	Site 2	11.8±1.5	5.40±0.40	0.50±0.20	12.0±1.0
	Site 3	29.4±1.5	6.80±0.40	0.2±0.1	−12.0±1.0
	Site 4	29.4±1.5	9.10±0.20	0.25±0.15	−12.5±0.5
<b>(2) AlPc(SPh)<sub>4</sub>Cl</b>					
	Site 1	30.3±1.5	10.0±0.2	0.10±0.10	28.0±2.0
	Site 2	9.1±1.5	5.40±0.40	0.50±0.20	12.0±1.0
	Site 3	30.3±1.5	6.45±0.20	0.10±0.10	−12.5±1.0
	Site 4	30.3±1.5	7.40±0.20	0.10±0.10	−12.5±1.0
<b>(3) AlNcCl</b>					
	Site 1	90.9±2.0	9.80±0.10	0.10±0.10	27.0±1.0
	Site 2	9.1±2.0	5.40±0.40	0.50±0.20	12.0±1.0

**Fig. 4.** Experimental QCPMG and solid-echo  $^{27}\text{Al}$  NMR spectra of a stationary powder sample of compound **3** acquired at 21.1 and 14.1 T. Spectra simulated using the experimental parameters with and without CSA are presented above the experimental spectra.

mental and theoretical values of the  $^{27}\text{Al}$  quadrupolar coupling constant. For both the RHF and DFT methods, all of the calculated  $C_Q$  values are significantly smaller than the experimental value. The largest predicted value of 7.96 MHz, which is obtained with the RHF/6–311+G(2d, p) level, is 18% smaller than the lower experimental limit value of 9.70 MHz. The data also show that for a given basis set, the calculations using RHF and B3LYP methods give similar results for  $C_Q$ , with the former method giving slightly larger values. This indicates that electron correlation is not important for the system under study. The calculations also indicate that the sign of  $C_Q$  is positive. The value of  $C_Q$  is also observed to increase as the size of the basis set is increased. The discrepancy between the calculated and observed values of  $C_Q$ , and of other reported  $^{27}\text{Al}$  NMR parameters as well, may be due to the fact that the atomic coordinates used in the calculations were obtained from a computationally optimized model of the compound, and not from the more realistic single-crystal XRD structure (which

are unavailable for this compound). Other important factors that may cause such discrepancies originate from the fact that calculations were performed on a single isolated rigid molecule in the gas phase (no rovibrational averaging included) and do not take into account the long-range intermolecular interactions in the solid state (which are believed to be very small for the Al site at the centre of the molecule). Also, the limited sizes of the basis sets used may be a factor. It is particularly satisfying to note that theoretical calculations predict an EFG tensor that is nearly axially symmetric, as shown in the tabulated values of the quadrupolar asymmetry parameter  $\eta$ . These are in good agreement with the observed value of  $0.1 \pm 0.1$ , especially with the B3LYP method employing large basis sets. The calculated B3LYP results for  $\eta$  converge to the value of 0.16, in excellent accord with experiment.

Aside from the isotropic chemical shift values, both RHF and B3LYP calculations of the  $^{27}\text{Al}$  CS tensor parameters show very good agreement with experiment. Both methods

**Table 2.** Experimental and calculated  $^{27}\text{Al}$  solid-state NMR parameters of compound **3**.

Method	Basis set	$C_Q$ (MHz)	$\eta$	$\delta_{\text{iso}}$ (ppm)	$\Omega$ (ppm)	$\kappa$	$\alpha$ ( $^\circ$ )	$\beta$ ( $^\circ$ )	$\gamma$ ( $^\circ$ )
Experimental		$9.80 \pm 0.10$	$0.10 \pm 0.10$	$27.0 \pm 1.0$	$120 \pm 10$	$0.85 \pm 0.10$	$100 \pm 20$	$5 \pm 1$	$45 \pm 20$
RHF	6-31G**	5.13	0.36	41	81	0.87	90	15	90
	6-31++G**	5.76	0.33	43	84	0.87	90	15	90
	6-311G**	7.51	0.29	47	100	0.88	90	12	90
	6-311++G**	7.59	0.29	46	100	0.88	90	13	90
	6-311+G(2d, p)	7.96	0.27	47	101	0.88	90	12	90
B3LYP	6-31G**	4.84	0.21	37	104	0.94	90	10	90
	6-31++G**	5.31	0.20	38	101	0.94	90	10	90
	6-311G**	7.26	0.16	41	137	0.95	90	8	90
	6-311++G**	7.32	0.16	40	136	0.94	90	9	90
	6-311+G(2d, p)	7.58	0.16	41	136	0.94	90	8	90

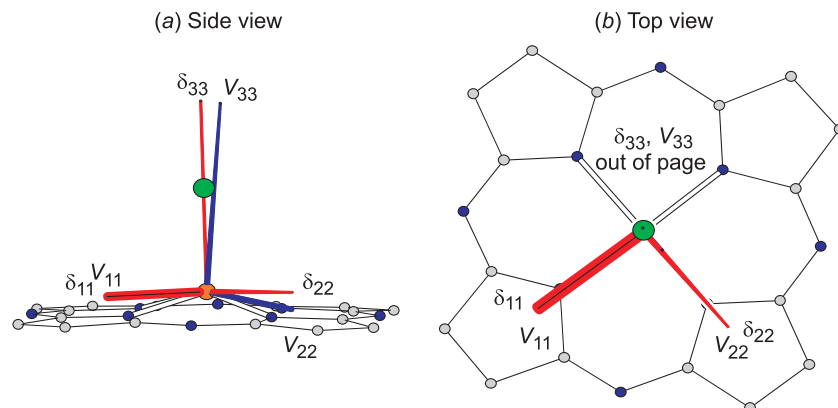
overestimate the isotropic chemical shift by at least 10 and 14 ppm for the B3LYP/6-31G\*\* and RHF/6-31G\*\* methods, respectively. With larger basis sets in both methods, the predicted values become even farther from that observed. The availability of an absolute shielding scale enables the most successful test of the ability of theoretical calculations to reproduce experimentally observed isotropic chemical shifts. In lieu of such a scale for  $^{27}\text{Al}$ , it is not surprising to find that the observed isotropic chemical shift,  $27.0 \pm 1.0$  ppm, is not well-reproduced by the calculations at both levels of theory. As mentioned in the Experimental section of this report, the calculated isotropic chemical shifts are derived by subtracting the calculated isotropic  $^{27}\text{Al}$  shielding constant in compound **3** from that in  $[\text{Al}(\text{H}_2\text{O})_6]^{3+}$ . Hence, the considerable difference between the predicted and observed values of  $\delta_{\text{iso}}$  is attributed to deficiencies in the geometrically optimized model of the reference cation. Geometry optimization using a larger basis set and (or) different theory than RHF (B3LYP or MP2) of this reference compound may be needed to establish better agreement between the experimental and calculated values of  $\delta_{\text{iso}}$ . Sykes et al. have reported a series of calculated isotropic shielding constants that converge near 613 ppm for  $[\text{Al}(\text{H}_2\text{O})_6]^{3+}$  at the RHF level<sup>77</sup> (an observation we have confirmed in our own calculations). Using their value as an absolute shielding reference for our calculated results gives  $\delta_{\text{iso}}$  values that are similar to those reported in Table 2, with values ranging from 20 to 47 ppm instead of 41 to 47 ppm at the RHF level, but, unsurprisingly, yields  $\delta_{\text{iso}}$  values that are in very poor agreement, ranging from 42 to 80 ppm at the B3LYP level (a different computational method) in going from the 6-31G\*\* to the 6-311+G(2d, p) basis sets. Our own results indicate a difference between the two computational methods, RHF vs. B3LYP, of calculating  $^{27}\text{Al}$  absolute chemical shielding ranging from 25 to 40 ppm, depending on the basis sets used.

As the size of the basis set is augmented, the calculated span of the aluminum CS tensor converges to a value of 100 ppm and 136 ppm at RHF and B3LYP levels, respectively. It is apparent that the DFT/B3LYP method yields span values that are closer to the observed one of  $120 \pm 10$  ppm than the RHF method. It is also interesting to find that both methods predict with high accuracy the skew of the aluminum CS tensor. All basis sets, in both methods, yield skew values that fall within the uncertainty limits indicated by the experimental value of  $0.85 \pm 0.10$ .

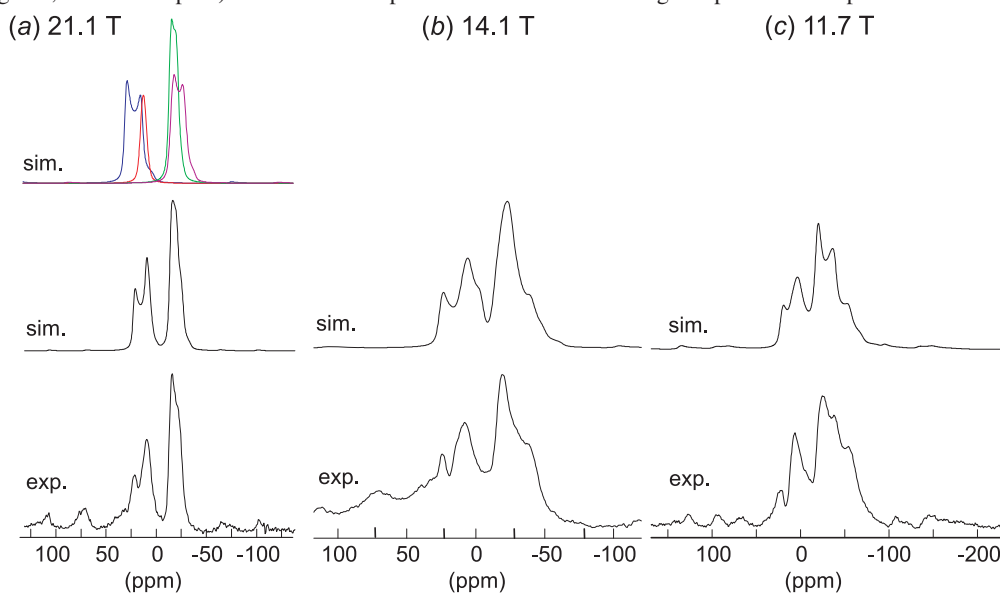
The calculated Euler angles, which define the rotations required to bring the PAS of the EFG tensor into coincidence with that of the CS tensor, are in good agreement with the experimental results at both levels of theory. In particular, calculations predict a small value for angle  $\beta$ , which is the angle between the largest EFG component ( $V_{33}$ ) and the most shielded CS component ( $\delta_{33}$ ), in close agreement with the observed value of  $5 \pm 1^\circ$ . Indeed, this is expected, as the observed and predicted pseudo-axial symmetry of both the EFG and CS tensors, with the skew of the latter being close to unity, dictate that approximate coincidence of their unique components,  $\delta_{33}$  and  $V_{33}$ . The absolute orientations of the  $^{27}\text{Al}$  EFG and CS tensors in the molecular framework, calculated at the B3LYP/6-311+G(2d, p) level, are shown in Fig. 5. The most shielded component of the chemical shift tensor,  $\delta_{33}$ , lies exactly along the Al–Cl bond axis, and the other two CS components,  $\delta_{11}$  and  $\delta_{22}$ , are perpendicular to it, and lie in the plane of the naphthalocyanine ring. The EFG tensor exhibits essentially the same orientation as the CS tensor, with  $V_{33}$  being  $8^\circ$  off the Al–Cl bond, and the other EFG components ( $V_{11}$  and  $V_{22}$ ) in the plane of the ring. On the basis of these results and the molecular structure of compound **3**, one can safely suggest that the Al–Cl bond acts as a pseudo- $C_4$  rotation axis, leading to aluminum being in an approximate square-pyramidal coordination environment. These orientations are in line with what has been observed in other phthalocyanine complexes with cobalt,<sup>11</sup> magnesium<sup>12</sup>, and gallium,<sup>13,14</sup> although ring geometry and coordination number can play an important role in the degree of axial symmetry displayed.

In contrast to the two sites observed in compound **3**, Figs. 2a and 2b reveal four distinct aluminum sites in each of compounds **1** and **2**. The presence of four non-equivalent sites, particularly for compound **1**, does not agree with its published crystal structure that reveals two unique and discrete  $\text{AlPcCl}$  molecules, in which each Al atom is involved in square-pyramidal coordination geometry.<sup>59</sup> Indeed, such disagreement is expected since the samples investigated here are in a poorly crystalline state. An attempt to understand the existence of additional sites in both compounds is discussed later in this report (vide infra). Estimated values for the isotropic chemical shift ( $\delta_{\text{iso}}$ ) and quadrupolar product ( $P_Q$ ) for each site in **1** and **2** were extracted from the sheared 3QMAS spectra using a combination of eq. [1] and the following equations for a spin-5/2 nucleus:<sup>78</sup>

**Fig. 5.** Calculated orientations of the  $^{27}\text{Al}$  chemical shift (in red) and electric field gradient (in blue) tensors in the molecular frame of compound **3**, as superimposed on views from the (a) side and (b) top. Only part of the molecular structure that depicts aluminum coordination environment is shown. Hydrogens are omitted for clarity. Aluminum is shown in orange, chlorine in green, nitrogen in blue, and carbon in grey.



**Fig. 6.** Experimental and simulated  $^{27}\text{Al}$  MAS NMR spectra of a powder sample of compound **1** acquired at three magnetic fields. Spinning rates are 20.0 kHz in (a) and (b), and 15.0 kHz in (c). The upper trace in (a) shows the simulation for each individual site (site 1: blue, site 2: red, site 3: green, and site 4: pink). All simulated spectra were calculated using the parameters reported in Table 1.



$$[2] \quad \delta_{\text{iso}} = \frac{17\delta_1 + 10\delta_2}{27}$$

$$[3] \quad P_Q = \nu_L \sqrt{-\frac{\delta_{\text{qis}}}{6000}} = \nu_L \sqrt{\frac{17(\delta_1 - \delta_2)}{162000}}$$

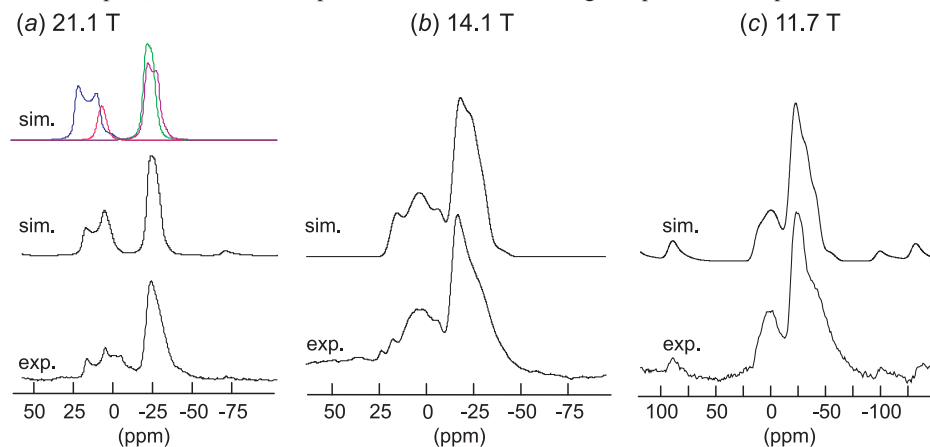
where  $\delta_1$  and  $\delta_2$  are the experimental chemical shifts of the centre of gravity of the peak in F1 and F2 dimensions of the sheared 3QMAS spectrum,  $\nu_L$  is the Larmor frequency,  $P_Q$  and  $\nu_L$  are in MHz, and  $\delta$  is in ppm. These estimated values were subsequently used in the simulation of the one-dimensional MAS spectra acquired at multiple fields. These spectra are shown in Figs. 6 and 7 for compounds **1** and **2**, respectively. The best-fit parameters obtained from the simultaneous simulation of the 1D MAS spectra at three fields are listed in Table 1.

Quantum chemical calculations were also performed on

compounds **1** and **2**, the results of which are given in Tables 3 and 4, respectively. Table 3 shows the calculated results obtained for the two  $\text{AlPcCl}$  molecules present in the asymmetric unit of compound **1**. Comparing these results with the experimental values obtained for site 1 of this compound, one observes fair agreement, within experimental error, between the experimental values of  $\delta_{\text{iso}}$ ,  $C_Q$ , and  $\eta$  and the calculated values at both the RHF and B3LYP levels. Most notably, the calculations predict an almost axially symmetric  $^{27}\text{Al}$  EFG tensor, in perfect accord with experiment. The same can be said about the predicted results of compound **2**, as shown in Table 4. The B3LYP calculations accurately reflect the experimental value of  $0.10 \pm 0.10$  for  $\eta$  observed for site 1 of **2** at all basis sets used, though it should be noted that they were carried out on a geometrically optimized model of **2** and not on an actual crystal structure, as none exists.



**Fig. 7.** Experimental and simulated  $^{27}\text{Al}$  MAS NMR spectra of a powder sample of compound **2** acquired at three magnetic fields. Spinning rates are 20.0 kHz in (a) and (b), and 15.0 kHz in (c). The upper trace in (a) shows the simulation for each individual site (site 1: blue, site 2: red, site 3: green, and site 4: pink). All simulated spectra were calculated using the parameters reported in Table 1.



**Table 3.** Calculated  $^{27}\text{Al}$  solid-state NMR parameters of compound **1**.

Method	Basis set	$C_Q$ (MHz)	$\eta$	$\delta_{\text{iso}}$ (ppm)	$\Omega$ (ppm)	$\kappa$	$\alpha$ ( $^\circ$ )	$\beta$ ( $^\circ$ )	$\gamma$ ( $^\circ$ )
<b>Molecule 1</b>									
RHF	6-31G**	6.07	0.10	33	102	0.98	158	1	21
	6-31++G**	6.77	0.09	36	106	0.97	145	0.7	29
	6-311G**	8.94	0.07	39	122	0.98	130	0.6	24
	6-311++G**	9.01	0.07	37	122	0.98	121	0.6	38
	6-311+G(2d, p)	9.39	0.07	39	124	0.98	117	0.6	41
B3LYP	6-31G**	5.83	0.09	33	108	0.98	7	1	172
	6-31++G**	6.38	0.08	43	109	0.92	35	0.8	169
	6-311G**	8.68	0.07	38	141	0.98	171	0.6	159
	6-311++G**	8.74	0.07	37	141	0.98	175	0.8	159
	6-311+G(2d, p)	9.01	0.07	38	141	0.98	173	0.6	159
<b>Molecule 2</b>									
RHF	6-31G**	7.51	0.09	34	99	0.97	133	2.5	39
	6-31++G**	8.24	0.08	36	104	0.95	138	2	32
	6-311G**	10.67	0.06	39	120	0.96	133	1.6	26
	6-311++G**	10.75	0.06	38	120	0.96	132	1.6	27
	6-311+G(2d, p)	11.13	0.06	39	122	0.96	134	1.5	25
B3LYP	6-31G**	7.10	0.08	33	106	0.97	134	2.3	40
	6-31++G**	7.68	0.08	35	106	0.95	116	2	59
	6-311G**	10.24	0.06	38	139	0.97	132	1.5	27
	6-311++G**	10.31	0.06	35	140	0.96	125	1.4	33
	6-311+G(2d, p)	10.58	0.06	37	140	0.96	128	1.4	32

**Table 4.** Calculated  $^{27}\text{Al}$  solid-state NMR parameters of compound **2**.

Method	Basis set	$C_Q$ (MHz)	$\eta$	$\delta_{\text{iso}}$ (ppm)	$\Omega$ (ppm)	$\kappa$	$\alpha$ ( $^\circ$ )	$\beta$ ( $^\circ$ )	$\gamma$ ( $^\circ$ )
RHF	6-31G**	5.39	0.35	39	86	0.87	87	14	93
	6-31++G**	6.05	0.31	41	91	0.88	87	13	93
	6-311G**	7.80	0.28	45	107	0.88	87	11	93
	6-311++G**	7.90	0.28	43	106	0.88	87	11	93
	6-311+G(2d, p)	8.25	0.27	44	106	0.88	87	11	93
B3LYP	6-31G**	5.11	0.21	35	108	0.94	86	9	94
	6-31++G**	5.64	0.19	37	107	0.94	86	9	93
	6-311G**	7.55	0.16	39	142	0.94	86	7	94
	6-311++G**	7.63	0.16	37	143	0.94	86	7	94
	6-311+G(2d, p)	7.88	0.16	38	142	0.94	86	7	94

**Table 5.** Calculated  $^{27}\text{Al}$  solid-state NMR parameters of a theoretical octahedral model of compound **1**, in which an additional axial chlorine is coordinated to Al.

Method	Basis set	$C_Q$ (MHz)	$\eta$	$\delta_{\text{iso}}$ (ppm)	$\Omega$ (ppm)	$\kappa$	$\alpha$ ( $^\circ$ )	$\beta$ ( $^\circ$ )	$\gamma$ ( $^\circ$ )
RHF	6-31G**	9.02	0.14	-15	33	0.83	91	0	89
	6-31++G**	10.05	0.13	-7	38	0.86	86	0	94
	6-311G**	12.62	0.13	+5	45	0.87	90	0	90
	6-311++G**	12.66	0.13	+7	48	0.88	91	0	89
	6-311+G(2d, p)	12.82	0.13	+8	46	0.87	90	0	90
B3LYP	6-31G**	7.99	0.08	+3	45	0.95	85	0	95
	6-31++G**	8.66	0.07	+8	34	0.93	125	0	55
	6-311G**	11.34	0.07	-1	74	0.97	92	0	88
	6-311++G**	11.31	0.07	0	59	0.96	97	0	83
	6-311+G(2d, p)	11.43	0.07	-1	52	0.96	102	0	78

**Table 6.** Calculated  $^{27}\text{Al}$  solid-state NMR parameters of a theoretical octahedral model of compound **1**, in which an additional axial  $\text{H}_2\text{O}$  is coordinated to Al.

Method	Basis set	$C_Q$ (MHz)	$\eta$	$\delta_{\text{iso}}$ (ppm)	$\Omega$ (ppm)	$\kappa$	$\alpha$ ( $^\circ$ )	$\beta$ ( $^\circ$ )	$\gamma$ ( $^\circ$ )
RHF	6-31G**	7.48	0.03	+3	76	0.99	174	1	74
	6-31++G**	8.15	0.02	+18	85	0.98	175	2	5
	6-311G**	9.87	0.02	+8	93	0.99	176	1	83
	6-311++G**	9.95	0.02	+16	93	0.99	176	1	85
	6-311+G(2d, p)	10.29	0.02	+17	94	0.99	175	1	84
B3LYP	6-31G**	7.36	0.02	+8	75	0.99	176	2	13
	6-31++G**	7.77	0.02	+17	80	0.92	174	2	7
	6-311G**	9.43	0.02	+14	106	0.99	177	2	88
	6-311++G**	9.52	0.02	+13	106	0.99	176	2	80
	6-311+G(2d, p)	9.76	0.02	+13	106	0.99	173	2	87

In light of this successful agreement between experiment and calculation for the major component of **3**, attempts were then made to use calculated predictions to guide interpretation of both the impurity peak common to all three compounds and to the additional sites apparent in compounds **1** and **2**. On the basis of both the simulated best-fit parameters for these additional sites, as given in Table 1, with  $^{27}\text{Al}$  chemical shifts falling in the expected range for octahedral Al species, and the chemical nature of these related dye molecular frameworks, it was appropriate to focus on possible octahedral derivatives of the parent penta-coordinate species. Calculated results were obtained for optimized structures composed of the original species with an additional axial ligand, either Cl or  $\text{H}_2\text{O}$ , completing the octahedral coordination of Al by occupying the empty site below the phthalocyanine ring. These calculated results are given in Tables 5 and 6. While exact agreement is not possible, it is clear that the trends are consistent with two likely assignments: sites 3 and 4 of compounds **1** and **2** are likely associated with additional Cl ligands interacting with the central Al, resulting in a low-frequency movement of the  $^{27}\text{Al}$  chemical shift to approximately -12 ppm; and site 2 of all three compounds is likely associated with a different ligand, possibly  $\text{H}_2\text{O}$  or another light coordinating atom (OH,  $\text{NH}_3$ , and so forth) resulting in a  $^{27}\text{Al}$  chemical shift near 10 ppm. In each case, it seems quite clear that a completion of the octahedral coordination sphere of Al may be responsible for the additional components.

## Conclusions

A combination of solid-state  $^{27}\text{Al}$  NMR experiments and quantum chemical calculations has been used to study anisotropic  $^{27}\text{Al}$  NMR interaction tensors in three commercially obtained aluminum-centered phthalocyanine dyes. The  $^{27}\text{Al}$  CS and EFG tensors, including their relative orientations, were determined for aluminum-2,3-naphthalocyanine chloride. The span of the aluminum chemical shift tensor in this compound is the largest measured directly by  $^{27}\text{Al}$  SSNMR spectroscopy. RHF and DFT calculations have provided more insight into the  $^{27}\text{Al}$  CS and EFG tensors, and their orientation with respect to the molecular frame, indicating that their largest components,  $\delta_{33}$  and  $V_{33}$ , are perpendicular to the macrocyclic ring of this compound. The use of a 21.1 T NMR spectrometer has offered an excellent opportunity for visible manifestation of the aluminum chemical shift anisotropy in experiments performed on stationary polycrystalline samples. In addition, the use of such an ultrahigh-field magnet, combined with the state-of-art triple-quantum MAS experiment, was vital for the resolution of the different non-equivalent aluminum sites present in powder samples of the three related compounds.

## Supplementary data

Supplementary data for this article are available on the journal Web site ([canjchem.nrc.ca](http://canjchem.nrc.ca)) or may be purchased from the Depository of Unpublished Data, Document Deliv-

ery, CISTI, National Research Council Canada, Ottawa, ON K1A 0R6, Canada. DUD 5313. For more information on obtaining material, refer to [cisti-icist.nrc-cnrc.gc.ca/cms/unpub\\_e.shtml](http://cisti-icist.nrc-cnrc.gc.ca/cms/unpub_e.shtml).

## Acknowledgements

The authors are grateful to the Natural Sciences and Engineering Research Council (NSERC) of Canada for financial support through Discovery and Equipment Grants to W.P.P. Access to the 900 MHz NMR spectrometer was provided by the National Ultrahigh-Field NMR Facility for Solids (Ottawa, Canada), a national research facility funded by the Canada Foundation for Innovation, the Ontario Innovation Trust, Recherche Québec, the National Research Council Canada, and Bruker BioSpin and managed by the University of Ottawa ([www.nmr900.ca](http://www.nmr900.ca)). NSERC is acknowledged for a Major Resources Support grant. Dr. Victor Terskikh and Dr. Eric Ye are thanked for NMR spectrometer assistance and for helpful remarks. We also thank Mr. Michael J. Ditty, Mrs. Janet Venne, and Dr. Claude Lemaire for their assistance on the NMR spectrometers at the University of Waterloo.

## References

- (1) Thomas, A. L. *Phthalocyanine Research and Applications*; CRC Press: Boston, 1990.
- (2) Kadish, K. M.; Smith, K. M.; Guillard, R., Eds. *The Porphyrin Handbook*; Academic Press: San Diego, 2003; Vol. 17–19.
- (3) Leznoff, C. C.; Lever, A. B. P., Eds. *Phthalocyanines Properties and Applications*; VCH Publishers: New York, 1996; Vol. 1–4.
- (4) Berezin, B. D. *Coordination Compounds of Porphyrins and Phthalocyanines*; John Wiley & Sons: New York, 1981.
- (5) McKeown, N. B. *Phthalocyanine Materials: Structure, Synthesis and Function*; Cambridge University Press: Cambridge, 1998.
- (6) Jiang, J.; Kasuga, K.; Arnold, D. P. In *Supramolecular Photosensitive and Electroactive Materials*; Nalwa, H. S., Ed.; Academic Press: New York, 2001; p. 113.
- (7) Schultz, H.; Lehmann, H.; Rein, M.; Hanack, M. *Structure and Bonding*. **1991**, 74, 41.
- (8) de la Torre, G.; Claessens, C. G.; Torres, T. *Chem. Commun. (Camb.)* **2007**, (20): 2000. doi:10.1039/b614234f. PMID: 17713062.
- (9) Kadish, K. M.; Smith, K. M.; Guillard, R., Eds. *The Porphyrin Handbook*, Vol. 5; Academic Press: San Diego, 2003.
- (10) Leznoff, C. C.; Lever, A. B. P., Eds. *Phthalocyanines Properties and Applications*, Vol. 2; VCH Publishers: New York, 1993.
- (11) Medek, A.; Frydman, V.; Frydman, L. *J. Phys. Chem. A* **1999**, 103 (25), 4830. doi:10.1021/jp990410d.
- (12) Wong, A.; Ida, R.; Mo, X.; Gan, Z.; Poh, J.; Wu, G. *J. Phys. Chem. A* **2006**, 110 (33), 10084. doi:10.1021/jp061350w. PMID: 16913682.
- (13) Tang, J. A.; O'Dell, L. A.; Aguiar, P. M.; Lucier, B. E.; Sakellariou, D.; Schurko, R. W. *Chem. Phys. Lett.* **2008**, 466 (4–6), 227. doi:10.1016/j.cplett.2008.10.044.
- (14) O'Dell, L. A.; Schurko, R. W. *Chem. Phys. Lett.* **2008**, 464 (1–3), 97. doi:10.1016/j.cplett.2008.08.095.
- (15) Kentgens, A. P. M. *Geoderma* **1997**, 80 (3–4), 271. doi:10.1016/S0016-7061(97)00056-6.
- (16) MacKenzie, K. J. D.; Smith, M. E. *Multinuclear Solid-State NMR of Inorganic Materials*; Pergamon Press: Amsterdam, 2002. Chap. 2–3.
- (17) Akit, J. W. *Prog. Nucl. Magn. Reson. Spectrosc.* **1989**, 21 (1–2), 1. doi:10.1016/0079-6565(89)80001-9.
- (18) Pyykkö, P. *Mol. Phys.* **2008**, 106 (16), 1965. doi:10.1080/00268970802018367.
- (19) Vega, A. J. In *Encyclopedia of Nuclear Magnetic Resonance*. Edited by D.M. Grant and R.K. Harris. Vol. 6. John Wiley & Sons, Chichester, UK. p. 3869. 1996.
- (20) Baugher, J. F.; Taylor, P. C.; Oja, T.; Bray, P. J. *J. Chem. Phys.* **1969**, 50 (11), 4914. doi:10.1063/1.1670988.
- (21) Cheng, J. T.; Edwards, J. C.; Ellis, P. D. *J. Phys. Chem.* **1990**, 94 (2), 553. doi:10.1021/j100365a014.
- (22) Power, W. P.; Wasylshen, R. E.; Mooibroek, S.; Pettitt, B. A.; Danchura, W. *J. Phys. Chem.* **1990**, 94 (2), 591. doi:10.1021/j100365a019.
- (23) MacKenzie, K. J. D.; Smith, M. E. *Multinuclear Solid-State NMR of Inorganic Materials*; Pergamon Press: Amsterdam, 2002. Chap. 5.
- (24) Lee, S. K.; Stebbins, J. F. *J. Phys. Chem. B* **2000**, 104 (17), 4091. doi:10.1021/jp994273w.
- (25) Züchner, L.; Chan, J. C. C.; Müller-Warmuth, W.; Eckert, H. *J. Phys. Chem. B* **1998**, 102 (23), 4495. doi:10.1021/jp980587s.
- (26) Chan, J. C. C.; Bertmer, M.; Eckert, H. *J. Am. Chem. Soc.* **1999**, 121 (22), 5238. doi:10.1021/ja983385i.
- (27) van Bokhoven, J. A.; Koningsberger, D. C.; Kunkeler, P.; van Bekkum, H.; Kentgens, A. P. M. *J. Am. Chem. Soc.* **2000**, 122 (51), 12842. doi:10.1021/ja002689d.
- (28) Lentz, P.; Carvalho, A. P.; Delevoye, L.; Fernandez, C.; Amoureux, J. P.; Nagy, J. B. *Magn. Reson. Chem.* **1999**, 37 (13), S55. doi:10.1002/(SICI)1097-458X(199912)37:13<S55::AID-MRC564>3.0.CO;2-F.
- (29) Chen, T. H.; Wouters, B. H.; Grobet, P. J. *J. Phys. Chem. B* **1999**, 103 (30), 6179. doi:10.1021/jp990215z.
- (30) Kentgens, A. P. M.; Iuga, D.; Kalwei, M.; Koller, H. *J. Am. Chem. Soc.* **2001**, 123 (12), 2925. doi:10.1021/ja005917c. PMID: 11456997.
- (31) Bodart, P. R.; Amoureux, J. P.; Pruski, M.; Bailly, A.; Fernandez, C. *Magn. Reson. Chem.* **1999**, 37 (13), S69. doi:10.1002/(SICI)1097-458X(199912)37:13<S69::AID-MRC533>3.0.CO;2-8.
- (32) Ashbrook, S. E.; Whittle, K. R.; Le Pollès, L.; Farnan, I. *J. Am. Ceram. Soc.* **2005**, 88 (6), 1575. doi:10.1111/j.1551-2916.2005.00294.x.
- (33) Ashbrook, S. E.; MacKenzie, K. J. D.; Wimperis, S. *Solid State Nucl. Magn. Reson.* **2001**, 20 (3–4), 87. doi:10.1006/snmr.2001.0032. PMID: 11846239.
- (34) Alemany, L. B.; Steuernagel, S.; Amoureux, J. P.; Callender, R. L.; Barron, A. R. *Solid State Nucl. Magn. Reson.* **1999**, 14 (1), 1. doi:10.1016/S0926-2040(99)00011-9. PMID: 10408271.
- (35) Alemany, L. B.; Callender, R. L.; Barron, A. R.; Steuernagel, S.; Iuga, D.; Kentgens, A. P. M. *J. Phys. Chem. B* **2000**, 104 (49), 11612. doi:10.1021/jp002066m.
- (36) Rocha, J. *J. Chem. Soc. Chem. Commun.* **1998**, 2489.
- (37) Rocha, J. *J. Phys. Chem. B* **1999**, 103 (44), 9801. doi:10.1021/jp991516b.
- (38) Rocha, J.; Morais, C. M.; Fernandez, C. *Clay Miner.* **2003**, 38 (3), 259. doi:10.1180/0009855033830094.
- (39) Smith, M. E. *Appl. Magn. Reson.* **1993**, 4 (1–2), 1. doi:10.1007/BF03162555.
- (40) Kemp, T. F.; Smith, M. E. *Solid State Nucl. Magn. Reson.* **2009**, 35 (4), 243. doi:10.1016/j.ssnmr.2008.12.003. PMID: 19186033.

- (41) Neuville, D. R.; Cormier, L.; Montouillout, V.; Florian, P.; Millot, F.; Rifflet, J. C.; Massiot, D. *Am. Mineral.* **2008**, *93* (11-12), 1721. doi:10.2138/am.2008.2867.
- (42) Neuville, D. R.; Cormier, L.; Massiot, D. *Geochim. Cosmochim. Acta* **2004**, *68* (24), 5071. doi:10.1016/j.gca.2004.05.048.
- (43) Frydman, L.; Harwood, J. S. *J. Am. Chem. Soc.* **1995**, *117* (19), 5367. doi:10.1021/ja00124a023.
- (44) Medek, A.; Harwood, J. S.; Frydman, L. *J. Am. Chem. Soc.* **1995**, *117* (51), 12779. doi:10.1021/ja00156a015.
- (45) Schurko, R. W.; Wasylishen, R. E.; Foerster, H. *J. Phys. Chem. A* **1998**, *102* (48), 9750. doi:10.1021/jp982367k.
- (46) Ashenhurst, J.; Wu, G.; Wang, S. *J. Am. Chem. Soc.* **2000**, *122* (11), 2541. doi:10.1021/ja992868z.
- (47) Ashenhurst, J.; Wang, S.; Wu, G. *J. Am. Chem. Soc.* **2000**, *122* (14), 3528. doi:10.1021/ja993613o.
- (48) Utz, M.; Nandagopal, M.; Mathai, M.; Papadimitrakopoulos, F. *Appl. Phys. Lett.* **2003**, *83* (19), 4023. doi:10.1063/1.1623945.
- (49) Nishiyama, Y.; Fukushima, T.; Takami, K.; Kusaka, Y.; Yamazaki, T.; Kaji, H. *Chem. Phys. Lett.* **2009**, *471* (1-3), 80. doi:10.1016/j.cplett.2009.02.012.
- (50) Schurko, R. W.; Hung, I.; Macdonald, C. L. B.; Cowley, A. H. *J. Am. Chem. Soc.* **2002**, *124* (44), 13204. doi:10.1021/ja020394p. PMID:12405849.
- (51) Tang, J. A.; Masuda, J. D.; Boyle, T. J.; Schurko, R. W. *ChemPhysChem* **2006**, *7* (1), 117. doi:10.1002/cphc.200500343. PMID:16404763.
- (52) Cheng, J. T.; Ellis, P. D. *J. Phys. Chem.* **1989**, *93* (6), 2549. doi:10.1021/j100343a061.
- (53) Larsen, F. H.; Jakobsen, H. J.; Ellis, P. D.; Nielsen, N. C. *J. Phys. Chem. A* **1997**, *101* (46), 8597. doi:10.1021/jp971547b.
- (54) Amoureux, J. P.; Fernandez, C.; Steuernagel, S. *J. Magn. Reson. A* **1996**, *123* (1), 116. doi:10.1006/jmra.1996.0221. PMID:8980071.
- (55) Bak, M.; Rasmussen, J. T.; Nielsen, N. C. *J. Magn. Reson.* **2000**, *147* (2), 296. doi:10.1006/jmre.2000.2179. PMID:11097821.
- (56) Massiot, D.; Fayon, F.; Capron, M.; King, I.; Le Calvé, S.; Alonso, B.; Durand, J.-O.; Bujoli, B.; Gan, Z.; Hoatson, G. *Magn. Reson. Chem.* **2002**, *40* (1), 70. doi:10.1002/mrc.984.
- (57) Frisch, M. J.; Trucks, G. W.; Schlegel, H. B.; Scuseria, G. E.; Robb, M. A.; Cheeseman, J. R.; Montgomery, J. A., Jr.; Vreven, T.; Kudin, K. N.; Burant, J. C.; Millam, J. M.; Iyengar, S. S.; Tomasi, J.; Barone, V.; Mennucci, B.; Cossi, M.; Scalmani, G.; Rega, N.; Petersson, G. A.; Nakatsuji, H.; Hada, M.; Ehara, M.; Toyota, K.; Fukuda, R.; Hasegawa, J.; Ishida, M.; Nakajima, T.; Honda, Y.; Kitao, O.; Nakai, H.; Klene, M.; Li, X.; Knox, J. E.; Hratchian, H. P.; Cross, J. B.; Bakken, V.; Adamo, C.; Jaramillo, J.; Gomperts, R.; Stratmann, R. E.; Yazyev, O.; Austin, A. J.; Cammi, R.; Pomelli, C.; Ochterski, J. W.; Ayala, P. Y.; Morokuma, K.; Voth, G. A.; Salvador, P.; Dannenberg, J. J.; Zakrzewski, V. G.; Dapprich, S.; Daniels, A. D.; Strain, M. C.; Farkas, O.; Malick, D. K.; Rabuck, A. D.; Raghavachari, K.; Foresman, J. B.; Ortiz, J. V.; Cui, Q.; Baboul, A. G.; Clifford, S.; Cioslowski, J.; Stefanov, B. B.; Liu, G.; Liashenko, A.; Piskorz, P.; Komaromi, I.; Martin, R. L.; Fox, D. J.; Keith, T.; Al-Laham, M. A.; Peng, C. Y.; Nanayakkara, A.; Challacombe, M.; Gill, P. M. W.; Johnson, B.; Chen, W.; Wong, M. W.; Gonzalez, C.; Pople, J. A. *Gaussian 03*, Revision C.02; Gaussian, Inc.: Wallingford, CT, 2004.
- (58) This work was made possible by the facilities of the Shared Hierarchical Academic Research Computing Network (SHARCNET: www.sharcnet.ca).
- (59) Hasegawa, M.; Sato, N. *Mol. Cryst. Liq. Cryst. (Phila. Pa.)* **1997**, *296* (1), 409. doi:10.1080/10587259708032337.
- (60) Engel, M. K. In *The Porphyrin Handbook*; Kadish, K. M., Smith, K. M., and Guillard, R., Eds.; Vol. 20; Academic Press: San Diego, 2003 p. 223.
- (61) Becke, A. D. *J. Chem. Phys.* **1993**, *98* (7), 5648. doi:10.1063/1.464913.
- (62) Lee, C.; Yang, W.; Parr, R. G. *Phys. Rev. B* **1988**, *37* (2), 785. doi:10.1103/PhysRevB.37.785.
- (63) Ditchfield, R. *Mol. Phys.* **1974**, *27* (4), 789. doi:10.1080/00268977400100711.
- (64) Wolinski, K.; Hinton, J. F.; Pulay, P. *J. Am. Chem. Soc.* **1990**, *112* (23), 8251. doi:10.1021/ja00179a005.
- (65) Adiga, S.; Aebi, D.; Bryce, D. L. *Can. J. Chem.* **2007**, *85*, 496. doi:10.1139/V07-069.
- (66) Harris, R. K.; Becker, E. D.; Cabral de Menezes, S. M.; Granger, P.; Hoffman, R. E.; Zilm, K. W. *Pure Appl. Chem.* **2008**, *80* (1), 59. doi:10.1351/pac200880010059.
- (67) Mason, J. *Solid State Nucl. Magn. Reson.* **1993**, *2* (5), 285. doi:10.1016/0926-2040(93)90010-K. PMID:7804782.
- (68) Duer, M. J. *Introduction to Solid-State NMR Spectroscopy*; Blackwell Science: Oxford, 2004; Chap. 5.
- (69) Amoureux, J. P.; Fernandez, C.; Granger, P. In *Multinuclear Magnetic Resonance in Liquids and Solids – Chemical Applications*, NATO ASI Series C, Vol. 322; Granger, P. and Harris, R. K., Eds. Kluwer Academic Publishers: Dordrecht, 1990; Chap. XXII.
- (70) Samoson, A. *Chem. Phys. Lett.* **1985**, *119* (1), 29. doi:10.1016/0009-2614(85)85414-2.
- (71) Arfken, G. *Mathematical Methods for Physicists*, 3rd ed.; Academic Press: New York, 1985.
- (72) Fernandez, C.; Amoureux, J. P.; Chezeau, J. M.; Delmotte, L.; Kessler, H. *Microporous Mater.* **1996**, *6* (5-6), 331. doi:10.1016/0927-6513(96)00040-5.
- (73) Fyfe, C. A.; Meyer zu Altenschildesche, H.; Wong-Moon, K. C.; Grondy, H.; Chezeau, J. M. *Solid State Nucl. Magn. Reson.* **1997**, *9* (2-4), 97. doi:10.1016/S0926-2040(97)00049-0. PMID:9477440.
- (74) Jansen, S. R.; Hintzen, H. T.; Metselaar, R.; de Haan, J. W.; van de Ven, L. J. M.; Kentgens, A. P. M.; Nachtegaal, G. H. *J. Phys. Chem. B* **1998**, *102* (31), 5969. doi:10.1021/jp981224v.
- (75) Schmücker, M.; Schneider, H. *J. Sol-Gel Sci. Technol.* **1999**, *15* (3), 191. doi:10.1023/A:1008786023100.
- (76) Bryant, P. L.; Harwell, C. R.; Wu, K.; Fronczek, F. R.; Hall, R. W.; Butler, L. G. *J. Phys. Chem. A* **1999**, *103* (27), 5246. doi:10.1021/jp990374i.
- (77) Sykes, D.; Kubicki, J. D.; Farrar, T. C. *J. Phys. Chem. A* **1997**, *101* (14), 2715. doi:10.1021/jp963891z.
- (78) Amoureux, J. P.; Huguenard, C.; Engelke, F.; Taulelle, F. *Chem. Phys. Lett.* **2002**, *356* (5-6), 497. doi:10.1016/S0009-2614(02)00398-6.



# 1D and 2D NMR investigations of the interaction between oppositely charged polymers and surfactants

Aleisha A. McLachlan and D. Gerrard Marangoni

**Abstract:** Proton chemical shifts and two-dimensional COSY and NOE spectroscopy (NOESY) experiments have been used to examine the interaction of various oppositely charged surfactant and polyelectrolyte systems, namely, the cationic surfactant dodecyltrimethylammonium bromide (DTAB) and a series of alkanediyl- $\alpha,\omega$ -bis(alkyldimethylammonium bromide) surfactants (Gem 12-*s*-12, where *s* is the length of the methylene spacer group) with the anionic polyelectrolyte poly(styrene sulfonate) or PSS. In all cases, we observe substantial aromatic-solute-induced chemical shifts (ASIS) in the surfactant peaks of the polymer/surfactant complexes versus that of the pure surfactant spectra. In the case of the DTAB/PSS system, the chemical-shift changes as a function of changing ratio of surfactant to polymer are interpreted in terms of structural changes that occur in the complex with increasing polymer concentration. For the Gem 12-*s*-12/PSS systems, the interaction of these gemini surfactants with the anionic polyelectrolyte, as deduced from the interpretation of the  $^1\text{H}$  ASIS shifts and the NOESY cross peaks, is dependent on the length of the methylene spacer. From the NOESY experiments, we observed significant NOESY cross peaks that correlated well with the expected mechanism of interaction as observed in the literature for the single-tailed surfactant/polymer system. NMR techniques are shown to provide information on the molecular arrangement of these molecules in aqueous solution.

**Key words:** polymers, surfactants, complexes, ASIS experiments, 2D NOESY.

**Résumé :** On a fait appel à des expériences déplacements chimiques du proton et de spectroscopie de corrélation bidimensionnelle (« COSY ») et de spectroscopie d'effets Overhauser nucléaire (NEOSY) pour étudier l'interaction entre divers systèmes formés d'un agent de surface et de polyélectrolytes de charges opposés, en particulier de micelles cationiques de l'agent de surface dodécyltriméthylammonium (DTAB) et une série de bromures d'alcanediyl- $\alpha,\omega$ -bis(alkyldiméthylammonium) (Gem 12-*s*-12 dans lesquels *s* correspond à la longueur du groupe espaceur méthylène) avec le polyélectrolyte anionique sulfonate de poly(styrène), SPS. Dans tous les cas, on observe d'importants déplacements anisotropiques induits par le solvant (DAIS) dans les pics des complexes polymère/agent de surface par rapport aux spectres de l'agent de surface pur. Dans le cas du système DTAB/SPS, les changements dans le déplacement chimique en fonction d'un changement dans le rapport d'agent de surface au polymère sont interprétés en fonction de changements structuraux qui se produisent dans le complexe avec une augmentation dans la concentration du polymère. Pour les systèmes Gem 12-*s*-12/SPS, l'interaction entre ces agents de surface jumeaux avec le polyélectrolyte anionique, telle que déduite de l'interprétation des déplacements anisotropiques induits par le solvant pour le  $^1\text{H}$  et des croisements de pics (NEOSY), est dépendante de la longueur de l'espaceur méthylène. À partir des expériences (NEOSY), on a observé des croisements de pics (NEOSY) importants qui donnent une bonne corrélation avec le mécanisme attendu d'interaction tel qu'observé dans la littérature pour le seul système agent de surface polymère étudié. On a donc démontré que les techniques de la RMN peuvent fournir de l'information relative à l'arrangement moléculaire de ces molécules dans une solution aqueuse.

**Mots-clés :** polymères, agents de surface, complexes, déplacements anisotropiques induits par le solvant (DAIS), spectroscopie d'effets Overhauser nucléaire bidimensionnelle (NEOSY).

[Traduit par la Rédaction]

## Introduction

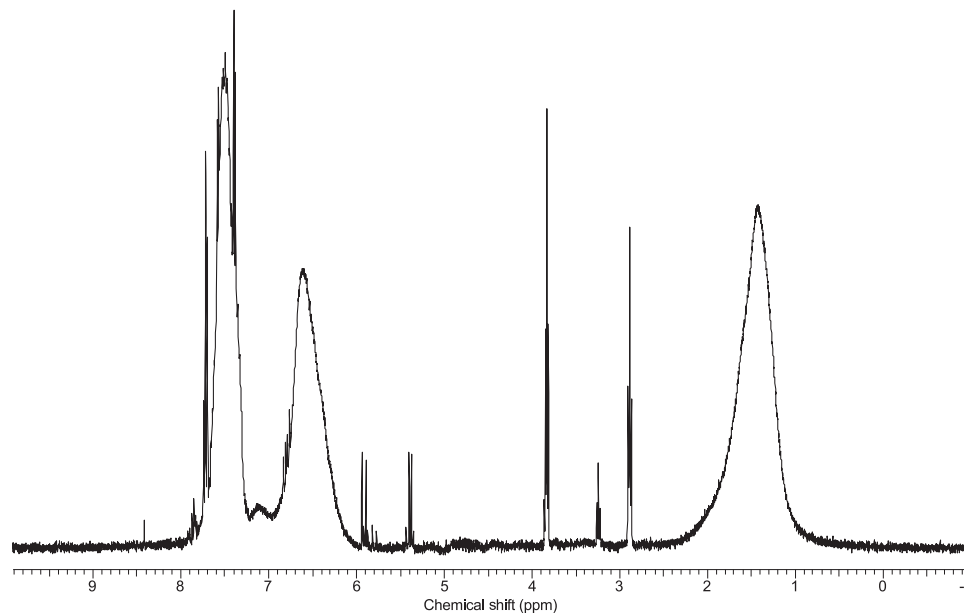
The interaction of polymers and surfactants has received a substantial amount of attention in the literature from both an academic and an industrial standpoint.<sup>1–28</sup> The manner in

which surfactants bind to polymers is critically dependent on the charges of the polymers and the surfactants. Oppositely charged polymer/surfactant complexes have been shown to be extremely surface-active, as evidenced by the efficient lowering of surface tension at very low concentrations of surfactant and polymer. Much of the literature has focused on the determination of the binding isotherms of the surfactants to the polymers via electromotive force measurements, NMR relaxation and chemical-shift studies, luminescence probing experiments, calorimetry, and partition-constant determinations. For example, the interactions between poly(styrenesulfonate) (PSS) and dodecyltrimethylammonium bromide (DTAB) have been investigated by sur-

Received 18 May 2009. Accepted 7 October 2009. Published on the NRC Research Press Web site at canjchem.nrc.ca on 19 January 2010.

A.A. McLachlan and D.G. Marangoni.<sup>1</sup> Department of Chemistry, St Francis Xavier University, P.O. Box 5000, Antigonish, NS B2G 2W5, Canada.

<sup>1</sup>Corresponding author (e-mail: g\_marangoni@colloid.stfx.ca).

**Fig. 1.**  $^1\text{H}$  NMR spectrum for the system 0.116 mol/L PSS.

factant-selective electrodes,<sup>29,30</sup> luminescence probing,<sup>31</sup> and NMR spectroscopy.<sup>32,33</sup>

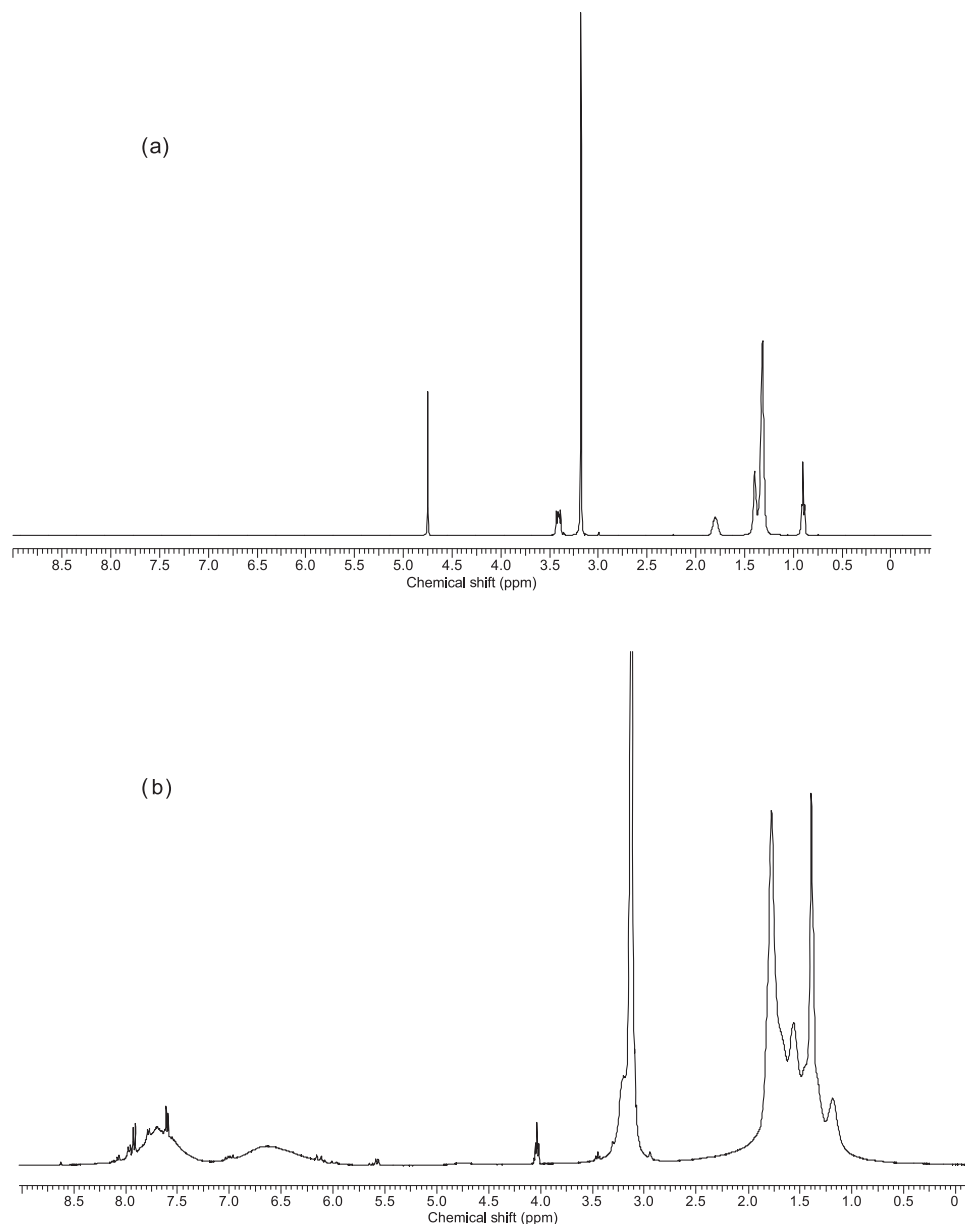
Dimeric and oligomeric surfactants are novel surfactants that are presently attracting considerable interest from both academic and industrial research groups. The term gemini surfactant, coined by Menger,<sup>34</sup> has become accepted in the surfactant literature for describing dimeric surfactants, that is, surfactant molecules that have two hydrophilic (chiefly ionic) groups and two tails per surfactant molecule.<sup>35</sup> Gemini surfactants possess a number of superior properties when compared with conventional single-headed, single-tailed surfactants, such as lower cmc values (by at least an order of magnitude) and increased surface activity ( $C_{20}$ ),<sup>36–38</sup> in addition to improved hard-water tolerance, superior wetting times, and better cold-water solubility. Cationic gemini surfactants of the *m-2-m* type have been investigated with luminescence probing and neutron scattering.<sup>39</sup> In all cases, the results are consistent with the combination of electrostatic and hydrophobic interactions being the driving forces in the formation of the polymer/surfactant aggregates.

A number of surfactant formulations often contain water-soluble polymers and additional surfactants. In most studies of polymer/surfactant systems, the binding of the surfactant to the polymers is discussed in terms of the nature and types of interactions; these depend greatly on the nature of the surfactant and polymer. Cooperative binding always occurs above a surfactant concentration referred to as *cac* (critical aggregation concentration), which is lower than the value of the surfactant cmc in a polymer-free system.<sup>29,30,40–42</sup> With surfactant/nonionic polymers, the *cac* is usually only slightly smaller than the cmc of the surfactant.<sup>43</sup> With ionic polymers like PSS, the *cac* can be as much as 100 to 1000 times smaller than the cmc.<sup>40</sup> Although a number of papers have examined the cooperativity of polymer/surfactant binding using various techniques, there are very few papers in the literature where detailed spectroscopic information is used to assess the manner in which these systems self-assemble.<sup>33,44</sup>

In the case of the *m-2-m* gemini surfactants/PSS systems, synergistic lowering of the surface tension at very low surfactant concentrations was observed, due to the electrostatic interactions between the positive surfactant head groups and sulfonate groups of the polymer.<sup>39</sup> This leads to both the surfactant and polymer adsorbing at the air/water interface, and forming highly surface-active complexes. However, the adsorption of gemini surfactants at the air/water interface depends greatly on the spacer length,<sup>37</sup> which would indicate that the manner in which gemini surfactants complex with PSS would also depend on spacer length.

Aromatic-solute-induced chemical shifts (ASIS effects) have been shown to be sensitive indicators of the structure in micellar and polymer/surfactant systems.<sup>44–48</sup> When coupled with two-dimensional nuclear Overhauser enhancement experiments (2D NOESY),  $^1\text{H}$  NMR experiments have been shown to provide significant information on both the intra- and inter-molecular proximity of protons.<sup>49</sup> There are a few papers in the literature dealing with the application of the 2D NOESY technique to probe micellar solubilization and polymer/surfactant systems.<sup>48–52</sup> In the case of oppositely charged surfactants and polymers, a detailed analysis of NOESY cross peaks should yield significant insights into the manner in which the polymer and surfactant interact with each other forming complexes and mixed micellar systems. In this paper, we report our results on the changes in the  $^1\text{H}$  NMR chemical shifts that occur when cationic surfactants are bound to the anionic polymer sodium poly(styrenesulfonate). The cationic surfactant systems investigated were (a) dodecyltrimethylammonium bromide (DTAB) and (b) alkanediyl- $\alpha,\omega$ -bis(alkyldimethylammonium bromide) (12-*s*-12). In all cases, we observe significant ASIS effects in the 1D NMR spectra. For the gemini cationic surfactants, the NMR chemical shifts indicate that the manner in which the gemini surfactants self-assemble with the polymer is dependent on the spacer length of the surfactant. The cross-peaks between the polymer and the surfactant protons in the NOESY con-

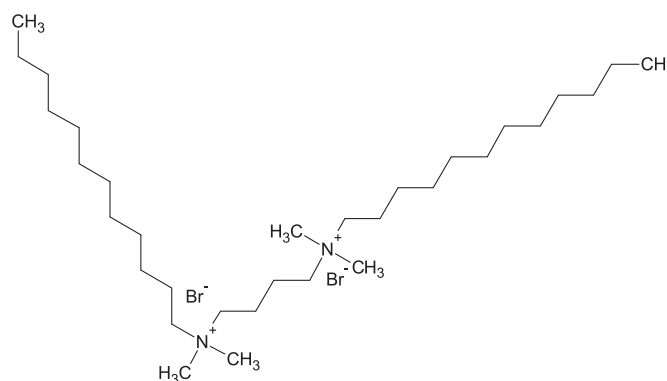
**Fig. 2.**  $^1\text{H}$  NMR spectrum for (a) 0.065 mol/L DTAB; (b) 0.065 mol/L DTAB/0.232 mol/L PSS.



four plots are consistent with the electrostatic interactions between the surfactant and polymer chains dominating the complex formation in micellar solution.

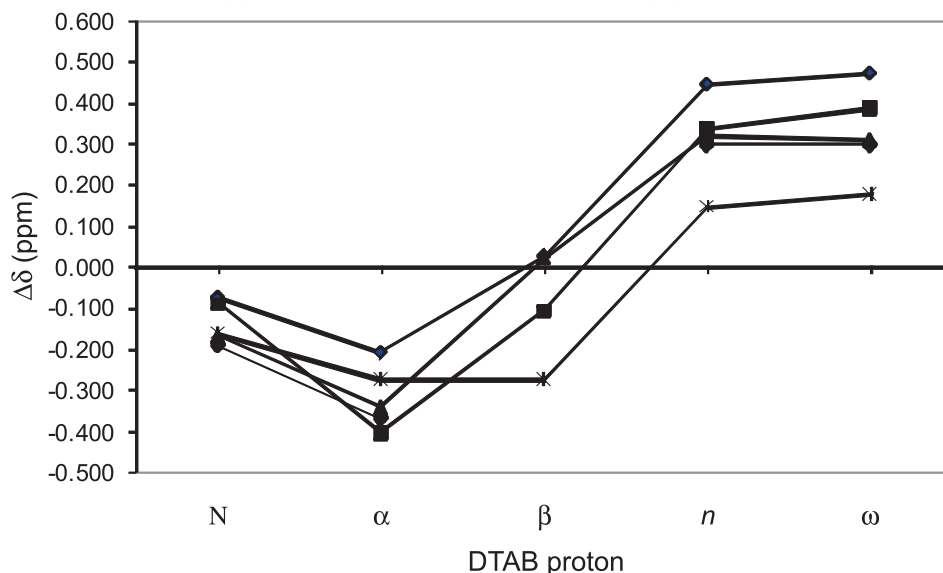
## Experimental

Dodecyltrimethylammonium bromide (DTAB) was obtained from the Sigma Chemical Company, and it was purified by at least three recrystallizations from an acetone/ethanol mixture. The gemini surfactants 12-*s*-12 were prepared by refluxing 2 mol equivalents of *N,N*-dimethyldodecyl amine (with a 10% excess) with the appropriate  $\alpha,\omega$ -dibromoalkane in either acetone or acetonitrile. The shorter spacer surfactants were recrystallized from acetonitrile, while the longer spacer gemini surfactants were recrystallized from acetone. The purity of the surfactants was confirmed by MS. The structure of the 12-4-12 gemini surfactant is given below.



High purity sodium poly(styrene sulfonate) was from Aldrich Chemical Company with a molecular mass of about

**Fig. 3.** Changes in proton chemical shifts of DTAB upon formation of DTAB/PSS aggregates ( $\Delta\delta = \delta(\text{DTAB/PSS}) - \delta(\text{DTAB})$ ) for varying concentrations and ratios of DTAB/PSS. (◆) 0.033 mol/L DTAB/0.116 mol/L PSS. (▲) 0.065 mol/L DTAB/0.116 mol/L PSS. (■) 0.065 mol/L DTAB/0.232 mol/L PSS. (\*) 0.130 mol/L DTAB/0.232 mol/L PSS. (●) Literature values from ref. 33.



70 000 g/mol; D<sub>2</sub>O (99.8%) was purchased from Aldrich or CDN Isotopes.

The 1D and 2D NMR spectra (<sup>1</sup>H) for the polymer/surfactant systems were obtained on a Bruker Avance 500 NMR spectrometer operating at 500.13 MHz for protons at the Atlantic Region Magnetic Resonance Centre (ARMRC) at Dalhousie University, or a Bruker Avance-II 400 NMR spectrometer operating at 400.13 MHz at St. Francis Xavier University. A typical <sup>1</sup>H spectrum for the system 0.116 mol/L PSS (in terms of the monomer concentration) is given in Fig. 1. The <sup>1</sup>H spectra were referenced to the HOD peak, which was assigned a value of  $\delta = 4.750$  ppm. For the phase-sensitive 2D NOESY spectra, 128 transients of either 8 or 16 scans over 512 complex data points were acquired with suppression of the HOD peak at 4.75 ppm. The mixing times were varied between 0.20 s and 1.5 s, and the delay times were kept fixed at 5.0 s. The data were zero-filled once in dimension 1 and multiplied by a shifted sine-bell function in F1 and F2 before transformation. Stock solutions of the surfactants and the polymers were prepared in sample vials; the appropriate quantities of the stock solutions were transferred to NMR tubes in the presence of a small amount of NaCl. All prepared solutions were clear and stable towards precipitation.

## Results and discussion

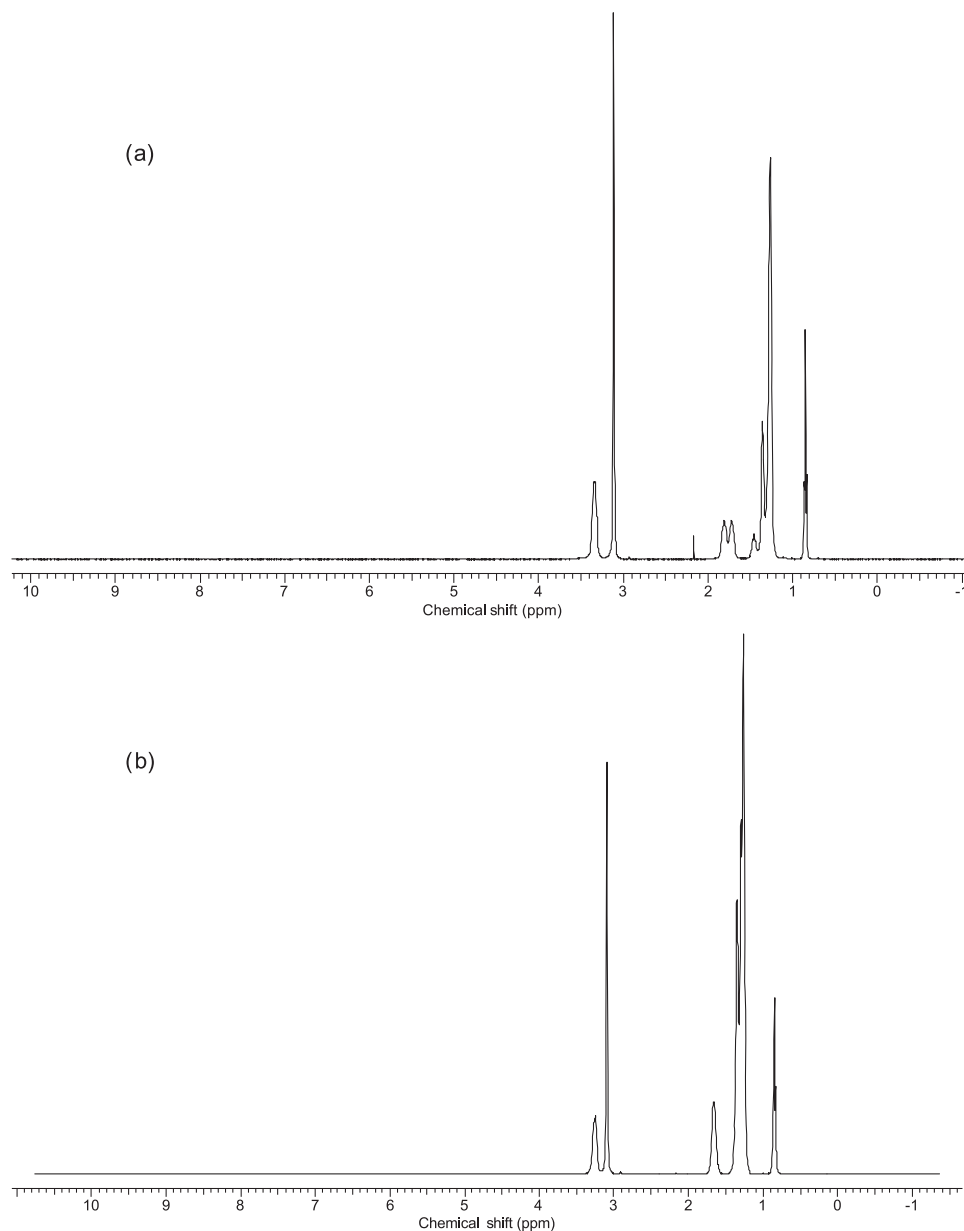
### <sup>1</sup>H chemical-shift changes

In Fig. 2, the <sup>1</sup>H NMR spectrum of a 0.065 mol/L DTAB solution is compared to the spectrum of the same concentration of surfactant mixed with 0.232 mol/L PSS. Significant broadening is seen in the DTAB resonances in the presence of the polymer, which is consistent with the NMR work of Gao et al.<sup>32</sup> We also note that there are considerable high- and low-frequency shifts for the DTAB protons in the polymer/surfactant complex, due to the presence of the aromatic head group in the polymer. Figure 3 gives the chemical-shift

differences for the protons of the DTAB surfactant in the presence and absence of the PSS polymer at various ratios of the polymer to surfactant concentrations. The intermolecular ring current shifts we observe here for the system 0.065 mol/L DTAB/0.116 mol/L PSS (i.e., at a polymer/surfactant ratio of 4:1) are identical to those reported by Gao et al.<sup>32,33</sup> In these oppositely charged polyelectrolyte/surfactant systems, the positively charged surfactant head groups are expected to be in the vicinity of the negatively charged aromatic head group; this will lead to large ring-current shifts for the chain protons on the surfactant molecules as well as for the  $-\text{CH}_3$  protons located in the surfactant head group. We note that for most of the concentrations of polymer and surfactant studied here, large high-frequency shifts are observed for the chain protons and the  $\omega$ -methyl protons, whereas large low-frequency shifts are obtained for the  $\alpha$ ,  $N$ -methyl, and  $\beta$  protons of the DTAB surfactant chain. We note that the magnitudes of the shift changes are almost identical at all the concentrations of polymer and surfactant investigated here, indicating that the microstructure of the polymer/surfactant complex does not vary significantly with changing amounts of polymer or surfactant. For the 0.130 mol/L DTAB/0.232 mol/L PSS system, high-frequency shifts are again observed for  $\omega$ -methyl protons and the chain protons, and low-frequency shifts are obtained for the  $\alpha$ ,  $\beta$ , and the  $N$ -methyl protons. However, it is worth noting that the magnitudes of the shift differences for all protons except the  $\beta$  protons are smaller than the shift differences observed for the other DTAB/PSS systems investigated here. This is consistent with a change in the orientation of the surfactant protons on DTAB with respect to the plane of the aromatic ring on the PSS backbone for the complex, due to a saturation of the polymer with surfactant chains or the interaction of small micelles with the polyanion.

The sign and the magnitude of aromatic-ring-current shifts are dependent on the orientation of the aromatic ring plane with respect to the various DTAB protons. For exam-

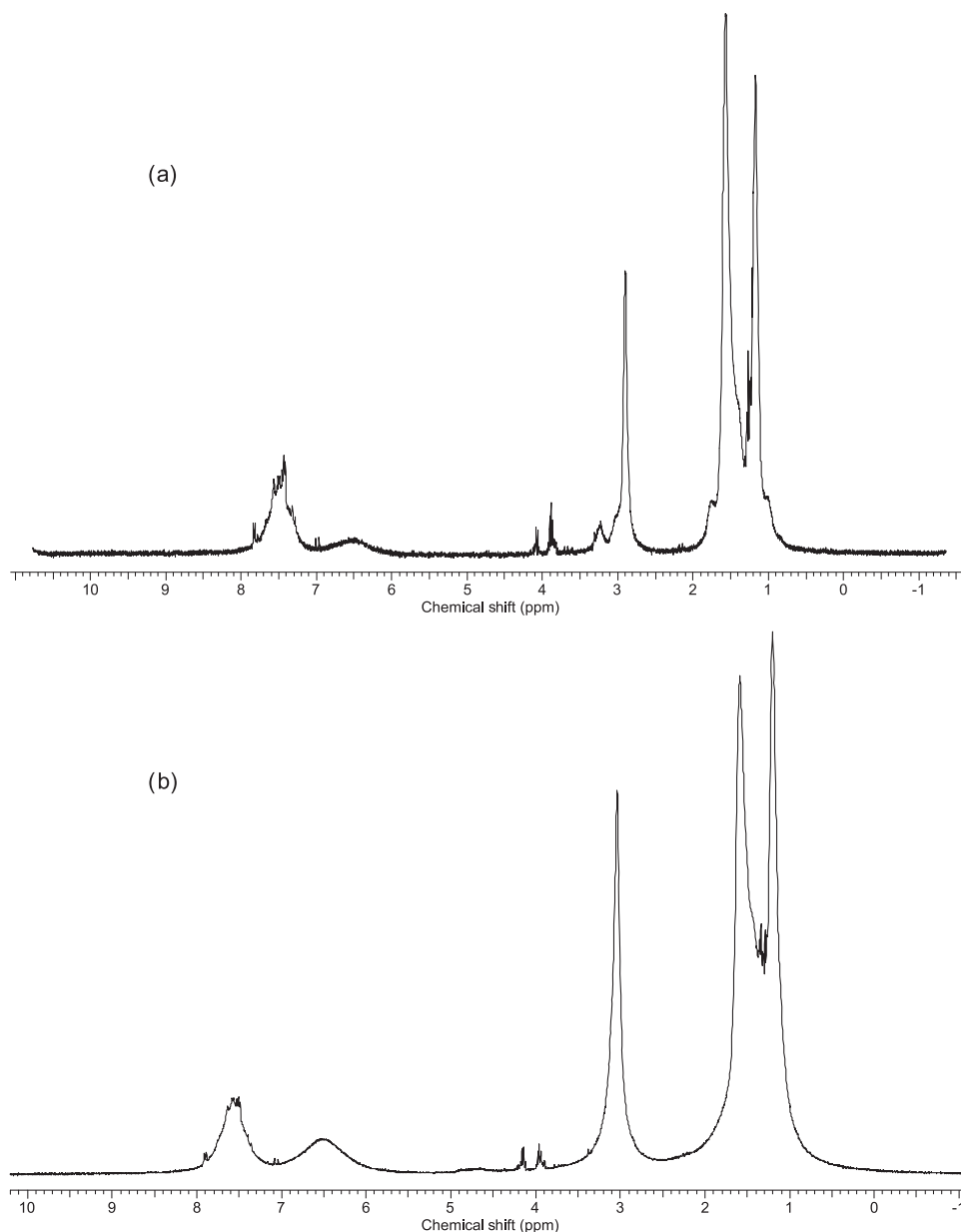


**Fig. 4.**  $^1\text{H}$  NMR spectrum for (a) 0.010 mol/L 12-5-12; (b) 0.0070 mol/L 12-12-12.

ple, if the protons on the DTAB chain are, on average, in the plane of the aromatic ring, their shielding constant is decreased and the result is a high-frequency chemical-shift change. On the other hand, if the average orientation of the protons is above the plane of the aromatic rings, their shielding constant is increased and a low-frequency shift change results. Hence, we can interpret Fig. 3 in terms of the structure of the polymer/surfactant aggregates. According to Gao et al.<sup>33</sup> and Abuin and Scaiano,<sup>31</sup> at the concentrations of surfactant and polymer investigated in this paper, we would expect that the aggregate sizes are small with the micelles interacting with the hydrophobic phenyl ring of the polymer. Hence, the large high-frequency shifts for the protons nearest the surfactant head group are consistent with the surfactant head group electrostatically interacting with the polyelectrolyte, while the  $\omega\text{-CH}_3$  and the chain protons

( $n$ -protons) are on average located in the plane of the aromatic group. We note that in most cases, as the ratio of the surfactant to polymer concentration is changed, the similarity in the ring-current shifts for the DTAB head-group protons indicates that the average orientation of the surfactant with respect to the polymer is essentially unchanged. This is in good agreement with the results of Gao et al.<sup>32,33</sup> However, the large differences in the ring-current shifts for the  $\beta$  protons in the 0.130 mol/L DTAB/0.232 mol/L PSS suggest that the environment of the DTAB protons is different at that concentration from the other complexes investigated here. This is consistent with a difference in the structure of the complexes as the amount of surfactant increases. Abuin and Scaiano<sup>31</sup> have stated that for higher ratios of polymer to surfactant, most of the surfactant ( $\geq 90\%$ ) is polymer-bound. Hence, in the case of the highest concentration of

**Fig. 5.**  $^1\text{H}$  NMR spectrum for (a) 0.010 mol/L 12-5-12/0.055 mol/L PSS; (b) 0.0070 mol/L 12-12-12/ 0.055 mol/L PSS.



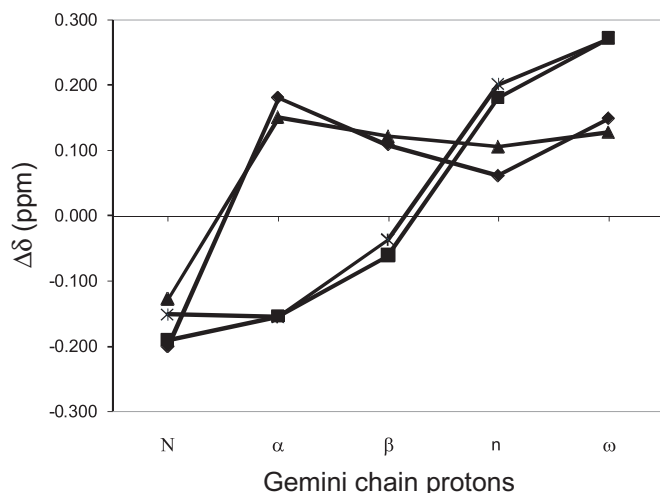
surfactant investigated here, the presence of additional amphiphile molecules likely leads to an almost complete saturation of the polymer, with the remaining surfactant self-assembling into free micelles. This is consistent with the fact that the magnitudes of all the chemical-shift differences for DTAB are somewhat reduced in this system, as the solutions will consist of a mixture of polymer/surfactant complexes of slightly larger surfactant aggregation numbers and some free-surfactant micelles. As the exchange between the complexes and the free micelles will be fast on the NMR timescale, the averaged NMR spectrum will reflect the distribution of surfactant molecules between the bound complexes and free micelles. The increase in the aggregation number of the surfactant in the polymer/surfactant complexes, coupled with the appearance of free micelles, leads to a more micelle-like environment in the complex with a

corresponding change in the ASIS chemical-shift profiles as a function of the surfactant concentration.

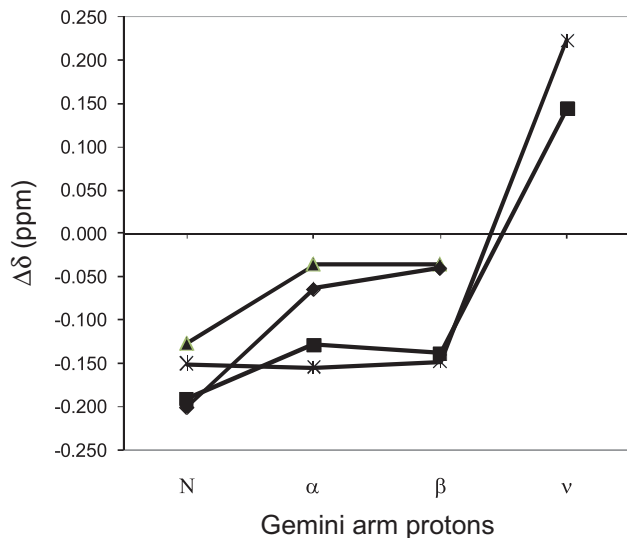
Typical  $^1\text{H}$  NMR spectra for the gemini surfactants 0.010 mol/L 12-5-12 and 0.0070 mol/L 12-12-12 are shown in Fig. 4. Indicated on the Figures are the chemical shifts of the protons on the 12-carbon chains of the gemini surfactants and in the  $n$ -methylene spacer groups.  $^1\text{H}$  NMR spectra for the same concentrations of both surfactants in a 0.055 mol/L solution of PSS are presented in Fig. 5. We can again clearly see that there are large ASIS effects induced for both the chain protons and for the spacer protons of the gemini surfactants in the presence of the anionic polyelectrolyte.

The  $^1\text{H}$  chemical shifts for the chain protons of the 12-s-12/PSS systems are presented in Fig. 6. From the plot of the  $\Delta\delta$  of the chain protons, we observe that there are differences in the manner in which the gemini surfactants in-

**Fig. 6.** Changes in proton chemical shifts of 12-*s*-12 gemini surfactant chain protons upon formation of 12-*s*-12/PSS aggregates ( $\Delta\delta = \delta(12\text{-}s\text{-}12/\text{PSS}) - \delta(12\text{-}s\text{-}12)$ ). (◆) 0.010 mol/L 12-4-12/0.055 mol/L PSS. (▲) 0.010 mol/L 12-5-12/0.055 mol/L PSS. (■) 0.0070 mol/L 12-10-12/0.055 mol/L PSS. (☆) 0.0070 mol/L 12-12-12/0.055 mol/L PSS.



**Fig. 7.** Changes in proton chemical shifts of 12-*s*-12 gemini surfactant spacer protons upon formation of 12-*s*-12/PSS aggregates ( $\Delta\delta = \delta(12\text{-}s\text{-}12/\text{PSS}) - \delta(12\text{-}s\text{-}12)$ ). (◆) 0.010 mol/L 12-4-12/0.055 mol/L. (▲) 0.010 mol/L 12-5-12/0.055 mol/L PSS. (■) 0.0070 mol/L 12-10-12/0.055 mol/L PSS. (☆) 0.0070 mol/L 12-12-12/0.055 mol/L PSS.



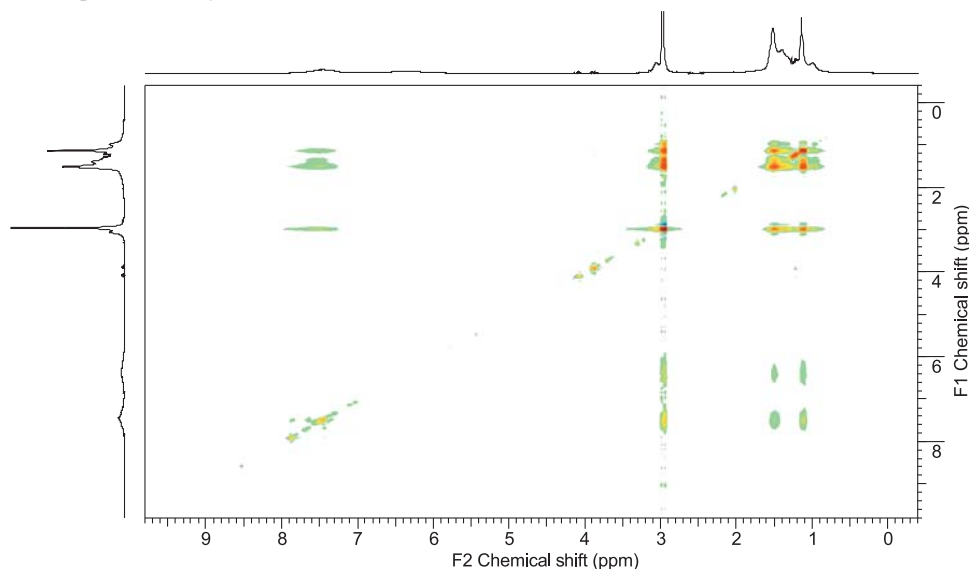
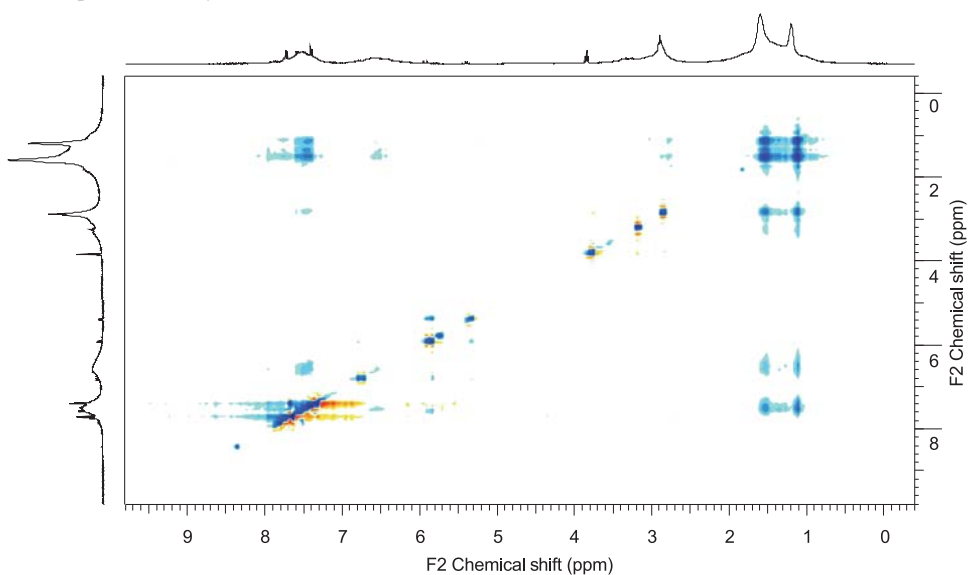
interact with the polyelectrolyte as a function of the length of the methylene spacer. For the shorter-spacer gemini surfactants 12-4-12 and 12-5-12, we note that the magnitude of the shift of the *N*-methyl protons is comparable to that of both DTAB and the longer-spacer gemini surfactants, whereas the chemical-shift differences for the  $\alpha$ -chain and the  $\beta$ -chain protons of the surfactant are different for the shorter- and longer-chain spacer gemini surfactants. This indicates that the manner in which the gemini surfactants self-assemble with the polyelectrolyte is different for short-

spacer gemini surfactants from longer-spacer gemini amphiphiles. In fact, when we examine the chemical-shift patterns for the chains of the longer-spacer gemini surfactants, they are identical to those of the DTAB/PSS systems shown above. This is consistent with the longer-spacer gemini surfactants self-assembling with the polyelectrolyte in a manner similar to DTAB, indicating that with the longer-spacer-length gemini surfactants, there is enough distance between the surfactant head groups that they behave essentially independently and are easily able to interact with adjacent PSS monomers on the polymer.

The chemical-shift differences for the spacer protons are presented in Fig. 7. We note that for the short-spacer-length gemini surfactants (12-4-12 and 12-5-12), very small changes are observed for the  $\alpha$  and  $\beta$  protons. However, as the spacer length increases (i.e., for 12-10-12 and 12-12-12), we note that the  $\Delta\delta$  values for the  $\alpha$ - and  $\beta$ -chain protons become more negative, indicating that the first few spacer protons are likely more constrained for the short gemini spacers than for the longer spacers. Given the short spacer length in the 12-4-12 and the 12-5-12 surfactants, when the cationic head groups interact with adjacent sulfonate groups on the polymer chain, this will lead to a more rigid environment for the spacer protons on the short-spacer gemini surfactants, keeping them in intimate contact with the aromatic chains. For the long-spacer gemini surfactants, the positive shift difference for those spacer protons in the middle of the chain indicate that they are outside of the ring current set up by the circulating  $\pi$  electrons, leading to a high-frequency shift for those protons. This would be consistent with the protons in the middle of the long-spacer chain having considerably more freedom of movement than the spacer protons of the short chains. We would expect that given the short spacer length of the 12-4-12 and the 12-5-12 system, the interactions with the two head groups of the gemini surfactant with the sulfonate groups on adjacent monomers would lead to crowding of the benzene rings on adjacent monomers in the complex; this steric crowding would lead to a decrease in the entropy of the system and would contribute to destabilization of the complex. For the long-spacer gemini surfactants, given the freedom of motion of the two chains that make up the cationic gemini surfactant, the reduction of the steric crowding in the complex would lead to an increase of the binding constants over those of the short-spacer gemini amphiphiles. We are currently determining the binding contacts for these species using emf measurements; they will be reported in a future publication. It should be noted that similar results were observed by Wettig et al. for the interaction of gemini surfactants of differing spacer lengths with DNA; their results indicated that the spacer length of the gemini impacted the manner in which cationic head groups were able to interact with negatively charged moieties at the surface of the DNA biopolymer. These subtle differences in binding resulted in differing transfection efficiencies for differing spacer lengths of their gemini-surfactant-based nanoparticles.<sup>53</sup>

### NOESY spectra

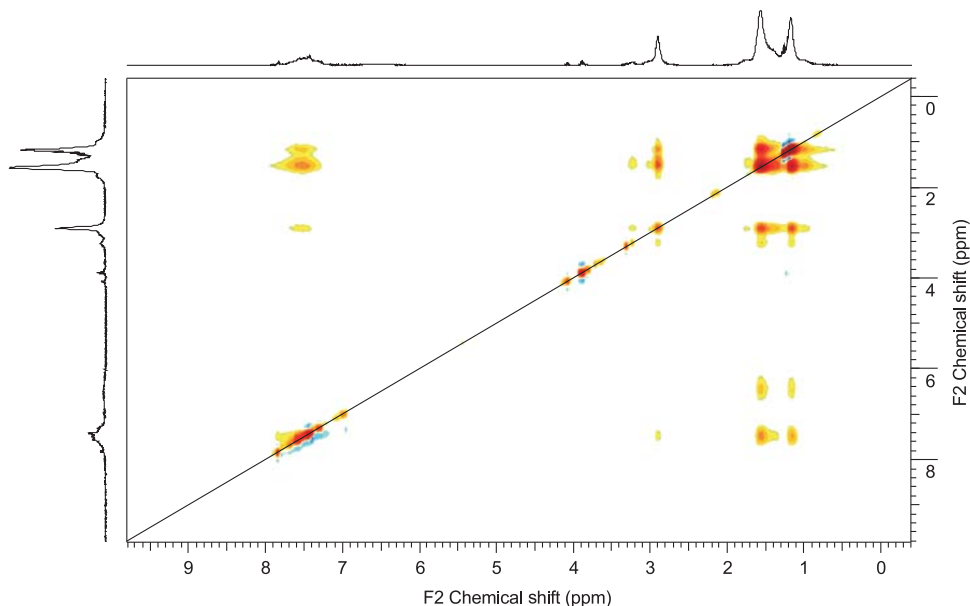
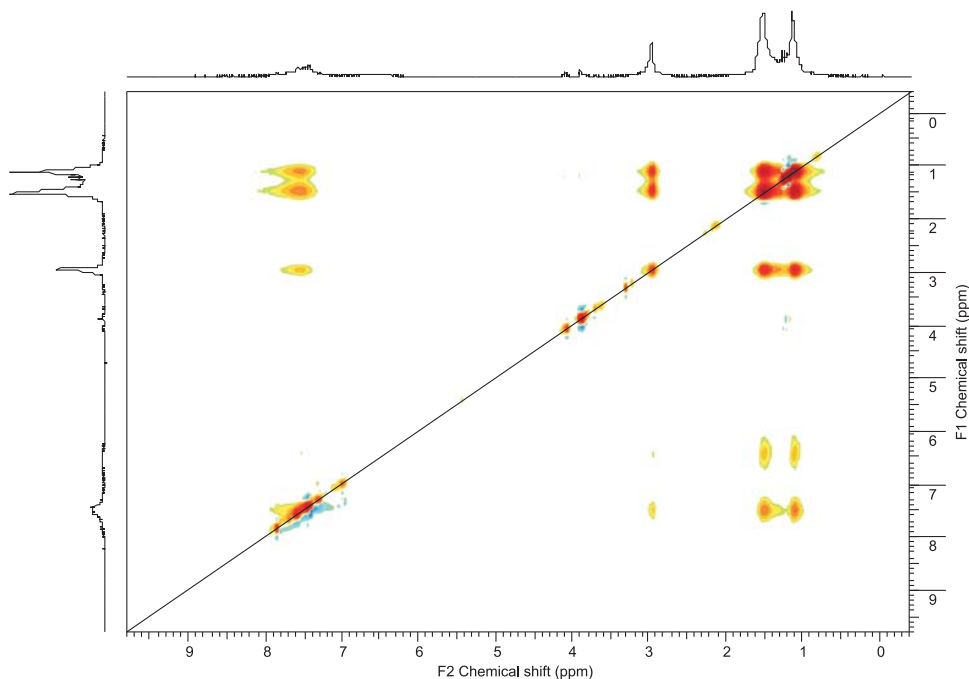
NMR NOESY experiments were performed for the following systems: 0.065 mol/L DTAB/0.116 mol/L PSS (Fig. 8), 0.010 mol/L 12-4-12/0.055 mol/L PSS (Fig. 9), 0.010 mol/L

**Fig. 8.** 2D NOESY contour plot for the system 0.065 mol/L DTAB/0.117 mol/L PSS.**Fig. 9.** 2D NOESY contour plot for the system 0.010 mol/L 12-4-12/0.055 mol/L PSS.

12-5-12/0.055 mol/L PSS (Fig. 10), 0.0070 mol/L 12-10-12/0.055 mol/L PSS (Fig. 11), 0.0070 mol/L 12-12-12/0.055 mol/L PSS (Fig. 12). 2D NOESY experiments have been shown to give excellent insights into the nature of the self-assembly process in a number of aggregated systems.<sup>48,50,52,54,55</sup> When we examine the NOESY contour plots for the system 0.065 mol/L DTAB /0.116 mol/L PSS (Fig. 8), it is clear that significant cross peaks occur between the protons of the surfactant and the polymer, indicating that at least some of the protons in both the polymer and the surfactant are within a spatial proximity of 0.5 nm. For the PSS/DTAB systems investigated here, we observe strong cross peaks between the aromatic protons of the polymer and the *N*-methyl protons of the DTAB, which we would expect for the presence of strong electrostatic interactions between the surfactant and polyanionic system. We note, as well, that there are

significant cross peaks between the chain protons of the surfactant and the charged head groups of the polymer, indicating that the chains of the surfactants are interacting strongly with the aromatic ring systems of the polymer. This is consistent with the condensation of a small number of molecules on the polymer backbone and the subsequent hydrophobic interactions of these molecules in the condensed structures. The very strong cross peaks that are observed between the terminal methyl group of the cationic surfactant and the aromatic ring systems signify the spatial proximity of these groups within the self-assembled complex. We note that when we compare the NOESY spectra of the individual 12-*s*-12 gemini systems with the polyanion, we observe very little difference in the nature of the cross peaks in all these systems, and also when compared to the DTAB/PSS system. This indicates that the manner in which these cationic surfactants self-

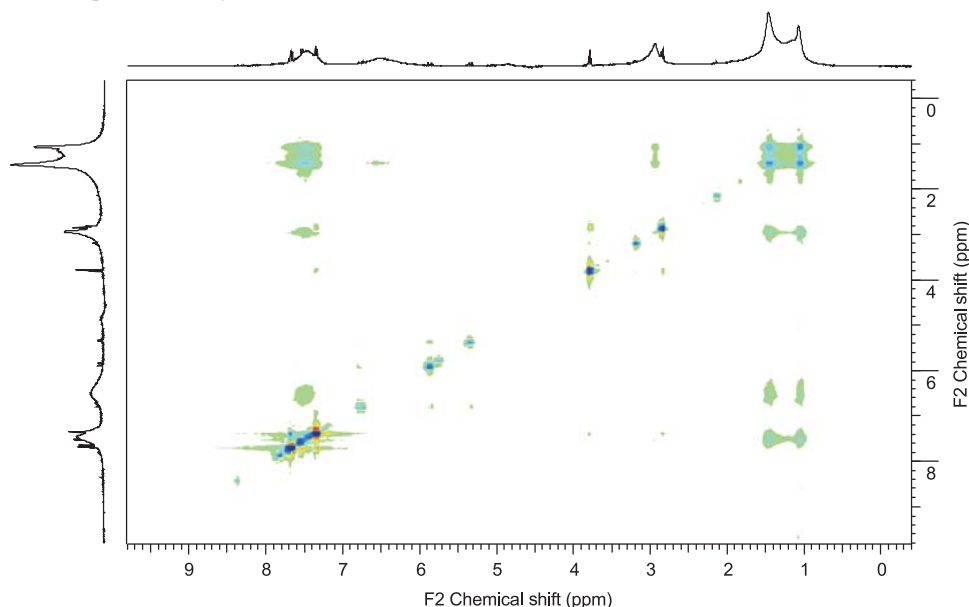


**Fig. 10.** 2D NOESY contour plot for the system 0.010 mol/L 12-5-12/0.055 mol/L PSS.**Fig. 11.** 2D NOESY contour plot for the system 0.0070 mol/L 12-10-12/0.055 mol/L PSS.

assemble with the polyanion is fundamentally identical. We also note that, in all cases, we observe cross peaks between many of the chain protons of the cationic surfactants and the aromatic ring of the polyanion, which is consistent with the ring-current shift measurements reported above. The existence of cross peaks between the aromatic resonances and the  $\omega$ -CH<sub>3</sub> protons in the cationic surfactants must indicate that these surfactant molecules have a significant amount of rotational freedom, in excellent agreement with the <sup>13</sup>C relaxation data of Gao et al.<sup>33</sup>

From the chemical-shift differences and the NOESY spectra of all the cationic surfactant PSS systems, we would con-

clude that the carbons near the head groups of all the cationic surfactants complexed with the PSS are more spatially restricted in the polymer/surfactant system than in the free surfactants themselves, in excellent agreement with the literature. Given the strong correlations in the 2D NOESY spectrum as well as the large, positive ASIS effects for the protons attached to the carbons near the end of the chain, we anticipate that the motions of the carbons in this region would be isotropic in nature. For the alkyl chain carbons near the head group, the strong NOESY correlations as well as the large, negative ASIS effects clearly indicate a spatially restricted environment for these groups in the complex

**Fig. 12.** 2D NOESY contour plot for the system 0.0070 mol/L 12-12-12/0.055 mol/L PSS.

compared to the micellar solution. Clearly, the binding between the polyanion and the cationic surfactants leads to a more rigid environment near the surface of the complexes compared to the DTAB micelle. These results suggest that the structure of all the cationic surfactant/PSS complexes are similar in that they consist of a highly ordered region near the aggregate surface and a much more micelle-like fluid hydrocarbon region in the core. The ASIS shifts appear to indicate that there are some additional constraints on the formation of these complexes when the spacer arm of the gemini surfactant is short.

## Summary

The  $^1\text{H}$  NMR chemical shifts and the NOESY spectra for a number of cationic surfactants complexed with an aromatic-containing polyanion (PSS) have been determined for several ratios of the surfactant and the polymer. All the NMR results support the existence of the structure where all the cationic surfactant/PSS complexes consist of a highly ordered region near the aggregate surface and a much more micelle-like fluid hydrocarbon region in the core. The  $^1\text{H}$  chemical differences indicate that the manner in which the DTAB and the long-spacer gemini surfactants interact with the PSS are fundamentally similar, whereas the shorter-spacer gemini surfactants have a different  $^1\text{H}$  chemical-shift difference pattern for the spacer and chain protons; this may indicate subtle differences in the nature of the binding of these cationic surfactants to the polyanion.

## Acknowledgements

The financial support of the Natural Sciences and Engineering Research Council of Canada (NSERC) (Discovery Grant, D.G.M., Research Capacity Development Grant, St. Francis Xavier) and St. Francis Xavier University (A.A.M) are greatly appreciated. We are grateful to Jan Kwak, Mike Lumsden, and Robert Berno for stimulating discussions.

## References

- (1) Herkstroeter, W. G.; Martic, P. A.; Hartman, S. E.; Williams, J. L. R.; Farid, S. J. *Polym. Sci. Polym. Chem. Ed.* **1983**, *21*, 2473.
- (2) Ananthapadmanabhan, K. P.; Leung, P. S.; Goddard, E. D. *Colloids Surf.* **1985**, *13*, 63. doi:10.1016/0166-6622(85)80006-8.
- (3) Hayakawa, K.; Ohyama, T.; Maeda, T.; Satake, I.; Sato, M.; Kwak, J. C. T. *Langmuir* **1988**, *4* (2), 481. doi:10.1021/la00080a041.
- (4) Mattai, J.; Kwak, J. C. T. *Macromolecules* **1986**, *19* (6), 1663. doi:10.1021/ma00160a031.
- (5) Pelton, R.; Lawrence, D. *Colloid Polym. Sci.* **1989**, *267* (10), 907. doi:10.1007/BF01410339.
- (6) Carlsson, A.; Lindman, B.; Watanabe, T.; Shirahama, K. *Langmuir* **1989**, *5* (5), 1250. doi:10.1021/la00089a022.
- (7) Hayakawa, K.; Satake, I.; Kwak, J. C. T.; Gao, Z. *Colloids Surf.* **1990**, *50*, 309. doi:10.1016/0166-6622(90)80272-6.
- (8) Sivadasan, K.; Somasundaran, P. *Colloids Surf.* **1990**, *49*, 229. doi:10.1016/0166-6622(90)80105-D.
- (9) Winnik, F. M.; Ringsdorf, H.; Venzmer, J. *Langmuir* **1991**, *7* (5), 905. doi:10.1021/la00053a016.
- (10) Winnik, F. M.; Winnik, M. A.; Ringsdorf, H.; Venzmer, J. *J. Phys. Chem.* **1991**, *95* (6), 2583. doi:10.1021/j100159a087.
- (11) Lindman, B.; Khan, A.; Marques, E.; Graca da Miguel, M.; Piculell, L.; Thalberg, K. *Pure Appl. Chem.* **1993**, *65* (5), 953. doi:10.1351/pac199365050953.
- (12) Wu, X. Y.; Pelton, R. H.; Tam, K. C.; Woods, D. R.; Hamielec, A. E. *J. Polym. Sci. Part Polym. Chem.* **1993**, *31* (4), 957. doi:10.1002/pola.1993.080310414.
- (13) Annable, T.; Buscall, R.; Ettelaie, R.; Shepherd, P.; Whittlestone, D. *Langmuir* **1994**, *10* (4), 1060. doi:10.1021/la00016a018.
- (14) Shimizu, T.; Kwak, J. C. T. *Colloids Surf. Physicochem. Eng. Aspects* **1994**, *82* (2), 163. doi:10.1016/0927-7757(93)02642-R.
- (15) Chang, Y.; Lochhead, R. Y.; McCormick, C. L. *Macromolecules* **1994**, *27* (8), 2145. doi:10.1021/ma00086a025.
- (16) Winnik, F. M.; Regismond, S. T. A.; Goddard, E. D. *Col-*

- oids and Surfaces A* **1996**, 106 (2-3), 243. doi:10.1016/0927-7757(95)03375-0.
- (17) Griffiths, P.; Stilbs, P.; Howe, A.; Whitesides, T. *Langmuir* **1996**, 12 (22), 5302. doi:10.1021/la960314t.
  - (18) Anthony, O.; Zana, R. *Langmuir* **1996**, 12 (8), 1967. doi:10.1021/la950817j.
  - (19) Anthony, O.; Zana, R. *Langmuir* **1996**, 12 (15), 3590. doi:10.1021/la960184o.
  - (20) Kevelam, J.; van Breemen, J. F. L.; Blokzijl, W.; Engberts, J. B. F. N.; *Langmuir* **1996**, 12 (20), 4709. doi:10.1021/la960300n.
  - (21) Bergfeldt, K.; Piculell, L. *J. Phys. Chem.* **1996**, 100 (14), 5935. doi:10.1021/jp953346i.
  - (22) Bloor, D.; Mwakibete, H. K. O.; Wyn-Jones, E. *J. Colloid Interface Sci.* **1996**, 178 (1), 334. doi:10.1006/jcis.1996.0121.
  - (23) Åbele, S.; Sjöberg, M.; Hamaide, T.; Zicmanis, A.; Guyot, A. *Langmuir* **1997**, 13 (2), 176. doi:10.1021/la960577n.
  - (24) Li, X.; Wettig, S. D.; Verrall, R. E. *Langmuir* **2004**, 20 (3), 579. doi:10.1021/la0350204. PMID:15773079.
  - (25) Guillemet, F.; Piculell, L. *J. Phys. Chem.* **1995**, 99 (22), 9201. doi:10.1021/j100022a038.
  - (26) Nowakowska, M.; Szczubialka, K.; Grebosz, M. *J. Colloid Interface Sci.* **2003**, 265 (1), 214. doi:10.1016/S0021-9797(03)00487-9. PMID:12927185.
  - (27) Wang, G.; Olofsson, G. *J. Phys. Chem. B* **1998**, 102 (46), 9276. doi:10.1021/jp9823446.
  - (28) Ritacco, H.; Kurlat, D. H. *Colloids Surf. Physicochem. Eng. Aspects* **2003**, 218, 27.
  - (29) Hayakawa, K.; Kwak, J. C. T. *J. Phys. Chem.* **1982**, 86 (19), 3866. doi:10.1021/j100216a032.
  - (30) Hayakawa, K.; Kwak, J. C. T. *J. Phys. Chem.* **1983**, 87 (3), 506. doi:10.1021/j100226a026.
  - (31) Abuin, E. B.; Scaiano, J. C. *J. Am. Chem. Soc.* **1984**, 106 (21), 6274. doi:10.1021/ja00333a028.
  - (32) Gao, Z.; Kwak, J. C. T.; Wasylishen, R. E. *J. Colloid Interface Sci.* **1988**, 126 (1), 371. doi:10.1016/0021-9797(88)90132-4.
  - (33) Gao, Z.; Wasylishen, R. E.; Kwak, J. C. T. *J. Phys. Chem.* **1990**, 94 (2), 773. doi:10.1021/j100365a048.
  - (34) Menger, F. M.; Littau, C. A. *J. Am. Chem. Soc.* **1991**, 113 (4), 1451. doi:10.1021/ja00004a077.
  - (35) Menger, F. M.; Keiper, J. S. *Angew. Chem. Int. Ed.* **2000**, 39 (11), 1906. doi:10.1002/1521-3773(20000602)39:11<1906::AID-ANIE1906>3.0.CO;2-Q.
  - (36) Rosen, M. J.; Tracy, D. J. *J. Surfact. Deterg.* **1998**, 1 (4), 547. doi:10.1007/s11743-998-0057-8.
  - (37) Zana, R. *Adv. Colloid Interface Sci.* **2002**, 97 (1-3), 203. doi:10.1016/S0001-8686(01)00069-0.
  - (38) Shukla, D.; Tyagi, V. K. *J. Oleo Sci.* **2006**, 55, 215.
  - (39) Yoshimura, T.; Nagata, Y.; Esumi, K. *J. Colloid Interface Sci.* **2004**, 275 (2), 618. doi:10.1016/j.jcis.2004.03.002. PMID:15178295.
  - (40) Malovikova, A.; Katumitu, H.; Kwak, J. C. T. In *Binding of Alkylpyridinium Cations by Anionic Polysaccharides; Structure/Performance Relationships in Surfactants*; American Chemical Society: WA, 1984; pp 225-239.
  - (41) Malovikova, A.; Hayakawa, K.; Kwak, J. C. T. *J. Phys. Chem.* **1984**, 88 (10), 1930. doi:10.1021/j150654a002.
  - (42) Hayakawa, K.; Santerre, J. P.; Kwak, J. C. T. *Macromolecules* **1983**, 16 (10), 1642. doi:10.1021/ma00244a017.
  - (43) Goddard, E. D.; Ananthapadmanabhan, K. P. In *Interactions of Surfactants With Polymers and Proteins*; CRC Press: Boca Raton, FL, 1993; p. 427.
  - (44) Gao, Z.; Wasylishen, R. E.; Kwak, J. C. T. *J. Colloid Interface Sci.* **1990**, 137 (1), 137. doi:10.1016/0021-9797(90)90050-X.
  - (45) Yuan, H. Z.; Tan, X. L.; Cheng, G. Z.; Zhao, S.; Zhang, L.; Mao, S. Z.; An, J. Y.; Yu, J. Y.; Du, Y. R. *J. Phys. Chem. B* **2003**, 107 (15), 3644. doi:10.1021/jp022185x.
  - (46) McCulloch, J. K.; Fornasiero, D.; Perera, J. M.; Murray, B. S.; Stevens, G. W.; Grieser, F. J. *Colloid Interface Sci.* **1993**, 157 (1), 180. doi:10.1006/jcis.1993.1174.
  - (47) Stilbs, P. *J. Colloid Interface Sci.* **1983**, 94 (2), 463. doi:10.1016/0021-9797(83)90286-2.
  - (48) Landry, J. M.; Marangoni, D. G.; Lumsden, M. D.; Berno, R. *Can. J. Chem.* **2007**, 85 (3), 202. doi:10.1139/V07-008.
  - (49) Wüthrich, K. In *Nmr of Proteins and Nucleic Acids*; Wiley VCH: New York, 1986; pp. 320.
  - (50) Mao, S. Z.; Du, Y. R. *Acta Physico-Chimica Sinica* **2003**, 19, 675.
  - (51) Roscigno, P.; Asaro, F.; Pellizer, G.; Ortona, O.; Paduano, L. *Langmuir* **2003**, 19 (23), 9638. doi:10.1021/la034928r.
  - (52) Hawrylak, B. E.; Marangoni, D. G. *Can. J. Chem.* **1999**, 77 (7), 1241. doi:10.1139/cjc-77-7-1241.
  - (53) Wettig, S. D.; Badea, I.; Donkuru, M.; Verrall, R. E.; Foldvari, M. *J. Gene Med.* **2007**, 9 (8), 649. doi:10.1002/jgm.1060. PMID:17654656.
  - (54) Yuan, H. Z.; Luo, L.; Zhang, L.; Zhao, S.; Mao, S. Z.; Yu, J. Y.; Shen, L. F.; Du, Y. R. *Colloid Polym. Sci.* **2002**, 280 (5), 479. doi:10.1007/s00396-001-0640-5.
  - (55) Landry, J. M.; Marangoni, D. G.; Arden, D. A.; MacLennan, I. J.; Kwak, J. C. T. *J. Surfact. Deterg.* **2009**, 12 (2), 155. doi:10.1007/s11743-009-1107-9.

# 1,3-Dibromo-5,5-dimethylhydantoin as an efficient homogeneous catalyst for the synthesis of 2-arylthiazolines and 2-arylimidazolines

Seyedeh Fatemeh Hojati, Iraj Mohammadpoor-Baltork, Behrooz Maleki, Mostafa Gholizadeh, Fatemeh Shafiezhadeh, and Mahnaz Haghdoust

**Abstract:** A simple, facile, and efficient procedure for the synthesis of 2-arylthiazolines and 2-arylimidazolines has been developed by the simple condensation of nitriles with 2-aminoethanethiol or ethylenediamine catalyzed by 1,3-dibromo-5,5-dimethylhydantoin under solvent-free conditions. Selective preparation of bithiazolines and monoimidazolines from dinitriles and also selective conversion of aryl nitriles to their corresponding 2-arylthiazolines or imidazolines in the presence of alkyl nitriles can be considered as considerable advantages of this method.

**Key words:** thiazoline, imidazoline, 1,3-dibromo-5,5-dimethylhydantoin, solvent-free

**Résumé :** On a mis au point une méthode simple, facile et efficace de réaliser la synthèse de 2-arylthiazolines et de 2-arylimidazolines impliquant une condensation simple de nitriles avec le 2-aminoéthanethiol ou l'éthylènediamine catalysée par la 1,3-dibromo-5,5-diméthylhydrantoïne dans des conditions sans solvant. La préparation sélective de bis-thiazolines et de mono-imidazolines, à partir de dinitriles, ainsi que la conversion sélective d'arylnitriles en 2-arylthiazolines ou 2-arylimidazolines, en présence d'alkylnitriles, peut être considérée comme un avantage considérable pour cette méthode.

**Mots-clés :** thiazoline, imidazoline, 1,3-dibromo-5,5-diméthylhydrantoïne, sans solvant

[Traduit par la Rédaction]

## Introduction

Thiazolines and imidazolines are very important structural moieties, because they are found in a large number of biologically active natural products.<sup>1,2</sup> The most significant examples are thiagazole,<sup>3</sup> tantazole B,<sup>3</sup> lissoclinamides,<sup>4</sup> curacin A,<sup>5</sup> naphazoline,<sup>6</sup> xylometazoline,<sup>7</sup> and oxymetazoline,<sup>8</sup> which are anti HIV-1 and 2, antineoplastic and antimicrobial agents,  $\alpha$ -adrenergic agonists, nasal decongestants, and  $\alpha$ -1 and  $\alpha$ -2 agonist topical decongestants, respectively. Antidiabetic,<sup>9</sup> antihypertensive,<sup>10</sup> antihypercholesterolemic,<sup>11</sup> and anti-inflammatory<sup>12</sup> activities are some other properties which have been reported for the natural and synthetic thiazoline and imidazoline containing compounds.

Optically active mono- and bis-derivatives of these heterocycles have been efficiently used as both auxiliaries and ligands in asymmetric transformations.<sup>13</sup> Furthermore, thiazoline derivatives have found industrial applications due to their ability to enhance the flavor and (or) aroma of various materials.<sup>14</sup>

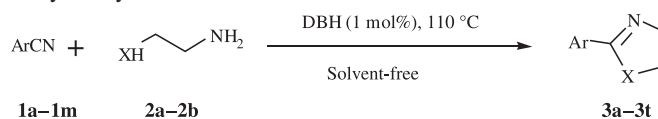
Different methods have been developed for the synthesis

of these biologically active heterocycles.<sup>15–21</sup> Various precursors, catalysts, and reaction conditions have been applied for this purpose. Although some of these protocols efficiently generate the desired compounds, most of them suffer from one or more drawbacks such as long reaction times,<sup>16</sup> harsh reaction conditions,<sup>17</sup> low yields of products,<sup>18</sup> use of expensive reagents<sup>17c,19</sup> or toxic solvents,<sup>20</sup> and using multi-step syntheses.<sup>15e,18b,21</sup> Therefore, the design of a new, simple, safe, and efficient method for the preparation of thiazolines and imidazolines is still challenging.

1,3-Dibromo-5,5-dimethylhydantoin (DBH) is a five-membered heterocycle, which had been known as a bromination agent,<sup>22</sup> but it has recently gained special attention as an efficient homogeneous catalyst in organic transformations.<sup>23</sup>

However, we were interested in examining the catalytic activity of DBH on our previous work<sup>15d,24</sup> on the synthesis of 2-arylthiazoline and 2-arylimidazoline derivatives (Scheme 1).

**Scheme 1.** Synthesis of 2-arylthiazolines and 2-arylimidazolines catalyzed by DBH.



## Results and discussion

The catalytic synthesis of thiazolines and imidazolines from nitriles by DBH was studied. At first, cyclocondensa-

Received 19 June 2009. Accepted 14 September 2009. Published on the NRC Research Press Web site at canjchem.nrc.ca on 29 January 2010.

S.F. Hojati,<sup>1</sup> B. Maleki, M. Gholizadeh, F. Shafiezhadeh, and M. Haghdoust. Department of Chemistry, Sabzevar Tarbiat Moallem University, Sabzevar 96179-76487, Iran.  
I. Mohammadpoor-Baltork. Department of Chemistry, Isfahan University, Isfahan 81746-73441, Iran.

<sup>1</sup>Corresponding author (e-mail: hojatee@yahoo.com).



tion of benzonitrile with 2-aminoethanethiol was carried out in the presence of different amounts of DBH. The temperature and solvent effects were also investigated (Table 1). The best result was obtained with 1:1.1:0.01 molar ratios of benzonitrile/2-aminoethanethiol/DBH at 110 °C under solvent-free conditions. 2-Phenylthiazolines was obtained in 95% yield after 7 min. To show the catalytic activity of DBH, when benzonitrile was reacted with 2-aminoethanethiol in the absence of catalyst under the same reaction conditions, only 15% yield was obtained after 7 min. Thus, DBH is an efficient homogeneous catalyst for the synthesis of 2-substituted thiazolines. Furthermore, the turnover number of the catalyst in the present reaction (TON = 95) exhibits the high catalytic activity of DBH in the synthesis of 2-thiazolines. The applicability of this method was investigated by the reaction of different nitriles with 2-aminoethanethiol in the presence of 1 mol% DBH. Results are summarized in Table 2 (entries 1–10). Nitrogen-containing analogues of thiazolines were also prepared satisfactorily by the current procedure (Table 2, entries 11–16). As shown in Table 2, both electron-donating and -withdrawing substituted nitriles reacted very well and produced corresponding 2-thiazolines and 2-imidazolines in good to excellent yields.

It is noteworthy that bisthiazolines and monoimidazolines were selectively generated by this method (Table 3). As illustrated in Table 3, reactions of 1,3- and 1,4-dicyanobenzene with 2-aminoethanethiol produced bisthiazolines in 97% and 85% yield, respectively, whereas the same substrates, when reacted with ethylenediamine, gave exclusively monoimidazolines in 96% and 95% yield, respectively. Bismidazolines were not obtained even by increasing the reaction times to 10 h.

It is also important to note that alkyl nitriles did not react with 2-aminoethanethiol and ethylenediamine under the same reaction conditions. So, several competitive reactions were performed between aryl nitriles and alkyl nitriles (Scheme 2), which showed an interesting selectivity. Only 2-arylthiazolines and 2-arylimidazolines were obtained after appropriate times, and alkyl nitriles remained intact in the reaction mixture. Consequently, the present method is potentially applicable for the chemoselective conversion of aryl nitriles to their corresponding 2-arylthiazolines and 2-arylimidazolines in the presence of alkyl nitriles.

Although the actual mechanism of the reaction is unclear, a reasonable explanation due to the high catalytic activity of DBH and mechanistic operation of DBH in similar reactions<sup>23c,25</sup> is shown in Scheme 3. 1,3-Dibromo-5,5-dimethylhydantion produces the bromonium ion (Br<sup>+</sup>) and activates the nitrile group by the formation of nitrogen cation **A**. The reaction follows by nucleophilic attack of 2-aminoethanethiol or ethylenediamine on activated nitrile **B** to afford **C** and **D** which are both N-activated by Br<sup>+</sup>. Finally, the corresponding 2-thiazoline or 2-imidazoline is produced by releasing NH<sub>3</sub> and bromonium ion, which returns to the catalytic cycle (Scheme 3).

In conclusion, we have demonstrated a mild and efficient protocol for the preparation of 2-arylthiazolines and 2-arylimidazolines using DBH as a homogeneous catalyst. Chemoselectivity, short reaction times, easy work-up, and high yields of products are noteworthy advantages of this protocol. Furthermore, the use of an inexpensive, approximately

**Table 1.** Investigation of temperature and solvent effects on the synthesis of 2-phenylthiazoline in the presence of DBH.

Entry	Solvent	Temperature (°C)	Time (min)	Yield <sup>a,b</sup> (%)
1	—	50	60	5
2	—	80	60	10
3	—	100	20	70
4	—	110	7	95
5	CH <sub>3</sub> OH	110	7	20
6	CH <sub>3</sub> CH <sub>2</sub> OH	110	7	25
7	CH <sub>2</sub> Cl <sub>2</sub>	110	7	75
8	Acetone	110	7	40
9	<i>n</i> -Hexane	110	7	30

<sup>a</sup>Reaction conditions: benzonitrile (1 mmol), 2-aminoethanethiol (1.1 mmol), and DBH (0.01 mmol).

<sup>b</sup>Isolated yields.

non-toxic, commercially available, and highly efficient catalyst under solvent-free conditions makes the current method economically acceptable and industrially applicable. We have also proposed a plausible mechanism for the present reaction.

## Experimental

All materials are commercial reagent grade and were obtained from Merck or Fluka. <sup>1</sup>H NMR spectra were recorded on a Bruker AVANCE 500 MHz or on a Bruker AW 80 MHz, and TMS was used as an internal standard in a 80 MHz spectrometer. Melting points were taken on a Stuart Scientific SMP2 apparatus. Elemental analyses were performed using a Heraeus CHN-O-Rapid analyzer. Mass spectra were recorded on a PLATFORM 8379E in 70 eV.

### General procedure for the preparation of 2-thiazolines and 2-imidazolines

A mixture of nitrile (2 mmol), 2-aminoethanethiol (2.2 mmol) or ethylenediamine (8 mmol), and DBH (0.02 mmol) was refluxed (110 °C) under solvent-free conditions for the appropriate time according to Table 2. After completion of the reaction as indicated by TLC (2:1 *n*-hexane/EtOAc for thiazolines and 4:1 EtOAc/CH<sub>3</sub>OH for imidazolines), the mixture was cooled to room temperature and the pure product was isolated by column chromatography.

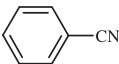
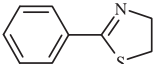
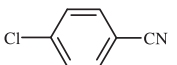
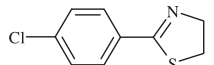
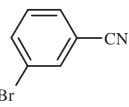
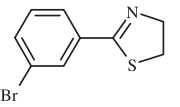
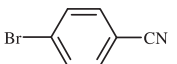
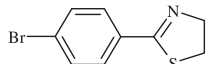

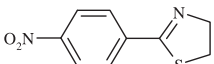
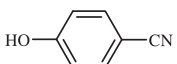
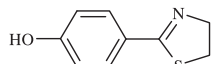
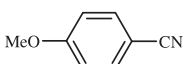
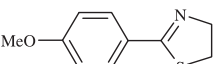
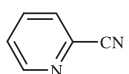
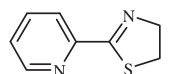
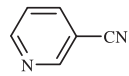
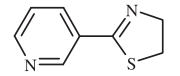
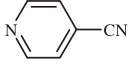
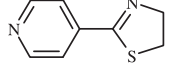
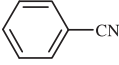
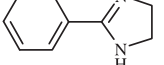
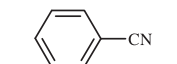
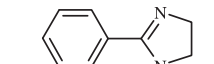

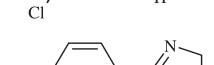
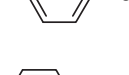
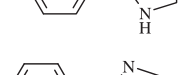
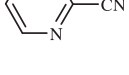
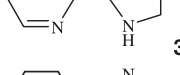
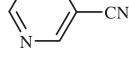
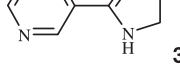
### General procedure for the synthesis of bisthiazolines and monoimidazolines

To a mixture of dinitrile (2 mmol) and 2-aminoethanethiol (5 mmol) or ethylenediamine (16 mmol) was added DBH (0.04 mmol) and the mixture stirred at 110 °C for the appropriate time according to Table 3. The progress of the reaction was monitored by TLC (2:1 *n*-hexane/EtOAc for thiazolines and 4:1 EtOAc/CH<sub>3</sub>OH for imidazolines). After completion of the reaction, the mixture was cooled to room temperature and the crude product purified via silica gel column chromatography.

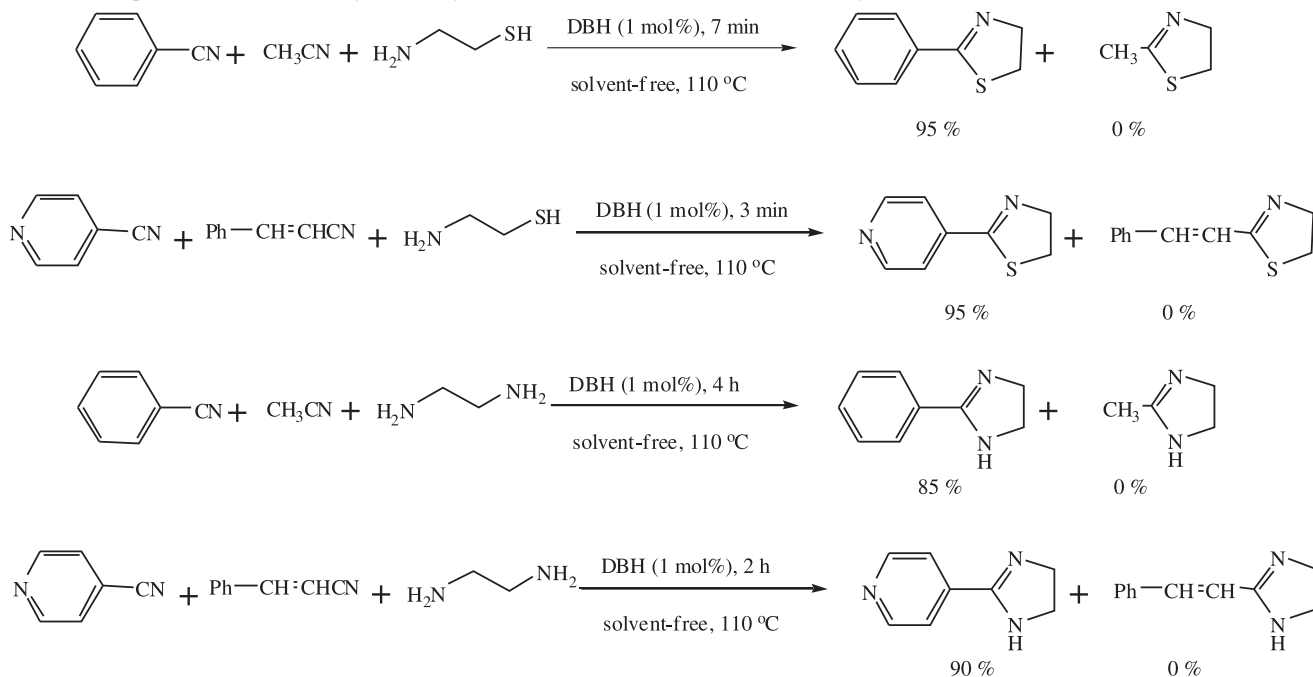
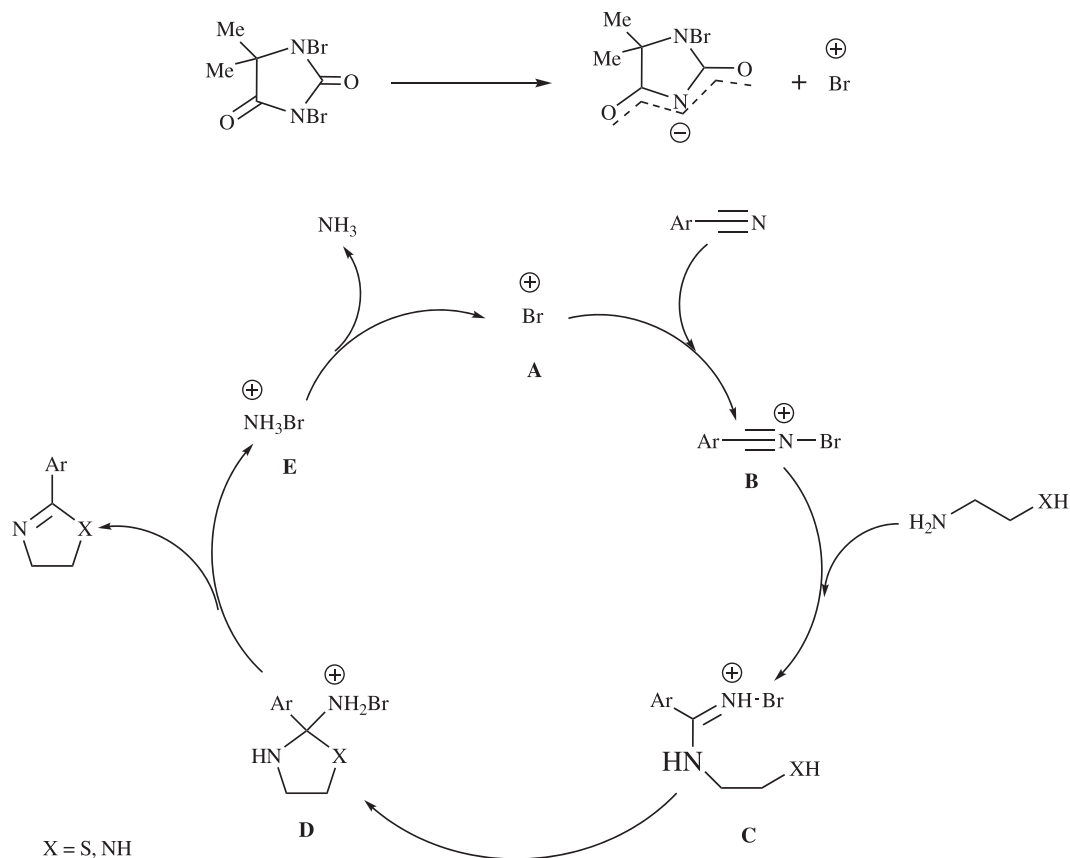
### 2-Phenylthiazoline (3a)

Solid; mp 126–128 °C. <sup>1</sup>H NMR (CDCl<sub>3</sub>, 500 MHz) δ: 3.40 (t, *J* = 8.3 Hz, 2H, CH<sub>2</sub>-S), 4.46 (t, *J* = 8.3 Hz, 2H, CH<sub>2</sub>-N), 7.38–7.49 (m, 3H, ArH), 7.85 (dd, *J* = 1.6 and

**Table 2.** Synthesis of 2-thiazolines and 2-imidazolines catalyzed by DBH.

Entry	Nitrile ( <b>1</b> )	Product ( <b>3</b> )	Time	Yield <sup>a,b</sup> (%)	Mp (°C), Ref.
1	 <b>1a</b>	 <b>3a</b>	7 min	95	126-128, 15a
2	 <b>1b</b>	 <b>3b</b>	3 min	90	53-55, 15b
3	 <b>1c</b>	 <b>3c</b>	9 min	83	Oil, 15c
4	 <b>1d</b>	 <b>3d</b>	3 min	94	Oil, 15c
5	 <b>1e</b>	 <b>3e</b>	8 min	82	151-153, 15b
6	 <b>1f</b>	 <b>3f</b>	3 min	90	176-178, 15d
7	 <b>1g</b>	 <b>3g</b>	9 min	60	52-54, 15b
8	 <b>1h</b>	 <b>3h</b>	8 min	95	92-94, 15e
9	 <b>1i</b>	 <b>3i</b>	6 min	85	110-112, 15f
10	 <b>1j</b>	 <b>3j</b>	3 min	96	74-76, 15d
11	 <b>1a</b>	 <b>3k</b>	4 h	87	100-102, 15g
12	 <b>1k</b>	 <b>3l</b>	2 h	88	134-136, 15h
13	 <b>1b</b>	 <b>3m</b>	4 h	70	186-188, 15g
14	 <b>1h</b>	 <b>3n</b>	0.5 h	97	100-102, 15h
15	 <b>1i</b>	 <b>3o</b>	2 h	65	106-108, 15i
16	 <b>1j</b>	 <b>3p</b>	2 h	90	134-136, 15i

<sup>a</sup> Products were identified by comparison of their physical and spectral data with those reported in the literature.<sup>b</sup> Isolated yields.

**Scheme 2.** Competitive reactions of aryl and alkyl nitriles with 2-aminoethanethiol or ethylenediamine.**Scheme 3.** Proposed mechanism for the synthesis of 2-arylthiazolines and 2-arylimidazolines catalyzed by DBH.

7.6 Hz, 2H, ArH). MS  $m/z$ : 163 [ $M^+$ ]. Anal. calcd. for  $C_9H_9NS$ : C 66.22, H 5.56, N 8.58; found C 66.28, H 5.63, N 8.48.

#### 2-(4-Chlorophenyl)thiazoline (3b)

Solid; mp 53–55 °C.  $^1\text{H}$  NMR ( $\text{CDCl}_3$ , 500 MHz)  $\delta$ : 3.45 (t,  $J$  = 8.4, 2H,  $\text{CH}_2\text{-S}$ ), 4.47 (t,  $J$  = 8.4 Hz, 2H,  $\text{CH}_2\text{-N}$ ),

**Table 3.** Selective synthesis of bis-thiazolines and mono-imidazolines using DBH.

Entry	Nitrile	Product	Time	Yield <sup>a,b</sup> (%)	Mp (°C), Ref.
1			9 min	97	111-113, 15d
2			14 min	85	105-107, 15b
3			2.5 h	96	133-134, 15d
4			3 h	95	207-209, 15j

<sup>a</sup> Products were identified by comparison of their physical and spectral data with those reported in the literature.

<sup>b</sup> Isolated yields.

7.40 (d,  $J = 8.6$  Hz, 2H, ArH), 7.79 (d,  $J = 8.6$  Hz, 2H, ArH). MS  $m/z$ : 197, 199 [ $M^+$ ]. Anal. calcd. for  $C_9H_8ClNS$ : C 54.68, H 4.08, N 7.08; found C 54.53, H 4.17, N 7.09.

### 2-(3-Bromophenyl)thiazoline (3c)

Oily Liquid.  $^1H$  NMR ( $CDCl_3$ , 500 MHz)  $\delta$ : 3.36 (t,  $J = 8.1$  Hz, 2H,  $CH_2-S$ ), 4.26 (t,  $J = 8.1$  Hz, 2H,  $CH_2-N$ ), 7.27 (t,  $J = 7.8$  Hz, 1H, ArH), 7.40 (d,  $J = 7.9$  Hz, 1H, ArH), 7.50 (d,  $J = 7.6$  Hz, 1H, ArH), 7.66 (s, 1H, ArH). MS  $m/z$ : 241, 243 [ $M^+$ ]. Anal. calcd. for  $C_9H_8BrNS$ : C 44.64, H 3.33, N 5.78; found C 44.67, H 3.37, N 5.72.

### 2-(4-Bromophenyl)thiazoline (3d)

Oily liquid.  $^1H$  NMR ( $CDCl_3$ , 500 MHz)  $\delta$ : 3.35 (t,  $J = 8.1$  Hz, 2H,  $CH_2-S$ ), 4.24 (t,  $J = 8.2$  Hz, 2H,  $CH_2-N$ ), 7.31 (d,  $J = 8.2$  Hz, ArH), 7.55 (d,  $J = 8.2$  Hz, 2H, ArH). MS  $m/z$ : 241, 243 [ $M^+$ ]. Anal. calcd. for  $C_9H_8BrNS$ : C 44.64, H 3.33, N 5.78; found C 44.69, H 3.26, N 5.81.

### 2-(4-Nitrophenyl)thiazoline (3e)

Solid; mp 151–153 °C.  $^1H$  NMR ( $CDCl_3$ , 500 MHz)  $\delta$ : 3.53 (t,  $J = 8.5$  Hz, 2H,  $CH_2-S$ ), 4.54 (t,  $J = 8.5$  Hz, 2H,  $CH_2-N$ ), 8.02 (d,  $J = 8.8$  Hz, 2H, ArH), 8.29 (d,  $J = 8.7$  Hz, 2H, ArH). MS  $m/z$ : 208 [ $M^+$ ]. Anal. calcd. for  $C_9H_8N_2O_2S$ : C 51.91, H 3.87, N 13.45; found C 51.88, H 3.80, N 13.52.

### 2-(4-hydroxyphenyl)thiazoline (3f)

Solid; mp 176–178 °C.  $^1H$  NMR ( $CDCl_3$ , 500 MHz)  $\delta$ : 3.43 (t,  $J = 8.3$  Hz, 2H,  $CH_2-S$ ), 3.85 (s, 1H, OH), 4.44 (t,  $J = 8.3$  Hz, 2H,  $CH_2-N$ ), 6.84 (d,  $J = 8.5$  Hz, 2H, ArH), 7.73 (d,  $J = 8.5$  Hz, 2H, ArH). MS  $m/z$ : 179 [ $M^+$ ]. Anal. calcd. for  $C_9H_9NOS$ : C 60.31, H 5.06, N 7.81; found C 60.43, H 5.00, N 7.78.

### 2-(4-Methoxyphenyl)thiazoline (3g)

Solid; mp 52–54 °C.  $^1H$  NMR ( $CDCl_3$ , 500 MHz)  $\delta$ : 3.42

(t,  $J = 8.2$  Hz, 2H,  $CH_2-S$ ), 3.86 (s, 3H, O- $CH_3$ ), 4.44 (t,  $J = 8.2$  Hz,  $CH_2-N$ ), 6.93 (d,  $J = 8.3$  Hz, 2H, ArH), 7.81 (d,  $J = 8.3$  Hz, 2H, ArH). MS  $m/z$ : 193 [ $M^+$ ]. Anal. calcd. for  $C_{10}H_{11}NOS$ : C 62.15, H 5.74, N 7.25; found C 62.17, H 5.75, N 7.21.

### 2-(2-Pyridyl)thiazoline (3h)

Solid; mp 92–94 °C.  $^1H$  NMR ( $CDCl_3$ , 500 MHz)  $\delta$ : 3.32 (t,  $J = 8.6$  Hz, 2H,  $CH_2-S$ ), 4.48 (t,  $J = 8.6$  Hz, 2H,  $CH_2-N$ ), 7.28–7.32 (m, 1H, ArH), 7.71 (m, 1H, ArH), 8.01 (d,  $J = 7.9$  Hz, 1H, ArH), 8.60 (d,  $J = 4.8$  Hz, 1H, ArH). MS  $m/z$ : 164 [ $M^+$ ]. Anal. calcd. for  $C_8H_8N_2S$ : C 58.51, H 4.91, N 17.06; found C 58.55, H 4.86, N 17.12.

### 2-(3-Pyridyl)thiazoline (3i)

Solid; mp 110–112 °C.  $^1H$  NMR ( $CDCl_3$ , 500 MHz)  $\delta$ : 3.37 (t,  $J = 8.4$  Hz, 2H,  $CH_2-S$ ), 4.39 (t,  $J = 8.4$  Hz, 2H,  $CH_2-N$ ), 7.27 (dd,  $J = 4.8$  and 8.0 Hz, 1H, ArH), 8.02 (dt,  $J = 1.9$  and 8.0 Hz, 1H, ArH), 8.60 (dd,  $J = 1.4$  and 4.8 Hz, 1H, ArH), 8.96 (d,  $J = 1.9$  Hz, 1H, ArH). MS  $m/z$ : 164 [ $M^+$ ]. Anal. calcd. for  $C_8H_8N_2S$ : C 58.51, H 4.91, N 17.06; found C 58.58, H 4.95, N 17.00.

### 2-(4-Pyridyl)thiazoline (3j)

Solid; mp 74–76 °C.  $^1H$  NMR ( $CDCl_3$ , 500 MHz)  $\delta$ : 3.48 (t,  $J = 8.5$  Hz, 2H,  $CH_2-S$ ), 4.51 (t,  $J = 8.5$  Hz, 2H,  $CH_2-N$ ), 7.68 (dd,  $J = 1.5$  and 4.5 Hz, 2H, ArH), 8.71 (dd,  $J = 1.5$  and 4.5 Hz, 2H, ArH). MS  $m/z$ : 164 [ $M^+$ ]. Anal. calcd. for  $C_8H_8N_2S$ : C 58.51, H 4.91, N 17.06; found C 58.49, H 4.85, N 17.13.

### 2-Phenylimidazoline (3k)

Solid; mp 100–102 °C.  $^1H$  NMR ( $CDCl_3$ , 80 MHz)  $\delta$ : 3.75 (s, 4H,  $2CH_2$ ), 4.8 (s, 1H, NH), 7.3–7.4 (m, 3H, ArH), 7.7–7.8 (m, 2H, ArH). MS  $m/z$ : 146 [ $M^+$ ]. Anal. calcd. for  $C_9H_{10}N_2$ : C 73.94, H 6.89, N 19.16; found C 73.95, H 6.85, N 19.18.



**2-(3-Chlorophenyl)imidazoline (3l)**

Solid; mp 134–136 °C.  $^1\text{H}$  NMR ( $\text{CDCl}_3$ , 80 MHz)  $\delta$ : 3.76 (s, 4H,  $2\text{CH}_2$ ), 4.25 (s, 1H, NH), 7.22–7.75 (m, 4H, ArH). MS  $m/z$ : 180, 182 [ $\text{M}^+$ ]. Anal. calcd. for  $\text{C}_9\text{H}_9\text{ClN}_2$ : C 59.84, H 5.02, N 15.51; found C 59.78, H 5.10, N 15.45.

**2-(4-Chlorophenyl)imidazoline (3m)**

Solid; mp 186–188 °C.  $^1\text{H}$  NMR ( $\text{CDCl}_3$ , 80 MHz)  $\delta$ : 3.75 (s, 4H,  $2\text{CH}_2$ ), 4.22 (s, 1H, NH), 7.3 (d, 2H, ArH), 7.93 (d, 2H, ArH). MS  $m/z$ : 180, 182 [ $\text{M}^+$ ]. Anal. calcd. for  $\text{C}_9\text{H}_9\text{ClN}_2$ : C 59.84, H 5.02, N 15.51; found C 59.88, H 5.06, N 15.49.

**2-(2-Pyridyl)imidazoline (3n)**

Solid; mp 100–102 °C.  $^1\text{H}$  NMR ( $\text{CDCl}_3$ , 80 MHz)  $\delta$ : 3.81 (s, 4H,  $2\text{CH}_2$ ), 5.38 (s, 1H, NH), 7.22–7.38 (m, 1H, ArH), 7.62–7.85 (m, 1H, ArH), 8.12 (d, 1H, ArH), 8.55 (d, 1H, ArH). MS  $m/z$ : 147 [ $\text{M}^+$ ]. Anal. calcd. for  $\text{C}_8\text{H}_9\text{N}_3$ : C 65.29, H 6.16, N 28.55; found C 65.20, H 6.17, N 28.61.

**2-(3-Pyridyl)imidazoline (3o)**

Solid; mp 106–108 °C.  $^1\text{H}$  NMR ( $\text{CDCl}_3$ , 80 MHz)  $\delta$ : 3.78 (s, 4H,  $2\text{CH}_2$ ), 4.54 (s, 1H, NH), 7.2–7.38 (m, 1H, ArH), 8.02–8.15 (m, 1H, ArH), 8.6–8.67 (m, 1H, ArH), 8.92 (s, 1H, ArH). MS  $m/z$ : 147 [ $\text{M}^+$ ]. Anal. calcd. for  $\text{C}_8\text{H}_9\text{N}_3$ : C 65.29, H 6.16, N 28.55; found C 65.25, H 6.14, N 28.63.

**2-(4-Pyridyl)imidazoline (3p)**

Solid; mp 134–136 °C.  $^1\text{H}$  NMR ( $\text{CDCl}_3$ , 80 MHz)  $\delta$ : 3.79 (s, 4H,  $2\text{CH}_2$ ), 4.3 (s, 1H, NH), 7.61 (d, 2H, ArH), 8.65 (d, 2H, ArH). MS  $m/z$ : 147 [ $\text{M}^+$ ]. Anal. calcd. for  $\text{C}_8\text{H}_9\text{N}_3$ : C 65.29, H 6.16, N 28.55; found C 65.33, H 6.21, N 28.49.

**2-(3-(Thiazolin-2-yl)phenyl)thiazoline (3q)**

Solid; mp 111–113 °C.  $^1\text{H}$  NMR ( $\text{CDCl}_3$ , 500 MHz)  $\delta$ : 3.46 (t,  $J = 8.4$  Hz, 4H,  $2\text{CH}_2\text{-S}$ ), 4.49 (t,  $J = 8.4$  Hz, 4H,  $2\text{CH}_2\text{-N}$ ), 7.48 (t,  $J = 7.8$  Hz, 1H, ArH), 7.95 (dd,  $J = 1.5$  and 7.8 Hz, 2H, ArH), 8.27 (s, 1H, ArH). MS  $m/z$ : 248 [ $\text{M}^+$ ]. Anal. calcd. for  $\text{C}_{12}\text{H}_{12}\text{N}_2\text{S}_2$ : C 58.03, H 4.87, N 11.28; found C 58.06, H 4.84, N 11.32.

**2-(4-(Thiazolin-2-yl)phenyl)thiazoline (3r)**

Solid; mp 105–107 °C.  $^1\text{H}$  NMR ( $\text{CDCl}_3$ , 500 MHz)  $\delta$ : 3.45 (t,  $J = 8.3$  Hz, 4H,  $2\text{CH}_2\text{-S}$ ), 4.49 (t,  $J = 8.3$  Hz, 4H,  $2\text{CH}_2\text{-N}$ ), 7.88 (s, 4H, ArH). MS  $m/z$ : 248 [ $\text{M}^+$ ]. Anal. calcd. for  $\text{C}_{12}\text{H}_{12}\text{N}_2\text{S}_2$ : C 58.03, H 4.87, N 11.28; found C 58.11, H 4.79, N 11.21.

**3-(Imidazolin-2-yl)benzonitrile (3s)**

Solid; mp 133–134 °C.  $^1\text{H}$  NMR ( $\text{CDCl}_3$ , 500 MHz)  $\delta$ : 3.81 (s, 4H,  $2\text{CH}_2$ ), 4.2 (s, 1H, NH), 7.51 (t,  $J = 7.8$  Hz, 1H, ArH), 7.71 (d,  $J = 7.7$  Hz, 1H, ArH), 8.01 (d,  $J = 7.9$  Hz, 1H, ArH), 8.05 (s, 1H, ArH). MS  $m/z$ : 171 [ $\text{M}^+$ ]. Anal. calcd. for  $\text{C}_{10}\text{H}_9\text{N}_3$ : C 70.16, H 5.30, N 24.54; found C 70.22, H 5.34, N 24.50.

**4-(Imidazolin-2-yl)benzonitrile (3t)**

Solid; mp 207–209 °C.  $^1\text{H}$  NMR ( $\text{CDCl}_3$ , 500 MHz)  $\delta$ : 3.83 (s, 4H,  $2\text{CH}_2$ ), 4.2 (s, 1H, NH), 7.71 (d,  $J = 8.4$  Hz, 2H, ArH), 7.90 (d,  $J = 8.4$  Hz, 2H, ArH). MS  $m/z$ : 171

[ $\text{M}^+$ ]. Anal. calcd. for  $\text{C}_{10}\text{H}_9\text{N}_3$ : C 70.16, H 5.30, N 24.54; found C 70.15, H 5.33, N 24.52.

**Acknowledgements**

The authors are grateful to the Research Council of Sabzevar Tarbiat Moallem University for partial support of this work.

**References**

- (1) Wipf, P. *Chem. Rev.* **1995**, 95 (6), 2115. doi:10.1021/cr00038a013.
- (2) Ferm, R. J.; Riebsomer, J. L. *Chem. Rev.* **1954**, 54 (4), 593. doi:10.1021/cr60170a002.
- (3) Boyce, R. J.; Mulqueen, G. C.; Pattenden, G. *Tetrahedron Lett.* **1994**, 35 (31), 5705. doi:10.1016/S0040-4039(00)77284-4.
- (4) Boden, C. D. J.; Pattenden, G.; Ye, T. *Synlett* **1995**, 417. doi:10.1055/s-1995-4993.
- (5) Lai, J.-Y.; Yu, J.; Mekonnen, B.; Falck, J. R. *Tetrahedron Lett.* **1996**, 37 (40), 7167. doi:10.1016/0040-4039(96)01616-4.
- (6) Podder, A.; Mukhopadhyay, B. P.; Dattagupta, J. K.; Saha, N. N. *Acta Crystallogr.* **1983**, C39, 495. doi:10.1107/S0108270183005259.
- (7) Khan, M. A.; Khan, A. A.; Faruqi, N. A. *J. Anat. Soc. India* **2005**, 54, 17.
- (8) Browning, S.; Housley, D.; Richards, R.; Eccles, R. *Acta Otolaryngol.* **1997**, 117 (6), 851. doi:10.3109/00016489709114213. PMID:9442826.
- (9) Rondou, F.; Le Bihan, G.; Wang, X.; Lamouri, A.; Touboul, E.; Dive, G.; Bellahsene, T.; Pfeiffer, B.; Renard, P.; Guardiola-Lemaitre, B.; Manechez, D.; Penicaud, L.; Ktorza, A.; Godfroid, J.-J. *J. Med. Chem.* **1997**, 40 (23), 3793. doi:10.1021/jm9608624. PMID:9371245.
- (10) Bousquet, P.; Feldman, J. *Drugs* **1999**, 58 (5), 799. doi:10.2165/00003495-199958050-00003. PMID:10595861.
- (11) Li, H.-Y.; Drummond, S.; DeLucca, I.; Boswell, G. A. *Tetrahedron* **1996**, 52 (34), 11153. doi:10.1016/0040-4020(96)00578-9.
- (12) Ueno, M.; Imaizumi, K.; Sugita, T.; Takata, I.; Takeshita, M. *Int. J. Immunopharmacol.* **1995**, 17 (7), 597. doi:10.1016/0192-0561(95)00057-9. PMID:8586488.
- (13) (a) Yamakuchi, M.; Matsunaga, H.; Tokuda, R.; Ishizuka, T.; Nakajima, M.; Kunieda, T. *Tetrahedron Lett.* **2005**, 46 (23), 4019. doi:10.1016/j.tetlet.2005.04.025.; (b) Osorio-Lozada, A.; Olivo, H. F. *Org. Lett.* **2008**, 10 (4), 617. doi:10.1021/ol702980p. PMID:18205374.; (c) Herrmann, W. A.; Goossen, L. J.; Spiegler, M. *Organometallics* **1998**, 17 (11), 2162. doi:10.1021/om970826i.
- (14) Spencer, M.; Parliment, T.; Gioadano, D. General food corporation. US Patent 4 355 049, 1982.
- (15) (a) Suzuki, N.; Fujita, Y.; Yamabayashi, T.; Deguchi, Y.; Izawa, Y. *J. Chem. Soc., Perkin Trans. 1* **1976**, (18): 1901. doi:10.1039/p19760001901.; (b) Katritzky, A. R.; Cai, C.; Suzuki, K.; Singh, S. K. *J. Org. Chem.* **2004**, 69 (3), 811. doi:10.1021/jo0355092. PMID:14750808.; (c) Robbe, Y.; Fernandez, J. P.; Chapat, J. P.; Sentenac-Roumanou, H.; Fatome, M. *Eur. J. Med. Chem.* **1985**, 20, 16; (d) Mohammad-poor-Baltork, I.; Moghadam, M.; Tangestaninejad, S.; Mirkhani, V.; Hojati, S. F. *Polyhedron* **2008**, 27 (2), 750. doi:10.1016/j.poly.2007.11.018.; (e) George, B.; Papadopoulos, E. P. *J. Org. Chem.* **1977**, 42 (3), 441. doi:10.1021/jo00423a011.; (f) Nakajima, T.; Kashiwabara, T.; Izawa, T.; Nakajima, S. *Bioorg. Med. Chem. Lett.* **1994**, 4 (20), 2485.

- doi:10.1016/S0960-894X(01)80415-7.; (g) Salgado-Zamora, H.; Campos, E.; Jimenez, R.; Cervantes, H. *Heterocycles* **1998**, *47* (2), 1043. doi:10.3987/COM-97-S(N)109.; (h) Mohammadpoor-Baltork, I.; Abdollahi-Alibeik, M. *Bull. Korean Chem. Soc.* **2003**, *44*, 1354; (i) Neef, G.; Eder, U.; Sauer, G. *J. Org. Chem.* **1981**, *46* (13), 2824. doi:10.1021/jo00326a055.; (j) Fujioka, H.; Murai, K.; Kubo, O.; Ohba, Y.; Kita, Y. *Tetrahedron* **2007**, *63* (3), 638. doi:10.1016/j.tet.2006.11.007.; (k) Kamila, S.; Biehl, E. R. *J. Heterocycl. Chem.* **2007**, *44* (2), 407. doi:10.1002/jhet.5570440220.
- (16) (a) Sayama, S. *Synlett* **2006**, *2006* (10), 1479. doi:10.1055/s-2006-941597.; (b) Levesque, G.; Gressier, J.-C.; Proust, M. *Synthesis* **1981**, *1981* (12), 963. doi:10.1055/s-1981-29659.
- (17) (a) Mahler, S. G.; Serra, G. L.; Antonow, D.; Manta, E. *Tetrahedron Lett.* **2001**, *42* (46), 8143. doi:10.1016/S0040-4039(01)01759-2.; (b) Helmkamp, G. K.; Pettitt, D. J.; Lowell, J. R., Jr.; Mabey, W. R.; Wolcott, R. G. *J. Am. Chem. Soc.* **1966**, *88* (5), 1030. doi:10.1021/ja00957a030.; (c) Forsberg, J. H.; Spaziano, V. T.; Balasubramanian, T. M.; Liu, G. K.; Kinsley, S. A.; Duckworth, C. A.; Poteruca, J. J.; Brown, P. S.; Miller, J. L. *J. Org. Chem.* **1987**, *52* (6), 1017. doi:10.1021/jo00382a009.
- (18) (a) Fernandez, X.; Fellous, R.; Lizzani-Cuvelier, L.; Loiseau, M.; Duñach, E. *Tetrahedron Lett.* **2001**, *42* (8), 1519. doi:10.1016/S0040-4039(00)02321-2.; (b) Sonn, A. German Patent 616227, 1935; *Chem. Abstr.* 1978, **30**, 478, 4313(c) Corbel, J. C.; Uriac, P.; Huet, J.; Martin, C. A. E.; Advenier, C. *Eur. J. Med. Chem.* **1995**, *30* (1), 3. doi:10.1016/0223-5234(96)88204-3.
- (19) Fernandez, X.; Fellous, R.; Duñach, E. *Tetrahedron Lett.* **2000**, *41* (18), 3381. doi:10.1016/S0040-4039(00)00419-6.
- (20) (a) Busacca, C. A.; Dong, Y.; Spinelli, E. M. *Tetrahedron Lett.* **1996**, *37* (17), 2935. doi:10.1016/0040-4039(96)00451-0.; (b) Almqvist, F.; Guillaume, D.; Hultgren, S. J.; Marshall, G. R. *Tetrahedron Lett.* **1998**, *39* (16), 2293. doi:10.1016/S0040-4039(98)00347-5.
- (21) Abrunhosa, I.; Gulea, M.; Levillain, J.; Masson, S. *Tetrahedron Asymmetry* **2001**, *12* (20), 2851. doi:10.1016/S0957-4166(01)00481-5.
- (22) (a) Shimizu, M.; Nakahara, Y.; Yoshioka, H. *J. Chem. Soc., Chem. Commun.* **1989**, (24): 1881. doi:10.1039/c39890001881.; (b) Chassaing, C.; Haudrechy, A.; Langlois, Y. *Tetrahedron Lett.* **1997**, *38* (25), 4415. doi:10.1016/S0040-4039(97)00943-X.
- (23) (a) Azarifar, D.; Bosra, H. G.; Tajbaksh, M. *J. Heterocycl. Chem.* **2007**, *44* (2), 467. doi:10.1002/jhet.5570440231.; (b) Azarifar, D.; Maleki, B.; Mohammadi, K. *Heterocycles* **2007**, *71* (3), 683. doi:10.3987/COM-06-10961.; (c) Madhusudan, S. K.; Misra, A. K. *Carbohydr. Res.* **2005**, *340* (3), 497. doi:10.1016/j.carres.2004.12.002. PMID:15680606.
- (24) (a) Mohammadpoor-Baltork, I.; Mirkhani, V.; Moghadam, M.; Tangestaninejad, S.; Zolfigol, M. A.; Abdollahi-Alibeik, M.; Khosropour, A. R.; Kargar, H.; Hojati, S. F. *Catal. Commun.* **2008**, *9* (5), 894. doi:10.1016/j.catcom.2007.09.017.; (b) Mohammadpoor-Baltork, I.; Moghadam, M.; Tangestaninejad, S.; Mirkhani, V.; Hojati, S. F. *Catal. Commun.* **2008**, *9* (6), 1153. doi:10.1016/j.catcom.2007.10.026.
- (25) Azarifar, D.; Ghasemnejad, H.; Ramzanian-Iehmali, F. *Mendeleev Commun.* **2005**, *15* (5), 209. doi:10.1070/MC2005v015n05ABEH002124.

# Threshold ionization and dissociation of *t*-butylamine

Paul M. Mayer, Martyn F. Guest, Emma E. Rennie, Louise Cooper,  
Larisa G. Shpinkova, David M.P. Holland, and David A. Shaw

**Abstract:** The threshold photoelectron spectrum of *t*-butylamine, recorded between 8 and 28 eV, is reported for the first time. The spectrum was compared to orbital ionization energies calculated at the OVGF/cc-pVTZ level of theory. The adiabatic and vertical ionization energies of the outermost orbital (made up primarily of the nitrogen p orbital) are  $8.48 \pm 0.02$  and  $9.40 \pm 0.02$  eV, respectively. Threshold photoelectron photoion coincidence spectra were recorded between 8.5 and 35 eV, and appearance energies for 15 fragment ions were obtained. The lowest energy dissociation is the loss of a methyl group to form the  $(\text{CH}_3)_2\text{CNH}_2^+$  ion. RRKM fitting of this dissociation leads to a  $\Delta_f H_{298}$  for  $(\text{CH}_3)_2\text{CNH}_2^+$  of  $603 \pm 3$  kJ mol<sup>-1</sup>. This value is  $\sim 10$  kJ mol<sup>-1</sup> higher than the previously derived value of Lossing et al. (based on an electron ionization appearance energy value) and the G3B3 estimate. Together with the proton affinity value of 932.3 kJ mol<sup>-1</sup>, the present  $\Delta_f H_{298}$  leads to a  $\Delta_f H_{298}$  for 2-propanimine  $(\text{CH}_3)_2\text{C}=\text{NH}$  of 5.3 kJ mol<sup>-1</sup>, which can be compared to a value of  $-5.7$  kJ mol<sup>-1</sup> (based on the Lossing et al.  $(\text{CH}_3)_2\text{CNH}_2^+$   $\Delta_f H_{298}$ ) and a G3B3 value of  $-0.3$  kJ mol<sup>-1</sup>. At photon energies above 26 eV, there is evidence for the dissociative double ionization of *t*-butylamine forming either the singlet or triplet state of the dication.

**Key words:** *t*-butylamine ions, ab initio molecular orbital calculations, density functional calculations, ionization energies, threshold photoelectron photoion coincidence spectroscopy, activation energies, activation entropies.

**Résumé :** Les spectres photoélectroniques de seuil de la *t*-butylamine ont été enregistrés entre 8 et 28 eV et sont rapportés pour la première fois. Les spectres sont comparés aux énergies d'ionisation des orbitales calculées au niveau OVGF/cc-pVTZ de la théorie. Les énergies d'ionisation adiabatique et verticale des orbitales les plus loin du noyau, qui comprennent principalement les orbitales p de l'azote, sont respectivement égales à  $8,48 \pm 0,02$  et  $9,40 \pm 0,02$  eV. Les spectres de coïncidence photoélectronique de seuil des photoions ont été enregistrés entre 8,5 et 35 eV et on a obtenu les énergies d'apparition de quinze fragments ioniques. La dissociation d'énergie la plus faible correspond à la perte d'un groupe méthyle conduisant à la formation de l'ion  $(\text{CH}_3)_2\text{C}=\text{NH}_2^+$ . Un ajustement de cette dissociation par la méthode de Rice, Ramsperger, Kassel et Marcus (RRKM) conduit à une valeur de  $603 \pm 3$  kJ mol<sup>-1</sup> pour le  $\Delta_f H_{298}$  de l'ion  $(\text{CH}_3)_2\text{C}=\text{NH}_2^+$ . Cette valeur est environ 10 kJ mol<sup>-1</sup> plus élevée que celle obtenue antérieurement par Lossing et al. sur la base de la valeur de l'énergie d'apparition d'une ionisation électronique ainsi que celle évaluée par la méthode G3B3. Combinée à la valeur de 932,3 kJ mol<sup>-1</sup> pour l'affinité du proton, la valeur de  $\Delta_f H_{298}$  trouvée dans cette étude conduit à une valeur de 5,3 kJ mol<sup>-1</sup> pour le  $\Delta_f H_{298}$  de la 2-propanimine,  $(\text{CH}_3)_2\text{C}=\text{NH}$ ; cette valeur est à comparer à la valeur de  $-5,7$  kJ mol<sup>-1</sup> rapportée par Lossing et al. sur la base de sa valeur du  $\Delta_f H_{298}$  pour l'ion  $(\text{CH}_3)_2\text{C}=\text{NH}_2^+$ , et à la valeur de  $-0,3$  kJ mol<sup>-1</sup> évaluée par la méthode G3B3. À des énergies photoniques supérieures à 26 eV, il y a des indications à l'effet qu'il se produit une double ionisation dissociative de la *t*-butylamine conduisant à l'état singulet ou triplet du dication.

**Mots-clés :** ions de la *t*-butylamine, calculs d'orbitales moléculaire ab initio, calculs de la fonctionnelle de la densité, énergies d'ionisation, spectroscopie de coïncidence photoélectronique de seuil des photoions, énergies d'activation, entropies d'activation.

[Traduit par la Rédaction]

Received 17 August 2009. Accepted 5 October 2009. Published on the NRC Research Press Web site at canjchem.nrc.ca on 29 January 2010.

**P.M. Mayer<sup>1</sup> and E.E. Rennie.<sup>2</sup>** Department of Chemistry, University of Ottawa, 10 Marie-Curie, Ottawa, Canada, K1N 6N5.

**M.F. Guest.** Advanced Research Computing, Cardiff University, Redwood Building, King Edward VII Avenue, Cardiff CF10 3NB Wales, UK.

**L. Cooper.** Department of Chemistry, Heriot-Watt University, Riccarton, Edinburgh, EH14 4AS, UK.

**L.G. Shpinkova.** Department of Nuclear Spectroscopy Methods, Institute of Nuclear Physics, Moscow State University, Moscow 119899, Russia.

**D.M.P. Holland and D.A. Shaw.** Daresbury Laboratory, Daresbury, Warrington, Cheshire, WA4 4AD, UK.

<sup>1</sup>Corresponding author (e-mail: pmmayer@uottawa.ca).

<sup>2</sup>Present address: Varian, Inc. 2700 Mitchell Drive Walnut Creek, CA 94598.

## Introduction

Primary amines such as *n*-butylamine and *iso*-butylamine display significant molecular ions ( $\sim 10\%$  of the base peak,  $m/z$  30  $\text{CH}_2\text{NH}_2^+$ ) in their electron ionization (EI) mass spectra, while the molecular ion of *sec*-butylamine is only  $\sim 1\%$  of the base peak ( $m/z$  44). *t*-Butylamine is one of many *t*-butyl-containing molecules that exhibit almost no molecular ion in their EI mass spectrum (the list includes *t*-butanol, *t*-butyl methyl ether, *t*-butyl halides, and related compounds such as *t*-pentylamine and trimethylsilylether, among others).<sup>1</sup> The lack of a molecular ion in  $(\text{CH}_3)_3\text{CR}$  systems is due primarily to a large geometry difference between the neutral and ionized molecule, in the form of a long C–C bond between the quaternary carbon and one of the methyl groups, driven by the formation of a stable  $(\text{CH}_3)_2\text{CR}$  moiety in the radical cation (when R is a charge/spin stabilizing group, such as  $\text{CH}_3$ ,<sup>2</sup>  $\text{NH}_2$  (see Results),  $\text{OH}$ ,<sup>3</sup>  $\text{OCH}_3$ ,<sup>2</sup> and  $\text{CN}$ <sup>4</sup>). Vertical ionization of the neutrals produces highly excited ions. Coupled with what are often small activation energies,  $E_0$ , for dissociation, the generated molecular ions simply cannot survive on the microsecond timescale of most mass spectrometers. To probe this issue further with *t*-butylamine, we have employed threshold photoelectron spectroscopy to explore the ionization of molecular orbitals with binding energies up to 28 eV and threshold photoelectron photoion coincidence spectroscopy to determine appearance energies for all ion dissociation channels up to a photon energy of 34 eV. The lowest energy dissociation channel, methyl radical loss, was modeled to extract thermochemical information for the  $(\text{CH}_3)_2\text{CNH}_2^+$  cation.

## Experimental procedures

The pulsed TPEPICO spectrometer<sup>5</sup> in which the dissociation, kinetic, and threshold photoelectron studies were performed, and the 5 m normal incidence monochromator,<sup>6</sup> attached to the Daresbury Laboratory synchrotron radiation source, have been described in detail previously. Briefly, the coincidence spectrometer employs a pulsed extraction technique,<sup>7</sup> the principal advantage of which is that threshold electrons can be detected with a high energy resolution, whilst also allowing the associated ions to be collected with a high mass resolution. In the present arrangement,<sup>5</sup> a very low electric field is applied initially across the interaction region to extract threshold electrons, the detection of which triggers the application of a high voltage ( $\sim 1$  kV) pulse across the interaction region to draw the ion towards the drift tube, initiating the (time-of-flight) TOF measurement. The time between the arrival of the electron and the associated ion is measured electronically, with the summation of many events producing a TOF spectrum. With the present apparatus, the minimum residence time has been measured as  $1.116 \pm 0.050$   $\mu\text{s}$ , using the experimental procedure described in Holland et al.<sup>5</sup>

The threshold photoelectron spectrum was recorded in the binding-energy range from 8 to 28 eV using only the electron-detection part of the coincidence spectrometer. The spectrum was normalized to the incident photon intensity using the signal from a photomultiplier monitoring the radiation after it impinged upon a sodium salicylate coated screen. The threshold photoelectron spectrum was measured

at a photon resolution of 0.1 nm FWHM ( $\sim 18$  meV at  $h\nu = 15$  eV). Lithium fluoride or indium filters could be inserted into the photon beam exiting the monochromator to help suppress higher order radiation. The binding-energy scale was calibrated by recording a threshold photoelectron spectrum of a gas mixture comprising *t*-butylamine, argon, and krypton.

## Computational procedures

Standard ab initio molecular orbital and density functional theory calculations<sup>8</sup> were carried out with the Gaussian 98 suite of programs.<sup>9</sup> Vibrational frequencies were calculated for all optimized geometries (B3-LYP/6–31+G(d,p)) to verify that they corresponded to equilibrium structures. Vibrational frequency scaling factors were chosen from the computational chemistry comparison and benchmark database.<sup>10</sup> Single-point energy calculations at the geometries specified in the text were performed with the G3B3<sup>11,12</sup> composite method, employing B3-LYP/6–31+G(d,p) geometries and zero-point vibrational energies (ZPEs). Neutral and ion enthalpies of formation were derived using the atomization method outlined by Nicholaides and Radom.<sup>13</sup> Thermal corrections incorporated standard  $(H_{298} - H_0)$  terms for the elements.

Vertical ionization energies and their relative spectral intensities (pole strengths) of *t*-butylamine were obtained using the outer valence Green's function (OVGF) approach.<sup>14</sup> The calculations employed the GAMESS-UK<sup>15,16</sup> suite of programs, with a variety of basis sets. For consistency, the geometries were fully optimized at the MP2 level using both cc-pVTZ and cc-pVDZ basis sets.<sup>17–20</sup> The OVGF calculations were performed at the cc-pVTZ-optimized equilibrium geometry of  $C_s$  symmetry using both the cc-pVDZ and cc-VTZ basis sets. Five inner-shell orbitals (the 1s functions on each C and N) were frozen. The cc-VTZ results are listed in Table 1, together with the distribution analysis derived from a Mulliken population analysis of the single configuration (the Hartree–Fock SCF wave function) generated at the same geometry used in the OVGF calculations.

The TPEPICO breakdown curve for the lowest energy-dissociation channel was modeled as described previously.<sup>21–27</sup> In the absence of a kinetic shift, the curve shape is dictated by the parent-ion thermal (rotational and vibrational) energy, the monochromator band pass function (photon resolution  $\sim 8$  meV), and the threshold electron analyzer transmission function ( $\sim 9$  meV full width at half-maximum) derived from a threshold electron spectrum obtained from the photoionization of krypton in the region of the  $^2\text{P}_{1/2}$  ionization limit under the conditions used in the TPEPICO measurements.<sup>21–23</sup> A kinetic step function is used to allow the activation energy,  $E_0$ , to be varied until a satisfactory fit to the experimental breakdown curves was obtained. This kinetic step function was obtained using an RRKM calculation<sup>28,29</sup> according to the standard equation:

$$[1] \quad k(E) = \frac{\sigma N^\ddagger (E - E_0)}{h \rho(E)}$$

where  $\sigma$  is the reaction symmetry number,  $h$  is Planck's constant, and  $N^\ddagger$  and  $\rho$  are the transition state sum-of-states and molecular ion density of states, respectively. The transition-



**Table 1.** Experimental and OVGF vertical ionization energies and charge-distribution analyses of *t*-butylamine.

Orbital	Ionization energy (eV)		Orbital character (% atomic population) <sup>a</sup>												
	OVGF	Experiment	(Me) <sub>3</sub> –					–C–			–NH <sub>2</sub>				
			Cs	Cp	Cdf	Hs	Hpd	Cs	Cp	Cdf	Ns	Np	Ndf	Hs	Hpd
1a'			11.2	2.1	0.2	1.7	0.1	22.4	1.7	0.3	46.8	1.8	0.1	10.6	1.0
2a'	24.88	23.9	37.8	1.9	0.3	10.9	0.4	12.5	5.5	0.5	19.8	1.8	0.1	8.0	0.6
3a'	22.78	21.9	62.3	0.9	0.3	26.8	0.8	0.0	7.9	0.4	0.1	0.5	0.0	0.0	0.0
1a''	22.78		60.8	1.0	0.2	26.6	0.8	0.0	9.1	0.3	0.0	0.6	0.0	0.4	0.0
4a'	18.56	18.3	12.7	21.5	1.1	21.0	0.7	19.9	0.5	0.0	1.0	14.7	0.4	6.1	0.4
2a''	16.54		1.5	14.5	0.3	9.5	0.5	0.0	8.7	0.2	0.0	35.5	0.3	28.1	0.8
5a'	15.84	15.79	0.7	37.1	0.7	25.4	1.1	0.7	16.3	0.1	0.1	13.9	0.1	3.8	0.4
6a'	15.20	15.14	0.6	45.3	0.6	31.1	1.3	0.0	14.8	0.1	1.0	5.1	0.2	0.0	0.2
3a''	14.75	14.65	0.2	43.3	0.4	33.0	1.1	0.0	3.6	0.8	0.0	9.6	0.1	7.8	0.2
7a'	14.01		0.0	49.6	0.7	40.9	1.2	0.0	0.6	1.1	0.6	4.6	0.0	0.5	0.1
4a''	13.52	13.57	0.0	45.4	1.1	41.3	1.0	0.0	0.8	0.2	0.0	5.1	0.2	4.7	0.1
5a''	13.13	13.03	0.0	50.5	1.8	46.5	1.1	0.0	0.0	0.1	0.0	0.0	0.0	0.0	0.0
8a'	12.74	12.81	0.1	31.1	1.7	29.7	0.6	0.5	9.4	1.6	1.0	19.0	0.2	4.9	0.3
9a'	11.91	11.92	0.2	38.8	2.0	24.7	1.0	0.0	17.5	1.1	0.2	13.3	0.2	0.5	0.4
6a''	11.60	11.42	0.7	45.0	2.0	20.3	1.2	0.0	23.7	1.6	0.0	1.8	0.3	3.4	0.0
10a'	9.41	9.40	0.6	12.5	0.2	5.7	0.3	0.2	5.9	2.1	4.4	64.5	0.0	2.0	1.7

<sup>a</sup>Cs refers to the s orbital on carbon, Cdf refers to d and f orbitals on carbon, and so forth.

state vibrational frequencies were chosen to be the same as those calculated for the molecular ion (see above), less one, arbitrarily chosen, mode to represent motion over the col. The calculated rotational constants of the molecular ion were used for both molecular ion and transition state when calculating the ro-vib densities and sums of states (which were calculated by the direct count algorithm).<sup>30</sup> The uncertainties quoted for  $E_0$  reflect (i) the uncertainty in the adiabatic IE chosen to convert photon energy to ion internal energy and (ii) the range of  $E_0$  values that gave satisfactory fits to the experimental breakdown curves.

## Results and discussion

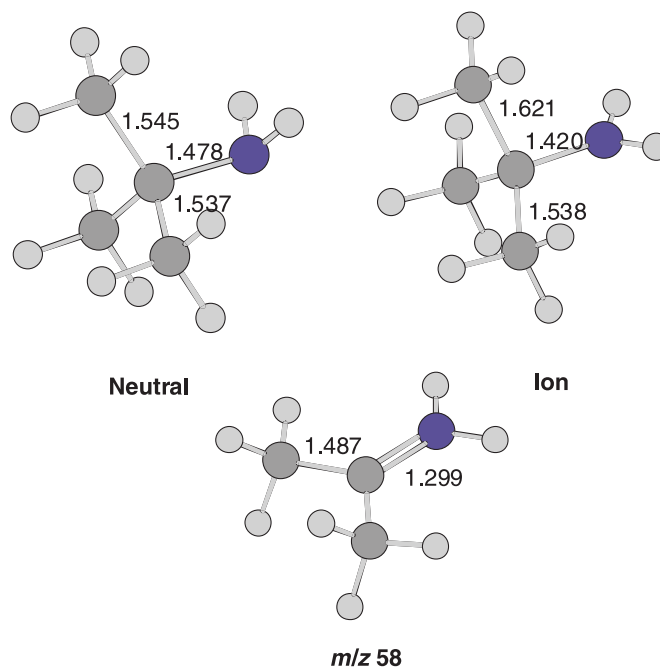
### The geometry of *t*-butylamine

The structures of neutral and ionized *t*-butylamine are shown in Fig. 1 along with selected geometrical parameters. As was previously found for *t*-butyl-containing species,<sup>2</sup> the ion exhibits a long C–C bond (1.621 Å) between the (CH<sub>3</sub>)<sub>2</sub>CNH<sub>2</sub> moiety and a methyl group. This is accompanied by an increased planarity of the carbons involved in the long bond and the amino group. The bond elongation allows the (CH<sub>3</sub>)<sub>2</sub>CNH<sub>2</sub> moiety to more closely resemble a delocalized system with a partial (CH<sub>3</sub>)<sub>2</sub>C–NH<sub>2</sub> double bond (evident from the bond length in Fig. 1).

### Threshold photoelectron spectrum

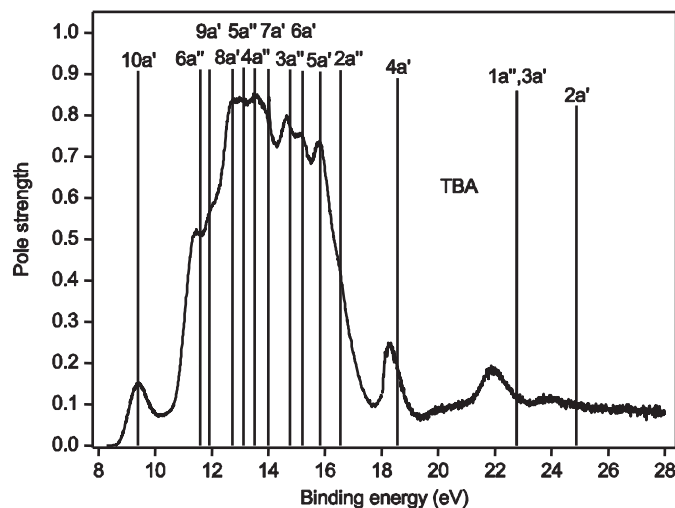
The valence-shell threshold photoelectron spectrum of *t*-butylamine is plotted in Fig. 2, together with the OVGF ionization energies and relative spectral intensities. The predicted ionization energies for the outer valence orbitals agree remarkably well with the observed values, thereby enabling structure in the experimental spectrum to be associated with ionization from specific molecular orbitals. A similar correlation is also feasible for the more tightly bound 4a', 1a'', 3a', and 2a' orbitals, although the calculated ionization energies of these inner valence orbitals are slightly higher than the experimental values. It is noticeable that the

**Fig. 1.** B3-LYP/6–31+G(d,p) optimized geometries for neutral and ionized *t*-butylamine and the fragmentation product  $m/z$  58, along with selected geometric parameters. Bond lengths are in Å.



peaks occurring at 18.3, 21.9, and 23.9 eV are less intense than those associated with the outer valence orbitals and are superimposed upon a continuum. This indicates that the molecular orbital model of ionization<sup>31</sup> no longer holds for these inner valence orbitals and that electron correlation leads to the intensity associated with a particular orbital being redistributed amongst numerous satellite states. It is the superposition of these satellites that results in the observed continuum. Table 1 lists the experimental vertical ionization energies (IE<sub>v</sub>) obtained through inspection of the threshold photoelectron spectrum.

**Fig. 2.** The threshold photoelectron spectrum of *t*-butylamine together with the theoretical results (Table 1). The height of the bar is proportional to the calculated relative spectral intensity (pole strength).



To the best of our knowledge, neither a HeI-excited nor a threshold photoelectron spectrum of *t*-butylamine has been published. Al-Joboury and Turner<sup>32</sup> quote adiabatic ionization energies ( $IE_a$ ) of 8.83, 9.81, 12.46, and 15.11 eV, but they neither show a spectrum nor attempt to relate these energies with specific orbitals. Their values do not agree well with either the present experimental or the calculated OVGf results. From inspection of the threshold photoelectron spectrum, we obtain adiabatic and vertical ionization energies of the outermost  $10a'$  orbital of  $8.48 \pm 0.02$  and  $9.40 \pm 0.02$  eV, respectively. The corresponding values given by Aue et al.<sup>33</sup> are 8.46 and 9.25 eV, respectively, and are thus in good agreement. The G3B3  $IE_a$  is significantly higher at 8.69 eV (Table 2). According to the OVGf calculations, the vertical ionization of the outermost orbital is  $\sim 2.2$  eV lower than that of the next ( $6a''$ ) orbital. These theoretical predictions correlate satisfactorily with the experimental spectrum because the peak at 11.42 eV, associated with the  $6a''$  orbital, leads to a separation of 2.0 eV between the bands corresponding with the  $10a'$  and  $6a''$  orbitals. It is noticeable that the threshold photoelectron yield remains finite across the Franck–Condon gap between the  $(10a')^{-1} \tilde{X}^2A'$  and the  $(6a'')^{-1} \tilde{A}^2A'$  state bands. This is due to resonant autoionization from super-excited states lying in the relevant energy region.

Ionization from the  $9a'$  orbital gives rise to a shoulder at 11.92 eV in the experimental spectrum. The next four orbitals ( $8a'$ ,  $5a''$ ,  $4a''$ , and  $7a'$ ) have similar binding energies and ionization results in overlapping bands, which form the most intense feature in the experimental spectrum. It should be noted that the very sharp peak at 14 eV is due to krypton, which was used to calibrate the energy scale. Ionization from each of the next three orbitals ( $3a''$ ,  $6a'$ , and  $5a'$ ) produces a distinct maximum (at 14.65, 15.14, and 15.79 eV, respectively), whereas ionization from the  $2a''$  orbital, with a predicted ionization energy of 16.54 eV, gives rise to no discernible feature.

The overall shape of the threshold photoelectron spectrum of *t*-butylamine is typical of those observed for small polyatomic molecules.<sup>34,35</sup> Experimentally, it has been found that

the relative intensities of photoelectron bands associated with weakly bound orbitals tend to be greater in conventional spectra than those in threshold photoelectron spectra, whereas the converse holds for the more tightly bound orbitals. The enhancement in the latter bands can be attributed to resonant autoionization from numerous super-excited (Rydberg or valence) states.

The charge-distribution analysis given in Table 1 may be used to characterize the molecular orbitals in terms of atomic populations. In molecules of low symmetry, such as the  $C_s$  symmetry applicable to *t*-butylamine, it is often useful to group together individual contributions into smaller molecular species relevant to that particular molecule. The charge distributions listed in Table 1 are presented in this manner. The results show that the electron density associated with the outermost  $10a'$  orbital is concentrated on the nitrogen atom and arises mainly from the 2p orbital. The electron densities for the following nine orbitals are similar to one-another, with the major contributions being C 2p and H 1s from the  $(Me)_3$  group. The composition of the next orbital ( $2a''$ ) is different in that the principal contributions arise from the N 2p and H 1s orbitals of atoms located at the opposite end of the molecule. The inner valence  $4a'$  orbital is the first to possess a significant C 2s component. Finally, the  $1a''$  and  $3a'$ , and to a lesser extent the  $2a'$ , orbitals contain substantial contributions from the C 2s and H 1s orbitals on the  $(Me)_3$  group whilst N 2s provides the principal component to the most tightly bound inner valence orbital  $1a'$ .

### Threshold photoelectron photoion coincidence spectroscopy

Threshold photoelectron photoion coincidence spectra were acquired from 8.54 to 34.04 eV. Table 3 lists the appearance energies (AEs) for each ion, obtained from inspection of their threshold for appearance. Breakdown curves for all ions except  $m/z$  73 (*t*-butylamine,  $(CH_3)_3CNH_2^+$ ) and 58 ( $(CH_3)_2CNH_2^+$ ) are shown in Fig. 3. The threshold region including  $m/z$  73 and 58 is presented in Fig. 4. The experimentally derived  $IE_a$  (Table 1) was employed to correct the experimental TPEPICO photon energy to ion internal energy

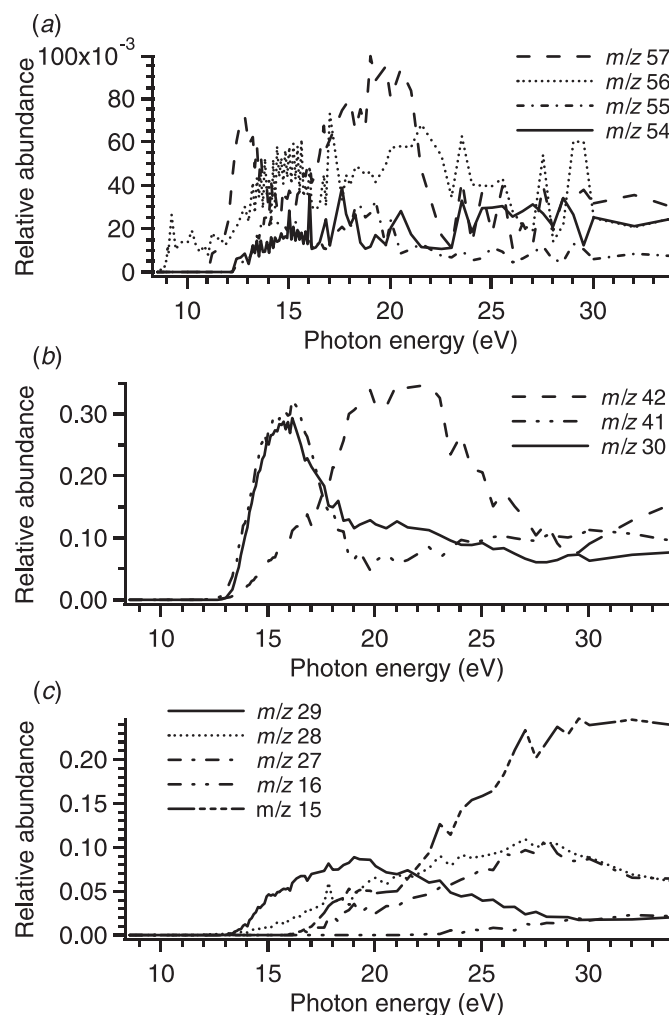
**Table 2.** Comparison of calculated and experimentally measured  $\Delta_f H$  values and relative energies.

	$\Delta_f H_{298}$ (kJ mol <sup>-1</sup> )			Relative energy (eV)		
	G3	Present	Literature <sup>a</sup>	G3	Present	Literature
(CH <sub>3</sub> ) <sub>3</sub> CNH <sub>2</sub>	-120 <sup>b</sup>	(-120.0±0.8) <sup>c</sup>	-120.0±0.8		0	0
(CH <sub>3</sub> ) <sub>3</sub> CNH <sub>2</sub> <sup>++</sup>	719	698±2	696	8.69	8.48±0.02	8.46±0.09, <sup>d</sup> 8.83, <sup>e</sup> 8.64 <sup>f</sup>
(CH <sub>3</sub> ) <sub>2</sub> CNH <sub>2</sub> <sup>+</sup>	592 <sup>g</sup>	603±4 <sup>h</sup>	592 <sup>i</sup>			
CH <sub>3</sub> <sup>•</sup>	142	(145.7) <sup>c</sup>	145.7			
(CH <sub>3</sub> ) <sub>2</sub> CNH <sub>2</sub> <sup>+</sup> + CH <sub>3</sub> <sup>•</sup>				8.80 (0 K) 8.85 (298 K)	8.96±0.04 (0 K) 9.01±0.04 (298 K)	8.89 <sup>i</sup>

<sup>a</sup>Taken from data in the NIST database<sup>1</sup> and Lias et al.<sup>45</sup><sup>b</sup> $\Delta_f H_0 = -83$  kJ mol<sup>-1</sup><sup>c</sup>Taken as the literature value.<sup>d</sup>Photoelectron spectroscopy, Aue et al.<sup>33</sup><sup>e</sup>Photoelectron spectroscopy, Al-Joboury and Turner.<sup>32</sup><sup>f</sup>Photoelectron spectroscopy, Watanabe et al.<sup>46</sup><sup>g</sup> $\Delta_f H_0 = 618$  kJ mol<sup>-1</sup><sup>h</sup> $\Delta_f H_0 = 631$  kJ mol<sup>-1</sup><sup>i</sup>Electron ionization appearance energy, Lossing et al.<sup>37</sup> Temperature is usually assumed to be 298 K.**Table 3.** Experimental AE values for *t*-butylamine.

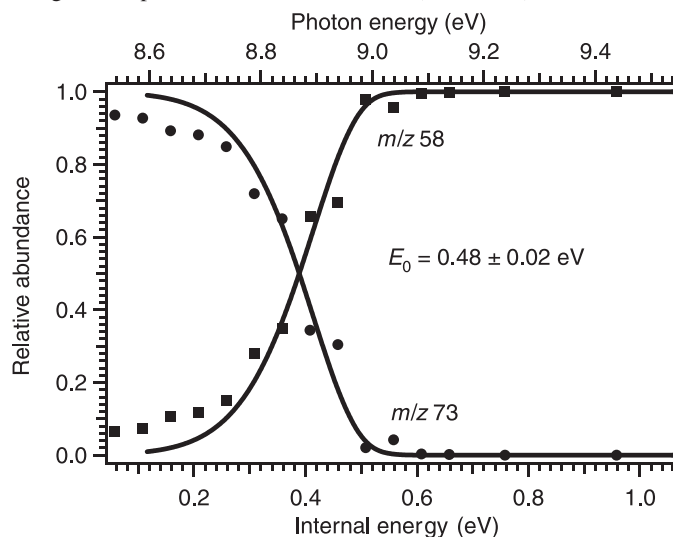
<i>m/z</i>	AE	
	This work	Reference 37
58	<8.5	8.89
57	11.2±0.2	
56	8.70±0.05	
55	20.0±0.5	
54	13.0±0.2	
43	13.3±0.1	
42	12.6±0.2	
41	12.4±0.2	
40	13.6±0.1	
38	23.0±0.5	
30	12.8±0.2	
29	13.0±0.2	
28	12.0±0.2	
27	16.3±0.2	
16	21.5±1.0	
15	16.0±0.1	

for subsequent data fitting. Ionized *t*-butylamine (*m/z* 73) dissociates by loss of a methyl radical to form (CH<sub>3</sub>)<sub>2</sub>CNH<sub>2</sub><sup>+</sup>, *m/z* 58. This is the analogous reaction to the formation of CH<sub>2</sub>NH<sub>2</sub><sup>+</sup> from ionized primary alkyl amines.<sup>36</sup> The reaction has no kinetic shift, and a fit was generated with the thermal population of neutral *t*-butylamine convoluted with the monochromator band pass and electron transmission functions. The latter shifts the precursor ion disappearance point higher than the true 0 K threshold, and so this threshold cannot be simply read straight off the breakdown curve in Fig. 4. The so-derived 0 K  $E_0$  of  $0.48 \pm 0.02$  eV corresponds to a 0 K energy of  $8.96 \pm 0.04$  eV relative to the neutral molecule (the 0 K appearance energy,  $AE_0$ ). This value can be corrected to a 298 K value of  $9.01 \pm 0.04$  eV employing the theoretical temperature corrections for the species involved. This AE can be used with the literature  $\Delta_f H$  values for neutral *t*-butylamine and the methyl radical (Table 2) to yield a  $\Delta_f H_{298}$  for (CH<sub>3</sub>)<sub>2</sub>CNH<sub>2</sub><sup>+</sup> of  $603 \pm 3$  kJ mol<sup>-1</sup>. This value is  $\sim 10$  kJ mol<sup>-1</sup> higher than

**Fig. 3.** TPEPICO breakdown curves for all observed ions other than *m/z* 73 and 58.

the previously derived value of Lossing et al.<sup>37</sup> (based on an electron ionization appearance energy value) and the G3B3 estimate. The  $\Delta_f H_{298}$  of CH<sub>2</sub>NH<sub>2</sub><sup>+</sup> is 750.3 kJ mol<sup>-1</sup> and

**Fig. 4.** Threshold breakdown curves for  $m/z$  73 and 58 (points) along with representative fits to the data (solid lines).



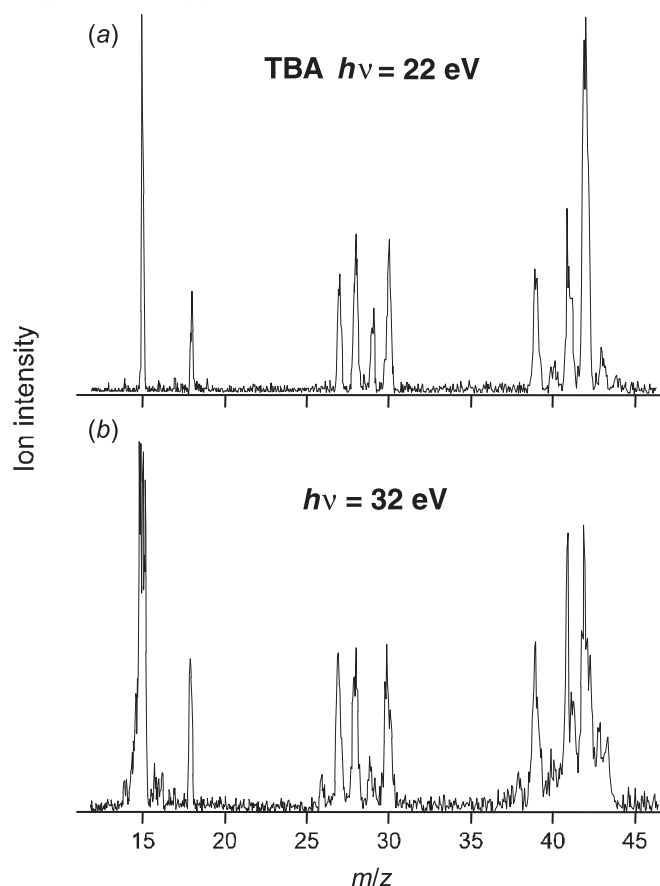
that of the mono-methyl-substituted ion  $\text{CH}_3\text{CHNH}_2^+$  is  $665 \pm 1.4 \text{ kJ mol}^{-1}$ .<sup>36,38</sup> These values indicate a successive methyl-substitution effect on the  $\text{CH}_2\text{NH}_2^+$  ion  $\Delta_f H_{298}$  of 85 and 62  $\text{kJ mol}^{-1}$ . This compares to, and is consistent with, the diminishing effect observed in the analogous alcohol system of  $\text{CH}_2\text{OH}^+$ ,  $\text{CH}_3\text{CHOH}^+$ , and  $(\text{CH}_3)_2\text{COH}^+$  of 119 and 90  $\text{kJ mol}^{-1}$  (based on their  $\Delta_f H_{298}$  values of 711, 592, and 502  $\text{kJ mol}^{-1}$ , respectively).<sup>39</sup> A  $\Delta_f H_{298}$  for  $(\text{CH}_3)_2\text{CNH}_2^+$  of 592  $\text{kJ mol}^{-1}$  (from the G3B3 calculations and the previous EI AE study) gives a somewhat smaller drop in the successive methyl-substitution effect of 85 and 73  $\text{kJ mol}^{-1}$ .

Employing a  $\Delta_f H_{298}$  for  $(\text{CH}_3)_2\text{CNH}_2^+$  of  $603 \pm 3 \text{ kJ mol}^{-1}$ , and the proton affinity (PA) value of  $932.3 \text{ kJ mol}^{-1}$ ,<sup>1</sup> leads to a  $\Delta_f H_{298}$  for 2-propanimine  $(\text{CH}_3)_2\text{C}=\text{NH}$  of  $5.3 \pm 3 \text{ kJ mol}^{-1}$ , which to our knowledge is the first report of this value. The  $\Delta_f H_{298}$  for  $(\text{CH}_3)_2\text{CNH}_2^+$  of 592  $\text{kJ mol}^{-1}$ , together with the experimental PA value of  $932.3 \text{ kJ mol}^{-1}$ ,<sup>1</sup> leads to a  $\Delta_f H_{298}$  for 2-propanimine of  $-5.7 \text{ kJ mol}^{-1}$ . Each compares well with, but are on opposite sides of, the G3B3  $\Delta_f H_{298}$  of  $-0.3 \text{ kJ mol}^{-1}$ . While it again would be useful to examine the methyl-substitution effect, this time on neutral methylenimine, the reported uncertainties in the  $\Delta_f H_{298}$  for  $\text{CH}_2\text{NH}$  ( $69 \pm 8 \text{ kJ mol}^{-1}$ )<sup>40</sup> and that of  $(\text{CH}_3)\text{CH}=\text{NH}$  ( $24 \pm 8 \text{ kJ mol}^{-1}$ )<sup>40</sup> are so large as to make the exercise impractical.

### Charge-separation reactions in doubly ionized *t*-butylamine cations

The G3B3 calculations predict vertical double-ionization energies of 26.4 and 26.6 eV for the singlet and triplet states, respectively, of the *t*-butylamine dication, whilst the corresponding adiabatic energies are 21.3 and 24.9 eV, respectively. For the singlet dication, the computations show that there is a large shift in geometry, putting one of the methyl groups over the  $\text{NH}_2$ . However, the doubly charged parent ion is not observed experimentally, indicating that it is unstable in relation to the microsecond timescale of the measurements, and fragments into two singly charged ions together with a neutral species.

**Fig. 5.** Ion TOF spectra of *t*-butylamine recorded at photon energies of (a) 22 eV and (b) 32 eV.



Ion TOF spectra of *t*-butylamine, recorded at photon energies of 22 and 32 eV, are plotted in Fig. 5, and it is noticeable that the widths of some of the peaks, particularly those associated with  $m/z$  15, 41, 42, and 43, are broader in the spectrum recorded at 32 eV than in that recorded at 22 eV. The peak width is dependent upon the fragment-ion initial kinetic energy and can be used to deduce double-ionization thresholds. In previous work,<sup>2,21,41,42</sup> we have shown that the width of the  $m/z$  15 peak provides a reliable estimate of the double-ionization threshold in molecules where the doubly charged parent ion is not observed experimentally because it appears that this fragment is often formed in combination with another small fragment ion in the dissociation of the doubly charged parent ion.

The TOF spectrum of *t*-butylamine recorded at 32 eV reveals two interesting features. First, the  $m/z$  15 peak profile contains several distinct components. One of these components coincides with the single peak observed in the TOF spectrum recorded at 22 eV, and therefore corresponds to an  $m/z$  15 fragment formed with very low kinetic energy. The appearance of the other components indicates that, at a photon energy of 32 eV,  $m/z$  15 fragments are produced through additional dissociation processes with the release of at least two distinct kinetic energies. Second, at 32 eV, the TOF peak profiles associated with the  $m/z$  41 and 43, and probably also 42, fragments are doublets. This is unusual at such relatively low excitation energies and demonstrates that these heavier fragment ions, presumably formed as the sec-



ond ionic species in the charge-separation reaction, carry away significant kinetic energy. In our previous charge-separation studies,<sup>2,21,41,42</sup> although the width of the TOF peak of the heavier ion was broader than that corresponding to a thermal ion, a doublet was not observed. The evidence from the TOF spectra of *t*-butylamine suggests that charge-separation reactions in the dication lead to the formation of fragment ions with *m/z* 15, together with *m/z* 41, 42 or 43, and an accompanying neutral species. Both the *m/z* 15 and the heavier fragment ion possess substantial kinetic energy.

The present results for *t*-butylamine show that the fragment peak broadening becomes evident at excitation energies of 26 eV, and above, thereby placing an upper limit on the double-ionization energy. Thus, the experimental value is in satisfactory agreement with the calculated vertical double-ionization energies of the singlet and triplet states of the dication. The present experimental result is also in accord with measurements of 26.1 eV for the vertical double-ionization energies of both the singlet and triplet states of *n*-butylamine.<sup>43,44</sup>

## Conclusion

The threshold photoelectron spectrum of *t*-butylamine was recorded between 8.5 and 28 eV. Threshold photoelectron photoion coincidence spectra were recorded between 8.5 and 35 eV and appearance energies for 15 fragment ions were obtained. The lowest energy dissociation is the loss of a methyl group to form the (CH<sub>3</sub>)<sub>2</sub>CNH<sub>2</sub><sup>+</sup> ion. RRKM fitting of this dissociation leads to a  $\Delta_f H_{298}$  for (CH<sub>3</sub>)<sub>2</sub>CNH<sub>2</sub><sup>+</sup> of 603 ± 3 kJ mol<sup>-1</sup>. This value is ~10 kJ mol<sup>-1</sup> higher than the previously EI-AE-derived value of Lossing et al.<sup>37</sup> and the G3B3 estimate. The present  $\Delta_f H_{298}$ , combined with the previously reported value and the results of G3B3 calculations, leads to a recommended  $\Delta_f H_{298}$  for 2-propanimine 0 ± 5 kJ mol<sup>-1</sup>, which to our knowledge is the first report of this value.

## Acknowledgements

The authors are grateful to the Council for the Central Laboratory of the Research Councils (UK) for the allocation of beam time at the Daresbury Laboratory Synchrotron Radiation Source. PMM thanks the Natural Sciences and Engineering Research Council of Canada (NSERC) for continuing financial support and the University of Ottawa for seed funds to undertake these experiments.

## References

- (1) NIST Chemistry Webbook. *NIST Standard Reference Database Number 69*; National Institute of Standards and Technology: Gaithersburg, MD, 2005.
- (2) Rennie, E. E.; Cooper, L.; Shpinkova, L. G.; Holland, D. M. P.; Shaw, D. A.; Guest, M. F.; Mayer, P. M. *J. Phys. Chem. A* **2009**, *113* (20), 5823. doi:10.1021/jp900991p. PMID: 19388684.
- (3) Beveridge, W.; Garioch, I. W.; Hunter, J. A.; Johnson, C. A. F.; Parker, J. E. *Org. Mass Spectrom.* **1991**, *26* (5), 416. doi:10.1002/oms.1210260510.
- (4) Mayer, P. M.; Guest, M. F.; Cooper, L.; Shpinkova, L. G.; Rennie, E. E.; Holland, D. M. P.; Shaw, D. A. *J. Phys.*

- Chem. A* **2010**, *114* (2), 867. doi:10.1021/jp9096524. PMID: 20000591.
- (5) Holland, D. M. P.; Shaw, D. A.; Sumner, I.; Hayes, M. A.; Mackie, R. A.; Wannberg, B.; Shpinkova, L. G.; Rennie, E. E.; Cooper, L.; Johnson, C. A. F.; Parker, J. E. *Nucl. Instrum. Meth. B* **2001**, *179* (3), 436. doi:10.1016/S0168-583X(01)00577-8.
- (6) Holland, D. M. P.; West, J. B.; MacDowell, A. A.; Munro, I. H.; Beckett, A. G. *Nucl. Instrum. Methods* **1989**, *B44*, 233.
- (7) Stockbauer, R. *Int. J. Mass Spectrom. Ion Phys.* **1977**, *25* (1), 89. doi:10.1016/0020-7381(77)80107-1.
- (8) Hehre, W. J.; Radom, L.; Schleyer, P. V.; Pople, J. A. *Ab initio Molecular Orbital Theory*; Wiley: New York, 1986.
- (9) Frisch, M. J.; Trucks, G. W.; Schlegel, H. B.; Scuseria, G. E.; Robb, M. A.; Cheeseman, J. R.; Zakrzewski, V. G.; Montgomery, J. A.; Stratmann, R. E.; Burant, J. C.; Dapprich, S.; Millam, J. M.; Daniels, A. D.; Kudin, K. N.; Strain, M. C.; Farkas, O.; Tomasi, J.; Barone, V.; Cossi, M.; Cammi, R.; Mennucci, B.; Pomelli, C.; Adamo, C.; Clifford, S.; Ochterski, J.; Petersson, G. A.; Ayala, P. Y.; Cui, Q.; Morokuma, K.; Malick, D. K.; Rabuck, A. D.; Raghavachari, K.; Foresman, J. B.; Cioslowski, J.; Ortiz, J. V.; Stefanov, B. B.; Liu, G.; Liashenko, A.; Piskorz, P.; Komaromi, I.; Gomperts, R.; Martin, R. L.; Fox, D. J.; Keith, T.; Al-Laham, M. A.; Peng, C. Y.; Nanayakkara, A.; Gonzalez, C.; Challacombe, M.; Gill, P. M. W.; Johnson, B.; Chen, W.; Wong, M. W.; Andres, J. L.; Gonzalez, C.; Head-Gordon, M.; Replogle, E. S.; Pople, J. A. *Gaussian 98*, rev. A.7; Gaussian Inc.: Pittsburgh PA, 1998.
- (10) NIST. Computational chemistry comparison and benchmark database. *NIST Standard Reference Database Number 101*; National Institute of Standards and Technology: Gaithersburg MD, 2006.
- (11) Baboul, A. G.; Curtiss, L. A.; Redfern, P. C. *J. Chem. Phys.* **1999**, *110* (16), 7650. doi:10.1063/1.478676.
- (12) Curtiss, L. A.; Raghavachari, K.; Redfern, P. C.; Rassolov, V.; Pople, J. A. *J. Chem. Phys.* **1998**, *109* (18), 7764. doi:10.1063/1.477422.
- (13) Nicolaides, A.; Rauk, A.; Glukhovtsev, M. N.; Radom, L. *J. Phys. Chem.* **1996**, *100* (44), 17460. doi:10.1021/jp9613753.
- (14) von Niessen, W.; Schirmer, J.; Cederbaum, L. S. *Comput. Phys. Rep.* **1984**, *1* (2), 57. doi:10.1016/0167-7977(84)90002-9.
- (15) Guest, M. F.; v Lenthe, J. H.; Kendrick, J.; Schoffel, K.; Sherwood, P. *Users Guide and Reference Manual*, version 7; Computing for Science Ltd.: CCLRC Daresbury Laboratory, 2005.
- (16) Guest, M. F.; Bush, I. J.; Van Dam, H. J. J.; Sherwood, P.; Thomas, J. M. H.; Van Lenthe, J. H.; Havenith, R. W. A.; Kendrick, J. *Mol. Phys.* **2005**, *103* (6-8), 719. doi:10.1080/00268970512331340592.
- (17) Dunning, T. H. *J. Chem. Phys.* **1989**, *90* (2), 1007. doi:10.1063/1.456153.
- (18) Wilson, A. K.; Woon, D. E.; Peterson, K. A.; Dunning, T. H. *J. Chem. Phys.* **1999**, *110* (16), 7667. doi:10.1063/1.478678.
- (19) Woon, D. E.; Dunning, T. H. *J. Chem. Phys.* **1993**, *98* (2), 1358. doi:10.1063/1.464303.
- (20) Woon, D. E.; Dunning, T. H. *J. Chem. Phys.* **1994**, *100* (4), 2975. doi:10.1063/1.466439.
- (21) Boulanger, A. M.; Rennie, E. E.; Holland, D. M. P.; Shaw, D. A.; Mayer, P. M. *J. Phys. Chem. A* **2008**, *112* (5), 866. doi:10.1021/jp077475y. PMID:18197646.
- (22) Rennie, E. E.; Boulanger, A.-M.; Mayer, P. M.; Holland, D. M. P.; Shaw, D. A.; Cooper, L.; Shpinkova, L. G. *J. Phys.*

- Chem. A* **2006**, *110* (28), 8663. doi:10.1021/jp0616866. PMID:16836427.
- (23) Boulanger, A.-M.; Rennie, E. E.; Holland, D. M. P.; Shaw, D. A.; Mayer, P. M. *J. Phys. Chem. A* **2007**, *111* (25), 5388. doi:10.1021/jp067863k. PMID:17539609.
- (24) Rabaev, M.; Boulanger, A.-M.; Holland, D. M. P.; Shaw, D. A.; Mayer, P. M. *J. Phys. Chem. A* **2009**, *113* (8), 1518. doi:10.1021/jp809404u.
- (25) Rennie, E. E.; Cooper, L.; Shpinkova, L. G.; Holland, D. M. P.; Shaw, D. A.; Guest, M. F.; Mayer, P. M. *J. Phys. Chem. A* **2009**, *113* (20), 5823. doi:10.1021/jp900991p. PMID:19388684.
- (26) Boulanger, A.-M.; Holland, D. M. P.; Shaw, D. A.; Mayer, P. M. *J. Am. Soc. Mass Spectrom.* **2009**, *20* (1), 20. doi:10.1016/j.jasms.2008.09.020. PMID:18926721.
- (27) Ferrier, B.; Boulanger, A.-M.; Holland, D. M. P.; Shaw, D. A.; Mayer, P. M. *Eur. J. Mass Spectrom. (Chichester, Eng.)* **2009**, *15* (2), 157. doi:10.1255/ejms.943. PMID:19423901.
- (28) Baer, T.; Hase, W. L. *Unimolecular Reaction Dynamics, Theory, and Experiments*; Oxford University Press: New York, 1996.
- (29) Baer, T.; Mayer, P. M. *J. Am. Soc. Mass Spectrom.* **1997**, *8* (2), 103. doi:10.1016/S1044-0305(96)00212-7.
- (30) Beyer, T.; Swinehart, D. F. *ACM Commun.* **1973**, *16* (6), 379. doi:10.1145/362248.362275.
- (31) Cederbaum, L. S.; Domcke, W.; Schirmer, J.; v Niessen, W. *Adv. Chem. Phys.* **1986**, *65*, 115. doi:10.1002/9780470142899.ch3.
- (32) Al-Joboury, M. I.; Turner, D. W. *J. Chem. Soc.* **1964**, 4434. doi:10.1039/jr9640004434.
- (33) Aue, D. H.; Webb, H. M.; Bowers, M. T. *J. Am. Chem. Soc.* **1976**, *98* (2), 311. doi:10.1021/ja00418a001.
- (34) Boulanger, A.-M.; Rennie, E. E.; Holland, D. M.; Shaw, D. A.; Mayer, P. M. *J. Phys. Chem. A* **2006**, *110* (27), 8563. doi:10.1021/jp0555854. PMID:16821842.
- (35) Rennie, E. E.; Cooper, L.; Johnson, C. A. F.; Parker, J. E.; Mackie, R. A.; Shpinkova, L. G.; Holland, D. M. P.; Shaw, D. A.; Hayes, M. A. *Chem. Phys.* **2001**, *263* (1), 149. doi:10.1016/S0301-0104(00)00346-3.
- (36) Bodi, A.; Kercher, J. P.; Bond, C.; Meteesatien, P.; Sztáray, B.; Baer, T. *J. Phys. Chem. A* **2006**, *110* (50), 13425. doi:10.1021/jp064739s. PMID:17165868.
- (37) Lossing, F. P.; Lam, Y.-T.; Maccoll, A. *Can. J. Chem.* **1981**, *59* (14), 2228. doi:10.1139/v81-322.
- (38) Traeger, J. C.; Harvey, Z. A. *J. Phys. Chem. A* **2006**, *110* (27), 8542. doi:10.1021/jp056409y. PMID:16821839.
- (39) Holmes, J. L.; Aubry, C.; Mayer, P. M. *Assigning Structures to Ions in Mass Spectrometry*; CRC Press: Boca Raton, FL, 2007.
- (40) Peerboom, R. A. L.; Ingemann, S.; Nibbering, N. M. M.; Liebman, J. F. *J. Chem. Soc., Perkin Trans. 2* **1990**, (11), 1825. doi:10.1039/p29900001825.
- (41) Cooper, L.; Shpinkova, L. G.; Rennie, E. E.; Holland, D. M. P.; Shaw, D. A. *Int. J. Mass Spectrom.* **2001**, *207* (3), 223. doi:10.1016/S1387-3806(01)00374-8.
- (42) Holland, D. M. P.; Shaw, D. A.; Sumner, I.; Bowler, M. A.; Mackie, R. A.; Shpinkova, L. G.; Cooper, L.; Rennie, E. E.; Parker, J. E.; Johnson, C. A. F. *Int. J. Mass Spectrom.* **2002**, *220* (1), 31. doi:10.1016/S1387-3806(02)00824-2.
- (43) Jeffreys, N.; Parry, D. E.; Harris, F. M. *Int. J. Mass Spectrom. Ion Process.* **1997**, *165/166*, 107. doi:10.1016/S0168-1176(97)00106-7.
- (44) Andrews, S. R.; Parry, D. E.; Harris, F. M. *J. Mass Spectrom.* **1995**, *30* (12), 1694. doi:10.1002/jms.1190301209.
- (45) Lias, S. G.; Bartmess, J. E.; Liebman, J. F.; Holmes, J. L.; Levin, R. D.; Mallard, W. G. *J. Phys. Chem. Ref. Data* **1988**, *17* (Suppl.1).
- (46) Watanabe, K.; Nakayama, T.; Mottl, J. *J. Quant. Spectrosc. Radiat. Transf.* **1962**, *2* (4), 369. doi:10.1016/0022-4073(62)90023-7.

# Task-specific ionic-liquid-catalyzed efficient synthesis of indole derivatives under solvent-free conditions

Sudarshan Das, Matiur Rahman, Dhiman Kundu, Adinath Majee, and Alakananda Hajra

**Abstract:** A sulfonic-acid-functionalized ionic liquid is used as a Brønsted acid catalyst for the efficient synthesis of indole derivatives in good-to-high yields at room temperature under solvent-free conditions. The catalyst can be reused for ten consecutive runs without significant loss of activity.

**Key words:** functionalized ionic liquid, indole derivatives, bis(indolyl)methanes, Michael adduct, recycling.

**Résumé :** On a utilisé un liquide ionique à base d'acide sulfonique fonctionnalisé comme catalyseur acide de Brønsted pour développer des synthèses efficaces de dérivés de l'indole obtenus avec des rendements allant de bons à élevés, dans des conditions sans solvant. Le catalyseur peut être réutilisé jusqu'à dix fois sans perte significative de son activité.

**Mots-clés :** liquide ionique fonctionnalisé, dérivés de l'indole, bis(indolyl)méthanés, adduit de Michael, recyclage.

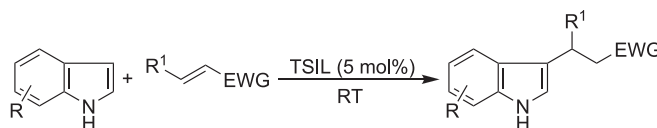
[Traduit par la Rédaction]

## Introduction

Michael reaction is one of the most important carbon-carbon bond-forming reactions.<sup>1</sup> The syntheses and the reactions of indole derivatives have received much interest for over a century because a number of their derivatives occur in nature and show versatile biological activities.<sup>2</sup> Since the 3-position of indole is the preferred site for electrophilic substitution reaction, 3-substituted indoles are versatile intermediates for the synthesis of a wide range of indole compounds.<sup>3</sup> Till date, several catalysts were used to catalyze the Michael addition of indoles to electron-deficient olefins; however, most of them were Lewis acids.<sup>4–20</sup> Many Lewis acids are deactivated or sometimes decomposed by nitrogen-containing reactants. Even when the desired reactions proceed, more than stoichiometric amounts of Lewis acids are required because the acids are deactivated by the nitrogen atom of indoles. However, the acid-catalyzed conjugate addition of indoles requires careful control of acidity to prevent side reactions such as dimerization and polymerization. For this reason, the need of a less expensive catalyst is desirable to secure catalytic activity, low toxicity, moisture, and air tolerance.

The application of Brønsted acidic task-specific ionic liquids (TSILs) as catalytic materials is growing continuously in the field of catalysis. Combining the useful charac-

Scheme 1.



teristics of solid acids and mineral acids, TSILs have been synthesized to replace traditional mineral liquid acids, such as hydrochloric acid and sulfuric acid, in chemical reactions. In view of green chemistry, the substitution of harmful liquid acids by reusable TSILs is the most promising catalytic system in chemistry.<sup>21–23</sup> Some “greener” halogen-free ionic liquids that involve phosphate or octyl sulfate anions have been reported, and effects of the anion and toxicology have been studied.<sup>24–26</sup> The use of Brønsted acidic TSILs to catalyze organic reactions is an area of ongoing activity and TSILs have been successfully used for various chemical transformations.<sup>27–29</sup> In continuation of our interest in ionic-liquid-mediated reactions,<sup>30</sup> we have explored the utility of a functionalized ionic liquid, 1-butane sulfonic acid-3-methylimidazolium tosylate, [BSMIM]Ts, as a catalyst for the conjugate addition of indoles with electron-deficient alkenes to produce 3-substituted indole derivatives under solvent-free conditions at room temperature (Scheme 1). To the best of our knowledge, this is the first report of a functionalized ionic liquid catalyzed Michael addition of various indoles to electron-deficient alkenes.

## Results and discussion

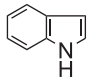
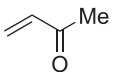
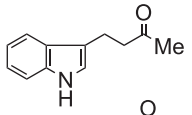
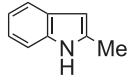
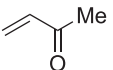
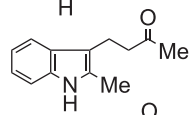
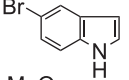
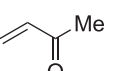
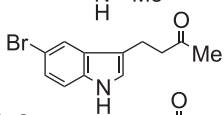
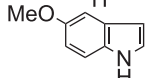
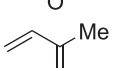
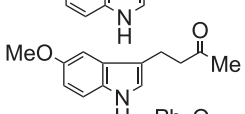
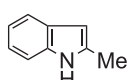
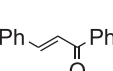
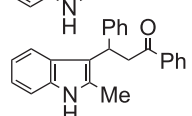
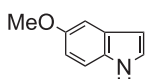
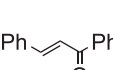
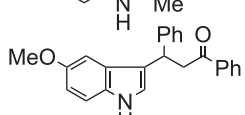
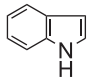
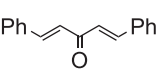
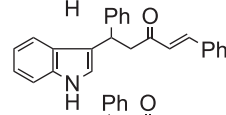
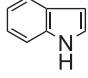
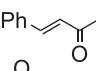
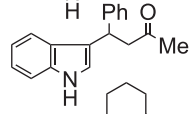
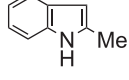

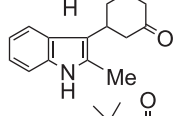
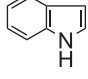
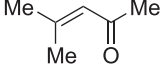
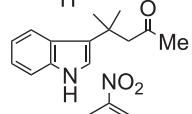
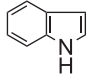
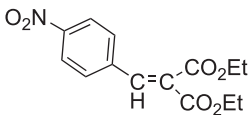
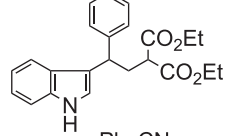
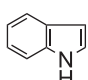
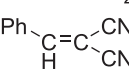
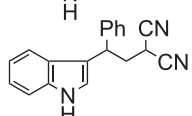
The experimental procedure is very simple. In a preliminary experiment, indole (2 mmol) was treated with methyl vinyl ketone (2 mmol) in the presence of TSIL (5 mol%) under solvent-free conditions at room temperature, providing the corresponding Michael adduct, exclusively, within 5 min

Received 23 July 2009. Accepted 5 October 2009. Published on the NRC Research Press Web site at canjchem.nrc.ca on 29 January 2010.

S. Das, M. Rahman, D. Kundu, A. Majee, and A. Hajra.<sup>1</sup>  
Department of Chemistry, Visva-Bharati University,  
Santiniketan 731235, India.

<sup>1</sup>Corresponding author (e-mail:  
alakananda.hajra@visva-bharati.ac.in).

**Table 1.** Conjugate addition of indoles with electron-deficient olefins.

Entry	Nucleophile	Electrophile	Product	Time (h)	Yield (%) <sup>a</sup>
1				5 min	95
2				5 min	88
3				10 min	85
4				10 min	82
5				2	85
6				5	64
7				1.5	82
8				8	50
9				1	76
10				13	70
11				10 min	82
12				17	40

<sup>a</sup> Yields refer to those of pure isolated products fully characterized by spectral and physical data.

in 95% yield. The structure of the product was settled from the spectral data. The crude product obtained after ether extraction was found to be pure, as there was no detectable amount of impurities or starting material in the <sup>1</sup>H NMR of the crude product. We next examined the generality of the present reaction conditions to a series of substituted indoles and electron-deficient alkenes. The results are summarized in Table 1.

Electron-deficient olefins, such as chalcone, benzalacetone, cyclohexenone, and dibenzylidene acetone, afforded the products in good-to-excellent yields. The reaction of dibenzylidene with indole gave mono-addition product in 82% yield. A hindered enone, mesityl oxide, which is difficult for conjugate addition, is also reacted to produce Michael ad-

duct in fairly good yield (Table 1, entry 10). By using substituted indoles, good-to-excellent yields were obtained. The substituents did not affect the reactivity of indoles significantly. The catalytic system also worked well with benzylidene malonate to produce the corresponding product in 82% yield (Table 1, entry 11). For benzylidene malononitrile, the corresponding Michael adduct was obtained in low yield under the same conditions even after a prolonged reaction time (Table 1, entry 12). The present protocol could be used on a 100 mmol scale using 2 mol% of the catalyst, which could be reused several times.

Generally, the reactions are clean, and the products are obtained in high yields without the formation of any side products, such as *N*-alkylation products. However, under the



present reaction conditions,  $\alpha,\beta$ -unsaturated aldehydes and esters did not afford the corresponding Michael addition products. Furthermore, the indole nitrogen did not require prior protection, and the avoidance of strong bases for deprotection permitted compatibility with a wide range of functional groups. The procedure did not require any inert atmospheric condition.

The efficacy and generality of the present protocol can be realized by comparing some of the results presented here with recently reported two ionic-liquid-based methods<sup>31,32</sup> as shown in Table 2, which compares reaction time, yields, and reaction conditions. Thus, it is clear from Table 2 that the present protocol can act as an effective method with respect to reaction times, yields, and reaction conditions.

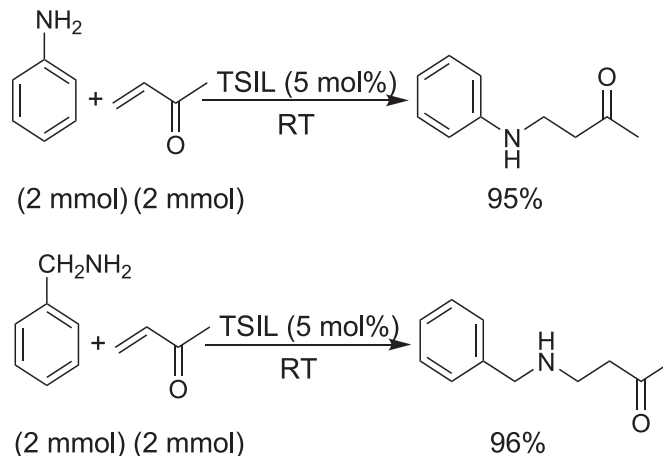
We extended the utility of catalyst for Michael addition of aniline and benzyl amine to methyl vinyl ketone under the present reaction conditions (Scheme 2). Surprisingly, both reactions proceeded very well in short times (25 min and 8 min, respectively), and the adducts were isolated in excellent yields. The results indicate that the catalyst can catalyze the Michael addition of both aromatic and aliphatic amines. This is a clear advantage over the recent reported ionic-liquid-catalyzed conjugate addition of aliphatic amines to electron-deficient alkenes.<sup>28</sup>

Synthesis of bis(indolyl)methanes is a subject of continuous interest to synthetic organic/medicinal chemists, as indoles and their derivatives have versatile biological activities and are widely present in various biologically active natural products.<sup>33</sup> The catalyst is also effective for the preparation of indole derivatives such as bis(indolyl)methane from benzaldehyde under present reaction conditions (Scheme 3). We found that 10 mg of the catalyst was sufficient to obtain the desired bis(indolyl)methane in 96% yield within 5 min at room temperature in neat conditions. Thus, this acidic ionic liquid is a versatile catalyst for various chemical transformations.

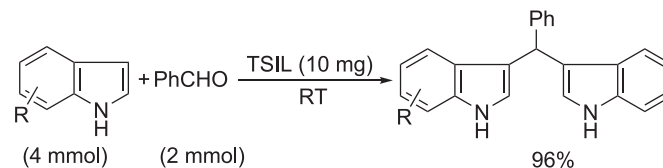
The reusability of the catalyst is an important benefit, especially for commercial applications. Thus, the recovery and reusability of the catalyst were investigated. After completion, the mixture was extracted with ether ( $3 \times 5$  mL) to obtain the desired products. The catalyst, left in the reaction vessel, was dried under vacuum and was reused for subsequent reactions. It showed the same activity as a fresh catalyst in term of yields. After ten recycles, the catalyst had a high activity and gave the desired product in fairly good yield (91%; Table 1, entry 1). Thus, this makes the process more cost-effective.

In conclusion, we have developed a mild, simple, environment-friendly, and cost-advantageous procedure for the Michael addition of indoles to electron-deficient alkenes using a recyclable task-specific acidic ionic liquid under solvent-free conditions. We believe that this procedure will provide a better and more practical alternative to the existing methodologies for the synthesis of 3-substituted indole derivatives. The catalyst is also effective for Michael addition of both aromatic and aliphatic amines as well as the synthesis of bis(indolyl)methane derivatives. Further procedures to broaden the scope of this methodology towards pharmaceuticals and biologically active compounds are under investigation.

Scheme 2.



Scheme 3.



## Experimental

The synthesis of the ionic liquid was carried out using a method similar to the reported.<sup>34</sup>

### Typical procedure for the synthesis of 4-(1*H*-indol-3-yl)-butan-2-one (Table 1, entry 1)

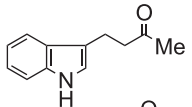
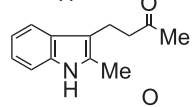
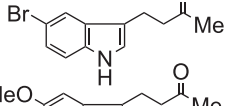
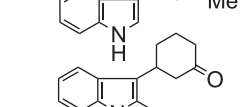
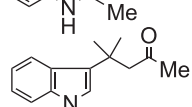
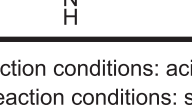
A mixture of indole (234 mg, 2 mmol) and MVK (162  $\mu$ L, 2 mmol) was stirred in presence of acidic ionic liquid (39 mg, 5 mol%) at room temperature for 5 min (TLC). After completion, the reaction mixture was extracted with diethyl ether ( $3 \times 10$  mL). Evaporation of solvent furnished the addition product as a solid (355 mg, 95%) whose spectroscopic data (IR and <sup>1</sup>H NMR) are in good agreement with those reported.<sup>5</sup> The catalyst left in the reaction vessel was dried under vacuum and was reused for the subsequent reaction. This procedure was followed for the synthesis of 3-substituted indoles listed in Table 1. Small amount of ethanol (0.5 mL) was added to the reaction mixture when both indoles and alkenes are solids. Analytically pure compound was obtained by silica gel chromatography using *n*-hexane/EtOAc as eluent. The spectral and elemental analyses of the compound, which are not readily available, are provided here.

The typical procedure for entry 1 (Table 1) was followed for 100 mmol scale reaction, taking a mixture of indole (11.7 g), MVK (8.1 mL), and acidic ionic liquid (780 mg). The pure product was obtained in 96% yield (17.90 g).

### 3-(5-Methoxy-1*H*-indol-3-yl)-1,3-diphenylpropan-1-one (Table 1, entry 6)

Solid; mp 150–151 °C. IR (cm<sup>-1</sup>)  $\nu$ : 3367, 1677, 1589, 1483, 1215. <sup>1</sup>H NMR (400 MHz, CDCl<sub>3</sub>)  $\delta$ : 7.95 (d, *J* = 0.7 Hz, 2H), 7.93 (d, *J* = 1.4 Hz, 1H), 7.55–7.17 (m, 10H), 6.97 (d, *J* = 2.3 Hz, 1H), 6.85–6.80 (m, 1H), 5.03 (t, *J* =

**Table 2.** Comparison of the present protocol with ionic-liquid-based reported methods.

Entry	Product	Present method		Reported method <sup>31</sup>		Reported method <sup>32</sup>	
		Time	Yield (%) <sup>a</sup>	Time (h)	Yield (%) <sup>b</sup>	Time (h)	Yield (%) <sup>c</sup>
1		5 min	95	24	96	3.5	90
2		5 min	88	16	88	3	93
3		10 min	85	12	95	—	—
4		10 min	82	12	92	—	—
5		1 h	76	20	70	4.5	87
6		13 h	70	—	—	—	—

<sup>a</sup> Present reaction conditions: acidic ionic liquid (5 mol%), RT, solvent-free (2 mmol scale).

<sup>b</sup> Reported reaction conditions: silica-supported sodium sulfonate with ionic liquid [DMIm]SbF<sub>6</sub> (11 – 14 mol%) in water, 30 °C (10 mmol scale).

<sup>c</sup> Reported reaction conditions: Cu(OTf)<sub>2</sub> (10 mol%) immobilized in ionic liquid [bmim]BF<sub>4</sub> (3 mL), RT (1 mmol scale).

7.1 Hz, 1H), 3.84–3.80 (m, 1H), 3.78 (s, 3H), 3.75–3.69 (m, 1H). <sup>13</sup>C NMR (100 MHz, CDCl<sub>3</sub>) δ: 198.5, 153.8, 144.1, 137.1, 132.9, 131.7, 128.5, 128.4 (2C), 128.1 (2C), 127.8 (2C), 127.0 (2C), 126.3, 122.1, 119.1, 112.2, 111.7, 101.5, 55.8, 45.1, 38.1. Anal. calcd. (%) for C<sub>24</sub>H<sub>21</sub>NO<sub>2</sub> (355.4): C 81.10, H 5.96, N 3.94; found: C 80.95, H 5.81, N 3.76.

## Acknowledgements

A. H. is pleased to acknowledge the financial support from the Department of Science and Technology (Grant No. SR/FTP/CS-107/2006). A. M. is pleased to acknowledge the financial support from the Council of Scientific and Industrial Research (CSIR) (Grant No. 01(2251)/08/EMR-II). D. K. thanks CSIR and M. R. thanks Visva-Bharati for their fellowships.

## References

- (1) Trost, B. M.; Fleming, I. *Comprehensive Organic Synthesis*; Pergamon: Oxford, 1991.
- (2) Sundberg, R. J. *The Chemistry of Indoles*; Academic Press: New York, 1996.
- (3) Moore, R. E.; Cheuk, C.; Patterson, G. M. L. *J. Am. Chem. Soc.* **1984**, *106* (21), 6456. doi:10.1021/ja00333a079.
- (4) Bandini, M.; Melchiorre, P.; Melloni, A.; Umani-Ronchi, A. *Synthesis* **2002**, 2002 (08), 1110. doi:10.1055/s-2002-31970.
- (5) Yadav, J. S.; Abraham, S.; Reddy, B. V. S.; Sabitha, G. *Synthesis* **2001**, 2001 (14), 2165. doi:10.1055/s-2001-18068.
- (6) Komoto, I.; Kobayashi, S. *J. Org. Chem.* **2004**, *69* (3), 680. doi:10.1021/jo0353177. PMID:14750791.
- (7) Harrington, P. E.; Kerr, M. A. *Synlett* **1996**, 1996 (11), 1047. doi:10.1055/s-1996-5685.
- (8) Zhan, Z. P.; Yang, R. F.; Lang, K. *Tetrahedron Lett.* **2005**, *46* (22), 3859. doi:10.1016/j.tetlet.2005.03.174.
- (9) Bartoli, G.; Bosco, M.; Giuli, S.; Giuliani, A.; Lucarelli, L.; Marcantoni, E.; Sambri, L.; Torregiani, E. *J. Org. Chem.* **2005**, *70* (5), 1941. doi:10.1021/jo048776w. PMID:15730329.
- (10) Firouzabadi, H.; Iranpoor, N.; Nowrouzi, F. *Chem. Commun. (Camb.)* **2005**, *6* (6), 789. doi:10.1039/b412653j. PMID:15685339.
- (11) Lin, C. C.; Hsu, J. M.; Sastry, M. N. V.; Fang, H. L.; Tu, Z. J.; Liu, J. T.; Yao, C. F. *Tetrahedron* **2005**, *61* (49), 11751. doi:10.1016/j.tet.2005.09.038.
- (12) Giuseppe, B.; Giustino, D. A.; Sandra, G.; Enrico, M.; Mauro, M. P.; Melissa, P. *Synthesis* **2008**, 320.
- (13) Hari, G. S.; Nagaraju, M.; Murthy, M. M. *Synth. Commun.* **2008**, *38* (1), 100. doi:10.1080/00397910701650815.
- (14) Das, B.; Chowdhury, N.; Damodar, K.; Reddy, K. R. *Helv. Chim. Acta* **2007**, *90* (2), 340. doi:10.1002/hlca.200790040.
- (15) Kusurkar, R. S.; Alkobati, N. A. H.; Gokule, A. S.; Chaudhari, P. M.; Waghchaure, P. B. *Synth. Commun.* **2006**, *36* (8), 1075. doi:10.1080/00397910500498788.
- (16) Chen, W.-Y.; Li, X.-S. *Synth. Commun.* **2009**, *39* (11), 2014. doi:10.1080/00397910802632555.
- (17) An, L.-T.; Zou, J.-P.; Zhang, L.-L.; Zhnag, Y. *Tetrahedron Lett.* **2007**, *48* (24), 4297. doi:10.1016/j.tetlet.2007.04.011.
- (18) Kawatsura, M.; Aburatani, S.; Uenishi, J. *Tetrahedron* **2007**, *63* (19), 4172. doi:10.1016/j.tet.2007.02.091.
- (19) Huang, Z.-H.; Zou, J.-P.; Jiang, W.-Q. *Tetrahedron Lett.* **2006**, *47* (45), 7965. doi:10.1016/j.tetlet.2006.08.108.
- (20) Firouzabadi, H.; Iranpoor, N.; Jafarpour, M.; Ghaderi, A. *J. Mol. Catal. Chem.* **2006**, *252* (1-2), 150. doi:10.1016/j.molcata.2005.11.025.

- (21) Cole, A. C.; Jensen, J. L.; Ntai, I.; Tran, K. L. T.; Weaver, K. J.; Forbes, D. C.; Davis, J. H., Jr. *J. Am. Chem. Soc.* **2002**, *124* (21), 5962. doi:10.1021/ja026290w. PMID: 12022828.
- (22) Fang, D.; Zhou, X.-L.; Ye, Z.-W.; Liu, Z.-L. *Ind. Eng. Chem. Res.* **2006**, *45* (24), 7982. doi:10.1021/ie060365d.
- (23) Leng, Y.; Wang, J.; Zhu, D.; Ren, X.; Ge, H.; Shen, L. *Angew. Chem. Int. Ed.* **2009**, *48* (1), 168. doi:10.1002/anie.200803567.
- (24) Wasserscheid, P.; Hal, R.; Bösmann, A. *Green Chem.* **2002**, *4*, 400. doi:10.1039/b205425f.
- (25) Fraga-Dubreuit, J.; Bourahla, K.; Rahmouni, M.; Bazureau, J. P.; Hamelin, J. *Catal. Commun.* **2002**, *3* (5), 185. doi:10.1016/S1566-7367(02)00087-0.
- (26) Garia, M. T.; Gathergood, N.; Scammells, P. J. *Green Chem.* **2005**, *7* (1), 9. doi:10.1039/b411922c.
- (27) Akbari, J.; Heydari, A. *Tetrahedron Lett.* **2009**, *50* (29), 4236. doi:10.1016/j.tetlet.2009.05.020.
- (28) Liang, X.; Wang, Y.; Gong, G.; Yang, J. *Catal. Commun.* **2008**, *10* (3), 281. doi:10.1016/j.catcom.2008.09.006.
- (29) Fang, D.; Shi, Q.-R.; Cheng, J.; Gong, K.; Liu, Z.-L. *Appl. Catal. Gen.* **2008**, *345* (2), 158. doi:10.1016/j.apcata.2008.04.037.
- (30) Ranu, B. C.; Dey, S. S.; Hajra, A. *Tetrahedron* **2003**, *59* (14), 2417. doi:10.1016/S0040-4020(03)00289-8.
- (31) Gu, Y.; Ogawa, C.; Kobayashi, S. *Org. Lett.* **2007**, *9* (2), 175. doi:10.1021/ol062446b. PMID:17217258.
- (32) Yadav, J. S.; Reddy, B. V. S.; Baishya, G.; Reddy, K. V.; Narasaiah, A. V. *Tetrahedron* **2005**, *61* (40), 9541. doi:10.1016/j.tet.2005.07.095.
- (33) Chakraborti, A. K.; Roy, S. R.; Kumar, D.; Chopra, P. *Green Chem.* **2008**, *10* (10), 1111. doi:10.1039/b807572g.
- (34) Du, Z.; Li, Z.; Deng, Y. *Synth. Commun.* **2005**, *35* (10), 1343. doi:10.1081/SCC-200057264.

# Circular dichroism and fluorescence spectroscopic study on the interaction of bisdemethoxycurcumin and diacetylbisdemethoxycurcumin with human serum albumin

Fakhrossadat Mohammadi, Abdol-Khalegh Bordbar, Khosro Mohammadi, Adeleh Divsalar, and Ali Akbar Saboury

**Abstract:** The interactions of bisdemethoxycurcumin (BDMC) as a bioactive constituent of turmeric and diacetylbisdemethoxycurcumin (DABC) as a novel synthetic derivative of curcumin with human serum albumin (HSA) have been investigated by fluorescence and circular dichroism (CD) spectroscopy. The binding parameters, including the number of substantive binding sites and the binding constants, have been estimated from the analysis of fluorescence measurements. The estimated binding parameters indicated that BDMC has higher affinity than DABC to bind HSA, suggesting the essential role of the phenolic OH groups of BDMC, which are acetylated in DABC. It was found that the binding site for BDMC and DABC is located in the vicinity of Trp-214 in subdomain IIA, which is the same as binding site for curcumin (CUR). The minor changes on the far-UV circular dichroism spectra resulted in partial changes in the calculated secondary structure contents of HSA. The negligible alteration in the secondary structure of HSA indicated that ligand-induced conformational changes are localized in the binding site and do not involve considerable changes in the protein folding. The visible CD spectra indicated that the optical activity observed during the ligand binding is due to induced-protein chirality.

**Key words:** bisdemethoxycurcumin (BDMC), diacetylbisdemethoxycurcumin (DABC), human serum albumin (HSA), fluorescence, circular dichroism (CD).

**Résumé :** Faisant appel à la spectroscopie de fluorescence et au dichroïsme circulaire (DC), on a étudié les interactions entre l'albumine sérique humaine (ASH) et le bisdéméthoxycurcumin (BDMC), un constituant bioactif de l'acide turmérique, ainsi que le diacétylbisdéméthoxycurcumin (DABC), un nouveau dérivé de synthèse du curcumin. Les paramètres de fixation, dont le nombre de sites de fixation substantifs ainsi que les constantes de fixation ont été évaluées à partir de l'analyse des mesures de fluorescence. Les paramètres de fixation évalués indiquent que l'affinité de fixation du BDMC pour l'ASH est plus élevée que celle du DABC ce qui suggère que les groupes phénoliques OH du BDMC, qui sont acétylés dans la DABC, sont essentiels. On a trouvé que le site de fixation pour le BDMC et le DABC est situé à proximité du Trp-214 dans la sous-domaine IIA; il s'agit du même site de fixation que celui pour le curcumin (CUR). Les changements mineurs dans les spectres de dichroïsme circulaire dans l'UV lointain résultent de changements partiels dans les teneurs en structure secondaire calculée de l'ASH. L'altération négligeable dans la structure secondaire de l'ASH indique que les changements conformationnels induits par le ligand sont localisés dans le site de fixation et n'impliquent pas de changements considérables dans le replis de la protéine. Les spectres de dichroïsme circulaire dans le visible indique que l'activité optique observée durant la fixation du ligand résulte d'une chiralité induite par la protéine.

**Mots-clés :** bisdéméthoxycurcumin (BDMC), diacétylbisdéméthoxycurcumin (DABC), albumine sérique humaine (ASH), fluorescence, dichroïsme circulaire (DC).

[Traduit par la Rédaction]

Received 2 March 2009. Accepted 13 October 2009. Published on the NRC Research Press Web site at canjchem.nrc.ca on 29 January 2010.

**Abbreviations:** HSA, human serum albumin; CUR, curcumin, DAC, diacetylcurcumin; DMC, demethoxycurcumin; BDMC, Bisdemethoxycurcumin; DABC, Diacetylbisdemethoxycurcumin; CD, circular dichroism.

**F. Mohammadi and A.-K. Bordbar.<sup>1</sup>** Laboratory of Biophysical Chemistry, Department of Chemistry, University of Isfahan, Isfahan 81746-73441, Iran.

**K. Mohammadi.** Department of Chemistry, College of Sciences, Persian Gulf University, Bushehr 75169, Iran.

**A. Divsalar.** Department of Biological Science, Tarbiat Moallem University, Tehran, Iran.

**A.A. Saboury.** Institute of Biochemistry and Biophysics, University of Tehran, Tehran, Iran.

<sup>1</sup>Corresponding author (e-mail: bordbar@chem.ui.ac.ir).



## Introduction

Curcumin, [1,7-bis(4-hydroxy-3-methoxyphenyl)1,6-heptadiene-3,5-dione] (Scheme 1a), is an active principle of the perennial herb *Curcuma longa* Linn. (commonly known as turmeric). The yellow-pigmented fraction of turmeric contains bioactive substances called curcuminoids, such as curcumin (CUR), demethoxycurcumin (DMC), bisdemethoxycurcumin (BDMC) (Scheme 1b), and the recently identified cyclocurcumin.<sup>1,2</sup> According to numerous studies, curcuminoids display anticarcinogenic,<sup>3,4</sup> antioxidant,<sup>5,6</sup> anti-inflammation,<sup>7</sup> and antiangiogenic properties,<sup>8,9</sup> and modulation of multi-drug-resistance gene and protein function.<sup>10,11</sup> The antimetastasis,<sup>12</sup> and also antitumor and antioxidant activity<sup>13</sup> of BDMC, is much greater than CUR and DMC. Hoehle et al.<sup>14</sup> studied the metabolism of CUR, DMC, and BDMC and their results on enzymatic hydrolysis under various conditions revealed that CUR and DMC are chemically less stable than BDMC, whereas reductive metabolites of all three curcuminoids are stable compounds. The anti-inflammatory properties of DMC and BDMC were attributed to the inhibition of inducible nitric oxide synthase (iNOS) and cyclooxygenase-2 (COX-2) expression, as initiated by the inhibition of nuclear factor-kappaB (NF-kappaB) activity. Additionally, both of them significantly inhibited carrageenan-induced paw edema in mice.<sup>15</sup> Diacetyl-bisdemethoxycurcumin (DABC) (Scheme 1c) is a new synthetic acetylated derivative of curcumin and has been shown to display moderate cytotoxicity ( $IC_{50} \sim 10 \mu\text{mol/L}$ ).<sup>16</sup>

Human serum albumin (HSA) is the major soluble protein constituent of blood plasma with many physiological functions. It contributes to colloid osmotic blood pressure and has an essential role in transport and disposition of many drugs, which are poorly soluble in water. The X-ray crystallographic measurements have shown that HSA is a globular protein and consists of a single polypeptide chain of 585 amino acid residues. HSA consists of three homologous domains (I, II and III). Each domain contains two separate helical subdomains (A and B), which are formed from six and four  $\alpha$ -helical, respectively. Terminal regions of sequential domains contribute to the formation of interdomain helices linking domain IB to IA, and IIB to IIIA, respectively. The secondary structure of HSA at pH 7.4 contains 65%  $\alpha$ -helix, 7%  $\beta$ -sheet, and 28% are the remaining structures (random coil and turn structures). The fluorophore groups of HSA include one tryptophan (residue 214 in domain IIA) and eleven tyrosine residues, of which seven are in domain I and four of them are in domain III. As can be deduced from the crystal structure of HSA, Trp-214 acts as an important stabilizer (by hydrophobic packing force) for the interface between subdomain IIA and IIIA. There are 35 cysteine residues in HSA, 34 of which form 17 disulfide bridges. Sixteen of these residues participate in the formation of eight so-called double disulfide bridges. Cys-34 does not participate in any disulfide bridge. The disulfide bridges, tryptophan, tyrosine, and phenylalanine residues, are the main chromophore groups in the circular dichroism spectra of HSA.<sup>17</sup> The crystal structure analyses have indicated that the principal regions of ligand binding sites of albumin are relocated in hydrophobic cavities in subdomain IIA (site I) and IIIA (site II). Remarkably, warfarin, an anticoagulant drug, and ibuprofen, a nonsteroidal anti-inflammatory agent, are considered stereotypical ligands for sites I and II, respec-

tively. HSA is capable of binding seven equivalents of long-chain fatty acids at multiple binding sites (IB, IIIA, IIIB, and subdomain interfaces) with different affinities.<sup>18–20</sup>

The serum albumin as a transport protein has an essential role in pharmacokinetic properties of drugs. Hence, study on the interaction of curcuminoids with HSA provides useful information for the formulation of these drugs. There are some reports on the interaction of curcumin with human and bovine serum albumin.<sup>21–27</sup> As a brief summary, these studies showed that the primary binding site of CUR is located in site I of HSA. The red-shifted absorption band and the binding of CUR to HSA in a right-handed chiral conformation is due to the dissociation of highly acidic phenolic OH groups of CUR. The interaction of diacetylcurcumin (DAC) and isoxazolcurcumin with BSA has been studied by Sahoo et al.<sup>28</sup> Their experimental results indicated minor conformational changes of BSA because of binding to these two derivatives of CUR and their binding location is in a hydrophobic cleft close to Trp-213.<sup>28</sup> However, there is no report on the interaction of BDMC and DABC with human serum albumin. In this research, we have studied the interaction of BDMC, as one of the natural polyphenol constituents of turmeric, and DABC, as a novel synthetic derivative of curcumin, with human serum albumin using fluorescence and circular dichroism (CD) spectroscopies.

## Experimental

### Materials

HSA (free fatty acid fraction V) was purchased from Sigma-Aldrich.

BDMC was separated from curcumin and DABC was synthesized based on a previously reported method.<sup>16</sup> Ethanol was obtained from Merck Company. All other materials and reagents were of analytical grade. Double distilled water was used for preparing the buffer solution.

### Preparation of the HSA solution

HSA was weighed and dissolved in 0.05 mol/L of pH 6.4 phosphate ( $\text{Na}_2\text{HPO}_4$  and  $\text{NaH}_2\text{PO}_4$ ) buffer solution. The exact concentrations of HSA were determined spectrophotometrically using the molar absorption coefficient of  $\epsilon_{278 \text{ nm}} = 35\,700 \text{ (mol/L}^{-1}\text{) cm}^{-1}$ .<sup>29</sup>

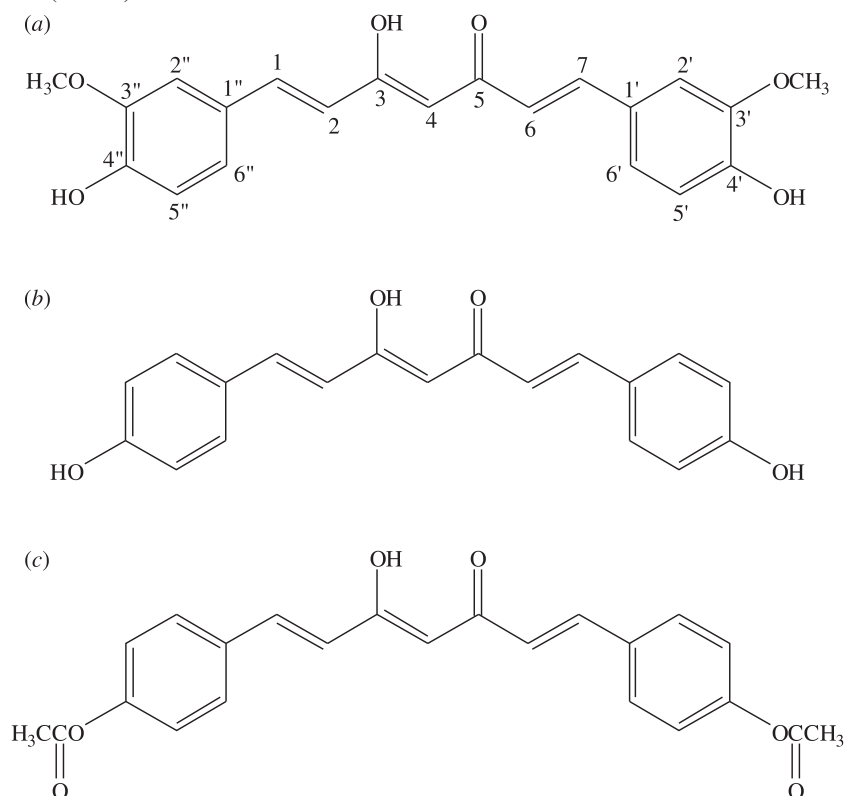
### Preparation of BDMC and DABC solutions

Stock solutions were prepared by dissolving BDMC and DABC in ethanol and different diluted solutions were made from the stock solutions with ethanol and their UV-vis absorption spectra were recorded between 250–600 nm. From the absorption versus concentration graph at the  $\lambda_{\text{max}}$  point (using the Beer-Lambert law), the molecular absorption coefficient of BDMC was found to be  $\epsilon_{417 \text{ nm}} = 46\,193 \text{ (mol/L}^{-1}\text{) cm}^{-1}$  and for DABC the result was  $\epsilon_{395 \text{ nm}} = 19\,122 \text{ (mol/L}^{-1}\text{) cm}^{-1}$ .

### Fluorescence measurements

HSA solution (3 mL, 3  $\mu\text{mol/L}$ ) in a 0.05 mol/L, pH 6.4 phosphate buffer was prepared in a 1 cm rectangular cell. BDMC and DABC solutions (1 mmol/L), which were prepared in ethanol, were consecutively added in  $\mu\text{L}$  volumes using a trace Hamiltonian syringe to the cell placed in the

**Scheme 1.** (a) Chemical structure of curcumin (CUR). (b) Chemical structure of bisdemethoxycurcumin (BDMC). (c) Chemical structure of diacetylbisdemethoxycurcumin (DABC).



sample chamber of the Shimadzu RF-5000 (Kyoto, Japan) spectrofluorimeter. Both the excitation and emission slit widths were set at 5 nm. The excitation wavelength was adjusted to 280 nm and the emission spectra were recorded for all of the samples in the range of 290–450 nm at 25 °C with a scan speed of 200 nm/min. Integration of spectra was done in the range of 290–390 nm to obtain the peak area. During the fluorescence measurements, ethanol that was added with the ligand never exceeded 3% (v/v). The presence of ethanol at 25% induces no major changes in the structure of HSA.<sup>30</sup> However, a control experiment was done on HSA with ethanol and proved the negligible effect of ethanol on the fluorescence intensity of HSA up to 3% (v/v) of ethanol (data are not shown). The other control experiments have also been done and proved that inner filter effect corrections are not required for the fluorescence data.

### CD measurements

All the CD spectra were recorded using Aviv spectropolarimeter model 215 (Proterion Corp., USA) at 25 °C. The scan speed was 20 nm/min and each spectrum was the average of four accumulated spectra. The CD spectra, recorded in the far-UV region (190–260 nm) using a 1 mm path length cell, were used to investigate the changes in the secondary structure of HSA. The protein concentration in the experiments for the far-UV region was 4.0 µmol/L. The results were expressed in molar ellipticity,  $[\theta]$  (deg cm<sup>2</sup> dmol<sup>-1</sup>). The CD software was used to predict the secondary structure of the protein according to the statistical method.<sup>31,32</sup>

The CD spectra recorded between 260–550 nm (near-UV

to visible range) using a cuvette of 1 cm path length were also studied. The induced CD is defined as the CD of the mixture of protein and ligand minus the CD of the protein alone at the same wavelengths and is displayed as  $\theta$  (ellipticity) in units of millidegrees (mdeg). The concentration of HSA solution in induced CD experiments was 15.04 µmol/L. During the CD spectroscopic measurements, ethanol content (added with the ligand) never exceeded 1.5% (v/v). It has been controlled and we observed no considerable changes due to the addition of alcohol.

## Results and discussion

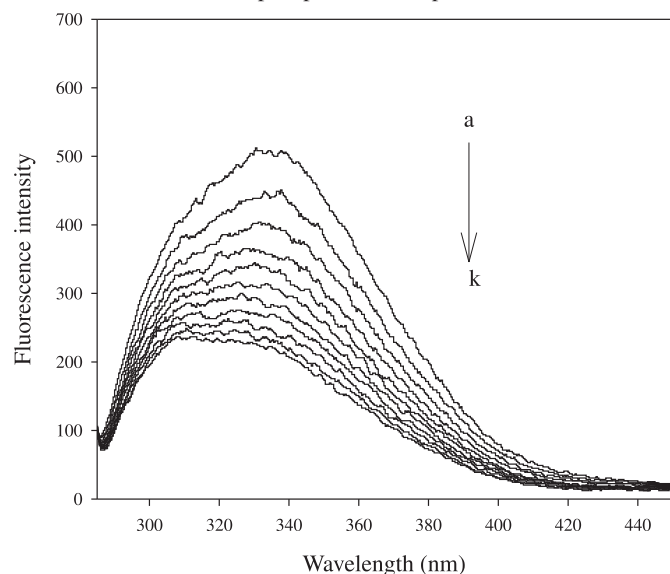
### Fluorescence studies

Fluorescence quenching is a procedure that decreases the fluorescence quantum yield of fluorophores by a variety of molecular interactions such as excited state reactions, energy transfer, molecular rearrangement, formation of a nonfluorescent ground state complex (static quenching), and collisional encounter between the fluorophore and quencher (dynamic quenching). The fluorescence quenching technique can reveal the nature of binding of small molecules with proteins. The fluorescence quenching data can be analyzed by the Stern–Volmer equation as follows:<sup>33</sup>

$$[1] \quad \frac{F_0}{F} = 1 + k_Q \tau_0 [Q] = 1 + K_{SV} [Q]$$

where  $F_0$  and  $F$  are the fluorescence intensities of fluorophore in the absence and presence of a quencher, respectively,  $[Q]$  is the quencher concentration, and  $K_{SV}$  is the Stern–Volmer quenching constant, which can be written as

**Fig. 1.** The fluorescence spectra of HSA (3  $\mu\text{mol/L}$ ) at different concentrations of BDMC: (a) 0  $\mu\text{mol/L}$ , (b) 0.7  $\mu\text{mol/L}$ , (c) 1.4  $\mu\text{mol/L}$ , (d) 2.2  $\mu\text{mol/L}$ , (e) 2.8  $\mu\text{mol/L}$ , (f) 3.5  $\mu\text{mol/L}$ , (g) 4.2  $\mu\text{mol/L}$ , (h) 4.9  $\mu\text{mol/L}$ , (i) 5.6  $\mu\text{mol/L}$ , (j) 6.3  $\mu\text{mol/L}$ , and (k) 7.0  $\mu\text{mol/L}$  measured in 0.050 mol/L phosphate buffer, pH 6.4,  $\lambda_{\text{ex}} = 280 \text{ nm}$ .



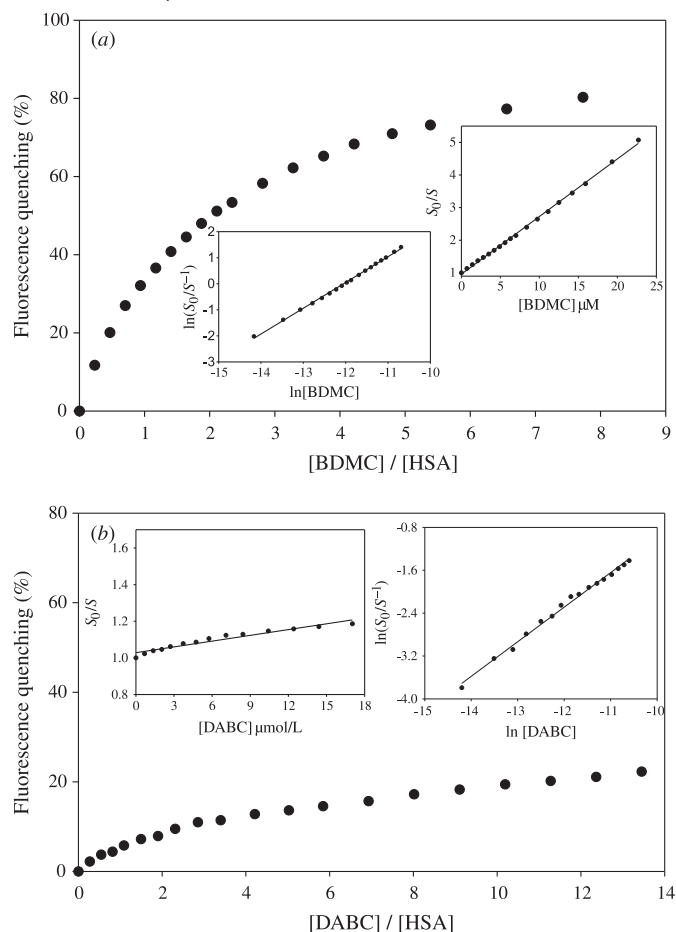
$K_{\text{SV}} = k_{\text{Q}}\tau_0$ , where  $k_{\text{Q}}$  is the bimolecule quenching rate constant and  $\tau_0$  is the average lifetime of the biomolecule without a quencher ( $\tau_0 = 10^{-8}\text{s}$ ).<sup>34</sup> The concentration of a quencher should be the free concentration, but in our experiments, the total concentration of the ligand (BDMC or DABC) was used. The total fluorescence intensity is usually expressed by the peak height, but it is more reasonable to use the total area of the fluorescence emission. So, in our results, we used the peak area of protein fluorescence spectra without or with ligand,  $S_0$  and  $S$ , respectively, instead of  $F_0$  and  $F$  in the Stern–Volmer equation.

It has been shown that both of the considered ligands in the current study (BDMC and DABC) have a quenching effect on the fluorescence emission of HSA. Only one tryptophan, Trp-214, located in subdomain IIA, is the predominant source of fluorescence emission in the UV region. However, minor contribution of tyrosine residue in fluorescence emission could be eliminated by adjusting the excitation wavelength at 295 nm. Figure 1 shows the quenching effect of BDMC on the fluorescence emission of HSA (data for DABC is not shown).

Figure 2 shows the percentage of quenching versus molar ratios of the ligand to protein (L/P) and the corresponding Stern–Volmer plots. As can be seen, the extent of quenching of HSA by BDMC is considerably greater than that by DABC. The estimated  $K_{\text{SV}}$  values are listed in Table 1. It is clear that quenching rate constants initiated by BDMC and DABC are greater than the maximum scatter quenching constant of various quenchers with the biopolymers ( $k_{\text{Q}} = 2 \times 10^{10} \text{ L mol}^{-1} \text{ s}^{-1}$ ).<sup>35</sup> So, the fluorescence quenching was not related to dynamic collision but it results from the formation of a nonfluorescent compound.

Based on the assumption that the fluorescence quenching of protein is a static process, and there are  $n$  substantive binding sites on protein to accommodate the ligand mole-

**Fig. 2.** Fluorescence quenching of HSA by (a) BDMC and (b) DABC in 0.050 mol/L phosphate buffer, pH 6.4,  $\lambda_{\text{ex}} = 280 \text{ nm}$  and  $[\text{HSA}] = 3 \mu\text{mol/L}$ .



**Table 1.** The Stern–Volmer constant,  $K_{\text{SV}}$ , bimolecule quenching rate constant,  $K_{\text{Q}}$ , number of substantive binding sites,  $n$ , and the binding constant,  $K_{\text{A}}$ , for the interaction of BDMC and DABC with HSA obtained from the fluorescence quenching measured in 0.050 mol/L phosphate buffer, pH 6.4 at  $\lambda_{\text{ex}} = 280 \text{ nm}$  and  $[\text{HSA}] = 3 \mu\text{mol/L}$ .

	BDMC	DABC
$K_{\text{SV}} ((\text{mol/L})^{-1})$	$1.77 \times 10^5$	$2.60 \times 10^4$
$K_{\text{Q}} ((\text{mol/L})^{-1} \text{ s}^{-1})$	$1.77 \times 10^{13}$	$2.60 \times 10^{12}$
$n$	0.99	0.63
$K_{\text{A}} ((\text{mol/L})^{-1})$	$1.49 \times 10^5$	$4.08 \times 10$

cules, the equilibrium between free and bound molecules can be given by the following equation:<sup>36</sup>

$$[2] \quad \ln \frac{F_0 - F}{F} = \ln K_{\text{A}} + n \ln [Q]$$

where  $F_0$ ,  $F$ , and  $[Q]$  are the same as the parameters in the Stern–Volmer equation.  $K_{\text{A}}$  is the apparent binding constant reflecting the reaction extent of protein and ligand. The value of  $n$  specifies the number of ligand molecules bound to a HSA macromolecule. The values of  $K_{\text{A}}$  and  $n$  derived from the intercept and slope of  $\ln \frac{F_0 - F}{F}$  versus  $\ln [Q]$  plot (Fig. 2) are listed in Table 1. From the values of  $n$ , it can be inferred

that there is one binding site on HSA for BDMC and DABC. The values of  $K_A$  reveal lower binding affinity of DABC than BDMC to HSA. The considerable different binding affinities of BDMC and DABC toward binding to HSA indicates the important role of the phenolic OH groups of BDMC, which are acylated in DABC, in the binding process.

We predict that the only fluorophore, Trp-214, is buried to some extent inside the protein in the hydrophobic environment. This prediction is based on the fact that the emission  $\lambda_{\max}$  of Trp-214 was 330 nm (Fig. 1), which is the emission region of hidden tryptophan molecules that are known to be usually around 320–325 nm,<sup>37</sup> while fluorescence emission of the exposed tryptophan molecules is around 340 nm due to solvent relaxation. The HSA conformation seems to bury Trp-214 in a hydrophobic environment. The alteration in fluorescence intensity of Trp-214 in the presence of a ligand may arise as a direct quenching effect or as a result of conformational changes induced after ligand binding. In the case of the DABC ligand, the emission  $\lambda_{\max}$  at 330 nm is not changed. No spectral shift was observed for the emission spectra upon DABC–HSA interaction, indicating that Trp-214 was not exposed to any alteration in polarity. For BDMC–HSA, the emission  $\lambda_{\max}$  slightly shifted to shorter wavelengths (Fig. 1). If the tryptophan residue becomes hydrogen bonded or exposed to water, the maximum emission shifts to longer wavelengths.<sup>32</sup> Hence, if tryptophan moves to a more hydrophilic environment upon binding to the drugs, it is expected to observe a redshift in the emission maximum. Due to the slightly blueshifted emission spectra of HSA in the presence of BDMC, it can be concluded that the binding of BDMC to HSA has changed the Trp-214 to a more hydrophobic environment.

Since there is no report on the interaction of BDMC and DABC with HSA, we compared our findings in the present work with the results of CUR or its derivatives binding to HSA. A recently published study by Mandeville et al.<sup>38</sup> revealed the moderate binding affinity of CUR to HSA with the association binding constant,  $K = 5.5 \times 10^4$  (mol/L)<sup>-1</sup>, which is comparable to the values reported by Pulla Reddy et al.,<sup>21</sup>  $K = 2.0 \times 10^5$  (mol/L)<sup>-1</sup>, Kunwar et al.,<sup>25</sup>  $K = 6.1 \times 10^4$  (mol/L)<sup>-1</sup>, and also Zsila et al.,<sup>22</sup>  $K = 0.93 \times 10^5$  (mol/L)<sup>-1</sup>. The results of these studies indicated that the most probable binding site for CUR on HSA is in the vicinity of Trp-214 in a hydrophobic cavity of subdomain IIA.

The order of the current calculated binding constant between BDMC and HSA,  $K = 1.49 \times 10^5$  (mol/L)<sup>-1</sup>, is comparable to that of CUR. Also, the number of substantive binding sites for BDMC,  $n = 0.99$ , is comparable to that of CUR ( $n = 1.33$ ) reported by Mandeville et al.<sup>38</sup> using the same double logarithmic plot of  $\ln \frac{F_0 - F}{F}$  versus  $\ln[Q]$ . Therefore, we deduced that the binding mode, binding affinity, and binding site of BDMC on HSA are very similar to those of CUR. This conclusion implies that the methoxy groups of CUR have a negligible role in the interaction with HSA, and the phenolic hydroxyl groups play an important role in the drug–protein interactions. This implication can be confirmed by comparing the results of a CUR derivative such as DABC, which lacks the methoxy groups and its phenolic OH groups are acetylated. Both the apparent binding constant value,  $K = 4.08 \times 10^5$  (mol/L)<sup>-1</sup>, and number of the

bound DABC to HSA,  $n = 0.63$ , reflect the weak drug–protein interaction.

In a similar way, we analyzed the binding interaction of CUR and DAC with HSA and BSA.<sup>39</sup> We showed that there was a great difference between CUR and DAC in their binding affinity toward both serum albumins. The association binding constants for DAC were of the order of  $10^2$ , whereas for CUR, they were in the range of  $10^5$ – $10^6$  (in accordance with the previous studies). So, the main conclusion on the essential role of the phenolic hydroxyl groups of CUR in the binding process can be confirmed on the basis of the great difference between binding parameters of CUR and DAC, and also BDMC and DABC. It is of considerable interest to notice that the difference between our approaches and that of others is that they have carried out the experiments at neutral and alkaline pH, in which CUR has low stability and decomposes relatively fast.<sup>40</sup> Though there is no evidence on the stability of CUR derivatives compounds such as BDMC, DAC, and DABC at different pHs, we have done all the experiments at pH 6.4 to remove the interference of probable decomposition products of CUR or its derivatives and also to gain logical comparison for the considered ligands. The interaction of DAC with BSA has been studied by Sahoo et al.<sup>28</sup> They obtained a binding constant in the range of  $10^5$  (mol/L)<sup>-1</sup>, which is in contrast with our results. This discrepancy may have arisen from the experimental procedures, for instance, they analyzed the UV absorption spectra to calculate the binding constant, whereas we analyzed the fluorescence spectra.

### Energy transfer from HSA to BDMC

The fluorescence quenching of HSA, after its binding with BDMC, indicated the occurrence of energy transfer between ligand and protein. It is important to recognize that the valuable parameters concerning the molecular details of the donor–acceptor pair can be obtained by using fluorescence resonance energy transfer (FRET).<sup>33</sup> FRET occurs whenever the emission spectrum of the fluorophore (donor) overlaps with the absorption spectrum of another molecule (acceptor). The extent of overlap between the emission spectrum of the donor (protein) and the absorption spectrum of the acceptor (ligand), and the relative orientation of the donor and acceptor transition dipoles determine the rate of energy transfer. Due to the important effect of the distance between the donor and acceptor on the extent of energy transfer, numerous applications of energy transfer in biochemical research have been found. According to Förster's theory, the efficiency of energy transfer,  $E$ , is described by the following equation:<sup>41</sup>

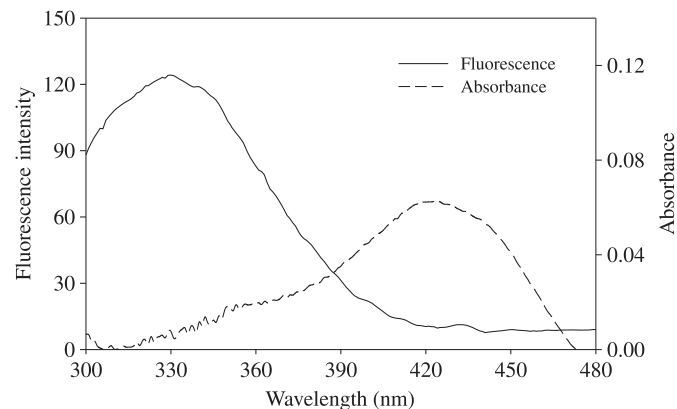
$$[3] \quad E = 1 - \frac{F}{F_0} = \frac{R_0^6}{R_0^6 + r^6}$$

where  $F$  and  $F_0$  are the fluorescence intensity of the donor in the absence and presence of an equal amount of acceptor,  $r$  is the distance from the bound ligand on protein to the tryptophan residue, and  $R_0$  is the Förster critical distance at which 50% of the excitation energy is transferred to the acceptor and can be calculated by the following equation:

$$[4] \quad R_0^6 = 8.8 \times 10^{-2} K^2 N^{-4} \Phi J$$



**Fig. 3.** Fluorescence emission and UV–vis absorption of solutions containing BDMC as ligand and HSA as protein measured in 0.050 mol/L phosphate buffer, pH 6.4,  $\lambda_{\text{ex}} = 280$  nm, and  $[\text{HSA}] = [\text{BDMC}] = 6 \mu\text{mol/L}$ .



where  $K^2$  is a factor describing the relative orientation of the transition dipoles of the donor and acceptor (for a random orientation as in fluids,  $K^2 = 2/3$ ),  $N$  is the average refractive index of the medium in the wavelength range where spectral overlap is significant,  $\Phi$  is the fluorescence quantum yield of the donor, and overlap integral,  $J$ , expresses the extent of overlap between the normalized fluorescence emission spectrum of the donor and the acceptor absorption spectrum.  $J$  is given by the following equation:

$$[5] \quad J = \frac{\sum F(\lambda)\varepsilon(\lambda)\lambda^4\Delta\lambda}{\sum F(\lambda)\Delta\lambda}$$

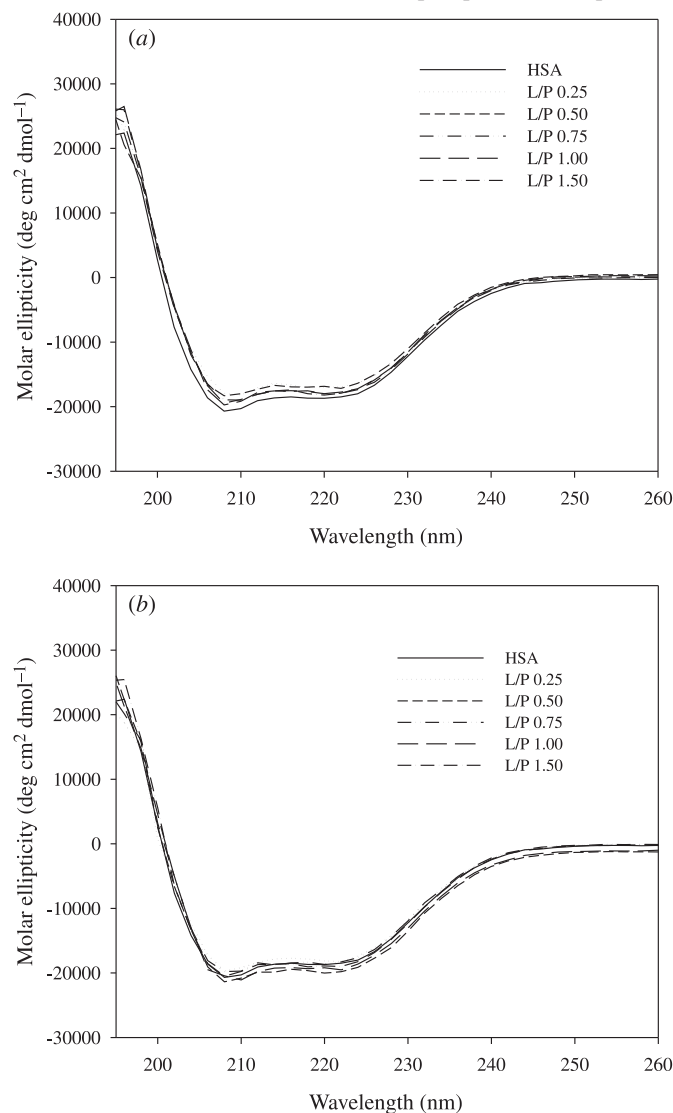
In this equation,  $F(\lambda)$  is the fluorescence intensity of the fluorescent donor at wavelength  $\lambda$  and is dimensionless,  $\varepsilon(\lambda)$  is the molar absorption coefficient of the acceptor at wavelength  $\lambda$ .

In our recent study, we prepared the solutions containing equimolar concentrations of ligand (BDMC or DABC) and HSA and recorded their UV–vis absorption spectra. As the fluorescence emission of protein is affected by the excitation light at 280 nm, the spectrum ranged from 300 to 500 nm and was chosen to obtain the overlapping integral. As shown in Fig. 3, the overlapping between the fluorescence emission of free HSA and absorption spectrum of BDMC is considerable. The UV–vis spectrum of the solution containing DABC and HSA did not show any absorption in the wavelength range of 300–500 nm (data are not shown), so, the energy transfer could not be calculated. The efficiency of energy transfer and overlapping integration can be easily calculated using eqs. [3] and [5]. For calculating the Förster critical distance in eq. [4],  $K^2$  is  $2/3$ ,  $N$  is 1.336, and  $\Phi$  is 0.118.<sup>42</sup> By using the obtained value for  $R_0$  from eq. [4] and  $E$  from eq. [3], the  $r$  value can be calculated. HSA has a single tryptophan residue (Trp-214) and the determined  $r$  is the distance from the bound ligand to this residue. The determined parameters for the interaction of human serum albumin with BDMC using FRET are reported in Table 2. It can be seen from this table that the distance from the bound ligand to tryptophan are less than 7 nm, indicating a nonradiative energy transfer mechanism for quenching.<sup>33</sup> However, the value of  $r$  is higher than the respective critical

**Table 2.** Förster critical distance,  $R_0$ , the binding distance to the tryptophan residue of protein,  $r$ , the overlap integral,  $J$ , and the energy transfer efficiency,  $E$ , upon the interaction of BDMC with HAS using fluorescence resonance energy transfer (FRET) measured in 0.050 mol/L phosphate buffer, pH 6.4,  $\lambda_{\text{ex}} = 280$  nm, and  $[\text{HSA}] = [\text{BDMC}] = 6 \mu\text{mol/L}$ .

$R_0$ (nm)	$r$ (nm)	$J$ ( $\text{cm}^3 \text{mol/L}$ )	$E$
2.167	2.816	$4.761 \times 10^{-15}$	0.172

**Fig. 4.** Far-UV circular dichroism spectra of 4.0  $\mu\text{mol/L}$  HSA in the absence and presence of different concentrations of (a) BDMC and (b) DABC measured in 0.050 mol/L phosphate buffer, pH 6.4.



distance ( $R_0$ ), so, the static quenching is more likely responsible for fluorescence quenching than the other mechanism of nonradiative energy transfer.

The  $R_0 = 2.167$  nm and  $r = 2.816$  nm for the binding of BDMC to HSA and are comparable to the  $R_0 = 2.744$  nm and  $r = 3.095$  nm for the case of CUR–HSA reported by Barik et al.,<sup>26</sup> which are in good agreement with our results for CUR–HSA ( $R_0 = 2.80$  nm and  $r = 3.10$  nm) and CUR–BSA ( $R_0 = 2.94$  nm and  $r = 3.16$  nm).<sup>39</sup> The calculated För-

**Table 3.** Content of the secondary structure of HSA upon interaction with (a) BDMC and (b) DABC in different molar ratios of ligand to protein measured in 0.050 mol/L phosphate buffer, pH 6.4 and [HSA] = 4.0  $\mu$ mol/L.

Ligand to protein molar ratios	(a) BDMC				(b) DABC			
	$\alpha$ -Helix (%)	$\beta$ -Sheet (%)	$\beta$ -Turn (%)	Random coil (%)	$\alpha$ -Helix (%)	$\beta$ -Sheet (%)	$\beta$ -Turn (%)	Random coil (%)
0	62.9	7.5	13.3	16.3	62.9	7.5	13.3	16.3
0.25	56.7	9.2	14.0	20.1	59.4	8.5	13.8	18.3
0.50	58.1	8.8	13.9	19.2	64.8	6.9	12.7	15.6
0.75	59.9	8.2	13.6	18.3	62.1	7.7	13.3	16.9
1.00	60.7	8.0	13.4	17.9	65.0	6.8	12.6	15.6
1.50	60.2	8.2	13.5	18.1	63.8	7.1	13.0	16.1

ster critical distance ( $R_0$ ) and distance between the donor and acceptor ( $r$ ) in the BDMC–HSA interaction are in the range of 2–3 nm, which are really close distances. This indicates that the energy transfer from Trp-214 to BDMC occurs with high possibility.

### Circular dichroism studies

Circular dichroism (CD) spectroscopy is a chiroptical method to study the binding of biologically active natural and synthetic compounds to biomacromolecules, including proteins, nucleic acids, and polysaccharides. Various aspects of protein structure and their ligand-binding characteristics can be explored by CD technique. The secondary structure of proteins can be investigated in the far-UV region (190–250 nm). The main absorbing groups in this region are peptide bonds. In the near-UV region, the aromatic amino acid side chains are placed in a chiral environment by the tertiary folding of the polypeptide chain and thus, rise to CD spectra, which can serve as characteristic finger prints of the native structure.<sup>43,44</sup> The induced optical activity of the achiral ligand molecules during the reversible binding interaction can be monitored by CD spectroscopy in the visible range of light absorption. The conformational adaptation of ligand to its asymmetric binding site(s), and also the interaction between ligand molecules held in chiral arrangement relative to each other by the protein sites, results in one or more induced CD bands with a different shape, sign, and intensity, which are called Cotton effects.<sup>45</sup>

The far-UV circular dichroism spectra of HSA in six L/P molar ratios (0, 0.25, 0.50, 0.75, 1.00, and 1.50) of two studied ligands in this research are shown in Figs. 4a and 4b and the secondary structure contents are listed in Table 3. The far-UV CD spectra of HSA exhibited characteristic features of the typical  $\alpha$ -helical structure of the protein and its complex to BDMC and DABC with negative bands at 208 nm and 220 nm (Figs. 4a and 4b). According to Fig. 4a and Table 3, the  $\alpha$ -helix content of HSA in the presence of different concentrations of BDMC is less than that of free HSA. The most decreasing in the  $\alpha$ -helix content is in the case of 0.25 L/P and with increasing the L/P ratios the  $\alpha$ -helix content gradually increases. The minor decrease in the  $\alpha$ -helix structure is accompanied by an increase in the  $\beta$ -sheet and random coil contents, whereas the turn content is not changed. Reduction of the  $\alpha$ -helix content and increase of the random coil structure represents the protein unfolding. The changes in the secondary structure contents of HSA in the presence of different concentrations of DABC

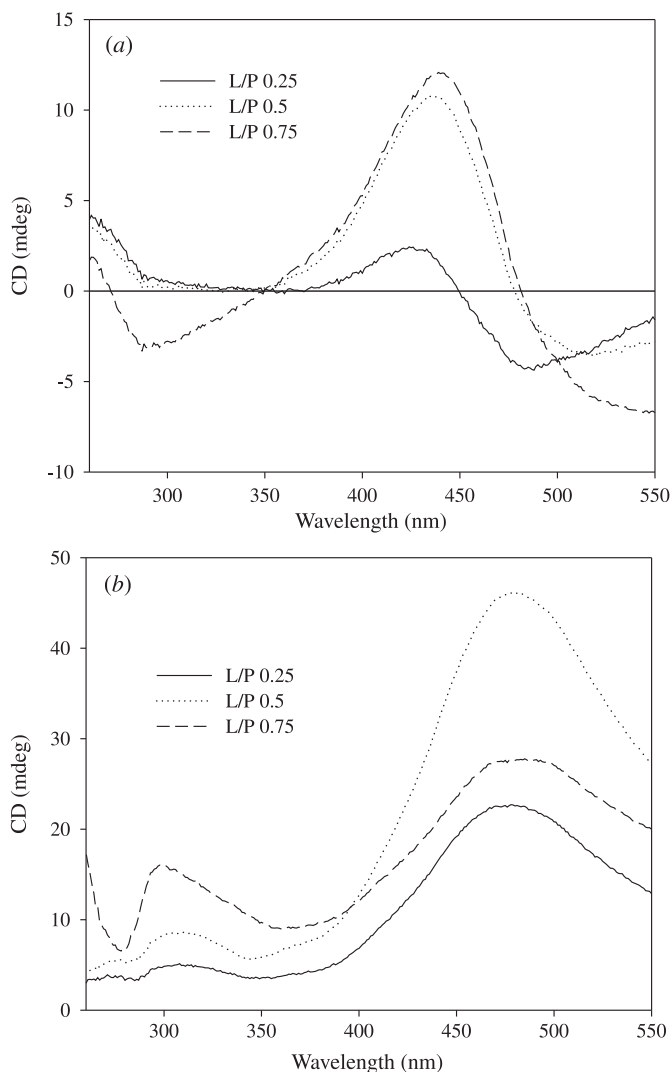
are not regular. The  $\alpha$ -helix content in 0.25 L/P is decreased, in the case of 0.75 L/P is not changed and in other L/P values is increased again. However, these unusual changes in the secondary structure of HSA during the binding to BDMC and DABC are not considerable. The minor changes in the secondary structure contents of HSA indicated that ligand-induced conformational changes are localized in the binding site and do not involve great alterations in protein folding.

The far-UV CD results that showed the minor alteration in the secondary structure content of HSA are consistent with the recent study on the CUR–HSA interaction by Mandeville et al.<sup>38</sup> The results of the binding of the two CUR derivatives, DAC and isoxazolcurcumin, to BSA also represented minor changes in BSA conformation during the binding process.<sup>28</sup>

The near-UV and visible range CD spectra (260–550 nm) in addition to the far-UV region, was investigated in the presence of the two studied ligands. The induced CD spectra are presented in Fig. 5. The results of control experiments show that both BDMC and DABC are achiral molecules and do not exhibit any CD spectra (data are not shown). The optical activities shown in Fig. 5 indicate the well-known phenomenon of protein-induced chirality, which arises from conformational adaptation to the asymmetric protein binding sites. This phenomenon can also be caused by the interaction between ligand molecules held in chiral arrangement relative to each other by the protein sites. Consequently, being bound to the protein, BDMC and DABC behave as chiral molecules and exhibit optical activities. From Fig. 5a, we can see that in the near-UV range (260–350 nm), there is a very weak positive band for 0.25 and 0.5 molar ratios. This positive band disappears and a new negative band appears at 0.75 L/P. In the visible range close to 350 nm, there are two opposite signed Cotton effects. The positive Cotton band is centered around 430 nm and its intensity increases with increasing L/P molar ratio. The negative Cotton band does not show a definite trend with increasing of L/P molar ratios.

From Fig. 5b, it can be seen that unlike BDMC, induced CD spectra of DABC have an intense positive Cotton effect centered at 480 nm. The intensity of this band has no regular increasing trend with increasing DABC concentration. Another positive Cotton band with much lower intensity in the near-UV region at 300 nm can be detected with considerable intensities in 0.5 and 0.75 L/P. The difference between the induced CD spectra of BDMC and DABC

**Fig. 5.** Induced CD spectra of HSA complex with (a) BDMC and (b) DABC measured in 0.050 mol/L phosphate buffer, pH 6.4 and [HSA] = 15.04  $\mu$ mol/L.



indicated the different configuration of these ligands in the binding site of HSA.

## References

- (1) Kiuchi, F.; Goto, Y.; Sugimoto, N.; Akao, N.; Kondo, K.; Tsuda, Y. *Chem. Pharm. Bull. (Tokyo)* **1993**, *41* (9), 1640. PMID:8221978.
- (2) Govindarajan, V. S.; Stahl, W. *CRC Crit. Rev. Food Sci. Nutr.* **1980**, *12* (3), 199. doi:10.1080/10408398009527278.
- (3) Limtrakul, P.; Lipigorngoson, S.; Namwong, O.; Apisariyakul, A.; Dunn, F. W. *Cancer Lett.* **1997**, *116* (2), 197. doi:10.1016/S0304-3835(97)00187-0. PMID:9215864.
- (4) Limtrakul, P.; Anuchapreeda, S.; Lipigorngoson, S.; Dunn, F. W. *BMC Cancer* **2001**, *1* (1), 1. doi:10.1186/1471-2407-1-1. PMID:11231886.
- (5) Masuda, T.; Hidaka, K.; Shinohara, A.; Maekawa, T.; Takeda, Y.; Yamaguchi, H. *J. Agric. Food Chem.* **1999**, *47* (1), 71. doi:10.1021/jf9805348. PMID:10563852.
- (6) Sreejayan, N.; Rao, M. N. *J. Pharm. Pharmacol.* **1997**, *49* (1), 105. PMID:9120760.
- (7) Singh, S.; Aggarwal, B. B. *J. Biol. Chem.* **1995**, *270* (42), 24995. doi:10.1074/jbc.270.42.24995. PMID:7559628.
- (8) Aggarwal, S.; Ichikawa, H.; Takada, Y.; Sandur, S. K.; Shishodia, S.; Aggarwal, B. B. *Mol. Pharmacol.* **2006**, *69* (1), 195. PMID:16219905.
- (9) Bae, M. K.; Kim, S. H.; Jeong, J. W.; Lee, Y. M.; Kim, H. S.; Kim, S. R.; Yun, I.; Bae, S. K.; Kim, K. W. *Oncol. Rep.* **2006**, *15* (6), 1557. PMID:16685395.
- (10) Limtrakul, P.; Anuchapreeda, S.; Buddhasukh, D. *BMC Cancer* **2004**, *4* (1), 13. doi:10.1186/1471-2407-4-13. PMID:15090070.
- (11) Limtrakul, P. *Adv. Exp. Med. Biol.* **2007**, *595*, 269. doi:10.1007/978-0-387-46401-5\_12. PMID:17569216.
- (12) Yodkeeree, S.; Chaiwangyen, W.; Garbisa, S.; Limtrakula, P. *J. Nutr. Biochem.* **2009**, *20* (2), 87. doi:10.1016/j.jnuthio.2007.12.003.
- (13) Ruby, A. J.; Kuttan, G.; Babu, K. D.; Rajasekharan, K. N.; Kuttan, R. *Cancer Lett.* **1995**, *94* (1), 79. doi:10.1016/0304-3835(95)03827-J. PMID:7621448.
- (14) Hoehle, S. I.; Pfeiffer, E.; Solyom, A. M.; Metzler, M. *J. Agric. Food Chem.* **2006**, *54* (3), 756. doi:10.1021/jf058146a. PMID:16448179.
- (15) Guo, L. Y.; Cai, X. F.; Lee, J. J.; Kang, S. S.; Shin, E. M.; Zhou, H. Y.; Jung, J. W.; Kim, Y. S. *Arch. Pharm. Res.* **2008**, *31* (4), 490. doi:10.1007/s12272-001-1183-8. PMID:18449507.
- (16) Mohammadi, K.; Thompson, K. H.; Patrick, B. O.; Storr, T.; Martins, C.; Polishchuk, E.; Yuen, V. G.; McNeill, J. H.; Orvig, C. *J. Inorg. Biochem.* **2005**, *99* (11), 2217. doi:10.1016/j.jinorgbio.2005.08.001. PMID:16171869.
- (17) Dockal, M.; Carter, D. C.; Rüker, F. *J. Biol. Chem.* **2000**, *275* (5), 3042. doi:10.1074/jbc.275.5.3042. PMID:10652284.
- (18) He, X. M.; Carter, D. C. *Nature* **1992**, *358* (6383), 209. doi:10.1038/358209a0. PMID:1630489.
- (19) Kragh-Hansen, U. *Pharmacol. Rev.* **1981**, *33* (1), 17. PMID:7027277.
- (20) Peters, T., Jr. *Adv. Protein Chem.* **1985**, *37*, 161. doi:10.1016/S0065-3233(08)60065-0. PMID:3904348.
- (21) Pulla Reddy, A. C.; Sudharshan, E.; Appu Rao, A. G.; Lokesh, B. R. *Lipids* **1999**, *34* (10), 1025. doi:10.1007/s11745-999-0453-x. PMID:10580329.
- (22) Zsila, F.; Bikádi, Z.; Simonyi, M. *Biochem. Biophys. Res. Commun.* **2003**, *301* (3), 776. doi:10.1016/S0006-291X(03)00030-5. PMID:12565848.
- (23) Zsila, F.; Bikádi, Z.; Simonyi, M. *Tetrahedron Asymmetry* **2003**, *14* (16), 2433. doi:10.1016/S0957-4166(03)00486-5.
- (24) Barik, A.; Priyadarsini, K. I.; Mohan, H. *Photochem. Photobiol.* **2003**, *77* (6), 597. doi:10.1562/0031-8655(2003)077<0597:PSOBC>2.0.CO;2. PMID:12870844.
- (25) Kunwar, A.; Barik, A.; Pandey, R.; Priyadarsini, K. I. *Biochim. Biophys. Acta* **2006**, *1760* (10), 1513. PMID:16904830.
- (26) Barik, A.; Mishra, B.; Kunwar, A.; Priyadarsini, K. I. *Chem. Phys. Lett.* **2007**, *436* (1–3), 239. doi:10.1016/j.cplett.2007.01.006.
- (27) Wang, F.; Yang, J.; Wu, X.; Liu, S. *Spectrochim. Acta, Part A* **2005**, *61* (11–12), 2650. doi:10.1016/j.saa.2004.10.007.
- (28) Sahoo, B. K.; Ghosh, K. S.; Dasgupta, S. *Biophys. Chem.* **2008**, *132* (2–3), 81. doi:10.1016/j.bpc.2007.10.007. PMID:18037556.
- (29) Pace, C. N.; Vajdos, F.; Fee, L.; Grimsley, G.; Gray, T. *Protein Sci.* **1995**, *4* (11), 2411. doi:10.1002/pro.5560041120. PMID:8563639.
- (30) Lin, S. Y.; Li, M. J.; Wei, Y. S. *Spectrochim. Acta, Part A*

- 2004**, *60* (13), 3107. doi:10.1016/j.saa.2004.03.001. PMID: 15477151.
- (31) Manavalan, P.; Johnson, W. C. J. R., Jr. *Anal. Biochem.* **1987**, *167* (1), 76. doi:10.1016/0003-2697(87)90135-7. PMID:3434802.
- (32) Yang, J. T.; Wu, C. S. C.; Martinez, H. M. *Methods Enzymol.* **1986**, *130*, 208. doi:10.1016/0076-6879(86)30013-2. PMID:3773734.
- (33) Lakowicz, J. R. *Principles of Fluorescence spectroscopy*; Kluwer Academic: New York, 1999.
- (34) Lakowicz, J. R.; Weber, G. *Biochemistry* **1973**, *12* (21), 4161. doi:10.1021/bi00745a020. PMID:4795686.
- (35) Ware, W. R. *J. Phys. Chem.* **1962**, *66* (3), 455. doi:10.1021/j100809a020.
- (36) Jiang, M.; Xie, M.-X.; Zheng, D.; Liu, Y.; Li, X.-Y.; Cheng, X. *J. Mol. Struct.* **2004**, *692* (1–3), 71. doi:10.1016/j.molstruc.2004.01.003.
- (37) Sulkowska, A. *J. Mol. Struct.* **2002**, *614* (1–3), 227. doi:10.1016/S0022-2860(02)00256-9.
- (38) Mandeville, J. S.; Froehlich, E.; Tajmir-Riahi, H. A. *J. Pharmaceut. Biomed.* **2009**, *49* (2), 468. doi:10.1016/j.jpba.2008.11.035.
- (39) Mohammadi, F.; Bordbar, A. K.; Divsalar, A.; Mohammadi, K.; Saboury, A. A. *Protein J.* **2009**, *28* (3–4), 117. doi:10.1007/s10930-009-9171-6. PMID:19189206.
- (40) Wang, F.; Yang, J.; Wu, X.; Liu, S. *Spectrochim. Acta, Part A* **2005**, *61* (11–12), 2650. doi:10.1016/j.saa.2004.10.007. PMID:16043060.
- (41) *Modern Quantum Chemistry*; Förster, T., Sinanoglu, O., Eds.; Academic Press: New York, 1996; p 93.
- (42) Epps, D. E.; Raub, T. J.; Caiolfa, V.; Chiari, A.; Zama, M. *J. Pharm. Pharmacol.* **1999**, *51* (1), 41. doi:10.1211/0022357991772079. PMID:10197416.
- (43) Kelly, S. M.; Price, N. C. *Curr. Protein Pept. Sci.* **2000**, *1* (4), 349. doi:10.2174/1389203003381315. PMID:12369905.
- (44) Kelly, S. M.; Price, N. C. *Biochim. Biophys. Acta* **1997**, *1338* (2), 161. PMID:9128135.
- (45) Zsila, F.; Bikádi, Z.; Fitos, I.; Simonyi, M. *Curr. Drug Discov. Technol.* **2004**, *1* (2), 133. doi:10.2174/1570163043335135. PMID:16472252.



# Silica-bonded *S*-sulfonic acid as a recyclable catalyst for the silylation of hydroxyl groups with hexamethyldisilazane (HMDS)

Khodabakhsh Niknam, Dariush Saberi, Hajar Molaei, and Mohammad Ali Zolfigol

**Abstract:** Silica-bonded *S*-sulfonic acid (SBSSA) was prepared by the reaction of 3-mercaptopropylsilica (MPS) and chlorosulfonic acid in *tert*-butylmethyl ether, and used as a catalyst for the silylation of hydroxyl groups. A good range of primary, secondary alcohols and phenolic hydroxyl groups were effectively converted into their corresponding trimethylsilyl ethers with hexamethyldisilazane (HMDS) in the presence of catalytic amounts of SBSSA under mild conditions at room temperature with short reaction times and in good-to-excellent yields. An excellent chemoselective silylation of hydroxyl groups in the presence of other functional groups was also observed. The heterogeneous catalyst was recycled for 30 runs upon the reaction of benzyl alcohol with HMDS without losing its catalytic activity.

**Key words:** silylation, silica-bonded *S*-sulfonic acid, hydroxyl groups, alcohols, catalyst.

**Résumé :** On a préparé de l'acide *S*-sulfonique lié à de la silice par (ASSLS) par réaction du 3-mercaptopropylsilicium (MPS) et de l'acide chlorosulfonique dans le éther de *tert*-butylméthyle et on l'a utilisé comme catalyseur pour la silylation de groupes hydroxyles. On a ainsi pu transformer un ensemble représentatif de groupes hydroxyles d'alcools primaires et secondaires et phénoliques en éthers triméthylsilyles correspondants par réaction avec de l'hexaméthylidisilazane (HMDS) en présence de quantités catalytiques d'acide *S*-sulfonique lié à de la silice, dans des conditions douces, à la température ambiante, avec des courts temps de réaction et avec des rendements allant de bons à excellents. On a pu aussi observer une excellent silylation chimiosélective de groupes hydroxyles en présence d'autres groupes fonctionnels. Le catalyseur hétérogène a pu être recyclé au moins trente fois, sans perte d'activité, pour la réaction de l'alcool benzylique avec le HMDS.

**Mots-clés :** silylation, acide *S*-sulfonique lié à de la silice, groupes hydroxyles, catalyseur.

[Traduit par la Rédaction]

## Introduction

In recent years, there has been much attention on the search for environmentally benign chemical processes or methodologies, because they are essential for the conservation of the global ecosystem. The development of heterogeneous catalysts for fine chemical synthesis has become a major area of research, as the potential advantages of these materials (facile recovery and reusability; the potential for incorporation in continuous reactors and micro reactors) over homogeneous systems can lead to novel environmentally benign chemical procedures for academia and industry.<sup>1</sup> Application of solid acids in organic transformations is desirable, owing to their simplicity in handling, decreased reactor and plant corrosion problems, and more environmentally safe disposal.<sup>2–10</sup> Green chemistry not only requires the use of environmentally benign reagents and solvents, but

also requires the use of recyclable catalysts. One way to overcome the problem of recyclability of the traditional acid catalysts is to chemically anchor their reactive center onto an inorganic solid carrier with a large surface area to create new organic–inorganic hybrid catalyst.<sup>5,6</sup> The reactive centers in these solid-supported catalysts are highly mobile similar to homogeneous catalysts, and at the same time have the advantage of recyclability like heterogeneous catalysts. In this view, several types of solid sulfonic-acid-functionalized silica (both amorphous and ordered) have been synthesized and applied as an alternative to traditional sulfonic acid resins and homogeneous acids in catalyzing chemical transformations.<sup>5,7</sup>

Herein, we wish to describe the preparation of silica-bonded *S*-sulfonic acid (SBSSA) as illustrated in Scheme 1, and its use as catalyst for the conversion of alcohols into corresponding trimethylsilyl ethers. Sulfur content of SBSSA by conventional elemental analysis was 16.12%. Typically, a loading at ~0.35 mmol/g is obtained. On the other hand, when the washed sulfonated product **2** was placed in an aqueous NaCl solution, the pH of the solution dropped virtually instantaneously to pH 1.85, as ion exchange occurred between protons and sodium ions (proton exchange capacity: 0.33 mmol/g of sulfonic acid **2**), which is in good agreement with the result obtained from TGA and titration.

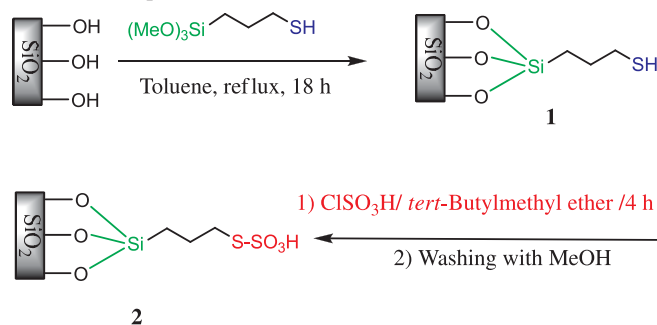
Protection and deprotection of functional groups are in-

Received 13 March 2009. Accepted 9 October 2009. Published on the NRC Research Press Web site at canjchem.nrc.ca on 29 January 2010.

**K. Niknam,<sup>1</sup> D. Saberi, and H. Molaei.** Chemistry Department, Faculty of Sciences, Persian Gulf University, Bushehr 75169, Iran.

**M.A. Zolfigol.** Faculty of Chemistry, Bu-Ali Sina University, P.O. Box 4135, Hamedan 6517838683, Iran.

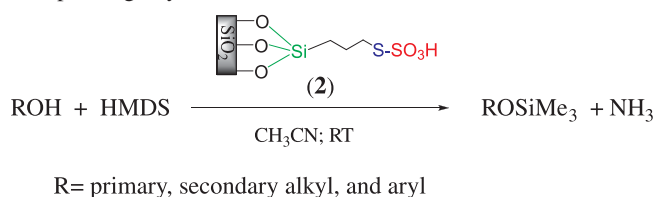
<sup>1</sup>Corresponding author (e-mail: khniknam@gmail.com).

**Scheme 1.** Preparation of silica-bonded S-sulfonic acid.

evitable processes for the synthesis of polyfunctional compounds. Silylation of alcohols and polyols is one of the most commonly used methods for their protection.<sup>11</sup> Trimethylsilylation is a classic way to produce volatile derivatives of alcohols and polyols, as required for their vapor-phase chromatography/mass spectrometric analysis.<sup>12</sup> Another application is the conversion of trimethylsilyl ethers into the corresponding ethers.<sup>13</sup> Generally, the formation of trimethylsilyl ethers has been carried out by treatment of alcohols with trimethylsilyl chloride or trimethylsilyl triflate in the presence of a base,<sup>14</sup>  $\text{Li}_2\text{S}$ ,<sup>15</sup> and sometimes a nonionic super base catalyst.<sup>16</sup> However, some of these methods have frequently suffered from drawbacks, such as lack of reactivity or the difficulty in removal of amine salts derived from the reaction of by-produced acid and co-bases during the silylation reaction. 1,1,1,3,3,3-Hexamethyldisilazane (HMDS) is a stable, commercially available, and inexpensive reagent for trimethylsilylation of hydrogen-labile substrates,<sup>17</sup> giving ammonia as the only byproduct. On the other hand, silylation, using this silazan-type reagent, is nearly neutral and does not need any special precautions. However, the weak silylating ability of HMDS is a main drawback for its application, which needs forceful conditions and long reaction times in many instances. A variety of catalysts, such as  $(\text{CH}_3)_3\text{SiCl}$ ,<sup>18</sup> silica chloride,<sup>19</sup>  $\text{ZnCl}_2$ ,<sup>20</sup>  $\text{LiClO}_4$ ,<sup>21</sup> H- $\beta$  zeolite,<sup>22</sup> tungstophosphoric acid,<sup>23</sup> poly(*N*-bromobenzene-1,3-disulfonamide),<sup>24</sup> ultrasound,<sup>25</sup>  $\text{CuSO}_4 \cdot 5\text{H}_2\text{O}$  and  $\text{Cu}(\text{OTf})_2$ ,<sup>26</sup>  $\text{Al}(\text{HSO}_4)_3$ ,<sup>27</sup>  $\text{KBr}$ ,<sup>28</sup> silica-supported perchloric acid,<sup>29</sup> sulfonic-acid-functionalized silica,<sup>30</sup> silica sulfuric acid,<sup>31</sup> 1,3-dibromo-5,5-diethylbarbituric acid,<sup>32</sup> tribromoiso-cyanuric acid and DABCO- $\text{Br}_2$ ,<sup>33</sup>  $\text{Fe}(\text{F}_3\text{CCO}_2)_3$ ,<sup>34</sup> tetrabutylammonium bromide,<sup>35</sup> tribromomelamine,<sup>36</sup> and alumina sulfuric acid<sup>37</sup> have been reported for the silylation of hydroxyl groups using HMDS. In addition to the previously reported procedures, the facile and general synthetic methodology for the silylation of alcohols under essentially neutral conditions is desirable, so this subject encouraged us to develop an efficient, convenient, and practical procedure for the protection of hydroxyl groups under mild and heterogeneous conditions.

## Results and discussion

The trimethylsilylation of hydroxyl groups is easily carried out at room temperature under mild conditions in the presence of SBSSA as a catalyst (Scheme 2). First, we studied the reaction of 4-bromobenzyl alcohol with HMDS

**Scheme 2.** Conversion of different kinds of hydroxyl groups into corresponding silyl ethers

in the presence of SBSSA in  $\text{CH}_3\text{CN}$  at room temperature. The optimal amount of the catalyst was 0.015 g per 1 mmol of 4-bromobenzyl alcohol and 0.8 mmol of HMDS. Next, we prepared a range of silyl ethers under the following reaction conditions: hydroxyl compound (1 mmol), HMDS (0.8 mmol), SBSSA (0.015 g), and acetonitrile (2 mL) (Table 1). A wide range of alcohols underwent silylation by this procedure to provide the corresponding TMS ethers in good-to-excellent yields. Generally, benzylic alcohols, phenols, and primary and secondary alcohols are faster than tertiary alcohols. Trimethylsilylation of hydroxyl groups produce corresponding trimethylsilylated compounds under these conditions, whereas substituted thiophenol, 1-butan-1-ol (Table 1, entries 8, 25, and 26), aniline derivatives, aliphatic amines (Table 1, entries 22–24), and *N*-phenyl acetamide (Table 1, entry 27) remained intact under the reaction conditions. It is worth mentioning that in the case of *p*-aminophenol, only the phenolic group reacted under these conditions and the amino group remains intact (Table 1, entry 19).

We investigated the selective silylation of different binary mixture of alcohols and also alcohols and phenols in the presence of amine, amide, and thiols. This method was shown to be highly selective for primary alcohols, such as benzyl alcohol and 2-phenylethanol. Primary alcohols were completely converted to the corresponding silyl ethers, while tertiary alcohols were converted to the corresponding silylated products with 0% yield (Scheme 3).

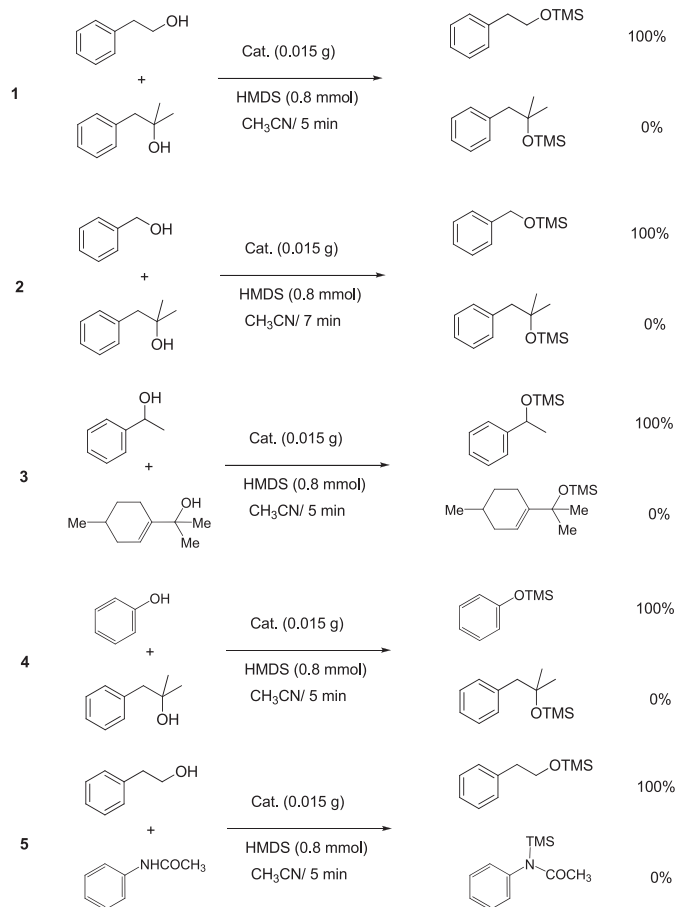
Excellent chemoselectivity was also observed for the conversion of secondary alcohols and phenols in the presence of tertiary alcohols such as  $\alpha$ -terpinene, 1-phenyl-2-methyl-2-propanol (Scheme 3). We also explored the chemoselectivity of SBSSA in the silylation method. Alcohols and phenols in the presence of an amine, amide, and thiols were completely converted to the corresponding trimethylsilyl ethers as sole product.

To show the efficiency of the SBSSA in comparison with previously reported procedures, Table 2 compares some of our results with  $\text{LiClO}_4/\text{SiO}_2$ ,<sup>21</sup> H- $\beta$  zeolite,<sup>22</sup>  $\text{HClO}_4/\text{SiO}_2$ ,<sup>29</sup> sulfonic-acid-functionalized silica,<sup>30</sup> silica sulfuric acid,<sup>31</sup> and alumina sulfuric acid<sup>37</sup> with respect to reaction times and yields of obtained products. It is clear from the results shown in Table 2, that silylation reactions carried out with SBSSA require shorter reaction times and lower catalyst loading.

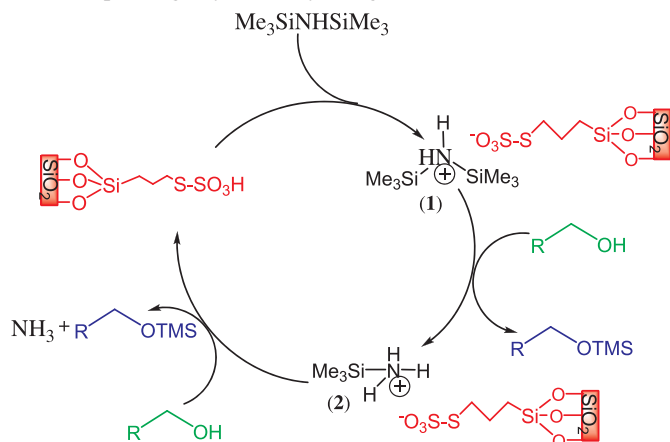
In all reactions studied, fast evolution of ammonia gas was observed (HMDS is stronger base than  $\text{NH}_3$ ). With this observation, we have proposed a mechanism in which the generation of  $\text{NH}_3$  and catalytic role of SBSSA in a catalytic cycle is clarified (Scheme 4).<sup>29,34</sup>

The possibility of recycling the catalyst was examined. For this purpose, the reaction of benzyl alcohol and HMDS

**Scheme 3.** Chemoselectivity between primary, secondary alcohols, and phenols in the presence of tertiary alcohols and amides using SBSSA with HMDS.

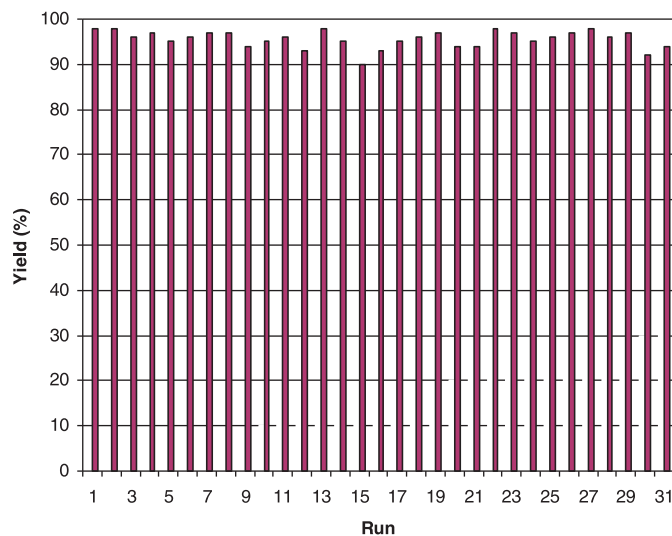


**Scheme 4.** Proposed mechanism for the conversion of alcohols into the corresponding silyl ether by using SBSSA.



was studied in acetonitrile at room temperature in the presence of SBSSA. When the reaction was complete, the mixture was filtered and the solid was washed with dichloromethane, and the recycled catalyst was saved for the next reaction. The recycled catalyst could be directly reused 30 times without any treatment. No observation of appreciable loss in its catalytic activities was noticed (Fig. 1).

**Fig. 1.** Recyclability of solid silica-bonded *S*-sulfonic acid as catalyst in the silylation reaction of benzyl alcohol (1 mmol) and HMDS (1 mmol) at room temperature. Reaction time = 5 min.



## Conclusion

In conclusion, a practical, efficient, and convenient method for the silylation of hydroxyl compounds was described. One major advantage of our described method is using very low molecular ratio of the catalysts in comparison with the reported procedures in the literature. Therefore, we think that this method can be a useful addition to the present methodologies for the silylation of hydroxy groups.

## Experimental

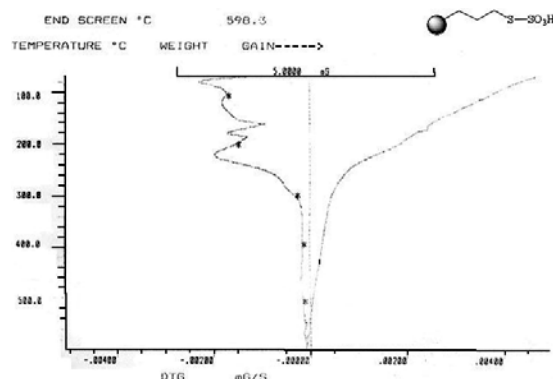
### General

Chemicals were purchased from Merck, Fluka, and Aldrich Chemical Companies. IR spectra were run on a Shimadzu IR-435 FTIR spectrophotometer.  $^1\text{H}$  NMR was run on JEOL NMR spectrometer (FX 90Q) and Bruker Avance (DRX 500 MHz). Melting points were recorded on a Melting Point SMP1 apparatus in open capillary tubes and are uncorrected. The progress of reaction was followed with TLC, using silica gel SILG/UV 254 plates. All the products are known and were characterized by comparison of their spectral (IR,  $^1\text{H}$  NMR), TLC, and physical data with those reported in the literature.<sup>22–36</sup> 3-Mercaptopropylsilica **1** (MPS) was prepared according to the previously reported procedure.<sup>5a</sup>

### Catalyst preparation

To a magnetically stirred mixture of 3-mercaptopropylsilica **1** (5 g) in *tert*-butylmethyl ether (20 mL), chlorosulfonic acid (1.00 g, 9 mmol) was added dropwise at 0 °C for 2 h. After addition was complete, the mixture was stirred for 2 h until HCl gas evolution was stopped. Then, the mixture was filtered and washed with methanol (30 mL) and dried at room temperature to obtain silica-bonded functionalized sulfonic acid **2** (SBSSA) as cream powder (5.22 g). Sulfur content of the samples was 16.12% by conventional elemental analysis. TGA analysis of SBSSA shows a first mass loss due to the desorption of water below 100 °C (Fig. 2). This

**Fig. 2.** TGA diagram for a sample of silica-bonded *S*-sulfonic acid under nitrogen stream.



is followed by a second mass loss starting at 140 °C, corresponding to the loss of the covalently bound organic group. From this mass loss, it is calculated that the loading of the organic group bound to silica surface was 1.78 mmol g<sup>-1</sup>.

#### **pH analysis of the SBSSA**

To an aqueous suspension of 0.1 g SBSSA, NaOH (1.8 mL, 0.1 mol/L) was added. This is equal to a loading of 1.8 mmol SO<sub>3</sub>H g<sup>-1</sup>. So, all of the SH functional groups in 3-mercaptopropylsilica **1** were sulfonated. According to previous reports,<sup>5</sup> the loading of 3-mercaptopropylsilica **1** is 0.33 mmol/g.

#### **General procedure for the silylation of alcohols**

To a stirred solution of the compound containing hydroxyl groups (1 mmol) and HMDS (0.8 mmol) in CH<sub>3</sub>CN (2 mL) was added SBSSA (0.015 g) and stirred at room temperature. When the reaction was complete by GC (or TLC, *n*-hexane/EtOAc, 9:1) analysis, CH<sub>2</sub>Cl<sub>2</sub> was added (10 mL), and SBSSA was removed by filtration. The solvent was evaporated and the trimethylsilyl ether was isolated almost as a pure crude product. Further purification was carried out by short column chromatography on silica gel eluting with ethyl acetate/petroleum ether, if necessary.

#### **Trimethyl(benzyloxy)silan (Table 1, entry 1)**

Purified on short column of silica gel using petroleum ether/ethyl acetate (10:1) as eluent. Colorless liquid;<sup>29</sup> bp 212 °C/760 torr (1 torr = 133.322 Pa). <sup>1</sup>H NMR (500 MHz, CDCl<sub>3</sub>, ppm) δ: 0.19 (s, 9H), 4.72 (s, 2H), 7.35–7.36 (m, 5H).

#### **Trimethyl(4-methoxybenzyloxy)silan (Table 1, entry 2)**

Purified on short column of silica gel using petroleum ether/ethyl acetate (10:1) as eluent. Colorless liquid;<sup>29</sup> bp 257–258 °C/760 torr. <sup>1</sup>H NMR (500 MHz, CDCl<sub>3</sub>, ppm) δ: 0.18 (s, 9H), 3.81 (s, 3H), 4.66 (s, 2H), 6.91 (d, 2H, *J* = 8.5 Hz), 7.44 (d, 2H, *J* = 8.4 Hz). <sup>13</sup>C NMR (125 MHz, CDCl<sub>3</sub>, ppm) δ: 0.30, 55.21, 64.41, 113.75, 128.13, 133.16, 158.90.

#### **Trimethyl(4-bromobenzyloxy)silan (Table 1, entry 3)**

Purified on short column of silica gel using petroleum ether/ethyl acetate (10:1) as eluent. Colorless liquid;<sup>36</sup> bp 250 °C/760 torr. <sup>1</sup>H NMR (90 MHz, CDCl<sub>3</sub>, ppm) δ: 0.17

(s, 9H), 4.65 (s, 2H), 7.20 (d, 2H, *J* = 8.4 Hz), 7.46 (d, 2H, *J* = 8.6 Hz).

#### **Trimethyl(4-chlorobenzyloxy)silan (Table 1, entry 4)**

Purified on short column of silica gel using petroleum ether/ethyl acetate (10:1) as eluent. Colorless liquid;<sup>36</sup> bp 228 °C/760 torr. <sup>1</sup>H NMR (90 MHz, CDCl<sub>3</sub>, ppm) δ: 0.19 (s, 9H), 4.68 (s, 2H), 7.28–7.30 (m, 4H).

#### **Trimethyl(4-nitrobenzyloxy)silan (Table 1, entry 5)**

Purified on short column of silica gel using petroleum ether/ethyl acetate (10:1) as eluent. Colorless liquid;<sup>25</sup> bp > 300 °C/760 torr. <sup>1</sup>H NMR (500 MHz, CDCl<sub>3</sub>, ppm) δ: 0.22 (s, 9H), 4.83 (s, 2H), 7.52 (d, 2H, *J* = 8.8 Hz), 8.22 (d, 2H, *J* = 8.7 Hz). <sup>13</sup>C NMR (125 MHz, CDCl<sub>3</sub>, ppm) δ: -0.10, 63.95, 123.95, 127.00, 147.49, 149.16.

#### **Trimethyl(2-phenylethoxy)silan (Table 1, entry 6)**

Purified on short column of silica gel using petroleum ether/ethyl acetate (10:1) as eluent. Colorless liquid;<sup>29</sup> bp 230 °C/760 torr. <sup>1</sup>H NMR (500 MHz, CDCl<sub>3</sub>, ppm) δ: 0.11 (s, 9H), 2.87 (t, 2H, *J* = 7.3 Hz), 3.81 (t, 2H, *J* = 7.3 Hz), 7.23–7.33 (m, 5H).

#### **Trimethyl(3-phenylpropyloxy)silan (Table 1, entry 7)**

Purified on short column of silica gel using petroleum ether/ethyl acetate (10:1) as eluent. Colorless liquid;<sup>25</sup> bp 245 °C/760 torr. <sup>1</sup>H NMR (500 MHz, CDCl<sub>3</sub>, ppm) δ: 0.22 (s, 9H), 1.92–1.98 (m, 2H), 2.77 (t, 2H, *J* = 7.8 Hz), 3.70 (t, 2H, *J* = 6.4 Hz), 7.26–7.29 (m, 3H), 7.35–7.38 (m, 2H). <sup>13</sup>C NMR (125 MHz, CDCl<sub>3</sub>, ppm) δ: 0.03, 32.60, 34.70, 62.36, 126.17, 128.75, 128.91, 142.58.

#### **Trimethyl(2-mercaptoethoxy)silan (Table 1, entry 8)**

Purified on short column of silica gel using petroleum ether/ethyl acetate (10:1) as eluent. Colorless liquid;<sup>38</sup> bp 146 °C/760 torr. <sup>1</sup>H NMR (90 MHz, CDCl<sub>3</sub>, ppm) δ: 0.06 (s, 9H), 1.43 (t, 1H, *J* = 8.1 Hz), 2.44–2.82 (m, 2H), 3.49–3.82 (m, 2H).

#### **Trimethyl(diphenylmethoxy)silan (Table 1, entry 9)**

Purified on short column of silica gel using petroleum ether/ethyl acetate (10:1) as eluent. Colorless liquid;<sup>29</sup> bp > 300 °C/760 torr. <sup>1</sup>H NMR (500 MHz, CDCl<sub>3</sub>, ppm) δ: 0.20 (s, 9H), 5.88 (s, 1H), 7.32 (t, 2H, *J* = 7.3 Hz), 7.40 (t, 4H, *J* = 7.6 Hz), 7.46 (t, 4H, *J* = 7.5 Hz). <sup>13</sup>C NMR (125 MHz, CDCl<sub>3</sub>, ppm) δ: 0.65, 77.00, 127.04, 127.53, 128.68, 145.35.

#### **Trimethyl(1-phenylethoxy)silan (Table 1, entry 10)**

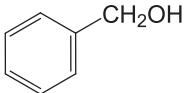
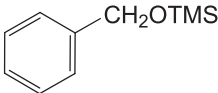
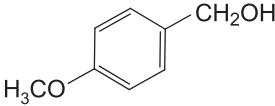
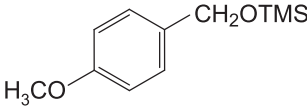
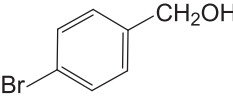
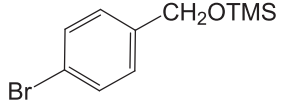
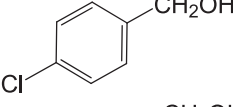
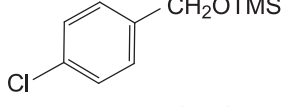
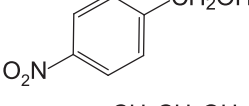
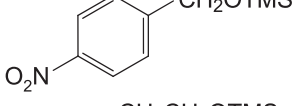
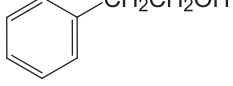
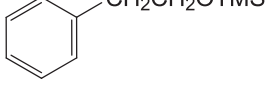
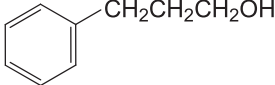
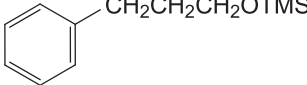
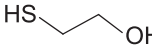
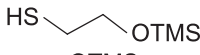
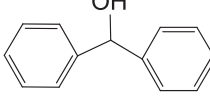
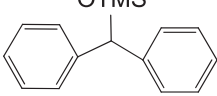
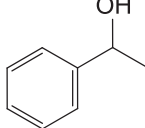
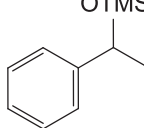
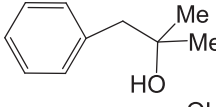
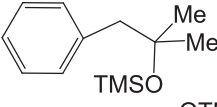
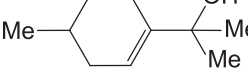
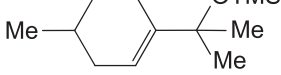
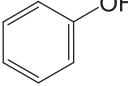
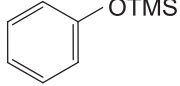
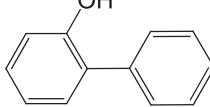
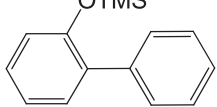
Purified on short column of silica gel using petroleum ether/ethyl acetate (10:1) as eluent. Colorless liquid;<sup>29</sup> bp 212 °C/760 torr. <sup>1</sup>H NMR (500 MHz, CDCl<sub>3</sub>, ppm) δ: 0.15 (s, 9H), 1.51 (d, 3H, *J* = 6.3 Hz), 4.93 (q, 1H, *J* = 6.3 Hz), 7.28 (t, 1H, *J* = 6.9 Hz), 7.34–7.40 (m, 4H).

#### **Trimethyl(1-phenyl-2-methyl-2-propyloxy)silan (Table 1, entry 11)**

Purified on short column of silica gel using petroleum ether/ethyl acetate (10:1) as eluent. Colorless liquid;<sup>36</sup> bp 245 °C/760 torr. <sup>1</sup>H NMR (90 MHz, CDCl<sub>3</sub>, ppm) δ: 0.05 (s, 9H), 1.20 (s, 6H), 2.71 (s, 2H), 7.12–7.38 (m, 5H).



**Table 1.** Silylation of alcohols, phenols, and naphthols with HMDS in the presence of SBSSA as catalyst at room temperature.

Entry	Substrate	Product	Time (min)	Yield <sup>b</sup> (%)
1			5	94
2			3	94
3			6	96
4			6	92
5			8	91
6			3	95
7			3	96
8			5	89
9			3	90
10			3	91
11			24 h	Trace
12			24 h	<30
13			3	93
14			15	90

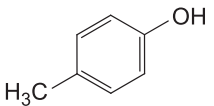
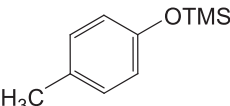
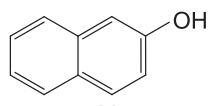
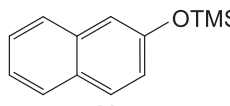
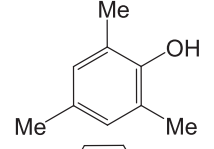
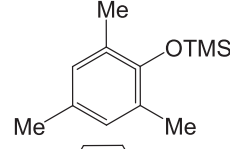
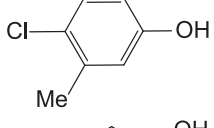
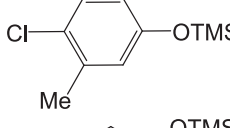
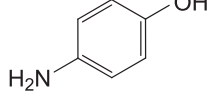
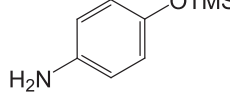
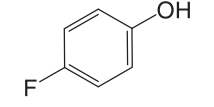
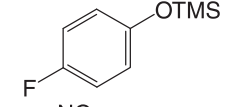
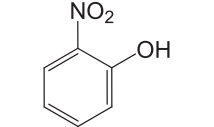
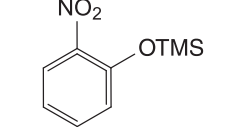
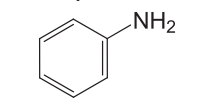
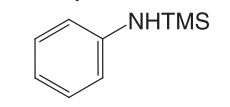
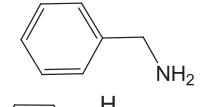
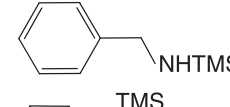
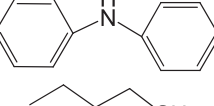
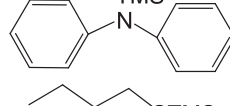
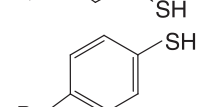
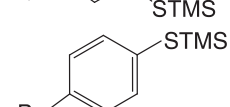
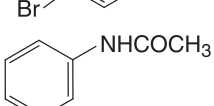
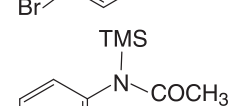
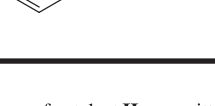
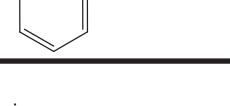
**Trimethyl[1-methyl-1-(4-methyl-cyclohex-1-enyl)ethoxy]silan (Table 1, entry 12)**

Purified on short column of silica gel using petroleum ether/ethyl acetate (10:1) as eluent. Colorless liquid;<sup>32</sup> bp 256 °C/760 torr. <sup>1</sup>H NMR (90 MHz, CDCl<sub>3</sub>, ppm) δ: 0.09 (s, 9H), 0.94–2.00 (m, 16H), 5.27–5.44 (m, 1H).

**Trimethylphenoxy silan (Table 1, entry 13)**

Purified on short column of silica gel using petroleum ether/ethyl acetate (10:1) as eluent. Colorless liquid;<sup>29</sup> bp 211 °C/760 torr. <sup>1</sup>H NMR (500 MHz, CDCl<sub>3</sub>, ppm) δ: 0.34 (s, 9H), 6.92 (d, 2H, *J* = 7.8 Hz), 7.02 (t, 1H, *J* = 7.3 Hz), 7.31 (t, 1H, *J* = 8.0 Hz).

**Table 1.** Concluded.

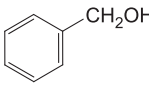
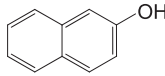
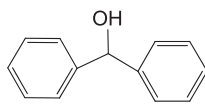
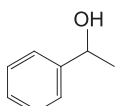
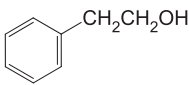
Entry	Substrate	Product	Time (min)	Yield <sup>b</sup> (%)
15			6	95
16			5	93
17			2	96
18			3	96
19			5	90
20			5	91
21			24 h	NR <sup>c</sup>
22			180	NR <sup>c</sup>
23			180	NR <sup>c</sup>
24			180	NR <sup>c</sup>
25			180	NR <sup>c</sup>
26			180	NR <sup>c</sup>
27			180	NR <sup>c</sup>

<sup>a</sup> Isolated yield.<sup>b</sup> The yields and times of catalyst **II** are written in parenthesis.<sup>c</sup> NR: No reaction.**Trimethyl(biphenyl-2-yloxy) silan (Table 1, entry 14)**

Purified on short column of silica gel using petroleum ether/ethyl acetate (10:1) as eluent. Colorless liquid;<sup>39</sup> bp 281 °C/760 torr. <sup>1</sup>H NMR (500 MHz, CDCl<sub>3</sub>, ppm) δ: 0.05 (s, 9H), 6.92 (dd, 1H, *J*<sub>1</sub> = 8.0 Hz, *J*<sub>2</sub> = 0.7 Hz), 7.06 (dt, 1H

*J*<sub>1</sub> = 7.5 Hz, *J*<sub>2</sub> = 0.8 Hz), 7.21–7.26 (m, 1H), 7.31 (t, 1H, *J* = 7.4 Hz), 7.36 (dd, 1H, *J*<sub>1</sub> = 7.5 Hz, *J*<sub>2</sub> = 1.5 Hz), 7.40 (t, 2H, *J* = 7.5 Hz), 7.54 (d, 2H, *J* = 8.3 Hz). <sup>13</sup>C NMR (125 MHz, CDCl<sub>3</sub>, ppm) δ: 0.51, 121.03, 122.35, 127.16, 128.26, 128.81, 130.06, 133.78, 139.49, 152.73.

**Table 2.** Comparison of the results of SBSSA (I) with LiClO<sub>4</sub>/SiO<sub>2</sub> (II),<sup>21</sup> H-β zeolite (III),<sup>22</sup> HClO<sub>4</sub>/SiO<sub>2</sub> (IV),<sup>29</sup> sulfonic-acid-functionalized silica (V),<sup>30</sup> silica sulfuric acid (VI),<sup>31</sup> and alumina sulfuric acid (VII)<sup>37</sup> in the synthesis of trimethylsilyl ether using HMDS.

Entry	Substrate	Time (min)/ yield (%) <sup>a</sup>						
		I	II	III	IV	V	VI	VII
1		5/94	5/98	300/95	2/98	80/100 <sup>b</sup>	10/93	2/98
2		5/93	120/84	20 h/67	4/100	420/80 <sup>b</sup>	5/86	4/95
3		3/90	50/87	—	4/89	60/98 <sup>b</sup>	10/85	7/89
4		3/91	30/89	—	4/91	—	15/89	8/91
5		3/95	—	—	2/97	40/100 <sup>b</sup>	—	12/97

**Note:** For I–VII, the equivalent ratios of substrate/ HMDS/ catalyst are 1/ 0.8/ 0.015 (g), 1/0.6/0.1 (g), 1/0.6/[10%(w/w)], 1/ 0.5/ 0.01, 1/ 0.6/ 0.003, 1/ 0.8/ 0.08 (g), 1/ 0.75/ 0.025 (g), respectively.

<sup>a</sup> Isolated Yield.

<sup>b</sup> GC Yield.

#### Trimethyl(4-methylphenoxy) silan (Table 1, entry 15)

Purified on short column of silica gel using petroleum ether/ethyl acetate (10:1) as eluent. Colorless liquid;<sup>29</sup> bp 206 °C/760 torr. <sup>1</sup>H NMR (500 MHz, CDCl<sub>3</sub>, ppm) δ: 0.32 (s, 9H), 2.33 (s, 3H), 6.80 (d, 2H, *J* = 8.1 Hz), 7.08 (d, 2H, *J* = 8.0 Hz).

#### Trimethyl(2-naphthalenoxy) silan (Table 1, entry 16)

Purified on short column of silica gel using petroleum ether/ethyl acetate (10:1) as eluent. Colorless liquid;<sup>29</sup> bp 282 °C/760 torr. <sup>1</sup>H NMR (500 MHz, CDCl<sub>3</sub>, ppm) δ: 0.41 (s, 9H), 7.18 (dd, 1H, *J*<sub>1</sub> = 8.8 Hz, *J*<sub>2</sub> = 2.3 Hz), 7.31 (d, 1H, *J* = 2.1 Hz), 7.41 (t, 1H, *J* = 7.3 Hz), 7.50 (dt, 1H, *J*<sub>1</sub> = 7.6 Hz, *J*<sub>2</sub> = 0.8 Hz), 7.77–7.85 (m, 3H).

#### Trimethyl(2,4,6-trimethylphenoxy) silan (Table 1, entry 17)

Purified on short column of silica gel using petroleum ether/ethyl acetate (10:1) as eluent. Colorless liquid;<sup>40</sup> bp 241 °C/760 torr. <sup>1</sup>H NMR (500 MHz, CDCl<sub>3</sub>, ppm) δ: 0.25 (s, 9H), 2.17 (s, 6H), 2.23 (s, 3H), 6.78 (s, 2H). <sup>13</sup>C NMR (125 MHz, CDCl<sub>3</sub>, ppm) δ: 1.37, 18.02, 20.94, 128.51, 129.47, 130.70, 150.63.

#### Trimethyl(4-chloro-3-methylphenoxy) silan (Table 1, entry 18)

Purified on short column of silica gel using petroleum ether/ethyl acetate (10:1) as eluent. Colorless liquid;<sup>39</sup> bp 243 °C/760 torr. <sup>1</sup>H NMR (500 MHz, CDCl<sub>3</sub>, ppm) δ: 0.26 (s, 9H), 2.32 (s, 3H), 6.62 (dd, 1H, *J*<sub>1</sub> = 8.6 Hz, *J*<sub>2</sub> = 2.8 Hz), 6.72 (d, 1H, *J* = 2.8 Hz), 7.17 (d, 1H, *J* = 7.9 Hz).

<sup>13</sup>C NMR (125 MHz, CDCl<sub>3</sub>, ppm) δ: 0.58, 20.60, 119.13, 122.96, 127.10, 130.03, 137.42, 154.14.

#### Trimethyl(4-aminophenoxy) silan (Table 1, entry 19)

Purified on short column of silica gel using petroleum ether/ethyl acetate (10:1) as eluent. Colorless liquid;<sup>29</sup> bp 255 °C/760 torr. <sup>1</sup>H NMR (500 MHz, CDCl<sub>3</sub>, ppm) δ: 0.22 (s, 9H), 3.34 (s, 2H), 6.51 (d, 2H, *J* = 8.5 Hz), 6.61 (d, 2H, *J* = 8.5 Hz).

#### Trimethyl(4-fluorophenoxy) silan (Table 1, entry 20)

Purified on short column of silica gel using petroleum ether/ethyl acetate (10:1) as eluent. Colorless liquid;<sup>29</sup> bp 208 °C/760 torr. <sup>1</sup>H NMR (500 MHz, CDCl<sub>3</sub>, ppm) δ: 0.25 (s, 9H), 6.75–6.77 (m, 2H), 6.89–6.92 (m, 2H). <sup>13</sup>C NMR (125 MHz, CDCl<sub>3</sub>, ppm) δ: 0.53, 116.10, 121.26, 151.52, 159.08.

## Acknowledgement

We are thankful to the Persian Gulf University Research Council for the partial support of this work.

## References

- (1) Choudhary, D.; Paul, S.; Gupta, R.; Clark, J. H. *Green Chem.* **2006**, 8 (5), 479. doi:10.1039/b601363e.
- (2) Riego, J. M.; Sedin, Z.; Zaldivar, J. M.; Marziano, N. C.; Tortato, C. *Tetrahedron Lett.* **1996**, 37 (4), 513. doi:10.1016/0040-4039(95)02174-4.
- (3) Firouzabadi, F.; Jafari, A. A. *J. Iran Chem. Soc.* **2005**, 2, 85.

- (4) (a) Salehi, P.; Ali Zolfigol, M.; Shirini, F.; Baghbanzadeh, M. *Curr. Org. Chem.* **2006**, *10* (17), 2171. doi:10.2174/138527206778742650.; (b) Zolfigol, M. A.; Shirini, P.; Salehi, P.; Abedini, M. *Curr. Org. Chem.* **2008**, *12* (3), 183. doi:10.2174/138527208783497475.
- (5) (a) Karimi, B.; Khalkhali, M. *J. Mol. Catal. A: Chem.* **2005**, *232* (1-2), 113. doi:10.1016/j.molcata.2005.01.028.; (b) Karimi, B.; Enders, D. *Org. Lett.* **2006**, *8* (6), 1237. doi:10.1021/ol060129z. PMID:16524312.; (c) Zareyee, D.; Karimi, B. *Tetrahedron Lett.* **2007**, *48* (7), 1277. doi:10.1016/j.tetlet.2006.12.030.; (d) Karimi, B.; Khalkhali, M. *J. Mol. Catal. A: Chem.* **2007**, *271* (1-2), 75. doi:10.1016/j.molcata.2007.02.018.
- (6) (a) Corma, A.; García, H. *Chem. Rev.* **2002**, *102* (10), 3837. doi:10.1021/cr010333u.; (b) Wight, A. P.; Davis, M. E. *Chem. Rev.* **2002**, *102* (10), 3589. doi:10.1021/cr010334m. PMID:12371895.
- (7) (a) Melerio, J. A.; van Grieken, R.; Morales, G. *Chem. Rev.* **2006**, *106* (9), 3790. doi:10.1021/cr050994h. PMID:16967921.; (b) Shimizu, K.-i.; Hayashi, E.; Hatamachi, T.; Kodama, T.; Higuchi, T.; Satsuma, A.; Kitayama, Y. *J. Catal.* **2005**, *231* (1), 131. doi:10.1016/j.jcat.2005.01.017.
- (8) (a) Niknam, K.; Zolfigol, M. A.; Khorramabadi-Zad, A.; Zare, R.; Shayegh, M. *Catal. Commun.* **2006**, *7* (7), 494. doi:10.1016/j.catcom.2006.01.004.; (b) Niknam, K.; Karami, B.; Zolfigol, M. A. *Catal. Commun.* **2007**, *8* (9), 1427. doi:10.1016/j.catcom.2006.12.011.; (c) Niknam, K.; Saberi, D.; Sefat, M. N. *Tetrahedron Lett.* **2009**, *50* (28), 4058. doi:10.1016/j.tetlet.2009.04.096.; (d) Niknam, K.; Saberi, D.; Mohagheghnejad, M. *Molecules* **2009**, *14* (5), 1915. doi:10.3390/molecules14051915. PMID:19471211.
- (9) (a) Niknam, K.; Zolfigol, M. A.; Sadabadi, T. *J. Iran Chem. Soc.* **2007**, *4*, 199; (b) Niknam, K.; Fatehi-Raviz, A. *J. Iran Chem. Soc.* **2007**, *4*, 438; (c) Niknam, K.; Zolfigol, M. A.; Hossieninejad, Z.; Daneshvar, N. *Chin. J. Catal.* **2007**, *28* (7), 591. doi:10.1016/S1872-2067(07)60051-5.; (d) Niknam, K.; Zolfigol, M. A.; Sadabadi, T.; Nejati, A. *J. Iran Chem. Soc.* **2006**, *3*, 318.
- (10) (a) Niknam, K.; Zolfigol, M. A.; Razavian, S. M.; Mohammadpoor-Baltork, I. *Heterocycles* **2005**, *65* (3), 657. doi:10.3987/COM-04-10302.; (b) Zolfigol, M. A.; Bagherzadeh, M.; Niknam, K.; Shirini, F.; Mohammadpoor-Baltork, I.; Choghamarani, A. G.; Baghbanzadeh, M. *J. Iran Chem. Soc.* **2006**, *3*, 73; (c) Niknam, K.; Zolfigol, M. A. *J. Iran Chem. Soc.* **2006**, *3*, 59; (d) Niknam, K.; Daneshvar, N. *Heterocycles* **2007**, *71* (2), 373. doi:10.3987/COM-06-10905.
- (11) Greene, T. W.; Wuts, P. G. M. *Greene's Protective Groups in Organic Synthesis*, 4th ed.; Wiley: New York, 2007.
- (12) Van Look, G.; Simchen, G.; Heberle, J. *Silylating Agents*, 2nd ed.; Fluka: Buchs, Switzerland, 1995.
- (13) Zolfigol, M. A.; Mohammadpoor-Baltork, I.; Habibi, D.; Mirjalili, B. F.; Bamoniri, A. *Tetrahedron Lett.* **2003**, *44* (44), 8165. doi:10.1016/j.tetlet.2003.09.036.
- (14) Corey, E. J.; Snider, B. B. *J. Am. Chem. Soc.* **1972**, *94* (7), 2549. doi:10.1021/ja00762a080. PMID:5016935.
- (15) Olah, G. A.; Gupta, B. G. B.; Narang, S. C.; Malhotra, R. *J. Org. Chem.* **1979**, *44* (24), 4272. doi:10.1021/jo01338a011.
- (16) D'Sa, B. A.; McLeod, D.; Verkade, J. G. *J. Org. Chem.* **1997**, *62* (15), 5057. doi:10.1021/jo9701492.
- (17) Lalonde, M.; Chan, T. H. *Synthesis* **1985**, *1985* (09), 817. doi:10.1055/s-1985-31361.
- (18) Gautret, P.; El-ghamarti, S.; Legrand, A.; Couturier, D.; Rigo, B. *Synth. Commun.* **1996**, *26* (4), 707. doi:10.1080/00397919608086745.
- (19) Shirini, F.; Zolfigol, M. A.; Mohammadi, K. *Phosphorus, Sulfur Silicon* **2003**, *178*, 1567.
- (20) Firouzabadi, H.; Sardarian, A. R.; Khayat, Z.; Karimi, B.; Tangestaninejad, S. *Synth. Commun.* **1997**, *27* (15), 2709. doi:10.1080/00397919708004140.
- (21) Azizi, N.; Yousefi, R.; Saidi, M. R. *J. Organomet. Chem.* **2006**, *691* (5), 817. doi:10.1016/j.jorganchem.2005.11.005.
- (22) Tillu, V. H.; Jadhav, V. H.; Borate, H. B.; Wakharkar, R. D. *Arkivoc* **2004**, *14*, 83.
- (23) Firouzabadi, H.; Iranpoor, N.; Amani, K.; Nowrouzi, F. *J. Chem. Soc., Perkin Trans. 1* **2002**, (23): 2601. doi:10.1039/b208202k.
- (24) Ghorbani-Vaghei, R.; Zolfigol, M. A.; Chegeny, M.; Veisi, H. *Tetrahedron Lett.* **2006**, *47* (26), 4505. doi:10.1016/j.tetlet.2006.03.157.
- (25) Mojtahedi, M. M.; Saeed Abaee, M.; Hamidi, V.; Zolfaghari, A. *Ultrason. Sonochem.* **2007**, *14* (5), 596. doi:10.1016/j.ultsonch.2006.09.009. PMID:17097324.
- (26) Akhlaghinia, B.; Tavakoli, S. *Synthesis* **2005**, *2005* (11), 1775. doi:10.1055/s-2005-865318.
- (27) Shirini, F.; Zolfigol, M. A.; Abedini, M. *Bull. Chem. Soc. Jpn.* **2005**, *78* (11), 1982. doi:10.1246/bcsj.78.1982.
- (28) Shirini, F.; Mollarazi, E. *Synth. Commun.* **2006**, *36* (8), 1109. doi:10.1080/00397910500501227.
- (29) Shaterian, H. R.; Shahrekipoor, F.; Ghashang, M. *J. Mol. Catal. A: Chem.* **2007**, *272* (1-2), 142. doi:10.1016/j.molcata.2007.03.036.
- (30) Zareyee, D.; Karimi, B. *Tetrahedron Lett.* **2007**, *48* (7), 1277. doi:10.1016/j.tetlet.2006.12.030.
- (31) Khazaei, A.; Zolfigol, M. A.; Rostami, A.; Choghamarani, A. G. *Catal. Commun.* **2007**, *8* (3), 543. doi:10.1016/j.catcom.2006.06.018.
- (32) (a) Khazaei, A.; Zolfigol, M. A.; Tanbakouchian, Z.; Shiri, M.; Niknam, K.; Saïen, J. *Catal. Commun.* **2007**, *8* (6), 917. doi:10.1016/j.catcom.2006.07.012.; (b) Khazaei, A.; Zolfigol, M. A.; Rostami, A.; Choghamarani, A. G. *Catal. Commun.* **2007**, *8* (3), 543. doi:10.1016/j.catcom.2006.06.018.
- (33) Niknam, K.; Zolfigol, M. A.; Chehardoli, G.; Dehghanian, M. *Chin. J. Catal.* **2008**, *29* (9), 901. doi:10.1016/S1872-2067(08)60072-8.
- (34) Firouzabadi, H.; Iranpoor, N.; Jafari, A. A.; Jafari, M. R. *J. Organomet. Chem.* **2008**, *693* (16), 2711. doi:10.1016/j.jorganchem.2008.05.018.
- (35) Shirini, F.; Abedini, M. *J. Iran Chem. Soc.* **2008**, *5*, S87.
- (36) Ghorbani-Choghamarani, A.; Zolfigol, M. A.; Hajjami, M.; Jafari, S. *J. Chin. Chem. Soc.* **2008**, *55*, 1208.
- (37) Shaterian, H. R.; Khorami, F.; Amirizadeh, A.; Ghashang, M.; Hosseinian, A. *Phosphorus Sulfur and Silicon* **2008**, *183* (10), 2584. doi:10.1080/10426500801967955.
- (38) Wada, M.; Sato, S. I.; Aritomi, M.; Harakawa, M.; Okawara, R. *J. Organomet. Chem.* **1972**, *39* (1), 99. doi:10.1016/S0022-328X(00)88908-1.
- (39) Speier, J. L. *J. Am. Chem. Soc.* **1952**, *74* (4), 1003. doi:10.1021/ja01124a039.
- (40) Olah, G. A.; Ernst, T. D. *J. Org. Chem.* **1989**, *54* (5), 1204. doi:10.1021/jo00266a041.



# Engineering of nanometer-sized cross-linked hydrogels for biomedical applications

Jung Kwon Oh

**Abstract:** Microgels/nanogels (micro/nanogels) are promising drug-delivery systems (DDS) because of their unique properties, including tunable chemical and physical structures, good mechanical properties, high water content, and biocompatibility. They also feature sizes tunable to tens of nanometers, large surface areas, and interior networks. These properties demonstrate the great potential of micro/nanogels for drug delivery, tissue engineering, and bionanotechnology. This mini-review describes the current approaches for the preparation and engineering of effective micro/nanogels for drug-delivery applications. It emphasizes issues of degradability and bioconjugation, as well as loading/encapsulation and release of therapeutics from customer-designed micro/nanogels.

**Key words:** microgels, nanogels, hydrogels, drug delivery, degradation, bioconjugation.

**Résumé :** Les microgels/nanogels (micro/nanogels) correspondent à des systèmes prometteurs d'administration des médicaments (SAM) en raison de leurs propriétés particulières, dont des structures physiques et chimiques accordables, de bonnes propriétés mécaniques, un niveau élevé d'eau et leur biocompatibilité. Ils comportent aussi des tailles ajustables jusqu'à des dizaines de nanomètres, des grandes surfaces de surface et des réseaux intérieurs. Ces propriétés démontrent le grand potentiel de micro/nanogels comme systèmes d'administration des médicaments, l'ingénierie des tissus et la bionanotechnologie. Cette minirevue décrit les approches actuelles à la préparation et à l'ingénierie de micro/nanogels adaptés pour les applications d'administration des médicaments. Elle fait ressortir les sujets de dégradabilité et de bioconjugaison ainsi que de chargement/encapsulation et de libération des produits thérapeutiques pour des microgels/nanogels répondant à des spécificités imposées par un client.

**Mots-clés :** microgels, nanogels, hydrogels, administration des médicaments, dégradation, bioconjugaison.

[Traduit par la Rédaction]

## Introduction

Hydrogels can form a cross-linked polymer network that has tunable chemical and physical structures, good mechanical properties, high water content, and biocompatibility. These unique properties suggest the enormous potential of their use in regenerative medicine, tissue engineering, biomedical implants, and drug delivery.<sup>1–7</sup> Recently, the design and preparation of unique hydrogels has also been explored

for the development of biosensors,<sup>8</sup> intracellular thermometry,<sup>9</sup> drug conjugates,<sup>10</sup> microfluidic biomaterials,<sup>11–13</sup> and photonic crystals.<sup>14</sup>

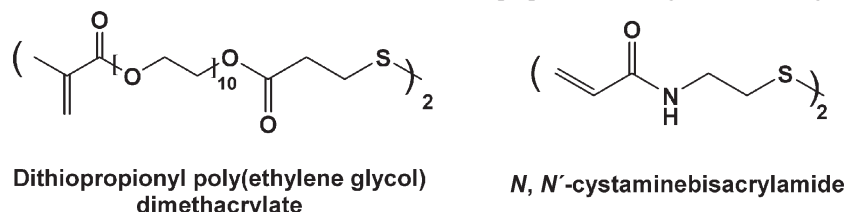
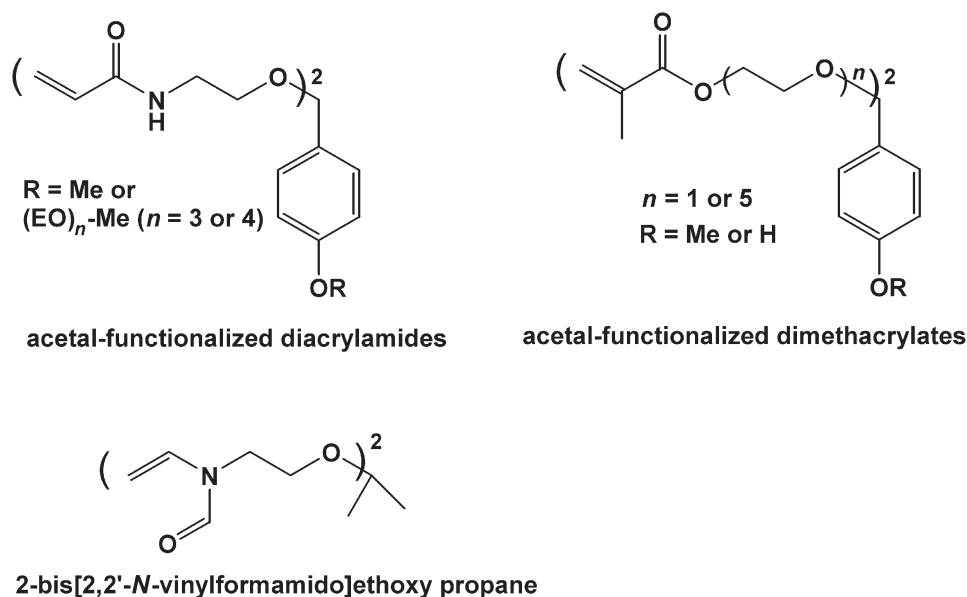
Microgels are a class of hydrogels that are submicron-sized cross-linked particulates.<sup>15</sup> The term “nanogel” is defined as a nanometer-sized microgel. While microgels share the unique properties of hydrogels, micro/nanogels have additional unique features: they are of a size tunable to tens of nanometers; have a large surface area; and possess an inte-

Received 26 August 2009. Accepted 14 October 2009. Published on the NRC Research Press Web site at canjchem.nrc.ca on 24 December 2009.

*This article is part of a Special Issue dedicated to Professor M. A. Winnik.*

**Abbreviations:** micro/nanogels, microgels/nanogels; biomicro/nanogels, biopolymer-based micro/nanogels; CS, chitosan; HA, hyaluronan; Dex, dextran; CeL, cellulose; PuL, pullulan; ChS, chondroitin sulfate; Alg, alginate; CRCP, controlled/living radical cross-linking polymerization; PEI, polyethyleneimine; TPP, sodium tripolyphosphate; PEO, poly(ethylene oxide); CyDex, cyclodextran; HECeL, hydroxyethylcellulose; CeL-Ac, cellulose; PuL-Ac, PuL acetate; PVP, poly(vinyl pyrrolidone); PAA-Cys, poly(acrylic acid)-cysteine; HPCeL, hydroxypropylcellulose; VEGF, vascular endothelial growth factor; FRP, free-radical polymerization; PNIPAM, poly(*N*-isopropylacrylamide); POEOMA, poly[oligo(ethylene glycol) monomethyl ether methacrylate]; LCST, lower critical solution temperature; MEO<sub>2</sub>MA, 2-(2-methoxyethoxy)ethyl methacrylate; PAAM, polyacrylamide; PEO-*b*-PPO-*b*-PEO, poly(ethylene glycol)-*b*-poly(propylene glycol)-*b*-poly(ethylene glycol); PFPE, photocurable perfluoropolyether; PEGDA, poly(ethylene glycol diacrylate); HEA, 2-hydroxyethyl acrylate; OH-EBiB, 2-hydroxyethyl 2-bromoisobutyrate; Dox, doxorubicin; PDT, photodynamic therapy; NPs, nanoparticles; QDs, quantum dots; MPS, mononuclear phagocyte system.

**J.K. Oh.** Dow Chemical Company, Midland, MI 48674, USA. (e-mail: jkoh2@dow.com).

**Fig. 1.** Chemical structures of disulfide-functionalized cross-linkers used for preparation of degradable microgels/nanogels.**Fig. 2.** Chemical structures of acetal-functionalized cross-linkers used for preparation of degradable microgels/nanogels.

rior network.<sup>16</sup> Micro/nanogels have great potential for various biorelated applications, including drug delivery, tissue engineering, and bionanotechnology, because of these properties.<sup>17–20</sup> Micro/nanogels are compositionally classified into two categories: synthetic and biopolymer-based.<sup>21</sup> Synthetic nanogels are based on hydrocarbon-based water-soluble or water-swelling (hydrophilic) polymers. In contrast, biopolymer-based micro/nanogels (biomicro/nanogels) are based on naturally occurring biopolymers including polysaccharides, such as chitosan (CS), hyaluronan (HA), dextran (Dex), cellulose (CeL), pullulan (PuL), chondroitin sulfate (ChS), and alginate (Alg), as well as proteins, gelatins, and poly(amino acids).<sup>22,23</sup> Such biopolymers are intrinsically biodegradable, abundant in nature, renewable, and nontoxic. They also possess a large amount of functional groups that can be utilized for further bioconjugation.<sup>24–26</sup>

Many strategies for the preparation of effective micro/nanogels have been developed. They have been designed and engineered to achieve a high degree of control over several criteria for in vitro and in vivo biomedical applications. Controllable features include dimension (diameter < 200 nm), degradability, bioconjugation to target disease cells, high-loading efficiency, and controllable release of encapsulated biomolecules (therapeutics), stability for prolonged circulation in blood, and non-toxicity to cells. This mini-review will describe the current approaches for the preparation and engineering of micro/nanogels for drug-delivery applications, with an emphasis on recent advances in

degradability, bioconjugation, loading/encapsulation, and release.

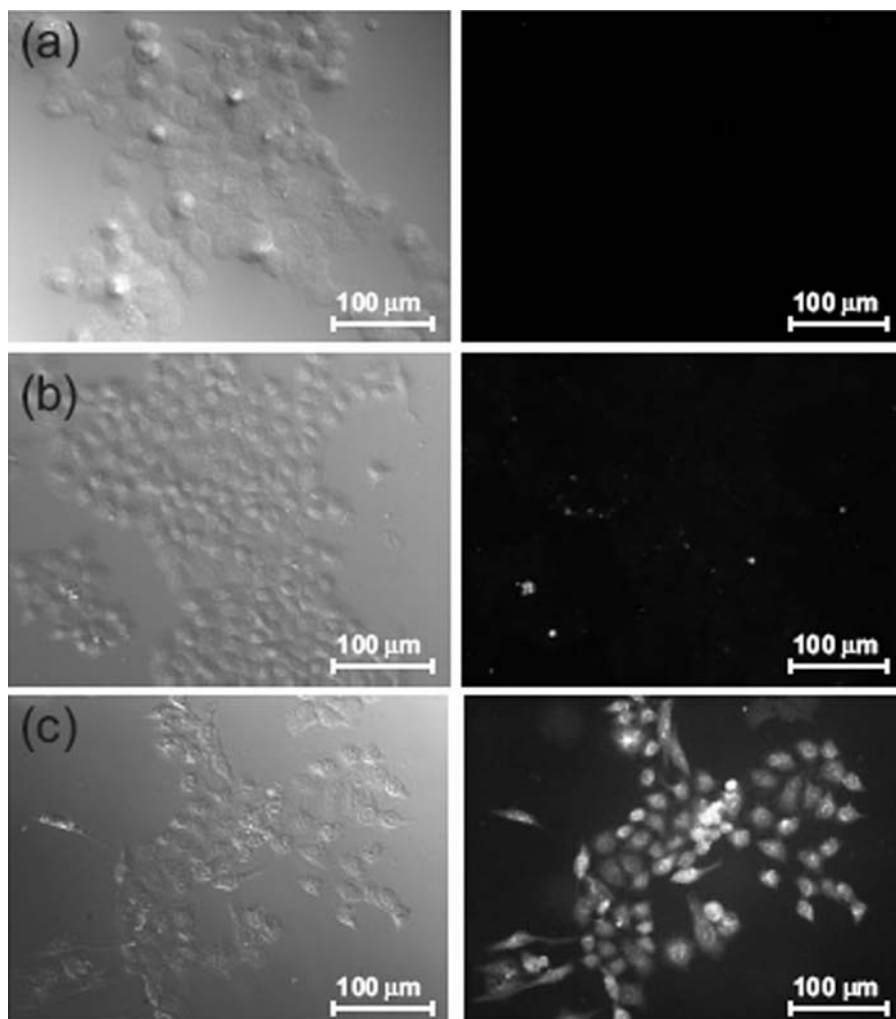
## Preparation of micro/nanogels

Current approaches for the preparation of cross-linked micro/nanogels can be largely classified into physical cross-linking, chemical cross-linking, and heterogeneous controlled/living radical cross-linking polymerization (CRCP).

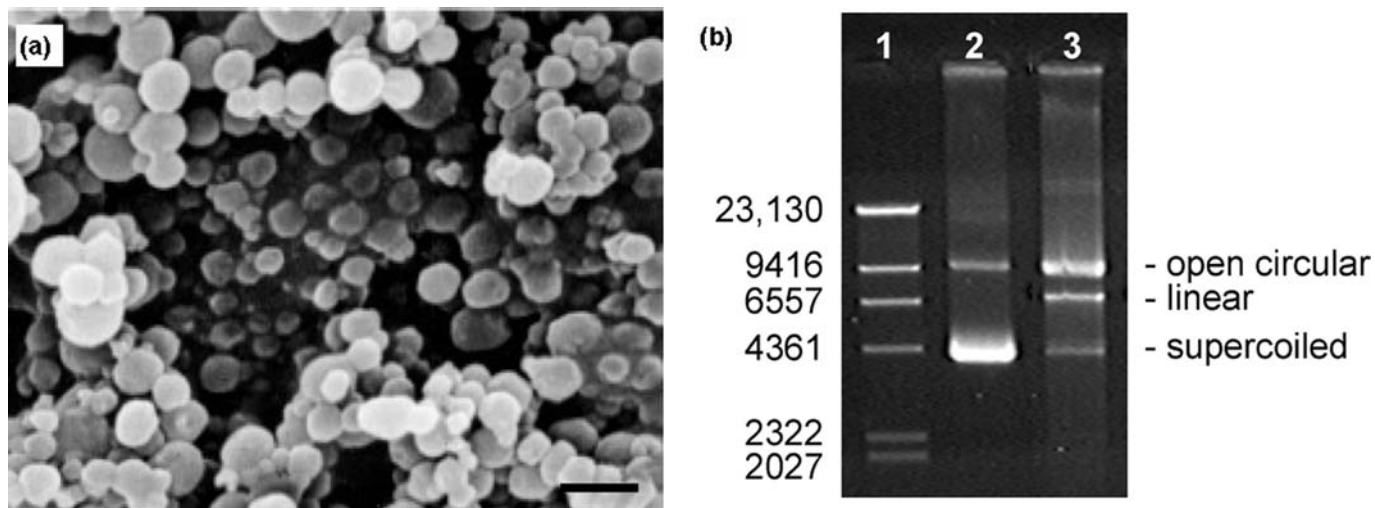
### Physical cross-linking approach

Physical cross-linking approach is achieved through electrostatic interactions, hydrogen bonds, crystallized domains, hydrophobic interactions, stereocomplexation, temperature-induced sol–gel transitions, host–guest interactions, aggregations, and self-assembly/self-associations. Physical cross-linking has two primary advantages: reversibility and no requirement that other chemicals be used to link chains. Several methods of physical cross-linking have been developed for the successful preparation of micro/nanogels. One general method involves aqueous homogeneous gelation. In most experiments, electrostatic interactions of polysaccharide-based polymers with various polyelectrolytes in water have been explored. These polyelectrolytes include polyethyleneimine (PEI),<sup>27</sup> sodium tripolyphosphate (TPP),<sup>28–30</sup> poly(ethylene oxide) (PEO)-*b*-poly(*N,N*-dimethylaminoethyl methacrylate) block copolymer,<sup>31</sup> and biopolymer-based polyelectrolyte<sup>32</sup> to yield CS-based nanogels. In addition, various other polysaccharide-based microgels have been

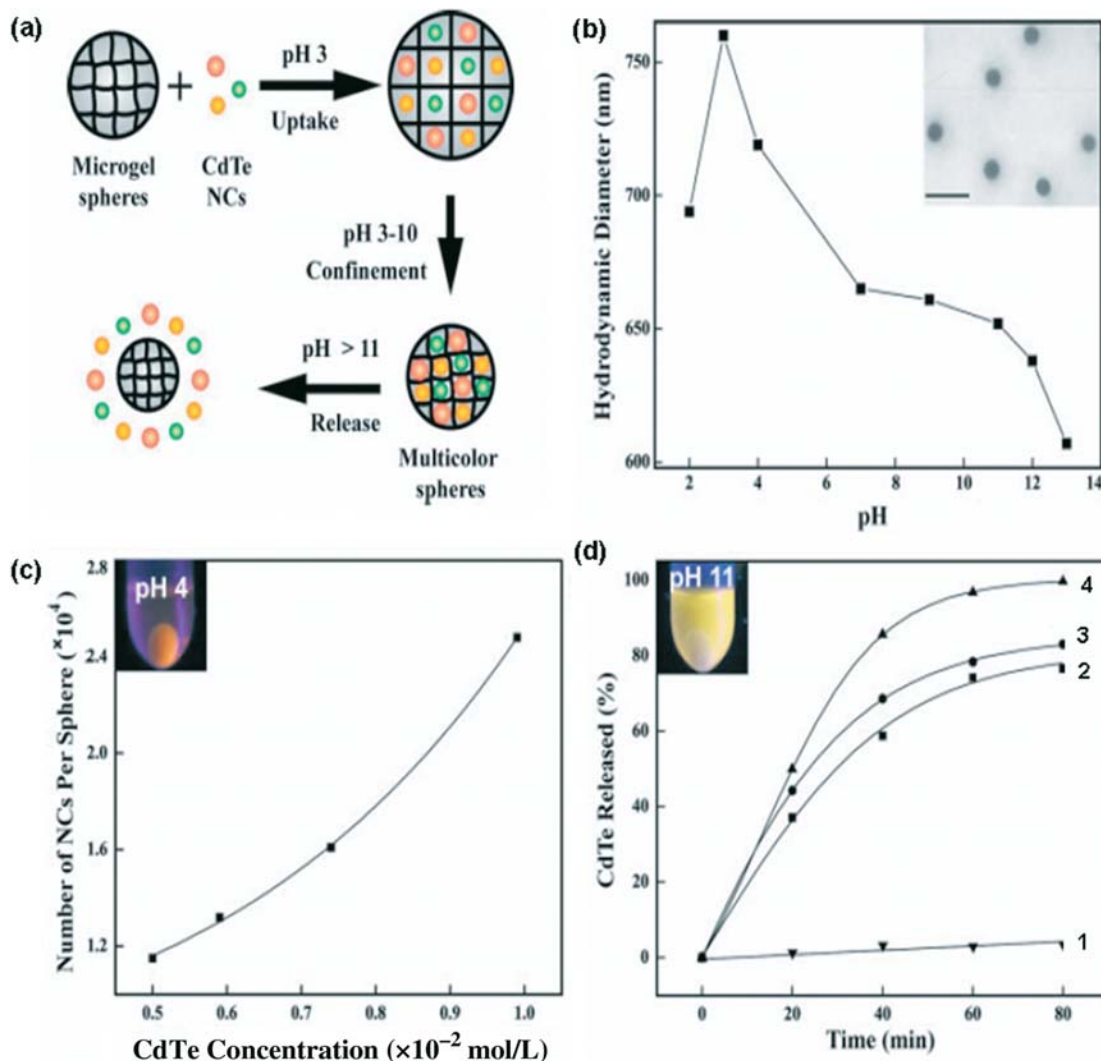
**Fig. 3.** Differential interference contrast (DIC) (left) and epifluorescent (right) images of HeLa cells after 24 h incubation with rhodamine 6G-loaded microgels that were not conjugated to any protein (a), conjugated to albumin (b), and conjugated to transferrin (c). Reprinted with permission from ref. 16. Copyright 2006 Wiley InterScience.



**Fig. 4.** Scanning electron micrograph of plasmid-loaded acid-labile PAAm microgels (a) and analysis of the released DNA by agarose gel electrophoresis. Line 1: Lambda Hind III ladder. Line 2: original plasmid DNA. Line 3: DNA released from microgels upon degradation. Reprinted with permission from ref. 149. Copyright 2004 American Chemical Society.



**Fig. 5.** Schematic illustration of the loading of CdTe QDs in P(NIPAM-VP) microgels and their release upon pH change (a). (b) Hydrodynamic diameter of microgels vs. pH in water at 25 °C (inset: TEM micrograph of microgels; scale bar = 500 nm). (c) Loading of 3 nm QDs into microgels (inset: fluorescence image of microgels loaded with QDs at pH = 4). (d) Release of 3 nm QDs from microgels vs. time at pH = 10 (1), 11 (2), 13 (3), and 13 with 0.05 mol/L NaCl (4) (inset: fluorescence image of microgels loaded with QDs at pH = 11). Reprinted with permission from ref. 179. Copyright 2005 Wiley InterScience.



prepared. They include cyclodextran (CyDex)-based nanogels and core-cross-linked Alg-based microcapsules for cell encapsulation in water,<sup>33,34</sup> mannose-bearing CS micro-spheres containing PEI/DNA complexes in emulsion,<sup>27</sup> and Dex-based microgels in double emulsion.<sup>35</sup>

A microfluidic method has also been employed for the preparation of physically cross-linked microgels. Microfluidic devices are designed with inlets for monomers, continuous liquids and optional cross-linkers, microchannels, and a tapered junction. Ionic cross-linking by external cross-linking appears to be a promising method for the microfluidic preparation of Alg-based microgels. Carboxylic acid residues (COOH) of Alg have been cross-linked with  $\text{Ca}^{2+}$  ions in droplets, yielding shape- and size-controlled Alg-microgels,<sup>36–38</sup> cell-encapsulated microgels,<sup>39</sup> and microcapsules with controlled morphology.<sup>40,41</sup>

Polysaccharide derivatives have also been modified with hydrophobic molecules or oligomers, yielding amphiphilic biopolymers that can self-assemble in water to form micellar

nanoparticles. Such nanoparticles include hydroxyethylcellulose (HECeL),<sup>42</sup> cellulose acetate (CeL-Ac),<sup>43</sup> PuL,<sup>44–47</sup> PuL acetate (PuL-Ac),<sup>48</sup> glycol CS,<sup>49</sup> and Dex.<sup>50</sup> Further, self-association of two polymers in water yields supramolecular nanogels. Examples include inclusion of  $\beta$ -CyDex with lauryl-modified Dex in water,<sup>51,52</sup> hydrogen bonds between poly(vinyl pyrrolidone) (PVP) and poly(acrylic acid)-cysteine (PAA-Cys),<sup>53</sup> HPCeL with carboxylic-acid-containing surfactant,<sup>54</sup> and temperature (or heat)-induced self-association of hydroxypropyl cellulose (HPCeL) in water.<sup>55–57</sup> In addition, the reverse micellar method has produced Alg-based microgels that are physically cross-linked with  $\text{Ca}^{2+}$  ions for the controlled delivery of vascular endothelial growth factor (VEGF).<sup>58</sup>

#### Chemical cross-linking approach

The chemical cross-linking approach is the general method for the preparation of micro/nanogels. Specific techniques of this approach have included polycondensation re-



actions as well as radical polymerizations in water and heterogeneous media. Polycondensation reactions are mainly utilized for the preparation of biomicro/nanogels. This is because functional groups are plentiful in polysaccharides, gelatins, and proteins and can react with external cross-linkers such as glutaraldehyde, divinyl sulfone, and adipic dihydrazide. In addition, the residual functional groups can be further used for bioconjugation with cell-targeting biomolecules, allowing for the exploration of specific biological processes. Various water-in-oil (W/O) heterogeneous gelation methods, including inverse miniemulsion,<sup>59–68</sup> inverse microemulsion,<sup>69,70</sup> and membrane emulsification,<sup>71–73</sup> have been explored for the preparation of HA, CS, and Alg-based micro/nanogels. Other methods include aqueous homogeneous gelation<sup>74,75</sup> and continuous reactive extrusion.<sup>76</sup> Details of these methods have been described in a recent review.<sup>21</sup>

Heterogeneous free-radical polymerization (FRP) of hydrocarbon-based water-soluble monomers in the presence of multifunctional cross-linkers has been extensively explored for the preparation of synthetic micro/nanogels. Typical FRP methods include precipitation, inverse (mini)emulsion, and inverse microemulsion polymerization. Precipitation polymerization in water has been utilized for the preparation of hydrogels and microgels based on poly(*N*-isopropylacrylamide) (PNIPAM)<sup>77–82</sup> and, more recently, poly[oligo(ethylene glycol) monomethyl ether methacrylate] (POEOMA) including its copolymers with 2-(2-methoxyethoxy)ethyl methacrylate (MEO<sub>2</sub>MA),<sup>83,84</sup> for biomedical applications. The thermosensitive properties of these polymers, which undergo volume change at a lower critical solution temperature (LCST) in water, make them good candidates for use in vivo. Above the LCST, they are hydrophobic and expel water; below LCST, they are hydrophilic and swell in water. These unique properties facilitate the loading of drugs into microgels and enhance the controllable release of encapsulated drugs.<sup>85</sup> In addition, copolymerization of NIPAM with various functional monomers under precipitation-polymerization conditions has been shown to yield functional microgels.<sup>86</sup> Examples of comonomers include more hydrophilic or hydrophobic monomers for tuning the volume phase transition of the resultant microgels<sup>87,88</sup> and acid-containing monomers such as AA, methacrylic acid, and undecanoic acid for targeted drug delivery<sup>16,89–91</sup> as well as for use as a glucose sensor.<sup>92–94</sup> (4-Vinyl-4'-methyl-2,2'-bipyridine)-bis(2,2'-bipyridine)ruthenium(II) complex has also been incorporated into PNIPAM-based nanogels for self-flocculating/self-dispersing oscillation.<sup>95</sup>

Inverse emulsion, miniemulsion, and microemulsion polymerization have been explored for the preparation of cross-linked micro/nanogels. This interest is due to the facile confinement of water-soluble drugs in aqueous droplets dispersed in continuous organic solvents. Examples include micro/nanogels based on PNIPAM,<sup>96</sup> polyacrylamide (PAAm),<sup>97</sup> acrylated triblock copolymer of poly(ethylene glycol)-*b*-poly(propylene glycol)-*b*-poly(ethylene glycol) (PEO-*b*-PPO-*b*-PEO),<sup>98</sup> poly(magnesium acrylate),<sup>99</sup> and diacrylated Pluronic-oligo(lactic acid) copolymer<sup>100,101</sup> by inverse (mini)emulsion polymerization. In addition, well-defined nanogels based on PAAm,<sup>102</sup> PVP,<sup>103,104</sup> poly(hydroxyethyl acrylate-*co*-2-acryloxyethyltrimethylammonium chloride),<sup>105</sup> and  $\alpha,\beta$ -poly(*N*-2-hydroxyethyl)-D,L-as-

partamide<sup>106</sup> have been prepared by inverse microemulsion polymerization.

Particle replication in nonwetting templates (PRINT)<sup>107</sup> was developed to fabricate submicron-sized microgels with control over particle size, shape, and composition. This method uses photolithography to create photocurable perfluoropolyether (PFPE) replica molds, in which various multifunctional monomers are cross-linked by photo-radical polymerization. PRINT has yielded monodisperse microgels of poly(ethylene glycol diacrylate) (PEGDA), triacrylate resin, polylactide (PLA), and polypyrrole, with sizes ranging from 200 nm to micron-scale in diameter and achieving various shapes, such as trapezoidal, bar, conical, and arrow.

### Heterogeneous controlled/living radical cross-linking polymerization

The utilization of controlled/living radical polymerization (CRP) techniques<sup>108–113</sup> allows for the development of cross-linked microgels, nanogels, and hydrogels with well-controlled polymer segments and high swelling ratios.<sup>114–119</sup> Few papers have reported on the use of CRP methods to prepare well-defined micro/nanogels. Atom transfer radical polymerization (ATRP)<sup>120,121</sup> in water has yielded PNIPAM nanogels at 25 °C.<sup>122</sup> Reversible addition fragmentation transfer (RAFT) polymerization<sup>123,124</sup> has produced poly(vinyl acetate)-based nanogels,<sup>125</sup> acid-cleavable core-shell nanoparticles,<sup>126</sup> and thermally responsive<sup>127</sup> and double hydrophilic<sup>128</sup> block copolymer nanogels. Recently, an effective method utilizing ATRP, inverse miniemulsion polymerization, and disulfide–thiol exchange has been developed for the preparation, functionalization, and application of well-defined biodegradable nanogels for the goal of targeted drug delivery. The novel approach has allowed for the preparation of biomaterials with many useful features. They include uniform network, high loading efficiency, novel distributed functionality of bromine end groups, and degradation by hydrolysis or through a disulfide–thiol exchange.<sup>129–135</sup> The details are reported elsewhere.<sup>136</sup>

### Degradation

Degradation cannot only modulate the release of encapsulated biomolecules, such as drugs, for a desired period of time, but also can enable the removal of an empty device after drug release from the body. Degradation is generally achieved by introducing degradable linkages as multifunctional cross-linkers into micro/nanogels. These degradable linkages are then cleaved in response to external stimuli, such as chemicals, pH, hydrolysis, enzymes, and light. Consequently, a significant amount of work has been directed toward the development of cross-linkers functionalized with degradable linkages, leading to degradable micro/nanogels for targeted drug-delivery applications.

Disulfides have been degraded into the corresponding thiols in the presence of water-soluble reducing agents, such as dithiothreitol<sup>137–139</sup> and glutathione,<sup>140</sup> through the disulfide–thiol change. In particular, glutathione is a biocompatible tripeptide found within cells at millimolar concentrations.<sup>141,142</sup> It has been reported that the viability of C2C12 cells in the presence of 10 mmol/L glutathione was over

91% for 2 days, suggesting that, at this concentration, glutathione exhibits insignificant cytotoxicity.<sup>130</sup> Nanogels prepared in the presence of disulfide-functionalized cross-linkers can be degraded in the presence of glutathione in cellular environments, releasing anticancer drugs to kill cancer cells. Well-defined nanogels of POEOMA have been prepared by inverse miniemulsion ATRP in the presence of dithiopropionyl poly(ethylene glycol) dimethacrylate.<sup>129,130</sup> Trojan horse PRINT particles have also been prepared in the presence of *N,N'*-cystamine bisacrylamide.<sup>143</sup> Figure 1 shows the chemical structures of disulfide-functionalized cross-linkers.

An acetal is an acid-labile linkage that can be degraded under acidic conditions ( $\text{pH} < 6.5$ ).<sup>144</sup> Acetal chemistry is extremely promising for targeted drug-delivery applications because acid-labile linkages can be sufficiently stable to sustain drugs in the bloodstream ( $\text{pH} = 7\text{--}7.5$ ), but then cleaved in cancer cells ( $\text{pH} < 5.7$ ), releasing drugs to kill a tumor.<sup>145,146</sup> Several reports have described the preparation of acetal-functionalized micro/nanogels mainly by inverse emulsion polymerization. Examples include nanogels based on PAAm and its copolymers prepared in the presence of acetal-functionalized diacrylamide cross-linkers,<sup>147–150</sup> poly(2-hydroxymethyl methacrylate) microgels with acetal-functionalized dimethacrylates,<sup>151</sup> and poly(*N*-vinylformamide) nanogels with 2-bis[2,2-*N*-vinylformamido]ethyl propane.<sup>152</sup> Figure 2 shows the chemical structures of acetal-functionalized cross-linkers.

Microgels cross-linked with oligolactate linkages have been prepared by inverse suspension polymerization of oligolactate-functionalized diacrylates. In this case, the microgels were degraded upon hydrolysis of oligolactate linkages in physiological conditions at  $\text{pH} = 7.0$  at  $37^\circ\text{C}$ .<sup>100</sup> Enzyme-responsive microgels were prepared by precipitation copolymerization of AAm with an amine-functionalized AAm derivative in water. The amine groups in the microgels reacted with enzyme-cleavable peptide linkers that were cleaved in the presence of a protease enzyme.<sup>80,81</sup> Light-responsive microgels were prepared by photo-induced dimerization ( $\lambda > 310\text{ nm}$ ) of coumarin groups in micellar nanoparticles produced from amphiphilic block copolymers consisting of PEO hydrophilic block and pendent coumarin-containing hydrophobic block.<sup>153</sup> Upon the irradiation of light ( $\lambda < 260\text{ nm}$ ), the dimers of coumarin side groups were cleaved, leading to microgel degradation.<sup>153</sup>

In addition, many reports have demonstrated the preparation of effective degradable hydrogels cross-linked with disulfides,<sup>140,154</sup> acetals,<sup>155,156</sup> peptides,<sup>157–160</sup> oligolactate esters,<sup>85,161–164</sup> and other degradable linkages, including periodates,<sup>165</sup> polyphosphoesters,<sup>166,167</sup> anhydrides,<sup>168</sup> polyperoxides,<sup>169</sup> and poly(3-hydroxybutyrate).<sup>170</sup>

## Bioconjugation

Bioconjugation of micro/nanogel surfaces with specific ligands that can recognize receptors on diseased cells has allowed for active targeting to specific cells. Effective ligands for cancer cells include folic acid derivatives, peptides, proteins, and antibodies. To achieve effective bioconjugation, a novel functionality must be incorporated into micro/nanogels. CS-based microgels physically cross-linked with TPP were prepared by aqueous homogeneous gelation. They

were bioconjugated with transferrin in water. The bioconjugation was characterized using ninhydrin solution.<sup>171</sup> Microgels of P(NIPAM-AA) had a hydrodynamic diameter of 110 and 156 nm at  $\text{pH} = 4.5$  and  $7.4$ , respectively. Acid groups in microgels reacted with amino groups of proteins, such as albumin and transferrin, yielding microgel–protein bioconjugates. Interestingly, only transferrin-conjugated microgels entered HeLa cancer cells through receptor-mediated endocytosis (Fig. 3).<sup>16</sup> The preparation of P(NIPAM-AA) microgels bioconjugated with folic acids have also been reported.<sup>89</sup>

Well-defined biodegradable OH-functionalized nanogels of POEOMA have been prepared by ATRP in inverse miniemulsion. Two approaches have been proposed: copolymerization of OEOMA with OH-functional monomers, particularly 2-hydroxyethyl acrylate (HEA),<sup>130</sup> and the use of OH-functionalized ATRP initiators such as 2-hydroxyethyl 2-biromisobutyrate (OH-EBiB).<sup>132</sup> Hydroxyl (OH) groups of nanogels have been reacted with carboxylic acid groups of biotins. The resulting biotin-functionalized nanogels were subsequently bioconjugated with avidin through a specific biotin–avidin interaction.<sup>130</sup> Biotin-functionalized nanogels can also be conjugated with an avidin-functionalized antibody for receptor-mediated endocytosis. In addition, OH groups in POEOMA nanogels have been converted to the corresponding carboxylic acids. The resulting COOH-POEOMA nanogels were subsequently conjugated with RGD-NH<sub>2</sub> tripeptide, yielding RGD-conjugated POEOMA nanogels.<sup>132</sup> Recently, the reversible surface switching of CS-based nanogels triggered by temperature was prepared by cross-linking reaction of CS with TPP at physiological  $\text{pH} = 7.4$ . The nanogels were conjugated with transferrin in aqueous media for receptor-mediated endocytosis.<sup>171,172</sup>

## Loading/encapsulation and release

Micro/nanogels have an interior network for the incorporation of biorelated molecules. Several methods have been utilized to incorporate various water-soluble and dispersible biomolecules into nanogels. They include physical loading and in situ physical incorporation. The entrapment of bioactive molecules in the polymeric network as well as their in vitro release have been extensively investigated as possible routes for drug delivery in biomedical applications. In general, load/release is achieved through electrostatic interactions, hydrophobic and hydrophilic interactions, stimuli response, and degradation.<sup>21</sup>

Physical loading has generally been utilized for low molecular weight bioactive molecules. Examples include anticancer drugs, like doxorubicin (Dox)<sup>16,143,173,174</sup> and methotrexate,<sup>75,171</sup> as well as polypeptides including insulin.<sup>175</sup> To accomplish physical loading, micro/nanogels are mixed with drugs in water. Excess drugs are removed by centrifugation or dialysis. In one study, a hydrophilic and hydrophobic interaction was utilized to load Dox into biodegradable POEOMA nanogels cross-linked with disulfide linkages in water. Here, the loading level of Dox was determined using the extinction coefficient of Dox ( $\epsilon = 7600\text{ mol/L}^{-1}\text{ cm}^{-1}$  at  $\lambda = 497\text{ nm}$ ) in water. It increased from 5.4 to 16.4 wt% as the initial ratio of Dox/nanogel in the mixture increased from 0.07/1 to 0.35/1.<sup>130</sup>

Results were similar to those for nanogels based on Pluronic F127 containing hydrophobic poly(propylene glycol). The amount of Dox loaded into the nanogels increased from 2.7 to 8.9 wt% as the initial ratio of Dox/nanogel increased from 0.1/1 to 0.2/1.<sup>98</sup> Thermoresponsiveness was also utilized to load Dox into P(NIPAM-AA) microgels at pH = 7.4 where the microgels were swollen. However, at pH = 4.5, the microgels shrank and Dox was then released.<sup>16</sup> The loading and release of insulin into PNIPAM-based microgels by thermal responsiveness has also been explored.<sup>175</sup>

In situ physical incorporation has been utilized to load relatively high molecular weight biomolecules, such as proteins, carbohydrates, and genes. In this case, the pore size of micro/nanogels is not sufficiently large to allow high molecular weight biomolecules to diffuse into the network. Two methods are generally employed. The more promising method involves the use of inverse (mini)emulsion and inverse microemulsion polymerization where water-soluble biomolecules are confined in water-soluble droplets. As an example, plasmid DNA was loaded into acid-labile PAAm-based microgels prepared by inverse emulsion polymerization. Subsequently, the plasmid DNA was released from the microgels upon degradation in response to pH change. The release behavior was characterized using agarose gel electrophoresis (Fig. 4).<sup>149</sup> In addition, ovalbumin,<sup>148</sup> BSA,<sup>133</sup> lysozyme,<sup>152</sup> and antisense<sup>105</sup> as well as various carbohydrate model drugs<sup>103,104,131</sup> have also been incorporated into micro/nanogels using the same method. The second method involves the use of aqueous gelation by physical cross-linking. Bioactive molecules are incorporated into micro/nanogels during gelation in aqueous solution. Examples include insulin loaded in microgels based on CS/CyDex hybrid<sup>34</sup> and PVP/PAA,<sup>53</sup> as well as BSA<sup>172</sup> and Dex<sup>29</sup> in CS-based microgels. Meta-tetra(hydroxyphenyl)chlorine has also been encapsulated into PAAm nanogels for photodynamic therapy (PDT).<sup>176</sup>

## Incorporation of inorganic nanoparticles into micro/nanogels

The incorporation of inorganic nanoparticles (NPs) into micro/nanogels allows for the retention of the unique structural and optical properties that have been attributed to nanoscale phenomena of inorganic NPs.<sup>177,178</sup> Examples of colloidal inorganic NPs include quantum dots (QDs) for fluorescent imaging, iron oxide NPs for magnetic resonance imaging (MRI), and silver and gold NPs for optical imaging and therapy. Three approaches are generally utilized: physical loading, in situ polymerization, and in situ formation.

For physical loading, the pH-responsive swelling property of P(NIPAM-VP) in water at pH = 3 has been utilized to incorporate water-soluble CdTe QDs into microgels, yielding CdTe-loaded microgels for multicolor-coded microspheres. At pH > 11, QDs have been released by thermal-responsiveness (shrinking) of P(NIPAM-VP) (Fig. 5).<sup>179</sup> Similarly, CdTe-loaded PNIPAM gels,<sup>180</sup> poly(NIPAM-AA),<sup>181</sup> and P(NIPAM-vinyl imidazole)<sup>182</sup> microgels have been prepared in response to temperature and pH stimuli. In addition, Au nanorods have been incorporated into P(NIPAM-AA) microgels for photodynamic therapy.<sup>183</sup> As an example of in situ polymerization, dispersion and inverse emulsion polymeriza-

tion of NIPAM in the presence of  $\gamma$ -Fe<sub>2</sub>O<sub>3</sub> NPs yielded magnetic PNIPAM-based microgels loaded with  $\gamma$ -Fe<sub>2</sub>O<sub>3</sub> NPs.<sup>184</sup> Magnetic PHEMA-based microgels have been similarly prepared.<sup>185</sup>

For in situ formation of inorganic NPs inside the microgel network, ionic precursors of inorganic NPs are added first to react with functional groups such as amines and carboxylic acids in microgels. A subsequent addition of counter ions yields inorganic NPs inside the microgel network. Examples include PNIPAM microgels loaded with Au NPs,<sup>186</sup> poly(*N*-vinyl caprolactam) microgels loaded with poly(3,4-ethylenedioxythiophene) nanorods,<sup>187</sup> P(NIPAM-AA) microgels with Ag NPs,<sup>188</sup> and P(NIPAM-AA-HEA) microgels with CdS QDs, Ag, and Fe<sub>3</sub>O<sub>4</sub> NPs.<sup>189</sup> Recently, magnetic P(NIPAM-AA-HEA) microgels containing Fe<sub>3</sub>O<sub>4</sub> NPs were utilized as stimuli-responsive emulsifiers for the remote control of separation and stability of oil-in-water emulsions.<sup>190</sup>

## Summary

Various methods for the preparation of micro/nanogels for drug-delivery applications have been developed using physical cross-linking, chemical cross-linking, and heterogeneous CRCP approaches. Micro/nanogels have been designed and engineered to achieve a high degree of control of properties for biomedical applications. To accomplish this high level of control, nanogel diameters should be <200 nm. This facilitates cellular uptake through receptor-mediated endocytosis to cross cell membranes, and reduces nanoparticle uptake by the mononuclear phagocyte system (MPS). Second, degradability enables modulation of drug release for a desired period of time and enables the removal of the empty device after drug release. This has generally been achieved by introducing degradable linkages as multifunctional cross-linkers into micro/nanogels. The degradable linkages can then be cleaved in response to external stimuli. Effective degradable linkages include disulfide (glutathione); acid-labile groups, including acetal, polyphosphoester, and hydrazone (pH change); oligolactate (hydrolysis); peptide (enzyme); and photo-cleavable groups (light). Third, functionality allows for the bioconjugation of microgel surfaces with specific ligands that can recognize receptors on diseased cells. Effective ligands for cancer cells include folic acid derivatives, peptides, proteins, and antibodies. Fourth, loading and release of biorelated molecules is achieved through electrostatic interactions, hydrophobic and hydrophilic interactions, stimuli-responsiveness, and degradation. General methods include (i) physical loading for both low molecular weight, bioactive molecules, and polypeptide, and (ii) in situ physical incorporation for relatively high molecular weight biomolecules, including proteins, carbohydrates, and genes. In addition, inorganic nanoparticles (NPs) have been incorporated into micro/nanogels for fluorescence, MRI, optical imaging, and therapy. In the future, more research effort will be directed toward the design and development of effective nanogels with better control over those criteria most critical for in vivo drug-delivery applications.

## References

- (1) Langer, R.; Vacanti, J. P. *Science* **1993**, 260 (5110), 920. doi:10.1126/science.8493529. PMID:8493529.



- (2) Hoffman, A. S. *J. Control. Release* **1987**, *6* (1), 297. doi:10.1016/0168-3659(87)90083-6.
- (3) Langer, R. *Science* **2001**, *293* (5527), 58. doi:10.1126/science.1063273. PMID:11441170.
- (4) Peppas, N. A.; Hilt, J. Z.; Khademhosseini, A.; Langer, R. *Adv. Mater.* **2006**, *18* (11), 1345. doi:10.1002/adma.200501612.
- (5) Choi, S.-W.; Xie, J.; Xia, Y. *Adv. Mater.* **2009**, *21* (29), 2997. doi:10.1002/adma.200803504.
- (6) Wang, Q.; Wang, L.; Detamore, M. S.; Berkland, C. *Adv. Mater.* **2008**, *20* (2), 236. doi:10.1002/adma.200702099.
- (7) Slaughter, B. V.; Khurshid, S. S.; Fisher, O. Z.; Khademhosseini, A.; Peppas, N. A. *Adv. Mater.* **2009**, *21* (32-33), 3307. doi:10.1002/adma.200802106.
- (8) Tanaka, H.; Isojima, T.; Hanasaki, M.; Ifuku, Y.; Takeuchi, H.; Kawaguchi, H.; Shiroya, T. *Macromol. Rapid Commun.* **2008**, *29* (15), 1287. doi:10.1002/marc.200800090.
- (9) Gota, C.; Okabe, K.; Funatsu, T.; Harada, Y.; Uchiyama, S. *J. Am. Chem. Soc.* **2009**, *131* (8), 2766. doi:10.1021/ja807714j.
- (10) Varghese, O. P.; Sun, W.; Hilborn, J.; Ossipov, D. A. *J. Am. Chem. Soc.* **2009**, *131* (25), 8781. doi:10.1021/ja902857b. PMID:19499915.
- (11) Cabodi, M.; Choi, N. W.; Gleghorn, J. P.; Lee, C. S. D.; Bonassar, L. J.; Stroock, A. D. *J. Am. Chem. Soc.* **2005**, *127* (40), 13788. doi:10.1021/ja054820t. PMID:16201789.
- (12) Golden, A. P.; Tien, J. *Lab Chip* **2007**, *7* (6), 720. doi:10.1039/b618409j. PMID:17538713.
- (13) Choi, N. W.; Cabodi, M.; Held, B.; Gleghorn, J. P.; Bonassar, L. J.; Stroock, A. D. *Nat. Mater.* **2007**, *6* (11), 908. doi:10.1038/nmat2022. PMID:17906630.
- (14) Kang, J.-H.; Moon, J. H.; Lee, S.-K.; Park, S.-G.; Jang, S. G.; Yang, S.; Yang, S.-M. *Adv. Mater.* **2008**, *20* (16), 3061. doi:10.1002/adma.200800141.
- (15) Oh, J. K.; Drumright, R.; Siegwart, D. J.; Matyjaszewski, K. *Prog. Polym. Sci.* **2008**, *33* (4), 448. doi:10.1016/j.progpolymsci.2008.01.002.
- (16) Das, M.; Mardiyani, S.; Chan, W. C. W.; Kumacheva, E. *Adv. Mater.* **2006**, *18* (1), 80. doi:10.1002/adma.200501043.
- (17) Hamidi, M.; Azadi, A.; Rafiei, P. *Adv. Drug Deliv. Rev.* **2008**, *60* (15), 1638. doi:10.1016/j.addr.2008.08.002. PMID:18840488.
- (18) Soussan, E.; Cassel, S.; Blanzat, M.; Rico-Lattes, I. *Angew. Chem. Int. Ed.* **2009**, *48* (2), 274. doi:10.1002/anie.200802453.
- (19) Raemdonck, K.; Demeester, J.; De Smedt, S. *Soft Matter* **2009**, *5* (4), 707. doi:10.1039/b811923f.
- (20) Kabanov, A. V.; Vinogradov, S. V. *Angew. Chem. Int. Ed.* **2009**, *48* (30), 5418. doi:10.1002/anie.200900441.
- (21) Oh, J. K.; Lee, D. I.; Park, J. M. *Prog. Polym. Sci.* **2009**, *34* (12), 1261. doi:10.1016/j.progpolymsci.2009.08001.
- (22) Laurent, T. C., Ed. *The Chemistry, Biology and Medical Applications of Hyaluronan and its Derivatives*; Wenner-Gren International Series, 1998; Vol. 72.
- (23) Berger, J.; Reist, M.; Mayer, J. M.; Felt, O.; Peppas, N. A.; Gurny, R. *Eur. J. Pharm. Biopharm.* **2004**, *57* (1), 19. doi:10.1016/S0939-6411(03)00161-9. PMID:14729078.
- (24) Liu, Z.; Jiao, Y.; Wang, Y.; Zhou, C.; Zhang, Z. *Adv. Drug Deliv. Rev.* **2008**, *60* (15), 1650. doi:10.1016/j.addr.2008.09.001. PMID:18848591.
- (25) Agnihotri, S. A.; Mallikarjuna, N. N.; Aminabhavi, T. M. *J. Control. Release* **2004**, *100* (1), 5. doi:10.1016/j.jconrel.2004.08.010. PMID:15491807.
- (26) Nanjawade, B. K.; Manvi, F. V.; Manjappa, A. S. *J. Control. Release* **2007**, *122* (2), 119. doi:10.1016/j.jconrel.2007.07.009. PMID:17719120.
- (27) Zhou, X.; Liu, B.; Yu, X.; Zha, X.; Zhang, X.; Chen, Y.; Wang, X.; Jin, Y.; Wu, Y.; Chen, Y.; Shan, Y.; Chen, Y.; Liu, J.; Kong, W.; Shen, J. *J. Control. Release* **2007**, *121* (3), 200. doi:10.1016/j.jconrel.2007.05.018. PMID:17630014.
- (28) Ko, J. A.; Park, H. J.; Hwang, S. J.; Park, J. B.; Lee, J. S. *Int. J. Pharm.* **2002**, *249* (1-2), 165. doi:10.1016/S0378-5173(02)00487-8. PMID:12433445.
- (29) Shu, X. Z.; Zhu, K. J. *Int. J. Pharm.* **2000**, *201* (1), 51. doi:10.1016/S0378-5173(00)00403-8. PMID:10867264.
- (30) Xu, Y.; Du, Y. *Int. J. Pharm.* **2003**, *250* (1), 215. doi:10.1016/S0378-5173(02)00548-3. PMID:12480287.
- (31) Mincheva, R.; Bougard, F.; Paneva, D.; Vachaudéz, M.; Fustin, C.-A.; Gohy, J.-F.; Manolova, N.; Rashkov, I.; Dubois, P. *J. Polym. Sci., Part A: Polym. Chem.* **2009**, *47* (8), 2105. doi:10.1002/pola.23315.
- (32) Boddohi, S.; Moore, N.; Johnson, P. A.; Kipper, M. J. *Biomacromolecules* **2009**, *10* (6), 1402. doi:10.1021/bm801513e. PMID:19371056.
- (33) Mazumder, M. A. J.; Burke, N. A. D.; Shen, F.; Potter, M. A.; Stöver, H. D. H. *Biomacromolecules* **2009**, *10* (6), 1365. doi:10.1021/bm801330j. PMID:19397289.
- (34) Teijeiro-Osorio, D.; Remuñán-López, C.; Alonso, M. J. *Biomacromolecules* **2009**, *10* (2), 243. doi:10.1021/bm800975j. PMID:19117404.
- (35) Jin, T.; Zhu, J.; Wu, F.; Yuan, W.; Geng, L. L.; Zhu, H. *J. Control. Release* **2008**, *128* (1), 50. doi:10.1016/j.jconrel.2008.02.010. PMID:18417240.
- (36) Liu, K.; Ding, H.-J.; Liu, J.; Chen, Y.; Zhao, X.-Z. *Langmuir* **2006**, *22*, 9468.
- (37) Sugiura, S.; Oda, T.; Izumida, Y.; Aoyagi, Y.; Satake, M.; Ochiai, A.; Ohkohchi, N.; Nakajima, M. *Biomaterials* **2005**, *26* (16), 3327. doi:10.1016/j.biomaterials.2004.08.029. PMID:15603828.
- (38) Choi, C.-H.; Jung, J.-H.; Rhee, Y. W.; Kim, D.-P.; Shim, S.-E.; Lee, C.-S. *Biomed. Microdevices* **2007**, *9* (6), 855. doi:10.1007/s10544-007-9098-7. PMID:17578667.
- (39) Tan, W.-H.; Takeuchi, S. *Lab Chip* **2008**, *8* (2), 259. doi:10.1039/b714573j. PMID:18231664.
- (40) Zhang, H.; Tumarkin, E.; Peerani, R.; Nie, Z.; Sullan, R. M. A.; Walker, G. C.; Kumacheva, E. *J. Am. Chem. Soc.* **2006**, *128* (37), 12205. doi:10.1021/ja0635682. PMID:16967971.
- (41) Zhang, H.; Tumarkin, E.; Sullan, R. M. A.; Walker, G. C.; Kumacheva, E. *Macromol. Rapid Commun.* **2007**, *28* (5), 527. doi:10.1002/marc.200600776.
- (42) Besheer, A.; Hause, G.; Kressler, J.; Mäder, K. *Biomacromolecules* **2007**, *8* (2), 359. doi:10.1021/bm0609487. PMID:17256901.
- (43) Hornig, S.; Heinze, T. *Biomacromolecules* **2008**, *9* (5), 1487. doi:10.1021/bm8000155. PMID:18393524.
- (44) Morimoto, N.; Hasegawa, U.; Sugawara, A.; Yamane, S.; Akiyoshi, K. *Nanotechnol. Carbohydr. Chem.* **2006**, 67.
- (45) Akiyoshi, K.; Deguchi, S.; Tajima, H.; Nishikawa, T.; Sunamoto, J. *Macromolecules* **1997**, *30* (4), 857. doi:10.1021/ma960786e.
- (46) Kuroda, K.; Fujimoto, K.; Sunamoto, J.; Akiyoshi, K. *Langmuir* **2002**, *18* (10), 3780. doi:10.1021/la011454s.
- (47) Akiyama, E.; Morimoto, N.; Kujawa, P.; Ozawa, Y.; Winnik, F. M.; Akiyoshi, K. *Biomacromolecules* **2007**, *8* (8), 2366. doi:10.1021/bm070136q. PMID:17630794.



- (48) Na, K.; Bum Lee, T.; Park, K.-H.; Shin, E.-K.; Lee, Y.-B.; Choi, H.-K. *Eur. J. Pharm. Sci.* **2003**, *18* (2), 165. doi:10.1016/S0928-0987(02)00257-9. PMID:12594010.
- (49) Hwang, H.-Y.; Kim, I.-S.; Kwon, I. C.; Kim, Y.-H. *J. Control. Release* **2008**, *128* (1), 23. doi:10.1016/j.jconrel.2008.02.003. PMID:18374444.
- (50) Liebert, T.; Hornig, S.; Hesse, S.; Heinze, T. *J. Am. Chem. Soc.* **2005**, *127* (30), 10484. doi:10.1021/ja052594h. PMID:16045324.
- (51) Gref, R.; Amiel, C.; Molinard, K.; Daoud-Mahammed, S.; Sébille, B.; Gillet, B.; Beloeil, J. C.; Ringard, C.; Rosilio, V.; Poupert, J.; Couvreur, P. *J. Control. Release* **2006**, *111* (3), 316. doi:10.1016/j.jconrel.2005.12.025. PMID:16504334.
- (52) Daoud-Mahammed, S.; Couvreur, P.; Bouchemal, K.; Cheron, M.; Lebas, G.; Amiel, C.; Gref, R. *Biomacromolecules* **2009**, *10* (3), 547. doi:10.1021/bm801206f.
- (53) Deutel, B.; Greindl, M.; Thaurer, M.; Bernkop-Schnürch, A. *Biomacromolecules* **2008**, *9* (1), 278. doi:10.1021/bm700916h. PMID:18159930.
- (54) Dou, H.; Tang, M.; Sun, K. *Macromol. Chem. Phys.* **2005**, *206* (21), 2177. doi:10.1002/macp.200500326.
- (55) Gao, J.; Haidar, G.; Lu, X.; Hu, Z. *Macromolecules* **2001**, *34* (7), 2242. doi:10.1021/ma001631g.
- (56) Xia, X.; Tang, S.; Lu, X.; Hu, Z. *Macromolecules* **2003**, *36* (10), 3695. doi:10.1021/ma0216728.
- (57) Cai, T.; Hu, Z.; Marquez, M. *Langmuir* **2004**, *20* (18), 7355. doi:10.1021/la049312w. PMID:15323473.
- (58) Jay, S. M.; Saltzman, W. M. *J. Control. Release* **2009**, *134* (1), 26. doi:10.1016/j.jconrel.2008.10.019. PMID:19027807.
- (59) Yun, Y. H.; Goetz, D. J.; Yellen, P.; Chen, W. *Biomaterials* **2004**, *25* (1), 147. doi:10.1016/S0142-9612(03)00467-8. PMID:14580918.
- (60) Laroui, H.; Grossin, L.; Léonard, M.; Stoltz, J.-F.; Gillet, P.; Netter, P.; Dellacherie, E. *Biomacromolecules* **2007**, *8* (12), 3879. doi:10.1021/bm700836y. PMID:18039001.
- (61) Kumbhar, S. G.; Kulkarni, A. R.; Aminabhavi, T. M. *J. Macroencapsulation* **2002**, *19* (2), 173. doi:10.1080/02652040110065422.
- (62) Denkbass, E. B.; Seyyal, M.; Piskin, E. *J. Macroencapsulation* **1999**, *16* (6), 741. doi:10.1080/026520499288681.
- (63) Al-Helw, A. A.; Al-Angary, A. A.; Mahrous, G. M.; Al-Dardari, M. M. *J. Macroencapsulation* **1998**, *15* (3), 373. doi:10.3109/02652049809006864.
- (64) Thanoo, B. C.; Sunny, M. C.; Jayakrishnan, A. *J. Pharm. Pharmacol.* **1992**, *44* (4), 283. PMID:1355537.
- (65) Sankar, C.; Rani, M.; Srivastava, A. K.; Mishra, B. *Pharmazie* **2001**, *56* (3), 223. PMID:11265588.
- (66) Jameela, S. R.; Kumary, T. V.; Lal, A. V.; Jayakrishnan, A. *J. Control. Release* **1998**, *52* (1-2), 17. doi:10.1016/S0168-3659(97)00187-9. PMID:9685932.
- (67) Lim, S. T.; Martin, G. P.; Berry, D. J.; Brown, M. B. *J. Control. Release* **2000**, *66* (2-3), 281. doi:10.1016/S0168-3659(99)00285-0. PMID:10742587.
- (68) Landfester, K. *Adv. Mater.* **2001**, *13* (10), 765. doi:10.1002/1521-4095(200105)13:10<765::AID-ADMA765>3.0.CO;2-F.
- (69) Mitra, S.; Gaur, U.; Ghosh, P. C.; Maitra, A. N. *J. Control. Release* **2001**, *74* (1-3), 317. doi:10.1016/S0168-3659(01)00342-X. PMID:11489513.
- (70) Jha, A. K.; Hule, R. A.; Jiao, T.; Teller, S. S.; Clifton, R. J.; Duncan, R. L.; Pochan, D. J.; Jia, X. *Macromolecules* **2009**, *42* (2), 537. doi:10.1021/ma8019442.
- (71) Wang, L.-Y.; Gu, Y.-H.; Zhou, Q.-Z.; Ma, G.-H.; Wan, Y.-H.; Su, Z.-G. *Colloids Surf. B Biointerfaces* **2006**, *50* (2), 126. doi:10.1016/j.colsurfb.2006.05.006. PMID:16787743.
- (72) Wang, L.-Y.; Ma, G.-H.; Su, Z.-G. *J. Control. Release* **2005**, *106* (1-2), 62. doi:10.1016/j.jconrel.2005.04.005. PMID:15922472.
- (73) Zhou, Q.-Z.; Wang, L.-Y.; Ma, G.-H.; Su, Z.-G. *J. Colloid Interface Sci.* **2007**, *311* (1), 118. doi:10.1016/j.jcis.2007.02.040. PMID:17362974.
- (74) Bodnar, M.; Hartmann, J. F.; Borbely, J. *Biomacromolecules* **2006**, *7* (11), 3030. doi:10.1021/bm0605053. PMID:17096528.
- (75) Shen, X.; Zhang, L.; Jiang, X.; Hu, Y.; Guo, J. *Angew. Chem. Int. Ed.* **2007**, *46* (37), 7104. doi:10.1002/anie.200701368.
- (76) Bloembergen, S.; McLennan, I.; Lee, D. I.; Van Leeuwen, J. *Paper* **2008**, *3*, 46.
- (77) Duracher, D.; Elaissari, A.; Pichot, C. *J. Polym. Sci., Part A: Polym. Chem.* **1999**, *37*, 1823. doi:10.1002/(SICI)1099-0518(19990615)37:12<1823::AID-POLA12>3.0.CO;2-#.
- (78) Hazot, P.; Chapel, J. P.; Pichot, C.; Elaissari, A.; Delair, T. *J. Polym. Sci., Part A: Polym. Chem.* **2002**, *40* (11), 1808. doi:10.1002/pola.10259.
- (79) Huang, G.; Gao, J.; Hu, Z.; St John, J. V.; Ponder, B. C.; Moro, D. *J. Control. Release* **2004**, *94* (2-3), 303. doi:10.1016/j.jconrel.2003.10.007. PMID:14744482.
- (80) Thornton, P. D.; Mart, R. J.; Ulijn, R. V. *Adv. Mater.* **2007**, *19* (9), 1252. doi:10.1002/adma.200601784.
- (81) Ulijn, R. V.; Bibi, N.; Jayawarna, V.; Thornton, P. D.; Todd, S. J.; Mart, R. J.; Smith, A. M.; Gough, J. E. *Mater. Today* **2007**, *10* (4), 40. doi:10.1016/S1369-7021(07)70049-4.
- (82) Keerl, M.; Pedersen, J. S.; Richtering, W. *J. Am. Chem. Soc.* **2009**, *131* (8), 3093. doi:10.1021/ja807367p.
- (83) Cai, T.; Marquez, M.; Hu, Z. *Langmuir* **2007**, *23* (17), 8663. doi:10.1021/la700923r. PMID:17658862.
- (84) Lutz, J.-F. *J. Polym. Sci., Part A: Polym. Chem.* **2008**, *46* (11), 3459. doi:10.1002/pola.22706.
- (85) Huang, X.; Lowe, T. L. *Biomacromolecules* **2005**, *6* (4), 2131. doi:10.1021/bm050116t. PMID:16004455.
- (86) Hoare, T.; Pelton, R. *Langmuir* **2004**, *20* (6), 2123. doi:10.1021/la0351562. PMID:15835661.
- (87) Leobandung, W.; Ichikawa, H.; Fukumori, Y.; Peppas, N. A. *J. Appl. Polym. Sci.* **2003**, *87* (10), 1678. doi:10.1002/app.11612.
- (88) Berndt, I.; Pedersen, J. S.; Lindner, P.; Richtering, W. *Langmuir* **2006**, *22* (1), 459. doi:10.1021/la052463u. PMID:16378460.
- (89) Nayak, S.; Lee, H.; Chmielewski, J.; Lyon, L. A. *J. Am. Chem. Soc.* **2004**, *126* (33), 10258. doi:10.1021/ja0474143. PMID:15315434.
- (90) Debord, J. D.; Lyon, L. A. *Bioconjug. Chem.* **2007**, *18* (2), 601. doi:10.1021/bc060248z. PMID:17323914.
- (91) Lee, C.-F.; Lin, C.-C.; Chiu, W.-Y. *J. Polym. Sci., Part A: Polym. Chem.* **2008**, *46* (17), 5734. doi:10.1002/pola.22887.
- (92) Zhang, Y.; Guan, Y.; Zhou, S. *Biomacromolecules* **2006**, *7* (11), 3196. doi:10.1021/bm060557s. PMID:17096551.
- (93) Hoare, T.; Pelton, R. *Macromolecules* **2007**, *40* (3), 670. doi:10.1021/ma062254w.
- (94) Hoare, T.; Pelton, R. *Biomacromolecules* **2008**, *9* (2), 733. doi:10.1021/bm701203r. PMID:18198833.
- (95) Suzuki, D.; Sakai, T.; Yoshida, R. *Angew. Chem. Int. Ed.* **2008**, *47* (5), 917. doi:10.1002/anie.200703953.
- (96) Dowding, P. J.; Vincent, B.; Williams, E. *J. Colloid Inter-*

- face Sci.* **2000**, 221 (2), 268. doi:10.1006/jcis.1999.6593. PMID:10631030.
- (97) Owens, D. E., III; Jian, Y.; Fang, J. E.; Slaughter, B. V.; Chen, Y.-H.; Peppas, N. A. *Macromolecules* **2007**, 40 (20), 7306. doi:10.1021/ma071089x.
- (98) Missirlis, D.; Tirelli, N.; Hubbell, J. A. *Langmuir* **2005**, 21 (6), 2605. doi:10.1021/la047367s. PMID:15752059.
- (99) Rubio-Retama, J.; Tamimi, F. M.; Heinrich, M.; López-Cabarcos, E. *Langmuir* **2007**, 23 (16), 8538. doi:10.1021/la700696h. PMID:17595123.
- (100) Zhu, W.; Wang, B.; Zhang, Y.; Ding, J. *Eur. Polym. J.* **2005**, 41 (9), 2161. doi:10.1016/j.eurpolymj.2005.04.006.
- (101) Zhang, Y.; Zhu, W.; Ding, J. *J. Biomed. Mater. Res. Part A* **2005**, 75A (2), 342. doi:10.1002/jbm.a.30437.
- (102) Gao, D.; Xu, H.; Philbert, M. A.; Kopelman, R. *Nano Lett.* **2008**, 8 (10), 3320. doi:10.1021/nl8017274. PMID:18788823.
- (103) Gaur, U.; Sahoo, S. K.; De, T. K.; Ghosh, P. C.; Maitra, A.; Ghosh, P. K. *Int. J. Pharm.* **2000**, 202 (1-2), 1. doi:10.1016/S0378-5173(99)00447-0. PMID:10915921.
- (104) Bharali, D. J.; Sahoo, S. K.; Mozumdar, S.; Maitra, A. *J. Colloid Interface Sci.* **2003**, 258 (2), 415. doi:10.1016/S0021-9797(02)00099-1. PMID:12618113.
- (105) McAllister, K.; Sazani, P.; Adam, M.; Cho, M. J.; Rubinstein, M.; Samulski, R. J.; DeSimone, J. M. *J. Am. Chem. Soc.* **2002**, 124 (51), 15198. doi:10.1021/ja027759q. PMID:12487595.
- (106) Craparo, E. F.; Cavallaro, G.; Bondi, M. L.; Mandracchia, D.; Giammona, G. *Biomacromolecules* **2006**, 7 (11), 3083. doi:10.1021/bm060570c. PMID:17096535.
- (107) Rolland, J. P.; Maynor, B. W.; Euliss, L. E.; Exner, A. E.; Denison, G. M.; DeSimone, J. M. *J. Am. Chem. Soc.* **2005**, 127 (28), 10096. doi:10.1021/ja051977c. PMID:16011375.
- (108) Matyjaszewski, K.; Davis, T. P., Eds. In *Handbook of Radical Polymerization*; John Wiley & Sons Inc., 2002.
- (109) Davis, K. A.; Matyjaszewski, K. *Adv. Polym. Sci.* **2002**, 159, 2.
- (110) Coessens, V.; Pintauer, T.; Matyjaszewski, K. *Prog. Polym. Sci.* **2001**, 26 (3), 337. doi:10.1016/S0079-6700(01)00003-X.
- (111) Braunecker, W. A.; Matyjaszewski, K. *Prog. Polym. Sci.* **2007**, 32 (1), 93. doi:10.1016/j.progpolymsci.2006.11.002.
- (112) Matyjaszewski, K.; Gaynor, S.; Greszta, D.; Mardare, D.; Shigemoto, T. *J. Phys. Org. Chem.* **1995**, 8 (4), 306. doi:10.1002/poc.610080414.
- (113) Matyjaszewski, K. *J. Phys. Org. Chem.* **1995**, 8 (4), 197. doi:10.1002/poc.610080403.
- (114) Ide, N.; Fukuda, T. *Macromolecules* **1997**, 30 (15), 4268. doi:10.1021/ma9700946.
- (115) Shim, S. E.; Oh, S.; Chang, Y. H.; Jin, M.-J.; Choe, S. *Polymer (Guildf.)* **2004**, 45 (14), 4731. doi:10.1016/j.polymer.2004.05.011.
- (116) Tsarevsky, N. V.; Matyjaszewski, K. *Macromolecules* **2005**, 38 (8), 3087. doi:10.1021/ma050020r.
- (117) Huang, J.; Cusick, B.; Pietrasik, J.; Wang, L.; Kowalewski, T.; Lin, Q.; Matyjaszewski, K. *Langmuir* **2007**, 23 (1), 241. doi:10.1021/la061683k. PMID:17190510.
- (118) Bencherif, S. A.; Srinivasan, A.; Sheehan, J. A.; Walker, L. M.; Gayathri, C.; Gil, R.; Hollinger, J. O.; Matyjaszewski, K.; Washburn, N. R. *Acta Biomater.* **2009**, 5 (6), 1872. doi:10.1016/j.actbio.2009.02.030. PMID:19328754.
- (119) Siegwart, D. J.; Bencherif, S. A.; Srinivasan, A.; Hollinger, J. O.; Matyjaszewski, K. *J. Biomed. Mater. Res. Part A* **2008**, 87A (2), 345. doi:10.1002/jbm.a.31708.
- (120) Wang, J.-S.; Matyjaszewski, K. *Macromolecules* **1995**, 28 (23), 7901. doi:10.1021/ma00127a042.
- (121) Wang, J.-S.; Matyjaszewski, K. *J. Am. Chem. Soc.* **1995**, 117 (20), 5614. doi:10.1021/ja00125a035.
- (122) Kim, K. H.; Kim, J.; Jo, W. H. *Polymer (Guildf.)* **2005**, 46 (9), 2836. doi:10.1016/j.polymer.2005.02.009.
- (123) Chiefari, J.; Chong, Y. K.; Ercole, F.; Krstina, J.; Jeffery, J.; Le, T. P. T.; Mayadunne, R. T. A.; Meijs, G. F.; Moad, C. L.; Moad, G.; Rizzardo, E.; Thang, S. H. *Macromolecules* **1998**, 31 (16), 5559. doi:10.1021/ma9804951.
- (124) Barner, L.; Davis, T. P.; Stenzel, M. H.; Barner-Kowollik, C. *Macromol. Rapid Commun.* **2007**, 28 (5), 539. doi:10.1002/marc.200600805.
- (125) Poly, J.; Wilson, D. J.; Destarac, M.; Taton, D. *Macromol. Rapid Commun.* **2008**, 29 (24), 1965. doi:10.1002/marc.200800542.
- (126) Chan, Y.; Bulmus, V.; Zareie, M. H.; Byrne, F. L.; Barner, L.; Kavallaris, M. *J. Control. Release* **2006**, 115 (2), 197. doi:10.1016/j.jconrel.2006.07.025. PMID:16996635.
- (127) Rieger, J.; Grazon, C.; Charleux, B.; Alaimo, D.; Jerome, C. *J. Polym. Sci., Part A: Polym. Chem.* **2009**, 47 (9), 2373. doi:10.1002/pola.23329.
- (128) Lutz, J.-F.; Börner, H. G. *Prog. Polym. Sci.* **2008**, 33 (1), 1. doi:10.1016/j.progpolymsci.2007.07.005.
- (129) Oh, J. K.; Tang, C.; Gao, H.; Tsarevsky, N. V.; Matyjaszewski, K. *J. Am. Chem. Soc.* **2006**, 128 (16), 5578. doi:10.1021/ja060586a. PMID:16620132.
- (130) Oh, J. K.; Siegwart, D. J.; Lee, H. I.; Sherwood, G.; Petteanu, L.; Hollinger, J. O.; Kataoka, K.; Matyjaszewski, K. *J. Am. Chem. Soc.* **2007**, 129 (18), 5939. doi:10.1021/ja069150l. PMID:17439215.
- (131) Oh, J. K.; Siegwart, D. J.; Matyjaszewski, K. *Biomacromolecules* **2007**, 8 (11), 3326. doi:10.1021/bm070381+. PMID:17894465.
- (132) Siegwart, D. J.; Oh, J. K.; Gao, H.; Bencherif, S. A.; Perineau, F.; Bohaty, A. K.; Hollinger, J. O.; Matyjaszewski, K. *Macromol. Chem. Phys.* **2008**, 209 (21), 2179. doi:10.1002/macp.200800337.
- (133) Siegwart, D. J.; Srinivasan, A.; Bencherif, S. A.; Karunanidhi, A.; Oh, J. K.; Vaidya, S.; Jin, R.; Hollinger, J. O.; Matyjaszewski, K. *Biomacromolecules* **2009**, 10 (8), 2300. doi:10.1021/bm9004904. PMID:19572639.
- (134) Bencherif, S. A.; Siegwart, D. J.; Srinivasan, A.; Horkay, F.; Hollinger, J. O.; Washburn, N. R.; Matyjaszewski, K. *Biomaterials* **2009**, 30 (29), 5270. doi:10.1016/j.biomaterials.2009.06.011. PMID:19592087.
- (135) Bencherif, S. A.; Washburn, N. R.; Matyjaszewski, K. *Biomacromolecules* **2009**, 10 (9), 2499. doi:10.1021/bm9004639. PMID:19711888.
- (136) Oh, J. K.; Bencherif, S. A.; Matyjaszewski, K. *Polymer (Guildf.)* **2009**, 50 (19), 4407. doi:10.1016/j.polymer.2009.06.045.
- (137) Zelikin, A. N.; Quinn, J. F.; Caruso, F. *Biomacromolecules* **2006**, 7 (1), 27. doi:10.1021/bm050832v. PMID:16398494.
- (138) Tsarevsky, N. V.; Matyjaszewski, K. *Macromolecules* **2002**, 35 (24), 9009. doi:10.1021/ma021061f.
- (139) Zhang, L.; Liu, W.; Lin, L.; Chen, D.; Stenzel, M. H. *Biomacromolecules* **2008**, 9 (11), 3321. doi:10.1021/bm800867n. PMID:18842025.
- (140) Li, C.; Madsen, J.; Armes, S. P.; Lewis, A. L. *Angew. Chem. Int. Ed.* **2006**, 45 (21), 3510. doi:10.1002/anie.200600324.
- (141) Carelli, S.; Ceriotti, A.; Cabibbo, A.; Fassina, G.; Ruvo, M.; Sitia, R. *Science* **1997**, 277 (5332), 1681. doi:10.1126/science.277.5332.1681. PMID:9287224.

- (142) Li, C.; Madsen, J.; Armes, S. P.; Lewis, A. L. *Angew. Chem. Int. Ed.* **2006**, *45* (21), 3510. doi:10.1002/anie.200600324.
- (143) Petros, R. A.; Ropp, P. A.; DeSimone, J. M. *J. Am. Chem. Soc.* **2008**, *130* (15), 5008. doi:10.1021/ja801436j. PMID: 18355010.
- (144) Tang, R.; Palumbo, R. N.; Ji, W.; Wang, C. *Biomacromolecules* **2009**, *10* (4), 722. doi:10.1021/bm9000475. PMID: 19281150.
- (145) Griset, A. P.; Walpole, J.; Liu, R.; Gaffey, A.; Colson, Y. L.; Grinstaff, M. W. *J. Am. Chem. Soc.* **2009**, *131* (7), 2469. doi:10.1021/ja807416t. PMID:19182897.
- (146) Zhang, L.; Bernard, J.; Davis, T. P.; Barner-Kowollik, C.; Stenzel, M. H. *Macromol. Rapid Commun.* **2008**, *29* (2), 123. doi:10.1002/marc.200700663.
- (147) Murthy, N.; Thng, Y. X.; Schuck, S.; Xu, M. C.; Fréchet, J. M. J. *J. Am. Chem. Soc.* **2002**, *124* (42), 12398. doi:10.1021/ja026925r. PMID:12381166.
- (148) Murthy, N.; Xu, M.; Schuck, S.; Kunisawa, J.; Shastri, N.; Fréchet, J. M. J. *Proc. Natl. Acad. Sci. U.S.A.* **2003**, *100* (9), 4995. doi:10.1073/pnas.0930644100. PMID:12704236.
- (149) Goh, S. L.; Murthy, N.; Xu, M.; Fréchet, J. M. J. *Bioconjug. Chem.* **2004**, *15* (3), 467. doi:10.1021/bc034159n. PMID:15149173.
- (150) Kwon, Y. J.; Standley, S. M.; Goh, S. L.; Fréchet, J. M. J. *J. Control. Release* **2005**, *105* (3), 199. doi:10.1016/j.jconrel.2005.02.027. PMID:15935507.
- (151) Bulmus, V.; Chan, Y.; Nguyen, Q.; Tran, H. L. *Macromol. Biosci.* **2007**, *7* (4), 446. doi:10.1002/mabi.200600258. PMID:17429806.
- (152) Shi, L.; Khondee, S.; Linz, T. H.; Berkland, C. *Macromolecules* **2008**, *41* (17), 6546. doi:10.1021/ma800812z.
- (153) He, J.; Tong, X.; Zhao, Y. *Macromolecules* **2009**, *42* (13), 4845. doi:10.1021/ma900665v.
- (154) Aliyar, H. A.; Hamilton, P. D.; Ravi, N. *Biomacromolecules* **2005**, *6* (1), 204. doi:10.1021/bm049574c. PMID: 15638522.
- (155) Themistou, E.; Patrickios, C. S. *Macromolecules* **2007**, *40* (14), 5231. doi:10.1021/ma070166l.
- (156) Kaihara, S.; Matsumura, S.; Fisher, J. P. *Macromolecules* **2007**, *40* (21), 7625. doi:10.1021/ma071297p.
- (157) Plunkett, K. N.; Berkowski, K. L.; Moore, J. S. *Biomacromolecules* **2005**, *6* (2), 632. doi:10.1021/bm049349v. PMID:15762623.
- (158) Kim, S.; Healy, K. E. *Biomacromolecules* **2003**, *4* (5), 1214. doi:10.1021/bm0340467. PMID:12959586.
- (159) Lévesque, S. G.; Shoichet, M. S. *Bioconjug. Chem.* **2007**, *18* (3), 874. doi:10.1021/bc0602127. PMID:17402704.
- (160) Perez, P.; Plieva, F.; Gallardo, A.; San Roman, J.; Aguilar, M. R.; Morfin, I.; Ehrburger-Dolle, F.; Bley, F.; Mikhailovsky, S.; Galaev, I. Y.; Mattiasson, B. *Biomacromolecules* **2008**, *9* (1), 66. doi:10.1021/bm7007668. PMID: 18067265.
- (161) Martens, P. J.; Bryant, S. J.; Anseth, K. S. *Biomacromolecules* **2003**, *4* (2), 283. doi:10.1021/bm025666v. PMID: 12625723.
- (162) Eichenbaum, K. D.; Thomas, A. A.; Eichenbaum, G. M.; Gibney, B. R.; Needham, D.; Kiser, P. F. *Macromolecules* **2005**, *38* (26), 10757. doi:10.1021/ma0518306.
- (163) Rice, M. A.; Sanchez-Adams, J.; Anseth, K. S. *Biomacromolecules* **2006**, *7* (6), 1968. doi:10.1021/bm060086+. PMID:16768421.
- (164) Leemhuis, M.; Kruijtz, J. A. W.; Nostrum, C. F.; Hennink, W. E. *Biomacromolecules* **2007**, *8* (9), 2943. doi:10.1021/bm700476h. PMID:17715961.
- (165) Nayak, S.; Lyon, L. A. *Angew. Chem. Int. Ed.* **2004**, *43* (48), 6706. doi:10.1002/anie.200461090.
- (166) Li, Q.; Wang, J.; Shahani, S.; Sun, D. D. N.; Sharma, B.; Elisseff, J. H.; Leong, K. W. *Biomaterials* **2006**, *27* (7), 1027. doi:10.1016/j.biomaterials.2005.07.019. PMID:16125222.
- (167) Du, J.-Z.; Sun, T.-M.; Weng, S.-Q.; Chen, X.-S.; Wang, J. *Biomacromolecules* **2007**, *8* (11), 3375. doi:10.1021/bm700474b. PMID:17902689.
- (168) Muggli, D. S.; Burkoth, A. K.; Keyser, S. A.; Lee, H. R.; Anseth, K. S. *Macromolecules* **1998**, *31* (13), 4120. doi:10.1021/ma980108n.
- (169) Kitamura, T.; Matsumoto, A. *Macromolecules* **2007**, *40* (17), 6143. doi:10.1021/ma0707537.
- (170) Neugebauer, D.; Rydz, J.; Goebel, I.; Dacko, P.; Kowalczyk, M. *Macromolecules* **2007**, *40* (5), 1767. doi:10.1021/ma062251j.
- (171) Zhang, H.; Mardiyani, S.; Chan, W. C. W.; Kumacheva, E. *Biomacromolecules* **2006**, *7* (5), 1568. doi:10.1021/bm050912z. PMID:16677040.
- (172) Zhang, H.; Oh, M.; Allen, C.; Kumacheva, E. *Biomacromolecules* **2004**, *5* (6), 2461. doi:10.1021/bm0496211. PMID:15530064.
- (173) Ghugare, S. V.; Mozetic, P.; Paradossi, G. *Biomacromolecules* **2009**, *10* (6), 1589. doi:10.1021/bm900185u. PMID: 19425550.
- (174) Cavalieri, F.; Chiessi, E.; Villa, R.; Viganò, L.; Zaffaroni, N.; Telling, M. F.; Paradossi, G. *Biomacromolecules* **2008**, *9* (7), 1967. doi:10.1021/bm800225v. PMID:18533701.
- (175) Nolan, C. M.; Gelbaum, L. T.; Lyon, L. A. *Biomacromolecules* **2006**, *7* (10), 2918. doi:10.1021/bm060718s. PMID: 17025370.
- (176) Gao, D.; Xu, H.; Philbert, M. A.; Kopelman, R. *Angew. Chem. Int. Ed.* **2007**, *46* (13), 2224. doi:10.1002/anie.200603927.
- (177) Cushing, B. L.; Kolesnichenko, V. L.; O'Connor, C. J. *Chem. Rev.* **2004**, *104* (9), 3893. doi:10.1021/cr030027b. PMID:15352782.
- (178) Tomczak, N.; Janczewski, D.; Han, M.; Vancso, G. J. *Prog. Polym. Sci.* **2009**, *34* (5), 393. doi:10.1016/j.progpolymsci.2008.11.004.
- (179) Kuang, M.; Wang, D.; Bao, H.; Gao, M.; Möhwald, H.; Jiang, M. *Adv. Mater.* **2005**, *17*, 267. doi:10.1002/adma.200400818.
- (180) Li, J.; Hong, X.; Liu, Y.; Li, D.; Wang, Y.; Li, J.; Bai, Y.; Li, T. *Adv. Mater.* **2005**, *17* (2), 163. doi:10.1002/adma.200400448.
- (181) Li, J.; Liu, B.; Li, J. *Langmuir* **2006**, *22* (2), 528. doi:10.1021/la052519k. PMID:16401098.
- (182) Shen, L.; Pich, A.; Fava, D.; Wang, M.; Kumar, S.; Wu, C.; Scholes, G. D.; Winnik, M. A. *J. Mater. Chem.* **2008**, *18* (7), 763. doi:10.1039/b713253k.
- (183) Das, M.; Sanson, N.; Fava, D.; Kumacheva, E. *Langmuir* **2007**, *23* (1), 196. doi:10.1021/la061596s. PMID: 17190504.
- (184) Macková, H.; Králová, D.; Horák, D. *J. Polym. Sci., Part A: Polym. Chem.* **2007**, *45* (24), 5884. doi:10.1002/pola.22341.
- (185) Horák, D.; Lednický, F.; Petrovský, E.; Kapicka, A. *Macromol. Mater. Eng.* **2004**, *289* (4), 341. doi:10.1002/mame.200300271.
- (186) Contreras-Cáceres, R.; Sánchez-Iglesias, A.; Karg, M.; Pastoriza-Santos, I.; Perez-Juste, J.; Pacifico, J.; Hellweg, T.; Fernández-Barbero, A.; Liz-Marzán, L. M. *Adv. Mater.* **2008**, *20* (9), 1666. doi:10.1002/adma.200800064.

- (187) Hain, J.; Eckert, F.; Pich, A.; Adler, H.-J. *Macromol. Rapid Commun.* **2008**, 29 (6), 472. doi:10.1002/marc.200700653.
- (188) Dong, Y.; Ma, Y.; Zhai, T.; Shen, F.; Zeng, Y.; Fu, H.; Yao, J. *Macromol. Rapid Commun.* **2007**, 28 (24), 2339. doi:10.1002/marc.200700483.
- (189) Zhang, J.; Xu, S.; Kumacheva, E. *J. Am. Chem. Soc.* **2004**, 126 (25), 7908. doi:10.1021/ja031523k. PMID:15212539.
- (190) Brugger, B.; Richtering, W. *Adv. Mater.* **2007**, 19 (19), 2973. doi:10.1002/adma.200700487.



# A sensitive fluorescence method for monitoring the kinetics of microemulsion polymerization

Haike Feng, Yi Dan, and Yue Zhao

**Abstract:** We present a fluorescence method that allows one to monitor the kinetics of microemulsion polymerization of very low monomer contents (water-to-monomer ratio can readily be superior to 1000). The microemulsion polymerization of methyl methacrylate (MMA) was investigated using *N*-(2-anthracene)methacrylamide (AnMA) as the probe whose fluorescence emission intensity was proportional to the conversion of MMA into the polymer. The real-time-measurement results show that in the regime of very low monomer contents, the surfactant exerted a profound effect on the kinetic process. In a microemulsion containing 0.1 wt% of MMA with respect to water, with the anionic surfactant of sodium dodecyl sulfate (SDS), the fast polymerization was preceded by an induction period whose length increased with reducing the concentration of the water-soluble initiator of potassium persulfate (KPS). By contrast, with the non-ionic surfactant of polyoxyethylene (20) oleyl ether (Brij98), the induction period was short and the decrease in the KPS concentration mainly resulted in a decrease of the reaction rate. The unprecedented sensitivity of this fluorescence method made it possible to access kinetic data of microemulsion polymerization with very low monomer contents for the first time, providing new insight into the effects of surfactant and initiator on this heterophase polymerization process.

**Key words:** microemulsion polymerization, reaction kinetics, fluorescence spectroscopy, characterization method.

**Résumé :** On a mis au point une méthode de fluorescence qui permet de suivre la cinétique de polymérisation en microémulsion à des teneurs très faibles de monomères dans lesquelles le rapport d'eau à monomère peut facilement être supérieur à 1000. On a étudié la polymérisation en microémulsion de méthacrylate de méthyle (MAM) en utilisant le *N*-(2-anthracène)méthacrylamide (AnMA) comme sonde dont l'intensité d'émission de fluorescence était proportionnelle à la conversion du méthacrylate de méthyle en polymère. Les résultats de mesures en temps réel montrent que dans le régime impliquant de très faibles teneurs en monomère, l'agent de surface exerce un effet important sur le processus cinétique. Dans une microémulsion contenant 0,1 % en poids de MAM par rapport à l'eau et du dodécylsulfate de sodium (DSS) comme agent de surface anionique, la polymérisation rapide est précédée d'une période d'induction dont la longueur augmente avec la réduction de la concentration du persulfate de potassium (PSK), l'initiateur soluble dans l'eau. Par opposition, avec l'éther oléyle du polyoxyéthylène (20) (Brij98), un agent de surface non ionique, la période d'induction est courte et une diminution de la concentration de persulfate de potassium conduit à une réduction de la vitesse de réaction. La sensibilité sans précédent de cette méthode de fluorescence permet d'obtenir pour la première fois des données cinétiques pour la polymérisation en microémulsion avec de très faibles teneurs en monomère et d'en tirer des conclusions sur les effets des agents de surface et de l'initiateur sur le processus de polymérisation en hétérophase.

**Mots-clés :** polymérisation en microémulsion, cinétique de la réaction, spectroscopie de fluorescence, méthode de caractérisation.

[Traduit par la Rédaction]

## Introduction

The kinetics of microemulsion polymerization has been extensively investigated.<sup>1–10</sup> Generally, to monitor the kinetics, aliquots of the oil (monomer) in water (o/w) reaction mixture are removed over the course of polymerization at

various time intervals; by measuring the polymer concentration formed over time, kinetic data can be obtained. Using this method, understandably, one needs a large volume of the reaction solution and a high monomer content (e.g., > 3 wt% with respect to water) to obtain data with an appreciable precision. There are also several real-time monitoring

Received 29 July 2009. Accepted 5 October 2009. Published on the NRC Research Press Web site at canjchem.nrc.ca on 19 January 2010.

*This article is part of a Special Issue dedicated to Professor M. A. Winnik.*

**H. Feng.** Département de chimie, Université de Sherbrooke, Sherbrooke, QC J1K 2R1, Canada; State Key Laboratory of Polymer Materials Engineering of China, Polymer Research Institute, Sichuan University, Chengdu 610065, China.

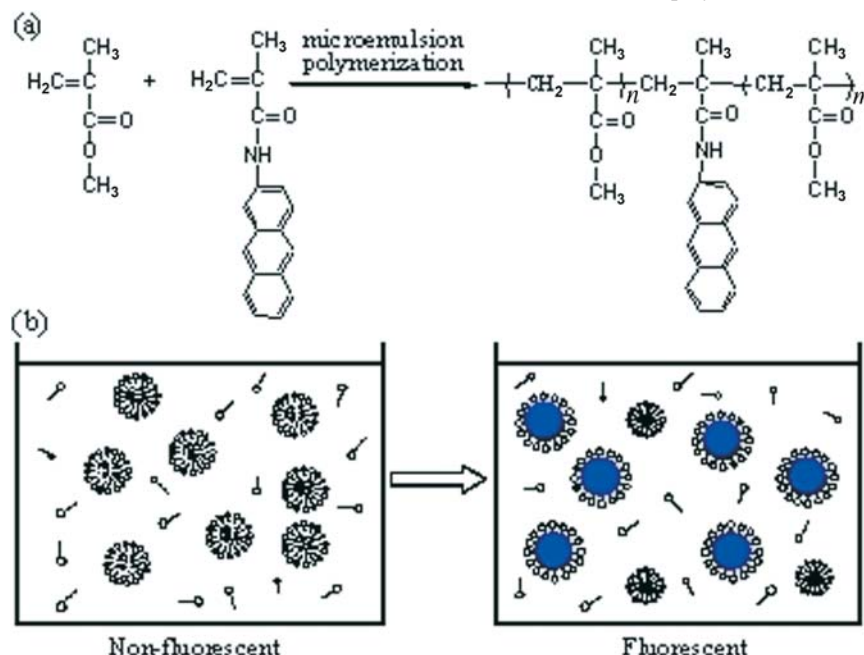
**Y. Dan.**<sup>1</sup> State Key Laboratory of Polymer Materials Engineering of China, Polymer Research Institute, Sichuan University, Chengdu 610065, China.

**Y. Zhao.**<sup>2</sup> Département de chimie, Université de Sherbrooke, Sherbrooke, QC J1K 2R1, Canada.

<sup>1</sup>Corresponding author (e-mail: danyi@scu.edu.cn).

<sup>2</sup>Corresponding author (e-mail: yue.zhao@usherbrooke.ca).

**Fig. 1.** Chemical structures of the monomers and schematic illustration of the microemulsion-polymerization-induced fluorescence emission.



techniques that have been utilized to study the kinetics of microemulsion (and miniemulsion) polymerizations. These include the dilatometry that measures the volume change of the reaction liquid in a capillary upon polymerization,<sup>3</sup> the reaction calorimetry that measures the heat released from the polymerization over time,<sup>8,9</sup> and the laser Raman spectroscopy that probes the breaking of C=C double bonds in a vinyl polymerization.<sup>2</sup> In terms of sensitivity, the calorimetric method is better, allowing the use of low monomer contents around 0.5 wt%.<sup>8</sup>

Although a microemulsion is a thermodynamically stable, transparent solution, the polymerization is a heterophase reaction process, since it takes place inside nanometer-sized monomer droplets (~5–10 nm) stabilized by a large number of surfactant molecules. In a microemulsion, there are also empty micelles, dissolved surfactant molecules, and either a water-soluble or monomer-soluble initiator.<sup>1–10</sup> It is of fundamental interest to know what happens when the monomer content becomes very low. For instance, is the polymerization kinetics affected by reducing the monomer concentration while keeping the same concentrations of surfactant and initiator? Can the kinetics reveal some sort of transition from a heterogeneous to homogeneous polymerization when the monomer concentration is extremely diluted? The above-mentioned experimental techniques cannot access this regime of very low monomer contents. In this paper, we report a very sensitive fluorescence-based method that can yield kinetic data on microemulsion (or miniemulsion) polymerization using monomer content as low as 0.0035 wt% (or water-to-monomer ratio of 28 000)!

The method used is based on previous reports of Warman and co-workers.<sup>11–14</sup> They have developed a series of fluorescent probes and used them to study radiation-induced polymerization. The fluorescent probes are polymerizable monomers (with a C=C double bond) and have the distinct feature to be completely nonfluorescent in the monomer

form but become fluorescent upon polymerization as the double bond is saturated. In particular, Frahn et al. showed that *N*-(2-anthracene)methacrylamide (AnMA) could be used as a fluorescent probe to monitor the Gamma-ray induced free-radical polymerization of methyl methacrylate (MMA) in bulk and in solution, and found that the ratio of the chain-propagating rate constants for the reactions of an MMA free radical with AnMA and with MMA is 0.96.<sup>14</sup> This means that the increase in the fluorescence emission intensity over time could reflect closely the kinetic process of the free-radical polymerization of MMA. In the present study, we used AnMA as the probe to investigate the microemulsion polymerization of MMA with very low monomer contents. The great sensitivity of the fluorescence appearing upon polymerization, as schematically illustrated in Fig. 1, allowed us to access kinetic data in this regime for the first time. Among the results, the real-time measurements show a more important effect of the used surfactant on the kinetics with very low monomer content than with relatively high monomer content.

## Experimental

### Materials

Unless otherwise stated, all chemicals were purchased from Aldrich. For the monomers, methyl methacrylate (MMA, 98%) was passed through a basic alumina column prior to use. *N*-(2-Anthracene)methacrylamide (AnMA) was synthesized using a literature method,<sup>13</sup> it was purified by recrystallization from a methylene chloride/hexane mixture (4:1, v/v). The two used surfactants were sodium dodecyl sulfate (SDS, 99%), which is an anionic surfactant, and polyoxyethylene (20) oleyl ether (Brij98, 99%), which is a non-ionic surfactant. For the free-radical initiators, the water-soluble potassium persulfate (KPS, 99.99%) was used as received, and the water-insoluble 2,2'-azobis(isobutyronitrile) (AIBN) (from Polysciences) was recrystallized twice from ethanol. For

other chemicals, tetrahydrofuran (THF, 99%) was distilled from sodium benzophenone, while hexadecane (99%) and hexyl alcohol (98%) were used without further purification.

### Preparation and monitoring of microemulsion polymerization

An example of experiment is detailed as follows: SDS (0.3 g, 1.04 mmol) was dissolved in 10 g of deionized water (0.56 mol) in a 25 mL round-bottom flask. AnMA (0.15 mg, 0.00057 mmol) was dissolved in a solution of hexyl alcohol, a costabilizer, (0.03 g, 0.29 mmol), and MMA (0.3 g, 3 mmol). Then, the liquid mixture of monomers containing AnMA was added dropwise into the aqueous solution at room temperature. After 5 min ultrasound sonication (60 W, 40 KHz), KPS (5 mg, 0.0185 mmol) was added. After another 1 min sonication, an aliquot of the microemulsion was transferred into a standard quartz fluorescence cuvette (1 cm × 1 cm × 3 cm), purged with argon gas for 15 min and sealed with a Teflon stopper and a Parafilm tape. Afterwards, the cuvette was placed in the spectrometer's sample holder, pre-heated to 60 °C, and the fluorescence emission (whole spectrum or intensity at a wavelength) was recorded after 1 min required for thermal equilibrium of the solution.

In case where Brij98 was the surfactant, hexadecane was used as costabilizer (10 wt% with respect to Brij98). In all reactions, the same extremely low fluorescent-probe concentration was used (0.19 mmol AnMA in 1 mol MMA) to ensure that AnMA remained part of the monomer even with a very low monomer content in the microemulsion. In the control test using relatively high monomer content, the increase in the amount of polymer over time was determined by using the conventional method. Aliquots of the reaction solution were taken at various time intervals, poured into cold methanol (cooled by ice), and the precipitated polymer was filtered, dried under vacuum, and weighed to calculate the monomer conversion defined as:  $\text{Conversion (\%)} = W_p/W_m \times 100\%$ , where  $W_p$  is the mass of the obtained PMMA and  $W_m$  is the known mass of the monomer. In this paper, the monomer content and the surfactant concentration are mass-percentages with respect to water, while the concentration of initiator is mass-percentage with respect to the monomer.

### Characterizations

Steady-state fluorescence emission spectra were recorded using a fluorescence spectrophotometer (Varian Cary Eclipse). The excitation and emission slit widths were set at 5 nm, and the scan rate was 10 nm s<sup>-1</sup>. Real-time monitoring of the emission intensity at a chosen wavelength could also be carried out. For all measurements, the excitation wavelength was 337 nm; and for the kinetic data, the emission intensity at 425 nm was measured. Unless otherwise stated, the reported fluorescence intensities were not scaled. They were recorded under the same conditions (same volume of reaction solution, same excitation and emission slit widths). Since the concentration of AnMA was kept constant in MMA, the different fluorescence intensities result from different monomer concentrations in the microemulsion.

## Results and discussion

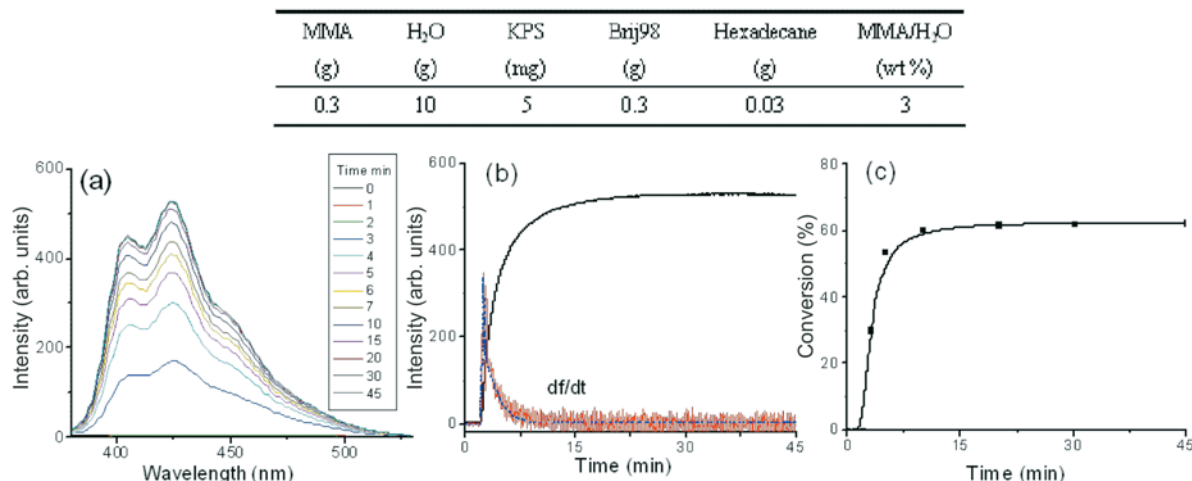
We first attempted to validate the fluorescence method by

using a microemulsion containing 3% of the monomer, with which the conventional method can be utilized to determine the reaction kinetics. Figure 2 shows the results, together with the composition of the solution. In Fig. 2a, the fluorescence emission spectra of the solution were recorded as a function of time. While the solution was virtually nonfluorescent before the reaction, the fluorescence emission increased over time, indicating a growing number of AnMA monomers polymerized with MMA. In Fig. 2b, the plot of fluorescence intensity,  $f$ , at 425 nm vs. time is given, showing a fast increase within the first 10 min before reaching a plateau. The first derivative of the plot,  $df/dt$ , yielded the change of the reaction rate over time (the profile of the rate curve is better seen from the smoothed line). The result is typical of a microemulsion polymerization, showing that the polymerization rate rose to a maximum value and then decreased to zero without an interval of constant reaction rate. Shown in Fig. 2c is the conversion curve obtained by measuring the polymer concentrations at various reaction times. It is seen that within experimental error, the plot of fluorescence intensity vs. time corroborates well the kinetics measured using the conventional method. However, it should be emphasized that the fluorescence result represents better the reaction kinetics due to its sensitivity. Using the conventional method, oligomers can be washed away upon polymer precipitation, while with the fluorescence method, they can be detected. Apparently, the maximum fluorescence intensity corresponds to a monomer conversion of about 60%. These results indicate that this fluorescent probe reveals correctly the kinetics of microemulsion polymerization of MMA. We mention that for the experiments with very low monomer contents to be discussed below, we were mainly focused on the kinetic aspects. Due to the few nanoparticles formed, the characterizations of actual conversion, molecular masses, and particle morphology could not be performed with certainty.

Before discussing the results obtained with low monomer contents, Fig. 3 is meant to emphasize that, with the used surfactant concentration, all polymerizations were performed with a microemulsion. The highest MMA content used was 3%, and with 3% of either SDS or Brij98, the solutions are basically transparent (Fig. 3, images A and B), in contrast with, for comparison, a solution with only 0.3% of SDS (Fig. 3, image C). However, the microemulsion with the non-ionic surfactant Brij98 appears less transparent than the solution with the anionic surfactant SDS, reflecting the difference between the two surfactants. The surfactant concentration was kept the same with lower MMA contents.

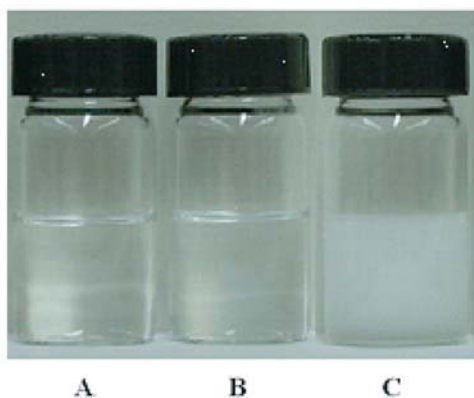
In a microemulsion, with the same concentrations of surfactant and water-soluble initiator, what could be the effect on the kinetics by diluting the monomer to a very low concentration? Fig. 4 shows the results obtained with a set of experiments designed to answer the question, using two different surfactants and, for each of them, three monomer concentrations (actual compositions of the solutions are shown in the figure). The fluorescence curves obtained with 0.5% and 0.1% of MMA are magnified by a factor as indicated in the figure, since a lower monomer content means less fluorescent AnMA units in the polymer. While the kinetics appears similar with the two surfactants at the rather high monomer content of 3%, it is drastically different at the low

**Fig. 2.** (a) Fluorescence emission spectra ( $\lambda_{\text{ex}} = 337$  nm) recorded at various polymerization times; (b) plots of fluorescence emission intensity at 425 nm, ( $f$ ) and the first derivative ( $df/dt$ ) vs. time; and (c) plot of conversion (%) vs. time for a microemulsion containing 3 wt% of MMA with respect to water (the composition of the reaction solution is indicated).



**Fig. 3.** Photographs of a microemulsion containing 3% MMA with 3% SDS (image A), a microemulsion containing 3% MMA with 3% Brij98 (image B), and an emulsion containing 3% MMA and 0.3% SDS (image C).

Sample	MMA (g)	Water (g)	SDS (g)	Brij98 (g)	Hexylalcohol (g)	Hexadecane (g)
A	0.3	10	0.3	0	0.03	0
B	0.3	10	0	0.3	0	0.03
C	0.3	10	0.03	0	0.003	0



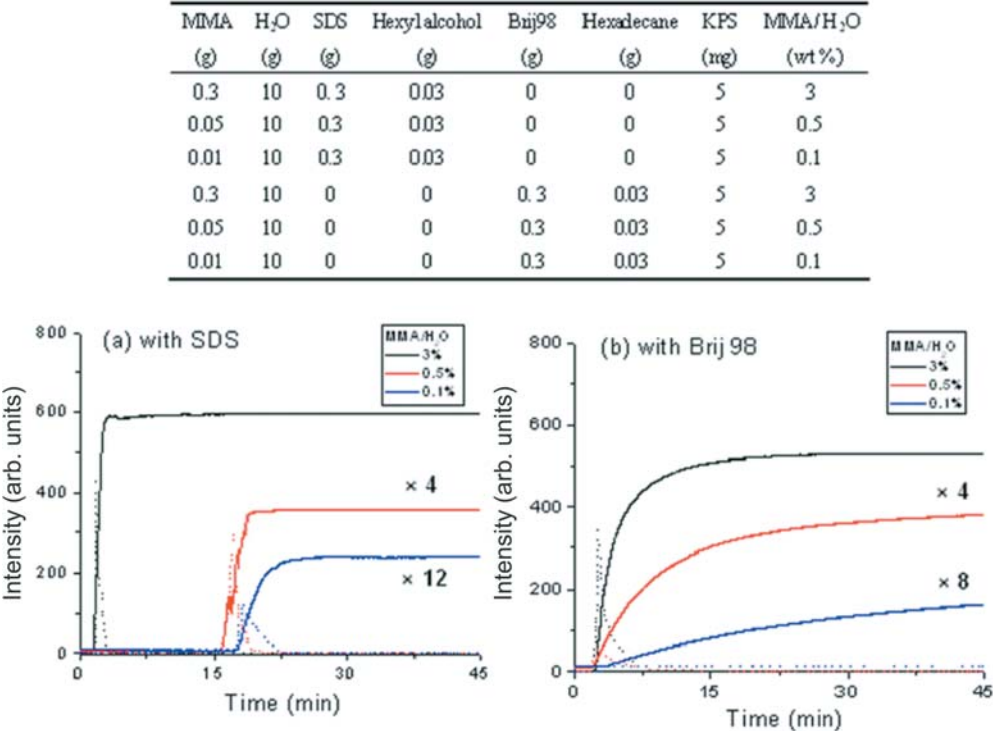
contents of 0.5% and 0.1%. With SDS as the surfactant, there appeared an induction period before the reaction took place, which became longer with reducing the monomer concentration. By contrast, using Brij98 as the surfactant, the reduction of the monomer concentration resulted in a decrease in the rate of polymerization. In all cases, the polymerization rate profiles (dotted lines) are also shown. A couple of analyses can be made. On the one hand, with the same surfactant, if only the number of monomer droplets was diminished with lower monomer content (more empty micelles in the solution), each droplet would be surrounded by initiator molecules of the same concentration and, consequently, the kinetics should not be changed. The results in Fig. 4 show that this is not the case, suggesting that at a very low concentration of monomer, the monomer droplet

size and the concentration of surfactant molecules adsorbed at the interface may be different, which changes the dynamic nature of the monomer-swollen micelles and the entry of primary free radicals in the droplets to initiate the polymerization. On the other hand, the very different kinetic behaviours observed with the two surfactants should reflect, among others, their different micellization abilities and interaction natures with MMA. The kinetic results indicate that the initiation of polymerization takes place more rapidly with Brij98 than with SDS, but after the initiation, the polymerization rate is slower with the former than with the latter. With SDS, the monomer droplets are covered by an outer layer of anionic sulfate groups, while with Brij98, they are surrounded with nonionic ethylene glycol units. The two surfactants are also very different in size (molar mass of 288 g for SDS as compared with about 1150 for Brij98), which means, at the same mass-based concentration, very different numbers of surfactant molecules interacting with the monomer droplets. These differences could affect the number and size of monomer droplets and the entry of primary radicals required to initiate the polymerization. It may appear more reasonable to use the same molar concentration for the two surfactants, but still this may just have a different effect on the number and size of monomer droplets, and on the density of adsorbed surfactant molecules. Clearly, it is the combination of those factors that dictates the reaction kinetics. At this point, we can only speculate the reasons for the observed differences; a clear understanding requires further studies by varying systematically the reaction conditions.

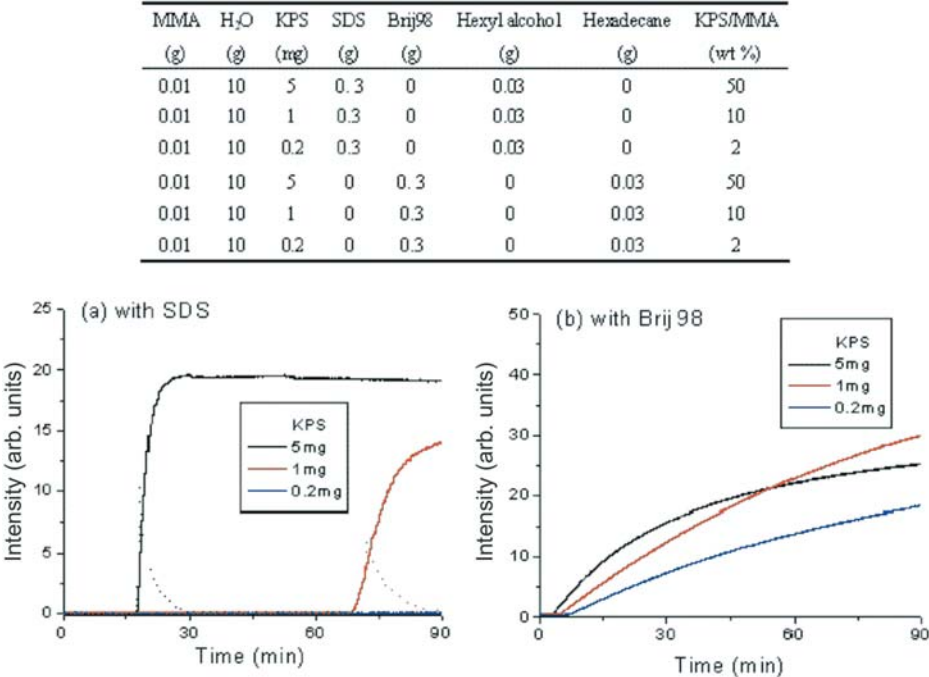
We then investigated the effect of the initiator concentration on the kinetic process with a very low monomer content of 0.1%, while keeping the surfactant concentration unchanged. Again, the two surfactants were utilized, and the results are shown in Fig. 5. With SDS as surfactant, the decrease of the water-soluble initiator concentration resulted in an increase in the induction period preceding the starting of polymerization and a slight decrease in the polymerization rate as well. At the lowest KPS concentration (2% with respect to the monomer), no polymerization was observed



**Fig. 4.** Fluorescence emission intensity at 425 nm ( $\lambda_{\text{ex}} = 337 \text{ nm}$ ) vs. reaction time for microemulsions containing 3%, 0.5%, and 0.1% MMA with (a) SDS and (b) Brij98 as surfactant. All solutions have the same surfactant and initiator (KPS) concentrations. The curves obtained at lower monomer contents are magnified by a factor as indicated in the figure.



**Fig. 5.** Fluorescence emission intensity at 425 nm ( $\lambda_{\text{ex}} = 337 \text{ nm}$ ) vs. reaction time for microemulsions containing 0.1% MMA and three different initiator (KPS) concentrations with (a) SDS and (b) Brij98 as surfactant. The compositions of all reaction solutions are shown.

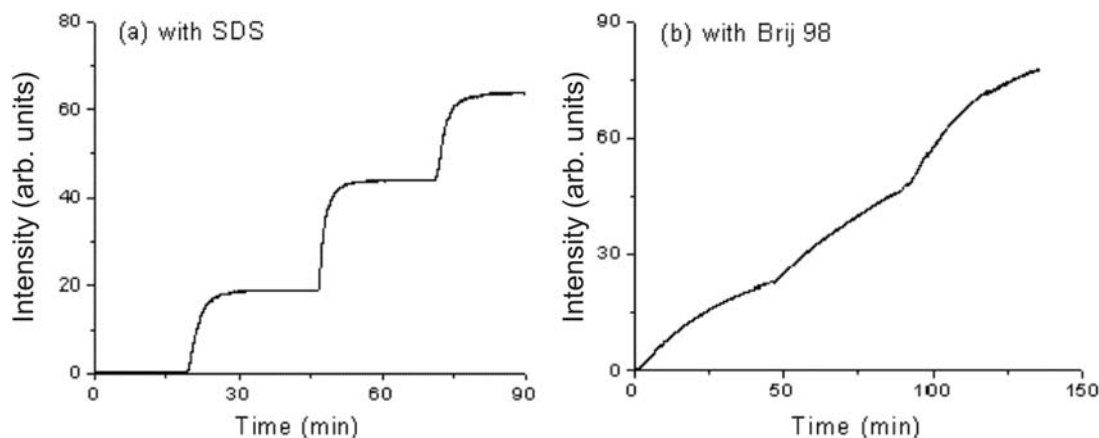


after 90 min, indicating the great difficulty in starting the polymerization when both monomer and initiator concentrations are small. While with Brij98 as surfactant, the decrease in the initiator concentration mainly resulted in a decrease in the polymerization rate and, on a closer inspection, a slight

increase of the induction period (the polymerization rate profiles are not shown for the sake of clarity). The effect of surfactant in this regime of very low monomer contents is evident for all initiator concentrations, but most strikingly at the lowest initiator concentration (2% with respect to mono-

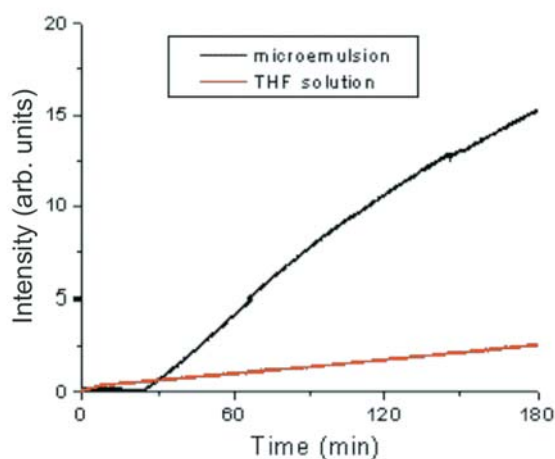
**Fig. 6.** Fluorescence emission intensity at 425 nm ( $\lambda_{\text{ex}} = 337$  nm) vs. reaction time for microemulsions containing 0.1% MMA with three successive additions of the monomer: (a) with SDS and (b) with Brij98 as surfactant.

MMA (g)	H <sub>2</sub> O (g)	KPS (mg)	SDS (g)	Brij98 (g)	Hexylalcohol (g)	Hexadecane (g)	MMA/H <sub>2</sub> O (wt %)
0.01	10	5	0.3	0	0.03	0	0.1
0.01	10	5	0	0.3	0	0.03	0.1



**Fig. 7.** Plots of fluorescence emission intensity at 425 nm ( $\lambda_{\text{ex}} = 337$  nm) vs. reaction time for a microemulsion containing 0.1% MMA with AIBN as initiator and for a THF solution containing 0.1% MMA with AIBN as initiator (the compositions of the two reaction solutions are indicated).

MMA (g)	H <sub>2</sub> O (g)	AIBN (mg)	THF (g)	Brij98 (g)	Hexadecane (g)	MMA/H <sub>2</sub> O (wt %)
0.01	10	1	0	0.3	0.03	0.1
0.01	0	1	10	0	0	0.1

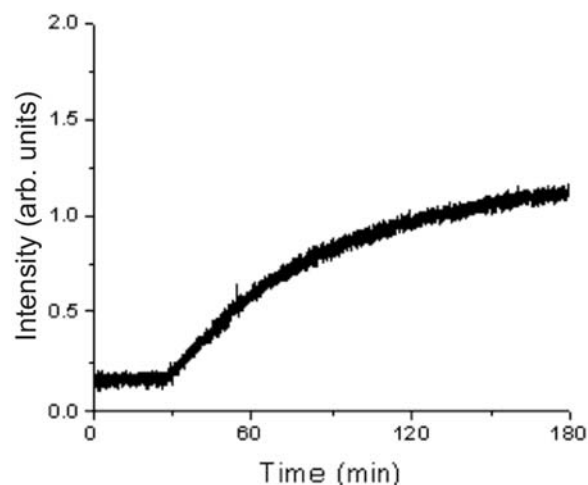


mer). We emphasize that all the experiments reported in Figs. 4 and 5 were carried out under the same experimental conditions, so that the induction period cannot be caused by the residual oxygen presented in the reaction solutions.

A microemulsion features an excess of surfactant molecules, and as the polymerization progresses, more empty micelles of the surfactant coexist with polymer latex particles.<sup>9</sup>

**Fig. 8.** Fluorescence emission intensity at 425 nm ( $\lambda_{\text{ex}} = 337$  nm) vs. reaction time for a microemulsion containing 0.0035% MMA (water-to-monomer ratio: 28 000) (the composition of the reaction solution is shown).

MMA (g)	H <sub>2</sub> O (g)	KPS (mg)	SDS (g)	Hexylalcohol (g)	MMA/H <sub>2</sub> O (wt %)
0.00035	10	5	0.3	0.03	0.0035



It is known that when more monomers are added into the solution at the end of a microemulsion polymerization, the reaction could resume, resulting in more polymer particles. We found that this could also happen with very low monomer contents. Figure 6 shows the result obtained with a solution containing 0.1% of MMA, with both SDS and Brij98 as the surfactant. In the case of SDS, after the fluorescence intensity reached the plateau level for some time, the same

amount of MMA was injected into the solution using a syringe through a parafilm covering the cuvette containing the solution; it took about 1 min before resuming the fluorescence intensity measurement (in other words, there was a 1 min delay between the cycles of polymerization). The result shows that within experimental error, at the end of the initial microemulsion polymerization, the two successive additions of more monomers proceeded with the same kinetics and a similar conversion degree, but with no induction period. This observation suggests that at the end of the first polymerization cycle, free radicals could be in empty micelles of the surfactant, so that once more monomers were added in the solution and solubilized by the micelles, new polymerization could take place immediately. Basically, the same conclusion can be drawn with Brij98 even though the kinetic process is different (slower polymerization rate with almost no induction period).

With an extremely low monomer content and in the presence of an excess amount of surfactant molecules, can the microemulsion polymerization get close to a homogeneous (single-phase) polymerization? An experiment was conducted with 0.1% MMA to get an answer to the question. Figure 7 compares the apparent kinetics of the polymerization of 0.1% MMA in a microemulsion with Brij98 as surfactant and in THF, with AIBN as initiator in both cases. The polymerization in THF solution started quickly but proceeded very slowly due to the low monomer concentration, while the microemulsion polymerization was much faster but started only after an induction period. These results indicate that at this low monomer content, the microemulsion polymerization is still a heterophase polymerization. The reaction inside monomer droplets is faster than the reaction in a homogeneous solution in which monomer molecules are much diluted. This result also gives a hint on the different kinetics by using SDS and Brij98 (Figs. 4 and 5). It would be possible that with very low monomer content, the reaction solution with Brij98 was closer to a homogeneous system than the solution with SDS, which accounts for the different induction periods. Finally, to highlight the unprecedented sensitivity of this fluorescence method in monitoring the kinetics of microemulsion polymerization, Fig. 8 shows the result obtained with 0.0035% of MMA, i.e., at a water-to-monomer ratio > 28 000! Even with this extremely low content of monomer, the typical kinetic process of the microemulsion polymerization of MMA with SDS as surfactant could still be detected, with of course a weak fluorescence signal. In principle, the sensitivity can further be improved by increasing the concentration of AnMA in the monomer.

## Conclusions

We presented a fluorescence method that made it possible to monitor the kinetics of microemulsion polymerization with very (or even extremely) low monomer contents. Using AnMA as the fluorescent probe, kinetic data of polymerization of MMA in a microemulsion with a water-to-monomer ratio as high as 28 000 could be obtained. The results show that with low monomer content, such as 0.1% of MMA with respect to water, the surfactant had a more profound effect on the kinetics than with a relatively high monomer content,

such as 3%. Using the anionic surfactant of SDS, the polymerization rate was fast, but there was an induction period, while with the non-ionic surfactant of Brij98, the polymerization started much earlier, but the reaction rate was slower. A decrease in the concentration of the water-soluble initiator KPS either further lengthened the induction period or slowed down the polymerization. With the unprecedented sensitivity, this fluorescence method is well-suited for kinetic study in the regime of low monomer contents. It can also be explored for monitoring polymerization systems, for which other methods are inaccessible or can be utilized with difficulties.

## Acknowledgement

YZ acknowledges financial support from the Natural Sciences and Engineering Research Council of Canada (NSERC) and le Fonds québécois de la recherche sur la nature et les technologies of Québec (FQRNT). YD acknowledges financial support from the National Natural Science Foundation of China (NO. 20374036). HKF thanks China Scholarship Council for a scholarship. YZ is a member of the FQRNT-funded Center for Self-Assembled Chemical Structures (CSACS).

## References

- (1) Guo, J. S.; Sudol, E. D.; Vanderhoff, J. W.; El-Aasser, M. S. *J. Polym. Sci. Part A: Polym. Chem.* **1992**, *30* (5), 691. doi:10.1002/pola.1992.080300501.
- (2) Feng, L.; Ng, K. Y. S. *Langmuir* **1990**, *23*, 1048.
- (3) Gan, L. M.; Lee, K. C.; Chew, C. H.; Ng, S. C. *Langmuir* **1995**, *11* (2), 449. doi:10.1021/la00002a014.
- (4) Morgan, J. D.; Lusvardi, K. M.; Kaler, E. W. *Macromolecules* **1997**, *30* (7), 1897. doi:10.1021/ma9613704.
- (5) Nomura, M.; Suzuki, K. *Macromol. Chem. Phys.* **1997**, *198* (10), 3025. doi:10.1002/macp.1997.021981004.
- (6) Antonietti, M.; Basten, R.; Lohmann, S. *Macromol. Chem. Phys.* **1995**, *196* (2), 441. doi:10.1002/macp.1995.021960201.
- (7) de Vries, R.; Co, C. C.; Kaler, E. W. *Macromolecules* **2001**, *34* (10), 3233. doi:10.1021/ma001247j.
- (8) Hermanson, K. D.; Kaler, E. W. *Macromolecules* **2003**, *36* (6), 1836. doi:10.1021/ma0216223.
- (9) Antonietti, M.; Landfester, K. *Prog. Polym. Sci.* **2002**, *27* (4), 689. doi:10.1016/S0079-6700(01)00051-X.
- (10) Antonietti, M.; Basten, R.; Lohmann, S. *Macromol. Chem. Phys.* **1995**, *196* (2), 441. doi:10.1002/macp.1995.021960201.
- (11) Warman, J. M.; Abellon, R. D.; Verhey, H. J.; Verhoeven, J. W.; Hofstraat, J. W. *J. Phys. Chem. B* **1997**, *101* (25), 4913. doi:10.1021/jp970642h.
- (12) Warman, J. M.; Abellon, R. D.; Luthjens, L. H.; Suykerbuyk, J. W. A.; Verhey, H. J.; Verhoeven, J. W. *Nucl. Instrum. Methods Phys. Res. B* **1999**, *151* (1-4), 361. doi:10.1016/S0168-583X(99)00113-5.
- (13) Frahn, M. S.; Abellon, R. D.; Jager, W. F.; Luthjens, L. H.; Warman, J. M. *Nucl. Instrum. Methods Phys. Res. B* **2001**, *185* (1-4), 241. doi:10.1016/S0168-583X(01)00837-0.
- (14) Frahn, M. S.; Luthjens, L. H.; Warman, J. M. *Polymer (Guildf.)* **2003**, *44* (26), 7933. doi:10.1016/j.polymer.2003.10.024.

# Design, synthesis, and properties of benzobisthiadiazole-based donor- $\pi$ -acceptor- $\pi$ -donor type of low-band-gap chromophores and polymers

Gang Qian and Zhi Yuan Wang

**Abstract:** A novel low-band-gap chromophore (**5**, 0.86 eV) having fluorene as a donor, benzobisthiadiazole (BBTD) as an acceptor, and pyrrole as a  $\pi$ -spacer was successfully designed and synthesized, to probe the effect of  $\pi$ -spacer on the band-gap level of the donor- $\pi$ -acceptor- $\pi$ -donor type of chromophores. Compared with the thiophene spacer analogue (in compound **3**), the intramolecular hydrogen bonding between the pyrrole and the neighboring BBTD unit pushes the absorption maximum and fluorescence emission of chromophore **5** into the near-infrared spectral region with a red shift of 172 and 158 nm, respectively. The same red-shift phenomenon can also be realized by addition of Lewis acid (e.g.,  $\text{BF}_3$ ) to the BBTD-containing chromophores with other spacers. Attempt of using low-band-gap chromophore **5** in bulk heterojunction (BHJ) solar cells was made, showing a non-optimized photovoltaic device with the power conversion efficiency of 0.01%. A precursor approach to introduction of the alkaline-labile BBTD acceptor into the polymer backbone has been demonstrated by successful synthesis of low-band-gap polymer **P2**. The same strategy can be in principle applied to the synthesis of a series of low-band-gap chromophores or polymers with strong acceptors.

**Key words:** donor- $\pi$ -acceptor- $\pi$ -donor, chromophore, low band gap, bulk heterojunction (BHJ), precursor polymer.

**Résumé :** Afin de pouvoir étudier l'effet d'un espaceur  $\pi$  sur le niveau d'énergie interbande des chromophores de type donneur- $\pi$ -accepteur- $\pi$ -donneur, on a développé et synthétisé un nouveau chromophore de basse énergie interbande (**5**, 0,86 eV) comportant un fluorène comme donneur, un benzobisthiadiazole (BBTD) comme accepteur et un noyau pyrrole comme espaceur  $\pi$ . Par comparaison avec l'analogue comportant un espaceur thiophène (dans le composé **3**), la liaison hydrogène intramoléculaire entre le pyrrole et l'unité adjacente BBTD déplace le maximum d'absorption et l'émission de fluorescence du chromophore **5** dans la région spectrale du proche infrarouge avec des déplacements vers le rouge de respectivement 172 et 158 nm. On peut observer le même phénomène de déplacement vers le rouge par l'addition d'un acide de Lewis (tel le  $\text{BF}_3$ ) à des chromophores comportant du BBTD et d'autres espaceurs. On a essayé d'utiliser le chromophore **5** à faible énergie interbande dans des cellules solaires à hétérojonction globale (HJG); on a obtenu un dispositif non voltaïque non optimisé ayant une efficacité de conversion de pouvoir de 0,01 %. On a démontré l'applicabilité d'une autre approche à l'introduction de l'accepteur BBTD labile aux produits alcalins dans le squelette d'un polymère en effectuant avec succès la synthèse du polymère **P2** de faible énergie interbande. En théorie, la même stratégie peut être appliquée à la synthèse d'une série de chromophores ou de polymères de faible énergie interbande avec des accepteurs forts.

**Mots-clés :** donneur- $\pi$ -accepteur- $\pi$ -donneur, chromophore, faible énergie interbande, hétérojonction globale (HJG), polymère précurseur.

[Traduit par la Rédaction]

## Introduction

Research on low-band-gap organic materials (e.g., chromophores and polymers), whose band-gap levels, defined as the difference between the highest occupied molecular orbital (HOMO) and the lowest unoccupied molecular orbital (LUMO) energy levels, are typically below 1.8 eV, has been the focal point in a number of technologically impor-

tant areas. Low-band-gap organic materials absorb light with wavelengths longer than 700 nm or within the near-infrared (NIR) spectral region of 750–2000 nm.

In the area of solar-energy conversion, it is essential that the absorption of the light-harvesting material matches the spectral characteristics of the sun.<sup>1</sup> For the polythiophene (P3HT)-based bulk heterojunction (BHJ) solar cells, P3HT has a band gap of ~1.90 eV and a rather narrow absorption

Received 30 August 2009. Accepted 13 October 2009. Published on the NRC Research Press Web site at canjchem.nrc.ca on 19 January 2010.

This article is part of a Special Issue dedicated to Professor M. A. Winnik.

G. Qian and Z.Y. Wang,<sup>1</sup> Department of Chemistry, Carleton University, 1125 Colonel By Drive, Ottawa, ON K1S 5B6, Canada.

<sup>1</sup>Corresponding author (e-mail: wayne\_wang@carleton.ca).



band (FWHM  $\approx$  150 nm) and can absorb only a limited fraction of the solar photons ( $\sim$ 30%). Thus, the NIR-absorbing chromophores and polymers have the possibility to improve the efficiency of organic BHJ solar cells owing to a better overlap with the solar spectrum.<sup>2</sup>

Near-infrared fluorescent organic materials may find applications as NIR-fluorescent tags for bio-imaging<sup>3</sup> and chemical sensing<sup>4</sup> or emitters in NIR light-emitting diodes (LED) for information-secured display and background lighting. To date, most of organic materials that have been shown to emit the light around 700–1000 nm are mainly with lanthanide complexes,<sup>5</sup> transition-metal complexes,<sup>6</sup> ionic dyes,<sup>7</sup> and low-band-gap polymers.<sup>8</sup> NIR organic photovoltaic materials have recently been demonstrated for use in NIR photodetectors.<sup>9</sup>

Among various types of low-band-gap organic materials, much effort has been focused on the design and synthesis of the chromophores and polymers consisting of powerful electron donor (D) and acceptor (A) units. Some of the best-performing BHJ organic solar cells are fabricated with the D–A type of conjugated polymers.<sup>10</sup> Some of these D–A polymers contain benzo-2,1,3-thiadiazole (BT) as the acceptor unit.<sup>11</sup> Recently, we have shown that the D– $\pi$ –A– $\pi$ –D type of chromophores, where  $\pi$  is a spacer or linking unit, can absorb light with the wavelength around 1000 nm and fluoresce above 1000 nm, such as compounds **1–3** in Fig. 1.<sup>12</sup> The band-gap levels of this class of chromophores depend on the strength of the donor and acceptor. Those containing a strong electron-withdrawing heterocyclic quinoid, namely, benzo[1,2-*c*:4,5-*c'*]bis([1,2,5]thiadiazole) (BBTD), tend to have a lower band gap than other acceptor-containing chromophores, since the BBTD unit is known to possess a substantial quinoidal character within a conjugated backbone, allowing for greater electron delocalization, and thus lowering the band gap.<sup>13</sup> However, the scope and limitations of the acceptor strength and the role of the spacer in tuning the band gap are still not fully understood. For example, a recent work shows that the band gap of the D–A type of benzothiadiazole (BT)-containing chromophores can be significantly lowered by the introduction of Lewis acids as a result of changing the electronic properties of the BT fragment via interactions with Lewis acids that bind nitrogen.<sup>14</sup>

Considering the D– $\pi$ –A– $\pi$ –D system such as compounds **1–3**, by diminishing the electron density on the nitrogen of the BBTD unit, a further decrease in band gap or red shift in absorption and emission spectra of the chromophores should be expected. Conceivably, the BBTD acceptor strength can be increased through either the intermolecular or intramolecular interaction by addition of Lewis acid or other electron-accepting species. In this work, we intend to show that by the introduction of pyrrole as a spacer, the band gap of the D– $\pi$ –A– $\pi$ –D chromophores can be further lowered due to the intramolecular hydrogen bonding with the neighboring BBTD unit, which is similar to the effect of adding a Lewis acid to the chromophores having other spacers. Accordingly, a new D– $\pi$ –A– $\pi$ –D chromophore (**5**, Fig. 1) is designed, synthesized, and characterized. Furthermore, for potential applications in thin-film devices, such as polymer BHJ solar cells, a new general approach to low-

band-gap polymers having the D– $\pi$ –A– $\pi$ –D unit in the backbone is demonstrated.

## Experimental section

### Materials

All chemicals and reagents were used as received from commercial sources without purification. Solvents for chemical synthesis were purified by distillation. All chemical reactions were carried out under an argon atmosphere. 2-Bromo-9,9-dioctylfluorene (**6**),<sup>15</sup> *N*-(*tert*-butoxycarbonyl)-2-(trimethylstannyl) pyrrole (**7**),<sup>16</sup> 4,8-dibromobenzo[1,2-*c*:4,5-*c'*]bis([1,2,5]thiadiazole) (**10**),<sup>13d</sup> 4,7-bis[4-(*N*-phenyl-*N*-(4-methylphenyl)amino)phenyl]-5,6-diamino-2,1,3-benzothiadiazole (**11**),<sup>12b</sup> and 9,9-dioctyl-2,7-bis(trimethyleneboronate)fluorene (**13**)<sup>17</sup> were prepared according to literature methods.

### Methods

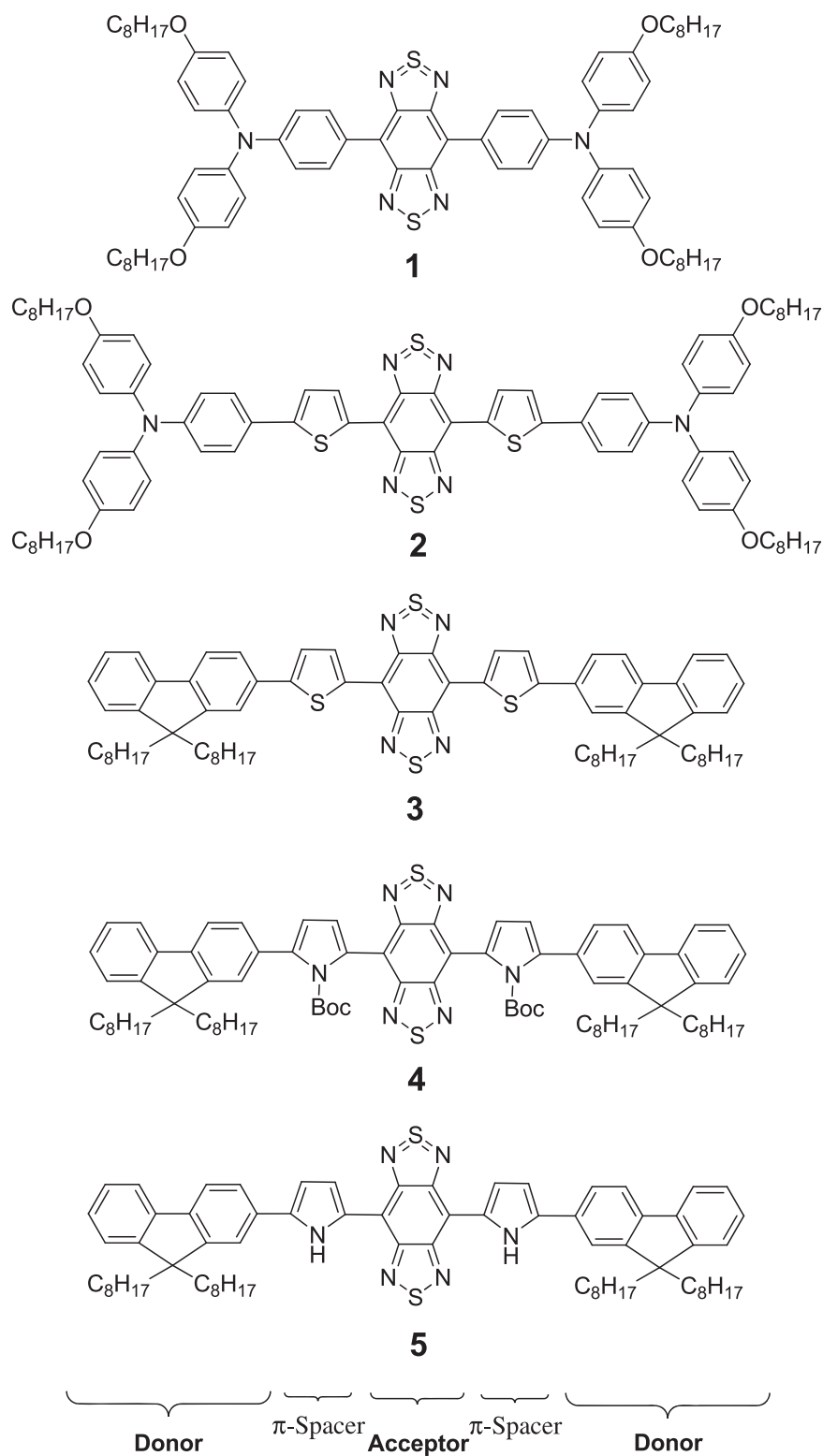
<sup>1</sup>H NMR spectra were recorded using a Bruker Avance 300 NMR spectrometer. The high-temperature NMR experiments were performed on a Varian Unity-400 MHz spectrometer. High-resolution mass spectrometry (HRMS) was obtained from 7.0 T Actively Shielded Fourier Transform Ion Cyclotron Resonance Mass Spectrometers. The number- and weight-average molecular weights of the polymers were determined by gel-permeation chromatography (GPC) with a Waters 410 instrument and polystyrene as a standard and THF as eluent. Absorption and fluorescence spectra were recorded with a Shimadzu UV-3600 or Lambda 900 Perkin-Elmer spectrophotometer and a PTI fluorescence spectrophotometer, respectively. IR spectra were recorded on a Bio-Rad FTS-135 spectrophotometer. Cyclic voltammetry (CV) was performed on a CHI660b electrochemical workstation, in dry dichloromethane containing *n*-Bu<sub>4</sub>NPF<sub>6</sub> (0.1 mol/L) with a scan rate of 50 mV/s at room temperature under argon, using a Pt disk (2 mm diameter) as the working electrode, a Pt wire as the counter electrode and a Ag/AgCl electrode as the reference electrode.

### Photovoltaic device fabrication and characterization

The solar-cell devices were fabricated with the device structure of [indium tin oxide (ITO)/poly(3,4-ethylene dioxathiophene):poly(styrenesulfonate) (PEDOT:PSS)/Compound **5**:PCBM/Al]. The ITO glass was pre-cleaned and coated with PEDOT:PSS. Then, the active layer was spin-coated from the chlorobenzene solution of compound **5** and PCBM (1:1, w/w) on the substrate. Finally, the Al cathode was deposited at a vacuum level of  $4 \times 10^{-4}$  Pa. The effective area of the unit cell is 16 mm<sup>2</sup>. The current–voltage (*I*–*V*) measurement of devices was conducted on a computer controlled Keithley 236 Source meter. A xenon lamp (500 W) with AM 1.5 filter was used as the white light source, and the optical power at the sample was 100 mW/cm<sup>2</sup>.

### *N*-(*tert*-Butoxycarbonyl)-2-(9,9-dioctylfluorene-2-yl)pyrrole (**8**)

2-Bromo-9,9-dioctylfluorene (**6**) (4.7 g, 10 mmol), *N*-(*tert*-butoxycarbonyl)-2-(trimethylstannyl)pyrrole (**7**) (6.6 g, 12 mmol), and tetrakis(triphenylphosphane) palladium(0) (115.5 mg, 0.1 mmol) were dissolved in a mixture of tol-

**Fig. 1.** Chemical structures of D- $\pi$ -A- $\pi$ -D chromophores **1–5**.

uene (20 mL) and a 1 mol/L aqueous solution of sodium carbonate (20 mL). The mixture was stirred at 110 °C for 60 h. After cooling, the resulting solution was extracted with dichloromethane. The combined organic layers were washed with water and dried with anhydrous  $\text{MgSO}_4$ . Evap-

oration of the solvent and subsequent column chromatography (silica gel, dichloromethane/petroleum ether = 1/5) afforded the product as pale yellow oil (1.1 g, 20%).  $^1\text{H}$  NMR (300 MHz,  $\text{CDCl}_3$ )  $\delta$  (ppm): 7.74–7.68 (m, 2H), 7.40–7.26 (m, 6H), 6.30–6.24 (m, 2H), 1.98 (t, 4H,  $J$  =

8.37 Hz), 1.41 (s, 9H), 1.40–1.10 (m, 20H), 0.89–0.87 (m, 6H), 0.73–0.61 (m, 4H).

**Tributyl[*N*-(*tert*-butoxycarbonyl)-5-(9,9-dioctylfluoren-2-yl)pyrrole-2-yl]stannane (9)**

A 100 mL three-necked flask was charged with dry THF (20 mL) and 2,2,6,6-tetramethylpiperidine (1.85 mL, 11 mmol). The mixture was cooled to  $-78^{\circ}\text{C}$  and *n*-BuLi (2.5 mol/L in hexane, 4.8 mL, 12 mmol) was added dropwise. The mixture was stirred at  $-78^{\circ}\text{C}$  for 10 min, then warmed to  $0^{\circ}\text{C}$  and stirred for additional 10 min. At this point, the mixture was cooled again to  $-78^{\circ}\text{C}$ , a solution of *N*-(*tert*-butoxycarbonyl)-2-(9,9-dioctylfluoren-2-yl)pyrrole (8) (5.5 g, 10 mmol) in dry THF (10 mL) was added, and the mixture was stirred for 1.5 h while keeping the temperature below  $-65^{\circ}\text{C}$ .  $\text{Bu}_3\text{SnCl}$  (3.7 mL, 13 mmol) was added dropwise. The mixture was stirred for 40 min at  $-75^{\circ}\text{C}$  and for additional 40 min at  $0^{\circ}\text{C}$ , and then for 12 h at room temperature. The mixture was poured into water and extracted with diethyl ether. The organic extracts were dried over anhydrous  $\text{MgSO}_4$ . Upon evaporation of the solvent, the crude product was obtained as pale yellow oil and used for the next step without further purification.  $^1\text{H}$  NMR (300 MHz,  $\text{CDCl}_3$ )  $\delta$  (ppm): 7.75–7.67 (m, 2H), 7.40–7.24 (m, 5H), 6.44 (d, 1H,  $J = 3.75$  Hz), 6.33 (d, 1H,  $J = 3.00$  Hz), 1.99 (t, 4H,  $J = 8.10$  Hz), 1.65–1.62 (m, 6H), 1.40–1.37 (m, 6H), 1.24 (s, 9H), 1.18–1.08 (m, 26H), 0.97–0.92 (m, 9H), 0.89–0.83 (m, 6H), 0.73–0.61 (m, 4H).

**4,8-Bis[*N*-(*tert*-butoxycarbonyl)-5-(9,9-dioctylfluoren-2-yl)-2-pyrrolyl]benzo[1,2-*c*:4,5-*c'*]bis([1,2,5]thiadiazole) (4)**

To a solution of compound 9 (1.0 g, 1.2 mmol) and 4,8-dibromobenzo[1,2-*c*:4,5-*c'*]bis([1,2,5]thiadiazole) (10) (0.18 g, 0.5 mmol) in toluene (40 mL) was added  $\text{Pd}(\text{PPh}_3)_4$  (71 mg, 0.061 mmol). The mixture was stirred for 36 h at  $110^{\circ}\text{C}$ . After cooling, the mixture was poured into water and extracted with dichloromethane. The organic layer was washed with saturated aqueous potassium fluoride and brine before being dried over anhydrous  $\text{MgSO}_4$ . After evaporation of the solvent, the residue was purified by column chromatography on silica gel with dichloromethane/petroleum ether (1:1) as the eluent to afford the product (0.13 g, 20%) as black solid.  $^1\text{H}$  NMR (400 MHz,  $o\text{-C}_6\text{D}_4\text{Cl}_2$ , 403 K)  $\delta$  (ppm): 7.78–7.72 (m, 4H), 7.54–7.46 (m, 4H), 7.41–7.35 (m, 6H), 7.05 (d, 2H,  $J = 3.5$  Hz), 6.56 (d, 2H,  $J = 3.5$  Hz), 2.05–2.00 (m, 8H), 1.59 (s, 18H), 1.29–1.00 (m, 40H), 0.86 (t, 12H,  $J = 6.7$  Hz), 0.70 (br, 8H).

**4,8-Bis[5-(9,9-dioctylfluoren-2-yl)-2-pyrrolyl]benzo[1,2-*c*:4,5-*c'*]bis([1,2,5]thiadiazole) (5)**

Thermolysis of compound 4 (98 mg) at  $200^{\circ}\text{C}$  under reduced pressure ( $10^{-5}$  torr, 30 min) (1 torr = 133.322 Pa) afforded 92 mg (94% yield) of product as black solid.  $^1\text{H}$  NMR (400 MHz,  $o\text{-C}_6\text{D}_4\text{Cl}_2$ , 403 K)  $\delta$  (ppm): 11.72 (br, 2H), 8.04 (br, 2H), 7.78–7.67 (m, 8H), 7.55–7.37 (m, 6H), 6.96 (br, 2H), 2.15–2.11 (m, 8H), 1.23–1.15 (m, 40H), 0.85–0.80 (m, 20H). HRMS (for  $[\text{M}]^+$ ) calcd.: 1100.65119; found: 1100.64015.

**4,7-Bis[4-(*N*-(4-bromophenyl)-*N*-(4-methylphenyl)amino)phenyl]-5,6-diamino-2,1,3-benzothiadiazole (12)**

A solution of tetrabutylammonium tribromide (0.96 g, 2.0 mmol) and 4,7-bis[4-(*N*-phenyl-*N*-(4-methylphenyl)amino)phenyl]-5,6-diamino-2,1,3-benzothiadiazole (11) (0.61 g, 9.0 mmol) in freshly distilled dichloromethane (45 mL) was stirred at room temperature for 3 h. The precipitates were filtrated and washed with dichloromethane. The solid was dried under vacuum to give the product as orange solid (0.55 g, 73%).  $^1\text{H}$  NMR (300 MHz,  $\text{CDCl}_3$ )  $\delta$  (ppm): 7.43 (d, 4H,  $J = 8.3$  Hz), 7.34 (d, 4H,  $J = 8.7$  Hz), 7.19 (d, 4H,  $J = 8.5$  Hz), 7.12 (d, 4H,  $J = 8.6$  Hz), 7.08 (d, 4H,  $J = 9.1$  Hz), 7.04 (d, 4H,  $J = 8.7$  Hz), 2.33 (s, 6H).

**Polymer P1**

To a mixture of 9,9-dioctyl-2,7-bis(trimethyleneboronate)-fluorene (13) (0.279 g, 0.500 mmol) and 4,7-bis[4-(*N*-(4-bromophenyl)-*N*-(4-methylphenyl)amino)phenyl]-5,6-diamino-2,1,3-benzothiadiazole (12) (0.419 g, 0.500 mmol) was added Aliquat 336 (0.120 g),  $\text{Pd}(\text{PPh}_3)_4$  (7.9 mg, 0.007 mmol), degassed toluene (7 mL), and aqueous 2 mol/L potassium carbonate (3 mL) under a dry argon atmosphere. The mixture was heated to  $95^{\circ}\text{C}$  and stirred in the dark for 48 h. After cooling, the mixture was poured into methanol. The precipitate was collected by filtration and then dissolved in dichloromethane. The solution was washed with water, dried with anhydrous  $\text{MgSO}_4$ , and then concentrated to an appropriate volume. The fiber-like brown polymer (0.500 g, 94%) was obtained by pouring the concentrated solution into methanol.  $^1\text{H}$  NMR (300 MHz,  $\text{CDCl}_3$ )  $\delta$  (ppm): 7.74 (d, 2H,  $J = 7.9$  Hz), 7.61–7.55 (m, 8H), 7.47 (d, 4H,  $J = 8.7$  Hz), 7.29–7.25 (m, 8H), 7.20–7.13 (m, 8H), 2.36 (s, 6H), 2.00 (br, 4H), 1.20–1.00 (m, 20H), 0.80–0.75 (m, 10H).

**Polymer P2**

To a solution of polymer P1 (0.107 g, 0.1 mmol) in dry pyridine (10 mL) was added *N*-sulfinylaniline (0.5 mL, 4 mmol) and chlorotrimethylsilane (0.5 mL, 3.6 mmol) in argon atmosphere. The mixture was heated to  $80^{\circ}\text{C}$  and stirred overnight. After workup, excess chlorotrimethylsilane was distilled off. The solution was concentrated to 5 mL and poured into methanol. The fiber-like dark blue polymer P2 (98.0 mg, 89%) was collected by filtration, washed with ethanol, and dried under vacuum.  $^1\text{H}$  NMR (300 MHz,  $\text{CDCl}_3$ )  $\delta$  (ppm): 8.20 (d, 4H,  $J = 8.5$  Hz), 7.75 (d, 2H,  $J = 7.4$  Hz), 7.63–7.56 (m, 8H), 7.34–7.16 (m, 16H), 2.37 (s, 6H), 2.06 (br, 4H), 1.06 (br, 20H), 0.80–0.75 (m, 10H).

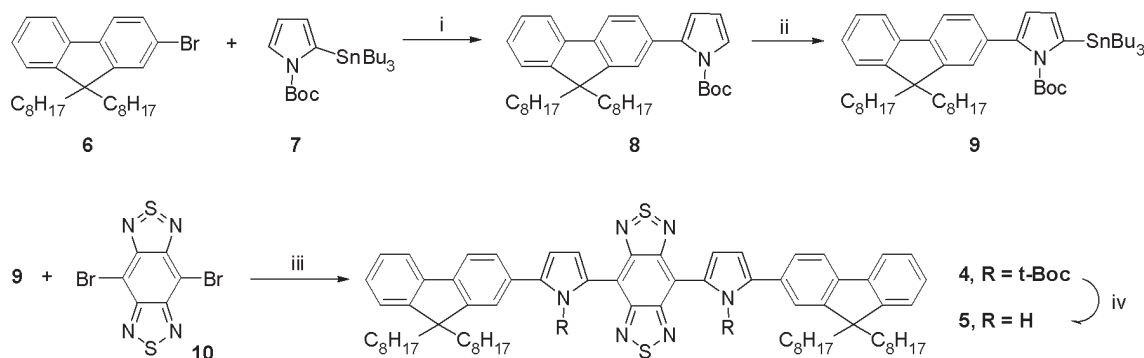
## Results and discussion

### Design and synthesis of low-band-gap chromophores

#### Design concept and synthesis

The concept for designing low-band-gap chromophores is based on the use of a strong electron acceptor, namely, benzobisthiadiazole, and electron donors that are linked through a  $\pi$ -conjugated spacer. In particular, the D- $\pi$ -A- $\pi$ -D type of chromophores, such as compounds 1–3 (Fig. 1), previously reported by our group,<sup>12a</sup> is the focal point of design

**Scheme 1.** Synthetic route to intermediates and chromophores **4** and **5**. Reagents and conditions: (i)  $\text{Pd}(\text{PPh}_3)_4$ ,  $\text{Na}_2\text{CO}_3$  (aq., 1 mol/L), toluene,  $110^\circ\text{C}$ , 60 h; (ii) *N*-lithium-2,2,6,6-tetramethylpiperidine,  $-70^\circ\text{C}$ ,  $(\text{Bu})_3\text{SnCl}$ , THF,  $-70^\circ\text{C}$  to room temperature; (iii)  $\text{Pd}(\text{PPh}_3)_4$ , toluene,  $110^\circ\text{C}$ , 36 h; (iv)  $200^\circ\text{C}$ , 30 min,  $10^{-5}$  torr.



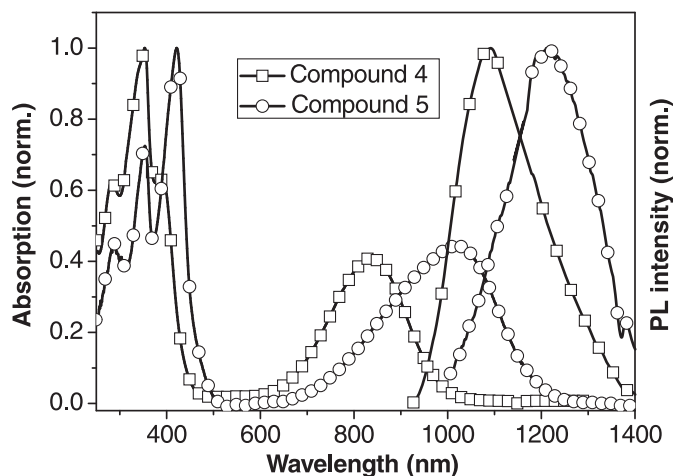
and study. With the same acceptor, the absorption wavelength of chromophores **1–3** varies according to the strength of donors and the nature of spacer. Between compounds **2** and **3**, the difference in band-gap levels is attributed to the different donors. However, a larger difference in the band-gap levels or absorption ( $\Delta\lambda_{\text{max}} = 157$  nm) between chromophores **1** and **2** is clearly due to the presence of different  $\pi$ -spacers (thiophene vs. benzene or nil). Therefore, the  $\pi$ -spacer or linking moiety in the D- $\pi$ -A- $\pi$ -D type of chromophores can play an important role in band-gap tuning, which may lead to further band-gap lowering or spectral red shift relative to chromophores **1–3**. Accordingly, in this work, pyrrole was introduced as  $\pi$ -spacer in a new chromophore **5** (Fig. 1) to study the scope and limitations of the  $\pi$ -spacer regarding the band-gap tuning. Any additional contribution to a better D-A interaction or lowering the LUMO level of the acceptor unit that may be brought by the use of a new  $\pi$ -spacer is likely to result in a further red shift in absorption in reference to the structurally analogous chromophore **3** ( $\lambda_{\text{max}} = 848$  nm).

Scheme 1 outlines the synthetic route to compounds **4** and **5**. Compound **4** was readily synthesized by the Stille coupling reaction of dibromo-BBTD **10** with tributyltin compounds **9** derived from the donor. It should be noted that aqueous sodium carbonate solution was not added, as required to suppress the C-Sn bond cleavage in the Stille coupling reaction,<sup>18</sup> due to instability of the BBTD group in alkaline solution, which caused a rather poor yield (20%) for compound **4**. Removal of the *tert*-butoxycarbonyl (*t*-Boc) protecting group in **4** by heating under reduced pressure afforded the target compound **5** with high yield.

#### Optical and electrochemical properties

The absorption and photoluminescence of compounds **4** and **5** in toluene are shown in Fig. 2, and the data are presented in Table 1. As for compounds **1–3**, compound **5** has mainly two absorption bands. The peaks from 300 to 500 nm are attributed to the  $\pi$ - $\pi^*$  transition and the possible  $n$ - $\pi^*$  transition of the conjugated aromatic segments, and those at longer wavelengths are due to the intramolecular charge transfer (ICT) transitions between the donor and acceptor. Compared with compound **3**, the maximum absorption of compound **4** is blue-shifted. Since pyrrole is more electron-donating than thiophene, the observed blue

**Fig. 2.** Normalized absorption ( $10^{-5}$  mol/L) and fluorescence emission ( $10^{-4}$  mol/L) spectra of compounds **4** and **5** in toluene.



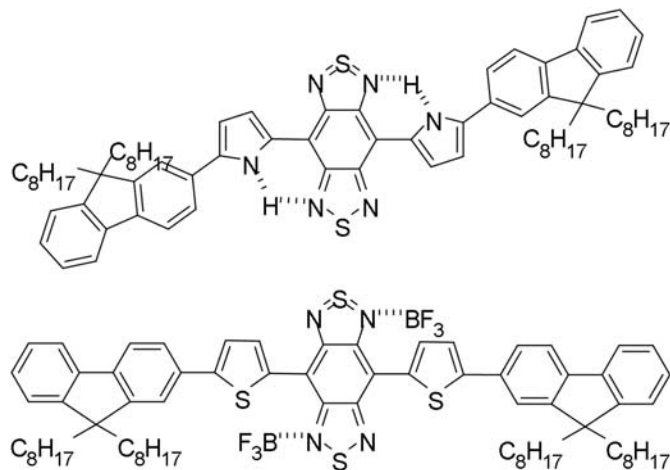
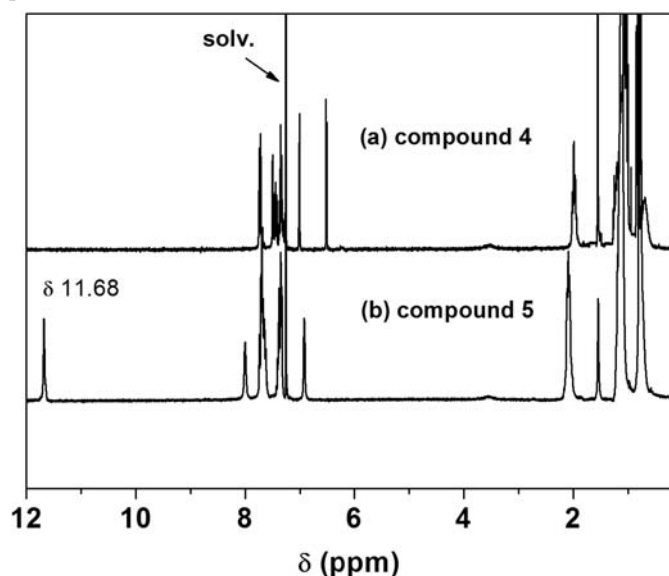
shift is mainly due to non-planarity between the BBTD and the pyrrole induced by *t*-Boc group. After removal of the *t*-Boc group, both the maximum absorption and emission wavelengths were red-shifted dramatically (about 183 and 121 nm, respectively; Fig. 2) relative to its precursor **4**. The pyrrole spacer and the neighboring BBTD core in compound **5** are expected to be completely coplanar by virtue of hydrogen bonding (Fig. 3), which should facilitate the charge transfer from donor to acceptor, and thus lowers the band-gap level. This intramolecular hydrogen bonding also contributes to altering the energy level of the BBTD acceptor by sharing or removing partial electrons on the nitrogen in BBTD. In the  $^1\text{H}$  NMR spectra of compound **5**, the pyrrole N-H signal is found at the low field ( $\delta = 11.68$ , Fig. 4), which is an indication for strong intramolecular hydrogen bonding.<sup>19</sup>

Similar to the effect of hydrogen-bonding interaction, addition of Lewis acids should also alter the band gap as a result of binding with the nitrogen in BBTD. Figure 5 shows the absorption spectra of compound **3** and a mixture of **3** with excess  $\text{BF}_3$ . The spectrum of compound **3** exhibits an absorption maximum ( $\lambda_{\text{max}}$ ) at 834 nm with an onset ( $\lambda_{\text{onset}}$ ) at 958 nm. Upon addition of an excess of  $\text{BF}_3$ , a color change took place immediately, going from yellowish green

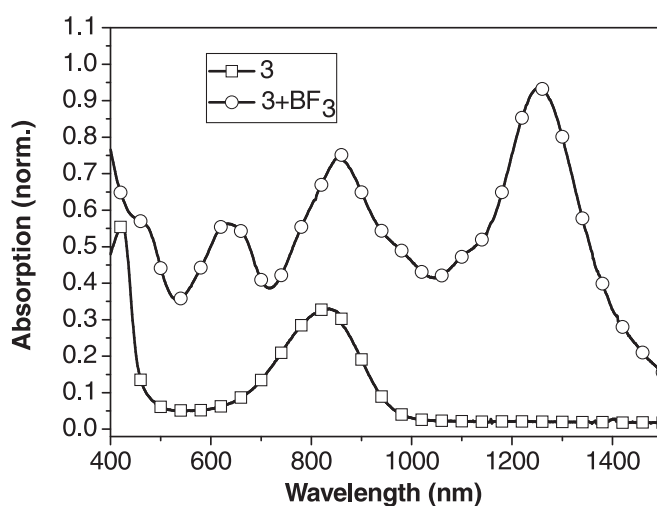


**Table 1.** Optical and electrochemical data of chromophores.

Compound	$\lambda_{\text{max}}^{\text{abs}}$ (nm) <sup>a</sup>	Log $\epsilon^a$	$\lambda_{\text{max}}^{\text{PL}}$ (nm) <sup>b</sup>	Stokes shift (nm)	$\Phi_f$ (%) <sup>c</sup>	HOMO (eV) <sup>d</sup>	LUMO (eV) <sup>d</sup>	Energy gap (eV)
<b>1</b> <sup>e</sup>	763	4.38	1065	302	7.1	4.95	3.76	1.19
<b>2</b> <sup>e</sup>	920	4.86	1125	205	5.3	4.77	3.94	0.83
<b>3</b> <sup>e</sup>	848	4.71	1055	207	18.5	5.14	3.99	1.15
<b>4</b>	837	4.53	1092	255	NA	4.96	3.85	1.11
<b>5</b>	1020	4.57	1213	193	0.3	4.75	3.89	0.86

<sup>a</sup>Measured in toluene with a concentration of  $10^{-5}$  mol/L.<sup>b</sup>Measured in toluene with a concentration of  $10^{-4}$  mol/L. Excitation wavelengths for **1–4** are at their maximum absorption wavelengths, and at 980 nm for **5**.<sup>c</sup>Fluorescence quantum yield measured relative to IR-125 ( $\Phi_f = 0.13$  in DMSO).<sup>d</sup>Calculated from the formula,  $E_{(\text{HOMO})} = -(E_{\text{ox}} + 4.34)$  (eV),  $E_{(\text{LUMO})} = -(E_{\text{red}} + 4.34)$  (eV).<sup>e</sup>See ref. 12a.**Fig. 3.** Hydrogen bonding in compound **5** and the **3**-BF<sub>3</sub> adduct.**Fig. 4.** <sup>1</sup>H NMR spectra (400 MHz, *o*-C<sub>6</sub>D<sub>4</sub>Cl<sub>2</sub>, 403 K) of compounds **4** and **5**.

to dark blue visually. Consequently, the  $\lambda_{\text{max}}$  and  $\lambda_{\text{onset}}$  of compound **3**-BF<sub>3</sub> adduct appeared at 1260 nm and 1580 nm, being red-shifted by 426 nm and 622 nm, respectively. According to the confirmed structure of the complex of benzothiadiazole derivatives with Lewis acid,<sup>14</sup> in the **3**-BF<sub>3</sub> adduct, BF<sub>3</sub> should bind to the nitrogen of each thia-

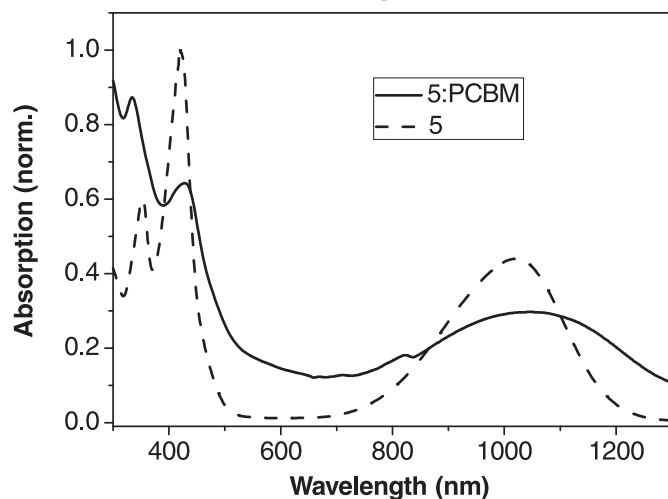
**Fig. 5.** Normalized absorption spectra of compound **3** ( $10^{-4}$  mol/L in THF) and a mixture of **3** with excess BF<sub>3</sub>.

diazole rings (Fig. 3), effectively pulling the electron density away from the BBTD unit, enhancing the ICT transition between peripheral donor and acceptor core, and thus leading to a significant bathochromic shift in absorption. Additionally, there is a synergistic lowering of the absolute energies of the two frontier molecular orbitals, thereby giving rise to the narrower band gap.

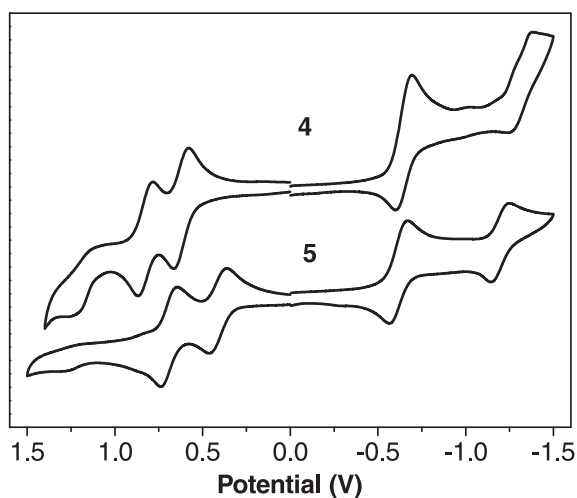
Considering the potential application of the D- $\pi$ -A- $\pi$ -D type of low-band-gap chromophores in photovoltaic cells, compound **5** was blended with PCBM and cast into films. Figure 6 shows the absorption spectrum of the blend film (1:1, w/w; solid line) and displays mainly three peaks centered at 333, 428, and 1046 nm, respectively. Compared with the absorption spectrum of **5**, the peak at 333 nm increases, which was due to the absorption of PCBM. Additionally, the ICT transition peak becomes broad and is red-shifted (about 26 nm). Thus, there is additional charge transfer interaction in the blend, which is likely due to the one between the acceptor and PCBM and similar to the effect of adding a Lewis acid to the chromophores.

The electrochemical properties of compounds **4** and **5** were investigated by CV (Fig. 7), and the data are summarized in Table 1. They are all electrochemically active, having two reversible oxidation and two reduction waves in the cyclic voltammogram, respectively. The first reduction potential is from the reduction of the BBTD core, and the first

**Fig. 6.** Absorption spectra of the blend film of compound **5** with PCBM (1:1, w/w; solid line) and compound **5**.



**Fig. 7.** Cyclic voltammograms of compounds **4** and **5** (1 mmol/L concentration).



oxidation wave is attributed to the oxidation of the donors and  $\pi$ -spacers. For chromophore **5**, the first oxidation potential increases significantly (about 0.2 eV); however, the reduction potentials keep nearly unchanged. The HOMO and LUMO levels of compounds **4** and **5** were calculated according to empirical equations of  $E_{(\text{HOMO})} = -(E_{\text{ox}} + 4.34)$  (eV) and  $E_{(\text{LUMO})} = -(E_{\text{red}} + 4.34)$  (eV), respectively. As shown, compound **5** has the band gap of 0.86 eV and absorbs at the longest wavelength (1020 nm) among chromophores **1–5**.

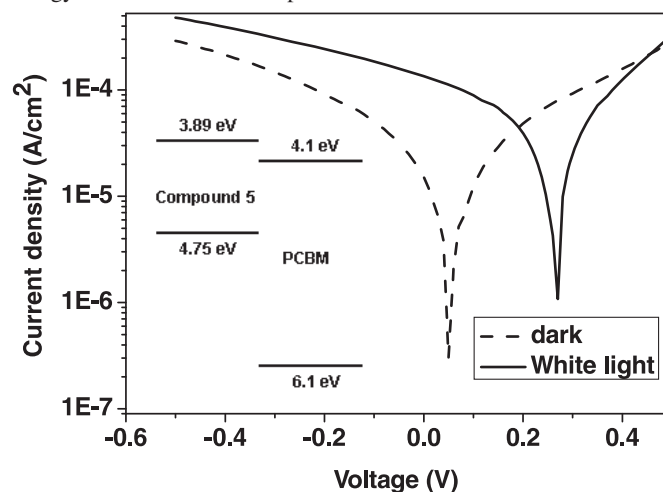
#### Photovoltaic property

Organic BHJ photovoltaic cells were fabricated using compound **5** as electron donor and PCBM as electron acceptor, with a structure configuration of ITO/PEDOT:PSS/**5**:PCBM/Al. Typical performance data of the devices are listed in Table 2, and the corresponding current–voltage curves are illustrated in Fig. 8. Without optimization, the device gave power conversion efficiency (PCE) of 0.01% with an open-circuit voltage ( $V_{\text{oc}}$ ) of 0.27 V and a short-circuit

**Table 2.** Performance of photovoltaic device under illumination of 100 mW/cm<sup>2</sup> white light.

Material	$V_{\text{oc}}$ (V)	$J_{\text{sc}}$ (mA/cm <sup>2</sup> )	FF	PCE (%)
<b>5</b> :PCBM (1:1, w/w)	0.27	0.13	0.28	0.01

**Fig. 8.** Current density–voltage curves of solar-cell devices in dark and under illumination of 100 mW/cm<sup>2</sup> white light. Inset: Proposed energy-level scheme of compound **5** and PCBM.

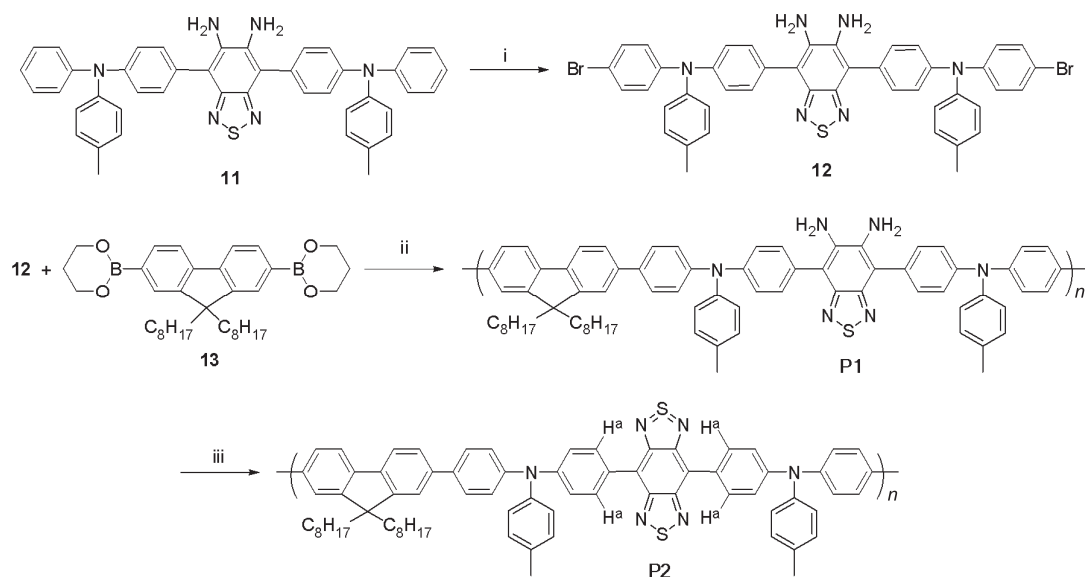


current ( $J_{\text{sc}}$ ) of 0.13 mA/cm<sup>2</sup> under AM 1.5 solar simulator (100 mW/cm<sup>2</sup>). Accordingly, a fill factor (FF) was calculated to be 0.28. For BHJ devices,  $V_{\text{oc}}$  is linearly correlated with the energy difference of the HOMO of the donor and the LUMO of the acceptor. Our result (0.27 V) coincides well with the empirical calculation.<sup>20</sup> The relatively low  $V_{\text{oc}}$  is likely due to the high HOMO level of the donor (Fig. 8, inset). The  $J_{\text{sc}}$  is determined by the amount of absorbed light and the internal conversion.<sup>21</sup> The absorption profile of the active layer shows a quiet mismatch to the solar photon flux, thus leading to the quite low  $J_{\text{sc}}$ . Nevertheless, the device based on low-band-gap chromophore **5** is still comparable well to some other solution-processed molecular BHJ solar cells.

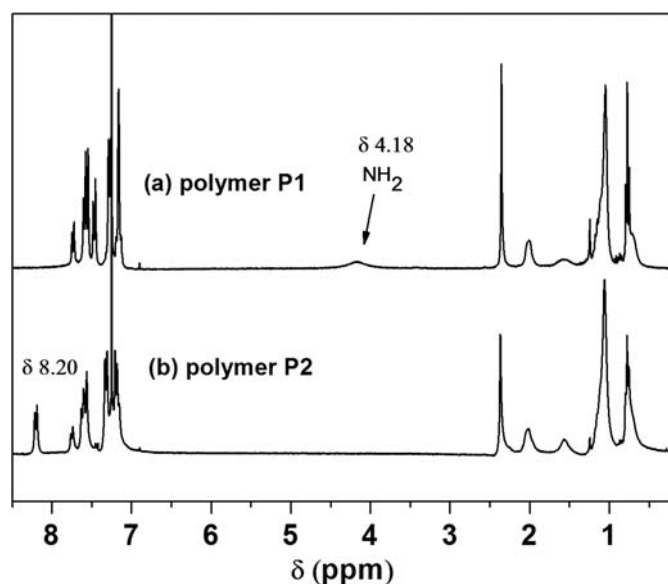
#### Design and synthesis of low-band-gap polymer

The band gap of polymers can be reduced by incorporating alternating donor and acceptor moieties in the polymer main chain. BBTD is a strong electron acceptor and can be used by design to construct many different kinds of low-band-gap polymers. However, because the BBTD unit is unstable in alkaline solution and readily attacked by nucleophiles (e.g., OH<sup>−</sup>), the polymers containing the BBTD moiety are often difficult to be synthesized by the Suzuki coupling reaction or other methods that need to use a base. Up to now, several polymers containing BBTD have been reported,<sup>22</sup> and are mainly synthesized by the Stille coupling reaction or electrochemical polymerization. However, the required tributylstannane monomers for the Stille polymerization are toxic and difficult to purify, and electrochemical polymerization is difficult to produce high-molecular-weight soluble polymers. Therefore, it remains a challenge to synthesize high-molecular-weight low-band-gap polymers containing BBTD unit.

**Scheme 2.** Synthetic routes to polymers **P1** and **P2**. Reagents and conditions: (i) Bu<sub>4</sub>NBr<sub>3</sub>, CH<sub>2</sub>Cl<sub>2</sub>, 25 °C, 3 h; (ii) Pd(PPh<sub>3</sub>)<sub>4</sub>, K<sub>2</sub>CO<sub>3</sub> (aq., 2 mol/L), toluene, Aliquat 336, 95 °C, 24 h; (iii) PhNSO, TMSCl, pyridine, 80 °C, overnight.

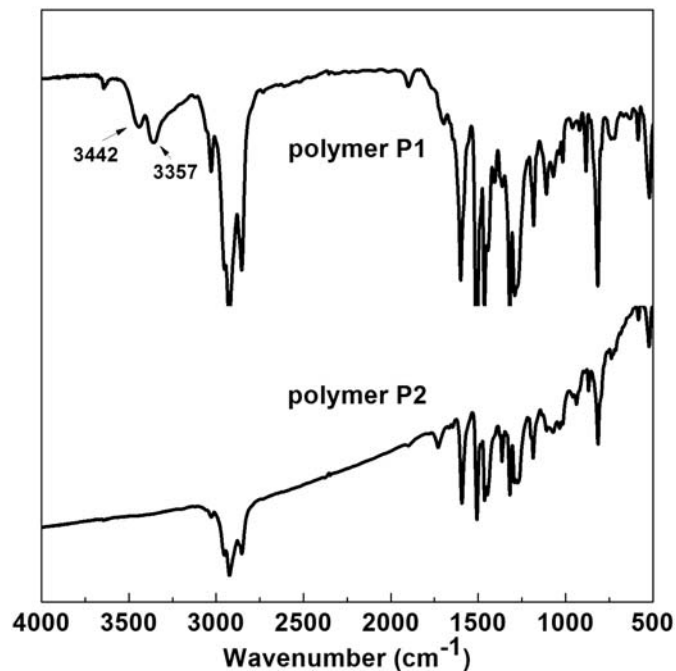


**Fig. 9.** <sup>1</sup>H NMR spectra (300 MHz, CDCl<sub>3</sub>) of polymers **P1** and **P2**.



In this work, we intend to explore a precursor approach to introduction of the BBTD unit in polymers. The feasibility of such a precursor approach is based on the fact that the monomers containing the 1,2-diaminophenylene group can be utilized in the Suzuki coupling reaction to produce high-molecular-weight polymers,<sup>23</sup> and the 1,2-diaminophenylene group can be converted into various electron-deficient groups (e.g., quinoxaline and benzothiadiazole).<sup>24</sup> Therefore, we demonstrated this precursor strategy by making the precursor polymer **P1** and subsequently converting to the BBTD-containing polymer **P2** (Scheme 2). The monomer **12** was prepared by bromination of compound **11** with tetrabutylammonium tribromide. Because of the presence of the

**Fig. 10.** IR spectra of polymers **P1** and **P2**.



methyl group on one of the two phenyl groups, bromination only takes place at one of the phenyl rings of the diphenylamino moiety in **11**. Using the Suzuki cross-coupling reaction, polymerization of monomers **12** and **13** gave the precursor polymer **P1**. By simple treatment of **P1** with *N*-sulfinylaniline and chlorotrimethylsilane in dry pyridine, the target low-band-gap polymer **P2** was readily obtained with high yield (89%).

#### Structural characterization

The chemical structures of polymers **P1** and **P2** were fully characterized by NMR and IR spectroscopic methods. Fig-

**Table 3.** Characterization of Polymers **P1** and **P2**.

Polymer	$M_n^a$ ( $\times 10^3$ )	$M_w^a$ ( $\times 10^3$ )	PDI	$\lambda_{\text{max}}^{\text{abs}}$ (nm) <sup>b</sup>	Log $\epsilon$	$\lambda_{\text{max}}^{\text{PL}}$ (nm) <sup>b</sup>	Stokes shifts (nm) <sup>b</sup>	Band gap (eV) <sup>c</sup>
<b>P1</b>	56	179	3.2	371, 440 (sh) <sup>d</sup>	NA	558	187	2.67
<b>P2</b>	28	75	2.7	749	4.39	980	231	1.41

<sup>a</sup>Determined by GPC.<sup>b</sup>Measured in chlorobenzene, excitation wavelengths for **P1** and **P2** are at their maximum absorption wavelengths.<sup>c</sup>Optical band gap, estimated from the onset wavelength of optical absorption spectra.<sup>d</sup>Shoulder peak.

ure 9a shows the  $^1\text{H}$  NMR spectrum of polymer **P1**. A peak at  $\delta$  4.18 ppm is assigned to the amine hydrogen and the aliphatic and aromatic hydrogens are observed at  $\delta$  0.6–2.5 and  $\delta$  7.1–7.7 ppm, respectively. After conversion of the diamine into the thiadiazole group, the peak at  $\delta$  4.18 disappeared (Fig. 9b), indicating that the transformation reaction was successful and the amino group was converted completely. A new peak at  $\delta$  8.20 is assigned to the hydrogens in the phenylene that is adjacent to the BBTD core ( $\text{H}^a$  shown in Scheme 2). Because of the strong electron-withdrawing BBTD unit, the signal of  $\text{H}^a$  shifted to a lower field. The observed chemical shift ( $\delta$  8.20) coincides well with that of a small compound with similar structure ( $\delta$  8.18),<sup>12b</sup> further demonstrating the formation of the BBTD unit in **P2**. The IR spectrum of polymer **P1** (Fig. 10) shows two distinct  $\nu(\text{NH})$  bands at 3442 and 3357  $\text{cm}^{-1}$ , which, as expected, are absent in the spectrum of **P2** (Fig. 10).

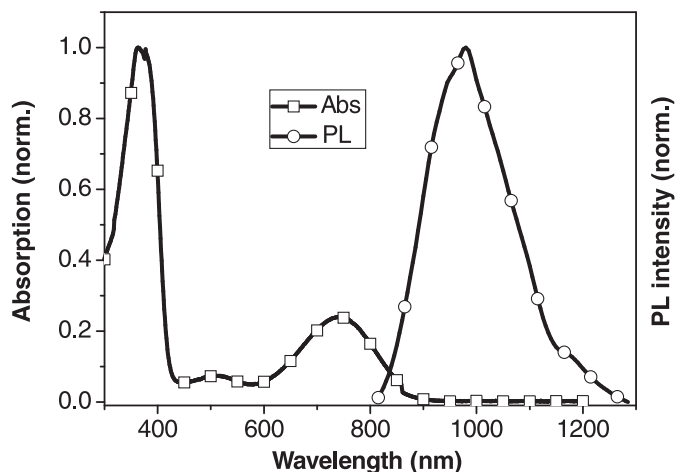
The molecular weights were estimated by gel-permeation chromatography (THF as eluent) relative to polystyrene standards. Polymer **P1** shows high molecular weight with the number-average molecular weight ( $M_n$ ) of 56 000 g/mol and a polydispersity index of 3.2 (Table 3). The apparent  $M_n$  of **P2** was found to be only 28 000 g/mol, although it should be the same or similar to that of **P1**, which was mainly due to poor solubility of the high-molecular-weight fraction of **P2** in THF.

### Optical property

The absorption and photoluminescence of polymers **P1** and **P2** were recorded in chlorobenzene. Without a strong acceptor or strong intramolecular charge transfer, **P1** absorbs in the visible spectral region with a maximum ( $\lambda_{\text{max}}$ ) at 440 nm and emits at 558 nm. In comparison, owing to the presence of the BBTD acceptor, the absorption and emission maxima of **P2** were red-shifted dramatically to 749 and 980 nm, respectively (Table 3 and Fig. 11). Similar to chromophores **1–5**, the absorption bands of polymer **P2** mainly have two parts. The peaks in the higher energy region are attributed to the  $\pi$ – $\pi^*$  and also possible  $n$ – $\pi^*$  transitions of the conjugated aromatic segments. The high molar extinction coefficient (Log  $\epsilon$  = 4.39) of the ICT band of **P2** is ideal for photovoltaic application. The optical band-gap levels of **P1** and **P2** were estimated from the onset wavelength ( $\lambda_{\text{onset}}$ ) of the optical absorption spectra to be 2.7 and 1.4 eV, respectively.

### Conclusions

A novel D– $\pi$ –A– $\pi$ –D type of low-band-gap (0.86 eV) chromophore **5** has been successfully designed and synthesized. The use of pyrrole as  $\pi$ -spacer is proven to be effective and beneficial in further lowering the band-gap level of

**Fig. 11.** Absorption and fluorescence emission of polymer **P2** in chlorobenzene.

and beneficial in further lowering the band-gap level of the D– $\pi$ –A– $\pi$ –D chromophores. Compared with the thiophene spacer (in compound **3**), the pyrrole spacer provides the intramolecular hydrogen bonding to the BBTD acceptor, which pushes the absorption maximum and fluorescence emission of chromophore **5** into the near-infrared spectral region with a red shift of 172 and 158 nm, respectively. A precursor approach to the introduction of the alkaline-labile BBTD acceptor into the polymer backbone has been demonstrated by successful synthesis of low-band-gap polymer **P2**. The same strategy can be in principle applied to the synthesis of a series of low-band-gap polymers with the structures and properties similar to chromophores **1–5**.

### Acknowledgement

This work was supported by the Natural Sciences and Engineering Research Council of Canada (NSERC).

### References

- (1) Roncali, J. *Macromol. Rapid Commun.* **2007**, 28 (17), 1761. doi:10.1002/marc.200700345.
- (2) (a) Dhanabalan, A.; van Duren, J. K. J.; van Hal, P. A.; van Dongen, J. L. J.; Janssen, R. A. J. *Adv. Funct. Mater.* **2001**, 11 (4), 255. doi:10.1002/1616-3028(200108)11:4<255::AID-ADFM255>3.0.CO;2-I; (b) van Duren, J. K. J.; Dhanabalan, A.; van Hal, P. A.; Janssen, R. A. J. *Synth. Met.* **2001**, 121 (1-3), 1587. doi:10.1016/S0379-6779(00)01307-2; (c) Neugebauer, H.; Kvarnström, C.; Brabec, C.; Sariciftci, N. S.; Kiebooms, R.; Wudl, F.; Luzzati, S. J. *Chem. Phys.* **1999**, 110 (24), 12108. doi:10.1063/1.479146.



- (3) Meek, S. T.; Nesterov, E. E.; Swager, T. M. *Org. Lett.* **2008**, *10* (14), 2991. doi:10.1021/ol800988w. PMID:18563902.
- (4) Qian, G.; Li, X.; Wang, Z. Y. *J. Mater. Chem.* **2009**, *19* (4), 522. doi:10.1039/b813478b.
- (5) (a) Kido, J.; Okamoto, Y. *Chem. Rev.* **2002**, *102* (6), 2357. doi:10.1021/cr010448y. PMID:12059271.; (b) Zang, F. X.; Hong, Z. R.; Li, W. L.; Li, M. T.; Sun, X. Y. *Appl. Phys. Lett.* **2004**, *84* (14), 2679. doi:10.1063/1.1695098.; (c) Slo-off, L. H.; Polman, A.; Cacialli, F.; Friend, R. H.; Hebbink, G. A.; van Veggel, F. C. J. M.; Reinhoudt, D. N. *Appl. Phys. Lett.* **2001**, *78* (15), 2122. doi:10.1063/1.1359782.; (d) Curry, R. J.; Gillin, W. P. *Appl. Phys. Lett.* **1999**, *75* (10), 1380. doi:10.1063/1.124700.; (e) Kang, T.-S.; Harrison, B. S.; Foley, T. J.; Knefely, A. S.; Boncella, J. M.; Reynolds, J. R.; Schanze, K. S. *Adv. Mater.* **2003**, *15* (13), 1093. doi:10.1002/adma.200304692.
- (6) (a) Borek, C.; Hanson, K.; Djurovich, P. I.; Thompson, M. E.; Aznavour, K.; Bau, R.; Sun, Y.; Forrest, S. R.; Brooks, J.; Michalski, L.; Brown, J. *J. Angew. Chem. Int. Ed.* **2007**, *46* (7), 1109. doi:10.1002/anie.200604240.; (b) Sun, Y.; Borek, C.; Hanson, K.; Djurovich, P. I.; Thompson, M. E.; Brooks, J.; Brown, J. J.; Forrest, S. R. *Appl. Phys. Lett.* **2007**, *90* (21), 213503. doi:10.1063/1.2740113.; (c) Cheng, C. H.; Fan, Z. Q.; Yu, S. K.; Jiang, W. H.; Wang, X.; Du, G. T.; Chang, Y. C.; Ma, C. Y. *Appl. Phys. Lett.* **2006**, *88* (21), 213505. doi:10.1063/1.2206678.; (d) Rosenow, T. C.; Walzer, K.; Leo, K. *J. Appl. Phys.* **2008**, *103* (4), 043105. doi:10.1063/1.2888362.; (e) Guo, Z.-G.; Cheng, C.-H.; Fan, Z.-Q.; He, W.; Yu, S.-K.; Chang, Y.-C.; Du, X.-G.; Wang, X.; Du, G.-T. *Chin. Phys. Lett.* **2008**, *25* (2), 715. doi:10.1088/0256-307X/25/2/098.
- (7) (a) Casalboni, M.; De Matteis, F.; Proposito, P.; Pizzoferrato, R. *Appl. Phys. Lett.* **1999**, *75* (15), 2172. doi:10.1063/1.124955.; (b) Suzuki, H. *Appl. Phys. Lett.* **2000**, *76* (12), 1543. doi:10.1063/1.126090.; (c) Suzuki, H. *Appl. Phys. Lett.* **2002**, *80* (18), 3256. doi:10.1063/1.1476711.; (d) Suzuki, H.; Ogura, K.; Matsumoto, N.; Proposito, P.; Schutzmann, S. *Mol. Cryst. Liq. Cryst. (Phila. Pa.)* **2006**, *444* (1), 51. doi:10.1080/15421400500379806.
- (8) (a) Yang, R.; Tian, R.; Yan, J.; Zhang, Y.; Yang, J.; Hou, Q.; Yang, W.; Zhang, C.; Cao, Y. *Macromolecules* **2005**, *38* (2), 244. doi:10.1021/ma047969i.; (b) Li, X.; Zeng, W.; Zhang, Y.; Hou, Q.; Yang, W.; Cao, Y. *Eur. Polym. J.* **2005**, *41* (12), 2923. doi:10.1016/j.eurpolymj.2005.05.039.; (c) Thompson, B. C.; Madrigal, L. G.; Pinto, M. R.; Kang, T.-S.; Schanze, K. S.; Reynolds, J. R. *J. Polym. Sci. Part Polym. Chem.* **2005**, *43* (7), 1417. doi:10.1002/pola.20578.; (d) Baigent, D. R.; Hamer, P. J.; Friend, R. H.; Moratti, S. C.; Holmes, A. B. *Synth. Met.* **1995**, *71* (1-3), 2175. doi:10.1016/0379-6779(94)03208-N.; (e) Chen, M.; Perzon, E.; Andersson, M. R.; Marcinkevicius, S.; Jönsson, S. K. M.; Fahlman, M.; Berggren, M. *Appl. Phys. Lett.* **2004**, *84* (18), 3570. doi:10.1063/1.1737064.
- (9) Yao, Y.; Liang, Y.; Shrotriya, V.; Xiao, S.; Yu, L.; Yang, Y. *Adv. Mater.* **2007**, *19* (22), 3979. doi:10.1002/adma.200602670.
- (10) Bundgaard, E.; Krebs, F. C. *Sol. Energy Mater. Sol. Cells* **2007**, *91* (11), 954. doi:10.1016/j.solmat.2007.01.015.
- (11) (a) Hou, J.; Chen, H. Y.; Zhang, S.; Li, G.; Yang, Y. *J. Am. Chem. Soc.* **2008**, *130* (48), 16144. doi:10.1021/ja806687u. PMID:18989961.; (b) Peet, J.; Kim, J. Y.; Coates, N. E.; Ma, W. L.; Moses, D.; Heeger, A. J.; Bazan, G. C. *Nat. Mater.* **2007**, *6* (7), 497. doi:10.1038/nmat1928. PMID:17529968.; (c) Kim, J. Y.; Lee, K.; Coates, N. E.; Moses, D.; Nguyen, T. Q.; Dante, M.; Heeger, A. J. *Science* **2007**, *317* (5835), 222. doi:10.1126/science.1141711. PMID:17626879.
- (12) (a) Qian, G.; Dai, B.; Luo, M.; Yu, D.; Zhan, J.; Zhang, Z.; Ma, D.; Wang, Z. Y. *Chem. Mater.* **2008**, *20* (19), 6208. doi:10.1021/cm801911n.; (b) Qian, G.; Zhong, Z.; Luo, M.; Yu, D.; Zhang, Z.; Wang, Z. Y.; Ma, D. *Adv. Mater.* **2009**, *21* (1), 111. doi:10.1002/adma.200801918.
- (13) (a) Ono, K.; Tanaka, S.; Yamashita, Y. *Angew. Chem. Int. Ed. Engl.* **1994**, *33* (19), 1977. doi:10.1002/anie.199419771.; (b) Karikomi, M.; Kitamura, C.; Tanaka, S.; Yamashita, Y. *J. Am. Chem. Soc.* **1995**, *117* (25), 6791. doi:10.1021/ja00130a024.; (c) Kitamura, C.; Tanaka, S.; Yamashita, Y. *Chem. Mater.* **1996**, *8* (2), 570. doi:10.1021/cm950467m.; (d) Yamashita, Y.; Ono, K.; Tomura, M.; Tanaka, S. *Tetrahedron* **1997**, *53* (29), 10169. doi:10.1016/S0040-4020(97)00356-6.
- (14) Welch, G. C.; Coffin, R.; Peet, J.; Bazan, G. C. *J. Am. Chem. Soc.* **2009**, *131* (31), 10802. doi:10.1021/ja902789w. PMID:19586021.
- (15) Belletête, M.; Beaupré, S.; Bouchard, J.; Blondin, P.; Leclerc, M.; Durocher, G. *J. Phys. Chem. B* **2000**, *104* (39), 9118. doi:10.1021/jp001349b.
- (16) Salman, H.; Abraham, Y.; Tal, S.; Meltzman, S.; Kapon, M.; Tessler, N.; Speiser, S.; Eichen, Y. *Eur. J. Org. Chem.* **2005**, *2005* (11), 2207. doi:10.1002/ejoc.200500012.
- (17) Yu, W.-L.; Pei, J.; Cao, Y.; Huang, W.; Heeger, A. J. *Chem. Commun* **1999**, 1837. doi:10.1039/a905482k.
- (18) Basarić, N.; Baruah, M.; Qin, W.; Metten, B.; Smet, M.; Dehaen, W.; Boens, N. *Org. Biomol. Chem.* **2005**, *3* (15), 2755. doi:10.1039/b505969k. PMID:16032354.
- (19) (a) van Mullekom, H. A. M.; Vekemans, J. A. J. M.; Meijer, E. W. *Chem. Eur. J.* **1998**, *4* (7), 1235. doi:10.1002/(SICI)1521-3765(19980710)4:7<1235::AID-CHEM1235>3.0.CO;2-4.; (b) Palmans, A. R. A.; Vekemans, J. A. J. M.; Meijer, E. W. *Recl. Trav. Chim. Pays Bas* **1995**, *114*, 277.; (c) Palmans, A. R. A.; Vekemans, J. A. J. M.; Fischer, H.; Hikmet, R. A.; Meijer, E. W. *Chem. Eur. J.* **1997**, *3* (2), 300. doi:10.1002/chem.19970030220.
- (20) Scharber, M. C.; Mühlbacher, D.; Koppe, M.; Denk, P.; Waldauf, C.; Heeger, A. J.; Brabec, C. J. *Adv. Mater.* **2006**, *18* (6), 789. doi:10.1002/adma.200501717.
- (21) Winder, C.; Sariciftci, N. S. *J. Mater. Chem.* **2004**, *14* (7), 1077. doi:10.1039/b306630d.
- (22) (a) Steckler, T. T.; Abboud, K. A.; Craps, M.; Rinzler, A. G.; Reynolds, J. R. *Chem. Commun. (Camb.)* **2007**, (46): 4904. doi:10.1039/b709672k. PMID:18361364. (b) Bundgaard, E.; Krebs, F. C. *Macromolecules* **2006**, *39* (8), 2823. doi:10.1021/ma052683e.
- (23) Yamaguchi, I.; Choi, B.-J.; Koizumi, T.-aki.; Kubota, K.; Yamamoto, T. *Macromolecules* **2007**, *40* (3), 438. doi:10.1021/ma062107y.
- (24) (a) Yamamoto, T.; Sugiyama, K.; Kanbara, T.; Hayashi, H.; Etori, H. *Macromol. Chem. Phys.* **1998**, *199* (9), 1807. doi:10.1002/(SICI)1521-3935(19980901)199:9<1807::AID-MACP1807>3.0.CO;2-2.; (b) Alam, M. M.; Jenekhe, S. A. *Chem. Mater.* **2002**, *14* (11), 4775. doi:10.1021/cm020600s.; (c) Tanimoto, A.; Shiraishi, K.; Yamamoto, T. *Bull. Chem. Soc. Jpn.* **2004**, *77* (3), 597. doi:10.1246/bcsj.77.597.; (d) Yamamoto, T.; Sugiyama, K.; Kushida, T.; Inoue, T.; Kanbara, T. *J. Am. Chem. Soc.* **1996**, *118*, 3930. doi:10.1021/ja954173d.; (e) Jenekhe, S. A.; Zhang, X.; Chen, X. L.; Choong, V.-E.; Gao, Y.; Hsieh, B. R. *Chem. Mater.* **1997**, *9* (2), 409. doi:10.1021/cm960474q.; (f) Ito, Y.; Miyake, T.; Hatano, S.; Shima, R.; Ohara, T.; Sugino, M. *J. Am. Chem. Soc.* **1998**, *120* (46), 11880. doi:10.1021/ja982500m.

# NMR imaging study of cross-linked high-amylose starch tablets — The effect of drug loading

Y.J. Wang, F. Ravenelle, and X.X. Zhu

**Abstract:** NMR imaging techniques were used to study the effect of drug loading in cross-linked high-amylose starch tablets. The tablets contained acetaminophen with loading levels from 10 to 40 wt%. The absolute amount of the drug released increased with a larger amount of drug loading, but the percentages of drug released had only minor differences for the different tablets, probably due to the rapid formation of a gel layer for all the tablets, which slowed down drug release significantly. The release of drugs from the tablets in all cases is dominated by a diffusion mechanism before the disappearance of the dry core of the tablets. Radial and axial swelling and water uptake were found to increase with the amount of drug loading. The diffusion rates of water were comparable at the initial stage for all the tablets with different loadings, but became faster later for the tablets with higher amounts of drug loading as water diffusion may be facilitated by the hydrophilicity of the drug.

**Key words:** NMR imaging, diffusion coefficient, high-amylose starch, drug loading.

**Résumé :** Les techniques d'imagerie RMN ont été utilisées pour étudier l'effet de la charge en médicament dans les tablettes d'amidon réticulés riche en amylose. Les tablettes contenaient un médicament, l'acétaminophène, de 10 à 40 pour-cent en poids. La quantité absolue du médicament libéré augmente avec une augmentation de la charge en médicament, mais les pourcentages de médicament libéré n'ont que des différences mineures pour les différentes tablettes, probablement à cause d'une formation rapide d'une couche de gel autour de toutes les tablettes qui ralentit d'une façon significative la libération du médicament. Les libérations de médicaments sont dominées dans tous les cas par un mécanisme de diffusion avant la disparition du cœur sec des tablettes. On a trouvé que les gonflements radiaux et axiaux ainsi que l'absorption d'eau augmentent avec une augmentation de la charge en médicament. Les vitesses de diffusion de l'eau dans la période initiale sont comparables pour toutes les tablettes comportant des charges différentes de médicament, mais plus tard elles deviennent plus rapides pour les tablettes portant une quantité plus élevée de médicament, probablement en raison du fait que la diffusion est peut-être facilitée par le caractère hydrophile du médicament.

**Mots-clés :** imagerie RMN, coefficient de diffusion, amidon à forte concentration d'amylose, charge en médicament.

## Introduction

Cross-linked high-amylose starch (CHAS) has been demonstrated to be an effective controlled release matrix.<sup>1-4</sup> Once the CHAS tablets are hydrated, a consistent gel layer is formed very rapidly around the tablet core, leading to retarded release of drugs.<sup>5</sup> The integrity of the CHAS tablets is sustained for over 48 h.<sup>6</sup> We have used NMR imaging to study the effects of tablet size, temperature, and drug loading on the tablet swelling and water diffusion.<sup>5-8</sup> The effect of moisture content on the swelling of high-amylose starch films was also studied by the use of NMR imaging by Russo et al.<sup>9</sup> In addition, the conversion from V-type (single helix) to B-type (double helices), which limits the swelling of starch, was also revealed by CP-MAS <sup>13</sup>C solid-state NMR spectroscopy.<sup>10</sup>

The drug release mechanism is classified into three cases:

diffusion mechanism, polymer relaxation mechanism, and a mechanism that lies between the two cases. It was found for ethyl cellulose tablets that drug release is controlled by a diffusion mechanism at a high loading of acetaminophen (APAP, 49.5 wt%), while the effect of the polymer relaxation becomes significant at a low loading (9.9 wt%).<sup>11</sup> In the case of poly(ethylene oxide) (PEO) tablets, the drug dissolution and diffusion through the swollen gel layer controlled the release at loading levels of 39% and 20%, respectively.<sup>12</sup> Previously, we have studied the release of two drugs, ciprofloxacin and acetaminophen, loaded at 10 wt% in CHAS.<sup>5</sup> The amount of drug loading may also have a significant effect on the amount released from the polymer tablets. APAP is an analgesic (pain reliever) and an antipyretic (fever reducer), which has been used as a probe to study controlled release properties of some matrices, including hydroxypropyl methyl cellulose (HPMC),<sup>13</sup>

Received 20 September 2009. Accepted 6 November 2009. Published on the NRC Research Press Web site at [canjchem.nrc.ca](http://canjchem.nrc.ca) on 6 February 2010.

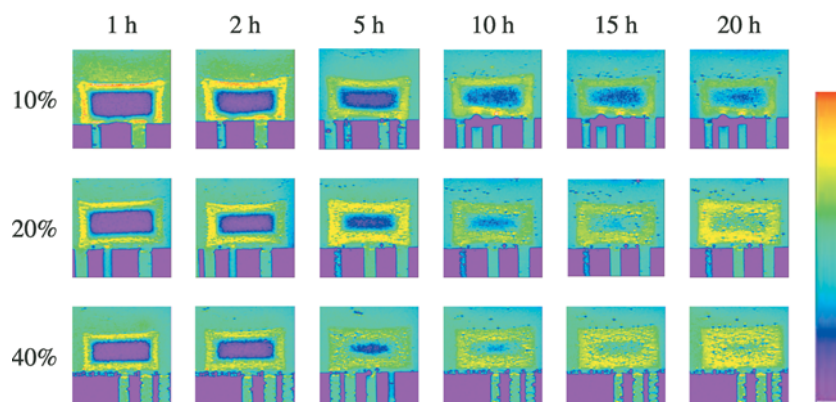
*This article is part of a Special Issue dedicated to Professor M. A. Winnik.*

**Y.J. Wang, F. Ravenelle,<sup>1</sup> and X.X. Zhu.<sup>2</sup>** Département de Chimie, Université de Montréal, C. P. 6128, Succursale Centre-ville, Montréal, QC H3C 3J7, Canada.

<sup>1</sup>Present address: Theratechnologies Inc., 2310 Boul. Alfred-Nobel, Montréal, QC H4S 2B4, Canada.

<sup>2</sup>Corresponding author (e-mail: [julian.zhu@umontreal.ca](mailto:julian.zhu@umontreal.ca)).

**Fig. 1.** NMR images of CHAS tablets immersed in water at 37 °C for 1, 2, 5, 10, 15, and 20 h. The purple part at the bottom of images is the Teflon support.



HPMC-polyvinylpyrrolidone,<sup>14</sup> and high-amylose sodium carboxymethyl starch matrices.<sup>15</sup> We also chose APAP in this study with loadings of 10, 20, and 40 wt% in the CHAS tablets. In vitro drug release from the matrix tablets was determined and the results were correlated with swelling and water uptake of the tablets. The diffusion coefficients of water can be obtained from profile fitting and diffusion-weighted NMR images.

## Experimental

### Preparation of tablets

The polymer (CHAS) was made of chemically modified high-amylose starch (70% amylose), cross-linked with 0.075 wt% phosphorous oxychloride in a mild alkaline medium first and further functionalized with 6 wt% of propylene oxide followed by washing and drying. Gelatinization of the starch under 160 °C and 5.5 bar (1 bar = 100 kPa) was then conducted immediately prior to spray drying. An appropriate amount of granulated acetaminophen (Compap, MW 151 g/mol,  $R_h$  0.37 nm) and CHAS were mixed for 4 min. The blend was compressed to form tablets of 200 mg, each with a dimension of 9.0 mm × 3.0 mm. To achieve the target weight and thickness for the tablets, the press parameters were adjusted to 1330 kg/cm<sup>2</sup> for 10–20 wt% drug loadings and 785 kg/cm<sup>2</sup> for 40 wt% drug loading along the axial direction. Dosages with drug loadings of 10, 20, and 40 wt% were obtained.

### NMR imaging

All NMR imaging experiments were carried out at 37.0 °C on a Bruker Advance-400 NMR spectrometer operating at a frequency of 400.27 MHz for protons equipped with a microimaging probe having a 20 mm inner diameter. A standard spin-echo pulse sequence was used to obtain spin density images of the tablets in a 20 mm o.d. NMR tube containing 20 mL of distilled water. A slice of 0.5 mm in thickness was selected either perpendicular or parallel to the main magnetic field using a sinc-shaped pulse. Eight scans were accumulated to obtain 128 × 128 pixel images for a field of view of 2.0 cm, leading to an in-plane resolution of 156 μm. An echo time (TE) of 3 ms and a repetition time (TR) of 1 s were fixed leading to an acquisition time of about 17 min for each image.

Diffusion-weighted images were acquired by combining the spin-echo pulse sequence with the pulsed-gradient spin-echo (PGSE) pulse sequence developed by Stejskal and Tanner.<sup>16</sup> The diffusion time ( $\Delta$ ) and the length of the gradient pulse ( $\delta$ ) were 10 ms and 2 ms, respectively. The gradient strength varied from 5 to 100 G/cm.

### Solubility tests of CHAS

The CHAS powder (300 mg) was mixed with 20 mL distilled water in a 50 mL centrifuge tube, which was then placed in a shaking bath and agitated at 100 rpm and 37 °C for 30 min. The samples were centrifuged (4000 rpm, 1 h) and the supernatant was collected and dried at 70 °C for soluble fraction quantification. The test was performed in triplicate.

### Water uptake experiments

Water uptake studies were carried out in a water bath at 37 °C with mild agitation. Each tablet was immersed in 20 mL distilled water and the weight was measured in triplicate at predetermined time intervals. The percentage of mass uptake is defined as

$$[1] \quad S_t = \frac{M_t - M_0}{M_0} \times 100\%$$

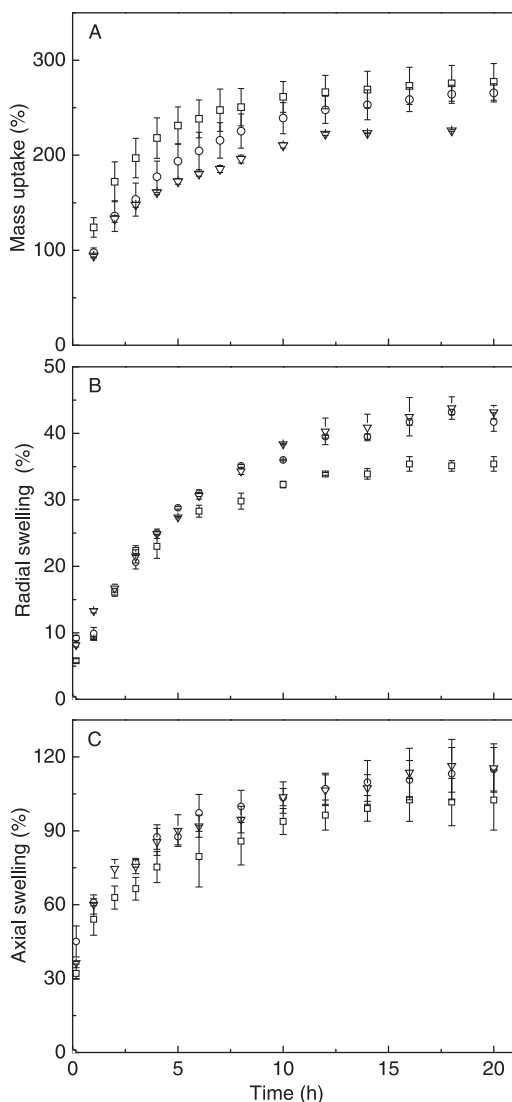
where  $S_t$  is the water uptake in percentage,  $M_0$  and  $M_t$  are the initial weight of a tablet and its weight at time  $t$ , respectively.

### In vitro drug release tests

The tablets were placed individually in 900 mL of distilled water at 37 °C in a U.S.P. XXIV dissolution apparatus 2 (Distek Premiere 5100 dissolution system) equipped with a rotating paddle (100 rpm). The amount of drug released from the tablet in 24 h was determined spectrophotometrically (244 nm) at intervals of 30 min. The sampling liquid flowed back to the vessels. All tablets were tested in triplicate.

The fitting of the data from NMR imaging experiments and of the drug release tests was carried out with Microsoft Excel 2003 using the Newton method to minimize the sum of the squared errors. A summation of 30 roots of the Bessel function was used.

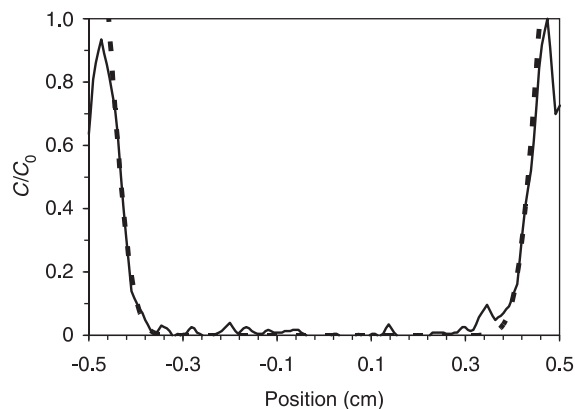
**Fig. 2.** (A) Mass uptake, (B) radial swelling, and (C) axial swelling of the CHAS tablets loaded with 10% ( $\square$ ), 20% ( $\circ$ ), and 40% ( $\nabla$ ) acetaminophen. Note that the mass uptake is the combined effect of the mass gain by the absorption of water and the mass loss by the release of the drug.



## Results and discussion

Figure 1 shows the NMR images of CHAS tablets acquired from 1 to 20 h in water at 37 °C. A gel layer formed quickly, within a few minutes after the tablets came into contact with water. All three images at 1 h clearly show the gel layer, the hydrated layer, and the dry core (with the lowest water signal). The formation of the gel layer is essential for the controlled release of the CHAS tablets. The apparent high water signal shown by the reddish periphery of the tablets is caused by the shorter longitudinal relaxation time,  $T_1$  (ca. 800 ms), of the hydrated layer compared with that of the free water (the green-bluish part, ca. 5 s). As the water front advanced towards the center, the dry core gradually diminished in dimension with immersion time. The effect of drug loading levels is visible on the images acquired at 5 h

**Fig. 3.** The water proton spin density profile (solid line) and the fit to eq. [2] (dashed line) of a CHAS tablet with 20% acetaminophen swelled in water at 37 °C for 30 min.



and onward. At 20 h, water is distributed almost evenly in the tablet of 40% APAP, while the tablet of 10% APAP is still far from reaching equilibrium (Fig. 1). NMR imaging experiments showed the tablets with 10% APAP loading reached equilibrium after 50 h. Therefore, the diffusion of water inside the tablets depends on the amount of APAP inside. It is to be noted that the movement of water into the tablet in the presence of the drug may not be strictly diffusional as the contribution of osmotic convection at the beginning stages of the process is present.

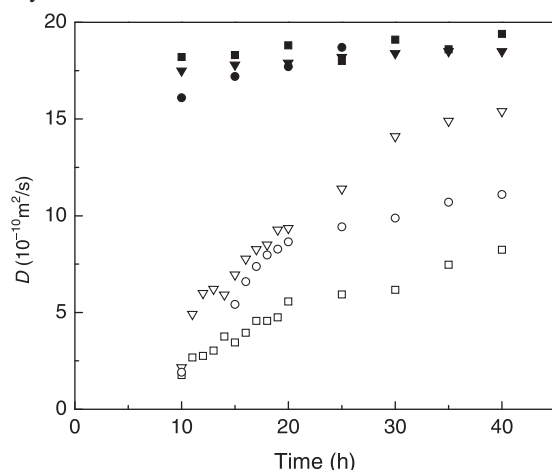
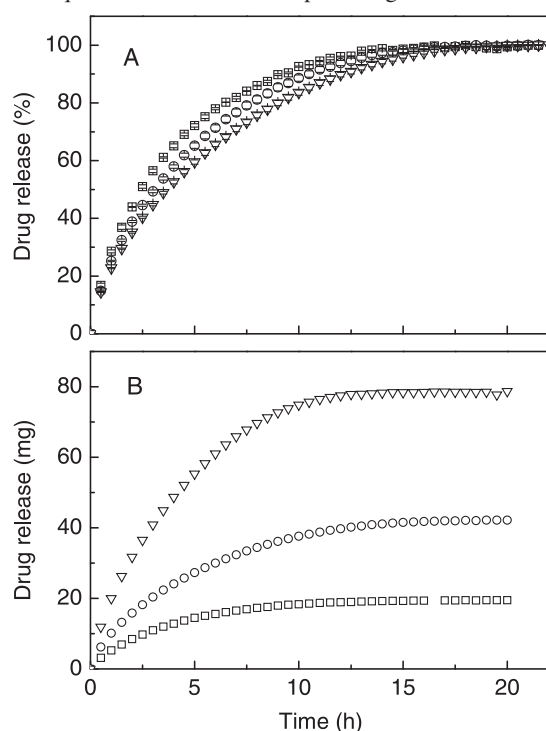
Figure 2A shows the mass uptake of tablets. Overall, the amount of mass change is contributed by the weight gain due to water diffused into the tablets and by the weight loss due to drug release from the tablets. The solubility of CHAS in water (2.6 mg/mL) is much lower than that of APAP (14.5 mg/mL, U.S.P. XXIV) so that the amount of dissolved CHAS can be neglected, but frequent manipulations may also cause weight loss and thus the mass uptake may be underestimated. In general, the tablets with a higher amount of drug loading had a lower gain in mass. The difference between the mass uptake at equilibrium is close to the difference between drug loading levels. The tablet with low drug loading had a faster increase in mass and reached an equilibrium earlier in time. Clearly, the tablets of 40% APAP undergo the highest weight loss due to drug release. In addition, the gel layers formed on these tablets are softer than the gel layers formed on tablets with lower drug loading levels, which is clearly visible, so these layers are less resistant to erosion.

Figures 2B and 2C show the radial and axial swelling of the tablets, respectively. The extent of axial swelling is almost three times that of the radial swelling for all the tablets, which has been observed for the CHAS tablets with and without the drug.<sup>5,6</sup> The higher axial swelling is caused by the compression along the axial direction during the preparation process. To prevent the floating and movement of the tablets in the liquid media, a piece of cotton ball was placed above the tablet to keep it in place during the NMR imaging experiments, which may have caused the relatively higher standard deviations of axial swellings in comparison to those of radial swellings. The tablets with 10% loading have the lowest swelling, while the other two swell at a similar rate and reached a similar size. The drug APAP has a



**Table 1.** The initial diffusion coefficients of water fitted to eq. [2] and the average diffusion coefficients fitted to eq. [5] in the CHAS tablets.

Drug loading (%)	Axial $D_0$	Radial $D_0$	$\bar{D}_0$ ( $10^{-11}$ m <sup>2</sup> s <sup>-1</sup> )	$\bar{D}_\infty$ ( $10^{-11}$ m <sup>2</sup> s <sup>-1</sup> )
10	6.50±0.16	5.15±1.06	2.38±0.21	13.6±2.1
20	7.11±0.45	3.32±0.62	1.82±0.04	12.3±0.1
40	7.63±0.30	4.19±0.53	1.98±0.19	16.2±2.5

**Fig. 4.** Diffusion coefficients of water in the inner core of the tablets loaded with 10% (□), 20% (○), and 40% (▽) acetaminophen obtained by diffusion-weighted imaging. The values corresponding to the hydrated gels of the tablets are shown by closed symbols.**Fig. 5.** Release of drugs of CHAS tablets loaded with 10% (□), 20% (○), and 40% (▽) acetaminophen. The amount of the drug released is quite different while the percentage remained similar.

higher hydrophilicity than the matrix, which facilitates the penetration of water and enhances the overall swelling in both axial and radial directions.

The measurement of diffusion coefficients of water ( $D$ ) inside of the CHAS tablets may provide quantitative information on the effect of drug loading on the mobility of the polymer matrix. The initial diffusion coefficient of water can be obtained from the water proton image profiles, an example of which is shown in Fig. 3. At the initial stage of swelling, a tablet can be treated as an infinite cylinder in which water diffusion follows Fick's second law of diffusion.<sup>6,17</sup> The initial diffusion coefficients of water (shown in Table 1) can be obtained from fitting the data to

$$[2] \quad \frac{C}{C_0} = 1 - 2 \sum_{n=1}^{\infty} \frac{J_0(x\alpha_n/r)}{\alpha_n J_1(\alpha_n)} e^{-D \frac{\alpha_n^2}{r^2} t}$$

where  $C$  and  $C_0$  are the concentrations of water at distance  $x$  and at the surface of the cylinder, respectively,  $r$  is the radius of the cylinder,  $D$  the diffusion coefficient of water,  $t$  the immersion time,  $J_0$  the Bessel function of the first kind of the order 0,  $J_1$  the Bessel function of the first kind of the order 1, and  $\alpha_n$  the  $n$ th root of  $J_0 = 0$ .<sup>18–21</sup>

At the beginning of immersion, the assumption of infinite cylinder is applicable and good fits to eq. [2] can be easily obtained, as exemplified by Fig. 3. The initial diffusion coefficients of water in CHAS tablets are comparable for all three tablets with different drug loading levels along both directions (Table 1). But the cylinder assumption becomes invalid with the further advancement of water inside the tablets. Alternatively, the average diffusion coefficient ( $\bar{D}$ ) can be calculated from the mass uptake by substituting the  $k_d$  value obtained from eq. [3] into eq. [4]:<sup>17,22</sup>

$$[3] \quad \frac{M}{M_\infty} = k_d t^n$$

$$[4] \quad \bar{D} = \left( \frac{k_d \pi r}{4} \right)^2$$

where  $M$  and  $M_\infty$  are the amount of water penetrated in a tablet at time  $t$  and at equilibrium, respectively, and  $k_d$  is a parameter related to the diffusion.

Mass uptake could be obtained from either gravimetric analyses or the integration of water signals in NMR images. The tablets become fragile after immersion in water, and manipulations during the weighing process may introduce errors, yielding less consistent results than the integration of signals of the NMR images. The latter method may also be difficult to apply for the system here since eq. [3] becomes invalid at ca. 60% of water uptake,<sup>9,23</sup> which can be accomplished within 3 h for the tablets. The rapid water uptake

during the first 3 h and the long acquisition time of each image with good S/N ratio (17 min) add up to the difficulty of obtaining an accurate  $\bar{D}$ .

To overcome such difficulties, diffusion-weighted images were acquired from which average diffusion coefficients may be obtained. This method produces images weighted with the local characteristics of water diffusion. The diffusion coefficients of both the gel part and the core of the tablets with various drug loading levels are shown in Fig. 4. Reliable values of  $D$  cannot be obtained for an immersion time of less than 10 h when the signal attenuation is too low to be accurately detected even if a high gradient strength is applied. Figure 4 shows that the self-diffusion coefficients of water in the outer gel changes only slightly with time and the values are comparable for different tablets, while those in the inner part of the tablets changed with time and vary significantly with different drug loading levels. The signal in the core for the tablets with 40% drug loading increased faster than the tablets of lower loadings. The faster water diffusion in these tablets agrees well with the faster swelling of the tablets. Since APAP is more hydrophilic than the CHAS matrix, a higher loading of APAP facilitates the diffusion of water towards the core.

The percentage of drug released at 37 °C (Fig. 5A) shows only minor differences among the tablets of different drug loading levels, even though the absolute amount of the drug released are very different (Fig. 5B). A small initial burst could be attributed to the release of the drug at the surface and surface erosion of the matrix prior to the formation of a gel layer. The drug release curves can be fitted to the equation  $F = kt^n$ . The value of the power index,  $n$ , serves as a criterion to determine whether the release is controlled by a diffusion mechanism ( $n = 0.5$ ) or polymer relaxation mechanism ( $n = 1$ ). For the CHAS tablets with 10%, 20%, and 40% APAP, the  $n$  values are found to be 0.51, 0.55, and 0.56, respectively, indicating the drug release process is dominated by a diffusion mechanism in all the tablets.

The average diffusion coefficients ( $\bar{D}$ ) may be obtained by fitting the dissolution test results to the following equation:<sup>24</sup>

$$[5] \quad \frac{M(t)}{M(\infty)} = 1 - \frac{8}{l^2 \alpha^2} \sum_m \alpha_m^{-2} \exp(-D\alpha_m^2 t) \times \sum_n \beta_n^{-2} \exp(-D\beta_n^2 t)$$

where  $M(t)$  and  $M(\infty)$  are the amount of drug released at time  $t$  and infinite time, respectively,  $l$  is the half-thickness of the tablet,  $r$  the radius, and  $D$  the diffusion coefficient;  $\alpha$  and  $\beta$  are parameters defined in  $J_0(r\alpha) = 0$  and  $\beta_n = \frac{(2n+1)\pi}{2l}$ , where  $J_0$  is a zero-order Bessel function. The model is applicable to tablets of a shape ranging from a flat disk to a cylinder. It is important to note that the validity of the equation is based on the hypotheses that there is no dimension change of the tablets, no variation of the diffusion coefficient of water from the outer gel to inner core, and no gradual increase of diffusion coefficients of water in the tablets over time. For comparison purposes, the fitting was performed on two stages, yielding the “initial” average diffusion coefficient ( $\bar{D}_0$ ) using the initial dimension of the tablet ( $l$  and  $r$ ) during the drug release of 0%–60% (cor-

responding to an immersion time from 0 to 3.5 or 4 h, depending on the amount of drug loading) and the average diffusion coefficient at equilibrium ( $\bar{D}_\infty$ ) using the final dimension during the drug release of 80%–100% (corresponding to an immersion time period of ca. 7–18 h). The results are shown in Table 1. The assumption of a constant diffusion coefficient leads to lower  $\bar{D}_0$  values than those obtained by spin density profile fitting, but still in the same order of magnitude. Moreover, the values for 10%–40% drug loadings are similar to each other, which is consistent with the trend obtained from NMRI profile fitting. At equilibrium, the water diffuses much faster than at the beginning and thus  $\bar{D}_\infty$  is almost an order of magnitude higher than  $\bar{D}_0$ . The trend is also reflected by the diffusion-weighted imaging experiments (Fig. 4). The difference between the two series of diffusion coefficients may be explained by the low repetition time used during the diffusion-weighted imaging experiments. Strictly speaking, this model is not applicable because of the gradual size change of the tablets and the heterogeneous diffusion process involved.

## Conclusion

We have studied the effect of drug loading for the case of cross-linked high-amylose starch with APAP. In this case, the amount of drug released is higher with a higher level of drug loading, but the percentage of the drug released remained similar, making the prediction of drug release easier. This is likely due to the formation of a protective gel layer upon hydration of the tablets, which serves as a key factor in such a controlled release process. The NMR imaging results also show that the radial and axial swelling and water uptake of the CHAS tablets increased with the drug loading level. Diffusion of water is faster for the tablets of high drug loadings due to the hydrophilicity of APAP, especially at a later stage of the release process. The dissolution tests demonstrated that the release of APAP from the CHAS tablets followed a diffusion mechanism. The results of this study may be useful in the study of the controlled release of drugs from pharmaceutical tablets made of starch.

## Acknowledgements

The financial support from the Natural Sciences and Engineering Research Council of Canada (NSERC), le Fonds québécois de la recherche sur la nature et les technologies (FQRNT) of Quebec, and the Canada Research Chair program is gratefully acknowledged. We thank Prof. Mircea A. Mateescu and Mr. Elias Assaad of Université du Québec à Montréal (UQAM) for their help with the dissolution tests. XXZ is indebted to Prof. Mitchell A. Winnik for introducing him to the field of diffusion studies.

## References

- (1) Mateescu, M. A.; Lenaerts, V.; Dumoulin, V. U.S. Patent 618,650, 1991.
- (2) Dumoulin, Y.; Alex, S.; Szabo, P.; Cartilier, L.; Mateescu, M. A. *Carbohydr. Polym.* **1998**, 37 (4), 361. doi:10.1016/S0144-8617(98)00058-7.
- (3) Lenaerts, V.; Moussa, I.; Dumoulin, Y.; Mebsout, F.; Chouinard, F.; Szabo, P.; Mateescu, M. A.; Cartilier, L.; Marches-

- sault, R. *J. Control. Release* **1998**, 53 (1–3), 225. doi:10.1016/S0168-3659(97)00256-3. PMID:9741930.
- (4) Lenaerts, V.; Beck, R. H. F.; Van Bogaert, E.; Chouinard, F.; Hopcke, R.; Desevaux, C. U.S. Patent 6,607,748, 2003.
  - (5) Thérien-Aubin, H.; Zhu, X. X.; Ravenelle, F.; Marchessault, R. H. *Biomacromolecules* **2008**, 9 (4), 1248. doi:10.1021/bm701256z. PMID:18357992.
  - (6) Thérien-Aubin, H.; Baille, W. E.; Zhu, X. X.; Marchessault, R. H. *Biomacromolecules* **2005**, 6 (6), 3367. doi:10.1021/bm0503930. PMID:16283767.
  - (7) Baille, W. E.; Malveau, C.; Zhu, X. X.; Marchessault, R. H. *Biomacromolecules* **2002**, 3 (1), 214. doi:10.1021/bm015621e. PMID:11866576.
  - (8) Malveau, C.; Baille, W. E.; Zhu, X. X.; Marchessault, R. H. *Biomacromolecules* **2002**, 3 (6), 1249. doi:10.1021/bm025576q. PMID:12425662.
  - (9) Russo, M. A. L.; Strounina, E.; Waret, M.; Nicholson, T.; Truss, R.; Halley, P. J. *Biomacromolecules* **2007**, 8 (1), 296. doi:10.1021/bm060791i. PMID:17206820.
  - (10) Thérien-Aubin, H.; Janvier, F.; Baille, W. E.; Zhu, X. X.; Marchessault, R. H. *Carbohydr. Res.* **2007**, 342 (11), 1525. doi:10.1016/j.carres.2007.04.014. PMID:17509547.
  - (11) Neau, S. H.; Howard, M. A.; Claudius, J. S.; Howard, D. R. *Int. J. Pharm.* **1999**, 179 (1), 97. doi:10.1016/S0378-5173(98)00391-3. PMID:10053206.
  - (12) Kim, C. J. *Drug Dev. Ind. Pharm.* **1998**, 24 (7), 645. doi:10.3109/03639049809082366. PMID:9876509.
  - (13) Cao, Q. R.; Choi, Y. W.; Cui, J. H.; Lee, B. J. *J. Control. Release* **2005**, 108 (2–3), 351. doi:10.1016/j.jconrel.2005.08.004. PMID:16154656.
  - (14) Ebube, N. K.; Hikal, A. H.; Wyandt, C. M.; Beer, D. C.; Miller, L. G.; Jones, A. B. *Pharm. Dev. Technol.* **1997**, 2 (2), 161. doi:10.3109/10837459709022621. PMID:9552442.
  - (15) Nabais, T.; Brouillet, F.; Kyriacos, S.; Mroueh, M.; Amores da Silva, P.; Bataille, B.; Chebli, C.; Cartilier, L. *Eur. J. Pharm. Biopharm.* **2007**, 65 (3), 371. doi:10.1016/j.ejpb.2006.12.001. PMID:17275270.
  - (16) Stejskal, E. O.; Tanner, J. E. *J. Chem. Phys.* **1965**, 42 (1), 288. doi:10.1063/1.1695690.
  - (17) Crank, J. *The Mathematics of Diffusion*, 2nd ed.; Oxford University Press: Oxford, 1975.
  - (18) Ghi, P. Y.; Hill, D. J. T.; Maillat, D.; Whittaker, A. K. *Polymer (Guildf.)* **1997**, 38 (15), 3985. doi:10.1016/S0032-3861(96)01071-3.
  - (19) Chowdhury, M. A.; Hill, D. J. T.; Whittaker, A. K. *Biomacromolecules* **2004**, 5 (3), 971. doi:10.1021/bm030079a. PMID:15132689.
  - (20) Chowdhury, M. A.; Hill, D. J. T.; Whittaker, A. K.; Braden, M.; Patel, M. P. *Biomacromolecules* **2004**, 5 (4), 1405. doi:10.1021/bm040003u. PMID:15244458.
  - (21) George, K. A.; Wentrup-Byrne, E.; Hill, D. J. T.; Whittaker, A. K. *Biomacromolecules* **2004**, 5 (4), 1194. doi:10.1021/bm034477p. PMID:15244430.
  - (22) Alfrey, T. J.; Gurnee, E. F.; Lloyd, W. G. *J. Polym. Sci. Polym. Symp.* **1966**, 12 (1), 249. doi:10.1002/polc.5070120119.
  - (23) Ghi, P. Y.; Hill, D. J. T.; Whittaker, A. K. *Biomacromolecules* **2001**, 2 (2), 504. doi:10.1021/bm000146q. PMID:11749213.
  - (24) Fu, J. C.; Hagemeir, C.; Moyer, D. L.; Ng, E. W. *J. Biomed. Mater. Res.* **1976**, 10 (5), 743. doi:10.1002/jbm.820100507. PMID:977604.

# Mixed micelles of poly(styrene-*b*-3-(methacryloylamino)propyltrimethylammonium chloride-*b*-ethylene oxide) and anionic amphiphiles in aqueous solutions

Jingjing Liu, Airi Yoneda, Dian Liu, Yuuichi Yokoyama, Shin-ichi Yusa, and Kenichi Nakashima

**Abstract:** The micelles of poly(styrene-*b*-3-(methacryloylamino)propyltrimethylammonium chloride-*b*-ethylene oxide) (PS-*b*-PMAPTAC-*b*-PEO) have been successfully prepared in aqueous solutions. The micelles have a PS core, cationic PMAPTAC shell, and PEO corona. Due to the short PS chain (degree of polymerization = 8), the formation of micelles is difficult at a low concentration, and the micelles are detected only at concentrations higher than 1 g L<sup>-1</sup>. The addition of anionic amphiphiles, such as sodium dodecyl sulfate (SDS) and poly(methacrylic acid) (PMAA), induces the formation of mixed micelles at a low concentration level of the polymer (~0.005 g L<sup>-1</sup>). This can be ascribed to insolubilization of the cationic PMAPTAC block due to charge neutralization by the anionic amphiphiles. The binding of SDS or PMAA to the PMAPTAC block is confirmed by zeta-potential measurements. The mixed micelles are characterized by dynamic light scattering (DLS), scanning electron microscopy (SEM), and fluorescence measurements. Based on DLS measurements, it is revealed that the hydrodynamic diameter of the mixed micelles falls in the range of 120–130 nm. SEM measurements provided clear pictures of mixed micelles with a spherical morphology. The kinetics of exchange of organic dyes between the micelle particles was investigated by fluorescence techniques. The result indicates that the exchange of the dyes between the micelle particles takes place within a time scale of seconds.

**Key words:** polymeric micelles, amphiphilic ABC triblock copolymer, mixed micelles, sodium dodecyl sulfate (SDS), poly(methacrylic acid) (PMAA).

**Résumé :** Opérant en solutions aqueuses, on a préparé avec succès des micelles de poly(styrène- chlorure de *b*-3-(méthacryloylamino)propyltriméthylammonium- *b*-oxyde d'éthylène) (PS-*b*-CPMAPTA-*b*-POE). Les micelles comportent un squelette de polyéthylène (PS), une coquille cationique de chlorure de polyméthacryloylaminopropyltriméthylammonium (CPMAPTA) et une couronne de polyoxyde d'éthylène (POE). En raison de la courte longueur de la chaise de polystyrène (degré de polymérisation = 8), la formation de micelles est difficile à faible concentration et les micelles ne peuvent être détectées qu'à des concentrations supérieures à 1 g L<sup>-1</sup>. L'addition d'amphiphiles anioniques, tel le dodécylsulfate de sodium (DSS) et l'acide poly(méthacrylique) (APMA), induisent la formation de micelles mixtes à des niveaux de concentration faible de polymère (environ 0.005 g L<sup>-1</sup>). Ce comportement peut être attribué à l'insolubilisation du bloc cationique de chlorure de polyméthacryloylaminopropyltriméthylammonium (CPMAPTA) provoquée par la neutralisation de la charge par les amphiphiles anioniques. La fixation du DSS ou de l'acide poly(méthacrylique) sur le bloc CPMAPTA est confirmée par des mesures de potentiel zêta. Les micelles mixtes ont été caractérisées par des mesures de diffraction dynamique de la lumière (DDL), de microscopie électronique à balayage (MEB) et de fluorescence. Sur la base de mesure de diffraction dynamique de la lumière, on a pu établir que le diamètre hydrodynamique des micelles mixtes se situe entre 120 et 130 nm. Les mesures de microscopie électronique à balayage permettent d'établir clairement que les micelles mixtes possèdent une morphologie sphérique. On a étudié les cinétiques d'échange de colorants organiques entre les particules de micelles par les techniques de fluorescence. Les résultats indiquent que l'échange des colorants entre les particules de micelles se fait sur une échelle de temps de secondes.

Received 31 August 2008. Accepted 9 October 2009. Published on the NRC Research Press Web site at canjchem.nrc.ca on 6 February 2010.

*This article is part of a Special Issue dedicated to Professor M. A. Winnik.*

**J. Liu, A. Yoneda, D. Liu, and K. Nakashima.**<sup>1</sup> Department of Chemistry, Faculty of Science and Engineering, Saga University, 1 Honjo-machi, Saga 840-8502, Japan.

**Y. Yokoyama and S. Yusa.** Department of Materials Science and Chemistry, University of Hyogo, 2167 Shosha, Himeji 671-2280, Japan.

<sup>1</sup>Corresponding author (e-mail: nakashik@cc.saga-u.ac.jp).



*Mots-clés* : micelles polymères, copolymère amphiphile à trois blocs ABC, micelles mixtes, dodécylsulfate de sodium (DSS), acide poly(méthacrylique) (APMA).

[Traduit par la Rédaction]

## Introduction

The synthesis of nanoparticles with a unique size and shape finds potential applications in areas such as optics, electronics, catalysis, and storage devices. For their synthesis, templates are often indispensable and it is an important issue to stabilize these nanoparticles or to arrange them into superstructures. For this purpose, amphiphilic block copolymers with hydrophilic and hydrophobic blocks turned out to be advantageous as each block performs different functions.<sup>1–4</sup> In most cases, the block copolymers are dissolved in a selective solvent that is poor for one block and good for the other block(s), which results in spherical micelles with a core-shell or multilayer structure.<sup>5</sup>

Very recently, core-shell-corona micelles from ABC triblock copolymers in aqueous solutions have attracted much attention. This type of micelle consists of a hydrophobic dense core surrounded by a hydrophilic shell, and an outer hydrophilic corona, which protects the micelles stability in an aqueous environment.<sup>6–9</sup> A typical example of a well-defined core-shell-corona micelle is the micelle of poly(styrene-*b*-2-vinylpyridine-*b*-ethylene oxide) (PS-*b*-P2VP-*b*-PEO) triblock copolymer, which has a PS core, P2VP shell, and PEO corona in aqueous solutions.<sup>10,11</sup> It was found that the micelles undergo a pH-sensitive morphological change from shrunken to extended spheres as the pH of the micellar solution is lowered below 5. This is due to the protonation of the P2VP block at a pH lower than 5, which causes an electrostatic repulsion between the protonated P2VP chains. Such a morphological change was also induced when the positive charge of the protonated P2VP was cancelled by the negative additives including dodecyl sulfate, dextran sulfate, and tungstate.<sup>12–15</sup>

It is important to note that the P2VP shell in the micelle of PS-*b*-P2VP-*b*-PEO is ionized only in a limited pH range, which restricts its potential applications in diverse material synthesis.<sup>16,17</sup> To overcome this difficulty, we synthesized a new ABC triblock copolymer, poly(styrene-*b*-3-(methacryloylamino)propyltrimethylammonium chloride-*b*-ethylene oxide) (PS-*b*-PMAPTAC-*b*-PEO) by a reversible addition-fragmentation chain transfer (RAFT) controlled radical polymerization.<sup>18</sup> We confirmed the formation of core-shell-corona micelles of PS-*b*-PMAPTAC-*b*-PEO in aqueous solutions.<sup>18</sup> The central PMAPTAC block is ionized over a wide pH range in contrast to the P2VP block, which is important when we employ these micelles as nanoreactors. The reactants can be incorporated into the PMAPTAC shell of the PS-*b*-PMAPTAC-*b*-PEO micelles at almost any pH in contrast to the P2VP shell of the PS-*b*-P2VP-*b*-PEO micelles.

In our previous study,<sup>18</sup> the micelles of PS-*b*-PMAPTAC-*b*-PEO with a longer PS chain (degree of polymerization, DP = 80) were already investigated in aqueous solutions. We now report the studies of micelles of the PS-*b*-PMAP-

TAC-*b*-PEO triblock copolymer with a short PS chain (DP = 8, Scheme 1). With a short PS chain, the formation of micelles is often quite difficult at low concentrations, and therefore the mixed micelle formation was also investigated in the presence of counter ions, such as sodium dodecyl sulfate (SDS) and poly(methacrylic acid) (PMAA). The counter ions with a negative charge are expected not only to stabilize the micelles through electrostatic binding with a positively charged PMAPTAC shell, but also to offer some interesting morphological changes to the micelles. Therefore, some new functional mixed micelles were also expected from these molecular self-assemblies. The micelles of the neat triblock copolymer and its mixed micelles were characterized by various techniques including dynamic light scattering (DLS), electrophoretic light scattering (ELS), scanning electron microscopy (SEM), and fluorescence spectroscopy.

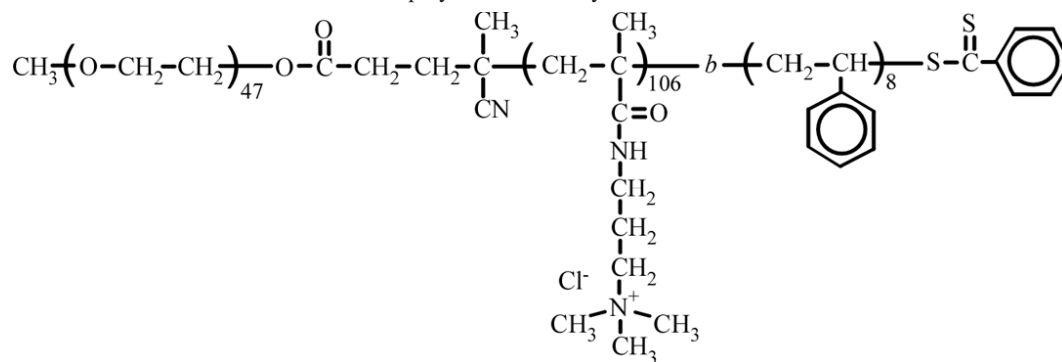
## Experimental

### Chemicals

(3-(Methacryloylamino)propyl)trimethylammonium chloride (MAPTAC) (50 wt% in water) from Sigma-Aldrich was passed through an inhibitor-remover column. 4,4'-Azobis(4-cyanopentanoic acid) (V-501) (98%) from Wako Pure Chemicals Industries, Ltd. (Wako) was used as received without further purification. 2,2'-Azobis(isobutyronitrile) (AIBN) (98%) from Wako was recrystallized from methanol. The styrene was washed with an aqueous alkaline solution and distilled from calcium hydride under reduced pressure. The *N,N*-dimethylformamide (DMF) was dried over 4 Å molecular sieves and distilled under reduced pressure. The methanol was dried over 4 Å molecular sieves and distilled. Pyrene (Sigma-Aldrich), titan yellow (TY, Wako), fluorescein (FL, Sigma-Aldrich), and SDS (Wako) were used without further purification. The PMAA homopolymer (Scientific Polymer Products, Inc.) was used as supplied. The molecular weight of PMAA is 15 000.

### Synthesis of PS-*b*-PMAPTAC-*b*-PEO

The poly(ethylene oxide) (PEO) based chain transfer agent (PEO-CTA) was synthesized according to the method reported by McCormick and co-workers.<sup>19</sup> The diblock copolymer, PEO-*b*-PMAPTAC, was synthesized via RAFT radical polymerization as previously reported.<sup>20</sup> The molecular weight distribution ( $M_w/M_n$ ) value determined by gel-permeation chromatography (GPC) was 1.02. The number-average degree of polymerization (DP) for the PEO and PMAPTAC blocks were estimated to be 47 and 106, respectively. A procedure for the synthesis of the triblock copolymer, PS-*b*-PMAPTAC-*b*-PEO is as follows: Styrene (525 mg, 5.04 mmol), 2,2'-azobis(isobutyronitrile) (3.30 mg, 0.02 mmol), and PEO-*b*-PMAPTAC (1.22 g, 0.05 mmol) were dissolved in methanol (105 mL). The mixture was de-

**Scheme 1.** The structure of PS-*b*-PMAPTAC-*b*-PEO employed in this study.

gassed by purging with Ar gas for 30 min. The polymerization was carried out at 60 °C for 24 h. The polymerization mixture was then poured into a large excess of ethyl acetate to precipitate the resulting polymer. The polymer was purified by reprecipitating from dimethyl sulfoxide (DMSO) into a large excess of ethyl acetate. The obtained triblock copolymer was dried in a vacuum oven for 24 h (1.02 g). The DP values for the PS block and number-average molecular weight ( $M_n$ ) of PS-*b*-PMAPTAC-*b*-PEO were 8 and  $2.65 \times 10^4$ , respectively, as estimated by  $^1\text{H}$  NMR in DMSO- $d_6$  at 100 °C. The detailed characterization method was described in our previous report.<sup>18</sup>

#### Gel-permeation chromatographic measurements

The gel-permeation chromatographic (GPC) measurements of PS-*b*-PMAPTAC-*b*-PEO were performed using a refractive index (RI) detector equipped with a Shodex 10  $\mu\text{m}$  bead size GPC K-806 mol/L column (exclusion limit  $\sim 10^7$ ) working at 40 °C. DMSO containing 10 mmol L<sup>-1</sup> LiBr was used as the eluent at a flow rate of 0.5 mL min<sup>-1</sup>.

PS-*b*-PMAPTAC-*b*-PEO cannot be completely dissolved except in DMSO. Although the unimodal GPC elution curve was detected for PS-*b*-PMAPTAC-*b*-PEO, the molecular weight could not be determined due to the insolubility of standard polystyrene samples in the eluent.

#### Dynamic light scattering measurements

The dynamic light scattering (DLS) was measured by an Otsuka ELS-800 at a fixed 90° scattering angle. Correlation functions were analyzed by a histogram method and used to determine the diffusion coefficient ( $D$ ) of the nanocomplexes in the test sample. The hydrodynamic diameter ( $D_h$ ) was calculated from  $D$  using the Stokes–Einstein equation:

$$[1] \quad D_h = \frac{k_B T}{3\pi\eta D}$$

where  $k_B$  is the Boltzmann constant,  $T$  is the absolute temperature, and  $\eta$  is the solvent viscosity.

#### Light scattering measurements

The light scattering measurements were carried out using a JASCO FP-6500 fluorescence spectrophotometer. The samples were irradiated with 400 nm light from a 150 W

Xe-lamp and the scattered light was detected at a right angle configuration.

#### Zeta-potential measurements

The electrophoresis mobility (EPM) was measured with an Otsuka ELS-800. The zeta potential was calculated from the EPM using Smoluchowski's equation:

$$[2] \quad \mu_E = \frac{\zeta \epsilon}{\eta}$$

where  $\mu_E$  is EPM,  $\zeta$  is the zeta potential, and  $\epsilon$  is the solvent permittivity.

#### Fluorescence spectroscopy

The fluorescence spectra were recorded by a JASCO FP-6500 fluorescence spectrophotometer using right-angle geometry.

#### Scanning Electron Microscopy

SEM measurements were carried out using a Hitachi S-3000N electron microscope at an accelerating voltage of 15 kV. The samples were prepared by dropping the micelle solution onto a carbon seal (Nisshin Em Co.) attached to the glass plate, followed by drying in air for 24 h.

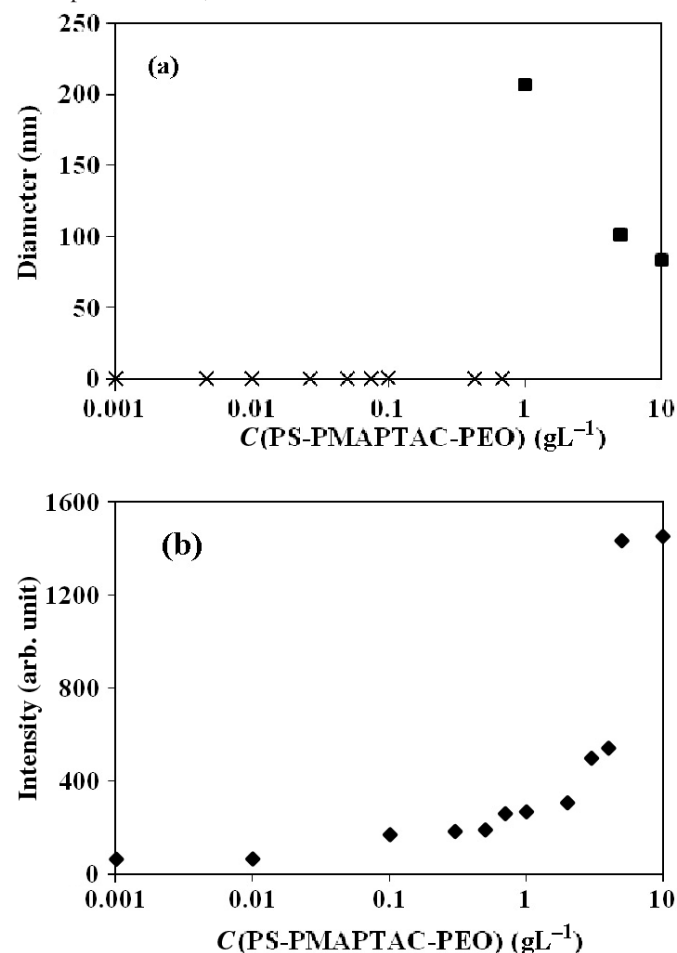
## Results and discussion

#### Micelle formation of PS-*b*-PMAPTAC-*b*-PEO

We first investigated the micellar behavior of PS-*b*-PMAPTAC-*b*-PEO in an aqueous solution without adding any amphiphiles. Figure 1a shows the hydrodynamic diameter ( $D_h$ ) of the micelles with respect to different polymer concentrations. For the polymer concentration ranging from 1 to 5 g L<sup>-1</sup>, reasonable hydrodynamic diameters were obtained by the DLS method and no reliable data were obtained for concentrations below 1 g L<sup>-1</sup>. The weak scattered light intensity is the reason for the lack of reliable data below 1 g L<sup>-1</sup> and it should be noted in Fig. 1a that the  $D_h$  values on the  $x$  axis do not correspond to 0 nm, but indicates that stable data were not obtained.

To determine the critical micelle concentration (cmc), an important parameter of polymeric micelles, we have carried out light scattering measurements because the sensitivity of the DLS measurement is not high enough to determine the

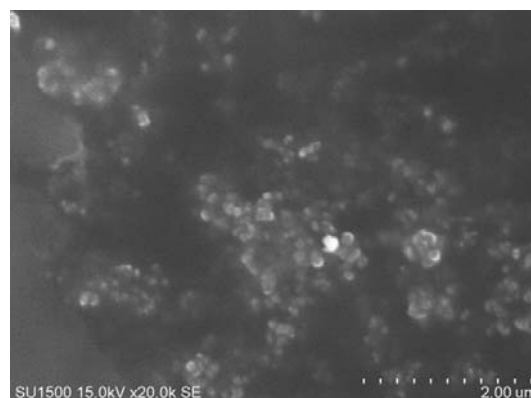
**Fig. 1.** (a) The hydrodynamic diameter ( $D_h$ ) of the micelles of PS-*b*-PMAPTAC-*b*-PEO as a function of the polymer concentration. (b) The light scattering intensity of micellar solutions of PS-*b*-PMAPTAC-*b*-PEO as a function of the polymer concentration. It should be noted that in Fig. 1a the  $D_h$  values on the  $x$  axis do not correspond to 0 nm, but indicate that stable data were not obtained.



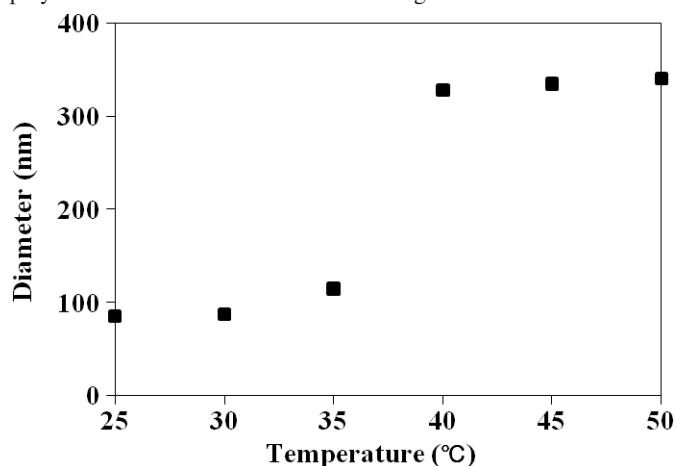
cmc. It is noted from Fig. 1b that the light intensity increased with the increasing polymer concentration, and a drastic change occurred at 5  $\text{g L}^{-1}$ . However, this value does not seem to be the cmc, because this concentration is almost the same as the concentration at which the DLS intensity was significantly enhanced.

As we could not get a clear cmc value from the DLS or from light scattering method, we carried out fluorescence measurements using pyrene as a probe.<sup>21</sup> It is reported by Winnik and co-workers<sup>21</sup> that the intensity ratio (so-called  $I_1/I_3$  ratio) between the 0–0 band (band 1) and the  $b_{1g}$  vibronic band (band 3) in monomer fluorescence gives the upper bound of the cmc of a polymeric micelle, and the excitation spectra gives an exact cmc value. However, we could not observe any significant change in both the  $I_1/I_3$  ratio and excitation spectra (see Fig. S1 in the Supplementary data). One of the possible reasons may be that the core of the micelles is not hydrophobic enough to provide a nonpolar environment to the pyrene molecule because the PS chain is very short.

**Fig. 2.** The SEM image of the micelles of PS-*b*-PMAPTAC-*b*-PEO. The SEM sample was prepared at 25 °C from a polymer solution with a concentration of 1  $\text{g L}^{-1}$ .



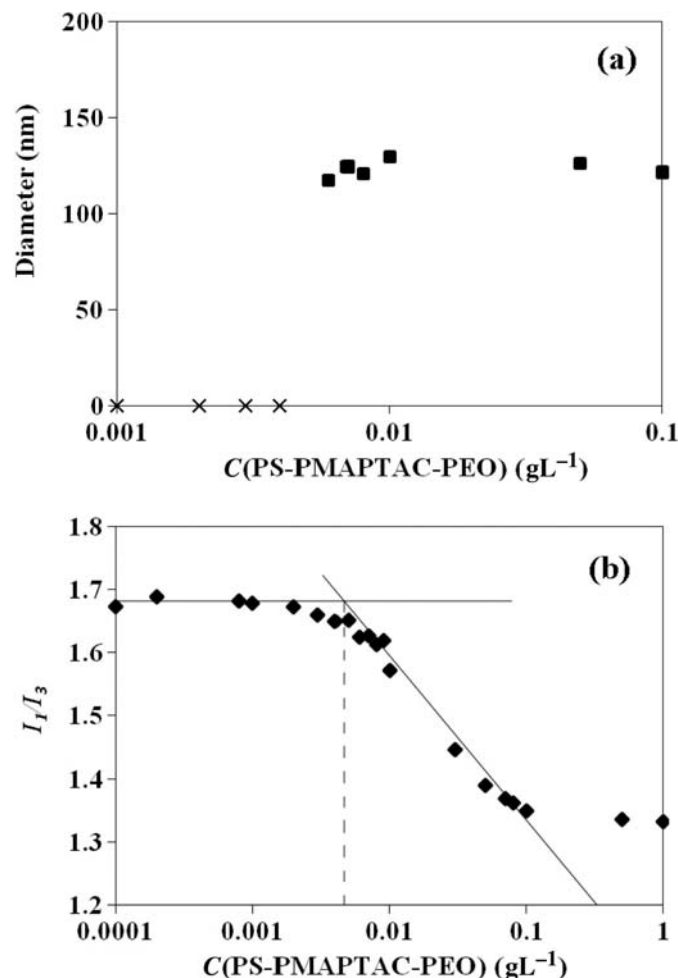
**Fig. 3.** Variation in the  $D_h$  of the micelles of PS-*b*-PMAPTAC-*b*-PEO vs temperature. All the measurements were made from a polymer solution at a concentration of 5  $\text{g L}^{-1}$ .



The micelle formation of the PS-*b*-PMAPTAC-*b*-PEO polymer was confirmed by SEM observations. Figure 2 shows the SEM image of the sample having spherical micelle particles. Thus, the SEM result provided concrete evidence for micelle formation of the present block copolymer and the estimated diameter from the SEM (around 100 nm) matches well with that obtained by DLS.

The temperature dependence of the hydrodynamic diameter of these polymeric micelles was also investigated and shown in Fig. 3. The diameter was measured by DLS at different temperatures starting from room temperature to 50 °C. Initially, the observed diameter was found to be approximately 100 nm until the temperature reached 35 °C. A further increase in temperature led to a sharp increase in the micelle's diameter up to 350 nm. The rapid increase in size may be due to the dehydration of the PEO block, which results in a secondary aggregation. The sharp increase in  $D_h$  around 35 °C may open some applications because this temperature is close to human body temperature.

**Fig. 4.** (a) The effect of concentration over the  $D_h$  for SDS/PS-*b*-PMAPTAC-*b*-PEO mixed micelles (ADN = 50%). (b) The effect of concentration over the  $I_1/I_3$  ratio of pyrene in SDS/PS-*b*-PMAPTAC-*b*-PEO solution (ADN = 50%). The fluorescence measurements were carried out at an excitation wavelength of 334 nm, and the excitation and emission band passes are 5 and 1 nm, respectively. It should be noted in Fig. 4a that the  $D_h$  values on the  $x$  axis do not correspond to 0 nm, but indicate that stable data were not obtained.

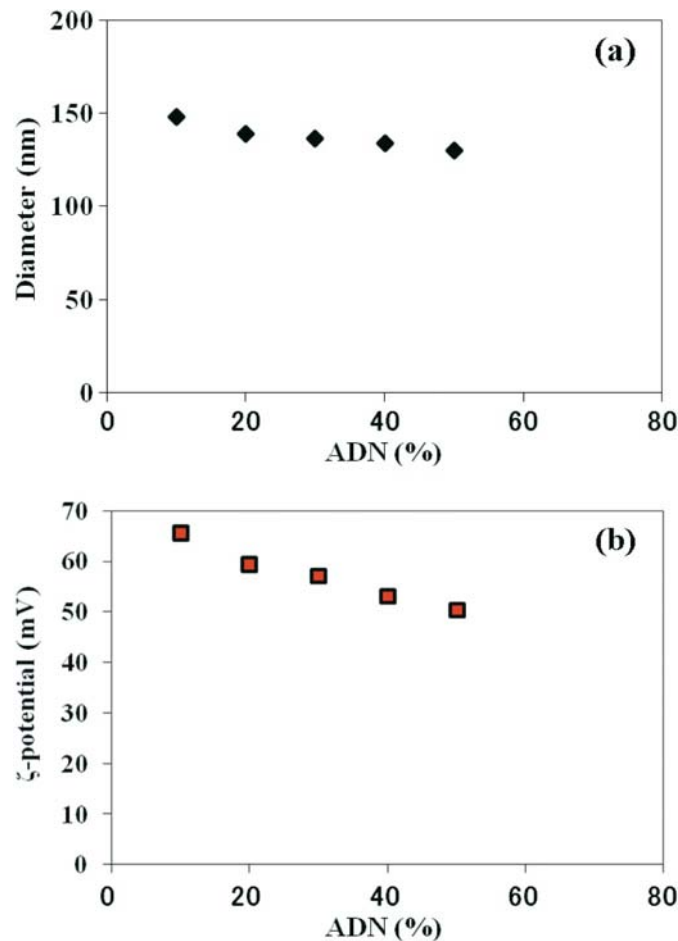


#### Mixed micelles of PS-*b*-PMAPTAC-*b*-PEO and SDS

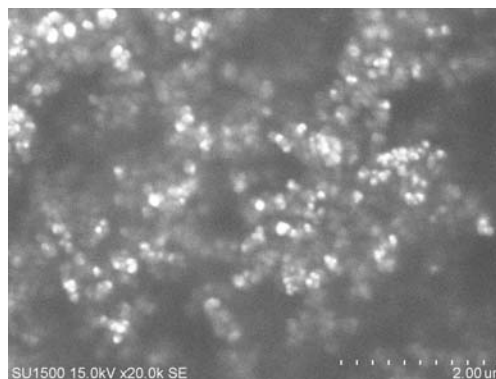
The formation of mixed micelles based on an electrostatic interaction between the positively charged PMAPTAC block in PS-*b*-PMAPTAC-*b*-PEO and the added surfactants was also examined in the present study. For the investigation, we employed an anionic surfactant (SDS), which is expected to interact with the positively charged PMAPTAC shell. To express the amount of added SDS, we introduced the concept of *apparent degree of neutralization* (ADN), which is defined by

$$[\text{3}] \quad \text{ADN (\%)} = \frac{\text{Amount of added SDS in mole unit}}{\text{Amount of trimethylammonium group of the PMAPTAC block in mole unit}} \times 100$$

**Fig. 5.** (a) Variation in the  $D_h$  and (b) zeta potential ( $\zeta$ ) of mixed micelles of SDS/PS-*b*-PMAPTAC-*b*-PEO as a function of ADN. The concentration of PS-*b*-PMAPTAC-*b*-PEO was fixed at 0.1 g L<sup>-1</sup> for both experiments.



**Fig. 6.** The SEM image of the micelles SDS/PS-*b*-PMAPTAC-*b*-PEO. The SEM sample was prepared from a polymer solution at the polymer concentration of 0.1 g L<sup>-1</sup> and ADN = 50%.





**Fig. 7.** Variation in the  $D_h$  for the mixed micelles of PMAA/PS-*b*-PMAPTAC-*b*-PEO with respect to concentration of PS-*b*-PMAPTAC-*b*-PEO (ADN = 50%). It should be noted that the  $D_h$  values on the  $x$  axis do not correspond to 0 nm, but indicate that stable data were not obtained.

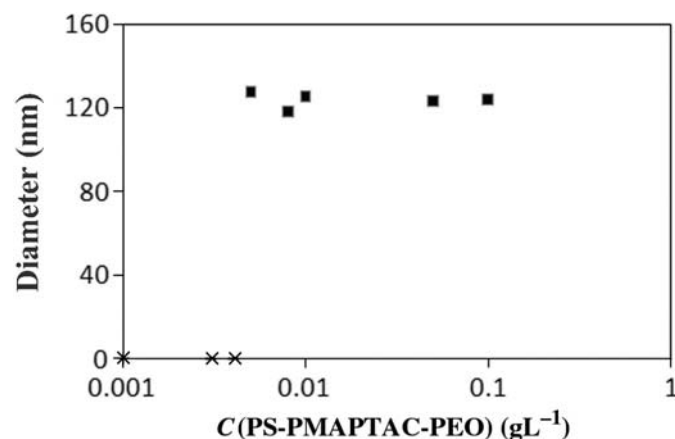


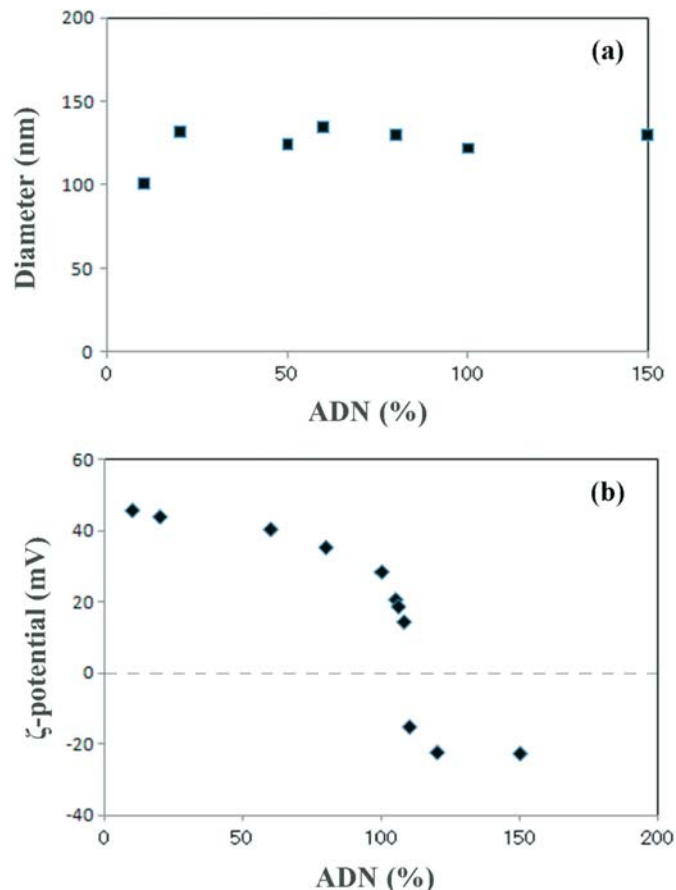
Figure 4a shows the  $D_h$  of the mixed micelles as a function of the polymer concentration at 50% ADN. A nearly uniform micelle size of about 125 nm was obtained when the polymer concentration level was above 0.006 g L<sup>-1</sup> and no reliable DLS data were obtained below that concentration. The formation of mixed micelles was also confirmed by the vibronic fine structure of the pyrene fluorescence spectra (Fig. 4b). The sudden decrease in the  $I_1/I_3$  ratio above 0.005 g L<sup>-1</sup> indicates the upper bound of the critical aggregate concentration (cac).<sup>21</sup> It should be noted that in the presence of SDS, the cac, value is significantly low indicating the smooth formation of the mixed micelles. The main significance of using SDS is that by neutralizing the positive charge of the PMAPTAC block, it increases the hydrophobicity, which facilitates the formation of core as well as stable micelles.

We have also explored the PS-*b*-PMAPTAC-*b*-PEO micelles for possible stimuli-induced morphological changes in the presence of SDS. In the absence of SDS, the PMAPTAC block of the PS-*b*-PMAPTAC-*b*-PEO micelles is expected to exist in an extended conformation due to the repulsion between the positive charges; whereas binding of SDS to the PMAPTAC block may lead to a shrunken conformation due to the cancellation of the charges. Figure 5a shows the variation in the hydrodynamic diameters of the mixed SDS/PS-*b*-PMAPTAC-*b*-PEO micelles with different ADN values. With the addition of SDS, the  $D_h$  gradually decreased and the solution turned turbid at 60% ADN. The reduction in the hydrodynamic diameter of the micelles clearly indicates that the SDS effectively binds with the cationic PMAPTAC and eliminates the repulsive forces between the PMAPTAC blocks.

The variation in the zeta potential with ADN is shown in Fig. 5b. The successive addition of SDS resulted in a continuous decrease in the zeta potential from 67.3 to 51.8 mV. This result indicates that the positive charges on the PS-*b*-PMAPTAC-*b*-PEO micelle particle are neutralized due to electrostatic binding of the oppositely charged species.

Figure 6 shows the SEM image of the SDS/PS-*b*-PMAP-

**Fig. 8.** Variation in the (a)  $D_h$  and (b) zeta-potential ( $\zeta$ ) of mixed micelles of PMAA/PS-*b*-PMAPTAC-*b*-PEO at different ADNs. The concentration of PS-*b*-PMAPTAC-*b*-PEO is fixed at 0.1 g L<sup>-1</sup> for both experiments.

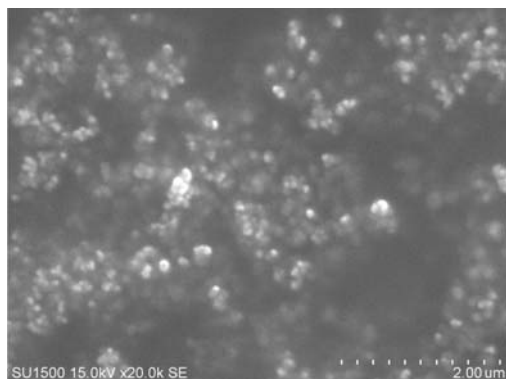


TAC-*b*-PEO mixed micelles at 50% ADN, and spherical particles with a good dispersivity are clearly observed. This image provides clear evidence for the formation of the mixed micelles of PS-*b*-PMAPTAC-*b*-PEO and SDS.

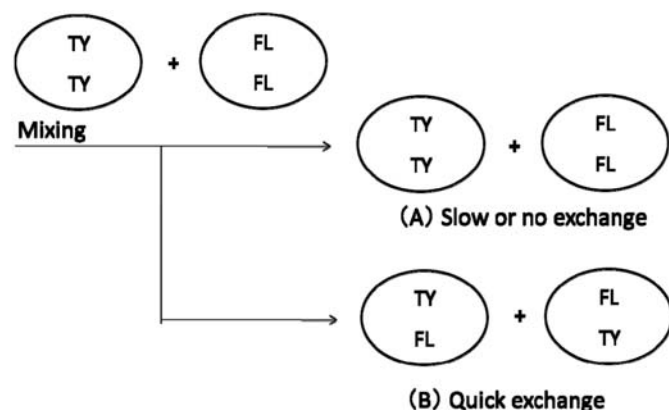
#### Mixed micelles of PS-*b*-PMAPTAC-*b*-PEO and PMAA

Impressed by the above results, we have extended our studies using the combination of the PS-*b*-PMAPTAC-*b*-PEO copolymer and PMAA, where the latter is expected to have application in biological and medical fields, e.g., controlled release of insulin after oral administration.<sup>22</sup> Figure 7 shows the  $D_h$  of mixed micelles over a range of polymer concentrations at 50% ADN. Nearly uniform micelles with a size of about  $120 \pm 5$  nm were obtained when the polymer concentration was raised above 0.006 g L<sup>-1</sup> indicating the formation of the mixed micelle in the presence of PMAA. Figure 8a shows the change in the hydrodynamic diameter of mixed micelles, PMAA/PS-*b*-PMAPTAC-*b*-PEO, at different ADNs. When PMAA was added to the aqueous solution of PS-*b*-PMAPTAC-*b*-PEO, the  $D_h$  rapidly increased to about 100 nm at 10% ADN and then the increase in the micelle size was rather slow with a further neutralization. The moderate increase in the  $D_h$  at a low degree of neutralization is attributed to the partial charge neutralization of the PMAPTAC blocks by PMAA. Unlike the case of SDS, no

**Fig. 9.** The SEM image of the mixed micelles of PMAA/PS-*b*-PMAPTAC-*b*-PEO. The SEM sample was prepared from a 0.1 g L<sup>-1</sup> polymer solution; ADN = 50%.



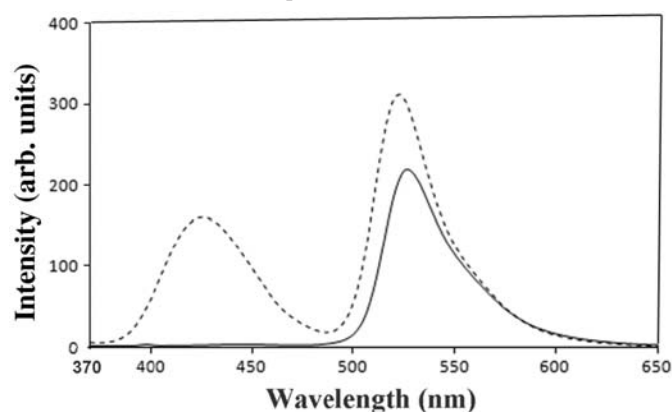
**Fig. 10.** The schematic representation for two model cases of the exchange of TY and FL dyes between the micelle particles.



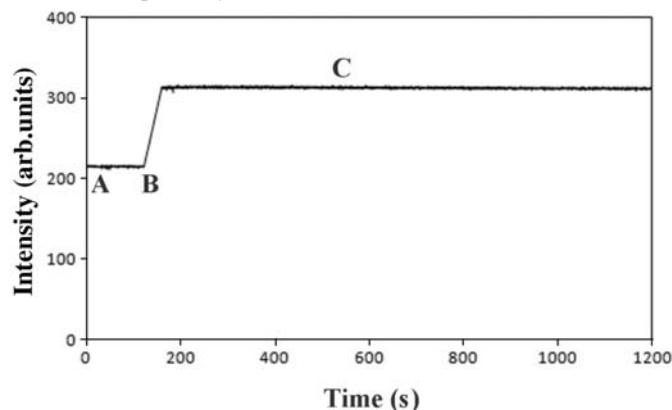
morphological change from the extended to shrunken conformation was observed, and also, the micellar solution did not become turbid even after 150% ADN. The lack of turbidity formation may be due to the hydrophilicity of the residual carboxyl groups present in the methacrylic acid after neutralization. The hydrophilic nature of the mixed micelles is implied from the change in the  $I_1/I_3$  ratio in the pyrene fluorescence spectra (see Fig. S2 in the Supplementary data). The  $I_1/I_3$  ratio shows a very slight change upon going from low (0.0001 g L<sup>-1</sup>) to high (0.1 g L<sup>-1</sup>) polymer concentrations.

Additional proof for the effective binding of PMAA was obtained from the zeta-potential measurements (Fig. 8b). The positive charge of the PS-*b*-PMAPTAC-*b*-PEO micelle particles is gradually neutralized during the binding of the oppositely charged PMAA resulting in a continuous decrease in the zeta potential up to 0 mV at about 100% ADN. However, the addition of more PMAA caused a further decrease in the zeta potential to -22.9 mV indicating the presence of excess negative charges in the mixed micelle system. The above results indicate that, in addition to the electrostatic interaction, there could be another type of interaction between the triblock copolymer and PMAA. Although the exact nature of the interaction is not known, it may be (1) a hydrophobic interaction between PMAA and

**Fig. 11.** The fluorescence spectra of FL and TY in the mixed micelles of PS-*b*-PMAPTAC-*b*-PEO and PMAA. The solid line indicates the fluorescence spectrum of FL (40 μmol/L) incorporated in the micelles. The dotted line shows the fluorescence spectra of TY (2 μmol/L) and FL (20 μmol/L), which are premixed before being incorporated in the micelles. The polymer concentration and ADN are fixed at 0.1 g L<sup>-1</sup> and 30%, respectively, throughout the experiments. The samples are excited at 350 nm, and both the excitation and emission band passes are 3 nm. It should be noted that the concentration of FL in the solid line spectrum is two times higher than that in the dotted line spectrum.



**Fig. 12.** Time dependence of FL fluorescence in the mixed micelle solutions of PMAA/PS-*b*-PMAPTAC-*b*-PEO. The concentration of PS-*b*-PMAPTAC-*b*-PEO is 0.1 g L<sup>-1</sup> and ADN is 30% throughout the experiment. The concentration of FL is 40 μmol L<sup>-1</sup> at point A. The concentrations of FL and TY at the end (at point C) are 20 and 2 μmol/L, respectively.



the PS-*b*-PMAPTAC-*b*-PEO or (2) hydrogen bonding between PMAA and the PEO block. The morphology and dispersivity of these mixed micelle systems is recorded by SEM, which is shown in Fig. 9.

#### Kinetics of the exchange of organic dyes between the micelle particles

It is interesting to investigate the kinetics of the exchange of organic dyes between the micelle particles, because the exchange kinetics can be related to the drug release from the container micelles. One of the methods to study the exchange kinetics is to use electronic energy transfer.<sup>23</sup> This

idea is schematically shown in Fig. 10. We prepared two kinds of micelle solutions: one only contains FL and the other only contains TY. It is known that the electronic energy of TY is transferred to FL by a dipole–dipole interaction, resulting in quenching of the TY fluorescence and the sensitization of the FL fluorescence.<sup>24,25</sup> The critical energy transfer distance is usually less than 10 nm. Therefore, the energy transfer quenching of the TY fluorescence and sensitization of the FL fluorescence will effectively occur when both TY and FL are incorporated in the same micelle particle, while they will not occur when TY and FL are partitioned among the different particles. We monitored the fluorescence intensity of FL before and after the mixing of the two micelle solutions. If the exchange of the incorporated dyes occurs within the time scale of seconds or less (case B in Fig. 10), then we will observe a quick increase in the fluorescence intensity of FL. If it takes hours or a much longer time for the exchange to occur (case A in Fig. 10), we will not observe any significant intensity change.

To investigate the exchange kinetics of the organic dyes between the micelle particles, we employed the mixed micelles of PS-*b*-PMAPTAC-*b*-PEO and PMAA. Before we examined the time profile of the fluorescence intensity of FL, we measured the fluorescence spectra of TY and FL in the mixed micelle solutions of PS-*b*-PMAPTAC-*b*-PEO and PMAA (Fig. 11). In the absence of TY (Fig. 11, solid line), there is only one band (around 520 nm) corresponding to the fluorescence of FL. When TY is also present in the micelle (Fig. 11, dotted line), we observe two bands, one is assigned to TY (around 425 nm), and the other is assigned to FL (around 520 nm). If we compare the two spectra (i.e., the solid and dotted lines), we realize that the fluorescence of FL is significantly sensitized by TY. This fact indicates that the energy transfer from TY to FL effectively occurs in the micelle particle, because such a high sensitization does not occur in the absence of the micelles (see Fig. S3 in the Supplementary data). In the bulk aqueous solution (i.e., in the absence of the micelles), the fluorescence of FL is not increased, but decreased by the presence of TY, because the intensity increase due to the sensitization by TY is much lower than the intensity decrease due to the inner filter effect of TY.

Figure 12 shows a time profile of the fluorescence intensity of FL in the mixed micelle solution. At point A in Fig. 12, the sample contains only FL. We quickly added the solution containing TY at point B in Fig. 12. The fluorescence intensity increased rapidly to the level of point C in Fig. 12, indicating that the TY and FL in different micelle particles rapidly mixed with each other in the same micelle particle. Therefore, we can conclude that the exchange of the incorporated dyes takes places within a time scale of seconds.

## Conclusions

The micelles of PS-*b*-PMAPTAC-*b*-PEO have been successfully prepared in aqueous solutions. Due to the short PS chain (DP = 8), the formation of micelles is difficult at low concentrations, and the micelles are detected by DLS and light scattering only at concentrations higher than 1 g L<sup>-1</sup>. This concentration is considerably higher than that (0.0015

g L<sup>-1</sup>) found previously for the same type of triblock copolymer with a longer PS chain (DP = 80).<sup>18</sup>

The addition of anionic amphiphiles, such as SDS and PMAA, induces the formation of mixed micelles at a low concentration level of the polymer (~0.005 g L<sup>-1</sup>). This can be ascribed to the insolubilization of the cationic PMAAPTAC block due to charge neutralization by the anionic amphiphiles. The binding of SDS or PMAA to the PMAAPTAC block is confirmed by the zeta-potential measurements. The zeta potential decreases with an increase in the amount of the added SDS or PMAA, reflecting the charge neutralization of the cationic PMAAPTAC block with anionic SDS or PMAA. The mixed micelles were characterized by DLS, SEM, and fluorescence measurements. The DLS measurements give  $D_h = 125$  nm for the SDS/PS-*b*-PMAPTAC-*b*-PEO mixed micelles and  $D_h = 120$  nm for the PMAA/PS-*b*-PMAPTAC-*b*-PEO mixed micelles. The SEM measurements provided clear pictures of the mixed micelles with a spherical morphology for both SDS/PS-*b*-PMAPTAC-*b*-PEO and PMAA/PS-*b*-PMAPTAC-*b*-PEO systems. The significant difference between the two systems is that the SDS/PS-*b*-PMAPTAC-*b*-PEO system undergoes precipitation when ADN exceeds 50%, while the PMAA/PS-*b*-PMAPTAC-*b*-PEO system does not undergo precipitation even after the ADN exceeds 100%. This difference may be attributed to the hydrophilicity of the residual carboxyl groups present in PMAA after neutralization.

The exchange kinetics of organic dyes between the micelle particles of the PMAA/PS-*b*-PMAPTAC-*b*-PEO system was investigated by a fluorescence technique, which is based on electronic energy transfer from TY to FL. This result indicated that the exchange of the dyes between the micelle particles takes places within a time scale of seconds.

## Supplementary data

Supplementary data for this article (additional figures of the dependence of the  $I_1/I_3$  ratio on the polymer concentration are available for the solution of PS-*b*-PMAPTAC-*b*-PEO micelles and PMAA/PS-*b*-PMAPTAC-*b*-PEO mixed micelles and fluorescence spectra of FL and TY in aqueous solutions) are available on the journal Web site (canjchem.nrc.ca) or may be purchased from the Depository of Unpublished Data, Document Delivery, CISTI, National Research Council Canada, Ottawa, ON K1A 0R6, Canada. DUD 5319. For more information on obtaining material, refer to [cisti-icist.nrc-cnrc.gc.ca/cms/unpub\\_e.shtml](http://cisti-icist.nrc-cnrc.gc.ca/cms/unpub_e.shtml).

## Acknowledgment

The present study was supported by a Grant-in-Aid for Scientific Research (20310054) from the Japan Society for the Promotion of Science (JSPS).

## References

- (1) Sapijeszko, R. S.; Matijevic, E. *J. Colloid Interface Sci.* **1980**, *74* (2), 405. doi:10.1016/0021-9797(80)90210-6.
- (2) Sakai, H.; Kawahara, H.; Shimazaki, M.; Abe, M. *Langmuir* **1998**, *14* (8), 2208. doi:10.1021/la970952r.
- (3) Khanal, A.; Inoue, Y.; Yada, M.; Nakashima, K. *J. Am. Chem. Soc.* **2007**, *129* (6), 1534. doi:10.1021/ja0684904. PMID:17283999.

- (4) Liu, X.; Basu, A. *J. Am. Chem. Soc.* **2009**, *131* (16), 5718. doi:10.1021/ja809619w. PMID:19351114.
- (5) Tuzar, Z.; Kratochvíl, P. *Surface and Colloid Science*; Plenum Press: New York, 1993; Chap. 1.
- (6) Kříž, J.; Masař, B.; Pleštil, J.; Tuzar, Z.; Pospíšil, H.; Doskocilová, D. *Macromolecules* **1998**, *31* (1), 41. doi:10.1021/ma9708003.
- (7) Patrickios, C. S.; Hertler, W. R.; Abbott, N. L.; Hatton, T. A. *Macromolecules* **1994**, *27* (4), 930. doi:10.1021/ma00082a008.
- (8) Zhou, Z.; Li, Z.; Ren, Y.; Hillmyer, M. A.; Lodge, T. P. *J. Am. Chem. Soc.* **2003**, *125* (34), 10182. doi:10.1021/ja036551h. PMID:12926935.
- (9) Nakashima, K.; Bahadur, P. *Adv. Colloid Interface Sci.* **2006**, *123-126*, 75. doi:10.1016/j.cis.2006.05.016.
- (10) Gohy, J. F.; Willet, N.; Varshney, S.; Zhang, J. X.; Jerome, R. *Angew. Chem. Int. Ed.* **2001**, *40* (17), 3214. doi:10.1002/1521-3773(20010903)40:17<3214::AID-ANIE3214>3.0.CO;2-F.
- (11) Gohy, J. F.; Willet, N.; Varshney, S.; Zhang, J. X.; Jerome, R. e-polymers 2002; No. 035.
- (12) Štěpánek, M.; Matejíček, P.; Humpolícková, J.; Procházka, K. *Langmuir* **2005**, *21* (23), 10783. doi:10.1021/la0516680. PMID:16262352.
- (13) Khanal, A.; Li, Y.; Takisawa, N.; Kawasaki, N.; Oishi, Y.; Nakashima, K. *Langmuir* **2004**, *20* (12), 4809. doi:10.1021/la049762o. PMID:15984235.
- (14) Li, Y.; Khanal, A.; Kawasaki, N.; Oishi, Y.; Nakashima, K. *Bull. Chem. Soc. Jpn.* **2005**, *78* (3), 529. doi:10.1246/bcsj.78.529.
- (15) Khanal, A.; Nakashima, K.; Kawasaki, N.; Oishi, Y.; Uehara, M.; Nakamura, H.; Tajima, Y. *Colloid Polym. Sci.* **2005**, *283* (11), 1226. doi:10.1007/s00396-005-1302-9.
- (16) Liu, D.; Nakashima, K.; Tuzar, Z.; Stepanek, P. *Polym. J.* **2009**, *41* (6), 492. doi:10.1295/polymj.PJ2009037.
- (17) Liu, D.; Nakashima, K. *Inorg. Chem.* **2009**, *48* (9), 3898. doi:10.1021/ic900078s. PMID:19323507.
- (18) Liu, J. J.; Liu, D.; Yokoyama, Y.; Yusa, S.; Nakashima, K. *Langmuir* **2009**, *25* (2), 739. doi:10.1021/la802690m. PMID:19072145.
- (19) Mitsukami, Y.; Donovan, M. S.; Lowe, A. B.; McCormick, C. L. *Macromolecules* **2001**, *34* (7), 2248. doi:10.1021/ma0018087.
- (20) Yusa, S.; Yokoyama, Y.; Morishima, Y. *Macromolecules* **2009**, *42* (1), 376. doi:10.1021/ma8021162.
- (21) Wilhelm, M.; Zhao, C. L.; Wang, Y.; Xu, R.; Winnik, M. A.; Mura, J. L.; Riess, G.; Croucher, M. D. *Macromolecules* **1991**, *24* (5), 1033. doi:10.1021/ma00005a010.
- (22) Victor, S. P.; Sharma, C. P. *J. Biomater. Appl.* **2002**, *17* (2), 125. doi:10.1106/088532802028583. PMID:12557998.
- (23) Li, Y.; Nakashima, K. *Langmuir* **2003**, *19* (3), 548. doi:10.1021/la0258852.
- (24) Li, G.; Tian, Y.; Liang, Y. *J. Chem. Soc. Faraday Trans* **1993**, *89* (9), 1365. doi:10.1039/ft9938901365.
- (25) Qi, H.; Xiao, W.; Wang, Q.; Li, G.; Yu, J.; Li, G. *J. Lumin.* **2007**, *124* (2), 195. doi:10.1016/j.jlumin.2006.02.014.



# How switching the substituent of a pyrene derivative from a methyl to a butyl affects the fluorescence response of polystyrene randomly labeled with pyrene

Mark Ingratta, Manoj Mathew, and Jean Duhamel

**Abstract:** A series of polystyrenes randomly labeled with 1-pyrenebutanol were prepared by copolymerizing styrene and 1-pyrenebutylacrylate yielding the CoBuE-PS series. Solutions of CoBuE-PS were prepared in nine organic solvents having viscosities ranging from 0.36 to 5.5 mPa·s and the fluorescence spectra and pyrene monomer and excimer fluorescence decays were acquired. Analysis of the fluorescence spectra yielded the  $I_E/I_M$  ratio, whereas analysis of the fluorescence decays with the fluorescence blob model (FBM) yielded the parameters  $N_{\text{blob}}^0$ ,  $\langle k_{\text{blob}} \times N_{\text{blob}} \rangle$ , and  $k_{\text{blob}}^0$ . These parameters were compared to those obtained with two other series of pyrene-labeled polystyrenes, which had been studied earlier, namely CoA-PS and CoE-PS where pyrene was attached to the polymer backbone via a methylamide and benzyl methyl-ether linker, respectively. Although the parameters  $I_E/I_M$ ,  $N_{\text{blob}}^0$ ,  $\langle k_{\text{blob}} \times N_{\text{blob}} \rangle$ , and  $k_{\text{blob}}^0$  took different values according to the specific nature of the linker connecting pyrene to the polystyrene backbone, they exhibited trends that were quite similar for all the pyrene-labeled polystyrene constructs. The excellent agreement between the parameters retrieved for the three different types of pyrene-labeled polystyrenes suggests that the FBM accounts satisfyingly for differences in the nature of the label used, while still retrieving information pertinent to the polymer of interest.

**Key words:** polymer chain dynamics, fluorescence, polystyrene, pyrene.

**Résumé :** La série CoBuE-PS de polystyrènes marqués aléatoirement par du 1-pyrènebutanol a été préparée par copolymérisation du styrène avec de l'acrylate de 1-pyrènebutyle. Des solutions de CoBuE-PS ont été préparées dans neuf solvants organiques dont les viscosités s'échelonnent de 0,36 à 5,5 mPa s. Les spectres de fluorescence ont été mesurés ainsi que les déclins de fluorescence du monomère et de l'excimère du pyrène. L'analyse des spectres de fluorescence a permis de déterminer les valeurs des rapports  $I_E/I_M$  alors que l'analyse des déclins de fluorescence à l'aide du modèle (« FBM ») conduit aux paramètres,  $N_{\text{blob}}^0$ ,  $\langle k_{\text{blob}} \times N_{\text{blob}} \rangle$  et  $k_{\text{blob}}^0$ . Ces paramètres ont été comparés à ceux obtenus avec deux autres séries de polystyrènes marqués par du pyrène étudiées antérieurement, soit les séries CoA-PS et CoE-PS dans lesquels les unités de pyrène étaient respectivement attachés à un squelette de polymère par des groupes méthylamide et oxide de benzométhyle. Même si les paramètres  $I_E/I_M$ ,  $N_{\text{blob}}^0$ ,  $\langle k_{\text{blob}} \times N_{\text{blob}} \rangle$  et  $k_{\text{blob}}^0$  varient suivant la nature spécifique des groupes qui relient le pyrène au squelette de polystyrène, ils présentent tous des tendances assez similaires pour tous les polymères de polystyrène marqué par du pyrène. L'excellent accord entre les paramètres obtenus à partir de trois types différents de polystyrènes marqués par du pyrène suggère que le modèle (« FBM ») permet d'expliquer d'une façon satisfaisante les différences dans la nature du marqueur utilisé tout en permettant d'en tirer l'information pertinente relative au polymère sous étude.

**Mots-clés :** dynamique de chaîne de polymère, fluorescence, polystyrène, pyrène.

## Introduction

In the late 1970s and early 1980s, the research groups of Winnik<sup>1-7</sup> in Toronto, Canada, and Cuniberti and Perico<sup>8,9</sup> in Genova, Italy, conducted pioneering experiments that demonstrated how the process of excimer formation between pyrene pendants covalently attached onto a polymer in solu-

tion provides information at the molecular level on the flexibility of the polymer backbone. Among the various scientific breakthroughs made during that period was the use by the Winnik group in Toronto<sup>1</sup> of time-resolved fluorescence decays to obtain a direct measure of the rate constant of pyrene encounters between two pyrenes attached at the opposite ends of a monodisperse polymer. The bulk of

Received 21 August 2009. Accepted 14 October 2009. Published on the NRC Research Press Web site at [canjchem.nrc.ca](http://canjchem.nrc.ca) on 10 February 2010.

*This article is part of a Special Issue dedicated to Professor M. A. Winnik.*

**M. Ingratta, M. Mathew, and J. Duhamel.**<sup>1</sup> Institute for Polymer Research, Department of Chemistry, University of Waterloo, 200 University Avenue West, Waterloo, ON N2L 3G1, Canada.

<sup>1</sup>Corresponding author (e-mail: [jduhamel@uwaterloo.ca](mailto:jduhamel@uwaterloo.ca)).

the work carried out by Winnik and co-workers<sup>1–7</sup> and Cuni-berti and Perico<sup>8,9</sup> was done with pyrene end-labeled monodisperse polymers to take advantage of the observation made in 1974 by Wilemski and Fixman<sup>10,11</sup> that the process of end-to-end cyclization can be described by a single rate constant,  $k_{cy}$ , if the chain is monodisperse.

The majority of these early cyclization experiments used pyrene due to its ability to form an excimer.<sup>12</sup> Upon excitation, an excited pyrene can either decay as a pyrene monomer with its lifetime,  $\tau_M$ , or it can encounter a ground-state pyrene to form an excimer that emits with a lifetime  $\tau_E$ . The pyrene monomer and excimer are two distinct species that represent, respectively, the reactants and the product of the cyclization undergone by a pyrene end-labeled polymer. Thus monitoring the rate of excimer formation provides a measure of  $k_{cy}$ . In turn, the cyclization experiments could draw from earlier studies conducted by Birks<sup>12</sup> that established the validity of a kinetic scheme now referred to as the Birks' scheme that provides a robust procedure to determine the rate constant of excimer formation from fluorescence decay measurements acquired for the pyrene monomer and excimer. Finally, the fact that pyrene acts both as the chromophore upon excitation and as the quencher while in the ground-state simplifies substantially the labeling chemistry since no special arrangement needs to be made in terms of reacting groups to ensure specific labeling of the chain with either the chromophore or the quencher.

As mentioned earlier, most cyclization experiments carried out with pyrene-labeled polymers used pyrene end-labeled monodisperse polymers due to the simplifications associated with the use of a unique rate constant,  $k_{cy}$ , to describe end-to-end cyclization.<sup>10,11</sup> As a matter of fact, the strict relationship predicted by Wilemski and Fixman<sup>10,11</sup> that was found to exist between polymer chain length and  $k_{cy}$  made it quite difficult to study end-labeled polydisperse polymers or randomly labeled polymers, since the process of excimer formation needed to be handled by a distribution of rate constants, with one rate constant corresponding to each and every polymer length spanning every two pyrenes. In turn, this complication prevented the use of randomly labeled polymers to study polymer chain dynamics in solution despite their easier preparation and dramatic enhancement of pyrene–pyrene encounters over what is typically observed with pyrene end-labeled monodisperse polymers.<sup>13</sup>

In 1999, this laboratory introduced the fluorescence blob model (FBM) as an analytical tool to study polymers randomly labeled with pyrene.<sup>14</sup> In a series of studies, the FBM was shown to be surprisingly robust, enabling the experimentalist to retrieve reliable quantitative information about polymer chain dynamics for different polymer backbones,<sup>15,16</sup> polymer architectures,<sup>17</sup> and in solutions of different solvent quality toward the polymer,<sup>13,15,16</sup> viscosity,<sup>18</sup> or polymer concentration.<sup>19</sup> In an interesting recent development, the rather complex FBM was found to yield trends in terms of polymer chain dynamics that perfectly matched those obtained with end-labeled monodisperse polymers, providing an appealing alternative to study polymers that cannot be easily prepared with a narrow molecular weight distribution and (or) end-labeled.<sup>13,18</sup>

So far, the entire work carried out by this laboratory on

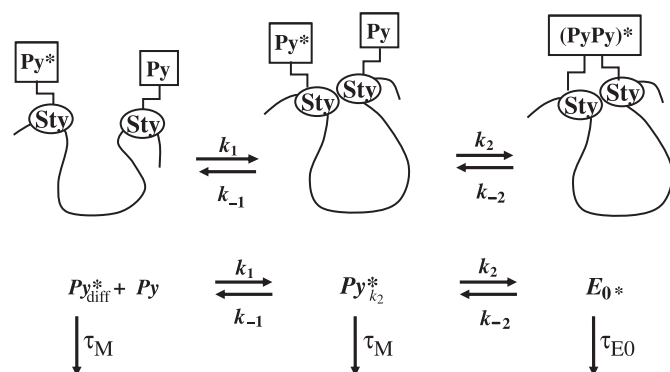
polymers randomly labeled with pyrene used a 1-pyrene-methyl derivative with an alcohol or amine functionality to label the polymer of interest, whereas a large number of studies found in the literature use a 1-pyrenebutyl derivative.<sup>20–29</sup> This state of affair is unfortunate because the fluorescence response of a given pyrene-labeled polymer construct has been found to be extremely sensitive, among other factors, to the nature of the linker connecting the pyrene derivative to the chain.<sup>17</sup> Although the FBM accounts for these differences, FBM analysis yields parameters that cannot be directly compared if two polymers are labeled with different linkers and pyrene derivatives. Consequently, the parameters retrieved from the analysis of fluorescence data acquired with polymers randomly labeled with pyrene will take different absolute values whether the polymer is labeled with a 1-pyrene-methyl or -butyl derivative, making direct comparison between such constructs difficult. This manuscript remedies this gap by conducting a FBM analysis on a series of polystyrene samples randomly labeled with pyrene (Py–PS) where pyrene is connected to the chain via a butyl ester linker. This type of Py–PS construct is referred to as CoBuE–PS in this report. The CoBuE–PS series was studied in nine organic solvents. The results obtained from the FBM analysis were compared to those obtained earlier with two other Py–PS constructs, the CoA–PS and CoE–PS series where pyrene is linked to the chain via a methyl amide and a benzyl methyl ether linker, respectively.<sup>13,17,18</sup> The results obtained with the CoA–PS and CoE–PS series have already been published,<sup>18</sup> but they are presented in this study to enable direct comparison between the results obtained with CoBuE–PS. Although the parameters retrieved from the FBM took different values for the three Py–PS constructs, the trends obtained with the FBM parameters pertaining to CoBuE–PS are quite similar to those obtained with CoA–PS and CoE–PS, demonstrating that the FBM accounts satisfyingly for the differences in chemical nature of the pyrene-to-backbone linker that were introduced in those Py–PS constructs. The results obtained with CoBuE–PS are expected to provide a useful reference point that can be used to compare the chain dynamics of other polymers labeled with the commonly encountered 1-pyrenebutyl derivative.

## Theory

Excimer formation between pyrenes covalently attached onto a polymer can be viewed as a two step mechanism as depicted in Scheme 1.<sup>17</sup> In the first step, the polymer chain brings two pyrenes via diffusion within striking range with a rate constant  $k_1$ . The second step corresponds to the rapid rearrangement of the pyrenes to form an excimer with a rate constant  $k_2$ . The first and second steps are controlled by the dynamics of the polymer backbone and that of the pyrene-to-backbone linker, respectively. Although Scheme 1 suggests that diffusive encounters between polymer segments can be described by a single rate constant,  $k_1$ , this is not the case when the fluorophores are attached randomly onto the polymer as for the case at hand.<sup>30–32</sup>

For randomly labeled polymers, an encounter between any two polymer segments bearing a pyrene label is characterized by a rate constant  $k_1$  that depends on the length of polymer spanning the two segments. As a result, there exists

**Scheme 1.** The effect of backbone and side chain motion on the kinetics of excimer formation.



a distribution of rate constants  $k_1$ , which somewhat complicates the analysis of the fluorescence data. In the case of excimer formation between pyrenes randomly attached onto a polymer, this distribution of rate constants  $k_1$  has been described by a function,  $f(t)$ , whose derivation follows from the fluorescence blob model (FBM).<sup>33</sup> Furthermore, Scheme 1 can be simplified by noting that pyrene excimer dissociation is negligible so that  $k_{-2}$  can be set equal to zero and that  $k_2$  being substantially larger than  $k_{-1}$ ,  $k_{-1}$  can be neglected.<sup>12</sup>

Based on Scheme 1, several pyrene species are expected to be present in solution.<sup>33</sup> They include those excited pyrenes ( $\text{Py}^*_{\text{diff}}$ ) that diffuse slowly in solution until they find themselves within striking range of a ground-state (GS) pyrene. Those nearby pyrene pairs constitute the species of excited pyrenes,  $\text{Py}^*_{k_2}$ , that forms an excimer,  $\text{E0}^*$ , rapidly with a rate constant  $k_2$ . Both  $\text{Py}^*_{\text{diff}}$  and  $\text{Py}^*_{k_2}$  emit with the monomer lifetime  $\tau_M$ , whereas  $\text{E0}^*$  emits with the excimer lifetime  $\tau_{\text{E0}}$ . Also, the random labeling of the polymer backbone induces the formation of pyrene-rich and pyrene-poor pockets where excimer formation is, respectively, enhanced or reduced. In the pyrene-poor pockets, some excited pyrenes will not be able to encounter a GS pyrene during their lifetime and they emit as isolated, unattached “free” pyrenes do and are thus referred to as  $\text{Py}^*_{\text{free}}$ . Finally, the steric constraints induced by the covalent attachment of a pyrene moiety onto the polymer has sometimes been found to generate some improper stacking of the pyrene moieties

resulting in the formation of either short- ( $\text{ES}^*$ ) or long- ( $\text{EL}^*$ ) lived pyrene dimers that emit with a lifetime  $\tau_{\text{ES}}$  and  $\tau_{\text{EL}}$ , respectively. The time-dependent behavior of the concentrations of the different pyrene species in solution can be described by the following set of differential equations.

$$[1] \quad \frac{d[\text{Py}^*_{\text{diff}}]}{dt} = -f(t) - \frac{1}{\tau_M} [\text{Py}^*_{\text{diff}}]$$

$$[2] \quad \frac{d[\text{Py}^*_{\text{free}}]}{dt} = -\frac{1}{\tau_M} [\text{Py}^*_{\text{free}}]$$

$$[3] \quad \frac{d[\text{Py}^*_{k_2}]}{dt} = f(t) - \left(k_2 + \frac{1}{\tau_M}\right) [\text{Py}^*_{k_2}]$$

$$[4] \quad \frac{d[\text{E0}^*]}{dt} = k_2 [\text{Py}^*_{k_2}] - \frac{1}{\tau_{\text{E0}}} [\text{E0}^*]$$

$$[5] \quad \frac{d[\text{ES}^*]}{dt} = -\frac{1}{\tau_{\text{ES}}} [\text{ES}^*]$$

$$[6] \quad \frac{d[\text{EL}^*]}{dt} = -\frac{1}{\tau_{\text{EL}}} [\text{EL}^*]$$

The concentration,  $[\text{Py}^*_{\text{diff}}]_{(t)}$ , is obtained by applying the FBM. The FBM postulates that while it remains excited, an excited pyrene probes a finite volume called a blob.<sup>14,32</sup> A blob is then taken as a volume unit, which is used to arbitrarily divide the polymer coil into a cluster of blobs. The random labeling of the chain with pyrene implies that the chromophores distribute themselves randomly among the blobs according to a Poisson distribution. The encounter between two polymer segments bearing a pyrene pendant occurs with a rate constant  $k_{\text{blob}}$ . The exchange of segments bearing pyrene moving in and out of the blobs is handled by  $k_e[\text{blob}]$ , which is the product of the exchange rate constant and the blob concentration inside the polymer coil. The average number of labels per blob is given by  $\langle n \rangle$ . Based on the above,  $[\text{Py}^*_{\text{diff}}]_{(t)}$  has been derived and its expression is given in eq. [7].<sup>14</sup>

$$[7] \quad [\text{Py}^*_{\text{diff}}]_{(t)} = [\text{Py}^*_{\text{diff}}]_0 \exp \left[ -\left(A_2 + \frac{1}{\tau_M}\right)t - A_3 \left(1 - \exp(-A_4 t)\right) \right]$$

In eq. [7], the parameters  $A_2$ ,  $A_3$ , and  $A_4$  are functions of  $k_{\text{blob}}$ ,  $\langle n \rangle$ , and  $k_e[\text{blob}]$  as shown in eq. [8].

$$[8] \quad A_2 = \langle n \rangle \frac{k_{\text{blob}} k_e [\text{blob}]}{k_{\text{blob}} + k_e [\text{blob}]} \quad A_3 = \langle n \rangle \frac{(k_{\text{blob}})^2}{(k_{\text{blob}} + k_e [\text{blob}])^2} \quad A_4 = k_{\text{blob}} + k_e [\text{blob}]$$

The same equation had already been derived to handle the exchange of chromophores between surfactant micelles.<sup>34</sup> Equation [7] can then be used to determine  $f(t)$  in eqs. [1] and [3]. Knowing  $f(t)$  allows one to integrate eq. [3] to get an expression for  $[\text{Py}^*_{k_2}]_{(t)}$ . Knowing the expression of  $[\text{Py}^*_{k_2}]_{(t)}$  enables one to integrate eq. [4] to get  $[\text{E0}^*]_{(t)}$ . Integration of eqs. [2], [5], and [6] is trivial. A more thorough description of the derivation used to find the overall time-dependent profile of the pyrene monomer  $[\text{Py}^*]_{(t)}$  and excimer  $[\text{E}^*]_{(t)}$  can be found in an earlier publication.<sup>33</sup> The final result is shown in eqs. [9] and [10].

$$\begin{aligned}
 [9] \quad [\text{Py}^*]_{(t)} &= [\text{Py}_{\text{diff}}^*]_{(t)} + [\text{Py}_{k_2}^*]_{(t)} + [\text{Py}_{\text{free}}^*]_{(t)} \\
 &= [\text{Py}_{\text{diff}}^*]_0 \exp \left( - \left( A_2 + \frac{1}{\tau_M} \right) t - A_3 \left( 1 - \exp(-A_4 t) \right) \right) \\
 &\quad + \left( [\text{Py}_{k_2}^*]_0 + [\text{Py}_{\text{diff}}^*]_0 e^{-A_3} \sum_{i=0}^{\infty} \frac{A_3^i}{i!} \frac{A_2 + iA_4}{A_2 + iA_4 - k_2} \right) \exp \left( - \left( k_2 + \frac{1}{\tau_M} \right) t \right) \\
 &\quad - [\text{Py}_{\text{diff}}^*]_0 e^{-A_3} \sum_{i=0}^{\infty} \frac{A_3^i}{i!} \frac{A_2 + iA_4}{A_2 + iA_4 - k_2} \exp \left( - \left( A_2 + iA_4 + \frac{1}{\tau_M} \right) t \right) + [\text{Py}_{\text{free}}^*]_0 \exp \left( - \frac{t}{\tau_M} \right)
 \end{aligned}$$

$$\begin{aligned}
 [10] \quad [\text{E}^*]_{(t)} &= [\text{E0}^*]_{(t)} + [\text{ES}^*]_{(t)} + [\text{EL}^*]_{(t)} \\
 &= k_2 \left( \left( [\text{Py}_{k_2}^*]_0 + [\text{Py}_{\text{diff}}^*]_0 e^{-A_3} \sum_{i=0}^{\infty} \frac{A_3^i}{i!} \frac{A_2 + iA_4}{A_2 + iA_4 - k_2} \right) \times \frac{\exp \left( - \frac{t}{\tau_{\text{E0}}} \right) - \exp \left( - \left( k_2 + \frac{1}{\tau_M} \right) t \right)}{k_2 + \frac{1}{\tau_M} - \frac{1}{\tau_{\text{E0}}}} \right. \\
 &\quad \left. + [\text{Py}_{\text{free}}^*]_0 e^{-A_3} \sum_{i=0}^{\infty} \frac{A_3^i}{i!} \frac{A_2 + iA_4}{A_2 + iA_4 - k_2} \frac{\exp \left( - \left( A_2 + iA_4 + \frac{1}{\tau_M} \right) t \right) - \exp \left( - \frac{t}{\tau_{\text{E0}}} \right)}{A_2 + iA_4 + \frac{1}{\tau_M} - \frac{1}{\tau_{\text{E0}}}} \right) \\
 &\quad + [\text{E0}^*]_0 \times \exp \left( \frac{t}{\tau_{\text{E0}}} \right) + [\text{ES}^*]_0 \times \exp \left( - \frac{t}{\tau_{\text{ES}}} \right) + [\text{EL}^*]_0 \times \exp \left( - \frac{t}{\tau_{\text{EL}}} \right)
 \end{aligned}$$

It must be noted that if  $k_2$  in Scheme 1 is very large, eq. [9] reverts back to eq. [11], which is the equation typically used for the FBM analysis of the fluorescence decays of the pyrene monomer.<sup>14,32</sup>

$$[11] \quad [\text{Py}^*]_{(t)} = [\text{Py}_{\text{diff}}^*]_0 \exp \left[ - \left( A_2 + \frac{1}{\tau_M} \right) t - A_3 \left( 1 - \exp(-A_4 t) \right) \right] + [\text{Py}_{\text{free}}^*]_0 \exp(-t/\tau_M)$$

Fitting the monomer decays with eq. [9] yields the fractions  $f_{\text{Mdiff}}$ ,  $f_{\text{Mk}_2}$ , and  $f_{\text{Mfree}}$ , which represent the molar fractions of the  $\text{Py}_{\text{diff}}^*$ ,  $\text{Py}_{k_2}^*$ , and  $\text{Py}_{\text{free}}^*$  species contributing to the monomer decays, whereas fitting the excimer decays with eq. [10] yields the fractions  $f_{\text{Ediff}}$ ,  $f_{\text{Ek}_2}$ ,  $f_{\text{EE0}}$ ,  $f_{\text{EES}}$ , and  $f_{\text{EEL}}$ , which represent the molar fractions of the  $\text{Py}_{\text{diff}}^*$ ,  $\text{Py}_{k_2}^*$ ,  $\text{Py}_{\text{free}}^*$ ,  $\text{E0}^*$ ,  $\text{ES}^*$ , and  $\text{EL}^*$  species contributing to the excimer decays. In turn, the fractions  $f_{\text{Mdiff}}$ ,  $f_{\text{Mk}_2}$ ,  $f_{\text{Mfree}}$ ,  $f_{\text{Ediff}}$ ,  $f_{\text{Ek}_2}$ ,  $f_{\text{EE0}}$ ,  $f_{\text{EES}}$ , and  $f_{\text{EEL}}$  can be rearranged to yield the molar fractions  $f_{\text{diff}}$ ,  $f_{k_2}$ ,  $f_{\text{free}}$ ,  $f_{\text{E0}}$ ,  $f_{\text{ES}}$ , and  $f_{\text{EL}}$  of all the pyrene species present in solution.

## Experimental

### Materials

Copolymerization of styrene with either 1-pyrenemethylacrylamide, 1-pyrenebutylacrylate, or 4-(1-pyrenyl)methoxymethylstyrene yielded the Py-PS constructs shown in Table 1 and are referred to as CoA-PS, CoBuE-PS, and CoE-PS, respectively. The polymerization of CoA-PS and CoE-PS has already been reported<sup>13,18</sup> along with their number-average molecular weight ( $M_n$ ), polydispersity index (PDI), molar fraction of pyrene-labeled monomer ( $x$ ), and pyrene content ( $\lambda_{\text{Py}}$  expressed in moles of pyrene per gram of polymer). The copolymerization of CoBuE-PS was conducted in the same manner as that of CoA-PS and CoE-PS using 1-pyrenebutylacrylate as the pyrene-labeled monomer. The synthesis of 1-pyrenebutylacrylate was conducted according to ref. 35. The  $M_n$ , PDI,  $x$ , and  $\lambda_{\text{Py}}$  values of the CoBuE-PS are listed in Table 2. Table 2 lists the solvents used

**Table 1.** Chemical structures of the pyrene-labeled polystyrenes.

CoE-PS	CoA-PS	CoBuE-PS

in this study and their quality towards polystyrene has been described in earlier publications.<sup>13,18</sup>

### Fluorescence measurements

Fluorescence spectra and decays of the CoBuE-PS samples were acquired and analyzed by following the same protocol used in earlier publications.<sup>13,18</sup> The pyrene monomer fluorescence decays were fitted with eq. [11], whereas the pyrene monomer and excimer fluorescence decays could be analyzed globally using eqs. [9] and [10]. The monomer lifetimes,  $\tau_M$ , used to fit the fluorescence decays are listed in Table 3. They were determined in earlier publications.<sup>13,18</sup>



**Table 2.** Number-average molecular weight ( $M_n$ ), polydispersity index (PDI), molar fraction of pyrene-labeled monomers ( $x$ ), and pyrene content ( $\lambda_{Py}$  in mol g<sup>-1</sup>) for the CoBuE-PS constructs.

$x$ (mol% pyrene)	$\lambda_{Py} \times 10^{-4}$ (mol g <sup>-1</sup> )	$M_n$ (kg mol <sup>-1</sup> )	PDI
2.1	1.9	46	1.65
3.1	2.8	43	1.67
4.5	3.9	49	1.62
5.4	4.7	53	1.69
6.0	5.1	46	1.68

**Table 3.** Solvent viscosities and monomer lifetimes ( $\tau_M$ ) in the different solvents.<sup>13,18</sup>

Solvent	Viscosity (mPa s) at 25 °C	$\tau_M$ (ns) for CoBuE-PS	$\tau_M$ (ns) for CoA-PS	$\tau_M$ (ns) for CoE-PS
Methyl acetate	0.36	198	250	250
Methyl ethyl ketone (MEK)	0.41	117	170	172
Dichloromethane (DCM)	0.41	105	152	144
Tetrahydrofuran (THF)	0.46	190	258	257
Toluene	0.56	172	241	230
<i>N,N</i> -Dimethylformamide (DMF)	0.79	160	220	220
Dioxane	1.18	175	243	242
<i>N,N</i> -Dimethylacetamide (DMA)	1.92	160	215	215
Benzyl Alcohol (BA)	5.47	133	198	180

**Simulations of fluorescence decays**

Equations [9] and [10] depend on 13 independent parameters which are  $k_{\text{blob}}$ ,  $\langle n \rangle$ ,  $k_e[\text{blob}]$ ,  $k_2$ ,  $\tau_{E0}$ ,  $\tau_{ES}$ ,  $\tau_{EL}$ , and the concentrations  $[\text{Py}^*_{\text{diff}}]_0$ ,  $[\text{Py}^*_{k_2}]_0$ ,  $[\text{Py}^*_{\text{free}}]_0$ ,  $[\text{E0}^*]_0$ ,  $[\text{ES}^*]_0$ , and  $[\text{EL}^*]_0$ . If no short- and long-lived dimer can be detected as is the case in the present study,  $[\text{ES}^*]_0$ ,  $[\text{EL}^*]_0$ ,  $\tau_{ES}$ , and  $\tau_{EL}$  do not need to be optimized and the number of independent parameters reduces to nine. Although one might question the reliability of fitting globally a monomer and excimer fluorescence decays with nine adjustable parameters, it must be pointed out that the same number of nine adjustable parameters is also used when fitting globally a monomer and excimer fluorescence decays with a sum of three exponentials, where the three decay times are coupled in the analysis. Global analysis of a monomer and excimer fluorescence decays with three exponentials has become a routine procedure in the scientific literature.<sup>36,37</sup>

Nevertheless, an error analysis of the parameters retrieved from the global analysis of the fluorescence decays was conducted as follows. The parameters retrieved from the global analysis of each pair of monomer and excimer fluorescence decays were used to generate 20 pairs of monomer and excimer decays having different Poisson noise patterns. The 20 pairs of decays were analyzed globally with eqs. [9] and [10]. The parameters retrieved from the analysis were averaged and their standard deviation was calculated. The errors on the parameters reported in Tables SI.1–SI.6 in the Supplementary data represent the larger value of the standard deviation or the difference between the actual input parameter minus the averaged value of the parameter retrieved from the analysis of the 20 pairs of simulated decays. Except for  $k_e[\text{blob}]$ , which is the parameter that always exhibits the largest errors,<sup>14</sup> and the fractions  $f_{M\text{free}}$  and  $f_{E0}$ , which took very small values, the errors on all the other parameters

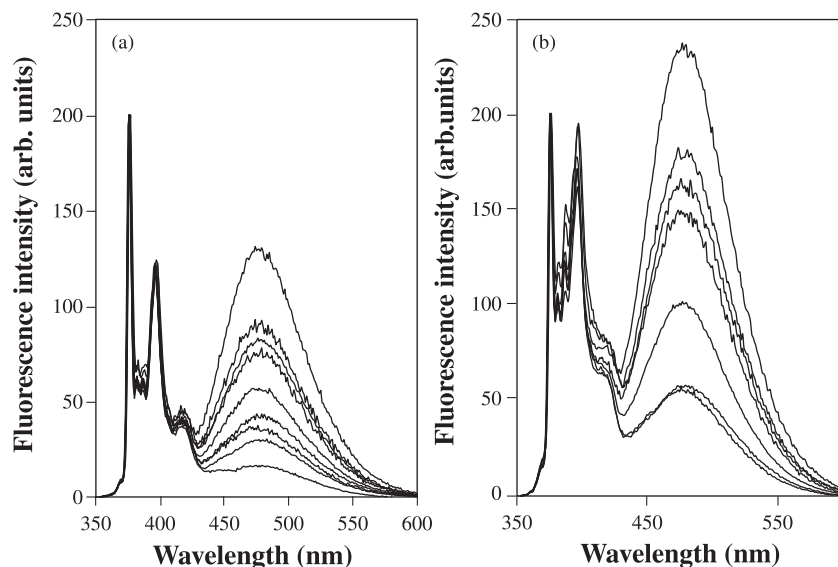
were smaller than 5% in the vast majority of cases, being as large as 10% in a few isolated cases.

**Results and discussion**

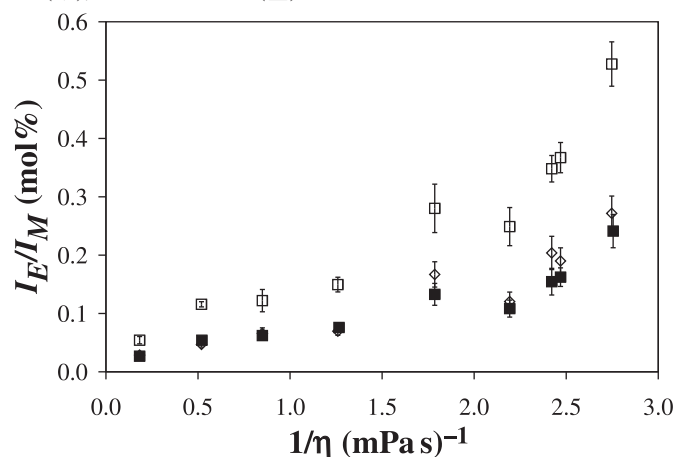
The structures of the three pyrene-labeled polystyrene constructs referred to as CoA-PS, CoBuE-PS, and CoE-PS are shown in Table 1. The pyrenyl pendants of CoE-PS are connected to the PS backbone via a flexible and long ether linker that holds the chromophore away from the backbone. In the CoA-PS constructs, pyrene is connected to the PS backbone via a short and rigid amide linker. Earlier studies of the pyrene fluorescence of CoA-PS and CoE-PS have reflected the differences in chemical structure of those constructs, showing that an excited pyrene attached to the CoE-PS backbone probes a larger volume than when attached to CoA-PS.<sup>17,18</sup> Furthermore, a 1-pyrenemethyl derivative was used to prepare CoA-PS and CoE-PS. In the case of CoBuE-PS, an ester bond was used to connect a 1-pyrenebutyl linker to the PS backbone.

As shown in Fig. 1, the fluorescence spectrum of the pyrene monomer observed between 370 and 430 nm is strongly affected by the nature of its substituent. The intensity ratio of the first to the third fluorescence peak, the  $I_1/I_3$  ratio, takes a value between 2.9 and 3.3 for all CoBuE-PS spectra shown in Fig. 1. By comparison, the  $I_1/I_3$  ratio of the CoA-PS samples takes a smaller value between 1.4 and 2.1. Similar  $I_1/I_3$  ratios were obtained for the CoE-PS series. In the case of molecular pyrene, the  $I_1/I_3$  ratio shows a clear correlation with solvent polarity increasing from 1.1 to 1.81, a 60% change as the solvent dielectric constant  $\epsilon$  increases from 2.4 in toluene to 36.7 in DMF.<sup>38</sup> This correlation is dampened and not as consistent for the 1-pyrenemethyl derivative where the  $I_1/I_3$  ratio of CoA-PS changes by less than 50% between dioxane ( $\epsilon = 2.2$ ) and DMA ( $\epsilon = 38.9$ )

**Fig. 1.** Fluorescence spectra of (A) CoEBu-PS with a pyrene content of 3.1 mol% and (B) CoA-PS with a pyrene content of 3.7 mol%. Solvents from top to bottom: methyl acetate, methyl ethyl ketone, dichloromethane, toluene, tetrahydrofuran, *N,N*-dimethylformamide, dioxane, dimethylacetamide, and benzyl alcohol.



**Fig. 2.** Plot of  $(I_E/I_M)/x$  as a function of  $\eta^{-1}$  for CoE-PS ( $\square$ ), CoA-PS ( $\diamond$ ), and CoBuE-PS ( $\blacksquare$ ).



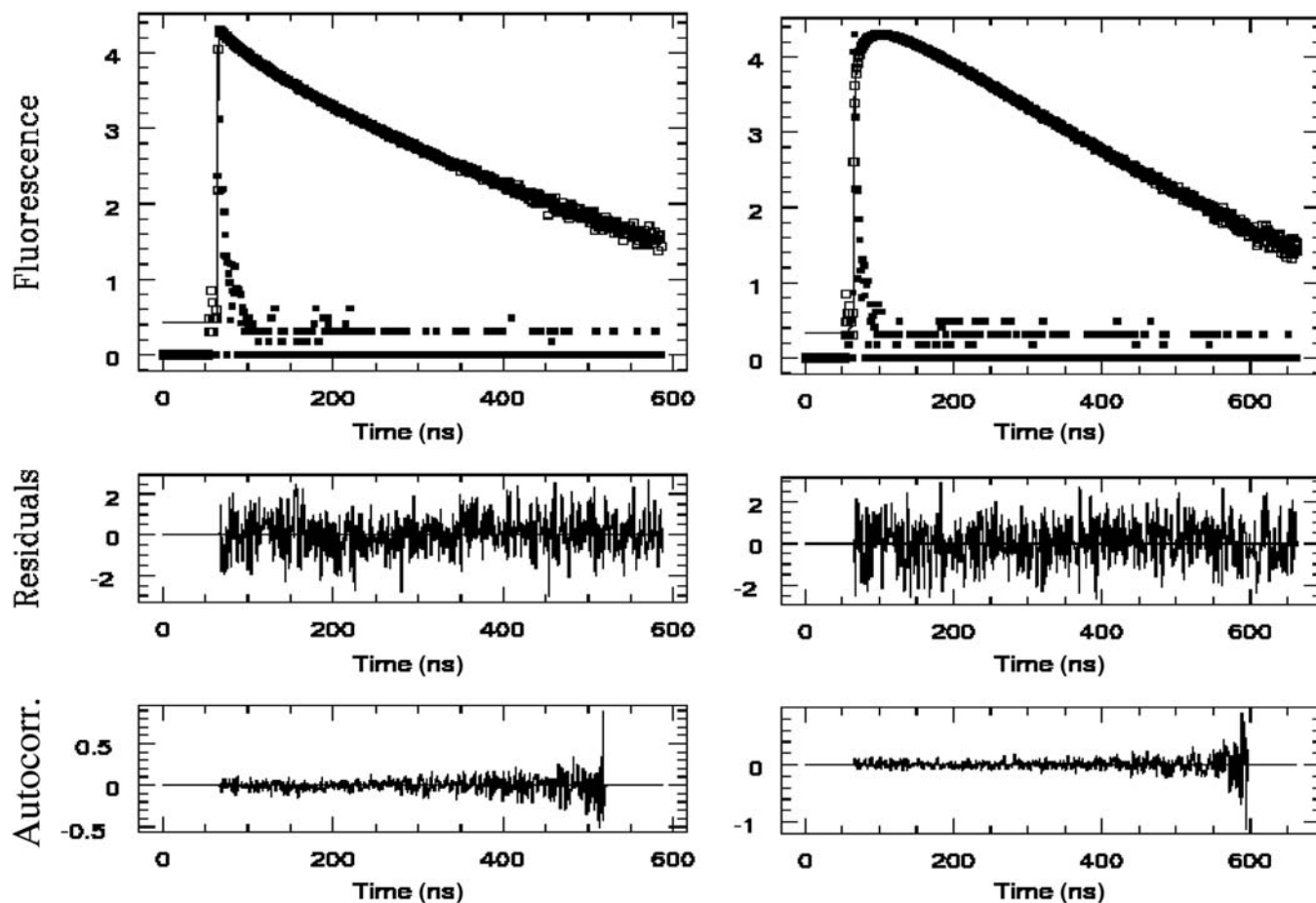
and is non-existent for the 1-pyrenebutyl pendant since the same change in  $\epsilon$  results in a 10% change for the  $I_1/I_3$  ratio of CoBuE-PS. These observations have already been reported.<sup>39,40</sup> The fluorescence emission corresponding to the  $I_1$  band at  $\sim 375$  nm has been reported as being symmetry forbidden and is repressed in apolar solvents for pyrene.<sup>41</sup> Aromatic<sup>41</sup> and polar<sup>38,42,43</sup> solvents appear to enhance the emission at 375 nm, as well as substituents that reduce the symmetry of pyrene such as the methyl<sup>44</sup> or butyl substituents of the 1-pyrenemethyl and 1-pyrenebutyl pendants used in this study. Spectral differences between the 1-pyrenemethyl and 1-pyrenebutyl pendants have also been compared for different constructs of pyrene-labeled poly(L-glutamic acid).<sup>45</sup>

Most importantly, the differences in the  $I_1/I_3$  ratio of CoA-PS and CoBuE-PS indicate that the spectral features of the 1-pyrenemethyl and 1-pyrenebutyl derivatives are different. Since the first peak of the pyrene monomer at  $\sim 375$  nm is taken as a measure of the pyrene monomer flu-

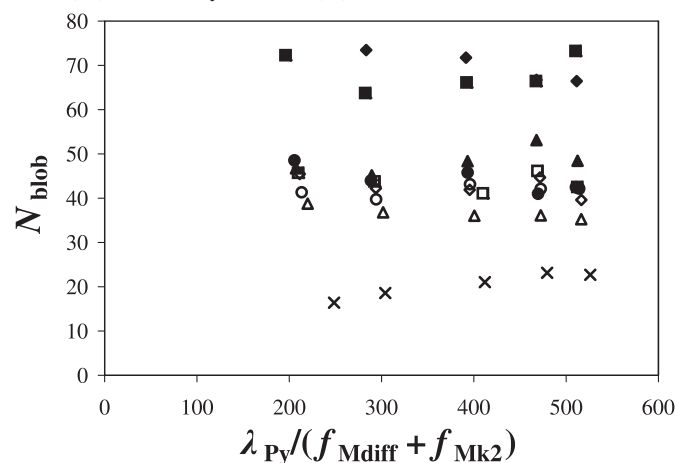
orescence intensity by any experimentalist dealing with pyrene fluorescence, the different spectral features exhibited by the two pyrene derivatives make it literally impossible to use the  $I_E/I_M$  ratio obtained from the steady-state fluorescence spectra to compare how much excimer is generated by a given polymer, whether or not that polymer has been labeled with a 1-pyrenemethyl or 1-pyrenebutyl derivative. As a matter of fact, a rapid analysis of the fluorescence spectra shown in Fig. 1 leads to the conclusion that CoBuE-PS generates less excimer than CoA-PS. This statement is confirmed in Fig. 2 that shows the  $I_E/I_M$  ratio of the three constructs as a function of the inverse of solvent viscosity ( $\eta^{-1}$ ). Although the  $I_E/I_M$  ratio increases with increasing  $\eta^{-1}$  regardless of the construct and as expected, since a smaller viscosity enhances excimer formation, it is noticeable that CoBuE-PS yields the smallest  $I_E/I_M$  ratio at all viscosities. Since the  $I_E/I_M$  ratio is typically taken as a measure of backbone flexibility, a smaller  $I_E/I_M$  ratio would suggest that CoBuE-PS is the construct that is the least efficient at producing excimer. In turn, this result is somewhat unexpected because the backbone being the same in both constructs, namely polystyrene, the longer and more flexible butyl ester linker of CoBuE-PS is expected to facilitate excimer formation when compared to the shorter and more rigid amide linker of CoA-PS. More realistically, the smaller  $I_E/I_M$  ratios obtained for CoBuE-PS must be a consequence of the larger  $I_M$  values obtained with the 1-pyrenebutyl derivative. The above discussion clearly illustrates the difficulties encountered when directly comparing the  $I_E/I_M$  ratios obtained with macromolecules labeled with different pyrene derivatives. In such a case, comparison of the process of excimer formation in CoA-PS, CoBuE-PS, and CoE-PS can only be achieved from the quantitative analysis of the monomer and excimer fluorescence decays.

To this end, the fluorescence decays of the pyrene monomer and excimer of all CoBuE-PS samples were acquired in nine organic solvents. The monomer decays could be fitted satisfyingly with eq. [11], but global analysis of the mono-

**Fig. 3.** Monomer (left,  $\lambda_{em} = 375$  nm) and excimer (right,  $\lambda_{em} = 510$  nm) decays acquired for the CoBuE-PS sample excited at 344 nm and labeled with 5.4% pyrene in dioxane. The decays were analyzed globally with eqs. [9] and [10] yielding  $\chi^2 = 1.02$ .

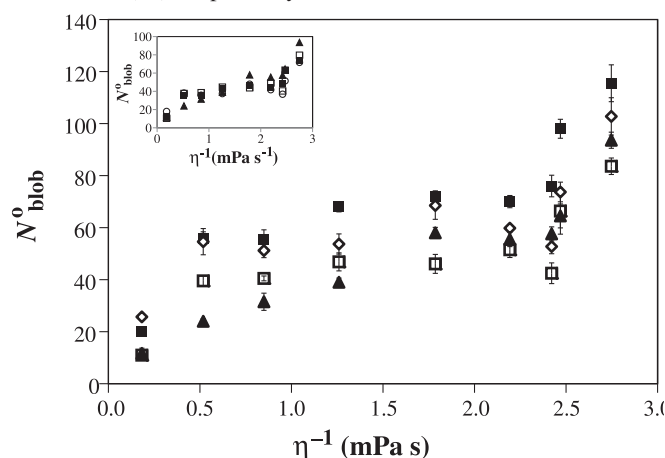


**Fig. 4.**  $N_{blob}$  as a function of the corrected pyrene content obtained through the global analysis of the monomer and excimer fluorescence decays with eqs. [9] and [10] in methyl acetate ( $\blacklozenge$ ), methyl ethyl ketone ( $\blacksquare$ ), dichloromethane ( $\blacktriangle$ ), tetrahydrofuran ( $\bullet$ ), toluene ( $\square$ ), dimethylformamide ( $\diamond$ ), dioxane ( $\triangle$ ), dimethylacetamide ( $\circ$ ), and benzyl alcohol ( $\times$ ).



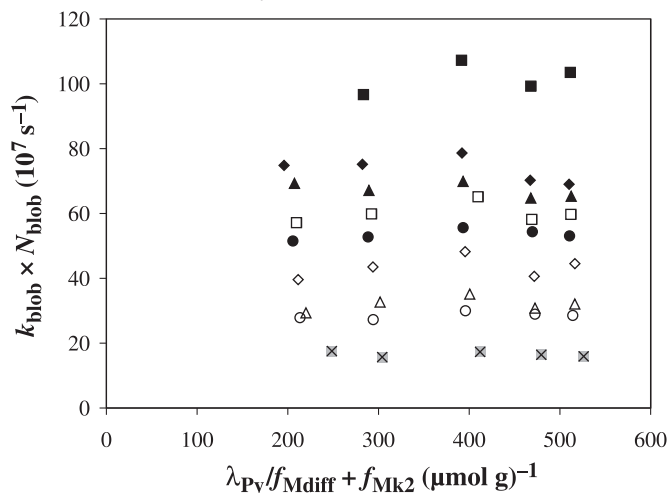
mer and excimer decays could only be achieved with the more complete eqs. [9] and [10], respectively. The presence of ground-state dimers  $ES^*$  and  $EL^*$  could not be detected

**Fig. 5.**  $N_{blob}^0$  as a function of  $\eta^{-1}$  for CoE-PS ( $\blacksquare$ ), CoBuE-PS ( $\diamond$ ), analysis of the monomer decays with eq. [11]), CoBuE-PS ( $\square$ ), global analysis of the monomer and excimer decays with eqs. [9] and [10]), and CoA-PS ( $\blacktriangle$ ). Inset:  $N_{blob}^0$  multiplied by 1.0, 0.95, 0.70, and 0.64 for CoA-PS ( $\blacksquare$ ), CoBuE-PS ( $\square$ ), analyzed globally with eqs. [9] and [10]), CoBuE-PS ( $\square$ ), analyzed with eq. [11]), and CoE-PS ( $\blacktriangle$ ), respectively.

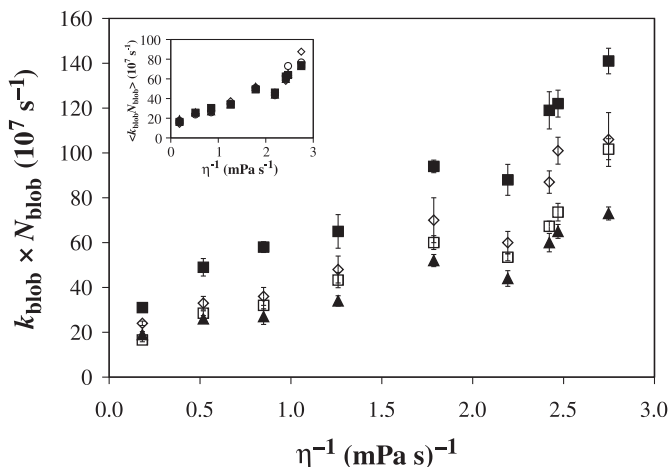


in our analysis and  $[ES^*]_0$  and  $[EL^*]_0$  were set equal to zero in eq. [10]. The global analysis of the fluorescence decays was conducted in two steps. In a first step, the mono-

**Fig. 6.**  $k_{\text{blob}} \times N_{\text{blob}}$  as a function of the corrected pyrene content obtained through the global analysis of the monomer and excimer fluorescence decays with eqs. [9] and [10] in methyl acetate (◆), methyl ethyl ketone (■), dichloromethane (▲), tetrahydrofuran (●), toluene (□), dimethylformamide (◇), dioxane (△), dimethylacetamide (○), and benzyl alcohol (×).

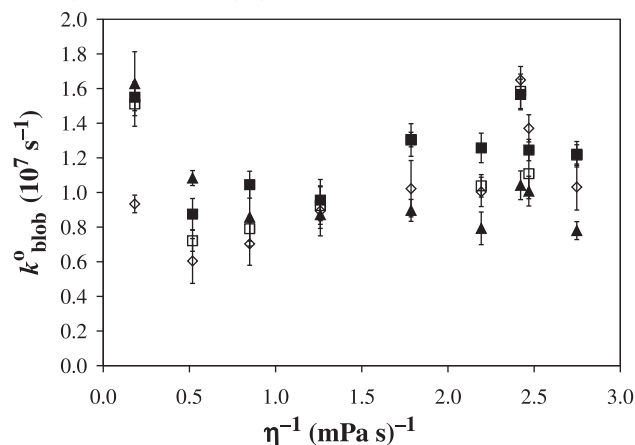


**Fig. 7.**  $k_{\text{blob}} \times N_{\text{blob}}$  as a function of  $\eta^{-1}$  for CoE-PS (■), CoBuE-PS (◇, analysis of the monomer decays with eq. [11]), CoBuE-PS (□, global analysis of the monomer and excimer decays with eqs. [9] and [10]), and CoA-PS (▲). Inset:  $k_{\text{blob}} \times N_{\text{blob}}$  multiplied by 0.52, 0.72, 0.86, and 1.0 for the trends obtained with CoE-PS (■), CoBuE-PS (◇, analyzed with eq. [11]), CoBuE-PS (□, analyzed globally with eqs. [9] and [10]), and CoA-PS (▲), respectively.



mer and excimer fluorescence decays of the five CoBuE-PS samples in each solvent were analyzed with eqs. [9] and [10] where the rate constant  $k_2$  was allowed to float. However, the  $k_2$  values retrieved in this manner showed some scatter. Consequently, the  $k_2$  values obtained for the five CoBuE-PS samples were averaged, and the averaged  $k_2$  was fixed in the analysis. In all cases, the fits were good with the analysis of the decays resulting in  $\chi^2$  smaller than 1.30 and residuals and autocorrelation function of the residuals randomly distributed around zero. The parameters retrieved from the analysis of the decays either globally with eqs. [9] and [10] or individually for the monomer decays with the FBM equation (i.e., eq. [11] with  $k_2 \rightarrow \infty$ ) are

**Fig. 8.**  $k_{\text{blob}}^0$  as a function of  $\eta^{-1}$  for CoE-PS (■), CoBuE-PS (◇, analysis of the monomer decays with eq. [11]), CoBuE-PS (□, global analysis of the monomer and excimer decays with eqs. [9] and [10]), and CoA-PS (▲).



listed in Tables SI.1–SI.8 in the Supplementary data. An example of the quality of the fits can be seen in Fig. 3.

For CoBuE-PS, the global analysis of the monomer and excimer fluorescence decays could only be achieved with eqs. [9] and [10], whereas for CoA-PS and CoE-PS, global analysis could be done with the simpler version of eqs. [9] and [10] obtained by assuming  $k_2 \gg k_1$  (i.e., eq. [11] for the pyrene monomer).<sup>13,18</sup> One reason why  $k_2$  could take smaller values for CoBuE-PS than for CoA-PS and CoE-PS might be due to the longer butyl linker used with CoBuE-PS compared to the short methyl linker used for CoA-PS and CoE-PS (Table 1). As shown in Scheme 1, the encounter of two polymer segments is followed by the quick rearrangement of the pyrene units into a conformation that allows optimal stacking of the pyrenes for excimer formation. The butyl linker might enable the pyrene pendants to adopt more conformations that do not lead to excimer formation, a process reflected by a smaller  $k_2$  value. The methylene linker used for CoA-PS and CoE-PS might reduce the number of inefficient conformations adopted by the pyrene pendants resulting in a faster rearrangement with  $k_2 \gg k_1$  in Scheme 1.

Analysis of the fluorescence decays yielded the average number of pyrenes per blob,  $\langle n \rangle$ , which was used with eq. [12] to determine the size of a blob as the number of styrene units making up a blob,  $N_{\text{blob}}$ .<sup>14,32</sup>

$$[12] \quad N_{\text{blob}} = \frac{\langle n \rangle}{[\lambda_{\text{Py}} / (1 - f_{\text{Mfree}})] \times [M_{\text{Py}}(x) + M_{\text{Sty}}(1 - x)]}$$

In eq. [12],  $\lambda_{\text{Py}}$  is the pyrene content in  $\text{mol} \cdot \text{g}^{-1}$  and  $f_{\text{Mfree}}$  is the fraction of pyrene monomer in the monomer fluorescence decays that do not form excimer (note that  $1 - f_{\text{Mfree}} = f_{\text{Mdiff}} + f_{\text{Mk}_2}$ ). In the case of CoBuE-PS,  $M_{\text{Py}}$  and  $M_{\text{Sty}}$  are the molar masses of a 1-pyrenebutyl acrylate and styrene units equal to 328 and 104  $\text{g} \cdot \text{mol}^{-1}$ , respectively, and  $x$  represents the molar fraction of pyrene labeled monomer in the polymer. A plot of  $N_{\text{blob}}$  as a function of the corrected pyrene content,  $\lambda_{\text{Py}} / (f_{\text{Mdiff}} + f_{\text{Mk}_2})$ , is shown in Fig. 4 when  $\langle n \rangle$  was retrieved from the global analysis of the monomer and excimer fluorescence decays. The trends shown in Fig. 4 in-



dicates that as the solvent viscosity increases and the motion of pyrene is hindered,  $N_{\text{blob}}$  decreases. The trends shown in Fig. 4 were extrapolated to zero-pyrene content to obtain the value of  $N_{\text{blob}}$  that an ideal unlabeled PS backbone would yield, which is referred to as  $N_{\text{blob}}^0$ . A similar procedure was applied to determine  $N_{\text{blob}}^0$  from the  $\langle n \rangle$  values retrieved from the analysis of the monomer decays with eq. [11]. The result of these analyses is shown in Fig. 5.

All trends in Fig. 5 show a similar behavior regardless of the polymer construct, as demonstrated in the inset of Fig. 5 where  $N_{\text{blob}}^0$  was scaled by 1.0, 0.95, 0.70, and 0.64 for CoA-PS, CoBuE-PS (analyzed globally with eqs. [9] and [10]), CoBuE-PS (analyzed with eq. [10]), and CoE-PS, respectively. The good overlap between the trends shown in the inset indicates that the FBM analysis of the fluorescence decays of the different Py-PS constructs satisfyingly handles differences in the nature of the linker and yields parameters such as  $N_{\text{blob}}^0$  and, as will be seen later on,  $\langle k_{\text{blob}} \times N_{\text{blob}} \rangle$ , that describe the chain dynamics of the polymer. The data in Fig. 5 show that  $N_{\text{blob}}^0$  increases with increasing  $\eta^{-1}$ , although that increase appears to be more pronounced for viscosities smaller and greater than 0.4 and 1.9 mPa·s, respectively. The overall increase of  $N_{\text{blob}}^0$  with  $\eta^{-1}$  reflects the enhanced restriction experienced by an excited pyrene moving in a more viscous solvent. In any solvent, CoE-PS yields the largest  $N_{\text{blob}}^0$  values, reflecting the longer reach enabled by the phenyl spacer between pyrene and the PS backbone, which allows pyrene to probe a larger volume,  $V_{\text{blob}}$ . CoA-PS and CoBuE-PS yield smaller  $N_{\text{blob}}^0$  values due to the shorter methyl and butyl pendants of the pyrene derivatives used to prepare these Py-PS constructs. Although the longer butyl linker of CoBuE-PS should theoretically yield a larger  $N_{\text{blob}}^0$  value than for CoA-PS, this is not always observed, certainly because the lifetime of the 1-pyrenebutyl derivative (Table 3) is usually about 50 ns smaller than that of the 1-pyrenemethyl derivative. Since  $V_{\text{blob}}$  is the volume probed by a chromophore while it remains excited, its value depends on both the lifetime and mobility of the excited chromophore. In the case of CoA-PS and CoBuE-PS, the longer lifetime of 1-pyrenemethyl with respect to that of 1-pyrenebutyl compensates to some extent for its reduced mobility associated with the shorter methylene linker.

Analysis of the monomer decays with eq. [11] yields  $N_{\text{blob}}^0$  values that are, on average, about 25% greater than those obtained by the global analysis of the CoBuE-PS decays with eqs. [9] and [10]. This difference in  $N_{\text{blob}}^0$  values appears to be inherent to the different types of analysis and will need to be taken into account when comparing trends obtained in future studies with other pyrene-labeled polymers.

As found in earlier reports,<sup>18,46</sup> the most informative parameter in a FBM analysis is the product  $k_{\text{blob}} \times N_{\text{blob}}$  because it is independent of pyrene content and it represents a measure of chain flexibility. It has also been shown to be much less sensitive to chromophore lifetime than the parameters  $N_{\text{blob}}$  and  $k_{\text{blob}}$ , which should facilitate comparison of the trends obtained with 1-pyrenemethyl and 1-pyrenebutyl.<sup>46</sup> It is plotted in Fig. 6 for CoBuE-PS in a series of solvents as a function of pyrene content using the results obtained from the global analysis of the monomer and excimer fluorescence decays. Similar trends were obtained when the monomer de-

cays were analyzed with eq. [11] (data not shown).  $k_{\text{blob}} \times N_{\text{blob}}$  in Fig. 6 is found to be independent of pyrene content. Its value can be averaged to yield  $\langle k_{\text{blob}} \times N_{\text{blob}} \rangle$ , which is given in Fig. 7 for both analyses as a function of  $\eta^{-1}$ .

For all constructs and analyses, the product  $\langle k_{\text{blob}} \times N_{\text{blob}} \rangle$  increases linearly with increasing  $\eta^{-1}$  within experimental error. When the trends are scaled by a multiplication factor of 1.0, 0.86, 0.72, and 0.52 for, respectively, CoA-PS, CoBuE-PS (analyzed globally with eqs. [9] and [10]), CoBuE-PS (analyzed with eq. [11]), and CoE-PS, the trends appear to overlap remarkably well (inset in Fig. 7), demonstrating that the FBM analysis yields parameters that describe the chain dynamics of PS regardless of the nature of the Py-PS construct. Furthermore, the product  $\langle k_{\text{blob}} \times N_{\text{blob}} \rangle$  appears to reflect accurately the differences in behavior expected for the Py-PS constructs. CoA-PS with a short and rigid amide linker yields the smallest  $\langle k_{\text{blob}} \times N_{\text{blob}} \rangle$  values in all solvents. The largest  $\langle k_{\text{blob}} \times N_{\text{blob}} \rangle$  is obtained for the CoE-PS constructs that have a long and flexible ether linker. Regardless of the type of analysis used,  $\langle k_{\text{blob}} \times N_{\text{blob}} \rangle$  takes intermediate values for CoBuE-PS whose butyl ester linker is longer and more flexible than that of CoA-PS but shorter and less flexible than that of CoE-PS. The  $\langle k_{\text{blob}} \times N_{\text{blob}} \rangle$  values obtained for CoBuE-PS from the analysis of the monomer decays with eq. [11] are, on average, 17% larger than those obtained with the global analysis of the monomer and excimer decays.

Since the rate constant for excimer formation inside a blob,  $k_{\text{blob}}$ , is often found to increase with pyrene content, it is obtained by taking the ratio  $\langle k_{\text{blob}} \times N_{\text{blob}} \rangle / N_{\text{blob}}^0$  and is referred to as  $k_{\text{blob}}^0$ .<sup>18,46</sup> The trends of  $k_{\text{blob}}^0$  as a function of  $\eta^{-1}$  are shown in Fig. 8 for all Py-PS constructs. Although scattered,  $k_{\text{blob}}^0$  remains relatively constant as a function of viscosity, taking an average value of  $1.0 \pm 0.3$ ,  $1.0 \pm 0.3$ ,  $1.1 \pm 0.3$ , and  $1.2 \pm 0.2 \times 10^7 \text{ s}^{-1}$  for CoA-PS, CoBuE-PS (analyzed with eq. [11]), CoBuE-PS (globally analyzed with eqs. [9] and [10]), and CoE-PS, respectively. Considering that the viscosity varies more than 10 fold from 0.36 mPa·s in methyl acetate to 5.5 mPa·s in benzyl alcohol, the small variations observed for  $k_{\text{blob}}^0$  with viscosity confirm that this parameter is relatively insensitive to solvent viscosity, an observation that has been already reported and rationalized within the framework of the FBM.<sup>16,18,19,46</sup>

Analysis of the monomer decays with eq. [11] yields  $N_{\text{blob}}^0$  and  $\langle k_{\text{blob}} \times N_{\text{blob}} \rangle$  values that are consistently 25% and 17% larger than those obtained from the global analysis of the monomer and excimer decays with eqs. [9] and [10]. One reason for this trend is that the introduction of  $k_2$  in eqs. [9] and [10] accounts for the early part of the monomer and excimer decays. It is this section of the decays that most affects  $\langle n \rangle$  and, to a lesser extent,  $k_{\text{blob}}$ . A steeper drop in the monomer decay accompanied by a rapid risetime in the excimer decay would result in larger  $\langle n \rangle$  values, and accordingly, larger  $N_{\text{blob}}$  and  $\langle k_{\text{blob}} \times N_{\text{blob}} \rangle$  values. Introducing  $k_2$  accounts for the fast early processes so that smaller  $\langle n \rangle$  values are obtained when using eqs. [9] and [10]. Although the absolute value of  $N_{\text{blob}}$  and  $\langle k_{\text{blob}} \times N_{\text{blob}} \rangle$  might not be known with an accuracy better than 25% and 17%, respectively, the present study demonstrates that a given analysis, either analysis of the monomer decays with eq. [11] or global analysis of the monomer and excimer decays with eqs. [9]

and [10], yields trends that are internally consistent (see insets in Figs. 5 and 7).

## Conclusions

The CoBuE-PS series of polystyrenes randomly labeled with 1-pyrenebutanol was prepared and their steady-state fluorescence spectra and monomer and excimer time-resolved fluorescence decays were acquired. The results obtained with the CoBuE-PS samples were compared with those obtained with the CoA-PS and CoE-PS series. The fluorescence spectra exhibited some noticeable differences in the spectral features of the pyrene monomer, whether or not the Py-PS construct was prepared with a 1-pyrenebutyl or a 1-pyrenemethyl derivative. In particular, the CoBuE-PS constructs prepared with the 1-pyrenebutyl derivative yielded larger  $I_M$  intensities than the Py-PS constructs obtained with the 1-pyrenemethyl derivative, which resulted in lower than expected  $I_E/I_M$  ratios. This observation highlighted the inherent difficulty of comparing trends obtained with polymers labeled with different pyrene derivatives.

If pyrene-labeled polymers are to be used to gain quantitative information on the chain dynamics of a given polymeric backbone in solution, the quantitative analysis of the pyrene monomer and excimer fluorescence decays must be carried out. This was done by using the FBM. FBM global analysis of the pyrene monomer and excimer fluorescence decays of CoBuE-PS highlighted another difference associated with the use of a 1-pyrenebutyl derivative. The rapid rearrangement step characterized by the rate constant  $k_2$  in Scheme 1 needed to be accounted for in the analysis. This had been found to be unnecessary for the CoA-PS and CoE-PS series<sup>17,18,46</sup> where a 1-pyrenemethyl derivative had been used to label polystyrene. Despite this mathematical modification needed to globally analyze the pyrene monomer and excimer fluorescence decays of CoBuE-PS, the trends obtained with the parameters  $N_{\text{blob}}^0$ ,  $\langle k_{\text{blob}} \times N_{\text{blob}} \rangle$ , and  $k_{\text{blob}}^0$  as a function of  $\eta^{-1}$  matched closely with those found earlier with CoA-PS and CoE-PS (see Figs. 5, 7, and 8). Comparison of the  $N_{\text{blob}}^0$  and  $\langle k_{\text{blob}} \times N_{\text{blob}} \rangle$  values obtained by fitting the monomer fluorescence decays with eq. [11] or the monomer and excimer fluorescence decays globally with eqs. [9] and [10] for CoBuE-PS showed that the former analysis yielded  $N_{\text{blob}}^0$  and  $\langle k_{\text{blob}} \times N_{\text{blob}} \rangle$  values that were, respectively, 25% and 17% larger than those obtained by the latter analysis.

The similar trends obtained for  $N_{\text{blob}}^0$  (Fig. 5),  $\langle k_{\text{blob}} \times N_{\text{blob}} \rangle$  (Fig. 7), and  $k_{\text{blob}}^0$  (Fig. 8) indicate that despite the various changes associated with the use of the 1-pyrenebutyl derivative in terms of a shorter lifetime and the need of a modified FBM analysis that accounts for the rapid rearrangement of the pyrene moieties, the FBM accounts satisfyingly for these changes and retrieves information that describes the behavior of the polymer, not that of the label. Since the 1-pyrenebutyl derivative seems to be commonly used to label macromolecules,<sup>20–29</sup> this study is expected to represent an important reference point to which the behavior of other polymers labeled with a 1-pyrenebutyl derivative can be compared.

## Supplementary data

Supplementary data for this article are available on the journal Web site (canjchem.nrc.ca) or may be purchased from the Depository of Unpublished Data, Document Delivery, CISTI, National Research Council Canada, Ottawa, ON K1A 0R6, Canada. DUD 5330. For more information on obtaining material, refer to cisti-icist.nrc-cnrc.gc.ca/cms/unpub\_e.shtml.

## Acknowledgements

The authors thank the Natural Sciences and Engineering Research Council of Canada (NSERC) for financial support.

## References

- (1) Winnik, M. A.; Redpath, T.; Richards, D. H. *Macromolecules* **1980**, *13* (2), 328. doi:10.1021/ma60074a023.
- (2) Redpath, A. E. C.; Winnik, M. A. *J. Am. Chem. Soc.* **1982**, *104* (21), 5604. doi:10.1021/ja00385a006.
- (3) Cheung, S.-T.; Winnik, M. A.; Redpath, A. E. C. *Makromol. Chem.* **1982**, *183* (7), 1815. doi:10.1002/macp.1982.021830720.
- (4) Svirskaya, P.; Danhelka, J.; Redpath, A. E. C.; Winnik, M. A. *Polymer (Guildf.)* **1983**, *24* (3), 319. doi:10.1016/0032-3861(83)90270-7.
- (5) Winnik, M. A. *Acc. Chem. Res.* **1985**, *18* (3), 73. doi:10.1021/ar00111a002.
- (6) Martinho, J. M. G.; Winnik, M. A. *Macromolecules* **1986**, *19* (8), 2281. doi:10.1021/ma00162a029.
- (7) Winnik, M. A.; Li, X.-B.; Guillet, J. E. *J. Polym. Sci. Polym. Symp.* **1985**, *73* (1), 113. doi:10.1002/polc.5070730116.
- (8) Cuniberti, C.; Perico, A. *Eur. Polym. J.* **1977**, *13* (5), 369. doi:10.1016/0014-3057(77)90097-0.
- (9) Cuniberti, C.; Perico, A. *Prog. Polym. Sci.* **1984**, *10* (4), 271. doi:10.1016/0079-6700(84)90007-8.
- (10) Wilemski, G.; Fixman, M. *J. Chem. Phys.* **1974**, *60* (3), 866. doi:10.1063/1.1681162.
- (11) Wilemski, G.; Fixman, M. *J. Chem. Phys.* **1974**, *60* (3), 878. doi:10.1063/1.1681163.
- (12) Birks, J. B. *Photophysics of Aromatic Molecules*; Wiley: New York, 1970; p 301.
- (13) Ingratta, M.; Hollinger, J.; Duhamel, J. *J. Am. Chem. Soc.* **2008**, *130* (29), 9420. doi:10.1021/ja800897m. PMID: 18582055.
- (14) Mathew, A.; Siu, H.; Duhamel, J. *Macromolecules* **1999**, *32* (21), 7100. doi:10.1021/ma990702c.
- (15) Kanagalingam, S.; Ngan, C. F.; Duhamel, J. *Macromolecules* **2002**, *35* (22), 8560. doi:10.1021/ma0207428.
- (16) Kanagalingam, S.; Spartalis, J.; Cao, T.-C.; Duhamel, J. *Macromolecules* **2002**, *35* (22), 8571. doi:10.1021/ma020784w.
- (17) Ingratta, M.; Duhamel, J. *Macromolecules* **2007**, *40* (18), 6647. doi:10.1021/ma070368h.
- (18) Ingratta, M.; Duhamel, J. *Macromolecules* **2009**, *42* (4), 1244. doi:10.1021/ma8019738.
- (19) Ironi, K.; Zhang, M.; Duhamel, J. *J. Phys. Chem. B* **2006**, *110* (6), 2628. doi:10.1021/jp055596x. PMID: 16471864.
- (20) Baker, L. A.; Crooks, R. M. *Macromolecules* **2000**, *33* (24), 9034. doi:10.1021/ma001379c.
- (21) Brauge, L.; Caminade, A.-M.; Majoral, J.-P.; Słomkowski, S.; Wolszczak, M. *Macromolecules* **2001**, *34* (16), 5599. doi:10.1021/ma0020077.
- (22) Danko, M.; Libiszowski, J.; Biela, T.; Wolszczak, M.; Duda,

- A. *J. Polym. Sci. Polym. Chem.* **2005**, *43* (19), 4586. doi:10.1002/pola.20932.
- (23) Kujawa, P.; Aseyev, V.; Tenhu, H.; Winnik, F. M. *Macromolecules* **2006**, *39* (22), 7686. doi:10.1021/ma061604b.
- (24) Barros, T. C.; Adronov, A.; Winnik, F. M.; Bohne, C. *Langmuir* **1997**, *13* (23), 6089. doi:10.1021/la970477x.
- (25) Winnik, F. M.; Regismond, S. T. A.; Goddard, E. D. *Langmuir* **1997**, *13* (1), 111. doi:10.1021/la9607159.
- (26) Kujawa, P.; Goh, C. C. E.; Calvet, D.; Winnik, F. M. *Macromolecules* **2001**, *34* (18), 6387. doi:10.1021/ma010384t.
- (27) Miyazawa, K.; Winnik, F. M. *J. Phys. Chem. B* **2003**, *107* (38), 10677. doi:10.1021/jp0347724.
- (28) Nishikawa, K.; Yekta, A.; Pham, H. H.; Winnik, M. A.; Sau, A. C. *Langmuir* **1998**, *14* (25), 7119. doi:10.1021/la980361g.
- (29) Relógio, P.; Martinho, J. M. G.; Farinha, J. P. S. *Macromolecules* **2005**, *38* (26), 10799. doi:10.1021/ma051701p.
- (30) Winnik, M. A.; Li, X.-B.; Guillet, J. E. *Macromolecules* **1984**, *17* (4), 699. doi:10.1021/ma00134a029.
- (31) Winnik, M. A.; Egan, L. S.; Tencer, M.; Croucher, M. D. *Polymer (Guildf.)* **1987**, *28* (9), 1553. doi:10.1016/0032-3861(87)90357-0.
- (32) Duhamel, J. *Acc. Chem. Res.* **2006**, *39* (12), 953. doi:10.1021/ar068096a. PMID:17176034.
- (33) Siu, H.; Duhamel, J. *J. Phys. Chem. B* **2008**, *112* (48), 15301. doi:10.1021/jp801105q. PMID:18989917.
- (34) Tachiya, M. *J. Chem. Phys.* **1982**, *76* (1), 340. doi:10.1063/1.442728.
- (35) Ge, Z.; Luo, S.; Liu, S. *J. Polym. Sci. Polym. Chem.* **2006**, *44* (4), 1357. doi:10.1002/pola.21261.
- (36) Seixas de Melo, J.; Costa, T.; da G. Miguel, M.; Lindman, B.; Schillén, K. *J. Phys. Chem. B* **2003**, *107* (46), 12605. doi:10.1021/jp0346054.
- (37) Costa, T.; Seixas de Melo, J.; Burrows, H. D. *J. Phys. Chem. B* **2009**, *113* (3), 618. doi:10.1021/jp806555x. PMID:19115817.
- (38) Kalyanasundaram, K.; Thomas, J. K. *J. Am. Chem. Soc.* **1977**, *99* (7), 2039. doi:10.1021/ja00449a004.
- (39) Duhamel, J. In *Molecular Interfacial Phenomena of Polymers and Biopolymers*; Chen, P., Ed.; Woodhead Publishing Company: Cambridge, UK, 2005; pp 214–248.
- (40) Anghel, D. F.; Alderson, V.; Winnik, F. M.; Mizusaki, M.; Morishima, Y. *Polymer (Guildf.)* **1998**, *39* (14), 3035. doi:10.1016/S0032-3861(97)10126-4.
- (41) Nakajima, A. *J. Lumin.* **1976**, *11* (5–6), 429. doi:10.1016/0022-2313(76)90027-2.
- (42) Dong, D. C.; Winnik, M. A. *Photochem. Photobiol.* **1982**, *35* (1), 17. doi:10.1111/j.1751-1097.1982.tb03805.x.
- (43) Dong, D. C.; Winnik, M. A. *Can. J. Chem.* **1984**, *62* (11), 2560. doi:10.1139/v84-437.
- (44) Lianos, P.; Georghiou, S. *Photochem. Photobiol.* **1979**, *30* (3), 355. doi:10.1111/j.1751-1097.1979.tb07368.x.
- (45) Ingratta, M.; Duhamel, J. *J. Phys. Chem. B* **2008**, *112* (30), 9209. doi:10.1021/jp8021248. PMID:18610962.
- (46) Ingratta, M.; Duhamel, J. *J. Phys. Chem. B* **2009**, *113* (8), 2284. doi:10.1021/jp8082858. PMID:19195988.

# Synthesis of *N*-vinylcarbazole-*N*-vinylpyrrolidone amphiphilic block copolymers by xanthate-mediated controlled radical polymerization

Chih-Feng Huang, Jeong Ae Yoon, and Krzysztof Matyjaszewski

**Abstract:** Amphiphilic block copolymers poly(*N*-vinylcarbazole)-*b*-poly(*N*-vinylpyrrolidone) (PNVK-*b*-PNVP) were prepared by xanthate-mediated reversible addition-fragmentation chain transfer (RAFT) polymerization. Both the PNVK and PNVP macroinitiators and the resulting block copolymers had molecular weights close to theoretical values, predicted for efficient initiation, in the range of  $M_n = 30\,000$  to  $90\,000$ . The block copolymers dissolved in several organic solvents but, depending on their composition, in methanol formed either micelles or large aggregates, as confirmed by dynamic light scattering. The presence of globular aggregates was confirmed by tapping mode atomic force microscopy.

**Key words:** amphiphilic block copolymer, RAFT, living radical polymerization, micelle.

**Résumé :** On a préparé des copolymères à bloc amphiphiles poly(*N*-vinylcarbazole)-*b*-poly(*N*-vinylpyrrolidone) (PNVK-*b*-PNVP) par une réaction de polymérisation de transfert de chaîne avec addition-fragmentation réversible (TCAR) catalysée par le xanthate. Les valeurs des poids moléculaires des deux macroinitiateurs PNVK et PNVP ainsi que des copolymères à bloc qui en ont résulté étaient proches des valeurs théoriques prévues pour une initiation efficace, de l'ordre de  $M_n = 30\,000$  à  $90\,000$ . Les copolymères à bloc se dissolvent dans plusieurs solvants organiques; toutefois, dans le méthanol, suivant leur composition, il y a formation de micelles ou de gros agrégats décelés par la diffusion dynamique de la lumière. La présence d'agrégats globulaires a aussi été confirmée par la spectroscopie en mode de forces atomiques.

**Mots-clés :** copolymère à bloc amphiphile, transfert de chaîne avec addition-fragmentation réversible (TCAR), polymérisation radicalaire vivante, micelle.

[Traduit par la Rédaction]

## Introduction

The preparation and properties of amphiphilic block copolymers, with hydrophilic and hydrophobic blocks, is currently an area of active study. Amphiphilic block copolymers form various supramolecular structures such as micelles, cylinders, or vesicles through self-organization and self-assembly and are being evaluated in numerous applications including emulsifiers, dispersants, and surfactants.<sup>1</sup> Potential uses also include microcontainers for delivery of hydrophobic materials or templates for syntheses of materials with nanosized features.

The aim of this study is to synthesize amphiphilic block copolymers using *N*-vinylcarbazole and *N*-vinylpyrrolidone (PNVK-*b*-PNVP). PNVK, a carbazole-containing polymer, is a photoconductive material with good charge-transport properties that has found applications as a photoreceptor, light-emitting diode, and photorefractive material.<sup>2</sup> On the other hand, PNVP, the water-soluble block, has been used

in medical, pharmaceutical, and cosmetic applications, due to its low toxicity and good biocompatibility.<sup>3</sup> This indicates that PNVK-*b*-PNVP could be an interesting conductive polymer which could be processed in water. The nanophase separation of the amphiphilic block copolymer could result in a conductive PNVK segment embedded in an insulating PNVP matrix. There are only a few reports on water processable conductive block copolymers because of the difficulties with synthesis.<sup>4</sup> To prepare well-defined amphiphilic block copolymers, a controlled/living polymerization technique is required.<sup>5</sup> Although both NVK and NVP can be polymerized by radical mechanisms, the controlled radical polymerizations of NVK and NVP have not been yet thoroughly studied due to the low reactivity of non-conjugated vinyl monomers.

In general, block copolymers can be prepared by three routes: sequential monomer addition;<sup>6</sup> chain-end coupling of separately prepared blocks;<sup>7</sup> or transformation of chain ends of polymers prepared by one mechanism into initiating moi-

Received 5 September 2009. Accepted 14 October 2009. Published on the NRC Research Press Web site at canjchem.nrc.ca on 10 February 2010.

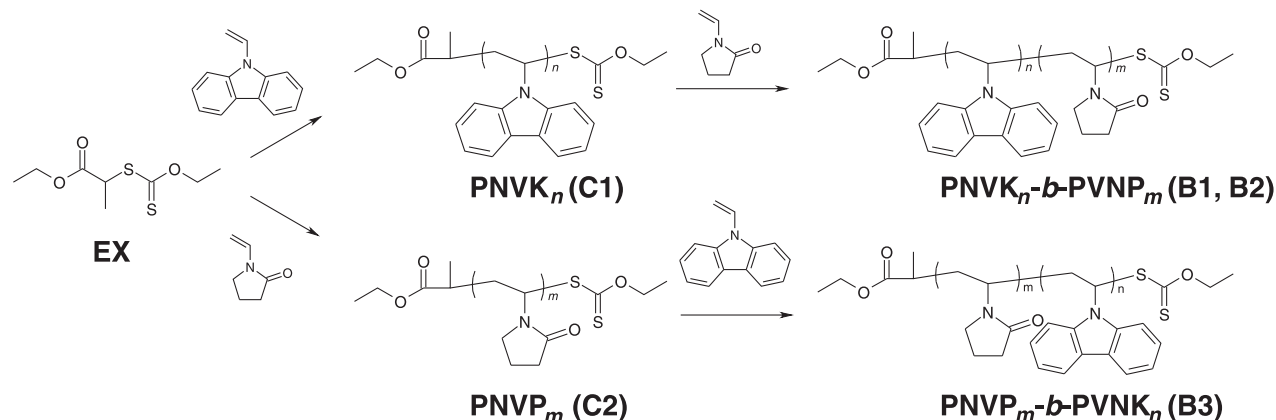
This article is part of a Special Issue dedicated to Professor M. A. Winnik.

**C. Huang.** Department of Chemistry, Carnegie Mellon University, 4400 Fifth Avenue, Pittsburgh, PA 15213, USA; Department of Applied Chemistry, National Chiao Tung University, Hsinchu 30050, Taiwan.

**J.A. Yoon and K. Matyjaszewski.**<sup>1</sup> Department of Chemistry, Carnegie Mellon University, 4400 Fifth Avenue, Pittsburgh, PA 15213, USA.

<sup>1</sup>Corresponding author (e-mail: km3b@andrew.cmu.edu).



**Scheme 1.** Synthesis of PNVK-*b*-PNVP amphiphilic block copolymers via xanthate-mediated RAFT polymerization.**Table 1.** Compositions and molecular weights of macroinitiators and block copolymers.

Entry	Composition <sup>f</sup>	$M_n$ , theory <sup>g</sup>	$M_n$ , NMR	$M_n$ , GPC	PDI
C1 <sup>a</sup>	PNVK <sub>31</sub>	6200	—	6300 <sup>h</sup>	1.28
C2 <sup>b</sup>	PNVP <sub>46</sub>	5200	—	5300 <sup>i</sup>	1.28
B1 <sup>c</sup>	PNVK <sub>31</sub> - <i>b</i> -PNVP <sub>269</sub>	39 200	35 800	35 400 <sup>i</sup>	1.35
B2 <sup>d</sup>	PNVK <sub>31</sub> - <i>b</i> -PNVP <sub>573</sub>	70 900	69 200	88 000 <sup>i</sup>	1.52
B3 <sup>e</sup>	PNVP <sub>46</sub> - <i>b</i> -PNVK <sub>139</sub>	32 400	32 100	21 700 <sup>i</sup>	1.35

<sup>a</sup>[NVK]/[EX]/[AIBN] = 43/1/0.5, 66 wt% of 1,4-dioxane to NVK, 60 °C, 4 h, conversion 71.0%.

<sup>b</sup>[NVP]/[EX]/[AIBN] = 150/1/0.35, 20 wt% of anisole to NVP, 60 °C, 4.5 h, conversion 30.1%.

<sup>c</sup>[NVP]/[C1]/[AIBN] = 600/1/0.5, 33 (v/v)% of anisole to NVP, 60 °C, 3.1 h, conversion 50.3%.

<sup>d</sup>[NVP]/[C1]/[AIBN] = 600/1/0.5, 33 (v/v)% of anisole to NVP, 60 °C, 20.9 h, conversion 98.1%.

<sup>e</sup>[NVK]/[C2]/[AIBN] = 150/1/0.5, 50 wt% of anisole to (NVK + C2), 60 °C, 26.2 h, conversion 93.9%.

<sup>f</sup>Homopolymer compositions were based on molecular weights measured by GPC. Block copolymer compositions were based on their macroinitiator composition and the NMR spectra of block copolymers.

<sup>g</sup>Molecular weights based on monomer conversion.

<sup>h</sup>GPC in THF, PS standards.

<sup>i</sup>GPC in DMF, PMMA standards.

eties for the chain propagation of the second monomer.<sup>8</sup> Previous attempts to prepare well-defined PNVK or PNVP homopolymers using one of the CRP methods has involved a degenerative transfer radical mechanism,<sup>9</sup> ATRP,<sup>10</sup> or Co-mediated polymerization.<sup>11</sup> Only a few studies describe chain extension from either PNVK or PNVP homopolymers to prepare block copolymers.<sup>12</sup> Regardless of the potentially interesting properties, block copolymers of PNVK and PNVP (PNVK-*b*-PNVP) have not been yet prepared, since the synthesis of well defined PNVK-*b*-PNVP block copolymers is challenging, owing to the low reactivity of both NVK and NVP. The low reactivity of NVK and NVP and the low stability of the propagating radicals indicate that a degenerative transfer process, such as reversible addition-fragmentation chain transfer (RAFT) polymerization, could be best suited for conducting a controlled polymerization. For this study, we selected a xanthate-type mediating agent, since it was successfully employed for RAFT polymerization of less active monomers in previous studies.<sup>12d</sup>

## Experimental

### Materials

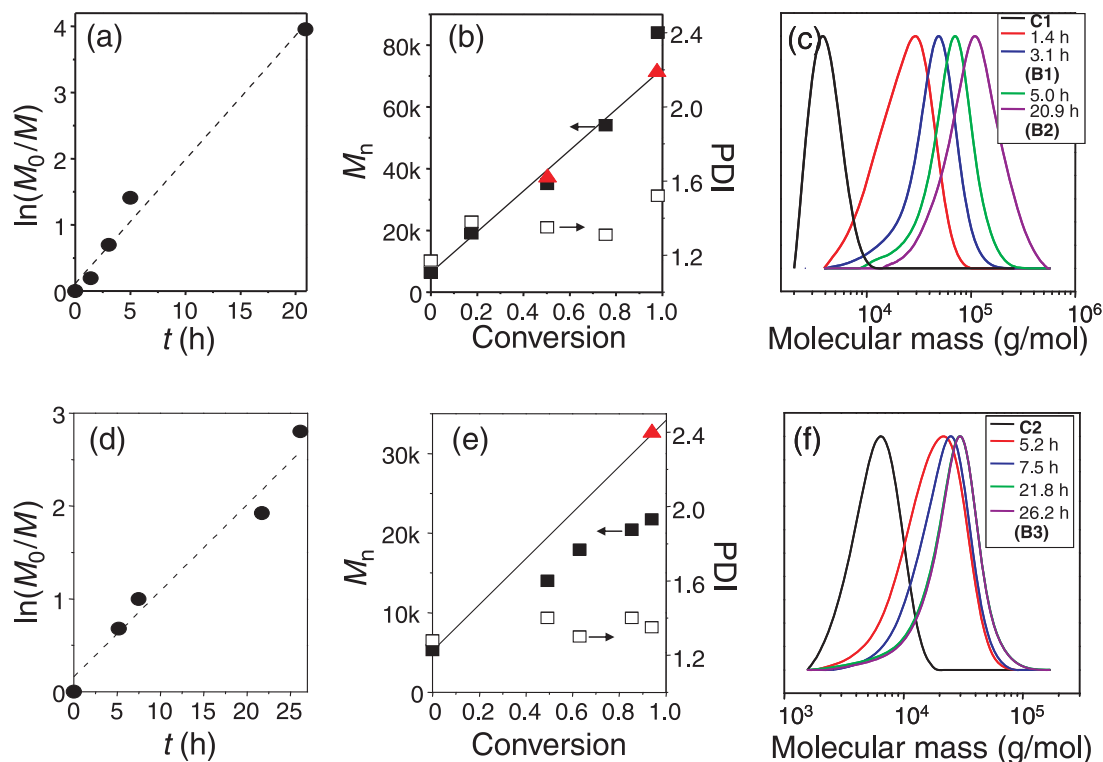
*N*-Vinylpyrrolidone (NVP, 99%, Sigma-Aldrich) was dried over anhydrous magnesium sulfate and purified by dis-

tillation under reduced pressure. *N*-vinylcarbazole (NVK, 97%, Sigma-Aldrich) and 2,2'-azobis(isobutyronitrile) (AIBN, 99%, Sigma-Aldrich) were recrystallized twice from methanol. All solvents were purified by distillation prior to use. *S*-(2-Ethyl propionate)-*O*-ethyl xanthate (EX)<sup>13</sup> was synthesized according to the literature procedure. Briefly, potassium *O*-ethyl xanthate (4.75 g, 2.9 × 10<sup>-2</sup> mol) was dissolved in 25 mL of ethanol with ethyl 2-bromopropionate (4.74 g, 5.3 × 10<sup>-2</sup> mol) for 20 h at room temperature. The crude product was purified by extraction with diethyl ether – water followed by column chromatography using hexane – ethyl acetate 95:5 (v/v) as eluent to give a yellow oil. Yield: 3.0 g (51%). <sup>1</sup>H NMR (300 MHz, CDCl<sub>3</sub>, ppm) δ: 4.63 (q, 2H), 4.37 (q, 1H), 4.20 (q, 2H), 1.56 (d, 3H), 1.41 (t, 3H), 1.28 (t, 3H).

### RAFT polymerization of NVK (C1)

3.41 g of NVK (17.6 mmol), 91.0 mg of EX (0.410 mmol), 34.0 mg of AIBN (0.207 × 10<sup>-3</sup> mmol), and 8 mL of anisole were charged to a Schlenk flask. The molar ratio of NVK–EX–AIBN was 43:1:0.5. The mixture was de-oxygenated by three freeze–pump–thaw cycles. The flask was placed in an oil bath thermostated at 60 °C for a required time period. Samples were withdrawn via a syringe for the measurement of monomer conversion and molecular

**Fig. 1.** Kinetic plots, evolution of molecular weights and polydispersities with conversion, and GPC traces for the synthesis of B1 and B2 (a, b, and c) and B3 (d, e, and f). Dashed lines (---) in (a) and (d) are least square linear fits. Solid lines (—) in (b) and (e) represent theoretical molecular weights vs. monomer conversion. Red triangles in (b) and (e) represent  $M_n$  values calculated based on block copolymer using  $^1\text{H}$  NMR.



**Table 2.** Hydrodynamic diameters (nm) measured in various solvents at room temperature.

Solvent	DC <sup>a</sup>	B1 (PNVK <sub>31</sub> - <i>b</i> -PNVP <sub>269</sub> )	B2 (PNVK <sub>31</sub> - <i>b</i> -PNVP <sub>573</sub> )	B3 (PNVP <sub>46</sub> - <i>b</i> -PNVK <sub>139</sub> )
Anisole	4.3	315 (1.751)	2377 (0.540)	10.3 (0.425)
CHCl <sub>3</sub>	4.8	7.86 (0.417)	12.9 (0.441)	9.34 (0.140)
THF	7.5	9.21 (0.390)	14.4 (0.304)	9.67 (0.170)
MeOH	33.0	44.0 (0.129)	64.0 (0.334)	774 + precipitation

**Note:** Average volume distribution. Numbers in parentheses are coefficients of variation.

<sup>a</sup>Dielectric constant.

weight of polymer by GPC with DMF or THF as eluent. The reaction was quenched by placing the flask in an ice bath, exposing to air, and diluting with THF to provide the PNVK-EX macromolecular chain transfer agent (C1). The crude polymer was purified by filtering through an alumina column followed by precipitation in hexane. Conversion = 71% (by NMR);  $M_{n, \text{theor}} = 6200$  g/mol,  $M_{n, \text{THF GPC}} = 6300$  g/mol (PDI = 1.28).

#### RAFT polymerization of NVP (C2)

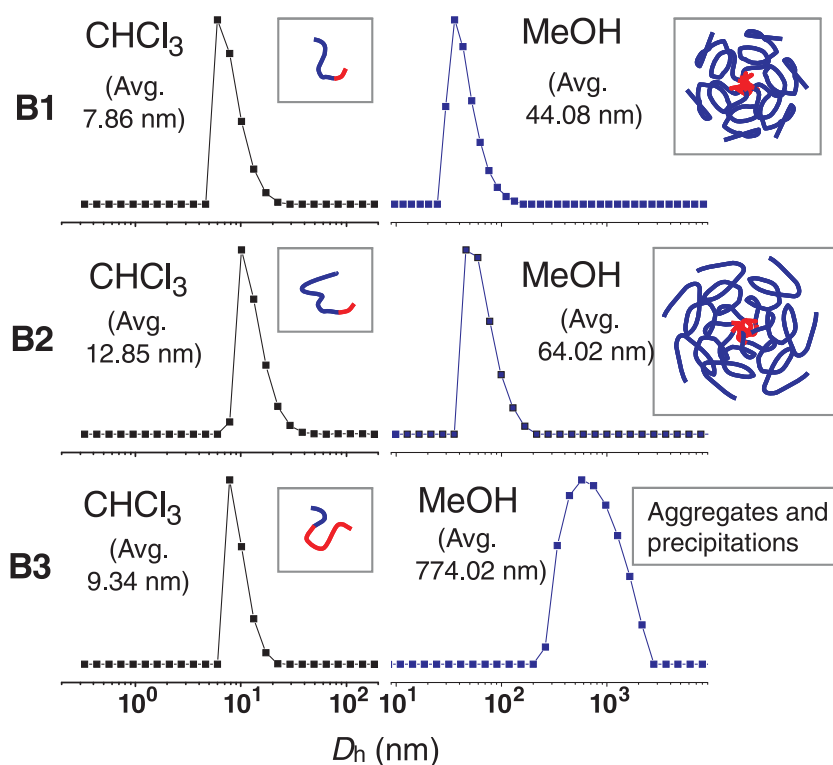
10.0 mL of NVP (10.4 g, 93.7 mmol), 139 mg of EX (0.626 mmol), 4.1 mg of AIBN (0.220 mmol), 2.5 mL of anisole were charged to a Schlenk flask. The mole ratio of NVP-EX-AIBN was 150:1:0.35. The mixture was deoxygenated by three freeze-pump-thaw cycles. The flask was placed in an oil bath thermostated at 60 °C for the desired time period. The rest of the procedure was the same as that for the

preparation of C1. Conversion = 30% (by NMR);  $M_{n, \text{theor}} = 5200$  g/mol,  $M_{n, \text{DMF GPC}} = 5300$  g/mol (PDI = 1.28).

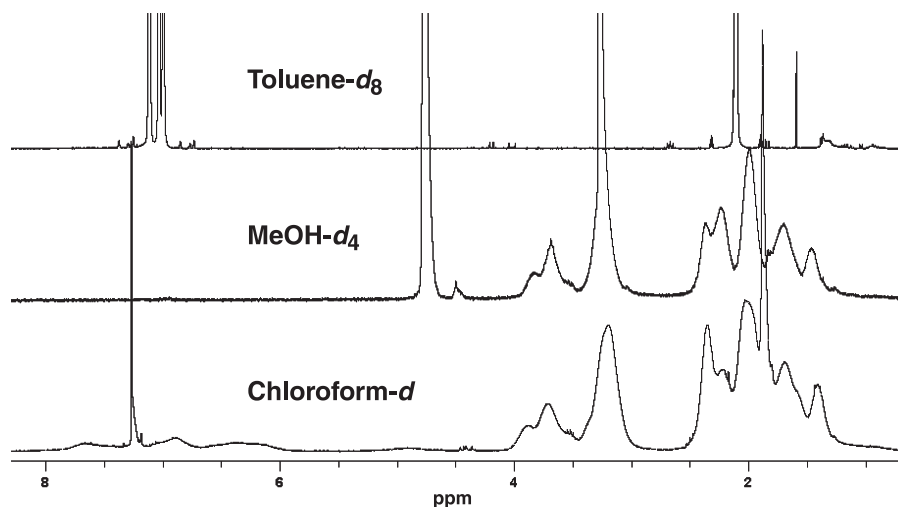
#### Chain extension of PNVK (C1) by RAFT polymerization of NVP forming a block copolymer

3.04 mL of NVP (3.18 g, 28.6 mmol), 0.300 g of C1 ( $M_{n, \text{THF GPC}} = 6300$  g/mol, PDI = 1.28,  $47.6 \times 10^{-3}$  mmol), 3.90 mg of AIBN ( $23.7 \times 10^{-3}$  mmol), and 1.56 mL of anisole were charged to a Schlenk flask. The mole ratio of NVP-C1-AIBN was 600:1:0.5. The mixture was deoxygenated by three freeze-pump-thaw cycles and then was placed in an oil bath thermostated at 60 °C for the required time period. Monomer conversion and molecular weight were tracked by GPC with DMF as eluent. At the desired conversion, the reaction was quenched and the polymer was purified by filtering through an alumina column followed by precipitation in hexane. B1 conversion = 50% (by GPC);  $M_{n, \text{theor}} = 39\,200$  g/mol,  $M_{n, \text{DMF GPC}} = 35\,400$  g/mol

**Fig. 2.** DLS profile for PNVK-*b*-PNVP block copolymer (**B1**, **B2**, and **B3**) in chloroform and methanol. Blue line: PNVP block, Red line: PNVK block.



**Fig. 3.**  $^1\text{H}$  NMR spectra of B1 in different solvents, toluene- $d_8$ , MeOH- $d_4$ , and chloroform- $d$ .



(PDI = 1.35). B2 conversion = 98% (by GPC);  $M_{n, \text{theor}} = 70\,900$  g/mol,  $M_{n, \text{DMF GPC}} = 88\,000$  g/mol (PDI = 1.52).

#### Chain extension of PNVP (C2) by RAFT polymerization of NVK

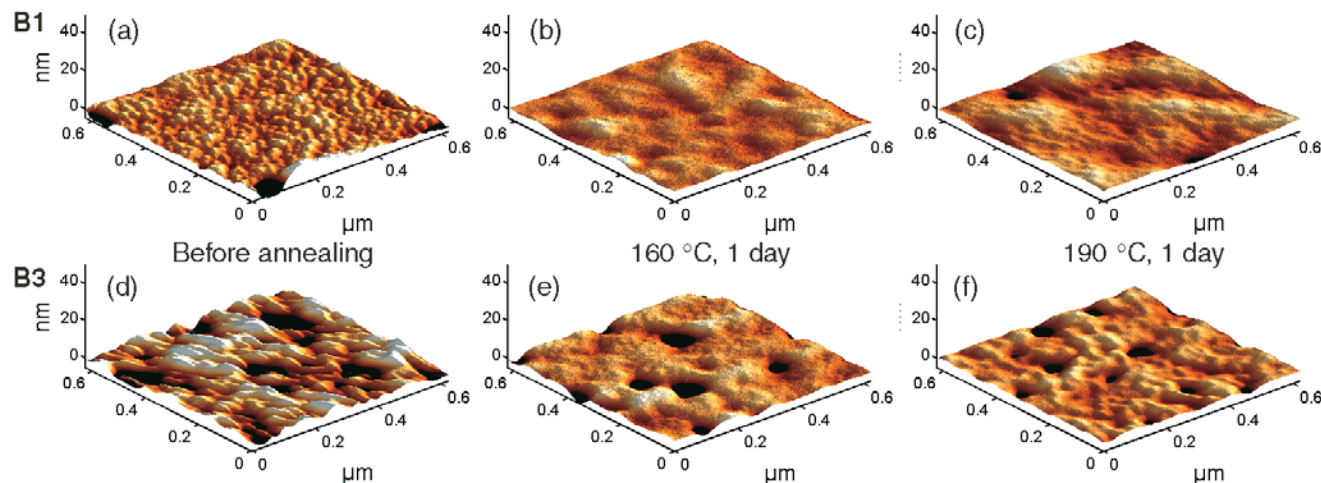
1.09 g of NVK (5.65 mmol), 0.200 of C2 ( $M_{n, \text{DMF}} = 5300$  g/mol, PDI = 1.28,  $37.7 \times 10^{-3}$  mmol), 3.10 mg of AIBN ( $18.9 \times 10^{-3}$  mmol), and 2.60 mL of anisole were charged to a Schlenk flask. The mole ratio of NVK–C2–AIBN was 150:1:0.5. The mixture was deoxygenated by three freeze–pump–thaw cycles. The flask was placed in an oil bath thermostated at 60 °C for the required time. The rest of the procedure was the same as that for the block copoly-

merization of NVP from PNVK described above. B3 conversion = 94% (by GPC);  $M_{n, \text{theor}} = 32\,400$  g/mol,  $M_{n, \text{DMF GPC}} = 21\,700$  g/mol (PDI = 1.35).

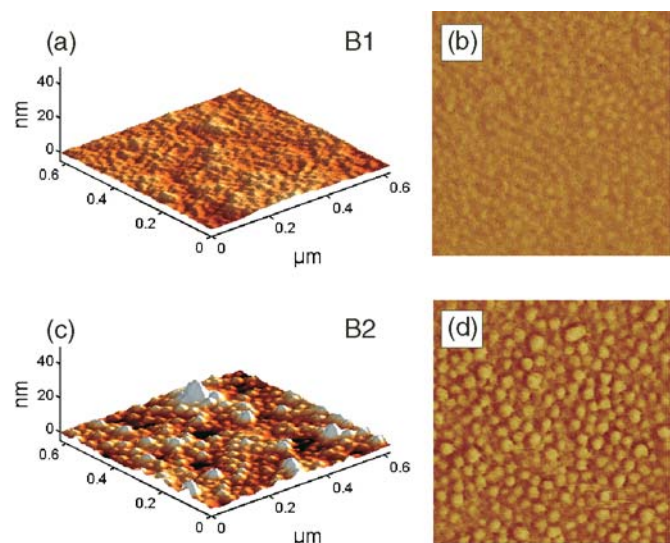
#### Analyses

The molecular weights and molecular-weight distributions were measured using GPC (Polymer Standards Services, columns (guard,  $10^5$ ,  $10^3$ , and  $10^2$  Å)) with DMF (containing 5 mmol/L LiBr) as eluent at 50 °C or with THF as eluent at 35 °C. The flow rate was kept at 1.00 mL/min and a differential refractive index (RI) detector (Waters, 2410) was used. Toluene was used as the internal standard to correct for any fluctuation in eluent flow rate. The molecular weight

**Fig. 4.** 3D images of height mode AFM at different conditions. B1: (a), (b), and (c), B3: (d), (e), and (f).



**Fig. 5.** 3D height mode AFM images (left column) and phase mode AFM images (right column) of B1 (a, b) and B2 (c, d) after drop casting of DMF solution and drying. Phase image size:  $0.6\ \mu\text{m} \times 0.6\ \mu\text{m}$ .



and the molecular-weight distribution were determined with a calibration curve based on linear PMMA (for DMF GPC line) or PS (for THF GPC line) standards using GPCWin software. Conversions were determined by NMR on a Bruker Avance™ 300 MHz instrument or by an internal standard addition, injecting a known amount of monomer into reaction mixtures and following the peak area changes in GPC traces. Particle size and size distribution were measured by dynamic light scattering (DLS) on High Performance Particle Sizer, Model HP5001 from Malvern Instruments, Ltd. DLS measurements provide average diameter,  $D_{\text{av}}$ , and size distribution index, CV (coefficient of variation), which is defined as  $\text{CV} = (S \times 100)/D_{\text{av}}$ , where  $D_{\text{av}}$  is the mean diameter and  $S$  is the size standard deviation. Tapping mode AFM experiments were carried out using a Multimode Nanoscope V system (Veeco instruments). The measurements were performed in air using commercial Si cantilevers with a nominal spring constant and resonance fre-

quency of 40 N/m and 330 kHz, respectively. The height and phase images were acquired simultaneously at a set-point ratio ( $A/A_0$ ), in the range of 0.7–0.9, where  $A$  and  $A_0$  refer, respectively, to the “tapping” and “free” cantilever amplitude.

## Results and discussions

### Synthesis

The synthesis of PNVK-*b*-PNVP block copolymers was conducted sequentially via the two alternative pathways shown in Scheme 1.

First, macromolecular chain transfer agents (CTAs), i.e., macroinitiators, were prepared by RAFT polymerizations using EX as a CTA. The molecular weights of the macroinitiators were measured by GPC and summarized in Table 1. The molecular weight of C1 measured by GPC (in THF using PS standards) ( $M_n = 6300$ ,  $\text{DP} = 31$ ) agreed well with the value estimated from monomer conversion ( $\Delta[M]/[\text{EX}]_0 = 43$ ,  $\text{DP} = 31$  at 71% conversion), assuming quantitative initiation. However, when the molecular weight was measured by GPC in DMF, a much smaller value ( $M_n = 3800$ ,  $\text{DP} = 19$ ) was obtained, presumably due to the formation of more compact polymer coils in DMF. A similar observation concerning a much smaller molecular weight of PS measured in DMF GPC, was reported previously.<sup>14</sup> The molecular weight of C2, determined by GPC (in DMF, PMMA standards), corresponded well to the theoretical molecular weight estimated from monomer conversion ( $\text{DP} = \Delta[M]/[\text{EX}]_0$ ) with the assumption of the quantitative initiation efficiency. The molecular weight of the macroinitiators measured by GPC (in DMF) compared well with the molecular weight calculated by end group analysis of  $^1\text{H}$  NMR spectra. For example, for another PNVP macroinitiator prepared under the same conditions as C2,  $M_n$  was calculated by end group analysis to be 4400 g/mol, and was measured by GPC to be 4500 g/mol (in DMF, PMMA standards). Furthermore, good agreement of experimental and theoretical molecular weights indicated that the number of new chains generated by decomposition of AIBN, coupling with CTA, and transfer process was small.

Chain extensions from the prepared macroinitiators were



performed by RAFT polymerization of the second monomer. The molecular weight and polydispersity of each block copolymer and the block copolymer composition determined by NMR are summarized in Table 1. Figure 1 displays the kinetic plots, the linear change of molecular weight with conversion, and the evolution of GPC traces over time for each block copolymer. The chain extension reactions were carried out to over 90% monomer conversion for both pathways. The molecular weights of B1 and B2 measured by GPC (in DMF, PMMA standards) were very similar to the calculated molecular weights based on monomer conversion and  $^1\text{H}$  NMR analyses. THF could not be used as GPC eluent for PNVP because it is isorefractive with PNVP. The molecular weight of B3, calculated from the  $^1\text{H}$  NMR spectrum, was very close to that based on monomer conversion, assuming quantitative initiation. The values differed from the  $M_n$  by GPC (in DMF, PMMA standard) which can be attributed to the compact structure of the PNVK block (83 wt% in B3) in DMF, as was the case with the PNVK macroinitiator. The observed first-order kinetic plots and the very high efficiency of the chain extensions suggested the negligible contribution of possible side reactions such as formation of NVP dimers or elimination of xanthate end groups.<sup>12e,15</sup> This could be attributed to the simple structure of xanthate (EX), use of purified reagents, and the mild polymerization temperature (60 °C).

### DLS and NMR studies

Particle-size distribution (volume vs. hydrodynamic diameter ( $D_h$ )) of each prepared block copolymer was studied by dynamic light scattering (DLS). Table 2 summarizes particle size distributions in various solvents having different polarities (represented in Table 2 by dielectric constant). The DLS profiles in two representative solvents, chloroform and methanol, are presented in Fig. 2.

All block copolymers displayed  $D_h$  values smaller than 15 nm in medium polarity solvents (chloroform and THF), implying dissolution of the block copolymers without formation of aggregates. However, when methanol was used as the solvent, the average particle size was much larger, ranging from 44 to 64 nm for B1 and B2, and resulted in larger aggregates ( $D_h > 700$  nm) for B3 (some precipitation was visually observed). Methanol, a non-solvent for PNVK and a good solvent for PNVP, resulted in formation of micelles with PNVP as the major block in the outer shell (B1 and B2). With PNVK as the major block (B3), larger aggregates were formed, accompanied by precipitation. Assuming full stretching of PNVP chains, the calculated size of micelles for B1 and B2 should range from 150 nm to 390 nm ( $\text{DP} \times (0.25 \text{ nm}) \times 2$ ), respectively. Observed smaller diameters suggest coiled chains of PNVP, due to a less dense micelle structures (Fig. 2, insets). In contrast to methanol, anisole is a good solvent for PNVK because of aromatic interactions and a poor solvent for PNVP because of its weak hydrogen-bonding ability. As a result, while B3 dissolved as individual chains ( $D_h = 10.3$  nm), B1 and B2, with PNVP as the major block, formed very large aggregates sized over 300 nm (cf. Table 2).

The change of solubility of the block copolymer in selective solvents was further confirmed by  $^1\text{H}$  NMR measurements. The  $^1\text{H}$  NMR spectra of B1 are shown in Fig. 3. In

the spectrum measured in chloroform-*d*, a good solvent for both blocks, peaks from both PNVK block (4.5–8 ppm) and PNVP block (0.5–4.5 ppm) are well resolved. However, the peaks of PNVK block disappear when measured in MeOH-*d*<sub>4</sub>, because of the insolubility of the PNVK block. Toluene-*d*<sub>8</sub> was selected as a nonpolar solvent instead of anisole. No appreciable peak was observed, proving the insolubility of the B1 to toluene owing to the large portion of polar PNVP block.

### AFM studies

The phase separation in block copolymers was also observed by tapping mode AFM (Fig. 4). The block copolymers B1 and B3 were dissolved in chloroform (1 mg/mL) and solutions were drop-cast onto silicon wafers (1 cm  $\times$  1 cm), followed by drying under vacuum at room temperature overnight. The films of block copolymers were studied by AFM. Globular morphologies with dimensions of 37 nm and 49 nm were observed for B1 and B3. Although the dilute chloroform solutions of B1 and B3 did not contain aggregates (cf. DLS studies), they formed aggregates as concentration increased during the solvent evaporation. The polymer films were then annealed at 160 °C (Figs. 4b and 4e) and 190 °C (Figs. 4c and 4f), i.e., above the  $T_g$  of PNVP block ( $\sim 120$  °C) under vacuum. Because the annealing was conducted below the  $T_g$  of the PNVK block ( $\sim 210$  °C), phase separation could not be enhanced by thermal annealing. The aggregates, formed during the film formation, relaxed, as seen from smoothed surfaces after annealing.

The hypothesis that the globular morphology was generated by aggregation of polymers during the drying process was supported by another experiment. This time, block copolymers B1 and B2, with the same PNVK block but different chain length of PNVP, were dissolved in DMF, a good solvent for both blocks. Since DMF evaporates at a slower rate than chloroform, it should provide sufficient time for the copolymers to attain lower-energy morphologies. The height and phase mode AFM images of B1 and B2 in Fig. 5 were measured after drop casting and drying of DMF in a vacuum oven at room temperature. The average domain sizes of B1 and B2, obtained by 2D isotropic power spectral density analysis of height images, were 28 and 33 nm, respectively, indicating that the increase in the size of the domains is correlated with the dimensions of the PNVP blocks ( $\text{DP} = 269$  vs.  $\text{DP} = 573$ ).

### Conclusion

Amphiphilic block copolymers with a hydrophobic PNVK block and a hydrophilic PNVP block were synthesized by xanthate-mediated RAFT polymerization by preparation of PNVK or PNVP macroinitiators and sequential chain extensions with the second monomer, i.e., NVP or NVK. The resulting block copolymers had low polydispersity and the molecular weight, measured by GPC and  $^1\text{H}$  NMR, agreed well with the theoretical values. The particle-size distributions of the prepared block copolymers were measured in various solvents with different polarities. Block copolymers B1 and B2, with longer PNVP blocks, formed micelles in methanol whereas B3, with PNVK as the major block,

formed larger aggregates and precipitates. AFM measurements of film samples revealed the block copolymers aggregated during the drying of films, even though the initial solution did not contain aggregates. Annealing the film samples at a temperature between the  $T_g$  of PNVK (210 °C) and PNVP (120 °C) yielded a smoother surface than before annealing but did not enhance the phase separation.

## Acknowledgements

C.-F. Huang acknowledges the National Science Council and National Chiao Tung University (NSC-096-2120-M-009-009 and NSC-096-2917-I-564-131) for postdoctoral fellowship support.

## References

- (1) (a) Discher, B. M.; Won, Y. Y.; Ege, D. S.; Lee, J. C. M.; Bates, F. S.; Discher, D. E.; Hammer, D. A. *Science* **1999**, *284* (5417), 1143. doi:10.1126/science.284.5417.1143. PMID:10325219.; (b) Discher, D. E.; Eisenberg, A. *Science* **2002**, *297* (5583), 967. doi:10.1126/science.1074972. PMID:12169723.; (c) Jain, S.; Bates, F. S. *Science* **2003**, *300* (5618), 460. doi:10.1126/science.1082193. PMID:12702869.; (d) Zhang, Q.; Remsen, E. E.; Wooley, K. L. *J. Am. Chem. Soc.* **2000**, *122* (15), 3642. doi:10.1021/ja993941o.; (e) Alexandridis, P.; Olsson, U.; Lindman, B. *Langmuir* **1998**, *14* (10), 2627. doi:10.1021/la971117c.
- (2) (a) Kido, J.; Hongawa, K.; Okuyama, K.; Nagai, K. *Appl. Phys. Lett.* **1993**, *63* (19), 2627. doi:10.1063/1.110402.; (b) Grazulevicius, J. V.; Strohriegel, P.; Pielichowski, J.; Pielichowski, K. *Prog. Polym. Sci.* **2003**, *28* (9), 1297. doi:10.1016/S0079-6700(03)00036-4.; (c) Wu, W.; Zhang, S.; Li, Y.; Li, J. X.; Liu, L. Q.; Qin, Y. J.; Guo, Z. X.; Dai, L. M.; Ye, C.; Zhu, D. B. *Macromolecules* **2003**, *36* (17), 6286. doi:10.1021/ma034513c.
- (3) (a) Haaf, F.; Sanner, A.; Straub, F. *Polym. J.* **1985**, *17* (1), 143. doi:10.1295/polymj.17.143.; (b) Benahmed, A.; Ranger, M.; Leroux, J. C. *Pharm. Res.* **2001**, *18* (3), 323. doi:10.1023/A:1011054930439. PMID:11442272.; (c) D'Souza, A. J. M.; Schowen, R. L.; Topp, E. M. *J. Control. Release* **2004**, *94* (1), 91. doi:10.1016/j.jconrel.2003.09.014. PMID:14684274.
- (4) (a) Kilbinger, A. F. M.; Feast, W. J. *J. Mater. Chem.* **2000**, *10* (8), 1777. doi:10.1039/b002899l.; (b) Henze, O.; Feast, W. J. *J. Mater. Chem.* **2003**, *13* (6), 1274. doi:10.1039/b212382g.; (c) Yan, L.; Tao, W. *J. Polym. Sci., Part A: Polym. Chem.* **2007**, *46* (1), 12. doi:10.1002/pola.22342.; (d) Hua, F.; Ruckenstein, E. *J. Polym. Sci., Part A: Polym. Chem.* **2004**, *42* (9), 2179. doi:10.1002/pola.20042.; (e) Bhadra, S.; Khastgir, D.; Singha, N. K.; Lee, J. H. *Prog. Polym. Sci.* **2009**, *34*, 783.
- (5) (a) Various living polymerizations and their application to the synthesis of block copolymers are covered in the following review articles: Matyjaszewski, K.; Müller, A. H. E. *Prog. Polym. Sci.* **2006**, *31* (12), 1039. doi:10.1016/j.progpolymsci.2006.09.002.; (b) Smid, J.; Van Beylen, M.; Hogen-Esch, T. E. *Prog. Polym. Sci.* **2006**, *31* (12), 1041. doi:10.1016/j.progpolymsci.2006.09.001.; (c) Hadjichristidis, N.; Iatrou, H.; Pitsikalis, M.; Mays, J. *Prog. Polym. Sci.* **2006**, *31* (12), 1068. doi:10.1016/j.progpolymsci.2006.07.002.; (d) Yagci, Y.; Tasdelen, M. A. *Prog. Polym. Sci.* **2006**, *31* (12), 1133. doi:10.1016/j.progpolymsci.2006.07.003.; (e) Bielawski, C. W.; Grubbs, R. H. *Prog. Polym. Sci.* **2007**, *32* (1), 1. doi:10.1016/j.progpolymsci.2006.08.006.; (f) Domski, G. J.; Rose, J. M.; Coates, G. W.; Bolig, A. D.; Brookhart, M. *Prog. Polym. Sci.* **2007**, *32* (1), 30. doi:10.1016/j.progpolymsci.2006.11.001.; (g) Braunecker, W. A.; Matyjaszewski, K. *Prog. Polym. Sci.* **2007**, *32* (1), 93. doi:10.1016/j.progpolymsci.2006.11.002.; (h) Yokozawa, T.; Yokoyama, A. *Prog. Polym. Sci.* **2007**, *32* (1), 147. doi:10.1016/j.progpolymsci.2006.08.001.; (i) Baskaran, D.; Mueller, A. H. E. *Prog. Polym. Sci.* **2007**, *32* (2), 173. doi:10.1016/j.progpolymsci.2007.01.003.; (j) Goethals, E. J.; Du Prez, F. *Prog. Polym. Sci.* **2007**, *32* (2), 220. doi:10.1016/j.progpolymsci.2007.01.001.; (k) Penczek, S.; Cypryk, M.; Duda, A.; Kubisa, P.; Slomkowski, S. *Prog. Polym. Sci.* **2007**, *32* (2), 247. doi:10.1016/j.progpolymsci.2007.01.002.; (l) *Controlled and Living Polymerizations: From Mechanisms to Materials*; Mueller, A. H. E., Matyjaszewski, K., Eds; Wiley-VCH: Weinheim, 2009.
- (6) (a) Wang, J. S.; Matyjaszewski, K. *J. Am. Chem. Soc.* **1995**, *117* (20), 5614. doi:10.1021/ja00125a035.; (b) Davis, K. A.; Matyjaszewski, K. *Adv. Polym. Sci.* **2002**, *159*, 1. doi:10.1007/3-540-45806-9\_1.; (c) Matyjaszewski, K.; Xia, J. *Chem. Rev.* **2001**, *101* (9), 2921. doi:10.1021/cr940534g. PMID:11749397.; (d) Tsarevsky, N. V.; Matyjaszewski, K. *Chem. Rev.* **2007**, *107* (6), 2270. doi:10.1021/cr050947p. PMID:17530906.; (e) Matyjaszewski, K.; Tsarevsky, N. V. *Nature Chem.* **2009**, *1* (4), 276. doi:10.1038/nchem.257.
- (7) (a) Hawker, C. J.; Wooley, K. L. *Science* **2005**, *309* (5738), 1200. doi:10.1126/science.1109778. PMID:16109874.; (b) Golas, P. L.; Matyjaszewski, K. *Qsar & Combin. Sci.* **2007**, *26* (11-12), 1116. doi:10.1002/qsar.200740059.
- (8) (a) Yagci, Y.; Tasdelen, M. A. *Prog. Polym. Sci.* **2006**, *31* (12), 1133. doi:10.1016/j.progpolymsci.2006.07.003.; (b) Coca, S.; Paik, H.-.; Matyjaszewski, K. *Macromolecules* **1997**, *30* (21), 6513. doi:10.1021/ma970637b.; (c) Gaynor, S. G.; Matyjaszewski, K. *Macromolecules* **1997**, *30* (14), 4241. doi:10.1021/ma970358o.; (d) Coca, S.; Matyjaszewski, K. *Macromolecules* **1997**, *30* (9), 2808. doi:10.1021/ma970073b.; (e) Matyjaszewski, K.; Beers, K. L.; Kern, A.; Gaynor, S. G. *J. Polym. Sci., Part A: Polym. Chem.* **1998**, *36* (5), 823. doi:10.1002/(SICI)1099-0518(19980415)36:5<823::AID-POLA15>3.0.CO;2-I.; (f) Shinoda, H.; Matyjaszewski, K. *Macromolecules* **2001**, *34* (18), 6243. doi:10.1021/ma0105791.; (g) Davis, K. A.; Charleux, B.; Matyjaszewski, K. *J. Polym. Sci., Part A: Polym. Chem.* **2000**, *38*, 2274; (h) Pintauer, T.; Matyjaszewski, K. *Coord. Chem. Rev.* **2005**, *249*, 1155; (i) Shinoda, H.; Miller, P. J.; Matyjaszewski, K. *Macromolecules* **2001**, *34*, 3186; (j) Kowalewski, T.; Tsarevsky, N. V.; Matyjaszewski, K. *J. Am. Chem. Soc.* **2002**, *124*, 10632; (k) Oh, J. K.; Drumright, R.; Siegwart, D. J.; Matyjaszewski, K. *Prog. Polym. Sci.* **2008**, *33*, 448.
- (9) (a) Ray, B.; Kotani, M.; Yamago, S. *Macromolecules* **2006**, *39* (16), 5259. doi:10.1021/ma060248u.; (b) Bilalis, P.; Pitsikalis, M.; Hadjichristidis, N. *J. Polym. Sci., Part A: Polym. Chem.* **2006**, *44* (1), 659. doi:10.1002/pola.21198.; (c) Devasia, R.; Bindu, R. L.; Borsali, R.; Moughin, N.; Gnanou, Y. *Macromol. Symp.* **2005**, *229* (1), 8. doi:10.1002/masy.200551102.; (d) Mori, H.; Ookuma, H.; Nakano, S.; Endo, T. *Macromol. Chem. Phys.* **2006**, *207* (12), 1005. doi:10.1002/macp.200600070.; (e) Iovu, M. C.; Matyjaszewski, K. *Macromolecules* **2003**, *36*, 9346; (f) Sheiko, S. S.; Sumerlin, B. S.; Matyjaszewski, K. *Prog. Polym. Sci.* **2008**, *33*, 759; (g) Debuigne, A.; Poli, R.; Jerome, C.; Jerome, R.; Detrembleur, C. *Prog. Polym. Sci.* **2009**, *34*, 211; (h) Lutz, J.-F.; Boerner, H. G. *Prog. Polym. Sci.* **2008**, *33*, 1.
- (10) (a) Lu, X. J.; Gong, S. L.; Meng, L. Z.; Li, C.; Yang, S.;

- Zhang, L. F. *Polymer (Guildf.)* **2007**, *48* (10), 2835. doi:10.1016/j.polymer.2007.03.048.; (b) Hua, J.; Chen, D. B.; Yu, Y. L.; Xu, L.; Zhang, Y. F.; Jing, X. K.; Wu, A. Q.; Shi, L. *Polym. Bull.* **2002**, *48* (2), 135. doi:10.1007/s00289-002-0023-1.; (c) Brar, A. S.; Kaur, S. *J. Polym. Sci., Part A: Polym. Chem.* **2006**, *44* (5), 1745. doi:10.1002/pola.21296.
- (11) Kaneyoshi, H.; Matyjaszewski, K. *Macromolecules* **2006**, *39* (8), 2757. doi:10.1021/ma052746t.
- (12) (a) Nguyen, T. L. U.; Eagles, K.; Davis, T. P.; Barner-Kowollik, C.; Stenzel, M. H. *J. Polym. Sci., Part A: Polym. Chem.* **2006**, *44* (15), 4372. doi:10.1002/pola.21518.; (b) Hussain, H.; Tan, B. H.; Gudipati, C. S.; Liu, Y.; He, C. B.; Davis, T. P. *J. Polym. Sci., Part A: Polym. Chem.* **2008**, *46* (16), 5604. doi:10.1002/pola.22882.; (c) Debuigne, A.; Willet, N.; Jerome, R.; Detrembleur, C. *Macromolecules* **2007**, *40* (20), 7111. doi:10.1021/ma0712908.; (d) Pound, G.; Aguesse, F.; McLeary, J. B.; Lange, R. F. M.; Klumperman, B. *Macromolecules* **2007**, *40* (25), 8861. doi:10.1021/ma0710075.; (e) Pound, G.; Eksteen, Z.; Pfukwa, R.; McKenzie, J. M.; Lange, R. F. M.; Klumperman, B. *J. Polym. Sci., Part A: Polym. Chem.* **2008**, *46* (19), 6575. doi:10.1002/pola.22968.; (f) Mori, H.; Ookuma, H.; Endo, T. *Macromolecules* **2008**, *41* (19), 6925. doi:10.1021/ma801266h.; (g) Morton, K.; Graffe, A.; Maric, M. *Macromol. Chem. Phys.* **2007**, *208* (5), 496. doi:10.1002/macp.200600560.
- (13) Kwak, Y.; Nicolay, R.; Matyjaszewski, K. *Macromolecules* **2009**, *42* (11), 3738. doi:10.1021/ma9005389.
- (14) (a) Dong, H.; Tang, W.; Matyjaszewski, K. *Macromolecules* **2007**, *40* (9), 2974. doi:10.1021/ma070424e.; (b) Guillaneuf, Y.; Castignolles, P. *J. Polym. Sci., Part A: Polym. Chem.* **2008**, *46* (3), 897. doi:10.1002/pola.22433.
- (15) Huang, C. F.; Nicolay, Y.; Kwak, Y.; Chang, F. C.; Matyjaszewski, K. *Macromolecules* **2009**, *42* (21), 8198. doi:10.1021/ma901578z.

# Synthesis, photophysics, and electrochemistry of thiophene–pyridine and thiophene–pyrimidine dyad comonomers

Andréanne Bolduc, Stéphane Dufresne, Garry S. Hanan, and W.G. Skene

**Abstract:** A series of new  $\pi$ -conjugated donor (D) and acceptor (A) dyad comonomers were prepared using Suzuki coupling protocols. The D–A comonomers consisting of thiophene/bithiophene as donors and pyridine/pyrimidine as acceptors were prepared to investigate their photophysical and electrochemical properties. The dyads were spectroscopically confirmed to be highly conjugated. This was further supported by the X-ray crystal structure of the bithiophene–pyridine dyad that showed all the heterocycles to be coplanar. It was further found that the fluorescence yields ( $\Phi_f$ ) of the dyads were highly dependent on the number of thiophenes. The bithiophene derivatives exhibited  $\Phi_f$  values  $\geq 0.3$  while the thiophene derivatives did not fluoresce. The suppressed fluorescence observed for the thiophene derivatives was due to their higher triplet energy resulting in efficient intersystem crossing (ISC) to the triplet state with  $\Phi_{ISC} \geq 0.8$ . This was confirmed both by time-resolved and steady-state measurements. The singlet excited state of both thiophene and bithiophene dyads was deactivated solely by either fluorescence and (or) ISC. Owing to their donor and acceptor character, the dyads could be oxidized and reduced both electrochemically and photochemically to afford the radical cation and anion, respectively.

**Key words:** comonomer, thiophene, pyridine, pyrimidine, photophysics, fluorescence.

**Résumé :** À l'aide d'un couplage de Suzuki, une série de comonomères conjugués contenant une fonction donneur d'électrons (D) et une fonction accepteur d'électrons (A) ont été préparés. Ces comonomères, dits D–A, qui utilisent le thiophène/bithiophène comme donneurs d'électrons et la pyridine/pyrimidine comme accepteurs d'électrons, ont été synthétisés dans le but d'analyser leurs propriétés photophysiques et électrochimiques. Il a été évalué spectroscopiquement que les dimères sont grandement conjugués. Ceci est d'ailleurs soutenu par la structure rayons-X du composé bithiophène–pyridine qui montre que tous les hétérocycles sont coplanaires. Il a été déterminé que les rendements quantiques de fluorescence ( $\Phi_f$ ) des composés dépendent du nombre de thiophènes présents dans la molécule. En effet, les dérivés du bithiophène ont des  $\Phi_f \geq 0,3$  tandis que les dérivés du thiophène ne fluorescent pas. Cette absence de fluorescence est causée par la formation d'un état triplet de haute énergie par croisement intersystème (ISC pour « intersystem crossing ») avec un  $\Phi_{ISC} \geq 0,8$ . L'état singulet excité des dimères de thiophène et de bithiophène est uniquement désactivé par la fluorescence ou le ISC. Grâce à leur caractéristique donneur/accepteur, les comonomères ont pu être oxydés et réduits électrochimiquement et chimiquement afin de former le radical cation et le radical anion.

**Mots-clés :** comonomère, thiophène, pyridine, pyrimidine, photophysique, fluorescence.

[Traduit par la Rédaction]

## Introduction

Conjugated materials have attracted much attention because of their electrochemical and photophysical properties that are ideally suited for plastic electronics, including organic field effect transistor,<sup>1–4</sup> photovoltaics,<sup>5,6</sup> emitting devices,<sup>7,8</sup> and conducting materials,<sup>9,10</sup> to name but a few. Thiophenes have been widely used in these electronic applications owing to their low oxidation potential and their possibility of undergoing electropolymerization resulting in conjugated polymers possessing extremely low oxidation potentials. However, homopolymers of thiophene and its deriv-

atives often have undesirably high HOMO–LUMO energy gaps ( $E_g$ ) and oxidation potentials ( $E_{pa}$ ) that are unsuitable for functional materials, as well as weak fluorescence.

The  $E_g$  and  $E_{pa}$  can be modulated by copolymerizing thiophene with different electron-donating and -accepting monomers. However, homopolymers are solely obtained if the oxidation potentials of both the monomer and thiophene are not closely matched. Although choosing monomers with  $E_{pa}$  that are closely matched to thiophene results in copolymers, the  $E_g$  and  $E_{pa}$  are similar to those of the homopolythiophene. This problem can be overcome with comonomers. The comonomer configuration consisting of a central aro-

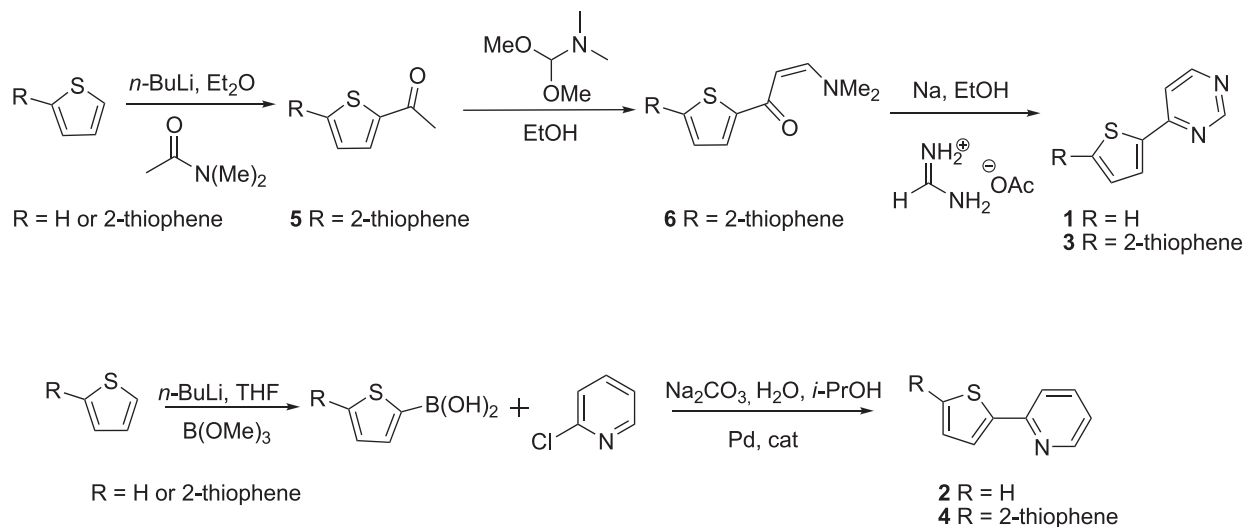
Received 26 August 2009. Accepted 5 October 2009. Published on the NRC Research Press Web site at canjchem.nrc.ca on 12 February 2010.

This article is part of a Special Issue dedicated to Professor M. A. Winnik.

A. Bolduc, S. Dufresne, G.S. Hanan, and W.G. Skene.<sup>1</sup> Centre for Self-Assembled Chemical Structures, Département de Chimie, Université de Montréal, CP 6128, Succ. Centre-ville, Montréal, QC H3C 3J7, Canada.

<sup>1</sup>Corresponding author (e-mail: w.skene@umontreal.ca).



**Scheme 1.** Synthetic scheme for **1** and **3** (top) and **2** and **4** (bottom).

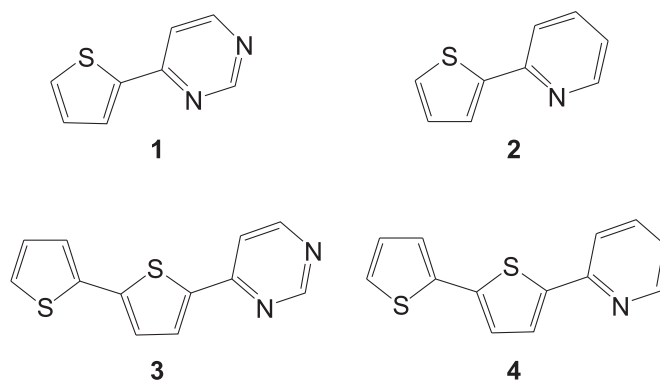
matic acceptor (A) core inserted between electron-rich donors (D) simplifies the electropolymerization process that would otherwise require two or three separate monomers to obtain analogous alternating copolymers via other coupling methods.<sup>11,12</sup> The same polymer can also be obtained by cathodic polymerization of a D–A–D comonomer.

Comonomers consisting of electron-deficient heterocycles, such as pyridine, pyrazine, and pyrimidines, are also interesting because they can coordinate with metals. This can be done either prior to- or post-polymerization, affording metal-containing polymers. Property tailoring for a given application is possible by coordinating different metals. *n*-Doping of the electron-deficient-containing compounds is further possible resulting in the both *p*- and *n*-type polymers.

Unlike the polymerization of D–A–D or A–D–A comonomers that can be done in one step, the polymerization of D–A comonomers requires two steps. This can either be done by anodic dimerization followed by cathodic polymerization or the reverse. The added advantage of the stepwise polymerization of D–A comonomers is that the anodically and cathodically coupled dimers can be characterized, and the metal complexes can be isolated and characterized as well. Structure–property relationships are therefore possible in addition to tailoring the properties for a given application. This is in contrast to their triad cousins that are insoluble when polymerized, precluding their spectroscopic and molecular-weight characterization.

Our ongoing investigation of conjugated polymers<sup>13–19</sup> and our previous endeavors in comonomer synthesis<sup>11,20</sup> prompted us to prepare a series of  $\pi$ -rich and  $\pi$ -poor dyad comonomers consisting of thiophenes and both pyridine and pyrimidine. These compounds are of particular interest because they are expected to exhibit mutual *p*- and *n*-doping properties allowing for selective stepwise anodic and cathodic coupling potentially leading to D–A–A–D and A–D–D–A comonomer products, respectively. These can then subsequently be electropolymerized. Furthermore, the  $\pi$ -donor/acceptor arrangement provides the means to tune the HOMO–LUMO energy levels and to tailor the spectroscopic and electrochemical properties.<sup>21–24</sup>

Herein, we present the preparation of new  $\pi$ -donor/acceptor

**Chart 1.** Comonomers synthesized.

dyad comonomers along with their steady-state and time-resolved photophysics and electrochemical characterization. The combined effect of thiophene and bithiophene  $\pi$ -donors coupled with pyridine and pyrimidine  $\pi$ -acceptors for comonomers is presented. Although such compounds are of interest for their electrochemical properties, little work has examined the photophysics for such dyads. Their structure–property relationships and the understanding of their fluorescence deactivation mechanisms are of interest for the design and property tuning of new compounds. For these reasons, the photophysical properties, including the emission yields and excited-state deactivation pathways, of these new comonomers are studied. The investigation of such properties provides valuable information for determining the suitability of such precursors for functional materials and for the design of future compounds.

## Synthesis

The comonomers **2** and **4** (Chart 1) were prepared by standard Suzuki coupling.<sup>25,26</sup> The 2-thiophene boronic acid and 2-bithiophene boronic acid precursors required for Suzuki coupling were obtained by standard aryl anion formation with *n*-BuLi followed by nucleophilic addition to triethylboronate ester starting from inexpensive thiophene and bithiophene, respectively.<sup>27</sup> The boronic acids were

**Table 1.** Details of crystal structure determination for **4**.

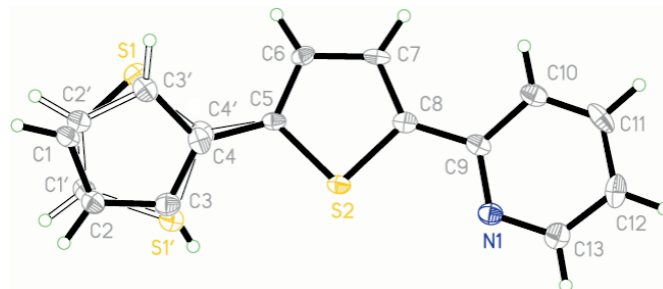
Formula	C <sub>13</sub> H <sub>9</sub> NS <sub>2</sub>
<i>M<sub>w</sub></i> (g/mol); <i>F</i> (000)	243.33 g/mol; 504
Crystal color and form	Yellow plate
Crystal size (mm)	0.15 × 0.07 × 0.05
<i>T</i> (K); <i>d</i> <sub>calcd.</sub> (g/cm <sup>3</sup> )	150 (2); 1.407
Crystal System	Orthorhombic
Space group	<i>Pna</i> 2 <sub>1</sub>
<i>a</i> (Å)	19.5336 (19)
<i>b</i> (Å)	10.1891 (10)
<i>c</i> (Å)	5.7716 (6)
$\alpha$ (°)	90.000
$\beta$ (°)	90.000
$\gamma$ (°)	90.000
<i>V</i> (Å <sup>3</sup> ); <i>Z</i>	1148.7 (2); 4
$\theta$ range (°); completeness	4.53–72.47; 0.852
Reflections: collected/independent; <i>R</i> <sub>int</sub>	8286/1783; 0.093
$\mu$ (mm <sup>-1</sup> )	3.930
Abs. Corr.	Semi-empirical
<i>R</i> 1( <i>F</i> ); <i>wR</i> ( <i>F</i> <sup>2</sup> ) [ <i>I</i> > 2σ ( <i>I</i> )]	0.0581; 0.1260
<i>R</i> 1( <i>F</i> ); <i>wR</i> ( <i>F</i> <sup>2</sup> ) (all data)	0.0725; 0.1321
GoF( <i>F</i> <sup>2</sup> )	1.065
Max. residual e <sup>-</sup> density	0.284 e <sup>-</sup> Å <sup>-3</sup>

coupled with a chloropyridine by Suzuki coupling in aqueous isopropanol, and this solvent led to homogenous reaction mixtures resulting in higher yields.<sup>11</sup> The reaction proceeded cleanly at 50 °C with only 1 mol% of catalyst. Conversely, **1** and **3** (Chart 1) were less straightforward to prepare, since the required 4-halogenopyrimidine commercially precursor is unavailable and the 2- and the 5-substituted derivatives are expensive. The required pyrimidine precursors for the synthesis of **1** and **3** were therefore prepared by a Michael reaction according to Scheme 1. This route unfortunately required a slow ring-closing step requiring 7 days for completion.<sup>28–30</sup>

## Crystallography

Confirmation of the formation of **4** was obtained by X-ray diffraction (Table 1). Suitable crystals for analysis were obtained from the slow evaporation of **4** in dichloromethane. The resolved structure is shown in Fig. 1. The resolved structure shows disorder of the terminal thiophene consisting of inversion of the thiophene. The thiophene (S1–C1–C2–C3–C4) weights are 76% for the structural representation with the two thiophene adopting an anti conformation. The remaining 24% is attributed to the minor isomer in which the two thiophenes are syn. It should be noted that the heterocycles are nearly coplanar, contributing in part to its high degree of conjugation (vide infra). The torsion angle between the pyridine and the central thiophene is 5.38° while that of two thiophenes is 9.75°, and is consistent with similar structures.<sup>11</sup>

The molecules of **4** in the crystal lattice align along the *a*–*b* axis in a zig-zag fashion as shown in Fig. 2. This arrangement is in part a result of non-conventional H-bonding occurring between C11–H and N1. The distance between C11 and N1 is 3.443 Å, which is within a suitable distance for such a weak interaction. Face-edge  $\pi$ -stacking also oc-

**Fig. 1.** X-ray structure of **4** and the numbering scheme adopted.

curs between S2–C5–C6–C7–C8 and the pyridine through C12 with the two being separated by 3.665 Å. C1 is also directed towards the N1–C9–C10–C11–C12–C13 ring, and they are separated by a distance of 3.427 Å (Fig. 3).

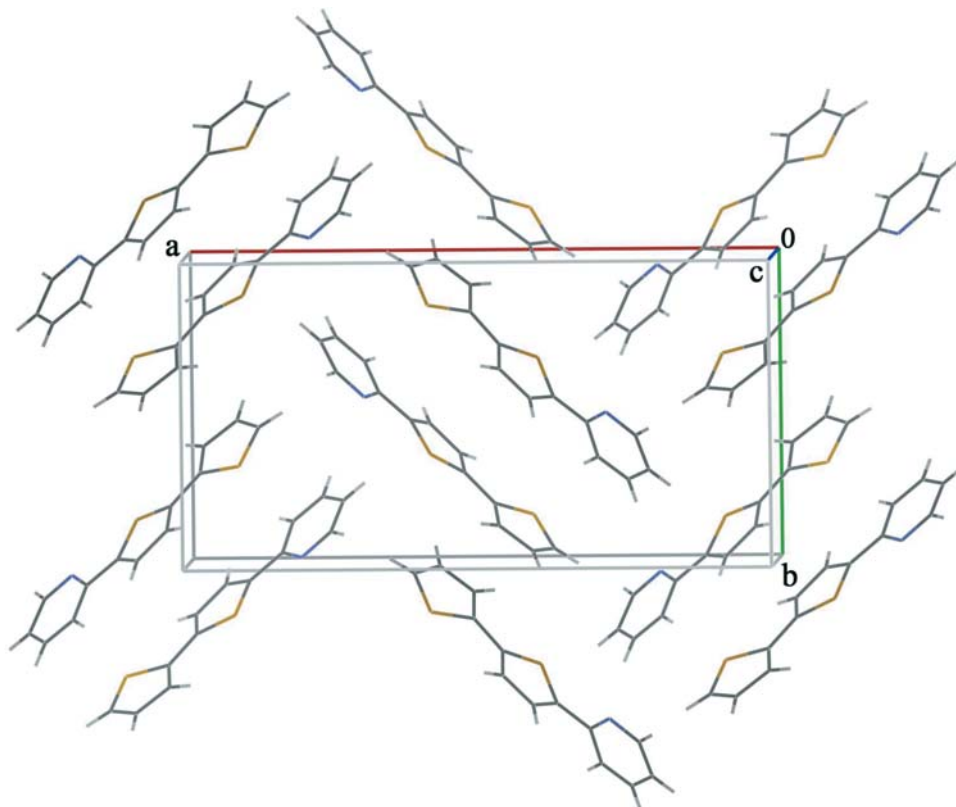
## Spectroscopy

The effect of the number of heterounits in the comonomer on the spectroscopic properties can be seen from the spectroscopic data in Table 2. Both the absorption and fluorescence maxima of **3** and **4** are bathochromically shifted relative to **1** and **2**. The bathochromic shifts imply an increased degree of conjugation resulting from the bithiophene unit relative to thiophene. The increased degree of conjugation of the bithiophene dyad relative to the thiophene is also evident from the *E<sub>g</sub>*, which is lower for **3** and **4** than for **1** and **2**. It is noteworthy that the *E<sub>g</sub>* is larger for pyridine-containing dyads compared with their pyrimidine analogues, owing to the more electron deficient nature of diazines, which perturbs the LUMO level.

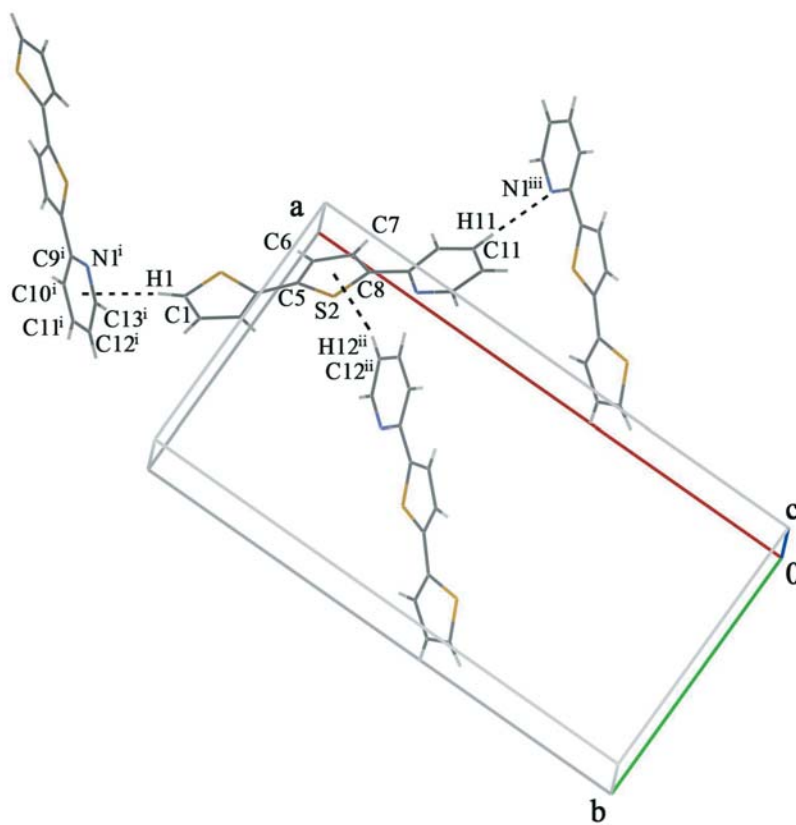
Functional materials with high fluorescence yields are of interest for emitting devices. High fluorescence yields are also desired for efficient ligand-to-metal energy transfer. For these reasons, we examined the fluorescence quantum yields for the comonomer dyads. Both the bithiophene dyads are highly fluorescent relative to their thiophene analogues. High fluorescence yields were confirmed by measuring the absolute emissions with an integrating sphere. The advantage of the integrating sphere is that references with similar absorption, emissions, and emission yields to the compounds of study are not required. Even though the fluorescence values measured for **1** and **2** are below the detection limit of the integrating sphere, accurate fluorescence measurements of **3** and **4** are possible. It can be concluded that **1** and **2** are nonfluorescent. The difference in fluorescence between the two sets of dyads implies two different deactivation pathways of the singlet excited state are present. Although both the thiophene and bithiophene dyads exhibit unimolecular fluorescence decays of approximately < 2 ns, an efficient deactivation mode competes with fluorescence for **1** and **2**, resulting in suppressed fluorescence.

Deactivation of the excited state by intramolecular charge transfer (ICT) can lead to suppressed fluorescence. ICT often results from charge separation occurring on separate donor–acceptor moieties. Charge separation can be visualized from the molecular orbitals, which can be accurately calculated by theoretical means. The HOMO and LUMOs of the comonomers were therefore investigated to afford insight into the different excited-state deactivation modes. As

**Fig. 2.** The three-dimensional network of **4** illustrating the zig-zag configuration along the  $a$ - $b$  axis.



**Fig. 3.** The interactions involved in the lattice of **4**. The disorder is omitted for clarity. (i)  $0.5 + x, 0.5 + y, z$ ; (ii)  $1.5 - x, 0.5 + y, 0.5 + z$ ; (iii)  $1.5 - x, -0.5 + y, 0.5 + z$ .

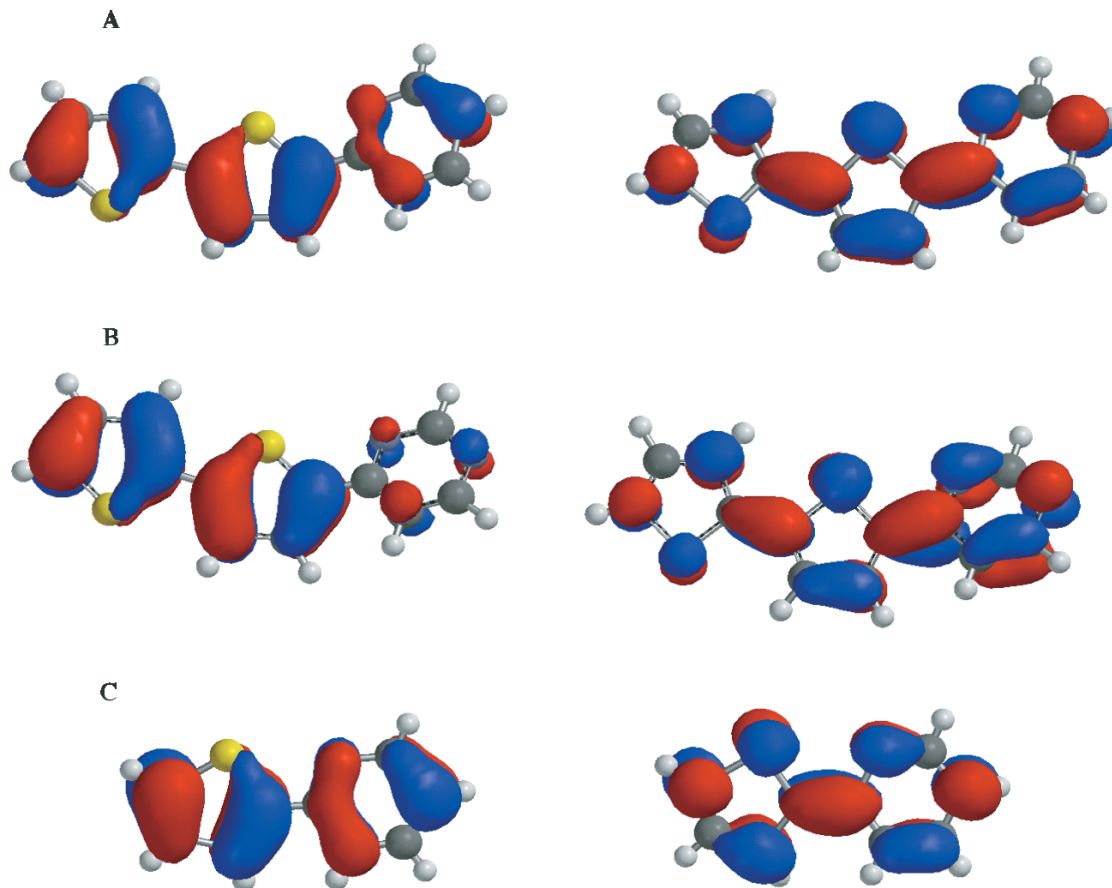


**Table 2.** Comonomer spectroscopic properties measured in anhydrous and deaerated dichloromethane.

Compound	$\lambda_{\text{abs}}$ (nm)	$\Delta E$ (eV)	$E_g$ (eV)	$\lambda_{\text{em}}$ (nm)	$\Phi_{\text{fl}}^a$	$\tau_{\text{fl}}$ (ns)	$\Delta G_{\text{et}}$ (kJ/mol) <i>N,N</i> -Dimethylaniline <sup>b</sup>	$\Delta G_{\text{et}}$ (kJ/mol) Benzoquinone <sup>b</sup>
1	306	3.7	3.3	380	<0.01 (0)	2.6	-79	-223
2	320	3.8	3.7	356	0.04 (0.08)	5.3	-69	-213
3	365	3.1	2.9	433	0.66 (0.86)	1.9	-2	-175
4	354	3.2	3.1	420	0.15 (0.30)	6.2	-11	-174

<sup>a</sup>Values in parentheses were measured using a calibrated integrating sphere.

<sup>b</sup>Calculated energetics of photoinduced electron transfer ( $\Delta G_{\text{et}}$ ) between the different comonomers and electron donors and acceptors.

**Fig. 4.** HOMO (left) and LUMO (right) energy levels calculated via DFT of **4** (A), **3** (B), and **2** (C).

seen in Fig. 4, the HOMO and LUMO orbitals calculated from DFT single-point energies from the X-ray crystal coordinates are not isolated on one heterocycles and they are evenly distributed across the heterocycles regardless of the dyad. ICT is therefore not responsible for the different fluorescence yields despite the  $\pi$ -donor/acceptor character.

The singlet excited state deactivation pathways of the comonomers were further investigated using various quenchers. In all cases, the comonomers were self-quenched with diffusion-controlled kinetics in acetonitrile ( $2 \times 10^{10} \text{ M}^{-1} \text{ s}^{-1}$ ).<sup>31</sup> All spectroscopic measurements were subsequently done at extremely low concentrations ( $10^{-6} \text{ mol/L}$ ) to avoid self-quenching. An electron acceptor (benzoquinone) and donor (*N,N'*-dimethylaniline) were added to determine whether the comonomers could undergo photoinduced electron transfer. Interestingly, all the comonomers studied were quenched at diffusion-controlled limits by both benzoquinone and *N,N'*-dimethylaniline (Fig. 5). This implies that the comonomers

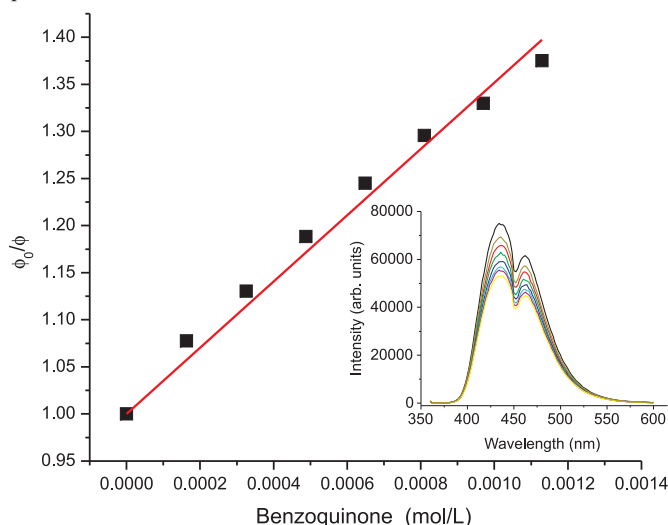
are capable of generating both radical cations and radicals. This is in contrast to thiophene derivatives that can generate only radical cations while pyridine and pyridimine afford uniquely radical anions. The photoinduced electron-transfer mechanism leading to radical ion intermediates is further supported by the exergonic  $\Delta G_{\text{et}}$  values calculated from the Rehm–Weller equation, shown in Table 2.<sup>31</sup> The dual quenching confirms that the comonomers can potentially be both oxidized and reduced while their increased degree of conjugation relative to their discrete monomers afford the means to tailor the spectroscopic and electrochemical properties.

### Laser flash photolysis

The donor–acceptor character of the comonomers can lead to radical ions upon photoirradiation, as observed by the fluorescence quenching with the electron donor and ac-



**Fig. 5.** Static Stern–Volmer analysis of **3** as a function of benzoquinone. Inset: Decrease in fluorescence intensity of **3** with benzoquinone addition in deaerated acetonitrile.



ceptor. Laser flash photolysis (LFP) was used for spectroscopically detecting these intermediates in addition to any triplets, either of which could be responsible for the reduced fluorescence of **1** and **2**. The transient absorption spectra for the dyads studied are found in the inset of Fig. 6. Both the thiophene and bithiophene comonomers exhibited transient spectra whose absorption maxima are dependent on the number of thiophenes. The unimolecular decay (Fig. 6) implies that the observed transients are triplets. Triplet assignment was further confirmed by the fast quenching of the transients with known triplet quenchers; oxygen, 1,3-cyclohexadiene,  $\beta$ -carotene, and 2-methylnaphthalene (Table 3). The unimolecular decay precludes the formation of radical ions that can be produced by intramolecular photoinduced electron transfer. The observed transients were further assigned to triplets, since they were not quenched by radical ion generators, benzoquinone, or *N,N*-dimethylaminopyridine.

Quantification of the triplet state is possible by LFP according to eq. [1]

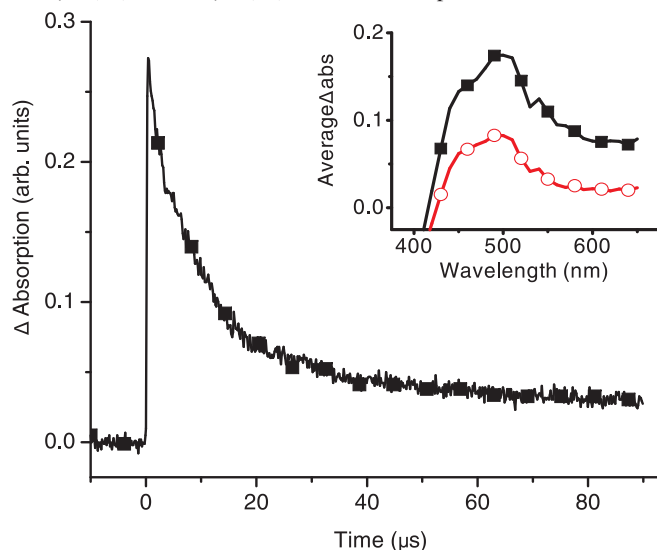
$$[1] \quad \Phi_x = \frac{\Delta \text{Abs}_x \cdot \Phi_{\text{ref}} \cdot \varepsilon_x}{\Delta \text{Abs}_{\text{ref}} \cdot \varepsilon_{\text{ref}}}$$

where  $\Phi_{\text{TT}}$  is the quantum yield of triplet formation,  $\varepsilon_{\text{TT}}$  is the triplet–triplet molar absorption coefficient,  $\Delta \text{Abs}$  is the signal intensity monitored at the maximum triplet absorption as a function of laser power, ref refers to the actinometer, and *x* refers to the corresponding comonomer. Either  $\Phi_{\text{TT}}$  or  $\varepsilon_{\text{TT}}$  can be derived by direct comparison of the comonomer triplet signal to the reference, xanthone. Equation [1] can be simplified to eq. [2] for calculating the triplet comonomer yield without knowing  $\varepsilon_{\text{TT}}$ , which is not normally precisely known.

$$[2] \quad \Phi_x = \frac{\Delta \text{Abs}_x \cdot \Phi_{\text{ref}}}{\Delta \text{Abs}_{\text{ref}} \cdot \Phi_x}$$

Equation [2] is valid if both the reference and the comonomer produce a common triplet. This is the case when 2-

**Fig. 6.** Kinetic decay of triplet **4** monitored at 490 nm after excitation at 355 nm. Inset: Transient absorption spectra of **4** monitored at 16  $\mu\text{s}$  (■) and 27  $\mu\text{s}$  (○) after the laser pulse of 355 nm.



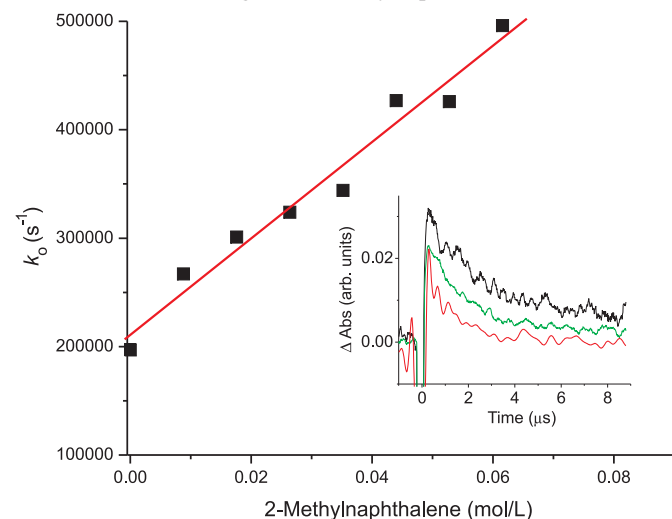
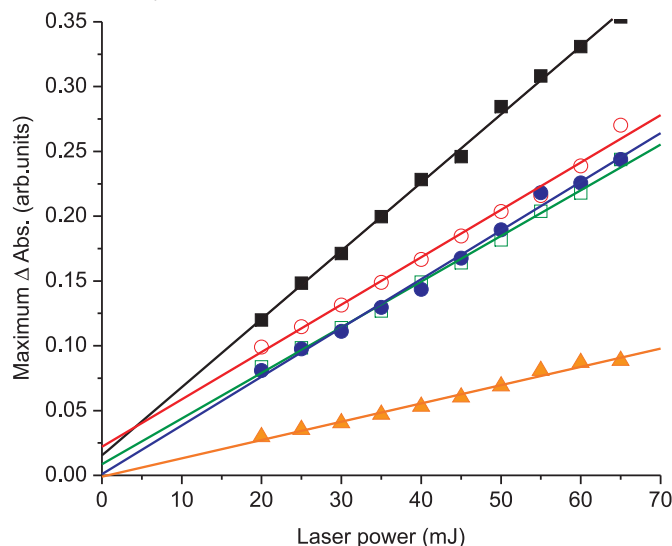
methylnaphthalene (MN) is added to both the reference and comonomer samples. In this case, MN quenches the comonomer and xanthone triplet by energy transfer to produce triplet MN that is observed at 420 nm. MN is the quencher of choice because its triplet cannot be produced by direct excitation. More importantly, its triplet can be detected by LFP and its absorption does not overlap with any of the comonomers or with xanthone. Equation [2] is valid if all the triplets produced within the laser pulse are rapidly quenched by energy transfer to produce the triplet methylnaphthalene. The amount of MN required for deactivating at least 95% of the comonomer and xanthone triplets can be calculated by the quenching rate constant derived from Fig. 7.

The  $\Phi_{\text{TT}}$  of the comonomers can be derived from the slope of the maximum triplet signal as a function of laser power relative to xanthone ( $\Phi_{\text{TT}} = 1$ ; Fig. 8) according to the simplified eq. [2] by observing the common triplet MN. The comonomer  $\varepsilon_{\text{TT}}$  can similarly be calculated from the slope of the maximum signal observed at the comonomer absorption maximum as a function of laser power versus xanthone in the absence of MN. The calculated triplet values found in Table 4 show that the  $\varepsilon_{\text{TT}}$  are larger for the bithiophene dyads than for the thiophene comonomers. The larger  $\varepsilon_{\text{TT}}$  implies the bithiophene triplets exhibit a higher degree of conjugation than **1** and **2**.

It is also evident from Table 3 that the comonomers produce appreciable amounts of triplet. From the energy conservation ( $1 = \Sigma \Phi_x = \Phi_{\text{fl}} + \Phi_{\text{ISC}} + \Phi_{\text{IC}}$ ) and the spectroscopic data, it can be concluded that the comonomers deactivate their singlet excited state predominately by two pathways: either fluorescence or intersystem crossing (ISC) to form their triplet state. In the case of the thiophene comonomers, the singlet excited manifold is deactivated predominately by ISC, supported by the fluorescence and LFP data. This is most likely a result of their higher triplet level favoring ISC. The higher triplet energy of **1** and **2** is confirmed by the phosphorescence emissions that are significantly hypsochromically shifted relative to **3** and **4** (Table 4 and

**Table 3.** Triplet-quenching rate constants for the different comonomers with various quenchers measured in anhydrous and deaerated acetonitrile.

Quencher	<b>1</b> ( $10^9 \text{ M}^{-1} \text{ s}^{-1}$ )	<b>2</b> ( $10^9 \text{ M}^{-1} \text{ s}^{-1}$ )	<b>3</b> ( $10^9 \text{ M}^{-1} \text{ s}^{-1}$ )	<b>4</b> ( $10^9 \text{ M}^{-1} \text{ s}^{-1}$ )
1,3-Cyclohexadiene	4.5	0.2	0.4	0.3
$\beta$ -Carotene	4.8	5.5	2.2	4.3
2-Methylnaphthalene	4.5	0.004	0.003	0.001
Self-quenching	3.8	8.4	19.9	16.4

**Fig. 7.** Variation of triplet rate constant of **1** with the addition of 2-methylnaphthalene measured at 390 nm. Inset: Effect of triplet transient of **1** monitored at 390 nm with 0 (black), 26 mmol/L (red), and 53 mmol/L (green) 2-methylnaphthalene.**Fig. 8.** Maximum absorption of triplet 2-methylnaphthalene as a function of laser power produced upon energy transfer from xanthone (■), **1** (○), **2** (●), **3** (□), and **4** (▲) monitored at 420 nm in anhydrous and deaerated acetonitrile.**Fig. 9.** The increased degree of conjugation resulting in splitting of the singlet–triplet energy levels is consistent with previous reports and further confirms that deactivation does not occur from intramolecular photoinduced electron transfer or other radiative means, such as internal conver-

sion.<sup>32,33</sup> The steady-state and time-resolved data collectively confirm that the fluorescence can be tuned as a function of comonomer structure and that the excited-state energy can be channeled to the emitting manifolds. Tuning of the spectroscopic properties as a function of structure is therefore possible.

## Electrochemistry

Cyclic voltammetry of each comonomer was done to determine their redox potentials. All the comonomers exhibited both oxidation and reduction potentials corresponding to the radical cation and anion, respectively. The electrochemical data also demonstrate the inherent dual *n*- and *p*-type character of the comonomers. This behaviour is corroborated by the fluorescence quenching data. The HOMO and LUMO values, and the corresponding energy gaps can be calculated from the measured redox potentials by standard methods leading to the values reported in Table 5.<sup>23</sup> It is evident from the calculated values that the  $\pi$ -donating thiophene group affects the LUMO of the  $\pi$ -accepting nitrogen-containing heterocycles. This is supported by the less-negative reductive potentials ( $E_{pc}$ ) of **1–4** compared with pyridine ( $E_{pc} = -2.6 \text{ V}$ ) and pyrimidine ( $E_{pc} = -2.4 \text{ V}$ ).<sup>34,35</sup> Conversely, the oxidation potentials ( $E_{pa}$ ) of the comonomers are unchanged compared to their thiophene ( $E_{pa} = 1.6 \text{ V}$ )<sup>36</sup> and bithiophene ( $E_{pa} = 1.3 \text{ V}$ ) monomers.<sup>37</sup> This is a result of the  $\pi$ -accepting character of the adjacent nitrogen heterocycle, further confirming that the comonomers are conjugated.

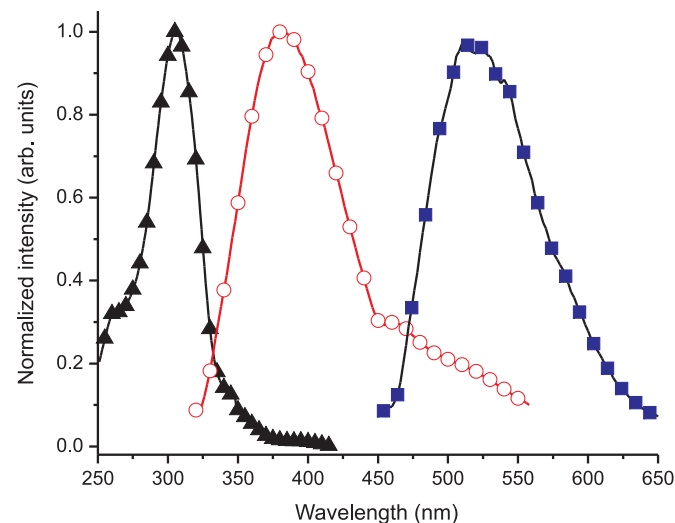
Both the reduction and oxidation processes of the comonomers are not reversible, as seen in Fig. 10. This is expected, since the radical ions are highly reactive and can cross-couple to form their corresponding dimers.<sup>38</sup> Electrochemical dimerization using a large-surface-area mesh electrode was used to afford sufficient quantities of dimers for characterization. Unfortunately, only products insoluble in standard organic solvents were obtained. This is most likely a result of multiple radical ion coupling on the same comonomer. This nonetheless confirms that the donor–acceptor dyads are electrochemically active and that D–A–A–D and A–D–D–A products are possible.

## Conclusion

A series of new donor–acceptor dyad comonomers were prepared. The spectroscopic and electrochemical properties can be modulated as a function of structure. The comonomers can both be photochemically and electrochemically oxidized and reduced resulting in radical ions. This dual active behaviour is a result of incorporating both  $\pi$ -donors and  $\pi$ -acceptors to form the comonomers. The singlet excited state was found to deactivate exclusively by either fluores-

**Table 4.** Triplet properties of the different comonomers measured in anhydrous and deaerated acetonitrile.

Compound	$\lambda_{\text{TT}}$ (nm)	$\tau_{\text{TT}}$ ( $\mu\text{s}$ )	$k_0$ ( $\text{s}^{-1}$ ) ( $10^{-5}$ )	$\varepsilon_{\text{TT}}$ ( $\text{M}^{-1} \text{cm}^{-1}$ )	$\Phi_{\text{TT}}$	$\lambda_{\text{phos}}$ (nm) <sup>a</sup>	$\tau_{\text{phos}}$ (ms) <sup>a</sup>
1	390	4.8	2.1	4000	0.79	522	190
2	380	7.9	1.3	8000	0.83	534	71
3	490	12.3	0.8	15 000	0.30	700	6
4	490	11.2	0.9	20 000	0.86	703	5

<sup>a</sup>Measured in a 4:1 ethanol/methanol matrix at 77 K.**Fig. 9.** Normalized absorbance ( $\blacktriangle$ ) and fluorescence ( $\circ$ ) of **1** measured in dichloromethane at room temperature and phosphorescence ( $\blacksquare$ ) measured at 77 K in 4:1 ethanol/methanol glass matrix.

cence or intersystem crossing. The deactivation pathway can be tailored by adjusting the triplet energy level, which in turn, is controlled by the degree of conjugation and the number of thiophenes. These novel comonomers are ideal candidates for emitting applications owing to their high fluorescence yields.

## Experimental

### Analyses

#### Spectroscopic measurements

Absorbance measurements were recorded on a Cary-500 spectrometer, while fluorescence measurements were performed with an Edinburgh Instruments FLS-920 fluorimeter after deaerating the sample for 20 min with nitrogen. Fluorescence quantum yields were measured at low sample concentration in dichloromethane by exciting the compounds close to their maximum absorption wavelength and by comparing the emission to bithiophene ( $\Phi_{\text{fl}} = 0.013$ ) at the same wavelength. Phosphorescence measurements were done on a Cary Eclipse at 77 K in a 4:1 ethanol/methanol solvent.

#### Laser flash photolysis (LFP) measurements

Laser flash photolysis experiments were done on a Luzchem mini-LFP system excited at 355 nm with the third harmonic of a Nd-YAG laser. The solutions were prepared with absorbances between 0.3 and 0.5 at the excitation wavelength. Triplet-state quantum yield and triplet–triplet molar absorption coefficients were measured against xanthone in

dichloromethane ( $\Phi_{\text{TT}} = 1$ ,  $\varepsilon_{\text{TT}} = 28\,000 \text{ mol/L}^{-1} \text{ s}^{-1}$ ) and were determined using standard techniques.<sup>39–42</sup>

#### Crystal structure determination

Diffraction data for **4** was collected on a Bruker Smart 6000 diffractometer using graphite-monochromatized Cu K $\alpha$  radiation with 1.54178 Å. The structures were solved by direct methods (SHELXS97). Disorder was found in the terminal thiophene and consisted of a flip of this heterounit. The weight of each isomer was optimized. All non-hydrogen atoms were refined based on Fobs2 (SHELXS97), while hydrogen atoms were refined on calculated positions with fixed isotropic U, using riding model techniques.

#### Electrochemical measurements

Cyclic voltammetry measurements were recorded with a Bio Analytical Systems Ec Epsilon potentiostat. The compounds of study were dissolved in anhydrous and deaerated dichloromethane with 0.1 mol/L TBAPF<sub>6</sub>. A platinum electrode was employed as the working electrode, while a platinum wire was used as the auxiliary electrode. The reference electrode was a saturated Ag/AgCl electrode.

### Syntheses

#### Thiophen-2-ylboronic acid

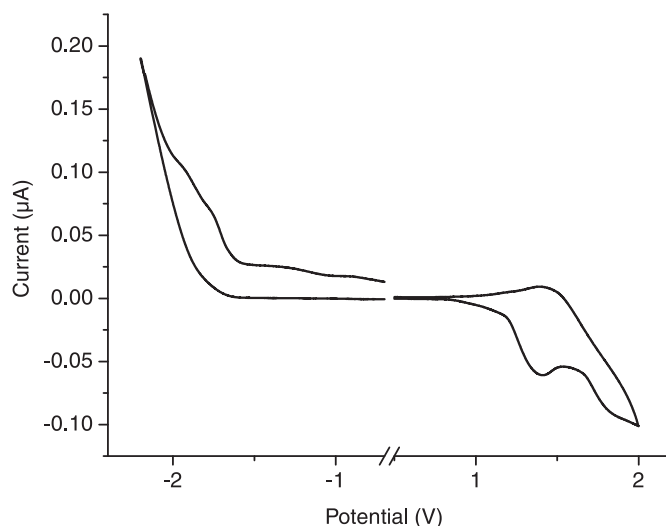
Thiophene (998 mg, 11 mmol) and butyl lithium 2.5 mol/L (5 mL, 12 mmol) were added to anhydrous THF (25 mL) at 0 °C under nitrogen. Trimethylborate (4.05 mL, 36 mmol) was added dropwise to the solution at –78 °C. The temperature was raised to room temperature, and the solution was stirred for 1 h before 10% H<sub>2</sub>SO<sub>4</sub> (20 mL) was added. The product was extracted with dichloromethane (20 mL), and the organic layer was then washed with 3 mol/L NaOH (50 mL). The pH of the aqueous layer was adjusted to 1 using 3.2 mol/L HCl, then it was washed with dichloromethane (60 mL). The product was isolated as a yellow-orange solid (840 mg, 55%) and was used without additional purification. Mp 137–139 °C. <sup>1</sup>H NMR (acetone-*d*<sub>6</sub>):  $\delta$  = 7.71 (d, 1H, <sup>3</sup>J = 4.4 Hz), 7.31 (s, 1H), 7.18 (t, 1H, <sup>3</sup>J = 4.1 Hz), 5.79 (s, 2H). <sup>13</sup>C NMR (acetone-*d*<sub>6</sub>):  $\delta$  = 136.1, 131.7, 128.4, 128.3.

#### 1-(2,2'-Bithiophen-5-yl)ethanone (**5**)

To anhydrous THF (20 mL) was added 2,2'-bithiophene (1.72 g, 10 mmol), and the reaction solution was cooled to –78 °C. *n*-Butyl lithium (10 mol/L, 1 mL, 10 mmol) was added under nitrogen, then the temperature was raised to room temperature and the mixture was allowed to stir for 1 h. *N,N*-Dimethylacetamide (0.93 mL, 10 mmol) was added, and the reaction was stirred for an additional 2 h at room temperature. The reaction was quenched with water

**Table 5.** Cyclic voltammetry data obtained in 1 mol/L TBAPF<sub>6</sub> in anhydrous and deaerated dichloromethane.

Compound	$E_{pa}$ (V)	$E_{pc}$ (V)	HOMO (eV)	LUMO (eV)	$E_g$ (eV)
<b>1</b>	1.5	−1.4	5.9	3.0	2.9
<b>2</b>	1.7	−1.6	6.1	2.8	3.3
<b>3</b>	1.4	−1.6	5.8	3.1	2.7
<b>4</b>	1.5	−1.6	5.9	3.2	2.7

**Fig. 10.** Cyclic voltammogram of **4** measured in anhydrous and deaerated dichloromethane with TBAPF<sub>6</sub> at 100 mV/s.

(50 mL), and the organic layer was extracted with dichloromethane (60 mL). The product was purified by flash chromatography eluted with hexanes/ethyl acetate (90:10, v/v) to give a yellow powder (451 mg, 21%). <sup>1</sup>H NMR (acetone-*d*<sub>6</sub>):  $\delta$  = 7.80 (d, 1H, <sup>3</sup>*J* = 4), 7.56 (dd, 1H, <sup>3</sup>*J* = 5.2, <sup>5</sup>*J* = 1.2), 7.46 (dd, 1H, <sup>3</sup>*J* = 3.6, <sup>5</sup>*J* = 0.8), 7.34 (d, 1H, <sup>3</sup>*J* = 4), 7.14 (dd, 1H, <sup>3</sup>*J* = 5.2 and 4), 2.52 (s, 3H).

**(2,2'-Bithiophen-5-yl)-3-(dimethylamino)prop-2-en-1-one (6)**

To a 2:1 ethanol/dichloromethane solution (3 mL) was added **5** (110 mg, 0.5 mmol), and the solution was then refluxed for 1 h. *N,N*-Dimethylformamide dimethyl acetal (225 mg, 1.9 mmol) was added, and the reaction was refluxed for 17 h. The reaction was cooled to room temperature, and then hexanes were added and the solution was left to cool in the freezer overnight. The precipitate was filtered to afford the product as an orange solid (102 mg, 75%). The compound was used without any further purification. <sup>1</sup>H NMR (acetone-*d*<sub>6</sub>):  $\delta$  = 7.68 (d, 1H, <sup>3</sup>*J* = 12.4), 7.65 (d, 1H, <sup>3</sup>*J* = 3.6), 7.49 (dd, 1H, <sup>3</sup>*J* = 5.2, <sup>5</sup>*J* = 1.2), 7.39 (dd, 1H, <sup>3</sup>*J* = 3.6, <sup>5</sup>*J* = 0.8), 7.27 (d, 1H, <sup>3</sup>*J* = 4), 7.13 (dd, 1H, <sup>3</sup>*J* = 5.2 and 3.6), 5.79 (d, 1H, <sup>3</sup>*J* = 12), 3.21 (s, 3H), 2.98 (s, 3H).

**4-(Thiophen-2-yl)pyrimidine (1)**

To absolute ethanol (25 mL) was added **6** (2.00 g, 11 mmol). The solution was brought to reflux after which time formamidine acetate (3.45 g, 33 mmol) was added, and the solution was refluxed for an additional 10 min. Sodium (0.77 g, 33 mmol) in absolute ethanol (2 mL) was then

added. The mixture was then refluxed for 16 h. The solvent was then evaporated, the solid washed with dichloromethane, and then filtered. The filtrate was purified by flash chromatography using hexanes/ethyl acetate (70:30, v/v) to afford the product as a yellow powder (541 mg, 31%). Mp 54–56 °C. <sup>1</sup>H NMR (acetone-*d*<sub>6</sub>):  $\delta$  = 9.05 (s, 1H), 8.74 (d, 1H, <sup>3</sup>*J* = 5.2 Hz), 7.99 (dd, 1H, <sup>3</sup>*J* = 4 Hz, <sup>5</sup>*J* = 1.2 Hz), 7.88 (dd, 1H, <sup>3</sup>*J* = 5.2 Hz, <sup>5</sup>*J* = 1.2 Hz), 7.75 (dd, 1H, <sup>3</sup>*J* = 4.8 Hz, <sup>5</sup>*J* = 0.8 Hz), 7.23 (dd, 1H, <sup>3</sup>*J* = 3.6 Hz and 1.2 Hz). <sup>13</sup>C NMR (acetone-*d*<sub>6</sub>):  $\delta$  = 160.8, 160.5, 159.4, 144.1, 132.5, 130.5, 130.0, 117.1. HR-MS(+) calculated for [C<sub>8</sub>H<sub>6</sub>N<sub>2</sub>S + H]<sup>+</sup>: 163.03245; found: 163.03303.

**2-Thiophene-2-yl-pyridine (2)**

To isopropanol (40 mL) was added a 2 mol/L Na<sub>2</sub>CO<sub>3</sub> solution in water (5 mL). Thiophene-2-yl-2-boronic acid (459 mg, 36 mmol) and 2-chloropyridine (408 mg, 36 mmol) were then added. Tetrakis (triphenylphosphine) palladium (101 mg, 0.36 mmol) was added under nitrogen under the cover of light. The temperature was raised to 50 °C, and the reaction was stirred at this temperature for 17 h. The product was extracted with dichloromethane and then purified by flash chromatography using hexanes/ethyl acetate (95:5, v/v) followed by 10% ethyl acetate. The product was isolated as a yellow solid (268 mg, 46%). Mp 56–58 °C. <sup>1</sup>H NMR (acetone-*d*<sub>6</sub>):  $\delta$  = 8.52 (d, 1H, <sup>3</sup>*J* = 4.8), 7.85 (dd, 1H, <sup>3</sup>*J* = 6.8, <sup>5</sup>*J* = 0.8), 7.79 (td, 1H, <sup>3</sup>*J* = 7.2, <sup>5</sup>*J* = 1.6), 7.74 (dd, 1H, <sup>3</sup>*J* = 4, <sup>5</sup>*J* = 1.2), 7.54 (dd, 1H, <sup>3</sup>*J* = 5.2, <sup>5</sup>*J* = 1.2), 7.24 (dd, 1H, <sup>3</sup>*J* = 4.8, <sup>5</sup>*J* = 1.2), 7.14 (dd, 1H, <sup>3</sup>*J* = 4 and 1.2). <sup>13</sup>C NMR (acetone-*d*<sub>6</sub>):  $\delta$  = 154.4, 151.3, 147.0, 138.7, 129.9, 126.5, 123.9, 120.3. HR-MS(+) calculated for [C<sub>9</sub>H<sub>7</sub>NS + H]<sup>+</sup>: 162.03719; found: 162.03711.

**4-(2,2'-Bithiophenyl-5-yl)pyrimidine (3)**

In ethanol (25 mL) was added 1-(2,2') bithiophenyl-5-yl-3-dimethylamino-propenone (178 mg, 0.67 mmol), and the solution was refluxed for 1 h. Formamidine acetate was then added (227 mg, 2 mmol), and the reaction was stirred for 10 min followed by the addition of sodium (57 mg, 2.5 mmol) in ethanol (2 mL). The slurry was then refluxed for 7 days. The solvent was evaporated, the product was taken up in dichloromethane, and the remaining inorganic salts were filtered. The product was purified by flash chromatography using hexanes/ethyl acetate (95:5, v/v) to afford the product as a bright yellow solid (144 mg, 87%). Mp 113–115 °C. <sup>1</sup>H NMR (acetone-*d*<sub>6</sub>):  $\delta$  = 9.06 (d, 1H, <sup>3</sup>*J* = 1.6), 8.74 (d, 1H, <sup>3</sup>*J* = 5.2), 7.96 (d, 1H, <sup>3</sup>*J* = 4), 7.90 (dd, 1H, <sup>3</sup>*J* = 5.6, <sup>5</sup>*J* = 1.6), 7.53 (dd, 1H, <sup>3</sup>*J* = 5.2, <sup>5</sup>*J* = 1.2), 7.45 (dd, 1H, <sup>3</sup>*J* = 3.6, <sup>5</sup>*J* = 0.8), 7.39 (d, 1H, <sup>3</sup>*J* = 4), 7.15 (dd, 1H, <sup>3</sup>*J* = 3.6 and 1.6). <sup>13</sup>C NMR (acetone-*d*<sub>6</sub>):  $\delta$  = 160.8, 160.1, 159.3, 143.7, 142.4, 131.0, 130.3, 128.0, 126.9,



126.8, 116.8. HR-MS(+) calculated for  $[C_{12}H_8N_2S_2 + H]^+$ : 245.02017; found: 245.02088.

### 2-(2,2') Bithiophenyl-5-yl-pyridine (4)

To ethanol (25 mL) was added 2 mol/L  $Na_2CO_3$  (5 mL) followed by (2,2') bithiophenyl boronic dimethyl ester (1.5 g, 7.27 mmol) and 2-chloropyridine (1.65 g, 14.54 mmol) under nitrogen. Tetrakis (triphenylphosphine) palladium (822 mg, 72.7 mmol) was then added under nitrogen and in the absence of light. The reaction mixture was heated to 50 °C for 16 h. The product was extracted with dichloromethane and was purified by flash chromatography using hexanes and increasing the polarity with hexanes/ethyl acetate (90:10, v/v). The product was isolated as a pale orange solid (656 mg, 40%). Mp 124–126 °C.  $^1H$  NMR (acetone- $d_6$ ):  $\delta$  = 8.53 (d, 1H,  $^3J$  = 4.8), 7.83 (d, 1H,  $^3J$  = 8), 7.81 (td, 1H,  $^3J$  = 7.6,  $^5J$  = 2), 7.68 (d, 1H,  $^3J$  = 3.6), 7.46 (dd, 1H,  $^3J$  = 5.2,  $^5J$  = 1.2), 7.37 (dd, 1H,  $^3J$  = 3.6,  $^5J$  = 1.2), 7.29 (d, 1H,  $^3J$  = 3.6), 7.25 (dd, 1H,  $^3J$  = 4.8,  $^5J$  = 0.8), 7.11 (dd, 1H,  $^3J$  = 3.6 and 1.2).  $^{13}C$  NMR (acetone- $d_6$ ):  $\delta$  = 154.0, 151.3, 145.8, 140.9, 139.1, 138.7, 130.1, 127.4, 127.0, 126.428, 126.0, 124.0, 120.2. HR-MS(+) calculated for  $[C_{13}H_9NS_2 + H]^+$ : 244.02492; found: 244.02546.

### Anodic dimerization

The comonomer **2** (20 mg, 0.12 mmol) was dissolved in anhydrous dichloromethane (12 mL) under nitrogen.  $FeCl_3 \cdot 6H_2O$  (166 mg, 0.61 mmol) was added, and the mixture was refluxed for 24 h. After refluxing, an insoluble precipitate formed. The soluble product was extracted with dichloromethane, the solvent evaporated, and taken up into THF for MS analysis.

### Supplementary data

Supplementary data for this article are available on the journal Web site (canjchem.nrc.ca) or may be purchased from the Depository of Unpublished Data, Document Delivery, CISTI, National Research Council Canada, Ottawa, ON K1A 0R6, Canada. DUD 5336. For more information on obtaining material, refer to cisti-icist.nrc-cnrc.gc.ca/cms/unpub\_e.shtml. CCDC 753448 contains the X-ray data in CIF format for this manuscript. These data can be obtained, free of charge, via [www.ccdc.cam.ac.uk/conts/retrieving.html](http://www.ccdc.cam.ac.uk/conts/retrieving.html) (Or from the Cambridge Crystallographic Data Centre, 12 Union Road, Cambridge CB2 1EZ, UK; fax +44 1223 336033; or [deposit@ccdc.cam.ac.uk](mailto:deposit@ccdc.cam.ac.uk)).

### Acknowledgments

The authors acknowledge financial support from the Natural Sciences and Engineering Research Council of Canada (NSERC), le Fonds de Recherche sur la Nature et les Technologies, Centre for Self-Assembled Chemical Structures, and additional equipment funding from the Canada Foundation for Innovation (CFI). Both S.D. and A.B. thank NSERC Canada for graduate and undergraduate scholarships, respectively.

### References

- (1) Thiem, H.; Strohhriegl, P.; Setayesh, S.; de Leeuw, D. *Synth.*

- Met.* **2006**, *156* (7-8), 582. doi:10.1016/j.synthmet.2006.02.005.
- (2) Dell'Aquila, A.; Mastorilli, P.; Nobile, C. F.; Romanazzi, G.; Suranna, G. P.; Torsi, L.; Tanese, M. C.; Acierno, D.; Amendola, E.; Morales, P. *J. Mater. Chem.* **2006**, *16* (12), 1183. doi:10.1039/b515583e.
- (3) Perepichka, I. F.; Perepichka, D. F.; Meng, H.; Wudl, F. *Adv. Mater.* **2005**, *17* (19), 2281. doi:10.1002/adma.200500461.
- (4) Levermore, P. A.; Chen, L.; Wang, X.; Das, R.; Bradley, D. D. C. *Adv. Mater.* **2007**, *19* (17), 2379. doi:10.1002/adma.200700614.
- (5) Colladet, K.; Fourier, S.; Cleij, T. J.; Lutsen, L.; Gelan, J.; Vanderzande, D.; Nguyen, L. H.; Neugebauer, H.; Sariciftci, S.; Aguirre, A.; Janssen, G.; Goovaerts, E. *Macromolecules* **2007**, *40* (1), 65. doi:10.1021/ma061760i.
- (6) Segura, J. L.; Martín, N.; Guldi, D. M. *Chem. Soc. Rev.* **2005**, *34* (1), 31. doi:10.1039/b402417f. PMID:15643488.
- (7) Brabec, C. J.; Sariciftci, N. S.; Hummelen, J. C. *Adv. Funct. Mater.* **2001**, *11* (1), 15. doi:10.1002/1616-3028(200102)11:1<15::AID-ADFM15>3.0.CO;2-A.
- (8) Veinot, J. G. C.; Marks, T. J. *Acc. Chem. Res.* **2005**, *38* (8), 632. doi:10.1021/ar030210r. PMID:16104686.
- (9) Dimitrakopoulos, C. D.; Malenfant, P. R. L. *Adv. Mater.* **2002**, *14* (2), 99. doi:10.1002/1521-4095(20020116)14:2<99::AID-ADMA99>3.0.CO;2-9.
- (10) MacDiarmid, A. G. *Angew. Chem. Int. Ed.* **2001**, *40* (14), 2581. doi:10.1002/1521-3773(20010716)40:14<2581::AID-ANIE2581>3.0.CO;2-2.
- (11) Dufresne, S.; Hanan, G. S.; Skene, W. G. *J. Phys. Chem. B* **2007**, *111* (39), 11407. doi:10.1021/jp075259j. PMID:17845027.
- (12) Ioachim, E.; Medlycott, E. A.; Skene, W. G.; Hanan, G. S. *Polyhedron* **2007**, *26* (17), 4929. doi:10.1016/j.poly.2007.06.025.
- (13) Bourdeaux, M.; Perez Guarin, S. A.; Skene, W. G. *J. Mater. Chem.* **2007**, *17*, 972. doi:10.1039/b615325a.
- (14) Pérez Guarin, S. A.; Tsang, D.; Skene, W. G. *N. J. Chem.* **2007**, *31* (2), 210. doi:10.1039/b611060f.
- (15) Guarin, S. A.; Bourdeaux, M.; Dufresne, S.; Skene, W. G. *J. Org. Chem.* **2007**, *72* (7), 2631. doi:10.1021/jo070100o. PMID:17343421.
- (16) Dufresne, S.; Bourdeaux, M.; Skene, W. G. *J. Mater. Chem.* **2007**, *17* (12), 1166. doi:10.1039/b616379c.
- (17) Bourdeaux, M.; Skene, W. G. *Macromolecules* **2007**, *40* (6), 1792. doi:10.1021/ma070292p.
- (18) Pérez Guarin, S. A.; Dufresne, S.; Tsang, D.; Sylla, A.; Skene, W. G. *J. Mater. Chem.* **2007**, *17*, 2801. doi:10.1039/b618098a.
- (19) Pérez Guarin, S. A.; Skene, W. G. *Mater. Lett.* **2007**, *61* (29), 5102. doi:10.1016/j.matlet.2007.04.015.
- (20) Hansford, K. A.; Perez Guarin, S. A.; Skene, W. G.; Lubell, W. D. *J. Org. Chem.* **2005**, *70* (20), 7996. doi:10.1021/jo0510888. PMID:16277320.
- (21) Guldi, D. M. R.; Rahman, G. M. A.; Zerbetto, F.; Prato, M. *Acc. Chem. Res.* **2005**, *38* (11), 871. doi:10.1021/ar040238i. PMID:16285709.
- (22) Galand, E. M.; Kim, Y.-G.; Mwaura, J. K.; Jones, A. G.; McCarley, T. D.; Shrotriya, V.; Yang, Y.; Reynolds, J. R. *Macromolecules* **2006**, *39* (26), 9132. doi:10.1021/ma061935o.
- (23) Zhu, Y.; Champion, R. D.; Jenekhe, S. A. *Macromolecules* **2006**, *39* (25), 8712. doi:10.1021/ma061861g.
- (24) Van De Wetering, K.; Brochon, C.; Ngov, C.; Hadziioannou,

- G. *Macromolecules* **2006**, 39 (13), 4289. doi:10.1021/ma060497i.
- (25) Fleckenstein, C. A.; Plenio, H. *J. Org. Chem.* **2008**, 73 (8), 3236. doi:10.1021/jo8001886. PMID:18355081.
- (26) Kondolff, I.; Doucet, H.; Santelli, M. *J. Mol. Cat. A* **2007**, 269 (1-2), 110. doi:10.1016/j.molcata.2007.01.011.
- (27) Hotta, S.; Katagiri, T. *J. Heterocycl. Chem.* **2003**, 40 (5), 845. doi:10.1002/jhet.5570400515.
- (28) Cherioux, F.; Guyard, L. *Adv. Funct. Mater.* **2001**, 11 (4), 305. doi:10.1002/1616-3028(200108)11:4<305::AID-ADFM305>3.0.CO;2-Y.
- (29) Ioachim, E.; Medlycott, E. A.; Polson, M. I. J.; Hanan, G. S. *Eur. J. Org. Chem.* **2005**, 2005 (17), 3775. doi:10.1002/ejoc.200500335.
- (30) Baraldi, P. G.; Fruttarolo, F.; Tabrizi, M. A.; Romagnoli, R.; Preti, D.; Ongini, E.; El-Kashef, H.; Carrión, M. D.; Borea, P. A. *J. Heterocycl. Chem.* **2007**, 44 (2), 355. doi:10.1002/jhet.5570440212.
- (31) Turro, N. J.; Ramamurthy, V.; Scaiano, J. C. *Principles of Molecular Photochemistry: An introduction*; University Science Books: Sausalito, 2009.
- (32) de Melo, J. S.; Silva, L. M.; Arnaut, L. G.; Becker, R. S. *J. Chem. Phys.* **1999**, 111 (12), 5427. doi:10.1063/1.479825.
- (33) Becker, R. S.; Seixas de Melo, J.; Maçanita, A. L.; Elisei, F. *J. Phys. Chem.* **1996**, 100 (48), 18683. doi:10.1021/jp960852e.
- (34) Meites, L. Z. P.; Rupp, E. *Handbook Series in Organic Electrochemistry*; CRC Press Inc., 1983.
- (35) Jenkins, I. H.; Salzner, U.; Pickup, P. G. *Chem. Mater.* **1996**, 8 (10), 2444. doi:10.1021/cm960207k.
- (36) Aeiyaich, S.; Bazzouai, E. A.; Lacaze, P.-C. *J. Electroanal. Chem.* **1997**, 434 (1-2), 153. doi:10.1016/S0022-0728(97)00044-2.
- (37) Cunningham, D. D.; Laguren-Davidson, L.; Mark, H. B., Jr.; Pham, C. V.; Zimmer, H. *J. Chem. Soc. Chem. Commun.* **1987**, 13, 1021. doi:10.1039/c39870001021.
- (38) Roncali, J. *Chem. Rev.* **1992**, 92 (4), 711. doi:10.1021/cr00012a009.
- (39) Carmichael, I.; Helman, W. P.; Hug, G. L. *J. Phys. Chem. Ref. Data* **1987**, 16 (2), 239. doi:10.1063/1.555782.
- (40) Bonneau, R.; Carmichael, I.; Hug, G. L. *Pure Appl. Chem.* **1991**, 63 (2), 289. doi:10.1351/pac199163020289.
- (41) Carmichael, I.; Hug, G. L. *J. Phys. Chem. Ref. Data* **1986**, 15, 1. doi:10.1063/1.555770.
- (42) Scaiano, J. C. *CRC Handbook of Organic Photochemistry*; CRC Press: Boca Raton, FL, 1989.

# The role of molecular volume and the shape of the hole transport molecule in the morphology of model charge transport composites

Ferdous Khan, Shalini Khanna, Ah-Mee Hor, and P.R. Sundararajan

**Abstract:** We present a study of the morphology and molecular interactions in a model charge transport composite with 1,1-bis(di-4-tolylaminophenyl) cyclohexane (TAPC) as the hole transport molecule in bisphenol-A polycarbonate (BPAPC) and cyclohexyl polycarbonate, also known as bisphenol-Z polycarbonate (PCZ). Solution NMR shows that while there is aromatic interaction between the phenyl groups of the polycarbonate and TAPC, the broadening of the peaks corresponding to the latter indicates a decrease in the rotational motion. FTIR spectroscopy also exhibits frequency shifts of the aromatic C–H absorption peaks, which parallels the extent of the depression of the glass transition temperature ( $T_g$ ) of the polycarbonate. These are compared with the previous results for *N,N*-diphenyl-*N,N*-bis(3-methylphenyl)-[1,1-biphenyl]-4,4-diamine (TPD) and tri-*p*-tolylamine (TTA), and the differences are rationalized on the basis of the molecular shape and van der Waals volume of the small molecules. It is proposed that when the polycarbonate is in a random coil conformation, spherical small molecules (e.g., TAPC and TTA) reduce the glass transition temperature much more than a rodlike small molecule (e.g., TPD). Annealing at a temperature just below the  $T_g$  of the polycarbonate was used as a means of simulating accelerated ageing. Upon annealing, phase separation and crystallization of TAPC occurs and leads to a recovery of the  $T_g$  of the polymer significantly. The  $T_g$  recovery in this case is much more significant than in the case of TPD. The average crystal sizes are about ten times smaller than the crystals obtained in the case of TPD for the same temperature of annealing. To enhance the charge mobility, it might actually be advantageous to induce submicron crystals of the small molecule, while keeping the film transparent.

**Key words:** hole transport, charge transport, polycarbonate, phase separation, solvent effect.

**Résumé :** On a étudié la morphologie et les interactions moléculaires dans un modèle de transport de charge composite comportant un 1,1-bis(di-4-tolylaminophényl)cyclohexane « TAPC » comme molécule du trou de transport dans un mélange de polycarbonate de bisphénol-A « BPAPC » et de polycarbonate de cyclohexyle, aussi connu sous le nom de polycarbonate de bisphénol-Z « PCZ ». Les spectres de RMN en solution montrent que, même s'il existe une interaction aromatique entre les groupements phényles du polycarbonate et le « TAPC », l'élargissement des pics correspondants aux derniers suggèrent qu'il se produit une diminution du mouvement rotationnel. Les spectres IR à transformée de Fourier présentent aussi des déplacements de fréquence des pics d'absorption des C–H aromatiques, parallèles au taux de dépression de la température  $T_g$  du polycarbonate. On a comparé ces résultats à ceux obtenus antérieurement avec la *N,N*-diphényl-*N,N*-bis(3-méthylphényl)-[1,1-biphényl]-4,4-diamine « TPD » et la tri-*p*-tolylamine « TTA » et on a rationalisé les différences sur la base de la forme moléculaire et du volume de van der Waals des petites molécules. On suggère que lorsque le polycarbonate se trouve dans une conformation pelote aléatoire, les petites molécules sphériques (telles le « TPAC » et la « TTA ») réduisent beaucoup plus la température de transition vitreuse qu'une petite molécule en forme de bâtonnet (telle la « TPD »). On a utilisé une température de recuisson juste inférieure à la valeur de  $T_g$  du polycarbonate dans le but de stimuler une accélération du vieillissement. Par recuisson, il se produit une séparation de phase et une cristallisation du « TAPC » qui conduit à une récupération significative de la  $T_g$  du polymère. La récupération de la  $T_g$  dans ce cas est beaucoup plus significative que dans le cas de la « TDP ». Les tailles moyennes des cristaux sont environ dix fois plus petites que celles des cristaux obtenus dans le cas de la « TDP » pour la même température de recuisson. Dans le but d'augmenter la mobilité de la charge, il pourrait être avantageux d'induire des cristaux sous-micron de la petite molécule tout en maintenant le film transparent.

Received 25 September 2009. Accepted 30 November 2009. Published on the NRC Research Press Web site at [canjchem.nrc.ca](http://canjchem.nrc.ca) on 13 February 2010.

*This article is part of a Special Issue dedicated to Professor M. A. Winnik.*

F. Khan,<sup>1</sup> S. Khanna,<sup>2</sup> A. Hor,<sup>3</sup> and P.R. Sundararajan.<sup>4</sup> Department of Chemistry, Carleton University, 1125 Colonel By Drive, Ottawa, ON K1S 5B6, Canada.

<sup>1</sup>Present address: School of Chemistry, The University of Edinburgh, Edinburgh, Scotland EH9 3JJ, UK.

<sup>2</sup>Present address: Microbial and Biochemical Evaluation Section, PMRA, Health Canada, 2720 Riverside Drive, Ottawa, ON K1A 0K9, Canada.

<sup>3</sup>Present address: Xerox Research Centre of Canada, 2660 Speakman Drive, Mississauga, ON L5K 2L1, Canada.

<sup>4</sup>Corresponding author (e-mail: [Sundar@Carleton.ca](mailto:Sundar@Carleton.ca)).

*Mots-clés* : transport par trou, transport de charge, polycarbonate, séparation de phase, effet de solvant.

[Traduit par la Rédaction]

## Introduction

Optoelectronic devices employ a complex mixture of functional small molecules dispersed in polymer matrices. Studies on the charge transport molecules (CTM) dissolved in a polymer matrix are of both technological and fundamental interests.<sup>1–3</sup> Such binary solid solution systems enable easy fabrication of films ( $\mu\text{m}$ – $\text{nm}$  thickness range) that are widely used in photoreceptors, organic light emitting diodes, and electrochromic devices. Charge transport occurs via charge transfer between adjacent donor or acceptor molecules, which is described as a one-electron oxidation–reduction process. The charge transport molecules contain one or more subunits, which are strong electron donors or acceptors.<sup>4,5</sup> Charge mobilities of hole transport molecules have strong electric field and temperature dependence.<sup>6–9</sup> It has been shown that the charge transport occurs by a hopping mechanism.<sup>10–13</sup> Several studies also showed that the host polymer has an influence on the charge transport properties of the devices.<sup>14–18</sup> For example, Yuh and Pai<sup>16,17</sup> found that the charge mobility of *N,N*-diphenyl-*N,N*-bis(3-methylphenyl)-[1,1-biphenyl]-4,4-diamine (TPD) was significantly higher with polystyrene than with polycarbonate as the matrix polymer. The charge transport properties of these materials were initially studied for applications in photoreceptor devices. A multilayered structure consisting of a charge transport layer (CTL) and a charge generation layer (CGL) has been commonly used in photoreceptor devices. A high concentration of the charge transport molecule is preferred to improve the overall sensitivity of the device and this must be accomplished without phase separation or crystallization of the charge transport molecule from the matrix.

Whereas the variation of the charge mobility was often interpreted in terms of the matrix–CTM interaction, morphological studies and the phase stability of these systems were not pursued at that time by this community. Several factors influence the phase separation and crystallization of the charge transport molecule, such as the type and nature of CTM and the polymer matrix, and to an extent, the solvent used for the preparation of composites. We<sup>19–22</sup> studied the stability of model CTLs with the two types of charge-transport molecules, such as TPD (*N,N*-diphenyl-*N,N*-bis(3-methylphenyl)-[1,1-biphenyl]-4,4-diamine) and TTA (tri-*p*-tolylamine) with different polymer binders. We used annealing as a means of simulating the ageing behaviour. The TTA-based charge transport composites were highly unstable in morphological aspects than those obtained from the TPD-based system. Using the results of the depression of the glass transition temperature ( $T_g$ ) of the polymer with the charge transport molecule, the FTIR spectroscopy, and molecular volumes, we interpreted the recovery of the  $T_g$  and the extent of phase separation and crystallization of the charge transport molecule, upon annealing, on the basis of molecular interactions. It was also shown that the conformational flexibility of the polymer significantly affects the stability. The type of solvent used

plays a role as well.<sup>22</sup> It was shown that polycarbonate exists in an extended conformation in 1,1,2,2-tetrachloroethane, and the composite films made with this solvent showed different morphological behavior than those made with dichloromethane. Thus, these results were rationalized in terms of the molecular volume of the charge transport molecule, polymer flexibility, and host–guest molecular level interactions.

The above organic semiconductors were originally developed for photoreceptor applications. Although the photoreceptor technology is now considered mature, the charge transport molecules of the type mentioned above are now being studied extensively, both experimentally and theoretically, for applications in organic light emitting diode (OLED) and organic photovoltaic devices.<sup>23</sup> Some recent publications include the studies of field and temperature dependence of hole mobility of TPD–polycarbonate,<sup>24</sup> and TPD–polystyrene,<sup>25</sup> the effect of a radical salt of TPD derivative,<sup>26</sup> the simulation of the effect of disorder and film morphology on charge transport,<sup>27</sup> and two in-depth reviews on charge transport of these organic semiconducting molecular materials.<sup>28,29</sup> Hence, as a continuation of our previous studies, we present the morphological aspects of another charge transport molecule, 1,1'-bis(di-4-tolylaminophenyl) cyclohexane (TAPC, Fig. 1), in polycarbonates and compare them with TPD and TTA.

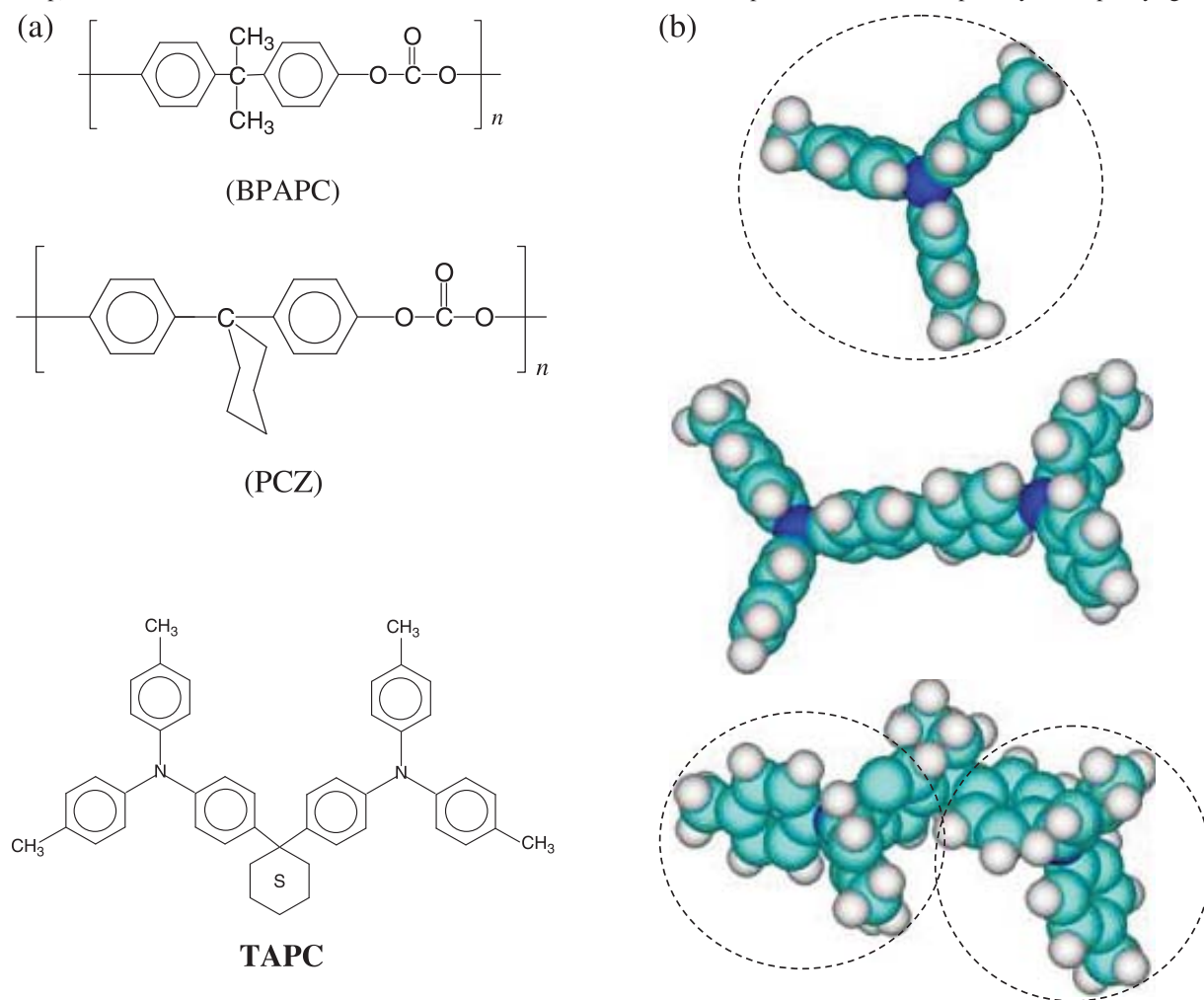
Borsenberger and co-workers<sup>9,18,30,31</sup> and Young<sup>32</sup> demonstrated that 1,1'-bis(di-4-tolylaminophenyl) cyclohexane (TAPC, Fig. 1) and TAPC-doped bisphenol-A-polycarbonate (BPAPC) are not susceptible to deep trapping as compared to the other hole charge transport molecules, over a wide range of temperatures and fields. This implied that devices could be fabricated over an extended concentration range without crystallization of TAPC.<sup>30</sup>

Although TPD, TTA, and TAPC are based on triphenyl amine groups, their molecular shapes are different. Although TPD is nonplanar, its molecular volume resembles a rodlike structure. The TTA, due to the nonplanarity of the three phenyl groups about the central nitrogen atom, has a spherical shape. The TAPC is a dimeric analog of the tri-*p*-tolylamine (TTA) moieties chemically bridged by a cyclohexane ring. Its molecular volume resembles two spheres anchored to a cyclohexyl group. Although the charge-transport sites of TAPC are identical to that of TTA,<sup>32</sup> their packing will be different due to their pairing in TAPC. From a morphological view, such differences in molecular shapes can be expected to lead to different stability properties when these molecules are dispersed in a polymer matrix.

In this paper, we discuss the molecular level interaction, phase separation, and morphological aspect of TAPC with different types of polycarbonates (PC). The differences and the similarities in morphological behavior of this charge transport molecule will be compared to those of TPD and TTA, which were discussed before.<sup>19–21</sup> Of the two types of polycarbonates, one is bisphenol-A polycarbonate (BPAPC) and the other, cyclohexyl polycarbonate (PCZ). Two differ-



**Fig. 1.** (a) Schematic of the structure of host polymers (BPAPC and PCZ) and the hole transport molecule (TAPC). (b) Molecular models of (from the top) TTA, TPD, and TAPC. The dotted circles are meant to indicate the spherical volume occupied by the triphenyl groups.



ent molecular weights of the latter were used, and these are denoted as PCZ-2 and PCZ-3. The PCZ polycarbonate has a higher  $T_g$  (e.g., between 160–180 °C) than BPAPC, depending on the molecular weight. It is known<sup>33–35</sup> that PCZ is conformationally more restricted compared to BPAPC. The conformational flexibility of these polymers has an influence on the phase separation and crystallization of the charge transport molecule as was demonstrated in Khan and Sundararajan's<sup>19,21</sup> previous investigations (TPD–PC and TTA–PC systems).

## Experimental section

Bisphenol-A polycarbonate (BPAPC) and cyclohexyl polycarbonate (PCZ) were purchased from Bayer Chemicals and Mitsubishi Gas Chemicals, respectively. The charge transport molecule (TAPC) was obtained from H.W. Sands Corporation, USA. The molecular weight ( $M_w$ ) and the polydispersity of the polymers, as measured by GPC, are presented in Table 1. The molecular structures of the materials used in this study are shown in Fig. 1. Films were prepared by dissolving the required amounts of TAPC and the polymer in dichloromethane ( $\text{CH}_2\text{Cl}_2$ ) or tetrachloroethane (TCE) of

laboratory grade. Concentrations ranging from 10 to 50 wt% of TAPC were used with the polycarbonates. Composite films were coated on a glass substrate using an electrically driven film coater and these were then dried at a very low rate of solvent evaporation at ambient conditions for at least 48 h. The thickness of the films was about 10–15  $\mu\text{m}$ . The annealing was performed using a vacuum oven with an accuracy of  $\pm 1$  °C.

A TA Instruments 2010 differential scanning calorimeter (DSC) was used for thermal analysis, at a heating rate of 10 °C  $\text{min}^{-1}$ . DSC thermograms were recorded with about 8–10 mg of sample, under a nitrogen flow of 50  $\text{mL min}^{-1}$ . The crystallinity of the samples was calculated as the ratio of the measured heat of fusion of the composite film corresponding to the melting endotherm of TAPC (normalized to the weight fraction of TAPC in the sample), and the heat of fusion of 100% TAPC.

Fourier transform infrared (FTIR) spectroscopic measurements were performed using a Michelson M120 BOMEM FTIR spectrometer. The BOMEM GRAMS/386 software was used for data collection and analysis. The spectrum of TAPC was obtained in the form of a transparent KBr pellet. A film sample holder was used to record the spectra of the

**Table 1.** Molecular weight and  $T_g$  of polycarbonates used in this study and their films with TAPC.

Sample	$M_w$	Polydispersity	$T_g$ (°C) (Onset)	$T_g$ (°C) (Midpoint)
BPAPC	250 860	1.7	148	154
TAPC–BPAPC (40/60)			65	68
TAPC–BPAPC (50/50)			52	56
PCZ-2	112 800	4.4	174	182
TAPC–PCZ-2 (40/60)			64	67
TAPC–PCZ-2 (50/50)			55	58
PCZ-3	365 500	1.8	178	184
TAPC–PCZ-3 (40/60)			60	62
TAPC–PCZ-3 (50/50)			57	59

polymers and composite films. For each experiment a background spectrum was taken with the identical sample holder and subtracted automatically. A heating stage built in our laboratory was used to investigate the phase transition for composites in the case of the FTIR spectroscopic kinetic study.

$^1\text{H}$  NMR solution spectra were obtained using a Bruker AMX-400 spectrometer. Samples of TAPC, BPAPC, or PCZ-3 (10 mg) were dissolved in deuterated dichloromethane at ambient conditions. In the case of composites (50% TAPC and PC), 5 mg of each was dissolved in the same solvent and conditions. Fourier transformation of 64 K transients and a 4.784 s acquisition time were used to obtain the net spectra.

X-ray diffraction was recorded using a Philips automated powder diffractometer Model PW 1710 with nickel-filtered Cu K $\alpha$  radiation ( $\lambda = 1.5418$  Å). The MDI Data Scan 3.2 software (Materials Data Inc., Livermore, CA) was used for data collection and MDI Jade 5 software to determine the crystallinity ( $X_c$ ). The  $X_c$  was calculated as the ratio of the intensity under the crystalline peaks above the background to the total intensity. A Zeiss Axioplan polarizing optical microscope was used to record optical micrographs. The Northern Eclipse software was used for image analysis.

The charge mobility was measured by the standard time-of-flight (TOF) method<sup>36</sup> with a nitrogen dye laser with a 10 ns pulse at  $\sim 680$  nm as the light source. The photoreceptor samples were prepared by solution coating a charge transport layer (the charge transport molecule/polymer) of thickness ( $L$ )  $\sim 20$  microns onto a phthalocyanine generator layer. Under the applied voltage ( $V$ ), the hole charge carrier is injected from the generator into the transport layer following laser excitation. The transit current versus time is recorded on a digital oscilloscope and the log–log plot of current–time yields the intersection, which defines the transit time ( $t_T$ ) for the arrival of the charge carrier at the counter electrode. The charge mobility ( $\mu$ ) is calculated from the equation

$$[1] \quad \mu = L^2/Vt_T$$

## Results and discussion

We will first discuss the depression of the glass transition temperature of the polymer by the charge transport molecule TAPC, the effect of molecular shape and volume, and the evidence from NMR and FTIR spectroscopy for molecular interaction between the small molecule and the polymer in

solution and in films, as well as the disorder. These results will be compared with those obtained previously with TPD and TTA as the charge transport molecules with the polycarbonates. We will then present the results of annealing and the recovery of the glass transition temperature upon phase separation of the charge transport molecule from the matrix.

### Depression of glass transition temperature

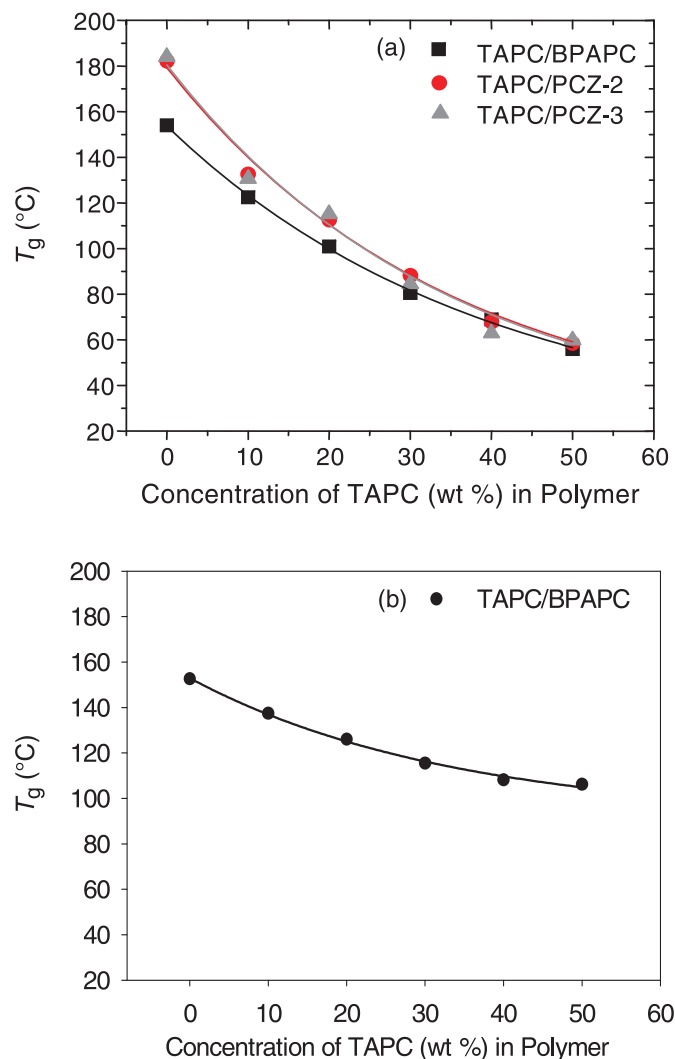
The molecular level interaction between two components is often quantified by measuring the  $T_g$  of the composite, as well as analyzing its dependence on composition. The polymers were amorphous and only glass transition temperatures were detected. Glass transition temperatures of the as-prepared films of BPAPC–, PCZ–, and TAPC–polymer composites are listed in Table 1. For the as-prepared films of BPAPC, PCZ-2, PCZ-3, the midpoint  $T_g$ s are 154, 182, and 184 °C, respectively (Table 1). The addition of TAPC lowers the  $T_g$  of the polymers, as expected. With lower concentrations (up to 30 wt%) of TAPC with BPAPC only a  $T_g$  was observed. However, with concentrations of  $\geq 40$  wt% TAPC an endothermic peak appeared at 178 °C, which corresponds to the melting of TAPC. At a concentration of 50 wt% of TAPC with PCZ-3, no endotherm was detected, and only  $T_g$  was detected for the as-prepared film.

The variation of the  $T_g$ s of BPAPC, PCZ-2, and PCZ-3 with different concentrations of TAPC for the as-prepared films with  $\text{CH}_2\text{Cl}_2$  as the solvent, is presented in Fig. 2a. The effect of the concentration of TAPC in BPAPC, with TCE as the solvent, is shown in Fig. 2b. The films were homogeneous and transparent up to 40 wt% of TAPC in the polymers, as will be discussed in the morphology section (see below).

For the films prepared with  $\text{CH}_2\text{Cl}_2$  (Fig. 2a), with 50 wt% of TAPC, the  $T_g$ s of BPAPC and PCZ-3 are depressed by 98 and 124 °C, respectively. The depression of the  $T_g$  caused by TAPC is less pronounced than with TTA (tri-*p*-tolylamine)<sup>21</sup> for the same concentration. With 50% of TTA with BPAPC and PCZ-3, the depression was 110 and 130 °C, respectively.<sup>21</sup> By comparison, Khan and Sundararajan's<sup>19</sup> studies of TPD–polycarbonate composites showed that the  $T_g$  depression for BPAPC and PCZ-3 was 74 and 88 °C, respectively, for a 50% concentration of the hole transport molecule.

The differences in the  $T_g$  depression mentioned above could be attributed to (i) molecular volume, (ii) the shape of the hole transport small molecule, and (iii) the polymer conformation, which would depend on the solvent used. The differences in the  $T_g$  depression caused by these small

**Fig. 2.** The variation of  $T_g$  of the polycarbonates (a) BPAPC, PCZ-2, and PCZ-3 based films using  $\text{CH}_2\text{Cl}_2$  and (b) BPAPC based films using TCE.



molecules could be due to their molecular packing differences and disorder. With respect to the molecular volume, TAPC is a dimeric analog of TTA with a cyclohexyl group. Using the HyperChem software (Hypercube Inc., Gainesville, FL) the calculated van der Waals volume of TAPC was  $638 \text{ \AA}^3$ , which is noticeably greater than that of TPD ( $513 \text{ \AA}^3$ ), and more than double that of TTA ( $298 \text{ \AA}^3$ ). The addition of the charge transport molecule increases the free volume of the polymer and this leads to enhanced mobility (not necessarily the conformational freedom) of the polymer and the depression of the  $T_g$ . Moreover, the change in free volume of the polymer can occur either on the segment level or at the molecular level as discussed before.<sup>19</sup> Thus, the size of the dopant molecule would have an effect on the extent of the reduction of the  $T_g$ . The differences in the  $T_g$  depression between the cases of TAPC and TTA could be attributed to the higher molecular volume of TAPC, which is about twice that of TTA. The smaller size of TTA would lead to a higher degree of dispersion.

As for the influence of the shape of the transport molecule, TPD is an almost linear rodlike molecule or dumbbell-

like (although nonplanar), whereas TTA is near spherical and TAPC is double spherical. The cyclohexyl group in the latter also enhances the bulkiness. Further, it was shown before<sup>22</sup> that the polycarbonate chain is in a coiled, globular shape in the  $\text{CH}_2\text{Cl}_2$  solution and in an extended shape in TCE. In the former case, spherical small molecules would be more effective in dispersing in the coil and increasing the free volume than a rodlike molecule such as TPD. Hence, the depression of the  $T_g$  by TAPC is larger than that caused by TPD.

As discussed before,<sup>26–28</sup> the PCZ is conformationally more restricted than BPAPC. The present results are in accord with the earlier observations that the higher the rigidity (greater the  $T_g$ ) of the polymer, the larger is the reduction in  $T_g$ . It appears that the free volume created by TAPC, or TTA, or TPD has a much larger effect in the case of PCZ than BPAPC. Such effect is higher in the case of TAPC than TPD.

As for the role of the polymer conformation, in a previous paper, Khan and Sundararajan<sup>22</sup> discussed the effect of the casting solvent on the  $T_g$  of the TPD–polymer composites. It was shown that the polycarbonate chain is in an extended conformation (stretched out) in TCE, and as a result, the depression of the  $T_g$  was larger (as compared with those cast from  $\text{CH}_2\text{Cl}_2$ ), due to the better intercalation of the rodlike TPD with the polymer. However, we find that the decrease in the  $T_g$  recorded for different composites of TAPC–BPAPC, prepared from TCE (Fig. 2b), is not as sharp as that observed in the case of composites prepared using dichloromethane. It is only about  $35^\circ\text{C}$  with 50% of TAPC. It is likely that the bulkiness of this spherical molecule hinders an effective intercalation, if the polymer is extended in its conformation.

The above observations would lead one to conclude that (i) since the BPAPC would be in a coiled conformation in  $\text{CH}_2\text{Cl}_2$ , packing of a near-spherical molecule such as TTA or TAPC would be more effective in the coil and lead to a larger depression of the  $T_g$  of the film than TPD, which is rodlike; (ii) likewise, the BPAPC chain is extended in TCE and the rodlike TPD would pack better than TAPC, which might be the cause of a small depression of the  $T_g$  of the film with TAPC.

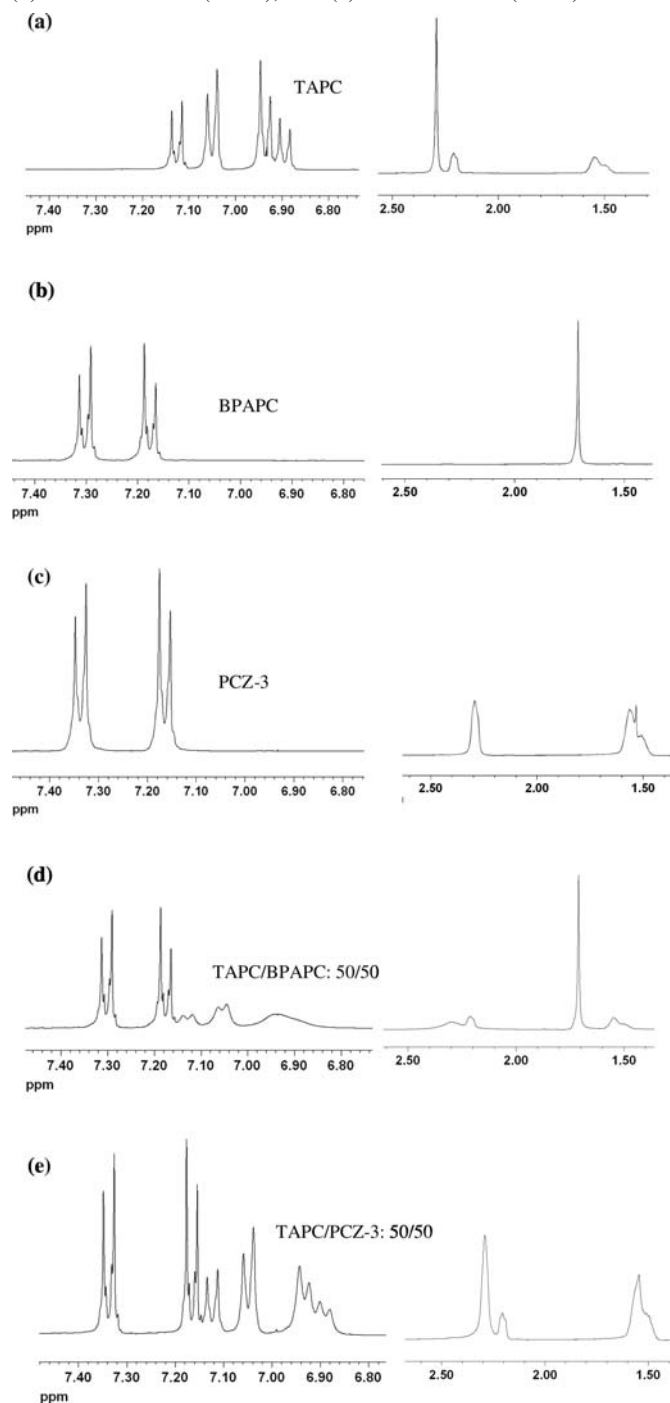
Several authors<sup>37</sup> have shown that the charge transport in polymers such as poly(3,4-ethylenedioxythiophene) (PEDOT), poly(3-methyl thiophene), polypyrroles, and polyanilines depend on the solvent used, and that the interactions that exist in solution (e.g., hydrogen bond, ion pairing, etc.) are manifested in the solid state. We feel that the case is similar with the films prepared from  $\text{CH}_2\text{Cl}_2$  and TCE: the solution conformation of the polycarbonate chain (i.e., a coiled conformation in the former) is retained when the film is cast.

### NMR spectra in solution

We used high-resolution proton nuclear magnetic resonance spectroscopy to probe the interactions, if any, between TAPC and the polycarbonates in solution. FTIR spectroscopy was used for this purpose with the solid films. Figure 3 presents the  $^1\text{H}$  NMR spectra of TAPC, BPAPC, PCZ-3, and mixtures of 50% TAPC with BPAPC and PCZ-3.

The comparison of the  $^1\text{H}$  NMR spectra of TAPC–

**Fig. 3.** The  $^1\text{H}$  NMR spectra of (a) TAPC, (b) BPAPC, (c) PCZ-3, (d) TAPC–BPAPC (50/50), and (e) TAPC–PCZ-3 (50/50).



BPAPC (50/50, Fig. 3d) with the spectra recorded for the individual components indicates that there is no noticeable change observed in the aromatic region of the BPAPC ranging from 7.31 to 7.16 ppm (Fig. 3b). The peaks appearing in the range from 7.1 to 6.9 ppm (Fig. 3d) correspond to the aromatic segments of TAPC. These peaks are broad and less intense as compared to the peaks recorded for individual TAPC (Fig. 3a). In addition, the peaks have shifted slightly downfield and the number of peaks is reduced on mixing with BPAPC (i.e., when TAPC was blended in solution

with BPAPC). In the upfield region ranging from 2.5 to 1.5 ppm there is no difference observed for the protons of  $\text{CH}_3$  groups of BPAPC at 1.7 ppm. However, the peak at 2.3 ppm in the TAPC spectrum becomes less intense on blending with BPAPC. The broadening can be interpreted as due to the decrease in the torsional mobility of the phenyl groups of TAPC due to their interaction with BPAPC.

Figures 3c and 3e show the spectra of PCZ-3 and TAPC–PCZ-3 (50/50) mixture, respectively. The aromatic protons of PCZ-3 give rise to four peaks at 7.35, 7.33, 7.18, and 7.15 ppm. When blended with TAPC, in addition to the peaks corresponding to PCZ-3, some extra peaks are seen at 7.34, 7.33, 7.3, 7.17, and 7.1 ppm. The TAPC spectra showed aromatic proton peaks in the range from 7.13 to 6.88 ppm (Fig. 3a). When TAPC was blended with PCZ-3, the peaks at 7.13, 7.12, and 7.1 ppm are not seen and the remaining peaks shifted slightly towards the upfield (Fig. 3e). Also, we observe a broadening and a reduction in the height of the peaks in the range from 6.94 to 6.88 ppm. The chemical shifts recorded in the range of 2.3 to 1.5 ppm for individual components (TAPC, Fig. 3a and PCZ-3, Fig. 3c) differ significantly in the case of mixtures. The change in the chemical shifts, peak heights, and the number of peaks indicate that molecular level interactions occur between TAPC and both the polycarbonates in solution.

#### Fourier transform IR spectroscopy

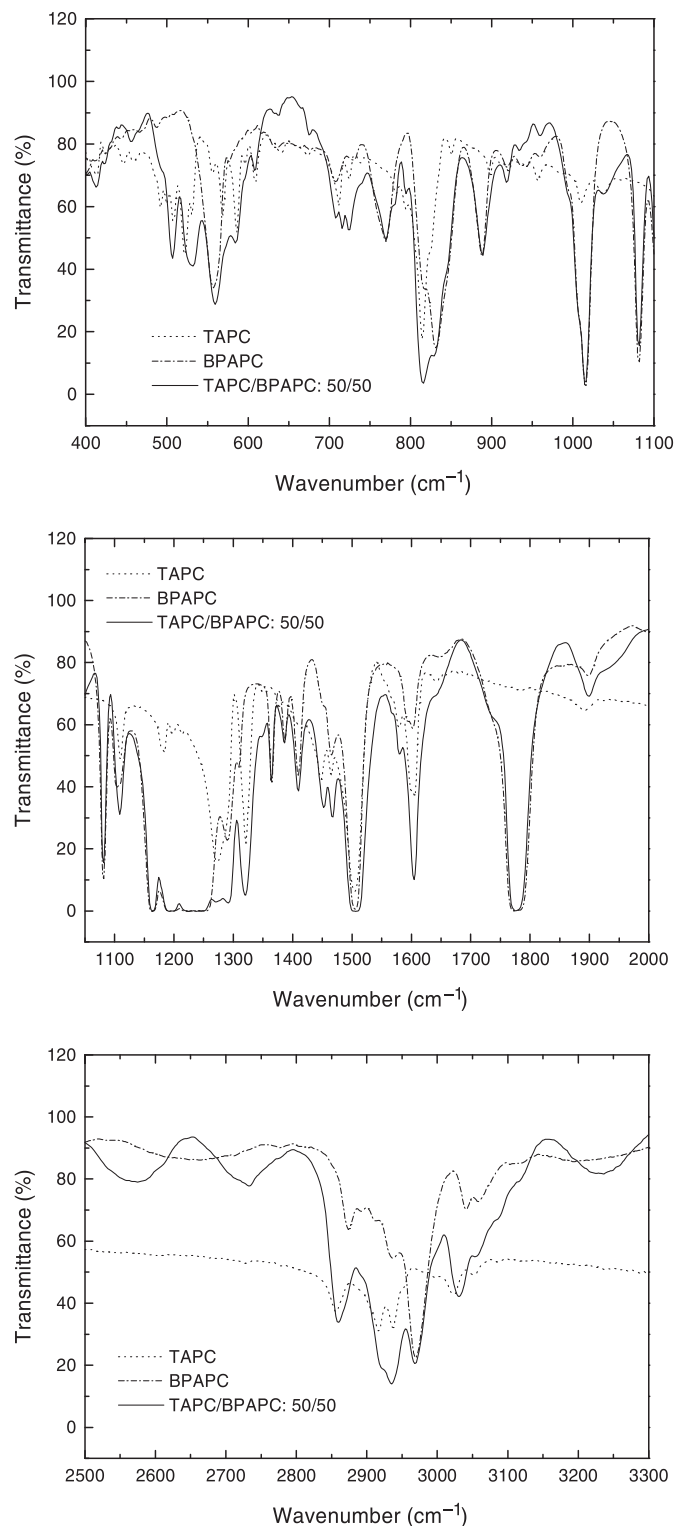
FTIR spectra were recorded with various concentrations of TAPC in the host polymer. Figure 4 shows the spectra for the composition of 50% TAPC with BPAPC along with the spectra of TAPC only and BPAPC films. The PCZ-3 spectra are not shown here. The medium absorption band at  $1602\text{ cm}^{-1}$  in both the BPAPC and TAPC spectra is attributed to the para-aromatic ring stretch,<sup>38</sup> which is shifted to a higher frequency by  $3\text{ cm}^{-1}$  with higher intensity along with a new shoulder at  $1581\text{ cm}^{-1}$  (due to TAPC) for the composites. In the case of PCZ-3 (not shown), the band at  $1604\text{ cm}^{-1}$  was shifted to  $1606\text{ cm}^{-1}$ , along with a shoulder at  $1580\text{ cm}^{-1}$ , with higher intensity. The peaks in the region  $3000\text{--}3200\text{ cm}^{-1}$  correspond to aromatic CH stretch.<sup>39</sup> A weak absorption band at  $3042\text{ cm}^{-1}$  in both BPAPC and PCZ-3 spectra shifted to a lower wavenumber, by  $12\text{ cm}^{-1}$ , with higher intensity. The peak at  $2874\text{ cm}^{-1}$  shifted to  $2860\text{ cm}^{-1}$  with higher intensity in TAPC–BPAPC. In this region ( $3000\text{--}3200\text{ cm}^{-1}$ ), such a change was noticeably higher in the case of TTA–BPAPC.<sup>21</sup>

In the BPAPC spectrum, a band at  $1104\text{ cm}^{-1}$  shifted to higher wavenumber by  $5\text{ cm}^{-1}$ . A broad band between  $1130$  and  $1335\text{ cm}^{-1}$  with several peaks at  $1310\text{ cm}^{-1}$ ,  $1290\text{ cm}^{-1}$ , and  $1163\text{ cm}^{-1}$  is attributed to the carbonate segment. This region became broader by  $27\text{ cm}^{-1}$  with a strong peak at  $1320\text{ cm}^{-1}$  and with small peaks at  $1274\text{ cm}^{-1}$ ,  $1192\text{ cm}^{-1}$ , and  $1164\text{ cm}^{-1}$ , similar to the case of TTA–BPAPC<sup>21</sup> and TPD–BPAPC.<sup>19</sup> Similar changes were observed in the case of TAPC–PCZ-3.

Thus, the FTIR spectra show a significant change in the absorption bands of the polycarbonates (both in the aromatic and carbonyl regions) by blending with TAPC. Figure 5a shows the increase in the wavenumber shift of the aromatic CH stretch ( $3042\text{ cm}^{-1}$ ) with TAPC concentration in PCs. A linear increase of peak absorption area of this peak with the



**Fig. 4.** FTIR spectra of TAPC, BPAPC, and TAPC–BPAPC (50/50) composite.



TAPC concentration in the host polymer is seen in Fig. 5b. Although there is no significant difference in the wavenumber shift between the two types of polycarbonates for the same concentration of TAPC, PCZ-3 showed a higher absorption area than the BPAPC. The wavenumber shift and peak absorption area are plotted as a function of  $\Delta T_g$  in

Figs. 5c and 5d, respectively. These results indicate specific interactions between the aromatic groups of the polycarbonate and the TAPC, i.e., the alignment of the phenyl group of the TAPC with those of the polycarbonates. The wavenumber shift observed here is more than that in the case of TPD, consistent with the larger  $T_g$  depression of the matrix. Similarly, the IR frequency shift in the case of TTA–BPAPC was larger than with TAPC or TPD, consistent with the larger  $T_g$  depression. The TPD–polystyrene system did not show significant IR frequency shifts, and the depression of the  $T_g$  was less.<sup>20</sup> Both the  $T_g$  reduction and the IR band shift depend on the concentration of TAPC. In the case of BPAPC, a larger shift for the  $\Delta T_g$  values is due to the smaller depression of the  $T_g$  of BPAPC as compared to the PCZ-3 for the same concentration of TAPC (see Fig. 2). Thus, the changes in the FTIR spectra show that while molecular interactions exist, the broadening of the peaks also indicate disordered packing with the TAPC.

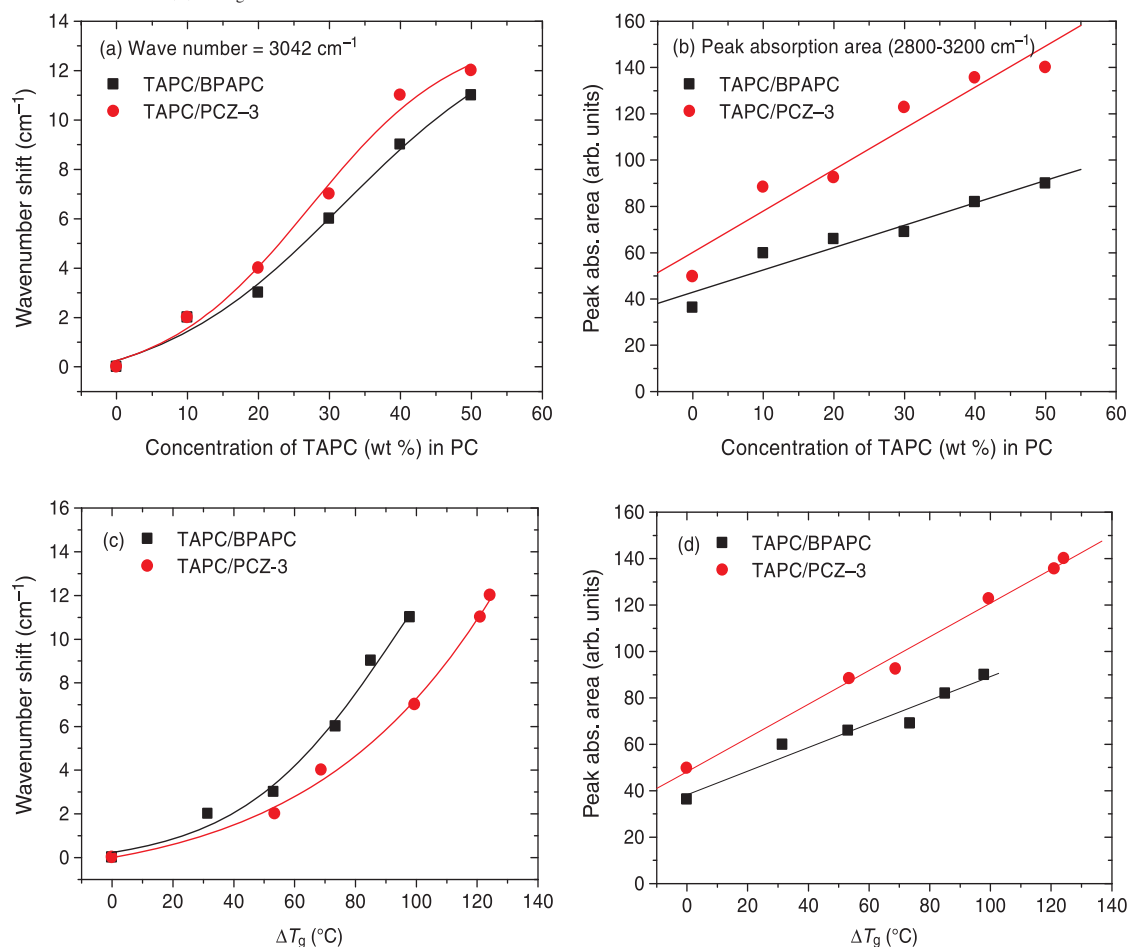
Hence, both NMR spectra in solution and FTIR analysis of the films indicate the presence of molecular interactions and disordered packing. The effect of disorder on the charge transport properties has been studied experimentally and via simulation.<sup>23a,23h,27</sup>

### Phase separation and $T_g$ recovery

Annealing is a common practice to understand the phase separation behavior and morphological stability of a small molecule (e.g., TAPC) in a polymer matrix. Accelerated thermal treatment has been used by several authors to study the ageing of polymers and polymer composites.<sup>40</sup> In previous publications, Khan and Sundararajan<sup>19–22</sup> discussed the annealing induced phase separation behaviour of the charge transport molecule from the host matrices, and rationalized them on the basis of molecular interactions and the molecular flexibility of the polymer. Annealing was performed at a few degrees below the  $T_g$  of the host polymer. We considered this to be similar to accelerated ageing. Although there might not be a standard testing procedure to estimate the ageing effect of charge transport layers, we used thermal annealing as a means to study the phase separation of the hole transport molecule from the charge transport layer. Other factors such as corona charging and other device conditions may also contribute to ageing.

Annealing was performed at 120, 130, and 140 °C for various times for TAPC–PC composites. The phase separation of TAPC from the polymer matrix would lead to a  $T_g$  recovery of the polymer. With a 40 wt% concentration of TAPC in BPAPC, the  $T_g$  recovery was 47 °C upon annealing at 140 °C for 4 h. The recovery of the  $T_g$  was more pronounced in the case of a 50 wt% TAPC concentration in polycarbonates. Figure 6 shows the increase in the  $T_g$  with annealing time and temperatures, for a TAPC concentration of 50 wt% in the two types of polycarbonates (BPAPC and PCZ-3). It is seen in Figs. 6a and 6b, that the rate of increase in the  $T_g$  is sharp during the first half hour of annealing, and it levels off beyond 2 h. The initial large increase indicates that the phase separation is profuse. Since the  $T_g$  recovers significantly during this initial period, further diffusion of the small molecule from the polymer matrix is retarded. With TAPC–BPAPC (50/50) composite, upon annealing at 120, 130, 140 °C for 4 h, the  $T_g$  increases from

**Fig. 5.** The infrared wavenumber shift ( $\text{cm}^{-1}$ ) as a function of (a) TAPC concentration and (c)  $\Delta T_g$ ; the absorption area as a function of (b) TAPC concentration and (d)  $\Delta T_g$ .



53 to 110, 128, and 134  $^{\circ}\text{C}$ , respectively (the onset  $T_g$ s are given here since the transitions were broad and determining the midpoint was difficult). Thus, a maximum  $T_g$  recovery of 81  $^{\circ}\text{C}$  was obtained (upon annealing at 140  $^{\circ}\text{C}$  for 2 and 4 h). This is a significantly higher recovery as compared to the case of 50 wt% TPD with BPAPC, in which the recovery was only 11  $^{\circ}\text{C}$  upon annealing for 4 h at 140  $^{\circ}\text{C}$ . The latter was rationalized on the basis that some of the sub-micron crystals formed during annealing actually exercise a plasticizing effect and keep the  $T_g$  lower.

Figure 6b for the case of TAPC–PCZ-3 (50/50) also shows that the  $T_g$  recovery is rapid in the first half hour of annealing. The maximum recovery is about 52  $^{\circ}\text{C}$  for PCZ-3 (for PCZ-2 also), after 4 h of annealing at 140  $^{\circ}\text{C}$ . Thus, the maximum recovery of  $T_g$  is lower by about 28  $^{\circ}\text{C}$  in the case of PCZ as compared with BPAPC. In contrast, the TPD–PCZ-3 system showed only a negligible 5  $^{\circ}\text{C}$  recovery in  $T_g$  when annealed at these temperatures.

For the case of TTA–BPAPC (50/50), the maximum  $T_g$  recovery was 92  $^{\circ}\text{C}$  when annealed at 140  $^{\circ}\text{C}$ , and it was 69  $^{\circ}\text{C}$  with TTA–PCZ-3. This is a higher  $T_g$  recovery when compared to the TAPC and TPD systems. Apart from the smaller molecular volume of TTA, its melting temperature (111  $^{\circ}\text{C}$ ) is also significantly lower than that of TAPC

(188  $^{\circ}\text{C}$ ) and TPD (171  $^{\circ}\text{C}$ ). The annealing temperatures used were above that of the melting of TTA and this resulted in sublimation of the small molecule.<sup>21</sup> Since TAPC is a dimeric analog of TTA, the  $T_g$  recovery is consistent with the higher van der Waals volume of TAPC when compared to TTA, which would lead to a lower diffusion rate and phase separation upon annealing.

It is expected that the  $T_g$  recovery would depend on the difference between the  $T_g$  of the polymer and the annealing temperature (i.e.,  $\Delta T = T_g - T_{\text{ann}}$ ). Figure 6c shows a plot of the  $T_g$  recovery as a function of  $\Delta T$  for BPAPC and PCZ-3, after annealing (for 4 h at 140  $^{\circ}\text{C}$ ). The trend can be expressed as follows.

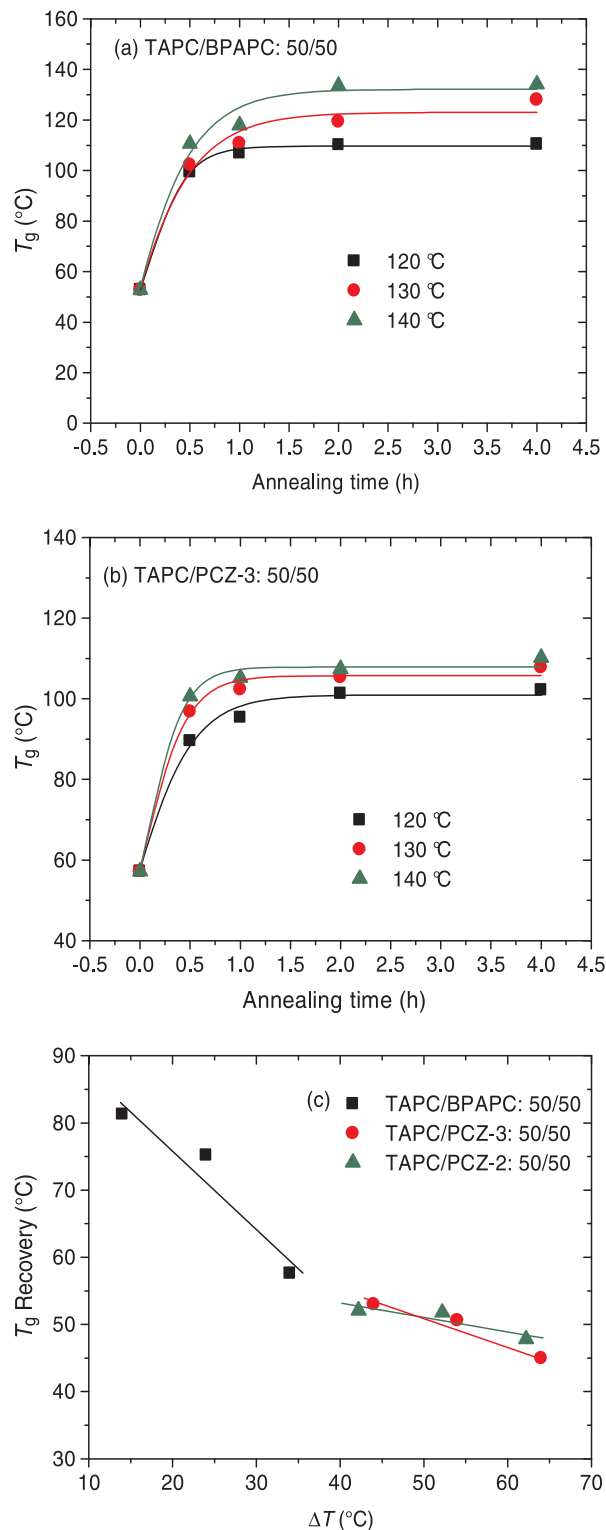
$$[2] \quad T_{g(\text{rec})} = 100 - 1.2\Delta T; (\text{TAPC–BPAPC})$$

$$[3] \quad T_{g(\text{rec})} = 62 - 0.2\Delta T; (\text{TAPC–PCZ-2})$$

$$[4] \quad T_{g(\text{rec})} = 71 - 0.4\Delta T; (\text{TAPC–PCZ-3})$$

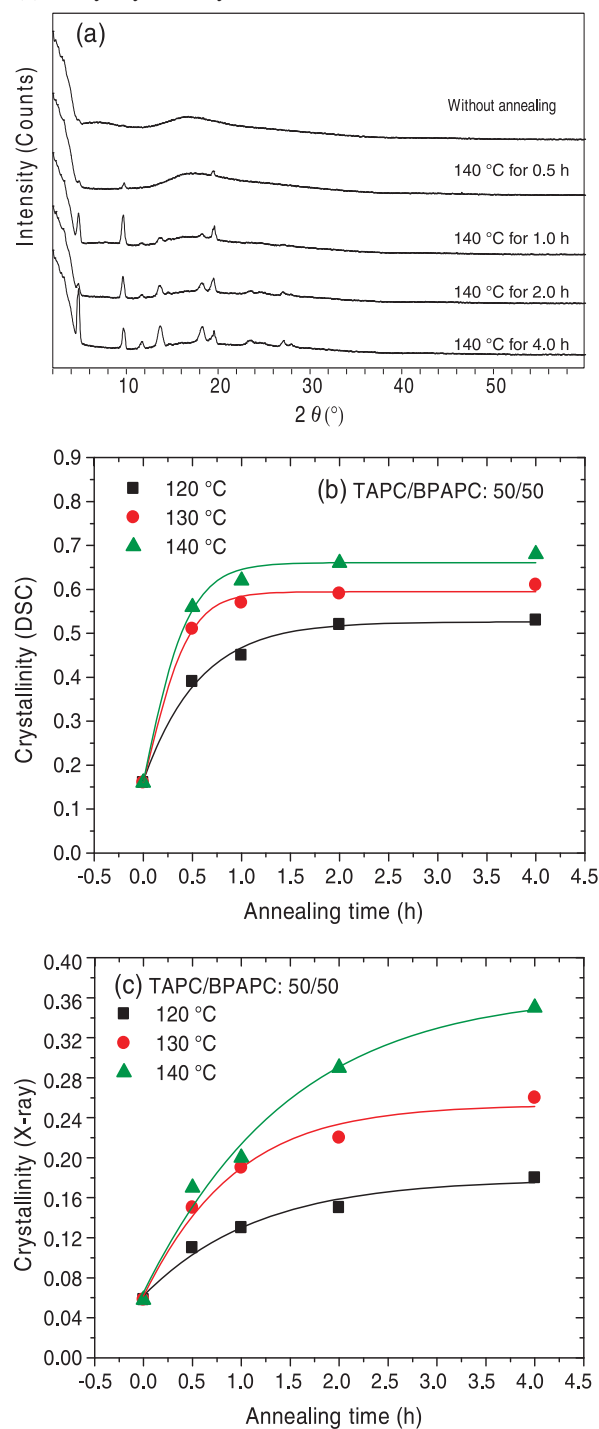
The slope corresponding to the BPAPC (eq. [2]) is higher than that of PCZ-3 (eq. [4]). These slopes were same in the case of TPD–BPAPC and TPD–PCZ-3 (see Fig. 8a and eq. [2] of ref. 19), which was  $-0.12$ .<sup>19</sup> In the case of the

**Fig. 6.** Recovery of the glass transition temperatures ( $T_g$ ) of (a) TAPC–BPAPC (50/50), (b) TAPC–PCZ-3 (50/50) with annealing time, and (c) the  $T_g$  recovery with  $\Delta T$  (the difference between the temperature of annealing and the  $T_g$  of the polymer).



TTA system, the rate of the  $T_g$  recovery was significantly higher than the TAPC and TPD systems. The corresponding slopes were  $-1.5$  and  $-0.8$  for TTA–BPAPC and TTA–PCZ-3.<sup>21</sup>

**Fig. 7.** Changes in the crystallinity upon annealing: (a) X-ray diffraction profiles, (b) DSC crystallinity of TAPC–BPAPC (50/50), and (c) X-ray crystallinity.



### Crystallinity of phase separated TAPC

The crystallinity was measured from the melting endotherm in the DSC thermogram and from the X-ray diffraction profiles, as described in the Experimental section. No resolved crystalline peak was seen in the X-ray diffraction profile for the as-prepared film. Figure 7a shows the X-ray diffraction profiles as the TAPC–BPAPC (50/50) film was annealed at 140 °C for various times. The crystalline peaks

corresponding to phase separated TAPC begin to appear within 30 min of the annealing time. A significant increase in intensity of such peaks is observed between 0.5 and 2 h. The crystallinities calculated from the DSC thermograms and X-ray diffraction profiles are shown in Figs. 7b and 7c, respectively. It is seen that the values of the crystallinity from X-ray diffraction are significantly lower than those obtained from the DSC measurements. Such a difference in the crystallinity measurement is expected while using two different methods. The trend in the variation of the crystallinity, however, is similar using both methods. The DSC crystallinity was measured with respect to the heat of fusion of TAPC, which is assumed to be that of 100% crystalline material. The results of X-ray diffraction suffer from the fact that the crystals that grow out of the polymer film are not necessarily perfect and not of uniform size. The crystallinities in the case of TAPC-PCZ were far less than those detected in the case of TAPC-BPAPC composites.

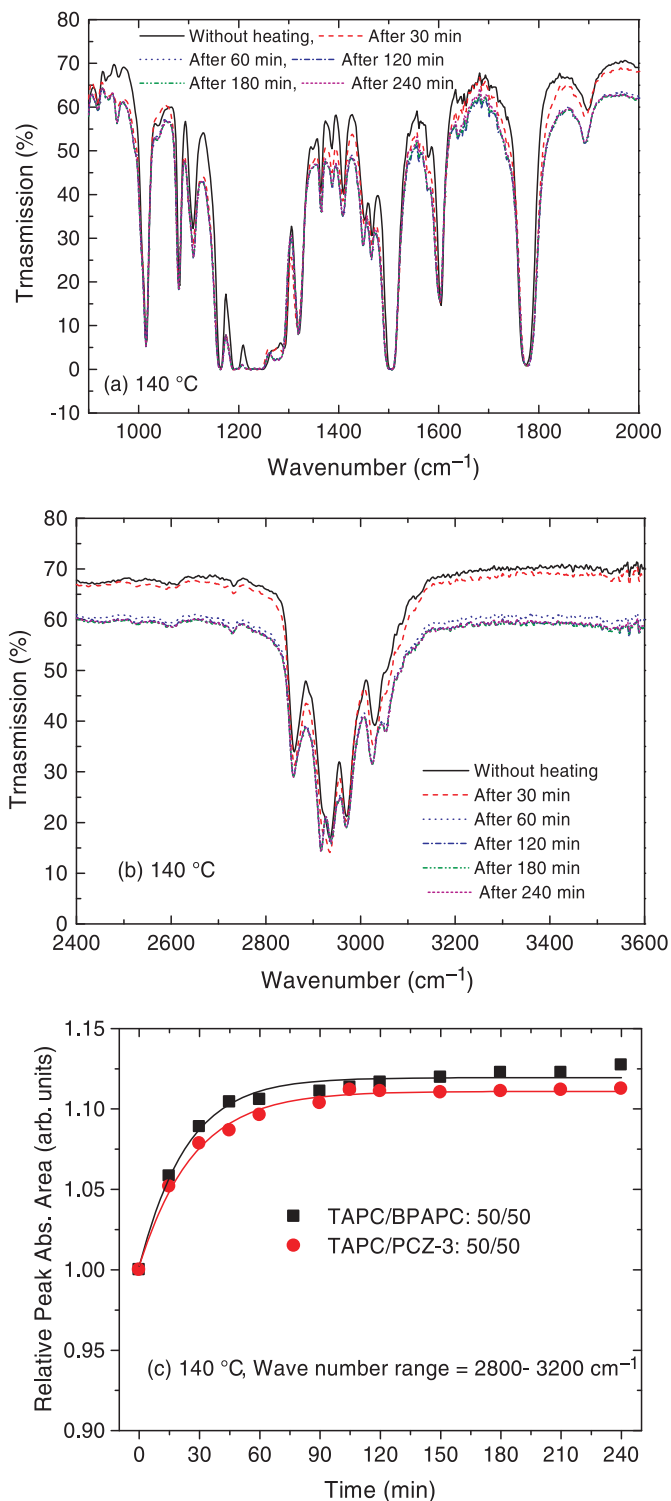
### Time dependence of FTIR spectra

It was seen in Fig. 5b that the peak absorption area corresponding to the aromatic CH stretch region increased with the concentration of TAPC in the polycarbonate matrices, indicating disordered packing. A kinetic study of the composite films was performed by keeping the films at 140 °C up to 4 h and collecting IR spectra at intervals of 15 min. Typical changes in the spectral shape with time are shown in Fig. 8, for a TAPC-BPAPC (50/50) film. It is seen in Figs. 8a and 8b that the transmission intensity of the bands decreased with prolonged annealing time. The change in intensity is more pronounced for the bands in the wavenumber range of 2800–3200  $\text{cm}^{-1}$ . These absorption areas were normalized with respect to that obtained from the as-prepared film, and the relative peak absorption areas are shown in Fig. 8c. Figure 8c shows that the increase of the peak absorption area is significantly high in the first hour of annealing time, which is consistent with the rate of increase of  $T_g$  upon annealing (Fig. 6). Annealing beyond this time does not cause any change in the absorption area or the  $T_g$ . The peak absorption area is higher in the case of BPAPC than PCZ-3, suggesting higher phase separation in the former case.

### Morphology of TAPC-polymer composites

Figure 9 shows the optical micrographs of the films under various conditions. We observed that the as-prepared films were transparent with up to 40 wt% of TAPC in the polymer. With 50 wt% of TAPC in BPAPC, PCZ-2, and PCZ-3, some crystals were detected for the as-prepared films (Figs. 9a and 9b). Most of these crystals were fairly uniform in size. The average crystal area was 13  $\mu\text{m}^2$  in the as-prepared film of TAPC-BPAPC (50/50), and it was slightly lower by about 4  $\mu\text{m}^2$  in the case of PCZ-2 and PCZ-3 with the same concentration of TAPC. On annealing these films, the number of crystals increases as seen in Figs. 9c and 9d. Figures 9c and 9d show that the phase separation of TAPC is pronounced in the case of BPAPC compared to PCZ. This could be attributed to the fact that BPAPC has a lower glass transition temperature than PCZ, and its conformation is also more flexible. The crystal size of TPD was about ten times larger in the case of TPD<sup>19</sup> (see also Fig. 8

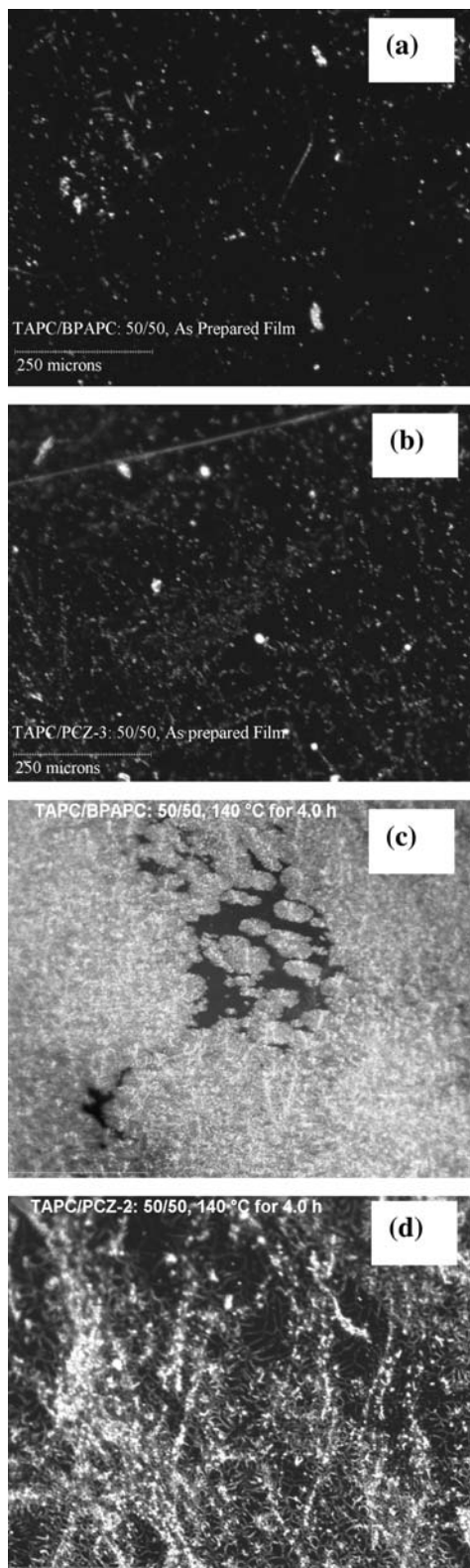
**Fig. 8.** (a) and (b) Changes in the FTIR spectra and (c) the absorption area as a function of annealing time at 140 °C for the TAPC-BPAPC (50/50) film.



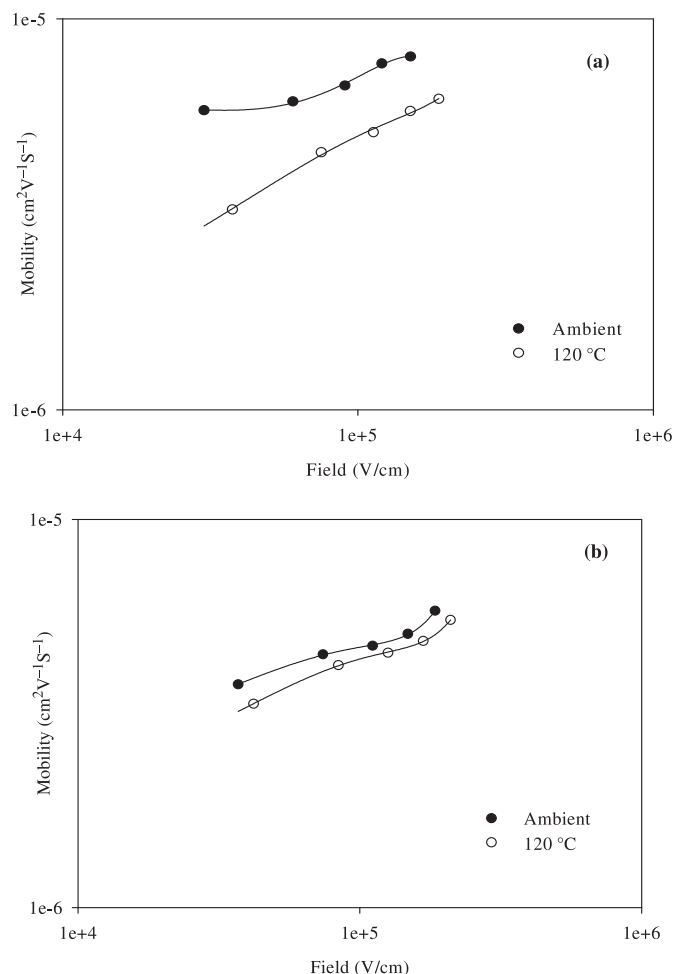
of ref. 20) as compared to TAPC. In the case of TTA-polymer composites, the phase separation was observed at temperatures as low as 80 °C upon annealing. This was attributed to the lower melting temperature of TTA as compared to TPD and TAPC.



**Fig. 9.** Optical micrographs of as-prepared films of (a) TAPC–BPAPC (50/50); (b) TAPC–PCZ-3 (50/50); (c) TAPC–BPAPC (50/50) film annealed at 140 °C for 4 h; (d) TAPC–PCZ-3 (50/50) film annealed at 140 °C for 4 h.



**Fig. 10.** Variation of the charge mobility for the as-prepared and annealed films with 40 wt% TAPC. (a) BPAPC. (b) PCZ-3.



### Charge mobility measurements

The effect of thermal annealing on the charge mobility depends on the type of polymer matrix. Figure 10 shows the charge mobility measurement results for 40 wt% TAPC–BPAPC and 40 wt% TAPC–PCZ composites before and after thermal annealing. After 2 h of annealing at 120 °C, TAPC–BPAPC showed a bigger drop, ~50% in mobility with respect to the unannealed sample. The TAPC–PCZ composite exhibited less than 10% change in mobility for the same treatment. The slower charge transport indicates a reduction of dispersed transport molecules in polymer matrix as they crystallized and phased separate. This seems to correlate very well with the fact that TAPC diffuses more readily in BPAPC and achieves greater phase separation than in PCZ.

It is seen in Fig. 10 that the charge mobility is higher in BPAPC than in PCZ-3. We find that even with 40 wt% TAPC, there is some phase separation with BPAPC as the matrix. The film was still transparent since the crystals were very small. It is likely that hopping between these sub-micron crystals enhances the mobility. Previously, we explained the enhanced charge mobility of TPD in polystyrene as due to the chaining of such submicron crystals.<sup>20</sup> If such is the case, it might actually be advantageous to induce sub-

micron crystals of the small molecule, while keeping the film transparent.

## Conclusions

The phase stability of model charge transport composites depend significantly on the shape of the charge transport molecule. We find that TAPC, which is double spherical and large compared to TPD is more effective in suppressing the  $T_g$  when the composite film is made with  $\text{CH}_2\text{Cl}_2$  as the solvent. The changes in the  $^1\text{H}$  NMR chemical shifts of TAPC and the polycarbonates in solution and the broadening of the peaks show that while aromatic interactions exist in the case of composites, the torsional mobility of TAPC is also reduced. Similarly, the IR spectra show frequency shifts indicative of aromatic interactions between TAPC and the polycarbonate and the areas of the absorption peaks also show an increase in the concentration of the small molecule in the composite.

As mentioned above, the polycarbonate is in an extended conformation in tetrachloroethane and in a random coil conformation in methylene chloride. Films made with TPD (a rodlike molecule) and BPAPC with the former solvent showed a larger depression of the  $T_g$  due to enhanced intercalation of the rodlike small molecule with a polymer in an extended conformation. Hence, our studies published so far indicate that the depression of the  $T_g$  caused by spherical small molecules (TTA and TAPC) in a random-coil polymer is more than that resulting by including a rodlike small molecule (TPD). Likewise, the rodlike TPD is more effective in reducing the  $T_g$  when the polymer is in an extended conformation. Using the spherical molecule (TAPC) with BPAPC in tetrachloroethane led to a smaller  $T_g$  depression of the film.

The crystallinity of TAPC that develops due to phase separation upon annealing is more pronounced in the case of BPAPC than PCZ as the matrix. The phase separation is nearly complete within the first half hour of annealing. The FTIR kinetic study also indicates that the phase separation is pronounced in the case of BPAPC compared to PCZ. The morphology of the crystals also depends on the type of transport molecule. The crystal sizes are about ten times smaller in the case of TAPC based composites as compared to the TPD–polymer composites. It is likely that the near-spherical and bulky shape of the TAPC prevents the growth of large crystals, as compared to the “rodlike” shape of TPD.

In the case of photoreceptors it has been necessary to use a concentration of 50 wt% of the charge transport molecule to achieve sufficient mobility. We show that at such concentrations, there is already some phase separation and that sub-micron crystals form. We suggest that the formation of such submicron crystals might itself be the reason for the enhanced mobility. This has been suggested in other studies as well.<sup>23a,23h,27</sup>

## Acknowledgements

This work was supported by the Natural Sciences and Engineering Research Council of Canada (NSERC) and Xerox Research Centre of Canada. The assistance of Greg McGuire (Xerox Research Centre of Canada) with electrical measurements is gratefully acknowledged.

## References

- (1) Schein, L. B. *Electrophotography and Development Physics*, 2nd ed.; Springer-Verlag: New York, 1992.
- (2) (a) Borsenberger, P. M.; Weiss, D. S. *Organic Photoreceptors for Xerography*, New York: Marcel Dekker Inc., 1998; (b) Melnyk, A.R.; Pai, D.M. In *Hard Copy and Printing Materials, Media and Process*; Gaynor, J., Ed.; Society of Photographic Instrumentation Engineers (SPIE): Bellingham, WA, USA, 1990; Vol. 1253; p 141.
- (3) Zhang, X.; Kale, D. M.; Jenekhe, S. A. *Macromolecules* **2002**, 35 (2), 382. doi:10.1021/ma0112164.
- (4) Stampor, W. *Chem. Phys.* **2000**, 256 (3), 351. doi:10.1016/S0301-0104(00)00123-3.
- (5) Gao, Z. Q.; Lee, C. S.; Bello, I.; Lee, S. T. *Synth. Met.* **2000**, 111–112 (1–2), 39. doi:10.1016/S0379-6779(99)00434-8.
- (6) Lin, L.-B.; Mason, M. G.; Young, R. H.; Schildkraut, D. E.; Borsenberger, P. M.; Jenekhe, S. A. In *Electrical, Optical, and Magnetic Properties of Organic Solid-State Materials IV*; Reynolds, J. R.; Jen, A. K.-Y.; Dalton, L. R.; Rubner, M. F.; Chiang, L. Y., Eds.; Materials Research Society Symposium Proceedings, Materials Research Society: Warrendale, PA, 1998; Vol. 488, p 689.
- (7) Zhang, X.; Shetty, A. S.; Jenekhe, S. A. *Acta Polym.* **1998**, 49 (1), 52. doi:10.1002/(SICI)1521-4044(199801)49:1<52::AID-APOL52>3.0.CO;2-V.
- (8) Gruenbaum, W. T.; Sorriero, L. J.; Borsenberger, P. M.; Zumbulyadis, N. *Jpn. J. Appl. Phys., Part 1* **1996**, 35 (5A), 2714. doi:10.1143/JJAP.35.2714.
- (9) Borsenberger, P. M.; Gruenbaum, W. T.; Sorriero, L. J.; Zumbulyadis, N. *Jpn. J. Appl. Phys., Part 2*, **1995**, 34 (12A), L1597. doi:10.1143/JJAP.34.L1597.
- (10) Haarer, D. *Angew. Makromol. Chem.* **1990**, 183 (1), 197. doi:10.1002/apmc.1990.051830111.
- (11) Abkowitz, M. A. *Philos. Mag. B* **1992**, 85, 817.
- (12) Borsenberger, P. M.; Aeiss, D. S. *Organic Photoreceptors for Imaging Systems*; Marcel Dekker: New York, 1993; p181.
- (13) Mylnikov, V. *Advances in Polymer Science*; Springer-Verlag: Berlin, 1994; Vol. 115, p 1.
- (14) Sasakawa, T.; Ikeda, T.; Tazuke, S. *J. Appl. Phys.* **1989**, 65 (7), 2750. doi:10.1063/1.342764.
- (15) Borsenberger, P. M. *J. Appl. Phys.* **1990**, 68 (10), 5188. doi:10.1063/1.347060.
- (16) Yuh, H.-J.; Pai, D. M. *Mol. Cryst. Liq. Cryst.* **1990**, 183 (1), 217. doi:10.1080/15421409008047459.
- (17) Yuh, H.-J.; Pai, D. M. *Philos. Mag. Lett.* **1990**, 62 (1), 61. doi:10.1080/09500839008203740.
- (18) Borsenberger, P. M.; Bäessler, H. J. *Chem. Phys.* **1991**, 95 (7), 5327. doi:10.1063/1.461646.
- (19) Khan, F.; Hor, A. M.; Sundararajan, P. R. *J. Phys. Chem. B* **2004**, 108 (1), 117. doi:10.1021/jp036306k.
- (20) Khan, F.; Hor, A. M.; Sundararajan, P. R. *Pure Appl. Chem.* **2004**, 76 (7–8), 1509. doi:10.1351/pac200476071509.
- (21) Khan, F.; Hor, A. M.; Sundararajan, P. R. *Synth. Met.* **2005**, 150 (2), 199. doi:10.1016/j.synthmet.2005.02.004.
- (22) Khan, F.; Sundararajan, P. R. *Org. Electron.* **2006**, 7 (5), 410. doi:10.1016/j.orgel.2006.05.004.
- (23) (a) Raj Mohan, S.; Joshi, M. P.; Singh, M. P. *Chem. Phys. Lett.* **2009**, 470, 279. doi:10.1016/j.cplett.2009.01.066; (b) Kalinowski, J.; Mezyk, J.; Meinardi, F.; Tubino, R.; Cocchi, M.; Virgili, D. J. *Chem. Phys.* **2008**, 128 (12), 124712. doi:10.1063/1.2841458. PMID:18376965; (c) Vragovic, I.; Calzado, E. M.; Diaz Garcia, M. A.; Hincinschi, C.; Gisslen, L.; Scholz, R. J. *Lumin.* **2008**, 128 (5–6), 845. doi:10.

- 1016/j.jlumin.2007.11.063.; (d) Deng, J.; Xie, G.; Yu, J.; Suo, F.; Li, W.; Jiang, Y. In *Advanced Optical Manufacturing Technologies*; Yang, L.; Chen, Y.; Kley, E.-B.; Li, R., Eds.; Proc. Society of Photographic Instrumentation Engineers (SPIE): Bellingham, WA, USA, 2007; Vol. 6722; p. 67223P.; (e) Kalinowski, J.; Stampor, W.; Szmytkowski, J.; Virgili, D.; Cocchi, M.; Fattori, V.; Sabatini, C. *Phys. Rev. B* **2006**, *74* (8), 085316. doi:10.1103/PhysRevB.74.085316.; (f) Virgili, D.; Cocchi, M.; Fattori, V.; Kalinowski, J.; Stampor, W. *Appl. Phys. Lett.* **2006**, *88* (5), 051102. doi:10.1063/1.2168508.; (g) Sakai, K.; Ichikawa, M.; Taniguchi, Y. *Chem. Phys. Lett.* **2006**, *420* (4–6), 405. doi:10.1016/j.cplett.2005.12.074.; (h) Sin, J. M.; Soos, Z. G. *Philos. Mag.* **2003**, *83* (7), 901. doi:10.1080/1364281021000045788.; (i) Lin, L.-B.; O'Reilly, J. M.; Magin, E. H.; Weiss, D. S.; Jenekhe, S. A. *J. Appl. Phys. (Berl.)* **2000**, *88* (6), 3501. doi:10.1063/1.1289781.; (j) Kadashchuk, A.; Weiss, D. S.; Borsenberger, P. M.; Ostapenko, N.; Zaika, V.; Skryshevski, Y. *Synth. Met.* **2000**, *109* (1–3), 177. doi:10.1016/S0379-6779(99)00233-7.
- (24) Raj Mohan, S.; Joshi, M. P.; Srivatsava, A. K. *Synth. Met.* **2005**, *155* (2), 372. doi:10.1016/j.synthmet.2005.09.016.
- (25) Raj Mohan, S.; Joshi, M. P. *Solid State Commun.* **2006**, *139* (4), 181. doi:10.1016/j.ssc.2006.05.020.
- (26) Vaddiraju, S. S.; Mathai, M.; Kymakis, E.; Papadimitrakopoulos, F. *Chem. Mater.* **2007**, *19* (16), 4049. doi:10.1021/cm070744c.
- (27) Raj Mohan, S.; Joshi, M. P.; Singh, M. P. *Org. Electron.* **2008**, *9* (3), 355. doi:10.1016/j.orgel.2007.12.005.
- (28) Coropceanu, V.; Cornil, J.; da Silva Filho, D. A.; Olivier, Y.; Silbey, R.; Brédas, J.-L. *Chem. Rev.* **2007**, *107* (4), 926. doi:10.1021/cr050140x. PMID:17378615.
- (29) Shirota, Y.; Kageyama, H. *Chem. Rev.* **2007**, *107* (4), 953. doi:10.1021/cr050143+. PMID:17428022.
- (30) Borsenberger, P. M.; Pautmeier, L.; Bäessler, H. *J. Chem. Phys.* **1991**, *94* (8), 5447. doi:10.1063/1.460506.
- (31) Borsenberger, P. M. *J. Appl. Phys.* **1992**, *72* (11), 5283. doi:10.1063/1.352012.
- (32) Young, R. H. *J. Chem. Phys.* **1995**, *103* (15), 6749. doi:10.1063/1.470354.
- (33) Sundararajan, P. R. *Macromolecules* **1989**, *22* (5), 2149. doi:10.1021/ma00195a025.
- (34) Sundararajan, P. R. *Macromolecules* **1993**, *26* (2), 344. doi:10.1021/ma00054a014.
- (35) Taylor, M. G.; Sundararajan, P. R. *Macromolecules* **1990**, *23* (9), 2602. doi:10.1021/ma00211a033.
- (36) Gill, W. D. *J. Appl. Phys.* **1972**, *43* (12), 5033. doi:10.1063/1.1661065.
- (37) (a) Kim, T. Y.; Kim, J. E.; Suh, K. S. *Polym. Int.* **2006**, *55* (1), 80. doi:10.1002/pi.1921.; (b) Pern, F. J.; Frank, A. J. *J. Electrochem. Soc.* **1990**, *137* (9), 2769. doi:10.1149/1.2087069.; (c) Cong, H. N.; Sene, C.; Chartier, P. *J. Chim. Phys. Phys. Chim. Biol.* **1995**, *92*, 979; (d) Joo, J.; Chung, Y. C.; Lee, J.-K.; Hong, J. K.; Lee, W. P.; Long, S. M.; Epstein, A. J.; Woo, H. S.; Jang, K. S.; Oh, E. J. *Synth. Met.* **1997**, *84* (1–3), 831. doi:10.1016/S0379-6779(96)04168-9.; (e) Joo, J.; Song, H. G.; Chung, Y. C.; Baeck, J. S.; Jeong, S. K.; Suh, J. S.; Oh, E. J. *J. Korean Phys. Soc.* **1997**, *30*, 230. doi:10.3938/jkps.30.230.
- (38) Heymans, N. *Polymer (Guildf.)* **1997**, *38* (14), 3435. doi:10.1016/S0032-3861(96)00929-9.
- (39) Noda, I.; Dowrey, A. E.; Haynes, J. L.; Marcott, C. *Physical Properties of Polymers Handbook*; Mark, J. E., Ed.; Springer: New York, 2007; pp 395.
- (40) (a) Hoffman, D. M.; Caley, L. E. *Org. Coatings Plast. Chem.* **1981**, *44*, 686.; (b) Ciutacu, S.; Budrugaec, P.; Mares, G.; Boconcios, I. *Polym. Degrad. Stabil.* **1990**, *29* (3), 321. doi:10.1016/0141-3910(90)90043-7.; (c) Tsotsis, T. K. *J. Comp. Mater.* **1995**, *29*, 410.; Bernstein, R.; Derzon, D. K.; Gillen, K. T. *Polym. Degrad. Stabil.* **2005**, *88* (3), 480. doi:10.1016/j.polymdegradstab.2004.11.020.

# A study of the intermolecular branch frequency dependence of tie-chain concentration in single-site linear low-density polyethylene blown films by a new FTIR method

Mingtao Wang, Nan Li, Phillip Choi, and Yaolin Zhang

**Abstract:** The relative concentrations of tie chains (TCs) in six single-site linear low-density polyethylene blown films (LLDPE) were measured using a polarized Fourier transform infrared (FTIR) technique along with a newly developed sample preparation strategy. Before the FTIR measurements, the films were first subjected to a tensile strain of 20% using a homemade appliance and then annealed at a temperature of 60 °C over a time period of 24 h to relax all nonTCs in the amorphous phase. The relative TC concentrations were inferred from the FTIR measurement of the orientation order of the amorphous chains in the stretched films. It is believed that a greater concentration of TCs leads to a higher orientation order for the amorphous chains. The results showed that the quantity of TCs is essentially determined by the chains with the appropriate branch frequency (~12 branches per 1000 backbone carbons based upon the films used in this work), especially those of the high molar mass chains as formation of TCs requires suitable ethylene sequence lengths between branches. The dart impact strength of the films appeared to be positively related to the relative concentration of TCs; films with greater concentrations showed higher dart impact strength. No clear correlations were observed between the relative concentration of TCs and the tear resistance of the films. However, the TC concentration seems to be related to the magnitude of the difference between the transverse direction and machine direction tear resistance.

**Key words:** tie chains, polarized Fourier transform infrared (FTIR), linear low-density polyethylene (LLDPE) blown films, dart impact.

**Résumé :** Faisant appel à la technique d'infrarouge à transformée de Fourier polarisée (IR-TF) et à une nouvelle stratégie de préparations des échantillons, on a étudié les concentrations relatives de chaînes liées (CL) de six films soufflés de polyéthylène de faible densité, linéaire et à site unique. Avant d'effectuer les mesures IR-TF, les films ont été soumis à une force tensile de 20 % à l'aide d'un appareil maison et ils ont ensuite été recuits à une température de 60 °C pour une période de 20 heures afin de détendre toutes les chaînes non liées dans la phase amorphe. Les concentrations relatives de chaînes liées ont été déduites de la mesure IR-TF de l'ordre d'orientation des chaînes amorphes dans les films étirés. On croit qu'une concentration plus élevée de chaînes liées conduit à un ordre d'orientation plus élevé pour les chaînes amorphes. Les résultats montrent que la quantité de chaînes liées est essentiellement déterminée par les chaînes comportant la fréquence appropriée de ramification (environ 12 branches par 1000 atomes de carbone dans le squelette si on se base sur les films utilisés dans cette étude), particulièrement pour les chaînes de masse moléculaire élevée puisque la formation de chaînes liées nécessite des longueurs appropriées de séquence d'éthylène entre les branches. Le force d'impact au dard des films semble être liée d'une façon positive à la concentration des chaînes liées; les films en comportant de plus grandes concentrations présentent une force d'impact au dard plus élevée. On n'a observé aucune corrélation entre la concentration relative des chaînes liées et la résistance aux déchirures des films. Toutefois, la concentration des chaînes liées semble être liée à l'amplitude de la différence entre la direction transverse et la direction mécanique de la résistance aux déchirures.

**Mots-clés :** chaînes liées, infrarouge à transformée de Fourier, films soufflés de polyéthylène de faible densité et linéaire, impact au dard.

[Traduit par la Rédaction]

Received 6 August 2009. Accepted 24 November 2009. Published on the NRC Research Press Web site at canjchem.nrc.ca on 12 February 2010.

*This article is part of a Special Issue dedicated to Professor M. A. Winnik.*

**M. Wang,** Department of Chemistry, University of Alberta, Edmonton, AB T6G 2G2, Canada; Department of Chemical & Materials Engineering, University of Alberta, Edmonton, AB T6G 2V4, Canada.

**N. Li and P. Choi.**<sup>1</sup> Department of Chemical & Materials Engineering, University of Alberta, Edmonton, AB T6G 2V4, Canada.

**Y. Zhang,** FPIInnovations – Forintek Divisions, 319 rue Franquet, Québec, QC G1P 4R4, Canada.

<sup>1</sup>Corresponding author (e-mail: phillip.choi@ualberta.ca).



## Introduction

Among the structural features in polyethylene blown films, tie chains (TCs) are believed to play a significant role in determining their physical properties as TCs bridge adjacent lamellae.<sup>1</sup> A high concentration of TCs results in a significant improvement in the resistance to low-temperature impact,<sup>2</sup> to creep,<sup>3</sup> to slow crack growth,<sup>4</sup> and to tear and puncture.<sup>5</sup> Without TCs, all lamellae would be held by relatively weak van der Waals forces leading to lower dart impact strength and tear resistance, the two most important performance properties of polyethylene blown films. The formation of TCs has been attributed to the random coil dimension in the molten state being larger than the thickness of crystallites formed in the solid state after crystallization.<sup>6,7</sup> Several crystalline lamellae can grow within the sphere of gyration of a chain provided the chain is sufficiently long. Therefore, a long-chain molecule can cross the noncrystalline region and provide the physical bridging for adjacent crystalline lamellae. Since not all chains emanating from a lamella would traverse through the amorphous regions and enter into another lamella, it is difficult to predict *a priori* the absolute concentration of TCs. In fact, some of the chains reenter the original lamella,<sup>8</sup> and others may simply end up in the amorphous regions as loose loops or dangling chains. Obviously, chains below a critical molar mass cannot participate in the TC formation process as these chains are not long enough to have at least two parts of it being involved in two different lamellae, which are connected by the remaining part of the chains. Also, optimal branch frequencies must exist for the formation of TCs for branched polyethylene chains of different lengths. In general, chains with low branch frequency tend not to form TCs even though their molar masses are high. All of the aforementioned findings regarding TCs have been summarized in a review article written by Seguela.<sup>9</sup> To formulate any structure–property relationship for polyethylene blown films, measurement of the absolute TC concentration is most desirable. Unfortunately, such measurement is difficult, if not impossible, as TCs are buried in the amorphous regions with other structural units, a situation that is hard for any analytical methods to differentiate and characterize them. Therefore, at present, no direct analytical method is available for such a purpose. In many cases, researchers tend to infer the relative concentration of TCs in a series of samples based on the measured mechanical properties such as the brittle fracture strength.<sup>10,11</sup> The quest for a reliable method for measuring the concentration of TCs, at least in a relative sense, is still of scientific and practical significance.

The orientation of amorphous chains in polyethylene blown films can be characterized by using a polarized infrared method.<sup>12</sup> Using polarized Fourier transform infrared (FTIR) spectroscopy, Lustiger and Ishikawa<sup>13</sup> measured the relative concentration of TCs in polyethylene blown films. In their work, the authors chlorinated the film specimens to differentiate the signals (peaks) of the amorphous orientation from those of the crystalline orientation.<sup>13</sup> A simpler method of differentiating the amorphous from the crystalline orientations was proposed by Kissin.<sup>14</sup> However, the method suffers from the problem that not all chlorinated branches are associated with the TCs. In fact, the amount of chlorinated

branches that are associated with TCs is unknown in this method. Also, extra efforts have to be spent for the chlorination process as highly toxic chlorinated chemicals must be used.

In the work presented here, we also used a polarized FTIR method employed by Kissin<sup>14</sup> to measure the relative concentration of TCs. However, a new simpler sample preparation strategy was applied to six single-site linear low-density polyethylene (ss-LLDPE) blown films with different molar mass dependence of branch frequency. The samples were chosen such that the experiments not only serve to test the proposed method but also allow us to investigate the effect of interchain branch frequency on the concentration of TCs.

## Theoretical background

When polyethylene blown films are stretched at a temperature above their glass transition temperature,  $T_g$ , both the crystalline and amorphous components oriented towards the stretching direction. Within the amorphous regions, the TCs and chains other than TCs (i.e., loose loops, dangling chains, nonbridging amorphous chains, collectively referred to as NTCs) would be aligned along the stretching direction. The NTCs, however, would relax back to the unoriented states provided that sufficient time and appropriate conditions are given. Since TCs act as bridges between lamellae, they cannot relax. Consequently, it can be assumed that upon relaxation, the orientation order of the amorphous regions mainly originates from the aligned TCs under stretch, and that measurement of the amorphous orientation order of a stretched sample upon relaxation can be directly related to the concentration of TCs. The comparison of such orders among film samples would yield information about which sample would have a relatively higher concentration of TCs. For a uniaxially stretched polyethylene blown film, the dichroic ratio,  $D$ , is defined as<sup>12</sup>

$$[1] \quad D = \frac{A_{//}}{A_{\perp}}$$

where  $A_{//}$  and  $A_{\perp}$  are the absorbance measured with the electric field vector of the polarized radiation parallel and perpendicular to the stretching direction, respectively. To characterize the orientation of the amorphous chains in the stretched samples, Herman orientation function,  $f$ , is used and defined as<sup>12</sup>

$$[2] \quad f = (3\langle \cos^2 \theta \rangle - 1)/2$$

where  $\theta$  is the angle between the stretching direction and the axis of the chain segments. The relationship between  $f$  and  $D$  for a given absorption band is given by eq. [3]:<sup>12</sup>

$$[3] \quad f = \frac{D - 1}{D + 2}$$

where  $D_0$  is given by eq. [4]:<sup>12</sup>

$$[4] \quad D_0 = 2\cos^2 \Phi$$

Here,  $\Phi$  is the angle between the chain axis and the transition moment direction of the vibration mode responsible for the infrared absorption.  $f$  is a function of both the degree of

**Table 1.** Characteristics of the ss-LLDPEs (A–F) and processing conditions used for producing the blown films.

	A	B	C	D	E	F
Solid-state density (g/cm <sup>3</sup> )	0.916	0.917	0.916	0.916	0.918	0.916
Melt index (g/10 min)	0.9	0.83	0.9	0.9	1.08	1.28
Comonomer type	1-Octene	1-Octene	1-Octene	1-Octene	1-Hexene	1-Hexene
Branch frequency (per 1000 backbone carbons)	15.4	16.3	15.4	15.4	12.3	11.7
$M_n$	33 200	28 200	33 200	33 200	52 700	48 600
$M_w$	96 200	110 300	96 200	96 200	102 100	92 300
$M_z$	212 400	359 600	212 400	212 400	171 000	145 700
Polydispersity index ( $M_w/M_n$ )	2.9	3.9	2.9	2.9	1.94	1.9
Die gap (mm)	50	50	50	50	50	50
Output (lb/h)	351	251	345	248	299	299
Blow up ratio	2.5	2.5	3.5	3.5	2.5	2.5
Frost line height (FLH, in)	30	20	30	22	24	23
Tear strength (g/mil)						
Machine direction	505	617	324	281	243	213
Transverse direction	561	743	421	370	363	403
Dart impact strength (g/mil)	371	577	713	983	1145	1159

**Note:** 1 lb = 0.45359237 kg; 1 in = 25.4 mm; 1 mil = 25.4  $\mu$ m.

orientation and the quantity of the orienting elements in a given film sample. Under comparable stretching conditions, the degree of orientation of the aligned elements in the amorphous regions in various films was assumed to be the same, and thus,  $f$  is an indicative of the relative concentration of TCs.

## Experimental

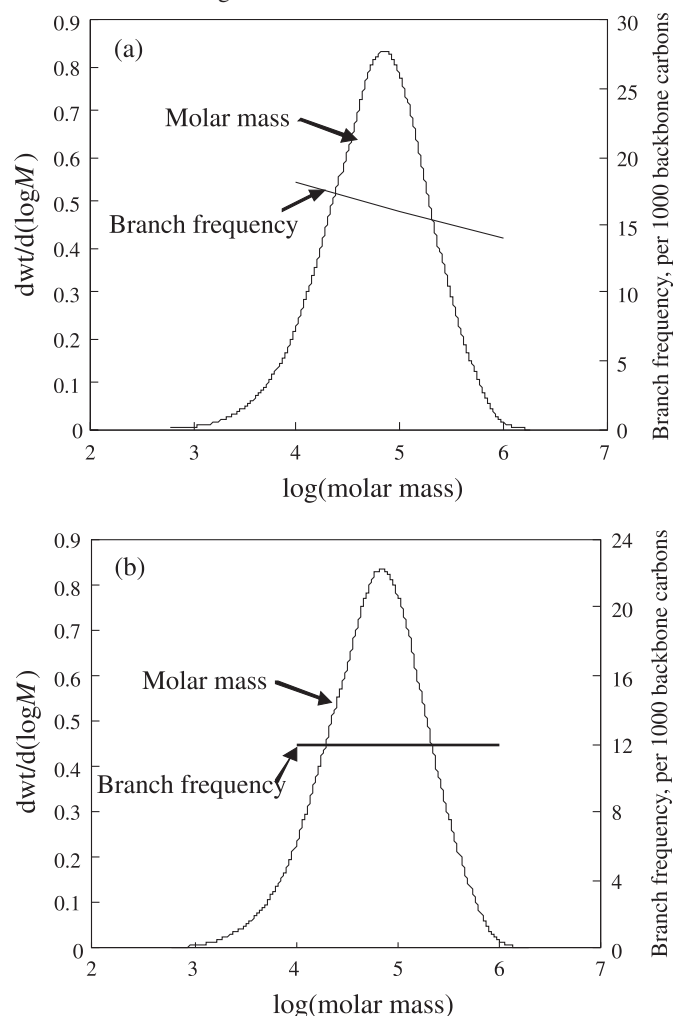
### Materials and blown film preparation

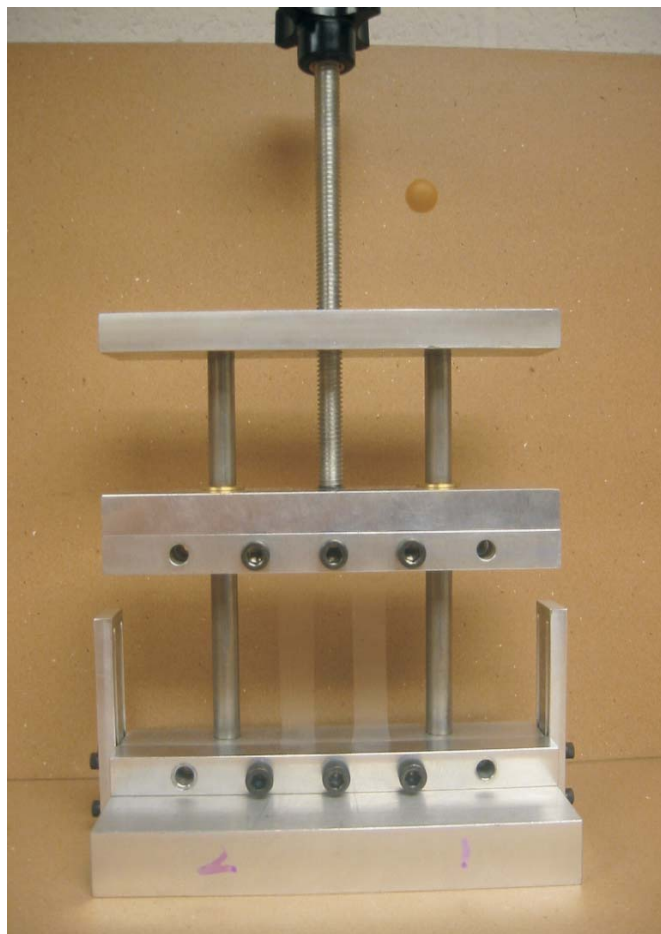
Six single-site linear low-density polyethylene (ss-LLDPE) blown films, hereafter referred to as films A, B, C, D, E, and F, exhibiting wide ranges of dart impact strength and tear resistance, were chosen to test the proposed FTIR method (see Table 1). They were provided by NOVA Chemicals Corporation (Calgary, AB). The films were made from resins with comparable solid-state densities and melt indices and their nominal thickness was about 25  $\mu$ m. As can be seen from Table 1, the molar mass averages and branch frequencies of the resins differ. It should be noted that the same resin was used for films A, C, and D but they were processed under different conditions. Another major difference between films A–D and E–F is their molar mass dependence of branch frequency (see schematics in Fig. 1). As shown, films A–D contain a greater portion of branches in their shorter chains (Fig. 1a), whereas the branches were more or less evenly distributed among chains in films E and F (Fig. 1b).

### Blown film deformation and relaxation of NTCs

The ss-LLDPE blown films were cut into 50 mm  $\times$  10 mm slices (machine direction  $\times$  transverse direction) in the rectangle geometry. The films were then placed in a homemade stretching device (see Fig. 2) and uniaxially stretched along the machine direction (MD) slowly to ensure uniform stretching. After the chosen strains were reached, the films were held in the stretching device and placed in an oven annealed at 60  $^{\circ}$ C for 24 h to relax the NTCs in their amorphous phase. The temperature was chosen so that it is not high enough to cause any destruction of the lamellae, and that it is not too low to result in unnecessary long

**Fig. 1.** Schematics of two types of molar mass dependence of branch frequency: (a) a greater portion of branches are located in shorter chains and (b) branches are evenly distributed among chains of different chain lengths.



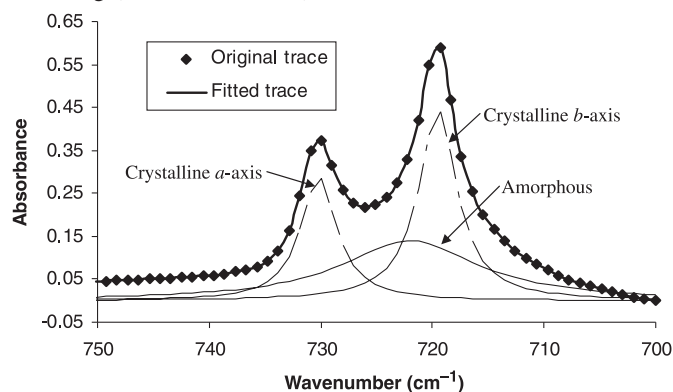
**Fig. 2.** An image of the homemade stretching device.

relaxation times. The relaxation time of 24 h was chosen based on the fact that longer relaxation times at 60 °C resulted in no significant changes to the FTIR spectra of the stretched films.

### FTIR measurements

Polarized FTIR measurements were carried out directly on the stretched films held in the fixture using a Nicolet 8700 FTIR spectrometer. The spectra were collected using a polarized beam parallel and perpendicular to the stretching machine direction with 128 scans at the resolution of 2.0 cm<sup>-1</sup>. Background spectra with the polarized beam at 0° and 90° were recorded before the acquisition of the parallel and perpendicular spectra of the stretched ss-LLDPE blown films. The strains of ss-LLDPE blown films along machine direction were reached stepwise (i.e., 0%, 5%, 10%, 15%, 20%, 30%, 50%, and 70%). The polarized FTIR spectra were collected for each relaxed film at each step.

A spectral range of 600–800 cm<sup>-1</sup> was used for the orientation measurements. This range includes three bands. Two of them, one at 730 cm<sup>-1</sup> and the other at 719 cm<sup>-1</sup>, characterize the rocking modes of the chains in the orthorhombic crystalline phase, with each transition moment parallel to the crystallographic *a* and *b* axes, respectively.<sup>12</sup> The third band, at 722 cm<sup>-1</sup>, is attributed to the transition moment perpendicular to the chain axes for the amorphous phase.<sup>12</sup> The doublet at 730/720 cm<sup>-1</sup> was fit with Lorentzian functions

**Fig. 3.** FTIR spectrum of film E with MD parallel to the polarized light. Three peaks at 730, 719, and 722 cm<sup>-1</sup> were resolved from the fitting (see text for details). *R*<sup>2</sup> = 0.992, standard error = 0.010.

into three peaks corresponding to three bands (730, 722, and 719 cm<sup>-1</sup>). Peak fitting was carried out using GRAMS/AI software from Thermal Fisher Scientific. Prior to the curve fitting, the baselines of the spectra were corrected using an offset function. The width of the crystalline bands is approximately 3~4 cm<sup>-1</sup>, and that of the amorphous band is 10~20 cm<sup>-1</sup>. The standard deviation errors of the fittings were smaller than the value of 0.01. Figure 3 shows a polarized FTIR spectrum of film E with the polarized beam parallel to the MD and the corresponding fitting curves.

Since the amorphous component of the 722 cm<sup>-1</sup> band has a transition moment lying perpendicular to the chain axis, the orientation factor (*f*<sub>722</sub>) of the TCs can be determined by eq. [5], which was obtained by combining eqs. [3] and [4]:

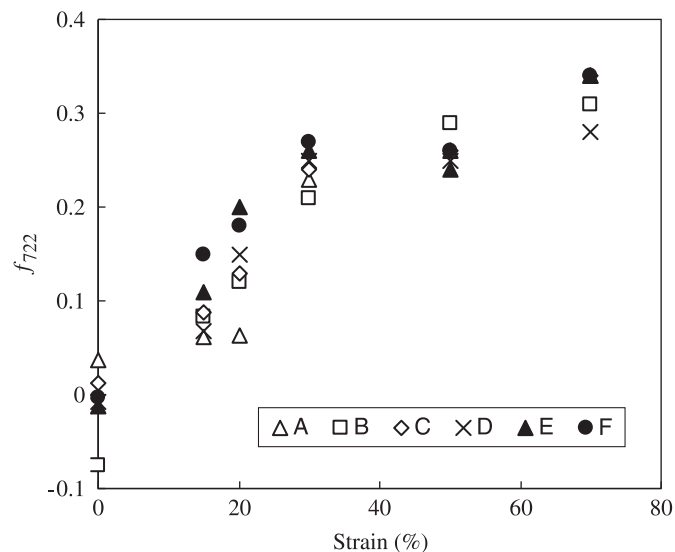
$$[5] \quad f_{722} = -2 \frac{D_{722} - 1}{D_{722} + 2}$$

## Results and discussion

### Relative concentration of TCs

The orientation order (*f*<sub>722</sub>) of the amorphous region of each film sample under different tensile strains was determined and the results are shown in Fig. 4. Note that, the *f*<sub>722</sub> values at low strains (5% and 10%) for all six film samples were measured and these values are close to those at 0%; in Fig. 4, only the *f*<sub>722</sub> values at 0% are shown. The near zero or slightly negative *f*<sub>722</sub> values observed at low strains (i.e., <~10%) for all six film samples indicate that their amorphous chains, including both TCs and NTCs, are essentially randomly oriented. As the tensile strain increases, the *f*<sub>722</sub> value increases. At tensile strains approximately above 10%, differences in the *f*<sub>722</sub> value start to manifest among the samples. In particular, films E and F exhibit greater *f*<sub>722</sub> values than do the remaining films. The differences start to diminish when the strain becomes greater than 20% although the *f*<sub>722</sub> values for all six samples keep increasing. It is believed that with strains greater than 20%, the disassembling of the crystalline chains occur, resulting in contributions to the *f*<sub>722</sub> value of the amorphous chains. Beyond 80% of stretching, the recrystallization process may occur because the pulled out crystalline chains start to realign.<sup>15</sup> From Fig. 4, it can be seen that the *f*<sub>722</sub> values are

**Fig. 4.** The orientation orders of the amorphous phases of six ss-LLDPE blown films at varying strains.

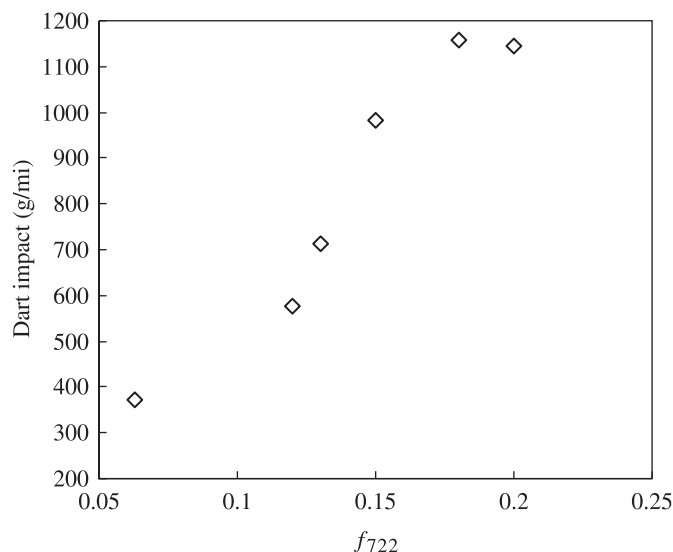


almost the same for all six films for strains ranging from 30% to 70%, indicating that portions of crystalline chains were pulled out of the lamellae and into the amorphous regions. This is further confirmed by the results obtained from the tensile testing experiments performed on the films using an INSTRON machine (results are not shown here; the yield strains of these samples are about 20%). Before yield, only the amorphous regions are being stretched leading to the separation of lamellae. Above the yield point, chains in the lamellae are being pulled out to allow higher strains; these chains enter the amorphous phase and increase the orientation order of the amorphous chains. The tensile testing results justified us to use the  $f_{722}$  values at a strain of 20% to signify the concentration of TCs. Finally, it should be noted that the determination of the fraction of each phase from the FTIR spectrum is possible if the corresponding extinction coefficient for each different phase is known. However, since such coefficients for the crystalline and amorphous phases would likely vary differently upon stretching, we did not measure them.

#### Effects of branch content and distribution

The existence, and thus the quantity of TCs are closely related to the content, and the inter- and intra-chain distribution patterns of the short-chain branches (SCBs). And it generally believed that the type of SCBs is of secondary importance in influencing the resultant structures when SCBs contain more than two methylene carbons. As shown in Fig. 4, films E and F made from resins with high  $M_n$  ( $\sim 50\,000$ ) and low branch frequency ( $\sim 12$  per 1000 backbone carbons) exhibited significantly higher  $f_{722}$  values (i.e., higher concentrations of TCs) than did the other four films made from resins with a  $M_n$  of  $\sim 30\,000$  and branch frequency of  $\sim 15$  per 1000 backbone carbons. This suggests that an ethylene sequence between adjacent SCBs should have an optimal length to form TCs, and that a sample consisting of a greater number of long chains and incorporating appropriate levels of SCBs into these long chains enhances the probability of generating more TCs, which are consistent

**Fig. 5.** The dart impact strength vs relative concentration of TCs for six ss-LLDPE blown films.



with the finding by Krishnaswamy et al.<sup>16</sup> On average, if SCBs are more clustered in shorter chains (films A, B, C, and D), a greater quantity of very long branch-free chain segments would occur and give rise to a greater probability of producing larger and thus fewer crystalline lamellae; the probability for shorter chains that contain too many branches to form lamellae is also greatly reduced.<sup>17</sup> These two factors decrease the number of TCs. In contrast, when SCBs are more evenly distributed among chains or a greater portion of SCBs are incorporated into longer chains (films E and F), more homogeneous crystalline lamellae would occur and the two aforementioned unfavorable conditions for the formation of TCs would be largely avoided. In fact, the molar mass dependency of SCBs in films E and F ensures a higher probability of producing lamellae across the whole molar mass range, the optimal condition for the formation of TCs. The data from Fig. 4 may also imply that a branch frequency of  $\sim 12$  per 1000 backbone carbons results in a greater probability of producing TCs than does a branch frequency of  $\sim 15$  per 1000 backbone carbons; this requires more investigations, however, since the average molar mass and branch distribution pattern for the two groups of films investigated here differ.

Results of films A, C, and D demonstrate that processing conditions also influence the formation of TCs to a certain degree. In particular, high blow up ratio and low output rate may increase the chance of forming more TCs. In the case of film B, it is speculated that it contains the appropriate level of branches (it must be less than  $\sim 16$  per 1000 backbone carbons as the average branch frequency of this sample is about 16) in the high molar mass chains (highest  $M_z$  among the resins), and it exhibited a reasonable dart impact and the highest tear resistance.

#### Relationship between the relative concentration of TCs and dart impact

The dart impact strength is an important physical property for LLDPE blown films, and it is closely related to the amount of TCs in the material. Figure 5 shows the relation-



ship between the dart impact strength and the measured relative concentration of TCs of the films used in this study. It is shown that the dart impact strength increases as the concentration of TCs increases. TCs play an important role in connecting different components to form a network in which the imbalance between different components and orientations is reduced. A greater amount of TCs leads to the formation of a high number of smaller crystallites that tend to be more randomly oriented than the larger ones in the unstretched film. As a result, such an isotropic morphology results in higher dart impact strengths.<sup>18</sup> The positive correlation between the dart impact strength and the concentration of TCs observed for six films shows that the presence and quantity of TCs play a major role, if not a dominant one, in determining the dart impact strength of the material.

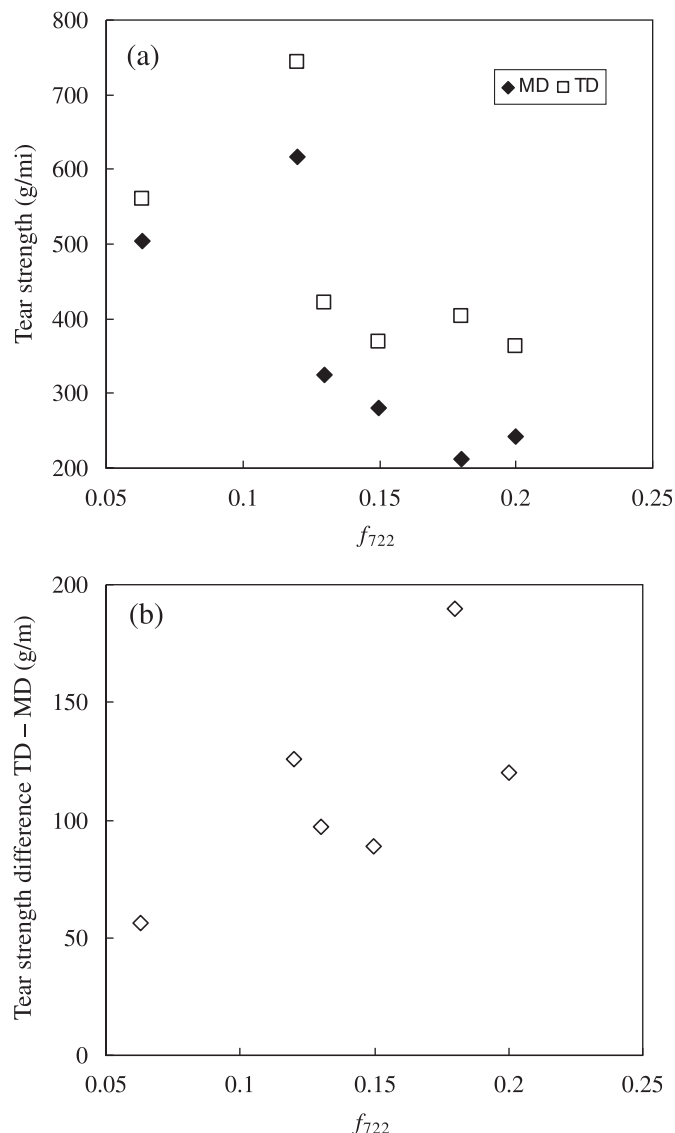
### Relationship between the relative concentration of TCs and tear strength

Tear resistance is another important physical property for LLDPE blown films. In the deformation, tear resistance reflects the energy that is dissipated in the growth of the crack. A certain amount of TCs (depending on machine direction (MD) or transverse direction (TD)) needs to be broken in order for the tear to propagate. As a result, if the crack propagation runs through a greater amount of TCs, stronger tear strength would follow owing to the covalent nature of the TC bonds. A clear correlation between the relative concentration of TCs and the tear resistance of the six films investigated here was not observed (Fig. 6a). Structural features other than TCs, such as the size and orientation of the crystalline lamellae, must be responsible for this observation. It is reported that larger lamellae being oriented along a certain direction result in good tear strengths in that direction.<sup>19</sup> A close examination of our data showed that the quantity of TCs may contribute to the tear resistance discrepancy between the MD and TD of the same film; it appeared that a higher concentration of TCs led to a larger discrepancy (Fig. 6b). This observation agrees with the finding of Chen et al.<sup>20</sup>

### Conclusions

The relative concentrations of tie chains (TCs) in six ss-LLDPE thin blown films were determined via the FTIR measurements of the amorphous orientation of the stretched films upon relaxation. The critical issues are the determination of an appropriate strain and the separation of the amorphous orientation from those of the crystalline chains. We demonstrated that at a strain of 20%, the amorphous chains (most importantly the TCs) were oriented to a significant degree, and the disturbance to the crystalline lamellar layer was limited to the minimum. The separation of the amorphous and crystalline orientations was solved by using the procedure reported by Kissin.<sup>14</sup> The average molar mass and the interchain distribution pattern of SCBs have significant effects on the amount of TCs. An optimal ethylene sequence length between SCBs must exist for the formation of TCs with other structural features remaining similar. The relationship between the relative concentration of TCs and the physical properties of the films showed that the quantity of TCs and the dart impact strength are positively related and

**Fig. 6.** (a) The tear strength vs relative concentration of TCs. (b) The tear strength difference (TD minus MD) vs relative concentration of TCs for six ss-LLDPE blown films.



that no clear correlation between the relative concentration of TCs and the tear strength was observed, indicating that other morphological features, such as lamellar size and orientation, may be more important in determining the tear resistance. The quantity of TCs may contribute to the discrepancy in MD and TD tear resistance of the films.

### Acknowledgements

We are grateful for the financial support from NOVA Chemicals Corporation and the Natural Sciences and Engineering Research Council of Canada through a collaborative research grant as well as to NOVA Chemicals Corporation for providing us the polyethylene film samples and the data shown in Table 1. We would also like to take this opportunity to thank the kind invitation from Professors Willie Leigh and Jean Duhamel at McMaster University and the University of Waterloo, respectively, for this submission to a special issue of the *Canadian Journal of Chemistry* to hon-

our the career contributions of Professor Mitchell A. Winnik at the University of Toronto.

## References

- (1) Brown, N.; Ward, I. M. *J. Mater. Sci.* **1983**, *18* (5), 1405. doi:10.1007/BF01111960.
- (2) Liu, T. M.; Baker, W. E. *Polym. Eng. Sci.* **1992**, *32* (14), 944. doi:10.1002/pen.760321406.
- (3) Ward, I. M.; Wilding, M. A. *J. Polym. Sci. Polym. Phys. Ed.* **2003**, *22* (4), 561. doi:10.1002/pol.1984.180220403.
- (4) Lustiger, A.; Markam, R. L. *Polymer (Guildf.)* **1983**, *24* (12), 1647. doi:10.1016/0032-3861(83)90187-8.
- (5) Schurzky, K. G. *J. Plast. Film Sheeting* **1985**, *1* (2), 142. doi:10.1177/875608798500100208.
- (6) Porter, R. S.; Johnson, J. F. *Chem. Rev.* **1966**, *66* (1), 1. doi:10.1021/cr60239a001.
- (7) Darras, O.; Séguéla, R. *Colloid Polym. Sci.* **1995**, *273* (8), 753. doi:10.1007/BF00658753.
- (8) Zhou, Z.; Lu, X.; Brown, N. *Polymer (Guildf.)* **1993**, *34* (12), 2520. doi:10.1016/0032-3861(93)90582-U.
- (9) Seguela, R. *J. Polym. Sci. Part B: Polym. Phys* **2005**, *43* (14), 1729. doi:10.1002/polb.20414.
- (10) Yeh, J. T.; Runt, J. *J. Polym. Sci. Part B: Polym. Phys* **2003**, *29* (3), 371. doi:10.1002/polb.1991.090290313.
- (11) Patel, R. M.; Sehanobish, K.; Jain, P.; Chum, S. P.; Knight, G. W. *J. Appl. Polym. Sci.* **1996**, *60* (5), 749. doi:10.1002/(SICI)1097-4628(19960502)60:5<749::AID-APP14>3.0.CO;2-U.
- (12) Read, B. E.; Stein, R. S. *Macromolecules* **1968**, *1* (2), 116. doi:10.1021/ma60002a004.
- (13) Lustiger, A.; Ishikawa, N. *J. Polym. Sci. Part B: Polym. Phys* **1991**, *29* (9), 1047. doi:10.1002/polb.1991.090290902.
- (14) Kissin, Y. V. *J. Polym. Sci. Part B: Polym. Phys* **1992**, *30* (10), 1165. doi:10.1002/polb.1992.090301011.
- (15) Peterlin, A. *J. Mater. Sci.* **1971**, *6* (6), 490. doi:10.1007/BF00550305.
- (16) Krishnaswamy, R. K.; Yang, Q.; Fernandez-Ballester, L.; Kornfield, J. A. *Macromolecules* **2008**, *41* (5), 1693. doi:10.1021/ma070454h.
- (17) Zhang, M. Z.; Yuen, F.; Choi, P. *Macromolecules* **2006**, *39* (24), 8517. doi:10.1021/ma060516o.
- (18) Krishnaswamy, R. K.; Sukhadia, A. M. *J. Plast. Film Sheeting* **2005**, *21* (2), 145. doi:10.1177/8756087905054148.
- (19) Lee, L.-B. W.; Register, R. A.; Dean, D. M. *J. Polym. Sci. Part B: Polym. Phys* **2005**, *43* (4), 413. doi:10.1002/polb.20350.
- (20) Chen, H. Y.; Bishop, M. T.; Landes, B. G.; Chum, S. P. *J. Appl. Polym. Sci.* **2006**, *101* (2), 898. doi:10.1002/app.23583.

# Conductivity percolation of carbon nanotubes (CNT) in polystyrene (PS) latex film

Ş. Uğur, Ö. Yargi, and Ö. Pekcan

**Abstract:** In this study, the effect of multiwalled carbon nanotubes (MWNT) on film formation behaviour and electrical conductivity properties of polystyrene (PS) latex film was investigated by using the photon transmission technique and electrical conductivity measurements. Films were prepared by mixing PS latex with different amounts of MWNTs, varying in the range between 0 and 20 wt%. After drying, MWNT content films were separately annealed above the glass transition temperature ( $T_g$ ) of PS, ranging from 100 to 270 °C, for 10 min. To monitor film formation behavior of PS–MWNT composites, transmitted light intensity,  $I_{tr}$ , was measured after each annealing step. The surface conductivity of annealed films at 170 °C was measured and found to increase dramatically above a certain fraction of MWNT (4 wt%) following the percolation theory. This fraction was defined as the percolation threshold of conductivity,  $R_c$ . The conductivity scales with the mass fraction of MWNT as a power law with exponent 2.27, which is extremely close to the value of 2.0 predicted by percolation theory. In addition, the increase in  $I_{tr}$  during annealing was explained by void closure and interdiffusion processes. Film formation stages were modeled and the corresponding activation energies were measured.

**Key words:** multiwalled carbon nanotubes, polystyrene, latex, nanocomposites, conductivity, transmission, percolation, film formation.

**Résumé :** Faisant appel à la technique de transmission photonique et à des mesures de conductivité électrique, on a étudié l'effet de nanotubes de carbone à parois multiples (NCPM) sur le comportement de formation de films et sur les propriétés de conductivité électrique de films de latex au polystyrène (PS). Les films ont été préparés en mélangeant du latex de PS avec diverses quantités de nanotubes de carbone à parois multiples allant de 0 à 20 % en poids. Après les avoir soumis au séchage, les films contenant des nanotubes de carbone à parois multiples ont été recuits séparément à une température supérieure à la celle de la de transition de verre ( $T_g$ ) du PS, de 100 à 270 °C, pendant dix minutes. Afin de suivre le comportement de formation des films composites PS/NCPM, on a mesuré l'intensité de la lumière transmise,  $I_{tr}$ , après chaque étape de recuisson. On a aussi mesuré la conductivité de surface des films recuits à 170 °C et on a observé une augmentation dramatique au-dessus d'une certaine fraction (4 % en poids), en accord avec la théorie de percolation. On a défini cette fraction comme le seuil de percolation de conductivité,  $R_c$ . Les échelles de conductivité utilisant la fraction massique des nanotubes de carbone à parois multiples avec une loi de puissance avec un exposant 2,27 sont très près de la valeur de 2,0 prédite par la théorie de la percolation. De plus, l'augmentation de  $I_{tr}$  durant la recuisson peut être expliquée par la fermeture du vide et des processus d'interdiffusion. On a calculé des modèles des stages de formation des films et on a mesuré les énergies d'activation correspondantes.

**Mots-clés :** nanotubes de carbone à parois multiples, polystyrène, latex, nanocomposites, conductivité, transmission, percolation, formation de film.

[Traduit par la Rédaction]

## Introduction

As a result of worldwide efforts by theorists and experimentalists, a very good understanding of the mechanisms of latex film formation has been achieved.<sup>1</sup> Traditionally, the film formation process of polymer latex is considered in terms of three sequential steps: (i) Water evaporation and subsequent packing of polymer particles. (ii) Deformation of the particles and close contact between the particles if

their glass transition temperature ( $T_g$ ) is less than or close to the drying temperature (soft or low  $T_g$  latex). Latex with a  $T_g$  above the drying temperature (hard or high  $T_g$  latex) stays undeformed at this stage. In the annealing of a hard latex system, deformation of particles first leads to void closure<sup>2–4</sup> and then after the voids disappear, diffusion across particle–particle boundaries starts, i.e., the mechanical properties of hard latex films evolve during annealing, after all solvent has evaporated and all voids have disappeared. (iii) Coales-

Received 13 August 2009. Accepted 16 November 2009. Published on the NRC Research Press Web site at canjchem.nrc.ca on 24 February 2010.

This article is part of a Special Issue dedicated to Professor M. A. Winnik.

Ş. Uğur and Ö. Yargi, Department of Physics Istanbul Technical University, Istanbul 34469, Turkey.  
Ö. Pekcan,<sup>1</sup> Kadir Has University, Cibali, Istanbul 34230, Turkey.

<sup>1</sup>Corresponding author (e-mail: pekcan@khas.edu.tr).

cence of the deformed particles to form a homogeneous film<sup>3</sup> where macromolecules belonging to different particles mix by interdiffusion.<sup>5,6</sup>

This understanding of latex film formation can now be exploited to underpin the processing of new types of coatings and adhesives. The blending of latex particles and inorganic nanoparticles provides a facile means of ensuring dispersion at the nanometer scale in composite coatings. Carbon nanotubes (CNT) and monodispersed nanoparticles are two of the most important building blocks proposed to create nanodevices. Recently, CNT-polymer nanocomposites have been widely investigated due to their remarkable mechanical,<sup>6</sup> thermal,<sup>7</sup> and electrical properties.<sup>8</sup> CNT have potential applications in many areas such as biosensors, conducting agents, field-effect transistors, and nanocomposites.<sup>9</sup> The polymeric or ceramic matrix of composites is usually considered nonconductive material because of its extremely low electrical conductivity (in the order of  $10^{-10}$ – $10^{-15}$  S/m). Dispersing conductive materials into the nonconductive matrix can form conductive composites. The electrical conductivity of a composite is strongly dependent on the volume fraction of the conductive phase. At low volume fractions, the conductivity remains very close to the conductivity of the pure matrix. When a certain volume fraction is reached, the conductivity of the composite drastically increases by many orders of magnitude. The phenomenon is known as percolation and can be well explained by percolation theory. The electrical percolation threshold of conductive reinforcements embedded in an insulating matrix is sensitive to the geometrical shape of the conductive phase. The small size and large aspect ratio (length/diameter) help lower the percolation threshold.<sup>10</sup> Depending on the matrix, the processing technique, and the nanotube type used, percolation thresholds ranging from 0.001 wt% to more than 10 wt% have been reported.<sup>11,12</sup> Because carbon nanotubes have tremendously large aspect ratios (100–10 000), many researchers have observed exceptionally low electrical percolation thresholds.<sup>12</sup> The electric current-carrying ability of CNTs may be 1000 times that of copper wires.<sup>13</sup> Due to the high aspect ratio of their external shapes, nanotubes can form percolated networks even at very low filler fractions (<5 wt%) to impart tremendous filler reinforcement effects. There have been many studies on low volume fraction composites where the addition of a very small amount of nanotubes substantially modifies the electrical properties of polymer matrices.<sup>13–16</sup> Thus, carbon nanotubes are excellent candidates to blend with polymers to produce electrostatic dissipative materials and other useful components in electronics.

As for the electrical properties of CNT-polymer composites, it was reported that the use of CNTs as conductive fillers in a polymer matrix implies a very low percolation threshold.<sup>13,15,17</sup> However, as CNTs are generally insoluble in common solvents and polymers, they tend to aggregate and disperse poorly in polymer matrix, resulting in deleterious effects. To overcome these difficulties, several methods have been developed to disperse CNTs in host polymers. CNTs could be dispersed in certain polymer solutions via ultrasonication<sup>18–22</sup> or in the presence of surfactants.<sup>23–25</sup> Several groups have reported electrical resistivity results for multiwalled nanotubes (MWNT) and single-walled nanotube (SWNT) ropes.<sup>26</sup> In a recent study, Gojny et al.<sup>27</sup> concluded

that multiwalled carbon nanotubes offer the highest potential for enhancement of electrical conductivity. The rationale behind this conclusion is that the multiwalled nanotubes usually have a better dispersability than single-walled nanotubes. Measured electrical conductivities for nanotube-based composites typically range from  $10^{-5}$  to  $10^{-2}$  S/m for nanotube contents above the percolation threshold.<sup>28</sup> However, electrical conductivity tailored to the range of 0.01–3480 S/m by varying the nanotube content from 0.11 to 15 wt% has also been reported.<sup>17</sup> Surely, the increase of the nanotube volume fraction can increase the electrical conductivity of composites. Previous studies indicate that the overall resistances of SWNT bundle networks and carbon nanotube-based composites are dominated by the contact resistance.<sup>29</sup> Measurements on crossed SWNTs<sup>30</sup> gave contact resistance of 100–400 k $\Omega$  for metal-metal or semiconducting-semiconducting SWNT junctions and values two orders higher for metal-semiconducting junctions.

Waviness is a dominant feature of carbon nanotubes in composites. Wavy nanotubes dispersed in a matrix tend to have more contact points than straight nanotubes, and therefore, have a considerable effect on electrical conductivity due to the dominant role of contact resistance. Previous studies have only investigated the effect of waviness on percolation threshold and elastic stiffness of composites.<sup>31–35</sup> The basic conclusion reached in these studies is that the waviness tends to increase the percolation threshold but reduces the elastic stiffness. To date, almost all the computational simulations of the electrical conductivity of nanotube-based composites assumed nanotubes as straight sticks.<sup>34</sup> More recently, Li et al.<sup>36</sup> simulated wavy nanotubes using elongated polygons, and the current carrying backbones of percolation clusters in the composite are identified by a direct electrifying algorithm.<sup>37</sup> The tunneling resistance due to an insulating film of matrix material between crossing nanotubes is considered. Results of Monte Carlo simulations indicate that the electrical conductivity of composites with wavy nanotubes is lower than that of composites with straight nanotubes. In experimental measurements of conductivities, researchers have strived to pursue composite systems with well dispersed fillers. Such an “ideal” system forms a basis for the comparison of conductivity percolation thresholds as influenced by factors such as filler aspect ratio, matrix materials, contact resistance, nanotube waviness, and so forth. The anisotropy of conductivity is strongly affected by nanotube alignment, especially when the nanotube contents are small. But the effect of alignment becomes weaker at larger nanotube contents.<sup>38,39</sup>

In the work reported here, we investigated the film formation behavior and electrical conductivity properties of polymer-CNTs depending on the CNTs content using the photon transmission technique and electrical conductivity measurements. In this work, MWNTs were chosen as conductive fillers rather than single-wall carbon nanotubes (SWNTs) since MWNTs are less expensive than SWNTs and polymer-MWNT composites may be more acceptable than polymer-SWNT composites in industrial application. Furthermore, MWNTs are easier to disperse in the polymer matrix compared to SWNTs. Polystyrene (PS) was used as the polymer matrix because its properties are well-known; it is easy to process, it is soluble in a broad range of solvents, and its



clarity allows dispersion of MWNTs to be optically observed at the micron scale. Films were prepared by mixing PS latex with MWNT particles in various compositions and annealing them at temperatures above the glass transition temperature of PS. After each annealing step, the transmitted light intensity,  $I_{tr}$ , was monitored to observe the film formation process. The increase in  $I_{tr}$  up to the healing temperature,  $T_h$ , and above  $T_h$  during annealing was explained by void closure and interdiffusion processes, respectively. From the measurements of the electrical conductivities of the composites, the percolation threshold of conductivity was found to be 4 wt% MWNT.

## Experimental

### Materials

PS particles were produced via surfactant free emulsion polymerization process. The polymerization was performed batch-wisely using a thermostatted reactor equipped with a condenser, thermocouple, mechanical stirring paddle, and nitrogen inlet. The agitation rate was 400 rpm and the polymerization temperature was controlled at 70 °C. Water (100 mL) and styrene (5 g) were first mixed in the polymerization reactor where the temperature was kept constant (at 70 °C). The potassium peroxydisulfate (KPS) initiator (0.1g), dissolved in small amount of water (2 mL), was then introduced to induce styrene polymerization. The polymerization was conducted during 18 h. The polymer has a high glass transition temperature ( $T_g = 105$  °C). The latex dispersion has an average particle size of 400 nm. Figure 1a shows a scanning electron microscope (SEM) image of the PS latex produced for this study.

Commercially available MWNTs (Cheap Tubes Inc., VT, USA, 10–30  $\mu\text{m}$  long, average inner diameter: 5–10 nm, outer diameter: 20–30 nm, the density is approximately 2.1 g/cm<sup>3</sup>, and purity is higher than 95 wt%) were used as supplied in black powder form without further purification. A stock solution of MWNTs was prepared following the manufacturers regulations: nanotubes were dispersed in de-ionized (DI) water with the aid of polyvinyl pyrrolidone (PVP) in the proportions of 10 parts MWNTs, 1–2 parts PVP, 2,000 parts DI water by bath sonication for 3 h. PVP is a good stabilizing agent for dispersions of carbon nanotubes, enabling preparation of polystyrene composites from dispersions of MWNT in polystyrene solution. Figure 1b shows the transmission electron microscope (TEM) image of MWNTs used in this study (www.cheaptubesinc.com).

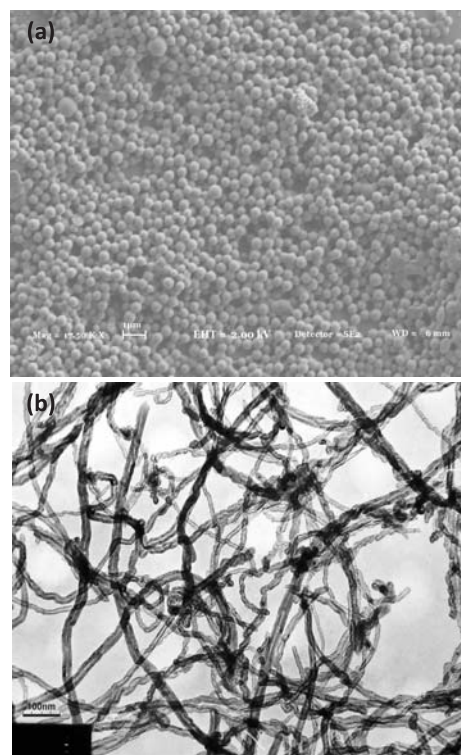
### Preparation of PS–MWNT composite films

A 15 g/L solution of polystyrene (PS) in water was prepared separately. The dispersion of MWNTs in water was mixed with the solution of PS yielding the required ratio,  $R$ , of MWNTs in PS latex by using the relation

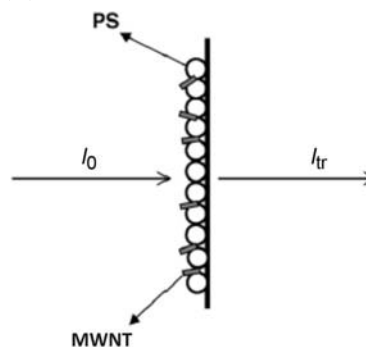
$$R = \frac{M_{\text{MWNT}}}{M_{\text{PS}} + M_{\text{MWNT}}}$$

where  $M_{\text{PS}}$  and  $M_{\text{MWNT}}$  represent the weight of PS and MWNTs in the mixture, respectively. Eighteen different mixtures were prepared with 0, 0.15, 0.45, 0.8, 1, 1.5, 1.8, 2, 2.5, 3, 4, 5, 8, 10, 13, 15, 18, 20 wt% MWNTs by using this relation. Each mixture was stirred for 1 h followed by

**Fig. 1.** (a) SEM image of PS latex and (b) TEM image of multi-walled nanotubes (MWNTs) (www.cheaptubesinc.com) used in this study.



**Fig. 2.** A schematic illustration of sample position and transmitted light intensity ( $I_{tr}$ ).



sonication for 30 min at room temperature. By placing the same number of drops on glass plates with similar surface areas ( $0.8 \times 2.5 \text{ cm}^2$ ) and allowing the water to evaporate at 60 °C in the oven, dry films were obtained. After drying, samples were separately annealed above the  $T_g$  of PS for 10 min at temperatures ranging from 100 to 270 °C. The temperature was maintained within  $\pm 2$  °C during annealing. After each annealing step, films were removed from the oven and cooled down to room temperature. The thickness of the films was determined from the weight and the density of samples and ranged from 6 to 10  $\mu\text{m}$ .

### Measurements

Photon transmission experiments were carried out using model Carry 100 bio UV–visible (UVV) spectrometer from Varian. The transmittances of the films were detected at

500 nm at which the composite's spectra is almost flat, i.e., at this wavelength polystyrene and carbon nanotubes have no specific absorption. This picture is quite common for the polymeric films studied using the optical transmission technique.<sup>40–42</sup> A glass plate was used as a standard for all UVV experiments. The sample position and the transmitted light intensity,  $I_{tr}$ , are presented in Fig. 2.

Scanning electron microscope (SEM) images were taken using LEO Supra VP35 FESEM.

Electrical conductivity was measured by a two-probe method using a Keithley Model 6517a Electrometer with an ultrahigh resistance meter. For the surface resistance measurements, the samples were coated onto thin rectangular glass slabs with typical dimensions of  $2.0 \times 3.0 \text{ cm}^2$ . The electrical contact was made using a silver paste. Electrical resistivities of the composite films were measured by alternating polarity technique with electrometer and a test fixture. The composite films were placed in the test fixture, which have disk shaped electrodes, then their surface resistivities,  $R_s$  ( $\Omega$ ), were measured for 15 s under 100 V alternating potential. All the resistivities of the composite films were determined for four different orientations and measurements were repeated many times to lower the error level. The surface resistivity was converted into surface conductivity.

## Results and discussion

### Film formation process of PS–MWNT composites

Transmitted light intensities,  $I_{tr}$ , versus annealing temperatures are plotted in Fig. 3 for the films with 0, 1.5, 3, 5, 10, and 15 wt% MWNT content. Upon annealing, the transmitted light intensity,  $I_{tr}$ , started to increase for all film samples except for 15 wt% MWNT content film. The increase in  $I_{tr}$  with annealing can be explained by the evaluation of the transparency of the films and surface smoothing upon annealing. Most probably, the increase in  $I_{tr}$  up to  $T_h$  corresponds to the void closure process,<sup>39,43–46</sup> i.e., the polystyrene starts to flow upon annealing and voids between particles can be filled. On the other hand, the increase in  $I_{tr}$  above  $T_h$  corresponds to the interdiffusion process. However, for 15 wt% MWNT content film,  $I_{tr}$  almost doesn't change with annealing, which means that no film formation process occurs, and light transmission is completely blocked by dispersion of the MWNTs in the composite film. On the other hand,  $I_{tr}$  decreases with increasing MWNT content in films at all annealing temperatures, predicting that less transparency occurs at high MWNT content films. The plots of the maximum values of  $(I_{tr})_{max}$  versus MWNT content in Fig. 4a also confirms this picture, i.e., as the MWNT content is increased,  $(I_{tr})_{max}$  first decreases continuously from 70% to 30% at 4 wt% MWNT, and then shows a slight decrease reaching its minimum value (10%) around 15 wt% MWNT.

To see dispersion of MWNTs in PS lattice during annealing, SEM micrographs of composite film with 15 wt% MWNT content were taken after annealing them at 100 and 150 °C (see Fig. 5), respectively. In Fig. 5a, for the 15 wt% MWNT film annealed at 100 °C no deformation in PS particles is observed and PS particles keep their original spherical shapes. After annealing treatment at 150 °C (Fig. 5b), SEM images show that complete particle coalescence has been achieved. It can be clearly seen that the composite

film consists of a network of bundles and indicates significant porosity, which results in strong scattering. The optical transmission of the films versus MWNT content above 15 wt% MWNT (Fig. 4a) is a good indicator of how finely nanotubes are dispersed in the matrix. This result is consistent with the microstructural analysis.

The increase in  $I_{tr}$  intensity below and above the  $T_h$  point in the 0–10 wt% MWNT range can be explained by void closure and interdiffusion processes, respectively.<sup>47</sup> To understand these phenomena, the following mechanisms and their formulations are proposed.

### Voids closure

Latex deformation and void closure between particles can be induced by shearing stress, which is generated by surface tension of the polymer, i.e., polymer–air interfacial tension. The void closure kinetics can determine the time for optical transparency and latex film formation.<sup>48</sup> To relate the shrinkage of a spherical void of radius  $r$  to the viscosity of the surrounding medium,  $\eta$ , an expression was derived and given by the following relation.<sup>48</sup>

$$[1] \quad \frac{dr}{dt} = -\frac{\gamma}{2\eta} \left( \frac{1}{\rho(r)} \right)$$

where  $\gamma$  is surface energy,  $t$  is time, and  $\rho(r)$  is the relative density. It has to be noted here that surface energy causes a decrease in void size and the term  $\rho(r)$  varies with the microstructural characteristics of the material, such as the number of voids, the initial particle size, and packing. Equation [1] is similar to one that was used to explain the time dependence of the minimum film formation temperature during latex film formation.<sup>49</sup> If the viscosity is constant in time, the integration of eq. [1] gives the relation as

$$[2] \quad t = -\frac{2\eta}{\gamma} \int_{r_0}^r \rho(r) dr$$

where  $r_0$  is the initial void radius at  $t = 0$ .

The dependence of the viscosity of the polymer melt on temperature is affected by the overcoming of the forces of macromolecular interaction, which enables the segments of the polymer chain to jump over from one equilibration position to another. This process happens at temperatures at which free volume becomes large enough and is connected with the overcoming of the potential barrier. The Frenkel–Eyring theory produces the following relation for the temperature dependence of viscosity.<sup>50–52</sup>

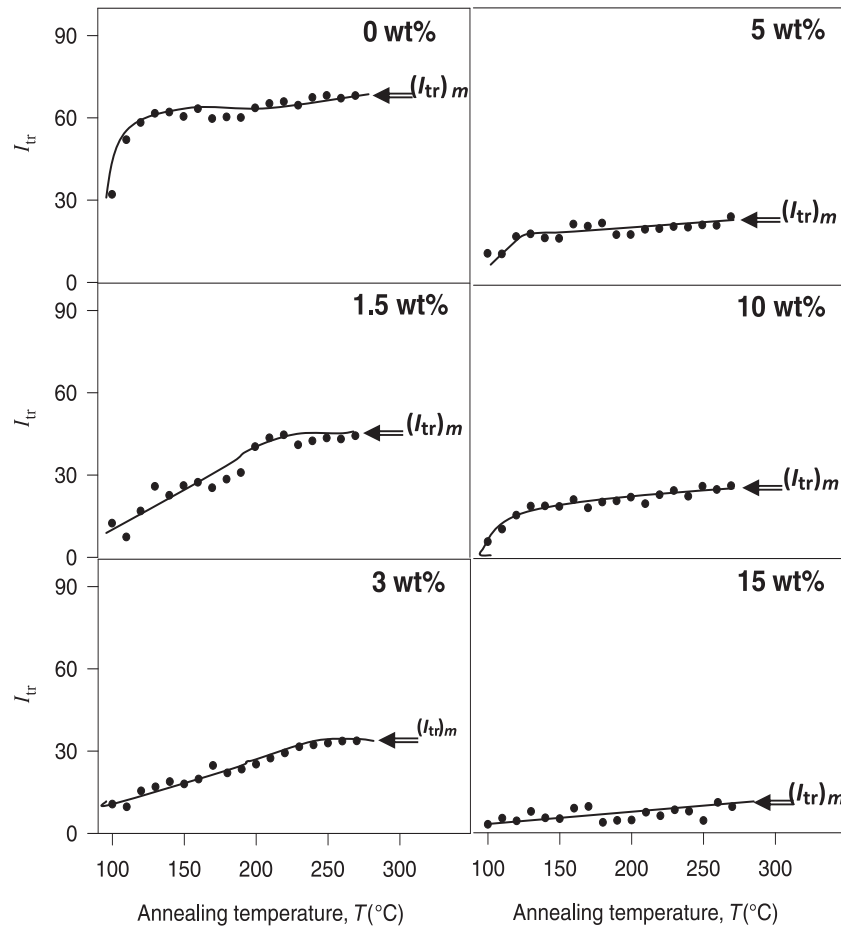
$$[3] \quad \eta = (N_0 h / V) \exp(\Delta G / kT)$$

where  $N_0$  is Avagadro's number,  $h$  is Planck's constant,  $V$  is the molar volume, and  $k$  is Boltzmann's constant. It is known that  $\Delta G = \Delta H - T\Delta S$ , then eq. [3] can be written as

$$[4] \quad \eta = A \exp(\Delta H / kT)$$

where  $\Delta H$  is the activation energy of viscous flow, i.e., the amount of heat that must be given to 1 mol of material for creating the act of a jump during viscous flow.  $\Delta S$  is the entropy of activation of viscous flow. Here,  $A$  represents a constant for the related parameters that do not depend on

**Fig. 3.** Plots of transmitted photon intensities,  $I_{tr}$ , vs. annealing temperatures depending on MWNT content in the films. The numbers on each figure show the MWNT content in the film.



temperature. Combining eq. [2] and [4] the following useful equation is obtained

$$[5] \quad t = -\frac{2A}{\gamma} \exp\left(\frac{\Delta H}{kT}\right) \int_{r_0}^r \rho(r) dr$$

To quantify the above results, eq. [5] can be employed by assuming that the interparticle voids are equal in size and the number of voids stay constant during film formation (i.e.,  $\rho(r) \propto r^{-3}$ ), then integration of eq. [5] gives the relation

$$[6] \quad t = \frac{2AC}{\gamma} \exp\left(\frac{\Delta H}{kT}\right) \left(\frac{1}{r^2} - \frac{1}{r_0^2}\right)$$

where  $C$  is a constant related to the relative density,  $\rho(r)$ .

To quantify the behavior of  $I_{tr}$  curves below  $T_h$  presented in Fig. 3, the void closure model can be applied, where a decrease in void size ( $r$ ) causes an increase in  $I_{tr}/(I_{tr})_{\max}$  ratios and vice versa. If the assumption is made that the  $I_{tr}/(I_{tr})_{\max}$  ratio is inversely proportional to the 6th power of the void radius,  $r$ , then eq. [6] can be written as

$$[7] \quad t = \frac{2AC}{\gamma} \exp\left(\frac{\Delta H}{kT}\right) \left(\frac{I_{tr}}{(I_{tr})_{\max}}\right)^{1/3}$$

Here,  $r_0^{-2}$  is omitted from the relation since it is very

small compared to  $r^{-2}$  values after a void closure process is started. Equation [7] can be solved for  $I_{tr}/(I_{tr})_{\max}$

$$[8] \quad I_{tr}(T) = S(t) \exp\left(\frac{-3\Delta H}{kT}\right)$$

where  $S(t) = (\gamma t / 2AC)^3$  and  $I_{tr} = I_{tr}/(I_{tr})_{\max}$ . For a given time the logarithmic form of eq. [8] can be written as follows

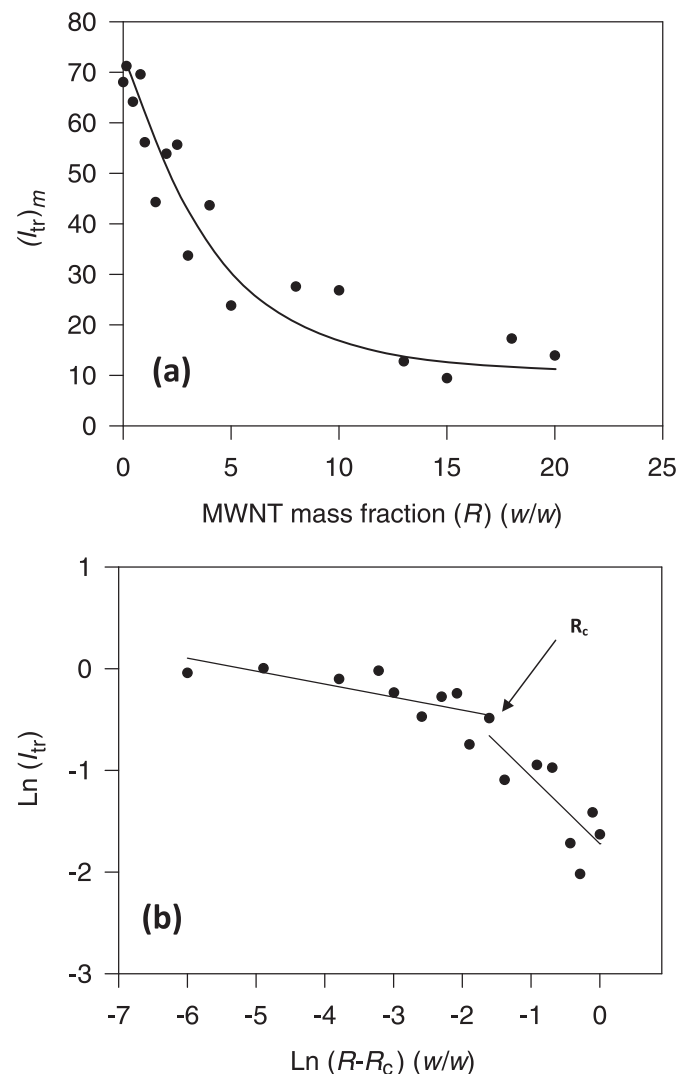
$$[9] \quad \ln I_{tr}(T) = \ln S(t) - \left(\frac{3\Delta H}{k_B T}\right)$$

Equation [9] can now be used to produce viscous flow activation energies,  $\Delta H$ .  $\ln I_{tr}$  versus  $T^{-1}$  plots and their fits to eq. [9] are presented in Fig. 6 (right hand side of the curves) from which  $\Delta H$  activation energies were obtained. The measured void closure,  $\Delta H$  activation energies are listed in Table 1, which are present at a minima around 4 wt%.

### Healing and interdiffusion

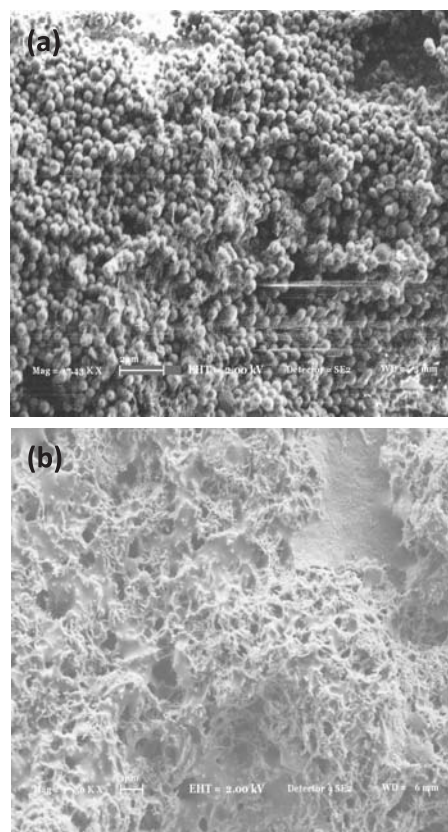
The decrease in  $I_{tr}$  was already explained in the previous section, by the increase in transparency of latex film due to the disappearance of deformed particle-particle interfaces. As the annealing temperature is increased above healing temperature,  $T_h$ , some part of the polymer chain may cross the junction surface and particle boundaries start to disappear, as a result,  $I_{tr}$  increases due to the shorter optical and

**Fig. 4.** (a) A plot of the maxima of transmitted light intensities,  $(I_{tr})_{max}$ , in Fig. 3 vs. MWNT content,  $R$  (w/w); (b) log-log plot of  $(I_{tr})_{max}$  vs.  $(R - R_c)$ .



long mean free paths of a photon.<sup>43–47</sup> To quantify these results, the Prager–Tirrell (PT) model<sup>53</sup> for the chain crossing density can be employed. These authors used de Gennes’s<sup>54</sup> “reptation” model to explain configurational relaxation at the polymer–polymer junction where each polymer chain is considered to be confined to a tube in which it executes a random back and forth motion. A homopolymer chain with  $N$  freely jointed segments of length  $L$  was considered by PT, which moves back and forth by one segment with a frequency,  $\nu$ . In time, the chain displaces down the tube by a number of segments,  $m$ . Here,  $\nu/2$  is called the “diffusion coefficient” of  $m$  in one-dimensional motion. PT calculated the probability of the net displacement with  $m$  during time  $t$  in the range of  $n - \Delta$  to  $n - (\Delta + d\Delta)$  segments. A Gaussian probability density was obtained for small times and large  $N$ . The total “crossing density”,  $\sigma(t)$  (chains per unit area), at the junction surface was then calculated from the contributions of  $\sigma_1(t)$  due to chains still retaining some portion of their initial tubes, plus a remainder,  $\sigma_2(t)$ . Here, the  $\sigma_2(t)$  contribution comes from chains that have relaxed at least

**Fig. 5.** SEM images of composite films prepared with 15% MWNT content and annealed for 10 min at (a) 100 and (b) 150 °C temperatures.



once. In terms of reduced time,  $\tau = 2\nu t/N^2$ , the total crossing density can be written as

$$[10] \quad \sigma(\tau)/\sigma(\infty) = 2\pi^{-1/2} \left\{ \tau^{1/2} + 2 \sum_{k=0}^{\infty} (-1)^k [\tau^{1/2} \exp(-k^2/\tau) - \pi^{-1/2} \operatorname{erfc}(k/\tau^{1/2})] \right\}$$

For small  $\tau$  values the summation term of the above equation is very small and can be neglected, which then results in

$$[11] \quad \sigma(\tau)/\sigma(\infty) = 2\pi^{-1/2} \tau^{1/2}$$

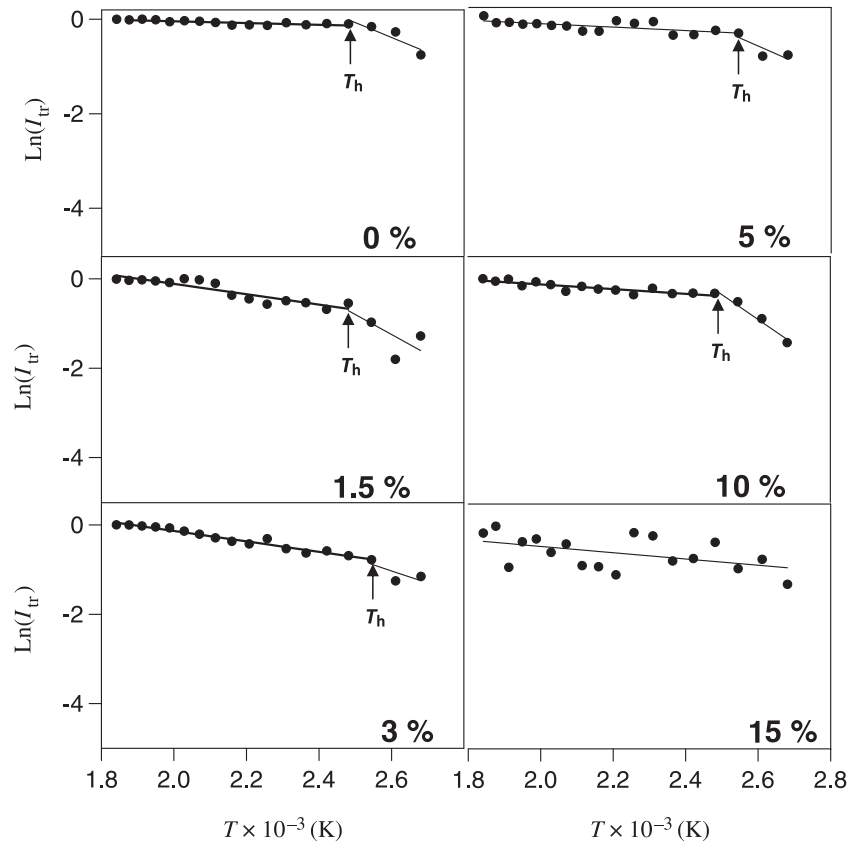
This was predicted by de Gennes<sup>54</sup> on the basis of scaling arguments. Here, it should be mentioned that the dependence on time,  $t$ , in eq. [10] goes as  $t^{1/4}$  at early times of healing.<sup>54,55</sup> To compare our results with the crossing density of the PT model, the temperature dependence of  $\sigma(\tau)/\sigma(\infty)$  can be modeled by taking into account the following Arrhenius relation for the linear diffusion coefficient

$$[12] \quad \nu = \nu_0 \exp(-\Delta E_b/kT)$$

Here,  $\Delta E_b$  is defined as the activation energy for backbone motion depending on the temperature interval. Combining eqs. [11] and [12], a useful relation is obtained as



**Fig. 6.** The  $\ln(I_{tr})$  vs.  $T^{-1}$  plots of the data in Fig. 3. The slope of the straight lines produces  $\Delta H$  and  $\Delta E$  activation energies, which are listed in Table 1.



**Table 1.** Experimentally determined activation energy values.

MWNT (wt%)	0	1.5	2	3	4	5	10	15
$\Delta H$ (kcal/mol)	2.1	3.0	1.1	1.8	0.8	2.2	3.7	—
$\Delta E$ (kcal/mol)	0.7	4.6	8.6	4.6	5.5	1.4	2.1	—

$$[13] \quad \sigma(\tau)/\sigma(\infty) = A_0 \exp(-\Delta E_b/2kT)$$

where  $A_0 = (8\nu_0 t/\pi N^2)^{1/2}$  is a temperature independent coefficient.

The increase in  $I_{tr}$  above  $T_h$  is already related to the disappearance of particle–particle interfaces, i.e., as annealing temperature is increased, more chains relax across the junction surface and as a result the crossing density increases. Now, it can be assumed that  $I_{tr}$  is proportional to the crossing density,  $\sigma(\tau)$ , in eq. [13] and then the phenomenological equation can be written as

$$[14] \quad I_{tr}(T)/I_{tr}(\infty) = A \exp(-\Delta E/2kT)$$

Logarithmic plots of  $I_{tr}$  versus  $T^{-1}$  are presented in Fig. 6 (left hand side of the curves) for various MWCNT content. The activation energies,  $\Delta E$ , are produced by least-squares fitting the data to eq. [14] and are listed in Table 1, where it is seen that  $\Delta E$  values present a maximum around 3 wt% MWNT content, while  $\Delta H$  values have a minimum about the same point. In other words, the interdiffusion of polymer chains needs more energy to cross over the junction surface than the amount of heat that was required by 1 mol of polymeric material to accomplish a jump during viscous flow. In

fact, these optimum points correspond to the percolation threshold for the electrical conductivity and for the optical transparency in composite film (see the next section).

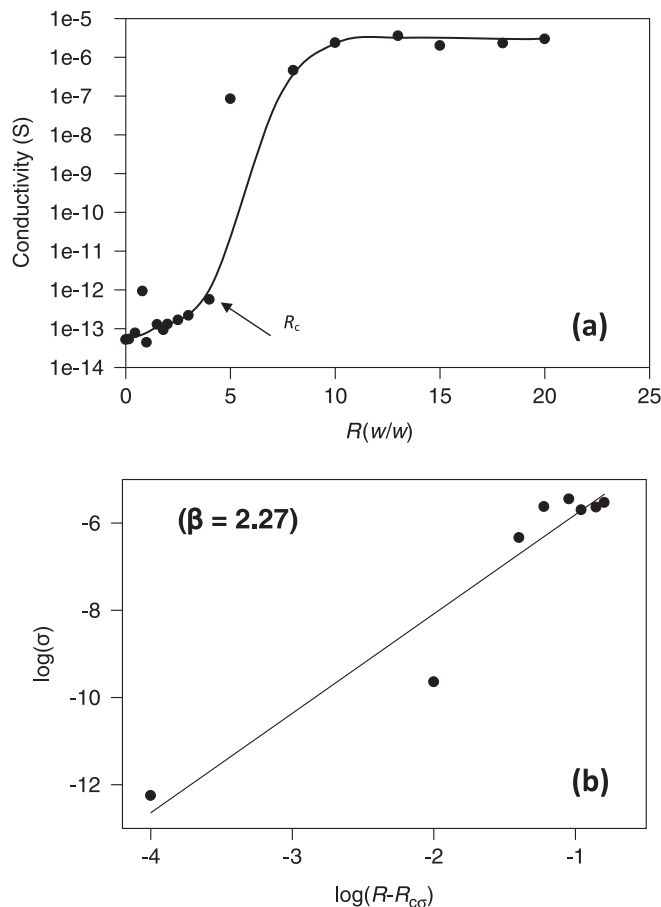
### Electrical conductivity of PS–MWNT composites

The surface conductivity properties of the films were measured at room temperature by using a two probe technique. Figure 7a shows the electrical conductivity ( $\sigma$ ) of PS–MWNT composite films and its best fit as a function of the MWNTs ratio,  $R$ . While low MWNT content composites ( $R < 0.04$ ) show similar conductivity between  $10^{-13}$ – $10^{-12}$  S, the conductivity of high MWNT content films ( $R > 0.04$ ) increase dramatically to  $\sim 10^{-7}$ – $10^{-6}$  S. In other words, above 0.04 MWNTs form an interconnected percolative network. However, below 0.04, clusters of MWNT become separated by the polystyrene layers. From here we could conclude that the electrical conductivity of the films exhibited a type of percolation<sup>56</sup> behavior since below a certain amount of MWNT, called the percolation threshold,  $R_{c\sigma}$  ( $= 0.04$ ), the conductivity exhibited only a very little change ( $10^{-13}$ – $10^{-12}$  S). While for a further increase of MWNTs to above  $R_{c\sigma} = 0.04$ , the conductivity shows a drastic increase ca. 6–7 orders of magnitude ( $10^{-7}$ – $10^{-6}$  S), as compared with low MWNTs content films. Zang and co-workers<sup>57,58</sup> found the percolation threshold is about 4 wt% MWNT for the MWNT–PS composites prepared by the polymerization filling method.

### Percolation theory

The basis of the percolation theory is to determine how a

**Fig. 7.** (a) Conductivity,  $\sigma$ , and its best fitted curve vs. MWNT content,  $R$  (w/w); (b) log-log plot of the best fitted curve of  $\sigma$  vs.  $(R - R_c)$ .

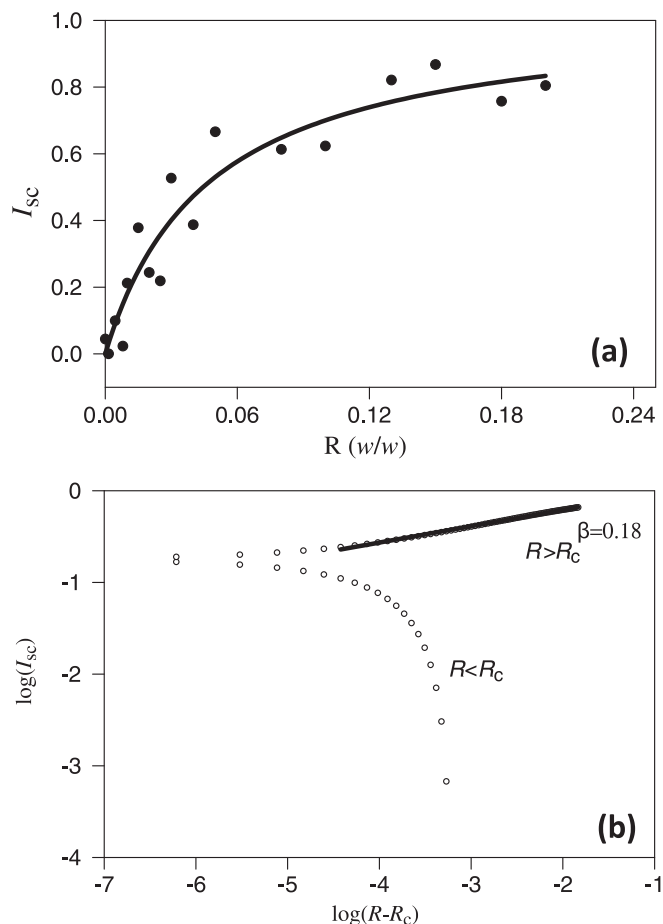


given set of sites, regularly or randomly positioned in some space, is interconnected.<sup>56</sup> At some critical probability, called the “percolation threshold ( $p_c$ )”, a connected network of sites is formed that spans the sample, causing the system to percolate. In 1957, Broadbent and Hammersley,<sup>59</sup> introduced the term “percolation theory” and used a geometrical and statistical approach to solve the problem of fluid flow through a static medium. Initial work focused on the determination of the percolation thresholds in simple two- and three-dimensional geometries. Two types of percolation were considered: site percolation, where sites in a lattice are either filled or empty, or bond percolation, where all the sites in a lattice are occupied, but are either connected or not.<sup>60</sup> Extensive simulations and theoretical work have shown that the percolation probability,  $P_\infty(p)$  vanishes as a power-law near  $p_c$ :

$$[15] \quad p_\infty(p) \approx (p - p_c)^\beta$$

For all volume fractions  $p > p_c$ , the probability of finding a spanning cluster extending from one side of the system to the other side is 1. The largest cluster spans the lattice connecting the left and right edges to the bottom edge, which is called “percolating cluster”. Whereas for all volume fractions  $p < p_c$ , the probability of finding such an infinite cluster is 0.

**Fig. 8.** (a) Scattering light intensity,  $I_{sc}$ , and its best fitted curve vs. MWNT content,  $R$  (w/w); (b) log-log plot of the best fitted curve of  $I_{sc}$  versus  $(R - R_c)$ .



The concept of percolation has been applied to many diverse applications, including the spread of disease in a population, flow through a porous medium, quarks in nuclear matter, and variable range hopping in amorphous semiconductors.<sup>61</sup> Percolation theory has been used to interpret the behaviour in a mixture of conducting and nonconducting components.<sup>62</sup> The sudden transition in such materials from insulator to conductor is evidence of a percolation threshold. The conductivity,  $\sigma$ , of a percolative system is generally described as a function of the mass fraction,  $R$ , by the scaling law in the vicinity of the percolation threshold ( $R_{c\sigma}$ ):

$$[16] \quad \sigma = \sigma_0(R - R_{c\sigma})^{\beta_\sigma}$$

where  $\sigma$  is the composite conductivity (in Siemens),  $\sigma_0$  is the self conductivity of MWNTs film and is equal to 1.  $R$  represents the weight fraction of MWNTs,  $R_{c\sigma}$  represents the percolation threshold of conductivity, and  $\beta_\sigma$  is the critical exponent. This equation is valid at concentrations above the percolation threshold, i.e., when  $R > R_{c\sigma}$ . The value of the critical exponents,  $\beta_\sigma$ , is dependent on the dimensions of the lattice.<sup>59</sup>

To calculate the percolation threshold, eq. [16] was transformed into the logarithmic form:

$$[17] \quad \log(\sigma) = \log(\sigma_0) + \beta_\sigma \log|R - R_c|$$

Then to produce an estimated value for  $R_{c\sigma}$  and the critical exponent  $\beta_\sigma$  we fitted the  $\log(\sigma) - \log|R - R_c|$  data in Fig. 7b for  $R > R_{c\sigma}$  to eq. [17]. Here, due to the limitation on getting more data in critical region, we used the continuous function fitted best to the experimental points in Fig. 7a. The goodness of the fit was around  $r^2 \approx 0.9$ . The value of  $\beta_\sigma$  has been determined from the slope of the linear relation of  $\log(\sigma) - \log|R - R_c|$  plot of the best fitted curve in Fig. 7b and found to be 2.27. This value agrees well with the universal scaling value of  $\beta_\sigma = 2.0$ . The difference between the theoretical and experimental values (13.5%) might be explained with the errors originating from the fitting. In three-dimensional lattice systems<sup>60</sup>  $\beta_\sigma$  values change from 1.3 to 3. The fact that  $\beta_\sigma$  is not significantly greater than 2.0 also suggests that the bundles are not separated by polymer tunneling barriers and shows that the polymer coating observed in Fig. 5 cannot simply coat individual bundles but must coat the network as a whole, allowing intimate contact between bundles at junction sites.

On the other hand, as seen in Fig. 4a, the inclusion of MWNTs into the PS lattice strongly decreases the transmitted light intensity. This finding can be rationalized by first assuming that  $\sigma$  is proportional to the scattered light intensity,  $I_{sc} = 1 - (I_{tr})_{max}$ , by obeying the following relation

$$[18] \quad I_{sc}(R) = (R - R_c)^\beta$$

Here, it should be realized that inclusions of MWNTs into the PS lattice creates a two phase heterogeneous structure, which causes light scattering from the composite film surface, while the conductivity increases in the same fashion. Equation [18] describes the percolation model for MWNTs distribution in the PS lattice where  $R_c$  was produced in Fig. 4b from the intersection of two broken straight lines. When  $R$  approaches  $R_c$ , the largest cluster of MWNTs appears by connecting the left and right edges to the bottom edge of the MWNTs.

The scattered light intensity,  $I_{sc}$ , versus MWNTs content and its best fit are plotted in Fig. 8a, where it is seen that  $I_{sc}$  has increased to large values for all samples above 4 wt% MWNT content. This behavior of scattering light intensity can be explained by percolating MWNT particles in the PS lattice. In Fig. 8b, the log-log plot of eq. [18] is fitted to the data in Fig. 8a, where the slope of the straight line produced the critical exponent,  $\beta = 0.18$ , above  $R_c = 0.04$ , which is not so far from the bond-percolation theory. In a simple cubic lattice  $\beta$  is found to be 0.25 for the bond percolation model.<sup>56</sup>

## Conclusions

We have reported an investigation of the film formation and electrical conductivity of PS-MWNT composites. Below 10 wt% MWNT content, two distinct film formation stages, which are named as void closure and interdiffusion, were observed. However, MWNT concentrations above 10 wt% MWNT, no film formation can be achieved. On the other hand, sample conductivities were observed to depend strongly on the MWNT contents, which are drastically changed with an increase of the MWNT content above the percolation threshold of 4 wt% MWNT. With the introduction of 4 wt% MWNTs, the conductivity presented an in-

crease by 6–7 orders of magnitude compared with low MWNT content films.

Void closure ( $\Delta H$ ) and interdiffusion ( $\Delta E$ ) activation energies presented optimum values around the threshold of the electrical conductivity and optical transparency percolation around 4 wt% MWNT content. Our results are quite similar to other reports on low conductance with CNTs amounts and start to saturate at higher CNTs content. Further investigation of electrical properties of the composite films is underway in our laboratory to understand the behaviors of ( $\Delta H$ ) and ( $\Delta E$ ) activation energies around the percolation point.

## Acknowledgement

Professor Pekcan would like to thank the Turkish Academy of Sciences for their partial support.

## References

- (1) *Film Formation in Waterborne Coatings*; Provder, T., Winnik, M. A., Urban, M. W., Eds., ACS Symposium Series 648; American Chemical Society: Washington, DC, 1996.
- (2) Sperry, P. R.; Snyder, B. S.; O'Dowd, M. L.; Lesko, P. M. *Langmuir* **1994**, *10* (8), 2619. doi:10.1021/la00020a021.
- (3) Mackenzie, J. K.; Shuttleworth, R. *Proc. Phys. Soc.* **1949**, *62B*, 833. doi:10.1088/0370-1301/62/12/310.
- (4) Keddie, J. L. *Mater. Sci. Eng.* **1997**, *R21*, 101.
- (5) Yoo, J. N.; Sperling, L. H.; Glinka, C. J.; Klein, A. *Macromolecules* **1991**, *24* (10), 2868. doi:10.1021/ma00010a036.
- (6) Pekcan, Ö. *Trends Polym. Sci.* **1994**, *2*, 236.
- (7) Baughman, R. H.; Zakhidov, A. A.; de Heer, W. A. *Science* **2002**, *297* (5582), 787. doi:10.1126/science.1060928. PMID: 12161643.
- (8) Coleman, J. N.; Khan, U.; Blau, W. J.; Gun'ko, Y. K. *Carbon* **2006**, *44* (9), 1624. doi:10.1016/j.carbon.2006.02.038.
- (9) Ajayan, P. M.; Zhou, O. Z. *Top. Appl. Phys.* **2001**, *80*, 391. doi:10.1007/3-540-39947-X\_14.
- (10) Bigg, D. M.; Stutz, D. E. *Polym. Compos.* **1983**, *4* (1), 40. doi:10.1002/pc.750040107.
- (11) Grunlan, J. C.; Mehrabi, A. R.; Bannon, M. V.; Bahr, J. L. *Adv. Mater.* **2004**, *16* (2), 150. doi:10.1002/adma.200305409.
- (12) Kymakis, E.; Alexandou, I.; Amaratunga, G. A. J. *Synth. Met.* **2002**, *127* (1–3), 59. doi:10.1016/S0379-6779(01)00592-6.
- (13) Sandler, J. K. W.; Kirk, J. E.; Kinloch, I. A.; Shaffer, M. S. P.; Windle, A. H. *Polymer (Guildf.)* **2003**, *44* (19), 5893. doi:10.1016/S0032-3861(03)00539-1.
- (14) Bin, Y.; Kitanaka, M.; Zhu, D.; Matsuo, M. *Macromolecules* **2003**, *36* (16), 6213. doi:10.1021/ma0301956.
- (15) Sandler, J.; Shaffer, M. S. P.; Prasse, T.; Bauhofer, W.; Schulte, K.; Windle, A. H. *Polymer (Guildf.)* **1999**, *40* (21), 5967. doi:10.1016/S0032-3861(99)00166-4.
- (16) Murphy, R.; Nicolosi, V.; Hernandez, Y.; McCarthy, D.; Rickard, D.; Vrbancic, D.; Mrzel, A.; Mihailovic, D.; Blau, W. J.; Coleman, J. N. *Scr. Mater.* **2006**, *54* (3), 417. doi:10.1016/j.scriptamat.2005.10.015.
- (17) Ramasubramaniam, R.; Chen, J.; Liu, H. Y. *Appl. Phys. Lett.* **2003**, *83* (14), 2928. doi:10.1063/1.1616976.
- (18) Barrau, S.; Demont, P.; Peigney, A.; Laurent, C.; Lacabanne, C. *Macromolecules* **2003**, *36* (14), 5187. doi:10.1021/ma021263b.
- (19) Ruan, S. L.; Gao, P.; Yang, X. G.; Yu, T. X. *Polymer (Guildf.)* **2003**, *44* (19), 5643. doi:10.1016/S0032-3861(03)00628-1.

- (20) Geng, H.; Rosen, R.; Zheng, B.; Shimoda, H.; Fleming, L.; Liu, J.; Zhou, O. *Adv. Mater.* **2002**, *14* (19), 1387. doi:10.1002/1521-4095(20021002)14:19<1387::AID-ADMA1387>3.0.CO;2-Q.
- (21) Jin, L.; Bower, C.; Zhou, O. *Appl. Phys. Lett.* **1998**, *73* (9), 1197. doi:10.1063/1.122125.
- (22) Qian, D.; Dickey, E. C.; Andrews, R.; Rantell, T. *Appl. Phys. Lett.* **2000**, *76* (20), 2868. doi:10.1063/1.126500.
- (23) Tang, B. Z.; Xu, H. *Macromolecules* **1999**, *32* (8), 2569. doi:10.1021/ma981825k.
- (24) Barrau, S.; Demont, P.; Perez, E.; Peigney, A.; Laurent, C.; Lacabanne, C. *Macromolecules* **2003**, *36* (26), 9678. doi:10.1021/ma030399m.
- (25) Jin, Z.; Huang, L.; Goh, S. H.; Xu, G.; Ji, W. *Chem. Phys. Lett.* **2000**, *332* (5–6), 461. doi:10.1016/S0009-2614(00)01294-X.
- (26) Schadler, L. S.; Giannaris, S. C.; Ajayan, P. M. *Appl. Phys. Lett.* **1998**, *73* (26), 3842. doi:10.1063/1.122911.
- (27) Gojny, F. H.; Wichmann, M. H. G.; Fiedler, B.; Kinloch, I. A.; Bauhofer, W.; Windle, A. H.; Schulte, K. *Polymer (Guildf.)* **2006**, *47* (6), 2036. doi:10.1016/j.polymer.2006.01.029.
- (28) McNally, T.; Pötschke, P.; Halley, P.; Murphy, M.; Martin, D.; Bell, S. E. J.; Brennan, G. P.; Bein, D.; Lemoine, P.; Quinn, J. P. *Polymer (Guildf.)* **2005**, *46* (19), 8222. doi:10.1016/j.polymer.2005.06.094.
- (29) Stadermann, M.; Papadakis, S. J.; Falvo, M. R.; Novak, J.; Snow, E.; Fu, Q.; Liu, J.; Fridman, Y.; Boland, J.; Superfine, R.; Washburn, S. *Phys. Rev. B* **2004**, *69* (20), 201402R. doi:10.1103/PhysRevB.69.201402.
- (30) Fuhrer, M. S.; Nygard, J.; Shih, L.; Forero, M.; Yoon, Y. G.; Mazzoni, M. S. C.; Choi, H. J.; Ihm, J.; Louie, S. G.; Zettl, A.; McEuen, P. L. *Science* **2000**, *288* (5465), 494. doi:10.1126/science.288.5465.494. PMID:10775104.
- (31) Yi, Y. B.; Berhan, L.; Sastry, A. M. *J. Appl. Phys.* **2004**, *96* (3), 1318. doi:10.1063/1.1763240.
- (32) Berhan, L.; Sastry, A. M. *Phys. Rev. E: Stat. Nonlinear Soft Matter Phys.* **2007**, *75* (4), 041121. PMID:17500879.
- (33) Fisher, F. T.; Bradshaw, R. D.; Brinson, L. C. *Compos. Sci. Technol.* **2003**, *63* (11), 1689. doi:10.1016/S0266-3538(03)00069-1.
- (34) Shi, D. L.; Feng, X. Q.; Huang, Y. G. Y.; Hwang, K. C.; Gao, H. J. *J. Eng. Mater. Technol.* **2004**, *126* (3), 250. doi:10.1115/1.1751182.
- (35) Wu, S.-H.; Masaharu, I.; Natsuki, T.; Ni, Q.-Q. *J. Reinf. Plast. Compos.* **2006**, *25* (18), 1957. doi:10.1177/0731684406069923.
- (36) Li, C. Y.; Thostenson, E. T.; Chou, T. W. *Compos. Sci. Technol.* **2008**, *68* (6), 1445. doi:10.1016/j.compscitech.2007.10.056.
- (37) Li, C. Y.; Chou, T. W. *J. Phys A: Math. Theor.* **2007**, *40*, 14679. doi:10.1088/1751-8113/40/49/004.
- (38) Du, F. M.; Fischer, J. E.; Winey, K. I. *J. Polym. Sci., Part B: Polym. Phys.* **2003**, *41* (24), 3333. doi:10.1002/polb.10701.
- (39) Du, F. M.; Fischer, J. E.; Winey, K. I. *Phys. Rev. B* **2005**, *72* (12), 121404. doi:10.1103/PhysRevB.72.121404.
- (40) Arda E, Bulmus V, Piskin E. *J. Colloid Interface Sci.* **1999**, *213* (1), 160. doi:10.1006/jcis.1998.6051.
- (41) Arda, E.; Pekcan, Ö. *Polymer (Guildf.)* **2001**, *42* (17), 7419. doi:10.1016/S0032-3861(01)00131-8.
- (42) Pekcan, Ö.; Arda, E.; Kesenci, K.; Pişkin, E. *J. Appl. Polym. Sci.* **2001**, *79*, 2014. doi:10.1002/1097-4628(20010314)79:11<2014::AID-APP1010>3.0.CO;2-3.
- (43) Pekcan, Ö.; Arda, E. *Encyclopedia of Surface and Colloid Science*; Marcel and Dekker: New York, 2002; p 2691.
- (44) Pekcan, Ö.; Arda, E.; Bulmuş, V.; Pişkin, E. *J. Appl. Polym. Sci.* **2000**, *77* (4), 866. doi:10.1002/(SICI)1097-4628(20000725)77:4<866::AID-APP21>3.0.CO;2-9.
- (45) Arda, E.; Özer, F.; Pişkin, E.; Pekcan, Ö. *J. Colloid Interface Sci.* **2001**, *233* (2), 271. doi:10.1006/jcis.2000.7234. PMID:11121276.
- (46) Arda, E.; Pekcan, Ö. *Polymer (Guildf.)* **2001**, *42* (17), 7419. doi:10.1016/S0032-3861(01)00131-8.
- (47) Uður, S.; Yargı, Ö.; Pekcan, Ö. *Compos. Interfaces* **2008**, *15* (4), 411. doi:10.1163/156855408784514748.
- (48) Keddie, J. L.; Meredith, P.; Jones, R. A. L.; Donald, A. M. *Film Formation in Waterborne Coatings*; Provdner, T., Winnik, M. A., Urban, M.W., Eds.; ACS Symposium Series 648; American Chemical Society: Washington, DC, 1996; pp 332–348.
- (49) Mc Kenna, G. B. In *Comprehensive Polymer Science*; Booth, C., Price C., Eds.; Pergamon Press: Oxford, UK, 1989; p 2.
- (50) Vogel, H. *Phys. Z.* **1925**, *22*, 645.
- (51) Fulcher, G. S. *J. Am. Ceram. Soc.* **1925**, *8* (6), 339. doi:10.1111/j.1151-2916.1925.tb16731.x.
- (52) Frenkel, J. *J. Phys. USSR* **1945**, *9*, 385.
- (53) (a) Prager, S.; Tirrell, M. *J. Chem. Phys.* **1981**, *75* (10), 5194. doi:10.1063/1.441871.; (b) Wool, R. P.; Yuan, B.-L.; McGarel, O. *J. Polym. Eng. Sci.* **1989**, *29* (19), 1340. doi:10.1002/pen.760291906.
- (54) de Gennes, P. G. *J. Chem. Phys.* **1982**, *76* (6), 3322. doi:10.1063/1.443329.
- (55) (a) Kim, Y. H.; Wool, R. P. *Macromolecules* **1983**, *16* (7), 1115. doi:10.1021/ma00241a013.; (b) Wool, R. P.; O'Connor, K. M. *J. Appl. Phys.* **1981**, *52* (10), 5953. doi:10.1063/1.328526.
- (56) Stauffer, D.; Aharony, A. *Introduction to Percolation Theory*; Taylor & Francis: London, 1994.
- (57) Dong, X. M.; Fu, R. W.; Zhang, M. Q.; Zhang, B.; Li, J. R.; Rong, M. Z. *Carbon* **2003**, *41* (2), 371. doi:10.1016/S0008-6223(02)00336-6.
- (58) Zhang, B.; Fu, R. W.; Zhang, M. Q.; Dong, X. M.; Lan, P. L.; Qiu, J. S. *Sens. Actuators, B* **2005**, *109* (2), 323. doi:10.1016/j.snb.2004.12.066.
- (59) Broadbent, S. R.; Hammersley, J. M. *Proc. Camb. Philos. Soc.* **1957**, *53* (03), 629. doi:10.1017/S0305004100032680.
- (60) Sahimi, M. *Applications of Percolation Theory* London: Taylor and Francis (1994).
- (61) Lux, F. *J. Mater. Sci.* **1993**, *28* (2), 285. doi:10.1007/BF00357799.
- (62) Kirkpatrick, S. *Rev. Mod. Phys.* **1973**, *45* (4), 574. doi:10.1103/RevModPhys.45.574.



# Biomaterials for neural-tissue engineering — Chitosan supports the survival, migration, and differentiation of adult-derived neural stem and progenitor cells

Vanessa I. Scanga, Alex Goraltchouk, Nasser Nussaiba, Molly S. Shoichet, and Cindi M. Morshead

**Abstract:** Neural precursor cells (NPCs or stem and progenitor cells) are promising in transplantation strategies to treat an injury to the central nervous system, such as a spinal cord injury (SCI), because of their ability to differentiate into neurons and glia. Transplantation studies to date have met with limited success for a number of reasons, including poor cell survival. One way to encourage cell survival in injured tissue is to provide the cells with a scaffold to enhance their survival, their integration, and potentially their differentiation into appropriate cell types. Towards this end, four amine-functionalized hydrogels were screened in vitro for adult murine NPC viability, migration, and differentiation: chitosan, poly(oligoethylene oxide dimethacrylate-co-2-amino ethyl methacrylate), blends of poly(oligoethylene oxide dimethacrylate-co-2-amino ethyl methacrylate), and poly(vinyl alcohol), and poly(glycerol dimethacrylate-co-2-amino ethyl methacrylate). The greatest cell viability was found on chitosan at all times examined. Chitosan had the greatest surface amine content and the lowest equilibrium water content, which likely contributed to the greater NPC viability observed over three weeks in culture. Only chitosan supported survival of multipotent stem cells and the differentiation of the progenitors into neurons, astrocytes, and oligodendrocytes. Plating intact NPC colonies revealed greater cell migration on chitosan relative to the other hydrogels. Importantly, long term cultures on chitosan showed no significant difference in total cell counts over time, suggesting no net cell growth. Together, these findings reveal chitosan as a promising material for the delivery of adult NPC cell-based therapies.

**Key words:** biomaterials, chitosan, hydrogels, stem cells, cell viability.

**Résumé :** Les cellules neurales précurseurs (CNP, cellules souches et progéniteurs) sont très prometteuses dans les stratégies de transplantation pour le traitement de blessures au système nerveux central, tel un traumatisme au cordon médullaire (TCM), en raison de leur habilité à différencier les neurones des cellules gliales. Jusqu'à maintenant, les études de transplantation n'ont eu que des succès mitigés en raison de divers facteurs, dont le faible taux de survie des cellules. Une façon d'augmenter ce taux de survie dans les tissus traumatisés est de fournir des cellules comportant un échafaudage permettant d'augmenter leur survie, leur intégration et éventuellement leur différenciation dans les divers types de cellules. À cette fin, quatre hydrogels portant des amines fonctionnalisées, le chitosane, le poly(diméthacrylate de l'oxyde d'oligoéthylène-co-2-aminométhacrylate d'éthyle), des mélanges de poly(diméthacrylate de l'oxyde d'oligoéthylène-co-2-aminométhacrylate d'éthyle) et d'alcool polyvinylique et du poly(diméthacrylate de glycérol-co-2-aminométhacrylate d'éthyle) ont été soumis à une évaluation in vitro, pour la migration, la différenciation et viabilité de cellules neurales précurseurs de murine adulte. Dans tous les cas, la viabilité la plus grande des cellules a été observée avec le chitosane. Le chitosane comporte le degré le plus élevé d'amine de surface et la quantité la plus faible d'eau en équilibre, ce qui a vraisemblablement contribué à la plus grande viabilité des cellules observée au cours de trois semaines en culture. Seul le chitosane a soutenu la survie de cellules souches multipotentes et la différenciation des progéniteurs en neurones, astrocytes et oligodendrocytes. Le plaqage de colonies intactes de NPC a révélé une migration plus grande sur le chitosane par rapport aux autres hydrogels. Importamment, les cultures à long terme sur le chitosane n'ont montré aucune différence significative dans les dénombrements de cellules au cours du temps, suggérant une croissance nette nulle. Ensemble, ces constatations révèlent le chitosane comme un matériau prometteur pour la délivrance de thérapies à base de cellules NPC adultes.

Received 1 September 2009. Accepted 16 November 2009. Published on the NRC Research Press Web site at [canjchem.nrc.ca](http://canjchem.nrc.ca) on 24 February 2010.

*This article is part of a Special Issue dedicated to Professor M. A. Winnik.*

**V.I. Scanga.** Institute of Medical Science, University of Toronto, Toronto, ON M5S 1A8, Canada; Department of Surgery, University of Toronto, Toronto, ON M5S 1A8, Canada.

**A. Goraltchouk.** Department of Chemical Engineering and Applied Chemistry, University of Toronto, Toronto, ON M5S 3E5, Canada; Institute of Biomaterials and Biomedical Engineering, University of Toronto, Toronto, ON M5S 3G9, Canada.

**N. Nussaiba.** Department of Surgery, University of Toronto, Toronto, ON M5S 1A8, Canada.

**M.S. Shoichet.**<sup>1</sup> Institute of Medical Science, University of Toronto, Toronto, ON M5S 1A8, Canada; Department of Chemical Engineering and Applied Chemistry, University of Toronto, Toronto, ON M5S 3E5, Canada; Institute of Biomaterials and Biomedical Engineering, University of Toronto, Toronto, ON M5S 3G9, Canada; Department of Chemistry, University of Toronto, Toronto, ON M5S 1A8, Canada.

**C.M. Morshead.** Institute of Medical Science, University of Toronto, Toronto, ON M5S 1A8, Canada; Department of Surgery, University of Toronto, Toronto, ON M5S 1A8, Canada; Institute of Biomaterials and Biomedical Engineering, University of Toronto, Toronto, ON M5S 3G9, Canada.

<sup>1</sup>Corresponding author (e-mail: [cindi.morshead@utoronto.ca](mailto:cindi.morshead@utoronto.ca)).

ment contribué à la plus grande viabilité des cellules neurales précurseurs sur une période de trois semaines dans les cultures. Seul le chitosane permet de supporter la survie de cellules souches à plusieurs composantes et de différencier les progéniteurs en neurones, astrocytes et oligodendrocytes. L'examen de plaques de colonies intactes de cellules neurales précurseurs met en évidence que la migration de ces cellules sur le chitosane est beaucoup plus rapide que sur les autres hydrogels. Les cultures à long terme sur le chitosane ne présentent pas de différences significatives dans les comptages totaux de cellules en fonction du temps; cette observation est importante puisqu'elle suggère qu'il ne supporte aucune croissance nette de cellules. Toutes ces observations mettent en évidence le fait que le chitosane est un matériau plein de promesses pour conduire à des thérapies basées sur les cellules neurales précurseurs adultes.

*Mots-clés* : biomatériaux, chitosane, hydrogels, cellules souches, viabilité des cellules.

[Traduit par la Rédaction]

## Introduction

Traumatic injury to the adult mammalian spinal cord causes irrevocable damage, producing an environment that inhibits regrowth of damaged axons.<sup>1–4</sup> The initial damage to the cord is compounded by a prolonged secondary cascade of injury including the disappearance of growth-promoting cues, the appearance of growth-inhibiting factors, apoptosis, and the formation of a glial scar. This series of post-injury cascades leads to the formation of a cystic cavity, axonal degeneration, and ultimately an inability of the adult cord to self-repair.<sup>5,6</sup> Regeneration of severed central-nervous-system (CNS) axons has been reported for both cellular bridges<sup>7–9</sup> and biomaterial implants;<sup>10–13</sup> however, functional recovery from these single application treatments has been limited. The complicated pathophysiology resulting from spinal cord injury (SCI) likely necessitates a combination strategy to promote axonal repair and regeneration. Neurons, astrocytes, and oligodendrocytes comprise the primary cell types of the CNS and because these cells die at the site of injury after SCI, cell replacement therapies will undoubtedly be key to combination strategies aimed at repairing the damaged spinal cord.

The therapeutic potential of CNS stem cells has received considerable attention.<sup>14–27</sup> The observation that stem-cell populations can be isolated from along the developing and adult neuroaxis<sup>28,29</sup> has led to the development of a number of cell-based therapies to treat SCI. In the context of developing regenerative-medicine strategies, the use of adult-derived populations is a significant step forward as it affords an approach that is independent of ethical concerns. Adult neural stem cells are maintained throughout the life of the animal in both the brain and spinal cord and have the capacity to self-renew and differentiate into astrocytes, oligodendrocytes, and neurons.<sup>28,30–33</sup> Neural stem cells can be isolated and propagated in vitro using a well-described colony-forming assay whereby individual stem cells proliferate in the presence of epidermal growth factor (EGF) and (or) fibroblast growth factor (FGF2) to form free-floating colonies of cells termed “neurospheres”. Individual neurospheres can be dissociated into single cells and replated in the presence of these growth factors to form new neurospheres thereby resulting in an expansion of neural stem-cell-derived cell populations, and demonstrating the cardinal stem cell property of self-renewal. Individual neurospheres are comprised of a mixed population of stem and progenitor cells<sup>31</sup> and are referred to collectively as neural precursor cells (NPCs). Upon exposure to differentiation conditions,

neurosphere-derived cells can differentiate into all of the neural phenotypes comprising the CNS (neurons, astrocytes, and oligodendrocytes), thereby illustrating their multipotentiality. The ability to proliferate and differentiate into CNS-specific cell types makes NPCs promising candidates for cell replacement strategies to replace cells lost after CNS injury.

The extracellular matrix during development influences cell adhesion, growth, differentiation, and motility<sup>34</sup> while at the same time contributing to tissue strength.<sup>35</sup> The regenerative ability in the damaged adult CNS is limited in large part due to the release of inhibitory matrix proteins and a breakdown in the structural scaffolding provided by the extracellular matrix to neurons, astrocytes, and oligodendrocytes.<sup>36,37</sup> Accordingly, bridging strategies provide attractive models of repair following damage to the nervous system and have included the use of nerve guides,<sup>38,39</sup> hydrogel scaffolds,<sup>40</sup> and tissue and cell transplants such as fetal tissue, Schwann cells, olfactory ensheathing glia, neural stem cells, and progenitor cells<sup>27,41–45</sup> as well as macrophages.<sup>46</sup> The partnership of some of these bridging strategies with the administration of neurotrophic<sup>47–49</sup> or survival<sup>50–53</sup> factors have clearly demonstrated the powerful effects of combination therapy in the treatment of this debilitating injury. However, these studies have shown only modest functional improvement. The extent of intrinsic cell renewal following the local delivery of mitogenic agents such as EGF and FGF2 to stimulate endogenous precursor cells<sup>47</sup> has also been insufficient in promoting significant recovery following SCI. Additionally, the poor survival rate of cells transplanted directly into the site of injury following SCI<sup>54</sup> reflects the need to provide a better environment for cell survival. Work by Karimi-Abdolrezaee et al.<sup>14</sup> has shown that combining NPC transplantation and the delivery of growth factors via an osmotic mini-pump leads to a dramatic increase in cell survival and differentiation and, moreover, leads to measurable functional recovery. Hence, we propose that a nerve guidance channel that is biodegradable, biocompatible, supportive of NPC survival and differentiation, and amenable to the incorporation of a drug delivery system will promote axon regeneration following SCI. Towards this end, we set out to identify the microenvironment, and specifically the matrix material, that met the specific criteria of NPC viability, migration, and differentiation.

Four polymeric biomaterials were screened using neurosphere-derived NPCs isolated from the forebrain of adult mice. These biomaterials were required to be biode-

gradable, amine-functionalized (to promote cell adhesion), non-cytotoxic, and capable of being processed into a nerve guidance channel. The following biomaterials were compared in terms of NPC viability, cell migration, and differentiation: (i) chitosan, a naturally-derived polysaccharide; (ii) poly(oligoethylene oxide dimethacrylate-*co*-2-amino ethyl methacrylate), P(PEG-*co*-AEMA); (iii) blends of P(PEG-*co*-AEMA) and poly(vinyl alcohol) (PVA), P(PEG-*co*-AEMA)-PVA; and (iv) poly(glycerol dimethacrylate-*co*-2-amino ethyl methacrylate), P(GDMA-*co*-AEMA). Chitosan was studied because it has already demonstrated some promise in neural-tissue engineering<sup>55</sup> and PEG-AEMA based polymers were synthesized with the understanding that PEG would be biocompatible<sup>56</sup> while AEMA would provide amine functional groups for enhanced cell adhesion.

## Materials and methods

### Materials

All reagents were purchased from Sigma-Aldrich and used as received unless otherwise stated. Poly(ethylene glycol) dimethacrylate (PEGDMA, molecular weight: 400 Da) and poly(vinyl alcohol) (PVA, molecular weight: 6000 Da, hydrolyzed to 80%) were purchased from PolySciences Inc. (Warrington, PA, USA). The MicroBCA Protein Assay Kit was purchased from Pierce (Rockford, IL, USA). Deionized water was obtained from Milli-RO 10 Plus and Milli-Q UF Plus (Bedford, MA, USA) and used at 18 M $\Omega$  resistance.

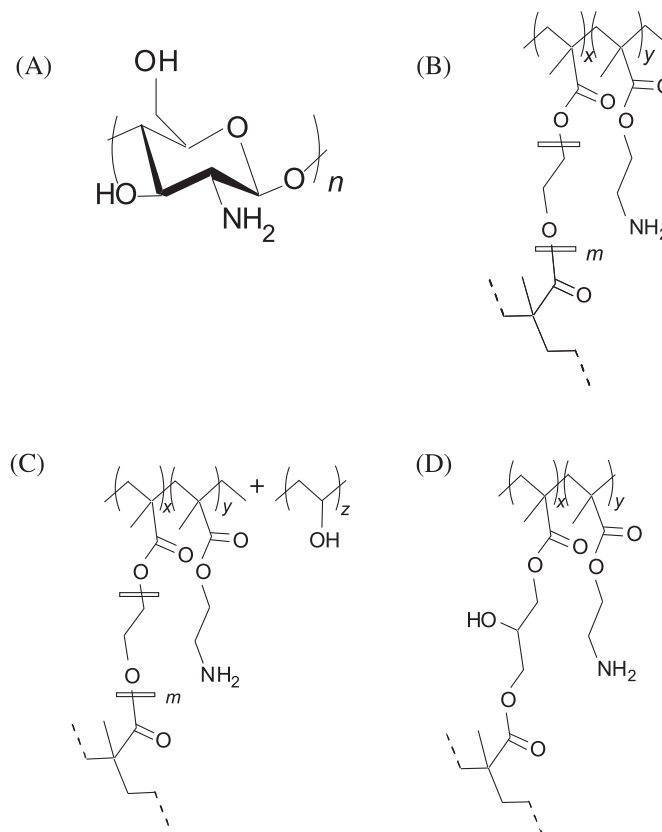
### Preparation of chitosan films

Deacetylated chitosan films were prepared from chitosan (NovaMatrix, Norway,  $M_w$ : approximately 150 000–400 000 g/mol) by two successive alkaline hydrolysis steps with 40 wt% NaOH solution at 100 °C for 1 h. The hydrolyzed flakes were washed to neutrality with water and lyophilized using the Thermo Savant ModulyoD freeze dryer at –50 °C and 1.5 mbar pressure. Following lyophilization, 5 g of deacetylated chitosan flakes were added to 166.7 mL of 2 wt% acetic acid in water solution (2/3 working solution). A stock neutralization solution was prepared by mixing 30 mL of ammonia with 70 mL of water and 900 mL of ethanol. Five to six g of the chitosan working solution was poured into a 10 cm Petri dish and allowed to stand uncovered for 24 h. The air-dried films were then washed twice with 20 mL of neutralization solution for 1 h each time. The neutralized films were then washed with PBS and allowed to dry overnight (Fig. 1A).

### Synthesis of PEGDMA-*co*-AEMA films

One g of PEGDMA was added to 20 mL of water in a 30 mL vial. The solution was vortexed and 20  $\mu$ L of concentrated phosphoric acid was added to keep the pH below 4.0. One gram of 2-amino ethyl methacrylate (AEMA) was added to the solution and allowed to completely dissolve. Stock solutions of 10 wt% ammonium persulfate (APS) and 10 wt% sodium metabisulfite (SMBS) in water were prepared. After complete dissolution of the monomers, 100  $\mu$ L of each of the APS and SMBS stock solutions were added, and the solution was vortexed and transferred to a 10 cm Petri dish for polymerization at 37 °C for 24 h (Fig. 1B).

**Fig. 1.** Four amine-functionalized polymer films were synthesized to assay neural precursor cell - matrix interaction: (A) chitosan, (B) poly(oligoethylene oxide dimethacrylate-*co*-2-amino ethyl methacrylate [P(PEGDMA-*co*-AEMA)], (C) physically blended poly(vinyl alcohol) and P(PEGDMA-*co*-AEMA) [P(PEGDMA-*co*-AEMA)-PVA], and (D) poly(glycerol dimethacrylate-*co*-2-amino ethyl methacrylate) [P(GDMA-*co*-AEMA)].



The disks were washed 3 times with PBS for 1 h each time and then washed in PBS overnight prior to use. We did not expect any adverse response due to residual APS-SMBS based on previously published results.<sup>55</sup>

### Synthesis of PEGDMA-*co*-AEMA-blend-PVA films

The identical method as described for the synthesis of PEGDMA-*co*-AEMA films was followed with the dissolution of the PEGDMA in 20 mL of a 5 wt% solution of PVA (6000 Da) in water instead of water alone in the first step (Fig. 1C).

### Preparation of GDMA-*co*-AEMA films

One g of glycerol dimethacrylate (GDMA) and 20  $\mu$ L of concentrated phosphoric acid were dissolved in a 1:1 (v/v) mixture of water and acetone. After the pH was lowered to pH < 4.0, to minimize rearrangement of the AEMA monomer via the acyl migration mechanism, 1 g of AEMA was added to the solution. Upon complete dissolution of all the monomers, 100  $\mu$ L of the APS and SMBS stock solutions were added, and the solution was vortexed and transferred to a 10 cm glass Petri dish covered with a glass slide. The dish with the polymerizing mixture was placed in an oven at 83 °C for 40 min. Soon after gelation, but prior to the



change in turbidity, the films were cooled to room temperature and 10 mL of water added (Fig. 1D).

### Analysis of polymer films

Polymer films were analyzed for equilibrium water content (EWC) according to eq. [1].

$$[1] \quad EWC = \frac{m_w - m_d}{m_d}$$

Wet mass ( $m_w$ ) was measured after allowing 5 mm disks of each material to swell in water for 2 weeks. Dry mass ( $m_d$ ) was measured after freeze-drying. The surface chemical composition was analyzed by X-ray photoelectron spectroscopy (XPS) in survey mode and for specific elements (C, N, O) using the Mg K $\alpha$  X-ray photoelectron spectrometer [Leybold (SPECS) Max 200].

### Isolation and culturing neural precursor cells

Neural precursor cells (NPCs) were isolated from the subependyma lining the lateral ventricles in the forebrain of adult CD1 mice (Charles River) as previously described.<sup>57</sup> Bulk cultures were maintained at clonal densities (10 cell/ $\mu$ L) in 1% penicillin–streptomycin serum-free medium (P/S-SFM) supplemented with EGF (20 ng/mL), FGF2 (10 ng/mL), and heparin (7.32 ng/mL) according to Tropepe et al. All supplements were purchased from Sigma-Aldrich (Oakville, ON, CA). The cultures were passaged weekly<sup>57</sup> to a maximum of three weeks.

### NPC plating and immunocytochemistry

Prior to cell plating, the polymer biomaterial films (8.6 mm<sup>2</sup>) were disinfected with 100% ethanol for 5 min, followed immediately by three serial washes in standard phosphate-buffered saline. The films were placed at 37 °C for 2–3 h prior to cell plating. Cell populations were plated at a density of  $3 \times 10^4$  single cells/film by slowly pipetting cells across the surface of the material. At 24 h, the plates were examined to ensure that there was no clumping of cells over the film surface. Cell migration studies involved plating 10 whole neurospheres onto the surfaces of each of the biomaterials tested and comparing to Matrigel™ controls. Cell counts were conducted in five non-overlapping areas of the polymer films as observed in 10 $\times$  fields of view of each sample area. An in-vitro experimental paradigm was established to analyze the viability of cells within a defined time course. Cell-seeded films were exposed to standard neurosphere-forming media described above followed by the addition of fetal bovine serum (+FBS) on day 2 post-plating to induce differentiation. Cultures were maintained for 2, 7, or 19 days after the addition of FBS and cell-seeded discs were analyzed at 4 (2 days with EFH + 2 days with FBS), 9 (2 + 7), and 21 (2 + 19) days post-seeding. Day-21 samples received new media every 7 days. Sample counts of Hoechst-positive cells were made at 10 $\times$  magnification per field of view. To compare cell counts over time and in the center and periphery of the film surfaces, 50% of the total film area was defined as the center area and 50% defined as the perimeter area. In all cases, 6–10 individual wells containing single material discs ( $n \geq 3$  independent trials) were analysed per group, per trial. In a separate set of experi-

ments, cell viability on chitosan was analysed and compared to Matrigel™ using a PicoGreen assay (Invitrogen) on d0, 2, 4, 9, and 21 post-plating ( $n = 3$  discs/trial from 3 independent trials). NPCs were plated in growth factor conditions for 2 days followed by 1% FBS for an additional 2, 7, or 19 days, similar to the Hoechst counting study described above. Cells were lysed off the films, and along with d0 samples, lysates were stored at –80 °C. Lysates were processed according to the manufacturer's instructions and DNA content was measured using a fluorescent microplate reader (excitation 480 nm, emission 520 nm). The concentration of dsDNA per lysate sample was converted to an estimation of total viable cells (6.05  $\mu$ g DNA / diploid mammalian cell).

To determine whether neural stem cells persisted on chitosan following exposure to differentiation conditions, cells plated on chitosan or Matrigel™ for 9 d were lifted from chitosan surfaces by washing three times with standard PBS followed by a 5 min incubation in 500  $\mu$ L of 0.25% trypsin-EDTA at 37 °C. Each well sample was triturated five times using a fire-polished glass pipette to dislodge the cells from chitosan surfaces. Cells were centrifuged for 5 min at 1500 rpm, and the supernatant was replaced with a 10 mg / 15  $\mu$ L solution of trypsin inhibitor (Roche) followed by centrifugation (5 min at 1500 rpm). The supernatant was replaced with 500  $\mu$ L SFM including EGF, FGF2, and heparin. Cells were replated onto non-adherent 24-well plates and neurosphere formation was assayed 7–9 days later. Recovered neurospheres were dissociated and passaged in standard neurosphere culture conditions and the presence of new neurospheres was assayed after 7 days. Neurosphere-derived cells were plated in 1% fetal bovine serum to examine their differentiation profile using standard immunocytochemistry as described below.

Immunocytochemistry was conducted as reported.<sup>57,58</sup> Briefly, single cells derived from dissociated neurospheres were plated onto the surfaces of biomaterials in 1% P/S-SFM containing FBS in the presence of growth factors following the culture conditions described above. Two, 7, and 19 days after plating the cell-seeded materials were fixed with 4% paraformaldehyde for 20 min. Cells were stained with antibodies to glial fibrillary acidic protein (GFAP, 1:400 rabbit polyclonal, Chemicon), nestin (1:1000 mouse monoclonal, Chemicon),  $\beta$ III tubulin (1:500 mouse monoclonal, Sigma-Aldrich) and O<sub>4</sub> (1:75 mouse monoclonal, Chemicon). Hoechst 33258 (0.725  $\mu$ L/mL, Sigma-Aldrich) was used to visualize the nuclei of plated cells to estimate the total number of cells as described above. To determine the percentages of differentiated cell types, the number of immunolabeled cells was counted and expressed as a percentage of the total number of Hoechst positive cells from 5 nonoverlapping fields of view per well ( $\geq 3$  wells/group/antibody,  $n \geq 3$  independent trials). Appropriate secondary antibodies (FITC or Alexa goat anti-rabbit, goat anti-mouse; FITC, or TRITC (1:200) from Jackson, Alexa (1:400) antibodies from Molecular Probes) were used. Secondary-only controls were prepared in the same manner as cell-plated biomaterials with 10% normal goat serum (Jackson) replacing primary antibodies. Cells were visualized on an Olympus IX70 fluorescent microscope with Olympus Microsuite Software.



### Statistical analysis

Student *t* test was performed for statistical analysis with 95% confidence using Microsoft Excel statistical software.

## Results

### Cell counts are greater on chitosan compared with P(PEGDMA-*co*-AEMA), P(PEGDMA-*co*-AEMA)-PVA blends and P(GDMA-*co*-AEMA)

A key limitation with cell transplantation is the poor rate of cell survival following implantation. For improved therapeutic efficacy following nervous system damage, an increased rate of cell survival is key to success. To determine which of the four biomaterials examined (chitosan, P(PEGDMA-*co*-AEMA), P(PEGDMA-*co*-AEMA)-PVA blend, or P(GDMA-*co*-AEMA)) best supports cell adhesion and viability of neurosphere-derived NPCs, the nuclear marker Hoechst was used to compare cell counts at 4 and 9 d post-plating. Cells showed a relatively even distribution on each material surface at 24 h post-plating; however this changed over time, depending on the material. As shown in Fig. 2A, at 4 d there were significantly more NPCs on chitosan at  $2.33 \pm 0.053 \times 10^3$  (comparable to Matrigel™ at  $2.00 \pm 0.01 \times 10^3$ ) than on the other hydrogel polymers studied, with the fewest number of NPCs found on P(GDMA-*co*-AEMA), followed by P(PEGDMA-*co*-AEMA), and P(PEGDMA-*co*-AEMA)-PVA. The low number of NPCs present on the synthetic polymer surfaces between d4 and d9 reflects either poorly maintained cell adhesion or poor cell survival. The lack of cell survival was further highlighted by the appearance of smaller nuclei,<sup>59</sup> which is indicative of poor cell viability, at both d4 and d9 on P(GDMA-*co*-AEMA), P(PEGDMA-*co*-AEMA), and P(PEGDMA-*co*-AEMA)-PVA (Figs. 2B and 2C). Both chitosan and Matrigel™ controls showed greater total numbers of cells surviving on d9 relative to d4, suggesting proliferation of NPCs between these two time points. This proliferation of NPCs observed on chitosan between d4 and d9 prompted the examination of longer survival times in culture because the continued proliferation of cells would be an undesirable attribute of the cell-material interaction. Cell counts on chitosan and Matrigel™ plated for 4, 9, and 21 d in vitro revealed that by d21 the total number of Hoechst-positive cells was not significantly different from the d4 counts on either matrix ( $p = 0.17$  for d4 compared to d21 on Matrigel™ and  $p = 0.21$  for d4 compared to d21 on chitosan). A PicoGreen assay was also performed at 2, 4, 9, and 21 days post-plating to determine the number of viable cells over time and relative to day 0. The assay employs a fluorochrome that selectively binds double-stranded DNA and can be used to extrapolate the numbers of viable cells per sample. We determined the numbers of viable cells at day 2 (prior to the addition of FBS) as a baseline to reflect the amount of cell death that occurred following initial plating. We observed a decrease in the numbers of cells on both chitosan and Matrigel™ on day 2 (Fig. 2D); however, between d4 and d9, we observed a 1.6- and 1.7-fold increase in the numbers of viable cells on chitosan and Matrigel™, respectively, and similar to what was observed with the Hoechst counts (Fig. 2A). As with the Hoechst analysis, the numbers of viable cells on day 21 was not

significantly different from the numbers present on d4. Overall, these data suggest that chitosan supports greater NPC survival and not uncontrolled cell proliferation. While chitosan and Matrigel™ demonstrated similar cell survival, Matrigel™ is derived from a mouse sarcoma and consists of a multitude of proteins and factors that would not be acceptable for implantation. Moreover, unlike chitosan, Matrigel™ cannot be easily processed into a nerve guidance channel. Taken together, these data suggest that chitosan is the most promising of the materials tested in terms of promoting cell adhesion and survival.

### XPS and EWC analyses

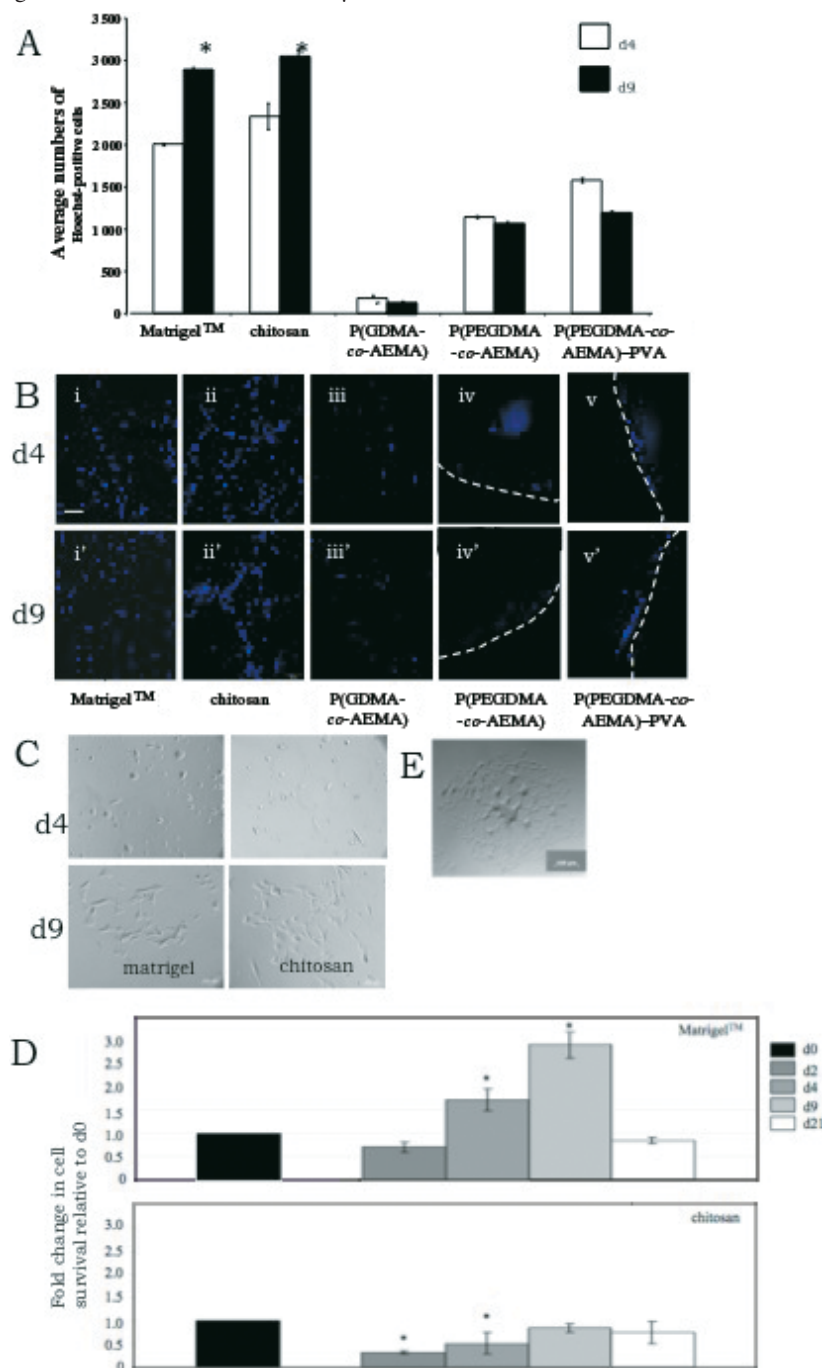
To better understand the NPC-matrix interaction, chitosan, P(GDMA-*co*-AEMA), P(PEGDMA-*co*-AEMA), and P(PEGDMA-*co*-AEMA)-PVA were analyzed by X-ray photoelectron spectroscopy (XPS) for surface composition and bulk equilibrium water content (EWC). As shown in Table 1, of the four biomaterials tested, chitosan had the highest nitrogen content ( $2.75 \pm 0.45$ ) and thus the highest amine surface concentration, reflecting that it is approximately  $99.2 \pm 0.5\%$  deacetylated chitin.<sup>60</sup> Interestingly, chitosan also had the lowest EWC. Our finding that NPC counts are greatest on chitosan is in agreement with Freier et al. who suggested that the higher amine content in chitosan results in increased cell viability relative to films with lower cationic ammonium charge, likely because of non-specific interactions with the negatively charged cell membranes.<sup>60</sup> P(GDMA-*co*-AEMA), P(PEGDMA-*co*-AEMA), and P(PEGDMA-*co*-AEMA)-PVA have significantly greater water content and thus were more hydrophilic than chitosan, reflecting the significant water capacity of PEG and AEMA hydrogels. PEG has been used repeatedly to limit cell adhesion<sup>61</sup> and protein adsorption;<sup>62</sup> thus, despite copolymerization with AEMA to introduce amine functional groups, the high water content likely contributed to the limited cell adhesion and viability observed.

### Neural precursor colony adhesion

Based on the XPS and EWC analysis performed, we hypothesized that a greater initial adhesion of NPCs to the chitosan surface relative to P(GDMA-*co*-AEMA), P(PEGDMA-*co*-AEMA), and P(PEGDMA-*co*-AEMA)-PVA may be a reason for the higher cell counts on chitosan. To test this, we plated 10 intact colonies of NPCs (neurospheres) on each biomaterial surface using identical culture conditions to those used for single cell plating, and examined the number of neurospheres that adhered to each surface at 9 days after cell plating. We observed a greater number of neurospheres adhering to the surface of chitosan relative to the hydrogel polymers (80% on chitosan versus 20%–30% on the other polymers tested). These differences support the hypothesis that the greater amine surface concentration and decreased water content of chitosan, relative to the synthetic hydrogels tested, led to greater cell adhesion and thus greater survival on chitosan.

The plating of whole neurospheres allowed us to look at cell migration on the surfaces of the polymer matrices. A prominent feature of NPCs and their progeny, both in vivo<sup>63–65</sup> and in vitro,<sup>26</sup> is their ability to migrate. We directly tested cell migration on all four biomaterial films

**Fig. 2.** (A) Cell viability was analyzed at d4 and d9 counting Hoechst-positive nuclei. Data are shown as mean  $\pm$  SEM,  $n = 3$  independent trials of 6–10 films. All synthetic materials have significantly reduced numbers of cells present at 4 and 9 days relative to Matrigel™ controls. \* indicates significant difference relative to day 4 ( $p < 0.05$ ) (B) At d4 (top row) and d9 (bottom row) most cells on P(GDMA-*co*-AEMA) (iii, iii'), P(PEG-*co*-AEMA) (iv, iv'), and P(PEG-*co*-AEMA)-PVA (v, v') were notably smaller and regionalized to the perimeter of the discs compared to chitosan (ii, ii') and Matrigel™ controls (i, i'). Dotted lines indicate the edge of the disk where cells were exclusively observed on P(PEG-*co*-AEMA) and P(PEG-*co*-AEMA)-PVA. (C) Bright phase images of cells on chitosan and Matrigel™ showing the morphology of the adherent cells on d4 and d9 post plating single cells. (D) Cell viability analyzed on Matrigel™ and chitosan at 2, 4, 9, and 21 days in culture using the PicoGreen assay and showing the fold change in the numbers of viable cells relative to the numbers of seeded cells on d0. Data represents means  $\pm$  sem. \* = significant difference relative to d0 ( $p < 0.05$ ). (E) Whole neurosphere on chitosan at d9 showing adhesion and migration of cells. Scale bar = 100  $\mu$ m.



compared to Matrigel™ controls by examining the diameter of adherent neurospheres (Fig. 2E). When intact neurospheres of equal diameter (100  $\mu$ m) were plated on day 0

and the diameter of the adherent colony was examined on d4, the cells migrated significantly more on chitosan relative to the other polymeric surfaces tested (chitosan:  $2.13 \pm$

**Table 1.** X-ray photoelectron spectroscopy and water equilibrium content analysis.

Material	Nitrogen surface concentration (%)	Equilibrium water content
Chitosan	2.75 ± 0.45	8.01 ± 1.37
P(GDMA- <i>co</i> -AEMA)	0.35 ± 0.05	56.74 ± 1.81
P(PEGDMA- <i>co</i> -AEMA)	1.65 ± 0.15	50.71 ± 3.51
P(PEGDMA- <i>co</i> -AEMA)-PVA	0.5 ± 0.20	54.68 ± 1.87

0.75 mm; P(GDMA-*co*-AEMA): 0.37 ± 0.18 mm; P(PEGDMA-*co*-AEMA): 0.49 ± 0.14 mm, and P(PEGDMA-*co*-AEMA)-PVA: 0.51 ± 0.36 mm). Hence, chitosan supports cell adhesion and migration to a greater extent than the other biomaterials tested herein, making it a promising material for cell delivery.

### NPC differentiation

Neural precursor cells have the potential to differentiate into astrocytes, oligodendrocytes, and neurons in vitro in the presence of serum on Matrigel<sup>TM</sup>.<sup>29,34</sup> To test the differentiation capacity of NPCs on the candidate matrices, we examined the differentiation profile using immunohistochemistry at various times post-plating. Single NPCs plated onto each biomaterial (and Matrigel<sup>TM</sup> controls) were immunostained for glial fibrillary acidic protein (GFAP) expression to assess for astrocyte formation;  $\beta$ III tubulin for neurons; and O<sub>4</sub> for oligodendrocytes (Figs. 3A and 3B). Strikingly, chitosan was the only candidate material of the four analyzed that supported NPC differentiation regardless of the time in culture (d4, d9, or d21). Moreover, chitosan supported the differentiation of all three cell types (astrocytes, neurons, and oligodendrocytes), similar to what is observed on Matrigel<sup>TM</sup> (Fig. 3A); however, the relative percentages of the differentiated phenotypes varied between the two substrates. Notably, neurons were observed on both chitosan and Matrigel<sup>TM</sup> at d9 and an increase in the percentage of neurons was observed on chitosan over time; oligodendrocytes were present at each time point and the percentage was not statistically different on chitosan over time; however the percentage of oligodendrocytes decreased on Matrigel<sup>TM</sup>, and astrocytes were present at each time point on both chitosan and Matrigel<sup>TM</sup> and comprised the major cell type at all time points. While it is still not known which cell type, or combination of cell types, is best suited for enhancing neural regeneration, the fact that all cell types can be formed on chitosan suggests that it may be advantageous for developing cell transplantation strategies using nerve guidance channels following nervous system damage.

### Neural stem cells persist on chitosan

The neurosphere-derived cells seeded onto the matrices were a mixed population of stem and progenitor cells. Having observed the multipotentiality of the progenitor cells on chitosan, we questioned whether neural stem cells (i.e., the neurosphere-forming cells) also persisted on the matrix. We assayed for the survival of stem cells by lifting the cells off the matrix 9 days post-plating and placing the cells in culture conditions that permit neurosphere formation. We examined the cells in terms of their ability to re-form neurospheres and for the expression of nestin (an intermediate fil-

ament protein that is expressed by virtually 100% of neurosphere-derived NPCs prior to differentiation and continues to be expressed following differentiation in vitro). We observed nestin expression following differentiation on chitosan at d4, d9, and d21 post-plating (Fig. 3), suggesting that undifferentiated precursors were maintained on chitosan. Notably, there was significant overlap in the GFAP- and nestin-expressing populations (ie. single cells expressed both markers) which may reflect an immature phenotype of astrocytes in culture.<sup>66,67</sup> Importantly, we isolated neurosphere-forming cells from chitosan cultures in comparable numbers to those observed on Matrigel<sup>TM</sup>. Similarly, the recovered neurospheres could be passaged and gave rise to neurons, astrocytes, and oligodendrocytes following differentiation. Hence, chitosan supports the differentiation of all three neural cell types in addition to the survival of multipotent stem cells.

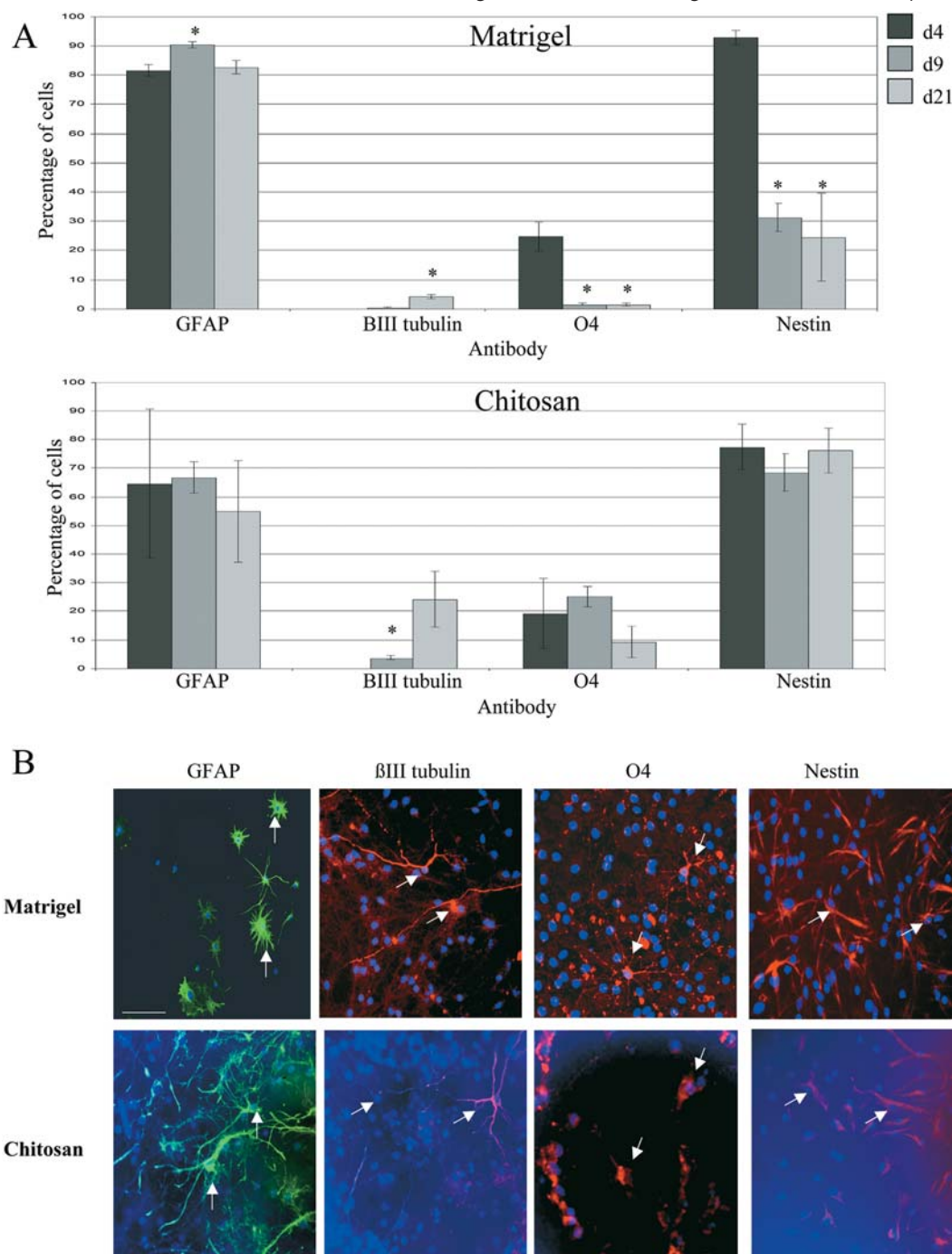
### Discussion

It has been shown that extrinsic factors originating from both diffusible factors<sup>68–71</sup> and cellular interactions<sup>72–74</sup> can regulate the proliferation and differentiation of cells. To our knowledge, this report is the first to show that cell viability, migration, and differentiation of adult murine NPCs differ over time on distinct amine-functionalized polymer surfaces. Moreover, the study identifies adult-derived NPCs and chitosan matrices as promising candidates for surgical implantation strategies aimed at restoring neurological deficits following injury to the nervous system.

Recently, Young et al.<sup>74</sup> reported that chitosan and poly(vinylidene fluoride) (PVDF) substrates could support the proliferation and differentiation of embryonic-derived cortical precursors. Interestingly, their observations using an embryonic-derived starting population of cells generated notable differences from our study when comparing the behaviour of cells plated on chitosan. Our starting population of single adult-derived cells was capable of differentiating into the three neural cell types on chitosan (Fig. 3), which differs from what was found using embryonic cortical precursor populations where single cells were inhibited from proliferating and differentiating on chitosan. This is a good example of the importance of considering both the material and the starting population of cells when designing strategies for tissue repair.

An important criterion in biomaterial selection in this study was the cell-biomaterial interaction. Irrespective of time in culture, NPC counts were significantly greater on chitosan than on the other synthetic hydrogels analyzed, demonstrating the importance of surface composition and water content which is consistent with the observations of others.<sup>27,75–77</sup> P(GDMA-*co*-AEMA), P(PEGDMA-*co*-AEMA), and P(PEGDMA-*co*-AEMA)-PVA hydrogels were either covalently or physically cross-linked to form highly water-swallowable polymer networks. The high water content of these polymeric hydrogels minimized protein adsorption and cell adhesion<sup>78,79</sup> reflecting the high water content associated with PEG.<sup>80</sup> To facilitate cell adhesion, amine-functionalized AEMA was copolymerized with GDMA and PEGDMA; however, this proved insufficient to overcome the low protein- and cell-adhesion properties associated with PEG. In-

**Fig. 3.** (A) The quantification of single-plated neural precursor cells for GFAP (astrocytes), neurons (βIII tubulin), oligodendrocytes (O4) and Nestin (undifferentiated cells) on Matrigel™ controls and chitosan on d4, d9, and d21. \* indicates significant difference relative to day 4 ( $p < 0.05$ ). (B) Immunohistochemistry of neural precursor cells plated on Matrigel™ and chitosan at d9 showing individual cells expressing GFAP (green), βIII tubulin (red), O4 (red), and Nestin (red) as indicated by arrows. Nuclei are Hoechst-positive (blue). Immunohistochemistry captured on chitosan exhibits an increased fluorescent background relative to Matrigel™. Scale bars = 100 μm.



terestingly, there was a progressive increase in cell viability and adhesion with decreasing water content in the polymer films studied and it was water content, not amine functionalization, that had the overriding effect on cell adhesion and thus viability. The low equilibrium water content, coupled with the amine functional groups present on chitosan, rendered chitosan cell-adhesive. Chitosan has also been shown

to be biocompatible and to degrade to non-cytotoxic products,<sup>60,81</sup> making it desirable for further investigation.

Adult NPCs are proliferative cells that migrate along a well-defined pathway to the olfactory bulb where they differentiate into neurons *in vivo*.<sup>58,63,82–85</sup> Proliferation, migration, and differentiation are also well-established characteristics of NPCs *in vitro*.<sup>86</sup> The cell behaviour observed



was dependent on the cell-matrix interaction and accordingly varied significantly between the matrices. Cell proliferation was observed on chitosan and control matrices between d4 and d9 and this coincided with an increase in the total numbers of cells in the center of the film. This mitogenic effect on chitosan surfaces has also been seen with human fibroblast and keratinocyte populations in vitro<sup>87</sup> and is thought to be the result of the highly deacetylated chitosan potentiating the effect of growth factors present in culture. Importantly, the total numbers of cells on d21 did not continue to increase, thereby reducing the likelihood of uncontrolled cell growth in vivo following implantation strategies after CNS damage. The ability of chitosan to promote the differentiation of all cell types (neurons, astrocytes, and oligodendrocytes) may be advantageous because its therapeutic potential as a delivery vehicle could be maximized for CNS injury repair and is attractive for developing regenerative medicine strategies. Importantly, chitosan is amenable to the incorporation of a drug delivery system that will further facilitate the development of specific cell types over time. Taken together, these features make chitosan a promising material for future development in the treatment of nervous system injury. More broadly, our findings provide the necessary framework for combining cellular therapeutics and implantation strategies in tissue engineering repair strategies of the damaged nervous system.

## Conclusions

Of four biomaterials screened, chitosan supported the greatest survival, migration, and multipotent differentiation of adult-derived neural precursors, making it a promising candidate material for cell-biomaterial transplantation studies in CNS applications. Importantly, chitosan supported the survival of multipotent, self-renewing stem cells without uncontrolled proliferation. Taken together, these findings provide the necessary framework for combining cellular therapeutics and implantation strategies to repair the damaged CNS.

## Acknowledgments

We thank Dr. Charles Tator for his insightful discussion and Howard Kim for preparation of chitosan films. We are grateful to the Canadian Institute of Health Research (MSS, CMM), the Natural Sciences and Engineering Research Council of Canada (MSS, CMM), the Ontario Neurotrauma Foundation (VS), CIHR Training in Regenerative Medicine (VS), the Ontario Graduate Scholarship in Science and Technology (AG), and the James F. Crothers Family (VS, AG) for financial support.

## References

- (1) Ramer, M. S.; Priestley, J. V.; McMahon, S. B. *Nature* **2000**, *403* (6767), 312. doi:10.1038/35002084. PMID:10659850.
- (2) Blesch, A.; Grill, R. J.; Tuszynski, M. H. *Prog. Brain Res.* **1998**, *117*, 473. doi:10.1016/S0079-6123(08)64033-9. PMID:9932426.
- (3) Grimpe, B.; Silver, J. *Prog. Brain Res.* **2002**, *137*, 333. doi:10.1016/S0079-6123(02)37025-0. PMID:12440376.
- (4) Schwab, M. E. *Science* **2002**, *295* (5557), 1029. doi:10.1126/science.1067840. PMID:11834824.
- (5) Fawcett, J. W.; Asher, R. A. *Brain Res. Bull.* **1999**, *49* (6), 377. doi:10.1016/S0361-9230(99)00072-6. PMID:10483914.
- (6) Silver, J.; Miller, J. H. *Nat. Rev. Neurosci.* **2004**, *5* (2), 146. doi:10.1038/nrn1326. PMID:14735117.
- (7) Paño, C. L.; Fernandez-Valle, C.; Bates, M. L.; Bunge, M. B. *J. Neurocytol.* **1994**, *23* (7), 433. doi:10.1007/BF01207115. PMID:7964912.
- (8) Pearse, D. D.; Pereira, F. C.; Marcillo, A. E.; Bates, M. L.; Berrocal, Y. A.; Filbin, M. T.; Bunge, M. B. *Nat. Med.* **2004**, *10* (6), 610. doi:10.1038/nm1056. PMID:15156204.
- (9) Barakat, D. J.; Gaglani, S. M.; Neravetla, S. R.; Sanchez, A. R.; Andrade, C. M.; Pressman, Y.; Puzis, R.; Garg, M. S.; Bunge, M. B.; Pearse, D. D. *Cell Transplant.* **2005**, *14* (4), 225. doi:10.3727/000000005783983106. PMID:15929557.
- (10) Liu, S.; Peulve, P.; Jin, O.; Boisset, N.; Tiollier, J.; Said, G.; Tadie, M. *J. Neurosci. Res.* **1997**, *49* (4), 425. doi:10.1002/(SICI)1097-4547(19970815)49:4<425::AID-JNR4>3.0.CO;2-A. PMID:9285519.
- (11) Deumens, R.; Koopmans, G. C.; Honig, W. M.; Maquet, V.; Jérôme, R.; Steinbusch, H. W.; Joosten, E. A. *Neurosci. Lett.* **2006**, *400* (3), 208. doi:10.1016/j.neulet.2006.02.050. PMID:16530957.
- (12) Tsai, E. C.; Dalton, P. D.; Shoichet, M. S.; Tator, C. H. *J. Neurotrauma* **2004**, *21* (6), 789. doi:10.1089/0897715041269687. PMID:15253805.
- (13) Tsai, E. C.; Dalton, P. D.; Shoichet, M. S.; Tator, C. H. *Biomaterials* **2006**, *27* (3), 519. doi:10.1016/j.biomaterials.2005.07.025. PMID:16099035.
- (14) Karimi-Abdolrezaee, S.; Eftekharpour, E.; Wang, J.; Morshead, C. M.; Fehlings, M. G. *J. Neurosci.* **2006**, *26* (13), 3377. doi:10.1523/JNEUROSCI.4184-05.2006. PMID:16571744.
- (15) Ishii, K.; Nakamura, M.; Dai, H.; Finn, T. P.; Okano, H.; Toyama, Y.; Bregman, B. S. *J. Neurosci. Res.* **2006**, *84* (8), 1669. doi:10.1002/jnr.21079. PMID:17044031.
- (16) Vroemen, M.; Caioni, M.; Bogdahn, U.; Weidner, N. *Cell Tissue Res.* **2007**, *327* (1), 1. doi:10.1007/s00441-006-0252-y. PMID:16941122.
- (17) Guo, J. S.; Zeng, Y. S.; Li, H. B.; Huang, W. L.; Liu, R. Y.; Li, X. B.; Ding, Y.; Wu, L. Z.; Cai, D. Z. *Spinal Cord* **2007**, *45* (1), 15. doi:10.1038/sj.sc.3101943. PMID:16773039.
- (18) Ke, Y.; Chi, L.; Xu, R.; Luo, C.; Gozal, D.; Liu, R. *Stem Cells* **2006**, *24* (4), 1011. doi:10.1634/stemcells.2005-0249. PMID:16339643.
- (19) Pallini, R.; Vitiani, L. R.; Bez, A.; Casalbore, P.; Facchiano, F.; Di Giorgi Gerevini, V.; Falchetti, M. L.; Fernandez, E.; Maira, G.; Peschle, C.; Parati, E. *Neurosurgery* **2005**, *57* (5), 1014, discussion 1014. doi:10.1227/01.NEU.0000180058.58372.4c. PMID:16284571.
- (20) Cummings, B. J.; Uchida, N.; Tamaki, S. J.; Salazar, D. L.; Hooshmand, M.; Summers, R.; Gage, F. H.; Anderson, A. J. *Proc. Natl. Acad. Sci. U.S.A.* **2005**, *102* (39), 14069. doi:10.1073/pnas.0507063102. PMID:16172374.
- (21) Okada, S.; Ishii, K.; Yamane, J.; Iwanami, A.; Ikegami, T.; Katoh, H.; Iwamoto, Y.; Nakamura, M.; Miyoshi, H.; Okano, H. J.; Contag, C. H.; Toyama, Y.; Okano, H. *FASEB J.* **2005**, *19* (13), 1839. PMID:16141363.
- (22) Enzmann, G. U.; Benton, R. L.; Woock, J. P.; Howard, R. M.; Tsoulfas, P.; Whittemore, S. R. *Exp. Neurol.* **2005**, *195* (2), 293. doi:10.1016/j.expneurol.2005.04.021. PMID:16087174.
- (23) Iwanami, A.; Kaneko, S.; Nakamura, M.; Kanemura, Y.; Mori, H.; Kobayashi, S.; Yamasaki, M.; Momoshima, S.; Ishii, H.; Ando, K.; Tanioka, Y.; Tamaoki, N.; Nomura, T.; Toyama, Y.; Okano, H. *J. Neurosci. Res.* **2005**, *80* (2), 182. doi:10.1002/jnr.20436. PMID:15772979.

- (24) Watanabe, K.; Nakamura, M.; Iwanami, A.; Fujita, Y.; Kanemura, Y.; Toyama, Y.; Okano, H. *Dev. Neurosci.* **2004**, *26* (2-4), 275. doi:10.1159/000082144. PMID:15711067.
- (25) Lang, B.; Liu, H. L.; Liu, R.; Feng, G. D.; Jiao, X. Y.; Ju, G. *Neuroscience* **2004**, *128* (4), 775. doi:10.1016/j.neuroscience.2004.06.033. PMID:15464285.
- (26) Kearns, S. M.; Laywell, E. D.; Kukekov, V. K.; Steindler, D. A. *Exp. Neurol.* **2003**, *182* (1), 240. doi:10.1016/S0014-4886(03)00124-9. PMID:12821394.
- (27) Teng, Y. D.; Lavik, E. B.; Qu, X.; Park, K. I.; Ourednik, J.; Zurakowski, D.; Langer, R.; Snyder, E. Y. *Proc. Natl. Acad. Sci. U.S.A.* **2002**, *99* (5), 3024. doi:10.1073/pnas.052678899. PMID:11867737.
- (28) Reynolds, B. A.; Weiss, S. *Science* **1992**, *255* (5052), 1707. doi:10.1126/science.1553558. PMID:1553558.
- (29) Weiss, S.; Dunne, C.; Hewson, J.; Wohl, C.; Wheatley, M.; Peterson, A. C.; Reynolds, B. A. *J. Neurosci.* **1996**, *16*, 7599. PMID:8922416.
- (30) Davis, A. A.; Temple, S. *Nature* **1994**, *372* (6503), 263. doi:10.1038/372263a0. PMID:7969470.
- (31) Morshead, C. M.; Benveniste, P.; Iscove, N. N.; van der Kooy, D. *Nat. Med.* **2002**, *8* (3), 268. doi:10.1038/nm0302-268. PMID:11875498.
- (32) Gritti, A.; Parati, E. A.; Cova, L.; Frolichsthal, P.; Galli, R.; Wanke, E.; Faravelli, L.; Morassutti, D. J.; Roisen, F.; Nickel, D. D.; Vescovi, A. L. *J. Neurosci.* **1996**, *16* (3), 1091. PMID:8558238.
- (33) Palmer, T. D.; Takahashi, J.; Gage, F. H. *Mol. Cell. Neurosci.* **1997**, *8* (6), 389. doi:10.1006/mcne.1996.0595. PMID:9143557.
- (34) Shen, Q.; Wang, Y.; Dimos, J. T.; Fasano, C. A.; Phoenix, T. N.; Lemischka, I. R.; Ivanova, N. B.; Stifani, S.; Morrisey, E. E.; Temple, S. *Nat. Neurosci.* **2006**, *9* (6), 743. doi:10.1038/nn1694. PMID:16680166.
- (35) Beningo, K. A.; Dembo, M.; Wang, Y. L. *Proc Natl Acad USA* **2004**, *101* (52), 18024. doi:10.1073/pnas.0405747102.
- (36) Steinmetz, M. P.; Horn, K. P.; Tom, V. J.; Miller, J. H.; Busch, S. A.; Nair, D.; Silver, D. J.; Silver, J. *J. Neurosci.* **2005**, *25* (35), 8066. doi:10.1523/JNEUROSCI.2111-05.2005. PMID:16135764.
- (37) Costa, S.; Planchenault, T.; Charriere-Bertrand, C.; Mouchel, Y.; Fages, C.; Juliano, S.; Lefrançois, T.; Barlovatz-Meimon, G.; Tardy, M. *Glia* **2001**, *37* (2), 105. doi:10.1002/glia.10015. PMID:11754209.
- (38) Ramón-Cueto, A.; Plant, G. W.; Avila, J.; Bunge, M. B. *J. Neurosci.* **1998**, *18* (10), 3803. PMID:9570810.
- (39) Fouad, K.; Schnell, L.; Bunge, M. B.; Schwab, M. E.; Liebscher, T.; Pearce, D. D. *J. Neurosci.* **2005**, *25* (5), 1169. doi:10.1523/JNEUROSCI.3562-04.2005. PMID:15689553.
- (40) Woerly, S.; Petrov, P.; Syková, E.; Roitbak, T.; Simonová, Z.; Harvey, A. R. *Tissue Eng.* **1999**, *5* (5), 467. doi:10.1089/ten.1999.5.467. PMID:10586102.
- (41) Houle, J. D.; Ziegler, M. K. *J. Neural Transplant. Plast.* **1994**, *5* (2), 115. doi:10.1155/NP.1994.115. PMID:7703291.
- (42) Oudega, M.; Gautier, S. E.; Chapon, P.; Frago, M.; Bates, M. L.; Parel, J. M.; Bunge, M. B. *Biomaterials* **2001**, *22* (10), 1125. doi:10.1016/S0142-9612(00)00346-X. PMID:11352092.
- (43) Lee, Y. S.; Hsiao, I.; Lin, V. W. *J. Neurotrauma* **2002**, *19* (10), 1203. doi:10.1089/08977150260338001. PMID:12427329.
- (44) Nakamura, M.; Houghtling, R. A.; MacArthur, L.; Bayer, B. M.; Bregman, B. S. *Exp. Neurol.* **2003**, *184* (1), 313. doi:10.1016/S0014-4886(03)00361-3. PMID:14637102.
- (45) Deng, C.; Gorrie, C.; Hayward, I.; Elston, B.; Venn, M.; Mackay-Sim, A.; Waite, P. *J. Neurosci. Res.* **2006**, *83* (7), 1201. doi:10.1002/jnr.20817. PMID:16498634.
- (46) Park, H. C.; Shim, Y. S.; Ha, Y.; Yoon, S. H.; Park, S. R.; Choi, B. H.; Park, H. S. *Tissue Eng.* **2005**, *11* (5-6), 913. doi:10.1089/ten.2005.11.913. PMID:15998231.
- (47) Namiki, J.; Kojima, A.; Tator, C. H. *J. Neurotrauma* **2000**, *17* (12), 1219. doi:10.1089/neu.2000.17.1219. PMID:11186234.
- (48) Taylor, L.; Jones, L.; Tuszynski, M. H.; Blesch, A. *J. Neurosci.* **2006**, *26* (38), 9713. doi:10.1523/JNEUROSCI.0734-06.2006. PMID:16988042.
- (49) Jimenez Hamann, M. C.; Tator, C. H.; Shoichet, M. S. *Exp. Neurol.* **2005**, *194* (1), 106. doi:10.1016/j.expneurol.2005.01.030. PMID:15899248.
- (50) Qiu, J.; Cai, D.; Dai, H.; McAtee, M.; Hoffman, P. N.; Bregman, B. S.; Filbin, M. T. *Neuron* **2002**, *34* (6), 895. doi:10.1016/S0896-6273(02)00730-4. PMID:12086638.
- (51) Lu, P.; Yang, H.; Jones, L. L.; Filbin, M. T.; Tuszynski, M. H. *J. Neurosci.* **2004**, *24* (28), 6402. doi:10.1523/JNEUROSCI.1492-04.2004. PMID:15254096.
- (52) Pearce, D. D.; Pereira, F. C.; Marcillo, A. E.; Bates, M. L.; Berrocal, Y. A.; Filbin, M. T.; Bunge, M. B. *Nat. Med.* **2004**, *10* (6), 610. doi:10.1038/nm1056. PMID:15156204.
- (53) Arias-Carrión, O.; Hernández-López, S.; Ibañez-Sandoval, O.; Bargas, J.; Hernández-Cruz, A.; Drucker-Colín, R. *J. Neurosci. Res.* **2006**, *84* (7), 1425. doi:10.1002/jnr.21068. PMID:17006899.
- (54) Horner, P. J.; Power, A. E.; Kempermann, G.; Kuhn, H. G.; Palmer, T. D.; Winkler, J.; Thal, L. J.; Gage, F. H. *J. Neurosci.* **2000**, *20* (6), 2218. PMID:10704497.
- (55) Yu, L. M. Y.; Kazazian, K.; Shoichet, M. S. *J. Biomed Mater. Res.: Part A* **2007**, *82*, 243. doi:10.1002/jbm.a.31069.
- (56) Hern, D. L.; Hubbell, J. A. *J. Biomed. Mater. Res.* **1998**, *39* (2), 266. doi:10.1002/(SICI)1097-4636(199802)39:2<266::AID-JBM14>3.0.CO;2-B. PMID:9457557.
- (57) Tropepe, V.; Sibilila, M.; Ciruna, B. G.; Rossant, J.; Wagner, E. F.; van der Kooy, D. *Dev. Biol.* **1999**, *208* (1), 166. doi:10.1006/dbio.1998.9192. PMID:10075850.
- (58) Chiasson, B. J.; Tropepe, V.; Morshead, C. M.; van der Kooy, D. *J. Neurosci.* **1999**, *19* (11), 4462. PMID:10341247.
- (59) Zhou, F. C.; Kelley, M. R.; Chiang, Y. H.; Young, P. *Exp. Neurol.* **2000**, *164* (1), 200. doi:10.1006/exnr.2000.7425. PMID:10877930.
- (60) Freier, T.; Koh, H. S.; Kazazian, K.; Shoichet, M. S. *Biomaterials* **2005**, *26* (29), 5872. doi:10.1016/j.biomaterials.2005.02.033. PMID:15949553.
- (61) Beringer, J. P.; Terrettaz, S.; Michel, R.; Tirelli, N.; Vogel, H.; Textor, M.; Hubbell, J. A. *Nat. Mater.* **2003**, *2* (4), 259. doi:10.1038/nmat851. PMID:12690400.
- (62) Tziampazis, E.; Kohn, J.; Moghe, P. V. *Biomaterials* **2000**, *21* (5), 511. doi:10.1016/S0142-9612(99)00212-4. PMID:10674816.
- (63) Fricker, R. A.; Carpenter, M. K.; Winkler, C.; Greco, C.; Gates, M. A.; Björklund, A. *J. Neurosci.* **1999**, *19* (14), 5990. PMID:10407037.
- (64) Kirschenbaum, B.; Doetsch, F.; Lois, C.; Alvarez-Buylla, A. *J. Neurosci.* **1999**, *19* (6), 2171. PMID:10066270.
- (65) Chazal, G.; Durbec, P.; Jankovski, A.; Rougon, G.; Cremer, H. *J. Neurosci.* **2000**, *20* (4), 1446. PMID:10662835.
- (66) Messam, C. A.; Hou, J.; Berman, J. W.; Major, E. O. *Brain Res. Dev. Brain Res.* **2002**, *134* (1-2), 87. doi:10.1016/S0165-3806(01)00325-X. PMID:11947939.
- (67) Wei, L. C.; Shi, M.; Chen, L. W.; Cao, R.; Zhang, P.; Chan, Y. S. *Brain Res. Dev. Brain Res.* **2002**, *139* (1), 9. doi:10.1016/S0165-3806(02)00509-6. PMID:12414089.

- (68) Cameron, H. A.; Hazel, T. G.; McKay, R. D. *J. Neurobiol.* **1998**, *36* (2), 287. doi:10.1002/(SICI)1097-4695(199808)36:2<287::AID-NEU13>3.0.CO;2-B. PMID:9712310.
- (69) Cattaneo, E.; McKay, R. *Nature* **1990**, *347* (6295), 762. doi:10.1038/347762a0. PMID:2172829.
- (70) Ciccolini, F.; Svendsen, C. N. *J. Neurosci.* **1998**, *18* (19), 7869. PMID:9742155.
- (71) Arsenijevic, Y.; Weiss, S.; Schneider, B.; Aebischer, P. *J. Neurosci.* **2001**, *21* (18), 7194. PMID:11549730.
- (72) Tsai, R. Y.; McKay, R. D. *J. Neurosci.* **2000**, *20* (10), 3725. PMID:10804214.
- (73) Hugnot, J. P.; Mellodew, K.; Pilcher, H.; Uwanogho, D.; Price, J.; Sinden, J. D. *J. Neurosci. Res.* **2001**, *65* (3), 195. doi:10.1002/jnr.1143. PMID:11494354.
- (74) Hung, C. H.; Lin, Y.-L.; Young, T. H. *Biomaterials* **2006**, *27* (25), 4461. doi:10.1016/j.biomaterials.2006.04.021. PMID:16687170.
- (75) Belkas, J. S.; Munro, C. A.; Shoichet, M. S.; Johnston, M.; Midha, R. *Biomaterials* **2005**, *26* (14), 1741. doi:10.1016/j.biomaterials.2004.05.031. PMID:15576148.
- (76) Lüthen, F.; Lange, R.; Becker, P.; Rychly, J.; Beck, U.; Nebe, J. G. *Biomaterials* **2005**, *26* (15), 2423. doi:10.1016/j.biomaterials.2004.07.054. PMID:15585246.
- (77) Gonzalez, A. L.; Gobin, A. S.; West, J. L.; McIntire, L. V.; Smith, C. W. *Tissue Eng.* **2004**, *10* (11-12), 1775. doi:10.1089/ten.2004.10.1775. PMID:15684686.
- (78) Hern, D. L.; Hubbell, J. A. *J. Biomed. Mater. Res.* **1998**, *39* (2), 266. doi:10.1002/(SICI)1097-4636(199802)39:2<266::AID-JBM14>3.0.CO;2-B. PMID:9457557.
- (79) Jenney, C. R.; Anderson, J. M. *J. Biomed. Mater. Res.* **1999**, *49* (4), 435. doi:10.1002/(SICI)1097-4636(20000315)49:4<435::AID-JBM2>3.0.CO;2-Y.
- (80) *Poly(Ethylene Glycol) Chemistry: Biotechnical and Biomedical Applications*; Harris, J. M., Ed.; Plenum Press: New York, 1991.
- (81) Silva, R. M.; Silva, G. A.; Coutinho, O. P.; Mano, J. F.; Reis, R. L. *J. Mater. Sci. Mater. Med.* **2004**, *15* (10), 1105. doi:10.1023/B:JMSM.0000046392.44911.46. PMID:15516871.
- (82) Morshead, C. M.; Reynolds, B. A.; Craig, C. G.; McBurney, M. W.; Staines, W. A.; Morassutti, D.; Weiss, S.; van der Kooy, D. *Neuron* **1994**, *13* (5), 1071. doi:10.1016/0896-6273(94)90046-9. PMID:7946346.
- (83) Herrera, D. G.; Garcia-Verdugo, J. M.; Alvarez-Buylla, A. *Ann. Neurol.* **1999**, *46* (6), 867. doi:10.1002/1531-8249(199912)46:6<867::AID-ANA9>3.0.CO;2-Z. PMID:10589539.
- (84) Luskin, M. B. *Neuron* **1993**, *11* (1), 173. doi:10.1016/0896-6273(93)90281-U. PMID:8338665.
- (85) Doetsch, F.; Caillé, I.; Lim, D. A.; García-Verdugo, J. M.; Alvarez-Buylla, A. *Cell* **1999**, *97* (6), 703. doi:10.1016/S0092-8674(00)80783-7. PMID:10380923.
- (86) Soares, S.; Sotelo, C. *Neuroscience* **2004**, *128* (4), 807. doi:10.1016/j.neuroscience.2004.07.031. PMID:15464288.
- (87) Howling, G. I.; Dettmar, P. W.; Goddard, P. A.; Hampson, F. C.; Dornish, M.; Wood, E. J. *Biomaterials* **2001**, *22* (22), 2959. doi:10.1016/S0142-9612(01)00042-4. PMID:11575470.

# Methods for probing the long-range dynamic of confined polymers in nanoparticles using small-angle neutron scattering

Y. Rharbi, M. Yousfi, Lionel Porcar, and Q. Nawaz

**Abstract:** Motivated by the recent advances in new technologies, a lot of effort has been dedicated to developing methods for quantifying the dynamic of nanoconfined polymers. Particularly, polymers confined in nanoparticles are an important system for several environment-friendly applications such as waterborne coatings and nanoblends. In this work, we discuss two methods to probe the large scale dynamic of nanoconfined polymers in nanoparticles in two situations: (i) nanoblends and (ii) the close-packed structure. In the methods we apply stress at the nanoscopic level around the polystyrene particles and we probe their deformation in real time using small-angle neutron scattering. These methods give new possibilities to probe, in a nonintrusive manner, the dynamic of confined polymers in nanoparticles, which could ultimately bring conclusive insight to this field.

**Key words:** polymer dynamic, confinement, nanoblends, polymer nanoparticles.

**Résumé :** Motivés par les développements récents dans les nouvelles technologies, beaucoup d'efforts ont été déployés dans le but de mettre au point des méthodes permettant de quantifier la dynamique des polymères nanoconfinés. En particulier, les polymères confinés dans des nanoparticules sont des systèmes importants pour plusieurs applications respectueuses de l'environnement, tels les enduits et les mélanges aqueux. Dans ce travail, on discute de deux méthodes d'étudier la dynamique à grande échelle des polymères nanoconfinés dans des nanoparticules, dans deux situations: (i) les nanomélanges et (ii) la structure à grande compacité. Dans ces méthodes, on applique un stress au niveau nanoscopique autour des particules de polystyrène et on étudie leur déformation en temps réel en faisant appel à la diffusion des neutrons à angles faibles. Ces méthodes fournissent de nouvelles possibilités pour étudier, d'une façon non intrusive, la dynamique des polymères confinés dans des nanoparticules et elles pourraient éventuellement permettre d'obtenir un éclairage conclusif pour comprendre ce champ.

**Mots-clés :** dynamique des polymères, confinement, nanomélanges, nanoparticules de polymère.

[Traduit par la Rédaction]

## Introduction

There are numerous indications that the dynamic of nanoconfined polymers near an interface deviates from that of the bulk.<sup>1–23</sup> This property is of great importance for several nano-technological applications such as the elaboration and stability of nanoscale polymer structures, adhesion, and environment-friendly coatings, among others. By far, thin film is the most studied nanoconfinement geometry<sup>1–19</sup> compared to the other geometries: nanospheres<sup>20–23</sup> and nanotubes.<sup>9</sup> Numerous studies determined the existence of an impressive depression of the nanoconfined glass transition temperature ( $T_g$ ) in supported and free-standing polystyrene (PS) thin films.<sup>1–6</sup> For supported films, the  $T_g$  was found to increase or decrease depending on the nature of the substrate and the polymer.<sup>1,2</sup>

The glass transition temperature in bulk polymers is usually linked to the segmental dynamic, thus, one expects the activation of the dynamic to accompany the observed  $T_g$  reduction in confined systems.<sup>1</sup> Therefore, several methods were proposed to monitor the dynamic of confined polymers at different length scales.<sup>7–19</sup> The segmental dynamic in free-standing PS films measured by means of dielectric relaxation was found to be faster than the bulk, which is coherent with the  $T_g$  reduction.<sup>7,8</sup> On the other hand, the numerous methods used to probe the large scale dynamic yielded different conclusions. For example, Reiter et al.<sup>10</sup> used the dynamic of dewetting of polystyrene on a solid substrate to extract information on the dynamics of polymer chains. Roth and Dutcher<sup>11</sup> investigated the dynamic of thin films using hole-opening experiments. Russell and co-workers<sup>12</sup> used fluorescence recovery after photobleaching to measure the chain

Received 20 September 2009. Accepted 14 December 2009. Published on the NRC Research Press Web site at canjchem.nrc.ca on 25 February 2010.

*This article is part of a Special Issue dedicated to Professor M. A. Winnik.*

**Y. Rharbi,<sup>1</sup> M. Yousfi, and Q. Nawaz.** Laboratoire de Rhéologie, UJF/INPG/CNRS, BP 53, Domaine universitaire 38041, Grenoble, France.

**L. Porcar.** Institut Laué-Langevin, BP 156 38042, Grenoble, France.

<sup>1</sup>Corresponding author (e-mail: rharbi@ujf-grenoble.fr).



diffusion in polystyrene thin films and found a reduction of the diffusion coefficient with decreasing film thickness. They concluded that chain adsorption on the substrate is what slows chain diffusion. O'Connell and McKenna<sup>13</sup> carried out mechanical tests using the "bubble inflation" technique on ultrathin films and suggested a strong reduction of rubbery compliance as the film thickness decreases, which could mean a higher entanglement density than in the bulk. Bodiguel and Fretigny<sup>14</sup> monitored the dynamic of contraction in free-standing thin films under the action of surface tension and did not find any variation of the rubbery plateau. However, they reported a reduction of the viscosity with decreasing film thickness.<sup>14</sup> Si et al.<sup>15</sup> performed stretching experiments on free-standing films and proposed that intra-chain entanglement decreases with decreasing film thickness. Recently, several researchers investigated the dynamics of the free surface layer of polystyrene films by looking at the time dependence of hole closure.<sup>16–19</sup> Reference 16 suggested that the relaxation of the free surface exhibits a bulk behavior for temperatures close to the bulk  $T_g$  and then strongly deviates from the bulk relaxation for temperatures below the  $T_g$ . To explain the discrepancy between the results of the literature there is still a need to develop new methods to precisely probe the dynamic of confined polymers.

The confinement of polymers in nanoparticles is important in many environmental applications:<sup>20,21</sup> blends, copolymers, nanocomposites, colloids, coatings, and so forth. One example is zero volatile organic compound (VOC) coatings, where polymer nanoparticles are used in the film-making process.<sup>22–26</sup> VOCs are used in coatings to lower the particle  $T_g$  and to soften the particle, which permits the fabrication of crack-free films at room temperature.<sup>20,21</sup> If the polymer dynamic is activated and the  $T_g$  decreases by decreasing the nanoparticle size, the use of VOCs could be avoided, which would have a positive impact on the environment. Another example is in nanoblends, where hard polymer nanoparticles are used to reinforce soft matrices. If confinement in this application causes the reduction of the hard particles'  $T_g$  and the activation of the polymer dynamics, reducing the particle size would be counterproductive for reinforcement since it would cause the softening of the hard particles.<sup>27,28</sup> Thus, there is a real need to develop appropriate methods to measure the dynamics of polymer in nanoparticles.

In this paper, we discuss two methods to monitor the large scale dynamic of polystyrene in nanoparticles in two situations: polymer particles in nanoblends and polymer particles in a close-packed structure. We apply stress to the particles at the nanoscopic level using various procedures and we probe the deformation of the particle in real time by means of small-angle neutron scattering. Particle deformation is then used to quantify the dynamic of confined polystyrene in nanoparticles. Recently, we proposed a method for probing the dynamic of polystyrene nanoparticles in nanoblends<sup>28</sup> and we applied it to a single particle size (80 nm). In the present paper, we first extend these results by discussing the effect of particle. Secondly, we discuss how the void closure between close packed particles could be used to monitor the absolute values of the relaxation time of polymer nanoparticles.

## Experimental

### Materials

Monomers, deuterated styrene ( $D_8$ , Sigma-Aldrich, 99%), nondeuterated styrene (Sigma-Aldrich, 99%), butyl acrylate (Sigma-Aldrich, 99%), butyl methacrylate (Sigma-Aldrich, 99%), and cross-linker, ethylene glycol dimethylacrylate (EGDMA), were used as received. The surfactant, sodium dodecyl sulfate (SDS, Sigma-Aldrich, 99%), the initiator, potassium persulfate (KPS, Sigma-Aldrich, 98%), and buffer sodium bicarbonate were used as received. Double deionized water was used in the emulsion polymerization.

### Synthesis

Poly(butyl methacrylate) (PBMA), poly(butyl acrylate) (PBA), deuterated polystyrene (dPS), and hydrogenated polystyrene (PS) particles were prepared using emulsion polymerization at 80 °C. The polymer concentrations in water were 10 wt% for the PBMA, 10 wt% PS, and 2 wt% for dPS. The PBMA particles were cross-linked at 10% using ethylene glycol dimethylacrylate (EGDMA) during the polymerization. The PBMA and PS nanoparticles were prepared in a standard three-neck round flask (500 mL) with a condenser and a nitrogen inlet. For the preparation of PBMA, the mixture (26 g) of the cross-linker (EGDMA) and monomer (BMA) were added to the predegassed SDS (3 g)/water (250 g) solution, which had previously been heated at 80 °C. The solution was vigorously agitated for 20 min before the initiator was added. A solution of the initiator KPS (33 mg) in water (1.7 g) was added to the reaction. After 4 h, another solution of the KPS (5.4 mg) in water (0.7 g) was added to polymerize all the nonreacted styrene monomer.

The dPS was either prepared from pure deuterated styrene ( $D_8$ ) or from a 50/50 wt% mixture of deuterated styrene ( $D_8$ ) and hydrogenated styrene. The dPS particles were prepared in a 50 mL minireactor equipped with a gas inlet and a homemade minicondenser. The size of the dPS particles was controlled by varying the added amount of surfactant in the reaction. The mixture of water (18 g) and SDS was heated to 80 °C, under nitrogen flux for 20 min and then 0.3 g of styrene monomer (50/50 wt% deuterated and hydrogenated) was added. A solution of the initiator KPS (14 mg) in water (0.5 g) was added to the reaction. After 4 h, another solution of the KPS (1.4 mg) in water (0.25 g) was added to polymerize all the nonreacted styrene monomer. The SDS concentration was varied to control the size of the particles.

The surfactant and free ions were removed from the dispersions using a mixture of anionic and cationic exchange resins (Dowex, Sigma-Aldrich). The suspensions were cleaned a few minutes prior to film preparation.

### Polymer and particle characterization

Particle diameters ( $D$ ) were measured using quasi elastic light scattering (QELS) (Malvern 5000) at a 90° angle. The molecular weight was measured using gas permeation chromatography (GPC) in tetrahydrofuran (THF). The molecular weight of PS-93 was found to be  $M_w \approx 280\,000$  kg/mol and its  $M_n \approx 92\,000$  kg/mol. For dPS-5 the  $M_w = 371\,000$  kg/mol and the  $M_n = 216\,000$  kg/mol.

The bulk glass transition temperature of polystyrene was measured by differential scanning calorimetry (DSC, Mettler

**Table 1.** Properties of the PBMA and PS samples.

	PBMA-10	PBA-10	dPS-5	dPS-6	dPS-1	PS-93
Cross-linking percentage	10%	10%	0%	0%	0%	0%
Particle diameter (nm)	55	50	80	77	30	93
$T_g$ (°C)	55		103	103	99	104.4

Toledo DSC 823) during the heating step at a rate of 10 K/min for polystyrene and 40 K/min for highly cross-linked PBMA. The powder dried at 45 °C, was added to the DSC pan, and annealed for 10 min at 140 °C to remove the thermal history before the first DSC scan. The  $T_g$  is taken as the midpoint in the DSC trace, and in Table 1, we report the  $T_g$  value from the first run. Also in Table 1, we list the properties of dPS and cross-linked PBMA.

### Preparation of the samples for the neutron scattering

The surfactant and free ions were removed from the dispersions using a mixture of anionic and cationic exchange resins (Dowex, Sigma-Aldrich). The dPS-5 suspension was annealed in a stainless steel bomb at 120 °C for 20 min to release their thermal histories.

The nanoblends were prepared by mixing dPS and PBMA dispersions to make dPS concentrations of 2 wt% of the solid PBMA. The blends containing dPS-1 and dPS-6 were prepared using PBMA (lot 2) and dPS-5 was prepared from a PBMA (lot 1). Cracked films were obtained after water evaporation at 56 °C. The hydrogenated PS samples were prepared by drying the PS suspension at 45 °C for 48 h. This yielded a cracked PS powder.

### SANS experiments

The small-angle neutron scattering (SANS) experiments were carried out on spectrometer PAXY of Laboratoire Léon Brillouin (LLB, Saclay, France) at the reactor Orphée Saclay and at D22 and D11 of Institut Laue-Langevin (ILL, Grenoble, France). The scattered neutrons, collected on an XY bidimensional multidetector, were circularly averaged to obtain spectra of intensities ( $I$ ) versus the magnitude of the scattering wave vector ( $Q$ ). Several configurations of the wavelengths and sample-to-detector distances were chosen to yield a range of  $Q$  values between  $2 \times 10^{-3}$  and  $1 \times 10^{-1} \text{ Å}^{-1}$ .

The nanoblend samples were prepared by gently grinding the cracked films into a powder with grains of 0.5 mm beads. This powder (105 mg) was then introduced between two quartz disks separated by a spacer of 12 mm inner diameter and 1.2 mm thickness. The nanoblends were annealed (in situ), the sample was positioned in the neutron beam in a homemade oven equipped with two quartz windows and was heated to the desired temperature during the SANS measurements. The sample temperatures were monitored using a thin thermocouple placed in the proximity of the sample. The sample temperature was found to reach the desired temperature within 2 min. Neutron spectra were taken for 1 min at various annealing times.

The PS samples were separated into several samples of 0.2 g placed in glass bottles. Each of these samples were annealed at  $100 \text{ °C} \pm 0.2 \text{ °C}$  for a given time between 1 min and 2 h. The samples were then gently grinded into 0.5 mm beads. This powder ( $0.09 \pm 0.002 \text{ g}$ ) was then placed between two pieces of aluminum scotch tape (0.1 mm thick)

separated by a spacer of 14 mm inner diameter and 0.8 mm thickness. The powder was then pressed using  $15 \text{ kgf/cm}^2$  ( $1 \text{ kgf/cm}^2 = 98.0665 \text{ kPa}$ ) to obtain a homogeneous film thickness of 0.8 mm.

## Results and discussion

A good protocol to monitor the dynamic of polymer nanoparticles requires (i) that a stress is applied to the particle at the nanoscopic level and (ii) a sensitive method to monitor the change in the particle shape during its deformation. From the time dependence of the particle shape one can deduce the relaxation time of the polymer and its dependence on the temperature and the confinement condition. We apply this procedure to probe the dynamic of polystyrene in two different environments: (i) polystyrene dispersed in nanoblends and (ii) close-packed polystyrene particles.

### Protocol for measuring the dynamic of polystyrene nanoparticles in nanoblends

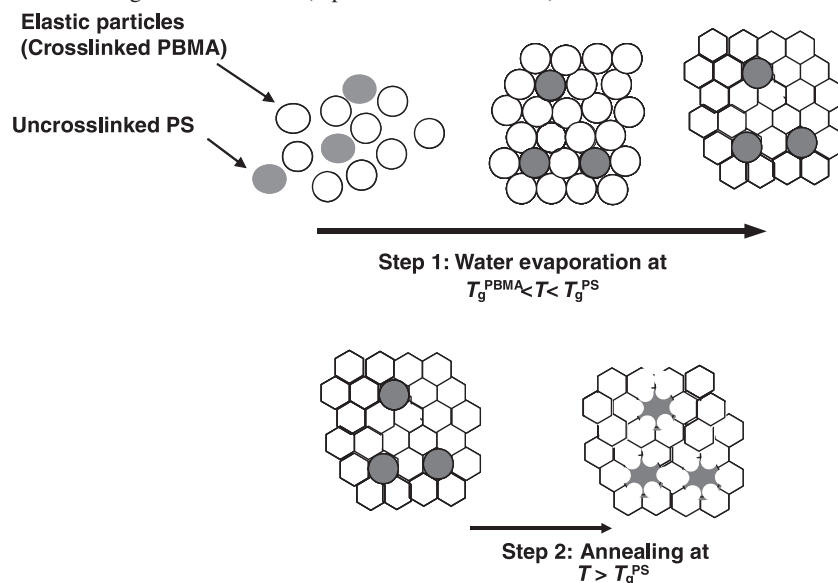
In a previous report, we proposed a new method to apply the stress locally to the polystyrene nanoparticles dispersed in nanoblends by using the following procedure:<sup>28</sup> Nanoblends composed of colloidal suspensions of cross-linked PBMA and 2% dPS nanoparticles were prepared via water evaporation, see Scheme 1. These blends were prepared at temperatures above the  $T_g$  of cross-linked PBMA particles ( $T_g^{\text{PBMA}}$ ) and well below the  $T_g$  of PS ( $T_g^{\text{PS}}$ ). This should lead to a deformation of the PBMA particles under capillary pressure ( $P_{\text{Lap}} = 12.9\gamma_{\text{aw}}/R \sim 23 \text{ MPa}$ , where  $\gamma_{\text{aw}}$  is the surface tension of air/water and  $R$  is the radius of the particle) filling the voids between them while the glassy dPS nanoparticles remain spherical. With  $P_{\text{Lap}} \sim 23 \text{ MPa}$ , the glassy PS particles with a modulus  $G \sim \text{GPa}$  should remain spherical at the temperature of film formation ( $T^f$ ). The cross-linked PBMA particles, which exhibit an elastic modulus of  $G < 23 \text{ MPa}$  are expected to deform under  $P_{\text{Lap}} \sim 23 \text{ MPa}$  for  $T^f > T_g^{\text{PBMA}}$ . This leads to storage of elastic energy within the PBMA nanoparticles.

After annealing the nanoblends above the  $T_g^{\text{PS}}$ , the PBMA around the PS release the stored elastic energy by partially regaining their spherical shape, which induces the deformation of the PS particles (Scheme 1). SANS is then used to monitor the evolution of the shape of the PS particle and to quantify the dynamic of the confined polystyrene.

### The adequate procedure to obtain individual nanoparticles in nanoblends

To properly study the confined PS in nanoblends, one should first succeed in making films containing PS particles individually dispersed within cross-linked matrices. When the PS and the matrix-forming particles are mixed at low concentrations, they remain stable in water because of electrostatic repulsion. The idealistic situation to obtain a con-

**Scheme 1.** Description of the procedure for measuring the dynamic of PS in nanoblends. Step 1 is the procedure of nanoblends preparation and step 2 is the procedure for annealing the nanoblends (reproduced from ref. 28).

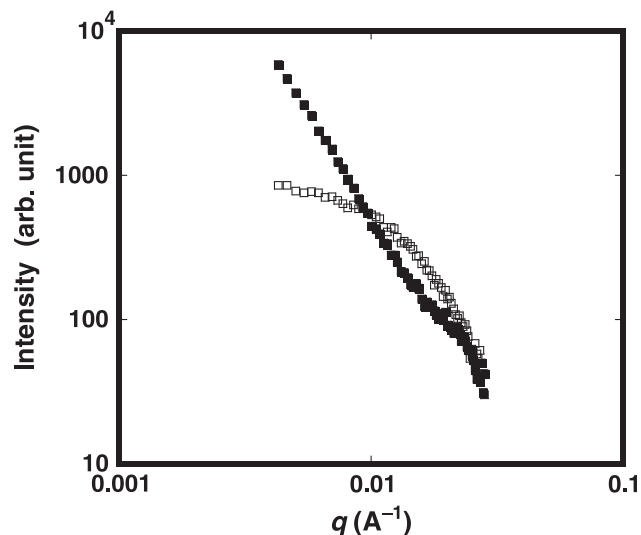


trolled dispersion at the nanoscopic level is that the two particles remain stable throughout the whole water evaporation process. During water evaporation the particle concentration increases, which could affect the stability of the different particles.

In Fig. 1, we compare the SANS spectra of 30 nm dPS particles dispersed in PBA and PBMA matrices. The spectra of dPS in a PBA matrix exhibit a strong scattering for  $q \rightarrow 0$ , which could be fitted to a power law with an exponent of  $-2.85$ . This suggests that dPS particles form large aggregates of dPS particles in the PBA matrix. On the other hand, the spectra of the same dPS particles in PBMA yields a low scattering intensity for  $q \rightarrow 0$ , which suggests that dPS are individually dispersed within the PBMA matrix. As we showed before when the PS and PBMA suspensions are cleaned using the ion exchange procedure, one can obtain nanoblends with perfect dispersion of the PS in the PBMA.<sup>27</sup> On the other hand, we could not obtain individual PS particles in the PBA even when both suspensions are cleaned in the same procedure as in the PS/PBMA. This shows that the ability to obtain nonaggregated particles in the blends depends on the physicochemical properties of the two particles during evaporation. In the following, we focus our discussion on the nanoblends of dPS in the PBMA matrix.

The SANS spectra of blends containing 2 wt% dPS (30, 77, and 80 nm) dispersed in a 10% cross-linked PBMA matrix exhibit a continuously decreasing scattering intensity,  $I(q)$  (Fig. 2). The  $I(q)$  were found to fit well to the  $P(q)$  of polydispersed hard spheres (Fig. 2). The best fit was found to yield for dPS-6 (77 nm) a mean particle diameter of 73 nm and for the dPS-1 (30 nm) a particle diameter of 28 nm. These diameters are similar to those from quasi elastic light scattering. This infers that the dPS nanoparticles are individually dispersed within the PBMA matrices and remain spherical in the blends. The intensity,  $I(q)$ , can be written as  $I(q) = P(q) \cdot S(q)$  where  $P(q)$  is the form factor and  $S(q)$  is the structure factor of the dPS particles.  $S(q) \approx 1$

**Fig. 1.** SANS spectra of films made from 2 wt% deuterated polystyrene particles (30 nm) dispersed in a 10% cross-linked PBA matrix (■) and in 10% cross-linked PBMA matrix (□). The films were prepared via evaporation at 56 °C of a mixture of dPS/PBMA (■) and dPS/PBA (□) suspensions.



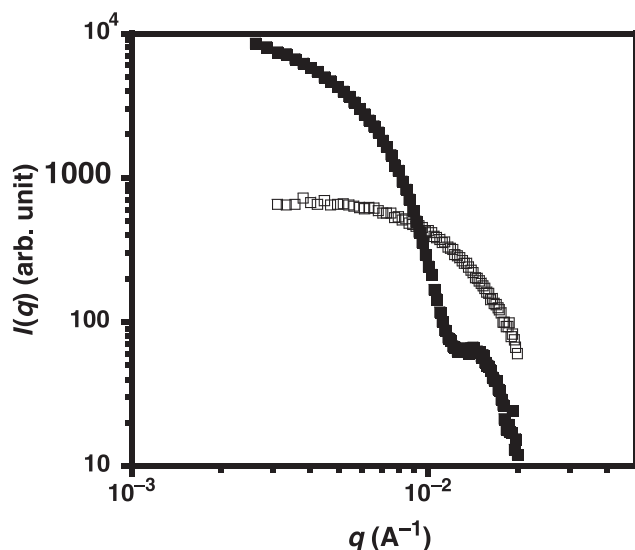
because of a low dPS concentration and the absence of selective aggregation. The spectra in Fig. 2 also imply that the cross-linked PBMA particles are deformed under Laplace pressure to fill the interstices. If not, a strong scattering peak from the PBMA matrix at  $q = 2\pi/D_{PBMA} = 0.01 \text{ Å}^{-1}$  would be visible, similar to that observed in glassy PS particles as will be discussed later.

#### Change of the shape of the particle after annealing

When the nanoblends of 77 nm dPS nanoparticles in 10% cross-linked PBMA are annealed above the bulk  $T_g$ , the shape of the dPS particles changes remarkably. The oscillations of the scattering spectra disappear and the intensity,  $I(q)$ , decreases for  $q < 0.01 \text{ Å}^{-1}$  and increases for



**Fig. 2.** SANS spectra of films made from 2 wt% deuterated polystyrene particles dispersed in a 10% cross-linked PBMA matrix: (a) 77 nm dPS (PS-6) and (b) 30 nm dPS (PS-1) particles. The films were prepared from a mixture of two suspensions: 10% cross-linked PBMA particles (56 nm) and dPS nanoparticles. The films were prepared by evaporation at 56 °C (above the  $T_g$  of PBMA and below  $T_g$  of dPS). The SANS curves are fitted to a form factor of (a) polydispersed spheres with a diameter of 73 nm and a polydispersity of PDI = 7% and (b) to polydispersed spheres with a diameter of 28 nm. (Insert: SANS of 80 nm particle (dPS-5) for a wide range of  $q$ , up to  $q = 0.1 \text{ \AA}^{-1}$ , fitted to a factor of spherical particle.)



$q > 0.01 \text{ \AA}^{-1}$ . This observation is found to be the same as the 80 nm dPS sample (dPS-5) reported previously.<sup>28</sup> The 30 nm particle also clearly shows the decrease of the intensity at  $q$  values after annealing. The evolution of the SANS spectra shows that the shape of the dPS nanoparticles evolves during the annealing process. We have shown previously that such change results from a deformation of the individual dPS particles during annealing.<sup>28</sup> One could imagine that the change in the SANS spectra results from penetration of deuterated polystyrene chains in the PBMA matrix or fusion of dPS particles. Fusion is unlikely because it results in large particles with a lower total surface area. This specific interface area between the dPS and the PBMA is estimated using the Porod law as  $q^4 \cdot I(q)$  at large  $q$  values. The average value of  $q^4 \cdot I(q)$  is found to triple after annealing, contrary to what is expected in fusion (Fig. 3 from ref. 28). Furthermore, since fusion yields large particles, a high scattering intensity for  $q \rightarrow 0$  is expected ( $I(0) \sim \phi \cdot V_{\text{part}}$ , where  $\phi$  is the volume fraction and  $V_{\text{part}}$  is the volume of the particles). In fact, the measured  $I(q)$  for low  $q$  after annealing is lower than  $I(q)$  of the nonannealed films in the range of  $q$  values investigated. This could mean that the volume of dPS particles remain unchanged despite the change in their shape. One could also imagine that the change in the SANS spectra results from penetration of deuterated polystyrene chains in the PBMA matrix. Polystyrene and uncross-linked PBMA form an interface which is a few nanometers thick,<sup>29</sup> whereas highly cross-linked PBMA is

likely to inhibit the interpenetration of the polymers. If penetration of dPS into the PBMA matrix is what causes the observed transformation in the SANS spectra, then the change should be more enhanced in low cross-linked PBMA matrices. In contrast with this, the spectra of films made of low cross-linked PBMA matrices remain slightly the same upon annealing (Fig. 4 from ref. 28). It is therefore clear that fusion of dPS nanoparticles and penetration of dPS into the PBMA matrix are not responsible for the observed transformation of the SANS spectra upon annealing. The change of SANS spectra most likely results from the deformation of individual polystyrene nanoparticles, which is dictated by the behavior of the surrounding cross-linked PBMA particles. During annealing, the cross-linked PBMA particles regain their spherical shape and squeeze the dPS particles between them. Such mechanism is likely to produce a dPS nanoparticle with an elongated shape with many branches. The simplest picture is that the dPS nanoparticles deform into a star-like shape with 12 branches according to Scheme 1.

#### *Dynamics of deformation of polystyrene confined in nanoblends at temperatures above the bulk glass transition*

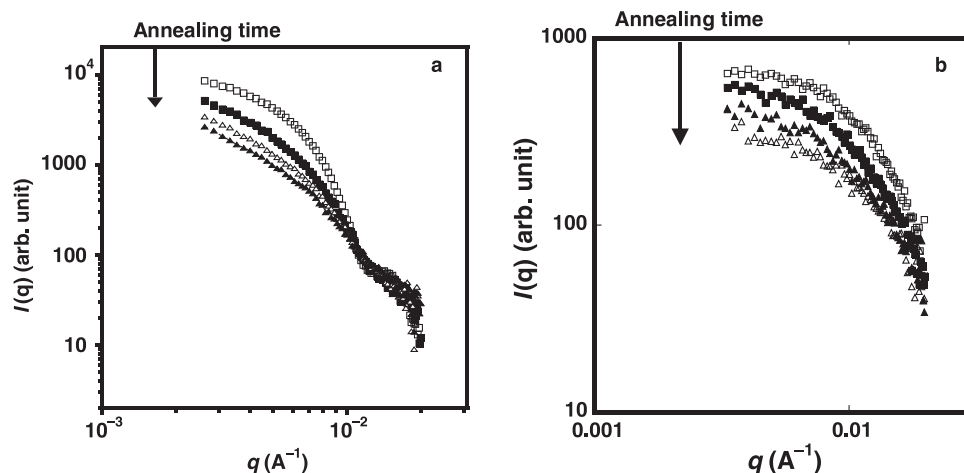
The shape of the spectra of 77 nm dPS in a 10% cross-linked PBMA matrix continuously changes during annealing at 140 °C: the intensity at low  $q$  decreases and that of large  $q$  increases (Fig. 3a). The evolution of the spectra with time reflects the change in the particles' shape during their deformation. Annealing the nanoblends with 30 nm particles at 140 °C gives the same behavior as the 77 nm particles (Fig. 3b): the intensity decreases in the low  $q$  range. This shows that this procedure can be used to test the dynamic of dPS particles in nanoblends for particles as small as 30 nm.

To quantify the dynamics of polystyrene particles in nanoblends, we can either use (i) the change of the scattering intensity at various  $q$  values,  $I(q,t)$ , or (ii) the variation of the gyration radius,  $R_g$ , of the dPS particle with time. In Fig. 4a, we show the scattering intensity at various  $q$  values for 77 nm dPS particles in 10% cross-linked PBMA matrix annealed at 140 °C. These plots fit perfectly to a stretched exponential with an exponent of  $\beta = 0.6$  (Fig. 5) and a relaxation time,  $\tau$ , which depends on the  $q$  value. The reliability of the fit and the estimation of the error bar in  $\beta$  and  $\tau$  are estimated from the width of the minimum of the least-squares plots versus  $\beta$  and  $\tau$ . The magnitude of change in the scattering intensity during annealing decreases when one approaches the minimum of  $P(q)$ , which makes it difficult to monitor the dynamic for  $q > 0.005 \text{ \AA}^{-1}$  for 77 nm and  $q > 0.01 \text{ \AA}^{-1}$  for 30 nm particles.

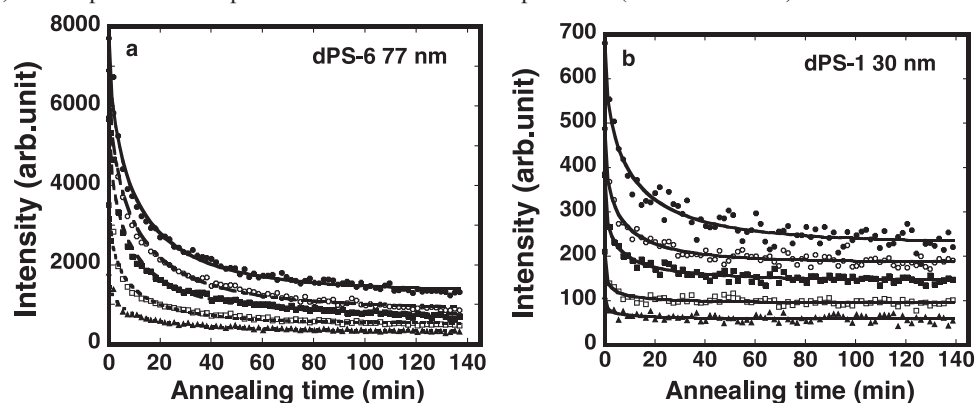
The  $R_g(t)$  at various annealing times is calculated by fitting the low  $q$  values of  $I(q)$  using the Guinier representation,  $\ln(I(q)) = \ln(I(0)) - q^2 \cdot R_g^2/3$ . The  $R_g(t)/R_g(0)$  decay for 77 nm dPS fits perfectly to a stretched exponential with a decay time of  $\tau_{R_g} = 25 \text{ min}$  and  $\beta = 0.64$  (Fig. 6). This behavior is exactly the same as that found previously on 80 nm particles;<sup>28</sup> however, the exponent was found to be  $\beta = 0.716 \pm 3\%$ , which is slightly higher than that found here. This infers that the exponent depends slightly on the property of the dPS particle and the surrounding matrix.



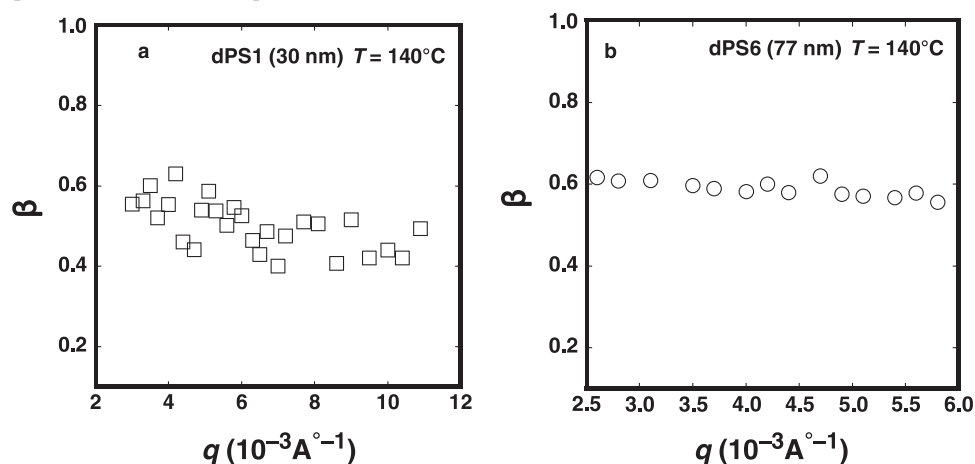
**Fig. 3.** (a) The scattering spectra plotted for various annealing times for 77 nm dPS nanoparticles in a 10% cross-linked PBMA matrix before annealing ( $\square$ ) and at 4 ( $\blacksquare$ ), 17 ( $\triangle$ ), and 37 min ( $\blacktriangle$ ). (b) The scattering spectra plotted for various annealing times for 30 nm dPS nanoparticles in a 10% cross-linked PBMA matrix. The films were annealed at 140 °C.



**Fig. 4.** The evolution of the scattering intensity at various  $q$  values, as a function of the annealing time for blends made from (a) 77 nm dPS nanoparticles and (b) 30 nm particles. The plot is fitted to a stretched exponential (continuous lines).



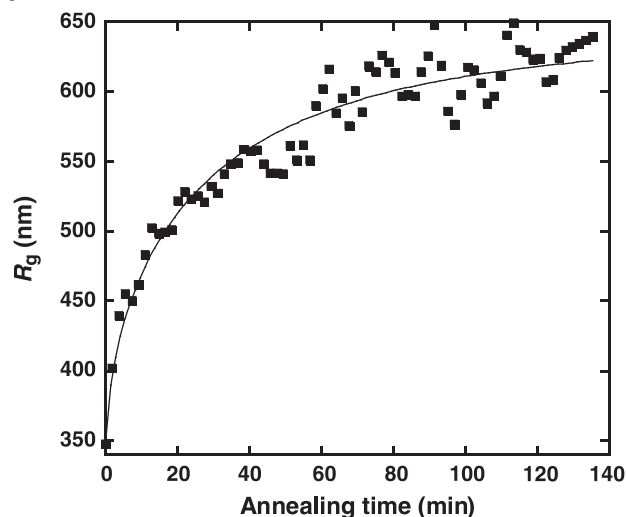
**Fig. 5.** The exponent  $\beta$  of the fit of the decays ( $I(q, t)$ ) in Fig. 4 to a stretched exponential ( $I(q, t) = I(q, 0) \exp - (t/\tau)^\beta$ ), plotted against the  $q$  values for (a) 30 nm particles and (b) 77 nm particles.



The time decay of the scattering intensity of the 30 nm particle was also found to fit to a stretched exponential with an exponent  $\beta = 5$  for  $q < 0.01 \text{\AA}^{-1}$ , which is slightly lower than that calculated in large particles (Fig. 5). The relaxation of the bulk PS is well-accepted to be a stretched exponential

with an exponent of 0.4.<sup>30</sup> The exponent,  $\beta$ , in our experiment reflects the change in the spreading mechanism of the dPS particle between the PBMA particles and therefore contains information on the exponent of the polymer relaxation as well as other parameters such as the particle size.

**Fig. 6.**  $R_g(t)$  vs. the annealing time for blends made from 77 nm dPS nanoparticles in 10% cross-linked PBMA annealed at 140 °C.  $R_g$  is calculated using the Guinier representation.



The appropriate parameter to characterize the stretched exponential dynamic is the average relaxation time,  $\langle\tau\rangle$ , which is calculated as  $\langle\tau\rangle = \int \exp(-(t/\tau)^\beta) dt$  using the  $\tau$  and  $\beta$  values.<sup>31</sup> The  $\langle\tau(q)\rangle$  in 77 nm dPS particles decreases with increasing  $q$  from 16.6 min to 11.4 min for  $q$  values between  $2.58 \times 10^{-3} \text{ \AA}^{-1}$  and  $5.1 \times 10^{-3} \text{ \AA}^{-1}$  (Fig. 7a). For 30 nm dPS  $\langle\tau\rangle$  was also found to decrease with increasing  $q$  in the same manner as the 77 nm particles (Fig. 7b). Such tendency is similar to that reported previously on dPS-6. Since  $I(q)$  at each  $q$  value portrays the density fluctuations with a size of  $\xi = 2\pi/q$ ,  $\langle\tau(q)\rangle$  also describes the relaxation dynamic of the density fluctuation with a size of  $\xi$ . Larger fluctuations would require more time to change than a smaller fluctuation. Therefore,  $\langle\tau(q)\rangle$  increases with increasing  $\xi$  and thus increases with decreasing  $q$ . For  $q$  approaching  $q = 0$ ,  $\langle\tau(q)\rangle$  converges toward the relaxation time of the gyration radius,  $\langle\tau_{R_g}\rangle$ , which is the largest size of the system,  $\langle\tau(q)\rangle_{R_g} = 34$  min.

The  $\langle\tau(q)\rangle$  of 30 nm particles is found to be larger than the  $\langle\tau(q)\rangle$  of 77 nm when measured at the same  $q$  values (Fig. 7b). The  $\langle\tau(q)\rangle$  and  $\langle\tau_{R_g}\rangle$  describe the dynamic of particle deformation under the applied stress,  $\sigma(t)$ , and depends directly on the relaxation time of the confined polymer ( $\tau_\alpha$ ). During the film formation, PBMA particles around smaller dPS particles undergo a small deformation as compared to around large particles, thus, they store less stress. Therefore, one expects smaller particles to deform more slowly than large ones if the PS behaves dynamically in the same manner in the two particles. To derive  $\tau_\alpha$  from  $\langle\tau(q)\rangle$  and  $\langle\tau_{R_g}\rangle$ , we assume the polymer to exhibit a single exponential relaxation with a time  $\tau_\alpha$  and use the following differential equation (eq. [1]).

$$[1] \quad \frac{d\sigma(t)}{dt} + \frac{\sigma(t)}{\tau_\alpha} = G \frac{d\varepsilon(t)}{dt}$$

where  $G$  is the high shear modulus and the deformation strain,  $\varepsilon(t)$ , defined by  $R_g(t)/R_g(0)$  or  $I(q,t)/I(q,0)$ . Equation [1] applies only if the time and the position dependence of

$\varepsilon(t)$  and  $\sigma(t)$  can be separated. It is easy to accept that the stored strain,  $\sigma(t)$ , decrease with increasing the time in the same manner as  $\varepsilon(t)$ . If we take  $\varepsilon(t)$  and  $\sigma(t)$  as exponential with relaxation time,  $\langle\tau(q)\rangle$  or  $\langle\tau_{R_g}\rangle$ , we found

$$[2] \quad \langle\tau\rangle \approx \frac{G}{\sigma(0)} \tau_\alpha$$

The PBMA particles around small dPS particles undergo a small deformation compared to around large dPS ones. Thus, one expects the stored stress,  $\sigma(0)$ , in the case of small dPS particles to be lower than that in large ones. If we take  $\sigma(0)$  to be proportional to the dPS particle diameter,  $D$  ( $\sigma(0) \propto D$ ), we found  $\tau_\alpha \propto \langle\tau\rangle \cdot D$ . In Fig. 8, we compare the plots  $\langle\tau\rangle \cdot D$  versus  $q$  for 77 nm and 30 nm dPS particles. The  $\langle\tau\rangle \cdot D$  of 30 nm particles is found to be lower than that of 77 nm, which could infer that the relaxation time of confined polystyrene,  $\tau_\alpha$ , of 30 nm is smaller than that of 77 nm.

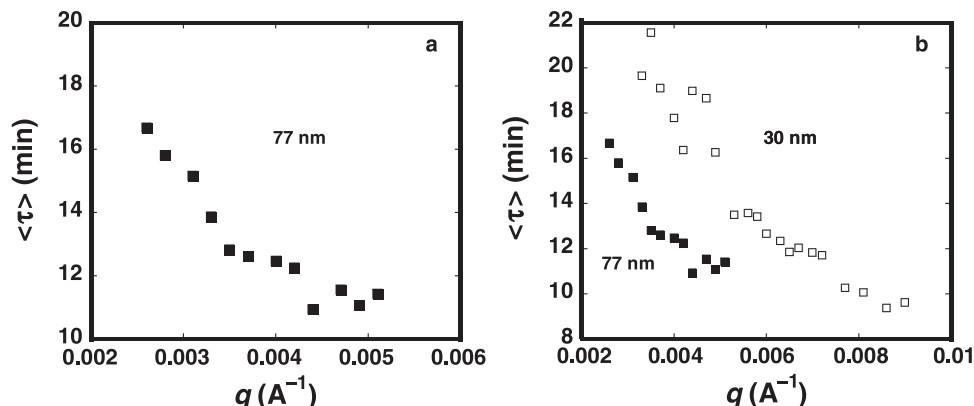
The decay times,  $\langle\tau(q)\rangle$  and  $\langle\tau_{R_g}\rangle$ , contain useful information about the relaxation time of the confined polystyrene in the nanoparticles in nanoblends. The evolution of these times with temperature and the particle size will be used to obtain information on the effect of confinement on the polymer dynamic.

#### Protocol for measuring the dynamic of polystyrene nanoparticles in a close-packed structure

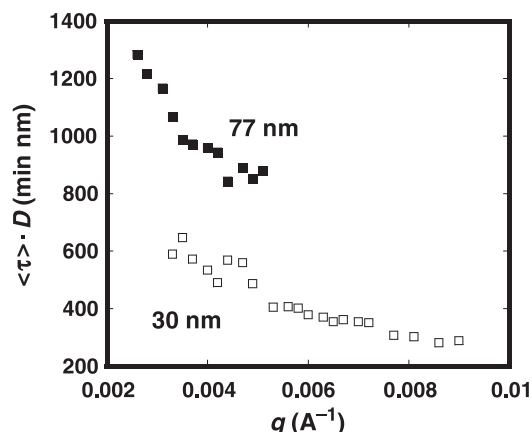
To apply the stress locally to polymer nanoparticles, we also propose the following procedure: When suspensions of polymer particles are evaporated below the glass transition temperature ( $T_g$ ) of the polymer, the particles remain spherical and form a close-packed structure separated with voids (Scheme 2, stage II). The presence of a large interface area (polymer/air) in the voids makes the particles a confined system, which could affect the polymer dynamic and, consequently, the kinetic of particle deformation and void closure. The presence of the voids applies Laplace pressure in the interstices due to the air/polystyrene surface tension ( $\gamma_{p/a}$ ),  $P_{\text{Lap}} = \alpha\gamma_{p/a}/R$ ,  $\gamma_{p/a} = 0.03 \text{ N/m}^2$ . This tends to deform the particle and close the voids to yield a bulk-like polymer (Scheme 2, stage III). If the particles are glassy, the voids should remain unaffected by Laplace pressure during the time of the experiment, and when the system is annealed above the polymer  $T_g$ , the particles deform and the voids close. If one can probe the closure of the interstices, then this can be used as a nonintrusive method to study the dynamic of confined polymers in nanoparticles. We used the small-angle neutron scattering technique to probe the deformation of the particles during annealing. Previous experiments used atomic force microscopy to monitor the change in the free surface corrugation during annealing of submicron size particles.<sup>32–35</sup> The dynamic of free surface corrugation in polyacrylate was found to be similar to the bulk dynamic.<sup>34,35</sup>

The SANS spectra of films made from 93 nm PS particles at 45 °C before annealing exhibit a well-defined narrow first peak followed by two small peaks (Fig. 9). The position of the first peak,  $q^*$ , corresponds to a characteristic distance of  $D^* = 2\pi(3/2)^{1/2}/q^* = 99 \text{ nm}$ , which is almost equal to the hydrodynamic diameter of the particles measured by dynamic light scattering. It is well-accepted that the drying of

**Fig. 7.** (a) Average relaxation time,  $\langle\tau(q)\rangle$ , plotted against  $q$  for blends of 77 nm dPS particles in 10% cross-linked PBMA matrix.  $\langle\tau(q)\rangle$  is calculated from the fit of the scattering intensities ( $I(q)$  vs. time) to a stretched exponential (Fig. 4). (b) Comparison of the plots  $\langle\tau(q)\rangle$  vs.  $q$  of the 77 nm (dPS-6) (■) and 30 nm dPS-1 (□) particles.  $\langle\tau(q)\rangle$  is calculated from the fit of the scattering intensities ( $I(q,t)$ ) to a stretched exponential.



**Fig. 8.** Relaxation time,  $\langle\tau(q)\rangle \cdot D$  plotted against  $q$  for 77 nm (dPS-6) (■) and 30 nm dPS-1 (□).  $\langle\tau(q)\rangle$  is calculated from the fit of the scattering intensities ( $I(q)$  vs. time) to a stretched exponential.



suspensions of monodispersed particles form a face centered cubic structure (FCC).<sup>25</sup> The contrast in the neutron scattering comes from the difference between the PS in the particles and the voids between them. The strong contrast in the SANS when the suspensions are dried below  $T_g$  infers that the particles remain spherical and separated with voids (Scheme 1, stage II).

#### Dynamic of void closure in 93 nm particles at the bulk $T_g$

When the PS samples are annealed at 100 °C both the first, second, and the third peaks decrease progressively and broaden during annealing (Fig. 9). After 30 min, the second peak disappears while the first peak turns into a broad maximum, and at 60 min both peaks have disappeared. The intensity measured at the first peak decreases steadily during annealing until it becomes purely the incoherent scattering from the PS (Fig. 10). The steady decrease of the intensity results from the progressive closure of the voids under the action of Laplace pressure. The scattering intensity varies as  $I(t) \propto (V_{\text{voids}}(t))^2$ , where  $V_{\text{voids}}$  is the volume of the voids between the particles. A random close-packed structure corresponds to a volume fraction of the solid of 0.64 and frac-

tion of the voids of 0.36.<sup>36</sup> Thus, the intensity can be written as  $I(t) \propto (V_{\text{voids}}(0))^2(0.36 - \varepsilon(t))^2$ , where  $\varepsilon(t)$  is the deformation strain of the sample and  $V_{\text{voids}}(0)$  is the initial volume of the voids or  $I(t)/I(0) \propto ((0.36 - \varepsilon(t))/(0.36 - \varepsilon(0)))^2$ .

Using a generalized Hertzian model<sup>37,38</sup> for the deformation of particles in a close-packed morphology, and assuming film shrinking occurs in the  $z$  direction, the governing equation can be written as eq. [3] when the deformation is averaged over all directions and over the entire film.<sup>36</sup>

$$[3] \quad \frac{6.69(1-\nu)\gamma_{p/a}}{R} = \int_0^t G(t-t') \frac{d\varepsilon^{3/2}}{dt'} dt'$$

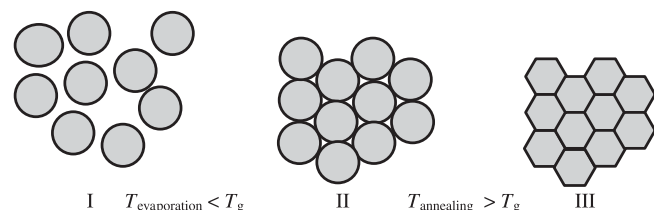
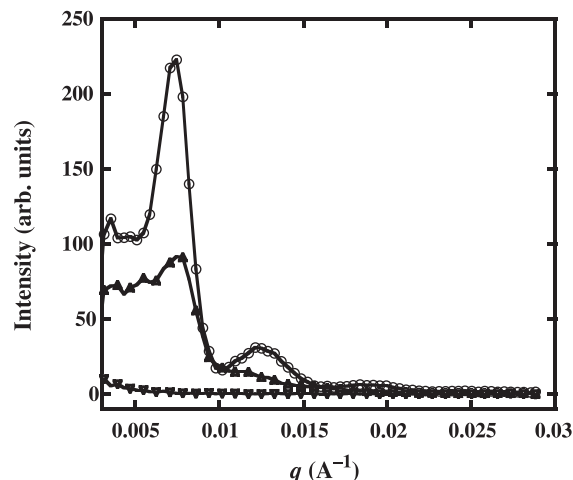
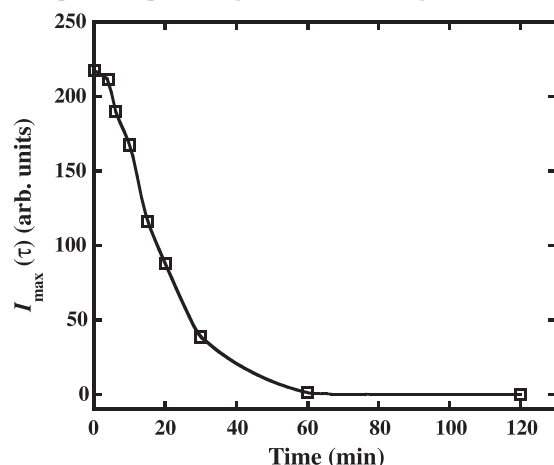
where  $G(t)$  is time dependent shear stress,  $\gamma_{p/a}$  is the surface tension between the PS and air,  $\nu$  is the Poisson's ratio of polystyrene ( $\nu = 0.33$ ), and  $R$  is the particle radius.

Near  $T_g$  and for short times, the compliance of PS is dominated by the glassy relaxation process.<sup>47</sup> If we assume the PS in this condition to exhibit a single relaxation time,  $\tau(G(t)$  is an exponential), the  $t_{\text{close}}$  can be calculated from eq. [3] as the time for which  $\varepsilon(t_{\text{close}}) = 0.36$  to give eq. [4]:

$$[4] \quad t_{\text{close}} \approx \frac{0.0479 G}{\gamma_{p/a}} R \cdot \tau$$

where  $G$  is the high frequency shear stress ( $G \sim 1$  GPa) and  $R$  the particle radius. From eq. [4], we can estimate  $\tau \approx 37$  s for  $D = 93$  nm. When the relaxation time was calculated by numerically resolving eq. [3], using the strain  $\varepsilon(t)$  from  $I(t)/I(0) \propto ((0.36 - \varepsilon(t))/(0.36 - \varepsilon(0)))^2$  we found  $\tau \approx 44$  s. The polystyrene dynamic in the glassy regime near the  $T_g$  is more likely to be a stretched exponential ( $G(t) = \exp(-(t/\tau)^\beta)$ ) with an exponent  $\beta = 0.4$ .<sup>30,39</sup> In this case, we estimated the average relaxation time,  $\langle\tau\rangle$  ( $\langle\tau\rangle = \int \exp(-(t/\tau)^\beta) dt$ ), by numerically resolving eq. [3] with  $\varepsilon(t)$  from  $I(t)/I(0) \propto ((0.36 - \varepsilon(t))/(0.36 - \varepsilon(0)))^2$ , which leads to  $\langle\tau\rangle \approx 47$  s. This shows that the various methods for calculating the relaxation time yield similar values.

Contrary to the first method described here, this method gives an absolute value of the relaxation time of the confined polystyrene in nanoparticles. The evolution of  $\langle\tau\rangle$  with a change in temperature and particle size will be used

**Scheme 2.** The three main steps of the film formation process.**Fig. 9.** SANS spectra of film made from 93 nm PS nanoparticles, annealed at 100 °C for various annealing times: 0 (○), 20 (▲), and 60 min (▼).**Fig. 10.** SANS intensity at the first scattering peak,  $I_{\max}(t)$ , of 93 nm PS particles plotted against the annealing time.

in further work to obtain information on the effect of confinement on the polymer dynamic.

## Conclusion

We presented two methods to probe the dynamic of polymers in nanoparticles in two different environments: (i) nanoblends and (ii) close-packed structures. We use neutron scattering to probe the kinetic of nanoparticle deformation under the action of applied stress at the nanoscopic level. For the nanoblends, we prepared the samples by water evaporation of suspensions of glassy PS and elastic PBMA (cross-linked) nanoparticles at  $T_g^{\text{PBMA}} < T^{\text{ev}} < T_g^{\text{PS}}$ . This

leads to storage of elastic stress in the cross-linked PBMA particles around the PS. During annealing at  $T_{\text{annealing}} > T_g^{\text{PS}}$ , the PS particles deform, and this deformation is probed by SANS. The characteristic time from this method can be used to obtain information on the relaxation time of confined PS nanoparticles in nanoblends. In the close-packed structure, the voids between the spherical particles apply Laplace pressure to the particles, which deforms the particle and closes the voids. The kinetic of void closure is used to obtain information on the dynamic of confined PS in nanoparticles. These two methods give new possibilities to probe, in a nonintrusive manner, the dynamic of confined polymers in nanoparticles, which ultimately could bring conclusive insight in this field.

## Acknowledgment

We Acknowledge the Pakistani ministry of education, the Higher Education Commission (HEC) of Pakistani and the French Société Française d'Exportation des ressources Éducatives (SFERE) program for Mr. Nawaz's scholarship. We also thank the French ministry of education and the Cluster Matériaux et Conception pour un Développement durable (MACODEV) program for their financial support. The French neutron facility at the Commissariat à l'Énergie Atomique (CEA) Saclay and the Laboratoire Léon Brillouin (LLB) are gratefully acknowledged for the neutron equipment. We thank Dr. F. Boué (LLB) and Dr. A. Lapp (LLB) for their help in the neutron scattering experiments and for the stimulating discussions. H. Galliard is also acknowledged for her help with these experiments.

## References

- (1) Alcoutlabi, M.; McKenna, G. B. *J. Phys. Condens. Matter* **2005**, *17* (15), R461. doi:10.1088/0953-8984/17/15/R01.
- (2) Forrest, J. A. *Eur. Phys. J. E* **2002**, *8* (2), 261. PMID: 15010978.
- (3) Forrest, J. A.; Dalnoki-Veress, K.; Stevens, J. R.; Dutcher, J. R. *Phys. Rev. Lett.* **1996**, *77* (10), 2002. doi:10.1103/PhysRevLett.77.2002. PMID:10061832.
- (4) Forrest, J. A.; Mattsson, J. *Phys. Rev. E Stat. Phys. Plasmas Fluids Relat. Interdiscip. Top.* **2000**, *61* (1), R53. PMID: 11046371.
- (5) Ellison, C. J.; Torkelson, J. M. *Nat. Mater.* **2003**, *2* (10), 695. doi:10.1038/nmat980. PMID:14502273.
- (6) Keddie, J. L.; Jones, R. A. L.; Cory, R. A. *Europhys. Lett.* **1994**, *27* (1), 59. doi:10.1209/0295-5075/27/1/011.
- (7) Fukao, K.; Miyamoto, Y. *Phys. Rev. E Stat. Phys. Plasmas Fluids Relat. Interdiscip. Top.* **2000**, *61* (2), 1743. PMID: 11046459.
- (8) Rotella, C.; Napolitano, S.; Wübbenhorst, M. *Macromolecules* **2009**, *42* (5), 1415. doi:10.1021/ma8027968.
- (9) Shin, K.; Obukhov, S.; Chen, J.-T.; Huh, J.; Hwang, Y.; Mok, S.; Dobriyal, P.; Thiagarajan, P.; Russell, T. P. *Nat. Mater.* **2007**, *6* (12), 961. doi:10.1038/nmat2031.
- (10) Reiter, G.; Hamieh, M.; Damman, P.; Sclavons, S.; Gabriele, S.; Vilmin, T.; Raphaël, E. *Nat. Mater.* **2005**, *4* (10), 754. doi:10.1038/nmat1484. PMID:16184173.
- (11) Roth, C. B.; Dutcher, J. R. *Phys. Rev. E Stat. Nonlin. Soft Matter Phys.* **2005**, *72* (2), 021803. PMID:16196593.
- (12) Frank, B.; Gast, A. P.; Russel, T. P.; Brown, H. R.; Hawker, C. *Macromolecules* **1996**, *29* (20), 6531. doi:10.1021/ma960749n.



- (13) O'Connell, P. A.; McKenna, G. B. *Science* **2005**, *307* (5716), 1760. doi:10.1126/science.1105658. PMID:15774754.
- (14) Bodiguel, H.; Fretigny, C. *Phys. Rev. Lett.* **2006**, *97* (26), 266105. doi:10.1103/PhysRevLett.97.266105. PMID:17280434.
- (15) Si, L.; Massa, M. V.; Dalnoki-Veress, K.; Brown, H. R.; Jones, R. A. L. *Phys. Rev. Lett.* **2005**, *94* (12), 127801. doi:10.1103/PhysRevLett.94.127801.
- (16) Fakhraai, Z.; Forrest, J. A. *Science* **2008**, *319* (5863), 600. doi:10.1126/science.1151205. PMID:18239120.
- (17) Qi, D.; Fakhraai, Z.; Forrest, J. A. *Phys. Rev. Lett.* **2008**, *101* (9), 096101. doi:10.1103/PhysRevLett.101.096101. PMID:18851624.
- (18) Papaléo, R. M.; Leal, R.; Carreira, W. H.; Barbosa, L. G.; Bello, I.; Bulla, A. *Phys. Rev. B* **2006**, *74* (9), 094203. doi:10.1103/PhysRevB.74.094203.
- (19) Gasemjit, P.; Johannsmann, D. *J. Polym. Sci., Part B: Polym. Phys.* **2006**, *44* (20), 3031. doi:10.1002/polb.20922.
- (20) Winnit, M. A. *Curr. Opin. Colloid Interface Sci.* **1997**, *2*, 192.
- (21) Steward, P. A.; Hearn, J.; Wilkinson, M. C. *Adv. Colloid Interface Sci.* **2000**, *86* (3), 195. doi:10.1016/S0001-8686(99)00037-8. PMID:10997764.
- (22) Sasaki, T.; Shimizu, A.; Mourey, T. H.; Thureau, C. T.; Ediger, M. D. *J. Chem. Phys.* **2003**, *119* (16), 8730. doi:10.1063/1.1613257.
- (23) Herminghaus, S.; Seemann, R.; Landfester, K. *Phys. Rev. Lett.* **2004**, *93* (1), 017801. doi:10.1103/PhysRevLett.93.017801.
- (24) Nawaz, Q.; Rharbi, Y. *Macromolecules* **2008**, *41* (15), 5928. doi:10.1021/ma7028049.
- (25) Chevalier, Y.; Pichot, C.; Graillat, C.; Joanicot, M.; Wong, K.; Maquet, J.; Lindner, P.; Cabane, B. *Colloid Polym. Sci.* **1992**, *270* (8), 806. doi:10.1007/BF00776153.
- (26) Rharbi, Y.; Boué, F.; Joanicot, M.; Cabane, B. *Macromolecules* **1996**, *29* (12), 4346. doi:10.1021/ma951142u.
- (27) Rharbi, Y. *Phys. Rev. E Stat. Nonlin. Soft Matter Phys.* **2008**, *77* (3), 031806. PMID:18517413.
- (28) Yousfi, M.; Porcar, L.; Lindner, P.; Boué, F.; Rharbi, Y. *Macromolecules* **2009**, *42* (6), 2190. doi:10.1021/ma802734j.
- (29) Spiro, J. G.; Yang, J.; Zhang, J. -X.; Winnik, M. A.; Rharbi, Y.; Vavasour, J. D.; Whitmore, M. D.; Jérôme, R. *Macromolecules* **2006**, *39* (20), 7055. doi:10.1021/ma0526037.
- (30) Ferry, J. D. *Viscoelastic Properties of Polymers*, 3rd ed.; Wiley: New York, 1980.
- (31) Dhinojwala, A.; Wong, G. K.; Torkelson, J. M. *J. Chem. Phys.* **1994**, *100* (8), 6046. doi:10.1063/1.467115.
- (32) Goudy, A.; Gee, M. L.; Biggs, S.; Underwood, S. *Langmuir* **1995**, *11* (11), 4454. doi:10.1021/la00011a045.
- (33) Pérez, E.; Lang, J. *Langmuir* **2000**, *16* (4), 1874. doi:10.1021/la990595f.
- (34) Pérez, E.; Lang, J. *Macromolecules* **1999**, *32* (5), 1626. doi:10.1021/ma9704121.
- (35) Lin, F.; Meier, D. J. *Langmuir* **1996**, *12* (11), 2774. doi:10.1021/la951554w.
- (36) Russel, W. B.; Wu, N.; Man, W. *Langmuir* **2008**, *24* (5), 1721. doi:10.1021/la702633t. PMID:18197713.
- (37) Hertz, H. *J. Reine Angew. Math.* **1881**, *92*, 156.
- (38) Hertz, H. *Gesammelte Werke* **1895**, *1*, 155.
- (39) Lin, Y. H.; *J. Phys. Chem. Br.* **2005**, *109*, 17654.

# Hybrid microspheres with alternating layers of a polymer and metal nanoparticles

Alla Petukhova, Andrew S. Paton, Ilya Gourevich, Selvakumar V. Nair, Harry E. Ruda, Alexander Shik, and Eugenia Kumacheva

**Abstract:** We studied the optical properties of hybrid multilayer microspheres (HMMs). We prepared multilayer particles with alternating radial layers of gold nanoparticles (NPs) and poly(methyl methacrylate) and achieved control over particle size, the thickness of particle layers, and the surface coverage of gold NPs. We showed the ability to tune the spectral characteristics of the HMMs, which was based on frequency dispersion of the dielectric constant of polymer–metal NP structures. Good agreement between experimental and theoretical extinction properties of the HMMs was obtained. In comparison with multilayer structures synthesized solely from polymers, hybrid multilayer microspheres have a larger refractive layer contrast between adjacent layers, which is important for practical applications in optoelectronic devices.

**Key words:** hybrid polymer–inorganic materials, polymer microspheres, gold nanoparticles, optical properties, extinction spectra.

**Résumé :** On a étudié les propriétés optiques de microsphères multicouches hybrides (MMH). On a préparé les particules à multicouches comportant des couches radiales alternantes de nanoparticules (NP) d'or et de poly(méthacrylate de méthyle) et on a pu contrôler la taille des particules des couches et la surface de la couverture des nanoparticules d'or. On a pu contrôler les caractéristiques spectrales des microsphères multicouches hybrides en ajustant la fréquence de dispersion de la constante de diélectrique des structures des nanoparticules polymère–métal. On a obtenu un bon accord entre les propriétés d'extinction expérimentales et théoriques des microsphères multicouches hybrides. Par comparaison avec les structures multicouches synthétisées uniquement à partir de polymères, les microsphères multicouches hybrides possèdent un plus grand contraste de réfraction par couche entre les couches, propriété importante pour les applications pratiques dans les appareils optoélectroniques.

**Mots-clés :** matériaux hybrides polymère–inorganique, microsphères de polymère, nanoparticules d'or, propriétés optiques, spectres d'extinction.

[Traduit par la Rédaction]

## Introduction

Polymer microspheres with a multilayer onion-like structure possess optical properties that are useful in photonic crystals,<sup>1,2</sup> optical data storage,<sup>3,4</sup> biometrics,<sup>5,6</sup> and, sensing and single-particle optical limiting.<sup>7–10</sup> Polymer multilayer particles with a radial modulation in the refractive index can also be used as optical-frequency resonators: due to Bragg reflection at the interfaces between the layers, light propagation in the particles at a given wavelength can be suppressed when reflection from the interfaces adds in phase and approaches unity.<sup>11</sup> For this application, the advantage of using polymer multilayer microspheres is their narrow size distribution and precisely controlled thickness of constituent layers, achieved in multistep polymerization proc-

esses.<sup>12,13</sup> The drawback of all-polymer particles is an inherent low refractive index contrast,  $\Delta n$ , between the layers, which requires a large number of layers to be incorporated in the multilayer structure, to achieve suppressed light propagation.<sup>11,14</sup> Fabrication of such multilayer structures, with specific properties of the layers, represents a cumbersome technological procedure. One of the promising approaches to such particles relies on an increase in the refractive index contrast between adjacent layers.

In the present work, this problem is solved by replacing all-polymer multilayer structures with metal–polymer, hybrid multilayer microspheres (HMMs). We synthesized and assembled multilayer particles with alternating layers of gold nanoparticles (NPs) and poly(methyl methacrylate)

Received 28 August 2009. Accepted 16 November 2009. Published on the NRC Research Press Web site at [canjchem.nrc.ca](http://canjchem.nrc.ca) on 26 February 2010.

*This article is part of a Special Issue dedicated to Professor M. A. Winnik.*

A. Petukhova and A. S. Paton contributed equally in this work.

**A. Petukhova, A.S. Paton, I. Gourevich, and E. Kumacheva.**<sup>1</sup> Department of Chemistry, University of Toronto, 80 Saint George street, Toronto, ON M5S 3H6, Canada.

**S.V. Nair, H.E. Ruda, and A. Shik.** Centre for Advanced Nanotechnology, University of Toronto, 170 College street, Toronto, ON M5S 3E4, Canada.

<sup>1</sup>Corresponding author (e-mail: [ekumache@chem.utoronto.ca](mailto:ekumache@chem.utoronto.ca)).

(PMMA). The use of layers of NPs (versus homogeneous gold layers) provided the ability to maintain a well-defined wavelength of absorption of the hybrid structures, in comparison with a red-shifted plasmonic resonance peak characteristic for dielectric particles with continuous gold shells.<sup>15</sup> In addition, a strong frequency dispersion of the dielectric constant of polymer-metal NP structures provided the ability to tune the spectral characteristics of the HMMs. We achieved control over particle size, the thickness of particle layers, and the surface density of gold NPs. Experimentally measured and theoretically predicted extinction properties of the HMMs were in good agreement.

## Experimental

### Materials

Methyl methacrylate (99%) was purchased from Fluka Canada. Ethylene glycol dimethacrylate (EGDMA, 98%), 4-vinylpyridine (4VP, 95%), 2,2'-azobis(2-methylpropionamide) dihydrochloride (V-50, 97%), poly(diallyldimethylammonium chloride) (PDDMAC, low molecular weight, 20 wt% in water), poly(sodium 4-styrenesulfonate) (PSS, average  $M_w \approx 70\,000$ ), hydrogen tetrachloroaurate(III) ( $\text{HAuCl}_4$ , 30 wt% solution in dilute hydrochloric acid, 99.99%), tetrakis(hydroxymethyl) phosphonium chloride (THPC, 80% solution in  $\text{H}_2\text{O}$ ) were purchased from Sigma-Aldrich Canada. All chemicals were used as received. Deionized water (18.2 M $\Omega$  cm) was purified by using a Millipore Milli-Q Plus purification system (Millipore Corp.).

### Synthesis of hybrid multilayer microspheres

#### Preparation of gold NPs

Negatively charged gold NPs were prepared by the reduction of tetrachloroauric acid with tetrakis(hydroxymethyl)phosphonium chloride, which was adapted from a method described elsewhere.<sup>16</sup> Briefly, to a vessel (e.g., a 125 mL erlenmeyer flask) containing 96 mL of deionized water, aqueous solutions of sodium hydroxide (1 mol/L, 1.0 mL) and the reducing agent THPC (1.29% w/w in water, 1.5 mL) were added under stirring. There were 4 min allowed between the addition of THPC and tetrachloroauric acid, and then  $\text{HAuCl}_4$  (28 mmol/L, 1 mL) was injected rapidly into the stirring solution. The color of the solution changed to dark brown, indicating the formation of small gold NPs. The NPs were aged for two weeks before the attachment to polymer particles.

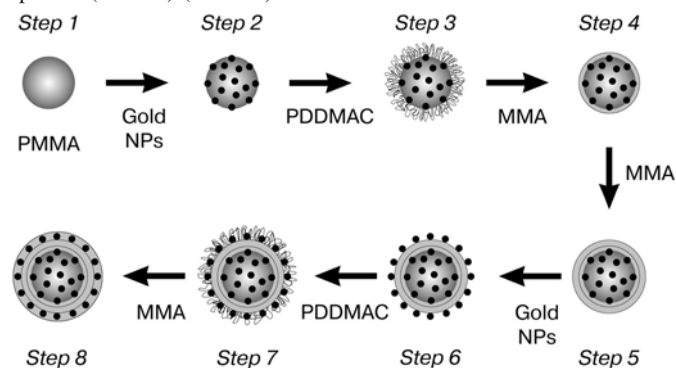
#### Synthesis of hybrid multilayer microspheres

The procedure of the synthesis of HMMs is shown schematically in Fig. 1. The latex particles were prepared using a surfactant-free emulsion polymerization procedure described elsewhere.<sup>12,14</sup> All reactions were carried out under nitrogen pressure in a double-walled three-neck flask equipped with a reflux condenser, a nitrogen inlet, and a mechanical stirrer at  $80 \pm 0.1^\circ\text{C}$ .

#### Step 1 — Synthesis of the polymer core

Positively charged 120 nm PMMA-co-P4VP particles (microspheres cores) were synthesized in a batch reaction. The reactor was charged with water (100 g) and mixture of methyl methacrylate (1.5 g), 4-vinylpyridine (0.015 g), and

**Fig. 1.** Schematics of the preparation of hybrid multilayer microspheres (HMMs) (see text).



the cross-linking agent EGDMA (0.015 g) and purged with nitrogen for 30 min. The temperature of the mixture was then increased to  $80 \pm 0.1^\circ\text{C}$ . An aqueous solution of V-50 (0.05 g) was injected into the reactor with a syringe. The reaction was carried out for 3 h. After the 30 min centrifugation cycle at 10 000 rpm (Eppendorf centrifuge 5417R), the supernatant was removed, the precipitated particles were redispersed in deionized water and sonicated for 2–3 min.

#### Step 2 — Attachment of gold NPs to PMMA-co-P4VP polymer particles

To achieve 30% surface coverage of the surface of polymer microspheres with gold NPs, 35 g of the solution of gold NPs were added at pH = 6.0 to 4 g of the dispersion of latex particles synthesized in Step 1 under vigorous stirring for 1 h. The system was then centrifuged at 8000 rpm for 30 min, the sediment was removed and diluted with water up to 50 mL and sonicated for 40 min. To achieve surface coverage lower than 30%, the solution of gold NPs was mixed with PSS with the concentration in the range of 0.01–0.001 wt% and this mixed solution was added to the dispersion of polymer particles, as described above.

#### Step 3 — Adsorption of PDDMAC

An aqueous solution of the cationic polyelectrolyte, PDDMAC (100 mL, 0.1%), was added dropwise at a rate 20 mL/h to the aqueous solution of hybrid microspheres from Step 2 using a fluid-metering pump. Excess PDDMAC was removed by centrifugation of the particles at 10 000 rpm for 30 min. The supernatant was removed and the precipitated particles were redispersed in deionized water and sonicated for 1 h.

#### Step 4 — Synthesis of the PMMA layer on the surface of hybrid particles

The PMMA layer on the surface of hybrid particles was prepared by using a multistage surfactant-free emulsion polymerization method.<sup>12,14</sup> The dispersion of hybrid microspheres (150 g) from Step 3 and water (10 g) were charged in the reaction flask and methyl methacrylate (1 g), EGDMA (0.01 g), and an aqueous solution of V-50 (0.05 g) were introduced using a syringe pump at a rate of 0.144 mL/h. The system was heated to  $80^\circ\text{C}$ , and the polymerization reaction was continued for 1 h after the feeding stage was complete. The latex was purified by centrifugation at 8000 rpm for 30 min, the supernatant was removed, and

the precipitated particles were redispersed in deionized water (100 g) and then sonicated for 2–3 min.

#### Step 5 — Synthesis of the PMMA-co-P4VP layer on the surface of hybrid particles

The synthesis of the PMMA-co-P4VP layer on the surface of hybrid particles was conducted in the same manner as in Step 4. Briefly, after mixing an aqueous solution of hybrid microspheres (70 g) from Step 4 and water (60 g) in the reaction flask, methyl methacrylate (2.5 g), EGDMA (0.025 g), 4-vinylpyridine (0.025 g), and an aqueous solution of V-50 (0.025 g) were introduced into the flask using a syringe pump at a rate of 0.4 mL/h. The system was heated to 80 °C, and the polymerization reaction was continued for 1 h. The centrifugation/redispersion step was repeated as in Step 4.

#### Steps 6–8 — Synthesis of alternating layers of gold and PMMA-co-P4VP layers

The synthesis of alternating layers of gold and PMMA-co-P4VP layers was conducted as in Steps 2–4.

### Characterization of hybrid multilayer microspheres

#### Characterization of particle size, shape, and morphology

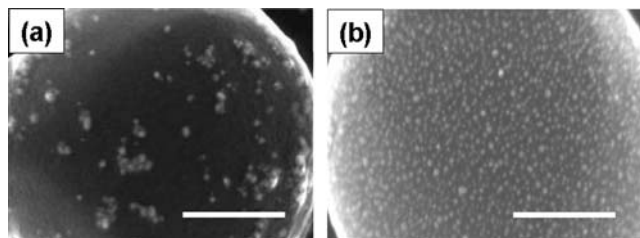
Scanning electron microscopy (SEM) imaging was performed on a Hitachi S-5200 microscope operating at an accelerating voltage of 1.0 kV and a current of 10 mA. A drop of dilute latex dispersion was dried on a carbon-coated copper transmission electron microscopy (TEM) grid. Scanning transmission electron microscopy (STEM) was carried out on Hitachi HD-2000 microscope using a high angle annular dark field imaging (HAADF-STEM) detector and operating at an acceleration voltage of 200.0 kV and a current of 40 mA. Prior to the STEM imaging, the microspheres were microtomed with a diamond knife using Leica Ultracut UCT microtome by embedding microbeads in the epoxy resin (5 min epoxy resin 12 Lepage, Henkel Canada Corporation). The 20 nm slices were then placed onto a carbon-coated copper TEM grid.

Particle size was determined by analyzing SEM images using the Image Tool software (University of Texas, Health Science Centre). The error of image analysis was  $\pm 1\%$ . The size distribution of the particles was characterized by the coefficient of variation as  $CV (\%) = (\sigma/D_m) \times 100$ , where  $D_m$  is the mean diameter of the particles and  $\sigma$  is the standard deviation of the particle diameter.

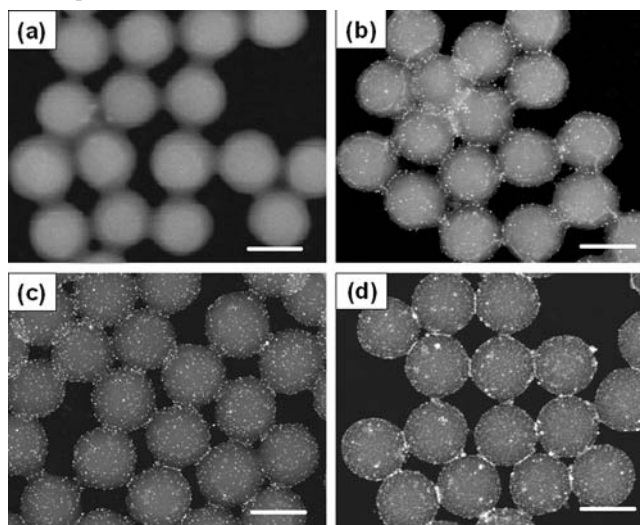
#### Characterization of the extinction properties of HMMs

The extinction spectra of the hybrid multilayer microspheres were recorded with a Varian UV-vis-NIR Cary 5000 spectrophotometer using water as the reference. Prior to the measurements, we ensured that the samples were sufficiently dilute to avoid multiple scattering. The extinction intensity was normalized by the path length of light (equal to 1 cm) and the concentration of particles (which was determined as the number of particles per unit volume). Typically, the concentration of particles varied in the range of  $10^7$  particles/mL (Step 8) to  $10^{10}$  particles/mL (Steps 1–3).

**Fig. 2.** SEM images of the surface of 120 nm diameter (a) PMMA and (b) PMMA-P4VP microspheres coated with gold NPs. The scale bar is 100 nm.



**Fig. 3.** DF-TEM images of (a) the PMMA particles synthesized in Step 1 and PMMA particles coated with (b) 5%, (c) 20%, and (d) 30% of gold NPs (Step 2), using the competition between electrostatically driven attraction of gold NPs and PDDMAC to the PMMA particles. The scale bar is 100 nm.



## Results and discussion

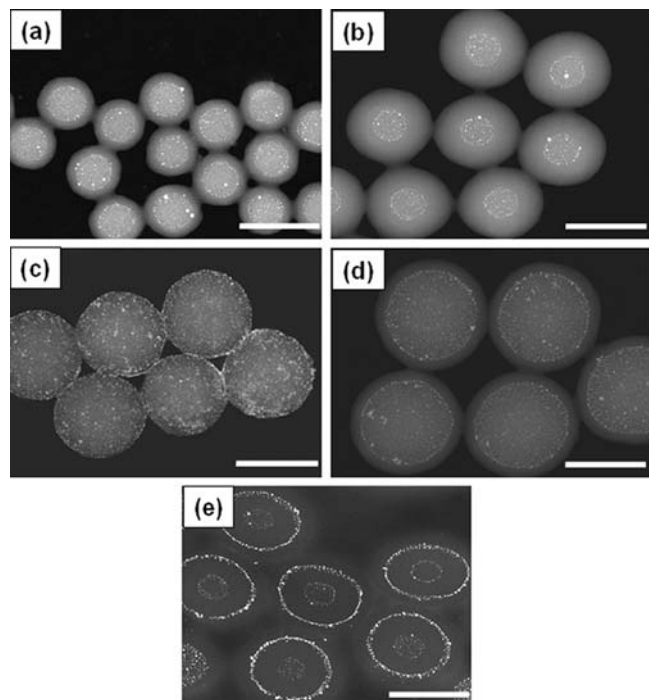
### Synthesis of hybrid microspheres

Figure 1 shows the schematic of the preparation of HMMs with a PMMA core, two alternating layers of gold NPs, and two alternating layers of PMMA. In Step 1, cationic 120 nm diameter latex microspheres were synthesized by emulsion polymerization by copolymerizing methyl methacrylate with 1 wt% of vinyl 4-pyridine (4VP) in the presence of a cationic water-soluble initiator, 2,2'-azo-bis(2-methylpropionamide) dihydrochloride (V-50). The negatively charged  $4 \pm 1$  nm diameter gold NPs stabilized with tetrakis (hydroxymethyl)phosphonium chloride were prepared using a method described elsewhere.<sup>16</sup> Using electrostatically mediated attraction between the anionic NPs and cationic microspheres, the NPs were deposited at pH = 6 on the surface of the latex particles (Fig. 1, Step 2). We stress that copolymerization of methyl methacrylate with a small amount of 4VP was critical to ensure the dense surface coverage and the uniform distribution of the gold NPs on the surface of the microspheres. Figure 2 shows that the positive charge of the latex particles originating solely from the use of the cationic initiator did not result in the dense attachment of gold NP to the particle surface.

Control of the fraction of the polymer surface covered



**Fig. 4.** Dark-field TEM images of HMMs synthesized in (a) Step 4, (b) Step 5, (c) Step 6, and (d) Step 8. Cross-sections of HMMs are shown in (e). Polymer and gold NPs appear dark and bright, respectively. The scale bar is 300 nm.



with gold NPs was achieved by depositing gold NPs on the microspheres in the presence of the anionic polyelectrolyte poly(sodium 4-styrenesulfonate), that is, by using the competition between the adsorption of gold NPs and the polyelectrolyte onto the cationic latex microspheres. When the relative concentration of poly(sodium 4-styrenesulfonate) in the solution of gold NPs changed from 0.01 to 0 wt%, the fraction of the surface of latex microspheres coated with gold NPs increased from 5% to 30%, as determined by the analysis of dark-field transmission electron microscopy images (DF-TEM) of the surface of HMMs (Fig. 3). In Steps 3–8 (Fig. 1) we used PMMA-*co*-P4VP particles with the highest (30%) surface coverage with gold NPs (later in the text, for simplicity, we will refer to these particles as PMMA particles). A cationic polymer poly(diallyldimethyl ammonium chloride) (PDDMAC) was adsorbed onto the polymer particles coated with gold NPs, to minimize the desorption of the NPs from the surface of microspheres in subsequent polymerization reactions. The PDDMAC-coated PMMA microspheres were used as seeds for the starve-fed interfacial polymerization of an outer polymer layer with thicknesses varying from 40 to 100 nm (Fig. 1, Steps 4 and 5, respectively).

To synthesize HMMs with two alternating layers of gold NP and two alternating polymer layers, the procedures of competitive adsorption of gold NPs and PDDMAC and interfacial copolymerization of methyl methacrylate and 4VP were repeated in Steps 6–8 (Fig. 1). The morphology of the microspheres and the presence and location of gold NPs in the HMMs were verified using DF-TEM. Figure 4 shows typical DF-TEM images of the hybrid microspheres produced in Steps 4–6 and Step 8. The multistep synthesis

yielded highly monodisperse HMMs with the alternating radial layers of gold NPs and PMMA-*co*-P4VP, as conceptualized and rationalized in Fig. 1. No evidence of aggregation in the system was observed. Gold NPs placed on the polymer surface were not desorbed in consecutive polymerization steps. Instead, they formed well-defined thin concentric layers. The characteristics of the HMMs such as the diameters and polydispersity of the HMMs and the thicknesses of the polymer and NP layers, all determined by the analysis of the SEM images, are provided in Table 1. We note that to examine the role of the thickness of polymer layers on the optical properties of HMMs, polymerizations in Steps 4 and 5 were carried out to produce the polymer layer with the same composition but with a different thickness.

### Optical properties of hybrid microspheres

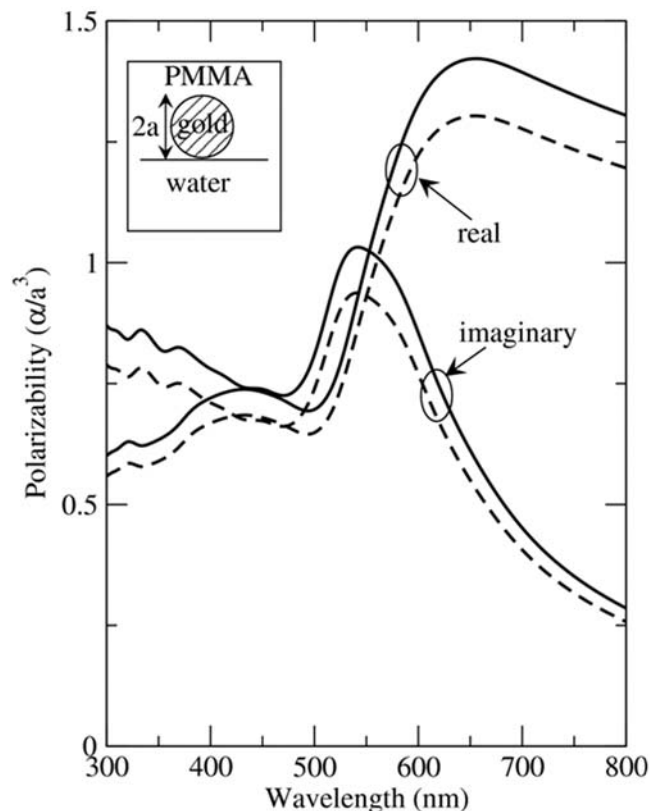
Optical properties of the HMMs were examined experimentally and theoretically. Theoretical calculations of the extinction spectra required the knowledge of the effective dielectric constant of the layers of gold NPs placed between the concentric polymer layers or localized at the water–polymer interface (e.g., for the HMMs produced in Steps 2 and 6). Following the procedure described in Appendix A, we obtained the polarizabilities of a gold NP placed at the PMMA–water interface. The calculated polarizabilities,  $\alpha_{\parallel}$  and  $\alpha_{\perp}$ , for the electric field oriented parallel and perpendicular to the interface of a 2 nm diameter gold NP are shown in Fig. 5. Due to anisotropy induced by the interface, the surface plasmon resonance was different for perpendicular and parallel polarizations.

Using the polarizability data we then computed the effective dielectric constant of the composite monolayer of gold NPs using the effective medium model described in Appendix A. For PMMA and water we used reported values of the dielectric constant.<sup>17</sup> Once the dielectric constants of each material constituting the HMMs were determined, the extinction spectra were calculated using an extension of Mie scattering theory to include the radial anisotropy of the dielectric constant of the gold NP layer. The calculated extinction spectra for the structures generated in Step 2 for the different coverage of the PMMA surface with gold NPs are shown as dashed lines in Fig. 6. Experimentally measured extinction spectra are also shown in Fig. 6 as solid lines. The results presented in Fig. 6 show that the magnitude of extinction of HMMs increased with increasing surface coverage of the PMMA particles with gold NPs. A very good agreement between the theoretical and experimental results was obtained for the spectral position of the plasmonic peaks, however, the magnitude of the plasmonic peak was higher in the theoretical spectra. This is most likely due to the approximations in our effective medium theory, which is strictly valid only for dilute composites. In fact, in three-dimensional metal–dielectric composites such effective medium theories are known to overestimate the surface plasmon resonance.<sup>18</sup>

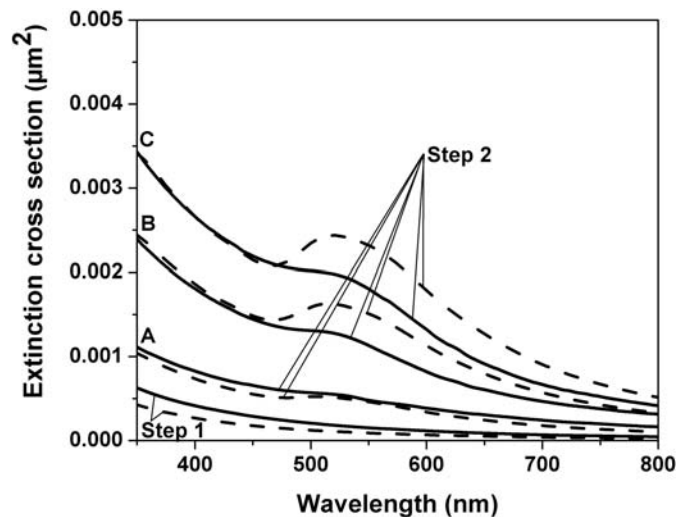
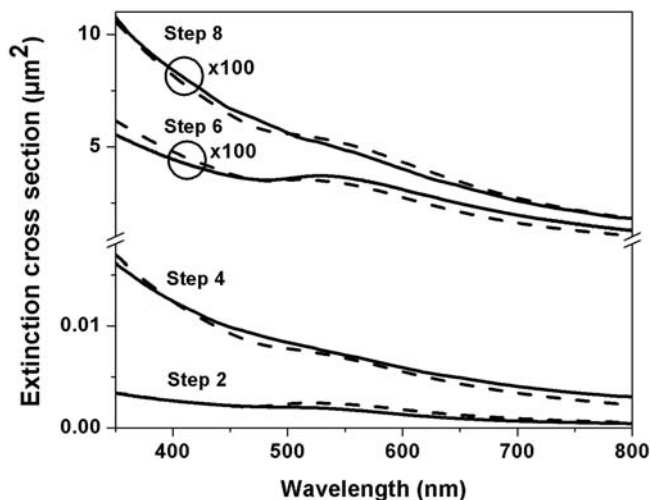
Furthermore, for the 30% coverage of the polymer surface with gold NPs we studied the evolution of the extinction spectra of HMMs by adding new polymer and NP layers (Fig. 1, Steps 3–8) and compared the results of calculations

**Table 1.** Mean diameter,  $D_m$ , coefficient of variation, CV, thickness of layers,  $\delta$ , and types of layers in HMMs.

Step numbers (as in Fig. 1)	1	2	4	5	6	8
Diameter of microspheres, $D_m$ , (nm)	120	120	200	322	322	430
Layer	—	Gold NPs	Polymer	Polymer	Gold NPs	Polymer
Thickness of the layer, $\delta$ (nm)	—	4–5	40	100	4–5	55
Coefficient of variation, CV (%)	3	3	3.3	2.8	2.8	2.65

**Fig. 5.** The real and imaginary parts of the polarizability,  $\alpha$ , of a spherical gold NP of radius  $a$  embedded in PMMA at an interface with water for polarization parallel (solid lines) and perpendicular (dashed lines) to the interface. The polarizability is shown scaled by  $a^3$ . The inset shows a schematic of the geometry.

and experiments. Figure 7 shows the following features: First, reasonably good agreement was achieved between the experimental and theoretical extinction spectra. Engulfment of the layer of gold NPs with the polymer layer (Step 2  $\rightarrow$  Step 4) resulted in a red-shift of the plasmon peak from 522 to 550 nm, which was caused by the dependence of the plasmon wavelength on the dielectric environment. The difference in the values of  $\epsilon$  of PMMA and water yielded the 5% shift in the position of plasmon maximum, in agreement with experimental results shown in Fig. 7. Further increase in the thickness of the polymer layer (Step 4  $\rightarrow$  Step 5) did not affect the dielectric environment around the NPs and the position of the plasmonic maximum did not change. The magnitude of the plasmon band increased for the HMMs synthesized in Step 6 and decreased in Step 8. Both of these changes were supported by theory. The experimentally measured and calculated positions of plasmon bands were also in reasonably good agreement.

**Fig. 6.** Comparison of experimental and calculated (solid and dashed lines, respectively) extinction spectra of HMMs dispersed in water for the polymer core (Fig. 1, Step 1) with different surface coverages of gold NPs (Fig. 1, Step 2): (A) 5%, (B) 20%, (C) 30%. The experimental spectra are normalized by the path length (1 cm) and the concentration of particles (the number of particles per unit volume).**Fig. 7.** Comparison of experimental and calculated (solid and dashed lines, respectively) extinction spectra of HMMs dispersed in water for Steps 2, 4, 6, and 8 in Fig. 1. The experimental spectra were normalized by the path length (1 cm) and the concentration of particles (the number of particles per unit volume). For clarity of presentation the data for Step 6 and Step 8 are scaled up by a factor of 100.

## Conclusion

To summarize, we conceptualized and synthesized hybrid multilayer polymer–inorganic microspheres comprising alternating concentric layers of a polymer and gold nanoparticles. The microspheres had a narrow size distribution and the thickness of the radial layers was well-defined. We experimentally characterized the extinction properties of the hybrid multilayer microspheres and compared the experimentally acquired spectra with the theoretical spectra calculated using a generalized classical Clausius–Mossotti (CM) theory. Good agreement was achieved between the experimental and theoretical results.

We emphasize that even in the HMMs with a single or two metal NP layers, the larger refraction index contrast results in noticeable changes in the extinction spectra, compared to all-polymer structures with similar size and number of layers.<sup>12c</sup> This makes the described hybrid multilayer microspheres promising objects for spherical resonators and other optoelectronic devices. For example, when combined with luminescent semiconductor quantum dots,<sup>12c</sup> they have the potential to be used as both passive and active types of devices.

## Acknowledgement

The authors acknowledge financial support from the Natural Sciences and Engineering Research Council of Canada (NSERC) under the Accelerator Grant for Exceptional New Opportunities (AGENO) program.

## References

- (1) Xu, S.; Zhang, J.; Paquet, C.; Lin, Y.; Kumacheva, E. *Adv. Funct. Mater.* **2003**, *13* (6), 468. doi:10.1002/adfm.200304338.
- (2) Rogach, A.; Susha, A.; Caruso, F.; Sukhorukov, G.; Kornowski, A.; Kershaw, S.; Mohwald, H.; Eychmüller, A.; Weller, H. *Adv. Mater.* **2000**, *12* (5), 333. doi:10.1002/(SICI)1521-4095(200003)12:5<333::AID-ADMA333>3.0.CO;2-X.
- (3) Kumacheva, E.; Kalinina, O.; Lilge, L. *Adv. Mater.* **1999**, *11* (3), 231. doi:10.1002/(SICI)1521-4095(199903)11:3<231::AID-ADMA231>3.0.CO;2-N.
- (4) Siwick, B.J.; Kalinina, O.; Kumacheva, E.; Miller, D. R. J.; Noolandi, J. *J. Appl. Phys.* **2001**, *90* (10), 5328. doi:10.1063/1.1406547.
- (5) Pham, H.; Gourevich, I.; Oh, J. K.; Jonkman, J. E. N.; Kumacheva, E. *Adv. Mater.* **2004**, *16* (6), 516. doi:10.1002/adma.200306156.
- (6) Pham, H.H.; Gourevich, I.; Jonkman, J. E. N.; Kumacheva, E. *J. Mater. Chem.* **2007**, *17* (6), 523. doi:10.1039/b614491h.
- (7) Radt, B.; Smith, T. A.; Caruso, F. *Adv. Mater.* **2004**, *16* (23–24), 2184. doi:10.1002/adma.200400920.
- (8) Chen, C.-W.; Chen, M.-Q.; Serizawa, T.; Akashi, M. *Adv. Mater.* **1998**, *10* (14), 1122. doi:10.1002/(SICI)1521-4095(199810)10:14<1122::AID-ADMA1122>3.0.CO;2-N.
- (9) Kato, N.; Caruso, F. *J. Phys. Chem. B* **2005**, *109* (42), 19604. doi:10.1021/jp052748f. PMID:16853535.
- (10) Shi, W.; Sahoo, Y.; Swihart, M. T.; Prasad, P. N. *Langmuir* **2005**, *21* (4), 1610. doi:10.1021/la047628y. PMID:15697315.
- (11) Brady, D.; Papen, G.; Sipe, J. E. *J. Opt. Soc. Am. B* **1993**, *10* (4), 644. doi:10.1364/JOSAB.10.000644.
- (12) (a) Alteheld, A.; Gourevich, I.; Field, L. M.; Paquet, C.; Kumacheva, E. *Macromolecules* **2005**, *38* (8), 3301. doi:10.1021/ma047446a.; (b) Gourevich, I.; Field, L. M.; Wei, Z.; Paquet, C.; Petukhova, A.; Alteheld, A.; Kumacheva, E.; Saarinen, J. J.; Sipe, J. E. *Macromolecules* **2006**, *39* (4), 1449. doi:10.1021/ma052167o.; (c) Petukhova, A.; Paton, A. S.; Wei, Z.; Gourevich, I.; Nair, S. V.; Ruda, H. E.; Shik, A.; Kumacheva, E. *Adv. Funct. Mater.* **2008**, *18* (13), 1961. doi:10.1002/adfm.200701441.
- (13) Takekoh, R.; Li, W.-H.; Burke, N. A. D.; Stöver, H. D. H. *J. Am. Chem. Soc.* **2006**, *128* (1), 240. doi:10.1021/ja055901s. PMID:16390152.
- (14) Petukhova, A.; Paton, A. S.; Gourevich, I.; Kumacheva, E.; Saarinen, J. J.; Sipe, J. E. *Appl. Phys. Lett.* **2006**, *89* (21), 211908. doi:10.1063/1.2397031.
- (15) Averitt, R. D.; Sarkar, D.; Halas, N. J. *Phys. Rev. Lett* **1997**, *78* (22), 4217. doi:10.1103/PhysRevLett.78.4217.
- (16) Duff, D. G.; Baiker, A.; Edwards, P. P. *Langmuir* **1993**, *9* (9), 2301. doi:10.1021/la00033a010.
- (17) (a) Brandrup, J.; Immergut, E. H.; Grulke, E. A. *Polymer Handbook*, 4th ed.; Wiley & Sons: New York, 1999; Vol. V, p 87; (b) Johnson, P. B.; Christy, R. W. *Phys. Rev. B* **1972**, *6* (12), 4370. doi:10.1103/PhysRevB.6.4370.
- (18) Sipe, J. E.; Boyd, R. W. *Optical Properties of Nanostructured Random Media*; Shalaev, V. M., Ed.; Springer: Berlin, 2002; p 450.

## Appendix A

We used a generalized classical Clausius–Mossotti (CM) theory to construct a model for the effective dielectric constant,  $\varepsilon_{\text{eff}}$ , of a monolayer of spherical NPs at an interface between two different dielectrics. We first consider a single particle of radius  $a$  and dielectric constant,  $\varepsilon_i$ , localized in a medium of the dielectric constant  $\varepsilon_b$  just above the interface with a substrate having the dielectric constant  $\varepsilon_s$ . The value of  $a$  is sufficiently small compared to the wavelength of light that the polarizability of the NP can be obtained from the quasistatic model by calculating the dipole moment induced in the NP by an applied electric field.

The induced dipole moment can be calculated by solving the Laplace equation for the situations when the electric field is either parallel or perpendicular to the interface. We used an analytical solution using bispherical coordinates.<sup>A1,A2</sup> Since the final expressions are cumbersome, we present the polarizability of NPs in the asymmetric system (the gold NPs localized at the interface of PMMA and water) in the numerical form.

We used the reported or experimentally measured values of the dielectric constant of water, PMMA,<sup>A3a</sup> and gold.<sup>A3b</sup> In the latter case, we corrected the experimental data to account for increased momentum relaxation due to the surface scattering as follows: We first fitted the experimentally measured dielectric constant of gold ( $\varepsilon_{\text{expt}}$ )<sup>A3b</sup> in the long-wavelength region to the Drude model and extracted the plasma frequency ( $\omega_p$ ) and relaxation time ( $\tau$ ). This fitting provided the values of  $\hbar\omega_p = 8.98$  eV and  $\hbar/\tau = 75$  meV. The value of  $\varepsilon_i$  of the NPs was then calculated as

$$[A1] \quad \varepsilon_i = \varepsilon_{\text{expt}} + \frac{\omega_p^2}{\omega(\omega - i/\tau)} - \frac{\omega_p^2}{\omega(\omega - i/\tau - i\eta v_F/a)}$$

where  $v_F$  is the Fermi velocity of bulk gold equal to

$1.57 \times 10^8$  cm/s and  $\eta$  is an adjustable parameter of the order 1. The calculated polarizability is shown in Fig. 5. We note that for gold NPs in a uniform background such as PMMA, the polarizability may be calculated using the well-known expression for the spherical particles in a dielectric medium.<sup>A4</sup>

In the next step, the CM theory was applied to the calculation of the effective dielectric constant  $\varepsilon_{\text{eff}}$  of a monolayer of NPs with surface density  $n$ . In terms of symmetry,  $\varepsilon_{\text{eff}}$  is a uniaxial tensor with the components  $\varepsilon_{\text{eff}}^{\perp}$  and  $\varepsilon_{\text{eff}}^{\parallel}$ , which had to be found separately for the applied electric field,  $E_0$ , perpendicular and parallel to the interface. The NPs were treated as point dipoles with a dipole moment,  $\alpha^{\perp\parallel}E_{\text{loc}}$ , where  $E_{\text{loc}}$  is the local electric field at the NP location.

### Perpendicular polarization

The effective dielectric constant of the NP layer,  $\varepsilon_{\text{eff}}^{\perp}$ , was determined by the ratio between the average polarization and the macroscopic electric field,  $E$ , inside the layer. To calculate  $E$ , the induced dipoles were treated as a two-dimensional dipole layer with the dipole density  $D = n\alpha^{\perp}E_{\text{loc}}$  and the thickness  $t$ , so that<sup>A4</sup>

$$[A2] \quad E = E_0 - \frac{4\pi n\alpha^{\perp}E_{\text{loc}}}{t}$$

The local field,  $E_{\text{loc}}$ , was calculated as the sum of the applied field and the field induced by the dipoles as

$$[A3] \quad E_{\text{loc}} = E_0 - \sum_n' \mu/r_n^3$$

where the sum is taken over all dipoles, except the one at the origin, where the local field is being computed,  $r_n$  is the distance from the origin and  $\mu = \alpha^{\perp}E_{\text{loc}}$  is the dipole moment of the  $n$ th dipole. The exact sum over dipoles depends on their microscopic arrangement but its ensemble average scales as  $\mu n^{3/2}\xi$ . The numerical constant,  $\xi$ , is weakly dependent on geometry and is 8.8927 or 9.0336 for the hexagonal or square lattices, respectively.<sup>A5</sup> For the random arrangement of NPs described in the present work, we used  $\xi = 9$ . By eliminating  $E_0$  from eqs. [A2] and [A3], we obtained the average local field

$$[A4] \quad \langle E_{\text{loc}} \rangle = \frac{E}{1 + n^{3/2}\alpha_{\perp}\xi - 4\pi n\alpha_{\perp}/t}$$

and obtained

$$[A5] \quad \varepsilon_{\text{eff}}^{\perp} = \varepsilon_b \left( 1 + \frac{4\pi n\alpha_{\perp}/t}{1 + n^{3/2}\alpha_{\perp}\xi - 4\pi n\alpha_{\perp}/t} \right)$$

### Parallel polarization

In this case, all the dipoles are oriented in the plane of the layer and the macroscopic field is equal to the applied field and

$$[A6] \quad E_{\text{loc}} = E_0 + \sum_n' \mu/2r_n^3$$

so that the effective dielectric constant is given by

$$[A7] \quad \varepsilon_{\text{eff}}^{\parallel} = \varepsilon_b \left( 1 + \frac{4\pi n\alpha_{\parallel}/t}{1 - n^{3/2}\alpha_{\parallel}\xi/2} \right)$$

In the calculations presented above, we assumed that  $t = 2a$ . Since the polarizability of spherical particles is proportional to  $a^3$ , the value of  $\varepsilon_{\text{eff}}$  depends on the geometrical parameters only through the NP area fraction,  $f = \pi a^2 n$ .

### References

- (A1) Aravind, P. K.; Metiu, H. *Surf. Sci.* **1983**, *124* (2–3), 506. doi:10.1016/0039-6028(83)90806-3.
- (A2) Ruppin, R. *Surf. Sci.* **1983**, *127* (1), 108. doi:10.1016/0039-6028(83)90402-8.
- (A3) (a) Brandrup, J.; Immergut, E. H.; Grulke, E. A. *Polymer Handbook*, 4th ed.; Wiley & Sons: New York, 1999; Vol. V, p 87; (b) Johnson, P. B.; Christy, R. W. *Phys. Rev. B* **1972**, *6* (12), 4370. doi:10.1103/PhysRevB.6.4370.
- (A4) Jackson, J. D. *Classical Electrodynamics*; John Wiley: New York, 1975; p 848.
- (A5) Topping, J. *Proc. R. Soc. London Ser. A* **1927**, *114* (766), 67. doi:10.1098/rspa.1927.0025.



## TRIBUTE

### A tribute to Mitch Winnik

Mitch Winnik was born in Milwaukee Wisconsin in 1943. He received his B.A. degree in Chemistry from Yale University in 1965. He carried out his doctoral research under the guidance of Professor Ronald Breslow at Columbia University and received his Ph.D. in organic chemistry in 1969. After postdoctoral studies with Professor George Hammond at the California Institute of Technology, he joined the faculty at the University of Toronto in September 1970 as an organic chemist. In those early days, he saw himself as a physical organic chemist and carried out research in the area of reaction mechanisms. He had a particular interest in intramolecular photochemical reactions of conformationally flexible molecules. Most of these experiments involved measurements of phosphorescence in solution of various benzophenone derivatives. Based on this work, he was promoted to Associate Professor with tenure in 1975. Two years later, while on a sabbatical in France, he met at a conference Walter Stockmayer, who persuaded him that his scientific life would be much richer if he would study similar processes in longer molecules. When he returned to Toronto in 1978, he and his postdoc Tony Redpath began a study of polymer cyclization in solution based upon time-resolved fluorescence measurements of excimer formation of pyrene attached to the chain ends. This turned out to be an enormously rich area of study, since it coincided with blossoming theoretical advances in the description of polymer conformation and dynamics in solution and new techniques to study those processes. It began Mitch's transformation from an organic chemist to a polymer chemist, and pyrene had now replaced benzophenone as his favourite luminescent chromophore.

In the early 1980s, Mitch began working with Mel Croucher at the Xerox Research Centre of Canada on polymer microparticles synthesized by dispersion polymerization. This interaction opened his eyes to the world of polymer materials, taught him about how to interact with scientists in industry, and led to the development of new techniques based upon fluorescence measurements for characterizing polymer morphology. Toward the end of the 1980s, a number of very exciting developments occurred in the Winnik research group. Jose Martinho joined his group and made major contributions to the study of diffusion-controlled reactions. Two key co-workers joined the group at this time, Cheng Le Zhao and Yongcai Wang. They pioneered efforts to apply fluorescence as a tool to study hydrophobically-modified polymers in water, work encouraged by David Bassett at Union Carbide because these polymers were important rheology modifiers for coatings. They also pioneered the Winnik group foray into the study of latex films, in which they developed techniques based upon fluorescence resonance energy transfer (FRET) to study the diffusion of polymer molecules across the boundaries between adjacent latex polymer nanoparticles as they pack in the film upon drying. This is the step that leads to the build-up of useful mechanical properties in the film. This work was initiated with support from ICI Paints and has continued for more than a decade in collaboration with scientists in many companies in the coatings field: ICI, Dow, Union Carbide, 3M, BASF, Air Products, Cytec, Johnson Polymers, and most recently, with Willie Lau at Rohm and Haas. This work has been widely recognized, for example by four First Place Roon awards (1991, 1995, 1998, and 2007) for the top publication in the coating

field, by an American Chemical Society Tess Award (1999), and by the Mattiello lecture award (2001) given by the Federation of Societies for Coatings Technology. These awards recognize that advances in fundamental science can also have an important impact on technology.

In the early 1990s, Ahmad Yekta and Jean Duhamel helped transform the Winnik group in a different direction. They recognized that data from FRET experiments carried out on dyes confined to nanometre-size domains could be interpreted to provide information about the size and shape of those domains. They brought a high level of mathematical rigour to these experiments. This in turn allowed a much deeper richness of information to be obtained from many studies in the Winnik group, on water-soluble polymers, on block copolymer micelles in solution, and on polymer diffusion in latex films. It also opened the possibility to study interfaces where polymers of different compositions meet. These interfaces have widths of only a few nanometers, larger than monomer units and smaller than polymer molecules, domain sizes that could be determined using the concept of energy transfer in restricted dimensions.

A collaboration with Ian Manners on micelles formed by polyferrocenylsilane (PFS) block copolymers began in the late 1990s with the co-supervision of Jason Massey's Ph.D. research. This system is surprisingly rich, with many unexpected discoveries. For example, this seems to be the only known block copolymer that forms fiber-like micelles by a mechanism similar to that of proteins, for example amyloid fibers. Many co-workers made critical contributions here. Several who stand out include Yahya Rharbi, who suggested that the PFS core might be crystalline, Xiaosong Wang, who discovered living self-assembly, Gerald Guerin, who contributed light scattering prowess, and Hai Wang who demonstrated that these nanofibres could serve as templates for the formation of arrays of metal nanoparticles.

A recent turning point in the Winnik group research interests began in 2005 when Mitch was invited to join a project in collaboration with Vladimir Baranov, Olga Ornatsky, and Mark Nitz, based upon the use of inductively coupled mass spectrometry (ICP-MS) for highly multiplexed bioassays. The idea is to use different (lanthanide) metal isotopes as labels to attach to antibodies, in much the same way that others attach fluorescent dyes. The initial focus was on phenotyping human leukemia cells. The Winnik group was asked to synthesize metal chelating polymers to carry many copies of a given metal or single isotope (like  $^{153}\text{Eu}$ ) so that each antibody would carry about 100 metal ions. The long term objective is to be able to measure quantitatively as few as 100 copies of a particular biomolecule in an individual cell. Recent experiments using the new technique of mass cytometry can detect and quantify more than 20 biomarkers cell-by-cell in a single assay.

Over the years, Mitch has been a Visiting Professor at the Université de Bordeaux (1977–1978), a world Trade Scholar at IBM (1982), a JSPS Fellow at the Tokyo Institute of Technology (1985–1986), an Alexander von Humboldt Fellow at the Max Planck Institute for Polymer Science (1996) in Mainz, Germany, and the holder of La Chaire de Paris-Sciences at l'Ecole Supérieure de Physique et Chimie Industrielle (2000) in Paris, France.

Mitch has received numerous awards including the CIC

Award in Polymer Science (1993), the Bell-Canada Forum Award for University-Industry interactions (1995), an Alexander von Humboldt Senior Scientist Award (1996), and the CIC Medal (2004). He was elected a Fellow of the Royal Society of Canada (1996) and of the Polymer and Material Sciences division of the American Chemical Society (2002). In 2006, he was listed as one of the most cited authors in chemistry by the ISI Web of Science. His 550+ publications have been cited more than 14 000 times ( $h^* = 57$ ). At the University of Toronto, he

holds the title University Professor, the University's highest award in recognition of academic excellence.

The number and quality of the papers submitted to this dedicated issue of the *Canadian Journal of Chemistry* attests to the breadth and reach of his influence in the chemistry and polymer science communities.

**Jean Duhamel**

## HOMMAGE

### Hommage à Mitch Winnik

Mitch Winnik est né à Milwaukee, au Wisconsin, en 1943. Il obtient son baccalauréat en chimie de l'Université Yale en 1965. Il poursuit ses études au programme de doctorat sous la direction du professeur Ronald Breslow de l'Université Columbia et reçoit son doctorat en chimie organique en 1969. Après ses études postdoctorales sous la supervision du professeur George Hammond au California Institute of Technology, il joint la faculté de l'Université de Toronto en septembre 1970 à titre d'organicien ou chimiste spécialiste de la chimie organique. À cette époque, il se voit plutôt comme spécialiste de la chimie organique physique et mène des travaux de recherche sur les mécanismes réactionnels, plus particulièrement sur les réactions photochimiques intramoléculaires des molécules présentant une mobilité conformationnelle. La plupart de ces expériences portent sur les mesures de phosphorescence de différents dérivés de la benzophénone en solution. De par ces travaux, il est nommé professeur agrégé permanent en 1975. Deux ans plus tard, alors qu'il est en congé sabbatique en France, il fait la rencontre, à l'occasion d'un congrès, de Walter Stockmayer qui le convainc que sa carrière scientifique serait d'autant plus riche s'il réorientait ses recherches sur les processus similaires dans des molécules plus longues. Dès son retour à Toronto, il entreprend en 1978, avec le concours de son étudiant postdoctoral Tony Redpath, une étude de la cyclisation des polymères en solution; étude qui repose sur des analyses de fluorescence – en temps résolu – de la formation d'excimères du pyrène attaché aux extrémités de la chaîne. Ce domaine d'étude s'avère extrêmement fertile en raison de l'effervescence concomitante d'avancées théoriques dans la description de la conformation et de la dynamique des polymères, et des nouvelles méthodes pour étudier ces processus. C'est ainsi que Mitch délaisse le domaine de la chimie organique au profit de la chimie des polymères, et la benzophénone cède la place au pyrène à titre de chromophore luminescent de prédilection.

Au début des années 1980, Mitch collabore avec Mel Croucher du Centre canadien de recherche Xerox sur la recherche des microparticules de polymères synthétisées par voie de polymérisation par dispersion. Pour lui, cette collaboration est plus qu'une ouverture sur le monde des matériaux polymères. En effet, elle donne lieu à des échanges privilégiés avec les scientifiques de l'industrie et à l'élaboration de nouvelles techniques axées sur les mesures de fluorescence pour la caractérisation de la morphologie des polymères. La fin des années 1980 est marquée par un nombre de changements très importants au sein du groupe de recherche de Winnik. En effet, Jose Martinho se joint au groupe et apporte des contributions majeures à l'étude de réactions contrôlées par la diffusion. De plus, Cheng Le Zhao et Yongcai Wang, deux autres contributeurs clés, se joignent alors au groupe. Ces chercheurs font œuvre de précurseurs en utilisant la fluorescence comme outil dans l'étude des polymères modifiés d'une façon hydrophobe dans l'eau; travail appuyé par David Bassett d'Union Carbide, car ces polymères sont d'importants modificateurs rhéologiques des revêtements. Cheng Le Zhao et Yongcai Wang sont également responsables de l'incursion du groupe de Winnik dans l'analyse des pellicules de latex, ce qui lui permet d'élaborer des techniques de transfert d'énergie par fluorescence de résonance (FRET) pour étudier la diffusion des molécules polymères transfrontalière entre les nano-

particules de latex polymères adjacentes durant leur agglomération en pellicule à l'assèchement. Cette étape mène ensuite à la découverte d'un assortiment de propriétés mécaniques pratiques pour les pellicules. Amorcé avec l'appui d'ICI Paints, ce travail se poursuit pendant plus de 10 ans en collaboration avec les chercheurs de l'industrie, y compris ICI, Dow, Union Carbide, 3M, BASF, Air Products, Cytec, Johnson Polymers, et plus récemment, avec Willie Lau de Rohm and Haas. Les efforts du groupe sont universellement reconnus et primés, comme en témoignent les quatre premières places du prix Roon (1991, 1995, 1998 et 2007) pour la meilleure publication dans le domaine des revêtements, le prix Tess de l'American Chemical Society (1999) et le prix de conférence Mattiello (2001) de la Federation of Societies for Coatings Technology. Ces prix reconnaissent non seulement l'importance des progrès en sciences fondamentales, mais aussi leurs répercussions sur les technologies.

Au début des 1990, Ahmad Yekta et Jean Duhamel insufflent une nouvelle orientation au groupe de Winnik en montrant que les données issues d'expériences par FRET sur des colorants confinés à des domaines de tailles nanométriques pouvaient être interprétées pour fournir des renseignements sur la taille et la forme de ces domaines. Ils inculquent une rigueur mathématique de haut niveau à ces travaux de recherche, ce qui se traduit par une plus grande richesse d'information pour bon nombre d'études réalisées par le groupe de Winnik, y compris les études sur les polymères hydrosolubles, sur les micelles de copolymères séquencés en solution et sur la diffusion des polymères dans les pellicules de latex. Par ailleurs, elle ouvre la voie aux études des interfaces où les polymères de composition variée interagissent. De l'ordre de quelques nanomètres, ces interfaces, qui ont une taille supérieure aux unités de monomères, mais inférieure aux molécules polymères, présentent des tailles de domaine pouvant être déterminées à l'aide du concept de transfert d'énergie dans des dimensions restreintes.

Alors qu'il participe à la supervision des travaux de recherche doctorale de Jason Massey à la fin des années 1990, il établit une collaboration avec Ian Manners sur l'étude des micelles de copolymères séquencés formées par le polyferrocénylsilane (PFS). Ces travaux s'avèrent étonnamment fertiles et débouchent sur un grand nombre de découvertes inattendues. À titre indicatif, il semble être le seul copolymère séquencé connu qui forme des micelles fibreuses par un mécanisme analogue à celui des protéines, comme les fibres amyloïdes. Bon nombre de chercheurs ont apporté des contributions considérables. Au nombre des chercheurs les plus mémorables, mentionnons Yahya Rharbi qui attribue une nature cristalline éventuelle au noyau du PFS; Xiaosong Wang qui découvre l'autoassemblage spontané; Gerald Guerin qui contribue aux prouesses techniques de la diffusion de la lumière; Hai Wang qui montre que ces nanofibres peuvent servir de matrices dans la formation d'une diversité de nanoparticules métalliques.

Un tournant dans les intérêts scientifiques du groupe de Winnik s'est amorcé en 2005 lorsque Mitch est invité à participer à un projet avec Vladimir Baranov, Olga Ornatsky et Mark Nitz; projet qui fait appel à la spectrométrie de masse avec plasma à couplage inductif (ICP-MS) pour les dosages biologiques hautement multiplexés. L'idée ici est d'utiliser différents isotopes métalliques (lanthanide) comme étiquettes pour mar-

quer des anticorps, de façon analogue à l'utilisation de fluorochromes. L'accent est porté initialement sur le phénotypage des cellules leucémiques humaines. On demande ensuite au groupe de Winnik de synthétiser des polymères métallifères pour porter de nombreuses copies d'un métal ou d'un isotope (comme  $^{153}\text{Eu}$ ) donné afin de munir chaque anticorps de quelque 100 ions métalliques. L'objectif à long terme est de mesurer de façon quantitative aussi peu que 100 copies d'une biomolécule particulière dans une cellule donnée. Des expériences récentes faisant appel à cette nouvelle technique de cytométrie de masse peuvent détecter et quantifier plus de 20 biomarqueurs pour chacune des cellules à l'aide d'une seule analyse.

Au fil des années, Mitch est professeur invité à l'Université de Bordeaux (1977–1978), éminent spécialiste du commerce à IBM (1982), boursier JSPS à l'Institut de technologie de Tokyo (1985–1986), boursier Alexander von Humboldt à l'Institut Max Planck pour la recherche sur les polymères (1996) à Mainz, Allemagne, ainsi que titulaire de la chaire de Paris-Sciences à l'École Supérieure de Physique et Chimie Industrielle (2000) de Paris, France.

Mitch est récipiendaire de nombreuses distinctions, y compris le prix de l'Institut de chimie du Canada (ICC) en science des polymères (1993), le prix Forum Bell Canada pour les interactions université-industrie (1995), le prix Alexander von Humboldt pour chercheur principal (1996) et la médaille de l'ICC (2004). Il devient membre de la Société royale du Canada (1996) et de la division des sciences des matériaux polymères de l'American Chemical Society (2002). En 2006, il figure comme l'un des auteurs les plus cités en chimie par le Web of Science de l'ISI Web of Science. Ses quelque 550 publications sont citées plus de 14 000 fois ( $h^* = 57$ ). À l'Université de Toronto, on lui décerne le titre de « Professeur Universitaire », le prix le plus prestigieux de cette université attribué en reconnaissance de l'excellence universitaire.

Le nombre et la qualité des articles de ce numéro dédié de la *Revue canadienne de chimie* sont des gages de l'étendue et la portée de son influence dans le milieu de la chimie et de la science des polymères.

**Jean Duhamel**



# Transfer hydrogenations of benzaldehyde using glycerol as solvent and hydrogen source

Dorith Tavor, Oxana Sheviev, Christina Dlugy, and Adi Wolfson

**Abstract:** Benzaldehyde was successfully reduced by catalytic transfer hydrogenation in glycerol using several ruthenium based complexes and bases. Glycerol was employed as a green solvent and hydrogen source, and it allowed for easy product separation and catalyst recycling and enabled the use of a microwave-assisted reaction.

**Key words:** transfer hydrogenation, catalysis, glycerol, green solvent, benzaldehyde.

**Résumé :** Le benzaldéhyde a été réduit avec succès par une hydrogénation de transfert catalytique, dans le glycérol, en présence de plusieurs complexes et bases à base de ruthénium. Le glycérol a été utilisé à la fois comme source d'hydrogène et de solvant écologique et il permet de séparer facilement le produit, de recycler le catalyseur et d'utiliser les micro-ondes pour faciliter la réaction.

**Mots-clés :** hydrogénation par transfert, catalyse, glycérol, solvant écologique, benzaldéhyde.

[Traduit par la Rédaction]

## Introduction

Carbonyl reduction is a fundamental organic transformation done using a variety of synthetic procedures.<sup>1–3</sup> Metal hydrides, and especially borohydrides, are cheap and simple reducing agents that can easily reduce many carbonyl compounds while producing characteristically high yields and selectivities, but their use is usually accompanied by large amounts of waste. Catalytic hydrogenation with molecular hydrogen, using different homogeneous and heterogeneous metal catalysts, is another potential route; however, it requires extra precautionary measures and special, high pressure equipment. Alternatively, transfer hydrogenation of carbonyl compounds using different organic molecules as the hydrogen source has also been intensively studied and reported in the literature.<sup>4–7</sup>

The transfer hydrogenation of aldehydes and ketones is usually performed in 2-propanol under a homogeneous mode with different ruthenium based complexes and organic or inorganic bases as cocatalysts.<sup>5,6</sup> To overcome the difficulties of the separation and recycling of homogeneous complexes, supported ruthenium catalysts were introduced.<sup>8,9</sup> We recently showed that 2-propanol can be replaced by glycerol, which served as green solvent and hydrogen donor in the transfer hydrogenation of various unsaturated organic compounds and which facilitated easy product separation and catalyst recycling.<sup>10</sup> The promising physical and chemical properties of glycerol enabled its application as a green solvent in many organic reactions, using various homogeneous and heterogeneous chemo- and bio-catalysts.<sup>11–13</sup> As the main byproduct of the conversion of oils and fats in oleochemical production, glycerol is becoming more plentiful,

which reduces its price, due to increases in the production and use of fatty acid derivatives in food, in the cosmetics and drugs industries, and in biofuel synthesis, i.e., biodiesel. As increasingly larger quantities of glycerol are generated by the biodiesel industry, it is vital that economical ways of utilizing glycerol be explored to further defray the cost of biodiesel production. In addition to glycerol's low environmental impact, its replacement of 2-propanol in transfer hydrogenation reactions allowed for experiments to be run at higher temperatures and facilitated easier product separation. Furthermore, during the reaction glycerol is dehydrogenated to dihydroxyacetone, which is a valuable ingredient in sunless tanning products.

In this study, glycerol was used as both solvent and hydrogen donor in the transfer hydrogenation of benzaldehyde as the representative carbonyl compound (Fig. 1). Various ruthenium complexes and different bases were tested as catalysts and promoters, respectively. The effects of catalyst and base types and of loading and reaction temperature on catalytic performance were tested. In addition, catalyst recycling tests and microwave-assisted reactions were also performed.

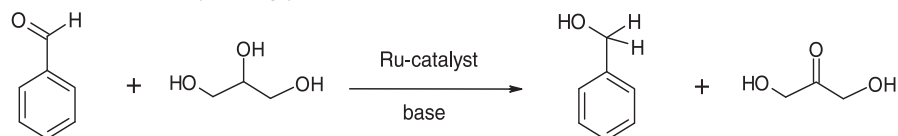
## Experimental

In a typical procedure, 2.2 mmol of benzaldehyde (0.22 g) and 270  $\mu$ mol of base (KOH, NaOH, or triethyl amine) were added to a vial with 4 g of glycerol (all purchased from Sigma-Aldrich). A corresponding amount of ruthenium catalyst was added, such that the molar ratio of benzaldehyde to ruthenium was in the range of 50–150. The mixture was

Received 25 August 2009. Accepted 4 November 2009. Published on the NRC Research Press Web site at canjchem.nrc.ca on 18 February 2010.

**D. Tavor, O. Sheviev, C. Dlugy, and A. Wolfson.**<sup>1</sup> Green Processes Center, Chemical Engineering Department, Sami Shamoon College of Engineering, Bialik/Basel Sts. Beer-Sheva, 84100 Israel.

<sup>1</sup>Corresponding author (e-mail: adiw@sce.ac.il).

**Fig. 1.** Transfer hydrogenation of benzaldehyde in glycerol.

placed in a preheated oil bath and heated to the required temperature (45–75 °C), after which it was magnetically stirred for 5–72 h. At the end of the reaction, the reaction mixture was cooled and extracted with 3 × 5 mL diethyl ether. The organic phase was concentrated under reduced pressure, and the resulting crude product was analyzed by gas chromatography (GC) analysis using an HP-5 column (30 m × 0.25 mm, 0.25 μm thick).

Catalyst recycling experiments were done in a 100 mL Erlenmeyer flask. For the first reaction cycle, 2 g benzaldehyde, 0.12 g Ru(*p*-cumene)Cl<sub>2</sub>-dimer, and 0.17 g KOH were dissolved in 25 g of glycerol, and the reaction mixture was heated in an oil bath to 70 °C for 18 h. At the end of the reaction, the product and the residual substrate were extracted with 3 × 25 mL diethyl ether and the catalyst was recycled by adding fresh benzaldehyde and running the reactions under conditions similar to those of the first run.

The transfer hydrogenation of benzaldehyde under microwave irradiation was carried out using a Ru(*p*-cumene)Cl<sub>2</sub>-dimer as the catalyst and KOH as the base. Experiments were conducted at atmospheric pressure in a domestic microwave oven (Crystal WP900, 900 W) in a 250 mL glass vessel covered with a watch glass. Benzaldehyde (2 g) was dissolved in 25 g of glycerol to which was added 0.12 g of the complex and 0.17 g of KOH. The vessel was covered with the watch glass, and the reaction mixture was heated in the microwave for 3 min from 26 to 72 °C. The vessel was then cooled to room temperature, and the reaction mixture was extracted with diethyl ether for GC analysis.

## Results and discussion

As previously mentioned, the homogeneous catalytic transfer hydrogenation of carbonyl compounds is usually performed with ruthenium complexes and a base. Thus, the investigation began by running the transfer hydrogenation of benzaldehyde in glycerol with different ruthenium catalysts and several bases (Table 1). As expected, performing the reaction in the absence of a base with all types of ruthenium catalysts did not yield any product. In contrast, running the reaction with potassium hydroxide but without a catalyst for 5 h resulted in a 20% yield of benzyl alcohol, but that yield did not change when the reaction was allowed to continue beyond 5 h (Table 1, entry 1). Increasing the amount of base while performing the reaction without catalyst resulted in a faster reaction, but did not change the final yield of benzyl alcohol. Replacing KOH with triethyl amine as a representative organic base and performing the reaction in the absence of the ruthenium complex failed to yield any product (Table 1, entry 2). It was previously reported that the role of the base in transfer hydrogenation–dehydrogenation reactions is to abstract the acidic proton of the hydrogen donor, thereby initiating the catalytic cycle.<sup>14</sup> In addition, it was found that soluble KOH by itself also catalyzed the

transfer hydrogenation of acetophenone in 2-propanol<sup>15</sup> and solid KOH and NaOH were successfully used in the dehydrogenation of aromatic alcohols.<sup>16</sup>

When ruthenium complex and KOH were added together to the reaction mixture, the yield of benzyl alcohol after 5 h was similar to the yield that was detected with KOH alone after 5 h (Table 1, entries 4–6), except in the case of the Ru(*p*-cumene)Cl<sub>2</sub>-dimer that exhibited a 40% higher yield of benzyl alcohol (Table 1, entry 3). Performing a comparative reaction in 2-propanol under similar conditions, using Ru(*p*-cumene)Cl<sub>2</sub>-dimer as catalyst and KOH as base, resulted in a 36% yield of benzyl alcohol, which is 33% higher than the yield in glycerol. It might be attributed to the lower viscosity of 2-propanol or to the difference in the structure of the two solvents that makes their affinity to the catalyst different and thus their ability to transfer proton and hydride. Although the yield of benzyl alcohol with KOH alone did not change after 5 h, the addition of all ruthenium complexes to KOH resulted in an increased yield after 24 h (Table 1, entries 3–6). These results imply that both the base and the ruthenium catalyst are necessary to maintain the catalytic cycle. In addition, no difference was found when the reaction was performed under an inert atmosphere.

The important reaction-initiating role of the base prompted us to test the effect of base type on benzyl alcohol yield (Table 1, entries 7–8). It was found that replacing KOH with either NaOH or triethyl amine did not change the yield. In addition, the yield of benzyl alcohol was only slightly changed at reaction temperatures in the range of 45–75 °C (Table 1, entry 9). Finally, replacing benzaldehyde with 2-octanone and running the reaction under similar reaction conditions resulted in a lower yield, as aliphatic ketones are less active in transfer hydrogenation reactions (Table 1, entry 10).

Reaction progress over time was tested with the Ru(*p*-cumene)Cl<sub>2</sub>-dimer and KOH (Fig. 2). The results show that increasing the reaction time led to a linear increase in the yield of benzyl alcohol. Benzaldehyde conversion was also affected by complex loading (Fig. 3). By decreasing the amount of the complex, thus increasing the substrate to catalyst ratio, the turnover frequency (TOF, the amount of substrate that was converted per each catalyst molecule per hour) increased linearly, thereby revealing that under these conditions, each molecule of complex undergoes more catalytic cycles per hour.

Finally, the efficacy of recycling the Ru(*p*-cumene)Cl<sub>2</sub>-dimer, KOH, and glycerol together was examined. The first reaction cycle was performed at 70 °C for 18 h, and at the end of the reaction the product and the residual substrate were extracted with diethyl ether to reveal a benzyl alcohol yield of 62%. Fresh benzaldehyde was then added to the reaction mixture for the second and third cycles, and the reaction was run under the same conditions as the first cycle. The yields of the second and the third cycles were 54% and

**Table 1.** Transfer hydrogenation of benzaldehyde in glycerol.

Entry	Catalyst type	Base type	Yield after 5 h (%)	Yield after 24 h (%)
1	—	KOH	20	20
2	—	Et <sub>3</sub> N	0	0
3	Ru( <i>p</i> -cumene)Cl <sub>2</sub> -dimer	KOH	27	45
4	RuCl <sub>3</sub> ·H <sub>2</sub> O	KOH	20	38
5	RuCl <sub>2</sub> (TPP) <sub>3</sub> <sup>a</sup>	KOH	20	48
6	RuCl <sub>2</sub> (TPPS) <sub>3</sub> <sup>b</sup>	KOH	20	39
7	Ru( <i>p</i> -cumene)Cl <sub>2</sub> -dimer	NaOH	20	20
8	Ru( <i>p</i> -cumene)Cl <sub>2</sub> -dimer	Et <sub>3</sub> N	19	19
9	Ru( <i>p</i> -cumene)Cl <sub>2</sub> -dimer <sup>c</sup>	KOH	25	42
10	Ru( <i>p</i> -cumene)Cl <sub>2</sub> -dimer <sup>d</sup>	KOH	—	27

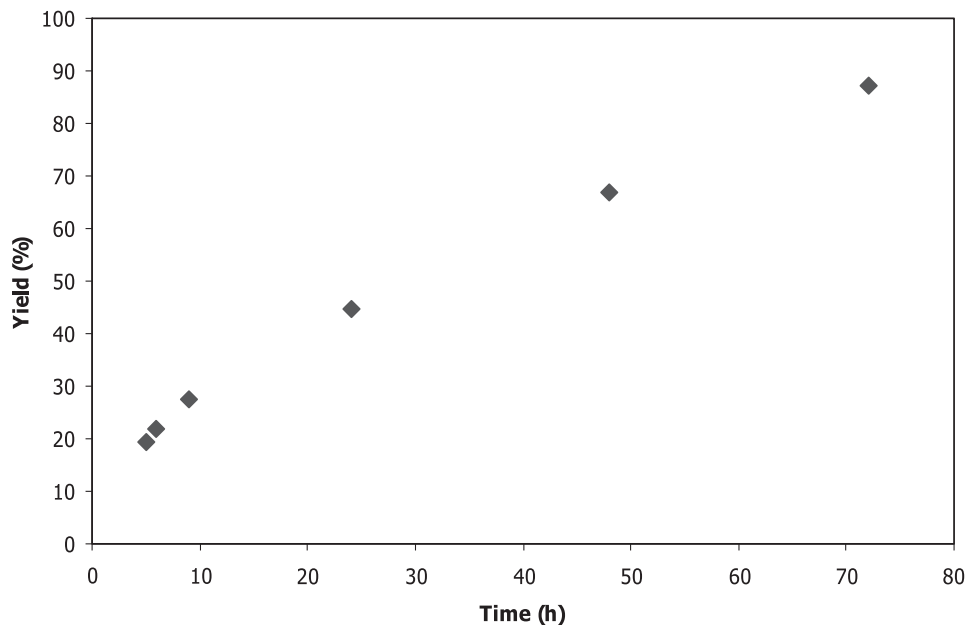
**Note:** Reaction conditions: 4 g glycerol, 0.22 g benzaldehyde, S/C = 100, 270 μmol base, 70 °C.

<sup>a</sup>TPP: triphenylphosphine.

<sup>b</sup>TPPS: tris-(3-sulfophenyl)-phosphine trisodium salt.

<sup>c</sup>45 °C.

<sup>d</sup>0.22 g 2-octanone.

**Fig. 2.** The progress of the reaction over time. Reaction conditions: 4 g glycerol, 0.22 g benzaldehyde, S/C = 100, 270 μmol KOH, 70 °C.

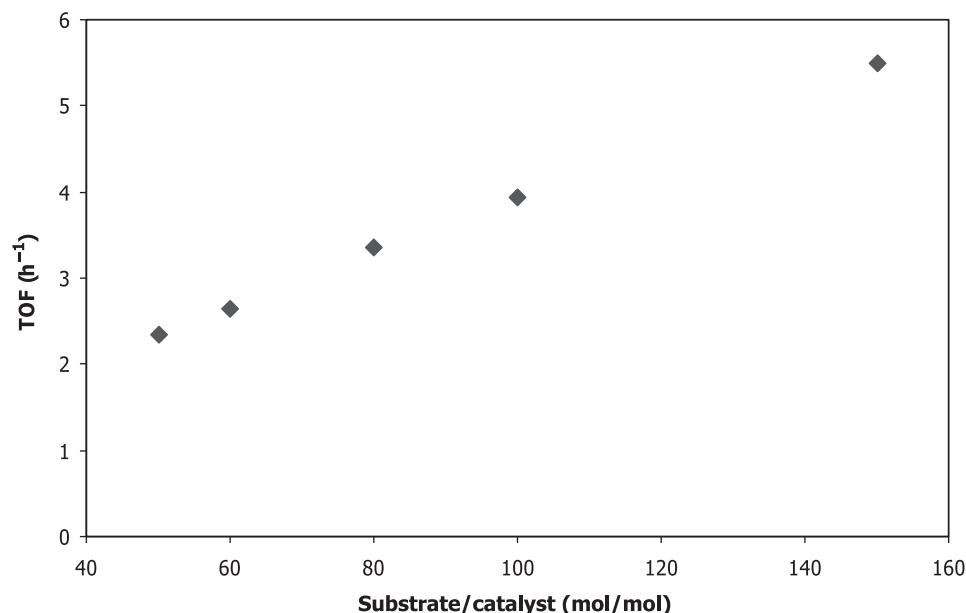
42%, respectively. The observed decline in yield may be attributable to partial deactivation of the catalyst or partial loss of base during the reaction. Thus, a recycling experiment with the addition of extra fresh KOH to the second reaction cycle was also tested. It resulted in a slightly higher benzyl alcohol yield of 59% instead of a yield of 54% when fresh base was not added. Finally, because transfer hydrogenation–dehydrogenation reactions are equilibrium reactions, glycerol's role as hydrogen donor could mean that part of it was already dehydrogenated in the former reaction cycles. If so, then the dehydrogenated glycerol would affect the conversion of benzaldehyde in the later cycles.

In addition to its roles as both solvent and hydrogen donor, glycerol also tolerated microwave-promoted heating.<sup>10–13</sup> Based on the ability of the solvent to absorb microwave energy and convert it into heat, microwave heating is ideally suited to the high dielectric constants and high boiling points

of polar solvents with hydroxyl substitution such as glycerol.<sup>17,18</sup> The transfer hydrogenation of unsaturated organic compounds under microwave irradiation has been studied previously.<sup>19–21</sup>

Microwave-promoted transfer hydrogenation of benzaldehyde in glycerol was carried out using a Ru(*p*-cumene)Cl<sub>2</sub>-dimer as the catalyst and KOH or triethyl amine as the base. The experiment was conducted in a domestic microwave oven at atmospheric pressure in a 250 mL glass vessel covered with a watch glass. Benzaldehyde (2 g) was dissolved in 25 g of glycerol after which 0.12 g of the complex and 0.17 g of the bases were added. The reaction mixture was heated in the microwave for 3 min from 26 to 72 °C. At the end of the reaction, the vessel was cooled to room temperature and the reaction mixture was extracted with diethyl ether for GC analysis. The yields were found to be 33% with KOH as the base and 25% with triethyl amine as

**Fig. 3.** The effect of the benzaldehyde to ruthenium complex ratio on catalytic performance. Reaction conditions: 4 g glycerol, 0.22 g benzaldehyde, 270  $\mu\text{mol}$  KOH, 70  $^{\circ}\text{C}$ , 5 h.



the base, but the reaction in the absence of catalyst yielded a much lower conversion. These yields are higher than those detected under conventional heating after 5 h.

## Conclusion

To conclude, benzaldehyde was successfully reduced to benzyl alcohol in catalytic transfer hydrogenation in glycerol using several ruthenium complexes as catalyst and using both organic and inorganic bases. Glycerol was employed as both a green solvent and also as the hydrogen source. As a solvent, glycerol also facilitated easy product separation and catalyst recycling, and it was amenable to microwave-promoted reactions.

## References

- (1) Buque, E. M.; Chin-Joe, I.; Straathof, A. J. J.; Jongejan, J. A.; Heijnen, J. J. *Enzyme Microb. Technol.* **2002**, 31 (5), 656. doi:10.1016/S0141-0229(02)00161-8.
- (2) Rylander, P. N. *Catalytic Hydrogenation in Organic Syntheses*; Academic Press: New York, 1979.
- (3) Nishimura, S. *Handbook of Heterogeneous Catalytic Hydrogenation for Organic Synthesis*; John Wiley & Sons: New York, 2001.
- (4) Johnstone, R. A. W.; Wilby, A. H.; Entwistle, I. D. *Chem. Rev.* **1985**, 85 (2), 129. doi:10.1021/cr00066a003.
- (5) Lundgren, R. J.; Rankin, M. A.; McDonald, R.; Schatte, G.; Stradiotto, M. *Angew. Chem. Int. Ed.* **2007**, 46 (25), 4732. doi:10.1002/anie.200700345.
- (6) Zhao, M.; Yu, Z.; Yan, S.; Li, Y. *Tetrahedron Lett.* **2009**, 50 (32), 4624. doi:10.1016/j.tetlet.2009.05.100.
- (7) Carrión, M. C.; Sepúlveda, F.; Jalón, F. A.; Manzano, B. R.; Rodríguez, A. M. *Organometallics* **2009**, 28 (13), 3822. doi:10.1021/om9001268.
- (8) Polshettiwar, V.; Baruwati, B.; Varma, R. S. *Green Chem.* **2009**, 11 (1), 127. doi:10.1039/b815058c.
- (9) Zeng, F.; Yu, Z. *Organometallics* **2008**, 27 (22), 6025. doi:10.1021/om8006213.
- (10) Wolfson, A.; Tavor, D.; Dlugy, C.; Shotland, Y. US Patent 61/137,239, 2008.
- (11) Wolfson, A.; Dlugy, C.; Shotland, Y. *Environ. Chem. Lett.* **2007**, 5 (2), 67. doi:10.1007/s10311-006-0080-z.
- (12) Wolfson, A.; Dlugy, C.; Tavor, D.; Blumenfeld, J.; Shotland, Y. *Tetrahedron Asymmetry* **2006**, 17 (14), 2043. doi:10.1016/j.tetasy.2006.07.026.
- (13) Wolfson, A.; Litvak, G.; Dlugy, C.; Shotland, Y.; Tavor, D. *Ind. Crops Prod.* **2009**, 30 (1), 78. doi:10.1016/j.indcrop.2009.01.008.
- (14) Zsigmond, Á.; Notheisz, F.; Csajnyik, G.; Bäckvall, J.-E. *Top. Catal.* **2002**, 19 (1), 119. doi:10.1023/A:1013893502340.
- (15) Le Page, M. D.; James, B. R. *Chem. Commun. (Camb.)* **2000**, 1647. doi:10.1039/b005338o.
- (16) Ben-Harush, K.; Wolfson, A.; Herskowitz, M. *Lett. Org. Chem.* **2006**, 3 (9), 664. doi:10.2174/157017806778699973.
- (17) Kappe, C. O. *Angew. Chem. Int. Ed.* **2004**, 43 (46), 6250. doi:10.1002/anie.200400655.
- (18) Tierney, J.; Lidström, P. *Microwave-Assisted Organic Synthesis*; Blackwell: Oxford, 2005.
- (19) Berthold, H.; Schotten, T.; Hönig, H. *Synthesis* **2002**, 1607. doi:10.1055/s-2002-33349.
- (20) Samec, J. S. M.; Mony, L.; Bäckvall, J.-E. *Can. J. Chem.* **2005**, 83 (6–7), 909. doi:10.1139/v05-103.
- (21) Sarkar, M. S.; Jin, M. J. *Solid State Phenomena* **2007**, 124–126, 1785. doi:10.4028/www.scientific.net/SSP.124-126.1785.



# Using the nitro group to induce $\pi$ -stacking in terthiophenes

Wendy A. Sears, Craig D. MacKinnon, Robert C. Mawhinney, Lauren C. Sinnemaki, Matthew J. Johnson, A. John Winter, and Craig M. Robertson

**Abstract:** A new synthetic route to mononitrated oligothiophenes is described, as well as the preparation of halogenated derivatives (Br, I) thereof. An unusual deep red colour is observed and explained, with the aid of DFT calculations, as arising from a significant quinoidal contribution to the molecular structure. The crystal structures of two compounds,  $\text{H}(\text{C}_4\text{H}_2\text{S})_3\text{NO}_2$  and  $\text{Br}(\text{C}_4\text{H}_2\text{S})_3\text{NO}_2$ , are presented. Both compounds have planar sheets held together by intermolecular short contacts (hydrogen bonds and, for the latter,  $\text{NO}_2\cdots\text{Br}$  interactions); the sheets do not directly superimpose, so the effect of the  $\pi$ -stacking is not maximized. Solid-state fluorescence and extended-Hückel band-structure calculations are also presented for these materials.

**Key words:** oligothiophene, organic semiconductor, crystal structure, band structure, nitro-substitution.

**Résumé :** On décrit une nouvelle méthode générale de synthèse des oligothiophènes mononitrés ainsi que la préparation de leurs dérivés bromés et iodés. On a observé une couleur rouge foncé inhabituelle et, en se basant sur des calculs de la théorie de la fonctionnelle de la densité (TFD), on suggère qu'elle résulte d'une importante contribution quinonoidale à la structure moléculaire. On a déterminé les structures cristallines des deux composés  $\text{H}(\text{C}_4\text{H}_2\text{S})_3\text{NO}_2$  et  $\text{Br}(\text{C}_4\text{H}_2\text{S})_3\text{NO}_2$ . Les deux composés se présentent sous la forme de feuillets plans maintenus en place par des contacts intermoléculaires courts (liaisons hydrogènes et, dans le deuxième cas, interactions  $\text{NO}_2\cdots\text{Br}$ ); les feuillets ne sont pas directement superposés et il en résulte que l'effet de superposition  $\pi$  n'est pas maximisé. On rapporte aussi les résultats obtenus pour la fluorescence à l'état solide de ces matériaux ainsi que les calculs étendus de Hückel de leur structure de bande.

**Mots-clés :** oligothiophène, semiconducteur organique, structure cristalline, structure de bande, substitution par un groupe nitro.

[Traduit par la Rédaction]

## Introduction

Organic materials are carbon-based small molecules or polymers with interesting electronic properties. Two of the most studied organic semiconductors are the oligothiophenes<sup>1–3</sup> and the acenes.<sup>4</sup> The promise of organic materials is held in the ability of the compounds to undergo “tuning” of the electronic structures through molecular substitution. Thus, an overwhelming variety of oligomers have been made, from dendrimers to polymers to molecules substituted at every position.

Unsubstituted organic semiconductors are mostly *p*-type (where the charge is carried by positive charges, or holes). Attachment of electron-withdrawing groups can convert them to *n*-type conductors (negative charge carriers), e.g., dihexylsexithiophene is *p*-type while bis(perfluorohexyl)sexithiophene is *n*-type.<sup>5</sup> The lowering of the frontier orbitals upon attachment also increases environmental stability because reactivity with oxygen in the air is reduced. Molecules

substituted with both an electronic acceptor and an electronic donor will contain an internal charge-transfer electronic transition that can be exploited for non-linear optical devices<sup>6,7</sup> or as light-emitting diode dyes.<sup>8</sup> These electronic consequences are well-documented; far less is known of the structural consequences. Perfluorination<sup>9</sup> and  $\alpha,\omega$ -cyano-substitution,<sup>10,11</sup> for example, both lead to a greater degree of  $\pi$ -stacking in the single-crystal structure, which is fortunately a beneficial outcome as  $\pi$ -stacking has been shown to increase mobility in standard device configurations.<sup>12,13</sup>

The nitro group is a typical example of a strong electron-withdrawing group that has been attached to molecular materials.<sup>14–17</sup> While the resultant materials have been well-studied electronically, structural investigations into the consequences of nitro substitution are sparse. Therefore, we have undertaken the synthesis and crystal growth of structurally simple nitro-substituted oligothiophenes. We chose to limit ourselves to mono-nitrated derivatives because these species are of greater synthetic interest, potentially allowing

Received 28 August 2009. Accepted 28 October 2009. Published on the NRC Research Press Web site at [canjchem.nrc.ca](http://canjchem.nrc.ca) on 4 March 2010.

W.A. Sears, C.D. MacKinnon,<sup>1</sup> R.C. Mawhinney, L.C. Sinnemaki, M.J. Johnson, and A.J. Winter. Department of Chemistry, Lakehead University, 955 Oliver Road, Thunder Bay, ON P7B 5E1, Canada.

C.M. Robertson.<sup>2</sup> Department of Chemistry, University of Waterloo, Waterloo, ON N2L 3G1, Canada.

<sup>1</sup>Corresponding author (e-mail: [craig.mackinnon@lakeheadu.ca](mailto:craig.mackinnon@lakeheadu.ca)).

<sup>2</sup>Present address: Department of Chemistry, University Science Laboratories, South Road, Durham DH1 3LE, United Kingdom.

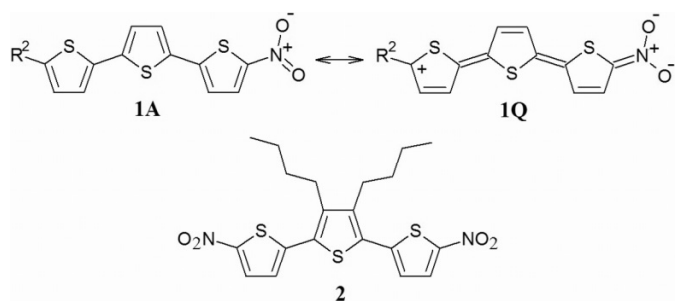
subsequent substitution to generate more complex molecules. The use of the letter "T" as an abbreviation for the 2,5-disubstituted thienyl ring is common in the oligothiophene literature (see Scheme 1). Using this abbreviation, we report herein the synthesis of several  $\text{XT}_n\text{NO}_2$  species, where  $\text{X} = \text{H}, \text{Br}, \text{or I}$ , and  $n = 2$  (bithiophene) and 3 (terthiophene). We also present the crystal structures of  $\text{HT}_3\text{NO}_2$  and  $\text{BrT}_3\text{NO}_2$ .

## Results and discussion

### Synthesis

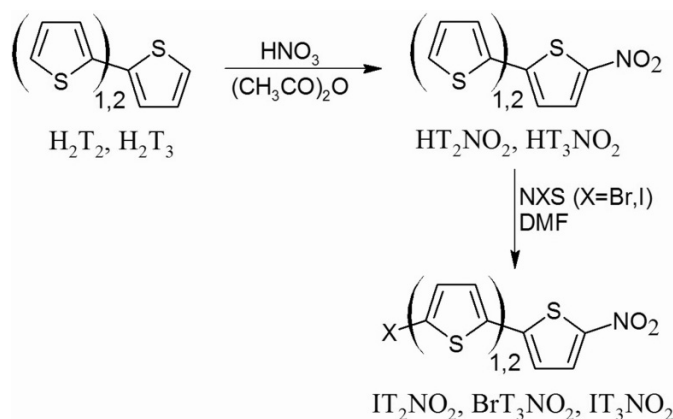
The compounds  $\text{HT}_3\text{NO}_2$  and  $\text{BrT}_3\text{NO}_2$  have been previously reported, but experimental details are scanty.<sup>18</sup> Further, we found the reported conditions to be excessively harsh, resulting in loss of regiochemical control, multiple nitrations, or oxidation of the thiophene ring.<sup>19</sup> Therefore, we report a new, milder synthesis of these species. We also report synthesis of the new species  $\text{BrT}_2\text{NO}_2$  and  $\text{IT}_3\text{NO}_2$ , which can be made the same way (although synthesis of  $\text{BrT}_2\text{NO}_2$  by the route  $\text{T}_2 \rightarrow \text{BrT}_2\text{H} \rightarrow \text{BrT}_2\text{NO}_2$  proved to have higher yield and purity). The reaction Scheme summarizes the syntheses. Nitration using nitric acid in acetic anhydride gave the best results, allowing us to heavily favour nitration at one (and only one) of the  $\alpha$ -sites on  $\text{H}_2\text{T}_2$  and  $\text{H}_2\text{T}_3$ . Unfortunately, this could not be extended to longer oligomers (the lack of solubility of  $\text{T}_4$ , for example, required heating the nitration step, leading to inseparable mixtures of regioisomers). Suzuki coupling<sup>20–22</sup> of  $\text{HT}_2\text{B(OH)}_2$  and  $\text{BrT}_2\text{NO}_2$  seemed to be a reasonable alternate route, but the low solubility of the product  $\text{HT}_4\text{NO}_2$  prevented purification by recrystallization or chromatography. Sublimation afforded some material but it was always accompanied by a significant amount of  $\text{H}_2\text{T}_4$  and unidentified decomposition product(s) (probably due to polymerization). The insolubility of  $\text{HT}_4\text{NO}_2$  also prevented the regioselective synthesis of halogenated derivatives. Stille coupling<sup>23–26</sup> was even less useful because it had the same problems as the Suzuki method, with the additional difficulty of stannyl contamination.

### Spectroscopic and computational studies



The most striking characteristic of the nitro-substituted terthiophenes is their deep red colour, in contrast to the pale yellow of unsubstituted  $\text{H}_2\text{T}_3$ . We<sup>10,27</sup> and others<sup>18,28–30</sup> have reported the UV–vis and fluorescence spectra in solution of a variety of oligothiophenes; some of the data are summar-

Scheme 1.



ized in Table 1. It is obvious from these data that the nitro group has an effect on  $\lambda_{\text{MAX}}$  that is larger than it should be based on a simple particle-in-a-box argument, i.e., the  $\text{NO}_2$  group should extend the molecule by only two bonds, the same as the nitrile group. Instead, the  $\lambda_{\text{MAX}}$  of  $\text{HT}_3\text{NO}_2$  is closest to that of  $\text{H}_2\text{T}_5$  (extending the conjugation by eight bonds). We conclude that the  $\text{NO}_2$  substituent helps rigidify the backbone by introducing a quinoidal resonance structure **1Q** to the molecule. This restricts the free rotation (it has a very small energy barrier<sup>35,36</sup>) about the  $\text{C5}–\text{C2}'$  and the  $\text{C5}'–\text{C2}''$  (ring–ring) bonds in the aromatic form **1A**. This rotation disrupts the extended conjugation of the oligomer and shortens the  $\lambda_{\text{MAX}}$ , so the restricted rotation in **1Q** increases the effective average conjugation length. Addition of a second nitro group (e.g., compound **2**) does not have the same effect, presumably because the quinoidalization has already occurred with the first  $\text{NO}_2$  group.

For verification, we turned to DFT calculations. If the resonance form **1Q** is significant, it should lead to a greater degree of  $\pi$ -bonding between C2 and C3 than is present in the aromatic form **1A**. The bonds  $\text{C1}–\text{C2}$  and  $\text{C3}–\text{C4}$  should also lengthen. The results are shown in Table 2, along with experimental bond lengths from crystal structures when available ( $\text{HT}_3\text{NO}_2$  and  $\text{BrT}_3\text{NO}_2$  are reported below for the first time, while the other species have been previously reported). Unfortunately, the ratio derived from the crystal structures is unconvincing, partly due to the fact that the ratio ( $\text{C2}–\text{C3}/\text{C1}–\text{C2}$ ) can vary widely due to crystal packing effects, and partly because the errors in the calculated ratios are within the statistical errors arising from the atomic ESDs. The computational results are more convincing, and may anyway be more representative of the structure in solution (i.e., in the absence of packing effects). For the computed structures, the  $\text{C2}–\text{C3}$  bond decreases in length by 0.012 Å on changing from an H to an  $\text{NO}_2$ . The  $\text{C1}–\text{C2}$  bond lengths also increase slightly, verifying that the resonance structure **1Q** does, in fact, have some influence on the structure of these molecules.

This change is essentially identical no matter what is happening at the other end of the molecule (independent of  $\text{R}^2$ ). This is somewhat counterintuitive because the quinoidal form **1Q** should be stabilized by lone pairs on  $\text{R}^2$ , which could occur when  $\text{R}^2 = \text{Br}$  but not when  $\text{R}^2 = \text{H}$ . We would conclude that the nitro group is such a strong electron-withdrawing substituent that a donor group at the other end is

**Table 1.** Absorption and fluorescence data for  $\text{XT}_n\text{NO}_2$  compounds. Solutions of  $\text{CH}_2\text{Cl}_2$  were used,  $\lambda_{\text{MAX}}$  values are reported in nm units. Literature values are in brackets.

Compound	UV-vis absorption	Fluorescence (solution) <sup>a</sup>	Fluorescence (solid) <sup>a</sup>	HOMO-LUMO gap <sup>b</sup>
$\text{H}_2\text{T}_3$	[354]	428, 420 [411, 433]	480, 505, 455 [471, 455, 505] <sup>32</sup>	318
$\text{H}_2\text{T}_4$	[390]	440, 465 [454, 484]	528, 552 [555, 526] <sup>33</sup>	
$\text{H}_2\text{T}_5$	417 [418, $\text{C}_6\text{H}_6$ ] <sup>29</sup>	496, 516 [482, 514, dioxane] <sup>30</sup>	669	
$\text{BrT}_2\text{NO}_2$	401	504	575 <sup>c</sup>	332
$\text{HT}_3\text{NO}_2$	[440]	581 [610]	643	379
$\text{BrT}_3\text{NO}_2$	[430]	581 [590]	669	383
$\text{IT}_3\text{NO}_2$	442	585	670	
Compound <b>2</b>	[444] <sup>31</sup>			
$\text{BrT}_3\text{CN}$	381	426	438	

**Note:** Literature values are also in  $\text{CH}_2\text{Cl}_2$  from ref. 18, unless otherwise stated.

<sup>a</sup>Italicized peaks are shoulders, peaks are listed in order of decreasing intensity.

<sup>b</sup>Using the PBE0/6-311++G(2df,pd) basis set, energy converted to equivalent wavelength in nm.

<sup>c</sup>Transition overlaps with a Raman scattering peak, which might alter the  $\lambda_{\text{MAX}}$  slightly.

**Table 2.** Selected bond lengths for  $\text{H}_2\text{T}_3$ ,  $\text{HT}_3\text{NO}_2$ ,  $\text{BrT}_3\text{NO}_2$ , compound **2**, and  $\text{T}_3\text{CN}_2$ ; calculated values are at the PBE0/6-311++G(2df,pd) level, distances in Å.

Compound		C1–C2	C2–C3	C3–C4	C4–C5	Ratio <sup>a</sup>
$\text{H}_2\text{T}_3$	Crystal structure <sup>b</sup>	1.374(13)	1.458(12)	1.422(11)	1.450(12)	
		1.359(13)	1.412(13)	1.398(12)	1.439(13)	
		1.385(12)	1.431(11)	1.426(11)	1.460(13)	
		1.3282(14)	1.407(13)	1.442(11)	1.447(12)	
		[1.375 (avg)]	[1.427 (avg)]	[1.422 (avg)]	[1.449 (avg)]	1.038
	Calculated	1.362	1.412	1.373	1.442	1.032
$\text{HT}_3\text{NO}_2$	Calculated <sup>c,d</sup>	1.368	1.423	1.380	1.457	1.040
	Crystal structure	1.354(3)	1.405(2)	1.369(2)	1.450(2)	1.038
	Calculated	1.366	1.400	1.382	1.437	1.025
$\text{BrT}_3\text{NO}_2$	Crystal structure	1.391(9)	1.404(9)	1.371(10)	1.464(9)	1.009
	Calculated	1.366	1.400	1.382	1.437	1.025
	Calculated <sup>c,d</sup>	1.373	1.409	1.392	1.450	1.026
Compound <b>2</b>	Crystal structure <sup>e</sup> 31	1.363(3)	1.404(3)	1.377(3)	1.461(3)	
		1.359(3)	1.402(3)	1.379(3)	1.451(3)	
		[1.361 (avg)]	[1.403 (avg)]	[1.378 (avg)]	[1.456 (avg)]	1.031
	Calculated <sup>c</sup>	1.373	1.410	1.391	1.452	1.027
$\text{T}_3(\text{CN})_2$	Crystal structure <sup>f</sup> 10	1.367(15)	1.389(16)	1.367(15)	1.461(14)	
		1.362(14)	1.424(13)	1.370(14)	1.362(14)	
		1.302(17)	1.376(16)	1.345(16)	1.447(14)	
		1.350(16)	1.417(14)	1.346(14)	1.450(14)	
		1.341(16)	1.384(14)	1.353(15)	1.469(14)	
		[1.344 (avg)]	[1.398 (avg)]	[1.356 (avg)]	[1.438 (avg)]	1.040

<sup>a</sup>The ratio of the bond lengths (C2–C3)/(C1–C2).

<sup>b</sup>There are two crystallographically independent  $\text{H}_2\text{T}_3$  molecules, neither of which have  $C_{2v}$  symmetry.

<sup>c</sup>At the B3LYP/631G\*\* level, from ref. 34.

<sup>d</sup>Calculated for the mononitrated equivalent of **2** (H or Br in place of one  $\text{NO}_2$ ).

<sup>e</sup>The molecule does not have  $C_{2v}$  symmetry in the crystal structure.

<sup>f</sup>There are 2.5 molecules in the asymmetric unit.

essentially irrelevant (or, put another way, the far thiophene ring acts as the donor group).

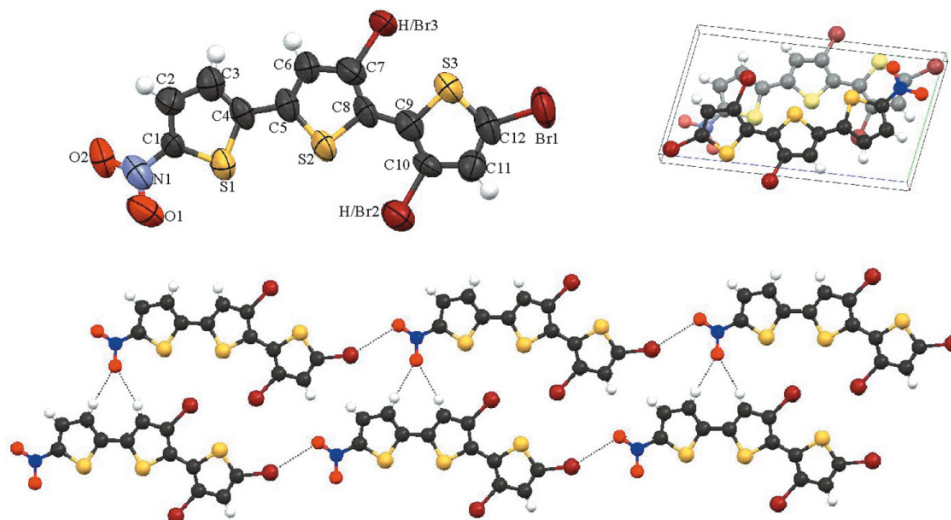
### Solid-state structures

Since we wished to determine the solid-state influence of the nitro group, crystals of both  $\text{HT}_3\text{NO}_2$  and  $\text{BrT}_3\text{NO}_2$  were grown, the former by sublimation and the latter from solution. The pertinent refinement data are given in Table 3. Unfortunately, the crystals for  $\text{BrT}_3\text{NO}_2$  were of low quality.

Because of its low solubility, conversion from  $\text{HT}_3\text{NO}_2$  to  $\text{BrT}_3\text{NO}_2$  required heating and a long reaction time, which created a mixture of brominated products. Purification by repeated recrystallization did not fully separate these substances, so consequently a small amount of disubstituted material remained, which was modeled using partial occupancies as shown in Fig. 1 (the atoms labeled “H/Br2” and “H/Br3” are the partially occupied sites). Repeated sublimation of the product did lead to pure  $\text{BrT}_3\text{NO}_2$  by combustion

**Table 3.** Crystallographic refinement information for HT<sub>3</sub>NO<sub>2</sub> and BrT<sub>3</sub>NO<sub>2</sub>.

Compound	HT <sub>3</sub> NO <sub>2</sub>	BrT <sub>3</sub> NO <sub>2</sub>
Empirical formula	C <sub>12</sub> H <sub>7</sub> NO <sub>2</sub> S <sub>3</sub>	C <sub>12</sub> H <sub>6</sub> BrNO <sub>2</sub> S <sub>3</sub>
Formula weight	293.37	476.53
Crystal system	Triclinic	Triclinic
Space group	<i>P</i> $\bar{1}$	<i>P</i> $\bar{1}$
<i>a</i> (Å)	6.3225(3)	7.3587(6)
<i>b</i> (Å)	7.6385(4)	7.8832(7)
<i>c</i> (Å)	13.2640(6)	13.7617(12)
$\alpha$ (°)	74.5191(10)	97.595(2)
$\beta$ (°)	83.4360(10)	96.644(2)
$\gamma$ (°)	87.3150(10)	113.5590(10)
<i>V</i> (Å <sup>3</sup> )	613.20(5)	712.77(11)
Formula units ( <i>Z</i> )	2	2
$\rho_{\text{calcd.}}$ (g cm <sup>-3</sup> )	1.589	2.222
$\mu$ (Mo K $\alpha$ ) (mm <sup>-1</sup> )	0.595	7.063
Crystal dimensions (mm)	0.40 × 0.24 × 0.14	0.22 × 0.08 × 0.04
<i>F</i> (000)	300	457
$\theta$ range (°)	3.21 < $\theta$ < 26.50	2.98 < $\theta$ < 25.99
Reflections collected	7285	8090
Unique reflections	2532	2795
<i>R</i> <sub>1</sub> [ <i>I</i> > 2 $\sigma$ ( <i>I</i> )]	0.0315	0.0537
<i>wR</i> <sub>2</sub> (all data)	0.0881	0.1084
Goodness of fit on <i>F</i> <sup>2</sup>	1.051	1.276

**Fig. 1.** Crystal structure of BrT<sub>3</sub>NO<sub>2</sub>. Top left: molecule showing atom numbering and thermal ellipsoids. Top right: two coplanar molecules showing the lack of face-to-face  $\pi$ -stacking between layers. Bottom: the two-dimensional sheet forcing coplanarity on the molecules, showing the short O $\cdots$ Br contacts and hydrogen bonds.

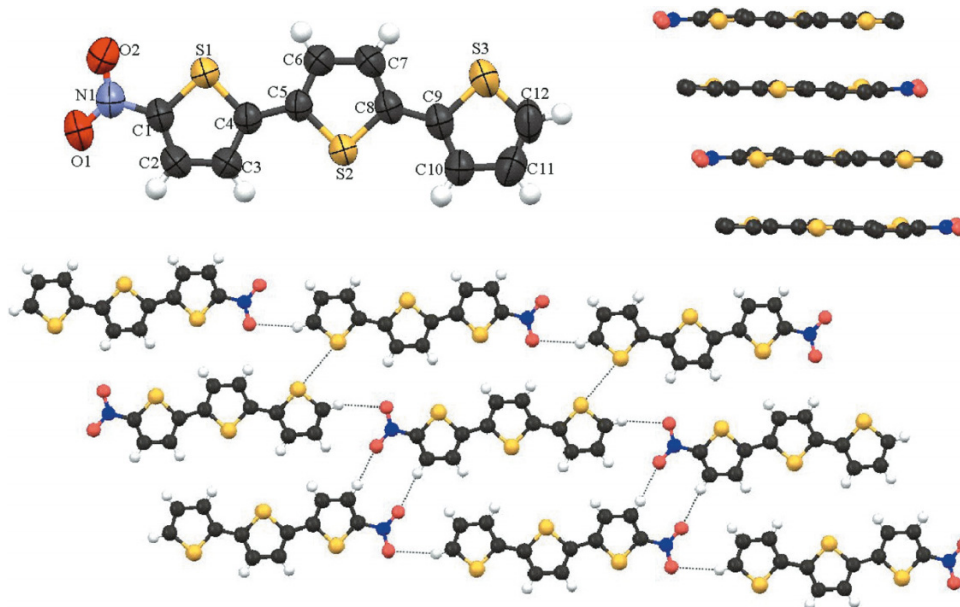
analysis. However, we were unable to obtain even low-quality single crystals of purified BrT<sub>3</sub>NO<sub>2</sub>. Fortunately, the gross structure does give the necessary information on atomic connectivities, and it shows the molecules forming ribbons held together by the halo-nitro supramolecular synthon.<sup>37,38</sup> Contact between the bromo and one oxygen on the nitro (as opposed to both oxygens equally) is typical.<sup>39</sup> The ribbons stack cofacially, but they are offset so that the  $\pi$ -systems overlap very little. Interestingly, rings 1 (C1–C4) and 2 (C5–C8) are mutually syn, while rings 2 and 3 (C9–C12) are anti to each other. While the syn orientation is less common, it is not unheard of (in fact, compound **2** also has mutually syn rings in its crystal structure<sup>31</sup>).

Figure 2 shows the crystal structure of HT<sub>3</sub>NO<sub>2</sub>. In this case, sublimation led to good-quality crystals. The molecules line up in head-to-tail ribbons joined by hydrogen bonds between each nitro oxygen and an aromatic hydrogen. There is also a cross-ribbon hydrogen bond, generating a two-dimensional sheet. These sheets stack in the third dimension, leading to  $\pi$ -stacks, the favored orientation for maximizing carrier mobility in molecular semiconductors. The  $\pi$ -stacking is not fully optimized, however, as consecutive ribbons run in opposite directions in the centrosymmetric space group.

Even though the  $\pi$ -stacking is not optimal in either structure, there are clearly intermolecular interactions that give



**Fig. 2.** Crystal structure of HT<sub>3</sub>NO<sub>2</sub>. Top left: molecule showing atom numbering scheme and thermal ellipsoids. Top right: side view of the  $\pi$ -stack; the top and bottom molecules have one S pointing at the viewer while the middle molecule has two, demonstrating the alternation in the sense of the stacking. Bottom: two-dimensional sheets held together with hydrogen bonds.



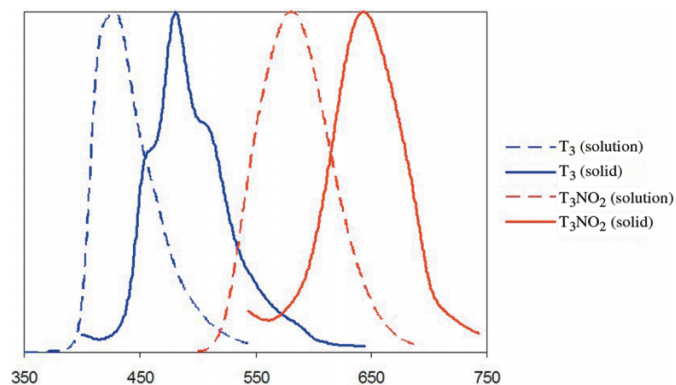
rise to intermolecular interactions between molecules in the solid state. The normalized fluorescence spectra for H<sub>2</sub>T<sub>3</sub> and HT<sub>3</sub>NO<sub>2</sub> (in both CH<sub>2</sub>Cl<sub>2</sub> solution and powder solid) are shown in Fig. 3. The  $\lambda_{\text{MAX}}$  for all the solid-state data were presented in Table 1, along with the solution data. The  $\lambda_{\text{MAX}}$  increases significantly for the solids compared with the solutions, demonstrating that the solid-state optical band gap is smaller than the molecular HOMO–LUMO gap.

The electrostatic hydrogen bonds connecting the molecules in the solid state do not contribute to the formation of an extended three-dimensional electronic structure. This is verified by Extended Hückel band structure calculations on RT<sub>3</sub>NO<sub>2</sub> (R = H, Br), the results of which are shown in Fig. 4, along with the same calculation on H<sub>2</sub>T<sub>3</sub>, using the literature crystal structure;<sup>35</sup> numerical data are given in Table 4. The bandwidths are narrow, with little dispersion along any of the reciprocal space axes. In triclinic space groups, in which all these structures crystallize, the directions *X*, *Y*, and *Z* do not correspond to the real-space axes *a*, *b*, and *c*; however, this does not affect the gross conclusion that the dispersion is small. The band gap is significantly lower in the nitro-substituted species than in the unsubstituted molecule, but this is a reflection of the change in the energies of the HOMO and LUMO not a reflection of an increase in the bandwidths. The bandwidths are much narrower than those published for H<sub>2</sub>T<sub>6</sub><sup>41</sup> but are comparable to H<sub>2</sub>T<sub>3</sub>, so longer nitro-substituted oligomers may have significantly larger bandwidths.

## Conclusions

The attachment of one nitro group to a terthiophene oligomer is possible by using the relatively mild conditions of nitric acid in acetic anhydride. The resultant product, HT<sub>3</sub>NO<sub>2</sub> has an unusually small HOMO–LUMO energy gap, which we attribute to the effect of the quinoidal reso-

**Fig. 3.** Normalized solution and powder fluorescence spectra for H<sub>2</sub>T<sub>3</sub> and HT<sub>3</sub>NO<sub>2</sub>.

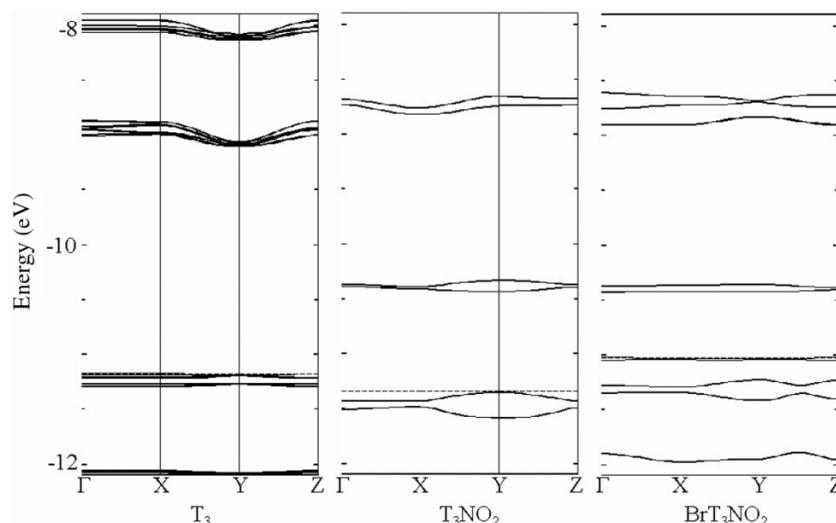


nance structure. The solid-state crystal structure consists of two-dimensional planes of molecules held together by hydrogen bonds. Although the sheets do not superimpose, there is some  $\pi$ -stacking between the sheets. Bromination and iodination of this molecule is possible, and the BrT<sub>3</sub>NO<sub>2</sub> molecule also has a  $\pi$ -sheet crystal structure, with hydrogen bonds and NO<sub>2</sub>...Br contacts. In this case, there is little  $\pi$ -interaction between the sheets. Neither solid has large dispersion in the band structure, but the bandwidths are similar to unsubstituted H<sub>2</sub>T<sub>3</sub>, so longer nitrated oligomers may have more electronically useful band structures. The band gap is significantly smaller in nitro-substituted species, but this is simply a reflection of the smaller HOMO–LUMO gap. These results suggest that the nitro group is a good candidate for inducing  $\pi$ -stacking in oligothiophenes.

## Experimental

### Materials

Starting reagents were purchased from Aldrich and used

**Fig. 4.** Extended-Hückel band structures of  $\text{H}_2\text{T}_3$ ,  $\text{HT}_3\text{NO}_2$ , and  $\text{BrT}_3\text{NO}_2$ . The dashed line is the Fermi level.**Table 4.** Band structures of selected oligothiophenes.

Compound	Band gap	Valence bandwidth	Conduction bandwidth	Reference
$\text{H}_2\text{T}_3$	2.08	0.013	0.11	This work <sup>a</sup>
$\text{HT}_3\text{NO}_2$	0.92	0.083	0.048	This work
$\text{BrT}_3\text{NO}_2^b$	0.60	0.016	0.023	This work
$\text{H}_2\text{T}_4$	2.24	0.52	0.44	40
$\text{H}_2\text{T}_6$	1.94	0.79	0.52	41

<sup>a</sup>The band structure calculation is new to this work, using the literature crystal structure (ref. 35).

<sup>b</sup>The crystal structure contains sites with partial Br occupancy; the band structure calculation has assumed 100% H for those sites.

without purification, except *N*-bromosuccinimide (NBS), which was recrystallized from water. Solvents were purchased from Anachemia or Caledon and purified prior to use: dichloromethane, diethyl ether, and tetrahydrofuran (THF) by passage through an alumina column under  $\text{N}_2$ ; alcohols by distillation from magnesium under  $\text{N}_2$ . Oligothiophenes 2,2'-bithiophene ( $\text{H}_2\text{T}_2$ ); 2,2':5',2''-terthiophene ( $\text{H}_2\text{T}_3$ ); 2,2':5',2'':5'',2'''-quaterthiophene ( $\text{H}_2\text{T}_4$ ); and 2,2':5',2'':5'',2'':5''',2''''-quinquethiophene ( $\text{H}_2\text{T}_5$ ) were synthesized by Grignard couplings of thienylmagnesium bromide ( $\text{HTMgBr}$ ) to 2-bromothiophene ( $\text{BrTH}$ ); 2,5-dibromothiophene ( $\text{Br}_2\text{T}$ ); 5,5'-dibromo-2,2'-bithiophene ( $\text{Br}_2\text{T}_2$ ); and 5,5'-dibromo-2,2':5',2''-terthiophene ( $\text{Br}_2\text{T}_3$ ), respectively, using the Kumada coupling catalyst ( $\text{Ni(dppp)Cl}_2$ ) [1,3-bis(diphenylphosphino)propane]dichloronickel(II).<sup>42</sup> The method of Bäuerle<sup>43</sup> was used for monobromination to create 5-bromo-2,2'-bithiophene ( $\text{BrT}_2\text{H}$ ), and for all dibrominations. 5-Bromo-2,2':5',2''-terthiophene-5'-carbonitrile ( $\text{BrT}_3\text{CN}$ ) was prepared by the literature route.<sup>10</sup> All reactions were performed under an atmosphere of  $\text{N}_2$  (using Schlenk conditions).

### Instruments

FTIR spectra were recorded as nujol mulls on a Nicolet 380 FTIR spectrometer; vibrational frequencies are reported as wavenumbers ( $\text{cm}^{-1}$ ), with an experimental resolution of  $4\text{ cm}^{-1}$ . NMR spectra were recorded on a Varian Unity Inova 500 at room temperature in  $\text{CDCl}_3$  or  $\text{DMSO}-d_6$  solutions, referenced to TMS added to the sample or to the residual protonated solvent peak. Fluorescence measurements were taken on a PerkinElmer LS50B luminescence

spectrometer, while UV-vis absorption spectra were recorded on a PerkinElmer Lambda 11 UV-vis spectrometer; both were recorded as  $\text{CH}_2\text{Cl}_2$  solutions. Combustion analyses were performed on a CEC (SCP) 240-XA Analyzer. Gradient vacuum sublimations and crystal growth for X-ray crystallography were performed on an Applied Test Systems model 3210 split tube furnace attached to a series 2404 three-zone temperature control system. Melting points were recorded on an Electrothermal 9100 apparatus and are uncorrected. Mass spectra were recorded on a Micromass VG Autospec electron impact mass spectrometer at Lakehead University or on a Bruker Reflex III laser desorption/ionization time-of-flight mass spectrometer at the Mass Spectrometry Facility in the Advanced Analysis Centre at the University of Guelph.

### X-ray crystallography

Single-crystal data were collected using the Smart Apex CCD (Bruker) equipped with an area detector utilizing graphite-monochromated  $\text{Mo K}\alpha$  radiation ( $\lambda = 0.71073\text{ \AA}$ ). The data were corrected for Lorentz and polarization effects. Absorption corrections were based on fitting a function to the empirical transmission surface as sampled by multiple equivalent measurements of numerous reflections using the scale function of the APEX II software. The space groups for all compounds were determined on the basis of the systematic absences using symmetry and space group of the APEX II package. Structure solution and refinement using the SHELXTL package of APEX II were successful in the chosen centrosymmetric space groups. The structure solution

via direct method led to the identification of the heavy atoms and the refinement on  $F^2$  using least-square method resulted in good  $R$  values. Full details of the structures have been deposited with the Cambridge Crystallographic Data Centre (see Supplementary data for details).

### Computational details

Calculations used the PBE0 hybrid functional<sup>44–46</sup> and the large basis set 6–311++G(2df, pd)<sup>47,48</sup> as implemented in the Gaussian 03 package.<sup>49</sup>

### Synthesis of 5-bromo-5'-nitro-2,2'-bithiophene ( $\text{BrT}_2\text{NO}_2$ )

Although this compound was often made in the method outlined in the Scheme 1, we found that the following method gave a higher-purity product. In 25 mL of acetic anhydride, 4.79 g (20 mmol) of  $\text{BrT}_2$  was dissolved, and the mixture was cooled to 0 °C. To this solution (maintaining 0 °C) was added dropwise with stirring a mixture of 1.50 g (24 mmol) of nitric acid in 20 mL of acetic anhydride. The resultant mustard-yellow solution was quenched with saturated sodium bicarbonate and extracted into dichloromethane. Rotary evaporation followed by recrystallization (from ethanol) and sublimation (two times) yielded 1.45 g (25.6%) of analytically pure material. Mp 190–193 °C.  $^1\text{H}$  NMR ( $\text{DMSO}-d_6$ )  $\delta$  (ppm): 8.12 (d,  $J_{\text{AB}}$  4.0 Hz, 1 H), 7.56 (d,  $J_{\text{AB}}$  4.0 Hz, 1 H), 7.45 (d,  $J_{\text{AB}}$  4.0 Hz, 1H), 7.36 (d,  $J_{\text{AB}}$  4.0 Hz, 1 H). Mass spectrum  $m/z$ : 291 ( $\text{M}^+$ , 98%), 261 ( $[\text{M} - \text{NO}]^+$ , 26%), 245 ( $[\text{M} - \text{NO}_2]^+$ , 23%), 201 ( $[\text{M} - \text{SCNO}_2]^+$ , 100%). Anal. calcd. for  $\text{C}_8\text{H}_4\text{BrNO}_2\text{S}_2$ : C 33.12, H 1.38, N 4.83; found: C 32.75, H 1.62, N 4.51%.

### Synthesis of 5-nitro-2,2':5',2''-terthiophene ( $\text{HT}_3\text{NO}_2$ )

In 100 mL of acetic anhydride, 8.75 g (35 mmol) of  $\text{H}_2\text{T}_3$  was dissolved, and the mixture was warmed until the oligothiophene dissolved. To this solution was added dropwise with stirring 2.75 g (44 mmol) of nitric acid. The dark-coloured solution was quenched with saturated sodium bicarbonate, at which time a dark-red precipitate formed. The solid was suction-filtered and washed with toluene and hexanes to give 3.19 g (31%) of an orange powder. Gradient sublimation in a tube furnace (95–70 °C) afforded analytically pure red crystals suitable for X-ray crystallography. Rotary evaporation followed by recrystallization (from ethanol) and sublimation (two times) yielded 1.45 g (25.6%) of analytically pure material. Mp 157–160 °C.  $^1\text{H}$  NMR ( $\text{DMSO}-d_6$ )  $\delta$  (ppm): 8.12 (d,  $J_{\text{AB}}$  4.5 Hz, 1 H), 7.69 (d,  $J_{\text{AB}}$  4.0 Hz, 1 H), 7.63 (d,  $J_{\text{AB}}$  6.0 Hz, 1H), 7.46 (d,  $J_{\text{AB}}$  4.5 Hz, 2 H), 7.41 (d,  $J_{\text{AB}}$  4.0 Hz, 1 H), 7.15 (dd,  $J_{\text{AB}} = J_{\text{AC}}$  4.5 Hz, 1 H). Mass spectrum  $m/z$ : 293 ( $\text{M}^+$ , 100%), 247 ( $[\text{M} - \text{NO}_2]^+$ , 25%), 203 (87%). Anal. calcd. for  $\text{C}_{12}\text{H}_7\text{NO}_2\text{S}_3$ : C 49.13, H 2.40, N 4.77; found: C 49.14, H 2.46, N 4.77%.

### Synthesis of 5-bromo-5'-nitro-2,2':5',2''-terthiophene ( $\text{BrT}_3\text{NO}_2$ )

In 100 mL of DMF was dissolved 0.78 g (2.7 mmol)  $\text{HT}_3\text{NO}_2$ . While stirring in the dark, 1.84 g (10 mmol) was added portionwise over the course of 2 h, after which the solution was stirred overnight. Crude material precipitated upon addition of water. The red solid was recrystallized from toluene and repeatedly sublimed (120–90 °C) to obtain analytically pure material. Mp 172–175 °C. Mass spec-

trum  $m/z$ : 373 ( $\text{M}^+$ , 100%), 327 ( $[\text{M} - \text{NO}_2]^+$ , 27%), 283 ( $[\text{M} - \text{SCNO}_2]^+$ , 73%), 145 (33%). Anal. calcd. for  $\text{C}_{12}\text{H}_6\text{BrNO}_2\text{S}_3$ : C 38.72, H 1.62, N 3.76; found: C 38.57, H 1.94, N 3.84%. Crystals suitable for X-ray crystallography were prepared by repeatedly recrystallizing the crude, i. e., isolating and redissolving material in toluene; this had the effect of concentrating the multibrominated byproducts, giving the structure as discussed in the text.

### Synthesis of 5-iodo-5'-nitro-2,2':5',2''-terthiophene ( $\text{IT}_3\text{NO}_2$ )

To a solution of 3.19 g (11 mmol)  $\text{HT}_3\text{NO}_2$  in 250 mL of DMF was added portionwise (in the dark) 2.48 g (11 mmol) of NIS. The mixture was then stirred overnight, followed by precipitation upon addition of water, giving 2.7 g (64%) of red-orange material. This material was purified by sublimation in vacuo. Mp 232–233 °C.  $^1\text{H}$  NMR ( $\text{CDCl}_3$ )  $\delta$  (ppm): 7.86 (d,  $J_{\text{AB}}$  4.5 Hz, 1 H), 7.26 (d,  $J_{\text{AB}}$  3.0 Hz, 1 H), 7.20 (d,  $J_{\text{AB}}$  4.0 Hz, 1 H), 7.09 (d,  $J_{\text{AB}}$  4.0 Hz, 1 H), 7.07 (d,  $J_{\text{AB}}$  4.0 Hz, 1 H), 6.91 (d,  $J_{\text{AB}}$  4.0 Hz, 1 H). Mass spectrum  $m/z$ : 419 ( $\text{M}^+$ , 100%), 373 ( $[\text{M} - \text{NO}_2]^+$ , 23%), 329 (40%), 293 ( $[\text{M} - \text{I}]^+$ , 11%). Anal. calcd. for  $\text{C}_{12}\text{H}_6\text{INO}_2\text{S}_3$ : C 34.38, H 1.44, N 3.34; found: C 34.50, H 1.65, N 3.11%.

### Supplementary data

Supplementary data for this article (computational data, including optimized geometries, orbital energies, and vertical excitation energies on the series  $\text{R}^1\text{T}_n\text{R}^2$  ( $n = 1–3$ ;  $\text{R}^1 = \text{H}$  or  $\text{Br}$ ,  $\text{R}^2 = \text{H}$  or  $\text{NO}_2$ ) and experimental information on the synthesis of  $\text{XT}_4\text{NO}_2$  ( $\text{X} = \text{H}$ ,  $\text{Br}$ )) are available on the journal Web site (<http://canjchem.nrc.ca>) or may be purchased from the Depository of Unpublished Data, Document Delivery, CISTI, National Research Council Canada, Ottawa, ON K1A 0R6, Canada. DUD 5327. For more information on obtaining material, refer to <http://cisti-icist.nrc-cnrc.gc.ca/eng/ibp/cisti/collection/unpublished-data.html>. CCDCs 739773 ( $\text{HT}_3\text{NO}_2$ ) and 739774 ( $\text{BrT}_3\text{NO}_2$ ) contain the X-ray data in CIF format for this manuscript. These data can be obtained, free of charge, via <http://www.ccdc.cam.ac.uk/conts/retrieving.html> (Or from the Cambridge Crystallographic Data Centre, 12 Union Road, Cambridge CB2 1EZ, UK; fax +44 1223 336033; or [deposit@ccdc.cam.ac.uk](mailto:deposit@ccdc.cam.ac.uk)).

### Acknowledgments

Funding for this research was primarily supplied by the Research Corporation (Cottrell College Science Award) and by Lakehead University. RCM would also like to thank SHARCNET for computational facilities. LCS was partially supported by the Natural Sciences and Engineering Research Council of Canada (NSERC) USRA Award. Thanks to Prof. William Sears in the Department of Physics at Lakehead University and to Dr. Abdeljalil Assoud in the Department of Chemistry at the University of Waterloo for some helpful discussions.

### References

- (1) Fichou, D. *Handbook of Oligo- and Polythiophenes*; Wiley-VCH: Weinheim, 1999.
- (2) Barbarella, G.; Melucci, M.; Sotgiu, G. *Adv. Mater.* **2005**, *17* (13), 1581. doi:10.1002/adma.200402020.



- (3) Mishra, A.; Ma, C.-Q.; Bäuerle, P. *Chem. Rev.* **2009**, *109* (3), 1141. doi:10.1021/cr8004229.
- (4) Anthony, J. E. *Chem. Rev.* **2006**, *106* (12), 5028. doi:10.1021/cr050966z. PMID:17165682.
- (5) Facchetti, A.; Deng, Y.; Wang, A.; Koide, Y.; Sirringhaus, H.; Marks, T. J.; Friend, R. H. *Angew. Chem. Int. Ed.* **2000**, *39* (24), 4547. doi:10.1002/1521-3773(20001215)39:24<4547::AID-ANIE4547>3.0.CO;2-J.
- (6) Rao, V. P.; Wong, K. Y.; Jen, A. K.-Y.; Drost, K. J. *Chem. Mater.* **1994**, *6* (12), 2210. doi:10.1021/cm00048a004.
- (7) Zhang, J. X.; Dubois, P.; Jérôme, R. *J. Chem. Soc., Perkin Trans. 2* **1997**, (6): 1209. doi:10.1039/a606547c.
- (8) Koumura, N.; Wang, Z.-S.; Mori, S.; Miyashita, M.; Suzuki, E.; Hara, K. *J. Am. Chem. Soc.* **2006**, *128* (44), 14256. doi:10.1021/ja0645640. PMID:17076489.
- (9) Sakamoto, Y.; Komatsu, S.; Suzuki, T. *J. Am. Chem. Soc.* **2001**, *123* (19), 4643. doi:10.1021/ja015712j. PMID:11457268.
- (10) Barclay, T. M.; Cordes, A. W.; MacKinnon, C. D.; Oakley, R. T.; Reed, R. W. *Chem. Mater.* **1997**, *9* (4), 981. doi:10.1021/cm960545l.
- (11) MacKinnon, C. D.; Parent, S. L. M.; Mawhinney, R. C.; As-soud, A.; Robertson, C. M. *CrystEngComm* **2009**, *11* (1), 160. doi:10.1039/b810479d.
- (12) Gao, X.; Wu, W.; Liu, Y.; Qiu, W.; Sun, X.; Yu, G.; Zhua, D. *Chem. Commun. (Camb.)* **2006**, (26): 2750. doi:10.1039/b603632e. PMID:17009451.
- (13) Ando, S.; Murakami, Y.; Nishida, J.; Tada, H.; Inoue, Y.; Tokito, S.; Yamashita, Y. *J. Am. Chem. Soc.* **2005**, *127* (43), 14996. doi:10.1021/ja055686f. PMID:16248617.
- (14) Prakash, M.; Radhakrishnan, T. P. *Chem. Mater.* **2006**, *18* (13), 2943. doi:10.1021/cm052607q.
- (15) Caruso, U.; Diana, R.; Fort, A.; Panunzi, B.; Roviello, A. *Macromol. Symp.* **2006**, *234* (1), 87. doi:10.1002/masy.200650212.
- (16) George, S.; Nangia, A.; Lam, C.-K.; Mak, T. C. W.; Nicoud, J.-F. *Chem. Commun. (Camb.)* **2004**, (10): 1202. doi:10.1039/b402050b. PMID:15136838.
- (17) Feng, K.; De Boni, L.; Misoguti, L.; Mendonça, C. R.; Meador, M.; Hsu, F.-L.; Bu, X. R. *Chem. Commun. (Camb.)* **2004**, (10): 1178. doi:10.1039/b402019g. PMID:15136827.
- (18) Garcia, P.; Pernaut, J. M.; Hapiot, P.; Wintgens, V.; Valat, P.; Garnier, F.; Delabouglise, D. *J. Phys. Chem.* **1993**, *97* (2), 513. doi:10.1021/j100104a040.
- (19) Soucy-Breau, C.; MacEachern, A.; Leitch, L. C.; Arnason, T.; Morand, P. *J. Heterocycl. Chem.* **1991**, *28* (2), 411. doi:10.1002/jhet.5570280239.
- (20) Oh-e, T.; Miyaura, N.; Suzuki, A. *J. Org. Chem.* **1993**, *58*, 2201. doi:10.1021/jo00060a041.
- (21) Chisaka, J.; Lu, M.; Nagamatsu, S.; Chikamatsu, M.; Yoshida, Y.; Goto, M.; Azumi, R.; Yamashita, M.; Yase, K. *Chem. Mater.* **2007**, *19* (10), 2694. doi:10.1021/cm0701658.
- (22) Lightowler, S.; Hird, M. *Chem. Mater.* **2005**, *17* (22), 5538. doi:10.1021/cm0512068.
- (23) Milstein, D.; Stille, J. K. *J. Am. Chem. Soc.* **1978**, *100* (11), 3636. doi:10.1021/ja00479a077.
- (24) Jousselm, B.; Blanchard, P.; Levillain, E.; Delaunay, J.; Alain, M.; Richomme, P.; Rondeau, D.; Gallego-Planas, N.; Roncali, J. *J. Am. Chem. Soc.* **2003**, *125* (5), 1363. doi:10.1021/ja026819p. PMID:12553839.
- (25) Liu, J.; Tanaka, T.; Sivula, K.; Alivisatos, A. P.; Fréchet, J. M. J. *J. Am. Chem. Soc.* **2004**, *126* (21), 6550. doi:10.1021/ja0489184. PMID:15161272.
- (26) Ellinger, S.; Kreyes, A.; Ziener, U.; Hoffmann-Richter, C.; Landfester, K.; Möller, M. *Eur. J. Org. Chem.* **2007**, 2007 (34), 5686. doi:10.1002/ejoc.200700566.
- (27) Sears, W. A.; Sears, W. M.; MacKinnon, C. D. *Synth. Met.* **2008**, *158* (1-2), 50. doi:10.1016/j.synthmet.2007.12.002.
- (28) Nakayama, J.; Konishi, T.; Murabayashi, S.; Hoshino, M. *Heterocycles* **1987**, *26* (7), 1793. doi:10.3987/R-1987-07-1793.
- (29) Sease, J. W.; Zechmeister, L. *J. Am. Chem. Soc.* **1947**, *69* (2), 270. doi:10.1021/ja01194a031.
- (30) Becker, R. S.; de Melo, J. S.; Maçanita, A. L.; Elisei, F. *J. Phys. Chem.* **1996**, *100* (48), 18683. doi:10.1021/jp960852e.
- (31) Pappenfus, T. M.; Raff, J. D.; Hukkanen, E. J.; Burney, J. R.; Casado, J.; Drew, S. M.; Miller, L. L.; Mann, K. R. *J. Org. Chem.* **2002**, *67* (17), 6015. doi:10.1021/jo025572b. PMID:12182637.
- (32) Choi, Y.; Tepavcevic, S.; Xu, Z.; Hanley, L. *Chem. Mater.* **2004**, *16* (10), 1924. doi:10.1021/cm0353052.
- (33) Hopmeier, M.; Gebauer, W.; Oestreich, M.; Sokolowski, M.; Umbach, E.; Mahrt, R. F. *Chem. Phys. Lett.* **1999**, *314* (1-2), 9. doi:10.1016/S0009-2614(99)01116-1.
- (34) Casado, J.; Pappenfus, T. M.; Miller, L. L.; Mann, K. R.; Ortí, E.; Viruela, P. M.; Pou-Amérigo, R.; Hernández, V.; López Navarrete, J. T. *J. Am. Chem. Soc.* **2003**, *125* (9), 2524. doi:10.1021/ja027835p. PMID:12603140.
- (35) Van Bolhuis, F.; Wynberg, H.; Havinga, E. E.; Meijer, E. W.; Staring, E. G. J. *Synth. Met.* **1989**, *30* (3), 381. doi:10.1016/0379-6779(89)90661-9.
- (36) Telesca, R.; Bolink, H.; Yunoki, S.; Hadzioannou, G.; Van Duijn, P. T.; Snijders, J. G.; Jonkman, H. T.; Sawatzky, G. A. *Phys. Rev. B* **2001**, *63* (15), o. 155112. doi:10.1103/PhysRevB.63.155112.
- (37) Kruszynski, R.; Czestkowski, W. *Acta Crystallogr.* **2002**, *E58*, o481.
- (38) Wagner, P.; Świerczek, K.; Kubicki, M. *Acta Crystallogr.* **2007**, *C63*, o445.
- (39) Thaimattam, R.; Sharma, C. V. K.; Clearfield, A.; Desiraju, G. R. *Cryst. Growth Des.* **2001**, *1* (2), 103. doi:10.1021/cg010286z.
- (40) Siegrist, T.; Kloc, C.; Laudise, R. A.; Katz, H. E.; Haddon, R. C. *Adv. Mater.* **1998**, *10* (5), 379. doi:10.1002/(SICI)1521-4095(199803)10:5<379::AID-ADMA379>3.0.CO;2-A.
- (41) Siegrist, T.; Fleming, R. M.; Haddon, R. C.; Laudise, R. A.; Lovinger, A. J.; Katz, H. E.; Bridenbaugh, P.; Davis, D. D. *J. Mater. Res.* **1995**, *10* (9), 2170. doi:10.1557/JMR.1995.2170.
- (42) Tamao, K.; Kodama, S.; Nakajima, I.; Kumada, M. *Tetrahedron* **1982**, *38* (22), 3347. doi:10.1016/0040-4020(82)80117-8.
- (43) Bäuerle, P.; Würthner, F.; Götz, G.; Effenberger, F. *Synthesis* **1993**, *1993* (11), 1099. doi:10.1055/s-1993-26009.
- (44) Perdew, J. P.; Burke, K.; Ernzerhof, M. *Phys. Rev. Lett.* **1996**, *77* (18), 3865. doi:10.1103/PhysRevLett.77.3865. PMID:10062328.
- (45) Perdew, J. P.; Burke, K.; Ernzerhof, M. *Phys. Rev. Lett.* **1997**, *78* (7), 1396. doi:10.1103/PhysRevLett.78.1396.
- (46) Perdew, J. P.; Ernzerhof, M.; Burke, K. *J. Chem. Phys.* **1996**, *105* (22), 9982. doi:10.1063/1.472933.
- (47) Hehre, W. J.; Ditchfield, R.; Pople, J. A. *J. Chem. Phys.* **1972**, *56* (5), 2257. doi:10.1063/1.1677527.
- (48) Francl, M. M.; Pietro, W. J.; Hehre, W. J.; Binkley, J. S.; Gordon, M. S.; Defrees, D. J.; Pople, J. A. *J. Chem. Phys.* **1982**, *77* (7), 3654. doi:10.1063/1.444267.
- (49) Frisch, M. J.; Trucks, G. W.; Schlegel, H. B.; Scuseria, G. E.; Robb, M. A.; Cheeseman, J. R.; Zakrzewski, V. G.; Montgomery, J. A.; Stratmann, R. E.; Burant, J. C.; Dapprich, S.;



Millam, J. M.; Daniels, A. D.; Kudin, K. N.; Strain, M. C.; Farkas, O.; Tomasi, J.; Barone, V.; Cossi, M.; Cammi, R.; Mennucci, B.; Pomelli, C.; Adamo, C.; Clifford, S.; Ochterski, J. W.; Petersson, G. A.; Ayala, P. Y.; Cui, Q.; Morokuma, K.; Salvador, P.; Dannenberg, J. J.; Malick, D. K.; Rabuck, A. D.; Raghavachari, K.; Foresman, J. B.; Cioslowski, J.; Ortiz, J. V.; Baboul, A. G.; Stefanov, B. B.; Liu,

G.; Liashenko, A.; Piskorz, P.; Komaromi, I.; Gomperts, R.; Martin, R. L.; Fox, D. J.; Keith, T.; Al-Laham, M. A.; Peng, C. Y.; Nanayakkara, A.; Challacombe, M.; Gill, P. M. W.; Johnson, B.; Chen, W.; Wong, M. W.; Andres, J. L.; Gonzalez, C.; Head-Gordon, M.; Replogle, E. S.; Pople, J. A. *Gaussian 03*, Revision E.01 ed.; Gaussian Inc.: Wallingford, CT, 2004.

# A halogenated pseudopterane diterpene from the Bahamian octocoral *Pseudopterogorgia acerosa*

Abhijeet S. Kate, Kelly Richard, Balaji Ramanathan, and Russell G. Kerr

**Abstract:** Two new pseudopterane diterpenes have been isolated from the gorgonian coral *Pseudopterogorgia acerosa* and have been characterized by NMR and mass spectrometry. These include 15-chlorodeoxypseudopterolide (**1**), the first halogenated pseudopterane diterpene, and 11-*epi*-pseudopteranol (**2**), an epimer of the previously described 11-pseudopteranol. In addition, six known diterpenes were also isolated from this collection including deoxypseudopterolide (**3**), pseudopteradiene (**4**), acerosolide (**5**), pseudopterolide-methanol adduct (**6**), 11-pseudopteranol (**7**), and isogorgiacerodiol (**8**). The cytotoxicity of these eight compounds towards three cancer cell lines (HeLa, PC-3, and HCT116) was assessed and the chlorinated pseudopterane **1** was found to have modest but selective activity against HCT116 (IC<sub>50</sub> 2.7 µmol/L), whereas its nonchlorinated derivative **3** was inactive. This indicates that the halo functionality can modify the cytotoxic activity of pseudopterane diterpenes and potentially other classes of diterpenes.

**Key words:** pseudopterane, diterpene, gorgonian, *Pseudopterogorgia acerosa*, marine natural product.

**Résumé :** On a isolé deux nouveaux diterpènes pseudoptéranoides du corail gorgonien *Pseudopterogorgia acerosa* et on les a caractérisés par MN et spectrométrie de masse. Il s'agit du 15-chlorodésoxypseudoptérolide (**1**), le premier diterpène pseudoptérané halogéné, et le 11-*épi*-pseudoptéranol (**2**), un épimère du 11-pseudoptéranol décrit antérieurement. On a isolé de plus six diterpènes connus à partir de cette collection, sont le désoxypseudoptérolide (**3**), le pseudoptéradène (**4**), l'acérosolide (**5**), l'adduit pseudoptérolide-méthanol (**6**), le 11-pseudoptéranol (**7**) et l'isogorgiacérodol (**8**). On a évalué la cytotoxicité de ces huit composés vis-à-vis de trois lignées de cellules cancéreuses (HeLa, PC-3 et HCT116) et on a trouvé que le pseudoptéranol chloré, **1**, présente une modeste, mais sélective, activité contre la HCT116 (IC<sub>50</sub>, 2,7 µmol/L) alors que son dérivé non chloré, **3**, est inactif. Ces résultats indiquent qu'une fonction halogénée peut modifier l'activité cytotoxique des pseudoptéranoides et éventuellement d'autres classes de diterpènes.

**Mots-clés :** pseudoptérané, diterpène, gorgonien, *Pseudopterogorgia acerosa*, produit marin naturel.

[Traduit par la Rédaction]

## Introduction

Pseudopterane diterpenes represent a biosynthetically intriguing family of diterpenes with a 12-membered carbocyclic skeleton. In 1982, Fenical and Clardy described pseudopterolide as the first pseudopterane and reported that this natural product exhibited considerable activity in the sea urchin antiproliferation assay.<sup>1</sup> Octocorals of the genus *Pseudopterogorgia* are well-known as a rich source of such pseudopterane diterpenes,<sup>2</sup> and *Pseudopterogorgia acerosa* collected from various locations has been found to be a source of a wide spectrum of such compounds.<sup>1–11</sup> We recently reported the isolation of a series of lipidyl pseudopteranes from *P. acerosa* which exhibit selective inhibitory activity against protein tyrosine phosphatase 1B.<sup>11</sup> An examination of the diterpene chemistry of a subsequent collection of *P. acerosa* from the Bahamas has led to the isolation of two new pseudopterane diterpenes along with

six previously described compounds. Herein, we report the isolation of the first halogenated pseudopterane diterpene 15-chlorodeoxypseudopterolide (**1**) and 11-*epi*-pseudopteranol (**2**), an epimer of a previously reported compound, along with six known compounds (**3–8**), five possessing the pseudopterane skeleton and one (**5**) with the 14-membered cembrane skeleton. A literature review revealed that cytotoxicities of only a few of these compounds have been reported,<sup>7,9</sup> and we therefore determined the cytotoxic activity against three cancer cell lines (PC-3, HCT116, and HeLa) for compounds **1–8** (Fig. 1).

## Results and discussion

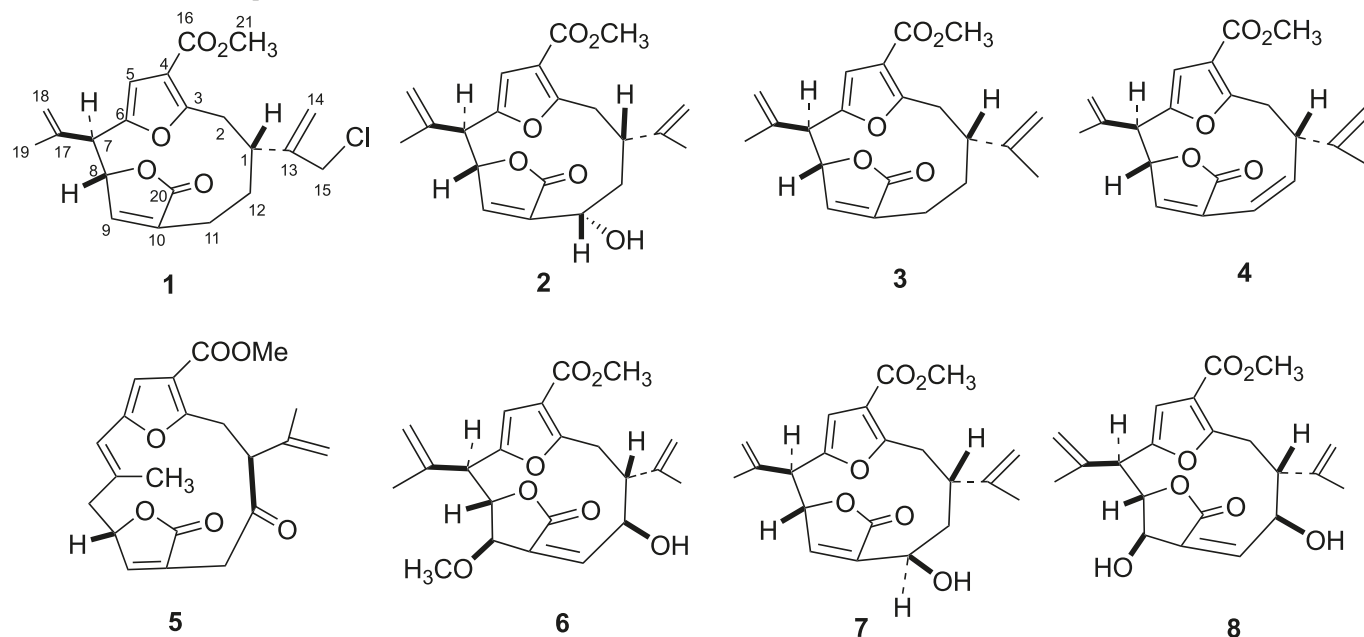
*Pseudopterogorgia acerosa* was collected from Grand Bahama Island, Bahamas in 2005. Dried material was extracted with ethyl acetate and methylene chloride to yield 26.7 g of crude extract which was subjected to flash column

Received 27 August 2009. Accepted 23 October 2009. Published on the NRC Research Press Web site at canjchem.nrc.ca on 4 March 2010.

**A.S. Kate and R.G. Kerr.**<sup>1</sup> Department of Chemistry, University of Prince Edward Island, Charlottetown, PE C1A 4P3, Canada; Department of Biomedical Sciences, Atlantic Veterinary College, University of Prince Edward Island, Charlottetown, PE C1A 4P3, Canada.

**K. Richard and B. Ramanathan.** Department of Biomedical Sciences, Atlantic Veterinary College, University of Prince Edward Island, Charlottetown, PE C1A 4P3, Canada.

<sup>1</sup>Corresponding author (e-mail: rkerr@upei.ca).

**Fig. 1.** Structures of compound 1–8.

chromatography over silica using hexanes to ethyl acetate affording 11 fractions. The mid-polar to polar range of these fractions were further purified by either preparative TLC or column chromatography (silica) followed by a semi-preparative HPLC leading to the isolation of eight pure diterpenes (**1–8**).  $^1\text{H}$  NMR, MS, and database searching (MARINLIT) were used to rapidly identify known compounds **3–8**.<sup>3–10</sup>

Compound **1** was obtained as a colorless oil with the molecular formula  $\text{C}_{21}\text{H}_{23}\text{ClO}_5$  suggested by HRESIMS analysis ( $[\text{M} + \text{Na}]^+$   $m/z$ : 413.1101; calculated 413.1126). The MS analysis also revealed the presence of the characteristic chlorine isotopic pattern. The IR spectrum indicated the presence of an unsaturated  $\gamma$ -lactone ( $1756\text{ cm}^{-1}$ ) and a  $\beta$ -carbomethoxyfuran ( $1722\text{ cm}^{-1}$ ) which are common to many pseudopterane diterpenes.<sup>7</sup>  $^1\text{H}$  and  $^{13}\text{C}$  NMR data (Table 1) showed a strong resemblance to that of deoxypseudopterolide (**3**),<sup>9</sup> a previously described metabolite from *P. acerosa*. Careful comparison of the  $^1\text{H}$  NMR of **1** and **3** showed that the olefinic methyl signal of **3** at  $\delta$  1.79 was absent in **1** and was replaced with a signal at  $\delta$  4.20 (2H, s). The chemical shifts of H-14a ( $\Delta 0.32$ ), H-14b ( $\Delta 0.55$ ), H-12a ( $\Delta 0.14$ ), H-12b ( $\Delta 0.14$ ), H-1 ( $\Delta 0.08$ ), H-2a ( $\Delta 0.1$ ), H-2b ( $\Delta 0.09$ ), and H-11b ( $\Delta 0.04$ ) were shifted downfield in **1** with respect to **3** while other signals were almost identical ( $< \Delta 0.02$ ).

The proton signal at  $\delta$  4.20 ppm (H-15) exhibited HMBC correlations with carbons at  $\delta$  39.5 (C-1), 115.8 (C-14), and 147.5 (C-13) confirming the position of the chlorine atom on C-15. Further, the  $^1\text{H}$  chemical shifts of H-15 and H-14 were in accordance with that for 3-chloro-2-methylpropene.<sup>12</sup> Further structural confirmation was achieved by COSY and HMBC correlations (Fig. 2).

The relative configurations of C-7, C-8, and C-1 were deduced by examination of the  $^1\text{H}$ – $^1\text{H}$  coupling constants and NOESY data, along with consideration of the established stereochemistry of known metabolite **3**,<sup>9</sup> the presumed biosynthetic precursor. Notably, the  $^1\text{H}$ – $^1\text{H}$  coupling constant

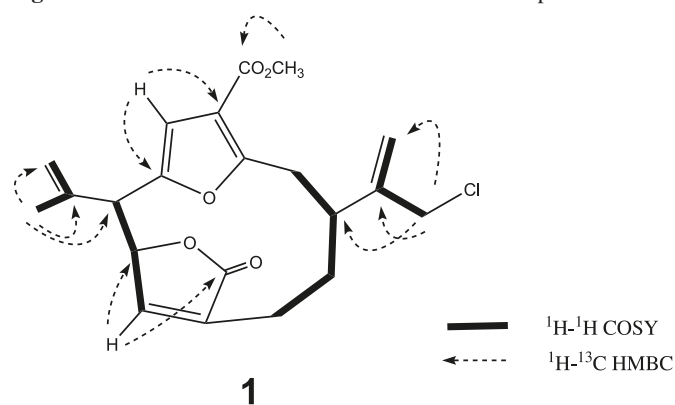
between H-7 and H-8 of 4.5 Hz was the same as that observed for **3**.

The planar structure of 11-*epi*-pseudopteranol (**2**) was assembled based on  $^1\text{H}$ ,  $^{13}\text{C}$  NMR, COSY, HMQC, HMBC, and MS data. HR-MS analysis of **2** revealed a molecular formula of  $\text{C}_{21}\text{H}_{24}\text{O}_6$  with  $m/z$  of 395.1452 as  $[\text{M} + \text{Na}]^+$  (calculated = 395.1465). The IR spectrum was similar to that of **1** and showed absorptions at  $1754\text{ cm}^{-1}$  and  $1723\text{ cm}^{-1}$  suggesting the presence of an unsaturated  $\gamma$  lactone ring as well as a  $\beta$ -carboxymethoxy furan moiety. The presence of an exchangeable proton in **2** was confirmed by a  $\text{D}_2\text{O}$  exchange experiment. The  $^1\text{H}$  NMR of **2** was found to be very similar to that of the known 11-pseudopteranol (**7**), in which the hydroxyl group at C-11 is in the  $\beta$  orientation and thus has the (*R*)-configuration. The  $^1\text{H}$  NMR showed differences in the proton chemical shifts: H-1 ( $\Delta 0.48\text{ ppm}$ ), H-12a ( $\Delta 0.37\text{ ppm}$ ), and H-11 ( $\Delta 0.15\text{ ppm}$ ) which were downfield in **2** with respect to **7**, while H-9 ( $\Delta 0.37\text{ ppm}$ ) was shifted upfield (Table 2). In compound **7**, the coupling constant between H-11 and H-12b of 11.3 Hz indicated a dihedral angle of approximately  $180^\circ$  while the  $J_{\text{HH}}$  value between the same protons in compound **2** was 3.5 Hz. An  $\alpha$  orientation is therefore suggested for the hydroxyl group at C-11 in **2**. The relative configuration of the other three stereocenters, C-7, C-8, and C-1, of compound **2** was established by comparing  $^1\text{H}$  and  $^{13}\text{C}$  chemical shifts and coupling constants with those of previously reported 11-pseudopteranol (**7**).<sup>10</sup> Assuming that compounds **1–8** share a common biosynthetic origin, it seems reasonable to suggest that the configurations at C-7, C-8, and C-1 are the same in **1** and **2**, and indeed in all members of this series.

Since the cytotoxic activity of many of the known compounds had not been reported, compounds **1–8** were evaluated in a cytotoxicity screen using SYBR Green<sup>13</sup> with HCT-116, HeLa, and PC-3 cells. None of the pseudopteroids showed any activity against PC-3 cells and only minimal activity was observed against the HeLa cell line.

**Table 1.**  $^1\text{H}$  and  $^{13}\text{C}$  NMR data of **1** and **3** in  $\text{CDCl}_3$ .

<b>1</b>			<b>3</b>	
Position	$^{13}\text{C}$ (mult.) <sup>a,b</sup>	$^1\text{H}$	$^{13}\text{C}$ (mult.) <sup>b</sup>	$^1\text{H}$
1	39.5 (CH)	2.87 (1H, nr)	41.6 (CH)	2.79 (1H, nr)
2	32.2 ( $\text{CH}_2$ )	3.41 (1H, ddd, $J = 14.7$ Hz, 13.6 Hz, 1.3 Hz) 2.83 (1H, nr)	31.5 ( $\text{CH}_2$ )	3.31 (1H, ddd, $J = 14.5$ Hz, 12.2 Hz, 2.5 Hz) 2.74 (1H, nr)
3	160.9 (C)		161.7 (C)	
4	115.7 (C)		115.4 (C)	
5	110.0 (CH)	6.38 (1H, s)	109.9 (CH)	6.36 (1H, s)
6	150.6 (C)		150.5 (C)	
7	48.6 (CH)	3.82 (1H, nr)	48.5 (CH)	3.83 (1H, nr)
8	80.7 (CH)	5.44 (1H, br d, $J = 4.5$ Hz)	80.6 (CH)	5.42 (1H, br d, $J = 4.4$ Hz)
9	146.9 (CH)	6.74 (1H, br s)	146.7 (CH)	6.72 (1H, br s)
10	140.7 (C)		137.3 (C)	
11	22.9 ( $\text{CH}_2$ )	2.44 (1H, ddd, $J = 14.1$ Hz, 13.2 Hz, 2.8 Hz) 2.25 (1H, br d, $J = 14.4$ Hz)	22.9 ( $\text{CH}_2$ )	2.42 (1H, ddd, $J = 14.1$ Hz, 13.5 Hz, 2.8 Hz) 2.21 (1H, ddd, $J = 13.6$ Hz, 4.5 Hz, 2.8 Hz)
12	36.4 ( $\text{CH}_2$ )	1.93 (1H, nr) 0.98 (1H, ddd, $J = 14.7$ Hz, 13.9 Hz, 2.6 Hz)	35.2 ( $\text{CH}_2$ )	1.79 (1H, nr) 0.84 (1H, ddd, $J = 14.5$ Hz, 13.7 Hz, 2.5 Hz)
13	147.5 (C)		147.3 (C)	
14	115.8 ( $\text{CH}_2$ )	5.35 (1H, nr) 5.34 (1H, nr)	111.4 ( $\text{CH}_2$ )	5.03 (1H, nr) 4.79 (1H, nr)
15	46.2 ( $\text{CH}_2$ )	4.20 (2H, s)	19.3 ( $\text{CH}_3$ )	1.79 (3H, s)
16	164.0 (C)		164.2 (C)	
17	141.2 (C)		141.4 (C)	
18	115.1 ( $\text{CH}_2$ )	5.05 (1H, s) 4.85 (1H, s)	114.9 ( $\text{CH}_2$ )	5.04 (1H, nr) 4.84 (1H, nr)
19	21.7 ( $\text{CH}_3$ )	1.98 (3H, s)	21.7 ( $\text{CH}_3$ )	1.98 (3H, s)
20	175.7 (C)		175.2 (C)	
21	51.2 ( $\text{CH}_3$ )	3.82 (3H, s)	51.4 ( $\text{CH}_3$ )	3.80 (3H, s)

<sup>a</sup> $^{13}\text{C}$  chemical shifts were obtained from  $^{13}\text{C}$  NMR, HMQC, and HMBC experiments.<sup>b</sup> $^{13}\text{C}$  multiplicities were based on DEPTQ and HMQC experiments; nr: not resolved.**Fig. 2.**  $^1\text{H}$ – $^1\text{H}$  COSY and HMBC correlations of compound **1**.

Interesting trends were observed in the activity of **1**–**8** against the HCT-116 cell line (Table 3).

The new chlorinated pseudopteranolide **1** was found to have an  $\text{IC}_{50}$  of 2.7  $\mu\text{mol/L}$  whereas the nonchlorinated analog **3** was inactive, thus indicating that incorporation of a halogen can greatly increase the cytotoxic activity of pseudopteranolides. A similar phenomenon may also hold true for other classes of diterpenes. It is also evident that pseudopteranolides

with an oxygen functionality at C-11 or C-12, or a C-11–C-12 double bond (**2**, **4**–**6**, **8**) generally exhibit modest cytotoxic activity, whereas the derivative that is not functionalized at these locations (**3**) is inactive.

## Experimental section

### General experimental procedures

$^1\text{H}$  (300 MHz and 400 MHz) and  $^{13}\text{C}$  (75 MHz and 100 MHz) NMR data were recorded in  $\text{CDCl}_3$  solution. Spectra were referenced with residual solvent signal with resonances at  $\delta_{\text{H}/^{13}\text{C}}$  at 7.27/77.00 ( $\text{CDCl}_3$ ). UV spectra were measured with a Beckman Coulter – DU 530, Life Science UV/VIS spectrophotometer. The optical rotation  $[\alpha]_{\text{D}}$  values were determined with a Digipol 781, Rudolph Instruments, and IR spectra were measured with Bruker–Equinox 55 (NaCl cell). Flash column chromatography was performed with Silica gel 200–425 mesh size and Silica gel 60  $\text{F}_{254}$  (Whatmann) pre-coated plates were used for preparative TLC. The HPLC experiments were carried out on a PerkinElmer system consisting of a Series 250 pump and LC-235 diode array detector for semi-preparative purpose. A Luna 5  $\mu$  Phenyl-Hexyl 250  $\times$  10 mm Phenomenex column was used for purification of compounds. Thermo Accela™ LC



**Table 2.**  $^1\text{H}$ ,  $^{13}\text{C}$  NMR, and  $1\text{H}-1\text{H}$  COSY of **2** and  $1\text{H}$  NMR of **7**.

<b>2</b>			<b>7</b>	
Position	$^{13}\text{C}$ (mult.) <sup>a</sup>	$^1\text{H}$	$^1\text{H}-^1\text{H}$ COSY	$^1\text{H}$
1	38.9 (CH)	3.28 (1H, m)	2a, 2b, 12a	2.80 (1H, m)
2	32.4 (CH <sub>2</sub> )	3.40 (1H, dd, $J$ = 15.1 Hz, 12.5 Hz) 2.74 (1H, dd, $J$ = 15.1 Hz, 4.3 Hz)	2b, 1 2a, 1	3.39 (1H, dd, $J$ = 15.3 Hz, 12.9 Hz) 2.70 (1H, dd, $J$ = 15.3 Hz, 4.3 Hz)
3	161.4 (C)			
4	115.8 (C)			
5	110.1 (CH)	6.37 (1H, s)		6.37 (1H, s)
6	150.1 (C)			
7	48.3 (CH)	3.85 (1H, d, $J$ = 4.3 Hz)	8, 18a, 18b, 19	3.86 (1H, d, $J$ = 4.3 Hz)
8	81.0 (CH)	5.47 (1H, dd, $J$ = 4.7 Hz, 1.2 Hz)	7, 9	5.48 (1H, ddd, $J$ = 4.3 Hz, 1.5 Hz, 1.5 Hz)
9	145.2 (CH)	6.65 (1H, dd, $J$ = 1.5 Hz, 0.7 Hz)	8	7.02 (1H, dd, $J$ = 1.5 Hz, 0.7 Hz)
10	135.6 (C)			
11	69.3 (CH)	4.79 (1H, ddd, $J$ = 10.5 Hz, 4.7 Hz, 3.5 Hz)	11 (-OH), 12a, 12b	4.64 (1H, ddd, $J$ = 11.3 Hz, 4.3 Hz, 0.7 Hz)
12	41.2 (CH <sub>2</sub> )	2.33 (1H, ddd, $J$ = 14.9 Hz, 6.7 Hz, 4.3 Hz) 1.02 (1H, ddd, $J$ = 14.9 Hz, 3.1 Hz, 1.9 Hz)	11, 1, 12b 11, 12a	1.96 (1H, ddd, $J$ = 13.1 Hz, 7.6 Hz, 4.3 Hz) 1.00 (1H, ddd, $J$ = 13.3 Hz, 11.3 Hz, 0.78 Hz)
13	148.7 (C)			
14	112.0 (CH <sub>2</sub> )	5.10 (1H, s) 4.85 (1H, s)	15 15	4.81 (1H, s) 5.03 (1H, s)
15	18.9 (CH <sub>3</sub> )	1.83 (3H, s)		1.81 (3H, s)
16	164.0 (C)			
17	140.8 (C)			
18	115.4 (CH <sub>2</sub> )	5.07 (1H, s) 4.85 (1H, s)	7, 19 7, 19	5.04 (1H, s) 4.81 (1H, s)
19	21.6 (CH <sub>3</sub> )	1.99 (3H, s)	7	1.96 (3H, s)
20	175.0 (C)			
21	51.5 (CH <sub>3</sub> )	3.81 (3H, s)		3.80 (3H, s)
OH <sup>b</sup>		4.20 (1H, d, $J$ = 10.9 Hz)	11	

<sup>a</sup> $^{13}\text{C}$  assignments and multiplicities were based on DEPTQ and HMQC experiments.<sup>b</sup>Exchangeable proton signal based on D<sub>2</sub>O exchange experiment.**Table 3.** Cytotoxic activity against HCT-116 and HeLa cell lines.

Compound	IC <sub>50</sub> values (μmol/L)	
	HCT-116	HeLa
<b>1</b>	2.7	29
<b>2</b>	38	>50
<b>3</b>	>50	>50
<b>4</b>	13	>50
<b>5</b>	11	>50
<b>6</b>	>50	34
<b>7</b>	>50	>50
<b>8</b>	12	21

system with LXQ linear ion trap mass spectrometer was used for low resolution mass spectrometry analysis.

### Collection and extraction procedure

Diterpenes **1–8** were isolated from the octocoral *Pseudopterogorgia acerosa*, collected at Grand Bahama Island, Bahamas in 2005. Sun-dried coral (367 g) was extracted with EtOAc–CH<sub>2</sub>Cl<sub>2</sub> (1:1) repeatedly until the extract was colorless (8 × 1L) to afford a dark brown oil (27.6 g). The crude extract was subjected to flash chromatography over silica using hexanes–EtOAc mixtures as mobile phase. A total of 11 fractions were collected and the 60% hexanes fraction was further subjected to column chromatography over silica with an isocratic solvent system of hexanes–CH<sub>2</sub>Cl<sub>2</sub>–acetone (64:27:9). Fractions were collected and combined based on TLC into fractions I–VIII. Fraction V was further separated by preparative TLC followed by semi-preparative HPLC to afford **3** (27.7 mg), **4** (3.0 mg), and **1** (1.0 mg). HPLC

purification of the 50% hexanes fraction led to the isolation of **5** (17.3 mg), and the 40% hexanes fraction was purified by preparative TLC and HPLC to give **6** (5.2 mg), and **2** (3.0 mg). HPLC purification of the 30% and the combined 20% and 10% hexane fractions led to **7** (4.0 mg) and **8** (1.9 mg), respectively.

### 15-Chlorodeoxypseudopterolide (1)

Colorless oil (1.0 mg).  $[\alpha]_D^{+122.2^\circ}$  (c 0.09, CHCl<sub>3</sub>). UV (acetonitrile)  $\lambda_{\max}$  (nm) ( $\epsilon$ ): 214 (13369), 254 (4553). IR (neat): 2930, 1756, 1722, 1443, 1078. For <sup>1</sup>H NMR and <sup>13</sup>C NMR (CDCl<sub>3</sub>) data, refer to Table 1. Mass (LR-MS)  $m/z$ : [M + H]<sup>+</sup> 390.96; MS<sup>2</sup> fragments (CID = 35) 359, 355(BP), 323. HR-ESIMS: calcd. [M + Na]<sup>+</sup> 413.1126, found 413.1101.

### 11-epi-Pseudopteranol (2)

Colorless oil (3.0 mg).  $[\alpha]_D^{+173.7^\circ}$  (c 0.12, CHCl<sub>3</sub>). UV (acetonitrile)  $\lambda_{\max}$  (nm) ( $\epsilon$ ): 216 (28407), 250 (4747). IR (neat): 2925, 1754, 1723, 1438, 1070. For <sup>1</sup>H NMR and <sup>13</sup>C NMR (CDCl<sub>3</sub>) data, refer to Table 2. Mass (LR-MS)  $m/z$ : [M + H]<sup>+</sup> 373.10; MS<sup>2</sup> fragments (CID = 35) 355(BP), 341, 323, 303, and 261. HR-ESIMS: calcd. [M + Na]<sup>+</sup> 395.1465, found 395.1452.

### Acknowledgements

Funding was provided by the Natural Sciences and Engineering Research Council of Canada (NSERC), the Canada Research Chair Program, the University of Prince Edward Island, the Canada Foundation for Innovation, the Atlantic Innovation Fund, and the Jeanne and Jean-Louis Lévesque Foundation. The assistance of T. Brück, L. Santiago, S. Withers, S. Jett, A. Kohl, and J. Frenz in specimen collection is gratefully acknowledged. We thank D. Lund, Department of Chemistry, University of Prince Edward Island for NMR and FTIR support. The HMBC experiment for 15-chlorodeoxypseudopterolide was performed by ARMRC, Dalhousie University, Halifax. A special thanks to A.

Thompson and A. Ali, Dalhousie University, Halifax, for polarimeter usage. HR-ESIMS spectral determination was performed by the Maritime Mass Spectrometry Laboratories at Dalhousie University, Halifax.

### References

- (1) Bandurraga, M. M.; Fenical, W.; Donovan, S. F.; Clardy, J. *J. Am. Chem. Soc.* **1982**, *104* (23), 6463. doi:10.1021/ja00387a059.
- (2) Berrue, F.; Kerr, R. G. *Nat. Prod. Rep.* **2009**, *26* (5), 681. doi:10.1039/b821918b. PMID:19387501.
- (3) Rodríguez, A. D.; Soto, J. J. *Chem. Pharm. Bull. (Tokyo)* **1996**, *44* (1), 91. PMID:8582045.
- (4) Tinto, W. F.; John, L.; Reynolds, W. F.; McLean, S. *Tetrahedron* **1991**, *47* (41), 8679. doi:10.1016/S0040-4020(01)96190-3.
- (5) Rodríguez, A. D.; Soto, J. J. *J. Nat. Prod.* **1998**, *61* (3), 401. doi:10.1021/np9703858. PMID:9544569.
- (6) Rodríguez, A. D.; Soto, J. J. *J. Org. Chem.* **1996**, *61* (13), 4487. doi:10.1021/jo951920g. PMID:11667361.
- (7) Montalvo, D.; Amade, P.; Funel-Le Bon, C.; Fernández, R.; Reyes, F. *Nat. Prod. Res.* **2006**, *20* (6), 548. doi:10.1080/14786410500183274. PMID:16835086.
- (8) Rodríguez, A. D.; Soto, J. J. *Tetrahedron Lett.* **1996**, *37* (16), 2687. doi:10.1016/0040-4039(96)00392-9.
- (9) Chan, W. R.; Tinto, W. F.; Laydoo, R. S.; Manchand, P. S.; Reynolds, W. F.; McLean, S. *J. Org. Chem.* **1991**, *56* (5), 1773. doi:10.1021/jo00005a022.
- (10) Tinto, W. F.; Laydoo, R. S.; Miller, S. L.; Reynolds, W. F.; McLean, S. *J. Nat. Prod.* **1995**, *58* (12), 1975. doi:10.1021/np50126a032.
- (11) Kate, A. S.; Aubry, I.; Tremblay, M. L.; Kerr, R. G. *J. Nat. Prod.* **2008**, *71* (12), 1977. doi:10.1021/np800544b. PMID:19061360.
- (12) Goren, Z.; Heeg, M. J.; Mobashery, S. *J. Org. Chem.* **1991**, *56* (25), 7186. doi:10.1021/jo00025a046.
- (13) Liu, T.; Hannafon, B.; Gill, L.; Kelly, W.; Benbrook, D. *Mol. Cancer Ther.* **2007**, *6* (6), 1814. doi:10.1158/1535-7163.MCT-06-0279. PMID:17575110.

# Heck-type hydroarylations and 1,3-dipolar cycloaddition reactions of new tricyclic hydrazones

Melek Gul and Nuket Ocal

**Abstract:** The C–C coupling of the new tricyclic hydrazones **3–7** with aryl and heteroaryl halides gave under reductive Heck conditions the tricyclic 1-(arylideneamino)pyrrolidine-2,5-diones **8–11a**, **9–11b**, **10c**, and **12**. The [3+2] cycloadditions of **3–7** with *p*-chlorophenyl nitrile oxide (**13**) yielded the bridged isoxazoline derivatives **14–18** with potential biological activity.

**Key words:** tricyclic hydrazone, reductive Heck reactions, C–C coupling, nitrile oxides, isoxazolines.

**Résumé :** Le couplage C–C des nouvelles hydrazones tricycliques **3–7** avec des halogénures d'aryles et d'hétéroaryles, dans les conditions réductrices de Heck, conduisent à la formation des 1-(arylidèneamino)pyrrolidine-2,5-diones tricycles **8–11a**, **9–11b**, **10c** et **12**. Les cycloadditions [3+2] des composés **3–7** avec l'oxyde du *p*-chlorophénylnitrile (**13**) conduisent à la formation des dérivés isoxazolines pontées **14–18** qui peuvent présenter une activité biologique.

**Mots-clés :** hydrazone tricyclique, réactions réductrices de Heck, couplage C–C, oxydes de nitriles, isoxazolines.

[Traduit par la Rédaction]

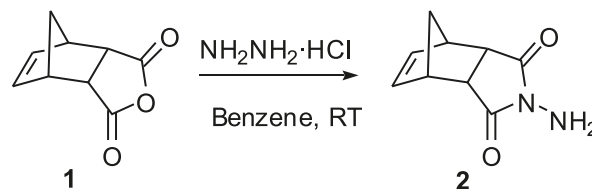
## Introduction

In a collaborative effort with Kaufmann and co-workers,<sup>1–3</sup> we reported palladium(II) acetate catalyzed asymmetric Heck-type hydroarylations of bicyclic and tricyclic alkenes, such as epibatidine analogs, and their domino–Heck applications by treating with aryl (or heteroaryl) iodides.<sup>4</sup> We then focused on reductive Heck reactions of tricyclic molecules containing a strained C=C bond and an acylamino imide or hydrazide group and possessing potential biological activity.<sup>5,6</sup>

Hydrazones are a versatile class of ligands that have extensive applications in various fields, possessing pronounced biological and pharmaceutical activities as antitumor,<sup>7,8</sup> antimicrobial,<sup>9</sup> antituberculosis,<sup>10</sup> and antimalarial agents.<sup>11</sup> These compounds play an important role in improving the antitumor selectivity and toxicity profile of antitumor agents by forming drug-carrier systems employing suitable carrier proteins.<sup>12</sup> Hydrazones, such as salicylaldehyde and heteroaryl substituted aldo hydrazones, act as orally effective drugs for treatment of iron-overload diseases or genetic diseases like  $\beta$ -thalassemia.<sup>13</sup>

In addition, five-membered heterocycles such as isoxazolines represent a class of compounds of great biological importance. For instance, isoxazolines possess a broad spectrum of biological activity, such as insecticidal, antibacterial, antibiotic, antitumor, and antifungal activities.<sup>14–16</sup>

Scheme 1. Preparation of compound **2**.



Isoxazolines are generally synthesized by 1,3-dipolar cycloadditions of alkenes onto nitrile oxides. 1,3-Dipolar cycloaddition reactions are useful tools for the construction of biologically potent five-membered heterocycles.<sup>17</sup>

There are a few reports in the literature of the synthesis of tricyclic hydrazones and practically no information on their structure analyses.<sup>18,19</sup> Therefore, we became interested in the synthesis of possible bioactive aryl- and hetero-aryl substituted tricyclic hydrazones by reductive Heck reactions and their isoxazoline derivatives via 1,3-dipolar cycloadditions.

## Results and discussion

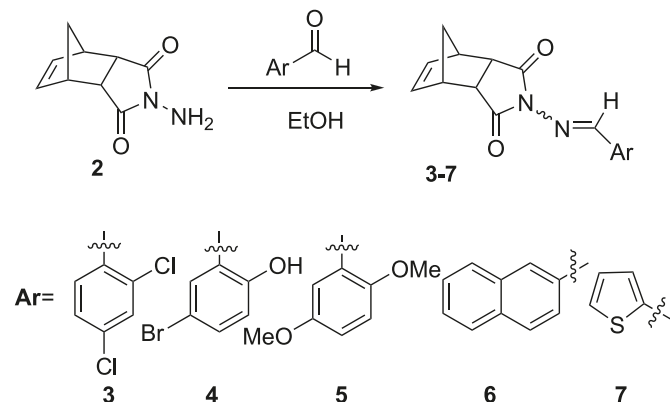
Our synthesis started with the reaction of *endo*-bicyclo[2.2.1]-hept-5-ene-2,3-dicarboxylic anhydride (**1**) and hydrazine hydrate. The reaction occurred in benzene at room temperature to give *N*-amino-bicyclo[2.2.1]hept-5-ene-2,endo-3-endo-dicarboximide (**2**) as colorless crystals in a yield of 87%<sup>19</sup> (Scheme 1).

Received 15 July 2009. Accepted 24 November 2009. Published on the NRC Research Press Web site at canjchem.nrc.ca on 4 March 2010.

This article is dedicated to Professor Dieter E. Kaufmann on the occasion of his 62nd birthday.

**M. Gul and N. Ocal.**<sup>1</sup> Yildiz Technical University, Faculty of Art and Sciences, Department of Chemistry, Davutpasa Campus, Esenler, Istanbul 34210, Turkey.

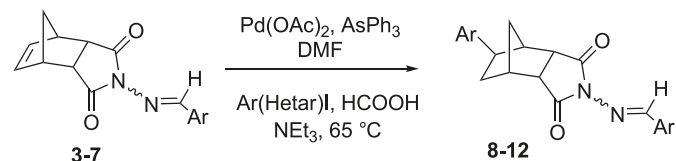
<sup>1</sup>Corresponding author (e-mail: nocal@yildiz.edu.tr).

**Scheme 2.** Synthesis of compounds **3–7**.

We carried out the condensation of **2** with aryl- or heteroaryl-substituted aldehydes in dry ethanol to obtain new tricyclic hydrazones (**3–7**) (Scheme 2). The structures of these synthesized compounds were elucidated using FTIR,  $^1\text{H}$  NMR,  $^{13}\text{C}$  NMR, and mass spectroscopic methods as well as elemental analysis.  $^1\text{H}$  NMR spectroscopy revealed that in  $\text{CDCl}_3$  **4–7** exist as an inseparable mixture of *E* and *Z* isomers pertaining to the stereochemistry about the carbon= nitrogen double bond; the major isomers were tentatively assigned the *E* configuration. In compounds **4–7**, varying ratios of *E/Z* isomers (93:7, 92:8, 78:22, 52:48, respectively) of the C=N bond were observed. The percentages of *E* and *Z* isomers were determined by integration of the  $\text{H}_8$  protons. Assignment of the stereochemistry was based upon the consideration that in the *E* isomer, the proton attached to C=N is in proximity to the imide nitrogen, resulting in an upfield shift compared with the chemical shift of the *Z* isomer. Further evidence for these structures were obtained from the phase-sensitive NOESY measurements. The NOESY experiment confirmed the assigned stereochemistries, showing an interaction between  $\text{H}_2$  and  $\text{H}_3$  and the  $\text{H}_8$ . In addition to the  $^{13}\text{C}$  NMR and FTIR spectral data and elemental analyses which were in agreement with the proposed structures, the mass spectra of all new compounds showed the expected molecular ion peaks.

Treatment of **3** with 4-chloro-1-iodobenzene and 4-methoxy-1-iodobenzene under reductive Heck conditions and subsequent column chromatography on silica gel gave **8a** and **8b** as single diastereomers in isolated yields of 55%–61%. The same reductive Heck arylation conditions were successfully applied to the reaction of **4** with 4-methoxy-1-iodobenzene and 2-chloro-5-iodopyridine to give the new *exo*-arylated heterocycles **9a** and **9b** in good yields after chromatographic separation. We also synthesized **10a**, **10b**, and **10c** from **5** with 2-iodothiophene, 4-chloro-1-iodobenzene, and 2-chloro-1-iodobenzene and prepared **11a** and **11b** from **6** with 1-iodobenzene and 2-iodothiophene (all obtained as *exo*-isomers) under the same conditions. This hydroarylation reaction was also applied successfully to **7** using 4-methoxy-1-iodobenzene to give **12** containing 4-methoxyphenyl group (Table 1 and Scheme 3). All new compounds were observed as *E* forms due to the isomerization of *Z* forms during hydroarylation conditions.

The stereochemistry for each Heck product was inferred from NMR spectra including diagnostic spin–spin interac-

**Scheme 3.** Synthesis of reductive Heck compounds **8–12**.

tions. (Table 2). The *exo*-position of the C–5 substituent was confirmed by the fact that  $\text{H}_5$  showed no significant interaction with  $\text{H}_1$ . The geminal protons on C–6 were identified by vicinal coupling to  $\text{H}_1$ .

Additionally,  $^1\text{H}$ – $^1\text{H}$  COSY spectra showed cross peaks between  $\text{H}_2$  and  $\text{H}_3$  and between  $\text{H}_5$  and  $\text{H}_6$ , respectively. In addition to the  $^{13}\text{C}$  NMR, NOESY, HSQC, and FTIR spectral data and elemental analyses which were in agreement with the proposed structures, the mass spectra of all new compounds showed the expected molecular ion peaks.

Norbornene and its derivatives have figured prominently in organic chemistry. The presence of a rigid bicyclic skeleton gives rise to stereoisomers with fixed spatial orientation of substituents. The double bond in substituted norbornenes is quite reactive toward cycloaddends, in particular toward nitrile oxides in 1,3-dipolar additions. We carried out the [3+2] cycloaddition of **3–7** with 4-chlorophenyl nitrile oxide **13** (generated in situ from 4-chlorobenzaldehyde with  $\text{NaOCl}$ ) to obtain the target compounds **14–18** (Scheme 4), respectively.

The  $^1\text{H}$  NMR spectra of **14–18** are in accord with the proposed structures. To identify the configuration of the isoxazolines with tricyclic hydrazone adducts, we have studied selective  $^1\text{H}$ – $^1\text{H}$  COSY and NOESY spectra obtained from these compounds (Table 3).

$^1\text{H}$ – $^1\text{H}$  COSY spectra show the cross peaks between resonances for  $\text{H}_2$  and  $\text{H}_3$ ;  $\text{H}_{5n}$  and  $\text{H}_{6n}$ . NOESY spectra show that there are appropriate cross-peak resonances ( $\text{H}_1$  and  $\text{H}_2$ ;  $\text{H}_1$  and  $\text{H}_{6n}$ ;  $\text{H}_4$  and  $\text{H}_3$ ;  $\text{H}_4$  and  $\text{H}_{5n}$ ;  $\text{H}_2$  and  $\text{H}_{6n}$ ;  $\text{H}_3$  and  $\text{H}_{5n}$ , respectively) verifying that the six protons are in close spatial proximity and syn. The EI-MS spectra of cycloadducts **14–18** showed the characteristic molecular ion peaks.

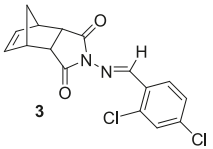
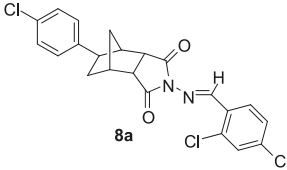
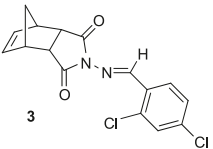
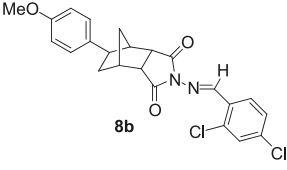
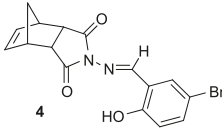
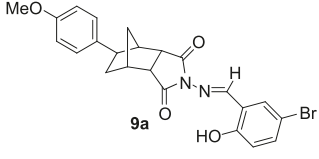
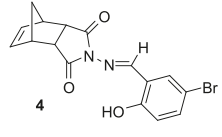
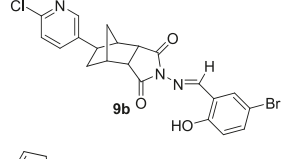
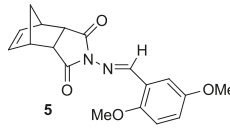
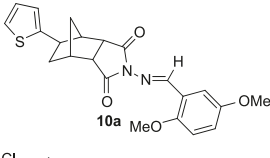
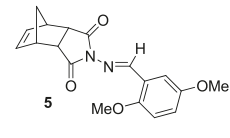
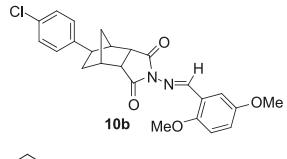
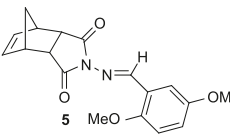
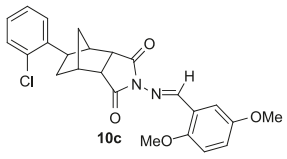
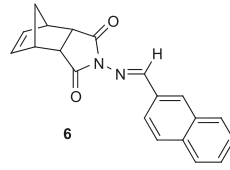
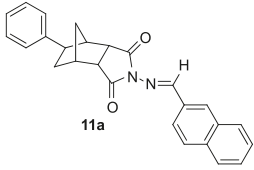
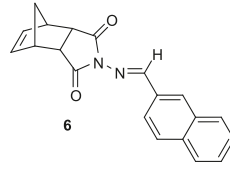
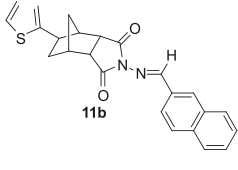
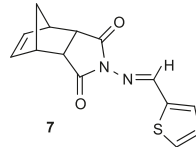
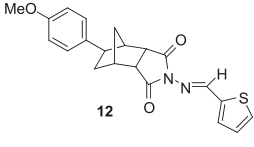
In summary, palladium(II) acetate catalyzed hydroarylation of the readily accessible tricyclic hydrazones **3–7**, in the presence of triphenylarsine as ligand, was shown to be a stereoselective, versatile, and high-yield approach to the synthesis of aryl and heteroaryl derivatives of tricyclic hydrazones. Our results have also demonstrated that the 1,3-dipolar cycloadditions of nitrile oxides onto bridged tricyclic hydrazone derivatives prove useful for the construction of novel heterocycles of potential pharmacological interest.

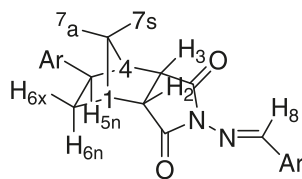
## Experimental

All the reactions were carried out under nitrogen atmosphere unless otherwise indicated. Reactions were monitored by thin-layer chromatography (TLC). Visualization of the developed chromatograms was performed either with UV light or  $\text{KMnO}_4$  stain. Products were purified by silica gel chromatography with a solvent gradient of 2:1 (ethyl acetate/*n*-hexane) to afford the title compounds. IR spectra were obtained with a PerkinElmer FTIR instrument, and absorption frequencies are reported in  $\text{cm}^{-1}$ . Melting points

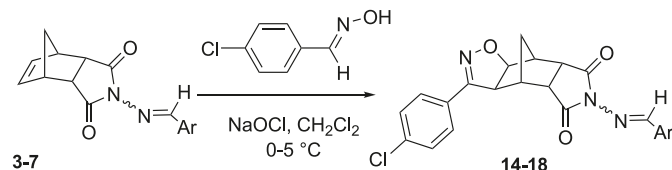


**Table 1.** Hydroarylation reactions of tricyclic hydrazones, 3–7.

Entry	Substrate 3-7	Product	Yield %
1			55
2			61
3			47
4			60
5			65
6			55
7			59
8			62
9			62
10			58

**Table 2.** Selected  $^1\text{H}$  NMR data for compounds **8–12**.

Entry	Compound	H <sub>7a</sub>	H <sub>4</sub>	H <sub>5n</sub>	H <sub>8</sub>
1	<b>8a</b>	1.63, d	3.02, brs	2.97–2.89, m	9.68, s
2	<b>8b</b>	1.51, d	2.91, brs	2.85–2.79, m	9.59, s
3	<b>9a</b>	1.60, d	2.95, brs	2.88–2.84, m	9.43, s
4	<b>9b</b>	1.62, d	2.98, brs	2.83, dd	9.35, s
5	<b>10a</b>	1.66, d	2.98, brs	3.29–3.19, m	9.34, s
6	<b>10b</b>	1.68–1.62, m	2.91, brs	3.16, ddd	9.27, s
7	<b>10c</b>	1.68–1.60, m	2.91, brs	3.16, ddd	9.21, s
8	<b>11a</b>	1.62, d	3.03, brs	3.03, brs	9.37, s
9	<b>11b</b>	1.67, d	3.01, brs	3.33–3.21, m	9.35, s
10	<b>12</b>	1.49, d	2.89, brs	2.85–2.82, m	9.24, s

**Scheme 4.** Synthesis of compounds **14–18**.

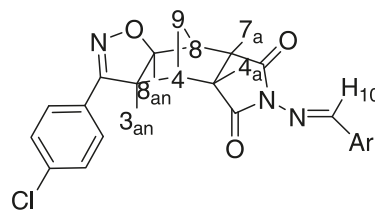
were determined with a Gallenkamp digital thermometer equipment. All melting points are uncorrected. NMR spectra were determined with a Bruker Ac-250 MHz NMR, Bruker Ac-400 MHz NMR, or Varian-INOVA-500 MHz instrument. 2D NMR experiments, such as COSY, 2D NOESY, HMBC, and HSQC, were performed with a Bruker Ac-400 MHz instrument. TMS (tetramethylsilane) was used as an internal standard and  $\text{CDCl}_3$  was used as the solvent. Signal multiplicities in the NMR spectra are reported as follows: s, singlet; brs, broad singlet; d, doublet; dd, doublet of doublets; and m, multiplet. Mass spectra were measured either with Agilent LC–MSD Trap SL or MS-ESI. Elemental analyses were carried out with a Thermo Flash EA 1112 Series apparatus.

#### Experimental procedure for the preparation of tricyclic hydrazones, **3–7**

A mixture of **2** (178.85 mg, 1 mmol) and aromatic or heteroaromatic aldehyde (1.00 mmol) in ethanol (50–70 mL) was heated at reflux for 10–12 h under nitrogen. The reaction mixture was concentrated and the residue was chromatographed on silica gel with ethyl acetate/*n*-hexane.

#### *N*-{[(2,4-dichlorophenyl)methylene]amino}-bicyclo[2.2.1]hept-5-ene-endo-2,endo-3-dicarboximide (**3**)

Colorless crystals, 65% yield. Mp 170 °C.  $R_f$  = 0.60 (2:1, ethyl acetate/*n*-hexane). FTIR ( $\text{cm}^{-1}$ ): 3010, 2995, 2941, 1732, 1710, 1618, 1582, 1471, 1380, 1183, 745, 728.  $^1\text{H}$  NMR (400 MHz)  $\delta$  (ppm): 9.50 (s, 1H, H<sub>8</sub>), 8.12 (d,  $J$  = 8.5 Hz, 1H, H<sub>aro</sub>), 7.43 (s, 1H, H<sub>aro</sub>), 7.30 (d,  $J$  = 7.2 Hz, 1H, H<sub>aro</sub>), 6.23 (s, 2H, H<sub>5</sub>–H<sub>6</sub>), 3.54 (brs, 2H, H<sub>1</sub>–H<sub>4</sub>), 3.36 (s, 2H, H<sub>2</sub>–H<sub>3</sub>), 1.79 (d,  $J$  = 8.8 Hz, 1H, H<sub>7s</sub>), 1.61 (d,  $J$  =

**Table 3.** Selected  $^1\text{H}$  NMR data for compounds **14–18**.

Entry	Compound	H <sub>3an</sub>	H <sub>8an</sub>	H <sub>9a</sub>	H <sub>10</sub>
1	<b>14</b>	3.61, dd	4.73, d	1.57, d	9.35, s
2	<b>15</b>	3.66, d	4.79, d	1.67, d	9.40, s
3	<b>16</b>	3.63, d	4.76, d	1.55, d	9.21, s
4	<b>17</b>	3.63, d	4.75, d	1.55, d	9.20, s
5	<b>18</b>	3.69, d	4.80, d	1.64, d	9.25, s

8.8, 1H, H<sub>7a</sub>).  $^{13}\text{C}$  NMR (100 MHz)  $\delta$  (ppm): 173.8 (2C, C=O), 156.4 (N=CH), 138.3 (C–Cl), 136.4 (C<sub>subst.</sub>), 134.7, 129.7 (C–Cl), 129.5, 128.9, 127.6, 51.8, 45.3, 44.0. MS-ESI (EI, 70 eV): 336 [ $\text{M}^+ + 1$ ], 335 [ $\text{M}^+$ ], 270.96, 197.86, 166.08, 147.86, 119.95. Anal. calcd. for  $\text{C}_{16}\text{H}_{12}\text{Cl}_2\text{N}_2\text{O}_2$ : C, 57.33; H, 3.61; N, 8.36. Found: C, 57.15; H, 3.44; N, 8.26.

#### *N*-{[(5-bromo-2-hydroxyphenyl)methylene]amino}-bicyclo[2.2.1]hept-5-ene-endo-2,endo-3-dicarboximide (**4**)

Colorless crystals, 52% yield. Mp 178 °C.  $R_f$  = 0.58 (2:1, ethyl acetate/*n*-hexane). FTIR ( $\text{cm}^{-1}$ ): 3316, 3005, 2970, 1730, 1700, 1623, 1563, 1475, 1364, 1180, 745, 728.  $^1\text{H}$  NMR (400 MHz)  $\delta$  (ppm): 11.12 (s, 1H, O–H, minor), 11.04 (s, 1H, O–H, major), 9.38 (s, 1H, H<sub>8</sub>, minor), 9.24 (s, 1H, H<sub>8</sub>, major), 7.46–7.40 (m, 2H, H<sub>aro</sub>), 6.89 (d,  $J$  = 8.8 Hz, 1H, H<sub>aro</sub>), 6.20 (s, 2H, H<sub>5</sub>–H<sub>6</sub>), 3.50 (s, 2H, H<sub>1</sub>–H<sub>4</sub>, major), 3.37 (s, 2H, H<sub>2</sub>–H<sub>3</sub>, major), 3.18 (brs, 2H, H<sub>1</sub>–H<sub>4</sub>, minor), 2.87 (brs, 2H, H<sub>2</sub>–H<sub>3</sub>, minor), 1.79 (d,  $J$  = 8.8 Hz, 1H, H<sub>7s</sub>, major), 1.58–1.67 (m, 2H, H<sub>7s</sub>minor – H<sub>7a</sub>major), 1.36 (d,  $J$  = 8.8 Hz, 1H, H<sub>7a</sub>, minor) (*E/Z*, 93:7).  $^{13}\text{C}$  NMR (100 MHz)  $\delta$  (ppm): 173.9 (2C, C=O, minor), 173.1 (2C, C=O, major), 160.4 (C–OH, minor), 160.2 (C–OH, major), 158.6 (N=CH, minor), 158.7 (N=CH, major), 136.1 (C–Br,

minor), 136.0 (C–Br, major), 134.7 (C<sub>subst.</sub>), 134.5 (minor), 134.5 (major), 119.6 (minor), 119.5 (major), 111.0 (C<sub>subst.</sub>, minor), 110.9 (C<sub>subst.</sub>, major), 51.9, 46.9 (minor), 45.3 (major), 44.0 (major), 41.8 (minor). LC–MSD: 362 [M<sup>+</sup> + 1], 361 [M<sup>+</sup>], 360 [M<sup>+</sup> – 1], 296, 266, 195, 162. Anal. calcd. for C<sub>16</sub>H<sub>13</sub>BrN<sub>2</sub>O<sub>3</sub>: C, 53.21; H, 3.63, N, 7.76. Found: C, 53.15; H, 3.49; N, 7.69.

**N-[(2,5-dimethoxyphenyl)methylene]amino}-bicyclo[2.2.1]hept-5-ene-endo-2,endo-3-dicarboximide (5)**

Colorless crystals, 45% yield. Mp 141 °C. *R*<sub>f</sub> = 0.47 (2:1, ethyl acetate/*n*-hexane). FTIR (cm<sup>-1</sup>): 3005, 2970, 2950, 1762, 1712, 1596, 1577 1495, 1463, 1180, 728, 716. <sup>1</sup>H NMR (400 MHz) δ (ppm): 9.30 (s, 1H, H<sub>8</sub>, minor), 9.19 (s, 1H, H<sub>8</sub>, major), 7.64 (d, *J* = 3.1 Hz, 1H, H<sub>aro.</sub>, minor), 7.58 (d, *J* = 3.1 Hz, H<sub>aro.</sub>, major), 7.01 (dd, *J* = 3.1 and 7.7 Hz, 2H, H<sub>aro.</sub>, major and minor), 6.86 (d, *J* = 8.8 Hz, 2H, H<sub>aro.</sub>, major–minor), 6.24 (s, 2H, H<sub>5</sub>–H<sub>6</sub>), 3.83 (s, 12H, –OCH<sub>3</sub>, major–minor), 3.49 (s, 2H, H<sub>1</sub>–H<sub>4</sub>, major), 3.34 (s, 2H, H<sub>2</sub>–H<sub>3</sub>, major), 3.16 (brs, 2H, H<sub>1</sub>–H<sub>4</sub>, minor), 2.86 (brs, 2H, H<sub>2</sub>–H<sub>3</sub>, minor), 1.78 (d, *J* = 8.8 Hz, 1H, H<sub>7s</sub>, minor), 1.58 (m, 2H, H<sub>7a</sub>–H<sub>7s</sub>, major–minor), 1.46 (d, *J* = 8.8 Hz, 1H, H<sub>7a</sub>, minor) (*E/Z*, 92:8). <sup>13</sup>C NMR (100 MHz) δ (ppm): 174.5 (2C, C=O, major), 173.8 (2C, C=O, minor), 159.6 (N=CH, major), 159.4 (N=CH, minor), 154.1 (C–OCH<sub>3</sub>, major), 154.0 (C–OCH<sub>3</sub>, minor), 153.6 (C–OCH<sub>3</sub>, major), 153.5 (C–OCH<sub>3</sub>, minor), 134.8 (minor), 134.7 (major), 121.6 (C<sub>subst.</sub>), 121.2 (major), 121.1 (minor), 112.7 (major), 112.6 (minor), 110.0 (minor), 109.9 (major), 56.2 (minor), 55.9 (major), 51.8 (major), 51.5 (minor), 45.1 (major), 45.0 (minor), 44.5 (minor), 44.1 (major). LC–MSD: 327 [M<sup>+</sup> + 1], 326 [M<sup>+</sup>], 325 [M<sup>+</sup> – 1], 266, 242. Anal. calcd. for C<sub>18</sub>H<sub>18</sub>N<sub>2</sub>O<sub>4</sub>: C, 66.25; H, 5.56; N, 8.58. Found: C, 66.12; H, 5.54; N, 8.55.

**N-[(2-naphthylmethylene)amino]-bicyclo [2.2.1]hept-5-ene-endo-2,endo-3-dicarboximide (6)**

Colorless crystals, 72% yield. Mp 158 °C. *R*<sub>f</sub> = 0.41 (2:1, ethyl acetate/*n*-hexane). FTIR (cm<sup>-1</sup>): 2967, 2963, 2860, 1734, 1710, 1603, 1568 1365, 1335, 1171, 756, 746. <sup>1</sup>H NMR (500 MHz) δ (ppm): 9.24 (s, 1H, H<sub>8</sub>, minor), 9.11 (s, 1H, H<sub>8</sub>, major), 8.04 (d, *J* = 5.8 Hz, 1H, H<sub>aro.</sub>), 7.99 (d, *J* = 8.8 Hz, 1H, H<sub>aro.</sub>), 7.77–7.84 (m, 3H, H<sub>aro.</sub>), 7.43–7.50 (m, 2H, H<sub>aro.</sub>), 6.17 (s, 2H, H<sub>5</sub>–H<sub>6</sub>), 3.44 (s, 2H, H<sub>2</sub>–H<sub>3</sub>, major), 3.23 (s, 2H, H<sub>1</sub>–H<sub>4</sub>, major), 3.10 (brs, 2H, H<sub>2</sub>–H<sub>3</sub>, minor), 2.81 (brs, 2H, H<sub>1</sub>–H<sub>4</sub>, minor), 1.72 (d, *J* = 8.8 Hz, 1H H<sub>7s</sub>, major), 1.56 (d, *J* = 8.8 Hz, 1H, H<sub>7s</sub>, minor), 1.52 (d, *J* = 8.8 Hz, 1H, H<sub>7a</sub>, major), 1.39 (d, *J* = 7.8 Hz, 1H, H<sub>7a</sub>, minor) (*E/Z*, 78:22). <sup>13</sup>C NMR (100 MHz) δ (ppm): 174.3 (2C, C=O, minor), 174.1 (2C, C=O, major), 161.9 (N=CH, minor), 161.7 (N=CH, major), 135.3 (minor), 135.2 (major), 134.7, 132.9 (minor), 132.8 (major), 131.6 (minor), 131.5 (major), 130.8 (minor), 130.7 (major), 128.9 (minor), 128.8 (major), 128.7 (minor), 128.6 (major), 127.9 (C<sub>subst.</sub>), 127.8 (minor), 127.8 (major), 126.7, 123.4 (minor), 123.3 (major), 51.8, 41.8, 39.6. LC–MSD: 339 [M<sup>+</sup> + Na], 317 [M<sup>+</sup> + 1], 316 [M<sup>+</sup>], 282, 244. Anal. calcd. for C<sub>20</sub>H<sub>16</sub>N<sub>2</sub>O<sub>2</sub>: C, 75.93; H, 5.10; N, 8.86. Found: C, 75.81; H, 4.98; N, 8.76.

**N-[(2-thienylmethylene)amino]-bicyclo[2.2.1]-hept-5-ene-endo-2,endo-3-dicarboximide (7)**

Colorless crystals, 59% yield. Mp 122 °C. *R*<sub>f</sub> = 0.49 (2:1,

ethyl acetate/*n*-hexane). FTIR (cm<sup>-1</sup>): 3104, 3011, 2972, 2935, 1764, 1738, 1696, 1589, 1427, 1373, 1180, 748, 719. <sup>1</sup>H NMR (250 MHz) δ (ppm): 9.12 (s, 1H, H<sub>8</sub>, minor), 9.07 (s, 1H, H<sub>8</sub>, major), 7.48–7.37 (m, 2H, H<sub>aro.</sub>), 7.05 (dd, *J* = 4.9 and 8.8 Hz, 1H, H<sub>aro.</sub>), 6.14 (s, 2H, H<sub>5</sub>–H<sub>6</sub>), 3.41 (brs, H<sub>3</sub>, major–minor), 3.35 (brs, 2H, H<sub>2</sub>, major–minor), 3.06 (brs, 2H, H<sub>4</sub>, major–minor), 2.78 (brs, 2H, H<sub>1</sub>, major–minor), 1.71 (d, *J* = 7.8 Hz, 2H, H<sub>7s</sub>, major–minor), 1.34 (d, *J* = 7.8 Hz, 2H, H<sub>7a</sub>, major–minor) (*E/Z*, 52:48). <sup>13</sup>C NMR (62.5 MHz) δ (ppm): 173.8 (2C, C=O, minor), 173.6 (2C, C=O, major), 155.7 (N=CH, minor), 155.6 (N=CH, major), 134.6, 133.7 (minor), 133.6 (major), 131.3 (minor), 131.2 (major), 129.0 (C<sub>subst.</sub>, minor), 128.8 (C<sub>subst.</sub>, major), 127.7 (minor), 127.6 (major), 51.8, 46.8, 45.3, 45.2, 44.0. LC–MSD: 295 [M<sup>+</sup> + Na], 273 [M<sup>+</sup> + 1], 272 [M<sup>+</sup>], 229, 163. Anal. calcd. for C<sub>14</sub>H<sub>12</sub>N<sub>2</sub>O<sub>2</sub>S: C, 61.75; H, 4.44; N, 10.29; S, 11.77. Found: C, 61.69; H, 4.29; N, 10.19; S, 11.88.

**Experimental procedure for the preparation of 8a–11a, 8b–11b, 10c, and 12**

A solution of Pd(OAc)<sub>2</sub> (5.6 mg, 0.025 mmol) and AsPh<sub>3</sub> (33.7 mg, 0.11 mmol) in dry DMF (3 mL) was stirred in a Schlenk flask under nitrogen at 65 °C for 15 min to form the catalyst complex. Then, aryl iodide (306 mg, 1.5 mmol), hydrazone (3–7; 1.00 mmol), triethylamine (354 mg, 3.5 mmol), and formic acid (138 mg, 3.0 mmol) were added. The mixture was heated to 65 °C for 24–48 h. After cooling down to RT, brine (50 mL) was added, the reaction mixture was extracted with ethyl acetate, and dried over MgSO<sub>4</sub>. The solvent was evaporated, and the residue was purified by chromatography.

**5-(4-Chlorophenyl)-N-[(2,4-dichlorophenyl)methylene]amino}-bicyclo[2.2.1]heptane-endo-2,endo-3-dicarboximide (8a)**

Light yellow crystals, 55% yield. Mp 157 °C. *R*<sub>f</sub> = 0.39 (2:1, ethyl acetate/*n*-hexane). FTIR (cm<sup>-1</sup>): 3068, 3025, 2963, 2875, 1789, 1714, 1616, 1582, 1491, 1469, 1416, 1384, 1098, 866, 800. <sup>1</sup>H NMR (400 MHz) δ (ppm): 9.68 (s, 1H, H<sub>8</sub>), 8.20 (d, *J* = 8.5 Hz, 1H, H<sub>aro.</sub>), 7.47 (d, *J* = 1.9 Hz, 1H, H<sub>aro.</sub>), 7.34 (dd, *J* = 1.9 and 8.5 Hz, 1H, H<sub>aro.</sub>), 7.28 (d, *J* = 4.0 Hz, 2H, H<sub>aro.</sub>), 7.13 (d, *J* = 8.4 Hz, 2H, H<sub>aro.</sub>) 3.33–3.23 (m, 2H, H<sub>2</sub>–H<sub>3</sub>), 3.02 (brs, 1H, H<sub>4</sub>), 2.97–2.89 (m, 2H, H<sub>1</sub>–H<sub>5n</sub>), 1.96–1.88 (m, 3H, H<sub>7s</sub>, H<sub>6x</sub> ve H<sub>6n</sub>), 1.63 (d, *J* = 10.7, 1H, H<sub>7a</sub>). <sup>13</sup>C NMR (100 MHz) δ (ppm): 174.2–174.1 (2C, C=O), 156.9 (N=CH), 142.6 (C<sub>subst.</sub>), 138.6 (C<sub>subst.</sub>), 136.6 (C–Cl), 132.0 (C–Cl), 129.8, 129.4 (C–Cl), 128.9, 128.5, 128.3, 127.7, 46.8, 46.3, 46.0, 41.2, 40.0, 39.0, 32.6. LC–MS: 447 [M<sup>+</sup>], 412, 390, 258, 171. Anal. calcd. for C<sub>22</sub>H<sub>17</sub>Cl<sub>3</sub>N<sub>2</sub>O<sub>2</sub>: C, 59.02; H, 3.83; N, 6.26. Found: C, 58.91; H, 3.71; N, 6.16.

**5-(4-Methoxyphenyl)-N-[(2,4-dichlorophenyl)methylene]amino}-bicyclo[2.2.1]heptane-endo-2,endo-3-dicarboximide (8b)**

Colorless crystals, 61% yield. Mp 184 °C. *R*<sub>f</sub> = 0.39 (2:1, ethyl acetate/*n*-hexane). FTIR (cm<sup>-1</sup>): 3037, 3015, 2975, 2960, 1771, 1711, 1596, 1582, 1497, 1471, 1454, 1377, 1275, 1260, 1174, 878, 867. <sup>1</sup>H NMR (500 MHz) δ (ppm): 9.59 (s, 1H, H<sub>8</sub>), 8.11 (d, *J* = 7.8 Hz, 1H, H<sub>aro.</sub>), 7.38–7.36 (m, 1H, H<sub>aro.</sub>), 7.26–7.24 (m, 1H, H<sub>aro.</sub>), 7.03 (d, *J* = 8.8 Hz,

2H, H<sub>aro.</sub>), 6.75 (d,  $J$  = 8.8 Hz, 2H, H<sub>aro.</sub>), 3.73 (s, 3H, OCH<sub>3</sub>), 3.19–3.13 (m, 2H, H<sub>2</sub>–H<sub>3</sub>), 2.91 (brs, 1H, H<sub>4</sub>), 2.85–2.79 (m, 2H, H<sub>1</sub>–H<sub>5n</sub>), 1.84–1.82 (m, 3H, H<sub>7s</sub>, H<sub>6n</sub>, H<sub>6x</sub>), 1.51 (d,  $J$  = 10.7 Hz, 1H, H<sub>7a</sub>). <sup>13</sup>C NMR (125 MHz)  $\delta$  (ppm): 174.3–173.2 (2C, C=O), 155.6–154.8 (N=CH), 136.8 (C<sub>subst.</sub>), 135.4 (C<sub>subst.</sub>), 132.7 (C–Cl), 130.3 (C–Cl), 128.0, 127.9, 127.0, 126.7, 112.8, 54.2, 45.8, 40.8, 40.0, 39.0, 38.6, 38.0, 31.6. LC–MS: 443 [M<sup>+</sup>], 374, 322, 268. Anal. calcd. for C<sub>23</sub>H<sub>20</sub>Cl<sub>2</sub>N<sub>2</sub>O<sub>3</sub>: C, 62.31; H, 4.55; N, 6.32. Found: C, 62.18; H, 4.39; N, 6.37.

**5-(4-Methoxyphenyl)-N-[(5-bromo-2-hydroxyphenyl)methylene]amino}-bicyclo[2.2.1]heptane-endo-2,endo-3-dicarboximide (9a)**

Light yellow crystals, 47% yield. Mp 187 °C.  $R_f$  = 0.60 (2:1, ethyl acetate/*n*-hexane). FTIR (cm<sup>-1</sup>): 3463, 3032, 3025, 2970, 2946, 1737, 1714, 1604, 1552, 1512, 1473, 1432, 1373, 1230, 1216, 1176, 822, 799, 777, 748. <sup>1</sup>H NMR (400 MHz)  $\delta$  (ppm): 11.14 (s, 1H, OH), 9.43 (s, 1H, H<sub>8</sub>), 7.48–7.46 (m, 2H, H<sub>aro.</sub>), 7.12 (d,  $J$  = 8.6 Hz, 2H, H<sub>aro.</sub>), 6.95 (d,  $J$  = 9.39 Hz, 1H, H<sub>aro.</sub>), 6.85 (d,  $J$  = 8.6 Hz, 2H, H<sub>aro.</sub>), 3.79 (s, 3H, OCH<sub>3</sub>), 3.32–3.19 (m, 2H, H<sub>2</sub>–H<sub>3</sub>), 2.95 (brs, 1H, H<sub>4</sub>), 2.88 (d,  $J$  = 6.8 Hz, 1H, H<sub>1</sub>), 2.88–2.84 (m, 1H, H<sub>5n</sub>), 1.95–1.89 (m, 3H, H<sub>7s</sub>, H<sub>6x</sub> ve H<sub>6n</sub>), 1.60 (d,  $J$  = 9.8 Hz, 1H, H<sub>7a</sub>). <sup>13</sup>C NMR (100 MHz)  $\delta$  (ppm): 174.5–174.4 (2C, C=O), 162.1 (N=CH), 144.3 (C<sub>subst.</sub>), 135.3, 132.9, 131.8, 130.7 (C<sub>subst.</sub>), 128.9, 128.7, 128.5, 127.9 (C–OCH<sub>3</sub>), 127.1, 126.7 (C–Br), 126.2, 123.3, 47.0, 46.5, 46.0, 41.8, 40.0, 39.1, 32.5. LC–MS: 470 [M<sup>+</sup> + 1], 469 [M<sup>+</sup>], 468 [M<sup>+</sup> – 1], 390, 374, 344, 296, 220, 180. Anal. calcd. for C<sub>23</sub>H<sub>21</sub>BrN<sub>2</sub>O<sub>4</sub>: C, 58.86; H, 4.51; N, 5.97. Found: C, 58.73; H, 4.40; N, 5.86.

**5-(6-Chloro-3-pyridyl)-N-[(5-bromo-2-hydroxyphenyl)methylene]amino}-bicyclo[2.2.1]heptane-endo-2,endo-3-dicarboximide (9b)**

Colorless crystals, 60% yield. Mp 175 °C.  $R_f$  = 0.59 (2:1, ethyl acetate/*n*-hexane). FTIR (cm<sup>-1</sup>): 3362, 3037, 2950, 2875, 1764, 1712, 1604, 1582, 1474, 1461, 1431, 1178, 825, 789, 740. <sup>1</sup>H NMR (500 MHz)  $\delta$  (ppm): 10.96 (s, 1H, OH), 9.35 (s, 1H, H<sub>8</sub>), 8.17 (d,  $J$  = 2.9 Hz, 1H, H<sub>aro.</sub>), 7.40–7.38 (m, 3H, H<sub>aro.</sub>), 7.19 (d,  $J$  = 8.8 Hz, 1H, H<sub>aro.</sub>), 6.86 (d,  $J$  = 8.8 Hz, 1H, H<sub>aro.</sub>), 3.27 (dd,  $J$  = 5.8, 9.8 Hz, 1H, H<sub>3</sub>), 3.20 (ddd,  $J$  = 1.9, 4.8, and 6.8 Hz, 1H, H<sub>2</sub>), 2.98 (brs, 1H, H<sub>4</sub>), 2.92 (d,  $J$  = 4.8 Hz, 1H, H<sub>1</sub>), 2.83 (dd,  $J$  = 5.8 and 8.8 Hz, 1H, H<sub>5n</sub>), 1.90 (ddd,  $J$  = 1.9, 8.8, and 10.7 Hz, 1H, H<sub>6n</sub>), 1.82–1.76 (m, 2H, H<sub>7s</sub>, H<sub>6x</sub>), 1.62 (d,  $J$  = 10.7 Hz, 1H, H<sub>7a</sub>). <sup>13</sup>C NMR (100 MHz)  $\delta$  (ppm): 172.2–172.1 (2C, C=O), 159.8 (N=CH), 157.8 (C–OH), 148.7 (C<sub>subst.</sub>), 147.3 (C<sub>subst.</sub>), 137.3 (C–Cl), 136.6 (C–Br), 135.4, 133.6, 123.0, 118.6, 117.4, 110.1, 45.7, 45.2, 44.5, 39.0, 38.2, 38.1, 31.6. LC–MS: 475 [M<sup>+</sup> + 1], 474 [M<sup>+</sup>], 473 [M<sup>+</sup> – 1], 395, 345, 282, 180. Anal. calcd. for C<sub>21</sub>H<sub>17</sub>BrClN<sub>3</sub>O<sub>3</sub>: C, 53.13; H, 3.61; N, 8.85. Found: C, 53.03; H, 3.70; N, 8.79.

**5-(2-Thienyl)-N-[(2,5-dimethoxyphenyl)methylene]amino}-bicyclo[2.2.1]heptane-endo-2,endo-3-dicarboximide (10a)**

Colorless crystals, 65% yield. Mp 167 °C.  $R_f$  = 0.42 (2:1, ethyl acetate/*n*-hexane). FTIR (cm<sup>-1</sup>): 3119, 3058, 2964, 2881, 2837, 1759, 1698, 1613, 1595, 1494, 1467, 1455,

1421, 1384, 1224, 1195, 815, 733, 711. <sup>1</sup>H NMR (400 MHz)  $\delta$  (ppm): 9.34 (s, 1H, H<sub>8</sub>), 7.66 (d,  $J$  = 2.8 Hz, 1H, H<sub>aro.</sub>), 7.15 (d,  $J$  = 5.2 Hz, 1H, H<sub>aro.</sub>), 7.05 (dd,  $J$  = 3.2 and 9.2 Hz, 1H, H<sub>aro.</sub>), 6.94 (dd,  $J$  = 3.6 and 4.8 Hz, 1H, H<sub>aro.</sub>), 6.88 (d,  $J$  = 9.2 Hz, 1H, H<sub>aro.</sub>), 6.83 (d,  $J$  = 3.2 Hz, 1H, H<sub>aro.</sub>), 3.85 (s, 3H, OCH<sub>3</sub>), 3.84 (s, 3H, OCH<sub>3</sub>), 3.29–3.19 (m, 3H, H<sub>2</sub>–H<sub>3</sub> and H<sub>5n</sub>), 2.98 (brs, 2H, H<sub>1</sub>–H<sub>4</sub>), 2.11–2.01 (m, 2H, H<sub>6x</sub>–H<sub>6n</sub>), 1.94–1.89 (m, 1H, H<sub>7s</sub>), 1.66 (d,  $J$  = 10.7 Hz, 1H, H<sub>7a</sub>). <sup>13</sup>C NMR (100 MHz)  $\delta$  (ppm): 174.0–173.9 (2C, C=O), 159.8 (N=CH), 154.1 (C–OCH<sub>3</sub>), 153.6 (C–OCH<sub>3</sub>), 149.3 (C<sub>subst.</sub>), 126.8, 123.5, 123.4 (C<sub>subst.</sub>), 121.5, 121.4, 112.7, 110.0, 55.9–56.2 (2C, OCH<sub>3</sub>), 47.4, 46.6, 46.2, 39.6, 39.5, 37.9, 34.9. LC–MS: 433 [M + Na<sup>+</sup>], 410 [M<sup>+</sup>], 409 [M<sup>+</sup> – 1], 274, 244, 218, 138. Anal. calcd. for C<sub>22</sub>H<sub>22</sub>N<sub>2</sub>O<sub>4</sub>S: C, 64.37; H, 5.40; N, 6.82; S, 7.81. Found: C, 64.20; H, 5.29; N, 6.71; S, 7.99.

**5-(4-Chlorophenyl)-[(2,5-dimethoxyphenyl)methylene]amino}-bicyclo[2.2.1]heptane-endo-2,endo-3-dicarboximide (10b)**

Colorless crystals, 55% yield. Mp 185 °C.  $R_f$  = 0.45 (2:1, ethyl acetate/*n*-hexane). FTIR (cm<sup>-1</sup>): 3058, 2969, 2947, 2878, 2839, 1737, 1706, 1614, 1598, 1493, 1462, 1423, 1376, 1217, 1189, 810, 792, 751. <sup>1</sup>H NMR (500 MHz)  $\delta$  (ppm): 9.27 (s, 1H, H<sub>8</sub>), 7.57 (d,  $J$  = 3.8 Hz, 1H, H<sub>aro.</sub>), 7.17 (d,  $J$  = 8.7 Hz, 2H, H<sub>aro.</sub>), 7.05 (d,  $J$  = 8.7 Hz, 2H, H<sub>aro.</sub>), 6.96 (dd,  $J$  = 3.8 and 8.6 Hz, 1H, H<sub>aro.</sub>), 6.79 (d,  $J$  = 8.7 Hz, 1H, H<sub>aro.</sub>), 3.76 (s, 3H, OCH<sub>3</sub>), 3.75 (s, 3H, OCH<sub>3</sub>), 3.25–3.21 (m, 2H, H<sub>2</sub>–H<sub>3</sub>), 3.16 (ddd,  $J$  = 1.9, 8.8, and 11.7 Hz, 1H, H<sub>5n</sub>), 2.98 (d,  $J$  = 4.8 Hz, 1H, H<sub>1</sub>), 2.91 (brs, 1H, H<sub>4</sub>), 2.08 (ddd,  $J$  = 1.9, 8.8, and 11.7 Hz, 1H, H<sub>6n</sub>), 1.89 (d,  $J$  = 9.7 Hz, 1H, H<sub>6x</sub>), 1.68–1.62 (m, 2H, H<sub>7a</sub> ve H<sub>7s</sub>). <sup>13</sup>C NMR (100 MHz)  $\delta$  (ppm): 173.1–173.0 (2C, C=O), 158.6 (N=CH), 153.1 (C–OCH<sub>3</sub>), 152.7 (C–OCH<sub>3</sub>), 141.8 (C–Cl), 130.9 (C<sub>subst.</sub>), 127.5, 127.4, 120.6 (C<sub>subst.</sub>), 120.2, 111.8, 109.1, 55.3–54.9 (2C, OCH<sub>3</sub>), 45.9, 45.2, 44.9, 40.2, 38.9, 38.0, 31.6. LC–MS: 439 [M<sup>+</sup> + 1], 438 [M<sup>+</sup>], 437 [M<sup>+</sup> – 1], 378, 322, 268, 246, 139. Anal. calcd. for C<sub>24</sub>H<sub>23</sub>ClN<sub>2</sub>O<sub>4</sub>: C, 65.68; H, 5.28; N, 6.38. Found: C, 65.53; H, 5.21; N, 6.43.

**5-(2-Chlorophenyl)-[(2,5-dimethoxyphenyl)methylene]amino}-bicyclo[2.2.1]heptane-endo-2,endo-3-dicarboximide (10c)**

Colorless crystals, 59% yield. Mp 126 °C.  $R_f$  = 0.39 (2:1, ethyl acetate/*n*-hexane). FTIR (cm<sup>-1</sup>): 3053, 2969, 2951, 2875, 1768, 1704, 1613, 1596, 1493, 1464, 1441, 1180, 837, 812, 792. <sup>1</sup>H NMR (500 MHz)  $\delta$  (ppm): 9.21 (s, 1H, H<sub>8</sub>), 7.59 (d,  $J$  = 3.9 Hz, 1H, H<sub>aro.</sub>), 7.29 (d,  $J$  = 7.8 Hz, 1H, H<sub>aro.</sub>), 7.18–7.13 (m, 2H, H<sub>aro.</sub>), 7.07 (ddd,  $J$  = 1.9, 8.8, and 14.6 Hz, 1H, H<sub>aro.</sub>), 6.96 (dd,  $J$  = 2.9 and 8.8 Hz, 1H, H<sub>aro.</sub>), 6.79 (d,  $J$  = 8.7 Hz, 1H, H<sub>aro.</sub>), 3.76 (s, 3H, OCH<sub>3</sub>), 3.75 (s, 3H, OCH<sub>3</sub>), 3.25–3.21 (m, 2H, H<sub>2</sub>–H<sub>3</sub>), 3.16 (ddd,  $J$  = 1.9, 8.7, and 11.7 Hz, 1H, H<sub>5n</sub>), 2.98 (d,  $J$  = 4.8 Hz, 1H, H<sub>1</sub>), 2.91 (brs, 1H, H<sub>4</sub>), 2.08 (ddd,  $J$  = 1.9, 8.7, and 11.7 Hz, 1H, H<sub>6n</sub>), 1.89 (d,  $J$  = 9.7 Hz, 1H, H<sub>6x</sub>), 1.68–1.60 (m, 2H, H<sub>7a</sub>–H<sub>7s</sub>). <sup>13</sup>C NMR (100 MHz)  $\delta$  (ppm): 173.1–172.8 (2C, C=O), 154.5 (N=CH), 156.1 (C–Cl), 154.5 (C<sub>subst.</sub>), 140.7 (C–OCH<sub>3</sub>), 138.1 (C<sub>subst.</sub>), 128.8, 127.1, 120.2, 125.2, 120.6, 111.6, 110.2, 55.4–55.2 (2C, OCH<sub>3</sub>), 46.1, 45.2, 43.6, 40.0, 39.0, 38.0, 32.2. LC–MS: 439 [M<sup>+</sup> +



1], 438 [M<sup>+</sup>], 437 [M<sup>+</sup> – 1], 378, 322, 268, 246, 139. Anal. calcd. for C<sub>24</sub>H<sub>23</sub>ClN<sub>2</sub>O<sub>4</sub>: C, 65.68; H, 5.28; N, 6.38. Found: C, 65.59; H, 5.23; N, 6.45.

**5-(Phenyl)-N-[[2-naphthylmethylene]amino]bicyclo[2.2.1]heptane-endo-2,endo-3-dicarboximide (11a)**

Light yellow crystals, 62% yield. Mp 132 °C. *R*<sub>f</sub> = 0.57 (2:1, ethyl acetate/*n*-hexane). FTIR (cm<sup>-1</sup>): 3053, 3012, 2970, 2921, 2882, 1737, 1724, 1703, 1605, 1587, 1512, 1455, 1433, 1178, 761, 738. <sup>1</sup>H NMR (400 MHz) δ (ppm): 9.37 (s, 1H, H<sub>8</sub>), 8.20 (s, 1H, H<sub>aro.</sub>), 8.16 (d, *J* = 8.7 Hz, 1H, H<sub>aro.</sub>), 7.94–7.87 (m, 3H, H<sub>aro.</sub>), 7.53–7.60 (m, 2H, H<sub>aro.</sub>), 7.33–7.19 (m, 5H, H<sub>aro.</sub>), 3.34–3.24 (m, 2H, H<sub>2</sub>–H<sub>3</sub>), 3.03 (brs, 3H, H<sub>1</sub>–H<sub>4</sub> and H<sub>5n</sub>), 2.05–1.94 (m, 3H, H<sub>7s</sub>, H<sub>6x</sub> ve H<sub>6n</sub>), 1.62 (d, *J* = 9.0 Hz, 1H, H<sub>7a</sub>). <sup>13</sup>C NMR (100 MHz) δ (ppm): 174.5–174.4 (2C, C=O), 162.1 (N=CH), 144.3 (C<sub>subst.</sub>), 135.3, 132.9, 131.8, 130.7, 128.9, 128.7, 128.5, 127.9, 127.0, 126.7, 126.2, 123.3, 47.0, 46.5, 46.0, 41.8, 40.0, 39.1, 32.5. LC–MS: 395 [M<sup>+</sup> + 1], 394 [M<sup>+</sup>], 393 [M<sup>+</sup> – 1], 332, 234, 206, 194, 167. Anal. calcd. for C<sub>26</sub>H<sub>22</sub>N<sub>2</sub>O<sub>2</sub>: C, 79.16; H, 5.62; N, 7.10. Found: C, 79.04; H, 5.70; N, 6.99.

**5-(2-Thienyl)-N-[[2-naphthylmethylene]amino]bicyclo[2.2.1]heptane-endo-2,endo-3-dicarboximide (11b)**

Light yellow crystals, 62% yield. Mp 145 °C. *R*<sub>f</sub> = 0.57 (2:1, ethyl acetate/*n*-hexane). FTIR (cm<sup>-1</sup>): 3058, 3045, 2953, 2921, 2875, 1734, 1700, 1607, 1569, 1467, 1438, 1350, 1180, 773, 760, 741, 697. <sup>1</sup>H NMR (400 MHz) δ (ppm): 9.35 (s, 1H, H<sub>8</sub>), 8.20 (brs, 1H, H<sub>aro.</sub>), 8.15 (d, *J* = 8.8 Hz, 1H, H<sub>aro.</sub>), 7.94–7.87 (m, 3H, H<sub>aro.</sub>), 7.53–7.60 (m, 2H, H<sub>aro.</sub>), 7.16 (d, *J* = 4.7 Hz, 1H, H<sub>aro.</sub>), 6.95–6.92 (m, 1H, H<sub>aro.</sub>), 6.84 (d, *J* = 3.4 Hz, 1H, H<sub>aro.</sub>), 3.33–3.21 (m, 3H, H<sub>2</sub>–H<sub>3</sub> and H<sub>5n</sub>), 3.01 (brs, 2H, H<sub>1</sub>–H<sub>4</sub>), 2.18–2.03 (m, 2H, H<sub>6x</sub>–H<sub>6n</sub>), 1.95–1.90 (m, 1H, H<sub>7s</sub>), 1.67 (d, *J* = 10.2 Hz, 1H, H<sub>7a</sub>). <sup>13</sup>C NMR (100 MHz) δ (ppm): 174.2–174.1 (2C, C=O), 162.2 (N=CH), 149.2 (C<sub>subst.</sub>), 135.3, 132.9, 131.8, 130.6 (C<sub>subst.</sub>), 128.9, 128.7, 127.9, 126.8, 126.7, 123.4, 123.3, 47.3, 46.6, 46.1, 39.6, 39.4, 38.0, 35.0. LC–MS: 400 [M<sup>+</sup>], 399 [M<sup>+</sup> – 1], 370, 234, 206, 167. Anal. calcd. for C<sub>24</sub>H<sub>20</sub>N<sub>2</sub>O<sub>2</sub>S: C, 71.98; H, 5.03; N, 6.99; S, 8.01. Found: C, 71.81; H, 5.19; N, 6.81; S, 8.08.

**5-(4-Methoxyphenyl)-N-[[2-thienylmethylene] amino]bicyclo[2.2.1]heptane-endo-2,endo-3-dicarboximide (12)**

Colorless crystals, 58% yield. Mp 177 °C. *R*<sub>f</sub> = 0.49 (2:1, ethyl acetate/*n*-hexane). FTIR (cm<sup>-1</sup>): 3082, 3032, 3068, 3053, 3012, 2955, 2886, 1764, 1713, 1609, 1581, 1511, 1464, 14434, 1373, 1247, 1170, 802, 744, 723. <sup>1</sup>H NMR (500 MHz) δ (ppm): 9.24 (s, 1H, H<sub>8</sub>), 7.48 (d, *J* = 4.8 Hz, 1H, H<sub>aro.</sub>), 7.43 (d, *J* = 2.9 Hz, 1H, H<sub>aro.</sub>), 7.05–7.02 (m, 3H, H<sub>aro.</sub>), 6.75 (d, *J* = 8.8 Hz, 2H, H<sub>aro.</sub>), 3.69 (s, 3H, OCH<sub>3</sub>), 3.18–3.09 (m, 2H, H<sub>2</sub>–H<sub>3</sub>), 2.89 (brs, 1H, H<sub>4</sub>), 2.85–2.82 (m, 2H, H<sub>1</sub>–H<sub>5n</sub>), 1.83–1.79 (m, 3H, H<sub>7s</sub>, H<sub>6n</sub>, H<sub>6x</sub>), 1.49 (d, *J* = 10.7 Hz, 1H, H<sub>7a</sub>). <sup>13</sup>C NMR (100 MHz) δ (ppm): 173.3–173.2 (2C, C=O), 157.0 (N=CH), 154.8 (C<sub>subst.</sub>), 136.8 (C<sub>subst.</sub>), 135.4, 132.7, 130.3, 127.0, 126.7, 112.8, 54.2 (C–OCH<sub>3</sub>), 45.9, 45.4, 45.3, 40.0, 38.9, 38.0, 31.6. LC–MS: 381 [M<sup>+</sup> + 1], 380 (M<sup>+</sup>), 379 [M<sup>+</sup> – 1], 366, 232, 206, 167. Anal. calcd. for C<sub>21</sub>H<sub>20</sub>N<sub>2</sub>O<sub>3</sub>S: C, 66.29; H, 5.30; N, 7.36; S, 8.43. Found: C, 66.08; H, 5.33; N, 7.23; S, 8.47.

**Experimental procedure for the preparation of 14–18**

To a solution of 4-chlorobenzaldoxime (202.25 mg, 1.3 mmol) in dichloromethane was added tricyclic hydrazone **3–7** (1 mmol), and the solution was cooled to 0 °C. Aqueous sodium hypochloride (5.25%, 3.5 g, 2.5 mmol) was added dropwise over 30 min, and the reaction was stirred overnight (0 °C – room temperature). The reaction mixture was extracted with either dichloromethane (3 × 10 mL) or diethyl ether and dried over MgSO<sub>4</sub>. The solvent was evaporated, and the residue was purified by chromatography.

**4,8-Methano-3-(4-chlorophenyl)-6-(2,4-dichloromethyleneamino)-4,4a,8,exo-8a-tetrahydro-exo-3aH-isoxazolo[5,4-f]isoindole-5,7(6H,7aH)-endo-dione (14)**

Colorless crystals, 80% yield. Mp 241 °C. *R*<sub>f</sub> = 0.60 (2:1, ethyl acetate/*n*-hexane). FTIR (cm<sup>-1</sup>): 3100, 3045, 2959, 2870, 1775, 1707, 1598, 1583, 1496, 1471, 1377, 1357, 1315, 1301, 1175, 900, 868, 827. <sup>1</sup>H NMR (400 MHz) δ (ppm): 9.35 (s, 1H, H<sub>10</sub>), 8.10 (d, *J* = 8.8 Hz, 1H, H<sub>aro.</sub>), 7.55 (d, *J* = 8.8 Hz, 2H, H<sub>aro.</sub>), 7.39 (d, *J* = 1.95 Hz, 1H, H<sub>aro.</sub>), 7.32 (d, *J* = 7.8 Hz, 2H, H<sub>aro.</sub>), 7.26 (dd, *J* = 1.9 and 7.8 Hz, 1H, H<sub>aro.</sub>), 4.73 (d, *J* = 7.8 Hz, 1H, H<sub>8an</sub>), 3.61 (dd, *J* = 1.4 and 7.8 Hz, 1H, H<sub>3an</sub>), 3.26–3.23 (m, 2H, H<sub>4a</sub>–H<sub>7a</sub>), 3.22 (brs, 1H, H<sub>8</sub>), 3.02 (brs, 1H, H<sub>4</sub>), 1.82 (d, *J* = 10.7 Hz, 1H, H<sub>9s</sub>), 1.57 (d, *J* = 9.0 Hz, 1H, H<sub>9a</sub>). <sup>13</sup>C NMR (100 MHz) δ (ppm): 172.0–171.1 (2C, C=O), 156.7 (C<sub>subst.</sub>), 154.2 (N=CH), 137.9 (C<sub>subst.</sub>), 135.7 (C<sub>subst.</sub>), 135.4 (C<sub>subst.</sub>), 128.9, 128.2, 128.0, 127.9, 127.0, 126.8, 125.5, 82.8, 51.4, 44.9, 43.8, 41.5, 41.2, 34.7. LC–MS: 491 [M<sup>+</sup> + 1], 488.75 [M<sup>+</sup>], 487 [M<sup>+</sup> – 1]. MS-ESI (EI, 70 eV): 490 [M<sup>+</sup>], 389.38, 363.31, 334.85, 317.14, 270.92, 220.07, 202.13, 167.23. Anal. calcd. for C<sub>23</sub>H<sub>16</sub>Cl<sub>3</sub>N<sub>3</sub>O<sub>3</sub>: C, 56.52; H, 3.30; N, 8.60. Found: C, 56.01; H, 3.33; N, 8.65.

**4,8-Methano-3-(4-chlorophenyl)-6-(5-bromo-2-hydroxy-phenylmethyleneamino)-4,4a,8,exo-8a-tetrahydro-exo-3aH-isoxazolo[5,4-f]isoindole-5,7(6H,7aH)-endo-dione (15)**

Colorless crystals, 78% yield. Mp 162 °C. *R*<sub>f</sub> = 0.58 (2:1, ethyl acetate/*n*-hexane). FTIR (cm<sup>-1</sup>): 3394, 3011, 2979, 2946, 1791, 1708, 1608, 1594, 1494, 1476, 1403, 1354, 1322, 1169, 741, 716. <sup>1</sup>H NMR (400 MHz) δ (ppm): 10.91 (s, 1H, O–H), 9.40 (s, 1H, H<sub>10</sub>), 7.62 (d, *J* = 8.5 Hz, 2H, H<sub>aro.</sub>), 7.50 (d, *J* = 7.8 Hz, 2H, H<sub>aro.</sub>), 7.41 (d, *J* = 8.5 Hz, 2H, H<sub>aro.</sub>), 6.95 (d, *J* = 9.0 Hz, 1H, H<sub>aro.</sub>), 4.79 (d, *J* = 8.0 Hz, 1H, H<sub>8an</sub>), 3.66 (d, *J* = 8.0 Hz, 1H, H<sub>3an</sub>), 3.34 (d, *J* = 3.7 Hz, 2H, H<sub>4a</sub>–H<sub>7a</sub>), 3.30 (brs, 1H, H<sub>8</sub>), 3.11 (brs, 1H, H<sub>4</sub>), 1.92 (d, *J* = 11.3 Hz, 1H, H<sub>9s</sub>), 1.67 (d, *J* = 11.3 Hz, 1H, H<sub>9a</sub>). <sup>13</sup>C NMR (100 MHz) δ (ppm): 172.3–171.7 (2C, C=O), 161.5 (N=CH), 158.8 (C<sub>subst.</sub>), 155.1 (C<sub>subst.</sub>), 136.6 (C<sub>subst.</sub>), 136.5 (C<sub>subst.</sub>), 134.7, 129.3, 128.0, 126.3, 119.7, 118.1, 111.2, 83.2, 52.5, 45.8, 44.7, 42.5, 42.1, 35.7. LC–MS: 516 [M<sup>+</sup> + 1], 515 [M<sup>+</sup>], 513 [M<sup>+</sup> – 1]. Anal. calcd. for C<sub>23</sub>H<sub>17</sub>BrClN<sub>3</sub>O<sub>4</sub>: C, 53.67; H, 3.33; N, 8.16. Found: C, 53.48; H, 3.41; N, 8.19.

**4,8-Methano-3-(4-chlorophenyl)-6-(2,5-dimethoxy-phenylmethyleneamino)-4,4a,8,exo-8a-tetrahydro-exo-3aH-isoxazolo[5,4-f]isoindole-5,7(6H,7aH)-endo-dione (16)**

Colorless crystals, 69% yield. Mp 211 °C. *R*<sub>f</sub> = 0.49 (2:1, ethyl acetate/*n*-hexane). FTIR (cm<sup>-1</sup>): 3053, 3009, 2970,

2947, 1767, 1704, 1610, 1599, 1496, 1468, 1422, 1406, 1378, 1225, 1184, 920, 900, 822.  $^1\text{H}$  NMR (400 MHz)  $\delta$  (ppm): 9.21 (s, 1H,  $\text{H}_{10}$ ), 7.57–7.56 (brs, 1H,  $\text{H}_{\text{aro}}$ ), 7.54 (d,  $J = 8.8$  Hz, 2H,  $\text{H}_{\text{aro}}$ ), 7.30 (d,  $J = 8.8$  Hz, 2H,  $\text{H}_{\text{aro}}$ ), 6.98 (dd,  $J = 2.9$  and 8.8 Hz, 1H,  $\text{H}_{\text{aro}}$ ), 6.80 (d,  $J = 9.7$  Hz, 1H,  $\text{H}_{\text{aro}}$ ), 4.76 (d,  $J = 8.8$  Hz, 1H,  $\text{H}_{8\text{an}}$ ), 3.77 (s, 3H, m-subst.,  $\text{OCH}_3$ ), 3.74 (s, 3H, o-substituted,  $\text{OCH}_3$ ), 3.63 (d,  $J = 8.8$  Hz, 1H,  $\text{H}_{3\text{an}}$ ), 3.21 (d,  $J = 3.9$  Hz, 2H,  $\text{H}_{4\text{a}}\text{--}\text{H}_{7\text{a}}$ ), 3.19 (brs, 1H,  $\text{H}_8$ ), 3.00 (brs, 1H,  $\text{H}_4$ ), 1.80 (d,  $J = 11.7$  Hz, 1H,  $\text{H}_{9\text{s}}$ ), 1.55 (d,  $J = 11.7$  Hz, 1H,  $\text{H}_{9\text{a}}$ ).  $^{13}\text{C}$  NMR (100 MHz)  $\delta$  (ppm): 172.0–171.1 (2C, C=O), 159.5 (N=CH), 154.3 ( $\text{C}_{\text{subst.}}$ ), 153.2 ( $\text{C}_{\text{subst.}}$ ), 152.7 ( $\text{C}_{\text{subst.}}$ ), 135.3 ( $\text{C}_{\text{subst.}}$ ), 128.2, 127.0, 125.5, 120.6, 120.1, 111.8, 109.0, 82.2, 55.2, 54.9, 51.5, 44.8, 43.9, 41.7, 41.1, 34.7. LC–MS: 481 [ $\text{M}^+ + 1$ ], 480 [ $\text{M}^+$ ]. Anal. calcd. for  $\text{C}_{25}\text{H}_{22}\text{ClN}_3\text{O}_5$ : C, 62.57; H, 4.62; N, 8.76. Found: C, 62.49; H, 4.59; N, 8.81.

**4,8-Methano-3-(4-chlorophenyl)-6-(2-naphthylmethyleneamino)-4,4a,8,exo-8a-tetrahydro-exo-3aH-isoxazolo[5,4-f]isoindole-5,7(6H,7aH)-endo-dione (17)**

Colorless crystals, 85% yield. Mp 135 °C.  $R_f = 0.41$  (2:1, ethyl acetate/*n*-hexane). FTIR ( $\text{cm}^{-1}$ ): 3027, 3011, 2958, 2916, 2850, 1767, 1706, 1625, 1606, 1593, 1493, 1468, 1366, 1346, 1178, 798, 738, 724.  $^1\text{H}$  NMR (400 MHz)  $\delta$  (ppm): 9.20 (s, 1H,  $\text{H}_{10}$ ), 8.01 (dd,  $J = 1.4$  and 8.8 Hz, 1H,  $\text{H}_{\text{aro}}$ ), 7.82–7.77 (m, 3H,  $\text{H}_{\text{aro}}$ ), 7.53 (d,  $J = 8.8$  Hz, 2H,  $\text{H}_{\text{aro}}$ ), 7.50–7.43 (m, 2H,  $\text{H}_{\text{aro}}$ ), 7.28 (d,  $J = 8.8$  Hz, 2H,  $\text{H}_{\text{aro}}$ ), 4.75 (d,  $J = 8.3$  Hz, 1H,  $\text{H}_{8\text{an}}$ ), 3.63 (d,  $J = 8.3$  Hz, 1H,  $\text{H}_{3\text{an}}$ ), 3.23 (d,  $J = 4.8$  Hz, 2H,  $\text{H}_{4\text{a}}\text{--}\text{H}_{7\text{a}}$ ), 3.20 (brs, 1H,  $\text{H}_8$ ), 2.99 (brs, 1H,  $\text{H}_4$ ), 1.80 (d,  $J = 11.2$  Hz, 1H,  $\text{H}_{9\text{s}}$ ), 1.55 (d,  $J = 11.2$  Hz, 1H,  $\text{H}_{9\text{a}}$ ).  $^{13}\text{C}$  NMR (100 MHz)  $\delta$  (ppm): 172.2–171.4 (2C, C=O), 161.8 ( $\text{C}_{\text{subst.}}$ ), 154.3 (N=CH), 135.3 ( $\text{C}_{\text{subst.}}$ ), 134.4 ( $\text{C}_{\text{subst.}}$ ), 131.8 ( $\text{C}_{\text{subst.}}$ ), 131.0, 129.3, 128.2, 127.9, 127.8, 127.1, 127.0, 125.8, 125.5, 122.0, 82.3, 52.4, 51.4, 44.8, 43.8, 41.6, 41.1. LC–MS: 471 [ $\text{M}^+ + 1$ ], 470 [ $\text{M}^+$ ], 469 [ $\text{M}^+ - 1$ ]. Anal. calcd. for  $\text{C}_{27}\text{H}_{20}\text{ClN}_3\text{O}_3$ : C, 69.01; H, 4.29; N, 8.94. Found: C, 69.19; H, 4.26; N, 8.78.

**4,8-Methano-3-(4-chlorophenyl)-6-(2-thienylmethyleneamino)-4,4a,8,exo-8a-tetrahydro-exo-3aH-isoxazolo[5,4-f]isoindole-5,7(6H,7aH)-endo-dione (18)**

Colorless crystals, 75% yield. Mp 169 °C.  $R_f = 0.47$  (2:1, ethyl acetate/*n*-hexane). FTIR ( $\text{cm}^{-1}$ ): 3088, 2976, 2921, 1769, 1701, 1592, 1514, 1494, 1343, 1319, 1184, 806, 728, 712.  $^1\text{H}$  NMR (400 MHz)  $\delta$  (ppm): 9.25 (s, 1H,  $\text{H}_{10}$ ), 7.62 (d,  $J = 8.3$  Hz, 2H,  $\text{H}_{\text{aro}}$ ), 7.59 (d,  $J = 5.0$  Hz, 1H,  $\text{H}_{\text{aro}}$ ), 7.53 (d,  $J = 3.6$  Hz, 1H,  $\text{H}_{\text{aro}}$ ), 7.38 (d,  $J = 8.2$  Hz, 1H,  $\text{H}_{\text{aro}}$ ), 7.15 (d,  $J = 4.0$  Hz, 2H,  $\text{H}_{\text{aro}}$ ), 4.80 (d,  $J = 8.3$  Hz, 1H,  $\text{H}_{8\text{an}}$ ), 3.69 (d,  $J = 8.3$  Hz, 1H,  $\text{H}_{3\text{an}}$ ), 3.32 (d,  $J = 3.7$  Hz, 2H,  $\text{H}_{4\text{a}}\text{--}\text{H}_{7\text{a}}$ ), 3.26 (brs, 1H,  $\text{H}_8$ ), 3.07 (brs, 1H,  $\text{H}_4$ ), 1.88 (d,  $J = 11.2$  Hz, 1H,  $\text{H}_{9\text{s}}$ ), 1.64 (d,  $J = 11.2$  Hz, 1H,  $\text{H}_{9\text{a}}$ ).  $^{13}\text{C}$  NMR (100 MHz)  $\delta$  (ppm): 173.0–171.3 (2C, C=O), 156.7 ( $\text{C}_{\text{subst.}}$ ), 155.3 (N=CH), 137.2 ( $\text{C}_{\text{subst.}}$ ), 136.3, 134.4, 131.9, 129.2, 128.1, 127.9, 126.4, 83.3, 52.4, 45.8, 44.7, 42.5, 42.1, 35.7. LC–MS: 427 [ $\text{M}^+ + 1$ ], 426 [ $\text{M}^+$ ], 425 [ $\text{M}^+ - 1$ ]. Anal. calcd. for  $\text{C}_{21}\text{H}_{16}\text{ClN}_3\text{O}_3\text{S}$ : C, 59.22; H, 3.79; N, 9.87; S, 7.53. Found: C, 59.01; H, 3.67; N, 9.75; S, 7.59.

## Acknowledgments

We gratefully acknowledge financial support of this work by the Yildiz Technical University Scientific Research Projects Coordination Department (Project No. 28–01–02–04). We thank Prof. Dr. I. Erden from San Francisco State University for fruitful discussions.

## References

- (1) Namyslo, J. C.; Kaufmann, D. E. *Chem. Ber.* **1997**, *130* (9), 1327. doi:10.1002/cber.19971300924.
- (2) Namyslo, J. C.; Kaufmann, D. E. *Synlett* **1999**, 1999 (6), 804. doi:10.1055/s-1999-2719.
- (3) Storsberg, J.; Yao, M.-L.; Ocal, N.; de Meijere, A.; Adam, A. E. W.; Kaufmann, D. E. *Chem. Commun. (Camb.)* **2005**, 45 (45), 5665. doi:10.1039/b507732j. PMID:16292383.
- (4) Yolacan, C.; Bagdatli, E.; Ocal, N.; Kaufmann, D. E. *Molecules* **2006**, *11* (8), 603. doi:10.3390/11080603. PMID:17971733.
- (5) Bagdatli, E.; Öcal, N.; Kaufmann, D. E. *Helv. Chim. Acta* **2007**, *90* (12), 2380. doi:10.1002/hlca.200790244.
- (6) Göksu, G.; Gül, M.; Öcal, N.; Kaufmann, D. E. *Tetrahedron Lett.* **2008**, *49* (17), 2685. doi:10.1016/j.tetlet.2008.02.171.
- (7) Terzioglu, N.; Gürsoy, A. *Eur. J. Med. Chem.* **2003**, *38* (7–8), 781. doi:10.1016/S0223-5234(03)00138-7. PMID:12932910.
- (8) Cocco, M. T.; Congiu, C.; Lilliu, V.; Onnis, V. *Bioorg. Med. Chem.* **2006**, *14* (2), 366. doi:10.1016/j.bmc.2005.08.012. PMID:16185883.
- (9) Vicini, P.; Zani, F.; Cozzini, P.; Doytchinova, I. *Eur. J. Med. Chem.* **2002**, *37* (7), 553. doi:10.1016/S0223-5234(02)01378-8. PMID:12126774.
- (10) Patole, J.; Sandbhor, U.; Padhye, S.; Deobagkar, D. N.; Anson, C. E.; Powell, A. *Bioorg. Med. Chem. Lett.* **2003**, *13* (1), 51. doi:10.1016/S0960-894X(02)00855-7. PMID:12467615.
- (11) Walcourt, A.; Loyevsky, M.; Lovejoy, D. B.; Gordeuk, V. R.; Richardson, D. R. *Int. J. Biochem. Cell Biol.* **2004**, *36* (3), 401. doi:10.1016/S1357-2725(03)00248-6. PMID:14687919.
- (12) Kratz, F.; Beyer, U.; Roth, T.; Tarasova, N.; Collery, P.; Lechenault, F.; Cazabat, A.; Schumacher, P.; Unger, C.; Falken, U. *J. Pharm. Sci.* **1998**, *87* (3), 338. doi:10.1021/js970246a. PMID:9523988.
- (13) Bernhardt, P. V.; Chin, P.; Sharpe, P. C.; Wang, J.-Y. C.; Richardson, D. R. *J. Biol. Inorg. Chem.* **2005**, *10* (7), 761. doi:10.1007/s00775-005-0018-0. PMID:16193304.
- (14) Umesha, K. B.; Ajay Kumar, K.; Lokanatha Rai, K. M. *Synth. Commun.* **2002**, *32* (12), 1841. doi:10.1081/SCC-120004066.
- (15) Houari, G. A.; Kerbal, A.; Bennani, B.; Baba, M. F.; Daoudi, M.; Hadda, T. B. *Arkivoc* **2008**, xii, 42.
- (16) Jayashankara, B.; Rai, K. M. L. *Arkivoc* **2008**, xi, 75.
- (17) Caramella, P.; Gruenanger, P. In *1,3-Dipolar Cycloaddition Chemistry*; Padwa, A., Ed.; Wiley Interscience: New York, 1984; Vol. 1.
- (18) Verma, S. M.; Rao, C. K. *Tetrahedron* **1972**, *28* (19), 5029. doi:10.1016/0040-4020(72)88155-9.
- (19) Kas'yan, L. I.; Tarabara, I. N.; Bondarenko, Ya. S.; Shishkina, S. V.; Shishkin, O. V.; Musatov, V. I. *Russ. J. Org. Chem.* **2005**, *41* (8), 1122. doi:10.1007/s11178-005-0305-9.

# Microwave-assisted, palladium-catalyzed carbonylative cyclization — Rapid synthesis of 2-quinolones from unprotected 2-iodoanilines and terminal alkynes

Jia-Rong Chen, Jie Liao, and Wen-Jing Xiao

**Abstract:** Palladium-catalyzed cyclocarbonylations of 2-iodoanilines with various terminal alkynes have been carried out by the use of commercially available molybdenum hexacarbonyl as a convenient and solid carbon monoxide source. The reactions were conducted at 160 °C for 30 min under microwave irradiation and in the presence of Et<sub>3</sub>N in THF, affording the corresponding 2-quinolone derivatives in good regioselectivities and yields.

**Key words:** microwave, palladium, carbonylation, 2-iodoaniline, 2-quinolone.

**Résumé :** Faisant appel à des catalyseurs de palladium et de l'hexacarbonyle de molybdène disponible commercialement comme source commode et solide de monoxyde de carbone, on a effectué des cyclocarbonylations de 2-iodoanilines avec divers alcynes en position terminale. Les réactions ont été effectuées à 160 °C, pendant 30 minutes, sous irradiations de micro-ondes et en présence de Et<sub>3</sub>N dans le THF et elles conduisent à la formation des 2-quinoléones correspondantes avec de bons rendements et de bonnes régiosélectivités.

**Mots-clés :** micro-onde, palladium, carbonylation, 2-iodoaniline, 2-quinoléone.

[Traduit par la Rédaction]

## Introduction

Undoubtedly, the transition-metal-catalyzed carbonylation has become one of the most important carbonyl-formation reactions in organic synthesis.<sup>1</sup> Particularly, palladium-catalyzed cyclocarbonylation of unsaturated substrates provides a unique, concise, and efficient approach toward carbo- and hetero-cycles bearing a carbonyl moiety.<sup>2</sup> For example, the insertion of CO into aryl–palladium bond leading to the formation of acylpalladium complex, which could react with various nucleophiles, is a ubiquitous process for the synthesis of aryl carbonyl compounds.<sup>3</sup> Representative examples include palladium-catalyzed carbonylative cyclizations of 2-iodophenols or 2-iodoanilines with unsaturated substrates, such as terminal alkynes, 1,2- and 1,3- dienes, and allenes by the use of gaseous CO.<sup>4</sup>

2-Quinolones are widely distributed in nature and in many biologically important alkaloids, which showed remarkable activities, such as anticancer,<sup>5</sup> antitumor, and antihypertensive properties.<sup>6</sup> In addition, they are useful intermediates in organic synthesis.<sup>7</sup> Conventional methods for the synthesis of 2-quinolones are usually based on the Friedländer synthesis via Schiff base condensation<sup>8</sup> and the Knorr synthesis through acid-catalyzed cyclization of  $\beta$ -ketoanilides.<sup>9</sup> Re-

cently, Kadnikov and Larock reported an elegant approach to 2-quinolones, which was based on palladium-catalyzed carbonylative annulation of terminal or internal alkynes with 2-iodoanilines.<sup>10</sup> However, relatively long reaction time and an additive (e.g., *n*-Bu<sub>4</sub>NCl) are usually required. Moreover, the amino group of 2-iodoanilines has to be protected in the reaction process. Therefore, the development of more rapid and flexible strategy for the synthesis of 2-quinolones is still highly desirable.

Microwave activation as a potential energy source has proven to be a very popular and useful technology in synthetic organic chemistry, especially in the synthesis of heterocyclic compounds.<sup>11</sup> Compared to the traditional heating, the microwave-accelerated reaction has the major advantages of shorter reaction times, cleaner product profiles, and minimal quantities of solvent. As part of our ongoing endeavors on carbo- and hetero-cycle-oriented organometallic catalysis,<sup>12</sup> we recently reported a rapid synthesis of chromen-2-one by microwave-accelerated, palladium-catalyzed carbonylative cyclization of 2-iodophenol with alkynes.<sup>13</sup> This method features the use of commercially available molybdenum hexacarbonyl as a convenient and solid carbon monoxide source.<sup>14</sup> Herein, we extend this carbonylative cyclization strategy as a practical and convenient synthesis

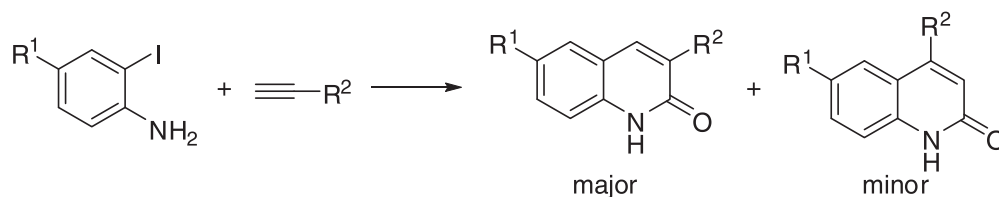
Received 6 August 2009. Accepted 26 November 2009. Published on the NRC Research Press Web site at canjchem.nrc.ca on 8 March 2010.

**J.-R. Chen, J. Liao, and W. Xiao.**<sup>1</sup> The Key Laboratory of Pesticide and Chemical Biology, Ministry of Education, College of Chemistry, Central China Normal University, 152 Luoyu Road, Wuhan, Hubei 430079, China.

<sup>1</sup>Corresponding author (e-mail: wxiao@mail.ccnu.edu.cn).



Scheme 1.



of 3- and 4-substituted 2-quinolones from 2-iodoanilines and terminal alkynes (Scheme 1).

## Results and discussion

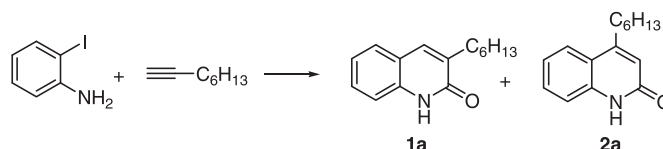
The reaction conditions previously used for the carbonylative cyclization reactions of 2-iodophenol with alkynes<sup>13a</sup> were initially applied to the reaction of 2-iodoaniline with 1-octyne (Table 1, entry 1). To our delight, the desired 2-quinolone was obtained in a 59% yield as a mixture of two regioisomers. The structure of 2-quinolone (**1a**) was proposed by NMR and unambiguously confirmed by X-ray crystallographic analysis (Figure 1) (see Supplementary data). Fortunately, these two isomers can easily be separated by flash column chromatography. To optimize the reaction conditions, the effects of the bases, catalysts, ligands, and solvents on the model reaction were further examined.

As can be seen from the results summarized in Table 1, both organic and inorganic bases were effective in this reaction. Among the organic bases screened, trialkylamine gave better results than secondary alkyl amines did (Table 1, entries 2 and 4 vs. entry 3). The use of unhindered pyridines or DMAP as the base resulted in decreased yields but with better regioselectivity (Table 1, entries 5 and 7). A similar effect was also observed in the case of DBU (Table 1, entry 6). The employment of inorganic bases led to low yields and moderate regioselectivity for this reaction. As a result, Et<sub>3</sub>N proved to be the best base, and the desired products were obtained in overall 60% yield with 3.5:1 regioselective ratio. Thereafter, different palladium catalysts, ligands, and solvents were also carefully examined to further improve the yields and regioselectivity with Et<sub>3</sub>N as the base.

Among the three palladium-PPh<sub>3</sub> systems examined, Pd(OAc)<sub>2</sub> exhibited good catalytic activity (Table 2, entry 2). Thus, other common phosphine ligands, such as DPPB, DPPP, DPPE, and DPPF were then examined. It was found that DPPE was the best choice in terms of regioselectivity and yield (**1a:2a** = 4:1, 60%) (Table 2, entry 6). The profile of solvent via reaction efficiency revealed that the reaction in THF gave higher yield and regioselectivity than in other solvents (Table 2, entries 8–12). Thus, the optimized reaction conditions for the microwave-accelerated carbonylative cyclization of 2-iodoaniline and alkynes with Mo(CO)<sub>6</sub> as the CO source have been determined to be 1 mmol of 2-iodoaniline, 2 equiv. of alkyne, 0.5 equiv. of Mo(CO)<sub>6</sub>, 5 mol% Pd(OAc)<sub>2</sub>, and 20 mol% DPPE in the presence of 2 equiv. of Et<sub>3</sub>N in 1 mL of THF under microwave irradiation at 160 °C for 30 min (**1a:2a** = 3.9:1, 62% yield) (Table 2, entry 8).

With the standard conditions in hand, we next investigated the scope and limitation of this process. A series of alkyl/aryl alkynes and differently substituted 2-iodoanilines were subjected to the optimized conditions. Generally, the carbon-

**Table 1.** Effects of the base on the carbonylative annulations of 2-iodoaniline with 1-octyne.



Entry	Base	Yield (%) <sup>a</sup>	Ratio of <b>1a:2a</b> <sup>b</sup>
1 <sup>c</sup>	DMAP–DIPEA	59	1.2:1
2	Et <sub>3</sub> N	60	3.5:1
3	Et <sub>2</sub> NH	38	3:1
4	DIPEA	62	1.5:1
5	Pyridine	39	3:1
6	DBU	23	3.5:1
7	DMAP	28	>10:1
8	Imidazole	35	4:1
9	K <sub>2</sub> CO <sub>3</sub>	44	4.6:1
10	Cs <sub>2</sub> CO <sub>3</sub>	29	1.5:1

**Note:** Representative experimental procedure: 2-iodoaniline (1 mmol), 1-octyne (2 mmol), base (2 mmol), Pd(OAc)<sub>2</sub> (5 mol%, 0.05 mmol), PPh<sub>3</sub> (20 mol%, 0.2 mmol), and Mo(CO)<sub>6</sub> (0.5 mmol); carried in THF (1 mL) under microwave irradiation at 60 °C for 10 min and then at 160 °C for 30 min.

<sup>a</sup>Isolated yield.

<sup>b</sup>The ratios were determined by GC.

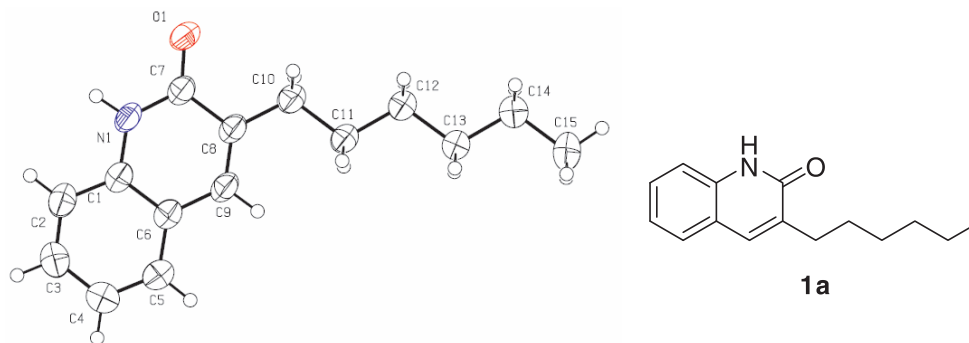
<sup>c</sup>DMAP (1 mmol) and DIPEA (1 mmol) were used.

ylative cyclization proceeded smoothly with good yields. For example, 1-octyne, 1-heptyne, and 1-hexyne were suitable for this protocol (Table 2, entries 16 and 17), affording the 2-quinolones **1** and **2** in 60%, 69%, and 70% overall yields, respectively (Table 3, entries 1–3). Aryl-substituted alkynes can also be employed in this transformation. Importantly, only one regioisomer was isolated in these cases, although the yield was moderate (Table 3, entries 4, 6, 8, and 10–12). Structural variation in the iodoanilines component is also possible. For example, methyl, Cl, and Br can be introduced on the benzene ring at the C(4) position without significant loss in reaction yield or efficiency (Table 3, entries 5–12). As shown in Table 3 (entries 5, 6, and 9–15), we have successfully utilized halogenated 2-iodoaniline substrates in this reaction. Moreover, these products should be valuable for further chemical transformations.<sup>15</sup> Note that the reaction has some limitations. Neither internal alkynes or N-protected 2-iodoanilines can be used in this carbonylative annulation.

## Conclusions

In summary, we have established a rapid and efficient synthesis of 3- or 4-substituted 2-quinolones starting from readily available unprotected 2-iodoanilines and alkynes



**Fig. 1.** Crystal structure of **1a**.**Table 2.** Optimization of reaction conditions for the carbonylative annulations.

Entry	Catalyst	Ligand	Solvent	Yield (%) <sup>a</sup>	Ratio of <b>1a:2a</b> <sup>b</sup>
1	PdCl <sub>2</sub>	PPh <sub>3</sub>	Dioxane	58	2.5:1
2	Pd(OAc) <sub>2</sub>	PPh <sub>3</sub>	Dioxane	60	3.5:1
3	Pd(PPh <sub>3</sub> ) <sub>4</sub>	PPh <sub>3</sub>	Dioxane	54	2.2:1
4	Pd(OAc) <sub>2</sub>	DPPB	Dioxane	59	2.4:1
5	Pd(OAc) <sub>2</sub>	DPPP	Dioxane	49	3.0:1
6	Pd(OAc) <sub>2</sub>	DPPE	Dioxane	60	4.0:1
7	Pd(OAc) <sub>2</sub>	DPPF	Dioxane	17	1.1:1
8	Pd(OAc) <sub>2</sub>	DPPE	THF	62	3.9:1
9	Pd(OAc) <sub>2</sub>	DPPE	DMF	25	>10:1
10	Pd(OAc) <sub>2</sub>	DPPE	CH <sub>3</sub> CN	15	>10:1
11	Pd(OAc) <sub>2</sub>	DPPE	CH <sub>2</sub> Cl <sub>2</sub>	28	2.4:1
12	Pd(OAc) <sub>2</sub>	DPPE	ClCH <sub>2</sub> CH <sub>2</sub> Cl	ND <sup>c</sup>	ND <sup>c</sup>

**Note:** Representative experimental procedure: iodoaniline (1 mmol), alkyne (2 mmol), Et<sub>3</sub>N (2 mmol), palladium catalyst (5 mol%, 0.05 mmol), ligand (20 mol%, 0.2 mmol), and Mo(CO)<sub>6</sub> (0.5 mmol); carried out in solvent (1 mL) under microwave irradiation at 60 °C for 10 min and then at 160 °C for 30 min.

<sup>a</sup>Isolated yield.

<sup>b</sup>The ratios were determined by GC.

<sup>c</sup>ND: no products were detected.

under microwave-irradiation conditions. The current methodology is attractive because of the short reaction time, the operational simplicity, and the absence of toxic gaseous carbon monoxide.

## Experimental section

### General methods

Unless otherwise noted, materials were purchased from commercial suppliers and used without further purification. Solvents and liquid organic bases were freshly distilled according to the known procedures.<sup>16</sup> Column chromatography was performed using 200–300 mesh silica gel. All melting points are uncorrected. <sup>1</sup>H NMR spectra were recorded on Varian Mercury 400 (400 MHz) spectrometers. Chemical shifts are reported in ppm from TMS with the solvent resonance as the internal standard (CDCl<sub>3</sub>: δ 7.24, DMSO: δ 2.50). Data are reported as follows: chemical shift, multiplicity (singlet (s), doublet (d), triplet (t), quartet (q), broad (br), or multiplet (m)), coupling constants (Hz). <sup>13</sup>C NMR spectra were recorded on Varian Mercury 400 (100 MHz) with complete proton decoupling spectrophotometers (CDCl<sub>3</sub>: δ 77.7, DMSO: δ 39.5). Elemental analysis was performed on a Vario EL III elemental analysis instrument.

Compounds **1b**, **1c**, **1d**, **1f**, **1j**, **2a**, **2b**, and **2c** are known compounds; and the data of these compounds have been found to be identical with those reported.<sup>10a,17</sup>

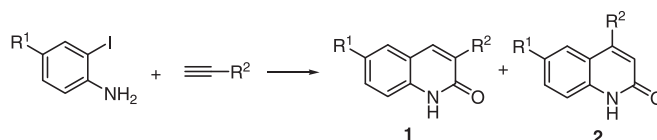
All experiments were performed in a Smith Synthesizer producing controlled irradiation at 2450 MHz with a power of 0–300 W.

### Representative procedure for the synthesis of 2-quinolones from unprotected 2-iodoanilines and terminal alkynes

To a 2.0–5.0 mL process vial were added 2-iodoaniline (1 mmol) and Pd(OAc)<sub>2</sub> (0.05 mmol), DPPE (0.2 mmol), Et<sub>3</sub>N (2 mmol), alkyne (2 mmol), Mo(CO)<sub>6</sub> (0.5 mmol), and anhydrous THF (1 mL). The vial was immediately capped with a Teflon septum under N<sub>2</sub> and irradiated with microwave at 60 °C for 10 min, then at 160 °C for another 30 min. After cooling to room temperature, the contents of the vessel were filtered through a short Celite pad, washed with acetone, and then concentrated under reduced pressure. The residue was purified by silica-gel chromatography to afford the desired products.

### 3-*n*-Hexyl-2-1*H*-quinoline (**1a**)

White solid (recrystallized from petroleum ether/acetone).

**Table 3.** Scope of the carbonylative annulations.

Entry	R <sup>1</sup>	R <sup>2</sup>	Product(s)	Yield (%) <sup>a</sup>	Ratio of 1:2 <sup>b</sup>
1	H	<i>n</i> -Hex	<b>1a</b> <b>2a</b>	60	3.9:1
2	H	<i>n</i> -Pen	<b>1b</b> <b>2b</b>	69	4.0:1
3	H	<i>n</i> -Bu	<b>1c</b> <b>2c</b>	70	6.7:1
4 <sup>c</sup>	H	Ph	<b>1d</b>	39	
5	Cl	<i>n</i> -Bu	<b>1e</b> <b>2e</b>	67	4.3:1
6 <sup>c</sup>	Cl	Ph	<b>1f</b>	29	
7	Me	<i>n</i> -Bu	<b>1g</b> <b>2g</b>	68	7.2:1
8 <sup>c</sup>	Me	Ph	<b>1h</b>	73	
9	Br	<i>n</i> -Bu	<b>1i</b> <b>2i</b>	66	10.7:1
10 <sup>c</sup>	Br	Ph	<b>1j</b>	29	
11 <sup>c</sup>	Br	4-MeC <sub>6</sub> H <sub>4</sub>	<b>1k</b>	46	
12 <sup>c</sup>	Br	3-FC <sub>6</sub> H <sub>4</sub>	<b>1l</b>	47	

**Note:** Representative experimental procedure: iodoaniline (1 mmol), alkyne (2 mmol), Et<sub>3</sub>N (2 mmol), Pd(OAc)<sub>2</sub> (5 mol%, 0.05 mmol), DPPE (10 mol%, 0.10 mmol), and Mo(CO)<sub>6</sub> (0.5 mmol); carried out in THF (1 mL) under microwave irradiation at 60 °C for 10 min and then at 160 °C for 30 min.

<sup>a</sup>Isolated yield.

<sup>b</sup>The ratios were determined by GC.

<sup>c</sup>Only the major isomers were detected.

Mp 113–116 °C. <sup>1</sup>H NMR (CDCl<sub>3</sub>, 400 MHz) δ: 11.04 (s, 1H), 7.60 (s, 1H), 7.44 (t, *J* = 7.6 Hz, 1H), 7.29 (t, *J* = 10.6 Hz, 1H), 7.19 (t, *J* = 7.6 Hz, 1H), 2.67 (t, *J* = 7.6 Hz, 2H), 1.69 (t, *J* = 7.6 Hz, 1H), 1.64 (s, 2H), 1.43 (s, 2H), 1.35 (m, 4H), 0.90 (t, *J* = 7.0 Hz, 3H). <sup>13</sup>C NMR (CDCl<sub>3</sub>, 100 MHz) δ: 164.5, 137.4, 136.5, 134.3, 129.2, 127.0, 122.3, 120.3, 115.6, 31.7, 30.2, 29.1, 28.3, 22.6, 14.1. MS *m/z*: 229 [M<sup>+</sup>]. Anal. calcd. for C<sub>15</sub>H<sub>19</sub>NO: C, 78.56; H, 8.35; N, 6.11. Found: C, 78.60; H, 8.30; N, 6.14.

#### 4-*n*-Hexyl-2-1*H*-quinoline (2a)

White solid (recrystallized from petroleum ether/acetone). Mp 155–157 °C. <sup>1</sup>H NMR (CDCl<sub>3</sub>, 400 MHz) δ: 12.33 (s, 1H), 7.73 (d, *J* = 8.0 Hz, 1H), 7.52–7.46 (m, 2H), 7.27–7.22 (m, 1H), 7.60 (s, 1H), 2.86 (t, *J* = 7.8 Hz, 2H), 1.83–1.69 (2H, m), 1.45 (t, *J* = 10.4 Hz, 2H), 1.83–1.69 (m, 2H), 1.36–1.33 (m, 4H), 0.95–0.88 (m, 3H). <sup>13</sup>C NMR (CDCl<sub>3</sub>, 100 MHz) δ: 164.7, 153.3, 138.7, 130.2, 124.0, 122.3, 119.8, 119.2, 116.9, 32.2, 31.5, 29.1, 28.7, 22.5, 14.0. MS *m/z*: 229 [M<sup>+</sup>]. Anal. calcd. for C<sub>15</sub>H<sub>19</sub>NO: C, 78.56; H, 8.35; N, 6.11. Found: C, 78.59; H, 8.34; N, 6.14.

#### 3-*n*-Pentyl-2-1*H*-quinoline (1b)

Brown solid (recrystallized from petroleum ether/acetone). Mp 133–136 °C. <sup>1</sup>H NMR (CDCl<sub>3</sub>, 400 MHz) δ: 11.83 (s, 1H), 7.62 (s, 1H), 7.53–7.18 (m, 4H), 2.69 (t, *J* = 7.6 Hz, 2H), 1.71 (t, *J* = 1.6 Hz, 2H), 1.43–1.40 (m, 4H), 0.93 (t, *J* = 7.0 Hz, 3H). <sup>13</sup>C NMR (CDCl<sub>3</sub>, 100 MHz) δ: 164.6, 137.4, 136.4, 134.2, 129.2, 126.9, 122.2, 120.3, 115.7, 31.6, 30.2, 28.0, 22.6, 14.0. MS *m/z*: 215 [M<sup>+</sup>]. Anal. calcd. for C<sub>14</sub>H<sub>17</sub>NO: C, 78.10; H, 7.96; N, 6.51. Found: C, 78.14; H, 7.92; N, 6.53.

#### 4-*n*-Pentyl-2-1*H*-quinoline (2b)

White solid (recrystallized from petroleum ether/acetone). Mp 142–145 °C. <sup>1</sup>H NMR (CDCl<sub>3</sub>, 600 MHz) δ: 12.75 (s, 1H), 7.71 (d, *J* = 8.0 Hz, 1H), 7.49 (d, *J* = 13.2 Hz, 2H), 7.25–7.21 (m, 1H), 6.59 (s, 1H), 2.84 (t, *J* = 7.6 Hz, 2H), 1.74–1.68 (2H, m), 1.50–1.44 (2H, m), 0.98 (t, *J* = 4.8 Hz, 3H). <sup>13</sup>C NMR (CDCl<sub>3</sub>, 100 MHz) δ: 164.6, 153.4, 138.5, 130.3, 124.1, 122.4, 119.8, 119.2, 116.8, 32.2, 31.6, 28.0, 22.5, 14.0. MS *m/z*: 215 [M<sup>+</sup>]. Anal. calcd. for C<sub>14</sub>H<sub>17</sub>NO: C, 78.10; H, 7.96; N, 6.51. Found: C, 78.13; H, 7.98; N, 6.50.

#### 3-*n*-Butyl-2-1*H*-quinoline (1c)

Brown solid (recrystallized from petroleum ether/acetone). Mp 151–154 °C. <sup>1</sup>H NMR (CDCl<sub>3</sub>, 400 MHz) δ: 12.20 (s, 1H), 7.62 (s, 1H), 7.53–7.40 (m, 2H), 7.21–7.17 (m, 1H), 2.70 (t, *J* = 7.4 Hz, 2H), 1.74–1.66 (m, 2H), 1.49–1.44 (m, 2H), 0.99 (t, 7.4 Hz, 3H). <sup>13</sup>C NMR (CDCl<sub>3</sub>, 100 MHz) δ: 164.6, 137.5, 136.4, 134.2, 126.9, 122.2, 120.3, 115.7, 30.5, 29.9, 22.5, 14.0. MS *m/z*: 201 [M<sup>+</sup>]. Anal. calcd. for C<sub>13</sub>H<sub>15</sub>NO: C, 77.58; H, 7.51; N, 6.96. Found: C, 77.60; H, 7.49; N, 6.99.

#### 4-*n*-Butyl-2-1*H*-quinoline (2c)

Brown solid (recrystallized from petroleum ether/acetone). Mp 112–115 °C. <sup>1</sup>H NMR (CDCl<sub>3</sub>, 400 MHz) δ: 12.77 (s, 1H), 7.72 (d, *J* = 5.2 Hz, 1H), 7.48 (d, *J* = 2.4 Hz, 2H), 7.24–7.21 (m, 1H), 6.60 (s, 1H), 2.85 (t, *J* = 5.2 Hz, 2H), 1.73–1.68 (m, 1H), 1.50–1.44 (m, 2H), 0.98 (t, *J* = 4.8 Hz, 3H). <sup>13</sup>C NMR (CDCl<sub>3</sub>, 100 MHz) δ: 164.6, 153.4, 138.5, 130.3, 124.1, 122.4, 119.8, 119.2, 116.9, 31.9, 30.9, 22.6, 14.0. MS *m/z*: 201 [M<sup>+</sup>]. Anal. calcd. for C<sub>13</sub>H<sub>15</sub>NO: C, 77.58; H, 7.51; N, 6.96.

C, 77.58; H, 7.51; N, 6.96. Found: C, 77.56; H, 7.53; N, 6.94.

### 3-*n*-Phenyl-2-1*H*-quinoline (1d)

White solid (recrystallized from petroleum ether/acetone). Mp 229–232 °C. <sup>1</sup>H NMR (DMSO, 400 MHz) δ: 11.98 (s, 1H), 8.11 (s, 1H), 7.78–7.73 (m, 3H), 7.51–7.20 (m, 6H). <sup>13</sup>C NMR (DMSO, 100 MHz) δ: 161.1, 138.4, 136.3, 131.6, 130.2, 128.7, 128.1, 128.0, 121.9, 119.6, 114.7. MS *m/z*: 221 [M<sup>+</sup>]. Anal. calcd. for C<sub>15</sub>H<sub>11</sub>NO: C, 81.43; H, 5.01; N, 6.33. Found: C, 81.46; H, 5.04; N, 6.30.

### 3-*n*-Butyl-6-chloro-2-1*H*-quinoline (1e)

White solid (recrystallized from petroleum ether/acetone). Mp 169–172 °C. <sup>1</sup>H NMR (CDCl<sub>3</sub>, 400 MHz) δ: 12.76 (s, 1H), 7.48 (d, *J* = 12.8 Hz, 2H), 7.39 (d, *J* = 8.8 Hz, 2H), 2.67 (t, *J* = 3.6 Hz, 2H), 1.69–1.63 (m, 2H), 1.50–1.40 (m, 2H), 0.98 (t, *J* = 7.2 Hz, 3H). <sup>13</sup>C NMR (CDCl<sub>3</sub>, 100 MHz) δ: 164.4, 135.9, 135.5, 135.2, 129.4, 127.5, 126.0, 121.2, 117.2, 30.4, 29.9, 22.5, 14.0. MS *m/z*: 238 [M<sup>+</sup>]. Anal. calcd. for C<sub>13</sub>H<sub>14</sub>ClNO: C, 66.24; H, 5.99; N, 5.94. Found: C, 66.26; H, 5.96; N, 5.92.

### 4-*n*-Butyl-6-chloro-2-1*H*-quinoline (2e)

White solid (recrystallized from petroleum ether/acetone). Mp 163–165 °C. <sup>1</sup>H NMR (DMSO, 400 MHz) δ: 11.75 (s, 1H), 7.76 (d, *J* = 2.0 Hz, 1H), 7.53 (1H, dd, *J* = 2.0, 2.0 Hz), 7.33 (d, *J* = 8.8 Hz, 1H), 6.60 (s, 1H), 2.79 (t, *J* = 7.6 Hz, 2H), 1.58 (t, *J* = 7.6 Hz, 2H), 1.42–1.37 (m, 2H), 0.93 (t, *J* = 7.2 Hz, 3H). <sup>13</sup>C NMR (DMSO, 100 MHz) δ: 161.4, 150.8, 137.6, 130.0, 125.8, 123.6, 120.9, 120.0, 117.5, 30.7, 30.4, 21.9, 13.7. MS *m/z*: 238 [M<sup>+</sup>]. Anal. calcd. for C<sub>13</sub>H<sub>14</sub>ClNO: C, 66.24; H, 5.99; N, 5.94. Found: C, 66.27; H, 5.97; N, 5.95.

### 3-Phenyl-6-chloro-2-2*H*-quinoline (1f)

Brown solid (recrystallized from petroleum ether/acetone). Mp 244–247 °C. <sup>1</sup>H NMR (DMSO, 400 MHz) δ: 12.11 (s, 1H), 8.09 (s, 1H), 7.84 (d, *J* = 2.4 Hz, 1H), 7.76 (t, *J* = 4.2 Hz, 1H), 7.56–7.34 (m, 5H). <sup>13</sup>C NMR (DMSO, 100 MHz) δ: 162.8, 137.3, 136.3, 135.6, 133.7, 130.5, 128.9, 128.4, 127.9, 127.0, 121.2, 116.9. MS *m/z*: 256 [M<sup>+</sup>]. Anal. calcd. for C<sub>15</sub>H<sub>10</sub>ClNO: C, 70.46; H, 3.94; N, 5.48. Found: C, 70.48; H, 3.96; N, 5.45.

### 3-Butyl-6-methyl-2-2*H*-quinoline (1g)

White solid (recrystallized from petroleum ether/acetone). Mp 144–147 °C. <sup>1</sup>H NMR (CDCl<sub>3</sub>, 400 MHz) δ: 11.67 (brs, 1H), 7.54 (s, 1H), 7.27 (m, 3H), 2.68 (t, *J* = 7.8 Hz, 2H), 2.43–2.38 (m, 3H), 1.72–1.65 (m, 2H), 1.50–1.41 (m, 2H), 1.02–0.96 (m, 3H). <sup>13</sup>C NMR (CDCl<sub>3</sub>, 100 MHz) δ: 164.4, 136.2, 135.4, 134.0, 131.7, 130.5, 126.5, 120.2, 115.6, 30.5, 29.9, 22.5, 20.9, 14.0. MS *m/z*: 215 [M<sup>+</sup>]. Anal. calcd. for C<sub>14</sub>H<sub>17</sub>NO: C, 78.10; H, 7.96; N, 6.51. Found: C, 78.14; H, 7.97; N, 6.49.

### 4-Butyl-6-methyl-2-1*H*-quinoline (2g)

Yellow solid (recrystallized from petroleum ether/acetone). Mp 171–174 °C. <sup>1</sup>H NMR (CDCl<sub>3</sub>, 400 MHz) δ: 12.52 (s, 1H), 7.56–7.49 (m, 1H), 7.38–7.26 (m, 2H), 7.24–7.21 (m, 1H), 6.59 (d, *J* = 9.6 Hz, 1H), 2.85 (t, *J* = 7.6 Hz,

2H), 2.47–2.42 (t, *J* = 10.0 Hz, 3H), 1.77–1.70 (m, 2H), 1.68–1.43 (m, 2H), 1.03–0.94 (m, 3H). <sup>13</sup>C NMR (CDCl<sub>3</sub>, 100 MHz) δ: 164.5, 153.0, 136.5, 131.8, 131.6, 123.6, 119.7, 119.1, 116.8, 31.8, 30.8, 22.5, 21.2, 13.9. MS *m/z*: 215 [M<sup>+</sup>]. Anal. calcd. for C<sub>14</sub>H<sub>17</sub>NO: C, 78.10; H, 7.96; N, 6.51. Found: C, 78.14; H, 7.97; N, 6.48.

### 3-Phenyl-6-methyl-2-1*H*-quinoline (1h)

White solid (recrystallized from petroleum ether/acetone). Mp 220–223 °C. <sup>1</sup>H NMR (DMSO, 400 MHz) δ: 11.90 (s, 1H), 8.02 (t, *J* = 10.0 Hz, 1H), 7.78–7.72 (m, 2H), 7.53 (d, *J* = 10.0 Hz, 1H), 7.46–7.22 (m, 5H), 2.36 (t, *J* = 9.8 Hz, 3H). <sup>13</sup>C NMR (DMSO, 100 MHz) δ: 161.0, 137.4, 136.4, 131.5, 130.9, 128.8, 128.0, 127.8, 127.6, 119.6, 114.7, 20.5. MS *m/z*: 235 [M<sup>+</sup>]. Anal. calcd. for C<sub>16</sub>H<sub>13</sub>NO: C, 81.68; H, 5.57; N, 5.95. Found: C, 81.70; H, 5.60; N, 5.92.

### 3-Butyl-6-bromo-2-1*H*-quinoline (1i)

White solid (recrystallized from petroleum ether/acetone). Mp 172–174 °C. <sup>1</sup>H NMR (DMSO, 400 MHz) δ: 12.36 (s, 1H), 7.65 (d, *J* = 2.4 Hz, 1H), 7.53 (d, *J* = 4.6 Hz, 2H), 7.28 (t, *J* = 8.2 Hz, 1H), 2.68 (t, *J* = 7.8 Hz, 2H), 1.71–1.63 (m, 2H), 1.48–1.42 (m, 2H), 0.98 (t, *J* = 7.2 Hz, 3H). <sup>13</sup>C NMR (DMSO, 100 MHz) δ: 164.3, 136.2, 135.6, 135.2, 132.0, 129.2, 121.7, 117.4, 114.9, 30.4, 29.9, 22.5, 14.0. MS *m/z*: 281 [M<sup>+</sup>]. Anal. calcd. for C<sub>13</sub>H<sub>14</sub>BrNO: C, 55.73; H, 5.04; N, 5.00. Found: C, 55.70; H, 5.08; N, 5.02.

### 4-Butyl-6-bromo-2-1*H*-quinoline (2i)

White solid (recrystallized from petroleum ether/acetone). Mp 181–184 °C. <sup>1</sup>H NMR (DMSO, 400 MHz) δ: 11.78 (1s, H), 7.89 (s, 1H), 7.66 (t, *J* = 4.4 Hz, 1H), 7.28 (d, *J* = 8.8 Hz, 1H), 6.4 (s, 1H), 2.79 (t, *J* = 7.4 Hz, 2H), 1.61–1.54 (m, 2H), 1.43–1.36 (m, 2H), 0.93 (t, *J* = 7.4 Hz). <sup>13</sup>C NMR (DMSO, 100 MHz) δ: 164.3, 136.2, 135.6, 135.2, 132.0, 129.2, 121.7, 117.4, 114.9, 30.4, 29.9, 22.5, 14.0. MS *m/z*: 281 [M<sup>+</sup>]. Anal. calcd. for C<sub>13</sub>H<sub>14</sub>BrNO: C, 55.73; H, 5.04; N, 5.00. Found: C, 55.70; H, 5.06; N, 5.01.

### 3-Phenyl-6-bromo-2-1*H*-quinoline (1j)

White solid (recrystallized from petroleum ether/acetone). Mp 256–259 °C. <sup>1</sup>H NMR (DMSO, 400 MHz) δ: 12.10 (s, 1H), 7.98 (d, *J* = 2.0 Hz, 1H), 7.74 (d, *J* = 7.2 Hz, 1H), 7.66 (dd, *J* = 2.0, 1.6 Hz, 1H), 7.47–7.40 (m, 3H), 7.28 (d, *J* = 8.8 Hz, 1H). <sup>13</sup>C NMR (DMSO, 100 MHz) δ: 160.8, 137.4, 136.4, 135.9, 132.7, 130.0, 128.7, 128.1, 128.0, 121.3, 116.8, 113.4. MS *m/z*: 300 [M<sup>+</sup>]. Anal. calcd. for C<sub>15</sub>H<sub>10</sub>BrNO: C, 60.02; H, 3.36; N, 4.67. Found: C, 60.04; H, 3.38; N, 4.65.

### 3-(*p*-Tolyl)-6-bromo-2-1*H*-quinoline (1k)

Yellow solid (recrystallized from petroleum ether/acetone). Mp 255–257 °C. <sup>1</sup>H NMR (DMSO, 400 MHz) δ: 12.07 (s, 1H), 8.06 (s, 1H), 7.96 (d, *J* = 2.4 Hz, 1H), 7.64 (dd, *J* = 8.0, 1.6 Hz, 3H), 7.29–7.24 (m, 3H), 2.23 (m, 3H). <sup>13</sup>C NMR (DMSO, 100 MHz) δ: 160.9, 137.5, 137.2, 135.8, 133.0, 132.3, 129.9, 128.7, 128.5, 121.4, 116.9, 116.7, 113.4, 21.0. MS *m/z*: 314 [M<sup>+</sup>]. Anal. calcd. for C<sub>16</sub>H<sub>12</sub>BrNO: C, 61.17; H, 3.85; N, 4.46. Found: C, 61.20; H, 3.83; N, 4.49.

### 3-(3-Fluorophenyl)-6-bromo-2-1H-quinoline (11)

White solid (recrystallized from petroleum ether/acetone). Mp 279–282 °C. <sup>1</sup>H NMR (DMSO, 400 MHz) δ: 12.16 (s, 1H), 8.19 (s, 1H), 7.98 (d, *J* = 1.6 Hz, 1H), 7.69–7.59 (m, 3H), 7.52–7.47 (m, 1H), 7.30–7.22 (m, 1H). <sup>13</sup>C NMR (DMSO, 100 MHz) δ: 163.0, 160.6, 138.1, 137.5, 133.0, 131.0, 130.0, 124.7, 121.1, 117.0, 115.6, 115.0, 113.5. MS *m/z*: 318 [M<sup>+</sup>]. Anal. calcd. for C<sub>15</sub>H<sub>9</sub>BrFNO: C, 56.63; H, 2.85; N, 4.40. Found: C, 56.67; H, 2.83; N, 4.43.

### Supplementary data

Supplementary data for this article are available on the journal Web site (canjchem.nrc.ca) or may be purchased from the Depository of Unpublished Data, Document Delivery, CISTI, National Research Council Canada, Ottawa, ON K1A 0R6, Canada. DUD 5355. For more information on obtaining material, refer to cisti-icist.nrc-cnrc.gc.ca/cms/unpub\_e.shtml.

### Acknowledgement

We are grateful to the Program for Academic Leader in Wuhan Municipality (200851430486) and the National Science Foundation of China (20672040 and 20872043) for support of this research.

### References

- (1) (a) Colquhoun, H. M.; Thompson, D. J.; Twigg, M. V. In *Carbonylation: Direct Synthesis of Carbonyl Compounds*; Plenum Press: New York, 1991; (b) Falbe, J. In *New Synthesis with Carbon Monoxide*; Springer: New York, 1980; (c) Khumtaveeporn, K.; Alper, H. *Acc. Chem. Res.* **1995**, 28 (10), 414. doi:10.1021/ar00058a003.; (d) El Ali, B.; Alper, H. In *Transition Metals for Organic Synthesis: Building Blocks and Fine Chemicals*; Beller, M., Bolm, C., Eds.; Wiley-VCH: New York, 1998; Vol. 1, p. 49; (e) Stille, J. K. In *Comprehensive Organic Synthesis*; Trost, B. M., Fleming, L., Eds.; Pergamon Press: New York, 1991; Vol. 4, p. 913.
- (2) (a) For reviews, see: El Ali, B.; Alper, H. In *Transition-Metal-Catalyzed reactions*; Murahashi, S.I., Davies, S.G., Eds.; Blackwell Science: Malden, Mass, 1999. p. 261; (b) Larock, R. C. *J. Organomet. Chem.* **1999**, 576 (1-2), 111. doi:10.1016/S0022-328X(98)01053-5.; (c) Tsuji, J. *Palladium Reagents and Catalysts*; Wiley: New York, 1995; (d) Khumtaveeporn, K.; Alper, H. *Acc. Chem. Res.* **1995**, 28 (10), 414. doi:10.1021/ar00058a003.
- (3) Tsuji, J. *Palladium Reagents and Catalysts; Innovations in Organic Synthesis*; John Wiley & Sons, Ltd.: Chichester, U.K., 1995.
- (4) (a) Moinet, C.; Fiaud, J. C. *Synlett* **1997**, 1997 (1), 97. doi:10.1055/s-1997-687.; (b) Grigg, R.; Khalil, H.; Levett, P.; Virica, J.; Sridharan, V. *Tetrahedron Lett.* **1994**, 35 (19), 3197. doi:10.1016/S0040-4039(00)76866-3.; (c) An, Z.-W.; Catellani, M.; Chiusoli, G. P. *J. Organomet. Chem.* **1989**, 371 (3), C51. doi:10.1016/0022-328X(89)85241-6.; (d) An, Z.-W.; Catellani, M.; Chiusoli, G. P. *Gazz. Chim. Ital.* **1990**, 120, 383; (e) Okuro, K.; Alper, H. *J. Org. Chem.* **1997**, 62 (6), 1566. doi:10.1021/jo962283c.; (f) Grigg, R.; Liu, A.; Shaw, D.; Suganthan, S.; Woodall, D.-E.; Yoganathan, G. *Tetrahedron Lett.* **2000**, 41 (36), 7125. doi:10.1016/S0040-4039(00)01176-X.
- (5) Ferrer, P.; Avendaño, C.; Söllhuber, M. *Liebigs Ann.* **1995**, 1995 (10), 1895. doi:10.1002/jlac.1995199510266.
- (6) Afonso, A.; Weinstein, J.; Gentles, M. J. (Schering Corp.). PCT Int. Appl. WO 9,203,327, 1992.
- (7) (a) Anzini, M.; Cappelli, A.; Vomero, S. *J. Heterocycl. Chem.* **1991**, 28 (7), 1809. doi:10.1002/jhet.5570280727.; (b) Godard, A.; Fourquez, J. M.; Tamion, R.; Marsais, F.; Quéguiner, G. *Synlett* **1994**, 1994 (04), 235. doi:10.1055/s-1994-22807.
- (8) (a) *Quinolines*; Jones, G., Ed.; John Wiley & Sons: London–New York–Sydney–Toronto, 1977; p. 181; (b) *Quinolines*; Jones, G., Ed.; John Wiley & Sons: London–New York–Sydney–Toronto, 1977; p. 191.
- (9) *Quinolines*; Jones, G., Ed.; John Wiley & Sons: London–New York–Sydney–Toronto, 1977; p. 151.
- (10) (a) Kadnikov, D. V.; Larock, R. C. *J. Organomet. Chem.* **2003**, 687 (2), 425. doi:10.1016/S0022-328X(03)00786-1.; (b) Kadnikov, D. V.; Larock, R. C. *J. Org. Chem.* **2004**, 69 (20), 6772. doi:10.1021/jo049149+. PMID:15387602.
- (11) (a) Lew, A.; Krutzik, P. O.; Hart, M. E.; Chamberlin, A. R. *J. Chem. Res.* **2002**, 4, 95; (b) Lidström, P.; Tierney, J.; Wathey, B.; Westman, J. *Tetrahedron* **2001**, 57 (45), 9225. doi:10.1016/S0040-4020(01)00906-1.; (c) Perreux, L.; Loupy, A. *Tetrahedron* **2001**, 57 (45), 9199. doi:10.1016/S0040-4020(01)00905-X.; (d) Mavandadi, F.; Lidström, P. *Curr. Top. Med. Chem.* **2004**, 4 (7), 773. doi:10.2174/1568026043451078. PMID:15032686.
- (12) (a) Yang, Q.; Alper, H.; Xiao, W.-J. *Org. Lett.* **2007**, 9 (5), 769. doi:10.1021/ol062959i. PMID:17279763.; (b) Yang, Q.; Xiao, W.-J.; Yu, Z.-K. *Org. Lett.* **2005**, 7 (5), 871. doi:10.1021/ol047356q. PMID:15727462.; (c) Yang, Q.; Li, X.-Y.; Wu, H.; Xiao, W.-J. *Tetrahedron Lett.* **2006**, 47 (23), 3893. doi:10.1016/j.tetlet.2006.03.164.; (d) Chen, J.-R.; Li, C.-F.; An, X.-L.; Zhang, J.-J.; Zhu, X.-Y.; Xiao, W.-J. *Angew. Chem. Int. Ed.* **2008**, 47 (13), 2489. doi:10.1002/anie.200705194.
- (13) (a) Cao, H.; Xiao, W.-J. *Can. J. Chem.* **2005**, 83 (6-7), 826. doi:10.1139/v05-094.; (b) For our other related palladium-catalyzed reactions, see: Xiao, W.-J.; Alper, H. *J. Org. Chem.* **1997**, 62 (11), 3422. doi:10.1021/jo970126n.; (c) Xiao, W.-J.; Vasapollo, G.; Alper, H. *J. Org. Chem.* **1998**, 63 (8), 2609. doi:10.1021/jo972121w. PMID:11672126.; (d) Xiao, W.-J.; Alper, H. *J. Org. Chem.* **1998**, 63 (22), 7939. doi:10.1021/jo9812328.; (e) Xiao, W.-J.; Vasapollo, G.; Alper, H. *J. Org. Chem.* **1999**, 64 (6), 2080. doi:10.1021/jo9824246. PMID:11674303.; (f) Xiao, W.-J.; Alper, H. *J. Org. Chem.* **1999**, 64 (26), 9646. doi:10.1021/jo9913098.; (g) Xiao, W.-J.; Vasapollo, G.; Alper, H. *J. Org. Chem.* **2000**, 65 (13), 4138. doi:10.1021/jo000231o. PMID:10866632.; (h) Xiao, W.-J.; Alper, H. *J. Org. Chem.* **2001**, 66 (19), 6229. doi:10.1021/jo0103773. PMID:11559167.; (i) Xiao, W.-J.; Alper, H. *J. Org. Chem.* **2005**, 70 (5), 1802. doi:10.1021/jo047938l. PMID:15730305.; (j) Cao, H.; Xiao, W.-J.; Alper, H. *Adv. Synth. Catal.* **2006**, 348 (14), 1807. doi:10.1002/adsc.200606213.; (k) Cao, Y.-J.; Lai, Y.-Y.; Cao, H.; Xing, X.-N.; Wang, X.; Xiao, W.-J. *Can. J. Chem.* **2006**, 84 (11), 1529. doi:10.1139/V06-151.
- (14) (a) Kaiser, N.-F. K.; Hallberg, A.; Larhed, M. *J. Comb. Chem.* **2002**, 4 (2), 109. doi:10.1021/cc010085f. PMID:11886283.; (b) Georgsson, J.; Hallberg, A.; Larhed, M. *J. Comb. Chem.* **2003**, 5 (4), 350. doi:10.1021/cc0201086. PMID:12857100.; (c) Wannberg, J.; Larhed, M. *J. Org. Chem.* **2003**, 68 (14), 5750. doi:10.1021/jo034382d. PMID:12839476.; (d) Yamazaki, K.; Kondo, Y. *J. Comb. Chem.* **2004**, 6 (1), 121. doi:10.1021/cc034029l. PMID:14714995.
- (15) (a) Ma, J.-A.; Cahard, D. *Chem. Rev.* **2004**, 104 (12), 6119.



- doi:10.1021/cr030143e. PMID:15584697.; (b) Littke, A. F.; Fu, G. C. *Angew. Chem. Int. Ed. Engl.* **1999**, 38 (16), 2411. doi:10.1002/(SICI)1521-3773(19990816)38:16<2411::AID-ANIE2411>3.0.CO;2-T. PMID:10458805.; (c) Hartwig, J. F. *Acc. Chem. Res.* **1998**, 31 (12), 852. doi:10.1021/ar970282g.
- (16) Armarego, W. L. F.; Perrin, D. D. *Purifications of Laboratory Chemicals*; Butterworth-Heinemann: Oxford, 1997.
- (17) (a) Park, K. K.; Jung J. Y. *Heterocycles* **2005**, 65, 2095; (b) Li H. -B.; Yang H.; Petersen J. L.; Wang K. K. *J. Org. Chem.* **2004**, 69, 4500 doi:10.1021/ar970282g.; (a) Reisch, J. *Angew. Chem.* **1963**, 75, 1203 doi:10.1021/cc034029l. PMID:14714995.; (b) Wolfe J. F.; Trimitsis G. B.; Morris D. R. *J. Org. Chem.* **1969**, 34, 3263. doi:10.1021/jo01263a009.

# AGOA hydration clusters produce the solvation effect on the aziridine...hydrofluoric acid complex — A modern proposal

Boaz G. Oliveira, Regiane C.M.U. Araújo, Antônio B. Carvalho, and Mozart N. Ramos

**Abstract:** The AGOA methodology was used to describe the hydration clusters of the  $C_2H_5N\cdots HF$  heterocyclic hydrogen-bonded complex. Using the TIP4P water-geometry model, the hydration clusters were generated by analyzing the finite gradients of the molecular electrostatic potential (MEP) of the solute ( $C_2H_5N\cdots HF$ ). The results obtained revealed high hydration energies ( $\Delta E^{HC-CORR}$ ) in the positive MEP field, indicating that the water molecules prefer to attack the methyl groups of the aziridine ring upon the formation of the  $C_2H_5N\cdots HF$  hydrogen-bonded complex. Although they are in accordance with the experimental behavior of the aziridine acid-catalyzed open-ring reaction, the theoretical results obtained here provide a new perspective on studies of the solvation effect because the AGOA protocol requires little computational effort to create the hydration-cluster structures.

**Key words:** hydrogen complexes, aziridine, AGOA, clusters, solvation.

**Résumé :** Afin de décrire les agrégats d'hydratation de complexes hétérocycliques  $C_2H_5N\cdots HF$  comportant une liaison hydrogène, on a fait appel à une méthode de calcul théorique dénommée, « AGOA », terme portugais signifiant à l'eau. Utilisant le modèle TIP4P pour la géométrie de l'eau, on a généré des agrégats d'hydratation en faisant une analyse des gradients finis du potentiel électrostatique moléculaire (PEM) du soluté ( $C_2H_5N\cdots HF$ ). Les résultats obtenus mettent en évidence la présence d'énergies d'hydratation élevées ( $\Delta E^{HC-CORR}$ ) dans le champ positif du PEM, ce qui indique que les molécules d'eau préfèrent s'attaquer aux groupements méthyles du noyau aziridine lors de la formation du complexe  $C_2H_5N\cdots HF$  comportant une liaison hydrogène. Même s'ils sont en accord avec le comportement expérimental de la réaction d'ouverture de l'aziridine catalysée par un acide, les résultats théoriques obtenus ici fournissent une nouvelle perspective pour les études d'effet de solvation puisque le protocole « AGOA » ne requiert que de faibles efforts de calculs pour générer les structures des agrégats d'hydratation.

**Mots-clés :** complexes d'hydrogène, aziridine, « AGOA », agrégats, solvation.

[Traduit par la Rédaction]

## Introduction

There can be no doubt that heterocyclic compounds are molecular structures that have properties essential to life,<sup>1</sup> and they are important sources of research into new pharmacological drugs,<sup>2</sup> the development of polymerization processes,<sup>3</sup> and the formation of amorphous metallic structures.<sup>4</sup> In the case of small rings,<sup>5,6</sup> in particular aziridine ( $C_2H_5N$ ), the capacity for reaction with nucleophiles in a basic or acid medium is well-known among organic chemists.<sup>7–10</sup> One example of this is the Wenker synthesis mechanism.<sup>11,12</sup> In short, the catalyzed open-ring reaction in acid medium occurs by a nucleophilic attack on the carbons of the aziridine ring,<sup>13</sup> as demonstrated in Fig. 1.

Using physicochemical studies, it has been demonstrated that acid species cause an acceleration in the reaction.<sup>14</sup> In this situation, the protonation of the aziridine ring weakens

its (C–N) adjacent bonds, inducing a rupture of the ring undergoing an  $S_N2$  mechanism, in which the aziridine cation (**2**) is the subsequent intermediate in the formation of the  $C_2H_5N\cdots HF$  hydrogen-bonded complex (**1**). According to this conjecture, the study of the solvent effect seems to be the key to better understanding of this reaction mechanism.

Over the years, the study of the solvent effect on the aziridine ring has been successfully developed by applying traditional methodologies.<sup>14</sup> In a recent proposal drawn up by Fang and co-workers,<sup>15</sup> interesting parameters relating to the solvent effect on aziridine in the acid-catalyzed open-ring reactions were obtained using SCRF continuum calculations. However, it is very important that a detailed description of the solvent effect be performed. This would involve explicit description of the action of the solvent molecules on the aziridine ring, which would seem to be essential to the

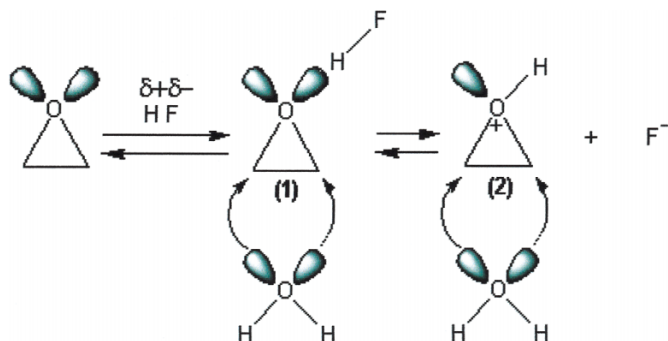
Received 6 May 2009. Accepted 4 November 2009. Published on the NRC Research Press Web site at [canjchem.nrc.ca](http://canjchem.nrc.ca) on 8 March 2010.

**B.G. Oliveira,<sup>1</sup> R.C.M.U. Araújo, and A.B. Carvalho.** Departamento de Química, Universidade Federal da Paraíba, 58059-900 João Pessoa, PB, Brazil.

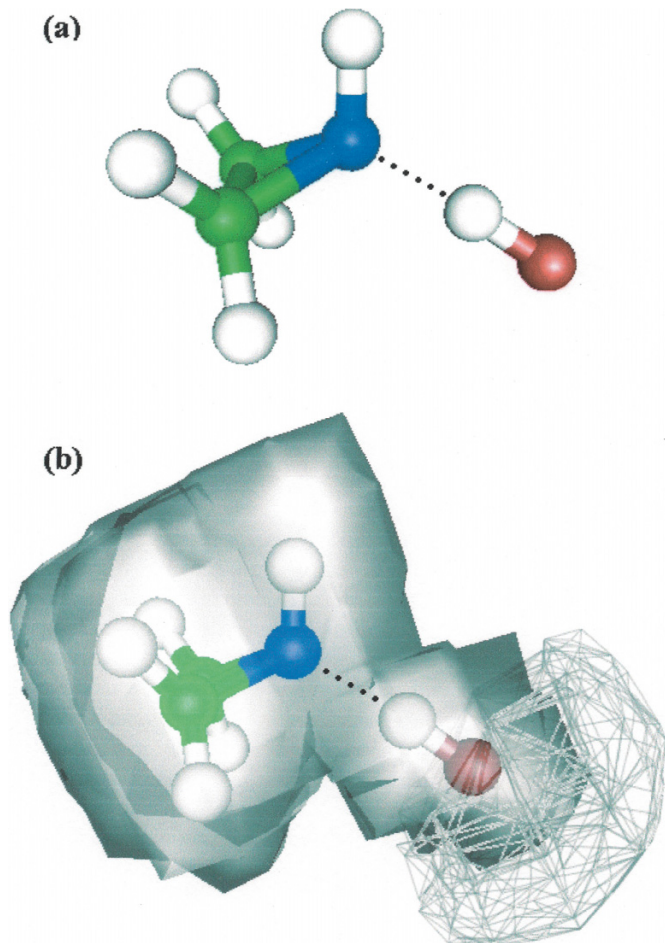
**M.N. Ramos.** Departamento de Química Fundamental, Universidade Federal de Pernambuco, 50739-901 Recife, PE, Brazil.

<sup>1</sup>Corresponding author (e-mail: [boazgaldino@gmail.com](mailto:boazgaldino@gmail.com)).

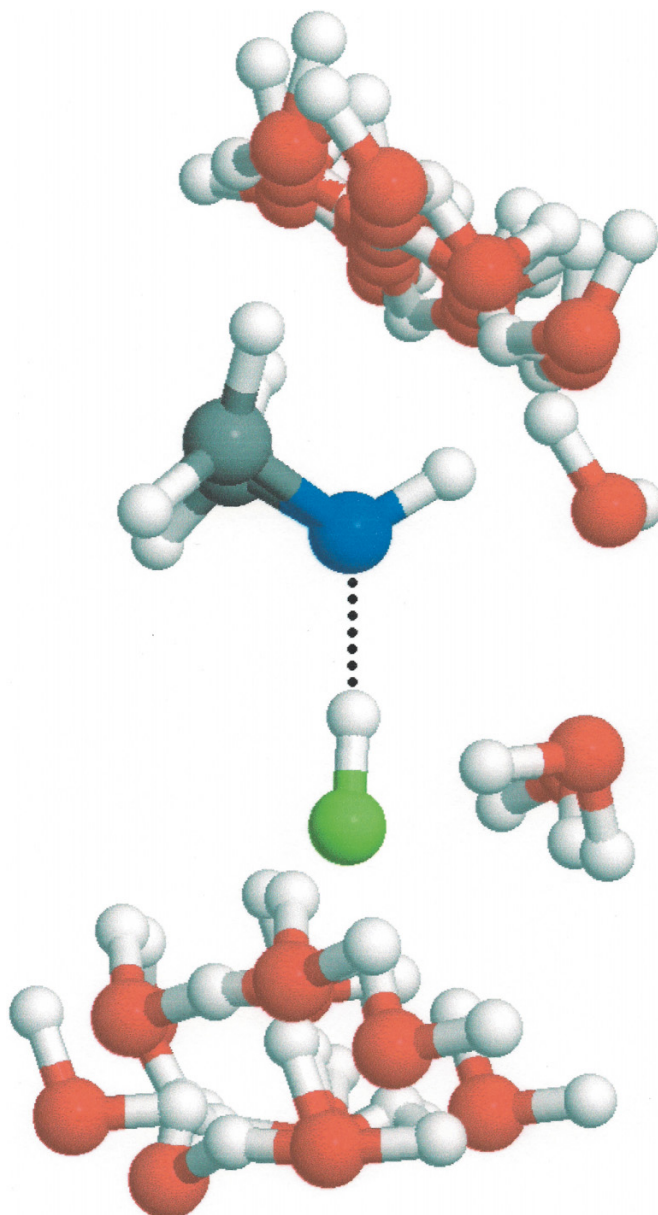
**Fig. 1.** Acid-catalyzed open-ring reaction of the aziridine: Protonated aziridine (2) and the  $C_2H_5N\cdots HF$  heterocyclic hydrogen-bonded complex (1) undergo the solvent effect.



**Fig. 2.** Optimized geometry of the  $C_2H_5N\cdots HF$  heterocyclic hydrogen-bonded complex (a) and its MEP surfaces (b). The potential-energy levels are +0.05 au and -0.05 au for transparent ( $MEP_{max}$ ) and meshed ( $MEP_{min}$ ) surfaces, respectively. MEP is given in atomic units (au).



**Fig. 3.** Hydration-cluster structures of the  $C_2H_5N\cdots HF$  heterocyclic hydrogen-bonded complex.



**Table 1.** AGOA internal default values for the cutoff radii.

Elements	Atomic cutoff radii
H	1.3
C	2.0
N	2.0
O	2.0
F	1.8

**Note:** All values are given in Å.

understanding of the acid-catalyzed open-ring reaction, even though it is not related to aziridine-ring protonation, but essentially occurs in the context of the  $C_2H_5N\cdots HF$  hydrogen-bonded complex. Given the ability of the continuum models, this is a task without promising results. A theoretical study of the solvent effect on the  $C_2H_5N\cdots HF$  hydrogen-

bonded complex, which discretely models the water molecules, should therefore be taken into account.<sup>16</sup>

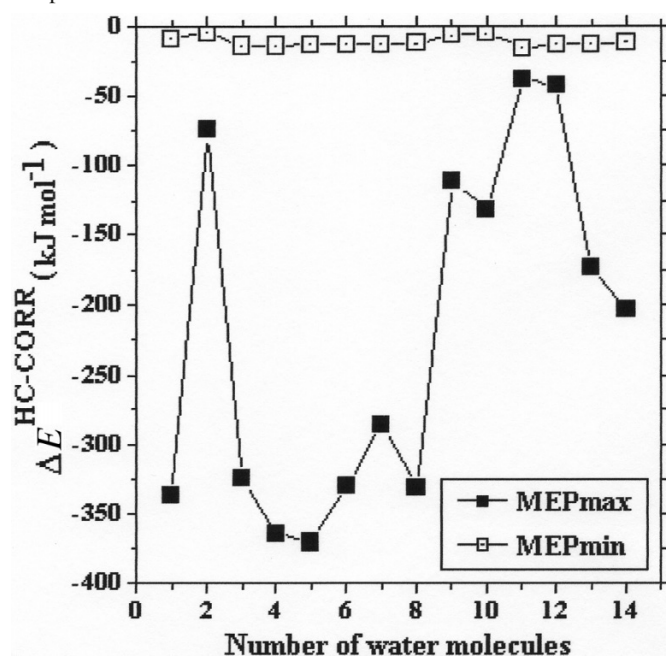
### The most adequate methodology

Historically, the first idea for evaluating the solvent effect

**Table 2.**  $\Delta E^{\text{HC-CORR}}$  hydration-clusters' energies of the  $\text{C}_2\text{H}_5\text{N}\cdots\text{HF}$  heterocyclic hydrogen-bonded complex.

Number of water molecules	$\text{C}_2\text{H}_5\text{N}\cdots\text{HF}$ heterocyclic hydrogen-bonded complex					
	$\Delta E^{\text{HC}}$ MEP <sub>max</sub>	BSSE MEP <sub>max</sub>	$\Delta E^{\text{HC-CORR}}$ MEP <sub>max</sub>	$\Delta E^{\text{HC-CORR}}$ MEP <sub>min</sub>	BSSE MEP <sub>min</sub>	$\Delta E^{\text{HC}}$ MEP <sub>min</sub>
1	-344.3	-7.4	-336.9	-12.4	-2.9	-9.5
2	-79.2	-4.9	-74.3	-7.8	-3.1	-4.7
3	-330.8	-6.1	-324.7	-16.3	-2.3	-14.0
4	-371.7	-7.1	-364.6	-16.3	-2.3	-14.0
5	-375.7	-5.1	-370.6	-15.7	-2.1	-13.6
6	-337.2	-7.2	-330.0	-15.8	-2.2	-13.6
7	-291.9	-6.0	-285.9	-16.1	-2.7	-13.4
8	-338.1	-6.8	-331.3	-15.7	-2.7	-13.0
9	-117.0	-6.0	-111.0	-10.3	-3.0	-7.3
10	-136.4	-4.9	-131.5	-8.8	-2.9	-5.9
11	-42.7	-4.8	-37.9	-18.6	-2.6	-16.0
12	-48.0	-5.1	-42.9	-15.7	-2.0	-13.7
13	-169.8	-3.7	-173.5	-15.7	-2.0	-13.7
14	-208.9	-5.6	-203.3	-14.4	-2.4	-12.0

Note: All values are given in  $\text{kJ mol}^{-1}$ .

**Fig. 4.** Relationship between hydration-cluster energies and the number of water molecules generated by AGOA to simulate the solvation effect in the  $\text{C}_2\text{H}_5\text{N}\cdots\text{HF}$  heterocyclic hydrogen-bonded complex.

in silico was based on the dielectric model,<sup>17,18</sup> and these were known as continuum methods. From theoretical formulations elaborated by Born,<sup>19</sup> Onsager,<sup>20</sup> and Kirkwood,<sup>21</sup> the continuum approach treats the solute using quantum mechanics, inserting it into a cavity molded as overlapping spheres. Recently, there has been intensive development of modern continuum implementations,<sup>22–24</sup> although these methodologies have serious limitations when it comes to describing specific interactions between solute and solvent.<sup>25</sup> These limitations can be partly overcome by the use of discrete models,<sup>26</sup> such as Monte Carlo or molecular dynamics.<sup>27–30</sup> These models provide an understanding of the real question regarding liquids, which is the association of a

large number of different configurations of the solvent. However, the application of these discrete methods has encountered a number of disadvantages, such as (i) the need for specific force fields, (ii) the dependence on the initial liquid configuration, and (iii) high computational cost.

It was therefore necessary to develop an alternative method of generating hydration clusters involving positioning the solvent molecules around the polar solutes without depending on specific force fields and (or) quantum-mechanical/molecular-mechanical calculations. The AGOA method was developed out of pioneering work carried out by Hernandez et al.,<sup>31</sup> as a way of generating liquid configurations by the analysis of the electrostatic potential of the solute. AGOA was further used to calibrate the force field for computational simulations. As a consequence, Hernandez and Longo<sup>32</sup> suggested another computational methodology called ab initio parametrization (AIPAR). In comparison to the OPLS data,<sup>33,34</sup> AIPAR has been successfully proven to simulate solvation in functional groups, such as methanol, acetone, methyl mercaptan, imidazole, oxazole, and furan. In the case of aziridine, however, the present study will not investigate the solvent effect in the  $\text{C}_2\text{H}_5\text{N}\cdots\text{HF}$  hydrogen-bonded complex using traditional discrete techniques, such as Monte Carlo or molecular dynamics. On the contrary, the aim here is to investigate the liquid configurations in the  $\text{C}_2\text{H}_5\text{N}\cdots\text{HF}$  hydrogen-bonded complex by way of AGOA. In this way, it is hoped that a suitable explanation of the aqueous stability of this complex will be found, thereby corroborating some aspects of the experimental aziridine acid-catalyzed open-ring reaction.<sup>35</sup>

## Computational details and procedure

The optimized geometry and molecular electrostatic potential (MEP)<sup>36</sup> of the  $\text{C}_2\text{H}_5\text{N}\cdots\text{HF}$  heterocyclic hydrogen-bonded complex were obtained using the density functional theory (DFT)<sup>37,38</sup> and the B3LYP hybrid functional.<sup>39–41</sup> The 6–311++G(d,p) basis set was used and all calculations were performed on the GAUSSIAN 98W program.<sup>42</sup> The hydration-cluster structures (solute:water) were generated by AGOA software, version 2.0.<sup>43</sup> Assuming that the electrostatic effects<sup>44</sup> are the most important interactions between



polar solutes and water molecules, AGOA interprets the MEP of the solute by plotting the solvent accessible surface area (SASA)<sup>45</sup> on a grid of  $20^3 = 8000$  points with the following dimensions:  $20 \times 20 \times 20 \text{ \AA}$ .

For notational purposes alone, the water molecules were distributed at equally spaced intervals in this cube. Single-point calculations for each hydration cluster ( $\Delta E^{\text{HC}}$ ) were then obtained as follows:

$$[1] \quad \Delta E^{\text{HC}} = E^{\text{TOTAL}} - E^{\text{SOLUTE}} - E^{\text{WATER}}$$

where  $E^{\text{TOTAL}}$ ,  $E^{\text{SOLUTE}}$ , and  $E^{\text{WATER}}$  correspond to the hydration-cluster energies of the dimer (solute:water), isolated solute ( $\text{C}_2\text{H}_5\text{N}\cdots\text{HF}$ ), and individual water molecules, respectively. All hydration-cluster energies  $\Delta E^{\text{HC}}$  were corrected using Boys and Bernardi's BSSE method,<sup>46</sup> and the values of the corrected hydration-cluster energies  $\Delta E^{\text{HC-CORR}}$  were then determined as follows:

$$[2] \quad \Delta E^{\text{HC-CORR}} = \Delta E^{\text{HC}} - \text{BSSE}$$

## Results and discussion

### Gas phase geometry and molecular electrostatic potential

First, it should be noted that the aim of this study is not to explore the potential-energy surface of the  $\text{C}_2\text{H}_5\text{N}\cdots\text{HF}$  heterocyclic hydrogen-bonded complex. Second, using the B3LYP/6-311++G(d,p) calculations to optimize the geometry of this complex, one particular minimum of the potential-energy surface was identified by analysis of the infrared spectrum in which no imaginary frequency had been detected. The optimized geometry of the  $\text{C}_2\text{H}_5\text{N}\cdots\text{HF}$  complex is illustrated in Fig. 2a.<sup>47,48</sup>

In accordance with the AGOA standard protocol,<sup>31</sup> the optimized geometry of the  $\text{C}_2\text{H}_5\text{N}\cdots\text{HF}$  complex was used to compute its MEP, whose surface can be seen in Fig. 2b. The maximum (+0.05 au) and minimum (−0.05 au) of the MEP regions are represented by transparent and meshed surfaces, respectively.

### Hydration clusters and interaction energies

AGOA describes hydration clusters by describing the MEP gradient (see eq. [3]) of the solute, and also uses the TIP4P geometry model to orient the water molecules around the solute.<sup>49</sup>

$$[3] \quad E(\text{H}_2\text{O}) = -\nabla\text{MEP}$$

The hydration clusters generated using AGOA for the  $\text{C}_2\text{H}_5\text{N}\cdots\text{HF}$  hydrogen-bonded complex are shown in Fig. 3. It can be seen that two groups of 14 water molecules were positioned in the maximum (max) and minimum (min) regions of the MEP, respectively. In this procedure, the AGOA program has internally stored default cutoff radii for the solute and solvent, whose values are listed in Table 1.

The hydration-clusters' structures were obtained in Cartesian coordinates and used to determine the hydration energies  $\Delta E^{\text{HC-CORR}}$ , whose results are presented in Table 2 and graphically illustrated in Fig. 4.

As can be seen in the region of maximum molecular electrostatic potential ( $\text{MEP}_{\text{max}}$ ), the orientation of the water molecules indicates that their oxygen atoms are interacting

with the hydrogen atoms of the methyl groups ( $-\text{CH}_2-$ ). On the other hand, in the region of minimum electrostatic potential ( $\text{MEP}_{\text{min}}$ ), the hydrogen atoms of the water molecules are directly aligned to the fluorine atom of hydrofluoric acid (HF).

Moreover, these hydration clusters provide better stability for the  $\text{MEP}_{\text{max}}$  field because the  $\Delta E^{\text{HC-CORR}}$  values computed in this region are higher, in the range of  $-364.6 \text{ kJ mol}^{-1}$ . This study may be considered consistent with the reproduction of the experimental behavior of aziridine, since cyclic amines are known to be highly reactive compounds.<sup>50</sup> Solely for comparative purposes, a similar experiment was performed to evaluate the solvent effect on the epoxide ring, in particular the  $\text{C}_2\text{H}_4\text{O}\cdots\text{HF}$  heterocyclic hydrogen-bonded complex.<sup>51</sup> Although the hydration-cluster energies of the  $\text{C}_2\text{H}_4\text{O}\cdots\text{HF}$  hydrogen-bonded complex showed values in the range of  $-292 \text{ kJ mol}^{-1}$ , it can be seen that aziridine is more reactive. In other words, the acid-catalyzed open-ring reaction occurs more easily if the formation of the  $\text{C}_2\text{H}_5\text{N}\cdots\text{HF}$  heterocyclic hydrogen-bonded complex is taken into account. The AGOA methodology provides a successful complementary description of the solvation effect, which not only produces interesting results, but can also be achieved at low computational cost, since the analysis of the solute MEP is the single criterion used to form the hydration clusters. In practice, it took only a few seconds to generate the hydration clusters for the  $\text{C}_2\text{H}_5\text{N}\cdots\text{HF}$  heterocyclic hydrogen-bonded complex.

## Conclusions and future research

The theoretical study of the solvation effect in the  $\text{C}_2\text{H}_5\text{N}\cdots\text{HF}$  heterocyclic hydrogen-bonded complex has proven that the presence of the water molecules is important for description of the acid-catalyzed open-ring reaction of aziridine. Analysis of the molecular electrostatic potential of the  $\text{C}_2\text{H}_5\text{N}\cdots\text{HF}$  complex revealed two important regions, which correspond to the methyl groups ( $\text{MEP}_{\text{max}}$ ) of the aziridine ( $\text{C}_2\text{H}_5\text{N}$ ) and the fluorine atom ( $\text{MEP}_{\text{min}}$ ) of the hydrofluoric acid, respectively. In the solvation structures generated by the AGOA methodology, the  $\Delta E^{\text{HC-CORR}}$  hydration-cluster energies are higher in the  $\text{MEP}_{\text{max}}$  region. This result concurs well with the experimental acid-catalyzed open-ring reaction, where the nucleophilic attack occurs through the interactions of the water molecules with the methyl groups of the aziridine ring. It should be noted that the AGOA software is for academic purposes,<sup>43</sup> but its potential has been successfully demonstrated<sup>31</sup> in areas such as the theoretical description of the acid/base equilibrium involving alkoxides and ammonium ions<sup>52,53</sup> and hydration-cluster studies of amino acids and protein fragments.<sup>54</sup> In future, we plan to undertake a study of hydration clusters in nanocompounds of biological interest, such as the quantum dots.

## Acknowledgement

The authors gratefully acknowledge partial financial support from the Brazilian Funding agencies Comissão de aperfeiçoamento de pessoal de ensino superior (CAPES), Conselho nacional de desenvolvimento científico e tecnológico (CNPq), and Financiadora de estudos e projetos (FINEP).

## References

- (1) Padwa, A.; Murphree, S. S.; Gribble, G. W.; Gilchrist, T. L. *Progress in Heterocyclic Chemistry*; Pergamon Press: Oxford, 2002.
- (2) Hayen, A.; Schmitt, M. A.; Ngassa, F. N.; Thomasson, K. A.; Gellman, S. H. *Angew. Chem. Int. Ed. Engl.* **2004**, *43* (4), 505. doi:10.1002/anie.200352125. PMID:14735547.
- (3) Staude, V. E. *Angew. Makromol. Chem.* **1970**, *13* (1), 163. doi:10.1002/apmc.1970.050130112.
- (4) Awazu, K.; Roorda, S.; Brebner, J. L.; Ishii, S.; Shima, K. *Jpn. J. Appl. Phys.* **2003**, *42* (Part 1, No. 6B), 3950. doi:10.1143/JJAP.42.3950.
- (5) Kudin, A. K. *Aziridines and Epoxides in Organic Synthesis*; Wiley-VCH: Weinheim, 2006.
- (6) Hu, X. E. *Tetrahedron* **2004**, *60* (12), 2701. doi:10.1016/j.tet.2004.01.042.
- (7) Fedotova, L. A.; Voronkov, M. G. *Chem. Heterocycl. Compd.* **1966**, *1* (6), 573. doi:10.1007/BF00472692.
- (8) Shomina, F. N.; Étlis, V. S.; Sineokov, A. P. *Chem. Heterocycl. Compd.* **1973**, *9*, 1105. doi:10.1007/BF00474782.
- (9) de Meijere, A. *Angew. Chem.* **1979**, *91* (11), 809. doi:10.1002/anie.197908093.
- (10) Greenberg, A.; Liebman, J. F. *Strained Organic Molecules*; Academic Press: New York, 1978.
- (11) Olofsson, B.; Wijnmans, R.; Somfai, P. *Tetrahedron* **2002**, *58* (30), 5979. doi:10.1016/S0040-4020(02)00610-5.
- (12) Bieber, L. W.; de Araujo, M. C. F. *Molecules* **2002**, *7* (12), 902. doi:10.3390/71200902.
- (13) Diao, T.; Sun, X.; Fan, R.; Wu, J. T.; Diao, T.; Sun, X.; Fan, R. *ChemInform* **2007**, *36*, 604.
- (14) Kotsuki, H.; Shimanouchi, T.; Ohshima, R. *Tetrahedron* **1998**, *54* (12), 2709. doi:10.1016/S0040-4020(98)83007-X.
- (15) Mu, W.-H.; Wang, C.; Fang, D.-C. *J. Mol. Struct. THEOCHEM* **2007**, *806* (1-3), 171. doi:10.1016/j.theochem.2006.11.024.
- (16) Chaplin, W. Available from [www.lsbu.ac.uk/water/index2.html](http://www.lsbu.ac.uk/water/index2.html) (accessed September, 2007).
- (17) Tomasi, J. *Theor. Chem. Acc.* **2000**, *103*, 196.
- (18) Luque, F. L.; López, J. M.; Orozco, M. *Theor. Chem. Acc.* **2000**, *103*, 343.
- (19) Born, M. *Phys. Z.* **1920**, *1* (1), 45. doi:10.1007/BF01881023.
- (20) Onsager, L. *J. Am. Chem. Soc.* **1936**, *58* (8), 1486. doi:10.1021/ja01299a050.
- (21) Kirkwood, J. J. *Chem. Phys.* **1935**, *3* (5), 300. doi:10.1063/1.1749657.
- (22) Miertuš, S.; Scrocco, E.; Tomasi, J. *Chem. Phys.* **1981**, *55* (1), 117. doi:10.1016/0301-0104(81)85090-2.
- (23) Klamt, A.; Schuurmann, G. *J. Chem. Soc. Perkin Trans.* **1993**, *2*, 799.
- (24) Cramer, C. J.; Truhlar, D. G. *J. Am. Chem. Soc.* **1991**, *113* (22), 8305. doi:10.1021/ja00022a017.
- (25) (a) Tapia, O. In *Molecular Interactions*; Orville-Thomas, J.W., Ratajczak, H., Eds.; John Wiley and Sons: Chichester, 1982.
- (26) Heermann, D. W. *Computer Simulation Methods in Theoretical Physics*; Springer-Verlag: New York, 1990.
- (27) Allen, M. P.; Tildesley, D. J. *Computer Simulation of Liquids*; Clarendon Press: Oxford, 1987.
- (28) Kalos, M. K.; Whitlock, P. A. *Monte Carlo Methods*; John Wiley and Sons: New York, 1986.
- (29) Metropolis, N.; Rosenbluth, A. W.; Rosenbluth, M. N.; Teller, A. H.; Teller, E. *J. Chem. Phys.* **1953**, *21* (6), 1087. doi:10.1063/1.1699114.
- (30) Hammond, B. L.; Lester, W. A., Jr.; Reybolds, P. J. *Monte Carlo Methods in Ab Initio Quantum Chemistry*; World Scientific: Singapore, 1994.
- (31) Hernandez, M. Z.; da Silva, J. B. P.; Longo, R. L. *J. Braz. Chem. Soc.* **2002**, *13* (1), 36. doi:10.1590/S0103-50532002000100005.
- (32) Hernandez, M. Z.; Longo, R. L. *J. Mol. Model.* **2005**, *11* (1), 61. doi:10.1007/s00894-004-0222-9. PMID:15592896.
- (33) Jorgensen, W. L.; Madura, J. D.; Swenson, C. J. *J. Am. Chem. Soc.* **1984**, *106* (22), 6638. doi:10.1021/ja00334a030.
- (34) Jorgensen, W. L.; Tirado-Rives, J. *J. Am. Chem. Soc.* **1988**, *110* (6), 1657. doi:10.1021/ja00214a001.
- (35) Prestat, G.; Baylon, C.; Heck, M.-P.; Mioskowski, C. *Tetrahedron Lett.* **2000**, *41* (20), 3829. doi:10.1016/S0040-4039(00)00496-2.
- (36) Gadre, S. R.; Kulkarni, S. A.; Shrivastava, I. H. *Chem. Phys. Lett.* **1992**, *96*, 5253.
- (37) Hohenberg, P.; Kohn, W. *Phys. Rev. B* **1964**, *136* (3B), B864. doi:10.1103/PhysRev.136.B864.
- (38) Kohn, W.; Sham, L. J. *Phys. Rev. A* **1965**, *140* (4A), A1133. doi:10.1103/PhysRev.140.A1133.
- (39) Becke, A. D. *J. Chem. Phys.* **1997**, *107* (20), 8554. doi:10.1063/1.475007.
- (40) Becke, A. D. *J. Chem. Phys.* **1993**, *98* (7), 5648. doi:10.1063/1.464913.
- (41) Lee, C.; Yang, W.; Parr, R. G. *Phys. Rev. B* **1988**, *37* (2), 785. doi:10.1103/PhysRevB.37.785.
- (42) Frisch, M. J.; Trucks, G. W.; Schlegel, H. B.; Scuseria, G. E.; Robb, M. A.; Cheeseman, J. R.; Zakrzewski, V. G.; Montgomery, J. A., Jr.; Stratmann, R. E.; Burant, J. C.; Dapprich, S.; Millam, J. M.; Daniels, A. D.; Kudin, K. N.; Strain, M. C.; Farkas, O.; Tomasi, J.; Barone, V.; Cossi, M.; Cammi, R.; Mennucci, B.; Pomelli, C.; Adamo, C.; Clifford, S.; Ochterski, J.; Petersson, G. A.; Ayala, P. Y.; Cui, Q.; Morokuma, K.; Rega, N.; Salvador, P.; Dannenberg, J. J.; Malick, D. K.; Rabuck, A. D.; Raghavachari, K.; Foresman, J. B.; Cioslowski, J.; Ortiz, J. V.; Baboul, A. G.; Stefanov, B. B.; Liu, G.; Liashenko, A.; Piskorz, P.; Komaromi, I.; Gomperts, R.; Martin, R. L.; Fox, D. J.; Keith, T.; Al-Laham, M. A.; Peng, C. Y.; Nanayakkara, A.; Challacombe, M.; Gill, P. M. W.; Johnson, B.; Chen, W.; Wong, M. W.; Andres, J. L.; Gonzalez, C.; Head-Gordon, M.; Replogle, E. S.; Pople, J. A. *Gaussian 98W*, Revision A.1; Gaussian, Inc.: Pittsburgh, PA, 1998.
- (43) Hernandez, M. Z. Available from <http://www.ufpe.br/farmacia/zaldini/agoa.html> (accessed June, 2004).
- (44) Umeyama, H.; Morokuma, K. *J. Am. Chem. Soc.* **1977**, *99* (5), 1316. doi:10.1021/ja00447a007.
- (45) Gaudio, A. C.; Takahata, Y. *Comput. Chem.* **1992**, *16* (4), 277. doi:10.1016/0097-8485(92)80047-4.
- (46) Boys, S. B.; Bernardi, F. *Mol. Phys.* **1970**, *19* (4), 553. doi:10.1080/00268977000101561.
- (47) Oliveira, B. G.; Santos, E. C. S.; Duarte, E. M.; Araújo, R. C. M. U.; Ramos, M. N.; Carvalho, A. B. *Spectrochim. Acta [A]* **2004**, *60* (8-9), 1883. doi:10.1016/j.saa.2003.10.006.
- (48) Oliveira, B. G.; Duarte, E. M.; Araújo, R. C. M. U.; Ramos, M. N.; Carvalho, A. B. *Spectrochim. Acta [A]* **2005**, *61* (3), 491. doi:10.1016/j.saa.2004.04.023.
- (49) Jorgensen, W. L.; Madura, J. D. *Mol. Phys.* **1985**, *56* (6), 1381. doi:10.1080/00268978500103111.
- (50) Acheson, R. M. *An Introduction to The Chemistry of Heterocyclic Compounds*; John Wiley and Sons: New York, 1967.
- (51) Oliveira, B. G.; Araújo, R. C. M. U.; Carvalho, A. B.; Ramos, M. N.; Hernandez, M. Z.; Cavalcante, K. R. *J. Mol.*

- Struct. THEOCHEM* **2007**, 802 (1-3), 91. doi:10.1016/j.theochem.2006.09.002.
- (52) de Oliveira, B. G.; De Almeida Vasconcellos, M. L. A. *J. Theor. Comput. Chem.* **2007**, 6 (2), 399. doi:10.1142/S0219633607002915.
- (53) Vasconcellos, M. L. A. A.; Oliveira, B. G.; Leite, L. F. C. C. *J. Mol. Struct. THEOCHEM* **2008**, 860 (1-3), 13. doi:10.1016/j.theochem.2008.03.023.
- (54) Cavalcante, K. R. Using the GRID Computation for Molecular Modeling in Biological Systems. M.Sc. Thesis, Centro de Informática, UFPE, Recife, Brazil, 2007.

# Triazene derivatives of (1,x)-diazacycloalkanes — Part IX. Synthesis and characterization of a series of 1,4-di[2-aryl-1-diazenyl]- 2,6-dimethylpiperazines

Naomi Hunter and Keith Vaughan

**Abstract:** A series of 1,4-di-[2-aryl-1-diazenyl]-2,6-dimethylpiperazines (**5a–5l**), have been synthesized by the reaction of 2,6-dimethylpiperazine with 2 equiv. of the appropriate diazonium salt. The products have been characterized by IR and NMR spectroscopy, and the molecular composition has been verified by high-resolution EI mass spectrometry with accurate mass measurement of the molecular ion. The presence of stereocenters at C2 and C6 of the piperazine ring in the bis-triazene **5** creates two unique pairs of diastereotopic protons in the methylene groups at positions 3 and 5 of the piperazine ring, as evidenced by the complexity of the NMR spectra, which nevertheless can be fully assigned in most cases. The assignment of the proton and carbon signals in the 1,4-di-[2-aryl-1-diazenyl]-2,6-dimethylpiperazines has been aided by the use of 2D NMR HSQC spectroscopy. These results compare favorably with assignments of proton and carbon signals reported previously for triazenes of type **1** and bis-triazenes of type **3**.

**Key words:** triazene, bis-triazene, piperazine, 2,6-dimethylpiperazine, diastereotopic protons, diazonium coupling, 2D NMR, HSQC.

**Résumé :** On a réalisé la synthèse d'une série de 1,4-di-[2-aryl-1-diazenyl]-2,6-diméthylpipérazines (**5a–5l**) par réaction de la 2,6-diméthylpipérazine avec deux équivalents du sel de diazonium approprié. Les produits ont été caractérisés par spectroscopies infrarouge et RMN et on a vérifié la composition moléculaire par spectrométrie de masse à haute résolution et ionisation électronique en effectuant la mesure exacte de la masse de l'ion moléculaire. La présence de stéréocentres dans les positions 2 et 6 du noyau pipérazine du bis-triazène **5** conduit à la création de deux paires distinctes de protons diastéréotopes dans les groupes méthylènes des positions 3 et 5 du noyau pipérazine qui sont mis en évidence par la complexité du spectre RMN qu'on peut toutefois assigner complètement dans la plupart des cas. L'attribution des signaux des atomes d'hydrogène et de carbone dans les 1,4-di-[2-aryl-1-diazenyl]-2,6-diméthylpipérazines a été rendue possible par l'utilisation de la spectroscopie RMN 2D avec corrélation à quantum unique hétéronucléaire (« HSQC »). Ces résultats se comparent favorablement avec les attributions des signaux des atomes d'hydrogène et de carbone rapportées antérieurement pour les triazènes du type **1** et les bis-triazènes de type **3**.

**Mots-clés :** triazène, bis-triazène, pipérazine, 2,6-diméthylpipérazine, protons diastéréotopes, couplage diazonium, RMN 2D, corrélation à quantum unique hétéronucléaire (« HSQC »).

[Traduit par la Rédaction]

## Introduction

This paper is the latest chapter in an extensive study of the synthesis of *N*-aryldiazenylpiperazines and the structural characterization of these triazenes. In Part I of this series,<sup>1</sup> the diazonium coupling reaction of 1-methylpiperazine was explored to synthesize the 4-methyl-1-(2-aryldiazen-1-yl)-piperazines (**1**) (Chart 1). The structure of one compound, namely methyl 4-[(*E*)-2-(4-methylpiperazino)-1-diazenyl]-benzoate, in this series has been verified by X-ray crystallography,<sup>2</sup> which showed that the piperazine ring adopts a

normal chair conformation. In the process of characterizing these triazenes by NMR spectroscopy, the chemical shift parameters of the protons and carbons in the piperazine ring were clearly established and verified by some classical 2D NMR work. This data was used to advantage in characterizing the 4-methyl-1-[aryldiazenyl]-homopiperazines (**2a**) (Chart 1), which have been described, along with the 1,4-di-(2-aryldiazen-1-yl)diazepanes (**2b**), in Part II of this series.<sup>3</sup> The bis-triazenes (**2b**) were obtained by reaction of homopiperazine with the diazonium salt in 1:2 molar proportion.

This bis-diazotization strategy was subsequently explored

Received 23 September 2009. Accepted 9 December 2009. Published on the NRC Research Press Web site at canjchem.nrc.ca on 4 March 2010.

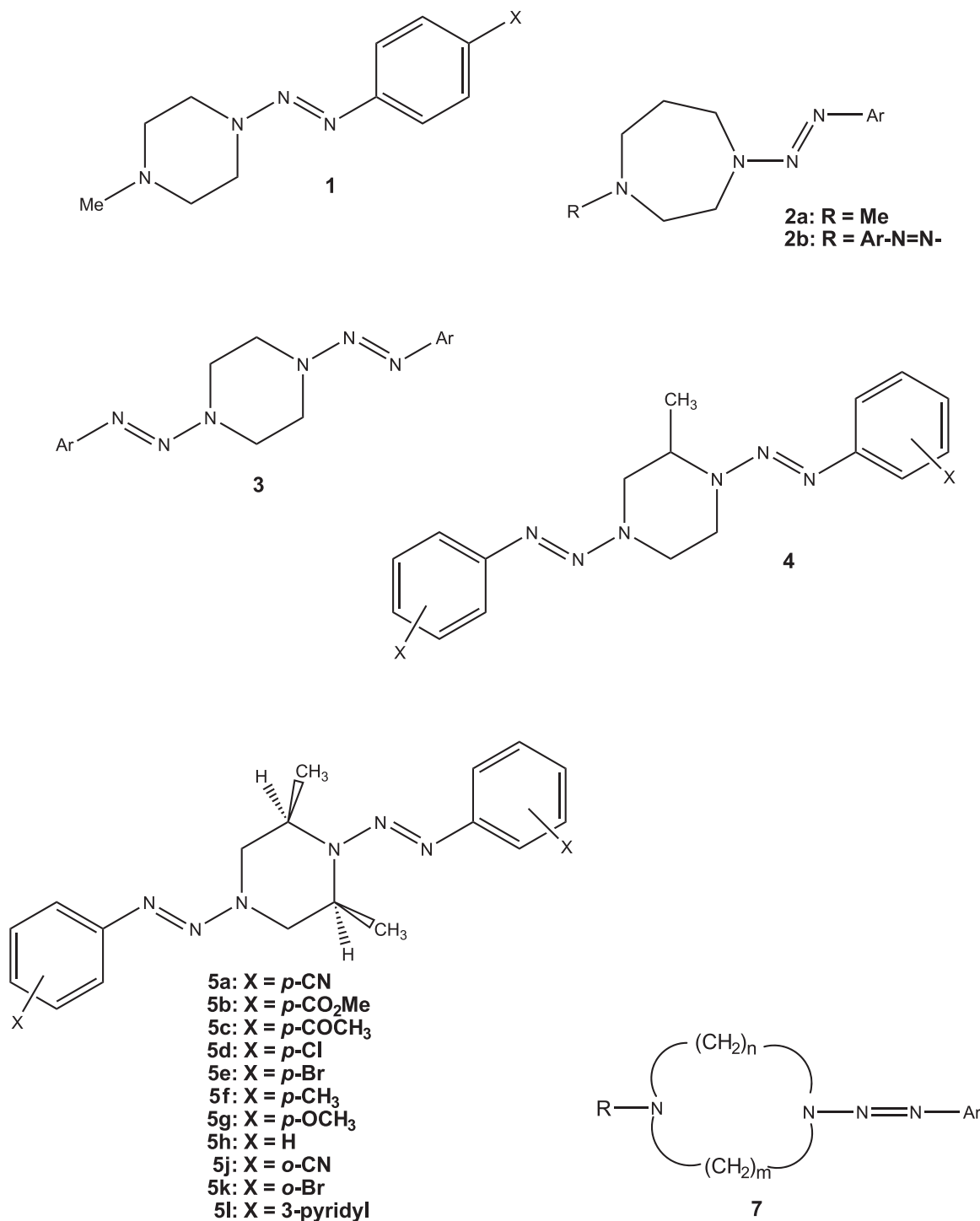
For Part VIII in this series, see ref. 6.

N. Hunter and K. Vaughan.<sup>1</sup> Department of Chemistry, Saint Mary's University, Halifax, NS B3M 3X6, Canada.

<sup>1</sup>Corresponding author (e-mail: keith.vaughan@smu.ca).



Chart 1.



with piperazine itself and the synthesis of a series of 1,4-di-(2-aryldiazen-1-yl)-piperazines (**3**) (Chart 1) was described in Part III of this series.<sup>4</sup> The bis-triazenes of type **3** were characterized by a range of spectroscopic techniques and the data was compared with some previously published work<sup>5</sup> in which several of the bis-aryldiazenyl-piperazines had already been described. Subsequently, we extended the study of bis-triazenes to the 1,4-di-[2-aryl-1-diazenyl]-2-methylpiperazines (**4**) (Chart 1), which were prepared by diazonium coupling to 2-methylpiperazine.<sup>6</sup>

The work described in this paper is a logical extension of

our previous study<sup>6</sup> of the synthesis of the unsymmetrical bis-triazenes of series **4** to the bis-triazene series **5** (Chart 1), in which an additional methyl substituent is introduced at position six of the piperazine ring. In characterizing the series of bis-triazenes (**3**), we observed that the eight protons of the piperazine ring occur as a single peak. The equivalence of all eight methylene protons in **3** is a little surprising in view of the potential for variation in chemical shift from either (*a*) axial versus equatorial proton environment, or (*b*) syn or anti orientation of the *N*-aryldiazenyl groups, or (*c*) a combination of both of these. We concluded that the

**Table 1.** Physical and IR spectroscopic data of the 1,4-di-[2-aryl-1-diazenyl]-2,6-dimethylpiperazines (**5a–5l**).

Compound No.	X	Yield (%)	Mp (°C)	Solvent	Crystal appearance	IR (cm <sup>-1</sup> )
<b>5a</b>	<i>p</i> -CN	61	185–186	EtOH	Off-white tiny needles	843, 851, 2220
<b>5b</b>	<i>p</i> -CO <sub>2</sub> Me	69	147–148	EtOH	Almost pure-white clumps	857, 1716
<b>5c</b>	<i>p</i> -COMe	32	196–199	EtOH	Lustrous red-brown prisms	841, 1673
<b>5d</b>	<i>p</i> -Cl	8	207–211	EtOH by trituration	Off-white powder	834
<b>5e</b>	<i>p</i> -Br	35	169–171	DMSO	Yellow needles	831.5
<b>5f</b>	<i>p</i> -CH <sub>3</sub>	15	94–96	EtOH by trituration	Tiny lilac-colored needles	823
<b>5g</b>	<i>p</i> -OCH <sub>3</sub>	30	182–184	EtOH	Lustrous golden-brown needles	840
<b>5h</b>	H	41	Oil	—	—	689, 752
<b>5j</b>	<i>o</i> -CN	53	157–159	EtOH	Pale yellow tiny needles	767, 2226
<b>5k</b>	<i>o</i> -Br	51	97–99	EtOH	Pale yellow tiny needles	758
<b>5l</b>	3-Pyridyl	48	Oil	—	—	707, 736

dynamic effects in molecules of type **3** must be occurring faster than the NMR time frame. The presence of a chiral centre at C2 of the piperazine ring in the bis-triazene series **4** created a multitude of diastereotopic protons in the methylene groups of the piperazine ring, as evidenced by the complexity of the NMR spectra, which nevertheless were fully assigned in some cases, such as the tolyl and phenyl derivatives. It was of interest to undertake the synthesis of the symmetrical meso bis-triazenes of series **5** to see the effect of the mirror-image stereocenters at C2 and C6 on the NMR features, in addition to the intellectual curiosity associated with the synthesis of any new molecules.

The presence of two stereocenters in the piperazine ring, as in structure **5**, might have some interesting consequences. In principle, the aryldiazenyl groups in **5** are in nonequivalent environments, and it is an intriguing challenge to see if high field NMR can resolve these nonequivalent aryl groups. Furthermore, there is an element of symmetry in the piperazine ring, which should result in equivalence of the two  $-\text{CH}_2\text{CH}(\text{CH}_3)-$  moieties on each side of the piperazine ring, potentially simplifying the NMR analysis. However, the C2/C6 carbons in **5** are stereocenters, creating the situation where the methylene hydrogens at C3 and C5 are diastereotopic. Thus, the resolution and interpretation of the NMR spectra of the bis-triazenes of type **5** has the potential for being an interesting exercise. These considerations prompted us to explore the effect of introducing two methyl substituents into the piperazine ring of the 1,4-bis(aryldiazenyl)piperazine system and this paper reports the synthesis and characterization of the series of 1,4-di[2-aryl-1-diazenyl]-2,6-dimethylpiperazines (**5a–5l**) (Chart 1), with an in-depth analysis of the NMR spectra of these novel compounds.

## Experimental

All reagents were reagent grade materials purchased from Sigma-Aldrich and were used without further purification. Melting points were determined on a Fisher–Johns melting point apparatus and are uncorrected. Infrared spectra were obtained using Nujol mulls with a Bruker Vector 22 spectrometer. <sup>1</sup>H and <sup>13</sup>C NMR spectra were obtained with either (i) Bruker 400 MHz and 500 MHz spectrometers at the Atlantic Regional Magnetic Resonance Center at Dalhousie

University (Halifax, NS), or (ii) the ANASAZI 60 MHz EFT spectrometer at Saint Mary's University (Halifax, NS). Chemical shifts were recorded in CDCl<sub>3</sub> or DMSO-*d*<sub>6</sub> solutions at 20 °C (as specified), and are relative to TMS as internal standard. Accurate mass measurements were made on a CEC 21-110B mass spectrometer operated at a mass resolution of 8000 (10% valley) by computer-controlled peak matching to appropriate PFK reference ions. Spectra were obtained using electron ionization at 70 V and a source temperature of 175 °C, with samples being introduced by means of a heatable quartz probe. The standard deviation of mass measurement is  $\pm 0.0008$  amu, which is an average of 3.6 ppm over the mass range of 100–300 amu.

## 1,4-Di-[2-aryl-1-diazenyl]-2,6-dimethylpiperazines (**5a–5l**)

### General procedure

The aromatic primary amine (0.01 mol) was dissolved in 12 mL of 3 mol/L hydrochloric acid, with the aid of heat if necessary, and the resulting solution was cooled in an ice/salt bath to 0 °C. The solution was diazotized with a solution of sodium nitrite (0.76 g) in water (10 mL) while maintaining the temperature below 5 °C, and then stirred for a further 0.5 h in the cold, reaching a starch–iodide end-point. A solution of 2,6-dimethylpiperazine (0.571 g), dissolved in water (10 mL), was added slowly to the mixture. After stirring for a further 0.5 h, the mixture was neutralized with saturated sodium carbonate solution and then left to stir until precipitation was deemed to be complete (about 1 h). The solid products were filtered under suction, dried and recrystallized from an appropriate solvent to give the 1,4-di-[2-aryl-1-diazenyl]-2,6-dimethylpiperazines (**5a–5g** and **5j–5k**) (Chart 1).

Compounds **5h** and **5l** were formed in the reaction mixture as oils, which were separated from the reaction mixture by extraction into dichloromethane. The dichloromethane solution was purified by washing with water and drying over anhydrous magnesium sulfate. The filtered solution was evaporated under vacuum to afford the compound, **5h** or **5l**, which were spectroscopically pure for characterization.

Physical data and IR spectroscopic bands are listed in Table 1. Table 2 shows the <sup>1</sup>H NMR spectral data (see Scheme 1 for labels), and <sup>13</sup>C NMR data are provided in Table 3 (see Scheme 2). High-resolution mass spectrometric results are tabulated in Table 4.

**Table 2.** <sup>1</sup>H NMR spectroscopic data of the 1,4-di-[2-aryl-1-diazenyl]-2,6-dimethylpiperazines (**5a–5l**) recorded at 300 K and 500 MHz.

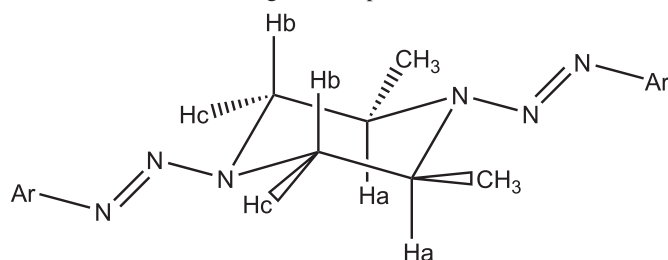
Compound No.	X	Aromatic	Methyl at C2 and C6	Methylene (H <sub>c</sub> )	Methylene (H <sub>b</sub> )	Methine (H <sub>a</sub> )	X
<b>5a</b>	<i>p</i> -CN (a)	7.51 (2H, d, <i>J</i> = 8.5 Hz), 7.54 (2H, d, <i>J</i> = 8.5 Hz), 7.64 (2H, d, <i>J</i> = 8.5 Hz), 7.65 (2H, d, <i>J</i> = 8.5 Hz)	1.45 (6H, d, <i>J</i> = 6.5 Hz)	3.99 (2H, br)	4.27 (2H, br d, <i>J</i> = 9.1 Hz)	4.87 (2H, br d, <i>J</i> = 4.7 Hz)	—
<b>5b</b>	<i>p</i> -CO <sub>2</sub> Me (b)	7.49 (2H, d, <i>J</i> = 5.7 Hz), 7.50 (2H, d, <i>J</i> = 5.7 Hz), 7.96 (2H, d, <i>J</i> = 3.8 Hz), 7.98 (2H, d, <i>J</i> = 3.8 Hz)	1.38 (6H, br d)	4.2 (2H, br d, <i>J</i> = 11 Hz)	4.38 (2H, v br)	4.85 (2H, br)	3.85 (6H, s) 2 × O-Me
<b>5c</b>	<i>p</i> -COMe (a)	7.50 (2H, d, <i>J</i> = 8.7), 7.53 (2H, d, <i>J</i> = 8.7 Hz), 7.96 (2H, d, <i>J</i> = 8.5 Hz), 7.98 (2H, d, <i>J</i> = 8.7 Hz)	1.46 (6H, br d)	3.97 (2H, v br)	4.29 (2H, br)	4.88 (2H, br)	2.60 (6H, s) Acetyl-Me
<b>5d</b>	<i>p</i> -Cl (b)	7.41 (4H, d, <i>J</i> = 8.8 Hz), 7.45 (4H, d, <i>J</i> = 8.9 Hz)	1.37 (6H, d, <i>J</i> = 6.3 Hz)	3.34 (2H, br)	3.40 (2H, v br)	4.55 (2H, v br)	—
<b>5e</b>	<i>p</i> -Br (a)	7.32 (2H, d, <i>J</i> = 8.7 Hz), 7.34 (2H, d, <i>J</i> = 8.5 Hz), 7.45 (2H, d, <i>J</i> = 8.7 Hz), 7.47 (2H, d, <i>J</i> = 8.7 Hz)	1.42 (6H, d, <i>J</i> = 6.6 Hz)	3.85 (2H, v br)	4.22 (2H, br d, <i>J</i> = 12.4 Hz)	4.80 (2H, br d, <i>J</i> = 5.4 Hz)	—
<b>5f</b>	<i>p</i> -CH <sub>3</sub> (a)	7.17 (2H, d, <i>J</i> = 8.0 Hz), 7.19 (2H, d, <i>J</i> = 8.0 Hz), 7.37 (2H, d, <i>J</i> = 8.2 Hz), 7.39 (2H, d, <i>J</i> = 8.2 Hz)	1.43 (6H, d, <i>J</i> = 6.5 Hz)	3.80 (2H, d, <i>J</i> = 11.6 Hz)	4.26 (2H, dd, <i>J</i> = 3.7, 13.5 Hz)	4.80 (2H, dq, <i>J</i> = 4.7, 6.6 Hz)	2.374 (3H, s), 2.369 (3H, s)
<b>5g</b>	<i>p</i> -OCH <sub>3</sub> (a)	6.90 (4H, d, <i>J</i> = 9.4 Hz), 7.41 (4H, d, <i>J</i> = 9.1 Hz)	1.67 (6H, d, <i>J</i> = 5.5 Hz)	3.39 (2H, br)	3.42 (2H, br)	4.56 (2H, d, <i>J</i> = 13.0 Hz)	3.84 (6H, s) 2 × O-Me
<b>5h</b>	H (a)	7.20–7.30 (2H, m), 7.37–7.42 (3H, m), 7.46–7.52 (3H, m), 10.20 (2H, b)	1.70 (6H, d, <i>J</i> = 6.0 Hz)	3.42 (2H, br)	3.51 (2H, t, <i>J</i> = 13.0 Hz)	4.65 (2H, d, <i>J</i> = 13.0 Hz)	—
<b>5j</b>	<i>o</i> -CN (b)	7.32 (1H, dd, <i>J</i> = 6.9, 12.9 Hz), 7.38 (1H, t, <i>J</i> = 7.5 Hz), 7.58 (1H, d, <i>J</i> = 8.4 Hz), 7.61 (1H, d, <i>J</i> = 7.9 Hz), 7.66 (1H, m), 7.70 (1H, dd, <i>J</i> = 1.4, 8.6 Hz), 7.80 (1H, ddd, <i>J</i> = 1.0, 2.7, 7.7 Hz), 7.84 (1H, dd, <i>J</i> = 1.0, 7.8 Hz)	1.37 (6H, d, <i>J</i> = 6.5 Hz)	3.48 (2H, br)	4.05 (1H, br), 4.24 (1H, br)	4.91 (2H, br)	—

Table 2 (concluded).

Compound No.	X	Aromatic	Methyl at C2 and C6	Methylene (H <sub>c</sub> )	Methylene (H <sub>b</sub> )	Methine (H <sub>a</sub> )	X
5k	<i>o</i> -Br (b)	7.11 (1H, dt, <i>J</i> = 1.7, 7 Hz), 7.12 (1H, dt, <i>J</i> = 1.6, 7 Hz), 7.35 (1H, dt, <i>J</i> = 1.2, 8.1 Hz), 7.36 (1H, dt, <i>J</i> = 1.3, 8.4 Hz), 7.40 (1H, dd, <i>J</i> = 1.5, 12.8 Hz), 7.42 (1H, dd, <i>J</i> = 1.5, 12.8 Hz), 7.64 (1H, t, <i>J</i> = 1.5 Hz), 7.65 (1H, t, <i>J</i> = 1.5 Hz)	1.40 (6H, br)	3.87/4.37 (2H, br)	4.20 (2H, br d, <i>J</i> = 9.5 Hz)	4.82 (2H, br)	—
5l	3-Pyridyl (a)	7.19–8.2 (8H, m)	1.44 (6H, d, <i>J</i> = 6.5)	3.82 (2H, br)	4.1 (2H, dd, <i>J</i> = 5, 8 Hz)	4.8 (2H, m)	—

Note: Recorded in either (a) CDCl<sub>3</sub> or (b) DMSO-*d*<sub>6</sub>.

Scheme 1. Proton labelling for interpretation of data in Table 2.



## Results and discussion

The target molecules, the 1,4-di-[2-aryl-1-diazenyl]-2,6-dimethylpiperazines (**5a–5l**), were synthesized by reacting 1 equiv. of 2,6-dimethylpiperazine with 2 equiv. of the appropriate diazonium salt. The products are mostly stable, crystalline solids, and the yields are variable in the range of 8%–69%. The products were first characterized by IR spectroscopy to confirm the presence of the aryl substituent, as indicated by the detection of bands from either carbonyl, nitrile, or nitro groups, and the OOP bending vibration characteristic of the substitution pattern. The molecular composition of eight compounds of the series was established by high-resolution EI mass spectrometry with accurate mass measurement of the molecular ion (see Table 4).

However, two compounds of the new series did not exhibit a molecular ion in the mass spectrum; these are the *p*-chloro derivative (**5d**) and the *p*-methoxy derivative (**5g**). Nevertheless, both of these compounds provided evidence in the mass spectra for a well-defined fragment (**6**) consistent with the 1,4-di-[2-aryl-1-diazenyl]-2,6-dimethylpiperazine structure. The common fragmentation pathway is shown in Scheme 3, in which the principle fragmentation is the cleavage of the N–N bond in one of the triazene moieties to give the aryldiazenylpiperazine fragment (**6**). The observed fragment of this pathway is observed at *m/e* 248 for **5g** and *m/e* 252/254 for **5d**. In the mass spectrum of **5g**, the base peak is found at *m/e* 135 (100%), which is assigned to the diazonium ion fragment (ArN<sub>2</sub><sup>+</sup>).

The essential features of the <sup>1</sup>H NMR data are consistent with the assigned structures (**5**). The first point to note is that the methyl groups at C2 and C6 are equivalent, and the signal is found in the range of 1.36–1.66 ppm. The second point is that the C2/C6 methyl signal is consistently a doublet with *J*, in the range of 5.5–7.0 Hz, due to the coupling with the adjacent methine proton, H<sub>a</sub>. The methine proton itself is observed as a broad hump in the range of 4.55–5.0 ppm. The extreme broadness of the methine proton signal, and some other protons, is a result of two factors: (a) the multiplicity of vicinal coupling with the methyl protons and with the diastereotopic methylene protons, H<sub>b</sub> and H<sub>c</sub>, and (b) the dynamic equilibrium associated with rotation around the N–N bond of the triazene moiety. In turn, the signals of the diastereotopic methylene protons, H<sub>b</sub> and H<sub>c</sub>, vary from extremely broad nondescript humps to broad doublets to well-defined doublets of doublets with coupling constants of ~6 and 13 Hz. The doublet of doublets is the expected multiplicity arising from the geminal coupling of H<sub>b</sub> with H<sub>c</sub> and the vicinal coupling (H<sub>a</sub> and H<sub>b</sub> or H<sub>a</sub> and H<sub>c</sub>).

The NMR spectra of the compounds **5b**, **5c**, **5f**, and **5g** also show the expected signals from protons of the substituents in the aryl groups. Indeed, the spectrum of the *p*-tolyl derivative **5f** is exceptional in showing two 3H signals for the tolyl methyl groups, which differ because of the nonequivalence of the aryl groups. The nonequivalence of the aryl groups is also evident from the analysis of the aromatic proton signals. Most of the *p*-substituted compounds in this series (**5a–5g**) show two distinct AA'BB' systems assigned to the two marginally different aryl rings, which arises because of the position of the C2/C6 methyl groups creating a dissymmetry in the molecule. The separation between the sets of signals averages out to ~0.02 ppm. The *o*-substituted analogues (**5j** and **5k**) also show two full sets of aromatic proton signals.

Further evidence for the nonequivalence of the aryl rings in **5** is supplied by analysis of the <sup>13</sup>C NMR spectra of these compounds (Table 2). Several of the *p*-substituted compounds in the series show clearly eight distinct frequencies



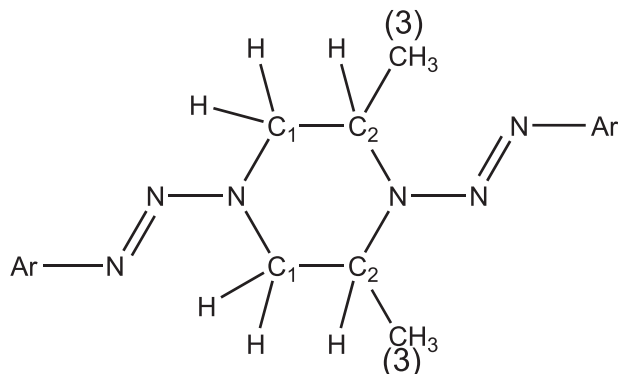
**Table 3.**  $^{13}\text{C}$  NMR spectroscopic data of the 1,4-di-[2-aryl-1-diazenyl]-2,6-dimethylpiperazines (**5a–5l**).

Compound No.	X	Aromatic	C1	C2	CH <sub>3</sub> (C3)	X
<b>5a</b>	<i>p</i> -CN (a)	119.7, 121.0, 133.1, 153.1 119.8, 120.9, 133.2, 153.5	51.0	53.3	17.0	107.7, 107.9
<b>5b</b>	<i>p</i> -CO <sub>2</sub> Me (b)	120.3, 126.1, 130.4, 153.7	51.5	52.7	17.9	52.2
<b>5c</b>	<i>p</i> -COMe (a)	120.7, 129.5, 134.7, 153.8	—	52.2	18.9(br)	26.5
<b>5d</b>	<i>p</i> -Cl (b)	121.8, 122.1, 129.0, 130.6, 148.1	50.3 (br)	—	15.4	—
<b>5e</b>	<i>p</i> -Br (a)	119.0, 122.5, 132.0, 148.5	50.2	51.6 (br)	15.15	—
<b>5f</b>	<i>p</i> -CH <sub>3</sub> (a)	120.5, 129.45, 135.5, 148.1 120.6, 129.5, 135.9, 148.5	51.6 <sup>a</sup>	51.6 <sup>a</sup>	19.2	21.0
<b>5g</b>	<i>p</i> -OCH <sub>3</sub> (a)	114.2, 121.8, 142.8, 158.3	50.2	49.2 (br)	15.2	54.85 (O-Me)
<b>5h</b>	H (a)	120.70, 121.0, 129.0, 149.2	52.1 <sup>b</sup>	49.8 (br) <sup>b</sup>	16.0	—
<b>5j</b>	<i>o</i> -CN (b)	117.3, 117.5, 125.76, 125.86, 126.5, 133.2, 133.3, 133.9, 151.6, 152.2, 152.7	51.0	54.1 (br)	16.0	106.5, 106.75
<b>5k</b>	<i>o</i> -Br (b)	118.8, 119.2, 128.0, 128.4, 132.9, 133.0, 146.7, 147.4	50.2 (br)	52.3 (br)	15.4	—
<b>5l</b>	3-Pyridyl (a)	123.4, 126.3, 143.2, 146.0	51.0 (br)	51.3 (br)	18.35	—

Note: Recorded in either (a) CDCl<sub>3</sub> or (b) DMSO-*d*<sub>6</sub>.

<sup>a</sup>Coincident signals, based on HSQC results.

<sup>b</sup>From HSQC spectrum.

**Scheme 2.** Carbon labels for interpretation of  $^{13}\text{C}$  NMR data.

in the aromatic region. The eight signals clearly fall into the pattern of two sets of four aromatic signals. Other features of the  $^{13}\text{C}$  NMR spectra are relevant to the interpretation of structure. The C-methyl carbon (at C3) is observed in the range of 15–19 ppm. The methine carbon (C2) is observed at 51–53 ppm and is always broadened due to the phenomenon of the dynamic equilibrium in the triazene moiety. The signal of the methylene carbon (C1) is also broad at ~50 ppm. Significantly, the nitrile carbons of the *o*-cyano derivative (**5j**) are distinguished at 106.5 and 106.75 ppm. The apparent reverse order of the C1 and C2 signals in **5h** is based on the HSQC spectrum.

The validity of the foregoing assignments is reinforced by the results acquired from the HSQC 2D NMR spectra of several of the compounds in the series **5a–5l**. For example, the HSQC spectrum of the *p*-tolyl derivative **5f** shows a clear correlation of the tolyl methyl carbon at 21.0 ppm with the tolyl methyl protons at 2.37 ppm. Also, in **5f** the methyl carbon signal of the C-methyl carbon at 19.2 ppm correlates with the doublet methyl signal at 1.43 ppm. The carbon peak at 51.6 ppm correlates with the proton signals of H<sub>a</sub> (3.86 ppm), H<sub>b</sub> (4.23 ppm), and H<sub>c</sub> (4.80 ppm), showing

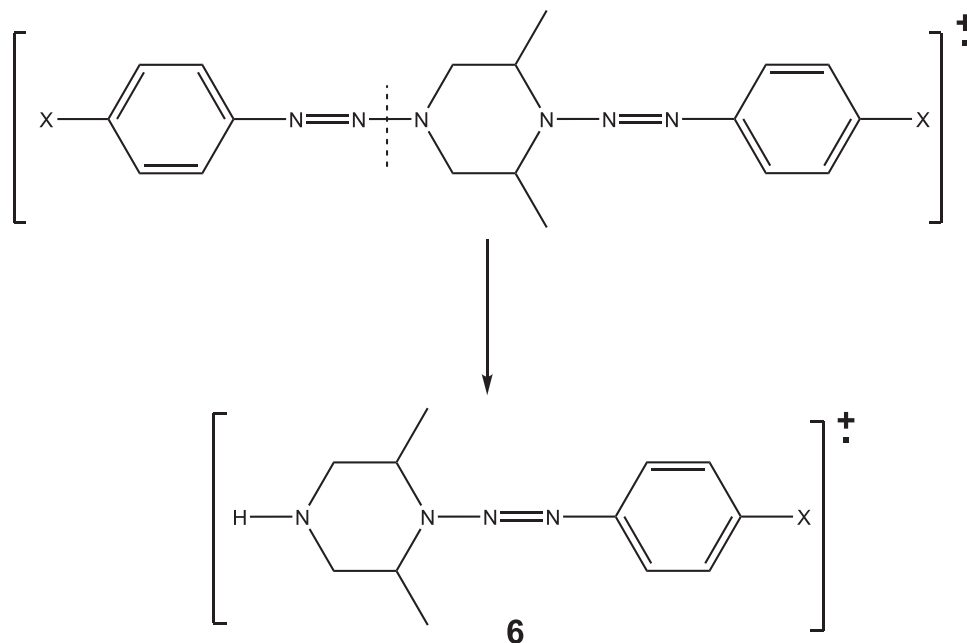
that the C1 and C2 carbon resonances are coincident at 51.6 ppm. The aromatic carbon signals at 120.5/120.6 ppm correlate with the aromatic protons at ~7.38 ppm, whereas the aromatic carbon signals at 129.45/129.50 ppm correlate with the aromatic protons at ~7.20 ppm.

Looking at the HSQC results in general, the aromatic carbon/aromatic hydrogen correlation is observed in the spectra of **5a**, **5b**, **5e**, **5f**, **5g**, **5h**, **5j**, and **5k**. All of the compounds exhibit peaks for the C2 methyl/proton correlation, and the correlation of the C1 signal with protons H<sub>b</sub> and H<sub>c</sub>. The C2/H<sub>a</sub> correlation is shown by compounds **5a**, **5e**, **5f**, **5g**, **5h**, **5j**, and **5k**. The C1/(H<sub>b</sub> + H<sub>c</sub>) correlation is also shown by compound **5a**, which for some reason did not show a C2 methyl/proton correlation. Correlations of the methyl carbon and methyl hydrogens of the substituent X were shown in compounds **5b**, **5f**, and **5g**.

These results compare favorably with the NMR parameters previously observed and assigned in the spectra of triazenes of types **1**,<sup>1</sup> **3**,<sup>4</sup> and **4**.<sup>6</sup> The methylene carbon in the piperazine ring of compounds of type **1** occurs at ~47 ppm, and the methylene protons of structure **1** give rise to proton signals at ~3.9 ppm. The assignments of the resonances of the methine carbons, C2, to the signal at 51–53 ppm, compares with the assignment of C2 in series **4** to the signal at ~53 ppm. The resonance of the equivalent C1 methylene carbon atoms in **5** is observed in the range of 50–51 ppm, which is a little different than the observed methylene resonance at ~46–47 ppm in the bis-triazenes of type **3** and at ~46 ppm in the series of type **4**. The 2 equiv. methyl substituents attached at C2 and C6 of the piperazine ring give rise to a  $^{13}\text{C}$  signal in the range of 15–19 ppm, compared to the methyl resonance at 16.0 ppm in triazenes of type **4**. In the symmetrical bis-triazenes of type **3**, the homotopic methylene protons of the piperazine ring give rise to a proton signal at ~4.1 ppm, which compares with the chemical shift assigned to the diastereotopic methylene protons in **5a–5l** in the range of 3.4–4.3 ppm. Thus, there is significant

**Table 4.** High-resolution mass spectral (EI) data for compounds in the series 1,4-di-[2-aryl-1-diazenyl]-2,6-dimethylpiperazines (**5a–5k**).

Compound No.	Substituent	Formula	Calculated mass (amu)	Found mass (amu)
<b>5a</b>	<i>p</i> -CN	C <sub>20</sub> H <sub>20</sub> N <sub>8</sub>	372.1811	372.1805
<b>5b</b>	<i>p</i> -CO <sub>2</sub> Me	C <sub>22</sub> H <sub>26</sub> N <sub>6</sub> O <sub>4</sub>	438.2015	438.2015
<b>5c</b>	<i>p</i> -COMe	C <sub>22</sub> H <sub>26</sub> N <sub>6</sub> O <sub>2</sub>	406.2117	406.2116
<b>5d</b>	<i>p</i> -Cl	C <sub>18</sub> H <sub>20</sub> N <sub>6</sub> Cl <sub>2</sub>	391.1204	No M <sup>+</sup>
<b>5e</b>	<i>p</i> -Br	C <sub>18</sub> H <sub>20</sub> N <sub>6</sub> Br <sub>2</sub>	478.0116	478.0119
<b>5f</b>	<i>p</i> -CH <sub>3</sub>	C <sub>20</sub> H <sub>26</sub> N <sub>6</sub>	350.2219	350.2213
<b>5g</b>	<i>p</i> -OCH <sub>3</sub>	C <sub>20</sub> H <sub>26</sub> N <sub>6</sub> O <sub>2</sub>	382.2117	No M <sup>+</sup>
<b>5h</b>	H	C <sub>18</sub> H <sub>22</sub> N <sub>6</sub>	322.1906	322.1905
<b>5j</b>	<i>o</i> -CN	C <sub>20</sub> H <sub>20</sub> N <sub>8</sub>	372.1811	372.1833
<b>5k</b>	<i>o</i> -Br	C <sub>18</sub> H <sub>20</sub> N <sub>6</sub> Br <sub>2</sub>	478.0116	478.0114

**Scheme 3.**

agreement in the NMR parameters among these compounds, but there is an additional degree of complexity in the spectra of compounds of series **5** due to the introduction of the stereocentres at C2 and C6, resulting in the diastereotopic methylene protons, H<sub>b</sub> and H<sub>c</sub>, giving rise to distinct NMR signals in the range of 3.4–4.0 and 4.2–4.4 ppm. However, there is insufficient data available to precisely assign the observed signals to either H<sub>b</sub> or H<sub>c</sub>.

## Conclusion

This paper is part IX in a series that describes the synthesis of a variety of triazenes and bis-triazenes that fit the general classification of 1-aryldiazenyl-(1,*x*)-diazacycloalkanes described by the general structure **7** (Chart 1), where *m* = 1 or 2 and *n* = 2, 3, 4, or 5. Previously, we reported new triazenes derived from imidazolidine (*m* = 1, *n* = 2),<sup>7</sup> hexahydropyrimidine (*m* = 1, *n* = 3),<sup>8</sup> piperazine (*m* = *n* = 2),<sup>1,4,6</sup> and homopiperazine (*m* = 2, *n* = 3).<sup>3</sup> The new piperazines of series **5** fit to the general structure **7** where *m* = 2 and *n* = 2. Future work in this field of chemistry will

endeavour to further extend the family of 1,4-di-(2-aryl-1-diazenyl)piperazines by preparing derivatives with a variety of substituents in the piperazine ring.

## Supplementary data

Supplementary data for this article are available on the journal Web site ([canjchem.nrc.ca](http://canjchem.nrc.ca)) or may be purchased from the Depository of Unpublished Data, Document Delivery, CISTI, National Research Council Canada, Ottawa, ON K1A 0R6, Canada. DUD 5358. For more information on obtaining material, refer to [cisti-icist.nrc-cnrc.gc.ca/cms/unpub\\_e.shtml](http://cisti-icist.nrc-cnrc.gc.ca/cms/unpub_e.shtml).

## Acknowledgements

The authors are grateful to the Natural Sciences and Engineering Research Council of Canada (NSERC) for a Discovery Grant to the principal author (KV) and an Undergraduate Summer Research Award (2004) to Naomi Hunter. We are also grateful to the Faculty of Graduate Studies and Research at Saint Mary's University for a Summer Research

Award (2005). We are also grateful to the Atlantic Region Magnetic Resonance Centre at Dalhousie University for providing NMR spectra, and to Dalhousie University for providing mass spectral data. In particular, we would like to thank Dr. Kathy Robertson for assistance with the NMR spectral data and Mr. Xiao Feng for assistance with mass spectra.

## References

- (1) Little, V. R.; Vaughan, K. *Can. J. Chem.* **2004**, *82* (8), 1294. doi:10.1139/v04-081.
- (2) Little, V. R.; Jenkins, H.; Vaughan, K. *J. Chem. Crystallogr.* **2008**, *38* (6), 447. doi:10.1007/s10870-008-9340-z.
- (3) Moser, S. L.; Vaughan, K. *Can. J. Chem.* **2004**, *82* (12), 1725. doi:10.1139/v04-153.
- (4) Little, V. R.; Tingley, R.; Vaughan, K. *Can. J. Chem.* **2005**, *83* (5), 471. doi:10.1139/v05-064.
- (5) Yanarates, E.; Disli, A.; Yildirim, Y. *Org. Prep. Proced. Int.* **1999**, *31* (4), 429. doi:10.1080/00304949909355733.
- (6) Hunter, N.; Tingley, R.; Peori, M. B.; Vaughan, K. *Can. J. Chem.* **2007**, *85* (3), 189. doi:10.1139/V07-013.
- (7) Glister, J. F.; Vaughan, K. *J. Heterocycl. Chem.* **2006**, *43* (1), 217. doi:10.1002/jhet.5570430134.
- (8) Moser, S. L.; Church, R.; Peori, M. B.; Vaughan, K. *Can. J. Chem.* **2005**, *83* (8), 1071. doi:10.1139/v05-131.

# Theoretical study of H bonds of HArF and HF with isoelectronic systems N<sub>2</sub>, CO, and BF

An Yong Li, Li Juan Cao, and Hong Bo Ji

**Abstract:** The H bonds of HArF and HF with N<sub>2</sub>, CO, and BF were studied at the MP2(full)/6-311++G(2d, 2p) level. The results show that only the complexes WY...HArF (WY = N<sub>2</sub>, OC) and WY...HF (WY = N<sub>2</sub>, OC, FB) are stable, the H-bonding WY...HArF leads to contraction of the HAr bond with a concomitant frequency blue shift, but the H-bonding WY...HF causes the HF bond to elongate with a frequency red shift. A quantity  $P$  is defined to measure polarization of the HX bond; the H bonding causes the  $P$  value of the HX bond (X = Ar, F) to increase. The HX bond length change and frequency shift in the H-bonding WY...HArF and WY...HF are mainly caused by intermolecular hyperconjugation,  $n(Y) \rightarrow \sigma^*(HX)$  (X = Ar, F), where electrostatic interaction has only a small contribution. In HArF, the strong intramolecular hyperconjugation,  $n(F) \rightarrow \sigma^*(HAr)$ , can adjust electron density on  $\sigma^*(HAr)$ ; upon formation of H bonding, the HAr stretching frequency blue shift is caused by a decrease of intramolecular hyperconjugation and an increase of the s character of the Ar hybrid in the HAr bond, induced by the intermolecular hyperconjugation. In the H bonds of HF without intramolecular hyperconjugation, the intermolecular hyperconjugation,  $n(Y) \rightarrow \sigma^*(HF)$ , leads to a red shift of the HF bond, although there is also large rehybridization.

**Key words:** H bonds, HArF, hyperconjugation, polarization of bonds.

**Résumé :** Faisant appel à des méthodes de calcul au niveau MP2(complet)/6-311++G(2d,2p), on a étudié les formations de liaisons entre les atomes d'hydrogène des HArF et HF avec N<sub>2</sub>, CO et BF. Les résultats montrent que seuls les complexes WY...HArF (WY = N<sub>2</sub>, OC) et WY...HF (WY = N<sub>2</sub>, OC, FB) sont stables, que la liaison hydrogène WY...HArF conduit à une contraction de la liaison HAr avec un déplacement concomitant de la fréquence vers le bleu alors que la liaison hydrogène WY...HF provoque une elongation de la liaison HF avec un déplacement vers le rouge. On a défini une quantité  $P$  pour mesurer la polarisation de la liaison HX; la liaison hydrogène provoque une augmentation de la valeur de  $P$  pour la liaison HX (X = Ar, F). Le changement de la longueur de la liaison HX et le déplacement de fréquence dans la liaison hydrogène WY...HArF et WY...HF sont causés principalement par une hyperconjugaison intermoléculaire  $n(Y) \rightarrow \sigma^*(HX)$  (X = Ar, F) alors que l'interaction électrostatique ne fait qu'une faible contribution. Dans HArF, la forte hyperconjugaison intramoléculaire  $n(F) \rightarrow \sigma^*(HAr)$  peut ajuster la densité électronique sur  $\sigma^*(HAr)$ ; par formation d'une liaison hydrogène, le déplacement vers le bleu de la fréquence d'elongation de HAr est provoqué par une diminution de l'hyperconjugaison intramoléculaire et une augmentation du caractère s de l'hybride Ar dans la liaison HAr induites par l'hyperconjugaison intermoléculaire. Dans les liaisons hydrogènes du HF sans hyperconjugaison intramoléculaire, l'hyperconjugaison intermoléculaire  $n(Y) \rightarrow \sigma^*(HF)$  conduit à un déplacement vers le rouge de la liaison HF, même s'il n'y a aucune réhybridisation importante.

**Mots-clés :** liaisons hydrogènes, HArF, hyperconjugaison, polarisations des liaisons.

[Traduit par la Rédaction]

## Introduction

Hydrogen bonding<sup>1-3</sup> and dihydrogen bonding<sup>4,5</sup> have extensive applications in chemistry and biology, and have been important topics in recent years. The most important spectroscopic criterion for the formation of a hydrogen bond, Y...H-X, is the elongation of the HX bond with a concomitant frequency red shift and an increase of IR intensity. It is well-known that a red shift of the HX bond in a H bond is mainly caused by two factors: (1) electrostatic attraction between the positive charge of H and the rich electron end of the proton acceptor and (2) electron density transfer from

the proton acceptor Y to the donor caused by the intermolecular hyperconjugation,  $n(Y) \rightarrow \sigma^*(HX)$ . However, the discovery of blue-shifted H bonds makes the problem much more complicated.<sup>6</sup> The physical and chemical essence of a stretching frequency blue shift of the HX bond in an improper H bond, Y...H-X, has being an important problem in the field of H bonding that remains unaddressed. Several valuable theories have been proposed to explain the blue shift, including the two-step mechanism of Hobza and Havlas,<sup>6</sup> the theory of the balance of attractive and repulsive interactions,<sup>7</sup> and the theory of hyperconjugation and rehybridization of

Received 13 October 2009. Accepted 14 December 2009. Published on the NRC Research Press Web site at canjchem.nrc.ca on 10 March 2010.

A.Y. Li,<sup>1</sup> L.J. Cao, and H.B. Ji. School of Chemistry and Chemical Engineering, Southwest University, Beibei District, Chongqing 400715, P. R. China.

<sup>1</sup>Corresponding author (e-mail: aylifnsy@swu.edu.cn).



Alabugin et al.<sup>8</sup> The last theory has attracted the attention of chemists and been developed by introducing intramolecular hyperconjugation.<sup>9</sup>

The H-bonding interaction includes electrostatic interaction, charge transfer and electron exchange repulsion, and so on. They induce changes in the internal electronic and molecular structures in the proton donor, which include the following: (i) Repolarization: polarization of the HX bond enhances, but the polarization strength of the HX bond does not correlate consistently with the strength and length of the HX bond. (ii) Rehybridization: the *s* character in the X hybrid orbital,  $h(sp^n)$ , of the HX bond increases, which causes contraction of the HX bond. (iii) Intramolecular hyperconjugation: as there exists strong intramolecular hyperconjugation,  $n(Z) \rightarrow \sigma^*(HX)$ , in the proton donor H–X–Z, the lone pair,  $n(Z)$ , is like an electron density reservoir and can adjust electron density in  $\sigma^*(HX)$  through the intramolecular hyperconjugation; in some cases, this causes occupancy on  $\sigma^*(HX)$  to decrease so that the HX bond enhances. The bond length change and frequency shift of the HX bond in the equilibrium H-bonding complex is a result of the balance of all these factors: intermolecular electrostatic interaction, charge transfer and repulsion, and adjustment of internal electronic and molecular structures in the proton donor. The decisive factor is different for different kinds of systems, especially for blue-shifted H bonds.

Since the compound HArF was detected in spectroscopy,<sup>10</sup> the rare gas compounds, HRgX (Rg = rare gas such as Ar and Kr, X is an element with high electronegativity), have attracted the attention of experimentalists and theorists.<sup>11–15</sup> Theoretical studies show that HArF contains a covalent bonding of the H–Ar bond and an ion bonding of the Ar–F bond, and has a ion-pair character,  $(HAr)^+F^-$ .<sup>16,17</sup>

HRgX can act as proton donor to participate in H bonding and dihydrogen bonding. It was found<sup>18</sup> that the linear  $N_2 \cdots HArCl$  hydrogen bonding leads to a large blue shift of  $113\text{ cm}^{-1}$  for the HAr bond stretch frequency, and the blue shift was attributed to the enhanced  $(HAr)^+Cl^-$  ion-pair character of the complex resulting in a stronger H–Ar covalent bond. Theoretical<sup>19–21</sup> and experimental<sup>22</sup> studies have shown that the HRg bond enhances and contracts with a concomitant frequency blue shift in the linear H-bonding  $N_2 \cdots HArF$  and  $N_2 \cdots HKrF$ . McDowell<sup>19–21</sup> attributed the blue shift to electron density transfer from  $\sigma^*(HAr)$  to  $n(F)$  caused by a negative quadrupole moment of  $N_2$ , which enhances the  $(HAr)^+F^-$  ion-pair character. This shortening of the HRg bond caused by electron density transfer exceeds elongation caused by electrostatic attraction between the protonated H and the negative-charge end of the quadrupole moment of  $N_2$ . However,  $P_2 \cdots HArF$  is a red-shifted H bond. The author rationalized the red shift by a charge transfer from  $n(F)$  to  $\sigma^*(HAr)$  caused by a positive quadrupole moment of  $P_2$ . This explanation of charge transfer caused by quadrupole moment does not work in the case of the dihydrogen bonding,  $HBeH \cdots HRgF$  (Rg=Ar, Kr).<sup>23</sup>  $HBeH$  has a large negative quadrupole moment three times larger than that of  $N_2$ ; however, the HRg bond weakens and elongates with a concomitant frequency red shift in these complexes. McDowell<sup>19–21</sup> attributed the red shift to the strong electrostatic attraction between the protonated H and the negative-charge end of the quadrupole moment of  $HBeH$ .

Although the H bond  $N_2 \cdots HArF$  is blue-shifted, it is well-known that the H bond  $N_2 \cdots HF$  is red-shifted. Obviously, the different frequency shift character in these two complexes is mainly due to the difference of the proton donors HArF and HF. Compared to the red-shifted dihydrogen bond  $HBeH \cdots HArF$  and H bond  $P_2 \cdots HArF$ , the proton acceptor  $N_2$  is crucial for a blue shift of  $N_2 \cdots HArF$ . What about the frequency shift of the H bonds if  $N_2$  is replaced by its isoelectronic molecules CO or BF? In this article, we theoretically study the H bonds of the proton donors HArF and HF with the acceptors  $N_2$ , CO, and BF, observing the frequency shift character and exploring the mechanism of frequency shift. One of the important purposes is to study the importance of the proton donor structure on frequency shift of the H bonds.

## Computation methods

All the calculations in this article were performed at the MP2(full)/6-311++G(2d, 2p) level by using the Gaussian 03 program.<sup>24</sup> The geometric structures of all the monomers and complexes were completely optimized without freezing any internal coordinate and the frequencies of normal vibrational modes were calculated. The interaction energies were computed with BSSE correction by means of the functional counterpoise method proposed by Boys and Bernardi.<sup>25</sup> We used the AIM2000 program to perform topological analysis of electron density and study properties of chemical bonds.<sup>26–28</sup> The NBO5.0 program<sup>29</sup> was applied to carry out natural bond orbital (NBO) analysis to study polarization of chemical bonds, hybridization of atomic orbitals, and interaction between molecular orbitals. Point charge models were used to mimic the electrostatic field of the proton acceptor and investigate contributions of electrostatic interaction and charge transfer to bond length change and frequency shift in the proton donor upon formation of H bonding.

## Results and discussion

### Changes of bond lengths, frequency shift, and interaction energies

The optimized structures of all the monomers and complexes are linear. The vibrational analysis shows that all the complexes have no imaginary frequency and so are minima in the potential energy surface, except for  $FB \cdots HArF$ , which has two imaginary frequencies and is equivalent to  $(F-B-H)^+ArF^-$ . The bond lengths and vibrational frequencies of the monomers and complexes are listed in Table 1. Upon formation of the H-bonding  $WY \cdots HArF$  with  $WY = N_2$ , CO, OC, and BF, the HAr bond contracts and its stretching frequency increases, and the ArF bond elongates and its stretch frequency decreases. However, the H-bonding  $WY \cdots HF$  with  $WY = N_2$ , CO, OC, BF, and FB leads to elongation of the HF bond with a concomitant frequency red shift. The blue shift of the HAr bond increases in the order of the proton acceptors  $WY = OC$ , BF, CO, and  $N_2$ , but the red shift of the HF bond increases in the order of  $WY = BF$ , CO,  $N_2$ , OC, and FB. Interestingly, in the two classes of complexes, the change of the proton acceptors is consistent. In the complexes  $WY \cdots HArF$  and  $WY \cdots HF$  with  $WY = BF$  and CO, the WY bond length increases and stretching fre-

**Table 1.** Bond lengths and vibrational frequencies of the monomers and complexes. The bond lengths and frequencies of N<sub>2</sub>, CO, and BF are 1.1127, 1.1367, and 1.2664 Å, and 2179, 2120, and 1401 cm<sup>-1</sup>, respectively.

(a) WY...HArF with WY = N <sub>2</sub> , CO, OC, and BF								
Systems	<i>r</i> (HAr)	<i>v</i> (HAr)	<i>r</i> (ArF)	<i>v</i> (ArF)	<i>v</i> (HArF) <sup>a</sup>	<i>r</i> (WY)	<i>v</i> (WY)	<i>r</i> (Y...H)
HArF	1.3263	2148	1.9964	480	743	—	—	—
OC...HArF	1.3245	2162	2.0673	411	828	1.1322	2149	1.9556
BF...HArF	1.3207	2226	2.0019	472	738	1.2763	1345	2.4088
CO...HArF	1.3152	2293	2.0118	462	733	1.1383	2112	2.2719
N <sub>2</sub> ...HArF	1.3141	2304	2.0275	447	739	1.1124	2180	2.1492
(b) WY...HF with WY = N <sub>2</sub> , CO, OC, BF, and FB								
Systems	<i>r</i> (HF)	<i>v</i> (HF)	<i>r</i> (WY)	<i>v</i> (WY)	<i>r</i> (Y...H)			
HF	0.9173	4170	—	—	—			
BF...HF	0.9177	4167	1.2745	1357	2.1445			
CO...HF	0.9186	4146	1.1376	2118	2.0961			
N <sub>2</sub> ...HF	0.9205	4100	1.1119	2187	2.0667			
OC...HF	0.9242	4010	1.1336	2146	2.0675			
FB...HF	0.9301	3865	1.2579	1460	2.1193			

<sup>a</sup>*ν*(HArF) is the frequency of bent vibration of the bond angle H–Ar–F.

quency decreases; but in the complexes of WY = N<sub>2</sub>, OC, and FB, the WY bond length decreases with a concomitant stretching frequency blue shift. In the red-shifted H-bonding WY...HF, the HF bond length and frequency is a linear correlation; in the blue-shifted H-bonding WY...HArF, the bond length and frequency of the HAr and ArF bonds are also linear correlations, as shown in Fig. 1.

The interaction energies,  $\Delta E_{\text{int}}$ , with BSSE correction and 0 K dissociation energies,  $D_0$ , with BSSE and ZPE corrections for the H bonding are listed in Table 2. In this article the interaction energy is calculated as the sum of energies of the monomers minus the energy of the complex, reversed the common convention, such that positive  $\Delta E_{\text{int}}$  indicates binding. The  $D_0$  value shows that only the five complexes WY...HArF with WY = N<sub>2</sub> and OC and WY...HF with WY = N<sub>2</sub>, OC, and FB are stable. Both for the blue-shifted H-bonding WY...HArF and the red-shifted H-bonding WY...HF, the energy increases in the order of the acceptors WY = BF, CO, N<sub>2</sub>, OC, and FB. This order is the same order of the red shift of the HF bond for the red-shifted H bonds, as shown in Fig. 1d, but is different from the order of the blue shift of the HAr bond for the blue-shifted H bonds, as shown in Fig. 1e.

### Topological analysis of electron density

Electron density topology based on the theory of atoms in molecules (AIM) can characterize chemical bonds. The calculated electron density and Laplacian at BCPs in the monomers and complexes are listed in Table 3. In the monomer HArF, electron density  $\rho > 0.1$  au and Laplacian  $\nabla^2\rho < 0$  at the HAr bond critical point (BCP) show that the HAr bond is a covalent bond, but  $\rho < 0.1$  au and Laplacian  $\nabla^2\rho > 0$  at the ArF BCP show that the ArF bond is a closed interaction, i.e., an ionic bond. The electron density and Laplacian at the intermolecular BCPs show that the H bonding is also a closed interaction.

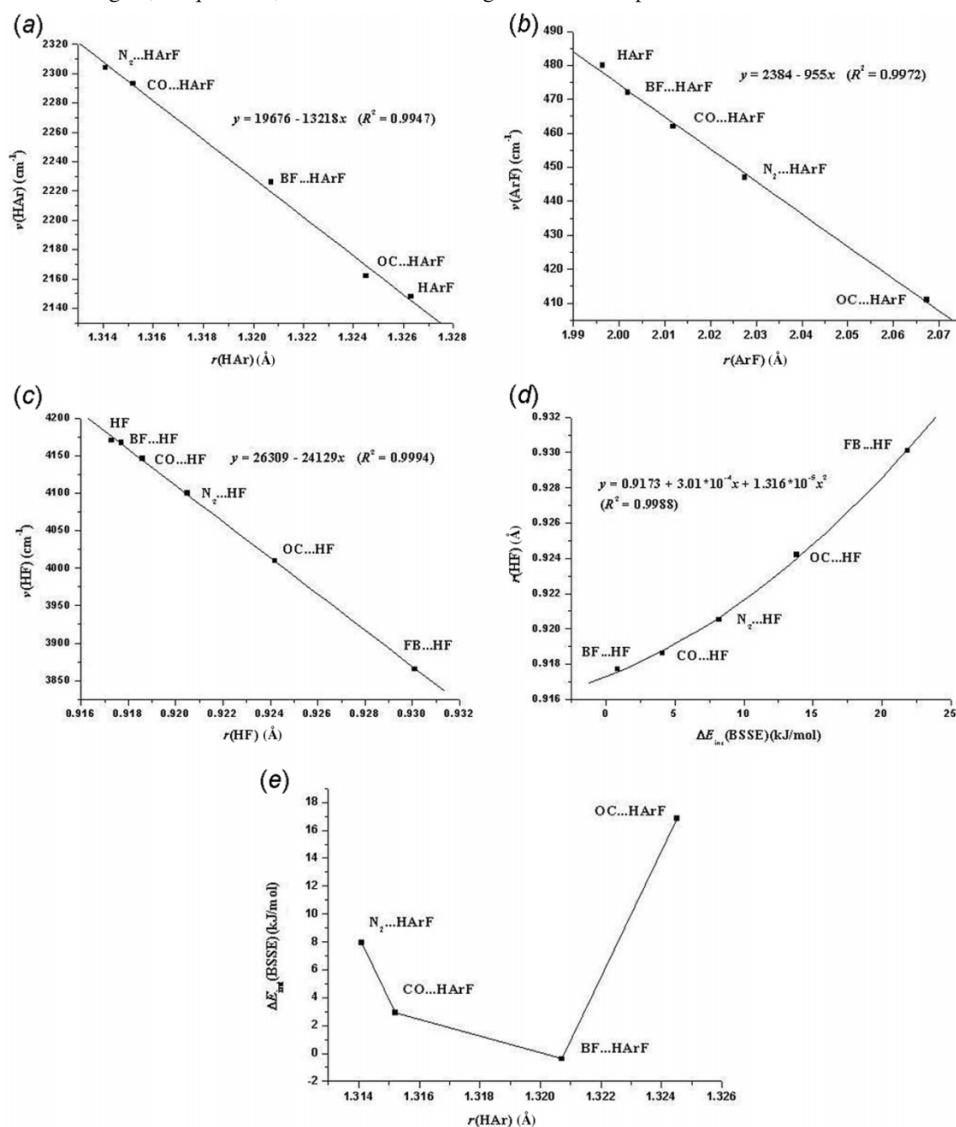
The magnitude of electron density at the BCP can characterize the strength of a chemical bond. In the complexes WY...HArF, electron density at the HAr BCP is larger than that in the monomer HArF, which is consistent with contrac-

tion and frequency blue shift of the HAr bond; electron density at the HAr BCP increases in the order of the blue shift, i.e., OC < BF < CO < N<sub>2</sub>. Moreover, electron density at the ArF bond is smaller than that in the monomer, which is consistent with the red shift of this bond; electron density at the ArF bond decreases in the order of the red shift, i.e., BF > OC > N<sub>2</sub> > CO. In the complexes WY...HF, electron density at the HF BCP is smaller than that in the monomer HF, which is consistent with the elongation and frequency red shift of the HF bond; electron density at the HF BCP decreases in the order of the red shift, i.e., BF > CO > N<sub>2</sub> > OC > FB. Similarly, an increase or decrease of electron density at the WY BCPs compared to the monomer is also consistent with a blue or red shift of this bond. Electron density at the Y...H BCP shows the strength of the H bonding and an increase with the interaction energy, i.e., BF < CO < N<sub>2</sub> < OC < FB. Here, we note that for red-shifted H bonding, changes in all kinds of properties are correlated with each other, but for blue-shifted H bonding, it is not the case. So, the blue-shifted H bonding is more complicated than the red-shifted H bonding.

### Charge transfer and inter- and intra-molecular hyperconjugations

The H-bonding interaction includes electrostatic interaction between permanent and induced multipole moments of the monomers, charge transfer, nuclear and electron exchange repulsions, and so on. The importance of these interactions is different for different kinds of H bonding. Generally, at larger intermolecular distance, there is only electrostatic attraction; at a smaller distance, repulsion is predominant; at equilibrium distance, attractive and repulsive interactions balance, and electrostatic interaction and charge transfer have important contributions to the interaction energy. We first discuss charge transfer.

In a H-bonding Y...HX, charge transfer is a result of intermolecular hyperconjugation between the electron donor,  $n(Y)$ , and acceptor,  $\sigma^*(HX)$ . The hyperconjugation energy is the second order perturbation energy,  $\Delta E^{(2)} = n(Y) \langle n | \text{Flo}^* \rangle^2 / (\epsilon_{\sigma^*} - \epsilon_n)$ , where  $n(Y)$  is the occupancy on

**Fig. 1.** Correlations of bond lengths, frequencies, and interaction energies in the complexes of HArF and HF.**Table 2.** Interaction Energies  $\Delta E_{\text{int}}$  (kJ/mol) with BSSE correction and 0K dissociation energies  $D_0$  (kJ/mol) with BSSE and ZPE corrections.

Systems	$\Delta E_{\text{int}}$	$D_0$
BF...HArF	-0.39	-2.64
CO...HArF	2.91	-0.21
N <sub>2</sub> ...HArF	7.96	4.09
OC...HArF	16.86	11.93
BF...HF	0.85	-4.22
CO...HF	4.11	-1.77
N <sub>2</sub> ...HF	8.19	1.23
OC...HF	13.83	5.58
FB...HF	21.86	13.22

the lone pair  $n(Y)$ ,  $\langle n|\text{F}| \sigma^* \rangle$  is the Fock matrix element, and  $\epsilon_{\sigma^*}$  and  $\epsilon_n$  are, respectively, the orbital energies of  $\sigma^*(\text{HX})$  and  $n(Y)$ . So, the larger the overlap between the two orbitals and the smaller their energy difference, the larger the hyperconjugation and charge transfer. In Table 4 we list the graphs, energies, and hybridization of the donor orbitals in

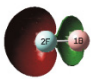
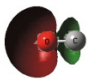
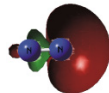
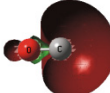
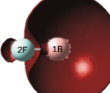
the proton acceptors N<sub>2</sub>, CO, and BF. From F to O to N to C to B, the donor orbital diffuses more and more so that its overlap with the acceptor orbital is larger and larger, and the absolute of energy of the donor orbital is smaller and smaller (the energy of the acceptor orbital is positive), therefore, the hyperconjugation is larger and larger. This conclusion is confirmed by the results of NBO analysis listed in Table 5. Electron density transfer (EDT),  $\Delta n(Y)$  (decrease of occupancy on the lone pair  $n(Y)$ ), and the hyperconjugation energy,  $E\{n(Y) \rightarrow \sigma^*(\text{HX})\}$  ( $X = \text{Ar}, \text{F}$ ), increase in the order of  $\text{WY} = \text{BF}, \text{CO}, \text{N}_2, \text{OC}$ , and  $\text{FB}$ . Since the orbital energy of  $\sigma^*(\text{HAr})$  in the monomer HArF, 0.1714 au, is smaller than that of  $\sigma^*(\text{HF})$  in the monomer HF, 0.7009 au, so  $\sigma^*(\text{HAr})$  is a stronger hyperconjugation acceptor than  $\sigma^*(\text{HF})$ . The hyperconjugation in the H-bonding  $\text{WY} \cdots \text{HArF}$  is larger than that in the H-bonding  $\text{WY} \cdots \text{HF}$  for the same WY.

One of the most important effects of intermolecular hyperconjugation on the monomers is to change occupancy on the involved orbitals. It transfers electron density from  $n(Y)$  to  $\sigma^*(\text{HX})$  so that occupancy on  $n(Y)$  decreases and occupancy

**Table 3.** Electron density and Laplacian at BCPs. The electron density and Laplacian at the BCPs of the monomers N<sub>2</sub>, CO, and BF are 0.6770 and −2.7628, 0.4948 and 0.3134, and 0.2342 and 1.5908, respectively.

<b>(a) HArF</b>								
Systems	$\rho(\text{HAr})$	$\nabla^2\rho(\text{HAr})$	$\rho(\text{ArF})$	$\nabla^2\rho(\text{HAr})$	$\rho(\text{Y}\cdots\text{H})$	$\nabla^2\rho(\text{Y}\cdots\text{H})$	$\rho(\text{WY})$	$\nabla^2\rho(\text{WY})$
HArF	0.2252	−0.6732	0.0859	0.3793	—	—	—	—
BF $\cdots$ HArF	0.2280	−0.7029	0.0845	0.3781	0.0060	0.0246	0.2245	1.5444
CO $\cdots$ HArF	0.2306	−0.7397	0.0822	0.3741	0.0094	0.0358	0.4908	0.2821
N <sub>2</sub> $\cdots$ HArF	0.2308	−0.7591	0.0791	0.3633	0.0155	0.0512	0.6750	−2.7328
OC $\cdots$ HArF	0.2219	−0.7595	0.0716	0.3397	0.0318	0.0559	0.4997	0.4115
<b>(b) HF</b>								
Systems	$\rho(\text{HF})$	$\nabla^2\rho(\text{HF})$	$\rho(\text{Y}\cdots\text{H})$	$\nabla^2\rho(\text{Y}\cdots\text{H})$	$\rho(\text{WY})$	$\nabla^2\rho(\text{WY})$		
HF	0.3814	−3.5877	—	—	—	—		
BF $\cdots$ HF	0.3800	−3.6091	0.0086	0.0448	0.2261	1.5587		
CO $\cdots$ HF	0.3777	−3.6172	0.0115	0.0548	0.4918	0.3021		
N <sub>2</sub> $\cdots$ HF	0.3749	−3.5944	0.0157	0.0647	0.6765	−2.7496		
OC $\cdots$ HF	0.3692	−3.5249	0.0208	0.0626	0.4982	0.3713		
FB $\cdots$ HF	0.3593	−4.2743	0.0238	0.0421	0.2418	1.6414		

**Table 4.** Graphs, energies, and hybridization of the donor orbitals  $n(\text{Y})$ .

Orbitals	$n(\text{F})$	$n(\text{O})$	$n(\text{N})$	$n(\text{C})$	$n(\text{B})$
Molecule	BF	CO	N <sub>2</sub>	CO	BF
Graph					
Energy (arb. unit)	−1.3477	−1.0424	−0.8553	−0.6687	−0.4658
Hybridization	sp <sup>0.77</sup>	sp <sup>0.85</sup>	sp <sup>0.62</sup>	sp <sup>0.36</sup>	sp <sup>0.16</sup>

**Table 5.** Charge transfer from WY to HXZ, changes of occupancies in the NBOs  $n(\text{Y})$  of WY,  $\sigma^*(\text{HX})$  and  $n(\text{Z})$  of HXZ, and the hyperconjugation energies,  $E\{n(\text{Z}) \rightarrow \sigma^*(\text{HX})\}$  and  $E\{n(\text{Y}) \rightarrow \sigma^*(\text{HX})\}$  (kcal/mol).

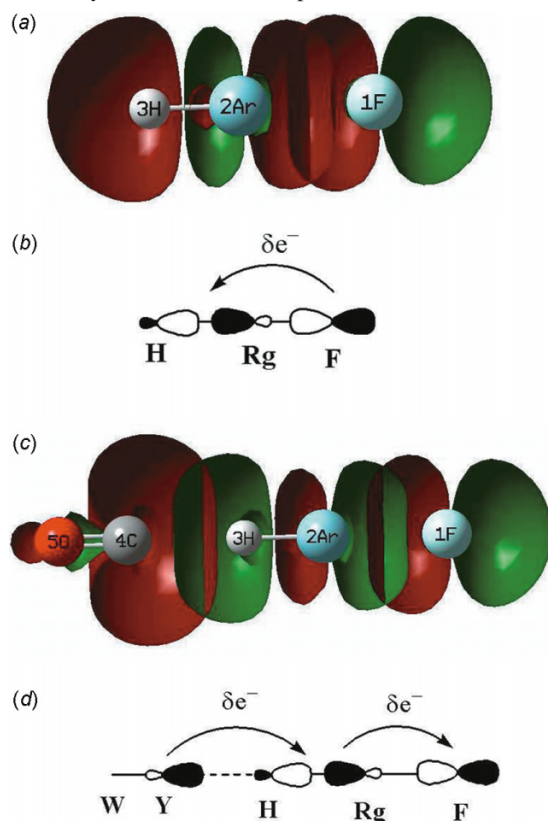
<b>(a) HArF: X = Ar, Z = F</b>					
Properties	BF $\cdots$ HArF	CO $\cdots$ HArF	N <sub>2</sub> $\cdots$ HArF	OC $\cdots$ HArF	
EDT	−0.00044	0.00265	0.01108	0.07942	
$\Delta n(\text{Y})$	−0.00059	−0.00237	−0.01131	−0.08038	
$\Delta\sigma^*(\text{HAr})$	−0.00549	−0.01243	−0.01036	0.03623	
$\Delta n(\text{F})$	0.00846	0.01871	0.02688	0.04803	
$E\{n(\text{F}) \rightarrow \sigma^*(\text{HAr})\}$	36.25	33.57	31.2	24.8	
$E\{n(\text{Y}) \rightarrow \sigma^*(\text{HAr})\}$	0.59	1.83	6.7	39.04	
<b>(b) HF: X = F</b>					
Properties	BF $\cdots$ HF	CO $\cdots$ HF	N <sub>2</sub> $\cdots$ HF	OC $\cdots$ HF	FB $\cdots$ HF
EDT	0.00080	0.00175	0.00487	0.02088	0.06055
$\Delta n(\text{Y})$	−0.00030	−0.00101	−0.00442	−0.02158	−0.05912
$\Delta\sigma^*(\text{HF})$	0.00081	0.00137	0.00486	0.02038	0.05625
$E\{n(\text{Y}) \rightarrow \sigma^*(\text{HF})\}$	0.4	1.02	3.32	12.36	27.7

on  $\sigma^*(\text{HX})$  increases. In the H-bonding WY $\cdots$ HF, electron density transfer caused by intermolecular hyperconjugation rationalizes elongation and frequency red shift of the HF bond. However, in the H-bonding WY $\cdots$ HArF, although the intermolecular hyperconjugation is larger than that in the H bonding of HF, the HAr bond length decreases and stretching frequency shifts to blue, which is because in HArF there exists intramolecular hyperconjugation between one lone pair  $n(\text{F})$  and  $\sigma^*(\text{HAr})$  in the ion pair  $(\text{HAr})^+\text{F}^-$ . In the free

monomer HArF, the lone pair on the anion  $\text{F}^-$ ,  $n(\text{sp}^{16.84}) = 0.2362\psi(2s) + 0.9712\psi(2p_z)$ , has large overlap with the antibonding orbital  $\sigma^*(\text{HAr}) = 0.5647h(\text{Ar}, \text{sp}^{15.58}) - 0.8253\psi(\text{H}, 1s)$ , as shown in Fig. 2a. So, the hyperconjugation is very large,  $E\{n(\text{F}) \rightarrow \sigma^*(\text{HAr})\} = 38.31\text{kcal/mol}$ , which transfers large electron density from  $n(\text{F})$  to  $\sigma^*(\text{HAr})$  so that  $\sigma^*(\text{HAr}) = 0.1093 \gg 0$  and  $n(\text{F}) = 1.8608 \ll 2$ , as shown in Fig. 2b. Upon formation of the H bonding, intermolecular hyperconjugation requires large overlap of  $n(\text{Y})$  with  $\sigma^*(\text{HAr})$  and so



**Fig. 2.** (a) Overlap of orbitals and (b) electron density transfer in free HArF. (c) Overlap of orbitals and (d) intra- and inter-molecular electron density transfer in the complex WY...HArF.



attracts the  $\sigma^*(\text{HAr})$  orbital polarizing towards H. Consequently, overlap between  $n(\text{F})$  and  $\sigma^*(\text{HAr})$  decreases, as shown in Fig. 2c, so that intramolecular hyperconjugation decreases and large electron density flows from  $\sigma^*(\text{HAr})$  back to  $n(\text{F})$ , as shown in Fig. 2d. The net change of occupancy on  $\sigma^*(\text{HAr})$  is decided by the two electron density transfers caused by the inter- and intra-molecular hyperconjugations. As shown in Table 5a, except for  $\text{OC}\cdots\text{HArF}$ ,  $\Delta\sigma^*(\text{HAr}) < 0$ , so the HAr bond enhances and contracts and its stretching frequency blue shifts. So, intramolecular hyperconjugation is a decisive factor for a blue shift in the H bonding of HArF. In  $\text{OC}\cdots\text{HArF}$ , intermolecular hyperconjugation is very large, even if intramolecular hyperconjugation also decreases largely, the occupancy on  $\sigma^*(\text{HAr})$  still increases, so that the blue shift in  $\text{OC}\cdots\text{HArF}$  is smallest; however, rehybridization has an important contribution to the blue shift.

Intramolecular hyperconjugation and charge transfer is induced by intermolecular hyperconjugation and charge transfer; the larger the latter, the larger the former. As the proton acceptor WY changes from BF to CO to  $\text{N}_2$  to OC, the intermolecular hyperconjugation energy,  $E\{n(\text{Y}) \rightarrow \sigma^*(\text{HAr})\}$ , is larger and larger so that the intramolecular hyperconjugation energy,  $E\{n(\text{F}) \rightarrow \sigma^*(\text{HAr})\}$ , is smaller and smaller, and intramolecular electron density transfer from  $\sigma^*(\text{HAr})$  to  $n(\text{F})$ ,  $\Delta n(\text{F})$  is larger and larger, as shown in Table 5.

Intermolecular interaction induces changes in the proton donor; generally, there are some electron structures in the donor to diminish these changes. As analyzed above, in the

H bonding of HArF, the intermolecular hyperconjugation,  $n(\text{Y}) \rightarrow \sigma^*(\text{HAr})$ , causes electron density on  $\sigma^*(\text{HAr})$  to increase; however, the intramolecular hyperconjugation,  $n(\text{F}) \rightarrow \sigma^*(\text{HAr})$  decreases and transfers electron density from  $\sigma^*(\text{HAr})$  to  $n(\text{F})$ . So, the lone pair  $n(\text{F})$  in HArF is like an electron density reservoir, which can adjust electron density on  $\sigma^*(\text{HAr})$  through intramolecular hyperconjugation. This self-adjustment in the proton donor HArF is very similar to Le Chatelier's principle on equilibrium shifting of chemical reaction.

### Polarization of the HX bond and hybridization of the X atom

The second important effect of intermolecular hyperconjugation and charge transfer on the proton donor in H-bond  $\text{Y}\cdots\text{HX}$  is to cause polarization of the HX bond to increase. In the free proton donor, the HX bond is formed by overlap of the 1s atomic orbital of H and the  $h(\text{sp}^n)$  hybrid orbital of X. The orthonormal bonding and antibonding orbitals are, respectively,  $\sigma(\text{HX}) = c_X h(\text{sp}^n) + c_H 1s_H$  and  $\sigma^*(\text{HX}) = c_H h(\text{sp}^n) - c_X 1s_H$ , where both  $c_X$  and  $c_H$  are positive. Since electronegativity of X is larger than that of H,  $c_X > c_H$ , the bonding orbital polarizes towards X and the antibonding orbital polarizes towards H. Polarization of the HX bond towards X causes X to be electronegative and H to be electropositive; in Table 6, Ar in HArF is positively charged because F has large electronegativity. Let occupancies on  $\sigma(\text{HX})$  and  $\sigma^*(\text{HX})$  be  $n(\sigma)$  and  $n(\sigma^*)$ , respectively, then electron populations on X and H are  $n(\sigma)|c_X|^2 + n(\sigma^*)|c_H|^2$  and  $n(\sigma)|c_H|^2 + n(\sigma^*)|c_X|^2$ , respectively, and their difference is  $[n(\sigma) - n(\sigma^*)][|c_X|^2 - |c_H|^2]$ . The polarization of the HX bond can be measured by the quantity  $P = [n(\sigma) - n(\sigma^*)][|c_X|^2 - |c_H|^2]/2$ . For diatomic molecules with similar nuclei,  $c_X = c_H = 1/2^{1/2}$ ,  $P = 0$ , and the HX bond is not polarized. For an ionic bond such as NaCl,  $c_X = 1$ ,  $c_H = 0$ , which expresses a lone pair on X; since generally  $n(\sigma) = 2$  and  $n(\sigma^*) = 0$ ,  $P = 1$ , and so the ionic bond has the largest polarization.

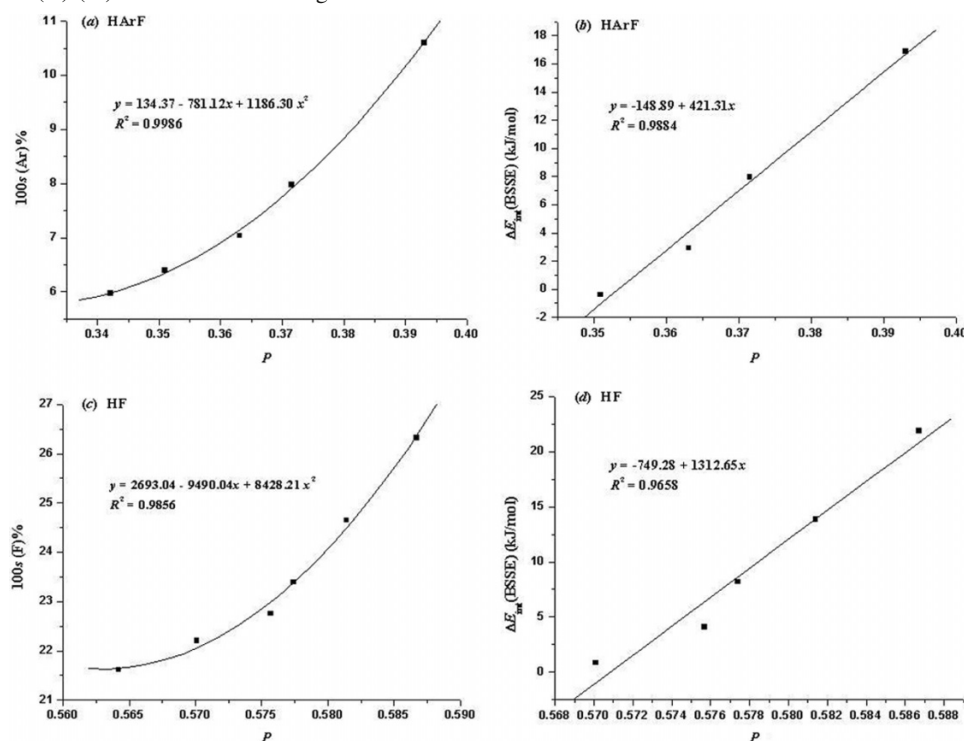
If electronegativity of X is less than H, such as Li, Be, and B, then  $c_X < c_H$ , and the HX bond polarizes towards H so that H is electronegative and X is electropositive. In this case,  $P$  is negative and in the range of  $0 \sim -1$ ; the larger the absolute of  $P$ , the larger the polarization of the HX bond. Weinhold and co-workers<sup>8</sup> use the polarization percentage,  $|c_X|^2$ , to express polarization of the HX bond, however, it cannot distinguish the two cases of the HX bond polarizing towards X and H. In addition, electronegativity of X and H can be quantitatively discussed and derived from electron densities at bond critical points.<sup>30</sup>

Upon formation of H bonding, the intermolecular hyperconjugation requires the largest overlap between  $n(\text{Y})$  and  $\sigma^*(\text{HX})$ , which causes the antibonding orbital  $\sigma^*(\text{HX})$  to further polarize towards H; correspondingly, since  $\sigma(\text{HX})$  and  $\sigma^*(\text{HX})$  are orthogonal,  $\sigma(\text{HX})$  will further polarize towards X. So, the coefficient  $c_X$  increases, the polarization percentage increases, and consequently, the  $P$  value of the HX bond increases, as shown in Table 6. It is observed that the change of occupancy on  $\sigma^*(\text{HX})$  has much less effect on  $P$  than  $c_X$ .

Upon formation of the H bonding, the third important effect of intermolecular hyperconjugation on the proton donor

**Table 6.** Natural atomic charge, the  $s$  character in the X hybrid of the HX bond, and the  $P$  value of the HX bond (X = Ar, F) in the proton donors and complexes.

Systems	$\sigma(\text{HX})$	$\sigma^*(\text{HX})$	$ \text{c}_{\text{X}} ^2$ (%)	$P$	$q_{\text{H}}$	$q_{\text{X}}$	$s(\text{X})$ (%)
HArF	1.9983	0.1093	68.11	0.3421	0.2838	0.5742	5.97
BF...HArF	1.9976	0.1038	68.53	0.3509	0.2956	0.5713	6.39
CO...HArF	1.9979	0.0969	69.10	0.3631	0.3108	0.5631	7.04
N <sub>2</sub> ...HArF	1.9974	0.0990	69.57	0.3715	0.3184	0.5550	7.98
OC...HArF	1.9978	0.1456	71.22	0.3930	0.3120	0.5143	10.60
HF	2.0000	0.0000	78.21	0.5642	0.5604	-0.5604	21.61
BF...HF	1.9996	0.0008	78.52	0.5701	0.5659	-0.5667	22.20
CO...HF	1.9996	0.0014	78.81	0.5757	0.5710	-0.5727	22.75
N <sub>2</sub> ...HF	1.9995	0.0049	78.95	0.5774	0.5706	-0.5755	23.39
OC...HF	1.9994	0.0204	79.38	0.5814	0.5659	-0.5868	24.65
FB...HF	1.9996	0.0563	80.19	0.5867	0.5493	-0.6098	26.32

**Fig. 3.** Correlations of  $s(\text{X})$  (%) and interaction energies with the  $P$  value of the HX bond.**Table 7.** The point charge models of the free proton acceptors N<sub>2</sub>, CO, and BF.

Molecule	Properties	CHelpG		NBO	Mulliken
		SCF density	MP2 density	SCF density	SCF density
N <sub>2</sub>	$q(\text{N})$ (au)				-0.2637
	$Q$ (D Å)				-0.7842
CO	$q(\text{C})$ (au)	0.08816	-0.01880	0.6099	0.1626
	$q(\text{O})$ (au)	-0.08816	0.01880	-0.6099	-0.1626
	$\mu$ (D)	-0.4813	0.1026	-3.3300	-0.3104
BF	$q(\text{B})$ (au)	-0.06278	-0.08754	0.6276	0.1419
	$q(\text{F})$ (au)	0.06278	0.08754	-0.6276	-0.1419
	$\mu$ (D)	0.3819	0.5325	-3.8176	-0.8199

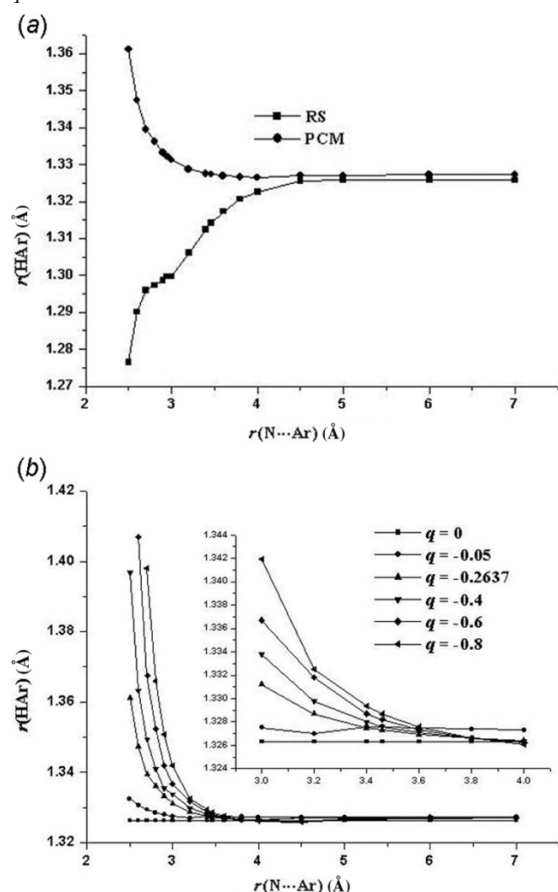
is that the  $s$  character in the X hybrid,  $h(\text{sp}^n)$ , of the HX bond increases, as shown in Table 6. According to Bent's rule,<sup>31</sup> an increase in the  $s$  character causes contraction of the HX bond, since the larger the  $s$  character, the stronger

the contraction of the  $h(\text{sp}^n)$  hybrid, and the shorter the HX bond to the largest overlap with the  $1s$  orbital of H. In the H-bonding WY...HF, elongation of the HF bond caused by intermolecular hyperconjugation exceeds the shortening

**Table 8.** Comparison of the RSs WY...HXZ and PCMs pc...HXZ at the intermolecular distance of equilibrium complexes.

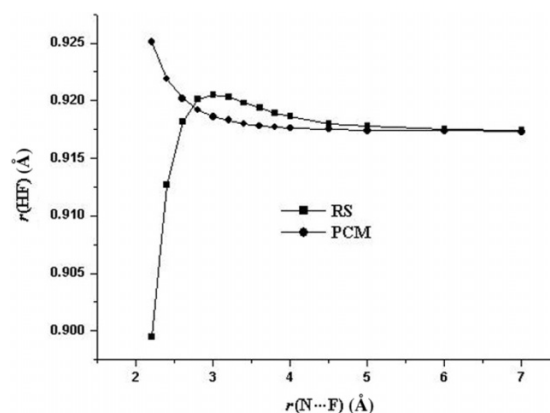
Systems	$\Delta r(\text{HX})$	$\Delta \nu(\text{HX})$	$\Delta \sigma^*(\text{HX})$	$\Delta  c_{\text{X}} ^2$	$\Delta P$	$\Delta q(\text{H})$	$\Delta s(\text{X})$ (%)	$\Delta n(\text{Z})$	$\Delta E_{\text{intra}}$
N <sub>2</sub> ...HArF	-0.0122	156	-0.0104	0.0146	0.0294	0.0346	2.01	0.0269	-7.11
pc...HArF	0.0010	-6	-0.0003	0.0006	0.0012	0.0012	0.02	0.0005	-0.29
OC...HArF	-0.0018	13	0.0362	0.0311	0.0509	0.0282	4.63	0.0480	-13.51
pc...HArF	-0.0004	4	-0.0003	0.0002	0.0004	0.0005	0.03	0.0004	-0.19
N <sub>2</sub> ...HF	0.0032	-70	0.0049	0.0074	0.0132	0.0102	1.78		
pc...HF	0.0014	-26	0.0000	0.0001	0.0002	0.0002	-0.08		
OC...HF	0.0069	-160	0.0204	0.0117	0.0172	0.0055	3.04		
pc...HF	0.0003	-5	0.0000	0.0000	0.0000	0.0000	-0.01		
FB...HF	0.0128	-304	0.0563	0.0198	0.0225	-0.0111	4.71		
pc...HF	0.0013	-24	0.0000	0.0001	0.0002	0.0002	-0.08		

Note: X = Ar, F; Z = F;  $E_{\text{intra}} = E\{n(\text{F}) \rightarrow \sigma^*(\text{HAr})\}$  (kcal/mol).

**Fig. 4.** (a) Correlation of  $r(\text{HAr})$  with  $r(\text{N}\cdots\text{Ar})$  for RS and PCM of N<sub>2</sub>...HArF; (b) correlation of  $r(\text{HAr})$  with  $r(\text{N}\cdots\text{Ar})$  for PCM with fixed  $q = 0 \sim -0.8$ .

caused by an increase of the s character, so the resulted H bond is red-shifted. In the H-bonding WY...HArF, shortening of the HAr bond caused by an increase of the s character and decrease of intramolecular hyperconjugation is larger than the elongation caused by the intermolecular hyperconjugation, and finally, the H bond is blue-shifted. In OC...HArF, especially, an increase of the s character has a large contribution to the blue shift.

The changes of structure and properties of the monomers in H bonds are induced by intermolecular interaction, so the larger the interaction energy, the larger the changes. For

**Fig. 5.** Correlation of  $r(\text{HF})$  with  $r(\text{N}\cdots\text{F})$  for RS and PCM of N<sub>2</sub>...HF.

example, the  $P$  value of the HX bond in H bonds increases with interaction energy, as shown in Fig. 3, so it can be used to express the strength of H bonding. The change of many properties of the proton donor increases with the  $P$  value of the HX bond, such as the s character as shown in Fig. 3, and the red shift for red-shifted H bonds (but for blue-shifted H bonds, the blue shift is not so).

### Electrostatic interaction

To explore the contribution of electrostatic interaction to structure change and frequency shift of the proton donor, we use point charge model (PCM) to mimic the electrostatic field of the free proton acceptor and investigate the change of the donor under this electric field. For CO and BF, two point charges,  $q$  and  $-q$ , are placed at the two atoms, respectively;  $q$  is deduced from the electrostatic potential of the free monomer by use of the CHelpG method with MP2 and SCF densities, or from orbital charge by means of NBO analysis or Mulliken population analysis with SCF density; the dipole moment,  $\mu = ql$ , with  $l$  equal to the bond length of the free monomer for CHelpG and NBO methods. For N<sub>2</sub> without a dipole moment, the electrostatic field of its quadrupole moment is mimicked by three charges,  $q$ ,  $q$ , and  $-2q$ , placed at the two ends and midpoint of free N<sub>2</sub>;  $q$  is deduced from the quadrupole moment,  $Q = ql^2/2$ , where  $l$  is the N–N bond length and  $Q$  is obtained using Mulliken population analysis. The results are listed in Table 7. We noted that for CO only the dipole moment of CHelpG with MP2 density is in good agreement with experimental data, 0.112 D,<sup>32</sup> so for

CO and BF, we use the PCMs obtained by this method to mimic their dipole fields.

In equilibrium structures of the complexes  $\text{WY}\cdots\text{HArF}$  and  $\text{WY}\cdots\text{HF}$ , the proton acceptor WY is replaced by the PCM obtained above; by then fixing the distance  $\text{Y}\cdots\text{X}$  ( $\text{X} = \text{Ar}, \text{F}$ ), we optimize the structure of the proton donor under the electric field of the point charges. The results are listed in Table 8; here we only study the five stable H-bonding complexes. In the PCMs of the H-bonds  $\text{WY}\cdots\text{HF}$ , the HF bond length increases and stretching frequency decreases, similar to the real systems (RSs), but the red shift is much smaller than that of the real system. In the PCM of  $\text{OC}\cdots\text{HArF}$ , the HAr bond contracts and vibrational frequency increases, but the blue shift is much smaller than that of the real system. In the PCM of  $\text{N}_2\cdots\text{HArF}$ , the HAr bond elongates and stretching frequency decreases, qualitatively opposite to the real system; the magnitude of the red shift is much smaller than that of the blue shift in the real system.

In the PCM, there is only electrostatic interaction (EI), without charge transfer and intermolecular hyperconjugation. The NBO analysis shows that EI does not lead to a change of electronic structure and many properties of the proton donors in these two kinds of H-bonding  $\text{WY}\cdots\text{HArF}$  and  $\text{WY}\cdots\text{HF}$ : (1) EI does not lead to repolarization, that is, does not enhance nor diminish the  $P$  value of the HX bond. (2) EI does not lead to rehybridization, i.e., does not change the  $s$  character of the X hybrid of the HX bond. (3) EI does not change the hydrogen atomic charge. (4) For HArF, EI does not induce a change of intramolecular hyperconjugation,  $n(\text{F}) \rightarrow \sigma^*(\text{HAr})$ , so does not change occupancies on  $\sigma^*(\text{HAr})$  and  $n(\text{F})$ . The result of McDowell,<sup>19</sup> that the negative quadrupole moment of  $\text{N}_2$  can cause electron density transfer from  $\sigma^*(\text{HAr})$  to  $n(\text{F})$  is opposite to our result. So, all of the above changes of electronic structure of the proton donors in these H bonds is caused by intermolecular hyperconjugation and charge transfer. The HX bond length change and frequency shift in these H bonds are mainly caused by charge transfer and intermolecular hyperconjugation. The electrostatic interaction has only a small contribution. In the PCM, electrostatic interaction includes attraction between the electropositive H and the negatively charged end of the multipole and repulsion between electron cloud of H and the negatively charged end of the multipole; for the complexes of HF and  $\text{N}_2\cdots\text{HArF}$ , attractive interaction is predominant, so the HX bond is red-shifted; but for  $\text{OC}\cdots\text{HArF}$ , the dipole moment and charge,  $q(\text{C})$ , is small, and the repulsive interaction is more important, so the HAr bond is blue-shifted.

For the complete electron system  $\text{N}_2\cdots\text{HArF}$  and its point charge model, we vary the distance of  $\text{Y}\cdots\text{Ar}$  from 2.5 Å to 7 Å; for each fixed  $\text{Y}\cdots\text{Ar}$  distance, we optimize the structure of the system. Figure 4a shows the correlation of the optimized bond length,  $r(\text{HAr})$ , with the  $\text{N}\cdots\text{Ar}$  distance for both RS and PCM. At large intermolecular distance, only electrostatic interaction works, so the two curves of RS and PCM coincide. As  $r(\text{N}\cdots\text{Ar}) < 4.5$  Å, the two curves begin to separate, so intermolecular hyperconjugation and charge transfer begin to work. For PCM,  $r(\text{HAr})$  increases as  $r(\text{N}\cdots\text{Ar})$  decreases, so electrostatic interaction always leads to a red shift of the HAr bond; however, for the real system,  $r(\text{HAr})$  decreases as  $r(\text{N}\cdots\text{Ar})$  decreases, so charge transfer

always causes a blue shift of the HAr bond. In the PCM, electrostatic interaction is mainly attraction between the negatively charged end of the quadrupole and the positive charge of H, which always causes elongation of the HAr bond. However, in the real system, intermolecular hyperconjugation induces a decrease of intramolecular hyperconjugation and an increase of the  $s$  character of the Ar hybrid of the HAr bond, which always leads to contraction of the HAr bond.

McDowell<sup>19</sup> mimicked the electric field of the quadrupole moment of  $\text{N}_2$  by also using similar PCM at the MP2/6-311G(d, p) level, but  $q = -0.624$  au, which is much larger than ours. He found that the quadrupole electric field leads to a blue shift of the HAr bond at the distance  $r(\text{N}\cdots\text{Ar})$  from 3.5 Å to 7 Å; this result is completely opposite to ours. Obviously, the difference is due to full electron correlation and the diffuse functions used by us. For further confirmation of our result, we vary the charge  $q$  from  $-0.05$  to  $-0.8$  au, but fix the N–N bond length,  $l$ , for the PCM, then optimize the structure of HArF under the quadrupole field for a series of fixed  $r(\text{N}\cdots\text{Ar})$  distances. Figure 4b shows the resulting correlation of the optimized bond length  $r(\text{HAr})$  with  $r(\text{N}\cdots\text{Ar})$  for different  $q$ . We noted that a negative quadrupole moment of the proton acceptor always leads to a red shift of the HAr bond.

For the complete electron system  $\text{N}_2\cdots\text{HF}$  and its PCM, we also vary  $r(\text{N}\cdots\text{F})$  from 2.2 Å to 7 Å; for each fixed  $r(\text{N}\cdots\text{F})$ , we optimize the structure of the system. Figure 5 shows correlation of  $r(\text{HF})$  with  $r(\text{N}\cdots\text{F})$  for RS and PCM. At large distances, the fact that the two curves coincide shows that only electrostatic interaction works. As  $r(\text{N}\cdots\text{F}) < 4.5$  Å, the two curves begin to separate, so charge transfer begins to work. For PCM,  $r(\text{HF})$  always increases with a decrease of  $r(\text{N}\cdots\text{F})$ , so electrostatic interaction always leads to elongation of the HF bond. But for RS,  $r(\text{HF})$  first increases and then decreases with a decrease of  $r(\text{N}\cdots\text{F})$ . At the moderate distance,  $r(\text{N}\cdots\text{F}) = 2.8 \sim 4.5$  Å, charge transfer causes the HF stretching frequency to more of a red shift; but as  $r(\text{N}\cdots\text{F}) < 2.8$  Å, exchange repulsion begins to work, which leads to contraction of the HF bond. Our result is consistent with that of McDowell.<sup>19</sup>

## Conclusions

Our theoretical calculated results on the H bonds of HArF and HF with  $\text{N}_2$ , CO, and BF show that the H bonding leads to a blue shift of the HAr bond but a red shift of the HF bond. The bond length change and frequency shift of the proton donor in the two kinds of H-bonds  $\text{WY}\cdots\text{HArF}$  and  $\text{WY}\cdots\text{HF}$  are mainly caused by intermolecular hyperconjugation and charge transfer; electrostatic interaction has only a small contribution. In HArF, there exists intramolecular hyperconjugation,  $n(\text{F}) \rightarrow \sigma^*(\text{HAr})$ , which can adjust electron density on  $\sigma^*(\text{HAr})$ ; upon the H bonding, intermolecular hyperconjugation induces a decrease of intramolecular hyperconjugation and an increase of the  $s$  character of the Ar hybrid of the HAr bond. These two factors lead to a blue shift of the HAr bond. In HF, however, there is no internal electron structure to adjust electron density on  $\sigma^*(\text{HF})$ , so charge transfer leads directly to an increase of



electron density on  $\sigma^*(\text{HF})$ , which exceeds the effect of re-hybridization so that the resulted H bond is red-shifted.

## Acknowledgements

We thank the National Natural Science Foundation of China for financial support (No. 20873103).

## References

- (1) Jeffrey, G. A. *An Introduction to Hydrogen Bonding*; Oxford University Press: New York, 1997.
- (2) Desiraju, G. R.; Steiner, T. *The Weak Hydrogen Bond*; Oxford University Press: Oxford, 1999.
- (3) Scheiner, S. *Hydrogen Bonding*; Oxford University Press: New York, 1997.
- (4) Custelcean, R.; Jackson, J. E. *Chem. Rev.* **2001**, *101* (7), 1963. doi:10.1021/cr000021b. PMID:11710237.
- (5) Bakhmutov, V. I. *Dihydrogen Bonds: Principles, Experiments, and Applications*; John Wiley & Sons, Inc.: Hoboken, NJ, 2008.
- (6) Hobza, P.; Havlas, Z. *Chem. Rev.* **2000**, *100* (11), 4253. doi:10.1021/cr990050q. PMID:11749346.
- (7) Li, X.; Liu, L.; Schlegel, H. B. *J. Am. Chem. Soc.* **2002**, *124* (32), 9639. doi:10.1021/ja020213j. PMID:12167060.
- (8) Alabugin, I. V.; Manoharan, M.; Peabody, S.; Weinhold, F. *J. Am. Chem. Soc.* **2003**, *125* (19), 5973. doi:10.1021/ja034656e. PMID:12733938.
- (9) Li, A. Y. *J. Chem. Phys.* **2007**, *126* (15), 154102. doi:10.1063/1.2715561. PMID:17461609.
- (10) Khriachtchev, L.; Pettersson, M.; Runeberg, N.; Lundell, J.; Räsänen, M. *Nature* **2000**, *406* (6798), 874. doi:10.1038/35022551. PMID:10972285.
- (11) Lundell, J.; Chaban, G. M.; Benny Gerber, R. *Chem. Phys. Lett.* **2000**, *331* (2–4), 308. doi:10.1016/S0009-2614(00)01180-5.
- (12) Khriachtchev, L.; Pettersson, M.; Lignell, A.; Räsänen, M. *J. Am. Chem. Soc.* **2001**, *123* (35), 8610. doi:10.1021/ja016197s. PMID:11525675.
- (13) Runeberg, N.; Pettersson, M.; Khriachtchev, L.; Lundell, J.; Rasanen, M. *J. Chem. Phys.* **2001**, *114* (2), 836. doi:10.1063/1.1331105.
- (14) Chaban, G. M.; Lundell, J.; Benny Gerber, R. *Chem. Phys. Lett.* **2002**, *364* (5), 628. doi:10.1016/S0009-2614(02)01411-2.
- (15) Bihary, Z.; Chaban, G. M.; Benny Gerber, R. *J. Chem. Phys.* **2002**, *116* (13), 5521. doi:10.1063/1.1455621.
- (16) Wong, M. W. *J. Am. Chem. Soc.* **2000**, *122* (26), 6289. doi:10.1021/ja9938175.
- (17) Benny Gerber, R. *Annu. Rev. Phys. Chem.* **2004**, *55* (1), 55. doi:10.1146/annurev.physchem.55.091602.094420. PMID:15117247.
- (18) Lignell, A.; Khriachtchev, L.; Pettersson, M.; Rasanen, M. *J. Chem. Phys.* **2002**, *117* (3), 961. doi:10.1063/1.1491403.
- (19) McDowell, S. A. C. *J. Chem. Phys.* **2003**, *118* (9), 4066. doi:10.1063/1.1540628.
- (20) McDowell, S. A. C. *Phys. Chem. Chem. Phys.* **2003**, *5* (5), 808. doi:10.1039/b211014h.
- (21) McDowell, S. A. C. *J. Chem. Phys.* **2003**, *118* (16), 7283. doi:10.1063/1.1564059.
- (22) Lignell, A.; Khriachtchev, L.; Pettersson, M.; Rasanen, M. *J. Chem. Phys.* **2003**, *118* (24), 11120. doi:10.1063/1.1575198.
- (23) McDowell, S. A. C. *J. Chem. Phys.* **2004**, *121* (12), 5728. doi:10.1063/1.1784449.
- (24) Frisch, M. J.; Trucks, G. W.; Schlegel, H. B.; Scuseria, G. E.; Robb, M. A.; Cheeseman, J. R.; Montgomery, J. J. A.; Vreven, T.; Kudin, K. N.; Burant, J. C.; Millam, S. S.; Iyengar, J. M.; Tomasi, J.; Barone, V.; Mennucci, B.; Cossi, M.; Scalmani, G.; Rega, N.; Petersson, G. A.; Nakatsuji, H.; Hada, M.; Ehara, M.; Toyota, K.; Fukuda, R.; Hasegawa, J.; Ishida, M.; Nakajima, T.; Honda, Y.; Kitao, O.; Nakai, H.; Klene, M.; Li, X.; Knox, J. E.; Hratchian, H. P.; Cross, J. B.; Adamo, C.; Jaramillo, J.; Gomperts, R.; Stratmann, R. E.; Yazyev, O.; Austin, A. J.; Cammi, R.; Pomelli, C.; Ochterski, J. W.; Ayala, P. Y.; Morokuma, K.; Voth, G. A.; Salvador, P.; Dannenberg, J. J.; Zakrzewski, V. G.; Dapprich, S.; Daniels, A. D.; Raghavachari, K.; Foresman, J. B.; Ortiz, J. V.; Cui, Q.; Baboul, A. G.; Clifford, S.; Cioslowski, J.; Stefanov, B. B.; Liu, G.; Liashenko, A.; Piskorz, P.; Komaromi, I.; Martin, R. L.; Fox, D. J.; Keith, T.; Al-Laham, M. A.; Peng, C. Y.; Nanayakkara, A.; Challacombe, M.; Gill, P. M. W.; Johnson, B.; Chen, W.; Wong, M. W.; Gonzalez, C.; Pople, J. A. *Gaussian 03*; Gaussian, Inc.: Pittsburgh, PA, 2003.
- (25) Boys, S. F.; Bernardi, F. *Mol. Phys.* **1970**, *19* (4), 553. doi:10.1080/00268977000101561.
- (26) Bader, R. F. W. *Atoms in Molecules: A Quantum Theory*; Clarendon Press: Oxford, 1990.
- (27) Matta, C. F.; Boyd, R. J. *The Quantum Theory of Atoms in Molecules*; Wiley-VCH Verlag GmbH & Co. KGaA: Weinheim, Germany, 2006.
- (28) Biegler-König, F.; Bader, R. F. W.; Tang, T.-H. *J. Comput. Chem.* **1983**, *3* (3), 317. doi:10.1002/jcc.540030306. Biegler-König, F. W.; Nguyen-Dang, T. T.; Tal, Y.; Bader, R. F. W. *Duke, A. J. J. Phys B* **1981**, *14* (16), 2739. The program AIM2000 has been modified by Keith, T. A.; Cheeseman, J. R.
- (29) Glendening, E. D.; Badenhoop, J. K.; Reed, A. E.; Carpenter, J. E.; Bohmann, J. A.; Weinhold, F. NBO 5.0; Theoretical Chemistry Institute, University of Wisconsin: Madison WI, 1996–2001.
- (30) Boyd, R. J.; Boyd, S. L. *J. Am. Chem. Soc.* **1992**, *114* (5), 1652. doi:10.1021/ja00031a018.
- (31) Bent, H. A. *Chem. Rev.* **1961**, *61* (3), 275. doi:10.1021/cr60211a005.
- (32) Gu, Q. Y.; Lou, S. C. *Table of Chemical Materials*; Jiangsu Science and Technology Press: P.R. China, 1998.

# Catalytic hypervalent iodine oxidation of alcohols to the corresponding carbonyl compounds using *N*-hydroxyphthalimide (NHPI) and *m*-chloroperbenzoic acid

Chenjie Zhu, Lei Ji, Qian Zhang, and Yunyang Wei

**Abstract:** An efficient, facile, and mild oxidation of alcohols to the corresponding carbonyl compounds with *m*-chloroperbenzoic acid (*m*CPBA) and *N*-hydroxyphthalimide (NHPI) in the presence of a catalytic amount of iodobenzene was reported. The oxidation proceeded in mixed solvent at room temperature to afford carbonyl compounds in excellent yields. A possible mechanism for the oxidation was proposed.

**Key words:** alcohols, oxidation, iodobenzene, *m*-chloroperbenzoic acid (*m*CPBA), *N*-hydroxyphthalimide (NHPI).

**Résumé :** On a mis au point une méthode efficace, facile et douce d'oxydation des alcools en dérivés carbonylés correspondants à l'aide de l'acide *m*-chloroperbenzoïque et le *N*-hydroxyphthalimide, en présence de quantités catalytiques d'iodobenzène. L'oxydation se produit en un solvant mixte, à la température ambiante et elle conduit à la formation des dérivés carbonylés avec d'excellents rendements. On propose un mécanisme possible pour la réaction.

**Mots-clés :** alcools, oxydation, iodobenzène, acide *m*-chloroperbenzoïque, *N*-hydroxyphthalimide.

[Traduit par la Rédaction]

## Introduction

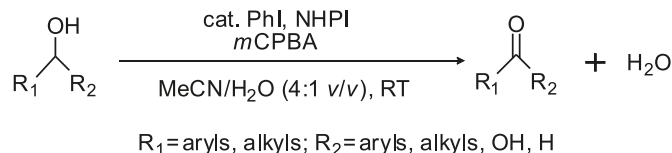
The selective oxidation of alcohols to the corresponding carbonyl compounds is a fundamental transformation both in laboratory synthesis and industrial production.<sup>1</sup> Numerous hypervalent iodine compounds (e.g., DMP, IBX, PhI(OAc)<sub>2</sub>, PhIO, and so forth) in stoichiometric amounts have been traditionally employed to accomplish this transformation.<sup>2</sup> However, some of these reagents are potentially explosive, and the use of stoichiometric amounts of iodine reagents leads to the production of equimolar amounts of organic iodine waste. From economic and environmental perspectives, the development of catalytic systems based on hypervalent iodine has received great attention.<sup>3</sup> Many highly efficient systems have been developed for catalytic hypervalent iodine oxidation using co-oxidants, such as *m*-chloroperbenzoic acid (*m*CPBA),<sup>4</sup> oxone (2KHSO<sub>5</sub>·KHSO<sub>4</sub>·K<sub>2</sub>SO<sub>4</sub>),<sup>5</sup> H<sub>2</sub>O<sub>2</sub>,<sup>6</sup> tetraphenyl-phosphonium monoperoxysulfate (TPPP),<sup>7</sup> NaBO<sub>3</sub>·H<sub>2</sub>O,<sup>8</sup> O<sub>2</sub>,<sup>9</sup> Ru,<sup>10</sup> peracetic acid,<sup>11</sup> or in combination with the nitroxyl radical 2,2,6,6-tetramethyl-piperidyl-1-oxy (TEMPO).<sup>12</sup>

On the other hand, it is well-known that nitroxyl radicals, such as 2,2,6,6-tetramethyl-1-piperidinyloxy free radical (TEMPO) and *N*-hydroxyphthalimide (NHPI) promote the oxidation of various alcohols to the corresponding carbonyl compounds effectively under mild reaction conditions.<sup>13</sup> Piancatelli and co-workers have reported a mild and selective method for the oxidation of primary and secondary alcohols

using TEMPO and stoichiometric bis(acetoxy)iodobenzene (PhI(OAc)<sub>2</sub>) as a reoxidant.<sup>14</sup> However, there are no reports concerning the use of hypervalent iodine as a reoxidant for NHPI.

In continuation of our interest in exploring systems on the oxidation of organic compounds,<sup>15</sup> here, we would like to report a facile procedure for the oxidation of alcohols to the corresponding carbonyl compounds with *m*CPBA in the presence of catalytic amounts of PhI and NHPI (Scheme 1).

**Scheme 1.** Oxidation of alcohols catalyzed by *m*CPBA/PhI/NHPI.



## Results and discussion

The initial experiments were carried out using 4-nitrobenzyl alcohol as the model substrate. When 4-nitrobenzyl alcohol was oxidized with *m*CPBA/PhI/NHPI at room temperature for 3 h, 97% conversion of the alcohol was observed (Table 1, entry 1). As control experiments, the same reaction was carried out in the absence of *m*CPBA, PhI, or NHPI,

Received 8 October 2009. Accepted 9 December 2009. Published on the NRC Research Press Web site at canjchem.nrc.ca on 9 March 2010.

C. Zhu, L. Ji, Q. Zhang, and Y. Wei.<sup>1</sup> School of Chemical Engineering, Nanjing University of Science and Technology, Nanjing 210094, China.

<sup>1</sup>Corresponding author (e-mail: ywei@mail.njust.edu.cn).

**Table 1.** Oxidation of 4-nitrobenzyl alcohol.

Entry	PhI (equiv.)	<i>m</i> CPBA (equiv.)	Additive	Conversion (%) <sup>a</sup>
1	0.1	2	NHPI	97
2	0.1	2	None	<10
3	0.1	None	NHPI	<10
4	None	2	NHPI	<10
5	0.05	2	NHPI	90
6 <sup>b</sup>	0.1	2	NHPI	24
7	0.1	2	CF <sub>3</sub> COOH	25
8	0.1	2	AcOH	29
9	0.1	2	(CF <sub>3</sub> CO) <sub>2</sub> O	<10
10	0.1	2	BF <sub>3</sub> ·Et <sub>2</sub> O	13
11 <sup>c</sup>	0.1	2	3 Å molecular sieves	<10

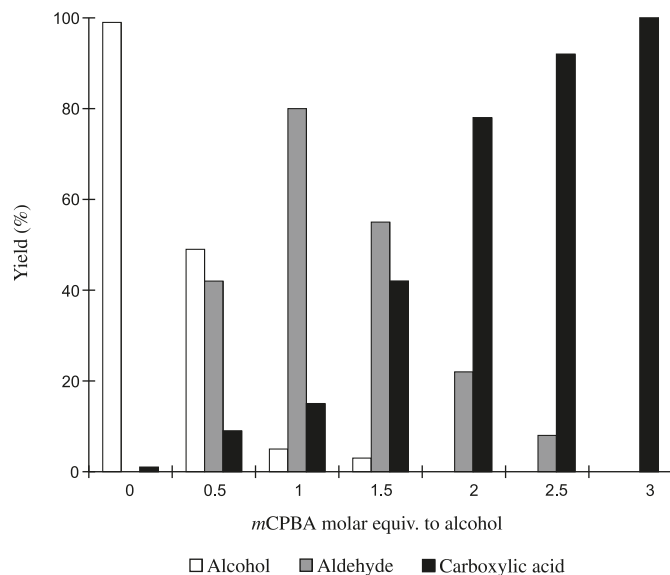
**Note:** Reactions were performed by using 4-nitrobenzyl alcohol (1 mmol), *m*CPBA (2 mmol), additive (0.2 mmol), and PhI (0.1 mmol) in MeCN/H<sub>2</sub>O (4:1, v/v) at room temperature for 3 h, unless otherwise noted.

<sup>a</sup>GC conversion.

<sup>b</sup>2,6-Di-*tert*-butylphenol (0.2 mmol) was added.

<sup>c</sup>0.1 g of 3 Å molecular sieves was added.

**Fig. 1.** Effect of the amount of *m*CPBA on the oxidation of 4-nitrobenzyl alcohol. Reaction conditions: 4-nitrobenzyl alcohol (1 mmol), *m*CPBA, NHPI (0.2 mmol), and PhI (0.1 mmol) in MeCN/H<sub>2</sub>O (4:1, v/v) at room temperature for 3 h.



respectively. In all cases, the conversion of the alcohol was less than 10% (Table 1, entries 2–4). It was possible to decrease the amount of PhI to as low as 0.05 equiv. without a significant loss in catalytic efficiency (Table 1, entry 5). Moreover, a range of additives were tested for this reaction; however, all of them were unsatisfactory except for NHPI (Table 1, entries 7–11). Besides, we also tested other co-oxidants, such as peracetic acid, NaBO<sub>3</sub>·H<sub>2</sub>O, K<sub>2</sub>S<sub>2</sub>O<sub>8</sub>, NaIO<sub>4</sub>, UHP, and Na<sub>2</sub>CO<sub>3</sub>·3H<sub>2</sub>O<sub>2</sub> in this experiment, all of them were unsuccessful.

To optimize the conditions of the oxidation, the role of *m*CPBA was studied using 1 mmol of 4-nitrobenzyl alcohol as substrate. It was found that the yield of 4-nitrobenzaldehyde reached to maximum when 1 equiv. of *m*CPBA was used. Using more than 1 equiv. of *m*CPBA led to the decrease of the yield of 4-nitrobenzaldehyde and increase of

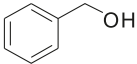
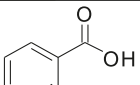
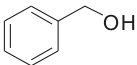
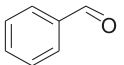
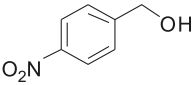
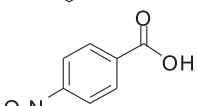
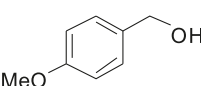
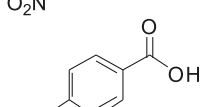
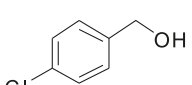
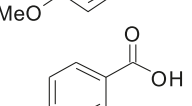
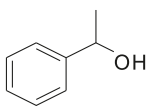
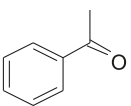
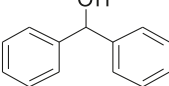
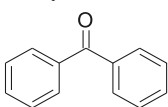
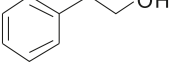
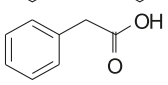
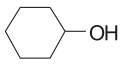
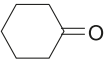
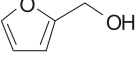
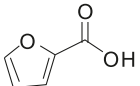
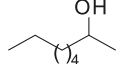
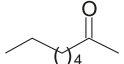
the yield of 4-nitrobenzoic acid. If 3 equiv. of *m*CPBA were used, quantitative yield of 4-nitrobenzoic acid was obtained (Fig. 1).

To evaluate the versatility of this novel catalytic system, we applied the procedure to the oxidation of a wide range of alcohols at room temperature. As shown in Table 2, most alcohols underwent oxidation to afford the corresponding carbonyl compounds in excellent yield. The present protocol afforded carboxylic acids from primary alcohols (Table 2, entries 1, 3–5, 8, 10, 11, and 13) and ketones from the secondary alcohols (Table 2, entries 6, 7, 9, and 12). The use of less amount of *m*CPBA and decreasing the reaction time in the oxidation of primary alcohols also led to the predominant formation of aldehydes (Table 2, entry 2). Benzylic alcohols underwent smooth oxidation (Table 2, entries 1–7). Even secondary alcohols, such as diphenylmethanol, were selectively oxidized to ketones effectively (Table 2, entry 7).

The electronic properties of the substituents in the aromatic ring had relatively minor influence on the oxidation of alcohols (Table 2, entries 3 and 4). Strong electron-withdrawing groups, such as nitro group, improve the oxidation of alcohol (Table 2, entry 3). Strong electron-donating group, such as –OCH<sub>3</sub> group, lowered the reaction rate (Table 2, entry 4). This is different from previously reported procedures, where –OCH<sub>3</sub> group favors alcohols oxidation.<sup>16</sup> It is worth mentioning that together with the good results with benzylic alcohols, the yields of ketones or acids obtained from the oxidation of aliphatic, alicyclic, or heterocyclic alcohols under the same conditions are also quite high (Table 2, entries 8–13).

Table 3 shows the results of the competitive oxidation of primary and secondary alcohols. The competing oxidation of an equimolar mixture of benzyl alcohol and 1-phenylethanol resulted in 95% yield of benzoic acid and less than 10% yield of acetophenone (Table 3, entry 1). Oxidation of an equimolar mixture of octan-1-ol and octan-2-ol gave 81% caprylic acid and less than 5% yield of hexyl methyl ketone, respectively (Table 3, entry 2). These results suggest that chemoselective oxidation of the primary alcoholic functionality in the presence of a secondary alcoholic functionality is possible with the present oxidation system.

**Table 2.** *m*CPBA/PhI/NHPI-catalyzed oxidation of alcohols.

Entry	Alcohols	Products	Time (h)	Yield <sup>a</sup> (%)
1			0.45	Quant.
2			0.5	81 <sup>b,c</sup>
3			3	Quant.
4			5	93
5			3	97
6			2.5	Quant.
7			5	95
8			8	88
9			8	83 <sup>d</sup>
10			4	Quant. <sup>d</sup>
11	$\text{CH}_3(\text{CH}_2)_7\text{OH}$	$\text{CH}_3(\text{CH}_2)_6\text{COOH}$	8	89
12			8	92 <sup>d</sup>
13	$n\text{-C}_{11}\text{H}_{23}\text{-CH}_2\text{OH}$	$n\text{-C}_{11}\text{H}_{23}\text{-COOH}$	10	96

**Note:** Reaction conditions: alcohol (1mmol), *m*CPBA (3mmol), PhI (0.1mmol), NHPI (0.2mmol) MeCN/H<sub>2</sub>O (4:1, v/v), at room temperature.

<sup>a</sup> Yields of isolated products unless otherwise noted. Quant.: Theoretical amount of product was obtained.

<sup>b</sup> *m*CPBA (1 equiv.) was used.

<sup>c</sup> Benzoic acid also formed in 19% yield.

<sup>d</sup> Yields were determined by GC.

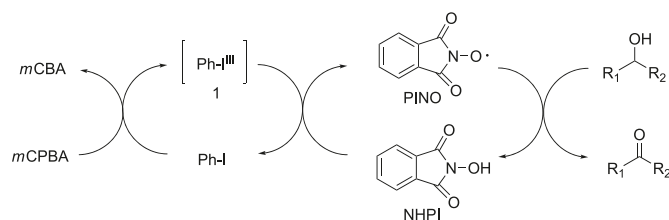
A plausible mechanism of this reaction is depicted in Scheme 2. PhI is initially oxidized by *m*CPBA to form the highly reactive hypervalent iodine(III) intermediate **1**, the role of **1** is to regenerate phthalimide-*N*-oxyl radical (PINO) from NHPI, then PINO is responsible for the actual oxidant in this reaction to oxidize alcohol to the corresponding carbonyl compound. Experimental evidence towards catalytic oxidation of PhI to **1** mediated by *m*CPBA has previously been documented,<sup>4a</sup> and the generation and identification of the highly reactive hypervalent iodine(III) intermediate **1** was reported in the literature.<sup>4d</sup> Addition of 2,6-di-*tert*-butylphenol, a free radical scavenger, to the reaction system led to the decrease of the conversion of 4-nitrobenzyl alcohol

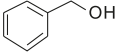
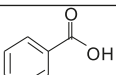
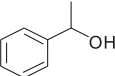
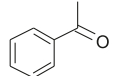
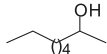
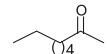
(Table 1, entry 6), which provides an experimental evidence for the generation of PINO during the reaction.

## Conclusion

In summary, a novel and mild catalytic system for the oxidation of alcohols to the corresponding carbonyl compounds with *m*CPBA/PhI/NHPI has been developed. PhI was oxidized by *m*CPBA in situ to highly active hypervalent iodine(III) species, a reoxidant of NHPI, which allowed the oxidation of various kinds of alcohols, including benzylic, aliphatic, alicyclic, and heterocyclic alcohols, to afford carbonyl compounds in excellent yields at room temperature.



**Scheme 2.** Tentative mechanism for the catalytic oxidation of alcohols with *m*CPBA/PhI/NHPI.**Table 3.** Competitive oxidation of primary and secondary alcohols.

Entry	Substrate	Product	Time (h)	Yield <sup>a</sup> (%)
1			0.5	95
				<10
	CH <sub>3</sub> (CH <sub>2</sub> ) <sub>7</sub> OH	CH <sub>3</sub> (CH <sub>2</sub> ) <sub>6</sub> COOH		81
2			4	<5

**Note:** The reactions were carried out on a 1:1 mixture of primary and secondary alcohols, on a 1 mmol scale.

<sup>a</sup>GC yield.

The procedure can be used for the synthesis of carboxylic acids and ketones from primary alcohols and secondary alcohols, respectively. By adjusting the dosage of *m*CPBA, aldehydes can also be obtained from primary alcohols. Selective oxidation of primary alcohols in the presence of secondary alcohols was also achieved.

## Experimental

### General

All chemicals (AR grade) were obtained from commercial sources and used without further purification. Gas chromatography (GC) analysis was performed on an Agilent GC-6820 chromatograph equipped with a 30 m × 0.32 mm × 0.5 μm HP-Innowax capillary column and a flame-ionization detector. Progress of the reactions was followed by TLC using silica-gel polygrams SIL G/UV 254 plates. Mass spectra were recorded on a Shimadzu GC MS-QP 1000 EX apparatus.

### Typical experimental procedure for oxidation of alcohols

To a solution of alcohol (1 mmol), iodobenzene (20 mg, 0.1 mmol), and NHPI (40 mg, 0.2 mmol) in MeCN/H<sub>2</sub>O (4:1, v/v) was added *m*CPBA (700 mg, 65% wet with H<sub>2</sub>O, 3 mmol). The mixture was stirred at room temperature for several hours while checking the reaction progress by gas or thin-layer chromatography. After completion, aqueous sodium thiosulfate and Et<sub>2</sub>O were sequentially added to the residue, and then the mixture was stirred vigorously for 10 min. The organic layer was separated, and the aqueous layer was extracted with Et<sub>2</sub>O. After evaporation, the residue was purified by column chromatography to provide the ana-

lytically pure product. The products were identified either by comparison with authentic samples using gas chromatography or by GC-MS analysis.

## Acknowledgement

We are grateful to Nanjing University of Science and Technology for financial support.

## References

- (1) (a) Tojo, G.; Fernández, M. *Oxidation of Primary Alcohols to Carboxylic Acids*; Springer: Berlin, 2006; (b) Tojo, G.; Fernández, M. *Oxidation of Alcohols to Aldehydes and Ketones*; Springer: Berlin, 2006; (c) Caron, S.; Dugger, R. W.; Ruggeri, S. G.; Ragan, J. A.; Ripin, D. H. B. *Chem. Rev.* **2006**, 106 (7), 2943. doi:10.1021/cr040679f. PMID: 16836305.
- (2) (a) Varvoglis, A. *Hypervalent Iodine in Organic Chemistry*; Academic Press: London, 1997; (b) Stang, P. J.; Zhdankin, V. V. *Chem. Rev.* **1996**, 96 (3), 1123. doi:10.1021/cr940424+. PMID:11848783.; (c) Wirth, T.; Hirt, U. H. *Synthesis* **1999**, 1999 (08), 1271. doi:10.1055/s-1999-3540.; (d) Moriarty, R. M.; Prakash, O. *Org. React.* **1999**, 54, 273; (e) Zhdankin, V. V.; Stang, P. J. *Chem. Rev.* **2008**, 108 (12), 5299. doi:10.1021/cr800332c. PMID:18986207.; (f) Ochiai, M. *Chem. Rec.* **2007**, 7 (1), 12. doi:10.1002/tcr.20104. PMID:17304588.; (g) Tohma, H.; Kita, Y. *Adv. Synth. Catal.* **2004**, 346 (23), 111. doi:10.1002/adsc.200303203.
- (3) (a) Richardson, R. D.; Wirth, T. *Angew. Chem. Int. Ed.* **2006**, 45 (27), 4402. doi:10.1002/anie.200601817.; (b) Ochiai, M.; Miyamoto, K. *Eur. J. Org. Chem.* **2008**, 2008 (25), 4229. doi:10.1002/ejoc.200800416.; (c) T. Dohi and Y. Kita. *Chem. Commun.* 2009, 2073; (d) Uyanik, M.; Ishihara, K. *Chem. Commun. (Camb.)* **2009**, (16), 2086. doi:10.1039/b823399c. PMID:19360158.; (e) Zhdankin, V. V. *Arkivoc* **2009**, i, 1.
- (4) (a) Dohi, T.; Maruyama, A.; Yoshimura, M.; Morimoto, K.; Tohma, H.; Kita, Y. *Angew. Chem. Int. Ed.* **2005**, 44 (38), 6193. doi:10.1002/anie.200501688.; (b) Ochiai, M.; Takeuchi, Y.; Katayama, T.; Sueda, T.; Miyamoto, K. *J. Am. Chem. Soc.* **2005**, 127 (35), 12244. doi:10.1021/ja0542800. PMID:16131201.; (c) Yamamoto, Y.; Togo, H. *Synlett* **2006**, 798; (d) Dohi, T.; Maruyama, A.; Minamitsuji, Y.; Takenaga, N.; Kita, Y. *Chem. Commun. (Camb.)* **2007**, (12), 1224. doi:10.1039/b616510a. PMID:17356763.; (e) Richardson, R. D.; Page, T. K.; Altermann, S.; Paradine, S. M.; French, A. N.; Wirth, T. *Synlett* **2007**, 538; (f) Akiike, J.; Yamamoto, Y.; Togo, H. *Synlett* **2007**, 2168; (g) Yamamoto, Y.; Kawano, Y.; Toy, P. H.; Togo, H. *Tetrahedron* **2007**, 63 (22), 4680. doi:10.1016/j.tet.2007.03.091.; (h) Richardson, R. D.; Desai, M.; Wirth, T. *Chem. Eur. J.* **2007**, 13 (23), 6745. doi:10.1002/chem.200700306.; (i) Moroda, A.; Togo, H. *Synthesis* **2008**, 1257; (j) Dohi, T.; Maruyama, A.; Takenaga, N.; Senami, K.; Minamitsuji, Y.; Fujioka, H.; Caemmerer, S. B.; Kita, Y. *Angew. Chem. Int. Ed.* **2008**, 47 (20), 3787. doi:10.1002/anie.200800464.; (k) Quideau, S.; Lyvinec, G.; Marguerit, M.; Bathany, K.; Ozanne-Beaudenon, A.; Buffeteau, T.; Cavagnat, D.; Chénéde, A. *Angew. Chem. Int. Ed.* **2009**, 48 (25), 4605. doi:10.1002/anie.200901039.; (l) Miyamoto, K.; Sei, Y.; Yamaguchi, K.; Ochiai, M. *J. Am. Chem. Soc.* **2009**, 131 (4), 1382. doi:10.1021/ja808829t. PMID:19133783.; (m) Uyanik, M.; Yasui, T.; Ishihara, K. *Med. Chem. Lett.* 2009.
- (5) (a) Thottumkara, A. P.; Bowsher, M. S.; Vinod, T. K. *Org. Lett.* **2005**, 7 (14), 2933. doi:10.1021/ol050875o. PMID:

- 15987173.; (b) Schulze, A.; Giannis, A. *Synthesis* **2006**, 257; (c) Lei, Z.; Yan, P.; Yang, Y. *Catal. Lett.* **2007**, 118 (1-2), 69. doi:10.1007/s10562-007-9147-0.; (d) Yakura, T.; Konishi, T. *Synlett* **2007**, 2007 (5), 0765. doi:10.1055/s-2007-970758.; (e) Yakura, T.; Tian, Y.; Yamauchi, Y.; Omoto, M.; Konishi, T. *Chem. Pharm. Bull. (Tokyo)* **2009**, 57 (3), 252. doi:10.1248/cpb.57.252. PMID:19252315.; (f) Yakura, T.; Omoto, M. *Chem. Pharm. Bull. (Tokyo)* **2009**, 57 (6), 643. doi:10.1248/cpb.57.643. PMID:19483353.; (g) Uyanik, M.; Akakura, M.; Ishihara, K. *J. Am. Chem. Soc.* **2009**, 131 (1), 251. doi:10.1021/ja807110n. PMID:19053813.; (h) Ojha, L. R.; Kudugunti, S.; Maddukuri, P. P.; Kommareddy, A.; Gunna, M. R.; Dokuparthi, P.; Gottam, H. B.; Botha, K. K.; Parapati, D. R.; Vinod, T. K. *Synlett* **2009**, 117.
- (6) (a) Sheng, J.; Li, X.; Tang, M.; Gao, B.; Huang, G. *Synthesis* **2007**, 1165.; (b) Dohi, T.; Minamitsuji, Y.; Maruyama, A.; Hirose, S.; Kita, Y. *Org. Lett.* **2008**, 10 (16), 3559. doi:10.1021/ol801321f. PMID:18616338.
- (7) Page, P. C. B.; Appleby, L. F.; Buckley, B. R.; Allin, S. M.; McKenzie, M. J. *Synlett* **2007**, 2007 (10), 1565. doi:10.1055/s-2007-982550.
- (8) Liu, H.; Tan, C.-H. *Tetrahedron Lett.* **2007**, 48 (46), 8220. doi:10.1016/j.tetlet.2007.09.078.
- (9) Mu, R.; Liu, Z.; Yang, Z.; Liu, Z.; Wu, L.; Liu, Z.-L. *Adv. Synth. Catal.* **2005**, 347 (10), 1333. doi:10.1002/adsc.200505102.
- (10) Yusubov, M. S.; Zagulyaeva, A. A.; Zhdankin, V. V. *Chem. Eur. J.* **2009**, 15 (42), 11091. doi:10.1002/chem.200901953.
- (11) Minamitsuji, Y.; Kato, D.; Fujioka, H.; Dohi, T.; Kita, Y. *Aust. J. Chem.* **2009**, 62 (7), 648. doi:10.1071/CH09148.
- (12) Herrerías, C. I.; Zhang, T. Y.; Li, C.-J. *Tetrahedron Lett.* **2006**, 47 (1), 13. doi:10.1016/j.tetlet.2005.10.123.
- (13) (a) Sheldon, R. A.; Arends, I. W. C. E. *Adv. Synth. Catal.* **2004**, 346 (910), 1051. doi:10.1002/adsc.200404110.; (b) Ishii, Y.; Sakaguchi, S. *Catal. Today* **2006**, 117 (1-3), 105. doi:10.1016/j.cattod.2006.05.006.; (c) Sheldon, R. A.; Arends, I. W. C. E. *J. Mol. Catal. Chem.* **2006**, 251 (1-2), 200. doi:10.1016/j.molcata.2006.02.016.; (d) Ishii, Y.; Sakaguchi, S.; Iwahama, T. *Adv. Synth. Catal.* **2001**, 343 (5), 393. doi:10.1002/1615-4169(200107)343:5<393::AID-ADSC393>3.0.CO;2-K.
- (14) De Mico, A.; Margarita, R.; Parlanti, L.; Vescovi, A.; Piancatelli, G. *J. Org. Chem.* **1997**, 62 (20), 6974. doi:10.1021/jo971046m.
- (15) (a) Wei, Y.; Cai, M.; Lu, C. *Catal. Lett.* **2003**, 90 (1/2), 81. doi:10.1023/A:1025824528577.; (b) Lin, L.; Juanjuan, M.; Liuyan, J.; Yunyang, W. *J. Mol. Catal. Chem.* **2008**, 291 (1-2), 1. doi:10.1016/j.molcata.2007.12.023.; (c) Lin, L.; Liuyan, J.; Yunyang, W. *Catal. Commun.* **2008**, 9 (6), 1379. doi:10.1016/j.catcom.2007.11.041.
- (16) (a) Ji, H. B.; Ebitani, K.; Mizugaki, T.; Kaneda, K. *Catal. Commun.* **2002**, 3 (11), 511. doi:10.1016/S1566-7367(02)00194-2.; (b) Ebitani, K.; Ji, H. B.; Mizugaki, T.; Kaneda, K. *J. Mol. Catal. A.* **2004**, 212 (1-2), 161. doi:10.1016/j.molcata.2003.10.036.

# Enantioselective fluorescent sensors for chiral carboxylates based on BINOL — Synthesis and chiral recognition

Kuo-xi Xu, Yu-xia Wang, Shu-yan Jiao, Jin Zhao, and Chao-jie Wang

**Abstract:** The four novel derivatives of 1,1'-bi-2-naphthol (BINOL) have been prepared, and the structures of these compounds have been characterized by IR, MS,  $^1\text{H}$  and  $^{13}\text{C}$  NMR spectroscopy, and elemental analysis. The enantioselective recognition of these receptors has been studied by fluorescence titration and  $^1\text{H}$  NMR spectroscopy. The receptors exhibited different chiral-recognition abilities towards some enantiomers of chiral materials and formed 1:1 complexes between host and guest. The receptors exhibit excellent enantioselective fluorescent-recognition ability towards the amino acid derivatives.

**Key words:** receptor, fluorescence, enantioselective recognition, anions, NMR spectroscopy.

**Résumé :** On a préparé quatre nouveaux dérivés du BINOL et on en a déterminé les structures par analyse élémentaire et par spectroscopies infrarouge, de masse et RMN du  $^1\text{H}$  et du  $^{13}\text{C}$ . On a étudié les propriétés de reconnaissance énantiosélective de ces récepteurs par titrage de fluorescence et par spectroscopie RMN du  $^1\text{H}$ . Les récepteurs présentent diverses capacités à reconnaître la chiralité de quelques énantiomères de produits chiraux et ils forment des complexes 1:1 entre molécules hôtes et invitées. Les récepteurs présentent une capacité excellente de reconnaître une fluorescence énantiosélective vis-à-vis des dérivés d'acides aminés.

**Mots-clés :** récepteur, fluorescence, reconnaissance énantiosélective, anions, spectroscopie RMN.

[Traduit par la Rédaction]

## Introduction

Molecular recognition, and in particular chiral recognition, is a fundamental characteristic in the biochemical systems. The study of synthetic model systems could contribute to the understanding of these processes and, at the same time, offer new perspectives for the development of pharmaceuticals, enantioselective sensors, catalysts, and other molecular devices.<sup>1</sup> The basis of any chiral recognition event is the formation of diastereomeric complexes composed of a chiral receptor and a chiral substrate possessing different stabilities.<sup>2</sup> The crucial points in the molecular design of chemosensors are how to achieve the specific recognition of a certain molecule and how to transduce the recognition event into a signal.<sup>3</sup> Many efforts involve the covalent linking of an optical signaling unit (a chromophore or a fluorophore) to a specific receptor for the chiral molecules.<sup>4</sup> Compared with other detection methods, such as NMR, HPLC, CD, or capillary electrophoresis, fluorescence techniques have often been used to study the interaction between enantiomers and receptors because of their sensitivity, selectivity, and versatility.<sup>5</sup> On the basis of their respective advantages, we attempt to design some receptors with optical

response to the enantiomers in the recognition interaction, which may offer a simple method to explore the recognition process for more information. The binaphthyl unit was especially eye-catching for its stable chiral configuration and tunable dihedral angle between the two naphthalene rings. Over the last two decades, binaphthyl derivatives have been shown to exhibit excellent enantioselectivities and turnovers in several types of asymmetric reactions, often matching the enantioselectivities traditionally regarded as being reserved for the enzyme realm.<sup>6</sup> As a naturally occurring chiral source, amino acids generally exhibit biological activity, and their recognition, in particular chiral recognition, attracts considerable interest.<sup>7</sup> Furthermore, they can be easily modified at the amino and carboxylic groups, which can also act as binding sites to form coordinate bonds with chiral molecules, so they were often used in the design and synthesis of artificial chiral receptors,<sup>8</sup> such as different types of acyclic compounds<sup>9</sup> as host molecules. We chose several familiar amino acids (e.g., alanine, phenylalanine) as chiral building blocks and introduced them into the 1,1'-bi-2-naphthol (BINOL) framework to construct the fluorescent receptors (Scheme 1). Herein, we describe the development of BINOL

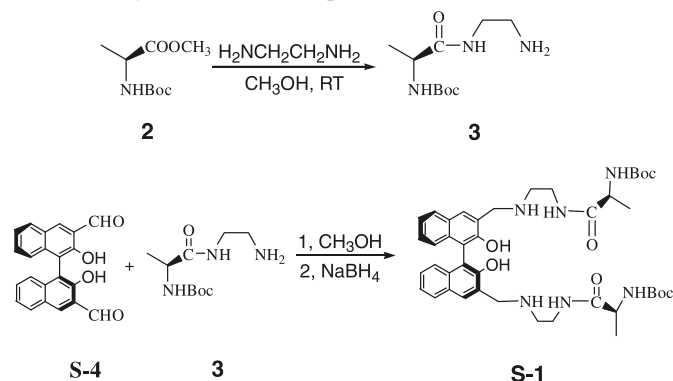
Received 30 July 2009. Accepted 7 December 2009. Published on the NRC Research Press Web site at canjchem.nrc.ca on 11 March 2010.

**K.-x. Xu and Y.-x. Wang.** College of Chemistry and Chemical Engineering, Henan University, Kaifeng 475004, China; Key Lab of Natural Medicinal and Immunol Engineering, Henan University, Kaifeng 475004, China.

**S.-y. Jiao.** College of Chemistry and Chemical Engineering, Henan University, Kaifeng 475004, China.

**J. Zhao and C.-j. Wang.**<sup>1</sup> Key Lab of Natural Medicinal and Immunol Engineering, Henan University, Kaifeng 475004, China.

<sup>1</sup>Corresponding author (e-mail: wcjsxq@henu.edu.cn).

**Scheme 1.** Synthesis of the receptor **S-1**.

derivatives bearing amino acid units, and their bonding properties with some enantiomers of chiral materials have been examined by using fluorescence titration experiments in  $\text{CHCl}_3$ . Receptors exhibited good enantioselective recognition abilities towards chiral materials and formed 1:1 complex with the guests in  $\text{CHCl}_3$ .  $^1\text{H}$  NMR experiments suggested that hydrogen-bonding interactions between the host and guest were the main factor in the recognition process.

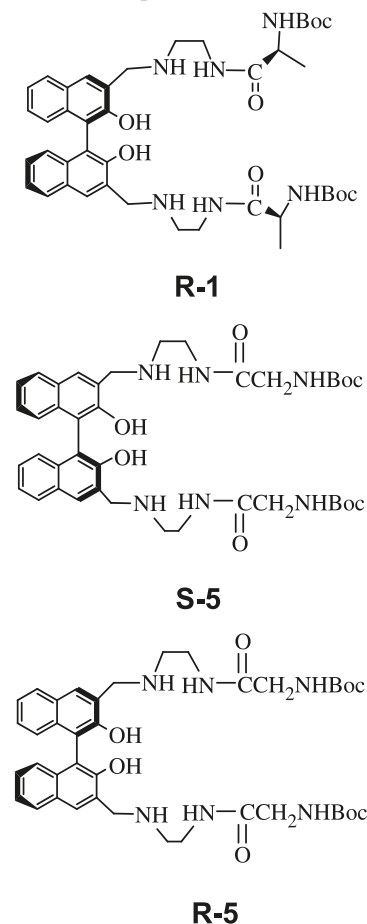
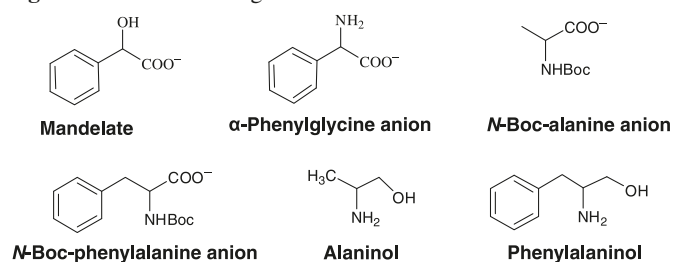
## Results and discussion

### Synthesis

The synthesis of receptor **S-1** is outlined in Scheme 1. The starting materials binaphthyl dialdehydes were prepared from BINOL.<sup>10</sup> *N*-Boc-protected alanine methyl ester (**2**) were synthesized according to the literature with high yield,<sup>11</sup> and then reacted with excess amount of ethylenediamine to obtain the compound (*S*)-*tert*-butyl-1-(2-aminoethylamino)-1-oxopropan-2-ylcarbamate (**3**). To avoid the partial racemization of **3** in this reaction, the compound **2** and ethylenediamine were dissolved in large amount of methanol and stirring was continued at room temperature. Especially at the end of reaction, the solvent and ethylenediamine should be evaporated under high vacuum at about  $30^\circ\text{C}$ , because a little higher temperature may lead the racemization of compound. Condensation of *S*-binaphthyl dialdehydes with compound **3**, followed by reduction, afforded the disubstituted BINOL **S-1** (Scheme 1). To study how the BINOL and amino acid units in **S-1** influenced the enantioselective fluorescent recognition, **R-1**, **S-5**, and **R-5** were also prepared (Fig. 1). They are readily soluble in common organic solvents, such as  $\text{CHCl}_3$ ,  $\text{CH}_2\text{Cl}_2$ ,  $\text{CH}_3\text{OH}$ , DMSO, and DMF. The structures of all these compounds were characterized by IR, MS,  $^1\text{H}$  and  $^{13}\text{C}$  NMR spectroscopy, and elemental analysis.

### Fluorescence spectra study

The properties of the chiral recognition of receptors **S-1** were investigated in the absence and presence of various chiral carboxylates (Fig. 2), such as (*S*)- and (*R*)-mandelate, the  $\alpha$ -phenylglycine anion, *N*-Boc-protected alanine anion (Ala), and *N*-Boc-protected phenylalanine anion (Phe), in which the amino groups were protected by the *tert*-butoxycarbonyl functionality. In each case, tetrabutylammonium was used as the counter cation, which could increase the reaction

**Fig. 1.** Structures of the receptors **R-1**, **S-5**, and **R-5**.**Fig. 2.** Structures of the guests.

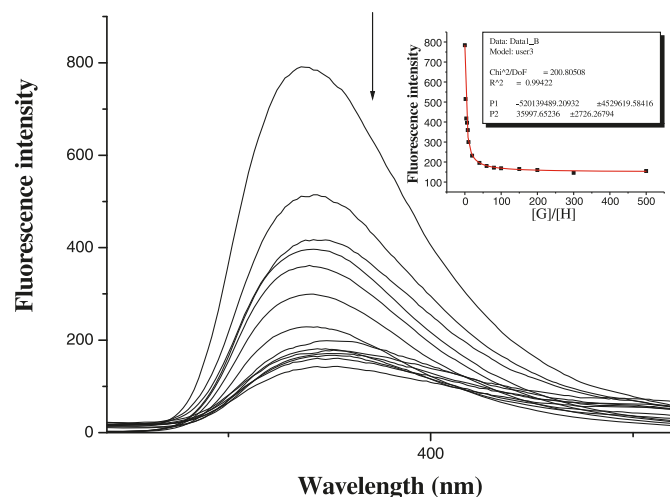
between the receptor and guest by hydrogen bondings.<sup>1c</sup> We also chose two amino alcohols, namely, alaninol and phenylalaninol, as guests to compare the associated abilities of the hosts to bind with neutral molecules.

The fluorescence spectra were recorded from a solution of sensor **S-1** ( $1.22 \times 10^{-5}$  mol  $\text{L}^{-1}$ ) in  $\text{CHCl}_3$  in the absence or presence of various enantiomers, (*R*)-, (*S*)-Ala, and Phe anions. Because there was almost no change observed on the UV-vis spectra of receptors upon addition of the anions, the interaction between host and anion was only evaluated by fluorescent spectra.

Upon addition of (*S*)- or (*R*)-Ala or Phe anions, different fluorescent-quenching degrees of **S-1** were observed. The quenching efficiencies of (*S*)-amino acid anions were much higher than the (*R*)-amino acid anions. Figure 3 and Fig. 4 show the fluorescence emission spectra of a mixture of **S-1**



**Fig. 3.** Fluorescence spectra of receptor **S-1** ( $1.22 \times 10^{-5}$  mol L $^{-1}$ ) with (*S*)-Ala anion in CHCl $_3$ . The anion equivalents are: 0, 2, 4, 6, 8, 10, 20, 40, 60, 80, 100, 150, 200, 300, and 500.  $\lambda_{\text{ex}} = 278$  nm. Inset: changes in the fluorescence intensity of **S-1** at 371 nm upon addition of (*S*)-Ala anion. The line shown is a line-fitted curve. The correlation coefficient (*R*) of the nonlinear curve fitting is 0.9994.



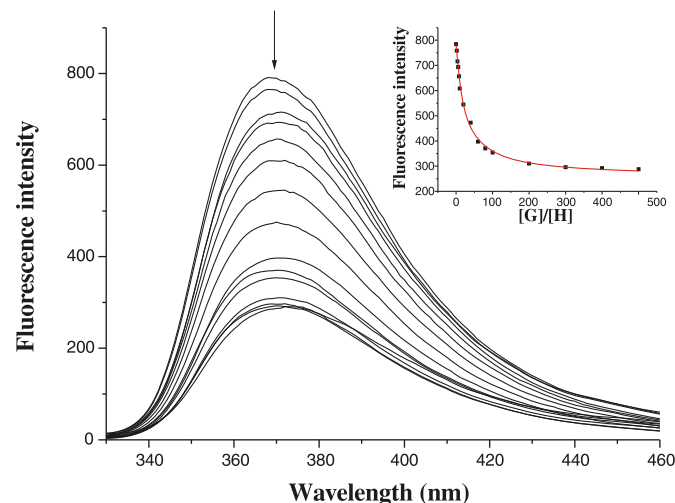
and different concentrations of the (*S*)- or (*R*)-Ala anion in CHCl $_3$  ( $\lambda_{\text{ex}} = 278$  nm), respectively. The graphs in the top right corners of Figs. 3 and 4 illustrate the fluorescence intensity change of receptor **S-1** upon addition of (*S*)- and (*R*)-Ala anions, respectively. Figure 5 shows the different fluorescence intensity changes when the same equiv. of (*S*)- or (*R*)-Ala anion were added to the solution of **S-1**, the quenching efficiency was 46.7% when 4 equiv. of (*S*)-Ala anion was added to the solution of **S-1**, while the quenching efficiency was only 8.7% when 4 equiv. of (*R*)-Ala anion was added. The quenched efficiencies ( $\Delta I_S/\Delta I_R = 5.37$ ) indicated that the host **S-1** has a good enantioselective recognition ability between the (*S*)- and (*R*)-Ala anions, respectively. Satisfactory nonlinear curve fitting (the correlation coefficient is over 0.99) confirmed that **S-1** and the (*S*)- or (*R*)-Ala formed a 1:1 complex (see the insets of Fig. 3 and Fig. 4). For a complex of 1:1 stoichiometry, the association constant ( $K_{\text{ass}}$ ) can be calculated by using eq. [1] from the Origin 7.5 software package<sup>12,13</sup>

$$[1] \quad X = X_0 + (X_{\text{lim}} - X_0)/2C_0\{C_H + C_G + 1/K_{\text{ass}} - [(C_H + C_G + 1/K_{\text{ass}})^2 - 4C_H C_G]^{1/2}\}$$

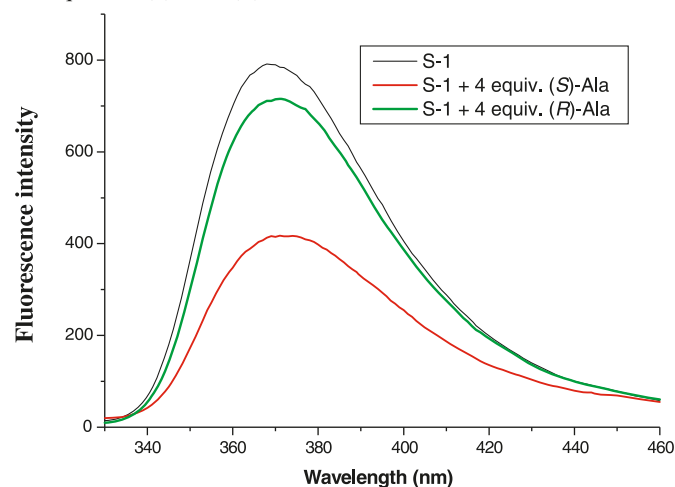
where *X* represents the fluorescence intensity,  $C_H$  and  $C_G$  are the host and guest concentrations, respectively, and  $C_0$  is the initial concentration of the host. The association constants ( $K_{\text{ass}}$ ) and correlation coefficients (*R*) obtained by a nonlinear least squares analysis of *X* vs.  $C_H$  and  $C_G$  are listed in Table 1.

The association constant for the interaction of **S-1** with the (*S*)- and (*R*)-Ala anion is  $(3.60 \pm 0.27) \times 10^4$  and  $(3.54 \pm 0.19) \times 10^3$  M $^{-1}$ , respectively. Receptor **S-1** gives an enantioselectivity  $K_{\text{ass}((S)\text{-Ala})}/K_{\text{ass}((R)\text{-Ala})} = 10.17$ . The dramatically different fluorescent responses and quenching efficiencies observed for the two enantiomers indicate that **S-1** has excellent enantioselective fluorescent-recognition ability towards the Ala anion. Similar phenomena were observed

**Fig. 4.** Fluorescence spectra of receptor **S-1** ( $1.22 \times 10^{-5}$  mol L $^{-1}$ ) with (*S*)-Ala anion in CHCl $_3$ . The anion equivalents are: 0, 2, 4, 6, 8, 10, 20, 40, 60, 80, 100, 200, 300, 400, and 500.  $\lambda_{\text{ex}} = 278$  nm. Inset: changes in the fluorescence intensity of **S-1** at 371 nm upon addition of (*S*)-Ala anion. The line shown is a line-fitted curve. The correlation coefficient (*R*) of the nonlinear curve fitting is 0.9994.



**Fig. 5.** Fluorescence spectra of host **S-1** ( $2.13 \times 10^{-6}$  mol L $^{-1}$ ) with 4.0 equiv. of (*S*)- and (*R*)-Ala anion in CHCl $_3$ .



when (*S*)- or (*R*)-Phe anions were added into a solution of **S-1**. The result of a nonlinear curve fitting (at 371 nm) indicates that a 1:1 complex was formed between receptor **S-1** and (*S*)- or (*R*)-Phe (see Table 1). In addition, the association constants ( $K_{\text{ass}}$ ) were different (see Table 1) ( $K_{\text{ass}((S))} = (3.17 \pm 0.11) \times 10^4$  M $^{-1}$ ,  $\Delta G_0 = -25.69$  kJ mol $^{-1}$ ;  $K_{\text{ass}((R))} = (3.09 \pm 0.08) \times 10^3$  M $^{-1}$ ,  $\Delta G_0 = -19.92$  kJ mol $^{-1}$ ), yielding an *S/R* selectivity [ $K_{\text{ass}((S))}/K_{\text{ass}((R))}$ ] of 10.26 for the Phe anions and a  $\Delta\Delta G_0$  value of  $-5.77$  kJ mol $^{-1}$ , demonstrating that **S-1** has good chiral recognition ability towards the enantiomers of Phe anions.

The binding of **S-1** with mandelate and  $\alpha$ -phenylglycine anion was also carried out, and the association constants of the host **S-1** with mandelate and  $\alpha$ -phenylglycine anion are also listed in Table 1. When **S-1** interacted with  $\alpha$ -phenylglycine anion, the receptor **S-1** exhibited weak enantioselective recognition ability to  $\alpha$ -phenylglycine anion that have been

**Table 1.** Association constants ( $K_{\text{ass}}$ ), correlation coefficients ( $R$ ), enantioselectivities ( $K_{\text{ass}(S)}/K_{\text{ass}(R)}$ ), Gibbs free energy changes ( $-\Delta G_0$ ), and  $\Delta\Delta G_0$  calculated from  $\Delta G_0$  for the complexation of receptors **S-1** and **R-1** with *S*-/*R*- guests in  $\text{CHCl}_3$  at 25 °C.

Entry	Host	Guest	$K_{\text{ass}}$ ( $\text{M}^{-1}$ ) <sup>a,b</sup>	$R$	$K_{\text{ass}(S)}/K_{\text{ass}(R)}$	$-\Delta G_0$ ( $\text{kJ mol}^{-1}$ )	$\Delta\Delta G_0$ ( $\text{kJ mol}^{-1}$ )
1	<b>S-1</b>	( <i>S</i> )-Ala <sup>c</sup>	$(3.60\pm0.27)\times10^4$	0.9971		26.01	
2	<b>S-1</b>	( <i>R</i> )-Ala <sup>c</sup>	$(3.54\pm0.19)\times10^3$	0.9984	10.17	20.26	−5.75
3	<b>S-1</b>	( <i>S</i> )-Phe <sup>c</sup>	$(3.17\pm0.11)\times10^4$	0.9927		25.69	
4	<b>S-1</b>	( <i>R</i> )-Phe <sup>c</sup>	$(3.09\pm0.08)\times10^3$	0.9928	10.26	19.92	−5.77
5	<b>S-1</b>	( <i>S</i> )-Mandelate	$(5.81\pm0.26)\times10^4$	0.9908		27.2	
6	<b>S-1</b>	( <i>R</i> )-Mandelate	$(1.04\pm0.13)\times10^4$	0.9946	5.87	22.93	−4.27
7	<b>S-1</b>	( <i>S</i> )-Phenylglycine	$(6.64\pm0.26)\times10^4$	0.9923		27.53	
8	<b>S-1</b>	( <i>R</i> )-Phenylglycine	$(3.91\pm0.19)\times10^4$	0.9931	1.70	26.22	−1.31
9	<b>S-1</b>	( <i>S</i> )-Alaninol	$(6.72\pm0.31)\times10^2$	0.9924		16.14	
10	<b>S-1</b>	( <i>R</i> )-Alaninol	$(4.31\pm0.05)\times10^2$	0.9902	1.56	15.04	−1.1
11	<b>S-1</b>	( <i>S</i> )-Phenylalaninol	$(5.98\pm0.21)\times10^2$	0.9944		15.85	
12	<b>S-1</b>	( <i>R</i> )-Phenylalaninol	$(1.99\pm0.15)\times10^2$	0.9919	3.01	13.12	−2.73
13	<b>R-1</b>	( <i>S</i> )-Ala <sup>c</sup>	$(3.26\pm0.22)\times10^3$	0.9903		20.06	
14	<b>R-1</b>	( <i>R</i> )-Ala <sup>c</sup>	$(3.02\pm0.13)\times10^4$	0.9912	1/9.26	25.57	5.51
15	<b>R-1</b>	( <i>S</i> )-Phe <sup>c</sup>	$(3.47\pm0.26)\times10^3$	0.9941		20.21	
16	<b>R-1</b>	( <i>R</i> )-Phe <sup>c</sup>	$(3.29\pm0.24)\times10^4$	0.9937	1/9.48	25.79	5.58
17	<b>R-1</b>	( <i>S</i> )-Mandelate	$(1.75\pm0.11)\times10^4$	0.9952		24.22	
18	<b>R-1</b>	( <i>R</i> )-Mandelate	$(7.81\pm0.51)\times10^4$	0.9917	1/4.46	27.93	3.71
19	<b>R-1</b>	( <i>S</i> )-Phenylglycine	$(2.98\pm0.22)\times10^4$	0.9962		25.54	
20	<b>R-1</b>	( <i>R</i> )-Phenylglycine	$(5.07\pm0.19)\times10^4$	0.9933	1/2.41	26.86	1.34
21	<b>R-1</b>	( <i>S</i> )-Alaninol	$(3.51\pm0.14)\times10^2$	0.9917		14.53	
22	<b>R-1</b>	( <i>R</i> )-Alaninol	$(6.94\pm0.29)\times10^2$	0.9951	1/1.98	16.22	1.69
23	<b>R-1</b>	( <i>S</i> )-Phenylalaninol	$(1.51\pm0.07)\times10^2$	0.9903		12.44	
24	<b>R-1</b>	( <i>R</i> )-Phenylalaninol	$(8.81\pm0.44)\times10^2$	0.9927	1/5.64	16.81	4.37
25	<b>S-5</b>	( <i>S</i> )-Ala <sup>c</sup>	$(4.53\pm0.18)\times10^4$	0.9989		26.58	
26	<b>S-5</b>	( <i>R</i> )-Ala <sup>c</sup>	$(9.71\pm0.52)\times10^3$	0.9946	4.67	22.76	−3.82
27	<b>S-5</b>	( <i>S</i> )-Phe <sup>c</sup>	$(4.19\pm0.24)\times10^4$	0.9938		26.39	
28	<b>S-5</b>	( <i>R</i> )-Phe <sup>c</sup>	$(8.62\pm0.29)\times10^3$	0.9913	4.86	22.47	−3.92
29	<b>S-5</b>	( <i>S</i> )-Mandelate	$(4.97\pm0.26)\times10^4$	0.9931		26.81	
30	<b>S-5</b>	( <i>R</i> )-Mandelate	$(1.54\pm0.39)\times10^4$	0.9911	3.23	23.91	−2.90
31	<b>S-5</b>	( <i>S</i> )-Phenylglycine	$(6.77\pm0.43)\times10^4$	0.9956		27.58	
32	<b>S-5</b>	( <i>R</i> )-Phenylglycine	$(4.34\pm0.39)\times10^4$	0.9931	1.56	26.47	−1.11
33	<b>S-5</b>	( <i>S</i> )-Alaninol	$(6.53\pm0.35)\times10^2$	0.9907		16.07	
34	<b>S-5</b>	( <i>R</i> )-Alaninol	$(3.37\pm0.39)\times10^2$	0.9916	1.94	14.43	−1.64
35	<b>S-5</b>	( <i>S</i> )-Phenylalaninol	$(6.01\pm0.35)\times10^2$	0.9907		15.86	
36	<b>S-5</b>	( <i>R</i> )-Phenylalaninol	$(2.32\pm0.39)\times10^2$	0.9921	2.59	13.50	−2.36
37	<b>R-5</b>	( <i>S</i> )-Ala <sup>c</sup>	$(1.27\pm0.10)\times10^4$	0.9934		23.43	
38	<b>R-5</b>	( <i>R</i> )-Ala <sup>c</sup>	$(4.02\pm0.18)\times10^4$	0.9940	1/3.17	26.28	2.85
39	<b>R-5</b>	( <i>S</i> )-Phe <sup>c</sup>	$(9.78\pm0.41)\times10^3$	0.9941		22.78	
40	<b>R-5</b>	( <i>R</i> )-Phe <sup>c</sup>	$(3.99\pm0.22)\times10^4$	0.9913	1/4.08	26.27	3.49
41	<b>R-5</b>	( <i>S</i> )-Mandelate	$(1.99\pm0.26)\times10^4$	0.9919		24.54	
42	<b>R-5</b>	( <i>R</i> )-Mandelate	$(4.82\pm0.39)\times10^4$	0.9934	1/2.42	26.73	2.19
43	<b>R-5</b>	( <i>S</i> )-Phenylglycine	$(3.98\pm0.43)\times10^4$	0.9926		26.26	
44	<b>R-5</b>	( <i>R</i> )-Phenylglycine	$(6.27\pm0.39)\times10^4$	0.9915	1/1.58	27.39	1.13
45	<b>R-5</b>	( <i>S</i> )-Alaninol	$(4.03\pm0.35)\times10^2$	0.9923		14.87	
46	<b>R-5</b>	( <i>R</i> )-Alaninol	$(5.99\pm0.39)\times10^2$	0.9908	1/1.49	15.86	0.99
47	<b>R-5</b>	( <i>S</i> )-Phenylalaninol	$(2.53\pm0.35)\times10^2$	0.9912		13.72	
48	<b>R-5</b>	( <i>R</i> )-Phenylalaninol	$(5.74\pm0.39)\times10^2$	0.9903	1/2.27	15.75	2.03

<sup>a</sup>The data were calculated from the results of fluorescence titrations in  $\text{CHCl}_3$ .<sup>b</sup>All error values were obtained from nonlinear curve fitting.<sup>c</sup>Ala and Phe tetrabutylammonium salts, the amino group was protected by a *tert*-butoxycarbonyl function.

tested (see Table 1). Upon the addition of alaninol or phenylalaninol into a solution of in  $\text{CHCl}_3$ , the fluorescence intensity of **S-1** was slightly quenched by both (*S*)- and (*R*)-enantiomers (see Table 1). This indicates that hydrogen bonding plays an important role in the interaction between

the host and guest and leads to the easier signal transductions of chiral recognition by fluorescence method.

The continuous variation methods were also employed to determine the stoichiometric ratio of the receptor **S-1** with guests [(*S*)- and (*R*)-Ala anions]. The total concentration of

host and guest was constant ( $1.0 \times 10^{-6}$  mol L $^{-1}$ ) in CHCl $_3$ , with a continuously variable molar fraction of host ( $[H]/([H] + [G])$ ). Figure 6 shows the Job plots of receptor **S-1** with (S)- and (R)-Ala anion (at 371 nm,  $\lambda_{\text{ex}} = 278$  nm). When the molar fraction of the host was 0.50, the fluorescence intensity reached a maximum, which demonstrated that receptor **S-1** formed a 1:1 complex with (S)- and (R)-Ala anions, respectively.<sup>14</sup>

The decrease in fluorescence intensity of the excimer upon addition of the anion is similar to the anion-induced fluorescence decrease reported previously.<sup>15</sup> Because of the similar structure of **S-1**, the fluorescent variations of **S-1** showed the same trend. Since there were no changes in the UV-vis spectra of the receptors when treated with (S)- or (R)-anions, a photoinduced electron transfer (PET) process might be responsible for the fluorescent quenching.<sup>16</sup> In the absence of anions, PET between the binaphthyl unit and the electron-withdrawing amide substituents might result in quenched fluorescence. In the presence of guest anions, the fluorescence quenching of receptors **S-1** most likely arose from the change of the free energy ( $\Delta G_{\text{PET}}$ ) of the electron transfer between the excited fluorophore and the receptor.<sup>17</sup> Therefore, fluorescence quenching was observed.

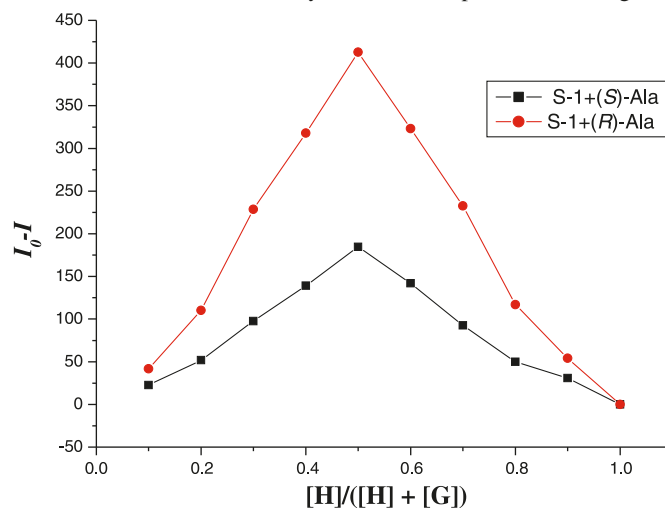
To study how the chirality of the amino acid unit and BINOL groups in **S-1** influenced the enantioselective fluorescent recognition, **R-1**, the diastereomeric compounds of **S-1**, **S-5**, and **R-5** were also prepared by similar methods. We also studied its interaction with mandelate, phenylglycine, Ala and Phe anions, alaninol, and phenylalaninol, which showed the opposite enantioselectivity. That is, the (R)-guest enantiomer quenched the fluorescence of **R-1** more efficiently than (S)-guest. The result of fluorescence titration indicated that a matched chirality between the guest anions center and the chiral BINOL unit led to the enantioselective recognition. The enantiomers of guest anions interacted with **R-1** and **S-1** in the same fashion.

According to Table 1, the interaction of **S-1** with the (S)-Ala and (S)-Phe anions is better than that with the (R)-Ala and (R)-Phe anions, which is probably due to the (S)-amino acid anions having a more complementary structure with receptors **S-1**. The receptors **S-1** and **R-1** all exhibit good chiral recognition ability towards the enantiomers of the Ala and Phe anions, which indicates that the preorganized structure of the chiral center of the binaphthyl unit plays important roles in the enantioselective recognition process.

### <sup>1</sup>H NMR study

<sup>1</sup>H NMR experiments were undertaken to assess the chiral-recognition properties between receptor **S-1** and chiral anionic guest because NMR spectroscopy can provide structural and dynamic information directly.<sup>18</sup> <sup>1</sup>H NMR chiral-recognition studies were carried out with a 400 MHz NMR spectrometer using receptor **S-1** in CDCl $_3$  as chiral solvating agent at room temperature. The spectra of receptor **S-1** and its complexes with equimolar amounts of racemic Ala anions are shown in Fig. 7. When treated with equimolar amounts of receptor **S-1**, the signal of the CH proton of the racemic Ala anion cleaved into a more complicated signal pattern (Fig. 7C) with a downfield shift. The interaction of receptor **S-1** with (S)-enantiomer showed that the CH proton has a larger downfield shift (from  $\delta = 3.85$  to 4.27 ppm,  $\Delta\delta =$

**Fig. 6.** Job plots of receptor **S-1** with (S)- and (R)-Ala anions (367 nm,  $\lambda_{\text{ex}} = 290$  nm). The total concentration of the host [H] and guest [G] is  $1.0 \times 10^{-6}$  mol L $^{-1}$  in CHCl $_3$ .  $I_0$ : fluorescence intensity of **S-1**;  $I$ : fluorescence intensity of **S-1** in the presence of the guest.

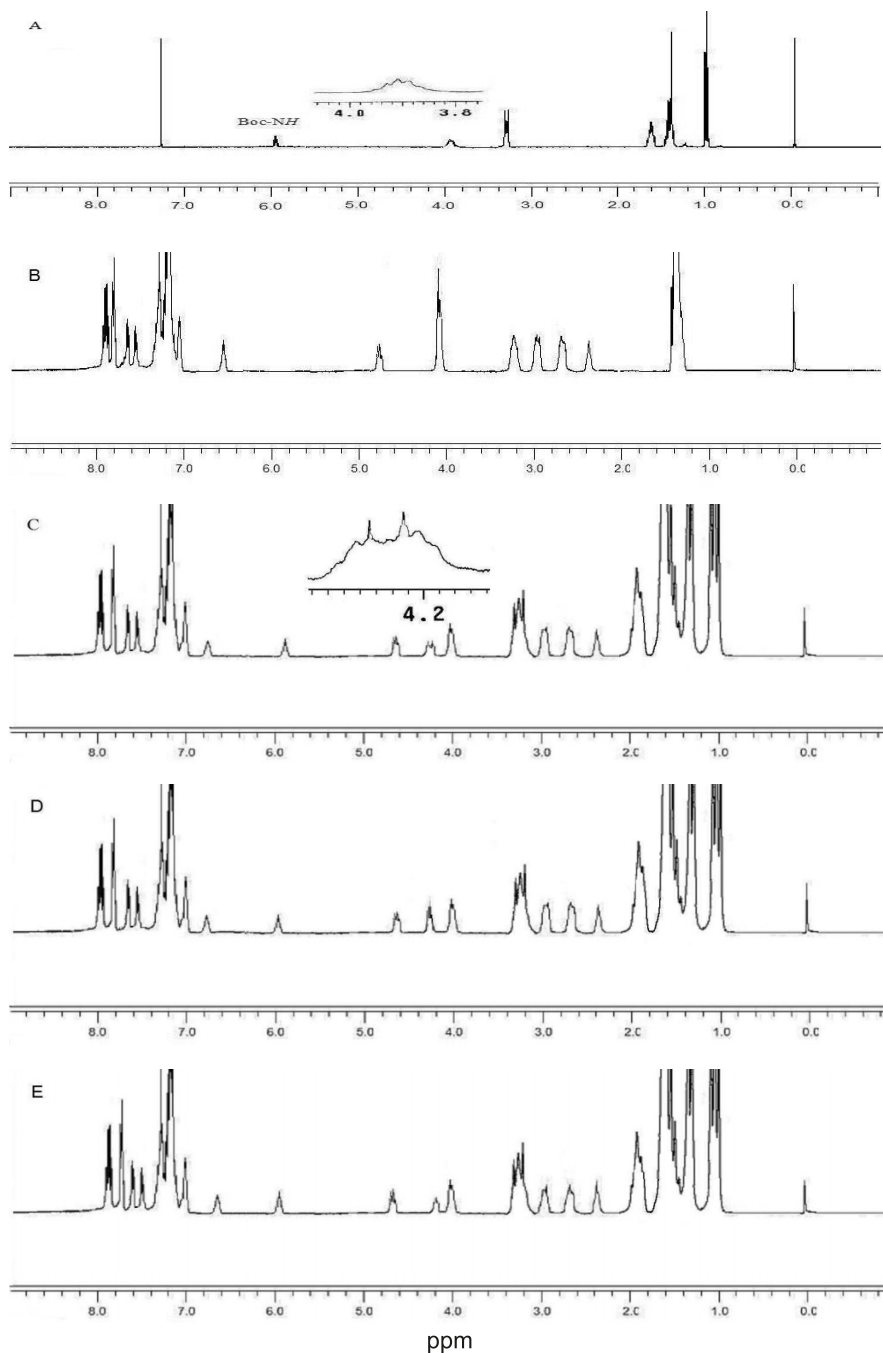


0.42 ppm, Fig. 7D) than that of the CH proton of the (R)-enantiomer (from  $\delta = 3.85$  to 4.19 ppm,  $\Delta\delta = 0.34$  ppm, Fig. 7E). Moreover, the signals of the -OH proton in the <sup>1</sup>H NMR spectra of the receptor **S-1** become weakened obviously and have downfield shift from 6.57 to 6.78 ppm ( $\Delta\delta = 0.21$  ppm, Fig. 7D) or 6.74 ppm ( $\Delta\delta = 0.17$  ppm, Fig. 7E) for (S)- or (R)-Ala anion, respectively, while the signals of the peaks of binaphthyl fragments are downfield-shifted and broadened with the addition of the guest. The signal of the amide (NH) group of Ala linked to the Boc moiety was also clearly downfield-shifted from  $\delta = 5.91$  to 5.98 ppm ( $\Delta\delta = 0.07$  ppm, Fig. 7D) and 5.94 ppm ( $\Delta\delta = 0.03$  ppm, Fig. 7E) for (S)- and (R)-Ala anion, respectively. The above results indicate that **S-1** has a stronger interaction with the (S)-Ala anion than with its (R)-enantiomer. This indicated that the interaction between the host and guest also happened by multiple hydrogen bondings. The results also illustrate that the nature of the receptor, multiple hydrogen-bonding interactions, and complementary chiral-center interactions maybe responsible for the enantiomeric recognition of the amino acid anion.<sup>19</sup>

### Conclusion

In summary, four chiral fluorescent receptors **S-1**, **R-1**, **S-5**, and **R-5** were synthesized, and their enantioselective recognition was studied by fluorescence titration and <sup>1</sup>H NMR spectroscopy. Receptors **S-1** and **R-1** exhibit different chiral-recognition abilities towards some enantiomers of chiral materials and form 1:1 complexes with the guest molecules. It is clear that the nature of the receptor, good structural preorganization, multiple hydrogen-bonding interactions, and complementary chiral-center interactions may be responsible for the enantiomeric recognition of anionic guests.<sup>19</sup> Receptors **S-1** and **R-1** are promising in their use as fluorescence sensors for amino acid anions. The remarkably different fluorescent responses that result from complexation reveal that **S-1** and **R-1** could be used as fluorescent chemosensors for the *N*-Boc-protected alanine anion or *N*-Boc-protected phenylalanine anion in the future.

**Fig. 7.** The  $^1\text{H}$  NMR spectra of **S-1** and its guest complexes at 25 °C ( $[\text{S-1}] = [\text{guest}] = 4.0 \times 10^{-3} \text{ mol L}^{-1}$ ) in  $\text{CDCl}_3$  at 400 MHz. (A) Racemic Ala anion; (B) receptor **S-1**; (C) receptor **S-1** + racemic Ala anion; (D) receptor **S-1** + (*S*)-Ala anion; (E) receptor **S-1** + (*R*)-Ala anion.



## Experimental section

### General

The reagents used were of commercial origin and were employed without further purification. Purifications by column chromatography were carried out over silica gel (230–400 mesh). The IR spectra were performed on a Nicolet 670 FTIR spectrophotometer.  $^1\text{H}$  and  $^{13}\text{C}$  NMR spectra were recorded on a Bruker AV-400 spectrometer. Mass spectra were determined by ESI recorded on a Esquire 3000 LC-MS mass instrument. Optical rotations were taken on a Per-

kinElmer Model 341 polarimeter. Fluorescence spectra were obtained with a F-7000 FL Spectrophotometer. Elemental analyses were performed by the Vario Elemental CHN-O microanalyzer. The anions were used as their tetrabutylammonium salts. The *N*-protected (by the *tert*-butoxycarbonyl functionality) amino acid derivatives were synthesized according to a literature method.<sup>20</sup>

### The synthesis of compound 3

Under  $\text{N}_2$ , excess ethylenediamine (0.60 g, 10 mmol) in 10 mL  $\text{CH}_3\text{OH}$  was added dropwise into a solution (20 mL)



of (*S*)-*N*-Boc-protected alanine methyl ester (**2**) (0.41 g, 2 mmol) in  $\text{CHCl}_3/\text{CH}_3\text{OH}$  (1:10, v/v) in an ice-bath. After the addition, the mixture was stirred at room temperature for 48 h. The solvent was evaporated, and the residual ethylenediamine was removed under reduced pressure. Then,  $\text{CHCl}_3$  (30 mL) was added and washed with  $\text{H}_2\text{O}$  (3  $\times$  30 mL); the organic layer was separated and dried over  $\text{Na}_2\text{SO}_4$ . After filtration, the solvent was removed under reduced pressure to give **3** as colorless ropy oil in 86% yield (0.40 g).  $[\alpha]_{\text{D}}^{20} + 21.84$  ( $c = 0.05$ ,  $\text{CHCl}_3$ ).  $^1\text{H}$  NMR ( $\text{CDCl}_3$ )  $\delta$  (ppm): 7.01 (s, 1 H, CONH), 5.47 (s, 1 H, NHBoc), 4.18 (CH), 3.31 (t,  $J = 6.4$  Hz, 2H,  $\text{CH}_2$ ), 2.82 (t,  $J = 6.4$  Hz, 2H,  $\text{CH}_2$ ), 1.72 (s, 2 H,  $\text{NH}_2$ ), 1.44 (s, 9 H,  $\text{CH}_3$ ), 1.35 (t,  $J = 6.8$  Hz, 3 H,  $\text{CH}_3$ ).  $^{13}\text{C}$  NMR ( $\text{CDCl}_3$ )  $\delta$  (ppm): 172.8, 155.2, 77.8, 54.1, 41.2, 40.3, 28.8, 27.9. ESI-MS  $m/z$  (%): 232 (100)  $[\text{M} + 1]^+$ .  $\text{C}_{10}\text{H}_{21}\text{N}_3\text{O}_3$  calcd.: C 51.93, H 9.15, N 18.17; found: C 51.66, H 9.22, N 18.04.

### The preparation of *tert*-butyl-2-(2-aminoethylamino)-2-oxoethylcarbamate

*Tert*-butyl-2-(2-aminoethylamino)-2-oxoethylcarbamate was prepared by the same method as that of compound **3** by starting with *N*-Boc-protected glycine methyl ester, and it gave 95% yield.  $^1\text{H}$  NMR ( $\text{CDCl}_3$ )  $\delta$  (ppm): 7.11 (s, 1H, CONH), 5.57 (s, 1H, NHBoc), 3.74 (s, 2H,  $\text{CH}_2$ ), 3.39 (t,  $J = 6.4$  Hz, 2H,  $\text{CH}_2$ ), 2.86 (t,  $J = 8.0$  Hz, 2H,  $\text{CH}_2$ ), 1.74 (s, 2 H,  $\text{NH}_2$ ), 1.44 (s, 9 H,  $\text{CH}_3$ ).  $^{13}\text{C}$  NMR ( $\text{CDCl}_3$ )  $\delta$  (ppm): 173.3, 155.9, 78.1, 55.7, 41.9, 40.7, 28.9. ESI-MS:  $m/z$  (%) = 218 (100)  $[\text{M} + 1]^+$ .  $\text{C}_9\text{H}_{19}\text{N}_3\text{O}_3$  calcd.: C 49.75, H 8.81, N 19.34; found: C 49.57, H 8.89, N 19.22.

### General procedure for the synthesis of compounds **R-1**, **S-1**, **R-5**, and **S-5**

A mixture of the (*R*) or (*S*)-binaphthyl dialdehyde (0.34 g, 1 mmol) and compound **3** or *tert*-butyl-2-(2-aminoethylamino)-2-oxoethylcarbamate (2.2 mmol) in  $\text{CH}_3\text{OH}$  (30 mL) was stirred for 48 h under  $\text{N}_2$  at room temperature until TLC showed the disappearance of the starting material.  $\text{NaBH}_4$  (0.19 g, 5 mmol) was then added to the mixture in three portions over 3 h, after which it was stirred under  $\text{N}_2$  for another 6 h at 50  $^\circ\text{C}$ . The mixture was poured into 30 mL of 10%  $\text{NaHCO}_3$  after removing the solvent under reduced pressure, and extracted three times with  $\text{CHCl}_3$ . The organic layers were combined and dried over anhydrous  $\text{Na}_2\text{SO}_4$ . After filtration, the solvent was evaporated under reduced pressure, and the residue was purified by column chromatography on silica gel [eluent:  $\text{CHCl}_3/\text{CH}_3\text{CH}_2\text{OH}$ , 50:1 (v/v)]. The pure product was obtained as a pale yellow solid.

### *S-1* and *R-1*

Yield (**S-1**): 76.8%;  $[\alpha]_{\text{D}}^{20} - 34.72$  ( $c = 0.05$ ,  $\text{CHCl}_3$ ). Yield (**R-1**): 79.3%;  $[\alpha]_{\text{D}}^{20} + 117.18$  ( $c = 0.05$ ,  $\text{CHCl}_3$ ).  $^1\text{H}$  NMR ( $\text{CDCl}_3$ )  $\delta$  (ppm): 7.87 (s, 2H, CONH), 7.83 (d,  $J = 8.0$  Hz, 2H, Ar-H), 7.76 (d,  $J = 9.6$  Hz, 2H, Ar-H), 7.61 (d,  $J = 8.1$  Hz, 2H, Ar-H), 7.28 (d,  $J = 7.6$  Hz, 2 H, Ar-H), 7.19 (d,  $J = 7.2$  Hz, 2H, Ar-H), 7.13–7.16 (t,  $J = 4.8$  Hz, 2H, Ar-H), 6.52 (s, 2H, OH), 4.76–4.68 (m, 2H,  $\text{CHCH}_2$ ), 4.10 (d,  $J = 8.0$  Hz, 4H, Ar- $\text{CH}_2$ ), 3.00–2.91 (m, 4H,  $\text{CH}_2$ ), 2.73–2.64 (m, 4H,  $\text{CH}_2$ ), 2.36 (s, 2H, NH), 1.42 (s, 18H,  $\text{CH}_3$ ), 1.28 (s, 3H,  $\text{CH}_3$ ), 1.22 (s, 3H,  $\text{CH}_3$ ).  $^{13}\text{C}$  NMR

( $\text{CDCl}_3$ )  $\delta$  (ppm): 172.39, 152.53, 152.51, 134.32, 133.76, 132.91, 132.69, 131.29, 130.69, 130.54, 130.12, 129.94, 128.34, 127.38, 126.95, 126.07, 125.86, 125.59, 125.22, 124.96, 121.02, 57.31, 57.09, 39.89, 24.95, 14.44, 14.14. ESI-MS  $m/z$  (%): 795 (100)  $[\text{M} + \text{Na}]^+$ .  $\text{C}_{42}\text{H}_{56}\text{N}_6\text{O}_8$  calcd.: C 65.26, H 7.30, N 10.87; found (**S-1**): C 65.11, H 7.21, N 10.99; found (**R-1**): C 65.07, H 7.19, N 11.02.

### *S-5* and *R-5*

Yield (**S-5**): 79.6%;  $[\alpha]_{\text{D}}^{20} = -68.32$  ( $c = 0.05$ ,  $\text{CHCl}_3$ ). IR (film,  $\text{cm}^{-1}$ )  $\nu$ : 3402, 3092, 2969, 1679, 1529, 1268, 1234, 752.  $^1\text{H}$  NMR ( $\text{CDCl}_3$ )  $\delta$  (ppm): 7.89 (s, 2H, CONH), 7.87 (d,  $J = 8.0$  Hz, 2H, Ar-H), 7.79 (d,  $J = 9.6$  Hz, 2H, Ar-H), 7.64 (d,  $J = 8.1$  Hz, 2H, Ar-H), 7.22 (d,  $J = 7.6$  Hz, 2H, Ar-H), 7.19 (d,  $J = 7.2$  Hz, 2H, Ar-H), 7.17–7.13 (t,  $J = 4.8$  Hz, 2H, Ar-H), 6.55 (s, 2H, OH), 4.12 (d,  $J = 8.0$  Hz, 4H, Ar- $\text{CH}_2$ ), 3.88 (s, 4H,  $\text{CH}_2$ ), 3.03–2.95 (m, 4H,  $\text{CH}_2$ ), 2.79–2.70 (m, 4H,  $\text{CH}_2$ ), 2.38 (s, 2H, NH), 1.44 (s, 18H,  $\text{CH}_3$ ).  $^{13}\text{C}$  NMR ( $\text{CDCl}_3$ )  $\delta$  (ppm): 174.03, 153.59, 153.31, 134.99, 133.96, 133.44, 133.17, 132.54, 131.06, 130.86, 130.58, 129.91, 128.71, 127.53, 126.62, 126.01, 125.93, 125.85, 125.73, 124.58, 74.09, 58.39, 58.49, 39.89, 24.92. ESI-MS  $m/z$  (%): 767 (100)  $[\text{M} + \text{Na}]^+$ .  $\text{C}_{40}\text{H}_{52}\text{N}_6\text{O}_8$  calcd.: C 64.50, H 7.04, N 11.28; found (**S-5**): C 64.29, H 7.09, N 11.19; found (**R-5**): C 64.33, H 7.11, N 11.15.

### Preparation of samples for fluorescence measurement

All solutions were prepared using volumetric syringes, pipettes, and volumetric flasks. The tetrabutylammonium salts were prepared by adding 1 equiv. of tetrabutylammonium hydroxide in methanol to a solution of the corresponding carboxylic acid in methanol, and stock solutions of the salts were prepared in  $\text{CHCl}_3$ . The resulting syrup was dried under high vacuum for 24 h, analyzed by NMR spectroscopy, and stored in a desiccator. Compounds **R-1** and **S-1** were prepared as stock solutions in  $\text{CHCl}_3$ . The test solutions were prepared by adding different volumes of anion solution to a series of test tubes, and then the same amount of stock solution of the host compound was added to each of the test tubes and diluted to 3.0 mL with  $\text{CHCl}_3$ . After being shaken for several minutes, the test solutions were analyzed immediately.

### Job Plots

Stock solutions of host **S-1** and the (*S*)- and (*R*)-Ala tetrabutylammonium salts in  $\text{CHCl}_3$  system (the total concentration of the host and guest is  $1.0 \times 10^{-6}$  mol  $\text{L}^{-1}$ ) were freshly prepared. The receptor and Ala solutions were added to the test tubes in ratios of 9:1, 8:2 to 0:10, respectively. After being shaken for several minutes, the working solution could be measured immediately.

### Acknowledgments

We thank the National Natural Science Foundation of China (Grant No. 20872027/B0206) and the Education Department of Henan Province of China (2010B150004) for financial support.

### References

- (1) (a) Lehn, J. M. *Supramolecular Chemistry: Concepts and Perspectives*; VCH: Weinheim, 1995; (b) Naemura, K.;

- Tobe, Y.; Kaneda, T. *Coord. Chem. Rev.* **1996**, *148*, 199. doi:10.1016/0010-8545(95)01189-7.; (c) Martínez-Mañez, R.; Sancenón, F. *Chem. Rev.* **2003**, *103* (11), 4419. doi:10.1021/cr010421e. PMID:14611267.; (d) Corradini, R.; Sforza, S.; Tedeschi, T.; Marchelli, R. *Chirality* **2007**, *19* (4), 269. doi:10.1002/chir.20372. PMID:17345563.; (e) Hembury, G. A.; Borovkov, V. V.; Inoue, Y. *Chem. Rev.* **2008**, *108* (1), 1. doi:10.1021/cr050005k. PMID:18095713.; (f) Liu, H.-L.; Hou, X.-L.; Pu, L. *Angew. Chem.* **2008**, *121* (2), 388. doi:10.1002/ange.200804538.
- (2) (a) Murakami, Y.; Kikuchi J.-i.; Hisaeda, Y.; Hayashida, O. *Chem. Rev.* **1996**, *96* (2), 721. doi:10.1021/cr9403704. PMID:11848771.; (b) Philp, D.; Stoddart, J. F. *Angew. Chem. Int. Ed. Engl.* **2003**, *35* (11), 1154. doi:10.1002/anie.199611541.
- (3) (a) Ward, T. J.; Hamburg, D. M. *Anal. Chem.* **2004**, *76* (16), 4635. doi:10.1021/ac040093t. PMID:15307771.; (b) Stibor, I.; Zlatuskova, P. *Top. Curr. Chem.* **2005**, *255*, 31.
- (4) (a) Ma, F.; Ai, L.; Shen, X.; Zhang, C. *Org. Lett.* **2007**, *9* (1), 125. doi:10.1021/ol062711t. PMID:17192101.; (b) Qing, G. Y.; He, Y. B.; Zhao, Y.; Hu, C. G.; Liu, S. Y.; Yang, X. *Eur. J. Org. Chem.* **2006**, *2006* (6), 1574. doi:10.1002/ejoc.200500704.; (c) Gasparrini, F.; Misiti, D.; Pierini, M.; Villani, C. *Org. Lett.* **2002**, *4* (23), 3993. doi:10.1021/ol026363g. PMID:12423069.
- (5) (a) Sessler, J. L.; Cho, D.-G.; Lynch, V. J. *Am. Chem. Soc.* **2006**, *128* (51), 16518. doi:10.1021/ja067720b. PMID:17177398.; (b) Pu, L. *Chem. Rev.* **2004**, *104* (3), 1687. doi:10.1021/cr030052h. PMID:15008630.; (c) Mei, X. F.; Wolf, C. *Chem. Commun. (Camb.)* **2004**, (18), 2078. doi:10.1039/b407718k. PMID:15367983.; (d) Tobey, S. L.; Jones, B. D.; Anslyn, E. V. *J. Am. Chem. Soc.* **2003**, *125* (14), 4026. doi:10.1021/ja021390n. PMID:12670205.
- (6) (a) Li, Z. B.; Lin, J.; Pu, L. *Angew. Chem. Int. Ed.* **2005**, *44* (11), 1690. doi:10.1002/anie.200462471.; (b) Kimaru, I. W.; Xu, Y. F.; McCarroll, M. E. *Anal. Chem.* **2006**, *78* (24), 8485. doi:10.1021/ac061335n. PMID:17165843.; (c) Trupp, S.; Schweitzer, A.; Mohr, G. J. *Org. Biomol. Chem.* **2006**, *4* (15), 2965. doi:10.1039/b604716e. PMID:16855745.; (d) Xu, K.-X.; Wu, X.-J.; He, Y.-B.; Liu, S.-Y.; Qing, G.-Y.; Meng, L.-Z. *Tetrahedron: Asymmetry* **2005**, *16* (4), 833. doi:10.1016/j.tetasy.2004.12.023.; (e) Xu, K.-X.; He, Y.-B.; Qin, H.-J.; Qing, G.-Y.; Liu, S.-Y. *Tetrahedron: Asymmetry* **2005**, *16* (18), 3042. doi:10.1016/j.tetasy.2005.08.014.
- (7) (a) Fitzmaurice, R. J.; Kyne, G. M.; Douheret, D.; Kilburn, J. D. *J. Chem. Soc., Perkin Trans. 1* **2002**, *7* (7), 841. doi:10.1039/b009041g.; (b) Rossi, S.; Kyne, G. M.; Turner, D. L.; Wells, N. J.; Kilburn, J. D. *Angew. Chem. Int. Ed. Engl.* **2002**, *41* (22), 4233. doi:10.1002/1521-3773(20021115)41:22<4233::AID-ANIE4233>3.0.CO;2-D. PMID:12434348.; (c) Folmer-Andersen, J. F.; Kitamura, M.; Anslyn, E. V. *J. Am. Chem. Soc.* **2006**, *128* (17), 5652. doi:10.1021/ja061313i. PMID:16637629.; (d) Ragusa, A.; Rossi, S.; Hayes, J. M.; Stein, M.; Kilburn, J. D. *Chem. Eur. J.* **2005**, *11* (19), 5674. doi:10.1002/chem.200500444.
- (8) (a) Kuroda, Y.; Kato, Y.; Higashioji, T.; Hasegawa, J.-.; Kawanami, S.; Takahashi, M.; Shiraishi, N.; Tanabe, K.; Ogoshi, H. *J. Am. Chem. Soc.* **1995**, *117* (44), 10950. doi:10.1021/ja00149a018.; (b) Bhattacharyya, T.; Nilsson, U. J. *Tetrahedron Lett.* **2001**, *42* (15), 2873. doi:10.1016/S0040-4039(01)00301-X.; (c) Narumi, F.; Hattori, T.; Matsumura, N.; Onodera, T.; Katagiri, H.; Kabuto, C.; Kameyama, H.; Miyano, S. *Tetrahedron* **2004**, *60* (36), 7827. doi:10.1016/j.tet.2004.06.074.
- (9) (a) Hayashida, O.; Sebo, L.; Rebek, J., Jr. *J. Org. Chem.* **2002**, *67* (24), 8291. doi:10.1021/jo0201171. PMID:12444605.; (b) Higashi, N.; Koga, T.; Niwa, M. *ChemBioChem* **2002**, *3* (5), 448. doi:10.1002/1439-7633(20020503)3:5<448::AID-CBIC448>3.0.CO;2-D. PMID:12007179.; (c) Breccia, P.; Van Gool, M.; Pérez-Fernández, R.; Martín-Santamaría, S.; Gago, F.; Prados, P.; de Mendoza, J. *J. Am. Chem. Soc.* **2003**, *125* (27), 8270. doi:10.1021/ja026860s. PMID:12837099.
- (10) (a) Zhang, H. C.; Huang, W. S.; Pu, L. *J. Org. Chem.* **2001**, *66* (2), 481. doi:10.1021/jo001276s. PMID:11429818.; (b) Stock, H. T.; Kellogg, R. M. *J. Org. Chem.* **1996**, *61* (9), 3093. doi:10.1021/jo952107o. PMID:11667172.
- (11) Qing, G. Y.; He, Y. B.; Wang, F.; Qin, H. J.; Hu, C. G.; Yang, X. *Eur. J. Org. Chem.* **2007**, *2007* (11), 1768. doi:10.1002/ejoc.200600917.
- (12) (a) Valeur, B.; Pouget, J.; Bourson, J.; Kaschke, M.; Ernsting, N. P. *J. Phys. Chem.* **1992**, *96* (16), 6545. doi:10.1021/j100195a008.; (b) Bernard, V. *Molecular Fluorescence: Principles and Applications*; Wiley-VCH: Weinheim, 2002; (c) Birks, J. B. *Photophysics of Aromatic Molecules*; Wiley: New York, 1970; p. 313.
- (13) (a) Kubo, Y.; Ishihara, S.; Tsukahara, M.; Tokita, S. *J. Chem. Soc., Perkin Trans. 1* **2002**, 1455; (b) Beer, P. D.; Timoshenko, V.; Maestri, M.; Passaniti, P.; Balzani, V. *Chem. Commun. (Camb.)* **1999**, (17), 1755. doi:10.1039/a905277a.; (c) Xu, K. X.; Qing, G. Y.; He, Y. B.; Qin, H. J.; Hu, L. *Supramolecular Chemistry* **2007**, *19* (6), 403. doi:10.1080/10610270601026586.; (d) Wu, F. Y.; Li, Z.; Wen, Z. C.; Zhou, N.; Zhao, Y. F.; Jiang, Y. B. *Org. Lett.* **2002**, *4* (19), 3203. doi:10.1021/ol026357k. PMID:12227749.
- (14) (a) Connors, K. A. *Binding Constants*; Wiley: New York, 1987; (b) Schneider, H. J.; Yatsimirsky, A. K. *Principles and Methods in Supramolecular Chemistry*; John Wiley & Sons: New York, 2000.
- (15) (a) Qing, G. Y.; He, Y. B.; Chen, Z. H.; Wu, X. J.; Meng, L. Z. *Tetrahedron Asymmetry* **2006**, *17* (22), 3144. doi:10.1016/j.tetasy.2006.11.043.; (b) Lu, Q. S.; Dong, L.; Zhang, J.; Li, J.; Jiang, L.; Huang, Y.; Qin, S.; Hu, C. W.; Yu, X. Q. *Org. Lett.* **2009**, *11* (3), 669. doi:10.1021/ol8027303. PMID:19143512.
- (16) (a) Gunnlaugsson, T.; Bichell, B.; Nolan, C. *Tetrahedron* **2004**, *60* (27), 5799. doi:10.1016/j.tet.2004.04.082.; (b) Wong, K. T.; Chen, H. F.; Fang, F. C. *Org. Lett.* **2006**, *8* (16), 3501. doi:10.1021/ol061227n. PMID:16869645.
- (17) (a) Amendola, V.; Fabbrizzi, L.; Mangano, C.; Pallavicini, P. *Acc. Chem. Res.* **2001**, *34* (6), 488. doi:10.1021/ar010011c. PMID:11412085.; (b) Gunnlaugsson, T.; Davis, A. P.; O'Brien, J. E.; Glynn, M. *Org. Lett.* **2002**, *4* (15), 2449. doi:10.1021/ol026004l. PMID:12123348.
- (18) Pirkle, W. H.; Pochapsky, T. C. *Chem. Rev.* **1989**, *89* (2), 347. doi:10.1021/cr00092a006.
- (19) (a) Zhang, X.; Guo, L.; Wu, F. Y.; Jiang, Y. B. *Org. Lett.* **2003**, *5* (15), 2667. doi:10.1021/ol034846u. PMID:12868885.; (b) Cho, E. J.; Moon, J. W.; Ko, S. W.; Lee, J. Y.; Kim, S. K.; Yoon, J.; Nam, K. C. *J. Am. Chem. Soc.* **2003**, *125* (41), 12376. doi:10.1021/ja036248g. PMID:14531658.
- (20) (a) Krapcho, A. P.; Kuell, C. S. *Synth. Commun.* **1990**, *20* (16), 2559. doi:10.1080/00397919008053205.; (b) Du, C. P.; You, J. S.; Yu, X. Q.; Liu, C. L.; Lan, J. B.; Xie, R. G. *Tetrahedron Asymmetry* **2003**, *14* (23), 3651. doi:10.1016/j.tetasy.2003.09.044.

# Electrochemical and in situ spectroelectrochemical investigations into the redox and aggregation behaviours of phthalocyanines bearing octyl 4-phenyloxyacetate moieties

İmran Koç, Meryem Çamur, Mustafa Bulut, and A. Riza Özkaya

**Abstract:** Electrochemical and spectroelectrochemical properties of phthalocyanines (H<sub>2</sub>Pc, ZnPc, NiPc, CuPc, and CoPc) involving octyl 4-phenyloxyacetate moieties have been investigated by cyclic voltammetry and differential pulse voltammetry on Pt in dimethylsulfoxide – tetrabutylammonium perchlorate. These measurements showed that the complexes undergo subsequent one-electron reduction and oxidation processes. In situ UV–vis spectroelectrochemical measurements enabled us to identify the ligand- and metal-based redox processes, and evaluate the effect of aggregation phenomena on these processes. The cobalt complex showed both metal-based and ring-based one-electron redox processes, while the other complexes displayed only ring-based one-electron couples. It was observed that the redox processes of H<sub>2</sub>Pc, NiPc, and CuPc are coupled by aggregation phenomenon, whereas those of ZnPc and especially CoPc are not, probably owing to the difference in their axial coordinating properties.

**Key words:** phthalocyanines, aggregation, electrochemistry, in situ spectroelectrochemistry.

**Résumé :** Faisant appel à la voltampérométrie cyclique et la voltampérométrie pulsée différentielle sur du Pt dans un mélange diméthylsulfoxyde – perchlorate de tétrabutylammonium, on a examiné les propriétés électrochimiques et spectroélectrochimiques de phthalocyanines (H<sub>2</sub>Pc, ZnPc, NiPc, CuPc et CoPc) impliquant des portions 4-phényloxyacétate d'octyle. Ces mesures ont montré que les complexes subissent des processus subséquents de réduction et d'oxydation à un électron. Des mesures spectroélectrochimiques UV–vis in situ ont permis d'identifier les processus redox à base de métal et de ligand et d'évaluer l'effet du processus d'agrégation alors que les autres complexes ne présentent que des couples à un électron à base du noyau. On a observé que les processus redox du H<sub>2</sub>Pc, du NiPc et du CuPc sont couplés par le phénomène d'agrégation alors que ceux du ZnPc et particulièrement celui de CoPc ne le sont probablement pas en raison de la différence dans leurs propriétés de coordination axiales.

**Mots-clés :** phthalocyanines, agrégation, électrochimie, spectroélectrochimie in situ.

[Traduit par la Rédaction]

## Introduction

There is a strong relationship between the redox properties of phthalocyanines (Pcs) and most of their industrial applications as semiconductors, photovoltaic cells, electrochromic displays, and catalysts, for example.<sup>1,2</sup> Accordingly, the electrochemistry of Pcs has received considerable interest in recent years. Small modifications in Pc molecules may remarkably influence their redox properties since these properties depend on various factors such as the type of the central metal, solvent, axial ligands, substituents, and aggregation.<sup>3–7</sup> It is well-known that Pcs may dimerize and even form larger and more complex aggregates, owing to the extended  $\pi$  system.<sup>8–14</sup> In most cases, the aggregation phenomenon is deleterious to the desired electrical,<sup>15,16</sup> spectroscopic,<sup>17–21</sup>

photophysical,<sup>22–27</sup> and electrochemical<sup>28,29</sup> properties of these compounds. On the other hand, the formation of well-defined Pc dimers and (or) aggregates is useful in materials and catalytic applications where the self-assembly of Pc cores in close proximity is beneficial.<sup>30–34</sup>

Voltammetry is the most widely used electrochemical method to determine the redox properties, whereas the aggregation process of Pcs can be probed using electronic spectroscopy. It is necessary to combine spectroscopic and electrochemical techniques, i.e., carry out in situ spectroelectrochemical measurements, to be able to identify thoroughly the effect of aggregation phenomenon on the redox processes. In most cases, the nature of the redox processes cannot be distinguished by voltammetric methods alone. In

Received 29 June 2009. Accepted 4 December 2009. Published on the NRC Research Press Web site at canjchem.nrc.ca on 12 March 2010.

İ. Koç, M. Çamur, M. Bulut, and A.R. Özkaya.<sup>1</sup> Chemistry Department, Marmara University, Goztepe, Kadikoy, Istanbul 34722, Turkey.

<sup>1</sup>Corresponding author (e-mail: aliozkaya@marmara.edu.tr).



situ spectroelectrochemical measurements allow us to determine whether the redox processes occur in the Pc ring or in the metal center.<sup>35–39</sup>

In a recent study, we have reported on the synthesis and characterization of metal-free and metal phthalocyanines (MPcs) with four 4-phenyloxyacetic acid groups on the periphery, prepared by cyclotetramerization of *p*-(3,4-dicyanophenoxy) phenyl-acetic acid and the corresponding divalent metal salts.<sup>40</sup> Further reactions of these products with thionylchloride and then benzylamine in tetrahydrofuran and octanol in pyridine, gave amide and ester derivatives, respectively. These complexes were observed to have a remarkable tendency to aggregation, a very useful feature for the fabrication of modified electrodes. In the present work, the redox and aggregation behaviours of the metal-free and metal Pcs, bearing octyl 4-phenyloxyacetate moieties and the effect of aggregation phenomena on their redox behaviour have been examined by voltammetry and in situ spectroelectrochemistry.

## Experimental

The electrochemical and in situ spectroelectrochemical measurements were monitored using a Gamry Reference 600 potentiostat–galvanostat controlled by an external PC and utilizing a three-electrode configuration at 25 °C. UV–vis absorption spectra were recorded by an Agilent 8453 diode array spectrophotometer equipped with the potentiostat–galvanostat. The electrochemical measurements were carried in extra pure dimethylsulfoxide (DMSO) containing electrochemical grade tetrabutylammonium perchlorate (TBAP) as the supporting electrolyte at a concentration of 0.10 mol dm<sup>−3</sup>. Metal-free and metal Pcs involving octyl 4-phenyloxyacetate moieties were prepared following a literature procedure<sup>40</sup> (Fig. 1).

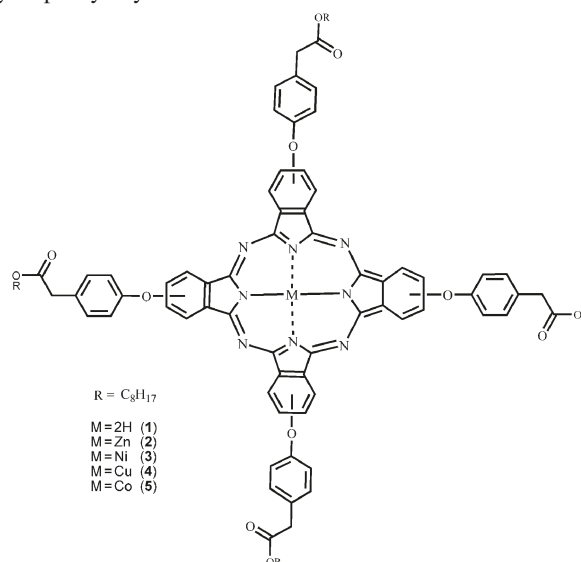
For cyclic voltammetry (CV) and differential pulse voltammetry (DPV) measurements, the working electrode was a Pt plate with a surface area of 0.10 cm<sup>2</sup>. A Pt spiral wire served as the counter electrode. A saturated calomel electrode (SCE) was employed as the reference electrode and separated from the bulk of the solution by a double bridge. High purity N<sub>2</sub> was used for deoxygenating the solution at least 20 min prior to each run and to maintain a nitrogen blanket during the measurements. Ferrocene was used as an internal reference, but the potentials were presented versus SCE.

The spectroelectrochemical measurements were carried out by utilizing a thin-layer quartz spectroelectrochemical cell at 25 °C in a three-electrode configuration. The working electrode was transparent Pt gauze. A Pt wire counter electrode separated by a glass bridge and an SCE reference electrode separated from the bulk of the solution by a double bridge were used.

## Results and discussion

Redox properties of the Pc compounds (1–5) in solution were studied by CV and DPV on a platinum working electrode in DMSO–TBAP. Table 1 lists the voltammetric data of the complexes which included the half-peak potentials ( $E_{1/2}$ ), the ratio of anodic to cathodic peak currents ( $I_{pa}/I_{pc}$ ), the peak-to-peak potential separations ( $\Delta E_p$ ), and the differ-

**Fig. 1.** The molecular structure of metal-free and metal Pcs bearing octyl 4-phenyloxyacetate moieties.



ence between the first oxidation and reduction processes ( $\Delta E_{1/2}$ ). Pc compounds undergo successive one-electron reduction and one-electron oxidation to yield the anion and cation radicals.

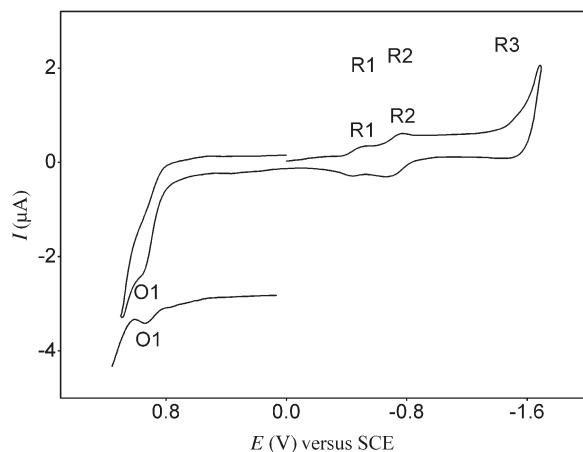
Figure 2 shows cyclic and differential pulse voltammograms of metal-free Pc **1**. Compound **1** gives a one-electron oxidation and three one-electron reduction processes. All redox processes in Fig. 2 are ring-based since compound **1** is a metal-free Pc. The values of  $I_{pa}/I_{pc}$  for the first and second reduction couples (R1 and R2, respectively, in Fig. 2) are close to unity at 0.010 V s<sup>−1</sup>. The peak-to-peak current ratios and (or) peak potential separations could not be determined for the first oxidation (Fig. 2, couple O1) and third reduction (Fig. 2, wave R3) processes since those occur at the ends of electrolyte-limited potential window.

The general voltammetric behaviour of **2** (ZnPc), **3** (NiPc), and **4** (CuPc) are similar to each other and to that of **1** (H<sub>2</sub>Pc). However, the redox processes of MPcs occur at more negative potential than those of **1** (Table 1). The differences between the  $E_{1/2}$  values can be attributed to the different polarizing powers of central atoms. On the other hand, the similarity in general redox behaviour between metal-free Pc **1** and MPcs **2–4** probably suggests that Zn(II), Ni(II), and Cu(II) behave as redox-inactive metal centers.<sup>41,42</sup> The  $\Delta E_{1/2}$  value corresponds to the energy difference between the highest occupied molecular orbital (HOMO) and the lowest unoccupied molecular orbital (LUMO) for metal-free Pcs, whereas it is related to HOMO–LUMO gap in MPc species, involving a redox-inactive metal center.  $\Delta E_{1/2}$  values ranging from 1.16 to 1.51 V for **1**, **2**, **3**, and **4** are generally consistent with the values reported in the literature.<sup>41,42</sup> The separation between the first and second ring reductions was found to be approximately 0.25–0.39 V for the complexes having a redox-inactive metal center. These peak separation values are also in agreement with the reported ones for redox processes in similar Pc compounds.<sup>5,41,42</sup> However, the comparison of the redox potentials of the Pcs **1–4** in DMSO (Table 1) with those of the relevant unsubstituted Pcs in a similar



**Table 1.** Voltammetric data for Pc compounds 1–5.

Complex		Ring oxidation	M <sup>II</sup> /M <sup>III</sup>	M <sup>II</sup> /M <sup>I</sup>	Ring reductions			$\Delta E_{1/2}^e$
<b>1</b> (H <sub>2</sub> Pc)	$E_{1/2}$ (V) <sup>a</sup> or $E_p^b$	0.89	—	—	–0.47	–0.72	–1.47 <sup>f</sup>	1.36
	$\Delta E_p$ (V) <sup>c</sup>	0.120	—	—	0.060	0.060	—	—
	$I_{pa}/I_{pc}^d$	—	—	—	0.97	1.07	—	—
<b>2</b> (ZnPc)	$E_{1/2}$ (V) <sup>a</sup> or $E_p^b$	0.81 <sup>f</sup>	—	—	–0.63	–1.00	–1.27	1.44
	$E_p$ (V) <sup>c</sup>	—	—	—	0.060	0.050	—	—
	$I_{pa}/I_{pc}^d$	—	—	—	1.00	1.00	—	—
<b>3</b> (NiPc)	$E_{1/2}$ (V) <sup>a</sup> or $E_p^b$	0.60	—	—	–0.62	–0.83	–1.54 <sup>f</sup>	1.20
	$\Delta E_p$ (V) <sup>c</sup>	—	—	—	0.050	0.090	—	—
	$I_{pa}/I_{pc}^d$	—	—	—	0.57	0.98	—	—
<b>4</b> (CuPc)	$E_{1/2}$ (V) <sup>a</sup> or $E_p^b$	1.00	—	—	–0.51	–0.90 <sup>g</sup>	–1.45	1.51
	$\Delta E_p$ (V) <sup>c</sup>	—	—	—	0.060	0.160	—	—
	$I_{pa}/I_{pc}^d$	—	—	—	0.96	1.08	—	—
<b>5</b> (CoPc)	$E_{1/2}$ (V) <sup>a</sup> or $E_p^b$	0.82	0.55	–0.30	–1.13	–1.70	—	0.85
	$\Delta E_p$ (V) <sup>c</sup>	0.060	0.120	0.120	0.070	0.100	—	—
	$I_{pa}/I_{pc}^d$	—	0.95	1.00	0.55	—	—	—

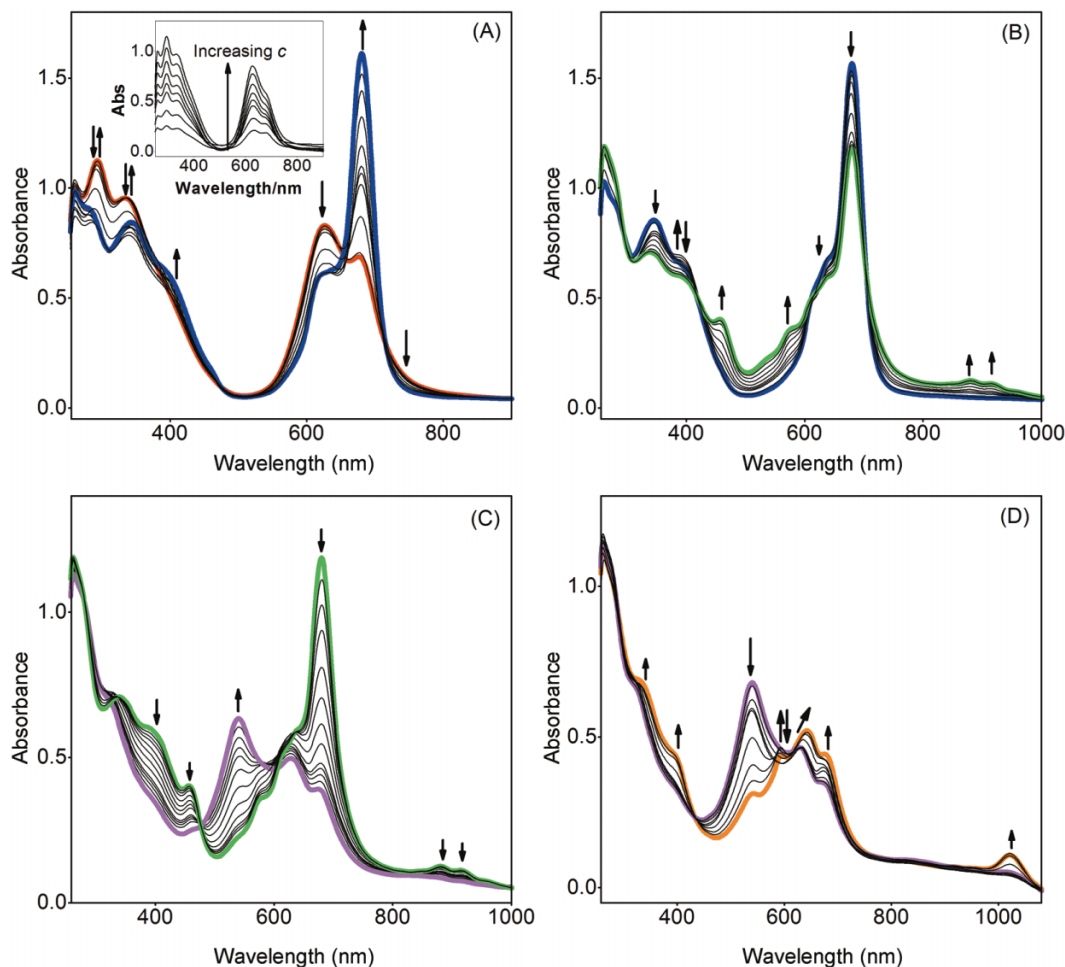
<sup>a</sup> $E_{1/2} = (E_{pa} + E_{pc})/2$  at 0.010 V s<sup>–1</sup>.<sup>b</sup>Cathodic or anodic peak potential for irreversible processes at 0.010 V s<sup>–1</sup>.<sup>c</sup> $E_p = E_{pa} + E_{pc}$  at 0.010 V s<sup>–1</sup>.<sup>d</sup> $I_{pa}/I_{pc}$  for reduction,  $I_{pc}/I_{pa}$  for oxidation processes at 0.010 V s<sup>–1</sup> scan rate. It could not be determined for some redox processes due to ill-defined redox waves.<sup>e</sup> $\Delta E_{1/2} = E_{1/2}$  (first oxidation) –  $E_{1/2}$  (first reduction). This value corresponds to the HOMO–LUMO gap for metal-free and metal Pcs having an electroinactive metal center, but it represents metal-to-ligand charge transfer (MLCT) or ligand-to-metal charge transfer (LMCT) transition gap for MPcs having a redox-active metal center.<sup>f</sup>The process could be recorded only with DPV.<sup>g</sup>Cathodic wave is split, probably due to electron transfer associated with the aggregation–disaggregation equilibrium.**Fig. 2.** Cyclic and differential pulse voltammograms of **1** ( $2.50 \times 10^{-4}$  mol/L) on Pt in DMSO–TBAP. DPV parameters: pulse time 0.050 s; pulse size 0.100 V; step size 0.005 V; sample period 0.100 s.

coordinating solvent, DMF, in the literature<sup>41,42</sup> showed clearly that the redox potentials of the former shift considerably to relatively more positive potentials, because of the electron-withdrawing effect of the octyl 4-phenyloxyacetate substituents. For example, in the case of **2**, the shift in redox potential is 0.23 V for the first reduction, 0.30 V for the second, 0.58 V for the third, and 0.14 V for the first oxidation. A similar behaviour was also observed previously for tetra-substituted Pcs bearing electron-withdrawing 4-phenyloxyacetic acid functionalities,<sup>40</sup> suggesting that the redox potentials, and thus the efficiency of Pcs in various applications, can be changed remarkably by peripheral substituents. For in-

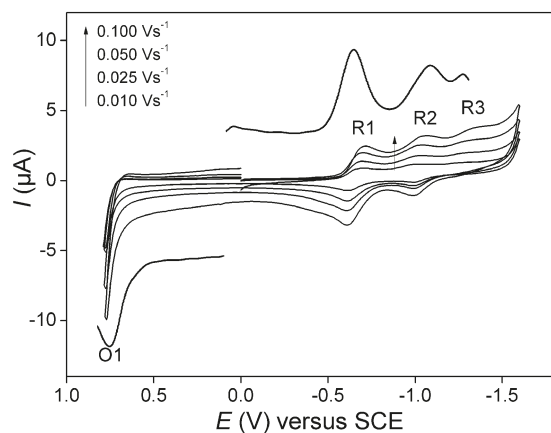
stance, the efficiency of MPcs in electrocatalytic applications is closely related to their redox potentials. The shift in redox potentials of octyl 4-phenyloxyacetate substituted **5** in DMSO towards more positive potentials, compared to those of unsubstituted CoPc in a similar coordinating solvent, DMF, in the literature was also observed.<sup>41,42</sup> However, the shift in the potential of the second reduction process (0.27 V), which is probably based on the Pc ring, was much higher than that in the potential of the first reduction process (0.07 V), which is probably metal-based. It appears that the electron-withdrawing effect of 4-phenyloxyacetate substituents at the periphery is probably more pronounced on the Pc ring than on the metal center.

The redox processes in MPcs are located at the ring and at the metal center.<sup>35–42</sup> Moreover, a general trend for some Pc compounds in this study was their aggregation character implied by splitting or broadening the redox waves. In most cases, it was not possible to identify the nature of the redox processes or to understand the possible aggregation effects on these processes in great detail on the basis of electrochemical measurements alone. For this reason, in situ spectroelectrochemical measurements during the controlled-potential electrolysis of the complexes at suitable potentials were also carried out to provide additional support for the assignment of redox processes and the identification of possible aggregation effects. The shape of the voltammetric peaks of metal-free Pc **1** in Fig. 2 suggests that the redox processes are not associated with the aggregation phenomenon. However, our observations during in situ spectroelectrochemical measurements, although carried out in relatively dilute solutions, indicated the coupling of the redox processes by aggregation–deaggregation transformations. The inset in Fig. 3A shows the effect of increasing concentration on the

**Fig. 3.** In situ UV-vis spectral changes during the controlled-potential electrolysis of **1** at (A)  $-0.56$  V, the former spectral changes (inset shows the effect of increasing concentration on the UV-vis spectra of **1**); (B)  $-0.56$  V, the latter spectral changes; (C)  $-1.00$  V; and (D)  $-1.65$  V vs. SCE.



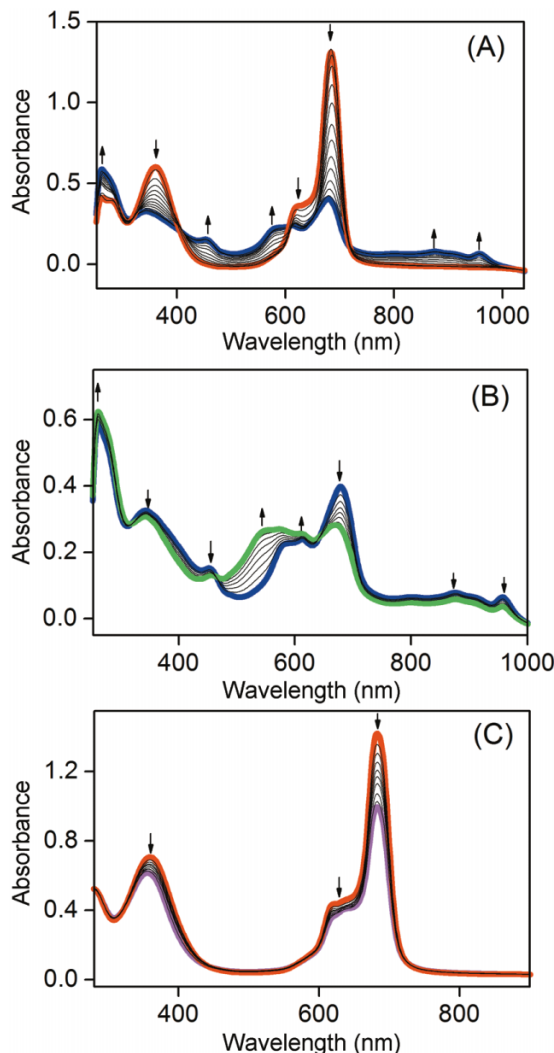
**Fig. 4.** Cyclic and differential pulse voltammograms of **2** ( $2.50 \times 10^{-4}$  mol/L) on Pt in DMSO-TBAP. DPV parameters: pulse time 0.050 s; pulse size 0.100 V; step size 0.005 V; sample period 0.100 s.



shape of the original UV-vis spectrum of **1**. There are two Q-band absorptions at 626 and 680 nm in its spectrum. As the concentration of **1** increases, the intensity of the band with the higher energy also increases and the absorption of

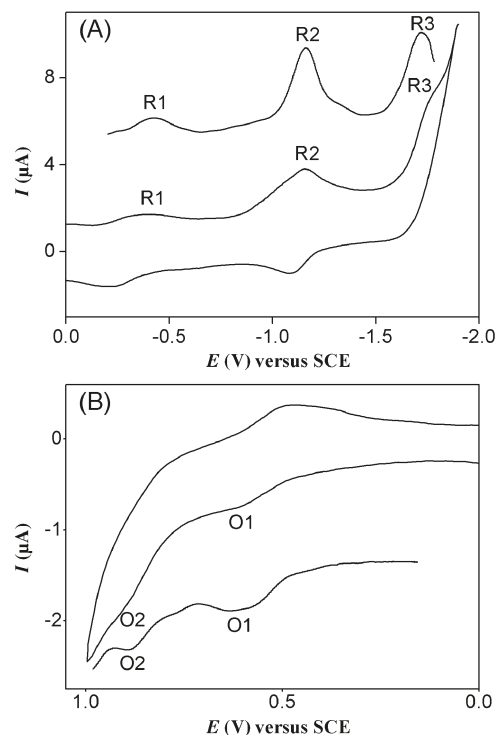
the band at 680 nm becomes a shoulder. This behaviour clearly suggests that the band at 626 nm corresponds to the aggregated species.<sup>43</sup> For metal-free Pcs, the symmetry is usually  $D_{2h}$  and therefore the main Q-band absorption is split. However, the main Q band of **1** at 680 nm is not split, even in the spectrum of the most diluted solution. One reason for the unsplit Q-band absorption is probably the aggregation phenomenon. Another reason is the high acidity of the inner pyrrole hydrogens in strongly basic solvents. When the inner pyrrole hydrogens are acidic enough, they dissociate, resulting in a charged  $Pc^{2-}$  system which becomes symmetric ( $D_{4h}$ ) and thus possesses an unsplit Q band. In situ UV-vis spectral changes during the controlled potential electrolysis of  $H_2Pc$  (**1**) at suitable potentials are shown in Fig. 3. When the working electrode is polarized at  $-0.56$  V vs. SCE, two groups of subsequent spectral changes were monitored. The former changes, accompanied by the formation of clear isosbestic points at 473, 654, and 713 nm, are shown in Fig. 3A. The band at 626 nm, assigned to the aggregated species, decreases in intensity and a new sharp single band at 680 nm appears. The decrease in intensity of the band at 626 nm probably suggests that the former spectral changes correspond to the reduction of aggregated species. During the latter spectral changes

**Fig. 5.** In situ UV-vis spectral changes during the controlled potential electrolysis of **2** at (A)  $-0.85$  V; (B)  $-1.10$  V; and (C)  $+0.80$  V vs. SCE.



(Fig. 3B), the Q-band absorptions at 680 and 626 nm, and the B-band absorption at 345 nm decrease while two new absorption bands appear at 459 and 574 nm. In addition, two weak absorption bands at 880 and 918 nm are observed. These spectral changes, accompanied by the formation of well-defined isosbestic points at 415, 612, and 704 nm, can be attributed to the reduction of disaggregated species. Similar spectroscopic changes for the first reduction of various metal-free Pcs were reported in the literature.<sup>7,37,44–46</sup> Some different spectral changes observed in this study may be attributed to the aggregation effects. During the potential application at  $-1.00$  V vs. SCE, the Q band at 680 nm decreases while two new bands at 540 and 630 nm appear (Fig. 3C), which is characteristic of ring reduction.<sup>43–46</sup> Therefore, the first reduction product,  $[\text{H}_2\text{Pc}(-3)]^-$  is reduced by one electron to form the  $[\text{H}_2\text{Pc}(-4)]^{2-}$  dianion during the second reduction process (couple R2 in Fig. 2). Moreover, the B band and the bands at 880 and 918 nm disappear. The Q band is split again after the second reduction. The spectral changes are accompanied by the formation of clear isosbestic points at 477 and 605 nm, confirming the forma-

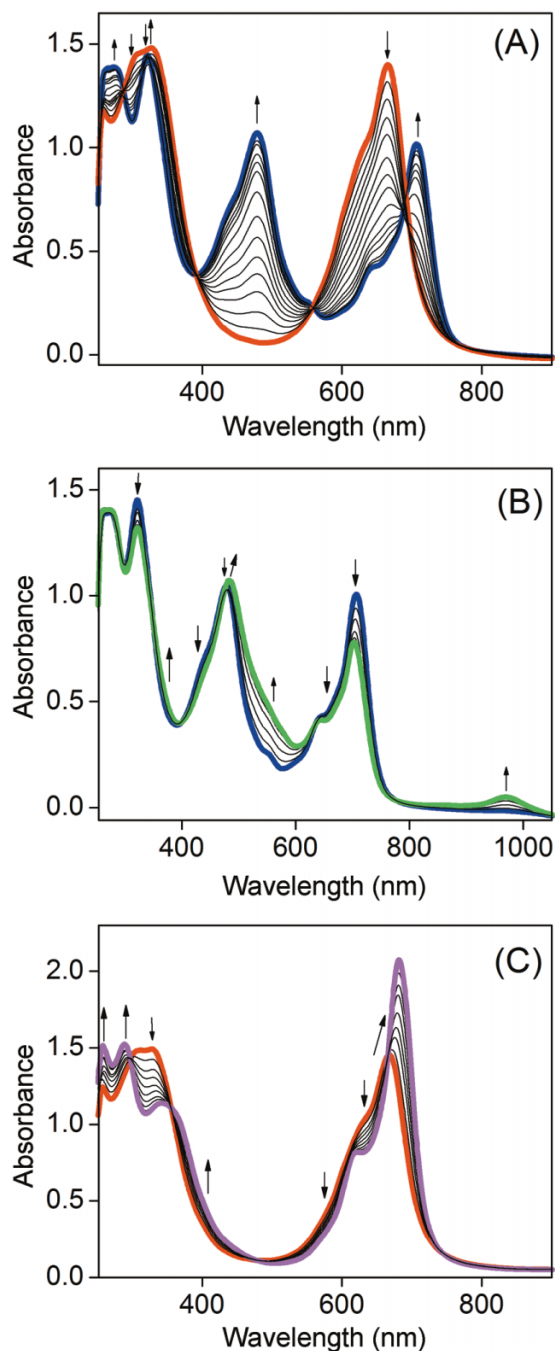
**Fig. 6.** Cyclic and differential pulse voltammograms of **5** ( $5.00 \times 10^{-4}$  mol/L) during (A) the negative potentials sweep and (B) the positive potentials sweep on Pt in DMSO-TBAP. DPV parameters: pulse time 0.050 s; pulse size 0.100 V; step size 0.005 V; sample period 0.100 s.



tion of  $[\text{H}_2\text{Pc}(-4)]^{2-}$  species. We observed net spectral changes even during the third reduction process (couple R3 in Fig. 2) with an applied potential of  $-1.65$  V vs. SCE (Fig. 3D), for the first time to the best of our knowledge. The band at 540 nm decreases in intensity while new bands at 340, 400, and 1022 nm appear. Moreover, the Q band increases with red shift from 630 to 643 nm while the band at 680 nm increases. These spectral changes are accompanied by the formation of clear isosbestic points at 434 and 617 nm, and can be assigned to the  $[\text{H}_2\text{Pc}(-4)]^{2-} \rightarrow [\text{H}_2\text{Pc}(-5)]^{3-}$  process. The spectrum of the triply reduced  $[\text{H}_2\text{Pc}(-5)]^{3-}$  species is split around the Q band region. The formation of a split Q band after the second and third reduction processes probably suggests the formation of completely disaggregated species. During the first oxidation process at 1.05 V vs. SCE, all the bands decreased in intensity without shift. This was probably due to the decomposition of the monocationic  $[\text{H}_2\text{Pc}(-2)]^+$  species after the oxidation, and is consistent with the observation of the relevant redox couple (O1 in Fig. 2) at the end of the solvent-limited potential window.

Figure 4 shows cyclic and differential pulse voltammograms of **2**. It undergoes a one-electron oxidation and three one-electron reductions. Anodic to cathodic peak separations ( $\Delta E_p$ ) of the first two reduction couples at  $0.010$  V s<sup>-1</sup> are approximately equal to 0.060 V, supporting reversible electron transfer. The unity of the  $I_{pa}/I_{pc}$  ratio with the scan rate and linear changes of  $I_{pc}$  with the square root of the scan rate for these couples indicated a purely diffusion-controlled electron transfer mechanism. The first oxidation process could be identified only by DPV, owing to its high positive

**Fig. 7.** In situ UV-vis spectral changes during the controlled potential electrolysis of **5** at (A)  $-0.65$  V, (B)  $-1.45$  V, and (C)  $+0.70$  V vs. SCE.



potential within the available potential range. The third reduction process was ill-defined without the anodic peak. However, well-defined reversible redox waves for the first two reduction processes imply that the redox processes of **2** are not coupled by the aggregation. In situ spectroelectrochemical changes during the controlled-potential electrolysis of **2** at suitable peak potentials are shown in Fig. 5. Figure 5A represents the spectral changes during the first oxidation process. As is clearly evident from an inspection of the spectrum of the original complex at the beginning, the Q-band absorption is rather narrow, suggesting that complex **2**

is in the form of monomers. Unlike compound **1**, the Zn(II) core in **2** probably binds donor DMSO molecules. Thus, the molecules of **2** are kept apart by the axially bound solvent molecules, preventing them from aggregating. After the first reduction at  $-0.85$  V vs. SCE, the absorption of the main Q band at 685 nm, the vibrational band at 616 nm and the B band at 362 nm decrease, while the new bands at 457, 581, 878, and 958 nm appear with the formation of well-specified isosbestic points at 313, 404, 608, and 718 nm. These spectral changes, especially the formation of a new band at 581 nm and the decrease of the Q band without shift, are characteristic for Pc ring reduction and thus confirm the voltammetric assignment of the couple R1 in Fig. 4 to  $\text{Zn(II)Pc}(-2)-[\text{Zn(II)Pc}(-3)]^-$ .<sup>36-39,47,48</sup> During the second reduction, with  $-1.10$  V potential application, the absorption of the main Q band continues to decrease without shift, while a new band around 544 nm appears and the bands at near-IR region decrease slightly without shift (Fig. 5B). These spectral changes, accompanied by the formation of well-defined isosbestic points, correspond to the second-ring reduction with the formation of the  $[\text{Zn(II)Pc}(-4)]^{2-}$  dianion species. During the oxidation at 0.80 V vs. SCE, the absorption of all bands decreases without formation of a new band, which is attributed to the decomposition of the complex immediately after the ring oxidation (Fig. 5C). This is an expected observation owing to the high positive oxidation potential.

Complexes **3** (NiPc) and **4** (CuPc) displayed a one-electron oxidation and three one-electron reduction processes (Table 1). Both electrochemical and spectroelectrochemical data showed that Pc ring-based electron transfer reactions of these complexes are complicated by the high aggregation tendency of these complexes (please see Supplementary data for the relevant figures and explanations).

Figure 6 shows the cyclic and differential pulse voltammograms of **5** (CoPc). The complex **5** undergoes two one-electron oxidations and three one-electron reductions. The  $\Delta E_p$  parameter of the redox couples takes the values within the range of 0.060–0.120 V at a  $0.010 \text{ V s}^{-1}$  scan rate, indicating the reversible or quasi-reversible character of electron-transfer processes. The unity of the peak current ratios ( $I_{pa}/I_{pc}$  for reduction and  $I_{pc}/I_{pa}$  for oxidation) with the scan rate and linear changes of peak currents with the square root of scan rate for the first reduction (R1) and first oxidation (O1) couples indicated a purely diffusion-controlled electron-transfer mechanism for these couples. The metal center in **5** probably prefers six-coordination and thus binds donor DMSO molecules. It is known that six-coordinate MPc species generally do not aggregate since they are kept apart by the axially bound ligands.<sup>41</sup> The peak current ratios for the third reduction (R3) and the second oxidation (O2) couples also appear to be unity. However, these values were not given in Table 1 since these couples, monitored at high potentials at the ends of the solvent-limited potential window, are ill-defined and thus peak current values could not be confirmed. Redox potentials of **5** are remarkably different compared with those of the other Pc compounds (Table 1). The  $\Delta E_{1/2}$  value of **5** is 0.85 V which is much lower than those of **1**, **2**, **3**, and **4**. Thus, it is reduced and oxidized more easily than the others. This distinctive behaviour of **5** can be attributed to the fact that the Co(II) center has



accessible d-orbital levels lying between the HOMO and LUMO gap of the Pc species, so that the metal center can be oxidized and reduced before the ring-based redox processes. However, the electrochemical behaviour of these Pc complexes can vary according to their environment, depending on whether there are any available coordinating species that would stabilize the Co(II) center. The main difference lies in whether the metal or the ring is oxidized first. Donor solvents strongly favour Co(III)Pc(–2) by coordinating along the axis to form six-coordinate species. If such donor solvents are absent, then oxidation to Co(III) is inhibited and ring oxidation occurs first. Thus, the first oxidation and the first reduction processes of **5** are probably metal-based and correspond to Co(II)Pc(–2)–[Co(III)Pc(–2)]<sup>+</sup> and Co(II)Pc(–2)–[Co(I)Pc(–2)]<sup>–</sup> redox couples, respectively, since the voltammetric measurements were carried out in DMSO–TBAP. On the other hand, it is also well-known from the literature that the other reduction processes and the second oxidation process are ring-based.<sup>41,42</sup> Spectroelectrochemical measurements were also carried out to assign the first reduction and the first oxidation processes of **5** with certainty. Figure 7A represents in situ UV–vis spectral changes during the first reduction of **5** at –0.65 V vs. SCE, corresponding to the redox process labeled R1 in Fig. 6. The Q band at 666 nm shifts to 707 nm, while a new band at 479 nm appears with a shoulder around 435 nm. The spectral changes have well-defined isosbestic points at 287, 393, 558, and 691 nm. The band at 479 nm and the shifting of the Q band indicate the formation of [Co(I)Pc(–2)]<sup>–</sup> species, confirming the CV assignment of the couple R1 to the Co(II)Pc(–2)–[Co(I)Pc(–2)]<sup>–</sup> process.<sup>36–39,47–50</sup> During the second reduction at –1.45 V vs. SCE, the Q band at 707 nm and the shoulder at 435 nm decrease without shift (Fig. 7B). At the same time, the absorption at 479 nm increases slightly in intensity with red shift to 484 nm, the absorption between 500 and 600 nm increases, and a new band at 970 nm appears. Clear isosbestic points were observed at 349, 400, 634, and 778 nm. These spectral changes at the potential of the couple R2 are characteristics of a ring-based reduction in a Co(II)Pc complex and confirm our voltammetric assignment of this process to [Co(I)Pc(–2)]<sup>–</sup>–[Co(I)Pc(–3)]<sup>2–</sup>. Figure 7C displays in situ UV–vis spectral changes during the first oxidation process. The Q band at 666 nm increases in intensity with red shift to 681 nm. This process gives clear isosbestic points at 297, 355, 479, and 666 nm. The increase of the Q band with red shift is typical of a metal-based oxidation in CoPc complexes and thus confirms the CV assignment of Co(II)Pc(–2)–[Co(III)Pc(–2)]<sup>+</sup> for couple O1 of **5** in Fig. 6.<sup>36–39,47–50</sup>

## Conclusion

The voltammetric measurements of the Pcs (H<sub>2</sub>Pc **1**, ZnPc **2**, NiPc **3**, CuPc **4**, and CoPc **5**) bearing octyl 4-phenyloxyacetate moieties showed that the compounds undergo one-electron reduction and oxidation processes. In situ spectroelectrochemical measurements enabled us to identify ligand- and metal-based redox processes. In addition, it was concluded from the results of this study that it is not possible to identify the effect of aggregation on the redox processes exactly, without in situ spectroelectrochemical measurements. In situ spectroelectrochemical measurements suggested that the redox processes of **1**, **3**, and **4** are coupled by aggregation

phenomenon, while those of **2** and especially **3** are not. Metal centers in **2** and **5** probably prefer six-coordination and bind donor DMSO molecules. Thus, they are kept apart by the axially bound solvent molecules. This prevents them from aggregating.

## Supplementary data

Supplementary data for this article are available on the journal Web site (canjchem.nrc.ca) or may be purchased from the Depository of Unpublished Data, Document Delivery, CISTI, National Research Council Canada, Ottawa, ON K1A 0R6, Canada. DUD 5361. For more information on obtaining material, refer to cisti-icist.nrc-cnrc.gc.ca/cms/unpub\_e.shtml.

## Acknowledgements

We thank the Scientific and Technical Research Council of Turkey (TUBITAK) for financial support (Project No.: 107T834).

## References

- (1) *Phthalocyanines: Properties and Applications*; Leznoff, C. C. and Lever, A. B. P., Eds.; VCH Publishers: New York, 1989, 1992, 1993, and 1996; Vols. 1–4.
- (2) McKeown, N. B. *Phthalocyanine Materials: Synthesis, Structure and Functions*; Cambridge University Press: Cambridge, England, 1998.
- (3) Esenpinar, A. A.; Özkaya, A. R.; Bulut, M. *Polyhedron* **2009**, 28 (1), 33. doi:10.1016/j.poly.2008.09.021.
- (4) Kulaç, D.; Bulut, M.; Altındal, A.; Özkaya, A. R.; Salih, B.; Bekaroğlu, Ö. *Polyhedron*, **2007**, 26 (18), 5432. doi:10.1016/j.poly.2007.08.015.
- (5) Kandaz, M.; Çetin, H. S.; Koca, A.; Özkaya, A. R. *Dyes and Pigm.* **2007**, 74 (2), 298. doi:10.1016/j.dyepig.2006.02.008.
- (6) Özer, M.; Altındal, A.; Özkaya, A. R.; Bulut, M.; Bekaroglu, Ö. *Synth. Met.* **2005**, 155 (1), 222. doi:10.1016/j.synthmet.2005.08.004.
- (7) Osmanbaş, Ö. A.; Koca, A.; Özçeşmeci, İ.; Okur, A. İ.; Gül, A. *Electrochim. Acta* **2008**, 53 (15), 4969. doi:10.1016/j.electacta.2008.02.021.
- (8) Choi, M. T. M.; Li Pearl, P. S.; Dennis, K. P. D. *Tetrahedron* **2000**, 56 (24), 3881. doi:10.1016/S0040-4020(00)00326-4.
- (9) Kostka, M.; Zimcik, P.; Miletin, M.; Klemra, P.; Kopecky, K.; Musil, Z. *J. Photochem. Photobiol. Chem.* **2006**, 178 (1), 16. doi:10.1016/j.jphotochem.2005.06.014.
- (10) Ng, D. K. P. C. R. *Chimie* **2003**, 6, 903. doi:10.1016/j.jrcr.2003.05.006.
- (11) Sessler, J. L.; Jayawickramarajah, J.; Gouloumis, A.; Dan Pantos, G.; Torres, T.; Guldí, D. M. *Tetrahedron* **2006**, 62 (9), 2123. doi:10.1016/j.tet.2005.05.110.
- (12) Durmus, M.; Ayhan, M. M.; Gürek, A. G.; Ahsen, V. *Dyes and Pigm.* **2008**, 77 (3), 570. doi:10.1016/j.dyepig.2007.08.010.
- (13) Durmus, M.; Nyokong, T. *Polyhedron* **2007**, 26 (12), 2767. doi:10.1016/j.poly.2007.01.018.
- (14) Wang, X.; Tang, D.; Zhen, Z.; Zhang, J.; Liu, X. *Dyes and Pigm.* **1999**, 41 (3), 193. doi:10.1016/S0143-7208(98)00082-5.
- (15) Law, K. Y. *J. Phys. Chem.* **1988**, 92 (14), 4226. doi:10.1021/j100325a046.

- (16) Deng, H.; Mao, H.; Lu, Z.; Xu, H. *Thin Solid Films* **1998**, 315 (1-2), 244. doi:10.1016/S0040-6090(97)00753-0.
- (17) Nevin, S. W. A.; Liu, W.; Lever, A. B. P. *Can. J. Chem.* **1987**, 65, 855. doi:10.1130/v87-144.
- (18) Schutte, W. J.; Sluyters-Rehbach, M.; Sluyters, J. H. *J. Phys. Chem.* **1993**, 97 (22), 6069. doi:10.1021/j100124a047.
- (19) Zelina, J. P.; Njue, C. K.; Rusling, J. F.; Kamau, G. N.; Masila, M.; Kibugu, J. *J. Porphyrins Phthalocyanines*, **1999**, 3, 188. doi:10.1002/(SICI)1099-1409(199903)3:3<188::AID-JPP122>3.0.CO;2-A.
- (20) Abkowitz, M.; Monahan, A. R. *J. Chem. Phys.* **1973**, 58 (6), 2281. doi:10.1063/1.1679503.
- (21) Kobayashi, N.; Higashi, R.; Ishii, K.; Hatsusaka, K.; Ohta, K. *Bull. Chem. Soc. Jpn.* **1999**, 72 (6), 1263. doi:10.1246/bcsj.72.1263.
- (22) Spikes, D. J. *Photochem. Photobiol.* **1986**, 43 (6), 691. doi:10.1111/j.1751-1097.1986.tb05648.x.
- (23) Simon, J.; Vacus, J. *Adv. Mater.* **1995**, 7 (9), 797. doi:10.1002/adma.19950070908.
- (24) Dhami, S.; Phillips, D. *J. Photochem. Photobiol. Chem.* **1996**, 100 (1-3), 77. doi:10.1016/S1010-6030(96)04438-3.
- (25) Howe, L.; Zhang, J. Z. *J. Phys. Chem. A* **1997**, 101 (18), 3207. doi:10.1021/jp9622445.
- (26) Lang, K.; Kubat, P.; Mosinger, J.; Wagnerova, D. M. *J. Photochem. Photobiol. Chem.* **1998**, 119 (1), 47. doi:10.1016/S1010-6030(98)00380-3.
- (27) Ng, A. C. H.; Li, X. Y.; Ng, D. K. P. *Macromolecules* **1999**, 32 (16), 5292. doi:10.1021/ma990367s.
- (28) Louati, A.; El Meray, M.; Andre, J. J.; Simon, J.; Kadish, K. M.; Gross, M.; Giraudeau, A. *Inorg. Chem.* **1985**, 24 (8), 1175. doi:10.1021/ic00202a012.
- (29) Isago, H.; Leznoff, C. C.; Ryan, M. F.; Metcalfe, R. A.; Davids, R.; Lever, A. B. P. *Bull. Chem. Soc. Jpn.* **1998**, 71 (5), 1039. doi:10.1246/bcsj.71.1039.
- (30) Baranton, S.; Coutanceau, C.; Garnier, E.; Leger, J. M. *J. Electroanal. Chem.* **2006**, 590 (1), 100. doi:10.1016/j.jelechem.2006.03.007.
- (31) Elzing, A.; Van der Putten, A.; Vissher, W.; Barendrecht, E. *J. Electroanal. Chem.* **1987**, 233 (1-2), 99. doi:10.1016/0022-0728(87)85009-X.
- (32) Cook, M. J.; Chambrier, I. In *The Porphyrin Handbook*; Kadish, K. M., Smith, K. M., and Guillard, R. Eds.; Academic: San Diego, 2003; Vol. 17, p. 37.
- (33) Law, K. Y. *Chem. Rev.* **1993**, 93 (1), 449. doi:10.1021/cr00017a020.
- (34) Fabian, J.; Nakazumi, H.; Matsuoka, M. *Chem. Rev.* **1992**, 92 (6), 1197. doi:10.1021/cr00014a003.
- (35) Özer, M.; Altındal, A.; Özkaya, A. R.; Salih, B.; Bulut, M.; Bekaroğlu, Ö. *Eur. J. Inorg. Chem.* **2007**, 2007 (22), 3519. doi:10.1002/ejic.200700141.
- (36) Koca, A.; Özkaya, A. R.; Arslanoğlu, Y.; Hamuryudan, E. *Electrochim. Acta* **2007**, 52 (9), 3216. doi:10.1016/j.electacta.2006.09.064.
- (37) Koca, A.; Özkaya, A. R.; Selçukoğlu, M.; Hamuryudan, E. *Electrochim. Acta* **2007**, 52 (7), 2683. doi:10.1016/j.electacta.2006.09.025.
- (38) Odabaş, Z.; Altındal, A.; Özkaya, A. R.; Bulut, M.; Salih, B.; Bekaroğlu, Ö. *Polyhedron* **2007**, 26 (3), 695. doi:10.1016/j.poly.2006.08.039.
- (39) Özer, M.; Altındal, A.; Özkaya, A. R.; Bulut, M.; Bekaroğlu, Ö. *Polyhedron* **2006**, 25 (18), 3593. doi:10.1016/j.poly.2006.07.011.
- (40) Çamur, M.; Özkaya, A. R.; Bulut, M. *Polyhedron* **2007**, 26 (12), 2638. doi:10.1016/j.poly.2007.01.010.
- (41) Lever, A. B. P.; Milaeva, E. R.; Speier, G. In *Phthalocyanines: Properties and Applications*; Leznoff, C. C. and Lever, A. B. P., Eds.; VCH: New York, 1993; Vol. 3, pp1-69.
- (42) Clack, D. W.; Hush, N. S.; Woolsey, I. S. *Inorg. Chim. Acta* **1976**, 19 (2), 129. doi:10.1016/S0020-1693(00)91084-3.
- (43) Arslan, S.; Yilmaz, I. *Polyhedron* **2007**, 26 (12), 2387. doi:10.1016/j.poly.2006.11.047.
- (44) Rollmann, L. D.; Iwamoto, R. T. *J. Am. Chem. Soc.* **1968**, 90 (6), 1455. doi:10.1021/ja01008a013.
- (45) Jin, Z.; Nolan, K.; McArthur, C. R.; Lever, A. B. P.; Leznoff, C. C. *J. Organomet. Chem.* **1994**, 468 (1-2), 205. doi:10.1016/0022-328X(94)80051-0.
- (46) Tse, Y.-H.; Goel, A.; Hu, M.; Lever, A. B. P.; Leznoff, C. C.; Van Lier, J. E. *Can. J. Chem.* **1993**, 71 (5), 742. doi:10.1139/v93-098.
- (47) George, R. D.; Snow, A. W.; Shirk, J. S.; Barger, W. R. *J. Porphyrins Phthalocyanines* **1998**, 2, 1. doi:10.1002/(SICI)1099-1409(199801/02)2:1<1::AID-JPP43>3.0.CO;2-L.
- (48) Martin, P. C.; Gouterman, M.; Pepich, B. V.; Renzoni, G. E.; Schindele, D. C. *Inorg. Chem.* **1991**, 30 (17), 3305. doi:10.1021/ic00017a016.
- (49) Stillman, M. J.; Thomson, A. J. *J. Chem. Soc., Faraday Trans. II* **1974**, 70, 790. doi:10.1039/f29747000790.
- (50) Day, P.; Hill, H. A. O.; Price, M. G. *J. Chem. Soc. A* **1968**, 90. doi:10.1039/j19680000090.

# Mean-field study of the synergic effect of the CO–NO reaction on a heterogeneous substrate of interconnected sectors

Joaquín Cortés and Eliana Valencia

**Abstract:** A mean-field theory study is made of the behaviour of a kinetic model of the reduction reaction of NO by CO catalyzed by a surface with simple heterogeneity consisting of two interconnected sectors that differ in their NO dissociation activation energy. A synergistic effect is manifested in the activity, apparent activation energy, and reaction order of the system. This situation, analogous to that observed in the literature in the case of a heterogeneous catalytic particle, is used in the paper to analyze a real case of a bimetallic catalyst.

**Key words:** mean-field model in superficial reaction, catalytic CO–NO reaction, surface heterogeneity in superficial reaction, superficial catalytic reaction, CO–NO reaction over palladium, steps–terraces superficial heterogeneity

**Résumé :** On a effectué une étude, à base de la théorie du champ moyen, du comportement d'un modèle cinétique de la réaction de réduction du NO par le CO, catalysée par une surface comportant une simple hétérogénéité formée de deux secteurs interreliés qui diffèrent par leur énergie d'activation de dissociation du NO. À part d'autres aspects, un effet synergique se manifeste dans l'activité du système, l'énergie d'activation apparente et l'ordre de la réaction. Cette situation, analogue à celle observée dans la littérature dans le cas d'une particule catalytique hétérogène, est utilisée dans ce travail pour analyser un cas réel de catalyseur bimétallique.

**Mots-clés :** modèle du champ moyen dans l'étude d'une réaction superficielle, réaction catalytique CO–NO, hétérogénéité en surface dans une réaction superficielle, réaction catalytique superficielle, réaction CO–NO sur du palladium, hétérogénéité superficielle en paliers et en terrasses

[Traduit par la Rédaction]

## Introduction

Over the last decades, great progress has been made in the knowledge of catalytic surface reactions, owing on the one hand to modern laboratory techniques and on the other to a better understanding of the behaviour of irreversible dynamic systems, of which surface reactions are an example. These kinds of systems have attracted the joint attention of chemists, because of their applications in catalysis, and of physicists, because they are good examples of nonequilibrium models that exhibit interesting complex phenomena such as oscillations, kinetics phase transitions, hysteresis, chaos, and dissipative structures.<sup>1</sup>

There have been advances in developing models and laboratory techniques in surface science to aid in the interpretation of the basic mechanisms of heterogeneous catalysis. In spite of these advances, however, there are still serious difficulties in interpreting the results of industrial catalysis, for two reasons. One reason is related to the fact that industrial experiments take place at about atmospheric pressure, while the models use certain parameters determined under ultra high vacuum conditions (UHV). This difficulty, which has been called the “pressure gap”, is directly related, among other factors, to the interpretation and the use of the con-

stants of the kinetic mechanism as well as to the introduction of lateral interactions between the adsorbed species in the model.

The second reason, called the “material gap”, is related to the fact that in technical catalysis we deal with nanometric metallic particles, as in the case of supported catalysts, while the parameters in model catalysis are usually determined over single crystals that expose a well-defined plane as the catalytic surface. This leads to difficulties in interpreting the heterogeneity existing in the real system, and this has been partially solved by the use of simulations, generally Monte Carlo (MC). However, the theoretical models commonly used by experimenters to interpret their data are, one way or another, mean-field schemes. This difficulty is what basically interests us in this paper.

Both types of techniques, mean field and MC, have been used extensively in the study of surface reactions, and they have been reviewed in some excellent articles by Evans,<sup>2</sup> Albano,<sup>3</sup> Zhdanov and Kasemo.<sup>4</sup> The theoretical study of the CO–NO reaction, which is not a concern in this paper, has an interesting history which began with Yaldran and Khan,<sup>5</sup> Brosilow and Ziff,<sup>6</sup> and Meng, Weinberg and Evans<sup>7</sup> using MC simulations and mean-field theories

Received 8 July 2009. Accepted 27 August 2009. Published on the NRC Research Press Web site at canjchem.nrc.ca on 16 March 2010.

J. Cortés<sup>1</sup> and E. Valencia. Facultad de Ciencias Físicas y Matemáticas, Universidad de Chile, Casilla 2777, Santiago, Chile.

<sup>1</sup>Corresponding author (e-mail: jcortes@dqf.uchile.cl).

(MFT) at the site level, and assuming a simplified mechanism that we have called the BZ model. This system showed an interesting surface-poisoning phenomenon<sup>6,7</sup> that was extended by our group to the study of disordered two- and three-dimensional substrates<sup>8</sup> using MC experiments. From the theoretical standpoint, our group extended the study of this reaction through the MFT model at the pairs level, a method introduced in a classical work by Dickmann for the (CO–O<sub>2</sub>) reaction,<sup>9</sup> for the BZ model,<sup>10</sup> and later for a complete kinetic mechanism,<sup>11</sup> confirming the MFT results with MC simulations. Later, Dickmann et al.<sup>12</sup> extended these analyses to different superficial lattices.

At our laboratory, we have been interested for some time in studying the kinetics of systems that also have practical importance in the catalytic control of motor-vehicle exhaust emissions, like the (CO–O<sub>2</sub>) and (CO–NO) reactions, which we have used as prototypes to relate various mean field models and MC simulations with experimental results.<sup>13,14</sup> Our interest in introducing the heterogeneous factor in a mean-field model, which dates back to our work in the field of adsorption on heterogeneous surfaces mentioned in the monograph of Rudzinski and Everett,<sup>15</sup> led us later to propose a mean-field theory of a surface reaction on a disordered substrate.<sup>16</sup> In the present paper, we propose both a sites and a pairs approximation, characterizing the substrate through set  $\{q_i\}$  of probability that the adsorbed site has  $i$  neighbors that belong to the substrate in the model.

An interesting different approach considered recently by Zhdanov and Kasemo (ZK approach),<sup>17–19</sup> introduces the heterogeneity of the substrate in a mean-field model that analyzes the kinetics of a heterogeneous reaction. The ZK scheme has been applied to the behavior of catalysts formed by particles on an inert support<sup>17,18</sup> and to the determination of the role of the steps of the catalytic surface in the case of the CO–NO reaction,<sup>17</sup> taking into account recent advances that use the density functional theory (DFT) approximation<sup>20</sup> to characterize the activation energy.

Motivated by this way of tackling the problem, in a recent paper, we have analyzed some consequences of the ZK approach.<sup>21</sup> In this paper we develop a mean-field scheme in the case of the CO–NO reaction catalyzed by a heterogeneous substrate consisting of a mixed surface formed by two interconnected sectors. Besides allowing us to analyze some general aspects of the model, such as its behavior with respect to the temperature and pressure of the gas phase, this approach has revealed a synergistic effect of the system that is of general interest.

The model can be applicable to some real systems. Zhdanov et al.<sup>17,18</sup> have used this approach to show that, owing to purely kinetic effects, the activity of a catalytic particle formed by a mixture of (111) and (100) faces can be higher than that calculated by the conventional approximation based on the assumption that the faces operate independently. This kind of synergism experienced by the particle is seen in the example given in the paper for what can be a bimetallic catalyst. The effect, however, may not occur, depending on the kinetic parameters involved. That is the case of the bimetallic catalyst studied in the experiments of Holles et al.<sup>22</sup> for the CO–NO reaction over Pd–Rh–Al<sub>2</sub>O<sub>3</sub>,

which we will analyze below as a possible application of the treatment developed in the paper.

## The kinetic scheme of the CO–NO reaction

The reduction reaction of NO by CO (CO–NO reaction) on rhodium has been studied extensively over the last decades, particularly because of its applications in catalytic converters of automobiles.<sup>23</sup> The determination of the kinetic mechanism of the CO–NO reaction on rhodium has a long and controversial history, since the first papers of Hecker and Bell<sup>24</sup> and followed, among others, by the studies of Oh,<sup>25</sup> Cho,<sup>26</sup> Chiang and Tan,<sup>27</sup> Peden,<sup>28</sup> and Permana,<sup>29</sup> and by those from our laboratory,<sup>30</sup> in the latter case considering recent experiments carried out by Zaera's group.<sup>31</sup> Scheme 1 shows the most frequently used kinetic mechanism, proposed by Peden<sup>28</sup> and Permana<sup>29</sup> for the CO–NO reaction on rhodium. Table 1 shows the parameters used in this paper, chosen from the above references indicated in the table and that we have used recently.<sup>30</sup> For the adsorption constants  $k_{\text{ads}}\{j\}$  of gas  $j$  we use the kinetic theory of gases expression

$$[1] \quad k_{\text{ads}}\{j\} = S_j \sigma (2\pi M_j RT)^{-1/2}$$

where  $M_j$  is the molar mass of  $j$ ,  $S_j$  is the corresponding sticking coefficient, which we have taken to be equal to 1 in this paper, and  $\sigma$  is the area occupied by one mole of metal atoms on the surface of the catalyst.

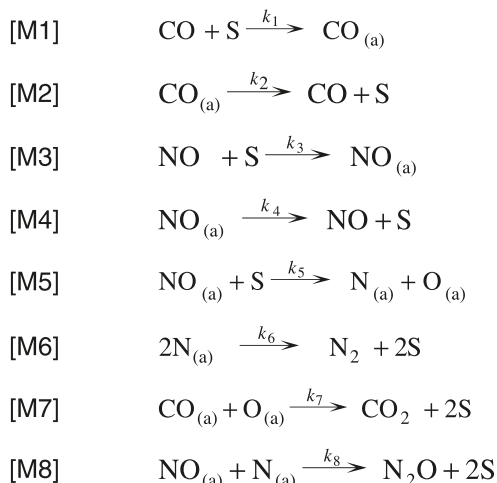
## The mean-field model

Appendix A shows the details of the analytic solution of a mean-field model published earlier by Cortés et al.<sup>14,30</sup> for the mechanism of Scheme 1. It corresponds to the development of the corresponding kinetics equations if it is considered that the surface of the catalyst is uniform. In general, a high superficial diffusion, assumed implicitly in models of the type with which we are concerned, ensure that the mean-field approximation can be a sufficient approximation. Also, if the adsorption–desorption steps are sufficiently fast, as they have been considered in the literature to be for this case,<sup>32</sup> it is possible to accept the approximation of assuming that the CO<sub>(a)</sub> and NO<sub>(a)</sub> adsorbates remain in equilibrium with the gas phase during the process, a condition that has been used to solve the kinetics equations in the previous model included in the appendix and in the procedure of concern in this paper.

The study of the ZK model is very interesting because it allows the application of a mean-field scheme to a catalytic surface with simple heterogeneity, made of few sectors with different energy characteristics. The most obvious examples are surfaces formed by different crystal faces<sup>17,18</sup> or surfaces that have step sites of different activity, presumably more active than the terrace sites of the rest of the surface.<sup>19</sup> The former case may be identified with a typical catalyst of a metal supported on an inert solid, where the surface of its particles is often conceived as a mixture of the most frequent crystal faces of the metal.<sup>33</sup> The latter was the case studied by ZK, motivated by the quantum studies that use the DFT to investigate the role of the steps in the heterogeneous catalysis phenomenon.<sup>20,34</sup>



**Scheme 1.** Mechanism of the CO–NO reaction used in the paper.



Below we will consider the mechanism of Scheme 1 for the CO–NO reaction in the case of a catalytic surface S12 formed by two regions, S1 and S2, that are interconnected. This can be understood if one imagines examples like bi-metallic catalysts, discussed below, or supported metal particles with different crystal faces, considered by Zhadanov.<sup>17,18</sup> The interconnection is defined in the model, for example, in the use of conservation equations applied to the whole surface, in contrast with the existence of some type of barrier in the case of unconnected sectors, in which case the equations are applied separately in each sector. The conservation eqs. [A5] and [A6] of the Appendix, however, which represent steady states for the adsorbed species  $\text{N}_{(\text{a})}$  and  $\text{O}_{(\text{a})}$  ( $d\theta_{\text{N}}/dt = 0$  and  $d\theta_{\text{O}}/dt = 0$ ), now have the following form:

$$\begin{aligned}
 [2] \quad & n^{\text{S2}} k_5^{\text{S2}} \theta_{\text{NO}}^{\text{S2}} \theta_{\text{S}}^{\text{S2}} + n^{\text{S1}} k_5^{\text{S1}} \theta_{\text{NO}}^{\text{S1}} \theta_{\text{S}}^{\text{S1}} = 2n^{\text{S2}} k_6^{\text{S2}} (\theta_{\text{N}}^{\text{S2}})^2 \\
 & + 2n^{\text{S1}} k_6^{\text{S1}} (\theta_{\text{N}}^{\text{S1}})^2 + n^{\text{S2}} k_8^{\text{S2}} \theta_{\text{NO}}^{\text{S2}} \theta_{\text{N}}^{\text{S2}} + n^{\text{S1}} k_8^{\text{S1}} \theta_{\text{NO}}^{\text{S1}} \theta_{\text{N}}^{\text{S1}} \\
 [3] \quad & n^{\text{S2}} k_5^{\text{S2}} \theta_{\text{NO}}^{\text{S2}} \theta_{\text{S}}^{\text{S2}} + n^{\text{S1}} k_5^{\text{S1}} \theta_{\text{NO}}^{\text{S1}} \theta_{\text{S}}^{\text{S1}} = n^{\text{S2}} k_7^{\text{S2}} \theta_{\text{CO}}^{\text{S2}} \theta_{\text{O}}^{\text{S2}} \\
 & + n^{\text{S1}} k_7^{\text{S1}} \theta_{\text{CO}}^{\text{S1}} \theta_{\text{O}}^{\text{S1}}
 \end{aligned}$$

$$[8] \quad F = \frac{(-A(k_8^{\text{S2}} + yk_8^{\text{S1}}) + (A^2(k_8^{\text{S2}} + yk_8^{\text{S1}})^2 + 8AB(k_6^{\text{S2}} + yk_6^{\text{S1}})(k_5^{\text{S2}} + yk_5^{\text{S1}}))^{1/2})}{4(k_6^{\text{S2}} + yk_6^{\text{S1}})}$$

and using conservation eq. [A7] we obtain for the coverage of  $\text{CO}_{(\text{a})}$

$$[9] \quad \theta_{\text{CO}} = 1/(1 + A + B + E + F)$$

The above equations allow the calculation of all the covered fractions  $\theta_i^j$  as a function of the kinetic parameters of the system, which make it possible to determine the average productions  $R_i$  of surface S12. If  $n^{\text{S1}}$  and  $n^{\text{S2}}$  are the number of sites of S1 and S2, respectively, then  $f = n^{\text{S1}}/(n^{\text{S1}} + n^{\text{S2}})$  is the fraction of sites belonging to sector S1. The total production  $R_i$  of species  $i$  will be equal to the weighted sum of productions of S1 and S2, respectively, so

$$[10] \quad R_{\text{CO}_2} = (1 - f)k_7^{\text{S2}} \theta_{\text{CO}} \theta_{\text{O}} + fk_7^{\text{S1}} \theta_{\text{CO}} \theta_{\text{O}}$$

where  $\theta_i$  is the fraction of covered surface and the superscripts refer to the respective sectors S1 and S2. In the development of the model we will assume a rapid diffusion of all the adsorbed species according to the ZK model.<sup>17–19,35</sup> As those authors point out, the values published<sup>35</sup> for the activation energies for the diffusion of adsorbed species, even atomic ones like N and O, are in general smaller than for the other stages  $M_i$  of the mechanism of Scheme 1. This leads to considering as an assumption of the model that the fraction of covered surface of species  $i$  is the same for all the heterogeneous surface S12, i.e.,  $\theta_i^{\text{S2}}$  is equal to  $\theta_i^{\text{S1}}$  for each species  $i$ .

Let us consider also a frequent situation of experimental interest, where the kinetic constants of CO and NO desorption are identical in both sectors. Since eq. [1] also assumes adsorption without activation energy, it means that eqs. [A1]–[A4] in Appendix A are valid for this case. Introducing eq. [A4] into eq. [2] and eq. [3] using the definition  $y = n^{\text{S1}}/n^{\text{S2}}$ , and recalling that  $\theta_i^{\text{S2}} = \theta_i^{\text{S1}} = \theta_i$ , we get

$$[4] \quad k_5^{\text{S2}} AB \theta_{\text{CO}}^2 + yk_5^{\text{S1}} AB \theta_{\text{CO}}^2 = 2k_6^{\text{S2}} \theta_{\text{N}}^2 + 2yk_6^{\text{S1}} \theta_{\text{N}}^2 + k_8^{\text{S2}} A \theta_{\text{N}} \theta_{\text{CO}} + yk_8^{\text{S1}} A \theta_{\text{N}} \theta_{\text{CO}}$$

$$[5] \quad k_5^{\text{S2}} AB \theta_{\text{CO}}^2 + yABk_5^{\text{S1}} \theta_{\text{CO}}^2 = k_7^{\text{S2}} \theta_{\text{CO}} \theta_{\text{O}} + yk_7^{\text{S1}} \theta_{\text{CO}} \theta_{\text{O}}$$

from which it is possible to obtain eq. [6] for the covered fraction of  $\text{O}_{(\text{a})}$

$$[6] \quad \theta_{\text{O}} = E \theta_{\text{CO}}$$

where

$$[7] \quad E = AB(k_5^{\text{S2}} + yk_5^{\text{S1}})/(k_7^{\text{S2}} + yk_7^{\text{S1}})$$

If we also define for  $\theta_{\text{N}}$ , the coverage  $N_{(\text{a})}$ ,  $\theta_{\text{N}} = F \theta_{\text{CO}}$ , from eq. [4] we get that

$$[11] \quad R_{\text{N}_2} = (1 - f)k_6^{\text{S2}} (\theta_{\text{N}})^2 + fk_6^{\text{S1}} (\theta_{\text{N}})^2$$

$$[12] \quad R_{\text{N}_2\text{O}} = (1 - f)k_8^{\text{S2}} \theta_{\text{NO}} \theta_{\text{N}} + fk_8^{\text{S1}} \theta_{\text{NO}} \theta_{\text{N}}$$

## Results and discussion

In this paper, to illustrate the model, we will study the interesting consequences derived from a particular case in which the regions differ only in the value of the activation energy  $E_5$  of the dissociation of NO, keeping unchanged the rest of the system's kinetic parameters. We will discuss the results of the model in the example described below. The kinetic parameters of sector S2 will be those corresponding to

**Table 1.** Kinetics parameters of the CO–NO reaction on Rh<sup>21</sup> and Pd<sup>23</sup> used in the paper.

Events	Activation energy $E_i$ (kcal/mol)		Frequency factor $\nu_i$ (sec <sup>-1</sup> )	
	Rh	Pd	Rh	Pd
CO desorption ( $k_2$ )	31.6		$1.6 \times 10^{14}$	
NO desorption ( $k_4$ )	29.7		$4.6 \times 10^{14}$	
NO dissociation ( $k_5$ )	17.5	34.2	$2.1 \times 10^{10}$	$2.7 \times 10^{14}$
N <sub>2</sub> production ( $k_6$ )	32.6	29	$4 \times 10^{12}$	$6.5 \times 10^{13}$
N <sub>2</sub> O production ( $k_8$ ) (ref. 21)	34.1	34.1	$5.3 \times 10^{13}$	$5.3 \times 10^{13}$
CO <sub>2</sub> production ( $k_7$ )	14.3	33.6	$10^{12}$	$7.1 \times 10^{15}$

Table 1 for Rh, and those of sector S1 differ from them in the value of the activation energy of NO dissociation,  $E_5$ , which we will consider as being 12 250 (cal/mol), 70% lower than that of sector S2. The kinetics mechanism of Scheme 1 is considered valid in both sector S1 and S2 and in the joint surface S12 of interconnected sectors. In this way, the equations that describe the kinetic behaviour of the CO–NO reaction will be given by Appendix A for the separate sectors S1 and S2, and by the model from the previous section for surface S12.

What is interesting here is the synergistic effect that appears in a system of interconnected sectors as a result of the mobility of the adsorbed phase particles, so the dissociation-energy difference chosen for this visualization will in some way be arbitrary. However, we can imagine real situations such as a supported particle whose surface has been conceived as a mixture of various crystalline faces<sup>33</sup> in the case studied by Zhdanov et al.<sup>17,18</sup> Although it is not easy to find in the literature reliable experimental values for the activation energies for the dissociation of NO on various crystalline faces, Michaelides et al.<sup>36</sup> have recently shown a linear relation between the activation energy of dissociation and the corresponding enthalpy changes in surface reactions. On the other hand, periodic density-functional calculations have been carried out for NO dissociation reactions on Rh(111) and Rh(100),<sup>37</sup> showing that the differences in order of magnitude used in our calculations for the hypothetical sectors S1 and S2 seem to be reasonable.

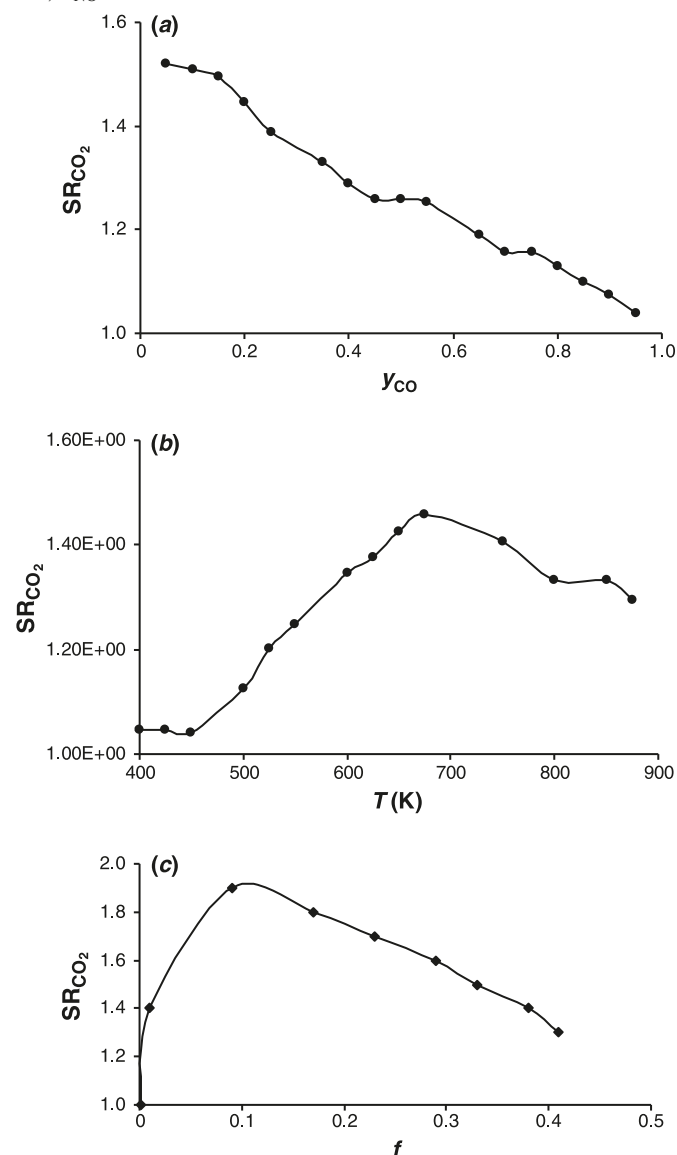
### Synergistic effect of the interconnected sectors system

Figure 1 shows the existence of a synergistic effect observed in the system studied, with changes in temperature, gas-phase concentration, and fraction of sites that belong to sector S1 of the surface. This effect, which we will refer to as the activity of CO<sub>2</sub>, will be described by means of the synergistic factor  $SR_{CO_2}$ , the quotient between the production of CO<sub>2</sub> in the interconnected-sectors system and what it would have if they were completely independent; that is

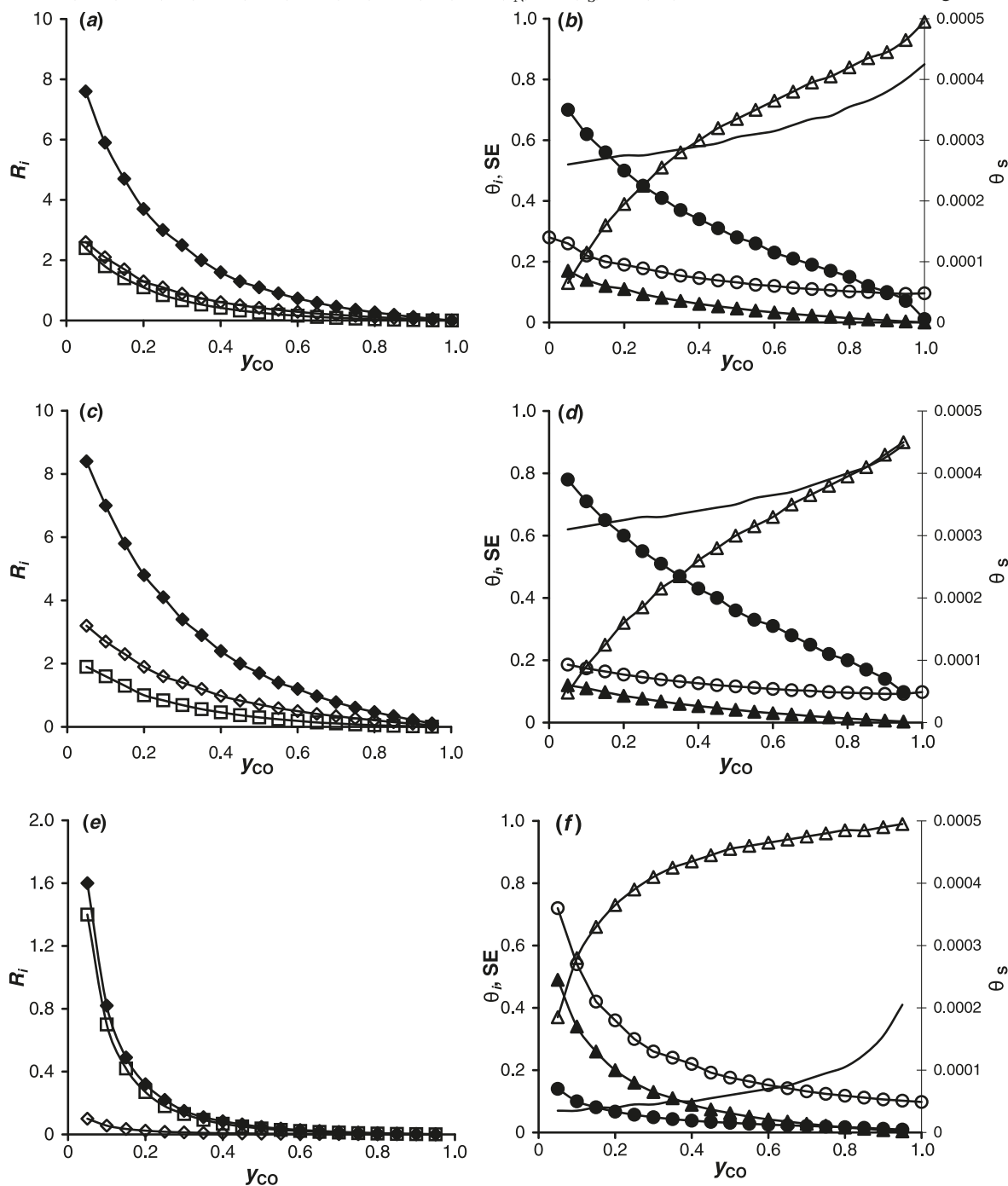
$$[13] \quad SR_{CO_2} = R_{CO_2}/RI_{CO_2}$$

where  $R_{CO_2}$  is determined from eq. [10], and  $RI_{CO_2}$  corresponds to the weighted sum with fraction  $f$  of the productions of both sectors S1 and S2 considered as independent, calculated from the equations of Appendix A using in each case the kinetics parameters corresponding to the sector. In general, the  $SR_{CO_2}$  quotient between the  $R_{CO_2}$  productions determined by the proposed model and  $RI_{CO_2}$  calculated

**Fig. 1.** Relation of CO<sub>2</sub> production between systems of interconnected sectors and sectors assumed to be independent ( $SR_{CO_2}$ ) (synergistic effect).  $E_{dis}(S1) = 12.25$  (kcal/mol),  $E_{dis}(S2) = 17.5$  (kcal/mol); (a) vs. CO concentration  $y_{CO}$ ,  $T = 600$  K,  $f = 0.5$ ; (b) vs. temperature  $T$ ,  $P_{CO} = 20.52$  torr (1 torr = 133.322 Pa),  $P_{NO} = 39.52$  torr,  $f = 0.5$ ; (c) vs. fraction  $f$  of sector S of the surface,  $T = 600$  K,  $P_{CO} = 20.52$  torr,  $P_{NO} = 39.52$  torr.



**Fig. 2.** Production ( $R_i$ ,  $y_{\text{CO}}$ ) and phase diagram ( $x_i$ ,  $y_{\text{CO}}$ ) vs. CO concentration in the gas ( $y_{\text{CO}}$ )  $T = 600$  K; (a, b) interconnected sectors S12,  $f = 0.5$ ,  $E_{\text{dis}}(\text{S1}) = 12.25$  kcal/mol,  $E_{\text{dis}}(\text{S2}) = 17.5$  kcal/mol; (c, d) uniform surface  $E_{\text{dis}} = 12.25$  kcal/mol; (e, f) uniform surface  $E_{\text{dis}} = 17.5$  kcal/mol.  $\blacklozenge$  ( $R_{\text{CO}_2}$ );  $\diamond$  ( $R_{\text{N}_2}$ );  $\square$  ( $R_{\text{N}_2\text{O}}$ );  $\triangle$  ( $\theta_{\text{CO}}$ );  $\blacktriangle$  ( $\theta_{\text{NO}}$ );  $\bullet$  ( $\theta_{\text{N}}$ );  $\circ$  ( $\theta_{\text{S}}$ ); — (SE); the lines have been drawn to guide the eye.



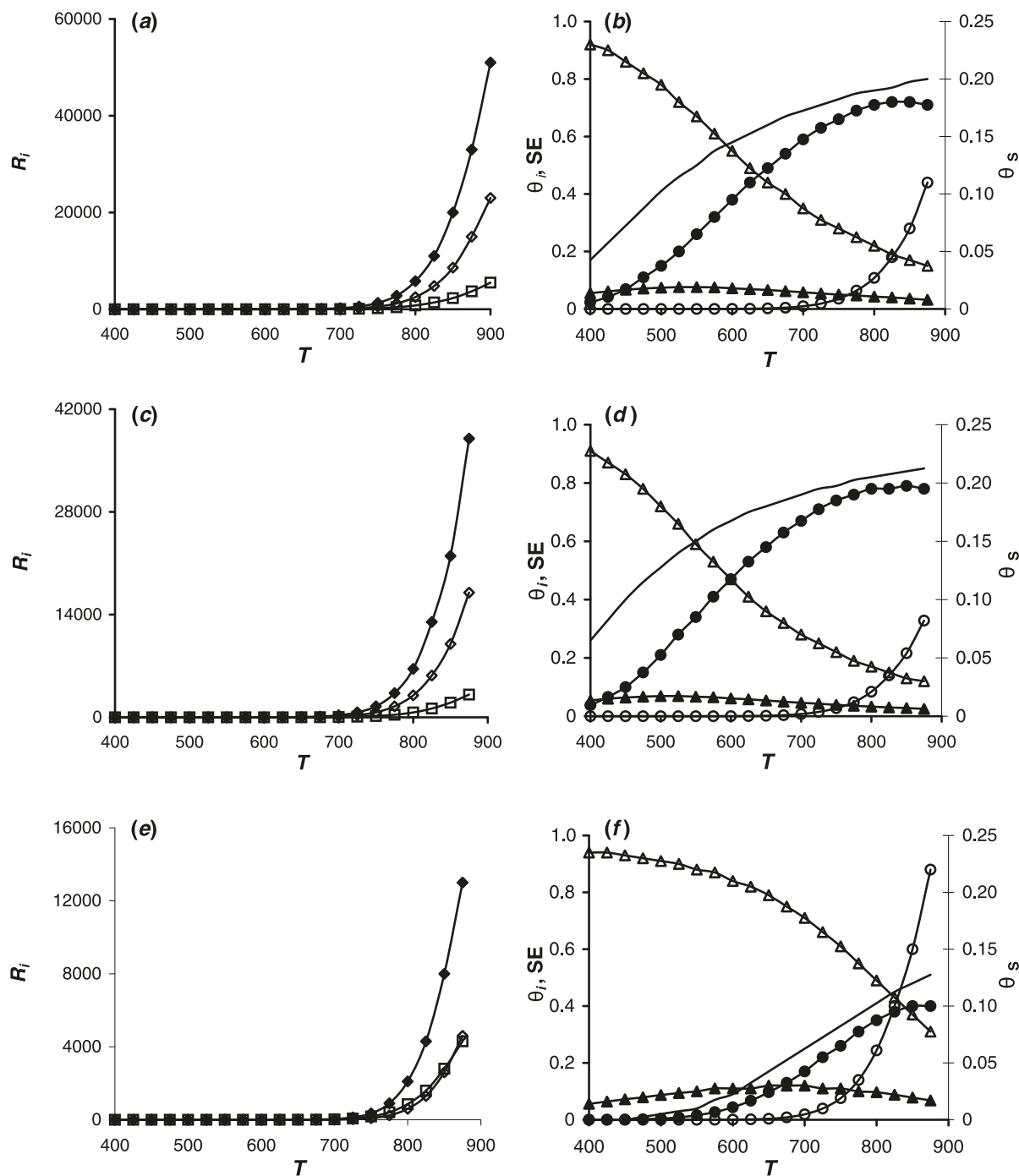
using the previous model developed in Appendix A shows some sensitivity, especially as a function of temperature, because of the rounding-off approximations of the numerical calculations made in each model.

Figure 1a shows an example at  $T = 600$  K, where it is observed that the synergistic effect is large for low concentrations of CO in the gas phase and decreases until it vanishes when that concentration increases up to the extreme situation of pure CO. Factor  $\text{SR}_{\text{CO}_2}$  becomes important when the  $\text{NO}_{(\text{a})}$  fraction of the surface is large. However, if the value

of  $\text{NO}_{(\text{a})}$  is low, which happens at high CO concentrations, the effect of the difference in the activation energy of dissociation on the synergistic effect decreases markedly, as seen in the figure.

On the other hand, Fig. 1b shows that  $\text{SR}_{\text{CO}_2}$  keeps the same order of magnitude for temperatures higher than about 650 K, decreasing at low temperatures. Figure 1c, finally, shows an interesting maximum value for  $\text{SR}_{\text{CO}_2}$  among the extreme situations corresponding to high and low values of fraction  $f$ , which indicate a decrease in the heterogeneity of

**Fig. 3.** The same as Fig. 2 vs. temperature  $T$ ;  $P_{\text{CO}} = 20.52$  torr,  $P_{\text{NO}} = 39.52$  torr.  $\blacklozenge$  ( $R_{\text{CO}_2}$ );  $\diamond$  ( $R_{\text{N}_2}$ );  $\square$  ( $R_{\text{N}_2\text{O}}$ );  $\triangle$  ( $\theta_{\text{CO}}$ );  $\blacktriangle$  ( $\theta_{\text{NO}}$ );  $\bullet$  ( $\theta_{\text{N}}$ );  $\circ$  ( $\theta_{\text{S}}$ ); — (SE).



the surface, and which finally turns uniform in the extreme situations of  $f = 0$  or 1, where  $\text{SR}_{\text{CO}_2} = 1$ .

### Production, selectivity, and phase diagram curves

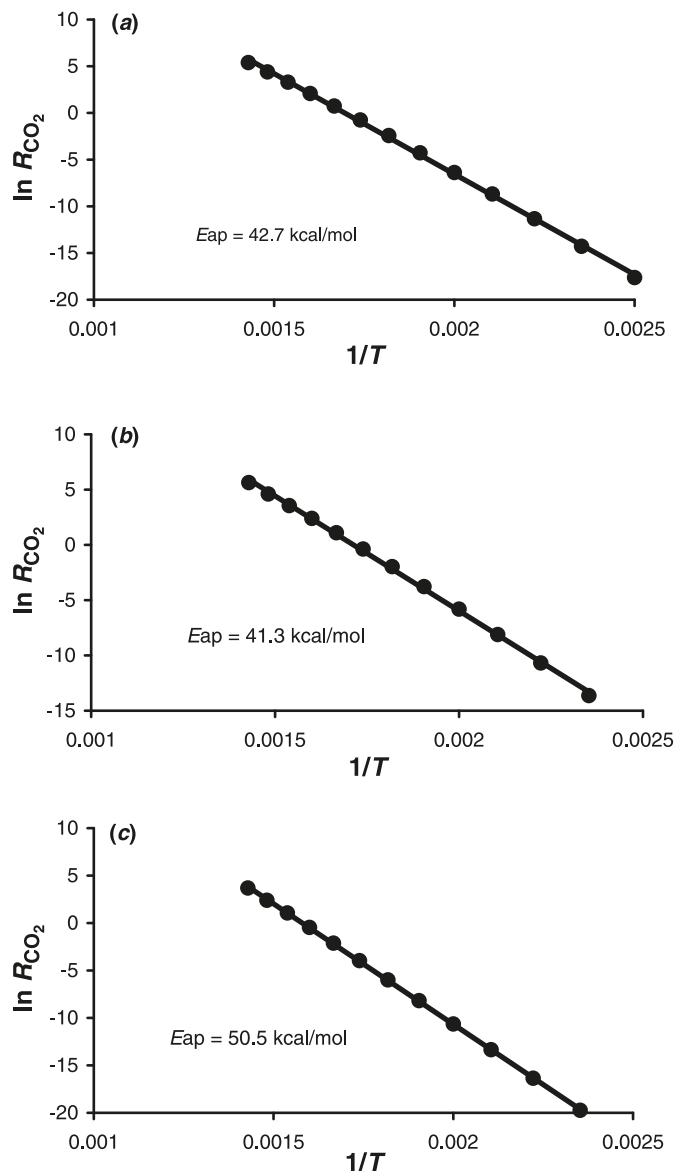
Figure 2 shows the behaviour at 600 K of production and the corresponding phase diagrams of both the heterogeneous system S12 in the case of  $f = 0.5$  and the separate sectors S1 and S2. The same situation is described in Fig. 3 when tem-

perature is varied while keeping CO and NO pressure constant.

Both figures indicate that the reaction, in the range of the kinetic parameters studied, occurs on a small fraction of vacant adsorbed sites. At high CO concentrations in the gas  $y_{\text{CO}}$  and low temperatures  $T$ , the surface is mostly occupied by particles of adsorbed CO. If  $y_{\text{CO}}$  decreases or  $T$  increases, there is an increase in the fraction of vacant sites on the surface  $\theta_{\text{S}}$  and in the particles of adsorbed atomic nitrogen  $\theta_{\text{N}}$ , that react between one another according to stage M6 of the



**Fig. 4.** Arrhenius behavior  $P_{\text{CO}} = 20.52$  torr)  $P_{\text{NO}} = 39.52$  torr; (a) interconnected sectors S12  $f = 0.5$ ,  $E_{\text{dis}}(\text{S1}) = 12.25$  kcal/mol,  $E_{\text{dis}}(\text{S2}) = 17.5$  kcal/mol; (b) uniform surface  $E_{\text{dis}} = 12.25$  kcal/mol; (c) uniform surface  $E_{\text{dis}} = 17.5$  kcal/mol.



kinetics mechanism. This effect is reflected in an increase in the activity of the system, accounting for the decrease in  $\text{CO}_2$  production with the decrease of  $y_{\text{CO}}$  and the decrease of  $T$ .

Comparing the figures corresponding to the uniform surfaces S1 and S2, the expected increase in the order of magnitude of production with the decrease of the activation energy of NO dissociation on surface S1 with respect to S2 is seen. The proportion of the increase of  $R_i$  is maintained at lower temperatures, as for example at 600 K, the temperature chosen in Fig. 2. The increase of  $R_i$ , as noted, correlates with the greater value of  $\theta_{\text{N}}$  on the surface. The greater value of  $\theta_{\text{N}}$  of substrate S1 with respect to S2, on the other hand, also explains the greater selectivity SE for nitrogen in S1, corresponding to the relations between the productions

$R_{\text{N}_2}$  and  $R_{\text{N}_2\text{O}}$ , as shown in both figures for the whole range of CO concentrations and temperatures.

Figures 2 and 3 also show the synergistic effect of the interconnected system S12, which is seen to have a surface configuration of the adsorbed phase similar to surface S1, as a result of the mobility of the adsorbates on the whole surface. This leads to a value greater than one for the synergistic factor  $\text{SR}_{\text{CO}_2}$ , as shown in Fig. 1.

### Arrhenius behavior and reaction orders

Figure 4 shows the Arrhenius straight lines of surfaces S1 and S2 and of the interconnected system S12, with a correlation better than 0.999 in all cases. The values of the apparent activation energy, shown in each of the graphs, is another way of observing the synergistic effect, because the system of interconnected sectors has an activation energy similar to that of sector S1, noticeably lower than that of sector S2.

In regard to the effect of pressure, experimenters usually present their data by means of a semiempirical expression like eq. [14], which in our case defines the order  $m$  with respect to CO and  $n$  with respect to NO:

$$[14] \quad R_{\text{CO}_2} = k_j p_{\text{CO}}^m p_{\text{NO}}^n$$

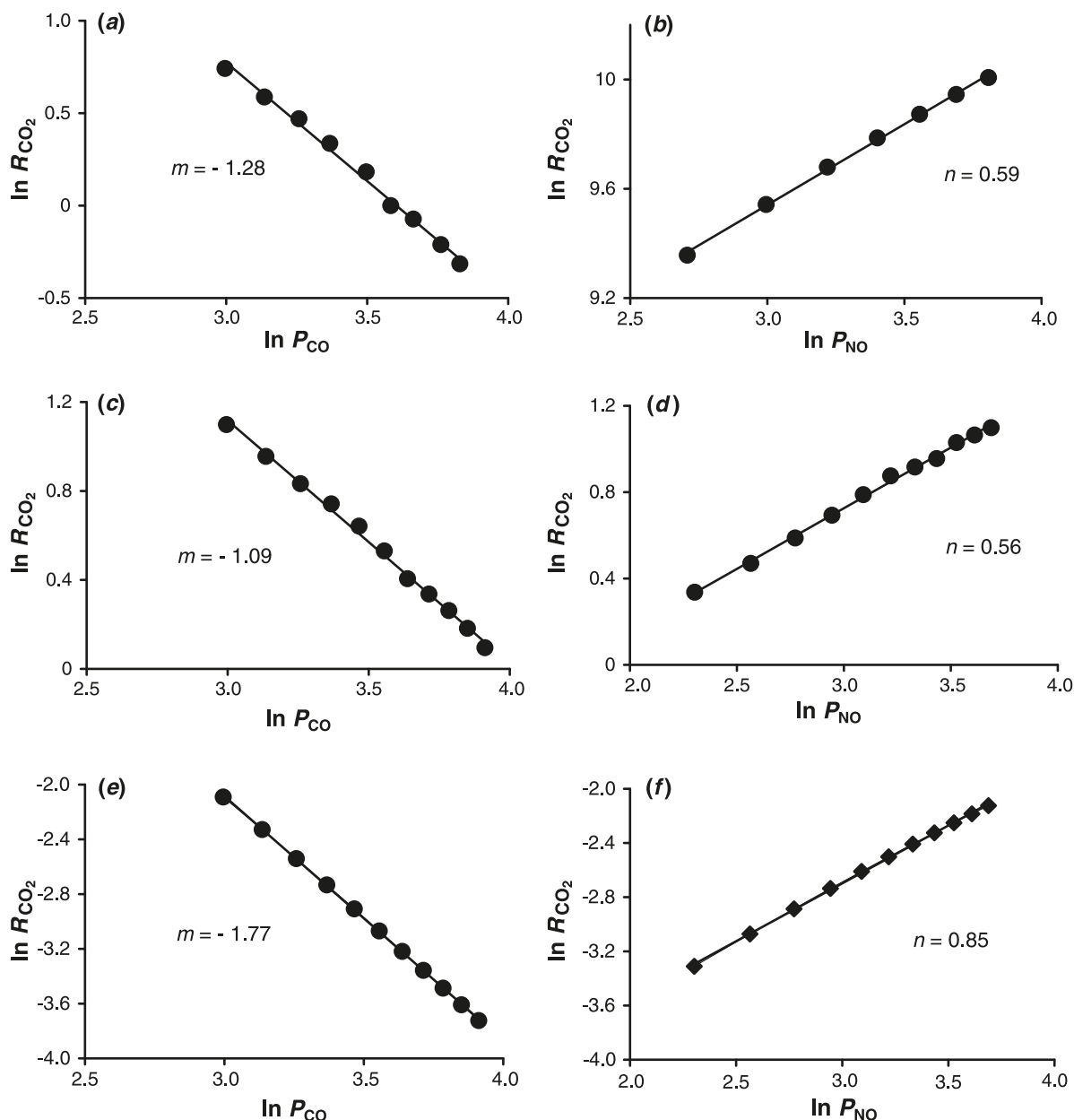
Figure 5 shows straight lines with a high correlation if the logarithm of production is plotted against the logarithm of the corresponding pressure while keeping the other pressure constant, allowing the determination of the corresponding parameters  $m$  and  $n$ . This indicates that on the three surfaces there is an order, decreasing with respect to CO ( $m < 0$ ) and increasing with respect to NO ( $n > 0$ ). The values of  $m$  and  $n$  given in each graph, however, show that the order with respect to both reagents in the interconnected-sector system S12 is similar to that of surface S1 and different from that of sector S2.

### Application of the model in the real case of a bimetallic catalyst

As mentioned in the Introduction, Zhdanov et al.<sup>17,18</sup> found that a catalytic particle shows a synergistic effect between the various faces that make up its surface. In this paper, we are interested in the general behavior of any heterogeneous surface, as in the example that we developed in a previous section, where the synergistic effect illustrated in Fig. 1 is observed. This may be the case of a bimetallic catalyst. However, depending on the parameters of the system, this synergistic effect may not be observed, as in the case of the experiments reported by Holles et al.<sup>22</sup> for the Those authors showed that the turnover frequency on Pd-Rh- $\text{Al}_2\text{O}_3$  was lower than that on either Pd- $\text{Al}_2\text{O}_3$  or Rh- $\text{Al}_2\text{O}_3$ , showing that there is no synergistic effect in that case.

Although Pd and Rh may form an alloy whose properties can explain the phenomenon, it is interesting to go through the exercise of analyzing the situation by means of the model considered in this paper, as shown in the results included in Table 2. It has been assumed that sector S1 corresponds to Pd and S2 to Rh, characterizing both surfaces by the kinetic parameters of stages (M5–M8) of Scheme 1,

**Fig. 5.** Reaction order (eq. [14]; (a)  $\text{CO}_2$  production as a function of CO pressure with a fixed NO pressure of 39.52 torr at 600 K, interconnected sectors S12,  $f = 0.5$ ,  $E_{\text{dis}}(\text{S1}) = 12.25$  kcal/mol, and  $E_{\text{dis}}(\text{S2}) = 17.5$  kcal/mol; (b) the same as (a) as a function of NO pressure with a fixed CO pressure of 20.53 torr; (c) the same as (a) with uniform surface,  $E_{\text{dis}} = 12.25$  kcal/mol; (d) the same as (b) with uniform surface,  $E_{\text{dis}} = 12.25$  kcal/mol; (e) the same of (a) with uniform surface,  $E_{\text{dis}} = 17.5$  kcal/mol; (f) the same as (b) with uniform surface,  $E_{\text{dis}} = 17.5$  kcal/mol.



**Table 2.** Activity  $R_i(\text{TON})$  of the CO–NO reaction on Pd, Rh, and the Pd–Rh bimetallic catalyst (interconnected system) according to the model of the paper;  $f = 0.5$ ,  $P_{\text{CO}} = 20.52$  torr,  $P_{\text{NO}} = 39.52$  torr,  $k_{\text{des}}/k_{\text{ad}}P = 10$ .

T	$R_{\text{CO}_2}$			$R_{\text{N}_2}$			$R_{\text{N}_2\text{O}}$		
	Pd	Rh	Pd–Rh	Pd	Rh	Pd–Rh	Pd	Rh	Pd–Rh
550	0.15	0.76	0.08	0.069	0.34	0.03	0.013	0.075	0.01
600	2	8.3	1.02	0.91	3.4	0.41	0.21	1.5	0.20
650	18	60	9.21	8	21	3.59	2.2	18	2.04
700	120	310	60.61	52	85	22.75	17	140	15.11

whose values are given in Table 1 for Pd and Rh, according to experimental data reported in the literature mentioned there. Given the characteristics of the model that we have developed, for the adsorption-desorption stages we have considered the simplification used by Zhdanov et al.,<sup>17–19</sup> using for the calculation the expression  $k_{\text{des}}/k_{\text{ad}}P = K$  for CO and NO, which implies the assumption that the adsorption equilibrium of both components in both sectors depend only on the corresponding pressures in the gas phase.

The values given in the table in the case of  $K = 10$ , which is the value used by Zhdanov, show the same situation as that reported by Holles et al.,<sup>22</sup> where the activities calculated for the assumption of interacting sectors are lower than on either Pd or Rh, so the bimetallic Rh–Pd system does not show synergism. A similar result, not shown in the paper, is obtained for values of  $K$  equal to 0.1 and 100.

The use of the development of the mean-field model in an experimental example shows the potential importance of using mean-field models on heterogeneous substrates in real situations, and that should encourage extending the frequent case in which the interpretation of the data is done by means of a system of kinetics equations for a catalytic surface assumed to be homogeneous.

## Conclusions

By mean-field theory, a study has been made of the behavior of a kinetic model of the reduction reaction of NO by CO catalyzed by a surface with simple heterogeneity consisting of two interconnected sectors that differ in the activation energy of NO dissociation. As a consequence of the mobility of the adsorbed phase assumed for the model, a synergic effect in the activity of the system is seen that changes with gas phase concentration, temperature, and the relation between the active sites of both sectors of the surface. The system shows an Arrhenius behavior and an order with respect to the pressure of CO and NO, with the effect of the synergy seen in both the apparent activation energy and the reaction orders, if the interacting sectors of the system are compared with the case in which they act independently. This situation, which is similar to that found by Zhdanov et al. in the case of catalytic particles formed by different crystal faces, is also used to explain, in the case of the same reaction on a real bimetallic catalyst, why no synergism was seen.

## Acknowledgments

The authors acknowledge the financial support of this work by Fondo Nacional de Desarrollo Científico y Tecnológico (FONDECYT) under Project No. 1070351.

## References

- (1) (a) Nicolis, G.; Prigogine, I. *Self-organization in Nonequilibrium Systems*; Wiley Interscience: New York, 1977; (b) Haken, H. *Synergetics*; Springer-Verlag: New York, 1977; (c) Marro, J.; Dickman, R. *Nonequilibrium Phase Transitions in Lattice Models*; University Press: Cambridge, 1999; (d) Imbühl, R.; Ertl, G. *Chem. Rev.* **1995**, 95 (3), 697. doi:10.1021/cr00035a012.
- (2) Evans, J. W. *Langmuir* **1991**, 7 (11), 2514. doi:10.1021/la00059a020.

- (3) (a) Albano, E. V. *Heterog. Chem. Rev.* **1996**, 3 (4), 389. doi:10.1002/(SICI)1234-985X(199612)3:4<389::AID-HCR68>3.0.CO;2-2.; (b) Albano, E. V.; Borowko, M. *Computational Methods in Surface and Colloid Science*; Marcel Dekker: New York, 2000; Chap. 8, pp 387–437.
- (4) Zhdanov, V. P.; Kasemo, B. *Surf. Sci. Rep.* **1994**, 20 (3), 113. doi:10.1016/0167-5729(94)90009-4.
- (5) Yaldram, K.; Khan, M. A. *J. Catal.* **1991**, 131 (2), 369. doi:10.1016/0021-9517(91)90271-5.
- (6) Brosilow, B. J.; Ziff, R. M. *J. Catal.* **1992**, 136 (1), 275. doi:10.1016/0021-9517(92)90130-A.
- (7) Meng, B.; Weinberg, W. H.; Evans, J. W. *Phys. Rev. E Stat. Phys. Plasmas Fluids Relat. Interdiscip. Topics* **1993**, 48 (5), 3577. PMID:9961015.
- (8) Cortés, J.; Valencia, E. *Phys. Rev. E Stat. Nonlin. Soft Matter Phys.* **2003**, 68 (1 Pt 2), o. 016111. PMID:12935204.
- (9) Dickman, R. *Phys. Rev. A* **1986**, 34 (5), 4246. doi:10.1103/PhysRevA.34.4246. PMID:9897772.
- (10) Cortés, J.; Puschmann, H.; Valencia, E. *J. Chem. Phys.* **1996**, 105 (14), 6026. doi:10.1063/1.472438.
- (11) Cortés, J.; Puschmann, H.; Valencia, E. *J. Chem. Phys.* **1998**, 109 (14), 6086. doi:10.1063/1.477235.
- (12) Dickman, A. G.; Grandi, B. C.; Figueiredo, W.; Dickman, R. *Phys. Rev. E Stat. Phys. Plasmas Fluids Relat. Interdiscip. Topics* **1999**, 59 (6), 6361. PMID:11969621.
- (13) (a) Valencia, E.; Cortés, J. *Surf. Sci.* **2000**, 470 (1-2), L109. doi:10.1016/S0039-6028(00)00859-1.; (b) Cortés, J.; Valencia, E. *Physica A* **2002**, 309 (1-2), 26. doi:10.1016/S0378-4371(02)00610-6.; (c) Cortés, J.; Valencia, E. *J. Phys. Chem. B* **2004**, 108, 2979. doi:10.1021/jp030803j.
- (14) Cortés, J.; Valencia, E.; Herrera, J.; Araya, P. *J. Phys. Chem. C* **2007**, 111, 7063. doi:10.1021/jp070697b.
- (15) (a) Cortés, J. *J. Chem. Phys.* **1989**, 91 (3), 1932. doi:10.1063/1.457099.; (b) Cortés, J. *Surf. Sci.* **1989**, 218 (1), L461. doi:10.1016/0039-6028(89)90615-8.; (c) Cortés, J.; Araya, P. *J. Coll. Inter. Sci.* **1987**, 115 (1), 271. doi:10.1016/0021-9797(87)90033-6.; (d) Cortés, J.; Araya, P. *J. Chem. Phys.* **1991**, 95 (10), 7741. doi:10.1063/1.461347.; (e) Rudzinski, W.; Everett, D. H. *Adsorption of Gases on Heterogeneous Surfaces*; Academic Press: London, 1992.
- (16) Cortés, J.; Narváez, A.; Puschmann, H.; Valencia, E. *Chem. Phys.* **2003**, 288 (1), 77. doi:10.1016/S0301-0104(02)01052-2.
- (17) (a) Zhdanov, V. P. *Phys. Rev. B* **2001**, 64 (19), o. 193406. doi:10.1103/PhysRevB.64.193406.; (b) Zhdanov, V. P.; Kasemo, B. *Surf. Sci.* **1998**, 405 (1), 27. doi:10.1016/S0039-6028(97)01078-9.
- (18) Zhdanov, V. P.; Kasemo, B. *Catal. Lett.* **2002**, 81 (3/4), 141. doi:10.1023/A:1016525022453.
- (19) Olsson, L.; Zhdanov, V. P.; Kasemo, B. *Surf. Sci.* **2003**, 529 (3), 338. doi:10.1016/S0039-6028(03)00275-9.
- (20) (a) Ge, Q. F.; Kose, R.; King, D. A. *Adv. Catal.* **2000**, 45, 207. doi:10.1016/S0360-0564(02)45015-8.; (b) Nørskov, J. K.; Bligaard, T.; Logadottir, A.; Bahn, S.; Hansen, L. B.; Bollinger, M.; Bengaard, H.; Hammaer, B.; Sljivancanin, Z.; Mavrikakis, M.; Xu, Y.; Dahl, S.; Jacobsen, C. J. H. *J. Catal.* **2002**, 209 (2), 275. doi:10.1006/jcat.2002.3615.
- (21) Cortés, J.; Valencia, E. *Can. J. Chem.* **2009**, 87 (4), 571. doi:10.1139/V09-016.
- (22) Holles, J. H.; Switzer, M. A.; Davis, R. J. *J. Catal.* **2000**, 190 (2), 247. doi:10.1006/jcat.1999.2780.
- (23) (a) Taylor, K. C. *Catal. Rev., Sci. Eng.* **1993**, 35, 457; doi:10.1080/01614949308013915.(b) Shelef, M.; Graham, G. *Catal. Rev., Sci. Eng.* **1994**, 36 (3), 433. doi:10.1080/

- 01614949408009468.; (c) Nieuwenhuys, B. E. *Adv. Catal.* **1999**, *44*, 259. doi:10.1016/S0360-0564(08)60514-3.; (d) Zhdanov, V. P.; Kasemo, B. *Surf. Sci. Rep.* **1997**, *29* (2), 31. doi:10.1016/S0167-5729(97)00009-5.
- (24) Hecker, W. C.; Bell, A. T. *J. Catal.* **1983**, *84* (1), 200. doi:10.1016/0021-9517(83)90098-2.
- (25) (a) Oh, S. H.; Fisher, G. B.; Carpenter, J. E.; Wayne, D. J. *J. Catal.* **1986**, *100* (2), 360. doi:10.1016/0021-9517(86)90103-X.; (b) Oh, S. H.; Eickel, C. C. *J. Catal.* **1991**, *128* (2), 526. doi:10.1016/0021-9517(91)90310-Z.
- (26) (a) Cho, B. K. *J. Catal.* **1992**, *138* (1), 255. doi:10.1016/0021-9517(92)90021-9.; (b) Cho, B. K. *J. Catal.* **1994**, *148* (2), 697. doi:10.1006/jcat.1994.1256.
- (27) Chuang, S. S. C.; Tan, C.-D. *J. Catal.* **1998**, *173* (1), 95. doi:10.1006/jcat.1997.1922.
- (28) Peden, C.; Belton, D.; Schmieg, S. J. *J. Catal.* **1995**, *155* (2), 204. doi:10.1006/jcat.1995.1204.
- (29) (a) Permana, H.; Ng, K. Y. S.; Peden, C. H. F.; Schmieg, S. J.; Belton, D. N. *J. Phys. Chem.* **1995**, *99* (44), 16344. doi:10.1021/j100044a022.; (b) Permana, H.; Simon, K.; Peden, C.; Schmieg, S. J.; Lambert, D. K.; Belton, D. J. *J. Catal.* **1996**, *164* (1), 194. doi:10.1006/jcat.1996.0375.
- (30) Cortés, J.; Valencia, E. *J. Phys. Chem. B* **2004**, *108* (9), 2979. doi:10.1021/jp030803j.
- (31) (a) Zaera, F.; Gopinath, Ch. S. *J. Chem. Phys.* **1999**, *111* (17), 8088. doi:10.1063/1.480142.; (b) Zaera, F.; Gopinath, Ch. S. *Chem. Phys. Lett.* **2000**, *332* (3-4), 209. doi:10.1016/S0009-2614(00)01247-1.; (c) Zaera, F.; Gopinath, Ch. S. *J. Chem. Phys.* **2002**, *116* (3), 1128. doi:10.1063/1.1426381.
- (32) Nakao, K.; Ito, S.; Tomishige, K.; Kunimori, K. *J. Phys. Chem. B* **2005**, *109* (37), 17579. doi:10.1021/jp052895d. PMID:16853249.
- (33) Prévot, G.; Meerson, O.; Piccolo, L.; Henry, C. R. *J. Phys. Condens. Matter* **2002**, *14* (16), 4251. doi:10.1088/0953-8984/14/16/315.
- (34) Hammer, B. *J. Catal.* **2001**, *199* (2), 171. doi:10.1006/jcat.2000.3147.
- (35) Barth, J. V. *Surf. Sci. Rep.* **2000**, *40* (3-5), 75. doi:10.1016/S0167-5729(00)00002-9.
- (36) Michaelides, A.; Liu, Z. P.; Zhang, C. J.; Alavi, A.; King, D. A.; Hu, P. *J. Am. Chem. Soc.* **2003**, *125* (13), 3704. doi:10.1021/ja027366r. PMID:12656593.
- (37) Loffreda, D.; Simon, D.; Sautet, P. *J. Chem. Phys.* **1998**, *108* (15), 6447. doi:10.1063/1.476051.

## Appendix A. Analytical solution of the reaction model used in the paper

In a manner similar to the development shown in one of our previous papers,<sup>14,30</sup> we will derive the equations used in this paper for the mechanism of Scheme 1. Since it is assumed that the CO<sub>(a)</sub> and NO<sub>(a)</sub> adsorbates are in equilibrium with the gas phase, it is possible to write the relations:

$$[A1] \quad \frac{k_1}{k_2} = K_{\text{CO}} = \frac{\theta_{\text{CO}}}{\theta_s P_{\text{CO}}}, \quad \frac{k_3}{k_4} = K_{\text{NO}} = \frac{\theta_{\text{NO}}}{\theta_s P_{\text{NO}}}$$

where the equilibrium constants are expressed as functions of the coverages  $\theta_{\text{CO}}$  and  $\theta_{\text{NO}}$ , and the partial pressures  $P_{\text{CO}}$  and  $P_{\text{NO}}$  of the gas phase, and  $\theta_s$  represents the coverage of the vacant surface sites. The procedure used consists in expressing the coverages  $\theta_i$  as functions of  $\theta_{\text{CO}}$ , for which, if we define

$$[A2] \quad A = \frac{P_{\text{NO}} K_{\text{NO}}}{P_{\text{CO}} K_{\text{CO}}}$$

$$[A3] \quad B = \frac{1}{P_{\text{CO}} K_{\text{CO}}}$$

it is possible to write the relations:

$$[A4] \quad \theta_{\text{NO}} = A\theta_{\text{CO}} \quad \theta_s = B\theta_{\text{CO}}$$

The following conservation equations can be written, where the first two represent the steady state for the surface species N<sub>(a)</sub> and O<sub>(a)</sub> ( $\frac{d\theta_N}{dt} = 0$  and  $\frac{d\theta_O}{dt} = 0$ ):

$$[A5] \quad k_5\theta_{\text{NO}}\theta_s - 2k_6\theta_N^2 - k_8\theta_{\text{NO}}\theta_N = 0$$

$$[A6] \quad k_5\theta_{\text{NO}}\theta_s - k_7\theta_{\text{CO}}\theta_O = 0$$

$$[A7] \quad \theta_s + \theta_{\text{CO}} + \theta_{\text{NO}} + \theta_N + \theta_O = 1$$

If we define the relations

$$[A8] \quad C = (-k_8A + ((k_8A)^2 + 8k_5k_6AB)^{1/2})/4k_6$$

$$[A9] \quad D = k_5AB/k_7$$

it is possible to write

$$[A10] \quad \theta_N = C\theta_{\text{CO}} \quad \theta_O = D\theta_{\text{CO}}$$

so that from eq. [A7] we have

$$[A11] \quad \theta_{\text{CO}} = 1/(1 + A + B + C + D)$$

Therefore, the productions  $R_i$  are the following:

$$[A12] \quad R_{\text{CO}_2} = k_7\theta_{\text{CO}}\theta_O \quad R_{\text{N}_2} = k_6\theta_N^2 \quad R_{\text{N}_2\text{O}} = k_8\theta_{\text{NO}}\theta_N$$

and the selectivity SE for the nitrogen is defined by

$$[A13] \quad \text{SE} = R_{\text{N}_2}/(R_{\text{N}_2} + R_{\text{N}_2\text{O}})$$



# Determining the maximum environmental release limit of the toxic dye, CHPD

Vimal K. Balakrishnan and Virginia Palabrica

**Abstract:** The *Canadian Environmental Protection Act, 1999* (CEPA, 1999) requires the Canadian government to categorize all substances on the Domestic Substances List (DSL). Under the Chemicals Management Plan, the Government of Canada addresses chemicals that had not previously undergone rigorous scientific assessment. One such compound, [[4-[[2-(4-cyclohexylphenoxy)ethyl]ethylamino]-2-methylphenyl]methylene]-, propanedinitrile, commonly known as CHPD (cyclohexylphenoxydinitrile), recently underwent a screening assessment and was declared to be “toxic” to the environment. As a result, the Government of Canada ordered the “virtual elimination” of CHPD from the environment. Thus, CHPD may not be present above the lowest concentration that can be accurately measured using sensitive, but routine, analytical methods. We present a solid-phase extraction (SPE) method to determine CHPD in water and wastewater effluent to establish the maximum environmental release limit for this toxic compound. Optimal extraction was attained using an ENVI-18 cartridge. Extracts were analyzed by HPLC–PDA and HPLC–MS/MS techniques; in both matrices, the PDA method had greater sensitivity, less susceptibility to matrix effects, lower limit of quantitation (LOQ) values, and could be successfully validated at multiple spike levels. The lowest concentration of CHPD that could accurately be measured was found to be 108 ng/L in extracts of pure water, using the HPLC–PDA system. Therefore, this value (108 ng/L) will inform regulations on the maximum environmental release limit for CHPD.

**Key words:** cyclohexylphenoxydinitrile (CHPD), dye, solid-phase extraction (SPE), HPLC–PDA, HPLC–MS, virtual elimination, maximum environmental release limit, Chemical Management Plan.

**Résumé :** La loi canadienne sur la protection de l'environnement (1999) [LCPE (1999)] mandate le gouvernement canadien, par le biais de son ministre de l'environnement, d'établir un registre de toutes les substances sur la liste des substances domestiques (LI et LE, liste intérieure et liste extérieure). Dans le cadre du plan de gestion des produits chimiques, le gouvernement du Canada examine les produits chimiques qui n'ont pas subi antérieurement d'évaluation scientifique rigoureuse. Un de ces produits, le [[4-[[2-(4-cyclohexylphénoxy)éthyl]éthylamino]-2-méthylphényl]méthylène]propanedinitrile, communément connu par l'abréviation « CHPD » (« cyclohexylphénoxydinitrile ») a récemment été soumis à une évaluation de criblage et, par la suite, il a été déclaré toxique pour l'environnement. En conséquence, le gouvernement du Canada a ordonné l'élimination virtuelle du CHPD de l'environnement. Le CHPD ne peut donc plus maintenant être présent dans l'environnement au-delà de la concentration la plus faible pouvant être mesurée à l'aide de méthodes analytiques sensibles, mais de routine. Dans ce travail on présente une méthode par extraction en phase solide (EPS) qui permet de déterminer le CHPD dans l'eau et dans les effluents d'eaux usées dans le but d'établir la limite environnementale maximale pour l'émission de ce produit toxique. L'extraction optimale est obtenue en utilisant une cartouche ENVU-18. Les extraits ont été analysés par des techniques de chromatographie liquide haute performance (CLHP) avec détecteur à barrette à photodiodes ou avec détecteur à SM/SM; dans les deux types de matrices, la méthode aux BPD présente la plus grande sensibilité, le moins de susceptibilité aux effets de matrice, les valeurs les plus faibles de la limite de quantification (LDQ) et elle pu être validée avec succès à de multiples niveaux d'ensemencement. Dans système CLHP–BPD, on a trouvé que pour des extraits dans de l'eau pure, la quantité la plus faible de CHPD qui peut être mesurée est égale à 108 ng/L. En conséquence, cette valeur (108 ng/L) sera utilisée dans les règlements sur la limite d'émission maximale de CHPD dans l'environnement.

**Mots-clés :** cyclohexylphénoxydinitrile (« CHPD »), colorant, extraction en phase solide (« EPS »), chromatographie liquide avec détecteur à barrette à photodiodes (« CL–BPD »), chromatographie liquide avec détecteur à SM/SM (« CL–SM/SM »), élimination virtuelle, limite d'émission maximale dans l'environnement, Plan de Gestion des Produits Chimiques.

[Traduit par la Rédaction]

Received 24 October 2009. Accepted 19 November 2009. Published on the NRC Research Press Web site at canjchem.nrc.ca on 12 March 2010.

**V.K. Balakrishnan<sup>1</sup> and V. Palabrica.** Aquatic Ecosystems Protection Research Division, Water Science and Technology Directorate, Environment Canada, 867 Lakeshore Road, Burlington, ON L7R 4A6, Canada.

<sup>1</sup>Corresponding author (e-mail: vimal.balakrishnan@ec.gc.ca).

## Introduction

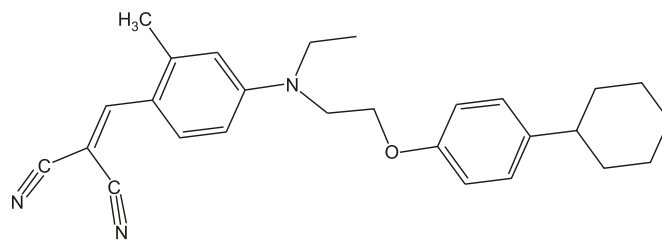
Synthetic dyes are extensively used in many fields, including textile industries,<sup>1</sup> leather tanning,<sup>2</sup> paper production,<sup>3</sup> food colouring,<sup>4</sup> and in personal care products<sup>5</sup> (e.g., hair colour, deodorant, and so forth). Furthermore, dyes are used in various engineering and scientific endeavours such as tracers for groundwater,<sup>6</sup> light-harvesting arrays<sup>7</sup> and photoelectrochemical cells.<sup>8</sup> Synthetic dyes exhibit considerable structural diversity, and their release into the environment is both a cause for public concern, and a serious challenge for environmental scientists. Because of their commercial importance, the impact and toxicity of dyes that are released into the environment must be carefully studied.

Many studies<sup>9–12</sup> have shown that dyes and pigments possess significant toxicity and are thus capable of having an impact on the environment. For example, the dye Direct Blue 14 has been shown to form a carcinogenic amine upon exposure to human skin bacteria,<sup>13</sup> while Oros et al.<sup>14</sup> found that 13 diazobenzene dyes had significant antifungal activity. In the course of manufacturing dyes, precursor compounds are often carried over into the final product<sup>15</sup> resulting in a complex mixture containing the dye itself and several other structurally similar compounds. Furthermore, many dyes (e.g., benzidine dyes) have been shown to undergo reduction in natural waterways, with degradation products that include amines, some of which are known carcinogens.<sup>16</sup> These precursors, intermediates, and degradation products are likely hazards due to their potential toxicity and (or) carcinogenicity, and thus knowledge of their environmental fate is of major interest from a risk assessment and risk management perspective. Adding to the complexity of managing the risks associated with environmental exposures to dyes and pigments is the fact that traditional wastewater treatment technologies have proven to be markedly ineffective for handling wastewater from dye manufacturing facilities.<sup>17</sup> Taken together, these findings highlight the importance of more fully evaluating the many dyes and pigments currently in commercial use.

In Canada, the *Canadian Environmental Protection Act, 1999* (CEPA, 1999) requires the Canadian government (through the federal Ministries of Health and Environment) to categorize all substances on the Domestic Substances List (DSL). Further to this activity, the CEPA requires that screening assessments be conducted for substances to determine whether these substances meet the definition of “toxic”, as set out in section 64 of CEPA, 1999. Under the Chemicals Management Plan (CMP), the Government of Canada plans to address legacy chemicals that had not previously undergone rigorous scientific assessment. As part of this plan, the Government of Canada challenged industry and other stakeholders (academics and nongovernmental organizations) to provide information on 193 priority chemical substances and how they are currently used in Canada. The information thus obtained under the CMP would thus facilitate a draft screening assessment under CEPA.

The substance, [[4-[[2-(4-cyclohexylphenoxy)ethyl]ethylamino]-2-methylphenyl]methylene]-, propanedinitrile, more commonly known as CHPD (cyclohexylphenoxydinitrile), was included in Batch 1 of the Challenge under the Chemicals Management Plan. CHPD (Fig. 1) is used as a colorant

**Fig. 1.** Chemical structure of [[4-[[2-(4-cyclohexylphenoxy)ethyl]ethylamino]-2-methylphenyl]methylene]-, propanedinitrile, more commonly known as cyclohexylphenoxydinitrile (CHPD).



in food packaging materials and is not naturally produced in the environment. The initial screening assessment report indicated that “CHPD entered or may be entering the environment in a quantity or a concentration or under conditions that have or may have an immediate or long-term harmful effect on the environment or its biological diversity.”<sup>18</sup> The final report concluded that CHPD met the criteria for persistence and bioaccumulation, and therefore, CHPD was declared a toxic substance.

Given the declaration of toxicity, the Government of Canada declared the ultimate environmental objective for CHPD to be virtual elimination (VE) as specified under subsections 65 and 77(4) of CEPA, 1999. Substances targeted for VE must be added to the Virtual Elimination List along with their level of quantification (LoQ). The LoQ is the lowest concentration that can be accurately measured using sensitive but routine sampling and analytical methods.

Since dyes are thermally unstable and nonvolatile; they are not readily amenable to analysis by GC.<sup>15</sup> Consequently, HPLC methods are typically used for measurements of dyes. The US Environmental Protection Agency (EPA) has validated a method<sup>19</sup> for a variety of azo- and anthra-quinone dyes, based on LC with UV or MS detection. Prior to analysis, samples are extracted using liquid–liquid extraction (LLE) with dichloromethane. However, given that LLE requires high volumes of organic solvent, much research has focused on developing less solvent-intensive alternatives, and applying those alternatives to environmentally relevant matrices.

One extraction technique that resolves problems in the determination of dyes is solid-phase extraction (SPE). For example, Brumley and Brownrigg<sup>20</sup> extracted a mixture of aromatic organic acids containing the sulfonated dyes Trip-tan Blue and Orange II followed by analysis using micellar electrokinetic chromatography, and obtained good recoveries of both from aqueous samples. Meanwhile, Franke et al.<sup>21</sup> applied SPE (using C-18 material) followed by HPLC–fluorescence analysis for the determination of the fluorescent tracers Uranine and Sulphorhodamine B in groundwater, with good recoveries (>80%), coefficients of variance (<20%), and low limits of detection (~300 ng/L). Similarly, SPE coupled to HPLC–FLD techniques were used for the determination of Rhodamine from surface waters.<sup>22</sup> The SPE methodologies used in these studies yielded good recoveries and detection limits in the environmentally relevant part-per-trillion range. Indeed, the robustness of SPE techniques was demonstrated by Mitrowska et al.,<sup>23</sup> who applied SPE (using SCX cartridges) as a clean-up and preconcentration step in

the extraction of malachite green and leucomalachite green from carp muscle.

To the best of our knowledge, no method exists for the determination of CHPD in environmental matrices. In this study, we report on the development and validation of the first solid-phase extraction technique for CHPD determination and we compare the performance of HPLC–PDA and tandem HPLC–MS instruments. Extractions were performed in pure (deionized) water and in wastewater effluent obtained from a water treatment plant in Burlington, ON. The limit of quantitation (LOQ) obtained as a result of this work will be used to establish the maximum environmental release limit for the virtual elimination of CHPD, as mandated under CEPA, 1999.

## Experimental

### Materials

[[4-[[2-(4-Cyclohexylphenoxy)ethyl]ethylamino]-2-methylphenyl]methylene]-, propanedinitrile (CHPD) was purchased (under the trade name Yellow 6G Gran) from Octochem Inc. (St. Louis, IL, lot number: CHSE55902, purity > 95%). A stock solution containing CHPD at a concentration of 100 mg/L was prepared in methanol (MeOH). Standard solutions were prepared by diluting the stock solution with MeOH.

Acetonitrile (CH<sub>3</sub>CN, HPLC grade) and methanol (MeOH, HPLC grade) were purchased from Caledon Laboratories (Georgetown, ON), while deionized water was obtained using a Milli-Q (Millipore) system.

Isotopically labelled <sup>13</sup>C<sub>3</sub>-caffeine was purchased from Cambridge Isotope Laboratories (Cambridge, MA).

### Solid-phase extraction procedures

Solid-phase extractions were performed at room temperature. Three sorbent phases were evaluated: OASIS MCX cartridges (6 mL; Waters Corporation, Milford, MA), STRATA-X cartridges (3 mL; Phenomenex, Torrance, CA), and ENVI-18 cartridges (6 mL, Supelco, Oakville, ON). Since wastewater contains undissolved organic matter, a sample clean-up step (filtration) was incorporated into our method and applied to wastewater samples and to our standard solutions.

The general SPE method used throughout this work was as follows. SPE cartridges were conditioned by passing the following sequence of solutions: methanol (MeOH, 5 mL), H<sub>2</sub>O (10 mL), MeOH/5% NaOH, and H<sub>2</sub>O adjusted to pH 3 (using H<sub>2</sub>SO<sub>4</sub>). Solutions (1 L) were filtered through a 3 cm bed of Celite 545 (Fisher Scientific) on a 1.2 µm GFC filter (VWR Scientific) after which the filtrate was passed through a 0.45 µm Metrical filter (VWR Scientific). The final filtrate was adjusted to pH 3 using concentrated HCl and loaded onto the SPE cartridge, which was then washed with 0.1 N HCl (4 mL). The SPE cartridge was eluted using 15 mL MeOH, a volume that was found to ensure that the CHPD was fully extracted from the sorbent phase (data not shown). The resulting eluate was evaporated under a stream of nitrogen to a final volume of 1 mL.

### Sample collection

Samples of wastewater effluent were collected from a

water treatment plant located in Burlington, ON. All samples were stored at 4 °C in 4 L amber glass bottles, spiked with the appropriate quantity of CHPD, and extracted within 3 d (vide supra). Upon extraction, samples were immediately analyzed as described below.

### Analytical methods

For comparison purposes, all samples were analyzed using two instruments. The first was an HPLC (Agilent LC1100), equipped with a PDA detector set at 423 nm, using a Phenomenex Ultracarb C-18 column (ODS 30, 150 mm × 4.6 mm ID × 5 µm) at 30 °C into which were injected 10 µL sample aliquots. Water (A) and acetonitrile (B) were used as mobile phase solvents for gradient elution at a flow rate of 0.5 mL/min. The gradient was increased from 75% B to 95% B within 1 min, held at 95% B for 10 min, and then immediately returned to the initial conditions (75% B) for the final 14 min of the run, giving a total run time of 25 min.

The second instrument used was a Quattro Ultima tandem LC triple quadrupole mass spectrometer (Micromass, Manchester, UK) equipped with a Z-Spray electrospray ionization (ESI) source and operated in the positive-ion mode. Nitrogen was used as the drying and nebulizing gas at flow rates of 500 and 70 L/h, respectively. Collision induced dissociations were conducted using  $2.5 \times 10^{-3}$  mbar Argon in a hexapole collision cell. MassLynx software (v. 4.1) (Waters Corporation: Milford, MA, 2005) was utilized for both data acquisition and processing. The MS was operated in multiple reaction monitoring (MRM) mode, with a dwell time of 100 ms per ion pair and an interchannel delay of 50 ms. For CHPD, at a cone voltage of 20 kV and collision energy of 15 eV, the precursor ion was found at  $m/z$  414.3, with product ions formed at  $m/z$  of 238.1 (quantitation) and 332.2 (confirmation). The source temperature was set to 120 °C, while that for desolvation was set to 350 °C. The MS apparatus was attached to an Acquity HPLC system (Waters, Milford, MA). Aliquots (10 µL) were injected onto a Phenomenex Ultracarb C-18 column (ODS 30, 150 mm × 4.6 mm ID × 5 µm) at 30 °C. Water (A) and acetonitrile (B) were used as mobile phase solvents for gradient elution at a flow rate of 0.5 mL/min, following the same elution profile as used for the HPLC–PDA runs.

Prior to sample injection, <sup>13</sup>C-labeled caffeine (50 mg/L, prepared in MeOH) was added as an internal standard, such that the final concentration of <sup>13</sup>C-labeled caffeine in all samples was 500 µg/L. MS responses presented throughout this work are normalized against <sup>13</sup>C-labeled caffeine, which had a precursor ion at  $m/z$  = 198.0 and a product ion at  $m/z$  140.0 (at a cone voltage of 30 kV and collision energy of 20 eV).

## Results and discussion

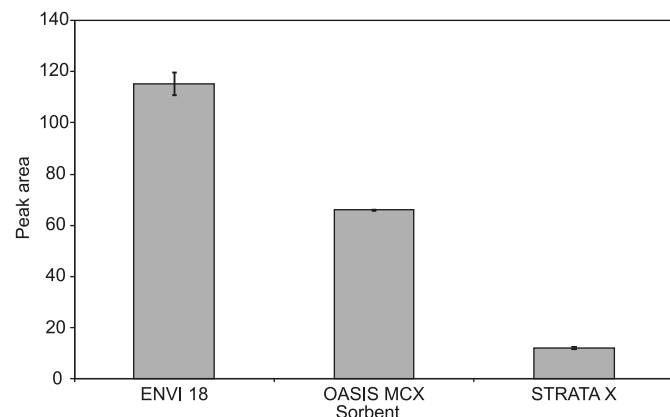
### Development of SPE method

Given that CHPD is a dye with an absorbance maximum at 423 nm, the initial method development was performed using the Agilent HPLC (PDA detector). Once SPE parameters were optimized, method performance samples were analyzed using both the PDA detector and the MS detector.

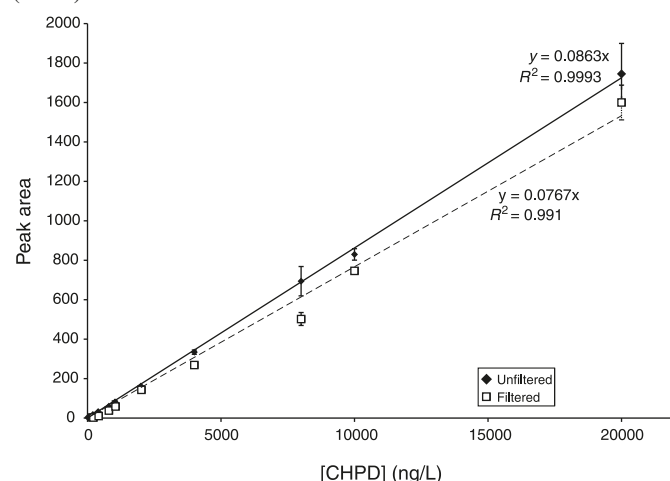
In SPE, arguably the most important systemic parameter



**Fig. 2.** Sorbent performance for the solid-phase extraction of a 1 L solution of CHPD at a concentration of 20  $\mu\text{g/L}$ , as determined using the PDA detector. Error bars denote the standard deviation about the mean response ( $n = 3$ ).



**Fig. 3.** The impact of filtering aqueous solutions of CHPD through Celite and 0.45  $\mu\text{m}$  filters, as determined using the PDA detector. Error bars denote the standard deviation about the mean response ( $n = 3$ ).



consists of the nature of the sorbent phase onto which the analyte of interest will be extracted. In this work, three sorbent phases were evaluated: ENVI-18 cartridges (reverse phase C-18 that has been polymerically linked to silica); OASIS MCX cartridges (a mixed mode sorbent composed of sulfonate groups, nominally 1 mequiv./g, on polydivinylbenzene-polyvinylpyrrolidone copolymers); and STRATA-X cartridges (a reverse phase polymeric sorbent designed for both polar and nonpolar compounds). When a 1 L aqueous sample of CHPD (20  $\mu\text{g/L}$ ) was passed through each of the sorbents, no evidence of breakthrough was observed. The relative extractability of the 20  $\mu\text{g/L}$  CHPD solution using each of these three sorbent phases is presented in Fig. 2, and was found to proceed as ENVI-18 > OASIS MCX >> STRATA-X. Accordingly, ENVI-18 cartridges were used for all subsequent SPE experiments presented in this work.

Since wastewater contains undissolved organic matter, and that SPE is not, by itself, considered a “clean-up” technique, we deemed it necessary to incorporate a sample clean-up step (filtration) into our method. Briefly, a solution

of CHPD was filtered through a 3 cm bed of Celite 545 on a 1.2  $\mu\text{m}$  GFC filter, after which the filtrate was passed through a 0.45  $\mu\text{m}$  Metrical filter. While the resulting calibration curves (Fig. 3) both had good linearity ( $R^2 > 0.99$ ), it is worth noting that the sensitivity (slope) of the filtered solutions (slope =  $(7.67 \pm 0.21) \times 10^{-2}$ ) was approximately 11% less than that of the unfiltered solutions (slope =  $(8.63 \pm 0.06) \times 10^{-2}$ ). Although small, the observed difference in sensitivity was found to be statistically significant at the 95% confidence interval, indicating that CHPD is somewhat retained by the filter material. Since unfiltered samples are unacceptable for injection into an HPLC column, the method calibration curve must include not only the solid-phase extraction, but also the sample filtration step to correct for the impact of the filter material.

## Method performance

### Calibration curves

In evaluating the SPE method performance, CHPD solutions were filtered through a 3 cm bed of Celite 545 on a 1.2  $\mu\text{m}$  GFC filter after which the filtrate was passed through a 0.45  $\mu\text{m}$  Metrical filter. Thereafter, the filtrate was passed through an ENVI-18 SPE cartridge, and eluted using methanol. A calibration curve was prepared in both deionized water and wastewater effluent containing CHPD at concentrations ranging between the 10 ng/L and 10 000 ng/L. For comparative purposes, extracts were analyzed using both PDA and MS detectors. Water and effluent blanks produced no signals in either detector that coeluted or, in the case of the MS detector, created “cross-talk” with the target analyte. The calibration curves resulting from triplicate measurements are provided in Figs. 4 and 5, and the corresponding figures of merit are given in Table 1.

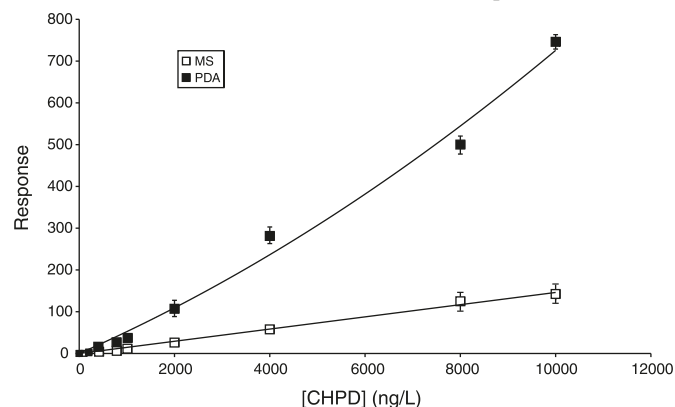
In general, the PDA response to CHPD in both deionized water and wastewater effluent adhered to a quadratic equation, while the MS detector produced a linear response throughout the entire calibration range. In all cases, coefficients of determination ( $R^2$ ) were found to exceed 0.99, denoting a strong correlation between experimental measurements and the fitted expressions.

In deionized water, it is readily apparent that the PDA detector provides a more sensitive response to CHPD than does the MS detector (Fig. 4). This is not surprising given that CHPD is a dye with a strongly absorbing chromophore. However, in wastewater effluent (Fig. 5), the sensitivity of the PDA detector towards CHPD decreased while the sensitivity of the MS detector increased (as evidenced by the slopes provided in Table 1). We attribute this dichotomous behaviour to matrix effects: for the PDA detector, the presence of other absorbing compounds in the effluent led to a higher background noise that resulted in the decreased sensitivity towards the target analyte; meanwhile, for the MS detector, the presence of effluent resulted in a matrix enhancement of CHPD.

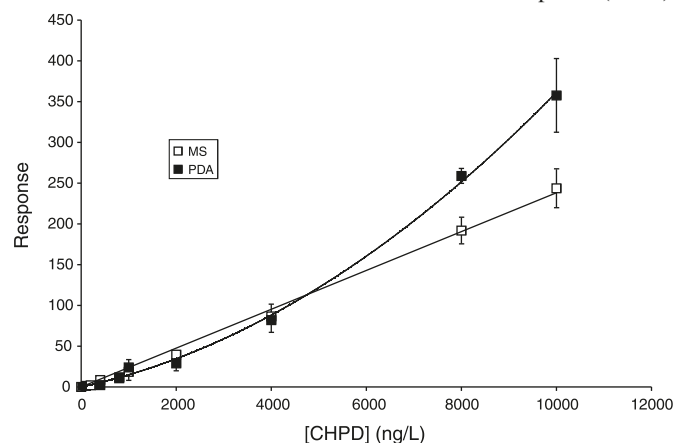
The matrix in which analytes are found is known to exert a powerful effect on electrospray MS by altering the extent to which the analytes of interest are ionized.<sup>24,25</sup> We suggest here that acid–base interactions between CHPD and the humic or fulvic acids normally found in the wastewater effluent enhanced CHPD ionization. Since analyte peak areas in



**Fig. 4.** Method calibration curves for the determination of CHPD in deionized water using both MS and PDA detectors. The response axis represents either the peak area at 423 nm in the case of PDA detection or an area corrected against  $^{13}\text{C}$ -labelled caffeine (500 ng/L) in those instances where an MS detector was used. Error bars denote the standard deviation about the mean response ( $n = 3$ ).



**Fig. 5.** Method calibration curves for the determination of CHPD in wastewater effluent using both MS and PDA detectors. The response axis represents either the peak area at 423 nm in the case of PDA detection or an area corrected against  $^{13}\text{C}$ -labelled caffeine (500 ng/L) in those instances where an MS detector was used. Error bars denote the standard deviation about the mean response ( $n = 3$ ).



electrospray mass spectroscopy are highly variable from one run to another, good laboratory practice dictates that each analyte peak be normalized against an internal standard of a known, constant concentration. Although matrix effects in MS are thought to be largely corrected by dilution using isotopically labelled analogues of the target analyte (i.e., CHPD) as an internal standard,<sup>26</sup> such a correction was not possible in this case given that isotopically labelled CHPD is not commercially available. Consequently, the fact that the selected internal standard ( $^{13}\text{C}_3$ -caffeine) interacts with the fulvic and humic acids in the effluent in a different manner than does CHPD means that the matrix effects will not be fully corrected, as is evident from the differing slopes obtained in deionized water and wastewater effluent (Figs. 4 and 5, Table 1). However, even in those instances where an isotopically labelled analogue of a target analyte is readily available as an internal standard, recent studies in our laboratory using various pharmaceuticals and personal care products

have shown that matrix effects cannot be entirely eliminated.<sup>27,28</sup> Therefore, we recommend that matrix matched calibration curves be employed to ensure the most accurate determination of CHPD in environmental samples.

#### Limits of detection and quantitation (LOD and LOQ)

Limit of detection (LOD) and limit of quantitation (LOQ) values (Table 1) were determined using both PDA and MS detectors by taking  $\text{LOD} = 3\sigma$  and  $\text{LOQ} = 10\sigma$ , where  $\sigma$  was the standard deviation about the mean of a measurement taken at a low CHPD concentration (i.e., where the CHPD concentration in the sample was no greater than ten times the LOD<sup>29</sup>). In deionized water, the measurement was performed at a CHPD concentration of 200 ng/L, whereas for wastewater effluent, the CHPD concentration was set at 500 ng/L.

In all cases, CHPD detection using the PDA detector yielded lower LOD and LOQ values. As expected, LOQ values were lower in deionized water than in wastewater effluent. Interestingly, the presence of wastewater had a greater impact on the MS detector than it did on the PDA detector. In fact, when using the MS detector, the LOQ in wastewater increased from that found for CHPD in pure water by 1160%, whereas the LOQ as determined using the PDA increased only 440%. While the increase in LOQ observed upon proceeding from deionized water to wastewater effluent can be attributed to the effect of a vastly more complicated matrix, the different extents by which the LOQ values increased suggests that the MS detector is more susceptible to matrix effects. In other words, even though CHPD in wastewater effluent is subject to *matrix enhancement* (i.e., increased sensitivity) when determined by MS and *matrix suppression* when determined by PDA (as shown by Figs. 4 and 5, and the slopes of the calibration curves (Table 1)), the MS detector had poorer LOQ results than did the PDA detector. Although this finding may seem counterintuitive, it appears that wastewater effluent enhances CHPD ionization in the MS detector (creating a matrix enhancement and increased sensitivity); the effluent itself is heterogeneous, producing a greater measure of imprecision, and hence, higher LOQs.

#### Method validation

The extraction method was validated at four different CHPD concentrations, in both deionized water and wastewater effluent. Once again, neither water nor effluent blanks produced any signals in either detector that coeluted or, in the case of the MS detector, created cross-talk with CHPD. CHPD was spiked such that the concentration in the sample was half the LOD, twice the LOD, five times greater than LOD, and 10 times greater than LOD. The LOD values used to calculate the spike levels for method validation were premised on the idea that establishing the lowest possible “maximum environmental release limit” and ensuring the virtual elimination of CHPD (as mandated under CEPA) would best be achieved by using the more sensitive PDA detector. Therefore, in deionized water, CHPD concentrations were spiked at 16.5, 66, 165, and 330 ng/L. Meanwhile, wastewater effluent was spiked at 87.5, 350, 875, and 1750 ng/L.

When CHPD was present at a concentration lower than

**Table 1.** SPE method performance for the determination of CHPD in Milli-Q water and wastewater effluent using ENVI-18 cartridges and both PDA and MS detectors.

Matrix	Detector	Equation ( $y = f(X)$ ), where $X = [\text{CHPD}]$	$n$	$R^2$	LOD* (ng/L)	LOQ* (ng/L)
Water	PDA	$(2.24 \times 10^{-6})X^2 + (5.01 \times 10^{-2})X$	9	0.991	32.3	108
	MS	$0.0146X$	9	0.997	46.2	154
Effluent	PDA	$(2.35 \times 10^{-6})X^2 + (1.26 \times 10^{-2})X$	8	0.998	175	583
	MS	$0.0238X$	8	0.996	602	2005

\*For determinations of LOD and LOQ, measurements were taken using a low concentration CHPD standard ( $n = 8$ ).

**Table 2.** Accuracy and precision ( $n = 4$ ) of the SPE method to extract CHPD from pure water and from wastewater effluent.

Matrix	Detector	Spike level (ng/L)	Recovery (%)	CV <sup>a</sup>
Water	PDA	16.5	ND <sup>b</sup>	NA <sup>c</sup>
		66	100.3	19.9
		165	94.9	3.15
		330	99.3	12.1
	MS	16.5	ND	NA
		66	92.7	12.6
		165	94.6	9.60
		330	99.2	3.93
Effluent	PDA	87.5	ND	NA
		350	91.3	16.2
		875	115	10.4
		1750	82.4	1.82
	MS	87.5	82.4	62.8
		350	75.0	51.0
		875	100	23.5
		1750	78.2	15.46

<sup>a</sup>CV = coefficient of variance.

<sup>b</sup>ND = not determined.

<sup>c</sup>NA = not applicable.

the Limit of Detection, CHPD was not found in any matrix (Table 2), except when using MS detection on an extract of wastewater effluent spiked at 87.5 ng/L CHPD. However, the Coefficient of Variance (CV) in that instance was unacceptably high (62.8%). Above the LOD (in both matrices), CHPD recoveries generally exceeded 75%. In fact, aqueous spike recoveries were generally above 90% with both MS and PDA detection at all spike levels above LOD. Furthermore, the CVs obtained in the recovery of aqueous extracts using both MS and PDA detection was typically less than 15%. However, at a spike concentration of 66 ng/L, the coefficient of variance using the PDA detector was 19.9%. Given that 66 ng/L represents a concentration of only twice the LOD, this is an acceptable degree of variance. Indeed, the fact that the method could be validated at only twice the LOD demonstrates the robustness of the method, since 66 ng/L is actually below the LOQ. Therefore, with method accuracy exceeding 80% and CVs no greater than 20%, the method developed herein meets the criteria for successful validation in deionized water.<sup>30</sup>

In analyzing extracts of wastewater effluent using the MS detector, we were unable to validate the method at any spike level. At 350 ng/L, neither the recovery (75%) nor the CV (51%) were acceptable. Meanwhile, at 875 ng/L, the recovery (100%) was acceptable, but the CV (23.5%) proved to be too large. At the final spike level (1750 ng/L), the CV (15.5%) was acceptable, but the recovery (78.2%) was not.

We attribute the failure of the method validation using the MS detector to the fact that the spike levels used in wastewater were all below the LOQ established for MS analyses (2005 ng/L, Table 1). However, when we used the PDA detector at all spike levels above the LOD, errors in accuracy and the CV values were always less than 20%. Hence, we conclude that the SPE extraction method when coupled with detection using a PDA detector is successfully validated.

## Conclusions and environmental implications

Our research has resulted in the development of an SPE extraction technique for the dye CHPD. We compared two HPLC detectors for CHPD determination, and concluded that CHPD is better determined (both in deionized water and wastewater) via SPE extraction using ENVI-18 cartridges followed by analysis on an HPLC–PDA apparatus rather than using an HPLC–MS/MS instrument. The PDA method was found to be more sensitive and less susceptible to matrix effects than was the MS method. Moreover, only determination by PDA could be fully validated in both matrices. Most importantly, the PDA detector produced lower LOQ values than did the MS detector. Accordingly, the PDA detector was used in the recommendation of a maximum environmental release limit for CHPD.

It was readily apparent that the presence of wastewater effluent had a significant impact on method performance, and

thus, we anticipate that the method performance will be impacted in all environmental matrices in a manner unique to each matrix. However, since the method we developed was robust enough to be validated in a matrix as complex as wastewater effluent, it should be readily applicable to the simpler matrices found in natural waters. Even when using matrix matched calibration curves, environmental matrices will tend to suppress the determination of CHPD via a PDA detector by raising the level of background noise. Therefore, any environmental determination of the contaminant would necessarily be at a level that exceeds the limit of quantitation established in pure water. *Consequently, it is our recommendation that the virtual elimination of CHPD (as mandated under the Canadian Environmental Protection Act (1999) and under the auspices of the Chemical Management Plan) is best accomplished by using the LOQ value obtained in pure water with a PDA detector, thereby setting a maximum environmental release limit of 108 ng/L.*

## Acknowledgements

Funding for this research was provided under the Government of Canada's Chemical Management Plan (2006). We gratefully thank Mr. John Toito (Environment Canada) for his valuable technical assistance.

## References

- (1) Gupta, G. S.; Shukla, S. P.; Prasad, G.; Singh, V. N. *Environ. Technol.* **1992**, *13* (10), 925. doi:10.1080/09593339209385228.
- (2) Tunay, O.; Kabdasli, I.; Eremektar, G.; Orhon, D. *Water Sci. Technol.* **1996**, *34* (11), 9.
- (3) Ivanov, K.; Gruber, E.; Schempp, W.; Kirov, D. *Das Papier* **1996**, *50*, 456.
- (4) Bhat, R. V.; Mathur, P. *Curr. Sci.* **1998**, *74*, 198.
- (5) Scarpi, C.; Ninci, F.; Centini, M.; Anselmi, C. *J. Chromatogr. A* **1998**, *796* (2), 319. doi:10.1016/S0021-9673(97)01015-7. PMID:9540212.
- (6) Field, M. S.; Wilhelm, R. G.; Quinlan, J. F.; Aley, T. J. *Environ. Monit. Assess.* **1995**, *38* (1), 75. doi:10.1007/BF00547128.
- (7) (a) Wagner, R. W.; Lindsey, J. S. *Pure Appl. Chem.* **1996**, *68* (7), 1373. doi:10.1351/pac199668071373.; (b) Abdallah, D.; Whelan, J.; Dust, J. M.; Hoz, S.; Buncel, E. *J. Phys. Chem. A* **2009**, *113* (24), 6640. doi:10.1021/jp901596t. PMID:19456113.
- (8) Wróbel, D.; Boguta, A.; Ion, R. M. *J. Photochem. Photobiol. Chem.* **2001**, *138* (1), 7. doi:10.1016/S1010-6030(00)00377-4.
- (9) Guaratini, C. C. I.; Zanoni, M. V. B. *Quim. Nova* **2000**, *23* (1), 71. doi:10.1590/S0100-40422000000100013.
- (10) Walthall, W. K.; Stark, J. D. *Environ. Pollut.* **1999**, *104* (2), 207. doi:10.1016/S0269-7491(98)00189-4.
- (11) Tsuda, S.; Murakami, M.; Matsusaka, N.; Kano, K.; Taniguchi, K.; Sasaki, Y. F. *Toxicol. Sci.* **2001**, *61* (1), 92. doi:10.1093/toxsci/61.1.92. PMID:11294979.
- (12) Hunger, K. *Pitt. Vernici. Eur* **1995**, *71*, 30.
- (13) Platzeck, T.; Lang, C.; Grohmann, G.; Gi, U. S.; Baltes, W. *Hum. Exp. Toxicol.* **1999**, *18* (9), 552. doi:10.1191/096032799678845061. PMID:10523869.
- (14) Oros, G.; Cserhati, T.; Forgacs, E. *Fresenius Environ. Bull.* **2001**, *10*, 319.
- (15) Barcelo, D. Environmental Analysis of Dyes. In *Encyclopedia of Analytical Chemistry*; John Wiley and Sons: New York, 2006; p 1.
- (16) Rinde, E.; Troll, W. J. *J. Natl. Cancer Inst.* **1975**, *55* (1), 181. PMID:808635.
- (17) Forgacs, E.; Cserhádi, T.; Oros, G. *Environ. Int.* **2004**, *30* (7), 953. doi:10.1016/j.envint.2004.02.001. PMID:15196844.
- (18) Publication After Screening Assessment of a Substance (Propanedinitrile, [[4-[[2-(4-cyclohexylphenoxy)ethyl]ethylamino]-2-methylphenyl]methylene]- (CHPD), CAS No. 54079-53-7) Specified on the Domestic Substances List [subsection 77(1) of the Canadian Environmental Protection Act, 1999]. *Canada Gazette*, **2008**, *142* (3) <http://www.gazette.gc.ca/rp-pr/p1/2008-01-19/html/index-eng.html> (accessed September 26, 2009).
- (19) *Solvent Extractable Nonvolatile Compounds by HPLC/TS/MS or UV detection, US EPA Method 8321A*; US Environmental Protection Agency: Washington, DC, 1995; p 1.
- (20) Brumley, W. C.; Brownrigg, C. M. *J. Chromatogr. A* **1993**, *646* (2), 377. doi:10.1016/0021-9673(93)83351-R.
- (21) Franke, C.; Westerholm, H.; Niessner, R. *Water Res.* **1997**, *31* (10), 2633. doi:10.1016/S0043-1354(97)00111-5.
- (22) Hofstraat, J. W.; Steendijk, M.; Vriezekolk, G.; Schreurs, W.; Broer, J. A. A.; Wijnstok, N. *Water Res.* **1991**, *25* (7), 883. doi:10.1016/0043-1354(91)90169-Q.
- (23) Mitrowska, K.; Posyniak, A.; Zmudzki, J. *J. Chromatogr. A* **2005**, *1089* (1-2), 187. doi:10.1016/j.chroma.2005.07.004. PMID:16130786.
- (24) Annesley, T. M. *Clin. Chem.* **2003**, *49* (7), 1041. doi:10.1373/49.7.1041. PMID:12816898.
- (25) Lindberg, R.; Jarnheimer, P.-A.; Olsen, B.; Johansson, M.; Tysklind, M. *Chemosphere* **2004**, *57* (10), 1479. doi:10.1016/j.chemosphere.2004.09.015. PMID:15519392.
- (26) Chu, S.; Metcalfe, C. D. *J. Chromatogr. A* **2007**, *1164* (1-2), 212. doi:10.1016/j.chroma.2007.07.024. PMID:17692856.
- (27) Balakrishnan, V. K.; Terry, K. A.; Toito, J. M. *J. Chromatogr. A* **2006**, *1131* (1-2), 1. doi:10.1016/j.chroma.2006.07.011. PMID:16879830.
- (28) Dussault, E. B.; Balakrishnan, V. K.; Solomon, K. R.; Sibley, P. K. *Can. J. Chem.* **2009**, *87* (5), 662. doi:10.1139/V09-042.
- (29) *Tests Methods SW-846, Part 1: Quality Control*; Office of Solid Waste, US Environmental Protection Agency: Washington, DC, 1992; p 1.
- (30) Bansal, S.; DeStefano, A. *Am. Assoc. Pharm. Sci. J.* **2007**, *9* (1), E109. doi:10.1208/aapsj0901011.



## OBITUARY / NÉCROLOGIE



**Keith Fagnou**, 38, associate professor of chemistry at the University of Ottawa and a rising star in the field of organic chemistry, died suddenly on Nov. 11, 2009. Keith received a B.Ed. from the University of Saskatchewan in 1995. He then earned an M.S. in 2000 and a Ph.D. in synthetic organic chemistry in 2002, both from the University of Toronto under the tutelage of Professor Mark Lautens. Upon completing his degree, he joined the faculty of the University of Ottawa. In 2007, he was promoted to associate professor and appointed University of Ottawa Research Chair in the Development of Novel Catalytic Transformations.

Keith's research program focused on the development of new reactions via the direct functionalization of C–H bonds, and applied these methods to the synthesis of medicinal compounds and small bioactive products. His seminal contributions in the generation of C–C bonds, especially in biaryl compounds, without the need for substrate preactivation, dramatically changed the way chemists approach the generation of carbon-carbon bonds. The excellence of his pioneering work was recognized internationally. He was a gifted lecturer at the undergraduate and graduate levels, and was a sought-after speaker by academic and industry. He gave several named lectures and received numerous awards, including the 2003 Polanyi Prize (Ontario), Sloan Research fellowship, Cottrell Research Scholarship, the Premier's Research Excellence Award (Ontario), and several accolades from pharmaceutical companies (Amgen, AstraZeneca, Boehringer Ingelheim, Eli Lilly, Merck). This past summer, he received the Organometallic Chemistry Directed Towards Organic Synthesis Award, which is presented every two years to a scientist under 40 for outstanding research contributions. In November 2009, Keith posthumously received the Rutherford Memorial

**Keith Fagnou**, 38 ans, professeur agrégé à l'Université d'Ottawa et étoile montante du domaine de la chimie organique, est décédé subitement le 11 novembre 2009. Titulaire d'un B. Éd. de l'Université de la Saskatchewan (1995), Keith a poursuivi ses études supérieures à l'Université de Toronto où il a obtenu une maîtrise (2000) et un doctorat en chimie organique synthétique en 2002, sous la direction du professeur Mark Lautens. Par la suite, il s'est joint à la faculté de l'Université d'Ottawa. En 2007, il est nommé professeur agrégé et occupe la chaire de recherche de l'Université d'Ottawa sur le développement de nouvelles transformations catalytiques.

Dans le cadre de son programme de recherche, il s'attaquait principalement à l'élaboration de nouvelles réactions par la fonctionnalisation directe des liaisons C–H au profit de la synthèse de composés médicinaux et de substances bioactives. L'apport indéniable et majeur de ses travaux à la génération de liaisons C–C, surtout en ce qui a trait aux composés biaryliques, sans préactivation des substrats, a profondément changé la façon dont les chimistes génèrent des liaisons carbone-carbone. L'excellence de ses travaux avant-gardistes est d'ailleurs reconnue mondialement. Il était un enseignant doué, tant au premier cycle qu'aux cycles supérieurs, et un conférencier très sollicité par les milieux universitaire et industriel. En plus d'être invité d'honneur de plusieurs congrès et colloques, Keith a remporté de nombreux prix, y compris le prix Polanyi 2003 (Ontario), une bourse Sloan, une bourse Cottrell, la Bourse du premier ministre pour l'excellence en recherche (Ontario), ainsi que plusieurs éloges d'établissements pharmaceutiques (Amgen, AstraZeneca, Boehringer Ingelheim, Eli Lilly, Merck). L'été dernier, il a remporté le prix « Organometallic Chemistry Directed Towards Organic Synthesis » [chimie organométallique appliquée à la synthèse



Medal of the Royal Society of Canada and was named one of "Canada's Top 40 under 40" by the *Globe & Mail*/Caldwell Partners. Keith was a modest person who was nonetheless a strong advocate for Canadian research excellence. On the personal side, Keith was a dedicated family man and was close to his friends. He will be missed by all. Keith is survived by his wife, Danielle Gervais-Fagnou, and three children, Zachary, Clara, and Samuel.

**Louis Barriault and André Beauchemin**

organique], remis aux deux ans à un scientifique de moins de 40 ans pour ses contributions exceptionnelles à la recherche. En novembre 2009, Keith a reçu, à titre posthume, la médaille commémorative de la Société royale du Canada et a été reconnu comme l'un des chefs de file canadiens avant l'âge de 40 ans « Canada's Top 40 under 40 » par le *Globe&Mail* et la société Caldwell Partners. Homme modeste, Keith était un ardent promoteur de l'excellence de la recherche canadienne. Sur une note plus personnelle, Keith était un père de famille dévoué et entretenait des relations étroites avec ses amis. Il manquera à tous ceux et celles qui l'ont connu. Keith laisse dans le deuil son épouse, Danielle Gervais-Fagnou, et ses trois enfants, Zachary, Clara et Samuel.

**Louis Barriault et André Beauchemin**

## AWARD LECTURE / CONFÉRENCE D'HONNEUR

# Absorption detection using optical waveguide cavities

Hans-Peter Loock, Jack A. Barnes, Gianluca Gagliardi, Runkai Li,  
Richard D. Oleschuk, and Helen Wächter

**Abstract:** Cavity ring-down spectroscopy is a spectroscopic method that uses a high quality optical cavity to amplify the optical loss due to the light absorption by a sample. In this presentation we highlight two applications of phase-shift cavity ring-down spectroscopy that are suited for absorption measurements in the condensed phase and make use of waveguide cavities. In the first application, a fiber loop is used as an optical cavity and the sample is introduced in a gap in the loop to allow absorption measurements of nanoliters of solution at the micromolar level. A second application involves silica microspheres as high finesse cavities. Information on the refractive index and absorption of a thin film of ethylene diamine on the surface of the microresonator is obtained simultaneously by the measurements of the wavelength shift of the cavity mode spectrum and the change in optical decay time, respectively.

**Key words:** cavity ring-down spectroscopy, microresonator, microsphere, fiber loop.

**Résumé :** La spectroscopie à cavité ring-down est une méthode spectroscopique qui utilise une cavité optique de haute qualité pour amplifier la perte optique due à l'absorption de lumière par l'échantillon. Durant cette présentation, nous mettons en évidence deux applications de la spectroscopie à cavité ring-down avec déplacement de phase qui convient aux mesures d'absorption en phase condensée et fait usage de cavités à guide d'onde. Dans la première application, une boucle de fibre est utilisée comme cavité optique et l'échantillon est introduit dans un intervalle de la boucle pour permettre des mesures d'absorption sur des nanolitres de solution au niveau micromolaire. Une seconde application est basée sur des microsphères de silice comme cavités à haute finesse. Des informations sur l'index de réfraction et l'absorption d'un film mince d'éthylène diamine sur la surface d'un micro-résonateur sont obtenues simultanément par des mesures de déplacement de longueur d'onde du spectre modal de la cavité et de changement de temps de décroissance optique, respectivement.

**Mots-clés :** spectroscopie à cavité ring-down, micro-résonateur, microsphère, boucle de fibre.

In the past years, absorption spectroscopy has undergone a rapid change and the absorption spectrometers that are developed in many research labs have little in common with the teaching instruments that most of us were trained on. Indeed, a typical UV-vis absorption spectrometer found in today's undergraduate labs shares many of its basic components with the "spectroscope" devised by Isaac Newton in 1666. It contains a dispersing element, such as a prism or grating, a sample compartment, and a detector that is either placed behind a slit or forms a detection array, such as a photographic plate or photodiode array. Since the experiments by Kirchhoff and Bunsen<sup>1,2</sup> in the 1860s, quantitative absorption spectroscopy relies on the accurate measurement

of a change of transmitted light intensity due to wavelength-dependent attenuation by the analyte of interest. Single pass "direct" absorption detection and spectroscopy remains popular to this day, since it is straightforward to implement and many analytes show absorption features in the UV-vis region of the spectrum, whereas many solvents do not. This makes UV-vis absorption an ideal "label-free" method for detection and quantification of analytes.

On the other hand, direct absorption measurements are not background free, in contrast to fluorescence, photoacoustics, resonant ionization, coherent anti-Stokes Raman spectroscopy (CARS), and other modern spectroscopy methods. Furthermore, as evident from the Beer-Lambert law,  $I/I_0 = \exp(-\epsilon C d)$ ,

Received 10 January 2009. Accepted 12 April 2009. Published on the NRC Research Press Web site at canjchem.nrc.ca on 26 March 2010.

W. A. E. McByrde Award Lecture, 2009.

**H.-P. Loock,<sup>1</sup> J.A. Barnes, R. Li, R.D. Oleschuk, and H. Wächter.** Department of Chemistry, Queen's University, Kingston, ON K7L 3N6, Canada.

**G. Gagliardi.** Consiglio Nazionale Delle Ricerche-Istituto Nazionale Di Ottica (INO), Via Campi Flegrei 34, Pozzuoli, Naples 80078, Italy.

<sup>1</sup>Corresponding author (e-mail: hploock@chem.queensu.ca).

the sensitivity of a direct absorption measurement  $dI/dC = -I_0\epsilon d \exp(-\epsilon Cd)$  depends critically on the stability of light sources, optical alignment, and detectors (all expressed through  $I_0$ ).

Because of the need to measure a small intensity change on top of a large, and possibly noisy, intensity background, direct absorption is rather insensitive for low concentrations and (or) short absorption paths. Therefore, a number of approaches have been developed to overcome this limitation, notably the use of multipass cells, preconcentration of the analyte, differential absorption measurements, etc. In gas-phase spectroscopy, only a few of these methods have had an impact comparable to that of the cavity ring-down (CRD) absorption technique, a method that was introduced in 1988 by O'Keefe and Deacon.<sup>3</sup>

### Cavity ring-down spectroscopy

In cavity ring-down spectroscopy, the sample is placed in an optical cavity that is usually made by opposing two highly reflective mirrors at distance  $d$  (Fig. 1). A laser light pulse that is coupled into the cavity will be trapped between the mirrors for a large number of roundtrips while its intensity decays exponentially. The characteristic decay time, or ring-down time,

$$[1] \quad \tau = \frac{t_R}{-2\ln R + \epsilon Cd}$$

depends on the pulses' round trip time,  $t_R = nd/c_0$ , and the reflectivity of the mirrors,  $R$ , but does not depend on the intensity of the light pulse that is coupled into the cavity or on slow fluctuations of the detector response. The ring-down time is large for high mirror reflectivity and decreases with the introduction of absorbing or scattering compounds into the cavity.<sup>4-6</sup> With commercially available "super mirrors", reflectivities higher than 99.99% ( $R > 0.9999$ ) may be achieved, which corresponds to a cavity finesse  $F \approx 2\pi/(1 - R) = 62\,800$ . Since this number can be roughly equated to the number of passes through the cavity medium, one can see that even a desktop cavity with length  $d = 1$  m is equivalent to an absorption cell with an effective path-length of over 60 km! In addition, the sensitivity of the ring-down time measurement,

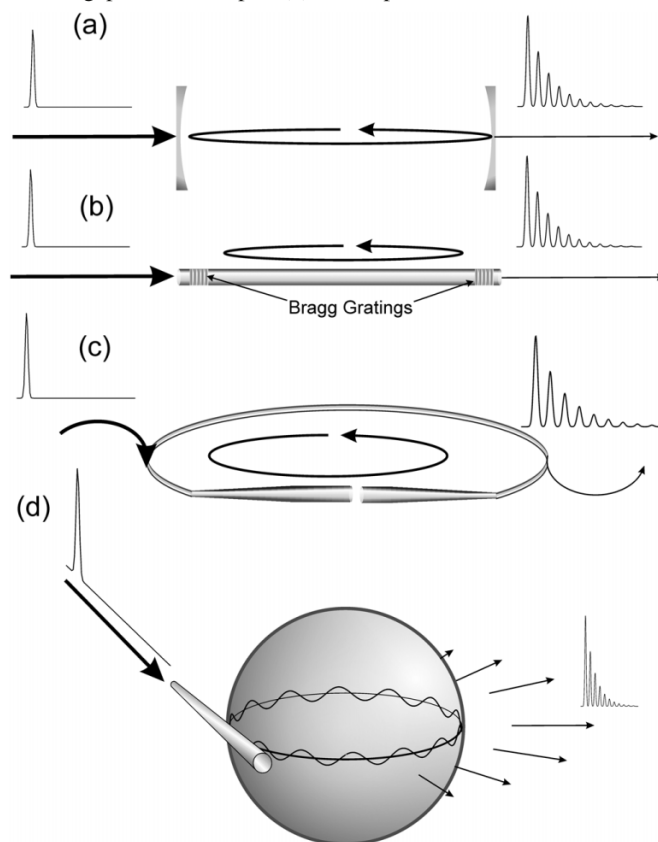
$$[2] \quad \frac{d\tau}{dC} = \frac{-\epsilon d t_R}{(-2\ln R + \epsilon Cd)^2}$$

increases quadratically with decreasing concentration and does not depend on intensity, which is a useful feature for an analytical spectroscopic method.

Not surprisingly, over the last twenty years, CRD spectroscopy and related cavity enhanced absorption methods have gained a larger and larger following, and the number of publications citing "cavity ring-down" in their title or abstract has increased from less than five in 1995 to over 150 in 2008. A large fraction of those publications is concerned with high resolution spectroscopy and detection of gases, of reactive intermediates, or of molecular beam-cooled samples. Since about 2002, an increasing number of research groups, including our own, attempt to adapt CRD detection to liquid samples.

CRD spectroscopy in liquids may be carried out simply by filling the entire optical cavity with liquid<sup>7</sup> or by insert-

**Fig. 1.** (a) Mirror-based cavity ring-down scheme; (b) optical cavity consisting of two fiber Bragg gratings; (c) fiber-loop CRD showing a small gap for the sample; (d) microsphere resonator.



ing a sample cuvette<sup>8-10</sup> or liquid jet<sup>11</sup> into the cavity. CRD detection for HPLC or other systems can similarly be realized by either constructing a very short cavity in which the mirrors are only separated by millimetres or by directing the effluent from the column across the optical axis of the cavity.<sup>12-16</sup> Both methods achieve impressive detection limits, which are limited by their baseline noise level to about  $10^{-5}$  to  $10^{-6}$  absorption units, depending on the mirrors, detection wavelength, and configuration. Also, both require careful optical alignment and a trained operator. In addition, the laser pulse width needs to be shorter than the roundtrip time. This means that millimetre long cavities can only be interrogated with picosecond laser pulses and with fast data acquisition systems. An excellent review describes the implementation of the CRD detection scheme to liquids with particular emphasis on the microliter-sized samples, which are relevant for HPLC.<sup>12</sup>

### CRD in waveguide cavities

In this presentation, we highlight two different types of optical cavities that are based on the waveguiding properties of silica and demonstrate their use for absorption measurements of small (nanoliter-sized) liquid samples.

In a simple analogy to the free-space optical cavity made of two mirrors, a strand of optical fiber that is gold coated at both end facets also acts as a high finesse optical cavity (Fig. 1b). Sigrist and co-workers<sup>17,18</sup> have used such a cavity to determine the concentration of  $H_2$  in the fiber core and to

measure bending losses occurring in the fiber optic cable. Instead of coatings applied to the fiber surface, one may also use fiber Bragg gratings (FBGs) as internal mirrors.<sup>19,20</sup> FBGs are periodic modulations of the refractive index written into the core of a sensitized fiber typically using UV laser radiation. They may have a reflectivity of up to 99.99%. Light propagating along the core of the fiber is reflected from these gratings when the Bragg condition is fulfilled, i.e., when the wavelength of the light is twice as large as the grating period.

An even simpler optical cavity may be formed by connecting the two ends of a strand of optical waveguide to form a continuous loop (Fig. 1c).<sup>21–25</sup> Once light is trapped inside the loop, it will circulate for many roundtrips before its intensity has decayed below the detection threshold. Compared to the linear cavity, the loop offers a number of advantages. First, the operating wavelengths are limited by the transmission spectrum of the waveguide, i.e., for silica from about 1700 nm to about 400 nm, whereas the FBGs have high reflectivity only in a 2–10 nm window, typically at around 1550 nm. Second, the gap between the fiber ends is a natural place to introduce a small liquid sample, for instance by using capillaries or channels in microfluidic devices. Third, the fiber-loop material and core diameter can be tailored to the application, whereas FBGs can be most easily written into single mode silica fibers. On the other hand, coupling light into the loop either requires couplers, which introduce cavity loss, or focusing of laser pulses onto the fiber core, which is a rather inefficient process. By contrast, FBG cavities can be simply spliced on the laser delivery fiber.

Both optical devices, the linear fiber cavity and the fiber loop, have been used in ring-down experiments. Similar to conventional free-space CRD, the ring-down time only depends on the optical loss in the cavity but is largely insensitive to lightsource power fluctuations or even detector response drifts, as long as those changes occur on timescales longer than the ring-down time. A recent review has highlighted the use of these cavities for mechanical and temperature measurements and, to a lesser extent, for refractive index measurements,<sup>26</sup> whereas we will focus on measurements of absorption induced by the interaction of the guided modes with an analyte. For a comprehensive review of cavity ring-down spectroscopic methods and in particular CRD using waveguides, the reader is directed to a 2009 book on cavity ring-down spectroscopy.<sup>6</sup>

### CRD phase-shift measurements

Before discussing different instruments in which waveguide based CRD measurements can be used, we should emphasize the differences between absorption measurements in flow systems and the “static” gas measurements in conventional cavities.

The optical loss in a fiber loop is much higher than in even a low-finesse optical cavity consisting of mirrors. With a mirror pair of a reflectivity of 99.9%, only 0.2% of the light is lost per roundtrip, whereas the insertion loss of fiber–fiber couplers, of fiber splices, and FBGs may easily add up to more than 5%. When measuring the absorption of a sample placed between the two ends of a fiber loop, the

loss is even higher: about 10%–30% of light is lost across the gap even when it is filled with nonabsorbing solvent! For a fiber cavity having the same roundtrip time as a conventional cavity, the ring-down time is therefore much shorter and the sensitivity to changes in the optical loss due to absorption by the analyte is correspondingly lower.

Also, in the analytical separation systems discussed below, the measurement has to take place in real time, while the analyte flows between the two fiber ends, with no opportunity to average multiple “events”. The data acquisition rate has to be matched to the flow rate and the detection volume, such that the detection volume is replaced at a rate that is about 10 times slower than the acquisition rate. Practically, we need to sample a ring-down event every 1–10 ms and determine the ring-down time ( $\tau = 0.1$ – $10 \mu\text{s}$ ) through exponential fitting at the same rate.

In our initial experiments, we used pulsed dye lasers operating at about 800 nm and were restricted in our data acquisition rate by the 10–100 Hz pulse repetition rate of our lasers.<sup>21,22</sup> Also, we had to average about 2000–6000 ring-down events to obtain a reliable ring-down time. The resulting data acquisition rate of  $1/3 \text{ min}^{-1}$  to  $1/10 \text{ min}^{-1}$  (one measurement every 3–10 min) is grossly inadequate for analytical flow measurements. While the rate can be increased considerably by switching to kHz repetition rate lasers, the main problem remains: the duty cycle of the experiment is woefully low. Assuming a 10 kHz repetition rate, light that is injected in the cavity rings down (in about  $10 \mu\text{s}$ ) only for a small fraction of the time, while the remaining time the system does nothing ( $90 \mu\text{s}$ ). Finally, it is neither trivial nor cheap to switch inexpensive lasers or other light sources, such as LEDs, on nanosecond timescales, and it is also costly to read out ring-down transients at high sampling rates.

All three concerns, the fast ring-down times, the poor duty cycle, and the high cost of (sub-)nanosecond switching and readout, may be addressed by applying a simple method that has been used in fluorescence lifetime measurements for many decades. Instead of monitoring the decay of a pulse in the time domain, one can also monitor the phase shift of an amplitude-modulated signal in the frequency domain (Fig. 2).<sup>27,28</sup> If an intensity-modulated signal is continuously fed into a high finesse cavity (or a fluorescent sample), the cavity (or sample) will emit light at the same modulation frequency,  $\omega$ , but with reduced modulation depth and with a phase shift that depends on the ring-down time,  $\tau$  (fluorescence lifetime). For a single exponential decay, the phase shift is<sup>28,29</sup>

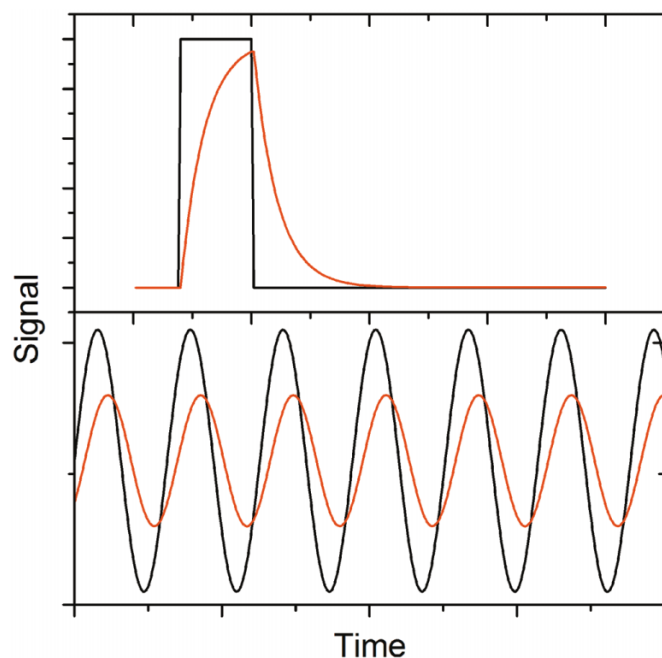
$$[3] \quad \tan(\phi - \phi_0) = -\omega\tau$$

Here,  $\phi$  is the phase shift between the light entering and exiting the fiber cavity and  $\phi_0$  is the phase shift resulting from instrumental factors such as electronic time constants and propagation delays. For multiexponential decays, the relation is more complicated but one can still determine the ring-down times and the relative amplitudes of each exponential component from phase-angle measurements at multiple modulation frequencies.<sup>30</sup>

The point is, phase-shift CRD measurements, introduced for spectral analysis by Engeln et al. in 1996,<sup>31</sup> are ideally



**Fig. 2.** Similar to a RC circuit, the response of an optical cavity is different to an impulse (DC, top) or an oscillating input (AC, bottom). An optical cavity, which is driven with a sinusoidally modulated input of angular frequency,  $\omega$ , will emit light with the same modulation frequency but reduced modulation depth and phase shifted to the input.



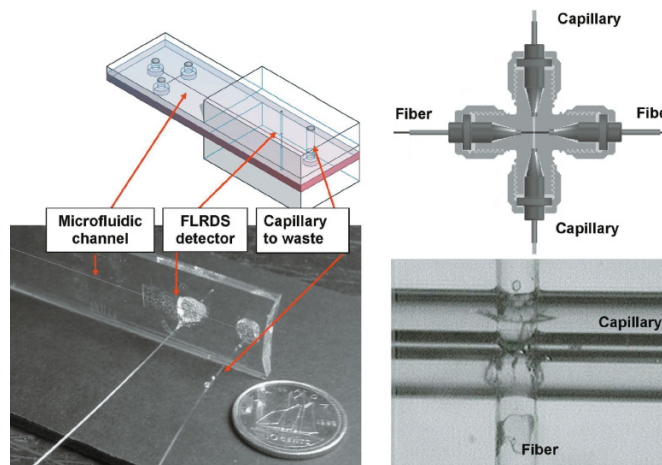
suited for transient absorption detection in low finesse optical cavities.<sup>32</sup> Phase-shift CRD is compatible with short ring-down times, since the modulation frequency may be set to the inverse of ring-down times. Changes in ring-down time as low as a few nanoseconds and picoseconds are readily measurable. Also, the duty cycle of the phase-shift measurement is unity, i.e., there is always light in the cavity. The readout rate is limited only by the ring-down time; “on the fly” exponential fitting is no longer required. Finally, phase comparators are also comparably inexpensive; simple integrated circuits with a  $1^\circ$  resolution may be bought for a few dollars.

Unfortunately, the ring-down times calculated from phase angles are sensitive to scattered light and are also less accurate compared to an exponential fit to a 10 000 point decay trace. Nevertheless, for our applications, the advantages, especially regarding data acquisition rate and cost, outweigh the disadvantages, and in all setups described below, the phase-shift CRD method was employed.

### Fiber-loop ring-down absorption detection

In a 2006 article, we presented three different interfaces between the fiber loop and the flow systems.<sup>33</sup> In one device, a commercial microcross was used to achieve fair coupling of light between the two ends of the fiber loop, which were fixed at a distance of 5–50  $\mu\text{m}$  from each other.<sup>34</sup> Two capillaries were inserted orthogonal to the optical fibers and used to flow samples of cyanine dyes in water between the fiber ends (Fig. 3). A detection limit of 200  $\mu\text{mol/L}$  corresponded to a minimal detectable absorption loss,  $\alpha_{\min}$ ,  $< 50 \text{ cm}^{-1}$ . The flow rate of 10  $\mu\text{L/min}$  and injection

**Fig. 3.** Three interfaces of the fiber loop with a fluidic system. Left: a microfluidic chip into which the fiber loop is inserted; right top: a commercial microcross with the fiber ends and capillary ends inserted normal to each other; right bottom: a 300  $\mu\text{m}$  capillary through which a hole was drilled to insert the two fiber ends. The fiber ends have hemispherical lenses at their ends.



volume of 2  $\mu\text{L}$  are compatible with capillary electrophoresis or micro-HPLC, but unfortunately, the limit of detection (LOD) is too large to be competitive with existing detection methods. Because it is difficult to optimize the optical alignment of the fibers in a microcross and thereby increase the sensitivity, we decided to use a second approach.

A 360  $\mu\text{m}$  capillary (ID: 100  $\mu\text{m}$ ) was embedded in a block of polymethyl methacrylate (PMMA) and a 150  $\mu\text{m}$  hole was drilled through the block and normal to the long axis of the capillary (Fig. 3, right bottom). The fiber ends were inserted to be flush with the inside wall of the capillary and about 60  $\mu\text{m}$  apart and then fixed using epoxy glue. The LOD was improved over the microcross to 50  $\mu\text{mol/L}$  ( $\alpha_{\min} = 10 \text{ cm}^{-1}$ ). The detection limit and sensitivity could be further improved by using hemispherical fiber ends instead of flat fiber end faces. This dramatically increases the coupling efficiency across the sample gap from 60% to about 90%.<sup>33</sup> To create hemispherical lenses, we heated the fiber ends in the electric arc of a fusion splicer.<sup>35</sup> The fiber ends were then inserted as before and placed 30  $\mu\text{m}$  apart before being glued in place. Using lensed fiber ends, the LOD was improved to 10  $\mu\text{mol/L}$  ( $\alpha_{\min} = 1.6 \text{ cm}^{-1}$ ) and protein detection became feasible.

A third interface was created to a microfluidic chip made of glass. Again, the flow channel was first sealed and encapsulated in PMMA and then a 150  $\mu\text{m}$  hole was drilled mechanically perpendicular to the channel. The flat-cut fiber ends were inserted and fixed at a distance of 14  $\mu\text{m}$ . The LOD of 30  $\mu\text{mol/L}$  ( $\alpha_{\min} < 10 \text{ cm}^{-1}$ ) was respectable, especially considering the short absorption path and the small detection volume of 700 pL. Note that the absolute quantity of detected analyte was only 21 fmol at the detection limit.<sup>33</sup>

All experiments above were conducted at 800 nm, i.e., a wavelength that was matched to the absorption maximum of the cyanine dye. At this wavelength, the fiber optic loss is quite low (3 dB/km) and the photomultiplier tubes used to detect scattered light from the loop show high sensitivity. Of course, a practical absorption detector for capillary elec-

trophoresis, microfluidics, or micro-HPLC needs to work at much shorter wavelengths. Because standard fiber optic cables have much reduced transmission at wavelengths shorter than 500 nm, it was believed that fiber-loop ring-down detection is not feasible at the important blue and UV wavelengths.

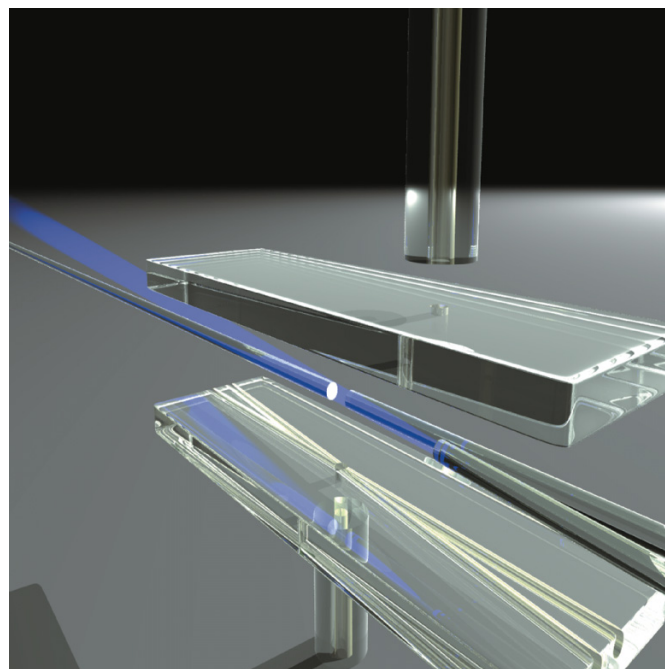
With recent advances in UV fiber optic materials, fiber CRD detection has now become possible, and in a recent publication we demonstrated the quantification of tartrazine dye, of myoglobin protein, and of a proprietary pharmaceutical ingredient using phase-shift fiber-loop ring-down detection at 405 nm.<sup>36</sup> The experiment was possible because of the low loss of the UV fiber optic loop ( $\alpha = 0.011 \text{ cm}^{-1}$ ) and of a specially designed fiber-optic-fluid interface (shown in Fig. 4), that combined a small detection volume (6 nL) with an even smaller dead volume (estimated at <2 nL). At the same interface, light from the 405 nm laser diode was introduced using a power delivery fiber that irradiated the gap between the fiber ends and thereby allowed for scattered blue light to enter the loop (Fig. 4). Despite the fact that the fiber ends were not lensed and comparatively far apart (190  $\mu\text{m}$ ), the detection limit is improved to 1  $\mu\text{mol/L}$  for myoglobin (Fig. 5) and the minimum detectable absorption loss is lower compared to our best earlier interface by almost an order of magnitude ( $\alpha_{\text{min}} = 0.11 \text{ cm}^{-1}$ ). This is likely due to the improved alignment between the fiber ends and the larger fiber core diameter, both leading to lower optical losses across the sample gap. More importantly, it is likely that the same setup will perform well at even shorter detection wavelengths and we plan to couple light from a 255 nm LED into the fiber loop in the near future.

With the interface displayed in Fig. 4, the detection of single micron-sized particles is also possible. The Mie scattering cross section increases with decreasing scattering wavelength and even the detection of transparent particles is possible if their refractive index differs by more than about 0.15 from the solvent. Indeed, we were able to detect single polystyrene particles of 5  $\mu\text{m}$  diameter that were suspended in water using a detergent (Fig. 5). Since these particles are comparable in size and refractive index to *Escherichia coli* cells, we expect that cytometry and single cell pathogen detection should be feasible using this very inexpensive and compact setup. Earlier experiments with an interface that was far from optimized and the 810 nm detection wavelength were conducted, and showed detection of yeast cells and *E. coli* cells, but not, yet, at the single cell level.<sup>37</sup>

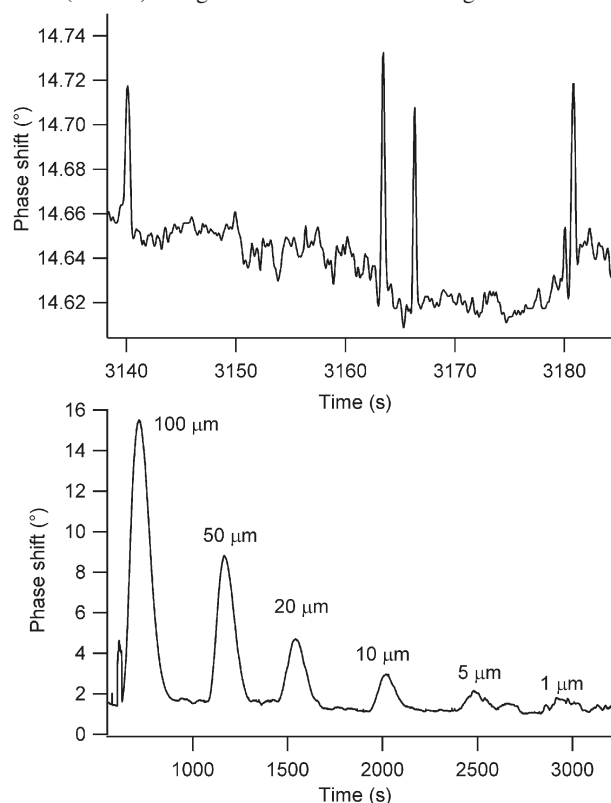
### Microsphere ring-down absorption detection

While the fiber loop is a “long roundtrip/low finesse” optical cavity, microresonators are optical cavities with very high finesse and extremely short roundtrip paths of typically less than a millimetre.<sup>38–41</sup> Microsphere resonators (shown schematically in Fig. 1d) have been used as chemical sensors for many years.<sup>42–52</sup> Light can be coupled tangentially into such a sphere, such that it travels along the “equator”. This so-called “whispering gallery mode (WGM)” can only be excited if the circumference of the sphere is an integer multiple of the excitation wavelength, and if the mode field

**Fig. 4.** Computer rendering of the optical–fluidic interface. The delivery fiber in the foreground illuminates the fiber gap. Capillaries attached to the top and bottom plate feed sample solution through small holes in front of the delivery fiber and out through a hole in the bottom plate.



**Fig. 5.** Detection of transparent 5  $\mu\text{m}$  diameter polystyrene particles (top trace) and detection of myoglobin in buffer solution at 405 nm (bottom) using the interface shown in Fig. 4.



of the whispering gallery mode overlaps with the mode field of the delivery waveguide. A whispering gallery mode can remain localized near the equator of the sphere for a very long time; in an analogy to the acoustic equivalent in the “whispering gallery” of, say, St. Paul’s Cathedral in London. Much like the sound of a whispered voice is guided along the inside of the Cathedral’s dome, light remains guided by total internal reflection. Light may be coupled into the sphere using, for example, tapered fibers (as we have done),<sup>53</sup> evanescent-field access blocks, angled fiber ends, or regular prisms.<sup>40</sup>

Refractive index measurements of analytes adsorbed on such microresonators are comparatively straightforward WGM frequency measurements. Since microresonators are very short, high-finesse cavities; they exhibit a sharp cavity mode spectrum, which depends strongly on the roundtrip length of the whispering gallery modes. The frequency of each WGM is, of course, influenced by the size of the microsphere, i.e., the circumference at the equator, but also by temperature and the refractive index of the immediate environment of the sphere. A thin layer of analyte adsorbed on the surface will effectively increase the circumference of the sphere. Of course, such an adsorbate may also attenuate the WGM intensity and reduce the number of roundtrips that one WGM experiences. Both quantities, the refractive index of the environment and its optical absorption, can therefore be obtained *simultaneously* from the frequency shift of the cavity fringes, and from their associated ring-down time, respectively.<sup>54</sup> Below, we intend to illustrate that such combined absorption and refractive index measurements using silica microsphere resonators are sensitive, but also quite simple.

In separate setups, silica resonators have already demonstrated superb performance for the measurements of both the refractive index and the optical absorption of adsorbed analytes. For example, researchers have used a toroidal microresonator to demonstrate the detection of a single interleukin-2 molecule through a combination of the induced refractive index change and optical absorption of the adsorbed molecule leading to heating and expansion of the sphere, the so-called thermoptic effect.<sup>52</sup> Simultaneous absorption and refractive index measurements of a few monolayers of an adsorbed species are easily feasible.<sup>55</sup> On the other hand, compared to the thermo-optic effect, cavity ring-down experiments provide a more direct measure of the optical absorption of an adsorbed layer but have, to our knowledge, not yet been used in chemical measurements. They were used, however, in characterizing the optical loss in microresonators. For example, Vahala and co-workers<sup>56</sup> conducted the CRD measurement in the time domain and obtained ring-down times of 43 ns for a 90  $\mu\text{m}$  diameter microresonator. The submicrosecond ring-down time highlights the fact that the roundtrip path for such devices is typically less than one millimetre and only about 280  $\mu\text{m}$  in this particular case. It is probably because of the short ring-down times, even for microresonators having a high finesse, that they have been used almost exclusively for refractive index measurements but not for absorption measurements.

On the other hand, a “large” square quartz monolith (7.5 mm  $\times$  7.5 mm  $\times$  5 mm) has been used as a high finesse cavity by Pipino<sup>57</sup> in 1999 and CRD absorption detec-

tion of 0.006% of a monolayer of  $\text{I}_2$  on the quartz surface was realized. Ring-down times of over a microsecond gave a finesse of over 12 500!

The finesse of the 300  $\mu\text{m}$  diameter silica microsphere cavities used in our group is between  $F = 5\,000$ – $100\,000$  and the ring-down times are correspondingly on the order of 4–70 ns, meaning that they will have to be measured with a resolution of picoseconds.

As in the fiber loop experiments, measurements of fast ring-down events at a high duty cycle may be achieved cost efficiently and simply through phase-shift CRD. By setting the modulation frequency,  $\omega = 1/\tau$ , we achieve optimal sensitivity to phase angle changes irrespective of the finesse or ring-down time of the cavity. While their appearance is very different, these microresonators show very similar behaviour compared to “regular” ring-down cavities consisting of two or more mirrors and to the above fiber-loop cavities. For example, in all three types of cavities the overall cavity loss depends on the losses inside the cavity medium *and* the losses that occur when light is coupled in and out of the cavity. The whispering gallery mode can interact with the sample through its evanescent field, i.e., the small part of the mode field that is located *outside* the sphere and decays exponentially over the distance of only a few 100 nm.

Recently, our group has demonstrated phase-shift CRD measurements on a 300  $\mu\text{m}$  microsphere and determined the attenuation that a WGM experiences.<sup>58</sup> In the following, we briefly describe the optical setup and highlight the theoretical and analytical aspects of this work.

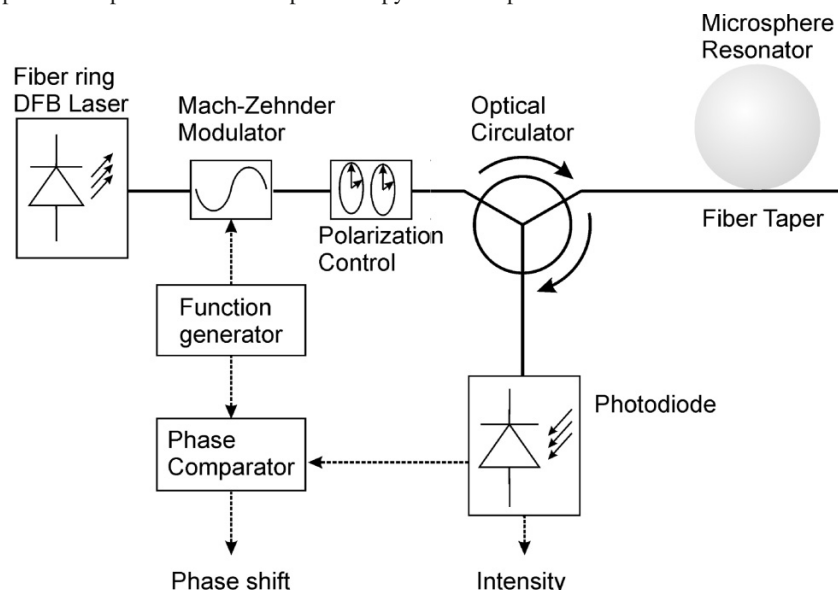
The silica microspheres were formed by fusing the end of a single-mode optical fiber (Corning, single mode fiber, SMF-28) to obtain a sphere with a nominal diameter of about 300  $\mu\text{m}$ . The residual optical fiber stem allows for manipulation and positioning of the microsphere. A tapered single-mode optical fiber, with a waist diameter of about 3–4  $\mu\text{m}$ , was used to couple light into the evanescent field of the microsphere WGM (Figs. 1 and 6). A detailed description of the experimental setup regarding the microsphere and tapered waveguide may be found elsewhere.<sup>53</sup>

Two different lasers were used. A tunable diode laser (Ando AQ 4320D, power: 3 mW) with a linewidth of about 200 MHz was used to optimize the coupling into the sphere and conduct proof-of-concept measurements of the phase angle associated with ring-down events on selected WGMs. An Er-doped fiber-ring DFB laser (Koheras Adjustik E15, linewidth < 1 kHz, power: 100 mW) was employed to interrogate the microsphere when ethylene diamine was deposited onto its surface.

The laser output was sinusoidally intensity modulated using a Mach–Zehnder modulator (JDS Uniphase) up to a modulation frequency of 2 MHz. A polarization controller, positioned after the modulator, allowed the TE and TM resonator modes to be selectively excited, although we were not able to distinguish between these two polarization states. Rayleigh back-scattering from imperfections in the silica microsphere quickly equilibrates degenerate counter-propagating cavity modes.<sup>59</sup> In our previously published work, WGM resonances were observed as dips in the delivery fiber transmission spectrum and as intensity peaks in the scattering spectrum from the microsphere. We also derived expressions (valid for angular modulation frequencies,  $\omega$ ,



**Fig. 6.** Scheme of the setup used for phase-shift CRD spectroscopy of microsphere resonators.



that are much lower than the carrier frequency) for the phase shifts that can be observed by recording the intensity modulated signal of the light transmitted through the fiber taper, and of the light scattered from the sphere.

$$[4] \quad \Delta\phi_{\text{trans}} \approx -\frac{2\omega n_{\text{eff}}L}{c} \frac{2\ln(\Gamma)}{(\ln\Gamma)^2 - (\alpha L/2)^2}$$

$$\Delta\phi_{\text{scatter}} \approx -\frac{2\omega n_{\text{eff}}L}{c} \frac{1}{-2\ln\Gamma + \alpha L}$$

Clearly, the two phase angles have a different dependence on the optical coupling,  $\Gamma$ , between the fiber and the resonator and the optical loss,  $\alpha L$ , of the WGM. Since both phase angles may be recorded simultaneously, we can obtain values for both  $\Gamma$  and  $\alpha L$  for each WGM. As for “regular” cavities, it is possible to transfer nearly all the power into the cavity, i.e., at “critical coupling”. This condition is achieved, here, when  $\Gamma_{\text{critical}} = 0.9998$  and  $\alpha_{\text{critical}} = 0.43 \text{ m}^{-1}$ . At this point, the phase angle of the transmitted light is infinite, and the intensity carried by the fiber taper drops to zero. Phase-angle measurements of the transmitted light are therefore biased to detect WGMs near critical coupling, whereas for scattered light, WGM with the lowest total loss ( $-\ln\Gamma + \alpha L$ ) show the largest phase angles.

With  $-\ln\Gamma$  and  $\alpha L$  one can easily calculate the nominal ring-down time

$$[5] \quad \tau = \frac{n_{\text{eff}}L}{c(-\ln\Gamma^2 + \alpha L)}$$

For the four WGMs that were investigated, we obtained  $\tau = 4 \text{ ns}$  to  $8 \text{ ns}$ , corresponding to quality factors (Q factors) of the order of  $10^6$ – $10^7$ . Most importantly for chemical detection, the attenuation term,  $\alpha$ , will change when an analyte is adsorbed to the microresonator surface and absorbs (or scatters) the WGM.

While the scattered light in previous work was collected through a microscope lens placed above the sphere, we also recorded WGM resonances that were detected through Rayleigh backscattered light. Conveniently, the Rayleigh

backscattered counterpropagating modes are partly coupled back into the delivery waveguide. A fiber optic circulator, positioned before the polarization controller, extracted the backscattered light and directed it to a fiber-coupled, 6 GHz bandwidth InGaAs detector (Thorlabs, Inc. SIR5). A radio-frequency lock-in amplifier (Stanford Research Systems Model SR844) processed the detector output, providing, simultaneously, an intensity and a phase-angle measurement that was referenced to the laser modulation. As the narrow band-width laser was slowly scanned, the lock-in amplifier’s outputs of intensity and phase shift were recorded. The entire optical setup was placed under a Plexiglas™ enclosure and purged with dry nitrogen to reduce contamination. Dry nitrogen was also used to sweep ethylene diamine (Sigma-Aldrich, used without purification) vapour from a flask into the plastic enclosure, with a partial pressure of about 10 Torr. Once a suitable shift in the WGM resonance was observed, the dosing was stopped and the chamber sealed. Ethylene diamine could be removed from the microsphere by purging the chamber with a continuous flow of dry nitrogen.

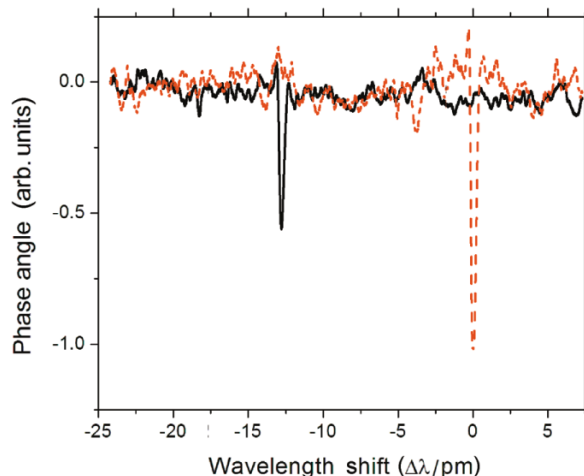
The presence of ethylene diamine in the vicinity of the silica microsphere surface manifests itself in two ways: through a shift in the cavity resonance position to longer wavelength and through a reduction in the optical lifetime (ring-down time) of the mode. Experimental results are shown in Figs. 7 and 8. The reduction of the ring-down time is also responsible for the decreased amplitude and larger linewidth in the phase-shift spectrum (Fig. 7). The magnitude of the phase shift has been measured for a number of modulation frequencies.

Previously, it has been shown that ethylene diamine adsorbs strongly to silica through interactions with surface silanol groups.<sup>60</sup> We assume, in our case, that the observed perturbations of the cavity resonance are due to adsorbed ethylene diamine, rather than vapour, by virtue of the method by which the compound was introduced. This assumption was confirmed in, as yet, unpublished calculations.

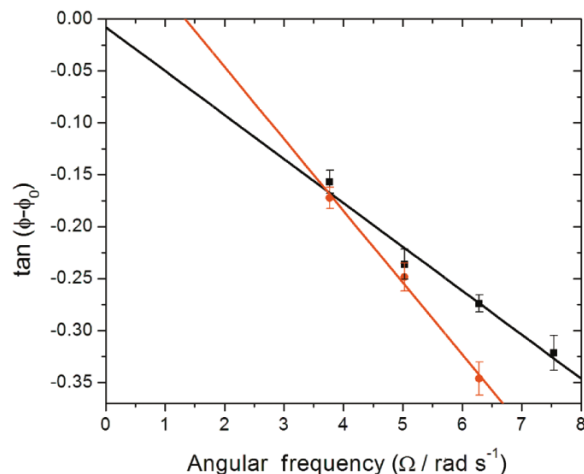
Arnold et al.<sup>43</sup> have derived an expression describing the wavelength shift of a WGM due to molecules adsorbed on a



**Fig. 7.** Redshift of the whispering gallery mode resonance at  $1.56\ \mu\text{m}$  (dashed red line) upon adsorption of ethylene diamine on the microsphere resonator (solid black). The phase shift was recorded at a modulation frequency of  $\omega = 3.77 \times 10^6\ \text{rad/s}$ .



**Fig. 8.** Phase shift of the Rayleigh backscattered light from the microsphere resonator as a function of modulation frequency measured with respect to the forward propagating modes. Due to the increased loss upon adsorption of ethylene diamine (black squares), the ring-down time, i.e., the slope, decreases.



microsphere surface. In our experiment, the observed shift of the WGM resonance upon dosing the microsphere with adsorbate was  $12.8 \pm 0.2\ \text{pm}$  from which a coverage of about 3 monolayers may be estimated using the polarizability of bulk ethylene diamine. Since water vapour is ubiquitous and is also strongly adsorbed on silica, the measured surface concentration of ethylene diamine also indicates that water has been displaced by ethylene diamine.

The surface coverage can also be obtained from the absorption measurement, i.e., from the decrease in phase shift (ring-down time) as the ethylene diamine concentration increases. For a single exponential decay, the phase shift of the intensity-modulated light is related to the ring-down time,  $\tau$ , by eq. [3]. From Fig. 8, the ring-down times with and without ethylene diamine present are  $\tau = 68 \pm 7\ \text{ns}$  and  $\tau_0 = 44 \pm 4\ \text{ns}$ , respectively. Note that this WGM has much lower loss compared to the WGM described previously by

our group.<sup>58</sup> From the ring-down times and using an estimate of the fraction of the evanescent field that can interact with the adsorbed layer, it is possible to again estimate the surface coverage of ethylene diamine as about seven monolayers using the absorption coefficient of bulk ethylene diamine (EDA).

The discrepancy of the value obtained through phase-shift CRD absorption, three monolayers ( $\Sigma_{\text{EDA}} = 3.6 \times 10^{15}\ \text{cm}^2$ ) with the value of seven monolayers ( $\Sigma_{\text{EDA}} = 1.5 \times 10^{15}\ \text{cm}^2$ ) that was obtained using the wavelength shift of the same WGM may be attributed to either a decrease of the ethylene diamine polarizability and (or) an increase of the absorption cross section of ethylene diamine compared to the bulk liquid. This is not surprising as it is well-known that the mid-infrared absorption cross section of ethylene diamine at silica surfaces is markedly higher than that of the bulk liquid.<sup>60</sup> Also, the alignment of the surface complex is normal to the sphere surface and is expected to cause further deviations of the absorption cross section and polarizability from the bulk liquid ethylene diamine values, both of which were obtained in isotropic samples.

In any case, it is possible to estimate the detection limit for the phase-shift CRD microsphere resonator detector. For our particular setup and WGM, we can measure a 10% change of the ring-down time (corresponding to best-fit errors of Fig. 8), and can therefore detect a surface coverage of  $\Sigma_{\text{EDA}} = 6.5 \times 10^{14}\ \text{cm}^2$  corresponding to less than 1.5 monolayers.

Future work will focus on improving this detection limit by using lasers with narrower line widths. Also, a careful survey of the WGM spectrum may yield better suitable WGM with higher Q factors. Finally, we require independent measurements of the surface refractive index and absorption of ethylene diamine to quantify the surface concentration with higher accuracy. Similar measurements should also be possible at different wavelengths, e.g., in the visible region of the spectrum or even in the mid-infrared region given the availability of narrow band lasers and waveguide materials.

While microsphere resonators are well-suited for the optical characterization of thin films, it would be much more difficult to use the optical cavity itself as a tool for chemical identification. Overtone absorption and refractive index of the film are both “broad band” spectroscopic features that carry little information on the exact identity of the chemical composition of the film. Chemical (bio-) detection of targeted molecules is possible, however, by functionalizing the surface such that the analyte of interest adsorbs and then interacts with the optical cavity.

## Conclusions

With this presentation, we intended to show the potential and limitations of two rather exotic applications of absorption spectroscopy. We concentrated this discourse on simple absorption measurements, but it is easily demonstrated that the fiber-loop ring-down method also has other applications, such as the measurements of refractive indices,<sup>61</sup> of loss in fiber optic components, of strain, temperature and pressure.<sup>62–64</sup> Here, the sensitivity of fiber optic devices such as

fiber Bragg gratings and long-period gratings to environmental parameters may be exploited.

Similarly, one can functionalize the surface of microspheres to obtain selectivity to analytes of interest. Refractive index measurements combined with thermooptic response of the cavity have already led to the detection of a single interleukin-2 molecule on silica microtoroid resonator.<sup>52,55</sup> Direct absorption measurements on functionalized spheres have not yet been conducted but are certainly in the realm of phase-shift CRD.

While it appears that CRD absorption measurements using waveguide loops or microresonators are only of limited use for measurements of trace gas concentrations (the strength of mirror-based CRD spectroscopy), and of "large liquid volume" absorption spectroscopy (the strength of direct absorption), the methods may evolve into a useful tool for the measurements of the absorption of small liquid volume and small amounts of adsorbed substances.

## Acknowledgements

The results shown in this presentation are the result of collaborative research initiatives that involved the groups of Professors Brown, Crudden, and Oleschuk (Queen's Chemistry), of Professor Fraser (Queen's Physics), and of Professor Yam (Electrical Engineering). We are particularly indebted to Professor Stephen Brown, who is the co-inventor of the original fiber-loop ring-down technique.

Many gifted students and postdoctoral fellows contributed to the experimental results that were presented here. Of those, we thank especially Zhaoguo Tong, Nicholas Trefiak, Jun Zhang, Mark Wilson, and Klaus Bescherer for their dedication and insights.

Funding for this work was provided by Queen's University, the Province of Ontario (Premier's Research Excellence Award, Photonics Research Ontario, Ontario Centres of Excellence), Canada (Natural Sciences and Engineering Research Council, Canadian Institute for Photonic Innovations), the Consiglio Nazionale delle Ricerche (CNR), Italy, and from industrial partners (Eli-Lilly Canada, PARTEQ Innovations, ITF Labs, Avensys Labs). GG acknowledges financial support by CNR RSTL project and Italian Ministry of Education, University and Research PON project. Finally, HPL thanks MDS Sciex for sponsoring the W.A.E. McBryde Medal and for their support of analytical chemistry research in Canada.

## References

- (1) Kirchhoff, G.; Bunsen, R. *Ann. Physik Chemie (Poggendorff)* **1860**, *186* (6), 161. doi:10.1002/andp.18601860602.
- (2) Meggers, W. F.; Tech, J. L. *J. Opt. Soc. Am.* **1960**, *50* (11), 1035. doi:10.1364/JOSA.50.001035.
- (3) O'Keefe, A.; Deacon, D. *Rev. Sci. Instrum.* **1988**, *59* (12), 2544. doi:10.1063/1.1139895.
- (4) Mazurenka, M.; Orr-Ewing, A. J.; Peverall, R.; Ritchie, G. A. D. *Annu. Rep. Prog. Chem.* **2005**, *101*, 100. doi:10.1039/b408909j.
- (5) Vallance, C. N. *J. Chem.* **2005**, *29* (7), 867. doi:10.1039/b504628a.
- (6) Lookock, H.-P. *Cavity Ring-Down Spectroscopy: Techniques and Applications*; Wiley-Blackwell: Hoboken, NJ, 2009.

- (7) Hallock, A. J.; Berman, E. S. F.; Zare, R. N. *Anal. Chem.* **2002**, *74* (7), 1741. doi:10.1021/ac011103i. PMID:12033270.
- (8) Bechtel, K. L.; Zare, R. N.; Kachanov, A. A.; Sanders, S. S.; Paldus, B. A. *Anal. Chem.* **2005**, *77* (4), 1177. doi:10.1021/ac048444r. PMID:15859003.
- (9) Snyder, K. L.; Zare, R. N. *Anal. Chem.* **2003**, *75* (13), 3086. doi:10.1021/ac0340152. PMID:12964755.
- (10) Hallock, A. J.; Berman, E. S. F.; Zare, R. N. *Appl. Spectrosc.* **2003**, *57* (5), 571. doi:10.1366/000370203321666614. PMID:14658685.
- (11) Alexander, A. J. *Anal. Chem.* **2006**, *78* (15), 5597. doi:10.1021/ac060571v. PMID:16878901.
- (12) van der Sneppen, L.; Ariese, F.; Gooijer, C.; Ubachs, W. *Annu. Rev. Anal. Chem.* **2009**, *2*, 13. doi:10.1146/annurev-anchem-060908-155301.
- (13) van der Sneppen, L.; Ariese, F.; Gooijer, C.; Ubachs, W. *J. Chromatogr. A* **2007**, *1148* (2), 184. doi:10.1016/j.chroma.2007.03.028. PMID:17383664.
- (14) van der Sneppen, L.; Wiskerke, A. E.; Ariese, F.; Gooijer, C.; Ubachs, W. *Appl. Spectrosc.* **2006**, *60* (8), 931. doi:10.1366/000370206778062101. PMID:16925931.
- (15) van der Sneppen, L.; Wiskerke, A.; Ariese, F.; Gooijer, C.; Ubachs, W. *Anal. Chim. Acta* **2006**, *558* (1–2), 2. doi:10.1016/j.aca.2005.11.022.
- (16) Bahnev, B.; van der Sneppen, L.; Wiskerke, A. E.; Ariese, F.; Gooijer, C.; Ubachs, W. *Anal. Chem.* **2005**, *77* (4), 1188. doi:10.1021/ac048428u. PMID:15859005.
- (17) Vogler, D. E.; Müller, M. G.; Sigrist, M. W. *Appl. Opt.* **2003**, *42* (27), 5413. doi:10.1364/AO.42.005413. PMID:14526828.
- (18) von Lerber, T.; Sigrist, M. W. *Appl. Opt.* **2002**, *41* (18), 3567. doi:10.1364/AO.41.003567. PMID:12078682.
- (19) Gupta, M.; Jiao, H.; O'Keefe, A. *Opt. Lett.* **2002**, *27* (21), 1878. doi:10.1364/OL.27.001878. PMID:18033388.
- (20) Andachi, M.; Nakayama, T.; Kawasaki, M.; Kurokawa, S.; Lookock, H. P. *Appl. Phys. B* **2007**, *88* (1), 131. doi:10.1007/s00340-007-2635-5.
- (21) Brown, R. S.; Kozin, I.; Tong, Z.; Oleschuk, R. D.; Lookock, H.-P. *J. Chem. Phys.* **2002**, *117* (23), 10444. doi:10.1063/1.1527893.
- (22) Tong, Z. G.; Jakubinek, M.; Wright, A.; Gillies, A.; Lookock, H. P. *Rev. Sci. Instrum.* **2003**, *74* (11), 4818. doi:10.1063/1.1614877.
- (23) Tarsa, P. B.; Rabinowitz, P.; Lehmann, K. K. *Chem. Phys. Lett.* **2004**, *383* (3–4), 297. doi:10.1016/j.cplett.2003.11.043.
- (24) Tarsa, P. B.; Wist, A. D.; Rabinowitz, P.; Lehmann, K. K. *Appl. Phys. Lett.* **2004**, *85* (19), 4523. doi:10.1063/1.1819520.
- (25) Pu, S. A.; Gu, X. J. *Opt. Lett.* **2009**, *34* (12), 1774. doi:10.1364/OL.34.001774. PMID:19529699.
- (26) Wang, C. *Sensors* **2009**, *9* (10), 7595. doi:10.3390/s91007595.
- (27) Gratton, E.; Jameson, D. *Anal. Chem.* **1985**, *57* (8), 1694. doi:10.1021/ac00285a041.
- (28) Lakowicz, J. R.; Laczko, G.; Cherek, H.; Gratton, E.; Limkeman, M. *Biophys. J.* **1984**, *46* (4), 463. doi:10.1016/S0006-3495(84)84043-6. PMID:6498264.
- (29) Herbelin, J. M.; McKay, J. A.; Kwok, M. A.; Ueunten, R. H.; Urevig, D. S.; Spencer, D. J.; Benard, D. J. *Appl. Opt.* **1980**, *19* (1), 144. doi:10.1364/AO.19.000144.
- (30) Bescherer, K.; Barnes, J. A.; Dias, S.; Gagliardi, G.; Lookock, H. P.; Trefiak, N. R.; Waechter, H.; Yam, S. *Appl. Phys. B* **2009**, *96* (1), 193. doi:10.1007/s00340-009-3429-8.
- (31) Engeln, R.; von Helden, G.; Berden, G.; Meijer, G. *Chem.*

- Phys. Lett.* **1996**, 262 (1–2), 105. doi:10.1016/0009-2614(96)01048-2.
- (32) Tong, Z.; Wright, A.; McCormick, T.; Li, R.; Oleschuk, R. D.; Loock, H. P. *Anal. Chem.* **2004**, 76 (22), 6594. doi:10.1021/ac0491253. PMID:15538782.
- (33) Loock, H.-P. *TrAC Trends Anal. Chem.* **2006**, 25 (7), 655. doi:10.1016/j.trac.2006.05.003.
- (34) Trefiak, N.; Barnes, J. A.; Rask, F.; Courtney, D. G.; Walford, R.; Li, R.; Oleschuk, R. D.; Loock, H. P. *Proc. SPIE* **2005**, 5969, 59690O. doi:10.1117/12.629756.
- (35) Li, R. K.; Loock, H.-P.; Oleschuk, R. D. *Anal. Chem.* **2006**, 78 (16), 5685. doi:10.1021/ac060289o. PMID:16906712.
- (36) Waechter, H.; Bescherer, K.; Dürr, C. J.; Oleschuk, R. D.; Loock, H.-P. *Anal. Chem.* **2009**, 81 (21), 9048. doi:10.1021/ac901696q. PMID:19813748.
- (37) Li, R. *Fiber-Loop Ring-Down Detection: A Novel Online Detection Method*. Ph.D. Dissertation, Queen's University, Kingston, ON, 2007.
- (38) Grudin, I. S.; Matsko, A. B.; Savchenkov, A. A.; Strekalov, D.; Ilchenko, V. S.; Maleki, L. *Opt. Commun.* **2006**, 265 (1), 33. doi:10.1016/j.optcom.2006.03.028.
- (39) Ilchenko, V. S.; Matsko, A. B. *IEEE J. Sel. Top. Quant. Electron.* **2006**, 12 (1), 15. doi:10.1109/JSTQE.2005.862943.
- (40) Matsko, A. B.; Ilchenko, V. S. *IEEE J. Sel. Top. Quant. Electron.* **2006**, 12 (1), 3. doi:10.1109/JSTQE.2005.862952.
- (41) Savchenkov, A. A.; Matsko, A. B.; Ilchenko, V. S.; Maleki, L. *Opt. Express* **2007**, 15 (11), 6768. doi:10.1364/OE.15.006768. PMID:19546987.
- (42) Farca, G.; Shopova, S. I.; Rosenberger, A. T. *Opt. Express* **2007**, 15 (25), 17443. doi:10.1364/OE.15.017443. PMID:19551038.
- (43) Arnold, S.; Khoshima, M.; Teraoka, I.; Holler, S.; Vollmer, F. *Opt. Lett.* **2003**, 28 (4), 272. doi:10.1364/OL.28.000272. PMID:12653369.
- (44) Arnold, S.; Ramjit, R.; Keng, D.; Kolchenko, V.; Teraoka, I. *Faraday Discuss.* **2008**, 137, 65. doi:10.1039/b702920a. PMID:18214098.
- (45) Noto, M.; Vollmer, F.; Keng, D.; Teraoka, I.; Arnold, S. *Opt. Lett.* **2005**, 30 (5), 510. doi:10.1364/OL.30.000510. PMID:15789719.
- (46) Teraoka, I.; Arnold, S.; Vollmer, F. *J. Opt. Soc. Am. B* **2003**, 20 (9), 1937. doi:10.1364/JOSAB.20.001937.
- (47) Vollmer, F.; Braun, D.; Libhaber, A.; Khoshima, M.; Teraoka, I.; Arnold, S. *Appl. Phys. Lett.* **2002**, 80 (21), 4057. doi:10.1063/1.1482797.
- (48) Rosenberger, A. T. *Opt. Express* **2007**, 15 (20), 12959. doi:10.1364/OE.15.012959. PMID:19550564.
- (49) Rosenberger, A. T.; Rezac, J. *Proc. SPIE* **2001**, 4265, 102. doi:10.1117/12.427962.
- (50) Armani, A. M.; Armani, D. K.; Min, B.; Vahala, K. J.; Spillane, S. M. *Appl. Phys. Lett.* **2005**, 87 (15), 151118. doi:10.1063/1.2099529.
- (51) Armani, A. M.; Vahala, K. J. *Opt. Lett.* **2006**, 31 (12), 1896. doi:10.1364/OL.31.001896. PMID:16729107.
- (52) Armani, A. M.; Kulkarni, R. P.; Fraser, S. E.; Flagan, R. C.; Vahala, K. J. *Science* **2007**, 317 (5839), 783. doi:10.1126/science.1145002. PMID:17615303.
- (53) Barnes, J.; Carver, B.; Fraser, J. M.; Gagliardi, G.; Loock, H. P.; Tian, Z.; Wilson, M. W. B.; Yam, S.; Yastrubshak, O. *Opt. Express* **2008**, 16 (17), 13158. doi:10.1364/OE.16.013158. PMID:18711554.
- (54) Of course, the optical absorption may also be obtained from the width and amplitude for the cavity fringes, if the cavity is well-characterized and the light source is very stable.
- (55) Vollmer, F.; Arnold, S. *Nat. Methods* **2008**, 5 (7), 591. doi:10.1038/nmeth.1221. PMID:18587317.
- (56) Armani, D. K.; Kippenberg, T. J.; Spillane, S. M.; Vahala, K. J. *Nature* **2003**, 421 (6926), 925. doi:10.1038/nature01371.
- (57) Pipino, A. C. R. *Phys. Rev. Lett.* **1999**, 83 (15), 3093. doi:10.1103/PhysRevLett.83.3093.
- (58) Barnes, J. A.; Carver, B.; Fraser, J. M.; Gagliardi, G.; Loock, H.-P.; Tian, Z.; Wilson, M. W.; Yam, S.-H.; Yastrubshak, O. *Opt. Express* **2008**, 16 (17), 13158. doi:10.1364/OE.16.013158. PMID:18711554.
- (59) Gorodetsky, M. L.; Pryamikov, A. D.; Ilchenko, V. S. *J. Opt. Soc. Am. B* **2000**, 17 (6), 1051. doi:10.1364/JOSAB.17.001051.
- (60) Xu, M.; Liu, D. F.; Allen, H. C. *Environ. Sci. Technol.* **2006**, 40 (5), 1566. doi:10.1021/es051537l. PMID:16568771.
- (61) Barnes, J. A.; Dreher, M.; Plett, K.; Brown, R.; Crudden, C. M.; Loock, H.-P. *Analyst (Lond.)* **2008**, 133 (11), 1541. doi:10.1039/b806129g.
- (62) Wang, C. J.; Mbi, A. *Meas. Sci. Technol.* **2006**, 17 (7), 1741. doi:10.1088/0957-0233/17/7/012.
- (63) Wang, C. J.; Scherrer, S. T. *Appl. Opt.* **2004**, 43 (35), 6458. doi:10.1364/AO.43.006458. PMID:15617282.
- (64) Wang, C. J.; Scherrer, S. T. *Opt. Lett.* **2004**, 29 (4), 352. doi:10.1364/OL.29.000352. PMID:14971750.

# ATRP grafting of oligo(ethylene glycol) methacrylates from gold surface — Effect of monomer size on grafted chain and EO unit densities

Zhilin Jin, John L. Brash, and Shiping Zhu

**Abstract:** Oligo(ethylene glycol) methacrylate (OEGMA) was grafted from Au surface via surface-initiated atom-transfer radical polymerization (s-ATRP). The initiator density was adjusted by the mole fractions of surface-attachable ATRP initiator and diluting agent. Three OEGMA monomers of  $M_r$  300, 475, and 1100 were used. The Au surfaces before and after modification were characterized by water contact angle and ellipsometry. The effect of monomer  $M_r$  and initiator density on surface chain density and EO unit density was investigated. It was found that at low initiator density (mole fraction of initiator of 2%–5%), poly(OEGMA) grafts had comparable surface chain density independent of OEGMA  $M_r$ . However, at high initiator density (mole fraction of initiator >10%), poly(OEGMA)<sub>1100</sub> had obviously lower chain densities than poly(OEGMA)<sub>300</sub> and poly(OEGMA)<sub>475</sub>, which could be attributed to the size difference of the monomers. The short chain length and low surface chain density of poly(OEGMA)<sub>1100</sub> resulted in its relatively low surface EO unit density.

**Key words:** Au surface, poly(ethylene glycol), atom transfer radical polymerization (ATRP), grafting, surface chain density, surface EO unit density, monomer  $M_r$ .

**Résumé :** On a greffé du méthacrylate d'oligo(éthylèneglycol) (MAOEG) sur une surface d'or par le biais d'une polymérisation radicalaire par transfert d'atome initié par la surface (PRTA-s). La densité de l'initiateur a été ajustée par les fractions molaires de l'initiateur de la PRTA qui peuvent être attachées à la surface et l'agent diluant. On a utilisé trois MAOEG de  $M_r$  300, 475 et 1100. On a caractérisé les surfaces d'or avant et après modification par l'angle de contact de l'eau et par ellipsométrie. On a étudié l'effet du poids moléculaire du monomère et la densité de l'initiateur sur la densité de la chaîne en surface et sur la densité de l'unité d'oligoéthylèneglycol. On a trouvé que pour des densités d'initiateur faibles (fraction molaire d'initiateur allant de 2 % à 5 %), la densité de chaîne en surface des greffes est indépendante du  $M_r$  du MAOEG. Toutefois, à des densités d'initiateur plus élevées (fraction molaire d'initiateur supérieure à 10 %), les densités de chaîne du poly(MAOEG)<sub>1100</sub> sont évidemment plus faibles que celles des poly(MAOEG)<sub>300</sub> et poly(MAOEG)<sub>475</sub> et cette situation peut être attribuée à une différence dans la taille des monomères. La courte longueur de la chaîne et la faible densité de la chaîne de surface du poly(MAOEG)<sub>1100</sub> résultent de la densité relativement faible de l'unité d'oligoéthylèneglycol.

**Mots-clés :** surface d'or, poly(éthylèneglycol), polymérisation radicalaire par transfert d'atome (PRTA), greffage, densité de la chaîne en surface, densité de l'unité d'oligoéthylèneglycol,  $M_r$  du monomère.

[Traduit par la Rédaction]

## Introduction

Poly(ethylene oxide) (PEO)- and oligo(ethylene glycol) (OEG)-containing polymers (e.g., poly(oligo(ethylene glycol) methacrylate) (poly(OEGMA))) have attracted much attention as a biomaterial coating because of its high ability to resist non-specific protein adsorption, biofouling, and its high biocompatibility.<sup>1</sup> It has been shown that many factors, including PEO chain length, surface chain density, polymer conformation, and surface EO unit density, have strong effects on the protein-resistant and biocompatible perform-

ance.<sup>2–4</sup> However, details of these effects are still a matter of debate. A significant barrier to elucidate these factors to protein resistance and (or) biocompatibility is the lack of techniques to control and accurately measure these properties.

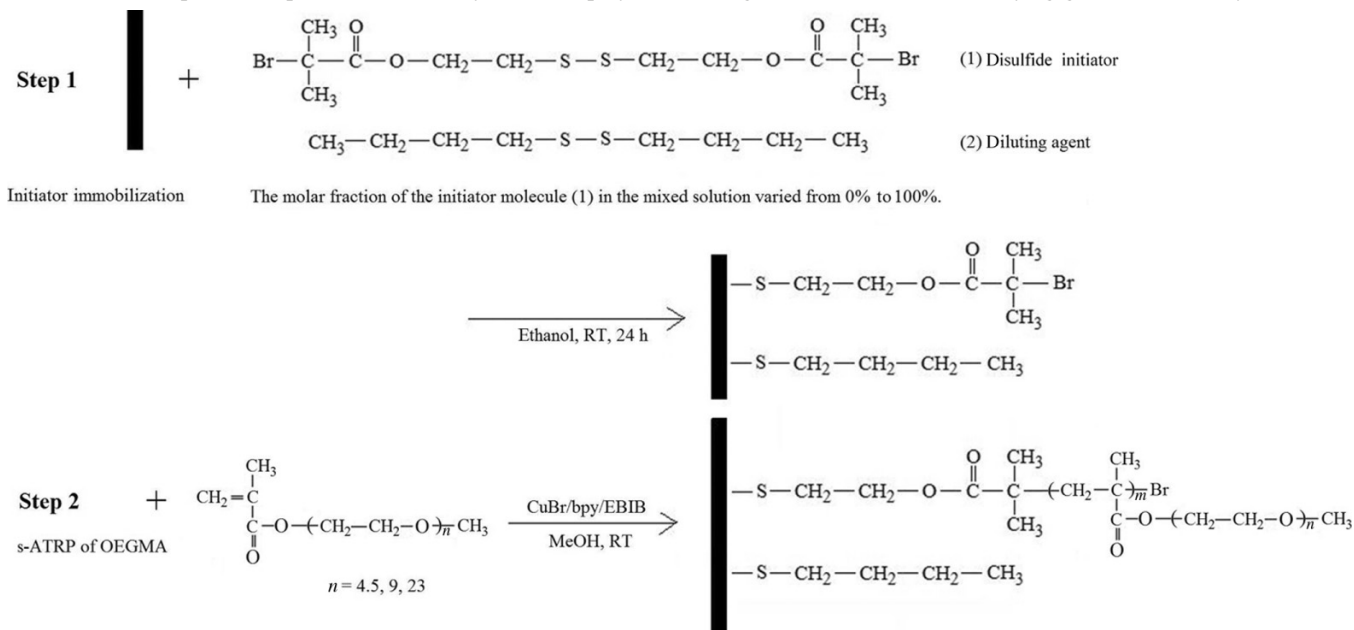
The recent development of atom-transfer radical polymerization (ATRP) method provides a facile way to achieve uniform and tunable graft chain length on surface.<sup>5–8</sup> It has also been found that chain density of polymer grafts can be varied by adjusting the initiator density on surface,<sup>9,10</sup> and

Received 5 October 2009. Accepted 19 January 2010. Published on the NRC Research Press Web site at canjchem.nrc.ca on 31 March 2010.

**Z. Jin, J.L. Brash, and S. Zhu.**<sup>1</sup> Department of Chemical Engineering and School of Biomedical Engineering, McMaster University, ON L8S 4L7, Canada.

<sup>1</sup>Corresponding author (e-mail: zhuship@mcmaster.ca).



**Scheme 1.** Two-step reaction procedure for the synthesis of poly(OEGMA)-grafted Au surface with varying graft chain density.

the monomer size has an effect on the polymer chain density formed via surface-initiated ATRP (s-ATRP).<sup>11</sup> Recently, the surface-initiated ATRP of PEO-containing molecules (such as OEGMA) has been performed on well-defined model substrates, such as silicon and gold,<sup>9,10</sup> which allow relatively accurate characterization of polymer grafts via ellipsometry and (or) AFM compared with other substrates, such as polymeric substrates. However, there is very little work where surface chain density and surface EO unit density are finely tuned by varying monomer  $M_r$  and initiator density, and where the effect of monomer  $M_r$  and initiator density was systematically studied.

In this study, oligo(ethylene glycol) methacrylate (OEGMA) was grafted from Au surface via s-ATRP with various initiator densities and three OEGMA monomers of  $M_r$  300, 475, and 1100 (equivalent to 5, 9, and 23 ethylene oxide residues, respectively). The effect of monomer  $M_r$  and initiator density on surface chain density and surface EO unit density was investigated.

## Experimental

### Materials

Gold-coated silicon wafers (500  $\mu\text{m}$  thickness, 100 mm diameter, Au coating layers of 100 nm thickness on both sides) were purchased from SVM (Silicon Valley Microelectronics, Inc.) and cut into 5  $\times$  5 mm pieces using a Micro Ace Series 3 dicer (Loadpoint Ltd., England). Hydrogen peroxide (30%), ammonia solution (30%), and methanol (HPLC grade) were obtained from Caledon Laboratories LTD and used as received. Bis[2-(2'-bromoisobutyryloxy) ethyl] disulfide (the structure shown in Scheme 1) was purchased from ATRP Solutions, Inc. and used as received. Butyl disulfide (97%), ethyl 2-bromoisobutyrate (EBIB) (98%), 2,2'-bipyridyl (bpy) (99%), and  $\text{Cu}^{\text{I}}\text{Br}$  (99.999%) were purchased from Sigma-Aldrich and used as received. OEGMAs with molecular weights ( $M_r$ ) of 300, 475, and 1100 were purchased

from Sigma-Aldrich and passed over a basic alumina column to remove inhibitor. Basic alumina (Brockman Activity 1, mesh 60–325) was purchased from Fisher Scientific and used as received. Deionized water used in this study had a resistivity of 18.2  $\text{M}\Omega\text{cm}$  and nitrogen gas was of ultrahigh-purity (UHP) grade.

### Pretreatment of Au surfaces

Gold-coated silicon chips (5  $\times$  5 mm) were immersed in a 1:1:5 solution of hydrogen peroxide:ammonium hydroxide:water at 80  $^{\circ}\text{C}$  for 5 min, sonicated for 1 min, and rinsed in deionized water to remove any carbonaceous contamination. After cleaning, the gold-coated chips were either used immediately for the formation of the initiator self-assembled monolayer (SAM) or stored in ethanol at room temperature.

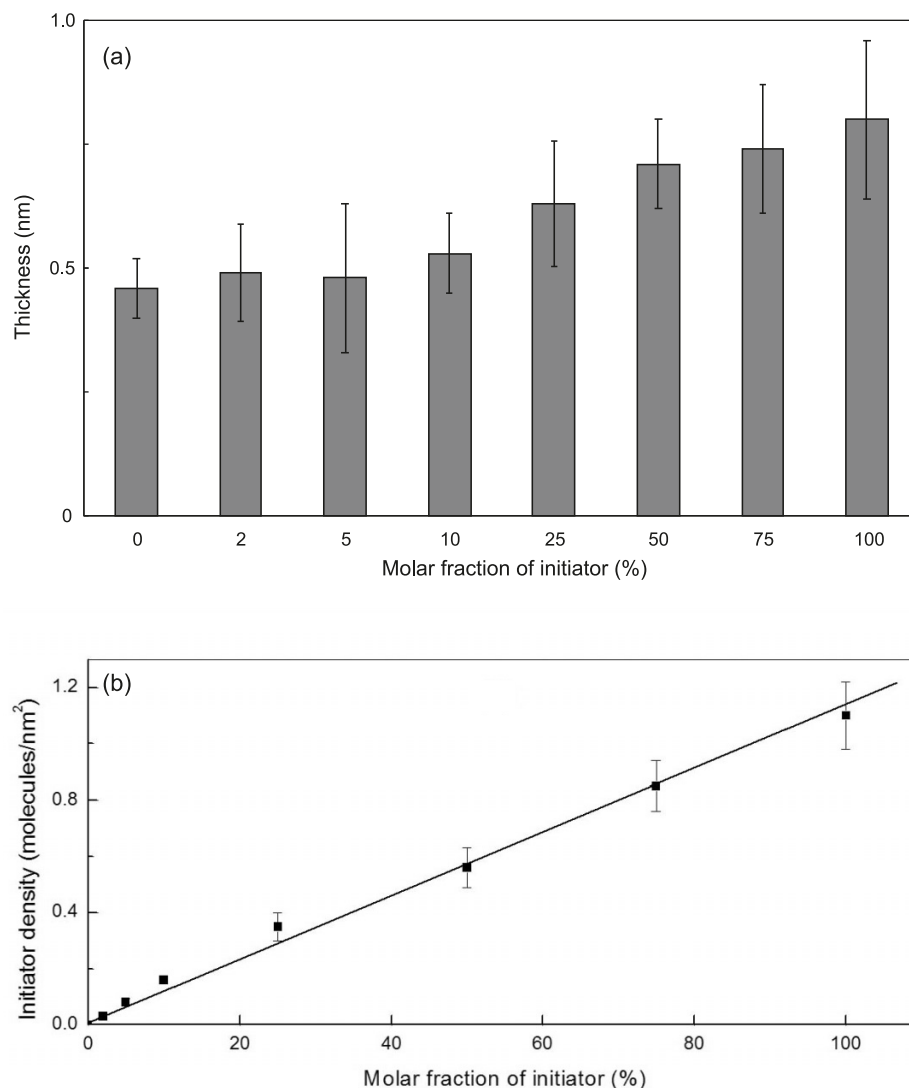
### Formation of initiator monolayer on Au surfaces

The self-assembled monolayer (SAM) of initiator was formed by soaking the freshly cleaned gold-coated chips in an ethanol solution (total concentration: 1 mmol/L) containing disulfides for 24 h without stirring at room temperature. The mixed disulfide solution contained bis[2-(2'-bromoisobutyryloxy) ethyl] disulfide (the initiator molecule **1** in Scheme 1) and butyl disulfide as a diluting agent. The mole fractions of the initiator varied from 0% to 100%. The surfaces were removed from the solution, cleaned ultrasonically for 1 min in pure ethanol, rinsed with THF, and then dried in a nitrogen stream. The gold surfaces with SAMs (referred to as Au/initiator) were either used immediately or stored in glass tubes under nitrogen at room temperature.

### s-ATRP of OEGMA from initiator-functionalized gold surfaces

Poly(OEGMA)s with various side-chain lengths (EO units) or monomer  $M_r$  values (300, 475, and 1100) were grafted from the Au/initiator surfaces via s-ATRP. The detailed procedure was described previously.<sup>12,13</sup> EBIB

**Fig. 1.** (a) Ellipsometric thickness of the mixed SAMs of initiator and diluting agent. (b) Surface density of initiator in the mixed SAMs. Error bars represent one standard deviation,  $n = 4$ .



**Table 1.** Conversion and molecular weight in s-ATRP of OEGMA from Au/initiator surfaces with sacrificial initiator in solution.

OEGMA $M_r$	Molar ratio (OEGMA/EBIB)	Conversion (%) <sup>a</sup>	Theoretical $M_n$ (kg/mol) <sup>b</sup>	$M_n$ , GPC (kg/mol) <sup>c</sup>	$M_w/M_n$
300	100	>99	30	28.7	1.06
475	100	>99	47.5	39.5	1.13
1100	100	48	52.8	49.0	1.05

<sup>a</sup>Conversion calculated from  $^1\text{H}$  NMR data.

<sup>b</sup>Calculated via conversion  $\times$  (molar ratio OEGMA/EBIB)  $\times$  (OEGMA  $M_r$ ).

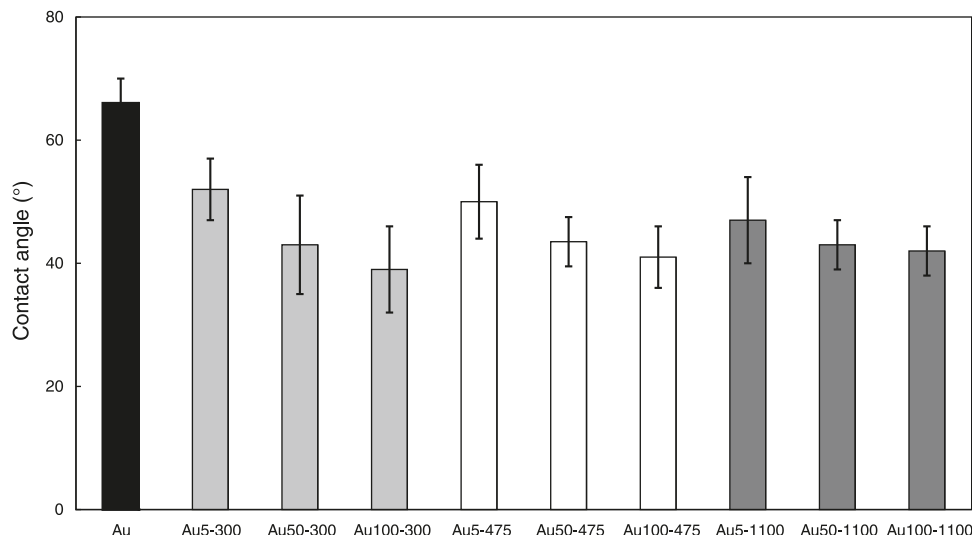
<sup>c</sup>Based on PEO calibration standards.

was used as a sacrificial initiator. The monomer concentration was fixed at 38% w/v and the molar ratio of OEGMA:EBIB:Cu<sup>I</sup>Br:bpy was 100:1:1:2, with methanol as solvent. 10 g OEGMA was used in an s-ATRP process with 40 pieces of gold-coated chips. The s-ATRP process was performed under nitrogen at room temperature for 48 h. The surfaces were then cleaned ultrasonically for 1 min in methanol, rinsed with methanol, and then dried in a nitrogen stream.

### Characterization

$^1\text{H}$  NMR spectroscopy (Bruker AC-P200 spectrometer, D<sub>2</sub>O solvent) was used to determine OEGMA conversion in the s-ATRP reactions. Gel permeation chromatography (GPC, Waters 2690 separations module with a Waters 2410 refractive index detector, PEO calibration standards) was used to determine the molecular weight and polydispersity index (PDI) of poly(OEGMA) formed in solution. Water contact angle measurements were performed on the gold surfaces

**Fig. 2.** Water contact angles (advancing) of poly(OEGMA)-grafted Au surfaces. The surfaces are named by the mole fraction of initiator (%) (first number) and the monomer  $M_r$  (second number). Error bars represent one standard deviation,  $n = 4$ .



with a Rame-Hart NRL goniometer (Mountain Lakes, NJ) at room temperature, using the sessile drop method.

An Exacta 2000 ellipsometer (Waterloo Digital Electronics) was used to determine the thicknesses of the initiator monolayer and poly(OEGMA) on the gold-coated substrates with single wavelength (6328 Å) and an incident angle of 70°. The gold-coated wafers were considered as the substrate, with refractive index ( $n_s$ ) and extinction coefficient ( $k_s$ ) of  $0.19 \pm 0.02$  and  $3.52 \pm 0.08$ , respectively. For the initiator-functionalized and poly(OEGMA)-grafted surfaces, the polarizer (P) and analyzer (A) angles for the null condition were measured and thickness values were determined using a three-layer air-grafts-gold model via the Exacta 2000 Variable Theta Simplex Fitting Program. A refractive index of 1.46 was used for initiator SAMs and poly(OEGMA) grafts.<sup>14,15</sup>

The surface chain densities of poly(OEGMA) as well as initiator/diluting agent were calculated based on the following equation:<sup>9,16</sup>

$$[1] \quad \sigma = \frac{h\rho N_A}{\bar{M}_n}$$

where  $\sigma$  is the surface chain density,  $h$  is the layer thickness determined by ellipsometry,  $\rho$  is the bulk density of the grafted layer (1.0 g/cm<sup>3</sup> was used for poly(OEGMA) and initiator SAMs),  $N_A$  is Avogadro's number, and  $\bar{M}_n$  is the number-average molecular weight ( $\bar{M}_{n, \text{GPC}}$  was used for poly(OEGMA)). The molecular weight of poly(OEGMA) formed on surface is assumed to be the same as that of poly(OEGMA) formed in solution, and the mole fraction of initiator in the SAMs is assumed to be the same as that in the mixed disulfide solution during initiator immobilization.

## Results and discussion

### Mixed SAMs formed on Au surfaces

Scheme 1 illustrates the two-step reaction procedure for the synthesis of poly(OEGMA)-grafted Au surfaces (referred to as Au/poly(OEGMA)). The chain density of poly(OEGMA) was controlled through the surface initiator density in the

SAMs. Bis[2-(2'-bromoisobutyryloxy) ethyl] disulfide (**1**) was used as the grafting initiator and butyl disulfide (**2**) as an inert "diluting agent" that chemisorbs to gold similarly to the initiator. The mole fractions of active initiator in the SAMs ranged from 2% to 100%.

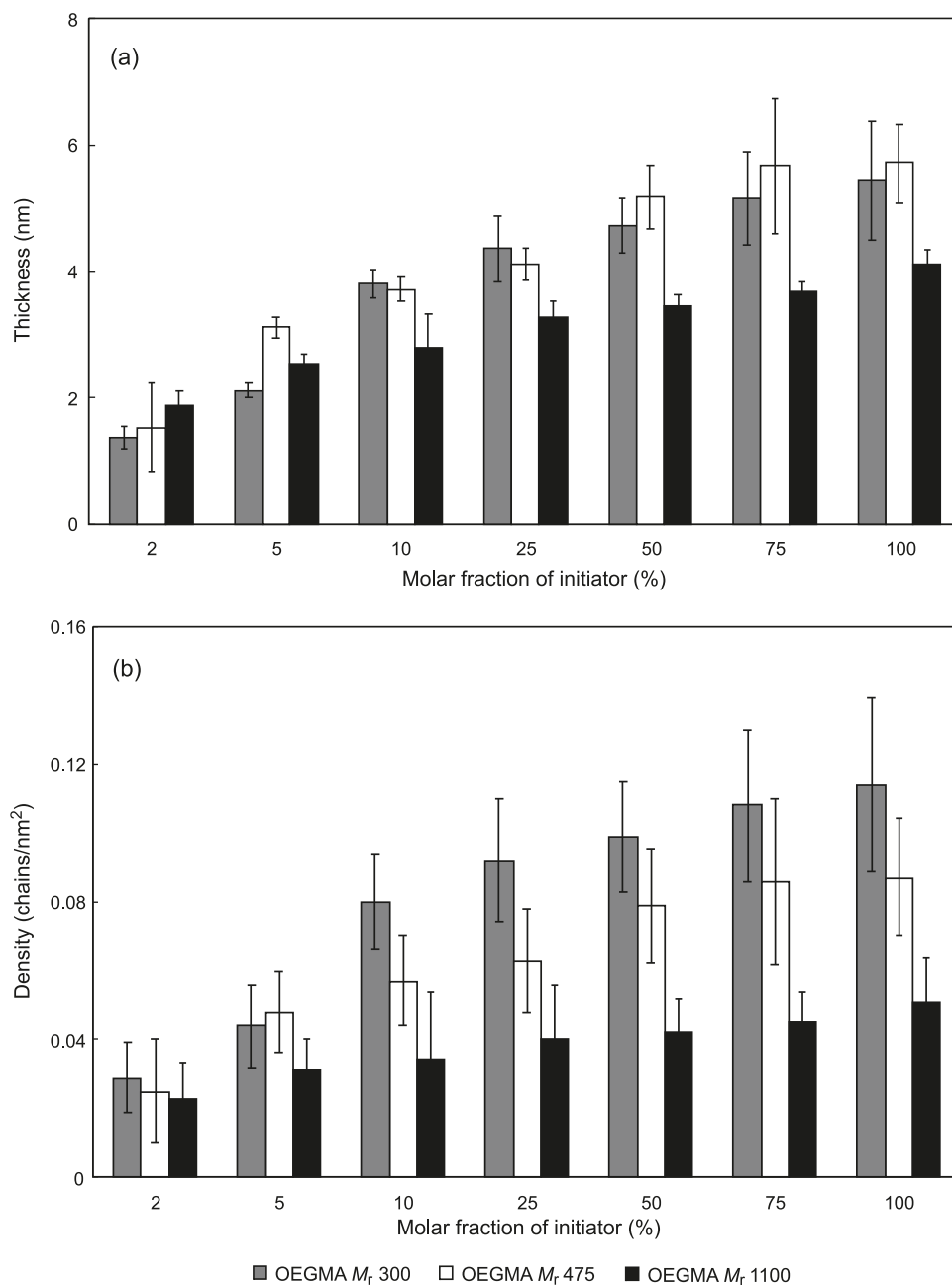
Figure 1a shows the ellipsometric thickness of the SAMs having various mole fractions of initiator; values were in the range of < 1 nm. The 100% initiator layer was significantly thicker than the 100% diluting agent layer, in agreement with the dimensions of the two molecules. The surface density (molecules/nm<sup>2</sup>) of the SAMs was calculated from the thickness data, and the initiator density was estimated from the SAM density and the mole fraction of initiator. The initiator density (Fig. 1b) was found to increase linearly with increasing mole fraction of initiator in the mixed disulfide solution.

### Poly(OEGMA) grafts via s-ATRP

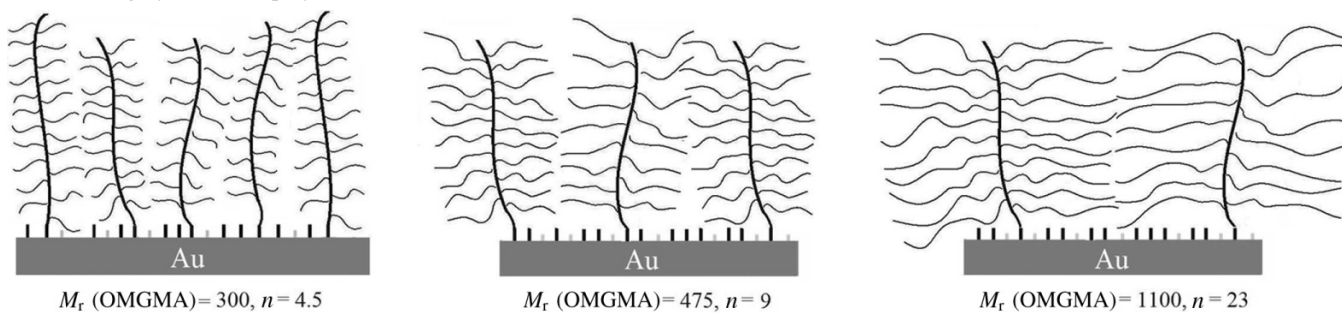
ATRP grafting of OEGMA was carried out on the Au/initiator surfaces with Cu(I)Br/2bpy complex as catalyst and free/sacrificial initiator (EBIB) in solution. The free initiator in solution was in very large amounts compared with the initiator covalently attached on surface. For a well-controlled ATRP process, the polymer chains formed by the free initiator in solution may be assumed to have the same chain length and distribution as the chains grafted on the surface.<sup>17</sup> The monomer conversion, molecular weight, and the polydispersity of the polymers formed in solution are shown in Table 1. Complete conversion was achieved for the ATRP grafting of OEGMA of  $M_r$  300 and 475. However, for OEGMA of  $M_r$  1100, the conversion was limited to ~48%. Polydispersities determined by GPC were in the range of 1.05 to 1.19, indicating good control of the ATRP process.

The advancing water contact angles ( $\theta_{\text{Adv}}$ ) of the Au surfaces before and after modification are shown in Fig. 2. The contact angle of unmodified Au surface was about 65° and clearly decreased after poly(OEGMA) grafting. For a given monomer  $M_r$ , especially for  $M_r$  of 300 and 475,  $\theta_{\text{Adv}}$  decreased slightly from ~55° to ~40° with increasing initiator

**Fig. 3.** (a) Ellipsometric thickness and (b) density (chains/nm<sup>2</sup>) of the poly(OEGMA) grafts with various OEGMA  $M_r$  300, 475, and 1100. Error bars represent one standard deviation,  $n = 4$ .

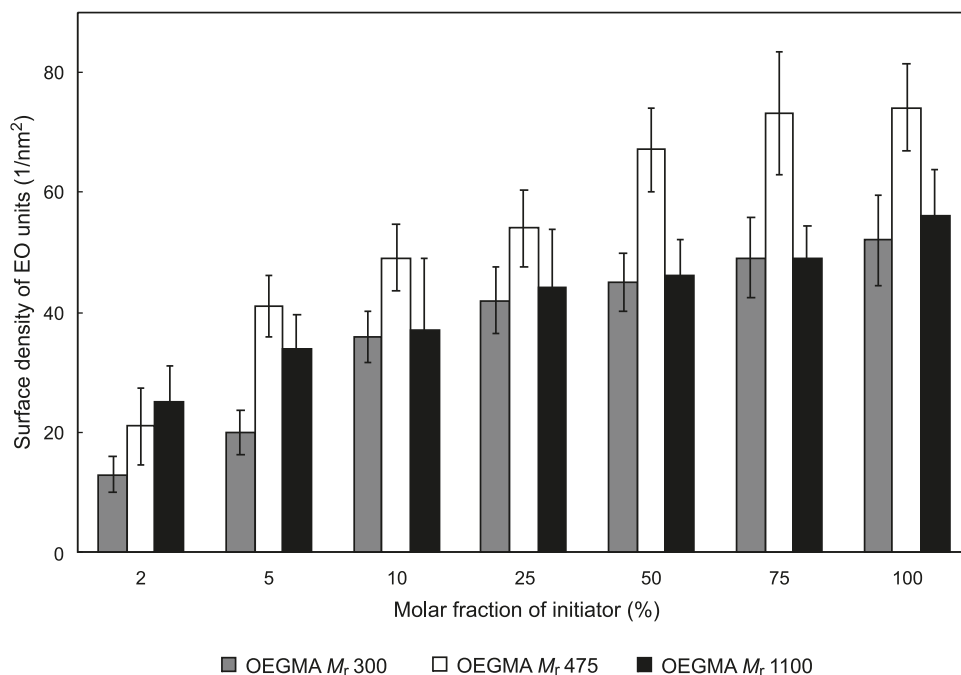


**Scheme 2.** Highly stretched poly(OEGMA) brushes with various OEGMA  $M_r$ .





**Fig. 4.** Surface density of EO units on Au surfaces with various OEGMA  $M_r$  and initiator density. Error bars represent one standard deviation,  $n = 4$ .



fraction from 2% to 100%, presumably due to the increased surface density of the hydrophilic EO units at higher initiator density. For OEGMA of  $M_r$  1100, the contact angle leveled off at initiator fraction > 50%; this is in agreement with the thickness and density variation of the poly(OEGMA) grafts (Fig. 3).

The thickness of poly(OEGMA) grafts was determined by ellipsometry, and the data are shown in Fig. 3a. For a given monomer  $M_r$ , the thickness of the grafts increased significantly with increasing initiator fraction or initiator density, and leveled off above an initiator fraction of 50%, especially for OEGMA of  $M_r$  1100. At relatively low surface initiator density (initiator fraction ~2%), poly(OEGMA)<sub>1100</sub> grafts showed a slightly higher thickness than poly(OEGMA)<sub>300</sub> presumably reflecting higher  $M_r$  but similar chain density. On surfaces with initiator fraction > 10%, the poly(OEGMA)<sub>1100</sub> layer was obviously thinner than the poly(OEGMA)<sub>300</sub> and poly(OEGMA)<sub>475</sub> for a given initiator density. The low DP (~48) or short backbone length of poly(OEGMA)<sub>1100</sub> is one possible reason for the relatively low thickness of poly(OEGMA)<sub>1100</sub> layers.

The surface densities (chains/nm<sup>2</sup>) of the poly(OEGMA) grafts calculated from the ellipsometric thickness data are shown in Fig. 3b. For a given monomer  $M_r$ , the poly(OEGMA) density increased significantly with increasing initiator fraction from 2% to ~50%, and leveled off at higher initiator fractions. At low initiator density (mole fraction 2%–5%), poly(OEGMA) grafts had comparable surface density (chains/nm<sup>2</sup>) independent of OEGMA  $M_r$ ; however, at high initiator density (mole fraction > 10%), significant differences were seen in the densities of poly(OEGMA) grafts for the different monomer  $M_r$  values. Poly(OEGMA)<sub>300</sub> and poly(OEGMA)<sub>475</sub> showed higher graft densities than poly(OEGMA)<sub>1100</sub>, possibly attributable to the size difference of the monomers. Scheme 2 shows a schematic of the stretched out structures of poly(OEGMA) brushes (the expected configuration at relatively high initia-

tor density) and the effect of monomer  $M_r$  on surface density of polymer chains. The larger monomer with larger footprint, once adsorbed, may restrict access of the catalyst complex and monomer to nearby initiator sites, thus reducing initiation efficiency and graft chain density.

The surface densities of EO repeat-unit residues (estimated from the monomer  $M_r$ , polymer chain length, and polymer chain density) are shown in Fig. 4. For a given monomer  $M_r$ , the surface EO unit density generally increased with increasing initiator density in the range investigated (0.03–1.1 chains/nm<sup>2</sup>). For a given high initiator density (initiator fraction > 10%), the poly(OEGMA)<sub>475</sub> layer had the highest EO unit density. The poly(OEGMA)<sub>300</sub> and poly(OEGMA)<sub>1100</sub> layers had similar EO unit density. The low DP and low surface chain density of poly(OEGMA)<sub>1100</sub> relative to poly(OEGMA)<sub>475</sub> and poly(OEGMA)<sub>300</sub> probably account for its relatively low surface EO unit density. Poly(OEGMA)<sub>300</sub> had a similar chain density to poly(OEGMA)<sub>475</sub> at the relatively low initiator density and obviously higher chain density than poly(OEGMA)<sub>475</sub> at the relatively high initiator density. However, poly(OEGMA)<sub>300</sub> had much shorter PEO side-chain length, about half of the side-chain length of poly(OEGMA)<sub>475</sub>, which resulted in a lower EO unit density than poly(OEGMA)<sub>475</sub>.

## Conclusions

Poly(OEGMA) was grafted from Au surface via a two-step procedure including initiator-chemisorption and surface-initiated ATRP. The initiator density was adjusted by mixing the initiator with an inert surface-attachable diluting agent. Three OEGMA monomers of  $M_r$  300, 475, 1100 were used. The Au surfaces were characterized by water contact angle and ellipsometry before and after modification. The data indicated successful formation of initiator and poly(OEGMA) layers with a range of surface densities.

The surface densities of initiator and poly(OEGMA) were calculated from the ellipsometric thickness of the layers. The initiator density was found to increase linearly with increasing mole fraction of initiator in the initiator – diluting agent mixture. For a given monomer  $M_r$ , the poly(OEGMA) thickness and density increased with increasing initiator fraction from 2% to ~50% and leveled off at higher initiator fractions. At low initiator density (mole fraction of initiator 2%–5%), poly(OEGMA) grafts had comparable surface chain density independent of the OEGMA  $M_r$ ; at high initiator density (mole fraction >10%), poly(OEGMA)<sub>1100</sub> showed lower graft densities than poly(OEGMA)<sub>300</sub> and poly(OEGMA)<sub>475</sub>, which could be attributed to the size difference of the monomers.

Surface EO unit density was estimated from the monomer's  $M_r$ , polymer chain length, and polymer chain density, and was found generally to increase with increasing initiator density in the range 0.03–1.1 chains/nm<sup>2</sup> for a given  $M_r$  value of the monomer. For a given high initiator density (initiator fraction >10%), poly(OEGMA)<sub>475</sub> layers showed the highest EO unit density. Poly(OEGMA)<sub>300</sub> and poly(OEGMA)<sub>1100</sub> layers showed similar, but lower, EO unit density.

## Acknowledgments

This work was supported by a Strategic Grant of the Natural Sciences and Engineering Research Council of Canada (NSERC). We also thank the Canada Foundation of Innovation (CFI) for supporting the research facilities in our laboratories.

## References

- (1) Harris, J. M., Ed. In *Poly(ethylene glycol) Chemistry: Biotechnical and Biomedical Applications*; Plenum Press: New York, 1992.
- (2) Szleifer, I. *Biophys. J.* **1997**, 72 (2), 595. doi:10.1016/S0006-3495(97)78698-3. PMID:9017189.
- (3) Jeon, S. I.; Andrade, J. D. J. *Colloid Interface Sci.* **1991**, 142 (1), 159. doi:10.1016/0021-9797(91)90044-9.
- (4) Unsworth, L. D.; Sheardown, H.; Brash, J. L. *Langmuir* **2005**, 21 (3), 1036. doi:10.1021/la047672d. PMID:15667186.
- (5) Liu, P.; Su, Z. *Polym. Bull.* **2005**, 55 (6), 411. doi:10.1007/s00289-005-0454-6.
- (6) Zhang, H.; Shouro, D.; Itoh, K.; Takata, T.; Jiang, Y. J. *Appl. Polym. Sci.* **2008**, 108 (1), 351. doi:10.1002/app.27619.
- (7) Ma, H.; Wells, M.; Beebe, T. P., Jr.; Chilkoti, A. *Adv. Funct. Mater.* **2006**, 16 (5), 640. doi:10.1002/adfm.200500426.
- (8) Feng, W.; Zhu, S.; Ishihara, K.; Brash, J. L. *Biointerphases* **2006**, 1 (1), 50. doi:10.1116/1.2187495.
- (9) Feng, W.; Brash, J. L.; Zhu, S. *Biomaterials* **2006**, 27 (6), 847. doi:10.1016/j.biomaterials.2005.07.006. PMID:16099496.
- (10) Ma, H.; Hyun, J.; Stiller, P.; Chilkoti, A. *Adv. Mater.* **2004**, 16 (4), 338. doi:10.1002/adma.200305830.
- (11) Ejaz, M.; Ohno, K.; Tsujii, Y.; Fukuda, T. *Macromolecules* **2000**, 33 (8), 2870. doi:10.1021/ma991927q.
- (12) Jin, Z.; Feng, W.; Beisser, K.; Zhu, S.; Sheardown, H.; Brash, J. L. *Colloids Surf. B Biointerfaces* **2009**, 70 (1), 53. doi:10.1016/j.colsurfb.2008.12.005. PMID:19150594.
- (13) Jin, Z.; Feng, W.; Zhu, S.; Sheardown, H.; Brash, J. L. *J. Biomed. Mater. Res. A* **2009**, 91 (4), 1189. PMID:19148931.
- (14) Kim, E.; Lee, B. S.; Pyo, H. B.; Song, H. W.; Kim, Y. P.; Choi, I. S.; Kim, H. S. *Biochip J* **2008**, 2, 103.
- (15) Lee, B. S.; Chi, Y. S.; Lee, K. B.; Kim, Y. G.; Choi, I. S. *Biomacromolecules* **2007**, 8 (12), 3922. doi:10.1021/bm7009043. PMID:18039000.
- (16) Feng, W.; Chen, R.; Brash, J. L.; Zhu, S. *Macromol. Rapid Commun.* **2005**, 26 (17), 1383. doi:10.1002/marc.200500335.
- (17) Pyun, J.; Kowalewski, T.; Matyjaszewski, K. *Macromol. Rapid Commun.* **2003**, 24 (18), 1043. doi:10.1002/marc.200300078.

# Competition between electrochemical advanced oxidation and electrochemical hypochlorination of acetaminophen at boron-doped diamond and ruthenium dioxide based anodes

Jordache Boudreau, Dorin Bejan, and Nigel J. Bunce

**Abstract:** This work was undertaken to distinguish four pathways for the electrochemical oxidation of acetaminophen as a model organic substrate: (i) direct electron transfer from the substrate to the anode, (ii) reaction of the substrate with HO• at boron-doped diamond anodes, (iii) non-radical (two-electron) oxidation of the substrate at Ti/RuO<sub>2</sub> anodes, and (iv) electrochemical hypochlorination if Cl<sup>-</sup> is present. Pathway (i) was isolated as a slow reaction when boron-doped diamond (BDD) was used as the anode in the range of water stability, whereas in the corresponding reaction with Ti/RuO<sub>2</sub> only pathway (iii) could be detected. Pathway (ii) predominated for BDD in the potential range of water oxidation, and was the only mechanism leading to mineralization of the substrate. Comparison between chemical hypochlorination and electrochemical oxidation at Ti/RuO<sub>2</sub> in the presence of chloride ion indicated that the latter process principally involves mediated hypochlorination. Oxidation at boron-doped diamond anodes in the presence of chloride was the most complex mechanistically, with competition between hypochlorination and the electrochemical “advanced oxidation process”; this led to the formation of chlorinated byproducts. The observation of mineralization under these conditions demonstrated cross-over between reaction pathways (ii) and (iv), even though hypochlorination appeared to be the initial pathway for loss of acetaminophen. The presence of chloride ion did not significantly retard mineralization of acetaminophen in the initial stages of oxidation, but significantly increased the energy requirement for complete mineralization. The results are discussed in the context of the use of electrochemical oxidation in waste management.

**Key words:** mineralization, electrochemical hypochlorination, electrochemical advanced oxidation, boron-doped diamond anode, acetaminophen.

**Résumé :** On a entrepris ce travail dans le but d'établir une distinction entre les quatre voies réactionnelles lors de l'oxydation électrochimique de l'acétaminophène utilisé comme substrat organique modèle : (i) transfert d'électron direct du substrat à l'anode; (ii) réaction du substrat avec le HO• au niveau des anodes de diamant dopées au bore; (iii) oxydation non radicalaire à deux électrons du substrat au niveau des anodes de Ti/RuO<sub>2</sub> et (iv) hypochloruration électrochimique si l'anion Cl<sup>-</sup> est présent. La voie réactionnelle (i) a été détectée sous la forme de réaction lente quand on utilise du diamant dopé au bore (DDB) comme anode dans la plage de stabilité de l'eau alors que pour la réaction correspondante avec des anodes de Ti/RuO<sub>2</sub> on n'a détecté que la voie (iii). La voie (ii) est prédominante pour le DDB dans la plage de potentiel d'oxydation de l'eau et c'est le seul mécanisme qui conduit à la minéralisation du substrat. Une comparaison entre l'hypochloruration chimique et l'oxydation électrochimique avec des anodes de Ti/RuO<sub>2</sub>, en présence d'ion chlorure, indique que le deuxième processus implique une hypochloruration catalysée. L'oxydation au niveau des anodes de diamant dopées au bore, en présence d'ion chlorure, est la réaction la plus complexe d'un point de vue mécanistique et elle implique une compétition entre l'hypochloruration et le processus d'oxydation électrochimique avancée; ceci conduit à la formation de sous-produits chlorés. L'observation d'une minéralisation dans ces conditions a permis de démontrer qu'il se produit un croisement entre les voies réactionnelles (ii) et (iv), même si l'hypochloruration semblait être la voie initiale pour la perte de l'acétaminophène. La présence d'ion chlorure ne retarde pas d'une façon significative la minéralisation de l'acétaminophène dans les étapes initiales de l'oxydation, mais elle augmente considérablement l'énergie requise pour arriver à une minéralisation complète. On discute des résultats dans le contexte d'une utilisation de l'oxydation électrochimique dans la gestion des déchets.

**Mots-clés :** minéralisation, hypochloruration électrochimique, oxydation électrochimique avancée, anode de diamant dopé au bore, acétaminophène.

[Traduit par la Rédaction]

Received 4 December 2009. Accepted 20 January 2010. Published on the NRC Research Press Web site at canjchem.nrc.ca on 24 March 2010.

**J. Boudreau, D. Bejan, and N.J. Bunce.**<sup>1</sup> Electrochemical Technology Centre, Chemistry Department, University of Guelph, 50 Stone Road East, Guelph, ON N1G 2W1, Canada.

<sup>1</sup>Corresponding author (e-mail: nbunce@uoguelph.ca).

## Introduction

Electrochemical oxidation of organic-contaminated wastewaters has received considerable research attention as a possible treatment method.<sup>1–7</sup> Much of this effort has focused on anodes with a high overpotential for oxygen evolution (inactive anodes), notably  $\beta$ -PbO<sub>2</sub>, Ti/SnO<sub>2</sub>, and boron-doped diamond (BDD), which are especially effective at producing sorbed hydroxyl radicals, also called “physisorbed active oxygen”.<sup>8,9</sup> These methods have been termed electrochemical advanced oxidation processes (EAOPs)<sup>10–12</sup> by analogy with conventional “advanced oxidation processes” (AOPs), which also involve hydroxyl radicals. Hydroxyl radicals have high and indiscriminate reactivity towards most organic compounds through addition and (or) hydrogen abstraction reactions,<sup>13</sup> leading to complete oxidation (mineralization) of recalcitrant organic contaminants by EAOP, or partial oxidation to render them more amenable to conventional biological oxidation.

Electrochemical oxidation of organic substrates is accelerated in the presence of chloride ion, which is a common constituent of industrial waste streams.<sup>14–17</sup> Chloride can be oxidized electrochemically to hypochlorous acid or hypochlorite ion, depending on the pH; the resulting free available chlorine (FAC) can effect electrochemical hypochlorination (EH) because FAC is both a chlorinating and an oxidizing agent. Hypochlorination does not lead to mineralization and may produce chlorinated byproducts that are more recalcitrant to remediation than the original contaminants. EH should predominate over EAOP at “active” anodes based on Ti/IrO<sub>2</sub> and Ti/RuO<sub>2</sub>, which function as oxidizing agents by a “higher oxide” (MO<sub>*n*+1</sub>) mechanism,<sup>18–20</sup> and which also promote efficient conversion of chloride to FAC.<sup>21</sup>

In principle, an organic contaminant might be electrochemically oxidized by several different reaction pathways when chloride ion is present. These are direct electron transfer from the substrate to the anode, EAOP by reaction of the substrate with HO• at inactive anodes, non-radical (two-electron) oxidation of the substrate by MO<sub>*n*+1</sub> at active anodes, and EH if Cl<sup>–</sup> is present.

We recently explored the relationship between some of these mechanisms using the antibiotic sulfamethoxazole (SMX) as a test substrate.<sup>22</sup> Most of the work was carried out using BDD anodes, at which EH and EAOP should occur competitively in the presence of chloride ion. The loss of SMX increased monotonically upon addition of chloride ion. Mineralization was not inhibited in the early stages of oxidation, but the formation of chlorinated intermediates greatly increased the charge needed for complete mineralization. The oxidation of SMX (with or without chloride) could not be studied at Ti/IrO<sub>2</sub>–Ta<sub>2</sub>O<sub>5</sub> anodes, which were rapidly inactivated due to electropolymerization through the aniline functional group. The present study was therefore initiated to remedy this limitation; the substrate selected was acetaminophen (AP), which has previously been shown to undergo oxidation in the absence of chloride at both active (Ti/IrO<sub>2</sub>–Ta<sub>2</sub>O<sub>5</sub>) and inactive (BDD) anodes using a plug-flow divided reactor.<sup>23</sup> AP offers a useful mechanistic distinction: whereas mineralization occurs smoothly at the inactive anode BDD, the chief product at the active anode

Ti/IrO<sub>2</sub>–Ta<sub>2</sub>O<sub>5</sub> is benzoquinone (BQ).<sup>23,24</sup> Brillas et al.<sup>25</sup> studied the mineralization of AP in the pH range of 1–12 with Na<sub>2</sub>SO<sub>4</sub> as supporting electrolyte using an undivided cell. Complete mineralization with release of NH<sub>4</sub><sup>+</sup> and NO<sub>3</sub><sup>–</sup> ions was achieved at a BDD anode, but mineralization was inefficient at Pt.

## Materials and methods

### Materials

Acetaminophen, *N*-(4-hydroxyphenyl)ethanamide (AP), 1,4-benzoquinone (BQ) 98%, potassium iodide 99%+, and sodium perchlorate 99%+ were supplied by Sigma-Aldrich (Oakville, ON). HPLC grade acetonitrile was obtained from Caledon Laboratories (Georgetown, ON); sodium chloride, sodium phosphate monobasic monohydrate, and sodium hydroxide were supplied by Fisher Scientific Company (Toronto, ON). “Ultra” bleach (6%) was purchased from No-Frills, Guelph ON, subsidiary of Loblaw's Inc, Toronto, ON. Solutions were prepared using a Millipore Milli-Q Reagent Water System with water having resistivity of about 18.2 MΩ cm. The Si/BDD anodes were obtained from the Swiss Center for Electronics and Microtechnology, Inc., Neuchâtel; titanium served as the cathode (Chemistry machine shop, University of Guelph).

### Apparatus and experimental procedures

Batch electrolyses were performed in a 150 mL beaker (Pyrex, USA) with a solution volume of 100 mL of 1 mmol/L AP or BQ; ionic strength was maintained at 0.1 mol/L with NaClO<sub>4</sub>. The immersed areas of both the titanium cathode and the Si/BDD anode were 3.75 cm<sup>2</sup>. Solutions were stirred during electrolysis using a Thermix stirrer (Fisher Scientific Model 120 MR). Voltage, electrode potential, and current were monitored using a Wavetek DM5XL Voltmeter and Mastercraft 052–0060–2 multimeter. Power to the electrochemical reactor was supplied by an EG&G Model 363 potentiostat/galvanostat. Cyclic voltammetry measurements were carried out at room temperature in a 50 mL beaker (solution volume 40 mL) using a BDD MDA 5–150/106 microelectrode array (Swiss Center for Electronics and Microtechnology, Inc., Neuchâtel) as the working electrode, platinum plate as the counter electrode, and saturated calomel reference electrode (Fisher Scientific, Toronto, ON). Data were obtained using an EG&G Model 273 Potentiostat/Galvanostat at a fixed sweep rate of 50 mV s<sup>–1</sup>, controlled using Power Suite version 2.12.1 software. Chemical hypochlorination was performed in a 150 mL beaker with a solution volume of 100 mL and a concentration of 1 mmol/L AP or BQ; injections of 40 μL bleach were added every 10 min. The bleach was standardized by iodometry: nominal concentration 6% w/v; actual 6.4%, 0.86 mol/L.

### Analytical measurements

The reactions were followed by HPLC, using a Waters 600E system equipped with a Waters 2487 dual λ absorbance detector set at 254 nm and a Supelco Discovery C18 column 150 × 4.6 mm (5 μm) equipped with a silica pre-column guard. An HPLC method was developed by using a mobile solvent of acetonitrile–water (30:70) (filtered through a 0.2 μm filter) at a flow rate of 1.0 mL min<sup>–1</sup> (retention times



of AP and BQ were ~2.5 min and ~4.0 min, respectively). Samples were manually injected into the 20  $\mu\text{L}$  sample loop of a Rheodyne injector. Total Organic Carbon (TOC) was analyzed as non-purgeable organic carbon (NPOC) with a Shimadzu TOC analyzer, model TOC-VCPN. Absorbable organic halide (AOX) analysis was provided by ALS Laboratory Services of Thunder Bay, ON, Canada.

## Results and discussion

### Voltammetry

Cyclic voltammetry of AP at a 5–150/106 BDD microelectrode array (Fig. 1) showed an irreversible voltammetric peak at +0.94 V vs. SCE with  $I_p \propto [\text{AP}]$ , in both the absence and presence of 100 mmol/L NaCl. Although  $E^\circ$  for oxidation of chloride ion to HOCl is +1.49 V and for  $\text{ClO}^-$  is 0.90 V,<sup>26,27</sup> there was no oxidation current for solutions of chloride alone, because of the large overpotential for this oxidation.<sup>28,29</sup> There was no oxidation current for *p*-benzoquinone (an oxidation product of AP) in the region of water stability nor did we observe the reduction peak for the immediate oxidation product of AP (*N*-acetylbenzoquinonimine) that had been observed by Nematollahi et al.<sup>30</sup> on a glassy carbon working electrode, Madsen et al.<sup>31</sup> on porous graphite, or Van Benschoten et al.<sup>32</sup> on carbon paste. At Ti/RuO<sub>2</sub>, the current at ~ +1.2 V vs. SCE due to solvent oxidation obscured the oxidation of AP itself (see Fig. 1 in the Supplementary data).

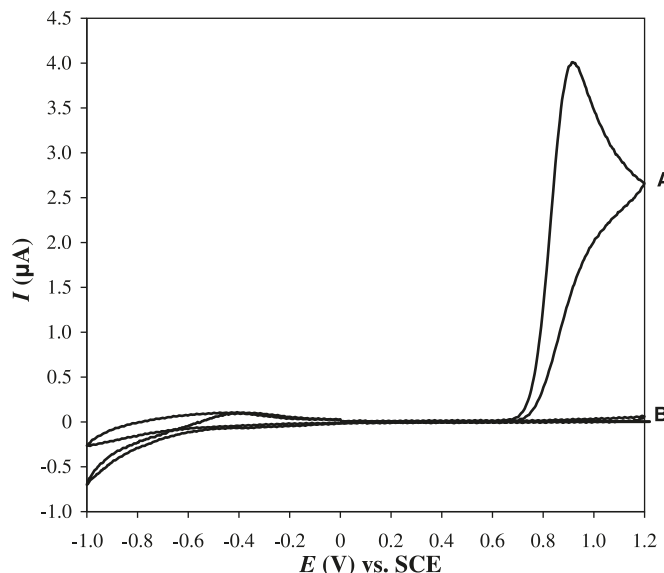
### Potentiostatic oxidation of AP in the presence of chloride ion

The oxidation of 1 mmol/L AP at Si/BDD was followed by HPLC within the range of water stability at +1.4 V vs. SCE, using 100 mmol/L NaClO<sub>4</sub> or NaCl as the supporting electrolyte in a divided cell. The loss of AP was very slow, whether or not chloride was present (Fig. 2A). Initial rates were 0.13  $\mu\text{mol min}^{-1}$  (NaClO<sub>4</sub>) and 0.10  $\mu\text{mol min}^{-1}$  (NaCl). The current was too low to be recorded accurately. No anode gas was observed, showing that there was no discharge of water at this potential and hence no production of hydroxyl radicals. The reaction was therefore attributed to direct oxidation of AP (pathway (i)). This conclusion was supported by the formation of a significant yield of benzoquinone, which is rapidly destroyed by hydroxyl radicals ( $1.2 \times 10^9 \text{ L mol}^{-1} \text{ s}^{-1}$  at pH 7).<sup>33</sup> At Ti/RuO<sub>2</sub>, the reaction was much faster because water is oxidized at this active anode, giving the surface oxide RuO<sub>3</sub>, which can oxidize either AP directly or  $\text{Cl}^-$  to hypochlorite; as a result, the loss of AP was faster in the presence of chloride (Fig. 2B). No mineralization occurred in any of these reactions.

### Amperostatic oxidation of AP

The electrochemical oxidation at 80 mA of AP at Si/BDD and at Ti/RuO<sub>2</sub> in the absence of chloride (NaClO<sub>4</sub> supporting electrolyte) is presented in Fig. 3, in which all data are shown in parts per million (mg L<sup>-1</sup>) of carbon. The loss of AP was slightly slower at Ti/RuO<sub>2</sub> and in both cases followed kinetics intermediate between pure current control (linear relationship between the concentration of AP remaining and time), and mass transport control (exponential loss of AP with time), tending to the latter towards the end of

**Fig. 1.** Cyclic voltammogram (0 V to +1.2 V to –1.0 V to 0 V) for 1 mmol/L AP at Si/BDD microelectrode array; sweep rate 50 mV s<sup>-1</sup>; supporting electrolyte 100 mmol/L NaClO<sub>4</sub>. (A) AP; (B) solvent.

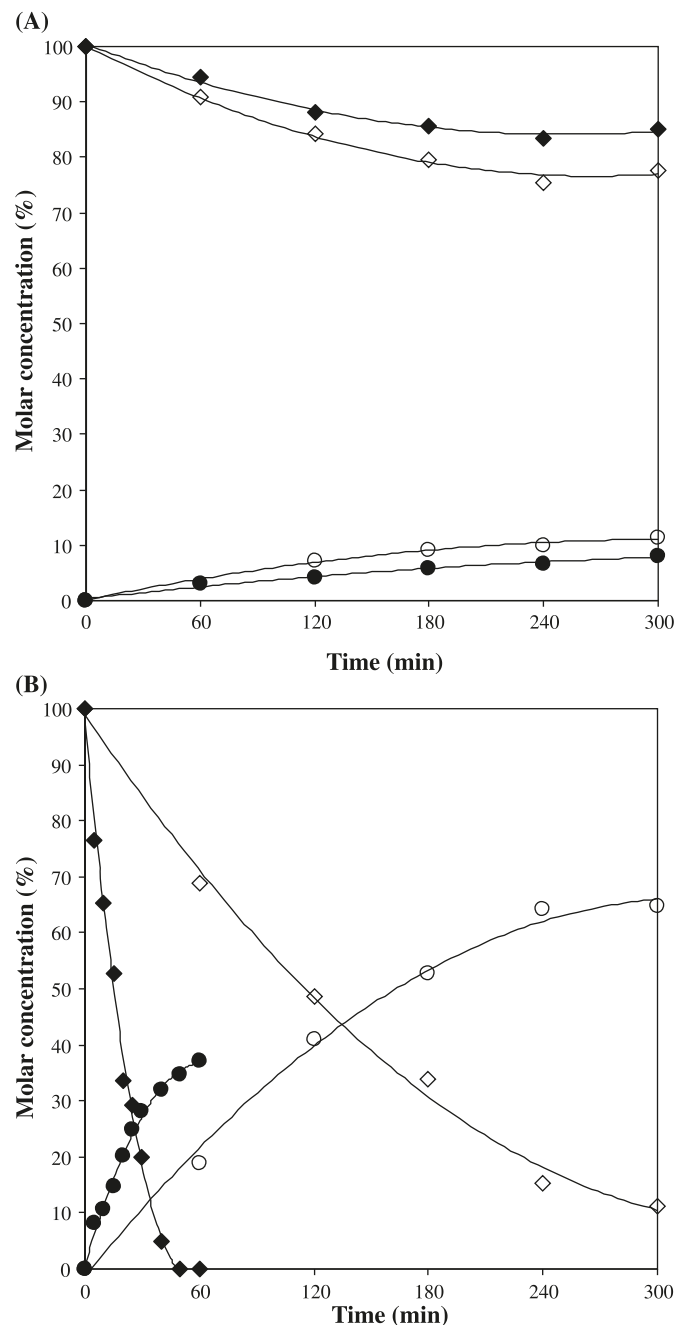


the reaction. Figure 2 in the Supplementary data shows the progress of the reaction according to the half-order kinetic model (between current control and mass transport control) developed in our previous work on the oxidation of sulfamethoxazole.<sup>34</sup>

Kapalka et al.<sup>8</sup> propose that for mass-transport limited reactions at inactive anodes such as BDD, the substrate undergoes multiple acts of HO•-induced oxidation without migrating from the anode into the bulk solution. At its extreme, this kinetic behaviour implies loss of substrate in parallel with loss of TOC. This was broadly true for the oxidation at BDD, where Fig. 3 shows that the course of mineralization, monitored as NPOC, only slightly lagged behind the loss of AP. (The deviation between the rates should be greater under pure current control, when the concentration of HO• radicals at the anode is insufficient to prevent migration of intermediates into the bulk solution.) The loss of AP was somewhat slower at Ti/RuO<sub>2</sub> but mineralization did not occur, consistent with oxidation at this active anode being a two-electron process; the observed formation of BQ supports this conclusion.

The presence of 100 mmol/L chloride ion greatly accelerated the loss of AP at both BDD and Ti/RuO<sub>2</sub> (Fig. 4), consistent with the involvement of EH. These reactions were first order in concentration of AP indicating that the principal electrochemical reaction is formation of FAC, followed by reaction between FAC and AP in the bulk solution. Mineralization occurred more slowly at the BDD anode when chloride was present (compare Figs. 3 and 4). AOX analysis showed the formation of chlorinated byproducts (Fig. 5), which were also detectable (though not specifically identified) by HPLC (see Fig. 3 in the Supplementary data, Panels A–C). Figure 5 shows the losses of AP and NPOC in mmol/L of carbon, and progression of AOX in mmol/L of chlorine. Under these conditions, mineralization could be initiated by hydroxyl radical attack on AP, with subsequent chlorination,

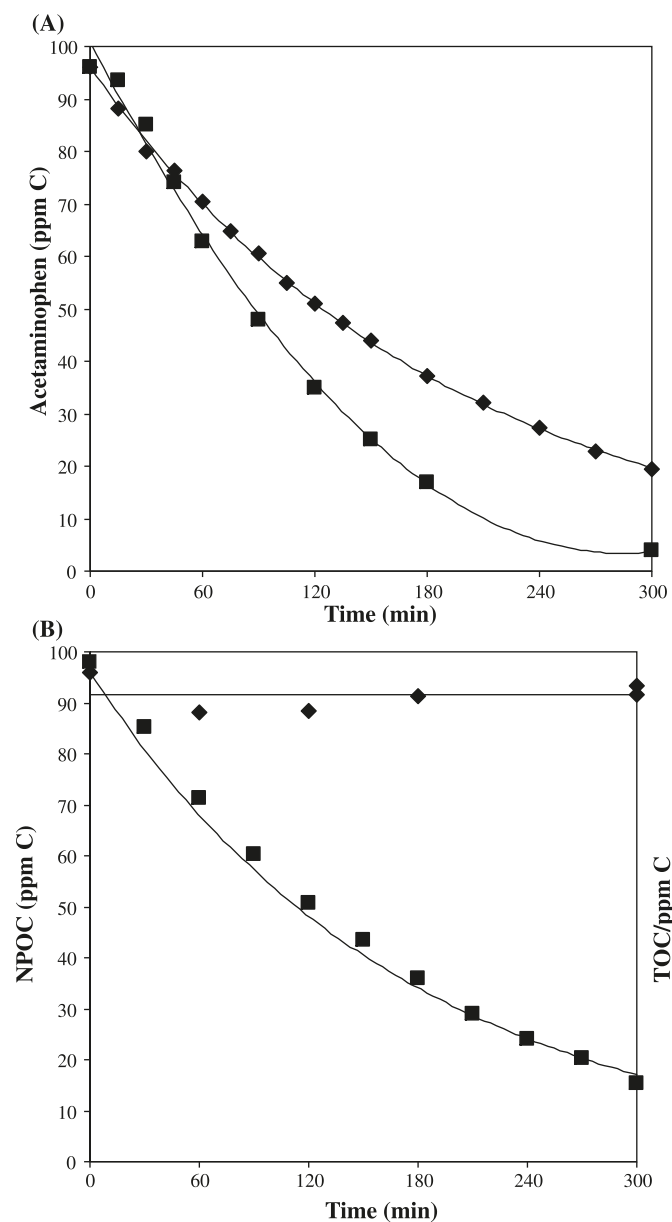
**Fig. 2.** Potentiostatic electrolysis of 1 mmol/L AP at +1.4 V (vs. SCE). Panel A: Si/BDD anode; panel B: Ti/RuO<sub>2</sub> anode. Symbols: ◇, AP; ○, BQ in 100 mmol/L NaClO<sub>4</sub>; ◆, AP; ●, BQ in 100 mmol/L NaCl.



and (or) by an initial hypochlorination and subsequent reaction with hydroxyl radicals. The mechanistic picture is further complicated by suggestions that adsorbed chloro and oxychloro radicals could participate in the oxidation process, though there appears to be no direct evidence for the intermediacy of these species.<sup>35–39</sup>

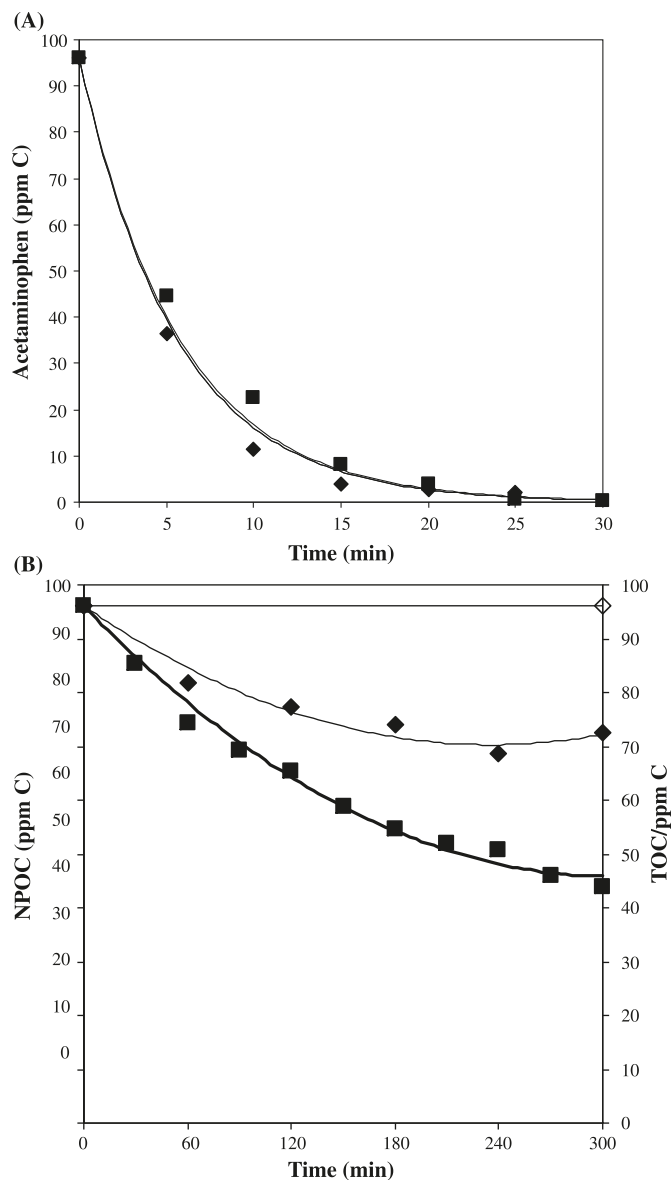
The chlorinated products were highly persistent; Fig. 5 shows that by the end of the electrolysis, the remaining organic material contained an average of one chlorine atom for every three carbon atoms. Complete mineralization of AP in the presence of chloride is thus much more energy-

**Fig. 3.** AP and NPOC loss during electrolysis at Si/BDD and Ti/RuO<sub>2</sub> anodes in the absence of chloride. Panel A: AP; panel B: NPOC. Symbols: ■, Si/BDD anode; ◆, Ti/RuO<sub>2</sub> anode. Supporting electrolyte: 100 mmol/L NaClO<sub>4</sub>; initial AP concentration: 1 mmol/L; current: 80 mA.



demanding than the corresponding chloride-free reaction (see Fig. 4 in the Supplementary data), as found previously for SMX.<sup>22</sup> The apparent partial mineralization of AP in the chloride-assisted oxidation at Ti/RuO<sub>2</sub>, shown in Fig. 4, Panel B, is an experimental artefact, caused by the fact that our TOC analyzer actually measures non-purgeable organic carbon (NPOC) rather than TOC. When correction was made for the purgeable organic carbon, it was found that no mineralization had occurred (see later for discussion of this point). These results support the hypothesis that at Ti/RuO<sub>2</sub> the principal reaction pathway is hypochlorination, whereas at BDD there is competition between EH and EAOP, with the initial products of EH being susceptible to EAOP and

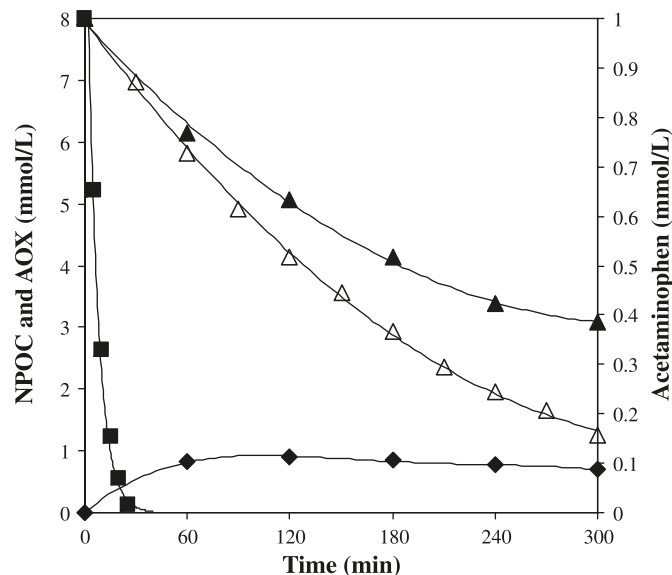
**Fig. 4.** AP and NPOC loss during electrolysis at Si/BDD and Ti/RuO<sub>2</sub> anodes in the presence of 100 mmol/L NaCl. Panel A: AP; panel B: NPOC and TOC. Symbols: ■, Si/BDD anode; ◆, Ti/RuO<sub>2</sub> anode; TOC: ◇, Ti/RuO<sub>2</sub> anode; supporting electrolyte. Initial AP concentration: 1 mmol/L; current: 80 mA.



vice versa. The latter hypothesis is supported by the observation that at BDD the loss of AP accelerated with increasing Cl<sup>-</sup> concentration, whereas the initial rate of mineralization was almost unaffected (see Fig. 5 in the Supplementary data; current 20 mA). At higher current, the initial loss of AP was faster (see Fig. 6 in the Supplementary data; current 80 mA), although the efficiency of mineralization per unit charge was lower, owing to more parasitic oxidation of water to O<sub>2</sub> (see Fig. 7 in the Supplementary data).

Electrooxidation of AP in the presence of chloride ion was compared with conventional chemical hypochlorination via FAC. Previously, Pinkston and Sedlak<sup>40</sup> showed that the pseudo first-order rate constant for reaction of AP with FAC changed by less than one log unit over the range pH 5–10. Bedner and MacCrehan<sup>41</sup> identified two initial

**Fig. 5.** Electrolysis of 1 mmol/L AP with a Si/BDD anode at 80 mA in the absence and presence of chloride. △, NPOC in the absence of chloride (100 mmol/L NaClO<sub>4</sub>); ■, AP; ▲, NPOC; ◆, AOX, all in the presence of 100 mmol/L NaCl.



reaction pathways: ring chlorination and oxidation to *N*-acetylbenzoquinonimine (and hence benzoquinone). We found that chemical hypochlorination was efficient on the basis of mol AP lost per mol FAC added (see Fig. 8 in the Supplementary data). No mineralization was observed, similar to the electrolysis at Ti/RuO<sub>2</sub> although the pattern of byproducts observed (see Fig. 3F in the Supplementary data) differed from those produced electrochemically at either Si/BDD or Ti/RuO<sub>2</sub> (see Fig. 3C and 3E in the Supplementary data). As in the electrochemical experiments, NPOC suggested that mineralization had occurred, but the missing material was again traceable to purgeable organic carbon (POC). The level of POC increased if NaOCl was added portion-wise (to mimic its electrochemical formation) rather than in a single aliquot, or if the solution pH was lowered from 6 to 5 (see Fig. 9 in the Supplementary data). We considered whether the purgeable material might be due to hydrolysis of the acetyl side chain of AP to acetate, but concluded that this was not the explanation because acetic acid was not purgeable under our analytical conditions.

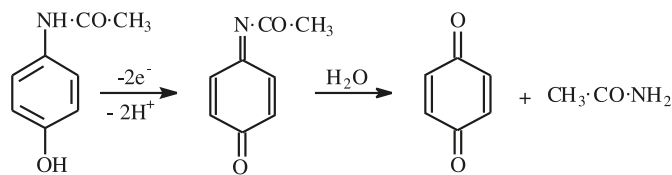
Because chemical hypochlorination is a common strategy for waste treatment,<sup>42–49</sup> we carried out a series of experiments to explore whether electrochemical oxidation could be useful for remediation after hypochlorination with FAC. The efficiency of mineralization was greater when NaClO<sub>4</sub> was used as the supporting electrolyte in the post-treatment rather than NaCl. However, mineralization remained most effective in the absence of chlorination (Fig. 6).

### Amperostatic oxidation of BQ

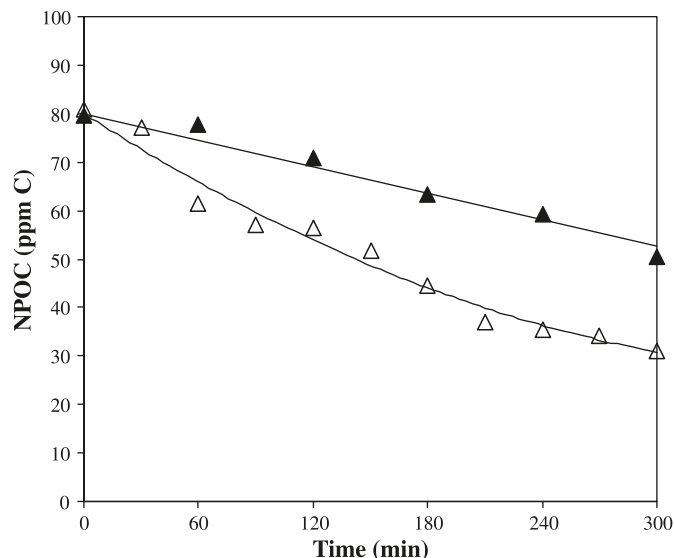
Previous work has shown that *p*-benzoquinone (BQ) is an intermediate in the oxidation of AP. Parallel to the metabolic chemistry of AP, the formation of BQ is believed to involve a two-electron oxidation of AP to a quinonimine followed by hydrolysis (Scheme 1).<sup>30,32</sup>

Yields of BQ are high when AP is oxidized at active electro-

Scheme 1.



**Fig. 6.** Comparison of chemically hypochlorinated AP and subsequent electrolysis with Si/BDD at 80 mA. Electrolysis of pre-hypochlorinated AP:  $\Delta$ , AP with 100 mmol/L NaClO<sub>4</sub>;  $\blacktriangle$ , AP with 100 mmol/L NaCl; initial AP concentration: 1 mmol/L.

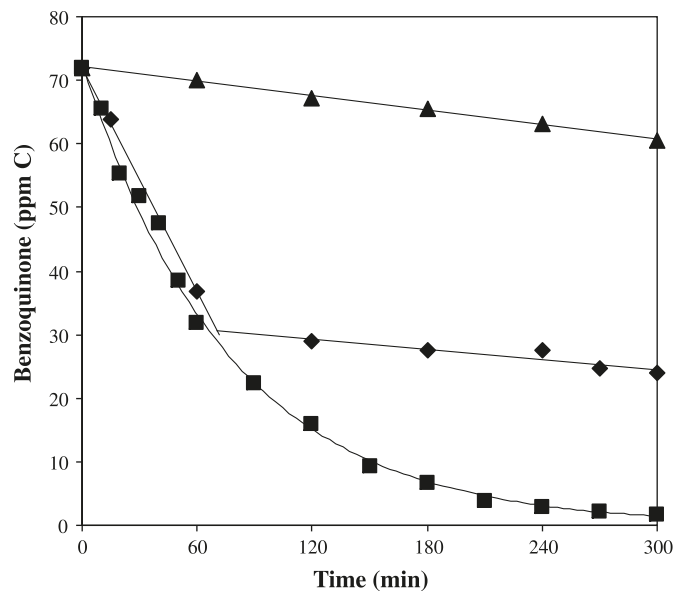


des, but low to negligible at inactive electrodes such as Si/BDD.<sup>23–25</sup> However, the formation of even low yields of BQ is less easily explained at an inactive anode such as Si/BDD, because Yang et al.<sup>50</sup> have indicated that addition to the phenolic ring is the primary reaction between AP and HO $\cdot$ . The voltammetric data reported above suggest that the low yield of BQ may arise by competing direct oxidation of AP. However, BQ is very susceptible to radical addition reactions and cannot build up to high concentrations when inactive anodes are used.

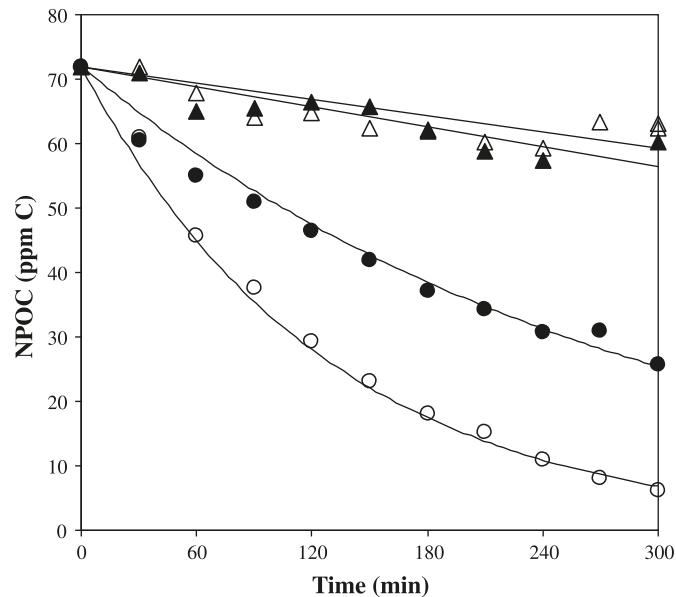
The voltammetric data also indicate that BQ should be stable to further oxidation at active electrodes, and this was essentially the case in earlier work carried out in a flow cell.<sup>23,24</sup> However, in the present work, which employed undivided batch reactors, BQ was at least as susceptible to reaction as AP at both Si/BDD and Ti/RuO<sub>2</sub> (see Fig. 10 in the Supplementary data). This phenomenon was traced to two factors: reduction of BQ at the cathode of the undivided cell and greater chemical stability at lower pH. Figure 7 demonstrates increased persistence of BQ upon electrolysis at Ti/RuO<sub>2</sub> in the order: undivided cell using NaClO<sub>4</sub> supporting electrolyte < undivided cell using H<sub>2</sub>SO<sub>4</sub> supporting electrolyte (pH 2) < divided cell using H<sub>2</sub>SO<sub>4</sub> supporting electrolyte (pH 2).

In many respects, the mineralization of BQ in the undivided batch reactor paralleled that of AP (compare Fig. 8 with Figs. 3 and 4). The rate of disappearance of BQ was comparable at Ti/RuO<sub>2</sub> and Si/BDD in the absence of chloride. Mineralization closely followed BQ loss at Si/BDD, but

**Fig. 7.** Electrolysis of 1 mmol/L *p*-benzoquinone with a Ti/RuO<sub>2</sub> anode at 80 mA. Symbols:  $\blacksquare$ , undivided cell (100 mmol/L NaClO<sub>4</sub>);  $\blacklozenge$ , undivided cell (H<sub>2</sub>SO<sub>4</sub>, pH 2);  $\blacktriangle$ , divided cell (conc. H<sub>2</sub>SO<sub>4</sub>, pH 2).



**Fig. 8.** NPOC loss during electrolysis of BQ with Si/BDD and Ti/RuO<sub>2</sub> at 80 mA in the absence and presence of chloride in an undivided cell. Si/BDD:  $\circ$ , 100 mmol/L NaClO<sub>4</sub>;  $\bullet$ , 100 mmol/L NaCl; Ti/RuO<sub>2</sub>:  $\Delta$ , 100 mmol/L NaClO<sub>4</sub>;  $\blacktriangle$ , 100 mmol/L NaCl; initial BQ concentration: 1 mmol/L.



there was almost no mineralization (based on NPOC) at Ti/RuO<sub>2</sub>. BQ is highly susceptible to hypochlorination, and in the presence of chloride, the rate of reaction at Ti/RuO<sub>2</sub> was greatly increased but again there was no mineralization. At Si/BDD, the presence of chloride increased the reactivity of BQ but substantially decreased the rate of mineralization; analysis by HPLC showed the presence of chlorinated byproducts.



## Conclusions

We introduced this work by identifying four distinct pathways for the electrochemical oxidation of an organic substrate, namely, (i) direct electron transfer from the substrate to the anode, (ii) EAOP by reaction of substrate with HO• at inactive anodes, (iii) non-radical (two electron) oxidation of substrate by MO<sub>n+1</sub> at active anodes, and (iv) EH if Cl<sup>-</sup> is present.

Acetaminophen is a valuable substrate for distinguishing these mechanisms. Its distinct voltammetric oxidation peak allowed the study of its direct electron transfer in the region of water stability. This reaction does not lead to mineralization in the absence or presence of chloride, even at the inactive anode Si/BDD, because hydroxyl radicals are not formed. It is inconveniently slow as a prospective remediation technology and rather inefficient; this mechanism probably contributes little to the overall chemistry except in the range of water stability.

Amperostatic oxidation in the region of water decomposition (O<sub>2</sub> evolution at the anode) showed an efficient mineralization reaction by the EAOP mechanism at Si/BDD in the absence of chloride; low yields of BQ at intermediate stages of the reaction were ascribed to the competing direct electron-transfer reaction. Comparison between chemical hypochlorination (FAC) and electrochemical oxidation at Ti/RuO<sub>2</sub> indicated that the latter process, which does not lead to mineralization, principally involves mediated hypochlorination. Oxidation at Si/BDD in the presence of chloride is the most complex mechanistically, with competition between EAOP and EH. Kinetic analysis suggested that chloride ion diverts the main pathway for initial destruction of AP to hypochlorination in the bulk even at BDD; this was confirmed by rather similar patterns of chlorinated byproducts at both electrodes. In contrast, different patterns of chlorinated byproducts were seen at Si/BDD and Ti/IrO<sub>2</sub>-Ta<sub>2</sub>O<sub>5</sub> in the degradation of SMX.<sup>22</sup> Even though EH appears to be the initial reaction for loss of AP, crossover between the EH and EAOP reaction sequences is evident by the occurrence of mineralization, albeit more slowly than in the absence of chloride.

Critically for the use of electrochemical oxidation in waste management, the presence of chloride ion as a constituent of the waste leads to the formation of persistent byproducts, whose removal significantly increases the energy requirement for complete mineralization at the inactive anode BDD (although the initial rate of mineralization is not retarded by chloride ion at low current). Although electrolysis can be considered as a post-treatment to the common industrial practice of chemical hypochlorination, mineralization under those circumstances is more energy-demanding.

## Supplementary data

Supplementary data for this article are available on the journal Web site (canjchem.nrc.ca) or may be purchased from the Depository of Unpublished Data, Document Delivery, CISTI, National Research Council Canada, Ottawa, ON K1A 0R6, Canada. DUD 5367. For more information on obtaining material, refer to cisti-icist.nrc-cnrc.gc.ca/cms/unpub\_e.shtml.

## Acknowledgements

We thank the Natural Sciences and Engineering Research Council of Canada (NSERC) for financial support.

## References

- (1) Martínez-Huitle, C. A.; Brillas, E. *Appl. Catal. B Environ.* **2009**, *87* (3–4), 105. doi:10.1016/j.apcatb.2008.09.017.
- (2) Anglada, A.; Urtiaga, A.; Ortiz, I. *J. Chem. Technol. Biotechnol.* **2009**, *84* (12), 1747. doi:10.1002/jctb.2214.
- (3) Cañizares, P.; Sáez, C.; Sánchez-Carretero, A.; Rodrigo, M. A. *J. Appl. Electrochem.* **2009**, *39* (11), 2143. doi:10.1007/s10800-009-9792-7.
- (4) Martínez-Huitle, C. A.; Alfaro, M. A. Q. *J. Environ. Econ. Manage.* **2008**, *18* (3), 155.
- (5) Busca, G.; Berardinelli, S.; Resini, C.; Arrighi, L. *J. Hazard. Mater.* **2008**, *160* (2–3), 265. doi:10.1016/j.jhazmat.2008.03.045. PMID:18455866.
- (6) Comninellis, C.; Kapalka, A.; Malato, S.; Parsons, S. A.; Poullos, I.; Mantzavinos, D. *J. Chem. Technol. Biotechnol.* **2008**, *83* (6), 769. doi:10.1002/jctb.1873.
- (7) Martínez-Huitle, C. A.; Ferro, S. *Chem. Soc. Rev.* **2006**, *35* (12), 1324. doi:10.1039/b517632h. PMID:17225891.
- (8) Kapalka, A.; Fóti, G.; Comninellis, C. *J. Appl. Electrochem.* **2008**, *38* (1), 7. doi:10.1007/s10800-007-9365-6.
- (9) Panizza, M.; Cerisola, G. *Chem. Rev.* **2009**, *109* (12), 6541. doi:10.1021/cr9001319. PMID:19658401.
- (10) Cañizares, P.; Paz, R.; Sáez, C.; Rodrigo, M. A. *J. Electrochem. Soc.* **2007**, *154* (11), E165. doi:10.1149/1.2772415.
- (11) Oturan, M. A.; Brillas, E. *Port. Electrochim. Acta* **2007**, *25* (1), 1. doi:10.4152/pea.200701001.
- (12) Brillas, E.; Arias, C.; Cabot, P.-L.; Centellas, F.; Garrido, J. A.; Rodríguez, R. M. *Port. Electrochim. Acta* **2006**, *24* (2), 159. doi:10.4152/pea.200602159.
- (13) Pignatello, J. J.; Oliveros, E.; MacKay, A. *Crit. Rev. Environ. Sci. Technol.* **2006**, *36* (1), 1. doi:10.1080/10643380500326564.
- (14) Wei, X.; Wang, Z.; Fan, F.; Wang, J.; Wang, S. *Desalination* **2010**, *251* (1–3), 167. doi:10.1016/j.desal.2009.08.005.
- (15) Fersi, C.; Dhahbi, M. *Desalination* **2008**, *222* (1–3), 263. doi:10.1016/j.desal.2007.01.171.
- (16) Snyder, S. A.; Adham, S.; Redding, A. M.; Cannon, F. S.; DeCarolis, J.; Oppenheimer, J.; Wert, E. C.; Yoon, Y. *Desalination* **2007**, *202* (1–3), 156. doi:10.1016/j.desal.2005.12.052.
- (17) Garcia, A.; Rivas, H. M.; Figueroa, J. L.; Monroe, A. L. *Desalination* **1995**, *102* (1–3), 255. doi:10.1016/0011-9164(95)00061-6.
- (18) Fierro, S.; Nagel, T.; Baltruschat, H.; Comninellis, C. *Electrochem. Solid-State Lett.* **2008**, *11* (7), E20. doi:10.1149/1.2912008.
- (19) Fierro, S.; Nagel, T.; Baltruschat, H.; Comninellis, C. *Electrochem. Commun.* **2007**, *9* (8), 1969. doi:10.1016/j.elecom.2007.05.008.
- (20) Fóti, G.; Gandini, D.; Comninellis, C.; Perret, A.; Haenni, W. *Electrochem. Solid-State Lett.* **1999**, *2* (5), 228. doi:10.1149/1.1390792.
- (21) Comninellis, C.; Nerini, A. *J. Appl. Electrochem.* **1995**, *25* (1), 23. doi:10.1007/BF00251260.
- (22) Boudreau, J.; Bejan, D.; Li, S.; Bunce, N. J. *Ind. Eng. Chem. Res.* **2010**, in press. doi:10.1021/ie900614d.
- (23) Waterston, K.; Wang, J. W.; Bejan, D.; Bunce, N. J. *J. Appl. Electrochem.* **2006**, *36* (2), 227. doi:10.1007/s10800-005-9049-z.

- (24) Bejan, D.; Malcolm, J. D.; Morrison, L.; Bunce, N. J. *Electrochim. Acta* **2009**, *54* (23), 5548. doi:10.1016/j.electacta.2009.04.057.
- (25) Brillas, E.; Sirés, I.; Arias, C.; Cabot, P. L.; Centellas, F.; Rodríguez, R. M.; Garrido, J. A. *Chemosphere* **2005**, *58* (4), 399. doi:10.1016/j.chemosphere.2004.09.028. PMID: 15620731.
- (26) Bratsch, S. G. *J. Phys. Chem. Ref. Data* **1989**, *18* (1), 1.
- (27) *CRC Handbook of Chemistry and Physics*; David, R. L., Ed.; CRC Press, 2000–2001; 81st ed.
- (28) Murata, M.; Ivandini, T. A.; Shibata, M.; Nomura, S.; Fujishima, A.; Einaga, Y. *J. Electroanal. Chem.* **2008**, *612* (1), 29. doi:10.1016/j.jelechem.2007.09.006.
- (29) Ferro, S.; De Battisti, A.; Duo, I.; Comninellis, C.; Haenni, W.; Perret, A. *J. Electrochem. Soc.* **2000**, *147* (7), 2614. doi:10.1149/1.1393578.
- (30) Nematollahi, D.; Shayani-Jam, H.; Alimoradi, M.; Niroo-mand, S. *Electrochim. Acta* **2009**, *54* (28), 7407. doi:10.1016/j.electacta.2009.07.077.
- (31) Madsen, K. G.; Olsen, J.; Skonberg, C.; Hansen, S. H.; Jurva, U. *Chem. Res. Toxicol.* **2007**, *20* (5), 821. doi:10.1021/tx700029u. PMID:17447796.
- (32) Van Benschoten, J. J.; Lewis, J. Y.; Heineman, W. R.; Roston, D. A.; Kissinger, P. T. *J. Chem. Educ.* **1983**, *60* (9), 772. doi:10.1021/ed060p772.
- (33) Buxton, G. V.; Greenstock, C. L.; Helman, W. P.; Ross, A. B. *J. Phys. Chem. Ref. Data* **1988**, *17* (2), 513.
- (34) Li, S.; Bejan, D.; McDowell, M. S.; Bunce, N. J. *J. Appl. Electrochem.* **2008**, *38* (2), 151. doi:10.1007/s10800-007-9413-2.
- (35) Scialdone, O.; Randazzo, S.; Galia, A.; Silvestri, G. *Water Res.* **2009**, *43* (8), 2260. doi:10.1016/j.watres.2009.02.014. PMID:19269668.
- (36) Martínez-Huitle, C. A.; Ferro, S.; Reyna, S.; Cerro-López, M.; De Battisti, A.; Quiroz, M. A. *J. Braz. Chem. Soc.* **2008**, *19* (1), 150. doi:10.1590/S0103-50532008000100021.
- (37) Martínez-Huitle, C. A.; Ferro, S.; De Battisti, A. *Electrochem. Solid-State Lett.* **2005**, *8* (11), D35. doi:10.1149/1.2042628.
- (38) Ferro, S.; De Battisti, A. *J. Phys. Chem. B* **2002**, *106* (9), 2249. doi:10.1021/jp012195i.
- (39) Bonfatti, F.; Ferro, S.; Lavezzo, F.; Malacarne, M.; Lodi, G.; De Battisti, A. *J. Electrochem. Soc.* **2000**, *147* (2), 592. doi:10.1149/1.1393238.
- (40) Pinkston, K. E.; Sedlak, D. L. *Environ. Sci. Technol.* **2004**, *38* (14), 4019. doi:10.1021/es035368l. PMID:15298214.
- (41) Bedner, M.; MacCrehan, W. A. *Environ. Sci. Technol.* **2006**, *40* (2), 516. doi:10.1021/es0509073. PMID:16468397.
- (42) Krasner, S. W.; Westerhoff, P.; Chen, B.; Rittmann, B. E.; Amy, G. *Environ. Sci. Technol.* **2009**, *43* (21), 8320. doi:10.1021/es901611m. PMID:19924963.
- (43) Krauss, M.; Longrée, P.; Dorusch, F.; Ort, C.; Hollender, J. *Water Res.* **2009**, *43* (17), 4381. doi:10.1016/j.watres.2009.06.048. PMID:19608213.
- (44) Wu, Q.-Y.; Hu, H.-Y.; Zhao, X.; Sun, Y.-X. *Environ. Sci. Technol.* **2009**, *43* (13), 4940. doi:10.1021/es8034329. PMID:19673289.
- (45) Wang, L. K. *Handbook of Environmental Engineering*; Humana Press Inc.: Totowa, NJ, 2008.
- (46) Winward, G. P.; Avery, L. M.; Stephenson, T.; Jefferson, B. *Water Res.* **2008**, *42* (1-2), 483. doi:10.1016/j.watres.2007.07.042. PMID:17904612.
- (47) Mezzanotte, V.; Antonelli, M.; Citterio, S.; Nurizzo, C. *Water Environ. Res.* **2007**, *79* (12), 2373. doi:10.2175/106143007X183763. PMID:18044353.
- (48) Blatchley, E. R., 3rd; Gong, W.-L.; Alleman, J. E.; Rose, J. B.; Huffman, D. E.; Otaki, M.; Lisle, J. T. *Water Environ. Res.* **2007**, *79* (1), 81. doi:10.2175/106143006X102024. PMID:17290975.
- (49) Macauley, J. J.; Qiang, Z.; Adams, C. D.; Surampalli, R.; Mormile, M. R. *Water Res.* **2006**, *40* (10), 2017. doi:10.1016/j.watres.2006.03.021. PMID:16678233.
- (50) Yang, L.; Yu, L. E.; Ray, M. B. *Environ. Sci. Technol.* **2009**, *43* (2), 460. doi:10.1021/es8020099. PMID:19238980.

# 5b,7b-Diaza-3b,9b-diborabenz[ghi]perylene

Michael J.D. Bosdet, Warren E. Piers, Ted S. Sorensen, and Masood Parvez

**Abstract:** Treatment of a precursor to the chelating Lewis acid 2,2'-diborabiphenyl with 2,6-bisalkynyl-substituted pyridazines, leads to elimination of 2 equiv. of ClSiMe<sub>3</sub>; subsequent treatment of the mixture with PtCl<sub>2</sub> catalyzes the cyclization of observable intermediates to the title 5b,7b-diaza-3b,9b-diborabenz[ghi]perylene compounds in low isolated yields. The compounds were characterized by NMR and UV-vis spectroscopies, and in one case, by X-ray crystallography. NICS(1) computations indicate that the inner ring is less aromatic than the outer rings.

**Key words:** polycyclic aromatic hydrocarbons, boron heterocycles, nitrogen heterocycles, X-ray structure.

**Résumé :** Le traitement d'un précurseur de l'acide de Lewis chélatant 2,2'-diborabiphényle avec des pyridazines substituées dans les positions 2,6 par des groupes bisalkynyles conduit à l'élimination de deux équivalents de ClSiMe<sub>3</sub>; le traitement subséquent du mélange avec du PtCl<sub>2</sub> catalyse la cyclisation des intermédiaires observables et à la formation des composés 5b,7b-diaza-3b,9b-diborabenz[ghi]pérylènes mentionnés dans le titre qui sont isolés avec de faibles rendements. Les composés ont été caractérisés par spectroscopies RMN et UV-vis et, dans un cas, par diffraction des rayons-X. Des calculs NICS(1) indiquent que le noyau interne est moins aromatique que les cycles externes.

**Mots-clés :** hydrocarbures aromatiques polycycliques, hétérocycles du bore, hétérocycles de l'azote, structure par diffraction des rayons X.

[Traduit par la Rédaction]

## Introduction

Transposition of C–C units for isoelectronic B–N modules in polycyclic aromatic hydrocarbons offers a means of altering opto-electronic, redox, and chemical properties of these important organic materials without dramatically affecting their gross structural features.<sup>1–3</sup> One of the most elementary examples is the BN-biphenyl analog **I** (Chart 1), the pyridine adduct of borabenzene, which has been known for many years.<sup>4</sup> Unlike biphenyl, **I** is susceptible to protonation by Brønsted acids at the carbon alpha to boron,<sup>5,6</sup> and facile Diels–Alder addition with moderately active dienophiles,<sup>7</sup> demonstrating the more reactive nature of the BN analog; indeed, **I** is quite air- and moisture-sensitive and needs to be handled accordingly.

We have been interested in this strategy as a means of producing novel organic electronic materials and have been developing synthetic methods to novel B<sub>x</sub>N<sub>x</sub> heterocyclic analogs of various PAH frameworks. For example, the BN-phenanthrene<sup>8</sup> and BN-pyrene<sup>9,10</sup> derivatives **II** and **III** (Chart 1) can be prepared via formation of borabenzene pyridine adducts wherein the pyridine unit is functionalized with alkynyl groups alpha to nitrogen. This buttressing of the B–N bond has a stabilizing effect, in that compounds **II** can be handled briefly in air, while pyrene analogs **III** can be stored under ambient atmosphere indefinitely; indeed, they are even unperturbed by treatment with aqueous HCl.

The B<sub>2</sub>N<sub>2</sub>-triphenylenes **IV** (Chart 1) are another class of

compounds we have studied extensively.<sup>11,12</sup> While they exhibit favorably modified redox and photophysical properties relative to the all-carbon triphenylenes, they do not have long-term stability to ambient conditions, limiting the scope of their utility. We thus sought to implement the buttressing strategy that was successful in stabilizing the BN-pyrenes **III** and protect the bay region of the triphenylenes **IV**. Herein, we report the synthesis of two examples of a 5b,7b-diaza-3b,9b-diborabenz[ghi]perylene framework, albeit in low yields. The limitations of the approach will be discussed along with the characterization of these intriguing compounds.

## Results and discussion

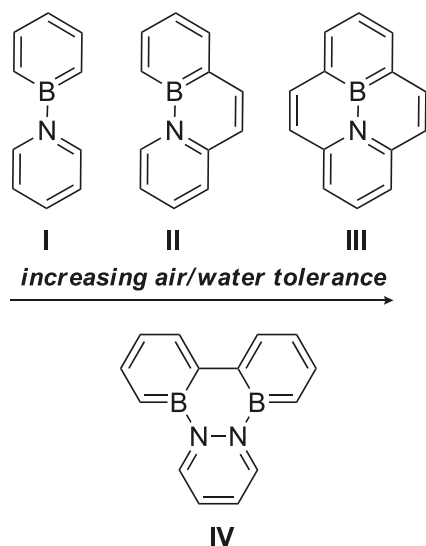
Engagement of the buttressing strategy for the stabilization of the C<sub>2</sub>B<sub>2</sub>N<sub>2</sub> heterocyclic core in compounds **IV** (Chart 1) required first the synthesis of 3,6-di(alkynyl)pyridazines **1a–1d**, which in our hands was best-accomplished by palladium-catalyzed coupling of 3,6-dichloropyridazine with alkynylzinc compounds,<sup>13</sup> as shown in Scheme 1. Terminal alkynes were first deprotonated with *n*BuLi at –78 °C, and subsequently transmetalated with ZnCl<sub>2</sub> to generate the required alkynylzinc reagents. The alkynylzinc compounds were transferred onto a THF solution of the aryl chloride and Pd catalyst and stirred for 24 h. After workup, the desired substrates were obtained in low but workable yields of ≈ 20%–25%. Alternatively, Sonogashira coupling pro-

Received 28 November 2009. Accepted 25 January 2010. Published on the NRC Research Press Web site at canjchem.nrc.ca on 26 March 2010.

M.J.D. Bosdet, W.E. Piers,<sup>1</sup> T.S. Sorensen, and M. Parvez. Department of Chemistry, University of Calgary, 2500 University Drive NW, Calgary, AB T2N 1N4, Canada.

<sup>1</sup>Corresponding author (e-mail: wpiers@ucalgary.ca).

Chart 1.



protocols could be employed, but dimerization of the terminal alkynes was a significant side reaction. The unsubstituted 3,6-bis(ethynyl)pyridazine (**1a**) was formed from the silyl derivative **1d** by desilylation with  $\text{KOH}_{(\text{aq})}$  in MeOH (Scheme 1).

With substrates **1** in hand, reactions with the methyl-substituted chloroboracyclic precursor, **2**,<sup>7</sup> were attempted (Scheme 2). In general, these reactions were not as clean as those previously observed for pyridazine bases without the acetylenic groups. While elimination of 2 equiv. of  $\text{Me}_3\text{SiCl}$  was observed, the reactions with pyridazines **1** appear to be prone to more side reactions, particularly for the parent derivative **1a**. Furthermore, the bis-acetylenic  $\text{B}_2\text{N}_2$ -triphenylene complexes (i.e., derivatives of **IV**), depicted in Scheme 2, were not detected in any of these reactions. Rather, one acetylenic group underwent spontaneous cyclization, and the major products observed for  $R = n\text{Bu}$  and Ph were the half-cyclized compounds **3b** and **3c**, presumably formed via intermediates **IV**. These polycyclic intermediates were not isolated in pure form, but carried forward to the fully cyclized compounds **4** using  $\text{PtCl}_2$  catalysis as shown in Scheme 2.<sup>14</sup> While not isolable in pure form, the nature of compounds **3** was supported by the  $^1\text{H}$  NMR spectral features observed for the butyl-substituted derivative **3b**. Two distinct methyl resonances were observed at 2.81 and 3.07 ppm in  $\text{C}_6\text{D}_6$  solution, highlighting the averaged  $\text{C}_s$  symmetry in **3b**. Further, two pairs of doublets, corresponding to H-6 and H-7 (5.97 and 6.25 ppm) and H-9 and H-10 (6.96 and 7.28 ppm) were observable, in addition to four aromatic singlets, for H-1 (9.16 ppm), H-3 (7.20 ppm), H-5 (6.56 ppm), and H-12 (8.57 ppm) (See Chart 2 for the numbering scheme).

Yields for the target heterocycles **4** were very low (trace–17%), but the compounds were isolated as moderately air- and moisture-tolerant, red-brown solids after purification via column chromatography. The majority of material loss apparently occurred in the catalyzed cycloisomerization step, since the mass balance in the production of crude **3b** was upwards of 70%. The inefficient synthesis was particularly evident in the attempted formation of **4a**; the amount

of product obtained was insufficient for NMR analysis, and while its presence may be inferred from a qualitative observation of pink–red fluorescence in solutions of the material off column, further analysis was precluded due to lack of material.

Although  $\text{B}_2\text{N}_2$ -benzo[ghi]perylene<sup>15</sup> **4b–4c** were available only in small quantities, we were able to characterize them reasonably thoroughly. Unlike the  $^1\text{H}$  NMR spectra for compounds **3b** and **3c**, those of **4b** and **4c** were much simpler, as expected for  $\text{C}_{2v}$  symmetric structures; the  $^1\text{H}$  NMR spectrum of **4b** is illustrated in Fig. 1. Each derivative gave rise to four aromatic singlets between 8.0 and 9.5 ppm for the  $\text{B}_2\text{N}_2$ -benzo[ghi]perylene framework, corresponding to H-1, H-3, H-5, and H-6, as well as a single methyl resonance at ~3.1 ppm, and the expected resonances for the R group. The  $^{11}\text{B}$  NMR spectrum showed a single resonance at 21 ppm, in agreement with other enclosed BN aromatic compounds (~22 ppm).

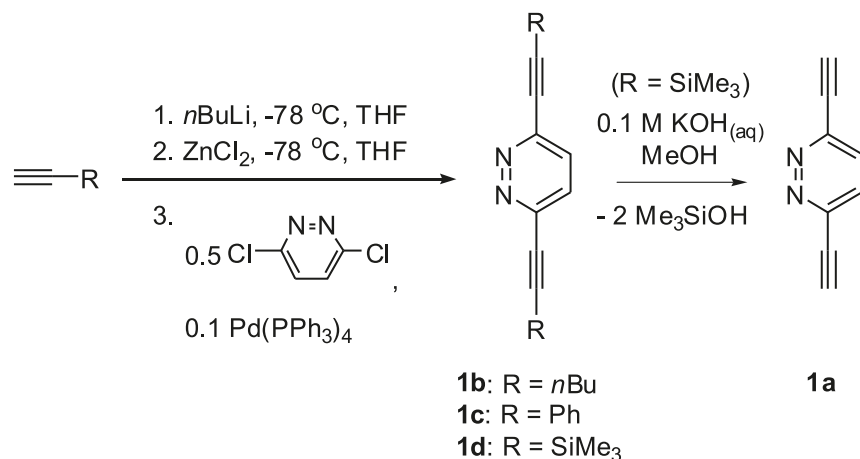
Slow evaporation of solvent from a diethyl ether solution of **4b** yielded crystals suitable for analysis via X-ray crystallography. The structure of **4b** is essentially planar, with a maximum dihedral angle of  $1.5^\circ$  within the ring system ( $\text{C}(18)\text{--C}(1)\text{--B}(1)\text{--C}(5)$ ) (Fig. 2 and Table 1). The B–N bond is short, at 1.452(2) Å, consistent with BN-pyrene **III** (1.456(4) Å) and the  $\text{B}_2\text{N}_2$ -triphenylene **IV** (1.464(4) Å),<sup>12</sup> and indicative of some  $\pi$ -character in this bond. However, in contrast to unbuttressed **IV**,<sup>12</sup> bond localization is evident throughout the carbon perimeter in **4b**, with alternating long and short C–C bonds within individual rings. Thus, in the borabenzene rings,  $\text{C}(1)\text{--C}(2)$  and  $\text{C}(3)\text{--C}(4)$  are short (1.390(3) Å avg.), whereas  $\text{C}(2)\text{--C}(3)$  and  $\text{C}(4)\text{--C}(5)$  are longer (1.414(3) Å avg.). The  $\pi$ -electron localization in the pyridazine ring in **4b** also differs from that in compounds **IV**, such that the short and long C–C bonds in the latter are reversed in **4b**. Specifically,  $\text{C}(8)\text{--C}(9)$  and  $\text{C}(9')\text{--C}(8')$  are 1.406 Å, while  $\text{C}(9)\text{--C}(9')$  is shortened to 1.346(3) Å; the corresponding lengths in unbuttressed **IV** are 1.345(5) Å and 1.433(6) Å. Additionally, the C–N bonds are shortened by ~0.02 Å (to 1.381(2) Å), suggesting better overall  $\pi$ -electron delocalization about this ring, in contrast to the cyclohexadiene-type bonding arrangement of heterocycles **IV**. The longest C–C bond in **4b** is  $\text{C}(1)\text{--C}(1')$ , at 1.456(3) Å, elongated by 2% relative to the same bond in  $\text{B}_2\text{N}_2$ -triphenylene **IV** but of similar length to the analogous bond in the all-carbon PAH benzo[ghi]perylene, at 1.484 Å.<sup>16</sup>

Overall then, the solid-state bond-length patterns suggests that the ring system is best-represented by resonance form **A** (Chart 3), in contrast to the dominant resonance form of triphenylene analogues **IV**, best-described by resonance form **B**. This is supported by NICS(1) calculations<sup>17</sup> performed on **4a**, which show a low aromaticity for the inner  $\text{C}_2\text{B}_2\text{N}_2$  ring in **4a**, but strong aromaticity for the outer rings. This is the inverse of trends noted for **IV**, and it thus appears that the effect of buttressing the system is to lower the aromatic stabilization of the inner ring relative to the unbuttressed system. Indeed, the all-carbon PAH benzo[ghi]perylene exhibits this pattern as well, with the inner ring having low aromatic character relative to the outer rings.<sup>18</sup>

Unlike the all-carbon frameworks, the  $\text{B}_2\text{N}_2$  compounds have molecular dipoles that are significant enough to influence



Scheme 1.



Scheme 2.

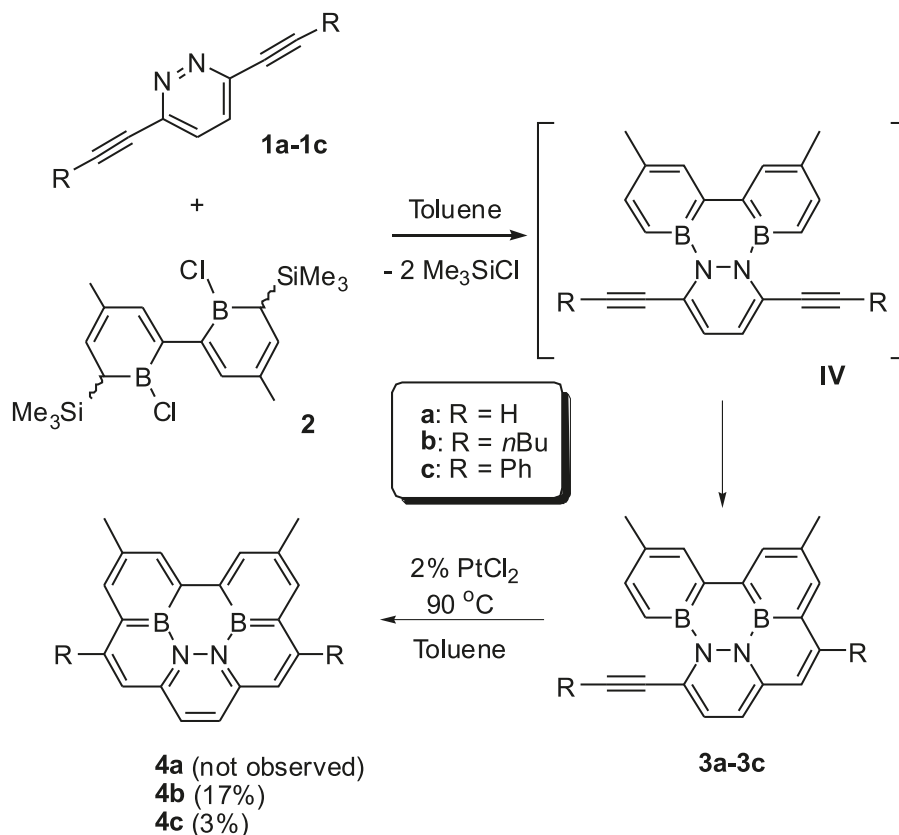
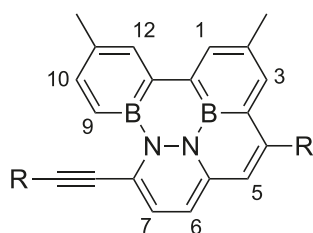


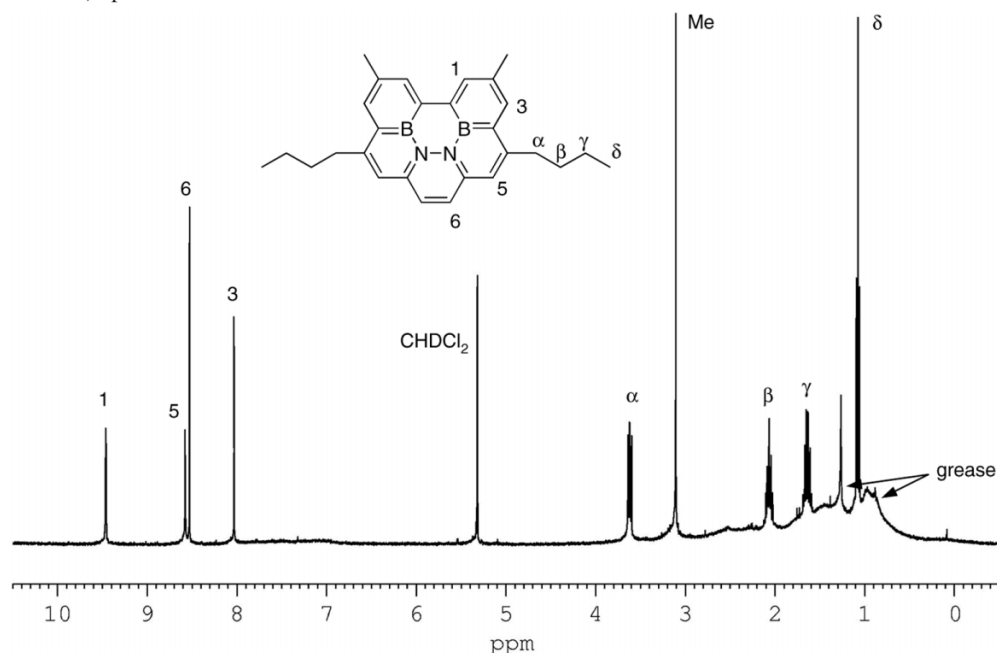
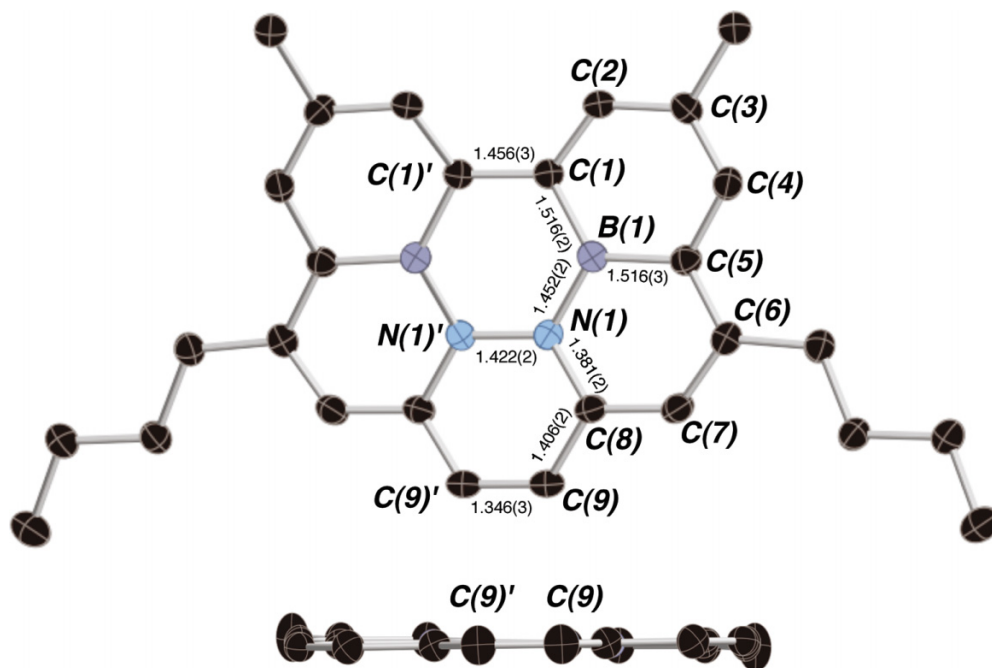
Chart 2.



packing in the solid state. The molecular packing of **4b**, shown in Fig. 3, features two molecules stacked with the dipoles (calculated to be 3.53 D in **4b**) aligned such that a

close non-bonding  $\text{B}\cdots\text{N}$  distance of 3.71 Å is observed. Intermolecular  $\pi$ -stacking distances of 3.42 Å exist between parallel sheets of **4b** molecules, which is very slightly shorter than the  $\pi$ - $\pi$  distance in crystalline benzo[ghi]perylene at 3.44 Å.

The unbuttressed  $\text{B}_2\text{N}_2$ -triphenylene compounds **IV** exhibit reversible one- and two-electron reduction process, and indeed the radical anion and dianions are stable and isolable.<sup>12</sup> It was therefore somewhat surprising to find that cyclic voltammetry on compounds **4a** and **4b** shows irreversible one-electron reductions, suggesting that the radical anions are unstable. This may be a reflection of the low aromaticity of the central rings in compounds **4** and a change in the character of the SOMO in the radical anions.

**Fig. 1.**  $^1\text{H}$  NMR (400 MHz) spectrum of **4b** in  $\text{CD}_2\text{Cl}_2$ .**Fig. 2.** Top: X-ray structure of **4b**. Numbers are bond lengths in Å. Bottom: **4b**, viewed along the molecular plane (perpendicular to the  $\text{N}(1)\text{--N}(1')$  bond), with butyl groups removed. Hydrogen atoms have been removed for clarity. Thermal ellipsoids are at the 50% probability level.

The absorption and emission spectra are indicative of lowered HOMO–LUMO gaps in comparison to triphenylene analogs **IV**, as may be expected by the extended conjugation afforded by the buttressing alkenyl groups. As for other  $\text{B}_x\text{N}_x$  analogs, both absorption and emission bands (621 and 630 nm for **4a** and **4b**, respectively) are red-shifted in these compounds in comparison to the all-carbon compound, but the emission quantum yields (0.023 and 0.015, respectively, relative to 9,10-diphenylanthracene in cyclohexane) are significantly lower than that of benzo[ghi]perylene (0.26).

## Conclusions

We have prepared and characterized two examples of 5b,7b-diaza-3b,9b-diborabenzo[ghi]perylene with a doubly buttressed  $\text{B}_2\text{N}_2\text{C}_2$  core. Although in previous work a doubly buttressed  $\text{B}_2\text{N}_2\text{C}_2$  core added stability to bora-aza analogs of PAHs, here the added benefit in this regard is minimal. This may stem from the fact that the core ring is of low aromaticity and therefore more reactive towards, for example, protic reagents and oxygen. Furthermore, the synthetic route

Chart 3.

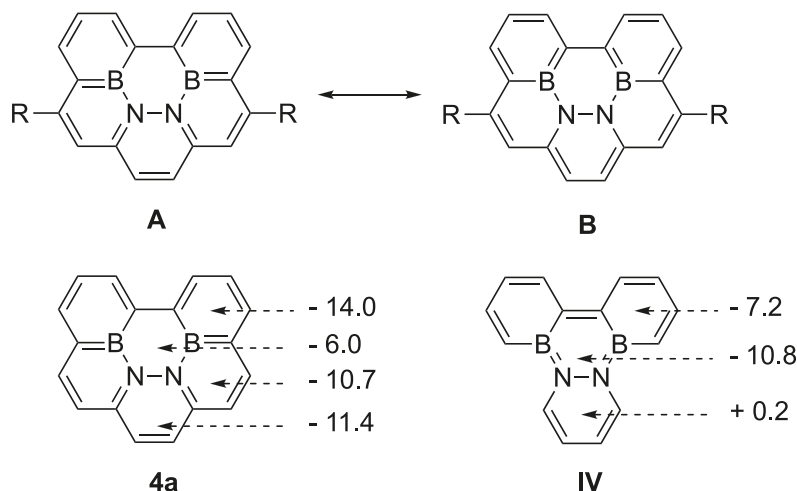


Table 1. Selected metrical parameters for 4b.

Bond lengths (Å)	
B(1)—N(1)	1.452(2)
B(1)—C(1)	1.516(2)
B(1)—C(5)	1.516(3)
C(1)—C(1)'	1.456(3)
C(1)—C(2)	1.391(2)
C(2)—C(3)	1.415(2)
N(1)—C(8)	1.381(2)
N(1)—N(1)'	1.422(2)
Bond angles (°)	
C(1)—B(1)—N(1)	122.63(14)
N(1)—B(1)—C(5)	117.23(14)
N(1)′—N(1)—B(1)	119.73(9)
B(1)—N(1)—C(8)	120.76(13)
B(1)—C(1)—C(1)′	117.63(9)
N(1)—C(8)—C(9)	119.80(14)
Torsion angles (°)	
C(8)—N(1)—B(1)—C(1)	179.74(14)

to these frameworks is inefficient (despite many attempts at improvements), and the photophysical properties are not unique enough to warrant further efforts directed towards discovery of more direct routes to the compounds. Nonetheless, the structural features and aromatic properties are of interest to add to the database of  $B_xN_x$  compounds in comparison to their all-carbon counterparts.

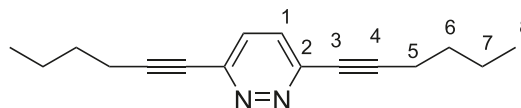
## Experimental section

General procedures have been described in detail elsewhere.<sup>12</sup> Celite 545<sup>®</sup> was purchased from Fisher Scientific and heated at 200 °C under high vacuum for 3 days prior to use. Neutral alumina (63–200  $\mu\text{m}$ , 70–230 Mesh ASTM) was purchased from EM Science and heated at 200 °C for 3 days under high vacuum prior to use. Silica-gel column chromatography was carried out on Geduran Silica 60 silica gel (particle size 40–63  $\mu\text{m}$ ).

Compound **2** was prepared as described previously.<sup>12</sup>  $\text{CuI}$ ,  $\text{BCl}_3$ ,  $\text{LiNMe}_2$ , pyridazine, 9,10-diphenylanthracene, and  $\text{Pd}(\text{PPh}_3)_4$  were purchased from Aldrich and used as re-

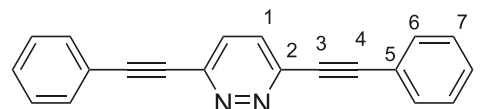
ceived. 3,6-Dichloropyridazine was purchased from Aldrich and sublimed prior to use. Phenylacetylene was purchased from Aldrich and passed through a column of alumina immediately prior to use. 1-Hexyne was purchased from Acros and used as received.  $\text{PtCl}_2$  was purchased from Alfa Aesar and used as received. Trimethylsilylacetylene was purchased from Petra Research, Inc. and distilled prior to use.  $^1\text{H}$  NMR assignments were made by comparison to known chemical shift patterns.<sup>5–9,11,12</sup>

## Synthesis of 3,6-bis(1-hexynyl)pyridazine, 1b



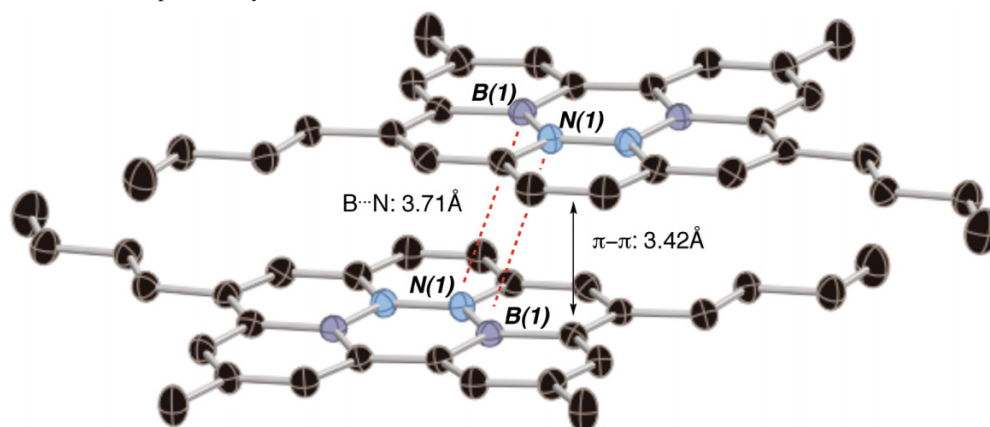
In a microwavable reaction tube, solid  $\text{Pd}(\text{PPh}_3)_4$  (8 mg, 7.1  $\mu\text{mol}$ ) and  $\text{CuI}$  (3 mg, 14.1  $\mu\text{mol}$ ) were added to a solution of 3,6-dichloropyridazine (50 mg, 0.33 mmol) in  $\text{NEt}_3$  (2 mL). This was immediately followed by the addition of a solution of 1-hexyne (58 mg, 0.71 mmol) in  $\text{NEt}_3$  (1 mL), and the mixture was heated in a microwave reactor (115 W, 150 °C) for 25 min. Once cooled, the crude product was extracted into  $\text{Et}_2\text{O}$  and gravity filtered. The solvent was removed in vacuo, and the orange material was dissolved in hexanes and loaded onto a column of neutral  $\text{Al}_2\text{O}_3$ . Gradient elution with hexanes/ $\text{Et}_2\text{O}$  ultimately gave the product as a yellow solid. Yield: 20 mg (25%).  $^1\text{H}$  NMR ( $\text{C}_6\text{D}_6$ )  $\delta$  (ppm): 6.62 (s, 2H, H-1), 2.12 (t, 4H,  $^3J_{\text{HH}} = 7$  Hz, H-5), 1.31 (m, 2 + 2H, H-6 + H-7), 0.76 (t, 6H,  $^3J_{\text{HH}} = 7$  Hz, H-). HR-MS for  $\text{C}_{16}\text{H}_{20}\text{N}_2$  ( $M^+$ ): 240.1626 (calcd.), 240.1624 (found).

## Synthesis of 3,6-bis(phenylethynyl)pyridazine, 1c



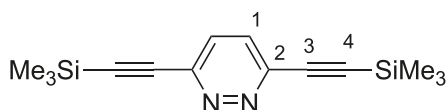
To a  $-78$  °C solution of phenylacetylene (1.33 g, 13.0 mmol) in THF (50 mL) was added a solution of *n*-butyl lithium in hexanes (1.6 mol/L, 8.12 mL, 13.0 mmol). After stirring at this temperature for 1 h, a solution of  $\text{ZnCl}_2$  (1.77 g, 13.0 mmol) in THF (50 mL) was transferred in via canula, and this mixture was stirred for another 45 min with

**Fig. 3.** Molecular packing of **4b**, including intermolecular B...N interactions (red dash). Hydrogen atoms have been removed for clarity. Thermal ellipsoids are at the 50% probability level.



the temperature maintained at  $-78^{\circ}\text{C}$ . The reaction mixture was then warmed to  $25^{\circ}\text{C}$ , and a solution of 3,6-dichloropyridazine (486 mg, 3.3 mmol) and  $\text{Pd}(\text{PPh}_3)_4$  (751 mg, 0.65 mmol) in THF (50 mL) was added. The mixture was stirred for 3 days, then quenched with saturated  $\text{NaHCO}_3(\text{aq})$  (75 mL), and filtered through Celite. After removing the organic layer, the aqueous layer was washed with  $\text{CHCl}_3$  ( $2 \times 20$  mL), and the combined organic fractions were dried with  $\text{MgSO}_4$ . The crude material obtained following gravity filtration and removal of volatiles in vacuo was purified by column chromatography, giving a white solid. Yield: 111 mg (12%).  $^1\text{H}$  NMR ( $\text{CDCl}_3$ )  $\delta$  (ppm): 7.65 (m, 4H, H-6), 7.61 (s, 2H, H-1), 7.41 (m, 2 + 1H, H-7 + H-8).  $^{13}\text{C}\{^1\text{H}\}$  NMR ( $\text{CDCl}_3$ )  $\delta$  (ppm): 146.00 (s, C-2), 132.38 (s, C-6), 129.92 (s, C-1), 129.01 (s, C-8), 128.72 (s, C-7), 121.59 (s, C-5), 95.67 (s, C-3/4), 86.10 (C-3/4). HR-MS for  $\text{C}_{20}\text{H}_{12}\text{N}_2$  ( $\text{M}^+$ ): 280.1000 (calcd.), 280.1001 (found).

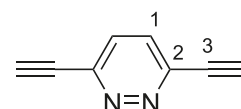
#### Synthesis of 3,6-bis(trimethyl-silylethynyl)pyridazine, **1d**



To a  $-78^{\circ}\text{C}$  solution of trimethylsilylacetylene (1.151 g, 11.7 mmol) in THF (50 mL) was added a solution of *n*-butyl lithium in hexanes (1.6 mol/L, 7.3 mL, 11.7 mmol). After stirring at this temperature for 1 h, a solution of  $\text{ZnCl}_2$  (1.60 g, 11.7 mmol) in THF (50 mL) was transferred in via canula, and this mixture was stirred for another 45 min with the temperature maintained at  $-78^{\circ}\text{C}$ . The reaction mixture was then warmed to  $25^{\circ}\text{C}$ , and a solution of 3,6-dichloropyridazine (436 mg, 2.9 mmol) and  $\text{Pd}(\text{PPh}_3)_4$  (338 mg, 0.29 mmol) in THF (40 mL) was added. The mixture was stirred for 3 days at  $35^{\circ}\text{C}$  and was then quenched with saturated  $\text{NaHCO}_3(\text{aq})$  (75 mL) and filtered through Celite. After removing the organic layer, the aqueous layer was washed with  $\text{CHCl}_3$  ( $2 \times 20$  mL), and the combined organic fractions were dried with  $\text{Na}_2\text{SO}_4$ . The crude material obtained following gravity filtration and removal of volatiles in vacuo was purified by column chromatography (5% EtOAc in hexanes), giving a white solid. Yield: 135 mg (17%).  $^1\text{H}$  NMR ( $\text{CDCl}_3$ )  $\delta$  (ppm): 7.44 (s, 2H, H-1), 0.17 (s, 18H,  $-\text{SiMe}_3$ ).

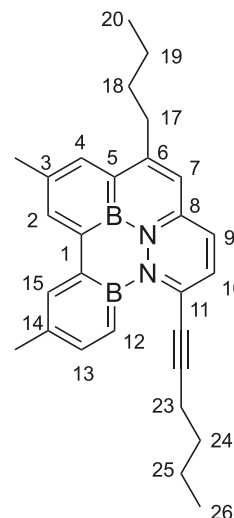
$^{13}\text{C}\{^1\text{H}\}$  NMR ( $\text{CDCl}_3$ )  $\delta$  (ppm): 145.46 (s, C-2), 129.02 (s, C-1), 102.09 (s, C-3/4), 100.42 (C-3/4),  $-0.53$  (s,  $\text{SiMe}_3$ ). HR-MS for  $\text{C}_{14}\text{H}_{20}\text{N}_2\text{Si}_2$  ( $\text{M}^+$ ): 272.1165 (calcd.), 272.1177 (found).

#### Synthesis of 3,6-bis(ethynyl)pyridazine, **1a**



Desilylation of 3,6-bis(trimethyl-silylethynyl)pyridazine was accomplished by the addition of  $\text{KOH}(\text{aq})$  (0.99 mol/L, 1.0 mL, 0.98 mmol) to a solution of **1d** (134 mg, 0.49 mmol) in MeOH (5 mL). After stirring for 1.5 h, the mixture was extracted into  $\text{CHCl}_3$  (20 mL) and washed with 6 mol/L  $\text{HCl}(\text{aq})$  ( $2 \times 10$  mL). The organic layer was dried over  $\text{MgSO}_4$ , filtered, and the solvent removed in vacuo to give **1a** as white crystals. Yield: 51 mg (81%).  $^1\text{H}$  NMR ( $\text{CDCl}_3$ )  $\delta$  (ppm): 7.56 (s, 2H, H-1), 3.52 (s, 2H, H-4).  $^{13}\text{C}\{^1\text{H}\}$  NMR ( $\text{CDCl}_3$ )  $\delta$  (ppm): 145.50 (s, C-2), 129.45 (s, C-1), 83.86 (s, C-3/4), 79.72 (C-3/4). HR-MS for  $\text{C}_8\text{H}_4\text{N}_2$  ( $\text{M}^+$ ): 128.0374 (calcd.), 128.0376 (found).

#### Synthesis/characterization of **3b**

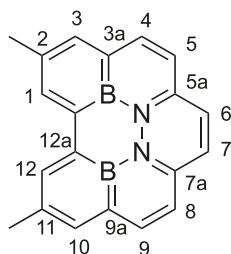


A solution of **2** (55 mg, 0.14 mmol) in toluene (1 mL) was added to a solution of **1b** (32 mg, 0.13 mmol) in tol-



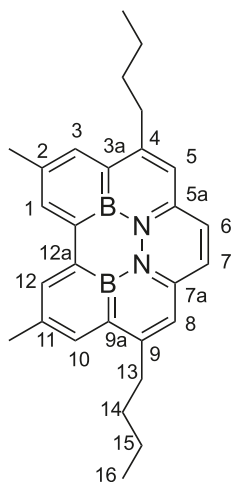
uene (5 mL) and stirred at 25 °C for 48 h. Volatiles were removed in vacuo, and the crude product was determined to be a mixture including the intermediate **3b** via  $^1\text{H}$  NMR spectroscopy.  $^1\text{H}$  NMR ( $\text{C}_6\text{D}_6$ )  $\delta$  (ppm): 9.16 (s, 1H, H-2), 8.57 (s, 1H, H-15), 7.28 (d, 1H,  $^3J_{\text{HH}} = 8$  Hz, H-13), 7.20 (s, 1H, H-4), 6.96 (d, 1H,  $^3J_{\text{HH}} = 8$  Hz, H-12), 6.56 (s, 1H, H-7), 6.25 (d, 1H,  $^3J_{\text{HH}} = 8$  Hz, H-10), 5.97 (d, 1H,  $^3J_{\text{HH}} = 8$  Hz, H-9), 3.25 (t, 2H,  $^3J_{\text{HH}} = 8$  Hz, C-17), 3.07 (s, 3H, C-3-Me), 3.04 (t, 2H,  $^3J_{\text{HH}} = 8$  Hz, C-23), 2.81 (s, 3H, C-14-Me), 2.35 (m, 2H, H-18), 2.21 (m, 2H, H-24), ~1.41 (m, H-19), ~1.38 (m, H-25), 0.99 (t, 3H,  $^3J_{\text{HH}} = 8$  Hz, C-20), 0.90 (t, 3H,  $^3J_{\text{HH}} = 8$  Hz, C-26).

#### Attempted synthesis of 4a



A solution of **2** (157 mg, 0.40 mmol) in toluene (3 mL) was added to a solution of **1a** (51 mg, 0.40 mmol) in toluene (10 mL) and stirred at 25 °C for 48 h. Volatiles were removed in vacuo and the crude material was re-dissolved in toluene and transferred onto  $\text{PtCl}_2$  (2 mg, 7  $\mu\text{mol}$ ). The mixture was stirred at 95 °C for 24 h, after which volatiles were removed, and the brown material was purified by flash chromatography through neutral  $\text{Al}_2\text{O}_3$ . The  $\text{Et}_2\text{O}$  fraction was observed to fluoresce pink-red upon irradiation at 365 nm, but an insufficient quantity for NMR characterization was obtained. Yield: trace.

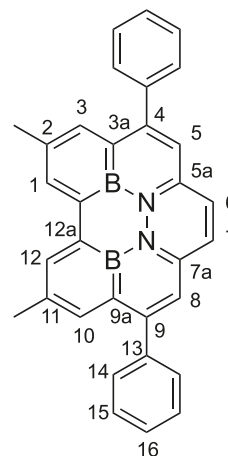
#### Synthesis of 4b



The crude material **3b** was re-dissolved in toluene and transferred onto  $\text{PtCl}_2$  (2 mg, 7  $\mu\text{mol}$ ). The mixture was stirred at 100 °C for 24 h, after which volatiles were removed, and the brown material was purified by flash chromatography through neutral  $\text{Al}_2\text{O}_3$ . Yield: 9 mg (17%).

UV-vis ( $\epsilon$  ( $10^4$  L mol $^{-1}$  cm $^{-1}$ ), cyclohexane)  $\lambda_{\text{max}}$  (nm): 261, 324, 413, 458, 511. Fluorescence (cyclohexane)  $\lambda_{\text{max}}$  (nm): 621, 667;  $\phi_f = 0.023$ ,  $\tau_f = 23$  ns.  $^1\text{H}$  NMR ( $\text{CD}_2\text{Cl}_2$ )  $\delta$  (ppm): 9.46 (s, 2H, H-1/12), 8.58 (s, 2H, H-3/10), 8.53 (s, 2H, H-5/8), 8.03 (s, 2H, H-6/7), 3.62 (t, 4H,  $^3J_{\text{HH}} = 8$  Hz, C-13), 3.11 (s, 6H, C-2/11-Me), 2.07 (m, 4H, H-14), 1.64 (m, 4H, H-15), 1.07 (t, 6H,  $^3J_{\text{HH}} = 8$  Hz, C-16) ppm.  $^{11}\text{B}\{^1\text{H}\}$  NMR ( $\text{C}_6\text{D}_6$ )  $\delta$  (ppm): 21 (br s). HR-MS for  $\text{C}_{32}\text{H}_{24}\text{B}_2\text{N}_2$  ( $\text{M}^+$ ): 418.27516 (calcd.), 418.27679 (found).

#### Synthesis of 4c



A solution of **2** (74 mg, 0.19 mmol) in toluene (1.5 mL) was added to a solution of **1c** (50 mg, 0.18 mmol) in toluene (5 mL) and stirred at 45 °C for 48 h. Volatiles were removed in vacuo and the crude product was re-dissolved in toluene and transferred onto  $\text{PtCl}_2$  (3 mg, 11  $\mu\text{mol}$ ). The mixture was stirred at 100 °C for 24 h, after which volatiles were removed, and the brown material was purified by flash chromatography through neutral  $\text{Al}_2\text{O}_3$ . Yield: 3 mg (3%). UV-vis ( $\epsilon$  ( $10^4$  L mol $^{-1}$  cm $^{-1}$ ), cyclohexane)  $\lambda_{\text{max}}$  (nm): 421, 523, 625. Fluorescence (cyclohexane)  $\lambda_{\text{max}}$  (nm): 630, 676;  $\phi_f = 0.015$ ,  $\tau_f = 23$  ns.  $^1\text{H}$  NMR ( $\text{CD}_2\text{Cl}_2$ )  $\delta$  (ppm): 9.54 (s, 2H, H-1/12), 8.64 (s, 2H, H-3/10), 8.48 (s, 2H, H-5/8 or 6/7), 8.19 (s, 2H, H-5/8 or 6/7), 7.92 (d, 4H,  $^3J_{\text{HH}} = 8$  Hz, H-14), (m, 4 + 2H, H-15 + H-16), 3.04 (s, 6H, C-2/11-Me). Cyclic voltammetry (vs. SCE)  $E_{1/2}$  (THF): -1.57 (rev.) V. HR-MS for  $\text{C}_{28}\text{H}_{32}\text{B}_2\text{N}_2$  ( $\text{M}^+$ ): 458.2126 (calcd.), 458.2109 (found).

#### X-ray crystallography

A deep-red – brown needle of  $\text{C}_{28}\text{H}_{32}\text{B}_2\text{N}_2$  was coated with Paratone 8277 oil (Exxon) and mounted on a glass fiber. All measurements were made on a Nonius KappaCCD diffractometer with graphite monochromated Mo  $\text{K}\alpha$  radiation. Details of crystal data and structure refinement have been provided in Table 2. The data were collected<sup>19</sup> using  $\omega$  and  $\phi$  scans. The data were corrected for Lorentz and polarization effects and for absorption using multi-scan method.<sup>20</sup>

The structure was solved by the direct methods<sup>21</sup> and expanded using Fourier techniques.<sup>22</sup> The H atoms were included at geometrically idealized positions and were not allowed to refine. The final cycle of full-matrix least-squares refinement using SHELXL97<sup>23</sup> converged with unweighted

**Table 2.** Crystal data and structure refinement for C<sub>28</sub>H<sub>32</sub>B<sub>2</sub>N<sub>2</sub>, **4b**.

Empirical formula	C <sub>28</sub> H <sub>32</sub> B <sub>2</sub> N <sub>2</sub>
Formula weight	418.18
Temperature	173(2) K
Wavelength	0.71073 Å
Crystal system	Monoclinic
Space group	<i>P2/c</i>
Unit cell dimensions	<i>a</i> = 12.473(5) Å <i>b</i> = 10.189(7) Å <i>c</i> = 9.339(8) Å $\beta$ = 108.70(3)°
Volume	1124.2(13) Å <sup>3</sup>
<i>Z</i>	2
Density (calc.d.)	1.235 Mg/m <sup>3</sup>
Absorption coefficient	0.070 mm <sup>-1</sup>
<i>F</i> (000)	448
Crystal size	0.32 × 0.11 × 0.10 mm <sup>3</sup>
$\theta$ range for data collection	3.45 to 27.48°
Index ranges	−16 ≤ <i>h</i> ≤ 16, −11 ≤ <i>k</i> ≤ 13, −12 ≤ <i>l</i> ≤ 12
Reflections collected	7866
Independent reflections	2555 [ <i>R</i> <sub>(int)</sub> = 0.0302]
Completeness to $\theta = 27.48^\circ$	99.1%
Absorption correction	Multi-scan method
Max. and min. transmission	0.9930 and 0.9779, respectively
Refinement method	Full-matrix least-squares on <i>F</i> <sup>2</sup>
Data/restraints/parameters	2555/0/147
Goodness-of-fit on <i>F</i> <sup>2</sup>	1.040
Final <i>R</i> indices [ <i>I</i> > 2σ( <i>I</i> )]	<i>R</i> <sub>1</sub> = 0.0531, <i>wR</i> <sub>2</sub> = 0.1288
<i>R</i> indices (all data)	<i>R</i> <sub>1</sub> = 0.0952, <i>wR</i> <sub>2</sub> = 0.1545
Largest diff. peak and hole	0.270 and −0.195 e Å <sup>-3</sup>

and weighted agreement factors, *R* = 0.0531 and *wR* = 0.1545 (all data), respectively, and goodness of fit, *S* = 1.040. The weighting scheme was based on counting statistics and the final difference Fourier map was essentially featureless. The figures were plotted with the aid of ORTEPII.<sup>24</sup>

## Supplementary data

Supplementary data for this article are available on the journal Web site (canjchem.nrc.ca) or may be purchased from the Depository of Unpublished Data, Document Delivery, CISTI, National Research Council Canada, Ottawa, ON K1A 0R6, Canada. DUD 5359. For more information on obtaining material, refer to cisti-icist.nrc-cnrc.gc.ca/cms/unpub\_e.shtml. CCDC 753114 (**4b**) contains the X-ray data in CIF format for this manuscript. These data can be obtained, free of charge, via www.ccdc.cam.ac.uk/conts/retrieving.html (Or from the Cambridge Crystallographic Data Centre, 12 Union Road, Cambridge CB2 1EZ, UK; fax +44 1223 336033; or deposit@ccdc.cam.ac.uk).

## Acknowledgements

Funding for this work was provided by the Xerox Foundation and the Natural Sciences and Engineering Research Council of Canada (NSERC) of Canada through a CRD grant to W.E.P. M.J.D.B. acknowledges NSERC and the Alberta Ingenuity Fund for postgraduate fellowship support.

## References

- (1) Bosdet, M. J. D.; Piers, W. E. *Can. J. Chem.* **2009**, *87* (1), 8. doi:10.1139/V08-110.
- (2) Marwitz, A. J. V.; Matus, M. H.; Zakharov, L. N.; Dixon, D. A.; Liu, S. Y. *Angew. Chem. Int. Ed.* **2009**, *48* (5), 973. doi:10.1002/anie.200805554.
- (3) Liu, L. J.; Marwitz, A. J. V.; Matthews, B. W.; Liu, S. Y. *Angew. Chem. Int. Ed.* **2009**, *48* (37), 6817. doi:10.1002/anie.200903390.
- (4) Boese, R.; Finke, N.; Keil, T.; Paetzold, P.; Schmid, G. Z. *Naturforsch. [B]* **1985**, *40*, 1327.
- (5) Ghesner, I.; Piers, W. E.; Parvez, M.; McDonald, R. *Organometallics* **2004**, *23* (13), 3085. doi:10.1021/om049800z.
- (6) Ghesner, I.; Piers, W. E.; Parvez, M.; McDonald, R. *Chem. Commun. (Camb.)* **2005**, (19): 2480. doi:10.1039/b502448j. PMID:15886777.
- (7) Wood, T. K.; Piers, W. E.; Keay, B. A.; Parvez, M. *Org. Lett.* **2006**, *8* (13), 2875. doi:10.1021/ol061201w. PMID:16774279.
- (8) Bosdet, M. J. D.; Jaska, C. A.; Piers, W. E.; Sorensen, T. S.; Parvez, M. *Org. Lett.* **2007**, *9* (7), 1395. doi:10.1021/ol070328y. PMID:17338544.
- (9) Bosdet, M. J. D.; Piers, W. E.; Sorensen, T. S.; Parvez, M. *Angew. Chem. Int. Ed.* **2007**, *46* (26), 4940. doi:10.1002/anie.200700591.
- (10) Liu, Z.; Marder, T. B. *Angew. Chem. Int. Ed.* **2008**, *47* (2), 242. doi:10.1002/anie.200703535.
- (11) Emslie, D. J. H.; Piers, W. E.; Parvez, M. *Angew. Chem. Int. Ed.* **2003**, *42* (11), 1252. doi:10.1002/anie.200390320.
- (12) Jaska, C. A.; Emslie, D. J. H.; Bosdet, M. J. D.; Piers, W. E.; Sorensen, T. S.; Parvez, M. *J. Am. Chem. Soc.* **2006**, *128* (33), 10885. doi:10.1021/ja063519p. PMID:16910684.
- (13) Chekmarev, D. S.; Stepanov, A. E.; Kasatkin, A. N. *Tetrahedron Lett.* **2005**, *46* (8), 1303. doi:10.1016/j.tetlet.2004.12.124.
- (14) Mamane, V.; Gress, T.; Krause, H.; Fürstner, A. *J. Am. Chem. Soc.* **2004**, *126* (28), 8654. doi:10.1021/ja048094q. PMID:15250709.
- (15) IUPAC: 5b,7b-diaza-3b,9b-diborabenz[ghi]perylene.
- (16) Trotter, J. *Acta Crystallogr.* **1959**, *12* (11), 889. doi:10.1107/S0365110X59002511.
- (17) Schleyer, P. R.; Maerker, C.; Dransfeld, A.; Jiao, H.; van Eikema Hommes, N. J. R. *J. Am. Chem. Soc.* **1996**, *118* (26), 6317. doi:10.1021/ja960582d.
- (18) Schulman, J. M.; Disch, R. L. *J. Phys. Chem. A* **1997**, *101* (48), 9176. doi:10.1021/jp972391i.
- (19) Otwinowski, Z.; Minor, W. *Methods Enzymol.* **1997**, *276*, 307. doi:10.1016/S0076-6879(97)76066-X.
- (20) Hooft, R. *COLLECT*; Nonius BV: Delft, The Netherlands, 1998.
- (21) Altomare, A.; Cascarano, M.; Giacovazzo, C.; Guagliardi, A. *J. Appl. Cryst.* **1993**, *26* (3), 343. doi:10.1107/S0021889892010331.
- (22) Smits, J. M. M. *The DIRDIF-94 program system*; Technical Report of the Crystallography Laboratory: The University of Nijmegen, Nijmegen, The Netherlands, 1994.
- (23) Sheldrick, G. M. *SHELXL97*; University of Göttingen: Göttingen, Germany, 1997.
- (24) Johnson, C. K. *ORTEPII*; Oak Ridge National Laboratory: Oak Ridge, TN, 1976.

# A DFT study on the electronic and redox properties of $[X_8V_{14}O_{50}]^{n-}$ ( $X = Si^{IV}, Ge^{IV}, P^V$ , and $As^V$ )

Muhammad Ramzan Saeed Ashraf Janjua, Zhong-Min Su, Wei Guan, Ahmad Irfan, Shabbir Muhammad, and Mudassir Iqbal

**Abstract:** The electronic and redox properties of the title polyanions have been calculated by means of density functional theory (DFT). These were unrestricted open-shell systems with electronic configuration of  $d^1$  of V. In this behalf, energies and compositions of  $\alpha$ -LUMO,  $\beta$ -LUMO,  $\alpha$ -HOMO, and  $\beta$ -HOMO were also analyzed. First of all, electronic and redox properties of vanadosilicate  $[Si_8V_{14}O_{50}]^{12-}$  (system **1**) were calculated and then  $Si^{IV}$  was substituted with  $Ge^{IV}$ ,  $P^V$ , and  $As^V$  for further investigations of systems **2**, **3**, and **4**, respectively. The substitution greatly modifies the electronic properties as  $\alpha$ -LUMOs are quite different in all the studied systems. The  $\alpha$ -LUMO is mainly composed of V and O in system **1**, V and Ge in system **2**, V and O in system **3**, and As, O, and V in system **4**. The alpha HOMO–LUMO energy gaps are greatly reduced in systems **2**, **3**, and **4** as compared with system **1**. The system **4**  $[As_8V_{14}O_{50}]^{4-}$  has minimal value of total bonding energy, whereas system **2**  $[Ge_8V_{14}O_{50}]^{12-}$  has maximal, so energetically system **4** is more favourable than the others. After the first reduction,  $\alpha$ -LUMO in  $[Si_8V_{14}O_{50}]^{14-}$  is made up of V and Si,  $\beta$ -LUMO in  $[Ge_8V_{14}O_{50}]^{13-}$  is concentrated on V and Ge,  $\beta$ -LUMO in  $[P_8V_{14}O_{50}]^{5-}$  is composed of V only, whereas  $\beta$ -LUMO in  $[As_8V_{14}O_{50}]^{5-}$  is delocalized over V, O, and As with almost the same contribution of all three atoms.

**Key words:** vanadium heteropolyanion, polyoxometalates (POM), electronic properties, redox properties, DFT.

**Résumé :** Faisant appel à la théorie de la fonctionnelle de la densité (TFD), on a calculé les propriétés électroniques et redox des polyanions mentionnés dans le titre. Ceux-ci correspondent à des systèmes en couches ouvertes sans restrictions avec une configuration électronique  $d^1$  pour le vanadium. À cette fin, on a aussi analysé les énergies et les compositions des orbitales moléculaires basses vacantes  $\alpha$  et  $\beta$  (BV- $\alpha$  et BV- $\beta$ ) ainsi que des orbitales moléculaires hautes occupées  $\alpha$  et  $\beta$  (HO- $\alpha$  et HO- $\beta$ ). Dans une première étape, on a calculé les propriétés électroniques et redox du vanadosilicate  $[Si_8V_{14}O_{50}]^{12-}$  (système **1**) et on a ensuite procédé à d'autres investigations en procédant à la substitution du  $Si^{IV}$  par du  $Ge^{IV}$ , du  $P^V$  et du  $As^V$  dans les systèmes respectivement **2**, **3** et **4**. La substitution modifie grandement les propriétés électroniques des BV- $\alpha$  qui sont très différentes dans chacun des systèmes étudiés. La BV- $\alpha$  est principalement formée de V et O dans le système **1**, de V et Ge dans le système **2**, de V et O dans le système **3** et de As, O et V dans le système **4**. Par comparaison avec le système **1**, la bande d'énergie entre les orbitales moléculaires OH- $\alpha$  et BV- $\alpha$  sont généralement réduites dans les systèmes **2**, **3** et **4**. L'énergie de liaison totale du système  $[As_8V_{14}O_{50}]^{4-}$  (système **4**) est la plus faible alors que celle du système  $[Ge_8V_{14}O_{50}]^{12-}$  (système **2**) est la plus élevée; d'un point de vue énergétique, le système **4** est donc plus favorable que les autres. Après une première réduction, l'orbitale OH- $\alpha$  du  $[Si_8V_{14}O_{50}]^{14-}$  est formée de V et Si, l'orbitale OH- $\beta$  du  $[Ge_8V_{14}O_{50}]^{13-}$  est concentrée sur le V et Ge, l'orbitale OH- $\beta$  du  $[P_8V_{14}O_{50}]^{5-}$  est composée que de V alors que l'orbitale OH- $\beta$  du  $[As_8V_{14}O_{50}]^{5-}$  est délocalisée sur le V, O et As avec des contributions pratiquement égales pour chacun des trois atomes.

**Mots-clés :** hétéropolyanion du vanadium, polyoxométalates, propriétés électroniques, propriétés redox, théorie de la fonctionnelle de la densité (TFD).

[Traduit par la Rédaction]

## Introduction

Polyoxometalates (POM) are a class of inorganic compounds with a remarkable degree of molecular and electronic tunabilities that have impact on disciplines as diverse

as catalysis,<sup>1</sup> medicine,<sup>2</sup> and materials science.<sup>3</sup> These compounds are molecular metal oxides mainly based on V, Mo, and W ions in their highest oxidation states. POMs are especially useful as model systems for the studies of magnetic

Received 6 December 2009. Accepted 9 February 2010. Published on the NRC Research Press Web site at canjchem.nrc.ca on 26 March 2010.

M.R.S.A. Janjua,<sup>1</sup> Z.-M. Su,<sup>2</sup> W. Guan, A. Irfan, and S. Muhammad. Northeast Normal University, Faculty of Chemistry, Jilin Province, Changchun 130024, P. R. China.

M. Iqbal. MESA+ Institute for Nanotechnology, University of Twente, P.O. Box 217, 7500 AE, Enschede, The Netherlands.

<sup>1</sup>Corresponding author (e-mail: Dr\_Janjua2010@yahoo.com).

<sup>2</sup>Corresponding author (e-mail: zmsu@nenu.edu.cn).

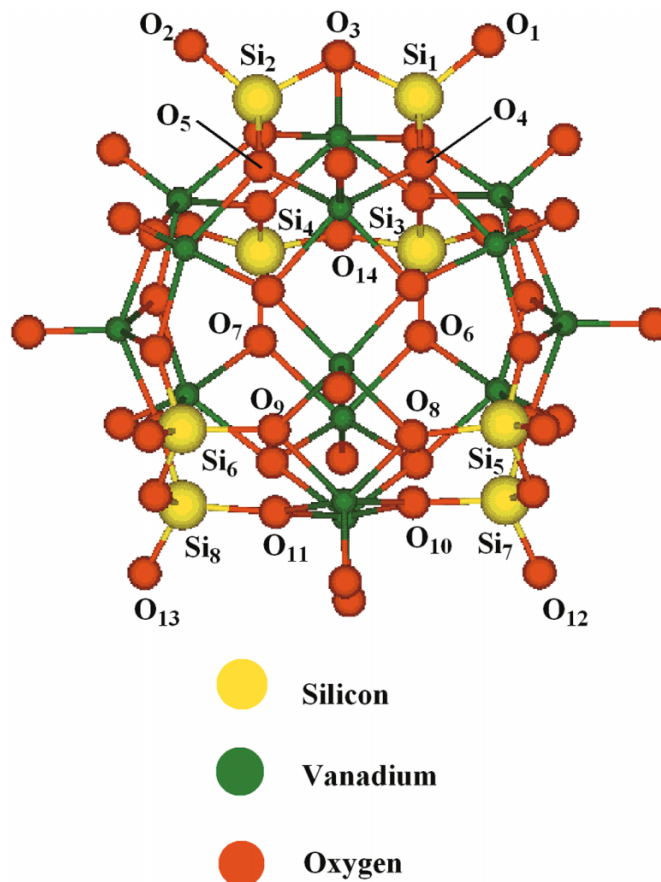
and electronic interactions owing to their cluster structures. Indeed, many of these structures allow the inclusion of well-isolated clusters of paramagnetic ions with various nuclearities and definite topologies and geometries.<sup>4</sup> On the other hand, they permit the controlled injection of electrons, giving rise to mixed-valence species in which delocalized electrons may coexist and interact with localized magnetic moments. Some typical structural types are the Lindqvist<sup>5</sup> ( $M_6O_{19}^{2-}$ ,  $M = Mo, W$ ), Keggin<sup>6</sup> ( $XM_{12}O_{40}^{m-}$ ,  $X = P, Si, Co, Ni$ , and so forth), and Dawson-Wells<sup>7</sup> ( $P_2M_{18}O_{62}^{n-}$ ). Polyoxometalates<sup>8,9</sup> and their transition-metal substituted derivatives are a large group of transformable anionic clusters that have multiple applications, many of which are related to their redox properties.<sup>10</sup> POMs are structures that contain arrays of corner and edge-sharing pseudo-octahedrally coordinated  $MO_6$  units, packed to form an ionic core, where the electronic configuration of the metal is usually  $d^0$  or  $d^1$  and is commonly called addenda or peripheral element. In this context, POMs provide unique systems for the development of new theories in the mixed valence area. One of the important applications of POMs is based on their potential to act as electron acceptors, which leads to the possibility of the formation of charge-transfer electron donor-acceptor materials with interesting electronic and magnetic properties.<sup>11,12</sup>

In this work, for the first time, polyoxovanadosilicate  $[Si_8V_{14}O_{50}]^{12-}$  has been studied theoretically and  $Si^{IV}$  was substituted with  $Ge^{IV}$ ,  $P^V$ , and  $As^V$  in system **1** leading to systems **2**, **3**, and **4**, respectively. Vanadosilicate has  $D_{2d}$  symmetry, which was reported by Tripathi et al.<sup>13</sup> However, several queries are considered to be answered. First, how does the germanium, phosphorous, and arsenic affect the structural and electronic properties? Second, where would be the first reduction of polyoxovanadates modified by  $Ge^{IV}$ ,  $P^V$ , and  $As^V$ ? Third, what would be the composition of  $\alpha$ -LUMO,  $\beta$ -LUMO,  $\alpha$ -HOMO, and  $\beta$ -HOMO of the aforementioned polyoxovanadates? Following our investigations of the electronic properties, bonding nature, stabilities, and nonlinear optical properties of POMs,<sup>14–18</sup> density functional theory (DFT), which has been proven to be a consequential tool for understanding and rationalizing the electronic and magnetic properties of polyanions,<sup>19–28</sup> was employed to pursue the questions mentioned above. Our main objective was to investigate the effect of substitution of  $Ge^{IV}$ ,  $P^V$ , and  $As^V$  with  $Si^{IV}$  in system **1** on the electronic and redox properties of POMs, which may open up possibilities for the experimentalists to synthesize other templated vanadosilicates as well as their heteropolyanions.

## Computational details

All calculations reported in this work were carried out with the ADF2006.01 program.<sup>29</sup> The local density approximation (LDA) characterized by the Vosko–Wilk–Nusair (VWN)<sup>30</sup> parameterization for correlation were used. Becke<sup>31</sup> and Perdew<sup>32</sup> gradient corrections were added for the exchange and correlation energy, respectively. Triple- $\zeta$  plus polarization Slater basis sets were employed to describe the electrons of elements. The cores (O: 1s; Si, P, V: 2p;

Fig. 1. The calculated model of  $[Si_8V_{14}O_{50}]^{12-}$ .



Ge, As: 3p) were kept frozen, and they were described by single Slater functions. The relativistic effects were taken into account by means of the zero-order regular approximation (ZORA).<sup>33</sup> We made spin-unrestricted calculations as our studied systems have open-shell configuration. All the polyanions reported here were optimized under the constraints of the  $D_{2d}$  point symmetry group. The functional and basis set choices for our studied systems were based on the research work that has already been published.<sup>34–38</sup> The structural and atom-labeling schemes for the studied polyanions are presented in Fig. 1. Fourteen V atoms and eight Si atoms in each structure have been denoted with green and yellow colors. The  $Si^{IV}$  was substituted with  $Ge^{IV}$ ,  $P^V$ , and  $As^V$  in system **1**, resulting in systems **2**, **3**, and **4**, respectively.

## Results and discussion

### Structural parameters

The optimized bond lengths and the experimental crystal structure's bond lengths<sup>13</sup> are shown in Table 1. The agreement between experimental and calculated metrical parameters of system **1** gives us confidence that the present study is consequential for this research work. However, bond lengths were shortened compared with the experimental values when there was phosphorous owing to its smaller atomic radius, which is 1.23 Å but bond lengths were increased with arsenic having an atomic radius of 1.33 Å, germanium and silicon have atomic radii 1.52 Å and 1.46 Å, respectively.



**Table 1.** Bond lengths (Å) of heteropolyanions calculated by LDA/TZP for systems **1–4**.

Metrical parameters	<b>1</b>	<b>2</b>	<b>3</b>	<b>4</b>
Si <sub>1</sub> —O <sub>1</sub>	1.601 (1.553) <sup>a</sup>	1.733	1.476	1.635
Si <sub>1</sub> —O <sub>3</sub>	1.684 (1.657)	1.827	1.641	1.815
Si <sub>1</sub> —O <sub>4</sub>	1.716 (1.615)	1.858	1.590	1.769
Si <sub>2</sub> —O <sub>2</sub>	1.601 (1.609)	1.733	1.476	1.635
Si <sub>2</sub> —O <sub>3</sub>	1.684 (1.606)	1.827	1.641	1.815
Si <sub>2</sub> —O <sub>5</sub>	1.716 (1.654)	1.858	1.590	1.769
Si <sub>3</sub> —O <sub>6</sub>	1.716 (1.654)	1.858	1.590	1.769
Si <sub>3</sub> —O <sub>14</sub>	1.684 (1.606)	1.827	1.641	1.815
Si <sub>4</sub> —O <sub>7</sub>	1.716 (1.615)	1.858	1.590	1.769
Si <sub>4</sub> —O <sub>14</sub>	1.684 (1.657)	1.827	1.641	1.815
Si <sub>5</sub> —O <sub>8</sub>	1.735 (1.648)	1.883	1.618	1.797
Si <sub>6</sub> —O <sub>9</sub>	1.735 (1.674)	1.883	1.618	1.797
Si <sub>7</sub> —O <sub>10</sub>	1.735 (1.674)	1.883	1.618	1.797
Si <sub>7</sub> —O <sub>12</sub>	1.601 (1.553)	1.733	1.476	1.635
Si <sub>8</sub> —O <sub>11</sub>	1.735 (1.648)	1.883	1.618	1.797
Si <sub>8</sub> —O <sub>13</sub>	1.601 (1.608)	1.733	1.476	1.635

Note: Si = Ge, P, and As for systems **2**, **3**, and **4**, respectively.

<sup>a</sup>The experimental values in parentheses are from ref. 13.

**Table 2.** Energies (eV), symmetry (S), and major composition of alpha frontier molecular orbitals of polyanions.

Polyanions	$\alpha$ -HOMO (energy)	S	Composition (%)	$\alpha$ -LUMO (energy)	S	Composition (%)	$\Delta E^\alpha$
[Si <sub>8</sub> V <sub>14</sub> O <sub>50</sub> ] <sup>12-</sup>	21.932	<i>a</i> <sub>1</sub>	V = 90.75 O = 3.27	23.044	<i>e</i>	V = 65.89 O = 21.18 Si = 2.2	1.112
[Ge <sub>8</sub> V <sub>14</sub> O <sub>50</sub> ] <sup>12-</sup>	21.528	<i>a</i> <sub>1</sub>	V = 90.13 O = 4.62	22.399	<i>a</i> <sub>1</sub>	V = 78.18 Ge = 13.59	0.871
[P <sub>8</sub> V <sub>14</sub> O <sub>50</sub> ] <sup>4-</sup>	3.344	<i>a</i> <sub>1</sub>	V = 87.86 O = 7.21	4.396	<i>e</i>	V = 65.86 O = 25.97	1.052
[As <sub>8</sub> V <sub>14</sub> O <sub>50</sub> ] <sup>4-</sup>	3.306	<i>a</i> <sub>1</sub>	V = 85.51 O = 8.59 As = 1.07	4.074	<i>a</i> <sub>1</sub>	As = 37.4 O = 32.29 V = 28.55	0.786
[Si <sub>8</sub> V <sub>14</sub> O <sub>50</sub> ] <sup>14-</sup>	26.866	<i>b</i> <sub>2</sub>	V = 72.78 Si = 25.25	26.923	<i>e</i> <sub>1</sub>	V = 65.94 Si = 21.15 O = 5.26	0.057
[Ge <sub>8</sub> V <sub>14</sub> O <sub>50</sub> ] <sup>13-</sup>	23.547	<i>a</i> <sub>1</sub>	V = 89.99 O = 4.63	24.190	<i>a</i> <sub>1</sub>	V = 77.84 Ge = 17.21	0.643
[P <sub>8</sub> V <sub>14</sub> O <sub>50</sub> ] <sup>5-</sup>	5.887	<i>a</i> <sub>1</sub>	V = 90.16 O = 5.22	7.297	<i>a</i> <sub>2</sub>	V = 70.84 O = 24.32	1.41
[As <sub>8</sub> V <sub>14</sub> O <sub>50</sub> ] <sup>5-</sup>	5.705	<i>a</i> <sub>1</sub>	V = 87.58 O = 6.12	6.412	<i>a</i> <sub>1</sub>	V = 33.19 O = 32.59 As = 32.48	0.707

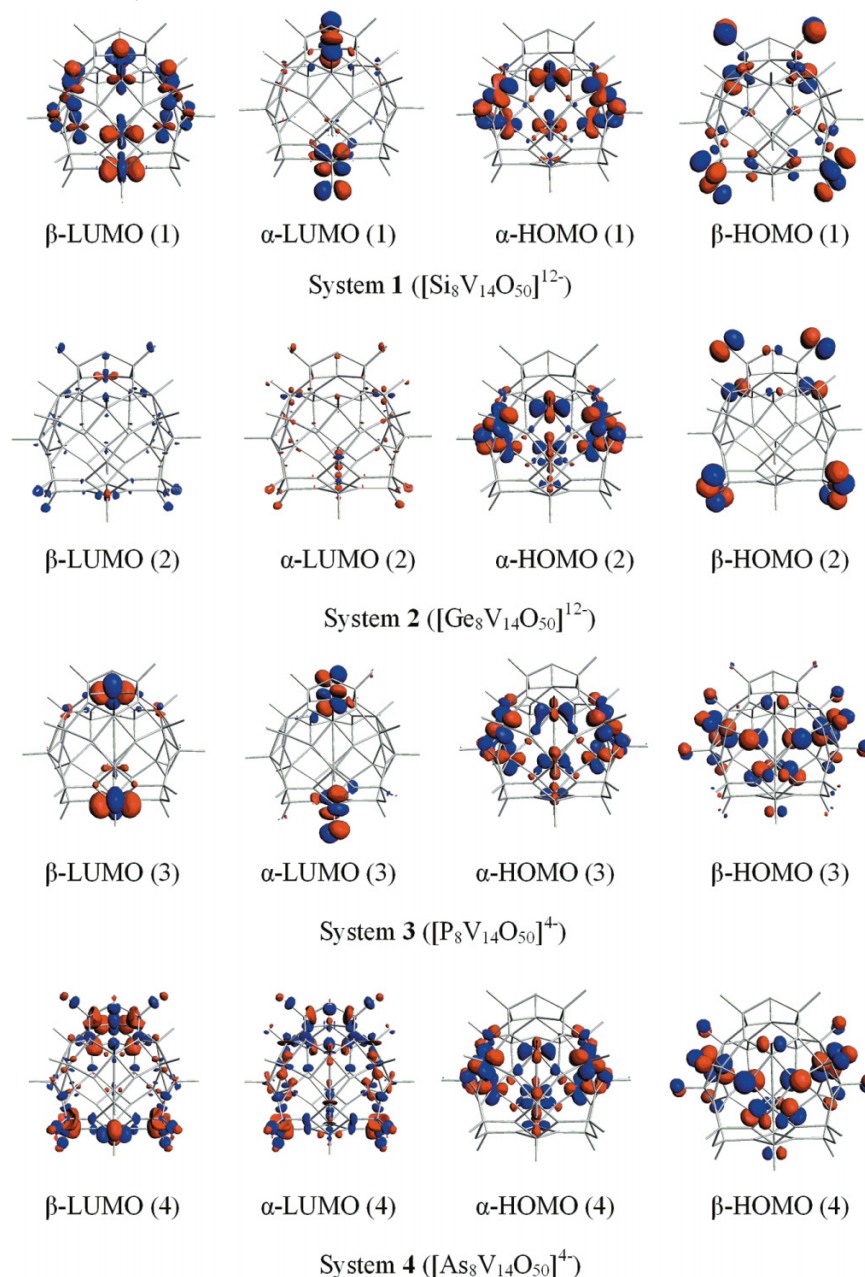
So, the bond lengths were increased compared with the experimental values. Furthermore, bond lengths of the polyanions of germanium were greater than silicon because of their higher atomic radii as illustrated in Table 1.

### Electronic properties of systems **1–4**

The Fig. 1 shows the calculation model for systems **1–4**, which are all open-shell systems. These systems are having 14  $\alpha$  electrons in their fully oxidized state. The  $\alpha$ -HOMOs are not affected by the substitution of Ge<sup>IV</sup>, P<sup>V</sup>, and As<sup>V</sup> because  $\alpha$ -HOMOs of systems **1–4** are mainly concentrated on V as depicted in Table 2 and Fig. 2. However, these substitu-

tions affect the composition of  $\alpha$ - and  $\beta$ -LUMOs of systems **2–4** (see Fig. 2).

The  $\alpha$ -LUMO of system **1** ([Si<sub>8</sub>V<sub>14</sub>O<sub>50</sub>]<sup>12-</sup>) is composed of 65.89% of V, 21.18% of O, and 2.2% of Si, and the  $\alpha$ -LUMO of system **2** ([Ge<sub>8</sub>V<sub>14</sub>O<sub>50</sub>]<sup>12-</sup>) consists of 78.18% of V and 13.59% of Ge. Moreover,  $\alpha$  HOMO–LUMO energy gap is also significantly decreased from 1.112 eV to 0.871 eV (see Table 2). In system **3**, ([P<sub>8</sub>V<sub>14</sub>O<sub>50</sub>]<sup>4-</sup>)  $\alpha$ -LUMO is composed of 65.86% of V and 25.97% of O, whereas in system **4** ([As<sub>8</sub>V<sub>14</sub>O<sub>50</sub>]<sup>4-</sup>)  $\alpha$ -LUMO is made up of 37.4% of As, 32.29% of O, and 28.55% of V. The values of  $\alpha$  HOMO–LUMO energy gaps are 1.052 eV and

**Fig. 2.** Frontier molecular orbitals of systems 1–4.

0.786 eV for systems 3 and 4, respectively, as shown in Table 2. However,  $\text{Si}^{\text{IV}}$  is participating while  $\text{P}^{\text{V}}$  has no contribution in the formation of  $\alpha$ -LUMO. Thus, it might be the reason that the  $\alpha$  HOMO–LUMO energy gap of system 1 is larger than that of system 3 in the following order:  $1 > 3 > 2 > 4$ . On the contrary, in the formation of  $\beta$ -LUMO,  $\text{Si}^{\text{IV}}$  has no contribution while  $\text{P}^{\text{V}}$  is participating, so it might be one reason due to which the beta HOMO–LUMO energy gap of system 3 is the largest, as  $3 > 1 > 2 > 4$ . The participation in the form of % of composition has also been mentioned in Tables 2 and 3. Moreover, on reduction of systems 1–4, we found a clue that the  $\beta$ -LUMO is favourable in systems 2–4 while  $\beta$ -LUMO is not suitable for system 1, so the above mentioned  $\beta$  HOMO–LUMO energy gap sequence of oxidized species  $3 > 1 > 2 > 4$  can be written as  $3 > 2 > 4$ ,

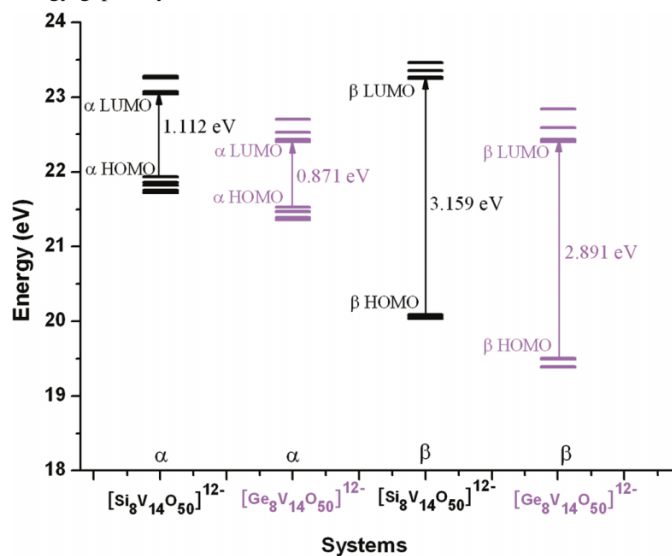
which is in accordance with the sequence of  $\alpha$  HOMO–LUMO energy gap of systems 2–4 (see Figs. 3 and 4). As far as the total bonding energy is concerned for systems 1–4, it is in the following order:  $2 > 1 > 3 > 4$  (see Table 4 and Fig. 5). The total steric interaction and Pauli repulsion along with total orbital interaction and electrostatic interaction of the studied systems (1–4) have been depicted in Figs. 5 and 6.

#### First reduction of systems 1–4

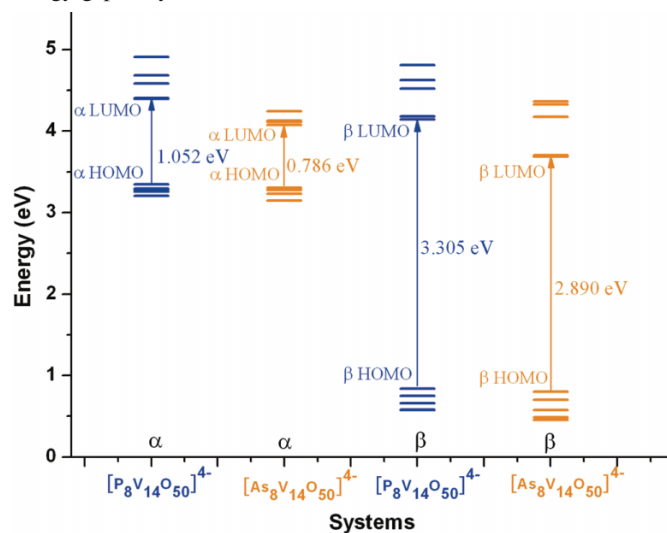
As far as the redox properties are concerned, it is well-known that the redox properties depend on the energy and composition of the LUMO. While the LUMO formally delocalizes over the metal atoms, which determines the redox properties of POMs.<sup>21</sup> In the first reduction of  $[\text{Si}_8\text{V}_{14}\text{O}_{50}]^{12-}$ , the  $\alpha$ -LUMO with symmetry  $e$  is available

**Table 3.** Energies (eV), symmetry (S), and major composition of beta frontier molecular orbitals of the polyanions.

Polyanions	$\beta$ -HOMO (energy)	S	Composition (%)	$\beta$ -LUMO (energy)	S	Composition (%)	$\Delta E^{\beta}$
$[\text{Si}_8\text{V}_{14}\text{O}_{50}]^{12-}$	20.087	$b_1$	O = 90.58 Si = 2.36	23.246	$a_1$	V = 86.19	3.159
$[\text{Ge}_8\text{V}_{14}\text{O}_{50}]^{12-}$	19.509	$a_2$	O = 91.62 Ge = 4.48	22.400	$a_1$	V = 73.55 Ge = 19.73 O = 1.18	2.891
$[\text{P}_8\text{V}_{14}\text{O}_{50}]^{4-}$	0.839	$a_2$	O = 96.43	4.144	$b_2$	V = 88.58 O = 3.08 P = 1.29	3.305
$[\text{As}_8\text{V}_{14}\text{O}_{50}]^{4-}$	0.798	$a_2$	O = 98.33	3.688	$a_1$	V = 35.54 O = 32.95 As = 32.63	2.89
$[\text{Si}_8\text{V}_{14}\text{O}_{50}]^{14-}$	24.067	$b_1$	O = 95.66	27.139	$a_1$	V = 84.27 Si = 12.5	3.072
$[\text{Ge}_8\text{V}_{14}\text{O}_{50}]^{13-}$	24.040	$a_1$	V = 73.29 Ge = 23.57	24.075	$b_2$	V = 54.14 Ge = 42.29 O = 2.08	0.035
$[\text{P}_8\text{V}_{14}\text{O}_{50}]^{5-}$	6.852	$b_2$	V = 88.07 P = 1.47 O = 1.43	6.874	$a_1$	V = 88.92 O = 1.07	0.022
$[\text{As}_8\text{V}_{14}\text{O}_{50}]^{5-}$	5.957	$a_1$	As = 36.14 O = 35.49 V = 27.67	5.996	$b_2$	As = 32.39 O = 32.76 V = 34.95	0.039

**Fig. 3.** Molecular orbital diagram and arrow indicates HOMO–LUMO energy gap of systems 1 and 2.

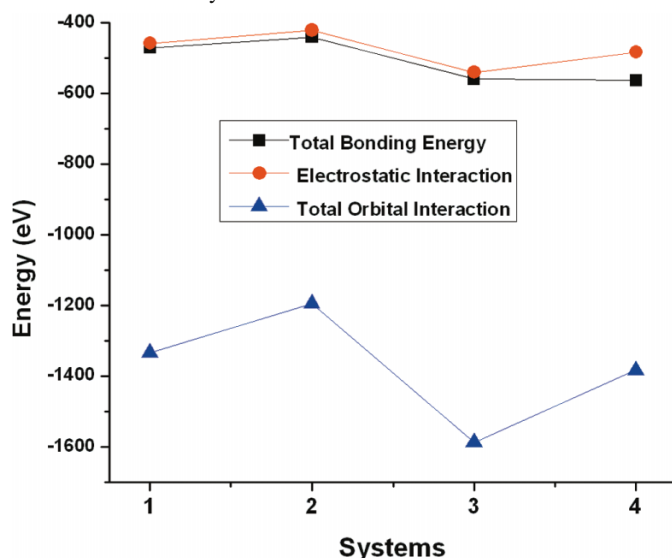
with a minimum energy of 23.04 eV. The question arises whether  $\alpha$ -LUMO or  $\beta$ -LUMO would accept an electron, it is obvious that the energy of  $\beta$ -LUMO is greater than that of  $\alpha$ -LUMO (see Tables 2 and 3), it means  $\alpha$ -LUMO is more favourable than  $\beta$ -LUMO, so 1 e will prefer to go to  $\alpha$ -LUMO. If 1 e goes to  $\beta$ -LUMO, then spin polarization becomes 13, and if an electron goes to  $\alpha$ -LUMO, the spin polarization becomes 15. We calculated both possibilities of  $[\text{Si}_8\text{V}_{14}\text{O}_{50}]^{13-}$  and found the total bonding energies, which were  $-445.81$  eV and  $-445.93$  eV for spin polarization 13 and 15, respectively. It was concluded that  $[\text{Si}_8\text{V}_{14}\text{O}_{50}]^{13-}$

**Fig. 4.** Molecular orbital diagram and arrow indicates HOMO–LUMO energy gap of systems 3 and 4.**Table 4.** Total bonding energies (eV) of systems 1– 4.

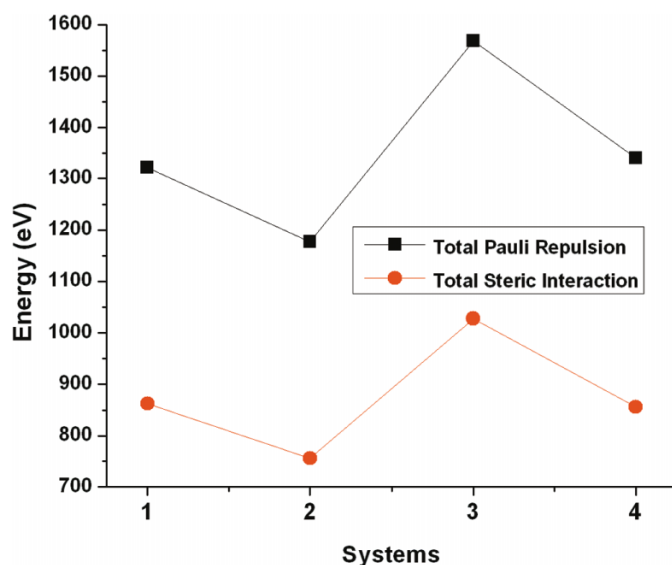
Systems	Total bonding energy (eV)
1	$-470.0956$
2	$-440.0773$
3	$-559.2619$
4	$-562.5542$

with spin polarization 15 is more favourable, so the first electron goes to  $\alpha$ -LUMO of symmetry  $e$  of  $[\text{Si}_8\text{V}_{14}\text{O}_{50}]^{12-}$  with 0.5 contribution to  $e_1$  and  $e_2$ . On second electron reduc-

**Fig. 5.** Total bonding energy, electrostatic interaction, and total orbital interaction of systems 1–4.



**Fig. 6.** Total Pauli repulsion and total steric interaction of systems 1–4.



tion  $\alpha$ -LUMO of symmetry  $e$  will be completed with two electrons resulting into  $[\text{Si}_8\text{V}_{14}\text{O}_{50}]^{14-}$  (see Fig. 7).

In one-electron reduction of  $[\text{Ge}_8\text{V}_{14}\text{O}_{50}]^{12-}$ , we have  $\alpha$ -LUMO and  $\beta$ -LUMO with very slight difference in energy (see Tables 2 and 3), i.e., the energy of  $\beta$ -LUMO is a little higher than that of  $\alpha$ -LUMO, and it seems that 1 e reduction will occur in  $\alpha$ -LUMO. The total bonding energies of  $[\text{Ge}_8\text{V}_{14}\text{O}_{50}]^{13-}$  have been observed as  $-417.02$  eV and  $-417.01$  eV for spin polarization 13 and 15, respectively. The total bonding energy with spin polarization 13 is less, so it is favourable, which means that 1 e will go to  $\beta$ -LUMO. Now, the question arises why is 1 e reduction favoured by  $\beta$ -LUMO? The answer of this question is that in  $\alpha$ -LUMO of  $[\text{Ge}_8\text{V}_{14}\text{O}_{50}]^{12-}$ , the contribution of V is 78.18%; on the contrary,  $\beta$ -LUMO is composed of 73.55% of V. So, it might be possible that 1 e goes to  $\beta$ -LUMO of  $[\text{Ge}_8\text{V}_{14}\text{O}_{50}]^{12-}$  to give it more electronic density. In 1 e

reduction of  $[\text{P}_8\text{V}_{14}\text{O}_{50}]^{4-}$ , an electron goes to  $\beta$ -LUMO due to its lower energy, as we also calculated total bonding energies of  $[\text{P}_8\text{V}_{14}\text{O}_{50}]^{5-}$ , which were  $-553.75$  eV and  $-553.43$  eV for spin polarization 13 and 15, respectively.  $[\text{P}_8\text{V}_{14}\text{O}_{50}]^{5-}$  with spin polarization 13 is more suitable, which means that the electron goes to  $\beta$ -LUMO of  $[\text{P}_8\text{V}_{14}\text{O}_{50}]^{4-}$ .

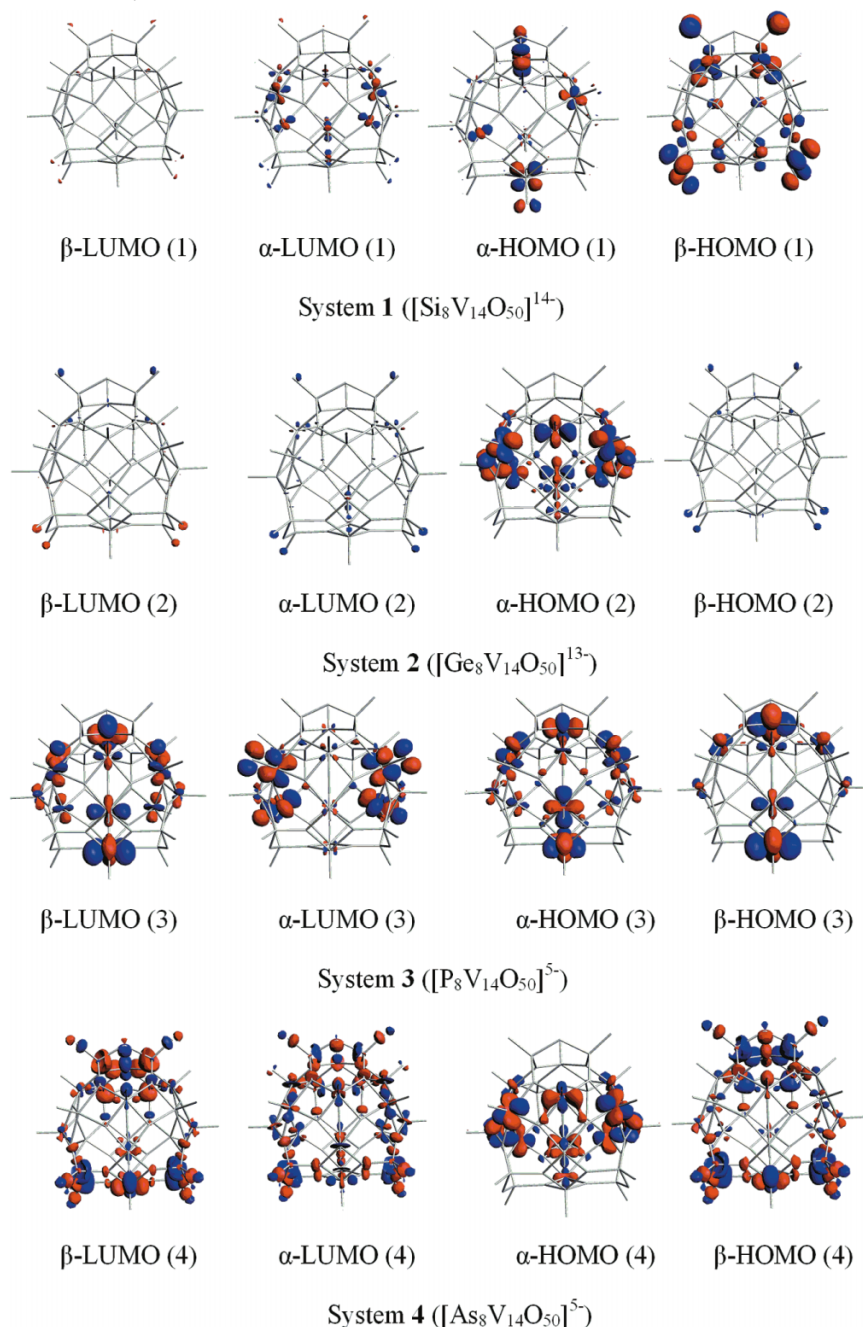
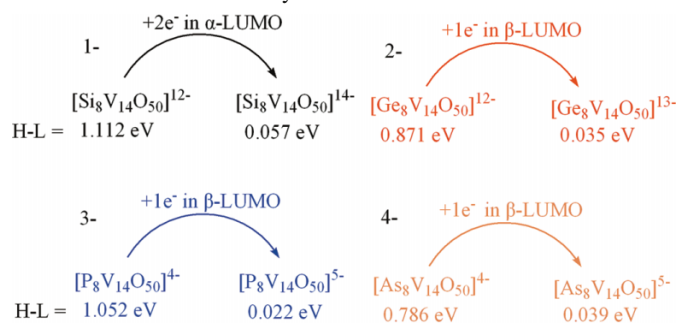
In the first reduction of  $[\text{As}_8\text{V}_{14}\text{O}_{50}]^{4-}$ , an electron goes to  $\beta$ -LUMO due to its low energy, which was further confirmed by the calculations of total bonding energies,  $-521.69$  eV and  $-521.32$  eV for spin polarization 13 and 15, respectively.  $[\text{As}_8\text{V}_{14}\text{O}_{50}]^{5-}$  with spin polarization 13 has less energy, which shows that 1 e goes to  $\beta$ -LUMO of  $[\text{As}_8\text{V}_{14}\text{O}_{50}]^{4-}$ . As far as energy gaps are concerned, the HOMO–LUMO energy gaps are significantly decreased after the first reduction of systems 1–4 as demonstrated in Scheme 1. The  $\alpha$ -LUMO in oxidized  $[\text{Si}_8\text{V}_{14}\text{O}_{50}]^{12-}$  is basically concentrated on V and O by 65.89% and 21.18%, respectively, whereas in reduced  $[\text{Si}_8\text{V}_{14}\text{O}_{50}]^{14-}$ , it is composed of V (65.94%) and Si (21.15%). The  $\alpha$ -LUMO in oxidized  $[\text{Ge}_8\text{V}_{14}\text{O}_{50}]^{12-}$  is delocalized over V (78.18%) and Ge (13.59%) while  $\beta$ -LUMO of  $[\text{Ge}_8\text{V}_{14}\text{O}_{50}]^{13-}$  is made up of V (54.14%) and Ge (42.29%). The  $\alpha$ -LUMO in oxidized  $[\text{P}_8\text{V}_{14}\text{O}_{50}]^{4-}$  is composed of 65.86% of V and 25.97% of O, whereas  $\beta$ -LUMO of  $[\text{P}_8\text{V}_{14}\text{O}_{50}]^{5-}$  is made up of 88.92% of V only (see Tables 2 and 3 with Figs. 2 and 7).

## Conclusions

In the present work, DFT calculations were carried out on vanadosilicate  $[\text{Si}_8\text{V}_{14}\text{O}_{50}]^{12-}$  and other related anions. The effect of substitution of  $\text{Ge}^{\text{IV}}$ ,  $\text{P}^{\text{V}}$ , and  $\text{As}^{\text{V}}$  with  $\text{Si}^{\text{IV}}$  on the electronic and redox properties was investigated. The above results can be summarized in following principal conclusions:

- (i) The substitution of  $\text{Si}^{\text{IV}}$  with  $\text{Ge}^{\text{IV}}$ ,  $\text{P}^{\text{V}}$ , and  $\text{As}^{\text{V}}$  has opened up possibilities for the experimentalists to synthesize other mimicked vanadosilicates, vanadogermenates, vandophosphates, and vandoarsenates as well as their heteropolyanions, respectively.
- (ii) The  $\alpha$ -LUMO is mainly concentrated on V and O in system 1, V and Ge in system 2, V and O in system 3, and As, O, and V in system 4.
- (iii) The substitution of  $\text{Ge}^{\text{IV}}$ ,  $\text{P}^{\text{V}}$ ,  $\text{As}^{\text{V}}$  with  $\text{Si}^{\text{IV}}$  in system 1 leads to decrease in the energy of LUMO and HOMO–LUMO energy gaps as well in systems 2, 3, and 4.
- (iv) The  $\alpha$  HOMO–LUMO energy gaps decrease in the following order: system 1 > 3 > 2 > 4.
- (v) The system 4 has a minimal value of the total bonding energy, whereas system 2 has a maximal value, so energetically system 4 is more favourable than the others. On the basis of total bonding energy, the formation of energetically favourable polyoxovanadates is in the following order: system 4 > 3 > 1 > 2.
- (vi) The bond lengths were shortened and lengthened because of the variable atomic radii of  $\text{Si}^{\text{IV}}$ ,  $\text{Ge}^{\text{IV}}$ ,  $\text{P}^{\text{V}}$ , and  $\text{As}^{\text{V}}$ .
- (vii) Phosphorous has the smallest atomic radius of 1.23 Å and germanium has the largest atomic radius of 1.52 Å among the afore mentioned polyoxovanadates,



**Fig. 7.** Frontier molecular orbitals of systems **1–4** after first reduction.**Scheme 1.** HOMO–LUMO energy gaps are significantly decreased after the first reduction of systems **1–4**.

and that is why bond lengths were maximum with the substitution of germanium while minimum with phosphorous.

(viii) Moreover, the bond lengths with  $\text{Ge}^{\text{IV}}$  were longer than with  $\text{Si}^{\text{IV}}$  due to the atomic radii of 1.52 Å and 1.46 Å, respectively, while the bond lengths with  $\text{As}^{\text{V}}$  were longer than with  $\text{P}^{\text{V}}$  due to atomic radii of 1.33 Å and 1.23 Å, respectively.

(ix) The first reduction would occur in the  $\alpha$ -LUMO of  $[\text{Si}_8\text{V}_{14}\text{O}_{50}]^{12-}$ ,  $\beta$ -LUMO of  $[\text{Ge}_8\text{V}_{14}\text{O}_{50}]^{12-}$ ,  $\beta$ -LUMO of  $[\text{P}_8\text{V}_{14}\text{O}_{50}]^{4-}$ , and  $\beta$ -LUMO of  $[\text{P}_8\text{V}_{14}\text{O}_{50}]^{4-}$  giving rise to reduced heteropolyanions of  $[\text{Si}_8\text{V}_{14}\text{O}_{50}]^{14-}$ ,  $[\text{Ge}_8\text{V}_{14}\text{O}_{50}]^{13-}$ ,  $[\text{P}_8\text{V}_{14}\text{O}_{50}]^{5-}$ , and  $[\text{As}_8\text{V}_{14}\text{O}_{50}]^{5-}$ , respectively.

(x) After the first reduction,  $\alpha$ -LUMO in  $[\text{Si}_8\text{V}_{14}\text{O}_{50}]^{14-}$  is composed of V and Si,  $\beta$ -LUMO in  $[\text{Ge}_8\text{V}_{14}\text{O}_{50}]^{13-}$  is concentrated on V and Ge,  $\beta$ -LUMO in  $[\text{P}_8\text{V}_{14}\text{O}_{50}]^{5-}$  is composed of V only, whereas  $\beta$ -LUMO in  $[\text{As}_8\text{V}_{14}\text{O}_{50}]^{5-}$  is made up of V, O, and As.

## Acknowledgements

The authors gratefully acknowledge the financial and technical support provided by Prof. Dr. Zhong-Min Su. Muhammad Ramzan Saeed Ashraf Janjua is also thankful to Muhammad Sareb Janjua, Dr. Muhammad Khan, Dr. Azhar Cheena, Dr. Abid Sheikh, Dr. Saeed Ahmad, Dr. Syed Manzar Abbas Shah, Dr. Muhammad Shahbaz Mustafai, Rauf Rufi, and Saqib Malik for their valuable support and encouragement.

## References

- (1) (a) Kozhevnikov, I. V. *Chem. Rev.* **1998**, 98 (1), 171. doi:10.1021/cr960400y. PMID:11851502.; (b) Mizuno, N.; Misono, M. *Chem. Rev.* **1998**, 98 (1), 199. doi:10.1021/cr960401q. PMID:11851503.; (c) Sadakane, M.; Steckhan, E. *Chem. Rev.* **1998**, 98 (1), 219. doi:10.1021/cr960403a. PMID:11851504.
- (2) Rhule, J. T.; Hill, C. L.; Judd, D. A.; Schinazi, R. F. *Chem. Rev.* **1998**, 98 (1), 327. doi:10.1021/cr960396q. PMID:11851509.
- (3) (a) Müller, A.; Peters, F.; Pope, M. T.; Gatteschi, D. *Chem. Rev.* **1998**, 98 (1), 239. doi:10.1021/cr9603946. PMID:11851505.; (b) Coronado, E.; Gómez-García, C. J. *Chem. Rev.* **1998**, 98 (1), 273. doi:10.1021/cr970471c. PMID:11851506.; (c) Klemperer, W. G.; Wall, C. G. *Chem. Rev.* **1998**, 98 (1), 297. doi:10.1021/cr9603993. PMID:11851507.; (d) Pope, M. T.; Müller, A. *Polyoxometalates: From Platonic Solids to Anti-Retroviral Activity*; Kluwer Academic Publishers: Dordrecht, The Netherlands, 1994.
- (4) Clemente-Juan, J. M.; Coronado, E. *Chem. Rev.* **1999**, 361, 193.
- (5) Lindquist, I. *Ark. Kemi* **1952**, 5, 247.
- (6) Keggin, J. F. *Nature* **1933**, 131 (3321), 908. doi:10.1038/131908b0.
- (7) Dawson, B. *Acta Crystallogr.* **1953**, 6 (2), 113. doi:10.1107/S0365110X53000466.
- (8) Pope, M. T. *Heteropoly and Isopoly Oxometalates*; Springer-Verlag: Berlin, 1983.
- (9) Hill, C. L. *Chem. Rev.* **1998**, 98 (1), 1. doi:10.1021/cr960395y. PMID:11851497.
- (10) Katsoulis, D. E. *Chem. Rev.* **1998**, 98 (1), 359. doi:10.1021/cr960398a. PMID:11851510.
- (11) Yamase, T. *Chem. Rev.* **1998**, 98 (1), 307. doi:10.1021/cr9604043. PMID:11851508.
- (12) Coronado, E.; Gómez-García, C. J. *Chem. Rev.* **1998**, 98 (1), 273. doi:10.1021/cr970471c. PMID:11851506.
- (13) Tripathi, A.; Hughbanks, T.; Clearfield, A. *J. Am. Chem. Soc.* **2003**, 125 (35), 10528. doi:10.1021/ja0365173. PMID:12940729.
- (14) Guan, W.; Yan, L. K.; Su, Z. M.; Liu, S. X.; Zhang, M.; Wang, X. *Inorg. Chem.* **2005**, 44 (1), 100. doi:10.1021/ic049830u. PMID:15627365.
- (15) Yan, L. K.; Su, Z. M.; Tan, K.; Zhang, M.; Qu, L. Y.; Wang, R. S. *Int. J. Quantum Chem.* **2005**, 105 (1), 37. doi:10.1002/qua.20675.
- (16) Yan, L. K.; Yang, G. C.; Guan, W.; Su, Z. M.; Wang, R. S. *J. Phys. Chem. B* **2005**, 109 (47), 22332. doi:10.1021/jp0542120. PMID:16853908.
- (17) Guan, W.; Yan, L. K.; Su, Z. M.; Wang, E. B.; Wang, X. H. *Int. J. Quantum Chem.* **2006**, 106 (8), 1860. doi:10.1002/qua.20965.
- (18) Yan, L. K.; Su, Z. M.; Guan, W.; Zhang, M.; Chen, G. H.; Xu, L.; Wang, E. B. *J. Phys. Chem. B* **2004**, 108 (45), 17337. doi:10.1021/jp0478256.
- (19) Maestre, J. M.; Lopez, X.; Bo, C.; Poblet, J. M.; Daul, C. *Inorg. Chem.* **2002**, 41 (7), 1883. doi:10.1021/ic0110676. PMID:11925184.
- (20) Rohmer, M.-M.; Bénard, M.; Blaudeau, J.-P.; Maestre, J.-M.; Poblet, J.-M. *Coord. Chem. Rev.* **1998**, 178-180, 1019. doi:10.1016/S0010-8545(98)00162-3.
- (21) Maestre, J. M.; Poblet, J. M.; Bo, C.; Casañ-Pastor, N.; Gomez-Romero, P. *Inorg. Chem.* **1998**, 37 (13), 3444. doi:10.1021/ic970195k.
- (22) López, X.; Maestre, J. M.; Bo, C.; Poblet, J. M. *J. Am. Chem. Soc.* **2001**, 123 (39), 9571. doi:10.1021/ja010768z. PMID:11572677.
- (23) Rohmer, M. M.; Devemy, J.; Wiest, R.; Benard, M. *J. Am. Chem. Soc.* **1996**, 118 (51), 13007. doi:10.1021/ja962259g.
- (24) Maestre, J. M.; Lopez, X.; Bo, C.; Poblet, J. M.; Casañ-Pastor, N. *J. Am. Chem. Soc.* **2001**, 123 (16), 3749. doi:10.1021/ja003563j. PMID:11457107.
- (25) Bridgeman, A. J.; Cavagliasso, G. *Inorg. Chem.* **2002**, 41 (13), 3500. doi:10.1021/ic0255510. PMID:12079470.
- (26) Bridgeman, A. J.; Cavagliasso, G. *J. Phys. Chem. A* **2003**, 107 (22), 4568. doi:10.1021/jp0340780.
- (27) Poblet, J. M.; López, X.; Bo, C. *Chem. Soc. Rev.* **2003**, 32 (5), 297. doi:10.1039/b109928k. PMID:14518183.
- (28) López, X.; Bo, C.; Poblet, J. M. *J. Am. Chem. Soc.* **2002**, 124 (42), 12574. doi:10.1021/ja020407z. PMID:12381202.
- (29) (a) Chemistry with ADF: te Velde, G.; Bickelhaupt, F. M.; Baerends, E. J.; Fonseca Guerra, C.; van Gisbergen, S. J. A.; Snijders, J. G.; Ziegler, T. *J. Comput. Chem.* **2001**, 22 (9), 931. doi:10.1002/jcc.1056.; (b) Fonseca Guerra, C.; Snijders, J. G.; te Velde, G.; Baerends, E. J. *Theor. Chem. Acc.* **1998**, 99 (6), 391. doi:10.1007/s002140050021.; (c) ADF2006.01. *SCM, Theoretical Chemistry*; Vrije Universiteit: Amsterdam, The Netherlands, 2006.
- (30) Vosko, S. H.; Wilk, L.; Nusair, M. *Can. J. Phys.* **1980**, 58, 1200. doi:10.1139/p80-159.
- (31) Becke, A. D. *Phys. Rev. A* **1988**, 38 (6), 3098. doi:10.1103/PhysRevA.38.3098. PMID:9900728.
- (32) Perdew, J. P. *Phys. Rev. B* **1986**, 33 (12), 8822. doi:10.1103/PhysRevB.33.8822.
- (33) (a) Chang, C.; Pelissier, M.; Durand, M. *Phys. Scr.* **1986**, 34 (5), 394. doi:10.1088/0031-8949/34/5/007.; (b) van Lenthe, E.; Baerends, E. J.; Snijders, J. G. *J. Chem. Phys.* **1993**, 99 (6), 4597. doi:10.1063/1.466059.; (c) van Lenthe, E.; Baerends, E. J.; Snijders, J. G. *J. Chem. Phys.* **1994**, 101 (11), 9783. doi:10.1063/1.467943.; (d) van Lenthe, E.; van Leeuwen, R.; Baerends, E. J.; Snijders, J. G. *Int. J. Quantum Chem.* **1996**, 57 (3), 281. doi:10.1002/(SICI)1097-461X(1996)57:3<281::AID-QUA2>3.0.CO;2-U.
- (34) Yan, L. K.; Dou, Z.; Guan, W.; Shi, S. Q.; Su, Z. M. *Eur. J. Inorg. Chem.* **2006**, 2006 (24), 5126. doi:10.1002/ejic.200600720.
- (35) Guan, W.; Yang, G. C.; Yan, L. K.; Su, Z. M. *Eur. J. Inorg. Chem.* **2006**, 2006 (20), 4179. doi:10.1002/ejic.200600450.
- (36) Guan, W.; Yang, G. C.; Yan, L. K.; Su, Z. M. *Inorg. Chem.* **2006**, 45 (19), 7864. doi:10.1021/ic061077c. PMID:16961379.

- (37) Janjua, M. R. S. A.; Liu, C. G.; Guan, W.; Zhuang, J.; Muhammad, S.; Yan, L. K.; Su, Z. M. *J. Phys. Chem. A* **2009**, *113* (15), 3576. doi:10.1021/jp808707q. PMID:19298074.
- (38) Carey, D. M. L.; Muñoz-Castro, A.; Bustos, C. J.; Manríquez, J. M.; Arratia-Pérez, R. *J. Phys. Chem. A* **2007**, *111* (28), 6563. doi:10.1021/jp0727594. PMID:17595070.

# Imino Diels–Alder reaction — An efficient synthetic protocol for 2-methyl-4-substituted tetrahydroquinolines catalyzed by copper dipyridine dichloride

C.S. Kavitha, K.M. Hosamani, and R.S. Harisha

**Abstract:** For the first time, copper dipyridine dichloride ( $\text{CuPy}_2\text{Cl}_2$ ) is used as an efficient and reusable catalyst for the imino Diels–Alder reaction of para-substituted anilines with *N*-vinylpyrrolidinone, *N*-vinylcarbazole, and *N*-vinylcaprolactam in acetonitrile to afford the corresponding 2-methyl-4-substituted-1,2,3,4-tetrahydroquinoline derivatives in excellent yields with good purity. The products were characterized by FTIR,  $^1\text{H}$  NMR,  $^{13}\text{C}$  NMR, MS, and elemental analysis.

**Key words:**  $\text{CuPy}_2\text{Cl}_2$ , reusable catalyst, aromatic amines, imino Diels–Alder reaction, 2-methyl-4-substituted tetrahydroquinolines.

**Résumé :** Le dichlorure de dipyridine cuivre ( $\text{CuPy}_2\text{Cl}_2$ ) a été utilisé pour la première fois comme catalyseur efficace et réutilisable pour la imino de Diels–Alder d'anilines para-substituées avec de la *N*-vinylpyrrolidone, du *N*-vinylcarbazole et du *N*-vinylcaprolactame, dans l'acétonitrile, pour conduire avec d'excellents rendements et un bonne pureté à la formation de dérivés correspondants, 2-méthyl-1,2,3,4-tétrahydroquinoléines substituées en position 4, qui ont été caractérisés par analyse élémentaire et par spectroscopies RMN du  $^1\text{H}$  et du  $^{13}\text{C}$ , par spectroscopie infrarouge à transformée de Fourier et par spectroscopie de masse.

**Mots-clés :**  $\text{CuPy}_2\text{Cl}_2$ , catalyseur réutilisable, amines aromatiques, réaction imino de Diels–Alder, 2-méthyl-1,2,3,4-tétrahydroquinoléines substituées en position 4.

[Traduit par la Rédaction]

## Introduction

One of the most challenging tasks in modern organic chemistry is the synthesis of natural products containing heterocyclic ring. Despite the considerable exploration to date within this field, there is still a need for further development of alternative methods for the synthesis of heterocyclic compounds. Among numerous families of natural products, tetrahydroquinolines seem to attract considerable attention because of their abundant presence in plants<sup>1</sup> along with their promising biological activities.<sup>2–8</sup> Therefore, their synthesis via newer and atom economical<sup>9</sup> approaches has been the subject of current research.<sup>10,11</sup> Since the pioneering work of Povarov,<sup>12</sup> this reaction has been extensively studied with use of different Lewis acids, such as  $\text{BF}_3\cdot\text{OEt}_2$ ,<sup>13</sup>  $\text{GaCl}_3$ ,<sup>14</sup>  $\text{InCl}_3$ ,<sup>15</sup>  $\text{LiClO}_4$ ,<sup>16,17</sup>  $\text{ZrCl}_4$ ,<sup>18</sup>  $\text{BiCl}_3$ ,<sup>19</sup> and  $\text{SbCl}_3$ ,<sup>20</sup> and protic acids, such as TFA,<sup>21</sup>  $\text{TsOH}$ ,<sup>22</sup> and  $(\text{COOH})_2$ .<sup>23</sup> Although the imino Diels–Alder reaction promoted by Lewis acid is known, many of these methods suffer from some limitations, such as more than stoichiometric amounts of the Lewis acid are required because of the coordination of the Lewis acid to the imine nitrogen. Further, most of these acids are moisture-sensitive and easily decom-

pose or become deactivated in the presence of water and are thus difficult to handle. Moreover, these reactions have some drawbacks like drastic reaction conditions, prolonged reaction time, tedious work-up procedures, and co-occurrence of side reactions, low yields, and expensive reagents/catalysts. Some of the catalysts are destroyed in the work-up procedure and cannot be recovered or reused. Furthermore, the disposal of these acids leads to environmental pollution. Therefore, the search continues for a better catalyst for the synthesis of tetrahydroquinolines in terms of operational simplicity, reusability of catalyst, low cost, and greater selectivity.

In continuation of our research work on imino Diels–Alder reaction by use of new catalysts,<sup>24,25</sup> we test copper dipyridine dichloride ( $\text{CuPy}_2\text{Cl}_2$ )<sup>26</sup> as an efficient Lewis acid catalyst. It is water-tolerant, reusable, and can effectively promote some of the organic reactions.<sup>27–29</sup>  $\text{CuPy}_2\text{Cl}_2$  is easier to handle than metal halides, such as  $\text{ZrCl}_4$ ,  $\text{BiCl}_3$ , and  $\text{SbCl}_3$ , and protic acids, such as TFA or  $\text{TsOH}$ . In the quest for developing a less toxic, potentially green catalyst, we thought of using  $\text{CuPy}_2\text{Cl}_2$  as a catalyst to synthesize the 2-methyl-4-substituted tetrahydroquinoline derivatives.

Received 19 August 2009. Accepted 25 January 2010. Published on the NRC Research Press Web site at canjchem.nrc.ca on 26 March 2010.

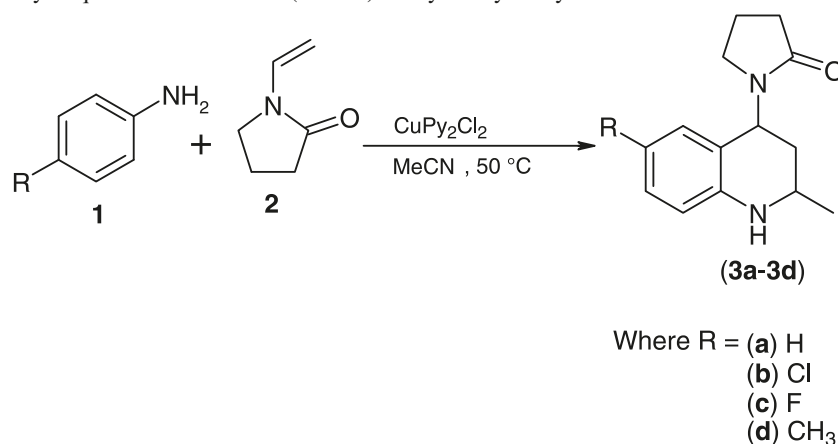
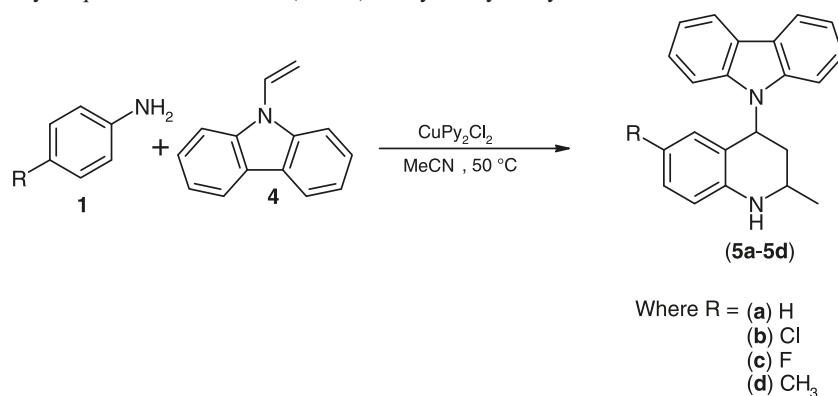
C.S. Kavitha, K.M. Hosamani,<sup>1</sup> and R.S. Harisha. P.G. Department of Studies in Chemistry, Karnatak University, Pavate Nagar, Dharwad 580 003, India.

<sup>1</sup>Corresponding author (e-mail: dr\_hosamani@yahoo.com).



**Table 1.** Effect of solvents on the synthesis of 2-methyl-4-substituted tetrahydroquinoline derivatives.

Entry	<i>p</i> -Chloroaniline(mmol)	NVP (mmol)	Solvent	Catalyst <sup>a</sup>	Temperature (°C)	Time (h)	Yield <sup>b</sup> (%)
1	5	12	CH <sub>2</sub> Cl <sub>2</sub>	CuPy <sub>2</sub> Cl <sub>2</sub>	25	15	55
2	5	12	CH <sub>3</sub> CN	CuPy <sub>2</sub> Cl <sub>2</sub>	25	10	60
3	5	12	CH <sub>3</sub> CN	CuPy <sub>2</sub> Cl <sub>2</sub>	50	3	90
4	5	12	Toluene	CuPy <sub>2</sub> Cl <sub>2</sub>	50	13	50
5	5	12	THF	CuPy <sub>2</sub> Cl <sub>2</sub>	50	18	60
6	5	12	MeOH	CuPy <sub>2</sub> Cl <sub>2</sub>	50	12	60
7	5	12	EtOH	CuPy <sub>2</sub> Cl <sub>2</sub>	50	12	60

<sup>a</sup>0.01 mmol CuPy<sub>2</sub>Cl<sub>2</sub> catalyst loaded.<sup>b</sup>Isolated yields.**Scheme 1.** Synthesis of tetrahydroquinoline derivatives (**3a–3d**) catalyzed by CuPy<sub>2</sub>Cl<sub>2</sub>.**Scheme 2.** Synthesis of tetrahydroquinoline derivatives (**5a–5d**) catalyzed by CuPy<sub>2</sub>Cl<sub>2</sub>.

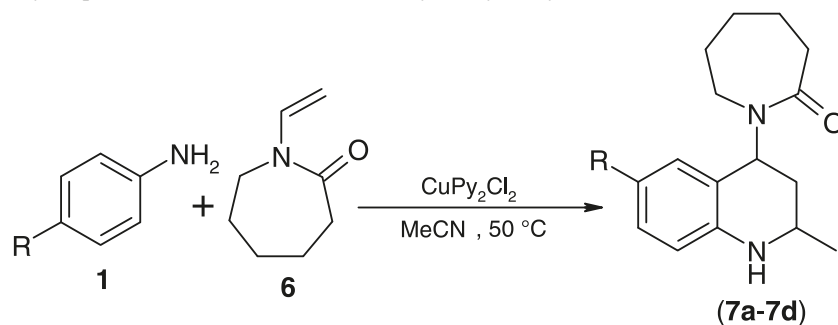
## Results and discussion

In view of the current trends in catalytic processes, there is merit in developing a truly catalytic method for the formation of 2-methyl-4-substituted tetrahydroquinolines. Now, we have found that an imino Diels–Alder reaction can be conveniently performed under neutral and mild conditions in the presence of a catalytic amount of CuPy<sub>2</sub>Cl<sub>2</sub>. Because of the presence of two pyridine rings, the electron deficiency increases on the nitrogen so it acts efficiently as a Lewis acid.<sup>26</sup>

Preliminary studies were carried out to study the effect of solvents and temperature on the model reaction of *p*-chloroaniline (5 mmol), and *N*-vinylpyrrolidinone (NVP) (12 mmol) in the presence of 0.01 mmol of CuPy<sub>2</sub>Cl<sub>2</sub>, and the results

are summarized (Table 1). Though the reaction proceeds at room temperature, the isolated yields are low and the reaction was sluggish. At 50 °C, the reaction proceeded smoothly and gave the desired products in excellent yields by using acetonitrile as solvent.

When the reaction was performed in different solvents such as dichloromethane, methanol, ethanol, THF and toluene, the observed yield was low (Table 1). However, when acetonitrile was used as solvent, the tetrahydroquinoline derivative was obtained in good yield with purity. However, the acetonitrile was found to be the best for the catalytic reaction in terms of yield and reaction time. In a control experiment, it was observed that in the absence of the catalyst, the reaction did not proceed neither at room temperature nor at higher temperatures.

**Scheme 3.** Synthesis of tetrahydroquinoline derivatives (**7a–7d**) catalyzed by  $\text{CuPy}_2\text{Cl}_2$ .

Thus, in the presence of 0.01 mmol of  $\text{CuPy}_2\text{Cl}_2$ , *p*-chloroaniline<sup>1</sup> was treated with NVP<sup>2</sup> in acetonitrile at 50 °C. After 2 h, the 1-(2-methyl-1,2,3,4-tetrahydroquinolin-4-yl)-pyrrolidin-2-one was obtained in good yield (Scheme 1). These compounds were established by IR, <sup>1</sup>H NMR, <sup>13</sup>C NMR, and mass spectral analysis.

Similarly, para-substituted anilines reacted smoothly with *N*-vinylpyrrolidinone, *N*-vinylcarbazole, and *N*-vinylcaprolactam (Scheme 1, Scheme 2, and Scheme 3, respectively) to give the corresponding tetrahydroquinolines (**3a–3d**, **5a–5d**, and **7a–7d**) in 80%–95% yields (Table 2) in the presence of 0.01 mmol of  $\text{CuPy}_2\text{Cl}_2$  in acetonitrile at 45–50 °C. In the IR spectra, the NH in all derivatives was observed at 3320–3360  $\text{cm}^{-1}$ , and C=O was observed from 1670.0 to 1678.3  $\text{cm}^{-1}$ . In <sup>1</sup>H NMR spectra, the NH peak was observed around 3–5 ppm, and NH proton disappeared on D<sub>2</sub>O addition and all the remaining protons were observed in the expected regions.

On the basis of previous reports<sup>30–32</sup> and the NMR data, all the substituted tetrahydroquinoline exist as *cis*-diastereomers. Their structural elucidation was based on <sup>1</sup>H NMR. The *J* values of H<sub>2</sub> and H<sub>4</sub> were found to be 7.88 and 6.80 Hz, respectively.

From these results, we propose the following possible mechanism to account for the reaction.<sup>24,25</sup> In a first step, the reaction must proceed by *N*-vinyl tautomerization to the iminium species and nucleophilic substitution at vinyl carbon, favoring the intermolecular proton transformation leading to the N–C bond formation. In a second step, the reaction of a second equivalent of the vinyl substrate leading to the Ar–C–C bond formation (Schemes 4–6).

## Conclusion

In conclusion, we are reporting that  $\text{CuPy}_2\text{Cl}_2$  is an efficient and reusable catalyst for the synthesis of 2-methyl-4-substituted tetrahydroquinoline derivatives. The present protocol provides easy work-up procedure, cost efficiency, providing reusability of the catalyst with excellent yields, which makes this method a valid contribution to the existing methodologies of tetrahydroquinolines.

## Experimental

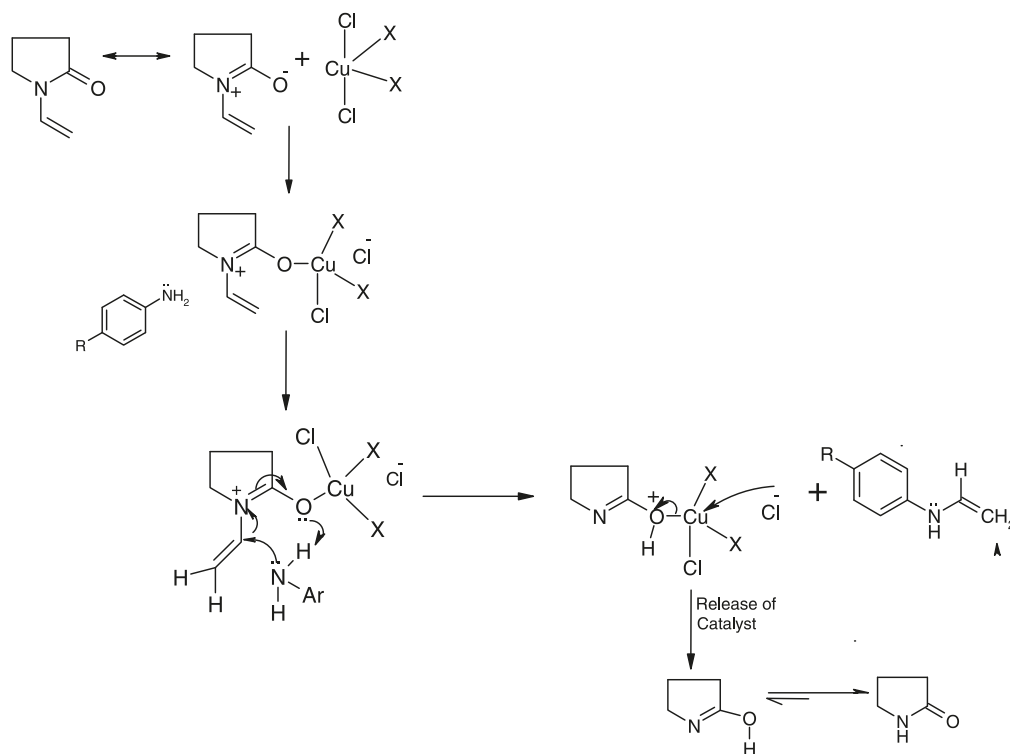
The melting points of the products were determined by open capillaries on a Buchi apparatus and are uncorrected. The IR spectra were recorded on a Nicolet Impact-5700 FTIR Spectrophotometer using KBr pellets. <sup>1</sup>H NMR and <sup>13</sup>C NMR spectra were recorded on a BRUKER AVANCE-300F 300 MHz spectrometer in  $\text{CDCl}_3$  using TMS as an internal standard with <sup>1</sup>H resonance frequency of 300 MHz and <sup>13</sup>C resonance frequency of 75 MHz. D<sub>2</sub>O exchange was applied to confirm the assignment of the signals of NH protons. The Mass spectra were recorded on a Shimadzu GC-2010. The elemental analysis was carried out by using HERAUS CHN rapid analyzer. The homogeneity of the compounds was described by TLC detected by UV light and iodine vapors. All chemical reagents were obtained from Fluka, sd fine, and Merck chemical companies and were used without purification.

### General procedure for the synthesis of 2-methyl-4-substituted tetrahydroquinoline derivatives in the presence of copper dipyrindine dichloride catalyst

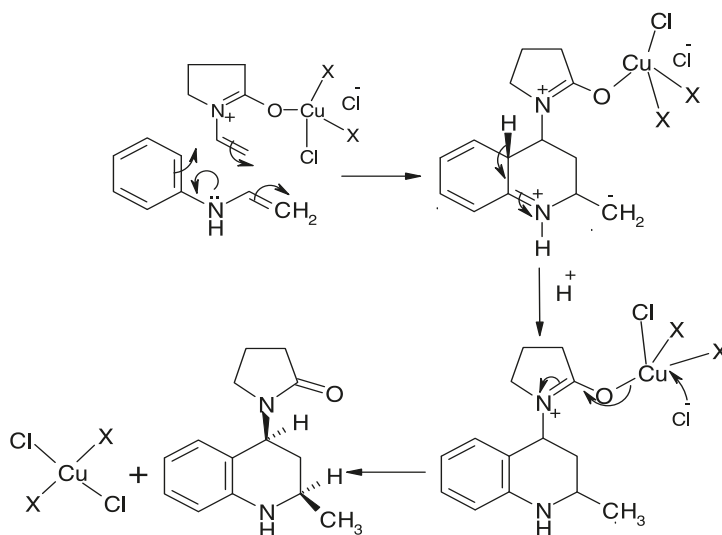
A mixture of the para-substituted anilines (**1**) (5 mmol), *N*-vinylpyrrolidin-2-one (**2**) (12 mmol), *N*-vinylcarbazole (**4**) (12 mmol), *N*-vinylcaprolactam (**6**) (12 mmol), and  $\text{CuPy}_2\text{Cl}_2$  (0.01 mmol) in acetonitrile (5 mL) was stirred at 45–50 °C for the appropriate time (Table 2). After completion of reaction as indicated by TLC, the reaction mixture was quenched with saturated aqueous  $\text{NaHCO}_3$  solution (20 mL) and extracted with ethyl acetate (2 × 15 mL). The combined organic layer was dried over anhydrous  $\text{Na}_2\text{SO}_4$  and concentrated under reduced pressure. After extraction, the water layer containing the catalyst could be evaporated under reduced pressure to give a catalyst back with blue colored sol id. The recovered catalyst was washed with ether and dried at 85 °C for 2 h under high pressure prior to further use in another reaction. The residue thus obtained was purified by column chromatography using silica gel (60–120 mesh) and eluted with petroleum ether:ethyl acetate (8:2) to afford tetrahydroquinoline derivatives (**3a–3d**, **5a–5d**, and **7a–7d**).

**Scheme 4.** Proposed plausible mechanistic pathway of the synthesis of tetrahydroquinoline derivatives (**3a–3d**) catalyzed by  $\text{CuPy}_2\text{Cl}_2$  (Scheme 1).

Step 1:



Step 2:



### Spectral data of the synthesized compounds

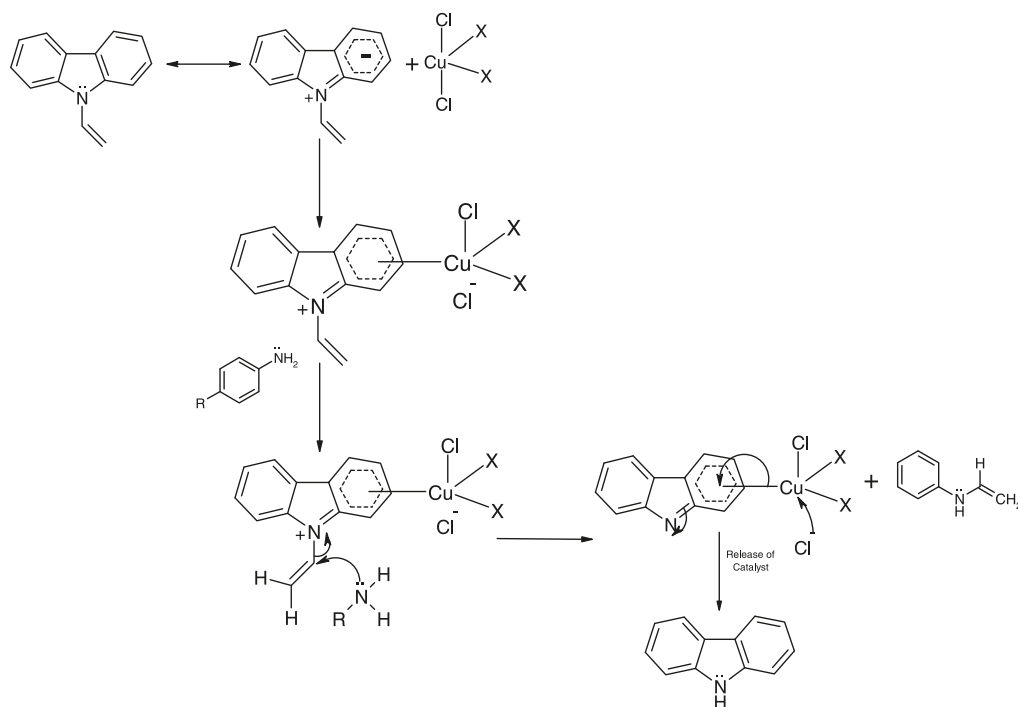
#### 1-(2-Methyl-1,2,3,4-tetrahydroquinolin-4-yl)pyrrolidin-2-one (**3a**)

Colorless crystalline solid. Yield: 90%, mp 72–74 °C (recrystallization solvent: chloroform). <sup>1</sup>H NMR (300 MHz,  $\text{CDCl}_3$ )  $\delta$  (ppm): 1.28 (d, 3H,  $J$  = 6.1 Hz), 1.67 (ddd, 1H,  $J$  = 12.2, 5.8, 1.9 Hz), 1.98 (ddd, 1H,  $J$  = 12.0, 6.0,

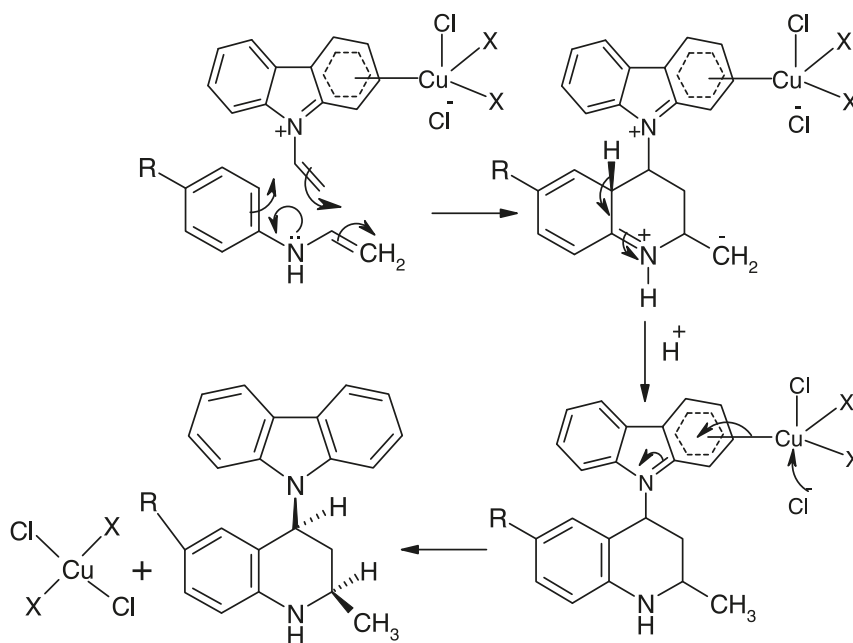
2.4 Hz), 1.99–2.16 (m, 2H), 2.44–2.68 (m, 2H), 2.98–3.13 (m, 2H), 3.43–3.54 (m, 1H), 4.5 (brs, 1H, NH), 5.65 (dd, 1H,  $J$  = 11.5, 6.0 Hz), 6.67 (td, 1H,  $J$  = 8.0, 1.1 Hz), 6.8 (t, 1H,  $J$  = 7.5 Hz), 6.99 (m, 2H). <sup>13</sup>C NMR (300 MHz,  $\text{CDCl}_3$ )  $\delta$  (ppm): 18.3, 22.1, 31.0, 33.6, 42.1, 47.3, 47.9, 114.1, 117.5, 122.6, 127.4, 128.8, 145.4, 175.6. IR (KBr)  $\nu$  ( $\text{cm}^{-1}$ ): 3346. MS  $m/z$ : 230. Anal. calcd. for  $\text{C}_{14}\text{H}_{18}\text{N}_2\text{O}$ : C, 73.01; H, 7.88; N, 12.16. Found: C, 72.95; H, 7.81; N, 12.01.

**Scheme 5.** Proposed plausible mechanistic pathway of the synthesis of tetrahydroquinoline derivatives (**5a–5d**) catalyzed by  $\text{CuPy}_2\text{Cl}_2$  (Scheme 2).

Step 1:



Step 2:



**1-(6-Chloro-2-methyl-1,2,3,4-tetrahydroquinolin-4-yl)pyrrolidin-2-one (3b)**

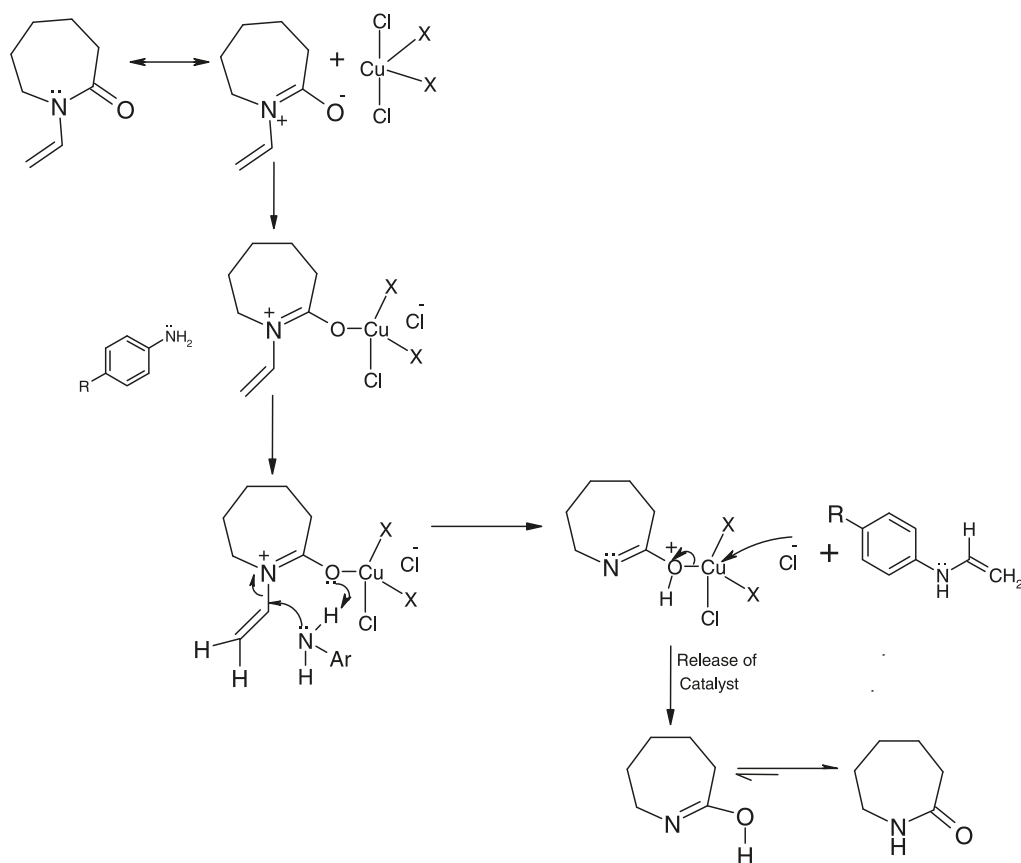
Colorless crystalline solid. Yield: 93%, mp 151–153 °C (recrystallization solvent: chloroform).  $^1\text{H}$  NMR (300 MHz,  $\text{CDCl}_3$ )  $\delta$  (ppm): 1.26 (d, 3H,  $J = 6.0$  Hz), 1.78 (ddd, 1H,  $J = 12.6, 5.3, 2.5$  Hz), 1.93 (ddd, 1H,  $J = 11.7,$

5.8, 26.4 Hz), 1.95–2.18 (m, 2H), 2.40–2.55 (m, 2H), 3.10–3.35 (m, 2H), 3.45–3.66 (m, 1H), 4.8 (brs, 1H, NH), 5.7 (dd, 1H,  $J = 12.0, 6.0$  Hz), 6.43 (d, 1H,  $J = 8.6$  Hz), 6.73 (s, 1H), 6.92 (dd, 1H,  $J = 8.8$  Hz, 2.4 Hz).  $^{13}\text{C}$  NMR (300 MHz,  $\text{CDCl}_3$ )  $\delta$  (ppm): 18.0, 22.2, 31.8, 33.4, 42.8, 47.6, 47.3, 116.3, 120.3, 122.2, 126.0, 129.6, 144.1, 175.4.

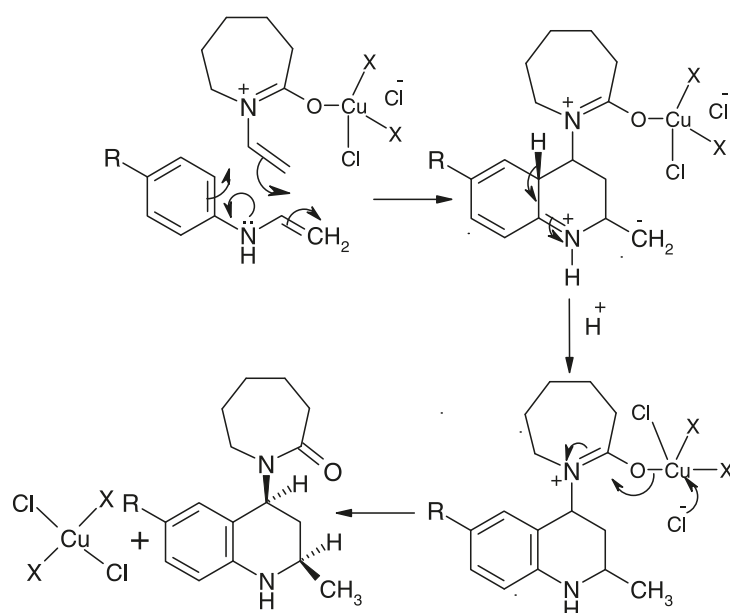


**Scheme 6.** Proposed plausible mechanistic pathway of the synthesis of tetrahydroquinoline derivatives (**7a–7d**) catalyzed by  $\text{CuPy}_2\text{Cl}_2$  (Scheme 3).

Step 1:



Step 2:



**Table 2.** CuPy<sub>2</sub>Cl<sub>2</sub>-catalyzed synthesis of 2-methyl-4-substituted tetrahydroquinoline.

Entry	Substrate	N-Vinyl Compound	Code	Product	Time (h)	Mp (°C) (CHCl <sub>3</sub> ) <sup>a</sup>	Yield <sup>b</sup> (%)	Yield <sup>c</sup> (%)
1			<b>3a</b> <sup>25</sup>		3.00	72–74	90	85
2			<b>3b</b> <sup>25</sup>		3.00	151–153	93	86
3			<b>3c</b> <sup>25</sup>		3.5	137–139	90	82
4			<b>3d</b> <sup>25</sup>		2.5	96–98	92	83
5			<b>5a</b>		2.0	124–126	90	85
6			<b>5b</b>		2.2	128–130	91	82
7			<b>5c</b>		2.5	131–133	91	86
8			<b>5d</b>		2.0	124–126	92	85
9			<b>7a</b>		2.0	118–120	92	86
10			<b>7b</b>		2.5	122–124	93	85
11			<b>7c</b>		2.5	128–130	90	86
12			<b>7d</b>		2.0	125–127	91	86

**Note:** 0.01 mmol CuPy<sub>2</sub>Cl<sub>2</sub> catalyst loaded.<sup>a</sup> Recrystallized solvent.<sup>b</sup> Isolated yield.<sup>c</sup> Isolated yield by use of recovered catalyst.

IR (KBr)  $\nu$  (cm<sup>-1</sup>): 3389. MS  $m/z$ : 264. Anal. calcd. for C<sub>14</sub>H<sub>17</sub>ClN<sub>2</sub>O: C, 63.51; H, 6.47; N, 10.58. Found: C, 63.47; H, 6.42; N, 10.52.

**1-(6-Fluoro-2-methyl-1,2,3,4-tetrahydroquinolin-4-yl)pyrrolidin-2-one (3c)**

Colorless crystalline solid. Yield: 90%, mp 137–139 °C

(recrystallization solvent: chloroform).  $^1\text{H}$  NMR (300 MHz,  $\text{CDCl}_3$ )  $\delta$  (ppm): 1.26 (d, 3H,  $J = 6.0$  Hz), 1.76 (m, 1H), 1.95 (ddd, 1H,  $J = 12.2, 5.7, 2.6$  Hz), 2.10–2.3 (m, 2H), 2.47–2.60 (m, 2H), 3.1–3.19 (m, 2H), 3.44–3.56 (m, 1H), 4.2 (brs, 1H, NH), 5.50 (dd, 1H,  $J = 11.7, 5.9$  Hz), 6.65 (m, 2H), 6.8 (d, 1H,  $J = 8.7, 2.8$  Hz).  $^{13}\text{C}$  NMR (300 MHz,  $\text{CDCl}_3$ )  $\delta$  (ppm): 17.8, 18.7, 21.8, 30.4, 33.0, 41.3, 46.6, 47.8, 116.2, 120.9, 122.6, 125.3, 128.9, 143.2, 175.3. IR (KBr)  $\nu$  ( $\text{cm}^{-1}$ ): 3255. MS  $m/z$ : 248. Anal. calcd. for  $\text{C}_{14}\text{H}_{17}\text{FN}_2\text{O}$ : C, 67.72; H, 6.90; N, 11.28. Found: C, 67.68; H, 6.82; N, 11.22.

### 1-(2,6-Dimethyl-1,2,3,4-tetrahydroquinolin-4-yl)pyrrolidin-2-one (3d)

Pale yellow crystalline solid. Yield: 92%, mp 96–98 °C (recrystallization solvent: chloroform).  $^1\text{H}$  NMR (300 MHz,  $\text{CDCl}_3$ )  $\delta$  (ppm): 1.2 (d, 3H,  $J = 5.6$  Hz), 1.66 (q, 1H,  $J = 11.8$  Hz), 1.74 (ddd, 1H,  $J = 12.1, 5.8, 2.5$  Hz), 1.93–2.10 (m, 2H), 2.24 (s, 3H), 2.25–2.45 (m, 2H), 2.95–3.21 (m, 2H), 3.39–3.58 (m, 1H), 5.25 (dd, 1H,  $J = 11.8, 5.9$  Hz), 5.46 (brs, 1H, NH), 6.42 (m, 2H), 6.70 (d, 1H,  $J = 8.1$  Hz).  $^{13}\text{C}$  NMR (300 MHz,  $\text{CDCl}_3$ )  $\delta$  (ppm): 17.70, 18.8, 20.2, 21.72, 30.64, 32.98, 41.2, 46.4, 47.4, 112.1, 125.2, 126.8, 127.8, 128.3, 143.9, 173.9. IR (KBr)  $\nu$  ( $\text{cm}^{-1}$ ): 3328. MS  $m/z$ : 244. Anal. calcd. for  $\text{C}_{15}\text{H}_{20}\text{N}_2\text{O}$ : C, 73.74; H, 8.25; N, 11.47. Found: C, 73.68; H, 8.19; N, 11.39.

### 9-(2-Methyl-1,2,3,4-tetrahydroquinolin-4-yl)-9H-carbazole (5a)

Colorless crystalline solid. Yield: 90%, mp 124–126 °C (recrystallization solvent: chloroform).  $^1\text{H}$  NMR (300 MHz,  $\text{CDCl}_3$ )  $\delta$  (ppm): 1.35 (d, 3H,  $J = 6.3$  Hz), 2.25 (dd, 2H,  $J = 11.7, 6.1, 2.0$  Hz), 3.15 (m, 1H), 4.97 (dd, 1H,  $J = 11.8, 6.2$  Hz), 4.4 (s, 1H, NH), 6.90 (d, 1H,  $J = 8.5$  Hz), 6.38 (d, 1H,  $J = 8.4$  Hz), 6.86 (d, 1H,  $J = 8.6$  Hz), 7.19–8.11 (m, 8H).  $^{13}\text{C}$  NMR (75 MHz,  $\text{CDCl}_3$ )  $\delta$  (ppm): 22.59, 35.16, 47.99, 52.08, 108.45, 110.90, 112.95, 114.93, 118.65, 119.25, 119.83, 120.78, 123.53, 123.76, 125.61, 126.06, 126.21, 128.12, 128.78, 139.89, 141.75, 145.66. IR (KBr)  $\nu$  ( $\text{cm}^{-1}$ ): 3417. MS  $m/z$ : 313. Anal. calcd. for  $\text{C}_{22}\text{H}_{20}\text{N}_2$ : C, 84.58; H, 6.45; N, 8.97. Found: C, 84.10; H, 6.40; N, 8.93.

### 9-(6-Chloro-2-methyl-1,2,3,4-tetrahydroquinolin-4-yl)-9H-carbazole (5b)

Colorless crystalline solid. Yield: 91%, mp 128–130 °C (recrystallization solvent: chloroform).  $^1\text{H}$  NMR (300 MHz,  $\text{CDCl}_3$ )  $\delta$  (ppm): 1.58 (d, 3H,  $J = 6.1$  Hz), 1.95 (dd, 2H,  $J = 11.4, 6.0, 2.6$  Hz), 3.45 (m, 1H), 5.5 (dd, 1H,  $J = 11.6, 6.0$  Hz), 4.1 (s, 1H, NH), 6.75 (s, 1H), 6.49 (d, 1H,  $J = 8.5$  Hz), 6.97 (d, 1H,  $J = 8.6$  Hz), 7.19–8.11 (m, 8H).  $^{13}\text{C}$  NMR (75 MHz,  $\text{CDCl}_3$ )  $\delta$  (ppm): 21.39, 37.0, 51.0, 55.1, 108.45, 110.90, 111.0, 112.1, 112.95, 115.1, 119.6, 119.83, 120.78, 121.7, 123.2, 126.05, 128.78, 129.55, 133.4, 141.75, 143.3, 145.66. IR (KBr)  $\nu$  ( $\text{cm}^{-1}$ ): 3417. MS  $m/z$ : 346. Anal. calcd. for  $\text{C}_{22}\text{H}_{19}\text{ClN}_2$ : C, 76.18; H, 5.52; N, 8.08. Found: C, 76.15; H, 5.48; N, 8.05.

### 9-(6-Fluoro-2-methyl-1,2,3,4-tetrahydroquinolin-4-yl)-9H-carbazole (5c)

Colorless crystalline solid. Yield: 91%, mp 131–133 °C (recrystallization solvent: chloroform).  $^1\text{H}$  NMR (300 MHz,

$\text{CDCl}_3$ )  $\delta$  (ppm): 1.49 (d, 3H,  $J = 6.5$  Hz), 1.84 (dd, 2H,  $J = 11.2, 6.3, 2.8$  Hz), 3.43 (m, 1H), 5.3 (dd, 1H,  $J = 11.4, 6.5$  Hz), 4.5 (s, 1H, NH), 6.71 (s, 1H), 6.46 (d, 1H,  $J = 8.9$  Hz), 6.93 (d, 1H,  $J = 8.9$  Hz), 7.14–8.16 (m, 8H).  $^{13}\text{C}$  NMR (75 MHz,  $\text{CDCl}_3$ )  $\delta$  (ppm): 22.61, 35.22, 48.12, 52.26, 108.64, 111.02, 112.76, 114.76, 118.61, 119.29, 119.68, 121.74, 123.29, 124.74, 125.89, 126.41, 127.18, 128.09, 128.76, 139.86, 141.72, 145.69. IR (KBr)  $\nu$  ( $\text{cm}^{-1}$ ): 3420. MS  $m/z$ : 330. Anal. calcd. for  $\text{C}_{22}\text{H}_{19}\text{FN}_2$ : C, 79.97; H, 5.80; N, 8.48. Found: C, 79.94; H, 5.75; N, 8.45.

### 9-(2,6-Dimethyl-1,2,3,4-tetrahydroquinolin-4-yl)-9H-carbazole (5d)

Colorless crystalline solid. Yield: 92%, mp 124–126 °C (recrystallization solvent: chloroform).  $^1\text{H}$  NMR (300 MHz,  $\text{CDCl}_3$ )  $\delta$  (ppm): 1.42 (d, 3H,  $J = 6.2$  Hz), 1.89 (dd, 2H,  $J = 11.6, 6.4, 2.6$  Hz), 2.35 (s, 3H), 3.21 (m, 1H), 4.95 (dd, 1H,  $J = 11.1, 6.0$  Hz), 4.5 (s, 1H, NH), 6.70 (s, 1H), 6.26 (d, 1H,  $J = 8.5$  Hz), 6.66 (d, 1H,  $J = 8.8$  Hz), 7.14–8.16 (m, 8H).  $^{13}\text{C}$  NMR (75 MHz,  $\text{CDCl}_3$ )  $\delta$  (ppm): 21.1, 21.3, 47.02, 51.0, 55.22, 108.64, 111.0, 111.02, 112.28, 112.76, 114.76, 115.1, 118.61, 119.6, 120.5, 121.74, 123.29, 125.89, 127.18, 128.09, 133.1, 140.3, 141.69. IR (KBr)  $\nu$  ( $\text{cm}^{-1}$ ): 3426. MS  $m/z$ : 326. Anal. calcd. for  $\text{C}_{23}\text{H}_{22}\text{N}_2$ : C, 84.63; H, 6.79; N, 8.58. Found: C, 84.58; H, 6.75; N, 8.55.

### 1-(2-Methyl-1,2,3,4-tetrahydroquinolin-4-yl)azepan-2-one (7a)

Light yellow crystalline solid. Yield: 92%, mp 118–120 °C (recrystallization solvent: chloroform).  $^1\text{H}$  NMR (300 MHz,  $\text{CDCl}_3$ )  $\delta$  (ppm): 1.23 (d, 3H,  $J = 6.3$  Hz), 2.09 (dd, 2H,  $J = 11.2, 6.3, 2.4$  Hz), 2.79 (m, 1H), 4.87 (dd, 1H,  $J = 11.5, 6.3$  Hz), 1.29 (t, 2H), 1.55 (m, 2H), 1.57 (m, 2H), 2.18 (t, 2H), 3.2 (t, 2H), 4.5 (s, 1H, NH), 6.49–6.91 (m, 4H).  $^{13}\text{C}$  NMR (75 MHz,  $\text{CDCl}_3$ )  $\delta$  (ppm): 21.3, 25.7, 31.8, 32.0, 32.2, 44.5, 46.6, 47.3, 50.7, 112.1, 116.7, 123.2, 126.5, 129.1, 143.3, 172.3. IR (KBr)  $\nu$  ( $\text{cm}^{-1}$ ): 3368, 1658. MS  $m/z$ : 258. Anal. calcd. for  $\text{C}_{16}\text{H}_{22}\text{N}_2\text{O}$ : C, 74.38; H, 8.58; N, 10.84. Found: C, 74.35; H, 8.50; N, 10.85.

### 1-(6-Chloro-2-methyl-1,2,3,4-tetrahydroquinolin-4-yl)azepan-2-one (7b)

Light yellow crystalline solid. Yield: 93%, mp 122–124 °C (recrystallization solvent: chloroform).  $^1\text{H}$  NMR (300 MHz,  $\text{CDCl}_3$ )  $\delta$  (ppm): 1.26 (d, 3H,  $J = 6.1$  Hz), 2.08 (dd, 2H,  $J = 11.1, 6.4, 2.8$  Hz), 2.79 (m, 1H), 4.87 (dd, 1H,  $J = 11.5, 6.3$  Hz), 1.29 (t, 2H), 1.55 (m, 2H), 1.57 (m, 2H), 2.18 (t, 2H), 3.2 (t, 2H), 4.5 (s, 1H, NH), 6.49–6.91 (m, 4H).  $^{13}\text{C}$  NMR (75 MHz,  $\text{CDCl}_3$ )  $\delta$  (ppm): 21.5, 25.7, 31.8, 32.0, 32.2, 44.0, 46.6, 47.3, 50.7, 113.5, 122.0, 126.9, 129.5, 129.6, 141.4, 172.0. IR (KBr)  $\nu$  ( $\text{cm}^{-1}$ ): 3362, 1654. MS  $m/z$ : 292. Anal. calcd. for  $\text{C}_{16}\text{H}_{21}\text{ClN}_2\text{O}$ : C, 65.63; H, 7.23; N, 9.57. Found: C, 65.59; H, 7.18; N, 9.52.

### 1-(6-Fluoro-2-methyl-1,2,3,4-tetrahydroquinolin-4-yl)azepan-2-one (7c)

Light yellow crystalline solid. Yield: 90%, mp 128–130 °C (recrystallization solvent: chloroform).  $^1\text{H}$  NMR (300 MHz,  $\text{CDCl}_3$ )  $\delta$  (ppm): 1.23 (d, 3H,  $J = 6.6$  Hz), 2.03 (dd, 2H,  $J = 11.0, 6.6, 2.4$  Hz), 2.79 (m, 1H), 4.85 (dd, 1H,  $J = 11.0, 6.6$  Hz), 1.27 (t, 2H), 1.53 (m, 2H), 1.58 (m, 2H),

2.20 (t, 2H), 3.5 (t, 2H), 4.2 (s, 1H, NH), 6.61 (s, 1H), 6.36 (d, 1H,  $J = 8.6$  Hz), 6.57 (d, 1H,  $J = 6.8$  Hz).  $^{13}\text{C}$  NMR (75 MHz,  $\text{CDCl}_3$ )  $\delta$  (ppm): 22.1, 25.6, 31.8, 32.6, 44.5, 44.6, 46.6, 47.3, 50.7, 113.5, 113.7, 116.1, 124.8, 138.9, 150.3, 172.9. IR (KBr)  $\nu$  ( $\text{cm}^{-1}$ ): 3366, 1657. MS  $m/z$ : 276. Anal. calcd. for  $\text{C}_{16}\text{H}_{21}\text{FN}_2\text{O}$ : C, 69.54; H, 7.66; N, 10.14. Found: C, 69.51; H, 7.62; N, 10.10.

### 1-(2,6-Dimethyl-1,2,3,4-tetrahydroquinolin-4-yl)azepan-2-one (7d)

Light yellow crystalline solid. Yield: 91%, mp 125–127 °C (Recrystallization solvent: chloroform).  $^1\text{H}$  NMR (300 MHz,  $\text{CDCl}_3$ )  $\delta$  (ppm): 1.28 (d, 3H,  $J = 6.0$  Hz), 2.35 (s, 2H,  $J = 11.1$ , 6.4, 2.8 Hz), 2.79 (m, 1H), 4.87 (dd, 1H,  $J = 11.5$ , 6.3 Hz), 1.29 (t, 2H), 1.55 (m, 2H), 1.57 (m, 2H), 2.18 (t, 2H), 3.2 (t, 2H), 4.5 (s, 1H, NH), 6.49–6.91 (m, 4H).  $^{13}\text{C}$  NMR (75 MHz,  $\text{CDCl}_3$ )  $\delta$  (ppm): 21.5, 25.7, 31.8, 32.0, 32.2, 44.0, 46.6, 47.3, 50.7, 113.5, 122.0, 126.9, 129.5, 129.6, 141.4, 172.0. IR (KBr)  $\nu$  ( $\text{cm}^{-1}$ ): 3368, 1651. MS  $m/z$ : 272. Anal. calcd. for  $\text{C}_{17}\text{H}_{24}\text{N}_2\text{O}$ : C, 74.96; H, 8.88; N, 10.28. Found: C, 74.90; H, 8.85; N, 10.23.

### Acknowledgments

This research work is financially supported by Council of Scientific and Industrial Research, New Delhi – 110 012 (Ref. No.: 01(2301)/09/EMR–II, dated 19 March 2009). Ms. C.S. Kavitha is grateful to UGC for the award of JRF (Ref. No.: KU/Sch/UGC/RFSM/2006–07/3236, dated 08 March 2007).

### References

- (1) (a) Konishi, M.; Ohkuma, H.; Tsuno, T.; Oki, T.; VanDuyne, G. D.; Clardy, J. *J. Am. Chem. Soc.* **1990**, *112*, 37153; (b) Omura, S.; Nakagawa, A. *Tetrahedron Lett.* **1981**, *22* (23), 2199. doi:10.1016/S0040-4039(01)90497-6.
- (2) (a) Michael, J. P. *Nat. Prod. Rep.* **1997**, *14* (6), 605. doi:10.1039/np9971400605; (b) Balasubramanian, M.; Keay, J. G. In *Comprehensive Heterocyclic Chemistry II*; McKillop, A., Ed.; Pergamon Press: Oxford, 1996; Vol. 5; Chapter 5; p. 245.
- (3) (a) Kouznetsov, V.; Palma, A.; Ewert, C.; Varlamov, A. *J. Heterocycl. Chem.* **1998**, *35* (4), 761. doi:10.1002/jhet.5570350402; (b) De Kimpe, N.; Keppens, M. *Tetrahedron* **1996**, *52* (10), 3705. doi:10.1016/0040-4020(96)00046-4.
- (4) (a) Padwa, A.; Brodney, M. A.; Liu, B.; Satake, K.; Wu, T. *J. Org. Chem.* **1999**, *64* (10), 3595. doi:10.1021/jo982453g. PMID:11674487; (b) Katritzky, A. R.; Rachwal, S.; Rachwal, B. *Tetrahedron* **1996**, *52* (48), 15031. doi:10.1016/S0040-4020(96)00911-8.
- (5) (a) Leeson, P. D.; Carling, R. W.; Moore, K. W.; Moseley, A. M.; Smith, J. D.; Stevenson, G.; Chan, T.; Baker, R.; Foster, A. C.; Grimwood, S.; Kemp, J. A.; Marshall, G. R.; Hoogsteen, K. *J. Med. Chem.* **1992**, *35* (11), 1954. doi:10.1021/jm00089a004. PMID:1534584; (b) Nagata, R.; Tanno, N.; Kodo, T.; Ae, N.; Yamaguchi, H.; Nishimura, T.; Antoku, F.; Tatsuno, T.; Kato, T.; Tanaka, Y.; Nakamura, M. I. *J. Med. Chem.* **1994**, *37* (23), 3956. doi:10.1021/jm00049a015. PMID:7966156.
- (6) (a) Kumar, M. B.; Potter, D. W.; Hormann, R. E.; Edwards, A.; Tice, C. M.; Smith, H. C.; Dipietro, M. A.; Polley, M.; Lawless, M.; Wolohan, P. R.; Kethidi, D. R.; Palli, S. R. *J. Biol. Chem.* **2004**, *279* (26), 27211. doi:10.1074/jbc.M403839200. PMID:15107428; (b) Kakihana, M.; Kato, K.; Mori, M.; Yamashita, T. *Heterocyclic Derivatives*. US Patent 6,930,104, 2005.
- (7) (a) Sikorski, J. A. *J. Med. Chem.* **2006**, *49* (1), 1. doi:10.1021/jm0582241; (b) Nakamura, I.; Yamamoto, Y. *Chem. Rev.* **2004**, *104* (5), 2127. doi:10.1021/cr020095i. PMID:15137788.
- (8) (a) Deiters, A.; Martin, S. F. *Chem. Rev.* **2004**, *104* (5), 2199. doi:10.1021/cr0200872. PMID:15137789; (b) McReynolds, M. D.; Dougherty, J. M.; Hanson, P. R. *Chem. Rev.* **2004**, *104* (5), 2239. doi:10.1021/cr020109k. PMID:15137790; (c) Zeni, G.; Larock, R. C. *Chem. Rev.* **2006**, *106* (11), 4644. doi:10.1021/cr0683966. PMID:17091931; (d) D'Souza, D. M.; Müller, T. J. J. *Chem. Soc. Rev.* **2007**, *36* (7), 1095. doi:10.1039/b608235c. PMID:17576477; (e) Mihovilovic, M. D.; Stanetty, P. *Angew. Chem.* **2007**, *46* (20), 3612. doi:10.1002/anie.200604743.
- (9) (a) Trost, B. M. *Science* **1991**, *254* (5037), 1471. doi:10.1126/science.1962206. PMID:1962206; (b) Trost, B. M. *Angew. Chem.* **1995**, *34* (3), 259. doi:10.1002/anie.199502591; (c) Sheldon, R. A. *Pure Appl. Chem.* **2000**, *72* (7), 1233. doi:10.1351/pac200072071233.
- (10) (a) Ma, D.; Xia, C.; Jiang, J.; Zhang, J. *Org. Lett.* **2001**, *3* (14), 2189. doi:10.1021/ol016043h. PMID:11440576; (b) Gallou-Dagommer, I.; Gastaud, P.; RajanBabu, T. V. *Org. Lett.* **2001**, *3* (13), 2053. doi:10.1021/ol016018b. PMID:11418047; (c) Goujon, J.-Y.; Zammattio, F.; Chrétien, J.-M.; Beaudet, I. *Tetrahedron* **2004**, *60* (18), 4037. doi:10.1016/j.tet.2004.03.010.
- (11) (a) Ding, K.; Flippen-Anderson, J.; Deschamps, J. R.; Wang, S. *Tetrahedron Lett.* **2004**, *45* (5), 1027. doi:10.1016/j.tetlet.2003.11.086; (b) Avemaria, F.; Vanderheiden, S.; Brase, S. *Tetrahedron* **2003**, *59* (35), 6785. doi:10.1016/S0040-4020(03)00915-3; (c) Fabio, R. D.; Alvaro, G.; Bertani, B.; Donati, D.; Giacobbe, S.; Marchioro, C.; Palma, C.; Lynn, S. M. *J. Org. Chem.* **2002**, *67* (21), 7319. doi:10.1021/jo020327d. PMID:12375961.
- (12) Povarov, L. S. *Russ. Chem. Rev.* **1967**, *36* (9), 656. doi:10.1070/RC1967v036n09ABEH001680.
- (13) Kametani, T.; Takeda, H.; Suzuki, Y.; Honda, T. *Synth. Commun.* **1985**, *15* (6), 499. doi:10.1080/00397918508063833.
- (14) Ma, Y.; Qian, C.; Xie, M.; Sun, J. *J. Org. Chem.* **1999**, *64* (17), 6462. doi:10.1021/jo982220p.
- (15) (a) Babu, G.; Perumal, P. T. *Tetrahedron Lett.* **1997**, *38* (28), 5025. doi:10.1016/S0040-4039(97)01060-5; (b) Zhang, J.; Li, C. J. *J. Org. Chem.* **2002**, *67* (11), 3969. doi:10.1021/jo020131d. PMID:12027728; (c) Zhang, J.; Li, C. J. *J. Org. Chem.* **2002**, *67* (11), 3969. doi:10.1021/jo020131d. PMID:12027728.
- (16) Charette, A. B. Lithium perchlorate. In *Encyclopedia of Reagents for Organic Synthesis*; John Wiley and Sons: New York, 2004.
- (17) Yadav, J. S.; Subba Reddy, B. V.; Srinivas, R.; Madhuri, C.; Ramalingam, T. *Synlett* **2001**, 1089.
- (18) Mahesh, M.; Venkateshwar Reddy, Ch.; Srinivasa Reddy, K.; Raju, P. V. K.; Narayana Reddy, V. V. *Synth. Commun.* **2004**, *34* (22), 4089. doi:10.1081/SCC-200036586.
- (19) Astrudillosaavedra, L.; Ramirez, M. C. *J. Chil. Chem. Soc.* **2004**, *49*, 319.
- (20) Maiti, G.; Kundu, P. *Tetrahedron* **2006**, *62*, 349.
- (21) (a) Boger, D. L.; Weinreb, S. M. In *Hetero Diels–Alder Methodology in Organic Synthesis*; Academic Press, 1987; Chapter 9; (b) Mellor, J. M.; Merriman, G. D.; Riviere, P.



- Tetrahedron Lett.* **1991**, 32 (48), 7103. doi:10.1016/0040-4039(91)85052-7.
- (22) Grieco, P. A.; Bahasas, A. *Tetrahedron Lett.* **1988**, 29 (46), 5855. doi:10.1016/S0040-4039(00)82208-X.
- (23) Nagarajan, R.; Perumal, P. T. *Synth. Commun.* **2001**, 31 (11), 1733. doi:10.1081/SCC-100103994.
- (24) Srinivasa, A.; Mahadevan, K. M.; Hosamani, K. M.; Hulikal, V. *Monatsh. Chem.* **2008**, 139 (2), 141. doi:10.1007/s00706-007-0765-4.
- (25) Srinivasa, A.; Mahadevan, K. M.; Hulikal, V. *Synth. Commun.* **2009**, 39 (1), 93. doi:10.1080/00397910802369653.
- (26) Dunitz, J. D. *Acta Crystallogr.* **1957**, 10 (4), 307. doi:10.1107/S0365110X57000894.
- (27) Rajitha, B.; Naveen Kumar, V.; Someshwar, P.; Venu Madhav, J.; Narsimha Reddy, P.; Thirupathi Reddy, Y. *Arkivoc* **2006**, 12, 23.
- (28) Naveen Kumar, V.; Someshwar, P.; Narsimha Reddy, P.; Thirupathi Reddy, Y.; Rajitha, B. *J. Heterocycl. Chem.* **2005**, 42 (5), 1017. doi:10.1002/jhet.5570420543.
- (29) Venu Madhav, J.; Naveen Kumar, V.; Someshwar, P.; Rajitha, B. *J. Heterocycl. Chem.* **2008**, 45, 119.
- (30) Vargas M, L. Y.; Castelli, M. V.; Kouznetsov, V. V.; Urbina G, J. M.; López, S. N.; Sortino, M.; Enriz, R. D.; Ribas, J. C.; Zacchino, S. *Bioorg. Med. Chem.* **2003**, 11 (7), 1531. doi:10.1016/S0968-0896(02)00605-3. PMID:12628677.
- (31) Kouznetsov, V. V.; Aliev, A. E.; Prostakov, N. S. *Khim. Geterotsikl. Soed.* **1994**, 1, 73; *Chem. Abstr.* **1994**, 121, 300.738.
- (32) Vargas Mendez, L. Y.; Kouznetsov, V. V.; Stashenko, E.; Bahsas, A.; Amaro-Luis, J. *Heterocycl. Commun.* **2002**, 7, 323.

# Effect of collision energy on cross sections and product alignments for the $C(^1D) + H_2$ ( $v = 0, j = 0$ ) insertion reactions

Lihua Kang and Bin Dai

**Abstract:** Quasi-classical trajectory (QCT) calculations of total reaction probabilities and vibrationally state-resolved reaction probabilities at total angular momentum  $J = 0$  as a function of collision energy for the  $C(^1D) + H_2$  ( $v = 0, j = 0$ ) reactions have been performed on an ab initio potential-energy surface [*J. Chem. Phys.* **2001**, *115*, 10701]. In addition, the integral cross sections as a function of collision energy have been carried out for the same reaction. The product rotational alignments have also been calculated, which are almost invariant with respect to collision energies.

**Key words:** cross sections, product alignments, insertion reactions, quasi-classical trajectory.

**Résumé :** On a effectué des calculs théoriques de trajectoire quasi-classique (TQC) sur une surface d'énergie potentielle ab initio [*J. Chem. Phys.* **2001**, *115*, 10701] pour évaluer les probabilités totales de réaction et les probabilités de réaction résolues en fonction de l'état vibrationnel, à un moment angulaire  $J = 0$  et en fonction de l'énergie de collision, des réactions  $C(^1D) + H_2$  ( $v = 0, j = 0$ ). De plus, pour la même réaction, on a aussi évalué les sections droites intégrales en fonction de l'énergie de collision. On a aussi calculé les alignements rotationnels qui sont pratiquement invariables avec les énergies de collision.

**Mots-clés :** sections droites, alignements du produit, réactions d'insertion, trajectoire quasi-classique.

## Introduction

In the past decades, a great deal of attention has been paid to the atom–diatom insertion reactions in which the potential energy surfaces are often dominated by deep wells rather than barriers.<sup>1</sup> The reaction between atomic carbon and molecular hydrogen belongs to this class of insertion reaction. Other thoroughly studied insertion reactions between electronically excited atoms and hydrogen molecules are  $O(^1D) + H_2$ ,<sup>2–7</sup>  $N(^2D) + H_2$ ,<sup>8–10</sup> and  $S(^1D) + H_2$ .<sup>11–14</sup> Unlike other members of the insertion reaction family, however,  $C(^1D) + H_2$  is considered to be a clean insertion reaction,<sup>15,16</sup> without involvement of abstraction pathways. The reaction between atomic carbon and molecular hydrogen  $C(^1D) + H_2$ , and its isotopic variants  $C(^1D) + HD$  and  $C(^1D) + D_2$ , play a central role in atmospheric and combustion chemistry. Because of its remarkable features, it has attracted much experimental<sup>15–19</sup> and theoretical attention.<sup>20,21</sup>

In crossed molecular-beam (CMB) experiments, Bergeat et al.<sup>15</sup> measured the product angular and time-of-flight (TOF) distributions for the  $C(^1D) + H_2$  reaction, and Balucani et al.<sup>19</sup> measured the product angular and velocity distributions.

Motivated by the crossed molecular-beam experiments,<sup>15</sup> Launay and co-workers<sup>21</sup> developed a global potential-energy surface (PES) for the first single state of  $^1A'$  symmetry for the  $CH_2$  system. The ab initio calculations were carried out over 1748 geometries and the resulting energies were fitted

to a many-body expansion. The potential energy surface has a well depth of 417.1 kJ/mol relative to the  $C(^1D) + H_2$  asymptote.

Theoretical studies of the title reaction have been stimulated by the availability of the high-quality potential-energy surface.<sup>21</sup> Launay and co-workers<sup>20,21</sup> performed QCT and QM calculations of reaction probabilities and cross sections. Since QM calculations are prohibitively expensive, the quantum integral cross section was calculated at a single collision energy ( $E_c$ ),  $E_c = 7.8$  kJ/mol (0.08 eV), and was found to be  $30.49 \text{ \AA}^2$ . At this  $E_c$ , previous QCT calculations were repeated and found to underestimate the value ( $22.48 \text{ \AA}^2$ ). For comparison, we also calculated the integral cross section at this  $E_c$  and found a value of  $25.75 \text{ \AA}^2$ .

Not only the scalar properties (such as integral cross section and product-branching ratios) but also the vector properties (such as velocities and angular momentum) can be obtained from QCT calculations.<sup>22</sup> For example, product alignments and orientations can be determined by QCT calculations.<sup>22–24</sup> And many experimental techniques, such as polarization-resolved chemiluminescence,<sup>25,26</sup> polarized laser-induced fluorescence,<sup>27</sup> and electric deflection methods,<sup>28</sup> can be used under molecular-beam and bulb conditions to determine the product alignments.<sup>29</sup> In the present work, we have performed QCT calculations of reaction probabilities and integral cross sections as well as product alignment for the title reaction. The calculated results have

Received 29 April 2009. Accepted 4 November 2009. Published on the NRC Research Press Web site at canjchem.nrc.ca on 31 March 2010.

L. Kang<sup>1</sup> and B. Dai. Shihezi University, Sch Chem & Chem Engrg, Shihezi, Xinjiang 832003, P. R. China.

<sup>1</sup>Corresponding author (e-mail: lhkang99@gmail.com).

been compared with the available QM and previous QCT results.

## Theoretical methods

All the QCT calculations have been carried out on the  $^1A'$   $\text{CH}_2$  ab initio PES of ref. 21. The general method for the calculation of QCT is the same as the one used in refs. 22, and 30–34, and the classical Hamilton's equations are integrated numerically for motion in three dimensions with the sixth-order symplectic integration.<sup>33</sup> The collision-energy dependence of the reaction probability at total angular momentum  $J = 0$ ,  $P^{J=0}(E_c)$ , for the  $\text{C}(^1\text{D}) + \text{H}_2$  ( $v = 0, j = 0$ ) reaction has been obtained by running batches of 100 000 trajectories randomly. The integration step size in the trajectories was chosen to be  $10^{-17}$  s, which guarantees the conservation of the total energy and total angular momentum. The trajectories were started at a distance of 1.0 nm between the incoming atom and the center of mass of the diatom. The maximum value of the impact parameter,  $b_{\text{max}}$ , was computed by calculating 100 000 trajectories at fixed values of the impact parameter  $b$  systematically increasing the value of  $b$  until no reactive trajectories were obtained. The reaction probability  $N_r/N$  is the ratio of the number of reactive trajectories to the total number of trajectories, and the reactive cross section is defined as  $\sigma_r = \pi b_{\text{max}}^2 \times (N_r/N)$ .

The product rotational-alignment calculations have been well studied by Han and co-workers.<sup>22</sup> Therefore, in addition to the scalar properties stated above, the average rotational alignment of the product CH has also been calculated using the method in ref. 22.

## Results and discussion

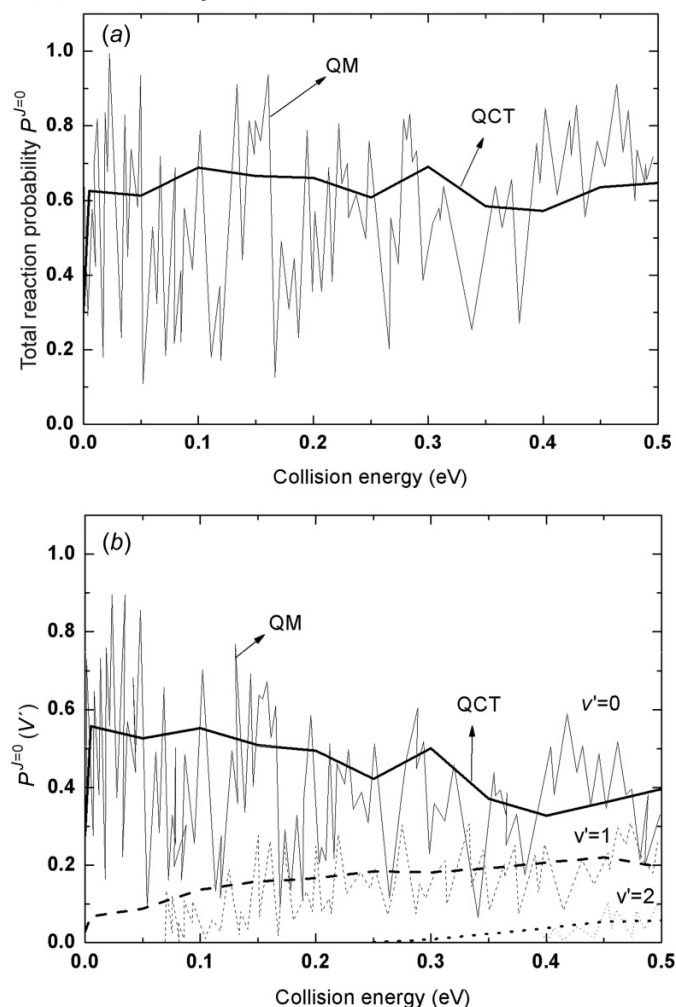
### Reaction probabilities

Figure 1 presents the QM<sup>21</sup> and QCT total and vibrationally state-resolved reaction probabilities of the final product  $\text{H} + \text{CH}$  ( $v' = 0, 1$ ) at total angular momentum  $J = 0$ ,  $P^{J=0}(E_c)$ , as a function of collision energy  $E_c$ , for the  $\text{C}(^1\text{D}) + \text{H}_2$  ( $v = 0, j = 0$ ) reaction. From Fig. 1, it can be seen that the results from the QCT and QM methods<sup>21</sup> agree with each other very well in the whole collision-energy range for the total and  $v'$  state-resolved reaction probabilities. This confirms that QCT and QM results are in good agreement for most reactions, as predicted in ref. 35. The QM and QCT total reaction probabilities for the reaction have no energy threshold as expected for a barrierless reaction with a deep well (417.1 kJ/mol).<sup>21,36</sup> Like the QM probabilities, the QCT reaction probabilities do not show any sharp peak structures. Instead, they follow the approximately average QM reaction probabilities. The  $v' = 0$  reaction probability dominates those for  $v' = 1$  and  $v' = 2$  over all the collision energy range. As shown in Fig. 1b, the  $v' = 0$  reaction probability decreases with increasing collision energy, whereas for the  $v' = 1$  and  $v' = 2$  reactions a smooth increasing probability is observed.

### Integral cross sections

Table 1 summarizes the trajectory details (maximum impact parameter, number of computed reactive trajectories) and the resulting cross sections of the reaction  $\text{C}(^1\text{D}) + \text{H}_2$  ( $v = 0, j = 0$ ). The QCT integral cross sections for the reac-

**Fig. 1.** QM (thin solid line) (see ref. 21) and QCT (thick solid line) total reaction probabilities (top panel) and vibrationally state-resolved reaction probabilities (bottom panel) as a function of collision energy, for total angular momentum  $J = 0$  calculated for the  $\text{C}(^1\text{D}) + \text{H}_2$  ( $v = 0, j = 0$ ) reaction.

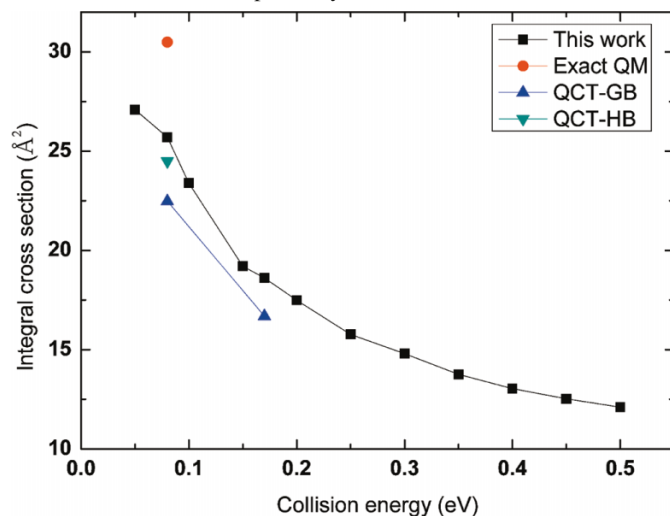


**Table 1.** Reactive cross section for the reaction  $\text{C}(^1\text{D}) + \text{H}_2$  ( $v = 0, j = 0$ ).

$E_c$ (eV)	$N$	$b_{\text{max}}$ (Å)	$N_r$	$\sigma_r \pm \sigma_{\sigma_r}$ (Å <sup>2</sup> )
0.05	100 000	3.70	63 060	27.091±0.003
0.08	100 000	3.51	66 558	25.698±0.002
0.10	100 000	3.40	64 442	23.391±0.002
0.15	100 000	3.00	67 939	19.200±0.002
0.20	100 000	2.80	71 041	17.489±0.002
0.25	100 000	2.63	72 584	15.765±0.002
0.30	100 000	2.55	72 465	14.796±0.002
0.35	100 000	2.45	72 972	13.754±0.002
0.40	100 000	2.40	72 100	13.040±0.002
0.45	100 000	2.37	71 006	12.523±0.002
0.50	100 000	2.30	72 841	12.099±0.002

tion  $\text{C}(^1\text{D}) + \text{H}_2$  ( $v = 0, j = 0$ ) are shown in Fig. 2 along with the QM results by Balucani et al.<sup>37</sup> As can be seen in Fig. 2, the QCT calculations yield cross sections somewhat lower than the QM at collision energy  $E_c = 7.8$  kJ/mol (0.08 eV). It seems reasonable that the QCT results are slightly smaller

**Fig. 2.** A comparison between the QCT-computed cross sections in this work and other theoretical cross sections for the  $C(^1D) + H_2$  ( $v = 0, j = 0$ ) reaction. The QM and QCT (HB,GB) results are taken from refs. 37 and 20, respectively.



than the accurate QM ones owing to the tunneling effect. The QCT method has a serious drawback in that it cannot handle the quantum mechanical questions of the system. As a result, the cross sections of the title reactions of the QM method are greater than those of the QCT method. As shown in Fig. 2, although the same PES was used in both calculations, the results of our work are greater than the results of Bañares et al.<sup>20</sup> at 7.8 kJ/mol collision energy. This may be ascribed to the fact that we chose  $10^{-17}$  s as the integration step size in the trajectories, whereas Bañares et al.<sup>20</sup> chose  $5 \times 10^{-17}$  s. The integral cross sections first decrease sharply at low collision energies and then level off at high energies. Similar observations have been found in theoretical studies of other insertion reactions.<sup>38–40</sup>

To understand the dynamics of the insertion reaction fully, the state-resolved quantities were obtained. In Fig. 3a, the product vibrational state as a function of collision energy is plotted for the  $C(^1D) + H_2$  ( $v = 0, j = 0$ )  $\rightarrow$   $CH$  ( $v' = 0, 1, j' = 0$ ) +  $H$  reaction. From Fig. 3a, we can see that the  $CH$  product is dominated by the ground vibrational states ( $v' = 0$ ). The  $v' = 0$  integral cross section decreases when the collision energy increases, whereas it increases for the  $v' = 1$  integral cross section.

In Fig. 3b, the resolved cross sections for the product rotational state are plotted against the collision energy for the  $C(^1D) + H_2$  ( $v = 0, j = 0$ )  $\rightarrow$   $CH$  ( $v' = 0, j' = 0, 5, 10, 15$ ) +  $H$  reaction. In Fig. 3b, for  $j' = 0, 5$ , and  $10$ , the integral cross section decreases with the increasing collision energy, whereas the trend is opposite for  $j' = 15$ .

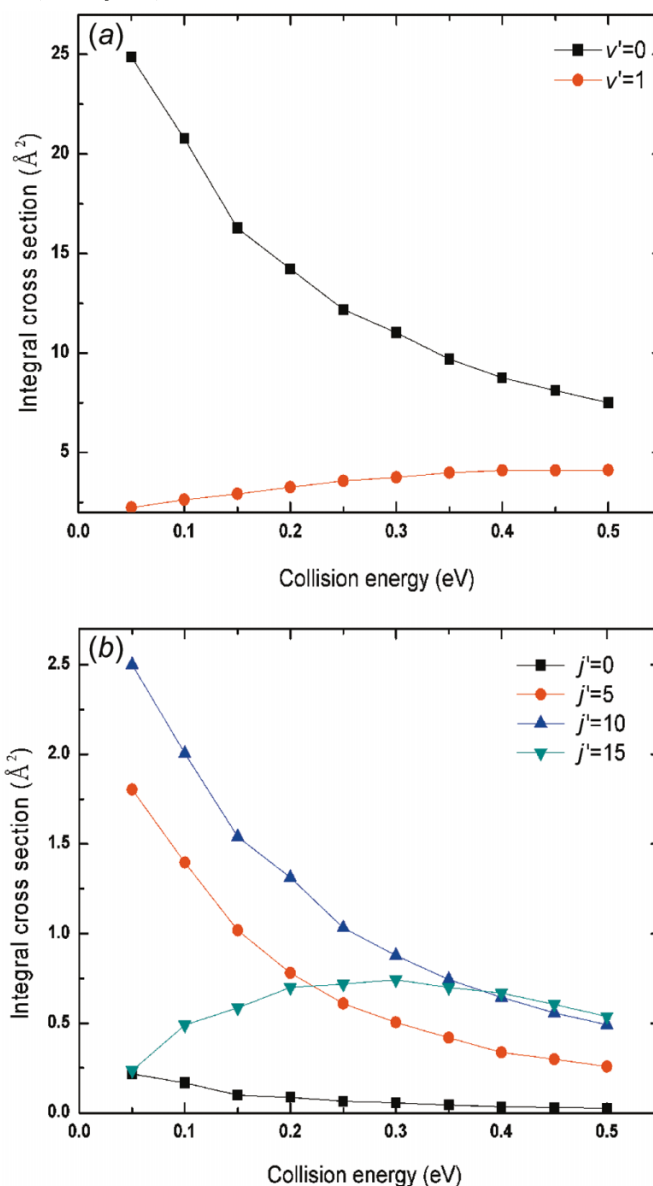
### Rotational alignment parameter

In a reactive encounter, the total angular momentum is conserved

$$[1] \quad j + l = j' + l'$$

where  $l$  and  $l'$  are the reagent and product orbital momenta, respectively. When the reagent angular momentum  $j$  is small, the product rotation can only result from  $l$ . The distribution

**Fig. 3.** Product vibrational state distributions ( $CH(v' = 0, 1, j' = 0) + H$ ) (a) and rotational state distributions ( $CH(v' = 0, j' = 0, 5, 10, 15) + H$ ) (b) as a function of collision energy for the  $C(^1D) + H_2$  ( $v = 0, j = 0$ ) reaction.



of the angular momentum  $j'$  of the product molecule is described by a function  $f(\theta)$ , where  $\theta$  is the angle between  $j'$  and  $k$  (the reagent relative velocity vector).  $f(\theta)$  can be represented by the Legendre polynomial<sup>22</sup>

$$[2] \quad f(\theta) = \sum a_n P_n(\cos \theta)$$

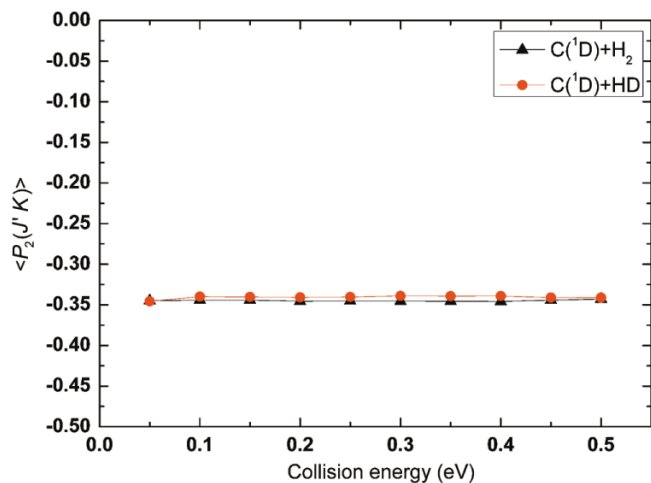
where  $n = 2$  indicates the product rotational alignment

$$[3] \quad \langle P_2(j' \cdot k) \rangle = 1/2 \langle \cos^2 \theta - 1 \rangle$$

where  $P_2$  is the second Legendre moment and the brackets indicate the average over the distribution of  $j'$  about  $k$ . In the present work, we calculate only the rotational alignment parameter of the product, since it alone has been measured in most of the experiments until now.



**Fig. 4.** CH product rotational alignment  $\langle P_2(j', k) \rangle$  for the reaction  $C(^1D) + H_2$  ( $v = 0, j = 0$ ) as a function of collision energy.



The dependence of the product rotational alignment on collision energies is shown in Fig. 4. It can be seen that the  $\langle P_2(j', k) \rangle$  values are almost invariant with respect to collision energies. Generally, the higher the collision energies, the stronger the rotational alignment of the products. However, in the present work, the  $\langle P_2(j', k) \rangle$  values calculated on the PES for the  $C(^1D) + H_2$  reaction are almost invariant as the collision energy increases. The reason is that the product orbital angular momentum is large, and the reactant orbital angular momentum has less influence on the molecular product rotational alignment. This is consistent with previous calculations.<sup>22,23</sup>

## Conclusion

In this paper, we have reported the QCT calculation of total and vibrationally state-resolved reaction probabilities at total angular momentum  $J = 0$  (zero-impact parameter) for reactions  $C(^1D) + H_2$  ( $v = 0, j = 0$ ) based on the ground  $^1A'$  state PES. The total reaction probability for the reaction was found to have no threshold. For the vibrational state-resolved reaction probabilities, the  $v' = 0$  reaction probabilities dominate those for  $v' = 1$  and  $v' = 2$  over the full collision energy range. The total integral cross sections as a function of collision energy have also been carried out for the same reaction. The total integral cross sections are decay functions of the collision energy, consistent with the barrierless insertion reaction. Comparing our QCT results with the quantum methods show that our QCT results are in reasonably good agreement with the QM results. In addition, the rotational alignment of the product is calculated, and  $\langle P_2(j', k) \rangle$  values are almost invariant with respect to collision energies. We look forward to more experimental studies of reaction probabilities, integral cross sections, and product rotational alignment effect on the  $C(^1D) + H_2$  reaction, so that a comparison of theory and experiment can be implemented.

## Acknowledgements

This work was supported by the National Natural Science Foundation of China under Grant No. 20363003.

## References

- (1) Rackham, E. J.; Gonzalez-Lezana, T.; Manolopoulos, D. E. *J. Chem. Phys.* **2003**, *119* (24), 12895. doi:10.1063/1.1628218.
- (2) Chu, T. S.; Zhang, X.; Han, K. L. *J. Chem. Phys.* **2005**, *122* (21), o. 214301. doi:10.1063/1.1924507. PMID:15974732.
- (3) Chu, T. S.; Zhang, Y.; Han, K. L. *Int. Rev. Phys. Chem.* **2006**, *25* (1-2), 201. doi:10.1080/01442350600677929.
- (4) Gray, S. K.; Balint-Kurti, G. G.; Schatz, G. C.; Lin, J. J.; Liu, X.; Harich, S.; Yang, X. *J. Chem. Phys.* **2000**, *113* (17), 7330. doi:10.1063/1.1313785.
- (5) Chu, T. S.; Han, K. L. *Phys. Chem. Chem. Phys.* **2008**, *10* (18), 2431. doi:10.1039/b715180b. PMID:18446243.
- (6) Aoiz, F. J.; Bañares, L.; Castillo, J. F.; Herrero, V. J.; Martinez-Haya, B.; Honvault, P.; Launay, J. M. *J. Chem. Phys.* **2002**, *116*, 10692. doi:10.1063/1.1478693.
- (7) Aoiz, F. J.; Bañares, L.; Castillo, J. F.; Herrero, V. J.; Martinez-Haya, B.; Honvault, P. *Phys. Chem. Chem. Phys.* **2002**, *4*, 4379. doi:10.1039/b203755f.
- (8) Rackham, E. J.; Huarte-Larranaga, F.; Manolopoulos, D. E. *Chem. Phys. Lett.* **2001**, *343* (3-4), 356. doi:10.1016/S0009-2614(01)00707-2.
- (9) Varandas, A. J. C.; Chu, T. S.; Han, K. L.; Caridade, P. J. S. B. *Chem. Phys. Lett.* **2006**, *421* (4-6), 415. doi:10.1016/j.cplett.2006.01.073.
- (10) Chu, T. S.; Han, K. L.; Varandas, A. J. C. *J. Phys. Chem. A* **2006**, *110* (4), 1666. doi:10.1021/jp054572n. PMID:16435830.
- (11) Bañares, L.; Castillo, J. F.; Honvault, P.; Launay, J.-M. *Phys. Chem. Chem. Phys.* **2005**, *7* (4), 627. doi:10.1039/b417368f. PMID:19787879.
- (12) Lee, S. H.; Liu, K. *J. Phys. Chem. A* **1998**, *102* (45), 8637. doi:10.1021/jp983220w.
- (13) Chu, T. S.; Han, K. L.; Schatz, G. C. *J. Phys. Chem. A* **2007**, *111* (34), 8286. doi:10.1021/jp075173q. PMID:17685502.
- (14) Lee, S. H.; Liu, K. *Chem. Phys. Lett.* **1998**, *290* (4-6), 323. doi:10.1016/S0009-2614(98)00535-1.
- (15) Bergeat, A.; Cartechini, L.; Balucani, N.; Capozza, G.; Phillips, L. F.; Casavecchia, P.; Volpi, G. G.; Bonnet, L.; Rayez, J. C. *Chem. Phys. Lett.* **2000**, *327* (3-4), 197. doi:10.1016/S0009-2614(00)00870-8.
- (16) Lin, S. Y.; Guo, H. *J. Phys. Chem. A* **2004**, *108* (46), 10066. doi:10.1021/jp046039y.
- (17) Fisher, W. H.; Carrington, T.; Sadowski, C. M.; Dugan, C. H. *Chem. Phys.* **1985**, *97* (2-3), 433. doi:10.1016/0301-0104(85)87051-8.
- (18) Sato, K.; Ishida, N.; Kurakata, T.; Iwasaki, A.; Tsuneyuki, S. *Chem. Phys.* **1998**, *237* (1-2), 195. doi:10.1016/S0301-0104(98)00183-9.
- (19) Balucani, N.; Capozza, G.; Segoloni, E.; Russo, A.; Bobbenkamp, R.; Casavecchia, P.; Gonzalez-Lezana, T.; Rackham, E. J.; Bañares, L.; Aoiz, F. J. *J. Chem. Phys.* **2005**, *122* (23), o. 234309. doi:10.1063/1.1930831. PMID:16008443.
- (20) Bañares, L.; Aoiz, F. J.; Honvault, P.; Bussery-Honvault, B.; Launay, J. M. *J. Chem. Phys.* **2003**, *118* (2), 565. doi:10.1063/1.1527014.
- (21) Bussery-Honvault, B.; Honvault, P.; Launay, J. M. *J. Chem. Phys.* **2001**, *115* (23), 10701. doi:10.1063/1.1417501.
- (22) Han, K. L.; He, G. Z.; Lou, N. Q. *J. Chem. Phys.* **1996**, *105* (19), 8699. doi:10.1063/1.472651.
- (23) Wang, M. L.; Han, K. L.; He, G. Z. *J. Chem. Phys.* **1998**, *109* (13), 5446. doi:10.1063/1.476522.
- (24) Wang, M. L.; Han, K. L.; He, G. Z. *J. Phys. Chem. A* **1998**, *102* (50), 10204. doi:10.1021/jp981738u.

- (25) Jonah, C. D.; Zare, R. N.; Ottinger, C. *J. Chem. Phys.* **1972**, *56* (1), 263. doi:10.1063/1.1676857.
- (26) Han, K. L.; Zhang, L.; Xu, D. L.; He, G. Z.; Lou, N. Q. *J. Phys. Chem. A* **2001**, *105* (13), 2956. doi:10.1021/jp002181x.
- (27) Li, R. J.; Han, K. L.; Li, F. E.; Lu, R. C.; He, G. Z.; Lou, N. Q. *Chem. Phys. Lett.* **1994**, *220* (3-5), 281. doi:10.1016/0009-2614(94)00174-X.
- (28) Case, D. A.; Herschbach, D. R. *Mol. Phys.* **1975**, *30* (5), 1537. doi:10.1080/00268977500103061.
- (29) Balucani, N.; Capozza, G.; Segoloni, E.; Russo, A.; Bobbenkamp, R.; Casavecchia, P.; Gonzalez-Lezana, T.; Rackham, E. J.; Bañares, L.; Aoiz, F. J. *J. Chem. Phys.* **2005**, *122* (23), 234309. doi:10.1063/1.1930831. PMID:16008443.
- (30) Murrell, J. N.; Carter, S.; Farantos, S. C.; Huxley, P.; Varandas, A. J. C. *Molecular Potential Energy Functions*; Wiley, 1984.
- (31) Truhlar, D. G.; Muckerman, J. T. In *Atom-Molecule Collision Theory*; Bernstein, R.B., Ed.; Plenum Press: NY, 1979.
- (32) Raff, L. M.; Thompson, D. L. In *Theory of Chemical Reaction Dynamics*; Baer, M., Ed.; CRC Press: Boca Raton, 1985.
- (33) Zhang, X.; Han, K.-L. *Inter. J. Quantum Chem.* **2006**, *106*, 1815. doi:10.1002/qua.20929.
- (34) Han, K. L.; Zheng, X. G.; Sun, B. F.; He, G. Z.; Zhang, R. Q. *Chem. Phys. Lett.* **1991**, *181* (5), 474. doi:10.1016/0009-2614(91)90383-K.
- (35) Ju, L. P.; Han, K. L.; Zhang, J. Z. H. *J. Comput. Chem.* **2009**, *30* (2), 305. doi:10.1002/jcc.21032. PMID:18615407.
- (36) Lin, S. Y.; Guo, H. *J. Chem. Phys.* **2003**, *119* (22), 11602. doi:10.1063/1.1624060.
- (37) Balucani, N.; Capozza, G.; Cartechini, L.; Bergeat, A.; Bobbenkamp, R.; Casavecchia, P.; Aoiz, F. J.; Bañares, L.; Honvault, P.; Bussery-Honvault, B.; Launay, J.-M. *Phys. Chem. Chem. Phys.* **2004**, *6*, 4957. doi:10.1039/b409327e.
- (38) Liu, K. *Int. Rev. Phys. Chem.* **2001**, *20* (2), 189. doi:10.1080/01442350110034057.
- (39) Gray, S. K.; Goldfield, E. M.; Schatz, G. C.; Balint-Kurti, G. *G. Phys. Chem. Chem. Phys.* **1999**, *1* (6), 1141. doi:10.1039/a809325c.
- (40) Schinke, R.; Lester, W. A. *J. Chem. Phys.* **1980**, *72* (6), 3754. doi:10.1063/1.439589.

# Medium-sized cyclophanes — Part 85: Benzylation by 8-(bromomethyl)[2.2]metacyclophanes. Through-space electronic interactions of [2.2]metacyclophane benzyl cations

Tomoe Shimizu, Kan Tanaka, Arjun Paudel, and Takehiko Yamato

**Abstract:**  $\text{TiCl}_4$ -mediated Friedel–Crafts benzylation of benzene with 8-(bromomethyl)[2.2]metacyclophanes to afford 8-benzyl[2.2]metacyclophanes is described. Substituent effect through space on the rate of the benzylation of benzene with a bromomethyl group attached on the opposite aromatic ring was first found in this investigation. Interestingly, the introduction of the substituents at the internal position 16 tends to promote the present benzylation reaction rate 1.8–3.8 times. It was found that the benzyl cation intermediate was stabilized by the direct through-space cation– $\pi$  interaction among the opposite benzene ring in the benzylation of [2.2]metacyclophane systems.

**Key words:** cyclophanes, Friedel–Crafts benzylation, benzyl cation intermediate, through-space electronic interaction.

**Résumé :** On décrit la réaction de benzylation du benzène par le 8-bromométhyl[2.2]métacyclophanes par la méthode de Friedel–Crafts catalysée par le  $\text{TiCl}_4$ . Dans ce travail, on a mis en évidence pour la première fois, un effet de substituant qui se fait sentir à travers l'espace sur la vitesse de benzylation du benzène en raison d'un groupe bromométhyle attachée sur le noyau aromatique opposé. Il est intéressant de noter que l'introduction de substituants à la position interne 16 tendent à accélérer les vitesses de réaction de benzylation par des facteurs allant de 1,8 à 3,8. On a trouvé que le cation benzylique intermédiaire est stabilisé par une interaction cation– $\pi$  directe à travers l'espace du noyau benzénique opposé dans la benzylation de systèmes [2.2]métacyclophanes.

**Mots-clés :** cyclophanes, benzylation suivant Friedel–Crafts, cation benzylique intermédiaire, interaction électronique à travers l'espace.

## Introduction

The geometry of the [2.2]metacyclophane ([2.2]MCP) skeleton is known in detail from an X-ray structural analysis.<sup>2,3</sup> The crystal consists of discrete molecules, each of which has a center of symmetry. The two halves of the molecule form a stepped system. It is interesting to note that the benzene rings are not planar, but have a boat conformation, with the result that the molecule evidently avoids the steric interaction of the central carbon atoms C(8) and C(16) and of the attached hydrogen atoms. The X-ray structural analysis of 8,16-dimethyl[2.2]MCP (**2**) confirms the increased strain in molecule **2** as compared with that in the parent hydrocarbon **1** (Fig.1).<sup>4–16</sup>

Although substituents at positions 8 and 16 in the [2.2]MCP system seem to have interesting chemical natures since they are covered by the opposite aromatic ring, there are few investigations concerning these problems.<sup>17,18</sup> Owing to electronic interaction between two benzene rings, the proximity of 8- and 16-positions, and the considerable strain

energy, [2.2]MCP is prone to giving transannular reaction products.<sup>19–21</sup> These are mostly explained by the initial formation of a cyclodehydrogenation reaction product, 4,5,9,10-tetrahydropyrene. It has been isolated under the electrophilic,<sup>22–25</sup> radical,<sup>26</sup> and photolytic reaction conditions,<sup>27</sup> together with other transformation products derived from tetrahydropyrene. Sato and co-workers<sup>28,29</sup> reported another type of iodine-induced reaction of [2.2]MCP, which gives 1,2,3,3a,4,5-hexahydropyrene. On the other hand, we have reported<sup>30,31</sup> the iodine-induced transannular cyclization of 8-methoxy[2.2]MCPs to give 4,5,9,10-tetrahydropyrenes with remarkable ease and with high selectivity. This novel transannular reaction might be attributed to the presence of the methoxy group at the 8-position, which increases the  $\pi$ -electron density of the benzene ring. Thus, these transannular reactions were ascribed to the through-space electronic interaction through the intra-annular 8,16-positions. As mentioned above, although two through-space electronic interactions, (i) interaction through the intra-annular 8- and 16-positions and (ii) direct through-space cation– $\pi$  interaction, are possi-

Received 9 March 2009. Accepted 1 December 2009. Published on the NRC Research Press Web site at canjchem.nrc.ca on 3 April 2010.

For Part 84, see ref. 1.

**T. Shimizu, K. Tanaka, A. Paudel, and T. Yamato.**<sup>1</sup> Department of Applied Chemistry, Faculty of Science and Engineering, Saga University, Honjo-machi 1, Saga-shi, Saga 840-8502, Japan.

<sup>1</sup>Corresponding author (e-mail: yamatot@cc.saga-u.ac.jp).

Scheme 1.

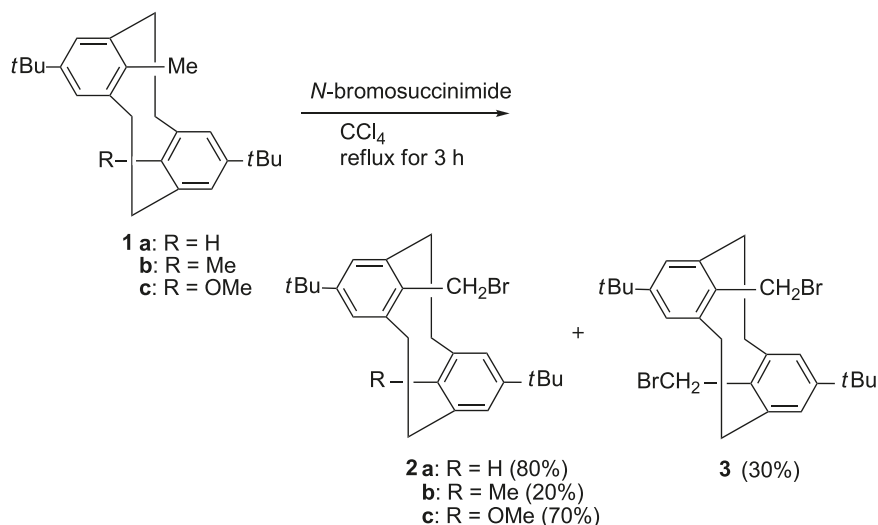
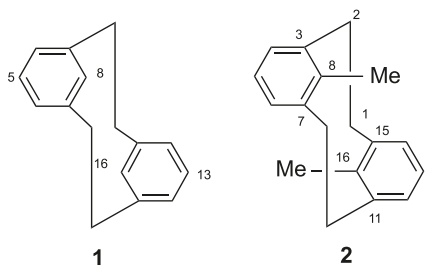
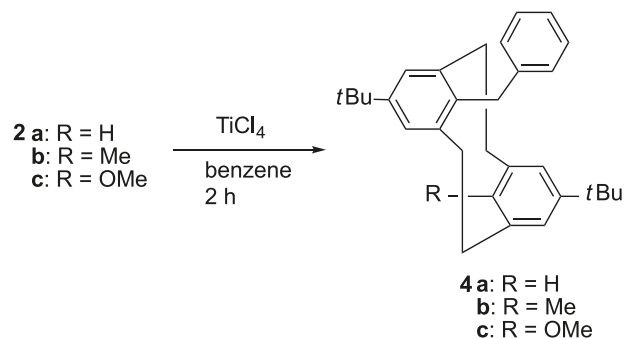


Fig. 1. Structure and numbering of [2.2]MCPs.



Scheme 2.



ble in the [2.2]MCP systems, the more favored interaction is not clear so far. Therefore, it is quite interesting to investigate the through-space electronic interaction on the rate of the benzoylation of bromomethyl groups attached on the opposite aromatic ring in the [2.2]MCP systems. We wish to report the benzoylation of benzene using cations derived from 8-(bromomethyl)[2.2]MCPs.

## Results and discussion

The preparative route of 8-(bromomethyl)[2.2]MCPs (**2a–2c**) is shown in Scheme 1. Bromination of **1a** and **1c**<sup>32–34</sup> with *N*-bromosuccinimide (NBS) in the presence of benzoyl peroxide under CCl<sub>4</sub> reflux for 3 h afforded the desired 8-(bromomethyl)[2.2]MCPs (**2a** and **2c**) in good yield. However, in the case of **1b**, 8,16-bis(bromomethyl)[2.2]MCP (**3**) was also obtained in 30% yield along with the recovery of the starting compound **1b** in 20% yield in spite of 1.2 equiv of NBS used. Isolation of the desired pure **2b** was unsuccessful. We have instead prepared 8-(bromomethyl)-16-methyl[2.2]MCP (**2b**) following our previously reported procedure.<sup>35,36</sup>

The TiCl<sub>4</sub>-mediated benzoylation of benzene with 8-(bromomethyl)-5,13-di-*tert*-butyl[2.2]MCPs (**2**) was carried out under various conditions of Scheme 2. The results are compiled in Table 1.

The TiCl<sub>4</sub>-mediated benzoylation of benzene with compound **2a** at room temperature (25 °C) for 2 h led to benzoylation reaction affording the desired 8-benzyl[2.2]MCP (**4a**)

Table 1. TiCl<sub>4</sub>-mediated benzoylation of benzene with **2**.

Run	Reaction temperature (°C)	Product yield (%) <sup>a</sup>	Recovery
1	25	<b>4a</b> (29)	<b>2a</b> (71)
2	50	<b>4a</b> (36) [25]	<b>2a</b> (64)
3	50	<b>4b</b> (52) [40]	<b>2b</b> (48)
4	25	<b>4c</b> (62) [51]	<b>2c</b> (28)
5	50	<b>4c</b> (85) [76]	<b>2c</b> (15)

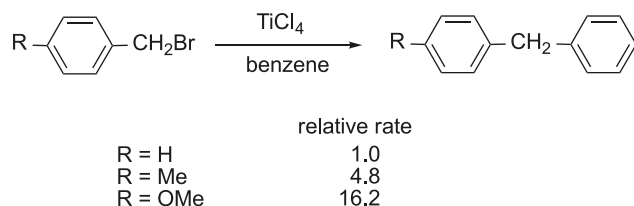
**Note:** [Benzene]/**2** = 30 (mol/mol), [TiCl<sub>4</sub>]/**2** = 1.5 (mol/mol).

<sup>a</sup>The yields were determined by GLC analysis. Isolated yields are shown in square brackets.

in 29% yield along with the recovery of the starting compound **2a** in 71% yield. The present benzoylation reaction was carried out at 50 °C under the same reaction conditions as above to increase the yield of 8-benzyl[2.2]MCP (**4a**) to 36%. Interestingly, in similar benzoylation of benzene with 16-methyl and 16-methoxy derivatives, much higher yields of the benzoylation products **4b** and **4c** resulted in 52% and 85% yields, respectively. The data in Table 1 clearly show that the substituents at the 16-position affected the yield of the benzoylation product of the 8-bromomethyl group in the opposite aromatic ring and that electron-donating groups, such as methyl and methoxy functions, increased the yield of the benzoylation product because of its high electron-donating ability like normal aromatic benzoylation.<sup>37</sup> Thus, such sub-



Scheme 3.

**Table 2.** Pseudo-first-order plots and rate constants on benzylation of benzene with **2**.

Compounds	R	$k \times 10^5 \text{ (sec}^{-1}\text{)}$	Relative rate
<b>2a</b>	H	6.21 ( $\pm 0.21$ )	1.0
<b>2b</b>	Me	10.99 ( $\pm 1.65$ )	1.8
<b>2c</b>	OMe	23.72 ( $\pm 1.14$ )	3.8

stituent effect through space on the rate of the benzylation of bromomethyl group attached on the opposite aromatic ring was first found in this investigation.

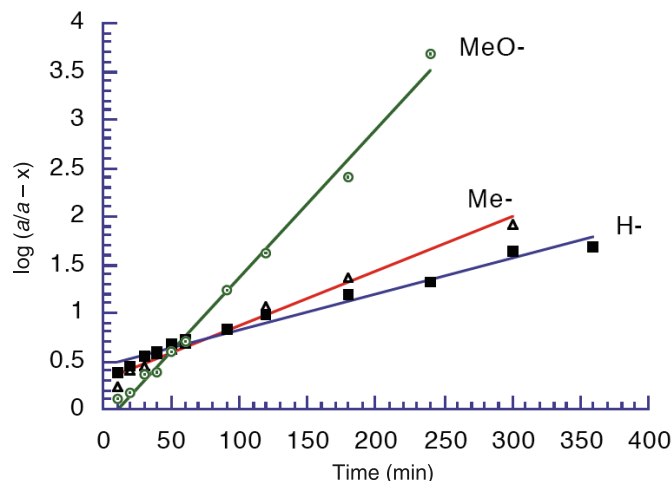
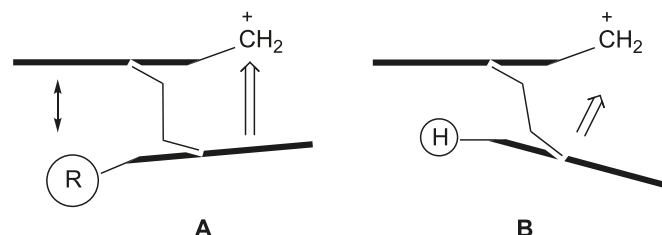
The structures of **4a–4c** were determined on the basis of their elemental analyses and spectral data. The  $^1\text{H}$  NMR spectrum of **4a** in  $\text{CDCl}_3$  shows a singlet at  $\delta$  2.15 ppm for the methylene protons of the benzyl group at 8-position, which is in a strongly shielded region of the opposite meta-bridged benzene ring, and  $\delta$  3.71 ppm for the internal aromatic proton at 16-position. Similar findings were observed in compounds **4b** and **4c**.

To study the present through-space electronic interactions in more detail, we have attempted to evaluate the rate of the benzylation of benzene with 8-(bromomethyl)[2.2]MCP (**2**) in the presence of  $\text{TiCl}_4$ . Pseudo-first-order plots on benzylation of benzene with **2a–2c** are shown in Fig. 2.

The  $\text{TiCl}_4$ -mediated benzylation rate constant of 8-(bromomethyl)[2.2]MCP **2a** with benzene is  $6.21 \times 10^5 \text{ s}^{-1}$  (Table 2). It was also found that the introduction of substituents at the internal position 16 tends to promote the present benzylation reaction rate 1.8–3.8 times. Thus, the rate of benzylation of internally substituted 8-(bromomethyl)[2.2]MCPs **2b** and **2c** are much larger than that of internally unsubstituted 8-(bromomethyl)[2.2]MCP **2a**, which is attributable to the electron-donating nature of 16-substituents, such as methyl and methoxy group. Although similar findings were also reported in the  $\text{TiCl}_4$ -catalyzed benzylation of benzene with 4-substituted benzyl bromide,<sup>38</sup> much smaller substituents effects on the benzylation were observed in the present [2.2]MCP systems than those of the reported benzylations of benzene with 4-substituted benzyl bromide (Scheme 3). This is ascribed to the smaller influence of the nature of a substituent on the remote aromatic ring by a direct through-space cation– $\pi$  interaction than that in 4-substituted benzyl bromide.

Considering the molecular model, it is concluded that the conformation of the benzyl cation intermediates in [2.2]MCPs should also be strongly affected by the size of the substituents at position 16.

As shown in Fig. 3, the interaction between the benzyl cation and the opposite benzene ring might be much more favorable for the 16-substituted [2.2]MCP **A** than the unsubstituted one **B**. Thus, the steric repulsion of 16-substituents,

**Fig. 2.** Pseudo-first-order plots on benzylation of benzene with **2a–2c**.**Fig. 3.** Proposed through-space electronic interactions of [2.2]MCP benzyl cation.

such as methyl and methoxy groups for the opposite benzene ring could shorten the distance between the benzyl cation and the opposite benzene ring, whereas the H– $\pi$  interaction could make this distance longer. The stabilization by the direct through-space cation– $\pi$  interaction is possible in the benzyl cations derived from 8-(bromomethyl)[2.2]MCPs. This result strongly suggests that the benzyl cation intermediate could be stabilized by the through-space electronic interaction among the opposite benzene ring as shown in Fig. 3. As previously mentioned, although two through-space electronic interactions, (i) interaction through the intraannular 8,16-positions and (ii) direct through-space cation– $\pi$  interaction, are possible in the [2.2]MCP systems, the latter interaction might be more favorable in the present systems.

## Conclusions

We have demonstrated the  $\text{TiCl}_4$ -mediated Friedel–Crafts benzylation of benzene with 8-(bromomethyl)[2.2]MCPs **2** to afford the corresponding 8-benzyl[2.2]MCPs **4**. The benzyl cation intermediate stabilized by the through-space electronic interaction from the opposite benzene ring was first demonstrated in the benzylation of [2.2]MCP systems. Further studies on the chemical properties of the benzylation products are now in progress.

## Experimental

All melting points were uncorrected.  $^1\text{H}$  NMR spectra were recorded on a Nippon Denshi JEOL FT-300 spectrometer. Chemical shifts are reported as  $\delta$  values (ppm) relative

to internal Me<sub>4</sub>Si. Mass spectra were obtained on a Nippon Denshi JIR-AQ20M mass spectrometer at an ionization energy of 70 eV using a direct-inlet system through GLC; *m/z* values reported include the parent ion peak. Infrared (IR) spectra were obtained on a Nippon Denshi JIR-AQ20M spectrophotometer as KBr disks. Elemental analyses were performed by Yanaco MT-5. GLC analyses were performed by Shimadzu gas chromatograph, GC-14A; silicone OV-1, 2 m; programmed temperature rise, 12 °C min<sup>-1</sup>; carrier gas nitrogen, 25 mL min<sup>-1</sup>.

## Materials

Preparation of 5,13-di-*tert*-butyl-8-substituted 16-methyl[2.2]metacyclopentane (**1a–1c**)<sup>32–34</sup> and 5,13-di-*tert*-butyl-8-(bromomethyl)-16-methyl[2.2]metacyclopentane (**2b**)<sup>35,36</sup> were previously described.

## Bromination of 8-methyl[2.2]metacyclopentanes (1) with *N*-bromosuccinimide

### Typical procedure

After a mixture of 5,13-di-*tert*-butyl-8-methoxy-16-methyl[2.2]metacyclopentane (**1c**; 500 mg, 1.4 mmol), *N*-bromosuccinimide (300 mg, 1.7 mmol), and benzoyl peroxide (50 mg, 0.21 mmol) in carbon tetrachloride (150 mL) had been refluxed for 3 h, the formed precipitates were filtered off. The filtrate was washed with 10% sodium hydroxide and water. The organic layer was dried over sodium sulfate and evaporated in vacuo to leave a colourless solid, which was recrystallized from *n*-hexane to give 5,13-di-*tert*-butyl-8-(bromomethyl)-16-methoxy[2.2]metacyclopentane (**2c**; 435 mg, 70%) as colorless prisms, mp 239–240 °C. IR (KBr, cm<sup>-1</sup>)  $\nu_{\max}$ : 3040, 2960, 1600, 1475, 1450, 1220, 1200, 1100, 1020, 880, 805, 780, 750. <sup>1</sup>H NMR (CDCl<sub>3</sub>)  $\delta$ : 1.26 (s, 18H, *t*-Bu), 2.85 (s, 3H, OMe), 2.68–3.02 (m, 8H, CH<sub>2</sub>), 3.08 (s, 2H, CH<sub>2</sub>), 7.04 (s, 2H, Ar-*H*), 7.06 (s, 2H, Ar-*H*). MS *m/z* (%): 442, 444 (M<sup>+</sup>). Anal. calcd. for C<sub>26</sub>H<sub>35</sub>BrO (443.47): C 70.42, H 7.96; found: C 70.13, H 7.84.

Bromination of **1a** and **1b** with *N*-bromosuccinimide was carried out using the same procedure as described above to afford **2a** and **2b** in 80% and 20% yields, respectively. However, in the case of **1b**, 8,16-bis(bromomethyl)[2.2]MCP (**3**) was also obtained in 30% yield along with the recovery of the starting compound **1b** in 20% yield in spite of 1.2 equiv of *N*-bromosuccinimide used.

## 8-(Bromomethyl)-5,13-di-*tert*-butyl[2.2]metacyclopentane (2a)

Colorless prisms (from *n*-hexane), mp 132–133 °C. IR (KBr, cm<sup>-1</sup>)  $\nu_{\max}$ : 3100, 2900, 1600, 1485, 1400, 1370, 1230, 1190, 1100, 1010, 950, 920, 890, 860, 820, 760, 730, 720, 660. <sup>1</sup>H NMR (CDCl<sub>3</sub>)  $\delta$ : 1.29 (s, 9H, *t*-Bu), 1.34 (s, 9H, *t*-Bu), 2.40–3.16 (m, 8H, CH<sub>2</sub>), 2.83 (s, 2H, CH<sub>2</sub>), 3.68 (broad s, 1H, Ar-*H*), 6.92–7.20 (m, 4H, Ar-*H*). MS *m/z* (%): 412, 414 (M<sup>+</sup>). Anal. calcd. for C<sub>25</sub>H<sub>33</sub>Br (413.45): C 72.63, H 8.05; found: C 72.41, H 7.76.

## 5,13-Di-*tert*-butyl-8-(bromomethyl)-16-methyl[2.2]metacyclopentane (2b)

Colorless prisms (from *n*-hexane), mp 272–275 °C. IR (KBr, cm<sup>-1</sup>)  $\nu_{\max}$ : 3020, 2940, 1580, 1445, 1350, 1270,

1215, 1180, 990, 730. <sup>1</sup>H NMR (CDCl<sub>3</sub>)  $\delta$ : 0.58 (s, 3H, Me), 1.28 (s, 18H, *t*-Bu), 2.76–3.02 (m, 8H, CH<sub>2</sub>), 3.07 (s, 2H, CH<sub>2</sub>), 7.06 (s, 2H, Ar-*H*), 7.12 (s, 2H, Ar-*H*). MS *m/z* (%): 426, 428 (M<sup>+</sup>). Anal. calcd. for C<sub>26</sub>H<sub>35</sub>Br (427.47): C 73.05, H 8.25; found: C 72.93, H 8.21.

## 5,13-Di-*tert*-butyl-8,16-bis(bromomethyl)[2.2]metacyclopentane (3)

Colorless prisms (from benzene), mp > 300 °C. IR (KBr, cm<sup>-1</sup>)  $\nu_{\max}$ : 3040, 2960, 1585, 1475, 1360, 1225, 1220, 1190, 890, 760, 665. <sup>1</sup>H NMR (CDCl<sub>3</sub>)  $\delta$ : 1.33 (18H, s, *t*-Bu), 2.75–3.11 (m, 8H, CH<sub>2</sub>), 3.04 (s, 4H, CH<sub>2</sub>), 7.16 (s, 4H, Ar-*H*). MS *m/z* (%): 504, 506, 508 (M<sup>+</sup>). Anal. calcd. for C<sub>26</sub>H<sub>34</sub>Br<sub>2</sub> (506.37): C 61.67, H 6.77; found: C 61.52, H 6.72.

## Benzylation of benzene with 8-(bromomethyl)-5,13-di-*tert*-butyl-16-substituted [2.2]metacyclopentane (2)

### Typical procedure

To a solution of 5,13-di-*tert*-butyl-8-(bromomethyl)-16-methyl[2.2]metacyclopentane (**2b**; 428 mg, 1.0 mmol) in benzene (2.67 mL, 30 mmol) was added TiCl<sub>4</sub> (0.16 mL, 1.5 mmol) at 0 °C. The reaction temperature was raised to room temperature by removing the ice bath. After the reaction mixture had been stirred at 50 °C for 2 h, it was poured into ice water and extracted with benzene. The extract was dried over anhydrous sodium sulfate and concentrated. The residue was subjected to silica-gel (Wako, C-300; 100 g) column chromatography using as eluent *n*-hexane–benzene (1:1) to give 8-benzyl-5,13-di-*tert*-butyl-16-methyl[2.2]metacyclopentane (**4b**; 170 mg, 40%) as colorless prisms (from *n*-hexane), mp 167–168 °C. <sup>1</sup>H NMR (CDCl<sub>3</sub>)  $\delta$ : 0.62 (s, 3H, Me), 1.27 (s, 9H, *t*-Bu), 1.35 (s, 9H, *t*-Bu), 2.39 (s, 2H, CH<sub>2</sub>), 2.68–3.00 (m, 8H, CH<sub>2</sub>), 6.36–6.52 (m, 2H, Ar-*H*), 6.88–7.04 (m, 3H, Ar-*H*), 7.13 (s, 2H, Ar-*H*), 7.18 (s, 2H, Ar-*H*). MS *m/z* (%): 424 (M<sup>+</sup>). Anal. calcd. for C<sub>32</sub>H<sub>40</sub> (424.68): C 90.51, H 9.49; found: C 90.31, H 9.58.

Benylation of benzene with **2a** and **2c** was carried out using the same procedure as described above and product yields are compiled in Table 1.

## 8-Benzyl-5,13-di-*tert*-butyl[2.2]metacyclopentane (4a)

Colorless prisms (from *n*-hexane), mp 195 °C. IR (KBr, cm<sup>-1</sup>)  $\nu_{\max}$ : 2964, 2864, 1594, 1478, 1477, 1454, 1359, 1275, 731. <sup>1</sup>H NMR (CDCl<sub>3</sub>)  $\delta$ : 1.36 (s, 18H, *t*-Bu), 2.15 (s, 2H, CH<sub>2</sub>), 2.17–3.07 (m, 8H, CH<sub>2</sub>), 3.71 (s, 1H, Ar-*H*), 6.60–7.09 (m, 5H, Ar-*H*), 7.07 (s, 2H, Ar-*H*), 7.19 (s, 2H, Ar-*H*). MS *m/z* (%): 410 (M<sup>+</sup>). Anal. calcd. for C<sub>31</sub>H<sub>38</sub> (410.65): C 90.67, H 9.33; found: C 90.57, H 9.35.

## 8-Benzyl-5,13-di-*tert*-butyl-16-methoxy[2.2]metacyclopentane (4c)

Colorless prisms (from *n*-hexane), mp 132 °C. IR (KBr, cm<sup>-1</sup>)  $\nu_{\max}$ : 2960, 2864, 1600, 1478, 1459, 1361, 1208, 1024, 727. <sup>1</sup>H NMR (CDCl<sub>3</sub>)  $\delta$ : 1.32 (s, 9H, *t*-Bu), 1.37 (s, 9H, *t*-Bu), 2.35 (s, 2H, CH<sub>2</sub>), 2.69–2.84 (m, 8H, CH<sub>2</sub>), 2.90 (s, 3H, OMe), 6.52–7.03 (m, 5H, Ar-*H*), 7.06 (s, 2H, Ar-*H*), 7.17 (s, 2H, Ar-*H*). MS *m/z* (%): 440 (M<sup>+</sup>). Anal. calcd. for C<sub>32</sub>H<sub>40</sub>O (440.68): C 87.22, H 9.15; found: C 87.33, H 9.74.

## The reaction rate determination for the benzylation of benzene with **2** in the presence of $\text{TiCl}_4$

### Typical procedure

To a solution of 5,13-di-*tert*-butyl-8-bromomethyl-16-methyl[2.2]metacyclopheane (**2b**; 100 mg, 0.2 mmol) in benzene (4.2 g, 54 mmol) was added a solution of  $\text{TiCl}_4$  in  $\text{CS}_2$  (0.10 mL, 0.14 mmol), which was prepared by dissolving  $\text{TiCl}_4$  (2.4 mL, 21.08 mmol) in  $\text{CS}_2$  (12.6 mL), by syringe at 25 °C. The reaction was monitored by  $^1\text{H}$  NMR. The reaction rate was determined by the following equations:



$$[2] \quad \frac{d[\text{MCP-CH}_2\text{Br}]}{dt} = k[\text{MCP-CH}_2\text{C}_6\text{H}_5]$$

$$[3] \quad \ln \frac{[\text{MCP-CH}_2\text{Br}]_0}{[\text{MCP-CH}_2\text{Br}] - [\text{MCP-CH}_2\text{C}_6\text{H}_5]} = kt$$

### References

- (1) Shimizu, T.; Hita, K.; Rahman, S.; Yamato, T. *J. Chem. Res.* **2009**, 293. doi:10.3184/030823409X447718.
- (2) Brown, C. J. *J. Chem. Soc.* **1953**, 3278. doi:10.1039/JR9530003278.
- (3) Shieh, C.-F.; McNally, D.; Boyd, R. H. *Tetrahedron* **1969**, 25 (17), 3653. doi:10.1016/S0040-4020(01)82898-2.
- (4) Hanson, A. W. *Acta Crystallogr.* **1962**, 15 (10), 956. doi:10.1107/S0365110X62002534.
- (5) Keehn, P. M.; Rosenfield, S. M., Eds. *Cyclophanes*; Academic Press: New York, 1983.
- (6) Wilson, D. J.; Boekelheide, V.; Griffin, R. W., Jr. *J. Am. Chem. Soc.* **1960**, 82 (24), 6302. doi:10.1021/ja01509a028.
- (7) Allinger, N. L.; Da Roo, M. A.; Hermann, R. B. *J. Am. Chem. Soc.* **1961**, 83 (8), 1974. doi:10.1021/ja01469a046.
- (8) Gutowsky, H. S.; Juan, C. *J. Chem. Phys.* **1962**, 37 (1), 120. doi:10.1063/1.1732932.
- (9) Sato, T.; Akabori, S.; Kainosho, M.; Hata, K. *Bull. Chem. Soc. Jpn.* **1966**, 39 (4), 856. doi:10.1246/bcsj.39.856.
- (10) Sato, T.; Akabori, S.; Kainosho, M.; Hata, K. *Bull. Chem. Soc. Jpn.* **1968**, 41 (1), 218. doi:10.1246/bcsj.41.218.
- (11) Fujimoto, M.; Sato, T.; Hata, K. *Bull. Chem. Soc. Jpn.* **1967**, 40 (3), 600. doi:10.1246/bcsj.40.600.
- (12) Burri, K.; Jenny, W. *Helv. Chim. Acta* **1967**, 50 (7), 1978. doi:10.1002/hlca.19670500731.
- (13) Allinger, N. L.; Gordon, B. J.; Hu, S.-E.; Ford, R. A. *J. Org. Chem.* **1967**, 32 (7), 2272. doi:10.1021/jo01282a040.
- (14) Flammang, R.; Figeys, H. P.; Martin, R. H. *Tetrahedron* **1968**, 24 (3), 1171. doi:10.1016/0040-4020(68)88065-2.
- (15) Blaschke, H.; Ramey, C. E.; Calder, I.; Boekelheide, V. *J. Am. Chem. Soc.* **1970**, 92 (12), 3675. doi:10.1021/ja00715a022.
- (16) Lindsay, W. S.; Stokes, P.; Humber, L. G.; Boekelheide, V. *J. Am. Chem. Soc.* **1961**, 83 (4), 943. doi:10.1021/ja01465a044.
- (17) Tashiro, M.; Arimura, T.; Yamato, T. *Chem. Pharm. Bull. (Tokyo)* **1983**, 31 (1), 370.
- (18) Yamato, T.; Fujita, K.; Shinoda, N.; Noda, K.; Nagano, Y.; Arimura, T.; Tashiro, M. *Res. Chem. Intermed.* **1996**, 22 (9), 871. doi:10.1163/156856796X00539.
- (19) Smith, B. H. *Bridged Aromatic Compounds*; Academic Press: New York, 1964.
- (20) Keehn, P. M.; Rosenfield, S. M., Eds. *Cyclophanes*; Academic Press: New York, 1983; Vols. 1 and 2.
- (21) Vögtle, F. *Cyclophane Chemistry*; Wiley: Chichester, UK, 1993.
- (22) Allinger, N. L.; Gordon, B. J.; Hu, S.-E.; Ford, R. A. *J. Org. Chem.* **1967**, 32 (7), 2272. doi:10.1021/jo01282a040.
- (23) Sato, T.; Yamada, E.-i.; Okamura, Y.; Amada, T.; Hata, K. *Bull. Chem. Soc. Jpn.* **1965**, 38 (6), 1049. doi:10.1246/bcsj.38.1049.
- (24) Fujimoto, M.; Sato, T.; Hata, K. *Bull. Chem. Soc. Jpn.* **1967**, 40 (3), 600. doi:10.1246/bcsj.40.600.
- (25) Sato, T.; Wakabayashi (née Fujimoto), M.; Okamura, Y.; Amada, T.; Hata, K. *Bull. Chem. Soc. Jpn.* **1967**, 40, 2363. doi:10.1246/bcsj.40.2363.
- (26) Sato, T.; Nishiyama, K. *J. Chem. Soc. Chem. Commun.* **1973**, 220. doi:10.1246/bcsj.44.2858.
- (27) Sato, T.; Nishiyama, K.; Shimada, S.; Hata, K. *Bull. Chem. Soc. Jpn.* **1971**, 44 (10), 2858. doi:10.1246/bcsj.44.2858.
- (28) Hayashi, S.; Sato, T. *Bull. Chem. Soc. Jpn.* **1972**, 45 (8), 2360. doi:10.1246/bcsj.45.2360.
- (29) Sato, T.; Nishiyama, K. *J. Org. Chem.* **1972**, 37 (21), 3254. doi:10.1021/jo00986a014.
- (30) Yamato, T.; Ide, S.; Tokuhisa, K.; Tashiro, M. *J. Org. Chem.* **1992**, 57 (1), 271. doi:10.1021/jo00027a048.
- (31) Yamato, T.; Matsumoto, J.; Ide, S.; Tokuhisa, K.; Suehiro, K.; Tashiro, M. *J. Chem. Res. (S)* **1992**, 420.
- (32) Tashiro, M.; Yamato, T. *Synthesis* **1978**, 435. doi:10.1055/s-1978-24769.
- (33) Tashiro, M.; Yamato, T. *J. Org. Chem.* **1981**, 46 (8), 1543. doi:10.1021/jo00321a005.
- (34) Tashiro, M.; Yamato, T. *J. Org. Chem.* **1981**, 46 (22), 4556. doi:10.1021/jo00335a047.
- (35) Tashiro, M.; Yamato, T. *Chem. Lett.* **1982**, 11 (1), 61. doi:10.1246/cl.1982.61.
- (36) Tashiro, M.; Yamato, T. *J. Chem. Soc. Perkin Trans. 1* **1984**, 2165. doi:10.1039/p19840002165.
- (37) Olah, G. A. *Acc. Chem. Res.* **1971**, 4 (7), 240. doi:10.1021/ar50043a002.
- (38) Olah, G. A.; Kobayashi, S.; Tashiro, M. *J. Am. Chem. Soc.* **1972**, 94 (21), 7448. doi:10.1021/ja00776a030.

# On the efficiency of phenol and cyclohexanone electrocatalytic hydrogenation — Effect of conditioning and working pH in acetic acid solution on palladium/fluorine-doped tin dioxide supported catalyst

Dihourahouni Tountian, Anne Brisach-Wittmeyer, Paul Nkeng, Gérard Poillerat, and Hugues Ménard

**Abstract:** The electrocatalytic hydrogenation (ECH) of phenol and cyclohexanone was performed on a conductive Pd/SnO<sub>2</sub>:F catalyst. The catalyst was obtained by the impregnation method. We studied the influence of the pH of the supporting electrolyte, the conditioning pH, and the quantity of the conditioning charge passed before hydrogenation. Fourier transform infrared spectroscopy analysis showed that the functionalization of the catalyst surface by the acetic acid electrolyte depends on the pH. A direct correlation was observed between the efficiency of the hydrogenation, the pH of the electrolyte, and the electrode conditioning charge. Phenol hydrogenation was favored in acidic media, whereas cyclohexanone hydrogenation needed an acidic medium for conditioning and a basic medium for hydrogenation. The ECH rate appeared to depend on the functionalization of the catalyst surface, the adsorption of the target organic molecule on the catalyst, and its structural modification with the pH.

**Key words:** electrocatalytic hydrogenation (ECH), functionalization, phenol, cyclohexanone, tin dioxide catalyst.

**Résumé :** L'hydrogénation électrocatalytique (HEC) du phénol et de la cyclohexanone a été réalisée avec un catalyseur de Pd sur SnO<sub>2</sub>:F conducteur obtenu par imprégnation. Les effets du pH de l'électrolyte support, du pH de conditionnement et de la quantité de charge utilisée pour le conditionnement ont été examinés. La spectroscopie infra rouge par transformée de Fourier a montré que la fonctionnalisation de la surface du catalyseur avec l'acide acétique dépend du pH de l'électrolyte. Une corrélation directe entre l'efficacité d'hydrogénation, le pH de l'électrolyte et la charge de conditionnement a été démontrée. L'hydrogénation du phénol est favorisée en milieu acide tandis que celle de la cyclohexanone nécessite un conditionnement en milieu acide et une HEC en milieu basique. Le taux d'HEC dépend ainsi de la fonctionnalisation de surface du catalyseur, de l'adsorption de la molécule cible sur la surface fonctionnalisée et de la structure de cette molécule en solution dépendamment du pH.

**Mots-clés :** hydrogénation électrocatalytique (HEC), fonctionnalisation, phénol, cyclohexanone, catalyseur de dioxyde d'étain.

## Introduction

Electrocatalytic hydrogenation (ECH) of organic compounds is industrially exploited to produce molecules that have applications as chemical intermediates.<sup>1,2</sup> This hydrogenation method is gradually replacing the catalytic hydrogenation (CH) process because of its easy implementation. Indeed, the reactions are carried out at ambient temperatures and pressures by producing chemisorbed hydrogen at a cath-

ode and by electrolyzing water. This method is applicable to hydrogenation of all kinds of unsaturated molecules, including aromatic rings, carbonyl, nitro, and nitrile compounds.<sup>3</sup>

The efficiency of the ECH is dependent on numerous parameters, such as the unsaturated molecule to be hydrogenated, the catalytic metal, the support of the metal, the supporting electrolyte and its pH, the presence of organic cosolvent or surfactant, and the current density.<sup>4</sup> Each of

Received 2 December 2009. Accepted 23 January 2010. Published on the NRC Research Press Web site at canjchem.nrc.ca on 6 April 2010.

**D. Tountian.** Laboratoire d'Électrochimie et de Chimie Physique du Corps Solide, Institut de Chimie- UMR 7177 CNRS- Université de Strasbourg, 4 rue Blaise Pascal, 67000 Strasbourg, France; Laboratoire Sciences de Matériaux d'Electrodes, Département de Chimie- Université de Sherbrooke, 2500 boul. de l'Université, Sherbrooke, QC J1K 2R1, Canada.

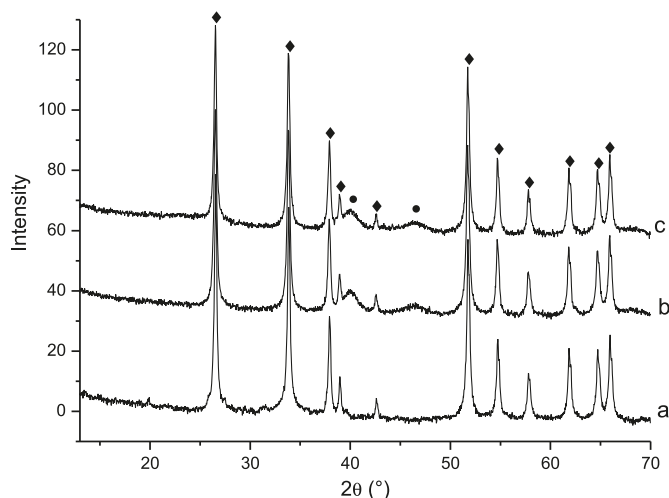
**A. Brisach-Wittmeyer<sup>1</sup> and H. Ménard.** Laboratoire Sciences de Matériaux d'Electrodes, Département de Chimie- Université de Sherbrooke, 2500 boul. de l'Université, Sherbrooke, QC J1K 2R1, Canada.

**P. Nkeng and G. Poillerat.** Laboratoire d'Électrochimie et de Chimie Physique du Corps Solide, Institut de Chimie- UMR 7177 CNRS- Université de Strasbourg, 4 rue Blaise Pascal, 67000 Strasbourg, France.

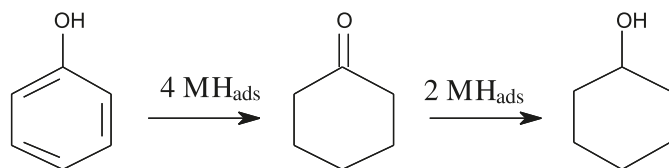
<sup>1</sup>Corresponding author (e-mail: Anne.Wittmeyer@USherbrooke.ca).



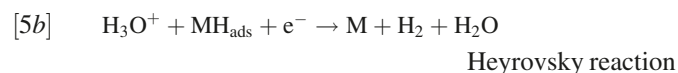
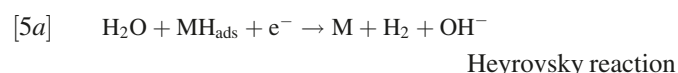
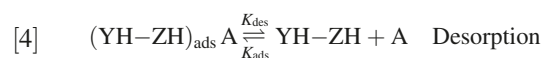
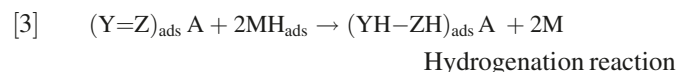
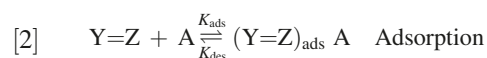
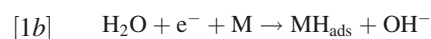
**Fig. 1.** X-ray diffraction patterns of Pd/SnO<sub>2</sub>:F catalyst (a) before and after ECH process at (b) pH 3 and (c) pH 12. (◆) SnO<sub>2</sub>:F, cassiterite structure; (♦) tetragonal PdO peaks at  $2\theta = 33.89$ ,  $46.66$ ,  $54.76$ , and  $71.48$  in diffractogram (a) are superposed to the SnO<sub>2</sub>:F peaks; (●) metallic Pd.



**Scheme 1.** Conversion of phenol into cyclohexanol via cyclohexanone.



these parameters has an influence on the mechanism of the ECH described below.



In this mechanism, three groups of reactions can be observed. The first one (reactions 1a and 1b) is relative to the

production of the chemisorbed hydrogen ( $\text{MH}_{\text{ads}}$ ) on the metallic surface (M) by the electroreduction of water (acidic or basic medium); the second (reactions 2–4) concerns the hydrogenation reaction, which starts with the adsorption of the unsaturated molecule ( $\text{Y}=\text{Z}$ ) on the support (A), which further reacts with the chemisorbed hydrogen; the last group of reactions (reactions 5 and 6), which concerns the hydrogen evolution reaction, is a competition reaction with hydrogenation. Depending on the parameters cited above, either the hydrogenation process or the hydrogen evolution will be predominant.

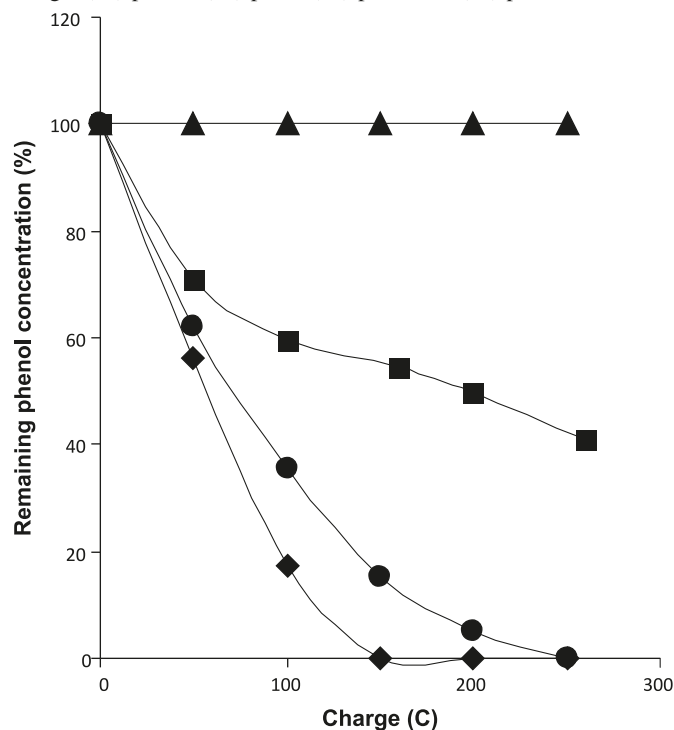
The behavior of a supported metal is different from the bulk metal, and the synergy effect of a metal supported on a matrix has been recently studied.<sup>5</sup> The adsorption of the unsaturated organic molecule is a key step. For the supported catalysts, this adsorption takes place on the support,<sup>6</sup> thus the efficiency of the ECH is relative to the nature of the catalyst matrix. To control both the adsorption of the unsaturated compound and the desorption of the hydrogenated product, recent studies have introduced new concepts: *ex situ*<sup>7</sup> and *in situ* functionalized<sup>8</sup> materials. They consisted of a modification of the catalyst matrix with organic functional molecules before and during the ECH process, respectively. These modifications controlled the adsorption of the target molecule as in reverse chromatography. It was demonstrated that the *in situ* modification of alumina surface depended on the pH of the electrolyte when acetic acid was used.<sup>9</sup>

Before the introduction of these new concepts, several studies had focused on phenol and cyclohexanone. On RaNi electrode, in alkaline media ( $\text{pH} > 13$ ), ECH of cyclohexanone led to excellent chemical yields and current efficiencies, the best results being obtained with NaOH 0.14 mol/L. However, when an acetate buffer was used, no hydrogenation took place.<sup>10</sup> The studies of Dubé et al.<sup>11</sup> in a phosphate buffer ( $\text{KH}_2\text{PO}_4 + \text{NaOH}$ ), pH 7, showed that Pd dispersed on both alumina and activated carbon presented a bad electrocatalytic activity compared with the other metals of the Pt group. They also demonstrated that the yield of cyclohexanone electrohydrogenation was strongly dependent on the nature of the non-conductive matrix used to disperse Ni nanoparticles. Santana et al.<sup>12</sup> found that the pH had no influence on the hydrogenation of 2-cyclohexen-1-one when a nickel sacrificial anode was used. This study concluded that the ECH of conjugated olefins or carbonyl groups is efficient, whereas for non-conjugated substrates (the case of cyclohexanone), it is not.

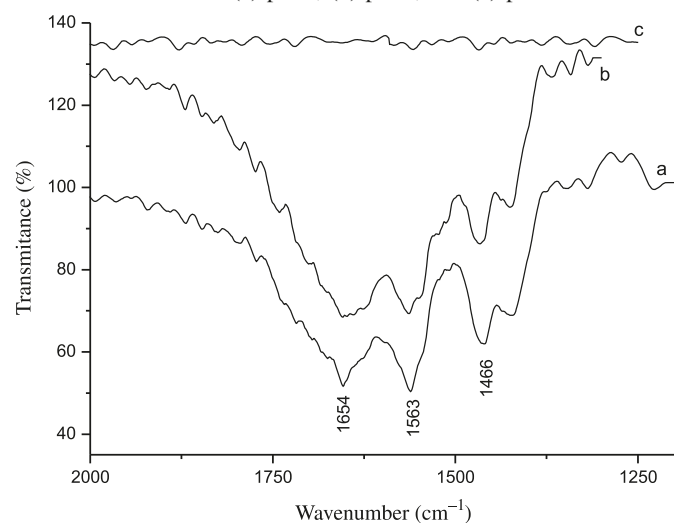
Fichter and al.<sup>13</sup> reported a poor yield for the reduction of phenol to cyclohexanol in 2 N  $\text{H}_2\text{SO}_4$  at a platinized Pt electrode. On the contrary, Misra et al.<sup>14</sup> showed that phenol was reduced electrochemically in a divided cell at a Pt cathode in 2 N  $\text{HClO}_4$ , in the presence of tetraethylammonium, with a 82.7% yield. More recently, the effect of pH on the kinetics of phenol ECH was investigated with  $\text{BaSO}_4$  as the adsorbent. The rate of reaction was considerably lower at pH 14, and remained unchanged between acidic and neutral media.<sup>15</sup> In acidic media ( $\text{H}_2\text{SO}_4$ ), Martel et al.<sup>4</sup> found that the phenol ECH depended on the catalyst material, whereas in neutral media the results were linked to the supporting electrolyte, i.e., the nature of ions in solution.

Current density also influences the hydrogenation product yield. This parameter acts as a balance between the two

**Fig. 2.** ECH of phenol on Pd/SnO<sub>2</sub>:F in aqueous solution of acetic acid (0.5 mol/L) as a function of the electrolyte pH and total charge: (▲) pH 12, (■) pH 6, (●) pH 5, and (◆) pH 3;  $I = 20$  mA.



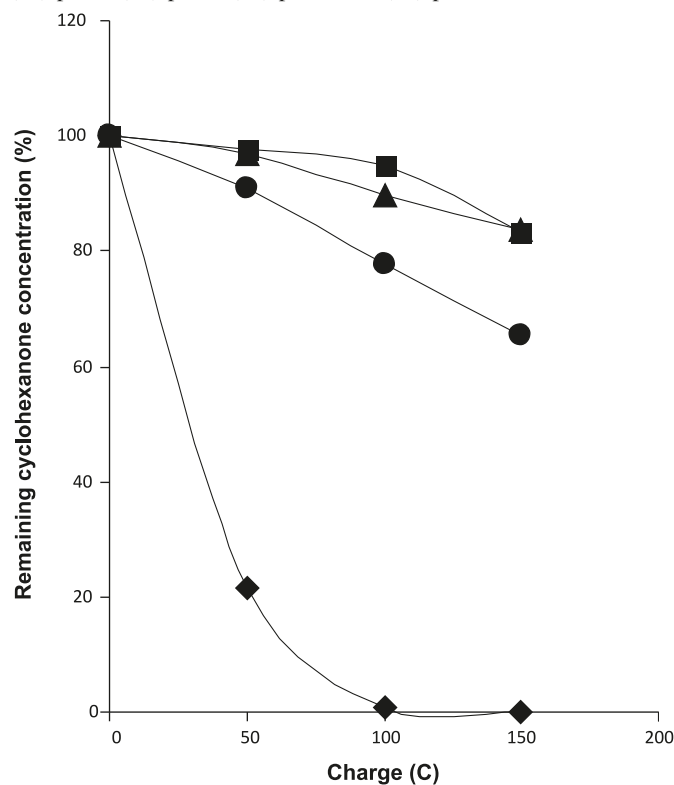
**Fig. 3.** FTIR spectra of SnO<sub>2</sub>:F powder subjected to aqueous solutions of acetic acid at (a) pH 3, (b) pH 6, and (c) pH 12.



competitive reactions (3 and 5a, 5b). A high current density favors the hydrogen evolution reaction, whereas a low current density improves the hydrogenation efficiency.<sup>16</sup>

This paper reports the results of a study on the effect of the pH (3 to 12) on the efficiency of phenol and cyclohexanone ECH in acetic acid as electrolyte using Pd deposited on conductive fluorine-doped tin dioxide (SnO<sub>2</sub>:F) as catalyst. Effectively, the ECH process implied a pH variation during its proceeding as stated by the mechanism (reactions 1 and 5), and also the functionalization of the catalyst is a pH-dependent phenomenon.<sup>9</sup>

**Fig. 4.** ECH of cyclohexanone on Pd/SnO<sub>2</sub>:F in aqueous solution of acetic acid (0.5 mol/L) as a function of the total charge, at different starting pH values without controlling the pH during the reaction: (■) pH 5, (◆) pH 6, (●) pH 8, and (▲) pH 12;  $I = 20$  mA.



As shown by the ECH mechanism, the efficiency of hydrogenation is linked to the production of chemisorbed hydrogen (reactions 1a and 1b) by electroreduction of water. Here, we present a study of the effect of quantity of charge used for the conditioning of the catalyst, before the ECH process, which determines the available quantity of chemisorbed hydrogen. We show that the ECH efficiency depends on the pH and the conditioning charge.

## Experimental

### Chemicals

Conductive fluorine-doped tin dioxide (SnO<sub>2</sub>:F) of ( $\rho < 5 \Omega\text{cm}$ ,  $S_{\text{BET}} = 6\text{--}10 \text{ m}^2 \text{ g}^{-1}$ ) was purchased from Keeling & Walker Limited. Also, Pd(OOCCH<sub>3</sub>)<sub>2</sub> as Pd precursor was purchased from Aldrich.

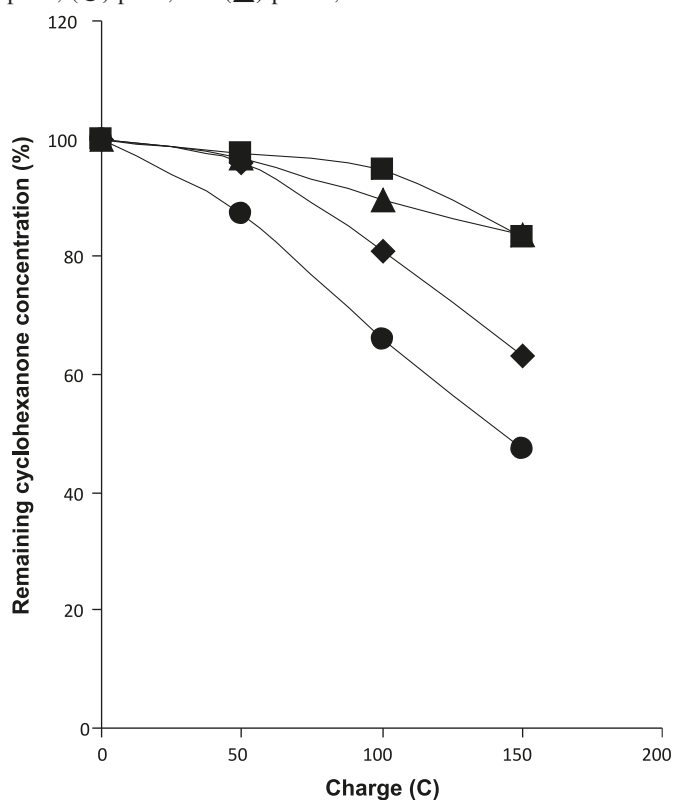
Phenol, cyclohexanone, cyclohexanone-oxime, cyclohexanol, and 3-methylcyclohexanol (Aldrich) were of +99% grade of purity and were used as received. High-purity water (from a Milli-Q unit) was used to prepare the solutions, and chloroform (Fisher, spectrophotometry-grade) was used for the solubilization of Pd(OOCCH<sub>3</sub>)<sub>2</sub> and the liquid-liquid extraction. Reticulated vitreous carbon (RVC, with 100 pores per inch) was purchased from Electrolytica Inc. and used as cathode. The electrolyte was prepared using glacial acetic acid from Aldrich.

### Catalyst preparation

Pd/SnO<sub>2</sub>:F catalyst was prepared by impregnating com-

**Table 1.** Evolution of the pH as a function of the starting pH and the quantity of charge passed.

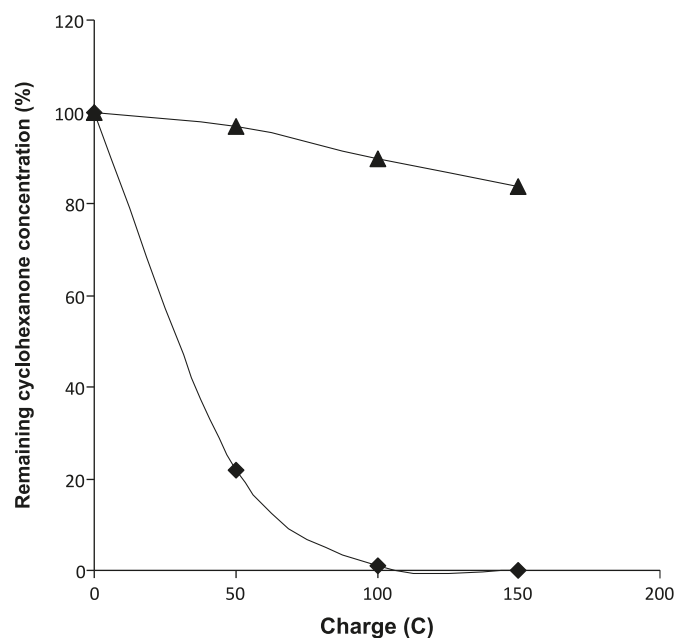
		Starting pH				
		3	5	6	8	12
Conditioning	7	3.0	5.0	6.1	10.0	12.0
	50	3.0	5.1	6.7	12.0	12.0
HEC process	20	3.1	5.1	11.2	12.1	12.0
	50	3.1	5.2	12.1	12.3	12.0
	100	3.1	5.2	11.9	12.0	12.1
	150	3.1	5.4	11.9	12.1	12.1

**Fig. 5.** ECH of cyclohexanone on Pd/SnO<sub>2</sub>:F in aqueous solution of acetic acid (0.5 mol/L) as a function of the total charge, at different starting pHs with pH control during the reaction: (■) pH 5, (◆) pH 6, (●) pH 8, and (▲) pH 12; *I* = 20 mA.

mercially available SnO<sub>2</sub>:F. Pd(OOCCH<sub>3</sub>)<sub>2</sub> was first solubilized in chloroform and poured in a flask containing SnO<sub>2</sub>:F. After 1 h of stirring, the chloroform was evaporated at low temperature. Water was added to the flask and it was maintained at 80 °C until the complete evaporation of water. The prepared catalyst with a nominal concentration of 10% of Pd was dried overnight at 90 °C in a stove.

### Catalyst characterization

Previous MEB characterization of the catalyst has been described elsewhere.<sup>17</sup> X-ray measurements were performed using an X'pert Pro MRD of Panalytical diffractometer with Cu K $\alpha$  (wavelength = 1.5406 Å) radiation. Diffractograms of powders were recorded in 2 $\theta$  scan configuration, in the 10–80 ° 2 $\theta$  range, at a fixed incident angle of 0.02 °. Fourier transform infrared spectroscopy (FTIR) of the SnO<sub>2</sub>:F pow-

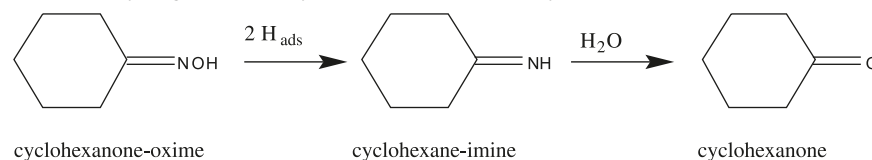
**Fig. 6.** ECH of cyclohexanone on Pd/SnO<sub>2</sub>:F in aqueous solution of acetic acid (0.5 mol/L) as a function of the total charge at two different conditioning pHs: (◆) pH 5, and (▲) pH 12; working pH = 12; *I* = 20 mA.

ders was recorded on a Bruker IFS 25 with a resolution of 4 cm<sup>-1</sup>. The powders were immersed in the aqueous supporting electrolyte solutions containing acetic acid at pH 3, 6, and 12. These pHs were adjusted with a NaOH (10 N) solution. The suspensions were filtered, and the powders were washed with water. After drying at 50 °C for 15 h, the powders were probed by FTIR using powder not exposed to the supporting electrolyte as a reference. The samples were dispersed in a KBr matrix and pressed in self-supporting disks.

Measurements of adsorption isotherms were carried out as described below. Cylindrical vials (25 mL) were thoroughly cleansed, rinsed with high purity water (from a Milli-Q unit), and dried. SnO<sub>2</sub>:F powder (1 g) was added to each vial, except to the vials serving as blanks, 10 mL of acetic acid solutions (0.5 mol/L) adjusted to pH 5 and 12 was added to each vial. After 1 h of stirring in the presence of SnO<sub>2</sub>:F powders, some of the vials at pH 5 were adjusted to pH 12. To each of these vials, cyclohexanone solution was added to obtain the desired concentrations. The total volume in each vial was 15 mL. The SnO<sub>2</sub>:F powders – cyclohexanone suspensions were then stirred with an orbital shaker at 320 trs/min and at ambient temperature (23 ± 2 °C). Adsorption isotherms were measured after 3 h (time required for one ECH experiment). A 0.5 mL aliquot was withdrawn from each vial, filtered, and analyzed by GC chromatography to determine cyclohexanone concentration.

### Electrocatalytic hydrogenation procedure

All electrocatalytic experiments were carried out in a two-compartment dynamic cell<sup>18</sup> under galvanostatic conditions at ambient temperature. The cathode compartment was filled with 29 mL of 0.5 mol/L solution of acetic acid in water at the desired pH. The anodic compartment was filled with the same solution. Prior to the ECH process, 200 mg of the cat-

**Scheme 2.** Reaction scheme for the hydrogenation of cyclohexanone-oxime to cyclohexanone.

alyst was suspended in the cathodic solution and dynamically circulated ( $\approx 1$  L/min) through the reticulated vitreous carbon cathode. The catalyst was then conditioned by passing a known quantity of charge. This quantity of charge served to reduce Pd(II) in the catalyst after preparation into metallic Pd and to saturate the cathode material with chemisorbed hydrogen. For our catalysts, containing theoretically 10% of Pd, 31 °C was normally necessary to reduce the oxidized Pd, assuming that Pd is totally in its oxidized form in the catalyst before conditioning. The reduction of oxidized Pd is kinetically faster than the formation of chemisorbed hydrogen.<sup>19</sup>

For phenol electrohydrogenation, the quantity of conditioning charge was fixed to 50 C for all the pH values, whereas for cyclohexanone this quantity varied from 5 C to 75 C.

After conditioning, the coulometer was reset to zero; a volume of 1 mL of an aqueous unsaturated organic compound solution (25.2 mg/mL of phenol or 26.3 mg/mL of cyclohexanone) was then added to the cathodic compartment, giving a total volume of 30 mL and an unsaturated compound concentration of  $8.94 \times 10^{-3}$  mol/L. During the ECH process, the constant current applied was 20 mA for phenol hydrogenation, 20 and 5 mA for cyclohexanone hydrogenation.

After passing different quantities of charge, 0.5 mL aliquots were withdrawn from the catholyte and added to 1 mL of chloroform, saturated with NaCl, and shaken together for the extraction of the organic compounds. The organic phase was removed and dried on  $\text{Na}_2\text{SO}_4$ . Finally, an internal standard chloroform solution was added to 0.4 mL of the organic phase, mixed, and 1  $\mu\text{L}$  of this solution was injected in the gas chromatograph. The GC analyses were carried out using an Agilent 6890 series chromatograph equipped with an MS detector and 5HS capillary column (30 m  $\times$  0.250 mm  $\times$  0.25  $\mu\text{m}$ ). Since hydroxide ions are produced (reaction 1) during the electrolysis, the pH can change depending on the quantity of charge, so we followed this pH in situ, or maintained its value using a concentrated acetic acid solution.

### Chemisorbed hydrogen quenching procedure

The quantity of chemisorbed hydrogen produced during the conditioning was estimated using cyclohexanone-oxime as a quencher. Open-circuit hydrogenation (catalytic hydrogenation)<sup>3</sup> of cyclohexanone oxime was done to determine the quantity of active atomic hydrogen in solution or adsorbed. After conditioning, the current was switched off, and 1 mL of cyclohexanone-oxime solution (30 mg/mL in 50/50 (v/v) water/methanol) was added to the cell. An aliquot was withdrawn from the cell at each hour, extracted with diethyl ether, and injected to GC chromatograph to

measure the quantity of cyclohexanone-oxime that disappeared from the solution in the cell.

## Results and discussion

As we study the influence of the pH on the ECH efficiency of phenol and cyclohexanone, we have to ensure that the properties of our catalysts are not modified by changing pH values. Indeed, XRD measurements carried out on the Pd/SnO<sub>2</sub>:F catalyst after the ECH process at pH 3 and pH 12 (Fig. 1) showed no change in the catalyst support (SnO<sub>2</sub>:F) structure, demonstrating that the catalyst support remained stable in acidic and basic media. The only change in the XRD peaks is linked to the electrochemical reduction of Pd(II) to metallic Pd during the process. As a result, SnO<sub>2</sub>:F is a good matrix, which allows the study of the pH effect in a large range, contrary to alumina for example, which is deteriorated in basic medium.<sup>15</sup>

Conversion of phenol can lead to cyclohexanone formation and eventually to cyclohexanol (Scheme 1), depending on the reaction conditions.

The ECH of phenol conducted on Pd/SnO<sub>2</sub>:F in acetic acid solution mainly led to the formation of cyclohexanone and presented different behaviors depending on the working pH (Fig. 2). Two observations can be made. First, at pH 12, the process was inefficient. Second, at pH 6 and below, the more acidic the pH, the more efficient the ECH process became. Considering the functionalization of the SnO<sub>2</sub>:F surface as a function of pH, the IR spectra were recorded. If functionalization of the catalyst by the acetic acid had occurred, three bands at 1654, 1563, and 1466  $\text{cm}^{-1}$  would appear. Figure 3 shows that this was not the case at pH 12. Therefore, it can be concluded that there was no acetic acid on the catalyst surface. That absence of functionalization at pH 12 is due to the competitive adsorption of the hydroxyl anions,<sup>20,21</sup> whereas at pH 3 and 6 (no excess of hydroxyl ions in solution), SnO<sub>2</sub>:F surface is well-functionalized. As shown by Cirtiu et al.,<sup>8</sup> the functionalization phenomenon enhances the hydrogenation process by improving the adsorption of the unsaturated molecule. That means that at pH 12, the catalyst surface is unable to adsorb phenol molecules because of the absence of functionalization. As shown in the ECH mechanism, the adsorption is an important step that will be the limiting reaction at this pH.

However, one also must take into account that the structure of phenol is pH-dependent, as its  $\text{pK}_a$  is 9.96. Thus, at pH 12, phenol exists as phenolate in solution. As ECH is totally inefficient at this pH, we suppose that this form (phenolate) does not adsorb onto the non-functionalized SnO<sub>2</sub>:F at all. Such a strong decrease in hydrogenation rate at high pH was pointed out by Wismeijer et al.<sup>22</sup> in the catalytic hydrogenation (CH) process when Pd/C was used. They attributed this effect to the absence of adsorption of the phenolate



**Table 2.** Quantity of H<sup>•</sup> available (mol) as a function of the charge passed for the conditioning.

Experimental conditions	pH	Entries	Theoretical H <sup>•</sup> quantity formed (mol) $N = Q/nF$	Cyclohexanone-oxime starting quantity (mol)	Cyclohexanone formed after 3 h (mol)	H <sup>•</sup> quantity available (mol)
With catalyst + 50 C charge	5	1	$5.18 \times 10^{-4}$	$2.27 \times 10^{-4}$	$2.20 \times 10^{-4}$	$4.40 \times 10^{-4}$
	12	2	$5.18 \times 10^{-4}$	$2.27 \times 10^{-4}$	$1.50 \times 10^{-4}$	$3.10 \times 10^{-4}$
Without catalyst, without charge	5	3	0	$2.27 \times 10^{-4}$	$0.45 \times 10^{-4}$	$0.90 \times 10^{-4}$
	12	4	0	$2.27 \times 10^{-4}$	0	0

on the catalyst. Phenolate molecules are preferably found in the aqueous phase because of the electrostatic repulsion with the negatively charged carbon surface due to the OH<sup>-</sup> ions. At pH < 10, we observed that the ECH process of phenol becomes efficient. Moreover, we showed that the more acidic the solution, the more efficient the hydrogenation. As there is a significant difference between conversion of phenol at pH 6 and at pH 3, we suggest the most acidic medium is favorable for phenol electrohydrogenation. Indeed, it is well-known that in a strong acid solution, the hydrogenation of phenol is facilitated by some decrease in its resonance stabilization energy.<sup>23</sup> Also, the rate of enhancement of aromatics hydrogenation in superacidic solutions was attributed to the removal of the aromatic resonance stabilization energy by Feiring<sup>24</sup> and Mador.<sup>25</sup>

Therefore, the ECH process of phenol on Pd/SnO<sub>2</sub>:F in an acetic solution will work, provided that the catalyst has been previously functionalized at a pH ≤ 6, and it will be more optimal in a more acidic medium. The pH values affected the catalyst/solution interface that has a great influence on the adsorption/desorption steps of the ECH process.

Cyclohexanone is the intermediate product in the complete ECH of phenol into cyclohexanol (Scheme 1), and it is interesting to study its reactivity as a function of pH when it is the starting product to see the influence of its adsorption and reactivity on the ECH efficiency. If we consider the ECH conducted at several pHs without controlling the pH (Fig. 4), we observe that the maximal efficiency is obtained for a starting pH equal to 6. Nevertheless, it is important to notice that, apart from the starting pH 5 and 12, which remained stable during the process, the other starting pH 6 and 8 change during the experiment for a final pH equal to 12 (Table 1). Maintaining the pH is especially important for values higher than 5.5 due to the loss of the buffer capacity of acetic acid, which has a pK<sub>a</sub> of 4.76. The speed of pH change increases when the starting pH increases (Table 1).

As observed for phenol hydrogenation, pH 12 is inefficient, owing to the non-functionalization of the catalyst surface. Surprisingly, pH 5 is the less efficient medium, although the surface is functionalized. In fact, Breitner et al.<sup>26</sup> had made the same observation in the CH process for rhodium and ruthenium catalysts, which hydrogenated carbonyl compounds rapidly in neutral and basic solutions and slowly in acid solutions. They also noted that palladium was ineffective to hydrogenate aliphatic ketones, but this becomes possible in our case by the ECH process.

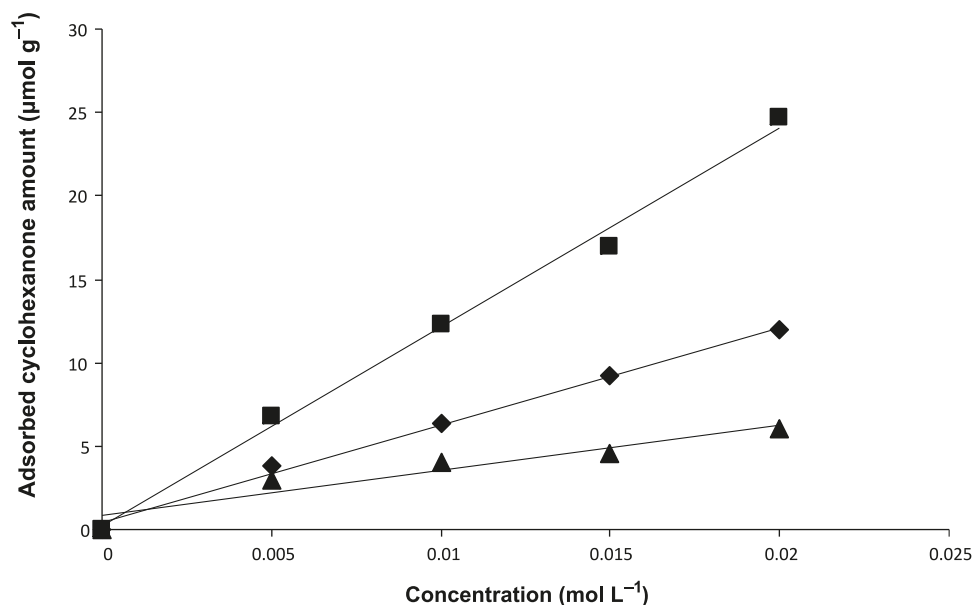
A starting pH of 6 with final pH equal to 12 seemed to be the best condition for ECH of cyclohexanone. Indeed, for a starting pH of 6, it remained slightly acidic at the end of the conditioning and went up to basic pH after a few quantity of charge (20 C) was passed for the ECH. When starting with a pH 8, only 7 C was sufficient to bring the pH to the basic range during the conditioning (Table 1).

Then, we decided to control the pH of the solution to know exactly the best working pH for cyclohexanone hydrogenation. We realized ECH of cyclohexanone at these different pHs with in situ control of the pH (Fig. 5), and we observed that the maximal efficiency was obtained for pH 8 and that it was near 50%. As a result, a starting pH of 6 was not the only reason for the ECH efficiency without pH control (Fig. 4) because this process was kinetically limited when the electrolyte was constantly maintained at pH 5 and 6. Even if the catalyst surface was functionalized at these pHs (Fig. 3), the process remained inefficient, which means that the functionalization is not the only sufficient condition.

Comparing Fig. 4 and Fig. 5, we can suppose that the starting pH must be acidic, whereas the working pH must be basic to get the best efficiency. This is the reason why the process is divided into two steps: the conditioning and the working parts. We verified the impact of the conditioning pH by conducting ECH of cyclohexanone with two different procedures (Fig. 6): First, we conditioned the catalyst at pH 5 during 50 C, and then adjusted the working pH to 12 before adding cyclohexanone. Second, we used pH 12 both in conditioning and working conditions. Figure 6 perfectly shows that catalyst must be conditioned at pH 5 to be able to convert cyclohexanone into cyclohexanol.

Then, it is important to know if there is a difference in the quantity of chemisorbed hydrogen produced in acidic and basic media. We know that the chemisorbed hydrogen's production kinetics depends upon the metal<sup>27</sup> and also the medium (acidic or basic).<sup>19</sup> To quantify the number of moles of H<sub>ads</sub> produced by the conditioning in acidic versus basic medium we used an H<sup>•</sup> quencher, which completely reacts with all the H<sup>•</sup> available. Before that, one must take into account that during the conditioning, some electrons are used to reduce the oxidized Pd and some to produce chemisorbed hydrogen (reaction 1). To determine the quantity of chemisorbed hydrogen produced during the conditioning, we made an open-circuit hydrogenation of cyclohexanone-oxime, which was added to the catholyte after switching off the current at the end of the conditioning. After a total time

**Fig. 7.** Adsorption isotherm for cyclohexanone after 3 h in contact with F-doped  $\text{SnO}_2$  powders in aqueous solution of acetic acid (0.5 mol/L) as a function of the initial pH: ( $\blacktriangle$ ) pH 12, ( $\blacklozenge$ ) pH 5, ( $\blacksquare$ ) 1 h of electrolyte– $\text{SnO}_2\text{:F}$  suspension stirring at pH 5 before adding cyclohexanone at pH 12.



of 4 h, the cyclohexanone-oxime CH ended, i.e., its reaction with active chemisorbed was total.

We calculated the theoretical quantity of  $\text{H}^\bullet$  formed during conditioning according to Scheme 2. Then, experiments were conducted in the presence and absence of a catalyst, and we determined the available quantities of active hydrogen (Table 2). This was done at a charge of 50 C during conditioning. Table 2 shows that the maximum quantity of  $\text{H}^\bullet$  produced is  $4.4 \times 10^{-4}$  mol (Table 2, entry 1) at pH 5 and 50 C conditioning of the electrocatalysis. We observed that at pH 12 (Table 2, entry 2), the available quantity of  $\text{H}^\bullet$  was less important. However, it is interesting to remark that without either a catalyst or a charge, little reactivity of cyclohexanone was observed at pH 5 (Table 2, entry 3), whereas no reaction at all took place at pH 12 (Table 2, entry 4). Consequently, we assume that only  $3.5 \times 10^{-4}$  mol of  $\text{H}^\bullet$  (corresponding to 33.7 C) are really produced at pH 5 on the catalyst over 50 C. In these conditions, the quantity of active hydrogen available at pH 5 or pH 12 is in the same range and the observed differences are in the experimental error range. Then, experimentally, a maximum of 20 C is used for the reduction of Pd(II) into Pd(0), which means that all the Pd is not in Pd(II) form in the catalyst before conditioning. We can assume that this quantity is always the same whatever the quantity of charge passed for conditioning.

From these observations, we can conclude that the difference in the efficiency of the ECH process due to the conditioning pH is not linked to the available quantity of  $\text{H}_{\text{ads}}$  because this quantity is the same in acidic and basic media. We can suppose that basic pH allows cyclohexanone to be activated and this activated form of cyclohexanone may have affinity with functionalized catalyst after conditioning in acidic medium (no functionalization in basic medium). Indeed, adsorption of cyclohexanone on  $\text{SnO}_2\text{:F}$  in presence of acetic acid (Fig. 7) is more favored at pH 5 than at

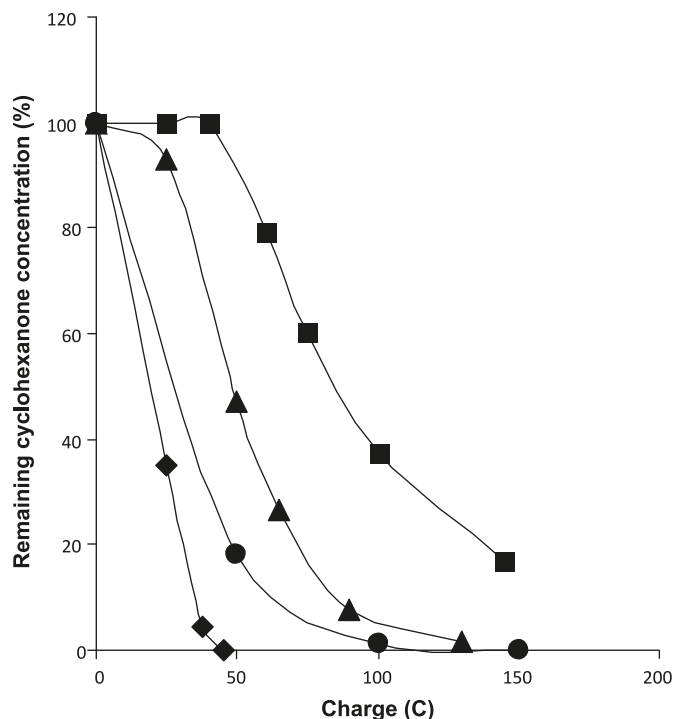
pH 12. Above that, its adsorption is maximal when the catalyst is conditioned at pH 5 (functionalization) and when cyclohexanone is introduced at pH 12. Hence, the activated cyclohexanone has a good adsorption onto the functionalized catalyst. This activation of cyclohexanone may be due to the solvation, which differs in acidic and basic environments. The keto–enol equilibrium is also more favorable in alkaline medium. Indeed, it was demonstrated that the alkene group is more reactive than the carbonyl group in the ECH process.<sup>12,26</sup> The increase in the rate of hydrogenation of cyclohexanone in KOH solution in the CH process was also observed by Wismeijer et al.<sup>22</sup> It was assumed that the promoted effect came from the reactive enolate anions or ionized hydrated cyclohexanone species formed in the presence of  $\text{OH}^-$ . In our case, the FTIR spectrum (not presented) of cyclohexanone at pH 12 shows an additional band compared with that of cyclohexanone at pH 5, that band was attributed to the enolate ion.

As pointed out by Dubé et al.,<sup>11</sup> the efficiency also depends on the kinetics of the transfer of a monoatomic hydrogen ( $\text{H}_{\text{ads}}$ ) from the metal site to the  $\pi$ -bond of the adsorbed organic molecule. This transfer can differ from acidic to basic medium depending on the configuration of the substrate in solution.

Because the quantity of the available  $\text{H}_{\text{ads}}$  can influence the hydrogenation, we were interested in studying its role in the ECH of cyclohexanone on the same catalyst in acetic acid electrolyte. For this study, the conditioning pH was 5 and the working pH was 12. To improve the efficiency of the reaction, the constant current applied after conditioning was 5 mA. As seen in the quenching of  $\text{H}_{\text{ads}}$ , the experimental quantity of charge necessary to reduce all the Pd(II) to Pd(0) was around 20 C. Then, we can estimate the approximate quantity of  $\text{H}_{\text{ads}}$  as a function of conditioning charge (Table 3). This table shows that if the quantity of charge for the conditioning increases, the quantity of  $\text{H}_{\text{ads}}$  available

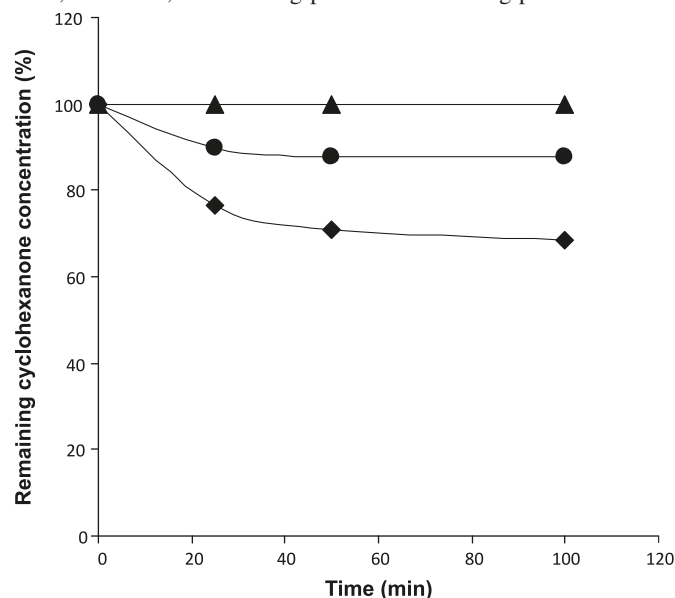
**Table 3.** Theoretical quantity of  $H^\bullet$  formed and available (mol) as a function of the conditioning charge.

Charge $Q$ passed for conditioning (C)	Experimental quantity of charge $Q_{Pd}$ necessary to reduce Pd(II) into Pd(0) (C)	Experimental quantity of charge $Q_{Hads}$ for chemisorbed hydrogen production with $Q_{Hads} = Q - Q_{Pd}$	Theoretical $H^\bullet$ quantity $N$ formed and available (mol) with $N = Q_{Hads}/(nF)$ and $n = 1$
5	20	0	None
25	20	5	$5.18 \times 10^{-5}$
50	20	30	$3.11 \times 10^{-4}$
75	20	55	$5.70 \times 10^{-4}$

**Fig. 8.** ECH of cyclohexanone on Pd/SnO<sub>2</sub>:F in aqueous solution of acetic acid (0.5 mol/L) as a function of the total charge for different quantities of conditioning charge: (■) 5 C, (▲) 25 C, (●) 50 C, and (◆) 75 C;  $I = 5$  mA; conditioning pH = 5 and working pH = 12.

increases. Indeed, the more the charge passed before the beginning of ECH, the faster the reaction (Fig. 8), which shows that the kinetics of cyclohexanone hydrogenation is affected. This observation can explain why a difference is noticed in the ECH process according to the nature of the metal used<sup>27</sup> or the conductivity of the matrix supporting the metallic nanoaggregates.<sup>17</sup> Indeed, the quantity of  $H_{ads}$  generated is linked to these parameters.

To study only the influence of the conditioning charge directly on cyclohexanone hydrogenation, CH of cyclohexanone was conducted at the end of each conditioning (Fig. 9). Cyclohexanone was added to the catholyte after the conditioning, i.e., in the presence of chemisorbed  $H_{ads}$  (demonstrated by the quenching), and then we verified whether or not it was hydrogenated after 100 min. Surprisingly, Fig. 9 shows that cyclohexanone hydrogenation took place and the quantity of  $H^\bullet$  (Table 3) produced during conditioning played an important role on the CH process. This result demonstrated that when chemisorbed hydrogen is produced (by the electroreduction of water), cyclohexanone could catalytically be hydrogenated on Pd catalyst. Never-

**Fig. 9.** CH of cyclohexanone on Pd/SnO<sub>2</sub>:F in aqueous solution of acetic acid (0.5 mol/L) as a function of the total charge for different quantities of conditioning charge: (▲) 25 C, (●) 50 C, and (◆) 75 C;  $I = 5$  mA; conditioning pH = 5 and working pH = 12.

theless, the catalytic hydrogenation of cyclohexanone, and most of aliphatic ketones, was impossible on palladium catalyst when hydrogen gas was used as source of chemisorbed hydrogen.<sup>12,26</sup> This is explained by the kinetic barrier (related to the low solubility and low dissociation of molecular hydrogen ( $H_2$ )) that is too high.<sup>28</sup> So, it can be said that the production of chemisorbed hydrogen is not systematic in CH conditions. The ECH offers soft conditions of work<sup>11</sup> in which the production of chemisorbed hydrogen is obvious as it was shown by the quenching. Additionally, in the ECH process, the polarization of the catalyst<sup>29</sup> and the cyclohexanone C=O bond takes place.<sup>9</sup>

## Conclusion

The in situ functionalization of the catalyst support affects the electrocatalytic hydrogenation of phenol and cyclohexanone. This functionalization takes place in an acidic medium ( $pH \leq 6$ ) with acetic acid as electrolyte. The effect of the pH on the ECH process is explained by the catalyst functionalization, which affects the catalyst/solution interface also by the structural changes of the target molecule.

Hydrogenation of phenol to cyclohexanone increases as the medium becomes more acidic. When the support surface is functionalized, cyclohexanone is hydrogenated only in a basic medium. For a complete hydrogenation of phenol

with good kinetics, it would be interesting to conduct the first step of hydrogenation, i.e., the formation of cyclohexanone in an acidic medium and then increase the pH to basic values to facilitate the formation of cyclohexanol. The conditioning charge influences the amount of chemisorbed hydrogen available for the hydrogenation of the organic compound. This work has identified yet another advantage of ECH versus CH, owing to the fact that the production of chemisorbed hydrogen is systematic in the ECH process.

## Acknowledgements

We are thankful to “Coopération France–Burkina Faso”, to the French Government Funding, and to Université de Sherbrooke for the financial and material support they provided.

## References

- (1) Ruest, L.; Ménard, H.; Moreau, V.; Laplante, F. *Can. J. Chem.* **2002**, *80* (12), 1662. doi:10.1139/v02-182.
- (2) Tsyganok, A. I.; Otsuko, K. *Appl. Cat. B Environ.* **1999**, *22* (1), 15. doi:10.1016/S0926-3373(99)00028-4.
- (3) Robin, D.; Comtois, M.; Martel, A.; Lemieux, R.; Cheong, A. K.; Belot, G.; Lessard, J. *Can. J. Chem.* **1990**, *68* (7), 1218. doi:10.1139/v90-189.
- (4) Martel, A.; Mahdavi, B.; Lessard, J.; Ménard, H.; Brossard, L. *Can. J. Chem.* **1997**, *75* (12), 1862. doi:10.1139/v97-619.
- (5) Jaksic, M. M. *Electrochim. Acta* **2000**, *19*, 4085.
- (6) Laplante, F.; Brossard, L.; Ménard, H. *Can. J. Chem.* **2003**, *81* (3), 258. doi:10.1139/v03-027.
- (7) St-Pierre, G.; Chagnes, A.; Bouchard, N.-A.; Harvey, P. D.; Brossard, L.; Ménard, H. *Langmuir* **2004**, *20* (15), 6365. doi:10.1021/la048977v. PMID:15248724.
- (8) Cirtiu, C. M.; Hassani, H. O.; Bouchard, N. A.; Rowntree, P. A.; Ménard, H. *Langmuir* **2006**, *22* (14), 6414. doi:10.1021/la0519002. PMID:16800708.
- (9) Cirtiu, C. M.; Brisach-Wittmeyer, A.; Ménard, H. *J. Catal.* **2007**, *245* (1), 191. doi:10.1016/j.jcat.2006.10.010.
- (10) Cheong, A. K.; Bolduc, Y.; Lessard, J. *Can. J. Chem.* **1993**, *71* (11), 1850. doi:10.1139/v93-232.
- (11) Dubé, P.; Kerdouss, F.; Laplante, F.; Proulx, P.; Brossard, L.; Ménard, H. *J. Appl. Electrochem.* **2003**, *33* (6), 541. doi:10.1023/A:1024495505252.
- (12) Santana, D. S.; Melo, G. O.; Lima, M. V. F.; Daniel, J. R. R.; Areias, M. C. C.; Navarro, M. J. *Electroanal. Chem.* **2004**, *569* (1), 71. doi:10.1016/j.jelechem.2004.02.015.
- (13) Fichter, F.; Stocker, R. *Ber. Bunsenges. Phys. Chem* **1914**, *47* (2), 2003. doi:10.1002/cber.19140470296.
- (14) Misra, R. A.; Sharma, B. L. *Electrochim. Acta* **1979**, *24* (6), 727. doi:10.1016/0013-4686(79)87058-9.
- (15) Laplante, F.; Brossard, L.; Ménard, H. *Can. J. Chem.* **2003**, *81* (3), 258. doi:10.1139/v03-027.
- (16) Mahdavi, B.; Chambion, P.; Binette, J.; Martel, E.; Lessard, J. *Can. J. Chem.* **1995**, *73* (6), 846. doi:10.1139/v95-105.
- (17) Tountian, D.; Brisach-Wittmeyer, A.; Nkeng, P.; Poillerat, G.; Ménard, H. *J. Appl. Electrochem.* **2009**, *39* (3), 411. doi:10.1007/s10800-008-9686-0.
- (18) Bannari, A.; Cirtiu, C.; Kerdouss, F.; Proulx, P.; Ménard, H. *Chem. Eng. Process.* **2006**, *45* (6), 471. doi:10.1016/j.cep.2005.11.007.
- (19) Weast, R. C., Ed. In *Handbook of Chemistry and Physics*, 56th ed.; 1975–1976; p. D-142.
- (20) Martinez, A. I.; Acosta, D. R.; Cedillo, G. *Thin Solid Films* **2005**, *490* (2), 118. doi:10.1016/j.tsf.2005.04.060.
- (21) Farrow, J. B.; Warren, L. J. *Colloids Surf.* **1988**, *34* (3), 255. doi:10.1016/0166-6622(88)80104-5.
- (22) Wismeijer, A. A.; Kieboom, A. P. G.; Van Bekkum, H. *Recl. Trav. Chim. Pays Bas* **1986**, *105*, 129.
- (23) Koeberg-Telder, A.; Lambrechts, H. J. A.; Cerfontain, H. *Recl. Trav. Chim. Pays Bas* **1983**, *102*, 293.
- (24) Feiring, A. E. *J. Org. Chem.* **1977**, *42* (20), 3255. doi:10.1021/jo00440a012.
- (25) Mador, I. L.; Rosan, A. M.; Crissey, R. K. *J. Catal.* **1984**, *87* (1), 276. doi:10.1016/0021-9517(84)90187-8.
- (26) Breitner, E.; Roginski, E.; Rylander, P. N. *J. Org. Chem.* **1959**, *24* (12), 1855. doi:10.1021/jo01094a004.
- (27) Wendt, H. In *Electrochemical Hydrogen Technologies*; Elsevier, Amsterdam, 1990.
- (28) Enyo, M. In *Comprehensive Treatise of Electrochemistry*; Conway, B. E.; Bockris, J. O'M., Yeager, E., and White, R. E., Eds.; Plenum Press: New York, 1983.
- (29) Kirilyus, I. V.; Zhuk, M. A. *Sov. Electrochem.* **1972**, *8*, 967.



# Synthesis and structures of isopropyl- $\beta$ -diketiminato copper(I) complexes

Paul O. Oguadinma and Frank Schaper

**Abstract:** The reaction of *N,N'*-diisopropyl-2-amino-4-iminopent-2-ene (nacnac<sup>*i*-Pr</sup>H, **1**) either with CuOt-Bu or with a mixture of mesityl copper and 10% CuOt-Bu afforded, in the presence of PPh<sub>3</sub>, CN(C<sub>6</sub>Me<sub>2</sub>H<sub>3</sub>), or MeCN, the Lewis base coordinated complexes nacnac<sup>*i*-Pr</sup>CuPPh<sub>3</sub>·0.5 C<sub>6</sub>H<sub>14</sub> (**2**), nacnac<sup>*i*-Pr</sup>CuCN(C<sub>6</sub>Me<sub>2</sub>H<sub>3</sub>) (**3**), and nacnac<sup>*i*-Pr</sup>Cu(NCMe) (**4**). Compounds **2**, **3**, and **4** were characterized by single-crystal X-ray diffraction studies. Compound **4** afforded two species in deuterated benzene in a 2:1 ratio, which were assigned to {nacnac<sup>*i*-Pr</sup>Cu}<sub>2</sub>( $\mu$ -NCMe) and nacnac<sup>*i*-Pr</sup>CuNCMe (**4**). Upon addition of 5 equiv. of MeCN, the two sets collapsed into that of **4**. No copper complexes were formed in the presence of styrene, stilbene, or diphenylacetylene.

**Key words:** diketiminate, copper, coordination chemistry.

**Résumé :** La réaction du *N,N'*-diisopropyl-2-amino-4-iminopent-2-ène (nacnac<sup>*i*-Pr</sup>H, **1**) avec le CuOt-Bu ou un mélange du mésityl-cuivre et du CuOt-Bu à 10 % a donné, en présence de PPh<sub>3</sub>, de CN(C<sub>6</sub>Me<sub>2</sub>H<sub>3</sub>) ou de MeCN, les complexes nacnac<sup>*i*-Pr</sup>CuPPh<sub>3</sub>·0,5 C<sub>6</sub>H<sub>14</sub> (**2**), nacnac<sup>*i*-Pr</sup>CuCN(C<sub>6</sub>Me<sub>2</sub>H<sub>3</sub>) (**3**), et nacnac<sup>*i*-Pr</sup>Cu(NCMe) (**4**). Les composés **2**, **3** et **4** ont été caractérisés par diffraction des rayons-X sur monocristaux. Le spectre RMN de **4** dans C<sub>6</sub>D<sub>6</sub> comporte deux séries de signaux selon un rapport 2:1, assignés à {nacnac<sup>*i*-Pr</sup>Cu}<sub>2</sub>( $\mu$ -NCMe) et à nacnac<sup>*i*-Pr</sup>CuNCMe (**4**). Après l'addition de 5 equiv. de MeCN, seuls les signaux de **4** ont été observés. Aucun complexe de cuivre n'a été obtenu en présence de styrène, de stilbène ou de diphenylacétylène.

**Mots-clés :** dikétiminate, cuivre, chimie de coordination.

## Introduction

Brookhart's demonstration in the mid 1990s that late transition-metal  $\alpha$ -diimine complexes of Pd and Ni were effective as catalysts in olefin polymerization<sup>1</sup> paved the way for the synthesis of the corresponding anionic diketiminate versions of these ligand systems.<sup>2</sup> Since then, interest in diketiminates has continued unabatedly, and today  $\beta$ -diketiminate represent one of the most extensively employed nitrogen-based, bidentate ligands in coordination chemistry.<sup>3</sup> The acronym "nacnac" is often used to describe 2-amino-4-iminopent-2-ene, which is the N-analogue of the ubiquitous acetylacetonate (acac). The nacnac ligands are monoanionic spectator ligands, which have assisted in the isolation of metal complexes in unusual oxidation states and (or) coordination numbers.<sup>4</sup> For copper in particular, Tolman and co-workers used diketiminate complexes to model the active site of metalloproteins.<sup>5</sup> Warren and co-workers isolated a nacnac copper carbene complex, which they employed in catalytic cyclopropanation, and used copper diketiminates for amination reactions.<sup>6–8</sup> While most applications of diketiminate ligands revolve around N-aryl substituents, their N-alkyl derivatives have not been well-exploited. For copper(I), they are limited to applications in atomic layer deposition<sup>9</sup> or analyses of copper–ligand bonding.<sup>10</sup> In continuation of previous work on diketiminate copper complexes with N-alkyl substituents,<sup>11,12</sup> we report here the

syntheses and characterization of *N,N'*-diisopropyl nacnac Cu<sup>I</sup> complexes. Just prior to submission of this manuscript, Arai et al. reported nacnac<sup>*i*-Pr</sup>Cu germylene complexes, using the same ligand.<sup>13</sup>

## Results and discussion

### Ligand and complex synthesis

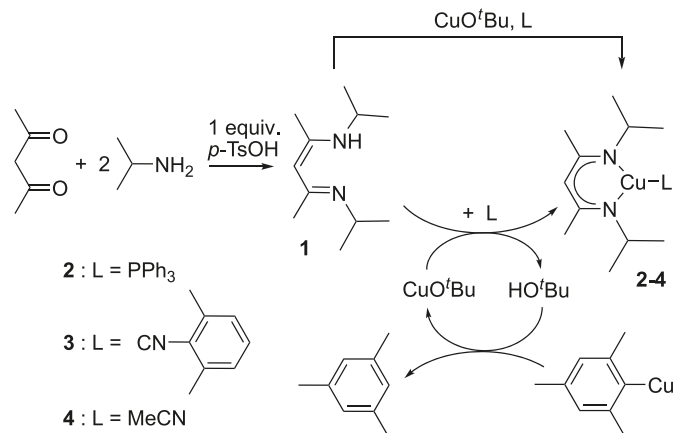
Ligand **1** has been obtained previously by a multi-step protocol, which is generally used to prepare *N*-alkyl diketiminates, either by employing Meerwein salt (32%–60% yield)<sup>14</sup> or dimethylsulfate (74% yield, from the aminoketone)<sup>15</sup> as O-alkylating agents. We employed a one-step procedure for condensation of acetylacetone with isopropylamine in the presence of equimolar amounts of *para*-toluenesulfonic acid,<sup>16</sup> which afforded **1** directly, albeit in a relatively low yield of 23% after 5 days of reflux (Scheme 1). The analogous ligands nacnac<sup>Bu</sup>H and nacnac<sup>*i*-Bu</sup>H, bearing primary alkyl groups, have been obtained in 1–2 days using the same procedure,<sup>12,17</sup> while the preparation of nacnac<sup>CH(Me)Ph</sup>H required 5 days.<sup>11</sup> Longer reaction times thus seem to be necessary for secondary amines. Complexes **2–4** were obtained as yellow air- and moisture-sensitive powders or crystals in 26%–84% yield by reaction of **1** in the presence of PPh<sub>3</sub>, xylol isocyanide, or acetonitrile either with CuOt-Bu, a procedure employed by Dai and Warren for preparing *N*-aryl nacnacCu<sup>I</sup> complexes,<sup>6</sup> or with mesityl copper and catalytic

Received 15 October 2009. Accepted 6 January 2010. Published on the NRC Research Press Web site at canjchem.nrc.ca on 10 April 2010.

P.O. Oguadinma and F. Schaper.<sup>1</sup> Département de chimie, Université de Montréal, Montréal, QC H3C 3J7, Canada.

<sup>1</sup>Corresponding author (e-mail: Frank.Schaper@umontreal.ca).

Scheme 1.



amounts of  $\text{CuO}^t\text{Bu}$  (Scheme 1). Mesityl copper in the absence of  $\text{CuO}^t\text{Bu}$  has been shown to be unreactive.<sup>11</sup> Though no major differences in terms of yields were observed between the use of  $\text{CuO}^t\text{Bu}$  or  $\text{MesCu}/\text{CuO}^t\text{Bu}$ , the complexes crystallized easier when  $\text{MesCu}/\text{CuO}^t\text{Bu}$  was used, probably due to the smaller amounts of *tert*-butanol present.

Compound **1** did not react with  $\text{CuO}^t\text{Bu}$  in the presence of styrene, stilbene, or diphenylacetylene. Identical observations were made with copper complexes carrying the chiral  $\text{nacnac}^{\text{CH}(\text{Me})\text{Ph}}$  ligand.<sup>11</sup> On the other hand, Cu–styrene complexes are readily obtained with  $\text{nacnac}^{\text{Mes}}$  ( $\text{Mes} = 2,4,6\text{-Me}_3\text{C}_6\text{H}_3$ )<sup>18</sup> or  $\text{nacnac}^{\text{dipp}}$  ( $\text{dipp} = 2,6\text{-}i\text{-Pr}_2\text{C}_6\text{H}_3$ , see Experimental section), one of the most sterically encumbered *N*-aryl diketiminates, as well as with  $\text{nacnac}^{\text{Bn}}$  or  $\text{nacnac}^i\text{-Bu}$ .<sup>12,17</sup> In-plane coordination of the two carbon atoms of an olefin is thus possible for diketimate ligands with aryl or primary alkyl substituents, but not if secondary alkyls are present on the nitrogen. The implied increased steric demand of  $\text{nacnac}^i\text{-Pr}$  compared with  $\text{nacnac}^{\text{dipp}}$  has to be set into contrast to observations for other systems. When compared with  $\text{nacnac}^{\text{dipp}}$ , diketimate ligands with secondary alkyl substituents on the nitrogen allow additional intramolecular  $\pi$ -coordination in Ti complexes<sup>19</sup> or coordination of a second  $\text{nacnac}$  to Zr.<sup>20</sup> When considering steric congestion imposed by diketimate ligands, it is thus important to differentiate between the first coordination sphere around the metal centre, where  $\text{nacnac}^i\text{-Pr}$  imposes a congested environment, and general steric demand in the (outer) coordination sphere, where it does not.

### Crystal structure studies

All three compounds are monomeric and crystallize in the  $P2_1/c$  space group with copper in a distorted trigonal-planar geometry. Complex **2** (Fig. 1) co-crystallizes with half a molecule of hexane. The methine hydrogen atoms of the *i*-Pr substituent point towards the methyl groups in the ligand backbone, even in the sterically encumbered **2**. C–N and C–C bond lengths of the diketimate ligand are in agreement with complete delocalization of the double bonds (Table 1). Cu–N bond distances in **3** and **4** are close to the average generally observed in  $\text{nacnacCu}$  complexes ( $1.94 \pm 0.06 \text{ \AA}$ ),<sup>21</sup> and the copper centre is found in the mean plane of the ligand. With the bulkier phosphine ligand in **2**, longer Cu–N distances and a displacement of C3 and the copper atom

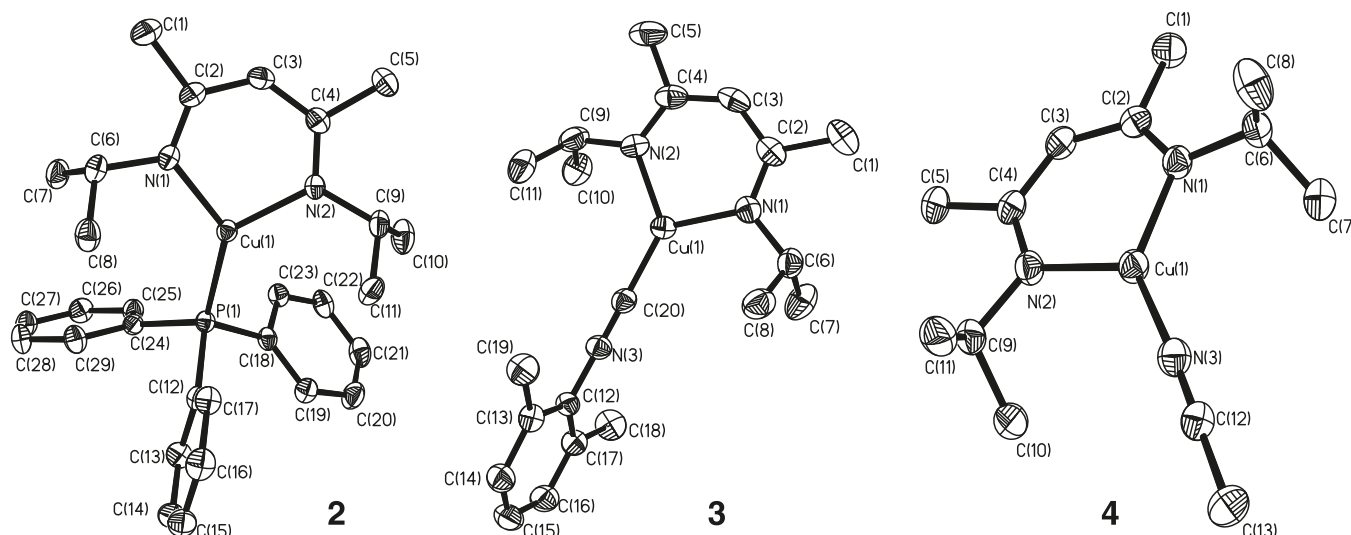
by 0.1 and 0.4  $\text{\AA}$ , respectively, out of the ligand mean plane are observed (plane defined by N1, N2, C2, and C4). While Cu–P and Cu–N bond distances (2.191(1)  $\text{\AA}$ ; 1.978(1) and 1.983(1)  $\text{\AA}$ ) are comparable to those in  $\text{nacnac}^{\text{CH}(\text{Me})\text{Ph}}\text{CuPPh}_3$  (2.195(1)  $\text{\AA}$ ; 1.972(1) and 1.983(1)  $\text{\AA}$ ),<sup>11</sup> they are longer than in  $\text{nacnac}^{\text{Ar}}\text{Cu}(\text{PPh}_3)$  complexes (2.16–2.18  $\text{\AA}$  and 1.94–1.97  $\text{\AA}$ )<sup>7,22–24</sup> in agreement with increased steric bulk introduced by a secondary alkyl substituent on the nitrogen atoms.

### Spectroscopic properties

The  $\text{PPh}_3$  resonance in the  $^{31}\text{P}$  NMR spectrum of compound **2** in  $\text{C}_6\text{D}_6$  was observed at  $\delta$  4.0. This value is intermediate between those of  $\text{nacnac}^{\text{Ar}}\text{CuPPh}_3$  complexes ( $\text{Ar} = \text{Me}_3\text{C}_6\text{H}_2$ : 5.2 ppm,<sup>7</sup>  $\text{Ar} = \text{Me}_2\text{C}_6\text{H}_3$ : 5.4 ppm,<sup>23</sup> and  $\text{Ar} = i\text{-Pr}_2\text{C}_6\text{H}_3$ : 3.6 ppm<sup>22</sup>) and  $\text{nacnac}^{\text{R}}\text{CuPPh}_3$  complexes ( $\text{R} = \text{Bn}$ : 3.5 ppm<sup>12</sup> and  $\text{R} = \text{CH}(\text{Me})\text{C}_6\text{H}_5$ : 3.9 ppm<sup>11</sup>). While *N*-aryl-substituted diketimate ligands tend to show  $^{31}\text{P}$  resonances at lower field, differences are too small to be correlated to the ligand properties. Similar to the behaviour observed for  $\text{nacnac}^{\text{CH}(\text{Me})\text{Ph}}\text{Cu}(\text{NCMe})$ ,<sup>11</sup> which also carries a secondary alkyl substituent on N, pure crystals of **4** dissolved in  $\text{C}_6\text{D}_6$  gave two sets of  $\text{nacnac}$  resonances in a ratio of 2:1 in its  $^1\text{H}$  NMR spectrum; the resonances of the major species being slightly broadened. Only one resonance was observed for MeCN. Fast exchange of coordinated and free Lewis base was observed before in  $\text{nacnacCuL}$  complexes,<sup>11,12,25</sup> and the amount of coordinated MeCN in the two species thus cannot be derived from NMR. Only one peak for  $\nu_{\text{CN}}$  was observed at 2259  $\text{cm}^{-1}$  in the IR spectrum of **4** in toluene solution, 5  $\text{cm}^{-1}$  higher than that of free MeCN.<sup>26</sup> Addition of excess MeCN (5 equiv.) caused the peaks to collapse to one set of resonances in its  $^1\text{H}$  and  $^{13}\text{C}$  spectra, belonging to the previously minor component. Changes in the overall concentration, on the other hand, did not affect the observed ratio, which rules out equilibrium [1] in Scheme 2. Complete MeCN redistribution (equilibrium [2] in Scheme 2) also seems unlikely, since bis(acetonitrile) complexes have not been reported for diketimate copper complexes and  $\text{nacnac}^i\text{-PrCu}$  complexes could not be obtained in the absence of ancillary ligands. We thus assign the species favoured at higher acetonitrile concentrations to the MeCN complex  $\text{nacnac}^i\text{-PrCuNCMe}$  (**4**), observed in the crystal structure, and the broadened peaks of the major species to the bridged complex  $\{\text{nacnac}^i\text{-PrCu}\}_2(\mu\text{-NCMe})$  (**4b**) (equilibrium [3] in Scheme 2). While bridging coordination of acetonitrile is rare, it is not unknown.<sup>27</sup> Monomer–dimer equilibria similar to equilibrium [3] in Scheme 2 have been observed for  $\text{nacnac}^{\text{Bn}}\text{Cu}$ , which forms a diphenylacetylene-bridged dimer in the solid state and a monomeric complex in solution when excess diphenylacetylene is present,<sup>12</sup> and for  $\text{nacnac}^{\text{Ar}}\text{Cu}$  complexes, which display an equilibrium between a monomeric and a dimeric benzene-coordinated complex in solution.<sup>7,25</sup> While single-crystal diffraction studies confirmed the formation of **4**, we were unable to obtain satisfactory elemental analyses, even from the crystalline material. Synthesis of **4** was reported at the time of submission of this article by Arii et al. from the reaction of  $[\text{Cu}(\text{NCMe})_4][\text{CF}_3\text{SO}_3]$  with  $\text{nacnac}^i\text{-PrLi}$ .<sup>13</sup> Although not discussed therein, they also observed a variable ratio of two products in NMR spectra of **4**.<sup>28</sup>

The stretching frequency  $\nu_{\text{CN}} = 2105 \text{ cm}^{-1}$  of the isocyanide

**Fig. 1.** Crystal structures of **2–4**. Hydrogen atoms and solvent are omitted for clarity. Thermal ellipsoids are drawn at the 50% probability level.



**Table 1.** Selected bond distances (Å) and bond angles (°) for **2**, **3**, and **4**.

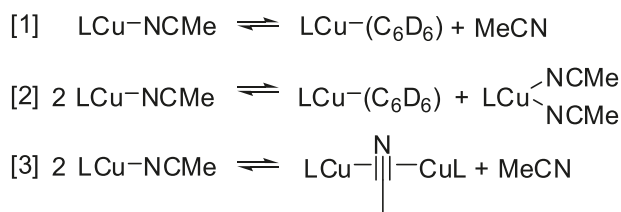
	<b>2</b>	<b>3</b>	<b>4</b>
<b>Bond distances (Å)</b>			
Cu1—N1	1.978(1)	1.939(2)	1.940(1)
Cu1—N2	1.987(1)	1.935(2)	1.961(2)
Cu1—X <sup>a</sup>	2.191(1)	1.822(2)	1.893(2)
N1—C2	1.323(2)	1.332(2)	1.326(3)
N2—C4	1.321(2)	1.331(2)	1.314(3)
C2—C3	1.408(2)	1.407(3)	1.413(3)
C3—C4	1.411(2)	1.407(3)	1.416(2)
X—Y <sup>b</sup>	1.839(2)	1.161(2)	1.148(3)
<b>Bond angles (°)</b>			
N1—Cu1—N2	97.7(1)	100.2(1)	100.6(1)
N1—Cu1—X <sup>c</sup>	132.6(1)	130.9(1)	134.7(1)
N2—Cu1—X <sup>c</sup>	129.4(1)	128.9(1)	124.8(1)

<sup>a</sup>Cu1—P1 (**2**), Cu1—C20 (**3**), and Cu1—N3 (**4**).

<sup>b</sup>Average of P1—C12, P1—C18, and P1—C24 (**2**), N3—C20 (**3**), N3—C12 (**4**).

<sup>c</sup>N1,2—Cu1—P1 (**2**), N1,2—Cu1—C20 (**3**), N1,2—Cu1—N3 (**4**).

## Scheme 2.



ligand in **3** is the lowest frequency observed in 2,6-xylyl isocyanide copper complexes with either N-alkyl-substituted ( $\nu_{\text{CN}} = 2111\text{--}2117 \text{ cm}^{-1}$ )<sup>11,12,17</sup> or N-aryl-substituted diketiminate ligands ( $\nu_{\text{CN}} = 2121\text{--}2126 \text{ cm}^{-1}$ )<sup>7,25,29</sup> indicating an increased, but still weak  $\pi$  back-donation (free isocyanide:  $\nu_{\text{CN}} = 2119 \text{ cm}^{-1}$ ).

In the course of preparing compound **3**, a minor side

product, **5**, was obtained. <sup>1</sup>H and <sup>13</sup>C NMR spectra of **5** showed resonances of the diketiminate ligand and isocyanide in a ratio of 1:2, which would suggest the formation of  $\text{nacnac}^i\text{-PrCu}(\text{CNC}_6\text{Me}_2\text{H}_3)_2$ . Satisfactory elemental analysis of **5**, however, could not be obtained and, more importantly, addition of 1 equiv. xylyl isocyanide did not transform **3** into **5**. Complex **5** showed the same stretching frequency in its IR spectrum as **3**. Taking also the low solubility of **5** in toluene into account, assignment as a bisisocyanide adduct seems improbable and the structure of **5** remains unclear.

## Conclusions

Copper complexes of  $\text{nacnac}^i\text{-Pr}$  were readily prepared if additional Lewis base was present to stabilize the complex. In agreement with observations made for  $\text{nacnac}^{\text{CH}(\text{Me})\text{Ph}}$ ,<sup>11</sup> diketiminate ligands with secondary alkyl substituents are slightly more Lewis-basic, but sterically more demanding in the first coordination sphere than diketiminates with aryl or primary alkyl substituents.

## Experimental section

All reactions, except ligand synthesis, were carried out under nitrogen atmosphere using Schlenk or glovebox techniques. Solvents were dried by passage through activated aluminum oxide (MBraun SPS) and de-oxygenated by repeated extraction with nitrogen.  $\text{C}_6\text{D}_6$  was distilled from Na and de-oxygenated by three freeze-pump-thaw cycles.  $\text{CuOt-Bu}^{30}$  and mesitylcopper<sup>31</sup> were synthesized as reported. All other chemicals were obtained from commercial suppliers and used as received. Elemental analyses were performed at the Laboratoire d'Analyse Élémentaire (Université de Montréal). NMR spectra were recorded on a Bruker ARX 400 MHz spectrometer and referenced to residual solvent ( $\text{C}_6\text{D}_5\text{H}$ :  $\delta$  7.15,  $\text{C}_6\text{D}_6$ :  $\delta$  128.02) or external reference (<sup>31</sup>P, 75%  $\text{H}_3\text{PO}_4$ ).

### $\text{nacnac}^i\text{-PrH}$ (**1**)<sup>14,15</sup>

Acetylacetone (4.0 mL, 38 mmol), *para*-toluenesulfonic

**Table 2.** Details of X-ray diffraction studies.

Complex	<b>2</b>	<b>3</b>	<b>4</b>
CCDC No.	764335	764336	764337
Formula	C <sub>29</sub> H <sub>36</sub> CuN <sub>2</sub> P·(C <sub>6</sub> H <sub>14</sub> ) <sub>0.5</sub>	C <sub>20</sub> H <sub>30</sub> CuN <sub>3</sub>	C <sub>13</sub> H <sub>24</sub> CuN <sub>3</sub>
<i>M<sub>r</sub></i> (g/mol); <i>d<sub>calcd.</sub></i> (g/cm <sup>3</sup> )	550.19; 1.247	376.01; 1.239	285.89; 1.277
<i>T</i> (K); <i>F</i> (000)	150 ; 1172	150; 800	150; 608
Crystal system	Monoclinic	Monoclinic	Monoclinic
Space group	<i>P</i> 2 <sub>1</sub> / <i>c</i>	<i>P</i> 2 <sub>1</sub> / <i>c</i>	<i>P</i> 2 <sub>1</sub> / <i>c</i>
Unit cell			
<i>a</i> (Å)	13.9417(4)	8.9807(3)	6.8103(1)
<i>b</i> (Å)	12.4813(4)	13.3632(4)	11.4563(3)
<i>c</i> (Å)	17.8496(6)	16.9799(5)	19.1252(3)
$\beta$ (°)	109.348(1)	98.320(1)	94.780(1)
<i>V</i> (Å <sup>3</sup> ); <i>Z</i>	2930.60(16); 4	2016.33(11); 4	1486.97(5); 4
$\theta$ range (°); completeness	3.36–73.61; 0.99	4.23–71.45; 0.99	4.50–67.82; 0.93
Reflections: collec./indep.; <i>R<sub>int</sub></i>	41989/5843; 0.037	24118/3879; 0.038	23408/2512; 0.034
$\mu$ (mm <sup>−1</sup> ); abs. corr.	1.72; SADABS	1.55; SADABS	1.93; SADABS
<i>R</i> <sub>1</sub> ( <i>F</i> ); <i>wR</i> ( <i>F</i> <sup>2</sup> ); GoF( <i>F</i> <sup>2</sup> ) <sup>a</sup>	0.0348; 0.0959; 1.052	0.0413; 0.1128; 1.00	0.0308; 0.0906; 1.067
Residual electron density	0.68; −0.38	0.32; −0.36	0.32; −0.51

<sup>a</sup>*R*<sub>1</sub>(*F*) based on observed reflections with *I* > 2σ(*I*), *wR*(*F*<sup>2</sup>) and GoF(*F*<sup>2</sup>) based on all data.

acid monohydrate (7.2 g, 38 mmol), and isopropylamine (6.1 mL, 76 mmol) were added to toluene (200 mL) and refluxed with the help of a Dean–Stark apparatus for 5 days, during which the yellow suspension turned brown. After cooling to room temperature, the brown precipitate formed was filtered. The precipitate was washed with toluene (100 mL) and transferred to a K<sub>2</sub>CO<sub>3</sub> solution (5 g in 100 mL of water). After stirring for 30 min, the aqueous phase was extracted with toluene (3 × 100 mL). The combined organic phases were dried over MgSO<sub>4</sub> and then filtered. The filtrate was evaporated to obtain brown oil (1.6 g, 23%), which was employed without further purification in subsequent synthesis.

<sup>1</sup>H NMR (CDCl<sub>3</sub>, 400 MHz)  $\delta$ : 11.44 (bs, 1H, NH), 4.38 (s, 1H, HC(C=N)<sub>2</sub>), 3.64 (sp, *J* = 6 Hz, 2H, CH(CH<sub>3</sub>)<sub>2</sub>), 1.89 (s, 6H, Me(C=N)<sub>2</sub>), 1.16 (d, *J* = 6 Hz, 12H, CH(CH<sub>3</sub>)<sub>2</sub>). <sup>13</sup>C NMR (CDCl<sub>3</sub>, 101 MHz)  $\delta$ : 158.5 (C=N), 93.5 (HC(C=N)<sub>2</sub>), 46.7 (CH(CH<sub>3</sub>)<sub>2</sub>), 24.7 (CH(CH<sub>3</sub>)<sub>2</sub>), 18.7 (Me(C=N)<sub>2</sub>). <sup>1</sup>H NMR (C<sub>6</sub>D<sub>6</sub>, 400 MHz)  $\delta$ : 11.63 (bs, 1H, NH), 4.46 (s, 1H, HC(C=N)<sub>2</sub>), 3.46 (sp, *J* = 6 Hz, 2H, CH(CH<sub>3</sub>)<sub>2</sub>), 1.71 (s, 6H, Me(C=N)<sub>2</sub>), 1.11 (d, *J* = 6 Hz, 12H, CH(CH<sub>3</sub>)<sub>2</sub>). <sup>13</sup>C NMR (C<sub>6</sub>D<sub>6</sub>, 101 MHz)  $\delta$ : 158.0 (C=N), 94.6 (HC(C=N)<sub>2</sub>), 47.0 (CH(CH<sub>3</sub>)<sub>2</sub>), 25.1 (CH(CH<sub>3</sub>)<sub>2</sub>), 18.8 (Me(C=N)<sub>2</sub>).

#### nacnac<sup>i</sup>-PrCuPPh<sub>3</sub>·0.5 C<sub>6</sub>H<sub>14</sub> (**2**)

nacnac<sup>i</sup>-PrH (300 mg, 1.65 mmol), mesitylcopper (301 mg, 1.65 mmol), CuOt-Bu (22 mg, 0.165 mmol), and PPh<sub>3</sub> (437 mg, 1.65 mmol) were dissolved in toluene (12 mL) to give a yellow-brown solution. After stirring for 1 h, the solution was filtered, concentrated to 1/5 of its volume and layered with hexane (5 mL). It was then kept at −35 °C. Yellow crystals together with powder formed after 3 day (700 mg, 84%).

<sup>1</sup>H NMR (C<sub>6</sub>D<sub>6</sub>, 400 MHz)  $\delta$ : 7.66–7.02 (m, 15H, PPh<sub>3</sub>), 4.67 (s, 1H, HC(C=N)<sub>2</sub>), 3.86 (sp, *J* = 6 Hz, 2H, CH(CH<sub>3</sub>)<sub>2</sub>), 2.10 (s, 6H, Me(C=N)<sub>2</sub>), 0.98 (d, *J* = 6 Hz, 12H, CH(CH<sub>3</sub>)<sub>2</sub>). <sup>13</sup>C NMR (C<sub>6</sub>D<sub>6</sub>, 101 MHz)  $\delta$ : 161.3 (C=N), 135.1 (d, *J* = 30 Hz, *ipso* PPh<sub>3</sub>), 134.7 (d, *J* = 14 Hz, *ortho* PPh<sub>3</sub>), 129.7 (*para* PPh<sub>3</sub>), 128.6 (d, *J* = 9 Hz, *ortho* PPh<sub>3</sub>), 95.4

(HC(C=N)<sub>2</sub>), 51.4 (CH(CH<sub>3</sub>)<sub>2</sub>), 26.7 (CH(CH<sub>3</sub>)<sub>2</sub>), 23.1 (Me(C=N)<sub>2</sub>). <sup>31</sup>P NMR (C<sub>6</sub>D<sub>6</sub>, 75 MHz)  $\delta$ : 4.0. Anal. Calcd. for C<sub>29</sub>H<sub>36</sub>N<sub>2</sub>PCu: C, 68.68; H, 7.15; N, 5.52. Found: C, 67.85; H, 7.48; N, 4.97.

#### nacnac<sup>i</sup>-PrCuCN(C<sub>6</sub>Me<sub>2</sub>H<sub>3</sub>) (**3**)

nacnac<sup>i</sup>-PrH (200 mg, 1.10 mmol), mesitylcopper (201 mg, 1.10 mmol), CuOt-Bu (15 mg, 0.11 mmol), and xylol isocyanide (151 mg, 1.15 mmol) were dissolved in toluene (4 mL). The yellow-brown solution was stirred for 1 h and then concentrated to half its volume to afford a yellow-brown suspension. The suspension was filtered, and the filtrate was layered with 4 mL of hexanes and kept at −35 °C. Yellow crystals of **3** formed after 1 day (190 mg, 46%).

IR (toluene)  $\nu_{\text{CN}}$ : 2114 cm<sup>−1</sup>. <sup>1</sup>H NMR (C<sub>6</sub>D<sub>6</sub>, 400 MHz)  $\delta$ : 6.75 (t, *J* = 8 Hz, 2H, *p*-CN(C<sub>6</sub>Me<sub>2</sub>H<sub>3</sub>)), 6.59 (d, *J* = 8 Hz, *m*-CN(C<sub>6</sub>Me<sub>2</sub>H<sub>3</sub>), 2H), 4.60 (s, 1H, HC(C=N)<sub>2</sub>), 4.01 (septet, *J* = 6 Hz, CH(CH<sub>3</sub>)<sub>2</sub>, 2H), 2.11 (s, 6H, Me(C=N)<sub>2</sub>), 2.08 (s, 6H, CN(C<sub>6</sub>Me<sub>2</sub>H<sub>3</sub>), 1.42 (d, 12H, *J* = 6 Hz, CH(CH<sub>3</sub>)<sub>2</sub>). <sup>13</sup>C NMR (C<sub>6</sub>D<sub>6</sub>, 101 MHz)  $\delta$ : 160.7 (C=N), 134.8, 94.8 (HC(C=N)<sub>2</sub>), 50.9 (CH(CH<sub>3</sub>)<sub>2</sub>), 27.5 (CH(CH<sub>3</sub>)<sub>2</sub>), 22.3 (Me(C=N)<sub>2</sub>), 18.8 (CN(C<sub>6</sub>Me<sub>2</sub>H<sub>3</sub>)). (CN(C<sub>6</sub>Me<sub>2</sub>H<sub>3</sub>) and three aromatic resonances were not detected). Anal. Calcd. for C<sub>20</sub>H<sub>30</sub>N<sub>3</sub>Cu: C, 63.88; H, 8.04; N, 11.17. Found: C, 63.83; H, 8.11; N, 11.12.

The solid obtained after filtration, **5**, gave the following data: IR (toluene)  $\nu_{\text{CN}}$ : 2114 cm<sup>−1</sup>. <sup>1</sup>H NMR (C<sub>6</sub>D<sub>6</sub>, 400 MHz)  $\delta$ : 6.69 (t, *J* = 8 Hz, *p*-CN(C<sub>6</sub>Me<sub>2</sub>H<sub>3</sub>), 2H), 6.52 (d, *J* = 8 Hz, *m*-CN(C<sub>6</sub>Me<sub>2</sub>H<sub>3</sub>), 4H), 4.61 (s, 1H, HC(C=N)<sub>2</sub>), 4.02 (septet, *J* = 6 Hz, CH(CH<sub>3</sub>)<sub>2</sub>, 2H), 2.14 (s, 12H, CN(C<sub>6</sub>Me<sub>2</sub>H<sub>3</sub>), 2.08 (s, 6H, Me(C=N)<sub>2</sub>), 1.43 (d, 12H, *J* = 6 Hz, CH(CH<sub>3</sub>)<sub>2</sub>). <sup>13</sup>C NMR (C<sub>6</sub>D<sub>6</sub>, 101 MHz)  $\delta$ : 160.7 (C=N), 135.4, 128.6, 128.1, 127.8, 94.8 (HC(C=N)<sub>2</sub>), 50.8 (CH(CH<sub>3</sub>)<sub>2</sub>), 27.5 (CH(CH<sub>3</sub>)<sub>2</sub>), 22.4 (Me(C=N)<sub>2</sub>), 18.8. (CN(C<sub>6</sub>Me<sub>2</sub>H<sub>3</sub>)). (CN(C<sub>6</sub>Me<sub>2</sub>H<sub>3</sub>) elusive).

#### nacnac<sup>i</sup>-PrCuNCMe (**4**)

nacnac<sup>i</sup>-PrH (75 mg, 0.41 mmol) and MeCN (41 mg,



0.82 mmol) were mixed and transferred to a vial containing a yellow solution of CuOt-Bu (69 mg, 0.41 mmol) in toluene (2 mL). The resulting yellow-brown solution was kept at  $-30\text{ }^{\circ}\text{C}$ . Colourless crystals formed after 1 h together with a brown precipitate (mirror) indicative of decomposition. Decantation of the brown suspension gave, after drying, 31 mg (26%) of yellow crystals, **4**.

Two species were observed in  $\text{C}_6\text{D}_6$  solutions of **4** (see text). IR (toluene)  $\nu_{\text{NC}}$ :  $2259\text{ cm}^{-1}$ . **4**:  $^1\text{H}$  NMR ( $\text{C}_6\text{D}_6$ , 400 MHz)  $\delta$ : 4.52 (s, 1H,  $\text{HC}(\text{C}=\text{N})_2$ ), 4.03 (septet,  $J = 6\text{ Hz}$ ,  $\text{CH}(\text{CH}_3)_2$ , 2H), 2.11 (s, 6H,  $\text{Me}(\text{C}=\text{N})_2$ ), 1.38–1.52 (m, 12H,  $\text{CH}(\text{CH}_3)_2$ ), 0.57 (NCMe).  $^{13}\text{C}$  NMR ( $\text{C}_6\text{D}_6$ , 101 MHz)  $\delta$ : 160.6 (C=N), 116.5 (NCMe), 65.9 ( $\text{HC}(\text{C}=\text{N})_2$ ), 50.7 ( $\text{CH}(\text{CH}_3)_2$ ), 26.9 ( $\text{CH}(\text{CH}_3)_2$ ), 22.3 ( $\text{Me}(\text{C}=\text{N})_2$ ) and 0.3 (NCMe). **4b**:  $^1\text{H}$  NMR ( $\text{C}_6\text{D}_6$ , 400 MHz)  $\delta$ : 5.29 (bs, 1H,  $\text{HC}(\text{C}=\text{N})_2$ ), 3.92–3.99 (featureless septet,  $\text{CH}(\text{CH}_3)_2$ , 2H), 2.56 (bs, 6H,  $\text{Me}(\text{C}=\text{N})_2$ ), 2.08 (s, 6H,  $\text{CN}(\text{C}_6\text{Me}_2\text{H}_3)$ ) and 1.38–1.52 (m, 12H,  $\text{CH}(\text{CH}_3)_2$ ) overlapping with that of **4**. Elemental analysis was unsatisfactory with varying results ( $\Delta\text{C} = 2\%–3\%$ ), which might be related to acetonitrile dissociation and complex decomposition.

#### NMR-scale preparation of $\text{nacnac}^{\text{dipp}}\text{Cu}(\text{styrene})$

A vial was charged with  $\text{nacnac}^{\text{dipp}}\text{H}$  ( $\text{dipp} = 2,6\text{-}i\text{-Pr}_2\text{C}_6\text{H}_3$ ) (10 mg, 24  $\mu\text{mol}$ ), CuOt-Bu (4 mg, 30  $\mu\text{mol}$ ), and styrene (3  $\mu\text{L}$ , 25  $\mu\text{mol}$ ).  $\text{C}_6\text{D}_6$  (0.6–0.7 mL) was added. After shaking thoroughly to obtain a homogeneous solution, the content was transferred to a J. Young tube and heated at  $60\text{ }^{\circ}\text{C}$  for 24 h.

$^1\text{H}$  NMR ( $\text{C}_6\text{D}_6$ , 400 MHz)  $\delta$ : 6.35–7.21 (m, 11H,  $2,6\text{-}i\text{-Pr}_2\text{C}_6\text{H}_3$  and styrene), 5.08 (dd,  $J = 9\text{ Hz}$  and  $14\text{ Hz}$ , 1H,  $\text{PhHC}=\text{C}$ ), 4.97 (s, 1H,  $\text{HC}(\text{C}=\text{N})_2$ ), 3.48–3.56 (m, 3H,  $\text{CH}(\text{CH}_3)_2$  and  $\text{cis H}_2\text{C}=\text{C}$ ), 3.34 (d,  $J = 9\text{ Hz}$ , 1H,  $\text{trans H}_2\text{C}=\text{C}$ ), 3.07 (sp,  $J = 7\text{ Hz}$ , 2H,  $\text{CH}(\text{CH}_3)_2$ ), 1.75 (s, 6H,  $\text{Me}(\text{C}=\text{N})_2$ ), 1.33 (d,  $J = 7\text{ Hz}$ , 6H,  $\text{CH}(\text{CH}_3)_2$ ), 1.15 (d,  $J = 7\text{ Hz}$ , 12H,  $\text{CH}(\text{CH}_3)_2$ ), 1.09 (d,  $J = 7\text{ Hz}$ , 6H,  $\text{CH}(\text{CH}_3)_2$ ).

#### X-ray diffraction studies

Compounds were crystallized by layering a toluene solution with hexane at  $-30\text{ }^{\circ}\text{C}$ , except for compound **4**, which crystallized directly from the toluene solution of the reaction at  $-30\text{ }^{\circ}\text{C}$ . Data sets for **2** and **3** were recorded on a Bruker SMART 6000 with Montel 200 monochromator, while that of compound **4** was collected on a Bruker Microstar-Proteum with Helios optics, both equipped with a rotating anode source for Cu  $K\alpha$  radiation ( $\lambda = 1.54178\text{ \AA}$ ). Cell refinement and data reduction were performed using APEX2.<sup>32</sup> Absorption corrections were applied using SADABS.<sup>33</sup> Structures were solved by direct methods using SHELXS97 and refined on  $F^2$  by full-matrix least squares using SHELXL97.<sup>34</sup> All non-hydrogen atoms were refined anisotropically. Hydrogen atoms were refined on calculated positions using a riding model. Further details can be found in Table 2.

#### Supplementary data

Supplementary data for this article are available on the journal Web site ([canjchem.nrc.ca](http://canjchem.nrc.ca)) or may be purchased from the Depository of Unpublished Data, Document Delivery, CISTI, National Research Council Canada, Ottawa, ON K1A 0R6, Canada. DUD 5390. For more information on ob-

taining material, refer to [cisti-icist.nrc-cnrc.gc.ca/cms/unpub\\_e.shtml](http://cisti-icist.nrc-cnrc.gc.ca/cms/unpub_e.shtml). CCDCs 764335–764337 contain the X-ray data in CIF format for this manuscript. These data can be obtained, free of charge, via [www.ccdc.cam.ac.uk/conts/retrieving.html](http://www.ccdc.cam.ac.uk/conts/retrieving.html) (Or from the Cambridge Crystallographic Data Centre, 12 Union Road, Cambridge CB2 1EZ, UK; fax +44 1223 336033; or [deposit@ccdc.cam.ac.uk](mailto:deposit@ccdc.cam.ac.uk)).

#### Acknowledgements

Financial support from the Natural Sciences and Engineering Research Council of Canada (NSERC) and the Université de Montréal is gratefully acknowledged.

#### References

- (1) Johnson, L. K.; Killian, C. M.; Brookhart, M. *J. Am. Chem. Soc.* **1995**, *117* (23), 6414. doi:10.1021/ja00128a054.
- (2) Feldman, J.; McLain, S. J.; Parthasarathy, A.; Marshall, W. J.; Calabrese, J. C.; Arthur, S. D. *Organometallics* **1997**, *16* (8), 1514. doi:10.1021/om960968x.
- (3) Bourget-Merle, L.; Lappert, M. F.; Severn, J. R. *Chem. Rev.* **2002**, *102* (9), 3031. doi:10.1021/cr010424r. PMID: 12222981.
- (4) (a) Lee, L. W. M.; Piers, W. E.; Elsegood, M. R. J.; Clegg, W.; Parvez, M. *Organometallics* **1999**, *18* (16), 2947. doi:10.1021/om9903801.; (b) Cui, C.; Roesky, H. W.; Schmidt, H.-G.; Noltemeyer, M.; Hao, H.; Cimpoesu, F. *Angew. Chem. Int. Ed. Engl.* **2000**, *39* (23), 4274. doi:10.1002/1521-3773(20001201)39:23<4274::AID-ANIE4274>3.0.CO;2-K.; (c) Hardman, N. J.; Eichler, B. E.; Power, P. P. *Chem. Commun. (Camb.)* **2000**, (20): 1991. doi:10.1039/b005686n.; (d) Smith, J. M.; Lachicotte, R. J.; Holland, P. L. *Chem. Commun. (Camb.)* **2001**, (17): 1542. doi:10.1039/b103635c. PMID:12240372.; (e) Smith, J. M.; Lachicotte, R. J.; Pittard, K. A.; Cundari, T. R.; Lukat-Rodgers, G.; Rodgers, K. R.; Holland, P. L. *J. Am. Chem. Soc.* **2001**, *123* (37), 9222. doi:10.1021/ja016094+.; (f) Fekl, U.; Kaminsky, W.; Goldberg, K. I. *J. Am. Chem. Soc.* **2001**, *123* (26), 6423. doi:10.1021/ja0156690.; (g) Neculai, A. M.; Neculai, D.; Roesky, H. W.; Magull, J.; Baldus, M.; Andronesi, O.; Jansen, M. *Organometallics* **2002**, *21* (13), 2590. doi:10.1021/om020090b.; (h) Kogut, E.; Wienko, H. L.; Zhang, L.; Cordeau, D. E.; Warren, T. H. *J. Am. Chem. Soc.* **2005**, *127* (32), 11248. doi:10.1021/ja0533186.
- (5) (a) Holland, P. L.; Tolman, W. B. *J. Am. Chem. Soc.* **1999**, *121* (31), 7270. doi:10.1021/ja991533e.; (b) Holland, P. L.; Tolman, W. B. *J. Am. Chem. Soc.* **2000**, *122* (26), 6331. doi:10.1021/ja001328v.; (c) Hong, S.; Gupta, A. K.; Tolman, W. B. *Inorg. Chem.* **2009**, *48* (14), 6323. doi:10.1021/ic900435p.; (d) York, J. T.; Llobet, A.; Cramer, C. J.; Tolman, W. B. *J. Am. Chem. Soc.* **2007**, *129* (25), 7990. doi:10.1021/ja071744g.
- (6) Dai, X.; Warren, T. H. *J. Am. Chem. Soc.* **2004**, *126* (32), 10085. doi:10.1021/ja047935q. PMID:15303885.
- (7) Badiei, Y. M.; Warren, T. H. *J. Organomet. Chem.* **2005**, *690* (24–25), 5989. doi:10.1016/j.jorganchem.2005.07.098.
- (8) Badiei, Y. M.; Dinescu, A.; Dai, X.; Palomino, R. M.; Heinemann, F. W.; Cundari, T. R.; Warren, T. H. *Angew. Chem. Int. Ed.* **2008**, *47* (51), 9961. doi:10.1002/anie.200804304.
- (9) Park, K.-H.; Bradley, A. Z.; Thompson, J. S.; Marshall, W. J. *Inorg. Chem.* **2006**, *45* (21), 8480. doi:10.1021/ic061016e. PMID:17029355.
- (10) Aullón, G.; Alvarez, S. *Eur. J. Inorg. Chem.* **2004**, 4430. doi:10.1002/ejic.200400206.; (b) Thompson, J. S.; Bradley,

- A. Z.; Park, K. H.; Dobbs, K. D.; Marshall, W. *Organometallics* **2006**, 25 (11), 2712. doi:10.1021/om060162p.
- (11) Oguadinma, P. O.; Schaper, F. *Organometallics* **2009**, 28 (14), 4089. doi:10.1021/om9002279.
- (12) Oguadinma, P. O.; Schaper, F. *Organometallics* **2009**, 28 (23), 6721. doi:10.1021/om900840f.
- (13) Arii, H.; Nakadate, F.; Mochida, K. *Organometallics* **2009**, 28 (17), 4909. doi:10.1021/om9006196.
- (14) (a) McGeachin, S. G. *Can. J. Chem.* **1968**, 46 (11), 1903. doi:10.1139/v68-315.; (b) Drees, D.; Magull, J. Z. *Anorg. Allg. Chem.* **1995**, 621 (6), 948. doi:10.1002/zaac.19956210608.; (c) Kuhn, N.; Fahl, J.; Fuchs, S.; Steimann, M.; Henkel, G.; Maulitz, A. H. Z. *Anorg. Allg. Chem.* **1999**, 625 (12), 2108. doi:10.1002/(SICI)1521-3749(199912)625:12<2108::AID-ZAAC2108>3.0.CO;2-K.; (d) Tian, X.; Goddard, R.; Pörschke, K. R. *Organometallics* **2006**, 25 (25), 5854. doi:10.1021/om0606486.
- (15) Bradley, A. Z.; Thorn, D. L.; Glover, G. V. *J. Org. Chem.* **2008**, 73 (21), 8673. doi:10.1021/jo801691m. PMID: 18844410.
- (16) Budzelaar, P. H. M.; de Gelder, R.; Gal, A. W. *Organometallics* **1998**, 17 (19), 4121. doi:10.1021/om980580x.
- (17) Ased, A.; Oguadinma, P. O.; Schaper, F. Unpublished results.
- (18) Dai, X.; Warren, T. H. *Chem. Commun. (Camb.)* **2001**, (19): 1998. doi:10.1039/b105244f.
- (19) Nikiforov, G. B.; Roesky, H. W.; Magull, J.; Labahn, T.; Vidovic, D.; Noltemeyer, M.; Schmidt, H.-G.; Hosmane, N. S. *Polyhedron* **2003**, 22 (19), 2669. doi:10.1016/S0277-5387(03)00345-0.
- (20) (a) El Zoghbi, I.; Latreche, S.; Schaper, F. *Organometallics* **2010**, in press. doi:10.1021/om900852y.; (b) El Zoghbi, I.; Verguet, E.; Oguadinma, P. O.; Schaper, F. *Inorg. Chem. Commun.* **2010**, 13, 529. doi:10.1016/j.inoche.2010.01.029.
- (21) Based on 32 nacnac copper(I) complexes with a non-chelating ancillary ligand in the Cambridge Structural Database: Allen, F. H. *Acta Crystallogr. B* **2002**, B58, 380.
- (22) Reynolds, A. M.; Lewis, E. A.; Aboelella, N. W.; Tolman, W. B. *Chem. Commun. (Camb.)* **2005**, (15): 2014. doi:10.1039/b418939f. PMID:15834490.
- (23) York, J. T.; Young, V. G., Jr.; Tolman, W. B. *Inorg. Chem.* **2006**, 45 (10), 4191. doi:10.1021/ic060050q. PMID: 16676981.
- (24) Aboelella, N. W.; Gherman, B. F.; Hill, L. M. R.; York, J. T.; Holm, N.; Young, V. G., Jr.; Cramer, C. J.; Tolman, W. B. *J. Am. Chem. Soc.* **2006**, 128 (10), 3445. doi:10.1021/ja057745v. PMID:16522125.
- (25) Oguadinma, P. O.; Schaper, F. *Inorg. Chim. Acta* **2009**, 362 (2), 570. doi:10.1016/j.ica.2008.05.008.
- (26) (a) Cho, H.-G.; Cheong, B.-S.; Kim, K.-W. *Bull. Korean Chem. Soc.* **1998**, 19, 909; (b) Jamroz, D.; Stangret, J.; Lindgren, J. *J. Am. Chem. Soc.* **1993**, 115 (14), 6165. doi:10.1021/ja00067a036.
- (27) (a) Eglin, J. L.; Marie Hines, E.; Valente, E. J.; Zubkowski, J. D. *Inorg. Chim. Acta* **1995**, 229 (1-2), 113. doi:10.1016/0020-1693(94)04235-N.; (b) Cotton, F. A.; Kuhn, F. E. *J. Am. Chem. Soc.* **1996**, 118 (24), 5826. doi:10.1021/ja954262q.; (c) Cotton, F. A.; Daniels, L. M.; Murillo, C. A.; Wang, X. *Polyhedron* **1998**, 17 (17), 2781. doi:10.1016/S0277-5387(97)00470-1.; (d) Li, B.; Xu, S.; Song, H.; Wang, B. *J. Organomet. Chem.* **2008**, 693 (1), 87. doi:10.1016/j.jorganchem.2007.10.026.
- (28) Arii, H.; Mochida, K. Personal communication, 2009.
- (29) Jazdzewski, B. A.; Holland, P. L.; Pink, M.; Young, V. G., Jr.; Spencer, D. J. E.; Tolman, W. B. *Inorg. Chem.* **2001**, 40 (24), 6097. doi:10.1021/ic010615c. PMID:11703106.
- (30) Tsuda, T.; Hashimoto, T.; Saegusa, T. *J. Am. Chem. Soc.* **1972**, 94 (2), 658. doi:10.1021/ja00757a069.
- (31) (a) Tsuda, T.; Yazawa, T.; Watanabe, K.; Fujii, T.; Saegusa, T. *J. Org. Chem.* **1981**, 46 (1), 192. doi:10.1021/jo00314a048.; (b) Haakansson, M.; Oertendahl, M.; Jagner, S.; Sigalas, M. P.; Eisenstein, O. *Inorg. Chem.* **1993**, 32 (10), 2018. doi:10.1021/ic00062a025.
- (32) APEX2, Release 2.1-0; Bruker AXS Inc.: Madison, USA, 2006.
- (33) Sheldrick, G. M. *SADABS*; Bruker AXS Inc.: Madison, USA, 1996 and 2004.
- (34) Sheldrick, G. M. *Acta Crystallogr.* **2008**, A64, 112.

# A novel approach towards the synthesis of tricyclic systems based on pyridine, pyran, thiopyran, azepine, oxepin, thiepin, and pyrimidine rings under different solvent conditions

Anand Sachar, Poonam Gupta, Shallu Gupta, and R.L. Sharma

**Abstract:** Synthesis of some oxygen, nitrogen, and sulfur based condensed heterocycles by the condensation of dimedone with aromatic monoaldehyde under different solvent conditions has been achieved.

**Key words:** dimedone, heterocyclization, dimerization.

**Résumé :** On a réalisé la synthèse de dérivés hétérocycliques à base d'oxygène, d'azote et de soufre par condensation de la dimédone avec un monoaldéhyde aromatique dans divers solvants.

**Mots-clés :** dimédone, hétérocyclisation, dimérisation.

[Traduit par la Rédaction]

## Introduction

1,3-Dicarbonyl derivatives constitute important synthetic intermediates, incorporating multiple functionalities that can be either nucleophilic or electrophilic species in a large variety of synthetic transformations.<sup>1</sup> Their versatility and effectiveness as potential multicomponent substrates were first discovered and utilized by Arthur Hantzsch<sup>2</sup> in 1882. Since then, 1,3-dicarbonyl compounds have been playing increasingly significant roles in the development of modern synthetic organic chemistry. Keeping these facts in view, we are studying the synthesis of some novel heterocyclic systems by investigating the effect of a change in solvent on the ring size of heterocyclic moiety via the condensation of a 1,3-dicarbonyl compound (dimedone) with an aromatic monoaldehyde. A literature survey revealed that a fair amount of work has been published in the condensation reactions of dimedone.<sup>3–8</sup> Because of our laboratory's long standing interest in the condensation reactions of active methylene compounds,<sup>9</sup> we extend our synthetic activity along these lines to include the synthesis of some pyran, pyridine, thiopyran, oxepin, azepine, and thiepin based condensed heterocycles by the condensation of dimedone with aromatic monoaldehyde under different solvent conditions.<sup>5,10–15</sup> The intermediates and the final heterocyclic products have been found to be highly potent pharmacologically in recent years, revealing some important conclusions regarding structure–activity relationships.<sup>16–19</sup>

## Results and discussion

When dimedone was treated with aromatic monoaldehyde

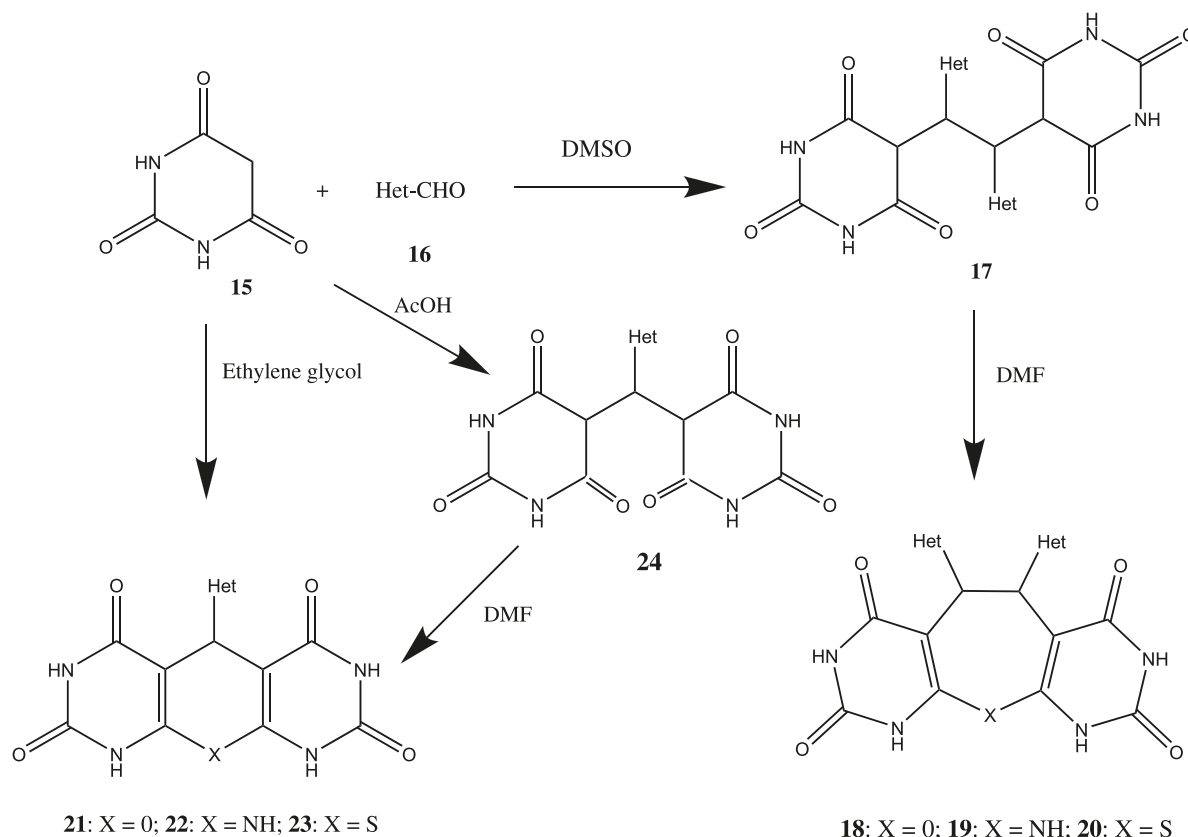
in ethylene glycol under different sets of conditions (as detailed in the Experimental section); some novel pyran, pyridine, and thiopyran based condensed heterocycles have been generated with dimedone moiety on the periphery of the molecule. The reaction probably takes place via the concerted mechanism in which Knoevenagel condensation occurs between dimedone (**1**) and aromatic aldehydes (**2**), Michael addition of the second dimedone molecule on the 2-arylidenedimedone probably formed in situ as a result of Knoevenagel condensation, and cyclodehydration of the probable Michael product (**9**)<sup>20,21</sup> takes place in single step. The products (**10–14**)<sup>20,22–25</sup> were obtained in excellent yield but the intermediate products, arylidenedimedone of Knoevenagel condensation, and product (**9**) of Michael addition could not be isolated. In another method using acetic acid as solvent in the initial step, the yield of the final products (**10–14**) was not as good and hardly comparable with that in the case of ethylene glycol. The added advantage in this method was the isolation of the intermediate product (**9**) in a reasonably good yield, which was probably in dienol form, and subsequently produced the products (**10–14**) with different reagents using DMF as solvent. The yield falls slightly in all the conversions of **9** to **10**, **11**, **12**, **13**, and **14** using DMF as solvent. Using DMSO as solvent, some interesting results were obtained in which arylidenedimedone moiety initially formed and underwent reductive dimerization to give the dimer (**3**) (Scheme 1). In each case, the dimer (**3**) was obtained as a mixture of a racemate and the inactive meso compound. The racemic mixture ( $\pm$ ) and the inactive meso compound could not be resolved and separated, respectively, by repeated efforts. The asymmetric synthesis of

Received 6 July 2009. Accepted 24 November 2009. Published on the NRC Research Press Web site at canjchem.nrc.ca on 15 April 2010.

A. Sachar, P. Gupta, S. Gupta, and R. Sharma.<sup>1</sup> Department of Chemistry, University of Jammu, Jammu – 180 006, India.

<sup>1</sup>Corresponding author (e-mail: rlsharma\_hod@rediffmail.com).

Scheme 1.



Het : 3-Indolyl, 2-Furfuryl

the enantiomers has almost been achieved in a separate study with good variety. Though it is still under active study, it may soon be submitted for publication. The dimers seemed to be very interesting for ring closure and as such were subjected to heterocyclization under different sets of conditions (as detailed in the Experimental section) in DMF to give some condensed heterocycles based on central oxepin, azepine, and thiopin moiety and the peripheral dimedone moiety. The condensed heterocyclic products (4–8) bearing seven membered central heterocyclic moiety were all obtained, again as single and pure meso compounds since the possibility of cyclization of the enantiomers of the racemic mixture of **3** resulting in the formation of a mixture of racemic (4–8) is not only highly difficult but almost impossible.

Exact quantities of  $\text{NH}_2\text{OH}\cdot\text{HCl}$  in the synthesis of *N*-hydroxy compounds,  $\text{NH}_2\cdot\text{NH}_2$  in the synthesis of *N*-amino compounds, and  $\text{P}_2\text{S}_5$  in the synthesis of thio compounds should be used lest their higher quantities should form corresponding oximino, hydrazino, and thioxo derivatives, respectively, of the respective carbonyl products (6–8, 12–14, 20, and 23).

To generalize these transformations and to derive the conclusions more confidently, reactions between a heterocyclic active methylene compound, barbituric acid (replacing dimedone), and heteroaromatic aldehydes, furfural and indole-3-carboxaldehyde (both replacing aromatic aldehydes), were also studied (Scheme 2). The results were exactly the same

as expected under different conditions of solvents and reagents.

All the compounds obtained (17–24) were analyzed for C, H, N, and S and were found to be in good agreement with the calculated values, which have been presented in Table 1, along with mps and yield. The structures were established on the basis of spectroscopic data and elemental analysis.

## Experimental

### General

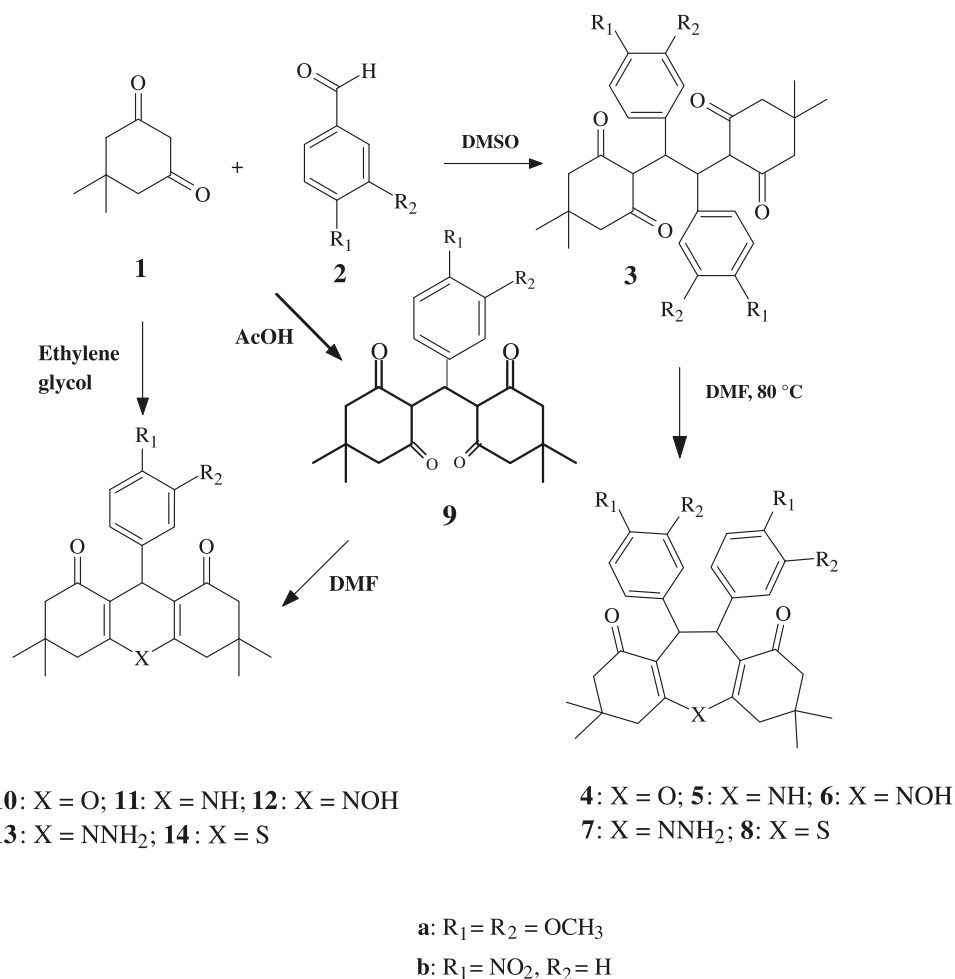
Thin layer chromatography was used to establish the homogeneity of the compounds. Column chromatography was performed over silica gel (60–120 mesh) using the ethyl acetate – petroleum ether system as eluent. All other reagents were commercially available and used without further purification. Melting points were determined in a capillary tube and are uncorrected. IR spectra were recorded on a PerkinElmer IR spectrometer using potassium bromide pellets. The  $^1\text{H}$  and  $^{13}\text{C}$  NMR spectra were run on Varian Unity 500 MHz NMR spectrometer using TMS as an internal standard (chemical shift in  $\delta$  ppm). Elemental analyses were performed on simple a CHNS analyzer.

### General procedure for the synthesis of 3

Dimedone (2 mmol) and aromatic aldehyde (2 mmol) were dissolved in dimethyl sulfoxide (1 mL) and the reaction mixture was refluxed for 30–40 min. The clear reaction



Scheme 2.



mixture was diluted with methanol (20 mL). The insoluble product was separated by filtration, washed with methanol (3 × 20 mL), and then finally dried at 100 °C for 1 h.

#### General procedure for the synthesis of 4–8

Compound **3** (0.01 mol) was stirred at 80° in DMF for 30 min (for **4**: as such; for **5**: 3 mmol NH<sub>4</sub>OAc; for **6**: 2 mmol NH<sub>2</sub>OH·HCl and 2 mmol NaOAc; for **7**: 2 mmol NH<sub>2</sub>·NH<sub>2</sub>·HCl and 2 mmol NaOAc; and for **8**: 2 mmol P<sub>2</sub>S<sub>5</sub> was added). The reaction mixture was cooled to room temperature, diluted with water, the insoluble product filtered and then the solid obtained was washed with water, dried, and crystallized from ethanol. Further purification was accomplished by running it through a short column of silica gel followed by recrystallization from hot ethanol.

#### General method for the synthesis<sup>20,21</sup> of 9a and 9b

Dimedone (0.02 mol) and an aromatic aldehyde (0.01 mol) were dissolved in glacial acetic acid (30 mL) and stirred at room temperature until TLC showed the disappearance of the starting material. The insoluble product was separated by filtration, washed with water (3 × 20 mL), dried, and crystallized from 95% ethanol. Further purification was accomplished by running it through a short column of silica gel followed by recrystallization from ethanol.

#### General procedure for the synthesis<sup>20,22–25</sup> of 10–14

Dimedone (4 mmol) and an aldehyde (2 mmol) were refluxed in an ethylene glycol (1 mL) for 8–10 min (for **10**: as such; for **11**: 3 mmol NH<sub>4</sub>OAc; for **12**: 2 mmol NH<sub>2</sub>OH·HCl and 2 mmol NaOAc; for **13**: 2 mmol NH<sub>2</sub>·NH<sub>2</sub>·HCl and 2 mmol NaOAc; and for **14**: 2 mmol P<sub>2</sub>S<sub>5</sub> was added). The reaction mixture was allowed to cool at room temperature, then poured into 50 mL of water. The solid that was separated was filtered and washed with water. The crude solid after drying was purified by recrystallization from 95% EtOH to give **10**, **11**, **12**, **13**, and **14**.

#### 2-[1,2-Bis(3,4-dimethoxyphenyl)-2-(4,4-dimethyl-2,6-dioxocyclohexyl)ethyl]-5,5-dimethylcyclohexane-1,3-dione (3a)

Recrystallized from methanol, mp 232–236 °C. IR (KBr, cm<sup>-1</sup>): 3410, 3040, 2944, 2860, 2594, 1580, 1460, 1410, 1370, 1296, 1235, 1132, 1050, 972, 870, 790. <sup>1</sup>H NMR (DMSO-*d*<sub>6</sub>) δ: 1.10 (s, 6H, 2 × CH<sub>3</sub>), 1.20 (s, 6H, 2 × CH<sub>3</sub>), 2.30–2.52 (m, 8H, 4 × CH<sub>2</sub>), 3.82 (s, 6H, OCH<sub>3</sub>), 3.86 (s, 6H, OCH<sub>3</sub>), 5.47 (d, 2H, *J* = 6.0 Hz), 5.70 (d, 2H, *J* = 6.0 Hz), 6.96–7.28 (m, 6H, ArH). <sup>13</sup>C NMR (DMSO-*d*<sub>6</sub>) δ: 15.9, 19.3, 27.1, 29.4, 47.4, 54.2, 58.3, 112.6, 115.2, 121.4, 133.5, 144.4, 147.5, 151.0, 160.0, 197.6. Anal. calcd. for C<sub>34</sub>H<sub>42</sub>O<sub>8</sub>: C 70.56, H 7.31; found: C 70.51, H 7.25.

**Table 1.** Physical and analytical data of compounds **17–24**.

Compound	Mp (°C) <sup>a</sup>	Yield (%)	Molecular formula	Analysis (% calcd./found)			
				C	H	N	S
<b>17a</b>	282–284	82	C <sub>26</sub> H <sub>20</sub> N <sub>6</sub> O <sub>6</sub>	60.93 60.89	3.90 3.88	16.40 16.35	
<b>17b</b> <sup>26</sup>	278–282	78	C <sub>18</sub> H <sub>14</sub> N <sub>4</sub> O <sub>8</sub>	52.17 52.12	3.38 3.34	13.52 13.48	
<b>18a</b>	276–282	80	C <sub>26</sub> H <sub>18</sub> N <sub>6</sub> O <sub>5</sub>	63.15 63.09	3.64 3.62	17.0 16.94	
<b>18b</b> <sup>26</sup>	286–290	82	C <sub>18</sub> H <sub>12</sub> N <sub>4</sub> O <sub>7</sub>	54.54 54.51	3.03 3.01	14.14 14.09	
<b>19a</b>	284–288	80	C <sub>26</sub> H <sub>19</sub> N <sub>7</sub> O <sub>4</sub>	63.28 63.23	3.85 3.84	19.87 19.82	
<b>19b</b>	282–286	82	C <sub>18</sub> H <sub>13</sub> N <sub>5</sub> O <sub>6</sub>	54.68 54.62	3.29 3.26	17.72 17.67	
<b>20a</b>	280–284	76	C <sub>26</sub> H <sub>18</sub> N <sub>6</sub> O <sub>4</sub> S	61.17 61.11	3.52 3.51	16.47 16.40	6.27 6.24
<b>20b</b>	286–290	74	C <sub>18</sub> H <sub>12</sub> N <sub>4</sub> O <sub>6</sub> S	52.42 52.36	2.91 2.88	13.59 13.52	6.27 6.25
<b>21a</b>	292–296	80	C <sub>17</sub> H <sub>11</sub> N <sub>5</sub> O <sub>5</sub>	55.89 55.84	3.01 2.98	19.17 19.11	
<b>21b</b> <sup>26</sup>	>300	78	C <sub>13</sub> H <sub>8</sub> N <sub>4</sub> O <sub>6</sub>	49.36 49.32	2.53 2.49	17.72 17.65	
<b>22a</b>	>300	80	C <sub>17</sub> H <sub>12</sub> N <sub>6</sub> O <sub>4</sub>	56.04 56.00	3.29 3.28	23.07 23.01	
<b>22b</b>	>300	82	C <sub>13</sub> H <sub>9</sub> N <sub>5</sub> O <sub>5</sub>	49.52 49.32	2.85 2.49	22.22 19.11	
<b>23a</b>	>300	78	C <sub>17</sub> H <sub>11</sub> N <sub>5</sub> O <sub>4</sub> S	53.54 53.49	2.88 2.84	18.37 18.31	8.39 8.35
<b>23b</b>	>300	76	C <sub>13</sub> H <sub>8</sub> N <sub>4</sub> O <sub>5</sub> S	46.98 46.92	2.40 2.36	16.86 16.81	9.63 9.61
<b>24a</b>	>300	80	C <sub>17</sub> H <sub>13</sub> N <sub>5</sub> O <sub>6</sub>	53.26 53.21	3.39 3.36	18.27 18.22	
<b>24b</b>	>300	84	C <sub>13</sub> H <sub>10</sub> N <sub>4</sub> O <sub>7</sub>	46.70 46.66	2.99 2.97	16.76 16.70	

Note: a: Het = 3-indolyl; b: Het = 2-furyl (Scheme 2).

<sup>a</sup>All compounds were recrystallized from hot ethanol.

**10,11-Bis(3,4-dimethoxyphenyl)-3,3,7,7-tetramethyl-1,2,3,4,6,7,8,9,10,11-decahydrodibenzo[*b,f*]oxepin-1,9-dione (4a)**

Recrystallized from hot ethanol, mp 240–244 °C. IR (KBr, cm<sup>-1</sup>): 3422, 3046, 2950, 2868, 2694, 1588, 1470, 1422, 1376, 1298, 1244, 1150, 1066, 972, 880, 700. <sup>1</sup>H NMR (DMSO-*d*<sub>6</sub>) δ: 1.11 (s, 6H, 2 × CH<sub>3</sub>), 1.24 (s, 6H, 2 × CH<sub>3</sub>), 2.34–2.54 (m, 8H, 4 × CH<sub>2</sub>), 3.80 (s, 6H, OCH<sub>3</sub>), 3.86 (s, 6H, OCH<sub>3</sub>), 5.44 (d, 2H, *J* = 6.0 Hz), 7.02–7.28 (m, 6H, ArH). <sup>13</sup>C NMR (DMSO-*d*<sub>6</sub>) δ: 15.9, 19.4, 27.1, 29.7, 47.7, 54.2, 56.3, 112.6, 115.0, 121.2, 133.4, 147.5, 160.4, 197.7. Anal. calcd. for C<sub>34</sub>H<sub>40</sub>O<sub>7</sub>: C 72.83, H 7.19; found: C 72.78, H 7.14.

**10,11-Bis(3,4-dimethoxyphenyl)-3,3,7,7-tetramethyl-2,3,4,5,6,7,8,9,10,11-decahydro-1*H*-dibenzo[*b,f*]azepine-1,9-dione (5a)**

Recrystallized from hot ethanol, mp 260–264 °C. IR (KBr, cm<sup>-1</sup>): 3420, 3056, 2950, 2862, 2684, 1578, 1475, 1422, 1366, 1290, 1248, 1155, 1068, 976, 880, 704. <sup>1</sup>H NMR (DMSO-*d*<sub>6</sub>) δ: 1.12 (s, 6H, 2 × CH<sub>3</sub>), 1.26 (s, 6H, 2 ×

CH<sub>3</sub>), 2.30–2.50 (m, 8H, 4 × CH<sub>2</sub>), 3.84 (s, 6H, OCH<sub>3</sub>), 3.88 (s, 6H, OCH<sub>3</sub>), 5.46 (d, 2H, *J* = 6.0 Hz), 7.02–7.26 (m, 6H, ArH), 8.20 (s, 1H, NH, exchangeable with D<sub>2</sub>O). <sup>13</sup>C NMR (DMSO-*d*<sub>6</sub>) δ: 15.4, 19.6, 27.7, 29.7, 47.7, 54.2, 56.3, 112.6, 115.0, 121.4, 134.4, 148.5, 160.2, 196.4. Anal. calcd. for C<sub>34</sub>H<sub>41</sub>NO<sub>6</sub>: C 72.96, H 7.38, N 2.50; found: C 72.78, H 7.34, N 2.46.

**10,11-Bis(3,4-dimethoxyphenyl)-5-hydroxy-3,3,7,7-tetramethyl-2,3,4,5,6,7,8,9,10,11-decahydro-1*H*-dibenzo[*b,f*]azepine-1,9-dione (6a)**

Recrystallized from hot ethanol, mp 240–242 °C. IR (KBr, cm<sup>-1</sup>): 3400, 3058, 2964, 2866, 2674, 1576, 1476, 1424, 1368, 1288, 1246, 1156, 1064, 976, 886, 710. <sup>1</sup>H NMR (DMSO-*d*<sub>6</sub>) δ: 1.12 (s, 6H, 2 × CH<sub>3</sub>), 1.26 (s, 6H, 2 × CH<sub>3</sub>), 2.30–2.50 (m, 8H, 4 × CH<sub>2</sub>), 3.84 (s, 6H, OCH<sub>3</sub>), 3.88 (s, 6H, OCH<sub>3</sub>), 5.46 (d, 2H, *J* = 6.0 Hz), 7.02–7.26 (m, 6H, ArH), 10.73 (bs, 1H, OH). <sup>13</sup>C NMR (DMSO-*d*<sub>6</sub>) δ: 15.4, 19.6, 27.4, 29.2, 47.8, 54.2, 56.3, 112.6, 115.1, 121.2, 132.4, 144.5, 161.1, 197.4. Anal. calcd. for C<sub>34</sub>H<sub>41</sub>NO<sub>7</sub>: C 70.93, H 7.17, N 2.43; found: C 72.89, H 7.14, N 2.38.

**5-Amino-10,11-bis(3,4-dimethoxyphenyl)-3,3,7,7-tetramethyl-2,3,4,5,6,7,8,9,10,11-decahydro-1H-dibenzo[*b,f*]azepine-1,9-dione (7a)**

Recrystallized from hot ethanol, mp 270–272 °C. IR (KBr,  $\text{cm}^{-1}$ ): 3410, 3050, 2954, 2865, 2676, 1578, 1466, 1416, 1366, 1286, 1242, 1158, 1066, 976, 880, 716.  $^1\text{H}$  NMR ( $\text{DMSO}-d_6$ )  $\delta$ : 1.14 (s, 6H,  $2 \times \text{CH}_3$ ), 1.22 (s, 6H,  $2 \times \text{CH}_3$ ), 2.34–2.54 (m, 8H,  $4 \times \text{CH}_2$ ), 3.82 (s, 6H,  $\text{OCH}_3$ ), 3.86 (s, 6H,  $\text{OCH}_3$ ), 5.42 (d, 2H,  $J = 6.0$  Hz), 7.02–7.24 (m, 6H, ArH), 8.25 (d, 2H, NH).  $^{13}\text{C}$  NMR ( $\text{DMSO}-d_6$ )  $\delta$ : 15.4, 19.2, 26.1, 29.6, 47.4, 54.2, 56.1, 112.6, 115.0, 121.2, 133.6, 147.2, 160.4, 197.4. Anal. calcd. for  $\text{C}_{34}\text{H}_{42}\text{N}_2\text{O}_6$ : C 71.05, H 7.36, N 4.87; found: C 72.01, H 7.31, N 4.81.

**10,11-Bis(3,4-dimethoxyphenyl)-3,3,7,7-tetramethyl-1,2,3,4,6,7,8,9,10,11-decahydrodibenzo[*b,f*]thiepin-1,9-dione (8a)**

Recrystallized from hot ethanol, mp 240–244 °C. IR (KBr,  $\text{cm}^{-1}$ ): 3426, 3056, 2960, 2864, 2694, 1588, 1470, 1422, 1376, 1298, 1244, 1156, 1068, 976, 880, 700.  $^1\text{H}$  NMR ( $\text{DMSO}-d_6$ )  $\delta$ : 1.11 (s, 6H,  $2 \times \text{CH}_3$ ), 1.24 (s, 6H,  $2 \times \text{CH}_3$ ), 2.34–2.54 (m, 8H,  $4 \times \text{CH}_2$ ), 3.82 (s, 6H,  $\text{OCH}_3$ ), 3.86 (s, 6H,  $\text{OCH}_3$ ), 5.44 (d, 2H,  $J = 6.0$  Hz), 7.02–7.28 (m, 6H, ArH).  $^{13}\text{C}$  NMR ( $\text{DMSO}-d_6$ )  $\delta$ : 15.7, 19.2, 27.2, 29.4, 47.1, 54.2, 56.3, 112.6, 115.0, 121.2, 132.4, 147.4, 160.2, 197.6. Anal. calcd. for  $\text{C}_{34}\text{H}_{40}\text{O}_6\text{S}$ : C 70.80, H 6.99, S 5.66; found: C 70.74, H 6.92, S 5.61.

**2-[(4,4-Dimethyl-2,6-dioxocyclohexyl)(3,4-dimethoxyphenyl)methyl]-5,5-dimethylcyclohexane-1,3-dione (9a)<sup>20</sup>**

Recrystallized from ethanol, mp 172–176 °C. IR (KBr,  $\text{cm}^{-1}$ ): 3440, 3090, 2844, 2866, 2564, 1590, 1470, 1440, 1300, 1292, 1232, 1144, 1040, 972, 870, 790.  $^1\text{H}$  NMR ( $\text{DMSO}-d_6$ )  $\delta$ : 1.12 (s, 6H,  $2 \times \text{CH}_3$ ), 1.20 (s, 6H,  $2 \times \text{CH}_3$ ), 2.30–2.52 (m, 8H,  $4 \times \text{CH}_2$ ), 3.82 (s, 3H,  $\text{OCH}_3$ ), 3.86 (s, 3H,  $\text{OCH}_3$ ), 5.47 (d, 2H,  $J = 6.0$  Hz), 5.70 (1H, s, CH), 6.96–7.28 (m, 3H, ArH).  $^{13}\text{C}$  NMR ( $\text{DMSO}-d_6$ )  $\delta$ : 15.4, 17.7, 26.2, 53.7, 56.4, 68.3, 112.8, 114.4, 119.2, 142.1, 144.4, 147.7, 208.4. Anal. calcd. for  $\text{C}_{24}\text{H}_{30}\text{O}_5$ : C 72.33, H 7.58; found: C 72.29, H 7.53.

**9-(3,4-Dimethoxyphenyl)-3,3,6,6-tetramethyl-2,3,4,5,6,7,8,9-octahydro-1H-xanthene-1,8-dione (10a)<sup>20</sup>**

Recrystallized from 95% ethanol, mp 186–188 °C. IR (KBr,  $\text{cm}^{-1}$ ): 3222, 3066, 2956, 2866, 2664, 1586, 1474, 1424, 1378, 1288, 1246, 1160, 1064, 976, 856, 740.  $^1\text{H}$  NMR ( $\text{DMSO}-d_6$ )  $\delta$ : 1.10 (s, 6H,  $2 \times \text{CH}_3$ ), 1.22 (s, 6H,  $2 \times \text{CH}_3$ ), 2.34–2.52 (m, 8H,  $4 \times \text{CH}_2$ ), 3.82 (s, 3H,  $\text{OCH}_3$ ), 3.86 (s, 3H,  $\text{OCH}_3$ ), 5.42 (d, 1H,  $J = 6.0$  Hz), 7.02–7.28 (m, 3H, ArH).  $^{13}\text{C}$  NMR ( $\text{DMSO}-d_6$ )  $\delta$ : 15.4, 25.2, 27.1, 47.4, 54.2, 56.1, 108.0, 114.4, 130.6, 159.7, 160.6, 198.4. Anal. calcd. for  $\text{C}_{25}\text{H}_{34}\text{O}_5$ : C 72.43, H 8.26; found: C 72.37, H 8.22.

**9-(3,4-Dimethoxyphenyl)-3,3,6,6-tetramethyl-1,2,3,4,5,6,7,8,9,10-decahydroacridine-1,8-dione (11a)<sup>22</sup>**

Recrystallized from 95% ethanol, mp 252–256 °C. IR (KBr,  $\text{cm}^{-1}$ ): 3424, 3066, 2954, 2864, 2686, 1576, 1478, 1422, 1366, 1290, 1248, 1166, 1070, 956, 840, 704.  $^1\text{H}$  NMR ( $\text{DMSO}-d_6$ )  $\delta$ : 1.12 (s, 6H,  $2 \times \text{CH}_3$ ), 1.24 (s, 6H,  $2 \times$

$\text{CH}_3$ ), 2.30–2.50 (m, 8H,  $4 \times \text{CH}_2$ ), 3.84 (s, 3H,  $\text{OCH}_3$ ), 3.88 (s, 3H,  $\text{OCH}_3$ ), 5.46 (d, 1H,  $J = 6.0$  Hz), 7.04–7.24 (m, 3H, ArH), 8.26 (s, 1H, NH, exchangeable with  $\text{D}_2\text{O}$ ).  $^{13}\text{C}$  NMR ( $\text{DMSO}-d_6$ )  $\delta$ : 16.4, 25.3, 27.7, 47.1, 54.2, 56.1, 108.0, 114.1, 130.2, 159.2, 161.6, 197.4. Anal. calcd. for  $\text{C}_{25}\text{H}_{35}\text{NO}_4$ : C 72.60, H 8.53, N 3.38; found: C 72.53, H 8.48, N 3.34.

**9-(3,4-Dimethoxyphenyl)-10-hydroxy-3,3,6,6-tetramethyl-1,2,3,4,5,6,7,8,9,10-decahydroacridine-1,8-dione (12a)<sup>24</sup>**

Recrystallized from 95% ethanol, mp 260–262 °C. IR (KBr,  $\text{cm}^{-1}$ ): 3410, 3068, 2954, 2866, 2674, 1566, 1466, 1428, 1364, 1280, 1260, 1146, 1074, 944, 880, 740.  $^1\text{H}$  NMR ( $\text{DMSO}-d_6$ )  $\delta$ : 1.16 (s, 6H,  $2 \times \text{CH}_3$ ), 1.22 (s, 6H,  $2 \times \text{CH}_3$ ), 2.34–2.54 (m, 8H,  $4 \times \text{CH}_2$ ), 3.84 (s, 3H,  $\text{OCH}_3$ ), 3.88 (s, 3H,  $\text{OCH}_3$ ), 5.46 (d, 1H,  $J = 6.0$  Hz), 7.02–7.26 (m, 3H, ArH), 10.73 (bs, 1H, OH).  $^{13}\text{C}$  NMR ( $\text{DMSO}-d_6$ )  $\delta$ : 15.1, 25.5, 27.2, 47.6, 54.4, 56.1, 108.0, 114.2, 130.2, 159.4, 160.4, 198.4. Anal. calcd. for  $\text{C}_{25}\text{H}_{35}\text{NO}_5$ : C 69.90, H 8.21, N 3.26; found: C 69.84, H 8.16, N 3.22.

**10-Amino-9-(3,4-dimethoxyphenyl)-3,3,6,6-tetramethyl-1,2,3,4,5,6,7,8,9,10-decahydroacridine-1,8-dione (13a)**

Recrystallized from 95% ethanol, mp 270–272 °C. IR (KBr,  $\text{cm}^{-1}$ ): 3420, 3042, 2960, 2864, 2672, 1562, 1462, 1424, 1360, 1284, 1242, 1158, 1066, 946, 882, 727.  $^1\text{H}$  NMR ( $\text{DMSO}-d_6$ )  $\delta$ : 1.14 (s, 6H,  $2 \times \text{CH}_3$ ), 1.22 (s, 6H,  $2 \times \text{CH}_3$ ), 2.34–2.54 (m, 8H,  $4 \times \text{CH}_2$ ), 3.84 (s, 3H,  $\text{OCH}_3$ ), 3.88 (s, 3H,  $\text{OCH}_3$ ), 5.44 (d, 1H,  $J = 6.0$  Hz), 7.06–7.26 (m, 3H, ArH), 8.28 (d, 2H, NH).  $^{13}\text{C}$  NMR ( $\text{DMSO}-d_6$ )  $\delta$ : 15.2, 25.4, 27.2, 47.5, 54.1, 56.2, 108.0, 114.4, 132.6, 159.4, 160.2, 197.4. Anal. calcd. for  $\text{C}_{25}\text{H}_{36}\text{N}_2\text{O}_4$ : C 70.06, H 8.46, N 6.53; found: C 70.01, H 8.48, N 6.48.

**9-(3,4-Dimethoxyphenyl)-3,3,6,6-tetramethyl-2,3,4,5,6,7,8,9-octahydro-1H thioxanthene-1,8-dione (14a)**

Recrystallized from 95% ethanol, mp 234–238 °C. IR (KBr,  $\text{cm}^{-1}$ ): 3426, 3056, 2960, 2864, 2694, 1588, 1470, 1422, 1376, 1298, 1244, 1156, 1068, 976, 880, 700.  $^1\text{H}$  NMR ( $\text{DMSO}-d_6$ )  $\delta$ : 1.11 (s, 6H,  $2 \times \text{CH}_3$ ), 1.24 (s, 6H,  $2 \times \text{CH}_3$ ), 2.34–2.54 (m, 8H,  $4 \times \text{CH}_2$ ), 3.80 (s, 3H,  $\text{OCH}_3$ ), 3.86 (s, 3H,  $\text{OCH}_3$ ), 5.44 (d, 1H,  $J = 6.0$  Hz), 7.02–7.28 (m, 3H, ArH).  $^{13}\text{C}$  NMR ( $\text{DMSO}-d_6$ )  $\delta$ : 15.2, 22.2, 27.4, 47.2, 54.2, 56.1, 108.0, 114.4, 130.6, 159.2, 160.4, 194.4. Anal. calcd. for  $\text{C}_{25}\text{H}_{34}\text{O}_4\text{S}$ : C 69.73, H 7.95, S 7.44; found: C 69.68, H 7.88, S 7.38.

**2-[1,2-Bis(4-nitrophenyl)-2-(4,4-dimethyl-2,6-dioxocyclohexyl)ethyl]-5,5-dimethylcyclohexane-1,3-dione (3b)**

Recrystallized from methanol, mp 238–240 °C. IR (KBr,  $\text{cm}^{-1}$ ): 3400, 3000, 2966, 2840, 2584, 1560, 1468, 1416, 1360, 1296, 1235, 1144, 1080, 976, 840, 786.  $^1\text{H}$  NMR ( $\text{DMSO}-d_6$ )  $\delta$ : 1.10 (s, 6H,  $2 \times \text{CH}_3$ ), 1.20 (s, 6H,  $2 \times \text{CH}_3$ ), 2.30–2.52 (m, 8H,  $4 \times \text{CH}_2$ ), 5.46 (d, 2H,  $J = 6.0$  Hz), 5.72 (d, 2H,  $J = 6.0$  Hz), 6.96–7.28 (m, 8H, ArH).  $^{13}\text{C}$  NMR ( $\text{DMSO}-d_6$ )  $\delta$ : 16.9, 20.3, 28.6, 30.4, 47.5, 112.5, 115.2, 122.4, 131.5, 142.4, 147.5, 150.2, 160.4, 198.6. Anal. calcd. for  $\text{C}_{30}\text{H}_{32}\text{N}_2\text{O}_8$ : C 65.68, H 5.87, N 5.10; found: C 65.62, H 5.81, N 5.06.

**10,11-Bis(4-nitrophenyl)-3,3,7,7-tetramethyl-1,2,3,4,6,7,8,9,10,11-decahydro-dibenzo[*b,f*]oxepin-1,9-dione (4b)**

Recrystallized from hot ethanol, mp 240–244 °C. IR (KBr,  $\text{cm}^{-1}$ ): 3422, 3046, 2950, 2868, 2694, 1588, 1470, 1422, 1376, 1298, 1244, 1150, 1066, 972, 880, 700.  $^1\text{H}$  NMR ( $\text{DMSO}-d_6$ )  $\delta$ : 1.11 (s, 6H,  $2 \times \text{CH}_3$ ), 1.24 (s, 6H,  $2 \times \text{CH}_3$ ), 2.34–2.54 (m, 8H,  $4 \times \text{CH}_2$ ), 5.42 (d, 2H,  $J = 6.0$  Hz), 7.02–7.28 (m, 8H, ArH).  $^{13}\text{C}$  NMR ( $\text{DMSO}-d_6$ )  $\delta$ : 15.9, 19.4, 27.1, 29.7, 47.7, 54.2, 112.6, 115.0, 121.2, 133.4, 147.5, 160.4, 197.7. Anal. calcd. for  $\text{C}_{30}\text{H}_{30}\text{N}_2\text{O}_7$ : C 67.91, H 5.69, N 5.28; found: C 67.87, H 5.64, N 5.23.

**10,11-Bis(4-nitrophenyl)-3,3,7,7-tetramethyl-2,3,4,5,6,7,8,9,10,11-decahydro-1H-dibenzo[*b,f*]azepine-1,9-dione (5b)**

Recrystallized from hot ethanol, mp 260–264 °C. IR (KBr,  $\text{cm}^{-1}$ ): 3420, 3056, 2960, 2862, 2684, 1578, 1475, 1422, 1366, 1290, 1248, 1155, 1068, 976, 880, 704.  $^1\text{H}$  NMR ( $\text{DMSO}-d_6$ )  $\delta$ : 1.12 (s, 6H,  $2 \times \text{CH}_3$ ), 1.26 (s, 6H,  $2 \times \text{CH}_3$ ), 2.30–2.50 (m, 8H,  $4 \times \text{CH}_2$ ), 5.46 (d, 2H,  $J = 6.0$  Hz), 7.02–7.26 (m, 8H, ArH), 8.24 (s, 1H, NH, exchangeable with  $\text{D}_2\text{O}$ ).  $^{13}\text{C}$  NMR ( $\text{DMSO}-d_6$ )  $\delta$ : 15.4, 19.6, 27.7, 29.7, 47.7, 54.2, 112.6, 115.0, 121.4, 134.4, 148.5, 160.2, 196.4. Anal. calcd. for  $\text{C}_{30}\text{H}_{31}\text{N}_3\text{O}_6$ : C 68.03, H 5.90, N 7.93; found: C 67.98, H 5.84, N 7.88.

**10,11-Bis(4-nitrophenyl)-5-hydroxy-3,3,7,7-tetramethyl-2,3,4,5,6,7,8,9,10,11-decahydro-1H-dibenzo[*b,f*]azepine-1,9-dione (6b)**

Recrystallized from hot ethanol, mp 240–242 °C. IR (KBr,  $\text{cm}^{-1}$ ): 3400, 3088, 2964, 2866, 2676, 1576, 1478, 1424, 1368, 1288, 1246, 1156, 1064, 976, 886, 710.  $^1\text{H}$  NMR ( $\text{DMSO}-d_6$ )  $\delta$ : 1.12 (s, 6H,  $2 \times \text{CH}_3$ ), 1.26 (s, 6H,  $2 \times \text{CH}_3$ ), 2.32–2.54 (m, 8H,  $4 \times \text{CH}_2$ ), 5.44 (d, 2H,  $J = 6.0$  Hz), 7.02–7.24 (m, 8H, ArH), 10.72 (bs, 1H, OH).  $^{13}\text{C}$  NMR ( $\text{DMSO}-d_6$ )  $\delta$ : 15.4, 19.6, 27.4, 29.2, 47.8, 54.2, 112.6, 115.1, 121.2, 132.4, 144.5, 161.1, 197.4. Anal. calcd. for  $\text{C}_{30}\text{H}_{31}\text{N}_3\text{O}_7$ : C 66.04, H 5.72, N 7.70; found: C 65.98, H 5.65, N 7.63.

**5-Amino-10,11-bis(4-nitrophenyl)-3,3,7,7-tetramethyl-2,3,4,5,6,7,8,9,10,11-decahydro-1H-dibenzo[*b,f*]azepine-1,9-dione (7b)**

Recrystallized from hot ethanol, mp 266–268 °C. IR (KBr,  $\text{cm}^{-1}$ ): 3410, 3050, 2954, 2865, 2676, 1578, 1466, 1416, 1366, 1286, 1242, 1158, 1066, 976, 880, 716.  $^1\text{H}$  NMR ( $\text{DMSO}-d_6$ )  $\delta$ : 1.14 (s, 6H,  $2 \times \text{CH}_3$ ), 1.22 (s, 6H,  $2 \times \text{CH}_3$ ), 2.34–2.54 (m, 8H,  $4 \times \text{CH}_2$ ), 5.46 (d, 2H,  $J = 6.0$  Hz), 7.02–7.24 (m, 8H, ArH), 8.22 (d, 2H, NH).  $^{13}\text{C}$  NMR ( $\text{DMSO}-d_6$ )  $\delta$ : 15.4, 19.2, 26.1, 29.6, 47.4, 54.2, 112.6, 115.0, 121.2, 133.6, 147.2, 160.4, 197.4. Anal. calcd. for  $\text{C}_{30}\text{H}_{32}\text{N}_4\text{O}_6$ : C 66.16, H 5.92, N 10.28; found: C 66.08, H 7.86, N 10.21.

**10,11-Bis(4-nitrophenyl)-3,3,7,7-tetramethyl-1,2,3,4,5,6,7,8,9,10,11-decahydro-dibenzo[*b,f*]thiepin-1,9-dione (8b)**

Recrystallized from hot ethanol, mp 240–244 °C. IR (KBr,  $\text{cm}^{-1}$ ): 3426, 3056, 2960, 2864, 1588, 1470, 1422, 1376, 1298, 1244, 1156, 1068, 976, 880, 700.  $^1\text{H}$  NMR

( $\text{DMSO}-d_6$ )  $\delta$ : 1.11 (s, 6H,  $2 \times \text{CH}_3$ ), 1.24 (s, 6H,  $2 \times \text{CH}_3$ ), 2.34–2.54 (m, 8H,  $4 \times \text{CH}_2$ ), 5.42 (d, 2H,  $J = 6.0$  Hz), 7.02–7.28 (m, 8H, ArH).  $^{13}\text{C}$  NMR ( $\text{DMSO}-d_6$ )  $\delta$ : 15.7, 19.2, 27.2, 29.4, 47.1, 54.2, 112.6, 115.0, 121.2, 132.4, 147.4, 160.2, 197.6. Anal. calcd. for  $\text{C}_{30}\text{H}_{30}\text{N}_2\text{O}_6\text{S}$ : C 65.91, H 5.53, N 5.12, S 5.86; found: C 65.85, H 5.48, N 5.05, S 5.80.

**2-[(4,4-Dimethyl-2,6-dioxocyclohexyl)(4-nitrophenyl)methyl]-5,5-dimethylcyclohexane-1,3-dione (9b)<sup>21</sup>**

Recrystallized from ethanol, mp 188 °C (decomp), 252 °C. IR (KBr,  $\text{cm}^{-1}$ ): 3440, 3090, 2834, 2868, 2544, 1590, 1472, 1446, 1320, 1282, 1230, 1146, 1060, 974, 870, 790.  $^1\text{H}$  NMR ( $\text{DMSO}-d_6$ )  $\delta$ : 1.14 (s, 6H,  $2 \times \text{CH}_3$ ), 1.22 (s, 6H,  $2 \times \text{CH}_3$ ), 2.34–2.52 (m, 8H,  $4 \times \text{CH}_2$ ), 5.47 (d, 2H,  $J = 6.0$  Hz), 5.70 (1H, s, CH), 7.02–7.24 (m, 4H, ArH).  $^{13}\text{C}$  NMR ( $\text{DMSO}-d_6$ )  $\delta$ : 15.4, 17.7, 26.2, 68.3, 112.8, 114.4, 119.2, 142.1, 144.4, 147.7, 208.4. Anal. calcd. for  $\text{C}_{23}\text{H}_{27}\text{NO}_6$ : C 66.81, H 6.58, N 3.38; found: C 66.76, H 6.54, N 3.34.

**9-(4-Nitrophenyl)-3,3,6,6-tetramethyl-2,3,4,5,6,7,8,9-octahydro-1H-xanthene-1,8-dione (10b)**

Recrystallized from 95% ethanol, mp 236–238 °C. IR (KBr,  $\text{cm}^{-1}$ ): 3222, 3066, 2956, 2866, 2664, 1586, 1474, 1424, 1378, 1288, 1246, 1160, 1064, 976, 856, 740.  $^1\text{H}$  NMR ( $\text{DMSO}-d_6$ )  $\delta$ : 1.10 (s, 6H,  $2 \times \text{CH}_3$ ), 1.22 (s, 6H,  $2 \times \text{CH}_3$ ), 2.34–2.52 (m, 8H,  $4 \times \text{CH}_2$ ), 5.44 (d, 1H,  $J = 6.0$  Hz), 7.02–7.26 (m, 4H, ArH).  $^{13}\text{C}$  NMR ( $\text{DMSO}-d_6$ )  $\delta$ : 15.4, 25.2, 27.1, 47.4, 54.2, 108.0, 114.4, 130.6, 159.7, 160.6, 198.4. Anal. calcd. for  $\text{C}_{23}\text{H}_{25}\text{NO}_5$ : C 69.85, H 6.37; found: C 69.78, H 6.31.

**9-(4-Nitrophenyl)-3,3,6,6-tetramethyl-1,2,3,4,5,6,7,8,9,10-decahydroacridine-1,8-dione (11b)<sup>23</sup>**

Recrystallized from 95% ethanol, mp 252–256 °C. IR (KBr,  $\text{cm}^{-1}$ ): 3424, 3066, 2954, 2864, 2686, 1576, 1478, 1422, 1366, 1290, 1248, 1166, 1070, 956, 840, 704.  $^1\text{H}$  NMR ( $\text{DMSO}-d_6$ )  $\delta$ : 1.12 (s, 6H,  $2 \times \text{CH}_3$ ), 1.24 (s, 6H,  $2 \times \text{CH}_3$ ), 2.30–2.50 (m, 8H,  $4 \times \text{CH}_2$ ), 5.46 (d, 1H,  $J = 6.0$  Hz), 7.04–7.24 (m, 4H, ArH), 8.26 (s, 1H, NH).  $^{13}\text{C}$  NMR ( $\text{DMSO}-d_6$ )  $\delta$ : 16.4, 25.3, 27.7, 47.1, 54.2, 108.0, 114.1, 130.2, 159.2, 161.6, 197.4. Anal. calcd. for  $\text{C}_{23}\text{H}_{26}\text{N}_2\text{O}_4$ : C 70.03, H 6.64, N 7.10; found: C 69.98, H 6.58, N 7.04.

**9-(4-Nitrophenyl)-10-hydroxy-3,3,6,6-tetramethyl-1,2,3,4,5,6,7,8,9,10-decahydroacridine-1,8-dione (12b)<sup>25</sup>**

Recrystallized from 95% ethanol, mp 260–262 °C. IR (KBr,  $\text{cm}^{-1}$ ): 3410, 3068, 2954, 2866, 2674, 1566, 1466, 1428, 1364, 1280, 1260, 1146, 1074, 944, 880, 740.  $^1\text{H}$  NMR ( $\text{DMSO}-d_6$ )  $\delta$ : 1.16 (s, 6H,  $2 \times \text{CH}_3$ ), 1.22 (s, 6H,  $2 \times \text{CH}_3$ ), 2.34–2.54 (m, 8H,  $4 \times \text{CH}_2$ ), 5.46 (d, 1H,  $J = 6.0$  Hz), 7.02–7.26 (m, 4H, ArH), 10.73 (bs, 1H, OH).  $^{13}\text{C}$  NMR ( $\text{DMSO}-d_6$ )  $\delta$ : 15.1, 25.5, 27.2, 47.6, 54.4, 108.0, 114.2, 130.2, 159.4, 160.4, 198.4. Anal. calcd. for  $\text{C}_{23}\text{H}_{26}\text{N}_2\text{O}_5$ : C 67.30, H 6.38, N 6.82; found: C 67.24, H 6.31, N 6.77.



**10-Amino-9-(4-nitrophenyl)-3,3,6,6-tetramethyl-1,2,3,4,5,6,7,8,9,10-decahydro acridine-1,8-dione (13b)**

Recrystallized from 95% ethanol, mp 270–272 °C. IR (KBr, cm<sup>-1</sup>): 3420, 3042, 2960, 2864, 2672, 1562, 1462, 1424, 1360, 1284, 1242, 1158, 1066, 946, 882, 727. <sup>1</sup>H NMR (DMSO-*d*<sub>6</sub>) δ: 1.14 (s, 6H, 2 × CH<sub>3</sub>), 1.22 (s, 6H, 2 × CH<sub>3</sub>), 2.34–2.54 (m, 8H, 4 × CH<sub>2</sub>), 5.44 (d, 1H, *J* = 6.0 Hz), 7.02–7.24 (m, 4H, ArH), 8.28 (d, 2H, NH). <sup>13</sup>C NMR (DMSO-*d*<sub>6</sub>) δ: 15.2, 25.4, 27.2, 47.5, 54.1, 108.0, 114.4, 132.6, 159.4, 160.2, 197.4. Anal. calcd. for C<sub>23</sub>H<sub>27</sub>N<sub>3</sub>O<sub>4</sub>: C 67.46, H 6.64, N 10.26; found: C 67.41, H 6.58, N 10.21.

**9-(4-Nitrophenyl)-3,3,6,6-tetramethyl-2,3,4,5,6,7,8,9-octahydro-1H-thioxanthene-1,8-dione (14b)**

Recrystallized from 95% ethanol, mp 234–238 °C. IR (KBr, cm<sup>-1</sup>): 3426, 3056, 2960, 2864, 2694, 1588, 1470, 1422, 1376, 1298, 1244, 1156, 1068, 976, 880, 700. <sup>1</sup>H NMR (DMSO-*d*<sub>6</sub>) δ: 1.11 (s, 6H, 2 × CH<sub>3</sub>), 1.24 (s, 6H, 2 × CH<sub>3</sub>), 2.34–2.54 (m, 8H, 4 × CH<sub>2</sub>), 3.80 (s, 3H, OCH<sub>3</sub>), 5.44 (d, 1H, *J* = 6.0 Hz), 7.02–7.28 (m, 4H, ArH). <sup>13</sup>C NMR (DMSO-*d*<sub>6</sub>) δ: 15.2, 22.2, 27.4, 47.2, 54.2, 108.0, 114.4, 130.6, 159.2, 160.4, 194.4. Anal. calcd. for C<sub>23</sub>H<sub>25</sub>N O<sub>4</sub>S: C 67.13, H 6.12, S 7.79; found: C 67.07, H 6.06, S 7.72.

**5-[1,2-Di(2-furyl)-2-(2,4,6-trioxohexahydropyrimidin-5-yl)ethyl]-hexahydropyrimidine-2,4,6-trione (17b)<sup>26</sup>**

<sup>1</sup>H NMR (DMSO-*d*<sub>6</sub>, 500 MHz) δ: 6.90–7.0 (6H, m, furan ring Hs), 8.45 (2H, d, *J* = 6.0 Hz), 8.48 (2H, d, *J* = 6.0 Hz), 11.26 (4H, s, NHs). <sup>13</sup>C NMR (DMSO-*d*<sub>6</sub>, 500 MHz) δ: 43.1 (barbituric acid C-5 carbon), 86.6 (benzyl carbon), 136.2, 137.7, 139.9, 142.3 (four different carbons for two furan moieties), 161.4, 162.1, 165.4 (three different carbonyl carbons from barbituric acid).

**5,6-Di(2-furyl)-5,6-dihydropyrimidino[5',4':6,7]oxepino[2,3-*d*]pyrimidine-2,4,7,9(1H,3H,8H,10H)-tetraone (18b)<sup>26</sup>**

<sup>1</sup>H NMR (DMSO-*d*<sub>6</sub>, 500 MHz) δ: 6.95–6.70 (6H, m, furan ring Hs), 8.46 (2H, d, *J* = 6.0 Hz), 11.10 (s, 2H, NHs), 11.23 (2H, s, NHs). <sup>13</sup>C NMR (DMSO-*d*<sub>6</sub>) δ: 43.2 (barbituric acid C-5 carbon), 139.9, 141.1, 144.2, 146.7 (four different carbons for two furan rings), 161.1, 163.4 (two different carbonyl carbons from barbituric acid).

**5-(2-Furyl)-5H-pyrimidino[5',4':5,6]pyrano[2,3-*d*]pyrimidine-2,4,6,8(1H,3H,7H,9H)-tetraone (21b)<sup>26</sup>**

<sup>1</sup>H NMR (DMSO-*d*<sub>6</sub>, 500 MHz) δ: 6.90–7.20 (3H, m, furan ring Hs), 8.68 (1H, s), 11.12 (s, 2H, NHs), 11.26 (s, 2H, NHs). <sup>13</sup>C NMR (DMSO-*d*<sub>6</sub>, 500 MHz) δ: 41.4 (barbituric acid C-5 carbon), 86.1 (benzyl carbon), 136.6, 137.2, 138.8, 141.4 (for carbons for furan ring), 162.3, 169.4 (two different carbonyl carbons for the barbituric acid moieties).

## References

- (1) Hantzsch, A. *Justus Liebigs Ann. Chem.* **1882**, 215 (1), 1. doi:10.1002/jlac.18822150102.
- (2) For some recent articles see: Benetti, S.; Romagnoli, R.; De Risi, C.; Spalluto, G.; Zanirato, V. *Chem. Rev.* **1995**, 95 (4),

1065. doi:10.1021/cr00036a007.; Langer, P. *Chem. Eur. J.* **2001**, 7 (18), 3858. doi:10.1002/1521-3765(20010917)7:18<3858::AID-CHEM3858>3.0.CO;2-V.; Langer, P. *Synthesis* **2002**, 441. doi:10.1055/s-2002-20954.
- (3) Kadutskii, A. P.; Kozlov, N. G. *Russ. J. Org. Chem.* **2006**, 42 (9), 1388. doi:10.1134/S1070428006090247.
- (4) Lipson, V. V.; Shirobokova, M. G.; Shishkin, O. V.; Shishkina, S. V. *Russ. J. Org. Chem.* **2006**, 42 (7), 1015. doi:10.1134/S1070428006070141.
- (5) Tu, S.; Gao, Y.; Miao, C.; Li, T.; Zhang, X.; Zhu, S.; Fang, F.; Shi, D. *Synth. Commun.* **2006**, 34 (7), 1289. doi:10.1081/SCC-120030317.
- (6) Tu, S.; Wei, Q.; Ma, H.; Shi, D.; Gao, Y.; Cui, G. *Synth. Commun.* **2001**, 31 (17), 2657. doi:10.1081/SCC-100105393.
- (7) Tu, S.; Gao, Y.; Miao, C.; Zhu, S.; Li, T.; Zhang, X.; Shi, D. *Synth. Commun.* **2004**, 34 (14), 2617. doi:10.1081/SCC-200025623.
- (8) Tu, S.; Miao, C.; Fang, F.; Youjian, F.; Li, T.; Zhuang, Q.; Zhang, X.; Zhu, S.; Shi, D. *Bioorg. Med. Chem. Lett.* **2004**, 14 (6), 1533. doi:10.1016/j.bmcl.2003.12.092.
- (9) Sachar, A.; Sharma, R. L.; Kumar, S.; Kaur, D.; Singh, J. J. *Heterocyclic Chem.* **2006**, 43 (5), 1177. doi:10.1002/jhet.5570430507.
- (10) Shi, D.; Wang, Y.; Lu, Z.; Dai, G. *Synth. Commun.* **2000**, 30 (4), 713. doi:10.1080/00397910008087374.
- (11) Ramachary, D. B.; Barbas, C. F. *Chem. Eur. J.* **2004**, 10 (21), 5323. doi:10.1002/chem.200400597.
- (12) Kolos, N. N.; Yurchenko, V. D.; Orlov, V. D.; Shishkina, S. V.; Shishkin, O. V. *Chem. Heterocycl. Compd.* **2004**, 40 (12), 1550. doi:10.1007/s10593-005-0098-3.
- (13) Tu, S.; Fang, F.; Zhu, S.; Li, T.; Zhang, X.; Zhuang, Q. J. *Heterocyclic Chem.* **2004**, 41 (5), 767. doi:10.1002/jhet.5570410519.
- (14) Jin, T.-S.; Zhang, J.-S.; Wang, A.-Q.; Li, T.-S. *Synth. Commun.* **2005**, 35 (17), 2339. doi:10.1080/00397910500187282.
- (15) Jin, T.-S.; Wang, A.-Q.; Zhang, J.-S.; Li, T.-S. *Indian. J. Chem.* **2006**, 45B, 470.
- (16) Kantevari, S.; Bantu, R.; Nagarapu, L. *J. Mol. Catal. A: Chem.* **2007**, 269, 53. doi:10.1016/j.molcata.2006.12.039.
- (17) Khan, K. M.; Maharvi, G. M.; Nawaz, S. A.; Perveen, S.; Choudhary, M. I. *Lett. Drug Des. Discovery* **2007**, 4 (4), 272. doi:10.2174/157018007784620004.
- (18) Khan, K. M.; Maharvi, G. M.; Nawaz, S. A.; Perveen, S.; Choudhary, M. I. *Lett. Drug Des. Discovery* **2008**, 5 (6), 423. doi:10.2174/157018008785777351.
- (19) Maharvi, G. M.; Ali, S.; Riaz, N.; Afza, N.; Malik, A.; Ashraf, M.; Iqbal, L.; Lateef, M. *J. Enzyme Inhib. Med. Chem.* **2008**, 23 (1), 62. doi:10.1080/14756360701408754.
- (20) Horning, E. C.; Horning, M. G. *J. Org. Chem.* **1946**, 11 (1), 95. doi:10.1021/jo01171a014.
- (21) Brown, J. D.; Taylor, E. C.; Wipf, P. *Indian J. Chem.* **1992**, 31B, 73.
- (22) Tu, S.-J.; Lu, Z.; Shi, D.; Yao, C.; Gao, Y.; Guo, C. *Synth. Commun.* **2002**, 32 (14), 2181. doi:10.1081/SCC-120005427.
- (23) Vanden Eynde, J. J.; D'Orazio, P.; Mayence, A.; Maguestiau, A.; Anders, E. *Tetrahedron* **1992**, 48 (7), 1263. doi:10.1016/S0040-4020(01)90788-4.
- (24) Shi, D.-Q.; Mou, J.; Zhuang, Q.-Y.; Wang, X.-S. *Chin. J. Chem.* **2005**, 23 (9), 1223. doi:10.1002/cjoc.200591223.
- (25) Tu, S.; Miao, C.; Gao, Y.; Fang, F.; Zhuang, Q.; Feng, Y.; Shi, D. *Synlett* **2004**, 255. doi:10.1055/s-2003-44981.
- (26) Sachar, A.; Sharma, R. L. *Indian J. Heterocycl. Chem.* **2008**, 17, 301.

# A novel and efficient cross-coupling of tris(fluorinated phenyl)boroxins with disulfides catalyzed by CuI/1,10-phenanthroline

Chuanming Yu, Beibei Jin, Zhenyu Liu, and Weihui Zhong

**Abstract:** Under an oxygen atmosphere, the cross-coupling of tris(fluorinated phenyl)boroxins and disulfides catalyzed by CuI/1,10-phenanthroline were smoothly achieved to produce the corresponding asymmetric fluorinated arylsulfides in good-to-excellent yields.

**Key words:** disulfide, tris(fluorinated phenyl)boroxin, fluorinated arylsulfide, cross-coupling, cuprous iodide.

**Résumé :** On a effectué sans difficulté le couplage croisé de tris(fluorophényl)boroxines et de disulfures, sous atmosphère d'oxygène et catalyse par du CuI/phénanthroline; on a pu isoler les arylsulfures fluorés asymétriques correspondants avec des rendements allant de bons à excellents.

**Mots-clés :** disulfure, tris(fluorophényl)boroxine, arylsulfure fluoré, couplage croisé, iodure cuivreux.

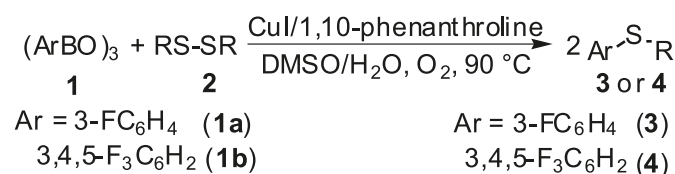
[Traduit par la Rédaction]

## Introduction

Transition-metal-catalyzed aryl carbon–sulfur formation reaction is an indispensable tool in synthetic organic chemistry. Aryl sulfides and their derivatives are a common functional group in numerous pharmaceutical and biological active compounds.<sup>1</sup> However, compared with metal-catalyzed formation of aryl C–N or aryl C–O bonds, transition-metal-mediated carbon–sulfur bonds formation have not received particular interest, which brought about a further research area.<sup>2</sup> In the 1980s, Migita and co-workers<sup>3</sup> first reported C–S bond formation through Pd(PPh<sub>3</sub>)<sub>4</sub> catalyzing the coupling reaction of aryl halides with thiols, but this method required considerable environmentally unfriendly PPh<sub>3</sub> as ligands. Later, various metal catalysts such as palladium,<sup>4</sup> nickel,<sup>5</sup> cobalt<sup>6</sup> and copper<sup>7</sup> have been developed among these reactions. While some synthetic difficulties must be addressed, for example, high temperatures, high catalyst loadings, and specially designed phosphine ligands,<sup>8</sup> it is gratifying to see that aryl triflates and organoboronic acids are sometimes used as good counterparts instead of aryl halides to overcome the disadvantages of the traditional reactions.<sup>9</sup> To the best of our knowledge, the preparation of asymmetric fluorinated arylsulfides via the cross-coupling of disulfide with tris(fluorinated phenyl)boroxin has not been reported.<sup>10</sup>

The arylation of tris(fluorinated phenyl)boroxins is of current interest because the unique properties conferred by the fluorine atoms might get some unexpected results and high biological activity compounds that are otherwise difficult to obtain.<sup>11</sup> Moreover, the analogous carbon–sulfur bond for-

Scheme 1.



mation without aryl halides should be desirable from the viewpoint of atom economy and the waste treatment of hydrogen halides.<sup>12</sup> Herein, we wish to report an efficient cross-coupling of tris(fluorinated phenyl)boroxins with disulfides catalyzed by the CuI/1,10-phenanthroline complex under oxygen atmosphere to give the corresponding fluorinated arylsulfides in good to excellent yields (Scheme 1).

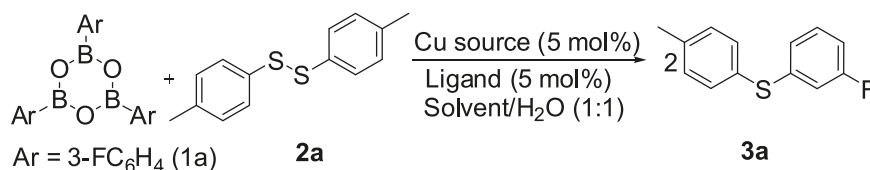
## Results and discussion

Initially, the cross-coupling reaction of tris(3-fluorophenyl)boroxin (**1a**) with 1,2-di-*p*-tolylsulfide (**2a**) was investigated under different conditions. Various factors including copper source and its amount, solvents, ligands, and reaction temperatures were screened. Firstly, this cross-coupling reaction was carried out in a mixture of DMSO and water (2:1) at 100 °C catalyzed by CuI in the presence of 2,2-bipyridyl,<sup>10</sup> the desired product (3-fluorophenyl)-4-tolylsulfide (**3a**) was obtained in only 26% yields (Table 1, entry 1) and most of **2a** was recovered. When we carried out the same reaction in an oxygen atmosphere, the yield of corresponding target product **3a** improved up to 68% (Table 1, entry 2),

Received 25 August 2009. Accepted 1 December 2009. Published on the NRC Research Press Web site at canjchem.nrc.ca on 15 April 2010.

C. Yu,<sup>1</sup> B. Jin, Z. Liu, and W. Zhong. Key Laboratory of Pharmaceutical Engineering of Ministry of Education, College of Pharmaceutical Sciences, Zhejiang University of Technology, Hangzhou 310014, P.R. China.

<sup>1</sup>Corresponding author (e-mail: pharmlab@zjut.edu.cn).

**Table 1.** Copper-catalyzed coupling of tris(3-fluorophenyl)boroxin with 1,2-di-*p*-tolyl disulfide.

Entry	[Cu]	Ligand	Solvent and ratios	Time (h)	<i>T</i> (°C)	Yield (%) <sup>a</sup>
1 <sup>b</sup>	CuI	<b>L1</b>	DMSO/H <sub>2</sub> O (2:1)	12	100	26
2	CuI	<b>L1</b>	DMSO/H <sub>2</sub> O (2:1)	12	100	68
3 <sup>c</sup>	CuI	<b>L1</b>	DMSO/H <sub>2</sub> O (2:1)	12	90	ND
4	CuI	—	DMSO/H <sub>2</sub> O (2:1)	24	120	ND
5	CuI	<b>L2</b>	DMSO/H <sub>2</sub> O (2:1)	8	90	93
6	CuI	<b>L3</b>	DMSO/H <sub>2</sub> O (2:1)	8	90	Trace
7	CuI	<b>L4</b>	DMSO/H <sub>2</sub> O (2:1)	8	90	ND
8	CuI	<b>L2</b>	DMSO/H <sub>2</sub> O (1:1)	8	90	94
9	CuI	<b>L2</b>	DMSO	8	90	93
10	CuI	<b>L2</b>	DMSO/H <sub>2</sub> O (1:2)	8	90	88
11	CuI	<b>L2</b>	1,4-Dioxane	8	90	56
12	CuI	<b>L2</b>	DMF	8	90	68
13	CuI	<b>L2</b>	2-Methyltetrahydrofuran	8	90	54
14	—	<b>L2</b>	DMSO/H <sub>2</sub> O (1:1)	8	90	ND
15	CuBr	<b>L2</b>	DMSO/H <sub>2</sub> O (1:1)	8	90	Trace
16	CuCl	<b>L2</b>	DMSO/H <sub>2</sub> O (1:1)	8	90	Trace
17	CuCl <sub>2</sub>	<b>L2</b>	DMSO/H <sub>2</sub> O (1:1)	8	90	Trace
18	Cu(OAc) <sub>2</sub>	<b>L2</b>	DMSO/H <sub>2</sub> O (1:1)	8	90	Trace

**Note:** Conditions: **1a** (1.5 mmol), **2a** (0.5 mmol), [Cu] (0.025 mmol), ligand (0.025 mmol) at 90 °C under oxygen atmosphere. ND = not determined.

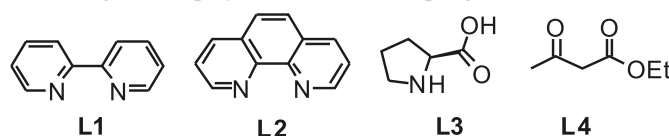
<sup>a</sup>Isolated yields based on **2a**.

<sup>b</sup>Under air atmosphere.

<sup>c</sup>Under nitrogen atmosphere.

while no desired product was observed under nitrogen atmosphere (Table 1, entry 3). Secondly, the effect of ligands was investigated (Fig. 1). The coupling reaction did not proceed in the absence of ligand (Table 1, entry 4), even by prolonging the reaction time or increasing the temperature. To our delight, the yield of product **3a** increased up to 94% when 1,10-phenanthroline (**L2**) was employed as ligand (Table 1, entries 5–7). Then, 1,10-phenanthroline (**L2**) was employed under Taniguchi's<sup>10</sup> conditions, and the reactions showed that this ligand was less stable than 2,2-bipyridyl (**L1**). Subsequently, we studied the effect of solvents, which have a negligible impact as compared to the reactions without additional water (Table 1, entries 5 and 8–9). A rate of DMSO and water of 1:1 was found not only to be an appropriate solvent for this reaction but also friendly to environment (Table 1, entries 5 and 8–13). Among these copper sources, CuI was the most effective (Table 1, entries 5 and 14–18). Therefore, the optimal conditions for the synthesis of fluorinated arylsulfides is by the treatment of disulfides and tri(fluorinated phenyl)boroxins in DMSO/H<sub>2</sub>O (1:1), under oxygen atmosphere at 90 °C, in the presence of only 5 mol% of CuI/**L2** (1,10-phenanthroline).

With the optimal conditions in hand, we decided to assess the scope of this reaction. Tris(fluorinated phenyl)boroxins were first investigated to react with a series of disulfides (see Table 2). It was found that both electron-donating and electron-withdrawing substituted disulfides were tolerated

**Fig. 1.** Ligands employed for the C–S coupling reaction.

well under the optimal reactions (Table 2, entries 1–9). The present process was shown to work well in the coupling of tris(fluorinated phenyl)boroxins with disulfides containing free *para*-hydroxyl or *meta*-amino groups to provide the desired products **3j**, **4j** and **3k**, **4k** in good yields (Table 2, entries 10 and 11). These compounds are very important intermediates.

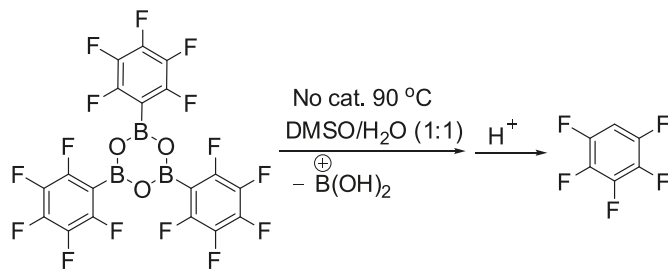
Unfortunately, as shown in Table 2, no expected product was detected when using benzothiazol-2-yl disulfide (**2l**) as substrate (Table 2, entry 12). The same result happened with **2m** (Table 2, entry 13). The possible reason was that the benzothiazol-2-yl group and carboxyl group had strong electron-donating effects and decreased the reactivities of corresponding disulfides.

Another interesting aspect of the reaction was when aliphatic disulfides as substrates were employed (Table 2, entry 14). While 1,2-dibenzyl disulfide (**2n**) was found to give the corresponding products **3n** and **4n** only in yields of 23% and 29%, respectively, the main products were bis(4-fluorophenyl)sulfide (**5a**) and bis(3,4,5-trifluorophenyl)sul-





Scheme 3.



reasonable explanation was that the basic catalyst system, or even the light basic solvent DMSO at 90 °C, may be decomposing tris(pentafluorophenyl)-boroxin (Scheme 3).<sup>14</sup>

## Conclusion

In summary, we have developed a practical protocol to asymmetric fluorinated arylsulfides via CuI catalyzed cross-coupling of tris(fluorinated phenyl)boroxins with disulfides in the presence of 1,10-phenanthroline under an oxygen atmosphere. The merits of our method are simple operation, short reaction times, good to excellent yields, and one-pot synthesis of asymmetric fluorinated phenylsulfides. Further studies on the application of fluorinated boronic acids are now in progress in our laboratory.

## Experimental section

### General method

All reagents are commercially available. Tris(4-fluorophenyl)boroxin, tris(3,4,5-trifluorophenyl)boroxin, and tris(pentafluorophenyl)boroxin were prepared from our own laboratory.<sup>15</sup> Melting points were measured on a digital melting-point apparatus WR-1B and were uncorrected. <sup>1</sup>H NMR, <sup>19</sup>F NMR, and <sup>13</sup>C NMR spectra were recorded on a Varian 400 MHz instrument using CDCl<sub>3</sub> as the solvent, and chemical shifts were expressed in parts per million (ppm) using TMS and trifluoroacetic acid as internal standards. Mass spectra were measured with a Trace Finnigan DSQ. High resolution mass spectra (HR-MS) analyses were measured on an Agilent 6210 TOF LC/MS using APCI (electrospray ionization) techniques. IR measurements were carried out with a Nicolet Aviator-370 instrument. Elemental analysis was performed on a VarioEL-III instrument. All spectral data of the products were identical to authentic samples.

### General procedure for the preparation of asymmetric fluorinated arylsulfides

To a solution of CuI (0.025 mmol) and 1,10-phenanthroline (**L2**, 0.025 mmol) in DMSO/H<sub>2</sub>O (1:1, 20 mL) were added disulfides (0.5 mmol) and tri(3-fluorophenyl)boroxin (1.5 mmol). The mixture was stirred at 90 °C under O<sub>2</sub> atmosphere for a given time. Then the reaction was quenched with brine and extracted with ethyl acetate (3 × 15 mL). The combined organic phase was dried over anhydrous Na<sub>2</sub>SO<sub>4</sub> and concentrated in vacuo and the crude product was purified by column chromatography on silica gel with petroleum ether as eluent to afford the desired product. All new compounds were identified by <sup>1</sup>H NMR, <sup>13</sup>C NMR, <sup>19</sup>F

NMR, and HR-MS. Data of known compounds have been found to be identical to those reported.

### (3-Fluorophenyl)-4-tolylsulfide (**3a**)

Colorless viscous oil. IR (KBr, cm<sup>-1</sup>): 3072, 2917, 1599, 1492, 881, 810, 774. <sup>1</sup>H NMR (400 MHz, CDCl<sub>3</sub>) δ: 2.33 (s, 3H), 6.77–6.85 (m, 2H), 6.95 (d, *J* = 7.6 Hz, 1H), 7.13 (d, *J* = 5.2 Hz, 3H), 7.34 (d, *J* = 8.0 Hz, 2H). <sup>13</sup>C NMR (100 MHz, CDCl<sub>3</sub>) δ: 21.0 (d, *J* = 15.7 Hz, 1C), 112.7 (d, *J* = 21.2 Hz, 1C), 115.2 (d, *J* = 23.2 Hz, 1C), 123.9, 128.4, 129.3, 129.7, 130.0–130.3 (m, 1C), 130.5, 133.5, 138.6, 140.5 (d, *J* = 7.5 Hz, 1C), 163.0 (d, *J* = 246.6 Hz, 1C). <sup>19</sup>F NMR (376 MHz, CDCl<sub>3</sub>) δ: –132.72 (dd, *J* = 15.4, 9.4 Hz, 1F). MS (EI) *m/z* (%): 218 (M<sup>+</sup>, 100), 203 (5). HR-MS calcd. for C<sub>13</sub>H<sub>11</sub>FS [M<sup>+</sup>]: 218.0565; found: 218.0553.

### (4-Bromophenyl)-3-fluorophenylsulfide (**3b**)

Colorless viscous oil. Lit. value<sup>16a</sup> bp 360.9 °C. <sup>1</sup>H NMR (400 MHz, CDCl<sub>3</sub>) δ: 6.89–6.97 (m, 2H), 7.05 (d, *J* = 7.6 Hz, 1H), 7.24 (dd, *J* = 15.2, 8.4 Hz, 3H), 7.45 (d, *J* = 8.8 Hz, 2H). <sup>19</sup>F NMR (376 MHz, CDCl<sub>3</sub>) δ: –110.83 (dd, *J* = 3.0, 2.0 Hz, 1F).

### (4-Chlorophenyl)-3-fluorophenylsulfide (**3c**)

Colorless viscous oil. IR (KBr, cm<sup>-1</sup>): 3064, 2925, 2839, 1598, 1580, 1474, 881, 821, 776. <sup>1</sup>H NMR (400 MHz, CDCl<sub>3</sub>) δ: 6.88–6.95 (m, 2H), 7.03 (d, *J* = 7.6 Hz, 1H), 7.23 (dd, *J* = 15.2, 7.2 Hz, 1H), 7.27–7.33 (m, 4H). <sup>13</sup>C NMR (100 MHz, CDCl<sub>3</sub>) δ: 114.2 (d, *J* = 20.5 Hz, 1C), 117.0 (d, *J* = 22.6 Hz, 1C), 125.7, 130.0, 130.7 (d, *J* = 9.0 Hz, 2C), 133.0, 133.8 (2C), 134.4, 138.8 (d, *J* = 7.2 Hz, 1C), 163.3 (d, *J* = 247.3 Hz, 1C). <sup>19</sup>F NMR (376 MHz, CDCl<sub>3</sub>) δ: –110.95 ~ –111.01 (m, 1F). MS (EI) *m/z* (%): 238 (M<sup>+</sup>, 100), 203 (45). HR-MS calcd. for C<sub>12</sub>H<sub>8</sub>ClFS [M<sup>+</sup>]: 238.0019; found: 238.0004.

### (3-Fluorophenyl)-4-fluorophenylsulfide (**3d**)

Yellow oil. Lit. value<sup>16b</sup> bp 313.7 °C. <sup>1</sup>H NMR (400 MHz, CDCl<sub>3</sub>) δ: 6.94 (td, *J* = 9.6, 2.0 Hz, 2H), 7.05 (d, *J* = 7.6 Hz, 1H), 7.25 (d, *J* = 8.0 Hz, 3H), 7.45 (d, *J* = 8.8 Hz, 2H). <sup>19</sup>F NMR (376 MHz, CDCl<sub>3</sub>) δ: –110.90 (dd, *J* = 15.1, 9.0 Hz, 2F).

### (3-Fluorophenyl)-4-nitrophenylsulfide (**3e**)

Yellow solid. Mp (recrystallization in petroleum ether) 71.5–73.5 °C (lit. value<sup>16c</sup> mp 71.0 °C). 71 °C. <sup>1</sup>H NMR (400 MHz, CDCl<sub>3</sub>) δ: 7.13–7.14 (m, 1H), 7.21–7.27 (m, 3H), 7.30 (d, *J* = 7.6 Hz, 1H), 7.41 (dd, *J* = 7.6, 5.6 Hz, 1H), 8.11 (d, *J* = 8.8 Hz, 2H). <sup>19</sup>F NMR (376 MHz, CDCl<sub>3</sub>) δ: –110.63 ~ –110.69 (m, 1F).

### (3-Fluorophenyl)phenylsulfide (**3f**)

Colorless viscous oil. Lit. value<sup>16c</sup> bp 302.2 °C. <sup>1</sup>H NMR (400 MHz, CDCl<sub>3</sub>) δ: 6.86 (td, *J* = 8.4, 2.4 Hz, 2H), 7.03 (d, *J* = 7.6 Hz, 1H), 7.20 (dd, *J* = 14.0, 8.0 Hz, 1H), 7.32 (dd, *J* = 15.6, 7.6 Hz, 3H), 7.41 (d, *J* = 7.2 Hz, 2H). <sup>19</sup>F NMR (376 MHz, CDCl<sub>3</sub>) δ: –111.51 (dd, *J* = 15.4, 9.4 Hz, 1F).

### (3-Fluorophenyl)-2,4-dimethylphenylsulfide (**3g**)

Colorless viscous oil. IR (KBr, cm<sup>-1</sup>): 3056, 2917, 1598, 1472, 880, 815, 773. <sup>1</sup>H NMR (400 MHz, CDCl<sub>3</sub>) δ: 2.33 (s, 6H), 6.68 (dt, *J* = 6.0, 2.0 Hz, 1H), 6.78 (td, *J* = 8.4,

1.6 Hz, 1H), 6.85 (d,  $J = 8.0$  Hz, 1H), 7.03 (d,  $J = 3.6$  Hz, 1H), 7.15 (dd,  $J = 14.0, 8.0$  Hz, 2H), 7.37 (d,  $J = 8.0$  Hz, 1H).  $^{13}\text{C}$  NMR (100 MHz,  $\text{CDCl}_3$ )  $\delta$ : 20.5, 21.1, 112.2 (d,  $J = 21.3$  Hz, 1C), 114.0 (d,  $J = 23.5$  Hz, 1C), 122.8, 127.7, 127.8, 130.7 (d,  $J = 8.4$  Hz, 1C), 131.8, 135.6, 139.6, 140.7 (d,  $J = 7.6$  Hz, 1C), 141.7, 163.1 (d,  $J = 246.6$  Hz, 1C).  $^{19}\text{F}$  NMR (376 MHz,  $\text{CDCl}_3$ )  $\delta$ : -132.07 (dd,  $J = 24.9, 9.4$  Hz, 1F). MS (EI)  $m/z$  (%): 127 (100), 137 (35), 232 ( $\text{M}^+$ , 5). HR-MS calcd. for  $\text{C}_{14}\text{H}_{13}\text{FS}$  [ $\text{M}^+$ ]: 232.0732; found: 232.0722.

### (3-Fluorophenyl)-4-isopropylphenylsulfide (3h)

Colorless viscous oil. IR (KBr,  $\text{cm}^{-1}$ ): 2962, 1598, 1473, 1426, 881, 828, 775, 678, 547.  $^1\text{H}$  NMR (400 MHz,  $\text{CDCl}_3$ )  $\delta$ : 1.24 (d,  $J = 6.8$  Hz, 6H), 2.88 (dd,  $J = 13.6, 7.2$  Hz, 1H), 6.80 (dd,  $J = 8.4, 8.4$  Hz, 1H), 6.88 (d,  $J = 9.6$  Hz, 1H), 6.97–7.04 (m, 1H), 7.12–7.21 (m, 3H), 7.37 (d,  $J = 8.4$  Hz, 2H).  $^{13}\text{C}$  NMR (100 MHz,  $\text{CDCl}_3$ )  $\delta$ : 23.8 (2C), 33.8 (d,  $J = 11.4$  Hz, 1C), 112.8 (d,  $J = 21.2$  Hz, 1C), 115.4 (d,  $J = 22.8$  Hz, 1C), 116.8, 122.7, 124.1 (2C), 127.2–128.1 (m, 1C), 129.7–130.4 (m, 1C), 133.4, 135.5 (d,  $J = 7.6$  Hz, 1C), 149.4, 163.0 (d,  $J = 246.5$  Hz, 1C).  $^{19}\text{F}$  NMR (376 MHz,  $\text{CDCl}_3$ )  $\delta$ : -111.32 ~ -111.36 (m, 1F). MS (EI)  $m/z$  (%): 246 ( $\text{M}^+$ , 95), 231 (100). HR-MS calcd. for  $\text{C}_{15}\text{H}_{15}\text{FS}$  [ $\text{M}^+$ ]: 246.0878; found: 246.0843.

### (3-Fluorophenyl)-2,3-dichlorophenylsulfide (3i)

Colorless viscous oil. IR (KBr,  $\text{cm}^{-1}$ ): 1597, 1474, 1399, 1086, 881, 781, 678.  $^1\text{H}$  NMR (400 MHz,  $\text{CDCl}_3$ )  $\delta$ : 6.89 (d,  $J = 8.0$  Hz, 2H), 7.02–7.13 (m, 2H), 7.20 (d,  $J = 8.0$  Hz, 1H), 7.31–7.40 (m, 2H).  $^{13}\text{C}$  NMR (100 MHz,  $\text{CDCl}_3$ )  $\delta$ : 116.0 (d,  $J = 20.8$  Hz, 1C), 120.0 (d,  $J = 22.4$  Hz, 1C), 127.9 (d,  $J = 28.1$  Hz, 1C), 128.5–129.0 (m, 1C), 129.9, 130.6, 131.2 (d,  $J = 7.9$  Hz, 1C), 131.7, 134.0, 134.8 (d,  $J = 7.5$  Hz, 1C), 138.4, 163.2 (d,  $J = 248.3$  Hz, 1C).  $^{19}\text{F}$  NMR (376 MHz,  $\text{CDCl}_3$ )  $\delta$ : -110.03 (dd,  $J = 13.9, 9.4$  Hz, 1F). MS (EI)  $m/z$  (%): 272 ( $\text{M}^+$ , 100), 202 (15). HR-MS calcd. for  $\text{C}_{12}\text{H}_7\text{Cl}_2\text{FS}$  [ $\text{M}^+$ ]: 271.9630; found: 271.9651.

### (3-Fluorophenyl)-4-hydroxyphenylsulfide (3j)

Colorless viscous oil. IR (KBr,  $\text{cm}^{-1}$ ): 3391, 2925, 1599, 1493, 878, 830, 774, 673.  $^1\text{H}$  NMR (400 MHz,  $\text{CDCl}_3$ )  $\delta$ : 5.44 (s, 1H), 6.75–6.80 (m, 2H), 6.85–6.92 (m, 3H), 7.16 (dd,  $J = 8.0, 8.0$  Hz, 1H), 7.40 (d,  $J = 8.8$  Hz, 2H).  $^{13}\text{C}$  NMR (100 MHz,  $\text{CDCl}_3$ )  $\delta$ : 112.4 (d,  $J = 21.3$  Hz, 1C), 114.1 (d,  $J = 23.5$  Hz, 2C), 116.7, 122.8 (2C), 130.1 (d,  $J = 8.3$  Hz, 2C), 136.5, 141.5, 156.4, 163.0 (d,  $J = 246.5$  Hz, 1C).  $^{19}\text{F}$  NMR (376 MHz,  $\text{CDCl}_3$ )  $\delta$ : -111.61 (dd,  $J = 15.4, 9.0$  Hz, 1F). MS (EI)  $m/z$  (%): 220 ( $\text{M}^+$ , 100), 201 (25). HR-MS calcd. for  $\text{C}_{12}\text{H}_9\text{FOS}$  [ $\text{M}^+$ ]: 220.0358; found: 220.0347.

### (3-Fluorophenyl)-2-aminophenylsulfide (3k)

Red viscous oil. IR (KBr,  $\text{cm}^{-1}$ ): 3469, 3375, 1609, 1479, 879, 750, 673.  $^1\text{H}$  NMR (400 MHz,  $\text{CDCl}_3$ )  $\delta$ : 4.24 (s, 2H), 6.70–6.79 (m, 4H), 6.85 (d,  $J = 8.0$  Hz, 1H), 7.15 (dd,  $J = 15.2, 7.2$  Hz, 1H), 7.20 (td,  $J = 8.4, 1.6$  Hz, 1H), 7.43 (d,  $J = 7.6$  Hz, 1H).  $^{13}\text{C}$  NMR (100 MHz,  $\text{CDCl}_3$ )  $\delta$ : 112.2 (d,  $J = 21.2$  Hz, 1C), 113.0 (d,  $J = 23.5$  Hz, 2C), 115.4, 118.8, 121.7, 130.1 (d,  $J = 8.3$  Hz, 1C), 131.6, 137.6, 139.5 (d,  $J = 6.8$  Hz, 1C), 148.9, 163.1 (d,  $J = 246.4$  Hz, 1C).  $^{19}\text{F}$  NMR (376 MHz,  $\text{CDCl}_3$ )  $\delta$ : -111.37 (dd,  $J = 15.1, 9.0$  Hz, 1F).

MS (EI)  $m/z$  (%): 219 ( $\text{M}^+$ , 100), 186 (25). HR-MS calcd. for  $\text{C}_{12}\text{H}_{10}\text{FNS}$  [ $\text{M}^+$ ]: 219.0518; found: 219.0505.

### (3-Fluorophenyl)benzylsulfide (3n)

White solid. Mp (recrystallization in petroleum ether) 30.5–31.4 °C. IR (KBr,  $\text{cm}^{-1}$ ): 3060, 2921, 1599, 1495, 773, 713, 697, 678.  $^1\text{H}$  NMR (400 MHz,  $\text{CDCl}_3$ )  $\delta$ : 4.13 (s, 2H), 6.86 (td,  $J = 8.4, 2.4$  Hz, 1H), 7.03 (dd,  $J = 22.0, 7.6$  Hz, 2H), 7.31–7.18 (m, 6H).  $^{13}\text{C}$  NMR (100 MHz,  $\text{CDCl}_3$ )  $\delta$ : 38.5, 110.4, 113.1 (t,  $J = 6.8$  Hz, 2C), 115.7–116.0 (m, 1C), 118.8, 124.6 (2C), 127.4–128.8 (m, 2C), 130.0 (d,  $J = 8.4$  Hz, 1C), 136.7, 161.5–164.0 (m, 1C).  $^{19}\text{F}$  NMR (376 MHz,  $\text{CDCl}_3$ )  $\delta$ : -111.65 ~ -111.73 (m, 1F). MS (EI)  $m/z$  (%): 218 ( $\text{M}^+$ , 100), 91 (75). HR-MS calcd. for  $\text{C}_{13}\text{H}_{11}\text{FS}$  [ $\text{M}^+$ ]: 218.0565; found: 218.0554.

### (3,4,5-Trifluorophenyl)-4-tolylsulfide (4a)

Colorless viscous oil. IR (KBr,  $\text{cm}^{-1}$ ): 2925, 1599, 1515, 1425, 1046, 878, 829, 760.  $^1\text{H}$  NMR (400 MHz,  $\text{CDCl}_3$ )  $\delta$ : 2.37 (s, 3H), 6.74 (dd,  $J = 8.0, 6.8$  Hz, 2H), 7.20 (d,  $J = 8.0$  Hz, 2H), 7.35 (d,  $J = 8.0$  Hz, 2H).  $^{13}\text{C}$  NMR (100 MHz,  $\text{CDCl}_3$ )  $\delta$ : 21.2, 112.0 (dd,  $J = 16.7, 6.1$  Hz, 2C), 128.3, 130.6 (2C), 134.0 (2C), 136.7, 139.5, 151.2 (d,  $J = 150.2$  Hz, 2C).  $^{19}\text{F}$  NMR (376 MHz,  $\text{CDCl}_3$ )  $\delta$ : -162.66 ~ -162.80 (m, 1F), -132.87 ~ -132.98 (m, 2F). MS (EI)  $m/z$  (%): 254 ( $\text{M}^+$ , 100), 239 (30). HR-MS calcd. for  $\text{C}_{13}\text{H}_9\text{FS}$  [ $\text{M}^+$ ]: 254.0377; found: 254.0357.

### (3,4,5-Trifluorophenyl)-4-bromophenylsulfide (4b)

White solid. Mp (recrystallization in petroleum ether) 56.0–58.0 °C. IR (KBr,  $\text{cm}^{-1}$ ): 3132, 1613, 1518, 855, 811, 759.  $^1\text{H}$  NMR (400 MHz,  $\text{CDCl}_3$ )  $\delta$ : 6.87 (d,  $J = 7.2$  Hz, 2H), 7.27 (d,  $J = 7.6$  Hz, 2H), 7.51 (d,  $J = 6.8$  Hz, 2H).  $^{13}\text{C}$  NMR (100 MHz,  $\text{CDCl}_3$ )  $\delta$ : 113.8 (dd,  $J = 16.7, 6.1$  Hz, 2C), 123.0, 132.3 (d,  $J = 16.7$  Hz, 1C), 132.9 (2C), 134.1 (2C), 137.5, 140.0, 151.3 (d,  $J = 247.3$  Hz, 2C).  $^{19}\text{F}$  NMR (376 MHz,  $\text{CDCl}_3$ )  $\delta$ : -132.11 ~ -132.19 (m, 2F), -160.92 ~ -161.07 (m, 1F). MS (EI)  $m/z$  (%): 318 ( $\text{M}^+$ , 100), 239 (10). HR-MS calcd. for  $\text{C}_{12}\text{H}_6\text{BrF}_3\text{S}$  [ $\text{M}^+$ ]: 317.9326; found: 317.9248.

### (3,4,5-Trifluorophenyl)-4-chlorophenylsulfide (4c)

Colorless viscous oil. IR (KBr,  $\text{cm}^{-1}$ ): 3134, 1614, 1516, 896, 841, 824, 759.  $^1\text{H}$  NMR (400 MHz,  $\text{CDCl}_3$ )  $\delta$ : 6.83 (dd,  $J = 6.8, 6.8$  Hz, 2H), 7.34 (s, 4H).  $^{13}\text{C}$  NMR (100 MHz,  $\text{CDCl}_3$ )  $\delta$ : 113.5 (dd,  $J = 16.7, 6.1$  Hz, 2C), 120.1, 129.4 (d,  $J = 18.2$  Hz, 1C), 129.9, 131.4, 132.5 (d,  $J = 50.8$  Hz, 1C), 134.0, 135.0, 138.7 (d,  $J = 243.4$  Hz, 1C), 151.3 (d,  $J = 247.2$  Hz, 2C).  $^{19}\text{F}$  NMR (376 MHz,  $\text{CDCl}_3$ )  $\delta$ : -132.11 ~ -132.19 (m, 2F), -160.92 ~ -161.07 (m, 1F). MS (EI)  $m/z$  (%): 274 ( $\text{M}^+$ , 100), 239 (40). HR-MS calcd. for  $\text{C}_{12}\text{H}_6\text{ClF}_3\text{S}$  [ $\text{M}^+$ ]: 273.981; found: 273.972.

### (3,4,5-Trifluorophenyl)-4-fluorophenylsulfide (4d)

Colorless viscous oil. IR (KBr,  $\text{cm}^{-1}$ ): 2964, 1614, 1517, 1425, 1047, 834, 759.  $^1\text{H}$  NMR (400 MHz,  $\text{CDCl}_3$ )  $\delta$ : 6.76 (dd,  $J = 3.6, 3.6$  Hz, 2H), 7.09 (dd,  $J = 11.6, 11.6$  Hz, 2H), 7.76 (dd,  $J = 11.6, 5.2$  Hz, 2H).  $^{13}\text{C}$  NMR (100 MHz,  $\text{CDCl}_3$ )  $\delta$ : 112.3 (dd,  $J = 17.1, 6.2$  Hz, 1C), 113.1 (d,  $J = 23.2$  Hz, 1C), 116.1–117.1 (m, 1C), 125.2, 127.4, 132.8 (d,  $J = 264.4$  Hz, 1C), 135.4, 136.0, 138.2 (d,  $J = 249.8$  Hz, 1C), 151.3 (d,  $J = 251.5$  Hz, 2C), 163.3 (d,  $J = 240.4$  Hz,

1C).  $^{19}\text{F}$  NMR (376 MHz,  $\text{CDCl}_3$ )  $\delta$ : -152.71 ~ -152.86 (m, 2F), -182.25 ~ -183.40 (m, 1F). MS (EI)  $m/z$  (%): 258 ( $\text{M}^+$ , 100), 238 (35). HR-MS calcd. for  $\text{C}_{12}\text{H}_6\text{F}_3\text{S}$  [ $\text{M}^+$ ]: 258.0126; found: 258.0114.

**(3,4,5-Trifluorophenyl)-4-nitrophenylsulfide (4e)**

Yellow solid. Mp (recrystallization in petroleum ether) 110.2–111.0 °C. IR (KBr,  $\text{cm}^{-1}$ ): 3130, 1617, 1505, 1401, 1087, 854, 739.  $^1\text{H}$  NMR (400 MHz,  $\text{CDCl}_3$ )  $\delta$ : 7.15 (dd,  $J$  = 6.8, 6.8 Hz, 2H), 7.26–7.31 (m, 2H), 8.15 (dd,  $J$  = 9.6, 4.4 Hz, 2H).  $^{13}\text{C}$  NMR (100 MHz,  $\text{CDCl}_3$ )  $\delta$ : 117.8–118.0 (m, 2C), 124.4 (2C), 128.4 (2C), 139.3, 141.8, 145.1, 146.4, 151.6 (d,  $J$  = 244.0 Hz, 2C).  $^{19}\text{F}$  NMR (376 MHz,  $\text{CDCl}_3$ )  $\delta$ : -130.60 (dd,  $J$  = 22.6, 9.0 Hz, 2F), -156.68 ~ -156.78 (m, 1F). MS (EI)  $m/z$  (%): 285 ( $\text{M}^+$ , 100), 238 (50), 255 (25). HR-MS calcd. for  $\text{C}_{12}\text{H}_6\text{F}_3\text{NO}_2\text{S}$  [ $\text{M}^+$ ]: 285.0071; found: 285.0060.

**(3,4,5-Trifluorophenyl)phenylsulfide (4f)**

Colorless viscous oil. Lit. value<sup>16d</sup> bp 316.3 °C.  $^1\text{H}$  NMR (400 MHz,  $\text{CDCl}_3$ )  $\delta$ : 6.81–6.84 (m, 2H), 7.37–7.74 (m, 5H).  $^{19}\text{F}$  NMR (376 MHz,  $\text{CDCl}_3$ )  $\delta$ : -161.80 (t,  $J$  = 19.3 Hz, 1F), -132.62 (t,  $J$  = 12.0 Hz, 2F).

**(3,4,5-Trifluorophenyl)-2,4-dimethylphenylsulfide (4g)**

Colorless viscous oil. IR (KBr,  $\text{cm}^{-1}$ ): 2917, 1613, 1515, 1424, 1317, 1046, 899, 875, 758.  $^1\text{H}$  NMR (400 MHz,  $\text{CDCl}_3$ )  $\delta$ : 2.34 (d,  $J$  = 9.2 Hz, 6H), 6.61 (dd,  $J$  = 7.2, 7.2 Hz, 2H), 7.04 (d,  $J$  = 7.6 Hz, 1H), 7.15 (s, 1H), 7.36 (d,  $J$  = 8.4 Hz, 1H).  $^{13}\text{C}$  NMR (100 MHz,  $\text{CDCl}_3$ )  $\delta$ : 20.8 (d,  $J$  = 24.9 Hz, 1C), 22.7, 110.7 (dd,  $J$  = 17.1, 6.1 Hz, 2C), 126.6, 128.1, 132.1, 134.7, 136.1 (d,  $J$  = 27.3 Hz, 1C), 138.8, 140.4, 142.0, 151.4 (d,  $J$  = 250.4 Hz, 2C).  $^{19}\text{F}$  NMR (376 MHz,  $\text{CDCl}_3$ )  $\delta$ : -153.34 (dd,  $J$  = 19.9, 16.9 Hz, 2F), -183.71 ~ -183.86 (m, 1F). MS (EI)  $m/z$  (%): 268 ( $\text{M}^+$ , 100), 91 (50), 218 (25). HR-MS calcd. for  $\text{C}_{14}\text{H}_{11}\text{F}_3\text{S}$  [ $\text{M}^+$ ]: 268.053; found: 268.133.

**(3,4,5-Trifluorophenyl)-4-isopropylphenylsulfide (4h)**

Colorless viscous oil. IR (KBr,  $\text{cm}^{-1}$ ): 2963, 1613, 1516, 1425, 1317, 1233, 897, 831, 758.  $^1\text{H}$  NMR (400 MHz,  $\text{CDCl}_3$ )  $\delta$ : 1.26 (t,  $J$  = 7.6 Hz, 6H), 2.30 (t,  $J$  = 7.2 Hz, 1H), 6.77 (dd,  $J$  = 8.4, 6.4 Hz, 2H), 7.25 (d,  $J$  = 8.8 Hz, 2H), 7.37 (d,  $J$  = 8.4 Hz, 2H).  $^{13}\text{C}$  NMR (100 MHz,  $\text{CDCl}_3$ )  $\delta$ : 23.8 (2C), 33.9, 112.2 (dd,  $J$  = 17.1, 6.1 Hz, 2C), 127.5 (d,  $J$  = 33.1 Hz, 1C), 128.7, 133.7 (d,  $J$  = 28.7 Hz, 1C), 134.6 (d,  $J$  = 4.8 Hz, 1C), 136.0, 136.8, 139.3, 150.2, 151.3 (d,  $J$  = 247.7 Hz, 2C).  $^{19}\text{F}$  NMR (376 MHz,  $\text{CDCl}_3$ )  $\delta$ : -153.17 ~ -153.28 (m, 2F), -182.87 ~ -183.00 (m, 1F). MS (EI)  $m/z$  (%): 282 ( $\text{M}^+$ , 100), 267 (95), 105 (35). HR-MS calcd. for  $\text{C}_{15}\text{H}_{13}\text{F}_3\text{S}$  [ $\text{M}^+$ ]: 282.0690; found: 282.0710.

**(3,4,5-Trifluorophenyl)-2,3-dichlorophenylsulfide (4i)**

Colorless solid. Mp (recrystallization in petroleum ether) 55.4–57.2 °C. IR (KBr,  $\text{cm}^{-1}$ ): 3131, 1616, 1518, 1401, 796, 770.  $^1\text{H}$  NMR (400 MHz,  $\text{CDCl}_3$ )  $\delta$ : 6.92–7.06 (m, 3H), 7.13 (dd,  $J$  = 16.0, 8.4 Hz, 1H), 7.39 (d,  $J$  = 8.0 Hz, 1H).  $^{13}\text{C}$  NMR (100 MHz,  $\text{CDCl}_3$ )  $\delta$ : 111.1 (d,  $J$  = 22.0 Hz, 1C), 116.5 (dd,  $J$  = 16.3, 6.0 Hz, 2C), 127.7, 129.3 (d,  $J$  = 26.2 Hz, 2C), 132.6, 134.2, 136.6, 140.0 (d,  $J$  = 245.0 Hz, 1C), 151.5 (d,  $J$  = 242.3 Hz, 2C).  $^{19}\text{F}$  NMR (376 MHz,  $\text{CDCl}_3$ )  $\delta$ : -131.44 (dd,  $J$  = 24.4, 20.3 Hz, 2F), -158.49 (dd,

$J$  = 26.3, 20.3 Hz, 1F). MS (EI)  $m/z$  (%): 238 (100), 308 ( $\text{M}^+$ , 40). HR-MS calcd. for  $\text{C}_{12}\text{H}_5\text{Cl}_2\text{F}_3\text{S}$  [ $\text{M}^+$ ]: 307.9441; found: 307.9462.

**(3,4,5-Trifluorophenyl)-4-hydroxyphenylsulfide (4j)**

White solid. Mp (recrystallization in petroleum ether) 68.7–70.1 °C. IR (KBr,  $\text{cm}^{-1}$ ): 3403, 3133, 1614, 1516, 1401, 1045, 832, 758, 619.  $^1\text{H}$  NMR (400 MHz,  $\text{CDCl}_3$ )  $\delta$ : 5.07 (s, 1H), 6.69 (dd,  $J$  = 13.2, 13.2 Hz, 2H), 6.88 (d,  $J$  = 5.2 Hz, 2H), 7.40 (d,  $J$  = 9.2 Hz, 2H).  $^{13}\text{C}$  NMR (100 MHz,  $\text{CDCl}_3$ )  $\delta$ : 110.0 (dd,  $J$  = 17.4, 6.1 Hz, 2C), 117.0 (2C), 122.1, 135.6, 136.2 (d,  $J$  = 31.90 Hz, 2C), 138.9, 151.3 (d,  $J$  = 250.3 Hz, 2C), 156.8.  $^{19}\text{F}$  NMR (376 MHz,  $\text{CDCl}_3$ )  $\delta$ : -153.25 ~ -153.37 (m, 2F), -183.69 (dd,  $J$  = 25.9, 19.9 Hz, 1F). MS (EI)  $m/z$  (%): 256 ( $\text{M}^+$ , 100), 195 (25). HR-MS calcd. for  $\text{C}_{12}\text{H}_7\text{F}_3\text{OS}$  [ $\text{M}^+$ ]: 256.0170; found: 256.0159.

**(3,4,5-Trifluorophenyl)-2-aminophenylsulfide (4k)**

Light yellow solid. Mp (recrystallization in petroleum ether) 66.5–66.9 °C. IR (KBr,  $\text{cm}^{-1}$ ): 3484, 3385, 3133, 1612, 1513, 1478, 1401, 832, 756, 607.  $^1\text{H}$  NMR (400 MHz,  $\text{CDCl}_3$ )  $\delta$ : 4.27 (s, 2H), 6.45 (dd,  $J$  = 7.2, 7.2 Hz, 2H), 6.76–6.82 (m, 2H), 7.25–7.30 (m, 1H), 7.41 (d,  $J$  = 8.8 Hz, 1H).  $^{13}\text{C}$  NMR (100 MHz,  $\text{CDCl}_3$ )  $\delta$ : 110.1 (dd,  $J$  = 17.5, 6.1 Hz, 1C), 112.4, 115.7, 119.1, 132.2, 133.5, 136.4, 137.7, 138.9, 149.0, 151.4 (d,  $J$  = 252.2 Hz, 2C).  $^{19}\text{F}$  NMR (376 MHz,  $\text{CDCl}_3$ )  $\delta$ : -152.36 (dd,  $J$  = 22.6, 15.0 Hz, 2F), -179.93 (dd,  $J$  = 21.4, 12.4 Hz, 1F). MS (EI)  $m/z$  (%): 255 ( $\text{M}^+$ , 100), 80 (30). HR-MS calcd. for  $\text{C}_{12}\text{H}_8\text{F}_3\text{NS}$  [ $\text{M}^+$ ]: 255.0330; found: 255.0315.

**(3,4,5-Trifluorophenylthio)-3-propanoic acid (4m)**

Yellow solid. Mp (recrystallization in petroleum ether) 68.9–71.2 °C. IR (KBr,  $\text{cm}^{-1}$ ): 3133, 1709, 1610, 1519, 1399, 1232, 1047, 810, 756, 656.  $^1\text{H}$  NMR (400 MHz,  $\text{CDCl}_3$ )  $\delta$ : 2.68–2.72 (m, 2H), 3.15 (t,  $J$  = 7.2 Hz, 2H), 7.00 (dd,  $J$  = 7.6, 6.8 Hz, 2H).  $^{13}\text{C}$  NMR (100 MHz,  $\text{CDCl}_3$ )  $\delta$ : 27.6, 33.4, 112.3 (d,  $J$  = 22.8 Hz, 1C), 117.8 (d,  $J$  = 17.5 Hz, 1C), 133.3, 136.9 (d,  $J$  = 253.5 Hz, 1C), 150.4 (d,  $J$  = 254.8 Hz, 2C), 172.5.  $^{19}\text{F}$  NMR (376 MHz,  $\text{CDCl}_3$ )  $\delta$ : -132.36 (dd,  $J$  = 24.4, 19.9 Hz, 2F), -161.00 ~ -161.13 (m, 1F). MS (EI)  $m/z$  (%): 236 ( $\text{M}^+$ , 100), 177 (45). HR-MS calcd. for  $\text{C}_9\text{H}_7\text{F}_3\text{O}_2\text{S}$  [ $\text{M}^+$ ]: 236.2109; found: 236.1989.

**(3,4,5-Trifluorophenyl)benzylsulfide (4n)**

White solid. Mp (recrystallization in petroleum ether) 50.0–50.9 °C. IR (KBr,  $\text{cm}^{-1}$ ): 3414, 3132, 1613, 1519, 1505, 1401, 1049, 823, 719, 694.  $^1\text{H}$  NMR (400 MHz,  $\text{CDCl}_3$ )  $\delta$ : 4.08 (s, 2H), 6.88 (dd,  $J$  = 7.2, 6.0 Hz, 2H), 7.21–7.33 (m, 5H).  $^{13}\text{C}$  NMR (100 MHz,  $\text{CDCl}_3$ )  $\delta$ : 39.5, 110.7, 113.5, 114.1 (d,  $J$  = 17.1 Hz, 1C), 116.4, 119.2, 127.9, 129.0, 132.6, 136.5, 151.3 (d,  $J$  = 26.0 Hz, 2C), 163.0–161.7 (m, 1C).  $^{19}\text{F}$  NMR (376 MHz,  $\text{CDCl}_3$ )  $\delta$ : -132.96 (m, 2F), -161.69 (d,  $J$  = 17.1 Hz, 1F). MS (EI)  $m/z$  (%): 254 ( $\text{M}^+$ , 100), 163 (15). HR-MS calcd. for  $\text{C}_{13}\text{H}_9\text{F}_3\text{S}$  [ $\text{M}^+$ ]: 254.0377; found: 254.0364.

**Bis(3-fluorophenyl)sulfide (5a)**

Yellow oil. IR (KBr,  $\text{cm}^{-1}$ ): 3064, 1597, 1472, 881, 815, 777, 677.  $^1\text{H}$  NMR (400 MHz,  $\text{CDCl}_3$ )  $\delta$ : 7.05 (dd,  $J$  = 10.4, 8.4 Hz, 2H), 7.22–7.26 (m, 2H), 7.31–7.41 (m, 4H).  $^{13}\text{C}$  NMR (100 MHz,  $\text{CDCl}_3$ )  $\delta$ : 110.4, 111.2 (dd,  $J$  = 15.7,



6.1 Hz, 1C), 113.2, 116.0, 118.9, 134.2, 139.9 (d,  $J$  = 252.3 Hz, 2C), 151.6 (dd,  $J$  = 249.4, 6.1 Hz, 2C), 162.8–161.9 (m, 2C).  $^{19}\text{F}$  NMR (376 MHz,  $\text{CDCl}_3$ )  $\delta$ : –117.87 (dd,  $J$  = 15.4, 9.0 Hz, 2F). MS (EI)  $m/z$  (%): 222 ( $\text{M}^+$ , 100), 203 (25). HR-MS calcd. for  $\text{C}_{12}\text{H}_8\text{F}_6\text{S}$  [ $\text{M}^+$ ]: 222.0315; found: 222.0322.

### Bis(3,4,5-trifluorophenyl)sulfide (5b)

White solid. Mp (recrystallization in petroleum ether) 87.8–89.1 °C. IR (KBr,  $\text{cm}^{-1}$ ): 3133, 1617, 1514, 1402, 1043, 690, 610, 478.  $^1\text{H}$  NMR (400 MHz,  $\text{CDCl}_3$ )  $\delta$ : 7.08–7.16 (m, 4H).  $^{13}\text{C}$  NMR (100 MHz,  $\text{CDCl}_3$ )  $\delta$ : 111.1 (dd,  $J$  = 16.1, 6.1 Hz, 4C), 134.3 (2C), 139.9 (d,  $J$  = 252.5 Hz, 2C), 151.6 (d,  $J$  = 249.80 Hz, 4C).  $^{19}\text{F}$  NMR (376 MHz,  $\text{CDCl}_3$ )  $\delta$ : –132.07 (t,  $J$  = 16.5 Hz, 4F), –159.54 ~ –159.69 (m, 2F). MS (EI)  $m/z$  (%): 294 ( $\text{M}^+$ , 100), 163 (95). HR-MS calcd. for  $\text{C}_{12}\text{H}_4\text{F}_6\text{S}$  [ $\text{M}^+$ ]: 293.9938; found: 293.9921.

### Acknowledgements

We thank the National Key Technology R&D Program (No. 2007BAI34B00), National Natural Science Foundation of China (20876147, 20676123), and Opening Foundation of Zhejiang Provincial Top Key Pharmaceutical Discipline for financial support.

### References

- (1) (a) Prim, D.; Campagne, J.-M.; Joseph, D.; Andrioletti, B. *Tetrahedron* **2002**, *58* (11), 2041. doi:10.1016/S0040-4020(02)00076-5.; (b) Hartwig, J. F. *Acc. Chem. Res.* **1998**, *31* (12), 852. doi:10.1021/ar970282g.; (c) Ley, S. V.; Thomas, A. W. *Angew. Chem. Int. Ed.* **2003**, *42* (44), 5400. doi:10.1002/anie.200300594.; (d) Kondo, T.; Mitsudo, T.-a. *Chem. Rev.* **2000**, *100* (8), 3205. doi:10.1021/cr9902749. PMID:11749318.; (e) Taniguchi, N. *J. Org. Chem.* **2007**, *72* (4), 1241. doi:10.1021/jo062131+. PMID:17288374.
- (2) (a) Caboni, P.; Sammelson, R. E.; Casida, J. E. *J. Agric. Food Chem.* **2003**, *51* (24), 7055. doi:10.1021/jf030439l. PMID:14611171.; (b) De Martino, G.; Edler, M. C.; La Regina, G.; Coluccia, A.; Barbera, M. C.; Barrow, D.; Nicholson, R. I.; Chiosis, G.; Brancale, A.; Hamel, E.; Artico, M.; Silvestri, R. *J. Med. Chem.* **2006**, *49* (3), 947. doi:10.1021/jm050809s. PMID:16451061.; (c) Mughesh, G.; du Mont, W.-W.; Sies, H. *Chem. Rev.* **2001**, *101* (7), 2125. doi:10.1021/cr000426w. PMID:11710243.; (d) Villalobos, J. M.; Srogl, J.; Liebeskind, L. S. *J. Am. Chem. Soc.* **2007**, *129* (51), 15734. doi:10.1021/ja074931n. PMID:18047333.
- (3) (a) Migita, T.; Shimizu, T.; Asami, Y.; Shiobara, J.; Kato, Y.; Kosugi, M. *Bull. Chem. Soc. Jpn.* **1980**, *53* (5), 1385. doi:10.1246/bcsj.53.1385.; (b) Kosugi, M.; Ogata, T.; Terada, M.; Sano, H.; Migita, T. *Bull. Chem. Soc. Jpn.* **1985**, *58* (12), 3657. doi:10.1246/bcsj.58.3657.
- (4) (a) Mispelaere-Canivet, C.; Spindler, J.-F.; Perrio, S.; Beslin, P. *Tetrahedron* **2005**, *61* (22), 5253. doi:10.1016/j.tet.2005.03.078.; (b) Itoh, T.; Mase, T. *Org. Lett.* **2004**, *6* (24), 4587. doi:10.1021/ol047996t. PMID:15548082.; (c) Murata, M.; Buchwald, S. L. *Tetrahedron* **2004**, *60* (34), 7397. doi:10.1016/j.tet.2004.05.044.
- (5) (a) Taniguchi, N. *J. Org. Chem.* **2004**, *69* (20), 6904. doi:10.1021/jo040184q. PMID:15387621.; (b) Jammi, S.; Barua, P.; Rout, L.; Saha, P.; Punniyamurthy, T. *Tetrahedron Lett.* **2008**, *49* (9), 1484. doi:10.1016/j.tetlet.2007.12.118.
- (6) Wong, Y.-C.; Jayanth, T. T.; Cheng, C.-H. *Org. Lett.* **2006**, *8* (24), 5613. doi:10.1021/ol062344l. PMID:17107085.
- (7) (a) Deng, W.; Zou, Y.; Wang, Y.-F.; Liu, L.; Guo, Q.-X. *Synlett* **2004**, 1254. doi:10.1055/s-2004-825584.; (b) Herrero, M. T.; SanMartin, R.; Domínguez, E. *Tetrahedron* **2009**, *65* (7), 1500. doi:10.1016/j.tet.2008.11.062.; (c) Chen, Y.-J.; Chen, H.-H. *Org. Lett.* **2006**, *8* (24), 5609. doi:10.1021/ol062339h. PMID:17107084.; (d) Zhu, D.; Xu, L.; Wu, F.; Wan, B. *Tetrahedron Lett.* **2006**, *47* (32), 5781. doi:10.1016/j.tetlet.2006.05.178.
- (8) Pârvulescu, V. I.; Hardacre, C. *Chem. Rev.* **2007**, *107* (6), 2615. doi:10.1021/cr050948h. PMID:17518502.
- (9) (a) Savarin, C.; Srogl, J.; Liebeskind, L. S. *Org. Lett.* **2002**, *4* (24), 4309. doi:10.1021/ol026948a. PMID:12443085.; (b) Herradura, P. S.; Pendola, K. A.; Guy, R. K. *Org. Lett.* **2000**, *2* (14), 2019. doi:10.1021/ol005832g. PMID:10891219.
- (10) (a) Taniguchi, N. *Synlett* **2006**, 1351. doi:10.1055/s-2006-939707.; (b) Luo, P.-S.; Wang, F.; Li, J.-H.; Tang, R.-Y.; Zhong, P. *Synthesis* **2009**, 921. doi:10.1055/s-0028-1083357.
- (11) (a) Camps, F.; Coll, J.; Fabrias, G.; Guerrero, A. *Tetrahedron* **1984**, *40* (15), 2871. doi:10.1016/S0040-4020(01)91296-7.; (b) Thenappan, A.; Burton, D. J. *J. Org. Chem.* **1990**, *55* (15), 4639. doi:10.1021/jo00302a030.; (c) McCarthy, J. R.; Jarvi, E. T.; Matthews, D. P.; Edwards, M. L.; Prakash, N. J.; Bowlin, T. L.; Mehdi, S.; Sunkara, P. S.; Bey, P. *J. Am. Chem. Soc.* **1989**, *111* (3), 1127. doi:10.1021/ja00185a052.; (d) Patrick, T. B.; Nadji, S. *J. Fluor. Chem.* **1990**, *49* (1), 147. doi:10.1016/S0022-1139(00)80371-1.
- (12) (a) Perutz, R. N.; Braun, T. In *Comprehensive Organometallic Chemistry III*; Crabtree, R., Mingos, D. M. P., Eds.; Elsevier: New York, 2007; Vol. 1, p 725; (b) Fukuzawa, S.-I.; Shimizu, E.; Atsuumi, Y.; Haga, M.; Ogata, K. *Tetrahedron Lett.* **2009**, *50* (20), 2374. doi:10.1016/j.tetlet.2009.02.214.
- (13) (a) Quach, T. D.; Batey, R. A. *Org. Lett.* **2003**, *5* (23), 4397. doi:10.1021/ol035681s. PMID:14602009.; (b) Kim, J. S.; Reibenspies, J. H.; Darensbourg, M. Y. *Inorg. Chim. Acta* **1996**, *250* (1–2), 283. doi:10.1016/S0020-1693(96)05237-1.
- (14) Zhong, W.; Liu, Z.; Yu, C.; Su, W. *Synlett* **2008**, 2888. doi:10.1055/s-0028-1083568.
- (15) Frohn, H.-J.; Adonin, N. Y.; Bardin, V. V.; Starichenko, V. F. *Z. Anorg. Allg. Chem.* **2002**, *628* (13), 2827. doi:10.1002/1521-3749(200213)628:13<2827::AID-ZAAC2827>3.0.CO;2-N.
- (16) (a) Suzuki, Y.; Yamanaka, T.; Tanaka, Y.; Niu, K.; Mizushima, M.; Ikeda, S.; Fujimoto, Y.; Yamabe, S. *Heterocycles* **1981**, *15* (2), 1233. doi:10.3987/S-1981-02-1233.; (b) Norris, T.; Leeman, K. *Org. Process Res. Dev.* **2008**, *12* (5), 869. doi:10.1021/op800098a.; (c) Sharghi, N.; Lalezari, I. *J. Chem. Eng. Data* **1963**, *8* (2), 276. doi:10.1021/je60017a041.; (d) Matsugi, M.; Murata, K.; Gotanda, K.; Nambu, H.; Anilkumar, G.; Matsumoto, K.; Kita, Y. *J. Org. Chem.* **2001**, *66* (7), 2434. doi:10.1021/jo001710q. PMID:11281785.



# Electrophilicity of a 9-aryl-9-fluorenyl cation in water — Kinetic evidence for antiaromaticity

Sarah Ward, Tammy Messier, and Matthew Lukeman

**Abstract:** The 9-(4-methoxyphenyl)-9-fluorenyl cation (**2**) has been generated in 100% water by laser flash photolysis of 9-(4-methoxyphenyl)-9-fluorenol (**3**), representing the first observation of a 9-fluorenyl cation in this solvent with lifetimes in the microsecond timescale. The relatively long lifetime permitted quenching studies with a number of anionic nucleophiles, and bimolecular rate constants for each were determined. For both bromide and iodide, rate data suggest that an equilibrium between the cation and trapped product is rapidly established, followed by slower, irreversible trapping of the cation by water. The bimolecular rate constants obtained show that the generated 9-fluorenyl cation is significantly more reactive towards nucleophilic attack, by two orders of magnitude, than related triarylmethyl cations that lack the  $4n \pi$ -system, lending support to the characterization of fluorenyl cations as antiaromatic.

**Key words:** 9-fluorenyl cation, laser flash photolysis, electrophilicity, carbocation, antiaromaticity.

**Résumé :** On a généré le cation 9-(4-méthoxyphényl)-9-fluorényle (**2**) dans un solvant à 100 % d'eau par photolyse éclair au laser du 9-(4-méthoxyphényl)-9-fluorénol (**3**); ceci correspond à la première observation du cation 9-fluorényle dans ce solvant avec un temps de vie de l'échelle de la microseconde. Le temps de vie relativement long a permis d'effectuer des études de piégeage avec un certain nombre de nucléophiles anioniques et on a déterminé les constantes de vitesses bimoléculaires pour chacune. Pour le bromure ainsi que pour l'iodure, les données de vitesse suggèrent qu'il s'établit rapidement un équilibre entre le cation et le produit piégé, suivi par un piégeage irréversible plus lent du cation par l'eau. Les constantes de vitesses bimoléculaires obtenues montrent que vis-à-vis des attaques nucléophiles, le cation 9-fluorényle généré est beaucoup plus réactif (au moins deux ordres de grandeur) que les réactions apparentées des cations triarylméthyles qui ne comportent pas de système  $4n \pi$ ; cette observation est en accord avec une caractérisation des cations fluorényles comme antiaromatiques.

**Mots-clés :** cation 9-fluorényle, photolyse éclair au laser, caractère électrophile, carbocation, antiaromaticité.

[Traduit par la Rédaction]

## Introduction

Antiaromaticity is a central concept in organic chemistry, and has been defined in thermodynamic terms: "If the structure is of higher energy (less stable) than such a hypothetical classical structure, the molecular entity is antiaromatic."<sup>1</sup> It can sometimes be difficult to assess antiaromaticity according to this definition, since energies of such hypothetical structures cannot be directly measured and can only be estimated. Comparisons between different but related structures are often used instead, and in addition to thermodynamic considerations, kinetic, electronic, geometric, spectroscopic, and magnetic data are frequently used to assess antiaromaticity.<sup>2</sup>

The potential antiaromaticity of the 9-fluorenyl cation (**1**) and its derivatives has been a source of interest for decades. Several observations support the notion that **1** is antiaromatic, including: the central ring possesses  $4n \pi$ -electrons, efforts to generate **1** thermally by dissolution of 9-fluorenol in strongly acidic media have failed,<sup>3</sup> and solvolysis reac-

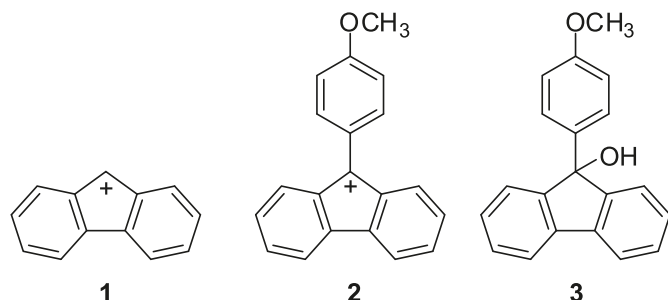
tions involving 9-fluorenyl cations proceed several orders of magnitude more slowly than analogues that do not involve  $4n \pi$ -systems.<sup>4</sup> Mills et al. have provided strong evidence in favour of the antiaromatic nature of the 9-fluorenyl cation ring when present as a component of fluorenylidene dications.<sup>5</sup> Amyes et al. determined that the  $pK_R$  value for **1** (−15.9) is more negative than that of the analogous diphenylmethyl cation ( $\text{Ph}_2\text{CH}^+$ ,  $pK_R = -11.7$ ), and based on these experiments and calculations, they estimate that **1** is destabilized by ~10 kcal/mol relative to the diphenylmethyl cation, which they claim is a relatively small difference that does not support the existence of antiaromatic character in **1**.<sup>6</sup> Magnetic susceptibility exaltation calculations carried out by Tidwell and co-workers at the ab initio and density functional theory levels also suggest that 9-fluorenyl cations do not have antiaromatic character, but are instead nonaromatic.<sup>7</sup> From the available studies, it appears that support for the antiaromaticity of **1** depends on which criterion is being considered. What is ultimately desired is a quantitative knowledge of the reactivity of 9-fluorenyl cations, such

Received 1 November 2009. Accepted 10 February 2010. Published on the NRC Research Press Web site at canjchem.nrc.ca on 20 April 2010.

S. Ward, T. Messier, and M. Lukeman.<sup>1</sup> Department of Chemistry, Acadia University, 6 University Avenue, Wolfville, NS B4P 4R6, Canada.

<sup>1</sup>Corresponding author (e-mail: mlukeman@acadiau.ca).

as **1**, so that their electrophilic character can be best understood. There remains a paucity of kinetic data involving electrophilic reactions of 9-fluorenyl cations, primarily because the typically fast reaction rates are difficult to measure. The current rate data available for 9-fluorenyl cations is largely limited to solvolysis reactions in fluorinated alcohols or water/organic solvent mixtures, since the very weak nucleophiles present in these cases give slow reactions that are more easily monitored. It was our desire at the outset of this project to address the lack of available kinetic data and enhance our knowledge of the reactivity of 9-fluorenyl cations by obtaining rate data for a wider suite of nucleophiles.



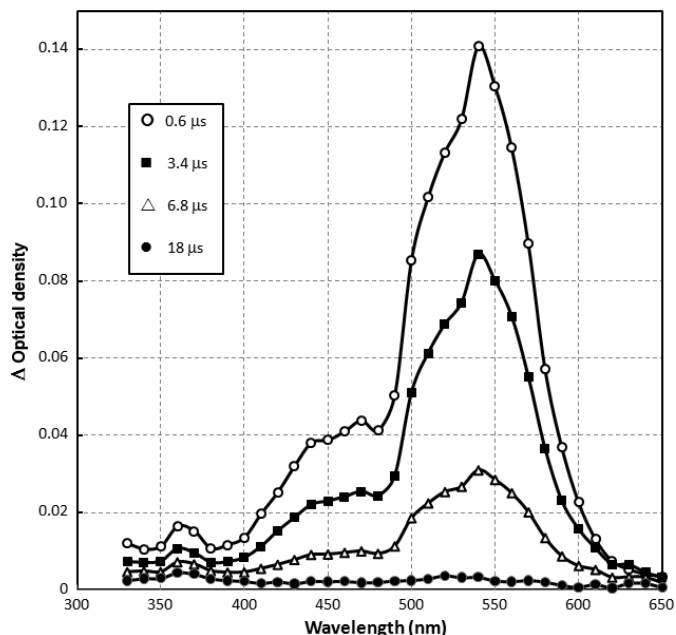
Wan and co-workers have uncovered a convenient photochemical route to 9-fluorenyl cations via photolysis of the corresponding 9-fluorenol derivatives.<sup>8</sup> 9-Fluorenyl cations generated in this way are generally very short-lived in aqueous solution ( $\tau < 20$  ps for **1**),<sup>9</sup> but can persist for much longer in non-nucleophilic protic solvents ( $\tau = 30$   $\mu$ s for **1** in 1,1,1,3,3,3-hexafluoro-2-propanol (HFIP)).<sup>10</sup> Many 9-substituted 9-fluorenyl cations have since been generated photolytically and characterized by LFP,<sup>11,12</sup> usually in polar protic organic solvents such as 1,1,1-trifluoroethanol (TFE) or HFIP, or in aqueous/organic solvent mixtures, but not in entirely aqueous solution. We were particularly interested in one such report<sup>11</sup> in which the 9-(4'-methoxyphenyl)-9-fluorenyl cation (**2**) is demonstrated to react with water (in 4:1 water/acetonitrile solution) with a rate constant of  $1.7 \times 10^5$  s<sup>-1</sup>, corresponding to a lifetime of 5.9  $\mu$ s that is easily accessible by nanosecond LFP. We expected that the cation would still be detectable in a 100% aqueous solvent, and that information regarding the electrophilicity of **2** could be determined through quenching studies with nucleophiles, thus providing for the first time comprehensive quantitative information on the electrophilicity of a substituted 9-fluorenyl cation.

## Results

The photochemical precursor to cation **2** is 9-(4'-methoxyphenyl)-9-fluorenol (**3**), which was readily prepared by the reaction of 4-methoxyphenylmagnesium bromide with 9-fluorenone in dry THF.

Water/acetonitrile mixtures are frequently used for the flash photolytic generation of organic cations, mainly because the organic co-solvent helps to solubilize the cation precursor. We were instead interested in using pure water as the solvent system in this study, since the nucleophilicity parameters ( $N^+$ ) of many nucleophiles are defined in this solvent.<sup>13</sup> The organic co-solvent was not needed in our

**Fig. 1.** Transient absorption spectrum obtained on LFP of **3** in Ar-purged water. Each trace corresponds to the time after laser pulse indicated in the legend.

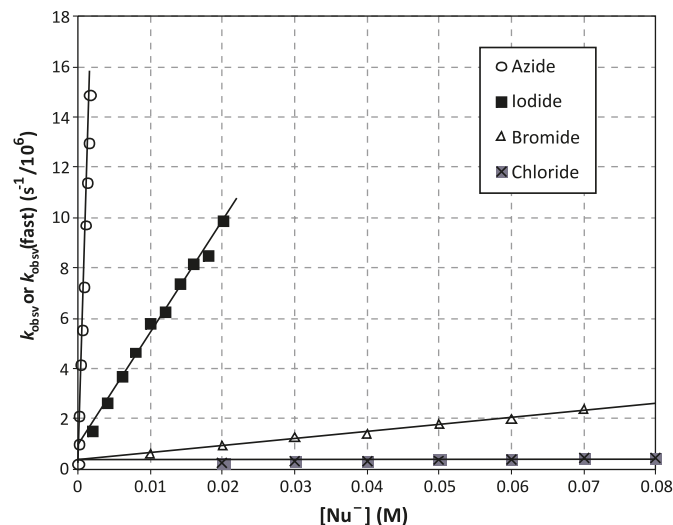


case to achieve sufficient concentrations of **3** for LFP studies. Nanosecond LFP of **3** in argon-bubbled water gave rise to a strongly absorbing transient with maxima at  $\lambda_{\text{max}} = 540$  and 460 nm (Fig. 1), very similar in appearance to that obtained in 4:1 H<sub>2</sub>O/CH<sub>3</sub>CN by McClelland and co-workers,<sup>11</sup> and is assigned to cation **2**. This transient decayed with first-order kinetics with a rate constant of  $2.7 \times 10^5$  s<sup>-1</sup> (20 °C), which is ~60% faster than the rate constant observed by McClelland and co-workers in 4:1 H<sub>2</sub>O/CH<sub>3</sub>CN, but is still sufficiently slow to allow for detailed quenching studies using nanosecond LFP. McClelland et al. measured the solvolysis rates of several diarylmethyl and triarylmethyl cations in water/acetonitrile mixtures with varying water content, and found that rate constants dropped slightly (by close to 20%) on moving from 20% water to pure water.<sup>14</sup> The 60% increase in rate constant we observe for **2** on moving from 80% to pure water is behaviour that is clearly different from that of the previously examined systems,<sup>14</sup> and shows that the presence of the organic co-solvent in some cases can indeed have a sizeable effect on the lifetime of organic cations. Quenching of this transient was carried out using a total of six anionic nucleophiles (bromide, iodide, chloride, fluoride, azide, and acetate) at a number of concentrations. Quenching plots were constructed for each of these nucleophiles, and data for selected nucleophiles are plotted in Fig. 2.

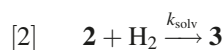
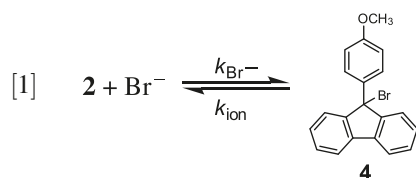
### Quenching by bromide

LFP of **3** in water containing 0.03 mol/L NaBr gave rise to a transient with an absorption profile identical in appearance to that shown in Fig. 1. The decay of this transient, however, was clearly not first-order, unlike the case in the absence of bromide (Fig. 3). The decay data fit well to a biexponential function, revealing two rate constants:  $k_{\text{obsd}}(\text{fast}) = 1.4 \times 10^6$  s<sup>-1</sup> and  $k_{\text{obsd}}(\text{slow}) = 6.5 \times 10^4$  s<sup>-1</sup>.

**Fig. 2.** Quenching plots indicating changes in  $k_{\text{obsd}}$  (or  $k_{\text{obsv}}(\text{fast})$ ) for  $\text{Br}^-$  and  $\text{I}^-$  at 300 K as a function of added nucleophile for the following nucleophiles:  $\text{NaN}_3$ ,  $\text{NaI}$ ,  $\text{NaBr}$ , and  $\text{NaCl}$ .



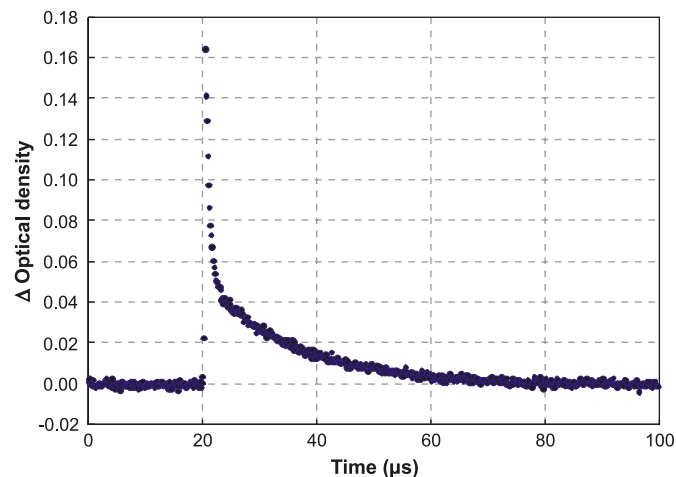
The rate constants and the pre-exponential factors remained constant at all wavelengths between 400 and 600 nm, suggesting that both decay components can be attributed to the same absorbing species (namely, cation **2**). As the bromide concentration was increased, the magnitude of the shorter component,  $k_{\text{obsd}}(\text{fast})$ , was increased and that of the longer component,  $k_{\text{obsd}}(\text{slow})$ , was reduced. This behaviour is consistent with the existence of an equilibrium between **2** and its 9-bromo adduct **4** (which does not absorb in the visible region), according to eq. [1] and eq. [2].<sup>15</sup> The fast decay component,  $k_{\text{obsd}}(\text{fast})$ , corresponds to establishment of the equilibrium (eq. [1]), while the slow component,  $k_{\text{obsd}}(\text{slow})$ , corresponds to the reaction of the equilibrium concentration of **2** with solvent water (eq. [2]). At bromide concentrations greater than 0.01 mol/L,  $k_{\text{obsd}}(\text{fast})$  exhibits a linear correlation with  $[\text{Br}^-]$ , according to eq. [3]. The data obtained from this correlation (plotted in Fig. 2) provides  $k_{\text{Br}^-} = 3.0 \times 10^7 \text{ M}^{-1}\text{s}^{-1}$  and  $k_{\text{ion}} = 4.8 \times 10^5 \text{ s}^{-1}$ . The ratio of these rates gives  $K_{\text{eq}} = 62 \text{ mol/L}^{-1}$ .



$$[3] \quad k_{\text{obsd}}(\text{fast}) = k_{\text{Br}^-}[\text{Br}^-] + k_{\text{ion}}$$

McClelland et al. observed similar equilibrium quenching of the trityl cation ( $\text{Ph}_3\text{C}^+$ ) with bromide,<sup>16</sup> and their analysis provided  $k_{\text{Br}^-} = 5.1 \times 10^6 \text{ M}^{-1}\text{s}^{-1}$ ,  $k_{\text{ion}} = 7.6 \times 10^6 \text{ s}^{-1}$ , and  $K_{\text{eq}} = 6.6 \text{ mol/L}^{-1}$  for that system. Comparison of these data with those obtained for **2** demonstrates the strong electrophilic nature of **2**. Bromide ion reacts with **2** faster than with the trityl cation, which is not a 4n system, despite the fact that **2** contains a stabilizing 4-methoxy group and the

**Fig. 3.** Transient absorption signal observed at 540 nm on LFP of **3** in water containing 0.03 mol/L  $\text{NaBr}$  with a clearly visible biphasic decay.



trityl cation does not. The lower stability of **2** relative to the trityl cation is also evident from the fact that  $K_{\text{eq}}$  is an order of magnitude larger in the case of **2**. It is indeed remarkable that **2** forms a detectable equilibrium with bromide, since this suggests that **4** should be a *thermal* source of the formally antiaromatic cation **2** in aqueous solution at room temperature.

The quenching experiments were repeated using two other bromide sources,  $\text{KBr}$  and  $\text{NH}_4\text{Br}$ , and no changes in the decay kinetics were observed, indicating that the cation behaves merely as a spectator ion and does not influence the anion–organic cation recombination.

### Quenching by iodide

Biphasic decay of **2** was also observed on LFP of **3** in aqueous solutions containing  $\text{NaI}$  ( $\geq 0.002 \text{ mol/L}$ ). A plot of  $k_{\text{obsd}}(\text{fast})$  vs.  $[\text{NaI}]$  (Fig. 2) was linear, and the data were treated by the same method as in the case of bromide giving  $k_{\text{I}^-} = 4.5 \times 10^8 \text{ M}^{-1}\text{s}^{-1}$ ,  $k_{\text{ion}} = 9.5 \times 10^5 \text{ s}^{-1}$ , and  $K_{\text{eq}} = 474 \text{ mol/L}^{-1}$ . The much larger  $k_{\text{Nu}^-}$  and  $K_{\text{eq}}$  values observed for quenching with iodide relative to bromide are consistent with the much greater nucleophilicity of iodide in aqueous solution.

### Quenching by other anionic nucleophiles

LFP of **3** in aqueous solution containing sodium chloride, sodium fluoride, sodium acetate, or sodium azide gave only the transient assigned to **2**, which in all cases showed clean first-order decay kinetics at all nucleophile concentrations examined. The absence of equilibrium behaviour (as was observed in the presence of bromide and iodide) for these nucleophiles is consistent with their comparatively lower leaving-group ability. Thus, when these nucleophiles are employed,  $k_{\text{ion}}$  is negligibly small, and the rate data can be described in a much simpler way (i.e., eq. [4]). Quenching plots of  $k_{\text{obsd}}$  vs.  $[\text{Nu}]$  were constructed for each of these four nucleophiles (plots for  $\text{NaN}_3$  and  $\text{NaCl}$  are shown in Fig. 2), and bimolecular quenching rate constants were obtained and appear in Table 1.

$$[4] \quad k_{\text{obsd}} = k_{\text{Nu}^-}[\text{Nu}^-] + k_{\text{s}}$$

**Table 1.** Rate and equilibrium constants for the reaction of **2** with nucleophiles at 300 K. Errors in values are estimated to be  $\pm 10\%$ .

Nu <sup>-</sup>	$k_{\text{Nu}^-}$ (M <sup>-1</sup> s <sup>-1</sup> )	$k_{\text{ion}}$ (s <sup>-1</sup> )	$K_{\text{eq}}$ (mol/L <sup>-1</sup> )
Br <sup>-</sup>	$3.0 \times 10^7$	$4.8 \times 10^5$	62
I <sup>-</sup>	$4.5 \times 10^8$	$9.5 \times 10^5$	474
Cl <sup>-</sup>	$3.3 \times 10^6$	—	—
F <sup>-</sup>	$3.8 \times 10^5$	—	—
OAc <sup>-</sup>	$4.3 \times 10^5$	—	—
N <sub>3</sub> <sup>-</sup>	$9.2 \times 10^9$	—	—
H <sub>2</sub> O	$2.7 \times 10^5$ s <sup>-1</sup> (293 K)	—	—

The bimolecular rate constants obtained for the reaction of the 9-(4-methoxyphenyl)-9-fluorenyl cation (**2**) span more than four orders of magnitude on moving from the weakest anionic nucleophile employed (fluoride) to the strongest (azide). The large value of  $9.2 \times 10^9$  M<sup>-1</sup>s<sup>-1</sup> for the reaction of **2** with azide is of interest, since it is significantly larger than the values obtained for the reaction of azide with other related arylmethyl cations:  $k(\text{N}_3^-) = 6.3 \times 10^9$  M<sup>-1</sup>s<sup>-1</sup> for the anthylium ion,<sup>17</sup>  $k(\text{N}_3^-) = 1.7 \times 10^8$  M<sup>-1</sup>s<sup>-1</sup> for the 9-phenylxanthylum ion,<sup>17</sup> and  $k(\text{N}_3^-) = 4.1 \times 10^9$  M<sup>-1</sup>s<sup>-1</sup> for the trityl cation.<sup>16</sup> To estimate the rate constants of various nucleophiles with phenethyl cations, Richard et al. have employed the reaction of these cations with azide ions as a “clock” with the estimated value of  $5 \times 10^9$  M<sup>-1</sup>s<sup>-1</sup> used as an upper limit.<sup>18</sup> The value we have obtained for the reaction of **2** with azide is nearly double this assumed upper limit.

### Activation energy determination

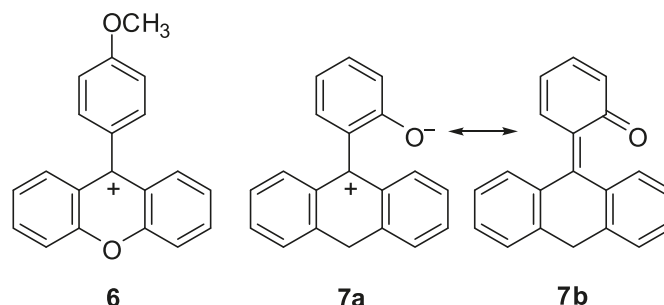
The reaction rate,  $k_{\text{solv}}$ , of **2** with water was measured at a variety of temperatures, and an Arrhenius plot of  $\log k_{\text{solv}}$  vs.  $1/T$  was constructed (Fig. 4). A linear fit was obtained providing an activation energy of 5.4 kcal/mol.

### Discussion

Several triarylmethyl cations have been previously generated and studied using LFP, providing many systems for comparison with the present data. Perhaps the most relevant is the methoxytrityl cation **5**, which is structurally comparable to cation **2**, but does not contain a 4n ring. This cation has been studied using stopped flow<sup>19</sup> and LFP<sup>14</sup> techniques, and reacts with water (in 1:2 CH<sub>3</sub>CN/H<sub>2</sub>O) with a rate constant of  $1.4 \times 10^3$  s<sup>-1</sup>. While data in pure water are not available for this cation, moving to this solvent might be reasonably expected to increase the rate constant for the reaction of **5** with water by approximately 60%, just as it did for **2**, giving an estimated pseudo-first-order rate constant of  $\sim 2 \times 10^3$  s<sup>-1</sup>. Thus, the 4-methoxytrityl cation (**5**) is two full orders of magnitude less reactive toward water than is the fluorenyl cation (**2**). This comparison provides support for the notion that 9-fluorenyl cations, such as **1** and **2**, possess enhanced reactivity consistent with antiaromatic destabilization.

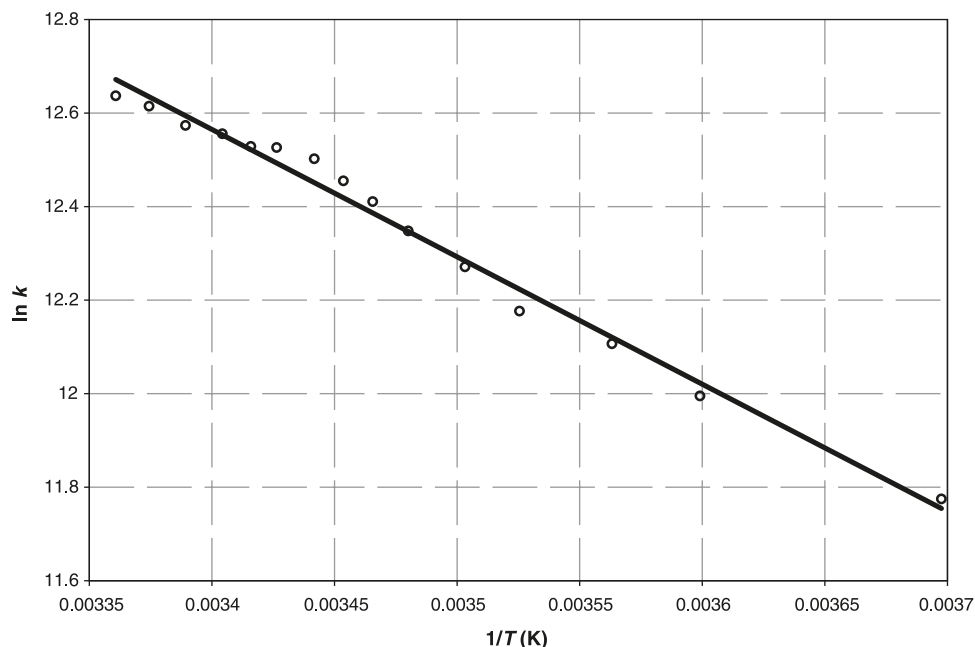
Direct comparison of the reactivities of **2** and **5** is complicated by the likelihood that the geometries of these cations are different, which introduces a steric component to the reactivity difference. Cation **2** likely has a more or less planar fluorenyl ring system with the 9-aryl group twisted out of the plane somewhat to relieve steric repulsion between the

1- and 8-fluorenyl hydrogens and the ortho hydrogens of the methoxyphenyl ring (Fig. 5).<sup>11</sup> Cation **5** is more likely to adopt a “paddlewheel” configuration, which might make the carbocation less sterically accessible, and thus less reactive toward nucleophiles. It is difficult to assess precisely how much of the reduced reactivity of **5** relative to **2** might result from steric differences, although a number of triaryl-methyl cations in which two rings are covalently bonded and thus constrained to be coplanar have been reported, and are available for comparison. The 9-(4'-methoxyphenyl)-9-xanthylum cation (**6**) is geometrically similar to **2**, but contains an aromatic central ring. Its reported reaction rate constant with water (in 1:4 CH<sub>3</sub>CN/water, 25 °C) of  $1.1 \times 10^1$  s<sup>-1</sup> is more than four orders of magnitude less than that of **2**.<sup>17</sup> Cation **7** has been generated in LFP experiments by Wan and co-workers,<sup>20</sup> and is a triarylmethyl cation related to **2** containing a central ring that is non-aromatic. This cation reacts very slowly with water (in 1:1 CH<sub>3</sub>CN/H<sub>2</sub>O) with a rate constant estimated to lie between  $10^0$  and  $10^{-2}$  s<sup>-1</sup>. The low value of the rate constant in this case might be partially rationalized by electron donation from the phenoxide ortho to the carbocation as is evident in resonance form **7b**, although the relative contribution of this resonance form is likely diminished by the expected twisting of the 9-aryl group out of the plane to relieve steric repulsion. It is clear from the examples of **6** and **7** that co-planarity of two aryl rings does not necessarily impart high reactivity to triarylmethyl cations, and that the reactivity is instead primarily a function of aromaticity and the ability of attached electron-donating groups to delocalize the charge. For this reason, we believe that the greatly increased reactivity of **2** relative to **5** is primarily due to antiaromatic character of the 4n central ring.

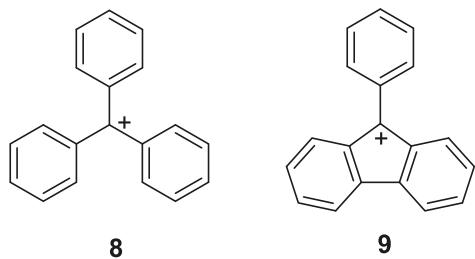


While **5** provides a natural basis for comparison of the reactivity of **2**, rate data for the reaction of **5** with other nucleophiles are not available. However, bimolecular rate constants for the reaction of the related trityl cation **8** with a wide variety of nucleophiles are available.<sup>16</sup> Reaction of **8** with water (in 1:2 CH<sub>3</sub>CN/H<sub>2</sub>O, 20 °C) occurs with a pseudo-first-order rate constant of  $1.50 \times 10^5$  s<sup>-1</sup>, a value that is approximately 100-fold faster than for **5**, a fact that can be almost entirely attributed to the absence of the stabilizing 4-methoxy group that is present only in **5**. Bimolecular rate constants for the reaction of **8** with several anionic nucleophiles also employed in the present work are available, including Br<sup>-</sup> ( $5 \times 10^6$  M<sup>-1</sup>s<sup>-1</sup>), Cl<sup>-</sup> ( $2.2 \times 10^6$  M<sup>-1</sup>s<sup>-1</sup>), F<sup>-</sup> ( $8.6 \times 10^5$  M<sup>-1</sup>s<sup>-1</sup>), AcO<sup>-</sup> ( $4 \times 10^5$  M<sup>-1</sup>s<sup>-1</sup>), and N<sub>3</sub><sup>-</sup> ( $4.1 \times 10^9$  M<sup>-1</sup>s<sup>-1</sup>).<sup>16</sup> The reaction rates of **8** with these nucleophiles are similar (within an order of magnitude) to those of **2** (Table 1). Because of the similarity in

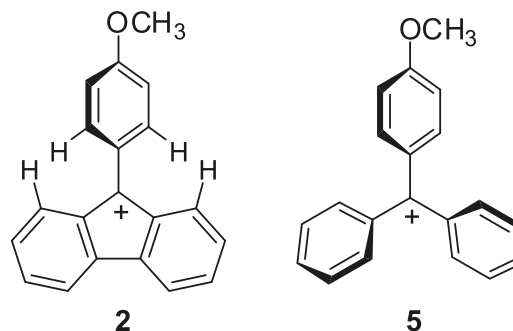


**Fig. 4.** Arrhenius plot of the reaction of **2** with water.

the reactivity of **2** and **8**, and the fact that **8** is roughly 100 times more reactive than **5** (at least towards the reaction with water), we can estimate that the increase in reactivity due to the presence of the formally antiaromatic 4n ring in **2** is roughly the same as the increase in reactivity experienced on removing a stabilizing 4-methoxy group. In fact, comparison of the pseudo-first-order rate constants of water with “antiaromatic” 9-phenyl-9-fluorenyl cation (**9**) ( $1.50 \times 10^7 \text{ s}^{-1}$ )<sup>11</sup> with **8** ( $1.50 \times 10^5 \text{ s}^{-1}$ )<sup>16</sup> reveals the same 100-fold difference in rates. This rate enhancement of two orders of magnitude has been noted previously for solvolysis reactions involving 4n rings,<sup>11</sup> and we now show that this enhancement is general for nucleophilic reactions with rate constants spanning more than five orders of magnitude, and might be general for other reactions of 9-fluorenyl cations.



The rates for the reaction of nucleophiles with cation **2** are slightly higher than for cation **8** for all nucleophiles examined except for fluoride, for which the reaction with the trityl cation is roughly twice as fast as for reaction with **2**.<sup>16</sup> This anomaly might result from the different solvent systems used in the two studies. Fluoride is especially well-solvated by water, a fact that greatly reduces its nucleophilicity when dissolved in this solvent. The reaction of **2** with fluoride studied in this work employed pure water as the solvent, and the fluoride ions would be expected to enjoy maximum solvation, leading to relatively low observed rates. In the case of the reaction of **8** with fluoride, the sol-

**Fig. 5.** Anticipated geometries of cations **2** and **5**.<sup>11</sup>

vent system contained 20% acetonitrile, which may have been responsible for decreased solvation of the fluoride anions, increasing their nucleophilicity and hence reaction rate with **8**. A similar effect would be less noticeable for the other anions that are not solvated by water as strongly as fluoride.

## Conclusion

We report for the first time kinetic data for a 4n cation (**2**) in water with a comprehensive series of nucleophiles, which span more than five orders of magnitude of reactivity. In the case of iodide and bromide nucleophiles, equilibrium behaviour was observed and equilibrium constants were determined. Comparison of the obtained rate data with known systems allows us to generalize that the presence of the 4n ring increases the reaction rate constants towards nucleophilic attack by approximately two orders of magnitude relative to related systems that do not possess a 4n ring, regardless of the nucleophile used. This rate increase resulting from the 4n ring is essentially the same as that observed on removing a 4-methoxy group. The kinetic data measured in this work support the notion that 9-fluorenyl cations indeed have antiaromatic character.

## Experimental

### General

LFP data was obtained with a LuzChem mLFP-111 system employing an Excimer laser (Xe/HCl) that supplied 308 nm pulses attenuated to ~10 mJ/pulse. Solutions were not flowed and were purged with argon gas prior to irradiation. Solutions' concentrations were adjusted to an absorbance value of 0.4 units at the laser wavelength (308 nm) and a 10 mm cell was used. NMR spectra were recorded in CDCl<sub>3</sub> purchased from Norell Inc. and run on a Bruker AVANCE 300 spectrometer. UV-vis spectra were recorded using a CARY 100 spectrometer.

### Materials

All fine chemicals were purchased from Sigma-Aldrich and used as received. Solvents were purchased from Caledon and used as received except for THF, which was distilled from sodium.

### 9-(4-Methoxyphenyl)-9-fluorenone (3)

To 9-fluorenone (5.0 g) dissolved in 20 mL dry THF was added 2 equiv. of 4-methoxyphenylmagnesium bromide, and the mixture was stirred at room temperature for 4 h. The reaction was quenched by addition of water and extracted with 20 mL CH<sub>2</sub>Cl<sub>2</sub>. The organic layer was separated and dried with MgSO<sub>4</sub>, and the solvent was removed by rotary evaporation. Compound **2** was obtained as a slightly yellow solid in 33% yield after recrystallization from cyclohexane. Mp 76–88 °C (lit.<sup>21</sup> mp 85–86 °C). <sup>1</sup>H NMR (300 MHz, CDCl<sub>3</sub>) δ (ppm): 2.67 (br s, 1H, OH), 3.77 (s, 3H, OCH<sub>3</sub>), 6.82 (d, 2H), 7.23–7.42 (m, 8H), 7.68 (d, 2H). <sup>13</sup>C NMR (75 MHz, CDCl<sub>3</sub>) δ (ppm): 55.60, 83.76, 114.00, 120.47, 125.14, 127.04, 128.83, 129.41, 135.75, 139.90, 151.00, 159.18.

### Acknowledgement

We thank the Natural Sciences and Engineering Research Council of Canada (NSERC), the Canadian Foundation for Innovation (CFI), and the Nova Scotia Research and Innovation Trust (NSRIT) for generous financial support. SW thanks NSERC for an Undergraduate Summer Research Award (USRA) and TM thanks Acadia University for a Huggins Summer Research Award (HSRA). Financial support was also provided by the Acadia University Research Fund. We also thank Dr. John Roscoe (Acadia University) for helpful discussions.

### References

- (1) Muller, P. *Pure Appl. Chem.* **1994**, *66* (5), 1077. doi:10.1351/pac199466051077.
- (2) Allen, A. D.; Tidwell, T. T. *Chem. Rev.* **2001**, *101* (5), 1333. doi:10.1021/cr990316t. PMID:11710224.
- (3) Olah, G. A.; Prakash, G. K. S.; Liang, G.; Westerman, P. W.; Kunde, K.; Chandrasekhar, J.; Schleyer, P. R. *J. Am. Chem. Soc.* **1980**, *102* (13), 4485. doi:10.1021/ja00533a030.
- (4) (a) Bolton, R.; Chapman, N. B.; Shorter, J. *J. Chem. Soc.* **1964**, 1895. doi:10.1039/jr9640001895.; (b) Eaborn, C.; Gollsworth, R. C.; Lilly, M. N. *J. Chem. Soc.* **1968**, 3052; (c) Friedrich, E. C.; Taggart, D. B. *J. Org. Chem.* **1978**, *43* (5), 805. doi:10.1021/jo00399a003.

- (5) (a) Malandra, J. L.; Mills, N. S.; Kadlecsek, D. E.; Lowery, J. A. *J. Am. Chem. Soc.* **1994**, *116* (25), 11622. doi:10.1021/ja00104a074.; (b) Mills, N. S.; Malandra, J. L.; Burns, E. E.; Green, A.; Unruh, K. E.; Kadlecsek, D. E.; Lowery, J. A. *J. Org. Chem.* **1997**, *62* (26), 9318. doi:10.1021/jo971716o.; (c) Mills, N. S.; Burns, E. E.; Hodges, J.; Gibbs, J.; Esparza, E.; Malandra, J. L.; Koch, J. *J. Org. Chem.* **1998**, *63* (9), 3017. doi:10.1021/jo972202s.; (d) Mills, N. S.; Malinky, T.; Malandra, J. L.; Burns, E. E.; Crossno, P. *J. Org. Chem.* **1999**, *64* (2), 511. doi:10.1021/jo981517k.; (e) Mills, N. S. *J. Am. Chem. Soc.* **1999**, *121* (50), 11690. doi:10.1021/ja9929032.; (f) Mills, N. S.; Benish, M. A.; Ybarra, C. *J. Org. Chem.* **2002**, *67* (7), 2003. doi:10.1021/jo001776l. PMID:11925203.; (g) Mills, N. S. *J. Org. Chem.* **2002**, *67* (20), 7029. doi:10.1021/jo026075y. PMID:12353996.; (h) Levy, A.; Rakowitz, A.; Mills, N. S. *J. Org. Chem.* **2003**, *68* (10), 3990. doi:10.1021/jo026924h. PMID:12737582.; (i) Mills, N. S.; Tirla, C.; Benish, M. A.; Rakowitz, A. J.; Bebell, L. M.; Hurd, C. M. M.; Bria, A. L. *J. Org. Chem.* **2005**, *70* (26), 10709. doi:10.1021/jo051599u. PMID:16355989.; (j) Piekarski, A. M.; Mills, N. S.; Yousef, A. *J. Am. Chem. Soc.* **2008**, *130* (44), 14883. doi:10.1021/ja8042323. PMID:18850706.
- (6) Amyes, T. L.; Richard, J. P.; Novak, M. *J. Am. Chem. Soc.* **1992**, *114* (21), 8032. doi:10.1021/ja00047a010.
- (7) Jiao, H.; Schleyer, P. von R.; Mo, Y.; McAllister, M. A.; Tidwell, T. T. *J. Am. Chem. Soc.* **1997**, *119* (30), 7075. doi:10.1021/ja970380x.
- (8) (a) Wan, P.; Krogh, E. *J. Chem. Soc. Chem. Commun.* **1985**, 1027; (b) Wan, P.; Krogh, E. *J. Am. Chem. Soc.* **1989**, *111* (13), 4887. doi:10.1021/ja00195a048.
- (9) (a) Mecklenburg, S. L.; Hilinski, E. F. *J. Am. Chem. Soc.* **1989**, *111* (14), 5471. doi:10.1021/ja00196a066.; (b) Gurzadyan, G. G.; Steenken, S. *Chem. Eur. J.* **2001**, *7* (8), 1808. doi:10.1002/1521-3765(20010417)7:8<1808::AID-CHEM18080>3.0.CO;2-8.
- (10) McClelland, R. A.; Mathivanan, N.; Steenken, S. *J. Am. Chem. Soc.* **1990**, *112* (12), 4857. doi:10.1021/ja00168a034.
- (11) Cozens, F. L.; Mathivanan, N.; McClelland, R. A.; Steenken, S. *J. Chem. Soc., Perkin Trans. 2* **1992**, (12): 2083. doi:10.1039/p29920002083.
- (12) (a) Johnston, L. J.; Kwong, P.; Shelemay, A.; Lee-Ruff, E. *J. Am. Chem. Soc.* **1993**, *115* (5), 1664. doi:10.1021/ja00058a009.; (b) Lew, C. S. Q.; McClelland, R. A.; Johnston, L. J.; Schepp, N. P. *J. Chem. Soc., Perkin Trans. 2* **1994**, (3): 395. doi:10.1039/p29940000395.; (c) Allen, A. D.; Colomvakos, J. D.; Tee, O. S.; Tidwell, T. T. *J. Org. Chem.* **1994**, *59* (24), 7185. doi:10.1021/jo00103a001.; (d) Lew, C. S. Q.; Wagner, B. D.; Angelini, M. P.; Lee-Ruff, E.; Luszyk, J.; Johnston, L. J. *J. Am. Chem. Soc.* **1996**, *118* (48), 12066. doi:10.1021/ja962066t.; (e) Lew, C. S. Q.; Wong, D. F.; Johnston, L. J.; Bertone, M.; Hopkinson, A. C.; Lee-Ruff, E. *J. Org. Chem.* **1996**, *61* (20), 6805. doi:10.1021/jo941685m. PMID:11667572.; (f) Creary, X.; Wolf, A. *J. Phys. Org. Chem.* **2000**, *13* (6), 337. doi:10.1002/1099-1395(200006)13:6<337::AID-POC249>3.0.CO;2-T.; (g) Mladenova, G.; Chen, L.; Rodriguez, C. F.; Siu, K. W. M.; Johnston, L. J.; Hopkinson, A. C.; Lee-Ruff, E. *J. Org. Chem.* **2001**, *66* (4), 1109. doi:10.1021/jo0009200. PMID:11312936.; (h) O'Neill, M. A.; Cozens, F. L.; Schepp, N. P. *Tetrahedron* **2000**, *56* (36), 6969. doi:10.1016/S0040-4020(00)00518-4.
- (13) Ritchie, C. D. *Can. J. Chem.* **1986**, *64* (12), 2239. doi:10.1139/v86-370.

- (14) McClelland, R. A.; Kanagasabapathy, V. M.; Banait, N. S.; Steenken, S. *J. Am. Chem. Soc.* **1989**, *111* (11), 3966. doi:10.1021/ja00193a031.
- (15) This approximation, also used by McClelland et al. in ref. 16, relies on two assumptions: (i) the concentration of bromide is much greater than that of **2** such that the bimolecular reaction is pseudo-first-order and (ii) trapping of **2** by water (eq. [2] has a negligible contribution to the fast decay component. We believe both approximations are valid in the present case.
- (16) McClelland, R. A.; Banait, N.; Steenken, S. *J. Am. Chem. Soc.* **1986**, *108* (22), 7023. doi:10.1021/ja00282a029.
- (17) McClelland, R. A.; Banait, N.; Steenken, S. *J. Am. Chem. Soc.* **1989**, *111* (8), 2929. doi:10.1021/ja00190a030.
- (18) Richard, J. P.; Rothenberg, M. E.; Jencks, W. P. *J. Am. Chem. Soc.* **1984**, *106* (5), 1361. doi:10.1021/ja00317a031.
- (19) Diefenbach, R. A.; Sano, K.; Taft, R. W. *J. Am. Chem. Soc.* **1966**, *88* (20), 4747. doi:10.1021/ja00972a054.
- (20) Flegel, M.; Lukeman, M.; Huck, L.; Wan, P. *J. Am. Chem. Soc.* **2004**, *126* (25), 7890. doi:10.1021/ja039078g. PMID: 15212537.
- (21) Toone, T. W.; Lee-Ruff, E.; Hopkinson, A. C. *Can. J. Chem.* **1975**, *53* (11), 1635. doi:10.1139/v75-230.

# Diffusion of oligomers in latex systems — A route to low volatile organic compound (VOC) coatings

David M. Fasano, Susan J. Fitzwater, Willie Lau, and Aurelia C. Sheppard

**Abstract:** We synthesize specially designed latex polymer systems by an in situ emulsion polymerization process that yields latex particles with both a high molecular weight polymer phase and a low molecular weight oligomer phase. The oligomer functions as a plasticizer by lowering the glass transition temperature ( $T_g$ ) of the polymer. A polymer system is prepared by blending soft latex and a hard latex where the hard mode consists of a hard, high molecular weight polymer and an oligomer, allowing for facile film formation at ambient conditions. Upon the soft and hard particles coming into contact during the film formation process, the oligomer preferentially diffuses from the hard polymer to the soft polymer, thus recovering the natural  $T_g$  of the hard polymer as described in a recent patent application. Oligomer diffusion allows a hard coalesced phase to be incorporated into a latex film without using a coalescing solvent, which would contribute to the volatile organic compound (VOC) content. A well-coalesced hard phase in a latex film contributes to a variety of desirable coatings properties, such as tack, print, block, and scrub resistance properties.

**Key words:** oligomers, diffusion, Designed Diffusion™ Technology, plasticization.

**Résumé :** On a effectué la synthèse de systèmes de polymères de latex conçus spécialement à cet effet en faisant appel à un processus de polymérisation en émulsion in situ qui conduit à la formation de particules de latex à la fois une phase de polymère de haut poids moléculaire et une phase d'oligomère de faible poids moléculaire. L'oligomère fonctionne comme plastifiant en réduisant la température de transition de verre ( $T_g$ ) du polymère. On prépare un système de polymère en procédant au mélange d'un latex mou et d'un latex dur dans lequel le mode dur est formé d'une polymère dur de poids moléculaire élevé et d'un oligomère qui permet de former facilement un film dans les conditions ambiantes. Lorsque les particules molles et dures viennent en contact durant le processus de formation du film, l'oligomère diffuse d'une façon préférentielle du polymère dur vers le polymère mou et il retrouve la  $T_g$  naturelle du polymère dur, tel que décrit dans une récente application pour un brevet. La diffusion de l'oligomère permet d'incorporer une phase dure ayant subi une coalescence d'être incorporée dans un film de latex sans utiliser de solvant de coalescence qui contribuerait à la teneur en composé organique volatil (COV). Une phase dure qui a subi une bonne coalescence dans un film de latex contribue à une variété de propriétés désirables des revêtements, telles que les propriétés résistance à la colle, à l'imprimerie, et au frotage.

**Mots-clés :** oligomère, diffusion, technologie Designed Diffusion™, plasticisation.

[Traduit par la Rédaction]

## Introduction

### Demand of low and no volatile organic compound (VOC) binders in latex paints

Water-borne latex coatings have been growing in popularity for decades as they offer performance, economic, and environmental advantages over solvent-borne coatings. Coatings contain a large number of ingredients that are designed to enhance their manufacture, storage, application, and final performance properties. One of the major ingredients in a typical architectural coatings formulation is the polymeric binder, which is responsible for forming the paint film and providing many of its final properties. Latex poly-

mers, aqueous dispersions of acrylic or vinyl polymer particles formed via emulsion polymerization, are the most commonly used binder polymers.

During the drying and curing process, the discrete polymer particles form a continuous film. Scheme 1 depicts the process of drying the latex polymer into a continuous film.<sup>1</sup> As water evaporates from the dispersion, polymer particles come into close contact with each other. Further drying results in the deformation of the particles increasing the contact surface between particles. The coalescing stage involves diffusion of the polymer chains across the particle boundaries, which results in a transparent and void-free polymer film. The diffusion of polymer chains across the particle

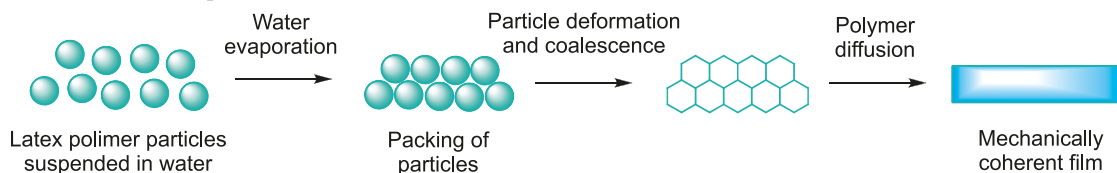
Received 24 September 2009. Accepted 19 January 2010. Published on the NRC Research Press Web site at canjchem.nrc.ca on 4 May 2010.

*This article is part of a Special Issue dedicated to Professor M. A. Winnik.*

**D.M. Fasano, S.J. Fitzwater, W. Lau,<sup>1</sup> and A.C. Sheppard.** Spring House Technology Center, The Dow Chemical Company, 727 Norristown Road, PO Box 904, Spring House, PA 19477, USA.

<sup>1</sup>Corresponding author (e-mail: wlau@dow.com).



**Scheme 1.** Latex film formation process.

boundaries directly affects both the extent of entanglement of the chains between particles and the resulting mechanical properties of the final film.<sup>1</sup> It is during this coalescing and curing stage that VOC components in the paint formulation are released from the film.

A polymer designed for use in architectural coatings must have a desirable balance of properties, which are often associated with both soft (glass transition temperature ( $T_g$ ) < ambient temperature) and hard ( $T_g$  > ambient temperature) polymer characteristics. The final polymer film needs to be hard to provide properties such as nontackiness, resistance to dirt pick up, block, and print. However, the film formation process demands a softer system for adequate particle deformation and chain diffusion across the particle boundaries during drying. In addition, some properties, such as film toughness, require a balance of both soft and hard properties.

In the past, this balance has been achieved by incorporating a coalescing agent in the formulation.<sup>2</sup> Typical coalescents are low molecular weight solvents, which are miscible with the polymer. Texanol ester alcohol, [2,2,4-trimethyl-1,3-pentanediol mono(2-methylpropanoate)], and Dowanol DPnB, [dipropylene glycol *n*-butyl ether], are commonly used commercial coalescents in latex coatings formulations.

A coalescent temporarily suppresses the  $T_g$  of the polymer to ensure good film formation. Coalescents plasticize high-molecular-weight polymers by affecting intermolecular interactions and therefore, chain relaxation dynamics, decreasing the internal friction coefficient among polymer chains. Once the coating has dried and the film is fully coalesced, the coalescent evaporates, leaving a harder, more durable film. This drying-induced  $T_g$  transition allows the polymer to behave in a soft or hard manner as required during the application, drying, and curing stages of the coating.

Coalescents must have a sufficiently high vapor pressure so that they almost completely evaporate in hours to weeks after the coating application, returning the polymer to its natural  $T_g$ . Increasing concern about and regulatory pressure on volatile organic compounds (VOC) have led to the investigation of alternative approaches to achieving satisfactory film formation and ultimate film properties.

One approach is to use softer polymer compositions, which do not require high coalescent levels to form a satisfactory film. Although VOC can be quite low in such systems, the overall performance can be compromised by the softer polymer.

The use of hard-soft systems is another approach in obtaining adequate performance from low-VOC coatings. It is known that some hardness properties can be achieved by the presence of hard domains in the polymer film.<sup>3–5</sup> These hard domains in a polymer film can be derived from a phase separated system or through the blending of hard and soft latex particles. While these systems showed enhanced hardness

properties with low coalescent demand, they often compromise other performance properties. For example, while the blending of hard with soft latex can provide enhanced mechanical properties, such blends often have decreased binding capacity because the hard polymers behave more like pigments than binders. It is believed that the reduced binding capacity is due to the inadequate interaction of the hard and soft particles, since the hard polymer will not undergo chain diffusion during film formation under ambient conditions without added coalescent.<sup>6</sup> As a result, properties such as gloss, durability, and film integrity are often compromised when this type of heterogeneous polymer system is used to reduce the solvent demand, especially when additional pigments and extenders, such as titanium dioxide, clay, silica, and calcium carbonate, are also present in the formulation.

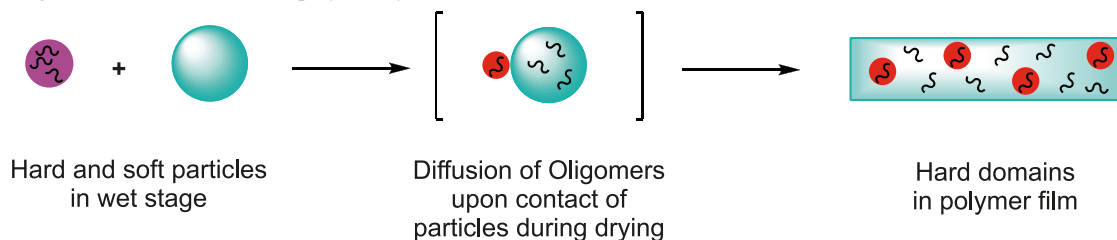
The objective of the research described here is to investigate a new approach to improve the performance of low VOC hard-soft blends, using oligomers as coalescing aids. Oligomers can suppress the  $T_g$  and film formation temperatures by behaving in a manner similar to coalescing solvents and plasticizers.<sup>7,8</sup> Further, by carefully controlling the composition of the polymer and oligomer phases, the oligomers can be designed to migrate from one polymer phase to another, thus providing the properties transition previously attained by evaporation of coalescing solvents.

### Oligomers

In general, polymers used as coatings binders are macromolecules having molecular weights ( $M_n$ ) of 10 000 or higher. The molecular weight of acrylic polymers prepared by emulsion polymerization can be upwards of 1 000 000. One of the key contributors to the mechanical properties of these polymers is derived from chain entanglement. For example, the average molecular weight between chain entanglements ( $M_e$ ) for poly(ethyl acrylate) and poly(*n*-butyl acrylate) were measured to be 11 000 and 16 000, respectively.<sup>9</sup> For a high molecular weight polymer, the multiple entanglements between the chains are directly related to the mechanical properties of the polymer.

Oligomers are macromolecules with molecular weights substantially below the respective entanglement molecular weights and carry a range of differentiated attributes compared to the equivalent composition at higher molecular weights. Most notable, and most useful in this application, is the capability in reducing the  $T_g$  of a high molecular weight polymer. In addition, for oligomers with molecular weights greater than 500, the room temperature evaporation rate is negligible and therefore these oligomers are not considered to be VOC.<sup>10</sup> This combination of properties allows low molecular weight oligomers to act as nonvolatile plasticizers in polymer systems.<sup>7,8</sup>

There is a broad range of oligomers being developed as

**Scheme 2.** Designed Diffusion<sup>TM</sup> in latex polymer systems.

intermediates in preparative polymer chemistry.<sup>11</sup> However, the utility of oligomers synthesized by emulsion polymerization has not been explored extensively due to the limitations of the synthetic method. The development of cyclodextrin as a chain transport catalyst enables the synthesis of a broad range of oligomer compositions and molecular weights.<sup>12</sup>

### Designed Diffusion<sup>TM</sup> Technology

This article describes a latex blend system (Scheme 2) in which the hard mode is plasticized by a carefully designed oligomer prepared in situ during emulsion polymerization. This plasticized hard mode is blended with a softer latex, which remains separate in the dispersion state until the drying stage. In this system, the oligomer is designed to be both an effective plasticizer for the hard polymer and to preferentially partition into the soft phase. As water evaporates, the hard and soft particles come into contact during the drying stage. The oligomer remains in the hard phase at this stage to facilitate coalescence. Chain entanglement can occur, which reinforces and strengthens the interfacial boundary between the particles. In a conventional system employing a coalescent that contributes to VOC, the polymer regains the intrinsic hardness when the volatile organic solvent evaporates after film formation. In the Designed Diffusion<sup>TM</sup> Technology systems, the hard polymer domains form when the oligomer diffuses from the coalesced hard particles into the softer continuous phase. In contrast to the conventional system, the oligomer remains in the film and does not contribute to the VOC level.

There are several key parameters that are critical in designing an effective system. These include (i) in situ preparation of the oligomer phase inside the hard mode; (ii) a molecular weight of oligomer that provides a sufficiently low  $T_g$  as well as facile diffusion in a mixed polymer system; (iii) a composition and molecular weight of oligomer that provides optimum plasticization and diffusion capability; and (iv) some minimum level of miscibility of oligomer in the hard phase and preferential miscibility in the soft phase to impact the direction of the diffusion during film formation process.

## Experimental section

### Materials

Butyl acrylate (BA), methyl methacrylate (MMA), and methacrylic acid (MAA) were commercial grade monomers used in latex products without further purification. Ammonium persulfate (APS), sodium carbonate ( $\text{Na}_2\text{CO}_3$ ), and *n*-dodecyl mercaptan (*n*-DDM) were purchased from Sigma-Aldrich and used as received. Methyl- $\beta$ -cyclodextrin (Me- $\beta$ -CD, Beta W7 M1.8) was supplied by Wacker Chemie AG as

a 50% solution in water. Sodium lauryl sulfate (SLS) and sodium dodecylbenzene sulfonate were supplied by the Stepan Company under the product name Polystep B-5 (28% solution) and Polystep A-16-22 (23% solution), respectively.

Materials used in paint formulations are as follows: Tamol 731A, Triton X-100, and Triton X-405 were obtained from the Dow Chemical Company; AMP-95 was obtained from the Angus Chemical Company; Nopco NDW was obtained from the Henkel Corporation; Ti-Pure R-706 was obtained from the E. I. du Pont de Nemours Company; and Natrosol 250 MR was obtained from Ashland Inc. and mixed with water to make a 2.5% solution.

All the polymer compositions are presented as weight percent of the monomer components. For example, 50 BA/49 MMA/1 MAA designates a polymer composition comprised of 50, 49, and 1 weight percent of BA, MMA, and MAA, respectively. The chain transfer agent (CTA) is presented as a part per 100 parts of the polymer in weight. 50 BA/49 MMA/1 MAA//11 *n*-DDM is comprised of 11 parts of *n*-DDM per 100 parts of the total polymer by weight. All the blend ratios are presented as parts by weight.

### Synthesis<sup>13,12b</sup>

#### Emulsion polymerization reaction vessel

The emulsion polymerizations were carried out in a four-neck 5 L round-bottom flask as the reaction vessel. The flask was fitted with a water-cooled reflux condenser with a nitrogen purge gas inlet, a thermocouple attached to a J-KEM Gemini temperature controller, and a glass stirring rod with a paddle connected to an IKA RW20 motor. The monomer emulsion (ME) and initiator were fed by a FMI QG-50 and Harvard syringe pump, respectively. The reaction mixture was heated using a heating mantle connected to a Variac voltage regulator. The temperature of the reaction mixture was regulated by raising and lowering the heating mantle placed on an I<sub>2</sub>R pot lifter connecting to the J-KEM temperature controller.

#### Synthesis of acrylic latex polymer

The monomer emulsion (ME) was prepared in a separate flask using a homogenizer. The ME for a 50 BA/49 MMA/1 MAA (weight percent) polymer was prepared by emulsification of a mixture of 735.0 g of deionized water, 16.8 g of SLS (28%), 936.0 g of BA, 917.5 MMA, and 18.7 g of MAA. The polymerization was carried out in the 5 L reaction vessel. Deionized water (853 g) and 16.8 g of SLS (28%) was added to the vessel and heated to 85 °C under a nitrogen sweep. At 85 °C, 6.3 g of APS in 26 g of water and 6.5 g of  $\text{Na}_2\text{CO}_3$  in 34 g of water were added to the reaction mixture. The ME was fed over

100 min together with an initiator solution consisting of 1.0 g of APS in 102.0 g of water. At the end of the ME feed, the reaction mixture was held at 85 °C for 20 min and cooled to room temperature. The latex was neutralized to pH 8.5 by ammonium hydroxide and filtered through a 325 mesh (45  $\mu\text{m}$ ) screen. The latex typically has a solids level of 50.0% and an average particle diameter between 100 and 130 nm.

### Synthesis of oligomeric latex

Latex polymers with different number average molecular weights ( $M_n$ ) were similarly prepared with a range of  $n$ -DDM levels. The monomer emulsion was prepared in a separate flask using a homogenizer to generate ME droplet size  $\sim 5$ –10  $\mu\text{m}$ . The ME for a 50 BA/49 MMA/1 MAA//11  $n$ -DDM (weight percent) polymer was prepared by emulsification of 735.0 g of deionized water, 16.8 g of SLS (28%), 936.0 g of BA, 917.5 g MMA, 18.7 g of MAA, and 205.9 g of  $n$ -DDM. Other molecular weight oligomer latices were prepared by adjusting the  $n$ -DDM levels in the ME accordingly. The polymerization was carried out in the 5 L reaction vessel. Deionized water (853.0 g), 16.8 g of SLS (28%), and 37.0 g of Me- $\beta$ -CD (50% solution) was added to the vessel and heated to 85 °C under a nitrogen sweep. At 85 °C, 6.3 g of APS in 26.0 g of water and 6.5 g of  $\text{Na}_2\text{CO}_3$  in 34.0 g of water were added to the reaction mixture. The ME was fed over 100 min together with an initiator solution consisting of 1.0 g of APS in 102.0 g of water. At the end of the ME feed, the reaction mixture was held at 85 °C for 20 min and cooled to room temperature. The latex was neutralized to pH 8.5 by ammonium hydroxide and filtered through a 325 mesh (45  $\mu\text{m}$ ) screen. The latex typically has a solids level of 50.0% and an average particle size of 115 nm.  $M_w$  and  $M_n$  were measured by size exclusion chromatography (SEC) to be 4060 and 3000, respectively. The  $T_g$  of the oligomer was measured by differential scanning calorimetry (DSC) to be  $-24.1$  °C.

### In situ synthesis of oligomers in high molecular latex particles

The oligomer is incorporated into a conventional latex particle by a two stage emulsion polymerization. The compositions of the oligomer and the high molecular weight polymer can be different, provided that the monomers and the high molecular weight polymer have sufficient miscibility. The two stage polymerization can be carried out by first polymerizing the high molecular weight polymer without  $n$ -DDM followed by the oligomer composition, or vice versa. There should be no new particles formed during the second stage polymerization. All of the oligomer was formed inside the polymer particles with the high molecular weight polymer.

A latex polymer with a higher molecular weight phase of 28 BA/71 MMA/1 MAA and an oligomer composition of 60 BA/39 MMA/1 MAA//17  $n$ -DDM was prepared with ingredients as shown in Table 1. Two monomer emulsions (ME) were prepared separately. The total monomers represent a 60/40 weight ratio of high molecular weight polymer to oligomer.

The polymerization was carried out in the 5 L reaction vessel. The reaction mixture was added to the vessel and heated to 85 °C under a nitrogen sweep. At 85 °C, 3.9 g of

**Table 1.** Ingredients for the in situ emulsion polymerization of oligomer in high molecular weight polymer particles.

Ingredients	ME I (g)	ME II (g)	Reaction mixture (g)
Deionized water	334.0	260.0	715.0
Polystep A-16-22	23.8	15.8	12.0
$\text{Na}_2\text{CO}_3$ /water			5.0/33.0
BA	247.0	353.5	
Me- $\beta$ -CD (50%)			29.4
MMA	625.0	229.0	
MAA	8.9	5.9	
$n$ -DDM		99.6	

**Note:** ME I produced the high molecular weight component and ME II produced the oligomer fraction in the polymer particle.

**Table 2.** UNIFAC group breakdowns for BA and MMA homopolymers.

Polymer	$-\text{CH}_3-$	$-\text{CH}_2-$	$-\text{CH}-$	$-\text{C}-$	$-\text{COO}-$
MMA <sup>a</sup>	2000	1000		1000	1000
BA <sup>b</sup>	781	3125	781		781

**Note:** The numbers in the table denote the total number of the chemical groups present in a 100 000 molecular weight homopolymers. For example, a 100 000 molecular weight MMA homopolymer contains 2000  $-\text{CH}_3$  moiety per chain.

<sup>a</sup>Methyl methacrylate homopolymer.

<sup>b</sup>Butyl acrylate homopolymer.

APS in 33.0 g of water was added to the reaction mixture. ME I was fed over 50 min together with an initiator solution consisting of 2.8 g of APS in 91.0 g of water. At the end of the ME I feed, ME feed was continued with ME II over 40 min. At the end of the ME feed, the reaction mixture was held at 85 °C for 20 min and cooled to room temperature. The latex was neutralized to pH 8.5 by ammonium hydroxide and filtered through a 325 mesh (45  $\mu\text{m}$ ) screen. Details of the characterization are included in the Results and discussion section.

### Characterization of latex particles

Particle size and size distribution were determined by capillary hydrodynamic fractionation (CHDF) using the CHDF-2000 particle size analyzer by Matec Applied Sciences. The calibration was carried out using particle size standards with diameters ranging between 40 and 800 nm. The samples were prepared by diluting two drops of the latex in 3 mL of carrier fluid. The solids content was determined gravimetrically.

### Characterization of latex polymers

#### Glass transition temperature

Glass transition temperature ( $T_g$ ) of the polymers was measured by differential scanning calorimetry (DSC). The measurement was performed on a TA model Q-2000 Auto DSC cooled by liquid nitrogen. Latex or blends of latex were air dried in DSC pans. Sufficient wet latex was added to the pan to yield 10–15 mg of dried polymer and oligomer in the pan. The pans were capped prior to running the DSC measurement. The test sample was equilibrated at  $-90$  °C for 2 min followed by heating at a rate of 20.0 °C/min to



150 °C. The Universal Analysis Software was used to determine the  $T_g$  at the inflection of the DSC curve.

### **Molecular weights and distributions**

Molecular weights and distributions were determined by size exclusion chromatography (SEC) in THF using an Agilent 1100 series instrument equipped with an evaporative light scattering detector and Polymer Laboratories mixed C 300 mm  $\times$  7.5 mm column. The calibration was carried out using polystyrene standards from Polymer Laboratories (PS-1) having a peak average molecular weight ranging from 580 to 7500,000 with narrow molecular weight distribution. Conversions from polystyrene to PMMA were made using Mark–Houwink constants.

### **Film morphology**

A Dimension 5000 scanning probe microscope (SPM; Veeco Instruments, Santa Barbara, CA) with a Nanoscope 4 controller was used for the analysis. The instrument was operated in the tapping mode to acquire phase and height images simultaneously. A silicon “TESP” probe (Veeco Instruments) with a spring constant of 20–80 N/m was operated near its fundamental harmonic frequency at approximately 300 kHz to collect the images. A setpoint of 0.80 was chosen to control the imaging force. Images and the analysis were carried out using Veeco Software, version 5.30.

Emulsion blend samples were casted onto a Mylar substrate and drawn into a film using a Bird applicator having a wet film thickness of 3 mil (3/1000 in; 1 in = 25.4 mm). The film was allowed to dry at room temperature and humidity for 5 d. Small 1/2 in<sup>2</sup> pieces were cut from the film. The pieces were mounted on SPM sample stubs and imaged under ambient conditions.

## **Modeling of miscibility and plasticization of oligomers**

### **Miscibility predictions**

Oligomer partitioning between phases was predicted from the condition that the oligomer chemical potentials in two phases must be equal at equilibrium:  $\mu(\text{phase 1}) = \mu(\text{phase 2})$ .

For phase separation predictions, phase #1 was defined as the hard phase and phase #2 as a small amount (<5%) of the total oligomer. These predictions are qualitative: they give an indication of potential phase separation problems but not a reliable quantitative estimate of the amount of phase separation. For the hard/soft partitioning predictions, phase #1 was defined as the hard phase and phase #2 as the soft phase. The partitioning predictions are at least semiquantitatively reliable.

For both types of predictions, we calculated oligomer chemical potentials using the universal functional activity coefficient (UNIFAC) method.<sup>12</sup> UNIFAC is a group contribution method. Each molecule is assumed to be composed of a series of chemical groups: methyl, methylene, carboxylate, etc. Table 2 shows the UNIFAC group breakdowns (group types and number of each) for 100 000 molecular weight MMA and BA homopolymers. UNIFAC assigns geometric and energetic parameters to each group, and combines these parameters to predict activities, activity coefficient, and chemical potential. UNIFAC accounts for

the effects of both molecular weight and chemistry upon mixing.

For the predictions described here, we used UNIFAC parameters for the aliphatic and carboxylic acid groups from 14a and the acrylic ester group (–COO–) parameters from 14b. We used the 14a parameters for the –CH<sub>2</sub>–O– group for the mercaptan –CH<sub>2</sub>–S– group. The ability to predict the preferential miscibility of oligomers is the critical link to the Designed Diffusion™ Technology.

### **Glass transition temperature ( $T_g$ ) predictions**

A mathematical model constructed by fitting measured  $T_g$ s of oligomers to the Fox equation was used to predict  $T_g$ s of oligomers and the mixed polymer systems. Table 3 compares model predictions with experimental  $T_g$ s for several oligomers.

### **Preparation of paints**

A typical aqueous semigloss trim formulation was used to prepare paints for testing of the polymer compositions. Paint formulation involves making a grind, which is a dispersion containing titanium dioxide and possibly other pigments and extenders. In this work, the only pigment used was titanium dioxide, which provides the hiding and gloss control of the paint film. An aqueous dispersion of the pigment is achieved by grinding the pigment under high shear using a Cowles mixer and appropriate wetting agents and dispersants. The rest of the formulation ingredients, referred to as the letdown, are mixed and added to the grind to form the aqueous coating compositions for the evaluation of the emulsion polymer examples. Tables 4 and 5 show the recipes for the grind and letdown used in this study. The paint is exemplified here for the case where the blend, latex I and II, contains soft phase particles and oligomer-modified hard phase particles. The final paint film upon drying contains 50.9% and 49.1% by weight of TiO<sub>2</sub> and polymer, respectively.

### **Testing of paints**

#### **Gloss**

A coating composition was drawn down on a Leneta chart (Leneta Company, Mahwah, NJ) using a 3 mil (3/1000 in; 1 in = 25.4 mm) Bird film applicator. The sample was dried at 24 °C and 50% relative humidity. Gloss (20° and 60°) was measured using a BYK-Gardner haze-gloss meter (BYK-Gardner, Columbia, MD). These gloss measurements follow guidelines established by the industry standards.<sup>5b</sup>

#### **Pendulum (Konig) hardness**

A coating composition was drawn down on an untreated aluminum panel using a 5 mil (5/1000 in) block applicator. The sample was dried at 24 °C and 50% relative humidity. Pendulum hardness was measured using a Byk Mallinckrodt König pendulum hardness tester (BYK-Gardner, Columbia, MD). The number of swings was multiplied by a factor of 1.4 s to obtain the pendulum hardness measured in seconds. Higher numbers reflect harder coatings.

#### **Zapon tack test**

A coating composition was drawn down on a Leneta chart



**Table 3.** Glass transition temperature (°C) comparison between DSC measurements (meas.) and the predictive model (pred.).

Compositions BA/MMA/MAA/ <i>n</i> -DDM <sup>a</sup>	<i>M<sub>n</sub></i>	<i>T<sub>g</sub></i> (meas.)	<i>T<sub>g</sub></i> (pred.)
98.5/0/1.5//15	2210	−71	−76
50/49/1//1	25200	14	12
50/49/1//4	6400	−2	9
50/49/1//11	2260	−48	−45
0/100/0//11	2250	29	31

<sup>a</sup>The compositions denote the weight percent of monomer in the polymer phase. The CTA (*n*-DDM) is expressed as parts per 100 parts of polymer in weight. For example, the polymer in row three has a composition of 50 BA/49 MMA/1 MM together with 4 parts of *n*-DDM per 100 parts of polymer to yield a polymer with a number average molecular weight (*M<sub>n</sub>*) of 6400.

**Table 4.** Preparation of pigment grind for aqueous semigloss trim paints.

Ingredients	Purpose	As supplied <sup>a</sup> (g)	Solids <sup>b</sup> (g)
Water		63.2	
Tamol 731A	Dispersant	15.0	
Triton X-100	Surfactant	2.2	
AMP-95	Base, pH adjuster	1.8	
Nopco NDW	Defoamer	0.9	
Ti-Pure R-706	Pigment (TiO <sub>2</sub> )	268.9	268.9
Total		352.0	268.9

**Note:** The ingredients were combined and mixed in a Cowles mixer to produce the grind.

<sup>a</sup>The ingredients are used as supplied from the supplier without dilution.

<sup>b</sup>The solids in the total grind composition assuming the other ingredients have negligible weights.

**Table 5.** Letdown compositions for aqueous semigloss trim paint.

Ingredients <sup>a</sup>	Formulation component	Amounts (g)	Solids (g)
Water		60.0	
Latex I <sup>b</sup>	Polymer	440.9	220.5
Latex II <sup>c</sup>	Polymer	78.8	39.4
Triton X-405	Surfactant	1.8	
Nopco NDW	Defoamer	0.9	
Natrosol 250 MR (2.5%)	Thickener	112.0	
Grind (Table 4)		268.9	
Pigment			
Total	Paint	1755.6	528.8

<sup>a</sup>The ingredients of the letdown were mixed materials with a low shear mixer.

<sup>b</sup>Latex I is the soft phase with a composition of 60 BA/39 MMA/1 MAA (total solids at 50%).

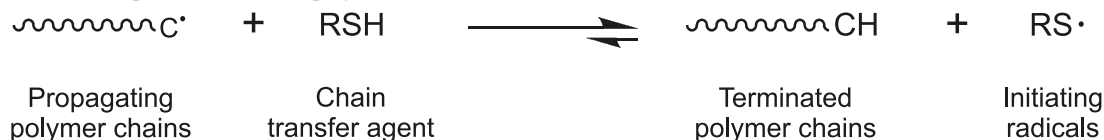
<sup>c</sup>Latex II is the oligomer modified hard phase with the hard composition containing 60 parts by weight of high molecular weight polymer (28 BA/71 MMA/1 MAA) and 40 parts by weight of oligomer (60 BA/39 MMA/1 MAA//17 *n*-DDM) synthesized by in situ emulsion polymerization (total solids at 50%).

(Leneta Company, Mahwah, NJ) using a 3 mil (3/1000 in) Bird film applicator. The sample was dried at 24 °C and 50% relative humidity. Tack was measured using an aluminum tack tester shaped like a bent L. The bottom of the tester was wrapped in smooth Al foil. Different weights (up to 500 g) were placed on the bottom of the tack tester for 10 s. If upon removal of a given weight the tack tester releases completely from the film, the given weight is given as the tack result. The higher the weight given, the less tacky the film. The foiled bottom of the tester was cleaned

with alcohol after each test.<sup>15</sup> The tests were carried out after the films were dried for both 4 and 8 h.

### Finger tack

A coating composition was drawn down on a Leneta chart (Leneta Company, Mahwah, NJ) using a 3 mil (3/1000 in) Bird film applicator. The sample was dried at 24 °C and 50% relative humidity. Tack was estimated by placing a finger on the film. Tests were carried out after the films were dried for both 4 and 8 h.

**Scheme 3.** Chain transfer process in radical polymerization.**Print resistance**

This test measures the ability of the coating to resist the imprint of another surface placed on it (such as flower pots on window sills). A coating composition was drawn down on an untreated aluminum panel using a 5 mil (5/1000 in) block applicator. The sample was dried at 24 °C and 50% relative humidity for 7 d. A small section of the panel was cut out, placed in a 60 °C oven, covered with cheesecloth, and topped with a rubber stopper and a 500 g weight. After 60 min, the panel was removed from the oven, and allowed to cool before removing the cheesecloth and evaluating for print. A scale of 0 to 10 was used to rate the depth and amount of the impression of the cheesecloth pattern, which was left on the paint film surface.

**Block resistance**

This test measures the resistance of paint films to sticking when they are placed in contact with each other, such as from the closing of a freshly painted window or door. A coating composition was drawn down on a Leneta chart (Leneta Company, Mahwah, NJ) using a 3 mil (3/1000 in) Bird film applicator. The sample was dried at 24 °C and 50% relative humidity for both 1 and 7 d. Two equal small sections of the chart were cut out and placed together with the paint surface face to face, then topped with a rubber stopper and a 1000 g weight. After either 0.5 or 16 h, the weight was removed and the film sections were separated slowly with steady force. Samples were rated on a scale of 0 to 10 according to the noise produced upon separation of blocked surfaces and the physical damage caused by the separation of blocked surfaces.<sup>16</sup>

**Scrub resistance**

This test measures the resistance of paint films to erosion caused by scrubbing such as it may occur when a film is repeatedly scrubbed to remove stains. A coating composition was drawn down on a black vinyl chart from the Leneta Company using a 5 mil (5/1000 in) block applicator. The sample was dried at 24 °C and 50% relative humidity for 7 d. The paint film was scrubbed using an abrasion tester (machine washability) from BYK-Gardner and an abrasive scrub medium, type SC-2, from the Leneta Company, until a cut was observed, and the number of scrub cycles required to erode the paint film to the substrate was recorded.<sup>17</sup>

**Results and discussion****Synthesis**

The efficient and precise molecular weight control of the polymer has a direct impact on the plasticization and diffusion capability of the oligomer. Mercaptan is among the most commonly used chain transfer agents (CTA) in radical polymerization due to the facile abstraction of a hydrogen atom from the thiol moiety by a carbon centered radical, a

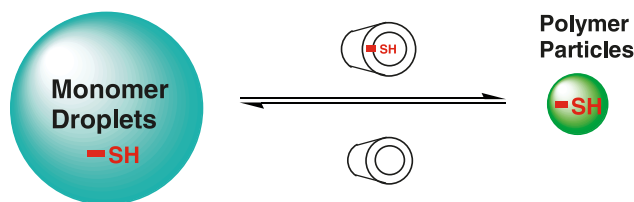
consequence of the relative C–H and S–H bond strengths (Scheme 3).<sup>18</sup>

*n*-Dodecyl mercaptan (*n*-DDM), a hydrophobic CTA with low water solubility, is the CTA of choice in emulsion polymerization.<sup>18a</sup> *n*-DDM is an effective chain transfer agent and partitions primarily into the organic phase due to its low solubility in water. Chain transfer is close to quantitative if *n*-DDM is present in the polymer phase (the site of the propagating radicals) during the polymerization. The quantitative consumption of *n*-DDM eliminates the unpleasant mercaptan odor in the latex. More hydrophilic mercaptans can partition into the water phase and create an odor issue in the final latex. In addition to the odor issue, CTA that partitions to the water phase does not participate in the chain transfer process since the propagating radicals are located in the polymer particles.

Although low levels of *n*-DDM (<0.5%) are commonly used in emulsion polymerization to control molecular weight and gel fraction, the use of high levels of *n*-DDM is impractical due to the poor diffusion between the monomer droplets and the polymer particles. This deficiency of hydrophobic CTAs is a consequence of the three phases present during an emulsion polymerization: the monomer droplets, the polymer particles, and the continuous water phase. The heterogeneous nature of emulsion polymerization requires the facile diffusion of molecules, monomers, and CTA, from the droplets, through the water phase, and into the polymer particles where the polymerization takes place. Adequate aqueous solubility of the monomer or CTA is essential for the diffusion process to occur effectively. Consequently, the use of high levels of *n*-DDM is not feasible due to its low water solubility. The solubility barrier can be overcome by the use of a catalytic level of cyclodextrin as a “phase transport catalyst”.<sup>12</sup> Cyclodextrin is capable of complexing hydrophobic molecules and rendering them water soluble. The complexation is reversible and the transport mechanism in emulsion polymerization is believed to involve a catalytic cycle in which the cyclodextrin continuously complexes the *n*-DDM molecules, transports them through the aqueous phase, and releases them to the polymer particles. This efficient transport allows the *n*-DDM to achieve a near quantitative chain transfer efficiency with a catalytic level of cyclodextrin (0.5 weight percent based on total monomer) in the reaction mixture (Scheme 4).

As the result of the quantitative chain transfer efficacy of *n*-DDM, molecular weight can be precisely controlled by the level of the CTA in the reaction mixture. For a quantitative chain transfer by CTA, (chain transfer constant (*C<sub>s</sub>*) = 1), every polymer chain is terminated by the abstraction of a hydrogen atom from the mercaptan and the resulting thio radical will start the propagation of another polymer chain. Table 6 shows molecular weights of several 50 BA /49 MMA /1 MAA latices prepared using a range of *n*-DDM levels in the presence of cyclodextrin to facilitate the *n*-DDM

**Scheme 4.** Cyclodextrin phase transport process of *n*-DDM (–SH) in emulsion polymerization. Note that the components of the scheme are for illustration and not drawn to scale. In the real system, the dimension of the monomer droplet, polymer particle, and cyclodextrin should be  $\sim 5\text{--}10\text{ }\mu\text{m}$ ,  $\sim 150\text{--}500\text{ nm}$ , and  $\sim 10\text{ }\text{\AA}$ , respectively.



transport. BA and MMA have adequate water solubility and will readily diffuse to the polymer particle.

The efficacy of chain transfer is close to quantitative as inferred from the linearity of the plot of  $M_n$  versus  $1/[n\text{-DDM}]$  (Fig. 1), a relationship as described by the Mayo equation.<sup>19</sup> In addition, all the latices have no mercaptan odor. With the low odor threshold of mercaptans, even low residual levels of mercaptan are noticeable and are not acceptable in commercial products. Without the cyclodextrin for the transport at high *n*-DDM levels sufficient to generate oligomer (see Table 6), the unreacted *n*-DDM stratified to the surface of the aqueous dispersion at the end of the polymerization. Consequently, the molecular weight was not controlled by the *n*-DDM levels.<sup>12a</sup>

Glass transition temperatures, as measured by DSC, drop precipitously for oligomers with  $M_n$  less than about 10 000, as shown in Fig. 2. Low oligomer  $T_g$  is essential for oligomers to function as effective plasticizers and to diffuse readily between polymer phases.

### Diffusion of oligomer

Effective diffusion of oligomers is the result of both thermodynamic and kinetic factors. Thermodynamically, oligomers will migrate to the more miscible phase. Kinetically, the molecular weight of the oligomers must be significantly below the entanglement molecular weight to allow diffusion to proceed under ambient conditions. Tomba et.al.<sup>20</sup> reported the diffusion of oligomers as a function of oligomer molecular weight by fluorescence resonance energy transfer (FRET). A high molecular weight acrylic latex was labeled with both a donor and an acceptor dye. When a donor located near an acceptor is irradiated, the excited donor can transfer part of the energy to the acceptor. The efficiency of the transfer, which can be derived from fluorescence decay measurements, is directly related to the distance between the donor and the acceptor.

The labeled latex was mixed with oligomer latices having a range of  $M_n$  between 2 400 and 139 000. The range is sufficiently broad to encompass molecular weights of oligomers through polymers. The mixed latices were dried and equilibrated under ambient conditions. If a significant amount of oligomer diffuses into the high molecular weight phase, then the total volume of the phase will increase. The volume increase results in an increase in the distance between the donor and the acceptor, which in turn reduces the amount of energy transfer. Figure 3 (from ref. 20) shows the quantum efficiency of energy transfer,  $\phi_{ET}$ , in the mixed la-

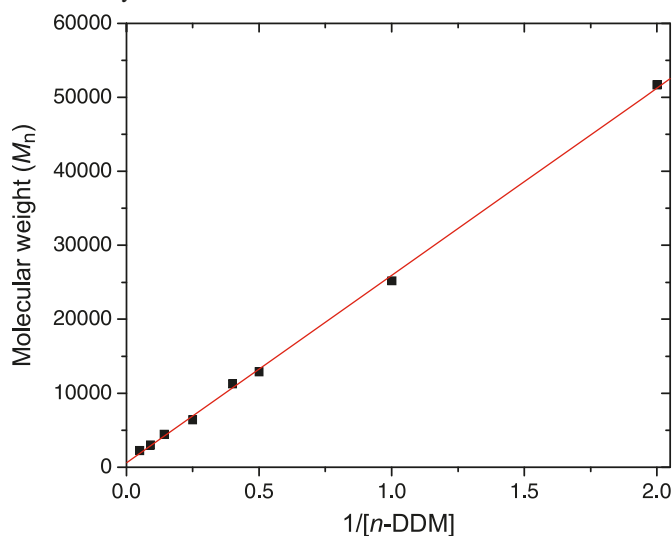
**Table 6.** Polymer molecular weights derived from CTA levels.

<i>n</i> -DDM (%) <sup>a</sup>	$T_g$ (°C)	P. S. (nm)	$M_w$ <sup>b</sup>	$M_n$ <sup>b</sup>
0.0	18.8	105	355 900	138 500
0.5	15.8	102	85 670	51 680
1	13.6	108	39 800	25 200
2	6.4	106	18 900	12 900
2.5	6.4	109	16 400	11 300
4	–1.5	110	9 300	6 400
7	–10.8	121	6 380	4 420
11	–22.6	112	4 100	3 000
20	–47.7	128	2 840	2 360

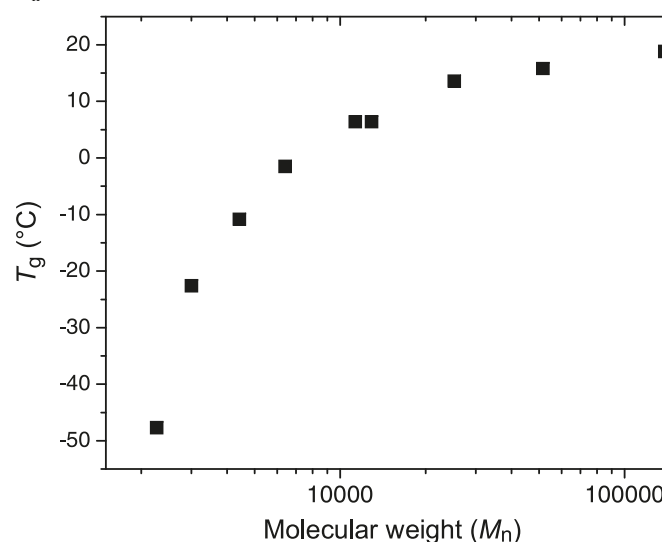
<sup>a</sup>The parts of *n*-DDM are in 100 parts of the polymer composition by weight (50 BA/49 MMA/1 MAA/*x* *n*-DDM).

<sup>b</sup>Measured by size exclusion chromatography.

**Fig. 1.** Relationship between  $M_n$  and *n*-DDM levels. *n*-DDM concentrations are in parts per 100 parts of total monomer and  $M_n$  are measured by SEC.



**Fig. 2.** Relationship between glass transition temperature ( $T_g$ ) and  $M_n$ .



tex systems. Energy transfer in the mixed latex system after film formation was compared to that in a solvent cast film, where the high molecular weight polymer and the oligomer should be fully mixed. Tetrahydrofuran (THF) was chosen as it is a very effective solvent for acrylic polymers. As expected, the solvent cast film showed a substantial decrease in  $\phi_{ET}$  and no dependence on oligomer molecular weight. Conversely, the latex films showed an increase in  $\phi_{ET}$  with the oligomer molecular weight. The increase in  $\phi_{ET}$  corresponds to a reduction of the oligomer mixing into the high molecular weight polymer. The  $\phi_{ET}$  value for the 136 000 mol/L<sub>n</sub> oligomer approaches the  $\phi_{ET}$  value where no dilution of the labeled polymer phase had taken place. The result suggests that there is no kinetic barrier to oligomer diffusion for oligomers with  $M_n$  of about 2 400.

### In situ synthesis of oligomer modified latex particles

In situ synthesis of oligomers inside a normal latex particle is a two stage semicontinuous emulsion polymerization where the second stage monomer emulsion contains the CTA (*n*-DDM) with levels predetermined for the targeted molecular weight.<sup>12b</sup> The lifetime of a free radical propagating polymer chain is relatively short due to the facile termination. In a semicontinuous emulsion polymerization under steady state conditions, the instantaneous composition of the polymer formed is close to the monomer composition being fed to the reaction mixture. In the two stage polymerization depicted in Scheme 5, the second stage monomer emulsion contains the CTA (*n*-DDM) for oligomer synthesis. If the monomer and CTA of the second stage are miscible with the polymer phase in the particle and there is no barrier for diffusion between the droplet and the particles, the second stage polymerization with the CTA will occur in the already formed polymer particles, which contain the high molecule weight polymer prepared in the first stage forming a oligomer phase fully mixed with the first stage polymer.

The evidence for a successful in situ synthesis of oligomer in the high molecular weight phase includes (i) the absence of new particle formation with continuous particle growth of existing particles and (ii) the presence of high and low molecular weight polymers as determined by SEC.

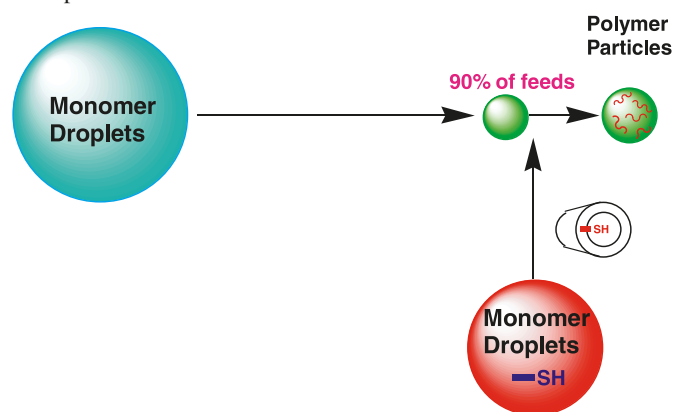
The final particle size of the in situ two stage synthesized latex was measured by CHDF (Fig. 4) and found to have a unimodal distribution of particles centered at 114 nm with no detectable new particles of a different size.

Conversely, the SEC result (Fig. 5) shows a bimodal molecular weight distribution with the high molecular weight fraction centered around 334 000 ( $M_n$ ) and the low molecular fraction at around 3 500 ( $M_n$ ).

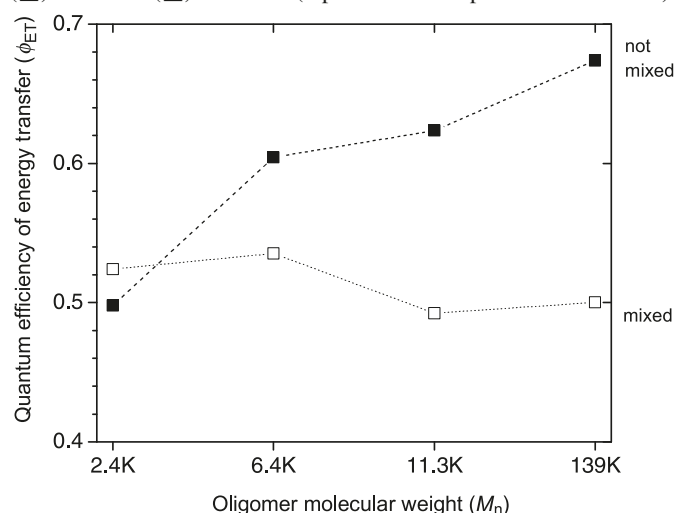
The plasticization effect of oligomers is shown by the  $T_g$  of the oligomer containing latex polymer. The two molecular weight fractions of the latex polymer have drastically different individual  $T_g$ s. However, there is only a single transition for the in situ oligomer containing latex polymer at a value between the  $T_g$ s of the two fractions. The result demonstrates the ability of the designed oligomer to be an effective plasticizer of the high molecular weight fraction (Table 7 and Fig. 6).

Collectively, the CHDF, SEC, and DSC results strongly support that the morphology of the particle depicted in

**Scheme 5.** In situ emulsion polymerization for oligomer modified latex particles.



**Fig. 3.** Quantum efficiency of energy transfer ( $\phi_{ET}$ ) showing the diffusion of oligomers at  $M_n$  2.4, 6.4, 11.3, and 136 K. The measurements were carried out with polymer film prepared from latex (■) and THF (□) solutions (reproduced with permission from 20).



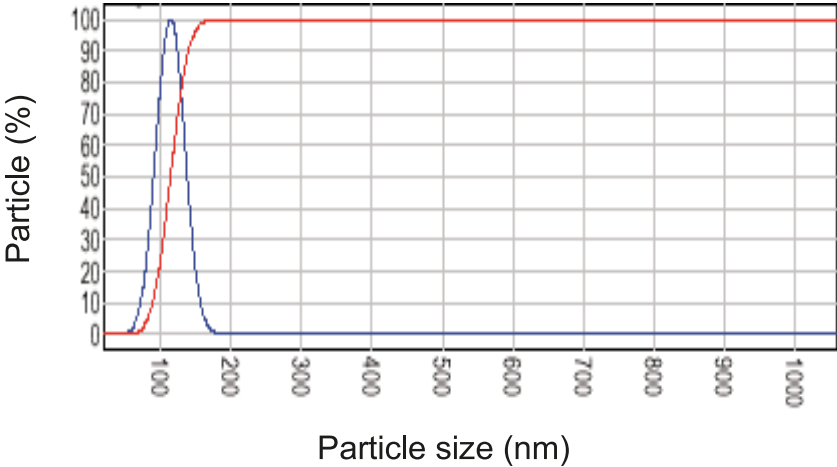
Scheme 5 from the “in situ” two stage emulsion polymerization is such that both high molecular weight polymer and oligomer coexisted in an individual particle.

### Diffusion of oligomer

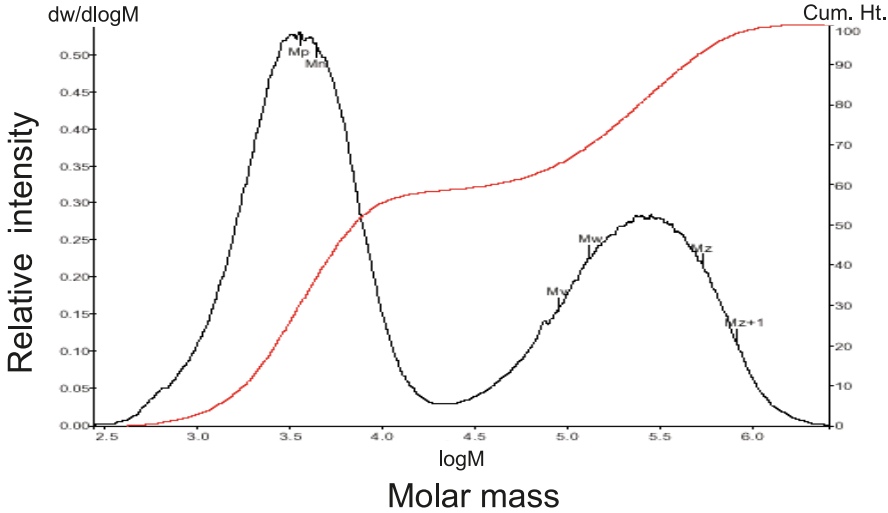
Our goal is to design an oligomer–polymer system where the oligomer is synthesized in a polymer phase and upon drying and film formation, diffuses to another polymer phase. The oligomer diffusion drives the desired  $T_g$  transition in the polymer phases. For the oligomer–polymer system to perform properly and bring value to a coatings system, it must meet several requirements: (i) The oligomer must be miscible in the hard phase. (ii) The oligomer must plasticize the hard phase, that is sufficiently decrease its  $T_g$ , to ensure good film formation. (iii) The oligomer must partition preferentially into the soft phase after the film has formed. (iv) The oligomer must diffuse from the hard to the soft phase over a time period of hours to a few days. (v) The  $T_g$  of the hard phase in the final equilibrated film must be high enough to enhance the performance of the polymer film.



**Fig. 4.** CHDF measurement of in situ oligomer modified latex particles.



**Fig. 5.** SEC determination of molecular weights and distribution of in situ oligomer modified latex particles.



**Table 7.** Glass transition temperature of single and polymer blends.

Composition	$M_n$	$T_g$ ( $^{\circ}\text{C}$ ) <sup>a</sup>
28 BA/71 MMA/1 MAA		54
80 BA/19 MMA/1 MAA//17 <i>n</i> -DDM	3000 <sup>b</sup>	-66
60 (28 BA/71 MMA/1 MAA)	<sup>c</sup>	10
40 (60 BA/39 MMA/1 MAA//17 <i>n</i> -DDM)		

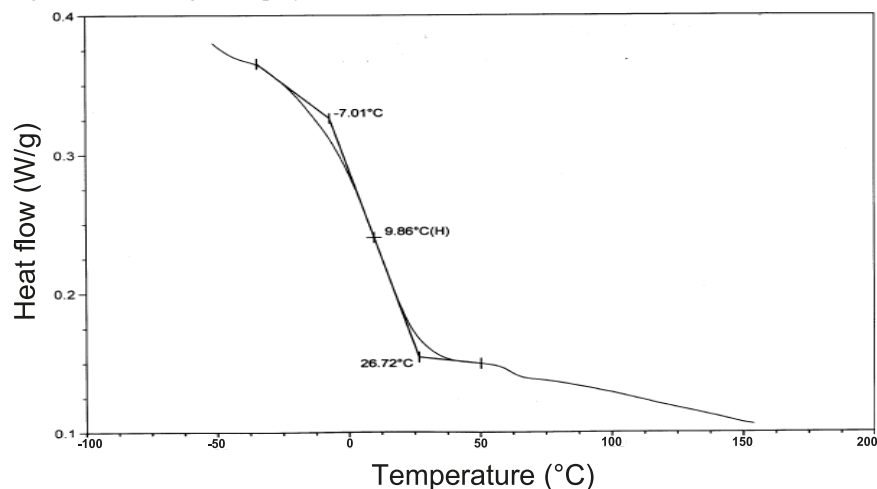
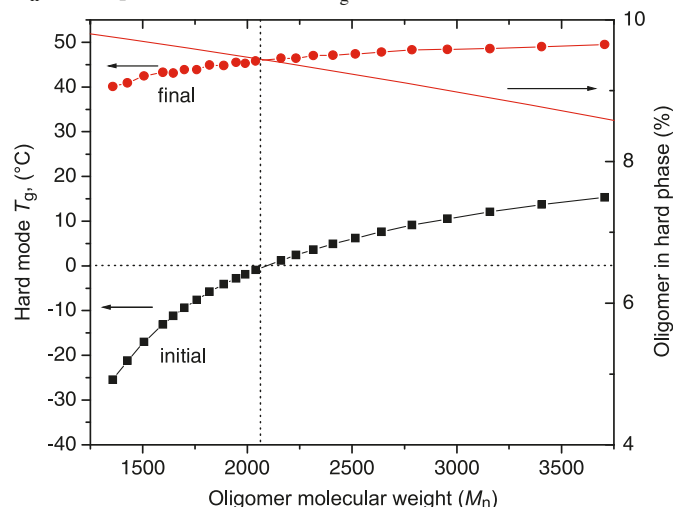
<sup>a</sup>Measured by DSC (see Fig. 6).  
<sup>b</sup>Measured by size exclusion chromatography (the theoretical  $M_n$  based on 17 parts of *n*-DDM is ~2000).  
<sup>c</sup>Bimodal molecular weight distribution (see Fig. 5).

Oligomer composition and molecular weight must be balanced carefully to meet all of these requirements. The  $T_g$  of the oligomer modified hard mode depends on the oligomer molecular weight, composition, and the level of oligomer in the hard mode. Clearly, the above requirements of low hard phase  $T_g$  during film formation (2) and high final hard phase  $T_g$  (5) necessitate some compromise on oligomer molecular weight.

The following example is an illustration of a Designed Diffusion™ polymer system. The hard and soft modes are

defined as follows: the hard mode is 60 parts hard phase (28 BA/71 MMA/1 MAA)// and 40 parts oligomer (60 BA/39 MMA/1 MAA//17 *n*-DDM) and the soft mode is 60 BA/39 MMA/1 MAA.

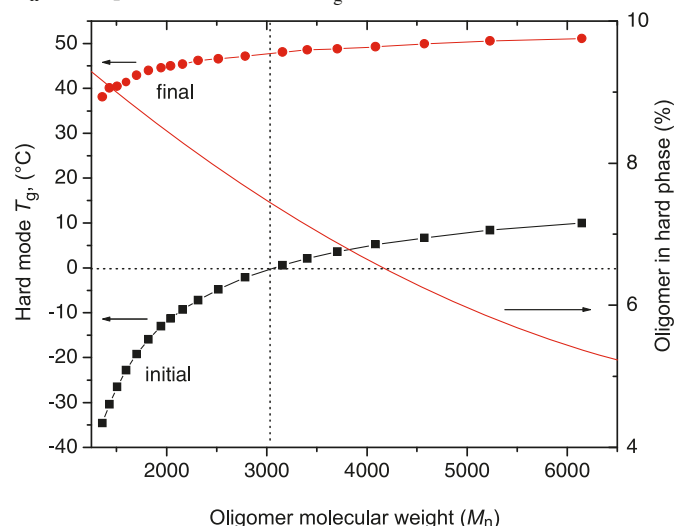
The heterogeneous latex blend contains 18.3 parts by weight of hard mode (11 hard phase, 7.3 oligomer) and 81.7 parts by weight of soft mode. Since most of the oligomer must end up in the soft phase, we need an oligomer composition that is more similar to the soft phase composition compared to the hard phase. The  $T_g$  of the unmodified hard phase is ~56 °C, so a significant  $T_g$  decrease

**Fig. 6.** DSC with in situ oligomer containing latex polymer.**Fig. 7.** Predicted initial (■) and final (●) hard mode  $T_g$ s, and predicted percent of total oligomer in the hard phase (—), for 60 BA/39 MMA/1 MMA oligomers in 81.7 parts soft mode and 18.3 parts hard mode blend. Intersection of dotted lines indicate the oligomer  $M_n$ , which produces hard mode  $T_g = 0^\circ\text{C}$ .

is needed for good film formation. The soft oligomer designed to lower the  $T_g$  of the hard phase has to be compatible to the hard phase.

The miscibility model was used for the oligomer design. For the first evaluation, we chose oligomer #1 with composition of 60 BA/39 MMA/1 MAA, the same as the soft phase composition to ensure complete miscibility. In the phase separation calculation, 97.5% of the oligomer (39 out of 40 g) was allowed to mix into the hard phase. The model predicts about 87.5% (about 35 out of 40 g) mixes into the hard phase, largely independent of oligomer molecular weight over the range studied. This is an indication that there will be no serious phase separation problems.

Figure 7 shows the initial and final hard mode  $T_g$ s and the percent oligomer in the hard phase as a function of oligomer #1 molecular weight. If we want the hard mode to have an initial  $T_g$  of about  $0^\circ\text{C}$ , the oligomer molecular weight must be about 2000 mol/L<sub>n</sub>. At equilibrium, about 9% of the

**Fig. 8.** Predicted initial (■) and final (●) hard mode  $T_g$ s, and predicted percent of total oligomer in hard phase (—), for 80 BA/19 MMA/1 MMA oligomers in 81.7 parts soft mode and 18.3 parts hard mode blend. Intersection of dotted lines indicates the oligomer  $M_n$  which produces hard mode  $T_g = 0^\circ\text{C}$ .

oligomer will remain in the hard mode, and the final  $T_g$  will be about  $46^\circ\text{C}$ .

We can attempt to increase the final hard mode  $T_g$  by changing oligomer composition so that more of the oligomer partitions into the soft phase. For our second evaluation, we chose oligomer #2 with composition 80 BA/19 MMA/1 MAA. We ran the phase separation calculation as before. The model predicts that about 50%–85% of the oligomer mixes into the hard phase, depending on the oligomer molecular weight. This result is an indication that there may be significant phase separation problems at higher oligomer molecular weights.

Figure 8 shows the initial and final hard mode  $T_g$ s and the percent oligomer in the hard phase as a function of oligomer #2 molecular weight. If we want the hard mode to have an initial  $T_g$  of about  $0^\circ\text{C}$ , the oligomer molecular weight must be about 3000 mol/L<sub>n</sub>. At this  $M_n$ , the model predicts that about 75% of the oligomer mixes into the hard phase, so

**Table 8.**  $T_g$  transitions derived from oligomer diffusion. Blends are based on weight ratios of the hard and soft mode.

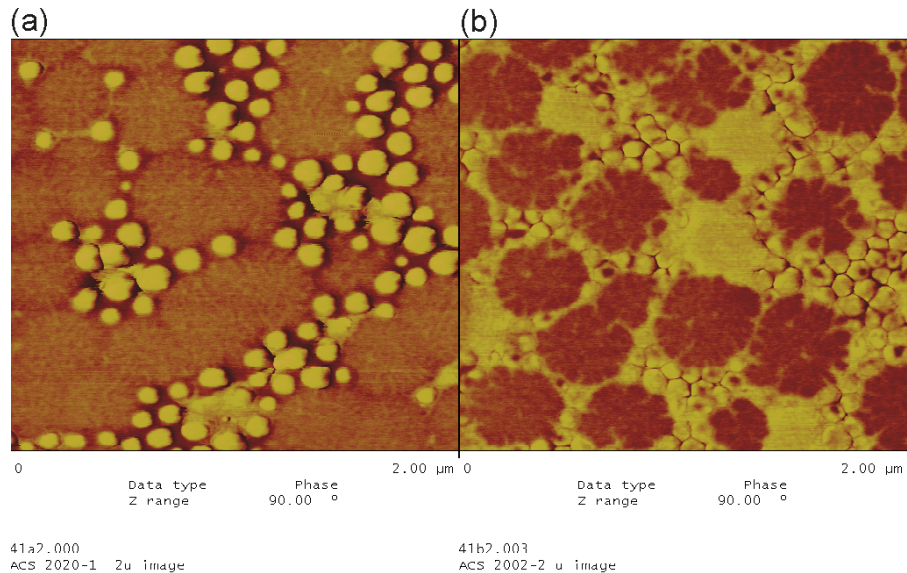
			50/50 Blend				80/20 Blend	
			Ambient dried		Heated (60 °C)		Ambient dried	
	Hard mode <sup>a</sup>	Soft mode <sup>b</sup>	T <sub>g</sub> (1) (°C)	T <sub>g</sub> (2) (°C)	T <sub>g</sub> (1) (°C)	T <sub>g</sub> (2) (°C)	T <sub>g</sub> (1) (°C)	T <sub>g</sub> (2) (°C)
Predicted	−1	2	27	−12	27	−12	44	−4
Measured	10	4	29	−5	43	−7	50	−2

**Note:** The blends show two glass transition temperatures with  $T_g$  (1) and  $T_g$  (2) corresponding to the hard and soft mode, respectively.

<sup>a</sup>The oligomer modified hard mode (60 parts 28 BA/71 MMA/1 MAA and 40 parts 60 BA/39 MMA/1 MAA//17 *n*-DDM). The DSC measurement of 28 BA/71 MMA/1 MAA without the oligomer modification is 54 °C and predicted to be 56 °C.

<sup>b</sup>The soft mode (60 BA/39 MMA/1 MAA).

**Fig. 9.** SPM of polymer film of latex polymer blends. The soft mode is blended with (a) unmodified hard node and (b) oligomer modified hard mode.



there are probably no significant phase separation problems. At equilibrium, about 7.5% of the oligomer will remain in the hard mode, and the final  $T_g$  of the hard mode will be about 47 °C.

Oligomer #2 does not give a significantly higher final hard mode  $T_g$ , but does have a higher probability of oligomer phase separation from the hard phase. We could try an oligomer composition with less than 60% BA, but this would require a lower molecular weight to give less partitioning into the soft phase and potentially lower final hard mode  $T_g$ .

Based on the modeling results, oligomer #1 (60 BA/39 MMA/1 MAA//17 *n*-DDM) was selected for further experimental evaluation.

### Designed Diffusion™ of latex

Experimental evidence for the oligomer diffusion from the hard to the soft mode was obtained using two different methods: (i) monitoring changes in the film  $T_g$  under different drying conditions and (ii) measuring surface hardness using SPM analysis of the dried films.

### Evidence of diffusion by monitoring of changes in film $T_g$

DSC was used to verify the concept of oligomer diffusion. The hard mode consisting of the 28 BA/71 MMA/1 MAA polymer and 60 BA/39 MMA/1 MAA//17 *n*-DDM in situ

oligomer and the soft mode consisting of the 60 BA/39 MMA/1 MAA polymer were blended at 50/50 and 80/20 weight ratios of latices. The total solids weight ratios in the blends are similar since the latices are at the same solid levels. Films were cast and then dried under two conditions: (i) at room temperature for two days and (ii) heated at 60 °C overnight. As shown in Table 8, the  $T_g$  of the soft mode shifted to a lower temperature while the  $T_g$  of the hard mode shifted to a higher temperature in both blend systems. This result demonstrates that the oligomer diffused from the hard mode to the soft mode after film formation. The partitioning and  $T_g$  models predict the experimental  $T_g$  shifts reasonably well. The difference between the temperature shift between the two systems (room temperature and 60 °C) may be the result of accelerated diffusion kinetics at the elevated temperature or a difference in the equilibrium point at the two temperatures.

### Evidence of diffusion by SPM analysis of films

Figure 9 shows the SPM phase images for films cast from (a) the blend of the soft mode and the hard mode without oligomer (89.2/10.8 weight ratio) and (b) the blend of the soft mode with the oligomer-modified hard mode (82.1/17.9 weight ratio). In both blends, the amount of hard 28 BA/71 MMA/1 MAA phase is the same (10.8% on total polymer). Films were dried at room temperature for five days before

**Table 9.** Effects of oligomer modification to polymer systems on gloss and pendulum hardness in semigloss paints.

Paint	Soft mode (SM)	Hard mode (HM)	Blend ratio (SM/HM)	Hard phase (%) <sup>c</sup>	Texanol (%)	Gloss (20/60) 7 d dry <sup>b</sup>	Pend. hard. 1/7 d dry <sup>c</sup>
1	60 BA/39 MMA/1 MAA	28 BA/71 MMA/1 MAA	89.2/10.8	10.8%	None	5/40	14/14
2	60 BA/39 MMA/1 MAA	28 BA/71 MMA/1 MAA	89.2/10.8	10.8%	20% <sup>d</sup>	4/39	—
3	60 BA/39 MMA/1 MAA	60 (28 BA/71 MMA/1 MAA) 40 (60 BA/39 MMA/1 MAA)/17 n-DDM	82.1/17.9	10.8%	None	25/73	14/14
4	60 BA/39 MMA/1 MAA	60 (28 BA/71 MMA/1 MAA) 40 (60 BA/39 MMA/1 MAA)/17 n-DDM	72.2/27.8	16.7%	None	24/70	20/20

<sup>a</sup>The total weight percent of the hard phase (28 BA/71 MMA/1 MAA) in the polymer excluding oligomer.<sup>b</sup>Gloss (20° and 60°) of the paint film after drying in room temperature for 7 d.<sup>c</sup>Pendulum hardness of the paint film after drying in room temperature for 1 and 7 d.<sup>d</sup>The weight percent of Texanol, a coalescent, based on total weight of the polymer.

SPM analysis. The contrast in these images is due predominantly to differences in the modulus or  $T_g$  of the materials. The harder material appears brighter in the image. In the absence of oligomer, the small hard particles are well-differentiated and pack around the large soft particles (Fig. 9a). In the case of the hard phase containing the oligomer (Fig. 9b), there is a significant decrease in the observed boundaries between particles, indicating a high degree of hard mode coalescence. Additionally, it is observed that the soft mode is darker in the oligomer-containing system, indicating that the modulus of the soft phase has dropped as the result of diffusion of the oligomer from the hard mode to the soft mode. Film surface roughness and imperfections (voids, pitting) are also decreased for the film based on the oligomer-containing system, which should be expected to correlate well with an increase in film gloss.<sup>21</sup> Since the SPM scans were carried out on the natural surface of the films, we were not able to determine the continuity of either phase in the bulk films from these images.

### Coatings performance

Semigloss paints were formulated according to the method described in the Experimental section with several blends of hard mode and soft mode, as described in Table 9. The polymer in the formulation included blends of a soft mode (60 BA/39 MMA/1 MAA) and hard modes with and without oligomer modification. The target is a semigloss coatings formulation that delivers good gloss and hardness properties while maintaining good film formation without the need of a coalescent. In general, hardness properties in a polymer or paint film can be enhanced by the blending of hard particles or pigments into a soft polymer that have good film formation characteristics. However, this approach is limited to low levels in which film formation is not being compromised without the use of coalescent. Loss of gloss is a good indicator of poor film formation. Table 9 compares gloss for paints 1–4. Paint 1 and 2 are blends of the soft mode with unmodified hard mode while paint 3 and 4 contain the oligomer modified hard mode. As shown in Table 9, paints 1 and 2 have inferior gloss for a semigloss paint. Incorporating up to 20% coalescent (paint 2) did not show an improvement suggesting the hard mode is not coalescing into a good film at that level. Applying Design Diffusion technology to the blend, an oligomer modified hard mode (paint 3) shows a good balance of gloss and hardness, indicative of good film formation. At the same level of hard phase (10.7%) and without coalescent, the oligomer-based blend has comparable pendulum hardness while providing significantly better gloss over the nonoligomer blend control. The hardness of the oligomer containing system can be further enhanced without sacrificing the gloss by increasing the level of the hard phase (paint 4).

Additional testing on the paints showed that the tack, print, block, and scrub resistance properties of the oligomer-modified systems were similar to those of the blend control without oligomer. Thus, the benefits reaped from the Designed Diffusion<sup>TM</sup> system do not carry a negative impact in the overall balance of properties.

The concept of Designed Diffusion<sup>TM</sup> Technology involving carefully designed oligomer modification of polymer systems can also be applied to blend systems other than the



ones described in this report. Incorporation of reactive functionalities in the polymer or diffusing oligomer that is capable of reacting with other reactive sites during or after film formation is attractive as a way to further enhance the hardness and resistance properties of a coating and is being explored.

## Conclusion

Latex polymers made with in situ oligomer modification are shown to offer a unique balance of performance properties required to meet the regulatory and environmental demands of the coatings industry. These oligomers are designed to enhance both the soft and hard properties necessary in coatings. Key design factors include a molecular weight, which sufficiently lowers the  $T_g$  of the oligomer, and a composition, which ensures that the oligomer, while miscible with both a hard and a soft polymer phases, preferentially partitions to the soft phase after film formation. Careful design of the composition and molecular weight of the oligomer phase ensures that it will transport between hard and soft polymer phases to achieve both film formation and final performance properties. The concept has been demonstrated to be effective in coating systems and is being applied to other applications. Theoretical modeling was demonstrated to be a viable tool in the design stage.

## Acknowledgements

The authors thank those who contributed to this work: Mr. Daniel Werner for the synthesis of most of the polymers and oligomers used in these studies, Mr. Thomas Machamer for preparing and testing most of the paint formulations, Dr. Jin Lu for much of the DSC work and miscibility calculations with polymer and oligomer blends, Dr. Robert Antrim for the SPM analysis, and Dr. Kathleen Koziski and Dr. Matthew Gebhard who were research colleagues through parts of this work. Additionally, the authors thank the Dow Chemical Company for support and publication of this research. The authors are grateful for the wealth of knowledge on polymer diffusion from the work of Professor Mitchell Winnik at the University of Toronto. This work has benefited from many helpful discussions with Professor Winnik. We wished to congratulate Professor Winnik on this occasion with this paper as a token of our appreciation.

## References

- (1) Steward, P. A.; Hearn, J.; Wilkinson, M. C. *Adv. Colloid Interface Sci.* **2000**, *86* (3), 195. doi:10.1016/S0001-8686(99)00037-8. PMID:10997764.
- (2) Toussaint, A.; De Wilde, M.; Molenaar, F.; Mulvihill, J. *Prog. Org. Coat.* **1997**, *30* (3), 179. doi:10.1016/S0300-9440(96)00685-6.
- (3) Winnik, M. A.; Feng, J. *J. Coat. Technol.* **1996**, *68* (852), 39.
- (4) (a) Heuts, M.; LeFebvre, R.; Van Hilst, J.; Overbeek, G. In *Influence of Morphology on Film Formation of Acrylic Dispersions*, Proceedings of the PMSE Symposium on Latex Film Formation, Chicago, IL, 1995; (b) Friel, J. European Patent Specification EP 466409, 1998.
- (5) (a) Eckersley, S.; Helmer, B. *J. Coat. Technol.* **1997**, *69* (1), 97. doi:10.1007/BF02696096.; (b) ASTM International. ASTM Standard D523-89. In *Standard Test Method for Specular Gloss*; ASTM International: West Conshohocken, PA, 1999.
- (6) Feng, J.; Odrobina, E.; Winnik, M. A. *Macromolecules* **1998**, *31* (16), 5290. doi:10.1021/ma980117w.
- (7) Marcilla, A.; Beltran, M. Mechanisms of Plasticizers Action. In *Handbook of Plasticizers*; Wypych, G., Ed.; ChemTec Pub.: Toronto, ON, 2004; pp 107–120.
- (8) Plante, M.; Bazuin, C. G. *Macromolecules* **1997**, *30* (9), 2613. doi:10.1021/ma961220t.
- (9) Tong, J.-D.; Jerome, R. *Macromolecules* **2000**, *33* (5), 1479. doi:10.1021/ma990404f.
- (10) Bokis, C. P.; Chen, C. C.; Orbey, H. *Fluid Phase Equilib.* **1999**, *155* (2), 193. doi:10.1016/S0378-3812(98)00458-0.
- (11) Uglea, C. V. *Oligomer Technology and Applications*, 1st ed.; Marcel Dekker, Inc.: New York, 1998.
- (12) (a) Lau, W. U.S. Patent 5,521,266, May 28, 1996; (b) Lau, W. U.S. Patent Application US2006/0183839 A1, August 17, 2006; (c) Lau, W. *Macromol. Symp.* **2002**, *182* (1), 283. doi:10.1002/1521-3900(200206)182:1<283::AID-MASY283>3.0.CO;2-H.
- (13) Sheppard, A. Aqueous Polymer Dispersions. US Patent Application 2006/0223935 A1, October 5, 2006.
- (14) (a) Fredenslund, A.; Jones, R. L.; Prausnitz, J. M. *AIChE J.* **1975**, *21* (6), 1086. doi:10.1002/aic.690210607.; (b) Macedo, E. A.; Weidlich, U.; Gmehling, J.; Rasmussen, P. *Ind. Eng. Chem. Process Des. Dev.* **1983**, *22* (4), 676. doi:10.1021/i200023a023.
- (15) Swartz, A. U.S. Patent 5,250,599, 1993.
- (16) ASTM International. ASTM Standard D4946-89. In *Standard Test Method for Blocking Resistance of Architectural Paints*; ASTM International: West Conshohocken, PA, 2008.
- (17) ASTM International. ASTM Standard D2486-06. ASTM International: West Conshohocken, PA, 2006.
- (18) (a) Moad, G.; Solomon, D. H. *The Chemistry of Free Radical Polymerization*, 1st ed.; Elsevier Science Inc.: New York, 1995; Chapter 5; (b) Gilbert, R. G. *Emulsion Polymerization: A Mechanistic Approach*, US Edition; Academic Press Inc.: San Diego, CA, 1995; Chapter 2,.
- (19) Mayo, F. R. *J. Am. Chem. Soc.* **1943**, *65* (12), 2324. doi:10.1021/ja01252a021.
- (20) Tomba, J. P.; Ye, X.; Li, F.; Winnik, M. A.; Lau, W. *Polymer (Guildf.)* **2008**, *49* (8), 2055. doi:10.1016/j.polymer.2008.02.024.
- (21) Tzitzinou, A.; Keddie, J. L.; Geurts, J. M.; Peters, A. C. I. A.; Satguru, R. *Macromolecules* **2000**, *33* (7), 2695. doi:10.1021/ma991372z.

# A solvent-free protocol for the green synthesis of arylalkylidene rhodanines in a task-specific ionic liquid

Abdolhamid Alizadeh, Mohammad M. Khodaei, and Ali Eshghi

**Abstract:** 2-Hydroxyethylammonium formate acts as a task-specific ionic liquid (TSIL) for the Knoevenagel condensation of carbonyl compounds with rhodanine to afford arylalkylidene rhodanines under solvent-free conditions and in good-to-excellent yields. Additionally, compared with those in organic solvents, the yields obtained in the presence of our ionic liquid (IL) were significantly increased. The detailed mechanism of the catalytic effect of TSIL is also reported for the first time.

**Key words:** 2-Hydroxyethylammonium formate, task-specific ionic liquids (TSILs), Knoevenagel condensation, arylalkylidene rhodanines.

**Résumé :** Dans des conditions n'impliquant aucun solvant, le formiate de 2-hydroxyéthylammonium agit comme liquide ionique pour une tâche spécifique (LITS) pour la condensation de Knoevenagel des composés carbonylés avec la rhodanine qui conduit aux arylalkylidènes de rhodanine avec des rendements allant de bons à excellents. De plus, par comparaison avec les rendements obtenus dans des solvants organiques, ceux obtenus en présence de notre liquide ionique sont nettement plus élevés. On propose pour la première fois un mécanisme détaillé de l'effet catalytique du LITS.

**Mots-clés :** formiate de 2-hydroxyéthylammonium, liquide ionique pour une tâche spécifique (LITS), condensation de Knoevenagel, arylalkylidènes de rhodanine.

[Traduit par la Rédaction]

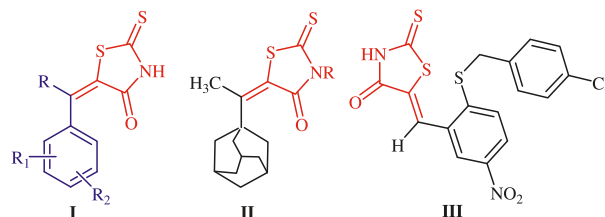
## Introduction

Rhodanine derivatives, especially arylalkylidene rhodanines (**I**) (Fig. 1), have proven to be attractive compounds because of their outstanding biological activities and have undergone rapid development as anticonvulsant, antibacterial, and anti-diabetic agents.<sup>1</sup> A series of arylalkylidene rhodanines have also been reported as Hepatitis C Virus (HCV) protease inhibitors (**II**)<sup>2</sup> (Fig. 1) or as novel inhibitors of UDP *N*-acetylmuramate/L-alanine ligase (**III**) (Fig. 1).<sup>3</sup>

For the preparation of 5-arylalkylidene rhodanines, various methods have been developed from acyclic building blocks or by functionalization of the thiazolone core.<sup>4</sup> In the second case, the Knoevenagel condensation of aldehydes at the nucleophilic C-5 position of rhodanine leads to the desired arylalkylidene rhodanine adducts. This reaction has been performed using sodium acetate in refluxing glacial acetic acid<sup>5a</sup> or piperidinium benzoate in refluxing toluene.<sup>5b</sup> Recently, Lee and Sim reported the synthesis of 5-arylalkylidene rhodanines by heating the reactants suspended in toluene at 110 °C for 3 days.<sup>6</sup> Also, Sing et al. reported the condensation of rhodanine with an aldehyde by heating in anhydrous EtOH for 6 h at 80 °C.<sup>7</sup>

The use of microwave irradiation (MW) as a clean and operationally simple technique has also been employed with

**Fig. 1.** Biologically active compounds bearing a 5-arylalkylidene rhodanine moiety.



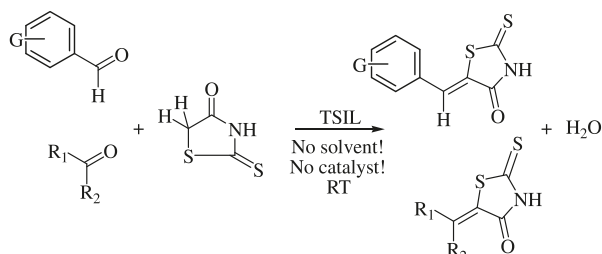
solid inorganic support (Al<sub>2</sub>O<sub>3</sub> or montmorillonite KSF clay)<sup>8,9</sup> but without control of the reaction temperature. Recently, Zhou et al. reported the use of MW and tetrabutylammonium bromide (TBAB) as phase-transfer catalyst in water.<sup>10</sup> In addition, despite their promising biological features, the synthesis of ketone derivatives of arylalkylidene rhodanine adducts has not been subjected to detailed investigations, and only a 60-year-old study of Brown and co-workers has reported the Knoevenagel condensation reaction of rhodanine with ketones in the presence of ammonium hydroxide and ammonium chloride in refluxing ethanol.<sup>11</sup> Similar to most conventional chemical transformations, all of the above-mentioned procedures involve harsh reaction conditions, large quantities of toxic solvents, long reaction

Received 15 October 2009. Accepted 4 January 2010. Published on the NRC Research Press Web site at canjchem.nrc.ca on 29 April 2010.

A. Alizadeh,<sup>1</sup> M.M. Khodaei,<sup>2</sup> and A. Eshghi. Faculty of Chemistry and Nanoscience & Nanotechnology Research Center (NNRC), Razi University, Kermanshah 67149, Iran.

<sup>1</sup>Corresponding author (e-mail: ahalizadeh2@hotmail.com).

<sup>2</sup>Corresponding author (e-mail: mmkhoda@razi.ac.ir).

**Scheme 1.** TSIL-catalyzed synthesis of 5-arylalkylidene rhodanines.

times, and unsatisfactory yields. Therefore, facile and green routes to arylalkylidene rhodanines would be of great interest.

Currently, ionic liquids (ILs) are being used as green solvents for laboratory as well as industrial use because of their desirable properties, such as good solvating ability, variable polarity, negligible vapor pressure, and ease of recyclability.<sup>12</sup> A literature survey revealed that ILs have not been utilized extensively for the Knoevenagel condensation of aldehydes or ketones with rhodanine, and only a study by Liu and co-workers utilizing a functionalized imidazolium-based IL has been reported.<sup>13</sup>

While considering ILs as reaction media and their use in industrial processes, one major concern is cost. The cost of the IL would be directly dependent on the price of the cations and anions that are used for their production.<sup>11</sup> Thus, the popular ILs incorporating expensive cations, such as alkyl methyl imidazolium and dialkyl imidazolium, are likely to remain expensive. Similarly, the anions that are frequently used in ILs, such as tetrafluoro borate and hexafluoro phosphate, are also expensive. This indicates that there is a need to develop and explore simple and cost-effective ILs.

Herein, we wish to report for the first time, a solvent-free and green procedure for the Knoevenagel condensation of aromatic aldehydes and ketones with rhodanine promoted with a low cost and task-specific IL (2-hydroxyethylammonium formate)<sup>14</sup> as an effective catalyst and reaction medium (Scheme 1).

To our knowledge, literature only shows one recent publication<sup>15</sup> related with the application of this new potential IL, but no further information is available about its application in chemical processes and organic syntheses. This IL can easily be synthesized from commercially available low cost chemicals (ethanolamine and formic acid) and has high conductivity and powerful solvating ability. Also, its low melting point ( $-82\text{ }^{\circ}\text{C}$ ) makes it an appropriate solvent for low temperature chemical transformations.

## Results and discussion

Our investigations on the Knoevenagel condensation reaction of rhodanine with carbonyl compounds began with the optimization of reaction conditions. Initially, the reaction of 1 mmol benzaldehyde with 1 mmol rhodanine in acetonitrile was tested in the absence of IL at room temperature. The reactants remained unchanged even after stirring for 20 h. Upon addition of only 1 mL of IL, condensation occurred and the reaction led to the desired product immediately after only 2 min in 94% yield without using any solvent or

catalyst at room temperature (Table 1, entry 1). Further increase in the reaction temperature did not result in a decrease in the reaction time or in an increase in the yield. Also, using 2 mmol of aldehyde (and 1 mmol of rhodanine) showed no change in the final product structure, and again, 5-benzylidene-2-thioxothiazolidine-4-one (Table 1, entry 1) was obtained as the final product.

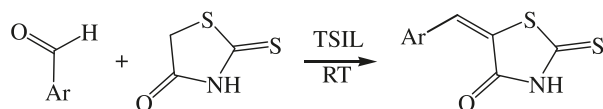
Thus, under this optimized mild condition, various structurally diverse aromatic aldehydes and ketones were tested with rhodanine, and the corresponding results are listed in Tables 1 and 2.

As shown in Table 1, the aryl aldehydes bearing electron-releasing and electron-withdrawing groups are effective for the aforementioned reaction and gave the desired products in excellent yields in the reaction time ranging from 1 to 6 min. For instance, aryl aldehydes such as 4-nitrobenzaldehyde and 4-fluorobenzaldehyde required relatively short reaction times (Table 1, entries 4 and 6), and in contrast, aryl aldehydes with electron-releasing groups required nearly longer reaction times (Table 1, entries 11 and 13).

In examining the scope and generality of the developed protocol as well as the influence of structural variation of carbonyl compounds on their reactivity toward rhodanine enolate, we studied the Knoevenagel condensation reaction of rhodanine with ketones in the conditions similar to that of aldehydes. It was found that the reaction proceeds in a similar fashion to that of aryl aldehydes except that ketones undergo nucleophilic attack of rhodanine enolate more slowly with relatively low yields. Entries 1–4 in Table 2 show that both cyclic and acyclic ketones can react with rhodanine enolate. In contrast, any effort to obtain Knoevenagel condensation adducts from the reaction of rhodanine enolate with benzophenone, benzamide, and 2,4-dimethyl-3-pentanone (diisopropylketone) was unsuccessful. We believe that benzophenone and benzamide do not participate in the condensation, presumably because of the resonance of the carbonyl moiety with the phenyl groups and nitrogen lone-pair electrons. Also, diisopropylketone has a steric hindrance around the carbonyl group, and hence, it does not react with rhodanine. The results are listed in Table 2.

A control experiment was also allowed to proceed under the developed conditions utilizing 1 mL of TSIL, 1 mmol of *p*-methylbenzaldehyde, and 1 mmol of acetophenone to evaluate the chemoselectivity of the TSIL. It was found that in the presence of 1 mL of the IL, rhodanine only reacts with *p*-methylbenzaldehyde, which leads to the formation of 4-methylbenzylidene rhodanine as the final product, and no adduct was obtained from the condensation of rhodanine with ketone (Scheme 2).

The obtained results allow us to propose a tentative mechanism for the TSIL-catalyzed Knoevenagel condensation reaction of aldehydes and ketones with rhodanine as depicted in Scheme 3. The structure of the IL used in this study (2-hydroxyethylammonium formate) has a specific feature bearing both acidic and basic sites. We believe that the acidic part of the IL (ammonium moiety) protonates the oxygen of the carbonyl group; this is a very suitable condition in nucleophilic additions to carbonyl compounds. On the other hand, rhodanine is a CH-acidic nucleophile and the anionic part of the IL (formate anion) is basic and easily deprotonates rhodanine at the C-5 position and causes the

**Table 1.** TSIL-catalyzed reaction of rhodanine with aromatic aldehydes.

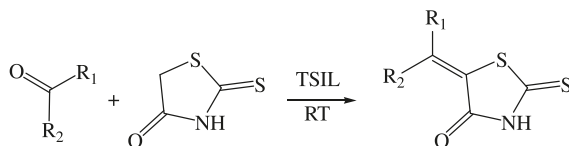
Entry	Ar	Time (min)	Mp (°C)		Yield (%) <sup>a,b</sup>
			Found	Reported	
1	C <sub>6</sub> H <sub>5</sub>	2	205	204 <sup>16</sup>	94
2	4-MeC <sub>6</sub> H <sub>4</sub>	2	221	220 <sup>16</sup>	95
3	4-MeOC <sub>6</sub> H <sub>4</sub>	2	251	251 <sup>16</sup>	96
4	4-NO <sub>2</sub> C <sub>6</sub> H <sub>4</sub>	1	255	250 <sup>16</sup>	98
5	4-ClC <sub>6</sub> H <sub>4</sub>	2	232	232 <sup>16</sup>	96
6	4-FC <sub>6</sub> H <sub>4</sub>	1	226	226 <sup>17</sup>	98
7	4-BrC <sub>6</sub> H <sub>4</sub>	1	230.5	231 <sup>17</sup>	97
8	2,4-ClC <sub>6</sub> H <sub>3</sub>	1	230	231 <sup>16</sup>	95
9	2,4-MeOC <sub>6</sub> H <sub>3</sub>	3	275 <sup>c</sup>	—	92
10	2-Furyl	2	230	229 <sup>16</sup>	95
11	4-N(Me) <sub>2</sub> C <sub>6</sub> H <sub>4</sub>	3	272	270 <sup>18</sup>	90
12	2-ClC <sub>6</sub> H <sub>4</sub>	4	191	192 <sup>16</sup>	94
13	2-OHC <sub>6</sub> H <sub>4</sub>	6	223	222 <sup>18</sup>	91
14	Cinammyl	1	227 <sup>c</sup>	—	98

**Note:** Reaction conditions: aldehyde (1 mmol), rhodanine (1 mmol), ionic liquid (1 mL), and RT.

<sup>a</sup>The products were characterized by comparison of their spectroscopic and physical data with those reported in the literature.

<sup>b</sup>Yields refer to pure isolated products.

<sup>c</sup>New compounds.

**Table 2.** TSIL-catalyzed reaction of rhodanine with ketones.

Entry	R <sub>1</sub>	R <sub>2</sub>	Time (min)	Mp (°C)		Yield (%) <sup>a</sup>
				Found	Reported	
1	(-CH <sub>2</sub> ) <sub>5</sub>	(-CH <sub>2</sub> ) <sub>5</sub>	20	175	173 <sup>11</sup>	87
2	(-CH <sub>2</sub> ) <sub>4</sub>	(-CH <sub>2</sub> ) <sub>4</sub>	15	195	195 <sup>11</sup>	90
3	C <sub>6</sub> H <sub>5</sub>	CH <sub>3</sub>	70	167	166 <sup>11</sup>	92
4	4ClC <sub>6</sub> H <sub>4</sub>	CH <sub>3</sub>	72	205	204 <sup>11</sup>	90
5	C <sub>6</sub> H <sub>5</sub>	C <sub>6</sub> H <sub>5</sub>				NR <sup>b</sup>
6	<i>i</i> -Pro	<i>i</i> -Pro				NR
7	C <sub>6</sub> H <sub>5</sub>	NH <sub>2</sub>				NR

**Note:** Reaction conditions: ketone (1 mmol), rhodanine (1 mmol), ionic liquid (1 mL), and RT.

<sup>a</sup>Yields refer to pure isolated products.

<sup>b</sup>NR: No reaction.

formation of nucleophilic rhodanine enolate. Subsequently, this enolate attacks the protonated aldehyde or ketone and gives an intermediate alcohol. Eventually, protonation of this alcohol, followed by a dehydration process, gives the desired products, recovered catalyst, and water as the only byproduct of the reaction.

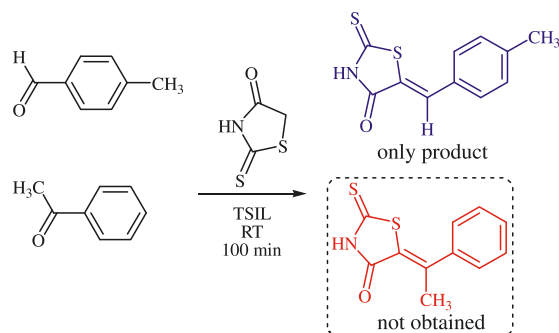
The ionic liquid was recovered and reutilized four times without the addition of extra ionic liquid; the results are shown in Fig. 2.

In conclusion, we have described a general, environment-

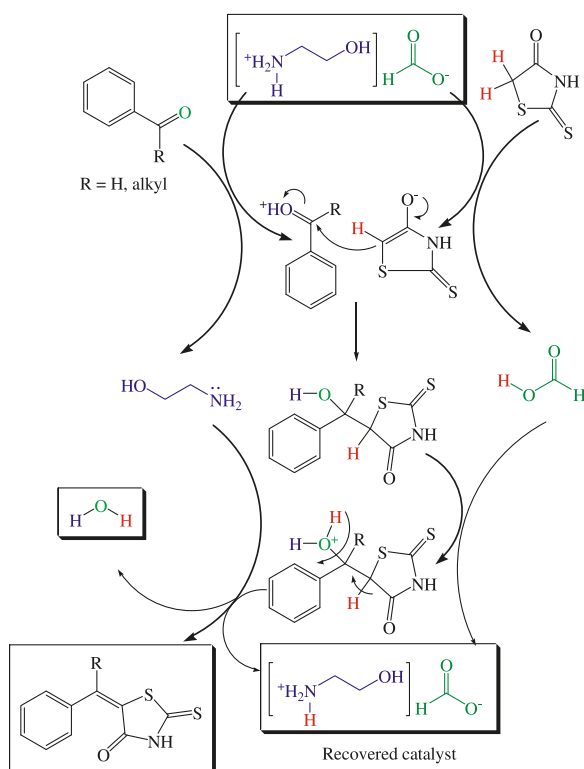
friendly, solvent-free, and reagentless protocol for the preparation of a series of arylalkylidene rhodanine derivatives using 2-hydroxyethylammonium formate as a task-specific ionic liquid. The ease of preparation of the IL from commercially available low cost starting materials, its high conductivity, powerful solvating ability, and low melting point make it an appropriate solvent for room temperature reactions. Furthermore, this method is applicable to both electron-rich as well as electron-deficient aldehydes. In all cases, the reaction proceeds smoothly under very mild con-



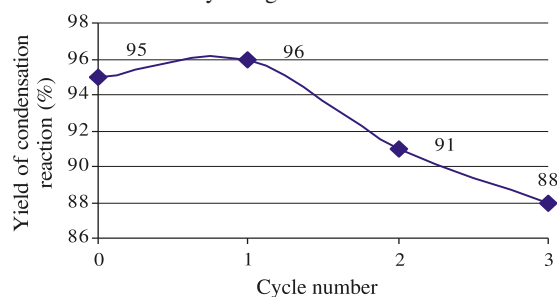
**Scheme 2.** Comparison of the reactions of rhodanine with benzaldehyde and acetophenone in the presence of TSIL.



**Scheme 3.** Representative mechanism of TSIL-promoted Knoevenagel condensation reaction of aldehydes and ketones with rhodanine.



**Fig. 2.** Successive trials by using the recoverable TSIL.



ditions without introducing any acid, base, or metal catalyst, and water is the only byproduct of the reaction. Compared with those obtained using traditional organic solvents, the

yields obtained in the presence of this TSIL are significantly increased. We believe that the low cost and the experimental simplicity of the method gives this green ionic-liquid-catalyzed procedure great potential, and it may find potential applications in synthetic organic chemistry, and more importantly, it can complement the existing chemical strategies.

## Experimental

All chemicals (ethanolamine, formic acid, rhodanine, aldehydes, and ketones) were reagent-grade materials, and they were used without further purification. Throughout all experiments, distilled water was used, and all the experiments were done at room temperature.  $^1\text{H}$  and  $^{13}\text{C}$  NMR spectra were recorded on a Bruker spectrometer operating at 200 and 50 MHz, respectively. Melting points were measured on a BI Branstead Electrothermal 9200 instrument and are uncorrected. FTIR spectra were recorded on a Rayleigh Wqf-510 spectrometer using a drop casting technique on KBr plates and are reported in wavenumbers ( $\text{cm}^{-1}$ ).

### Synthesis of arylalkylidene rhodanines: general procedure

Rhodanine (1 mmol) and 2-hydroxyethylammonium formate (1 mL) were mixed together and stirred at room temperature for 2 min after which 1 mmol of aromatic aldehyde or ketone was added to the reaction mixture. After completion of the reaction (monitored by TLC), a mixture of water and ethanol (50:50 v/v) was added to the reaction flask, and the obtained precipitates were easily filtered leading to the final pure products while no extra purification was needed. Evaporating the water of the filtrate gave the pure IL, which could be reused for further reactions. Selected characterization data for some of the arylalkylidene rhodanines prepared are given below.

#### 5-Phenyl-2-thioxothiazolidin-4-one

Yellow powder, mp 205 °C (lit.<sup>16</sup> mp 204 °C).  $^1\text{H}$  NMR (DMSO- $d_6$ , 200 MHz)  $\delta$  (ppm): 7.51–7.85 (m, 5H,  $\text{H}_{\text{ar}}$ ), 7.68 (s, 1H, vinyl), 13.87 (s, 1H, NH).  $^{13}\text{C}$  NMR (DMSO- $d_6$ , 50 MHz)  $\delta$  (ppm): 125.9, 127.4, 129.8, 130.8, 131.1, 131.9, 169.8, 196.1.

#### 5-(4-Methylbenzyliden)-2-thioxothiazolidin-4-one

Yellow powder, mp 221 °C (lit.<sup>16</sup> mp 220 °C).  $^1\text{H}$  NMR (DMSO- $d_6$ , 200 MHz)  $\delta$  (ppm): 2.40 (s, 3H,  $\text{CH}_3$ ), 7.40 (d, 2H,  $\text{H}_{\text{ar}}$ ), 7.53 (d, 2H,  $\text{H}_{\text{ar}}$ ), 7.65 (s, 1H, vinyl), 13.88 (s, 1H, NH).  $^{13}\text{C}$  NMR (DMSO- $d_6$ , 50 MHz)  $\delta$  (ppm): 21.5, 124.7, 130.4, 130.6, 130.9, 132.1, 141.5, 169.9, 196.1.

#### 5-(2,4-Dimethoxybenzyliden)-2-thioxothiazolidin-4-one

Orange powder, mp 275 °C. IR (KBr)  $\nu$  ( $\text{cm}^{-1}$ ): 3452, 1707, 1621, 1564, 1445, 1117.  $^1\text{H}$  NMR (DMSO- $d_6$ , 200 MHz)  $\delta$  (ppm): 3.86 (s, 3H,  $\text{OCH}_3$ ), 3.91 (s, 3H,  $\text{OCH}_3$ ), 6.70–6.75 (m, 2H,  $\text{H}_{\text{ar}}$ ), 7.33 (d, 1H,  $\text{H}_{\text{ar}}$ ), 7.74 (s, 1H, vinyl), 13.72 (s, 1H, NH).  $^{13}\text{C}$  NMR (DMSO- $d_6$ , 50 MHz)  $\delta$  (ppm): 55.7, 55.9, 98.7, 106.5, 115.5, 123.0, 126.7, 130.6, 159.7, 162.7, 163.2, 199.1. Anal. calcd. for  $\text{C}_{12}\text{H}_{11}\text{NO}_3\text{S}_2$ : C, 51.23%; H, 3.94%; N, 4.98%; S, 22.79%. Found: C, 48.2%; H, 5.0%; N, 6.6%; S, 19.1%.

### 5-[(E)-3-Phenylallylidene]-2-thioxothiazolidin-4-one

Orange powder, mp 227 °C. IR (KBr)  $\nu$  (cm<sup>-1</sup>): 3458, 1691, 1624, 1573, 1448, 1150. <sup>1</sup>H NMR (DMSO-*d*<sub>6</sub>, 200 MHz)  $\delta$  (ppm): 7.01 (m, 1H, vinyl), 7.31 (d, 1H, vinyl), 7.40–7.47 (m, 5H, H<sub>ar</sub>), 7.67 (d, 1H, vinyl), 13.64 (s, 1H, NH). <sup>13</sup>C NMR (DMSO-*d*<sub>6</sub>, 50 MHz)  $\delta$  (ppm): 124.6, 128.0, 128.9, 129.8, 130.8, 132.9, 136.4, 145.5, 169.6, 196.2. Anal. calcd. for C<sub>12</sub>H<sub>9</sub>NOS<sub>2</sub>: C, 58.27%; H, 3.67%; N, 5.66%; S, 25.93%. Found: C, 58.2%; H, 4.1%; N, 6.1%; S, 24.1%.

### Supplementary data

Supplementary data for this article are available on the journal Web site (canjchem.nrc.ca).

### Acknowledgment

Financial support for this work by Razi University is hereby appreciated.

### References

- (1) (a) Ohishi, Y.; Mukai, T.; Nagahara, M.; Yajima, M.; Kajikawa, N.; Miyahara, K.; Takano, T. *Chem. Pharm. Bull. (Tokyo)* **1990**, *38* (7), 1911. PMID:2125247.; (b) Momose, Y.; Meguro, K.; Ikeda, H.; Hatanaka, C.; Oi, S.; Sohda, T. *Chem. Pharm. Bull. (Tokyo)* **1991**, *39* (6), 1440. PMID:1934164.
- (2) Sudo, K.; Matsumoto, Y.; Matsushima, M.; Fujiwara, M.; Konno, K.; Shimotohno, K.; Shigeta, S.; Yokota, T. *Biochem. Biophys. Res. Commun.* **1997**, *238* (2), 643. doi:10.1006/bbrc.1997.7358. PMID:9299567.
- (3) Sim, M. M.; Ng, S. B.; Buss, A. D.; Crasta, S. C.; Goh, K. L.; Lee, S. K. *Bioorg. Med. Chem. Lett.* **2002**, *12* (4), 697. doi:10.1016/S0960-894X(01)00832-0. PMID:11844704.
- (4) (a) Brown, F. C. *Chem. Rev.* **1961**, *61* (5), 463. doi:10.1021/cr60213a002.; (b) Singh, S. P.; Parmar, S. S.; Raman, K. V.; Stenberg, I. *Chem. Rev.* **1981**, *81* (2), 175. doi:10.1021/cr00042a003.
- (5) (a) Cutshall, N. S.; O'Day, C.; Prezhdo, M. *Bioorg. Med. Chem. Lett.* **2005**, *15* (14), 3374. doi:10.1016/j.bmcl.2005.05.034. PMID:15961311.; (b) Lohray, B. B.; Bhushan, V.; Rao, P. B.; Madhavan, G. R.; Murali, N.; Rao, K. N.; Reddy, K. A.; Rajesh, B. M.; Reddy, P. G.; Chakrabarti, R.; Rajagopalan, R. *Bioorg. Med. Chem. Lett.* **1997**, *7* (7), 785. doi:10.1016/S0960-894X(97)00118-2.
- (6) Lee, C. L.; Sim, M. M. *Tetrahedron Lett.* **2000**, *41* (30), 5729. doi:10.1016/S0040-4039(00)00866-2.
- (7) Sing, W. T.; Lee, C. L.; Yeo, S. L.; Lim, S. P.; Sim, M. M. *Bioorg. Med. Chem. Lett.* **2001**, *11* (2), 91. doi:10.1016/S0960-894X(00)00610-7. PMID:11206478.
- (8) (a) Zhang, L. *Chem. J. Chin. Univ.* **1994**, *15*, 1647; (b) Bourgrin, K.; Soufiaoui, M. N. *J. Chem.* **1998**, *22*, 809.
- (9) Bourahla, K.; Derdour, A.; Rahmouni, M.; Carreaux, F.; Bazureau, J. P. *Tetrahedron Lett.* **2007**, *48* (33), 5785. doi:10.1016/j.tetlet.2007.06.078.
- (10) Zhou, J. F.; Zhu, F. X.; Song, Y. Z.; Zhu, Y. L. *Arkivoc* **2006**, *iv*, 175.
- (11) Brown, F. C.; Bradsher, C. K.; McCallum, S. G.; Potter, M. *J. Org. Chem.* **1950**, *15* (1), 174. doi:10.1021/jo01147a028.
- (12) Wasserscheid, P.; Welton, T., Eds. *Ionic Liquids in Synthesis*; Wiley-VCH Verlag GmbH & Co. KGaA, 2003. doi:10.1002/3527600701.fmatter\_indsub.
- (13) Gong, K.; He, Z. W.; Xu, Y.; Fang, D.; Liu, Z. L. *Monatsh. Chem.* **2008**, *139* (8), 913. doi:10.1007/s00706-008-0871-y.
- (14) Bicak, N. *J. Mol. Liq.* **2005**, *116* (1), 15. doi:10.1016/j.molliq.2004.03.006.
- (15) Sharma, Y. O.; Degani, M. S. *J. Mol. Catal. Chem.* **2007**, *277* (1-2), 215. doi:10.1016/j.molcata.2007.07.053.
- (16) Luo, J.; Li, Y.; Zhou, M. *J. Chem. Int.* **2006**, *8*, 17.
- (17) Sortino, M.; Delgado, P.; Juárez, S.; Quiroga, J.; Abonía, R.; Insuasty, B.; Nogueras, M.; Rodero, L.; Garibotto, F. M.; Enriz, R. D.; Zaccchino, S. A. *Bioorg. Med. Chem.* **2007**, *15* (1), 484. doi:10.1016/j.bmc.2006.09.038. PMID:17049255.
- (18) Zhou, J. F.; Zhu, F. X.; Song, Y. Z.; Zhu, Y. *Arkivoc* **2006**, *xiv*, 175.

# Feruloyl sucrose derivatives from *Bistorta manshuriensis*

Ki Hyun Kim, Sang Wook Chang, and Kang Ro Lee

**Abstract:** *Bistorta manshuriensis* is a well-known Korean medicinal plant traditionally used to treat diarrhea. Phytochemical investigation of the aerial parts of *B. manshuriensis* led to the isolation of two new feruloyl sucrose derivatives, bistoroside A (**1**) and bistoroside B (**2**), together with three known compounds, helonioside A (**3**), helonioside B (**4**), and smilaside L (**5**). The structures of the new compounds were elucidated as (3,6-di-*O*-*Z*-feruloyl)- $\beta$ -D-fructofuranosyl-(1 $\rightarrow$ 2)- $\alpha$ -D-glucopyranoside (**1**) and (3,6-di-*O*-*Z*-feruloyl)- $\beta$ -D-fructofuranosyl-(1 $\rightarrow$ 2)-(6'-*O*-acetyl)- $\alpha$ -D-glucopyranoside (**2**) on the basis of extensive analysis of 1D and 2D NMR (HMQC and HMBC), HR-FAB-MS, and chemical evidence.

**Key words:** *Bistorta manshuriensis*, Polygonaceae, feruloyl sucrose derivatives, bistoroside A, bistoroside B.

**Résumé :** La *Bistorta manshuriensis* est une plante médicinale coréenne bien connue pour le traitement traditionnel de la diarrhée. Une étude phytochimique des parties aériennes du *B. manshuriensis* a permis d'isoler deux nouveaux dérivés féruloyle du sucrose, le bistoroside A (**1**) et le bistoroside B (**2**) aux côtés de trois composés connus, l'hélonioside A (**3**), l'hélonioside B (**4**) et le smilaside L (**5**). En se basant sur des études extensives de RMN 1D et 2D, de spectrométrie de masse à haute résolution et bombardement avec des atomes rapides (SM-HR-BAR) et de données chimiques, on a établi que le composé **1** est le (3,6-di-*O*-*Z*-féruloyle)- $\beta$ -D-fructofuranosyl-(1 $\rightarrow$ 2)- $\alpha$ -D-glucopyranoside alors que le composé **2** est le (3,6-di-*O*-*Z*-féruloyle)- $\beta$ -D-fructofuranosyl-(1 $\rightarrow$ 2)-(6'-*O*-acétyl)- $\alpha$ -D-glucopyranoside.

**Mots-clés :** *Bistorta manshuriensis*, polygonacée, dérivés féruloyle du sucrose, bistoroside A, bistoroside B.

[Traduit par la Rédaction]

## Introduction

*Bistorta manshuriensis* KOM (Polygonaceae) (Korean name: Bum-ko-ri) is an erect perennial herb that is widely distributed throughout Korea.<sup>1</sup> The scientific name of this plant has also been used in China in combination with *Polygonum bistorta*. The rhizomes of *B. manshuriensis* have been used in traditional Korean medicine for the treatment of diarrhea.<sup>1</sup> In Chinese folk medicine, its rhizomes have been used to treat dysentery with bloody stools in acute gastroenteritis, acute respiratory infection, and venomous snake bite.<sup>2</sup> It has been reported that the crude extract of *P. bistorta* exhibits several potent pharmacological activities, including antibacterial, anti-inflammatory activities, and antimutagenic effect of 3-amino-1,4-dimethyl-5*H*-pyrido[4,3-*b*]indole (Trp-P-1).<sup>3–6</sup> Previous phytochemical investigation of *P. bistorta* revealed the presence of triterpenoids, flavones, coumarins, and phenolic acids.<sup>5–10</sup> Despite several studies on *P. bistorta*, little is known about the phytochemical constituents of *B. manshuriensis*. Therefore, as a part of our continuing search for novel secondary metabolites from Korean medicinal plants, we investigated the constituents of the aerial parts of *B. manshuriensis* and isolated cerebroside, flavonoids, and phenolic constituents from this source.<sup>11</sup> Herein, we report the further isolation and struc-

ture elucidation of two new feruloyl sucrose derivatives, bistoroside A (**1**) and bistoroside B (**2**), as well as three previously reported compounds, helonioside A (**3**), helonioside B (**4**), and smilaside L (**5**).

## Results and discussion

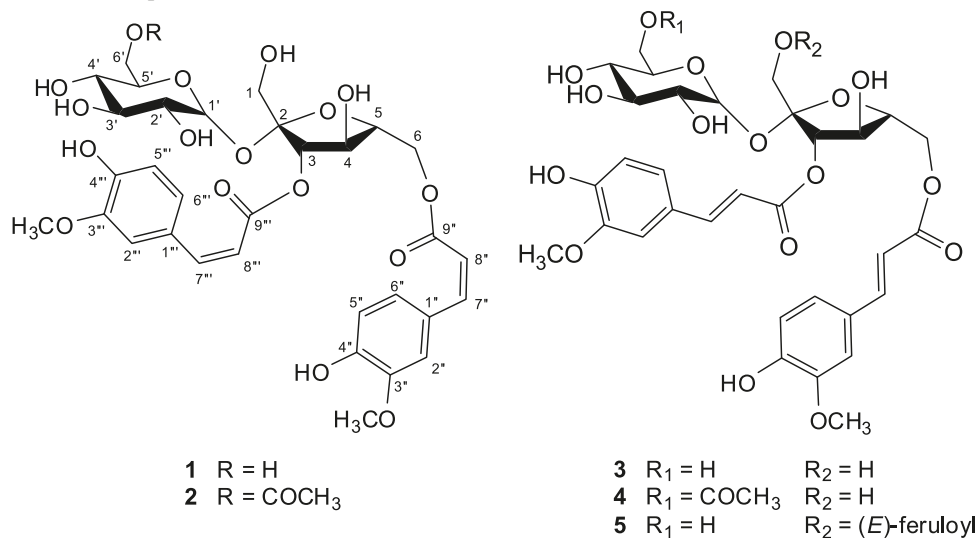
The EtOAc-soluble portion of the 80% MeOH extract of the aerial parts of *B. manshuriensis* was subjected to repeated column chromatography on silica gel to afford two new feruloyl sucrose derivatives (**1–2**), together with three known compounds (**3–5**) (Fig. 1). Their structures were elucidated by 1D and 2D NMR, HR-FAB-MS, and comparison with published data.

Bistoroside A (**1**) was isolated as a yellowish gum with a molecular formula of C<sub>32</sub>H<sub>38</sub>O<sub>17</sub> on the basis of the [M + H]<sup>+</sup> peak at *m/z* 695.2180 (calcd. for C<sub>32</sub>H<sub>39</sub>O<sub>17</sub>: 695.2187) in the HR-FAB-MS. Its IR and UV spectra displayed absorption bands for the hydroxyl and  $\alpha,\beta$ -unsaturated aromatic ester groups. The <sup>1</sup>H NMR spectrum (Table 1) of **1** showed two pairs of olefinic protons at  $\delta$  6.92 and 5.90 (each 1H, d, *J* = 13.0 Hz, H-7'', 8''), 6.89 and 5.83 (each 1H, d, *J* = 13.0 Hz, H-7''', 8'''), and two aromatic moieties with ABX coupling patterns at  $\delta$  6.82 (d, *J* = 8.5 Hz, H-5''), 7.16 (dd, *J* = 8.5, 2.0 Hz, H-6''), and 7.83 (d, *J* = 2.0 Hz, H-2'') and at  $\delta$  6.78 (d, *J* = 8.5 Hz, H-5'''), 7.13 (dd, *J* = 8.5,

Received 27 January 2010. Accepted 5 March 2010. Published on the NRC Research Press Web site at canjchem.nrc.ca on 5 May 2010.

**K.H. Kim, S.W. Chang, and K.R. Lee.**<sup>1</sup> Natural Products Laboratory, School of Pharmacy, Sungkyunkwan University, 300 Chonchondong, Jangsan-ku, Suwon 440-746, Korea.

<sup>1</sup>Corresponding author (e-mail: krlee@skku.ac.kr).

**Fig. 1.** Chemical structures of compounds **1**–**5**.

2.0 Hz, H-6'''), and 7.83 (d,  $J = 2.0$  Hz, H-2'''). The coupling constant (13.0 Hz) of the proton signals at  $\delta$  6.92/5.90 and 6.89/5.83 suggested the presence of two pairs of *cis*-olefinic protons.<sup>12</sup> The above <sup>1</sup>H NMR data, along with two methoxy groups at the aromatic moieties as determined from the HMBC spectrum, indicated the presence of two *cis*-feruloyl units in **1**.<sup>13</sup> In addition, signals for eight oxygenated methines at  $\delta$  5.47 (d,  $J = 8.0$  Hz, H-3), 4.42 (t,  $J = 7.0$  Hz, H-4), 4.16 (m, H-5), 5.42 (d,  $J = 4.0$  Hz, H-1'), 3.42 (dd,  $J = 10.0$ , 4.0 Hz, H-2'), 3.67 (t,  $J = 10.0$  Hz, H-3'), 3.40 (t,  $J = 10.0$  Hz, H-4'), and 3.95 (m, H-5'), three oxygenated methylenes at  $\delta$  3.60 and 3.65 (each 1H, d,  $J = 12.0$  Hz, H-1), 4.48 (dd,  $J = 12.0$ , 4.0 Hz, H-6a), 4.54 (dd,  $J = 12.0$ , 7.0 Hz, H-6b), 3.78 (dd,  $J = 12.0$ , 6.0 Hz, H-6'a), and 3.91 (dd,  $J = 12.0$ , 2.5 Hz, H-6'b) were observed in the <sup>1</sup>H NMR spectrum. A characteristic anomeric signal at  $\delta$  5.42 with a small coupling constant (d,  $J = 4.0$  Hz, H-1'), together with 12 oxygenated carbon signals containing two anomeric carbons ( $\delta$  105.1 and 93.3) in the <sup>13</sup>C NMR spectrum, suggested that **1** possessed a disaccharide moiety. Alkaline hydrolysis of **1** gave methyl (*Z*)-ferulate,<sup>13</sup> together with sucrose [ $\alpha$ -D-Glc-(1→2)- $\beta$ -D-Fru], which was confirmed by HMBC analysis indicating linkage of the two sugars and by comparing HPLC and optical rotation data with those of an authentic sample.<sup>14</sup> On further inspection of the HMBC spectrum, each (*Z*)-feruloyl moiety at C-3 and at C-6 in fructose (Fru) could be assigned unambiguously. The correlations between H-3 ( $\delta$  5.47) and H-6 ( $\delta$  4.48 and 4.54) of fructose and the corresponding carbonyl carbons ( $\delta$  168.3 and 168.4) of (*Z*)-ferulate were observed in the HMBC spectrum, respectively (Fig. 2). Thus, the structure of **1** was determined as (3,6-di-*O*-*Z*-feruloyl)- $\beta$ -D-fructofuranosyl-(1→2)- $\alpha$ -D-glucopyranoside, and it was named bistoroside A (Fig. 1).

Bistoroside B (**2**) was isolated as a yellowish gum. Its molecular formula was determined as C<sub>34</sub>H<sub>40</sub>O<sub>18</sub> from the [M + H]<sup>+</sup> peak at  $m/z$  737.2298 (calcd. for C<sub>34</sub>H<sub>41</sub>O<sub>18</sub>: 737.2293) in the HR-FAB-MS spectrum. The <sup>1</sup>H and <sup>13</sup>C NMR spectra of **2** were almost identical to those of **1** (Table 1), except for the presence of an acetyl group signal. This indicated that **2** possessed a structure similar to **1**, con-

taining glucose (Glc) and fructose (Fru) units, two (*Z*)-feruloyl moieties, and one additional acetyl group. Acetylation of **2** yielded an octaacetate (**2a**) identical to that obtained from acetylation of **1**, indicating that the two (*Z*)-feruloyl moieties were located at C-3 and C-6 of the fructose unit in **2**, as in the structure of **1**. In the <sup>1</sup>H and <sup>13</sup>C NMR spectra of **2**, the signals of H-6' and C-6' in **2** were shifted to lower field ( $\delta$  4.13,  $\delta$  4.48, and  $\delta$  65.5 for **2**;  $\delta$  3.78,  $\delta$  3.91, and  $\delta$  62.6 for **1**), while that of C-5' was shifted to higher field ( $\delta$  71.7 for **2**;  $\delta$  74.5 for **1**) when comparing the NMR spectra of **1** and **2**. This supported the assignment of the acetyl group at C-6' of glucose. The HMBC experiment of **2** displayed correlations between the protons at  $\delta$  4.13 and 4.48 (H-6' of Glc) and the carbonyl carbon at  $\delta$  172.5, confirming that the acetyl group was located at C-6' of Glc. On the basis of this evidence, the structure of **2** was determined as (3,6-di-*O*-*Z*-feruloyl)- $\beta$ -D-fructofuranosyl-(1→2)-(6'-*O*-acetyl)- $\alpha$ -D-glucopyranoside, and it was named bistoroside B (Fig. 1).

Three other known compounds obtained in this investigation were identified as helonioside A (**3**),<sup>14</sup> helonioside B (**4**),<sup>14</sup> and smilaside L (**5**)<sup>15</sup> by comparison of their spectroscopic data with those published in the literature (Fig. 1). Although several sucrose phenylpropanoid esters have previously been isolated from *Polygonum* sp.,<sup>16</sup> this is the first report of compounds from this class being isolated from a medicinal plant from the genus *Bistorta*.

## Experimental

### General experimental procedures

Optical rotations were measured on a Jasco P-1020 polarimeter in MeOH. IR spectra were recorded on a Bruker IFS-66/S FTIR spectrometer. UV spectra were recorded with a Shimadzu UV-1601 UV-vis spectrophotometer. FAB and HR-FAB mass spectra were obtained on a JEOL JMS700 mass spectrometer. NMR spectra, including <sup>1</sup>H-<sup>1</sup>H COSY, HMQC, and HMBC experiments, were recorded on a Varian UNITY INOVA 500 NMR spectrometer operating at 500 MHz (<sup>1</sup>H) and 125 MHz (<sup>13</sup>C) with chemical shifts given in ppm ( $\delta$ ). Preparative HPLC was conducted using a

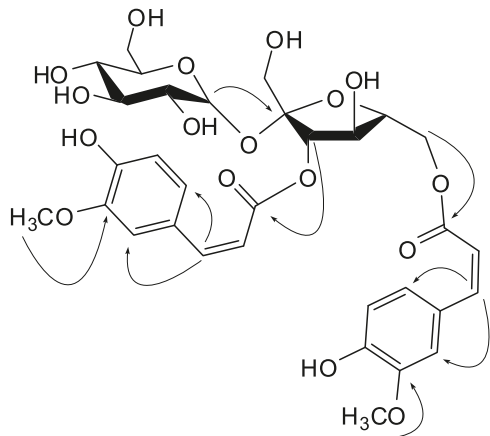


**Table 1.** <sup>1</sup>H and <sup>13</sup>C NMR spectral data of compounds **1** and **2** in CD<sub>3</sub>OD.

	<b>1</b>		<b>2</b>	
Position	<sup>1</sup> H ( <i>J</i> = Hz)	<sup>13</sup> C	<sup>1</sup> H ( <i>J</i> = Hz)	<sup>13</sup> C
β-D-Fru 1	3.60 d (12.0) 3.65 d (12.0)	65.3	3.59 d (12.0) 3.64 d (12.0)	65.2
2		105.1		104.4
3	5.47 d (8.0)	79.1	5.49 d (8.0)	78.4
4	4.42 t (7.0)	75.0	4.45 t (7.0)	73.8
5	4.16 m	81.3	4.15 m	80.8
6	4.48 dd (12.0, 4.0) 4.54 dd (12.0, 7.0)	66.3	4.49 dd (12.0, 4.0) 4.52 dd (12.0, 7.0)	65.3
α-D-Glc 1'	5.42 d (4.0)	93.3	5.43 d (4.0)	92.2
2'	3.42 dd (10.0, 4.0)	73.3	3.44 dd (10.0, 4.0)	72.6
3'	3.67 t (10.0)	74.9	3.64 t (10.0)	74.3
4'	3.40 t (10.0)	71.4	3.26 t (10.0)	71.5
5'	3.95 m	74.5	4.18 m	71.7
6'	3.78 dd (12.0, 6.0) 3.91 dd (12.0, 2.5)	62.6	4.13 dd (12.0, 6.0) 4.48 dd (12.0, 2.5)	65.5
Feruloyl 1''		128.2		127.6
2''	7.83 d (2.0)	115.17	7.82 d (2.0)	114.84
3''		147.93		147.93
4''		149.89		149.3
5''	6.82 d (8.5)	116.65	6.81 d (8.5)	115.26
6''	7.16 dd (8.5, 2.0)	127.1	7.16 dd (8.5, 2.0)	126.6
7''	6.92 d (13.0)	146.29	6.91 d (13.0)	145.5
8''	5.90 d (13.0)	115.9	5.89 d (13.0)	115.29
9''		168.4		167.7
OCH <sub>3</sub>	3.89 s	56.68	3.88 s	56.1
Feruloyl 1'''		128.1		127.5
2'''	7.83 d (2.0)	115.16	7.81 d (2.0)	114.81
3'''		147.91		147.91
4'''		149.81		149.2
5'''	6.78 d (8.5)	116.63	6.78 d (8.5)	115.24
6'''	7.13 dd (8.5, 2.0)	127.0	7.11 dd (8.5, 2.0)	126.5
7'''	6.89 d (13.0)	146.26	6.86 d (13.0)	145.4
8'''	5.83 d (13.0)	115.8	5.82 d (13.0)	115.6
9'''		168.3		167.4
OCH <sub>3</sub>	3.87 s	56.64	3.86 s	56.0
OAc-6'				172.5
			2.10 s	20.5

**Note:** NMR data were obtained at 500 MHz for <sup>1</sup>H and at 125 MHz for <sup>13</sup>C.

**Fig. 2.** Key HMBC (→) correlations of **1**.



Gilson 306 pump with Shodex refractive-index detector and Apollo Silica 5 μm column (250 × 10 mm). Silica gel 60 (Merck, 70–230 mesh and 230–400 mesh) and RP-C<sub>18</sub> silica gel (Merck, 230–400 mesh) were used for column chromatography. The packing material for molecular-sieve column chromatography was Sephadex LH-20 (Pharmacia Co.). Low pressure liquid chromatography was carried out over a LiChroprep Lobar®-A RP-18 (240 × 10 mm) column with a FMI QSY-0 pump (ISCO). Merck precoated Silica gel F<sub>254</sub> plates and RP-18 F<sub>254s</sub> plates were used for TLC. Spots were detected on TLC under UV light or by heating after spraying with 10% H<sub>2</sub>SO<sub>4</sub> in C<sub>2</sub>H<sub>5</sub>OH (v/v).

**Plant material**

The aerial parts of *B. manshuriensis* (2.9 kg) were collected from Mount Daeduk, Gangwon Province, Korea, in June 2008. The plants were authenticated by one of the au-

thors (K.R.L.). A voucher specimen (SKKU-2008-6) of the plant was deposited in the herbarium of the School of Pharmacy, Sungkyunkwan University, Suwon, Korea.

### Extraction and isolation

The dried aerial parts of *B. manshuriensis* (2.9 kg) were extracted three times at room temperature with 80% MeOH over a period of 3 days and evaporated under reduced pressure to give a crude extract (219 g). The crude extract was dissolved in distilled water (800 mL) and successively extracted with *n*-hexane, CH<sub>2</sub>Cl<sub>2</sub>, EtOAc, and *n*-BuOH to provide *n*-hexane (10 g), CH<sub>2</sub>Cl<sub>2</sub> (2 g), EtOAc (9 g), and *n*-BuOH extracts (32 g). The EtOAc-soluble extract (9 g) was subjected to normal-phase column chromatography (CC) over silica gel using CHCl<sub>3</sub>/MeOH of increasing polarity (7:1 to 1:1) to give six fractions (E1–E6). Fraction E2 (1.1 g) was subjected to reversed-phase column chromatography over an RP-C<sub>18</sub> silica gel using MeOH/H<sub>2</sub>O (3:2) to provide five subfractions (E21–E25). Subfraction E21 (220 mg) was chromatographed on LiChroprep Lobar®-A RP-18 using MeOH/H<sub>2</sub>O (1:1) to give four subfractions (E211–E214). Subfraction E213 (45 mg) was separated on Sephadex LH-20 column using 100% MeOH to yield bistoroside A (**1**, 8 mg) and helonioside A (**3**, 5 mg). Subfraction E22 (130 mg) was subjected to LiChroprep Lobar®-A RP-18 column using MeOH/H<sub>2</sub>O (7:3) to afford three subfractions (E221–E223). Subfraction E223 (52 mg) was separated by preparative normal-phase HPLC using a solvent system of CHCl<sub>3</sub>/MeOH (6:1) over 30 min at a flow rate of 2.0 mL/min to obtain bistoroside B (**2**, 26 mg) and helonioside B (**4**, 5 mg). Subfraction E23 (150 mg) was separated over LiChroprep Lobar®-A RP-18 column using MeOH/H<sub>2</sub>O (1:1) to afford smilaside L (**5**, 8 mg).

### Bistoroside A (1)

Yellowish gum.  $[\alpha]_D^{25} - 6.5$  (*c* 0.25, MeOH). UV  $\lambda_{\max}$  (MeOH) nm: 326, 299 (sh), 235, 217. IR (KBr)  $\nu_{\max}$ : 3354, 2945, 2833, 1699, 1453, 1597, 1278, 1030 cm<sup>-1</sup>. <sup>1</sup>H (500 MHz) and <sup>13</sup>C (125 MHz) NMR data: see Table 1. HR-FAB-MS *m/z*: 695.2180 [M + H]<sup>+</sup> (calcd. for C<sub>32</sub>H<sub>39</sub>O<sub>17</sub>: 695.2187).

### Bistoroside B (2)

Yellowish gum.  $[\alpha]_D^{25} - 4.7$  (*c* 0.65, MeOH). UV  $\lambda_{\max}$  (MeOH) nm: 327, 299 (sh), 235, 218. IR (KBr)  $\nu_{\max}$ : 3357, 2945, 2833, 1701, 1598, 1518, 1453, 1278, 1121, 1029 cm<sup>-1</sup>. <sup>1</sup>H (500 MHz) and <sup>13</sup>C (125 MHz) NMR data: see Table 1. HR-FAB-MS *m/z*: 737.2298 [M + H]<sup>+</sup> (calcd. for C<sub>34</sub>H<sub>41</sub>O<sub>18</sub>: 737.2293).

### Alkaline hydrolysis of 1 and 2

Compounds (**1**: 2.5 mg and **2**: 6.0 mg) were hydrolyzed with 3% KOH/MeOH (3 mL) at room temperature for 15 min. The reaction mixture was neutralized with 2N HCl (monitored with indicator paper) and filtered. The filtrate was concentrated under reduced pressure to give a residue that was chromatographed over Sephadex LH-20 (100% MeOH) and preparative normal-phase HPLC (CHCl<sub>3</sub>/MeOH/H<sub>2</sub>O, 9:7:1.5) to afford methyl (Z)-ferulate<sup>13</sup> (0.3 mg from **1**; 1.2 mg from **2**) and sucrose (0.8 mg from **1**; 2.7 mg from **2**). The sucrose was identified by comparison of its optical

rotation value,  $[\alpha]_D^{25} + 26.6$  (*c* 0.15, MeOH) with that of an authentic sample<sup>14</sup> and by co-TLC comparison with an authentic sample (CHCl<sub>3</sub>/MeOH/H<sub>2</sub>O, 9:7:1.5; *R<sub>f</sub>* = 0.31). The sucrose was detected by co-injection of an authentic sample on preparative normal-phase HPLC using a solvent system of CHCl<sub>3</sub>/MeOH/H<sub>2</sub>O (9:7:1.5) at a flow rate of 2.0 mL/min in the same manner above, giving a single peak at 11.03 min.

### Acetylation of 1 and 2

To each compound (**1**: 3.0 mg; **2**: 3.0 mg) mixed with pyridine (1 mL), acetic anhydride (1 mL) was added. Each solution was stirred at room temperature for 24 h. Each reaction solution was extracted with CHCl<sub>3</sub> three times to give each octaacetate, which was purified by a silica gel Waters Sep-Pak® Vac 6cc (hexane/EtOAc, 5:1). Octaacetate of **1** (**1a**): colorless gum. FAB-MS *m/z*: 1031 [M + H]<sup>+</sup>. <sup>1</sup>H NMR (CDCl<sub>3</sub>, 500 MHz)  $\delta$ : 7.93, 7.91 (1H each, d, *J* = 2.0 Hz, H-2'', H-2'''), 7.34–7.10 (4H, m, H-5'', H-5''', H-6'', H-6'''), 7.02, 6.97 (1H each, d, *J* = 13.0 Hz, H-7'', H-7'''), 5.95, 5.88 (1H each, d, *J* = 13.0 Hz, H-8'', H-8'''), 5.71 (1H, d, *J* = 3.5 Hz, H-1'), 5.63 (1H, d, *J* = 6.0 Hz, H-3), 5.55 (1H, t, *J* = 6.0 Hz, H-4), 5.45 (1H, t, *J* = 9.5 Hz, H-3'), 5.01 (1H, t, *J* = 9.5 Hz, H-4'), 4.90 (1H, dd, *J* = 9.5, 3.5 Hz, H-2'), 4.40, 4.17 (1H each, d, *J* = 12.0 Hz, H<sub>2</sub>-1), 4.55–4.15 (6H, m, H-5, H<sub>2</sub>-6, H-5', H<sub>2</sub>-6'), 3.91, 3.88 (3H each, s, OCH<sub>3</sub>), 2.30, 2.28 (3H each, s, OAc  $\times$  2), 2.13, 2.12, 2.10, 2.05, 1.97, 1.81 (3H each, s, OAc  $\times$  6). Octaacetate of **2** (**2a**) was identical to **1a** in terms of <sup>1</sup>H NMR and TLC.

### Acknowledgements

The authors would like to thank Mr. Do Kyun Kim, Dr. Eun Jung Bang, and Dr. Jung Ju Seo at the Korea Basic Science Institute for the NMR and MS spectra measurements.

### References

- (1) Natural Products Research Institute. *Medicinal Plants in the Republic of Korea*; World Health Organization: Seoul, 1998; p. 53.
- (2) Editorial Committee of the Pharmacopoeia of People's Republic of China. *The Pharmacopoeia of People's Republic of China, Part 1*; Chemical Industry Press: Beijing, 2000; p. 239.
- (3) Duwiewjua, M.; Zeitlin, I. J.; Waterman, P. G.; Gray, A. I. *J. Pharm. Pharmacol.* **1994**, 46 (4), 286. PMID:8051612.
- (4) Niikawa, M.; Wu, A. F.; Sato, T. *Nat. Med.* **1995**, 49, 329.
- (5) Duwiewjua, M.; Zeitlin, I. J.; Gray, A. I.; Waterman, P. G. *Planta Med.* **1999**, 65 (4), 371. doi:10.1055/s-2006-960791. PMID:10364846.
- (6) Ahn, J. S.; Kwon, Y. S.; Kim, C. M. *Korean J. Pharmacogn.* **1999**, 30, 345.
- (7) Manoharan, K. P.; Benny, T. K. H.; Yang, D. *Phytochemistry* **2005**, 66 (19), 2304. doi:10.1016/j.phytochem.2005.07.008. PMID:16112695.
- (8) Liu, X.; Chen, F.; Wu, L.; Wang, S.; Li, W. *Shenyang Yaoke Daxue Xuebao* **2004**, 21, 187.
- (9) Xiao, K.; Xuan, L.; Xu, Y.; Bai, D. *Zhongcaoyao* **2003**, 34, 203.
- (10) Choi, S. Y.; Kwon, Y. S.; Kim, C. M. *Korean J. Pharmacogn.* **2000**, 31, 426.
- (11) Chang, S. W.; Kim, K. H.; Lee, I. K.; Choi, S. U.; Ryu, S. Y.; Lee, K. R. *Nat. Prod. Sci.* **2009**, 15 (4), 234.

- (12) Bergman, M.; Varshavsky, L.; Gottlieb, H. E.; Grossman, S. *Phytochemistry* **2001**, 58 (1), 143. doi:10.1016/S0031-9422(01)00137-6. PMID:11524124.
- (13) Shen, Y.-C.; Lin, S.-L.; Chein, C.-C. *Phytochemistry* **1997**, 44 (5), 891. doi:10.1016/S0031-9422(96)00641-3.
- (14) Nakano, K.; Murakami, K.; Takaishi, Y.; Yomimatsu, T. *Chem. Pharm. Bull. (Tokyo)* **1986**, 34, 5005.
- (15) Zhang, L.; Liao, C. C.; Huang, H. C.; Shen, Y. C.; Yang, L. M.; Kuo, Y. H. *Phytochemistry* **2008**, 69 (6), 1398. doi:10.1016/j.phytochem.2008.01.002. PMID:18329678.
- (16) Sun, X.; Zimmermann, M. L.; Campagne, J. M.; Sneden, A. T. *J. Nat. Prod.* **2000**, 63 (8), 1094. doi:10.1021/np000055e. PMID:10978204.

# Interactions of cytidine with N<sup>2</sup>-functionalized guanosines and cytidine–cytidine exchange involving a GC pair — NMR and fluorescence spectroscopic study

Sanela Martić, Gang Wu, and Suning Wang

**Abstract:** Two N<sup>2</sup>-functionalized guanosines by diphenylaminobiphenyl and di(2-pyridyl)aminobiphenyl have been found to act as the effective probes for G–C interactions in organic media. Because of the highly emissive nature of the N<sup>2</sup>-functionalized guanosines in the visible region, the GC base pair formation event accompanied by distinct fluorescence quenching can be readily monitored by fluorescence spectroscopy. NMR and fluorescence results confirm that the N<sup>2</sup>-arylguanosines form H-bonded pairs with cytidine, selectively. An unusual exchange pathway between non-bound cytidine and bound cytidine, in the GC pair, has been identified and extensively studied by NMR methods.

**Key words:** N<sup>2</sup>-guanosine, GC pair and cytidine exchange, fluorescence, NMR, hydrogen bonding.

**Résumé :** On a trouvé que deux guanosines fonctionnalisées en N<sup>2</sup> par des groupes diphénylaminobiphényle et di(2-pyridyl)aminobiphényle peuvent agir comme sondes efficaces pour les interactions G–C dans des milieux organiques. En raison du grand pouvoir émetteur des guanosines fonctionnalisées en N<sup>2</sup> dans la région visible, il est très facile par le biais de la spectroscopie de fluorescence de détecter la fluorescence distincte de piégeage qui accompagne la formation d'une paire de base GC. Les résultats de la RMN et de la fluorescence confirment que les N<sup>2</sup>-arylguanosines forment sélectivement des paires avec la cytidine, par le biais de liaisons hydrogènes. Faisant appel à des études par RMN, on a identifié et étudié une voie d'échange inhabituelle entre la cytidine non liée et la cytidine liée, dans la paire GC.

**Mots-clés :** N<sup>2</sup>-guanosine, paire GC, échange de cytidine, fluorescence, RMN, liaison hydrogène.

[Traduit par la Rédaction]

## Introduction

Among the nucleobases, guanine displays the most versatile H-bonding patterns, including Hoogsteen or Watson–Crick interactions, or combination thereof, and is thus a valuable building block in supramolecular chemistry.<sup>1</sup> In addition, the hydrogen-bonding motifs of guanine, such as G-quartets, are also known to have important and unique biological functions.<sup>2</sup> Hence, developing new functionalized guanosines to facilitate the study of various H-bonding patterns and self-assembled structures involving guanine has been a very active research area. We have shown recently that the attachment of an aryl group, such as a non-emissive *n*-butylphenyl group, at the N<sup>2</sup> site of the guanosine does not disrupt the formation of G-quartet and G-octamer via H-bonds in the presence of alkaline or alkaline-earth metal ions.<sup>3</sup> Building on this knowledge, we have reported recently a class of new luminescent hydrophilic N<sup>2</sup>-arylguanosines including **G1** and **G2** shown in Chart 1.<sup>4</sup> Because of the highly emissive nature of the N<sup>2</sup>-functionalized guanosines and their strong absorptions in the visible spectra, we have shown that they can be used effectively in studying interactions of guanosines with metal ions such as Zn(II) via a

combination of fluorescence, CD, and NMR spectroscopic methods.<sup>4</sup> In addition, the complementary base for guanine in Watson–Crick interactions is cytosine; hence, various functionalized guanosines or cytidines have been used previously to study the formation of the GC base pair and the charge-transfer phenomenon via the GC pair between fluorescent donor and acceptor.<sup>5</sup> To our best knowledge, however, there have been no reports on GC base pairs involving fluorescent N<sup>2</sup>-functionalized guanosines.<sup>6</sup> To examine the impact of N<sup>2</sup>-functionalization of guanosine on GC pair formation, we investigated the interactions of the native cytidine with **G1** and **G2** by both NMR and fluorescent spectroscopic methods. However, because **G1** and **G2** have poor solubilities in organic solvents and are sparingly soluble in water or the mixture of water and alcohols, which also compete for H bonds with guanosine and cytidine leading to complex H-bond patterns, no meaningful data could be obtained. To overcome this problem, we converted **G1** and **G2** to lipophilic guanosines by protecting OH moieties with acetyl groups, which greatly improved their solubility. The resulting **G1A** and **G2A** guanosines display selective H-bonding with cytidine in solvents such as CH<sub>2</sub>Cl<sub>2</sub> that

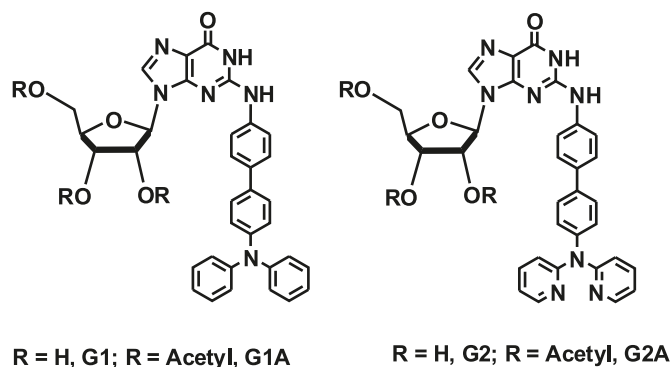
Received 3 December 2009. Accepted 28 February 2010. Published on the NRC Research Press Web site at canjchem.nrc.ca on 5 May 2010.

S. Martić, G. Wu, and S. Wang.<sup>1</sup> Department of Chemistry, Queen's University, Kingston, ON K7L 3N6, Canada.

<sup>1</sup>Corresponding author (e-mail: wangs@chem.queensu.ca).



Chart 1.



can be monitored by both NMR and fluorescent spectra. The key results are reported herein.

## Experimental section

All reagents were purchased from Aldrich Chemical Co. and used without further purification unless stated otherwise. Acetic anhydride, triethylamine, and acetonitrile were freshly distilled under  $N_2$  prior to acetylation reactions. Low-resolution and high-resolution mass spectrometry experiments were performed using the electrospray ionization mode on QSTAR XL MS/MS Systems using Analyst QS Method. Excitation and emission spectra were recorded on a Photon Technologies International QuantaMaster Model C-60 spectrometer. Molecular orbital and molecular geometry calculations were performed using Gaussian 03 program suite. Calculations were carried out at the B3LYP level of theory using 6-31G\*\* as the basis set for all atoms.

### Fluorescence experiments

Excitation and emission spectra were recorded on a Photon Technologies International QuantaMaster Model C-60 spectrometer. To the prepared solutions of **G1A** ( $2.5 \times 10^{-5}$  mol/L) and **G2A** ( $2.5 \times 10^{-5}$  mol/L) in  $CH_2Cl_2$ , the solution of **4-C** ( $6.0 \times 10^{-3}$  mol/L) was added in 5  $\mu$ L aliquots.

### NMR experiments

All 1D and 2D NMR experiments were recorded on Bruker Avance 400 MHz or 600 MHz spectrometer at 298 K, unless otherwise specified.  $^1H$  NMR titrations were performed using the solutions of **G1A** ( $6.8 \times 10^{-4}$  mol/L) or **G2A** ( $1.6 \times 10^{-2}$  mol/L) in  $CD_2Cl_2$  with the solution of **4-C** in  $CD_2Cl_2$  being added in 10  $\mu$ L aliquots. DOSY NMR experiments were carried out with Bruker Avance-600 MHz spectrometer using the pulse sequence of longitudinal eddy current delay (LED) with bipolar-gradient pulses. The diffusion period was varied from 50 to 90 ms. Calibration of the field gradient strength was achieved by measuring the value of translational diffusion coefficient ( $D_t$ ) for the residual  $^1H$  signal in  $D_2O$ ,  $D_t = 1.91 \times 10^{-9}$  m<sup>2</sup>/s. All NOESY spectra at 298 K were acquired using a mixing time of 0.3 or 0.4 s and the 10 s recycling delay. Phase-sensitive NOESY experiment at 195 K was performed using a mixing time of 0.1 s and a 2 s recycling delay. Phase-sensitive ROESY NMR spectra were recorded on 400 MHz spectrometer at 195 K

using a variable mixing times of 0.08, 0.1, and 0.3 s and the 3 s relaxation delay.

### Synthesis of 2',3',5'-O-triacetyl-*N*<sup>2</sup>-(*p*-4,4'-biphenyldiphenylamino)guanosine (**G1A**)

To a suspension of *N*<sup>2</sup>-(*p*-4,4'-biphenyldiphenylamino)-guanosine, **G1**, (0.34 g, 0.57 mmol) and dimethylaminopyridine (0.005 g, 0.04 mmol) in dry acetonitrile (10 mL), freshly distilled triethylamine (0.30 mL, 2.21 mmol) was added. After stirring for 5 min, freshly distilled acetic anhydride (0.19 mL, 2.00 mmol) was added dropwise over 5 min, and the mixture was stirred for 2 h at room temperature. The reaction mixture was quenched with methanol (5 mL), and the organic solvents were removed to dryness. The residue was treated using the chromatographic column on  $CH_2Cl_2$  and  $CH_2Cl_2/MeOH$  (95:5, v/v) as the eluents to give **G1A** as the white solid. Yield: 0.17 g (43%). Mp > 300 °C. UV absorption  $\lambda_{max}$  ( $CH_2Cl_2$ ), nm ( $\epsilon$  dm<sup>3</sup>mol<sup>-1</sup>cm<sup>-1</sup>): 236 (24 040) and 343 (36 272). Fluorescence ( $CH_2Cl_2$ ):  $\lambda_{ex}$  = 362 nm and  $\lambda_{em}$  = 410 nm.  $^1H$  NMR (400 MHz, DMSO-*d*<sub>6</sub>, 298 K)  $\delta$  (ppm): 10.82 (1H, br s, N<sub>1</sub>H), 8.96 (1H, br s, N<sub>2</sub>H), 8.00 (1H, s), 7.61–7.58 (6H, m,  $J$  = 5.8, 8.6 Hz, Ph), 7.32 (4H, t,  $J$  = 7.9 Hz, Ph), 7.05 (8H, m,  $J$  = 7.8, 8.5 Hz, Ph), 6.02 (1H, d,  $J$  = 5.0 Hz, 1'-H), 6.00 (1H, t,  $J$  = 5.8 Hz, 2'-H), 5.37 (1H, t,  $J$  = 5.7 Hz, 3'-H), 4.28 (1H, dd,  $J$  = 4.4, 5.3 Hz, 4'-H), 4.20 (1H, m,  $J$  = 4.1, 12.1 Hz, 5'-H), 4.13 (1H, m,  $J$  = 4.1, 12.4 Hz, 5'-H), 2.07 (3H, s, CH<sub>3</sub>), 2.05 (3H, s, CH<sub>3</sub>), 1.84 (3H, s, CH<sub>3</sub>).  $^{13}C$  NMR (500 MHz, MeOD)  $\delta$  (ppm): 171.2, 170.1, 169.9, 148.1, 138.1, 134.3, 129.6 (6C), 127.6 (2C), 127.1 (2C), 124.6 (6C), 124.1 (2C), 123.3 (2C), 122.3 (2C), 121.1, 115.6, 96.8 (2C), 87.5 (C<sub>1'</sub>), 80.1 (C<sub>4'</sub>), 72.6 (C<sub>2'</sub>), 70.9 (C<sub>3'</sub>), 63.1 (C<sub>5'</sub>), 19.6 (CH<sub>3</sub>), 19.5 (CH<sub>3</sub>), 19.4 (CH<sub>3</sub>). ESI-MS<sup>+</sup>  $m/z$ : 729.2465 [M + H]<sup>+</sup>. HRMS-EI<sup>+</sup>  $m/z$  calcd. for C<sub>40</sub>H<sub>36</sub>N<sub>6</sub>O<sub>8</sub>: 728.2594, found: 728.2538.

### Synthesis of 2',3',5'-O-triacetyl-*N*<sup>2</sup>-(*p*-4,4'-biphenyldipyridylamino)guanosine (**G2A**)

**G2A** was obtained using the same procedure as for **G1A** with **G2** as the starting material. Yield: 0.08 g (40%). Mp 241–250 °C. UV absorption  $\lambda_{max}$  ( $CH_2Cl_2$ ), nm ( $\epsilon$  dm<sup>3</sup>mol<sup>-1</sup>cm<sup>-1</sup>): 235 (24 003) and 319 (50 240). Fluorescence ( $CH_2Cl_2$ ):  $\lambda_{ex}$  = 344 nm and  $\lambda_{em}$  = 386 nm.  $^1H$  NMR (400 MHz, DMSO-*d*<sub>6</sub>, 298 K)  $\delta$  (ppm): 10.83 (1H, br s, N<sub>1</sub>H), 8.97 (1H, br s, N<sub>2</sub>H), 8.25 (2H, d,  $J$  = 3.7 Hz, Py), 8.02 (1H, s, 8-H), 7.72–7.65 (8H, m,  $J$  = 7.8, 8.4 Hz, Ph), 7.16 (2H, d,  $J$  = 8.4 Hz, Ph), 7.04 (2H, d,  $J$  = 5.3 Hz, Py), 6.99 (2H, d,  $J$  = 8.8 Hz, Py), 6.08 (1H, d,  $J$  = 5.3 Hz, 1'-H), 6.01 (1H, t,  $J$  = 5.8 Hz, 2'-H), 5.39 (1H, t,  $J$  = 5.7 Hz, 3'-H), 4.28 (1H, m,  $J$  = 4.3, 9.6 Hz, 4'-H), 4.22 (1H, m,  $J$  = 3.9, 12.4 Hz, 5'-H), 4.19 (1H, m,  $J$  = 3.9, 12.3 Hz, 5'-H), 2.09 (3H, s, CH<sub>3</sub>), 2.06 (3H, s, CH<sub>3</sub>), 1.85 (3H, s, CH<sub>3</sub>).  $^{13}C$  NMR (500 MHz, MeOD)  $\delta$  (ppm): 170.9, 170.2, 170.1, 158.2, 150.4, 147.9 (3C), 144.1, 138.8 (3C), 138.4, 138.1, 137.6, 136.4, 127.9 (3C), 127.3 (2C), 127.2 (3C), 122.5 (2C), 119.0 (2C), 117.9 (2C), 87.6 (C<sub>1'</sub>), 80.0 (C<sub>4'</sub>), 72.5 (C<sub>2'</sub>), 70.8 (C<sub>3'</sub>), 62.8 (C<sub>5'</sub>), 19.3 (CH<sub>3</sub>), 19.2 (CH<sub>3</sub>), 19.1 (CH<sub>3</sub>). ESI-MS<sup>+</sup>  $m/z$ : 731.8851 [M + H]<sup>+</sup>. HRMS-ESI<sup>+</sup>  $m/z$  calcd. for C<sub>38</sub>H<sub>34</sub>N<sub>8</sub>O<sub>8</sub> + H: 731.2572, found: 731.2578.

### Synthesis of 2',3',5'-*O*,*N*<sup>2</sup>-tetraacetyl-*N*<sup>2</sup>-(*p*-4,4'-biphenyldipyridylamino)guanosine (**G2B**)

**G2B** was isolated as a side product from the same reaction for **G2A**. Yield: 0.03 g (18%). Mp 156–164 °C. <sup>1</sup>H NMR (400 MHz, CD<sub>3</sub>CN, 298 K) δ (ppm): 12.98 (broad, N<sub>1</sub>H, 1H), 8.24 (d, *J* = 4.5 Hz, 2H), 7.82 (d, *J* = 8.4 Hz, 2H), 7.73 (s, 1H, H<sub>8</sub>), 7.72 (d, *J* = 6.5 Hz, 2H), 7.65 (dt, *J* = 1.8, 9.1 Hz, 2H), 7.48 (d, *J* = 8.4 Hz, 2H), 7.21 (d, *J* = 8.5 Hz, 2H), 7.02 (m, 4H), 5.75 (d, *J* = 4.6 Hz, 1H, H<sub>1'</sub>), 5.57 (t, *J* = 4.9 Hz, 1H, H<sub>2'</sub>), 4.41 (t, *J* = 6.0 Hz, 1H, H<sub>3'</sub>), 4.05 (m, *J* = 5.1, 11.5 Hz, 1H, H<sub>4'</sub>), 3.71 (m, 2H, H<sub>5'</sub>, H<sub>5''</sub>), 2.03 (s, CH<sub>3</sub>, 3H), 1.94 (s, CH<sub>3</sub>, 3H), 1.88 (s, CH<sub>3</sub>, 3H), 1.86 (s, CH<sub>3</sub>, 3H). <sup>13</sup>C NMR (400 MHz, CD<sub>3</sub>CN, 298 K) δ (ppm): 175.7, 170.2, 169.4, 169.3, 158.1 (2C), 155.3, 150.5, 148.3, 147.5 (2C), 145.4, 140.7, 139.4, 138.0 (2C), 137.7 (2C), 135.9, 129.7 (2C), 128.4 (2C), 127.9 (2C), 127.3 (2C), 121.9, 118.6 (2C), 117.3, 87.9 (C<sub>1</sub>), 79.4 (C<sub>4</sub>), 71.9 (C<sub>2</sub>), 70.7 (C<sub>3</sub>), 63.8 (C<sub>5</sub>), 25.8 (CH<sub>3</sub>), 19.8 (CH<sub>3</sub>), 19.6 (CH<sub>3</sub>), 19.5 (CH<sub>3</sub>). HRMS-ESI<sup>+</sup> *m/z* calcd. for C<sub>40</sub>H<sub>36</sub>N<sub>8</sub>O<sub>9</sub>·H<sup>+</sup>: 773.2678, found: 773.2666.

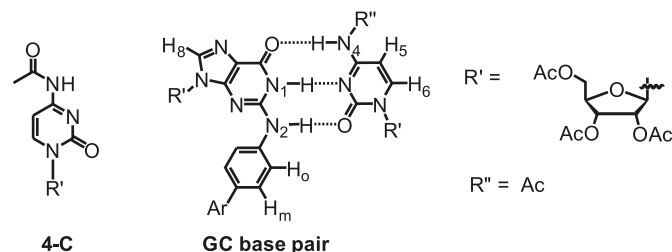
## Results and discussion

### NMR measurements

#### GC base pair formation

The structure of the cytidine (**4-C**) used in the study and the GC base pair with labels are shown in Chart 2. <sup>1</sup>H NMR spectra indicated that in the absence of **4-C**, **G1A** and **G2A** exist predominantly as monomers in CD<sub>2</sub>Cl<sub>2</sub> at 298 K. The addition of **4-C** to the solution of **G1A** or **G2A** in CD<sub>2</sub>Cl<sub>2</sub> results in upfield shifts of the imino and amino resonances of the guanine and cytosine units, indicative of H-bonding. As shown in Fig. 1, upon [**G1A**]:[**4-C**] base pair formation, a slight change was observed for the phenyl protons (H<sub>6</sub>) directly attached to the N<sup>2</sup>-site of guanine, while the H<sub>8</sub> signal of the guanine ring remains virtually unchanged. The most significant change is observed for the H<sub>6</sub> and H<sub>5</sub> resonances of **4-C**, which shift ~ 0.1–0.3 ppm upfield. Upon cooling to 228 K, the [**G1A**]:[**4-C**] dimer can be clearly identified through the sharp peaks at ~ 13.1, 12.2, and 10.7 ppm that can be assigned to the N<sub>1</sub>H (**G1A**), N<sub>4</sub>H (**4-C**), and N<sub>2</sub>H (**G1A**), respectively, as presented in Fig. 2. At 228 K, the NOE cross peaks are of the same phase as the diagonal peaks. The key NOE cross peaks between the N<sub>1</sub>H (**G1A**) with N<sub>4</sub>H (**4-C**) in the GC base pair were observed in the NOESY NMR spectrum, confirming the GC pair formation. The GC pair formation was further supported by ESI-MS data, with a peak at *m/z* 1140 identified as [**G1A**:**4-C** + H]<sup>+</sup> (see Fig. S1 in the Supplementary data). Similar NMR and ESI-MS data were also obtained for the [**G2A**]:[**4-C**] base pair (see Figs. S2–S4 in the Supplementary data). The relative ribose stereogeometry of the GC base pair was assigned by NOESY NMR and was found to be syn for both N<sup>2</sup>-arylguanosines, owing to the strong NOE cross peak between its H<sub>1</sub> and H<sub>8</sub>, and anti for **4-C**, judging from the strong NOE between its H<sub>2</sub> and H<sub>6</sub> protons.<sup>7</sup> An association constant could not be determined by NMR dilution method because of the strong GC association. As a control study, we also examined the interaction of 2',3',5'-*O*,*N*<sup>2</sup>-tetraacetyl-*N*<sup>2</sup>-(*p*-4,4'-biphenyldipyridylamino)guanosine (**G2B**) with **4-C**,

Chart 2.

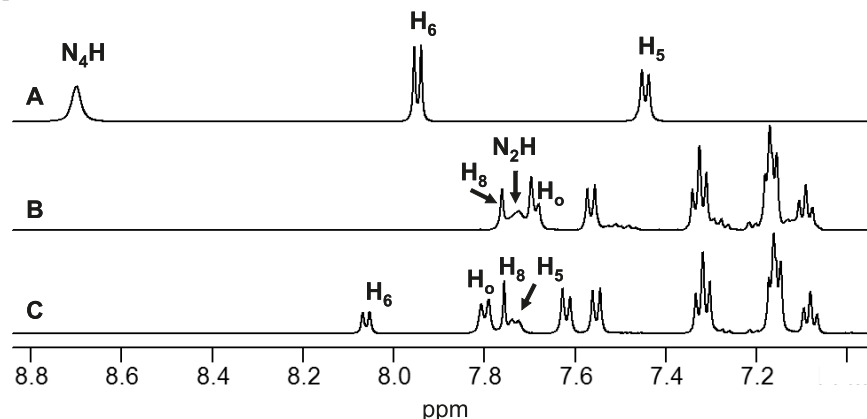
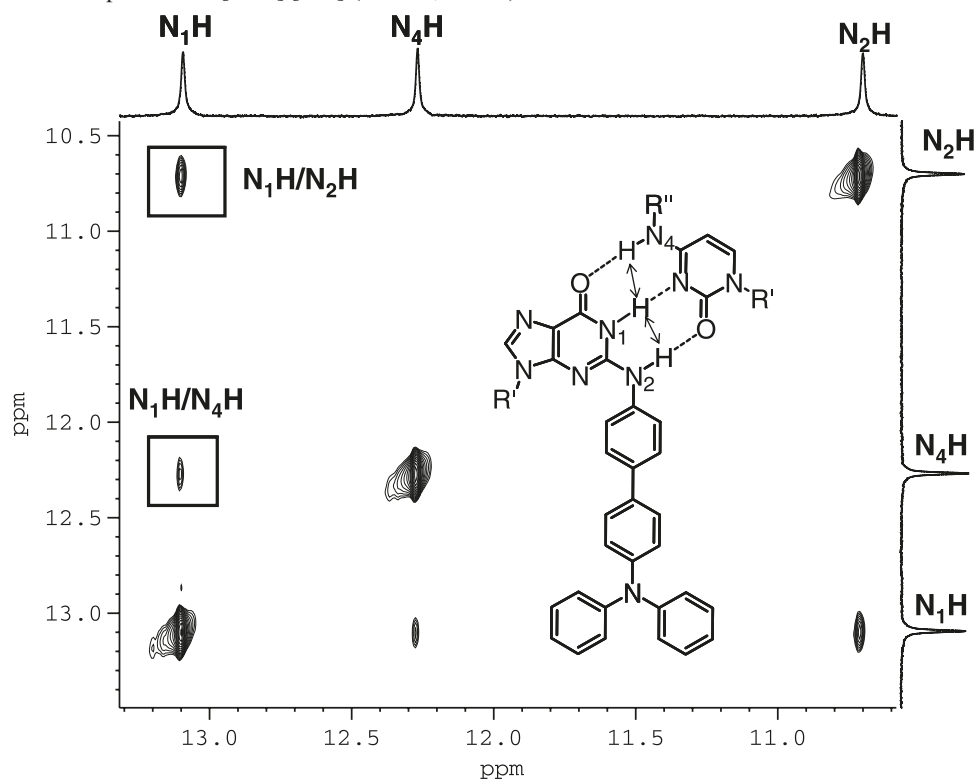


where the H-donor site of the N<sup>2</sup> group is blocked by an acetyl group. Not surprisingly, **G2B** did not form a GC dimer as confirmed by NMR (see Fig. S5 in the Supplementary data for NMR). Thus, the NMR data established unequivocally that the N<sup>2</sup>-functionalization by an aryl group does not impede the ability of the guanosine to form a H-bonded base pair with cytidine.

#### Dynamic exchange of non-bound and bound **4-C** in the GC pair

Although the GC base pair formation has been extensively investigated, little is known about the interaction and the exchange mechanism of a GC pair with non-bound G or C. A previous NMR study on the interaction of a GC pair with free guanosine has identified a GCG trimer.<sup>8</sup> However, the exact nature of the interactions between the GC pair and free cytidine remains unclear. The GC pair formed by **G1A** and **G2A** with **4-C** provided us an opportunity to study such interactions by NMR methods. As shown in Fig. 3, the addition of more than 1 equiv. of **4-C** to the solution of **G1A** results in the sharpening of the N<sup>1</sup>H and N<sub>2</sub>H (**G1A**) resonances along with a slight downfield shift. Surprisingly, the N<sub>4</sub>H (**4-C**) proton is shifted upfield (~3 ppm) and broadened, indicating a dynamic process. The overall chemical shift positions and the sharpness of the exchangeable **G1A** protons indicate the complex formation by H-bonds. At [**G1A**]:[**4-C**] ≈ 1:4 ratio, the chemical shifts of the **G1A** protons are similar to those of [**G1A**]:[**4-C**] = 1:1, while the chemical shifts of **4-C** exhibit significant changes. These findings support that in the presence of excess amount of **4-C**, **G1A** remains involved in the H-bonding in the GC pair while cytidine undergoes some dynamic exchange. Similar trends were also observed for **G2A** when treated with excessive **4-C** (see Fig. S6 in the Supplementary data). DOSY NMR study on [**G2A**]:[**4-C**] and [**G2A**]:[**4-C**]<sub>2</sub> shows that the diffusion coefficients *D*<sub>i</sub> of these two species are similar (see Fig. S7 in the Supplementary data), thus supporting that the stable GCC trimer species is unlikely, but it may be involved in a dynamic process.

Variable temperature NMR experiments were performed for [**G1A**]:[**4-C**]<sub>4</sub> to further probe the chemical-exchange process. As shown in Fig. 4, at temperatures below 208 K, one type of **G1A** and two types of **4-C** peaks (denoted as **4-C** and **4-C\***) were observed. The sharp peaks between 10.5 and 13.4 ppm are assigned to N<sub>2</sub>H (**G1A**), N<sub>1</sub>H (**G1A**), and N<sub>4</sub>H (**4-C**) of the GC pair. The broad resonance at 10.2 ppm can be assigned to a N<sub>4</sub>H\* of the non-bound **4-C\***. Since the N<sub>4</sub>H\* proton remains broad and below 12 ppm, we can conclude that it does not belong to the typical [**4-C**]<sub>2</sub> dimer. Further lowering of the temperature to <188 K results in the

**Fig. 1.** Partial  $^1\text{H}$  NMR spectra of (A) **4-C**, (B) **G1A**, and (C) **[G1A]:[4-C]** ( $\text{CD}_2\text{Cl}_2$ , 298 K).**Fig. 2.** Partial NOESY NMR spectrum of **[G1A]:[4-C]** ( $\text{CD}_2\text{Cl}_2$ , 228 K).

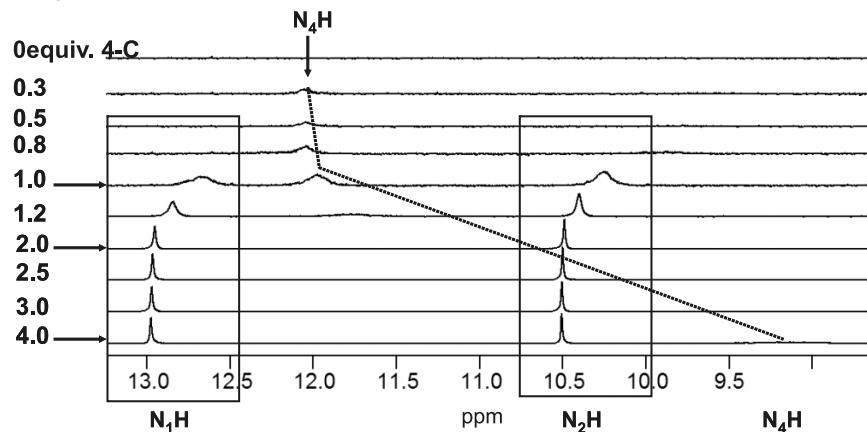
splitting of all non-exchangeable protons into **4-C** and **4-C\*** as well.

To gain structural information about the dynamics of this system and to establish the connectivity between the GC pair and the non-bound **4-C\***, COSY, NOESY, and ROESY NMR experiments were performed on the mixture of **[G1A]:[4-C]**<sub>2</sub> and **[G2A]:[4-C]**<sub>2</sub>. The spectroscopic data for **G2A** are presented here because of the higher resolution and spectral quality compared with those for **G1A**. Complete spectral assignment for **G2A** and **4-C** resonances in **[G2A]:[4-C]**<sub>2</sub> was established using COSY. NOESY NMR was performed at 195 K, allowing the identification of closely related protons. Figure 5 shows the strong NOE signature cross peaks for **[G2A]:[4-C]**<sub>2</sub> between  $\text{N}_1\text{H}$  (**G2A**)/ $\text{N}_4\text{H}$  (**4-C**) protons indicative of Watson–Crick H-bonding. It is also worth noting that the NOE cross peaks observed

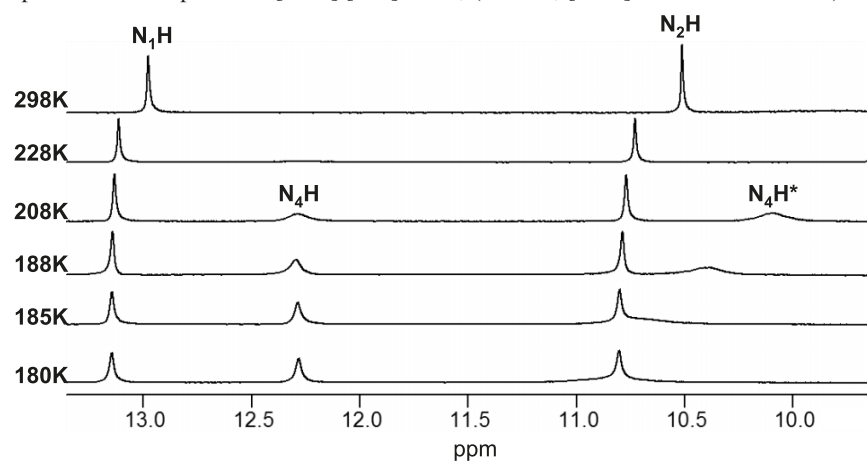
between  $\text{N}_1\text{H}$  (**G2A**),  $\text{N}_4\text{H}$  (**4-C**), and  $\text{N}_4\text{H}^*$  (**4-C\***) with  $\text{N}_4\text{Ac}$  (**4-C**) and  $\text{N}_4\text{Ac}^*$  (**4-C\***) indicate that these protons are in close proximity to each other (see Fig. S8 in the Supplementary data). In the presence of excessive cytidine, all the cross peaks in the NOESY spectrum are of the same phase as the diagonal peaks.

To confirm NOE correlations and to distinguish them from chemical-exchange cross peaks, a 2D ROESY NMR spectrum was recorded at 195 K (Fig. 6), which reveals clear NOE cross peaks between the bound **4-C** and non-bound **4-C\*** (e.g.,  $\text{N}_4\text{H}$  (**4-C**)/ $\text{N}_4\text{Ac}^*$  (**4-C\***) and  $\text{N}_4\text{H}^*$  (**4-C\***)/ $\text{N}_4\text{Ac}$  (**4-C**)). In addition, the ribose protons associated with **4-C** in the **[G2A]:[4-C]** base pair are found to be in close proximity to  $\text{H}_6^*$  (**4-C\***) proton and vice versa. Furthermore, the  $\text{H}_6$  proton (**4-C**) exhibits a NOE cross peak with the  $\text{H}_5^*$  (**4-C\***) proton. In addition, the chemical-exchange

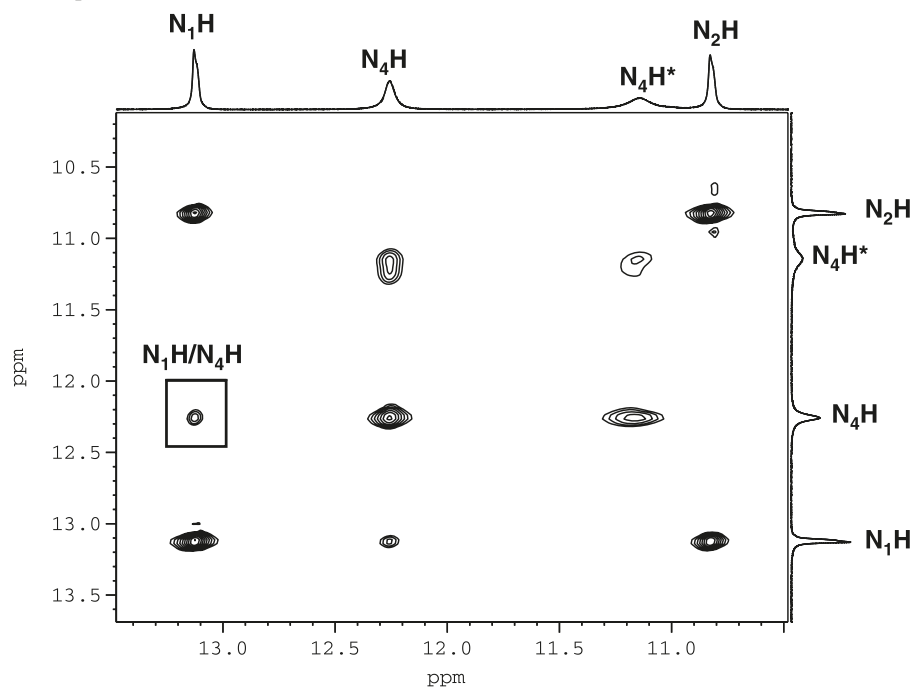
**Fig. 3.**  $^1\text{H}$  NMR spectral change of **G1A** with the addition of **4-C** ( $\text{CD}_2\text{Cl}_2$ , 298 K,  $[\text{G1A}] = 6.8 \times 10^{-4}$  mol/L).



**Fig. 4.** Partial variable temperature NMR spectra of  $[\text{G1A}]:[\text{4-C}] = 1:4$ , ( $\text{CD}_2\text{Cl}_2$ ,  $[\text{G1A}] = 6.8 \times 10^{-4}$  mol/L).

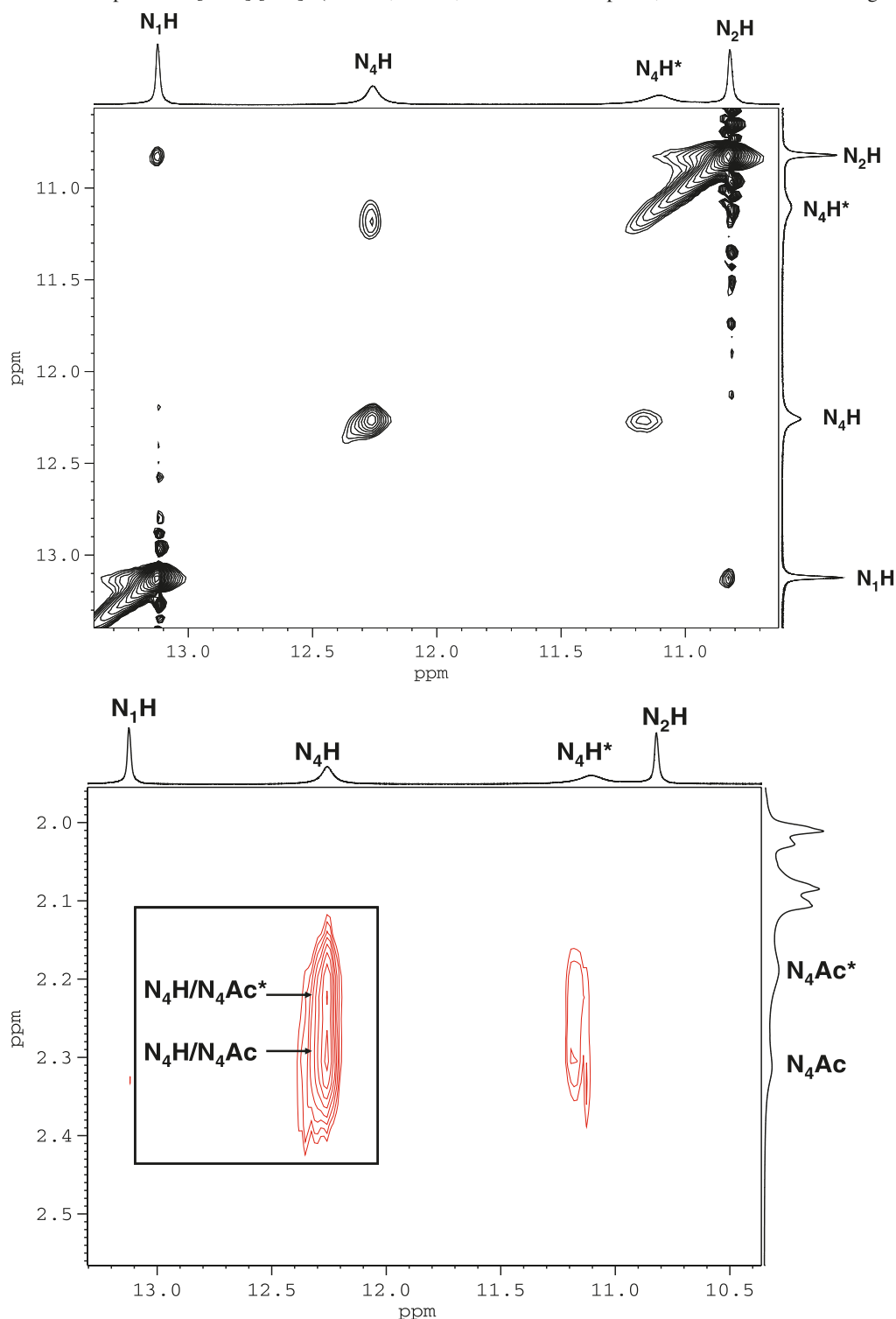


**Fig. 5.** Partial NOESY NMR spectrum of  $[\text{G2A}]:[\text{4-C}]_2$  ( $\text{CD}_2\text{Cl}_2$ , 195 K).





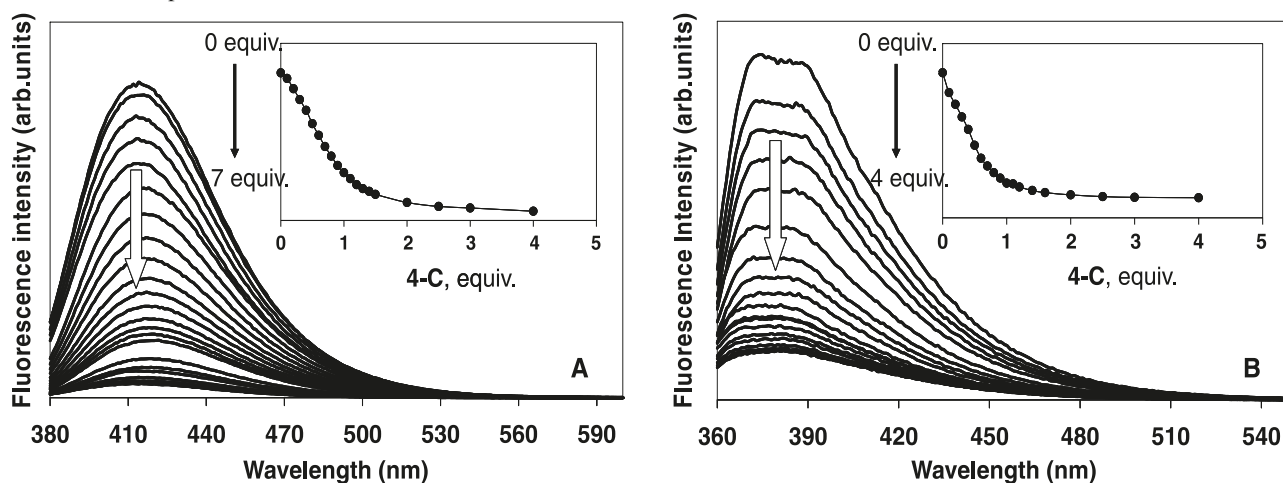
**Fig. 6.** Partial ROESY NMR spectra of [G2A]:[4-C]<sub>2</sub> (CD<sub>2</sub>Cl<sub>2</sub>, 195 K, red: NOE cross peaks, black: chemical-exchange cross peaks).



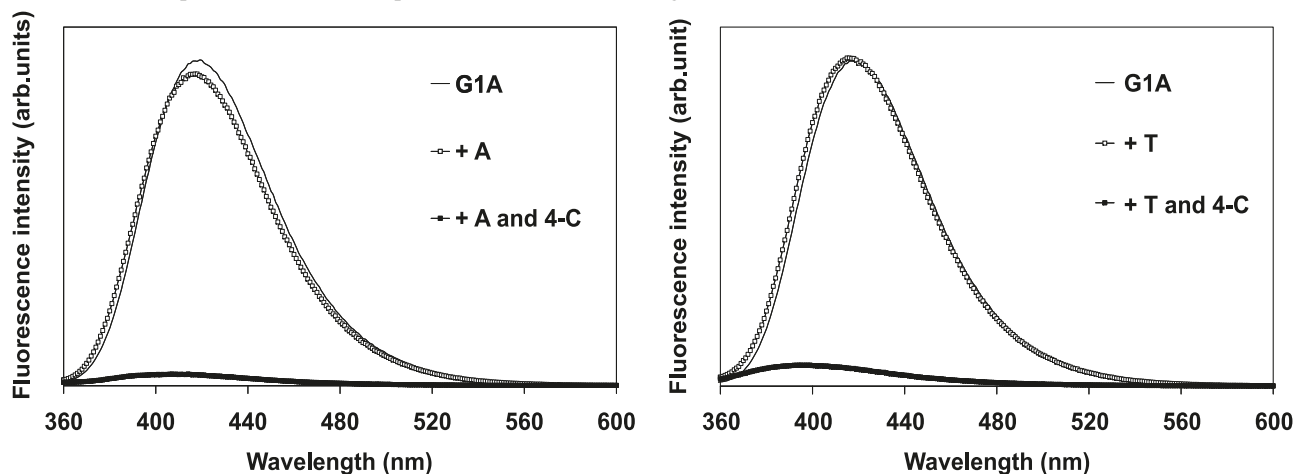
interaction was observed between the proton pairs of H<sub>6</sub> (4-C)/H<sub>6</sub>\* (4-C\*) and H<sub>5</sub> (4-C)/H<sub>5</sub>\* (4-C\*). The key protons that are involved in GC base pair formation all undergo chemical exchange with each other, which makes the complete assignment of the final structure difficult. However, on the basis of the relative chemical shifts of non-exchangeable protons and the specific NOE interactions shown in Fig. 6, it can be concluded that there are two types of cytidines,

non-bound 4-C\* and bound 4-C with G2A, which undergo chemical exchange with each other, leading to the averaging of the 4-C signals at above 208 K. These findings are consistent with the presence of  $\pi$ - $\pi$  stacking interactions between 4-C in the [G2A]:[4-C] pair and non-bound 4-C\*. Since G2A does not exhibit NOE with H<sub>6</sub>\* (4-C\*) and H<sub>5</sub>\* (4-C\*) protons the possibilities of  $\pi$ - $\pi$  interactions between G2A in the [G2A]:[4-C] pair and 4-C\* can be ruled out.

**Fig. 7.** Fluorescence titrations of (A) **G1A** and (B) **G2A** with **4-C** ( $\text{CH}_2\text{Cl}_2$ ,  $2.5 \times 10^{-5}$  mol/L,  $\lambda_{\text{ex}} = 362$  nm (**G1A**) and 344 nm (**G2A**). Inset: Stern–Volmer plots at  $\lambda_{\text{max}}$ .



**Fig. 8.** Fluorescence spectra of **G1A** in the presence of A (left) or T (right) nucleosides with or without **4-C** ( $\text{CH}_2\text{Cl}_2$ ).



Using the variable temperature NMR data, the exchange rate  $k_c$  and the activation free energy  $\Delta G^\ddagger$  for the exchange process were estimated to be  $88 \text{ s}^{-1}$  and  $43 \text{ kJ mol}^{-1}$ , respectively, at 208 K.

### Fluorescence measurement

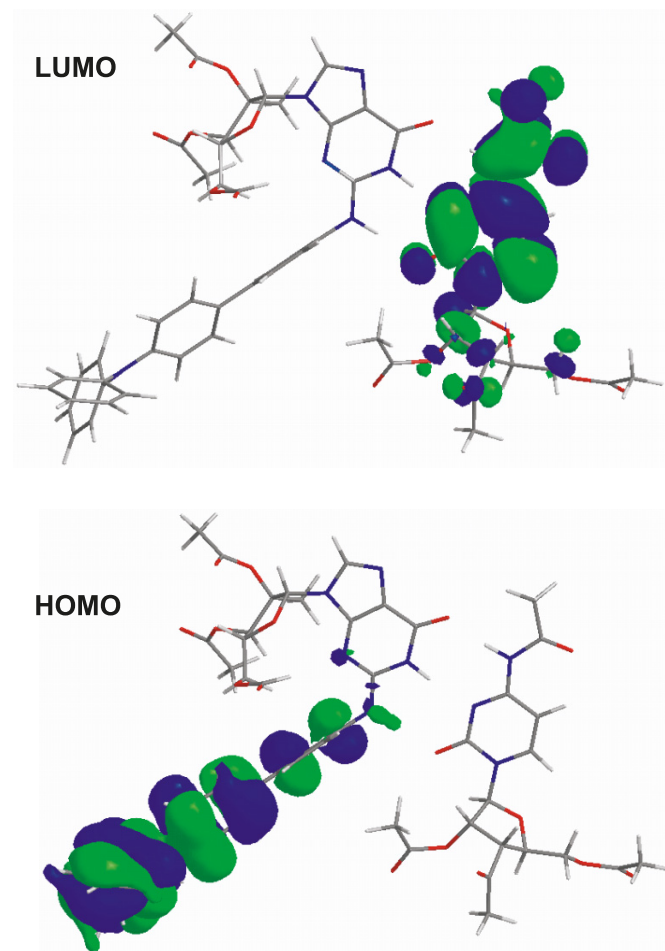
In contrast to the non-functionalized guanosines, which are weakly emissive in the UV region, **G1A** and **G2A** are highly emissive in the visible region, thus making it possible to monitor the G–C interactions by fluorescence spectroscopy as well. As shown in Fig. 7, the addition of **4-C** to the solution of **G1A** or **G2A** in  $\text{CH}_2\text{Cl}_2$  results in quenching of the fluorescence emission of the  $N^2$ -arylguanosines. The Stern–Volmer plots support the formation of a stable 1:1 species with **4-C** (Fig. 6, inset), which is most likely responsible for the quenching of the guanosine emission. The binding constants for the GC pairs were determined to be  $5 \times 10^5 \text{ M}^{-1}$  and  $2 \times 10^6 \text{ M}^{-1}$  for **G1A** and **G2A**, respectively (see Fig. S9 in the Supplementary data).<sup>9</sup> These binding constants are in agreement with those reported in the literature for other GC pairs.<sup>10</sup>

As a control study, the fluorescence titration of **G2B** with **4-C** was also carried out (see Fig. S10 in the Supplementary

data), which, not surprisingly, does not show any fluorescent quenching, thus further supporting the role of selective H-bonding between **G2A** and **4-C** in the fluorescence quenching. The selectivity of the fluorescence response of **G1A** and **G2A** toward cytidine was further confirmed by the competition experiments of 2',3',5'-O-triacetyladenosine (A) and 3',5'-O-diacetylthymidine (T) with **4-C** for binding with **G1A** and **G2A**. As shown in Fig. 8, both A and T have no impact at all on the fluorescent spectrum of **G1A**. Similar results were also obtained for **G2A** (see Fig. S11 in the Supplementary data).

### Molecular orbital calculations

Our previous TD-DFT calculations have established that the lowest electronic transitions and the fluorescence of **G1A** and **G2A** are  $\pi$ – $\pi^*$  transitions centered on guanine and the biphenyl- $\text{NAr}_2$  group.<sup>4</sup> To understand the origin of the fluorescence quenching upon GC pair formation, DFT calculations were performed for the [**G1A**]:[**4-C**] pair. The ground-state structure of the [**G1A**]:[**4-C**] pair was fully optimized at a B3-LYP/6–31G\*\* level of theory and is presented in Fig. 9 along with the diagrams of the HOMO and LUMO levels.<sup>11</sup> The HOMO level of [**G1A**]:[**4-C**] consists

**Fig. 9.** HOMO and LUMO orbitals of the [G1A]:[4-C] base pair.

of  $\pi$  orbitals of the biphenyl-NPh<sub>2</sub> group while the LUMO level is made of entirely the  $\pi^*$  orbitals of the cytosine ring. Hence, in contrast to **G1A**, where the lowest electronic transition is from a  $\pi$ - $\pi^*$  transition localized on the same part of the molecule, the lowest electronic transition of [G1A]:[4-C] is a charge transfer from the N<sup>2</sup> substituent to the cytosine ring. The low lying LUMO of the cytosine in the GC pair is therefore clearly responsible for quenching the emission of **G1A**. The guanine ring has no contributions to either the HOMO or the LUMO level of the GC pair, and probably acts as a bridge to facilitate H-bonds and electronic transitions between the N<sup>2</sup> substituent and the cytosine ring. Many examples of fluorescence quenching via intramolecular charge transfer in donor-acceptor types of GC base pair facilitated by H-bonding are known in the literature.<sup>12</sup> Our compounds are however the first example showing charge-transfer fluorescence quenching via the GC pair involving N<sup>2</sup>-functionalized guanines.

In summary, the aryl group at the N<sup>2</sup> site of guanines **G1A** and **G2A** does not impede the selective formation of the H-bonding pair with cytidine. In fact, it facilitates the study of the G-C interactions via fluorescence spectroscopy owing to its highly fluorescent nature and the high sensitivity of the fluorescence spectrum toward G-C pair formation. An unusual exchange pathway between bound and free cyti-

dine molecules and a potential  $\pi$ -stacked intermediate have been identified by NMR data.

## Supplementary data

Supplementary data for this article are available on the journal Web site (canjchem.nrc.ca).

## Acknowledgement

We thank the Natural Sciences and Engineering Research Council of Canada (NSERC) for financial support.

## References

- (1) (a) Alberti, P.; Bourdoncle, A.; Saccà, B.; Lacroix, L.; Mergny, J.-L. *Org. Biomol. Chem.* **2006**, *4* (18), 3383. doi:10.1039/b605739j. PMID:17036128.; (b) Sivakova, S.; Rowan, S. J. *Chem. Soc. Rev.* **2005**, *34* (1), 9. doi:10.1039/b304608g. PMID:15643486.; (c) Zhong, C.; Wang, J.; Wu, N.; Wu, G.; Zavalij, P. Y.; Shi, X. *Chem. Commun. (Camb.)* **2007**, (30): 3148. doi:10.1039/b704756h. PMID:17653370.; (d) Nikan, M.; Sherman, J. C. *J. Org. Chem.* **2009**, *74* (15), 5211. doi:10.1021/jo9001245. PMID:19518105.; (e) Koyogoku, Y.; Lord, R. C.; Rich, A. *Science* **1966**, *154* (748), 518. PMID:5916945.
- (2) (a) Zakian, V. A. *Science* **1995**, *270* (5242), 1601. doi:10.1126/science.270.5242.1601. PMID:7502069.; (b) Guschlbauer, W.; Chanton, J. F.; Thiele, D. *J. Biomol. Struct.* **1990**, *8*, 91.; (c) Parkinson, G. N.; Lee, M. P.; Neidle, S. *Nature* **2002**, *417* (6891), 876. doi:10.1038/nature755. PMID:12050675.
- (3) (a) Liu, X. Y.; Kwan, I. C. M.; Wang, S.; Wu, G. *Org. Lett.* **2006**, *8* (17), 3685. doi:10.1021/ol061236w. PMID:16898792.; (b) Martić, S.; Liu, X. Y.; Wang, S.; Wu, G. *Chem. Eur. J.* **2008**, *14* (4), 1196. doi:10.1002/chem.200701411.
- (4) Martić, S.; Wu, G.; Wang, S. *Inorg. Chem.* **2008**, *47* (18), 8315. doi:10.1021/ic800899b. PMID:18710219.
- (5) (a) Harriman, A.; Magda, D. J.; Sessler, J. L. *J. Phys. Chem.* **1991**, *95* (4), 1530. doi:10.1021/j100157a005.; (b) Sessler, J. L.; Jayawickramarajah, J.; Gouloumis, A.; Pantos, G. D.; Torres, T.; Guldi, D. M. *Tetrahedron* **2006**, *62* (9), 2123. doi:10.1016/j.tet.2005.05.110.; (c) Sessler, J. L.; Jayawickramarajah, J.; Gouloumis, A.; Pantos, G. D.; Torres, T.; Guldi, D. M. *Chem. Soc. Rev.* **2007**, *36* (2), 314. doi:10.1039/b604119c. PMID:17264932.; (d) Sessler, J. L.; Sathiosatham, M.; Brown, C. T.; Rhodes, T. A.; Wiederrecht, G. *J. Am. Chem. Soc.* **2001**, *123* (16), 3655. doi:10.1021/ja005547s. PMID:11457097.; (e) Sessler, J. L.; Wang, B.; Harriman, A. *J. Am. Chem. Soc.* **1993**, *115* (22), 10418. doi:10.1021/ja00075a091.
- (6) Kim, H. Y. H.; Cooper, M.; Nechev, L. V.; Harris, C. M.; Harris, T. M. *Chem. Res. Toxicol.* **2001**, *14* (9), 1306. doi:10.1021/tx010086p. PMID:11559047.
- (7) Neidle, S.; Balasubramanian, S. *Quadruplex Nucleic Acids*; RCS Publishing: Cambridge, 2006.
- (8) (a) Williams, L. D.; Chawla, B.; Shaw, B. R. *Biopolymers* **1987**, *26* (4), 591. doi:10.1002/bip.360260411.; (b) Williams, N. G.; Williams, L. D.; Shaw, B. R. *J. Am. Chem. Soc.* **1989**, *111* (18), 7205. doi:10.1021/ja00200a046.; (c) Williams, L. D.; Williams, N. G.; Shaw, B. R. *J. Am. Chem. Soc.* **1990**, *112* (2), 829. doi:10.1021/ja00158a050.
- (9) (a) de la Peña, A. M.; Salinas, F.; Gómez, M. J.; Acedo, M. I.; Peña, M. S. *J. Inclusion Phenom. Mol. Recogn. Chem.*

- 1993**, *15* (2), 131 doi:10.1007/BF00710222.; (b) Connors, K. A. *Binding Constants*; John Wiley & Sons: New York, 1987.
- (10) (a) Encinas, S.; Simpson, N. R.; Andrews, M. D.; Ward, C. M.; White, C. M.; Armaroli, N.; Barigelletti, F.; Houlton, A. N. *J. Chem.* **2000**, *24* (12), 987. doi:10.1039/b006503j.; (b) Sessler, J. L.; Jayawickramarajah, J.; Gouloumis, A.; Torres, T.; Guldi, D. M.; Maldonado, S.; Stevenson, K. J. *Chem. Commun. (Camb.)* **2005**, (14): 1892. doi:10.1039/b418345b. PMID:15795778.; (c) Harriman, A.; Kubo, Y.; Sessler, J. L. *J. Am. Chem. Soc.* **1992**, *114* (1), 388. doi:10.1021/ja00027a074.
- (11) Fisch, M. J.; Trucks, G. W.; Schlegel, H. B.; Scuseria, G. E.; Robb, M. A.; Cheesman, J. R., Jr.; Montgomery, J. A.; Vreven, T.; Kudin, K. N.; Burant, J. C.; Millam, J. M.; Iyengar, S. S.; Tomasi, J.; Barone, V.; Mennucci, B.; Cossi, M.; Scalmani, G.; Rega, N.; Petersson, G. A.; Nakatsuji, H.; Hada, M.; Ehara, M.; Toyota, K.; Fukuda, R.; Hasegawa, J.; Ishida, M.; Nakajima, T.; Honda, Y.; Kitao, O.; Nakai, H.; Li, M.; Klene, X.; Knox, J. E.; Hratchian, H. P.; Cross, J. B.; Bakken, V.; Adamo, C.; Jaramillo, J.; Gomperts, R.; Stratmann, R. E.; Yazyev, O.; Austin, A. J.; Cammi, R.; Pomelli, C.; Ochterski, J. W.; Ayala, P. Y.; Morokuma, K.; Voth, G. A.; Salvador, P.; Dannenberg, J. J.; Zakrzewski, V. G.; Dapprich, S.; Daniels, D.; Strain, M. C.; Farkas, O.; Malick, D. K.; Rabuck, A. D.; Raghavachari, K.; Foresman, J.; Ortiz, J. V.; Cui, Q.; Baboul, A. G.; Clifford, S.; Cioslowski, J.; Stefanov, B. B.; Liu, G.; Liashenko, A.; Piskorz, P.; Komaromi, I.; Martin, R. L.; Fox, D. J.; Keith, T.; Al-Laham, M. A.; Peng, C. Y.; Nanayakkara, A.; Challacombe, M.; Gill, P. M. W.; Johnson, B.; Chen, W.; Wong, M. W.; Bonzales, C.; Pople, J. A. *Gaussian 03, Revision C.02*; Gaussian Inc.: Wallingford, CT, 2004.
- (12) (a) Mallajosyula, S. S.; Datta, A.; Pati, S. K. *Synth. Met.* **2005**, *155* (2), 398. doi:10.1016/j.synthmet.2005.09.022.; (b) Schwalb, N. K.; Temps, F. *J. Am. Chem. Soc.* **2007**, *129* (30), 9272. doi:10.1021/ja073448+. PMID:17622153.; (c) Ohshiro, T.; Umezawa, Y. *Proc. Natl. Acad. Sci. U.S.A.* **2006**, *103* (1), 10. doi:10.1073/pnas.0506130103. PMID: 16373509.



# Determination of diltiazem based on the reduction of Cu(II)–BCA complexes in micellar medium

Larissa Zupardo Lacerda Sabino, Daniele Cestari Marino, and  
Horacio Dorigan Moya

**Abstract:** A simple method was developed for determining microquantities of diltiazem, based on the reduction of copper(II) in buffered solution (pH 7.0) and the use of a micellar medium containing 4,4'-dicarboxy-2,2'-biquinoline acid. The copper(I) produced reacts with 4,4'-dicarboxy-2,2'-biquinoline acid and the complexes formed are spectrophotometrically measured at 558 nm. A typical calibration graph shows good linearity ( $r = 0.993$ ) from 20 to 100  $\mu\text{g mL}^{-1}$  of diltiazem. The limit of detection and relative standard deviation were calculated as 12  $\mu\text{g mL}^{-1}$  (99% confidence level) and 3.5% (40  $\mu\text{g mL}^{-1}$ ;  $n = 6$ ), respectively, with a mean recovery value of 96.5% found in pharmaceutical dosages. A straightforward and effective way to recycle the reagents is addressed. The hazardous aspects of the Cu(I)–BCA reaction are presented as well.

**Key words:** diltiazem, Cu(I), 4,4'-dicarboxy-2,2'-biquinoline acid (bicinchoninic acid), spectrophotometry.

**Résumé :** On a développé une méthode simple pour déterminer des microquantités de diltiazem basée sur la réduction du cuivre(II), dans une solution tamponnée (pH de 7,0) et un milieu micellaire contenant de la 4,4'-dicarboxy-2,2'-biquinolène. Le cuivre(I) qui est produit réagit avec l'acide 4,4'-dicarboxy-2,2'-biquinolène et les complexes qui se forment peuvent être mesurés d'une façon spectrophotométrique à 558 nm. Un graphique de calibration typique présente une bonne linéarité ( $r = 0.993$ ) pour des concentrations allant de 20 à 100  $\mu\text{g mL}^{-1}$  de diltiazem. On a calculé que la limite de détection et la déviation standard relative sont respectivement égales à 12  $\mu\text{g mL}^{-1}$  (niveau de confiance de 99 %) et de 3,5 % (40  $\mu\text{g mL}^{-1}$ ;  $n = 6$ ) avec une valeur moyenne de récupération de 96,5 % des dosages présents dans des formulations pharmaceutiques. On présente les risques associés à l'utilisation de la réaction Cu(I)/ABC ainsi qu'une méthode simple et efficace de recycler les réactifs utilisés.

**Mots-clés :** diltiazem, Cu(I), acide 4,4'-dicarboxy-2,2'-quinoléine (acide bicinchoninique, ABC), spectrophotométrie.

[Traduit par la Rédaction]

## Introduction

Only a few ligands, including neocuproine and bathocuproine, are able to stabilize Cu(I) in aqueous solution; this stabilization results from the formation of the respective Cu(I) charge-transfer transition complexes.<sup>1</sup> However, because of the low solubility of these compounds in water, the aqueous solution is not used on a wide scale in the analysis of drugs; instead, the Cu(I)–neocuproine complexes in ethanolic medium are used for the determination of ascorbic acid,<sup>2</sup>  $\alpha$ -tocopherol,<sup>3</sup> ceftazidime,<sup>4</sup> and isoniazid<sup>5</sup> in pharmaceutical preparations. The Cu(I)–bathocuproine complexes were recently used to quantify some dibenzazepine drugs.<sup>6</sup>

The 4,4'-dicarboxy-2,2'-biquinoline acid (bicinchoninic acid), or BCA, is a weak organic acid ( $\text{p}K_{\text{a}1} = 1.87$ ;  $\text{p}K_{\text{a}2} = 2.85$ ) derived from quinoline (Fig. 1a), which acts as a specific chelating agent for Cu(I) in aqueous solution forming violet soluble complexes showing absorption maxima at 357 ( $\varepsilon = 4.2 \times 10^4 \text{ L mol}^{-1} \text{ cm}^{-1}$ ) and 558 nm ( $\varepsilon = 7.7 \times 10^3 \text{ L mol}^{-1} \text{ cm}^{-1}$ ).<sup>7</sup> It was initially used to determine copper in

different samples, such as alloys,<sup>8</sup> minerals,<sup>9</sup> and blood.<sup>10</sup> The determination was based on the reduction of Cu(II) using hydroxylamine hydrochloride as the reducing agent. It has also been used to quantify the total level of protein,<sup>11</sup> reducing sugars,<sup>12</sup> and uric<sup>13</sup> and ascorbic<sup>14</sup> acids. In our previous work,<sup>15</sup> it was shown that polyphenols reduced Cu(II) to Cu(I) in a buffered ammonium acetate solution (pH 7.0) containing BCA. This work also presented an alternative analytical method for determining tannins in wines and teas by flow injection analysis, with a limit of detection of 10 nmol L<sup>-1</sup> (99.7% confidence level) and a linear range from 0.5 to 5  $\mu\text{mol L}^{-1}$  of tannic acid.

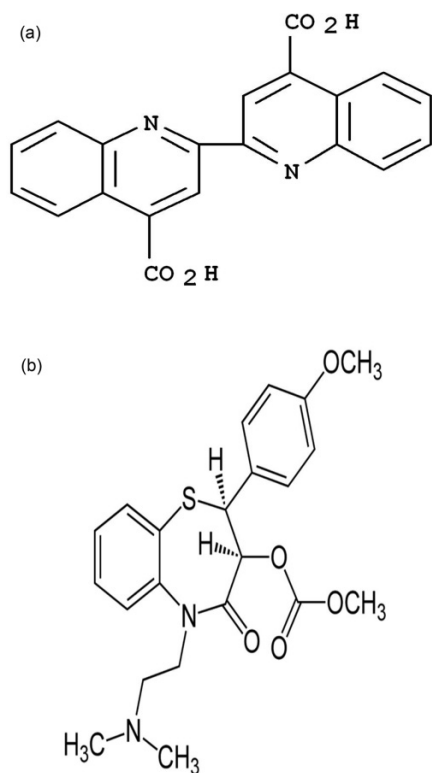
The British Pharmacopeia<sup>16</sup> recommends a non-aqueous titration technique for determining the drug 3-acetyloxy-5-(2-(dimethylamino)ethyl)-2,3-dihydro-2-(4-methoxyphenyl)-1,5-benzothiazepin-4(5H)one (Fig. 1b), known as diltiazem, which is one of the pharmaceutical compounds most widely used as Ca<sup>2+</sup>-blocking drugs. However, as this method is based on acid–base properties, other weak acids or bases (e.g., stearate or acetate) present in the samples may inter-

Received 29 October 2009. Accepted 11 February 2010. Published on the NRC Research Press Web site at canjchem.nrc.ca on 6 May 2010.

**L.Z.L. Sabino, D.C. Marino, and H.D. Moya.**<sup>1</sup> Faculdade de Medicina da Fundação do ABC, Centro de Estudos, Pesquisa, Prevenção e Tratamento em Saúde, CEP- 09060-650 Santo André, SP, Brazil.

<sup>1</sup>Corresponding author (e-mail: hdmoya@fmabc.br).

**Fig. 1.** (a) Structure of 4,4'-dicarboxy-2,2'-biquinoline acid (BCA); (b) structure of diltiazem.



fere. Moreover, this procedure presents some disadvantages, such as higher reagent consumption and large amounts of waste.

Table 1 shows a selection of some suggested alternative methods for diltiazem quantification including voltametric,<sup>17</sup> potentiometric,<sup>18,19</sup> chromatographic,<sup>20–24</sup> and spectrophotometric techniques.<sup>25–33</sup> Despite the good analytical parameters obtained in the voltametric and chromatographic methods, they demanded more expensive pieces of equipment, which are not always available in quality control laboratories. Potentiometric techniques could be more useful for this purpose but they use either organic solvents<sup>16</sup> or selective electrodes, which must be previously assembled.<sup>18,19</sup> In contrast, chromatographic techniques have been preferentially used for diltiazem determination in biological samples such as human plasma<sup>20,22,24</sup> or urine.<sup>24</sup>

It can be also seen from Table 1 that most of the methods presented are based on spectrophotometric analysis, probably because of its simplicity, low cost, and the roughness of the spectrophotometric technique. However, many of them use extractive procedures with organic solvents<sup>26–28</sup> or have some analytical steps that take a long time to be completed.<sup>31</sup> Other methods use hazardous reagents demanding proper disposal.<sup>32,33</sup>

This study presents a new spectrophotometric method for the determination of diltiazem, which reduces Cu(II) to Cu(I) in the presence of BCA forming Cu(I)–BCA complexes at pH 7.0 (maintained with ammonium acetate buffer) in a micellar medium containing dodecyltrimethylammonium bromide (Fig. 2). The absorbance measurement at 558 nm, characteristic of the Cu(I)–BCA complexes,<sup>7</sup> is proportional to the drug concentration. The proposed method is faster

than some spectrophotometric procedures and does not require any organic solvent. Additionally, it presents advantages when compared to the official method:<sup>16</sup> it is a less-demanding method and it significantly minimizes waste generation.

## Experimental

### Apparatus, reagents, and chemicals

The spectrophotometric measurements were made in a HPUV 8453 spectrophotometer using 1.00 cm glass cuvettes.

All reagents were of AR or CP grade from Merck, Sigma-Aldrich, or Fluka Chemie A.G. Deionized water was used in all solutions.

Pharmaceutical grade diltiazem·HCl, C<sub>22</sub>H<sub>26</sub>N<sub>2</sub>O<sub>4</sub>S·HCl, was generously supplied as a gift from Farmalab Ind. Químicas e Farmacêuticas Ltda., São Paulo, Brazil. Stock standard solution 1.0 × 10<sup>−2</sup> mol L<sup>−1</sup> was prepared by dissolution in water just before use. Commercial drugs containing diltiazem·HCl with 30 mg per tablet and 90, 120, and 180 mg per capsule were used as samples.

Copper(II) nitrate, Cu(NO<sub>3</sub>)<sub>2</sub>·6H<sub>2</sub>O, 1.0 mol L<sup>−1</sup>, stock solution was prepared from direct dissolution of the salt in water. A 1.0 × 10<sup>−2</sup> mol L<sup>−1</sup> working solution was prepared by suitable dilution in water. Standardization was carried out by complexometric titration with EDTA.

BCA 3.0 × 10<sup>−2</sup> mol L<sup>−1</sup> stock solution was prepared by dissolution of the disodium salt of 4,4'-dicarboxy-2,2'-biquinoline, Na<sub>2</sub>C<sub>20</sub>H<sub>10</sub>N<sub>2</sub>O<sub>4</sub>, in water.

Stock solutions of DTAB (dodecyltrimethylammonium bromide, CH<sub>3</sub>(CH<sub>2</sub>)<sub>11</sub>N(CH<sub>3</sub>)<sub>3</sub>Br), 0.33 mol L<sup>−1</sup>, and ammonium acetate, CH<sub>3</sub>CO<sub>2</sub>NH<sub>4</sub>, 2.0 mol L<sup>−1</sup> were prepared by dissolution in water.

### Sample preparation

Samples were prepared from two forms currently found in the local pharmaceutical market: tablets and capsules. For the first form, 30 mg tablets were used. The second one was prepared from three different alternatives: 180 mg, 120 mg, and 90 mg capsules.

To compensate for the different drug quantity present in the different versions of the capsules (180, 120, and 90 mg), one 180-mg capsule; two 120-mg capsules. or three 90-mg capsules were used.

Regardless of the sample form, all drug samples were filtered through filter paper into a 25.0 mL volumetric flask and diluted with deionized water.

### Procedures

The calibration graph of the proposed procedure was obtained by preparing six sets of solutions containing 250 µL Cu(II) 1.0 × 10<sup>−2</sup> mol L<sup>−1</sup>, 2.0 mL ammonium acetate 2.0 mol L<sup>−1</sup> (to keep the pH of the solution at 7.0), 250 µL BCA 3.0 × 10<sup>−2</sup> mol L<sup>−1</sup>, and 120 µL DTAB 0.33 mol L<sup>−1</sup> added in the sequence described. Each solution was transferred into a 5.00 mL volumetric flask. Aliquots with volumes ranging from 25 to 120 µL of diltiazem·HCl stock standard solution 1.0 × 10<sup>−2</sup> mol L<sup>−1</sup> were added to the flasks which were then filled to the mark with deionized water. The resulting solutions were mixed well and placed

**Table 1.** Analytical parameters of some selected methods for diltiazem determination in pure or dosage forms.

Method	LR ( $\mu\text{g mL}^{-1}$ )	LOD ( $\mu\text{g mL}^{-1}$ )	Remarks	Reference
Voltametry	0.045–0.406	$2.7 \times 10^{-3a}$	Adsorptive stripping was used to determine the drug in phosphate buffer (pH 7.0) with an adsorptive cathodic peak observed at $-1.72$ V vs. Ag–AgCl.	17
Potentiometry	4.51–45100	3.2	Based on a membrane containing the drug and tetraphenylborate (slope $55.5$ mV/pC).	18
Potentiometry	4.51–451	0.45	Based on incorporation of DNNS along with the drug into a PVC membrane (slope $60.1$ mV/pC).	19
Chromatography	0–0.3	$3 \times 10^{-3b}$	A reversed phase HPLC method with extn. of the drug in a mixture of hexane, $\text{CHCl}_3$ and isopropanol (60:40:5 v/v) and hydromethanolic solution (80:20 v/v) as mobile phase with UV detection at $239$ nm.	20
Chromatography	$(5-25) \times 10^4$	$5 \times 10^{3c}$	Based on a solid phase extraction coupled with reversed-phase HPLC with UV detection.	21
Chromatography	0.02–0.5	$5 \times 10^{-3b}$	HPLC method for detn. of the drug based on a solid-phase and liq.-liq. extraction for the drug using acetonitrile – $0.025$ mol $\text{L}^{-1}$ $\text{KH}_2\text{PO}_4$ (pH 5.5), 35:65 (v/v) as mobile phase with UV detection at $215$ nm.	22
Chromatography	0.092–0.431	0.028	Based in a hybrid micellar as mobile phase of $0.05$ mol $\text{L}^{-1}$ SDS – 5% pentanol; UV detection at $220$ nm.	23
Chromatography	0–0.4	$2 \times 10^{-3ab}$	HPLC method using $\text{MeOH}-\text{CH}_2\text{Cl}_2$ –hexane as the mobile phase and UV detection at $240$ nm.	24
Spectrophotometry	2.5–20.0 (BTB)	NA	Based on the formation of ion-pair complexes of the drug with acid–base indicators in acidic medium, with extraction in $\text{CHCl}_3$ and measurements at $415$ nm.	25
Spectrophotometry	2.5–10.0 (BPB)	NA	—	26
	2.5–12.5 (BCG)	NA	—	
	40–200	NA	Based on the formation of an ion-assocn. complex from the reaction of the drug and Erythrosin B with extraction in $\text{CHCl}_3$ and measurements at $491$ nm.	
Spectrophotometry	8–40	NA	Based on the alkaline hydrolysis of the drug with MBTH and measurements at $593$ nm.	27
Spectrophotometry	50–170	NA	Based on the formation of a ternary complex with extraction in $\text{CH}_2\text{Cl}_2$ and measurements at $536.8$ nm.	28
	60–600 (CT)	NA	Based on the formation of complex of the drug with cobalt thiocyanate (CT) or methyl orange (MO), extd. into org. solvents, and measured at $630$ nm and $420$ nm, respectively.	
	5–60 (MO)	NA		
Spectrophotometry	500–3500	NA	Based on the reaction with ammonium reineckate reagent and the ppt. formed isolated and dissolved in acetone with measurements $525$ nm.	29
Spectrophotometry	12–32	NA	Based on the oxidn. of the drug with Fe(III) in acidic medium in presence of 1,10-phen. with measurements $510$ nm.	30
Spectrophotometry	2.5–25	0.12	Based on the reaction of the drug with $\text{NaClO}$ ; destruction of the excess $\text{NaClO}$ by $\text{NaNO}_2$ ; reaction of drug chloro deriv. with starch and KI in $\text{NaHCO}_3$ medium, with measurements at $540$ nm.	31
Spectrophotometry	0–50	0.02	Based on the reaction of the drug with boiling solution of $\text{NaVO}_3$ in $\text{H}_2\text{SO}_4$ medium ( $11$ mol $\text{L}^{-1}$ ) for $20$ min and measurements at $750$ nm.	32
Spectrophotometry	3.5–7.0 (C2R)	0.007	Based on the addn. of excess of $(\text{NH}_4)_2\text{Ce}(\text{SO}_4)_3 \cdot 2\text{H}_2\text{O}$ in a medium containing the drug and detn. of the unconsumed oxidant by a decrease of C2R at $528$ nm or by a decrease of Rh6G at $525$ nm.	33
Spectrophotometry	3.5–6.3 (Rh6G)	0.024	—	This work
	20–100	12	Based on the reduction of Cu(II) to Cu(I) by the drug in a buffered ammonium acetate medium (pH = 7.0) in presence of the ligand BCA in a micellar medium containing DTAB.	

**Note:** LR = linear range; LOD = limit of detection; NA = not available; DNNS = dinonylnaphthalene sulfonic acid; SDS = sodium dodecyl sulfate; BTB = bromothymol blue; BPB = bromophenol blue; BCG = bromocresol green; DDQ = 2,3-dichloro-5,6-dicyano-benzoquinone; MBTH = 3-methylbenzothiazolonehydrazone; C2R = chromotrope 2R; 1,10-phen = 1,10-phenantroline; Rh6G = rhodamine 6G.

<sup>a</sup>Also in urine sample.

<sup>b</sup>Also in human plasma sample.

<sup>c</sup>Gel sample.

in a boiling water bath for 5 min. After the solutions were cooled, the absorbance was measured at 558 nm using a mixture containing 0.5 mmol L<sup>-1</sup> Cu(II), 1.5 mmol L<sup>-1</sup> BCA, 8.0 mmol L<sup>-1</sup> DTAB, and 0.8 mol L<sup>-1</sup> ammonium acetate as reference solution (Fig. 3).

The multiple standard addition method was used to analyze the samples. Fifty  $\mu$ L of the prepared sample solution was transferred to five 5.0 mL volumetric flasks. Each flask contained 250  $\mu$ L Cu(II)  $1.0 \times 10^{-2}$  mol L<sup>-1</sup>, 2.0 mL ammonium acetate 2.0 mol L<sup>-1</sup>, 250  $\mu$ L BCA  $3.0 \times 10^{-2}$  mol L<sup>-1</sup>, and 120  $\mu$ L DTAB 0.33 mol L<sup>-1</sup>. Diltiazem HCl  $1.0 \times 10^{-2}$  mol L<sup>-1</sup> standard solution was not added to the first of the five flasks. To the second, third, fourth, and fifth flasks were added 23, 36, 45 and 67,  $\mu$ L, respectively (Fig. 3).

The reference procedure, based on a non-aqueous titration, was carried out as described in the British Pharmacopoeia.<sup>16</sup>

## Results and discussion

Diltiazem undergoes oxidation by Cu(II) in the presence of BCA in a buffered ammonium acetate medium (pH 7.0). However, the reaction requires a very long time (more than 20 h) for completion at room temperature (Fig. 4, curve II) and a light green precipitate of Cu(II)-BCA was formed in the bottom of the cuvette. Initial efforts to accelerate this reaction by carrying it out in a micellar medium (Fig. 4, curve III) decreased the reaction time to four hours but did not avoid the formation of the same precipitate. However, heating this solution accelerated the reaction and also prevented the formation of any precipitates. The highest analytical signal, using the Cu(I)-BCA complexes at 558 nm, was achieved in a solution containing 0.5 mmol L<sup>-1</sup> Cu(II), 1.5 mmol L<sup>-1</sup> BCA, and 8.0 mmol L<sup>-1</sup> DTAB in 0.8 mol L<sup>-1</sup> ammonium acetate medium (pH 7.0) and by heating the mixture in a boiling water bath for 5 min. No bathochromic effect was observed after this treatment. After the reaction completion, the absorbance value of the complexes remained constant at room temperature for 24 h in the dark refrigerator.

Variations in the concentration of Cu(II) and BCA were tested providing a Cu(II):BCA proportion of 1:3. The Cu(II)-BCA light green precipitate was formed when the concentrations were Cu(II) 1.0 mmol L<sup>-1</sup> and BCA 3.0 mmol L<sup>-1</sup>. A decrease of about 30% in the absorbance values in much lower concentrations (e.g., Cu(II) 0.05 mmol L<sup>-1</sup> and BCA 0.15 mmol L<sup>-1</sup>) was observed.

The buffer solution used is essential for this diltiazem determination providing its addition is made after Cu(II) in the following order: (Cu(II) + buffer + BCA) + DTAB + diltiazem. In the majority of analytical studies with the Cu(I)-BCA complexes, an acetic acid – sodium acetate buffer solution was used to keep the pH 7.0,<sup>9,10,13,14</sup> though it is far from its buffering capacity. Thus, some buffer solutions had to be tested for this reaction. When potassium citrate (pH 7.4) and sodium citrate (pH 7.5) solutions were used, the absorbance signal decreased by 70% and 65%, respectively, probably because of the Cu(II)-citrate complex formation ( $\log \beta = 14$ ).<sup>34</sup> Potassium phosphate (pH 7.0) and Na<sub>2</sub>B<sub>4</sub>O<sub>7</sub>-HCl buffer solutions (pH 7.4) could be used but a green turbid solution was observed before adding BCA.

In the tannin determination mentioned above,<sup>15</sup> a 0.03 mol L<sup>-1</sup> ammonium hydroxide solution was used as a carrier to avoid precipitation of Cu(II)-BCA. Under this condition, a stable baseline was observed without affecting sensitivity and reproducibility. Taking all of this into consideration, a reasonable decision was the use of ammonium acetate to adjust the pH to 7.0. At this pH, NH<sub>3</sub> is present as ammonium ion. At the same pH, acetate ion does not complex Cu(II) in a pronounced way ( $\log \beta_1 = 1.70$ ;  $\log \beta_2 = 2.69$ ;  $\log \beta_3 = 3.0$ ;  $\log \beta_4 = 2.9$ ).<sup>34</sup> The influence of ammonium acetate concentration was then investigated. It was found that in ammonium acetate 1.0 mol L<sup>-1</sup> the absorbance value decreased about 50%, probably because of the formation of [Cu(NH<sub>3</sub>)<sub>4</sub>]<sup>2+</sup> complex ( $\log \beta_4 = 12$ ).<sup>34</sup> At lower concentrations such as 0.5 mol L<sup>-1</sup>, a slightly green turbid solution was formed and the absorbance value decreased 60% (Fig. 5).

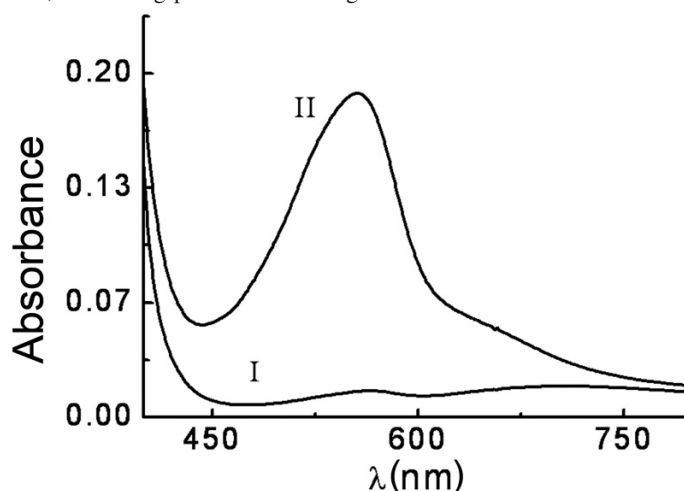
Several surfactants were tested to accelerate this reaction (all tests were performed over heating). Anionic surfactants, such as sodium lauryl ethersulphate and sodium laurylsulphate, did not prevent the precipitation at all. Nonionic surfactant such as Triton X-100 and Tween 20 did prevent it. However, the reference solution remained markedly violet, which would represent no advantage regarding the absorbance measurements. A cationic surfactant based on quaternary ammonium cations like CTAB (hexadecyltrimethylammonium bromide) or CTAC (hexadecyltrimethylammonium chloride) prevents the precipitation. However, CTAB and CTAC produce deeper violet reference solutions than DTAB (dodecyltrimethylammonium bromide). Because DTAB was the only surfactant tested that did not strongly react with Cu(II)-BCA under the experimental conditions addressed in the article, different final concentrations were tested, namely 4, 6, 8, 10, 50, and 100 mmol L<sup>-1</sup>. The best analytical signal was achieved with 8 mmol L<sup>-1</sup>, which is below the DTAB critical micellar concentration (15 mmol L<sup>-1</sup>) (Fig. 6).

Under these optimized conditions (Cu(II) = 0.5 mmol L<sup>-1</sup>, BCA = 1.5 mmol L<sup>-1</sup>, DTAB = 8.0 mmol L<sup>-1</sup>, ammonium acetate = 0.8 mol L<sup>-1</sup>, and heating this mixture in a boiling water bath for 5 min), the calibration graph was linear for diltiazem-HCl concentrations from 20 to 100  $\mu$ g mL<sup>-1</sup>, which is described by the regression equation  $A = 0.06003 + 0.00203 \times [D]$ ,  $r = 0.993$ , where A is the absorbance measured at 558 nm and [D] is the diltiazem-HCl concentration in  $\mu$ g mL<sup>-1</sup> (Fig. 3). The limit of detection, defined as three times the standard deviation of the linear coefficient divided by the angular coefficient value, was estimated as 12  $\mu$ g mL<sup>-1</sup> at 99% confidence level, which is significantly lower than that required for the determination of diltiazem in all of the pharmaceutical formulations. The relative standard deviation was estimated as 3.5% for 5 measurements of a 40  $\mu$ g mL<sup>-1</sup> diltiazem standard solution, which can be considered satisfactory. The analytical results obtained are summarized in Table 2 and they are well aligned with the official method,<sup>16</sup> demonstrating that the procedure suggested here can be used as an alternative method for diltiazem-HCl quantification in dosage forms.

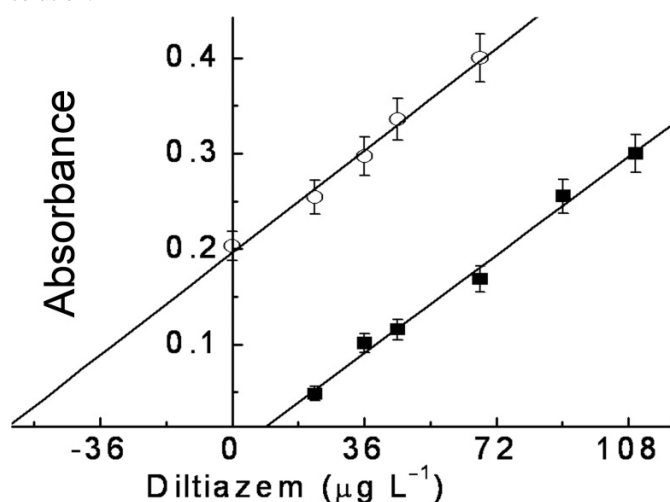
To confirm the consistency of the proposed method, drug samples were spiked with diltiazem-HCl (50, 80, 100, and 150  $\mu$ mol L<sup>-1</sup>), and the recovery of diltiazem-HCl was estimated. Data presented in Table 3 show recoveries from 87.8



**Fig. 2.** Absorption spectra of: I = Cu(II) 0.5 mmol L<sup>-1</sup> + BCA 1.5 mmol L<sup>-1</sup> + 8.0 mmol L<sup>-1</sup> DTAB + 0.8 mol L<sup>-1</sup> ammonium acetate; II = solution I + 80 µg mL<sup>-1</sup> diltiazem-HCl, after being placed in a boiling water bath for 5 min. Water as reference solution.



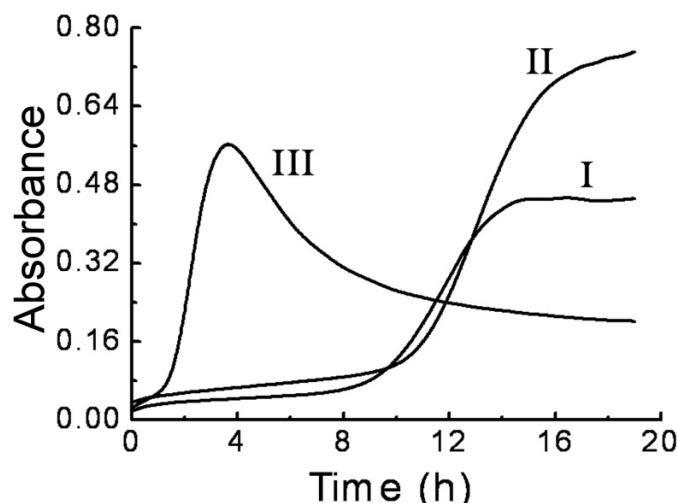
**Fig. 3.** (■) Calibration ( $A = 0.06003 + 0.00203 \times [D]$ ,  $r = 0.993$ ,  $n = 6$ ) and (○) the multiple standard addition method ( $A = 0.02071 + 0.00212 \times [D]$ ,  $r = 0.990$ ,  $n = 5$ ) curves obtained for diltiazem determination using the Cu(I)-BCA complexes. Sample = one 180 mg capsule of diltiazem-HCl. Cu(II) = 0.5 mmol L<sup>-1</sup>; BCA = 1.5 mmol L<sup>-1</sup>; DTAB = 8.0 mmol L<sup>-1</sup>; and ammonium acetate = 0.8 mol L<sup>-1</sup>. All spectrophotometric measurements at 558 nm after being placed in a boiling water bath for 5 min. Water as reference solution.



to 103%, with a mean value of 96.5%. Additionally, the curve obtained by the multiple standard addition method for the samples was parallel when compared with the one described by the calibration graph (slope differences between 5%–8%). These curves indicate that matrix effects on the proposed procedure can be negligible (Fig. 3).

The influence of common additives found in tablets and capsules was tested for their possible interferences in this reaction for diltiazem determination. It was observed that talc, starch, and magnesium stearate did not interfere because they remain insoluble after dissolution of the samples. The effects of glucose, lactose, and sucrose were also investigated since they are usually found as adjuvants in pharmaceutical preparations. Thus, solutions containing

**Fig. 4.** Variation of absorbance at 558 nm of solutions containing: I = Cu(II) 0.5 mmol L<sup>-1</sup> + BCA 1.5 mmol L<sup>-1</sup> + 0.8 mol L<sup>-1</sup> ammonium acetate + 8.0 mmol L<sup>-1</sup> DTAB; II = Cu(II) 0.5 mmol L<sup>-1</sup> + BCA 1.5 mmol L<sup>-1</sup> + 0.8 mol L<sup>-1</sup> ammonium acetate + 40 µg mL<sup>-1</sup> diltiazem-HCl; III = Cu(II) 0.5 mmol L<sup>-1</sup> + BCA 1.5 mmol L<sup>-1</sup> + 0.8 mol L<sup>-1</sup> ammonium acetate + 8.0 mmol L<sup>-1</sup> DTAB + 40 µg mL<sup>-1</sup> diltiazem-HCl. All measurements at room temperature, with water as reference solution.

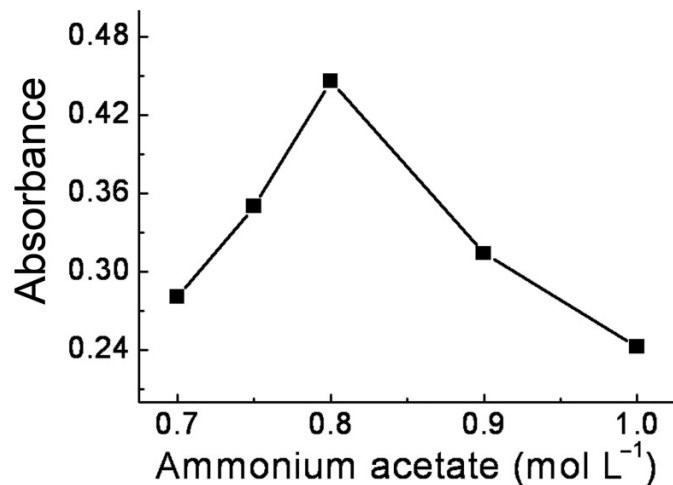


50 µmol L<sup>-1</sup> diltiazem-HCl and three known concentrations (0.05, 0.5, and 2.5 mmol L<sup>-1</sup>) of these substances were analyzed by the proposed procedure. No interference was observed up to 50-fold excess of glucose, lactose, and sucrose. As the samples containing diltiazem-HCl are diluted 100-fold (see Experimental), those substances present in the levels usually found in dosage forms will probably not interfere. The results observed in the interference study and the good recoveries estimated for three drug-spiked concentrations in the four kinds of samples (Table 3) confirmed that the proposed method can be used as an alternative method for diltiazem-HCl.

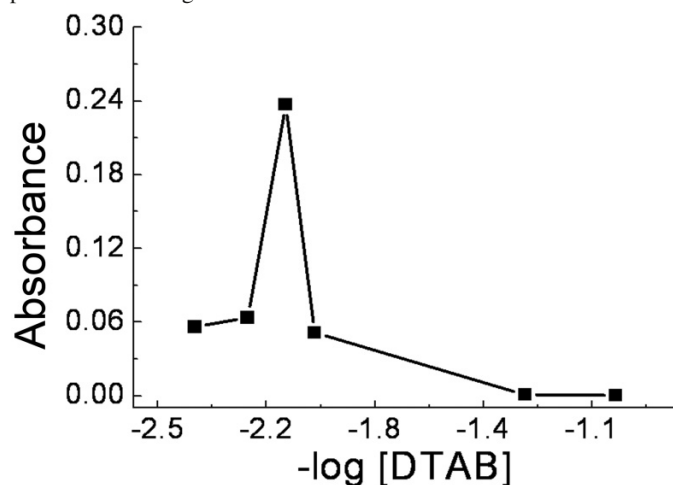
#### Hazardous aspects of the Cu(I)-BCA reaction

The toxicological properties of BCA have not been fully

**Fig. 5.** Variation of absorbance at 558 nm of solutions containing Cu(II) 0.5 mmol L<sup>-1</sup> + BCA 1.5 mmol L<sup>-1</sup> + 8.0 mmol L<sup>-1</sup> DTAB + 150 µg mL<sup>-1</sup> diltiazem-HCl and ammonium acetate. All measurements made after being placed in a boiling water bath for 5 min. Water as reference solution.



**Fig. 6.** Variation of absorbance at 558 nm of solutions containing Cu(II) 0.5 mmol L<sup>-1</sup> + BCA 1.5 mmol L<sup>-1</sup> + 0.8 mol L<sup>-1</sup> ammonium acetate + 100 µg mL<sup>-1</sup> diltiazem-HCl and DTAB. Reference solution: Cu(II) 0.5 mmol L<sup>-1</sup> + BCA 1.5 mmol L<sup>-1</sup> + 0.8 mol L<sup>-1</sup> ammonium acetate and DTAB. All measurements made after being placed in a boiling water bath for 5 min.



**Table 2.** Determination of diltiazem-HCl in pharmaceutical forms by the reference and the present methods.

Sample	Diltiazem-HCl (mg) <sup>a</sup>		
	Informed value	Reference method <sup>16</sup>	Present method
Tablets	30	30.5±0.3	29.3±0.8
Capsule	90	90.7±0.7	89.2±0.9
Capsule	120	122±1	119±2
Capsule	180	179±2	182±1

<sup>a</sup>Mean and relative standard deviation results obtained with the average of three analyses.

**Table 3.** Recovery rates from diluted samples of diltiazem formulations obtained with four different quantities of spiked concentrations using the Cu(I)-BCA complexes.

Sample	Diluted sample	Diltiazem concentration (µg mL <sup>-1</sup> )		
		Added	Found	Recovery (%)
Tablets of 30 mg	48	22.5	63.0	87.8
		36.0	75.8	90.2
		45.0	89.0	95.6
		67.5	114	98.7
Capsules of 90 mg	108	67.5	176	100
		22.5	132	101
		36.0	148	103
		67.5	179	102
Capsules of 120 mg	96	45.0	130	92.3
		22.5	114	96.7
		36.0	129	98.3
		67.5	155	94.8
Capsules of 180 mg	72	36.0	99.7	92.3
		22.5	90.1	95.3
		45.0	114	97.5
		67.5	137	98.0

studied so far but it may cause sore eyes and affect mucous membranes, and it is expected to be internally toxic, so it must be appropriately disposed of.

The total waste volume of Cu(II), BCA, DTAB, and ammonium acetate for each determination (5 mL) were approximately 0.16, 2.9, 12, and 310 mg, respectively. However, the waste obtained after many BCA analysis can be recycled using a simple procedure. First, the solution should be alkalinized to pH 12 with 3.0 mol L<sup>-1</sup> NaOH solution to precipitate all of the copper ion. After removing the copper hydroxocompounds by filtration, the solution remaining is acidified with a 2.0 mol L<sup>-1</sup> HCl solution to protonate (pK<sub>a1</sub> = 1.87; pK<sub>a2</sub> = 2.85) and separate all the BCA present. The insoluble H<sub>2</sub>BCA obtained is then filtered and must be recrystallized before new use.

## Conclusion

The procedure presented here is a simple and accurate alternative method for diltiazem-HCl determination in dosage forms. It provides good sensitivity when compared with most of the spectrophotometric methods previously reported for this drug. The colored Cu(I)-BCA complexes formed are stable for more than 24 h, which makes the method more practicable. Besides, the validity of the proposed method is well demonstrated by analyzing various dosage forms of diltiazem-HCl. Additionally, as it is free from interference by common additives, it can be used for routine quality control.

Although there are already several methods for determining diltiazem-HCl determination, this is the first report of an analytical procedure based on the reduction of Cu(II) to Cu(I) by this drug in the presence of BCA in a micellar medium containing DTAB. Among its advantages are low cost of the technique, low reagent consumption, and no need for organic solvents. In addition, the possibility of the recovery of

the BCA and Cu(II) makes this procedure more attractive from the environmental point of view.

## Acknowledgements

The authors acknowledge the financial support of FAPESP (Fundação de Amparo à Pesquisa do Estado de São Paulo) and NEPAS (Núcleo de Ensino, Pesquisa e Assessoria a Saúde da FMABC).

## References

- (1) Pietrzyk, D. J.; Frank, C. W. *Analytical Chemistry: An Introduction*; Academic Press: New York, 1974; p. 131.
- (2) Güçlü, K.; Sözen, K.; Tütem, E.; Ozyürek, M.; Apak, R. *Talanta* **2005**, *65* (5), 1226. doi:10.1016/j.talanta.2004.08.048. PMID:18969936.
- (3) Tütem, E.; Apak, R.; Günaydı, E.; Sözen, K. *Talanta* **1997**, *44* (2), 249. doi:10.1016/S0039-9140(96)02041-3. PMID:18966741.
- (4) Moreno, A. H.; Salgado, H. R. N. *Anal. Lett.* **2008**, *41* (12), 2143. doi:10.1080/00032710802240818.
- (5) Safavi, A.; Karimi, M. A.; Nezhad, M. R. H.; Kamali, R.; Saghir, N. *Spectrochim. Acta, Part A Mol. Biomol. Spectrosc.* **2004**, *60* (4), 765. doi:10.1016/S1386-1425(03)00288-9.
- (6) Keshavachar, N. G.; Syeda, A.; Pasha, M. A.; Syed, A. A. *Indian J. Pharm. Sci.* **2005**, *67* (2), 175.
- (7) Gershuns, A. L.; Koval, V. L. *Visnik Kharkivs'kogo Univ.* **1970**, *46* (1), 64.
- (8) Arkhangel'skaya, A. S.; Batalina, G. P. *Zavod. Lab* **1968**, *34* (4), 408.
- (9) Lapin, N. N.; Vovk, A. I. *Khim. Khim. Tekhnol* **1966**, *9* (1), 27.
- (10) Noskova, N. N. *Mikrochem. Sib* **1974**, *9*, 159.
- (11) Smith, P. K.; Krohn, R. I.; Hermanson, G. T.; Mallia, A. K.; Gartner, F. H.; Provenzano, M. D.; Fujimoto, E. K.; Goeke, N. M.; Olson, B. J.; Klenk, D. C. *Anal. Biochem.* **1985**, *150* (1), 76. doi:10.1016/0003-2697(85)90442-7. PMID:3843705.
- (12) McFeeters, R. F. *Anal. Biochem.* **1980**, *103* (2), 302. doi:10.1016/0003-2697(80)90614-4. PMID:7386863.
- (13) Li, S. Y.; Rei, I. C.; Shou, S. Y.; Sai, Y. F.; Woo, T. K.; Ho, F. S.; Kuo, M. E.; Juan, J. L.; Chan, H. T. Japan Patent Application 166466, 2000.
- (14) Pustovar, P. Ya.; Gershuns, A. L. *Vestn. Khar'k. Unta.* **1983**, *242*, 40.
- (15) Moya, H. D.; Dantoni, P.; Rocha, F. R. P.; Coichev, N. *Microchem. J.* **2008**, *88* (1), 21. doi:10.1016/j.microc.2007.08.006.
- (16) *British Pharmacopoeia*, 5th ed.; Council of Europe: Strasbourg, 1999; Vol. 1, Pt. 1, p. 516.
- (17) Ghandour, M. A.; Aboul Kasim, E.; Ali, A. M. M.; El-Haty, M. T.; Ahmed, M. M. *J. Pharm. Biomed. Anal.* **2001**, *25* (3-4), 443. doi:10.1016/S0731-7085(00)00594-X. PMID:11377024.
- (18) Ganjali, M. R.; Razavi, T.; Dinarvand, R.; Riahi, S.; Norouzi, P. *Int. J. Electrochem. Sci* **2008**, *3* (12), 1543.
- (19) Cunningham, L.; Freiser, H. *Anal. Chim. Acta* **1984**, *157* (1), 157. doi:10.1016/S0003-2670(00)83616-8.
- (20) Li, K.; Zhang, X.; Zhao, F. *Biomed. Chromatogr.* **2003**, *17* (8), 522. doi:10.1002/bmc.270. PMID:14648609.
- (21) Buur, J. L.; Baynes, R. E.; Yeatts, J. L.; Davidson, G.; De-francesco, T. C. *J. Pharm. Biomed. Anal.* **2005**, *38* (1), 60. PMID:15907620.
- (22) Zendelovska, D.; Stafilov, T.; Stefova, M. *Anal. Bioanal. Chem.* **2003**, *376* (6), 848. doi:10.1007/s00216-003-1996-9. PMID:12811463.
- (23) Gil-Agustí, M. S.; Carda-Broch, S.; Capella-Peiró, M. E.; Esteve-Romero, J. *J. Pharm. Biomed. Anal.* **2006**, *41* (4), 1235. doi:10.1016/j.jpba.2006.03.005. PMID:16647237.
- (24) Kinney, C. D.; Kelly, J. G. *J. Chromatogr. A* **1986**, *382*, 377.
- (25) Rahman, N.; Hejaz-Azmi, S. N. *J. Pharm. Biomed. Anal.* **2000**, *24* (1), 33. doi:10.1016/S0731-7085(00)00409-X. PMID:11108537.
- (26) Salama, F. M. *Al-Azhar J. Pharm. Sc.* **1998**, *21*, 75.
- (27) Hassanein, H. H.; Mostafa, S.; Gomaa, M. S. *Egyptian J. Biomed. Sci.* **2005**, *17*, 268.
- (28) Shivramachandra, K.; Rao, B. E. *Indian J. Pharm. Sci.* **1992**, *54* (6), 218.
- (29) Bindu, R.; Chandrasekharan, A. K. *East. Pharm.* **1993**, *36* (429), 123.
- (30) Ayad, M. M.; Shalaby, A.; Abdellatef, H. E.; Hosny, M. M. *Anal. Bioanal. Chem.* **2003**, *376* (5), 710. doi:10.1007/s00216-003-1954-6. PMID:12750873.
- (31) Rahman, N.; Azmi, S. N. H.; Ahmad, Y. *J. Chin. Chem. Soc.* **2007**, *54* (2), 419.
- (32) Rahman, N.; Azmi, S. N. H.; Ahmad, Y. *Microchem. J.* **2000**, *65* (1), 39. doi:10.1016/S0026-265X(00)00025-4.
- (33) El-Didamony, A. M. *Cent. Eur. J. Chem.* **2005**, *3* (3), 520. doi:10.2478/BF02479280.
- (34) Smith, R. M.; Martell, A. E. *NIST Critically Selected Stability Constants of Metal Complexes, Database 46*, Version 8.0; NIST: Gaithersburg, MD, 2004.

# Removal of Cd(II) and Pb(II) complexes with glycolic acid from aqueous solutions on different ion exchangers

Justyna Jachuła, Dorota Kołodyńska, and Zbigniew Hubicki

**Abstract:** The sorption of Cd(II) and Pb(II) ions from aqueous solutions on different ion exchangers was investigated by using glycolic acid (GA) as a complexing agent. Glycolic acid is useful for organic synthesis in oxidation–reduction, esterification, and long-chain polymerization. The experiments were carried out by using the following chelating ion exchangers: Purolite S-930, Purolite S-940, Purolite S-950, Diaion CR-20, and Wofatit MC-50 and the cationic ion exchangers: Purolite C-104, Lewatit CNP-80, and Lewatit SP-112. The influence of the initial concentration of Cd(II) and Pb(II) and glycolic acid, pH of the solution, and phase contact time on the sorption percentage was determined in the batch experiments. Pseudo-first-order and pseudo-second-order kinetic models were used to describe the kinetic data, and the rate constants were evaluated. The experimental data, fitted using the Langmuir and Freundlich adsorption models, were applied to describe the equilibrium isotherms and determined the isotherm constants. The Cd(II) and Pb(II) concentrations in the raffinate were determined by the AAS method.

**Key words:** heavy-metal ions, ion exchangers, glycolic acid, sorption, removal.

**Résumé :** Utilisant l'acide glycolique (AG) comme agent complexant, on a étudié la sorption des ions Cd(II) et Pb(II) présents dans diverses solutions aqueuses sur différents échangeurs d'ions. L'acide glycolique est aussi utile en synthèse organique pour les réactions d'oxydation et de réduction, d'estérification et de polymérisation de longues chaînes. Dans le cadre de notre travail, les expériences ont été effectuées à l'aide des échangeurs d'ions chélatants Purolite S-930, Purolite S-940, Purolite S-950, Diaion CR-20, Wofatit MC-50 ainsi que des échangeurs cationiques Purolite C-104, Lewatit CNP-80 et Lewatit SP-112. Par le biais d'expériences par lots, on a déterminé l'influence de la concentration initiale des ions Cd(II) et Pb(II) et de l'acide glycolique ainsi que du temps de contact sur le pourcentage de sorption. On a utilisé des modèles cinétiques du pseudo-premier ordre et du pseudo-deuxième ordre pour décrire les données cinétiques ainsi que les constantes de vitesse. Les données expérimentales ajustées en faisant appel aux modèles d'adsorption de Langmuir et de Freundlich ont été appliquées pour décrire les isothermes d'équilibre et pour déterminer les constantes isothermes. Les concentrations de cadmium(II) et de plomb(II) dans les raffinats ont été déterminées par une méthode de spectroscopie d'absorption atomique (SAA).

**Mots-clés :** ions de métaux lourds, échangeurs d'ions, acide glycolique, sorption, élimination.

[Traduit par la Rédaction]

## Introduction

The need for clean water increases year by year, and yet water sources are reduced by pollution of our waterways with industrial chemicals.<sup>1</sup> The disposal of effluents containing heavy metals is related to a wide range of industrial operations, such as electroplating, chemical manufacturing, leather tanning, and especially mining and mineral processing. The removal of such contaminants up to the levels approved by national or international agencies could not be entirely solved by conventional methods like precipitation, coagulation, and so forth.<sup>2</sup> Recently, sorption processes have proved to be effective for the removal of pollutants from wastewaters.<sup>3–6</sup>

In recent years, the use of  $\alpha$ -hydroxy acids especially in cosmetic products has greatly expanded.<sup>7–9</sup> The most commonly used in skin products is glycolic acid (hydroxyacetic acid). It is manufactured by bubbling carbon monoxide through formaldehyde, by the action of sodium hydroxide on monochloroacetic acid ( $\text{ClCH}_2\text{CO}_2\text{H} + \text{NaOH} \rightarrow \text{HOCH}_2\text{CO}_2\text{H} + \text{NaCl}$ ), and by the electrolytic reduction of oxalic acid. It is available pure and in aqueous solution. It can be isolated from natural sources, such as sugarcane. Glycolic acid is used in various skin-care products because of its excellent capability of skin penetration. It is also useful for organic synthesis in a range of reactions, including oxidation–reduction, esterification, and long-chain polymerization. It is used as a monomer in the preparation of poly-

Received 2 November 2009. Accepted 10 February 2010. Published on the NRC Research Press Web site at canjchem.nrc.ca on 6 May 2010.

**J. Jachuła, D. Kołodyńska, and Z. Hubicki.**<sup>1</sup> Department of Inorganic Chemistry, Faculty of Chemistry, Maria Curie-Skłodowska University, Maria Curie-Skłodowska Sq. 2, 20-031 Lublin, Poland.

<sup>1</sup>Corresponding author (e-mail: zbigniew.hubicki@poczta.umcs.lublin.pl).



glycolic acid and other biocompatible copolymers (e.g., PLGA).<sup>10</sup> Among others, this compound finds employment in the textile industry, food processing, and ink and paint production.

Previous research confirms the fact that due to the hydroxyl group at the  $\alpha$ -position of the carboxylic acid, hydroxyacetic acid has higher acidity ( $pK_a$  3.83) and stronger chelating properties toward metal ions than an unfunctionalized carboxylic acid ( $pK_a$  4.8).<sup>11–15</sup> Thus, it is used industrially for rust removal, degreasing, and so forth. Novel glycolic acid/platinum complexes have antitumor activity comparable to or more potent than that of *cis*-platinum. It should be added that its nephrotoxicity is very low.<sup>16</sup>

As for the removal of heavy-metal ions from water, among numerous separation techniques, sorption processes can be very useful in terms of technical and economical feasibility. This is attributed to its low cost, easy availability of sorbents, simplicity of design, high efficiency, and easiness of operation.<sup>17</sup>

The aim of this work is to determine the influence of the complexing agent, which is glycolic acid, on the removal of heavy-metal ions from waters and wastewaters. Its influence on the effectiveness of sorption was tested for the chelating ion exchangers: Purolite S-930, Purolite S-940, Purolite S-950, Diaion CR-20, and Wofatit MC-50, and the cationic ion exchangers: Purolite C-104, Lewatit CNP-80, and Lewatit SP-112. The evaluation of different chemical conditions on the ion-exchange capacity and on the kinetics of Cd(II) and Pb(II) complexes with glycolic acid permitted the optimization of heavy-metal removal.

## Materials and methods

### Resin

The chelating ion exchangers Purolite S-930, Purolite S-940, Purolite S-950 (Purolite Int. Ltd.), Diaion CR-20 (Mitsubishi Chemical Corp.), and Wofatit MC-50 (Lanxess) were used together with the cationic ion exchangers Purolite C-104 (Purolite Int. Ltd.), Lewatit CNP-80, and Lewatit SP-112 (Lanxess). Their main characteristics are presented in Table 1. The exchangers were washed with 1 mol/L NaOH and 1 mol/L HCl to remove organic and inorganic impurities and then washed several times with deionised water prior to use.

### Chemicals

Cd(II) and Pb(II) nitrates were obtained from POCh Gliwice. Cd(II) and Pb(II) solutions were prepared by dissolving their nitrates in distilled water. They were diluted to get the solutions of various concentrations. Then, the appropriate amount of glycolic acid solution (denoted in this paper as GA), obtained from PP-H-U Domena Poland, was added.

The initial pH values of the solutions were in the range 3.0 to 3.5. All chemicals used were of analytical reagent-grade. It is well-known that M(II) ions are octahedrally coordinated by one carboxylate O atom and one hydroxyl O atom from each glycolate ligand and two water O atoms in *cis* positions. The general formula of the formed complexes is  $[M(\text{HOCH}_2\text{COO})_2(\text{H}_2\text{O})_2]$ .<sup>18–20</sup>

## Column studies

The breakthrough curves of the Cd(II) and Pb(II) ions in the presence of glycolic acid were determined using 10 mL of the swollen ion exchanger packed in 10 mm diameter glass column with a glass-wool stopper. The prepared solutions of complexed metal ions were passed continuously downwards through the resin beds keeping the flow rate at 0.6 mL/min. The effluent was collected in fractions in which the metal(II) content was determined. The mass ( $D_g$ ) and volume ( $D_v$ ) distribution coefficients as well as the working ( $C_w$ ) and total ( $C_t$ ) ion-exchange capacities were calculated from the determined breakthrough curves according to eqs. [1–3]<sup>21</sup>

$$[1] \quad D_g = \frac{\bar{V} - (V_0 + V_i)}{m_j}$$

$$[2] \quad D_v = \frac{\bar{V} - (V_0 + V_i)}{V_j}$$

$$[3] \quad C_w = \frac{V_e c_0}{V_j}$$

where  $\bar{V}$  is the volume of effluent at  $c = c_0/2$  (determined graphically) (mL),  $V_0$  is the dead volume in the column (liquid volume in the column between the bottom edge of ion-exchanger bed and the outlet) (mL), and  $V_i$  is the void (interparticle) ion-exchanger-bed volume, which amounts to ~40% of the bed volume (mL),  $m_j$  is the dry ion-exchanger mass (g),  $V_j$  is the bed volume (mL),  $V_e$  is the effluent volume to the break point (L), and  $c_0$  is the initial concentration of M(II) solution (mg/L).

The total ion-exchange capacities ( $C_t$ ) were calculated by integration along the curve.

## Batch studies

The sorption of Pb(II) and Cd(II) ions in the presence of glycolic acid on the above-mentioned ion exchangers was investigated by batch operation as a function of the initial concentration of the metal and glycolic acid, pH of the solution, and contact time. The experiments were performed to determine the concentration of the analyzed metals at the equilibrium ( $q_e$ ), at a specific time ( $q_t$ ), and sorption percent ( $S\%$ ). The resin phase concentrations of M(II) at the equilibrium,  $q_e$  (mg/g), at a specific time,  $q_t$  (mg/g), and sorption percent ( $S\%$ ) were obtained according to<sup>22</sup>

$$[4] \quad q_e = \frac{(c_0 - c_e)V}{m}$$

$$[5] \quad q_t = \frac{(c_0 - c_t)V}{m}$$

$$[6] \quad S(\%) = \frac{c_0 - c_t}{c_t} \times 100$$

where  $c_e$  is the concentration of M(II) in the aqueous phase at equilibrium (mg/L),  $c_t$  is the concentration of M(II) in the aqueous phase at time  $t$  (mg/L),  $V$  is the volume of the solution (mL or L),  $m$  is the mass of the ion exchanger (g).

**Table 1.** Characteristics of the ion exchangers.

Ion exchanger	Typical properties				
	Matrix	Active groups	Delivery form	Bead size (mm)	Total capacity (equiv./L)
Purolite C-104	PS-DVB (gel)	Carboxylic	H <sup>+</sup>	0.3–1.2	4.2
Lewatit CNP-80	PA-DVB (macroporous)	Carboxylic	H <sup>+</sup>	0.3–1.6	4.3
Lewatit SP-112	PS-DVB (macroporous)	Sulfonic	Na <sup>+</sup>	0.65	1.7
Purolite S-930	PS-DVB (macroporous)	Iminodiacetic	Na <sup>+</sup>	0.3–1.0	1.6
Purolite S-940	PS-DVB (macroporous)	Aminophosphonic	Na <sup>+</sup>	0.4–0.85	20 g Ca/L
Purolite S-950	PS-DVB (macroporous)	Aminophosphonic	Na <sup>+</sup>	0.3–1.2	2.0
Diaion CR-20	PS-DVB (gel)	Polyamine	H <sup>+</sup>	0.3–0.55	0.8
Wofatit MC-50	PS-DVB (gel)	Iminodiacetic	Na <sup>+</sup>	0.3–1.2	1.2

In the case of the equilibrium and kinetic experiments, 0.2 g of the ion exchanger was added into 100 mL flasks and mixed in 20 mL solution of Pb(II) and Cd(II) ions in the presence of GA. The initial concentration of each solution was  $1 \times 10^{-3}$  mol/L. The flasks were shaken at the constant temperature of 25 °C. The samples were collected at the defined time or at different time intervals. After completion of each batch of experiments, the solution was filtered. The filtrate was analyzed by atomic absorption spectrometry (AAS) to determine the amount of metal left after sorption. The experiments were conducted in the three parallel series. The reproducibility of the measurements was within 5%.

### Adsorption studies

Adsorption isotherm studies were carried out using the batch equilibrium technique. Initial concentrations of the studied solutions were prepared in the range from  $1 \times 10^{-3}$  mol/L to  $2.5 \times 10^{-2}$  mol/L. Ion-exchanger samples (0.2 g) and 20 mL solutions of Cd(II) and Pb(II) ions in the presence of glycolic acid were mixed in 100 mL flasks until equilibrium was reached. The adsorption equilibrium data were fitted into the Langmuir and Freundlich models, which were represented as<sup>23</sup>

$$[7] \quad q_e = \frac{q_0 K_L c_e}{1 + K_L c_e}$$

$$[8] \quad q_e = K_F c_e^{1/n}$$

where  $q_e$  is the equilibrium M(II) ions concentration on the ion exchanger (mg/g),  $q_0$  is the monolayer capacity of the ion exchanger (mg/g),  $K_L$  is the Langmuir adsorption constant (L/mg) related to the free energy of adsorption (L/mg),  $K_F$  is the Freundlich adsorption capacity (mg/g (L/mg)<sup>1/n</sup>), and  $1/n$  is the Freundlich constant related to the surface heterogeneity.

### Desorption studies

To investigate the possibility of repetitive use of the ion exchangers Purolite S-940 and Lewatit SP-112, desorption experiments were conducted under batch experimental conditions, and desorption efficiencies were compared. Samples (0.5 g) of the above-mentioned ion exchangers saturated with Pb(II) ions in the presence of glycolic acid were in contact with 50 mL of different regeneration agents for 2 h. The use of demineralized water showed insignificant metal ions desorption capacity. Therefore, 1 mol/L NaCl, HCl,

HNO<sub>3</sub>, and H<sub>2</sub>SO<sub>4</sub> solutions were selected as the optimal regeneration agents for the systems studied. The amount of metal ions eluted from the solution was then determined and expressed as a desorption efficiency.

### Instruments

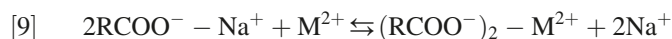
A mechanical shaker (Elpin type 357, Elpin-Plus, Poland) was used for the batch experiments. A pH meter (PHM 84, Radiometer, Denmark) with the glass REF 451 and calomel pHG 201–8 electrodes was used for pH measurements. An atomic absorption spectrometer (ContrAA, Analytic Jena, Germany) was used for quantitative determination of Cd(II) and Pb(II) ions concentrations. An FTIR spectrometer (ALPHA model, including a platinum ATR sampling module with a single-bounce diamond crystal and deuterated triglycine sulfate (DTGS) detector (Bruker Optik GmbH, Germany)) was used to record the FTIR spectra of Lewatit C-104 and Purolite S-930 before and after loading of Pb(II) in the presence of GA in the spectral range 400–4000 cm<sup>-1</sup>.

## Results and discussion

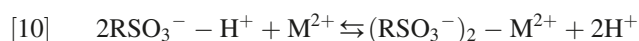
### The spectroscopic analysis

An FTIR spectrometer with ATR module was used to record the IR spectra of the samples. They are presented in Figs. 1 and 2.

In the spectra of the cation exchanger Purolite C-104 (similar to Lewatit CNP-80), which possesses the carboxylic functional groups, appear the bands which are characteristic of the carbonyl group vibrations at about 1698 cm<sup>-1</sup>. After the sorption of Pb(II) ions, a band appears in the range from 1216 to 1163 cm<sup>-1</sup> associated with asymmetric and symmetric vibrations of the carboxylate anion, indicating an ion-exchange mechanism of sorption (Fig. 1). Thus, one can suppose that decomposition of the Pb(II)–GA complex takes place, and the sorption of metal ions occurs

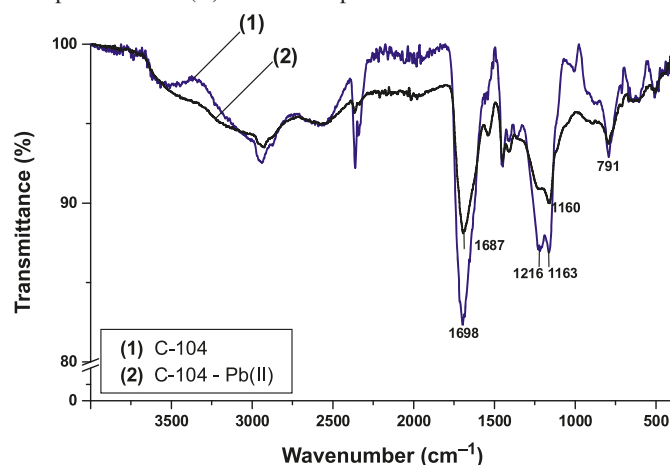


where R is the cation-exchange skeleton. An analogous ion-exchange mechanism can be assumed in the case of Lewatit SP-112 with the sulfonic acid functional groups

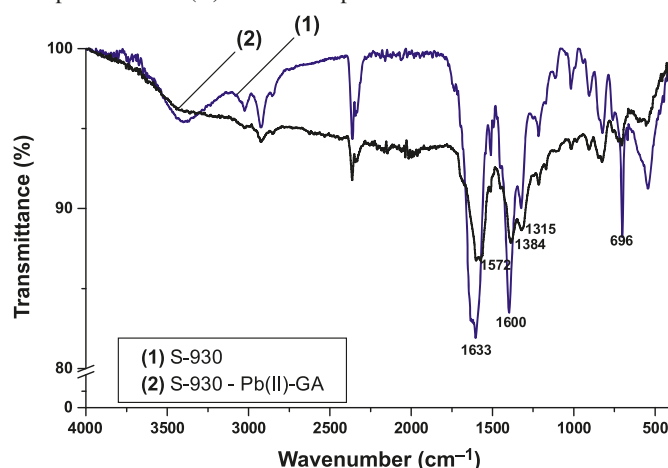


In the case of the chelating ion exchanger Purolite S-930 (Fig. 2) (and Wofatit MC-50) with iminodiacetic functional groups, the bands connected with the presence of carboxyl

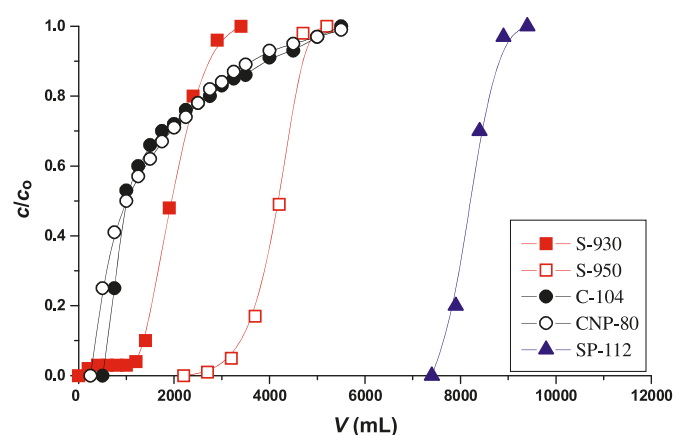
**Fig. 1.** FTIR spectrum of Purolite C-104 before and after the sorption process of Pb(II) ions in the presence of GA.



**Fig. 2.** FTIR spectrum of Purolite S-930 before and after the sorption process of Pb(II) ions in the presence of GA.

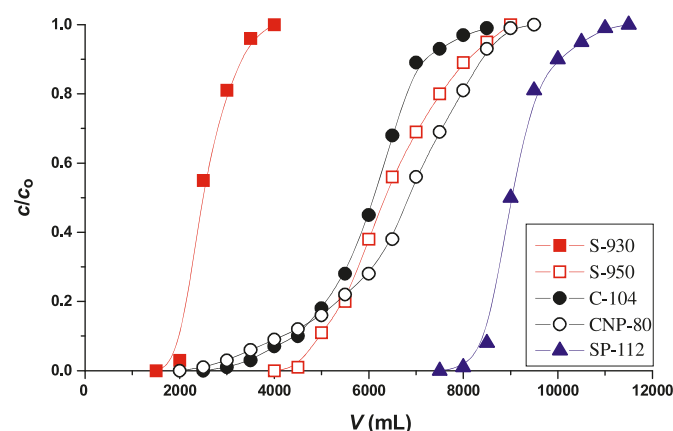


**Fig. 3.** Breakthrough curves of Cd(II) in the presence of GA on Purolite S-930, Purolite S-950, Purolite C-104, Lewatit CNP-80, and Lewatit SP-112.



groups occurring at 1633 cm<sup>-1</sup> and 1601 cm<sup>-1</sup>, respectively, are overlapped by those characteristic of vibrations of the –NH bond observed in the range 1500 to 1650 cm<sup>-1</sup>. After

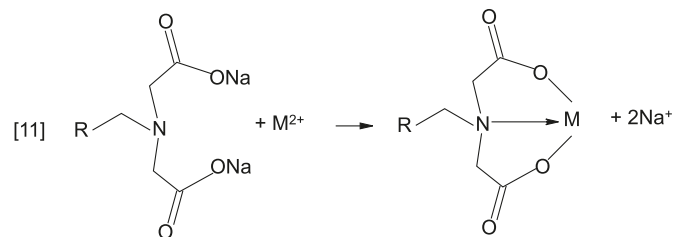
**Fig. 4.** Breakthrough curves of Pb(II) in the presence of GA on Purolite S-930, Purolite S-950, Purolite C-104, Lewatit CNP-80, and Lewatit SP-112.



**Table 2.** Mass ( $D_g$ ) and volume ( $D_v$ ) distribution coefficients as well as working ( $C_w$ ) and total ( $C_r$ ) ion-exchange capacities for Cd(II) and Pb(II) in the presence of GA on Purolite C-104, Lewatit CNP-80, Lewatit SP-112, Purolite S-930, and Purolite S-950.

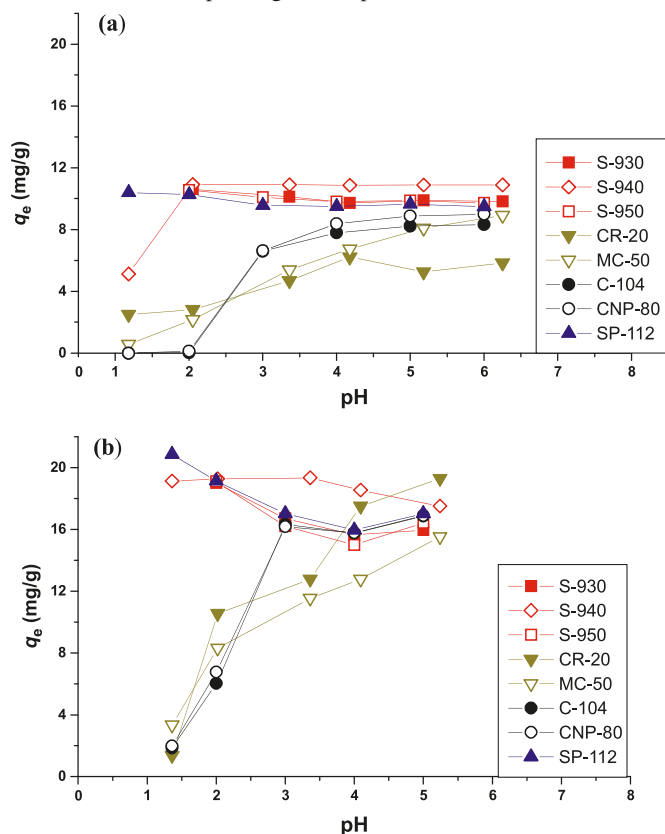
Ion exchanger	$D_g$	$D_v$	$C_w$	$C_r$
<b>Cd(II)</b>				
C-104	501.30	100.76	0.0006	0.0019
CNP-80	560.90	101.24	0.0001	0.0017
SP-112	4394.36	819.94	0.0083	0.0092
S-930	1359.15	193.03	0.0001	0.0022
S-950	2726.18	415.55	0.0025	0.0046
<b>Pb(II)</b>				
C-104	3035.37	610.08	0.0052	0.0123
CNP-80	3782.31	682.67	0.0041	0.0136
SP-112	4838.59	902.83	0.0155	0.0189
S-930	1745.04	193.26	0.0001	0.0024
S-950	4164.25	634.76	0.0083	0.0134

sorption the bands connected with the presence of carboxylate groups are shifted from 1399 cm<sup>-1</sup> and 1328 cm<sup>-1</sup> to 1381 cm<sup>-1</sup> and 1321 cm<sup>-1</sup>. It is well-known that the iminodiacetic functional groups in sodium or hydrogen form chelate heavy-metal ions by ion attraction to the dicarboxylic functionality and electron donation from nitrogen<sup>24</sup>

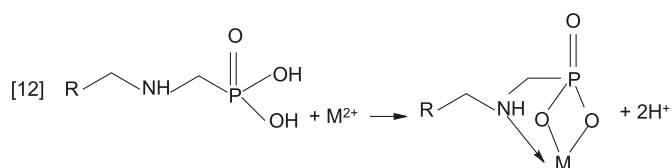


For Purolite S-940 and Purolite S-950 with the amino-phosphonic functional groups, the most favourable model of chelation when the pH increases into the weak-acid region is the formation of a four-membered ring. In this case, these

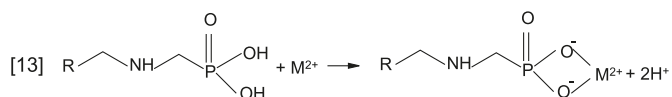
**Fig. 5.** Comparison of the resin phase concentrations of (a) Cd(II) and (b) Pb(II) ions in the presence of GA on the ion exchangers under discussion, depending on the pH value of the solution.



functional groups can act as tridentate ligands and the structure of complexes can be as follows:<sup>25</sup>



In acidic conditions, because of strong protonation, the amino-nitrogen atom does not participate in the bond formation, and complexes without amine-group contribution can also be formed. The most frequent structure is



As for Diaion CR-20 with polyamine functional groups, in the pH range from 4 to 10, it acts as a chelating ion exchanger,<sup>26,27</sup> whereas in acid medium, it behaves as a basic anion exchanger. For Pb(II) and Cd(II) ions in the presence of glycolic acid at pH in the range from 3.0 to 3.5, the sorption process can be analogous to that previously presented for Purolite C-104 or Lewatit SP 112.

## Sorption of Cd(II) and Pb(II) in the presence of glycolic acid

### Dynamic method

As evident from the plots presented in Figs. 3 and 4 and the comparison of the mass ( $D_g$ ) and volume ( $D_v$ ) distribution coefficients as well as the working ( $C_w$ ) and total ( $C_T$ ) ion-exchange capacities of Cd(II) and Pb(II) ions in the presence of GA (Table 2), the highest values of  $D_g$  were obtained on Lewatit SP-112 with the sulfonic acid functional groups. The smallest values were obtained in the case of sorption of Cd(II) in the presence of GA on Lewatit C-104.  $D_v$  values are identical for both Cd(II) and Pb(II) ions in the presence of glycolic acid sorbed on Purolite S-930. The results are also in agreement with the selectivity order of the above-mentioned ion exchangers, which is as follows:

**Purolite C-104** (and also Lewatit CNP-80):  $\text{H}^+ > \text{Ra}^{2+} > \text{Ba}^{2+} > \text{Pb}^{2+} > \text{Sr}^{2+} > \text{Cu}^{2+} > \text{Ca}^{2+} > \text{Zn}^{2+} > \text{Fe}^{2+} > \text{Mg}^{2+} > \text{K}^+ > \text{NH}_4^+ > \text{Na}^+$ .

**Lewatit SP-112:**  $\text{Ba}^{2+} > \text{Pb}^{2+} > \text{Sr}^{2+} > \text{Cu}^{2+} > \text{Ca}^{2+} > \text{Zn}^{2+} > \text{Fe}^{2+} > \text{Mg}^{2+} > \text{K}^+ > \text{NH}_4^+ > \text{Na}^+ > \text{H}^+$ .

**Purolite S-930** (and also Wofatit MC-50):  $\text{Cr}^{3+} > \text{Cu}^{2+} > \text{Ni}^{2+} > \text{Zn}^{2+} > \text{Co}^{2+} > \text{Cd}^{2+} > \text{Fe}^{2+} > \text{Mn}^{2+} > \text{Ca}^{2+} \gg \text{Na}^+$ .

**Purolite S-940** (and also Purolite S-950):  $\text{Pb}^{2+} > \text{Cu}^{2+} > \text{U}^{4+}, \text{Zn}^{2+}, \text{Al}^{3+} > \text{Mg}^{2+} > \text{Sr}^{2+} > \text{Ca}^{2+} > \text{Cd}^{2+} > \text{Na}^+ > \text{Ba}^{2+}$ .

**Diaion CR-20:**  $\text{Hg}^{2+} > \text{Pb}^{2+} > \text{Fe}^{3+} > \text{Cu}^{2+} > \text{Zn}^{2+} > \text{Cd}^{2+} > \text{Ni}^{2+} > \text{Co}^{2+} > \text{Ag}^+ > \text{Mn}^{2+}$ . The Pb(II) ions exhibit higher affinity for these ion exchangers than Cd(II) ions.

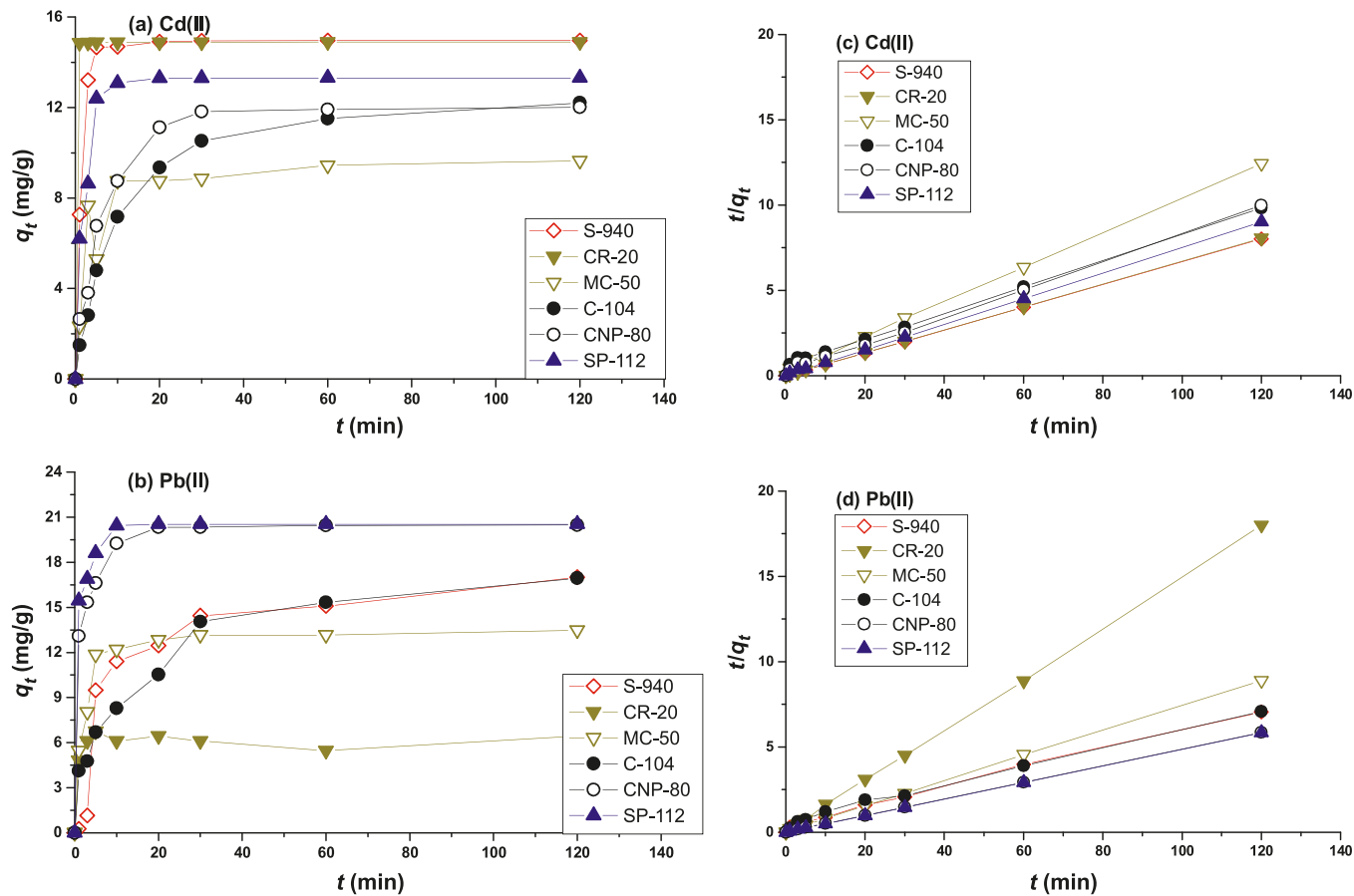
### Batch method

Earlier studies on heavy-metal ion sorption have shown that pH is an important parameter affecting the sorption process. Most metal ions are soluble in water in appropriate pH ranges and are quite insoluble in other cases. Even within the optimal pH ranges for solubility, most metal ions are soluble to only a limited extent. In the presence of complexing agents, the metal ions are capable of remaining in the solution. It was observed that the efficiency of removal of selected heavy-metal complexes does not depend on the pH in all cases. Figures 5a and 5b show the variation of the resin phase concentrations at the equilibrium of Cd(II) and Pb(II) ions in the presence of GA as a function of pH for Purolite S-930, Purolite S-940, Purolite S-950, Diaion CR-20, Wofatit MC-50, Purolite C-104, Lewatit CNP-80, and Lewatit SP-112.

For Purolite S-930, Purolite S-940, Purolite S-950, and Lewatit SP-112, the sorption of Cd(II) ions in the presence of GA slightly depends on the pH. Maximum sorption capacity (6.23 mg/g) for Cd(II) was observed for Diaion CR-20 at pH 4.0. In this case, the sorption percentage ( $S\%$ ) was 57%. For Wofatit MC-50, the highest sorption percentage (81.6% for Cd(II) ions) was observed in the pH range from 4 to 6. For Purolite C-104, the sorption capacities of Cd(II) ions were from 0.03 mg/g at the pH 2.0 to 8.33 mg/g at pH 6.0. For Lewatit CNP-80, the sorption capacities increase from 0.13 mg/g at the pH 2.0 to 9.00 mg/g at pH 6.0. A similar situation was found for the sorption of Pb(II) ions in the presence of GA on the above-mentioned ion exchangers.



**Fig. 6.** Comparison of the sorption capacities (a–b) and the pseudo-second-order kinetic (c–d) for the M(II) ions in the presence of the GA on the chelating ion exchangers Purolite S-940, Diaion CR-20, and Wofatit MC-50 and cationic ion exchangers Purolite C-104, Lewatit CNP-80, and Lewatit SP-112, depending on the phase contact time.



**Table 3.** Kinetic parameters for the M(II) ions in the presence of GA on Purolite S-940, Diaion CR-20, Wofatit MC-50, Purolite C-104, Lewatit CNP-80, and Lewatit SP-112.

Ion exchanger	S-940	CR-20	MC-50	C-104	CNP-80	SP-112
<b>Cd(II) (pseudo-second-order)</b>						
$q_{e,exp}$	14.96	14.90	9.65	12.21	12.02	13.31
$q_2$	15.02	14.92	9.90	13.16	12.35	13.33
$k_2$	0.18	4.50	0.04	0.01	0.03	0.93
$h$	1.39	1.00	4.42	1.68	4.97	1.66
$R^2$	0.999	1.000	0.999	0.999	0.999	1.000
<b>Cd(II) (intraparticle diffusion)</b>						
$k_i$	0.10	0.01	0.53	1.08	0.92	0.52
$R^2$	1.000	0.824	0.499	0.812	0.675	0.409
<b>Pb(II) (pseudo-second-order)</b>						
$q_{e,exp}$	15.09	6.44	13.49	16.95	20.49	20.54
$q_2$	15.02	6.41	13.70	18.87	20.83	20.95
$k_2$	0.633	0.077	0.06	0.01	0.12	0.23
$h$	14.85	3.14	10.99	1.450	2.63	1.00
$R^2$	1.000	0.998	0.999	0.998	1.000	0.999
<b>Pb(II) (intraparticle diffusion)</b>						
$k_i$	1.59	0.04	0.61	1.38	0.65	0.42
$R^2$	0.694	0.045	0.498	0.909	0.590	0.490

**Table 4.** Isotherm parameter values for Cd(II) and Pb(II) ions in the presence of GA in the (1:1) system on Purolite S-930, Purolite S-940, Diaion CR-20, Wofatit MC-50, Purolite C-104, Lewatit CNP-80, and Lewatit SP-112.

Ion exchanger	Langmuir constants			Freundlich constants		
	$q_0$	$K_L$	$R^2$	$K_F$	$n$	$R^2$
<b>Cd(II)</b>						
S-930	111.11	0.066	0.999	9.42	2.39	0.437
S-940	142.85	0.089	0.999	37.58	4.78	0.760
CR-20	35.79	0.002	0.974	0.50	1.78	0.981
MC-50	36.88	0.002	0.813	0.95	2.11	0.906
C-104	40.18	0.005	0.979	1.34	2.11	0.959
CNP-80	16.02	0.025	0.999	4.56	5.43	0.959
SP-112	171.29	0.651	0.993	48.08	5.02	0.636
<b>Pb(II)</b>						
S-930	250.00	0.042	0.999	33.88	3.28	0.681
S-940	357.14	0.007	0.997	12.42	2.15	0.809
CR-20	64.19	0.002	0.977	1.66	2.24	0.883
C-104	94.26	0.004	0.998	1.41	1.76	0.962
CNP-80	70.81	0.008	0.995	10.19	3.94	0.966
SP-112	476.19	0.024	0.998	91.83	4.44	0.669

It was also found that the sorption equilibrium was reached after 120 min, depending on the initial metal ion concentration (Figs. 6a and 6b). For the kinetic data, kinetic analysis was performed with the aid of the pseudo-first- and the pseudo-second-order equations:<sup>28,29</sup>

$$[14] \quad \frac{dq}{dt} = k_1(q_e - q)$$

$$[15] \quad \frac{dq}{dt} = k_2(q_e - q)^2$$

where  $q_e$  and  $q$  are the removal amount of M(II) ions per unit mass of the ion exchanger at equilibrium and time  $t$ , respectively. Figures 6c and 6d show a plot of the linearized form of the pseudo-second-order model according to the equation:

$$[16] \quad \frac{t}{q} = \frac{t}{q_e} + \frac{1}{k_2 q_e^2}$$

for the sorption of M(II) ions in the presence of GA on the chelating ion exchangers Purolite S-940, Diaion CR-20, and Wofatit MC-50 and the cationic ion exchangers Purolite C-104, Lewatit CNP-80, and Lewatit SP-112. As follows from the data presented in Table 3, the correlation coefficients ( $R^2$ ) for the pseudo-second-order kinetic plots were above 0.998 and the calculated sorption capacities ( $q_2$ ) values are also in agreement with experimental values ( $q_{e,exp}$ ). In contrast to the pseudo-second-order kinetic model, the pseudo-first-order model gives a poor correlation ( $R^2$ ) for the sorption of Cd(II) and Pb(II) ions in the presence of GA, and these data are not presented.

In addition to the pseudo-second-order rate equation, the intraparticle diffusion model is commonly used for examining the steps involved during adsorption. It can be expressed as<sup>30</sup>

$$[17] \quad q_t = k_i t^{0.5}$$

where  $k_i$  is the diffusion coefficient ( $\text{mg/g min}^{0.5}$ ).

The results show also that the intraparticle diffusion model does not adequately describe the sorption results of M(II) ions in the presence of GA on the ion exchangers under discussion (Table 3).

#### Adsorption studies

Two important isotherms are selected in this study to optimize the design of adsorption systems. The Langmuir adsorption isotherm assumes that adsorption occurs in specific homogeneous sites within the adsorbent and has found successful application in many adsorption studies of monolayer adsorption. The Freundlich isotherm is an empirical equation employed to describe the heterogeneous system.<sup>28</sup>

Table 4 shows that the values of  $R^2$  suggest that the Langmuir isotherm provides a good model of the sorption system with Purolite S-930, Purolite S-940, Purolite C-104, Lewatit CNP-80, and Lewatit SP-112. For the other ion exchangers, the Freundlich isotherm is more suitable. The sorption capacity for Cd(II) in the presence of GA is the highest in the case of Lewatit SP-112 and Purolite S-940, but the sorption constant,  $K_L$  is the largest for Purolite S-940. For Pb(II) in the presence of GA, the sorption capacity is also high in the case of Lewatit SP-112. The sorption constant,  $K_L$  is the largest for Purolite S-930.

In the case of Cd(II)–GA (1:2) system, the experimental sorption capacities ( $q_{e,exp}$ ) were 103.6 mg/g for Purolite S-930, 133.2 mg/g for Purolite S-940, 32.33 mg/g for Diaion CR-20, 34.23 mg/g for Wofatit MC-50, 34.05 mg/g for Purolite C-104, 12.04 mg/g for Lewatit CNP-80, and 181.16 mg/g for Lewatit SP-112. They are in good agreement with the calculated capacities ( $q_0$ ). In the Pb(II)–GA (1:2) system, the experimental sorption capacities were 243.39 mg/g for Purolite S-930, 332.80 mg/g for Purolite S-940, 62.41 mg/g for Diaion CR-20, 89.95 mg/g for Purolite C-104, 68.21 mg/g for Lewatit CNP-80, and 474.83 mg/g for Lewatit SP-112, and they are also in agreement with the obtained capacities.

The sorption capacity order for the Cd(II)–GA complexes is Lewatit SP-112 > Purolite S-940 > Purolite S-930 > Purolite C-104 > Wofatit MC-50 > Diaion CR-20 > Lewatit CNP-80, and for the Pb(II)–GA complexes, the order is Lewatit SP-112 > Purolite S-940 > Purolite S-930 > Purolite C-104 > Lewatit CNP-80 >> Diaion CR-20.

### Desorption of Pb(II) in the presence of glycolic acid

The desorption process was carried out for the Lewatit SP 112 and Purolite S-940 for which the sorption process was the most effective. From the investigations, the use of 1 mol/L solutions of NaCl, HCl, HNO<sub>3</sub>, and H<sub>2</sub>SO<sub>4</sub> resulted in recovery efficiencies of about 37.8%, 24.8%, 96.4%, and 2% for Pb(II) ions from Lewatit SP 112, respectively. In the case of Purolite S-940, these values were 8.8%, 35.6%, 91.2%, and 1.5%, respectively.

### Conclusion

The present study demonstrates the significant effect of glycolic acid on the removal of Cd(II) and Pb(II) from wastewater. The results reveal the possibly efficient removal of these heavy-metal ions using the chelating ion exchangers Purolite S-940 and Purolite S-930 and the strongly acidic polystyrene cation exchanger Lewatit SP-112.

The sorption process in the presence of glycolic acid as a complexing agent on these ion exchangers was studied as a function of the pH, contact time, and concentration of metal solutions. The pH and initial metal concentration were found to influence the effectiveness of Cd(II) and Pb(II) sorption. Batch equilibrium was reached after about 120 min of the contact. The ion-exchange process, which is pH-dependent, showed the maximum removal of heavy-metal ions in the pH range 4.0–6.0. The experimental data have been analyzed using the Langmuir and Freundlich isotherm models.

The sorption of the studied metal ions in the presence of GA on Purolite S-940, Diaion CR-20, Wofatit MC-50, Purolite C-104, Lewatit CNP-80, and Lewatit SP-112 followed the pseudo-second-order reversible kinetics. Nitric acid was found to be the most effective regenerating agent.

### References

- (1) Todtheide, V.; Laufenberg, G.; Kunz, B. *Desalination* **1997**, *110* (3), 213. doi:10.1016/S0011-9164(97)00100-8.
- (2) Padilla, A. P.; Tavani, E. L. *Desalination* **1999**, *126* (1-3), 219. doi:10.1016/S0011-9164(99)00178-2.
- (3) Ho, Y. S.; McKay, G. *Can. J. Chem. Eng.* **1998**, *76* (4), 822. doi:10.1002/cjce.5450760419.
- (4) Ho, Y. S.; Porter, J. F.; McKay, G. *Water Air Soil Pollut.* **2002**, *141* (1/4), 1. doi:10.1023/A:1021304828010.
- (5) Sarkar, M.; Acharya, P. K.; Bhattacharya, B. *J. Colloid Interface Sci.* **2003**, *266* (1), 28. doi:10.1016/S0021-9797(03)00551-4. PMID:12957578.
- (6) Ho, Y. S. *Carbon* **2004**, *42* (10), 2115. doi:10.1016/j.carbon.2004.03.019.
- (7) Stiller, M. J.; Bartolone, J.; Stern, R.; Smith, S.; Kollias, N.; Gillies, R.; Drake, L. A. *Arch. Dermatol.* **1996**, *132* (6), 631. doi:10.1001/archderm.132.6.631. PMID:8651713.
- (8) Smith, W. P. *Int. J. Cosmet. Sci.* **1996**, *18* (2), 75. doi:10.1111/j.1467-2494.1996.tb00137.x. PMID:19245467.
- (9) Scalia, S.; Callegari, R.; Villani, S. *J. Chromatogr. A* **1998**, *795* (2), 219. doi:10.1016/S0021-9673(97)00973-4. PMID:9528100.
- (10) Rivas, B. L.; Maureira, A. *Inorg. Chem. Commun.* **2007**, *10* (2), 151. doi:10.1016/j.inoche.2006.10.005.
- (11) Zelitch, I. *McGraw-Hill Encyclopedia of Science and Technology*, 7th ed.; New York, 1992; Vol. 13, pp 705–710.
- (12) Guilherme, L. R.; Massabni, A. C.; Cuin, A.; Oliveira, L. A. A.; Castellano, E. E.; Heinrich, T. A.; Costa-Neto, C. M. *J. Coord. Chem.* **2009**, *62*, 1561. doi:10.1080/00958970802663555.
- (13) Ohshima, T.; Yamamoto, Y.; Takaki, U.; Inoue, Y.; Saeki, T.; Itou, K.; Maegawa, Y.; Iwasaki, T.; Mashima, K. *Chem. Commun. (Camb.)* **2009**, (19): 2688. doi:10.1039/b902729g. PMID:19532922.
- (14) Thakkar, A. J.; Kassimi, N. E. B.; Hu, S. *Chem. Phys. Lett.* **2004**, *387* (1-3), 142. doi:10.1016/j.cplett.2004.02.012.
- (15) Calderia, M.; Ramos, M. L.; Gil, V. M. S. *Can. J. Chem.* **1987**, *65*, 827.
- (16) Komura, M. Novel Glycolic Acid Platinum Complexes. European Patent EP0112591, 1986 (Available from www.freepatentsonline.com/EP0112591B1.html) (accessed July, 2009).
- (17) Dorfner, K., Ed.. *Ion Exchangers*; W. de Gruyter: Berlin, New York, 1991.
- (18) Lis, T. *Acta Crystallogr. B* **1980**, *36* (3), 701. doi:10.1107/S0567740880004190.
- (19) Medina, G.; Gasque, L.; Bernés, S. *Acta Crystallogr. C* **2000**, *56* (Pt 6), 637. doi:10.1107/S010827010000161X. PMID:10902001.
- (20) Gao, S.; Huo, L.-H.; Zhang, Z.-Y.; Zhao, H.; Zhao, J.-G. *Acta Cryst.* **2004**, *E60*, 1278.
- (21) Dybczyński, R. *Separation and Preconcentration Methods in Inorganic Trace Analysis*; John Wiley & Sons: New York, 1982.
- (22) McKay, G.; Ho, Y. S.; Ng, J. C. Y. *Separ. Purif. Methods* **1999**, *28* (1), 87. doi:10.1080/03602549909351645.
- (23) Hongxia, Z.; Yongxin, X.; Zuyi, T. *Colloids Surf. A* **2005**, *252* (1), 1. doi:10.1016/j.colsurfa.2004.10.005.
- (24) Sahni, S. K.; Reedijk, J. *Coord. Chem. Rev.* **1984**, *59* (1), 1. doi:10.1016/0010-8545(84)85053-5.
- (25) Arden, T. V. Ion exchangers. In *Principles and Applications, Ullman's Encyclopedia of Industrial Chemistry*, 6th ed.; Wiley-VCH Verlag GmbH, 2001; pp 1–70.
- (26) Okada, T. *Anal. Chim. Acta* **1995**, *303* (2-3), 193. doi:10.1016/0003-2670(94)00541-S.
- (27) Bhandari, V. M.; Yonemoto, T.; Juvekar, V. A. *Chem. Eng. Sci.* **2000**, *55* (24), 6197. doi:10.1016/S0009-2509(00)00212-8.
- (28) Sun, Q. Y.; Lu, P.; Yang, L. Z. *Environ. Geochem. Health* **2004**, *26* (2-3), 311. doi:10.1023/B:EGAH.0000039595.12014.6b. PMID:15499788.
- (29) Tunali, S.; Özcan, A. S.; Özcan, Ö.A.; Gedikbey, T. *J. Hazard. Mater. B* **2006**, *135* (1-3), 141. doi:10.1016/j.jhazmat.2005.11.033.
- (30) Kumar, D.; Singh, A.; Gaur, J. P. *Bioresour. Technol.* **2008**, *99* (17), 8280. doi:10.1016/j.biortech.2008.03.008. PMID:18411047.

# The dehydrogenation of combined organic and inorganic hydrogen-storage carriers

Dominik Wechsler, Boyd Davis, and Philip G. Jessop

**Abstract:** A thermally balanced H<sub>2</sub> storage system can be created by combining an H<sub>2</sub> carrier that releases H<sub>2</sub> endothermically with one that releases H<sub>2</sub> exothermically. Here, we describe combinations of H<sub>2</sub> carriers wherein both carriers release H<sub>2</sub> by dehydrogenation rather than by hydrolysis. The endothermic carriers tested were heterocyclic organic liquids, while the exothermic carriers were amine-borane compounds. The options of having the two carriers chemically bound together or merely physically mixed together were explored. With both options, the exothermic carrier inhibited the endothermic carrier, either by chemically affecting the heterocyclic ring of the endothermic carrier or by decreasing the activity of the heterogeneous dehydrogenation catalyst.

**Key words:** hydrogen storage, dehydrogenation, amine-borane, N-heterocycle, heterogeneous catalyst.

**Résumé :** On peut créer un système de stockage d'hydrogène (H<sub>2</sub>) thermiquement équilibré en combinant un porteur de H<sub>2</sub> qui dégage du H<sub>2</sub> d'une façon endothermique avec un autre qui dégage de l'hydrogène d'une façon exothermique. Dans ce travail, on décrit la combinaison de deux porteurs d'hydrogène qui dégagent de l'hydrogène par déshydrogénation plutôt que par hydrolyse. Les porteurs d'hydrogène endothermiques qui ont été évalués sont des liquides organiques hétérocycliques alors que les porteurs d'hydrogène exothermiques sont des composés amine-borane. On a examiné les options d'utiliser deux porteurs d'hydrogène chimiquement liés ou simplement mélangés d'un point de vue physique. Quelle que soit l'option retenue, le porteur exothermique inhibe le porteur endothermique en affectant d'une façon chimique le noyau hétérocyclique du porteur endothermique ou par une diminution de l'activité du catalyseur hétérogène de déshydrogénation.

**Mots-clés :** entrepose d'hydrogène, déshydrogénation, amine-borane, hétérocycle azoté, catalyseur hétérogène.

[Traduit par la Rédaction]

## Introduction

Increasing concerns about pollution from the use of fossil fuels has resulted in much attention being paid towards renewable energy sources and clean energy carriers, such as hydrogen.<sup>1,2</sup> While fuel cell technologies are advancing,<sup>2,3</sup> the development of hydrogen-storage systems is being stymied by significant technological roadblocks. Currently, several hydrogen-storage systems are being developed, e.g., physical systems involving compressed or adsorbed H<sub>2</sub> and chemical systems, such as metal hydrides and organic liquids.<sup>4-6</sup>

The use of organic liquids<sup>7</sup> (e.g., cyclohexanes, piperidines<sup>8-14</sup>) as hydrogen carriers would be desirable for their ease of transportation, their pumpability, and the reversibility of their dehydrogenation. These can be categorized as endothermic carriers because they release H<sub>2</sub> endothermically, which makes the release more controllable. However, a drawback for implementing these endothermic systems is the energy that must be supplied to satisfy the enthalpy of dehydrogenation (this can significantly detract from the effective energy storage density).

Inorganic hydrogen carriers, such as metal hydrides and boron hydrides, on the other hand, are solids and therefore generally more difficult to handle and impossible to pump. Hydrogen release from these compounds is typically exothermic, and proceeds by either dehydrogenation or hydrolysis. The advantages of these carriers are the significantly higher gravimetric hydrogen-storage densities and the lack of a requirement for heat to be supplied on-board. However, they would require more complicated on-board engineering because they are solids and because the exothermic release of hydrogen results in heat-management issues and the risk of overheating or runaway reaction.

Combining an endothermic (organic) carrier and an exothermic (inorganic) carrier creates a hybrid system that has the advantages of both. The heat released from the exothermic release of H<sub>2</sub> could be transferred to the endothermic carrier, minimizing the need for an external heat source for the release of H<sub>2</sub> from the latter. Dissolving the inorganic carrier in the organic carrier would eliminate the engineering difficulties associated with the use of a solid. The low hydrogen-storage density of the endothermic carrier would be improved by the addition of the exothermic hydrogen

Received 11 August 2009. Accepted 8 October 2009. Published on the NRC Research Press Web site at canjchem.nrc.ca on 11 May 2010.

**D. Wechsler and P.G. Jessop.**<sup>1</sup> Department of Chemistry, Queen's University, Kingston, ON K7L 3N6, Canada.

**B. Davis.** Queen's-RMC Fuel Cell Research Centre, Queen's University, 945 Princess St, 2nd Floor, Kingston, ON K7L 5L9, Canada.

<sup>1</sup>Corresponding author (e-mail: jessop@chem.queensu.ca).



carrier. Finally, the use of a liquid carrier to dissolve the solid carrier means that there is no need for an inert solvent for the latter. In short, the combination of two carriers could solve many of the problems that plague the individual carriers.

We recently reported the production of hydrogen from just such a combination of endothermic (organic) and exothermic (inorganic) hydrogen carriers. Endothermic dehydrogenation of indoline and exothermic hydrolysis of amino boranes (triethylamine-borane, dimethylamine-borane (DMAB), and amino-borane) were achieved together at 100 °C in the presence of palladium on carbon (Pd/C) catalyst. In these successful combinations, the exothermic and endothermic carriers were physically mixed together. When, however, an exothermic carrier was covalently bonded to an endothermic carrier, the H<sub>2</sub> release from the latter was prevented.<sup>15</sup>

We now describe our efforts to produce hydrogen from a similar combination of hydrogen carriers but using dehydrogenation, rather than hydrolysis, of the exothermic carrier. Dehydrogenation is preferred because hydrolysis of boranes puts the products into a large thermodynamic well so that regeneration of the hydrolyzed carrier is chemically challenging and energetically intensive.

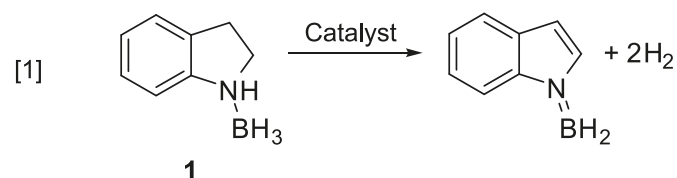
Two separate approaches were considered for combining the two carriers: (i) having both carriers in the same molecule through a chemical bond and (ii) having a physical mixture of the two carriers. Having both carriers in the same molecule is advantageous because accidental phase separation of the two carriers is impossible, energy transfer from the exothermic to the endothermic carrier is facile, and the ratio of exothermic to endothermic carriers is fixed. In our previous study,<sup>15</sup> some inhibition of the indoline dehydrogenation was observed, which could also be a concern with this approach.

Alternatively, having the two carriers physically mixed together, rather than chemically bonded to each other, makes it possible to adjust the molar ratio of the two carriers; this is advantageous to achieve an overall heat balance within the system. The drawback is that new Lewis acid/Lewis base adducts could be formed during the reaction.

## Results and discussion

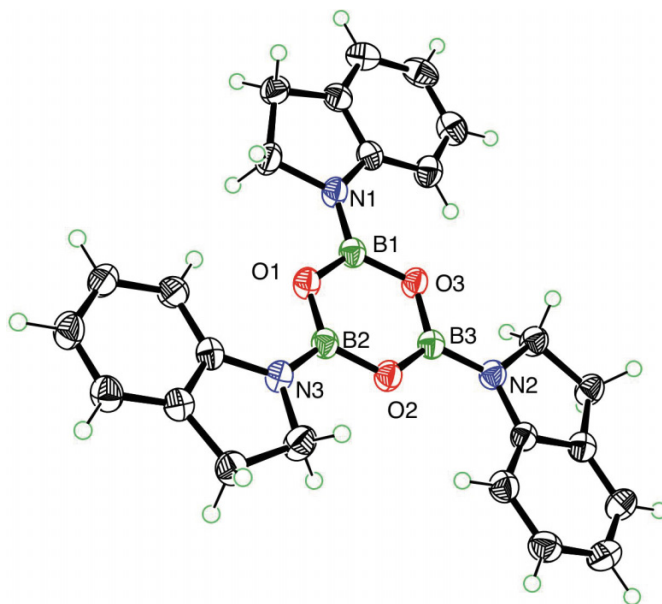
### Exothermic carrier chemically bound to the endothermic carrier

The known<sup>15</sup> indoline-BH<sub>3</sub> adduct (**1**) was first explored for the potential release of 2 equiv. of H<sub>2</sub> in the presence of a heterogeneous catalyst under anhydrous conditions (eq. [1]).



The dehydrogenation of compound **1** was first attempted in toluene in the presence of different heterogeneous platinum-group catalysts (ruthenium on carbon (Ru/C), palladium on carbon (Pd/C), and platinum on carbon (Pt/C)) at 100 °C. In each case, <sup>1</sup>H NMR spectroscopy showed that

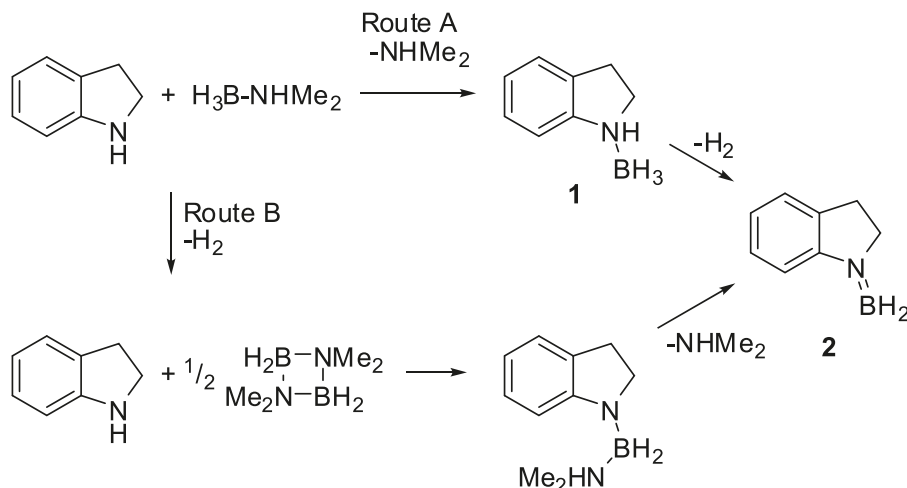
**Fig. 1.** ORTEP diagram of compound **3**, shown with 50% probability ellipsoids.



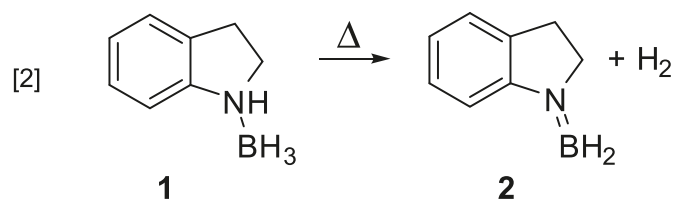
compound **1** had been converted to indoline; the borane fragment had been removed and yet no dehydrogenation of the C–C single bond was observed. No boron-containing species were observed in the liquid phase of the final reaction mixture by <sup>11</sup>B NMR spectroscopy. Once the boron moiety is cleaved from the indoline, one would have expected that the unbound indoline should be easily dehydrogenated. The lack of dehydrogenation must be due to inhibition of the catalyst by boron-containing species.

When rhodium on carbon (Rh/C) was used as the catalyst, a new single boron shift at 20.7 ppm was observed in the <sup>11</sup>B NMR spectrum, while in the <sup>1</sup>H NMR spectrum, several indoline-related compounds were observed including free indoline and compound **1**, but neither indole nor any indole derivatives were observed. No further characterization was attempted because of the mixture of products in the <sup>1</sup>H NMR spectrum. This shows that dehydrogenation of the C–C bond was again inhibited, although in this case it might have been due to boron-induced electronic changes in the indoline ring rather than inhibition of the catalyst.

Because of the loss of the borane moiety in the presence of three catalysts (Ru/C, Pd/C, and Pt/C), we explored the reactivity of **1** without catalyst at 100 °C. Several different atmospheric reaction conditions such as continuous flow of argon, static atmosphere of nitrogen, and under partial vacuum were explored. Evaluation by <sup>1</sup>H and <sup>11</sup>B NMR spectroscopy revealed a change in the chemical shifts of the borane protons and the boron atom. The methylene peaks of **1** (four distinct multiplets) changed to two distinct triplets corresponding to a new compound (**2**) (eq. [2]). The connectivity of **2** was confirmed by standard NMR experiments (<sup>1</sup>H, <sup>13</sup>C{<sup>1</sup>H}, <sup>11</sup>B, <sup>1</sup>H–<sup>1</sup>H COSY, <sup>1</sup>H–<sup>13</sup>C HSQC, and <sup>1</sup>H–<sup>13</sup>C HMB) as well as <sup>1</sup>H{<sup>11</sup>B} and <sup>1</sup>H–<sup>1</sup>H NOESY NMR experiments. In the <sup>1</sup>H{<sup>11</sup>B} spectra, (Fig. S3 in the Supplementary data), the boron moiety was decoupled resulting in a singlet at 5.05 ppm. The structure was further confirmed by through-space <sup>1</sup>H–<sup>1</sup>H NOESY correlations (Fig. S4 in

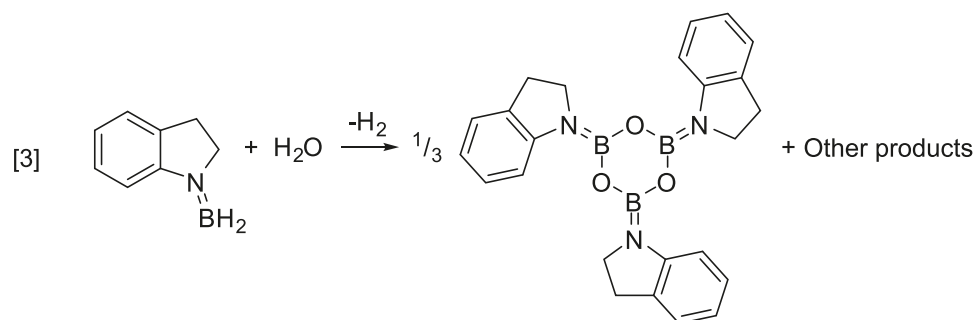
**Scheme 1.** Two possible mechanisms for the reaction between indoline and DMAB.

the Supplementary data) between the aryl protons and the borane protons as well as the methylenes. The formation of analogous compounds  $\text{R}_2\text{NBH}_2$  has been reported previously.<sup>16–19</sup>



Compound **2** is very air- and moisture-sensitive; upon exposure to air for just a few minutes, borane hydrolysis occurs. This has been followed by IR (Fig. S2 in the

Supplementary data) where complete hydrolysis is achieved within 20 min. The addition of 1 (or more) equiv. of water to compound **2** resulted in the loss of the borane moiety and the formation of unbound indoline. However, extremely slow exposure of a solution of **2** in chloroform to air over weeks generated crystals of compound **3**, which were analyzed crystallographically. The suggested chemical transformation is shown in eq. [3]. The ORTEP<sup>20</sup> diagram (Fig. 1) shows that **3** is a trimeric structure having planar geometry at N ( $359.97^\circ$ ) and having an N–B bond length ( $1.411(2) \text{ \AA}$ ) significantly shorter than in  $\text{R}_2\text{HN-BH}_3$  complexes ( $\sim 1.60 \text{ \AA}$ )<sup>15,21–23</sup> but comparable to that in a literature  $[\text{R}_2\text{N-B(OR)}]_2\text{O}$  structure ( $1.407(4) \text{ \AA}$ ).<sup>24</sup> Several attempts to form compound **3** in bulk have been met with no success.



The lack of dehydrogenation at the C–C single bond of **1** shows that having the two carriers in close proximity within the same molecule has its limitations. Therefore, our next strategy was to physically mix an endothermic carrier and an exothermic carrier, rather than chemically attach them to each other.

#### Inorganic carrier physically mixed with the organic carrier

Indoline, DMAB, and Pd/C were combined under an inert

atmosphere<sup>25</sup> and heated at  $100^\circ\text{C}$  for 2 h. By  $^1\text{H}$  NMR spectroscopy, compound **2** was observed with quantitative conversion. Heating indoline and DMAB to  $100^\circ\text{C}$  in the absence of catalyst also resulted in the formation of **2** in greater than 95% yield. At room temperature, no interaction is observed between the two compounds. Two possible pathways for the formation of **2** are depicted in Scheme 1. The first pathway (route A in the scheme) corresponds to the displacement of the dimethylamine moiety by indoline resulting in the in situ formation of **1** followed by B–N dehydrocoupling.

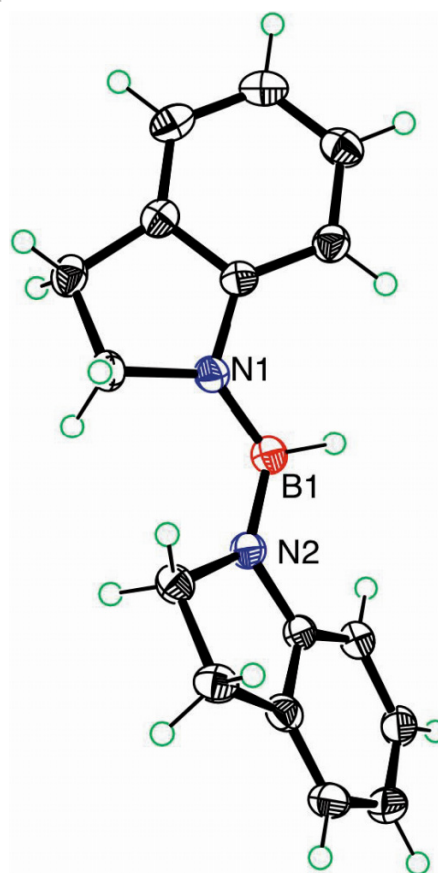
Alternatively (route B), if the DMAB dimer ( $[\text{Me}_2\text{N}-\text{BH}_2]_2$ ) forms first and then indoline breaks up the dimer, the depicted intermediate could be formed followed by the loss of the dimethylamine moiety to form compound **2**.

To determine whether route B is viable, dimethylaminoborane dimer ( $[\text{Me}_2\text{N}-\text{BH}_2]_2$ ) was combined with indoline in chloroform-*d*. Heating the mixture at 55 °C for 2 h provided a second set of indoline peaks as well as new methyl peaks in the  $^1\text{H}$  NMR spectrum. In the  $^{11}\text{B}$  NMR spectrum, two new boron peaks appeared. Upon heating for 20 h, all of the starting materials were consumed. According to the  $^1\text{H}$ ,  $^{13}\text{C}\{^1\text{H}\}$ , and  $^{11}\text{B}$  NMR spectra, there appear to be two major products; in the  $^1\text{H}$  NMR spectrum, a minor product is also observed. In the  $^{11}\text{B}$  NMR spectrum, two equally intense peaks are observed, which correlate to separate proton peaks in the  $^1\text{H}$  NMR spectrum as shown by  $^1\text{H}\{^{11}\text{B}\}$  NMR experiments. In the  $^1\text{H}$  NMR spectrum, there seem to be two major and one minor methyl peaks, while in the  $^{13}\text{C}$  NMR spectrum, two separate methyl carbons with different intensities are observed. Several standard 2D NMR (COSY,  $^1\text{H}-^{13}\text{C}$  HSQC,  $^1\text{H}-^{13}\text{C}$  HMBC),  $^1\text{H}-^1\text{H}$  NOESY, and variable-temperature  $^1\text{H}$  NMR experiments have been performed, but no distinct compound could be characterized.

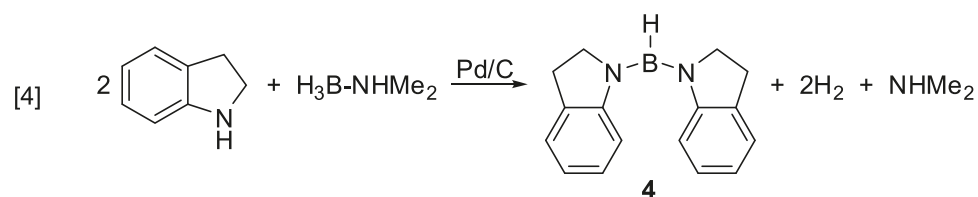
To determine if the dimethylamine moiety can be lost, the mixture of products was taken up in toluene and heated to 100 °C in the presence of Pd/C for 2 h. By NMR spectroscopy, the dimethylamine moiety is still present as well as the methylene peaks of an unidentified boron-adduct of indoline. Because this treatment did not generate compound **2**, we suggest that route B is not viable; route A is therefore considered likely.

The reactivity of indoline with DMAB was also explored at a 2:1 ratio. When 2 equiv. of indoline were combined with DMAB in the presence of Pd/C and heated at 100 °C for 2 h followed by extraction into dichloromethane and cooling at -19 °C, compound **4** was crystallized. Equation [4] shows the assumed stoichiometry. This reaction can also be performed at room temperature; when all reagents are combined, gas evolution is observed within a few minutes. Upon completion of the reaction, the reaction mixture solidified and the product was isolated from the catalyst by extraction with dichloromethane followed by filtration and

**Fig. 2.** ORTEP structure of compound **4**, shown with 50% probability ellipsoids.



removal of solvent in vacuo. The chemical shifts in the  $^1\text{H}$  and  $^{11}\text{B}$  NMR spectra are close to those for **2**. In the crystal structure (Fig. 2), the N atoms are planar [N(1): 359.62(16)° and N(2): 359.59(16)°] and the N–B bond lengths [B(1)–N(1): 1.416(2) Å and B(1)–N(2): 1.412(2) Å] are close to those in compound **3** and to those observed in the literature for hydroboranes with a similar core structure of  $\text{R}_2\text{N}-\text{BH}-\text{NR}_2$  [1.405(3) to 1.428(3) Å].<sup>26</sup>



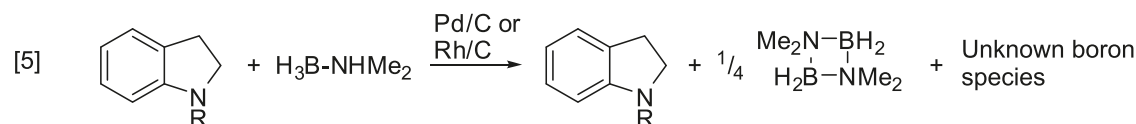
These experiments show that there is a strong tendency for the two hydrogen carriers to chemically combine. One of the reagents needs to be altered to avoid the formation of a Lewis acid/Lewis base adduct.

To determine if adduct formation can be inhibited by making the N atom of the indoline more sterically hindered,

*N*-butylindoline, and *N*-trimethylsilylindoline were synthesized and then heated with DMAB at 100 °C for 2 h over Pd/C. The  $^1\text{H}$  NMR spectrum showed that the *N*-alkylindoline was unchanged; neither dehydrogenation of the C–C bond nor formation of an adduct of *N*-alkylindoline with a boron moiety occurred. The loss of some of the dimethyl-

amine moiety of DMAB was observed by  $^1\text{H}$  NMR spectroscopy. The DMAB dimer and small quantities of boron species (20–28 ppm) were observed by  $^{11}\text{B}$  NMR spectroscopy. When Rh/C was used instead of Pd/C, similar results were obtained except that roughly equal intensities of DMAB dimer and other boron species (26–28 ppm) were observed by  $^{11}\text{B}$  NMR spectroscopy (eq. [5], where the 1:4 ratio of dimer to indoline is based on NMR observations rather than predicted stoichiometry). In the absence of DMAB, com-

plete dehydrogenation of *N*-butylindoline and *N*-trimethylsilylindoline was achieved with Pd/C. The fact that the *N*-alkylindoline did not form an adduct is an indication that the alkyl groups may have added enough steric bulk to prevent the formation of an adduct. Nevertheless, the free *N*-alkylindoline was not dehydrogenated in the presence of DMAB, showing that the catalyst is inhibited by a boron species.



Similar observations have been reported by Manners and co-workers<sup>27</sup> in the dehydrogenation of DMAB, where the heterogeneous metal catalysts were poisoned by “ $\text{BH}_3$ ” generated in metal-assisted adduct dissociation reactions.

## Conclusion

In this paper, we explored two approaches (chemically bound and physically mixed) to combining two independent hydrogen carriers. Attempts to release hydrogen from both carriers, without resorting to hydrolysis, were only partly successful. Hydrogen release from the borane group was achieved while dehydrogenation of the organic carrier was not.

This work has shown that compound **1** (chemically bound inorganic and organic carriers) decomposes in the presence of several catalysts (Ru/C, Pt/C, and Pd/C) to indoline and unknown boron species. The dehydrogenation of the free indoline does not take place, indicating that some boron species is poisoning the catalyst. In the case of Rh/C, although the B–N bond was not cleaved, the indoline dehydrogenation was still inhibited, most likely due to the electron-withdrawing effect of the borane group. In the absence of catalyst, only 1 equiv. of  $\text{H}_2$  was released by dehydrogenation of the B–N bond, forming compound **2**.

The strategy of having the two carriers physically mixed together but chemically separate has also shown limited success. Whenever indoline and DMAB were combined under a variety of conditions, compound **2** was formed. When an extra equivalent of indoline was employed, a 2:1 complex (**4**) was formed. Thus, again, dehydrogenation of the borane was achieved while dehydrogenation of the C–C bond was not.

In an attempt to prevent the borane binding to the organic (endothermic) carrier, *N*-substituted indoline derivatives (*N*-butylindoline and *N*-trimethylsilylindoline) were tested in place of indoline. In the absence of a borane, complete indoline dehydrogenation is achieved in the presence of catalyst. When borane is added, the indoline dehydrogenation is prevented, which suggests that some boron species is inhibiting the catalyst.

This shows that this approach of dehydrogenation of a combination of organic and inorganic hydrogen carriers con-

taining boron does not work because of boron inhibition of the catalyst and possibly electronic effects on the endothermic carrier.

## Experimental methods

### General considerations

Manipulations of air-sensitive compounds were conducted in the absence of oxygen and water under an atmosphere of  $\text{N}_2$  by the use of standard Schlenk methods, utilizing glassware that was oven-dried ( $130^\circ\text{C}$ ) and evacuated while hot prior to use. Indoline (Aldrich) was dried in vacuo at  $80^\circ\text{C}$  for 2 h prior to use. Palladium (10%) on activated carbon (dry powder, Strem Chemicals), platinum (5%) on activated carbon (dry powder, Alfa Aesar), rhodium (5%) on activated carbon (dry powder, Alfa Aesar), ruthenium (5%) on activated carbon (dry powder, Alfa Aesar), and dimethylamine-borane (Alfa Aesar) were used as received. Compound **1** was synthesized via literature methods.<sup>15</sup> Tetrahydrofuran and toluene were obtained from Fisher Scientific and passed through a double-column solvent-purification system purchased from Innovative Technologies, Inc., degassed using three freeze–pump–thaw cycles, and stored over activated molecular sieves (4 Å) prior to use. Dichloromethane ( $\text{CH}_2\text{Cl}_2$ ) (Fisher Scientific) and  $\text{CDCl}_3$  (Aldrich Chemicals) were stirred over  $\text{CaH}_2$  for 7 days, followed by three freeze–pump–thaw cycles, and vacuum transferred into a new flask and stored over activated molecular sieves (4 Å).

$^1\text{H}$ ,  $^{13}\text{C}$ , and  $^{11}\text{B}$  NMR spectra were collected at 300 K on a Bruker AV-400 spectrometer operating at 400.3, 100.7, and 128.4 MHz, respectively, with chemical shifts reported in ppm downfield of  $\text{SiMe}_4$  (for  $^1\text{H}$  and  $^{13}\text{C}$ ) or  $\text{BF}_3\text{--Et}_2\text{O}$  (for  $^{11}\text{B}$ ) unless otherwise stated.  $^1\text{H}$  and  $^{13}\text{C}$  NMR chemical shift assignments were made on the basis of data obtained from  $^1\text{H}$ – $^1\text{H}$  COSY,  $^1\text{H}$ – $^{13}\text{C}$  HSQC, and  $^1\text{H}$ – $^{13}\text{C}$  HMBC NMR experiments.  $^1\text{H}\{^{11}\text{B}\}$  and  $^1\text{H}$ – $^1\text{H}$  NOESY NMR experiments were performed at 300 K on a Bruker AV-600 spectrometer at 600.2 MHz. In some cases, fewer than expected unique  $^{13}\text{C}\{^1\text{H}\}$  NMR resonances were observed. Infrared spectra were recorded with a Nicolet Avatar 360 FTIR E.S.P. instrument using potassium bromide plates.



## Preparation of 1-borylindoline, 2

### Method A

To a round-bottom flask charged with a stir bar, compound **1** (0.036 g, 0.27 mmol) was added and heated at 100 °C under a flow of argon or nitrogen for 1 h. The flask was cooled to room temperature giving a white solid.

### Method B

To a Schlenk flask charged with a stir bar was added indoline (0.397 mL, 3.54 mmol), DMAB (0.209 g 3.54 mmol), and Pd/C (0.075g, 0.070 mmol) followed by heating at 100 °C for 2 h under argon flow. The residue was taken up in chloroform and filtered through a plug of diatomaceous earth. The solvent was removed in vacuo and solid-washed with hexanes yielding a white solid (0.402 g, 3.07 mmol, 87%).

IR:  $\nu$  2490.01  $\text{cm}^{-1}$  for B–H stretch.  $^1\text{H}$  NMR ( $\text{CDCl}_3$ ):  $\delta$  7.30–7.18 (m, 3H, C4–H, C7–H, and C5–H or C6–H), 6.97 (t,  $^3J_{\text{HH}} = 7.4$  Hz, 1H, C5–H or C6–H), 5.17 (v br s, BH<sub>2</sub>), 4.14 (t,  $^3J_{\text{HH}} = 8.5$  Hz, 2H, C2–H<sub>2</sub>), 3.16 (t,  $^3J_{\text{HH}} = 8.5$  Hz, 2H, C3–H<sub>2</sub>).  $^{13}\text{C}\{^1\text{H}\}$  NMR ( $\text{CDCl}_3$ ):  $\delta$  150.6 (C3a), 131.6 (C7a), 127.3 (C5), 124.6 (C4), 120.7 (C6), 111.5 (C7), 49.2 (C2), 30.0 (C3).  $^{11}\text{B}$  NMR ( $\text{CDCl}_3$ ):  $\delta$  25.7.

## Preparation of compound 4

In a Schlenk flask charged with a stir bar, DMAB (0.048 g, 0.81 mmol), and 10% Pd/C (0.026 mg) was added indoline (0.18 mL, 1.62 mmol). The flask was heated at 100 °C for 2 h. Alternatively, if the reaction mixture is left at room temperature, gas evolution is observed over the course of ~1 h followed by the solidifying of the reaction mixture. The product was then extracted with dichloromethane and filtered through diatomaceous earth to remove the catalyst. Removal of the solvent in vacuo resulted in a white solid (0.17 g, 0.70 mmol, 73%). X-ray quality crystals were grown from a solution of dichloromethane at –19 °C under an inert atmosphere.  $^1\text{H}$  NMR ( $\text{CDCl}_3$ ):  $\delta$  7.17–7.05 (m, 3H, C4–H, C7–H and C5–H or C6–H), 6.84 (t,  $^3J_{\text{HH}} = 7.2$  Hz, 1H, C5–H or C6–H), 5.17 (v br s, BH), 4.10 (t,  $^3J_{\text{HH}} = 8.5$  Hz, 2H, C2–H<sub>2</sub>), 3.09 (t,  $^3J_{\text{HH}} = 8.5$  Hz, 2H, C3–H<sub>2</sub>).  $^{13}\text{C}\{^1\text{H}\}$  NMR ( $\text{CDCl}_3$ ):  $\delta$  150.5 (C3a), 131.4 (C7a), 127.1 (C5), 124.5 (C4), 120.6 (C6), 111.4 (C7), 49.1 (C2), 29.9 (C3).  $^{11}\text{B}$  NMR ( $\text{CDCl}_3$ ):  $\delta$  25.4.

## Preparation of N-1-butyldindoline

To a round-bottom Schlenk flask charged with a stir bar, NaH (1.4 g, 0.060 mol), and THF (10 mL) was added indoline (6.7 mL, 0.060 mol). The mixture was allowed to stir overnight (16 h), resulting in a yellow solution. Bromobutane (6.4 mL, 0.060 mol) was slowly added and the reaction mixture was stirred for 4 h resulting in a colorless liquid and a white precipitate. The solvent was removed in vacuo and the product was distilled away from the precipitate under reduced pressure, yielding a colorless liquid (6.9 g, 0.039 mol, 68%).

$^1\text{H}$  NMR ( $\text{CDCl}_3$ ):  $\delta$  7.14–7.10 (m, 2H, aryl–Hs), 6.69 (t,  $^3J_{\text{HH}} = 7.3$  Hz, 1H, aryl–H), 6.53 (d,  $^3J_{\text{HH}} = 8.0$  Hz, 1H, aryl–H), 3.39 (t,  $^3J_{\text{HH}} = 8.3$  Hz, 2H, C2–H<sub>2</sub>), 3.11 (t,  $^3J_{\text{HH}} = 7.3$  Hz, 2H, CH<sub>2</sub>CH<sub>2</sub>CH<sub>2</sub>CH<sub>3</sub>), 3.01 (t,  $^3J_{\text{HH}} = 8.2$  Hz, 2H, C3–H<sub>2</sub>), 1.66 (m, 2H, CH<sub>2</sub>CH<sub>2</sub>CH<sub>2</sub>CH<sub>3</sub>), 1.49 (m, 2H,

CH<sub>2</sub>CH<sub>2</sub>CH<sub>2</sub>CH<sub>3</sub>), 1.04 (t,  $^3J_{\text{HH}} = 7.4$  Hz, 3H, CH<sub>2</sub>CH<sub>2</sub>CH<sub>2</sub>CH<sub>3</sub>).  $^{13}\text{C}\{^1\text{H}\}$  NMR ( $\text{CDCl}_3$ ):  $\delta$  153.0 (quat), 130.1 (quat), 127.4 (aryl–C), 124.5 (aryl–C), 117.3 (aryl–C), 106.9 (aryl–C), 53.2 (CH<sub>2</sub>), 49.1 (CH<sub>2</sub>), 29.7 (CH<sub>2</sub>), 28.7 (CH<sub>2</sub>), 20.6 (CH<sub>2</sub>), 14.2 (CH<sub>3</sub>). NMR data match those reported in the literature.<sup>28,29</sup>

## Preparation of N-trimethylsilylindoline

To a round-bottom Schlenk flask charged with a stir bar, NaH (0.94 g, 0.039 mol), and THF (10 mL) was added indoline (4.4 mL, 0.039 mol). The mixture was allowed to stir overnight (16 h), resulting in a yellow solution. Chlorotrimethylsilane (5.0 mL, 0.039 mol) was added slowly and the reaction mixture was stirred for 4 h resulting in a colorless liquid and a white precipitate. The solvent was removed in vacuo and the product was distilled away from the precipitate under reduced pressure, yielding a colorless oil (6.4 g, 0.033 mol, 86%).  $^1\text{H}$  NMR ( $\text{CDCl}_3$ ):  $\delta$  6.97 (d,  $^3J_{\text{HH}} = 6.8$  Hz, 1H, aryl–H), 6.89 (t,  $^3J_{\text{HH}} = 7.6$  Hz, 1H, aryl–H), 6.54–6.48 (m, 2H, aryl–Hs), 3.52 (t,  $^3J_{\text{HH}} = 8.8$  Hz, 2H, C2–H<sub>2</sub>), 2.91 (t,  $^3J_{\text{HH}} = 8.8$  Hz, 2H, C3–H<sub>2</sub>), 0.20 (s, 9H, Me<sub>3</sub>Si).  $^{13}\text{C}\{^1\text{H}\}$  NMR ( $\text{CDCl}_3$ ):  $\delta$  152.3 (quat), 131.9 (quat), 127.2 (aryl–C), 124.7 (aryl–C), 116.9 (aryl–C), 109.0 (aryl–C), 49.2 (CH<sub>2</sub>), 30.0 (CH<sub>2</sub>), –0.5 (SiMe<sub>3</sub>). The NMR data match those reported in the literature.<sup>30</sup>

## General procedure for dehydrogenation of indoline and amine borane

In a glovebox, a Schlenk flask was charged with a stir bar, catalyst, amine-borane, and indoline and sealed with a rubber septum. The flask was brought out of the glovebox and flushed with argon using a low flow. The flask was then lowered into a preheated 100 °C oil bath, and magnetic stirring was initiated. After 2 h, the flask was removed from the oil bath and allowed to cool to room temperature. Once cooled, the headspace was evacuated and the flask was brought back into the glovebox. The reaction mixture was extracted with  $\text{CDCl}_3$  and analyzed by NMR spectroscopy.

## Crystallographic characterization of 3 and 4

A crystal of the compound was mounted on a glass fiber with grease and cooled to –93 °C in a stream of nitrogen gas controlled with Cryostream Controller 700. Data collection was performed on a Bruker SMART APEX II X-ray diffractometer with graphite-monochromated Mo K $\alpha$  radiation ( $\lambda = 0.71073$  Å), operating at 50 kV and 30 mA over 2 $\theta$  ranges of 4.82–52.00°. No significant decay was observed during the data collection.

Data were processed on a PC using the Bruker AXS Crystal Structure Analysis Package.<sup>31</sup> Data collection: APEX2; cell refinement: APEX2; data reduction: SAINT and XPREP; program used to solve structure: SHELXTL; program used to refine structure: SHELXTL; molecular graphics: SHELXTL; software used to prepare material for publication: SHELXTL. Neutral atom scattering factors were taken from Cromer and Waber.<sup>32</sup> The structures were solved by direct methods. Full-matrix least-square refinements minimizing the function  $\Sigma w(F_o^2 - F_c^2)^2$  were applied to the compounds. All non-hydrogen atoms were refined anisotropically. All of the H atoms were placed in geometrically calculated positions, with C–H = 0.95 (aromatic) and

0.99 (CH<sub>2</sub>) Å, and refined as riding atoms, with  $U_{\text{iso}}(\text{H}) = 1.2 U_{\text{eq}}(\text{C})$ . For compound **4**, the H on the B atom was located from the difference Fourier map and refined without restriction.

Additional crystallographic information is provided in the accompanying CIF files (see Supplementary data).

## Supplementary data

Supplementary data (<sup>13</sup>C{<sup>1</sup>H} NMR spectra for **2** and **4**; <sup>1</sup>H, <sup>13</sup>C{<sup>1</sup>H} and <sup>1</sup>H{<sup>11</sup>B} NMR spectra for indoline-dimethylamino borane adduct; and single-crystal X-ray diffraction data in CIF format for **3** and **4**) for this article are available on the journal Web site (canjchem.nrc.ca). CCDCs 766954 and 766955 contain the X-ray data in CIF format for this manuscript. These data can be obtained, free of charge, via [www.ccdc.cam.ac.uk/conts/retrieving.html](http://www.ccdc.cam.ac.uk/conts/retrieving.html) (Or from the Cambridge Crystallographic Data Centre, 12 Union Road, Cambridge CB2 1EZ, UK; fax +44 1223 336033; or deposit@ccdc.cam.ac.uk).

## Acknowledgement

The authors gratefully acknowledge financial support from the Natural Sciences and Engineering Research Council of Canada (NSERC), the Ontario Centres of Excellence (Energy), Defense Research and Development Canada, AUTO21, Chrysler Canada, the Canada Research Chairs program, Queen's University, and the Ministry of Research and Innovation Ontario.

## References

- Schlapbach, L.; Züttel, A. *Nature* **2001**, *414* (6861), 353. doi:10.1038/35104634. PMID:11713542.
- Felderhoff, M.; Weidenthaler, C.; von Helmolt, R.; Eberle, U. *Phys. Chem. Chem. Phys.* **2007**, *9* (21), 2643. doi:10.1039/b701563c. PMID:17627309.
- Janssen, L. J. J. *J. Appl. Electrochem.* **2007**, *37* (11), 1383. doi:10.1007/s10800-007-9347-8.
- Ni, M. *Energy Explor. Exploit.* **2006**, *24* (3), 197. doi:10.1260/014459806779367455.
- Ross, D. K. *Vacuum* **2006**, *80* (10), 1084. doi:10.1016/j.vacuum.2006.03.030.
- Gray, E. M. *Adv. Appl. Ceram.* **2007**, *106* (1), 25. doi:10.1179/174367607X152380.
- For selected references on hydrogen storage liquids, see: (a) Tsuji, T.; Shinya, Y.; Hiaki, T.; Itoh, N. *Fluid Phase Equilib.* **2005**, *228–229*, 499. doi:10.1016/j.fluid.2004.07.013.; (b) Kariya, N.; Fukuoka, A.; Ichikawa, M. *Appl. Catal. Gen.* **2002**, *233* (1–2), 91. doi:10.1016/S0926-860X(02)00139-4.; (c) Hama, S.; Li, X.; Yukawa, K.; Saito, Y. *Chem. Lett.* **1992**, *21* (12), 2463. doi:10.1246/cl.1992.2463.; (d) Davtyan, O. K.; Burshtein, I. I. *Arm. Khim. Zh.* **1971**, *24*, 1044; (e) Cacciola, G.; Giordano, N.; Restuccia, G. *Int. J. Hydrogen Energy* **1984**, *9* (5), 411. doi:10.1016/0360-3199(84)90062-4.; (f) Touzani, A.; Klvana, D.; Belanger, G. *Int. J. Hydrogen Energy* **1984**, *9* (11), 929. doi:10.1016/0360-3199(84)90158-7.; (g) Klvana, D.; Touzani, A.; Chaouki, J.; Belanger, G. *Int. J. Hydrogen Energy* **1991**, *16* (1), 55. doi:10.1016/0360-3199(91)90060-V.; (h) Pez, G. P.; Scott, A. R.; Cooper, A. C.; Cheng, H.; Bagzis, L. D.; Appleby, J. B. EP 1 660 404, 2006.
- Pez, G. P.; Scott, A. R.; Cooper, A. C.; Cheng, H. US Patent 7,429,372, 2008.
- Moore, A.; Poyatos, M.; Luo, Y.; Crabtree, R. H. *New J. Chem.* **2006**, *30* (11), 1675. doi:10.1039/b608914c.
- Clot, E.; Eisenstein, O.; Crabtree, R. H. *Chem. Commun. (Camb.)* **2007**, (22): 2231. doi:10.1039/b705037b. PMID:17534500.
- Cui, Y.; Kwok, S.; Bucholtz, A.; Davis, B.; Whitney, R. A.; Jessop, P. G. *New J. Chem.* **2008**, *32* (6), 1027. doi:10.1039/b718209k.
- Crabtree, R. H. *Energy Environ. Sci.* **2008**, *1* (1), 134. doi:10.1039/b805644g.
- Pez, G. P.; Scott, A. R.; Cooper, A. C.; Cheng, H.; Wilhelm, F. C.; Abdourazak, A. H. Air Products. US Patent 7 351 395, 2008.
- Toseland, B.; Pez, G.; Puri, P. US Patent 7,485,161, 2009.
- Wechsler, D.; Cui, Y.; Dean, D.; Davis, B.; Jessop, P. G. *J. Am. Chem. Soc.* **2008**, *130* (50), 17195. doi:10.1021/ja806721s. PMID:19053482.
- Euzenat, L.; Horhant, D.; Ribourdouille, Y.; Duriez, C.; Alcaraz, G.; Vaultier, M. *Chem. Commun. (Camb.)* **2003**, (18): 2280. doi:10.1039/b306874a. PMID:14518874.
- Jaska, C. A.; Temple, K.; Lough, A. J.; Manners, I. *J. Am. Chem. Soc.* **2003**, *125* (31), 9424. doi:10.1021/ja030160l. PMID:12889973.
- Jaska, C. A.; Manners, I. *J. Am. Chem. Soc.* **2004**, *126* (31), 9776. doi:10.1021/ja0478431. PMID:15291581.
- Clark, T. J.; Russell, C. A.; Manners, I. *J. Am. Chem. Soc.* **2006**, *128* (30), 9582. doi:10.1021/ja062217k. PMID:16866483.
- Farrugia, L. J. ORTEP-3 for Windows - a version of ORTEP-III with a Graphical User Interface (GUI). *J. Appl. Crystallogr.* **1997**, *30* (5), 565. doi:10.1107/S0021889897003117.
- Amezcu, C. A.; Bell, K. E.; Kelly, H. C. *Inorg. Chim. Acta* **1999**, *290* (1), 80. doi:10.1016/S0020-1693(99)00118-8.
- Chitsaz, S.; Breyhan, T.; Pauls, S.; Neumuller, B. *Z. Anorg. Allg. Chem.* **2002**, *628* (5), 956. doi:10.1002/1521-3749(200206)628:5<956::AID-ZAAC956>3.0.CO;2-4.
- Khasnis, D. V.; Lattman, M.; Siriwardane, U. *J. Chem. Soc. Chem. Commun.* **1989**, 538.
- Tapia-Benavides, A. R.; Cruz, E. M. *Heteroatom Chem.* **2005**, *18*, 513.
- When DMAB and Pd/C were combined in air, immediate release of heat and H<sub>2</sub> was observed showing that if any moisture is present, hydrolysis will occur before the loss of H<sub>2</sub> of DMAB and in turn the dimerization. An inert atmosphere is required.
- Segawa, Y.; Suzuki, Y.; Yamashita, M.; Nozaki, K. *J. Am. Chem. Soc.* **2008**, *130* (47), 16069. doi:10.1021/ja8057919. PMID:18980311.
- Cory, A.; Jaska, C. A.; Clark, T. J.; Clendenning, S. B.; Grozea, D.; Turak, A.; Lu, Z.; Manners, I. *J. Am. Chem. Soc.* **2008**, *130*, 5116.
- Omar-Amrani, R.; Thomas, A.; Brenner, E.; Schneider, R.; Fort, Y. *Org. Lett.* **2003**, *5* (13), 2311. doi:10.1021/ol034659w. PMID:12816436.
- Beller, M.; Breindl, C.; Riermeier, T. H.; Tillack, A. *J. Org. Chem.* **2001**, *66* (4), 1403. doi:10.1021/jo001544m. PMID:11312973.
- Brown, K. L.; Chandra, T.; Zou, S.; Valente, E. J. *Nucleosides Nucleotides Nucleic Acids* **2005**, *24* (8), 1147. doi:10.1081/NCN-200067398. PMID:16270659.
- (a) Bruker AXS Crystal Structure Analysis Package: Bruker. *SHELXT*, version 6.14; Bruker AXS Inc.: Madison, WI,

2000; (b) Bruker. *XPREP*, version 2005/2; Bruker AXS Inc.: Madison, WI, 2005; (c) Bruker. *SAINT*, version 7.23A; Bruker AXS Inc.: Madison, WI, 2005; (d) Bruker. *APEX2*, version 2.0-2; Bruker AXS Inc.: Madison, WI, 2006.

- (32) Waber, J. T. *International Tables for X-ray Crystallography*; Kynoch Press: Birmingham, UK, 1974.

# ESR analysis of the oxidation reactions of phosphorus-containing nitrone-type spin traps with gold(III) ion

Akira Nakajima, Emiko Matsuda, Yuto Ueda, and Kunihiro Tajima

**Abstract:** Phosphorus-containing cyclic nitrones, such as DEPMPO, CYPMPO, and DPPMPO, were oxidized by hydrogen tetrachloroaurate(III) to DEPMPOX, CYPMPOX, and DPPMPOX with the precipitation of Au(0). The reaction was depressed by the addition of chloride or hydroxide ions. The peculiar pH dependency was observed in DEPMPOX, CYPMPOX, and DPPMPOX formation, which should be caused by the diethoxyphosphoryl group in DEPMPO, the 1,3-propoxy cyclophosphoryl group in CYPMPO, and the diphenylphosphinoyl group in DPPMPO. The oxidation of the nitrones proceeded through the ligand exchange of  $\text{Cl}^-$  in  $\text{AuCl}_4^-$  with  $>\text{N}^+-\text{O}^-$  in nitrone and the nucleophilic addition of the water molecule to the C-2 position in the nitrones, the stepwise intra-molecular transfer of three electrons from the nitrones to Au(III), and the release of the resulting Au(0). The phosphoryl group in the nitrones suppressed the first ligand-exchange interaction by its electronegativity, while the group promoted the electron transfer from the nitrones to Au(III) by its inductive effect.

**Key words:** ESR, spin traps, DMPOX, DEPMPO, CYPMPO, DPPMPO, Au(III) ion.

**Résumé :** Phosphore-contenant les nitrones cycliques, tels que DEPMPO, CYPMPO, et DPPMPO, ont été oxydés par le tetrachloroaurate(III) d'hydrogène à DEPMPOX, à CYPMPOX, et à DPPMPOX avec la précipitation d'Au(0). La réaction a été diminuée par l'addition des ions de chlorure ou d'hydroxyde. La dépendance particulière de pH a été observée dans DEPMPOX, CYPMPOX, et la formation de DPPMPOX, qui devrait être causée par le groupe de diethoxyphosphoryl dans DEPMPO, le 1,3-propoxy groupe de cyclophosphoryl dans CYPMPO, et le groupe de diphenylphosphinoyl dans DPPMPO. L'oxydation du nitrones a parcouru les étapes l'interaction d'échange de ligand de  $\text{Cl}^-$  dans  $\text{AuCl}_4^-$  avec  $>\text{N}^+-\text{O}^-$  dans nitrone et l'addition de nucleophilic de la molécule d'eau au C2 position dans le nitrones, le transfert dans-moléculaire disposé en gradins de trois électrons du nitrones à Au(III), et le relâchement du résultant Au(0). Le groupe de phosphoryl dans les nitrones a supprimé la première interaction d'échange de ligand par son electronegativity, alors que le groupe favorisait le transfert d'électron à partir des nitrones à l'Au(III) par son effet inductif.

**Mots-clés :** RPE, piège à spin, DMPOX, DEPMPO, CYPMPO, DPPMPO, ion Au(III).

## Introduction

Phosphorus-containing nitrone-type spin traps should be useful for the trapping of superoxides. First, a spin trap containing phosphorus atom, 5-diethoxyphosphoryl-5-methyl-1-pyrroline *N*-oxide (DEPMPO), was developed for superoxide trapping.<sup>1</sup> Recently, two spin traps containing phosphorus atom, such as 5-(2,2-dimethyl-1,3-propoxycyclophosphoryl)-5-methyl-1-pyrroline *N*-oxide (CYPMPO)<sup>2</sup> and 2-(diphenylphosphinoyl)-2-methyl-3,4-dihydro-2*H*-pyrrole 1-oxide (DPPMPO),<sup>3</sup> were developed and actively used for superoxide trapping.<sup>4-10</sup> The fact that DEPMPO was oxidized to the 5-diethoxyphosphoryl-5-methyl-1-pyrrolid-2-one-*N*-oxyl (DEPMPOX) radical in the biosystems<sup>11</sup> in a manner similar to 5,5-dimethyl-1-pyrroline-*N*-oxide (DMPO)<sup>12-18</sup> required that we analyze the characteristics

of the oxidation reaction of these spin traps containing phosphorus atom.

Previously, we found that cyclic nitrones, such as 5,5-dimethyl-1-pyrroline-*N*-oxide (DMPO), 4-phenyl-5,5-dimethyl-1-pyrroline-*N*-oxide (PDMPO), and 3,3,5,5-tetramethyl-1-pyrroline-*N*-oxide (M4PO), were oxidized by hydrogen tetrachloroaurate(III) ( $\text{HAuCl}_4$ ) to 5,5-dimethyl-1-pyrrolid-2-one-*N*-oxyl (DMPOX), 4-phenyl-5,5-dimethyl-1-pyrrolid-2-one-*N*-oxyl (PDMPOX), and 3,3,5,5-tetramethyl-1-pyrrolid-2-one-*N*-oxyl (M4POX), respectively, through three electron-transfer reactions.<sup>19</sup> As  $\text{HAuCl}_4$  oxidizes the nitrone to DMPOX-type aminoxyl radicals<sup>20</sup> directly without any other radicals, the nitrone- $\text{HAuCl}_4$  system is suitable for the analysis of the mechanism of nitrone oxidation.

Received 5 December 2009. Accepted 22 February 2010. Published on the NRC Research Press Web site at canjchem.nrc.ca on 13 May 2010.

**A. Nakajima.**<sup>1</sup> Section of Obstetrics and Gynecology, Department of Reproductive and Developmental Medicine, Faculty of Medicine, University of Miyazaki, Kiyotake, Miyazaki 889-1692, Japan.

**E. Matsuda.** Section of Chemistry, Department of Medical Science, Faculty of Medicine, University of Miyazaki, Kiyotake, Miyazaki 889-1692, Japan.

**Y. Ueda.** Department of Psychiatry, Faculty of Medicine, University of Miyazaki, Kiyotake, Miyazaki 889-1692, Japan.

**K. Tajima.** Department of Biomolecular Engineering, Kyoto Institute of Technology, Matsugasaki, Sakyo-ku, Kyoto 606-8585, Japan.

<sup>1</sup>Corresponding author (e-mail: akanaka@med.miyazaki-u.ac.jp).



In the present study, we examined the oxidation reaction of spin traps containing phosphorus atoms, such as DEPMPO, CYPMPO, and DPPMPO, with  $\text{HAuCl}_4$  and discussed the reaction profiles of the formation of DMPOX-type aminoxyl radicals.

## Experimental

### Chemicals

Hydrogen tetrachloroaurate(III) ( $\text{HAuCl}_4$ ) dihydrate and other chemicals were obtained from Nacalai Tesque, Kyoto, Japan. DEPMPO was obtained from Alexis Biochemicals, Enzo Life Sciences, Inc., USA; CYPMPO was obtained from Radical Research, Inc., Tokyo, Japan; and DPPMPO was obtained from DOJINDO, Kumamoto, Japan. The molecular structures of the nitrones used in this study are shown in Fig. 1. All nitrones used were examined by ESR, and no radical species were observed.

### ESR measurements

ESR measurements were conducted using procedures nearly identical to those described previously,<sup>19</sup> namely, 40  $\mu\text{L}$  of a  $\text{HAuCl}_4$  solution (1.25 mmol/L) and 40  $\mu\text{L}$  of a nitron solution (1.25 mmol/L) were mixed at pH 4. As DPPMPO formed far smaller amounts of DPPMPOX than other nitrones, experiments were conducted in a solution containing 6.25 mmol/L of  $\text{HAuCl}_4$  and DPPMPO. In the nitron concentration experiments, the desired amounts of the nitrones were mixed with  $\text{HAuCl}_4$  (1.25 mmol/L for DEPMPO and CYPMPO and 6.25 mmol/L for DPPMPO). After aspirating the mixture into a capillary tube, its ESR spectrum was immediately recorded using an X-band ESR spectrometer (JES TE-100, JEOL, Ltd., Tokyo, controlled by a WIN-RAD ESR data analyzer, Radical Research, Inc., Tokyo) under the conditions described previously.<sup>19</sup> For the observation of the hyperfine structure of methyl protons, the modulation width was set to 0.025 mT and the time was set to 8 min. The solution pH was adjusted to the desired value with 0.1 N  $\text{HNO}_3$  and 0.1 N  $\text{NaOH}$  solutions. To avoid the photochemical reduction of Au(III), the reaction was conducted in the darkness. The concentration of the DMPOX-type radical was calibrated using TEMPOL as a standard after double integration of the observed ESR signal. A computer simulation of each ESR spectrum was also conducted using a WIN-RAD ESR data analyzer.

### Gold determination

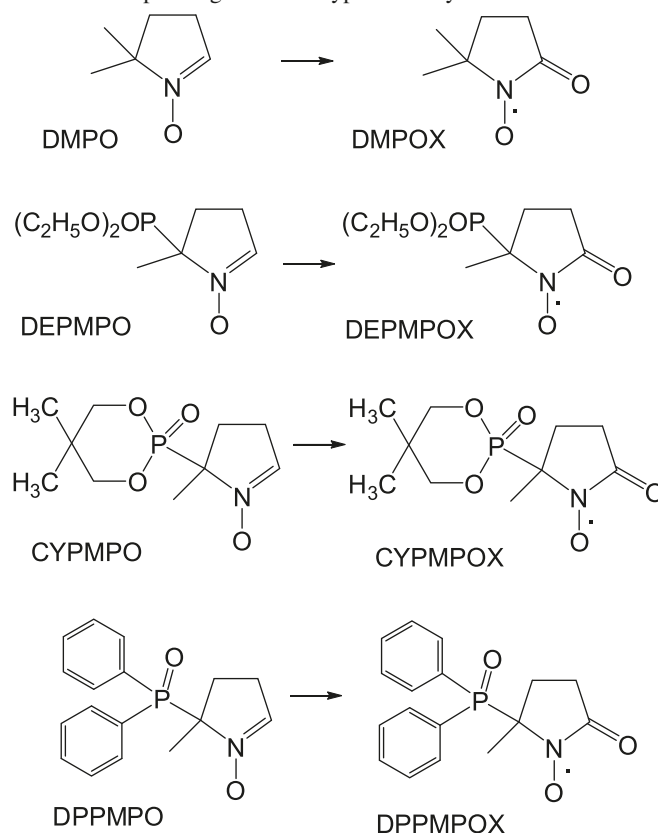
The total amounts of the Au(III) species in the reaction mixture and the resulting amounts of Au(0) were determined as described previously.<sup>19</sup>

## Results

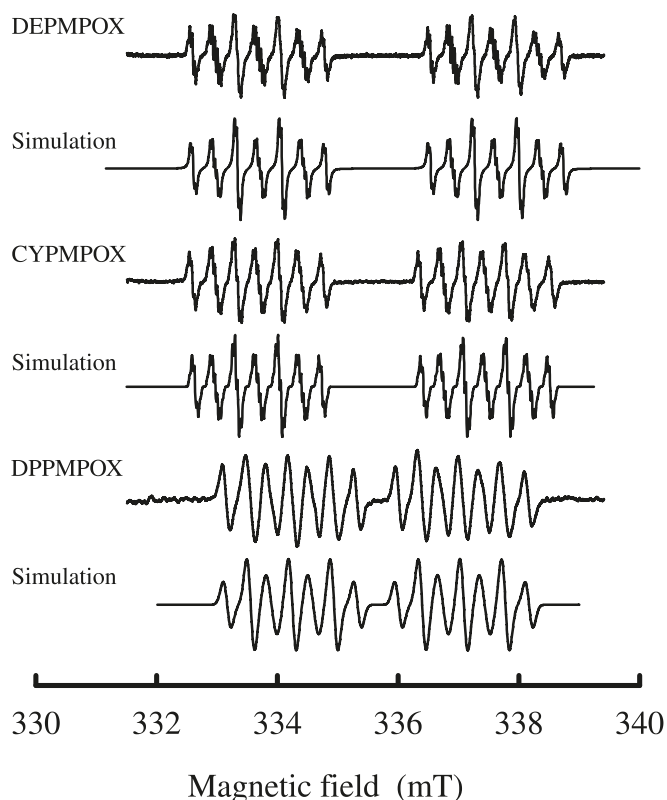
### Formation of aminoxyl radicals in phosphorus-containing nitron- $\text{HAuCl}_4$ solutions

When solutions of phosphorus-containing cyclic nitrones, such as DEPMPO, CYPMPO, and DPPMPO, were mixed with a hydrogen tetrachloroaurate(III) ( $\text{HAuCl}_4$ ) solution at pH 4, ESR signals indicating a large doublet with seven lines appeared (Fig. 2). Two former spectra had some additional small hyperfine structures. Their hyperfine coupling

**Fig. 1.** Molecular structure of phosphorous-containing spin traps and the corresponding DMPOX-type aminoxyl radicals.



**Fig. 2.** ESR spectra of DEPMPOX, CYPMPOX, and DPPMPOX and their computer simulations.



**Table 1.** Hyperfine coupling constants of DMPOX-type aminoxyl radicals.

Aminoxyl radical	Hyperfine coupling constant (mT)				Reference
	$a_N$	$a_{3H^a}$	$a_{H-Me}$	$a_P$	
DMPOX	0.70	0.39			Ref. 19
DEPMPOX	0.67	0.37	0.04	3.78	Present
	0.71	0.30			
CYPMPOX	0.74	0.40	0.04	3.93	Present
		0.33			
DPPMPOX	0.69	0.40		2.84	Present
		0.39			

**Note:** As the C-5 atom in nitrones containing phosphorus atom are chiral, protons combined with C-3 atom are not equivalent in the two isomers.

<sup>a</sup>Hyperfine coupling constant for protons combined with the C-3 atom in nitron.

constants, estimated from a computer simulation, are listed in Table 1. Simulation spectra for the three are shown in Fig. 2 in comparison with the ones observed. From these values, the resultant radicals were identified to be DMPOX-type aminoxyl radicals, DEMPOX, CYPMPOX, and DPPMPOX. The assumed structures of the DMPOX-type aminoxyl radicals containing DMPOX are depicted in Fig. 1 with the corresponding nitrones.

No other free radical species, except DMPOX-type ones, were observed in DEPMPO-Au(III) and CYPMPO-Au(III) solutions for a period of 2 h after the reaction was started. On the other hand, in the DPPMPO-Au(III) solution, an ESR signal with seven lines appeared, superposed upon the DPPMPOX signal. In the present work, we concentrated on DPPMPOX after subtracting the effect of the signal.<sup>21</sup>

### Aspects of DMPOX-type radical formation in cyclic nitron-HAuCl<sub>4</sub> solutions

#### Time course of radical formation

The time course of DMPOX-type aminoxyl radical formation was examined using the mixture of nitrones and HAuCl<sub>4</sub> at pH 4. As shown in Fig. 3, the amounts of DMPOX-type aminoxyl radicals increased with the passing of time and reached a maximum value within 40 min for DEMPOX, 50 min for CYPMPOX, and 15 min for DPPMPOX. As the time courses of the amounts of DMPOX-type aminoxyl radicals indicate the combination of the sigmoid-type curves  $\{1/[1 + \exp(-a(t - b))]\}$  and the exponential decay  $[\exp(-ct)]$ , the reaction mechanisms should be very complicated. However, the decrease of the Au(III) ion in the reaction mixtures obeyed the second-order kinetics, eq. [1], as shown previously<sup>19</sup>

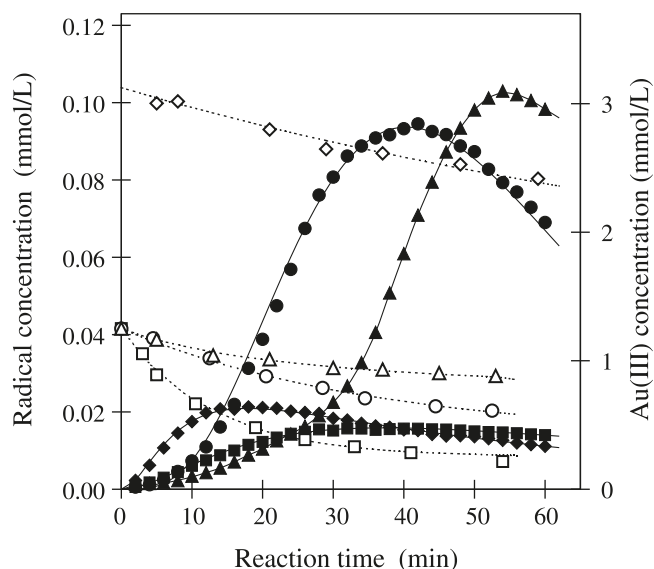
$$[1] \quad d[\text{Au(III)}]/dt = C/[kCt + 1]$$

The kinetic constant,  $k$ , for each nitron is listed in Table 2, as well as the amounts of the DMPOX-type aminoxyl radicals at 60 min after the start of the reaction. As shown in Table 2, the magnitudes of  $k$  are in the order of DMPO > DEPMPO > CYPMPO >> DPPMPO. The amounts of DMPOX-type aminoxyl radicals are in the order of CYPMPO > DEPMPO >> DMPO >> DPPMPO.

#### Effect of solution pH

The effects of the solution pH on the formation of DEPM-

**Fig. 3.** Time course of the aminoxyl radical concentrations and Au(III) concentration in the mixtures of nitrones (1.25 mmol/L and 6.25 mmol/L for DPPMPO) and HAuCl<sub>4</sub> (1.25 mmol/L and 6.25 mmol/L for DPPMPO). The closed circle indicates the amount of DEPMPOX; the closed triangle indicates the amount of CYPMPOX; the closed diamond indicates the amount of DPPMPOX; and the closed square indicates the amount of DMPOX. The open circle indicates the Au(III) concentration in the DEPMPO solution; the open triangle indicates the Au(III) concentration in the CYPMPO solution; the open diamond indicates the Au(III) concentration in the DPPMPO solution; and the open square indicates the Au(III) concentration in the DMPO solution.



POX, CYPMPOX, and DPPMPOX were examined using a mixture of nitrones and HAuCl<sub>4</sub>. As shown in Fig. 4, the amounts of DEPMPOX indicated a maximum at around pH 4 and abruptly decreased above and below pH 4. The amounts of CYPMPOX indicated a maximum at around pH 3 and abruptly decreased above and below pH 3. The amounts of DPPMPOX were far smaller than those of DEPMPOX and CYPMPOX and indicated a maximum at pH 2. The ratios of the chemical species, AuCl<sub>4</sub><sup>-</sup>, Au(OH)Cl<sub>3</sub><sup>-</sup>, Au(OH)<sub>2</sub>Cl<sub>2</sub><sup>-</sup>, Au(OH)<sub>3</sub>Cl<sup>-</sup>, and Au(OH)<sub>4</sub><sup>-</sup>, in the solution, depicted in Fig. 4, were calculated using the parameters listed by Sillen and Martell.<sup>22</sup> As the ratios of AuCl<sub>4</sub><sup>-</sup> and Au(OH)<sub>4</sub><sup>-</sup> in the reaction mixture increased, the

**Table 2.** Second-order rate constants and amounts of DMPOX-type aminoxyl radical formed.

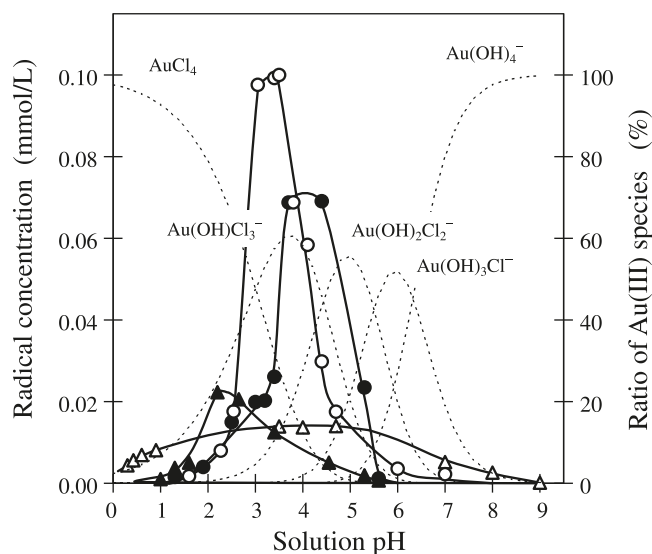
Nitron	$k$ ( $\text{M}^{-1}\text{s}^{-1}$ )	Amounts of free radical at 60 min ( $\text{mmol/L}$ ) <sup>a</sup>	Reference
DMPO	0.043	0.014	Ref. 19
DEPMPO	0.016	0.069	Present
CYPMPO	0.0076	0.098	Present
DPPMPO	0.0017	0.011 <sup>b</sup>	Present

Note:  $[\text{Au(III)}] = C/[kCt + 1]$ .

<sup>a</sup>The initial concentration of each nitron was 2.5 mmol/L and  $\text{HAuCl}_4$ , 2.5 mmol/L.

<sup>b</sup>DPPMPO was 6.25 mmol/L and  $\text{HAuCl}_4$ , 6.25 mmol/L.

**Fig. 4.** Effect of the solution pH on the formation of DMPOX-type aminoxyl radicals in the mixtures of nitrones (1.25 mmol/L for DEPMPO and CYPMPO and 6.25 mmol/L for DPPMPO) and  $\text{HAuCl}_4$  (1.25 mmol/L for DEPMPO and CYPMPO and 6.25 mmol/L for DPPMPO) at each pH for 1 h. The closed circle indicates the amount of DEPMPOX; the open circle indicates the amount of CYPMPOX; the closed triangle indicates the amount of DPPMPOX; and the open triangle indicates the amount of DMPOX. The dotted line indicates the ratios of  $\text{AuCl}_4^-$  and  $\text{Au(OH)}_4^-$  calculated using the formation constants listed by Sillen and Martell.<sup>22</sup>

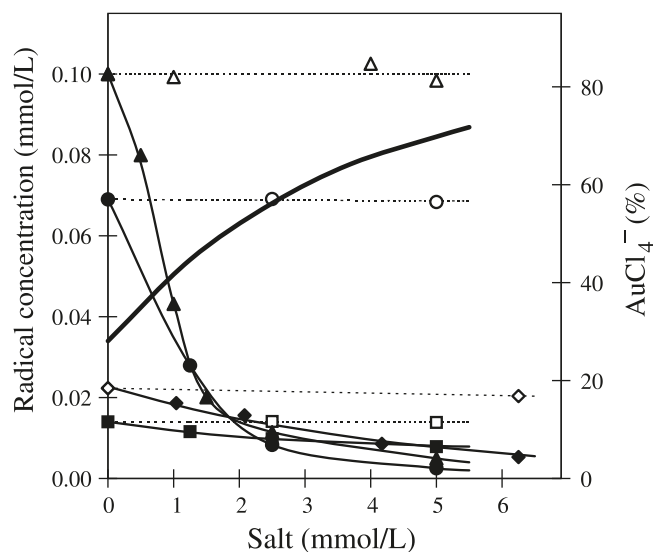


ESR signal intensities decreased. Figure 4 indicates that DMPOX-type aminoxyl radical formations in DEPMPO and CYPMPO solutions were so pH-sensitive that radicals only formed in a very narrow pH range. In other words, the formations of DEPMPOX and CYPMPOX were strongly affected by  $\text{AuCl}_4^-$  and  $\text{Au(OH)}_4^-$ . These results were quite different from those of DMPOX, which formed in a wide pH range.

#### Effect of co-existing salts

The addition of sodium chloride to the reaction mixture markedly decreased the amounts of DEPMPOX, CYPMPOX, and DPPMPOX, while no effect was observed by the addition of  $\text{NaNO}_3$  (Fig. 5). The amounts of  $\text{AuCl}_4^-$  in the solution, depicted in Fig. 5, were calculated using the formation constants listed by Sillen and Martell.<sup>22</sup> As shown in Fig. 5, the formation of a stable complex anion,  $\text{AuCl}_4^-$ , suppressed the redox reaction as described previously.<sup>19</sup> DEPMPOX and CYPMPOX decreased much more heavily with the increase

**Fig. 5.** Effect of sodium salts on the formation of DMPOX-type aminoxyl radicals in the mixtures of nitrones (1.25 mmol/L for DEPMPO, CYPMPO, and DMPO and 6.25 mmol/L for DPPMPO),  $\text{HAuCl}_4$  (1.25 mmol/L for DEPMPO, CYPMPO, and DMPO and 6.25 mmol/L for DPPMPO), and the desired amounts of sodium salts for 1 h. In the  $\text{NaCl}$  solution, the closed circle indicates the amount of DEPMPOX; the closed triangle indicates the amount of CYPMPOX; and the closed diamond and closed square indicate the amount of DMPOX. In the  $\text{NaNO}_3$  solution, the open circle indicates DEPMPOX; the open triangle indicates CYPMPOX; the open diamond indicates DPPMPOX; and the open square indicates DMPOX. The solid thick line indicates the ratio of  $[\text{AuCl}_4^-]$  calculated as described in the legend of Fig. 4.

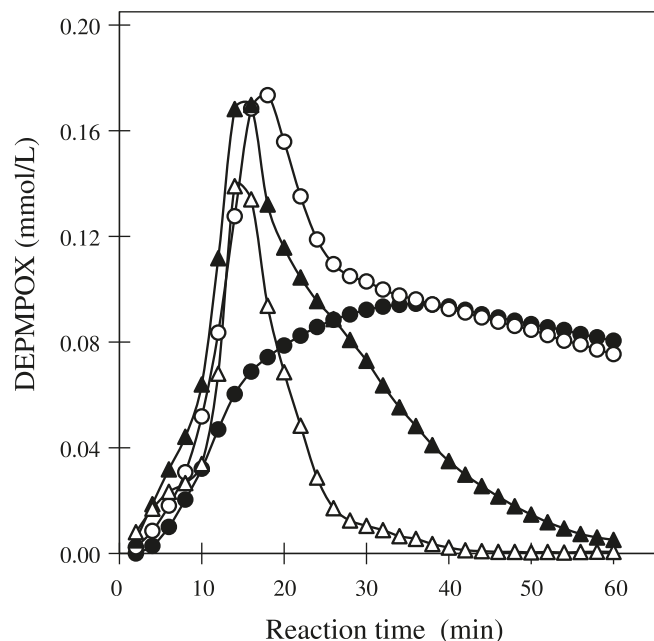


of the  $\text{NaCl}$  concentration than did DMPOX. These results indicated that the formations of DEPMPOX and CYPMPOX were strongly affected by  $\text{AuCl}_4^-$ , as described previously.

#### Effect of nitron concentration

The amounts of DEPMPOX in the solution containing 1.25 mmol/L of DEPMPO increased gradually with time and reached a maximum 40 min after the start of the reaction (Fig. 6). However, in the 3.75 mmol/L DEPMPO solution, the amounts of DEPMPOX reached a maximum 20 min after the start of the reaction and then gradually decreased, in accordance with the decay curve of those in the 1.25 mmol/L DEPMPO solution. In 6.25 and 12.5 mmol/L DEPMPO solutions, the amounts of DEPMPOX reached a maximum 20 min after the start of the reaction and then abruptly decreased to about 0. A similar anomalous nitron concentration effect was found in the DMPOX formation.<sup>19</sup>

**Fig. 6.** Effect of the DEPMPO concentration on the formation of DEPMPOX in the mixtures of desired amounts of DEPMPO and 1.25 mmol/L of  $\text{HAuCl}_4$ . The closed circle indicates 1.25 mmol/L; the open circle indicates 3.75 mmol/L; the closed triangle indicates 6.25 mmol/L; and the open triangle indicates 12.5 mmol/L DEPMPO.



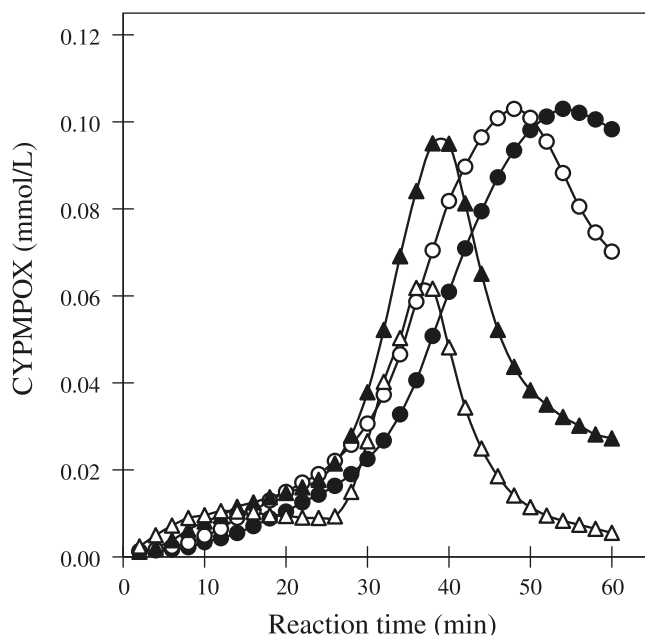
The amounts of CYPMPOX in the solution containing 1.25 mmol/L of CYPMPO increased gradually with time and reached a maximum 54 min after the start of the reaction (Fig. 7). The time required to reach a maximum decreased with a higher CYPMPO concentration (48, 38–40, 36–38 min for 2.5, 6.25, and 12.5 mmol/L CYPMPO, respectively), while the maximum amounts became smaller (0.103, 0.095, and 0.062 mmol/L CYPMPOX for 2.5, 6.25, and 12.5 mmol/L CYPMPO, respectively). The amounts of DPPMPOX in the solution containing 1.25–12.5 mmol/L of DPPMPO increased gradually and reached a maximum 18–20 min after the start of the reaction (Fig. 8). The amounts of DPPMPOX linearly increased with the increase of DPPMPO.

## Discussion

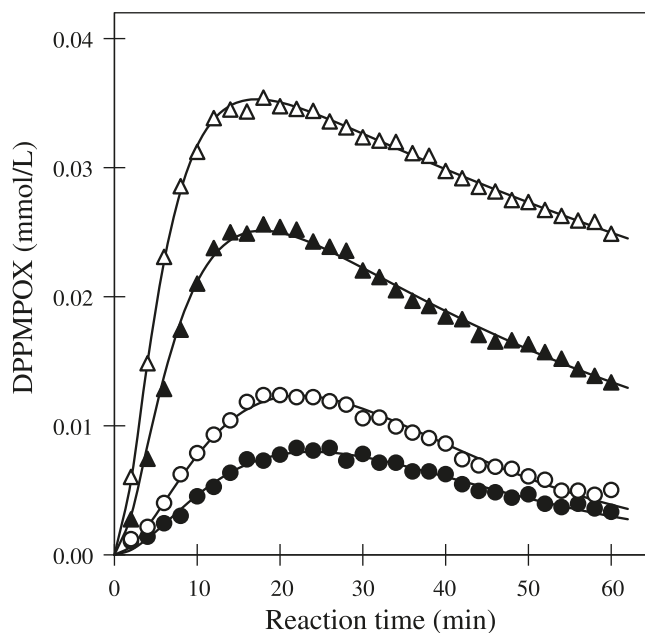
The hyperfine coupling constants of phosphorus in DEPMPOX and CYPMPOX were larger than those of DPPMPOX, while those of nitrogen and  $\beta$ -hydrogen were almost identical among three nitrones. As phosphorus in DPPMPOX belongs to the phosphine oxide group containing only one oxygen atom, the inductive effect of the group is smaller than that of the phosphonic acid group with three oxygen atoms found in DEPMPOX and CYPMPOX. Furthermore, the resonance effect caused by the diphenyl-phosphinoyl group in DPPMPOX also decreases the electron density of the phosphorus atom. The hyperfine coupling constant of phosphorus in DPPMPOX, therefore, becomes smaller than that of the other two, DEPMPOX and CYPMPOX.

In previous work, we showed that the formation of DMPOX-type aminoxyl radicals should proceed through the

**Fig. 7.** Effect of the CYPMPO concentration on the formation of CYPMPOX in the mixtures of CYPMPO (1.25–12.5 mmol/L) and 1.25 mmol/L of  $\text{HAuCl}_4$ . The closed circle indicates 1.25 mmol/L; the open circle indicates 2.5 mmol/L; the closed triangle indicates 6.25 mmol/L; and the open triangle indicates 12.5 mmol/L CYPMPO.

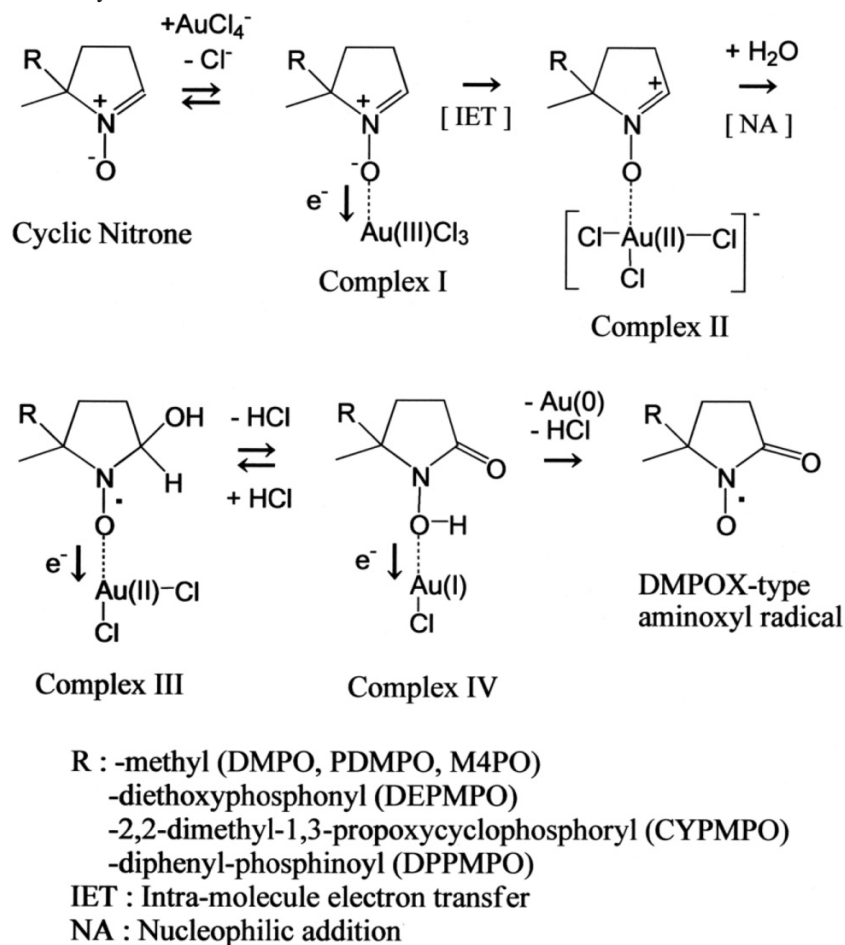


**Fig. 8.** Effect of the DPPMPO concentration on the formation of DPPMPOX in the mixtures of DPPMPO (1.25–12.5 mmol/L) and 6.25 mmol/L of  $\text{HAuCl}_4$ . The closed circle indicates 1.25 mmol/L; the open circle indicates 2.5 mmol/L; the closed triangle indicates 6.25 mmol/L; and the open triangle indicates 12.5 mmol/L DPPMPO.



scheme (Fig. 9) of a ligand exchange of  $\text{Cl}^-$  in  $\text{AuCl}_4^-$  with  $>\text{N}^+-\text{O}^-$  in nitron, a nucleophilic addition of a water molecule to nitron, and a stepwise intramolecular transfer of three electrons from nitron to  $\text{Au(III)}$ .<sup>19</sup> Previously, we showed that substituent groups added to DMPO affected the



**Fig. 9.** Overall reaction scheme of cyclic nitrones and  $\text{HAuCl}_4$ .

reaction aspects. The present results indicated that the substituents had drastic effects.

The first step of the reaction is a ligand exchange interaction of  $\text{Cl}^-$  in  $\text{AuCl}_4^-$  with  $>\text{N}^+-\text{O}^-$  in nitron. As DEPMPO and CYPMPO have large bulky substituents, such as diethoxyphosphonyl and 2,2-dimethyl-1,3-propoxycyclophosphoryl, the steric effect of these substituents hindered the ligand exchange. Furthermore, the inductive effects of these substituents also weakened the ligand exchange. These effects caused the retardation of DMPOX-type radical formation. Therefore, the magnitudes of  $k$  are in the order of  $\text{DMPO} > \text{DEPMPO} > \text{CYPMPO} \gg \text{DPPMPO}$ .

Once the ligand exchange was established, the inductive effect of the phosphonyl group promoted the nucleophilic addition of the water molecule, which caused the formation of large amounts of DEPMPOX and CYPMPOX. On the other hand, DPPMPO, being so hydrophobic and having a large resonance effect by the phosphine group, donated electrons to  $>\text{N}-\text{O}$  against the weak inductive effect, which caused the rapid but smaller formation of DPPMPOX. These discussions successfully explained the facts that the amounts of DMPOX-type aminoxyl radicals are in the order of  $\text{CYPMPO} > \text{DEPMPO} \gg \text{DMPO} \gg \text{DPPMPO}$ .

As the ratios of  $\text{AuCl}_4^-$  and  $\text{Au(OH)}_4^-$  in the reaction mixture increased, the amounts of DMPOX-type radical decreased. These results suggest that the formation of stable complex anions, such as  $\text{AuCl}_4^-$  and  $\text{Au(OH)}_4^-$ , suppresses

the redox reaction, as described previously.<sup>19</sup> As DEPMPOX and CYPMPOX were formed in a very narrow pH range, their formations were strongly affected by  $\text{AuCl}_4^-$ , as observed for the salt effects. As described above, the initial ligand exchange of  $\text{Cl}^-$  in  $\text{AuCl}_4^-$  with  $>\text{N}^+-\text{O}^-$  in nitron was heavily affected by the addition of a phosphonyl group.

Large amounts of DEPMPOX (0.14–0.17 mmol/L) formed rapidly in the solution containing a concentration of DEPMPO higher than 1.25 mmol/L, and a slower increase and decrease were observed with 1.25 mmol/L of DEPMPO, as for the formation of DMPOX.<sup>19</sup> For CYPMPOX formation, a similar rapid increase and decrease were only observed in 1.25 mmol/L of CYPMPO. However, DPPMPOX indicated a slower increase and decrease in the DPPMPO concentration range of 1.25 to 12.5 mmol/L. Previously, we proposed two possible reaction schemes: (i) the elimination of DMPOX by excess amounts of DMPO described by Hill and Thornalley<sup>23</sup> and (ii) the dimerization of DMPOX. Only small amounts of DPPMPOX were formed at a very high DPPMPO concentration; for such a case, scheme (i) was not applicable, and scheme (ii) became more predominant.

## Conclusion

The formation of DMPOX-type aminoxyl radicals in phosphorus-containing cyclic nitrones should proceed through the scheme of the ligand exchange between  $\text{AuCl}_4^-$

and  $>\text{N}^+-\text{O}^-$  in nitron, the nucleophilic addition of a water molecule to nitron, and the stepwise intramolecular transfer of three electrons from nitron to Au(III). Although the phosphonyl groups in DEPMPO and CYPMPO retard the initial step of the reaction, they promote the nucleophilic addition of the water molecule, and, finally, large amounts of DEMPOX and CYPMPOX are formed. DPPMPO, being hydrophobic, formed only small amounts of DPPMPOX. Care should be taken with the oxidation reaction and the formation of DMPOX-type aminoxyl radical in the use of DEPMPO and CYPMPO as spin traps in biosystems. On the other hand, the phosphine group resists the oxidation reaction, which becomes a merit of DPPMPO as a spin trap.

Our former and present investigations on the oxidation of cyclic nitrones with  $\text{HAuCl}_4$  are summarized as follows: From the results of the oxidation reaction of DMPO and HDMPN, a precursor of DMPOX, by  $\text{HAuCl}_4$ , we proposed a reaction scheme containing the ligand exchange between  $\text{Cl}^-$  in  $\text{AuCl}_4^-$  and  $>\text{N}^+-\text{O}^-$  in nitron, the nucleophilic addition of a water molecule to nitron, the stepwise intramolecular transfer of three electrons from nitron to Au(III), and the production of DMPOX-type aminoxyl radical after the release of Au(0). Taking electronic properties, such as the steric and the inductive effects, and hydrophobicity of substituents in cyclic nitrones into consideration, the reaction scheme proposed can explain the behavior for DMPOX-type aminoxyl radical formation with  $\text{HAuCl}_4$  not only for cyclic nitrones having 3,3-dimethyl group, such as PDMPO and M4PO, but also for phosphorus-containing cyclic nitrones, such as DEPMPO, CYPMPO, and DPPMPO. These facts, therefore, give us important information on side reaction of spin trapping.

## Acknowledgements

This work was supported by the Cooperative Grant for Innovative Technology and Advanced Research in Evolutional Areas from the Ministry of Education, Science, Sports, and Culture of Japan, and it was also supported by the Research for Promoting Technological Seeds, No. 1223, Japan Science and Technology Agency.

## References

- (1) Frejaville, C.; Karoui, H.; Tuccio, B.; Le Moigne, F.; Culcasi, M.; Pietri, S.; Lauricella, R.; Tordo, P. *J. Med. Chem.* **1995**, 38 (2), 258. doi:10.1021/jm00002a007. PMID: 7830268.
- (2) Kamibayashi, M.; Oowada, S.; Kameda, H.; Okada, T.; Inanami, O.; Ohta, S.; Ozawa, T.; Makino, K.; Kotake, Y. *Free Radic. Res.* **2006**, 40 (11), 1166. doi:10.1080/10715760600883254. PMID: 17050170.
- (3) Nishizawa, M.; Shioji, K.; Kurauchi, Y.; Okuma, K.; Kohno, M. *Bull. Chem. Soc. Jpn.* **2007**, 80 (3), 495. doi:10.1246/bcsj.80.495.
- (4) Ogura, A.; Oowada, S.; Kon, Y.; Hirayama, A.; Yasui, H.; Meike, S.; Kobayashi, S.; Kuwabara, M.; Inanami, O. *Can. J. Chem.* **2009**, 87 (1), 64. doi:10.1016/j.canlet.2008.11.021. PMID: 19117669.
- (5) Nakamoto, K.; Takayama, F.; Mankura, M.; Hidaka, Y.; Egashira, T.; Ogino, T.; Kawasaki, H.; Mori, A. *J. Clin. Biochem. Nutr.* **2009**, 44 (3), 239. doi:10.3164/jcbrn.08-256. PMID: 19430612.
- (6) Houghton, E. A.; Nicholas, K. M. *J. Biol. Inorg. Chem.* **2009**, 14 (2), 243. doi:10.1007/s00775-008-0444-x. PMID: 18975018.
- (7) Saito, K.; Takahashi, M.; Kamibayashi, M.; Ozawa, T.; Kohno, M. *Free Radic. Res.* **2009**, 43 (7), 668. doi:10.1080/10715760902988850. PMID: 19479584.
- (8) Shioji, K.; Iwashita, H.; Shimomura, T.; Yamaguchi, T.; Okuma, K. *Bull. Chem. Soc. Jpn.* **2007**, 80 (4), 758. doi:10.1246/bcsj.80.758.
- (9) Shimamura, T.; Fujimura, Y.; Ukeda, H. *Anal. Sci.* **2007**, 23 (10), 1233. doi:10.2116/analsci.23.1233. PMID: 17928673.
- (10) Karakawa, T.; Sato, K.; Muramoto, Y.; Mitani, Y.; Kitamada, M.; Iwanaga, T.; Nabeshima, T.; Maruyama, K.; Nakagawa, K.; Ishida, K.; Sasamoto, K. *Biochem. Biophys. Res. Commun.* **2008**, 370 (1), 93. doi:10.1016/j.bbrc.2008.03.048. PMID: 18355451.
- (11) Clement, J.-L.; Gilbert, B. C.; Rockenbauer, A.; Tordo, P. *J. Chem. Soc., Perkin Trans.* **2001**, 2, 1463.
- (12) Floyd, R. A.; Soong, L. M. *Biochem. Biophys. Res. Commun.* **1977**, 74 (1), 79. doi:10.1016/0006-291X(77)91377-8. PMID: 189765.
- (13) Thornalley, P. J.; Trotta, R. J.; Stern, A. *Biochim. Biophys. Acta* **1983**, 759 (1-2), 16. PMID: 6309246.
- (14) Bernofsky, C.; Bandara, B. M. R.; Hinojosa, O. *Free Radic. Biol. Med.* **1990**, 8 (3), 231. doi:10.1016/0891-5849(90)90068-T. PMID: 2160410.
- (15) Shi, X.; Dalal, N. S.; Kasprzak, K. S. *Arch. Biochem. Biophys.* **1992**, 299 (1), 154. doi:10.1016/0003-9861(92)90257-W. PMID: 1332613.
- (16) Makino, K.; Hagi, A.; Ide, H.; Murakami, A.; Nishi, M. *Can. J. Chem.* **1992**, 70 (11), 2818. doi:10.1139/v92-358.
- (17) Mao, G. D.; Thomas, P. D.; Poznansky, M. J. *Free Radic. Biol. Med.* **1994**, 16 (4), 493. doi:10.1016/0891-5849(94)90127-9. PMID: 8005534.
- (18) Ozawa, T.; Miura, Y.; Ueda, J. *Free Radic. Biol. Med.* **1996**, 20 (6), 837. doi:10.1016/0891-5849(95)02092-6. PMID: 8728032.
- (19) Nakajima, A.; Ueda, Y.; Endoh, N.; Tajima, K.; Makino, K. *Can. J. Chem.* **2005**, 83 (8), 1178. doi:10.1139/v05-132.
- (20) Hereafter, DMPOX derivatives are referred to as DMPOX-type aminoxyl radicals.
- (21) As the concentration of the free radical with seven lines is about 10% of DPPMPOX, it should be a byproduct of the oxidation reaction of DPPMPO by  $\text{HAuCl}_4$  rather than an impurity of DPPMPO synthesis. Precise information regarding the radical will be provided in subsequent research.
- (22) Sillen, L. G.; Martell, L. A. E. *Stability Constants of Metal-Ion Complexes*; Suppl. 1, Part I: Inorganic Ligands; The Chemical Society: London, 1971.
- (23) Hill, H. A. O.; Thornalley, P. J. *Inorg. Chim. Acta* **1982**, 67, L35. doi:10.1016/S0020-1693(00)85024-0.

# An efficient and selective method for the preparation of triphenylmethyl ethers of alcohols and nucleosides

Negar Zekri and Reza Fareghi Alamdari

**Abstract:** A very simple and efficient method is described for the protection of alcohols and nucleosides with benzyl monomethoxytrityl and benzyl dimethoxytrityl ethers in the presence of diethylazodicarboxylate and a catalytic amount of ceric triflate. High selectivity was observed for the tritylation of 5'-OH function of nucleosides.

**Key words:** selective hydroxyl-group protection, benzyl dimethoxytrityl ether, ceric triflate, nucleosides.

**Résumé :** On a développé une méthode très simple et efficace de protéger des alcools et des nucléosides par formation d'éthers benzylmonométhoxytrityle et benzyldiméthoxytrityle, en présence d'azodicarboxylate de diéthyle et d'une quantité catalytique de triflate cérique. On a observé une grande sélectivité lors de la tritylation de la fonction 5'-OH des nucléosides.

**Mots-clés :** protection sélective d'un groupe hydroxyle, éther benzyldiméthoxytrityle, triflate cérique, nucléosides.

[Traduit par la Rédaction]

## Introduction

Hydroxyl-group protection is important in the synthesis of some organic molecules. One way to protect hydroxyl groups is to transform the molecules to their corresponding trityl (Tr) ethers.<sup>1</sup> Distinctive features of the trityl group are the following: (i) owing to its bulkiness, selective protection of polyols as monotritylated ethers is easily achieved, (ii) removal (deprotection) of the trityl group is easily affected by the action of mild acids such as formic acid<sup>2</sup> or Amberlyst resin.<sup>3</sup> There are several methods for the preparation of trityl ethers from the corresponding alcohols. Use of trityl chlorides in the presence of pyridine as a base and a solvent seems to be the most popular method for the preparation of trityl ethers.<sup>4,5</sup> This method requires the use of pyridine as a solvent, which is a toxic compound with high boiling point, and needs an aqueous work-up. In addition, this method suffers from prolonged reaction time. Other reagents for the tritylation of alcohols include a complex of trityl chloride and 4-dimethoxytrityl pyridine (DMAP) prepared beforehand.<sup>6</sup>

Selective protection of hydroxyl groups is an important synthetic strategy for the preparation of nucleoside derivatives. This work has been performed with varying degrees of success. The general procedure used for the tritylation of nucleosides is on the basis of that originally developed by Khorona.<sup>7</sup> Using Khorona's procedure for the tritylation of nucleosides, a mixture of monotritylated materials (i.e., 5'-OTr, 2'-OTr, and 3'-OTr) and ditritylated materials (2',5'-OTr, 3',5'-OTr, and 2',3'-OTr) was obtained, and the separation of unreacted remaining starting materials with column

chromatography was very difficult. Hakimelahi et al. reported a method for the tritylation of alcohols and nucleosides by the use of silver ion as catalyst.<sup>8</sup> The use of silver ion for the tritylation of alcohols and nucleosides increased the rate of tritylation, so the selectivity of the tritylation of nucleosides decreased. Recent work has included variations and improvements of the well-established tritylation procedures and the discovery and application of entirely new methods. The use of different reagents and media, such as acid-washed molecular sieves for the tritylation of saccharidic hydroxyls,<sup>9</sup> tetrabutyl ammonium bromide medium for the dimethoxy-tritylation of -OH function of nucleosides,<sup>10</sup> and 1-butyl-3-methylimidazolium chloride for the tritylation of cellulose,<sup>11</sup> is reported. Several other reagents, such as TrODT-TrTCI<sub>5</sub>,<sup>12</sup> AgOTf-TrCl,<sup>13</sup> prenyl trityl ether (PTE)-DDQ,<sup>14</sup> and B(C<sub>6</sub>F<sub>5</sub>)<sub>3</sub>,<sup>15</sup> are also available. However, most of these methods suffer from one or more disadvantages, including long reaction times, vigorous reaction conditions, and poor yields of the products in many cases. Oikawa et al. reported benzyl trityl ether and DDQ as alternative tritylation reagents.<sup>16</sup> However, the conditions of that reaction have been found to have limited applicability, and it is used only for the tritylation of alcohols and not for any nucleosides.

We have reported the deprotection of trityl ethers by the use of a catalytic amount of ceric triflate [Ce(OTf)<sub>4</sub>], and we showed that the rate-determining step of that reaction is involved in the production of trityl cation step.<sup>17</sup> So, we decided to study the tritylation of alcohols and nucleosides by

Received 21 September 2009. Accepted 23 November 2009. Published on the NRC Research Press Web site at canjchem.nrc.ca on 17 May 2010.

**N. Zekri and R.F. Alamdari.**<sup>1</sup> Department of Chemistry and Chemical Engineering, Faculty of Material and Chemical Engineering, Malek-Ashtar University of Technology (MUT), Lavizan, Tehran, P.O. Box 16765-3454, Iran.

<sup>1</sup>Corresponding author (e-mail: reza\_fareghi@yahoo.com).

**Table 1.** Investigation of the effect of various cerium anions and the presence of DEAD on the dimethoxytritylation of alcohols in acetonitrile at room temperature.

$$\text{Ph-CH}_2\text{CH}_2\text{CH}_2\text{OH} + \text{BDTE} \xrightarrow{\text{CH}_3\text{CN, RT}} \text{Ph-CH}_2\text{CH}_2\text{CH}_2\text{ODMT}$$

Entry	Molar Ratio					Time (min)	Yield (%)
	BDTE	DEAD	Ce(OTf) <sub>4</sub>	Ce(NO <sub>3</sub> ) <sub>6</sub> (NH <sub>4</sub> ) <sub>2</sub>	Ce(SO <sub>4</sub> ) <sub>3</sub> (NH <sub>4</sub> ) <sub>2</sub>		
1	1.2	—	0.05	—	—	120	—
2	1.2	1.2	—	—	—	120	—
3	1.2	1.2	0.02	—	—	120	42
4	1.2	1.0	0.05	—	—	120	73
5	1.2	1.2	0.05	—	—	15	95
6	1.2	1.2	—	0.02	—	120	15
7	1.2	1.2	—	0.05	—	90	85
8	1.2	1.2	—	—	0.02	120	27
9	1.2	1.2	—	—	0.05	50	93

the use of benzyl trityl ether (BTE) as well as benzyl monomethoxytrityl (BMTE) and benzyl dimethoxytrityl (BDTE) ethers. In this work, we report a new, mild, and efficient method for hydroxyl-group protection by the reaction of primary, secondary, and tertiary alcohols and nucleosides with BMTE or BDTE ethers and ceric triflate in the presence of diethylazodicarboxylate (DEAD). We found that Ce(OTf)<sub>4</sub> catalyzes the efficient tritylation of alcohols and nucleosides with BMTE and BDTE in the presence of DEAD.

## Experimental

The chemicals were either prepared in our laboratories or purchased from Fluka or Merck Chemical Companies. All yields refer to isolated products after column chromatography. The products were characterized by their spectral data. NMR spectra were recorded on a Bruker advanced DPX-250 MHz, FTNMR spectrometer. Melting points were determined on a Buchi 510 in open capillary tubes circulating oil melting point in open apparatus and are uncorrected. The purity of the substance and the progress of the reactions were monitored by TLC on silica gel polygram SILG/UV254 plates. Column chromatography was carried out on the medium column of silica gel 60 Merck (30–270 mesh) in glass column (1 or 2 cm diameter) using 10–20 g of silica gel per 1 g of mixture.

### General procedure for protection of alcohols and nucleosides with BDTE or BMTE in the presence of Ce(OTf)<sub>4</sub> and DEAD

A solution of alcohol (5 mmol), DEAD (1.05 g, 6 mmol), and BDTE (2.46 g, 6 mmol) or BMTE (2.25 g, 6 mmol) in CH<sub>3</sub>CN (50 mL) was prepared. Ce(OTf)<sub>4</sub> (0.37 g, 0.5 mmol) and activated molecular sieves (4 Å, 2 g) were added to this solution, and the mixture was stirred for a specified time at room temperature. When either the alcohol or BDTE was completely consumed (TLC was used for monitoring), the reaction was quenched by the addition of 50 mL of 5% NaHCO<sub>3</sub>.

The mixture was extracted with chloroform (3 × 35 mL), and the combined extract was dried over Na<sub>2</sub>SO<sub>4</sub>. After evaporation of the solvent, the resulting mixture was introduced into a silica gel column eluted with CH<sub>2</sub>Cl<sub>2</sub>. The pure trityl ethers were obtained in 75%–95% yields (Tables 1

and 2). The effect of different solvents on the yield of the reaction is presented in Table 3.

### A typical procedure for the preparation of diphenylmethyl dimethoxytrityl ether with BDTE and DEAD in the presence of Ce(OTf)<sub>4</sub>

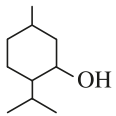
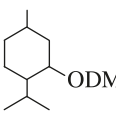
A solution of benzhydrol (0.92 g, 5 mmol), DEAD (1.05 g, 6 mmol), and BDTE (2.46 g, 6 mmol) in CH<sub>3</sub>CN (50 mL) was prepared. Ce(OTf)<sub>4</sub> (0.37 g, 0.5 mmol) and activated molecular sieves (4 Å, 2 g) were added to this solution, and the mixture was stirred for a specified time (1.5 h) at room temperature. When either the alcohol or BDTE was completely consumed (TLC was used for monitoring), the reaction was quenched by the addition of 50 mL of 5% NaHCO<sub>3</sub>. The mixture was extracted with chloroform (3 × 35 mL), and the combined extract was dried over Na<sub>2</sub>SO<sub>4</sub>. After evaporation of the solvent, the resulting mixture was introduced into a silica gel column eluted with CH<sub>2</sub>Cl<sub>2</sub>. The pure diphenylmethyl dimethoxytrityl ether was obtained as a pale yellow solid in 82% yield (Table 2); mp 62 °C. *R*<sub>f</sub> (EtOAc:*n*-hexane, 8:2): 0.3. <sup>1</sup>H NMR (CDCl<sub>3</sub>, ppm) δ: 7.49–6.91 (m, 23H, Ph–), 5.36 (s, 1H, CH–), 3.77 (s, 6H, CH<sub>3</sub>–).

### Preparation of 5'-*O*-monomethoxytrityl thymidine with BMTE and DEAD in the presence of Ce(OTf)<sub>4</sub>

A suspension of thymidine (0.48 g, 2 mmol), DEAD (0.42 g, 2.4 mmol), and BMTE (0.9 g, 2.4 mmol) in CH<sub>3</sub>CN (50 mL) was prepared. Ce(OTf)<sub>4</sub> (147.2 mg, 0.2 mmol) and activated molecular sieves (4 Å, 2 g) were added to this solution, and the mixture was stirred for the specified time at room temperature. When either the alcohol or BMTE was completely consumed (TLC was used for monitoring), the reaction was quenched by the addition of 50 mL of 5% NaHCO<sub>3</sub>. The mixture was extracted with chloroform (3 × 35 mL), and the combined extract was dried over Na<sub>2</sub>SO<sub>4</sub>. After evaporation of the solvent, the resulting mixture was introduced into a silica gel column eluted with EtOAc. The pure 5'-*O*-monomethoxytrityl thymidine was obtained as a white solid in 70% yield (Table 4); mp 103 °C (lit.<sup>18</sup> mp 103–105 °C). <sup>1</sup>H NMR (CDCl<sub>3</sub>, ppm) δ: 9.64 (s, 1H, NH), 7.64 (s, 1H, H-6), 7.45–7.26 (m, 14H, Ph–), 6.88 (d, 2H, CH<sub>2</sub>-5'), 6.45 (t, 1H, H-1'), 4.61 (s, 1H,



**Table 2.** Dimethoxytritylation of alcohols by BDTE and DEAD in the presence of Ce(OTf)<sub>4</sub> in acetonitrile at room temperature.

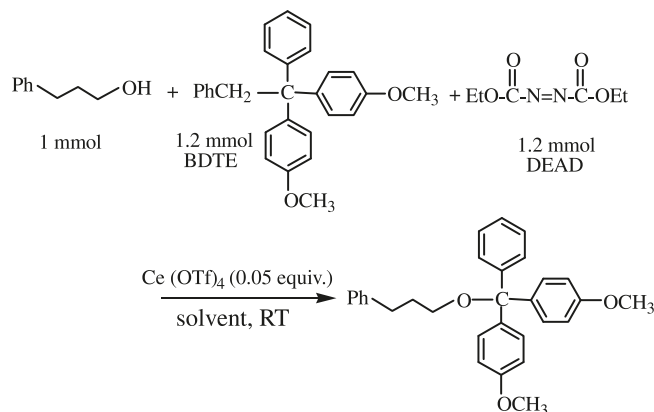
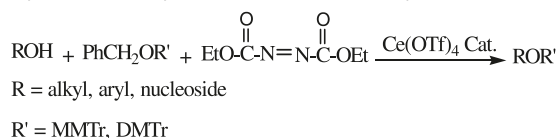
Entry	Substrate	Product	Time (min)	Yield <sup>a</sup> (%)
1	4-CH <sub>3</sub> OC <sub>6</sub> H <sub>4</sub> CH <sub>2</sub> OH	4-CH <sub>3</sub> OC <sub>6</sub> H <sub>4</sub> CH <sub>2</sub> ODMT	12 <sup>b</sup>	90
2	4-NO <sub>2</sub> C <sub>6</sub> H <sub>4</sub> CH <sub>2</sub> OH	4-NO <sub>2</sub> C <sub>6</sub> H <sub>4</sub> CH <sub>2</sub> ODMT	15 <sup>b</sup>	88
3	Ph-CH <sub>2</sub> -CH <sub>2</sub> -OH	Ph-CH <sub>2</sub> -CH <sub>2</sub> -ODMT	15 <sup>b</sup>	95
4	Ph-CH(OH)-CH <sub>3</sub>	Ph-CH(ODMT)-CH <sub>3</sub>	45 <sup>b</sup>	87
5	Ph-CH(OH)-Ph	Ph-CH(ODMT)-Ph	90 <sup>b</sup>	82
6			90 <sup>c</sup>	85
7	(Ph) <sub>2</sub> C(OH)-CH <sub>3</sub>	(Ph) <sub>2</sub> C(ODMT)-CH <sub>3</sub>	120 <sup>c</sup>	75
8	CH <sub>3</sub> -CH(OH)-CH <sub>2</sub> OH	CH <sub>3</sub> -CH(ODMT)-CH <sub>2</sub> ODMT	60	90

<sup>a</sup> Isolated yield after column chromatography.<sup>b</sup> The molar ratio of BDTE/DEAD/Ce(OTf)<sub>4</sub> is 1.2:1.2:0.05.<sup>c</sup> The molar ratio of BDTE/DEAD/Ce(OTf)<sub>4</sub> is 1.5:1.5:0.1.**Table 3.** The effect of different solvents on the protection of –OH group of 3-phenyl propanol with benzyl dimethoxytrityl ether.

Entry	Solvent	Time	Yield (%)
1	CH <sub>2</sub> Cl <sub>2</sub>	24 h	40
2	THF	24 h	85
3	CH <sub>3</sub> NO <sub>2</sub>	15 min	90
4	CH <sub>3</sub> CN	15 min	95

**Table 4.** Selective protection of nucleosides with benzyl trityl ethers (BTE, BDTE, and BMTE) in the presence of DEAD and Ce(OTf)<sub>4</sub> (0.1 equiv.).

Entry	Substrate	Reagent	Product	Time (h)	Yield <sup>a</sup> (%)
1	<b>1a</b>	BDTE	<b>2a</b>	2	87
2	<b>1b</b>	BDTE	<b>2b</b>	3	90
3	<b>1c</b>	BMTE	<b>2c</b>	7	75
4	<b>1d</b>	BMTE	<b>2d</b>	7.5	70
5	<b>1e</b>	BTE	<b>2e</b>	12	45
6	<b>1f</b>	BTE	<b>2f</b>	10	57
7	<b>1g</b>	BTE	<b>2g</b>	10	18

**Note:** The molar ratio of substrate/reagent/DEAD is 1:1.2:1.2.<sup>a</sup> Isolated yield after column chromatography.**Fig. 1.** The effect of different solvents used in the dimethoxytritylation of 3-phenyl propanol in the presence of diethylazodicarboxylate and Ce(OTf)<sub>4</sub> catalyst.**Scheme 1.** Tritylation of alcohols and nucleosides in the presence of diethylazodicarboxylate and Ce(OTf)<sub>4</sub> catalyst.

OH), 4.22–4.11 (m, 1H, H-3'), 3.82 (s, 3H, OCH<sub>3</sub>), 3.47–3.36 (m, 3H, CH<sub>2</sub>-2', H-4'), 2.38 (s, 3H, CH<sub>3</sub>–).

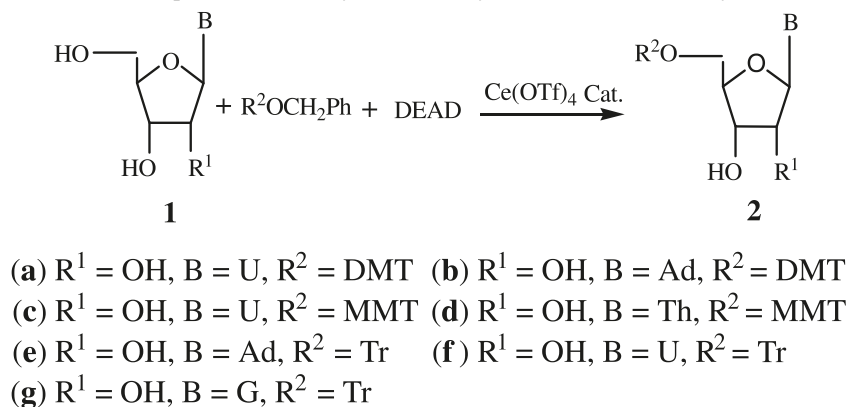
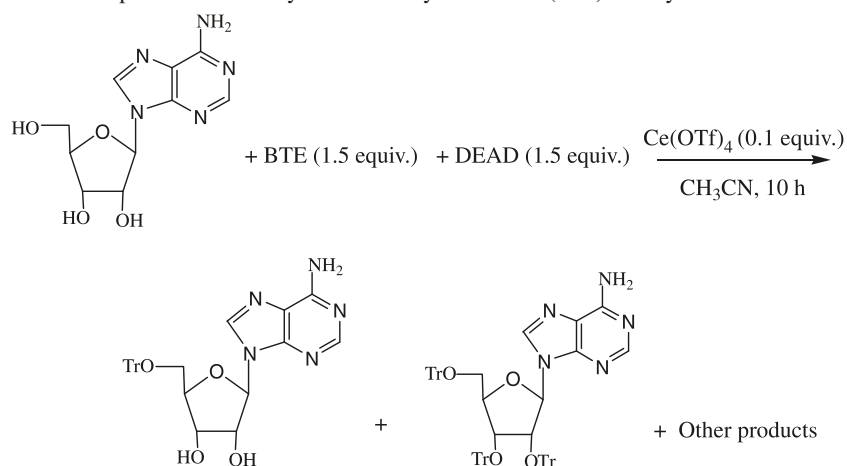
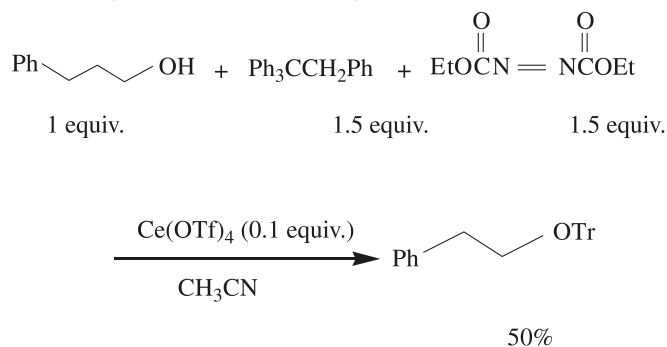
## Results and discussion

Different alcohols and nucleosides were subjected to the tritylation reaction in the presence of diethylazo-dicarboxylate and a catalytic amount of ceric triflate at room temper-

ature. The choice of solvent in the protection of –OH group with Ce(OTf)<sub>4</sub> is important, so the dimethoxytritylation of 3-phenyl propanol in different solvents was investigated (Fig. 1). On the basis of our results, which are shown in Table 3, Ce(OTf)<sub>4</sub> acts more efficiently in polar solvents, such as CH<sub>3</sub>CN.

The experiments were carried out in 1:1.2:1.2 molar ratio of alcohol/DEAD/BMTE (or BDTE) (Scheme 1).



**Scheme 3.** Tritylation of nucleosides in the presence of diethylazodicarboxylate and Ce(OTf)<sub>4</sub> catalyst.**Fig. 2.** Tritylation of adenosine in the presence of diethylazodicarboxylate and Ce(OTf)<sub>4</sub> catalyst.**Fig. 3.** Tritylation of 3-phenyl propanol in the presence of diethylazodicarboxylate and Ce(OTf)<sub>4</sub> catalyst.

To verify the proposed mechanism, tritylation of 3-phenyl propanol with BTE was carried out. Using 1.5 equiv. of BTE and 1.5 equiv. of DEAD in the presence of 0.1 equiv. of Ce(OTf)<sub>4</sub> at room temperature, this reaction proceeded at a slower rate than those with BDTE (Fig. 3). After 5 h, the product was obtained in only 50% yield. This shows that the rate of these reactions is dependent on the stability of the trityl cations.

Mechanistically, since the reaction rate is affected by the exchange of Tr by DMT and MMT, we believe in a mechanism that involves heterolytic cleavage of C–O benzilic bond to form the trytil cation.

In conclusion, a very simple and efficient method for the protection of alcohols and nucleosides is described. It should be mentioned that high rate of the reaction, high yields of the products, accompanied with high selectivity, easy work-up, and the use of a catalytic amount of Ce(OTf)<sub>4</sub> are advantages of the presented method. The Khorona's method for the tritylation of nucleosides suffers from prolonged reaction times and time-consuming work-up due to the presence of pyridine, which must be removed by repeated extraction of the reaction mixture with water. Elimination of pyridine, which is a toxic solvent, accompanied with an easy work-up, are worthy of mention as additional advantages for this method in the laboratory.

## Acknowledgment

Financial support for this work by the Research Council of Malek-Ashtar University of Technology, Tehran, Iran, is gratefully acknowledged.

## References

- (1) Greene, T. W. Wuts., P. G. M. *Protective Groups in Organic Synthesis*, 4th ed.; John Wiley and Sons. Inc., 2006.
- (2) Bessodes, M.; Komiotis, D.; Antonakis, K. *Tetrahedron Lett.* **1986**, 27 (52), 579. doi:10.1016/S0040-4039(00)84045-9.
- (3) Yang, S. M.; Lagu, B.; Wilson, L. J. *J. Org. Chem.* **2007**, 72 (21), 8123. doi:10.1021/jo701411d. PMID:17880142.

- (4) Chaudhary, S. K.; Hernandez, O. *Tetrahedron Lett.* **1979**, 20 (28), 99. doi:10.1016/S0040-4039(01)85893-7.
- (5) Reddy, M. P.; Rampal, J. B.; Becaucage, S. L. *Tetrahedron Lett.* **1987**, 28 (1), 23. doi:10.1016/S0040-4039(00)95639-9.
- (6) Hernandez, O.; Chaudhary, S. K.; Cox, R. H.; Proter, J. *Tetrahedron Lett.* **1981**, 22 (16), 1491. doi:10.1016/S0040-4039(01)90358-2.
- (7) Khorana, H. G. *Some Recent Developments in The Chemistry of Phosphate Esters of Biological Interest*; John Wiley and Sons: New York, 1961; pp 93–140.
- (8) Hakimelahi, G. H.; Kunju, K.; Lin, L. C.; Tsay, S.-C. *Bull. Inst. Chem. Acad. Sin.* **1993**, 40, 11.
- (9) Adinolfi, M.; Barone, G.; Iadonisi, A.; Schiattarella, M. *Tetrahedron Lett.* **2003**, 44 (19), 3733. doi:10.1016/S0040-4039(03)00758-5.
- (10) Khalafi-Nezhad, A.; Mokhtari, B. *Tetrahedron Lett.* **2004**, 45 (36), 6737. doi:10.1016/j.tetlet.2004.07.054.
- (11) Erdmenger, T.; Haensch, C.; Hoogenboom, R.; Schubert, U. S. *Macromol. Biosci.* **2007**, 7 (4), 440. doi:10.1002/mabi.200600253. PMID:17429805.
- (12) Inman, C. E.; Reed, S. M.; Hutchison, J. E. *Langmuir* **2004**, 20 (21), 9144. doi:10.1021/la049627b. PMID:15461499.
- (13) Lundquist, J. T., 4th; Satterfield, A. D.; Pelletier, J. C. *Org. Lett.* **2006**, 8 (18), 3915. doi:10.1021/ol0614018. PMID:16928037.
- (14) Jyothi, Y.; Mahalingam, A. K.; Ilangovan, A.; Sharma, G. V. M. *Synth. Commun.* **2007**, 37 (12), 2091. doi:10.1080/00397910701357833.
- (15) Reddy, C. R.; Rajesh, G.; Balaji, S. V.; Chethan, N. *Tetrahedron Lett.* **2008**, 49 (6), 970. doi:10.1016/j.tetlet.2007.12.020.
- (16) Oikawa, M.; Yoshizaki, H.; Kusumoto, S. *Synlett* **1998**, 1998 (7), 757. doi:10.1055/s-1998-1777.
- (17) Khalafi-Nezhad, A.; Fareghi Alamdary, R. *Tetrahedron* **2001**, 57 (31), 6805. doi:10.1016/S0040-4020(01)00616-0.
- (18) Schaller, H.; Weimann, G.; Lerch, B.; Khorana, H. G. *J. Am. Chem. Soc.* **1963**, 85 (23), 3821. doi:10.1021/ja00906a021.



# Redox reactions of reactive oxygen species in aqueous solutions as the probe for scanning electrochemical microscopy of single live T24 cells

Xiaocui Zhao, Mengni Zhang, Yitao Long, and Zhifeng Ding

**Abstract:** The redox reactions of two main components of reactive oxygen species (ROS), superoxide and hydrogen peroxide, along with oxygen in aqueous solutions were investigated using a conventional electrochemical technique, differential pulse voltammetry (DPV). Superoxide undergoes oxidation at a Pt working electrode biased at 0.055 V versus Ag/AgCl, while hydrogen peroxide can be oxidized and reduced at 0.817 and −0.745 V, respectively. Oxygen in the solutions is reduced at the electrode with an applied potential of −0.455 V. Based on these results, hydrogen peroxide and superoxide released from live cells can be successfully monitored, identified, and mapped using scanning electrochemical microscopy (SECM) at different potentials. Single human bladder (T24) cells were imaged using a 5 μm diameter SECM probe biased at −0.400, −0.600, and −0.800 V. Oxygen reduction that seems an interference can be discriminated from that of hydrogen peroxide by means of SECM.

**Key words:** live cells, scanning electrochemical microscopy, reactive oxygen species, differential pulse voltammetry.

**Résumé :** Faisant appel à une technique électrochimique conventionnelle, la voltampérométrie pulsée différentielle (PD), on a étudié les réactions d'oxydoréduction des deux composants principaux des espèces réactives de l'oxygène (ERO), le superoxydes et le peroxyde d'hydrogène avec également celle de l'oxygène. Le superoxydes subit une oxydation au niveau d'une électrode de travail de Pt biaisée à 0,055 V vs. Ag/AgCl, tandis que le peroxyde d'hydrogène peut être oxydé et réduit respectivement à 0,817 et −0,745 V. En solutions, l'oxygène est réduit à l'électrode par un potentiel appliqué de −0,455 V. Sur la base de ces résultats, le peroxyde d'hydrogène et le superoxyde émis par des cellules vivantes peuvent facilement être détectés, identifiés et localisés en faisant appel à la microscopie électrochimique à balayage (MECB), à divers potentiels. On a pu produire des images des cellules uniques de vessie humaine (T24) en utilisant cette technique à l'aide d'une sonde de diamètre 5 μm, biaisée à −0,400, −0,600 et −0,800 V. La réduction de l'oxygène qui semble une interférence peut être différenciée de celle du peroxyde d'hydrogène grâce à la MECB.

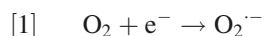
**Mots-clés :** cellules vivantes, microscopie électrochimique à balayage, espèces d'oxygène réactives, voltampérométrie pulsée différentielle.

## Introduction

Reactive oxygen species (ROS) play critical roles in the physiological processes of live cells. They are involved in a wide variety of cellular activities<sup>1</sup> such as cell adhesion,<sup>2</sup> inflammatory response,<sup>3</sup> and cell proliferation and apoptosis<sup>4</sup> when they are constantly generated at relatively low concentrations in normal healthy cells. However, they can damage key macromolecules such as DNA in the cells and induce various diseases, such as cancer, if they are persistently produced in excess.<sup>5–9</sup> Therefore, ROS are gaining attention in a large number of research areas.<sup>4</sup>

ROS can be generated in the intracellular region and extracellular field. Mitochondria and other nucleus related or-

ganelles are the major intracellular sources of ROS by delivering electrons to oxygen molecules:<sup>10</sup>



The superoxide anions are subsequently converted to hydrogen peroxide, through a reaction catalyzed by superoxide dismutase (SOD):<sup>11</sup>



Superoxide anions are confined to their generation sites inside of cells. However, hydrogen peroxide generated dur-

Received 15 February 2010. Accepted 28 March 2010. Published on the NRC Research Press Web site at [canjchem.nrc.ca](http://canjchem.nrc.ca) on 17 May 2010.

**X. Zhao and Z. Ding.**<sup>1</sup> Department of Chemistry, The University of Western Ontario, London, ON N6A 5B7, Canada.

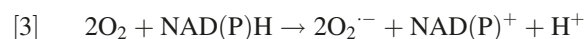
**M. Zhang.** Department of Chemistry, The University of Western Ontario, London, ON N6A 5B7, Canada; Department of Chemistry, East China University of Science and Technology, Shanghai 200237, China.

**Y. Long.** Department of Chemistry, East China University of Science and Technology, Shanghai 200237, China.

<sup>1</sup>Corresponding author (e-mail: [zfding@uwo.ca](mailto:zfding@uwo.ca)).

ing the dismutated reaction can pass through cell membranes and enter the extracellular fluid.<sup>12</sup>

The most significant extracellular source of ROS is NAD(P)H oxidase:<sup>13</sup>



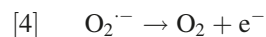
Thus, the main ROS released by live cells are superoxide anions and hydrogen peroxide.

In situ detection and identification of ROS is challenging due to their short chemical life time: as reported,  $\text{H}_2\text{O}_2$  exists for milliseconds and superoxide exists for microseconds in certain physiological environments.<sup>14</sup> Electrochemical methods, specifically scanning electrochemical microscopy (SECM), present facile tools of direct examination of ROS released from cells, utilizing well-positioned ultramicroelectrodes (UMEs) or modified electrodes.<sup>5,8,9,15–22</sup> In SECM, the UME was held in a bulk solution or moved in the close proximity of the substrate immersed in the solution containing a redox mediator. The electrochemical current due to the reduction or oxidation of the mediator flowing through the UME is measured. Since the current is proportional to the concentration of a redox species at the substrate, which can be live cells or metal alloys, any change in their chemical activities will perturb the electrochemical responses of the probe. This perturbation provides information about the nature and activities of the substrate. Standard redox mediators are often used to precisely control the separation distance between the probe and the substrate.<sup>23,24</sup> Here, we used ferrocenemethanol because it is a standard redox mediator widely used in biosystems.<sup>25–27</sup> Since ferrocenemethanol can be oxidized at 0.244 V versus Ag/AgCl,<sup>28</sup> the probe was biased at 0.350 V where the oxidation current of ferrocenemethanol is diffusion controlled. When the probe is far away from the substrate, the current detected by the UME ( $I_\infty$ ) is independent of the separation distance between the electrode and the substrate. As the tip is moving down toward the substrate, which in our case is a live cell, the current will decrease due to the hindered diffusion by the cell. The closer the tip to the cell, the smaller the current. The cell shows “negative feedback”. The curve of normalized current ( $I/I_\infty$ ) versus normalized distance (UME-to-substrate distance divided by UME radius) is called the probe approach curve (PAC), which is independent of the UME size in this negative feedback case. In our SECM experiments, the tip was being moved down until the current was reduced by 35% (i.e.,  $I = 0.65I_\infty$ ). That means that the separation distance between the electrode surface and the cell is 3.3  $\mu\text{m}$ , as read from the theoretical PAC.<sup>23,24,29</sup> In such a close approximate, ROS flux in the extracellular fluid can be immediately detected by recording the corresponding current at appropriate potentials under physiological conditions without disturbing the biological mechanisms. Thus, real-time information can be acquired concerning extracellular ROS. Furthermore, different types of ROS species can be identified by amperometry methods at different electrode potentials. Amatore’s group<sup>30,31</sup> recorded oxidative currents of reactive nitrogen species (RNS), hydrogen peroxide released by macrophages and phagocytes. They also detected the immediate ROS burst using amperometric detection with a platinized carbon fiber microelectrode via puncturing the cell cytoplasmic membrane with the microelectrode.<sup>8,9,18,22</sup>

Matsue’s group<sup>19</sup> also detected ROS release with an electrochemistry method and chemiluminescence method using phorbol myristate acetate (PMA)-differentiated cells. It should be mentioned that SECM has become a more and more popular technique to acquire the chemical and topographical information in the vicinity of live cells for the following reasons: it is noninvasive to live cells, it can identify different species released from the cells with varied potentials applied to the UME, and it can locate the species released from the different locations of the same cell.<sup>17,32–38</sup> SECM has been proven to be a powerful tool for mapping cell topography,<sup>39–41</sup> monitoring the respiration function,<sup>42–46</sup> investigating the pathway of transmembrane charge transfer,<sup>47,48</sup> and detecting short life time species such as  $\text{ROS}^{23}$  and nitric oxide<sup>49</sup> released from live cells. Our group<sup>46</sup> has previously shown that SECM can be used to study the effect of Cd-induced stress on single stomata in *Brassica juncea*.

However, almost all the groups mentioned above except ours<sup>23</sup> detected the ROS through oxidation using electrochemical methods in the positive potential region. The mediator, ferrocenemethanol, used to precisely control the probe-to-cell distance has a drastic interference when the applied potential is larger than 0.200 V. It is desirable to be able to determine ROS in the potential range that is more negative than 0.200 V. Systematic investigations in this aspect are scarce due to the irreversibility of the ROS reactions at large electrodes, their possible slow reaction rates, and the interference of the oxygen reduction.

Predominant extracellular ROS should be hydrogen peroxide and superoxide, since other ROS, such as hydroxide radicals, are too reactive to survive long enough to be detected. Superoxide can be oxidized by the SECM probe in the designated potential region while hydrogen peroxide can be reduced.



Oxygen reduction is unavoidable in the potential range whereby hydrogen peroxide is reduced.

In the present work, redox reactions of hydrogen peroxide and superoxide along with oxygen in aqueous solutions were systematically studied using differential pulse voltammetry (DPV). Although the redox reactions of these two species and oxygen were studied by other groups before, their experimental conditions were too different from the physiological environment of live cells (e.g., pH).<sup>50–55</sup> And the redox potentials of these species are largely dependent on pH, the electrode material, and the property of the solvent. Thus, it is necessary for us to verify the reduction potential of each species at our experiment condition, which is similar to the physiological environment of live cells. Hydrogen peroxide and nominal oxygen profiles in the vicinity of single T24 cells were imaged using SECM with a 5  $\mu\text{m}$  diameter UME with various bias potentials.

## Experimental section

### Chemicals

Culture media, serum, antibiotics, and glutamine were purchased from Gibco (Invitrogen Canada, Inc., Burlington,

ON). Deionized water with 18.2 mol/L  $\Omega$  resistivity (Milli-Q, Millipore, Bedford, MA) was used to prepare all aqueous solutions.  $\text{H}_2\text{O}_2$  solution (30%) was obtained from EMD Chemicals, Inc. (Darmstadt, Germany). Catalase from bovine liver, superoxide dismutase from bovine liver, potassium chloride, potassium superoxide, and ferrocenemethanol were purchased from Sigma-Aldrich (Mississauga, ON).

### Cell culture

T24 cells, which originate from human bladder carcinoma cells, were supplied by American Type Culture Collection, Manassas, VA. The T24 cells were cultured in DMEM supplemented with 4 mmol/L L-glutamine, 100 units/mL of penicillin, and 10% fetal bovine serum. The cells were incubated at 37 °C and 5%  $\text{CO}_2$  in an incubator (Sanyo Canada, Ltd. Concord, ON). Cell culture was performed with 50 mL plastic tissue culture flasks (Becton, Dickinson and Company, Mississauga, ON). T24 cells were detached from plastic walls of the flasks for subcultures with 0.25% Trypsin-EDTA (Gibco. Invitrogen Canada, Burlington, ON). Cells were detached, transferred, and subcultured onto Petri dishes one day prior to experiments.

### Electrochemistry procedures for DPV

A two-electrode system containing a 10  $\mu\text{m}$  diameter Pt UME as the working electrode and a saturated KCl Ag/AgCl electrode as the reference and counter electrode was employed in the DPV experiment. All potentials reported here are referred to the Ag/AgCl reference electrode. For comparison, the oxidation potential of ferrocenemethanol was determined as 0.236 V. The potential value was checked at the end of each experiment and was found to be very constant. DPV was recorded with a potentiostat, CHI 610A (CH Instruments, Austin, TX). Typical experimental parameters for DPVs are 0.05 V as pulse height, 50 ms pulse width, 200 ms period, and 0.02 V/s scan rate.<sup>56</sup> For the deaerated experiment, the stream of Argon (Ar) gas was continuously bubbled into the solution for at least 20 min prior to the experiment and a stream of Ar was maintained over the solution during the experiment to minimize the oxygen concentration in solution. For the oxygen-rich experiments, pure  $\text{O}_2$  gas was bubbled in the solution for 20 min prior to the experiment and a flow of oxygen was kept over the solution during the experiment.

### SECM setup

The detailed SECM procedure was described in one of our recent publications.<sup>23</sup> In brief, SECM setup was adapted from Alpha-SNOM by replacing the objective with an electrode holder and a homemade Pt electrode. This electrode serves as the working electrode and an Ag/AgCl electrode is used as the reference and counter electrode. In the experiments, the SECM electrode, applied at a certain potential, was brought closer to the cells and positioned at a desired height while the current was monitored. At this fixed height, the working electrode was scanned in a plane by moving the scanning stage. Constant height SECM images can be obtained by recording current versus lateral coordinates in the scanning plane. All the SECM measurements were performed with a potentiostat (Compactstat Electrochemical Interface, IVIUM Technologies, Netherlands) driven by the

IviumStat Control software (IVIUM Technologies), from which the electrochemical current was directed into a data acquisition channel of the Alpha-SNOM microscope (WITec, Germany) connected to a computer. WITec software for confocal microscopy was adopted for the SECM imaging. The integration time at each image pixel was 0.01 s. The acquisition time of each image was around 12 min with a resolution of  $256 \times 256$  pixels for one image.

## Results and discussion

### Oxygen reduction reaction (ORR)

ORR at the Pt microelectrode was studied with DPV in the potential range of  $-0.850$  to  $0.000$  V in the air-saturated electrolyte solution containing 50 mmol/L KCl (Fig. 1). A peak potential was observed at  $-0.430$  V due to oxygen reduction when the applied potential was scanned from  $0.000$  to  $-0.850$  V (top solid curve in Fig. 1). The maximum potential appeared at  $-0.490$  V while scanning the potential in the reverse direction (bottom solid wave in Fig. 1). Oxygen was reduced to  $\text{H}_2\text{O}$  through a four-electron process<sup>57</sup> as shown in eq. [6].



Assuming that the diffusion coefficients of the reactant and product are approximately the same, the formal potential for ORR can be determined by eq. [7].<sup>58,59</sup>

$$[7] \quad E^0 = E_{\text{max}} + \Delta E/2$$

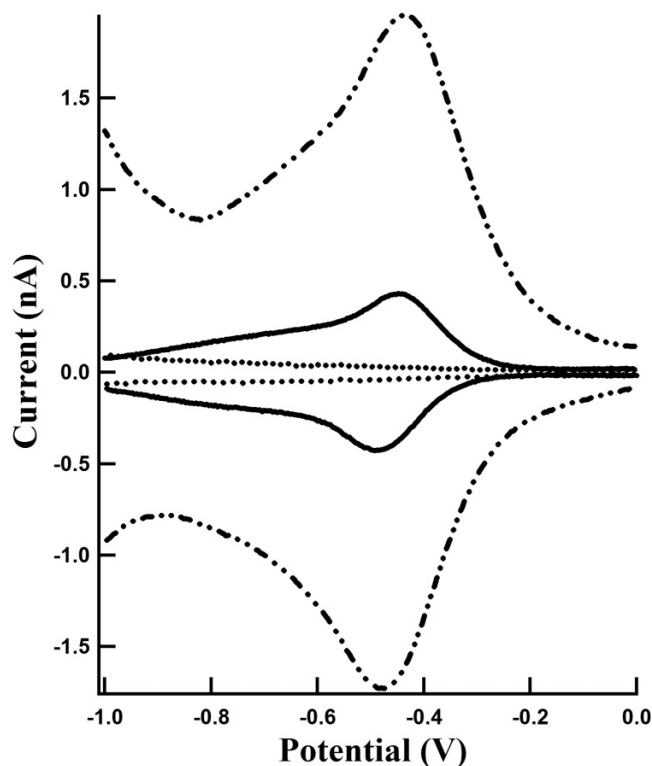
where  $E_{\text{max}}$  is the peak potential in the DPV and  $\Delta E$  is the pulse height (50 mV). The formal reduction potential was determined from the forward and reverse scans as  $-0.455$  and  $-0.465$  V, respectively. From the difference of the obtained formal potential, it is plausible that the reduction reaction is not reversible and the reaction kinetics is slow. However, with the microelectrode, it is still possible to measure the steady-state current that is proportional to the oxygen concentration.<sup>46,60</sup> Tsionsky et al. (Bard's laboratory).<sup>60</sup> reported the oxygen reduction at the surface of a 7  $\mu\text{m}$  carbon electrode by recording cyclic voltammograms.<sup>60</sup> Our group<sup>46</sup> and Bard's laboratory<sup>60</sup> monitored the ORR using cyclic voltammetry at platinum and carbon microelectrodes and detected the oxygen released from photosynthetic processes by setting an applied potential at which the diffusion controlled steady-state current can be obtained.

These DPV peaks disappeared after the solution was deaerated with Ar gas (dotted voltammograms in Fig. 1) and the peak current increased in the oxygen-saturated solution (dotted and dashed curves in Fig. 1). This confirmed that the peaks were due to the electron transfer between oxygen and the electrode.

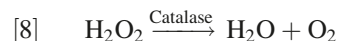
### Redox behaviours of $\text{H}_2\text{O}_2$

The reduction behaviour of  $\text{H}_2\text{O}_2$  in deaerated 50 mmol/L KCl solution was recorded (solid lines in Fig. 2A) and a pair of peaks appeared at potentials of  $-0.720$  and  $-0.750$  V, respectively, when the applied potential was scanned from  $0.200$  to  $-0.900$  V and subsequently reversed. These peaks gave a formal potential of  $-0.745$  or  $-0.725$  V based on eq. [7]. Hydrogen peroxide undergoes a reduction reaction

**Fig. 1.** Differential pulse voltammograms within a potential range between 0.000 and  $-0.800$  V for oxygen at a  $10\text{ }\mu\text{m}$  diameter Pt electrode in air-saturated (solid lines), oxygen-saturated (dotted and dashed lines), and deaerated (dotted lines) electrolyte solutions. KCl (50 mmol/L) was used as the supporting electrolyte in all solutions.



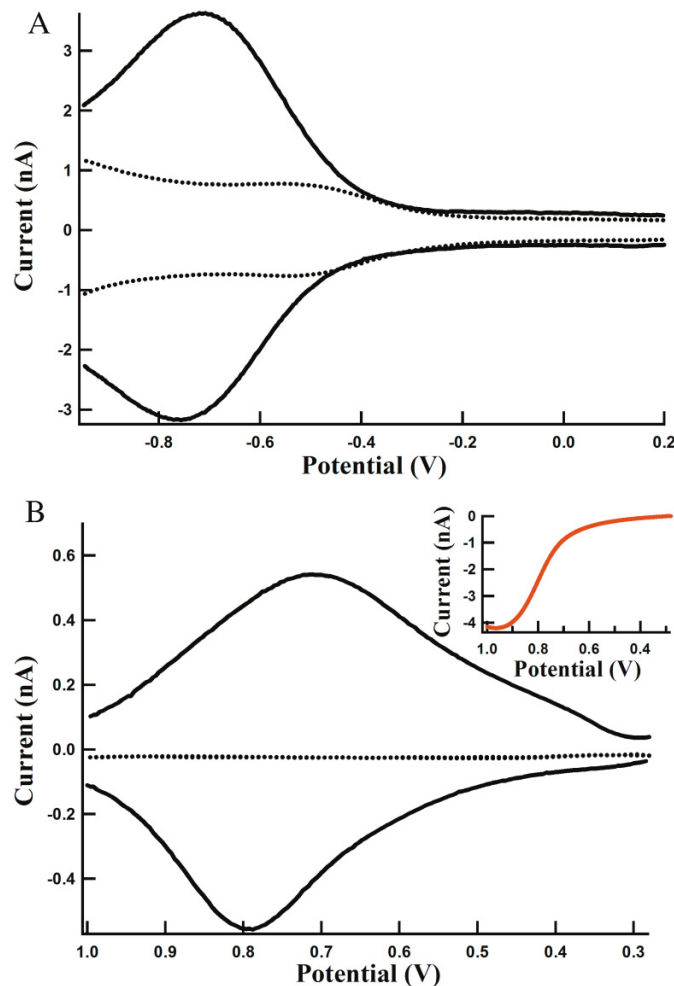
via eq. [5]. To confirm that the observed reduction peaks are due to the electron transfer of  $\text{H}_2\text{O}_2$  and its counter part, an enzyme, catalase, which can convert  $\text{H}_2\text{O}_2$  to oxygen and water, was added to the above solution. Differential pulse voltammograms were recorded immediately without purging Ar gas into the solution after catalase was mixed thoroughly with the solution. The coupled peaks at  $-0.720/-0.750$  V in forward/reverse scans disappeared and the waves for oxygen reduction were determined to be  $-0.430/-0.490$  V (dotted line in Fig. 2A). This demonstrates that the reduction peaks at  $-0.720/-0.750$  V were due to the electrochemical reaction of  $\text{H}_2\text{O}_2$ . The low current after the catalase addition can be attributed to the limited solubility of oxygen in the solution and disproportionation reaction of hydrogen peroxide with the aid of catalase as described by eq. [8].



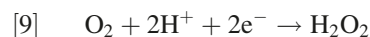
The detection of  $\text{H}_2\text{O}_2$  reduction was discriminated from ORR by polarography.<sup>61</sup> The formal potential was also determined to be  $-0.8$  V (vs Ag/AgCl) with DPV at a mercury electrode.<sup>62</sup> It is clear from our results and those in the literature that trace concentrations of hydrogen peroxide in aqueous solutions can be determined by means of electrochemistry.

In addition, our experimental results (not presented here) revealed that the reduction peaks shifted slightly with higher concentrations of  $\text{H}_2\text{O}_2$  in the solution, due to the pH change caused by the concentration. It is interesting to note that the

**Fig. 2.** (A) Differential pulse voltammograms within a potential range between 0.200 and  $-0.880$  V for 3.4 mmol/L hydrogen peroxide at a  $10\text{ }\mu\text{m}$  diameter Pt electrode in deaerated  $\text{H}_2\text{O}_2$  solution containing 50 mmol/L KCl electrolyte (solid lines) and in  $\text{H}_2\text{O}_2$  solution containing 50 mmol/L KCl electrolyte in the presence of catalase (dotted lines). (B) Differential pulse voltammograms with a potential range from 0.280 and 1.000 V for hydrogen peroxide at a  $5\text{ }\mu\text{m}$  diameter Pt electrode in a deaerated solution containing 50 mmol/L KCl electrolyte in the presence (solid lines) and absence (dotted lines) of 1.2 mmol/L hydrogen peroxide. The inset is the linear voltammograms of the same hydrogen peroxide solutions with the applied potential scanned from 0.280 to 1.000 V.



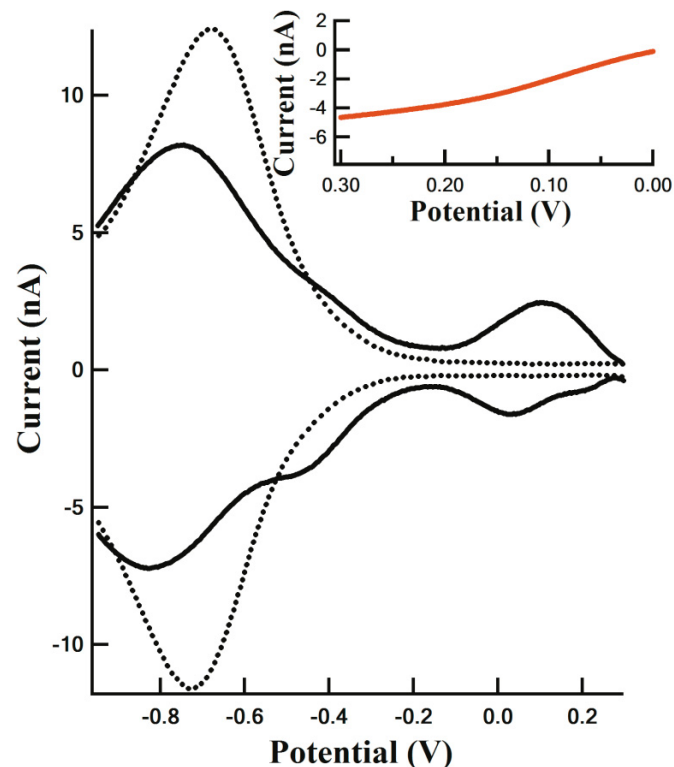
reduction waves of oxygen became broad and can be deconvoluted into two successive reductions (dot-dashed curves in Fig. 1) when the KCl electrolyte solution was purged with pure oxygen. The second reduction peak potential agrees very well with that of  $\text{H}_2\text{O}_2$  reduction. The reduction of oxygen can therefore follow a pathway of two two-electron transfer processes when the oxygen concentration was high.



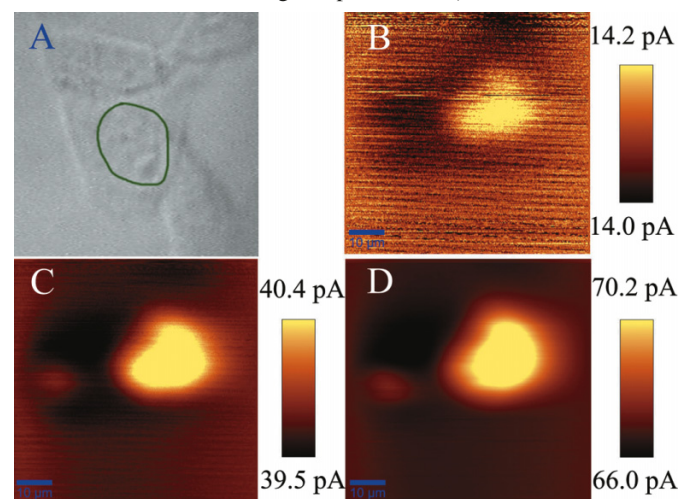
This observation agrees well with the fact that oxygen reduction current at a mercury electrode was enhanced via the reaction in eq. [8] by adding catalase.<sup>61</sup> Furthermore, the



**Fig. 3.** Differential pulse voltammograms within a potential range between 0.160 and  $-0.880$  V at a  $10\text{ }\mu\text{m}$  diameter Pt electrode for potassium superoxide in  $\text{KO}_2$  solution containing  $50\text{ mmol/L}$  KCl electrolyte in the absence (solid lines) and presence (dashed lines) of superoxide dismutase. The inset is the linear voltammograms of the same solutions with the applied potential scanned from  $0.000$  to  $0.300$  V.



**Fig. 4.** Microscopic picture of (A) a live T24 cell and the SECM images of the T24 cell using a  $5\text{ }\mu\text{m}$  diameter Pt electrode biased at (B)  $-0.400$  V, (C)  $-0.600$  V, and (D)  $-0.800$  V vs Ag/AgCl. The microelectrode ratio of the glass sheath diameter to that of Pt (RG) is 5. The scale bar in the images represents  $10\text{ }\mu\text{m}$ .



two-electron transfer process in the acidic solution was also observed by Bard's group<sup>63</sup> at a Hg/Au electrode.

The oxidation of hydrogen peroxide was also investigated by means of DPV as shown in Fig. 2B. The voltammograms

showed a peak potential at  $0.792$  V when the applied potential was scanned from  $0.280$  to  $1.000$  V and one at  $0.712$  V when the potential scan direction was reversed. The cyclic voltammogram demonstrated a dramatic hysteresis (not shown) between the forward and backward scans. All these observations prove the irreversibility of the oxidation reaction. The negative sign current was recorded in a linear voltammogram running from  $0.280$  to  $1.000$  V in the presence of hydrogen peroxide (inset in Fig. 2B), which provided the further proof of the oxidation of hydrogen peroxide. The formal potential was then calculated as  $0.817$  V from the DPV curve when the applied potential was scanned from low to high. Amatore's group<sup>8,18</sup> reported the oxidation potential at  $0.6$  V versus Ag/AgCl with a platinized carbon fiber microelectrode and monitored this oxidant release using macrophages at the level of a single cell, in real time and quantitatively.

### Oxidation of superoxide

Superoxide is not stable and is easily decomposed in the aqueous solution to hydrogen peroxide and oxygen.



Therefore, the detection using electrochemical methods were constrained to organic solutions, which greatly differ from the natural environment of live cells.<sup>64–66</sup> In our experiment, our strategy to detect superoxide in aqueous solutions was to use a microelectrode in the presence of superoxide dismutase. In the DPV of superoxide (solid lines in Fig. 3), in addition to the peaks for oxygen reduction ( $-0.430/-0.490$  V) and hydrogen reduction ( $-0.750/-0.830$  V), a new pair of peaks appeared at  $0.120/0.030$  V. The redox nature was further verified by recording the linear scan voltammogram of the superoxide (shown in the inset in Fig. 3). By conventional American standards, the negative current sign in the inset depicted oxidation behaviour. The formal oxidation potential was calculated as  $0.055$  V based on eq. [7] with the DPV curve when the applied potential was scanned from negative to positive (bottom solid line in Fig. 3). A further experiment was conducted to confirm the electrochemical activity of superoxide by adding superoxide dismutase (SOD) into the solution. The DPV result is shown by the dotted waves in Fig. 3. Superoxide can be completely converted to hydrogen peroxide in the presence of SOD according to eq. [2]. The superoxide oxidation peaks at  $0.120$  and  $0.030$  V disappeared, which further indicates that this peak pair was from electrochemical reactions of superoxide. Furthermore, the peak currents attributed to  $\text{H}_2\text{O}_2$  reduction increased from  $8.2$  to  $12.4$  nA due to the augmented  $\text{H}_2\text{O}_2$  concentration via reaction by means of SOD. Our experimental data agreed well with a published paper<sup>21</sup> in which anodic current due to superoxide oxidation was recorded at  $0.1$  V versus Ag/AgCl using a carbon fiber electrode.

### Detection of $\text{H}_2\text{O}_2$ released from T24 cells at different potentials with SECM

As can be seen from the DPV results, it is possible to detect the two most common ROS, hydrogen peroxide and superoxide, by setting appropriate potentials at a microelectrode. SECM probes are advantageous as they can be positioned in the vicinity of a live cell to determine ROS

immediately after being released from the cell. Therefore, we attempted to map out the hydrogen peroxide concentration profile above single T24 cells at variable potentials from  $-0.400$  to  $-0.800$  V. These experiments should provide the rationale as to whether we can discriminate the release of hydrogen peroxide from oxygen that has an approximate concentration of  $0.2$  mmol/L.<sup>46</sup>

The bottom view of the cell in the inverted microscope is shown in Fig. 4A. First, a  $5\text{ }\mu\text{m}$  diameter Pt SECM probe electrode with a biased potential of  $0.350$  V was positioned above a T24 cell in the medium containing  $0.45$  mmol/L ferrocenemethanol. There is minimal interaction between the SECM mediator and the live cell so that the SECM probe approach curve (PAC) is expected to show a negative feedback.<sup>23,47</sup> Based on the SECM principle, a probe-to-cell distance of  $3.25\text{ }\mu\text{m}$  was reached, where the normalized current at the probe is  $0.65I_{\infty}$ .<sup>23,46</sup> Following this, the bias potential was switched to  $-0.400$  V and the SECM probe was rastered above the cell. The SECM image as shown in Fig. 4B was obtained by recording the probe current versus its coordinates. The dark area in the image (Fig. 4B) illustrates low current while the bright region indicates high current. From the DPV results for oxygen reduction, one can see that oxygen can be partially reduced at  $-0.400$  V. The middle of the cell in Fig. 4B is relatively brighter, which can be attributed to higher current and therefore a higher concentration of oxygen. Oxygen is not released directly by cells and the close distance between the probe and the cell causes blockage of the oxygen diffusion to the probe by the cell. However, oxygen concentration can be relatively high above the cell due to the decomposition of hydrogen peroxide. From the high current in the middle of the cell image in Fig. 4B, it is evident that the indirect oxygen generation overwhelmed the blockage. With the biased potential of  $-0.600$  V at the microelectrode, the SECM image of the same T24 cell demonstrated a much better contrast (Fig. 4C). At this applied potential, the SECM probe reached a steady-state current, which is proportional to the local oxygen concentration. It is therefore expected to see higher current due to the oxygen reduction. It can be seen from the scale bars beside the images (Figs. 4B and 4C) that the maximum reduction current increased from  $14.2$  to  $40.4$  pA. Furthermore, the applied potential was moved to be more negative at  $-0.800$  V where oxygen and hydrogen peroxide can both be reduced. The highest current was monitored as  $70.2$  pA, and the highest image contrast was obtained among images at probe potentials of  $-0.400$ ,  $-0.600$ , and  $-0.800$  V (Figs. 4B–4D). It can be concluded that in the vicinity of the cell, hydrogen peroxide has a higher concentration than oxygen. It is therefore possible to determine this ROS using SECM even though it may decompose on its way to travelling to the surface of the electrode. SECM has the advantage to approach live cells at a very short distance and catch ROS before their decay to other species. As discussed in the Introduction, mitochondria in cells can generate superoxide, which mutates to hydrogen peroxide simultaneously or enzymatically. This is not the case in our experiments. It is plausible that hydrogen peroxide was mainly produced above the nucleus. The production pathways might be extracellular (via the enzymes at the cell surface) or intracellular (via inner organelles and diffusion through the cell membrane).

## Conclusions

The SECM probe, consisting of a custom-made platinum microelectrode, is efficient to determine the redox reactions of the two major ROS, hydrogen peroxide and superoxide, along with oxygen in aqueous solutions. DPV determined the formal reduction potential of oxygen as  $-0.455$  V versus saturated KCl Ag/AgCl. It was found that hydrogen peroxide undergoes reduction at  $-0.745$  V and oxidation at  $0.817$  V versus the same reference electrode. Superoxide can be oxidized with a formal potential of  $0.055$  V versus the Ag/AgCl. This work provides the fundamentals for further SECM studies on live T24 cells using nominal oxygen concentrations or hydrogen peroxide as the extracellular marker. The successful application of SECM experiments to single live cells presents the tremendous potential of ROS as a promising extracellular indicator for studies on the physiological activities of live cells. Moreover, the noninvasive nature of SECM is ideal for a real-time investigation on almost all single live cells while maintaining their physiological environment without adding any extraneous indicator.

## Acknowledgments

We appreciate the financial support for this research from the Canadian Institute for Photonic Innovations (CIPI), the Natural Sciences and Engineering Research Council of Canada (NSERC), the Ontario Photonics Consortium (OPC), the Canada Foundation for Innovation (CFI), the Ontario Innovation Trust (OIT), the Premier Research Excellence Award (PREA), and the University of Western Ontario (UWO; Academic Development Fund (ADF) as well as a Start-up Fund). Our lab is part of the Centre of Chemical Physics (CCP) and Western Institute of Nano Science (WINS) at UWO. Technical assistance from John Vanstone, Jon Aukema, Sherrie McPhee, and Mary Lou Hart is gratefully acknowledged.

## References

- (1) Khan, A. U.; Wilson, T. *Chem. Biol.* **1995**, 2 (7), 437. doi:10.1016/1074-5521(95)90259-7. PMID:9383446.
- (2) Roy, S.; Sen, C. K.; Packer, L. *Methods Enzymol.* **1999**, 300, 395. doi:10.1016/S0076-6879(99)00144-5. PMID:9919540.
- (3) Hehner, S. P.; Breitkreutz, R.; Shubinsky, G.; Unsoeld, H.; Schulze-Osthoff, K.; Schmitz, M. L.; Dröge, W. *J. Immunol.* **2000**, 165 (8), 4319. PMID:11035067.
- (4) Bedard, K.; Krause, K.-H. *Physiol. Rev.* **2007**, 87 (1), 245. doi:10.1152/physrev.00044.2005. PMID:17237347.
- (5) Chang, S.-C.; Pereira-Rodrigues, N.; Henderson, J. R.; Cole, A.; Bédoui, F.; McNeil, C. J. *Biosens. Bioelectron.* **2005**, 21 (6), 917. doi:10.1016/j.bios.2005.02.015. PMID:16257661.
- (6) Griendling, K. K.; FitzGerald, G. A. *Circulation* **2003**, 108 (16), 1912. doi:10.1161/01.CIR.0000093660.86242.BB. PMID:14568884.
- (7) Hamilton, M. L.; Van Remmen, H.; Drake, J. A.; Yang, H.; Guo, Z. M.; Kewitt, K.; Walter, C. A.; Richardson, A. *Proc. Natl. Acad. Sci. U.S.A.* **2001**, 98 (18), 10469. doi:10.1073/pnas.171202698. PMID:11517304.
- (8) Arbault, S.; Pantano, P.; Sojic, N.; Amatore, C.; Best-Belpomme, M.; Sarasin, A.; Vuillaume, M. *Carcinogenesis* **1997**, 18 (3), 569. doi:10.1093/carcin/18.3.569. PMID:9067558.
- (9) Arbault, S.; Sojic, N.; Bruce, D.; Amatore, C.; Sarasin, A.;

- Vuillaume, M. *Carcinogenesis* **2004**, 25 (4), 509. doi:10.1093/carcin/bgh046. PMID:14688028.
- (10) Richter, C.; Gogvadze, V.; Laffranchi, R.; Schlapbach, R.; Schweizer, M.; Suter, M.; Walter, P.; Yaffee, M. *Biochim. Biophys. Acta Mol. Basis Dis.* **1995**, 1271 (1), 67. doi:10.1016/0925-4439(95)00012-S.
  - (11) Fridovich, I. *Annu. Rev. Biochem.* **1995**, 64 (1), 97. doi:10.1146/annurev.bi.64.070195.000525. PMID:7574505.
  - (12) Antunes, F.; Cadenas, E. *FEBS Lett.* **2000**, 475 (2), 121. doi:10.1016/S0014-5793(00)01638-0. PMID:10858501.
  - (13) Babior, B. M. *Blood* **1999**, 93 (5), 1464. PMID:10029572.
  - (14) Nindl, G. *Cellscience* **2004**, 1, 1.
  - (15) Chang, S.-C.; Rodrigues, N. P.; Zurgil, N.; Henderson, J. R.; Bedioui, F.; McNeil, C. J.; Deutsch, M. *Biochem. Biophys. Res. Commun.* **2005**, 327 (4), 979. doi:10.1016/j.bbrc.2004.12.108. PMID:15652491.
  - (16) Amatore, C.; Arbault, S.; Chen, Y.; Crozatier, C.; Tapsoba, I. *Lab Chip* **2007**, 7 (2), 233. doi:10.1039/b611569a. PMID:17268626.
  - (17) Amemiya, S.; Guo, J.; Xiong, H.; Gross, D. A. *Anal. Bioanal. Chem.* **2006**, 386 (3), 458. doi:10.1007/s00216-006-0510-6. PMID:16855816.
  - (18) Arbault, S.; Pantano, P.; Jankowski, J. A.; Vuillaume, M.; Amatore, C. *Anal. Chem.* **1995**, 67 (19), 3382. doi:10.1021/ac00115a004. PMID:8686890.
  - (19) Kasai, S.; Shiku, H.; Torisawa, Y.-.; Noda, H.; Yoshitake, J.; Shiraishi, T.; Yasukawa, T.; Watanabe, T.; Matsue, T.; Yoshimura, T. *Anal. Chim. Acta* **2005**, 549 (1–2), 14. doi:10.1016/j.aca.2005.06.034.
  - (20) Mesároš, Š.; Vaňková, Ž.; Mesárošová, A.; Tomčík, P.; Grunfeld, S. *Bioelectrochem. Bioenerg.* **1998**, 46 (1), 33. doi:10.1016/S0302-4598(98)00107-X.
  - (21) Isogai, Y.; Tsuyama, T.; Osada, H.; Iizuku, T.; Tanaka, K. *FEBS Lett.* **1996**, 380 (3), 263. doi:10.1016/0014-5793(96)00068-3. PMID:8601437.
  - (22) Lachgar, A.; Sojic, N.; Arbault, S.; Bruce, D.; Sarasin, A.; Amatore, C.; Bizzini, B.; Zagury, D.; Vuillaume, M. *J. Virol.* **1999**, 73 (2), 1447. PMID:9882350.
  - (23) Zhao, X.; Petersen, N. O.; Ding, Z. *Can. J. Chem.* **2007**, 85 (3), 175. doi:10.1139/V07-007.
  - (24) Zhu, R.; Ding, Z. *Can. J. Chem.* **2005**, 83 (10), 1779. doi:10.1139/v05-189.
  - (25) Li, X.; Bard, A. J. *J. Electroanal. Chem.* **2009**, 628 (1–2), 35. doi:10.1016/j.jelechem.2009.01.002.
  - (26) Yasukawa, T.; Uchida, I.; Matsue, T. *Biochim. Biophys. Acta Biomembr.* **1998**, 1369 (1), 152. doi:10.1016/S0005-2736(97)00220-4.
  - (27) Guo, J.; Amemiya, S. *Anal. Chem.* **2005**, 77 (7), 2147. doi:10.1021/ac048370j. PMID:15801749.
  - (28) Arning, M. D.; Menteer, S. D. In *Handbook of Electrochemistry*; Zoski, C. G.; Elsevier: Amsterdam, 2007; p 819.
  - (29) Bard, A. J. In *Scanning Electrochemical Microscopy*; Bard, A. J., Mirkin, M. V.; Marcel Dekker: New York, 2001; p 1.
  - (30) Amatore, C.; Arbault, S.; Bouton, C.; Coffi, K.; Drapier, J.-C.; Ghandour, H.; Tong, Y. *ChemBioChem* **2006**, 7 (4), 653. doi:10.1002/cbic.200500359. PMID:16502474.
  - (31) Verchier, Y.; Lardy, B.; Nguyen, M. V. C.; Morel, F.; Arbault, S.; Amatore, C. *Biochem. Biophys. Res. Commun.* **2007**, 361 (2), 493. doi:10.1016/j.bbrc.2007.07.041. PMID:17655824.
  - (32) Sun, P.; Laforge, F. O.; Mirkin, M. V. *Phys. Chem. Chem. Phys.* **2007**, 9 (7), 802. doi:10.1039/b612259k. PMID:17287874.
  - (33) Bard, A. J.; Li, X.; Zhan, W. *Biosens. Bioelectron.* **2006**, 22 (4), 461. doi:10.1016/j.bios.2006.04.028. PMID:16797958.
  - (34) Yasukawa, T.; Kaya, T.; Matsue, T. *Electroanalysis* **2000**, 12 (9), 653. doi:10.1002/1521-4109(200005)12:9<653::AID-ELAN653>3.0.CO;2-S.
  - (35) Schulte, A.; Schuhmann, W. *Angew. Chem. Int. Ed.* **2007**, 46 (46), 8760. doi:10.1002/anie.200604851.
  - (36) Honda, A.; Komatsu, H.; Kato, D.; Ueda, A.; Maruyama, K.; Iwasaki, Y.; Ito, T.; Niwa, O.; Suzuki, K. *Anal. Sci.* **2008**, 24 (1), 55. doi:10.2116/analsci.24.55. PMID:18187850.
  - (37) Stoica, L.; Neugebauer, S.; Schuhmann, W. *Adv. Biochem. Eng. Biotechnol.* **2008**, 109, 455. PMID:17922101.
  - (38) Roberts, W. S.; Lonsdale, D. J.; Griffiths, J.; Higson, S. P. J. *Biosens. Bioelectron.* **2007**, 23 (3), 301. doi:10.1016/j.bios.2007.06.020. PMID:17869090.
  - (39) Kurulugama, R. T.; Wipf, D. O.; Takacs, S. A.; Pongmayteegul, S.; Garriss, P. A.; Baur, J. E. *Anal. Chem.* **2005**, 77 (4), 1111. doi:10.1021/ac048571n. PMID:15858993.
  - (40) Liebetrau, J. M.; Miller, H. M.; Baur, J. E.; Takacs, S. A.; Anupunpisit, V.; Garriss, P. A.; Wipf, D. O. *Anal. Chem.* **2003**, 75 (3), 563. doi:10.1021/ac026166v. PMID:12585485.
  - (41) Wang, W.; Xiong, Y.; Du, F.-Y.; Huang, W.-H.; Wu, W.-Z.; Wang, Z.-L.; Cheng, J.-K.; Yang, Y.-F. *Analyst (Lond.)* **2007**, 132 (6), 515. doi:10.1039/b701880k.
  - (42) Holt, K. B.; Bard, A. J. *Biochemistry* **2005**, 44 (39), 13214. doi:10.1021/bi0508542. PMID:16185089.
  - (43) Lee, C.; Kwak, J.; Bard, A. J. *Proc. Natl. Acad. Sci. U.S.A.* **1990**, 87 (5), 1740. doi:10.1073/pnas.87.5.1740. PMID:2308933.
  - (44) Shiku, H.; Shiraishi, T.; Ohya, H.; Matsue, T.; Abe, H.; Hoshi, H.; Kobayashi, M. *Anal. Chem.* **2001**, 73 (15), 3751. doi:10.1021/ac010339j. PMID:11510844.
  - (45) Takii, Y.; Takoh, K.; Nishizawa, M.; Matsue, T. *Electrochim. Acta* **2003**, 48 (20–22), 3381. doi:10.1016/S0013-4686(03)00408-0.
  - (46) Zhu, R.; Macfie, S. M.; Ding, Z. *J. Exp. Bot.* **2005**, 56 (421), 2831. doi:10.1093/jxb/eri275. PMID:16216848.
  - (47) Liu, B.; Rotenberg, S. A.; Mirkin, M. V. *Proc. Natl. Acad. Sci. U.S.A.* **2000**, 97 (18), 9855. doi:10.1073/pnas.97.18.9855. PMID:10963658.
  - (48) Cai, C.; Liu, B.; Mirkin, M. V.; Frank, H. A.; Rusling, J. F. *Anal. Chem.* **2002**, 74 (1), 114. doi:10.1021/ac010945e. PMID:11795778.
  - (49) Isik, S.; Schuhmann, W. *Angew. Chem. Int. Ed.* **2006**, 45 (44), 7451. doi:10.1002/anie.200601708.
  - (50) Saveant, J.-M. *J. Phys. Chem. C* **2007**, 111 (7), 2819. doi:10.1021/jp068322y.
  - (51) AlNashef, I. M.; Leonard, M. L.; Matthews, M. A.; Weidner, J. W. *Ind. Eng. Chem. Res.* **2002**, 41 (18), 4475. doi:10.1021/ie010787h.
  - (52) Orive, A. G.; Creus, A. H.; Grumelli, D.; Benitez, G. A.; Andirini, L.; Requejo, F. G.; Bonazzola, C.; Salvarezza, R. C. *J. Phys. Chem. C* **2009**, 113 (39), 17097. doi:10.1021/jp905560d.
  - (53) Weber, M. F.; Dignam, M. J.; Park, S. M.; Venter, R. D. *J. Electrochem. Soc.* **1986**, 133 (4), 734. doi:10.1149/1.2108665.
  - (54) Okuda, M.; Tsuruta, T.; Katayama, K. *Phys. Chem. Chem. Phys.* **2009**, 11 (13), 2287. doi:10.1039/b817695g. PMID:19305903.
  - (55) Shleev, S.; Wetterö, J.; Magnusson, K.-E.; Ruzgas, T. *Biosens. Bioelectron.* **2006**, 22 (2), 213. doi:10.1016/j.bios.2005.12.017. PMID:16442792.
  - (56) Bard, A. J.; Ding, Z.; Myung, N. *Struct. Bond.* **2005**, 118, 1. doi:10.1007/b137239.
  - (57) Li, X.; Heryadi, D.; Gewirth, A. A. *Langmuir* **2005**, 21 (20), 9251. doi:10.1021/la0508745. PMID:16171359.

- (58) Bard, A. J.; Faulkner, L. R. *Electrochemical methods, fundamentals and applications*, 2nd ed.; John Wiley & Sons Inc.: New York, 2001.
- (59) Girault, H. H. *Électrochimie Physique et Analytique*; Presses Polytechniques et Universitaires Romandes: Laussane, Switzerland, 2001.
- (60) Tsionsky, M.; Cardon, Z. G.; Bard, A. J.; Jackson, R. B. *Plant Physiol.* **1997**, *113* (3), 895. PMID:12223651.
- (61) Heyrovský, J.; Kuta, J. *Principles of Polarography*; Academic Press: New York, 1966.
- (62) Navrátil, T.; Novotný, L. *Fresenius' J. Anal. Chem.* **2000**, *366* (3), 249. doi:10.1007/s002160050049.
- (63) Sánchez-Sánchez, C. M.; Rodríguez-López, J.; Bard, A. J.; *Anal. Chem.* **2008**, *80* (9), 3254. doi:10.1021/ac702453n. PMID:18355084.
- (64) Tsushima, M.; Tokuda, K.; Ohsaka, T. *Anal. Chem.* **1994**, *66* (24), 4551. doi:10.1021/ac00096a024.
- (65) Vasudevan, D.; Wendt, H. J. *Electroanal. Chem.* **1995**, *392* (1–2), 69. doi:10.1016/0022-0728(95)04044-O.
- (66) Araki, T.; Kitaoka, H. *Chem. Pharm. Bull. (Tokyo)* **2001**, *49* (5), 541. doi:10.1248/cpb.49.541. PMID:11383603.



# Theoretical study of the electron spectra of *s*-triazine vapour

Delano P. Chong

**Ref.:** *Can. J. Chem.* **2009**, 87 (8), 1148.

For the removal of an electron from the degenerate MOs of a molecule, there are two ways to describe the cation: (i) using fractional electrons to maintain full symmetry, and (ii) removing an electron from one of the degenerate MOs. For more reliable prediction of vertical ionization energies (VIEs) using the method abbreviated as  $\Delta$ PBE0(SAOP) in the above-mentioned paper,<sup>1</sup> the latter choice should have been used, except for nonperhalo molecules,<sup>2</sup> instead of which choice (i) was incorrectly employed. In Table 1 below, the results for both choices are shown, together with

the deviations from experiment in parentheses, as well as the results from a larger basis set known as even-tempered valence quadruple-zeta (et-pVQZ) of Slater-type orbitals.<sup>3</sup>

It can be seen that the aug-TZP basis set is sufficiently large for VIEs. In addition, the assignment of the bands at 17.8 and 18.2 to  $1a_2'$  and  $4a_1'$ , respectively, is uncertain.<sup>4</sup> Since my  $\Delta$ PBE0(SAOP) procedure has been so successful in predicting VIEs, I offer the alternative of interchanging the two assignments in Table 1, with the result of smaller average absolute deviations (AADs).

**Table 1.** Comparison of calculated vertical ionization energies, in eV, of gas-phase *s*-triazine (with deviations in parentheses).

Species	Observed <sup>a</sup>	$\Delta$ PBE0(SAOP)/aug-TZP		$\Delta$ PBE0(SAOP)/et-pVQZ
		(i) Full symmetry	(ii) Integer occupations	(ii) Integer occupations
6e'	10.39	10.84 (+ 0.45)	10.43 (+0.04)	10.42 (+0.03)
1e''	11.69	12.43 (+0.74)	11.91 (+0.22)	11.92 (+0.23)
5a <sub>1</sub> '	13.23	13.38 (+0.15)	13.38 (+0.15)	13.36 (+0.13)
5e'	14.66	15.14 (+0.48)	14.79 (+0.13)	14.78 (+0.12)
1a <sub>2</sub> ''	14.87	15.42 (+0.15)	15.42 (+0.55)	15.43 (+0.56)
1a <sub>2</sub> '	17.8/18.2	18.22 (+0.4 <sub>2</sub> /+0.0 <sub>2</sub> )	18.22 (+0.4 <sub>2</sub> /+0.0 <sub>2</sub> )	18.19 (+0.3 <sub>9</sub> /-0.0 <sub>1</sub> )
4a <sub>1</sub> '	18.2/17.8	18.07 (-0.1 <sub>3</sub> /+0.2 <sub>7</sub> )	18.07 (-0.1 <sub>3</sub> /+0.2 <sub>7</sub> )	18.05 (-0.1 <sub>5</sub> /+0.2 <sub>5</sub> )
4e'	22.2	22.45 (+0.2 <sub>5</sub> )	21.99 (-0.2 <sub>1</sub> )	21.96 (-0.2 <sub>4</sub> )
3e'		28.69	28.20	28.17
3a <sub>1</sub> '		31.64	31.64	31.60
AAD	0.00	0.40/0.36	0.23/0.20	0.23/0.20

<sup>a</sup>Best estimate from different experiments. See Table 1 of ref. 1.

## References

- (1) Chong, D. P. *Can. J. Chem.* **2009**, 87 (8), 1148. doi:10.1139/V09-084.
- (2) Segala, M.; Chong, D. P. *J. Electron Spectrosc. Relat. Phenom.* **2009**, 171 (1-3), 18. doi:10.1016/j.elspec.2008.12.006.
- (3) Chong, D. P.; van Lenthe, E.; Van Gisbergen, S.; Baerends, E. *J. J. Comput. Chem.* **2004**, 25 (8), 1030. doi:10.1002/jcc.20030. PMID:15067678.
- (4) Fridh, C.; Åsbrink, L.; Jonsson, B. Ö.; Lindholm, E. *Int. J. Mass Spectrom. Ion Phys.* **1972**, 8 (2), 85. doi:10.1016/0020-7381(72)80001-9.

Received 30 April 2010. Accepted 30 April 2010. Published on the NRC Research Press Web site at canjchem.nrc.ca on 18 May 2010.

**D.P. Chong.** Department of Chemistry, 2036 Main Mall, The University of British Columbia, Vancouver, BC V6T 1Z1, Canada.

# Stereoelectronic interaction effects on the conformational properties of 5-methyl-5-aza-1,3-dithiacyclohexane and its analogous containing N, P, O, and Se atoms — A hybrid density functional theory (DFT), ab initio study, and natural bond orbital (NBO) analysis

Davood Nori-Shargh, Neda Hassanzadeh, Meisam Kosari, Parvin Rabieikarahrudi, Hooriye Yahyaei, and Sasan Sharifi

**Abstract:** Natural bond orbital (NBO) analysis, hybrid density functional theory (hybrid DFT: B3LYP/6-311+G\*\*//B3LYP/6-311+G\*\*), and ab initio molecular orbital (MO: MP2/6-311+G\*\*//B3LYP/6-311+G\*\*) based methods were used to study the electronic delocalization energy (DE), dipole–dipole interactions, and steric repulsions on the conformational properties of 5-methyl-5-aza-1,3-dioxacyclohexane (**1**) (-phospha- (**2**), -arsena- (**3**)), 5-methyl-5-aza-1,3-dithiacyclohexane (**4**) (-phospha- (**5**), -arsena- (**6**)), and 5-methyl-5-aza-1,3-diselenacyclohexane (**7**) (-phospha- (**8**), -arsena- (**9**)). The MP2/6-311+G\*\*//B3LYP/6-311+G\*\* and B3LYP/6-311+G\*\*//B3LYP/6-311+G\*\* results revealed that the axial stereoisomers of compounds **1–9** are more stable than their equatorial stereoisomers. In this regard, the obtained results showed an egregious axial preference for compounds **1**, **4**, and **7**. Importantly, the results showed that the energy differences between the axial and equatorial stereoisomers decrease from compounds **1** → **3**, **4** → **6**, and also, **7** → **9**. The NBO analysis of donor–acceptor interactions revealed that the calculated DE for compounds **1–3** are  $-21.50$ ,  $-7.84$ , and  $-4.38$  kcal mol<sup>-1</sup>, respectively. The decrease of the calculated DE values from compound **1** to compound **3** could reasonably explain the decrease of the energy differences between the axial and equatorial stereoisomers from compound **1** to compound **3**. The correlation between the DE, dipole–dipole interactions, structural parameters, and conformational behaviors of compounds **1–9** has been investigated.

**Key words:** anomeric effects, molecular modeling, ab initio, natural bond orbital (NBO), 5-methyl-5-aza-1,3-dithiacyclohexane.

**Résumé :** On a fait appel à des méthodes d'analyse à base de l'orbitale de liaison neutre (OLN), de la théorie de la fonctionnelle de densité hybride (TFD-hybride : B3LYP/6–311+G\*\*//B3LYP/6–311+G\*\*) et l'orbitale moléculaire ab initio (OM : MP2/6–311+G\*\*//B3LYP/6–311+G\*\*) pour étudier l'énergie de délocalisation (ED) électronique, les interactions dipôle-dipôle et les répulsions stériques sur les propriétés conformationnelles du 5-méthyl-5-aza-1,3-dioxacyclohexane (**1**) [-phospha- (**2**), -arséna- (**3**)], 5-méthyl-5-aza-1,3-dithiacyclohexane (**4**) [-phospha- (**5**), -arséna- (**6**)] et 5-méthyl-5-aza-1,3-disélenacyclohexane (**7**) [-phospha- (**8**), -arséna- (**9**)]. Les résultats obtenus avec les méthodes MP2/6–311+G\*\*//B3LYP/6–311+G\*\* et B3LYP/6–311+G\*\*//B3LYP/6–311+G\*\* révèlent que les stéréoisomères axiaux des composés **1–9** sont plus stables que les stéréoisomères équatoriaux. Dans cette optique, les résultats obtenus montrent une préférence globale pour les composés **1**, **4** et **7**. De plus, les résultats montrent que les différences d'énergie entre les stéréoisomères axiaux et équatoriaux diminuent dans les composés **1** → **3**, **4** → **6** et aussi **7** → **9**. L'analyse de l'OLN des interactions donneur-accepteur révèle que l'énergie de délocalisation pour les composés **1–3** sont respectivement de  $-21,50$ ,  $-7,84$  et  $-4,38$  kcal mol<sup>-1</sup>. La diminution des valeurs calculées d'ED en allant du composé **1** au composé **3** pourrait facilement être expliquée par une diminution dans les différences d'énergie entre les stéréoisomères axiaux et équatoriaux des composés **1** à **3**. On a étudié la corrélation entre les ED, les interactions dipôle-dipôle, les paramètres de structure et les comportements conformationnels des composés **1–9**.

**Mots-clés :** effets anomères, modelage moléculaire, ab initio, orbitale de liaison neutre (OLN), 5-méthyl-5-aza-1,3-dithiacyclohexane.

[Traduit par la Rédaction]

Received 2 September 2009. Accepted 14 December 2009. Published on the NRC Research Press Web site at canjchem.nrc.ca on 24 May 2010.

**D. Nori-Shargh.**<sup>1</sup> Chemistry Department, Science and Research Branch, Islamic Azad University, Hesarak, Poonak, Tehran, Iran.

**N. Hassanzadeh.** Chemistry Department, Ahvaz Branch, Islamic Azad University, Ahvaz, Iran; Chemistry Department, Science Faculty, Arak Branch, Islamic Azad University, Arak, Iran.

**M. Kosari, P. Rabieikarahrudi, and S. Sharifi.** Chemistry Department, Science Faculty, Arak Branch, Islamic Azad University, Arak, Iran.

**H. Yahyaei.** Chemistry Department, Zanjan Branch, Islamic Azad University, P.O. Box 49195-467, Zanjan, Iran.

<sup>1</sup>Corresponding author (e-mail: nori\_ir@yahoo.com).

## Introduction

The knowledge about conformational properties of heterocyclic compounds should be of very general interest since saturated heterocyclic compounds comprise a large segment of organic and inorganic chemistry and are quite widespread in nature (e.g., in alkaloids, carbohydrates, and plant growth regulators, among other compounds).

It is well-known that the stereoelectronic interactions are expected to play an important role on the conformational properties of heterocyclic compounds.<sup>1,2</sup> In this context, Angiolini et al.<sup>3</sup> have described that the methyl group in 5-methyl-5-aza-1,3-dithiacyclohexane (**1**) is largely axial. There is a substantial disfavoring factor in the equatorial conformation of compound **1** (unshared electron pairs are parallel (e.g., the “rabbit-ear effect”)).<sup>4,5</sup> On the other hand, the axial orientation of the methyl group at the nitrogen atom in compound **1** has been explained in terms of favorable  $LP_N \rightarrow \sigma^*_{C-S}$  (LP = lone pair) orbital interactions.<sup>6,7</sup>

It should be noted that the anomeric effect (AE) is in favor of the axial conformation of a six-membered saturated ring in opposition to the steric effect, which normally leads to a preference for the equatorial conformation. In this context, there is a stereoelectronic preference for conformations in which the best donor lone pair is antiperiplanar to the best acceptor bond.<sup>8,9</sup> Therefore, we could stress that the delocalization energy (DE) associated with electronic delocalizations must be considered as the difference between the sum of the equatorial and axial delocalization energies:

$$[1] \quad DE = \Sigma DE_{eq} - \Sigma DE_{ax}$$

Based on this argument, there is a direct relationship between the DE and AE.

The origin of the generalized anomeric effects in methanediol and its sulfur, selenium, and tellurium derivatives were examined by ab initio calculations<sup>10,11</sup> and NBO<sup>12–17</sup> analysis. Also, the conformational preferences of methanediol, dithoxymethane, and methanediamine were analyzed within the framework of the quantum theory of atom in molecule (QTAIM) method.<sup>18,19</sup> In addition, the NBO analysis was performed to study the conformational stability of  $CH_2(XH_2)_2$  (X = N, P, As) compounds.<sup>20</sup>

There is sufficient published experimental information about the stereoelectronic and steric interactions in compound **1**,<sup>3,6,7</sup> but there is no published experimental or quantitative theoretical data about the donor–acceptor delocalization effects on the conformational properties of compounds **1–9**. In this work, the stereoelectronic interactions associated with the DE, dipole–dipole interactions, and also the confor-

mational and structural properties of compounds **1–9** have been investigated computationally using both ab initio molecular orbital (MO) and density functional theory (DFT) methods (see Scheme 1).<sup>21–25</sup>

Also, the stabilization energies ( $E_2$ ) associated with  $LP_{eqX5} \rightarrow \sigma^*_{C6-Y1}$  and  $LP_{axX5} \rightarrow \sigma^*_{C6-Y1}$  delocalizations (see Figs. 1 and 2) and their influences on the conformational properties of compounds **1–9** were quantitatively investigated by the NBO (natural bond orbital) analysis.<sup>26</sup> The resonance energies associated with donor  $\rightarrow$  acceptor electronic delocalizations are proportional to  $S^2/\Delta E$  where  $S$  is the orbital overlap and  $\Delta E$  is the energy differences between the LP and  $\sigma^*$  orbitals.<sup>27</sup>

$$E_2 \text{ (stabilization or resonance energy)} \propto (S^2/\Delta E)$$

In addition, the stabilization energy ( $E_2$ ) associated with  $i \rightarrow j$  delocalization is explicitly estimated by the following equation:

$$[2] \quad E_2 = q_i \frac{F^2(i,j)}{\varepsilon_j - \varepsilon_i}$$

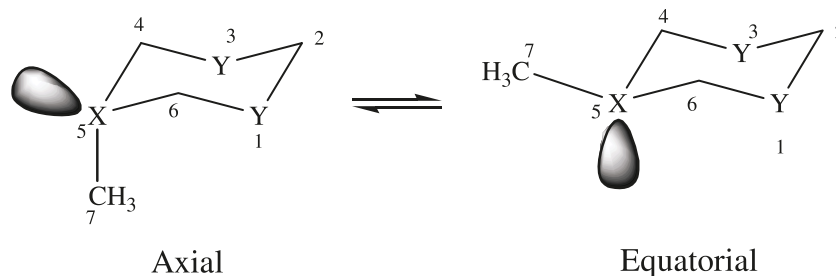
where  $q_i$  is the  $i$ th donor orbital occupancy,  $\varepsilon_i$  and  $\varepsilon_j$  are diagonal elements (orbital energies), and  $F(i,j)$  are off-diagonal elements associated with the NBO Fock matrix. Therefore, there is a direct relationship between  $F(i,j)$  off-diagonal elements and the orbital overlap ( $S$ ).

The successful application of DFT-based methods broadened the applicability of the computational methods and now represents an interesting approach for determining activation barrier and molecular energies.<sup>22–25</sup> On the other hand, the B3LYP method combines Becke’s three-parameter exchange function with the correlation function of Lee et al.<sup>23</sup> Our recent studies showed that the NBO analysis is a sufficient approach to investigate the stereoelectronic interactions on the reactivity and dynamic behaviors of chemical compounds.<sup>28–31</sup>

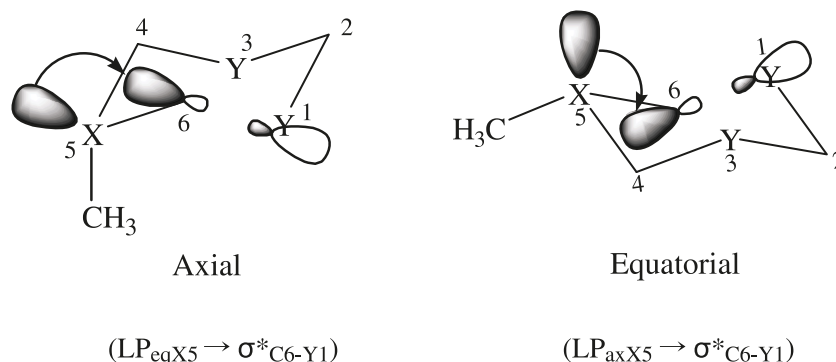
## Computational details

Ab initio calculations were carried out using MO (MP2/6-311+G\*\*//B3LYP/6-311+G\*\*) and hybrid DFT (B3LYP/6-311+G\*\*//B3LYP/6-311+G\*\*) based methods with the Gaussian 98 package of programs.<sup>21</sup> Also, B3LYP/6-311+G\*\* level of theory was used for optimizing the initial estimated structural geometries of compounds **1–9**. Energy minimum molecular geometries were located by minimizing energy with respect to all geometrical coordinates without imposing any symmetry constraints. The nature of the stationary points

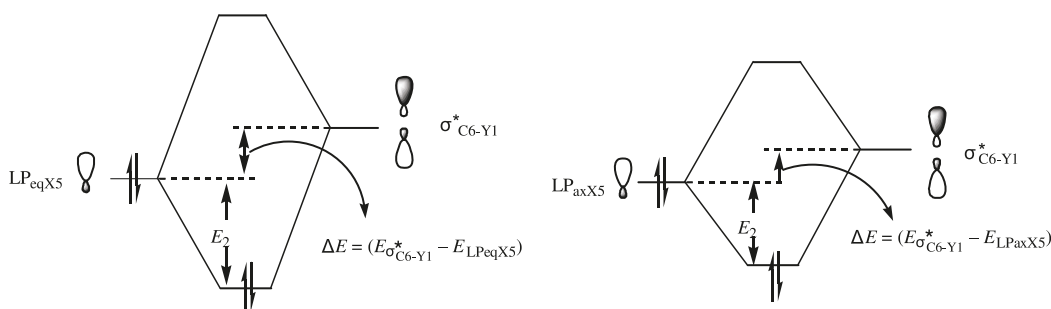
**Scheme 1.** Schematic representation of the stereoisomers of compounds **1–9**.



**Fig. 1.** Schematic representation of the electronic delocalization between nonbonding and antibonding orbitals (i.e.,  $\text{LP}_{\text{eqX5}} \rightarrow \sigma^*_{\text{C6-Y1}}$  and  $\text{LP}_{\text{axX5}} \rightarrow \sigma^*_{\text{C6-Y1}}$ ) in compounds **1–9**.



**Fig. 2.** Schematic representation of stabilization energy (resonance energy;  $E_2$ ) associated with donor (nonbonding)–acceptor (antibonding) interactions.



for compounds **1–9** has been determined by means of the number of imaginary frequencies. For minimum state structures, only all real frequency values were accepted.<sup>32,33</sup>

An NBO analysis was then performed using the B3LYP/6-311+G\*\* level for the axial and trans forms of compounds **1–9** by the NBO 3.1 program<sup>26</sup> included in the Gaussian 98 package of programs.<sup>21</sup>

The bonding and antibonding orbital occupancies in the axial and equatorial conformations of compounds **1–9**, and also the stabilization energies associated with  $\text{LP}_{\text{eqX5}} \rightarrow \sigma^*_{\text{C6-Y1}}$  and  $\text{LP}_{\text{axX5}} \rightarrow \sigma^*_{\text{C6-Y1}}$  delocalizations, were calculated using NBO analysis. The stabilizing orbital interactions is inversely proportional to the energy difference between the interacting orbitals; therefore, the strongest stabilizing interactions will take place between the most effective donors and the most effective acceptors (see Fig. 2).

The thermodynamic functions (all corrected for the zero-point energy), i.e.,  $E_0$ , enthalpy,  $H$  (sum of the electronic and the thermal enthalpy), Gibbs free energy,  $G$  (sum of the electronic and thermal free energy), and entropy,  $S$ , were calculated according to the following relation:  $E = E_0 + E_{\text{vib}} + E_{\text{rot}} + E_{\text{trans}}$ ,  $H = E + RT$ ,  $G = H - TS$ . Finally, using the corresponding calculated thermodynamic data for ground and transition states,  $\Delta G$ ,  $\Delta H$ , and  $\Delta S$  were also determined.

## Results and discussion

The zero point (ZPE) and total electronic ( $E_{\text{el}}$ ) energies ( $E_0 = E_{\text{el}} + \text{ZPE}$ ) for the axial and equatorial stereoisomers of compounds **1–9**, as calculated by the DFT (B3LYP/6-311+G\*\* level of theory) are given in Table 1. For single-

point energy calculations, the ab initio molecular orbital (MP2/6-311+G\*\*//B3LYP/6-311+G\*\*) method was used (see Table 1). Table 2 shows the value of the thermodynamic functions,  $H$ ,  $S$ , and  $G$ , and the  $\Delta G$ ,  $\Delta S$  and  $\Delta H$  parameters. The calculated  $\Delta S$  values are relatively small, so that the calculated  $\Delta H$  and  $\Delta G$  parameters are close to the  $\Delta E_0$  values.

The B3LYP/6-311+G\*\*//B3LYP/6-311+G\*\* results revealed that the axial stereoisomers of compounds **1–3** are more stable than their equatorial stereoisomers by 3.39, 1.03, and 2.18 kcal mol<sup>-1</sup>, respectively. Also, the axial stereoisomers of compounds **1–3** are more stable than their equatorial stereoisomers by 4.03, 4.00, and 3.12 kcal mol<sup>-1</sup>, respectively, as calculated at the MP2/6-311+G\*\*//B3LYP/6-311+G\*\* level of theory (see Table 1). In addition, the Gibbs free energy difference ( $G_{\text{equatorial}} - G_{\text{axial}}$ ) values (i.e.,  $\Delta G_{\text{eq-ax}}$ ) between the axial and equatorial stereoisomers decrease from compound **1** to compound **3**. The calculated  $\Delta G_{\text{eq-ax}}$  values for compounds **1–3** are 3.32, 3.22, and 2.07 kcal mol<sup>-1</sup>, respectively, as calculated at the B3LYP/6-311+G\*\*//B3LYP/6-311+G\*\* level of theory (see Table 2).

Importantly, the MO and hybrid DFT results revealed that the energy differences between the axial and equatorial stereoisomers of compound **4** are more than those for the corresponding stereoisomers of compound **1**. Contrary to the observed trend for compound **4**, the energy differences between the axial and equatorial stereoisomers of compounds **5** and **6** are less than those for the corresponding stereoisomers of compounds **2** and **3**, respectively (see Table 1). In addition, the  $\Delta G_{\text{eq-ax}}$  values decreases from compound **4** to compound **6** (see Table 2).



**Table 1.** B3LYP/6-311+G\*\*//B3LYP/6-311+G\*\* and MP2/6-311+G\*\*//B3LYP/6-311+G\*\* calculated total energies,  $E$  (in hartree), zero-point energies, ZPE (in hartree, from B3LYP/6-311+G\*\* level), and relative energies,  $\Delta E$  ( $E_h$ , in hartree), for the equatorial and axial conformations of compounds **1–9**.

Method	B3LYP/6-311+G**//B3LYP/6-311+G**				MP2/6-311+G**//B3LYP/6-311+G**		
Geometry	ZPE	$E_{el}$	$E_0$	$\Delta E_0^a$	$E_{el}$	$E_0$	$\Delta E_0^a$
1-eq	0.13824	–363.11272	–362.97448	(3.39) <sup>b</sup>	–362.11336	–361.97512	(4.03) <sup>b</sup>
1-ax	0.13907	–363.11894	–362.97987	0.00000	–362.12061	–361.98154	0.00000
2-eq	0.13151	–649.72975	–649.59824	(3.28) <sup>b</sup>	–648.34037	–648.20886	(4.00) <sup>b</sup>
2-ax	0.13170	–649.73517	–649.60347	0.00000	–648.346936	–648.21523	0.00000
3-eq	0.12975	–2544.22886	–2544.09910	(2.18) <sup>b</sup>	–2541.74144	–2541.61169	(3.12) <sup>b</sup>
3-ax	0.12998	–2544.23255	–2544.10257	0.00000	–2541.74664	–2541.61667	0.00000
4-eq	0.13076	–1009.06485	–1008.9341	(5.52) <sup>b</sup>	–1007.30501	–1007.17425	(5.10) <sup>b</sup>
4-ax	0.13145	–1009.07433	–1008.94289	0.00000	–1007.31383	–1007.18238	0.00000
5-eq	0.12397	–1295.69751	–1295.57354	(1.25) <sup>b</sup>	–1293.54869	–1293.42472	(0.95) <sup>b</sup>
5-ax	0.124187	–1295.69972	–1295.57553	0.000000	–1293.5504148	–1293.426228	0.000000
6-eq	0.12213	–3190.19696	–3190.07484	0.00082	–3186.95158	–3186.82945	(0.71) <sup>b</sup>
6-ax	0.12231	–3190.19796	–3190.07565	0.00000	–3186.95289	–3186.83058	0.00000
7-eq	0.12797	–5015.72864	–5015.60067	(6.94) <sup>b</sup>	–5011.80205	–5011.67408	(6.89) <sup>b</sup>
7-ax	0.12888	–5015.74061	–5015.61173	0.00000	–5011.81394	–5011.68506	0.00000
8-eq	0.12127	–5302.36378	–5302.24251	(1.15) <sup>b</sup>	–5298.05159	–5297.93033	(0.75) <sup>b</sup>
8-ax	0.12151	–5302.36586	–5302.24435	0.00000	–5298.05303	–5297.93152	0.00000
9-eq	0.11950	–7196.86294	–7196.74344	(0.31) <sup>b</sup>	–7191.45446	–7191.33496	(0.42) <sup>b</sup>
9-ax	0.11956	–7196.86350	–7196.74394	0.00000	–7191.45518	–7191.33562	0.00000

<sup>a</sup>Relative to the most stable conformation.

<sup>b</sup>Numbers in parentheses are the corresponding thermodynamic function values in kcal mol<sup>–1</sup>.

**Table 2.** B3LYP/6-311+G\*\*//B3LYP/6-311+G\*\* calculated thermodynamic functions for the equatorial and axial conformations of compounds **1–9**.

Geometries	$H$ (hartree)	$S$ (cal mol <sup>–1</sup> K <sup>–1</sup> )	$G$ (hartree)	$\Delta H$ (hartree) <sup>a</sup>	$\Delta S$ (cal mol <sup>–1</sup> K <sup>–1</sup> ) <sup>a</sup>	$\Delta G$ (hartree) <sup>a</sup>
1-eq	–362.96707	78.96	–363.00459	0.00055 (3.45) <sup>b</sup>	0.43	0.00529 (3.32) <sup>b</sup>
1-ax	–362.97257	78.52	–363.00988	0.00000	0.00	0.00000
2-eq	–649.58971	84.70	–649.62996	0.00527 (3.30) <sup>b</sup>	0.28	0.00513 (3.22) <sup>b</sup>
2-ax	–649.59498	84.42	–649.63509	0.00000	0.000	0.00000
3-eq	–2544.09033	88.71	–2544.13218	0.00353 (2.22) <sup>b</sup>	0.49	0.00330 (2.07) <sup>b</sup>
3-ax	–2544.09356	88.22	–2544.13548	0.00000	0.00	0.00000
4-eq	–1008.92545	86.08	–1008.96634	0.00881 (5.53) <sup>b</sup>	0.26	0.00868 (5.45) <sup>b</sup>
4-ax	–1008.93425	85.82	–1008.97503	0.00000	0.00	0.00000
5-eq	–1295.56378	91.42	–1295.60722	0.00196 (1.23) <sup>b</sup>	0.00	0.00202 (1.27) <sup>b</sup>
5-ax	–1295.56575	91.54	–1295.60924	0.000000	0.12	0.00000
6-eq	–3190.06445	95.90	–3190.11001	0.00078 (0.49) <sup>b</sup>	0.00	0.00089 (0.56) <sup>b</sup>
6-ax	–3190.06523	96.11	–3190.11090	0.00000	0.21	0.00000
7-eq	–5015.59110	93.85	–5015.63569	0.01116 (7.00) <sup>b</sup>	0.91	0.01073 (6.73) <sup>b</sup>
7-ax	–5015.60226	92.94	–5015.64642	0.00000	0.00	0.00000
8-eq	–5302.23194	98.32	–5302.27866	0.00178 (1.12) <sup>b</sup>	0.00	0.00193 (1.21) <sup>b</sup>
8-ax	–5302.23372	98.63	–5302.28058	0.00000	0.31	0.00000
9-eq	–7196.73228	102.38	–7196.78092	0.00038 (0.24) <sup>b</sup>	0.00	0.00084 (0.53) <sup>b</sup>
9-ax	–7196.73265	103.35	–7196.78176	0.00000	0.97	0.00000

<sup>a</sup>Relative to the ground state.

<sup>b</sup>Numbers in parentheses are the corresponding thermodynamic function values in kcal mol<sup>–1</sup>.

Importantly, the B3LYP/6-311+G\*\*//B3LYP/6-311+G\*\* and MP2/6-311+G\*\*//B3LYP/6-311+G\*\* results revealed that the energy difference between the axial and equatorial stereoisomers of compound **7** is more than those for the corresponding stereoisomers of compounds **1** and **4**. Based on B3LYP/6-311+G\*\*//B3LYP/6-311+G\*\* results, the axial stereoisomer of compounds **7–9** are more stable than their

equatorial stereoisomers by 6.94, 1.15, and 0.31 kcal mol<sup>–1</sup>, respectively. Also, the axial stereoisomers of compounds **7–9** are more stable than their equatorial stereoisomers by about 6.89, 0.75, and 0.42 kcal mol<sup>–1</sup>, respectively, as calculated at the MP2/6-311+G\*\*//B3LYP/6-311+G\*\* level of theory (see Table 1). In addition, the calculated  $\Delta G_{eq-ax}$  values decreases from compound **7** to compound **9**. The calculated

**Table 3.** NBO calculated stabilization energies ( $E_2$ ), delocalization energy (DE) associated with  $LP_{eqX5} \rightarrow \sigma^*_{C6-Y1}$  and  $LP_{axX5} \rightarrow \sigma^*_{C6-Y1}$  electronic delocalizations and dipole moments for the equatorial and axial conformations of compounds **1–9**, based on the geometry optimized at the B3LYP/6-311+G\*\* level of theory.

	Stabilization energy (resonance energy) (kcal mol <sup>-1</sup> )							
	1		2		3		4	
Donor $\rightarrow$ acceptor	eq	ax	eq	ax	eq	ax	eq	ax
$LP_{eqX5} \rightarrow \sigma^*_{C6-Y1}$	—	2(13.19)	—	2(3.93)	—	2(2.19)	—	2(16.61)
( $LP_{eqX5} \rightarrow \sigma^*_{C4-Y3}$ )		[0.078] <sup>a</sup>		[0.046] <sup>a</sup>		[0.037] <sup>a</sup>		[0.075] <sup>a</sup>
$LP_{axX5} \rightarrow \sigma^*_{C6-Y1}$	2(2.44)	—	—	—	—	—	2(2.50)	—
( $LP_{axX5} \rightarrow \sigma^*_{C4-Y3}$ )	[0.034] <sup>a</sup>						[0.030] <sup>a</sup>	
$\Sigma DE$	4.88	26.38	—	7.84	—	4.38	5.00	33.22
DE	—	-21.50	—	-7.84	—	-4.38	—	-28.22
$\mu$ (D)	2.650	1.194	2.965	0.945	2.769	1.088	2.628	1.722

<sup>a</sup>Off-diagonal elements.

**Table 3 (concluded).**

	Stabilization energy (resonance energy) (kcal mol <sup>-1</sup> )									
	5		6		7		8		9	
Donor $\rightarrow$ acceptor	eq	ax	eq	ax	eq	ax	eq	ax	eq	ax
$LP_{eqX5} \rightarrow \sigma^*_{C6-Y1}$	—	2(6.53)	—	2(4.21)	—	2(19.48)	—	2(7.61)	—	2(4.97)
( $LP_{eqX5} \rightarrow \sigma^*_{C4-Y3}$ )		[0.054]		[0.047]		[0.075]		[0.054]		[0.048]
$LP_{axX5} \rightarrow \sigma^*_{C6-Y1}$	—	—	—	—	2(3.97)	—	—	—	—	—
( $LP_{axX5} \rightarrow \sigma^*_{C4-Y3}$ )					[0.035]					
$\Sigma DE$	—	13.06	—	8.42	7.94	38.96	—	15.22	—	9.94
DE	—	-13.06	—	-8.42	—	-31.02	—	-15.22	—	-9.94
$\mu$ (D)	2.965	0.945	2.760	1.1856	2.508	1.953	2.653	0.746	2.472	0.976

<sup>a</sup>Off-diagonal elements.

$\Delta G_{eq-ax}$  for compounds **7–9** are 6.73, 1.21 and 0.53 kcal mol<sup>-1</sup>, respectively, as calculated at the B3LYP/6-311+G\*\*//B3LYP/6-311+G\*\* level of theory (see Table 2). Accordingly, the axial preference for compound **7** is more than compounds **4** and **1**. In addition, the axial preference dwindling from compound **1** to **3** is more than those for compounds **4–6** and also compounds **7–9** (see Tables 1 and 2).

According to the NBO results, the axial and equatorial stereoisomers of compounds **1–9** benefit from  $LP_{eqX5} \rightarrow \sigma^*_{C6-Y1}$  and  $LP_{axX5} \rightarrow \sigma^*_{C6-Y1}$  donor–acceptor interactions. Based on the optimized ground state geometries using the B3LYP/6-311+G\*\* method, the NBO analysis of donor–acceptor interactions showed that the stabilization energies associated with  $LP_{eqX5} \rightarrow \sigma^*_{C6-Y1}$  electronic delocalizations for the axial stereoisomers of compounds **1–3** are 13.19, 3.92, and 2.19 kcal mol<sup>-1</sup>, respectively (see Table 3). Also, the stabilization energies associated with  $LP_{eqX5} \rightarrow \sigma^*_{C6-Y1}$  electronic delocalizations decrease from the axial stereoisomers of compound **4** to compound **6** and also compound **7** to compound **9** (see Table 3). Interestingly, the decrease of axial preference from compounds **1**  $\rightarrow$  **3**, **4**  $\rightarrow$  **6**, and **7**  $\rightarrow$  **9** could be fairly explained by the decrease of the stabilization energies associated with  $LP_{eqX5} \rightarrow \sigma^*_{C6-Y1}$  electronic delocalizations. It should be noted that there is no  $LP_{eqX5} \rightarrow \sigma^*_{C6-Y1}$  electronic delocalization for the equatorial stereoisomer of compounds **1–9**.

Also, the NBO analysis revealed that there is  $LP_{axX5} \rightarrow \sigma^*_{C6-Y1}$  electronic delocalization only for the equatorial stereoisomers of compounds **1**, **4**, and **7**, and it is not observed for the axial and equatorial stereoisomers of compounds **2**,

**3**, **5**, **6**, **8**, and **9**. In this regard, the stabilization energies associated with  $LP_{axX5} \rightarrow \sigma^*_{C6-Y1}$  electronic delocalizations for the equatorial stereoisomers of compounds **1**, **4**, and **7** are 2.44, 2.50, and 3.97 kcal mol<sup>-1</sup>, respectively.

Based on the eq. [1], the DE associated with  $LP_{axX5} \rightarrow \sigma^*_{C6-Y1}$  and  $LP_{eqX5} \rightarrow \sigma^*_{C6-Y1}$  electronic delocalizations decreases from compound **1** to compound **3**. The calculated DE for compounds **1–3** are -21.50, -7.84, and -4.38 kcal mol<sup>-1</sup>, respectively (see Table 3). Along this line, the NBO analysis revealed the calculated DE associated with  $LP_{axX5} \rightarrow \sigma^*_{C6-Y1}$  and  $LP_{eqX5} \rightarrow \sigma^*_{C6-Y1}$  electronic delocalization decreases from compound **4** to compound **6** and also compound **7** to compound **9**. Effectively, the decrease of the DE can explain the decrease of the calculated  $\Delta G_{eq-ax}$  from compounds **1**  $\rightarrow$  **3**, **4**  $\rightarrow$  **6**, and **7**  $\rightarrow$  **9** (see Table 2).

Similar to the larger DE values in the axial stereoisomers of compounds **1–9**, these forms are more stable than their equatorial stereoisomers. From a structural point of view, it seems that the axial stereoisomers of compounds **1–9** could be less stable than their equatorial stereoisomers. The primary reason for this argument is based on the nonbonding gauche repulsions between the methyl group of X5 atoms and 1- and 3-Y atoms of rings. Accordingly, these interactions (steric repulsions) should be weaker than the stabilization energies associated with the DE (associated with  $LP_{axX5} \rightarrow \sigma^*_{C6-Y1}$  electronic delocalizations). Consequently, this fact could justify the stability of the axial stereoisomers of compounds **1–9** compared to their equatorial stereoisomers.

On the other hand, the NBO results showed that the  $LP_{axX5}$  nonbonding orbital occupancies in the axial stereo-

**Table 4.** Calculated nonbonding and antibonding orbital occupancies for the equatorial and axial conformations of compounds **1–9** using NBO analysis, based on the optimized structures by B3LYP/6-311+G\*\* level of theory.

Occupancy	LP <sub>eqX5</sub>	LP <sub>axX5</sub>	$\sigma^*_{C6-Y1}$
1-eq	—	1.8705	0.0261
1-ax	1.8488	—	0.0556
2-eq	—	1.9587	0.0174
2-ax	1.9445	—	0.0320
3-eq	—	1.9776	0.0164
3-ax	1.9677	—	0.0252
4-eq	—	1.8664	0.0312
4-ax	1.7984	—	0.0802
5-eq	—	1.9567	0.0180
5-ax	1.9177	—	0.0427
6-eq	—	1.9763	0.0166
6-ax	1.9508	—	0.0317
7-eq	—	1.8492	0.0421
7-ax	1.7646	—	0.1011
8-eq	—	1.9753	0.0201
8-ax	1.8983	—	0.0538
9-eq	—	1.9753	0.0184
9-ax	1.9390	—	0.0391

isomers of compounds **1–3** are 1.8488, 1.9445, and 1.9677, respectively (see Table 4). Similar to the observed trend for compounds **1–3**, the LP<sub>axX5</sub> nonbonding orbital occupancies increase from the axial stereoisomers of compound **4** to compound **6** and also compound **7** to compound **9**. Contrary to the increase of the LP<sub>axX5</sub> nonbonding orbital occupancies from the axial stereoisomers of compound **1** to compound **3**, compound **4** to compound **6** and compound **7** to compound **9**, the  $\sigma^*_{C6-Y1}$  antibonding orbital occupancies of these stereoisomers decrease. In this regard, NBO results revealed that the  $\sigma^*_{C6-Y1}$  antibonding orbital occupancies in the axial stereoisomers of compounds **1–3** are 0.0556, 0.0320, and 0.0252, respectively. This trend was observed for compounds **4–6** and also compounds **7–9** (see Table 4).

Importantly, the increase of the LP<sub>axX5</sub> nonbonding and the decrease of the  $\sigma^*_{C6-Y1}$  antibonding orbital occupancies in the axial stereoisomers of compounds **1–9** could be justified by the decrease of the LP<sub>axX5</sub>  $\rightarrow$   $\sigma^*_{C6-Y1}$  electronic delocalizations from the axial stereoisomers of compounds **1**  $\rightarrow$  **3**, **4**  $\rightarrow$  **6** and **7**  $\rightarrow$  **9**. Therefore, it can be concluded that the donor-acceptor interaction is an effective factor on the nonbonding and antibonding orbital occupancies of the equatorial and axial stereoisomers of compounds **1–9**.

It has to be noted that the LP  $\rightarrow$   $\sigma^*$  resonance energies are proportional to  $S^2/\Delta E$  where  $S$  is the orbital overlap and  $\Delta E$  is the energy differences between the LP nonbonding and  $\sigma^*$  antibonding orbitals. In this regard, the stereoelectronic orbital interactions are anticipated to be more effective for the anti rather than the syn or gauche arrangement between the donor (LP) and acceptor ( $\sigma^*$ ) orbitals, and the stabilization should increase as the anti-bonding orbital  $\sigma^*$  energy decreases and the nonbonding orbital LP energy increases. The energy difference between donor ( $E_{LPaxX5}$ ) and acceptor ( $E_{\sigma^*C6-Y1}$ ) orbitals ( $\Delta(E_{\sigma^*C6-Y1} - E_{LPaxX5})$ ) for the axial stereoisomers of compounds **1–3** are 0.5778, 0.7045,

and 0.7974 au, respectively, as calculated by NBO analysis. Effectively, the energy differences between donor ( $E_{LPaxX5}$ ) and acceptor ( $E_{\sigma^*C6-Y1}$ ) orbitals ( $\Delta(E_{\sigma^*C6-Y1} - E_{LPaxX5})$ ) increased from the axial stereoisomers of compounds **1**  $\rightarrow$  **3**, **4**  $\rightarrow$  **6**, and **7**  $\rightarrow$  **9**. It can be concluded that the rich acceptor  $\sigma^*_{C6-Y1}$  antibonding orbitals of the axial stereoisomers of compounds **1**, **4** and **7**, compared to those in compounds **2**, **3**, **4**, **5** and **7**, **8** may give rise to strong DE. Also, the decrease of the orbital overlap ( $S$ ) (off-diagonal elements ( $F_{ij}$ )) values could reduce the DE (see Tables 3 and 5). The NBO calculated off-diagonal elements ( $F_{ij}$ ) for LP<sub>axX5</sub>  $\rightarrow$   $\sigma^*_{C6-Y1}$  electronic delocalizations in the axial stereoisomers of compounds **1–3** are 0.078, 0.046, and 0.037, respectively (see Table 5). In this regard, the calculated off-diagonal elements ( $F_{ij}$ ) for LP<sub>axX5</sub>  $\rightarrow$   $\sigma^*_{C6-Y1}$  electronic delocalizations decrease from the axial-stereoisomers of compound **4** to compound **6** and also compound **7** to compound **9**. The decrease of the orbital overlap ( $S$ ) values could be justified by the increase of X5 atom radius from compounds **1**  $\rightarrow$  **3**, **4**  $\rightarrow$  **6**, and **7**  $\rightarrow$  **9**.

In addition, it is well-known that there is a preference for the conformation with the smallest resultant dipole moment. Especially in the gas phase, it is generally found that the conformation with the larger dipole moment has the larger electrostatic energy. Therefore, the conformation with the larger dipole moment has an increased overall energy.<sup>34</sup> Table 3 presents the calculated dipole moments for the axial and equatorial conformations of compounds **1–9**. The B3LYP/6-311+G\*\* results showed that the dipole moments for the equatorial stereoisomers of compounds **1–9** (the rabbit-ear effect) are larger than those in the axial stereoisomers. Accordingly, the rationalization of the conformation preference solely in terms of dipole–dipole interactions succeeds in accounting qualitatively for the axial stereoisomers preferences in compounds **1–9**.

Representative structural parameters for the axial and equatorial stereoisomers of compounds **1–9**, as calculated by B3LYP/6-311+G\*\* level of theory, are shown in Table 6. Although, due to the nature of the various approximations involved in these theoretical calculations, it is not expected, in principal, to obtain exactly the experimental values;<sup>35</sup> however, it is possible to carry out theoretical calculations, from which many properties and structures can be obtained with an accuracy that is competitive with experiments.<sup>35–38</sup> Importantly, considering the structures of compounds **1–9** (optimized by B3LYP/6-311+G\*\* method) gave evidence that in the axial stereoisomers of these compounds the  $\sigma_{X5-C6}$  bond lengths are significantly contracted compared to those in the equatorial stereoisomers. Based on the B3LYP/6-311+G\*\* results, the  $\sigma_{X5-C6}$  bond lengths in the equatorial and axial stereoisomers of compound **1** are 1.456 and 1.445 Å, respectively (see Table 6). Similarly, the  $\sigma_{X5-C6}$  bond lengths in the equatorial and axial stereoisomers of compound **2** are 1.892 and 1.881 Å, respectively, as calculated by B3LYP/6-311+G\*\* level of theory. In this context, the B3LYP/6-311+G\*\* results showed that the  $\sigma_{X5-C6}$  bond lengths in the equatorial and axial stereoisomers of compound **3** are 2.022 and 2.014 Å, respectively.

Along this line, the  $\sigma_{X5-C6}$  bond lengths decrease from the equatorial stereoisomers of compounds **4–9** to their axial stereoisomers. Also, the  $\sigma_{C6-Y1}$  bond lengths of the axial

**Table 5.** Calculated nonbonding and antibonding orbital energies (au) for the equatorial and axial conformations of compounds **1–9** using NBO analysis, based on the optimized structures by B3LYP/6-311+G\*\* level of theory.

Energy	LP <sub>eqX5</sub>	LP <sub>axX5</sub>	$\sigma^*_{C6-Y1}$	$\Delta(E_{\sigma^*C6-Y1} - E_{LP_{eqX5}})$	$\Delta(E_{\sigma^*C6-Y1} - E_{LP_{axX5}})$
1-eq	—	−0.28950	0.29319	—	0.58269
1-ax	−0.28437	—	0.29346	0.57783	—
2-eq	—	−0.42083	0.29421	—	0.71504
2-ax	−0.40923	—	0.29529	0.70452	—
3-eq	—	−0.51192	0.29515	—	0.80707
3-ax	−0.50149	—	0.29587	0.79736	—
4-eq	—	−0.28436	0.14098	—	0.42534
4-ax	−0.27633	—	0.13873	0.41506	—
5-eq	—	−0.41935	0.13829	—	0.55764
5-ax	−0.40213	—	0.13892	0.54105	—
6-eq	—	−0.51695	0.13895	—	0.65590
6-ax	−0.50055	—	0.14037	0.64092	—
7-eq	—	−0.27647	0.08788	—	0.36435
7-ax	−0.27496	—	0.08660	0.36156	—
8-eq	—	−0.51513	0.08508	—	0.60021
8-ax	−0.39657	—	0.08459	0.48116	—
9-eq	—	−0.51513	0.08508	—	0.60018
9-ax	−0.49691	—	0.08604	0.58295	—

conformations decrease from compounds **1** → **3**, **4** → **6**, and **7** → **9**. The B3LYP/6-311+G\*\* results showed that the  $\sigma_{C6-N1}$  bond lengths in the axial stereoisomers of compounds **1–3** are 1.438, 1.428, and 1.423 Å, respectively (see Table 6). This observation is in agreement with the decrease of the LP<sub>axX5</sub> →  $\sigma^*_{C6-Y1}$  electronic delocalization from the axial stereoisomers from compound **1** to compound **3**, compound **4** to compound **6**, and compound **7** to compound **9**. The decrease of the LP<sub>axX5</sub> →  $\sigma^*_{C6-Y1}$  electronic delocalizations can produce the contracted  $\sigma_{C6-Y1}$  bond lengths by decreasing the  $\sigma^*_{C6-Y1}$  antibonding orbital occupancies.

In addition, Table 6 shows that the  $\theta_{5-6-1}$  bond angles increase from the equatorial stereoisomers of compounds **1–9** to their corresponding axial stereoisomers. Also, the  $\phi_{4-5-6-1}$  torsion (dihedral) angles decrease from the equatorial stereoisomers of compounds **1–9** to their corresponding axial stereoisomers. The increase of the  $\theta_{5-6-1}$  bond angles and the decrease of the  $\phi_{4-5-6-1}$  torsion angles from the equatorial stereoisomers of compounds **1–9** to their corresponding axial stereoisomers could be justified by the increase of the X5–C6 bond orders. The LP<sub>eqX5</sub> →  $\sigma^*_{C6-Y1}$  electronic delocalizations can reasonably explain the increase of the X5–C6 bond orders in the axial stereoisomers of compounds **1–9** compared to their corresponding equatorial stereoisomers.

## Conclusion

The above reported ab initio calculations and NBO analysis provided a reasonable picture from structural, energetic, bonding, and stereoelectronic points of view for the conformational preference in compounds **1–9**. Effectively, B3LYP/6-311+G\*\*// B3LYP/6-311+G\*\* results revealed that the calculated  $\Delta G_{eq-ax}$  decreases from compounds **1** → **3**, **4** → **6**, and **7** → **9**. In addition, the dwindling axial preference for compounds **1** → **3** is more than those for compounds **4** → **6** and also compounds **7** → **9**.

In addition NBO results revealed that (i) the stabilization energies associated with LP<sub>eqX5</sub> →  $\sigma^*_{C6-Y1}$  delocalizations for the axial stereoisomers decreases from compounds **1** → **3**, **4** → **6**, and **7** → **9**. (ii) The decrease of the donor–acceptor interactions associated with LP<sub>eqX5</sub> →  $\sigma^*_{C6-Y1}$  delocalizations could fairly explain the increase of occupancies of LP<sub>eqX5</sub> nonbonding orbitals and the decrease of occupancies of  $\sigma^*_{C6-Y1}$  antibonding orbitals from the axial stereoisomers of compounds **1** → **3**, **4** → **6**, and **7** → **9**. (iii) The energy difference between donor ( $E_{LP_{axX5}}$ ) and acceptor ( $E_{\sigma^*C6-Y1}$ ) orbitals ( $\Delta(E_{\sigma^*C6-Y1} - E_{LP_{axX5}})$ ) increased from the axial stereoisomers of compounds **1** → **3**, **4** → **6**, and **7** → **9**. It can be concluded that the rich acceptor antibonding orbital may give rise to strong DE. Also, the decrease of the orbital overlap ( $S$ ) (off-diagonal elements ( $F_{ij}$ )) values could reduce the DE. (iv) The rationalization of the conformation preference solely in terms of dipole–dipole interactions succeeds in accounting qualitatively for the axial stereoisomers preferences in compounds **1–9**.

Also, the  $\sigma_{C6-Y1}$  bond lengths decrease from the axial stereoisomers from compounds **1** → **3**, **4** → **6**, and **7** → **9**. This observation is consistent with the decrease of the LP<sub>axX5</sub> →  $\sigma^*_{C6-Y1}$  electronic delocalization from the axial stereoisomers of compounds **1** → **3**, **4** → **6**, and **7** → **9**, which produce the contracted  $\sigma_{C6-Y1}$  bonds by decreasing the  $\sigma^*_{C6-Y1}$  antibonding orbital occupancies. It can be concluded that the decrease of the DE can reasonably explain the decrease of the calculated  $\Delta G_{eq-ax}$  from compounds **1** → **3**, **4** → **6**, and **7** → **9**. Interestingly, the decrease of axial preference from compounds **1** → **3**, **4** → **6**, and **7** → **9** could be reasonably explained by the decrease of the stabilization energies associated with LP<sub>eqX5</sub> →  $\sigma^*_{C6-Y1}$  electronic delocalizations. Effectively, this fact demonstrates that the order of the anomeric effects (AE) for M–C–N fragments are as follows: N–C–O > P–C–O > As–C–O; N–C–S > P–C–S > As–C–S; N–C–Se > P–C–Se > As–C–Se.



**Table 6.** B3LYP/6-311+G\*\* calculated structural parameters for the equatorial and axial conformations of compounds **1–9**.

Com- pound	<b>1</b>		<b>2</b>		<b>3</b>		<b>4</b>		<b>5</b>		<b>6</b>		<b>7</b>		<b>8</b>		<b>9</b>	
State	eq	ax	eq	ax	eq	ax	eq	ax	eq	ax	eq	ax	eq	ax	eq	ax	eq	ax
<b>Bond lengths (Å°)</b>																		
$r_{1-2}$	1.408	1.412	1.407	1.407	1.407	1.407	1.826	1.833	1.827	1.828	1.828	1.827	1.970	1.977	1.970	1.971	1.971	1.970
$r_{2-3}$	1.408	1.412	1.407	1.407	1.407	1.407	1.826	1.833	1.827	1.828	1.828	1.827	1.970	1.977	1.970	1.971	1.971	1.970
$r_{3-4}$	1.414	1.438	1.425	1.428	1.421	1.422	1.835	1.873	1.831	1.838	1.826	1.828	1.993	2.038	1.978	1.990	1.973	1.977
$r_{4-5}$	1.456	1.445	1.892	1.881	2.022	2.014	1.452	1.438	1.877	1.873	2.007	2.007	1.443	1.428	1.870	1.864	2.000	2.000
$r_{5-6}$	1.456	1.445	1.892	1.881	2.022	2.014	1.452	1.438	1.877	1.873	2.007	2.007	1.443	1.428	1.870	1.864	2.000	1.999
$r_{6-1}$	1.414	1.438	1.425	1.428	1.421	1.423	1.835	1.873	1.831	1.838	1.826	1.828	1.993	2.038	1.978	1.990	1.973	1.977
$r_{5-7}$	1.455	1.468	1.864	1.859	1.992	1.984	1.462	1.461	1.867	1.853	1.995	1.978	1.462	1.459	1.870	1.851	1.997	1.977
<b>Bond angles (°)</b>																		
$\theta_{1-2-3}$	111.9	112.2	113.7	113.5	114.0	113.7	113.8	114.8	117.2	116.9	118.0	117.5	113.8	114.6	117.0	116.6	117.9	117.4
$\theta_{2-3-4}$	110.6	109.8	113.1	113.0	113.8	113.8	97.2	96.5	99.3	99.4	99.9	100.1	95.0	94.3	96.9	97.0	97.5	97.7
$\theta_{3-4-5}$	110.4	112.5	109.8	114.5	109.9	113.9	114.2	116.2	113.6	120.2	113.4	119.7	114.5	116.6	114.2	121.3	113.9	120.9
$\theta_{4-5-6}$	109.5	108.5	92.1	93.8	88.9	90.6	112.9	114.1	97.9	100.7	95.0	98.0	113.9	115.7	99.2	102.3	96.4	99.8
$\theta_{5-6-1}$	110.4	112.5	109.8	114.5	109.9	113.9	114.2	116.2	113.6	120.2	113.4	119.7	114.5	116.6	114.2	121.3	113.9	120.9
$\theta_{6-1-2}$	110.6	109.8	113.1	113.0	113.8	113.8	97.2	96.5	99.3	99.4	99.9	100.1	95.0	94.3	96.9	97.0	97.5	97.7
$\theta_{7-5-6}$	112.4	113.9	99.5	100.1	97.4	97.4	111.8	115.5	98.3	102.1	96.4	99.6	113.2	116.1	97.9	102.7	96.1	100.2
$\theta_{7-5-4}$	112.4	113.9	99.5	100.1	97.5	97.4	111.8	115.5	98.3	102.1	96.4	99.6	113.2	116.1	97.9	102.7	96.1	100.2
<b>Torsion angles (°)</b>																		
$\phi_{1-2-3-4}$	58.3	57.6	66.7	68.0	69.9	71.4	58.9	59.0	65.1	66.9	67.4	69.8	57.2	57.9	63.3	65.4	65.5	68.1
$\phi_{2-3-4-5}$	-57.1	-56.5	-65.5	-60.0	-66.5	-61.2	-60.3	-58.6	-65.9	-60.0	-66.8	-60.4	-60.8	-59.0	-66.5	-60.8	-67.4	-61.0
$\phi_{3-4-5-6}$	56.2	54.6	55.2	44.9	52.8	43.4	70.5	67.1	68.2	54.1	66.7	52.3	75.3	70.8	72.0	57.0	70.7	55.3
$\phi_{4-5-6-1}$	-56.2	-54.6	-55.1	-44.9	-52.8	-43.4	-70.5	-67.1	-68.2	-54.1	-66.7	-52.3	-75.3	-70.8	-72.0	-57.0	-70.7	-55.3
$\phi_{5-6-1-2}$	57.1	56.5	65.4	60.0	66.4	61.1	60.3	58.6	66.0	60.0	66.8	60.4	60.8	59.0	66.5	60.7	67.3	61.0
$\phi_{6-1-2-3}$	-58.3	-57.6	-66.6	-68.0	-69.8	-71.4	-58.9	-59.0	-65.1	-66.9	-67.4	-69.8	-57.2	-57.9	-63.3	-65.4	-65.5	-68.1
$\phi_{7-5-6-1}$	-178.1	73.3	-155.2	56.0	-150.2	54.1	-162.4	70.3	-167.8	50.9	-163.7	48.9	-153.5	70.65	-171.4	49.3	-167.5	47.0
$\phi_{7-5-4-3}$	178.1	-73.3	155.2	-56.0	150.2	-54.1	-62.4	-70.4	167.8	-50.9	163.7	-48.9	153.5	-70.5	171.4	-49.3	167.5	-47.0

## References

- (1) Wilen, S. H. *Stereochemistry of Organic Compounds*; Wiley: New York, 1994.
- (2) Cuevas, G. *The Anomeric Effect*; CRC Press Inc.: Boca Raton, FL, 1995.
- (3) Angiolini, L.; Duke, R. P.; Jones, R. A. Y.; Katritzky, A. R. *J. Chem. Soc. Perkin Trans. 2* **1972**, 674. doi:10.1039/P29720000674.
- (4) Hutchins, R. O.; Kopp, L. D.; Eliel, E. L. *J. Am. Chem. Soc.* **1968**, 90 (25), 7174. doi:10.1021/ja01027a078.
- (5) Eliel, E. L. *Angew. Chem. Int. Ed. Engl.* **1972**, 11 (9), 739. doi:10.1002/anie.197207391.
- (6) Juaristi, E.; Gonzalez, E. A.; Pinto, B. M.; Johnston, B. D.; Nagelkerke, R. *J. Am. Chem. Soc.* **1989**, 111 (17), 6745. doi:10.1021/ja00199a038.
- (7) Pinto, B. M.; Johnston, B. D.; Nagelkerke, R.; Juaristi, E.; González, E. A. *Can. J. Chem.* **1989**, 67 (12), 2067. doi:10.1139/v89-321.
- (8) Kirby, A. J. *The Anomeric Effects and Related Stereoelectronic Effects at Oxygen*; Springer-Verlag: Berlin, 1983.
- (9) Praly, J.-P.; Lemieux, R. U. *Can. J. Chem.* **1987**, 65 (1), 213. doi:10.1139/v87-034.
- (10) Salzner, U.; Schleyer, P. R. *J. Am. Chem. Soc.* **1993**, 115 (22), 10231. doi:10.1021/ja00075a044.
- (11) Schleyer, P. R.; Jemmis, E. D.; Spitznagel, G. W. *J. Am. Chem. Soc.* **1985**, 107 (22), 6393. doi:10.1021/ja00308a041.
- (12) Reed, A. E.; Weinstock, R. B.; Weinhold, F. *J. Chem. Phys.* **1985**, 83 (2), 735. doi:10.1063/1.449486.
- (13) Reed, A. E.; Curtiss, L. A.; Weinhold, F. *Chem. Rev.* **1988**, 88 (6), 899. doi:10.1021/cr00088a005.
- (14) Foster, J. P.; Weinhold, F. *J. Am. Chem. Soc.* **1980**, 102 (24), 7211. doi:10.1021/ja00544a007.
- (15) Brunck, T. K.; Weinhold, F. *J. Am. Chem. Soc.* **1979**, 101 (7), 1700. doi:10.1021/ja00501a009.
- (16) Reed, A. E.; Weinhold, F. *J. Chem. Phys.* **1985**, 83 (4), 1736. doi:10.1063/1.449360.
- (17) Reed, A. E.; Schleyer, P. R. *J. Am. Chem. Soc.* **1987**, 109 (24), 7362. doi:10.1021/ja00258a020.
- (18) Vila, A.; Mosquera, R. A. *J. Comput. Chem.* **2007**, 28 (9), 1516. doi:10.1002/jcc.20585. PMID:17330885.
- (19) Eskandari, K.; Vila, A.; Mosquera, R. A. *J. Phys. Chem. A* **2007**, 111 (34), 8491. doi:10.1021/jp073801y. PMID:17685599.
- (20) Carballeira, L.; Pérez-Juste, I. *J. Phys. Chem. A* **2000**, 104 (41), 9362. doi:10.1021/jp001937p.
- (21) Frisch, M. J.; Trucks, G. W.; Schlegel, H. B.; Scuseria, G. E.; Robb, M. A.; Cheeseman, J. R.; Zakrzewski, V. G.; Montgomery, J. A.; Stratmann, R. E., Jr.; Burant, J. C.; Dapprich, S.; Millam, J. M.; Daniels, A. D.; Kudin, K. N.; Strain, M. C.; Farkas, O.; Tomasi, J.; Barone, V.; Cossi, M.; Cammi, R.; Mennucci, B.; Pomelli, C.; Adamo, C.; Clifford, S.; Ochterski, J.; Petersson, G. A.; Ayala, P. Y.; Cui, Q.; Morokuma, K.; Malick, D. K.; Rabuck, A. D.; Raghavachari, K.; Foresman, J. B.; Cioslowski, J.; Ortiz, J. V.; Stefanov, B. B.; Liu, G.; Liashenko, A.; Piskorz, P.; Komaromi, I.; Gomperts, R.; Martin, R. L.; Fox, D. J.; Keith, T.; Al-Laham, M. A.; Peng, C. Y.; Nanayakkara, A.; Gonzalez, C.; Challacombe, M.; Gill, P. M. W.; Johnson, B.; Chen, W.; Wong, M. W.; Andres, J. L.; Head-Gordon, M.; Replogle, E. S.; Pople, J. A. *Gaussian 98*, revision A.3; Gaussian Inc.: Pittsburgh, PA, 1998.
- (22) Becke, A. D. *J. Chem. Phys.* **1993**, 98 (7), 5648. doi:10.1063/1.464913.
- (23) Lee, C.; Yang, W.; Parr, R. G. *Phys. Rev. B* **1988**, 37 (2), 785. doi:10.1103/PhysRevB.37.785.
- (24) Hehre, W. J.; Radom, L.; Schleyer, P. v. R.; Pople, J. A. *Ab Initio Molecular Orbital Theory*; Wiley: New York, 1986.
- (25) Seminario, J. M.; Politzer, P., Eds. *Modern Density Function Theory. In A Tool for Chemistry*; Elsevier: Amsterdam, 1995.
- (26) Glendening, E. D.; Reed, A. E.; Carpenter, J. E.; Weinhold, F. *NBO*, version 3.1. Theoretical Chemistry Institute, University of Wisconsin: Madison, WI, 2001.
- (27) Dionne, P.; St-Jacques, M. *J. Am. Chem. Soc.* **1987**, 109 (9), 2616. doi:10.1021/ja00243a012.
- (28) Nori-Shargh, D.; Roohi, F.; Deyhimi, F.; Naeem-Abyaneh, R. *J. Mol. Struct. THEOCHEM* **2006**, 763 (1–3), 21. doi:10.1016/j.theochem.2006.01.011.
- (29) Nori-Shargh, D.; Malekhsosseini, M.; Deyhimi, F. *J. Mol. Struct. THEOCHEM* **2006**, 763 (1–3), 187. doi:10.1016/j.theochem.2006.01.032.
- (30) Nori-Shargh, D.; Deyhimi, F.; Boggs, J. E.; Jameh-Bozorghi, S.; Shakibazadeh, R. *J. Phys. Org. Chem.* **2007**, 20 (5), 355. doi:10.1002/poc.1154.
- (31) Nori-Shargh, D.; Abbasi, A.; Jameh-Bozorghi, S.; Deyhimi, F.; Naeem-Abyaneh, R.; Sarkar, F. *Phosphorus Sulfur Silicon Relat. Elem.* **2006**, 181 (1), 75. doi:10.1080/104265090968983.
- (32) McIver, J. W., Jr. *Acc. Chem. Res.* **1974**, 7 (3), 72. doi:10.1021/ar50075a002.
- (33) Ermer, O. *Tetrahedron* **1975**, 31 (16), 1849. doi:10.1016/0040-4020(75)87040-2.
- (34) Wiberg, K. B.; Murcko, M. A. *J. Phys. Chem.* **1987**, 91 (13), 3616. doi:10.1021/j100297a030.
- (35) Freeman, F.; Phornvoranunt, A.; Hehre, W. J. *J. Phys. Org. Chem.* **1998**, 11 (11), 831. doi:10.1002/(SICI)1099-1395(199811)11:11<831::AID-POC75>3.0.CO;2-P.
- (36) Gilbert, T. M. *Tetrahedron Lett.* **1998**, 39 (50), 9147. doi:10.1016/S0040-4039(98)02105-4.
- (37) Strickland, D.; Caldwell, R. A. *J. Phys. Chem.* **1993**, 97 (50), 13394. doi:10.1021/j100152a053.
- (38) Arnason, I.; Thorarinnsson, G. K.; Matern, E. *J. Mol. Struct. THEOCHEM* **1998**, 454, 91. doi:10.1016/S0166-1280(98)00234-6.

# The Meisenheimer model for predicting the principal site for nucleophilic substitution in aromatic perfluorocarbons — Generalization to include ring-nitrogen atoms and non-fluorine ring substituents

Jon Baker and Max Muir

**Abstract:** Our recent simple model for predicting the principal site for nucleophilic substitution in aromatic perfluorocarbons (*J. Fluorine Chem.* **2005**, 126, 727) is generalized to include both ring-nitrogen atoms and non-fluorine ring substituents. The model is based on the relative stabilities of the Meisenheimer complexes as calculated using Hartree–Fock theory with a modest basis set. Calculations on a wide range of fluorine-containing aromatics demonstrate the general applicability of the model; in over 70 systems examined, we found only one where the predicted primary substitution site did not agree with the experimental findings. We demonstrate that criticism by Chambers et al. to the effect that the model is incapable of reproducing experimental substitution patterns, and, in particular, cannot distinguish between the different activating effects of *ortho*- and *para*-fluorines, are entirely unfounded. The observed substitution patterns for six reactions involving attack by aniline on perfluoropyridine and various non-fluorine-substituted derivatives, selected by Chambers et al. to highlight the failings of our model, are, on the contrary, accurately predicted by it.

**Key words:** nucleophilic substitution, fluorine-containing hetero-aromatics, Meisenheimer model.

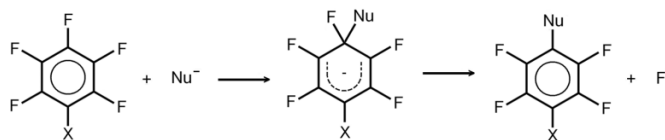
**Résumé :** On a généralisé le modèle simple qu'on a proposé récemment (*J. Fluorine Chem.* **2005**, 126, 727) pour prédire le site principal de la substitution nucléophile dans des dérivés perfluorocarbonés aromatiques de façon à inclure aussi bien les atomes d'azote dans le cycle que des atomes non fluorés attachés comme substituants. Le modèle est basé sur les stabilités relatives des complexes de Meisenheimer tels que calculés par la théorie de Hartree–Fock à l'aide d'un ensemble de base modeste. Les calculs sur une grande variété des dérivés aromatiques contenant du fluor démontrent le domaine général dans lequel le modèle peut être appliqué; dans plus de 70 systèmes examinés, on en a trouvé qu'un dans lequel le site de substitution primaire prédit ne correspond pas aux données expérimentales. On a démontré que les critiques émises par Chambers et al. à l'effet que le modèle ne permet pas de reproduire les patrons expérimentaux de substitution et, en particulier, ne permet pas de distinguer entre les différents effets activants des atomes de fluor en positions *ortho* et *para* sont non fondées. Les patrons de substitution observés pour six réactions impliquant une attaque par l'aniline sur la perfluoropyridine et sur divers dérivés portant des substituants non fluorés choisis par Chambers et al. pour mettre en évidence les déficiences de notre modèle sont, au contraire, prédits correctement par celui-ci.

**Mots-clés :** substitution nucléophile, noyaux hétéroaromatiques contenant du fluor, modèle de Meisenheimer.

[Traduit par la Rédaction]

## Introduction

In an earlier work,<sup>1</sup> we provided a simple calculational model for predicting the primary substitution site for nucleophilic substitution in aromatic perfluorocarbons. This model was based on the standard two-stage description of nucleophilic substitution involving the formation of a negatively charged intermediate, known as a Meisenheimer complex,<sup>2</sup> which is the anionic equivalent of the Wheland intermediate in electrophilic substitution.<sup>3</sup>

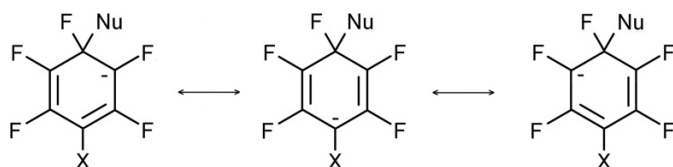


The negative charge in the Meisenheimer complex is delocalized into the aromatic  $\pi$ -system, which, like the Wheland intermediate, can be considered as a resonance hybrid of multiple canonical forms.

Received 2 December 2009. Accepted 29 January 2010. Published on the NRC Research Press Web site at canjchem.nrc.ca on 26 May 2010.

**J. Baker<sup>1</sup> and M. Muir.** Parallel Quantum Solutions, 2013 Green Acres Road, Suite A, Fayetteville, Arkansas 72703, USA.

<sup>1</sup>Corresponding author (e-mail: baker@pqcs-chem.com).



Basically, the model considers the relative stability of all possible Meisenheimer complexes, as determined by calculation (using the fluoride ion itself as a “typical” nucleophile), with the most stable complex corresponding to the preferred site for nucleophilic substitution. As such, it is an extension of previous, even simpler models, which attempted to predict the stabilities of the various Meisenheimer complexes without recourse to any serious calculation at all. A fairly successful early model along these lines was Burdon’s “ $I_{\pi}$ -repulsion” theory,<sup>4</sup> based upon electron repulsions in the Meisenheimer complexes, specifically the destabilizing effect of the repulsion between the filled p-orbital of a planar carbanion and the filled p-orbital of a substituent. This was later extended (as “amplified  $I_{\pi}$ -repulsion” theory) by Burdon and Parsons,<sup>5</sup> with the aid of simple Hückel theory.

All of these models involve essentially a purely thermodynamic rationale, i.e., the thermodynamically most stable Meisenheimer complex is the one most likely to form, and the substitution pattern follows directly from that. The underlying assumptions are, first, that the substitution reaction is indeed two-step, involving an at least meta-stable Meisenheimer complex as intermediate; second, that barrier heights (both from reactant to intermediate and intermediate to product) are either more or less identical in all cases, and can therefore be ignored, or reflect the thermodynamic stability in the Meisenheimer complex so that considering only the latter gives the correct substitution pattern; and third, that varying the reaction conditions, principally the solvent and the actual nucleophile itself, makes no difference to the preferred substitution site, i.e., the mechanism is essentially the same for all nucleophiles in all solvents.

Note that even in cases where the reaction kinetics (i.e., transition-state barrier heights) are dominant, the model can still be usefully applied. For example, if *decomposition* of the Meisenheimer complex (to give the products) is the rate-determining step, then any intermediate Meisenheimer complex can decompose back to reactants many times before finally going over to products; this will favor the formation of the thermodynamically most-stable complex, exactly as required by the model. Only in reactions where *formation* of the Meisenheimer complex is rate-determining will the model formally have no predictive capability.

Now, there is obviously no chance of such a simple model predicting the correct outcome under all circumstances; indeed, many examples are known of nucleophiles reacting differently depending on the reaction conditions, e.g., whether the nitrite ion attacks predominantly through the nitrogen or the oxygen atom is heavily influenced by the solvent,<sup>6</sup> and there are suggestions that at least some nucleophilic substitution reactions may be just one-step,<sup>7</sup> i.e., proceed directly from reactants to products *without* involving a Meisenheimer complex as intermediate. Nonetheless, the success of this simple model, as exemplified by our

study on aromatic perfluorocarbons,<sup>1</sup> suggests that the model is sound in many situations, especially involving “standard” reaction conditions (NaOMe/MeOH or an amine in dioxan or ether).

In this article, we extend this simple model to cover systems with both ring-nitrogen atoms and (or) non-fluorine ring substituents. Can the Meisenheimer model predict the experimentally observed substitution patterns in these types of compounds?

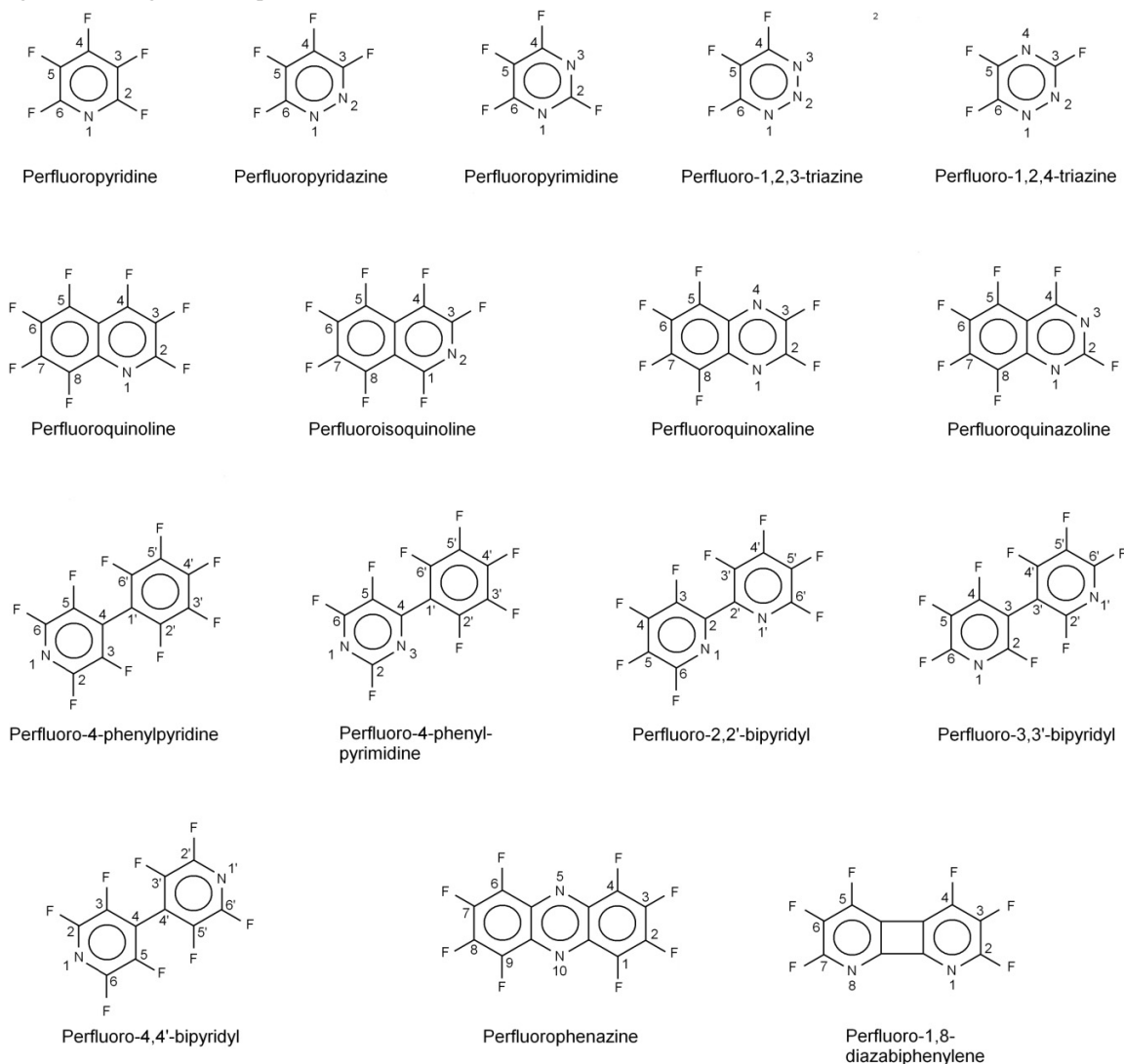
## Results and discussion

Figure 1 depicts schematically the structures of 16 nitrogen-containing aromatic perfluorocarbons, covering most systems of size around 25 atoms or less, for which we were able to find at least some data in the regular literature. Much of the experimental work dates from the late 1960s to the early 1970s and was carried out by the Durham (UK) group headed by Musgrave and (later) Chambers. These compounds are perfluoropyridine,<sup>8</sup> perfluoropyridazine,<sup>9</sup> perfluoropyrimidine,<sup>10,11</sup> perfluoro-1,2,3-triazine,<sup>12</sup> perfluoro-1,2,4-triazine,<sup>13</sup> perfluoroquinoline,<sup>14–16</sup> perfluoroisquinoline,<sup>14–16</sup> perfluoroquinoxaline,<sup>17</sup> perfluoroquinazoline,<sup>18</sup> perfluoro-(4-phenylpyridine),<sup>19,20</sup> perfluoro-(4-phenylpyrimidine),<sup>21</sup> perfluoro-2,2'-bipyridyl,<sup>22</sup> perfluoro-3,3'-bipyridyl,<sup>23</sup> perfluoro-4,4'-bipyridyl,<sup>19</sup> perfluorophenazine,<sup>24</sup> and perfluoro-1,8-diazabiphenylene.<sup>25</sup>

We have carried out calculations on all 16 of these compounds, computing all distinct Meisenheimer intermediates for all systems using a fluoride ion as the attacking nucleophile. This is exactly analogous to our previous calculations on aromatic perfluorocarbons.<sup>1</sup> In ref. 1, we demonstrated that essentially the same results were obtained using a number of theoretical approaches: HF/6–31G\*, HF/6–31+G\*, MP2/6–31G\*, and B3LYP/6–31G\* all gave identical predictions of the preferred site for nucleophilic substitution and, indeed, gave the same relative energy ordering for each system’s Meisenheimer complexes. The addition of diffuse functions to the basis set (as with the 6–31+G\* basis) made no difference to the results, nor did the inclusion of electron correlation (via MP2 and the B3LYP density functional). This strongly suggested, and was noted in ref. 1, that basic Hartree–Fock theory (HF/6–31G\*) was a perfectly adequate model for our purposes. At the time, however, we selected B3LYP/6–31G\* for our standard model based upon its ability to reproduce experimental geometries and energetics better than Hartree–Fock theory.

We have subsequently discovered some rather disturbing artefacts with density functional theory (certainly with the B3LYP functional, but we suspect with DFT in general); namely, a marked tendency to converge to symmetrical structures, which occasionally results in geometries that make no sense chemically. For example, if attempts are made to add a second pyrazolyl substituent to 1-pyrazolyl-2,4,5-trifluorobenzene at the B3LYP/6–31G\* level, then Meisenheimer complexes can readily be formed at positions 4 and 5, but attempts to add at position 2 results in a symmetrical structure with a fluorine atom midway between carbon atoms 1 and 2. This does not occur with Hartree–Fock theory, which gives standard Meisenheimer complexes at all three positions. Because of this, and similar calculational artefacts for other systems, we have replaced DFT in our



**Fig. 1.** Nitrogen-containing aromatic perfluorocarbons.

standard model by Hartree–Fock. All the calculations presented in this work were done with HF/6–31G\*.

Table 1 presents our results for the 16 nitrogen-containing aromatic perfluorocarbons shown in Fig. 1. For each system, we give the relative energies (in kcal/mol) of each possible Meisenheimer complex, with the lowest energy complex (and hence the predicted most favorable site for nucleophilic substitution) taken as the energy zero. Now, it is tempting (a temptation we avoided in our previous study<sup>1</sup>) to look at the relative energies and suggest that if any additional Meisenheimer complexes are close in energy to the lowest one, e.g., within, say, a few kcal/mol, this may indicate a secondary substitution site. The closer the relative energies are to each other, the more likely it is that there will be significant secondary substitution.

We also show in Table 1 the experimentally determined substitution sites, including secondary substitution sites where these were reported (p = primary, s = secondary). In all cases, the secondary substitution site corresponds to the second lowest Meisenheimer complex, and these in turn are typically within a few kcal/mol of the lowest-energy complex. For ex-

ample, Brooke et al. have reported<sup>16</sup> that while the primary substitution site in perfluoroisquinoline is position 1 for MeO<sup>−</sup> in methanol (and also for many other oxygen nucleophiles), sulfur nucleophiles (e.g., HS<sup>−</sup>, MeS<sup>−</sup>) prefer position 6. Similar results are observed for perfluoroquinoline with respect to sites 2 and 4. Under the circumstances, our own results for these two systems (see Table 1), which show the lowest energy for the MeO<sup>−</sup> primary site, with a close-lying secondary site corresponding to the primary site for the sulfur nucleophiles, are really remarkably good and the best that can be expected for such a simple model.

The experimental data for perfluoro-(4-phenylpyridine) are conflicting, with Green et al.<sup>19</sup> reporting that substitution occurs primarily at position 4' in the phenyl ring (in agreement with our own findings), whereas Banks et al.<sup>20</sup> find that substitution occurs predominantly at position 2 in the pyridyl ring. Green et al.'s study<sup>19</sup> was primarily concerned with the chemistry of the metal carbonyls, and the nucleophiles they used were somewhat esoteric (e.g., [( $\pi$ -C<sub>2</sub>H<sub>5</sub>)Fe(CO)<sub>2</sub>]<sup>−</sup> and [Re(CO)<sub>5</sub>]<sup>−</sup>); Banks et al. on the other hand used sodium methoxide in methanol.<sup>20</sup> Assuming both

**Table 1.** Relative energies (kcal/mol) of the various Meisenheimer complexes for nitrogen-containing aromatic perfluorocarbons (see Fig. 1) with experimentally observed substitution sites.

<b>Perfluoropyridine (C<sub>5</sub>NF<sub>5</sub>)</b>		
2-F	7.4	
3-F	23.5	
4-F	0.0	p <sup>a</sup>
<b>Perfluoropyridazine (C<sub>4</sub>N<sub>2</sub>F<sub>4</sub>)</b>		
3-F	12.7	
4-F	0.0	p
<b>Perfluoropyrimidine (C<sub>4</sub>N<sub>2</sub>F<sub>4</sub>)</b>		
2-F	6.8	
4-F	0.0	p
5-F	37.5	
<b>Perfluoro-1,2,4-triazine (C<sub>3</sub>N<sub>3</sub>F<sub>3</sub>)</b>		
3-F	19.8	
5-F	0.0	p
6-F	26.8	
<b>Perfluoro-1,2,3-triazine (C<sub>3</sub>N<sub>3</sub>F<sub>3</sub>)</b>		
4-F	0.0	p
5-F	4.8	
<b>Perfluoroquinoline (C<sub>9</sub>NF<sub>7</sub>)</b>		
2-F	5.0	s <sup>b</sup>
3-F	18.0	
4-F	0.0	p
5-F	13.0	
6-F	19.6	
7-F	11.7	
8-F	21.5	
<b>Perfluoroisoquinoline (C<sub>9</sub>NF<sub>7</sub>)</b>		
1-F	0.0	p
3-F	6.0	
4-F	19.2	
5-F	14.4	
6-F	0.2	s
7-F	13.8	
8-F	2.3	
<b>Perfluoroquinazoline (C<sub>8</sub>N<sub>2</sub>F<sub>6</sub>)</b>		
2-F	12.2	
4-F	0.0	p
5-F	12.9	
6-F	31.2	
7-F	10.6	
8-F	32.4	
<b>Perfluoroquinoxaline (C<sub>8</sub>N<sub>2</sub>F<sub>6</sub>)</b>		
2-F	0.0	p
5-F	18.0	
6-F	15.4	
<b>Perfluoro-(4-phenylpyridine) (C<sub>11</sub>NF<sub>9</sub>)</b>		
2-F	7.7	p <sup>*c</sup>
3-F	13.9	
2'-F	6.6	
3'-F	17.9	
4'-F	0.0	p <sup>*</sup>
<b>Perfluoro-(4-phenylpyrimidine) (C<sub>10</sub>N<sub>2</sub>F<sub>8</sub>)</b>		
2-F	11.3	
5-F	28.6	

**Table 1 (concluded).**

6-F	0.0	p
2'-F	12.1	
3'-F	28.9	
4'-F	7.0	
<b>Perfluoro-2,2'-bipyridyl (C<sub>10</sub>N<sub>2</sub>F<sub>8</sub>)</b>		
3-F	7.8	
4-F	0.0	p
5-F	2.7	
6-F	9.1	
<b>Perfluoro-3,3'-bipyridyl (C<sub>10</sub>N<sub>2</sub>F<sub>8</sub>)</b>		
2-F	8.0	
4-F	0.0	p
5-F	31.0	
6-F	1.8	s
<b>Perfluoro-4,4'-biphenyl (C<sub>10</sub>N<sub>2</sub>F<sub>8</sub>)</b>		
2-F	0.0	p
3-F	1.7	
<b>Perfluorophenazine (C<sub>12</sub>N<sub>2</sub>F<sub>8</sub>)</b>		
1-F	4.1	
2-F	0.0	p
<b>Perfluoro-1,8-diazabiphenylene</b>		
2-F	4.3	
3-F	8.8	
4-F	0.0	p

<sup>a</sup>p: Experimental primary substitution site.<sup>b</sup>s: Secondary substitution site; primary for some nucleophiles.<sup>c</sup>p\*: Conflicting experimental data for perfluoro-(4-phenylpyridine); see text.

sets of authors are correct, this clearly shows (not that there was any doubt) the very strong influence of the nucleophile and the experimental conditions on the substitution site.

The results we have presented in Table 1 demonstrate that the Meisenheimer model can be reliably extended to include nitrogen atoms in the aromatic ring. We now look at some examples where the initial perfluorocarbon has already had at least one fluorine substituted. Can the model mimic the directional effects (if any) of the substituent and predict which fluorine will be substituted next?

Our principal example is C<sub>6</sub>F<sub>5</sub>X (1-substituted hexafluorobenzene). A large number of papers have been published on the directional effects of various substituents (X) in this system. The most common site for nucleophilic attack is para to X; this is the site predicted by the *p*-difluoride rule derived from Burdon's "I<sub>π</sub>-repulsion" theory,<sup>4</sup> and also from an observation by Chambers and co-workers that the most favorable substitution site should have the maximum number of neighboring *ortho*- and *meta*-fluorines.<sup>26</sup> The fact that not all substituents direct para clearly shows the limitations of these simple empirical rules. We have selected a dozen substituents (X), including some which have been shown experimentally to direct meta. (Ortho substitution often occurs as a secondary substitution site together with para. It is possible to obtain exclusively ortho substitution with polar substituents (X) containing carbon or sulfur multiple bonds to nitrogen or oxygen in reactions with metal-containing reagents, e.g., LiAlH<sub>4</sub>. This is the result of

specific interactions between the substituent and the metal center in the nucleophile and is outside the purview of our model.) The substituents  $X$  we have chosen are:  $-H$ ;<sup>27</sup>  $-CH_3$ ;<sup>28</sup>  $-CF_3$ ;<sup>29</sup>  $-CHO$ ;<sup>30</sup>  $-OH$ ;<sup>28</sup>  $-NO_2$ ;<sup>31</sup>  $-NH_2$ ,  $-NH(CH_3)$ , and  $-N(CH_3)_2$ ;<sup>32</sup>  $-CH=CH_2$ ;<sup>33</sup>  $-CH_2OH$ ;<sup>34</sup> and  $-SCH_3$ .<sup>35</sup> Can the Meisenheimer model predict the marked preference for para substitution and yet identify those substituents that direct meta?

The short answer to the above question is a resounding yes. The relative energies of the three Meisenheimer complexes (ortho, meta, and para) for each substituent are given in Table 2. Ten of the 12 direct para, but two  $-NH_2$  and  $-OH$  direct meta and are correctly predicted to do so by our model. The dominance of para substitution almost (but not quite) regardless of the substituent  $X$  is notable:  $H$ ,  $CH_3$ , and  $CF_3$  all direct para despite their very different electron-donating/withdrawing properties.

Figure 2 shows a further selection of fluorine- and ring-substituted aromatic perfluorocarbons taken more-or-less at random from the literature: hexafluoro-1-aminoisquinoline;<sup>36</sup> perfluorothiophene;<sup>37</sup> perfluorobenzophenone and octafluoro-2,2'-dihydrobenzophenone;<sup>38</sup> perfluorodibenzofuran, perfluorodibenzothiophen, and perfluoro-9-fluorenone;<sup>39</sup> 5-phenyl-octafluorodibenzophosphole and 5-phenyl-octafluorodibenzophosphole-5-oxide;<sup>40</sup> various methoxy-substituted derivatives of perfluoroacenaphthylene;<sup>41</sup> perfluoropyrene<sup>42</sup> and perfluorofluoranthene;<sup>43</sup> 4,5,6,7-tetrafluorobenzo(*b*)thiophen;<sup>44</sup> 2-methoxy-heptafluoronaphthalene;<sup>45</sup> and 2-amino-heptafluoronaphthalene.<sup>46</sup> These examples were chosen to give a range of functional groups (O, S, P, and C=O in the ring) and a large number of different substitution sites (as many as nine following single-substitution in the methoxy-substituted aromatic perfluorocarbons). This represents a thorough test for the model with plenty of scope for error.

Our results are shown in Table 3. As can be seen in every case, the model correctly predicts the primary substitution site. There was some mild controversy at the time with both perfluorodibenzothiophen and perfluoro-9-fluorenone as initially Chambers and Spring reported that the principal sites for nucleophilic substitution in these systems were at position 2<sup>38</sup> (note that this represents a *different* ring position in the two compounds owing to the different labelling conventions; see Fig. 2). These predictions became increasingly incompatible with results reported by others for related systems<sup>47</sup> (and specifically by Burdon et al.<sup>48</sup>), and the same authors subsequently reported (correctly, see Table 3) that substitution in fact occurred at position 3.<sup>39</sup>

The substitution patterns reported by Burdon et al. following attack by methoxide ion on perfluoroacenaphthylene, perfluoropyrene, and perfluorofluoranthene are reproduced exactly by our model. For perfluoroacenaphthylene, substitution occurs first at position 3, followed by positions 8, 5, and 6, in that order.<sup>41</sup> It was already predicted in ref. 1 that the primary site for nucleophilic substitution in perfluoroacenaphthylene was position 3. Starting from the 3-substituted derivative, our model correctly predicts that subsequent attack occurs primarily at position 8 (see Table 3), starting from the 3,8-substituted derivative attack then occurs at position 5 and from the 3,5,8-substituted derivative at position 6. Similar results are obtained for perfluorofluoranthene, which

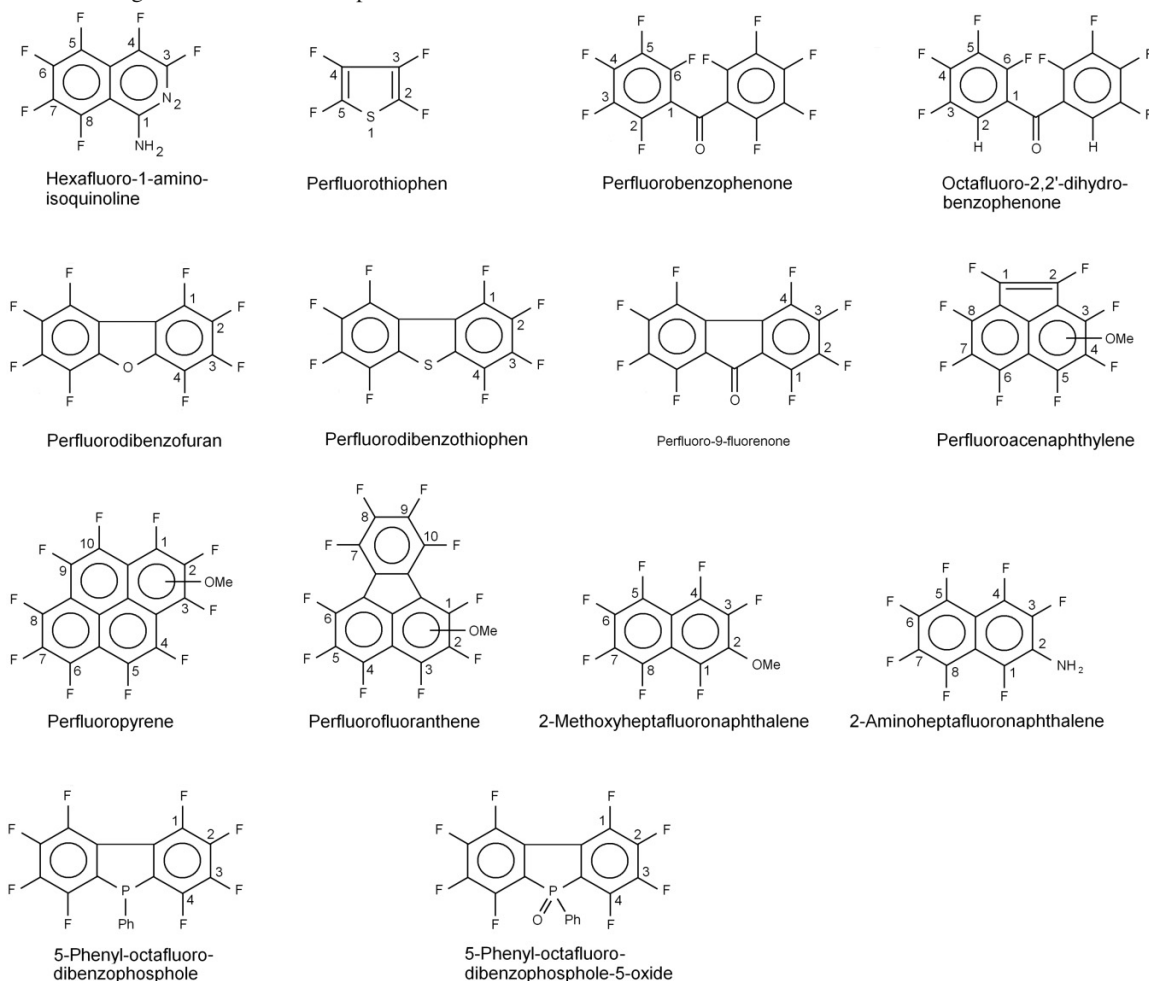
**Table 2.** Relative Energies (kcal/mol) of the various Meisenheimer complexes for reactions involving substituted perfluorobenzenes ( $C_6F_5X$ ).

<b>X = H</b>		
2-F	3.9	
3-F	9.0	
4-F	0.0	p <sup>a</sup>
<b>X = CH<sub>3</sub></b>		
2-F	3.1	
3-F	6.5	
4-F	0.0	p
<b>X = CF<sub>3</sub></b>		
2-F	3.9	
3-F	16.3	
4-F	0.0	p
<b>X = CHO</b>		
2-F	6.4	
3-F	25.4	
4-F	0.0	p
<b>X = OH</b>		
2-F	2.1	
3-F	0.0	p
4-F	1.9	
<b>X = NO<sub>2</sub></b>		
2-F	3.5	
3-F	23.2	
4-F	0.0	p
<b>X = NH<sub>2</sub></b>		
2-F	1.9	
3-F	0.0	p
4-F	3.1	
<b>X = NHCH<sub>3</sub></b>		
2-F	2.1	
3-F	3.7	
4-F	0.0	p
<b>X = N(CH<sub>3</sub>)<sub>2</sub></b>		
2-F	3.2	
3-F	7.8	
4-F	0.0	p
<b>X = CH = CH<sub>2</sub></b>		
2-F	5.1	
3-F	14.5	
4-F	0.0	p
<b>X = CH<sub>2</sub>OH</b>		
2-F	2.3	
3-F	9.2	
4-F	0.0	p
<b>X = SCH<sub>3</sub></b>		
2-F	4.5	
3-F	15.0	
4-F	0.0	p

<sup>a</sup>p: Experimental primary substitution site.

substitutes first at position 1, and then at positions 6, 3, and 4,<sup>43</sup> exactly as predicted by our model.

The subsequent substitution sites in these particular compounds can already be seen from the relative energies of the

**Fig. 2.** Fluorine- and ring-substituted aromatic perfluorocarbons.

various Meisenheimer complexes for the singly substituted derivative. For example, it is obvious from the calculations on 1-methoxy-nonafluorofluoranthene that the most activated sites are positions 3, 4, and 6; the only question is the precise order. Likewise for 3-methoxy-heptafluoroacenaphthylene where the activated sites are clearly positions 5, 6, and 8.

With perfluoropyrene, substitution takes place first at position 1, and then at a mixture of positions 3, 6, and 8. Burdon et al. report<sup>42</sup> that the dimethoxy compounds were clearly a mixture with about 5%–10% of the 1,3-dimethoxy and the rest 1,6- and 1,8-dimethoxy in roughly equal amounts. The energetics of the various Meisenheimer complexes for 1-methoxy-nonafluoropyrene reported in Table 3 could hardly agree better with this observation; in particular, the complexes at positions 6 and 8 have virtually identical energies (differing by only 0.1 kcal/mol). 1,3,6-Trimethoxy-heptafluoropyrene is reported<sup>42</sup> to further substitute (this is obvious after the initial calculation) at position 8, and this is also reproduced by our model.

2-Substituted-heptafluoronaphthalenes substitute predominantly at position 6.<sup>45</sup> Recently, Rodionov and co-workers reported that amination of 2-amino-heptafluoronaphthalene in liquid ammonia affords a mixture of isomeric forms with considerable prevalence of the 2,7-isomer (70%). They claim that this is the first example of the predominant sub-

stitution at position 7 in 2-substituted polyfluoronaphthalenes.<sup>46</sup> Once again the Meisenheimer model fully agrees with the experimental findings, with 2-methoxy-heptafluoronaphthalene (a typical example) predicted to substitute predominantly at position 6, while 2-amino-heptafluoronaphthalene substitutes predominantly at position 7 (see Table 3).

This simple and very successful Meisenheimer model has been extensively criticized in a recent paper by Chambers et al.,<sup>49</sup> who claim that it is incapable of reproducing experimentally observed substitution patterns, and, in particular, cannot distinguish between the different activating effects of *ortho*- and *para*-fluorines. They provide six examples (in their Fig. 6) of nucleophilic substitution involving attack by aniline on perfluoropyridine and various substituted derivatives to illustrate this. We reproduce this figure with all six reactions as Fig. 3.

Table 4 presents our results using the Meisenheimer model for the six reactions specifically mentioned by Chambers et al. in ref. 49. Our predictions for both the primary and secondary fluorine substitution sites could hardly be better. We predict the correct primary substitution site in all six cases and, in those reactions with substantial secondary substitution, there is a low-lying Meisenheimer complex within a few kcal/mol of that for the primary substitution site.



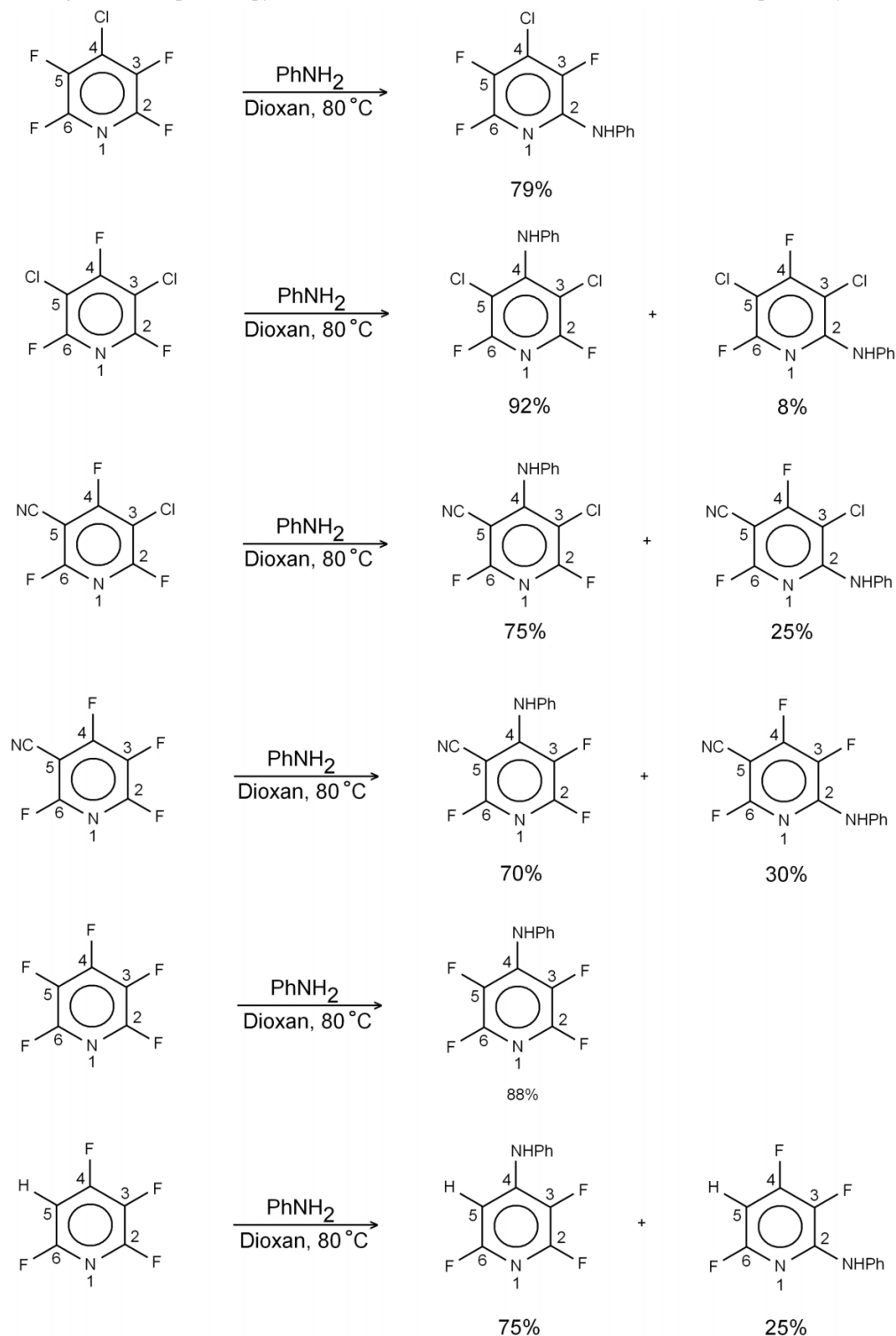
**Table 3.** Relative Energies (kcal/mol) of the various Meisenheimer complexes for several substituted aromatic perfluorocarbons (see Fig. 2) with experimentally observed substitution sites.

<b>Hexafluoro-1-aminoisoquinoline</b>		
3-F	7.5	
4-F	28.4	
5-F	13.0	
6-F	0.0	p <sup>a</sup>
7-F	12.1	
8-F	0.9	
<b>Perfluorothiophene</b>		
2-F	0.0	p
3-F	12.2	
<b>Perfluorobenzophenone</b>		
2-F	5.9	
3-F	26.8	
4-F	0.0	p
5-F	26.5	
6-F	4.3	
<b>Octafluoro-2,2'-dihydrobenzophenone</b>		
3-F	22.3	
4-F	0.0	p
5-F	16.6	
6-F	6.2	
<b>Perfluorodibenzofuran</b>		
4-F	11.9	
3-F	0.0	p
2-F	15.2	
1-F	1.6	
<b>Perfluorodibenzothiophen</b>		
4-F	11.7	
3-F	0.0	p
2-F	11.8	
1-F	2.4	
<b>Perfluoro-9-fluorenone</b>		
1-F	4.7	
2-F	8.0	
3-F	0.0	p
4-F	11.2	
<b>5-Phenyl-octafluorodibenzophosphole</b>		
4-F	7.5	
3-F	0.0	p
2-F	3.4	
1-F	3.0	
<b>5-Phenyl-octafluorodibenzophosphole-5-oxide</b>		
4-F	5.8	
3-F	2.7	
2-F	0.0	p
1-F	5.5	
<b>3-Methoxy-heptafluoroacenaphthylene</b>		
1-F	17.3	
2-F	17.4	
4-F	28.0	
5-F	1.6	
6-F	1.0	
8-F	0.0	p
<b>3,8-Dimethoxy-hexafluoroacenaphthylene</b>		
1-F	14.2	
4-F	25.4	
5-F	0.0	p
<b>3,5,8-Trimethoxy-pentafluoroacenaphthylene</b>		
1-F	12.9	
2-F	13.7	
4-F	24.7	

**Table 3 (concluded).**

6-F	0.0	p
7-F	24.7	
<b>1-Methoxy-nonafluoropyrene</b>		
2-F	14.1	
3-F	1.8	s <sup>b</sup>
4-F	13.6	
5-F	12.9	
6-F	0.1	p
7-F	13.3	
8-F	0.0	p
9-F	13.2	
10-F	13.6	
<b>1,3,6-Trimethoxy-heptafluoropyrene</b>		
2-F	14.8	
4-F	12.7	
5-F	11.9	
7-F	13.9	
8-F	0.0	p
9-F	12.0	
10-F	12.4	
<b>1-Methoxy-nonafluorofluoranthene</b>		
2-F	27.1	
3-F	1.2	
4-F	0.4	
5-F	25.4	
6-F	0.0	p
7-F	20.7	
8-F	17.4	
9-F	17.4	
10-F	20.3	
<b>1,6-Dimethoxy-octafluorofluoranthene</b>		
2-F	24.8	
3-F	0.0	p
7-F	17.6	
8-F	14.7	
<b>1,3,6-Trimethoxyheptafluorofluoranthene</b>		
2-F	24.4	
4-F	0.0	p
5-F	24.2	
7-F	16.8	
8-F	13.6	
9-F	13.8	
10-F	16.6	
<b>4,5,6,7-Tetrafluorobenzo(b)thiophen</b>		
4-F	1.5	
5-F	5.5	
6-F	0.0	p
7-F	5.0	
<b>2-Methoxy-heptafluoronaphthalene</b>		
1-F	1.8	
3-F	1.5	
4-F	3.7	
5-F	2.3	
6-F	0.0	p
7-F	1.7	
8-F	0.8	
<b>2-Amino-heptafluoronaphthalene</b>		
1-F	4.0	
3-F	2.2	
4-F	1.5	
5-F	0.6	
6-F	1.3	
7-F	0.0	p
8-F	1.9	

<sup>a</sup>p: Experimental primary substitution site.<sup>b</sup>s: Secondary substitution site.

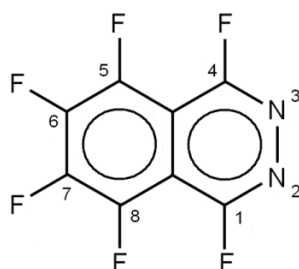
**Fig. 3.** Reactions involving substituted perfluoropyridines that Chambers and co-workers claim cannot be explained by the Meisenheimer model.

Rather than demonstrate the failings of the model, these six reactions show just how applicable it actually is.

Is our model infallible? Of course not! As we have already mentioned, we originally developed and used it to predict the most likely site(s) for nucleophilic substitution in aromatic perfluorocarbons. In this work, we have generalized it to include systems with heteroatoms (particularly nitrogen) in the aromatic ring and non-fluorine ring substitu-

ents. The model works very well in both of these cases. Additionally, it does a good job in predicting secondary substitution sites. We have deliberately kept the model simple; there are no factors in it to account for specific nucleophile or specific solvent effects, and therefore it obviously *cannot* account for changes in the substitution pattern due to changes in the solvent or use of a different nucleophile. But within its limitations, it is extremely successful.

So far, we have found just one example where the basic model fails: perfluorophthalazine.



Perfluorophthalazine

According to Chambers et al.,<sup>50</sup> methanolic sodium methoxide progressively replaces all six fluorine atoms in perfluorophthalazine, with positions 1 and 4 being the most reactive and 5 and 8 the least. Our calculations predict that position 6 (and 7) is the primary substitution site; experimentally, this is, at best, a secondary site. We have no reason to doubt the results presented in ref. 50 and clearly the model is just plain wrong for this molecule.

We have already noted that the standard Meisenheimer model incorporates no specific nucleophile or solvent effects. It might be possible to extend the basic model to include such effects; for example, by using the actual nucleophile during the calculation of the Meisenheimer intermediates rather than the fluoride ion, and by including either a continuous solvation model or explicit solvent molecules or a combination of both. However, we believe that the initial model, together with the generalizations we have made here, has clear predictive capability as it stands, and attempts to extend it, particularly via the incorporation of solvent effects, will destroy its essential simplicity without necessarily offering any real improvements.

## Conclusions

A simple model for predicting which fluorine atom will be replaced by an attacking nucleophile in nitrogen-containing and (or) substituted aromatic perfluorocarbons has been presented. This is a generalization of an existing model for aromatic perfluorocarbons only,<sup>1</sup> in which the energies of all possible Meisenheimer complexes were computed at HF/6-31G\* with full geometry optimization using the fluoride ion as a model nucleophile. The lowest energy Meisenheimer complex indicates the most likely substitution site.

This model was used to predict the position for nucleophilic attack in 17 nitrogen-containing aromatic perfluorocarbons, 12 substituted perfluorobenzenes ( $C_6F_5X$ ) and 20 other assorted fluorine-containing aromatics for which the primary substitution site was known experimentally. For only one compound, perfluorophthalazine, was the prediction not in accord with the experimental results. Additionally, predictions for six further nucleophilic substitution reactions, specifically selected by Chambers et al. to highlight alleged failings in the model,<sup>49</sup> agreed 100% with the experimental observations.

Including the 17 aromatic perfluorocarbons in the original paper,<sup>1</sup> we have presented calculations on over 70 systems, covering a range of fluorine-containing aromatics with a va-

**Table 4.** Relative Energies (kcal/mol) of the various Meisenheimer complexes for reactions involving substituted perfluoropyridines with aniline selected by Chambers and co-workers to demonstrate the failings of the Meisenheimer model (see Fig. 3).

<b>2,3,5,6-Tetrafluoro-4-chloropyridine</b>		
2-F	0.0	p <sup>a</sup>
3-F	9.8	
<b>2,4,6-Trifluoro-3-chloro-5-cyanopyridine</b>		
2-F	1.0	s <sup>b</sup>
4-F	0.0	p
6-F	5.0	
<b>2,3,4,6-Tetrafluoro-5-cyanopyridine</b>		
2-F	1.0	s
3-F	35.8	
4-F	0.0	p
6-F	7.7	
<b>2,4,6-Trifluoro-3,5-dichloropyridine</b>		
2-F	5.2	
4-F	0.0	p
<b>Perfluoropyridine</b>		
2-F	7.4	
3-F	23.5	
4-F	0.0	p
<b>2,3,4,6-Tetrafluoropyridine</b>		
2-F	3.4	s
3-F	27.9	
4-F	0.0	p
6-F	8.0	

<sup>a</sup>p: Experimental primary substitution site.

<sup>b</sup>s: Experimental secondary substitution site.

riety of substituents and non-carbon (N, O, P, and S) ring atoms. The wide applicability of the standard Meisenheimer model (using the fluoride ion as a generic attacking nucleophile) is abundantly clear. We emphasize that we have *not* carefully selected the systems that we have presented, discarding those which our model fails to predict correctly; for the original set of 17 perfluorocarbons and the ring-nitrogen systems in this work (Fig. 1), we used every system we could find in the literature for which the substitution site was known experimentally.

The circumstances under which the standard Meisenheimer model is expected to work well have been outlined in the Introduction. The reason why the model is so successful is simply because these circumstances apply in the vast majority of nucleophilic substitution reactions involving aromatic perfluorocarbons. A huge number of these reactions do indeed proceed via a two-stage process involving a Meisenheimer complex as intermediate, and theory is more than capable of predicting the relative stability of the Meisenheimer intermediates, which is why the model works. Hasegawa et al. have recently observed the ionized Meisenheimer intermediate in the reaction between perfluorobenzene and ammonia using IR spectroscopy.<sup>51</sup> Theoretical calculations greatly assisted in the identification of the complex.

## Acknowledgements

We thank Dr. Vladimir Sorokin, Department of Organic Chemistry, Rostov State University, Rostov-on-Don, Russia, for providing synopses (in English) of several articles originally published in Russian.

## References

- (1) Muir, M.; Baker, J. *J. Fluor. Chem.* **2005**, *126* (5), 727. doi:10.1016/j.jfluchem.2005.02.018.
- (2) Meisenheimer, J. *Justus Liebigs Ann. Chem.* **1902**, 323 (2), 205. doi:10.1002/jlac.19023230205.
- (3) Wheland, G. W. *J. Am. Chem. Soc.* **1942**, *64* (4), 900. doi:10.1021/ja01256a047.
- (4) Burdon, J. *Tetrahedron* **1965**, *21* (12), 3373. doi:10.1016/S0040-4020(01)96958-3.
- (5) Burdon, J.; Parsons, I. W. *J. Am. Chem. Soc.* **1977**, *99* (23), 7445. doi:10.1021/ja00465a007.
- (6) Broxton, T. J.; Muir, D. M.; Parker, A. J. *J. Org. Chem.* **1975**, *40* (22), 3230. doi:10.1021/jo00910a015.
- (7) Renfrew, A. H. M.; Taylor, J. A.; Whitmore, J. M. J.; Williams, A. J. *Chem. Soc., Perkin Trans. 2* **1993**, (10): 1703. doi:10.1039/p29930001703.
- (8) Chambers, R. D.; Hutchinson, J.; Musgrave, W. K. R. *J. Chem. Soc.* **1964**, 3736. doi:10.1039/jr9640003736.
- (9) Chambers, R. D.; MacBride, J. A. H.; Musgrave, W. K. R. *J. Chem. Soc. C* **1968**, 2116.
- (10) Chambers, R. D.; MacBride, J. A. H.; Musgrave, W. K. R. *Chem. Ind.* **1966**, 1721.
- (11) Banks, R. E.; Field, D. S.; Haszeldine, R. N. *J. Chem. Soc. C* **1967**, 1822.
- (12) Chambers, R. D.; Tamura, M.; Howard, J. A. K.; Johnson, O. *J. Chem. Soc. Chem. Commun.* **1987**, (22): 1697. doi:10.1039/c39870001697.
- (13) Barlow, M. G.; Haszeldine, R. N.; Simon, C.; Simpkin, D. J.; Ziervogel, G. *J. Chem. Soc., Perkin Trans. 1* **1982**, 1251. doi:10.1039/p19820001251.
- (14) Chambers, R. D.; Hole, M.; Musgrave, W. K. R.; Storey, R. A.; Iddon, B. *J. Chem. Soc. C* **1966**, 2331.
- (15) Bell, S. L.; Chambers, R. D.; Daniels, R.; Holmes, T. F.; Silvester, M. J. *J. Fluor. Chem.* **1986**, *32* (4), 403. doi:10.1016/S0022-1139(00)81948-X.
- (16) Brooke, G. M.; Chambers, R. D.; Drury, C. J.; Bower, M. J. *J. Chem. Soc., Perkin Trans. 1* **1993**, (18): 2201. doi:10.1039/p19930002201.
- (17) Allison, C. G.; Chambers, R. D.; MacBride, J. A. H.; Musgrave, W. K. R. *J. Fluor. Chem.* **1971/72**, *1* (1), 59. doi:10.1016/S0022-1139(00)82534-8.
- (18) Allison, C. G.; Chambers, R. D.; MacBride, J. A. H.; Musgrave, W. K. R. *Tetrahedron Lett.* **1970**, *11* (23), 1979. doi:10.1016/S0040-4039(01)98132-8.
- (19) Green, M.; Taunton-Rigby, A.; Stone, F. G. A. *J. Chem. Soc. A* **1968**, 2762. doi:10.1039/j19680002762.
- (20) Banks, R. E.; Barlow, M. G.; Haszeldine, R. N.; Phillips, E. *J. Chem. Soc. C* **1971**, 1957.
- (21) Banks, R. E.; Barlow, M. G.; Haszeldine, R. N.; Massey, J. C. *J. Fluor. Chem.* **1978**, *12* (1), 53. doi:10.1016/S0022-1139(00)82892-4.
- (22) Chambers, R. D.; Lomas, D.; Musgrave, W. K. R. *Tetrahedron* **1968**, *24* (16), 5633. doi:10.1016/0040-4020(68)88161-X.
- (23) Chambers, R. D.; Lomas, D.; Musgrave, W. K. R. *J. Chem. Soc. C* **1968**, 625.
- (24) Birchall, J. M.; Haszeldine, R. N.; Kemp, J. E. G. *J. Chem. Soc. C* **1970**, 449.
- (25) Adams, D. B.; Kilcoyne, J. P.; MacBride, J. A. H.; Muir, M. *J. Chem. Res. (S)* **1990**, 6, 172.
- (26) Chambers, R. D.; Close, D.; Williams, D. L. H. *J. Chem. Soc., Perkin Trans. 2* **1980**, (5): 778. doi:10.1039/p29800000778.
- (27) Burdon, J.; Coe, P. L.; Marsh, C. R.; Tatlow, J. C. *Tetrahedron* **1966**, *22* (4), 1183. doi:10.1016/S0040-4020(01)99407-4.
- (28) Burdon, J.; Hollyhead, W. B.; Tatlow, J. C. *J. Chem. Soc.* **1965**, 5152. doi:10.1039/jr9650005152.
- (29) Alsop, D. J.; Burdon, J.; Tatlow, J. C. *J. Chem. Soc.* **1962**, 1801. doi:10.1039/jr9620001801.
- (30) Aroskar, E. V.; Brown, P. N. J.; Plevvey, R. G.; Stephens, R. *J. Chem. Soc. C* **1968**, 1569.
- (31) Allen, J. G.; Burdon, J.; Tatlow, J. C. *J. Chem. Soc.* **1965**, 1045. doi:10.1039/jr9650001045.
- (32) Allen, J. G.; Burdon, J.; Tatlow, J. C. *J. Chem. Soc.* **1965**, 6329. doi:10.1039/jr9650006329.
- (33) Burdon, J.; Westwood, W. T. *J. Chem. Soc. C* **1970**, 1271.
- (34) Gerasimova, T. N.; Lokshina, E. G.; Barkhash, V. A.; Vorozhtsov, N. N. *Zh. Obshch. Khim.* **1967**, *37*, 1296.
- (35) Robson, P.; Smith, T. A.; Stephens, R.; Tatlow, J. C. *J. Chem. Soc.* **1963**, 3692. doi:10.1039/jr9630003692.
- (36) Chambers, R. D.; Hole, M.; Musgrave, W. K. R.; Storey, R. A.; Iddon, B. *J. Chem. Soc. C* **1966**, 2331.
- (37) Burdon, J.; Campbell, J. G.; Parsons, J. W.; Tatlow, J. C. *J. Chem. Soc., Chem. Commun.* **1969**, 27.
- (38) Chambers, R. D.; Spring, D. J. *Tetrahedron* **1969**, *25* (3), 565. doi:10.1016/S0040-4020(01)83267-1.
- (39) Chambers, R. D.; Spring, D. J. *Tetrahedron* **1971**, *27* (3), 669. doi:10.1016/S0040-4020(01)90735-5.
- (40) Chambers, R. D.; Spring, D. J. *J. Fluor. Chem.* **1971/72**, *1* (3), 309. doi:10.1016/S0022-1139(00)83228-5.
- (41) Burdon, J.; Harrison, D.; Stephens, R. *Tetrahedron* **1965**, *21* (5), 927. doi:10.1016/0040-4020(65)80030-8.
- (42) Burdon, J.; Parsons, I. W.; Gill, H. S. *J. Chem. Soc., Perkin Trans. 1* **1979**, 1351. doi:10.1039/p19790001351.
- (43) Burdon, J.; Gill, H. S.; Parsons, I. W.; Tatlow, J. C. *J. Chem. Soc., Perkin Trans. 1* **1980**, 1726. doi:10.1039/p19800001726.
- (44) Castle, M. D.; Plevvey, R. G.; Tatlow, J. C. *J. Chem. Soc. C* **1968**, 1225.
- (45) Price, D.; Suschitzky, H.; Hollies, J. I. *J. Chem. Soc. C* **1969**, 1967.
- (46) Vaganova, T. A.; Kusov, S. Z.; Rodionov, V. I.; Shundrina, I. K.; Sal'nikov, G. E.; Mamatyuk, V. I.; Malykhin, E. V. *J. Fluor. Chem.* **2008**, *129* (4), 253. doi:10.1016/j.jfluchem.2007.11.010.
- (47) De Pasquale, R. J.; Tamborski, C. *J. Org. Chem.* **1967**, *32* (10), 3163. doi:10.1021/jo01285a051.
- (48) Burdon, J.; Kane, B. L.; Tatlow, J. C. *J. Fluor. Chem.* **1971/72**, *1* (2), 185. doi:10.1016/S0022-1139(00)83212-1.
- (49) Chambers, R. D.; Martin, P. A.; Sandford, G.; Williams, D. L. H. *J. Fluor. Chem.* **2008**, *129* (10), 998. doi:10.1016/j.jfluchem.2008.04.009.
- (50) Chambers, R. D.; McBride, J. A. H.; Musgrave, W. K. R.; Reilly, I. S. *Tetrahedron Lett.* **1970**, *11* (1), 57. doi:10.1016/S0040-4039(01)87564-X.
- (51) Hasegawa, H.; Mizuse, K.; Hachiya, M.; Matsuda, Y.; Mikami, N.; Fujii, A. *Angew. Chem. Int. Ed.* **2008**, *47*, 6008.



# Catalyst-free, direct, high regio-, and chemo-selective conversion of epoxides to 2-thiocyanatoalkyl alkanoates under neutral and solvent-free conditions

Ghasem Aghapour and Razieh Hatefipour

**Abstract:** A catalyst-free, direct, high regio-, and chemo-selective method is reported for the facile conversion of a wide variety of epoxides to their corresponding 2-thiocyanatoalkyl alkanoates, which contain two important functional groups (ester and thiocyanate), using a mixture of tetrabutylammonium rhodanide ((*n*-Bu)<sub>4</sub>NSCN) and an aliphatic or aromatic carboxylic anhydride under neutral and solvent-free conditions.

**Key words:** epoxide, 2-thiocyanatoalkyl alkanoate, carboxylic anhydride, tetrabutylammonium rhodanide.

**Résumé :** On a mis au point une méthode hautement régio- et chimio-sélective directe et n'impliquant aucun catalyseur pour la transformation facile d'une grande variété d'époxydes en alcanates de 2-thiocyanatoalkyles correspondants qui contiennent deux groupes fonctionnels importants (ester et thiocyanate); elle comporte l'utilisation d'un mélange de rhodanide de tétrabutylammonium (*n*-Bu)<sub>4</sub>NSCN et l'anhydride d'un acide carboxylique aliphatique ou aromatique, dans des conditions neutres et sans solvant.

**Mots-clés :** époxyde, alcanate de 2-thiocyanatoalkyle, anhydride d'acide carboxylique, rhodanide de tétrabutylammonium.

[Traduit par la Rédaction]

## Introduction

Epoxides are important intermediates in organic synthesis.<sup>1</sup> Their facile regio- and stereo-selective ring-opening reactions with a wide variety of nucleophiles provide a powerful strategy in organic chemistry.<sup>1–6</sup> However, in most of the epoxide ring-opening reactions under acidic conditions, the formation of a mixture of regioisomers and polymerization is observed.

On the other hand, thiocyanates have gained considerable importance in various areas of organosulfur chemistry.<sup>7</sup> For example, these compounds are important intermediates in agricultural and pharmaceutical chemistry: the thiocyanato group occurs as an important functionality in certain anticancer natural products formed by deglycosylation of glucosinolates derived from cruciferous vegetables.<sup>8,9</sup>

Also, synthesis of esters has played an important role in organic synthesis from its infancy.<sup>10</sup> This importance stemmed from its utility in diverse fields both in the laboratory and in industry. Ester moieties, irrespective of whether acyclic or cyclic, constitute major backbones, as well as functional groups of chemical significance, in numerous natural products and synthetic compounds. Ester groups also play versatile temporary roles in organic synthesis for the protection of carboxylic acids and hydroxy groups. Therefore, the acetylation of alcohols is one of the most widely used procedure for the protection of hydroxy groups, which

is routinely carried out by acid anhydrides or acid chlorides in the presence of tertiary amines,<sup>11</sup> protic or Lewis acids,<sup>12</sup> or sometimes solid acid catalysts.<sup>13</sup> Also, many other different reagents or catalysts have been introduced in various conditions for the esterification reactions.<sup>10</sup>

It is obvious that with respect to the importance of thiocyanato and ester functional groups, 2-thiocyanatoalkyl alkanoates, which contain both these groups, represent an interesting and important subclass and have multiple modes of reactivity. Although, there are several reports concerning the preparation of  $\beta$ -hydroxy thiocyanates from epoxides using different reagents or catalysts,<sup>14–16</sup> as far as we know, there is no report in the literature about the direct synthesis of 2-thiocyanatoalkyl alkanoates from epoxides. Even the reports on the stepwise conversion of epoxides to 2-thiocyanatoalkyl alkanoates are scarce.

In one method, epoxide was first converted to its corresponding  $\beta$ -hydroxy thiocyanate using NH<sub>4</sub>SCN in the presence of 18-crown-6, followed by a treatment with acetylchloride in reflux conditions to convert the hydroxy group into an ester group.<sup>17</sup> A second method involves the reaction of triphenylphosphine-thiocyanogen (TPPT) with epoxide at  $-40\text{ }^{\circ}\text{C}$  under argon and then at room temperature overnight. Then, in the second step, the resulted  $\beta$ -hydroxy thiocyanate was treated with benzoyl chloride and triethylamine producing the final desired product.<sup>15b</sup> In addition, in

Received 2 November 2009. Accepted 25 March 2010. Published on the NRC Research Press Web site at canjchem.nrc.ca on 27 May 2010.

G. Aghapour<sup>1</sup> and R. Hatefipour. School of Chemistry, Damghan University of Basic Sciences, Damghan, 36715-364, Iran.

<sup>1</sup>Corresponding author (e-mail: Gh\_Aghapour@dubs.ac.ir).

a different work for obtaining of these compounds, epoxides were treated with thiocyanic acid as described by van Tame-len,<sup>14a</sup> producing  $\beta$ -hydroxy thiocyanates, which on treatment with acetyl chloride in pyridine gave the corresponding 2-thiocyanatoalkyl alkanoates.<sup>18</sup> Furthermore, in this report, the formation of these compounds has also been described via treatment of thiocyanogen chloride with alkenes in the presence of a radical inhibitor in acetic acid in the dark as minor products.<sup>18</sup>

On the other hand, waste prevention and environmental protection are major requirements in an overcrowded world with increasing demands. Synthetic chemistry continues to develop various techniques for obtaining better products with less environmental impact. One of the more promising approaches is solvent-free organic synthesis.<sup>19</sup> These reactions have many advantages: reduced pollution, low costs, and simplicity in process and handling. These factors are especially important in industry.<sup>20</sup>

Thus, on the basis of the above descriptions, the development of simple and efficient methods for the preparation of 2-thiocyanatoalkyl alkanoates from epoxides, especially in neutral and solvent-free conditions, is desirable.

## Results and discussion

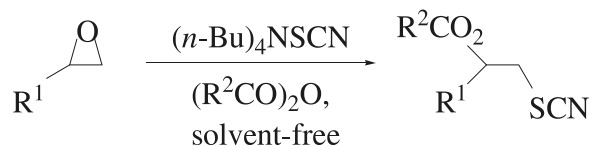
In our previous works,<sup>21</sup> we have reported the conversion of epoxides to  $\beta$ -halohydrins and now in continuation of our recent work<sup>22</sup> on the catalyst-free conversion of epoxides to  $\beta$ -hydroxy thiocyanates and also with consideration of advantages of solvent-free reactions, we report a direct and catalyst-free method for the conversion of epoxides to 2-thiocyanatoalkyl alkanoates using a mixture of tetrabutylammonium rhodanide ( $(n\text{-Bu})_4\text{NSCN}$ ) and an aliphatic or aromatic carboxylic anhydride under neutral and solvent-free conditions (Scheme 1).

First, we took 1,2-epoxytetradecane as an example, and optimized the reaction conditions for its conversion to 1-dodecyl-2-thiocyanatoethyl acetate (**1**) using thiocyanate anion in the presence of acetic anhydride ( $\text{Ac}_2\text{O}$ ). We found that no desired product (**1**) was formed using  $\text{NH}_4\text{SCN}$  as a source of thiocyanate anion in various conditions. Thus, we tried to perform this conversion using  $(n\text{-Bu})_4\text{NSCN}$ . The results are shown in Table 1. It must be noted that in all of these reactions epoxide was added to a stirring mixture of  $(n\text{-Bu})_4\text{NSCN}$  and acetic anhydride in the absence of a catalyst and stirring was continued for stated times.

As shown in Table 1, this reaction was unsuccessful in  $\text{CH}_2\text{Cl}_2$  and  $\text{CH}_3\text{CN}$  as solvents even under reflux conditions (Table 1, entries 1–3). Also, **1** was obtained in only 30%–40 % yield at room temperature after 24 h under solvent-free conditions (Table 1, entries 4 and 5). However, the yield of this reaction was increased by increasing the reaction temperature (60 °C) under solvent-free conditions (Table 1, entry 6). Finally, the best result was obtained in the case of entry 7 (Table 1) so that **1** was produced in 80 % yield using a mixture of  $(n\text{-Bu})_4\text{NSCN}:(\text{CH}_3\text{CO})_2\text{O}$  in a 1.2 :0.5 molar ratio at 60 °C after 6 h under solvent-free conditions.

We therefore used these conditions (Table 1, entry 7) for the conversion of other epoxides to their corresponding 2-thiocyanatoalkyl acetates. The results are shown in Table 2.

**Scheme 1.** Direct and catalyst-free method for the conversion of epoxides to 2-thiocyanatoalkyl alkanoates using tetrabutylammonium rhodanide ( $(n\text{-Bu})_4\text{NSCN}$ ) in the presence of an aliphatic or aromatic carboxylic anhydride under neutral and solvent-free conditions.



As shown in Table 2, epoxides are directly and efficiently converted to 2-thiocyanatoalkyl acetates by a mixture of  $(n\text{-Bu})_4\text{NSCN}:(\text{CH}_3\text{CO})_2\text{O}$  in a 1.2:0.5 molar ratio at 60 °C under neutral and solvent-free conditions and without using a catalyst.

It is possible to obtain other 2-thiocyanatoalkyl alkanoates using another carboxylic anhydride in this method. We found that epoxides can be converted to 2-thiocyanatoalkyl benzoates by using benzoic anhydride as an aromatic anhydride instead of acetic anhydride (Table 2, entries 8 and 9). However, benzoic anhydride (0.85 equiv.) must be used slightly more than acetic anhydride (0.5 equiv.), probably due to its lower reactivity compared to acetic anhydride.

Except for the case of styrene oxide, which produced two regioisomers (Table 2, entry 2), the reaction of other unsymmetrical epoxides occurred with high regioselectivity, and the thiocyanate anion attacked the less-hindered side of the epoxide ring due to the combination of steric and electronic factors. Under these reaction conditions, the ethereal bonds, phenyl ring, carbon–halogen bonds, and carbon–carbon double bonds as functional groups that are present in the epoxide molecules remain intact.

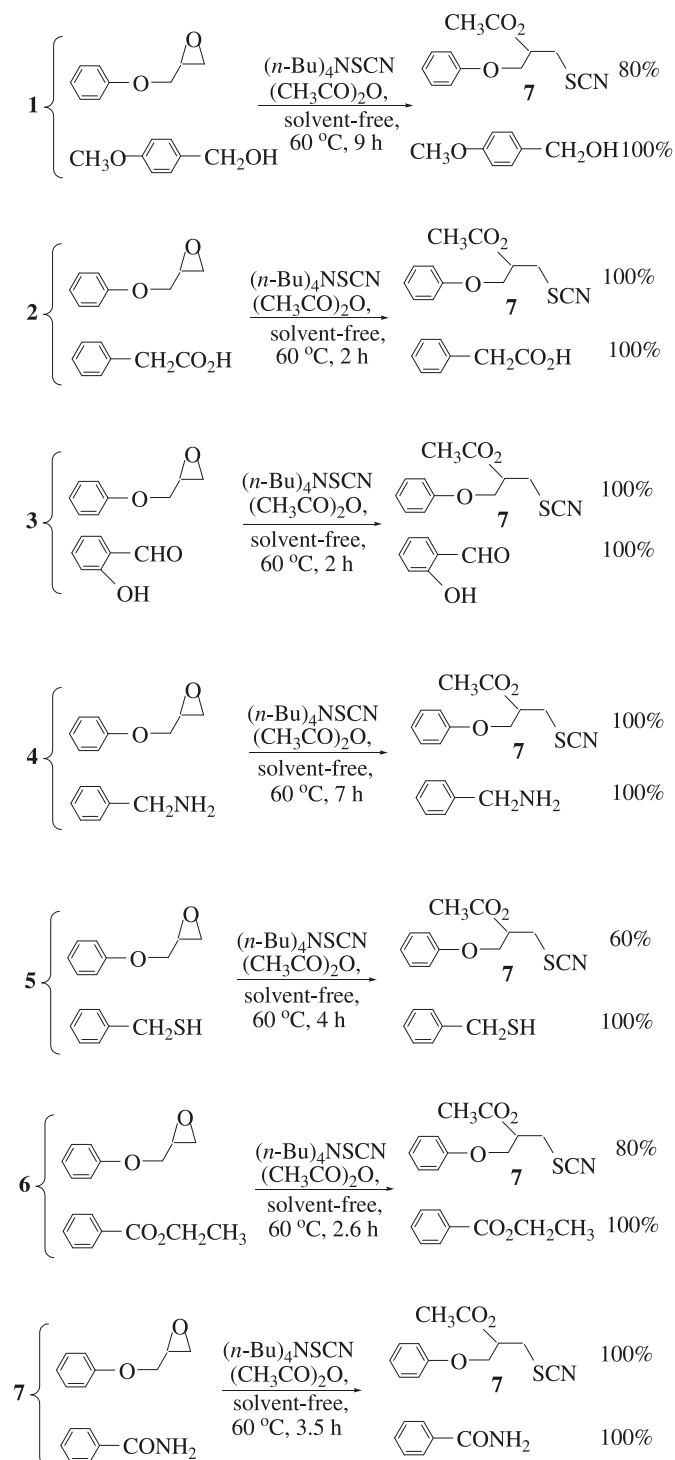
In order to have more insight into the applicability, selectivity, and limitations of the present method, we studied the possibility of the conversion of epoxides to 2-thiocyanatoalkyl alkanoates in the presence of some other functional groups in binary mixtures. For this purpose, a binary mixture of glycidyl phenyl ether and another organic compound (1:1) was treated with a stirring mixture of  $(n\text{-Bu})_4\text{NSCN}$  (1.2 equiv) and  $(\text{CH}_3\text{CO})_2\text{O}$  (0.5 equiv) in a flask at 60 °C under solvent-free conditions. The conversion yields obtained for these selective reactions of different binary mixtures are shown in Scheme 2.

In addition to the various selectivities mentioned above, as shown in Scheme 2, epoxides can be efficiently converted to their corresponding 2-thiocyanatoalkyl alkanoates in the presence of alcohols, carboxylic acids, aldehydes, amines, thiols, esters, and amides with excellent selectivity using the present method so that these functional groups remain completely intact.

## Conclusion

In conclusion, the present investigation has demonstrated that the use of tetrabutylammonium rhodanide ( $(n\text{-Bu})_4\text{NSCN}$ ) in the presence of aliphatic or aromatic carboxylic anhydrides offers a direct, simple, and efficient method, avoiding the use of a catalyst for the regioselective conversion of a wide variety of epoxides to their corresponding 2-thiocyanatoalkyl alkanoates, which have two important func-

**Scheme 2.** Chemoselectivities in the reaction of 2,3-epoxypropyl phenyl ether with  $(n\text{-Bu})_4\text{NSCN}$  in the presence of acetic anhydride at 60 °C under neutral and solvent-free conditions.



tional groups (ester and thiocyanate) under solvent-free conditions. This method can be efficiently used for preparation of 2-thiocyanatoalkyl alkanoates even in the presence of many other functional groups with excellent chemoselectivity. Easy work up and operation under neutral and solvent-free conditions without using a catalyst are considered other advantages of this method.

## Experimental

Solvents, reagents, and chemicals were obtained from Merck (Germany) and Fluka (Switzerland) Chemical Companies. Some products are known compounds and data of these compounds (such as bp, mp,  $^1\text{H}$  and  $^{13}\text{C}$  NMR, IR, mass) have been found to be identical to those reported.<sup>17,18</sup> Also, other products were characterized by their physical or spectral data. FTIR spectra were recorded on a PerkinElmer RXI spectrophotometer. Nuclear magnetic resonance spectra were recorded on a Bruker Avance DRX-500 spectrometer. Mass spectra were determined on a HP 5973 msd at 70 eV. Thin layer chromatography (TLC) was carried out on silica gel 254 analytical sheets obtained from Fluka.

### Typical procedure for the conversion of 2,3-epoxypropyl phenyl ether to 1-phenoxy-3-thiocyanatopropan-2-yl acetate (7) using $(n\text{-Bu})_4\text{NSCN}$ in the presence of acetic anhydride

Acetic anhydride (0.047 mL, 0.5 mmol) was added to a flask containing tetrabutylammonium rhodanide (0.36 g, 1.2 mmol) in an oil bath at 60 °C under solvent-free conditions. This mixture was stirred for 15 min so that a homogeneous mixture was formed. Then 2,3-epoxypropyl phenyl ether (0.135 mL, 1 mmol) was added and the reaction mixture was stirred until TLC showed the completion of the reaction (2.5 h). The crude product was subjected to column chromatography on silica gel using *n*-hexane-ethyl acetate (60:1) as eluent affording **7** (0.226 g, 90% yield). Oil. FTIR (neat,  $\text{cm}^{-1}$ ): 2157 (m, CN), 1743 (s, C=O).  $^1\text{H}$  NMR ( $\text{CDCl}_3$ , 500 MHz, ppm)  $\delta$ : 2.15 (s, 3H ( $\text{CH}_3$ )), 3.30–3.35 (dd, 1H ( $\text{CHCH}_a\text{H}_b\text{S}$ ),  $J_{\text{H}_a\text{H}_b} = 14.2$  Hz,  $J_{\text{H}_a\text{CH}} = 6.7$  Hz), 3.40–3.43 (dd, 1H ( $\text{CHCH}_a\text{H}_b\text{S}$ ),  $J_{\text{H}_b\text{CH}} = 4.3$  Hz), 4.12–4.16 (dd, 1H ( $\text{OCHcHdCH}$ ),  $J_{\text{H}_c\text{H}_d} = 10.2$  Hz,  $J_{\text{H}_c\text{CH}} = 5.8$  Hz), 4.17–4.20 (dd, 1H ( $\text{OCHcH}_d\text{CH}$ ),  $J_{\text{H}_d\text{CH}} = 4.5$  Hz), 5.40–5.44 (m, 1H (CH)), 6.89–6.91 (m, 2H (Ph)), 6.95–7.01 (m, 1H (Ph)), 7.26–7.32 (m, 2H (Ph)).  $^{13}\text{C}$  NMR ( $\text{CDCl}_3$ , 125.77 MHz, ppm)  $\delta$ : 21.17, 34.83, 66.83, 70.56, 112.15, 114.99, 122.19, 130.07, 158.28, 170.49. Mass spectra  $m/z$ : 251 (M, 3%), 208 (M –  $\text{CH}_3\text{CO}$ , 0.3%), 193 (M – SCN, 0.37%), 158 (M – PhO, 100%), 43 ( $\text{CH}_3\text{CO}$ , 43%).

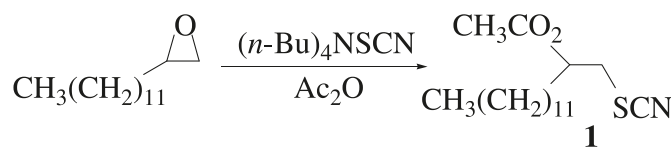
### Spectroscopic data

#### 1-Phenyl-2-thiocyanatoethyl acetate (2)

Oil. FTIR (neat,  $\text{cm}^{-1}$ ): 2156 (m, CN), 1744 (s, C=O).  $^1\text{H}$  NMR ( $\text{CDCl}_3$ , 500 MHz, ppm)  $\delta$ : 2.17 (s, 3H ( $\text{CH}_3$ )), 3.28–3.31 (dd, 1H ( $\text{CH}_a\text{H}_b$ ),  $J_{\text{H}_a\text{H}_b} = 14$  Hz,  $J_{\text{H}_a\text{CH}} = 4.4$  Hz), 3.34–3.39 (dd, 1H ( $\text{CH}_a\text{H}_b$ ),  $J_{\text{H}_b\text{CH}} = 8.1$  Hz), 6.02–6.05 (m, 1H (CH)), 7.32–7.41 (m, 5H (Ph)).  $^{13}\text{C}$  NMR ( $\text{CDCl}_3$ , 125.77 MHz, ppm)  $\delta$ : 21.30, 39.51, 74.24, 112.05, 126.82, 129.40, 129.59, 137.57, 170.15. Mass spectra  $m/z$ : 221 (M, 0.31%), 178 (M –  $\text{CH}_3\text{CO}$ , 0.21%), 161 (M –  $\text{CH}_3\text{CO}_2\text{H}$ , 10.6%), 149 (M –  $\text{CH}_2\text{SCN}$ , 64%), 107 (M –  $\text{CH}_2\text{SCN}$  –  $\text{CH}_2\text{CO}$ , 100%), 43 ( $\text{CH}_3\text{CO}$ , 72.96%).

#### 2-Phenyl-2-thiocyanatoethyl acetate (3)

Oil. FTIR (neat,  $\text{cm}^{-1}$ ): 2156 (m, CN), 1744 (s, C=O).  $^1\text{H}$  NMR ( $\text{CDCl}_3$ , 500 MHz, ppm)  $\delta$ : 2.11 (s, 3H ( $\text{CH}_3$ )), 4.26–4.30 (dd, 1H ( $\text{CH}_a\text{H}_b$ ),  $J_{\text{H}_a\text{H}_b} = 11.9$  Hz,  $J_{\text{H}_a\text{CH}} = 8.04$  Hz), 4.32–4.35 (dd, 1H ( $\text{CH}_a\text{H}_b$ ),  $J_{\text{H}_b\text{CH}} = 3.9$  Hz), 4.58–4.62 (m, 1H (CH)), 7.32–7.41 (m, 5H (Ph)).  $^{13}\text{C}$  NMR ( $\text{CDCl}_3$ ,

**Table 1.** Conversion of 1,2-epoxytetradecane to 1-dodecyl-2-thiocyanatoethyl acetate (**1**) using (*n*-Bu)<sub>4</sub>NSCN/Ac<sub>2</sub>O in various conditions.

Entry	Solvent	Molar ratio <sup>a</sup>	Temperature (°C)	Time (h)	Yield (%)
1	CH <sub>2</sub> Cl <sub>2</sub>	1:1.2:1	RT	46	10
2	CH <sub>2</sub> Cl <sub>2</sub>	1:1.2:1	Reflux	46	10
3	CH <sub>3</sub> CN	1:1.2:1	Reflux	46	20
4	—	1:1.2:2	RT	24	40
5	—	1:1.2:0.5	RT	24	30
6	—	1:1.2:1	60	5.5	78
7	—	1:1.2:0.5	60	6	80
8	—	1:1.2:0.25	60	6	20

<sup>a</sup>The molar ratio is related to epoxide:(*n*-Bu)<sub>4</sub>NSCN:Ac<sub>2</sub>O.

125.77 MHz, ppm)  $\delta$ : 21.19, 51.86, 65.93, 111.08, 127.13, 129.08, 129.79, 136.94, 170.48. Mass spectra *m/z*: 221 (M, 0.15%), 163 (M – SCN, 54.44%), 104 (M – SCN – CH<sub>3</sub>CO<sub>2</sub>, 31.84%), 43 (CH<sub>3</sub>CO, 100%).

#### 1-Isopropoxy-3-thiocyanatopropan-2-yl acetate (**4**)

Oil. FTIR (neat, cm<sup>-1</sup>): 2156 (m, CN), 1743 (s, C=O). <sup>1</sup>H NMR (CDCl<sub>3</sub>, 500 MHz, ppm)  $\delta$ : 1.13–1.14 (d, 6H (2 × CH<sub>3</sub>), *J*<sub>CH-CH</sub> = 6.1 Hz), 2.12 (s, 3H (CH<sub>3</sub>)), 3.18–3.22 (dd, 1H (CHCH<sub>a</sub>H<sub>b</sub>S), *J*<sub>H<sub>a</sub>H<sub>b</sub></sub> = 14 Hz, *J*<sub>H<sub>a</sub>CH</sub> = 6.3 Hz), 3.31–3.35 (dd, 1H (CHCH<sub>a</sub>H<sub>b</sub>S), *J*<sub>H<sub>b</sub>CH</sub> = 4.2 Hz), 3.51–3.62 (m, 1H ((CH<sub>3</sub>)<sub>2</sub>CHO) + 2H (OCH<sub>2</sub>CH)), 5.14–5.19 (m, 1H (CHOC=O)). <sup>13</sup>C NMR (CDCl<sub>3</sub>, 125.77 MHz, ppm)  $\delta$ : 21.22, 22.37, 35.11, 66.92, 71.22, 73.06, 112.52, 170.55. Mass spectra *m/z*: 217 (M, 0.35%), 174 (M – CH<sub>3</sub>CO, 0.23%), 159 (M – SCN, 3.03%), 158 (M – (CH<sub>3</sub>)<sub>2</sub>CHO or M – CH<sub>3</sub>CO<sub>2</sub>, 29.99%), 99 (M – (CH<sub>3</sub>)<sub>2</sub>CHO – HSCN, 31.82%), 43 (CH<sub>3</sub>CO, 100%). Anal. calcd. for C<sub>9</sub>H<sub>15</sub>NO<sub>3</sub>S: C 49.75, H 6.96, N 6.45; found: C 49.87, H 6.91, N 6.51.

#### 1-Allyloxy-3-thiocyanatopropan-2-yl acetate (**5**)

Oil. FTIR (neat, cm<sup>-1</sup>): 2157 (m, CN), 1747 (s, C=O). <sup>1</sup>H NMR (CDCl<sub>3</sub>, 500 MHz, ppm)  $\delta$ : 2.13 (s, 3H (CH<sub>3</sub>)), 3.19–3.23 (dd, 1H (CHCH<sub>a</sub>H<sub>b</sub>S), *J*<sub>H<sub>a</sub>H<sub>b</sub></sub> = 14 Hz, *J*<sub>H<sub>a</sub>CH</sub> = 6.4 Hz), 3.31–3.35 (dd, 1H (CHCH<sub>a</sub>H<sub>b</sub>S), *J*<sub>H<sub>b</sub>CH</sub> = 4.4 Hz), 3.58–3.66 (m, 2H (OCH<sub>2</sub>)), 4.00–4.02 (m, 2H (CH<sub>2</sub>O)), 5.20–5.29 (m, 1H (CH) + 2H (CH<sub>2</sub>=)), 5.82–5.90 (m, 1H (=CH)). <sup>13</sup>C NMR (CDCl<sub>3</sub>, 125.77 MHz, ppm)  $\delta$ : 21.22, 34.92, 68.82, 70.97, 72.86, 112.35, 118.35, 134.25, 170.52. Mass spectra *m/z*: 215 (M, 0.36%), 172 (M – CH<sub>3</sub>CO, 2.94%), 158 (M – C<sub>3</sub>H<sub>5</sub>O, 78.92%), 115 (M – C<sub>3</sub>H<sub>5</sub>O – CH<sub>3</sub>CO, 4.4%), 100 (M – C<sub>3</sub>H<sub>5</sub>O – SCN, 4.5%), 98 (M – C<sub>3</sub>H<sub>5</sub>O – CH<sub>3</sub>CO<sub>2</sub>H, 7.3%), 43 (CH<sub>3</sub>CO, 100%). Anal. calcd. for C<sub>9</sub>H<sub>13</sub>NO<sub>3</sub>S: C 50.21, H 6.09, N 6.51; found: C 50.29, H 6.14, N 6.45.

#### trans-2-Thiocyanatocyclohexyl acetate (**6**)

Bp 101–102 °C/0.2 mmHg (1 mmHg = 133.322 Pa) (lit. value<sup>18</sup> bp 102–103 °C/0.2 mmHg). FTIR (neat, cm<sup>-1</sup>): 2153 (s, CN), 1741 (s, C=O). <sup>1</sup>H NMR (CDCl<sub>3</sub>, 500 MHz,

ppm)  $\delta$ : 1.31–1.43 (m, 3H (ring), 1.63–1.71 (m, 1H (ring)), 1.79–1.85 (m, 2H (ring)), 2.10 (s, 3H (CH<sub>3</sub>)), 2.15–2.17 (m, 1H (ring)), 2.27–2.31 (m, 1H (ring)), 3.17–3.22 (m, 1H (CHS)), 4.74–4.79 (m, 1H (CHO)). <sup>13</sup>C NMR (CDCl<sub>3</sub>, 125.77 MHz, ppm)  $\delta$ : 21.36, 24.03, 25.98, 32.60, 32.86, 51.74, 75.06, 111.21, 170.44. Mass spectra *m/z*: 199 (M, 0.22%), 156 (M – CH<sub>3</sub>CO, 2.87%), 139 (M – CH<sub>3</sub>CO<sub>2</sub>H, 94.98%), 81 (M – CH<sub>3</sub>CO<sub>2</sub>H – SCN, 81.87%), 43 (CH<sub>3</sub>CO, 100%).

#### 1-Dodecyl-2-thiocyanatoethyl acetate (**1**)

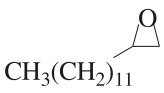
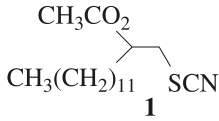
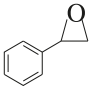
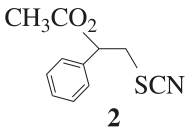
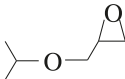
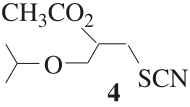
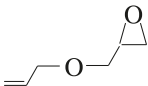
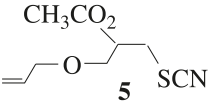
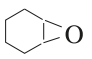
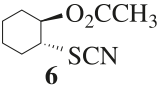
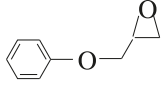
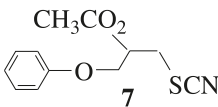
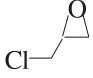
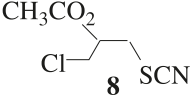
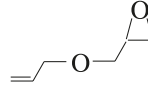
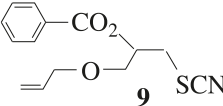
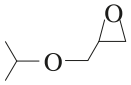
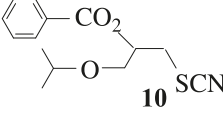
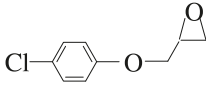
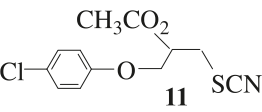
Oil. FTIR (neat, cm<sup>-1</sup>): 2158 (m, CN), 1745 (s, C=O). <sup>1</sup>H NMR (CDCl<sub>3</sub>, 500 MHz, ppm)  $\delta$ : 0.86–0.88 (t, 3H (CH<sub>3</sub>CH<sub>2</sub>), *J* = 7.06 Hz), 1.25–1.30 (m, 20H (10 × CH<sub>2</sub>)), 1.59–1.65 (m, 1H (CH<sub>a</sub>H<sub>b</sub>CH)), 1.69–1.74 (m, 1H (CH<sub>a</sub>H<sub>b</sub>CH)), 2.11 (s, 3H (CH<sub>3</sub>CO)), 3.04–3.08 (dd, 1H (CHCH<sub>a</sub>H<sub>b</sub>S), *J*<sub>H<sub>a</sub>H<sub>b</sub></sub> = 13.93 Hz, *J*<sub>H<sub>a</sub>CH</sub> = 6.55 Hz), 3.22–3.26 (dd, 1H (CHCH<sub>a</sub>H<sub>b</sub>S), *J*<sub>H<sub>b</sub>CH</sub> = 3.83 Hz), 5.04–5.13 (m, 1H (CH)). <sup>13</sup>C NMR (CDCl<sub>3</sub>, 125.77 MHz, ppm)  $\delta$ : 14.51, 21.26, 23.09, 25.50, 29.65, 29.75, 29.79, 29.83, 29.90, 29.93, 30.04, 32.32, 33.23, 38.00, 72.29, 112.43, 170.82. Mass spectra *m/z*: 313 (M, 0.32%), 255 (M – SCN, 1.5%), 253 (M – CH<sub>3</sub>CO<sub>2</sub>H, 4.5%), 196 (M – SCN – CH<sub>3</sub>CO<sub>2</sub>, 6.06%), 43 (CH<sub>3</sub>CO, 100%). Anal. calcd. for C<sub>17</sub>H<sub>31</sub>NO<sub>2</sub>S: C 65.13, H 9.97, N 4.47; found: C 65.09, H 10.02, N 4.45.

#### 1-Chloro-3-thiocyanatopropan-2-yl acetate (**8**)

Oil. FTIR (neat, cm<sup>-1</sup>): 2159 (m, CN), 1747 (s, C=O). <sup>1</sup>H NMR (CDCl<sub>3</sub>, 500 MHz, ppm)  $\delta$ : 2.12 (s, 3H (CH<sub>3</sub>)), 2.99–3.05 (m, 2H (CH<sub>2</sub>S)), 3.75–3.77 (m, 2H (ClCH<sub>2</sub>)), 5.26–5.31 (m, 1H (CH)). <sup>13</sup>C NMR (CDCl<sub>3</sub>, 125.77 MHz, ppm)  $\delta$ : 21.28, 34.87, 43.29, 71.48, 112.12, 170.54. Mass spectra *m/z*: 195 (M + 2, 0.17%), 193 (M, 0.5%), 135 (M + 2 – CH<sub>3</sub>CO<sub>2</sub>H or M – SCN, 5.86%), 133 (M – CH<sub>3</sub>CO<sub>2</sub>H, 16.51%), 98 (M + 2 – CH<sub>3</sub>CO<sub>2</sub>H – <sup>37</sup>Cl or M – CH<sub>3</sub>CO<sub>2</sub>H – <sup>35</sup>Cl, 12.72%), 77 (M + 2 – CH<sub>3</sub>CO<sub>2</sub>H – SCN, 3.03%), 75 (M – CH<sub>3</sub>CO<sub>2</sub>H – SCN, 9.33%), 43 (CH<sub>3</sub>CO, 100%). Anal. calcd. for C<sub>6</sub>H<sub>8</sub>NO<sub>2</sub>SCl: C 37.21, H 4.16, N 7.23; found: C 37.10, H 4.19, N 7.25.



**Table 2.** Catalyst-free conversion of epoxides to 2-thiocyanatoalkyl alkanoates using  $(n\text{-Bu})_4\text{NSCN}$  (1.2 equiv.)/carboxylic anhydride at 60 °C under neutral and solvent-free conditions.

Entry	Epoxide	Product	Time (h)	Yield (%) <sup>a</sup>
1		 <b>1</b>	6	80
2		 <b>2</b> + <b>(3)</b>	3	58(23) <sup>b</sup>
3		 <b>4</b>	2.5	66
4		 <b>5</b>	3	77
5		 <b>6</b>	1	80
6		 <b>7</b>	2.5	90
7		 <b>8</b>	1	60
8		 <b>9</b>	1.5	72
9		 <b>10</b>	2	70
10		 <b>11</b>	2.5	85

**Note:** Acetic anhydride (0.5 equiv.) or benzoic anhydride (0.85 equiv.) were used in these reactions.

<sup>a</sup> Isolated yields.

<sup>b</sup> Yields are based on NMR analysis. The number in parenthesis is related to 2-phenyl-2-thiocyanatoethyl acetate as regioisomeric product.

**1-Allyloxy-3-thiocyanatopropan-2-yl benzoate (9)**

Oil. FTIR (neat,  $\text{cm}^{-1}$ ): 2157 (m, CN), 1722 (s, C=O), 1601 (m, Ph).  $^1\text{H}$  NMR ( $\text{CDCl}_3$ , 500 MHz, ppm)  $\delta$ : 3.38–3.42 (dd, 1H ( $\text{CHCH}_a\text{H}_b\text{S}$ ),  $J_{\text{H}_a\text{H}_b} = 14$  Hz,  $J_{\text{H}_a\text{CH}} = 6.3$  Hz), 3.46–3.50 (dd, 1H ( $\text{CHCH}_a\text{H}_b\text{S}$ ),  $J_{\text{H}_b\text{CH}} = 4.5$  Hz), 3.73–3.76 (dd, 1H ( $\text{OCH}_c\text{H}_d\text{CH}$ ),  $J_{\text{H}_c\text{H}_d} = 10.4$  Hz,  $J_{\text{H}_c\text{CH}} = 5.8$  Hz), 3.78–3.81 (dd, 1H ( $\text{OCH}_c\text{H}_d\text{CH}$ ),  $J_{\text{H}_d\text{CH}} = 4.4$  Hz), 4.04–4.06 (m, 2H ( $\text{CH}_2\text{O}$ )), 5.20–5.22 (dd, 1H ( $\text{H}_a\text{H}_b\text{C}=\text{CH}$ ),  $J_{\text{H}_a\text{CH}} = 10.36$  Hz,  $J_{\text{H}_a\text{H}_b} = 1.2$  Hz), 5.26–5.30 (dd, 1H ( $\text{H}_a\text{H}_b\text{C}=\text{CH}$ ),  $J_{\text{H}_b\text{CH}} = 17$  Hz), 5.45–5.49 (m, 1H (CH)), 5.84–5.92 (m, 1H ( $=\text{CH}$ )), 7.44–7.48 (m, 2H (Ph)), 7.57–7.60 (m, 1H (Ph)), 8.06–8.09 (m, 2H (Ph)).  $^{13}\text{C}$  NMR ( $\text{CDCl}_3$ , 125.77 MHz, ppm)  $\delta$ : 35.35, 68.81, 71.41, 72.91, 112.47, 118.35, 128.95, 129.56, 130.39, 134.01, 134.31, 166.02. Mass spectra  $m/z$ : 277 (M, 0.3%), 220 (M –  $\text{C}_3\text{H}_5\text{O}$ , 51.72%), 162 (M –  $\text{C}_3\text{H}_5\text{O}$  – SCN, 1.4%), 105 (PhCO, 100%). Anal. calcd. for  $\text{C}_{14}\text{H}_{15}\text{NO}_3\text{S}$ : C 60.63, H 5.45, N 5.05; found: C 60.69, H 5.48, N 5.02.

**1-Isopropoxy-3-thiocyanatopropan-2-yl benzoate (10)**

Oil. FTIR (neat,  $\text{cm}^{-1}$ ): 3020 (w, Ph-H), 2157 (m, CN), 1723 (s, C=O), 1601 (w, C=C).  $^1\text{H}$  NMR ( $\text{CDCl}_3$ , 500 MHz, ppm)  $\delta$ : 1.16–1.17 (d, 6H ( $2 \times \text{CH}_3$ ),  $J_{\text{CH}_3\text{CH}} = 6.1$  Hz), 3.37–3.41 (dd, 1H ( $\text{CHCH}_a\text{H}_b\text{S}$ ),  $J_{\text{H}_a\text{H}_b} = 13.95$  Hz,  $J_{\text{H}_a\text{CH}} = 6.2$  Hz), 3.47–3.51 (dd, 1H ( $\text{CHCH}_a\text{H}_b\text{S}$ ),  $J_{\text{H}_b\text{CH}} = 4.3$  Hz), 3.62–3.67 (m, 1H ( $(\text{CH}_3)\text{CHO}$ )), 3.68–3.71 (dd, 1H ( $\text{OCH}_c\text{H}_d\text{CH}$ ),  $J_{\text{H}_c\text{H}_d} = 10.1$  Hz,  $J_{\text{H}_c\text{CH}} = 6.46$  Hz), 3.76–3.79 (dd, 1H ( $\text{OCH}_c\text{H}_d\text{CH}$ ),  $J_{\text{H}_d\text{CH}} = 4.42$  Hz), 5.41–5.44 (m, 1H (CH)), 7.44–7.48 (m, 2H (Ph)), 7.57–7.60 (m, 1H (Ph)), 8.07–8.09 (m, 2H (Ph)).  $^{13}\text{C}$  NMR ( $\text{CDCl}_3$ , 125.77 MHz, ppm)  $\delta$ : 22.39, 35.57, 66.91, 71.64, 73.16, 112.66, 128.94, 129.65, 130.37, 133.96, 166.07. Mass spectra  $m/z$ : 279 (M, 0.2%), 220 (M –  $\text{C}_3\text{H}_7\text{O}$ , 15.5%), 162 (M –  $\text{C}_3\text{H}_7\text{O}$  – SCN, 0.8%), 105 (PhCO, 100%). Anal. calcd. for  $\text{C}_{14}\text{H}_{17}\text{NO}_3\text{S}$ : C 60.19, H 6.13, N 5.02; found: C 60.12, H 6.09, N 5.10.

**1-(4-Chlorophenoxy)-3-thiocyanatopropan-2-yl acetate (11)**

Mp 44–45  $^{\circ}\text{C}$  (lit. value<sup>17</sup> mp 43–44  $^{\circ}\text{C}$ ). FTIR (neat,  $\text{cm}^{-1}$ ): 2156 (m, CN), 1743 (s, C=O).  $^1\text{H}$  NMR ( $\text{CDCl}_3$ , 500 MHz, ppm)  $\delta$ : 2.15 (s, 3H ( $\text{CH}_3$ )), 3.30–3.34 (dd, 1H ( $\text{CHCH}_a\text{H}_b\text{S}$ ),  $J_{\text{H}_a\text{H}_b} = 13.9$  Hz,  $J_{\text{H}_a\text{CH}} = 6.4$  Hz), 3.41–3.44 (dd, 1H ( $\text{CHCH}_a\text{H}_b\text{S}$ ),  $J_{\text{H}_b\text{CH}} = 4.3$  Hz), 4.11–4.14 (dd, 1H ( $\text{OCH}_c\text{H}_d\text{CH}$ ),  $J_{\text{H}_c\text{H}_d} = 10.3$  Hz,  $J_{\text{H}_c\text{CH}} = 5.5$  Hz), 4.17–4.20 (dd, 1H ( $\text{OCH}_c\text{H}_d\text{CH}$ ),  $J_{\text{H}_d\text{CH}} = 4.4$  Hz), 5.40–5.43 (m, 1H (CH)), 6.85–7.33 (m, 4H (ph)).  $^{13}\text{C}$  NMR ( $\text{CDCl}_3$ , 125.77 MHz, ppm)  $\delta$ : 20.66, 34.19, 66.57, 69.84, 111.57, 115.74, 126.60, 129.42, 156.32, 169.98.

**Acknowledgements**

We gratefully acknowledge the support of this work by the Damghan University of Basic Sciences Research Council.

**References**

- (1) Behrens, C. H.; Ko, S. Y.; Sharpless, K. B.; Walker, F. J. *J. Org. Chem.* **1985**, *50* (26), 5687–5696. doi:10.1021/jo00350a050.
- (2) Nugent, W. A. *J. Am. Chem. Soc.* **1992**, *114* (7), 2768–2769. doi:10.1021/ja00033a090.
- (3) Tokunaga, M.; Larrow, J. F.; Kakiuchi, F.; Jacobsen, E. N. *Science* **1997**, *277* (5328), 936–938. doi:10.1126/science.277.5328.936. PMID:9252321.

- (4) Bonini, C. R.; Righi, G. *Synthesis* **1994**, 225–238. doi:10.1055/s-1994-25445.
- (5) Gorzynski Smith, J. *Synthesis* **1984**, 629–656. doi:10.1055/s-1984-30921.
- (6) Yamada, J.; Yumoto, M.; Yamamoto, Y. *Tetrahedron Lett.* **1989**, *30* (32), 4255–4258. doi:10.1016/S0040-4039(01)80704-8.
- (7) Guy, R. G. *The Chemistry of the Cyanates and Their Thio Derivatives*; Patai, S., Ed.; Wiley Interscience: New York, 1977; p 819.
- (8) Shahidi, F. *Sulphur Compounds in Foods*. Mussinan, C. J., Keelan, M. E., Eds.; American Chemical Society: Washington, DC, 1994; p 106.
- (9) Mehta, R. G.; Liu, J.; Constantinou, A.; Thomas, C. F.; Hawthorne, M.; You, M.; Gerhäuser, C.; Pezzuto, J. M.; Moon, R. C.; Moriarty, R. M. *Carcinogenesis* **1995**, *16* (2), 399–404. doi:10.1093/carcin/16.2.399. PMID:7859373.
- (10) Otera, J. *Esterification, Methods, Reactions and Applications*; WILEY-VCH Verlag GmbH & Co. KGaA: Weinheim, 2003.
- (11) (a) Greene, T. W.; Wuts, P. G. M. *Protective Groups in Organic Synthesis*, 2nd ed.; Wiley: New York, 1991; (b) Kocienski, P. J. *Protecting Groups*; Thieme: Stuttgart, 1994.
- (12) (a) Larock, R. C. *Comprehensive Organic Transformations*; VCH Publishers Inc.: New York, 1989; p 980; (b) For more references, see: Saravanan, P.; Singh, V. K. *Tetrahedron Lett.* **1999**, *40* (13), 2611–2614. doi:10.1016/S0040-4039(99)00229-4; (c) Chandrasekhar, S.; Ramachander, T.; Takhi, M. *Tetrahedron Lett.* **1998**, *39* (20), 3263–3266. doi:10.1016/S0040-4039(98)00465-1; (d) Damen, E. W. P.; Braamer, L.; Scheeren, H. W. *Tetrahedron Lett.* **1998**, *39* (33), 6081–6082. doi:10.1016/S0040-4039(98)01253-2; (e) Orita, A.; Mitsutome, A.; Otera, J. *J. Org. Chem.* **1998**, *63* (8), 2420–2421. doi:10.1021/jo9800412. PMID:11672094; (f) Breton, G. W. *J. Org. Chem.* **1997**, *62* (25), 8952–8954. doi:10.1021/jo971367y; (g) Orita, A.; Sakamoto, K.; Hamada, Y.; Mitsutome, A.; Otera, J. *Tetrahedron* **1999**, *55* (10), 2899–2910. doi:10.1016/S0040-4020(99)00072-1.
- (13) (a) Li, T. S.; Li, A. X. *J. Chem. Soc. Perkin Trans. 1* **1998**, 1913–1918. doi:10.1039/a802051e; (b) Ballini, R.; Bosica, G.; Carloni, L.; Maggi, R.; Sartori, G. *Tetrahedron Lett.* **1998**, *39* (33), 6049–6052. doi:10.1016/S0040-4039(98)01244-1; (c) Bhaskar, P. M.; Loganathan, D. *Tetrahedron Lett.* **1998**, *39* (15), 2215–2218. doi:10.1016/S0040-4039(98)00178-6.
- (14) (a) van Tamelen, E. E. *J. Am. Chem. Soc.* **1951**, *73* (7), 3444–3448. doi:10.1021/ja01151a132; (b) Choudary, B. M.; Rani, S. S.; Kantam, M. L. *Synth. Commun.* **1990**, *20* (15), 2313–2317. doi:10.1080/00397919008053174.
- (15) (a) Nájera, C.; Sansano, J. M. *Tetrahedron* **1991**, *47* (28), 5193–5202. doi:10.1016/S0040-4020(01)87131-3; (b) Tamura, Y.; Kawasaki, T.; Yasuda, H.; Gohda, N.; Kita, Y. *J. Chem. Soc. Perkin Trans. 1* **1981**, 1577–1581. doi:10.1039/p19810001577; (c) Olszewski-Ortar, A.; Gros, P.; Fort, Y. *Tetrahedron Lett.* **1997**, *38* (50), 8699–8702. doi:10.1016/S0040-4039(97)10338-0.
- (16) (a) Sharghi, H.; Beni, A. S.; Khalifeh, R. *Helv. Chim. Acta* **2007**, *90* (7), 1373–1385. doi:10.1002/hlca.200790139; (b) Sharghi, H.; Nejad, A. H.; Nasser, M. A. *New J. Chem.* **2004**, *28* (8), 946–951. doi:10.1039/b316880h; (c) Sawant, S.; Youssef, D.; Mayer, A.; Sylvester, P.; Wali, V.; Arant, M.; El Sayed, K. *Chem. Pharm. Bull. (Tokyo)* **2006**, *54* (8), 1119–1123. doi:10.1248/cpb.54.1119. PMID:16880655; (d) Yadav, J. S.; Reddy, B. V. S.; Reddy, Ch. S. *Tetrahedron*

- Lett.* **2004**, *45* (6), 1291–1293. doi:10.1016/j.tetlet.2003.11.102.
- (17) Łukowska, E.; Plenkiewicz, J. *Tetrahedron Asymmetry* **2005**, *16* (12), 2149–2156. doi:10.1016/j.tetasy.2005.05.007.
- (18) Guy, R. G.; Pearson, I. *J. Chem. Soc., Perkin Trans. 1* **1973**, 281–284. doi:10.1039/p19730000281.
- (19) Tanaka, K. *Solvent-Free Organic Synthesis*; WILEY-VCH Verlag GmbH & Co. KGaA: Weinheim, 2003.
- (20) Tanaka, K.; Toda, F. *Chem. Rev.* **2000**, *100* (3), 1025–1074. doi:10.1021/cr940089p. PMID:11749257.
- (21) (a) Iranpoor, N.; Firouzabadi, H.; Aghapour, G.; Nahid, A. *Bull. Chem. Soc. Jpn.* **2004**, *77* (10), 1885–1891. doi:10.1246/bcsj.77.1885.; (b) Aghapour, G.; Afzali, A.; Salek, F. *Indian J. Chem.* **2009**, *48B* (2), 231–236.
- (22) Aghapour, G.; Hatefipour, R. *Synth. Commun.* **2009**, *39* (10), 1698–1707. doi:10.1080/00397910802578626.

# Organocatalysis in the stereoselective bromohydrin reaction of alkenes

Sukanta Bar

**Abstract:** An efficient regio- and stereo-selective (>99:1) trans-bromohydration (bromohydroxylation and bromomethoxylation) of alkenes including  $\alpha,\beta$ -unsaturated carbonyl compounds with *N*-bromosuccinimide (NBS) has been achieved by using 1.0 mol% of *N,N'*-diarylthiourea catalyst.

**Key words:** thiourea, *N*-halosuccinimide, alkene.

**Résumé :** On a pu réaliser des bromohydrations trans (bromohydroxylation et bromométhoxylation) d'alcènes régio- et stéréo-sélectives (>99:1) efficaces, y compris des composés carbonylés  $\alpha,\beta$ -insaturés, sous l'action du *N*-bromosuccinimide (NBS), en présence de 1,0 mole % de *N,N'*-diarylthiourée comme catalyseur.

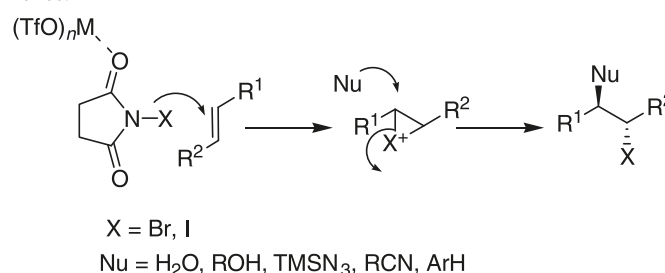
**Mots-clés :** thiourée, *N*-halosuccinimide, alcène.

[Traduit par la Rédaction]

1,2-Halofunctionalization of olefins, for example, halohydrin reaction (halohydroxylation and haloalkoxylation) is an important transformation in organic chemistry.<sup>1</sup> The resulting 1,2-halohydroxy and alkoxyhalide compounds are versatile precursors in organic, medicinal, as well as industrial chemistry.<sup>2</sup> Owing to the immense importance of vicinal halohydrins, a number of methods have been developed for the reaction of aqueous (alcoholic) solutions of alkenes with molecular halogens, *N*-halosuccinimides (NXSs),<sup>3</sup>  $\text{TsNBr}_2$ ,<sup>4</sup> *N*-halosaccharin,<sup>5</sup> and metal halides along with an oxidizing agent.<sup>6</sup> Cheap and available NXSs, in particular *N*-bromosuccinimide (NBS) and *N*-chlorosuccinimide (NCS), are the choice of halogen sources over other hazardous reagents. However, longer reaction times and low yields, especially of electron-deficient alkenes, are major hitches. Some attempts are made to improve the reaction by performing in ionic liquids.<sup>7</sup> Herein, we report highly efficient *N,N'*-diarylthiourea-catalyzed (1.0 mol% of *N,N'*-diarylthiourea (PhNHCSNHPh)) 1,2-bromohydrin reaction of alkenes, including  $\alpha,\beta$ -unsaturated carbonyl compounds with high regio- and diastereo-selectivity (>99:1).

Recently, organocatalysis has become a vast area of research, while interest in catalysis of thiourea has grown.<sup>8</sup> In my continued efforts towards the development of new catalytic methods for the regio- and stereo-selective 1,2-halofunctionalization of alkenes, Lewis acids like metal triflates were found to activate NXS for the transfer of halogen to alkenes (Scheme 1).<sup>9</sup> This led us to anticipate that unlike Lewis acid, thiourea derivatives having hydrogen-bonding capability with carbonyl oxygen might catalyze the electrophilic halogen transfer from NXS to the olefins (Fig. 1). Recently, thiourea-catalyzed ( $\text{H}_2\text{NCSNH}_2$ ; 20 mol%) chlorohydrin reaction of alkenes was reported by Bentley et al. with poor-to-moderate stereoselectivity and yields.<sup>10</sup>

**Scheme 1.** Lewis acid catalyzed 1,2-halofunctionalization of alkenes.



In search for an effective thiourea catalyst for the bromohydrin reaction, we first studied the reaction of *trans*-stilbene **1a** with NBS in aqueous  $\text{CH}_3\text{CN}$  with *N,N'*-diarylthiourea **3** and simple thiourea, and the results are presented in Table 1. Compared with the non-catalytic reaction (5 h, 56% yield; Table 1, entry 1), *N,N'*-diphenylthiourea-catalyzed bromohydrin reaction of stilbene **1a** proceeded very fast at RT, and within 5 min, it afforded the desired bromohydroxylation product **2a** in 86% yield (Table 1, entry 3) along with 8% of 1,2-dibromostilbene. Further improvement of the yield as well as product distribution was observed when the reaction was performed at 0 °C, and no 1,2-dibromostilbene was detected by <sup>1</sup>H NMR spectrum analysis of the crude reaction mixture (Table 1, entry 4). There was no appreciable change in the reactivity and selectivity with thiourea **3b**, and **3c** containing electron-rich and electron-deficient arenes, respectively (Table 1, entries 5 and 6), while Thiourea **3d** provided the desired product, with 65% yield along with 16% of the 1,2-dibromostilbene.

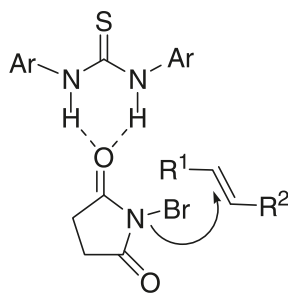
In search for an appropriate solvent for the bromohydrin reaction, we first studied the reaction of *trans*-stilbene (**1a**) and NBS with 1 mol% *N,N'*-diarylthiourea (PhNHCSNHPh, **3a**) in different solvents. Common organic solvents were used

Received 15 December 2009. Accepted 25 March 2010. Published on the NRC Research Press Web site at canjchem.nrc.ca on 28 May 2010.

S. Bar. Department of Chemistry, Indian Institute of Technology, Kharagpur 721 302, India. (e-mail: sukantachem@yahoo.com).



**Fig. 1.** Proposed activation of *N*-bromosuccinimide (NBS) by *N,N'*-diarylthiourea.



for this purpose. Acetone, THF, 1,4-dioxane, and 1,2-dimethoxyethane gave 45%–61% yield of the desired product along with 1,2-dibromostilbene as the byproduct. Other solvents gave very poor results. Acetonitrile was found to be the best solvent with 95% yield of the desired product. Detailed results of the solvent study are summarized in Table 2.

Thus, the best result was obtained when substrate **1a** was treated with 0.01 equiv. of thiourea (PhNHCSNHPh, **3a**) and 1.2 equiv. of NBS in 20% aqueous acetonitrile at 0 °C for 1 h. To establish the generality of the thiourea-catalyzed bromohydrin reaction, it was investigated on other alkenes, namely,  $\beta$ -propylstyrene, 1,2-dihydronaphthalene, and indene. All underwent smooth reaction at 0 °C and provided corresponding bromohydrins in excellent yields within an hour (Table 1, entries 8, 10, and 12).

When these alkenes were subjected to bromohydrin reaction at 25 °C, reactions were completed within 5 min but with 8%–10% less yields, which is due to the formation of dibromide as the byproduct (Table 1, entries 7, 9, and 11). In all the above cases, these reactions were anti-selective and no cis-isomer was formed as revealed by the <sup>1</sup>H NMR spectrum of the crude mixture.

Unfortunately for compounds containing isolated double bonds like cyclohexene, the reaction was less satisfying, as a messy reaction mixture was obtained. Similar result was obtained for ethyl acrylate.

$\alpha,\beta$ -Unsaturated carbonyls usually undergo slow bromohydrin reaction with poor yields of the desired bromohydrins. So, this catalytic method was studied for a large number of  $\alpha,\beta$ -unsaturated carbonyls like cinnamates and chalcones (Table 2). Reaction of methyl cinnamate **4a** under the catalytic conditions afforded the desired bromohydrin in 91% yield at RT after 5 h (Table 3, entry 1) compared with 60% yield after 18 h for the non-catalytic reaction carried out with 1.6 equiv. of NBS (not shown in Table 3). Electron-rich cinnamates **4b** and **4c** provided corresponding bromohydrins in excellent yields at 0 °C (Table 3, entries 2 and 3).

3,4-Methylenedioxycinnamate (**4d**) behaved similar to cinnamate (**4a**) (Table 3, entry 4). Similar trend was also observed for chalcones. Thus, electron-rich substrates preferred to show clean reaction at 0 °C, while other substrates reacted at RT (Table 3, entries 5–10).

To increase the scope of the reaction, we decided to study the bromomethoxylation reaction of a variety of alkenes. When methanolic solutions of alkenes, including  $\alpha,\beta$ -unsaturated carbonyls, were subjected to *N,N'*-diarylthiourea-catalyzed bromomethoxylation reaction with NBS, they produced methoxybromides in excellent yields (Table 4).

In summary, we have developed an efficient and general catalytic method for the bromohydrin reaction (bromohydroxylation and bromomethoxylation) of alkenes in the presence of only 1.0 mol% of *N,N'*-diarylthiourea using NBS as halogen source with excellent anti-selectivity and yields.

## Experimental section

### General methods

Commercial-grade reagents were used without further purification. Solvents were dried and distilled following usual protocols. Flash chromatography was carried out using Rankem Silica gel (230–400 mesh) purchased from Rankem, India. TLC was performed on aluminium-backed plates coated with Silica gel 60 with F254 indicator (Merck).

The <sup>1</sup>H NMR spectra were measured on Bruker-200 (200 MHz) and Bruker-400 (400 MHz) spectrometers, and <sup>13</sup>C NMR spectra were measured on Bruker-200 (50 MHz) and Bruker-400 (100 MHz) spectrometers using CDCl<sub>3</sub>. <sup>1</sup>H NMR chemical shifts are expressed in ppm ( $\delta$ ) downfield to CHCl<sub>3</sub> ( $\delta$  = 7.26), and <sup>13</sup>C NMR chemical shifts are expressed in ppm ( $\delta$ ) relative to the central CDCl<sub>3</sub> resonance ( $\delta$  = 77.0). Coupling constants in <sup>1</sup>H NMR are in Hz. Elemental analyses were carried out on a PerkinElmer 2400-II, Department of Chemistry, Indian Institute of Technology, Kharagpur. Melting points were measured in Toshniwal (India) melting point apparatus. IR spectra were recorded using PerkinElmer Spectrum R  $\times$  I FTIR Spectrometer.

### General procedure for the *N,N'*-diarylthiourea-catalyzed halohydrin reaction of alkenes

#### Bromohydrination of stilbene **1a**

To a well-stirred solution of *trans*-stilbene (**1a**) (0.10 g, 0.55 mmol) in 2.75 mL CH<sub>3</sub>CN:H<sub>2</sub>O (4:1), PhNHCSNHPh (1.2 mg, 0.0055 mmol) and NBS (0.118 g, 0.66 mmol) were added, and the reaction mixture was allowed to stir at 0 °C under argon atmosphere. Progress of the reaction was monitored by TLC. After 1 h, the solvent was evaporated under reduced pressure at RT. The crude reaction mass was subjected to purification by flash column chromatography using 5% EtOAc in petroleum ether (60–80 °C) to obtain ( $\pm$ )-**2a**<sup>11</sup> (0.146 g, 95%) as a white solid; mp 83–86 °C (lit.<sup>11</sup> mp 83–84 °C). <sup>1</sup>H NMR (200 MHz, CDCl<sub>3</sub>)  $\delta$ : 2.18 (bs, 1H), 5.10 (d, *J* = 6.8 Hz, 1H), 5.21 (d, *J* = 6.8 Hz, 1H), 7.36 (m, 10H). Bromohydrin compounds **2b**,<sup>12</sup> **2c**,<sup>13</sup> **2d**,<sup>14</sup> **5a**,<sup>15</sup> **5b**,<sup>15</sup> and **5e**<sup>16</sup> were characterized by <sup>1</sup>H and <sup>13</sup>C NMR and compared with the reported literature data.

#### 2-Bromo-3-(3,4-dimethoxyphenyl)-3-hydroxy-propionic acid methyl ester (**5c**)

Yield: 95%; white solid; mp 133 °C. *R*<sub>f</sub> (25% EtOAc/petroleum ether): 0.16. IR (KBr, cm<sup>-1</sup>)  $\nu$ : 751, 819, 872, 1021, 1037, 1142, 1156, 1244, 1274, 1462, 1508, 1747, 3457. <sup>1</sup>H NMR (200 MHz, CDCl<sub>3</sub>)  $\delta$ : 3.1 (d, *J* = 4.8 Hz, 1H), 3.82 (s, 3H), 3.88 (s, 3H), 3.90 (s, 3H), 4.36 (d, *J* = 8.0 Hz, 1H), 5.04 (dd, *J* = 8.0, 4.8 Hz, 1H), 6.86 (d, *J* = 8.0 Hz, 1H), 6.93 (m, 2H). <sup>13</sup>C NMR (100 MHz, CDCl<sub>3</sub>)  $\delta$ : 47.6, 53.1, 55.79, 55.83, 74.9, 109.5, 110.7, 119.6, 131.5, 148.9, 149.2, 169.8. Anal. calcd. for C<sub>12</sub>H<sub>15</sub>BrO<sub>5</sub>: C, 45.16; H, 4.74. Found: C, 45.32; H, 4.51.

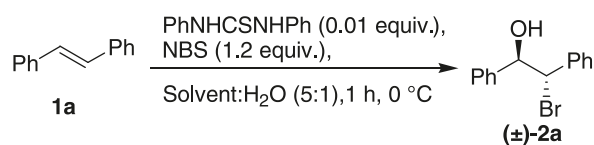
**Table 1.** *N,N'*-diarylthiourea-catalyzed bromohydrin of alkenes **1**.

$\text{1} \xrightarrow[\text{MeCN:H}_2\text{O (5:1)}]{\text{3 (0.01 equiv.), NBS (1.2 equiv.)}} (\pm)\text{-2}$

$\text{Ar-NH-C(=S)-NH-Ar}$   
**3a:** Ar = C<sub>6</sub>H<sub>5</sub>  
**3b:** Ar = 4-MeOC<sub>6</sub>H<sub>4</sub>  
**3c:** Ar = 3,5-CF<sub>3</sub>C<sub>6</sub>H<sub>3</sub>  
**3d:** Ar = H

Entry	Substrate	Catalyst	<i>T</i> (°C)	Time	Product	Yield of <b>2</b> <sup>a</sup> (%)
1		None	25	5 h		52
2		None	0	12 h		56
3		<b>3a</b>	25	5 min		86
4		<b>3a</b>	0	1 h	(±)- <b>2a</b>	95
5		<b>3b</b>	0	1 h		91
6		<b>3c</b>	0	1 h		91
7		<b>3d</b>	0	1 h		65
8		<b>3a</b>	25	5 min		80
9	<b>1b</b>	<b>3a</b>	0	1 h	(±)- <b>2b</b>	89
10		<b>3a</b>	25	5 min		84
11	<b>1c</b>	<b>3a</b>	0	1 h	(±)- <b>2c</b>	92
12		<b>3a</b>	25	5 min		84
13	<b>1d</b>	<b>3a</b>	0	1 h	(±)- <b>2d</b>	94

<sup>a</sup> Determined from the <sup>1</sup>H NMR spectra of the crude reaction mixture with naphthalene as an internal standard.

**Table 2.** *N,N'*-Diarylthiourea-catalyzed bromohydrin of alkene **1a** with different solvents.

Entry	Substrate	Solvent	Yield of <b>2</b> <sup>a</sup> (%)	Yield of 1,2-dibromo stilbene <sup>a</sup> (%)
1	<b>1a</b>	CH <sub>3</sub> CN	95	0
2	<b>1a</b>	(CH <sub>3</sub> ) <sub>2</sub> CO	56	17
3	<b>1a</b>	CH <sub>2</sub> Cl <sub>2</sub>	12	15
4	<b>1a</b>	CH <sub>3</sub> Cl	18	10
5	<b>1a</b>	CCl <sub>4</sub>	10	9
6	<b>1a</b>	Cl(CH <sub>2</sub> ) <sub>2</sub> Cl	21	12
7	<b>1a</b>	OMe(CH <sub>2</sub> ) <sub>2</sub> OMe	45	18
8	<b>1a</b>	Toluene	8	4
9	<b>1a</b>	THF	61	19
10	<b>1a</b>	1,4-Dioxane	48	16

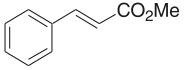
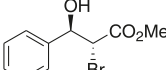
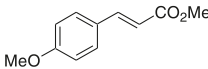
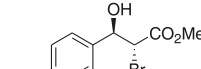
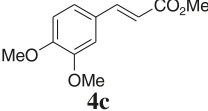
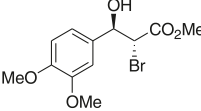
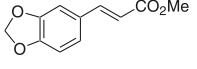
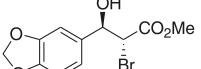
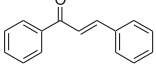
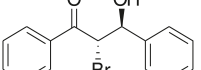
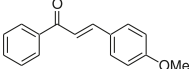
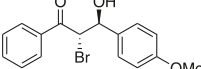
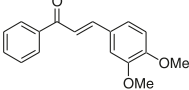
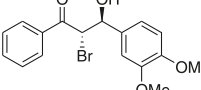
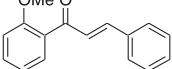
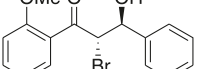
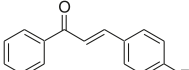
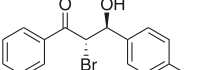
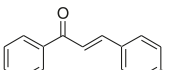
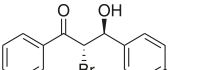
<sup>a</sup> Determined from the <sup>1</sup>H NMR spectra of the crude reaction mixture with naphthalene as an internal standard.

### 3-Benzo[1,3]dioxol-5-yl-2-bromo-3-hydroxypropionic acid methyl ester (**5d**)

Yield: 91%; white solid; mp 75 °C. *R*<sub>f</sub> (10% EtOAc/petroleum ether): 0.18. IR (KBr, cm<sup>-1</sup>): 814, 929, 1009, 1042, 1249, 1297, 1440, 1488, 1504, 1717, 1741, 3418 (br). <sup>1</sup>H

NMR (200 MHz, CDCl<sub>3</sub>): 3.82 (s, 3H), 4.31 (d, *J* = 8.6 Hz, 1H), 5.0 (d, *J* = 8.6 Hz, 1H), 5.98 (s, 2H), 6.82 (m, 3H). <sup>13</sup>C NMR (100 MHz, CDCl<sub>3</sub>) δ: 47.5, 53.2, 74.9, 101.2, 107.0, 108.1, 120.9, 132.8, 147.7, 147.8, 169.8. Anal. calcd. for C<sub>11</sub>H<sub>11</sub>BrO<sub>5</sub>: C, 43.59; H, 3.66. Found: C, 43.67; H, 3.65.

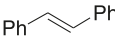
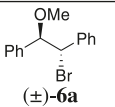
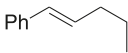
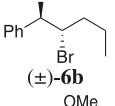
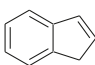
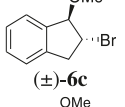
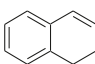
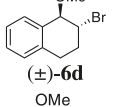
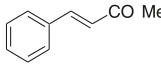
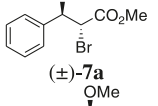
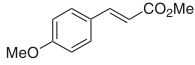
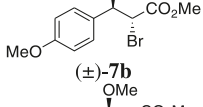
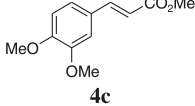
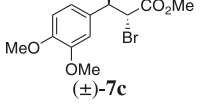
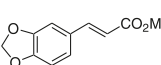
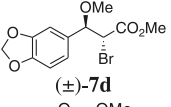
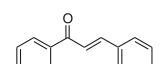
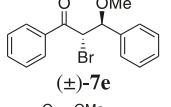
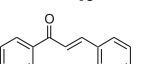
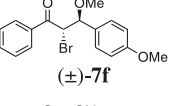
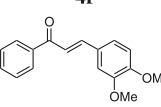
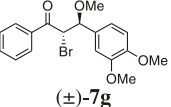
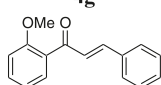
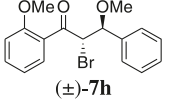
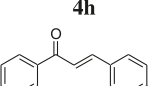
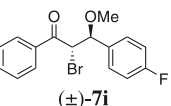
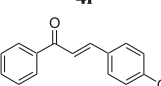
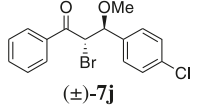
**Table 3.** *N,N'*-Diarylthiourea-catalyzed bromohydration of  $\alpha,\beta$ -unsaturated carbonyls with NBS in 20% aqueous  $\text{CH}_3\text{CN}$ .

$  \begin{array}{c}  \text{R}^1 \\    \\  \text{R}^2 - \text{C}_6\text{H}_4 - \text{CH}=\text{CH} - \text{C}(=\text{O})\text{R}^3 \\  \mathbf{4}  \end{array}  \xrightarrow[\text{CH}_3\text{CN:H}_2\text{O (4:1)}]{\begin{array}{c} \mathbf{3a} \text{ (0.01 equiv.)}, \\ \text{NBS (1.2 equiv.)} \end{array}}  \begin{array}{c}  \text{R}^1 \\    \\  \text{R}^2 - \text{C}_6\text{H}_4 - \text{CH}(\text{OH}) - \text{CH}(\text{Br}) - \text{C}(=\text{O})\text{R}^3 \\  (\pm)\text{-}\mathbf{5}  \end{array}  $					
Entry	Substrate	<i>T</i> (°C)	Time (h)	Product	Yield of <b>5</b> (%) <sup>a</sup>
1	 <b>4a</b>	25	5	 <b>(±)-5a</b>	91
2	 <b>4b</b>	0	2.5	 <b>(±)-5b</b>	95
3	 <b>4c</b>	0	2	 <b>(±)-5c</b>	95
4	 <b>4d</b>	25	5	 <b>(±)-5d</b>	91
5	 <b>4e</b>	20	2.5	 <b>(±)-5e</b>	92
6	 <b>4f</b>	0	2	 <b>(±)-5f</b>	95
7	 <b>4g</b>	0	2	 <b>(±)-5g</b>	94
8	 <b>4h</b>	20	2.5	 <b>(±)-5h</b>	93
9	 <b>4i</b>	20	1.5	 <b>(±)-5i</b>	93
10	 <b>4j</b>	20	3	 <b>(±)-5j</b>	94

**Note:** Bromohydrin synthesis from olefins (1.0 equiv.) was performed with  $\text{PhNHCSNHPh}$  (0.01 equiv.), 1.2 equiv. NBS in 20% aqueous acetonitrile at 0–25 °C.

<sup>a</sup>Isolated yield of the respective bromohydrin after column chromatography.

**Table 4.** *N,N'*-Diarylthiourea-catalyzed bromomethoxylation of alkenes with NBS in MeOH.

Entry	Substrate	<i>T</i> (°C)	Time (h)	Product	Yield of <b>6</b> (%) <sup>a</sup>
1	 <b>1a</b>	0	1	 (±)- <b>6a</b>	95
2	 <b>1b</b>	0	1	 (±)- <b>6b</b>	87
3	 <b>1c</b>	0	1	 (±)- <b>6c</b>	95
4	 <b>1d</b>	0	1	 (±)- <b>6d</b>	93
5	 <b>4a</b>	25	5	 (±)- <b>7a</b>	91
6	 <b>4b</b>	0	2.5	 (±)- <b>7b</b>	95
7	 <b>4c</b>	0	2	 (±)- <b>7c</b>	95
8	 <b>4d</b>	25	5	 (±)- <b>7d</b>	91
9	 <b>4e</b>	20	2.5	 (±)- <b>7e</b>	92
10	 <b>4f</b>	0	2	 (±)- <b>7f</b>	95
11	 <b>4g</b>	0	2	 (±)- <b>7g</b>	94
12	 <b>4h</b>	20	2.5	 (±)- <b>7h</b>	93
13	 <b>4i</b>	20	1.5	 (±)- <b>7i</b>	93
14	 <b>4j</b>	20	3	 (±)- <b>7j</b>	94

**Note:** Bromomethoxylation of olefins (1.0 equiv.) was performed with PhNHCSNHPh (0.01 equiv.), 1.2 equiv. NBS in methanol at 0–25 °C.

<sup>a</sup>Isolated yield of **6** and **7** after column chromatography.



**2-Bromo-3-hydroxy-3-(4-methoxyphenyl)-1-phenylpropan-1-one (5f)**

Yield: 95%; white solid; mp 58 °C.  $R_f$  (15% EtOAc/petroleum ether): 0.16. IR (KBr,  $\text{cm}^{-1}$ ): 625, 684, 811, 834, 1002, 1037, 1176, 1217, 1251, 1282, 1449, 1516, 1594, 1611, 1679, 2836, 3466 (br).  $^1\text{H}$  NMR (200 MHz,  $\text{CDCl}_3$ )  $\delta$ : 3.45 (d,  $J$  = 4.6 Hz, 1H), 3.82 (s, 3H), 5.2 (d,  $J$  = 8.4 Hz, 1H), 5.31 (dd,  $J$  = 8.6, 4.6 Hz, 1H), 6.92 (m, 2H), 7.37–7.66 (m, 5H), 8.03 (m, 2H).  $^{13}\text{C}$  NMR (100 MHz,  $\text{CDCl}_3$ )  $\delta$ : 48.2, 55.2, 74.2, 113.8 (2C), 128.4 (2C), 128.8 (2C), 128.9 (2C), 131.6, 134.1, 134.5, 159.7, 194.6. Anal. calcd. for  $\text{C}_{16}\text{H}_{15}\text{BrO}_3$ : C, 57.33; H, 4.51. Found: C, 57.21; H, 4.22.

**2-Bromo-3-(3,4-dimethoxyphenyl)-3-hydroxy-1-phenylpropan-1-one (5g)**

Yield: 94%; white solid; mp 130 °C.  $R_f$  (20% EtOAc/petroleum ether): 0.22. IR (KBr,  $\text{cm}^{-1}$ ): 635, 690, 812, 979, 1027, 1135, 1229, 1251, 1463, 1447, 1511, 1595, 1685, 3498.  $^1\text{H}$  NMR (200 MHz,  $\text{CDCl}_3$ )  $\delta$ : 3.45 (d,  $J$  = 4.4 Hz, 1H), 3.89 (s, 3H), 3.92 (s, 3H), 5.2 (d,  $J$  = 8.2 Hz, 1H), 5.3 (dd,  $J$  = 8.8, 4.0 Hz, 1H), 6.87 (d,  $J$  = 8.4 Hz, 1H), 7.03 (m, 2H), 7.49 (m, 2H), 7.63 (m, 1H), 8.02 (m, 2H).  $^{13}\text{C}$  NMR (100 MHz,  $\text{CDCl}_3$ )  $\delta$ : 48.2, 55.81, 55.87, 74.5, 109.9, 110.7, 119.8, 128.8 (2C), 128.9 (2C), 131.9, 134.1, 134.5, 148.8, 149.0, 194.6. Anal. calcd. for  $\text{C}_{17}\text{H}_{17}\text{BrO}_4$ : C, 55.91; H, 4.69. Found: C, 56.06; H, 4.64.

**2-Bromo-3-hydroxy-1-(2-methoxyphenyl)-3-phenylpropan-1-one (5h)**

Yield: 93%; gummy liquid.  $R_f$  (10% EtOAc/petroleum ether): 0.20. IR (KBr,  $\text{cm}^{-1}$ ): 567, 756, 930, 979, 1031, 1176, 1250, 1356, 1448, 1514, 1613, 1675, 2054, 2838, 3470 (br).  $^1\text{H}$  NMR (200 MHz,  $\text{CDCl}_3$ )  $\delta$ : 3.90 (s, 3H), 5.27 (d,  $J$  = 7.8 Hz, 1H), 5.62 (d,  $J$  = 7.8 Hz, 1H), 7.0 (m, 2H), 7.31–7.55 (m, 6H), 7.78 (dd,  $J$  = 7.8, 1.8 Hz, 1H).  $^{13}\text{C}$  NMR (100 MHz,  $\text{CDCl}_3$ )  $\delta$ : 48.2, 55.2, 74.2, 113.8 (2C), 128.5 (2C), 128.8 (2C), 128.9 (2C), 131.6, 134.1, 134.5, 159.6, 194.4. Anal. calcd. for  $\text{C}_{16}\text{H}_{15}\text{BrO}_3$ : C, 57.33; H, 4.51. Found: C, 57.41; H, 4.43.

**2-Bromo-3-(4-fluorophenyl)-3-hydroxy-1-phenylpropan-1-one (5i)**

Yield: 93%; white solid; mp 80 °C.  $R_f$  (5% EtOAc/petroleum ether): 0.20. IR (KBr,  $\text{cm}^{-1}$ ): 548, 686, 814, 836, 1009, 1159, 1231, 1281, 1449, 1594, 1608, 1682, 3298 (br).  $^1\text{H}$  NMR (200 MHz,  $\text{CDCl}_3$ )  $\delta$ : 3.47 (bs, 1H), 5.15 (d,  $J$  = 8.4 Hz, 1H), 5.33 (d,  $J$  = 8.4 Hz, 1H), 7.08 (t,  $J$  = 8.4 Hz, 2H), 7.48 (m, 3H), 7.63 (t,  $J$  = 7.6 Hz, 2H), 8.02 (d,  $J$  = 8.0 Hz, 2H).  $^{13}\text{C}$  NMR (100 MHz,  $\text{CDCl}_3$ )  $\delta$ : 48.0, 73.9, 115.2, 115.4, 128.8 (2C), 129 (3C), 129.1, 134.3, 134.4, 135.2, 162.7 (d,  $J$  = 245.5 Hz, 1C), 194.4. Anal. calcd. for  $\text{C}_{15}\text{H}_{12}\text{BrFO}_2$ : C, 55.75; H, 3.74. Found: C, 56.29; H, 3.51.

**2-Bromo-3-(4-chlorophenyl)-3-hydroxy-1-phenylpropan-1-one (5j)**

Yield: 94%; white solid; mp 96 °C.  $R_f$  (10% EtOAc/petroleum ether): 0.15. IR (KBr,  $\text{cm}^{-1}$ ): 544, 646, 682, 779, 808, 834, 1012, 1089, 1219, 1277, 1293, 1376, 1449, 1594, 1680, 3449 (br).  $^1\text{H}$  NMR (200 MHz,  $\text{CDCl}_3$ )  $\delta$ : 3.49 (d,  $J$  = 4.4 Hz, 1H), 5.10 (d,  $J$  = 8.4 Hz, 1H), 5.29 (dd,  $J$  = 8.2, 4.0 Hz, 1H), 7.23–7.50 (m, 6H), 7.60 (m, 1H), 7.90 (d,  $J$  = 7.0 Hz, 2H).  $^{13}\text{C}$  NMR (100 MHz,  $\text{CDCl}_3$ )  $\delta$ : 47.7, 73.9,

128.5 (2C), 128.7 (2C), 128.8 (2C), 128.9 (2C), 134.28, 134.31 (2C), 137.8, 194.3. Anal. calcd. for  $\text{C}_{15}\text{H}_{12}\text{BrClO}_2$ : C, 53.05; H, 3.56. Found: C, 53.42; H, 3.17.

**Bromomethoxylation of stilbene 1a**

To a well-stirred solution of *trans*-stilbene (**1a**) (0.10 g, 0.55 mmol) in 2.75 mL MeOH,  $\text{PhNHCSNHPH}$  (1.2 mg, 0.0055 mmol) and NBS (0.118 g, 0.66 mmol) were added, and the reaction mixture was allowed to stir at 0 °C under argon atmosphere. Progress of the reaction was monitored by TLC. After 1 h, the solvent was evaporated at RT under reduced pressure. The crude reaction mass was subjected to purification by flash column chromatography using 5% EtOAc in petroleum ether (60–80 °C) to obtain ( $\pm$ )-**6a**<sup>6d</sup> (0.153 g, 95%) as a white solid; mp 115–118 °C (lit.<sup>17</sup> mp 116–118 °C).  $^1\text{H}$  NMR (200 MHz,  $\text{CDCl}_3$ )  $\delta$ : 3.20 (s, 3H), 4.65 (d,  $J$  = 6.8 Hz, 1H), 5.04 (d,  $J$  = 6.8 Hz, 1H), 7.30 (m, 10H). Spectral data of compounds **6c**,<sup>18</sup> **6e**, and **6i** are consistent with the reported literature data.

**(2-Bromo-methoxypentyl)-benzene (6b)**

Yield: 87%; gummy liquid.  $R_f$  (3% EtOAc/petroleum ether): 0.45. IR (KBr,  $\text{cm}^{-1}$ ): 585, 624, 702, 760, 956, 1093, 1134, 1168, 1188, 1454, 1494, 2933, 2960.  $^1\text{H}$  NMR (200 MHz,  $\text{CDCl}_3$ )  $\delta$ : 0.92 (t,  $J$  = 7.2 Hz, 3H), 1.37–1.94 (m, 4H), 3.34 (s, 3H), 4.19 (m, 1H), 4.40 (d,  $J$  = 5.6 Hz, 1H), 7.39 (m, 5H).  $^{13}\text{C}$  NMR (100 MHz,  $\text{CDCl}_3$ )  $\delta$ : 13.3, 20.8, 34.9, 57.5, 59.5, 86.7, 127.6 (2C), 128.1, 128.16 (2C), 138.5. Anal. calcd. for  $\text{C}_{12}\text{H}_{17}\text{BrO}$ : C, 56.04; H, 6.66. Found: C, 56.13; H, 6.59.

**2-Bromo-1-methoxy-1,2,3,4-tetrahydronaphthalene (6d)**

Yield: 93%; liquid.  $R_f$  (3% EtOAc/petroleum ether): 0.62. IR (KBr,  $\text{cm}^{-1}$ ): 601, 748, 817, 937, 1078, 1117, 1214, 1438, 1455, 1492, 2821, 2928.  $^1\text{H}$  NMR (200 MHz,  $\text{CDCl}_3$ )  $\delta$ : 2.12–2.25 (m, 1H), 2.42–2.56 (m, 1H), 2.77–2.88 (m, 1H), 2.90–3.15 (m, 1H), 3.54 (s, 3H), 4.48 (d,  $J$  = 4.0 Hz, 1H), 4.65 (m, 1H), 7.13–7.35 (m, 4H).  $^{13}\text{C}$  NMR (100 MHz,  $\text{CDCl}_3$ )  $\delta$ : 25.8, 26.9, 49.6, 57.4, 81.4, 126.2, 128.3, 128.8, 130.2, 132.9, 135.6. Anal. calcd. for  $\text{C}_{11}\text{H}_{13}\text{BrO}$ : C, 54.79; H, 5.43. Found: C, 54.64; H, 5.34.

**2-Bromo-3-methoxy-3-(4-methoxyphenyl)-propionic acid methyl ester (7b)**

Yield: 95%; white solid; mp 46 °C.  $R_f$  (3% EtOAc/petroleum ether): 0.25. IR (KBr,  $\text{cm}^{-1}$ ): 578, 833, 1031, 1074, 1095, 1150, 1182, 1246, 1281, 1316, 1379, 1438, 1516, 1612, 1742, 2940.  $^1\text{H}$  NMR (200 MHz,  $\text{CDCl}_3$ )  $\delta$ : 3.19 (s, 3H), 3.82 (s, 3H), 3.84 (s, 3H), 4.21 (d,  $J$  = 9.8 Hz, 1H), 4.50 (d,  $J$  = 10.0 Hz, 1H), 6.92 (m, 2H), 7.28 (m, 2H).  $^{13}\text{C}$  NMR (100 MHz,  $\text{CDCl}_3$ )  $\delta$ : 47.3, 52.9, 55.1, 57.3, 83.6, 113.7 (2C), 128.7, 129.1 (2C), 159.9, 169.4. Anal. calcd. for  $\text{C}_{12}\text{H}_{15}\text{BrO}_4$ : C, 47.54; H, 4.99. Found: C, 47.77; H, 4.98.

**2-Bromo-3-(3,4-dimethoxyphenyl)-3-methoxypropionic acid methyl ester (7c)**

Yield: 95%; white solid; mp 75 °C.  $R_f$  (10% EtOAc/petroleum ether): 0.30. IR (KBr,  $\text{cm}^{-1}$ ): 646, 817, 855, 1021, 1074, 1104, 1143, 1170, 1236, 1238, 1261, 1294, 1447, 1464, 1517, 1593, 1748, 2936, 2964.  $^1\text{H}$  NMR (200 MHz,  $\text{CDCl}_3$ )  $\delta$ : 3.22 (s, 3H), 3.85 (s, 3H), 3.89 (s, 6H), 4.22 (d,  $J$  = 10.0 Hz, 1H), 4.49 (d,  $J$  = 9.8 Hz, 1H), 6.88 (m, 3H).

$^{13}\text{C}$  NMR (100 MHz,  $\text{CDCl}_3$ ):  $\delta$  47.3, 52.9, 55.74, 55.81, 57.4, 83.9, 109.8, 110.4, 121.1, 129.0, 149.0, 149.3, 169.4. Anal. calcd. for  $\text{C}_{13}\text{H}_{17}\text{BrO}_5$ : C, 46.86; H, 5.14. Found: C, 47.28; H, 5.15.

**3-Benzo[1,3]dioxol-5-yl-2-bromo-3-methoxypropionic acid methyl ester (7d)**

Yield: 91%; white solid; mp 74 °C.  $R_f$  (5% EtOAc/petroleum ether): 0.32. IR (KBr,  $\text{cm}^{-1}$ ): 559, 631, 655, 818, 924, 961, 1017, 1036, 1066, 1091, 1159, 1251, 1274, 1447, 1489, 1501, 1744.  $^1\text{H}$  NMR (200 MHz,  $\text{CDCl}_3$ ):  $\delta$  3.17 (s, 3H), 3.81 (s, 3H), 4.13 (d,  $J = 9.8$  Hz, 1H), 4.42 (d,  $J = 9.8$  Hz, 1H), 5.95 (s, 2H), 6.81 (m, 3H).  $^{13}\text{C}$  NMR (100 MHz,  $\text{CDCl}_3$ ):  $\delta$  47.3, 53, 57.4, 83.9, 101.2, 107.5, 107.9, 122.4, 130.7, 147.9, 148.1, 169.4. Anal. calcd. for  $\text{C}_{12}\text{H}_{13}\text{BrO}_5$ : C, 45.45; H, 4.13. Found: C, 45.06; H, 4.0.

**2-Bromo-3-methoxy-3-(4-methoxyphenyl)-1-phenylpropan-1-one (7f)**

Yield: 95%; white solid; mp 90 °C.  $R_f$  (5% EtOAc/petroleum ether): 0.25. IR (KBr,  $\text{cm}^{-1}$ ): 578, 685, 806, 832, 1038, 1074, 1175, 1219, 1254, 1305, 1279, 1373, 1446, 1516, 1611, 1685, 2929.  $^1\text{H}$  NMR (200 MHz,  $\text{CDCl}_3$ ):  $\delta$  3.18 (s, 3H), 3.85 (s, 3H), 4.80 (d,  $J = 9.8$  Hz, 1H), 5.12 (d,  $J = 9.8$  Hz, 1H), 6.96 (dd,  $J = 6.6, 2.0$  Hz, 2H), 7.39 (dd,  $J = 6.6, 2.0$  Hz, 2H), 7.50–7.62 (m, 3H), 8.06 (d,  $J = 7.0$  Hz, 2H).  $^{13}\text{C}$  NMR (100 MHz,  $\text{CDCl}_3$ ):  $\delta$  47.6, 55.2, 57.4, 82.8, 113.7 (2C), 128.76 (2C), 128.79 (2C), 129.3 (2C), 129.7, 133.7, 135.2, 159.9, 193.2. Anal. calcd. for  $\text{C}_{17}\text{H}_{17}\text{BrO}_3$ : C, 58.47; H, 4.91. Found: C, 58.40; H, 4.98.

**2-Bromo-3-(3,4-dimethoxyphenyl)-3-methoxy-1-phenylpropan-1-one (7g)**

Yield: 94%; gummy liquid.  $R_f$  (10% EtOAc/petroleum ether): 0.25. IR (KBr,  $\text{cm}^{-1}$ ): 577, 686, 806, 832, 1039, 1073, 1095, 1175, 1219, 1254, 1279, 1304, 1373, 1446, 1517, 1611, 1685, 2929.  $^1\text{H}$  NMR (200 MHz,  $\text{CDCl}_3$ ):  $\delta$  3.19 (s, 3H), 3.91 (s, 3H), 3.93 (s, 3H), 4.8 (d,  $J = 10.0$  Hz, 1H), 5.11 (d,  $J = 9.8$  Hz, 1H), 6.88–7.05 (m, 3H), 7.41–7.65 (m, 3H), 8.04 (m, 2H).  $^{13}\text{C}$  NMR (100 MHz,  $\text{CDCl}_3$ ):  $\delta$  47.5, 55.8, 55.9, 57.5, 83.1, 110.4, 110.5, 121.1, 128.73 (2C), 128.76 (2C), 130.1, 133.6, 135.2, 148.9, 149.3, 193.1. Anal. calcd. for  $\text{C}_{18}\text{H}_{19}\text{BrO}_4$ : C, 57.01; H, 5.05. Found: C, 57.19; H, 4.90.

**2-Bromo-3-methoxy-1-(2-methoxyphenyl)-3-phenylpropan-1-one (7h)**

Yield: 93%; gummy liquid.  $R_f$  (5% EtOAc/petroleum ether): 0.30. IR (KBr,  $\text{cm}^{-1}$ ): 701, 754, 771, 1082, 1162, 1249, 1312, 1439, 1486, 1597, 1683, 2945.  $^1\text{H}$  NMR (200 MHz,  $\text{CDCl}_3$ ):  $\delta$  3.20 (s, 3H), 3.93 (s, 3H), 4.82 (d,  $J = 9.8$  Hz, 1H), 5.43 (d,  $J = 9.8$  Hz, 1H), 7.03 (m, 2H), 7.34–7.56 (m, 6H), 7.84 (dd,  $J = 7.6, 1.8$  Hz, 1H).  $^{13}\text{C}$  NMR (100 MHz,  $\text{CDCl}_3$ ):  $\delta$  52.6, 55.8, 57.6, 84.1, 111.9, 120.9, 126.3, 128.2 (4C), 128.5, 131.5, 134.5, 138.1, 158.7, 194.9. Anal. calcd. for  $\text{C}_{17}\text{H}_{17}\text{BrO}_3$ : C, 58.47; H, 4.91. Found: C, 58.63; H, 4.89.

**2-Bromo-3-(4-fluorophenyl)-3-methoxy-1-phenylpropan-1-one (7i)**

Yield: 93%; white solid; mp 62 °C.  $R_f$  (3% EtOAc/petroleum ether): 0.45. IR (KBr,  $\text{cm}^{-1}$ ): 567, 637, 686, 808,

833, 1071, 1094, 1157, 1225, 1298, 1370, 1446, 1511, 1604, 1684, 2934.  $^1\text{H}$  NMR (200 MHz,  $\text{CDCl}_3$ ):  $\delta$  3.15 (s, 3H), 4.81 (d,  $J = 9.8$  Hz, 1H), 5.05 (d,  $J = 9.8$  Hz, 1H), 7.08 (m, 2H), 7.38–7.63 (m, 5H), 8.01 (m, 2H).  $^{13}\text{C}$  NMR (100 MHz,  $\text{CDCl}_3$ ):  $\delta$  47.2, 57.6, 82.5, 115.2, 115.4, 128.7 (4C), 129.7, 129.8, 133.59, 133.62, 135, 162.9 (d,  $J = 245.6$  Hz, 1C), 192.8. Anal. calcd. for  $\text{C}_{16}\text{H}_{14}\text{BrFO}_2$ : C, 56.99; H, 4.19. Found: C, 57.39; H, 3.97.

**2-Bromo-3-(4-chlorophenyl)-3-methoxy-1-phenylpropan-1-one (7j)**

Yield: 94%; white solid; mp 90 °C.  $R_f$  (5% EtOAc/petroleum ether): 0.35. IR (KBr,  $\text{cm}^{-1}$ ): 686, 807, 991, 1015, 1070, 1094, 1221, 1301, 1370, 1446, 1489, 1596, 1685, 2933.  $^1\text{H}$  NMR (200 MHz,  $\text{CDCl}_3$ ):  $\delta$  3.19 (s, 3H), 4.83 (d,  $J = 9.8$  Hz, 1H), 5.07 (d,  $J = 10.0$  Hz, 1H), 7.41 (s, 4H), 7.43–7.66 (m, 3H), 8.03 (m, 2H).  $^{13}\text{C}$  NMR (100 MHz,  $\text{CDCl}_3$ ):  $\delta$  46.9, 57.7, 82.6, 128.6 (2C), 128.8 (4C), 129.5 (2C), 133.8, 134.5, 135.0, 136.4, 192.7. Anal. calcd. for  $\text{C}_{16}\text{H}_{14}\text{BrClO}_2$ : C, 54.34; H, 3.99. Found: C, 54.73; H, 3.84.

**Supplementary data**

Supplementary data for this article ( $^1\text{H}$  and  $^{13}\text{C}$  NMR spectra of compounds **5c–5d**, **5f–5j**, **6b**, **6d**, and **7b–7j**) are available on the journal Web site (canjchem.nrc.ca).

**Acknowledgments**

I thank the Department of Science and Technology (DST), New Delhi, for providing financial support for this work, and I also thank the Council of Science and Industrial Research (CSIR), New Delhi, for my fellowship.

**References**

- (1) (a) Trost, B. M.; Fleming, I.; Semmelhalk, M. F., Eds.; In *Comprehensive Organic Synthesis*; Pergamon: Oxford, 1991; pp 344–347, Vol. 4; (b) March, J. *Advanced Organic Chemistry*, 4th ed.; Wiley: New York, 1992; p. 815; (c) Carey, F.; Sundberg, R. *Advanced Organic Chemistry*, Part B, 4th ed.; Plenum: New York, 2001; p. 203.
- (2) (a) Christophersen, C.; Bazin, H.; Heikkilä, J.; Chattopadhyaya, J.; Kupryszewski, G.; Wigilius, B. *Acta Chem. Scand. A* **1985**, 38b, 517. doi:10.3891/acta.chem.scand.39b-0517.; (b) Ueda, Y.; Mayrand, S. C. *Tetrahedron Lett.* **1988**, 29 (41), 5197. doi:10.1016/S0040-4039(00)80715-7.; (c) Konopelski, J. P.; Boehler, M. A.; Tarasow, T. M. *J. Org. Chem.* **1989**, 54 (20), 4966. doi:10.1021/jo00281a049.; (d) *Ullmann's Encyclopedia of Industrial Chemistry*, 6th ed.; Electronic Release, 1998; (e) Cabanal-Duvillard, I.; Berrier, J. F.; Royer, J.; Husson, H. P. *Tetrahedron Lett.* **1998**, 39 (29), 5181. doi:10.1016/S0040-4039(98)01017-X.
- (3) (a) Laock, R. C., Ed.; *Comprehensive Organic Transformation: A Guide to Functional Group Preparation*, 2nd ed.; Wiley-VCH: New York, 1999; pp 629–640; (b) Damin, B.; Garapon, J.; Sillion, B. *Synthesis* **1981**, 1981 (5), 362. doi:10.1055/s-1981-29447.; (c) Rolston, J. H.; Yates, K. *J. Am. Chem. Soc.* **1969**, 91 (6), 1469. doi:10.1021/ja01034a033.; (d) Dalton, D. R.; Dutta, V. P.; Jones, D. C. *J. Am. Chem. Soc.* **1968**, 90 (20), 5498. doi:10.1021/ja01022a030.; (e) Hanzlik, R. P. *Organic Syntheses*; Wiley & Sons: New York, 1988; pp 560–564, Collect. Vol. 6; (f) Sweeney, J. B.; Knight, J. R.; Thobhani, S. *Tetrahedron* **2006**, 62 (50),

11565. doi:10.1016/j.tet.2006.08.076.; (g) Heasley, V. L.; Wade, K. E.; Aucoin, T. G.; Gipe, D. E.; Shellhamer, D. F. *J. Org. Chem.* **1983**, *48* (8), 1377. doi:10.1021/jo00156a054.; (h) Narender, M.; Reddy, M. S.; Nageswar, Y. V. D.; Rao, K. R. *J. Mol. Catal. Chem.* **2006**, *258* (1–2), 10. doi:10.1016/j.molcata.2006.05.009.; (i) Das, B.; Venkateswarlu, K.; Damodar, K.; Suneel, K. *J. Mol. Catal. A: Chem.* **2007**, *269* (1–2), 17.
- (4) Phukan, P.; Chakraborty, P.; Katak, D. *J. Org. Chem.* **2006**, *71* (20), 7533. doi:10.1021/jo0600611. PMID:16995656.
- (5) Urankar, D.; Rutar, B.; Modec, B.; Dolenc, D. *Eur. J. Org. Chem.* **2005**, *2005* (11), 2349. doi:10.1002/ejoc.200400829.
- (6) (a) Nair, V.; Panicker, S. B.; Augustine, A.; George, T. G.; Thomas, S.; Vairamani, M. *Tetrahedron* **2001**, *57* (34), 7417. doi:10.1016/S0040-4020(01)00712-8.; (b) Kabalka, G. W.; Yang, K.; Reddy, N. K.; Narayana, C. *Synth. Commun.* **1998**, *28* (5), 925. doi:10.1080/00032719808006492.; (c) Dieter, R. K.; Nice, L. E.; Velu, S. E. *Tetrahedron Lett.* **1996**, *37* (14), 2377. doi:10.1016/0040-4039(96)00295-X.; (d) Dewkar, G. K.; Narina, S. V.; Sudalai, A. *Org. Lett.* **2003**, *5* (23), 4501. doi:10.1021/ol0358206. PMID:14602035.; (e) Agrawal, M. K.; Adimurthy, S.; Ganguly, B.; Ghosh, P. K. *Tetrahedron* **2009**, *65* (14), 2791. doi:10.1016/j.tet.2009.01.095.
- (7) Yadav, J. S.; Reddy, B. V. S.; Baishya, G.; Harshavardhan, S. J.; Chary, Ch. J.; Gupta, M. K. *Tetrahedron Lett.* **2005**, *46* (20), 3569. doi:10.1016/j.tetlet.2005.03.108.
- (8) (a) Taylor, M. S.; Jacobsen, E. N. *Angew. Chem. Int. Ed.* **2006**, *45* (10), 1520. doi:10.1002/anie.200503132.; (b) Sigman, M. S.; Jacobsen, E. N. *J. Am. Chem. Soc.* **1998**, *120* (19), 4901. doi:10.1021/ja980139y.; (c) Wenzel, A. G.; Jacobsen, E. N. *J. Am. Chem. Soc.* **2002**, *124* (44), 12964. doi:10.1021/ja028353g. PMID:12405820.; (d) Tillman, A. L.; Ye, J.; Dixon, D. J. *Chem. Commun. (Camb.)* **2006**, (11): 1191. doi:10.1039/b515725k. PMID:16518487.; (e) Joly, G. D.; Jacobsen, E. N. *J. Am. Chem. Soc.* **2004**, *126* (13), 4102. doi:10.1021/ja0494398. PMID:15053588.; (f) Taylor, M. S.; Jacobsen, E. N. *J. Am. Chem. Soc.* **2004**, *126* (34), 10558. doi:10.1021/ja046259p. PMID:15327311.; (g) Sohtome, Y.; Tanatani, A.; Hashimoto, Y.; Nagasawa, K. *Chem. Pharm. Bull. (Tokyo)* **2004**, *52* (4), 477. doi:10.1248/cpb.52.477. PMID:15056971.; (h) Okino, T.; Hoashi, Y.; Takemoto, Y. *J. Am. Chem. Soc.* **2003**, *125* (42), 12672. doi:10.1021/ja036972z. PMID:14558791.; (i) Vakulya, B.; Varga, S.; Csámpai, A.; Soós, T. *Org. Lett.* **2005**, *7* (10), 1967. doi:10.1021/ol050431s. PMID:15876031.; (j) Maher, D. J.; Connon, S. J. *Tetrahedron Lett.* **2004**, *45* (6), 1301. doi:10.1016/j.tetlet.2003.11.062.; (k) Wang, J.; Li, H.; Yu, X.; Zu, L.; Wang, W. *Org. Lett.* **2005**, *7* (19), 4293. doi:10.1021/ol051822+. PMID:16146410.; (l) Fuerst, D. E.; Jacobsen, E. N. *J. Am. Chem. Soc.* **2005**, *127* (25), 8964. doi:10.1021/ja052511x. PMID:15969569.; (m) Takemoto, Y. *Org. Biomol. Chem.* **2005**, *3* (24), 4299. doi:10.1039/b511216h. PMID:16327888.
- (9) (a) Hajra, S.; Bar, S.; Sinha, D.; Maji, B. *J. Org. Chem.* **2008**, *73* (11), 4320. doi:10.1021/jo8003937. PMID:18459808.; (b) Hajra, S.; Maji, B.; Bar, S. *Org. Lett.* **2007**, *9* (15), 2783. doi:10.1021/ol070813t. PMID:17585769.; (c) Hajra, S.; Bhowmick, M.; Maji, B.; Sinha, D. *J. Org. Chem.* **2007**, *72* (13), 4872. doi:10.1021/jo070614n. PMID:17542637.; (d) Hajra, S.; Bhowmick, M.; Sinha, D. *J. Org. Chem.* **2006**, *71* (24), 9237. doi:10.1021/jo061593k. PMID:17109556.; (e) Hajra, S.; Sinha, D.; Bhowmick, M. *Tetrahedron Lett.* **2006**, *47* (39), 7017. doi:10.1016/j.tetlet.2006.07.110.; (f) Hajra, S.; Bhowmick, M.; Karmakar, A. *Tetrahedron Lett.* **2005**, *46* (17), 3073. doi:10.1016/j.tetlet.2005.03.014.
- (10) Bentley, P. A.; Mei, Y.; Du, J. *Tetrahedron Lett.* **2008**, *49* (8), 1425. doi:10.1016/j.tetlet.2007.11.211.
- (11) Dalton, D. R.; Langman, A. W. *Org. Synth.* **1980**, *59*, 16.
- (12) Li, L.; Cai, P.; Guo, Q.; Xue, S. *J. Org. Chem.* **2008**, *73* (9), 3516. doi:10.1021/jo800231s. PMID:18380443.
- (13) McEwen, I.; Roennqvist, M.; Ahlberg, P. *J. Am. Chem. Soc.* **1993**, *115* (10), 3989. doi:10.1021/ja00063a019.
- (14) Voets, M.; Antes, I.; Scherer, C.; Müller-Vieira, U.; Biemel, K.; Marchais-Oberwinkler, S.; Hartmann, R. W. *J. Med. Chem.* **2006**, *49* (7), 2222. doi:10.1021/jm060055x.
- (15) Anand, N.; Kapoor, A.; Koul, S.; Taneja, S. C.; Sharma, R. L.; Qazi, G. N. *Tetrahedron Asymmetry* **2004**, *15* (19), 3131. doi:10.1016/j.tetasy.2004.08.026.
- (16) Imamoto, T.; Kusumoto, T.; Yokoyama, M. *Tetrahedron Lett.* **1983**, *24* (47), 5233. doi:10.1016/S0040-4039(00)88405-1.
- (17) House, H. O.; Ro, R. S. *J. Am. Chem. Soc.* **1958**, *80* (1), 182. doi:10.1021/ja01534a046.
- (18) Kirby, A. J.; Williams, N. H. *J. Chem. Soc., Perkin Trans. 2* **1994**, (4): 643. doi:10.1039/p29940000643.



# Étude DFT des réactions d'hydrogénation des cyclohexènes disubstitués en position 2 et 3

Sameh Ayadi et Manef Abderrabba

**Résumé :** Dans ce travail, nous avons étudié théoriquement les réactions d'hydrogénation des cyclohexènes disubstitués par une voie chimique par le (Z)-1,2-diazène (**1**) et le (E)-1,2-diazène (**1'**). Nous avons discuté de point de vue thermodynamique la possibilité et la stéréosélectivité de ces réactions. Les états de transition de la réaction entre les cyclohexènes de type (**2a–2c**) et le (Z)-1,2-diazène (**1**) ont été déterminés.

**Mots-clés :** cyclohexène, théorie de la fonctionnelle de densité (« DFT »), hydrogénation.

**Abstract:** The purpose of this work is to conduct a theoretical study of the hydrogenation reaction between disubstituted cyclohexenes (**2a–2c**) and (Z)-1,2-diazene (**1**) and the reaction between disubstituted cyclohexenes (**2a–2c**) and (E)-1,2-diazene (**1'**). From a thermodynamic point of view, we discuss the reactivity and the stereoselectivity of these reactions. Activation barriers of the reaction between cyclohexenes (**2a–2c**) and the (Z)-1,2-diazene (**1**) have been calculated and discussed.

**Key words:** cyclohexene, density functional theory (DFT), hydrogenation.

## Introduction

Les réactions d'hydrogénation des cycloalcènes substitués possèdent une grande importance en synthèse organique.<sup>1–16</sup> Nous avons trouvé intéressant d'effectuer une étude théorique sur la possibilité et la stéréosélectivité des réactions d'hydrogénation des cyclohexènes disubstitués (**2a–2c**) par le (Z)-1,2-diazène (**1**) et par le (E)-1,2-diazène (**1'**) (fig. 1).

Dans le but de comparer l'influence des substituants de **2b–2c** sur la réactivité de ces réactions d'hydrogénation, nous avons commencé par étudier la réaction entre le cyclohexène **2a** et **1'**. Par la suite, nous avons étudié de point de vue cinétique et thermodynamique la réaction entre **1** et **2a**. Dans chaque cas, nous avons vérifié que ces réactions sont sous le contrôle des orbitales frontières. Enfin, nous avons étudié de point de vue thermodynamique et cinétique la possibilité et la stéréosélectivité de ces réactions d'hydrogénation entre **1** et **2b–2c**.

## Les méthodes de calcul

Cette étude a été réalisée en utilisant le programme Gaussian 03.<sup>17</sup> Les calculs ont été effectués au niveau DFT (théorie de la fonctionnelle de densité) avec les bases standard 6–31G\* et 3–21G. Nous avons utilisé la fonctionnelle B3LYP dans laquelle l'énergie d'échange est calculée par la méthode de Becke à trois paramètres et la corrélation est calculée par la méthode de Lee, Yang et Paar.<sup>18–20</sup> En effet, il a été établi que cette méthode de calcul DFT est une des plus performantes pour ce type des molécules organiques.<sup>21</sup>

Reçu le 11 décembre 2009. Accepté le 20 avril 2010. Publié sur le site Web des Presses scientifiques du CNRC, au [revcanchim.cnr.ca](http://revcanchim.cnr.ca), le 4 juin 2010.

**S. Ayadi<sup>1</sup> et M. Abderrabba.** Unité de recherche Physico-chimie moléculaire, Institut préparatoire aux études scientifiques et techniques (IPEST), B.P. 51, 2070 la Marsa, Tunisie.

1. Auteur correspondant (courriel : [sameh\\_ayadi2003@yahoo.fr](mailto:sameh_ayadi2003@yahoo.fr)).

## Résultats et discussion

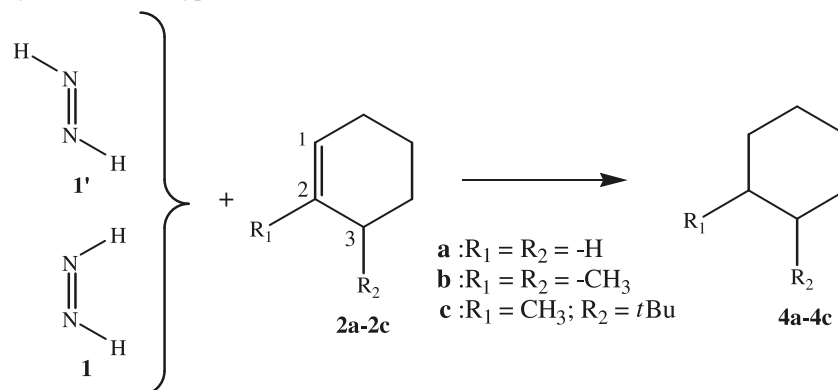
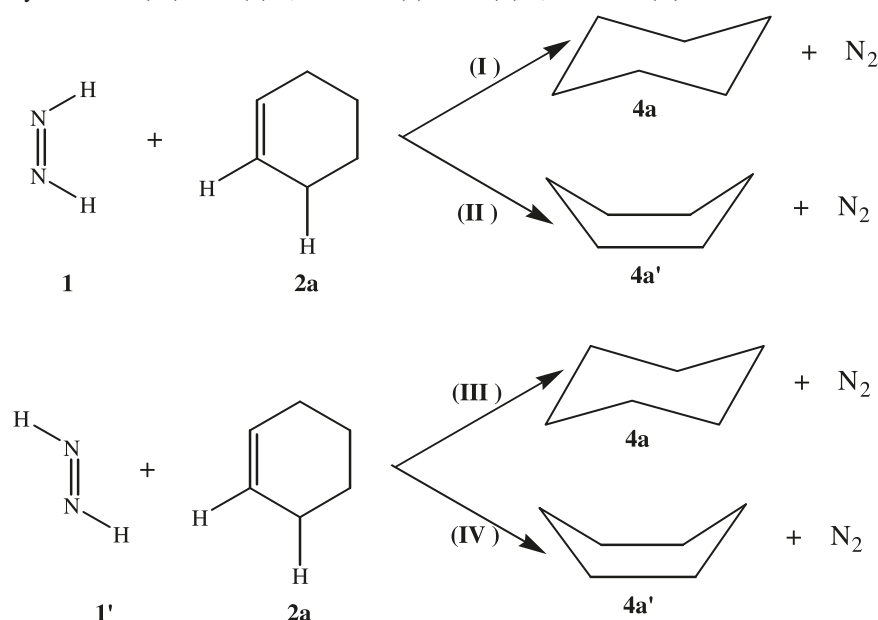
### Étude de la réaction d'hydrogénation du cyclohexène

#### Étude thermodynamique

Nous avons étudié thermodynamiquement la possibilité et la stéréosélectivité de la réaction entre **1** et **2a** et la réaction entre **1'** et **2a** (fig. 2). En utilisant la méthode de calcul DFT/B3LYP avec les bases standard 6–31G\* et 3–21G, nous avons déterminé dans les conditions standard de température et de pression (15 K et 1 atm (1 atm = 101,325 kPa)) les variations d'énergie réactionnelle  $\Delta E_r$ , les variations d'enthalpie libre réactionnelle  $\Delta G_r$ , les variations d'enthalpie réactionnelle  $\Delta H_r$  et le ZPE (« zero-point energy ») qui correspond aux réactions (I), (II), (III) et (IV).

Comme le montre le tableau 1, les variations d'enthalpie libre réactionnelle  $\Delta G_r$  sont toutes négatives, par conséquent ces réactions sont possibles et favorisées thermodynamiquement. Nous avons remarqué que les valeurs de la variation d'enthalpie libre réactionnelle qui correspond aux réactions (I) et (II) sont respectivement supérieures en valeur absolue aux valeurs des réactions (III) et (IV). Ce qui nous a permis de dire que la réaction entre **1** et **2a** est plus favorisée thermodynamiquement que la réaction entre **1'** et **2a**. De plus, nous avons remarqué que la valeur de la variation d'enthalpie libre réactionnelle  $\Delta G_r$  qui correspond à la réaction (I) est supérieure en valeur absolue à la valeur de  $\Delta G_r$  de la réaction (II). Ce qui nous a permis de dire que le conformère chaise (**4a**) est plus stable thermodynamiquement que le conformère bateau (**4a'**). De la même manière pour les réactions (III) et (IV), nous avons remarqué que la valeur d'enthalpie libre réactionnelle  $\Delta G_r$  qui correspond à la formation de **4a** est supérieure en valeur absolue à la valeur de  $\Delta G_r$  qui correspond à la formation de **4a'**. Nous avons aussi remarqué que les valeurs de la variation de l'énergie  $\Delta E_r$  qui correspond aux réactions (I) et (III) sont respectivement plus importantes que celles de la variation de l'énergie qui



**Fig. 1.** Réactions entre les cyclohexènes de type (**2a–2c**) et le (*Z*)-1,2-diazène (**1**) ou le (*E*)-1,2-diazène (**1'**).**Fig. 2.** Réactions entre le cyclohexène (**2a**) et le (*Z*)-1,2-diazène (**1**) ou le (*E*)-1,2-diazène (**1'**).**Tableau 1.** Valeurs calculées ( $\text{kcal mol}^{-1}$ ) des variations d'énergie réactionnelle  $\Delta E_r$ , des variations d'enthalpie libre réactionnelle  $\Delta G_r$ , des variations d'enthalpie réactionnelle  $\Delta H_r$  et le « zero-point energy » ZPE.

Réactions	Produits	$\Delta E_r$	$\Delta E_r + \text{ZPE}$	$\Delta G_r$
<b>B3LYP/6–31G*</b>				
Réaction (I)	<b>4a</b>	–92,09	–92,09	–88,61
Réaction (II)	<b>4a</b>	–88,98	–88,99	–82,05
<b>B3LYP/3–21G</b>				
Réaction (III)	<b>4a</b>	–85,95	–85,96	–82,76
Réaction (IV)	<b>4a</b>	–82,86	–82,85	–76,20

correspond aux réactions (II) et (IV). Ce qui confirme de nouveau que la formation de **4a** est le produit majoritaire de la réaction entre **2a** et **1** et de la réaction entre **2a** et **1'**.

Nos résultats théoriques confirment bien que **4a** est plus stable thermodynamiquement que **4a'**.

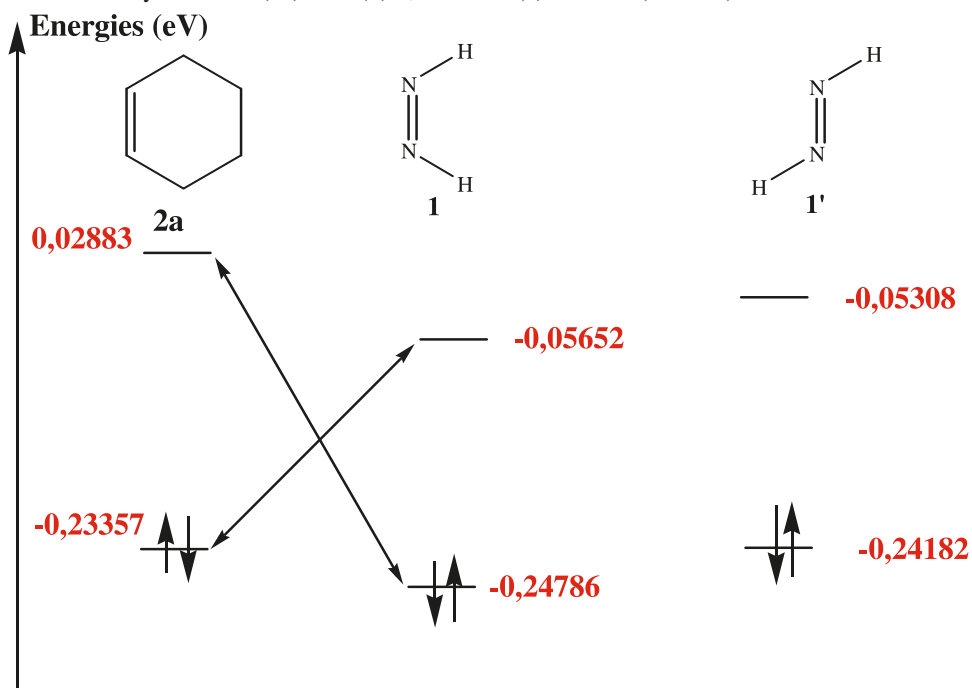
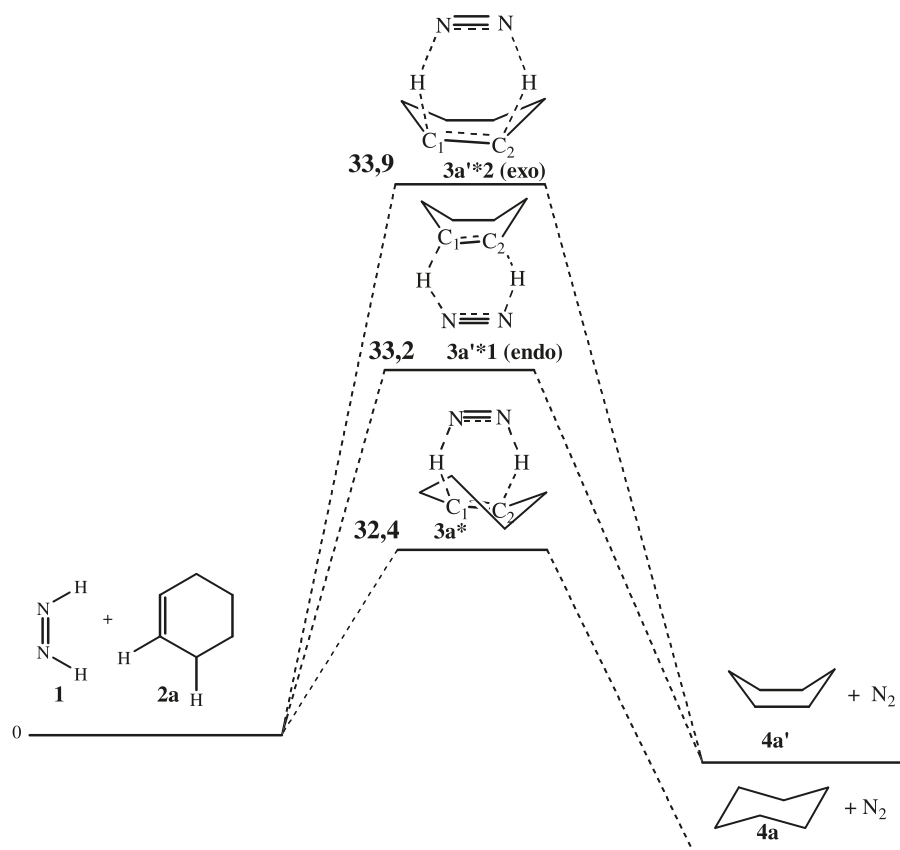
#### Étude des orbitales frontières

En utilisant la méthode de calculs DFT/B3LYP avec les bases standard 6–31G\* et 3–21G, nous avons déterminé les

**Tableau 2.** Les énergies (eV) de la LUMO et de la HOMO du cyclohexène (**2a**), du (*Z*)-1,2-diazène (**1**) et du (*E*)-1,2-diazène (**1'**).

	B3LYP (6–31G*)		B3LYP (3–21G)	
	LUMO	HOMO	LUMO	HOMO
<b>1</b>	–0,056 52	–0,247 86	–0,054 11	–0,2493
<b>1'</b>	–0,053 08	–0,241 82	–0,051 98	–0,2441
<b>2a</b>	0,028 830	–0,233 57	0,028 71	–0,2412

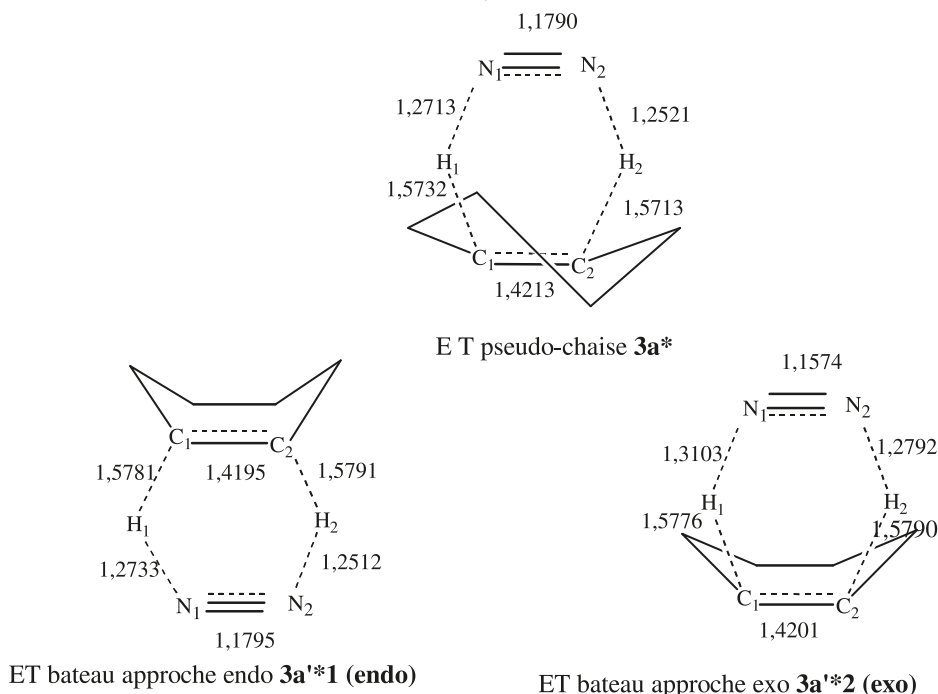
énergies de la LUMO et de la HOMO de **2a** ainsi que les énergies de la LUMO et de la HOMO de **1** et de **1'** (voir tableau 2). D'après la théorie des orbitales frontières, lors de l'interaction entre deux molécules, les orbitales frontières à considérer sont la HOMO de l'une et la LUMO de l'autre, choisies de telle sorte que l'écart énergétique  $\Delta E$  qui les sépare soit le plus faible possible.<sup>22</sup> Comme le montre la figure 3, le diagramme orbitalaire donne une bonne indication qualitative quant à la réactivité de notre système. Nous avons remarqué que l'interaction principale se fait entre l'énergie de la LUMO de **1** et l'énergie de la HOMO de **2a**. De plus, nous avons remarqué que la variation d'énergie  $\Delta E$

**Fig. 3.** Diagramme orbitalaire du cyclohexène (**2a**) et le (Z)-1,2-diazène (**1**). B3LYP (6–31G\*).**Fig. 4.** Profil énergétique des réactions conduisant aux conformères chaise (**4a**) et bateau (**4a'**) en DFT/B3LYP avec la base standard 6–31G\* (énergie en kcal mol<sup>-1</sup>).

entre la LUMO de **1** et la HOMO de **2a** est inférieure à la variation d'énergie  $\Delta E$  entre la LUMO de **1'** et la HOMO de **2a**. Ce qui explique bien que la réaction entre **1** et **2a** est plus réactive que dans le cas de la réaction entre **1'** et **2a**.

#### Calcul des états de transition

Nous avons optimisé les états de transition de la réaction de **2a** et **1**. Nous avons obtenu trois conformations différentes des états de transitions : l'état de transition pseudo-chaise **3a\***

**Fig. 5.** États de transition de la réaction entre le (Z)-1,2-diazène et le cyclohexène, distance en Å (1 Å = 0,1 nm). B3LYP (6–31G\*).**Tableau 3.** Énergies relatives  $E^*$  (kcal mol<sup>-1</sup>) des états de transition par rapport aux énergies des réactifs (calculées avec la méthode DFT/B3LYP).

	DFT/B3LYP(6–31G*)	DFT/B3LYP (3–21G)
<b>1</b>		
<b>2</b>		
<b>3a*</b>	32,4	33,1
<b>3a*1</b>	33,2	34,3
<b>3a*2</b>	33,9	35,2

Nota : **1**, **2**, **3a\***, **3a\*1** (endo); **3a\*2** (exo).

**Tableau 4.** Longueurs des liaisons en formation C<sub>1</sub>–H<sub>1</sub> et C<sub>2</sub>–H<sub>2</sub> dans l'état de transition de la réaction du (Z)-1,2-diazène (**1**) et le cyclohexène (**2a**).

	B3LYP (6–31G*)		B3LYP (3–21G)	
	C <sub>1</sub> –H <sub>1</sub>	C <sub>2</sub> –H <sub>2</sub>	C <sub>1</sub> –H <sub>1</sub>	C <sub>2</sub> –H <sub>2</sub>
<b>3a*</b>	1,5732	1,5713	1,5685	1,5811
<b>3a*1</b>	1,5781	1,5791	1,5732	1,5752
<b>3a*2</b>	1,5776	1,5790	1,5723	1,5761

Nota : **3a\***, **3a\*1** (endo); **3a\*2** (exo).

et les états de transitions bateau tels que **3a\*1** (endo) et **3a\*2** (exo) obtenus respectivement avec une approche de **1** en endo de **2a** et avec une approche de **1** en exo de **2a** (fig. 4).

Les calculs théoriques montrent que la formation de **4a** est favorisée par rapport à la formation de **4a'**. En utilisant la méthode de calcul DFT/B3LYP avec les bases standard 6–31G\* et 3–21G, nous avons trouvé pour **4a'** une grande énergie d'activation respectivement de 33,9 kcal mol<sup>-1</sup> et 35,2 kcal mol<sup>-1</sup> aux niveaux du calcul citées précédemment. Ces valeurs sont plus grandes que celles trouvées pour les états de transition conduisant à la formation de **4a** (tableau 3). Ce qui confirme de nouveau que **4a** est plus stable que **4a'**. Ces valeurs de l'énergie d'activation sont du même ordre de grandeur que celle trouvée par McKee et al. pour la réaction entre **1** et l'éthène.<sup>23</sup> La comparaison des profils énergétiques des réactions conduisant respectivement à **4a** et **4a'** est donnée sur la figure 4.

Nous avons déterminé les états de transition bateau avec une approche du (Z)-1,2-diazène en endo et avec une approche du (Z)-1,2-diazène en exo. Les résultats montrent que la forme endo est favorisée par rapport à la forme exo. La géométrie des trois états de transitions **3a\***, **3a\*1** (endo) et **3a\*2** (exo) est présentée sur la figure 5.

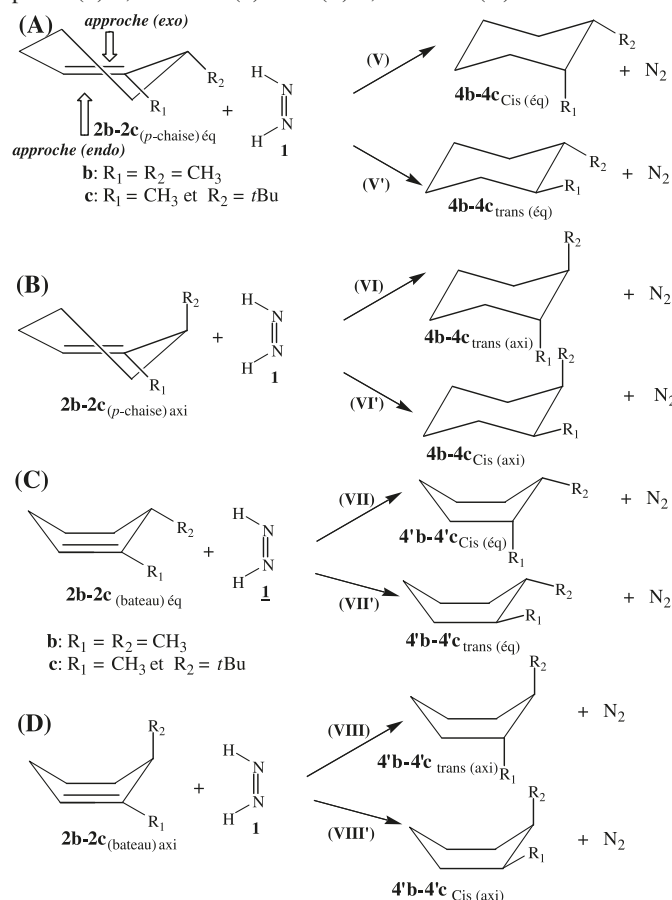
Nous avons remarqué que le cycle de l'état de transition est quasi plan. Si on compare les longueurs des liaisons en formation, on constate que la liaison C<sub>1</sub>–H<sub>1</sub> est plus courte que la liaison C<sub>2</sub>–H<sub>2</sub> (tableau 4).

### Étude de la réaction entre le (Z)-1,2 diazène et les cyclohexènes disubstitués

Dans la deuxième partie de ce travail, nous avons étudié thermodynamiquement les réactions entre **1** et **2b–2c** dans les différentes conformations possibles tels que les conformères pseudo-chaire et les conformères bateau (fig. 6). Dans chaque cas, une des approches endo et exo de **1** sur **2b–2c** conduit au stéréoisomère cis et l'autre au stéréoisomère trans.

### Étude thermodynamique

Dans le but d'étudier la possibilité et la stéréosélectivité de la réaction d'hydrogénation de **2b–2c** par **1**, nous avons étudié de point de vue thermodynamique les réactions entre **1** et **2b–2c** dans les différentes conformations possibles telles que les conformations pseudo-chaire **2b–2c**<sub>(p-chaire)éq</sub> et **2b–2c**<sub>(p-chaire)axi</sub> et les conformations bateau **2b–2c**<sub>(bateau)éq</sub> et **2b–2c**<sub>(bateau)axi</sub> (fig. 6).

**Fig. 6.** Réactions d'hydrogénation des cyclohexènes disubstitués par le (Z)-1,2-diazène (**1**) et le (E)-1,2-diazène (**1'**).

Dans chaque cas, une des approches endo et exo de **1** sur **2b-2c** conduit au stéréoisomère cis tels que **4b-4c**<sub>cis(éq)</sub>, **4b-4c**<sub>cis(axi)</sub>, **4'b-4'c**<sub>cis(éq)</sub> et **4'b-4'c**<sub>cis(axi)</sub> et l'autre conduit au stéréoisomère trans tels que **4b-4c**<sub>trans(éq)</sub>, **4b-4c**<sub>trans(axi)</sub>, **4'b-4'c**<sub>trans(éq)</sub> et **4'b-4'c**<sub>trans(axi)</sub>.

Dans chaque cas de ces réactions, nous avons trouvé des valeurs des enthalpies libres réactionnelles négatives (tableau 5). Ces réactions sont possibles théoriquement et, par conséquent, elles sont favorisées thermodynamiquement. De plus, nous avons remarqué que les valeurs des enthalpies libres réactionnelles qui correspondent aux réactions (V), (V'), (VI) et (VI') sont plus importantes en valeur absolue que celles qui correspondent aux réactions (VII), (VII'), (VIII) et (VIII'). Ceci nous a permis de dire que les conformères chaise sont plus stables thermodynamiquement que les conformères bateau.

Nous avons aussi remarqué que la formation de **4b-4c**<sub>trans(éq)</sub> est plus favorisée que la formation de **4b-4c**<sub>cis(éq)</sub> provenant respectivement des approches endo et exo de **1** sur **2b-2c** (p-chaire)éq. Par contre, dans le cas de la réaction B, lors des approches respectivement en endo et exo du **1** sur **2b-2c** (p-chaire)axi, nous avons trouvé que la formation de **4b-4c**<sub>cis(axi)</sub> est plus favorisée que celle de **4b-4c**<sub>trans(axi)</sub> (tableau 5).

Dans le cas des approches endo et exo de **1** sur **2b-2c** (bateau)éq, nous avons remarqué que la formation de **4b-4c**<sub>trans(éq)</sub> est plus favorisée respectivement par rapport

**Tableau 5.** Valeurs calculées (kcal mol<sup>-1</sup>) des variations d'énergie réactionnelle  $\Delta E_r$ , des variations d'enthalpie libre réactionnelle  $\Delta G_r$ , des variations d'enthalpie réactionnelle  $\Delta H_r$  et le ZPE.

	Les produits	$\Delta E_r$	$\Delta E_r + \text{ZPE}$	$\Delta G_r$
<b>B3LYP/6-31G*</b>				
Réaction (V)	<b>4b</b> <sub>cis(éq)</sub>	-81,79	-81,75	-77,66
	<b>4c</b> <sub>cis(éq)</sub>	-78,12	-78,11	-72,21
Réaction (V')	<b>4b</b> <sub>trans(éq)</sub>	-84,05	-84,06	-80,07
	<b>4c</b> <sub>trans(éq)</sub>	-80,93	-80,92	-77,34
Réaction (VI)	<b>4b</b> <sub>trans(axi)</sub>	-80,34	-80,34	-76,32
	<b>4c</b> <sub>trans(axi)</sub>	-76,41	-76,41	-75,02
Réaction (VI')	<b>4b</b> <sub>cis(axi)</sub>	-81,68	-81,67	-77,75
	<b>4c</b> <sub>cis(axi)</sub>	-76,93	-76,93	-76,45
Réaction (VII)	<b>4'b</b> <sub>cis(éq)</sub>	-51,27	-51,28	-48,51
	<b>4'c</b> <sub>cis(éq)</sub>	-49,87	-49,87	-45,29
Réaction (VII')	<b>4'b</b> <sub>trans(éq)</sub>	-69,31	-69,30	-65,29
	<b>4'c</b> <sub>trans(éq)</sub>	-50,24	-50,23	-47,71
Réaction (VIII)	<b>4'b</b> <sub>trans(axi)</sub>	-48,31	-48,31	-42,87
	<b>4'c</b> <sub>trans(axi)</sub>	-43,27	-43,28	-40,39
Réaction (VIII')	<b>4'b</b> <sub>cis(axi)</sub>	-50,23	-50,23	-45,81
	<b>4'c</b> <sub>cis(axi)</sub>	-46,78	-46,77	-41,90
<b>B3LYP/3-21G</b>				
Réaction (V)	<b>4b</b> <sub>cis(éq)</sub>	-80,17	-80,16	-76,29
	<b>4c</b> <sub>cis(éq)</sub>	-76,23	-76,22	-73,13
Réaction (V')	<b>4b</b> <sub>trans(éq)</sub>	-83,93	-83,92	-79,11
	<b>4c</b> <sub>trans(éq)</sub>	-80,06	-80,07	-75,32
Réaction (VI)	<b>4b</b> <sub>trans(axi)</sub>	-69,12	-69,14	-61,32
	<b>4c</b> <sub>trans(axi)</sub>	-68,74	-68,74	-65,86
Réaction (VI')	<b>4b</b> <sub>cis(axi)</sub>	-79,14	-79,14	-75,63
	<b>4c</b> <sub>cis(axi)</sub>	-75,80	-75,81	-73,19
Réaction (VII)	<b>4'b</b> <sub>cis(éq)</sub>	-57,22	-57,23	-43,34
	<b>4'c</b> <sub>cis(éq)</sub>	-49,20	-49,21	-42,52
Réaction (VII')	<b>4'b</b> <sub>trans(éq)</sub>	-58,38	-58,38	-51,91
	<b>4'c</b> <sub>trans(éq)</sub>	-54,12	-54,12	-49,87
Réaction (VIII)	<b>4'b</b> <sub>trans(axi)</sub>	-48,12	-48,12	-40,91
	<b>4'c</b> <sub>trans(axi)</sub>	-42,10	-42,11	-38,32
Réaction (VIII')	<b>4'b</b> <sub>cis(axi)</sub>	-48,71	-48,72	-42,87
	<b>4'c</b> <sub>cis(axi)</sub>	-43,93	-42,92	-40,36

à **4b-4c**<sub>cis(éq)</sub>. Par contre dans le cas de la réaction D, lors de l'addition de **1** sur **2b-2c** (bateau)axi dans les deux approches endo et exo. Les résultats théoriques montrent que la formation de **4'b-4'c**<sub>cis(axi)</sub> est plus stable thermodynamiquement que celle de **4'b-4'c**<sub>trans(axi)</sub>.

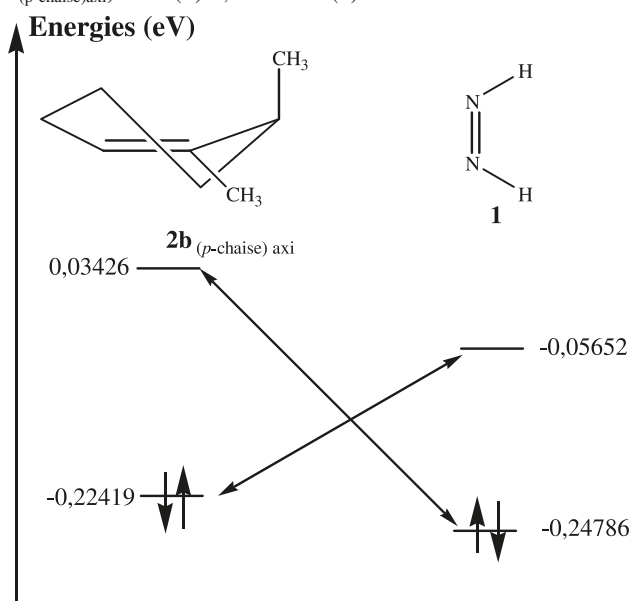
### Étude des orbitales frontières

En utilisant la méthode de calcul DFT/B3LYP avec les bases standard 6-31G\* et 3-21G, nous avons déterminé les énergies de la LUMO et de la HOMO des cyclohexènes disubstitués dans les différentes conformations possibles pseudo-chaire et bateau (tableau 6). Le diagramme orbitalaire des réactifs entre **1** et **2b** (p-chaire)axi, calculé au niveau DFT/B3LYP et la base standard 6-31G\*, est donné sur la figure 7. Ce diagramme orbitalaire donne une bonne indication qualitative quant à la réactivité de notre système. D'après la théorie des orbitales frontières,<sup>22</sup> l'interaction principale se produit entre la HOMO de **2b-2c** (p-chaire)axi et la HOMO de **1**.



**Tableau 6.** Les énergies (eV) de la LUMO et de la HOMO des cyclohexènes disubstitués.

	B3LYP/6-31G*		B3LYP/3-21G	
	LUMO	HOMO	LUMO	HOMO
<b>2b</b> <sub>(p-chaîse)éq</sub>	0,035 86	-0,224 91	0,035 73	-0,213 45
<b>2b</b> <sub>(p-chaîse)axi</sub>	0,034 26	-0,224 19	0,035 61	-0,213 67
<b>2c</b> <sub>(p-chaîse)éq</sub>	0,034 38	-0,224 23	0,035 67	-0,213 81
<b>2c</b> <sub>(p-chaîse)axi</sub>	0,034 45	-0,224 61	0,035 53	-0,213 84
<b>2b</b> <sub>(bateau)éq</sub>	0,036 28	-0,216 89	0,036 34	-0,217 14
<b>2b</b> <sub>(bateau)axi</sub>	0,036 14	-0,221 43	0,035 25	-0,226 32
<b>2c</b> <sub>(bateau)éq</sub>	0,035 93	-0,223 15	0,035 73	-0,225 46
<b>2c</b> <sub>(bateau)axi</sub>	0,035 87	-0,223 36	0,035 79	-0,226 48

**Fig. 7.** Diagramme orbitalaire du 2,3-diméthylcyclohexène (**2b**<sub>(p-chaîse)axi</sub>) et le (Z)-1,2-diazène (**1**). B3LYP/6-31G\*.

### Calcul des états de transition

Dans le but de déterminer la stéréospécificité de la réaction entre **1** et **2b–2c**, nous avons déterminé les états de transition correspondant à l'addition du **1** sur **2b–2c**<sub>(p-chaîse)éq</sub> et **2b–2c**<sub>(p-chaîse)axi</sub> dans les deux approches endo et exo.<sup>24</sup> Nous avons aussi déterminé les états de transition correspondant à l'addition du **1** sur **2b–2c**<sub>(bateau)éq</sub> et **2b–2c**<sub>(bateau)axi</sub> dans les deux approches endo et exo. Les énergies correspondantes sont reportées dans le tableau 7.

Comme le montre le tableau 7, dans chaque cas des réactions A, B, C et D, la forme endo correspond à une énergie d'activation inférieure à celle de la forme exo. Ce qui nous a permis de dire que la forme endo est plus favorisée par rapport à la forme exo.

Nos résultats théoriques montrent que dans le cas de la réaction A, les formes endo donnent **4b–4c**<sub>trans(éq)</sub> qui sont thermodynamiquement plus stables que **4b–4c**<sub>cis(éq)</sub> provenant des formes exo. Ceci nous a permis de dire que **4b–4c**<sub>trans(éq)</sub> sont les produits cinétique et thermodynamique de la réaction A.

De la même manière, nous avons trouvé dans le cas de la réaction C que les formes endo donnent **4b–4c**<sub>trans(éq)</sub> qui sont plus stables de point de vue thermodynamique et cinétique

**Tableau 7.** Énergies relatives  $E^*$  (kcal mol<sup>-1</sup>) des états de transition par rapport aux énergies des réactifs (calculées avec la méthode DFT/B3LYP).

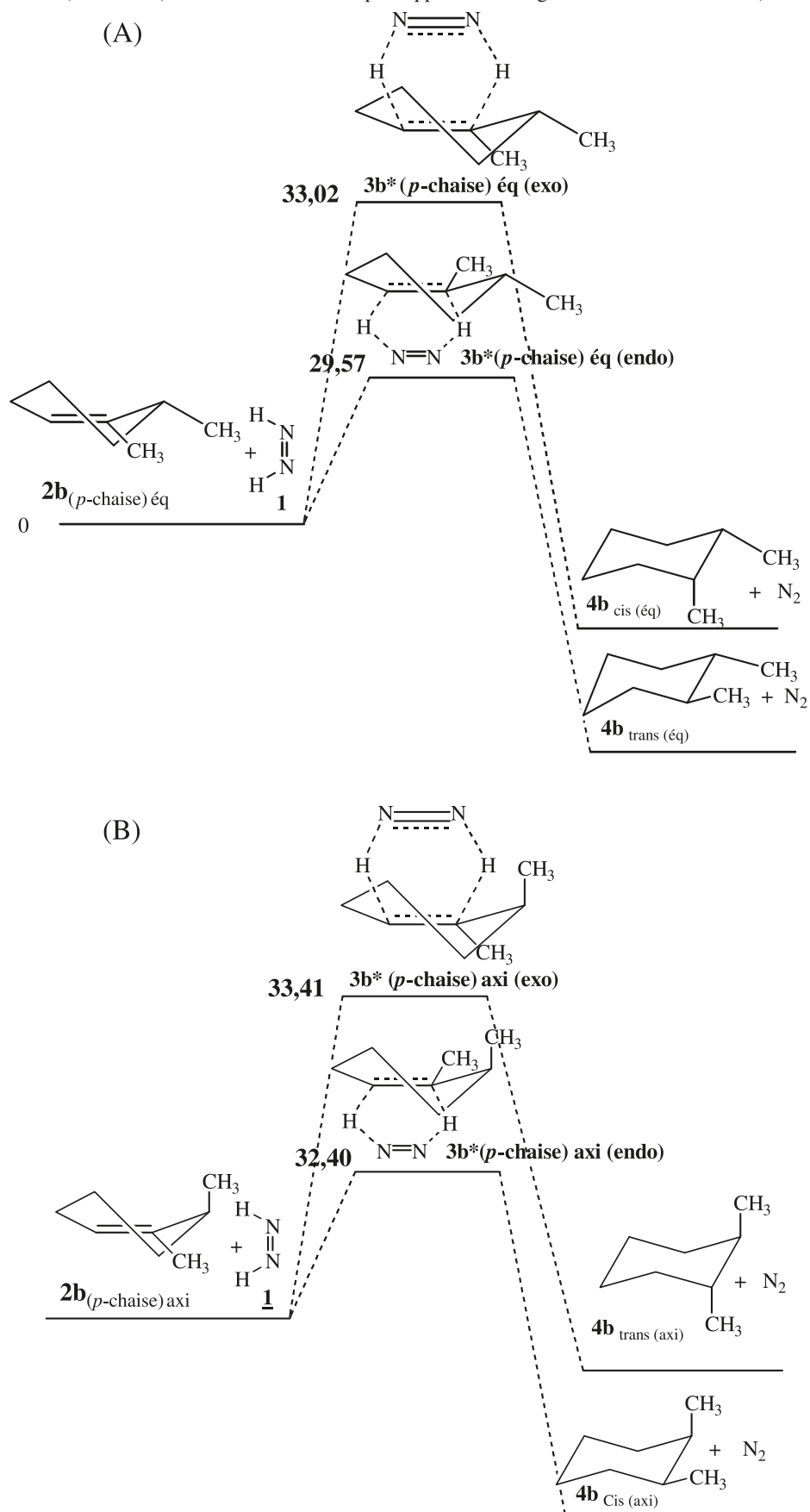
	B3LYP (6-31G*)	B3LYP (3-21G)
<b>Réaction A</b>		
<b>1</b>		
<b>2b</b> <sub>(p-chaîse)éq</sub>		
<b>3b</b> <sup>*</sup> <sub>(p-chaîse)éq</sub> (endo)	29,57	28,91
<b>3b</b> <sup>*</sup> <sub>(p-chaîse)éq</sub> (exo)	33,02	32,75
<b>2c</b> <sub>(p-chaîse)éq</sub>		
<b>3c</b> <sup>*</sup> <sub>(p-chaîse)éq</sub> (endo)	29,81	29,12
<b>3c</b> <sup>*</sup> <sub>(p-chaîse)éq</sub> (exo)	32,97	32,81
<b>Réaction B</b>		
<b>1</b>		
<b>2b</b> <sub>(p-chaîse)éq</sub>		
<b>3b</b> <sup>*</sup> <sub>(p-chaîse)éq</sub> (endo)	32,40	32,15
<b>3b</b> <sup>*</sup> <sub>(p-chaîse)éq</sub> (exo)	33,41	33,21
<b>2c</b> <sub>(p-chaîse)éq</sub>		
<b>3c</b> <sup>*</sup> <sub>(p-chaîse)éq</sub> (endo)	32,70	32,81
<b>3c</b> <sup>*</sup> <sub>(p-chaîse)éq</sub> (exo)	33,91	33,95
<b>Réaction C</b>		
<b>1</b>		
<b>2b</b> <sub>(bateau)éq</sub>		
<b>3b</b> <sup>*</sup> <sub>(bateau)éq</sub> (endo)	31,73	31,91
<b>3b</b> <sup>*</sup> <sub>(bateau)éq</sub> (exo)	32,47	32,86
<b>2c</b> <sub>(bateau)éq</sub>		
<b>3c</b> <sup>*</sup> <sub>(bateau)éq</sub> (endo)	32,13	32,10
<b>3c</b> <sup>*</sup> <sub>(bateau)éq</sub> (exo)	33,75	33,57
<b>Réaction D</b>		
<b>1</b>		
<b>2b</b> <sub>(bateau)axi</sub>		
<b>3b</b> <sup>*</sup> <sub>(bateau)axi</sub> (endo)	33,97	33,91
<b>3b</b> <sup>*</sup> <sub>(bateau)axi</sub> (exo)	34,12	34,06
<b>2c</b> <sub>(bateau)axi</sub>		
<b>3c</b> <sup>*</sup> <sub>(bateau)axi</sub> (endo)	33,98	33,96
<b>3c</b> <sup>*</sup> <sub>(bateau)axi</sub> (exo)	34,57	34,42

que **4b–4c**<sub>cis(éq)</sub> provenant des formes exo. Par contre dans le cas des réactions B et D, nous avons trouvé que les formes endo donnent respectivement **4b–4c**<sub>cis(axi)</sub> et **4b–4c**<sub>cis(axi)</sub> qui sont respectivement plus stables thermodynamiquement et cinétiquement que **4b–4c**<sub>trans(axi)</sub> et **4b–4c**<sub>trans(axi)</sub> provenant des formes exo.

La comparaison des profils énergétiques des réactions A et B conduisant respectivement à **4b**<sub>trans(éq)</sub> et **4b**<sub>cis(éq)</sub> et à **4b**<sub>cis(axi)</sub> et **4b**<sub>trans(axi)</sub> est donnée sur la figure 8.

Nous avons comparé nos résultats avec d'autres études antérieures.<sup>23–27</sup> Ces études ont été réalisées sur l'hydrogénation des alcènes non cycliques tels que les molécules d'éthène et de propène. Dans le cas d'hydrogénation de **2b–2c** par **1**, lors de l'approche des réactifs, il y a des effets de gêne stérique qui apparaissent. Cette gêne est différente selon la face de l'alcène dont s'approche **1**.

Nous avons comparé les longueurs des liaisons en formation; on constate que la liaison C<sub>1</sub>–H<sub>1</sub> est plus courte que la liaison C<sub>2</sub>–H<sub>2</sub>. Ces distances sont assez proches de celle trouvée par McKee et al. pour la réaction entre **1** et l'éthène<sup>23</sup> (tableau 8).

**Fig. 8.** Énergies relatives  $E^*$  (kcal mol<sup>-1</sup>) des états de transition par rapport aux énergies des réactifs. B3LYP (6-31G\*).

**Tableau 8.** Longueurs des liaisons en formation C<sub>1</sub>–H<sub>1</sub> et C<sub>2</sub>–H<sub>2</sub> dans l'état de transition pour la formation des conformères chaise et bateau.

	B3LYP/6–31G*		B3LYP/3–21G	
	C <sub>1</sub> –H <sub>1</sub>	C <sub>2</sub> –H <sub>2</sub>	C <sub>1</sub> –H <sub>1</sub>	C <sub>2</sub> –H <sub>2</sub>
<b>Réaction A</b>				
<b>3b*</b> <sub>(p-chaise)éq</sub> (endo)	1,5612	1,5741	1,5670	1,5731
<b>3b*</b> <sub>(p-chaise)éq</sub> (exo)	1,5613	1,5754	1,5654	1,5745
<b>3c*</b> <sub>(p-chaise)éq</sub> (endo)	1,5620	1,5742	1,5676	1,5750
<b>3c*</b> <sub>(p-chaise)éq</sub> (exo)	1,5617	1,5732	1,5682	1,5766
<b>Réaction B</b>				
<b>3b*</b> <sub>(p-chaise)axi</sub> (endo)	1,5622	1,5756	1,5668	1,5761
<b>3b*</b> <sub>(p-chaise)axi</sub> (exo)	1,5625	1,5753	1,5660	1,5756
<b>3c*</b> <sub>(p-chaise)axi</sub> (endo)	1,5611	1,5761	1,5686	1,5754
<b>3c*</b> <sub>(p-chaise)axi</sub> (exo)	1,5634	1,5730	1,5674	1,5747
<b>Réaction C</b>				
<b>3b*</b> <sub>(bateau)éq</sub> (endo)	1,5623	1,5755	1,5676	1,5737
<b>3b*</b> <sub>(bateau)éq</sub> (exo)	1,5615	1,5742	1,5664	1,5735
<b>3c*</b> <sub>(bateau)éq</sub> (endo)	1,5612	1,5745	1,5672	1,5771
<b>3c*</b> <sub>(bateau)éq</sub> (exo)	1,5626	1,5733	1,5671	1,5750
<b>Réaction D</b>				
<b>3b*</b> <sub>(bateau)axi</sub> (endo)	1,5614	1,5756	1,5663	1,5745
<b>3b*</b> <sub>(bateau)axi</sub> (exo)	1,5635	1,5753	1,5652	1,5743
<b>3c*</b> <sub>(bateau)axi</sub> (endo)	1,5612	1,5742	1,5686	1,5760
<b>3c*</b> <sub>(bateau)axi</sub> (exo)	1,5611	1,5765	1,5682	1,5756

## Conclusion

Dans ce travail, nous avons réalisé une étude théorique permettant de prévoir la stéréochimie et la réactivité des réactions d'hydrogénation de **2a–2c** par **1** et par **1'**.

Les résultats de calculs théoriques par la méthode DFT avec la fonctionnelle B3LYP et les bases standard 6–31G\* et 3–21G montrent que ces réactions sont possibles théoriquement, et par conséquent elles sont favorisées thermodynamiquement.

Les résultats montrent aussi que les conformères chaise sont plus stables thermodynamiquement que les conformères bateau. De plus, nous avons trouvé que les réactions entre **2a–2c** et **1** sont plus réactives que les réactions entre **2a–2c** et **1'**. Les calculs des états de transition montrent que les produits cinétiques de la réaction d'hydrogénation sont les conformères chaise **4a–4c**, et en plus les stéréoisomères provenant de la forme endo sont plus favorisés que les stéréoisomères provenant de la forme exo.

## Bibliographie

- (1) Yoshimura, M.; Ishibashi, Y.; Miyata, K.; Bessho, Y.; Tsukamoto, M.; Kitamura, M. *Tetrahedron* **2007**, *63* (46), 11399. doi:10.1016/j.tet.2007.08.071.
- (2) Tanyeli, C.; Özçubukçu, O. *Tetrahedron Asymmetry* **2003**, *14* (9), 1167. doi:10.1016/S0957-4166(03)00161-7.
- (3) Alonso, F.; Radivoy, G.; Yus, M. *Tetrahedron* **2000**, *56* (44), 8673. doi:10.1016/S0040-4020(00)00797-3.
- (4) Francisco, C. G.; Freire, R.; Herrera, A. J.; Pérez-Martín, I.; Suárez, E. *Tetrahedron* **2007**, *63* (36), 8910. doi:10.1016/j.tet.2007.06.023.
- (5) Macaev, F. Z.; Malkov, A. V. *Tetrahedron* **2006**, *62* (1), 9. doi:10.1016/j.tet.2005.09.001.
- (6) Armstrong, P.; O'Mahony, G.; Stevenson, P. J.; Walker, A. D. *Tetrahedron Lett.* **2005**, *46* (47), 8109. doi:10.1016/j.tetlet.2005.09.133.
- (7) Larsen, J. W.; Freund, M.; Kim, K. Y.; Sidovar, M.; Stuart, J. L. *Carbon* **2000**, *38* (5), 655. doi:10.1016/S0008-6223(99)00155-4.
- (8) Fonseca, G.; Seoane, G. *Tetrahedron Asymmetry* **2005**, *16* (7), 1393. doi:10.1016/j.tetasy.2005.02.012.
- (9) Kumarraja, M.; Pitchumani, K. *Appl. Catal. Gen.* **2004**, *265* (2), 135. doi:10.1016/j.apcata.2004.01.009.
- (10) Pasto, D. J. *Organic Reactions*; John Wiley and Sons: New York, 1991; Vol. 40.
- (11) Haviari, G.; Célérier, J. P.; Petit, H.; Lhomme, G. *Tetrahedron Lett.* **1993**, *34* (10), 1599. doi:10.1016/0040-4039(93)85017-Q.
- (12) Siegel, S.; Foreman, G. M.; Johnson, D. J. *Org. Chem.* **1975**, *40* (24), 3589. doi:10.1021/jo00912a028.
- (13) Siegel, S. Dans *Heterogeneous Catalysis and Fine Chemicals II*; M. Guisnet et al., Eds.; Elsevier Science Publishers: Amsterdam, 1991.
- (14) Haviari, G.; Célérier, J. P.; Petit, H.; Lhomme, G.; Gardette, D.; Gramain, J. C. *Tetrahedron Lett.* **1992**, *33* (30), 4311. doi:10.1016/S0040-4039(00)74247-X.
- (15) Agraftiotis, D. K.; Rzepa, H. J. *Am. Chem. Soc., Perkin Trans. 2* **1989**, (5): 475. doi:10.1039/p29890000475.
- (16) Cioslowsky, J.; Sauer, J.; Hetzenegger, J.; Karcher, T.; Hierstetter, T. *J. Am. Chem. Soc.* **1993**, *115* (4), 1353. doi:10.1021/ja00057a019.
- (17) Frisch, M. J.; Trucks, G. W.; Schlegel, H. B.; Scuseria, G. E.; Robb, M. A.; Cheeseman, J. R.; Montgomery, J. A., Jr.; Vreven, T.; Kudin, K. N.; Burant, J. C.; Millam, J. M.; Iyengar, S. S.; Tomasi, J.; Barone, V.; Mennucci, B.; Cossi, M.; Scalmani, G.; Rega, N.; Peterson, G. A.; Nakatsuji, H.; Hada, M.; Ehara, M.; Toyota, K.; Fukuda, R.; Hasegawa, J.;

- Ishida, M.; Nakajima, T.; Honda, Y.; Kitao, O.; Nakai, H.; Klene, M.; Li, X.; Knox, J. E.; Hratchian, H. P.; Cross, J. B.; Adamo, C.; Jaramillo, J.; Gomperts, R.; Stratmann, R. E.; Yazyev, O.; Austin, A. J.; Cammi, R.; Pomelli, C.; Ochterski, J. W.; Ayala, P. Y.; Morokuma, K.; Voth, G. A.; Salvador, P.; Dannenberg, J. J.; Zakrzewski, V. G.; Dapprich, S.; Daniels, A. D.; Strain, M. C.; Farkas, O.; Malick, D. K.; Rabuck, A. D.; Raghavachari, K.; Foresman, J. B.; Ortiz, J. V.; Cui, Q.; Baboul, A. G.; Clifford, S.; Cioslowski, J.; Stefanov, B. B.; Liu, G.; Liashenko, A.; Piskorz, P.; Komaromi, I.; Martin, R. L.; Fox, D. J.; Keith, T.; Al-Laham, M. A.; Peng, C. Y.; Nanayakkara, A.; Challacombe, M.; Gill, P. M. W.; Johnson, B.; Chen, W.; Wong, M. W.; Gonzalez, C.; Pople, J. A. *Gaussian 03*, Revision A1; Gaussian, Inc.: Pittsburgh, PA, 2003.
- (18) Lee, C.; Yang, W.; Parr, R. G. *Phys. Rev. B* **1988**, 37 (2), 785. doi:10.1103/PhysRevB.37.785.
- (19) Becke, A. D. *Phys. Rev. A* **1988**, 38 (6), 3098. doi:10.1103/PhysRevA.38.3098. PMID:9900728.
- (20) Becke, A. D. *J. Chem. Phys.* **1993**, 98 (7), 5648. doi:10.1063/1.464913.
- (21) Goldstein, E.; Beno, B.; Houk, K. N. *J. Am. Chem. Soc.* **1996**, 118 (25), 6036. doi:10.1021/ja9601494.
- (22) Louis, J. Rivial, *éléments de chimie quantique à l'usage des chimistes*; Éditions C.N.R.S., 1994.
- (23) McKee, M. L.; Squillacote, M. E.; Stanbury, D. M. *J. Phys. Chem.* **1992**, 96 (8), 3266. doi:10.1021/j100187a017.
- (24) Garbisch, E. W., Jr.; Sprecher, C. M.; McCallum, R. J. Dans *Reaction Transition States*, Proceeding of the 21th Annual Meeting of the Société de Chimie Physique Paris, 1970; J.E. Dubois, Ed.; Gorgon and Breach, 1972.
- (25) Garbisch, E. W., Jr.; Schildcrout, S. M.; Patterson, D. B.; Sprecher, C. M. *J. Am. Chem. Soc.* **1965**, 87 (13), 2932. doi:10.1021/ja01091a025.
- (26) Pasto, D. J.; Chipman, D. M. *J. Am. Chem. Soc.* **1979**, 101 (9), 2290. doi:10.1021/ja00503a007.
- (27) Cioslowsky, J.; Sauer, J.; Hetzenegger, J.; Karcher, T.; Hiersteller, T. *J. Am. Chem. Soc.* **1993**, 115 (4), 1353. doi:10.1021/ja00057a019.



# Novel lariat calix[4]-1,3-aza-crowns with two branched chains — The excellent phase transfer catalysts for nucleophilic substitution reaction

Fafu Yang, Yanhua Wang, Hongyu Guo, Jianwei Xie, and Zhiqiang Liu

**Abstract:** By reacting calix[4]-1,3-diethoxylaminoethyl derivative (**2**) with phenyl isothiocyanate, novel dendritic calix[4]-arene derivative (**3**) with two different branched chains was synthesized in a yield of 78%. By reacting compound **2** with 1,6-diisocyanatohexane or *N,N'*-bis(2-chloroacetamide)ethylene in a “1 + 1” intermolecular addition mode, novel lariat calix[4]-1,3-aza-crowns (**4** and **5**, respectively) with two branched ethoxyl chains were prepared in reasonable yields. The composition, structures, and conformations of all new compounds were confirmed by elemental analyses, IR, ESI-MS, <sup>1</sup>H NMR, and so forth. The liquid–liquid extraction experiments showed that all new hosts possessed good extraction abilities towards soft and hard metal cations. The liquid membrane transport experiments suggested that they had good transport abilities for K<sup>+</sup> and Ag<sup>+</sup>. The experiments of phase transfer catalysis indicated that they possessed excellent catalytic properties of aromatic nucleophilic substitution reaction and benzyl nucleophilic substitution. The optimum yields of products in catalytic reaction were as high as approximately 100%.

**Key words:** calix[4]crown, lariat, synthesis, liquid membrane transport, phase transfer catalysis.

**Résumé :** La réaction du dérivé **2** du calix[4]-1,3-diéthoxylaminoéthyle avec l'isothiocyanate d'éthyle a permis de réaliser la synthèse, avec un rendement de 78 %, du nouveau dérivé dendritique du calix[4]arène portant deux chaînes ramifiées différentes. La réaction du composé **2** avec le 1,6-diisocyanatohexane ou le *N,N'*-bis(2-chloroacétamide)éthylène dans un mode d'addition intermoléculaire « 1 + 1 », il est aussi possible de préparer avec des rendements raisonnables de nouveaux éthers lariats, des calix[4]-1,3-azacouronnes (**4** et **5**) portant des chaînes ramifiées éthoxyles. La composition, les structures et les conformations de tous les nouveaux produits ont été confirmées par analyse élémentaire, spectrométrie de masse avec ionisation par électronébulisation (SM-IEN), RMN du <sup>1</sup>H et autres. Des expériences d'extraction liquide–liquide ont montré que toutes les nouvelles molécules hôtes possèdent de bonnes habilités pour l'extraction des cations métalliques durs et mous. Des expériences de transport dans une membrane liquide suggère qu'elles possèdent de bonnes habilités pour le transport des ions K<sup>+</sup> et Na<sup>+</sup>. Les expériences en catalyse de transfert de phase indiquent qu'elles possèdent d'excellentes propriétés catalytiques dans les réactions de substitution nucléophile aromatique et de substitution nucléophile benzylique. Les rendements optimaux de produits dans les réactions catalytiques vont jusqu'à environ 100 %.

**Mots-clés :** calix[4]couronne, lariat, synthèse, transport dans une membrane liquide, catalyse par transfert de phase.

[Traduit par la Rédaction]

## Introduction

The importance of calixarenes in the family of host macrocycles is now well-established.<sup>1–3</sup> Since the first calix-crown was reported in 1983,<sup>4</sup> much research attention had been paid to the synthesis of calixcrowns and the study of their molecular and ion recognition to use them in the design of ion selective electrodes, liquid supported membranes and catalyst, and so forth.<sup>5–7</sup> All kinds of calixcrowns containing only oxygen donor atoms were synthesized and exhibited excellent recognition towards hard metal ions or some soft metal ions, and calixcrowns containing heteroatoms such as aza and sulfur groups usually showed outstanding complexation abilities for soft metal cations.<sup>8–17</sup>

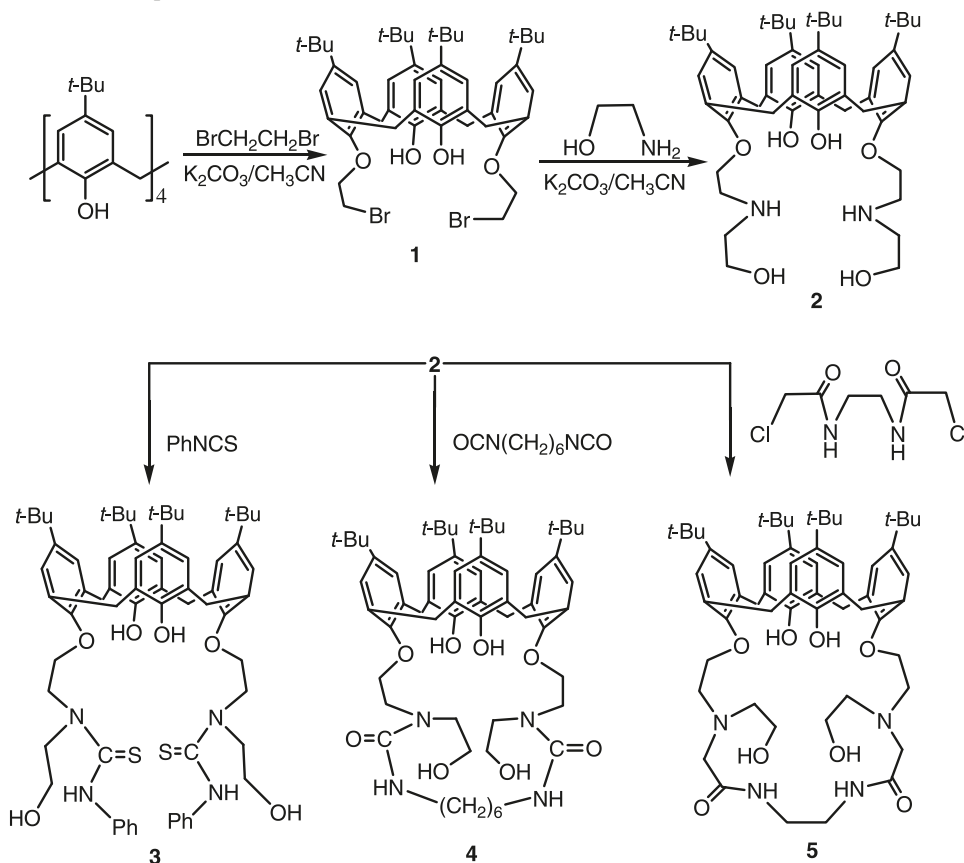
In the field of crown ethers, it is well-known that the lariat crown ethers with branched chains usually show outstanding complexation abilities for guest due to the coordinated recognition of crown ether chains and branched chains. However, in the field of calixcrowns, although many calixcrowns were reported, only Bitter and co-workers<sup>18,19</sup> and Bond et al.<sup>20</sup> reported several lariat calix[4]-aza-crowns with one amino-branched chain. These lariat calix[4]-aza-crowns exhibited excellent recognition properties due to the favorable synergistic complexation<sup>18–19</sup> but they were not concerned with their phase catalytic properties. Thus, it is interesting to study the syntheses and properties of novel lariat calixcrowns with other functional groups and more branched chains. In this paper, we report the syntheses of

Received 31 January 2010. Accepted 21 April 2010. Published on the NRC Research Press Web site at canjchem.nrc.ca on 6 June 2010.

**F. Yang,<sup>1</sup>** College of Chemistry and Materials, Fujian Normal University, Fuzhou 350007, P.R. China; Fujian Key Laboratory of Polymer Materials, Fuzhou 350007, P.R. China.

**Y. Wang, H. Guo, J. Xie, and Z. Liu.** College of Chemistry and Materials, Fujian Normal University, Fuzhou 350007, P.R. China.

<sup>1</sup>Corresponding author (e-mail: yangfafu@fjnu.edu.cn).

**Scheme 1.** Synthetic routes for compounds **2**, **3**, **4**, and **5**.

two novel lariat calix[4]-1,3-aza-crowns with two branched ethoxyl chains and a novel dendritic calix[4]arene derivative with two different branched chains. Also, their interesting properties of metal ion extraction, liquid membrane transport, and phase transfer catalysis were studied.

## Results and discussion

### Syntheses and characterization of products

The synthetic routes are shown in Scheme 1. 1,3-Broethoxyl-calix[4]arene (**1**) was prepared according to the published procedures.<sup>21</sup> By refluxing compound **1** with excess ethanolamine (molar ratio = 1:10) in  $\text{K}_2\text{CO}_3/\text{MeCN}$  for 48 h, the calix[4]-1,3-diethoxylaminoethyl derivative (**2**) was obtained in a yield of 73% after recrystallization in  $\text{CH}_3\text{OH}/\text{H}_2\text{O}$ . By further reacting compound **2** with phenyl isothiocyanate under room temperature, novel dendritic calix[4]arene derivative (**3**) with two different branched chains was obtained in a yield of 78% after recrystallization in  $\text{CHCl}_3$ /petroleum ether ( $60\sim 90^\circ\text{C}$ ). On the other hand, by refluxing compound **2** with 1,6-diisocyanatohexane in high diluted  $\text{CHCl}_3$  solution over night, novel lariat calix[4]-1,3-aza-crown (**4**) with two branched ethoxyl chains was prepared with a yield of 62% in a “1 + 1” addition mode after recrystallization in  $\text{CHCl}_3$ /petroleum ether ( $60\sim 90^\circ\text{C}$ ). Also, by refluxing compound **2** with *N,N'*-bis(2-chloroacetamide)ethylene in  $\text{K}_2\text{CO}_3/\text{MeCN}$  for 72 h, novel lariat calix[4]-1,3-aza-crown (**5**) with two branched ethoxyl chains was obtained in a yield of 42% in a “1 + 1” condensation mode after column chromatography. In

this condensation reaction, no catalyst, such as KI, was added to avoid the reaction of *N,N'*-bis(2-chloroacetamide)ethylene with the phenolic hydroxyl groups of compound **2**. Moreover, to test the reaction activity of phenolic hydroxyl groups of compound **2** in this reaction, compound **1** was refluxed with *N,N'*-bis(2-chloroacetamide)ethylene with the same reaction conditions, but no materials took part in the reaction in 72 h (if KI was added, materials took part in reaction). This result certainly suggested that it was not the phenolic hydroxyl groups but the amino groups of compound **2** taking part in the condensation reaction as showed in Scheme 1. To the best of our knowledge, compound **3** was the novel dendritic calix[4]arene derivative with two different branched chains, and compounds **4** and **5** were the first examples of lariat calix[4]-1,3-aza-crowns with two branched ethoxyl chains.

All new compounds were tested by elemental analyses, IR, ESI-MS, and  $^1\text{H}$  NMR spectra. The ESI-MS spectra of compounds **2**, **3**, **4**, and **5** clearly showed molecular ion peaks ( $\text{M}^+$ ,  $\text{MH}^+$ , or  $\text{MNa}^+$ ) at 824.0, 1116.0, 990.3, and 985.8, respectively. In the  $^1\text{H}$  NMR spectra, all of the compounds showed two singlets (1:1) for the *tert*-butyl groups and one pair of doublets (1:1) for the methylene bridges of the calix[4]arene skeleton. Comparing with the similar  $^1\text{H}$  NMR spectra of the other calix[4]arene 1,3-bisubstituted or 1,3-bridged derivatives in cone conformation,<sup>8–11</sup> all these  $^1\text{H}$  NMR spectra data of the new compounds **2–5** were in accordance with the assigned structures and indicated that the calix[4]arene units adopted cone conformation as shown in Scheme 1.

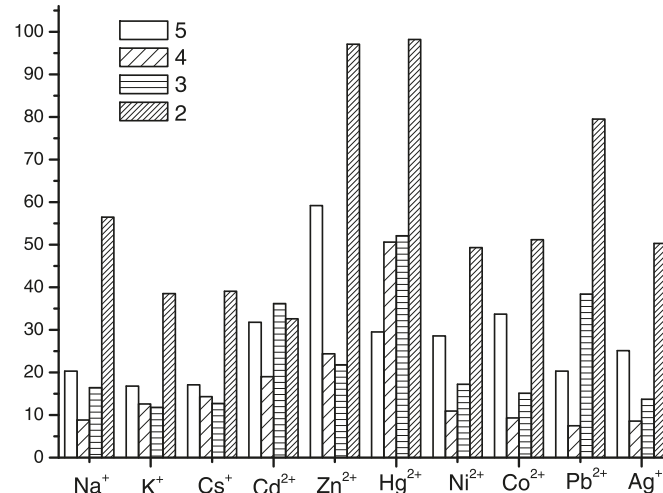
### Liquid-liquid extraction for metal cations

The complexation abilities of compounds **2**, **3**, **4**, and **5** towards a series of metal cations were studied by two-phase extraction experiments ( $\text{H}_2\text{O}/\text{CHCl}_3$ ) of metal cation picrate salts. The results were summarized in Fig. 1. Compounds **2**, **3**, **4**, and **5** exhibited good extraction abilities for both soft and hard metal cations. These results were in accordance with the "soft and hard acids and bases" concept, i.e., amino groups and hydroxyl groups were favorable for binding soft and hard metal cations, respectively. It is worthy to note that the extraction percentage of compound **2** for  $\text{Zn}^{2+}$  and  $\text{Hg}^{2+}$  were as high as 100%. On the other hand, hosts **4** and **5** showed lower extraction percentages but higher extraction selectivities than that of hosts **2** and **3**. For example, the extraction selectivity of host **4** for  $\text{Hg}^{2+}/\text{Ag}^+$  was 6.75 (extraction percentage of  $\text{Hg}^{2+}$ /extraction percentage of  $\text{Ag}^+$  = 50.6/7.5). These extraction results might suggest that the crown structures of compounds **4** and **5** were more favorable for producing the complexation selectivity than that of the open-chain structures of compounds **2** and **3**.

### Liquid membrane transport for $\text{K}^+$ , $\text{Zn}^{2+}$ , and $\text{Ag}^+$

To investigate the potential application of new hosts **2**, **3**, **4**, and **5**, they were studied by liquid membrane transport experiments. Based on the extraction experiments, the  $\text{K}^+$ ,  $\text{Zn}^{2+}$ , and  $\text{Ag}^+$  were chosen as representative usual metal cations of hard and soft cations, and representative extraction abilities with variational extraction percentages (from 10% to 100%) in extraction experiments. The fluorinion was chosen as the anion of these metal salts because F<sup>-</sup> plays an important role in the nucleophilic substitution reaction of preparing fluorine compounds. The transport results were summarized in Table 1. It could be seen that the salt concentration in the receiving phase increased with prolonging the running times. It was interesting that hosts **2**, **3**, **4**, and **5** possessed transport abilities for cations in the similar order of  $\text{K}^+ \approx \text{Ag}^+ > \text{Zn}^{2+}$ . For example, in compound **5**, the salts concentrations in the receiving phase of  $\text{K}^+$  and  $\text{Ag}^+$  in 20 h were  $8.9 \times 10^{-3}$  mol/L and  $7.8 \times 10^{-3}$  mol/L, respectively. However, the salt concentration of  $\text{Zn}^{2+}$  was as low as  $4.3 \times 10^{-3}$  mol/L under the same transport conditions. On the other hand, hosts **4** and **5** showed far higher transport amounts than that of hosts **2** and **3** in the running times over 20 h. For example, the concentrations of  $\text{K}^+$  in the receiving phase using hosts **4** and **5** as carriers in 20 h were  $6.8 \times 10^{-3}$  mol/L and  $8.9 \times 10^{-3}$  mol/L, respectively. However, the concentrations of  $\text{K}^+$  in the receiving phase using hosts **2** and **3** were as low as  $1.8 \times 10^{-3}$  mol/L and  $1.7 \times 10^{-3}$  mol/L, respectively, under the same transport conditions. These results of liquid membrane transport were utterly different from the results of two phase extraction experiments. It was known that the liquid membrane transport ability relied on the balance of the complexation ability of the host for guest and the decomplexing ability of the complexes.<sup>22,23</sup> These results of liquid membrane transport might suggest that complex  $2\text{M}^+(\text{and } 2\text{M}^{2+}, 3\text{M}^+, 3\text{M}^{2+})$  possessed stronger stabilities and lower decomplexing abilities in comparison with the corresponding complexes with hosts **4** and **5**. Thus, although the two phase extraction abilities of hosts **4** and **5** were lower than that of hosts **2** and **3**, the lower stabilities of the complexes with **4** and **5** led to higher de-

Fig. 1. Percentage extraction (%) of **2**, **3**, **4**, and **5** towards picrate salts.



complexing abilities and then higher speeds of liquid membrane transport than that of **2** and **3**.

### The phase transfer catalysis of the nucleophilic substitution reaction

Based on the experiment results of liquid membrane transport, the phase transfer catalytic properties of aromatic nucleophilic substitution reactions were studied. Aromatic fluorine compounds have important applications in insecticidal and refined chemicals.<sup>24</sup> The replacement of aromatic Cl by F in nucleophilic substitution reactions was chosen as a reaction system to evaluate the phase transfer catalytic abilities of new hosts **2**, **3**, **4**, and **5**. The experiment results are shown in Table 2. It can be seen that the yield of the product was as low as 8.5% when the reaction was performed without a catalyst (Table 2, entry 1). As catalysts were added, the yields greatly increased. Under the same reaction conditions, hosts **4** and **5** showed higher catalytic activity than that of hosts **2** and **3** (Table 2, entries 2–5). These results were in accordance with the results of the liquid membrane transport experiment. Using  $\text{AgF}$  instead of  $\text{KF}$ , hosts **4** and **5** still keep the high catalytic activity, although the yields of the product decreased a little (Table 2, entries 6–7). On the other hand, the yields of the products were over 90% when the reaction time was prolonged to 24 h and 36 h (Table 2, entries 8–11). Also, *p*-nitrochlorobenzene, having an electron withdrawing group (1,2-dichloro-4-nitrobenzene or 2,4-dinitrochlorobenzene), offered higher yields (Table 2, entries 12–13), which were attributed to the favorable influence of the electron withdrawing group for an aromatic nucleophilic substitution reaction. The yields were as high as 100% when using 2,4-dinitrochlorobenzene as material.

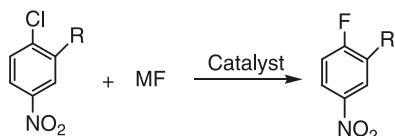
Also, the replacement of aliphatic Cl by a nitrile group in a benzyl nucleophilic reaction was studied by using new hosts **2**, **3**, **4**, and **5** as phase transfer catalysts. The experiment results are shown in Table 3, which are similar to the results in Table 2. The yields of products were greatly increased from 6.4% to approximately 90% when catalysts were added. Although hosts **4** and **5** showed higher catalytic activities than that of hosts **2** and **3**, the differences in yields were not remarkable. The yields were as high as almost

**Table 1.** Salts concentrations (in the receiving phase) change with running times for different carriers in cation transport.

Carriers <sup>a</sup>	K <sup>+</sup> (10 <sup>-3</sup> mol/L)				Zn <sup>2+</sup> (10 <sup>-3</sup> mol/L)				Ag <sup>+</sup> (10 <sup>-3</sup> mol/L)			
	2 h	5 h	10 h	20 h	2 h	5 h	10 h	20 h	2 h	5 h	10 h	20 h
<b>2</b>	0.5	1.1	1.5	1.8	0.2	0.6	0.9	1.1	0.4	1.0	1.6	1.9
<b>3</b>	0.4	0.8	1.4	1.7	0.5	1.0	1.4	1.6	0.4	0.9	1.5	1.7
<b>4</b>	2.3	4.5	5.8	6.3	1.4	3.1	4.5	5.5	2.0	4.1	5.3	6.5
<b>5</b>	3.0	5.6	7.2	8.9	0.8	1.8	3.2	4.3	2.6	4.9	6.6	7.8

**Note:** The source aqueous solution: 0.05 mol/L of each salt.

<sup>a</sup>Membrane:  $5.0 \times 10^{-4}$  mol/L carrier in CHCl<sub>3</sub>. For a blank experiment, no transport rate was detected in the absence of carriers during more than 12 h of continuous running.

**Table 2.** Catalytic investigation of compounds **2**, **3**, **4**, and **5** in aromatic nucleophilic reactions.

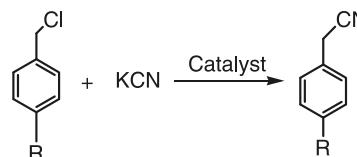
Entry	R	M <sup>+</sup>	Catalyst	Run time (h)	Yield (%)
1	H	K <sup>+</sup>	None	12	8.5
2	H	K <sup>+</sup>	<b>2</b>	12	72.5
3	H	K <sup>+</sup>	<b>3</b>	12	79.3
4	H	K <sup>+</sup>	<b>4</b>	12	88.2
5	H	K <sup>+</sup>	<b>5</b>	12	90.5
6	H	Ag <sup>+</sup>	<b>4</b>	12	86.4
7	H	Ag <sup>+</sup>	<b>5</b>	12	88.6
8	H	K <sup>+</sup>	<b>4</b>	24	94.3
9	H	K <sup>+</sup>	<b>5</b>	24	96.7
10	H	K <sup>+</sup>	<b>4</b>	36	97.8
11	H	K <sup>+</sup>	<b>5</b>	36	98.2
12	Cl	K <sup>+</sup>	<b>5</b>	24	98.8
13	NO <sub>2</sub>	K <sup>+</sup>	<b>5</b>	24	99.2

**Note:** Reaction conditions: *p*-nitrochlorobenzene or its derivatives (5 mmol), potassium fluoride or silver fluoride (10 mmol), catalyst (3.0 mol%), DMSO as solvent (12 mL), reaction temperature (40 °C).

100% when the reaction time was prolonged to 24 h. All these catalytic results in Table 2 and Table 3 indicate that novel lariat calix[4]-1,3-aza-crowns (**4** and **5**) are excellent phase transfer catalysts for nucleophilic substitution reactions.

## Conclusion

Novel dendritic calix[4]arene derivative (**3**) with two different branched chains was prepared by reacting calix[4]-1,3-diethoxylaminoethyl derivative (**2**) with phenyl isothiocyanate. Novel lariat calix[4]-1,3-aza-crowns (**4** and **5**) with two branched ethoxyl chains were prepared by reacting compound **2** with 1,6-diisocyanatohexane or *N,N'*-bis(2-chloroacetamide)ethylene in a "1 + 1" intermolecular addition mode. The composition, structures, and conformations of all new compounds were confirmed by elemental analyses, IR, ESI-MS, <sup>1</sup>H NMR, and so forth. The liquid-liquid extraction experiment showed that all new hosts possessed good complexation abilities towards soft metal cations and hard metal cations. The liquid membrane transport experiments suggested that they had good transport abilities for both K<sup>+</sup> and Ag<sup>+</sup>. The experiments of phase transfer cataly-

**Table 3.** Catalytic investigation of compounds **2**, **3**, **4**, and **5** in benzyl nucleophilic substitution.

Entry	R	Catalyst	Run time (h)	Yield (%)
1	H	None	12	6.4
2	H	<b>2</b>	12	84.2
3	H	<b>3</b>	12	88.5
4	H	<b>4</b>	12	93.6
5	H	<b>5</b>	12	97.4
6	H	<b>4</b>	24	98.6
7	H	<b>5</b>	24	98.9
8	CH <sub>3</sub>	<b>4</b>	12	92.1
9	CH <sub>3</sub>	<b>5</b>	12	88.4
10	CH <sub>3</sub>	<b>4</b>	24	98.5
11	CH <sub>3</sub>	<b>5</b>	24	98.2

**Note:** Reaction conditions: benzyl chloride or *p*-methylbenzyl chloride (5 mmol), potassium cyanide (10 mmol), catalyst (3.0 mol%), DMSO as solvent (12 mL), reaction temperature (40 °C).

sis exhibited that they possessed excellent catalytic properties of aromatic nucleophilic substitution reaction and benzyl nucleophilic substitution. The yields of products in catalytic reaction were as high as approximately 100%.

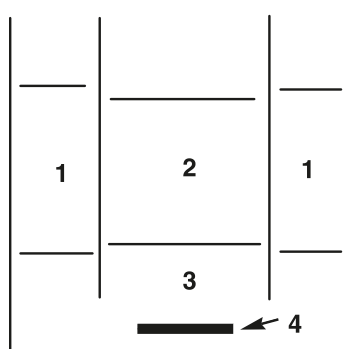
## Experimental section

### Instruments

Melting points are uncorrected. <sup>1</sup>H NMR spectra were recorded in CDCl<sub>3</sub> on a Bruker-ARX 500 instrument, using TMS as a reference. ESI-MS spectra were obtained from a DECAX-30000 LCQ Deca XP mass spectrometer in MeCN, setting the ESI capillary at 3.5 kV and the cone voltage at 40 V. Elemental analyses were performed at a Vario EL III elemental analyzer. The UV-vis measurements were performed on a Varian UV-vis spectrometer. The gas chromatography was performed on a Varian 450-GC/240-MS instrument. Atomic absorption was measured on a WFX-II spectrograph. All solvents were purified by standard procedures. 1,3-Broethoxyl-calix[4]arene (**1**) was prepared according to the published procedures.<sup>21</sup> The picrate salts were prepared according to literature.<sup>25,26</sup>



**Fig. 2.** Liquid membrane cell: (1) source phase, (2) receiving phase, (3) membrane phase, and (4) magnetic stirring bar.



### Syntheses of calix[4]-1,3-diethoxylaminoethyl derivative (2)

Under  $N_2$  atmosphere, a mixture of compound **1** (0.430 g, 0.5 mmol), ethanolamine (0.30 mL, 5 mmol), and  $K_2CO_3$  (0.280 g, 2 mmol) was stirred in refluxing dry acetonitrile (30 mL) for 48 h. Thin layer chromatography (TLC) detection showed the disappearance of compound **1**. After distilling off the solvent under reduced pressure, the residue was treated with 30 mL HCl (10%) and a white precipitate separated out. The precipitate was filtered and recrystallized by MeOH/H<sub>2</sub>O. Compound **2** was obtained as a white powder in a yield of 73%; mp 204–206 °C. IR (KBr,  $cm^{-1}$ ): 3421 (OH and NH).  $^1H$  NMR ( $CDCl_3$ , 500 MHz)  $\delta$ : 0.97 (s, 18H,  $C(CH_3)_3$ ), 1.23 (s, 18H,  $C(CH_3)_3$ ), 3.28 (bs, 8H,  $ArCH_2Ar$  and  $OCH_2$ ), 3.49~3.53 (bs, 8H,  $NH_2$  and  $OCH_2$ ), 3.88~3.92 (bs, 4H,  $NCH_2$ ), 4.16 (s, 4H, OH and NH), 4.24 (d, 4H,  $J = 13.5$  Hz,  $ArCH_2Ar$ ), 6.85 (s, 4H, ArH), 7.01 (s, 4H, ArH), 7.24 (s, 2H, ArOH). ESI-MS  $m/z$  (%): 824.0 ( $MH^+$ , 100). Anal. calcd. for  $C_{52}H_{74}N_2O_6$ : C 75.87, H 9.06, N 3.40; found: C 75.77, H 9.15, N 3.29.

### Synthesis of novel dendritic calix[4]arene derivative (3)

A mixture of compound **2** (0.205 g, 0.25 mmol) and phenyl isothiocyanate (0.3 mL, 2 mmol) was stirred in 10 mL  $CHCl_3$  for 4 h under room temperature. TLC detection indicated the disappearance of compound **2**. The solvent was removed under reduced pressure at room temperature. The residue was treated with 10 mL petroleum ether (60~90 °C) and a white precipitate separated out. The precipitate was filtered and recrystallized by  $CHCl_3$ /petroleum ether (60~90 °C). Compound **3** was obtained as a white powder in a yield of 78%; mp 213–216 °C. IR (KBr,  $cm^{-1}$ ): 1239 (C=S).  $^1H$  NMR (500 MHz,  $CDCl_3$ )  $\delta$ : 0.95 (s, 18H,  $C(CH_3)_3$ ), 1.21 (s, 18H,  $C(CH_3)_3$ ), 3.22 (t, 4H,  $OCH_2$ ), 3.38 (d, 4H,  $J = 14.5$  Hz,  $ArCH_2Ar$ ), 3.57 (t, 4H,  $OCH_2$ ), 3.82 (t, 4H,  $NCH_2$ ), 3.96~4.01 (m, 4H,  $NCH_2$ ), 4.28 (d, 4H,  $J = 14.5$  Hz,  $ArCH_2Ar$ ), 6.79 (s, 2H, ArH), 6.96 (d, 4H,  $J = 7.5$  Hz, ArH), 7.15 (s, 4H, ArH), 7.32 (m, 8H, ArH), 7.18, 7.40, 9.48 (s, each, 2H, each, OH and NH). MS  $m/z$  (%): 1116.0 ( $MNa^+$ , 100). Anal. calcd. for  $C_{66}H_{84}N_4S_2O_6$ : C 72.50, H 7.74, N 5.12; found: C 72.33, H 7.83, N 5.01.

### Synthesis of novel lariat calix[4]-1,3-aza-crown (4)

A mixture of compound **2** (0.205 g, 0.25 mmol) and 1,6-diisocyanatohexane (0.048 mL, 0.3 mmol) was refluxed in 100 mL  $CHCl_3$  for 12 h. TLC detection indicated the disappearance of compound **2**. The solvent was removed under

reduced pressure. The residue was treated with 10 mL petroleum ether (60 °C~90 °C) and a white precipitate separated out. The precipitate was filtered and recrystallized by  $CHCl_3$ /petroleum ether (60~90 °C). Compound **4** was obtained as a white powder in a yield of 62%; mp 232–234 °C. IR (KBr,  $cm^{-1}$ ): 1703 (C=O).  $^1H$  NMR ( $CDCl_3$ , 500 MHz)  $\delta$ : 0.90 (s, 18H,  $C(CH_3)_3$ ), 1.31 (s, 18H,  $C(CH_3)_3$ ), 1.42 (bs, 4H,  $CH_2$ ), 1.86 (bs, 4H,  $CH_2$ ), 3.16~3.30 (m, 8H,  $NCH_2$  and  $OCH_2$ ), 3.32 (d, 4H,  $J = 12.5$  Hz,  $ArCH_2Ar$ ), 3.49~4.11 (m, 12H,  $NH_2$  and  $OCH_2$ ), 4.18 (d, 4H,  $J = 12.5$  Hz,  $ArCH_2Ar$ ), 4.90, 6.34, 6.54 (s, each, 2H, each, OH and NH), 6.66 (s, 4H, ArH), 7.08 (s, 4H, ArH). ESI-MS  $m/z$  (%): 990.3 ( $M^+$ , 100). Anal. calcd. for  $C_{60}H_{86}N_4O_8$ : C 72.69, H 8.74, N 5.65; found: C 72.58, H 8.82, N 5.55.

### Synthesis of novel lariat calix[4]-1,3-aza-crown (5)

Under  $N_2$  atmosphere, a mixture of compound **2** (0.205 g, 0.25 mmol), *N,N'*-bis(2-chloroacetamide)ethylene (0.064 g, 0.3 mmol), and  $K_2CO_3$  (0.280 g, 2 mmol) was stirred in refluxing dry acetonitrile (30 mL) for 72 h. The TLC detection indicated the disappearance of compound **2**. After distilling off the solvent under reduced pressure, the residue was purified by column chromatography (50 cm  $\times$  3 cm,  $SiO_2$  100–200 mesh, acetone/ $CH_2Cl_2$  (3:2, v/v) as eluant, 500 mL). Compound **5** was then obtained as a white powder in a yield of 42%; mp 241–244 °C. IR (KBr,  $cm^{-1}$ ): 1653 (C=O).  $^1H$  NMR ( $CDCl_3$ , 500 MHz)  $\delta$ : 0.89 (s, 18H,  $C(CH_3)_3$ ), 1.30 (s, 18H,  $C(CH_3)_3$ ), 3.26~3.36 (m, 12H,  $ArCH_2Ar$ ,  $NCH_2$ , and  $OCH_2$ ), 3.65~4.06 (m, 8H,  $NH_2$  and  $OCH_2$ ), 4.12 (d, 4H,  $J = 12.5$  Hz,  $ArCH_2Ar$ ), 4.14~4.33 (m, 8H,  $OCH_2CO$  and  $NCH_2$ ), 6.61 (s, 4H, ArH), 7.08 (s, 4H, ArH), 6.82, 7.01, 8.52 (s, each, 2H, each, OH and NH). ESI-MS  $m/z$  (%): 985.8 ( $MNa^+$ , 100). Anal. calcd. for  $C_{58}H_{82}N_4O_8$ : C 72.31, H 8.58, N 5.81; found: C 72.21, H 8.66, N 5.70.

### Procedures for two phase extraction experiments of metallic picrates

According to the reported method,<sup>25</sup> 3 mL of chloroform solution containing calixarene derivatives ( $2.0 \times 10^{-5}$  mol/L) and 3 mL of aqueous solution containing metallic picrate ( $2.0 \times 10^{-5}$  mol/L) were placed in a flask (Caution: metallic picrates are hazardous materials; avoid fire, extrusion, high temperature, and so forth). The pH of 6.9~7.1 of these aqueous solutions suggests that little hydrolysis happened. The mixture was shaken for 5 min and stored for 2 h at room temperature. The extraction ability was not affected by further shaking, indicating that the equilibrium had been attained within 2 h. The aqueous phase was separated and subjected to the analysis by UV absorption spectrometry in near 357 nm. The extracting percentage ( $E\%$ ) was determined by the decrease of the picrate concentration in the aqueous phase,  $E\% = \{([Pic]_{blank} - [Pic]_{water})/[Pic]_{blank}\} \times 100$ , where  $[Pic]_{blank}$  denoted the picrate concentrations in the aqueous phase after extraction with pure chloroform, and  $[Pic]_{water}$  denoted the picrate concentrations in the aqueous phase after extraction with chloroform solution containing calixarene derivatives as extractants. The average of the twice-independent experiments was carried out. Control ex-

periments showed that no picrate extraction occurred in the absence of the calixarene derivatives.

### Procedures for metal ion transport experiments

According to the reported method,<sup>27</sup> liquid membrane transport experiments were conducted using the bulk liquid membrane apparatus presented in Fig. 2. The membrane phase was the  $\text{CHCl}_3$  solution of new host with a concentration of  $5.0 \times 10^{-4}$  mol/L. The membrane phase (25.0 mL) was added to the bottom of the vessel and stirred magnetically at 200 rpm. An aqueous salt solution (15 mL) with a concentration of 0.05 mol/L (source phase, fluorides) and 15 mL of doubly distilled deionized water (receiving phase) were poured on top of the organic phase. The two water phases were separated by a cylindrical glass cell holding a glass tube. The interface between the membrane phase and the source phase (or the receiving phase) was 7.5 cm<sup>2</sup>. The measurements were performed at a constant temperature of 25 °C. The concentration of salt in the receiving phase was determined by atomic absorption spectrography. The pH value of the source phase and receiving phase changed in the scope of 6.9~7.2, which indicated that little hydrolysis happened in the metal ion transport experiments. Blank experiment showed that no transport was detected in the absence of host during more than 12 h of continuous running. Each experiment was repeated three times. The cation concentration in the receiving phase was reported as the mean of the determination and the relative standard deviation from the mean was less than 5%.

### The procedures of phase transfer catalysis of a nucleophilic substitution reaction

A typical nucleophilic substitution reaction was conducted by mixing reactant (5 mmol) and corresponding inorganic salt (10 mmol) in 12 mL of DMSO. The catalyst (3.0 mol%) was added and the reaction was stirred (800 rpm) for a stipulated time period (Table 2 and Table 3) at 40 °C. The yields of product were analyzed by gas chromatography (Varian 450-GC/240-MS).

### Acknowledgements

Financial support from the National Natural Science Foundation of China (No. 20402002), the Fujian Natural Science Foundation of China (No. 2009J01019), and the Program for New Century Excellent Talents in the University of Fujian Province are greatly acknowledged.

### References

- (1) Asfari, Z.; Böhmer, V.; Harrowfield, J.; Vicens, J. *Calixarenes 2001*; Kluwer Academic Publishers: Dordrecht, the Netherlands, 2001.
- (2) Ikeda, A.; Shinkai, S. *Chem. Rev.* **1997**, 97 (5), 1713. doi:10.1021/cr960385x. PMID:11851464.
- (3) Oueslati, I. *Tetrahedron* **2007**, 63 (44), 10840. doi:10.1016/j.tet.2007.06.128.
- (4) Alfieri, C.; Dradi, E.; Pochini, A.; Ungaro, R.; Andreetti, G. D. *J. Chem. Soc. Chem. Commun.* **1983**, 1075. doi:10.1039/c39830001075.

- (5) Cacciapaglia, R.; Casnati, A.; Mandolini, L.; Ungaro, R. *J. Am. Chem. Soc.* **1992**, 114 (27), 10956. doi:10.1021/ja00053a040.
- (6) Casnati, A.; Pochini, A.; Ungaro, R.; Bocchi, C.; Ugozzoli, F.; Egberink, R. J. M.; Struijk, H.; Lugtenberg, R.; de Jong, F.; Reinhoudt, D. N. *Chem. Eur. J.* **1996**, 2 (4), 436. doi:10.1002/chem.19960020413.
- (7) Pappalardo, S.; Parisi, M. F. *Tetrahedron Lett.* **1996**, 37 (9), 1493. doi:10.1016/0040-4039(96)00047-0.
- (8) Guan, B.; Gong, S.; Wu, X.; Li, Z.; Chen, Y. *J. Incl. Phenom. Macrocycl. Chem.* **2006**, 54 (1–2), 81. doi:10.1007/s10847-005-4601-3.
- (9) Oueslati, I.; Thuéry, P.; Shkurenko, O.; Suwinska, K.; Harrowfield, J.; Abidi, R.; Vicens, J. *Tetrahedron* **2007**, 63 (1), 62. doi:10.1016/j.tet.2006.10.047.
- (10) He, Y.; Xiao, Y.; Meng, L.; Zeng, Z.; Wu, X.; Wu, C. T. *Tetrahedron Lett.* **2002**, 43 (35), 6249. doi:10.1016/S0040-4039(02)01322-9.
- (11) Yang, Y.; Cao, X.; Surowiec, M.; Bartsch, R. A. *Tetrahedron* **2010**, 66 (2), 447. doi:10.1016/j.tet.2009.11.058.
- (12) Surowiec, M.; Custelcean, R.; Surowiec, K.; Bartsch, R. *Tetrahedron* **2009**, 65 (37), 7777. doi:10.1016/j.tet.2009.07.006.
- (13) Yang, F. F.; Chen, Y. Y. *Eur. J. Org. Chem.* **2001**, 2001 (2), 365. doi:10.1002/1099-0690(200101)2001:2<365::AID-EJOC365>3.0.CO;2-N.
- (14) Yang, F. F.; Chen, Y. Y. *Supramol. Chem.* **2001**, 12 (4), 445. doi:10.1080/10610270108027476.
- (15) Yang, F. F.; Chen, X. L.; Guo, H. Y.; Cai, X. Q.; Lin, S. *Synth. Commun.* **2004**, 34 (19), 3513. doi:10.1081/SCC-200030980.
- (16) Yang, F. F.; Huang, C. Y.; Guo, H. Y.; Lin, J. R.; Peng, Q. *J. Incl. Phenom. Macrocycl. Chem.* **2007**, 58 (1–2), 169. doi:10.1007/s10847-006-9139-5.
- (17) Yang, F.; Wang, Y.; Hong, B.; Chai, X. *J. Incl. Phenom. Macrocycl. Chem.* **2009**, 64 (1–2), 67. doi:10.1007/s10847-009-9537-6.
- (18) Bitter, I.; Grün, A.; Tóth, G.; Balázs, B.; Tóke, L. *Tetrahedron* **1997**, 53 (28), 9799. doi:10.1016/S0040-4020(97)00627-3.
- (19) Balázs, B.; Tóth, G.; Horváth, G.; Grün, A.; Csokai, V.; Tóke, L.; Bitter, I. *Eur. J. Org. Chem.* **2001**, 61. doi:10.1002/1099-0690(200101)2001:1<61::AID-EJOC61>3.0.CO;2-E.
- (20) Bond, A. D.; Creaven, B. S.; Donlon, D. F.; Gernon, T. L.; McGinley, J.; Toftlund, H. *Eur. J. Inorg. Chem.* **2007**, 749. doi:10.1002/ejic.200601000.
- (21) Li, Z. T.; Ji, G. Z.; Zhao, C. X.; Yuan, S. D.; Ding, H.; Huang, C.; Du, A. L.; Wei, M. *J. Org. Chem.* **1999**, 64 (10), 3572. doi:10.1021/jo9824100. PMID:11674484.
- (22) Alpaydin, S.; Yilmaz, M.; Ersoz, M. *Sep. Sci. Technol.* **2005**, 39 (9), 2189. doi:10.1081/SS-120039310.
- (23) Saf, A. Ö.; Alpaydin, S.; Sirit, A. *J. Membr. Sci.* **2006**, 283 (1–2), 448. doi:10.1016/j.memsci.2006.07.023.
- (24) Finger, G. C.; Kruse, C. W. *J. Am. Chem. Soc.* **1986**, 78, 6034.
- (25) Arnaud-Neu, F.; Collins, E. M.; Deasy, M.; Ferguson, G.; Harris, S. J.; Kaitner, B.; Lough, A. J.; McKervy, M. A.; Marques, E. *J. Am. Chem. Soc.* **1989**, 111 (23), 8681. doi:10.1021/ja00205a018.
- (26) Zhong, Z. L. *Syntheses and Complexation Properties of Calix[4]crowns*. Ph.D. Thesis, Wuhan University, Wuhan, China, 1996.
- (27) Li, H.; Chen, Y.; Tian, D.; Gao, Z. *J. Membr. Sci.* **2008**, 310 (1–2), 431. doi:10.1016/j.memsci.2007.11.013.

# Synthesis and biological evaluation of acyclic nucleotide analogues with a furo[2,3-*d*]pyrimidin-2(3*H*)-one base

Zlatko Janeba, Antonín Holý, Radek Pohl, Robert Snoeck, Graciela Andrei, Erik De Clercq, and Jan Balzarini

**Abstract:** As a part of a broader structure–activity relationship (SAR) study of bicyclic nucleoside analogues (BCNAs) [anti-varicella-zoster virus (anti-VZV) and anti-human cytomegalovirus (anti-HCMV) agents], a novel series of 2-(phosphonomethoxy)ethyl (PME) substituted furo[2,3-*d*]pyrimidin-2(3*H*)-ones was synthesized. The target acyclic nucleotide analogues were prepared by Sonogashira coupling of protected 5-iodo-1-[2-(phosphonomethoxy)ethyl]uracil with various 1-alkynes, followed by in situ Cu(I)-promoted intramolecular cyclization and standard removal of the isopropyl ester groups. None of the prepared PME analogues were active at subtoxic concentrations against VZV thymidine kinase competent (TK<sup>+</sup>), VZV thymidine kinase deficient (TK<sup>−</sup>), HCMV, or any other viruses tested.

**Key words:** Sonogashira reaction, intramolecular cyclization, acyclic nucleotide analogues, phosphonates, bicyclic nucleoside analogues (BCNAs).

**Résumé :** Dans le cadre d'une large étude des analogues bicycliques de nucléotides (ABCN) [des agents actifs contre le virus de varicelle-zoster (anti-VVZ) et contre le cytomégalo-virus humain (anti-CMVH)], on a réalisé la synthèse d'une nouvelle série de furo[2,3-*d*]pyrimidin-2(3*H*)-ones portant un substituant 2-(phosphonométhoxy)éthyle (PME). On a préparé les analogues acycliques de nucléotides voulus par un couplage de Sonogashira du 5-iodo-1-[2-(phosphonométhoxy)éthyl]uracile avec divers 1-alcynes, suivi d'une cyclisation in situ intramoléculaire, catalysée par du Cu(I), et finalement d'une élimination standard des groupes esters isopropyles. Aucun des analogues PME n'est actif, à des concentrations sous-toxiques, contre le virus de varicelle-zoster (anti-VVZ), contre le cytomégalo-virus humain (anti-CMVH) ou contre tout autre virus testé.

**Mots-clés :** réaction de Sonogashira, cyclisation intramoléculaire, analogues acycliques de nucléotide (ABCN), phosphonate.

[Traduit par la Rédaction]

## Introduction

Antiviral drugs currently belong to the most widely used medications. The majority of them now available are designed to help deal with infections caused by herpes simplex virus (HSV), human immunodeficiency virus (HIV), hepatitis B virus (HBV), hepatitis C virus (HCV), and cytomegalovirus (CMV). Prominent among the antiviral drugs are nucleoside and nucleotide analogues, mainly for their ability to inhibit viral DNA polymerases and reverse transcriptases. Nowadays, research of nucleic acid components steadily continues to provide new compounds with interesting biological activities and high potential in the management of viral infections.

While studying 5-substituted pyrimidines as potential inhibitors of thymidylate synthase and thus prospective antiviral agents, 6-*n*-butyl-3-methylfuro[2,3-*d*]pyrimidin-2(3*H*)-one was reported by Robins and Barr<sup>1</sup> in 1981 as a byproduct (9% yield) of Sonogashira cross-coupling of 5-iodo-1-methyluracil with 1-hexyne. The same compound was formed

in 92% yield by treatment of 5-hexynyl-1-methyluracil with CuI in refluxing triethylamine/methanol mixture.<sup>1</sup> Two years later, the same authors described the preparation of the 6-*n*-butylfuro[2,3-*d*]pyrimidin-2(3*H*)-one 2'-deoxynucleoside analogue.<sup>2</sup>

Two decades later, the remarkably potent and selective activity against varicella-zoster virus (VZV) was discovered with furo[2,3-*d*]pyrimidin-2(3*H*)-one 2'-deoxynucleoside analogues with longer alkyl chains at the C-6 position (e.g., compound **1**, Fig. 1).<sup>3</sup> Subsequent extensive structure–activity relationship (SAR) studies of these bicyclic nucleoside analogues (BCNAs) followed<sup>4</sup> and identified compound Cf 1743 (compound **3**, Fig. 1) as one of the most potent antiviral agents that have ever been reported.<sup>5</sup> Its promising prodrug FV100 (5'-valine ester of Cf 1743) is currently in phase II of clinical development against herpes zoster (shingles).<sup>6</sup>

While SAR studies<sup>4</sup> of BCNAs showed that some structural modifications of the furo[2,3-*d*]pyrimidin-2(3*H*)-one

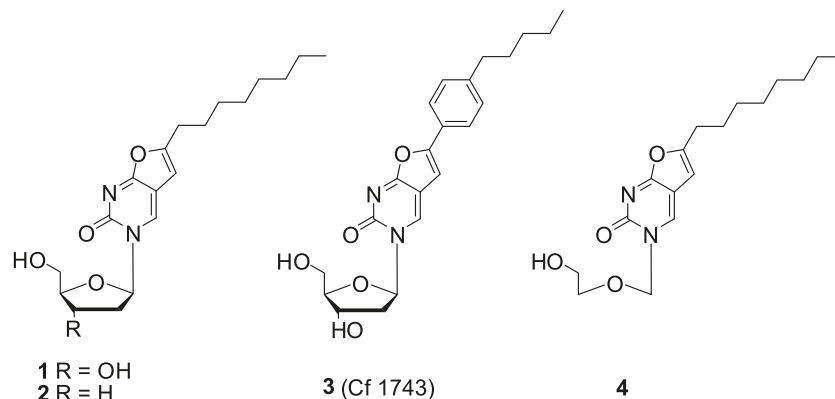
Received 13 January 2010. Accepted 22 March 2010. Published on the NRC Research Press Web site at canjchem.nrc.ca on 10 June 2010.

**Z. Janeba,<sup>1</sup> A. Holý, and R. Pohl.** Institute of Organic Chemistry and Biochemistry, Academy of Sciences of the Czech Republic, Flemingovo nám. 2, CZ-166 10 Prague 6, Czech Republic.

**R. Snoeck, G. Andrei, E. De Clercq, and J. Balzarini.** Rega Institute for Medical Research, Minderbroedersstraat 10, Leuven B-3000, Belgium.

<sup>1</sup>Corresponding author (e-mail: janeba@uochb.cas.cz).



**Fig. 1.** Bicyclic nucleoside analogues.

base or the substituent at the C-6 position are tolerated, sugar modifications of BCNAs are not acceptable for maintaining potent anti-VZV activity. Thus, while 2'-deoxyribosides are potent and selective anti-VZV agents, their ribo- and arabino-analogues are significantly less active.<sup>4</sup> Furthermore, 2',3'-dideoxy analogues (e.g., compound **2**, Fig. 1)<sup>7</sup> and N-3 alkyl derivatives<sup>8</sup> showed poor activity against VZV but they surprisingly exhibited activity against human cytomegalovirus (HCMV). Replacement of the sugar at the N-3 position by the (2-hydroxyethoxy)methyl group (present in the antiherpes drug acyclovir) afforded compounds (e.g., compound **4**, Fig. 1) with weak activity against both VZV and HCMV.<sup>9</sup>

Although not sufficient as a requirement, phosphorylation of the furo[2,3-*d*]pyrimidin-2(3*H*)-one nucleoside analogues by the VZV thymidine kinase (TK) is a prerequisite for their eventual anti-VZV activity.<sup>4,10</sup> This fact is supported by the complete absence of antiviral activity of BCNAs in the thymidine kinase deficient VZV TK<sup>-</sup> assays. Thus, the anti-VZV activity of 2'-deoxyriboside BCNAs follows the activation pathway characteristic for thymidine nucleosides (nucleoside mechanism mode of action). On the other hand, BCNAs with modified sugar moiety that inhibit HCMV replication do so by a non-nucleoside mechanism of action, at an early stage of the viral life cycle, possibly affecting viral entry into the cells.<sup>10</sup>

In 1986, De Clercq et al.<sup>11</sup> described broad spectrum antiviral activity of (*S*)-9-(3-hydroxy-2-phosphonmethoxy)propyladenine (HPMPA) and 9-(2-phosphonmethoxy)ethyladenine (PMEA), compounds belonging to a group of acyclic nucleoside phosphonates (ANPs). ANPs possess a phosphonate group attached to the acyclic moiety of the nucleoside through a stable P–C bond so they are resistant towards degradation by cellular enzymes. Due to “by-passing” of the first phosphorylating step, a number of ANPs proved to be active against a broad range of DNA viruses and retroviruses, and during the course of some 30 years, they have become a key class of antiviral agents.<sup>12</sup>

To further elucidate the mechanism of antiviral action of BCNAs, which still remains unclear, we decided to synthesize a novel series of 2-(phosphonmethoxy)ethyl (PME) furo[2,3-*d*]pyrimidin-2(3*H*)-ones,<sup>13</sup> stable analogues of nucleotides that by-pass the first phosphorylation step. It is the first time that a combination of the furo[2,3-*d*]pyrimidin-2(3*H*)-one base and the acyclic nucleoside phosphonate moiety is reported.

## Results and discussion

### Chemistry

The furo[2,3-*d*]pyrimidin-2(3*H*)-one nucleoside analogues are usually prepared by the Sonogashira coupling of various alkynes with 5-iodouracils, followed by Cu(I)-promoted intramolecular cyclization.<sup>1–3</sup> This procedure, with some modifications and optimization, was applied in the present work.

Recently, 5-bromouracil derivative was used to modify 1-[2-(phosphonmethoxy)ethyl]uracil (PMEU) analogues in the C-5 position of the uracil moiety via Pd-catalysed Suzuki–Miyaura coupling.<sup>14</sup> No record of the protected 5-iodo-1-[2-(phosphonmethoxy)ethyl]uracil intermediate was found in the literature even though the 5-iodouracil compounds could be expected to be more reactive toward cross-coupling reactions compared to their 5-bromouracil counterparts. Thus, we decided to prepare the novel 5-iodouracil analogue as a suitable starting material for subsequent syntheses.

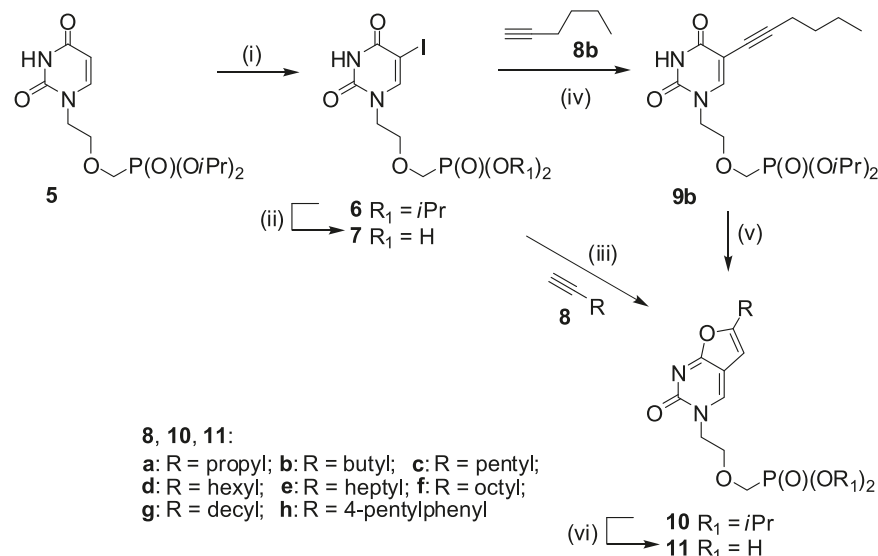
Starting PMEU compound **5** was prepared by a previously described procedure:<sup>15</sup> reaction of 4-methoxypyrimidin-2(1*H*)-one<sup>16</sup> with diisopropyl [(2-chloroethoxy)methyl]phosphonate<sup>17</sup> in the presence of sodium hydride followed by hydrolysis in aqueous methanol using Dowex 50 (H<sup>+</sup> form). A much improved yield was obtained during the alkylation step (79%) compared to the original procedure (49%).<sup>15</sup> The major difference in our procedure seems to be neutralization of the reaction mixture before the work-up (evaporation of solvents) to avoid possible product decomposition, since a slight excess of NaH is used for the alkylation reaction.

The desired 5-iodouracil derivative (**6**) was prepared by the reaction of compound **5** with iodine and ammonium cerium(IV)nitrate (CAN) in refluxing acetonitrile (Scheme 1).<sup>18</sup> This reactive intermediate can be conveniently prepared as a white product by recrystallization in 90% yield. Treatment of compound **6** with bromo(trimethyl)silane in a mixture of acetonitrile/2,6-lutidine (~5:1) afforded the free phosphonic acid (**7**). The presence of the sterically hindered mild base 2,6-lutidine is required to neutralize forming HBr and thus prevent exchange of iodine atom in the C-5 position for bromine or proton during the reaction and (or) its work-up.

Furo[2,3-*d*]pyrimidin-2(3*H*)-ones (**10**) were prepared in moderate to high yields (50%–90% isolated yields for two in situ steps) by the Sonogashira coupling of various terminal alkynes (**8**) with 5-iodouracil derivative (**6**), followed by in situ Cu(I)-promoted intramolecular cyclization (Scheme 1).



**Scheme 1.** Reagents: (i)  $I_2$ , CAN,  $CH_3CN$ , 80 °C; (ii)  $(CH_3)_3SiBr$ , 2,6-lutidine,  $CH_3CN$ , RT; (iii)  $Pd(Ph_3P)_4$ , CuI,  $Et_3N$ , DMF, 50 °C, then CuI and 90 °C; (iv)  $Pd(Ph_3P)_4$ , CuI,  $Et_3N$ , DMF (or THF), 50 °C; (v) CuI,  $Et_3N$ , MeOH, reflux; (vi)  $(CH_3)_3SiBr$ ,  $CH_3CN$ , RT.



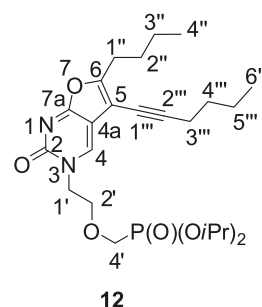
The lower yields can be attributed to difficult crystallization/precipitation of highly lipophilic compounds (**10**). Nevertheless, the purity of diesters (**10**) proved to be very important to ultimately obtain the pure final products (**11**). Also, extraction of the reaction mixture with aqueous EDTA solution during the work-up is necessary to get pure diesters (**10**) with matching elemental analyses since phosphonates strongly bind metal ions. Finally, the free phosphonic acids (**11**) were prepared by standard treatment of compounds **10** with bromo(trimethyl)silane in acetonitrile followed by hydrolysis.

Similarly, as during the BCNAs synthesis,<sup>1-3</sup> 5-alkynyl intermediates (**9**) were not isolated. Formation of compounds **9** and their conversion to fluorescent bicyclic products (**10**) was monitored by thin-layer chromatography (TLC). There were often fluorescent and nonfluorescent byproducts observed, so we tried to optimize the reaction conditions. The best yields of compounds **10** were obtained by the addition of fresh CuI (0.5 equiv.) and by increasing the reaction temperature from 50–90 °C after the starting compound **6** was completely consumed (TLC, ~1 h).

In spite of the fact that Sonogashira coupling and in situ cyclization is a very practical procedure, which gives high overall yields of furo[2,3-*d*]pyrimidin-2(3*H*)-ones (**10**), we decided to prepare, isolate, and fully characterize one of the intermediate 5-alkynyluracils and use it as pure starting compound in the next cyclization step. Thus, coupling of the 5-iodouracil derivative (**6**) with 1.3 equiv. of 1-hexyne (**8b**) under standard Sonogashira coupling conditions ( $Pd(Ph_3P)_4$ , CuI,  $Et_3N$ , DMF, 50 °C, 2 h) afforded the 5-hexynyluracil derivative (**9b**) in 82% yield (Scheme 1). Fluorescent byproduct was clearly visible on the TLC plate and the corresponding 6-butylfuro[2,3-*d*]pyrimidin-2(3*H*)-one (**10b**) was isolated from the reaction mixture in 2% yield.

Treatment of the 5-hexynyluracil derivative (**9b**) with CuI (1 equiv.) in a mixture of MeOH/ $Et_3N$  (3:2) at reflux gave the cyclized product **10b** in 90% yield. The calculated overall yield of compound **10b** starting from 5-iodouracil derivative (**6**) was 74% and is comparable to the yield of

**Fig. 2.** Structure of compound **12** with atom numbering of the substituted furo[2,3-*d*]pyrimidin-2(3*H*)-ones used for assignment of NMR signals.

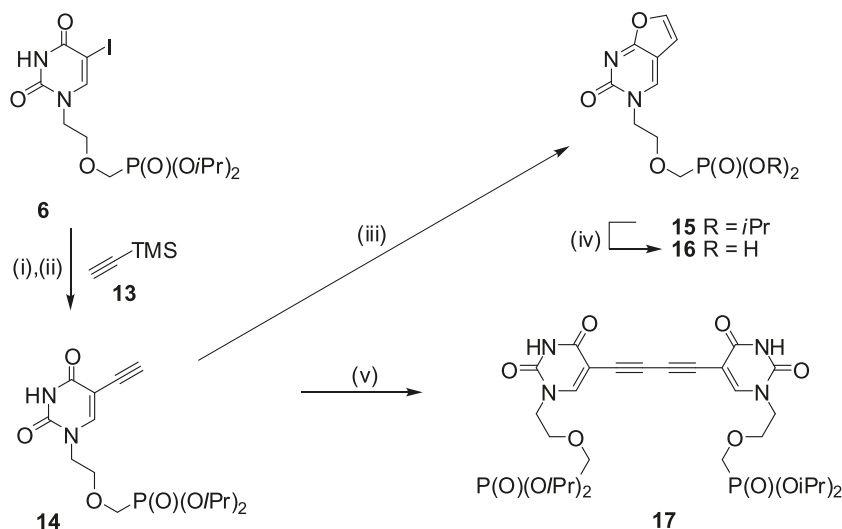


compound **10b** (78%) prepared by the standard in situ synthesis in the DMF/ $Et_3N$  mixture. Although, not all reaction steps were optimized, the comparison of the results of the in situ procedure with the two-pot-reaction sequence clearly shows that the in situ approach for general preparation of furo[2,3-*d*]pyrimidin-2(3*H*)-ones is preferable and more economic.

For comparison, the Sonogashira coupling of the 5-iodouracil derivative (**6**) with 1-hexyne (**8b**) was carried out using THF as a solvent instead of DMF. In this case, the 5-hexynyluracil derivative (**9b**) was isolated only in 59% yield (compared to 82% in DMF) together with 5,6-disubstituted furo[2,3-*d*]pyrimidin-2(3*H*)-one (**12**) as a byproduct (Fig. 2). Formation of a similar type of byproduct during synthesis of bicyclic nucleoside analogues was previously reported by the group of McGuigan.<sup>19</sup>

To prepare the parent furo[2,3-*d*]pyrimidin-2(3*H*)-one derivative unsubstituted at the C-6 position, ethynyl(trimethyl)silane (**13**) was coupled with the starting 5-iodouracil compound (**6**) followed by deprotection of the trimethylsilyl group with TBAF/THF (Scheme 2). The desired 5-ethynyluracil derivative (**14**) was obtained in 63% yield, but its subsequent cyclization with CuI did not proceed well and the reactions usually afforded complex mixtures. The best

**Scheme 2.** Reagents: (i) Pd(Ph<sub>3</sub>P)<sub>4</sub>, CuI, Et<sub>3</sub>N, DMF, 70 °C; (ii) TBAF, THF, RT; (iii) CuI, Et<sub>3</sub>N, EtOAc, reflux; (iv) (CH<sub>3</sub>)<sub>3</sub>SiBr, CH<sub>3</sub>CN, RT; (v) CuI, Et<sub>3</sub>N, MeOH, reflux.



yield (38%) of the furo[2,3-*d*]pyrimidin-2(3*H*)-one (**15**) was achieved by the Cu(I)-promoted intramolecular cyclization in an EtOAc/Et<sub>3</sub>N mixture. Similar reaction of compound **14** with 1 equiv. of CuI in the MeOH/Et<sub>3</sub>N mixture gave a complex mixture from which only a dimeric product of Eglinton coupling,<sup>20</sup> compound **17**, was isolated in 10% yield (Scheme 2). Finally, free phosphonic acid (**16**) was prepared from compound **15** by the standard procedure in 74% yield (Scheme 2).

### Biological activity

All the final 3-[2-(phosphonomethoxy)ethyl]furo[2,3-*d*]pyrimidin-2(3*H*)-ones (**11**) and **16** were evaluated for their inhibitory activity against a variety of DNA viruses including herpes simplex virus type 1 (KOS) (HSV-1), HSV-2 (G), varicella-zoster virus (VZV) (thymidine kinase (TK) competent (TK<sup>+</sup>) and TK deficient (TK<sup>-</sup>)), vaccinia virus (Lederle), human cytomegalovirus (HCMV) (Davis) and the lentiviruses, and human immunodeficiency virus type 1 (HIV-1) (III<sub>B</sub>) and HIV-2 (ROD). Interestingly, none of the compounds tested were active at subtoxic concentrations, including **11f** and **11h**, which represent the corresponding analogues of the BCNA prototypes Cf 1368 and Cf 1743.<sup>3,5</sup> These data revealed that the acyclic nucleotide analogues of furo[2,3-*d*]pyrimidin-2(3*H*)-ones (**11**) and **16**, designed to by-pass the first phosphorylation step necessary for the anti-VZV activity of BCNAs, may not be further metabolized to their active antiviral metabolites and (or) the compounds may not be recognized as an inhibitor at their eventual antiviral target.

### Conclusions

In conclusion, novel series of the 2-(phosphonomethoxy)ethyl derivatives of 6-alkylfuro[2,3-*d*]pyrimidin-2(3*H*)-ones was effectively synthesized by a convenient one-pot procedure consisting of Sonogashira coupling of the 5-iodouracil compound (**6**) with 1-alkynes (**8**) and subsequent Cu(I)-promoted cyclization. For this purpose, protected 5-iodo-1-[2-(phosphonomethoxy)ethyl]uracil (**6**) was prepared as a suitable

starting compound. An example of Sonogashira reaction product, the 5-hexynyluracil derivative (**9b**) was isolated and fully characterized, as well as the product **12**, which was formed during the coupling procedure in THF. Bearing in mind the same overall yields of 6-butylfuro[2,3-*d*]pyrimidin-2(3*H*)-one derivative (**10b**), the in situ coupling-intramolecular cyclization is clearly preferable to two-pot synthesis with isolation of the 5-hexynyluracil intermediate (**9b**). Coupling of the 5-iodouracil derivative (**6**) with ethynyl(trimethyl)silane (**13**) under the Sonogashira reaction conditions, followed by removal of the TMS group, afforded the 5-ethynyluracil derivative (**14**). Intramolecular cyclization of compound **14** in EtOAc gave the desired furo[2,3-*d*]pyrimidin-2(3*H*)-one (**15**), while a similar reaction in MeOH only afforded a dimer (**17**) in very low yield. Free phosphonic acids (**11** and **16**) were obtained by the standard deprotection of the corresponding diesters (**10** and **15**). None of the compounds tested were active in any of the antiviral assays.

### Experimental section

Solvents were dried by standard procedures. Tetrahydrofuran (THF) was freshly distilled from sodium/benzophenone under argon. All 1-alkynes, Pd(Ph<sub>3</sub>P)<sub>4</sub>, and CuI are commercially available from Sigma-Aldrich. TLC was performed on plates of Kieselgel 60 F254 (Merck). If not stated otherwise, NMR spectra were recorded on Bruker Avance 400 (<sup>1</sup>H at 400.0 MHz, <sup>13</sup>C at 100.6 MHz) in CDCl<sub>3</sub>, DMSO-*d*<sub>6</sub>, or D<sub>2</sub>O. NMR spectra of several compounds were recorded on Bruker Avance 600 spectrometer (<sup>1</sup>H at 600.0 MHz, <sup>13</sup>C at 150.9 MHz) or Bruker Avance 500 (<sup>1</sup>H at 500.0 MHz, <sup>13</sup>C at 125.8 MHz). Chemical shifts (in ppm, δ scale) were referenced to the solvent signal (CDCl<sub>3</sub> δ: 7.26 ppm for <sup>1</sup>H NMR and δ: 77.0 ppm for <sup>13</sup>C NMR, DMSO-*d*<sub>6</sub> for <sup>1</sup>H NMR δ: 2.5 ppm and for <sup>13</sup>C δ: 39.7 ppm). Chemical shifts in D<sub>2</sub>O were referenced to 1,4-dioxane for <sup>1</sup>H NMR δ: 3.75 ppm and for <sup>13</sup>C NMR δ: 67.19 ppm. Melting points were determined on a Büchi melting point B-545 apparatus and are uncorrected. UV spectra were measured on a DU spectrophotometer with solutions

in MeOH. Mass spectra were measured on a LCQ classic spectrometer using electrospray ionization (ESI). All new compounds were fully characterized by mass spectrometry, NMR spectroscopy, and elemental analysis (or HR mass spectrometry in the case of compounds **6**, **10h**, **12**, and **17**). Complete assignment of all NMR signals using a combination of  $^1\text{H}$ - $^1\text{H}$  COSY,  $^1\text{H}$ - $^{13}\text{C}$  HSQC, and  $^1\text{H}$ - $^{13}\text{C}$  HMBC methods is provided.

### 1-{2-[(Diisopropoxyphosphoryl)methoxy]ethyl}-5-iodouracil (**6**)

A solution of **5** (8.28 g, 24.78 mmol), CAN (6.79 g, 12.39 mmol), and iodine (8.18 g, 32.22 mmol) in dry acetonitrile (240 mL) was stirred at 80 °C under an inert atmosphere until the starting material was completely consumed after 3 h as monitored by TLC analysis (5% MeOH/ $\text{CHCl}_3$ ). Volatiles were evaporated, and the residue was dissolved in EtOAc (250 mL) and washed with ice cold 5%  $\text{Na}_2\text{S}_2\text{O}_3$  (aq., 130 mL) and brine (50 mL). Organics were dried ( $\text{MgSO}_4$ ), filtered, and solvents evaporated. The crude product was crystallized (EtOAc) to give **6** (10.40 g, 87%) as white crystals; mp 114 °C.  $^1\text{H}$  NMR ( $\text{DMSO}-d_6$ )  $\delta$ : 11.66 (bs, 1H, NH), 8.07 (s, 1H, H-6), 4.56 (dh, 2H,  $J_{\text{H,P}} = 7.7$  Hz,  $J_{\text{vic}} = 6.2$  Hz, POCH), 3.87 (m, 2H, H-1'), 3.77 (d, 2H,  $J_{\text{H,P}} = 8.3$  Hz, H-4'), 3.69 (m, 2H, H-2'), 1.23 and 1.21 (2  $\times$  d, 2  $\times$  6H,  $J_{\text{vic}} = 6.2$  Hz,  $\text{CH}_3$ ).  $^{13}\text{C}$  NMR ( $\text{DMSO}-d_6$ )  $\delta$ : 161.1 (C-4), 150.7 (C-2), 150.5 (C-6), 70.3 (d,  $J_{\text{C,P}} = 6.4$  Hz, POC), 69.9 (d,  $J_{\text{C,P}} = 11.6$  Hz, C-2'), 67.7 (C-5), 64.9 (d,  $J_{\text{C,P}} = 163.8$  Hz, C-4'), 47.4 (C-1'), 23.9 (d,  $J_{\text{C,P}} = 3.8$  Hz,  $\text{CH}_3$ ), 23.8 (d,  $J_{\text{C,P}} = 4.5$  Hz,  $\text{CH}_3$ ). MS (ESI)  $m/z$ : 459  $[\text{M} - \text{H}]^-$ . HR-MS (ESI)  $m/z$ :  $\text{C}_{13}\text{H}_{21}\text{N}_2\text{IO}_6\text{P}$   $[\text{M} - \text{H}]^-$ . Anal. calcd.: 459.0176; found: 459.0181.

### 5-Iodo-1-[2-(phosphonomethoxy)ethyl]uracil (**7**)

A mixture of compound **6** (230 mg, 0.50 mmol), bromo-(trimethyl)silane (0.90 mL, 1.04 g, 6.82 mmol), and 2,6-lutidine (0.70 mL, 648 mg, 6.00 mmol) in acetonitrile (5 mL) was stirred overnight at room temperature. The mixture was concentrated in vacuo and then codistilled with acetonitrile (3  $\times$  5 mL). The residue was dissolved in 50% aqueous methanol (20 mL) and concd HCl was added until the pH was between 2 and 3. After 1 h at room temperature, the solvents were evaporated to dryness and the residue was purified using HPLC (20%–100% aq. MeOH) and crystallized ( $\text{H}_2\text{O}$ ) to give **7** (70 mg, 37%) as white crystals; mp 194 °C. UV-vis  $\lambda_{\text{max}}$  (nm) ( $\epsilon$  ((mol/L) $^{-1}$  cm $^{-1}$ ): 286 (16 300).  $^1\text{H}$  NMR ( $\text{DMSO}-d_6$ )  $\delta$ : 11.64 (bs, 1H, NH), 8.10 (s, 1H, H-6), 3.85 (m, 2H, H-1'), 3.68 (m, 2H, H-2'), 3.57 (d, 2H,  $J_{\text{H,P}} = 8.4$  Hz, H-4').  $^{13}\text{C}$  NMR ( $\text{DMSO}-d_6$ )  $\delta$ : 161.1 (C-4), 150.8 (C-2), 150.5 (C-6), 69.7 (d,  $J_{\text{C,P}} = 9.8$  Hz, C-2'), 67.8 (C-5), 66.5 (d,  $J_{\text{C,P}} = 159.7$  Hz, C-4'), 47.1 (C-1'). MS (ESI)  $m/z$ : 374.9  $[\text{M} - \text{H}]^-$ . Anal. calcd. for  $\text{C}_7\text{H}_{10}\text{N}_2\text{IO}_6\text{P} \cdot 2/3\text{H}_2\text{O}$  (388.05): C 21.67, H 2.94, N 7.22, I 32.70, P 7.98; found: C 21.67, H 3.13, N 6.92, I 32.96, P 7.77.

### Sonogashira coupling of 5-iodouracil derivative (**6**) with 1-hexyne (**8b**)

#### Method A

A stirred suspension of **6** (690 mg, 1.50 mmol),  $\text{Pd}(\text{Ph}_3\text{P})_4$  (87 mg, 75  $\mu\text{mol}$ ), CuI (87 mg, 0.46 mmol), and 1-hexyne

(**8b**, 0.22 mL, 160 mg, 1.95 mmol) in dry and deoxygenated DMF/ $\text{Et}_3\text{N}$  (10:1, 20 mL) was heated under argon at 50 °C for 2 h. Volatiles were flash evaporated, the residue was extracted with hot MeOH (3  $\times$  30 mL), and the solid was filtered off. Volatiles were evaporated, the residue was dissolved in  $\text{CHCl}_3$  (50 mL) and washed (2  $\times$  30 mL of saturated EDTA (aq.), 1  $\times$  20 mL  $\text{H}_2\text{O}$ ). Organics were dried ( $\text{MgSO}_4$ ) and filtered. Flash chromatography (4% MeOH in  $\text{CHCl}_3$ ) afforded compounds **9b** (512 mg, 82%) as brownish oil and **10b** (11 mg, 2%) as yellow foam.

### 1-{2-[(Diisopropoxyphosphoryl)methoxy]ethyl}-5-(1-hexynyl)uracil (**9b**)

$^1\text{H}$  NMR ( $\text{CDCl}_3$ )  $\delta$ : 9.00 (bs, 1H, NH), 7.48 (s, 1H, H-6), 4.73 (dh, 2H,  $J_{\text{H,P}} = 7.7$  Hz,  $J_{\text{vic}} = 6.2$  Hz, POCH), 3.93 (m, 2H, H-1'), 3.79 (m, 2H, H-2'), 3.73 (d, 2H,  $J_{\text{H,P}} = 8.4$  Hz, H-4'), 2.36 (t, 2H,  $J_{\text{vic}} = 7.1$  Hz, H-3''), 1.57–1.50 (m, 2H, H-4''), 1.46–1.36 (m, 2H, H-5''), 1.35–1.28 (m, 12H,  $\text{CH}_3$ ), 0.90 (t, 3H,  $J_{\text{vic}} = 7.3$  Hz, H-6'').  $^{13}\text{C}$  NMR ( $\text{CDCl}_3$ )  $\delta$ : 162.1 (C-4), 149.8 (C-2), 147.4 (C-6), 100.2 (C-5), 95.2 (C-2''), 71.2 (d,  $J_{\text{C,P}} = 6.7$  Hz, POC), 70.8 (C-1''), 70.7 (d,  $J_{\text{C,P}} = 10.5$  Hz, C-2'), 66.2 (d,  $J_{\text{C,P}} = 167.8$  Hz, C-4'), 48.8 (C-1'), 30.6 (C-3''), 24.02 (d,  $J_{\text{C,P}} = 3.8$  Hz,  $\text{CH}_3$ ), 23.96 (d,  $J_{\text{C,P}} = 4.5$  Hz,  $\text{CH}_3$ ), 22.0 (C-4''), 19.3 (C-5''), 13.6 (C-6''). MS (ESI)  $m/z$ : 415  $[\text{M} + \text{H}]^+$ . HR-MS (ESI)  $m/z$ :  $\text{C}_{19}\text{H}_{31}\text{N}_2\text{O}_6\text{P}$ -Na  $[\text{M} + \text{Na}]^+$ . Anal. calcd.: 437.1810; found: 437.1812.

### 6-Butyl-3-{2-[(diisopropoxyphosphoryl)methoxy]ethyl}furo[2,3-d]pyrimidin-2(3H)-one (**10b**)

$^1\text{H}$  and  $^{13}\text{C}$  NMR data were identical with compound **10b** prepared from compound **6** by the General Procedure A.

#### Method B

A stirred suspension of **6** (230 mg, 0.50 mmol),  $\text{Pd}(\text{Ph}_3\text{P})_4$  (29 mg, 25  $\mu\text{mol}$ ), CuI (20 mg, 0.11 mmol), 1-hexyne (0.17 mL, 122 mg, 1.49 mmol), and  $\text{Et}_3\text{N}$  (0.21 mL) in dry and deoxygenated THF (10 mL) was stirred under argon at 50 °C for 3 h. Volatiles were flash evaporated, the residue was extracted with hot MeOH (3  $\times$  30 mL), and the solid was filtered off. Volatiles were evaporated, the residue was dissolved in EtOAc (30 mL) and washed (2  $\times$  10 mL of saturated EDTA (aq.), 1  $\times$  10 mL  $\text{H}_2\text{O}$ ). Organics were dried ( $\text{MgSO}_4$ ) and filtered. Flash chromatography (5% MeOH/ $\text{CHCl}_3$ ) afforded compounds **9b** (246 mg, 59%) as a yellow oil and **12** as a yellowish oil (60 mg, 12%).

### 1-{2-[(Diisopropoxyphosphoryl)methoxy]ethyl}-5-(1-hexynyl)uracil (**9b**)

$^1\text{H}$  and  $^{13}\text{C}$  NMR data were identical with compound **9b** prepared by Method A.

### Diisopropyl {(2-[6-butyl-2-oxo-5-(hexyn-1-yl)furo[2,3-d]pyrimidin-3(2H)-yl]ethoxy)methyl}phosphonate (**12**)

$^1\text{H}$  NMR (500.0 MHz,  $\text{CDCl}_3$ )  $\delta$ : 7.89 (s, 1H, H-4), 4.68 (dh, 2H,  $J_{\text{H,P}} = 7.7$  Hz,  $J_{\text{vic}} = 6.2$  Hz, POCH), 4.21 (m, 2H, H-1'), 3.91 (m, 2H, H-2'), 3.69 (d, 2H,  $J_{\text{H,P}} = 8.6$  Hz, H-4'), 2.73 (t, 2H,  $J_{\text{vic}} = 7.4$  Hz, H-1''), 2.41 (t, 2H,  $J_{\text{vic}} = 7.1$  Hz, H-3''), 1.68 (m, 2H, H-2''), 1.57 and 1.46 (2  $\times$  m, 2  $\times$  2H, H-4''' and H-5'''), 1.36 (m, 2H, H-3'''), 1.28 and 1.24 (2  $\times$  d, 2  $\times$  6H,  $J_{\text{vic}} = 6.2$  Hz,  $\text{CH}_3$ ), 0.94 (t, 3H,  $J_{\text{vic}} = 7.4$  Hz, H-6'''), 0.93 (t, 3H,  $J_{\text{vic}} = 7.3$  Hz, H-4'').  $^{13}\text{C}$  NMR (125.8 MHz,  $\text{CDCl}_3$ )  $\delta$ : 170.7 (C-7a), 162.0 (C-6), 155.3 (C-2), 140.8 (C-



4), 107.7 (C-4a), 97.8 (C-5), 97.2 (C-2'''), 71.1 (d,  $J_{C,P}$  = 6.6 Hz, POCH), 70.3 (d,  $J_{C,P}$  = 11.6 Hz, C-2'), 68.2 (C-1'''), 66.1 (d,  $J_{C,P}$  = 168.2 Hz, C-4'), 52.1 (C-1'), 30.6 (C-4'''), 29.0 (C-2''), 26.8 (C-1''), 24.0 (d,  $J_{C,P}$  = 3.8 Hz, CH<sub>3</sub>), 23.9 (d,  $J_{C,P}$  = 4.6 Hz, CH<sub>3</sub>), 22.0 (C-5''' and C-3''), 19.2 (C-3'''), 13.6 (C-6''' and C-4''). MS (ESI)  $m/z$ : 495 [M + H]<sup>+</sup>. HR-MS (ESI)  $m/z$ : C<sub>25</sub>H<sub>40</sub>N<sub>2</sub>O<sub>6</sub>P [M + H]<sup>+</sup>. Anal. calcd.: 495.2618; found: 495.2616.

### 6-Butyl-3-{2-[(diisopropoxyphosphoryl)methoxy]ethyl}furo[2,3-d]pyrimidin-2(3H)-one (10b)

A stirred suspension of **9b** (438 mg, 1.06 mmol) and CuI (200 mg, 1.05 mmol) in a mixture of MeOH (30 mL) and Et<sub>3</sub>N (20 mL) was refluxed for 2 h. Volatiles were flash evaporated, the residue was extracted with hot MeOH (3 × 30 mL), and the solid was filtered off. Volatiles were evaporated, the residue was dissolved in CHCl<sub>3</sub> (50 mL) and washed (2 × 30 mL of saturated EDTA (aq.)), 1 × 20 mL H<sub>2</sub>O). Organics were dried (MgSO<sub>4</sub>), filtered, and the product was isolated by flash chromatography (4% MeOH/CHCl<sub>3</sub>) and crystallized (EtOAc/Et<sub>2</sub>O) to give **10b** (375 mg, 90%) as white crystals; mp 142 °C. <sup>1</sup>H and <sup>13</sup>C NMR data were identical with compound **10b** prepared from compound **6** by General procedure A.

### Synthesis of furo[2,3-d]pyrimidin-2(3H)-ones (10) by Sonogashira coupling of 5-iodouracil derivative (6) with 1-alkynes (8) followed by in situ intramolecular cyclization

#### General procedure A

A stirred suspension of **6**, Pd(Ph<sub>3</sub>P)<sub>4</sub> (0.05 equiv.), CuI (0.5 equiv.), and 1-alkyne (**8**; 1.3 equiv.) in dry and deoxygenated DMF/Et<sub>3</sub>N was stirred under argon at 50 °C for 2–3 h. TLC (5% MeOH/CHCl<sub>3</sub>) showed complete conversion to a faster-migrating product. CuI (0.5 equiv.) was added and the reaction mixture was stirred at 90 °C for 2–4 h. TLC (5% MeOH/CHCl<sub>3</sub>) showed complete conversion of the intermediate 6-alkynyl derivative to a fluorescent product (**10**). Volatiles were flash evaporated, the residue was dissolved in hot MeOH, and the solid filtered off. Volatiles were evaporated and the residue was dissolved in CHCl<sub>3</sub> (80 mL). Organics were washed (2 × 10 mL of saturated EDTA (aq.)), 1 × 10 mL H<sub>2</sub>O) and dried (MgSO<sub>4</sub>). After filtration and evaporation, the product was isolated by flash chromatography (5% MeOH/CHCl<sub>3</sub>) and crystallized from a mixture of EtOAc with other organic solvents (hexanes, EtOH, Et<sub>2</sub>O).

### 3-{2-[(Diisopropoxyphosphoryl)methoxy]ethyl}-6-propylfuro[2,3-d]pyrimidin-2(3H)-one (10a)

Treatment of **6** (690 mg, 1.50 mmol) with 1-pentyne (**8a**; 0.19 mL, 133 mg, 1.95 mmol) by General procedure A gave **10a** (402 mg, 67%) as white crystals (EtOAc/hexanes 1:1); mp 128 °C. <sup>1</sup>H NMR (500.0 MHz, CDCl<sub>3</sub>) δ: 7.94 (s, 1H, H-4), 6.09 (t, 1H,  $J_{5,1''}$  = 1.1 Hz, H-5), 4.68 (dh, 2H,  $J_{H,P}$  = 7.7 Hz,  $J_{vic}$  = 6.2 Hz, POCH), 4.22 (m, 2H, H-1'), 3.91 (m, 2H, H-2'), 3.70 (d, 2H,  $J_{H,P}$  = 8.6 Hz, H-4'), 2.63 (td, 2H,  $J_{vic}$  = 7.4 Hz,  $J_{1'',5}$  = 1.1 Hz, H-1''), 1.72 (h, 2H,  $J_{vic}$  = 7.4 Hz, H-2''), 1.29 and 1.25 (2 × d, 2 × 6H,  $J_{vic}$  = 6.2 Hz, CH<sub>3</sub>), 0.99 (t, 3H,  $J_{vic}$  = 7.4 Hz, H-3''). <sup>13</sup>C NMR

(125.8 MHz, CDCl<sub>3</sub>) δ: 172.1 (C-7a), 159.6 (C-6), 155.4 (C-2), 140.5 (C-4), 107.4 (C-4a), 98.5 (C-5), 71.1 (d,  $J_{C,P}$  = 6.7 Hz, POC), 70.6 (d,  $J_{C,P}$  = 11.8 Hz, C-2'), 66.0 (d,  $J_{C,P}$  = 168.8 Hz, C-4'), 51.5 (C-1'), 30.1 (C-1''), 24.0 (d,  $J_{C,P}$  = 3.9 Hz, CH<sub>3</sub>), 23.9 (d,  $J_{C,P}$  = 4.6 Hz, CH<sub>3</sub>), 20.2 (C-2''), 13.5 (C-3''). MS (ESI)  $m/z$ : 399 [M – H]<sup>–</sup>. Anal. calcd. for C<sub>18</sub>H<sub>29</sub>N<sub>2</sub>O<sub>6</sub>P (400.41): C 53.99, H 7.30, N 7.00, P 7.74; found: C 53.94, H 7.35, N 6.86, P 8.02.

### 6-Butyl-3-{2-[(diisopropoxyphosphoryl)methoxy]ethyl}furo[2,3-d]pyrimidin-2(3H)-one (10b)

Treatment of **6** (690 mg, 1.50 mmol) with 1-hexyne (**8b**; 0.22 mL, 160 mg, 1.95 mmol) by General procedure A gave **10b** (485 mg, 78%) as white crystals (EtOAc/Et<sub>2</sub>O); mp 139 °C. <sup>1</sup>H NMR (CDCl<sub>3</sub>) δ: 7.91 (s, 1H, H-4), 6.06 (s, 1H, H-5), 4.66 (dh, 2H,  $J_{H,P}$  = 7.7 Hz,  $J_{vic}$  = 6.2 Hz, POCH), 4.20 (m, 2H, H-1'), 3.88 (m, 2H, H-2'), 3.68 (d, 2H,  $J_{H,P}$  = 8.6 Hz, H-4'), 2.63 (t, 2H,  $J_{vic}$  = 7.5 Hz, H-1''), 1.68–1.61 (m, 2H, H-2''), 1.42–1.31 (m, 2H, H-3''), 1.27 and 1.23 (2 × d, 2 × 6H,  $J_{vic}$  = 6.2 Hz, CH<sub>3</sub>), 0.92 (t, 3H,  $J_{vic}$  = 7.4 Hz, H-4''). <sup>13</sup>C NMR (CDCl<sub>3</sub>) δ: 172.1 (C-7a), 159.7 (C-6), 155.3 (C-2), 140.4 (C-4), 107.3 (C-4a), 98.4 (C-5), 71.0 (d,  $J_{C,P}$  = 6.7 Hz, POC), 70.6 (d,  $J_{C,P}$  = 11.8 Hz, C-2'), 66.1 (d,  $J_{C,P}$  = 168.8 Hz, C-4'), 51.5 (C-1'), 28.8 (C-1''), 27.9 (C-2''), 24.0 (d,  $J_{C,P}$  = 3.9 Hz, CH<sub>3</sub>), 23.9 (d,  $J_{C,P}$  = 4.6 Hz, CH<sub>3</sub>), 22.0 (C-3''), 13.6 (C-4''). MS (ESI)  $m/z$ : 415 [M + H]<sup>+</sup>. Anal. calcd. for C<sub>19</sub>H<sub>31</sub>N<sub>2</sub>O<sub>6</sub>P (414.43): C 55.06, H 7.54, N 6.76, P 7.47; found: C 55.12, H 7.63, N 6.70, P 7.69.

### 3-{2-[(Diisopropoxyphosphoryl)methoxy]ethyl}-6-pentylfuro[2,3-d]pyrimidin-2(3H)-one (10c)

Treatment of **6** (464 mg, 1.01 mmol) with 1-heptyne (**8c**; 0.17 mL, 126 mg, 1.31 mmol) by General procedure A gave **10c** (343 mg, 79%) as white crystals (EtOAc/EtOH); mp 120 °C. <sup>1</sup>H NMR (CDCl<sub>3</sub>) δ: 7.91 (s, 1H, H-4), 6.06 (s, 1H, H-5), 4.65 (dh, 2H,  $J_{H,P}$  = 7.7 Hz,  $J_{vic}$  = 6.2 Hz, POCH), 4.20 (m, 2H, H-1'), 3.89 (m, 2H, H-2'), 3.68 (d, 2H,  $J_{H,P}$  = 8.6 Hz, H-4'), 2.62 (t, 2H,  $J_{vic}$  = 7.2 Hz, H-1''), 1.70–1.63 (m, 2H, H-2''), 1.35–1.29 (m, 4H, H-3'' and H-4''), 1.25 and 1.21 (2 × d, 2 × 6H,  $J_{vic}$  = 6.2 Hz, CH<sub>3</sub>), 0.88 (t, 3H,  $J_{vic}$  = 7.0 Hz, H-5''). <sup>13</sup>C NMR (CDCl<sub>3</sub>) δ: 172.1 (C-7a), 159.8 (C-6), 155.3 (C-2), 140.4 (C-4), 107.4 (C-4a), 98.4 (C-5), 71.0 (d,  $J_{C,P}$  = 6.8 Hz, POC), 70.6 (d,  $J_{C,P}$  = 11.8 Hz, C-2'), 66.1 (d,  $J_{C,P}$  = 168.8 Hz, C-4'), 51.5 (C-1'), 31.1 (C-1''), 28.2 (C-2''), 26.4 (C-3''), 24.0 (d,  $J_{C,P}$  = 3.9 Hz, CH<sub>3</sub>), 23.9 (d,  $J_{C,P}$  = 4.6 Hz, CH<sub>3</sub>), 22.2 (C-4''), 13.9 (C-5''). MS (ESI)  $m/z$ : 429 [M + H]<sup>+</sup>. Anal. calcd. for C<sub>20</sub>H<sub>33</sub>N<sub>2</sub>O<sub>6</sub>P (428.21): C 56.06, H 7.76, N 6.54, P 7.23; found: C 56.11, H 7.89, N 6.47, P 7.49.

### 3-{2-[(Diisopropoxyphosphoryl)methoxy]ethyl}-6-hexylfuro[2,3-d]pyrimidin-2(3H)-one (10d)

Treatment of **6** (920 mg, 2.00 mmol) with 1-octyne (**8d**; 0.38 mL, 287 mg, 2.60 mmol) by General procedure A gave **10d** (586 mg, 64%) as white crystals (EtOAc/hexanes); mp 118 °C. <sup>1</sup>H NMR (CDCl<sub>3</sub>) δ: 7.92 (s, 1H, H-4), 6.06 (s, 1H, H-5), 4.65 (dh, 2H,  $J_{H,P}$  = 7.7 Hz,  $J_{vic}$  = 6.2 Hz, POCH), 4.20 (m, 2H, H-1'), 3.89 (m, 2H, H-2'), 3.68 (d, 2H,  $J_{H,P}$  = 8.6 Hz, H-4'), 2.62 (t, 2H,  $J_{vic}$  = 7.2 Hz, H-1''), 1.70–1.62 (m, 2H, H-2''), 1.40–1.19 (m, 18H, H-3'' and H-4'' and H-5'' and CH<sub>3</sub>), 0.87 (t, 3H,  $J_{vic}$  = 6.9 Hz, H-6''). <sup>13</sup>C NMR (CDCl<sub>3</sub>) δ: 172.1



(C-7a), 159.8 (C-6), 155.3 (C-2), 140.4 (C-4), 107.4 (C-4a), 98.4 (C-5), 71.0 (d,  $J_{C,P}$  = 6.8 Hz, POC), 70.6 (d,  $J_{C,P}$  = 11.8 Hz, C-2'), 66.1 (d,  $J_{C,P}$  = 168.8 Hz, C-4'), 51.5 (C-1'), 31.4 (C-1''), 28.6 (C-2''), 28.2 (C-3''), 26.7 (C-4''), 24.0 (d,  $J_{C,P}$  = 3.9 Hz, CH<sub>3</sub>), 23.9 (d,  $J_{C,P}$  = 4.6 Hz, CH<sub>3</sub>), 22.5 (C-5''), 14.0 (C-6''). MS (ESI)  $m/z$ : 441 [M - H]<sup>-</sup>. Anal. calcd. for C<sub>21</sub>H<sub>35</sub>N<sub>2</sub>O<sub>6</sub>P (442.49): C 57.00, H 7.97, N 6.33, P 7.00; found: C 56.84, H 8.09, N 6.24, P 7.17.

### 3-{2-[(Diisopropoxyphosphoryl)methoxy]ethyl}-6-heptylfuro[2,3-d]pyrimidin-2(3H)-one (10e)

Treatment of **6** (460 mg, 1.00 mmol) with 1-nonyne (**8e**; 0.21 mL, 162 mg, 1.30 mmol) by General procedure A gave **10e** (226 mg, 50%) as white crystals (EtOAc/Et<sub>2</sub>O); mp 116 °C. <sup>1</sup>H NMR (CDCl<sub>3</sub>) δ: 7.92 (s, 1H, H-4), 6.06 (s, 1H, H-5), 4.67 (dh, 2H,  $J_{H,P}$  = 7.7 Hz,  $J_{vic}$  = 6.2 Hz, POCH), 4.21 (m, 2H, H-1'), 3.90 (m, 2H, H-2'), 3.69 (d, 2H,  $J_{H,P}$  = 8.6 Hz, H-4'), 2.63 (t, 2H,  $J_{vic}$  = 7.3 Hz, H-1''), 1.71–1.63 (m, 2H, H-2''), 1.35–1.23 (m, 20H, H-3'' and H-4'' and H-5'' and H-6'' and CH<sub>3</sub>), 0.87 (t, 3H,  $J_{vic}$  = 6.9 Hz, H-7''). <sup>13</sup>C NMR (CDCl<sub>3</sub>) δ: 172.2 (C-7a), 159.9 (C-6), 155.4 (C-2), 140.3 (C-4), 107.4 (C-4a), 98.4 (C-5), 71.1 (d,  $J_{C,P}$  = 6.9 Hz, POC), 70.6 (d,  $J_{C,P}$  = 11.8 Hz, C-2'), 66.2 (d,  $J_{C,P}$  = 168.8 Hz, C-4'), 51.5 (C-1'), 31.7 (C-1''), 29.0 (C-2''), 28.9 (C-3''), 28.2 (C-4''), 26.8 (C-5''), 24.01 (d,  $J_{C,P}$  = 3.9 Hz, CH<sub>3</sub>), 23.96 (d,  $J_{C,P}$  = 4.6 Hz, CH<sub>3</sub>), 22.6 (C-6''), 14.0 (C-7''). MS (ESI)  $m/z$ : 457 [M + H]<sup>+</sup>. Anal. calcd. for C<sub>22</sub>H<sub>37</sub>N<sub>2</sub>O<sub>6</sub>P (456.51): C 57.88, H 8.17, N 6.14, P 6.78; found: C 57.67, H 8.14, N 5.99, P 7.05.

### 3-{2-[(Diisopropoxyphosphoryl)methoxy]ethyl}-6-octylfuro[2,3-d]pyrimidin-2(3H)-one (10f)

Treatment of **6** (992 mg, 2.16 mmol) with 1-decyne (**8f**; 0.51 mL, 390 mg, 2.82 mmol) by General procedure A gave **10f** (491 mg, 49%) as white crystals (EtOAc/Et<sub>2</sub>O); mp 114–115 °C. <sup>1</sup>H NMR (CDCl<sub>3</sub>) δ: 7.92 (s, 1H, H-4), 6.06 (s, 1H, H-5), 4.68 (dh, 2H,  $J_{H,P}$  = 7.7 Hz,  $J_{vic}$  = 6.2 Hz, POCH), 4.21 (m, 2H, H-1'), 3.90 (m, 2H, H-2'), 3.69 (d, 2H,  $J_{H,P}$  = 8.6 Hz, H-4'), 2.63 (t, 2H,  $J_{vic}$  = 7.5 Hz, H-1''), 1.72–1.62 (m, 2H, H-2''), 1.39–1.21 (m, 22H, H-3'' and H-4'' and H-5'' and H-6'' and H-7'' and CH<sub>3</sub>), 0.87 (t, 3H,  $J_{vic}$  = 6.8 Hz, H-8''). <sup>13</sup>C NMR (CDCl<sub>3</sub>) δ: 172.1 (C-7a), 159.9 (C-6), 155.3 (C-2), 140.4 (C-4), 107.4 (C-4a), 98.4 (C-5), 71.1 (d,  $J_{C,P}$  = 6.9 Hz, POC), 70.6 (d,  $J_{C,P}$  = 11.8 Hz, C-2'), 66.1 (d,  $J_{C,P}$  = 168.8 Hz, C-4'), 51.5 (C-1'), 31.8 (C-1''), 29.2 (C-2''), 29.1 (C-3''), 29.0 (C-4''), 28.2 (C-5''), 26.8 (C-6''), 24.2 (d,  $J_{C,P}$  = 3.9 Hz, CH<sub>3</sub>), 24.0 (d,  $J_{C,P}$  = 4.6 Hz, CH<sub>3</sub>), 22.6 (C-7''), 14.1 (C-8''). MS (ESI)  $m/z$ : 471 [M + H]<sup>+</sup>. Anal. calcd. for C<sub>23</sub>H<sub>39</sub>N<sub>2</sub>O<sub>6</sub>P (470.54): C 58.71, H 8.35, N 5.95, P 6.58; found: C 58.59, H 8.43, N 5.88, P 6.77.

### 6-Decyl-3-{2-[(diisopropoxyphosphoryl)methoxy]ethyl}furo[2,3-d]pyrimidin-2(3H)-one (10g)

Treatment of **6** (800 mg, 1.74 mmol) with 1-dodecyne (**8g**; 0.48 mL, 376 mg, 2.26 mmol) by General procedure A gave **10g** (700 mg, 81%) as white crystals (EtOAc/hexanes); mp 112 °C. <sup>1</sup>H NMR (CDCl<sub>3</sub>) δ: 7.91 (s, 1H, H-4), 6.05 (s, 1H, H-5), 4.65 (dh, 2H,  $J_{H,P}$  = 7.7 Hz,  $J_{vic}$  = 6.2 Hz, POCH), 4.20 (m, 2H, H-1'), 3.88 (m, 2H, H-2'), 3.68 (d, 2H,  $J_{H,P}$  = 8.6 Hz, H-4'), 2.61 (t, 2H,  $J_{vic}$  = 7.4 Hz, H-1''), 1.72–1.60

(m, 2H, H-2''), 1.33–1.19 (m, 26H, H-3'' and H-4'' and H-5'' and H-6'' and H-7'' and H-8'' and H-9'' and CH<sub>3</sub>), 0.86 (t, 3H,  $J_{vic}$  = 6.9 Hz, H-10''). <sup>13</sup>C NMR (CDCl<sub>3</sub>) δ: 172.1 (C-7a), 159.8 (C-6), 155.3 (C-2), 140.4 (C-4), 107.4 (C-4a), 98.4 (C-5), 71.0 (d,  $J_{C,P}$  = 7.0 Hz, POC), 70.6 (d,  $J_{C,P}$  = 11.8 Hz, C-2'), 66.1 (d,  $J_{C,P}$  = 168.8 Hz, C-4'), 51.5 (C-1'), 31.8 (C-1''), 29.5 (C-2''), 29.4 (C-3''), 29.24 (C-4''), 29.20 (C-5''), 29.0 (C-6''), 28.2 (C-7''), 26.8 (C-8''), 24.0 (d,  $J_{C,P}$  = 3.9 Hz, CH<sub>3</sub>), 23.9 (d,  $J_{C,P}$  = 4.6 Hz, CH<sub>3</sub>), 22.6 (C-9''), 14.1 (C-10''). MS (ESI)  $m/z$ : 521 499 [M + H]<sup>+</sup>. Anal. calcd. for C<sub>25</sub>H<sub>43</sub>N<sub>2</sub>O<sub>6</sub>P (498.59): C 60.22, H 8.69, N 5.62, P 6.21; found: C 59.93, H 8.75, N 5.49, P 6.46.

### 3-{2-[(Diisopropoxyphosphoryl)methoxy]ethyl}-6-(4-pentylphenyl)furo[2,3-d]pyrimidin-2(3H)-one (10h)

Treatment of **6** (460 mg, 1.00 mmol) with (4-pentylphenyl)acetylene (**8h**; 0.25 mL, 224 mg, 1.30 mmol) by General procedure A gave **10h** (232 mg, 46%) as white crystals (EtOAc/hexanes); mp 172 °C. <sup>1</sup>H NMR (500.0 MHz, CDCl<sub>3</sub>) δ: 8.08 (s, 1H, H-4), 7.69–7.67 (m, 2H, *o*-Ph), 7.28–7.26 (m, 2H, *m*-Ph), 6.65 (s, 1H, H-5), 4.70 (dh, 2H,  $J_{H,P}$  = 7.7 Hz,  $J_{vic}$  = 6.2 Hz, POCH), 4.27–4.25 (m, 2H, H-1'), 3.95–3.94 (m, 2H, H-2'), 3.72 (d, 2H,  $J_{H,P}$  = 8.6 Hz, H-4'), 2.67–2.64 (m, 2H, H-1''), 1.66–1.63 (m, 2H, H-2''), 1.37–1.34 (m, 4H, H-3'' and H-4''), 1.30 and 1.27 (2 × d, 2 × 6H,  $J_{vic}$  = 6.2 Hz, CH<sub>3</sub>), 0.92–0.89 (m, 3H, H-5''). <sup>13</sup>C NMR (125.8 MHz, CDCl<sub>3</sub>) δ: 171.9 (C-7a), 155.9 (C-6), 155.3 (C-2), 145.1 (C-*p*-Ph), 141.2 (C-4), 129.0 (C-*m*-Ph), 125.8 (C-*i*-Ph), 124.9 (C-*o*-Ph), 108.0 (C-4a), 96.3 (C-5), 71.1 (d,  $J_{C,P}$  = 6.7 Hz, POC), 70.5 (d,  $J_{C,P}$  = 11.6 Hz, C-2'), 66.1 (d,  $J_{C,P}$  = 168.9 Hz, C-4'), 51.6 (C-1'), 35.8 (C-1''), 31.4 and 30.9 (C-2'' and C-3''), 24.00 (d,  $J_{C,P}$  = 3.9 Hz, CH<sub>3</sub>), 23.95 (d,  $J_{C,P}$  = 4.6 Hz, CH<sub>3</sub>), 22.5 (C-4''), 14.0 (C-5''). MS (ESI)  $m/z$ : 505 [M + H]<sup>+</sup>. HR-MS (ESI)  $m/z$ : C<sub>26</sub>H<sub>38</sub>N<sub>2</sub>O<sub>6</sub>P [M + H]<sup>+</sup>. Anal. calcd.: 505.2462; found: 505.2463.

## Transformation of esters (10) to free phosphonic acids (11)

### General procedure B

The dried starting esters (**10**; 1 mmol), bromo(trimethyl)silane (1.75 mL, 2.03 g, 13.26 mmol), and acetonitrile (10 mL) were stirred at room temperature overnight. The mixture was concentrated in vacuo and then codistilled with a mixture of water/EtOH (9:1, 2 × 5 mL). The residue was crystallized (2 crops) to give free phosphonic acids (**11**).

### 3-{2-(Phosphonomethoxy)ethyl}-6-propylfuro[2,3-d]pyrimidin-2(3H)-one (11a)

Treatment of **10a** (250 mg, 0.62 mmol) gave **11a** (167 mg, 85%) as white crystals (EtOAc/EtOH 3:1); mp 165 °C. UV-vis  $\lambda_{max}$  (nm) ( $\epsilon$  ((mol/L)<sup>-1</sup> cm<sup>-1</sup>): 329 (5400), 242 (8900). <sup>1</sup>H NMR (DMSO-*d*<sub>6</sub>) δ: 8.36 (s, 1H, H-4), 6.41 (s, 1H, H-5), 4.11 (m, 2H, H-1'), 3.78 (m, 2H, H-2'), 3.57 (d, 2H,  $J_{H,P}$  = 8.5 Hz, H-4'), 2.61 (t, 2H,  $J_{vic}$  = 7.4 Hz, H-1''), 1.71–1.58 (m, 2H, H-2''), 0.94 (t, 3H,  $J$  = 7.4 Hz, H-3''). <sup>13</sup>C NMR (DMSO-*d*<sub>6</sub>) δ: 171.5 (C-7a), 157.9 (C-6), 154.6 (C-2), 142.8 (C-4), 106.0 (C-4a), 99.7 (C-5), 69.4 (d,  $J_{C,P}$  = 10.5 Hz, C-2'), 66.5 (d,  $J_{C,P}$  = 159.9 Hz, C-4'), 50.2 (C-1'), 29.4 and 20.0 and 13.5 (6-propyl). MS (ESI)  $m/z$ : 315 [M - H]<sup>-</sup>. Anal. calcd. for C<sub>12</sub>H<sub>17</sub>N<sub>2</sub>O<sub>6</sub>P·1/5H<sub>2</sub>O (319.85): C 45.06, H 5.48, N 8.76, P 9.68; found: C 45.21, H 5.45, N 8.64, P 9.90.

### 6-Butyl-3-[2-(phosphonomethoxy)ethyl]furo[2,3-d]pyrimidin-2(3H)-one (**11b**)

Treatment of **10b** (200 mg, 0.48 mmol) gave **11b** (110 mg, 69%) as white crystals (H<sub>2</sub>O); mp 144 °C. UV-vis  $\lambda_{\text{max}}$  (nm) ( $\epsilon$  ((mol/L)<sup>-1</sup> cm<sup>-1</sup>): 329 (7000), 243 (13 500). <sup>1</sup>H NMR (DMSO-*d*<sub>6</sub>)  $\delta$ : 8.36 (s, 1H, H-4), 6.40 (s, 1H, H-5), 4.11 (m, 2H, H-1'), 3.77 (m, 2H, H-2'), 3.58 (d, 2H,  $J_{\text{H,P}}$  = 8.6 Hz, H-4'), 2.64 (t, 2H,  $J_{\text{vic}}$  = 7.4 Hz, H-1''), 1.68–1.50 (m, 2H, H-2''), 1.42–1.27 (m, 2H, H-3''), 0.90 (t, 3H,  $J$  = 7.4 Hz, H-4''). <sup>13</sup>C NMR (DMSO-*d*<sub>6</sub>)  $\delta$ : 171.5 (C-7a), 158.1 (C-6), 154.6 (C-2), 142.9 (C-4), 106.1 (C-4a), 99.6 (C-5), 69.4 (d,  $J_{\text{C,P}}$  = 10.5 Hz, C-2'), 66.5 (d,  $J_{\text{C,P}}$  = 159.9 Hz, C-4'), 50.3 (C-1'), 28.7 and 27.2 and 21.7 and 13.8 (6-butyl). MS (ESI)  $m/z$ : 329 [M – H]<sup>-</sup>. Anal. calcd. for C<sub>13</sub>H<sub>19</sub>N<sub>2</sub>O<sub>6</sub>P (330.27): C 47.28, H 5.80, N 8.48, P 9.38; found: C 47.14, H 5.76, N 8.33, P 9.59.

### 3-[2-(Phosphonomethoxy)ethyl]-6-pentylfuro[2,3-d]pyrimidin-2(3H)-one (**11c**)

Treatment of **10c** (250 mg, 0.58 mmol) gave **11c** (160 mg, 80%) as white crystals (H<sub>2</sub>O); mp 156 °C. UV-vis  $\lambda_{\text{max}}$  (nm) ( $\epsilon$  ((mol/L)<sup>-1</sup> cm<sup>-1</sup>): 329 (6700), 243 (13 600). <sup>1</sup>H NMR (DMSO-*d*<sub>6</sub>)  $\delta$ : 8.36 (s, 1H, H-4), 6.40 (s, 1H, H-5), 4.11 (m, 2H, H-1'), 3.77 (m, 2H, H-2'), 3.58 (d, 2H,  $J_{\text{H,P}}$  = 8.6 Hz, H-4'), 2.63 (t, 2H,  $J_{\text{vic}}$  = 7.3 Hz, H-1''), 1.61 (m, 2H, H-2''), 1.37–1.26 (m, 4H, H-3'' and H-4''), 0.87 (t, 3H,  $J$  = 6.9 Hz, H-5''). <sup>13</sup>C NMR (DMSO-*d*<sub>6</sub>)  $\delta$ : 171.5 (C-7a), 158.1 (C-6), 154.6 (C-2), 142.9 (C-4), 106.1 (C-4a), 99.6 (C-5), 69.4 (d,  $J_{\text{C,P}}$  = 10.5 Hz, C-2'), 66.5 (d,  $J_{\text{C,P}}$  = 159.9 Hz, C-4'), 50.3 (C-1'), 30.8 and 27.5 and 26.2 and 21.9 and 14.1 (6-pentyl). MS (ESI)  $m/z$ : 343 [M – H]<sup>-</sup>. Anal. calcd. for C<sub>14</sub>H<sub>21</sub>N<sub>2</sub>O<sub>6</sub>P (344.30): C 48.84, H 6.15, N 8.14, P 9.00; found: C 48.53, H 5.97, N 7.99, P 9.06.

### 6-Hexyl-3-[2-(phosphonomethoxy)ethyl]furo[2,3-d]pyrimidin-2(3H)-one (**11d**)

Treatment of **10d** (490 mg, 1.11 mmol) gave **11d** (283 mg, 71%) as white crystals (H<sub>2</sub>O); mp 159–160 °C. UV-vis  $\lambda_{\text{max}}$  (nm) ( $\epsilon$  ((mol/L)<sup>-1</sup> cm<sup>-1</sup>): 329 (5900), 243 (11 100). <sup>1</sup>H NMR (DMSO-*d*<sub>6</sub>)  $\delta$ : 8.36 (s, 1H, H-4), 6.39 (s, 1H, H-5), 4.11 (m, 2H, H-1'), 3.78 (m, 2H, H-2'), 3.58 (d, 2H,  $J_{\text{H,P}}$  = 8.5 Hz, H-4'), 2.63 (t, 2H,  $J_{\text{vic}}$  = 7.4 Hz, H-1''), 1.69–1.54 (m, 2H, H-2''), 1.39–1.18 (m, 6H, H-3'' and H-4'' and H-5''), 0.85 (t, 3H,  $J$  = 6.7 Hz, H-6''). <sup>13</sup>C NMR (DMSO-*d*<sub>6</sub>)  $\delta$ : 171.5 (C-7a), 158.1 (C-6), 154.7 (C-2), 142.9 (C-4), 106.1 (C-4a), 99.6 (C-5), 69.4 (d,  $J_{\text{C,P}}$  = 10.5 Hz, C-2'), 66.5 (d,  $J_{\text{C,P}}$  = 159.9 Hz, C-4'), 50.3 (C-1'), 31.1 and 28.3 and 27.6 and 26.5 and 22.2 and 14.1 (6-hexyl). MS (ESI)  $m/z$ : 357 [M – H]<sup>-</sup>. Anal. calcd. for C<sub>15</sub>H<sub>23</sub>N<sub>2</sub>O<sub>6</sub>P (358.33): C 50.28, H 6.47, N 7.82, P 8.64; found: C 49.97, H 6.52, N 7.70, P 8.85.

### 6-heptyl-3-[2-(phosphonomethoxy)ethyl]furo[2,3-d]pyrimidin-2(3H)-one (**11e**)

Treatment of **10e** (270 mg, 0.59 mmol) gave **11e** (187 mg, 84%) as white crystals (H<sub>2</sub>O/EtOH); mp 162–163 °C; UV-vis  $\lambda_{\text{max}}$  (nm) ( $\epsilon$  ((mol/L)<sup>-1</sup> cm<sup>-1</sup>): 328 (7900), 243 (14 700). <sup>1</sup>H NMR (500.0 MHz, DMSO-*d*<sub>6</sub>)  $\delta$ : 8.35 (s, 1H, H-4), 6.40 (t, 1H,  $J_{5,1''}$  = 1.1 Hz, H-5), 4.11 (m, 2H, H-1'), 3.77 (m, 2H, H-2'), 3.58 (d, 2H,  $J_{\text{H,P}}$  = 8.5 Hz, H-4'), 2.63 (td, 2H,  $J_{\text{vic}}$  = 7.4 Hz,  $J_{1'',5}$  = 1.1 Hz, H-1''), 1.68–1.52 (m, 2H,

H-2''), 1.36–1.20 (m, 8H, H-3'' and H-4'' and H-5'' and H-6''), 0.85 (t, 3H,  $J$  = 6.9 Hz, H-7''). <sup>13</sup>C NMR (125.8 MHz, DMSO-*d*<sub>6</sub>)  $\delta$ : 171.6 (C-7a), 158.2 (C-6), 154.7 (C-2), 143.0 (C-4), 106.2 (C-4a), 99.7 (C-5), 69.5 (d,  $J_{\text{C,P}}$  = 10.5 Hz, C-2'), 66.5 (d,  $J_{\text{C,P}}$  = 159.9 Hz, C-4'), 50.3 (C-1'), 31.4 and 28.59 and 28.55 and 27.6 and 26.6 and 22.3 and 14.2 (6-heptyl). MS (ESI)  $m/z$ : 371 [M – H]<sup>-</sup>. Anal. calcd. for C<sub>16</sub>H<sub>25</sub>N<sub>2</sub>O<sub>6</sub>P·1/4 H<sub>2</sub>O (376.86): C 50.99, H 6.82, N 7.43, P 8.22; found: C 51.12, H 6.77, N 7.41, P 8.40.

### 6-Octyl-3-[2-(phosphonomethoxy)ethyl]furo[2,3-d]pyrimidin-2(3H)-one (**11f**)

Treatment of **10f** (166 mg, 0.35 mmol) gave **11f** (126 mg, 90%) as white crystals (H<sub>2</sub>O/EtOH); mp 164 °C. UV-vis  $\lambda_{\text{max}}$  (nm) ( $\epsilon$  ((mol/L)<sup>-1</sup> cm<sup>-1</sup>): 329 (5900), 243 (11 000). <sup>1</sup>H NMR (DMSO-*d*<sub>6</sub>)  $\delta$ : 8.36 (s, 1H, H-4), 6.40 (s, 1H, H-5), 4.11 (m, 2H, H-1'), 3.77 (m, 2H, H-2'), 3.57 (d, 2H,  $J_{\text{H,P}}$  = 8.6 Hz, H-4'), 2.63 (t, 2H,  $J_{\text{vic}}$  = 7.3 Hz, H-1''), 1.68–1.52 (m, 2H, H-2''), 1.38–1.15 (m, 10H, H-3'' and H-4'' and H-5'' and H-6'' and H-7''), 0.85 (t, 3H,  $J$  = 6.8 Hz, H-8''). <sup>13</sup>C NMR (DMSO-*d*<sub>6</sub>)  $\delta$ : 171.5 (C-7a), 158.1 (C-6), 154.6 (C-2), 142.8 (C-4), 106.1 (C-4a), 99.6 (C-5), 69.4 (d,  $J_{\text{C,P}}$  = 10.5 Hz, C-2'), 66.5 (d,  $J_{\text{C,P}}$  = 159.9 Hz, C-4'), 50.2 (C-1'), 31.4 and 28.73 and 28.67 and 28.5 and 27.5 and 26.5 and 22.2 and 14.1 (6-octyl). MS (ESI)  $m/z$ : 385 [M – H]<sup>-</sup>. Anal. calcd. for C<sub>17</sub>H<sub>27</sub>N<sub>2</sub>O<sub>6</sub>P·1/2 H<sub>2</sub>O (395.39): C 51.64, H 7.14, N 7.09, P 7.83; found: C 51.58, H 7.18, N 7.02, P 8.11.

### 6-Decyl-3-[2-(phosphonomethoxy)ethyl]furo[2,3-d]pyrimidin-2(3H)-one (**11g**)

Treatment of **10g** (250 mg, 0.50 mmol) gave **11g** (187 mg, 90%) as white crystals (H<sub>2</sub>O/EtOH); mp 166–167 °C. UV-vis  $\lambda_{\text{max}}$  (nm) ( $\epsilon$  ((mol/L)<sup>-1</sup> cm<sup>-1</sup>): 329 (6900), 243 (13 000). <sup>1</sup>H NMR (DMSO-*d*<sub>6</sub>)  $\delta$ : 8.36 (s, 1H, H-4), 6.40 (s, 1H, H-5), 4.11 (m, 2H, H-1'), 3.77 (m, 2H, H-2'), 3.58 (d, 2H,  $J_{\text{H,P}}$  = 8.5 Hz, H-4'), 2.63 (t, 2H,  $J_{\text{vic}}$  = 7.1 Hz, H-1''), 1.66–1.54 (m, 2H, H-2''), 1.37–1.15 (m, 14H, H-3'' and H-4'' and H-5'' and H-6'' and H-7'' and H-8'' and H-9''), 0.85 (t, 3H,  $J$  = 6.7 Hz, H-10''). <sup>13</sup>C NMR (DMSO-*d*<sub>6</sub>)  $\delta$ : 171.5 (C-7a), 158.1 (C-6), 154.6 (C-2), 142.8 (C-4), 106.1 (C-4a), 99.6 (C-5), 69.4 (d,  $J_{\text{C,P}}$  = 10.5 Hz, C-2'), 66.5 (d,  $J_{\text{C,P}}$  = 159.9 Hz, C-4'), 50.2 (C-1'), 31.4 and 29.1 and 29.0 and 28.8 and 28.5 and 27.5 and 26.5 and 22.2 and 14.1 (6-decyl). MS (ESI)  $m/z$ : 413 [M – H]<sup>-</sup>. Anal. calcd. for C<sub>19</sub>H<sub>31</sub>N<sub>2</sub>O<sub>6</sub>P·1/4H<sub>2</sub>O (418.94): C 54.47, H 7.58, N 6.69, P 7.39; found: C 54.52, H 7.53, N 6.61, P 7.70.

### 6-(4-Pentylphenyl)-3-[2-(phosphonomethoxy)ethyl]furo[2,3-d]pyrimidin-2(3H)-one (**11h**)

Treatment of **10h** (130 mg, 0.26 mmol) gave **11h** (85 mg, 78%) as white crystals (H<sub>2</sub>O/EtOH); mp 243–245 °C (dec). UV-vis  $\lambda_{\text{max}}$  (nm) ( $\epsilon$  ((mol/L)<sup>-1</sup> cm<sup>-1</sup>): 351 (16 400), 279 (20 500). <sup>1</sup>H NMR (DMSO-*d*<sub>6</sub>)  $\delta$ : 8.54 (s, 1H, H-4), 7.73 (m, 2H, *o*-Ph), 7.32 (m, 2H, *m*-Ph), 7.19 (s, 1H, H-5), 4.15 (m, 2H, H-1'), 3.81 (m, 2H, H-2'), 3.60 (d, 2H,  $J_{\text{H,P}}$  = 8.6 Hz, H-4'), 2.61 (t, 2H,  $J_{\text{vic}}$  = 7.6 Hz, H-1''), 1.64–1.53 (m, 2H, H-2''), 1.36–1.20 (m, 4H, H-3'' and H-4''), 0.86 (t, 3H,  $J$  = 7.0 Hz, H-5''). <sup>13</sup>C NMR (DMSO-*d*<sub>6</sub>)  $\delta$ : 171.3 (C-7a), 154.6 (C-6), 153.7 (C-2), 144.1 (C-*p*-Ph), 144.0 (C-4), 129.1 (C-*m*-Ph), 126.1 (C-*i*-Ph), 124.7 (C-*o*-Ph), 106.6 (C-4a), 98.6 (C-5), 69.3 (d,  $J_{\text{C,P}}$  = 10.5 Hz, C-2'), 66.5 (d,  $J_{\text{C,P}}$  =

160 Hz, C-4'), 50.4 (C-1'), 35.1 and 31.0 and 30.5 and 22.1 and 14.0 (*p*-pentyl). MS (ESI) *m/z*: 419 [M - H]<sup>-</sup>. Anal. calcd. for C<sub>20</sub>H<sub>25</sub>N<sub>2</sub>O<sub>6</sub>P (420.40): C 57.14, H 5.99, N 6.66, P 7.37; found: C 56.96, H 6.01, N 6.53, P 7.61.

### 1-{2-[(Diisopropoxyphosphoryl)methoxy]ethyl}-5-ethynyluracil (**14**)

TMSA (**13**; 0.9 mL, 640 mg, 6.51 mmol) and then Et<sub>3</sub>N (5.5 mL) were added to a suspension of **6** (2 g, 4.34 mmol), Pd(Ph<sub>3</sub>P)<sub>4</sub> (251 mg, 0.22 mmol), and CuI (83 mg, 0.44 mmol) in deoxygenated DMF (20 mL). The reaction was sealed with a septum and stirred at 45 °C for 1 h. Volatiles were evaporated in vacuo, and toluene was added to the residue and then evaporated (2 × 5 mL). The residue was flash chromatographed (4% MeOH/CHCl<sub>3</sub>) to give a yellowish solid upon drying. The TMS intermediate was dissolved in dry THF (40 mL), TBAF (1 mol/L THF solution, 5 mL) was added, and the reaction mixture was stirred at ambient temperature for 0.5 h. Volatiles were evaporated, the residue was dissolved in CHCl<sub>3</sub> (50 mL), and the solution was washed (saturated EDTA (aq.), and H<sub>2</sub>O) and dried (MgSO<sub>4</sub>). Volatiles were evaporated, and the residue was chromatographed (4% MeOH/CHCl<sub>3</sub>) and crystallized to give **14** (1.04 g, 63%) as white crystals (EtOAc/hexanes); mp 147–148 °C. <sup>1</sup>H NMR (600 MHz, DMSO-*d*<sub>6</sub>) δ: 11.64 (bs, 1H, NH), 7.97 (s, 1H, H-6), 4.55 (dh, 2H, *J*<sub>H,P</sub> = 7.7 Hz, *J*<sub>vic</sub> = 6.2 Hz, POCH), 4.08 (s, 1H, HC≡C), 3.90–3.87 (m, 2H, H-1'), 3.77 (d, 2H, *J*<sub>H,P</sub> = 8.3 Hz, H-4'), 3.72–3.69 (m, 2H, H-2'), 1.22 and 1.20 (2 × d, 2 × 6H, *J*<sub>vic</sub> = 6.2 Hz, CH<sub>3</sub>). <sup>13</sup>C NMR (150.9 MHz, DMSO-*d*<sub>6</sub>) δ: 162.4 (C-4), 150.5 (C-6), 150.1 (C-2), 96.6 (C-5), 83.7 (HC≡C), 76.5 (C≡CH), 70.4 (d, *J*<sub>C,P</sub> = 6.4 Hz, POC), 69.9 (d, *J*<sub>C,P</sub> = 11.5 Hz, C-2'), 64.9 (d, *J*<sub>C,P</sub> = 164 Hz, C-4'), 47.7 (C-1'), 24.0 (d, *J*<sub>C,P</sub> = 3.7 Hz, CH<sub>3</sub>), 23.9 (d, *J*<sub>C,P</sub> = 4.4 Hz, CH<sub>3</sub>). MS (ESI) *m/z*: 381 [M + Na]<sup>+</sup>. Anal. calcd. for C<sub>15</sub>H<sub>23</sub>N<sub>2</sub>O<sub>6</sub>P·1/4 EtOAc (380.35): C 50.52, H 6.63, N 7.37, P 8.14; found: C 50.28, H 6.68, N 7.20, P 8.43.

### 3-{2-[(Diisopropoxyphosphoryl)methoxy]ethyl}furo[2,3-*d*]pyrimidin-2(3*H*)-one (**15**)

A stirred suspension of **14** (620 mg, 1.63 mmol), CuI (310 mg, 1.63 mmol), Et<sub>3</sub>N (60 mL), and EtOAc (200 mL) was refluxed under argon for 12 h. Volatiles were evaporated, the residue was dissolved in hot MeOH (50 mL), and the solid filtered off. Volatiles were evaporated and the residue dissolved in CHCl<sub>3</sub> (80 mL). Organics were washed (2 × 30 mL of saturated EDTA (aq.), 1 × 20 mL H<sub>2</sub>O) and dried (MgSO<sub>4</sub>). Isolation by flash chromatography (8% MeOH/CHCl<sub>3</sub>) and crystallization afforded compound **15** (236 mg, 38%) as white crystals (EtOAc); mp 168 °C. <sup>1</sup>H NMR (500.0 MHz, DMSO-*d*<sub>6</sub>) δ: 8.54 (s, 1H, H-4), 7.73 (d, 1H, *J*<sub>6,5</sub> = 2.7 Hz, H-6), 6.81 (d, 1H, *J*<sub>5,6</sub> = 2.7 Hz, H-5), 4.49 (dh, 2H, *J*<sub>H,P</sub> = 7.7 Hz, *J*<sub>vic</sub> = 6.2 Hz, POCH), 4.17 (m, 2H, H-1'), 3.80 (m, 2H, H-2'), 3.77 (d, 2H, *J*<sub>H,P</sub> = 8.2 Hz, H-4'), 1.16 and 1.12 (2 × d, 2 × 6H, *J*<sub>vic</sub> = 6.2 Hz, CH<sub>3</sub>). <sup>13</sup>C NMR (125.8 MHz, DMSO-*d*<sub>6</sub>) δ: 171.7 (C-7a), 154.6 (C-2), 145.2 (C-4), 144.8 (C-6), 105.1 (C-5), 104.5 (C-4a), 70.3 (d, *J*<sub>C,P</sub> = 6.3 Hz, POC), 69.4 (d, *J*<sub>C,P</sub> = 11.4 Hz, C-2'), 64.8 (d, *J*<sub>C,P</sub> = 163.8 Hz, C-4'), 50.9 (C-1'), 23.9 (d, *J*<sub>C,P</sub> = 3.7 Hz, CH<sub>3</sub>), 23.8 (d, *J*<sub>C,P</sub> = 4.6 Hz, CH<sub>3</sub>). MS (ESI) *m/z*: 359 [M + H]<sup>+</sup>.

Anal. calcd. for C<sub>15</sub>H<sub>23</sub>N<sub>2</sub>O<sub>6</sub>P (358.13): C 50.28, H 6.47, N 7.82, P 8.64; found: C 50.22, H 6.53, N 7.69, P 8.98.

### 3-[2-(Phosphonomethoxy)ethyl]furo[2,3-*d*]pyrimidin-2(3*H*)-one (**16**)

A mixture of compound **15** (150 mg, 0.42 mmol), bromo(trimethyl)silane (1.00 mL, 1.16 g, 7.58 mmol), and acetonitrile (5 mL) was stirred at room temperature overnight. The mixture was concentrated in vacuo and then codistilled with a mixture of water/ethanol (9:1, 2 × 5 mL). The residue was crystallized to give **16** (85 mg, 74%) as yellowish crystals (EtOAc/EtOH 3:1), dec. over 200 °C. UV-vis λ<sub>max</sub> (nm) (ε ((mol/L)<sup>-1</sup> cm<sup>-1</sup>): 325 (5200), 238 (8700). <sup>1</sup>H NMR (500.0 MHz, D<sub>2</sub>O) δ: 8.55 (s, 1H, H-4), 7.58 (d, 1H, *J*<sub>6,5</sub> = 2.7 Hz, H-6), 6.80 (d, 1H, *J*<sub>5,6</sub> = 2.7 Hz, H-5), 4.31 (m, 2H, H-1'), 3.94 (m, 2H, H-2'), 3.71 (d, 2H, *J*<sub>H,P</sub> = 8.7 Hz, H-4'). <sup>13</sup>C NMR (125.8 MHz, D<sub>2</sub>O) δ: 174.3 (C-7a), 159.6 (C-2), 148.3 (C-4 and C-6), 110.4 (C-4a), 107.8 (C-5), 72.5 (d, *J*<sub>C,P</sub> = 11.7 Hz, C-2'), 69.0 (d, *J*<sub>C,P</sub> = 158.7 Hz, C-4'), 54.4 (C-1'). MS (ESI) *m/z*: 273 [M - H]<sup>-</sup>. Anal. calcd. for C<sub>9</sub>H<sub>11</sub>N<sub>2</sub>O<sub>6</sub>P·1/3H<sub>2</sub>O (280.17): C 38.58, H 4.20, N 10.00, P 11.06; found: C 38.80, H 4.33, N 9.66, P 10.82.

### 5,5'-Buta-1,3-diyne-1,4-diylbis{(1-{2-[(diisopropoxyphosphoryl)methoxy]ethyl}-uracil)} (**17**)

A stirred suspension of **14** (400 mg, 1.11 mmol), CuI (213 mg, 1.11 mmol), Et<sub>3</sub>N (6 mL), and MeOH (14 mL) was refluxed for 5 h. Reddish gel was formed. DMF (2 mL) was added and the reaction stirred at room temperature overnight. TLC (20% MeOH/CHCl<sub>3</sub>) showed complex mixture. Volatiles were flash evaporated and the residue codistilled with toluene (2 × 5 mL). Flash chromatography (15% MeOH/CHCl<sub>3</sub>) and crystallization gave compound **17** (82 mg, 10%) as yellow crystals (EtOAc/EtOH), dec. over 240 °C. <sup>1</sup>H NMR (500.0 MHz, DMSO-*d*<sub>6</sub>) δ: 11.77 (bs, 2H, NH), 8.15 (s, 2H, H-6), 4.56 (dh, 4H, *J*<sub>H,P</sub> = 7.7 Hz, *J*<sub>vic</sub> = 6.2 Hz, POCH), 3.90 (t, 4H, *J*<sub>1',2'</sub> = 4.8 Hz, H-1'), 3.78 (d, 4H, *J*<sub>H,P</sub> = 8.3 Hz, H-4'), 3.71 (t, 4H, *J*<sub>2',1'</sub> = 4.8 Hz, H-2'), 1.23 and 1.21 (2 × d, 2 × 12H, *J*<sub>vic</sub> = 6.2 Hz, CH<sub>3</sub>). <sup>13</sup>C NMR (125.8 MHz, DMSO-*d*<sub>6</sub>) δ: 162.3 (C-4), 152.0 (C-6), 149.9 (C-2), 95.8 (C-5), 76.7 (C≡C-C≡C), 75.4 (C≡C-C≡C), 70.4 (d, *J*<sub>C,P</sub> = 6.4 Hz, POC), 69.8 (d, *J*<sub>C,P</sub> = 11.6 Hz, C-2'), 64.9 (d, *J*<sub>C,P</sub> = 163.7 Hz, C-4'), 48.0 (C-1'), 24.0 (d, *J*<sub>C,P</sub> = 3.7 Hz, CH<sub>3</sub>), 23.9 (d, *J*<sub>C,P</sub> = 4.5 Hz, CH<sub>3</sub>). MS (ESI) *m/z*: 737 [M + Na]<sup>+</sup>. HR-MS (ESI) *m/z*: C<sub>30</sub>H<sub>45</sub>N<sub>4</sub>O<sub>12</sub>P<sub>2</sub> [M + H]<sup>+</sup>. Anal. calcd.: 715.2504; found: 715.2504.

## Antiviral activity assays

Varicella-zoster virus (VZV) drug susceptibility tests were performed on confluent hen egg lysozyme (HEL) cells in 96-well microtiter plates by the plaque reduction assay. Monolayers were infected with 20 plaque forming units (PFU) of cell-associated virus per well. For each assay, virus controls (infected–untreated cells) were included. After a 2 h incubation period, the virus inoculum was removed and the media replaced by the different dilutions (in duplicate) of the tested molecules. Serial dilutions of test compounds were incubated with the infected monolayers for 5 d. After a 5 d incubation period, the cells were fixed and stained



with Giemsa, and the level of virus-induced cytopathic effect was determined by counting the number of plaques for each dilution. Activity was expressed as EC<sub>50</sub> (effective compound concentration required to reduce virus plaque formation by 50%) compared to the untreated control.

For the HCMV assays, confluent HEL fibroblasts were grown in 96-well microtiter plates and infected with the human cytomegalovirus strains Davis and AD-169 at 100 PFU per well. After a 2 h incubation period, residual virus was removed and the infected cells were further incubated with medium containing different concentrations of the test compounds (in duplicate). After incubation for 7 d at 37 °C, virus-induced cytopathogenicity was monitored microscopically after ethanol fixation and staining with Giemsa. Antiviral activity was expressed as the EC<sub>50</sub> or compound concentration required to reduce virus-induced cytopathogenicity by 50%.

To examine the inhibitory effect of the compounds against virus-induced cytopathicity in HEL cells (herpes simplex virus type 1 (HSV-1), HSV-2 (G), vaccinia virus, and vesicular stomatitis virus), confluent cell cultures in microtiter 96-well plates were inoculated with 100 CCID<sub>50</sub> of virus (1 CCID<sub>50</sub> being the virus dose to infect 50% of the cell cultures). After a 1 h virus adsorption period, residual virus was removed, and the cell cultures were incubated in the presence of varying concentrations (200, 40, 8, ... μmol/L) of the test compounds. Viral cytopathicity was recorded as soon as it reached completion in the control virus-infected cell cultures that were not treated with the test compounds.

The methodology of the anti-HIV assays was as follows: human T-lymphocyte CEM (~3 × 10<sup>5</sup> cells/cm<sup>3</sup>) cells were infected with 100 CCID<sub>50</sub> of HIV-1(III<sub>B</sub>) or HIV-2(ROD)/mL and seeded in 200 μL wells of a microtiter plate containing appropriate dilutions of the test compounds. After 4 d of incubation at 37 °C, HIV-induced CEM giant cell formation was examined microscopically.

## Acknowledgments

This study was performed as a part of research project (OZ40550506) of the Institute of Organic Chemistry and Biochemistry, v.v.i. This study was supported by the Center for New Antivirals and Antineoplastics (IM0508) by the Ministry of Education, Youth and Sports of the Czech Republic, and by Gilead Sciences and the Institute of Organic Chemistry and Biochemistry (IOCB) Research Centre. The research of JB was supported by the "Geconcerteerde Onderzoeksacties Vlaanderen" (GOA no. 05/19). We thank Leentje Persoons, Vicky Broeckx, Frieda De Meyer, Anita Camps, Lies Van den Heurck, Steven Carmans, and Leen Ingels for excellent technical assistance.

## References

- (1) Robins, M. J.; Barr, P. J. *Tetrahedron Lett.* **1981**, 22 (52), 421. doi:10.1016/0040-4039(81)80115-3.
- (2) Robins, M. J.; Barr, P. J. *J. Org. Chem.* **1983**, 48 (11), 1854. doi:10.1021/jo00159a012.
- (3) McGuigan, C.; Yarnold, C. J.; Jones, G.; Velázquez, S.; Barucki, H.; Branciale, A.; Andrei, G.; Snoeck, R.; De Clercq, E.; Balzarini, J. *J. Med. Chem.* **1999**, 42 (22), 4479. doi:10.1021/jm990346o. PMID:10579812.
- (4) Reviews:(a) McGuigan, C.; Branciale, A.; Barucki, H.; Srinivasan, S.; Jones, G.; Pathirana, R. N.; Blewett, S.; Alvarez,

- R.; Yarnold, C. J.; Carangio, A.; Velázquez, S.; Andrei, G.; Snoeck, R.; De Clercq, E.; Balzarini, J. *Drugs Future* **2000**, 25, 1151; (b) Balzarini, J.; McGuigan, C. *J. Antimicrob. Chemother.* **2002**, 50 (1), 5. doi:10.1093/jac/dkf037. PMID:12096000; (c) De Clercq, E. *Med. Res. Rev.* **2003**, 23 (3), 253. doi:10.1002/med.10035. PMID:12647310; (d) McGuigan, C.; Balzarini, J. *Antiviral Res.* **2006**, 71 (2–3), 149. doi:10.1016/j.antiviral.2006.04.001. PMID:16712966.
- (5) (a) McGuigan, C.; Barucki, H.; Blewett, S.; Carangio, A.; Erichsen, J. T.; Andrei, G.; Snoeck, R.; De Clercq, E.; Balzarini, J. *J. Med. Chem.* **2000**, 43 (26), 4993. doi:10.1021/jm000210m. PMID:11150169; (b) McGuigan, C.; Barucki, H.; Carangio, A.; Blewett, S.; Srinivasan, S.; Andrei, G.; Snoeck, R.; De Clercq, E.; Balzarini, J. *Nucleosides Nucleotides Nucleic Acids* **2001**, 20 (4–7), 287. doi:10.1081/NCN-100002299. PMID:11563040.
- (6) (a) McGuigan, C.; Pathirana, R. N.; Migliore, M.; Adak, R.; Luoni, G.; Jones, A. T.; Díez-Torrubia, A.; Camarasa, M.-J.; Velázquez, S.; Henson, G.; Verbeken, E.; Sienaaert, R.; Nae-sens, L.; Snoeck, R.; Andrei, G.; Balzarini, J. *J. Antimicrob. Chemother.* **2007**, 60 (6), 1316. doi:10.1093/jac/dkm376. PMID:17956908; (b) De Clercq, E. *Future Virol.* **2008**, 3 (4), 393. doi:10.2217/17460794.3.4.393; (c) De Clercq, E. *Nucleosides Nucleotides Nucleic Acids* **2009**, 28 (5), 586. doi:10.1080/15257770903054159. PMID:20183603.
- (7) McGuigan, C.; Pathirana, R. N.; Snoeck, R.; Andrei, G.; De Clercq, E.; Balzarini, J. *J. Med. Chem.* **2004**, 47 (7), 1847. doi:10.1021/jm030857h. PMID:15027877.
- (8) (a) Kelleher, M. R.; McGuigan, C.; Andrei, G.; Snoeck, R.; De Clercq, E.; Balzarini, J. *Nucleosides Nucleotides Nucleic Acids* **2005**, 24 (5–7), 639. doi:10.1081/NCN-200060118. PMID:16248003; (b) Robins, M. J.; Miranda, K.; Rajwan-shi, V. K.; Peterson, M. A.; Andrei, G.; Snoeck, R.; De Clercq, E.; Balzarini, J. *J. Med. Chem.* **2006**, 49 (1), 391. doi:10.1021/jm050867d. PMID:16392824.
- (9) Janeba, Z.; Balzarini, J.; Andrei, G.; Snoeck, R.; De Clercq, E.; Robins, M. J. *J. Med. Chem.* **2005**, 48 (14), 4690. doi:10.1021/jm050291s. PMID:16000005.
- (10) De Clercq, E. *Nucleosides Nucleotides Nucleic Acids* **2004**, 23 (1–2), 457. PMID:15043166.
- (11) De Clercq, E.; Holý, A.; Rosenberg, I.; Sakuma, T.; Balzarini, J.; Maudgal, P. C. *Nature* **1986**, 323 (6087), 464. doi:10.1038/323464a0. PMID:3762696.
- (12) Reviews:(a) De Clercq, E. *Clin. Microbiol. Rev.* **2003**, 16 (4), 569. doi:10.1128/CMR.16.4.569-596.2003. PMID:14557287; (b) De Clercq, E.; Holý, A. *Nat. Rev. Drug Discov.* **2005**, 4 (11), 928. doi:10.1038/nrd1877. PMID:16264436; (c) Holý, A. *Antiviral Res.* **2006**, 71 (2–3), 248. doi:10.1016/j.antiviral.2006.06.002. PMID:16857275; (d) De Clercq, E. *Antiviral Res.* **2007**, 75 (1), 1. doi:10.1016/j.antiviral.2006.10.006. PMID:17116336.
- (13) Janeba, Z.; Holý, A.; Snoeck, R.; Andrei, G.; De Clercq, E.; Balzarini, J. *Antiviral Res.* **2009**, 82 (2), A58. doi:10.1016/j.antiviral.2009.02.139.
- (14) Pomeisl, K.; Holý, A.; Pohl, R. *Tetrahedron Lett.* **2007**, 48 (17), 3065. doi:10.1016/j.tetlet.2007.02.107.
- (15) Pomeisl, K.; Votruba, I.; Holý, A.; Pohl, R. *Collect. Czech. Chem. Commun.* **2006**, 71 (4), 595. doi:10.1135/cccc20060595.
- (16) Holý, A.; Ivanova, G. S. *Nucleic Acids Res.* **1974**, 1 (1), 19. doi:10.1093/nar/1.1.19. PMID:10793656.
- (17) Dvořáková, H.; Holý, A. *Collect. Czech. Chem. Commun.* **1993**, 58 (6), 1419. doi:10.1135/cccc19931419.
- (18) Asakura, J.; Robins, M. J. *Tetrahedron Lett.* **1988**, 29 (23), 2855. doi:10.1016/0040-4039(88)85229-8.



- (19) Luoni, G.; McGuigan, C.; Andrei, G.; Snoeck, R.; De Clercq, E.; Balzarini, J. *Bioorg. Med. Chem. Lett.* **2005**, *15* (16), 3791. doi:10.1016/j.bmcl.2005.05.071. PMID:15993062.
- (20) Eglinton, G.; Galbraith, A. R. *J. Chem. Soc.* **1959**, 889. doi:10.1039/jr9590000889.

# A new family of bent-core $C_2$ -symmetric liquid crystals

Kyle A. Hope-Ross, Paul A. Heiney, and John F. Kadla

**Abstract:** A series of  $C_2$ -symmetric compounds with different core sizes and varying lengths and numbers of alkoxy side chains were prepared, and the factors influencing their liquid crystalline mesophase behaviour were investigated. The compounds studied were based on benzophenone, dibenzylidene-acetone, and 1,9-diphenyl-nona-1,3,6,8-tetraen-5-one cores with either 1 or 2 linear alkoxy side chains. The side chains were varied in length from  $C_6H_{13}$  to  $C_{12}H_{25}$ . The liquid crystalline mesophase behaviour of the compounds was investigated using differential scanning calorimetry, polarizing optical microscopy, and small-angle X-ray scattering (SAXS). It was found that a number of the molecules were able to self-assemble into smectic and nematic liquid crystalline phases.

**Key words:** mesophase,  $C_2$  symmetric, SAXS, benzophenone, dibenzylidene-acetone and 1,9-diphenyl-nona-1,3,6,8-tetraen-5-one.

**Résumé :** On a réalisé la synthèse d'une série de composés de symétrie  $C_2$  comportant des coeurs de tailles différentes et des quantités diverses de chaînes latérales alcoyles de longueurs variables et on a étudié les facteurs qui influencent leur comportement comme mésophase de cristal liquide. Les composés étudiés ont des coeurs à base de benzophénone, de dibenzylidèneacétone et de 1,9-diphényl-1,3,6,8-tétraén-5-one et des chaînes latérales alcoyles linéaires en positions 1 ou 2. Les longueurs de chaînes latérales varient de  $C_6H_{13}$  à  $C_{12}H_{25}$ . On a étudié leur comportement comme mésophase de cristal liquide en faisant appel à la calorimétrie à balayage différentiel, à la microscopie optique polarisante et par la diffusion des rayons-X à angle faible (DXAF). On a trouvé qu'un certain nombre de molécules peuvent s'autoassembler en phases de cristal liquide smectique et nématique.

**Mots-clés :** mésophase, symétrie  $C_2$ , diffusion des rayons X à angle faible (DXAF), benzophénone, dibenzylidèneacétone, 1,9-diphényl-1,3,6,8-tétraén-5-one.

[Traduit par la Rédaction]

## Introduction

Liquid crystals are a growing field of research with applications in a wide variety of devices, including photovoltaic solar cells,<sup>1</sup> light-emitting diodes,<sup>2</sup> and displays.<sup>3</sup>

Traditionally, molecules displaying liquid crystalline mesophases display a structure that consists of a flat, rigid (usually aromatic) core with multiple, usually aliphatic, flexible side chains.<sup>4</sup> Liquid crystalline molecules can consist of disc-like,<sup>5</sup> linear<sup>6</sup> or bent-shaped<sup>7</sup> core structures. In addition, owing to their inherent ability to self-assemble, based largely on  $\pi$ -stacking interactions, any factor that influences the electronic structure of the core will affect the ability of the molecules to form liquid crystalline mesophases.<sup>8</sup> It has been shown that alkyl side-chain length,<sup>9,10</sup> electronics,<sup>11</sup> and core size<sup>12</sup> all have an impact on molecular self-assembly. To fully exploit the potential applications of liquid crystalline materials, we must fully understand the variables that have an effect on mesophase formation.

Herein, we report the synthesis and characterization of a

new family of bent-core  $C_2$ -symmetric molecules, and discuss various factors that affect their ability to self-assemble into liquid crystalline mesophases. The compounds prepared were based on a benzophenone (**1**), dibenzylidene acetone (**2**), and 1,9-diphenyl-nona-1,3,6,8-tetraen-5-one (**3**) core (Fig. 1) with either one or two linear alkoxy side chains varying in length from  $C_6H_{13}$  to  $C_{12}H_{25}$ .

## Experimental section

All chemicals were purchased from Sigma-Aldrich (Oakville, ON) and used without further purification unless otherwise noted.

### General procedure for the synthesis of 4,4'-bis(alkyloxy)benzophenones (**1a–1d**)

#### 4,4'-Bis(hexyloxy)benzophenone (**1a**)

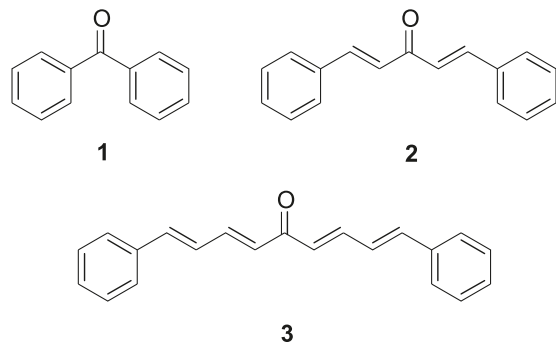
To a solution of 4,4'-dihydroxybenzophenone (0.50 g, 2.33 mmol) and potassium carbonate (1.29 g, 9.34 mmol) in ace-

Received 1 October 2009. Accepted 30 March 2010. Published on the NRC Research Press Web site at canjchem.nrc.ca on 15 June 2010.

**K.A. Hope-Ross and J.F. Kadla.**<sup>1</sup> Advanced Biomaterials Chemistry Laboratory, Department of Wood Science, The University of British Columbia, Vancouver, BC V6T 1Z4, Canada.

**P.A. Heiney.** Department of Physics and Astronomy and Laboratory for Research on the Structure of Matter, University of Pennsylvania, Philadelphia, PA 19104, USA.

<sup>1</sup>Corresponding author (e-mail: john.kadla@ubc.ca).

**Fig. 1.** Core structures studied: **1**, **2**, and **3**.

tone (25 mL) was added 1-bromohexane (1.54 g, 9.34 mmol) dropwise. The resulting mixture was heated and allowed to reflux. After 48 h, the reaction mixture was poured into water (200 mL) and extracted with  $\text{CH}_2\text{Cl}_2$  ( $3 \times 75$  mL). The combined organic layers were washed with water (300 mL), dried over  $\text{MgSO}_4$ , filtered, and the solvent was removed in vacuo. Recrystallization from acetone afforded **1a** (0.86 g, 97%) as white crystals, mp 102–105 °C. IR (thin film,  $\text{cm}^{-1}$ ): 2955, 2938, 2863, 1636, 1604, 1256, 853, 764.  $^1\text{H}$  NMR (300 MHz,  $\text{CDCl}_3$ )  $\delta$ : 7.79 (d,  $J$  = 8.66 Hz, 4H), 6.96 (d,  $J$  = 8.66 Hz, 4H), 4.05 (t,  $J$  = 6.58 Hz, 4H), 1.84 (quin.,  $J$  = 6.58 Hz, 4H), 1.56–1.31 (m, 12H), 0.94 (t,  $J$  = 6.58 Hz, 6H).  $^{13}\text{C}$  NMR (300 MHz,  $\text{CDCl}_3$ )  $\delta$ : 194.5, 162.4, 132.2, 130.6, 113.9, 68.2, 31.6, 29.1, 25.7, 22.6, 14.0. Anal. calcd. for  $\text{C}_{25}\text{H}_{34}\text{O}_3$ : C, 78.49; H, 8.96. Found: C, 78.58; H, 8.73.

#### General procedure for the synthesis of 3,3',4,4'-tetrakis(alkoxy)benzophenones (**1e–1h**)

##### 3,3',4,4'-Tetrakis(hexyloxy)benzophenone (**1e**)

To a solution of 3,4-bis(hexyloxy)benzoic acid (**9e**, 0.34 g, 1.06 mmol) and diethylamine (0.50 mL) in  $\text{CH}_2\text{Cl}_2$  was added  $\text{SOCl}_2$  (5 mL) dropwise. The resulting solution was heated to reflux for 1.5 h. Excess  $\text{SOCl}_2$ , diethylamine, and  $\text{CH}_2\text{Cl}_2$  were removed in vacuo, and the resultant acid chloride was added as a solution in  $\text{CH}_2\text{Cl}_2$  (15 mL) to a mixture of  $\text{AlCl}_3$  (0.14 g, 1.06 mmol) and 1,2-bis(hexyloxy)benzene (**5e**, 0.29 g, 1.06 mmol) in  $\text{CH}_2\text{Cl}_2$  (15 mL) at 0 °C under  $\text{N}_2$  atmosphere. The reaction mixture was stirred for 1 h, warmed to RT, and stirred overnight. The green solution was quenched with  $\text{H}_2\text{O}$  (10 mL), poured into 2.0 mol/L HCl (200 mL), and the organic phase was separated. The aqueous layer was extracted with  $\text{CH}_2\text{Cl}_2$  ( $3 \times 75$  mL), and the combined organic phases were washed with  $\text{H}_2\text{O}$  (200 mL) and brine (200 mL), dried over  $\text{MgSO}_4$ , filtered, and the solvent was removed in vacuo. Recrystallization from acetone afforded **1e** (0.37 g, 60%) as a white powder, mp 44–48 °C. IR (thin film,  $\text{cm}^{-1}$ ): 2931, 2860, 1649, 1595, 1513, 1428, 1266, 1135, 1017, 760.  $^1\text{H}$  NMR (300 MHz,  $\text{CDCl}_3$ )  $\delta$ : 7.42 (d,  $J$  = 1.86 Hz, 2H), 7.37 (dd,  $J_1$  = 8.33 Hz,  $J_2$  = 1.86 Hz, 2H), 6.90 (d,  $J$  = 8.33 Hz, 2H), 4.09 (t,  $J$  = 6.58 Hz, 4H), 4.06 (t,  $J$  = 6.58 Hz, 4H), 1.93–1.79 (m, 8H), 1.58–1.30 (m, 24H), 0.93 (t,  $J$  = 6.58 Hz, 6H), 0.92 (t,  $J$  = 6.58 Hz, 6H).  $^{13}\text{C}$  NMR (300 MHz,  $\text{CDCl}_3$ )  $\delta$ : 194.6, 152.8, 148.7, 130.7, 124.7, 114.7, 111.5, 69.3, 69.1,

31.58, 31.56, 29.2, 29.1, 25.69, 25.66, 22.6 (4C), 14.0 (4C). Anal. calcd. for  $\text{C}_{37}\text{H}_{58}\text{O}_5$ : C, 76.25; H, 10.03. Found: C, 76.06; H, 10.09.

#### General procedure for the synthesis of 1,5-bis(4-alkoxyphenyl)-penta-1,4-dien-3-ones (**2a–2d**)

##### 1,5-Bis(4-hexyloxy-phenyl)-penta-1,4-dien-3-one (**2a**)

A solution of sodium hydroxide (0.39 g, 9.75 mmol) in water (5 mL) and ethanol (5 mL) was cooled to 0 °C for 30 min. To this solution was added acetone (0.11 g, 1.95 mmol) and 4-hexyloxy-benzaldehyde (**11a**, 0.80 g, 3.90 mmol). The resulting solution was allowed to stir at room temperature. After 3 days, the reaction mixture was poured into 2.0 mol/L HCl (200 mL), and the organic phase was separated. The aqueous phase was extracted with dichloromethane ( $2 \times 150$  mL) and washed with water (250 mL). The combined organic phases were dried over  $\text{MgSO}_4$ , filtered, and the solvent was removed in vacuo. Recrystallization from EtOH afforded **2a** as yellow crystals (0.49 g, 58%), mp 97–100 °C. IR (thin film,  $\text{cm}^{-1}$ ): 2934, 2869, 1651, 1599, 1574, 1512, 1177, 1030, 983.  $^1\text{H}$  NMR (300 MHz,  $\text{CDCl}_3$ )  $\delta$ : 7.72 (d,  $J$  = 15.78 Hz, 2H), 7.58 (d,  $J$  = 8.66 Hz, 4H), 6.97 (d,  $J$  = 15.78 Hz, 2H), 6.94 (d,  $J$  = 8.66 Hz, 4H), 4.02 (t,  $J$  = 6.58 Hz, 4H), 1.82 (quin.,  $J$  = 6.58 Hz, 4H), 1.54–1.29 (m, 12H), 0.93 (t,  $J$  = 6.58 Hz, 6H).  $^{13}\text{C}$  NMR (300 MHz,  $\text{CDCl}_3$ )  $\delta$ : 188.9, 161.2, 142.7, 130.1, 127.4, 123.4, 114.9; 68.2, 31.6, 29.1, 25.7, 22.6, 14.0. Anal. calcd. for  $\text{C}_{29}\text{H}_{38}\text{O}_3$ : C, 80.14; H, 8.81. Found: C, 80.03; H, 8.64.

#### General procedure for the synthesis of 1,5-bis(3,4-bis(alkoxy-phenyl))-penta-1,4-dien-3-ones (**2e–2h**)

##### 1,5-Bis(3,4-bis(hexyloxy-phenyl))-penta-1,4-dien-3-one (**2e**)

To a solution of 4-(3,4-bis(hexyloxy-phenyl))-but-3-en-2-one (**12e**, 0.50 g, 1.44 mmol) and 3,4-bis(hexyloxy)benzaldehyde (**11e**, 0.44 g, 1.44 mmol) in methanol (20 mL) was added sodium methoxide (25 wt% solution in MeOH, 0.94 mL, 4.33 mmol) dropwise. The resulting solution was heated to reflux. After 48 h, the reaction mixture was poured into 2.0 mol/L HCl (200 mL), and the organic phase was separated. The aqueous phase was extracted with  $\text{CH}_2\text{Cl}_2$  ( $3 \times 75$  mL). The combined organics were washed with  $\text{H}_2\text{O}$  ( $2 \times 200$  mL), dried over  $\text{MgSO}_4$ , filtered, and the solvent was removed in vacuo. Recrystallization from acetone afforded **2e** (0.52 g, 57%) as a yellow powder, mp 62–65 °C. IR (thin film,  $\text{cm}^{-1}$ ): 2955, 2931, 2860, 1648, 1618, 1595, 1511, 1468, 1432, 1258, 1234, 1172, 1137, 1095, 1017.  $^1\text{H}$  NMR (300 MHz,  $\text{CDCl}_3$ )  $\delta$ : 7.69 (d,  $J$  = 15.78 Hz, 2H), 7.21–7.15 (m, 4H), 6.95 (d,  $J$  = 15.78 Hz, 2H), 6.90 (d,  $J$  = 8.33 Hz, 2H), 4.07 (t,  $J$  = 6.58 Hz, 4H), 4.06 (t,  $J$  = 6.58 Hz, 4H), 1.87 (quin.,  $J$  = 6.58 Hz, 4H), 1.86 (quin.,  $J$  = 6.58 Hz, 4H), 1.56–1.26 (m, 24H), 0.94 (t,  $J$  = 6.58 Hz, 6H), 0.93 (t,  $J$  = 6.58 Hz, 6H).  $^{13}\text{C}$  NMR (300 MHz,  $\text{CDCl}_3$ )  $\delta$ : 188.8, 151.6, 149.2, 143.1, 127.8, 123.5, 123.1, 113.0, 112.6, 69.4, 69.1, 31.59, 31.56, 29.2, 29.1, 25.71, 25.67, 22.62, 22.59, 14.03, 14.01. Anal. calcd. for  $\text{C}_{41}\text{H}_{62}\text{O}_5$ : C, 77.56; H, 9.84. Found: C, 77.57; H, 9.75.

## General procedure for the synthesis of 1,9-bis(4-alkoxy-phenyl)-nona-1,3,6,8-tetraen-5-ones (3a–3d)

### 1,9-Bis(4-hexyloxy-phenyl)-nona-1,3,6,8-tetraen-5-one (3a)

To a solution of 6-(4-hexyloxy-phenyl)-hexa-3,5-dien-2-one (**18a**, 0.20 g, 0.73 mmol) and 4-hexyloxy-cinnamaldehyde (**17a**, 0.17 g, 0.73 mmol) in THF (15 mL) was added NaOMe (25 wt% in MeOH, 0.48 mL, 2.20 mmol) dropwise. The resulting dark orange solution was allowed to stir at RT. After 30 min, the reaction mixture was poured into 2.0 mol/L HCl (100 mL), and the organic phase was separated. The aqueous phase was extracted with CH<sub>2</sub>Cl<sub>2</sub> (3 × 75 mL), and the combined organics were washed with H<sub>2</sub>O (2 × 200 mL), dried over MgSO<sub>4</sub>, filtered, and the solvent was removed in vacuo. Recrystallization from acetone afforded **3a** as a green/yellow solid (0.22 g, 62%), mp 147–151 °C. IR (thin film, cm<sup>-1</sup>): 2926, 2851, 1655, 1592, 1509, 1464, 1359, 1257, 1174, 1071, 1005, 854, 821. <sup>1</sup>H NMR (300 MHz, CDCl<sub>3</sub>) δ: 7.48 (dd, *J*<sub>1</sub> = 15.13 Hz, *J*<sub>2</sub> = 10.41 Hz, 2H), 7.44 (d, *J* = 8.66 Hz, 4H), 6.95 (d, *J* = 15.46 Hz, 2H), 6.90 (d, *J* = 8.66 Hz, 4H), 6.84 (dd, *J*<sub>1</sub> = 15.46 Hz, *J*<sub>2</sub> = 10.41 Hz, 2H), 6.53 (d, *J* = 15.13 Hz, 2H), 4.0 (t, *J* = 6.58 Hz, 4H), 1.81 (quin., *J* = 6.58 Hz, 4H), 1.55–1.30 (m, 12H), 0.91 (t, *J* = 6.58 Hz, 6H). <sup>13</sup>C NMR (300 MHz, CDCl<sub>3</sub>) δ: 189.0, 160.2, 143.3, 141.2, 128.8, 128.7, 128.1, 124.8, 114.9, 68.2, 31.6, 29.2, 25.7, 22.6, 14.0. Anal. calcd. for C<sub>33</sub>H<sub>42</sub>O<sub>3</sub>: C, 81.44; H, 8.70. Found: C, 80.56; H, 8.68.

### Characterization

Small-angle X-ray scattering (SAXS) measurements employed a Bruker-Nonius FR591 rotating-anode generator with a copper anode operated at 3.4 kW. The beam was collimated and focused with Osmic confocal optics and pinholes, and the scattered radiation was detected using a Bruker Hi-Star wire (area) detector.<sup>13</sup> Samples were sealed in 1 mm diameter glass capillaries. Measurements were made at fixed sample–detector distances of 54 and 11 cm; the presence or absence of crystalline (three-dimensional order) was established from the 11 cm data sets, while the final refinement of the liquid crystal unit cell parameters was made using the data from the 54 cm configuration. In situ temperature-dependent measurements employed a Linkam heating cell. Primary data analysis was performed using Datasqueeze.<sup>14</sup>

Differential scanning calorimetry (DSC) measurements were performed on a TA Instruments Q1000 DSC. All experiments were run with 1–3 mg of sample in aluminum hermetic pans at heating rates of 10 °C/min and cooling rates of 5 °C/min unless otherwise noted. The samples were initially analyzed at temperatures between –90 °C and 250 °C with subsequent runs performed only in the temperature range displaying phase transitions.

<sup>1</sup>H and <sup>13</sup>C NMR spectra were recorded using a 300 MHz Bruker Avance Ultrashield NMR Spectrometer (300.13 and 75.03 MHz, respectively) at concentrations of approximately 10 mg/mL and referenced to CDCl<sub>3</sub> (7.28 ppm) or acetone-*d*<sub>6</sub> (2.05 ppm). The number of scans used was 16 for <sup>1</sup>H NMR and 3072 for <sup>13</sup>C NMR.

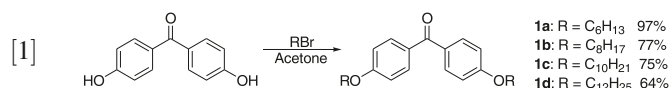
Polarizing optical microscopy (POM) was performed on an Olympus BX41 Microscope equipped with an Instec

HCS402 Hot Stage and STC200 Temperature Controller. All samples that exhibited multiple endothermic transitions on heating or multiple exothermic transitions on cooling by DSC analysis were characterized by POM. In a typical experiment, 5–10 mg of sample was heated to the clearing point, which was estimated by DSC, and cooled slowly to observe the liquid crystalline textures. POM images were captured with a Lumenera Infinity1 Digital Camera and were recorded and analyzed using InfinityCapture software.

## Results and discussion

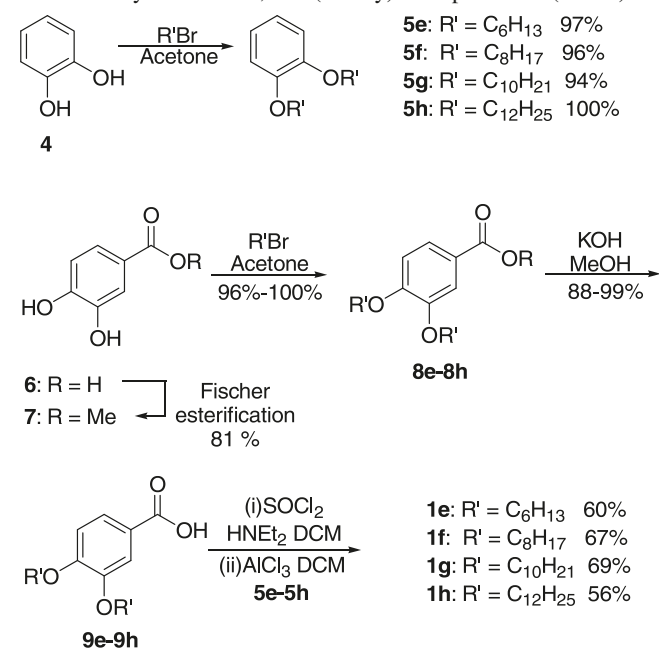
### Synthesis

The synthesis of the mono-alkoxy-substituted benzophenones **1a–1d** simply involved appending the alkoxy chains onto commercially available 4,4'-dihydroxy-benzophenone using the Williamson ether synthesis<sup>15</sup> (eq. [1]).

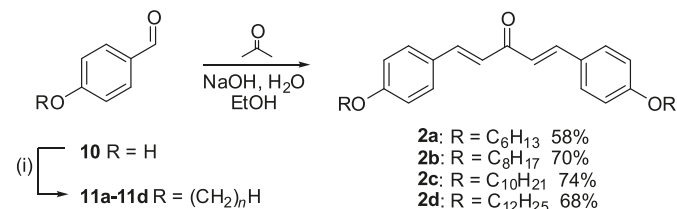


The synthesis of the bis(alkoxy)benzophenones (**1e–1h**) involved a Friedel–Crafts acylation<sup>16</sup> between 3,4-bis(alkoxy)-benzoic acids (**9e–9h**) and 3,4-bis(alkoxy)benzenes (**5e–5h**) (Scheme 1). The 3,4-bis(alkoxy)benzenes (**5e–5h**) were achieved via a Williamson ether synthesis between catechol (**5**) and the appropriate *n*-alkyl bromides (94%–100%). The substituted benzoic acids were achieved in three steps from 3,4-dihydroxybenzoic acid (**7**). First, **6** was protected as its methyl ester **7** by Fischer esterification,<sup>17</sup> then Williamson conditions were used to append the alkoxy chains to achieve esters **8e–8h**<sup>18</sup> in yields ranging from 96% (C<sub>6</sub>) to 100% (C<sub>8</sub>). Finally, saponification of **8e–8h**<sup>19</sup> afforded the benzoic acid coupling precursors **9e–9h** in yields from 88% (C<sub>10</sub>) to 99% (C<sub>8</sub>). Benzoic acids **9e–9h** were first converted to their respective acid chlorides using thionyl chloride and diethylamine.

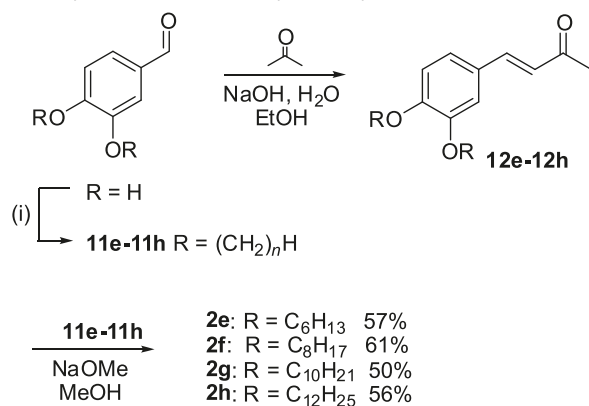
**Scheme 1.** Synthesis of 3,4-bis(alkoxy)benzophenones (**1e–1h**).





**Scheme 2.** Synthesis of mono-alkoxy dibenzylidene-acetones **2a–2d**.

Reagents and conditions: (i) RBr, K<sub>2</sub>CO<sub>3</sub>, DMF (86%–100%)

**Scheme 3.** Synthesis of bis(alkoxy)dibenzylidene-acetones (**2e–2h**).

Reagents and conditions: (i) RBr, K<sub>2</sub>CO<sub>3</sub>, DMF (89%–100%)

The acid chlorides were then added to a solution containing **5e–5h** and AlCl<sub>3</sub>. The benzophenones **1e–1h** were achieved in five steps with overall yields from 40% (C<sub>12</sub>) to 52% (C<sub>8</sub>).

The synthesis of the mono-alkoxy-substituted dibenzylidene acetones **2a–2d** involved a bidirectional aldol condensation between 1 equiv. of acetone and 2 equiv. of 4-alkoxybenzaldehydes (**11a–11d**), which were achieved again using a Williamson ether synthesis between 4-hydroxybenzaldehyde (**10**) and the appropriate *n*-alkyl bromides<sup>20</sup> (Scheme 2).

The attempted procedure of a bidirectional aldol condensation to achieve the di-alkoxy-substituted dibenzylidene acetones **2e–2h** in a method analogous to that of **2a–2d** proved difficult, with the reaction yielding an inseparable mixture of the mono- and bis-aldol condensation products. Instead, two stepwise aldol condensations were employed, the first reaction between 1 equiv. of acetone and 1 equiv. of 3,4-alkoxybenzaldehydes (**11e–11h**), and the second reaction between the resulting 4-(4-alkoxy-phenyl)but-3-en-2-ones (**12e–12h**) and a second equiv. of benzaldehydes **11e–11h** (Scheme 3).

The synthesis of mono-alkoxy 1,9-diphenyl-nona-1,3,6,8-tetraen-5-ones (**3a–3d**) was performed in a method analogous to that of **2e–2h**, employing stepwise aldol condensations between acetone and 4-alkoxy cinnamaldehydes. The latter were obtained, after various functional group interconversions, from commercially available *p*-coumaric acid (Scheme 4). The synthesis proceeded in six linear steps with overall yields of 42% (C<sub>10</sub>) to 56% (C<sub>12</sub>).

First, *p*-coumaric acid (**13**) was converted to its methyl ester **14** by Fischer esterification in 97% yield. The alkoxy

**Table 1.** Phase behaviour of **1a–1h**.

		Phase $\xrightarrow{T_1 (^{\circ}\text{C})^a}$ Phase	
<b>1a</b>	Cr <sub>1</sub>	$\xrightleftharpoons[62.8]{66.3}$	Cr <sub>2</sub>
	Cr <sub>2</sub>	$\xrightleftharpoons[93.4]{103.6}$	I
<b>1b</b>	Cr <sub>1</sub>	$\xrightleftharpoons[87.5]{89.9}$	Cr <sub>2</sub>
	Cr <sub>2</sub>	$\xrightleftharpoons[90.8]{98.2}$	I
<b>1c</b>	Cr	$\xrightleftharpoons[93.7]{100.2}$	I
<b>1d</b>	Cr	$\xrightleftharpoons[98.9]{103.2}$	I
<b>1e</b>	Cr <sub>1</sub>	$\xrightleftharpoons[-14.9]{-16.5}$	Cr <sub>2</sub>
	Cr <sub>2</sub>	$\xrightleftharpoons[45.8]{26.4}$	SmA
<b>1f</b>	Cr	$\xrightleftharpoons[11.3]{56.9}$	I
<b>1g</b>	Cr	$\xrightleftharpoons[39.7]{64.2}$	I
<b>1h</b>	Cr	$\xrightleftharpoons[47.0]{71.8}$	I

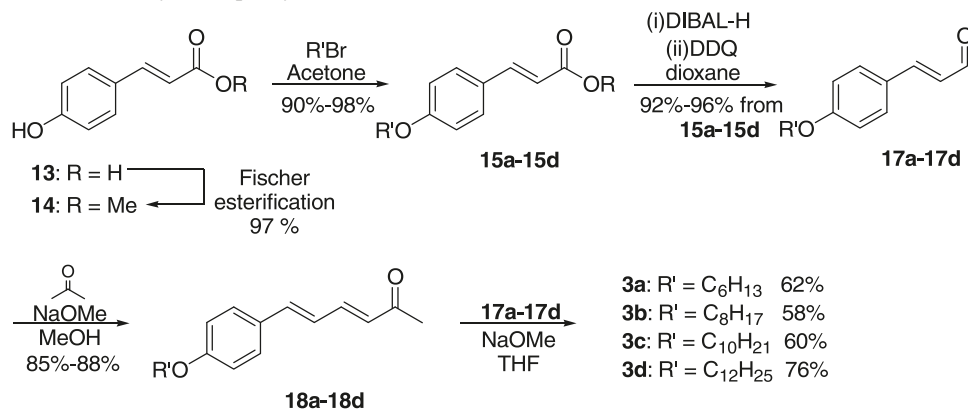
Note: Transition temperatures were determined by DSC.

<sup>a</sup>Cr = crystalline, Sm = Smectic, I = Isotropic.

chains were appended by the Williamson ether synthesis to afford **15a–15d** in yields from 90% to 98%. Attempted DIBAL reduction to the aldehydes **17a–17d**<sup>21</sup> led to a 1:1 mixture of completely reduced alcohol **16a–16d** and unreacted ester **15a–15d**. Instead, a strategy of complete reduction to the alcohol and subsequent reoxidation to the aldehyde was employed. The attempted reduction using LAH<sup>22</sup> resulted in reduction of esters **15a–15d** as well as hydrogenation of the olefin; a known result that seems to be limited to cinnamic acid derivatives.<sup>23</sup> A reduction using an excess of DIBAL afforded the cinnamyl alcohols **16a–16d** in yields ranging from 93% to 96%. Oxidation using the Corey–Suggs reagent PCC<sup>24</sup> led to both the desired α,β-unsaturated aldehydes **17a–17d** (minor) as well as the oxidative olefin cleavage byproduct<sup>23</sup> benzaldehyde (major). Instead, an oxidation using DDQ in dioxane<sup>25</sup> gave **17a–17d** in excellent yields (97% to 100%). Stepwise aldol condensations; the first between 1 equiv. of aldehydes **17a–17d** and acetone, and the second between the resulting 6-(4-alkoxy-phenyl)-hexa-3,5-dien-2-ones (**18a–18d**) and a second equiv. of **17a–17d**, gave the desired 1,9-diphenyl-nona-1,3,6,8-tetraen-5-ones (**3a–3d**) in yields of 49% to 67% over two steps.

### Characterization

It was found that neither the mono-alkoxybenzophenone derivatives **1a–1d** nor the bis(alkoxy)benzophenones (**1e–1h**) were mesogenic. Of the bis(alkoxy)benzophenones, **1e** was seen in SAXS measurements to undergo a crystal-to-

**Scheme 4.** Synthesis of mono-alkoxy 1,9-diphenyl-1,3,6,8-tetra-en-5-ones (**3a–3d**).**Table 2.** Phase behaviour of **2a–2h**.

Phase		$T_t$ (°C) <sup>a</sup>	Phase
<b>2a</b>	Cr	109.8	I
		101.6	
<b>2b</b>	Cr <sub>1</sub>	81.5	Cr <sub>2</sub>
		92.4	I
<b>2c</b>	Cr <sub>1</sub>	90.9	Cr <sub>2</sub>
		94.8	I
<b>2d</b>	Cr	95.4	I
		90.7	
<b>2e</b>	Cr	54.8	N
		31.4	I
<b>2f</b>	Cr <sub>1</sub>	3.2	Cr <sub>2</sub>
		23.0	I
<b>2g</b>	Cr <sub>1</sub>	39.1	Cr <sub>2</sub>
		26.6	I
<b>2h</b>	Cr <sub>1</sub>	51.2	Cr <sub>2</sub>
		31.4	I

Note: Transition temperatures were determined by DSC.  
<sup>a</sup>Cr = crystalline, N = Nematic, I = Isotropic.

**Table 3.** Phase behaviour of **3a–3d**.

Phase		$T_t$ (°C) <sup>a</sup>	Phase
<b>3a</b>	Cr	149.7	I
		128.5	
<b>3b</b>	Cr <sub>1</sub>	11.6	Cr <sub>2</sub>
		8.0	I
<b>3c</b>	Cr <sub>1</sub>	34.9	Cr <sub>2</sub>
		33.2	I
<b>3d</b>	Cr	121.1	N
		62.9	I

Note: Transition temperatures were determined by DSC.  
<sup>a</sup>Cr = crystalline, N = Nematic, I = Isotropic.

crystal transition at ~50 °C and to melt at ~100 °C. The phase behaviour of **1a–1h** is outlined in Table 1.

It was found the mono-alkoxy dibenzylidene acetone derivatives **2a–2d** were non-mesogenic. By contrast, the C<sub>6</sub>, C<sub>8</sub>, and C<sub>10</sub> bis(alkoxy)dibenzylidene acetones **2e**, **2f**, and **2g** were found to self-assemble into nematic mesophases. Figure 2 displays POM images of **2e** and **2f** taken at a magnification of 10×, and the phase behaviour of **2a–2h** is outlined in Table 2.

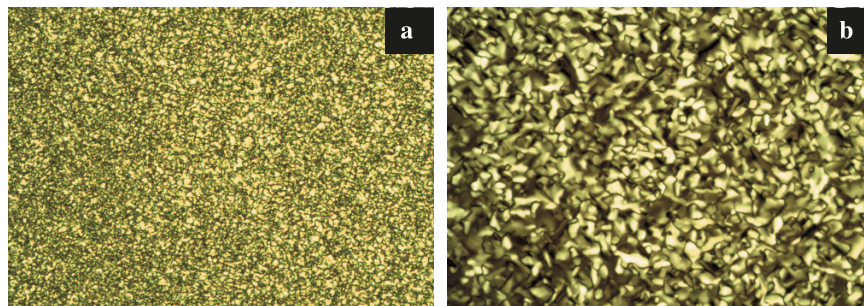
SAXS measurements confirm the assignments of **2e**, **2f**, and **2g** to nematic mesophases above room temperature. A diffuse maximum in the scattering from **2e** is consistent

with a nematic phase with a typical dimension of the cybotatic group of 2.1 nm and a correlation that increases upon cooling from 1.2 nm near the clearing point to 3.0 nm at room temperature. Compound **2f** shows similar behaviour, with a cybotatic dimension of 2.4 nm and a correlation length of 2.0 nm, and similarly **2g** has a nematic cybotatic dimension of 2.6 nm and a correlation length of ~2 nm.

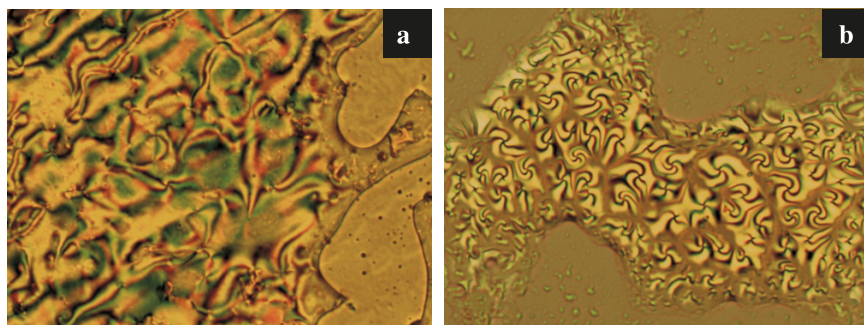
It was found that all four 1,9-diphenyl-nona-1,3,6,8-tetra-en-5-one derivatives self-assembled into nematic liquid crystalline phases. Figure 3 displays POM images of **3b** and **3d** in the nematic phase taken at a magnification of 10×, and the phase behaviour of **3a–3d** is outlined in Table 3.

SAXS on **3a** and **3b** were consistent with nematic phases at high temperature, but low signal levels precluded accurate measurement of cybotatic dimensions or correlation length. However, SAXS measurements on **3c** and **3d** showed sharp diffraction peaks with lamellar *d* spacings of 3.3 nm (**3c**) and 3.5 nm (**3d**), clearly indicating a smectic phase and inconsistent with the nematic texture observed in POM (Fig. 3). The reasons for this discrepancy are unclear, but are likely related to differences either in thermal history or anchoring effects by the glass slides and glass capillaries used in the two measurements.

**Fig. 2.** Polarized optical micrographs of (a) **2e** at 55 °C and (b) **2f** at 62 °C (10× magnification).



**Fig. 3.** Polarized optical micrographs of (a) **3b** at 136 °C and (b) **3d** at 122 °C (10× magnification).



## Conclusions

In summary, we have synthesized a new series of  $C_{2\text{-symmetric}}$  compounds, which display liquid crystalline mesophase behaviour. It was determined that the size of the rigid core, the length of the alkoxy side chain, and the number of alkoxy side chains have an impact on the ability of the molecules to self-assemble into liquid crystalline mesophases. Increasing the core size as well as increasing the number of side chains helped induce mesophase formation. In addition, increasing the length of the alkoxy side chain expanded the temperature range of the mesophase for the 1,9-diphenyl-nona-1,3,6,8-tetraen-5-ones.

## Supplementary data

Supplementary data for this article (detailed experimental procedures as well as spectral and analytical data, including  $^1\text{H}$  and  $^{13}\text{C}$  NMR spectra, DSC thermograms, and POM micrographs) are available on the journal Web site (canjchem.nrc.ca).

## Acknowledgement

The authors thank the Natural Science and Engineering Research Council of Canada (NSERC) for financial support (RGPAS 364426). We thank Dr. Mark MacLachlan for helpful discussions. We also thank Emilie Voisin and Dr. Vance Williams for assistance with mesophase characterization. Structural work at the University of Pennsylvania was supported by the MRSEC program of the National Science Foundation (Grant No. DMR05–20020).

## References

- (1) Schmidt-Mende, L.; Fechtenkötter, A.; Müllen, K.; Moons, E.; Friend, R. H.; MacKenzie, J. D. *Science* **2001**, 293 (5532), 1119. doi:10.1126/science.293.5532.1119. PMID:11498585.
- (2) (a) Shirota, Y. *J. Mater. Chem.* **2000**, 10 (1), 1. doi:10.1039/a908130e.; (b) Freudenmann, R.; Behnisch, B.; Hanack, M. *J. Mater. Chem.* **2001**, 11 (6), 1618. doi:10.1039/b100083g.
- (3) Christ, T.; Glösen, B.; Greiner, A.; Kettner, A.; Sander, R.; Stümpflen, V.; Tsukruk, V.; Wendorff, J. H. *Adv. Mater.* **1997**, 9, 48. doi:10.1002/adma.19970090110.
- (4) Grolik, J.; Sieron, L.; Eilmes, J. *Tetrahedron Lett.* **2006**, 47 (47), 8209. doi:10.1016/j.tetlet.2006.09.134.
- (5) Jeong, M. J.; Park, J. H.; Lee, C.; Chang, J. Y. *Org. Lett.* **2006**, 8 (11), 2221. doi:10.1021/ol060479l. PMID:16706491.
- (6) Park, Y. S.; Kim, D.; Lee, H.; Moon, B. *Org. Lett.* **2006**, 8 (21), 4699. doi:10.1021/ol061711q. PMID:17020281.
- (7) Yang, P.-J.; Lin, H.-C. *Liq. Cryst.* **2006**, 33 (5), 587. doi:10.1080/02678290600633394.
- (8) Foster, E. J.; Jones, R. B.; Lavigneur, C.; Williams, V. E. *J. Am. Chem. Soc.* **2006**, 128 (26), 8569. doi:10.1021/ja0613198. PMID:16802823.
- (9) Lai, C. K.; Liu, H.-C.; Li, F.-J.; Cheng, K.-L.; Sheu, H.-S. *Liq. Cryst.* **2005**, 32 (1), 85. doi:10.1080/02678290512331324048.
- (10) Engel, M. K.; Bassoul, P.; Bosio, L.; Lehmanns, H.; Hanacks, M.; Simon, J. *Liq. Cryst.* **1993**, 15 (5), 709. doi:10.1080/02678299308036489.
- (11) Wang, C.-S.; Wang, I.-W.; Cheng, K.-L.; Lai, C. K. *Tetrahedron* **2006**, 62 (40), 9383. doi:10.1016/j.tet.2006.07.058.
- (12) van de Craats, A. M.; Warman, J. M. *Adv. Mater.* **2001**, 13 (2), 130. doi:10.1002/1521-4095(200101)13:2<130::AID-ADMA130>3.0.CO;2-L.
- (13) See [www.lrsr.upenn.edu/lrsr/facMAXS.html](http://www.lrsr.upenn.edu/lrsr/facMAXS.html) for additional details.
- (14) See [www.datasqueezesoftware.com](http://www.datasqueezesoftware.com) for more details.
- (15) Williamson, A. W. *J. Chem. Soc.* **1852**, 4, 229.
- (16) (a) Friedel, C.; Crafts, J. M. *C. R. Chim.* **1877**, 84, 1392; (b) Friedel, C.; Crafts, J. M. *C. R. Chim.* **1877**, 84, 1392; (c) Xiao, S.; Tang, J.; Beetz, T.; Guo, X.; Tremblay, N.; Siegr-

- ist, T.; Zhu, Y.; Steigerwald, M.; Nuckolls, C. *J. Am. Chem. Soc.* **2006**, *128* (33), 10700. doi:10.1021/ja0642360. PMID: 16910663.
- (17) Fischer, E.; Speier, A. *Chem. Ber.* **1895**, *28* (3), 3252. doi:10.1002/cber.189502803176.
- (18) Percec, V.; Rudick, J. G.; Peterca, M.; Wagner, M.; Obata, M.; Mitchell, C. M.; Cho, W.-D.; Balagurusamy, V. S. K.; Heiney, P. A. *J. Am. Chem. Soc.* **2005**, *127* (43), 15257. doi:10.1021/ja055406w. PMID:16248668.
- (19) (a) Rowe, K. E.; Bruce, D. W. *J. Mater. Chem.* **1998**, *8* (2), 331. doi:10.1039/a706400d.; (b) Suárez, S.; Mamula, O.; Scopelliti, R.; Donnio, B.; Guillon, D.; Terazzi, E.; Piguet, C.; Buenzli, J.-C. *G. N. J. Chem.* **2005**, *29* (10), 1323. doi:10.1039/b503591k.; (c) Ropponen, J.; Nummelin, S.; Rissanen, K. *Org. Lett.* **2004**, *6* (15), 2495. doi:10.1021/ol049555f. PMID:15255674.
- (20) (a) Tang, Y.; Mei, C.; Li, S.; Wang, Y.; Wang, X.; Wang, L.; Yan, D.; Ye, C. *Chin. Sci. Bull.* **2005**, *50* (17), 1849. doi:10.1360/982005-6.; (b) Brun, A.; Etemad-Moghadam, G. *Synthesis* **2002**, (10): 1385. doi:10.1055/s-2002-33111.; (c) Lensen, M. C.; Elemans, J. A. A. W.; van Dingenen, S. J. T.; Gerritsen, J. W.; Speller, S.; Rowan, A. E.; Nolte, R. J. M. *Chem. Eur. J.* **2007**, *13* (28), 7948. doi:10.1002/chem.200700131.
- (21) Winterfeldt, F. *Synthesis* **1975**, *7*, 617.
- (22) (a) Finholt, A. E.; Bond, A. C., Jr.; Schlesinger, H. I. *J. Am. Chem. Soc.* **1947**, *69* (5), 1199. doi:10.1021/ja01197a061.; (b) Nystrom, R. F.; Brown, W. G. *J. Am. Chem. Soc.* **1947**, *69* (5), 1197. doi:10.1021/ja01197a060.
- (23) Nystrom, R. F.; Brown, W. G. *J. Am. Chem. Soc.* **1947**, *69* (10), 2548. doi:10.1021/ja01202a082.
- (24) Corey, E. J.; Suggs, J. W. *Tetrahedron Lett.* **1975**, *16* (31), 2647. doi:10.1016/S0040-4039(00)75204-X.
- (25) Kumar, N. S. S.; Varghese, S.; Narayan, G.; Das, S. *Angew. Chem. Int. Ed.* **2006**, *45* (38), 6317. doi:10.1002/anie.200602088.



# Radiolysis of supercritical water at 400 °C and liquid-like densities near 0.5 g/cm<sup>3</sup> — A Monte Carlo calculation

Jintana Meesungnoen, David Guzonas, and Jean-Paul Jay-Gerin

**Abstract:** Monte Carlo simulations are used to calculate the primary radical yields  $g(e_{aq}^-)$ ,  $g(^{\bullet}OH)$ , the sum  $[g(e_{aq}^-) + g(^{\bullet}OH) + g(H^{\bullet})]$ , and the ratio  $g(H^{\bullet})/g(e_{aq}^-)$  in the low linear energy transfer (LET) radiolysis of supercritical water (SCW) at 400 °C in the high-density, liquid-like region near  $\sim 0.5$  g/cm<sup>3</sup>. Using all the currently available information on the reactivities and diffusion coefficients of the radiation-induced species under these conditions, and assuming the aqueous medium to be a “continuum”, a good accord is found between our calculations and the available experimental data. In particular, our computed  $e_{aq}^-$  yields at 60 ps and 1 ns compare very well with recently reported direct time-dependent  $e_{aq}^-$  yield measurements in SCW (D<sub>2</sub>O) at 400 °C and 0.570 g/cm<sup>3</sup> using picosecond pulse radiolysis experiments.

**Key words:** supercritical water, radiolysis, hydrated electron,  $^{\bullet}OH$  radical,  $H^{\bullet}$  atom, rate constants, diffusion coefficients, primary radiolytic yields ( $g$  values), Monte Carlo track structure simulations.

**Résumé :** À l'aide de simulations Monte Carlo, nous avons calculé, pour des rayonnements de faible transfert d'énergie linéique (TEL), les rendements primaires radicalaires ( $g(e_{aq}^-)$ ),  $g(^{\bullet}OH)$ , la somme  $[g(e_{aq}^-) + g(^{\bullet}OH) + g(H^{\bullet})]$  et le rapport  $g(H^{\bullet})/g(e_{aq}^-)$  intervenant lors de la radiolyse de l'eau à l'état supercritique (ESC) à 400 °C dans la région de haute densité de type liquide autour de  $\sim 0,5$  g/cm<sup>3</sup>. En utilisant toute les renseignements actuellement disponibles sur les réactivités et les coefficients de diffusion des espèces radio induites dans ces conditions et en considérant le milieu aqueux comme un « continuum », un bon accord a été trouvé entre nos calculs et les données expérimentales existantes. En particulier, nos rendements calculés en électrons hydratés ( $e_{aq}^-$ ) à 60 ps et 1 ns s'accordent très bien avec les mesures directes obtenues en radiolyse pulsée picoseconde du rendement en  $e_{aq}^-$  dans l'ESC (D<sub>2</sub>O) à 400 °C et 0 570 g/cm<sup>3</sup>.

**Mots-clés :** eau supercritique, radiolyse, électron hydraté, radical  $^{\bullet}OH$ , atome  $H^{\bullet}$ , constantes de vitesse de réaction, coefficients de diffusion, rendements primaires radiolytiques (valeurs  $g$ ), simulations Monte Carlo de structure de trajectoire.

## Introduction

While experiments showing that water is decomposed by X-rays and radium date back to the early 20th century, various quantitative aspects of this radiolysis are still not fully resolved (for example, see refs. 1–3). The operation of water-cooled nuclear reactors, which use water in various process systems around the reactor core, including the primary heat transport system, as a neutron moderator and as a biological shield,<sup>4</sup> requires the ability to predict and mitigate the effects of this water radiolysis. The Generation IV (Gen IV) supercritical water-cooled reactor (SCWR) designs currently under consideration for deployment in the 2025 time-frame<sup>5–10</sup> would operate at core outlet temperatures as high as 625 °C and at a pressure of 25 MPa, i.e., well beyond the thermodynamic critical point of water (H<sub>2</sub>O:  $t_c = 373.95$  °C,  $P_c = 22.06$  MPa or 217.7 atm,  $\rho_c = 0.322$  g/cm<sup>3</sup>; D<sub>2</sub>O:  $t_c = 370.74$  °C,  $P_c = 21.67$  MPa or 213.9 atm,  $\rho_c = 0.358$  g/cm<sup>3</sup>).<sup>11</sup> Thermodynamic cycle efficiencies as high as  $\sim 49\%$  (vs.  $\sim 33\%$  for existing water reactors) have been

calculated for reactors operating with a supercritical water (SCW) coolant, thus generating lower-cost electricity.

A greatly enhanced understanding of the effects of radiation on aqueous systems in future SCWR designs will be required to specify a chemistry control strategy that will minimize unwanted degradation of components in the SCWR core and of piping downstream of the core resulting from the radiolytic formation of oxidizing products such as  $^{\bullet}OH$ , H<sub>2</sub>O<sub>2</sub>, O<sub>2</sub>, and O<sub>2</sub> $^{\bullet-}$  (or HO<sub>2</sub> $^{\bullet}$  depending on the pH).<sup>8–10,12</sup> These oxidizing products are highly reactive with most metal alloys at the elevated temperatures proposed for the SCWR core outlet. In current pressurized water reactor (PWR) designs, one commonly used chemistry control measure to prevent the net radiolytic production of oxidizing species in the water is to add a small overpressure of excess H<sub>2</sub> to the reactor coolant. It is still unclear, however, whether this strategy, or some variant on the same theme, would also be effective under SCWR conditions.<sup>9</sup>

The combination of extreme conditions of high tempera-

Received 14 January 2010. Accepted 19 April 2010. Published on the NRC Research Press Web site at canjchem.nrc.ca on 18 June 2010.

**J. Meesungnoen and J.-P. Jay-Gerin.**<sup>1</sup> Département de Médecine Nucléaire et de Radiobiologie, Faculté de Médecine et des Sciences de la Santé, Université de Sherbrooke, Sherbrooke, QC J1H 5N4, Canada.

**D. Guzonas.** Reactor Chemistry and Corrosion Branch, Atomic Energy of Canada Limited, Chalk River Laboratories, Chalk River, ON K0J 1J0, Canada.

<sup>1</sup>Corresponding author (e-mail: jean-paul.jay-gerin@USherbrooke.ca).

ture and pressure and the intense flux of ionizing radiations (fast neutrons,  $\gamma$ -rays, recoil protons/deuterons and heavy ions), which are the main source of the oxidizing products,<sup>9,10,13,14</sup> make the experimental characterization of water radiolysis under expected SCWR operating conditions very difficult. As a result, theoretical models and computer simulations of the radiation chemistry of the SCWR coolant are an important route of investigation.<sup>9,10,14,15</sup> However, a large amount of input information on the reaction rate constants ( $k$ ) of radiation-induced species, reaction mechanisms, diffusion coefficients ( $D$ ), and radiolytic yields ( $g$  values) in subcritical water and in the SCW regime is needed to create such models. This information is important since preliminary studies suggest, in many cases, a markedly different behavior of the effects of radiation at SCW conditions compared to what one would predict from simplistic extrapolations of experimental data originally measured at lower temperatures. Key examples here include the rate constants of a growing number of chemical reactions that are found to exhibit, at elevated temperatures, negative Arrhenius activation energies (i.e., the temperature dependence of  $k$  actually decreases gradually with temperatures above a certain temperature), so that earlier attempts to extrapolate existing experimental data on reactivities from their measured ranges (mostly less than 250–310 °C; see, for example, refs. 15–18) to the temperatures of interest, assuming simple Arrhenius behavior, should be viewed with caution.<sup>9,19–24</sup> Since about 2000, there has been a revival in the study of the high-temperature, radiolysis of water driven, in large part, by the need for information on (light and heavy) water in the supercritical regime. Generally, these studies have been able to extend the measurements of both reaction rates and  $g$  values to higher temperatures than the original investigations, thereby reducing or, in some cases, eliminating the need to extrapolate the data.<sup>24,25</sup> More recently, the need to model chemistry in a SCWR has initiated concerted national and international experimental programs that are now underway in several laboratories to generate the necessary radiation chemistry data. Currently, however, only limited experimental data are available on the radiation chemistry and reaction kinetics of transients in SCW.<sup>8,9,13,19,20,26–36</sup>

The present work is a first attempt to extend our previous Monte Carlo track structure simulations in liquid water at high temperatures<sup>37</sup> to the study of the low linear energy transfer (LET) radiolysis of SCW (H<sub>2</sub>O) at 400 °C. It represents an initial effort to obtain data to help elucidate mechanisms by which radiation interacts with water in its supercritical regime. The calculations reported herein incorporate all the currently available information on the reactivities and diffusion coefficients of the radiolytically produced free radicals and molecular products ( $e_{aq}^-$ , H<sup>+</sup>, OH<sup>-</sup>, H<sup>•</sup>, H<sub>2</sub>, •OH, H<sub>2</sub>O<sub>2</sub>, O<sub>2</sub><sup>•-</sup> (or HO<sub>2</sub>•), etc.)<sup>1,38–40</sup> and on the physicochemical properties (density, viscosity, static dielectric constant,  $K_w$ , etc.) of water at this temperature. To our knowledge, no theoretical modeling of the radiolysis of water at such elevated temperatures has been reported so far. It should be pointed out that even if uncertainties abound throughout, and many steps remain to be studied before a complete theoretical foundation exists for describing the radiolysis of SCW, we have used parameters that appear reasonable to us. Rather than waiting until better data be-

come available, our first objective is to push the calculation to the point at which we can compare calculated  $g$  values for radiolysis yields with existing experimental observations. Of course, the final objective is a track model that agrees with all experimental chemical data.

The organization of the paper is as follows. We first briefly describe the main features of our simulation approach, and then present and discuss, in the light of the available experimental data, the results of our calculated yields of the free radical products  $e_{aq}^-$  (hydrated electron), •OH, and H<sup>•</sup> atom in irradiated SCW at 400 °C in the liquid-like density region around  $\sim 0.5$  g/cm<sup>3</sup>. We conclude with a short summary and final remarks.

## Monte Carlo simulations

The radiolysis of SCW has been modeled using an extended version of our Monte Carlo track structure simulation code called IONLYS-IRT, which simulates irradiations (by high-energy protons or heavier ions) of pure liquid water or (dilute) aqueous solutions at ambient<sup>41–44</sup> and elevated<sup>37</sup> temperatures. A detailed description of our simulation methodology and reaction scheme used to model the radiation chemistry of water can be found in refs. 37 and 41–44. In brief, the IONLYS program models, on an event by event basis, all the events of the early “physical” ( $<10^{-15}$  s) and “physicochemical” ( $\sim 10^{-15}$ – $10^{-12}$  s) stages<sup>45</sup> in the track development. The complex spatial distribution of reactants present at the end of the physicochemical stage, which is provided as an output of the IONLYS program, is then used directly as the starting point for the subsequent “nonhomogeneous chemical” stage.<sup>45</sup> This third and final stage (from  $\sim 10^{-12}$  s up to about  $10^{-7}$ – $10^{-6}$  s at room temperature), during which the various radiolytic species diffuse randomly and react with one another or with dissolved solutes (if any) present at the time of irradiation, until all spur/track processes are complete, is covered by our IRT program. This program employs the “independent reaction times” (IRT) method,<sup>46,47</sup> a computer-efficient stochastic simulation technique that is used to simulate reaction times without having to follow the trajectories of the diffusing species. The IRT method relies on the approximation that the reaction time for each pair of reactants is independent of the presence of other reactants in the system. Such an approximation has been found to be accurate in solvents of high dielectric constant, where the Coulomb forces between the ions are weak (as is the case with ordinary water), but the method has also been used in intermediate and low-permittivity solvents (such as water at elevated temperatures, alcohols, and hydrocarbons).<sup>37,48–50</sup> Within the framework of this approach, the competition between the reactions is simply described via a sorting out of the stochastically sampled reaction times for each of the potentially reactive pairs of reactants. The implementation of this program has been described in detail previously<sup>42,44</sup> and its ability to give accurate time-dependent chemical yields has been validated by comparison with full random flight Monte Carlo simulations that do follow the reactant trajectories in detail.<sup>51,52</sup>

In the present version of IONLYS-IRT, the rate constants of the dominant chemical and acid/base equilibrium reactions involved in the radiolysis of SCW at 400 °C in the

**Table 1.** Main spur/track reactions and values at 400 °C and in the liquid-like density region near  $\sim 0.5 \text{ g/cm}^3$  for the corresponding rate constants ( $k$ ) used in our simulations.

Symbol	Reaction	$k$ ( $10^{10} (\text{mol/L})^{-1} \text{ s}^{-1}$ )
R1	$\bullet\text{OH} + \text{e}_{\text{aq}}^- \rightarrow \text{OH}^-$	$45^a$
R2	$\bullet\text{OH} + \text{H}^\bullet \rightarrow \text{H}_2\text{O}$	$4.4^b$
R3	$\bullet\text{OH} + \bullet\text{OH} \rightarrow \text{H}_2\text{O}_2$	$0.85^a$
R4	$\bullet\text{OH} + \text{HO}_2^\bullet \rightarrow \text{O}_2 + \text{H}_2\text{O}$	$3^a$
R5	$\text{OH} + \text{H}_2 \rightarrow \text{H}^\bullet + \text{H}_2\text{O}$	$0.06^a$
R6	$\text{e}_{\text{aq}}^- + \text{H}^+ \rightarrow \text{H}^\bullet$	$300^{a,c}$
R7	$\text{e}_{\text{aq}}^- + \text{H}^\bullet \rightarrow \text{H}_2 + \text{OH}^-$	$79^a$
R8	$\text{H}^\bullet + \text{OH}^- \rightarrow \text{e}_{\text{aq}}^- + \text{H}_2\text{O}$	$2.2^a$
R9	$\text{H}^+ + \text{OH}^- \rightarrow \text{H}_2\text{O}$	$200^a$
R10	$\text{e}_{\text{aq}}^- + \text{e}_{\text{aq}}^- \rightarrow \text{H}_2 + 2\text{OH}^-$	$21^d$
R11	$\text{H}^\bullet + \text{H}^\bullet \rightarrow \text{H}_2$	$15^e$
R12	$\text{H}^\bullet + \text{O}_2 \rightarrow \text{HO}_2^\bullet$	$6.7^a$
R13	$\text{H}^\bullet + \text{HO}_2^\bullet \rightarrow 2\bullet\text{OH}$	$34^a$
R14	$\text{H}^\bullet + \text{H}_2\text{O}_2 \rightarrow \bullet\text{OH} + \text{H}_2\text{O}$	$0.23^a$
R15	$\text{e}_{\text{aq}}^- + \text{H}_2\text{O}_2 \rightarrow \bullet\text{OH} + \text{OH}^-$	$46^a$
R16	$\bullet\text{OH} + \text{H}_2\text{O}_2 \rightarrow \text{HO}_2^\bullet + \text{H}_2\text{O}$	$0.06^a$
R17	$\text{e}_{\text{aq}}^- + \text{O}_2 \rightarrow \text{O}_2^{\bullet-}$	$25^{a,f}$

<sup>a</sup>Extrapolated from ref. 24.

<sup>b</sup>From Fig. 2 of ref. 20. See also ref. 24.

<sup>c</sup>See also ref. 53.

<sup>d</sup>Extrapolated from Fig. 3 of ref. 16, assuming reaction R10 is diffusion controlled and using the experimental data up to 150 °C. See also ref. 37.

<sup>e</sup>Extrapolated from Fig. 7 of ref. 16, assuming reaction R11 is diffusion controlled. See also ref. 24.

<sup>f</sup>See also ref. 28.

liquid-like density region studied have generally been obtained by extrapolating the experimental data recently compiled by Elliot and Bartels<sup>24</sup> from their measured ranges (mostly 20–350 °C). In some cases, however, the kinetic data of Ghandi and Percival<sup>20</sup> inferred from muon spin spectroscopy measurements in subcritical water and SCW (up to 450 °C) have also been used. The corresponding  $k$  values employed in our simulations are listed in Table 1. Note the particular case of the self-reaction of  $\text{e}_{\text{aq}}^-$  (reaction R10) whose temperature dependence in near-neutral solution is still a subject of discussion<sup>16–18,23,24</sup> that requires clarification. Its rate constant has been chosen here by following the extrapolation procedure previously proposed by Elliot,<sup>16</sup> and employed in ref. 37, which assumes that this reaction is diffusion controlled at temperatures above 150 °C. The validity of this assumption is confirmed by the good agreement of the calculated and experimental  $g(\text{e}_{\text{aq}}^-)$  values up to 350 °C (data not shown). In contrast, if the abrupt decrease in this rate constant observed in alkaline solution above 150 °C is included in our simulations, a sharp downward discontinuity in  $g(\text{H}_2)$  is predicted,<sup>37</sup> see also refs. 54 and 55, which is not observed experimentally.<sup>24</sup> This abrupt drop needs to be confirmed at near-neutral pH values, as it may be a function of the pH of the solution.<sup>16–18</sup> For the other reactions, whose rate constants have been measured only up to 200 or 250 °C (many of these data have been collected and summarized in refs. 15–18 and 24 for both light and heavy water), the available data for  $k$  have been extrapolated above their experimentally studied temperature range as described previ-

**Table 2.** Values at 400 °C for the diffusion coefficients ( $D$ ) of reactive species in SCW in the high-density region around  $\sim 0.5 \text{ g/cm}^3$ .

Species	$D$ ( $10^{-9} \text{ m}^2 \text{ s}^{-1}$ )
$\text{H}_2^a$	146
$\text{H}_2\text{O}_2^a$	70
$\text{H}^\bullet^a$	213
$\bullet\text{OH}^a$	67
$\text{e}_{\text{aq}}^-$	$420^b$
$\text{H}_3\text{O}^+$	$56^c$
$\text{OH}^-$	$58^c$
$\text{H}_2\text{O}^a$	70

<sup>a</sup>The diffusion coefficients of  $\text{H}_2$ ,  $\text{H}_2\text{O}_2$ ,  $\text{H}^\bullet$ , and  $\bullet\text{OH}$ , explicitly determined at 25 °C but essentially unknown at 400 °C, are assumed to scale with the self-diffusion of water above room temperature.<sup>16–18,23,37,54</sup> The values of  $D$  at 25 °C for the various reactants are taken from refs. 16 and 37.  $D_{\text{H}_2\text{O}}(25^\circ\text{C}) = 2.299 \times 10^{-9} \text{ m}^2 \text{ s}^{-1}$ .<sup>56</sup> The self-diffusion coefficient of compressed SCW at 400 °C and  $\sim 0.5 \text{ g/cm}^3$  is taken to be  $70 \times 10^{-9} \text{ m}^2 \text{ s}^{-1}$  from the measurements of Lamb et al.<sup>57</sup>

<sup>b</sup>Extrapolated from the data of Schmidt et al.<sup>58</sup> up to 90 °C and the estimate of Marin et al.<sup>23</sup> at 300 °C ( $\sim 240 \times 10^{-9} \text{ m}^2 \text{ s}^{-1}$ ).

<sup>c</sup>Obtained by extrapolation of the experimental data reported by Elliot and Bartels (Figs. 4–27 of ref. 24) over the 0–350 °C temperature range.

ously.<sup>37</sup> Due to the lack of experimental data, we have simply assumed that the reaction rate constants remain constant with water density on the 400 °C isotherm of interest. This approximation would most likely not be too severe, taking into account the limited range of densities (around  $\sim 0.5 \text{ g/cm}^3$ ) investigated here.<sup>28</sup>

The diffusion coefficients used in the simulations for the main reactive species are listed in Table 2. The values of the viscosity ( $\eta \sim 58.6 \text{ } \mu\text{Pa s}$ ), static dielectric constant ( $\epsilon_0 \sim 9.6$ ), and molar concentration ( $\sim 27.8 \text{ mol/L}$ ) of SCW at 400 °C and  $\sim 0.5 \text{ g/cm}^3$  have been taken from the NIST Chemistry WebBook<sup>11</sup> while the ionic product of water ( $K_w$ ) has been obtained from Bandura and Lvov.<sup>59</sup> Finally, from a microscopic viewpoint, we have ignored here the heterogeneous molecular structure of SCW originating from the existence of density fluctuations (or water “clustering”) that are associated with the high compressibility of water in the vicinity of the critical point (e.g., see refs. 60–65 and refs. cited therein). In our simulations, we assume that the overall instantaneous picture of SCW can simply be viewed as a *continuum* medium with a mean density equal to the density of bulk water. This approximation is thought to be reasonable at the liquid-like SCW densities considered in this study<sup>61,63</sup> and it seems to be justified by the agreement we have obtained between model and experiment (see below).

To reproduce the effects of  $^{60}\text{Co}$   $\gamma$ -rays or fast electrons, we use short ( $\sim 100 \text{ } \mu\text{m}$ ) segments of  $\sim 300 \text{ MeV}$  proton tracks, over which the LET is essentially constant and equal to  $\sim 0.3 \text{ keV}/\mu\text{m}$  in normal liquid water at 25 °C. Such an analysis thus gives “track segment” yields<sup>66</sup> as a function of time from picoseconds to, typically, microseconds. The number of proton histories ( $\sim 150$ ) is chosen so as to ensure only small statistical fluctuations when calculating average yields, while keeping acceptable computer time limits.

**Table 3.** Comparison of available experimental data of  $g(e_{aq}^-)$ ,  $g(\bullet OH)$ ,  $(g(e_{aq}^-) + g(\bullet OH) + g(H^\bullet))$ , and  $g(H^\bullet)/g(e_{aq}^-)$  in the low-LET radiolysis of SCW at 400 °C and in the liquid-like density region near  $\sim 0.5 \text{ g/cm}^3$  with the results of our Monte Carlo simulations.

Yield	Experiment	This work <sup>a</sup>
$g(e_{aq}^-)$	$3.48 \pm 0.2^b$ at $0.570 \text{ g/cm}^3$ and $\sim 60 \text{ ps}^{35,36}$ $2.46 \pm 0.2^b$ at $0.570 \text{ g/cm}^3$ and $\sim 1 \text{ ns}^{35,36}$ $2.29$ at $0.523 \text{ g/cm}^3$ <sup>31</sup> $2.36$ at $0.502 \text{ g/cm}^3$ <sup>31</sup> $2.45^c$ at $0.475 \text{ g/cm}^3$ <sup>31</sup>	$3.15$ at $60 \text{ ps}$ $2.55$ at $1 \text{ ns}$  $2.26$
$g(e_{aq}^-) + g(\bullet OH) + g(H^\bullet)$	$9.45$ at $0.523 \text{ g/cm}^3$ <sup>31</sup> $9.35$ at $0.502 \text{ g/cm}^3$ <sup>31</sup> $9.55$ at $0.475 \text{ g/cm}^3$ <sup>31</sup> $9.38$ at $0.523 \text{ g/cm}^3$ <sup>34</sup> $10.08$ at $0.475 \text{ g/cm}^3$ <sup>34</sup>	$9.07$
$g(\bullet OH)$	$5.41^d$ at $0.523 \text{ g/cm}^3$ <sup>33</sup> $5.63^d$ at $0.475 \text{ g/cm}^3$ <sup>33</sup>	$4.91$
$g(H^\bullet)/g(e_{aq}^-)$	$0.996^e$ at $0.523 \text{ g/cm}^3$ $1.11^e$ at $0.475 \text{ g/cm}^3$	$0.84$

**Note:** Most data reported here are derived from scavenged yields of species measured in steady-state experiments and supposed ideally to be close to the “escape” yields from the spur.<sup>24,39,66</sup> The precision of these measurements is estimated to be on the order of 10%.<sup>31,33,34</sup> Unless otherwise indicated, our calculated yields are all obtained assuming a scavenging time of  $\sim 10 \text{ ns}$ .<sup>13</sup> The  $g$  values are expressed here in units of molecules per 100 eV. For conversion into SI units (mol/J): 1 molecule/100 eV  $\approx 0.10364 \mu\text{mol/J}$ .<sup>1</sup>

<sup>a</sup>All yield values are computed for a SCW density of  $0.5 \text{ g/cm}^3$ .

<sup>b</sup>Direct observation using picosecond pulse radiolysis experiments in supercritical  $D_2O$ .

<sup>c</sup>Janik et al.<sup>13</sup> also measured the  $e_{aq}^-$  escape yields in SCW at 400 and 380 °C as a function of density using  $N_2O$  as a specific scavenger for  $e_{aq}^-$  rather than the *tert*-BuOH/methyl viologen scavenging system used in the experiments of Lin et al.<sup>31</sup> At their highest densities studied ( $\sim 0.42\text{--}0.55 \text{ g/cm}^3$ ), their  $e_{aq}^-$  yields ( $\sim 1.48\text{--}3.12$  molecules/100 eV) are comparable with those measured by Lin et al.<sup>31</sup> In contrast, the value of  $g(e_{aq}^-) = 0.8$  molecule/100 eV found by Sims<sup>27</sup> in  $\gamma$ -irradiated SCW at 400 °C and  $0.45 \text{ g/cm}^3$  from a reanalysis of data previously published by Burns and Marsh<sup>26</sup> is a factor of  $\sim 3$  lower than that measured by Lin et al.<sup>31</sup>

<sup>d</sup>Average over several determinations. Note that there are at present no experimental data from other groups with which to compare our results.

<sup>e</sup>Obtained from different product yield measurements without taking account of the scavenging time of the two species.<sup>67</sup> Note that similar values of this ratio have also been reported at 380 °C in the density regime studied here by Janik et al.<sup>13</sup> (see also ref. 28). For comparison, the value for  $g(H^\bullet)/g(e_{aq}^-)$  in the low-LET radiolysis of ordinary liquid water at 25 °C is  $\sim 0.22$ .<sup>24</sup>

## Results and discussion

Table 3 compares our calculated values of  $g(e_{aq}^-)$ ,  $g(\bullet OH)$ , the sum  $(g(e_{aq}^-) + g(\bullet OH) + g(H^\bullet))$ , and the ratio  $g(H^\bullet)/g(e_{aq}^-)$  with available experimental data<sup>13,26,27,31,33–36</sup> for the low-LET radiolysis of pure, deaerated SCW at 400 °C and  $\sim 0.5 \text{ g/cm}^3$ . As we can see, there is good overall agreement between calculated and experimental  $g$  values. Among the results emerging from this study, let us note below the following points.

First, there is at present only limited information with which to compare our results on the radiation yields of transient species in water under supercritical conditions. In fact, published data mainly concern  $g$  values for  $e_{aq}^-$ ,<sup>9,13,26–28,31,32,35,36</sup>  $H^\bullet$  atom,<sup>9,13,28</sup>  $H_2$ ,<sup>9,13</sup> and  $\bullet OH$ <sup>33</sup> production in low-LET radiolysis up to 400 °C. Most of these studies employ steady-state radiolysis experiments with various specific scavengers, assuming that they (and the products formed) are thermally stable in SCW. However, because of the lack of precise determination of the rate constants for the reactions between radicals and scavengers, the

scavenging time (i.e., the reciprocal of the “scavenging power”, defined as the product of  $k$  and the scavenger concentration) corresponding to the  $g$  values reported at high temperature, and a fortiori in the supercritical regime, is not well-known and may differ appreciably depending on the experimental conditions. In fact, to ensure minimal scavenging in the spur/track, experimentalists generally use scavenger concentrations such that the scavenging time at room temperature is about  $10^{-7} \text{ s}$ .<sup>16,24,31–33</sup> In the calculations reported in Table 3, we have assumed that, in the temperature/density regime investigated, the scavenging time in those yield experiments is of the order of  $10 \text{ ns}$ .<sup>13,68</sup> This choice is consistent with our Monte Carlo calculations, which show that, in liquid water for low-LET radiation and under ordinary irradiation conditions, the lifetime of the spur (i.e., the time at which the nonhomogeneous chemical stage is completed) diminishes with increasing temperature, reaching a value close to  $2 \times 10^{-8} \text{ s}$  at 350 °C.<sup>37,69</sup>

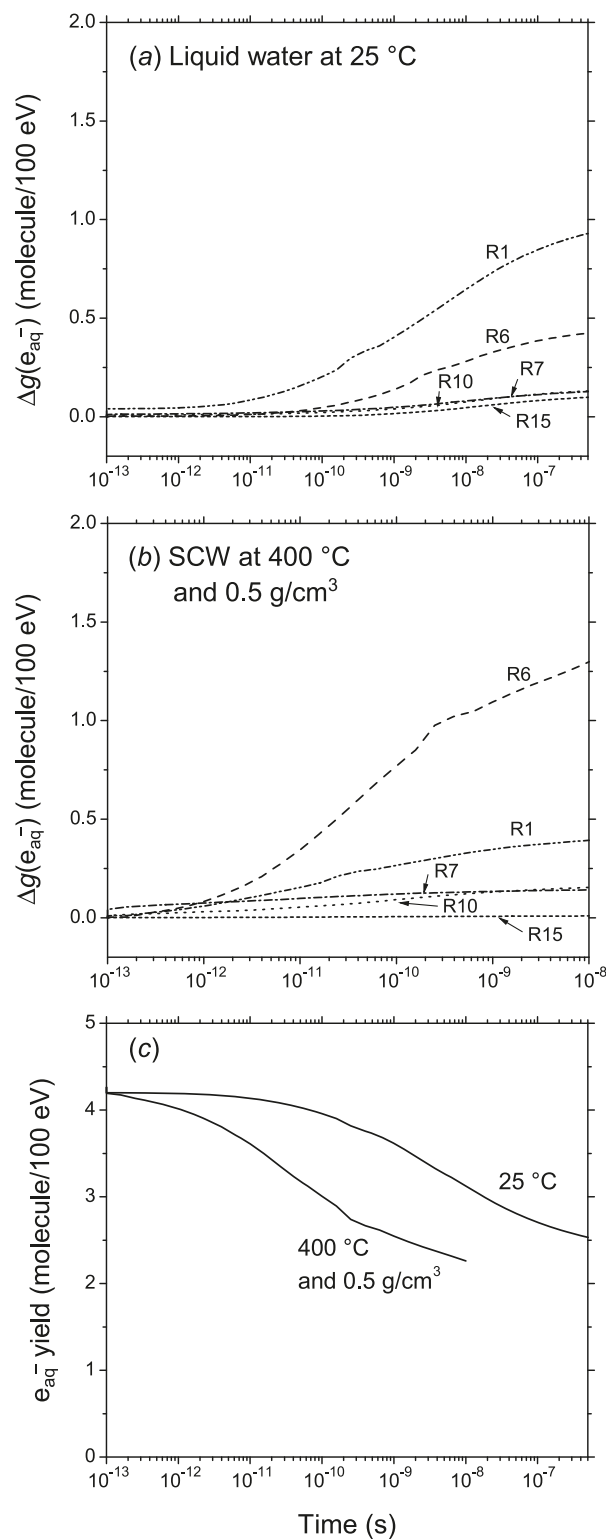
Second, in an effort to overcome the difficulties posed by the scavenging method, Muroya et al.<sup>35</sup> have recently measured, for the first time, the time-dependent yield of hydrated



**Fig. 1.** Time dependence of the extents  $\Delta g(e_{aq}^-)$  (in molecule/100 eV) of the main spur/track reactions R1, R6, R7, R10, and R15 (listed in Table 1) that contribute to the decay of  $e_{aq}^-$ , calculated from our Monte Carlo simulations of the radiolysis of (a) pure, deaerated liquid water at 25 °C and (b) SCW at 400 °C and 0.5 g/cm<sup>3</sup>. The time intervals chosen here correspond to the estimated lifetimes of spurs in the two considered cases. Simulations are carried out with 300 MeV incident protons (corresponding to an LET of  $\sim 0.3$  keV/ $\mu$ m in ordinary liquid water at 25 °C). Note that, in the case of reaction R10 involving two hydrated electrons, the  $\Delta g$  value that is shown accounts for the fact that each reaction eliminates two reactants. For the sake of comparison, Fig. 1c shows the time dependences of the yield of  $e_{aq}^-$  computed at 25 °C, and at 400 °C and 0.5 g/cm<sup>3</sup> over the considered spur lifetimes. As we can see, the kinetics of the decay of  $e_{aq}^-$  is significantly accelerated with increasing temperature, a result in agreement with the recent picosecond time-resolved experiments in SCW of Muroya et al.<sup>35</sup>

electrons in SCW (D<sub>2</sub>O) at 400 °C and various water densities between  $\sim 0.182$  and 0.570 g/cm<sup>3</sup>, using picosecond pulse radiolysis experiments. As shown in Table 3, at the highest density studied by these authors,<sup>35</sup> a good agreement is observed between our computed  $e_{aq}^-$  yields at 60 ps and 1 ns and their corresponding measured  $g$  values.<sup>36</sup> In this context, it is interesting to note that these *direct* time-dependent  $e_{aq}^-$  yield measurements<sup>35,36</sup> compare well with Lin et al.'s<sup>31,32</sup> previous studies that used scavenging methods.

Finally, our third point concerns the contribution of the various reactions to the yield of  $e_{aq}^-$  in irradiated SCW at 400 °C, and in particular the importance of the charge-recombination reaction, R6 (see Table 1). In fact, the rate constant for this reaction is known only up to 350 °C;<sup>24</sup> at 25 °C, it is  $2.1 \times 10^{10}$  (mol/L)<sup>-1</sup> s<sup>-1</sup> while it reaches the value of  $\sim 2 \times 10^{12}$  (mol/L)<sup>-1</sup> s<sup>-1</sup> at 350 °C.<sup>16,24,53</sup> However, the recent measurements of Muroya et al.<sup>35</sup> have suggested that reaction R6 at 400 °C is even faster than that at 350 °C. In view of these results, we have examined the sensitivity of our simulated radiolytic yields on variations in the value of the rate constant for this reaction. As expected,<sup>13,35</sup> reaction R6 does have a major impact on the calculated yields of  $g(e_{aq}^-)$  and  $g(H^\bullet)$ . For example, at 400 °C and 0.5 g/cm<sup>3</sup>, the ratio  $g(H^\bullet)/g(e_{aq}^-)$  at 10 ns varies from 0.74 to 1.26 when the rate constant of reaction R6 is varied from 2.5 to  $5 \times 10^{12}$  (mol/L)<sup>-1</sup> s<sup>-1</sup>. By contrast,  $g(\bullet OH)$  and  $g(H_2)$  are found to be rather insensitive to this parameter. The importance of reaction R6 is further illustrated in Fig. 1 where we compare the time dependence of the cumulative yield variations,  $\Delta g(e_{aq}^-)$ , of the main spur/track reactions that contribute to the decay of  $e_{aq}^-$  in the low-LET radiolysis of liquid water at 25 °C and of SCW at 400 °C and 0.5 g/cm<sup>3</sup>. As can be seen, at 25 °C, the decay of the  $e_{aq}^-$  yield is mainly due to the reaction R1 (see Table 1) of  $e_{aq}^-$  with  $\bullet OH$  radicals; about 54% of electrons decay in this reaction and about 25% in reaction R6 with protons (Fig. 1a). Under supercritical conditions, reaction R1 loses its efficiency and reaction R6 becomes largely predominant; at  $\sim 10^{-8}$  s, this latter reaction contributes about 65% to the decay of  $e_{aq}^-$ , while only 20% of electrons are lost because of reaction R1 (Fig. 1b). The total contribution of reactions R7, R10, and R15 (see Table 1) does not exceed 15%. As a consequence



of this predominance of reaction R6 in irradiated SCW, there are more  $H^\bullet$  atoms available to either react in other spur/track reactions or escape into the bulk solution. This, in large part, supports the marked increase in the ratio  $g(H^\bullet)/g(e_{aq}^-)$  observed during the radiolysis of SCW at 380–400 °C in the density regime studied (see Table 3), compared to its value ( $\sim 0.22$ ) in ordinary liquid water at 25 °C.<sup>24</sup>

## Conclusion

In this work, we have presented the results of our calculated yields of the primary free-radical products  $e_{aq}^-$ ,  $\bullet OH$  radical, and  $H^\bullet$  atom in the low-LET radiolysis of SCW at 400 °C and liquid-like densities around  $\sim 0.5 \text{ g/cm}^3$ . Assuming the aqueous medium to be a "continuum" and using all the currently available information on the rate constants for the main reactions involved in the radiolysis of water under these conditions, our Monte Carlo simulations are found to reproduce well the available experimental data. In particular, our computed  $e_{aq}^-$  yields at 60 ps and 1 ns compare very well with recently reported time-dependent yields of hydrated electrons in SCW at 400 °C and  $0.570 \text{ g/cm}^3$  measured directly using picosecond pulse radiolysis experiments. This good overall accord between experiment and theory shows that Monte Carlo simulations offer a most promising avenue at present to further develop our understanding of temperature/pressure (density) effects in the radiolysis of SCW under various thermodynamic conditions. Currently, work is in progress at our laboratory to calculate the  $g$  values in SCW at 400 °C in the low-density, gas-like region near  $\sim 0.15 \text{ g/cm}^3$ .

## Acknowledgements

We thank Professor D. M. Bartels, Professor M. Boero, Dr. A. J. Elliot, Professor K. Ghandi, Dr. C. D. Jonah, Professor Y. Katsumura, Dr. M. Lin, Professor P. W. Percival, Dr. C. R. Stuart, and the late Professor D. A. Armstrong for useful discussions and correspondence, and for kindly sending us their experimental data prior to publication. Financial support from the Atomic Energy of Canada Limited, the Natural Sciences and Engineering Research Council of Canada (NSERC), and Natural Resources Canada is gratefully acknowledged.

## References

- (1) Ferradini, C.; Jay-Gerin, J.-P. *Can. J. Chem.* **1999**, *77* (9), 1542. doi:10.1139/cjc-77-9-1542.
- (2) Department of Energy (DOE). *Research Needs and Opportunities in Radiation Chemistry Workshop*, Proceedings of the Indian Oaks Conference Center, Chesterton, IN, April 19–22, 1998; Report DOE/SC-0003, U.S. Department of Energy: Germantown, MD, 1999. Available from <http://www.science.doe.gov/production/bes/chm/Publications/RadRprt.pdf>.
- (3) Garrett, B. C.; Dixon, D. A.; Camaioni, D. M.; Chipman, D. M.; Johnson, M. A.; Jonah, C. D.; Kimmel, G. A.; Miller, J. H.; Rescigno, T. N.; Rossky, P. J.; Xantheas, S. S.; Colson, S. D.; Laufer, A. H.; Ray, D.; Barbara, P. F.; Bartels, D. M.; Becker, K. H.; Bowen, Jr., K. H.; Bradforth, S. E.; Carmichael, I.; Coe, J. V.; Corrales, L. R.; Cowin, J. P.; Dupuis, M.; Eienthal, K. B.; Franz, J. A.; Gutowski, M. S.; Jordan, K. D.; Kay, B. D.; LaVerne, J. A.; Lymar, S. V.; Madey, T. E.; McCurdy, C. W.; Meisel, D.; Mukamel, S.; Nilsson, A. R.; Orlando, T. M.; Petrik, N. G.; Pimblott, S. M.; Rustad, J. R.; Schenter, G. K.; Singer, S. J.; Tokmakoff, A.; Wang, L.-S.; Wittig, C.; Zwieter, T. S. *Chem. Rev.* **2005**, *105* (1), 355. doi:10.1021/cr030453x. PMID:15720157.
- (4) Cohen, P. *Water Coolant Technology of Power Reactors*; American Nuclear Society: La Grange Park, IL, 1980.
- (5) Oka, Y.; Koshizuka, S. *Prog. Nucl. Energy* **1998**, *32* (1–2), 163. doi:10.1016/S0149-1970(97)00014-0.
- (6) Department of Energy (DOE). *A Technology Roadmap for*

- Generation IV Nuclear Energy Systems*; Report GIF-002-00, U.S. DOE Nuclear Energy Research Advisory Committee and the Generation IV International Forum: Washington, DC, 2002.
- (7) Khartabil, H. F.; Duffey, R. B.; Spinks, N.; Diamond, W. In *Proceedings of the International Congress on Advances in Nuclear Power Plants (ICAPP 05)*, Seoul, Korea, May 15–19, 2005; Paper 5564, 2005.
  - (8) Katsumura, Y. In *Charged Particle and Photon Interactions With Matter: Chemical, Physical, and Biological Consequences with Applications*; Mozumder, A., Hatano, Y., Eds.; Marcel Dekker: New York, 2004; p. 697.
  - (9) Bartels, D. M.; Anderson, M.; Wilson, P.; Allen, T.; Sridharan, K. *Supercritical Water Radiolysis Chemistry. Supercritical Water Corrosion*. Available from [http://nuclear.inl.gov/deliverables/docs/uwnd\\_scw\\_level\\_ii\\_sep\\_2006\\_v3.pdf](http://nuclear.inl.gov/deliverables/docs/uwnd_scw_level_ii_sep_2006_v3.pdf).
  - (10) (a) Guzonas, D.; Tremaine, P.; Jay-Gerin, J.-P. In *Proceedings of the International Conference on Water Chemistry of Nuclear Reactor Systems*, Berlin, Germany, September 15–18, 2008; VGB PowerTech e.V. TB 430-08; Paper L15-1, 2008; (b) Guzonas, D.; Tremaine, P.; Jay-Gerin, J.-P. *Power Plant Chem.* **2009**, *11*, 284.
  - (11) Linstrom, P. J., Mallard, W. G., Eds. *NIST chemistry webbook. NIST Standard Reference Database No. 69*; National Institute of Standards and Technology: Gaithersburg, MD, 2005. Available from <http://webbook.nist.gov>.
  - (12) Was, G. S.; Ampornrat, P.; Gupta, G.; Teyseyre, S.; West, E. A.; Allen, T. R.; Sridharan, K.; Tan, L.; Chen, Y.; Ren, X.; Pister, C. J. *Nucl. Mater.* **2007**, *371* (1–3), 176. doi:10.1016/j.jnucmat.2007.05.017.
  - (13) Janik, D.; Janik, I.; Bartels, D. M. *J. Phys. Chem. A* **2007**, *111* (32), 7777. doi:10.1021/jp071751r. PMID:17645317.
  - (14) McCracken, D. R.; Tsang, K. T.; Laughton, P. J. *Aspects of the Physics and Chemistry of Water Radiolysis by Fast Neutrons and Fast Electrons in Nuclear Reactors*; Report AECL-11895, Atomic Energy of Canada Ltd.: Chalk River, ON, 1998.
  - (15) Christensen, H. *Fundamental Aspects of Water Coolant Radiolysis*; SKI Report 2006:16, Swedish Nuclear Power Inspectorate: Stockholm, Sweden, 2006.
  - (16) Elliot, A. J. *Rate Constants and g-Values for the Simulation of the Radiolysis of Light Water Over the Range 0–300 °C*; Report AECL-11073, Atomic Energy of Canada Ltd.: Chalk River, ON, 1994.
  - (17) Elliot, A. J.; Ouellette, D. C.; Stuart, C. R. *The Temperature Dependence of the Rate Constants and Yields for the Simulation of the Radiolysis of Heavy Water*; Report AECL-11658, Atomic Energy of Canada Ltd.: Chalk River, ON, 1996.
  - (18) Stuart, C. R.; Ouellette, D. C.; Elliot, A. J. *Pulse Radiolysis Studies of Liquid Heavy Water at Temperatures up to 250 °C*; Report AECL-12107, Atomic Energy of Canada Ltd.: Chalk River, ON, 2002.
  - (19) (a) Ghandi, K.; Addison-Jones, B.; Brodovitch, J.-Cl.; Kerman, S.; McKenzie, I.; Percival, P. W. *Physica B* **2003**, *326* (1–4), 55. doi:10.1016/S0921-4526(02)01572-7; (b) Percival, P. W.; Brodovitch, J.-Cl.; Ghandi, K.; McCollum, B. M.; McKenzie, I. *Radiat. Phys. Chem.* **2007**, *76* (8–9), 1231. doi:10.1016/j.radphyschem.2007.02.010.
  - (20) Ghandi, K.; Percival, P. W. *J. Phys. Chem. A* **2003**, *107* (17), 3005. doi:10.1021/jp027858q.
  - (21) Janik, I.; Bartels, D. M.; Marin, T. W.; Jonah, C. D. *J. Phys. Chem. A* **2007**, *111* (1), 79. doi:10.1021/jp065140v. PMID:17201391.
  - (22) Janik, I.; Bartels, D. M.; Jonah, C. D. *J. Phys. Chem. A* **2007**, *111* (10), 1835. doi:10.1021/jp065992v. PMID:17309240.

- (23) Marin, T. W.; Takahashi, K.; Jonah, C. D.; Chemerisov, S. D.; Bartels, D. M. *J. Phys. Chem. A* **2007**, *111* (45), 11540. doi:10.1021/jp074581r. PMID:17929904.
- (24) Elliot, A. J.; Bartels, D. M. *The Reaction Set, Rate Constants and g-Values for the Simulation of the Radiolysis of Light Water Over the Range 20 to 350 °C Based on Information Available in 2008*; Report AECL-153-127160-450-001, Atomic Energy of Canada Ltd.: Chalk River, ON, 2009.
- (25) Baldacchino, G.; de Waele, V.; Monard, H.; Sorgues, S.; Gobert, F.; Larbre, J. P.; Vigneron, G.; Marignier, J. L.; Pommeret, S.; Mostafavi, M. *Chem. Phys. Lett.* **2006**, *424* (1–3), 77. doi:10.1016/j.cplett.2006.04.061.
- (26) Burns, W. G.; Marsh, W. R. *J. Chem. Soc. Faraday Trans. I* **1981**, *77* (1), 197. doi:10.1039/f19817700197.
- (27) Sims, H. E. *Radiat. Phys. Chem.* **2006**, *75* (9), 1047. doi:10.1016/j.radphyschem.2006.01.010.
- (28) Cline, J.; Takahashi, K.; Marin, T. W.; Jonah, C. D.; Bartels, D. M. *J. Phys. Chem. A* **2002**, *106* (51), 12260. doi:10.1021/jp0270250.
- (29) Takahashi, K.; Bartels, D. M.; Cline, J. A.; Jonah, C. D. *Chem. Phys. Lett.* **2002**, *357* (5–6), 358. doi:10.1016/S0009-2614(02)00549-3.
- (30) Katsumura, Y., Ed. *Proceedings of the Workshop on Radiation Effects on Water Chemistry of Supercritical Water-Cooled Reactor*, University of Tokyo: Tokyo, Japan, 18–19 September, 2003; 2003, 156 pp.
- (31) Lin, M.; Katsumura, Y.; Muroya, Y.; He, H.; Wu, G.; Han, Z.; Miyazaki, T.; Kudo, H. *J. Phys. Chem. A* **2004**, *108* (40), 8287. doi:10.1021/jp048854j.
- (32) Lin, M.; Katsumura, Y.; He, H.; Muroya, Y.; Han, Z.; Miyazaki, T.; Kudo, H. *J. Phys. Chem. A* **2005**, *109* (12), 2847. doi:10.1021/jp044590p. PMID:16833600.
- (33) Lin, M.; Katsumura, Y.; Muroya, Y.; Han, Z. In *Program and Abstracts, Proceedings of the 7th International Symposium on Advanced Science Research on Charged Particle and Photon Interactions with Matter*, Tokai, Ibaraki, Japan, 6–9 November, 2007; Paper OR41, 2007.
- (34) Lin, M.; Katsumura, Y.; Muroya, Y.; He, H.; Miyazaki, T.; Hiroishi, D. *Radiat. Phys. Chem.* **2008**, *77* (10–12), 1208. doi:10.1016/j.radphyschem.2008.05.017.
- (35) Muroya, Y.; Lin, M.; de Waele, V.; Hatano, Y.; Katsumura, Y.; Mostafavi, M. *J. Phys. Chem. Lett.* **2010**, *1* (1), 331. doi:10.1021/jz900225a.
- (36) Lin, M. Personal communication, 2010.
- (37) (a) Hervé du Penhoat, M.-A.; Goulet, T.; Frongillo, Y.; Fraser, M.-J.; Bernat, Ph.; Jay-Gerin, J.-P. *J. Phys. Chem. A* **2000**, *104* (50), 11757. doi:10.1021/jp001662d.; (b) Hervé du Penhoat, M.-A.; Meesungnoen, J.; Goulet, T.; Filali-Mouhim, A.; Mankhetkorn, S.; Jay-Gerin, J.-P. *Chem. Phys. Lett.* **2001**, *341* (1–2), 135. doi:10.1016/S0009-2614(01)00462-6.; (c) Meesungnoen, J.; Jay-Gerin, J.-P.; Filali-Mouhim, A.; Mankhetkorn, S. *Can. J. Chem.* **2002**, *80* (7), 767. doi:10.1139/v02-088.
- (38) Allen, A. O. *The Radiation Chemistry of Water and Aqueous Solutions*; D. Van Nostrand Co.: Princeton, NJ, 1961.
- (39) Spinks, J. W. T.; Woods, R. J. *An Introduction to Radiation Chemistry*, 3rd ed.; Wiley: New York, 1990.
- (40) Buxton, G. V. In *Charged Particle and Photon Interactions With Matter: Chemical, Physical, and Biological Consequences with Applications*; Mozumder, A., Hatano, Y., Eds.; Marcel Dekker: New York, 2004; p 331.
- (41) Cobut, V.; Frongillo, Y.; Patau, J. P.; Goulet, T.; Fraser, M.-J.; Jay-Gerin, J.-P. *Radiat. Phys. Chem.* **1998**, *51* (3), 229. doi:10.1016/S0969-806X(97)00096-0.
- (42) Frongillo, Y.; Goulet, T.; Fraser, M.-J.; Cobut, V.; Patau, J. P.; Jay-Gerin, J.-P. *Radiat. Phys. Chem.* **1998**, *51* (3), 245. doi:10.1016/S0969-806X(97)00097-2.
- (43) Muroya, Y.; Meesungnoen, J.; Jay-Gerin, J.-P.; Filali-Mouhim, A.; Goulet, T.; Katsumura, Y.; Mankhetkorn, S. *Can. J. Chem.* **2002**, *80* (10), 1367. doi:10.1139/v02-173.
- (44) (a) Meesungnoen, J.; Jay-Gerin, J.-P. *J. Phys. Chem. A* **2005**, *109* (29), 6406. doi:10.1021/jp058037z. PMID:16833985.; (b) Meesungnoen, J.; Jay-Gerin, J.-P. *Radiat. Res.* **2005**, *164* (5), 688. doi:10.1667/RR3459.1. PMID:16238448.; (c) Meesungnoen, J.; Jay-Gerin, J.-P. In *Charged Particle and Photon Interactions With Matter: Recent Advances, Applications, and Interfaces*; Hatano, Y., Katsumura, Y., Mozumder, A., Eds.; Taylor & Francis: Boca Raton, FL, 2010. In press.
- (45) Platzman, R. L. In *Radiation Biology and Medicine. Selected Reviews in the Life Sciences*; Claus, W. D., Ed.; Addison-Wesley: Reading, MA, 1958; p 15.
- (46) Clifford, P.; Green, N. J. B.; Oldfield, M. J.; Pilling, M. J.; Pimblott, S. M. *J. Chem. Soc. Faraday Trans. I* **1986**, *82* (9), 2673. doi:10.1039/f19868202673.
- (47) Pimblott, S. M.; Pilling, M. J.; Green, N. J. B. *Radiat. Phys. Chem.* **1991**, *37*, 377.
- (48) Bégusová, M.; Pimblott, S. M. *Radiat. Prot. Dosimetry* **2002**, *99* (1–4), 73. PMID:12194364.
- (49) Green, N. J. B.; Pilling, M. J.; Pimblott, S. M.; Clifford, P. *J. Phys. Chem.* **1989**, *93* (24), 8025. doi:10.1021/j100361a014.
- (50) Pimblott, S. M.; Green, N. J. B. In *Research in Chemical Kinetics*; Compton, R. G., Hancock, G., Eds.; Elsevier: Amsterdam, 1995; Vol. 3, p 117.
- (51) Goulet, T.; Fraser, M.-J.; Frongillo, Y.; Jay-Gerin, J.-P. *Radiat. Phys. Chem.* **1998**, *51* (1), 85. doi:10.1016/S0969-806X(97)00060-1.
- (52) Plante, I. Ph.D. Thesis, Université de Sherbrooke, Sherbrooke, QC, 2009.
- (53) Stanisky, C. M.; Bartels, D. M.; Takahashi, K. *Radiat. Phys. Chem.* **2010**, *79* (1), 64. doi:10.1016/j.radphyschem.2009.08.032.
- (54) LaVerne, J. A.; Pimblott, S. M. *J. Phys. Chem.* **1993**, *97* (13), 3291. doi:10.1021/j100115a034.
- (55) (a) Swiatla-Wojcik, D.; Buxton, G. V. *J. Phys. Chem.* **1995**, *99* (29), 11464. doi:10.1021/j100029a026.; (b) Swiatla-Wojcik, D.; Buxton, G. V. *Res. Chem. Intermed.* **2001**, *27* (7), 875. doi:10.1163/15685670152622149.
- (56) Mills, R. *J. Phys. Chem.* **1973**, *77* (5), 685. doi:10.1021/j100624a025.
- (57) Lamb, W. J.; Hoffman, G. A.; Jonas, J. J. *Chem. Phys.* **1981**, *74* (12), 6875. doi:10.1063/1.441097.
- (58) Schmidt, K. H.; Han, P.; Bartels, D. M. *J. Phys. Chem.* **1995**, *99* (26), 10530. doi:10.1021/j100026a016.
- (59) Bandura, A. V.; Lvov, S. N. *J. Phys. Chem. Ref. Data* **2006**, *35* (1), 15. doi:10.1063/1.1928231.
- (60) Jortner, J.; Gaathon, A. *Can. J. Chem.* **1977**, *55* (11), 1801. doi:10.1139/v77-253.
- (61) Ohtaki, H.; Radnai, T.; Yamaguchi, T. *Chem. Soc. Rev.* **1997**, *26* (1), 41. doi:10.1039/cs9972600041.
- (62) Tucker, S. C. *Chem. Rev.* **1999**, *99* (2), 391. doi:10.1021/cr9700437. PMID:11848986.
- (63) Akiya, N.; Savage, P. E. *Chem. Rev.* **2002**, *102* (8), 2725. doi:10.1021/cr000668w. PMID:12175266.
- (64) Boero, M.; Terakura, K.; Ikeshoji, T.; Liew, C. C.; Parri-nello, M. *J. Chem. Phys.* **2001**, *115* (5), 2219. doi:10.1063/1.1379767.
- (65) Jay-Gerin, J.-P.; Lin, M.; Katsumura, Y.; He, H.; Muroya,

- Y.; Meesungnoen, J. *J. Chem. Phys.* **2008**, *129* (11), 114511. doi:10.1063/1.2978955. PMID:19044973.
- (66) (a) LaVerne, J. A. *Radiat. Res.* **2000**, *153* (5), 487. doi:10.1667/0033-7587(2000)153[0487:TEOHII]2.0.CO;2. PMID: 10790268.; (b) LaVerne, J. A. In *Charged Particle and Photon Interactions With Matter: Chemical, Physical, and Biological Consequences With Applications*; Mozumder, A., Hatano, Y., Eds.; Marcel Dekker: New York, 2004; p 403.
- (67) Lin, M. Personal communication, 2008.
- (68) Takahashi, K.; Ohgami, S.; Koyama, Y.; Sawamura, S.; Marin, T. W.; Bartels, D. M.; Jonah, C. D. *Chem. Phys. Lett.* **2004**, *383* (5–6), 445. doi:10.1016/j.cplett.2003.11.050.
- (69) Sanguanmith, S.; Tippayamontri, T.; Meesungnoen, J.; Jay-Gerin, J.-P. Manuscript submitted to this journal.



# Synthesis and characterization of chalcone-substituted phosphazenes

Zainab Ngaini and Norashikin I. Abdul Rahman

**Abstract:** A series of mono[(*E*)-1-(4-alkyloxyphenyl)-3-(4-hydroxyphenyl)prop-2-en-1-one]cyclotriphosphazenes and hexakis[(*E*)-1-(4-alkyloxyphenyl)-3-(4-hydroxyphenyl)prop-2-en-1-one]cyclotriphosphazenes have been synthesized. A convenient synthetic method was performed from the reaction of hexachlorocyclotriphosphazenes with 1 and 6 equiv. of (*E*)-1-(4-alkyloxyphenyl)-3-(4-hydroxyphenyl)prop-2-en-1-one (**2a–2c**) to afford (**3a–3c**) in 17%–19% and (**4a–4c**) in 70%–82%, respectively. The compounds differ in the length of alkyl groups,  $C_nH_{2n+1}$ , where  $n = 10, 12$ , and  $14$ .

**Key words:** hexachlorocyclotriphosphazenes, chalcones, alkyloxy, condensation.

**Résumé :** On a réalisé la synthèse d'une série de mono[(*E*)-1-(4-alkyloxyphényl)-3-(4-hydroxyphényl)prop-2-én-1-one]cyclotriphosphazènes et de hexakis[(*E*)-1-(4-alkyloxyphényl)-3-(4-hydroxyphényl)prop-2-én-1-one]cyclotriphosphazènes. On a exécuté une méthode de synthèse appropriée par réaction d'hexachlorocyclotriphosphazènes avec 1 et 6 equiv. de (*E*)-1-(4-alkyloxyphényl)-3-(4-hydroxyphényl)prop-2-én-1-one (**2a–2c**) qui ont conduit respectivement aux produits (**3a–3c**) avec des rendements allant de 17 à 19 % et aux produits (**4a–4c**) avec des rendements allant de 70 à 82. Les composés diffèrent par la longueur des groupes alkyles,  $C_nH_{2n+1}$ , dans lesquels  $n = 10, 12$  et  $14$ .

**Mots-clés :** hexachlorocyclotriphosphazènes, chalcones, alkyloxy, condensation.

## Introduction

Phosphazenes are compounds containing a framework of alternating phosphorus and nitrogen atoms, either in cyclic or linear form.<sup>1</sup> Linear, cyclic, and poly phosphazenes have been widely investigated. These compounds are reported to possess interesting biomedical properties<sup>2</sup> and promising application as effective flame retardants for fiber materials.<sup>3</sup> Nucleophilic substitution reactions on hexachlorocyclotriphosphazenes have been widely reported.<sup>4–6</sup> The synthesis of cyclotriphosphazenes, bearing 4-oxychalcones<sup>6</sup> as side groups, has been studied for photosensitive phosphazenes that could undergo photo-cross-linking reaction under UV irradiation.

In photochemistry, chalcone derivatives were reported to possess outstanding nonlinear optic property for optical communications and optical electronics,<sup>7</sup> liquid crystal displays,<sup>8,9</sup> and alignment film.<sup>10</sup> Chalcones were also reported to promote excellent blue-light transmittance and good crystallability,<sup>11,12</sup> high photosensitivity, and thermal stability for various crystalline electro-optical devices.

Recently, we reported a very convenient method for the preparation of trimeric aryloxyphosphazenes directly from  $[N_3P_3Cl_6]$  and (*E*)-3-(4-(alkyloxy)phenyl)-1-(4-hydroxyphenyl)prop-2-en-1-one using  $K_2CO_3$  in acetone.<sup>13</sup> This prompted us to try the reaction of cyclotriphosphazenes with other para-substituted hydroxy chalcones. We herein describe the synthesis of cyclotriphosphazenes incorporated with hydroxylated chalcones (*E*)-1-[4-(alkyloxy)phenyl]-3-[4-hydroxyphenyl] prop-2-en-1-one

(**2a–2c**), which could be used as model reactions for various crystalline electro-optical devices.

## Results and discussion

The series of chalcone derivatives (*E*)-1-[4-(alkyloxy)phenyl]-3-[4-hydroxyphenyl] prop-2-en-1-one (**2a–2c**) was prepared via Claisen–Schmidt condensation of **1a–1c** and 4-hydroxybenzaldehyde by the route depicted in Scheme 1.

The structural assignments of compounds **2a–2c** were based on the analytical and spectral data. The IR spectra of the hydroxylated chalcones **2a–2c** showed the presence of bands at  $2921$ – $2852\text{ cm}^{-1}$ , which were attributed to the introduction of the long alkyl chain via etherification of 4-hydroxyacetophenone. The presence of a new  $C=O$  stretching frequency at  $1651\text{ cm}^{-1}$  substantiated the formation of the title compound. The chemical structures of **2a–2c** were found to be consistent with  $^1H$  NMR and  $^{13}C$  NMR spectroscopic data and showed the peaks corresponding to the structures. In  $^1H$  NMR spectra, the coupling constant,  $J_{ab} = 15.0$ – $16.0\text{ Hz}$ , indicated all chalcones obtained were in trans-configuration.

The synthetic route for the preparation of mono- $(N_3P_3Cl_5[OC_6H_4CH=CHC(O)C_6H_4OC_nH_{2n+1}])$  (**3a–3c**) and hexa-substituted cyclotriphosphazenes  $(N_3P_3[OC_6H_4CH=CHC(O)C_6H_4OC_nH_{2n+1}]_6)$  (**4a–4c**) is illustrated in Scheme 2.

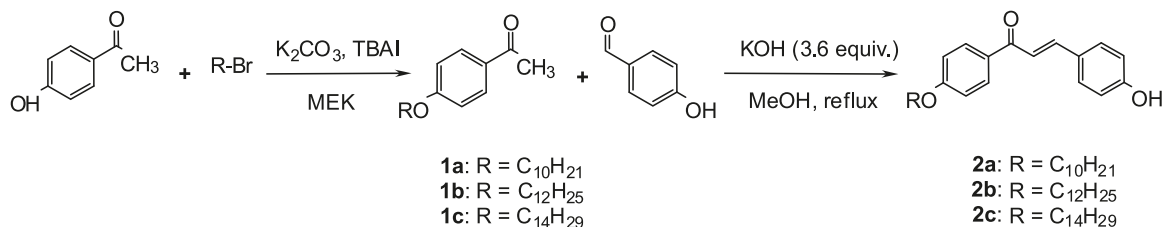
Mono-substituted cyclotriphosphazenes **3a–3c** were obtained from the reaction of hexachlorocyclotriphosphazenes with 1 equiv. of chalcone derivatives **2a–2c** in the presence of  $K_2CO_3$  in acetone. The higher polarity of the

Received 29 November 2009. Accepted 21 April 2010. Published on the NRC Research Press Web site at canjchem.nrc.ca on 18 June 2010.

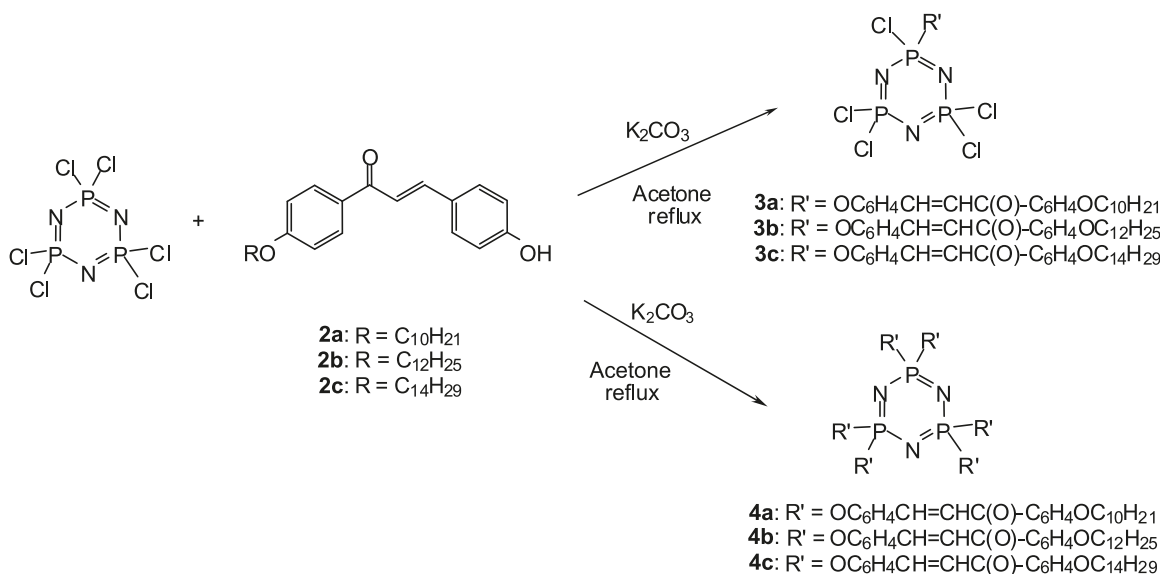
**Z. Ngaini<sup>1</sup> and N.I. Abdul Rahman.** Department of Chemistry, Faculty of Resource Science and Technology, Universiti Malaysia Sarawak 94300, Kota Samarahan, Sarawak, Malaysia.

<sup>1</sup>Corresponding author (e-mail: nzainab@frst.unimas.my).

Scheme 1.



Scheme 2.



acetone<sup>14</sup> was believed to increase the rate of reaction compared with THF<sup>6</sup> and dioxane.<sup>15</sup> The IR spectra showed P=N stretching vibrations at  $1183\text{ cm}^{-1}$ , which are characteristic of cyclotriphosphazenes.<sup>16,17</sup> The absorption bands observed at  $871\text{ cm}^{-1}$  were attributed to the presence of the P-O-C bond.<sup>18</sup>  $^{31}\text{P}$  NMR spectra showed two resonances as a triplet and a doublet at 12.74 ppm and 23.27 ppm, respectively, with a coupling constant,  $J = 60\text{ Hz}$ , which implied the replacement of one chlorine from the cyclotriphosphazenes ring for the mono-substituted phosphazenes.<sup>19</sup>  $^1\text{H}$  and  $^{13}\text{C}$  NMR data also confirmed the substitution of 2a-2c, with the chemical shifts moving slightly downfield.

The reaction of hexachlorocyclotriphosphazenes with 6 equiv. of 2a-2c under the same conditions afforded 4a-4c in high yields. The IR spectra showed the characteristic absorption bands at  $1180\text{ cm}^{-1}$ , which were attributed to P=N stretching vibrations. The absorption bands observed at  $881\text{ cm}^{-1}$  in 4a-4c were attributed to the presence of P-O-C bond.  $^{31}\text{P}$  NMR showed a single resonance at  $\delta\ 8.84\text{ ppm}$ , which implied complete chlorine replacement.<sup>19</sup> The data obtained from elemental analysis,  $^1\text{H}$ , and  $^{13}\text{C}$  NMR showed good agreement to the corresponding structures.

## Conclusion

In summary, this research has demonstrated the nucleophilic substitution of (*E*)-1-[4-(alkyloxy)phenyl]-3-[4-hydroxyphenyl] prop-2-en-1-one (2a-2c) onto cyclotriphosphazenes, which afforded new mono{(*E*)-1-[4-(alkyloxy)phenyl]-3-[4-hydroxyphenyl]prop-2-en-1-one}cyclotriphosphazenes (3a-3c)

and hexakis{(*E*)-1-[4-(alkyloxy)phenyl]-3-[4-hydroxyphenyl]prop-2-en-1-one}cyclotriphosphazenes (4a-4c). Compounds 3a-3c gave lower melting points, whereas compounds 4a-4c possessed higher melting points than the hydroxylated chalcones (2a-2c). These findings could potentially be used as model reactions for various crystalline electrooptical devices.

## Experimental

### General

4-Hydroxybenzaldehyde, 4-hydroxyacetophenone, and 1-bromoalkanes were obtained from Merck Company and used as received. Hexachlorocyclotriphosphazenes was provided by Aldrich and were recrystallized from hexane. Acetone was distilled from calcium hydride under nitrogen before use. All other reagents and solvents were used as received. The reactions were performed under dry nitrogen. Melting points were determined in open capillaries and are uncorrected. Infrared spectra were recorded on (FTIR) 1605 Shimadzu Spectrometer using KBr pellets.  $^1\text{H}$  NMR spectra were recorded on a 500 MHz Jeol Delta 2-NMR, and  $^{13}\text{C}$  NMR was recorded on a 125.77 MHz using TMS as the internal standard.

### Synthesis of alkyloxyphenyl-ethanone (1a-1c)

#### General procedure

Bromoalkane (72 mmol), 4-hydroxyacetophenone (72 mmol),  $K_2CO_3$  (72 mmol), and TBAI (6 mmol) in MEK (200 mL)

were heated at reflux for 5 h. The mixture was filtered and cooled to room temperature. Water (30 mL) was added to the filtrate, and the layers separated. The aqueous layer was extracted with dichloromethane ( $2 \times 30$  mL). The combined layers were washed with water ( $2 \times 20$  mL), dried ( $\text{MgSO}_4$ ), filtered, and concentrated in vacuo. The crude was recrystallized from ethanol to give **1a–1c**.

#### *1-(4-Decyloxyphenyl)-ethanone (1a)*

Compound **1a** was obtained as colorless crystals. Yield: 89. FTIR and NMR data were consistent with the reported literature.<sup>20</sup>

#### *1-(4-Dodecyloxyphenyl)-ethanone (1b)*

Compound **1b** was obtained as colorless crystal. Yield: 78%; mp 52–53 °C. FTIR (thin films,  $\text{cm}^{-1}$ )  $\nu_{\text{max}}$ : 2954, 2918, 2849 (C–H), 1676 (C=O), 1606 (aromatic), 1253 (alkyl aryl ethers).  $^1\text{H}$  NMR (500 MHz,  $\text{CDCl}_3$ )  $\delta_{\text{H}}$ : 0.85 (3H, t,  $1 \times \text{CH}_3$ ), 1.24–1.77 (20H, m,  $8 \times \text{CH}_2$ ), 2.52 (3H, s,  $1 \times \text{CH}_3$ ), 3.98 (2H, t,  $\text{OCH}_2$ ), 6.87 (2H, d,  $J = 9.2$  Hz, Ar–H), 7.88 (2H, d,  $J = 9.2$  Hz, Ar–H).  $^{13}\text{C}$  NMR (125.77 MHz,  $\text{CDCl}_3$ )  $\delta_{\text{C}}$ : 14.06, 22.63, 25.91, 26.24, 29.03, 29.29, 29.50, 29.53, 39.58, 29.60, 29.60, 31.86, 68.19, 114.06, 130.01, 130.50, 163.06, 196.71. Anal. calcd. (%)  $\text{C}_{20}\text{H}_{32}\text{O}_2$ : C, 78.90; H, 10.59. Found (%): C, 78.73; H, 10.45.

#### *1-(4-Tetradecyloxyphenyl)-ethanone (1c)*

Compound **1c** was obtained as colorless crystals. Yield: 94%; mp 58–59 °C. FTIR (thin films,  $\text{cm}^{-1}$ )  $\nu_{\text{max}}$ : 2954, 2917, 2849 (C–H), 1676 (C=O), 1605 (aromatic), 1253 (alkyl aryl ether).  $^1\text{H}$  NMR (500 MHz,  $\text{CDCl}_3$ )  $\delta_{\text{H}}$ : 0.84 (3H, t,  $1 \times \text{CH}_3$ ), 1.23–1.76 (24H, m,  $10 \times \text{CH}_2$ ), 2.50 (3H, s,  $1 \times \text{CH}_3$ ), 3.96 (2H, t,  $\text{OCH}_2$ ), 6.86 (2H, d,  $J = 8.0$  Hz, Ar–H), 7.87 (2H, d,  $J = 8.0$  Hz, Ar–H).  $^{13}\text{C}$  NMR (125.77 MHz,  $\text{CDCl}_3$ )  $\delta_{\text{C}}$ : 14.02, 22.60, 25.88, 26.16, 29.01, 29.28, 29.28, 29.47, 29.51, 29.57, 29.57, 29.59, 31.83, 68.13, 114.00, 129.97, 130.44, 163.02, 196.55. Anal. calcd.  $\text{C}_{22}\text{H}_{36}\text{O}_2$ : C, 79.46; H, 10.91. Found (%): C, 79.23; H, 10.51.

### Synthesis of (alkyloxy)phenyl-hydroxyphenyl]prop-2-en-1-one (**2a–2c**)

#### *General procedure*

A mixture of 4-hydroxybenzaldehyde (12.5 mmol) and **1a** (12.5 mmol) in 35 mL of methanol was added under stirring to a solution of KOH (2.52 g) in methanol (10 mL). The mixture was heated at reflux for 10 h. The reaction was cooled to room temperature and acidified with cold diluted HCl (2 N). The resulting precipitate was filtered, washed, and dried. The crude was recrystallized from hexane:ethanol (7:1) to give **2a–2c**.

#### *(E)-1-[4-(Decyloxy)phenyl]-3-[4-hydroxyphenyl]prop-2-en-1-one (2a)*

Compound **2a** was obtained as yellow crystals. Yield: 34. FTIR and NMR data were consistent with the reported literature.<sup>20</sup>

#### *(E)-1-[4-(Dodecyloxy)phenyl]-3-[4-hydroxyphenyl]prop-2-en-1-one (2b)*

Compound **2b** was obtained as yellow crystals. Yield: 44%; mp 110.6–111.2 °C. FTIR (thin films,  $\text{cm}^{-1}$ )  $\nu_{\text{max}}$ :

3195 (OH), 2921, 2852 (C–H), 1651 (C=O), 1581 (aromatic), 1223 (alkyl aryl ether), 990 (C=C).  $^1\text{H}$  NMR (500 MHz,  $\text{CDCl}_3$ )  $\delta_{\text{H}}$ : 0.81 (3H, t,  $1 \times \text{CH}_3$ ), 1.21–1.87 (20H, m,  $10 \times \text{CH}_2$ ), 3.95 (2H, t,  $\text{OCH}_2$ ), 6.83 (2H, d,  $J = 8.6$  Hz, Ar–H), 6.86 (2H, d,  $J = 8.6$  Hz, Ar–H), 7.32 (1H, d,  $J = 15.45$  Hz,  $1 \times$  olefinic H), 7.45 (2H, d,  $J = 8.0$  Hz, Ar–H), 7.67 (1H, d,  $J = 15.45$  Hz,  $1 \times$  olefinic H), 7.94 (2H, d,  $J = 8.0$  Hz, Ar–H).  $^{13}\text{C}$  NMR (125.77 MHz,  $\text{CDCl}_3$ )  $\delta_{\text{C}}$ : 14.10, 22.67, 25.96, 29.08, 29.33, 29.55, 29.58, 29.61, 30.96, 31.89, 68.29, 114.30, 116.09, 119.03, 127.24, 130.45, 130.84, 144.66, 158.75, 163.12, 189.62. Anal. calcd.  $\text{C}_{27}\text{H}_{36}\text{O}_3$ : C, 79.37; H, 8.88. Found (%): C, 79.52; H, 8.90.

#### *(E)-1-[4-(Tetradecyloxy)phenyl]-3-[4-hydroxyphenyl]prop-2-en-1-one (2c)*

Compound **2c** was obtained as yellow crystals. Yield: 39%; mp 107–108 °C. FTIR (thin films,  $\text{cm}^{-1}$ )  $\nu_{\text{max}}$ : 3208 (OH), 2918, 2850 (C–H), 1646 (C=O), 1585 (aromatic), 1223 (alkyl aryl ether), 990 (C=C).  $^1\text{H}$  NMR (500 MHz,  $\text{DMSO}-d_6$ )  $\delta_{\text{H}}$ : 0.82 (3H, t,  $1 \times \text{CH}_3$ ), 1.24–1.71 (24H, m,  $12 \times \text{CH}_2$ ), 4.04 (2H, t,  $\text{OCH}_2$ ), 6.81 (2H, d,  $J = 8.6$  Hz, Ar–H), 7.02 (2H, d,  $J = 9.15$  Hz, Ar–H), 7.61 (1H, d,  $J = 15.45$  Hz,  $1 \times$  olefinic H), 7.69 (1H, d,  $J = 15.45$  Hz,  $1 \times$  olefinic H), 7.70 (2H, d,  $J = 9.15$  Hz, Ar–H), 8.09 (2H, d,  $J = 8.60$  Hz, Ar–H), 10.04 (1H, s, OH).  $^{13}\text{C}$  NMR (125.77 MHz,  $\text{DMSO}-d_6$ )  $\delta_{\text{C}}$ : 13.93, 22.09, 25.42, 28.54, 28.72, 28.97, 28.97, 29.02, 29.05, 30.67, 31.29, 67.81, 114.28, 115.76, 118.36, 125.90, 130.60, 130.65, 130.81, 143.52, 159.92, 162.44, 187.12. Anal. calcd. (%)  $\text{C}_{29}\text{H}_{40}\text{O}_3$ : C, 79.77; H, 9.23. Found (%): C, 78.83; H, 9.04.

### Synthesis of mono-substituted cyclotriphosphazene (**3a–3c**)

#### *General procedure*

A mixture of hexachlorocyclotriphosphazenes (2.01 mmol), **2a** (2.01 mmol), and  $\text{K}_2\text{CO}_3$  (4.02 g) in acetone (60 mL) was heated at reflux for 1 h. The mixture was allowed to cool to room temperature and filtered. The filtrate was dried, filtered, and concentrated in vacuo. The crude solid was recrystallized from acetone to afford **3a–3c**.

#### *Preparation of $\text{N}_3\text{P}_3\text{Cl}_5[\text{OC}_6\text{H}_4\text{CH}=\text{CHC}(\text{O})\text{C}_6\text{H}_4\text{OC}_{10}\text{H}_{21}]$ (**3a**)*

Compound **3a** was obtained as pale yellow solid. Yield: 17%; mp 74–75 °C. FTIR (thin films,  $\text{cm}^{-1}$ )  $\nu_{\text{max}}$ : 1183 (P=N), 871 (P–O–C).  $^1\text{H}$  NMR (500 MHz,  $\text{CDCl}_3$ )  $\delta_{\text{H}}$ : 0.81 (3H, t,  $1 \times \text{CH}_3$ ), 1.21–1.75 (16H, m,  $8 \times \text{CH}_2$ ), 3.97 (2H, t,  $\text{OCH}_2$ ), 6.89 (2H, d,  $J = 9.15$  Hz, Ar–H), 7.24 (2H, d,  $J = 8.0$  Hz, Ar–H), 7.44 (1H, d,  $J = 16.05$ ,  $1 \times$  olefinic H), 7.60 (2H, d,  $J = 8.55$  Hz, Ar–H), 7.68 (1H, d,  $J = 15.50$  Hz,  $1 \times$  olefinic H), 7.95 (2H, d,  $J = 8.60$  Hz, Ar–H).  $^{13}\text{C}$  NMR (125.77 MHz,  $\text{CDCl}_3$ )  $\delta_{\text{C}}$ : 14.09, 22.65, 25.96, 29.08, 29.29, 29.33, 29.52, 31.86, 31.91, 68.30, 114.34, 121.86, 122.71, 129.85, 130.55, 130.82, 133.78, 141.98, 150.31, 163.23, 188.25.  $^{31}\text{P}$  NMR (200 MHz,  $\text{CDCl}_3$ )  $\delta_{\text{P}}$ : 12.74 (t,  $J = 60.0$  Hz,  $\text{P}_a\text{–P}$ ), 23.27 (d,  $J = 60.0$  Hz,  $\text{P}_b\text{–P}$ ). Anal. calcd. (%)  $\text{N}_3\text{P}_3\text{Cl}_5\text{C}_{25}\text{H}_{31}\text{O}_3$ : C, 43.41; H, 4.52; N, 6.07. Found (%): C, 43.06; H, 4.44; N, 6.03.

#### *Preparation of $\text{N}_3\text{P}_3\text{Cl}_5[\text{OC}_6\text{H}_4\text{CH}=\text{CHC}(\text{O})\text{C}_6\text{H}_4\text{OC}_{12}\text{H}_{25}]$ (**3b**)*

Compound **3b** was obtained as pale yellow solid. Yield:

19%; mp 60–62 °C. FTIR (thin films,  $\text{cm}^{-1}$ )  $\nu_{\text{max}}$ : 1183 (P=N), 871 (P–O–C).  $^1\text{H}$  NMR (500 MHz,  $\text{CDCl}_3$ )  $\delta_{\text{H}}$ : 0.86 (3H, t,  $1 \times \text{CH}_3$ ), 1.26–1.80 (20H, m,  $10 \times \text{CH}_2$ ), 4.02 (2H, t,  $\text{OCH}_2$ ), 6.94 (2H, d,  $J = 8.60$  Hz, Ar–H), 7.29 (2H, d,  $J = 8.60$  Hz, Ar–H), 7.48 (1H, d,  $J = 15.45$  Hz,  $1 \times$  olefinic H), 7.65 (2H, d,  $J = 8.0$  Hz, Ar–H), 7.74 (1H, d,  $J = 15.45$  Hz,  $1 \times$  olefinic H), 8.01 (2H, d,  $J = 8.0$  Hz, Ar–H).  $^{13}\text{C}$  NMR (125.77 MHz,  $\text{CDCl}_3$ )  $\delta_{\text{C}}$ : 14.12, 22.68, 25.97, 29.00, 29.09, 29.25, 29.34, 29.42, 29.49, 29.58, 31.90, 68.32, 114.36, 121.87, 122.70, 129.86, 130.58, 130.83, 133.80, 141.95, 151.24, 163.25, 188.27.  $^{31}\text{P}$  NMR (200 MHz,  $\text{CDCl}_3$ )  $\delta_{\text{P}}$ : 12.74 (t,  $J = 60.0$  Hz,  $\text{P}_a$ –P), 23.27 (d,  $J = 60.0$  Hz,  $\text{P}_b$ –P). Anal. calcd. (%)  $\text{N}_3\text{P}_3\text{Cl}_5\text{C}_{27}\text{H}_{35}\text{O}_3$ : C, 45.06; H, 4.90; N, 5.84. Found (%): C, 45.03; H, 4.83; N, 5.76.

#### Preparation of $\text{N}_3\text{P}_3\text{Cl}_5[\text{OC}_6\text{H}_4\text{CH}=\text{CHC}(\text{O})\text{C}_6\text{H}_4\text{OC}_{14}\text{H}_{29}]$ (3c)

Compound **3c** was obtained as pale yellow solid. Yield: 18%; mp 68–71 °C. FTIR (thin films,  $\text{cm}^{-1}$ )  $\nu_{\text{max}}$ : 1184 (P=N), 871 (P–O–C).  $^1\text{H}$  NMR (500 MHz,  $\text{CDCl}_3$ )  $\delta_{\text{H}}$ : 0.87 (3H, t,  $1 \times \text{CH}_3$ ), 1.25–1.80 (24H, m,  $12 \times \text{CH}_2$ ), 4.03 (2H, t,  $\text{OCH}_2$ ), 6.95 (2H, d,  $J = 8.60$  Hz, Ar–H), 7.29 (2H, d,  $J = 8.60$  Hz, Ar–H), 7.49 (1H, d,  $J = 16.00$  Hz,  $1 \times$  olefinic H), 7.66 (2H, d,  $J = 8.60$  Hz, Ar–H), 7.73 (1H, d,  $J = 15.45$  Hz,  $1 \times$  olefinic H), 8.00 (2H, d,  $J = 8.05$  Hz, Ar–H).  $^{13}\text{C}$  NMR (125.77 MHz,  $\text{CDCl}_3$ )  $\delta_{\text{C}}$ : 14.09, 22.66, 25.95, 29.08, 29.33, 29.33, 29.53, 29.50, 29.62, 29.62, 29.63, 29.66, 31.89, 68.31, 114.34, 121.89, 122.71, 129.85, 130.56, 130.81, 133.78, 141.97, 150.32, 163.23, 188.26.  $^{31}\text{P}$  NMR (200 MHz,  $\text{CDCl}_3$ )  $\delta_{\text{P}}$ : 12.74 (t,  $J = 60.0$  Hz,  $\text{P}_a$ –P), 23.27 (d,  $J = 60.0$  Hz,  $\text{P}_b$ –P). Anal. calcd. (%)  $\text{N}_3\text{P}_3\text{Cl}_5\text{C}_{29}\text{H}_{39}\text{O}_3$ : C, 46.58; H, 5.26; N, 5.62. Found (%): C, 46.43; H, 5.14; N, 5.59.

### Synthesis of hexasubstituted cyclotriphosphazene (4a–4c)

#### General procedure

A mixture of hexachlorocyclotriphosphazenes (2.01 mmol), **2a** (12.06 mmol), and  $\text{K}_2\text{CO}_3$  (24.12 g) in acetone (60 mL) was heated at reflux for 1 h. The mixture was allowed to cool to room temperature and filtered. The filtrate was dried, filtered, and concentrated in vacuo. The crude solid was recrystallized from acetone to afford **4a–4c**.

#### Preparation of $\text{N}_3\text{P}_3[\text{OC}_6\text{H}_4\text{CH}=\text{CHC}(\text{O})\text{C}_6\text{H}_4\text{OC}_{10}\text{H}_{21}]_6$ (4a)

Compound **4a** was obtained as pale yellow solid. Yield: 82%; mp 143–145 °C. FTIR (thin films,  $\text{cm}^{-1}$ )  $\nu_{\text{max}}$ : 3067 (CH in aromatic), 1180 (P=N), 881 (P–O–C).  $^1\text{H}$  NMR (500 MHz,  $\text{CDCl}_3$ )  $\delta_{\text{H}}$ : 0.81 (3H, t,  $1 \times \text{CH}_3$ ), 1.22–1.71 (16H, m,  $8 \times \text{CH}_2$ ), 3.97 (2H, t,  $\text{OCH}_2$ ), 6.89 (2H, d,  $J = 9.15$  Hz, Ar–H), 7.20 (2H, d,  $J = 8.60$  Hz, Ar–H), 7.25 (1H, d,  $J = 15.45$  Hz,  $1 \times$  olefinic H), 7.41 (2H, d,  $J = 8.60$  Hz, Ar–H), 7.62 (1H, d,  $J = 15.45$  Hz,  $1 \times$  olefinic H), 7.95 (2H, d,  $J = 9.15$  Hz, Ar–H).  $^{13}\text{C}$  NMR (125.77 MHz,  $\text{CDCl}_3$ )  $\delta_{\text{C}}$ : 14.09, 22.66, 25.99, 29.12, 29.31, 29.38, 29.55, 30.92, 31.87, 68.25, 114.29, 121.37, 121.88, 129.58, 130.47, 130.73, 132.35, 142.18, 151.65, 163.12, 188.01.  $^{31}\text{P}$  NMR (200 MHz,  $\text{CDCl}_3$ )  $\delta_{\text{P}}$ : 8.86 (s, 3P,  $\text{N}_3\text{P}_3$  ring). Anal. calcd. (%)  $\text{N}_3\text{P}_3\text{C}_{150}\text{H}_{186}\text{O}_{18}$ : C, 74.69; H, 7.77; N, 1.74. Found (%): C, 73.86; H, 7.60; N, 1.83.

#### Preparation of $\text{N}_3\text{P}_3[\text{OC}_6\text{H}_4\text{CH}=\text{CHC}(\text{O})\text{C}_6\text{H}_4\text{OC}_{12}\text{H}_{25}]_6$ (4b)

Compound **4b** was obtained as pale yellow solid. Yield: 72%; mp 141–143 °C. FTIR (thin films,  $\text{cm}^{-1}$ )  $\nu_{\text{max}}$ : 3064 (C–H in aromatic), 1180 (P=N), 883 (P–O–C).  $^1\text{H}$  NMR (500 MHz,  $\text{CDCl}_3$ )  $\delta_{\text{H}}$ : 0.86 (3H, t,  $1 \times \text{CH}_3$ ), 1.25–1.78 (20H, m,  $10 \times \text{CH}_2$ ), 3.97 (2H, t,  $\text{OCH}_2$ ), 6.87 (2H, d,  $J = 7.45$  Hz, Ar–H), 7.00 (2H, d,  $J = 8.00$  Hz, Ar–H), 7.41 (1H, d,  $J = 16.00$  Hz,  $1 \times$  olefinic H), 7.46 (2H, d,  $J = 8.00$  Hz, Ar–H), 7.71 (1H, d,  $J = 16.00$  Hz,  $1 \times$  olefinic H), 7.91 (2H, d,  $J = 7.45$  Hz, Ar–H).  $^{13}\text{C}$  NMR (125.77 MHz,  $\text{CDCl}_3$ )  $\delta_{\text{C}}$ : 14.09, 22.66, 25.99, 29.12, 29.33, 29.38, 29.56, 29.59, 29.61, 29.64, 31.89, 68.25, 114.29, 121.36, 121.88, 129.58, 130.47, 130.73, 132.34, 142.19, 120.64, 163.13, 188.03.  $^{31}\text{P}$  NMR (200 MHz,  $\text{CDCl}_3$ )  $\delta_{\text{P}}$ : 8.84 (s, 3P,  $\text{N}_3\text{P}_3$  ring). Anal. calcd. (%)  $\text{N}_3\text{P}_3\text{C}_{162}\text{H}_{210}\text{O}_{18}$ : C, 75.41; H, 8.20; N, 1.63. Found (%): C, 74.87; H, 8.17; N, 2.16.

#### Preparation of $\text{N}_3\text{P}_3[\text{OC}_6\text{H}_4\text{CH}=\text{CHC}(\text{O})\text{C}_6\text{H}_4\text{OC}_{14}\text{H}_{29}]_6$ (4c)

Compound **4c** was obtained as pale yellow solid. Yield: 70%; mp 137–138 °C. FTIR (thin films,  $\text{cm}^{-1}$ )  $\nu_{\text{max}}$ : 3068 (C–H in aromatic), 1177 (P=N), 880 (P–O–C).  $^1\text{H}$  NMR (500 MHz,  $\text{CDCl}_3$ )  $\delta_{\text{H}}$ : 0.87 (3H, t,  $1 \times \text{CH}_3$ ), 1.25–1.80 (24H, m,  $12 \times \text{CH}_2$ ), 4.03 (2H, t,  $\text{OCH}_2$ ), 6.95 (2H, d,  $J = 8.60$  Hz, Ar–H), 7.29 (2H, d,  $J = 8.60$  Hz, Ar–H), 7.49 (1H, d,  $J = 16.00$  Hz,  $1 \times$  olefinic H), 7.66 (2H, d,  $J = 8.60$  Hz, Ar–H), 7.73 (1H, d,  $J = 15.45$  Hz,  $1 \times$  olefinic H), 8.00 (2H, d,  $J = 8.05$  Hz, Ar–H).  $^{13}\text{C}$  NMR (125.77 MHz,  $\text{CDCl}_3$ )  $\delta_{\text{C}}$ : 14.09, 22.66, 25.95, 29.08, 29.33, 29.33, 29.53, 29.50, 29.62, 29.62, 29.63, 29.66, 31.89, 68.31, 114.34, 121.89, 122.71, 129.85, 130.56, 130.81, 133.78, 141.97, 150.32, 163.23, 188.26.  $^{31}\text{P}$  NMR (200 MHz,  $\text{CDCl}_3$ )  $\delta_{\text{P}}$ : 8.86 (s, 3P,  $\text{N}_3\text{P}_3$  ring). Anal. calcd. (%)  $\text{N}_3\text{P}_3\text{C}_{174}\text{H}_{234}\text{O}_{18}$ : C, 76.03; H, 8.58; N, 1.53. Found (%): C, 75.90; H, 8.31; N, 1.70.

### Acknowledgements

We are grateful to the Universiti Malaysia Sarawak and the Ministry of Science, Technology, and Innovation (MOSTI) for the financial support through FRGS/01(03)/608/2006(41).

### References

- (1) Allcock, H. R. *Phosphorus-Nitrogen Compounds*; Academic Press: New York, 1972.
- (2) Giavaresi, G.; Tschon, M.; Borsari, V.; Daly, J. H.; Liggat, J. J.; Fini, M.; Bonazzi, V.; Nicolini, A.; Carpi, A.; Morra, M.; Cassinelli, C.; Giardino, R. *Biomed. Pharmacother.* **2004**, *58* (8), 411. PMID:15464867.
- (3) Allen, C. W. *J. Fire Sci.* **1993**, *11* (4), 320. doi:10.1177/073490419301100404.
- (4) Carriedo, G. A.; García Alonso, F. J.; López Vizcaíno, S.; Díaz Valenzuela, C.; Yutronic, N. *Phosphorus Sulfur Silicon Relat. Elem.* **2003**, *178* (7), 1549. doi:10.1080/10426500307869.
- (5) Allcock, H. R.; Cameron, C. G. *Macromolecules* **1994**, *27* (12), 3125. doi:10.1021/ma00090a002.
- (6) Allcock, H. R.; Cameron, C. G. *Macromolecules* **1994**, *27* (12), 3131. doi:10.1021/ma00090a003.



- (7) Indira, J.; Karat, P. P.; Sarojini, B. K. *J. Cryst. Growth* **2002**, 242 (1-2), 209. doi:10.1016/S0022-0248(02)01306-4.
- (8) Thaker, B. T.; Patel, D. M.; Tandel, P. K.; Jesani, M. S.; Vyas, C. J.; Vansadia, A. D. *Phase Transit.* **2005**, 78 (6), 521. doi:10.1080/01411590500189130.
- (9) Jung, K. H.; Hyun, S. Y.; Song, D. M.; Shin, D. M. *Opt. Mater.* **2003**, 21 (1-3), 663. doi:10.1016/S0925-3467(02)00219-7.
- (10) Mihara, T.; Tsutsumi, M.; Koide, N. *Mol. Cryst. Liq. Cryst. (Phila. Pa.)* **2004**, 412 (1), 247. doi:10.1080/15421400490439879.
- (11) Zhou, B.; Lu, W.-Q.; Zhou, Z.-H.; Wu, Y. *J. Mater. Chem.* **2000**, 10 (7), 1513. doi:10.1039/a909757k.
- (12) Fichou, D.; Watanabe, T.; Takeda, T.; Miyata, S.; Goto, Y.; Nakayama, M. *Jpn. J. Appl. Phys.* **1988**, 27 (Part 2, No. 3), L429. doi:10.1143/JJAP.27.L429.
- (13) Ngaini, Z.; Rahman, N. I. A. *Phosphorus Sulfur Silicon Relat. Elem.* **2010**, 185 (3), 628. doi:10.1080/10426500902893217.
- (14) Carriedo, G. A.; Fernández-Catuxo, L.; García-Alonso, F. J.; Elipe, P. G.; González, P. A.; Sánchez, G. *J. Appl. Polym. Sci.* **1996**, 59 (12), 1879. doi:10.1002/(SICI)1097-4628(19960321)59:12<1879::AID-APP9>3.0.CO;2-N.
- (15) Kajiwar, M.; Saito, H. *Angew. Makromol. Chem.* **1985**, 132 (1), 197. doi:10.1002/apmc.1985.051320115.
- (16) Moriya, K.; Masuda, T.; Suzuki, T.; Yano, S.; Kajiwar, M. *Mol. Cryst. Liq. Cryst. (Phila. Pa.)* **1998**, 318 (1), 267. doi:10.1080/10587259808045389.
- (17) Çil, E.; Arslan, M.; Gorgulu, A. O. *Polyhedron* **2006**, 25 (18), 3526. doi:10.1016/j.poly.2006.07.009.
- (18) Tarassoli, A.; Shushizadeh, M. R. *Phosphorus Sulfur Silicon Relat. Elem.* **2003**, 178 (4), 803. doi:10.1080/10426500307787.
- (19) Lee, K. H.; Lee, D. C. *Polym. Bull.* **1999**, 42 (5), 543. doi:10.1007/s002890050500.
- (20) Nam, S. W.; Kang, S. H.; Chang, J. Y. *Macromol. Res.* **2007**, 15 (1), 74.

# TiO<sub>2</sub>/biscyanine and CdS/biscyanine heterostructures — Influence of the structural composition on the photocatalytic activity

I. Kobasa, I. Kondratyeva, and L. Odosiy

**Abstract:** This paper deals with investigation of a character of the light reflection and absorption of some newly synthesized heterostructural materials based on TiO<sub>2</sub> or CdS semiconductors and bisquinocyanine dyes (carbocyanine and styryle). Changes in spectral parameters of the heterostructures caused by adding the dye to the semiconducting material have also been investigated. The changes in the spectra can be caused by different chromophores disposition induced by influence of the semiconductor on the electron configuration in the dye molecules. A well-known test reaction of methylene blue reduction has been used to detect the photocatalytic activity of the materials, which was found directly depending on the efficiency of the mutual influence of the components of the heterostructures. The heterostructures containing a dye, which causes more significant spectral changes, ensure higher photocatalytic activity.

**Key words:** titanium dioxide, cadmium sulfide, biscyanine dyes, photocatalytic activity, mutual influence of components.

**Résumé :** Dans ce travail, on a étudié un caractère de la réflexion et de l'absorption de nouveaux matériaux de synthèse hétérostructuraux à base de TiO<sub>2</sub>, de semiconducteurs CdS et de colorants de la bisquinocyanine (carbocyanine et styrile). On a aussi étudié les changements dans les paramètres spectraux des hétérostructures provoqués par l'addition du colorant au matériel semiconducteur. Les changements dans les spectres peuvent être provoqués par diverses dispositions de chromophores induites par l'influence du semiconducteur sur la configuration électronique dans les molécules de colorant. On a utilisé une réaction bien connue de réduction du bleu de méthylène comme test pour détecter l'activité photocatalytique des matériaux et on a trouvé qu'elle dépend directement sur l'efficacité de l'influence mutuelle des composants des hétérostructures. Les hétérostructures contenant un colorant, qui cause les changements spectraux les plus significatifs, assurent une plus grande activité photocatalytique.

**Mots-clés :** dioxyde de titane, sulfure de cadmium, colorants de la biscyanine, activité photocatalytique, influence mutuelle des composants.

[Traduit par la Rédaction]

## Introduction

Electrochemical and electrophysical parameters of any photocatalytic material should mutually agree to keep needful electron-transfer processes thermodynamically allowed and ensure high driving force of the process. This condition should be observed for the effective designing of photocatalytic systems or their components.<sup>1,2</sup> This is a necessary, yet not sufficient condition for designing the highly effective photocatalysts, since photocatalytic activity (PA) also depends on kinetic, adsorption, and other factors.<sup>1</sup> The initial raise in PA caused by better light absorption is followed by depression of the photocatalyst's efficiency that has been reported in refs. 3–5 for a number of heterostructures (HS) containing cyanine dyes sensitizers. Such dependence of a material activity on its composition can be caused by changes in the dye's association level. Spectral data prove that mutual influence of the dye and the semiconductor is gradually weakening with raise in the dye content. This effect can cause depression of the PA for the HS with higher

dye concentration as reported in ref.6. Detailed investigation of the dependence of PA on various physical and physicochemical parameters is a topical task, since this information is necessary for the development of new complex photoactive materials with pre-assigned properties.

This paper reports the results of the comparative investigation of the spectral and photochemical characteristics of heterostructures consisting of titanium dioxide or cadmium sulfide with biscyanine/cyanine dye-sensitizer with two conjugated chromophores. Any electronic or steric factors can change the conformation of the HS molecules and result in significant spectral changes in the light absorption pattern. That is why such materials can be suitable objects for investigation of the structural changes in the semiconductors occurring at the formation of HS. Two biscyanine compounds (styryle and monocarbocyanine) were used as HS components because they have different auxochromes and substitutes in the polymethine chains. Our electrochemical measurements proved similarity of redox potentials of both

Received 19 November 2009. Accepted 13 April 2010. Published on the NRC Research Press Web site at canjchem.nrc.ca on 18 June 2010.

I. Kobasa,<sup>1</sup> I. Kondratyeva, and L. Odosiy. Chernivtsi National University, 2 Kotsiubinsky Street, Chernivtsi 58012, Ukraine.

<sup>1</sup>Corresponding author (e-mail: imk-11@hotmail.com).

biscyanines. As reported in refs. 1 and 2, such similarity ensures that close values of thermodynamic advantage are gained when electrons are injected to the conductivity band and, consequently, similar values of PA.

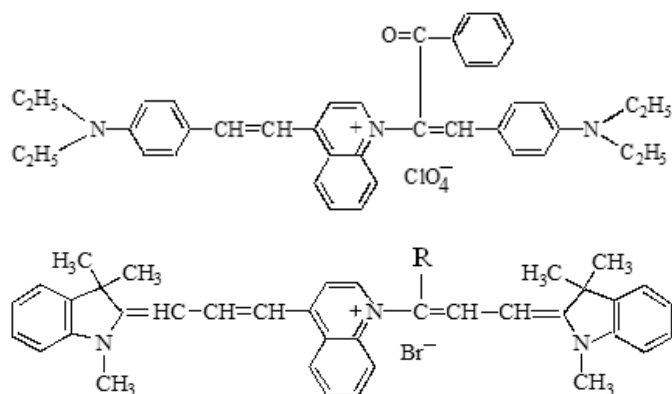
An "energetic agreement" contribution into PA can be eliminated using the above-mentioned principle of the components selection for HS. Therefore, any difference in PA for the HS with the similar content of the two dyes can be caused only by different types of interaction between the dyes and semiconductor.

## Experimental

All heterostructural materials have been synthesized using the following method:<sup>3,6</sup> a dye-sensitizer has been deposited upon a particle of some semiconducting dispersion. Then, the HS was covered with the polyepoxypropylcarbazole (PEPC) film to prevent its dissolution. This method ensures synthesis of heterogeneous structures, which consist of a semiconductor nucleus covered with separate molecules, or the uniformal layer of the dye, and a protecting polymer film (Fig. 1). Such structural composition can be obtained because positive dye particles do not dissolve in benzene solution of the polymer used in this method.

The polymer film can slightly influence the electron-transfer processes and photocatalytic activity. As reported in ref. 6, the PEPC film (PEPC content: 0.02–0.2 mg/g) completely stops the dissolution of the dye; however, it does not thwart any electron-transfer processes at the interface boundary. PA drops to 20% if the PEPC content reaches 1.8 mg/g.

The following dyes have been used as sensitizers: *N*-(benzoyl-diethylaminostyryl)-4-*n*-diethylaminostyrylquinolinium perchlorate (Dye I) and (*N*-[ $\alpha$ -coumarine-3-yl]carbo(1,3,3-trimethyl-2-indolynylidene)propenyl](4-quinolyne)1,3,3-trimethyl-2-indolynyliden) trimethyncyanine bromide (Dye II). Synthesis of Dye I has been carried out according to ref. 7, and Dye II was synthesized according to ref. 8. Details of the dye synthesis, yields, and characteristics of the dyes are reported in refs. 7 and 8.

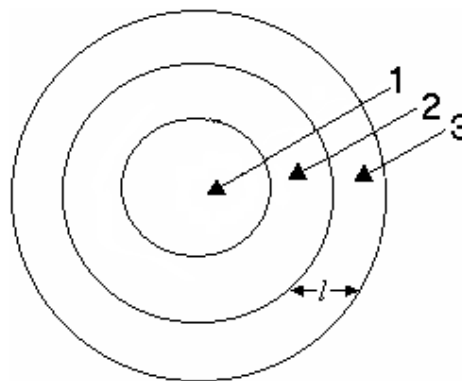


R: 3-coumarinyl

Both dyes were applied to the following semiconductors:

- (i) Titanium dioxide with specific surface area  $S_{sp} = 50.0 \text{ m}^2/\text{g}$  has been synthesized by the original method<sup>9</sup> through  $\text{TiCl}_4$  vapour hydrolysis in the air-

**Fig. 1.**  $\text{TiO}_2/\text{D}/\text{PEPC}$  and  $\text{CdS}/\text{D}/\text{PEPC}$  heterostructures: 1, semiconductor particle; 2, dye-sensitizer; and 3, protective polymer film ( $l$ : thickness of the polymer layer).



hydrogen flame at 1170–1370 K.  $\text{TiO}_2$  particles size ranged from 20 to 40 nm;

- (ii) Ultrapure cadmium sulfide with  $S_{sp} = 4.0 \text{ m}^2/\text{g}$  (particle size was 100  $\mu\text{m}$ ).

All particle sizes were measured using Scanning Electronic Microscope ZEISSEVO50XVP.

Cyclic voltammetry<sup>10</sup> of the dye ethanolic solution ( $C = 1.25 \times 10^{-4} \text{ mol/L}$ ) was used to determine values of  $E_{D/D^+}^*$  and  $E_{D/D^-}^*$ . A LOMO-made spectrophotometer SF-46 has been used to record the optical spectra of the dyes. Diffusive reflection spectra of the oxide semiconductors and the HS of  $\text{TiO}_2$  and  $\text{CdS}$  with the dyes have been recorded using PerkinElmer Lambda Bio-40 spectrophotometer equipped with integrating sphere and then transformed into absorption spectra using Kubelka–Munk method.<sup>11</sup> A value  $(1 - R^2)/2R$ , which is proportional to optical density, where  $R$  (%) (diffusive reflection at the given wavelength) was calculated to apply this method of transformation.

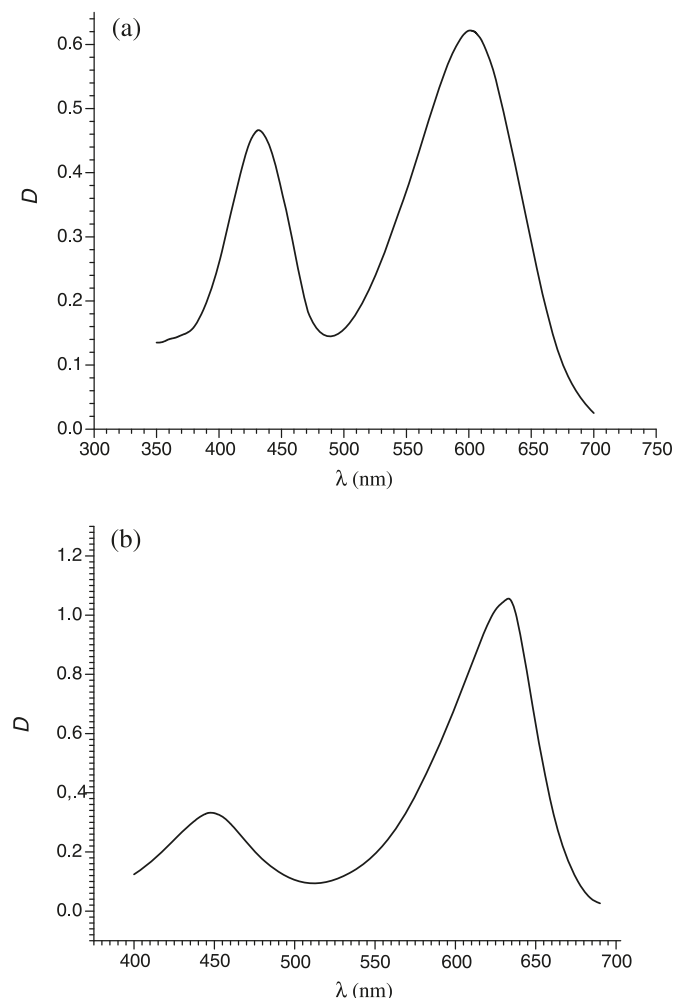
The PA of the heterostructures has been determined through acceleration of methylene blue (MB) photodegradation running in an oxygen-free aqueous solution with formaldehyde as a reducing agent.<sup>5,6</sup> A regular 500 W incandescent lamp and the mercury lamp DRT-1000 were used as light sources for the photodegradation. The following color filters: UFS-2 ( $\lambda = 310\text{--}400 \text{ nm}$ ), ZhS-11 ( $\lambda > 400 \text{ nm}$ ), FS-1 ( $\lambda < 520 \text{ nm}$ ), or OS-13 ( $\lambda > 560 \text{ nm}$ ) were used to filter the needed light bands. A value of PA has been calculated as  $\text{PA} = (C_0 \times 1000)/(\tau_{1/2} S m)$ ,<sup>5</sup> where PA means a value of PA ( $\text{mg}/(\text{mL min m}^2)$ ),  $C_0$ : initial concentration of MB ( $\text{mg/mL}$ ),  $\tau_{1/2}$ : half-discoloration time (min),  $S$ : specific surface area of a sample ( $\text{m}^2/\text{g}$ ), and  $m$ : weight of a sample (g).

## Results

### Dye I (D I) and the heterostructure $\text{TiO}_2/\text{D I}/\text{PEPC}$

There are two light absorption bands in the visible light spectrum of the Dye I, which is common for all biscyanines. Peaks of these bands are located for the ethanolic solution at  $\lambda_{\text{max}} = 432 \text{ nm}$  ( $\log \varepsilon = 4.75$ ) and  $\lambda_{\text{max}} = 603 \text{ nm}$  ( $\log \varepsilon = 4.97$ ) (Fig. 2). The width of the shortwave band at 2/3 of its height is  $\Delta = 56 \text{ nm}$ , and  $\Delta = 80 \text{ nm}$  for the longwave band. The ratio between the intensities of the bands is  $I_{sw}/I_{lw} = 0.76$ .

**Fig. 2.** Light absorption spectra for the ethanolic solutions of the dyes-sensitizers: (a) Dye I, (b) Dye II ( $C = 10^{-5}$  mol/L). Optical density ( $D$ ) vs. light wavelength ( $\lambda$ ).

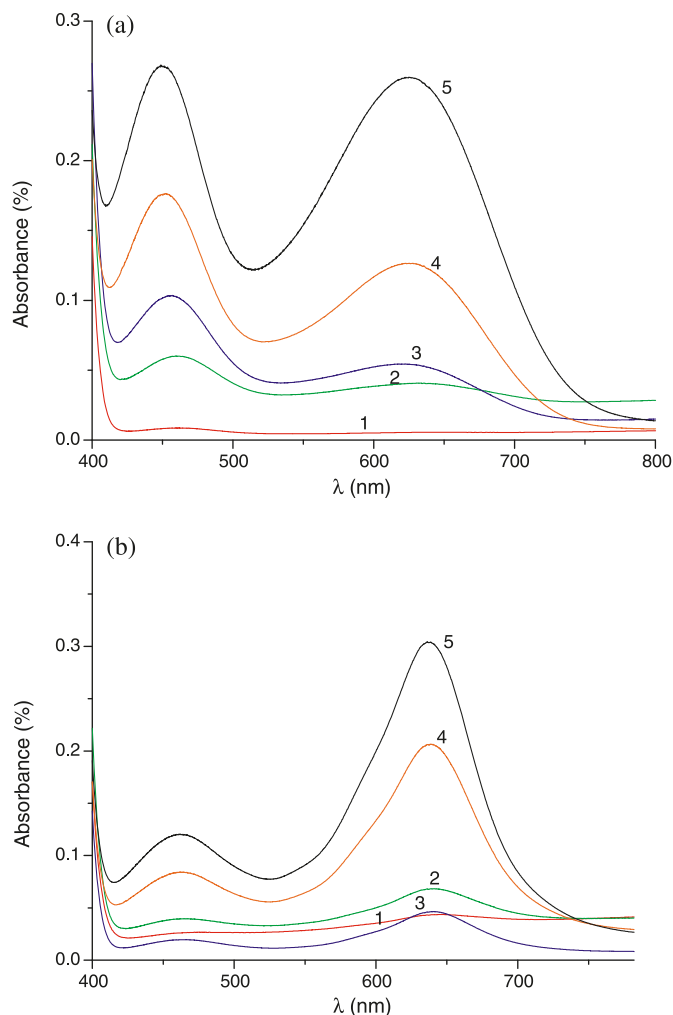


All the above-mentioned parameters undergo significant changes for a spectrum of the dye deposit on the surface of the HS (see Fig. 3a and Table 1). Table 1 also represents potentials of oxidation  $E_{D/D^+}^*$  and reduction  $E_{D/D^-}^*$  of the excited molecule of the dye after absorbing a longwave quantum with energy  $E^*$ . The potentials were calculated according to the equations:<sup>12</sup>  $E_{D/D^+}^* = E_{D/D^+} - E^*$  and  $E_{D/D^-}^* = E_{D/D^-} + E^*$ . Dark redox potentials were obtained using a cyclic voltammetry:<sup>10</sup>  $E_{D/D^+}^* = +0.86$  V,  $E_{D/D^-}^* = +0.008$  V.

#### Dye II (D II) and the heterostructure TiO<sub>2</sub>/D II/PEPC

A spectrum of the Dye II also shows two visible light absorption bands. Peaks of these bands are located at  $\lambda_{\max} = 446$  nm ( $\log \varepsilon = 4.52$ ) and  $\lambda_{\max} = 632$  nm ( $\log \varepsilon = 5.03$ ). Width of the shortwave band at 2/3 of its height ( $\Delta$ ) is 53 nm, and  $\Delta = 42$  nm for the longwave band. The ratio between the intensities of the bands is  $I_{sw}/I_{lw} = 0.33$ . All parameters of the absorption spectrum also change at the formation of a heterostructure from Dye II and TiO<sub>2</sub>. However, Fig. 3b and Table 2 prove that the width of both bands ( $\Delta$ ) increases similarly to the previous material while increase of  $\lambda_{\max}$  and  $I_{sw}/I_{lw}$  here is much less than the D I

**Fig. 3.** Light absorption spectra for TiO<sub>2</sub>-based heterostructures: (a) TiO<sub>2</sub>/D I/PEPC, (b) TiO<sub>2</sub>/D II/PEPC. Dye content in the HS (mg/g): 1, 0.019; 2, 0.094; 3, 0.188; 4, 0.94; and 5, 1.88.



material. Values of  $E_{D/D^+} = +0.89$  V,  $E_{D/D^-} = +0.012$  V, and  $E^*$  for the longwave band calculated from the experimental data are represented in Table 2.

#### Heterostructures D I and D II with CdS

Absorption spectra of such materials are less informative because the shortwave band is completely hidden behind the wide absorption band of CdS (see Fig. 4). Electrochemical parameters of this material  $E_{D/D^+}$  and  $E_{D/D^-}$  have been determined similarly to TiO<sub>2</sub>-based materials.

#### Photocatalytic activity of the heterostructures

Photocatalytic activities of various heterostructures are shown in Tables 3 and 4, and the dependence of PA on some spectral parameters is represented in Fig. 5.

#### Energy transformation diagrams for various photocatalytic systems based on heterostructures

Energy transformation diagrams have been built for various HS to identify the thermodynamically allowed electron-transfer processes, which can occur at exposure to light from various spectral ranges. The diagrams were composed based



**Table 1.** Spectral and electrochemical parameters of the heterostructures TiO<sub>2</sub>/D I/PEPC, sw and lw: shortwave and longwave absorption bands, respectively,  $I_{sw}/I_{lw}$ : the ratio between the intensities of the bands,  $\Delta$  (nm): width of the band at 2/3 of its height,  $E_{D/D^{*+}}^{*}(lw)$  and  $E_{D/D^{*-}}^{*}(lw)$ : potentials of oxidation  $E_{D/D^{*+}}^{*}$  and reduction  $E_{D/D^{*-}}^{*}$  of the excited molecule of the dye after absorbing a longwave quantum with energy  $E^*$  (eV).

Sample	Dye content in the HS, mg/g <sup>a</sup>	$\lambda_{1max}$ , nm ( $\Delta$ , nm)	$\lambda_{2max}$ , nm ( $\Delta$ , nm)	$I_{sw}/I_{lw}$	$E_{D/D^{*+}}^{*}(lw)$ , eV	$E_{D/D^{*-}}^{*}(lw)$ , eV
3	0.188	456	630	1.87	-1.11	+2.06
4	0.94	452	626	1.38	-1.12	+2.06
5	1.88	451 (68)	624 (117)	1.02	-1.19	+2.07
Solution	$1 \times 10^{-5}$ mol/L	432 (56)	603 (80)	0.76	-1.20	+2.14

<sup>a</sup>mg/g means weight of the dye (mg) per 1 g of the HS.

**Table 2.** Spectral and electrochemical parameters of the heterostructures TiO<sub>2</sub>/D II/PEPC, sw and lw: shortwave and longwave absorption bands, respectively,  $I_{sw}/I_{lw}$ : the ratio between the intensities of the bands,  $\Delta$  (nm): width of the band at 2/3 of its height,  $E_{D/D^{*+}}^{*}(lw)$  and  $E_{D/D^{*-}}^{*}(lw)$ : potentials of oxidation  $E_{D/D^{*+}}^{*}$  and reduction  $E_{D/D^{*-}}^{*}$  of the excited molecule of the dye after absorbing a longwave quantum with energy  $E^*$  (eV).

Sample	Dye content in the HS, mg/g	$\lambda_{1max}$ , nm ( $\Delta$ , nm)	$\lambda_{2max}$ , nm ( $\Delta$ , nm)	$I_{sw}/I_{lw}$	$E_{D/D^{*+}}^{*}(lw)$ , eV	$E_{D/D^{*-}}^{*}(lw)$ , eV
3	0.88	465	642	0.44	-1.04	+1.94
4	0.94	463	639	0.40	-1.05	+1.95
5	1.88	461 (81)	637 (63)	0.39	-1.06	+1.96
Solution	$1 \times 10^{-5}$ mol/L	446 (53)	632 (48)	0.33	-1.07	+1.97

**Table 3.** Photocatalytic activity (PA, mg/mL min m<sup>2</sup>) of heterostructures TiO<sub>2</sub>/D I/PEPC and TiO<sub>2</sub>/D II/PEPC for various contents of the dyes and exposition to light from different spectral bands.

No.	Dye content in the HS, mg/g	PA: light absorbed by a semiconductor, $\lambda = 310\text{--}400$ nm		PA: light absorbed by the dyes, $\lambda > 400$ nm	
		TiO <sub>2</sub> /D I/PEPC	TiO <sub>2</sub> /D II/PEPC	TiO <sub>2</sub> /D I/PEPC	TiO <sub>2</sub> /D II/PEPC
0	without dye	$1.6 \times 10^{-1}$	$1.6 \times 10^{-1}$	0	0
1	0.019	$8.4 \times 10^{-2}$	$8.5 \times 10^{-2}$	$6.9 \times 10^{-2}$	$1.8 \times 10^{-2}$
2	0.094	$4.7 \times 10^{-2}$	$2.7 \times 10^{-2}$	$5.4 \times 10^{-1}$	$1.4 \times 10^{-1}$
3	0.188	$2.3 \times 10^{-2}$	$1.0 \times 10^{-2}$	$8.7 \times 10^{-1}$	$2.6 \times 10^{-1}$
4	0.94	$6.3 \times 10^{-3}$	$6.4 \times 10^{-3}$	$4.3 \times 10^{-1}$	$1.1 \times 10^{-1}$
5	1.88	$3.2 \times 10^{-3}$	$4.1 \times 10^{-3}$	$9.8 \times 10^{-3}$	$4.6 \times 10^{-3}$

**Note:** PA of pure TiO<sub>2</sub> (without any dye and PEPC) was similar to the values in line 0:  $1.6 \times 10^{-1}$  and 0 for irradiation with the light with  $\lambda = 310\text{--}400$  nm and  $\lambda > 400$  nm, respectively.

**Table 4.** Photocatalytic activity (PA, mg/mL min m<sup>2</sup>) of heterostructures CdS/D I/PEPC and CdS/D II/PEPC for various contents of the dyes and exposition to the light from different spectral bands.

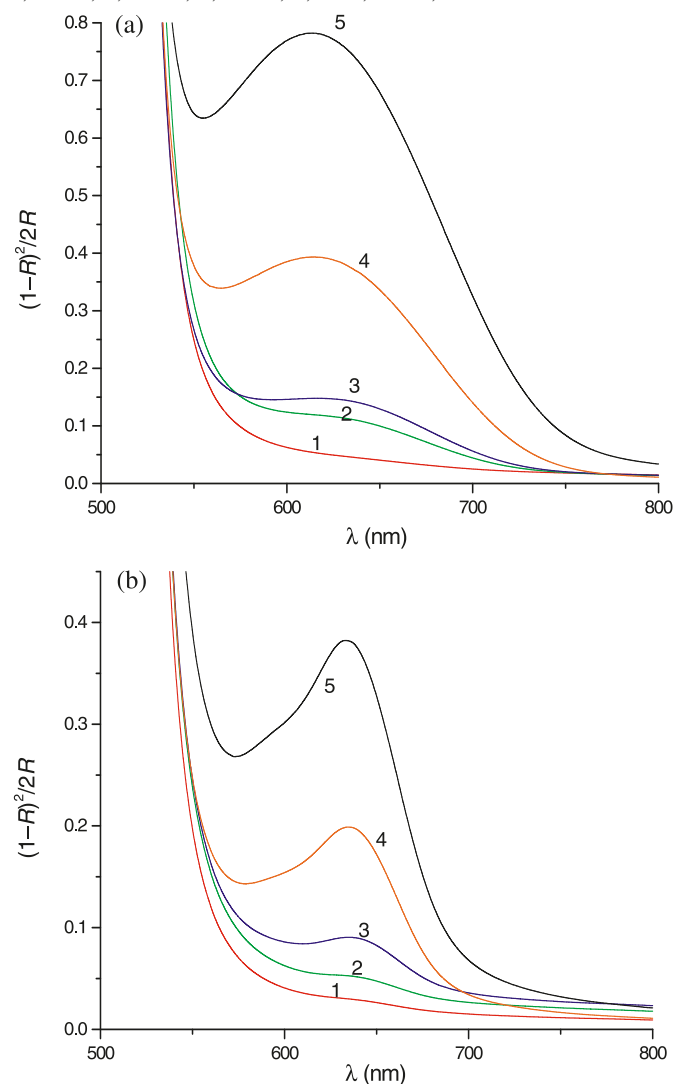
No.	Dye content in the HS, mg/g	PA: light absorbed by a semiconductor, $\lambda = 310\text{--}400$ nm		PA: light absorbed by the dyes, $\lambda > 400$ nm	
		CdS/D I/PEPC	CdS/D II/PEPC	CdS/D I/PEPC	CdS/D II/PEPC
0	without dye	1.1	1.1	0	0
1	0.019	$7.1 \times 10^{-1}$	$7.5 \times 10^{-1}$	$4.0 \times 10^{-2}$	$1.1 \times 10^{-2}$
2	0.094	$2.1 \times 10^{-1}$	$4.9 \times 10^{-1}$	$9.1 \times 10^{-2}$	$6.9 \times 10^{-2}$
3	0.188	$8.4 \times 10^{-2}$	$7.0 \times 10^{-2}$	$6.7 \times 10^{-1}$	$3.2 \times 10^{-1}$
4	0.94	$1.3 \times 10^{-2}$	$5.8 \times 10^{-2}$	$3.3 \times 10^{-1}$	$1.9 \times 10^{-1}$
5	1.88	$9.1 \times 10^{-3}$	$8.1 \times 10^{-3}$	$7.2 \times 10^{-3}$	$1.6 \times 10^{-3}$

**Note:** PA of pure CdS (without any dye and PEPC) was similar to the values in line 0: 1.1 and 0 for irradiation with the light with  $\lambda = 310\text{--}400$  nm and  $\lambda > 400$  nm, respectively.

upon the redox potentials (Tables 1 and 2), potentials of conductivity bands of TiO<sub>2</sub> ( $E_{CB} = -0.54$  V<sup>13,14</sup>) and CdS ( $E_{CB} = -0.80$  V<sup>2,14</sup>), reduction potential of methylene blue

( $E_{MB/MB^{*+}} = +0.11$  V<sup>15</sup>), oxidation potential of formaldehyde ( $E_{F/F^{*+}} = -0.5$  V<sup>16</sup>), and PEPC ( $E_{P/P^{*+}} = 1.28$  V<sup>1</sup>). The diagrams are represented in Figs. 6–8.

**Fig. 4.** Light absorption spectra for CdS-based heterostructures: (a) CdS/D I/PEPC, (b) CdS/D II/PEPC. Dye content in the HSs (mg/g): 1, 0.019; 2, 0.094; 3, 0.188; 4, 0.94; and 5, 1.88.



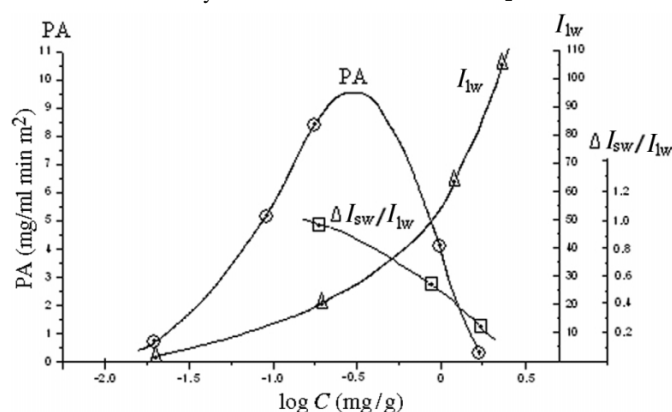
## Discussion

### Energy characteristics of photocatalytic systems and photocatalytic activity of the heterostructures in the reduction of methylene blue

#### Effect of the light absorption in the range 310–400 nm: Light is absorbed mainly by a semiconductor

As seen from the energy transformation diagrams (Fig. 6), the following processes can be thermodynamically allowed in the HS after generating an electron-hole pair in  $\text{TiO}_2$  or CdS: (process 1) an electron can be transferred from the conductivity band to the reducing agent; (process 2) a hole in the valence band can be filled with an electron from the reducing agent, either directly (process 3) or through the PEPC molecule (processes 4 and 5). Energy gaps  $\Delta E$  between potentials of all reactants in the above processes are wide enough, and all the processes should run efficiently and ensure high PA of the HS. However, the energy diagrams prove that there is another electron-transfer option

**Fig. 5.** Dependence of PA and spectral parameters  $I_{\text{lw}}$  and  $\Delta I_{\text{sw}}/I_{\text{lw}}$  on the content of Dye I in the heterostructure  $\text{TiO}_2/\text{D I}/\text{PEPC}$ .



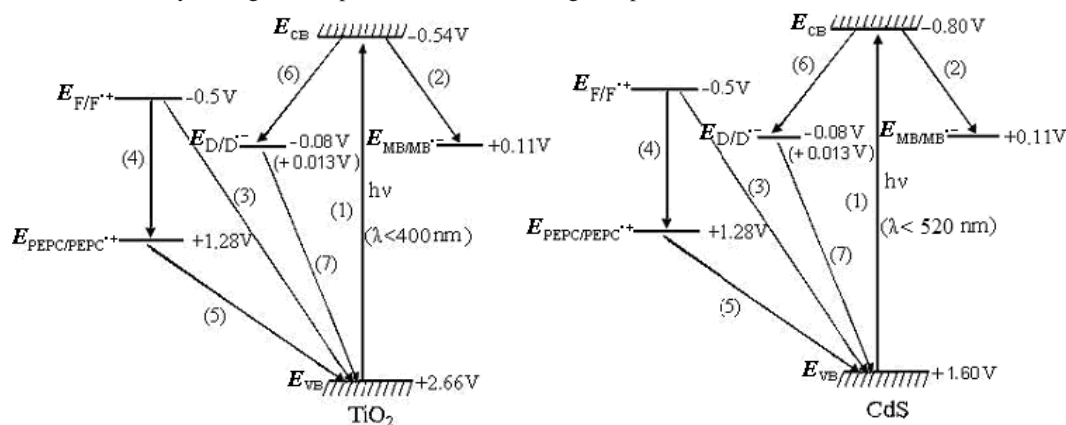
available for each HS: an electron can be transferred from the conductivity band to the dye molecule (process 6). This process and the process 7 together can be considered as an indirect electron-hole recombination. Reduction potentials for MB, D I, and D II are very close, and these agents can effectively intercept electrons from the conductivity band. Therefore, the rise in the dye-sensitizer content should result in lowering the PA of a material and slowing down the MB reduction on the interface boundary. Experimental data from Tables 3 and 4 confirm this assumption: adding 0.019 mg/g of D I or D II results in a 50% decrease of the PA of  $\text{TiO}_2$  followed by further lowering after adding next portions of the sensitizer. A CdS-based material exhibits the same effect (see Table 4).

#### Effect of the light absorption at $\lambda > 400$ nm, where the light is absorbed mainly by the dyes — HS: $\text{TiO}_2/\text{D I}/\text{PEPC}$ and $\text{TiO}_2/\text{D II}/\text{PEPC}$

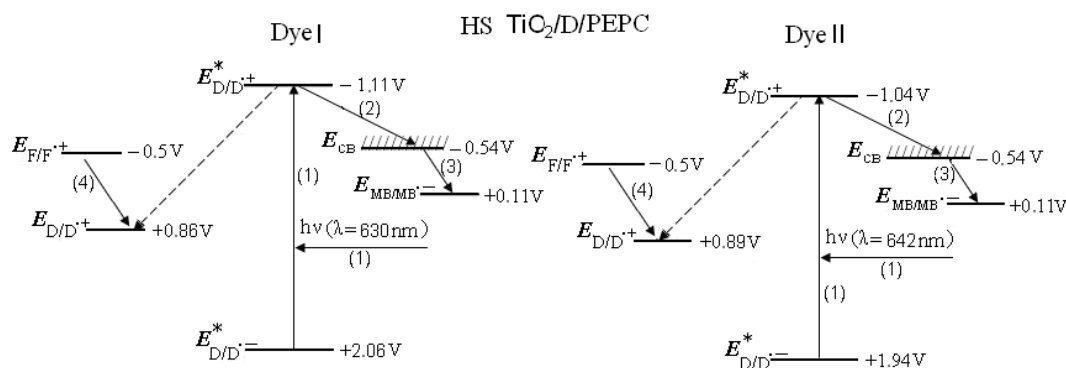
It is known<sup>1,17</sup> that injection of electrons from excited molecules of a dye into the conductivity band is a basic process, which governs sensitizing semiconductors by the dyes. An energy gap  $\Delta E = E_{\text{CB}} - E_{\text{D/D}^+}$  determines the thermodynamic efficiency of this process. As seen from the energetic diagrams of the photocatalytic systems with a dye content of 0.188 mg/g (Fig. 6), such gaps are wide enough even for photoexcitation by the visible light from the long-wave dye absorption bands. Comparison to the data from Table 1 proves that efficiency of the electron injection into the conductivity band cannot be significantly influenced by the shifting effect of changes in the HS composition on the positions of such bands. This shifting only leads to small changes of some hundredth parts in the value of  $E_{\text{D/D}^+}$ .

Therefore, the “longwave” photoexcitation (Fig. 7, process 1) should induce the injection of electrons into the conductivity band (process 2) at any composition of the HSs  $\text{TiO}_2/\text{D I}/\text{PEPC}$  and  $\text{TiO}_2/\text{D II}/\text{PEPC}$ . The following processes are thermodynamically allowed and can have needful driving force: interface electron transfer (i) from the conductivity band (process 3) to MB molecules and (ii) from formaldehyde (process 4) to cation-radicals  $\text{D}^{\bullet+}$  (formed in process 2 from  $\text{D}^*$ ; see the broken lines in Fig. 7). The photoactive form of the photocatalyst is regenerated in the latter process. Similar analysis of the energy transformation diagrams

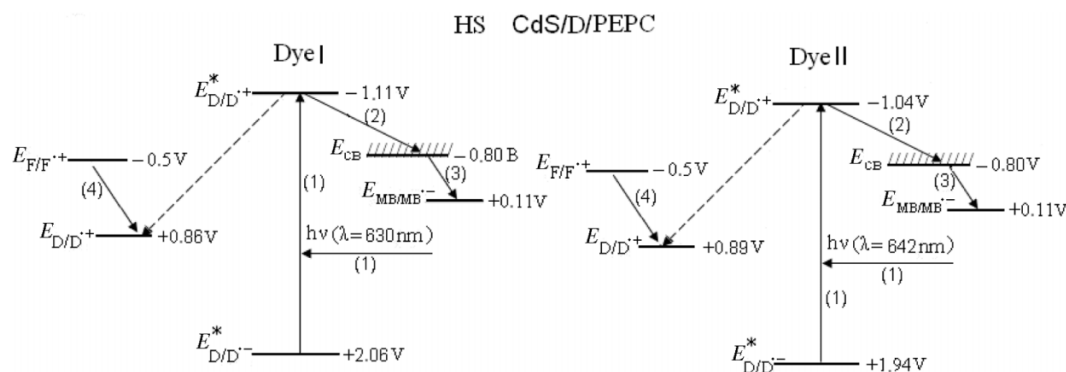
**Fig. 6.** Energy transformation diagrams for photocatalytic systems with  $\text{TiO}_2$ - and  $\text{CdS}$ -based heterostructures comprising D I and schemes of electronic processes induced by the light absorption on semiconducting compounds.



**Fig. 7.** Energy transformation diagrams for the photocatalytic systems with  $\text{TiO}_2/\text{D I/PEPC}$  and  $\text{TiO}_2/\text{D II/PEPC}$  heterostructures. Schemes of the electronic processes induced after the light absorption by a dye-sensitizer ( $\lambda > 400$  nm, calculations were made for a sample with  $C = 0.188$  mg/g).



**Fig. 8.** Energy transformation diagrams for photocatalytic systems with  $\text{CdS}/\text{D I/PEPC}$  and  $\text{CdS}/\text{D II/PEPC}$  heterostructures. Schemes of the electronic processes induced after the light absorption by a dye-sensitizer ( $\lambda > 400$  nm, calculations were made for a sample with  $C = 0.188$  mg/g).



proves that the above electron-transfer processes 1–4 are also thermodynamically allowed for HSs  $\text{CdS}/\text{D I/PEPC}$  and  $\text{CdS}/\text{D II/PEPC}$  (see Fig. 8).

Hence, both dyes D I and D II should exhibit close sensitizing efficiency (if there are no other side effects influencing their sensitizing) resulting in a very close photocatalytic activity of HSs  $\text{TiO}_2/\text{D I/PEPC}$  and  $\text{TiO}_2/\text{D II/PEPC}$  as well as  $\text{CdS}/\text{D I/PEPC}$  and  $\text{CdS}/\text{D II/PEPC}$ . The value of the HS photocatalytic activity should increase if the content of D I or D II raises and then remains stable at further raise in the

dye's content. However, this conclusion does not agree with the experimental data. D I-based HS exhibits significantly higher photocatalytic activity compared with the D II-based materials (see Tables 3 and 4) even though both dyes have very close values of  $E_{\text{D/D}^+}$  and should provide very close efficiency of the electron injection, resulting in similar PA values. Moreover, initial raise in PA tends to decrease as the concentration of the dye increases. This unexpected deviation from thermodynamically predicted characteristics can be explained by the following analysis of the HS spectra.

### ***Spectral changes resulting from the deposition of the dyes on semiconducting particles — Dependence on photocatalytic activity of the heterostructure***

As we mentioned above, the location of the light absorption bands, their width, and intensity ratio can change as a result of deposition of both dyes on the surface of TiO<sub>2</sub> particles. Similar changes probably occur at the formation of CdS-based HS, but they are mostly hidden behind overlapping light absorption bands of CdS. Therefore, we shall confine further consideration to TiO<sub>2</sub>-based materials only.

As seen from Table 1, deposition of D I on the surface of the HS causes shifting of both shortwave and longwave light absorption peaks. This shifting reaches 24 and 27 nm, respectively, for sample 3 ( $C = 0.188$  mg/g). The shifting values decrease to 19 and 21 nm, respectively, if a dye content is larger by one order of magnitude (sample 5,  $C = 1.88$  mg/g). Similarly,<sup>6</sup> such spectral changes can be explained as a result of the strong influence of titanium dioxide on the electron system of the dye molecules on the surface of TiO<sub>2</sub>. The more dye molecules deposited on the surface, the larger would be the distance between the newly deposited molecules and the surface. This effect causes weakening of further spectral changes at the deposition of new portions of the dye. Such weakening can be proved by changes in ratio between the intensities of the shortwave and longwave light absorption bands  $I_{sw}/I_{lw}$  (see Table 1). According to the theory by A. I. Kiprianov,<sup>18,19</sup> this parameter characterizes the spatial orientation of the biscyanine's chromophores. This orientation can be changed by steric and electronic factors.

The value of  $I_{sw}/I_{lw}$  for the D I solution is 0.76. According to ref. 18, this value evidences the obtuse angle between the chromophores (calculations from ref. 7 gave the value of this angle  $\theta = 113^\circ$ ). For a remote-from-surface molecule of D I (sample 5), this value is  $\theta \approx 90^\circ$  ( $I_{sw}/I_{lw} \approx 1$ ) while for a surface and, probably, near-to-surface molecule of the dye, this angle is acute and  $I_{sw}/I_{lw} = 1.38$  and  $1.87$ , respectively (see samples 4 and 3).

The parameter  $\Delta I_{sw}/I_{lw}$  is calculated as the difference between  $I_{sw}/I_{lw}$  values for the dye deposited on TiO<sub>2</sub> and the dissolved dye molecules, and it represents a character of the given semiconductor influence on the dye molecules in the ground state. This parameter can also characterize processes, which occur at the photoexcitation of the HS after a molecule of the dye absorbs the light quantum. This characterization grounds on unavoidable deterioration of conditions of injecting the electrons into the conductivity band and considerable lowering of PA due to weakening of the mutual influence of the dye and semiconductor. As seen in Fig. 5, values of  $\Delta I_{sw}/I_{lw}$  and PA show similar changes for all the samples with  $C_{D\ I} > 0.188$  mg/g. Moreover, the photocatalytic activity shows significant decrease even though a value of  $I_{lw}$  raises, which causes quantitative rise of the light absorption.

Bathochromic shifting of the dye absorption bands also occurs at the formation of a HS from TiO<sub>2</sub> and D II. However, the value of such shifting is significantly lower than the value for TiO<sub>2</sub>/D I heterostructure (see Tables 1 and 2). For example, such values are 10 and 27 nm, respectively, for sample 3. Only the angle between the chromophores differs significantly for these HSs. The ratio between the val-

ues of intensities of the absorption bands shows that this angle decreases though remaining obtuse at the deposition of D II on TiO<sub>2</sub>.

We use the parameter  $\Delta I_{sw}/I_{lw}$  as a characteristic of the dye-semiconductor interaction. The maximal value of  $\Delta I_{sw}/I_{lw} = 1.11$  is reached for sample 3 with  $C_{D\ I} = 0.188$  mg/g while this parameter is only 0.11 for TiO<sub>2</sub>/D II/PEPC. Data from Table 3 prove that PA values of these samples differ more than three times. We consider this difference as an evidence of more intense interaction between TiO<sub>2</sub> and D I compared with TiO<sub>2</sub> and D II.

A joint analysis of the spectral bands shifting and PA values for the HS with CdS, D I, and D II also proves strong dependence of the dyes sensitizing activity on the influence of a semiconductor on their electronic structure and light absorption spectra. For example, more active material (sample 3,  $C_{D\ I} = 0.188$  mg/g) ensures shifting of the HS light absorption band for 24 nm from its position for the dye solution (from 603 to 627 nm, see Fig. 4a) and shows high PA =  $6.7 \times 10^{-1}$  mg/mL min m<sup>2</sup> (see Table 4). A heterostructure with D II has weaker interaction with CdS and shows lower band shifting of 8 nm (from 632 to 640 nm, see Fig. 4b) and lower PA =  $3.2 \times 10^{-1}$  mg/mL min m<sup>2</sup> (see Table 4). The width of the light absorption bands is mainly determined by intermolecular interaction.<sup>20</sup> Therefore, widening of the HS bands compared with the bands of the dye solution can be caused by much stronger interaction between the surface dye molecules compared with the interaction in the solutions.

Both electron-donating and electron-accepting organic molecules can be adsorbed on the semiconductors (for example, TiO<sub>2</sub> or CdS) with partial or complete transfer of the biscyanine electron. Taking into account the presence of both donors (like -NR<sub>2</sub> groups) and accepting (like quaternary nitrogen or a carbonyl group) active centres in a dye molecule, we can assume that they can react with the semiconductor substrate either by donating or accepting mechanisms. Detailed clarification of such processes requires more specialized investigation.

## **Conclusions**

A series of the heterostructures based on TiO<sub>2</sub> and CdS and sensitized with bisquinocyanine dyes have been synthesized. We have determined the photocatalytic activity of these materials and found a character of its dependence on quantitative composition, spectral, and energetic parameters.

It was found that the sensitizing activity of the dyes with similar spectral and oxidation-reduction properties may differ depending on their bonding force with a semiconductor in the HS.

## **References**

- (1) Kryukov, A. I.; Kuchmii, S. Ya.; Pokhodenko, V. D. *Theor. Exp. Chem.* **1995**, *30* (4), 141. doi:10.1007/BF00534653.
- (2) Kryukov, A. I.; Kuchmii, S. Ya.; Pokhodenko, V. D. *Theor. Exp. Chem.* **2000**, *36* (2), 63. doi:10.1007/BF02529022.
- (3) Kuchmii, S. Ya.; Korzhak, A. V.; Guba, N. F.; Kulik, S. V.; Kryukov, A. I. *Theor. Exp. Chem.* **1996**, *31* (6), 309. doi:10.1007/BF00531245.
- (4) Kobasa, I. M. *Functional Materials* **2003**, *10*, 276.



- (5) Kobasa, I. M. *Theor. Exp. Chem.* **2003**, 39 (1), 53. doi:10.1023/A:1022954328611.
- (6) Kobasa, I. M.; Kondratyeva, I. V. *Pol. J. Chem.* **2008**, 82, 1639.
- (7) Yagodinets, P. I. *J. Gen. Chem.* **1997**, 67, 1576.
- (8) Cherniuk, I. N.; Yagodinets, P. I.; Pridan, V. E. *J. Gen. Chem.* **1997**, 67, 459.
- (9) Kobasa, I. M.; Strus, V. J.; Kovbasa, M. A. WO Patent No. WO/2008/076308, 2008.
- (10) Elzayat, M. Y.; Saed, A. O.; El-Dessouki, M. S. *Sol. Energy Mater. Sol. Cells* **2002**, 71 (1), 27. doi:10.1016/S0927-0248(01)00042-3.
- (11) Delgass, W. N.; Haller, C. L.; Kellerman, R.; Lunsford, J. H. *Spectroscopy in Heterogenous Catalysis*; Academic Press: NY, San-Francisco, London, 1979; p. 341.
- (12) Chibisov, A. K. *Adv. Chem* **1981**, 50, 1169.
- (13) Kamat, P. V. *J. Chem. Soc., Faraday Trans. I* **1985**, 81 (2), 509. doi:10.1039/f19858100509.
- (14) Xu, J.; Schoonen, M. A. A. *Am. Mineral.* **2002**, 85, 543.
- (15) Kamat, P. V. *Chem. Rev.* **1993**, 93 (1), 267. doi:10.1021/cr00017a013.
- (16) Salkauskas, M.; Vashkylis, A. *Chemical Metallization of Plastics*; Khimiya: Leningrad, 1977; p. 117.
- (17) Kalyanasundaram, K.; Gratzel, M. *Curr. Sci.* **1994**, 66, 706.
- (18) Kiprianov, A. I. *Introduction to Electronic Theory of Organic Compounds*; Naukova Dumka: Kiev, 1975; Chapter 3.
- (19) Kiprianov, A. I. *Color and Composition of the Cyanine Dyes*; Naukova Dumka: Kiev, 1979; Chapter 2–4.
- (20) Ischenko, A. A. *Composition, Spectral and Luminescence Properties of the Polymethine Dyes*; Naukova Dumka: Kiev, 1994; pp. 66–97.

# Ortho-phenylene-bridged aryloxy phosphine ligands and their coordination chemistry with tantalum(V)

Christopher D. Carmichael and Michael D. Fryzuk

**Abstract:** The lithium complexes  $\text{RP}(3,5\text{-}^t\text{Bu}_2\text{C}_6\text{H}_2\text{OLi})_2(\text{THF})_4$ , where  $\text{R} = \text{Ph}$  or  $^i\text{Pr}$ , ( $^{\text{R}}[\text{OPO}]\text{Li}_2$ )(THF)<sub>4</sub>, can be converted quantitatively into the protonated forms,  $^{\text{R}}[\text{OPO}]\text{H}_2$ , by reaction with  $\text{Et}_3\text{NHCl}$ . Reaction of the protonated compounds with  $\text{KH}$  yields the potassium complexes  $^{\text{Ph}}[\text{OPO}]\text{K}_2(\text{THF})_6$  and  $(^i\text{Pr})[\text{OPO}]\text{K}_2(\text{THF})_3$ . The reaction of  $^{\text{R}}[\text{OPO}]\text{H}_2$  with  $\text{TaCl}_5$  yields the sparingly soluble tantalum trichloride complexes  $^{\text{R}}[\text{OPO}]\text{TaCl}_3$  via elimination of  $\text{HCl}$ . Reaction of  $^{\text{Ph}}[\text{OPO}]\text{H}_2$  with  $\text{TaMe}_3\text{Cl}_2$  leads to the monomethyl complex  $^{\text{Ph}}[\text{OPO}]\text{TaMeCl}_2$ , or the dimethyl halide complex,  $^{\text{Ph}}[\text{OPO}]\text{TaMe}_2\text{Cl}$ , via protonolysis, and the potassium complex  $(^{\text{Ph}}[\text{OPO}]\text{K}_2)_2(\text{THF})_6$  yields the trimethyl complex,  $^{\text{Ph}}[\text{OPO}]\text{TaMe}_3$  by a metathesis process.

**Key words:** tantalum, phosphine, potassium, aryloxy, tridentate ligand, alkyl.

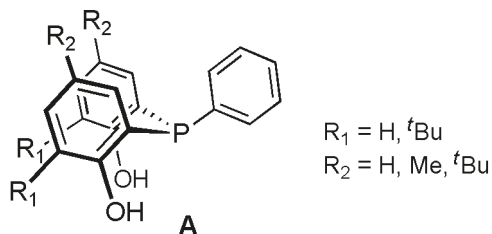
**Résumé :** Les complexes du lithium  $\text{RP}(3,5\text{-}^t\text{Bu}_2\text{C}_6\text{H}_2\text{OLi})_2(\text{THF})_4$  dans lesquels  $\text{R} = \text{Ph}$  ou  $^i\text{Pr}$ , ( $^{\text{R}}[\text{OPO}]\text{Li}_2$ )(THF)<sub>4</sub> peuvent être transformés quantitativement en formes protonées,  $^{\text{R}}[\text{OPO}]\text{H}_2$  par réaction avec le  $\text{Et}_3\text{NHCl}$ . La réaction des composés protonés avec le  $\text{KH}$  conduit à la formation des complexes de potassium  $(^{\text{Ph}}[\text{OPO}]\text{K}_2)_2(\text{THF})_6$  et  $(^i\text{Pr})[\text{OPO}]\text{K}_2(\text{THF})_3$ . La réaction du  $^{\text{R}}[\text{OPO}]\text{H}_2$  avec du  $\text{TaCl}_5$  conduit à la formation de complexes du trichlorure de tantale,  $^{\text{R}}[\text{OPO}]\text{TaCl}_3$ , qui sont très peu solubles et qui résultent d'une élimination de  $\text{HCl}$ . La réaction du  $^{\text{Ph}}[\text{OPO}]\text{H}_2$  avec du  $\text{TaMe}_3\text{Cl}_2$  conduit, par le biais d'une protonolyse, à la formation de complexes monométhylés,  $^{\text{Ph}}[\text{OPO}]\text{TaMeCl}_2$ , ou biméthylés,  $^{\text{Ph}}[\text{OPO}]\text{TaMe}_2\text{Cl}$  alors que celle du complexe potassique  $(^{\text{Ph}}[\text{OPO}]\text{K}_2)_2(\text{THF})_6$  conduit, par un processus de métathèse, à la formation du complexe triméthylé,  $^{\text{Ph}}[\text{OPO}]\text{TaMe}_3$ .

**Mots-clés :** tantale, phosphine, potassium, aryloxy, ligand tridentate, alkyle.

[Traduit par la Rédaction]

## Introduction

For some time, we have been interested in examining the coordination chemistry of mixed-donor multidentate ligands.<sup>1,2</sup> By combining hard donors, such as amido ( $\text{NR}_2^-$ ), with soft phosphines ( $\text{PR}_3$ )<sup>3–7</sup> or arsines ( $\text{AsR}_3$ )<sup>8,9</sup> into chelating arrays, we have been able to prepare transition-metal complexes that can activate molecular nitrogen in certain cases.<sup>2,10–13</sup> We have extended this mixed-donor ligand approach to include the hard aryloxy ( $\text{ArO}^-$ ) moiety with phosphines to generate OPO ligand sets with *o*-phenylene linkers.<sup>14</sup> The general family of OPO ligand precursors **A** is shown below with the various substitution patterns that have been examined.



Rhenium and technetium complexes supported by the parent ligand, bis(*o*-phenoxy)phenylphosphine (**A** with  $\text{R}_1 = \text{R}_2 = \text{H}$ ), have drawn interest for their potential use as radiopharmaceutical agents.<sup>15,16</sup> With group 4, the heptacyclic, tetranuclear titanium complex,  $\{(^i\text{PrO})_2\text{Ti}(\mu^3\text{-O})\text{TiCl}(\text{PrO})[(\text{OC}_6\text{H}_4)_2\text{PPh}]\}_2$ , was obtained,<sup>17</sup> likely a result of the lack of steric bulk around the OPO donor set.

Bis(3-*tert*-butyl-5-methyl-2-phenoxy)phenylphosphine (**A**,  $\text{R}_1 = ^t\text{Bu}$ ,  $\text{R}_2 = \text{Me}$ ), which has a sterically bulky *tert*-butyl group ortho to the phenoxy group, has been complexed to titanium<sup>18</sup> and chromium.<sup>19</sup> These complexes were found to be highly active for the polymerization of ethylene.

Bis(3,5-*tert*-butyl-2-phenoxy)phenylphosphine was first reported in 2000;<sup>20</sup> in this report, we abbreviate it as  $^{\text{Ph}}[\text{OPO}]\text{H}_2$  (**A**,  $\text{R}_1 = \text{R}_2 = ^t\text{Bu}$ ), where the Ph superscript refers to the substituent at phosphorus that is not a substituted phenol. Despite the presence of two bulky *tert*-butyl substituents on the phenolic units, the donor set readily forms bis(ligand) complexes with several transition metals, including cobalt and nickel, although in these complexes one phe-

Received 11 January 2010. Accepted 22 March 2010. Published on the NRC Research Press Web site at canjchem.nrc.ca on 24 June 2010.

**C.D. Carmichael and M.D. Fryzuk.**<sup>1</sup> Department of Chemistry, The University of British Columbia, 2036 Main Mall, Vancouver, BC V6T 1Z1, Canada.

<sup>1</sup>Corresponding author (e-mail: fryzuk@chem.ubc.ca).

nol arm of the ligand remains protonated.<sup>20</sup> Vanadium(IV) complexes supported by  $\text{Ph}[\text{OPO}]$  can be synthesized by reaction of the protonated phenol with  $\text{VCl}_3(\text{THF})_3$ ;<sup>21</sup> a short exposure to oxygen is necessary to oxidize V(III) to V(IV). Lithium and potassium salts, supported by the chelating donor solvent DME (1,2-dimethoxyethane) have been recently reported.<sup>22</sup>

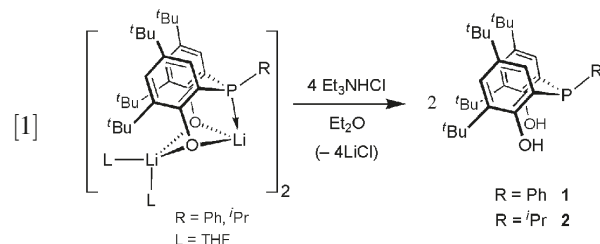
Several group-4 metal complexes have been prepared using  $\text{Ph}[\text{OPO}]\text{H}_2$ , including  $\text{Ph}[\text{OPO}]\text{TiCl}_2(\text{THF})$ , and the bis(ligand) derivatives  $\text{Ph}[\text{OPO}]_2\text{M}(\text{OH}_2)$  ( $\text{M} = \text{Zr}, \text{Hf}$ ) and  $\text{Ph}[\text{OPO}]_2\text{Ti}$ .<sup>23</sup> The bis(ligand) complex is so readily formed in the titanium system that a comproportionation reaction between  $\text{Ph}[\text{OPO}]_2\text{Ti}$  and  $\text{TiCl}_4(\text{THF})_2$  was found to be the best method for the preparation of  $\text{Ph}[\text{OPO}]\text{TiCl}_2(\text{THF})$ . Similar reactions with  $\text{SnCl}_4$  did not produce the bis(ligand) complex, instead leading to the clean formation of  $\text{Ph}[\text{OPO}]\text{SnCl}_2$ .<sup>24</sup>

A very recent report details the synthesis and structures of a series of bis(ligand) complexes of Ta(V) having the formula  $\text{Ph}[\text{OPO}]_2\text{TaX}$ , where  $\text{X} = \text{Cl}, \text{H}, \text{Me}, \text{Et}$ , and  $\text{OH}$ .<sup>25</sup> Of relevance to this work was the observation that the monoligand complexes  $\text{Ph}[\text{OPO}]\text{TaX}_3$  were not accessible despite a number of different synthetic strategies attempted.

We have recently reported the structural variety of lithium aryloxy complexes based on the  $\text{R}[\text{OPO}]$  donor set<sup>14</sup> utilizing phenyl and *iso*-propyl substituents on phosphorus. We present herein an extension of this bis(aryloxy)phosphine chemistry by reporting an improved synthesis of the protonated compounds  $\text{R}[\text{OPO}]\text{H}_2$  from the lithium salts, the synthesis of THF-supported potassium salts,  $(\text{Ph}[\text{OPO}]\text{K}_2)_2(\text{THF})_6$  (**3**) and  $(i\text{Pr}[\text{OPO}]\text{K}_2)_3(\text{THF})_3$  (**4**), and their reactions with the tantalum precursors  $\text{TaCl}_5$  and  $\text{TaMe}_3\text{Cl}_2$ . We also describe the preparation of the elusive monoligand complexes  $\text{R}[\text{OPO}]\text{TaCl}_3$  ( $\text{R} = \text{Ph}, i\text{Pr}$ ).

## Results and discussion

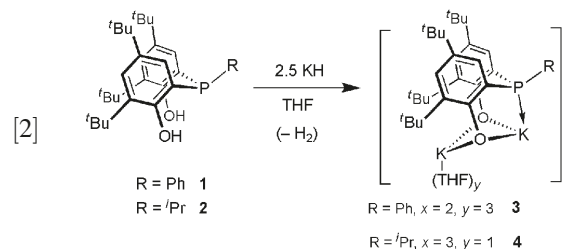
Reaction of the lithium complexes,  $\text{RP}(3,5\text{-}t\text{Bu}_2\text{C}_6\text{H}_2\text{OLi})_2(\text{THF})_4$ , where  $\text{R} = \text{Ph}$  or  $i\text{Pr}$ ,  $(\text{R}[\text{OPO}]\text{Li})_2(\text{THF})_4$ , with 4 equiv. of  $\text{Et}_3\text{NHCl}$  in diethyl ether, eq. [1], gives the desired products,  $\text{Ph}[\text{OPO}]\text{H}_2$  (**1**) or  $i\text{Pr}[\text{OPO}]\text{H}_2$  (**2**), in 97% and 96% isolated yields, respectively.  $^1\text{H}$  and  $^{31}\text{P}\{^1\text{H}\}$  NMR spectra of **1** are consistent with literature values.<sup>20</sup> The  $^{31}\text{P}\{^1\text{H}\}$  NMR spectrum of **2** displays a singlet at  $\delta -61.6$ , slightly upfield from that observed for **1**, reflecting the more basic nature of the alkyl phosphine. The  $^1\text{H}$  NMR spectrum of **2** contains two singlet resonances for the *tert*-butyl groups, and a characteristic doublet of septets for the methine proton of the *iso*-propyl group coupled to phosphorus and the methyl protons, which appear as a doublet of doublets.



X-ray quality crystals of **1** containing 3 equiv. of the co-crystallized solvent were grown by slow evaporation of a saturated benzene solution. The solid-state structure is pre-

sented in Fig. 1, and selected bond distances and angles are collected in Table 1. The unit cell parameters are identical to those reported for the related phosphine oxide compound.<sup>20</sup> This may seem surprising at first; however, Fig. 1 shows how the oxygen of a phosphine oxide would fit easily into the molecule, while not altering the overall size of the molecule. In addition, the phenolic hydrogens, which were located in the diffraction pattern and refined isotropically, are well-positioned to engage in hydrogen bonding to a phosphine oxide. Phosphine/phosphine oxide systems with identical cell parameters are known,<sup>26</sup> and solid-state structures have been reported with partial oxidation of the phosphine, and thus fractional occupation in the crystal lattice.<sup>27–29</sup> The phenol rings in **1** are twisted with respect to each other by  $23^\circ$ .

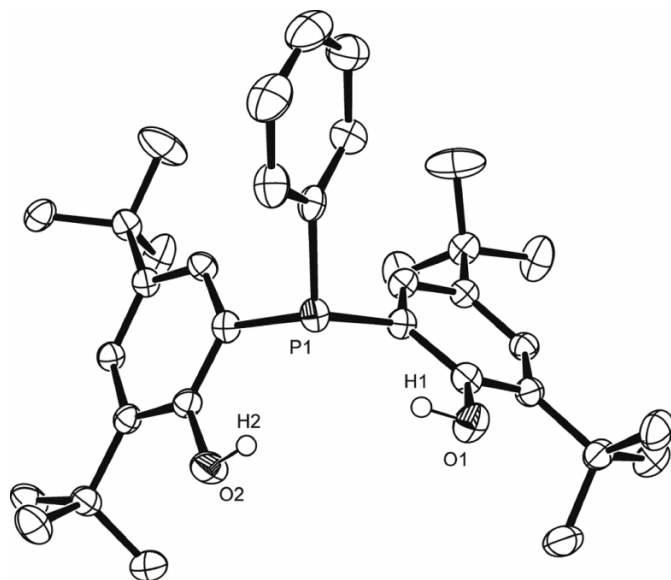
The synthesis of the  $\text{R}[\text{OPO}]$  potassium derivatives is outlined in eq. [2]. Reaction of the protonated ligands **1** or **2** with an excess of KH in THF affords the products  $(\text{Ph}[\text{OPO}]\text{K}_2)_2(\text{THF})_6$  (**3**) and  $(i\text{Pr}[\text{OPO}]\text{K}_2)_3(\text{THF})_3$  (**4**) in 92% and 71% yield, respectively. NMR studies indicate that **3** has a symmetric structure in solution as evidenced by two distinct singlet resonances in the  $^1\text{H}$  NMR spectra at  $\delta 1.64$  and  $\delta 1.33$ , which correspond to the two different *tert*-butyl protons on each ring; the  $^{31}\text{P}\{^1\text{H}\}$  NMR spectrum shows a singlet for the  $^{31}\text{P}$  nuclei at  $-29.6$  ppm. Mass spectral analysis indicates that the complex is dimeric in the bulk material.



X-ray quality crystals of **3** containing three molecules of the co-crystallized solvent were grown by slow evaporation of a saturated THF solution at  $-40^\circ\text{C}$ . The solid-state structure is presented in Fig. 2, and selected bond distances and angles are collected in Table 2. Structurally, **3** is a symmetrical dimer, in agreement with the solution and mass spectral data, with two crystallographically related fragments. The core of the structure is virtually identical to the DME-supported complex,  $\text{Ph}[\text{OPO}]\text{K}_2(\text{DME})_2$ , reported recently.<sup>22</sup> The only significant differences are a direct consequence of the difference in coordinating solvent. In both complexes, a single molecule of solvent is bound to K(2); however, the bidentate nature of DME results in longer bonds to the surrounding oxygen atoms than are present in **3**, where a monodentate THF is coordinated. Two solvent oxygens are coordinated to K(1) in both complexes, a single DME in  $\text{Ph}[\text{OPO}]\text{K}_2(\text{DME})_2$  and both terminal and bridging THF molecules in **3**. Although the observed K–O bond distances in the structure of **3** vary by almost  $0.4 \text{ \AA}$ , they agree well with the DME structure<sup>22</sup> and other literature values,<sup>30–32</sup> as do the K–P bond distances.<sup>33–35</sup> With regard to the phosphine to potassium distances in the solid state, it is clear that these are weak interactions and the connectivities only indicate close interactions.

Slow diffusion of hexanes into a benzene solution of **4** af-

**Fig. 1.** Molecular structure (ORTEP) of  $\text{Ph}[\text{OPO}]\text{H}_2$ , **1**. Ellipsoids are drawn at 50% probability. Co-crystallized solvent was omitted for clarity. Modeled *t*-butyl disorder was also omitted for clarity.



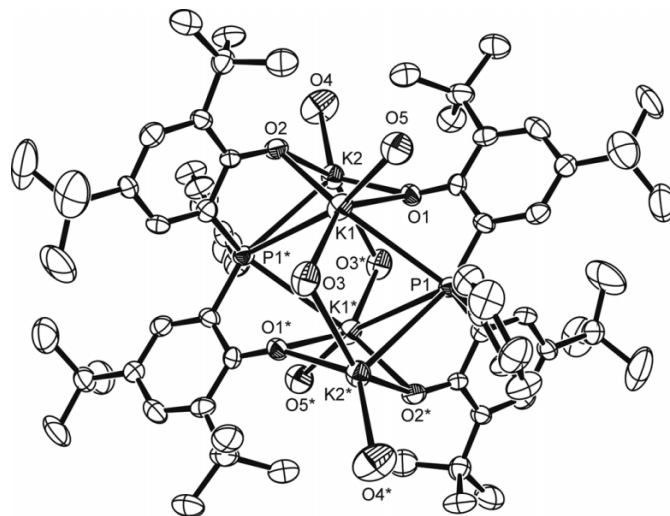
**Table 1.** Selected bond distances (Å), bond angles (°), and dihedral angles (°) for  $\text{Ph}[\text{OPO}]\text{H}_2$ , **1**.

Bond distances (Å)	
P(1)—C(1)	1.828(2)
P(1)—C(7)	1.826(2)
O(1)—H(1)	0.901(2)
O(2)—H(2)	0.950(2)
O(1)—C(2)	1.375(2)
O(2)—C(8)	1.377(2)
P(1)—C(13)	1.824(2)
Bond angles (°)	
C(1)—P(1)—C(7)	102.31(9)
C(7)—P(1)—C(13)	106.01(9)
C(1)—P(1)—C(13)	107.03(10)
C(2)—O(1)—H(1)	107.04(10)
C(8)—O(2)—H(2)	105.46(10)

forded X-ray quality crystals that have been structurally characterized as the benzene adduct ( $^{\text{tPr}}[\text{OPO}]\text{K}_2(\text{THF})_3(\eta^6\text{-C}_6\text{H}_6)$  (**4-C<sub>6</sub>H<sub>6</sub>**) containing four molecules of co-crystallized benzene and two molecules of co-crystallized hexane per unit cell. The solid-state structure of **4** is presented in Fig. 3. The structure is that of an asymmetric trimer, and one molecule of benzene is  $\pi$ -bonded in a  $\eta^6$  fashion to a potassium atom, K(5), a motif that has been reported in other potassium complexes.<sup>36–38</sup> Unfortunately, extreme disorder in the co-crystallized and coordinated solvent results in very weak data, insufficient to support a more detailed discussion of the structure. A cif file is included in the Supplementary data.

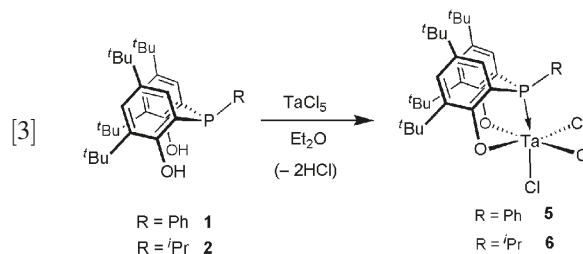
The  $^1\text{H}$  and  $^{31}\text{P}\{^1\text{H}\}$  NMR spectra of **4** show a symmetrical solution structure, which is at odds with the asymmetrical nature of the solid-state structure. A mass spectrum of **4** could not be obtained, presumably due to the high molecular weight of the trimer. One likely explanation for the symmetrical NMR spectra is that the trimer exists only in the solid

**Fig. 2.** Molecular structure (ORTEP) of  $(^{\text{tPr}}[\text{OPO}]\text{K}_2)_2(\text{THF})_6$ , **3**. Ellipsoids are drawn at 50% probability. Carbon atoms of the THF ligands and co-crystallized solvent were removed for clarity. Modeled *t*-butyl disorder was also omitted for clarity.



state and it breaks up in solution forming monomeric species. However, the  $^1\text{H}$  NMR spectrum indicates that THF exists in two different environments, with distinct multiplets attributable to one THF molecule, and broad singlets attributable to two THF molecules. The distinct multiplets indicate that one THF molecule is strongly bound and not undergoing exchange. The broad singlets indicate two THF molecules are undergoing exchange, which is unusual, given the apparent lack of donors in the system, as evidenced by the coordinated benzene in the solid-state structure.

Synthesis of the tantalum chloride complexes  $\text{Ph}[\text{OPO}]\text{-TaCl}_3$  (**5**) and  $^{\text{tPr}}[\text{OPO}]\text{TaCl}_3$  (**6**) is outlined in eq. [3]. Reaction of **1** with  $\text{TaCl}_5$  in diethyl ether under reduced pressure affords a thick mixture of a yellow solid and a yellow solution. Filtration of the mixture and drying of the solid in vacuo affords **5** as a bright yellow powder in 92% isolated yield. The *iso*-propyl derivative is prepared in 82% yield by the analogous reaction of **2** with  $\text{TaCl}_5$ . The complexes were characterized by  $^1\text{H}$  and  $^{31}\text{P}\{^1\text{H}\}$  NMR spectroscopy, mass spectrometry, and elemental analysis. Both complexes display a singlet resonance in the  $^{31}\text{P}\{^1\text{H}\}$  NMR spectrum, **5** at  $\delta$  33.5 and **6** at  $\delta$  31.9.  $^1\text{H}$  NMR spectra indicate that the complexes are  $C_s$ -symmetric, with two resonances due to the *tert*-butyl protons; **6** also displays a diagnostic doublet of septets for the *iso*-propyl methine proton and a doublet of doublets for the *iso*-propyl methyl protons.



The synthesis of **5** and **6** is strongly linked to the concentration of the reagents in the reaction mixture. For example, reaction of **1** with  $\text{TaCl}_5$  in highly concentrated solution

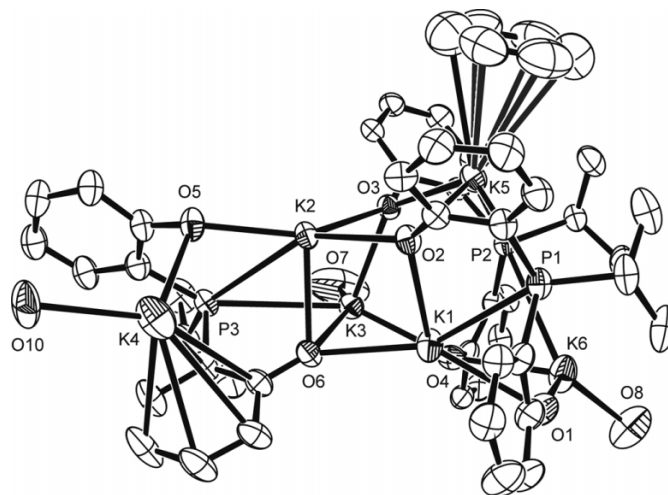


**Table 2.** Selected bond distances (Å) and bond angles (°) for  $(\text{Ph}[\text{OPO}]\text{K}_2)_2(\text{THF})_6$ , **3**.

Bond distances (Å)	
K(1)—O(1)	2.690(6)
K(1)—O(2)	2.673(6)
K(1)—O(3)	2.913(7)
K(1)—O(5)	2.748(7)
K(1)—P(1)	3.361(3)
K(1)—P(1*)	3.507(3)
K(2)—O(1)	2.591(6)
K(2)—O(2)	2.551(6)
K(2)—O(3*)	2.909(7)
K(2)—O(4)	2.667(8)
K(2)—P(1*)	3.343(3)
Bond angles (°)	
P(1)—K(1)—O(1)	56.57(13)
P(1)—K(1)—O(2)	137.15(15)
P(1)—K(1)—O(3)	88.29(14)
P(1)—K(1)—O(5)	89.41(16)
P(1)—K(1)—P(1*)	106.25(7)
O(1)—K(1)—O(2)	84.49(18)
O(1)—K(1)—O(3)	144.73(19)
O(1)—K(1)—O(5)	98.6(2)
O(1)—K(1)—P(1*)	92.58(14)
O(2)—K(1)—O(3)	127.0(2)
O(2)—K(1)—O(5)	115.8(2)
O(2)—K(1)—P(1*)	53.88(14)
O(3)—K(1)—O(5)	82.5(2)
O(3)—K(1)—P(1*)	94.93(15)
O(1)—K(2)—O(2)	89.04(19)
O(1)—K(2)—O(3*)	77.76(19)
O(1)—K(2)—O(4)	131.4(2)
O(1)—K(2)—P(1*)	98.29(14)
O(2)—K(2)—O(3*)	141.29(19)
O(2)—K(2)—O(4)	106.4(2)
O(2)—K(2)—P(1*)	57.00(14)
O(3*)—K(2)—P(1*)	88.69(15)
K(1)—P(1)—K(1*)	73.75(7)
K(1)—P(1)—K(2*)	76.57(7)
K(1)—O(3)—K(2*)	91.02(18)
K(1)—O(1)—K(2)	88.18(18)
K(1)—O(2)—K(2)	89.38(18)
K(1)—P(1*)—K(2)	64.84(6)

leads to the formation of the known bis(OPO) complex,  $\text{Ph}[\text{OPO}]_2\text{TaCl}$  (**7**),<sup>25</sup> which can be easily separated from **5** by filtration, owing to its significantly increased solubility. Reaction of 2 equiv. of **1** furnishes the highest yield of **7**; however, the reaction does not go to completion.

The synthesis of **5–7** is somewhat unusual in that it proceeds via direct protonolysis of the Ta–Cl bond producing reactive HCl as the byproduct. Salt metathesis routes to early transition-metal coordination complexes are driven to completion by the formation of simple alkali metal salts such as lithium chloride. The formation of HCl does not offer the same driving force as the formation of an alkali metal salt. However, it is likely that the protonolysis reaction is controlled by the oxophilic nature of tantalum and the formation of strong tantalum–oxygen bonds. Alternative routes to traditional salt metathesis in tantalum halide chem-

**Fig. 3.** Molecular structure (ORTEP) of  $(i^{\text{Pr}}[\text{OPO}]\text{K}_2)_3(\text{THF})_3(\eta^6\text{-C}_6\text{H}_6)$ , **4-C}\_6\text{H}\_6**. Ellipsoids are drawn at 50% probability. Carbon atoms of the THF ligands and *t*-butyl groups were removed for clarity.

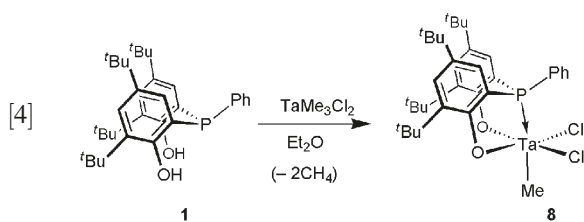
istry are known, particularly in the synthesis of cyclopentadienyl derivatives containing alkyl silane or stannane functionalities that are then eliminated as silyl chlorides<sup>39,40</sup> or stannyl chlorides,<sup>41,42</sup> respectively. However, the pathway utilized in the synthesis of **5–7** is very rare,<sup>43,44</sup> presumably due to the sensitivity of Ta–O bonds to HCl.<sup>45</sup>

Complexes **5–7** are tantalum halides supported by tridentate mixed-donor ligands, something that could not be achieved with the amidophosphine ligand  $\text{Ph}[\text{NPN}]$ ,<sup>3</sup> where  $\text{Ph}[\text{NPN}] = [\text{PhP}(\text{CH}_2\text{SiMe}_2\text{NPh})_2]$ . With the tantalum-halide species reported here, it should be possible to investigate reduction of the halide in the presence of dinitrogen, a technique that has proven useful in synthesizing dinitrogen complexes of group-4 metals supported by amidophosphine ligands.<sup>11–13</sup> However, typical reduction protocols of complexes **5–7** utilizing  $\text{KC}_8$  or  $\text{Na/Hg}$  in the presence of one or four atmospheres of dinitrogen resulted in the formation of dark brown solids that solution NMR spectral and mass spectral data indicate are composed of several different materials, none of which can be positively identified as a dinitrogen complex. It is possible that the lack of steric bulk around the metal center in these complexes opens alternative reactivity pathways for the reduced metal complex, potentially including the formation of metal–metal bonded species.<sup>46,47</sup>

Another route to dinitrogen complexes that has proven useful with  $[\text{NPN}]$  tantalum complexes is the hydrogenation of alkyl derivatives.<sup>3,48</sup> Reactions of **5** and **6** with alkylating agents such as  $(\text{PhCH}_2)\text{MgCl}$  and  $\text{CH}_3\text{MgCl}$  at  $-40^\circ\text{C}$  and  $-78^\circ\text{C}$  yield only mixtures of products, from which the desired alkyl could not be cleanly isolated. However, in the absence of tantalum halide complexes supported by  $[\text{NPN}]$ , work with that ligand turned to reaction of ligand precursors with tantalum alkyl halide materials, particularly  $\text{TaMe}_3\text{Cl}_2$ .

The synthesis of **5** has shown that phenols react with Ta–Cl bonds, so it was of interest to examine the reaction of **1** with  $\text{TaMe}_3\text{Cl}_2$  where either HCl or  $\text{CH}_4$  could be released. Addition of an ethereal solution of  $\text{TaMe}_3\text{Cl}_2$  to **1** in  $\text{Et}_2\text{O}$  affords a pale yellow solid that solution NMR spectroscopy,

mass spectrometry, and elemental analysis indicate is the monomethyl complex  $\text{Ph}[\text{OPO}]\text{TaMeCl}_2$  (**8**), formed via elimination of two equivalents of methane, as shown in eq. [4]. In the  $^1\text{H}$  NMR spectrum, the methyl ligand appears as a phosphorus-coupled doublet at  $\delta$  2.08 ( $^3J_{\text{PH}} = 9.8$  Hz) integrating to three protons; the  $^{31}\text{P}\{^1\text{H}\}$  NMR spectrum shows a singlet at  $\delta$  38.8. A structure with a trans orientation of the Ta–Me, and the Ta–P is supported by the rather large three-bond P–H coupling constant observed in the  $^1\text{H}$  NMR spectrum. For example, the bis(OPO) complex  $\text{Ph}[\text{OPO}]_2\text{TaMe}$  displays a singlet for the Ta–Me protons in the  $^1\text{H}$  NMR spectrum, indicative of the cis disposition of phosphine groups compared to the methyl on Ta.<sup>25</sup>



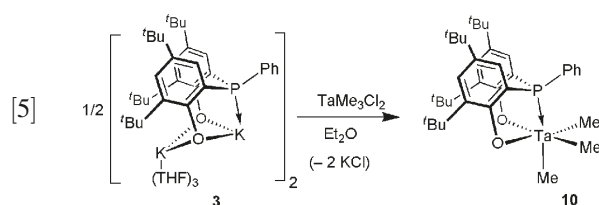
Mixed methyl chloride coordination complexes are known in tantalum chemistry, supported by various ligands, including cyclopentadienyl-based ligands,<sup>49–51</sup> and a biphenolate pincer ligand.<sup>52</sup> Although most coordination compounds of this nature are formed via salt metathesis routes, other examples of alkane elimination routes are known.<sup>52,53</sup>

Further reactivity of **8** has not produced results to date. Attempts to create mixed alkyl species through reaction of **8** with  $(\text{PhCH}_2)\text{MgCl}$  result in dark solids that are composed of several materials. A similar result is observed when **8** is reduced in the presence of dinitrogen. Much like the reduction of **7**, reductions produce dark brown materials, from which no dinitrogen complexes could be identified. Hydrogenation of **8** under 4 atm (1 atm = 101.325 kPa) of hydrogen produces a mixture of products, and no resonances attributable to tantalum hydrides can be observed in a  $^1\text{H}$  NMR spectrum.

When a substoichiometric amount of **1** is reacted with  $\text{TaMe}_3\text{Cl}_2$ , an impurity is observed in solution NMR spectra that can be separated from **8** by crystallization. Slow evaporation of the reaction solution deposits bright yellow crystals of X-ray quality. These have been structurally characterized as  $\text{Ph}[\text{OPO}]\text{TaMe}_2\text{Cl}$  (**9**). The solid-state molecular structure is presented in Fig. 4, and selected bond distances and angles are collected in Table 3. There is a distorted octahedral geometry about the tantalum, with the chloride trans to the phosphine and the two aryloxides trans to the methyl carbons. Ta–O, Ta–P, and Ta–Cl bond distances compare well to those of similar complexes reported recently.<sup>25</sup> The tantalum methyl bond distances are very similar to those of  $\text{Ph}[\text{NAsN}]\text{TaMe}_3$ <sup>9</sup> and  $\text{Ph}[\text{NPN}]\text{TaMe}_3$ .<sup>3</sup> In the  $^1\text{H}$  NMR spectrum, the methyl hydrogen resonances are superimposed upon one set of *t*-butyl resonances, but integrate to six protons when the *t*-butyl protons are subtracted. The  $^{31}\text{P}\{^1\text{H}\}$  NMR spectrum shows the expected singlet at  $\delta$  40.6. The origin of **9** is likely a result of a redistribution reaction between the monomethyl  $\text{Ph}[\text{OPO}]\text{TaMeCl}_2$  (**8**) and unreacted  $\text{TaMe}_3\text{Cl}_2$ .

Salt metathesis has proven productive for the synthesis of  $\text{Ph}[\text{OPO}]\text{TaMe}_3$  (**10**), which is outlined in eq. [5]. Reaction of  $\text{TaMe}_3\text{Cl}_2$  with **3** in  $\text{Et}_2\text{O}$  furnishes the product as an off-

white solid in moderate yield (68%). The synthesis can also be carried out using the lithium salt  $(\text{Ph}[\text{OPO}]\text{Li})_2(\text{THF})_4$ ; however, the potassium salt affords a cleaner transformation. In solution, the  $^{31}\text{P}\{^1\text{H}\}$  NMR spectrum of **10** displays a single resonance at  $\delta$  13.0, and the *t*-butyl protons appear as a pair of singlets in the  $^1\text{H}$  NMR spectrum at  $\delta$  1.60 and  $\delta$  1.25, and the methyl protons appear as a phosphorus-coupled doublet ( $^3J_{\text{PH}} = 4.4$  Hz) at  $\delta$  1.53. The methyl carbons appear at  $\delta$  63.5 in the  $^{13}\text{C}\{^1\text{H}\}$  NMR spectrum. The solid-state structure of **10** has not been determined to date; however, a mass spectrum indicates the complex is monomeric. Thus, a distorted octahedral structure similar to **9** would be expected. The observation of three equivalent Ta–Me groups by NMR spectroscopy is likely a result of a fluxional process, similar to that previously reported for  $\text{Ph}[\text{NPN}]\text{TaMe}_3$ .<sup>3</sup>



Reaction of **10** with 4 atm of hydrogen results in the formation of a dark orange solid. NMR spectroscopy indicates the solid is a mixture of different compounds with no resonances attributable to hydrides identifiable.

## Conclusions

In this report, an improved synthesis of the bis(aryloxy)-phosphines  $\text{Ph}[\text{OPO}]\text{H}_2$  and  $i\text{Pr}[\text{OPO}]\text{H}_2$  has been developed by reaction of precursor lithium salts with  $\text{Et}_3\text{NHCl}$ . Conversion of the protonated compounds to potassium salts was accomplished by reaction with KH, furnishing  $(\text{Ph}[\text{OPO}]\text{K}_2)(\text{THF})_6$  and  $(i\text{Pr}[\text{OPO}]\text{K}_2)_3(\text{THF})_3$ .

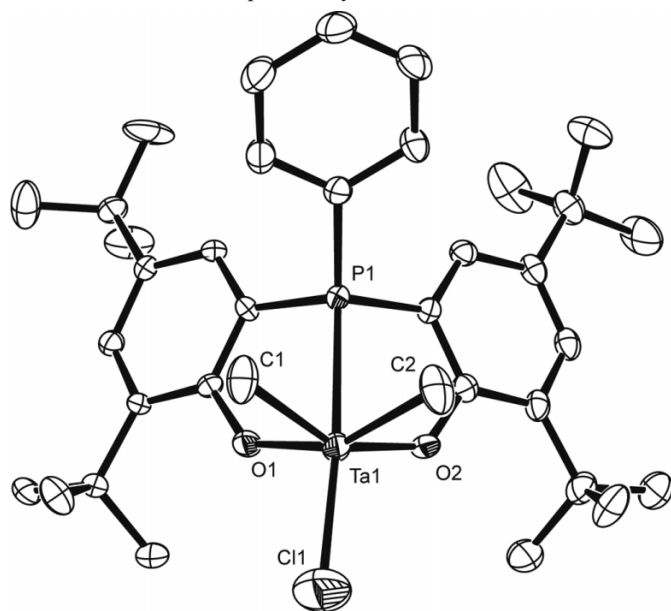
Tantalum complexes supported by [OPO] were synthesized by reaction of [OPO] precursors with  $\text{TaCl}_5$  and  $\text{TaMe}_3\text{Cl}_2$ . Reactions with  $\text{TaCl}_5$  produce the halide complexes  $\text{Ph}[\text{OPO}]\text{TaCl}_3$  and  $i\text{Pr}[\text{OPO}]\text{TaCl}_3$ , and a bis(ligand) complex,  $\text{Ph}[\text{OPO}]_2\text{TaCl}$ , was synthesized through manipulation of reaction concentration. Reaction with  $\text{TaMe}_3\text{Cl}_2$  furnishing the mixed methyl chloride complexes  $\text{Ph}[\text{OPO}]\text{TaMeCl}_2$  and  $\text{Ph}[\text{OPO}]\text{TaMe}_2\text{Cl}$  by methane elimination, and the trimethyl complex  $\text{Ph}[\text{OPO}]\text{TaMe}_3$  by salt metathesis with the potassium salt  $(\text{Ph}[\text{OPO}]\text{K}_2)_2(\text{THF})_6$ .

## Experimental section

### General procedures

Unless otherwise stated, all manipulations were performed under an atmosphere of dry, oxygen-free dinitrogen or argon by means of standard Schlenk or glovebox techniques (Vacuum Atmospheres HE-553–2 glovebox equipped with a MO-40–2H purification system and a  $-40^\circ\text{C}$  freezer), unless specified. Anhydrous hexanes and toluene were purchased from Aldrich, sparged with dinitrogen, and further dried by passage through a tower of silica followed by passage through a tower of Ridox (or Q-5) catalyst prior to use.<sup>54</sup> Anhydrous pentane, benzene, tetrahydrofuran, and diethyl ether were purchased from Aldrich, sparged with dinitrogen.

**Fig. 4.** Molecular structure (ORTEP) of  $\text{Ph}[\text{OPO}]\text{TaMe}_2\text{Cl}$ , **9**. Ellipsoids are drawn at 50% probability.



**Table 3.** Selected bond distances (Å), bond angles (°), and dihedral angles (°) for  $\text{Ph}[\text{OPO}]\text{TaMe}_2\text{Cl}$  (**9**).

Bond distances (Å)	
Ta(1)—P(1)	2.6331(13)
Ta(1)—C(1)	2.196(6)
Ta(1)—C(2)	2.179(5)
Ta(1)—O(1)	1.939(3)
Ta(1)—O(2)	1.943(4)
Ta(1)—Cl(1)	2.300(2)
Bond angles (°)	
P(1)—Ta(1)—Cl(1)	172.35(6)
P(1)—Ta(1)—C(1)	81.72(17)
P(1)—Ta(1)—C(2)	84.05(18)
P(1)—Ta(1)—O(1)	72.30(10)
P(1)—Ta(1)—O(2)	72.58(10)
C(1)—Ta(1)—C(2)	82.8(2)
C(1)—Ta(1)—O(1)	86.82(19)
C(1)—Ta(1)—O(2)	152.5(2)
C(1)—Ta(1)—Cl(1)	99.75(19)
O(1)—Ta(1)—O(2)	155.3(2)

trogen, and passed through an Innovative Technologies SPS-PureSolv-400-4 apparatus. Water was distilled and thoroughly degassed prior to use. All organic solvents were tested with addition of sodium benzophenone ketyl prior to use to ensure absence of oxygen and water. Alternatively, anhydrous diethyl ether was stored over sieves and distilled from sodium benzophenone ketyl under argon; tetrahydrofuran was refluxed over  $\text{CaH}_2$  prior to distillation from sodium benzophenone ketyl under argon, and pentane was stored over sieves and distilled from sodium benzophenone ketyl solubilized by tetraglyme under dry dinitrogen prior to storage over a potassium mirror. Nitrogen gas was dried and deoxygenated by passage through a column containing activated molecular sieves and  $\text{MnO}$ .

Deuterated benzene was dried by refluxing with molten

sodium/potassium alloy in a sealed vessel under partial pressure, then trap-to-trap distilled, and freeze-pump-thaw-degassed three times. Deuterated tetrahydrofuran and toluene were dried by refluxing with molten potassium metal or sodium-potassium alloy in a sealed vessel under vacuum, then trap-to-trap distilled, and freeze-pump-thaw-degassed three times.  $^1\text{H}$ ,  $^{31}\text{P}$ ,  $^1\text{H}\{^{31}\text{P}\}$ ,  $^{31}\text{P}\{^1\text{H}\}$ ,  $^{13}\text{C}\{^1\text{H}\}$ , and  $^7\text{Li}\{^1\text{H}\}$  NMR spectra were recorded on either a Bruker AMX-500 instrument operating at 500.13 MHz for  $^1\text{H}$  spectra, a Bruker AVA-400 instrument operating at 400.13 MHz for  $^1\text{H}$  spectra, or a Bruker AVA-300 instrument operating at 300.13 MHz for  $^1\text{H}$  spectra.  $^1\text{H}$  NMR spectra were referenced to residual protons in deuterated solvent as follows:  $\text{C}_6\text{D}_5\text{H}$  ( $\delta$  7.15),  $\text{C}_4\text{D}_7\text{HO}$  ( $\delta$  3.58), and  $\text{C}_7\text{D}_7\text{H}$  ( $\delta$  2.09) with respect to tetramethylsilane at  $\delta$  0.0.  $^{13}\text{C}$  NMR spectra were referenced to 1% tetramethylsilane in  $\text{CDCl}_3$  at  $\delta$  0.0.  $^{31}\text{P}$  NMR spectra were referenced to either external or internal  $\text{P}(\text{OMe})_3$  ( $\delta$  141.0 with respect to 85%  $\text{H}_3\text{PO}_4$  at  $\delta$  0.0).  $^7\text{Li}$  NMR spectra were referenced to external  $\text{LiCl}$  (0.3 mol/L solution in  $\text{MeOH}$  at  $\delta$  0.0). Elemental analyses were performed by Mr. P. Borda and Mr. M. Lakha, and mass spectrometry (EI/MS on a Kratos MS 50 unless otherwise stated) was performed by Mr. M. Lapawa, all at the Department of Chemistry, the University of British Columbia.

## Materials

The complexes  $(\text{Ph}[\text{OPO}]\text{Li}_2)_2(\text{THF})_4$  and  $(i\text{Pr}[\text{OPO}]\text{Li}_2)_2(\text{THF})_4$  were prepared by the literature procedure.<sup>14</sup>  $\text{Et}_3\text{NHCl}$  was prepared by the reaction of triethylamine and aqueous hydrochloric acid, and recrystallized from ethanol. Potassium hydride was purchased from Acros Chemicals and used as received;  $\text{TaCl}_5$  was purchased from STREM and sublimed prior to use.  $\text{TaMe}_3\text{Cl}_2$  was prepared according to published methods.<sup>55</sup>

## Synthesis of $\text{Ph}[\text{OPO}]\text{H}_2$ (**1**)

To an intimate mixture of  $(\text{Ph}[\text{OPO}]\text{Li}_2)_2(\text{THF})_4$  (5.00 g, 7.41 mmol) and  $\text{Et}_3\text{NHCl}$  (2.01 g, 14.8 mmol) was added  $\text{Et}_2\text{O}$  (150 mL). The solution was stirred for 12 h, and then the solvent was removed under vacuum. The residue was extracted into toluene (50 mL), the solution filtered through Celite, and then evaporated to dryness. The colourless solid was washed with minimal pentane and dried under vacuum. Yield: 3.74 g (97%). X-ray quality crystals of **1** containing three equivalents of co-crystallized solvent were grown by slow evaporation of a saturated benzene solution.  $^1\text{H}$  NMR (500 MHz,  $\text{C}_6\text{D}_6$ , 25 °C)  $\delta$ : 7.64 (d,  $^3J_{\text{HH}} = 2.3$  Hz, 1H, *p*-PPh), 7.35 (m, 4H, *o*/*m*-PPh), 7.23 (s, 2H, Ph), 7.02 (m, 2H, Ph), 6.50 (d,  $^4J_{\text{PH}} = 8.9$  Hz, OH), 1.61 (s, 18H, *o*- $\text{PhC}(\text{CH}_3)_3$ ), 1.26 (s, 18H, *p*- $\text{PhC}(\text{CH}_3)_3$ ).  $^{31}\text{P}\{^1\text{H}\}$  NMR (121.4 MHz,  $\text{C}_6\text{D}_6$ , 25 °C)  $\delta$ : -50.23 (s).  $^1\text{H}$  NMR (300 MHz,  $\text{C}_4\text{D}_8\text{O}$ , 25 °C)  $\delta$ : 7.33 (d,  $^3J_{\text{HH}} = 2.4$  Hz, 2H, Ph-*H*), 7.27 (m, 7H, Ph-*H*), 6.84 (dd,  $^4J_{\text{HH}} = 2.4$  Hz,  $^4J_{\text{PH}} = 5.5$  Hz, 2H, OH), 1.42 (s, 18H, *o*- $\text{PhC}(\text{CH}_3)_3$ ), 1.12 (s, 18H, *p*- $\text{PhC}(\text{CH}_3)_3$ ).  $^{31}\text{P}\{^1\text{H}\}$  NMR (121.4 MHz,  $\text{C}_4\text{D}_8\text{O}$ , 25 °C)  $\delta$ : -47.18 (s).

## Synthesis of $i\text{Pr}[\text{OPO}]\text{H}_2$ (**2**)

Following the procedure for **1**,  $\text{Et}_2\text{O}$  (150 mL) was added to an intimate mixture of  $\text{Et}_3\text{NHCl}$  (1.95 g, 14.18 mmol) and  $(i\text{Pr}[\text{OPO}]\text{Li}_2)_2(\text{THF})_4$  (4.54 g, 7.09 mmol). Yield: 3.27 g



(96%).  $^1\text{H}$  NMR (300 MHz,  $\text{C}_6\text{D}_6$ , 25 °C)  $\delta$ : 7.58 (dd,  $^3J_{\text{PH}} = 4.5$  Hz,  $^4J_{\text{HH}} = 2.2$  Hz, 2H, *o*-OPh), 7.50 (d,  $^4J_{\text{HH}} = 2.2$  Hz, 2H, *p*-OPh), 7.00 (d,  $^4J_{\text{PH}} = 11.2$  Hz, OH), 2.88 (ds,  $^2J_{\text{PH}} = 12.4$  Hz,  $^3J_{\text{HH}} = 6.9$  Hz, 1H, P-CH(CH<sub>3</sub>)<sub>2</sub>), 1.50 (s, 18H, *o*-PhC(CH<sub>3</sub>)<sub>3</sub>), 1.29 (s, 18H, *p*-PhC(CH<sub>3</sub>)<sub>3</sub>), 0.92 (dd,  $^3J_{\text{PH}} = 18.2$  Hz,  $^3J_{\text{HH}} = 6.9$  Hz, 6H, P-CH(CH<sub>3</sub>)<sub>2</sub>).  $^{31}\text{P}\{^1\text{H}\}$  NMR (121.4 MHz,  $\text{C}_6\text{D}_6$ , 25 °C)  $\delta$ : -61.65 (s). MS (EI)  $m/z$  (%): 484 (100) [M]<sup>+</sup>. Anal. calcd. for  $\text{C}_{31}\text{H}_{49}\text{O}_2\text{P}$ : C, 76.82; H, 10.19. Found: C, 76.62; H, 9.96.

#### Synthesis of $(^{\text{Ph}}[\text{OPO}]\text{K}_2)(\text{THF})_6$ (3)

Potassium hydride (1.16 g, 28.9 mmol) was added in portions over 30 min to a solution of  $^{\text{Ph}}[\text{OPO}]\text{H}_2$  (5.0 g, 9.6 mmol) in THF (100 mL) with stirring. The solution was then placed under partial vacuum until the evolution of hydrogen ceased, stirred 12 h under static partial vacuum, filtered through Celite, and then evaporated to dryness. The resulting pale yellow residue was washed with minimal hexanes to give **3** as a colourless solid. Yield: 7.13 g (92%). X-ray quality crystals of **3** containing three equivalents of co-crystallized solvent were grown from a saturated THF solution at -40 °C.  $^1\text{H}$  NMR (300 MHz,  $\text{C}_6\text{D}_6$ , 25 °C)  $\delta$ : 7.52–6.96 (m, 18H, Ph), 3.62 (m, 24H, THF-OCH<sub>2</sub>CH<sub>2</sub>), 1.64 (s, 36H, *o*-PhC(CH<sub>3</sub>)<sub>3</sub>), 1.48 (m, 24H, THF-OCH<sub>2</sub>CH<sub>2</sub>), 1.33 (s, 36H, *p*-PhC(CH<sub>3</sub>)<sub>3</sub>).  $^{31}\text{P}\{^1\text{H}\}$  NMR (121.4 MHz,  $\text{C}_6\text{D}_6$ , 25 °C)  $\delta$ : -29.59 (s). MS (EI)  $m/z$  (%): 1188 (6) [M - (THF)<sub>6</sub>]<sup>+</sup>, 516 (80) [OPO]<sup>+</sup>. Anal. calcd. for  $\text{C}_{92}\text{H}_{138}\text{K}_4\text{O}_{10}\text{P}_2 \cdot 2\text{C}_4\text{H}_8\text{O}$ : C, 67.99; H, 8.79. Found: C, 68.38; H, 8.65.

#### Synthesis of $(^{\text{iPr}}[\text{OPO}]\text{K}_2)(\text{THF})_3$ (4)

Following the procedure for **3**, KH (0.21 g, 5.19 mmol) was added to a solution of **2** (1.00 g, 2.017 mmol) in THF (25 mL). Yield: 0.93 g (71%). X-ray quality crystals of the benzene adduct **4**· $\text{C}_6\text{H}_6$  containing one equivalent of co-crystallized benzene and half a molecule of co-crystallized hexane were grown from slow diffusion of hexanes into a benzene solution. Crystals of **4**· $\text{C}_6\text{H}_6$  were dried and used for elemental analysis.  $^1\text{H}$  NMR (300 MHz,  $\text{C}_6\text{D}_6$ , 25 °C)  $\delta$ : 7.15 (d,  $^3J_{\text{HH}} = 2.6$  Hz, 6H, Ph), 6.94 (d,  $^3J_{\text{HH}} = 2.6$  Hz, 6H, Ph), 3.62 (m, 4H, THF-OCH<sub>2</sub>CH<sub>2</sub>), 3.58 (s, 8H, THF-OCH<sub>2</sub>CH<sub>2</sub>), 2.28 (m, 3H, P-CH(CH<sub>3</sub>)<sub>2</sub>), 1.78 (m, 4H, THF-OCH<sub>2</sub>CH<sub>2</sub>), 1.73 (s, 8H, THF-OCH<sub>2</sub>CH<sub>2</sub>), 1.39 (s, 54H, *o*-PhC(CH<sub>3</sub>)<sub>3</sub>), 1.21 (s, 54H, *p*-PhC(CH<sub>3</sub>)<sub>3</sub>), 1.00 (dd,  $^3J_{\text{PH}} = 14.4$  Hz,  $^3J_{\text{HH}} = 6.6$  Hz, 18H, P-CH(CH<sub>3</sub>)<sub>2</sub>).  $^{31}\text{P}\{^1\text{H}\}$  NMR (121.4 MHz,  $\text{C}_6\text{D}_6$ , 25 °C)  $\delta$ : -37.41 (s). Anal. calcd. for  $\text{C}_{105}\text{H}_{165}\text{K}_6\text{O}_9\text{P}_3 \cdot 1/3\text{C}_6\text{H}_6$ : C, 67.43; H, 8.72. Found: C, 67.08; H, 8.61.

#### Synthesis of $^{\text{Ph}}[\text{OPO}]\text{TaCl}_3$ (5)

To an intimate mixture of **1** (2.86 g, 3.86 mmol) and TaCl<sub>5</sub> (1.38 g, 3.86 mmol) was added diethyl ether (100 mL) with stirring. The bright yellow solution was stirred for 12 h under reduced static pressure during which time a yellow solid was deposited. The solution was filtered through Celite and evaporated to dryness. The residue was washed with hexanes and dried under vacuum to yield **5** as a bright yellow solid. Yield: 2.86 g (92%).  $^1\text{H}$  NMR (300 MHz,  $\text{C}_6\text{D}_6$ , 25 °C)  $\delta$ : 7.60 (m, 6H, Ph), 7.05 (m, 3H, Ph), 1.57 (s, 18H, *o*-PhC(CH<sub>3</sub>)<sub>3</sub>), 1.16 (s, 18H, *p*-PhC(CH<sub>3</sub>)<sub>3</sub>).  $^{31}\text{P}\{^1\text{H}\}$  NMR (121.4 MHz,  $\text{C}_6\text{D}_6$ , 25 °C)  $\delta$ :

33.46 (s). MS (EI)  $m/z$  (%): 802 (100) [M]<sup>+</sup>. Anal. calcd. for  $\text{C}_{34}\text{H}_{45}\text{Cl}_3\text{O}_2\text{PTa}$ : C, 50.79; H, 5.64. Found: C, 50.90; H, 5.76.

#### Synthesis of $^{\text{iPr}}[\text{OPO}]\text{TaCl}_3$ (6)

With the same procedure described above for **5**, **2** (1.00 g, 2.07 mmol) was reacted with TaCl<sub>5</sub> (0.743 g, 2.07 mmol), giving **6** as a bright yellow solid. Yield: 1.31 g (82%).  $^1\text{H}$  NMR (300 MHz,  $\text{C}_6\text{D}_6$ , 25 °C)  $\delta$ : 7.52 (m, 2H, Ph), 7.21 (m, 2H, Ph), 3.03 (dsep,  $^2J_{\text{PH}} = 5.8$  Hz,  $^3J_{\text{HH}} = 6.9$  Hz, 1H, P-CH(CH<sub>3</sub>)<sub>2</sub>), 1.50 (s, 18H, *o*-PhC(CH<sub>3</sub>)<sub>3</sub>), 1.35 (dd,  $^3J_{\text{PH}} = 19.2$  Hz,  $^3J_{\text{HH}} = 6.9$  Hz, 6H, P-CH(CH<sub>3</sub>)<sub>2</sub>), 1.23 (s, 18H, *p*-PhC(CH<sub>3</sub>)<sub>3</sub>).  $^{31}\text{P}\{^1\text{H}\}$  NMR (121.4 MHz,  $\text{C}_6\text{D}_6$ , 25 °C)  $\delta$ : 31.88 (s). MS (EI)  $m/z$  (%): 768 (100) [M]<sup>+</sup>. Elemental analysis was not obtained.

#### Synthesis of $^{\text{Ph}}[\text{OPO}]_2\text{TaCl}$ (7)

A solution of **1** (2.00 g, 3.87 mmol) in toluene (10 mL) was added dropwise to a suspension of TaCl<sub>5</sub> (0.693 g, 1.93 mmol) in toluene (10 mL) with stirring. The resulting yellow solution was stirred for 24 h then evaporated to dryness. The residue was extracted into hexanes (5 mL), filtered through Celite, and the solvent was removed under vacuum, furnishing **7** as a bright yellow powder. Yield: 1.09 g (45%).  $^1\text{H}$  NMR (300 MHz,  $\text{C}_6\text{D}_6$ , 25 °C)  $\delta$ : 7.70–7.04 (m, 18H, Ph), 1.49 (s, 36H, *o*-PhC(CH<sub>3</sub>)<sub>3</sub>), 1.14 (s, 36H, *p*-PhC(CH<sub>3</sub>)<sub>3</sub>).  $^{31}\text{P}\{^1\text{H}\}$  NMR (121.4 MHz,  $\text{C}_6\text{D}_6$ , 25 °C)  $\delta$ : 37.85 (s). MS (EI)  $m/z$  (%): 1249 (30) [M]<sup>+</sup>. Anal. calcd. for  $\text{C}_{68}\text{H}_{90}\text{ClO}_4\text{P}_2\text{Ta}$ : C, 65.35; H, 7.26. Found: C, 65.56; H, 7.43.

#### Synthesis of $^{\text{Ph}}[\text{OPO}]\text{TaMeCl}_2$ (8)

A solution of TaMe<sub>3</sub>Cl<sub>2</sub> (0.12 g, 0.39 mmol) in Et<sub>2</sub>O (10 mL) was added dropwise to a solution of **1** (0.20 g, 0.39 mmol) in Et<sub>2</sub>O (50 mL) at -78 °C, and the resulting pale yellow solution was stirred at -78 °C for 1 h. Removal of the cold bath, slow warming for 40 min, followed by removal of the solvent under vacuum gave a pale yellow residue that was washed with minimal pentane and dried under vacuum to give **8** as a pale yellow solid. Yield: 0.21 g (70%).  $^1\text{H}$  NMR (300 MHz,  $\text{C}_6\text{D}_6$ , 25 °C)  $\delta$ : 7.58 (m, 6H, Ph), 7.09 (m, 3H, Ph), 2.08 (d,  $^3J_{\text{PH}} = 9.8$  Hz, 3H, Ta-CH<sub>3</sub>), 1.56 (s, 18H, PhC(CH<sub>3</sub>)<sub>3</sub>), 1.23 (s, 6H, PhC(CH<sub>3</sub>)<sub>3</sub>), 1.19 (s, 12H, PhC(CH<sub>3</sub>)<sub>3</sub>).  $^{31}\text{P}\{^1\text{H}\}$  NMR (121.4 MHz,  $\text{C}_6\text{D}_6$ , 25 °C)  $\delta$ : 38.79 (s). MS (EI)  $m/z$  (%): 782 (100) [M]<sup>+</sup>. Anal. calcd. for  $\text{C}_{35}\text{H}_{48}\text{Cl}_2\text{O}_2\text{PTa}$ : C, 53.65; H, 6.17. Found: C, 53.87; H, 6.23.

#### Synthesis of $^{\text{Ph}}[\text{OPO}]\text{TaMe}_2\text{Cl}$ (9)

A solution of TaMe<sub>3</sub>Cl<sub>2</sub> (0.056 g, 0.188 mmol) in Et<sub>2</sub>O (5 mL) was added dropwise to a solution of **1** (0.076 g, 0.147 mmol) in Et<sub>2</sub>O (5 mL) at -78 °C. After 1 h, the solution was warmed to room temperature, concentrated to about half volume, and allowed to slowly evaporate, affording **9** as yellow crystals of X-ray quality. Yield: 0.025 g (22% from **1**).  $^1\text{H}$  NMR (300 MHz,  $\text{C}_6\text{D}_6$ , 25 °C)  $\delta$ : 7.64 (m, 5H, Ph), 7.12 (m, 4H, Ph), 1.56 (br s, 24H, Ta-CH<sub>3</sub> and *o*-PhC(CH<sub>3</sub>)<sub>3</sub>), 1.22 (s, 18H, *p*-PhC(CH<sub>3</sub>)<sub>3</sub>).  $^{31}\text{P}\{^1\text{H}\}$  NMR (121.4 MHz,  $\text{C}_6\text{D}_6$ , 25 °C)  $\delta$ : 40.65 (s). Elemental analysis was not recorded.



### Synthesis of *Ph*[OPO]TaMe<sub>3</sub> (**10**)

A solution of TaMe<sub>3</sub>Cl<sub>2</sub> (0.040 g, 0.135 mmol) in Et<sub>2</sub>O (10 mL) was added dropwise to a solution of **3** (0.100 g, 0.067 mmol) in Et<sub>2</sub>O (50 mL) at –78 °C, and the resulting pale solution was stirred at –78 °C for 1 h. Removal of the cold bath, slow warming for 40 min, followed by removal of the solvent under vacuum gave a pale yellow solid. The residue was extracted into toluene (20 mL), the solution filtered through Celite, and evaporated to dryness yielding a solid that was washed with minimal pentane and dried under vacuum to give **10** as an off-white solid. Yield: 0.068 g (68%). <sup>1</sup>H NMR (300 MHz, C<sub>6</sub>D<sub>6</sub>, 25 °C) δ: 7.82 (m, 1H, *p*-PPh), 7.65 (dd, <sup>3</sup>J<sub>HH</sub> = 2.2 Hz, <sup>3</sup>J<sub>PH</sub> = 6.1 Hz, 2H, *o*-PPh), 7.58 (d, <sup>3</sup>J<sub>HH</sub> = 2.2 Hz, 2H, *m*-PPh), 7.11 (m, 4H, Ph), 1.60 (s, 18H, *o*-PhC(CH<sub>3</sub>)<sub>3</sub>), 1.53 (d, <sup>3</sup>J<sub>PH</sub> = 4.4 Hz, 9H, Ta–CH<sub>3</sub>), 1.25 (s, 18H, *p*-PhC(CH<sub>3</sub>)<sub>3</sub>). <sup>31</sup>P{<sup>1</sup>H} NMR (121.4 MHz, C<sub>6</sub>D<sub>6</sub>, 25 °C) δ: 12.98 (s). <sup>13</sup>C{<sup>1</sup>H} NMR (75.4 MHz, C<sub>7</sub>D<sub>8</sub>, 0 °C) δ: 166.2 (s, *o*Ph *i*-C), 145.4 (d, <sup>1</sup>J<sub>PC</sub> = 4.0 Hz, PPh *i*-C), 138.3 (d, <sup>1</sup>J<sub>PC</sub> = 5.7 Hz, P–PhC(CH<sub>3</sub>)<sub>3</sub> *i*-C), 132.2 (s, PPh *o*-C), 132.0 (s, PPh *o*-C), 129.6–123.7 (Ph–C), 63.5 (s, Ta–(CH<sub>3</sub>)<sub>3</sub>), 35.3 (s, *o*-PhC(CH<sub>3</sub>)<sub>3</sub>), 34.7 (s, *p*-PhC(CH<sub>3</sub>)<sub>3</sub>), 31.5 (s, *o*-PhC(CH<sub>3</sub>)<sub>3</sub>), 29.6 (s, *p*-PhC(CH<sub>3</sub>)<sub>3</sub>). MS (EI) *m/z* (%): 742 (100) [M]<sup>+</sup>. Anal. calcd. for C<sub>37</sub>H<sub>54</sub>O<sub>2</sub>PTa: C, 59.83; H, 7.33. Found: C, 59.75; H, 7.45.

### Crystallography

In all cases, suitable crystals were selected and mounted on a glass fibre using Paratone-N oil or an acceptable substitute and frozen to –100 °C.

Measurements for structure **1** were made on a Rigaku/ADSC CCD area detector with graphite monochromated Mo K $\alpha$  radiation. The data were processed using the d\*TREK<sup>56</sup> module, part of the CrystalClear software package, version 1.3.6 SP0,<sup>57</sup> and corrected for Lorentz and polarization effects and absorption. Neutral atom scattering factors for all non-hydrogen atoms were taken from Cromer and Waber.<sup>58</sup> Anomalous dispersion effects were included in *F*<sub>calcd</sub>.<sup>59</sup>

Measurements for structures **3**, **4**, and **9** were made on a Bruker X8 area detector with monochromated Mo K $\alpha$  radiation. The data were processed and integrated using the Bruker SAINT software package<sup>60</sup> and corrected for absorption effects using the multi-scan technique (SADABS).<sup>61</sup>

All structures were solved by direct methods using the programs SIR97<sup>62</sup> or SIR2002.<sup>63</sup> All non-hydrogen atoms were refined anisotropically by least-squares procedures on *F*<sup>2</sup> using SHELXL-97.<sup>64</sup> Hydrogen atoms were included but not refined; their positional parameters were calculated with fixed C–H bond distances of 0.99 Å for sp<sup>2</sup> C, 0.98 Å for sp<sup>3</sup> C, and 0.95 Å for aromatic sp C, with *U*<sub>iso</sub> set to 1.2 × *U*<sub>eq</sub> of the attached sp or sp<sup>2</sup> C and *U*<sub>iso</sub> set to 1.5 × *U*<sub>eq</sub> values of the attached sp<sup>3</sup> C atom. Methyl hydrogen torsion angles were determined by electron density. Structure solution and refinements were conducted using the WinGX software package, version 1.64.05.<sup>65</sup> Structural illustrations were created using ORTEP-III for Windows.<sup>66</sup>

### Supplementary data

Supplementary data for this article are available on the journal Web site (canjchem.nrc.ca). CCDCs 756433–756437

contain the X-ray data in CIF format for this manuscript. These data can be obtained, free of charge, via [www.ccdc.cam.ac.uk/conts/retrieving.html](http://www.ccdc.cam.ac.uk/conts/retrieving.html) (Or from the Cambridge Crystallographic Data Centre, 12 Union Road, Cambridge CB2 1EZ, UK; fax +44 1223 336033; or [deposit@ccdc.cam.ac.uk](mailto:deposit@ccdc.cam.ac.uk)).

### Acknowledgement

Dr. B. O. Patrick is gratefully thanked for crystallography assistance. We thank the Natural Sciences and Engineering Research Council of Canada (NSERC) for generous financial support.

### References

- (1) Fryzuk, M. D. *Can. J. Chem.* **1992**, 70 (12), 2839. doi:10.1139/v92-361.
- (2) Fryzuk, M. D. *Acc. Chem. Res.* **2009**, 42 (1), 127. doi:10.1021/ar800061g. PMID:18803409.
- (3) Fryzuk, M. D.; Johnson, S. A.; Patrick, B. O.; Albinati, A.; Mason, S. A.; Koetzle, T. F. *J. Am. Chem. Soc.* **2001**, 123 (17), 3960. doi:10.1021/ja0041371. PMID:11457146.
- (4) Fryzuk, M. D.; Kozak, C. M.; Mehrkhodavandi, P.; Morello, L.; Patrick, B. O.; Rettig, S. J. *J. Am. Chem. Soc.* **2002**, 124 (4), 516. doi:10.1021/ja012100q. PMID:11804471.
- (5) Fryzuk, M. D.; MacNeil, P. A.; Rettig, S. J.; Secco, A. S.; Trotter, J. *Organometallics* **1982**, 1 (7), 918. doi:10.1021/om00067a006.
- (6) Fryzuk, M. D.; Montgomery, C. D.; Rettig, S. J. *Organometallics* **1991**, 10 (2), 467. doi:10.1021/om00048a025.
- (7) MacLachlan, E. A.; Fryzuk, M. D. *Organometallics* **2005**, 24 (6), 1112. doi:10.1021/om049165x.
- (8) Carmichael, C. D.; Fryzuk, M. D. *Dalton Trans.* **2005**, (3), 452. doi:10.1039/b415976d. PMID:15672188.
- (9) Carmichael, C. D.; Shaver, M. P.; Fryzuk, M. D. *Can. J. Chem.* **2006**, 84 (12), 1667. doi:10.1139/V06-173.
- (10) Fryzuk, M. D.; Haddad, T. S.; Rettig, S. J. *J. Am. Chem. Soc.* **1990**, 112 (22), 8185. doi:10.1021/ja00178a063.
- (11) MacLachlan, E. A.; Hess, F. M.; Patrick, B. O.; Fryzuk, M. D. *J. Am. Chem. Soc.* **2007**, 129 (35), 10895. doi:10.1021/ja073753v. PMID:17685617.
- (12) Morello, L.; Ferreira, M. J.; Patrick, B. O.; Fryzuk, M. D. *Inorg. Chem.* **2008**, 47 (4), 1319. doi:10.1021/ic701599t. PMID:18179167.
- (13) Morello, L.; Yu, P.; Carmichael, C. D.; Patrick, B. O.; Fryzuk, M. D. *J. Am. Chem. Soc.* **2005**, 127 (37), 12796. doi:10.1021/ja054467r. PMID:16159262.
- (14) Carmichael, C. D.; Fryzuk, M. D. *Dalton Trans.* **2008**, (6), 800. doi:10.1039/b710506a. PMID:18239836.
- (15) Luo, H.; Setyawati, I.; Rettig, S. J.; Orvig, C. *Inorg. Chem.* **1995**, 34 (9), 2287. doi:10.1021/ic00113a008.
- (16) Cavell, R. G.; Hilt, R. W.; Luo, H.; McDonald, R. *Inorg. Chem.* **1999**, 38 (5), 897. doi:10.1021/ic980304a. PMID:11670861.
- (17) Priya, S.; Balakrishna, M. S.; Mague, J. T. *Chem. Lett.* **2004**, 33 (3), 308. doi:10.1246/cl.2004.308.
- (18) Hanaoka, H.; Imamoto, Y.; Hino, T.; Oda, Y. *Oganomet, J. Chem.* **2006**, 691 (23), 4968. doi:10.1016/j.jorgchem.2006.08.036.
- (19) Hanaoka, H.; Imamoto, Y.; Hino, T.; Kohno, T.; Yanagi, K.; Oda, Y. *J. Polym. Sci., Part A: Polym. Chem.* **2007**, 45 (16), 3668. doi:10.1002/pola.22116.
- (20) Siefert, R.; Weyermüller, T.; Chaudhuri, P. *J. Chem. Soc., Dalton Trans.* **2000**, (24), 4656. doi:10.1039/b005693f.

- (21) Paine, T. K.; Weyhermüller, T.; Slep, L. D.; Neese, F.; Bill, E.; Bothe, E.; Wieghardt, K.; Chaudhuri, P. *Inorg. Chem.* **2004**, *43* (23), 7324. doi:10.1021/ic040052f. PMID: 15530082.
- (22) Chang, Y.-N.; Liang, L.-C. *Inorg. Chim. Acta* **2007**, *360* (1), 136. doi:10.1016/j.ica.2006.07.050.
- (23) Liang, L.-C.; Chang, Y.-N.; Lee, H. M. *Inorg. Chem.* **2007**, *46* (7), 2666. doi:10.1021/ic062314e. PMID: 17298057.
- (24) Liang, L.-C.; Chang, Y.-N.; Chen, H.-S.; Lee, H. M. *Inorg. Chem.* **2007**, *46* (18), 7587. doi:10.1021/ic701006r. PMID: 17663548.
- (25) Liang, L.-C.; Cheng, L.-C.; Tsai, T.-L.; Hu, C.-H.; Guo, W.-H. *Inorg. Chem.* **2009**, *48* (13), 5697. doi:10.1021/ic802125z.
- (26) Bennett, M. A.; Copley, C. J.; Rae, A. D.; Wenger, E.; Willis, A. C. *Organometallics* **2000**, *19* (8), 1522. doi:10.1021/om990749m.
- (27) Hitchcock, P. B.; Lee, T. H.; Leigh, G. J. *Dalton Trans.* **2003**, (11), 2276. doi:10.1039/b300596h.
- (28) Atkinson, R. C.; Gibson, V. C.; Long, N. J.; White, A. J. P.; Williams, D. J. *Dalton Trans.* **2004**, (12), 1823. doi:10.1039/b403862b. PMID: 15381986.
- (29) Burger, S.; Therrien, B.; Suss-Fink, G. *Inorg. Chim. Acta* **2004**, *357* (4), 1213. doi:10.1016/j.ica.2003.09.036.
- (30) Brooker, S.; Edelmann, F. T.; Kottke, T.; Roesky, H. W.; Sheldrick, G. M.; Stalke, D.; Whitmire, K. H. *J. Chem. Soc. Chem. Commun.* **1991**, (3), 144. doi:10.1039/c39910000144.
- (31) Evans, W. J.; Ansari, M. A.; Ziller, J. W.; Khan, S. I. *J. Organomet. Chem.* **1998**, *553* (1-2), 141. doi:10.1016/S0022-328X(97)00635-9.
- (32) Boyle, T. J.; Andrews, N. L.; Rodriguez, M. A.; Campana, C.; Yiu, T. *Inorg. Chem.* **2003**, *42* (17), 5357. doi:10.1021/ic034222k. PMID: 12924908.
- (33) Fermin, M. C.; Ho, J.; Stephan, D. W. *Organometallics* **1995**, *14* (9), 4247. doi:10.1021/om00009a030.
- (34) Beswick, M. A.; Hopkins, A. D.; Kerr, L. C.; Mosquera, M. E. G.; Palmer, J. S.; Raithby, P. R.; Rothenberger, A.; Wheatley, A. E. H.; Wright, D. S.; Stalke, D.; Steiner, A. *Chem. Commun. (Camb.)* **1998**, (15), 1527. doi:10.1039/a803834a.
- (35) Wolf, R.; Schisler, A.; Lonnecke, P.; Jones, C.; Hey-Hawkins, E. *Eur. J. Inorg. Chem.* **2004**, *2004* (16), 3277. doi:10.1002/ejic.200400153.
- (36) Hu, J.; Barbour, L. J.; Gokel, G. W. *Chem. Commun. (Camb.)* **2002**, (17), 1808. doi:10.1039/b204338f. PMID: 12271619.
- (37) Forbes, G. C.; Kennedy, A. R.; Mulvey, R. E.; Roberts, B. A.; Rowlings, R. B. *Organometallics* **2002**, *21* (23), 5115. doi:10.1021/om020596u.
- (38) Pu, L.; Phillips, A. D.; Richards, A. F.; Stender, M.; Simons, R. S.; Olmstead, M. M.; Power, P. P. *J. Am. Chem. Soc.* **2003**, *125* (38), 11626. doi:10.1021/ja035711m. PMID: 13129367.
- (39) Lancaster, S. J.; Hughes, D. L. *Dalton Trans.* **2003**, (9), 1779. doi:10.1039/b300552f.
- (40) Gómez, M.; Gomez-Sal, P.; Hernandez, J. M. *Eur. J. Inorg. Chem.* **2006**, *2006* (24), 5106. doi:10.1002/ejic.200600633.
- (41) Gibson, V. C.; Bercaw, J. E.; Bruton, W. J.; Sanner, R. D. *Organometallics* **1986**, *5* (5), 976. doi:10.1021/om00136a023.
- (42) Chirik, P. J.; Zubris, D. L.; Ackerman, L. J.; Henling, L. M.; Day, M. W.; Bercaw, J. E. *Organometallics* **2003**, *22* (1), 172. doi:10.1021/om020628d.
- (43) Davies, H. O.; Jones, A. C.; Motevalli, M. A.; McKinnell, E. A.; O'Brien, P. *Inorg. Chem. Commun.* **2005**, *8* (7), 585. doi:10.1016/j.inoche.2005.03.025.
- (44) Kawaguchi, H.; Matsuo, T. *J. Organomet. Chem.* **2005**, *690* (23), 5333. doi:10.1016/j.jorganchem.2005.05.002.
- (45) Jernakoff, P.; De Meric de Bellefon, C.; Geoffroy, G. L.; Rheingold, A. L.; Geib, S. J. *Organometallics* **1987**, *6* (6), 1362. doi:10.1021/om00149a042.
- (46) Cotton, F. A.; Diebold, M. P.; Roth, W. J. *J. Am. Chem. Soc.* **1987**, *109* (18), 5506. doi:10.1021/ja00252a033.
- (47) Scioly, A. J.; Leukens, M. L., Jr.; Wilson, R. B., Jr.; Huffman, J. C.; Sattelberger, A. P. *Polyhedron* **1987**, *6* (4), 741. doi:10.1016/S0277-5387(00)86882-5.
- (48) Ballmann, J.; Munhá, R. F.; Fryzuk, M. D. *Chem. Commun. (Camb.)* **2010**, *46* (7), 1013. doi:10.1039/b922853e. PMID: 20126700.
- (49) Galakhov, M. V.; Gomez, M.; Gomez-Sal, P.; Velasco, P. *Organometallics* **2005**, *24* (5), 848. doi:10.1021/om049110v.
- (50) Gómez, M.; Gomez-Sal, P.; Hernandez, J. M. *J. Organomet. Chem.* **2007**, *692* (11), 2291. doi:10.1016/j.jorganchem.2007.01.057.
- (51) Cloke, F. G. N.; Hitchcock, P. B.; Kuchta, M. C.; Morley-Smith, N. A. *Polyhedron* **2004**, *23* (17), 2625. doi:10.1016/j.poly.2004.06.015.
- (52) Agapie, T.; Bercaw, J. E. *Organometallics* **2007**, *26* (12), 2957. doi:10.1021/om700284c.
- (53) Bazinet, P.; Yap, G. P. A.; Richeson, D. S. *Organometallics* **2001**, *20* (20), 4129. doi:10.1021/om0105167.
- (54) Pangborn, A. B.; Giardello, M. A.; Grubbs, R. H.; Rosen, R. K.; Timmers, F. J. *Organometallics* **1996**, *15* (5), 1518. doi:10.1021/om9503712.
- (55) Schrock, R. R.; Sharp, P. R. *J. Am. Chem. Soc.* **1978**, *100* (8), 2389. doi:10.1021/ja00476a022.
- (56) Pflugrath, J. W. *Acta Crystallogr. D Biol. Crystallogr.* **1999**, *55* (10), 1718. doi:10.1107/S090744499900935X. PMID: 10531521.
- (57) Rigaku. *CrystalClear: An Integrated Program for the Collection and Processing of Area Detector Data*; Rigaku Corporation, 1997–2004.
- (58) Cromer, D. T.; Waber, J. T. *International Tables for X-ray Crystallography*; Kynoch Press: Birmingham, 1974.
- (59) Ibers, J. A.; Hamilton, W. C. *Acta Crystallogr.* **1964**, *17* (6), 781. doi:10.1107/S0365110X64002067.
- (60) Bruker AXS. *SAINT*; Bruker AXS Inc.: Madison, WI, 1997–2003.
- (61) Bruker AXS. *Bruker Nonius Area Detector Scaling and Absorption Correction*; Bruker AXS Inc.: Madison, WI, 2003.
- (62) Altomare, A.; Burla, M. C.; Camalli, M.; Cascarano, G. L.; Giacovazzo, C.; Guagliardi, A.; Moliterni, A. G. G.; Polidori, G.; Spagna, R. *J. Appl. Cryst.* **1999**, *32* (1), 115. doi:10.1107/S0021889898007717.
- (63) Burla, M. C.; Camalli, M.; Carrozzini, B.; Cascarano, G. L.; Giacovazzo, C.; Polidori, G.; Spagna, R. *J. Appl. Cryst.* **2003**, *36* (4), 1103. doi:10.1107/S0021889803012585.
- (64) Sheldrick, G. M. *SHELX97 [includes SHELXS97, SHELXL97, and CIFTAB] (programs for crystal structure analysis)*, release 97–02; University of Gottingen: Gottingen, Germany, 1998.
- (65) Farrugia, L. J. *J. Appl. Cryst.* **1999**, *32* (4), 837. doi:10.1107/S0021889899006020.
- (66) Farrugia, L. J. *J. Appl. Cryst.* **1997**, *30* (5), 565. doi:10.1107/S0021889897003117.

# Electrochemical reduction of sunset yellow at a multiwalled carbon nanotube (MWCNT)-modified glassy carbon electrode and its analytical application

Yuan-Zhi Song

**Abstract:** The electrochemical reduction of sunset yellow at a multiwalled carbon nanotube (MWCNT)-modified glassy carbon electrode is investigated using cyclic voltammetry. A simple, sensitive, and inexpensive method for determination of sunset yellow in soft drinks is proposed and the accuracy and reproducibility of this determination method are evaluated. This method is satisfactorily applied for the determination of sunset yellow in soft drinks in the concentration range of 1.2–125.0 mg L<sup>-1</sup> and 125.0–265.0 mg L<sup>-1</sup>, with a detection limit of 0.5 mg L<sup>-1</sup>.

**Key words:** sunset yellow, multiwalled carbon nanotube (MWCNT), cyclic voltammetry, glassy carbon electrode.

**Résumé :** Faisant appel à la voltampérométrie cyclique, on a étudié la réduction électrochimique du jaune soleil à une électrode de carbone vitreux modifiée par un nanotube de carbone à surfaces multiples. On propose une méthode simple, sensible et peu coûteuse de déterminer le jaune soleil dans les boissons gazeuses et on en a évalué la reproductibilité et l'exactitude. Cette méthode peut être appliquée d'une façon satisfaisante pour la détermination du jaune soleil dans les boissons gazeuses à des concentrations allant de 1,2 à 125,0 mg L<sup>-1</sup> et de 125,0 à 265,0 mg L<sup>-1</sup> avec une limite de détection de 0,5 mg L<sup>-1</sup>.

**Mots-clés :** jaune soleil, nanotube de carbone à surfaces multiples, voltampérométrie cyclique, électrode de carbone vitreuse.

[Traduit par la Rédaction]

## Introduction

Sunset yellow is an azo compound that is found in common food products such as candies, beverages, bakery products, and dairy products. As the genetic toxicity of some azo dyes has been confirmed,<sup>1,2</sup> accurate and reliable methods for the determination of synthetic dyes in foodstuff are required. Although spectrophotometry,<sup>3–6</sup> thin-layer chromatography,<sup>7–9</sup> reversed-phase liquid chromatography (RPLC),<sup>10,11</sup> ion-pair RPLC,<sup>12,13</sup> capillary electrophoresis,<sup>14–18</sup> and anion-exchange chromatography<sup>19–21</sup> have been used for the determination of various water-soluble synthetic dyes, many of these methods are time-consuming.

Since carbon nanotubes (CNTs) were discovered in 1991,<sup>22</sup> they have attracted much attention from researchers. The modification of electrode substrates with multiwalled carbon nanotubes (MWCNTs) has been shown to result in high sensitivities, electron-transfer promotion, resistance to surface fouling, and reduction of overpotentials. It has been reported that CNT modified electrodes can be successfully applied in the determination of many organic molecules.<sup>23–29</sup>

This paper concerns the electrochemical reduction of sunset yellow at multiwalled carbon nanotube-modified glassy carbon electrode (MWCNT/GCE) and the development of a

simple, rapid, and effective method for the determination of sunset yellow in drinks.

## Experimental

### Chemicals and reagents

Tartrazine, amaranth, ponceau 4R, sunset yellow, and brilliant blue FCF were purchased from the National Research Center for Certified Reference Materials (CRMs; Beijing, China). MWCNTs were purchased from Shenzhen Nanotechnologies Port Co. Ltd. (China). All other reagents were analytical grade. Double-distilled water was used throughout. Phosphate buffer solution (PBS; 0.1 mol/L) was prepared by dissolving 0.1 mol NaCl and 0.1 mol Na<sub>2</sub>HPO<sub>4</sub> in 1 L of double-distilled water and adjusting the pH using 6 mol/L aq HCl or 1 mol/L NaOH solution.

### Instrumentation

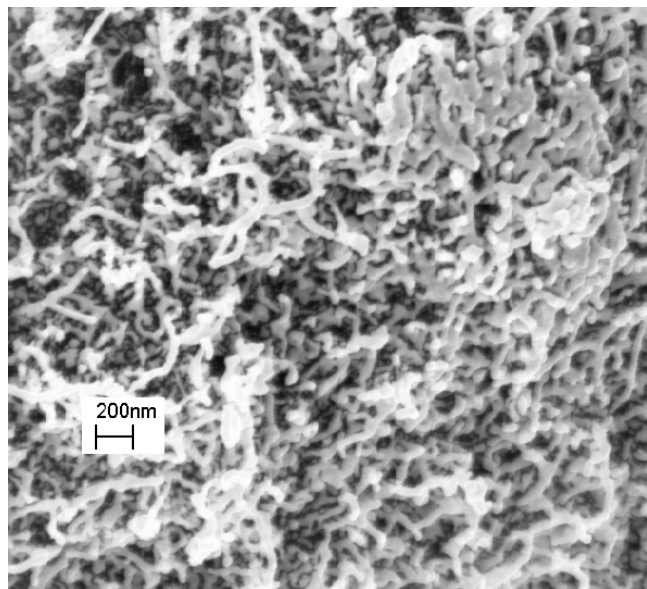
For all electrochemical experiments, a CHI660B electrochemical analyzer (CH Instruments, Inc., USA) was employed. The electrochemical cells consisted of a three electrode, a 3 mm diameter glassy carbon disc electrode, and a MWCNT composite modified GCE were used as the working electrode, a platinum wire served as the counter electrode, and a saturated calomel electrode (SCE) was used

Received 4 November 2009. Accepted 31 March 2010. Published on the NRC Research Press Web site at canjchem.nrc.ca on 24 June 2010.

**Y.-Z. Song,** Jiangsu Province Key Laboratory for Chemistry of Low-Dimensional Materials, School of Chemistry & Chemical Engineering, Huaiyin Normal University, Huai An 223300, People's Republic of China. (e-mail: songyuanzhi@sina.com).



**Fig. 1.** TEM image of the purified MWCNTs.



as the reference electrode. The MWCNTs were characterized by transmission electron microscopy (TEM) (JEM 2100, JEOL Ltd., Japan).

#### Preparation of MWCNTs and modified GCE

The MWCNTs were purified in boiling concentrated nitric acid for 3 h, followed by rinsing with deionized water, and drying under ambient atmosphere. Open-end MWCNTs with hydrophilic surfaces were thus obtained. The TEM image of purified MWCNTs is shown in Fig. 1; many nanocarbon tubes with diameters ranging from 20 to 30 nm were observed. Before modification, the GCE was polished with 0.05  $\mu\text{m}$  alumina slurry on a polishing cloth, rinsed thoroughly with double-distilled water, and then sonicated in ethanol and double-distilled water for 10 min, sequentially. The modifier suspension was prepared by dispersing the MWCNTs in 5.0 mL of *N,N*-dimethylformamide under sonication for 30 min. The MWCNT modified GCE was prepared by casting 5  $\mu\text{L}$  of the above-mentioned black suspension on the GCE surface using a micropipette and left to dry at room temperature. Before the cyclic voltammetric measurements, the modified electrode was cycled between  $-1$  and  $1$  V (scan rate  $100 \text{ mV s}^{-1}$ ) in  $0.1 \text{ mol/L}$  PBS for several times until acquiring the reproducible responses.

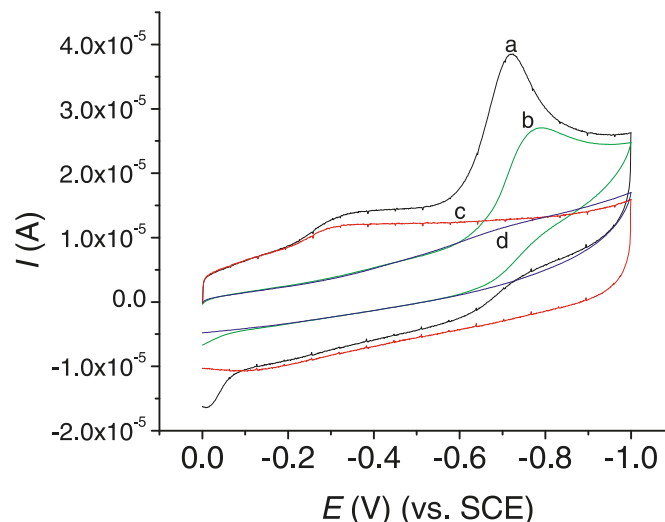
## Results and discussion

#### Electrochemical behavior of sunset yellow at MWCNT/GCE

The cyclic voltammograms (CVs) of sunset yellow at bare GCE and MWCNT/GCE in purged  $\text{N}_2$   $0.1 \text{ mol/L}$  PBS of pH 8.3 are shown in Fig. 2. It can be seen that the reduction peak for sunset yellow at bare GCE and MWCNT/GCE are observed at  $-0.780 \text{ V}$  and  $-0.721 \text{ V}$ , respectively, the reduction potential of sunset yellow at MWCNT/GCE shifted to positive potentials, and the peak current increased.

These results indicate that the MWCNT modified electrode promoted the electrochemical reduction of sunset yellow

**Fig. 2.** CVs of  $50.0 \text{ mg L}^{-1}$  sunset yellow at (a) MWCNT/GCE and (b) bare GCE; CVs of (c) MWCNT/GCE and (d) bare GCE. Scan rate:  $100 \text{ mV s}^{-1}$ ; supporting electrolyte:  $0.1 \text{ mol/L}$  PBS of pH 8.3;  $5 \mu\text{L}$  accumulation volume of  $1.0 \text{ mg mL}^{-1}$  MWCNT suspension.



low by considerably accelerating the rate of electron transfer. Purified MWCNTs are functionalized with  $-\text{OH}$  and  $-\text{COOH}$ , which could interact with hydroxyl and sulfonyl in sunset yellow to form a hydrogen bond. The  $\pi$ - $\pi$  conjugated bonds between MWCNTs and the sunset yellow probably increase the reduction current. The MWCNT interface has a large surface area, a great deal of active sites, better conductivity, and favorable electrocatalytic power; all of them led to the dissimilar conjugation effect of sunset yellow with the bare electrode interface.

#### Amount of the modifier

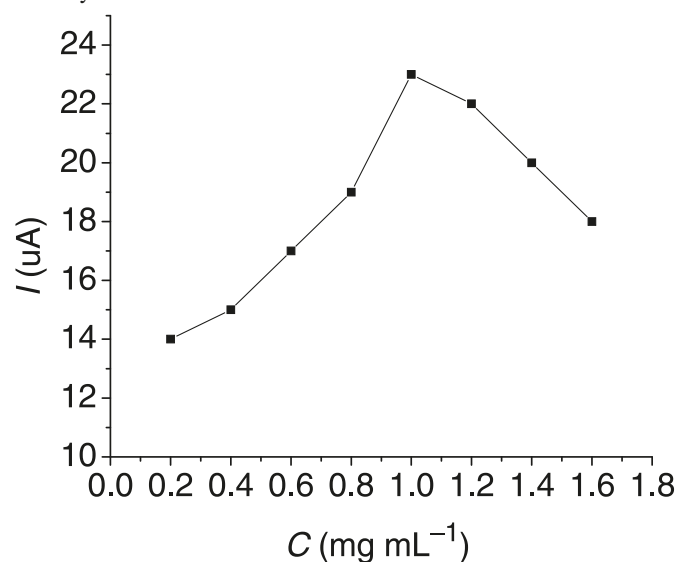
The reduction current of sunset yellow at a modified electrode can be affected by the amount of MWCNTs on the electrode surface. This can be controlled by using the same volume ( $5.0 \mu\text{L}$ ) of the suspensions with the different concentrations of MWCNTs, casted on the surface of the GCE. The experiments showed that the reduction peak current for  $50.0 \text{ mg L}^{-1}$  sunset yellow increased quickly by increasing the concentration of MWCNT suspension deposited on the surface of the GCE up to  $1.0 \text{ mg mL}^{-1}$  (Fig. 3). A further increase caused a gradual decrease in the cathodic peak current of sunset yellow with an increase in background current. As a result,  $5.0 \mu\text{L}$  of  $1.0 \text{ mg mL}^{-1}$  MWCNT suspension was selected as the optimum volume for preparation of the modified electrode.

#### Influence of pH

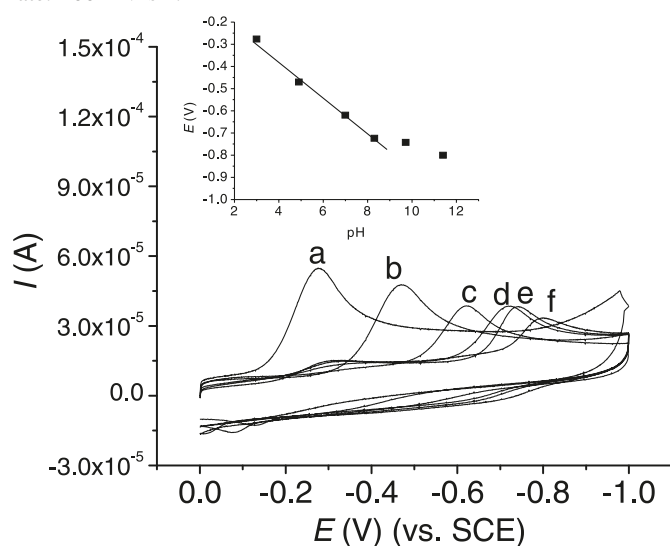
The influence of pH on the electrochemical behavior of sunset yellow was investigated at different pH values in the range of 2.0 to 11.4. Figure 4 shows the CVs of  $50.0 \text{ mg L}^{-1}$  sunset yellow on the surface of the modified electrode over the discussed pH range at the scan rate of  $100 \text{ mV s}^{-1}$ . It was found that the peak potential ( $E_p$ ) shifted negatively with pH increasing and a good linear relationship was observed between the  $E_p$  and pH values in the range of 3.0 to 8.3 with the following equation:  $E_p (\text{V}) = -0.0681\text{pH} - 0.0404$  ( $R$ : correlation coefficient;  $R^2 = 0.988$ ).



**Fig. 3.** Dependence of the reduction peak current of 50.0 mg L<sup>-1</sup> sunset yellow on the amount of the modifier.



**Fig. 4.** Influence of pH on the shape of the cathodic peak of 50.0 mg L<sup>-1</sup> sunset yellow; pH: (a) 3.0, (b) 5.0, (c) 7.0, (d) 8.3, (e) 9.7, and (f) 11.4. Insert: Plot of the peak potential against pH; Scan rate: 100 mV s<sup>-1</sup>.

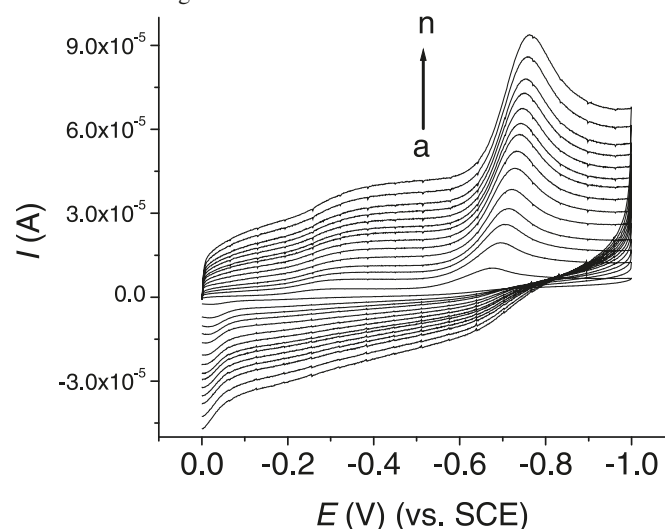


A value of about -68.1 mV per pH unit indicates that equal numbers of electrons and protons are involved in the electroreduction of sunset yellow on the surface of the modified electrode. On the other hand, the peak current was shown to be increased by the pH from 11.4 to 3.0. To avoid the influence of oxygen on the reduction reaction of sunset yellow, 0.1 mol/L PBS of pH 8.3 was used as the supporting electrolyte in all voltammetric determinations.

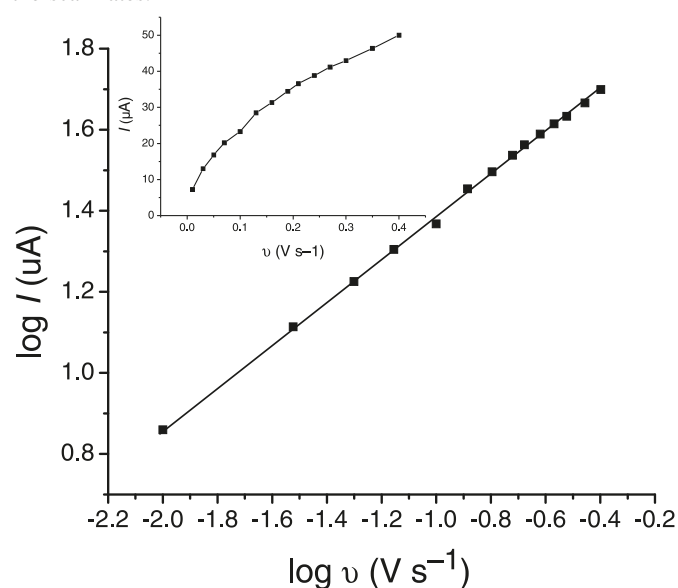
#### Effect of the potential scan rate

The information involving electrochemical mechanisms can usually be obtained from the investigation of CVs in the different potential sweep rates. Therefore, the CVs investigations for 50.0 mg L<sup>-1</sup> sunset yellow were performed

**Fig. 5.** CVs of 50.0 mg L<sup>-1</sup> sunset yellow at MWCNT/GCE with different scan rates. (a–n) are 10, 30, 50, 70, 100, 130, 160, 190, 210, 240, 270, 300, 350, and 400 mV s<sup>-1</sup>, respectively. Other conditions are as in Fig. 1.



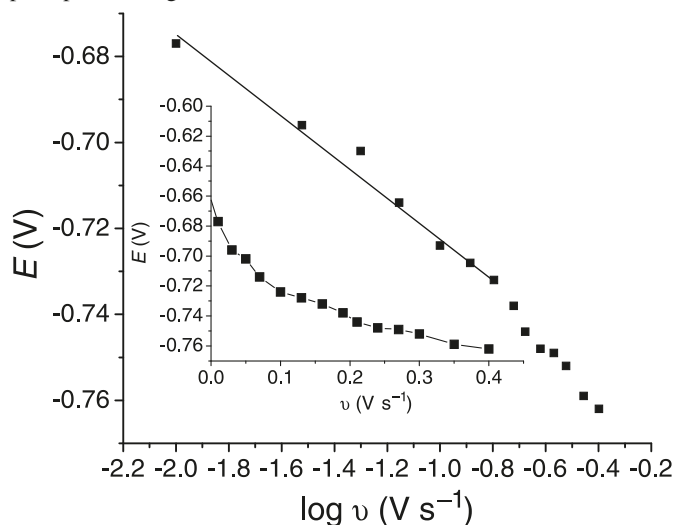
**Fig. 6.** Dependence of the logarithm of the peak current on the logarithm of the scan rates. Insert: plot of the peak current against the scan rates.



on the surface of the MWCNT/GCE in a buffer solution of pH 8.3 at different potential sweep rates. Figure 5 illustrates the influence of the scan rate on the CVs of 50.0 mg L<sup>-1</sup> sunset yellow in the range of 10–400 mV s<sup>-1</sup>. The linear relation between the log(*I*) and the log(*v*) (Fig. 6, where *I* = peak current and *v* = scan rate) indicates a mixed adsorption–diffusion controlled process on the surface of the modified electrode; the regression equation for this relationship was given as log(*I*) = 0.5259 log(*v*) + 1.9116 (*R*<sup>2</sup> = 0.999, *I*: μA, *v*: V s<sup>-1</sup>).

The relationship between the reduction peak potential and logarithm of the scan rate is shown in Fig. 7. It can be seen that the reduction peak potential shifts negatively with an increasing scan rate. Such a behavior revealed the irreversible

**Fig. 7.** Dependence of the reduction peak potential of 50.0 mg L<sup>-1</sup> sunset yellow on the logarithm of the scan rates. Insert: plot of the peak potential against scan rates.



nature of the electrochemical process for sunset yellow. The regression equation for this relationship was obtained as  $E_p = -0.047 \log(\nu) - 0.7687$  ( $R^2 = 0.981$ ,  $E_p$ : V,  $\nu$ : V s<sup>-1</sup>).

As for an irreversible electrode process,  $E_p$  is given by the following equation:<sup>30,31</sup>

$$[1] \quad E_p = E^{o'} + \frac{2.303RT}{\alpha nF} \log \frac{RTk^o}{\alpha nF} - \frac{2.303RT}{\alpha nF} \log \nu$$

where  $\alpha$  is the transfer coefficient,  $k^o$  is the standard heterogeneous rate constant of the reaction,  $n$  is the number of electrons transferred,  $\nu$  is the scan rate, and  $E^{o'}$  is the formal redox potential. Thus, the value of  $\alpha n$  can be easily calculated. The  $\alpha n$  was calculated to be 1.2583. According to Bard and Faulkner,<sup>32</sup>  $\alpha$  can be obtained as

$$[2] \quad \alpha = \frac{47.7}{|E_p - E_{p/2}|} mV$$

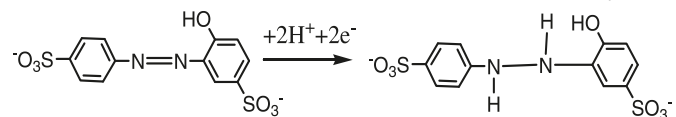
where  $E_{p/2}$  is the potential where the current is at half the peak value. The  $\alpha$  is calculated to be 0.6446. Furthermore, the number of electrons transferred ( $n$ ) in the electroreduction of sunset yellow was calculated to be  $1.95 \pm 0.20$ . The value of  $E^{o'}$  could be obtained from the intercept of the  $E_p$  versus  $\nu$  curve by extrapolating to the vertical axis at  $\nu = 0$ .<sup>33</sup> The intercept for the  $E_p$  versus  $\log \nu$  plot was  $-0.7687$  V and the  $E^{o'}$  was  $-0.664$  V (Fig. 7, insert), thus,  $k^o$  is calculated to be  $0.29$  s<sup>-1</sup>.

It is generally admitted that azo molecules are reduced at the mercury drop in two steps:<sup>34</sup> step 1:  $R-N=N-R' + 2e^- + 2H^+ = R-NH-NH-R'$ , step 2:  $R-NH-NH-R' + 2e^- + 2H^+ = R-NH_2 + R'-NH_2$ .

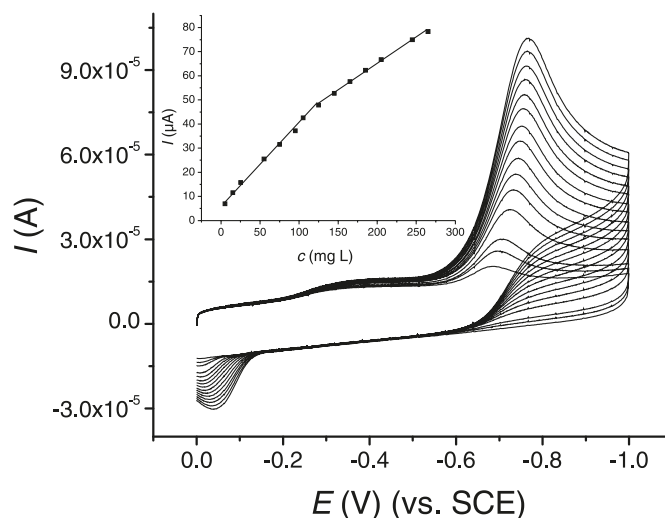
When the pH value is below 3, steps 1 and 2 occur simultaneously, while for media close to neutrality, the second step does not occur. Consequently, reduction potentials and intensities are strongly influenced by the media pH.

Taking into account that sunset yellow contains a N=N group, which presents a basic center of electron and proton acceptors, we may, therefore, assume that the reduction step

**Fig. 8.** Mechanism for the electrochemical reduction of sunset yellow.



**Fig. 9.** CVs of different concentrations of sunset yellow. Insert: plot of the peak current against the concentration. Other conditions are as in Fig. 1.



of sunset yellow is located on the N=N group. The sunset yellow accepts two protons and two electrons. The mechanism is shown in Fig. 8.

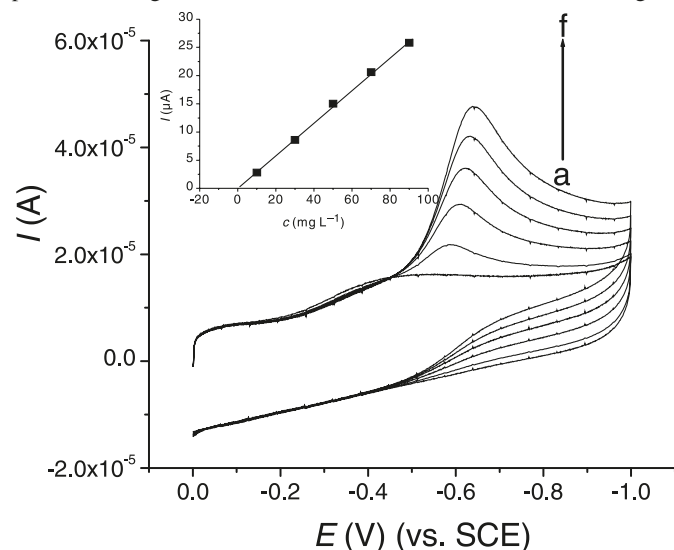
### Linearity range and the detection limit

The relationship between the reduction peak current and the concentration ( $c$ ) of sunset yellow was examined by CVs on the surface of MWCNT/GCE (Fig. 9). Under the previously mentioned optimum conditions, the reduction peak currents were proportional to sunset yellow concentrations over two intervals in the range of  $1.2$ – $125.0$  mg L<sup>-1</sup> and  $125.0$ – $265.0$  mg L<sup>-1</sup> in  $0.1$  mol/L PBS of pH 8.3. Two linear regression equations were obtained as  $I$  (μA) =  $0.3348c$  (mg L<sup>-1</sup>) +  $6.4803$  ( $R^2 = 0.997$ ) and  $I$  (μA) =  $0.2186c$  (mg L<sup>-1</sup>) +  $21.2890$  ( $R^2 = 0.997$ ). The detection limit ( $3\sigma/s$ , where  $\sigma$  is the standard deviation of the intercept and  $s$  is the slope of the calibration curve) observed for sunset yellow was  $0.5$  mg L<sup>-1</sup>.

### Repeatability of the modified electrode

The repeatability of the modified electrode was investigated by repetitive recording at a fixed sunset yellow concentration of  $50.0$  mg L<sup>-1</sup>. The relative standard deviation (RSD) for the peak currents in CVs based on six replicates was  $1.5\%$ , indicating excellent repeatability of the response of the modified electrode. Also, on using the MWCNT/GCE daily and storing under ambient conditions over a period of two weeks, the electrode retained  $96.3\%$  of its initial peak current response for a sunset yellow concentration of  $50.0$  mg L<sup>-1</sup>. The results indicate that the modified electrode has an excellent repeatability.

**Fig. 10.** CVs of (a) a sample and (b–f) added standard samples. The concentration of the added standard sunset yellow were (b) 10.0, (c) 30.0, (d) 50.0, (e) 70.0, and (f) 90.0 mg L<sup>-1</sup>. Insert: plot of the peak current against concentration. Other conditions are as in Fig. 1.



**Table 1.** Recoveries and relative standard deviations (RSD, %) for sunset yellow in soft drinks by the proposed method.

No.	Sample (mg L <sup>-1</sup> ) <sup>a</sup>	RSD (%), <i>n</i> = 6	Added (mg L <sup>-1</sup> )	Found (mg L <sup>-1</sup> ) <sup>a</sup>	Recovery (%)
1	0.0	1.2	20.0	20.6	103.0
2	5.6	3.0	30.0	36.5	103.0
3	16.7	2.1	40.0	55.1	96.0
4	18.1	2.7	50.0	70.3	104.4
5	19.1	2.0	60.0	80.2	101.8
6	50.3	1.5	80.0	134.0	104.6

<sup>a</sup>Average of six replicate measurements (*n* = 6).

### Determinations of sunset yellow in soft drinks

To assess the applicability of the proposed method, the MWCNT/GCE was used to determine the content of sunset yellow in soft drinks by applying the CV method.

The CVs of a sample and added standard samples are shown in Fig. 10. Soft drinks (2.00 mL) were diluted to 5.0 mL with 0.1 mol/L PBS of pH 8.3 and the linear regression equation was obtained as  $c$  (mg L<sup>-1</sup>) =  $3.4459I$  (μA) – 0.27 ( $R^2 = 0.999$ ). The determination results using the standard addition method are shown in Table 1. The recoveries ranged from 96.0% to 104.4% and the content for sunset yellow in soft drinks was 0.0 ~ 50.3 mg L<sup>-1</sup> with a RSD of 1.2% ~ 3.0% (*n* = 6).

### Interference

The influence of some organic compounds was tested. If the presence of an interferent altered the average current signal of 50.0 mg L<sup>-1</sup> sunset yellow concentration by less than ±5%, we considered that caused no interference. The results showed a 100-fold of glucose, 50-fold of ascorbic acid, indigotine, brilliant blue FCF, amaranth, erythrosine, cane sugar, sorbic acid, and saccharin sodium did not interfere with the determination, while ponceau 4R and tartrazine

interfered severely. This suggests that the modified electrode had certain resistance to some interferences.

### Conclusion

In the present work, it was demonstrated that modification of GCE with MWCNTs is a simple and effective method for the determination of sunset yellow in soft drinks. The procedure enables preparation of highly stable and reproducible uniform modifier films, which leads to a considerable enhancement in repeatability and reproducibility in the voltammetric measurements. High sensitivity and improved detection limit of the MWCNT/GCE are promising for the determination of trace amounts of sunset yellow in soft drinks.

### Acknowledgement

This research was supported by the National Science Foundation of China (No. 20872046/B020901), Opened Foundation of Key Laboratory for the Synthesis and Application of Organic Functional Molecules of the Ministry of Education of China, Opened Foundation of Jiangsu Province Key Laboratory for Chemistry of Low-Dimensional Materials (Grant No.JSKC08049), the Science Foundation of Huai-An City (Grant No.SN0675), and the Science Foundation of the Education Department of Jiangsu Province of China (Grant No. 07KJD610028).

### References

- (1) Combes, R. D.; Haveland-Smith, R. B. *Mutat. Res.* **1982**, 98 (2), 101. doi:doi:10.1016/0165-1110(82)90015-X.
- (2) Rajaguru, P.; Fairbairn, L. J.; Ashby, J.; Willington, M. A.; Turner, S.; Woolford, L. A.; Chinnasamy, N.; Rafferty, J. A. *Mutat. Res.* **1999**, 444 (1), 175. doi:doi:10.1016/S1383-5718(99)00081-9.
- (3) Vidotti, E. C.; Cancino, J. C.; Oliveira, C. C.; Rollemberg, M. C. E. *Anal. Sci.* **2005**, 21 (2), 21. doi:doi:10.2116/analsci.21.149.
- (4) Blanco, C. C.; Campaña, A. M. G.; Barrero, F. A. *Talanta* **1996**, 43 (7), 1019. doi:doi:10.1016/0039-9140(96)01847-4.
- (5) Berzas Nevado, J. J.; Cabanillas, C. G.; Salcedo, A. M. C. *Talanta* **1995**, 42 (12), 2043. doi:doi:10.1016/0039-9140(95)01695-3.
- (6) Capitán-Vallvey, L. F.; Fernández, M. D., de Orbe, I.; Avidad, R. *Talanta* **1998**, 47 (4), 861. doi:doi:10.1016/S0039-9140(98)00159-3.
- (7) Berzas Nevado, J. J.; Rodríguez Flores, J.; Villaseñor Llerena, M. J. *Talanta* **1997**, 44 (3), 467. doi:doi:10.1016/S0039-9140(96)02105-4.
- (8) Dugar, S. M.; Leibowitz, J. N.; Dyer, R. H. *J. Assoc. Off. Anal. Chem.* **1994**, 77, 1335.
- (9) Oka, H.; Ikaia, Y.; Ohno, T.; Kawamura, N.; Hayakawa, J.; Harada, K.; Suzuki, M. *J. Chromatogr. A* **1994**, 674 (1–2), 301. doi:doi:10.1016/0021-9673(94)85235-9.
- (10) Greenway, G. M.; Kometa, N.; Macrae, R. *Food Chem.* **1992**, 43 (2), 137. doi:doi:10.1016/0308-8146(92)90227-S.
- (11) Hann, J. T.; Gilkison, I. S. *J. Chromatogr. A* **1987**, 395, 317. doi:doi:10.1016/S0021-9673(01)94120-2.
- (12) White, P. C.; Harbin, A. M. *Analyst (Lond.)* **1989**, 114 (8), 877. doi:doi:10.1039/AN9891400877.
- (13) Chen, Q.-c.; Mou, S.-f.; Hou, X.-p.; Riviello, J. M.; Ni, Z.m.

- J. Chromatogr. A* **1998**, 827 (1), 73. doi:doi:10.1016/S0021-9673(98)00759-6.
- (14) Huang, H.-Y.; Chuang, C.-L.; Chiu, C.-W.; Chung, M.-C. *Electrophoresis* **2005**, 26 (4), 867. doi:doi:10.1002/elps.200410279.
- (15) Liu, H.; Zhu, T.; Zhang, Y.; Qi, S.; Huang, A.; Sun, Y. *J. Chromatogr. A* **1995**, 718 (2), 448. doi:doi:10.1016/0021-9673(95)00682-6.
- (16) Thompson, C. O.; Trenerry, V. C. *J. Chromatogr. A* **1995**, 704 (1), 195. doi:doi:10.1016/0021-9673(95)00165-J.
- (17) Razee, S.; Tamura, A.; Masujima, T. *J. Chromatogr. A* **1995**, 715 (1), 179. doi:doi:10.1016/0021-9673(95)00586-C.
- (18) Suzuki, S.; Shirao, M.; Aizawa, M.; Nakazawa, H.; Sasa, K.; Sasagawa, H. *J. Chromatogr. A* **1994**, 680 (2), 541. doi:doi:10.1016/0021-9673(94)85153-0.
- (19) Bailey, J. E.; Cox, E. A. *J. Assoc. Off. Anal. Chem.* **1975**, 58, 609.
- (20) Singh, M. *J. Assoc. Off. Anal. Chem.* **1977**, 60, 173.
- (21) Bailey, J. E.; Cox, E. A. *J. Assoc. Off. Anal. Chem.* **1976**, 59, 5.
- (22) Iijima, S. *Physica B* **2002**, 324 (1-4), 1. doi:doi:10.1016/S0921-4526(02)00869-4.
- (23) Siswana, M. P.; Ozoemena, K. I.; Nyokong, T. *Electrochim. Acta* **2006**, 52 (1), 114. doi:doi:10.1016/j.electacta.2006.03.090.
- (24) Moraes, F. C.; Mascaro, L. H.; Machado, S. A. S.; Brett, C. M. A. *Talanta* **2009**, 79 (5), 1406. doi:doi:10.1016/j.talanta.2009.06.013.
- (25) Hegde, R. N.; Shetti, N. P.; Nandibewoor, S. T. *Talanta* **2009**, 79 (2), 361. doi:doi:10.1016/j.talanta.2009.03.064.
- (26) Fang, B.; Wei, Y.; Li, M. G.; Wang, G. F.; Zhang, W. *Talanta* **2007**, 72 (4), 1302. doi:doi:10.1016/j.talanta.2007.01.039.
- (27) Ghalkhani, M.; Shahrokhian, S.; Ghorbani-Bidkorbeh, F. *Talanta* **2009**, 80 (1), 31. doi:doi:10.1016/j.talanta.2009.06.019.
- (28) Zeng, B.; Huang, F. *Talanta* **2004**, 64 (2), 380. doi:doi:10.1016/j.talanta.2004.02.024.
- (29) Zhang, W.; Liu, T.; Zheng, X.; Huang, W.; Wan, C. *Colloids Surf. B Interfaces* **2009** (1), 74, 28. doi:doi:10.1016/j.colsurfb.2009.06.016.
- (30) Laviron, E. *J. Electroanal. Chem.* **1974**, 52 (3), 355. doi:doi:10.1016/S0022-0728(74)80448-1.
- (31) Laviron, E. *J. Electroanal. Chem.* **1979**, 101 (1), 19. doi:doi:10.1016/S0022-0728(79)80075-3.
- (32) Bard, A. J.; Faulkner, L. R. *Electrochemical Methods, Fundamentals and Application*, 2nd ed.; Wiley & Sons: New York, 2001; p. 236.
- (33) Wu, Y.; Ji, X.; Hu, S. *Bioelectrochemistry* **2004**, 64 (1), 91. doi:doi:10.1016/j.bioelechem.2004.03.005.
- (34) Kolthoff, I. M.; Lingane, J. J. *Polarography*; Interscience Publishers: New York, 1952; Vol. 2; p. 768.



# A kinetic study of dimethyl sulfoxide reductase based on density functional theory

Elizabeth Hernandez-Marin and Tom Ziegler

**Abstract:** We present a density functional theory study on the oxygen atom transfer (OAT) reaction of dimethyl sulfoxide (DMSO) with model complexes resembling a functional synthetic analogue of the molybdoenzyme DMSO reductase. The good agreement between our calculated Gibbs free energy profile and data derived from experimental kinetic parameters supports the reaction mechanisms of the oxygen atom transfer proposed in this study. When the mechanism involves the formation of a DMSO-bound intermediate, the calculations on the free energy surface provide valuable information that explains the origin of the apparent contradiction between the experimental findings and previous theoretical calculations with respect to the rate-limiting step of the reaction mechanism. The enzymatic mechanism of the OAT reaction is more complex than the mechanism of any synthetic analogue, mainly due to the formation of an enzyme-substrate adduct prior to the appearance of the substrate-bound intermediate. This study also presents a possible mechanism for the formation of such an adduct and the subsequent oxygen atom transfer. The mechanism involves a proton transfer to and from the substrate.

**Key words:** dimethyl sulfoxide (DMSO) reductase, oxygen atom transfer, density functional theory.

**Résumé :** On présente une étude basée sur la théorie de la fonctionnelle de densité pour la réaction de transfert de l'atome d'oxygène à partir du diméthylsulfoxyde (DMSO), en utilisant des complexes modèles ressemblant à un analogue de synthèse du molybdoenzyme de la réductase de DMSO. Le bon accord entre le profil d'énergie libre de Gibbs calculé et les données dérivées de paramètres cinétiques expérimentaux supporte les mécanismes réactionnels proposés dans cette étude pour le transfert de l'atome d'oxygène. Quand le mécanisme implique la formation d'un intermédiaire lié au DMSO, les calculs de la surface d'énergie libre fournissent une information utile qui explique l'origine de la contradiction apparente entre les données expérimentales et les calculs théoriques antérieurs relative à l'étape cinétiquement limitante du mécanisme réactionnel. Le mécanisme enzymatique de la réaction de transfert de l'atome d'oxygène est plus complexe que le mécanisme de tout analogue de synthèse, principalement en raison de la formation d'un adduit enzyme substrat avant l'apparition de l'intermédiaire lié au substrat. Cette étude présente aussi un mécanisme potentiel pour la formation d'un tel adduit et le transfert subséquent de l'atome d'oxygène. Le mécanisme implique un transfert de proton vers, et à partir du substrat.

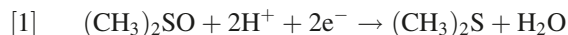
**Mots-clés :** réductase de diméthylsulfoxyde (DMSO), transfert d'atome d'oxygène, théorie de la fonctionnelle de densité.

[Traduit par la Rédaction]

## Introduction

Dimethyl sulfide (DMS) in seawater has been proposed to serve as a seed for cloud condensation over the oceans and can as such have a possible effect on the climate.<sup>1</sup> For this reason, knowledge of the processes that regulate DMS concentrations in seawater is of considerable interest. Among those processes, the interconversion occurring between DMS and dimethyl sulfoxide (DMSO) is believed to be important.<sup>2</sup> In this regard, DMSO in seawater has been found to arise from DMS oxidation via photochemical and bacterial oxidation processes. On the other hand, some bacteria are able to reduce DMSO to DMS.<sup>3</sup> A reductase for DMSO from *Escherichia coli* has been isolated and characterized as

an iron-sulfur molybdoenzyme.<sup>4</sup> A simpler molybdoenzyme (without other prosthetic groups such as flavin or iron-sulfur centers) is found in bacteria of the genus *Rhodobacter*.<sup>5,6</sup> The enzymes that possess a molybdenum center as their sole redox-active center belong to the DMSO reductase (DMSOR) family.<sup>7</sup> DMSOR serves as a terminal reductase in the bacterial respiratory chain where dimethyl sulfoxide is used as an electron acceptor,<sup>8</sup> undergoing the overall reaction



The molybdenum active center participates in an oxygen (oxo) atom transfer (OAT) reaction

Received 3 June 2009. Accepted 21 August 2009. Published on the NRC Research Press Web site at canjchem.nrc.ca on 27 February 2010.

This article is part of a Special Issue dedicated to Professor R. J. Boyd.

**E. Hernandez-Marin and T. Ziegler.**<sup>1</sup> Department of Chemistry, University of Calgary, 2500 University Drive, Calgary, AB T2N 1N4, Canada.

<sup>1</sup>Corresponding author (e-mail: ziegler@ucalgary.ca).



Multiple spectroscopic studies on DMSOR from bacterial sources have been carried out to determine its structure.<sup>9–13</sup> As a result, there is a considerable body of information about the coordination geometry of the molybdenum center in DMSOR. It has been established that the oxidized active site of DMSOR consists of the metal coordinated by two molybdopterin (metal binding pyranopterin ene-1,2-dithiolate) ligands, one oxo group, and one oxygen atom from the side chain of a serinyl residue.<sup>14</sup>

Synthetic molybdenum complexes with structural and functional behavior similar to that of the DMSOR have been developed<sup>15–18</sup> as one approach to understand the enzymatic oxo-transfer reaction. Density functional theory (DFT) methods have been used as well to investigate the OAT reaction above. Webster and Hall<sup>19</sup> employed the complex  $[\text{Mo}(\text{OMe})(\text{S}_2\text{C}_2\text{Me}_2)_2]^-$  as a model for the  $[\text{Mo}^{\text{IV}}]$  species. Thapper et al.<sup>20</sup> based their modeling on a  $[\text{Mo}(\text{OMe})(\text{S}_2\text{C}_2(\text{CN})_2)_2]^-$  complex, while  $[\text{Mo}(\text{OMe})(\text{S}_2\text{C}_2\text{Me}_2)_2]^-$  was used by Hillier and co-workers.<sup>21</sup> In the present DFT study, we reinvestigate the OAT reaction involving DMSO and the model complexes  $[\text{Mo}(\text{OR})(\text{S}_2\text{C}_2\text{H}_2)_2]^-$  with  $\text{R} = \text{Me}, \text{Ph}$ . Our investigation was prompted by a recent experimental study on the kinetics of DMSOR<sup>22</sup> and by the apparent contradiction between the theoretical calculations and the conclusions drawn from experimental results with respect to the nature of the rate-limiting step in the OAT reaction for synthetic analogues.<sup>23</sup> Thus, we shall calculate the kinetic parameters of the OAT between the model complexes and DMSO and compare them to available experimental data for the actual enzyme and some synthetic analogues. It is hoped that the current study will give a more detailed and direct comparison between DFT calculations and experimental kinetic data on the OAT in synthetic analogues than has been provided in the past. We shall finally discuss how synthetic or computational studies on the OAT in model systems relate to experimental investigations of the kinetics for OAT in the actual enzyme. In this discussion, we shall elaborate on a possible mechanism for OAT in the actual enzyme involving a proton transfer to and from DMSO.

## Computational details and methods

All calculations were based on DFT as implemented in the ADF (Amsterdam density functional) program version 2006.01.<sup>24</sup> Use was made of the Becke–Perdew exchange–correlation (XC) functional (BP86)<sup>25–27</sup> and a standard triple- $\zeta$  STO basis with one set of polarization functions for all atoms. The 1s electrons of C, N, and O; the 1s2s2p electrons of S; and the 1s2s2p3s3p3d electrons of Mo were treated as frozen cores. For all the optimizations and linear transit calculations, the protein matrix was represented by making use of the dielectric continuum model COSMO (conductor-like screening model)<sup>28</sup> as implemented in ADF, with a dielectric constant of  $\epsilon = 5$ . The continuum model was used in accordance with common practice<sup>29,30</sup> to simulate the polarizable background of the protein matrix.

The crystal structure of the reduced DMSO reductase from *Rhodobacter capsulatus* with bound DMSO substrate is available (PDB code 4DMR).<sup>31</sup> This structure represents

a good candidate for an intermediate in the oxygen atom transfer reaction. The Cartesian coordinates provided by the crystallographic data were used to construct the starting geometry for a computationally convenient model complex,  $[\text{Mo}(\text{OMe})(\text{S}_2\text{C}_2\text{H}_2)_2 \cdots \text{DMSO}]^-$ . The coordinates of the oxygen and carbon of the OMe group, and of the sulfur and carbon atoms of the dithiolate groups were taken as those of Ser 147 and the pterin cofactors, respectively, from the crystal structure. After the starting geometry was fully optimized, two approximate transition states were located by performing linear transit calculations. One linear transit considered the increment of the Mo–O<sub>DMSO</sub> distance. The other linear transit calculation allowed for the increment of the distance between S and O from the DMSO ligand. Starting from those approximate transition state geometries, both stationary points were then fully optimized<sup>32,33</sup> as transition states. Finally, the reactants,  $[\text{Mo}(\text{OR})(\text{S}_2\text{C}_2\text{H}_2)_2]^-$  and DMSO, as well as the products,  $[\text{Mo}(\text{OR})\text{O}(\text{S}_2\text{C}_2\text{Me}_2)_2]^-$  and DMS, were optimized separately. Subsequent gas-phase harmonic frequency analysis calculations were conducted to ensure that all optimized structures represented either true minima or transition states. The reported enthalpies and free energies were computed using the entropy and internal energy values calculated via standard statistical mechanics.

## Results and discussion

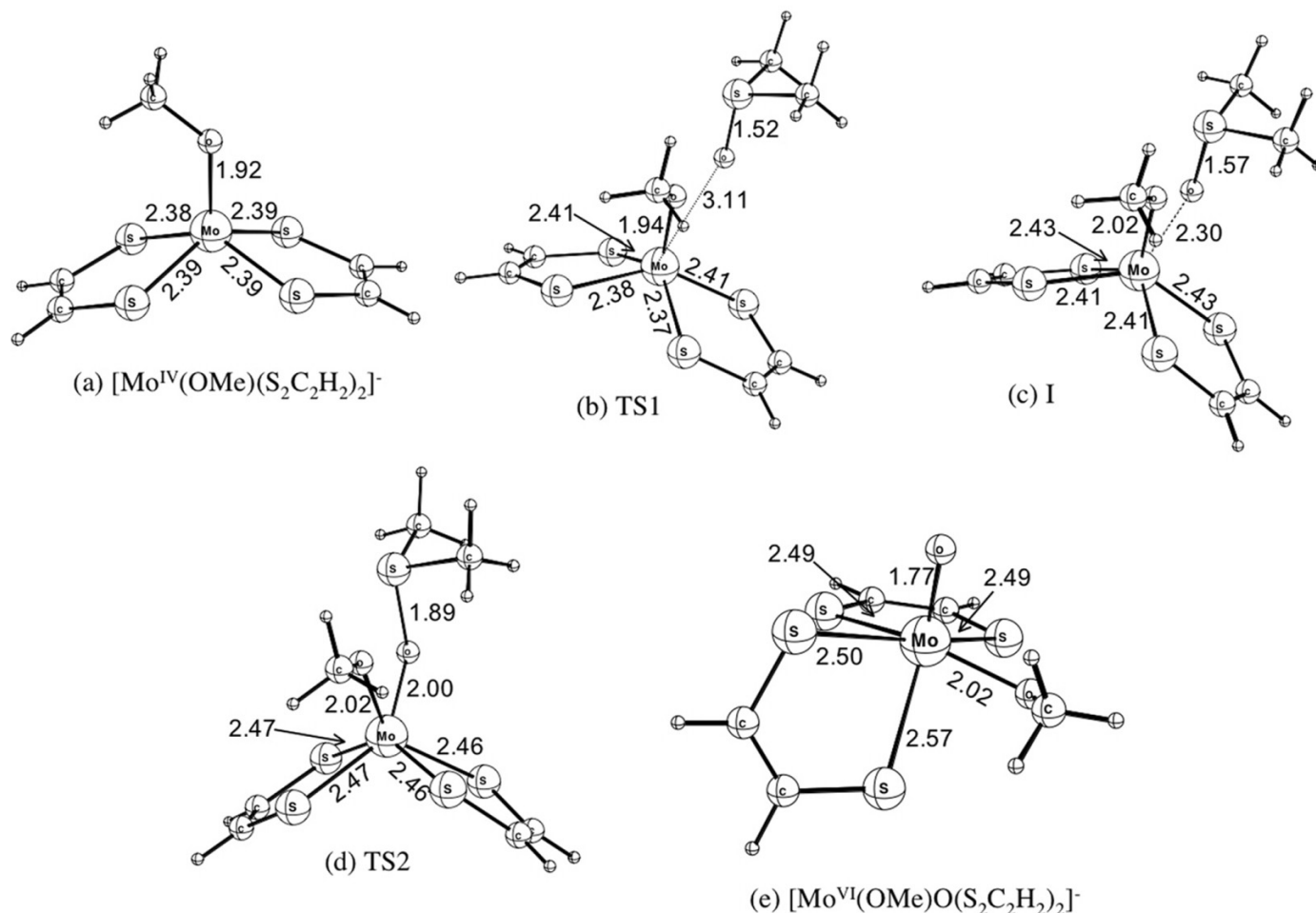
### Theoretical modeling of synthetic analogues

Holm and co-workers<sup>15–18</sup> have prepared molybdenum and tungsten functional analogues of the DMSOR active site. One of those analogues is structurally similar to the enzymatic metal center:  $[\text{M}(\text{OPh})(\text{S}_2\text{C}_2\text{Me}_2)_2]^-$  ( $\text{M} = \text{Mo}, \text{W}$ ).<sup>17</sup> The crystallographic structure of the desoxo complex had a square-pyramidal geometry but despite considerable efforts, Holm and co-workers<sup>17</sup> were not able to isolate the oxidized  $[\text{Mo}^{\text{VI}}]$  complex, in contrast to the tungsten oxo complex  $[\text{W}(\text{OPh})\text{O}(\text{S}_2\text{C}_2\text{Me}_2)_2]^-$  that was analyzed via X-ray crystallography. However, the in situ formation of  $[\text{Mo}(\text{OPh})\text{O}(\text{S}_2\text{C}_2\text{Me}_2)_2]^-$  was established by comparing spectroscopic properties of the reaction mixture with the absorption spectrum of the tungsten complex.

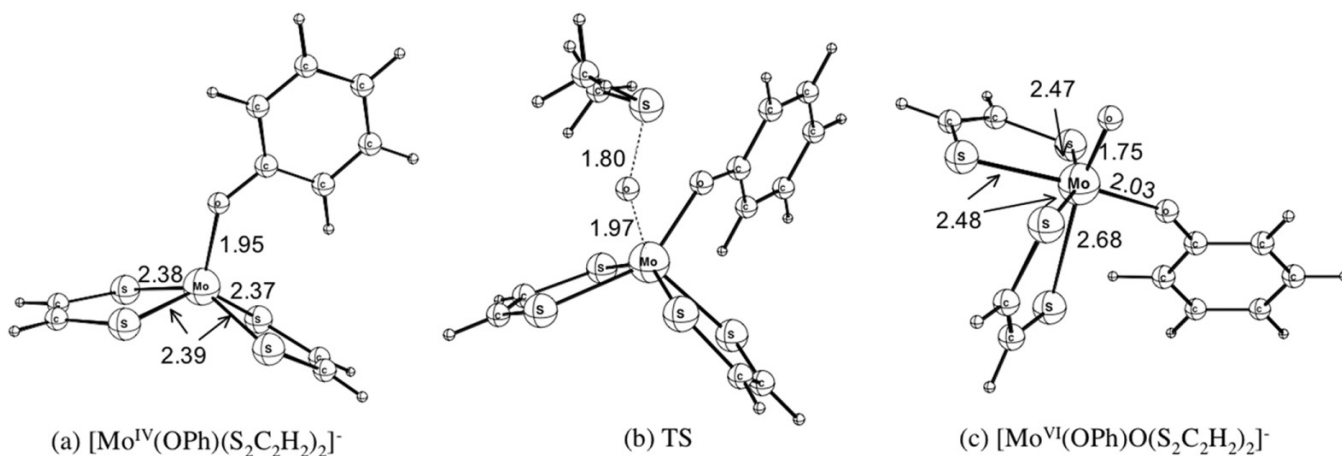
We have optimized the geometry of  $[\text{Mo}(\text{OR})(\text{S}_2\text{C}_2\text{Me}_2)_2]^-$  for  $\text{R} = \text{Me}$  used in previous theoretical studies to model DMSOR and for  $\text{R} = \text{Ph}$  used in the synthetic DMSOR analogue by Holm and co-workers.<sup>17</sup> Figure 1a shows the optimized geometry of  $[\text{Mo}(\text{OMe})(\text{S}_2\text{C}_2\text{Me}_2)_2]^-$ , whereas that of  $[\text{Mo}(\text{OPh})(\text{S}_2\text{C}_2\text{Me}_2)_2]^-$  is displayed in Fig. 2a. The optimized models have a square-pyramidal geometry, and the S–Mo and Mo–O bond distances are 2.39 Å and 1.92 Å, respectively, for  $\text{R} = \text{Me}$  and 2.38 Å and 1.96 Å, respectively, for  $\text{R} = \text{Ph}$ . Figures 1 and 2 reveal that the structural parameters of the optimized complexes for  $\text{R} = \text{Me}$  and  $\text{Ph}$  are in good agreement with those of the synthetic analogue given in Table 1.

We shall now discuss our calculated energy profiles for the OAT reaction starting with  $\text{R} = \text{Me}$ . According to the oxo transfer hypothesis,<sup>8</sup> the substrate (DMSO in our case), will approach cis to the  $\text{Mo}^{\text{IV}}(\text{OMe})$  group. This way of attack is adopted in our calculations. We find one transition state, TS1, for the formation of an intermediate I. The optimized structure of TS1, Fig. 1b, indicates a weak interaction

**Fig. 1.** Optimized geometries for the reaction between  $[\text{Mo}(\text{OMe})(\text{S}_2\text{C}_2\text{H}_2)_2]^-$  and DMSO. (a)  $\text{Mo}^{\text{IV}}$  complex. (b) First transition state. (c) Intermediate. (d) Second transition state (oxygen transfer). (e)  $\text{Mo}^{\text{VI}}$  complex.



**Fig. 2.** Optimized geometries for the reaction between  $[\text{Mo}(\text{OPh})(\text{S}_2\text{C}_2\text{H}_2)_2]^-$  and DMSO. (a)  $\text{Mo}^{\text{IV}}$  complex. (b) Oxygen transfer transition state. (c)  $\text{Mo}^{\text{VI}}$  complex.



between DMSO and the metal. The  $\text{Mo}-\text{O}_{\text{DMSO}}$  distance is 3.11 Å, while the  $\text{Mo}-\text{S}_{\text{dith}}$  distances remain the same (compared with the  $\text{Mo}^{\text{IV}}$  complex).

The intermediate I, Fig. 1c, now shows the DMSO bound to the metal. The  $\text{Mo}-\text{O}_{\text{DMSO}}$  distance has decreased to

2.30 Å and the  $\text{Mo}-\text{S}_{\text{dith}}$  distances start to slightly increase. Additionally, the distance between the sulfur and the oxygen in DMSO increases to 1.57 Å compared with 1.53 Å in free DMSO. The intermediate I features a six-coordinated metal center with a trigonal prismatic geometry. Our geometric pa-

**Table 1.** Selected bond distances (Å) for DMSO reductase, a synthetic analogue, and optimized model structures.

	Complex	Mo—S (mean)	Mo—O	Mo=O	Reference
Synthetic analogue DMSOR	[Mo(OPh)(S <sub>2</sub> C <sub>2</sub> Me <sub>2</sub> ) <sub>2</sub> ] <sup>−</sup>	2.32	1.90	NA	17
	Reduced DMSOR (EXAFS)	2.33	2.16 <sup>a</sup> 1.92 <sup>b</sup>	NA	12
Optimized models	Oxidized DMSOR (EXAFS)	2.44	1.92	1.68	12
	Oxidized DMSOR (X-ray)	2.43	1.84	1.76	9
	[Mo <sup>IV</sup> (OMe)(S <sub>2</sub> C <sub>2</sub> H <sub>2</sub> ) <sub>2</sub> ] <sup>−</sup>	2.39	1.92	NA	This work
	[Mo <sup>IV</sup> (OPh)(S <sub>2</sub> C <sub>2</sub> H <sub>2</sub> ) <sub>2</sub> ] <sup>−</sup>	2.38	1.95	NA	This work
	[Mo <sup>IV</sup> (OMe)OH(S <sub>2</sub> C <sub>2</sub> H <sub>2</sub> ) <sub>2</sub> ] <sup>2−</sup>	2.44	2.10 <sup>c</sup> 2.08 <sup>d</sup>	NA	This work
	[Mo <sup>IV</sup> (OMe)(H <sub>2</sub> O)(S <sub>2</sub> C <sub>2</sub> H <sub>2</sub> ) <sub>2</sub> ] <sup>−</sup>	2.41	2.05 <sup>c</sup> 2.41 <sup>d</sup>	NA	This work
	[Mo <sup>VI</sup> (OMe)O(S <sub>2</sub> C <sub>2</sub> H <sub>2</sub> ) <sub>2</sub> ] <sup>−</sup>	2.49 <sup>e</sup> 2.57 <sup>f</sup>	2.02	1.77	This work
	[Mo <sup>VI</sup> (OPh)O(S <sub>2</sub> C <sub>2</sub> H <sub>2</sub> ) <sub>2</sub> ] <sup>−</sup>	2.48 <sup>e</sup> 2.68 <sup>f</sup>	2.03	1.75	This work

**Note:** NA: Not applicable.<sup>a</sup>Assigned to a Mo—O<sub>ser</sub> bond.<sup>b</sup>Assigned to a Mo—OH bond.<sup>c</sup>From the Mo—OMe bond.<sup>d</sup>From the Mo—OH (OH<sub>2</sub>) bond.<sup>e</sup>Mean value from three Mo—S bonds.<sup>f</sup>Mo—S trans to the Mo=O bond. See Fig. 1d.**Table 2.** Calculated distances of the different species along the energy profile of the OAT process from previous and present studies.

Complex	Mo—S	Mo—O	Mo=O	Mo—O <sub>DMSO</sub>	(S—O) <sub>DMSO</sub>	Reference
[Mo(OMe)(S <sub>2</sub> C <sub>2</sub> Me <sub>2</sub> ) <sub>2</sub> ] <sup>−</sup>	2.38	2.37	NA	NA	NA	19
Int	—	—	NA	2.27	1.56	19
TS2	—	—	NA	1.93	1.88	19
[Mo(OMe)O(S <sub>2</sub> C <sub>2</sub> Me <sub>2</sub> ) <sub>2</sub> ] <sup>−</sup>	—	—	1.72	NA	NA	19
[Mo(OMe)(S <sub>2</sub> C <sub>2</sub> (CN) <sub>2</sub> ) <sub>2</sub> ] <sup>−</sup>	2.32	1.85	NA	NA	NA	20
TS1	2.33	1.87	NA	2.99	1.53	20
Int	2.35	1.98	NA	2.17	1.57	20
TS2	2.40	2.03	NA	1.85	1.99	20
[Mo(OMe)O(S <sub>2</sub> C <sub>2</sub> (CN) <sub>2</sub> ) <sub>2</sub> ] <sup>−</sup>	2.42	1.92	1.74	NA	NA	20
	2.54					20
[Mo(OMe)(S <sub>2</sub> C <sub>2</sub> H <sub>2</sub> ) <sub>2</sub> ] <sup>−</sup>	2.39	1.89	NA	NA	NA	21
TS1	2.40	1.95	NA	2.81	1.52	21
Int	2.42	2.26	NA	2.27	1.65	21
TS2	2.46	2.01	NA	1.93	1.85	21
[Mo(OMe)O(S <sub>2</sub> C <sub>2</sub> H <sub>2</sub> ) <sub>2</sub> ] <sup>−</sup>	2.47	1.95	1.72	NA	NA	21
	2.66					21
[Mo(OMe)(S <sub>2</sub> C <sub>2</sub> H <sub>2</sub> ) <sub>2</sub> ] <sup>−</sup>	2.39	1.92	NA	NA	—	This work
TS1	2.39	1.94	NA	3.11	1.52	This work
Int	2.42	2.02	NA	2.30	1.57	This work
TS2	2.47	2.03	NA	1.96	1.89	This work
[Mo(OMe)O(S <sub>2</sub> C <sub>2</sub> H <sub>2</sub> ) <sub>2</sub> ] <sup>−</sup>	2.49	2.02	1.77	NA	—	This work
	2.57					This work

**Note:** All values in Å. NA: Not applicable.

rameters of the transition state TS1 are similar to those found in other theoretical studies,<sup>19–21</sup> as can be seen from Table 2.

After the formation of the intermediate I, a second transition state, TS2, that maintains a trigonal prismatic geometry,

Fig. 1d, is found. In this species, the oxygen atom has been almost transferred to the molybdenum center. The bond between oxygen and sulfur in DMSO is almost broken (1.89 Å) while the Mo—O<sub>DMSO</sub> distance has decreased to 2.00 Å. The relatively long Mo—O<sub>DMSO</sub> distance might indi-



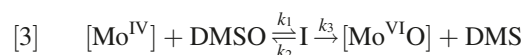
cate that molybdenum is still in the reduced state because the EXAFS (extended X-ray absorption fine structure) and X-ray data show that the typical Mo<sup>VI</sup>–O bond distance is in the range between 1.68 and 1.76 Å.<sup>9,12</sup> The Mo–S bond distance increases to 2.47 Å.

Finally, Fig. 1e displays the six-coordinated optimized structure of the oxidized [Mo(OMe)O(S<sub>2</sub>C<sub>2</sub>H<sub>2</sub>)<sub>2</sub>]<sup>–</sup> complex that has adopted a distorted octahedral geometry. The Mo–S distance of the sulfur trans to the Mo=O bond is 2.57 Å while the other Mo–S bonds are around 2.50 Å and thus much shorter. The longer Mo–S distance is in agreement with an expected value of 2.6 Å attributable to the trans effect due to Mo=O.<sup>34</sup> As it was mentioned earlier, crystallographic data are not available for the oxidized molybdenum complex but its formation was well-established by spectroscopic comparison with [W(OPh)O(S<sub>2</sub>C<sub>2</sub>Me<sub>2</sub>)<sub>2</sub>]<sup>–</sup> for which X-ray data are available. The tungsten complex had a distorted octahedral geometry and the trans effect from W=O was also present. In the tungsten complex, the average W–S bond distance of the sulfur atoms not trans to the oxo ligand was 2.42 Å, whereas the W–S distance of the sulfur trans to W=O was 2.49 Å.<sup>17</sup>

### Comparison between experimental and theoretical kinetic parameters for OAT carried out by synthetic analogues

The calculated energy profile for the overall reaction of DMSO with [Mo(OMe)(S<sub>2</sub>C<sub>2</sub>H<sub>2</sub>)<sub>2</sub>]<sup>–</sup> is shown in Fig. 3. We find that the formation of the intermediate I proceeds with an activation enthalpy of 9 kcal/mol. The formation of the intermediate is an endothermic process with  $\Delta H = 8.1$  kcal/mol and the OAT reaction,  $I \rightarrow \text{Mo}^{\text{VI}} + \text{DMS}$ , has an activation enthalpy of 8.5 kcal/mol. Further, the overall enthalpy of reaction from separated reactants to separated products is exothermic with  $\Delta H = -13$  kcal/mol. These results are consistent with those of previous theoretical calculations<sup>19–21</sup> summarized in Table 3.

Our mechanism for the OAT reaction can be written as



By making use of the steady state condition for the intermediate I the rate law for the consumption of [Mo<sup>IV</sup>] is

$$[4] \quad -\frac{d[\text{Mo}^{\text{IV}}]}{dt} = \left( \frac{k_1 k_3}{k_2 + k_3} \right) [\text{Mo}^{\text{IV}}][\text{DMSO}] = k[\text{Mo}^{\text{IV}}][\text{DMSO}]$$

where the overall rate constant  $k$  is

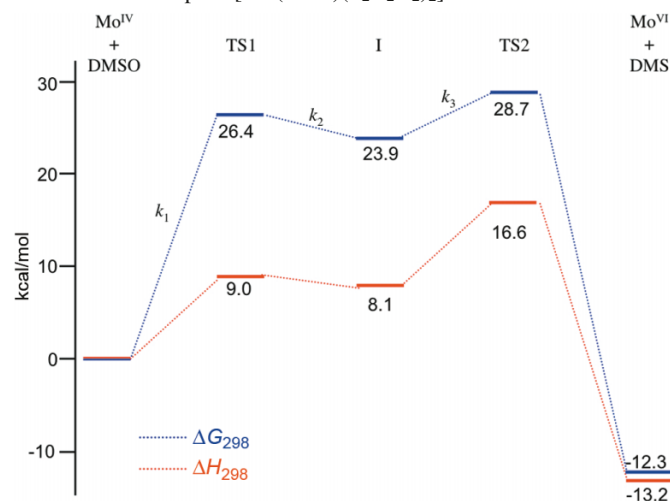
$$[5] \quad k = \frac{k_1 k_3}{k_2 + k_3}$$

It is possible to determine the rate constants  $k_1$ ,  $k_2$ , and  $k_3$  by using the calculated thermodynamic data and the transition state theory as

$$[6] \quad k = \frac{k_B T}{h} \exp \left( \frac{-\Delta G^\ddagger}{RT} \right)$$

where  $k_B$ ,  $h$ , and  $R$  are the Boltzmann, Planck, and gas con-

**Fig. 3.** Energy profile for the oxygen atom transfer reaction between model complex [Mo(OMe)(S<sub>2</sub>C<sub>2</sub>H<sub>2</sub>)<sub>2</sub>]<sup>–</sup> and DMSO.



stants, respectively;  $T$  is the temperature and  $\Delta G^\ddagger$  corresponds to the free energy of activation. The results are summarized in Table 4. The overall rate constant,  $k$ , is easily found by substituting the calculated values of  $k_i$  into eq. [5]. Once  $k$  is calculated, the overall free energy of activation as well as  $\Delta S^\ddagger$  can be determined. For  $R = \text{Me}$ ,  $\Delta G^\ddagger = 28.7$  kcal/mol, which is the highest point on the energy surface and represents the oxygen transfer transition state, TS2, of Fig. 3. TS1 is only 2.3 kcal/mol lower in free energy than TS2, but on the potential energy surface TS2 is 7.6 kcal/mol higher in energy than TS1.

The data in Table 5 show that our calculated kinetic parameters for the model system, [Mo(OR)(S<sub>2</sub>C<sub>2</sub>H<sub>2</sub>)<sub>2</sub>]<sup>–</sup>, with  $R = \text{Me}$  are in good agreement with those measured for the synthetic analogue, [M(OPh)(S<sub>2</sub>C<sub>2</sub>H<sub>2</sub>)<sub>2</sub>]<sup>–</sup>. The overall enthalpy of activation is 16.6 kcal/mol and the overall entropy of activation is calculated to be  $-40$  eu; the corresponding experimental values are 14.8 kcal/mol and  $-36$  eu, respectively.

It follows from Fig. 3 and Table 4 that the internal barriers of intermediate formation ( $\Delta H_1^\ddagger$ ) and oxygen transfer ( $\Delta H_3^\ddagger$ ) differ by only 0.5 kcal/mol. However, the difference between the two internal barriers on the free energy surface is substantial. Thus,  $\Delta G_1^\ddagger = 26.4$  and  $\Delta G_3^\ddagger = 4.8$  kcal/mol. As a consequence, the formation of the intermediate I has a much smaller rate constant,  $k_1$ , than the oxygen transfer step ( $k_3$ ), see Table 4. This finding is in line with the conclusions by Sung and Holm,<sup>18</sup> based on a series of synthetic analogues of the form [W(OR')(S<sub>2</sub>C<sub>2</sub>R<sub>2</sub>)<sub>2</sub>]<sup>–</sup> where  $R' = p\text{-C}_6\text{H}_4\text{X}'$  and  $R = p\text{-C}_6\text{H}_4\text{X}$ , and the substituents  $X$  and  $X'$  were electron-donating groups (EDG) or electron-withdrawing groups (EWG). Sung and Holm<sup>18</sup> found that the rate constants exhibited the order  $k_{\text{EWG}} > k_{\text{EDG}}$  and their measurement of reversible redox potentials showed that EWGs increased the oxidation potentials ( $E_{\text{EWG}} > E_{\text{EDG}}$ ) i.e., it is easier to oxidize a complex coordinated by EDGs. Further, Sung and Holm<sup>18</sup> considered that the relationship in the oxidation potentials may be extended to the intrinsic ease of oxidation of the metal center in the transition state such as, in principle, the rate constant for a complex with EDG substituents should be larger than for a complex with EWGs.

**Table 3.** Calculated energies of the oxygen atom transfer reaction from the present study and previous computational studies.

XC functional	$E_I$	$\Delta E_{\text{reactants} - I}$	$\Delta E_{\text{TS1} - I}$	$\Delta E_{\text{TS2} - I}$	$\Delta E_{\text{rxn}}^a$	Reference
B3LYP	0 <sup>b</sup> (1.0) <sup>c</sup>	NA	NA	8.9 (7.9)	-19.9 (-11.9)	20
BP86	0 (9.3) <sup>d</sup>	-10.5 <sup>b</sup>	7.4	15.1 (2.2)	-1.2	21
	0	-9.6 <sup>e</sup>	5.7	13.9	-12.0	21
B3LYP	0	-11.1 <sup>b</sup>	1.2	8.2	-23.1	22
BP86	0	-10.0 <sup>b</sup>	3.0	6.9	-17.6	This work
	0	-8.2 <sup>f</sup>	2.8	8.7	-12.8	This work

**Note:** Energies in kcal/mol, relative to the intermediate complex with bound DMSO. NA: Not applicable.

<sup>a</sup>The difference between separated reactants and separated products.

<sup>b</sup>Gas phase values.

<sup>c</sup>In parenthesis, results from a recalculation considering complexes with the sulfur ligands constrained to have the same orientation as in the transition state (TS2).

<sup>d</sup>In parenthesis, results from calculations considering a complex with bound DMSO, where the DMSO was rotated to be in line with the orientation of the substrate in the X-ray structure of the enzyme in ref. 31.

<sup>e</sup>Values calculated with COSMO model and  $\epsilon = 1$ .

<sup>f</sup>Values calculated with COSMO model and  $\epsilon = 5$ .

**Table 4.** Calculated kinetic parameters for the oxo transfer reaction of the model complex  $[\text{Mo}(\text{OR})(\text{S}_2\text{C}_2\text{H}_2)_2]^-$  with DMSO.

R	Reaction <sup>a</sup>	$\Delta H^\ddagger$	$T\Delta S^\ddagger$ (kcal/mol)	$\Delta G^\ddagger$	$k^b$ (s <sup>-1</sup> )
Me	(1) $[\text{Mo}^{\text{IV}}] + \text{DMSO} \rightarrow \text{I}$	9.0	-17.4	26.4	$2.71 \times 10^{-7}$ <sup>c</sup>
	(2) $\text{I} \rightarrow [\text{Mo}^{\text{IV}}] + \text{DMSO}$	0.9	-1.6	2.5	$9.11 \times 10^{10}$ <sup>d</sup>
	(3) $\text{I} \rightarrow [\text{Mo}^{\text{VI}}] + \text{DMS}$	8.5	3.7	4.8	$1.82 \times 10^9$ <sup>e</sup>
Ph	$[\text{Mo}^{\text{IV}}] + \text{DMSO} \rightarrow [\text{Mo}^{\text{VI}}] + \text{DMS}$	15.5	-10.6	26.1	$3.80 \times 10^{-7}$

<sup>a</sup>The numbers 1, 2, 3 refer to the reaction depicted in Fig. 3.

<sup>b</sup> $T = 298$  K.

<sup>c</sup>Rate constant  $k_1$  of Fig. 3.

<sup>d</sup>Rate constant  $k_2$  of Fig. 3.

<sup>e</sup>Rate constant  $k_3$  of Fig. 3.

**Table 5.** Calculated and experimental kinetic parameters (at  $T = 298$  K) for the oxo transfer reaction between the  $\text{Mo}^{\text{IV}}$  complex (or actual enzyme) and DMSO.

	Complex	Process	$k^a$ ((mol/L) <sup>-1</sup> s <sup>-1</sup> )	$\Delta H^\ddagger$ (kcal/mol)	$\Delta S^\ddagger$ (eu)
Calculated <sup>b</sup>	$[\text{Mo}(\text{OMe})(\text{S}_2\text{C}_2\text{H}_2)_2]^-$	$[\text{Mo}^{\text{IV}}] + \text{DMSO} \rightarrow [\text{Mo}^{\text{VI}}] + \text{DMS}$	$5.3 \times 10^{-9}$ , <sup>c</sup>	16.6	-41
Calculated <sup>b</sup>	$[\text{Mo}(\text{OPh})(\text{S}_2\text{C}_2\text{H}_2)_2]^-$	$[\text{Mo}^{\text{IV}}] + \text{DMSO} \rightarrow [\text{Mo}^{\text{VI}}] + \text{DMS}$	$3.8 \times 10^{-7}$	15.5	-35
Experimental <sup>d</sup>	$[\text{Mo}(\text{OPh})(\text{S}_2\text{C}_2\text{Me}_2)_2]^-$	$[\text{Mo}^{\text{IV}}] + \text{DMSO} \rightarrow [\text{Mo}^{\text{VI}}] + \text{DMS}$	$1.3 \times 10^{-6}$	14.8	-36
Experimental <sup>e</sup>	Enzyme	$\text{E} + \text{DMSO} \rightleftharpoons \text{M}^f$	$\Delta G_F = -4.9^g$	ND	ND
		$\text{M} \rightarrow \text{ES}$	1000 <sup>h</sup>	ND	ND
		$\text{ES} \rightarrow \text{E}' + \text{DMS}$	38	15.6 <sup>i</sup>	6.3 <sup>i</sup>

**Note:** ND: Not determined.

<sup>a</sup>At  $T = 298$  K.

<sup>b</sup>This work.

<sup>c</sup>This value of  $k$  was calculated with eq. [5].

<sup>d</sup>Reference 10.

<sup>e</sup>Reference 22.

<sup>f</sup>See eq. [7].

<sup>g</sup>The experimental data available was the dissociation constant  $K_D = 155$   $\mu\text{mol/L}$ ; therefore, the listed value of  $\Delta G$  corresponds to the free energy of formation of the M species.

<sup>h</sup> $T = 278$  K.

<sup>i</sup>Experimental values from the Arrhenius plot.

Following that consideration, they proposed that the lack of correlation between the ease of oxidation and the rate constants indicated that the oxidation of the metal center associated with the oxygen atom transfer was not the rate-determining step.<sup>18</sup> Previous theoretical studies reported only barriers on the potential energy surface<sup>19–21</sup> where the oxygen transfer and not the formation of the intermediate

had the highest internal activation barrier. This has lead to an apparent contradiction between the theoretical calculations and the experimental conclusions. It is not surprising that the formation of the intermediate I has a large negative activation entropy since this step is an associative process.

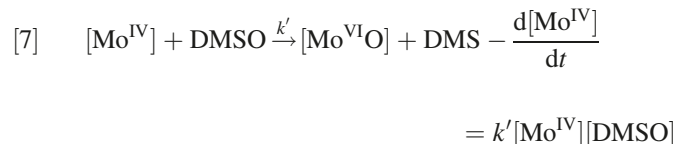
We have also examined the complex  $[\text{Mo}(\text{OR})(\text{S}_2\text{C}_2\text{H}_2)_2]^-$  with  $\text{R} = \text{Ph}$ , which keeps a close resemblance to one of the

synthetic analogues studied by Holm and co-workers.<sup>17</sup> As for the model system with R = Me, we adopted the same approach with DMSO toward the metal center. In contrast to R = Me, we find only one transition state (TS). This transition state has a trigonal prismatic geometry, Fig. 2b, where the bond between the metal and the oxygen from DMSO is forming with a Mo–O distance of 1.97 Å, while a S–O distance of 1.80 Å indicates the weakening of the S–O bond. The six-coordinated oxidized product,  $[\text{Mo}(\text{OPh})\text{O}(\text{S}_2\text{C}_2\text{H}_2)_2]^-$ , Fig. 2c, has a distorted octahedral geometry where the trans effect from Mo=O is evident because the Mo–S distance of the sulfur trans to the O ligand is 2.68 Å, while the remaining Mo–S bonds average a shorter distance of 2.48 Å.

The energy profile in Fig. 4 shows that the OAT reaction for R = Ph takes place in one associative step with an activation enthalpy of 15.5 kcal/mol and a corresponding activation entropy of –35 eu. These parameters are similar to the respective experimental values of  $\Delta H^\ddagger = 14.8$  kcal/mol and  $\Delta S^\ddagger = -36$  eu. The formation of the products, DMS and  $[\text{Mo}(\text{OPh})\text{O}(\text{S}_2\text{C}_2\text{H}_2)_2]^-$ , is exothermic with  $\Delta H = -18.0$  kcal/mol. Experimentally, Sung and Holm<sup>18</sup> found that  $k_{\text{EWG}} > k_{\text{EDG}}$ .

Because the phenoxy ligand may be considered to be slightly more electron-withdrawing than the methoxy ligand, the correlation  $\Delta G_{\text{OPh}}^\ddagger < \Delta G_{\text{OMe}}^\ddagger$  is reasonable. In line with this expectation, the overall activation energy for R = Me (28.7 kcal/mol) is calculated to be slightly larger than for R = Ph (26.1 kcal/mol), making  $k_{\text{OPh}} > k_{\text{OMe}}$ .

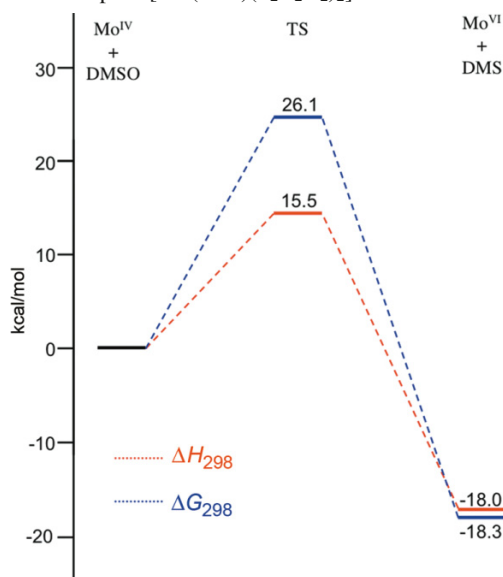
The rate law for the process depicted in Fig. 4 is similar to that of eq. [4]:



The kinetic studies on the OAT reaction of the  $[\text{M}(\text{OPh})(\text{S}_2\text{C}_2\text{Me}_2)_2]^-$  complexes conducted by Holm and co-workers<sup>17</sup> were found to follow the second-order rate law,  $d[\text{Mo}^{\text{IV}}]/dt = -k[\text{Mo}^{\text{IV}}][\text{DMSO}]$ , and the negative entropy of activation is consistent with an associative mechanism.<sup>35</sup>

The agreement between our results and the measured experimental kinetic parameters allows us to propose that the OAT reaction between the synthetic analogue  $[\text{M}(\text{OPh})(\text{S}_2\text{C}_2\text{Me}_2)_2]^-$  and DMSO for R = Ph occurs in a single step where the  $[\text{Mo}^{\text{IV}}]$  species reacts with DMSO associatively to yield the  $[\text{Mo}^{\text{VI}}]$  species and DMS, such as it was found in posterior kinetic studies on the OAT reaction of  $[\text{M}(\text{OPh})(\text{S}_2\text{C}_2\text{Me}_2)_2]^-$  with  $\text{SeO}_4^{2-}$  and  $(\text{CH}_2)_4\text{SO}$  where the presence of an intermediate was not detected.<sup>23</sup> The transition state is predicted to involve a species where a bond between the metal and the oxygen from the substrate is being created while the S–O bond in the substrate weakens. Holm and co-workers<sup>23</sup> hypothesized that the transition state should be mainly metal-substrate bond-making in character. Our calculations indicate that when the reaction proceeds without the formation of an intermediate, the transition state resembles mostly TS2 from the two-step reaction involving R = Me. Further, TS of Fig. 2 exhibits substantial Mo–O bond formation with a bond distance of 1.97 Å as well as a

**Fig. 4.** Energy profile for the oxygen atom transfer reaction between model complex  $[\text{Mo}(\text{OPh})(\text{S}_2\text{C}_2\text{H}_2)_2]^-$  and DMSO.



considerable S–O bond stretching with a S–O distance of 1.80 Å.

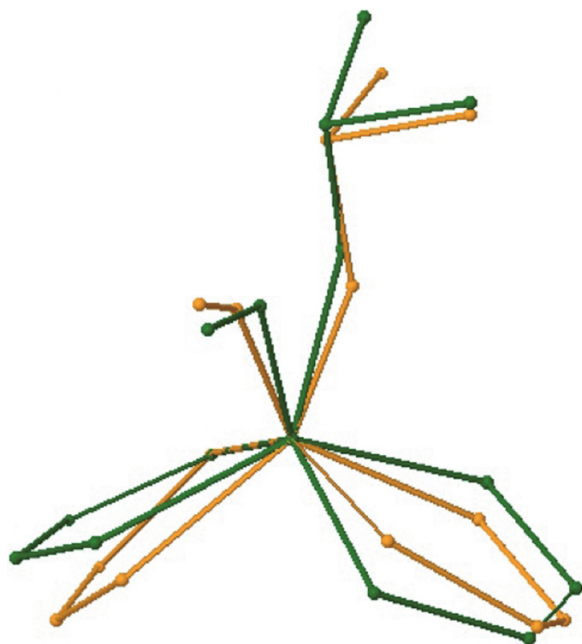
According to the energy profile in Fig. 3, when the axial ligand OR in  $[\text{Mo}(\text{OR})(\text{S}_2\text{C}_2\text{Me}_2)_2]^-$  changes from R = Ph to R = Me, one intermediate is formed. This intermediate, with the substrate bound to the reduced metal, will subsequently decompose to form DMS and the oxidized  $[\text{Mo}^{\text{VI}}]$  species. The isolation of a crystalline structure of the actual enzyme with the bound substrate<sup>31</sup> is a good indication that the OAT reaction in the actual enzyme proceeds via the formation of an intermediate. Figure 5 reveals that the orientation of the coordinated DMSO in our optimized intermediate resembles that found in the actual enzyme, allowing a possible comparison between the results from our investigation and the kinetic studies on the actual enzyme with respect to the OAT reaction, i.e., the  $k_3$  step in eq. [3].

The comparison of our results to other theoretical studies of synthetic analogues is as follows: our calculations, as well as those by Hall and Webster<sup>19</sup> and Hillier and co-workers<sup>21</sup> estimated the energy of activation,  $\Delta E_{\text{TS2} \rightarrow 1}$ , to be approximately 9 kcal/mol. However, Thapper et al.<sup>20</sup> located a more stable intermediate with a different orientation of the DMSO molecule, see Fig. 6. It should be noted that they used the complex  $[\text{Mo}(\text{OMe})(\text{S}_2\text{C}_2(\text{CN})_2)_2]^-$ . In addition, we investigated the possibility of finding a more stable intermediate, I', for  $[\text{Mo}(\text{OMe})(\text{S}_2\text{C}_2\text{H}_2)_2]^-$ , based on the intermediate found by Thapper et al.,<sup>20</sup> but when the CN groups are substituted by H, the new intermediate is only 1 kcal/mol more stable. Furthermore, it seems clear from the X-ray structure of DMSOR with bound DMSO<sup>31</sup> that the alternative orientation of DMSO depicted in Fig. 6b cannot occur in the actual enzyme due to the presence of the Trp 116 indole side chain.

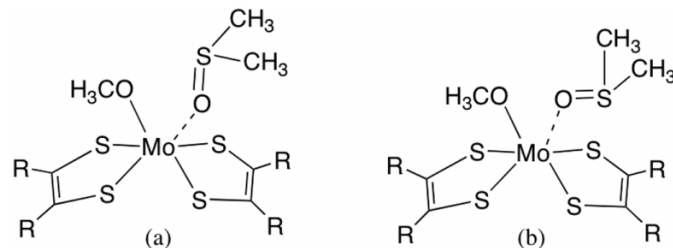
### Kinetics of the OAT process in the actual enzyme

In spite of the functional similarity between synthetic analogues and the enzyme, kinetics studies on enzymes such as DMSOR from *R. sphaeroides*<sup>22</sup> have revealed some mecha-

**Fig. 5.** Superposition of the optimized intermediate I (green) and the structure from crystallographic data<sup>31</sup> of the DMSO-bound DMSOR (yellow). Hydrogens were removed for clarity.



**Fig. 6.** Two possible intermediates for the association of  $[\text{Mo}(\text{O-Me})(\text{S}_2\text{C}_2\text{R}_2)_2]^-$  and DMSO. When  $\text{R} = \text{H}$ , the intermediate (b) is 1 kcal/mol more stable than (a); for  $\text{R} = \text{CN}$  the intermediate to the right is more stable by 9 kcal/mol.<sup>20</sup>



nistic features that are not present in the systems studied by Holm and co-workers.<sup>15–17,23</sup> In the case of the enzyme, the experimental kinetic data were consistent with the fast formation of a prior enzyme-substrate complex (Michaelis complex, M) before the formation of an intermediate enzyme-substrate (ES) complex. This ES complex decays, in the second phase, to yield the reduced substrate (DMS) and the oxidized enzyme,  $\text{E}'$ .<sup>22</sup> Thus, the proposed mechanism for the reduction of DMSO by DMSOR can be described as



This scheme differs from those of the functional analogue of Holm and co-workers<sup>17</sup> and our theoretical model in that the intermediate I (similar to ES) is formed by direct association of DMSO and the molybdenum species. The experimental rate constant for the fast phase (formation of the ES complex) was determined to be  $k'_2 = 1000 \text{ s}^{-1}$ , while the dissociation constant for the pre-equilibrium between M and  $\text{E} + \text{DMSO}$  was  $K_D = 155 \text{ } \mu\text{mol/L}$ . The slow phase (decay of ES) had a rate constant of  $k'_3 = 35 \text{ s}^{-1}$ . From an Arrhenius

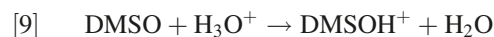
plot of the second phase, it was found that  $\Delta H_3^\ddagger \approx 15 \text{ kcal/mol}$ , and  $\Delta H_3^\ddagger = 6.5 \text{ eu}$ .<sup>22</sup> Results in Table 4 show that our calculated enthalpy of activation of  $\Delta H_3^\ddagger = 8.5 \text{ kcal/mol}$  is rather small when compared with the experimental value for the enzyme of  $\Delta H_3^\ddagger \approx 15 \text{ kcal/mol}$ . We found the activation entropy to be small and positive ( $\Delta S_3^\ddagger = 12.4 \text{ eu}$ ), as it was the case for the enzyme ( $\Delta S_3^\ddagger = 6.5 \text{ eu}$ ).

#### Possible structure of the Michaelis complex (M) involving the reduced $[\text{Mo}^{\text{IV}}]$ species

According to eq. [1], the enzymatic reduction of DMSO involves the transfer of two  $\text{H}^+$  species. In a general reaction mechanism, it has been proposed that the transfer of a  $\text{H}^+$ , the departure of a water molecule, and the addition of the substrate can occur in one step.<sup>36</sup> After the OAT reaction has been completed, the oxidized active site,  $[\text{Mo}^{\text{VI}}\text{O}]$ , is subjected to a one-electron reduction and another  $\text{H}^+$  is transferred to the oxygen atom to form  $[\text{Mo}^{\text{V}}\text{OH}]$ , such species have been detected by EPR spectroscopy.<sup>13</sup> The formation of the Michaelis complex (M) in eq. [8] was deduced experimentally from plots of observed rate constant versus substrate concentration.<sup>22</sup> We have explored the possibility that the formation of such a Michaelis complex (M) may involve some residues that do not belong to the immediate coordination sphere of the metal.

The full X-ray structures of the oxidized and DMSO-bound enzymes overlap almost entirely, except for the residues 385–390. In the case of the DMSO-bound structure, the Trp 388 is sitting above the DMSO molecule around 8.5 Å apart from the metal center. In the oxidized enzyme, the same residues appear oriented toward the surface of the protein and far away (25 Å) from the molybdenum. Based on the coordinates of residues 386–388, plus those of the metal center, Ser 147 and sulfurs from the MPT cofactor, two different models were constructed and optimized. The model in Fig. 7a will be referred to as the “open” structure and was created from the oxidized enzyme (PDB code 1DMR).<sup>10</sup> We have assumed that the orientation of the residues 385–390 in the reduced enzyme should be similar to the open structure. The second model, or “closed” structure, was constructed from the bound DMSO enzyme (PDB code 4DMR).<sup>9</sup>

Further, we propose that the carrier of one of the protons in eq. [1] will be the DMSO molecule<sup>37</sup>:

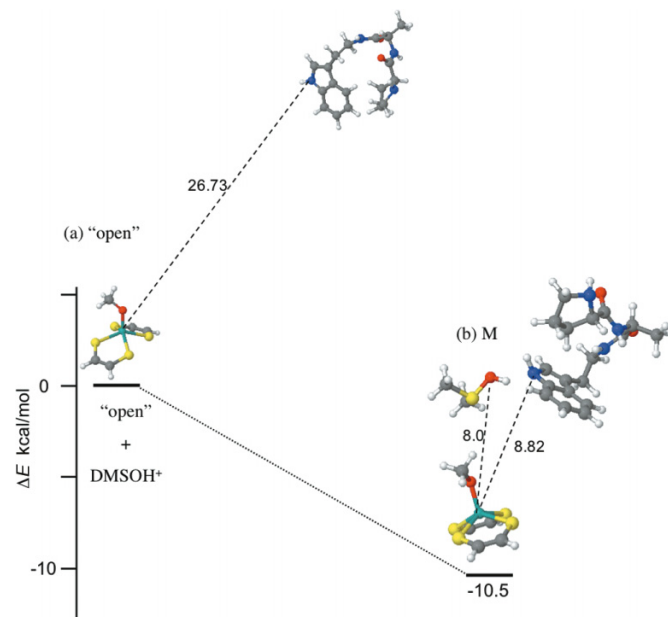


The protonated DMSO will then interact with some residues of the enzyme. It is known that the 780 polypeptide chain of the *Rhodobacter* DMSO reductases is folded to shape an ellipsoidal molecule with a “funnel-like” depression on one side. The funnel is lined by aromatic residues and the molybdenum is located at the bottom of this funnel.<sup>14</sup> On the other hand, it has been established that interactions of DMSO with aromatic and hydrophobic amino acid side chains are favorable;<sup>38</sup> these interactions between the protonated substrate and the residues in the funnel may cause the enzyme to change from the open to the closed conformations.

We have investigated a possible pathway for the formation of the Michaelis complex (M) that involves the loss of



**Fig. 7.** Optimized structures. (a) Molybdenum (IV) in “open” configuration (initial coordinates taken from PDB file code 1DMR). (b) Possible configuration of the Michaelis intermediate (M) formed with the addition of a protonated DMSO molecule to the “closed” configuration (initial coordinates for the closed configuration are from the PDB file code 4DMR). The peptidic chain was constructed using the coordinates of the following residues: Pro 386, Glu 387, and Trp 388.



a water molecule from the metal center prior to the substrate association. This model assumes that the loss of a water molecule is due to the transfer of a proton to the hydroxide ligand in the initial six-coordinated metal center, Fig. 8a, leaving a five-coordinated metal center and the enzyme in the open conformation, Fig. 7a. Subsequently, the  $\text{DMSOH}^+$  species associates to the enzyme inducing a change in conformation and the new structure M, Fig. 7b. The results from the optimizations of both structures indicate that M (closed conformation with the associated protonated substrate) is 10.5 kcal/mol more stable with respect to the separate open structure and  $\text{DMSOH}^+$  as indicated in the potential energy profile in Fig. 7. The dissociation constant for the pre-equilibrium between M and the separate reduced enzyme and DMSO was experimentally found to be  $K_D = 155 \mu\text{mol/L}$  at  $5^\circ\text{C}$  and  $\text{pH} = 6.0$ .<sup>22</sup> Using  $\Delta G^\circ = -RT \ln(1/K_D)$ , the corresponding value of free energy of formation for M is  $\Delta G^\circ = -4.9 \text{ kcal/mol}$ . We calculate  $\Delta E$  for the formation of M to be  $-10.5 \text{ kcal/mol}$  and the corresponding  $\Delta G$  value is likely to be reduced in absolute terms relative to  $\Delta E$  as the entropy change for the association of the substrate with the enzyme is expected to be negative. In the suggested structure of M, the substrate is located 8 Å apart from the active site (Fig. 7b). With such a conformation M would, in the actual enzyme, prepare the substrate for the attack on the active site.

Next, we consider such an attack in a linear transit calculation that involves the model complex  $[\text{Mo}(\text{OMe})(\text{S}_2\text{C}_2\text{H}_2)_2]^-$ , Fig. 1a, and  $\text{DMSOH}^+$  as the separate reactants. Our calculation indicates that the proton migrates from the oxygen of DMSO to a sulfur of one dithiolate ligand prior to the forma-

tion of the intermediate I'. This intermediate (I') would represent ES in the actual enzyme. Figure 9a shows the intermediate I' with the DMSO bound to the metal at a Mo–O distance of 2.24 Å. The S–O bond is 1.59 Å and the H–S distance is 1.37 Å. This S–H bond distance remains constant for the rest of the OAT reaction. One consequence of the migration of the proton to one of the sulfurs is the elongation of the Mo–S bond distance to 2.56 Å, while the other three Mo–S distances stay in the range 2.36–2.41 Å. After the formation of I' (ES), the final oxygen transfer step takes place leading to DMS and the oxidized species. The transition state, TS2', for the last OAT step maintains the trigonal prismatic geometry of the intermediate I', Fig. 9b. In TS2', the O–S bond in DMSO is almost broken (1.86 Å) while the Mo–O<sub>DMSO</sub> distance has decreased to 1.98 Å. The final product, oxidized  $[\text{Mo}(\text{OMe})\text{O}(\text{HS}_2\text{C}_2\text{H}_2)_2]^-$ , adopts a distorted octahedral geometry. The Mo–S distance of the sulfur trans to the Mo=O bond is 2.59 Å. The Mo–S bond distance of the protonated sulfur is 2.66 Å. This distance is rather long compared with the experimental distances in the crystallographic data, Table 1. It might be probable that in the actual enzyme the proton migrates to a different location during the spectroscopic measurements; for example, to the basic residue histidine 649 that lies around 3 Å apart from one of the sulfurs of a molybdopterin cofactor in the X-ray structure. The estimated  $\Delta E$  for such process is around  $-10 \text{ kcal/mol}$ .

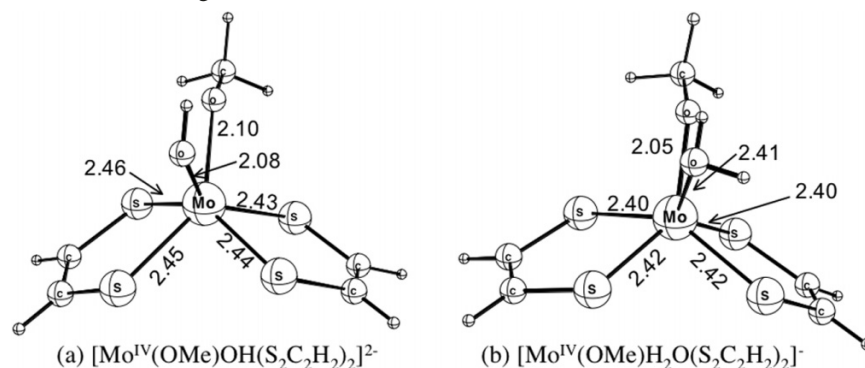
With the exception of the Mo–SH distances, the geometric parameters are very similar to those previously discussed when the substrate was DMSO. The potential energy surface in Fig. 10 shows similar activation energy for the OAT ( $\Delta E^\ddagger = 5.4 \text{ kcal/mol}$ ). Recalling that the experimental value for the enthalpy of activation is 15 kcal/mol, the discrepancy might suggest that the activation energy in the actual enzyme includes not only the interactions at the active site and the first sphere of coordination. Perhaps a change in conformation is also involved alongside the oxygen transfer to the metal. The fact that the enzyme with bound DMSO was crystallized suggests that such intermediate is somehow stable. The optimized intermediate I' is more stable than the separate products, unlike intermediate I in Fig. 3.

## Concluding remarks

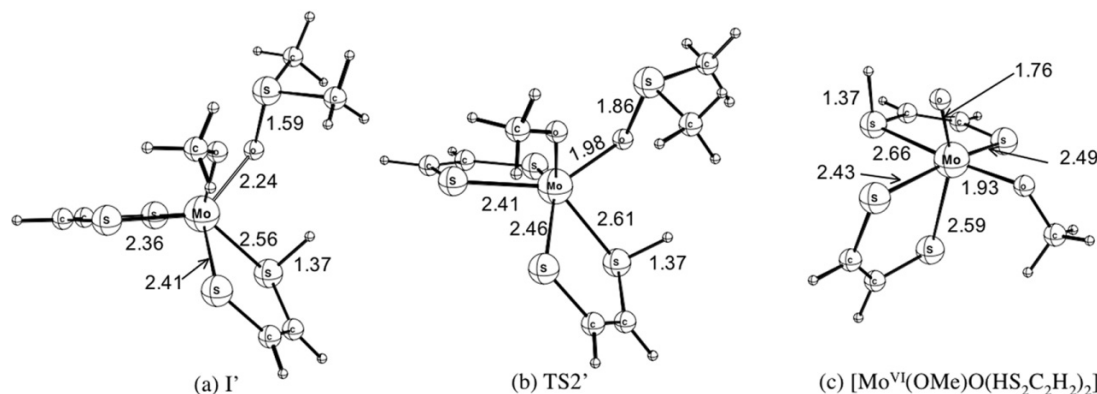
According to our calculations, the reaction between DMSO and the model complex  $[\text{Mo}(\text{OPh})(\text{C}_2\text{S}_2\text{H}_2)_2]^-$  proceeds in one associative step. In the optimized transition state, the bond between the metal and DMSO is being formed through the oxygen atom of DMSO, while the S–O bond in the substrate is weakening. The good agreement between the experimental kinetic data for the functional synthetic analogue,  $[\text{Mo}(\text{OPh})(\text{C}_2\text{S}_2\text{Me}_2)_2]^-$ ,<sup>17</sup> and our calculated free energy surface, seems to indicate that our theoretical method is suitable for the type of OAT process under investigation here.

When the substituent of the axial ligand (–OR) is changed from R = Ph to R = Me (a slightly less electron-withdrawing species, compared with Ph), an intermediate is formed. In this intermediate, the substrate binds the molybdenum prior to the oxygen atom transfer step. We have found that on the Gibbs free energy surface, the rate constant for the formation of the intermediate is smaller than the rate constant of

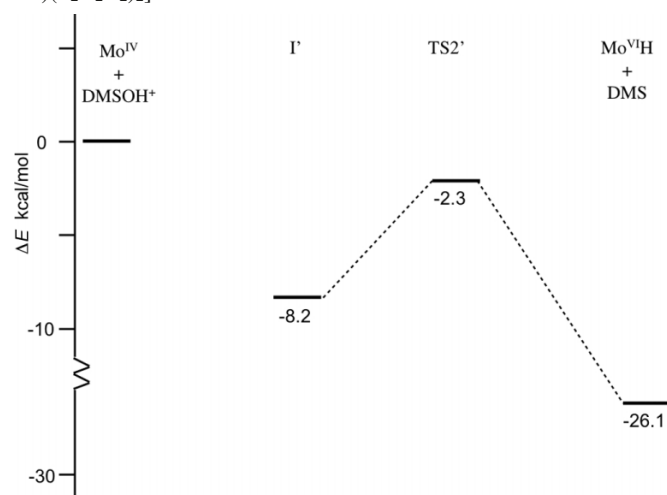
**Fig. 8.** (a) Optimized geometry of a six-coordinated  $\text{Mo}^{\text{IV}}$  complex where  $\text{OH}^-$  is the sixth ligand. (b) Optimized geometry of a six-coordinated  $\text{Mo}^{\text{IV}}$  complex with  $\text{H}_2\text{O}$  as the sixth ligand.



**Fig. 9.** Optimized geometries for the reaction between  $[\text{Mo}(\text{OMe})(\text{S}_2\text{C}_2\text{H}_2)_2]^-$  and  $\text{DMSOH}^+$ . (a) Intermediate  $\text{I}'$ . (b)  $\text{TS2}'$ , transition state for the oxygen transfer step. (c)  $\text{Mo}^{\text{VI}}\text{H}$  complex.



**Fig. 10.** Potential energy surface for the reaction between  $[\text{Mo}(\text{OMe})(\text{S}_2\text{C}_2\text{H}_2)_2]^-$  and  $\text{DMSOH}^+$ .



the final OAT step. This result is in line with the experimental findings by Holm and co-workers.<sup>17,23</sup> The large negative entropic contribution in the associative step (formation of the intermediate) appears to be the key element in the difference between the rate constants. Previous theoretical studies considered only the potential energy surface,<sup>22</sup> leading to an apparent contradiction with the experimental findings.

Although the complexes prepared by Holm and co-

workers<sup>23</sup> are functional analogues to the enzyme, their OAT reaction mechanism is different from the enzymatic one. In the enzymatic mechanism, the formation of a prior enzyme-substrate complex  $\text{M}$  occurs before the appearance of an intermediate  $\text{ES}$  where the substrate is bound to the metal center in the active site.<sup>22</sup> We propose that in the initial conformation of the reduced enzyme, the residues 385–390 are far away from the active site and that one proton might be transferred to the hydroxide ligand in the active site to promote the loss of one water molecule. The subsequent formation of the complex  $\text{M}$  may involve a protonated DMSO molecule positioned around 5 Å from the metal center. The substrate molecule might be carried out to the vicinity of the active site from the surface of the enzyme by a change in conformation involving mainly the residues 385–390. The calculations show that such a complex ( $\text{M}$ ) is more stable than the separate reactants, as it should according to the experimental kinetic studies.<sup>22</sup> Moreover, we propose that before the formation of the intermediate  $\text{ES}$ , the proton from the substrate should migrate to a suitable location in the enzyme. In the case of our model complex, the proton migrated to a sulfur of one of the dithiolate ligands.

## Acknowledgement

All calculations made use of the Western Canada Research Grid computing resources ([www.westgrid.ca](http://www.westgrid.ca)). This work was supported by the Natural Sciences and Engineer-

ing Research Council of Canada (NSERC). T.Z. thanks the Canadian government for a Canada Research Chair.

## References

- (1) Charlson, R. J.; Lovelock, J. E.; Andreae, M. O.; Warren, S. G. *Nature* **1987**, 326 (6114), 655. doi:10.1038/326655a0.
- (2) Lee, P. A.; de Mora, S.; Levasseur, M. *Atmos.-Ocean* **1999**, 37 (4), 439.
- (3) Zinder, S. H.; Brock, T. D. *J. Gen. Microbiol.* **1978**, 335, 655.
- (4) Weiner, J. H.; Rothery, R. A.; Sambasivarao, D.; Trieber, C. A. *Biochim. Biophys. Acta* **1992**, 1102 (1), 1. doi:10.1016/0005-2728(92)90059-B. PMID:1324728.
- (5) Satoh, T.; Kurihara, F. N. *J. Biochem.* **1987**, 102 (1), 191. PMID:2822679.
- (6) McEwan, A. G.; Wetzstein, H. G.; Ferguson, S. J.; Jackson, J. B. *Biochim. Biophys. Acta* **1985**, 806 (3), 410. doi:10.1016/0005-2728(85)90248-8.
- (7) Hille, R. *Chem. Rev.* **1996**, 96 (7), 2757. doi:10.1021/cr950061t. PMID:11848841.
- (8) Schultz, B. E.; Hille, R.; Holm, R. H. *J. Am. Chem. Soc.* **1995**, 117 (2), 827. doi:10.1021/ja00107a031.
- (9) Li, H.; Temple, C.; Rajagopalan, K.; Schindelin, H. *J. Am. Chem. Soc.* **2000**, 122 (32), 7673. doi:10.1021/ja000643e.
- (10) McAlpine, A.; McEwan, A.; Shaw, A.; Bailey, S. *J. Biol. Inorg. Chem.* **1997**, 2 (6), 690. doi:10.1007/s007750050185.
- (11) George, G. N.; Hilton, J.; Temple, C.; Prince, R.; Rajagopalan, K. *J. Am. Chem. Soc.* **1999**, 121 (6), 1256. doi:10.1021/ja982843k.
- (12) George, G. N.; Hilton, J.; Rajagopalan, K. V. *J. Am. Chem. Soc.* **1996**, 118 (5), 1113. doi:10.1021/ja953317l.
- (13) Raitsimring, A. M.; Astashkin, A. V.; Feng, C.; Enemark, J. H.; Nelson, K. J.; Rajagopalan, K. V. *J. Biol. Inorg. Chem.* **2003**, 8 (1–2), 95. doi:10.1007/s00775-002-0393-8. PMID:12459903.
- (14) Tunney, J. M.; McMaster, J.; Garner, C. D. *Comprehensive Coordination Chemistry II*; McClevery, J. A., Meyer, T. J., Eds.; Elsevier - Pergamon: New York, 2003; Vol. 8, p 459.
- (15) Berg, J.; Holm, R. *J. Am. Chem. Soc.* **1985**, 107 (4), 925. doi:10.1021/ja00290a030.
- (16) Caradonna, J.; Reddy, P.; Holm, R. *J. Am. Chem. Soc.* **1988**, 110 (7), 2139. doi:10.1021/ja00215a022.
- (17) Lim, B. S.; Sung, K.-M.; Holm, R. *J. Am. Chem. Soc.* **2000**, 122 (30), 7410. doi:10.1021/ja001197y.
- (18) Sung, K.-M.; Holm, R. H. *J. Am. Chem. Soc.* **2002**, 124 (16), 4312. doi:10.1021/ja012735p. PMID:11960460.
- (19) Webster, C. E.; Hall, M. B. *J. Am. Chem. Soc.* **2001**, 123 (24), 5820. doi:10.1021/ja0156486. PMID:11403624.
- (20) Thapper, A.; Deeth, R. J.; Nordlander, E. *Inorg. Chem.* **2002**, 41 (25), 6695. doi:10.1021/ic020385h. PMID:12470064.
- (21) McNamara, J. P.; Hillier, I. H.; Bhachu, T. S.; Garner, C. D. *Dalton Trans.* **2005**, (21), 3572. doi:10.1039/b507206a. PMID:16234940.
- (22) Cobb, N.; Conrads, T.; Hille, R. *J. Biol. Chem.* **2005**, 280 (12), 11007. doi:10.1074/jbc.M412050200. PMID:15649898.
- (23) Wang, J.-J.; Tessier, C.; Holm, R. H. *Inorg. Chem.* **2006**, 45, 2970.
- (24) te Velde, G.; Bickelhaupt, F. M.; Baerends, E. J.; Fonseca Guerra, C.; van Gisbergen, S. J. A.; Snijders, J. G.; Ziegler, T. *J. Comput. Chem.* **2001**, 22 (9), 931. doi:10.1002/jcc.1056; Amsterdam density functional (ADF) software. *ADF2006.01*; SCM, Theoretical Chemistry: Vrije Universiteit, Amsterdam, The Netherlands, 2006. Available at <http://www.scm.com>.
- (25) Becke, A. D. *Phys. Rev. A: At. Mol. Opt. Phys.* **1988**, 38 (6), 3098. doi:10.1103/PhysRevA.38.3098.
- (26) Perdew, J. *Phys. Rev. B* **1986**, 33 (12), 8822. doi:10.1103/PhysRevB.33.8822.
- (27) Perdew, J. *Phys. Rev. B* **1986**, 34 (10), 7406. doi:10.1103/PhysRevB.34.7406.
- (28) Klamt, A.; Schüürmann, G. *J. Chem. Soc., Perkin Trans. 2* **1993**, 5, 799. doi:10.1039/p29930000799.
- (29) Blomberg, M. R. A.; Siegbahn, P. *J. Phys. Chem. B* **2001**, 105 (39), 9375. doi:10.1021/jp010305f.
- (30) Lovell, T.; Himo, F.; Han, W.-G.; Noodleman, L. *Coord. Chem. Rev.* **2003**, 238–239, 211. doi:10.1016/S0010-8545(02)00331-4.
- (31) McAlpine, A. S.; McEwan, A. G.; Bailey, S. *J. Mol. Biol.* **1998**, 275 (4), 613. doi:10.1006/jmbi.1997.1513. PMID:9466935.
- (32) Versluis, L.; Ziegler, T. *J. Chem. Phys.* **1988**, 88 (1), 322. doi:10.1063/1.454603.
- (33) Fan, L.; Ziegler, T. *J. Am. Chem. Soc.* **1992**, 114 (27), 10890. doi:10.1021/ja00053a027.
- (34) Das, S. K.; Chaudhury, P. K.; Biswas, D.; Sarkar, S. *J. Am. Chem. Soc.* **1994**, 116 (20), 9061. doi:10.1021/ja00099a024.
- (35) Atwood, J. D. *Inorganic and Organometallic Reaction Mechanisms*, 2nd ed.; VCH: New York, 1997.
- (36) Cobb, N.; Hemann, C.; Polsinelli, G. A.; Ridge, J. P.; McEwan, A. G.; Hille, R. *J. Biol. Chem.* **2007**, 282 (49), 35519. doi:10.1074/jbc.M704458200. PMID:17921142.
- (37) Tureček, F. *J. Phys. Chem. A* **1998**, 102 (24), 4703. doi:10.1021/jp980940u.
- (38) Arakawa, T.; Kita, Y.; Timasheff, S. N. *Biophys. Chem.* **2007**, 131 (1–3), 62. doi:10.1016/j.bpc.2007.09.004. PMID:17904724.

# Do corresponding coupling constants in hydrogen-bonded homo- and hetero-chiral dimers differ?

Janet E. Del Bene, Ibon Alkorta, and José Elguero

**Abstract:** Ab initio equation-of-motion coupled cluster singles and doubles (EOM-CCSD) calculations have been carried out to evaluate spin-spin coupling constants in six pairs of homo- and hetero-chiral dimers: (HOOH)<sub>2</sub>, (H<sub>2</sub>NNH<sub>2</sub>)<sub>2</sub>, (FOOH)<sub>2</sub>, (FHNNH<sub>2</sub>)<sub>2</sub>, (HOOOH)<sub>2</sub>, and (FOOOH)<sub>2</sub>. Corresponding spin-spin coupling constants in these isomeric pairs of C<sub>2</sub> and C<sub>i</sub> symmetry may differ, but these differences are small and may not be detectable experimentally. For the complexes with O1-H...O and O1-H...F hydrogen bonds, <sup>1</sup>J(O1-H) has a larger absolute value in the C<sub>2</sub> isomer. For the same set of complexes, <sup>1</sup>J(O1-O2) has a larger absolute value in the C<sub>i</sub> isomer. No distinguishable patterns could be discerned in the remaining spin-spin coupling constants in the C<sub>2</sub> and C<sub>i</sub> isomers of these complexes, nor in complexes with N-H...N hydrogen bonds.

**Key words:** spin-spin coupling constants, homo- and hetero-chiral dimers, hydrogen bond.

**Résumé :** Des calculs ab initio EOM-CCSD ont été effectués pour évaluer les constantes de couplage spin-spin dans six paires de dimères homo- et heterochiral : (HOOH)<sub>2</sub>, (H<sub>2</sub>NNH<sub>2</sub>)<sub>2</sub>, (FOOH)<sub>2</sub>, (FHNNH<sub>2</sub>)<sub>2</sub>, (HOOOH)<sub>2</sub>, et (FOOOH)<sub>2</sub>. Les correspondantes constantes de couplage spin-spin dans les paires d'isomères sont, en général, différentes mais les différences sont faibles au point, pour certaines d'entre elles, de ne pas pouvoir être détectées expérimentalement. Pour les complexes avec des liaisons hydrogène O-H...O et O-H...F, <sup>1</sup>J(O1-H) a une plus large valeur absolue dans l'isomère C<sub>2</sub>. Pour le même ensemble des complexes, <sup>1</sup>J(O1-O2) a une plus large valeur absolue dans l'isomère C<sub>i</sub>. On ne trouve pas des règles générales pour les restantes constantes de couplage spin-spin dans les isomères C<sub>2</sub> et C<sub>i</sub> de ces complexes et non plus dans les complexes avec des liaisons hydrogène N-H...N.

**Mots-clés :** constantes de couplage spin-spin, homo- et hetero-chiral dimères, liaisons hydrogène.

## Introduction

Chiral distinction or "chiral recognition" has been a topic of interest to both theorists and experimentalists. In the past, we have devoted several papers to the topic of chiral distinction in which we focused primarily on energy differences between enantiomers.<sup>1</sup> Experimental NMR studies of nuclear shielding have been reported and used to characterize and analyze chiral discrimination in complexes formed by a molecule of known chirality and a mixture of enantiomeric compounds.<sup>2-4</sup> In the present paper, we ask for the first time whether or not corresponding spin-spin coupling constants for hydrogen-bonded hetero- and homo-chiral dimers differ, and if so, do patterns exist that would distinguish one isomer from the other as a tool for chiral distinction.<sup>5,6</sup> To answer this question, we have carried out ab initio equation-of-motion coupled cluster singles and doubles (EOM-CCSD) calculations to evaluate spin-spin coupling constants for the C<sub>2</sub> (homochiral; optically active) and C<sub>i</sub>

(heterochiral; optically inactive) isomers of six hydrogen-bonded dimers: (HOOH)<sub>2</sub>, (H<sub>2</sub>NNH<sub>2</sub>)<sub>2</sub>, (FOOH)<sub>2</sub>, (FHNNH<sub>2</sub>)<sub>2</sub>, (HOOOH)<sub>2</sub>, and (FOOOH)<sub>2</sub>. In this paper, we present the results of these calculations, and our conclusions about relationships between corresponding spin-spin coupling constants in the isomeric pairs.

## Methods

The structures of the monomers and complexes were optimized at second-order Møller-Plesset perturbation theory (MP2)<sup>7-10</sup> with the 6-311++G(d,p) basis set.<sup>11-13</sup> Frequencies were computed to insure that each isomer corresponds to a local minimum on its potential surface. The geometries of some of the systems have been reported by us in a previous article.<sup>14</sup> Coupling constants were evaluated using the equation-of-motion coupled cluster singles and doubles (EOM-CCSD) method in the CI (configuration interaction)-like approximation<sup>15,16</sup> with all electrons correlated. For these

Received 1 October 2009. Accepted 30 November 2009. Published on the NRC Research Press Web site at canjchem.nrc.ca on 12 March 2010.

*This article is part of a Special Issue dedicated to Professor R. J. Boyd. This paper is dedicated to our friend and colleague Russell Boyd.*

**J.E. Del Bene.**<sup>1</sup> Department of Chemistry, Youngstown State University, Youngstown, Ohio 44555, USA.

**I. Alkorta and J. Elguero.** Instituto de Química Médica, CSIC (Consejo Superior de Investigaciones Científicas), Juan de la Cierva, 3, E-28006 Madrid, Spain.

<sup>1</sup>Corresponding author (e-mail: jedelbene@ysu.edu).



calculations, the Ahlrichs and co-workers<sup>17</sup> qzp basis set was placed on <sup>15</sup>N, <sup>17</sup>O, and <sup>19</sup>F, and the qz2p basis set was placed on the hydrogen-bonded <sup>1</sup>H. All other H atoms were described using the Dunning<sup>18</sup> cc-pVDZ basis set, and no coupling constants are reported for these hydrogens. The EOM-CCSD method with the Ahlrichs (qzp,qz2p) basis set has been shown to yield coupling constants in good agreement with experimental values for molecules.<sup>19–22</sup> Its application to hydrogen-bonded complexes has provided insight into experimentally determined coupling constants,<sup>23</sup> and the predicted relationship between <sup>2h</sup>J(N–N) and the N–N distance for N–H...N hydrogen bonds<sup>24</sup> has been verified experimentally.<sup>25</sup> Finally, the computed signs and magnitudes of <sup>2h</sup>J(X–Y), <sup>1h</sup>J(H–Y), and <sup>1</sup>J(X–H) for X–H...Y hydrogen bonds have been used successfully to characterize hydrogen-bond type.<sup>26,27</sup>

In the Ramsey approximation, the total coupling constant (*J*) is a sum of four contributions: the paramagnetic spin-orbit (PSO), diamagnetic spin-orbit (DSO), Fermi contact (FC), and spin-dipole (SD).<sup>28</sup> All terms have been computed for all molecules. The MP2 calculations were carried out using the Gaussian 03 suite of programs<sup>29</sup> on the computers at the CSIC (Consejo Superior de Investigaciones Científicas). EOM-CCSD calculations were done with ACES II<sup>30</sup> on the IBM Cluster 1350 (Glenn) at the Ohio Supercomputer Center.

## Results and discussion

### Structures and binding energies

Table 1 presents the hydrogen-bonding coordinates *R*(X–Y), *R*(X–H), *R*(H...Y), and the angle H–X–Y for the *C*<sub>2</sub> and *C*<sub>i</sub> isomers of the six dimers with X–H...Y hydrogen bonds, and the binding energies of these complexes. The complexes (HOOH)<sub>2</sub> and (HOOH)<sub>2</sub> are stabilized by O–H...O hydrogen bonds, with O–O distances varying from 2.814 to 2.841 Å. The (FOOH)<sub>2</sub> and (FOOH)<sub>2</sub> dimers are stabilized by O–H...F hydrogen bonds. The O–F distances in the *C*<sub>2</sub> and *C*<sub>i</sub> structures of (FOOH)<sub>2</sub> are 2.811 and 2.755 Å, respectively. The corresponding distances are much longer in (FOOH)<sub>2</sub>, at 3.616 and 3.031 Å, respectively. (H<sub>2</sub>NNH<sub>2</sub>)<sub>2</sub> and (FHNNH<sub>2</sub>)<sub>2</sub> are stabilized by N–H...N hydrogen bonds, with N–N distances between 3.084 and 3.146 Å. Except for the O–F distances in (FOOH)<sub>2</sub>, these intermolecular distances are not unusual. However, the hydrogen bonds in these dimers are not linear, and in some cases the deviation from linearity is significant, as evident from Table 1. The dimers with hydrogen bonds that exhibit the smallest deviation from linearity are the isomers of (HOOH)<sub>2</sub>, for which the H–O–O angle is approximately 10°. It is also interesting to note that the *C*<sub>2</sub> and *C*<sub>i</sub> isomers of this dimer have the greatest binding energies of 10.9 and 11.2 kcal mol<sup>–1</sup>, respectively. The largest deviation from linearity is 40° in the *C*<sub>i</sub> isomer of (FOOH)<sub>2</sub>. Although this isomer has a shorter O–F distance than the *C*<sub>2</sub> isomer, it is less stable by 1.2 kcal mol<sup>–1</sup>. The large deviation from linearity makes it debatable as to whether the *C*<sub>i</sub> isomer can even be described as hydrogen bonded, since it may gain stability from electrostatic interactions, including an antiparallel alignment of O–H bond dipole moments, as shown in Fig. 1. It is noteworthy that the

(FOOH)<sub>2</sub> dimer is the only dimer for which the *C*<sub>2</sub> isomer is more stable than *C*<sub>i</sub>.

The other dimers that have significantly nonlinear hydrogen bonds are the isomers of (FHNNH<sub>2</sub>)<sub>2</sub>. These dimers have the F atom bonded to the proton donor N1–H, with binding energies of 5.8 and 6.6 kcal mol<sup>–1</sup> for the *C*<sub>2</sub> and *C*<sub>i</sub> structures, respectively. These isomers have the weakest hydrogen bonds, except for the *C*<sub>i</sub> isomer of (FOOH)<sub>2</sub>. It might have been anticipated that substituting F on the donor N1–H would make HFNNH<sub>2</sub> a stronger proton donor, and (FHNNH<sub>2</sub>)<sub>2</sub> would be more stable than (H<sub>2</sub>NNH<sub>2</sub>)<sub>2</sub>, but this is obviously not the case since the (H<sub>2</sub>NNH<sub>2</sub>)<sub>2</sub> isomers have binding energies of 7.0 and 7.5 kcal mol<sup>–1</sup>. The reduced stabilities of the (FHNNH<sub>2</sub>)<sub>2</sub> dimers may reflect the significant nonlinearity of the hydrogen bonds in the *C*<sub>2</sub> and *C*<sub>i</sub> isomers, which have H–N–N angles of 32° and 35°, respectively.

### Spin–spin coupling constants

In the Introduction to this paper we asked the question whether or not corresponding spin–spin coupling constants for hydrogen-bonded hetero- and homo-chiral dimers are different, and if so, do patterns exist that would distinguish one isomer from the other. The one- and two-bond coupling constants <sup>1</sup>J(X–H), <sup>1h</sup>J(H–Y), and <sup>2h</sup>J(X–Y) across the X–H...Y hydrogen bonds are reported in Table 2. The two-bond coupling constants <sup>2h</sup>J(X–Y) are very small, ranging from 0.42 Hz in the *C*<sub>i</sub> isomer of (HOOH)<sub>2</sub> to 3.09 Hz in the *C*<sub>2</sub> isomer of (FOOH)<sub>2</sub>. However, when comparing coupling constants involving different atoms, it is the reduced coupling constants that should be used to eliminate the dependence of the coupling constant on the magnetogyric ratios of the coupled atoms. The reduced coupling constants are given in Table 3. From Table 3 it can be seen that the reduced two-bond coupling constants for the dimers with N–H...N hydrogen bonds are significantly greater than the reduced two-bond coupling constants across O–H...O and O–H...F hydrogen bonds. Moreover, although the reduced two-bond coupling constants for O–H...O and N–H...N hydrogen bonds are positive, the reduced two-bond coupling constants across the O–H...F hydrogen bonds are negative, and like the two-bond F–F coupling constant for (HF)<sub>2</sub>, are exceptions to the generalization that reduced two-bond coupling constants across hydrogen bonds are positive.<sup>31</sup>

There is no correlation between the two-bond coupling constant <sup>2h</sup>J(X–Y) and the corresponding X–Y distance, most probably due in part to the varying degree of nonlinearity of the hydrogen bonds. Although for each dimer <sup>2h</sup>J(X–Y) values are different in the *C*<sub>2</sub> and *C*<sub>i</sub> isomers, there is no recognizable pattern to these differences. For example, <sup>2h</sup>J(O–O) is greater for the *C*<sub>2</sub> isomer of (HOOH)<sub>2</sub>, but it is greater for the *C*<sub>i</sub> isomer of (HOOH)<sub>2</sub>. It might be tempting to suggest that this difference may be related to the number of bonds between the proton-donor and the proton-acceptor oxygen atoms (1 vs 2). However, <sup>2h</sup>J(O–F) is also greater for the *C*<sub>2</sub> isomer of (FOOH)<sub>2</sub> and the *C*<sub>i</sub> isomer of (FOOH)<sub>2</sub>, in which case there are two and three bonds, respectively, between the proton-donor and the proton-acceptor atoms. With such relationships, there are too few cases for generalization.

From Table 2 it may also be seen that the one-bond X–H

**Table 1.** Distances (Å), H–X–Y angles (°), and binding energies (kcal mol<sup>−1</sup>) of hydrogen-bonded hetero- and homo-chiral dimers.

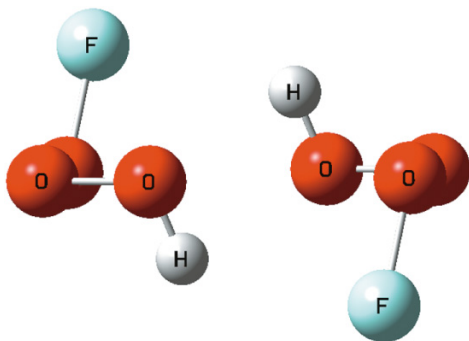
Complex	Symmetry	<i>R</i> (X–Y)	<i>R</i> (X–H)	<i>R</i> (H···Y)	<H–X–Y	Δ <i>E</i> <sub>e</sub> <sup>a</sup>
(HOOH) <sub>2</sub>	<i>C</i> <sub>2</sub>	2.833	0.972	1.929	18	9.2
O–H···O	<i>C</i> <sub>i</sub> *	2.841	0.973	1.932	17	9.4
Monomer			0.965			
(HOOOH) <sub>2</sub>	<i>C</i> <sub>2</sub>	2.814	0.976	1.885	9	10.9
O–H···O	<i>C</i> <sub>i</sub> *	2.820	0.976	1.866	10	11.2
Monomer			0.969			
(FOOH) <sub>2</sub>	<i>C</i> <sub>2</sub>	2.811	0.978	1.882	15	9.0
O–H···F	<i>C</i> <sub>i</sub> *	2.755	0.979	1.847	15	9.4
Monomer			0.971			
(FOOOH) <sub>2</sub>	<i>C</i> <sub>2</sub> *	3.616	0.972	2.680	13	7.0
O–H···F	<i>C</i> <sub>i</sub>	3.031	0.973	2.364	40	5.8
Monomer			0.969			
(H <sub>2</sub> NNH <sub>2</sub> ) <sub>2</sub>	<i>C</i> <sub>2</sub>	3.142	1.018	2.216	20	7.0
N–H···N	<i>C</i> <sub>i</sub> *	3.128	1.018	2.207	21	7.5
Monomer			1.012 <sup>b</sup>			
(FHNNH <sub>2</sub> ) <sub>2</sub> <sup>c</sup>	<i>C</i> <sub>2</sub>	3.146	1.021	2.339	32	5.8
N–H···N	<i>C</i> <sub>i</sub> *	3.084	1.021	2.317	35	6.6
Monomer			1.019			

**Note:** The more stable isomer is denoted by \*.

<sup>a</sup>Δ*E*<sub>e</sub> is the negative of the electronic energy for the reaction in which two monomers form a dimer.

<sup>b</sup>The N–H that is subsequently hydrogen bonded in the dimers.

<sup>c</sup>F is bonded to the proton donor N–H.

**Fig. 1.** The *C<sub>i</sub>* structure of (FOOOH)<sub>2</sub> illustrating the nonlinearity of possible hydrogen bonds and the antiparallel alignment of O–H bond dipole moments.

coupling constant  $^1J(X-H)$  always increases in absolute value upon complexation as the X–H distance also increases. Such behavior has been observed previously.<sup>32,33</sup> Although this increase may be as great as 6 Hz for  $^1J(O-H)$  in (FOOH)<sub>2</sub>, the difference between  $^1J(X-H)$  in the *C*<sub>2</sub> and *C<sub>i</sub>* isomers is small. Nevertheless,  $^1J(O-H)$  has a greater absolute value in the *C<sub>i</sub>* isomers, with a difference that ranges from 0.03 Hz for (HOOOH)<sub>2</sub> to 0.5 Hz for (FOOOH)<sub>2</sub>. This pattern does not hold for dimers with N–H···N hydrogen bonds since the absolute value of  $^1J(N-H)$  is 0.4 Hz greater for the *C*<sub>2</sub> isomer of (H<sub>2</sub>NNH<sub>2</sub>)<sub>2</sub> but 0.3 Hz smaller for the *C<sub>i</sub>* isomer of (FHNNH<sub>2</sub>)<sub>2</sub>.

The reduced one-bond coupling constants  $^1hK(H-Y)$  across the hydrogen bonds are always negative, indicating that such bonds are traditional (normal) hydrogen bonds.<sup>34</sup> A pattern would not be anticipated for  $^1hK(H-Y)$ , since this coupling constant may have a maximum absolute value be-

fore it asymptotically approaches 0 Hz as the H–Y distance increases. Thus, it may have the same value at two different H–Y distances.

While small differences are evident in the coupling constants  $^1J(X-H)$  and  $^2hJ(X-Y)$  for the *C*<sub>2</sub> and *C<sub>i</sub>* isomers of these dimers, the lack of systematic differences is really not surprising. The isomers of the six dimers investigated in this study can be very different structurally, particularly with respect to the arrangement of the heavy atoms in the complex and the degree of nonlinearity of the hydrogen bonds. For example, the hydrogen-bonded O and H atoms in the *C<sub>i</sub>* isomer of (HOOH)<sub>2</sub> are essentially coplanar but deviate to some extent from coplanarity in the *C*<sub>2</sub> isomer. In the *C<sub>i</sub>* isomer of (HOOOH)<sub>2</sub>, the hydrogen-bonded O and H atoms are essentially coplanar, but the oxygen that is bonded to both proton-donor and proton-acceptor oxygens does not lie in this plane. In contrast, there is no hydrogen-bonding plane in the *C*<sub>2</sub> isomer. Finally, one might even question whether hydrogen bonds exist in the *C<sub>i</sub>* isomer of (FOOOH)<sub>2</sub>, which is illustrated in Fig. 1, or in the isomers of (FHNNH<sub>2</sub>)<sub>2</sub>, given the nonlinearity of these bonds as indicated by the values of the H–X–Y angles reported in Table 1. All of these differences are likely sources of the lack of distinguishable patterns for corresponding coupling constants involving hydrogen-bonded atoms in the *C*<sub>2</sub> and *C<sub>i</sub>* isomers.

Are there any other easily identifiable pairs of atoms that might have distinguishable coupling constants for the two isomers? Our search for these yielded only one pair, O1–O2, where O1 is the proton-donor oxygen. Table 4 presents O1–O2 distances and  $^1J(O1-O2)$  for the monomers and the *C*<sub>2</sub> and *C<sub>i</sub>* isomers of dimers with O1–H···O and O1–H···F hydrogen bonds.  $^1J(O1-O2)$  are positive for HOOH and the two isomers of (HOOH)<sub>2</sub> but negative for the other monomers and dimers. It is interesting to note that dimer formation makes

**Table 2.** Coupling constants  ${}^{2h}J(X-Y)$ ,  ${}^{1h}J(H-Y)$ ,  ${}^1J(X-H)$ , and  $\Delta J$  (Hz) for coupling across  $X-H\cdots Y$  hydrogen bonds in homo- and hetero-chiral dimers.

Complex	Symmetry	${}^{2h}J(X-Y)$	$\Delta {}^{2h}J(X-Y)^a$	${}^1J(X-H)$	$\Delta {}^1J(X-H)^a$	${}^{1h}J(H-Y)$	$\Delta {}^{1h}J(H-Y)^a$
(HOOH) <sub>2</sub>	<i>C</i> <sub>2</sub>	0.65	0.23 (O–O)	–61.84	0.13 (O–H)	5.40	0.41 (H–O)
O–H $\cdots$ O	<i>C<sub>i</sub></i> *	0.42		–61.94		4.99	
Monomer				–60.46			
(HOOOH) <sub>2</sub>	<i>C</i> <sub>2</sub>	1.16	–0.46 (O–O)	–63.97	0.03 (O–H)	6.66	–1.00 (H–O)
O–H $\cdots$ O	<i>C<sub>i</sub></i> *	1.62		–64.00		7.66	
Monomer				–59.70			
(FOOH) <sub>2</sub>	<i>C</i> <sub>2</sub>	3.09	2.09 (O–F)	–67.11	0.10 (O–H)	–28.32	2.89 (H–F)
O–H $\cdots$ F	<i>C<sub>i</sub></i> *	1.00		–67.21		–31.21	
Monomer				–61.00			
(FOOOH) <sub>2</sub>	<i>C</i> <sub>2</sub> *	0.61	–0.41 (O–F)	–57.82	0.49 (O–H)	–1.48	2.26 (H–F)
O–H $\cdots$ F	<i>C<sub>i</sub></i>	1.02		–58.31		–3.74	
Monomer				–56.24			
(H <sub>2</sub> NNH <sub>2</sub> ) <sub>2</sub>	<i>C</i> <sub>2</sub>	1.62	–0.65 (N–N)	–72.23	–0.39 (N–H)	1.83	–0.05 (H–N)
N–H $\cdots$ N	<i>C<sub>i</sub></i> *	2.27		–71.84		1.88	
Monomer				–69.50			
(FHNNH <sub>2</sub> ) <sub>2</sub>	<i>C</i> <sub>2</sub>	0.77	–0.84 (N–N)	–66.72	0.32 (N–H)	1.17	0.04 (H–N)
N–H $\cdots$ N	<i>C<sub>i</sub></i> *	1.61		–67.04		1.13	
Monomer				–64.40			

**Note:** The more stable isomer is denoted by \*.

${}^a\Delta J = J(C_2) - J(C_i)$ .

**Table 3.** Reduced coupling constants  ${}^{2h}K(X-Y)$ ,  ${}^{1h}K(H-Y)$ , and  ${}^1K(X-H)$  ( $K \times 10^{19}$  N A<sup>–2</sup> m<sup>–3</sup>) across  $X-H\cdots Y$  hydrogen bonds in homo- and hetero-chiral dimers.

Complex	Symmetry	${}^{2h}K(X-Y)$	${}^1K(X-H)$	${}^{1h}K(H-Y)$
(HOOH) <sub>2</sub>	<i>C</i> <sub>2</sub>	2.94	37.96	–3.32
O–H $\cdots$ O	<i>C<sub>i</sub></i> *	1.90	38.02	–3.06
Monomer			37.14	
(HOOOH) <sub>2</sub>	<i>C</i> <sub>2</sub>	5.25	39.27	–4.09
O–H $\cdots$ O	<i>C<sub>i</sub></i> *	7.33	39.29	–4.70
Monomer			36.65	
(FOOH) <sub>2</sub>	<i>C</i> <sub>2</sub>	–2.02	41.20	–2.50
O–H $\cdots$ F	<i>C<sub>i</sub></i> *	–0.65	41.26	–2.76
Monomer			37.45	
(FOOOH) <sub>2</sub>	<i>C</i> <sub>2</sub> *	–0.40	35.50	
O–H $\cdots$ F	<i>C<sub>i</sub></i>	–0.67	35.80	–0.33
Monomer			34.50	
(H <sub>2</sub> NNH <sub>2</sub> ) <sub>2</sub>	<i>C</i> <sub>2</sub>	13.13	59.32	–1.50
N–H $\cdots$ N	<i>C<sub>i</sub></i> *	18.39	59.00	–1.54
Monomer			57.08	
(FHNNH <sub>2</sub> ) <sub>2</sub>	<i>C</i> <sub>2</sub>	6.24	54.80	–0.96
N–H $\cdots$ N	<i>C<sub>i</sub></i> *	13.04	67.04	–0.93
Monomer			52.89	

**Note:** The more stable isomer is denoted by \*.

${}^1J(O1-O2)$  less positive for (HOOH)<sub>2</sub> as the O1–O2 distance remains essentially constant.  ${}^1J(O1-O2)$  for the remaining dimers becomes more negative, that is, it increases in absolute value as the O1–O2 distance decreases upon dimer formation. The largest change in the O1–O2 distance and in  ${}^1J(O1-O2)$  upon dimer formation is found for (FOOH)<sub>2</sub>. The absolute value of  ${}^1J(O1-O2)$  is always greater in the *C<sub>i</sub>* isomer, with differences varying from 0.6 to 1.4 Hz. Unfortunately, the nuclear spin of 5/2 for <sup>17</sup>O makes it unlikely that such small differences could be detected experimentally.

**Table 4.** O1–O2 distances (Å) and  ${}^1J(O1-O2)$  (Hz) for monomers and hetero- and homo-chiral dimers with O2–O1–H $\cdots$ Y hydrogen bonds.

Complex	Monomer	<i>C</i> <sub>2</sub> isomer	<i>C<sub>i</sub></i> isomer
<i>R</i> (O1–O2)			
(HOOH) <sub>2</sub>	1.450	1.450	1.451
(HOOOH) <sub>2</sub>	1.423	1.413	1.411
(FOOH) <sub>2</sub>	1.361	1.325	1.323
(FOOOH) <sub>2</sub>	1.439	1.436	1.438
${}^1J$ (O1–O2)			
(HOOH) <sub>2</sub>	17.42	13.36	14.71
(HOOOH) <sub>2</sub>	–13.84	–16.97	–17.66
(FOOH) <sub>2</sub>	–38.59	–57.44	–58.67
(FOOOH) <sub>2</sub>	–13.38	–15.12	–15.70

No patterns are observed for the values of  ${}^1J(N1-N2)$  in the *C*<sub>2</sub> and *C<sub>i</sub>* isomers of dimers with N–H $\cdots$ N hydrogen bonds.

The  $\Delta J$  values reported in Table 2 correspond to what is termed *chiral anisogamy*, meaning a difference in corresponding coupling constants in a pair of chiral isomers.<sup>35</sup> Could such differences be detected experimentally? To answer this question, it is necessary to first consider the spins of the nuclei involved. Since couplings between nuclei both of which have  $I > 1/2$  cannot be measured, all of the O–O couplings are eliminated. Couplings between one nucleus that has  $I = 1/2$  and another with  $I > 1/2$  can be measured, but small differences are not detectable. This is the situation for O–H and O–F couplings. However, progress is being made in this area.<sup>36</sup> With ultrahigh resolution NMR, couplings between nuclei with  $I = 1/2$  can be measured to a precision better than 0.1 Hz,<sup>37</sup> which means that even small couplings involving H, N, and F could be detected. However, experimental studies of the particular dimers investigated in this study would be difficult both in solution where



they would need to form and remain stable, and in the solid state with the very low temperatures required. The most promising candidate for experimental investigation would be a strongly-bound complex with a  $^{15}\text{N}$ -labeled hydrazine derivative, which is a solid at room temperature and shows X-ray crystallographic evidence for the existence of hydrogen bonds.

## Conclusions

Corresponding spin–spin coupling constants for hydrogen-bonded atoms in isomeric pairs of homo- and hetero-dimers of  $\text{C}_2$  and  $\text{C}_i$  symmetry may differ, but the differences are small and would probably be difficult to detect experimentally. For the four complexes with  $\text{O}\cdots\text{H}\cdots\text{X}$  hydrogen bonds,  $^1\text{J}(\text{O1}\cdots\text{H})$  has a larger absolute value in the  $\text{C}_2$  isomer. For the same set of complexes,  $^1\text{J}(\text{O1}\cdots\text{O2})$  has a larger absolute value in the  $\text{C}_i$  isomer. No distinguishable patterns could be discerned in corresponding spin–spin coupling constants in the  $\text{C}_2$  and  $\text{C}_i$  isomers of complexes with  $\text{N}\cdots\text{H}\cdots\text{N}$  hydrogen bonds.

## Acknowledgments

This work was carried out with financial support from the Ministerio de Educación y Ciencia (Project No. CTQ2009-13129-C02-02) and Comunidad Autónoma de Madrid (Project MADRISOLAR, ref. S-0505/PPQ/0225). Thanks are given to the Ohio Supercomputer Center for its continued support and to the CTI (Centro Técnico de Informática; CSIC: Consejo Superior de Investigaciones Científicas) for an allocation of computer time.

## References

- (1) (a) Alkorta, I.; Elguero, J. *J. Am. Chem. Soc.* **2002**, *124* (7), 1488. doi:10.1021/ja011348c. PMID:11841319.; (b) Picazo, O.; Alkorta, I.; Elguero, J. *J. Org. Chem.* **2003**, *68* (19), 7485. doi:10.1021/jo035026y. PMID:12968904.; (c) Alkorta, I.; Elguero, J. *J. Mol. Struct. THEOCHEM* **2004**, *680* (1–3), 191. doi:10.1016/j.theochem.2004.04.030.; (d) Rozas, I.; Alkorta, I.; Elguero, J. *J. Phys. Chem. A* **2006**, *110* (49), 13310. doi:10.1021/jp064386x. PMID:17149851.; (e) Alkorta, I.; Elguero, J.; Zborowski, K. *J. Phys. Chem. A* **2007**, *111* (6), 1096. doi:10.1021/jp0669916. PMID:17286362.
- (2) Dobashi, A.; Saito, N.; Motoyama, Y.; Hara, S. *J. Am. Chem. Soc.* **1986**, *108* (2), 307. doi:10.1021/ja00262a027.
- (3) Giordano, C.; Restelli, A.; Villa, M.; Annunziata, R. *J. Org. Chem.* **1991**, *56* (6), 2270. doi:10.1021/jo00006a064.
- (4) Wagger, J.; Grdadolnik, S. G.; Groselj, U.; Meden, A.; Stanovnik, B.; Svete, J. *Tetrahedron Asymmetry* **2007**, *18* (4), 464. doi:10.1016/j.tetasy.2007.02.010.
- (5) (a) Agranat, I.; Sarel, S. *Enantiomer* **1996**, *1*, 249; (b) Garten, S.; Biedermann, P. U.; Agranat, I.; Topiol, S. *Chirality* **2005**, *17* (S1), S159. doi:10.1002/chir.20136. PMID:15849802.
- (6) For a recent review of chiral distinction in hydrogen-bonded clusters, see: Alkorta, I.; Elguero, J. *Chirality and Chiral Recognition*. In *Practical Aspects of Computational Chemistry*; Leszczynski, J., Shukla, M. K., Eds.; Springer-Verlag: New York, 2010.
- (7) Pople, J. A.; Binkley, J. S.; Seeger, R. *Int. J. Quantum Chem.* **1976**, *10* (S10), 1. doi:10.1002/qua.560100802.
- (8) Krishnan, R.; Pople, J. A. *Int. J. Quantum Chem.* **1978**, *14* (1), 91. doi:10.1002/qua.560140109.
- (9) Bartlett, R. J.; Silver, D. M. *J. Chem. Phys.* **1975**, *62* (8), 3258. doi:10.1063/1.430878.
- (10) Bartlett, R. J.; Purvis, G. D. *Int. J. Quantum Chem.* **1978**, *14* (5), 561. doi:10.1002/qua.560140504.
- (11) Frisch, M. J.; Pople, J. A.; Krishnan, R.; Binkley, J. S. *J. Chem. Phys.* **1984**, *80* (7), 3265. doi:10.1063/1.447079.
- (12) Spitznagel, G. W.; Clark, T.; Chandrasekhar, J.; Schleyer, P. R. *J. Comput. Chem.* **1982**, *3* (3), 363. doi:10.1002/jcc.540030311.
- (13) Clark, T.; Chandrasekhar, J.; Spitznagel, G. W.; Schleyer, P. R. *J. Comput. Chem.* **1983**, *4* (3), 294. doi:10.1002/jcc.540040303.
- (14) Alkorta, I.; Elguero, J. *J. Chem. Phys.* **2002**, *117* (14), 6463. doi:10.1063/1.1504710.
- (15) Perera, S. A.; Sekino, H.; Bartlett, R. J. *J. Chem. Phys.* **1994**, *101* (3), 2186. doi:10.1063/1.467725.
- (16) Perera, S. A.; Nooijen, M.; Bartlett, R. J. *J. Chem. Phys.* **1996**, *104* (9), 3290. doi:10.1063/1.471092.
- (17) Schäfer, A.; Horn, H.; Ahlrichs, R. *J. Chem. Phys.* **1992**, *97* (4), 2571. doi:10.1063/1.463096.
- (18) Dunning, T. H., Jr. *J. Chem. Phys.* **1989**, *90* (2), 1007. doi:10.1063/1.456153.
- (19) Del Bene, J. E.; Alkorta, I.; Elguero, J. *J. Chem. Theory Comput.* **2008**, *4* (6), 967. doi:10.1021/ct800111j.
- (20) Del Bene, J. E.; Provasi, P. F.; Alkorta, I.; Elguero, J. *Magn. Reson. Chem.* **2008**, *46* (11), 1003. doi:10.1002/mrc.2304. PMID:18792421.
- (21) Del Bene, J. E.; Alkorta, I.; Elguero, J. *J. Chem. Theory Comput.* **2009**, *5* (1), 208. doi:10.1021/ct800321b.
- (22) Del Bene, J. E.; Alkorta, I.; Elguero, J. *J. Phys. Chem. A* **2009**, *113* (45), 12411. doi:10.1021/jp902089g. PMID:19462958.
- (23) Del Bene, J. E.; Bartlett, R. J.; Elguero, J. *Magn. Reson. Chem.* **2002**, *40* (12), 767. doi:10.1002/mrc.1103.
- (24) Del Bene, J. E.; Bartlett, R. J. *J. Am. Chem. Soc.* **2000**, *122* (42), 10480. doi:10.1021/ja002735+.
- (25) Söntjens, S. H. M.; van Genderen, M. H. P.; Sijbesma, R. P. *J. Org. Chem.* **2003**, *68* (23), 9070. doi:10.1021/jo034889o. PMID:14604382.
- (26) Del Bene, J. E. *Calculation of NMR and EPR Parameters*; Kaupp, M., Bühl, M., Malkin, V., Eds.; Wiley-VCH: Weinheim, 2004; pp 353–370.
- (27) Del Bene, J. E.; Elguero, J. *Computational Chemistry: Reviews of Current Trends*; Leszczynski, J., Ed.; World Scientific Publishing Co. Pte, LTD.: Singapore, 2006; Vol. 10, pp 229–264.
- (28) Kirpekar, S.; Jensen, H. J. A.; Oddershede, J. *J. Chem. Phys.* **1994**, *100* (2–3), 171. doi:10.1016/0301-0104(94)00260-6.
- (29) Frisch, M. J.; Trucks, G. W.; Schlegel, H. B.; Scuseria, G. E.; Robb, M. A.; Cheeseman, J. R.; Montgomery, J. A., Jr.; Vreven, T.; Kudin, K. N.; Burant, J. C.; Millam, J. M.; Iyengar, S. S.; Tomasi, J.; Barone, V.; Mennucci, B.; Cossi, M.; Scalmani, G.; Rega, N.; Petersson, G. A.; Nakatsuji, H.; Hada, M.; Ehara, M.; Toyota, K.; Fukuda, R.; Hasegawa, J.; Ishida, M.; Nakajima, T.; Honda, Y.; Kitao, O.; Nakai, H.; Klene, M.; Li, X.; Knox, J. E.; Hratchian, H. P.; Cross, J. B.; Adamo, C.; Jaramillo, J.; Gomperts, R.; Stratmann, R. E.; Yazyev, O.; Austin, A. J.; Cammi, R.; Pomelli, C.; Ochterski, J. W.; Ayala, P. Y.; Morokuma, K.; Voth, G. A.; Salvador, P.; Dannenberg, J. J.; Zakrzewski, V. G.; Dapprich, S.; Daniels, A. D.; Strain, M. C.; Farkas, O.; Malick, D. K.; Rabuck, A. D.; Raghavachari, K.; Foresman, J. B.; Ortiz, J. V.; Cui, Q.; Baboul, A. G.; Clifford, S.; Cioslowski, J.; Stefanov, B. B.; Liu, G.; Liashenko, A.; Piskorz, P.; Komaromi,



- I.; Martin, R. L.; Fox, D. J.; Keith, T.; Al-Laham, M. A.; Peng, C. Y.; Nanayakkara, A.; Challacombe, M.; Gill, P. M. W.; Johnson, B.; Chen, W.; Wong, M. W.; Gonzalez, C.; Pople, J. A. *Gaussian 03*; Gaussian, Inc.: Pittsburgh PA, 2003.
- (30) Stanton, J. F.; Gauss, J.; Watts, J. D.; Nooijen, M.; Oliphant, N.; Perera, S. A.; Szalay, P. G.; Lauderdale, W. J.; Gwaltney, S. R.; Beck, S.; Balkova, A.; Bernholdt, D. E.; Baeck, K.-K.; Tozyczko, P.; Sekino, H.; Huber, C.; Bartlett, R. J. ACES II; Quantum Theory Project, University of Florida: Gainesville, FL. Integral packages included are VMOL (Almlöf, J., Taylor, P. R.), VPROPS (Taylor, P. R.), ABACUS (Helgaker, T., Jensen, H. J. Aa., Jørgensen, P., Olsen, J., Taylor, P. R.). Brillouin–Wigner perturbation theory was implemented by J. Pittner.
- (31) Del Bene, J. E.; Elguero, J. *Magn. Reson. Chem.* **2004**, *42* (5), 421. doi:10.1002/mrc.1386. PMID:15095377.
- (32) Del Bene, J. E.; Elguero, J. *J. Phys. Chem. A* **2006**, *110* (23), 7496. doi:10.1021/jp0613642. PMID:16759141.
- (33) Del Bene, J. E.; Elguero, J.; Alkorta, I. *J. Phys. Chem. A* **2007**, *111* (17), 3416. doi:10.1021/jp068695z. PMID:17425291.
- (34) Del Bene, J. E.; Elguero, J. *J. Phys. Chem. A* **2004**, *108* (52), 11762. doi:10.1021/jp040544d.
- (35) Nasipuri, D. *Stereochemistry of Organic Compounds: Principles and Applications*; New Age International: New Dehli, 2007.
- (36) Appelt, S.; Kühn, H.; Häsing, F. W.; Blümich, B. *Nat. Phys.* **2006**, *2* (2), 105. doi:10.1038/nphys211.
- (37) (a) Maple, S. R.; Allerhand, A. *J. Am. Chem. Soc.* **1987**, *109* (1), 56. doi:10.1021/ja00235a009.; (b) Raynes, W. T.; Stevens, S. J. *Magn. Reson. Chem.* **1992**, *30* (2), 124. doi:10.1002/mrc.1260300206.

# Intramolecular hydroamination of unactivated alkenes with secondary alkylamines catalyzed by iridium phosphino–phenolate complexes

Kevin D. Hesp, Robert McDonald, and Mark Stradiotto

**Abstract:** The phosphino–phenolate complex ( $\kappa^2$ -{2-*i*-Pr<sub>2</sub>PC<sub>6</sub>H<sub>4</sub>}O)Ir(COD) (COD =  $\eta^4$ -1,5-cyclooctadiene; **1**) is shown to be an effective precatalyst for the intramolecular hydroamination of unactivated alkenes with pendant secondary alkylamines, providing either pyrrolidine or piperidine heterocycles in high isolated yields. While monitoring the progress of a selected test reaction of this type, a significant induction period (~3 h) was observed; variable-temperature <sup>1</sup>H and <sup>31</sup>P NMR studies (25–100 °C) under catalytically relevant conditions revealed no new metal-containing species. In an effort to develop an enantiopure variant of **1**, a synthetic route to the chiral ( $\kappa^2$ -*P,O*)Ir(COD) complex (**7**), which features a 1-aryl-2,5-dialkylphospholane structure derived from (2*S*,5*S*)-2,5-hexanediol cyclic sulfate, was developed. The structure of **7** was confirmed by use of single-crystal X-ray diffraction techniques. While **7** failed to provide enantioselectivity in the intramolecular hydroamination of unactivated alkenes with pendant secondary alkylamines, the activity of **7** was found to be comparable to that of **1**.

**Key words:** catalysis, hydroamination, iridium, ligand design.

**Résumé :** On montre que le complexe phosphino–phénolate, ( $\kappa^2$ -{2-*i*-Pr<sub>2</sub>PC<sub>6</sub>H<sub>4</sub>}O)Ir(COD) (**1**), est un précatalyseur efficace pour l'hydroamination intramoléculaire d'alcènes non activés portant des chaînes latérales avec des alkylamines secondaires qui conduit à la formation d'hétérocycles pyrrolidine ou pipéridine avec des rendements élevés en produits isolés. En observant le progrès d'une réaction de ce type choisie comme représentative, on a observé une période d'induction significative (environ 3 heures); des études de RMN du <sup>1</sup>H et du <sup>31</sup>P à température variable (25 à 100 °C), dans des conditions catalytiquement appropriées ont révélé qu'il n'y a pas de nouvelles espèces contenant un métal. Dans un effort pour développer une variété énantiomériquement pure du composé **1**, on a mis au point une voie de synthèse du complexe chiral ( $\kappa^2$ -*P,O*)Ir(COD), **7**, qui inclut une structure 1-aryl-2,5-dialkylphospholane obtenue à partir du sulfate cyclique du (2*S*,5*S*)-hexane-2,5-diols. La structure du composé **7** a été confirmée par des techniques de diffraction des rayons X par un cristal unique. Même si le composé **7** n'a pas permis d'obtenir d'énantiosélectivité dans l'hydroamination intramoléculaire d'alcènes non activés portant des chaînes latérales avec des alkylamines secondaires, l'activité de ce produit est comparable à celle du produit **1**.

**Mots-clés :** Catalyse, hydroamination, iridium, développement d'un ligand.

## Introduction

The prevalence of nitrogen-containing moieties in both naturally occurring and biologically active molecules has prompted the development of efficient methods for the formation of C–N bonds, including the use of transition-metal catalysis.<sup>1</sup> Notwithstanding the tremendous success of Buchwald–Hartwig amination and related cross-coupling chemistry,<sup>1b,c</sup> the inherent lack of atom economy associated with such procedures has prompted the development of hydroamination protocols that enable C–N bond formation via the direct addition of N–H bonds to unsaturated substrates.<sup>1d</sup> In particular, intramolecular hydroamination involving N–H bond addition to an unactivated alkene offers an attractive

route to nitrogen-containing heterocycles. However, while catalyst systems employing Brønsted acids,<sup>2</sup> rare earth elements and actinides,<sup>3</sup> alkali and alkaline earth metals,<sup>4</sup> group 4 metals,<sup>5</sup> and groups 8–11 metals<sup>6,7</sup> have all proven capable of mediating the intramolecular hydroamination of such unactivated aminoalkenes, general methods for promoting the cyclization of these challenging substrates under mild conditions and with broad substrate scope remain elusive.

We recently reported on the use of [Ir(COD)Cl]<sub>2</sub> (COD =  $\eta^4$ -1,5-cyclooctadiene) as a precatalyst for the intramolecular addition of a variety of secondary alkyl- or aryl- amines to unactivated alkenes, without the requirement of added ligands or cocatalysts<sup>7a</sup>; notably, this represents one of only a

Received 25 September 2009. Accepted 17 November 2009. Published on the NRC Research Press Web site at canjchem.nrc.ca on 15 April 2010.

This article is part of a Special Issue dedicated to Professor R. J. Boyd. We dedicate this article to Professor Russ Boyd in recognition of his widespread contributions to the Department of Chemistry at Dalhousie University as well as to the Canadian chemical community.

**K.D. Hesp and M. Stradiotto.**<sup>1</sup> Department of Chemistry, Dalhousie University, Halifax, NS B3H 4J3, Canada.

**R. McDonald.** X-Ray Crystallography Laboratory, Department of Chemistry, University of Alberta, Edmonton, AB T6G 2G2, Canada.

<sup>1</sup>Corresponding author (e-mail: mark.stradiotto@dal.ca).

**Table 1.** Intramolecular hydroamination of unactivated alkenes by secondary alkylamines employing **1** as a precatalyst.

Entry	Aminoalkene	Product	mol% <b>1</b> (time, h)	Yield <sup>a</sup>
1	R = Ph		1.0 (16)	92
2	R = 4 - C <sub>6</sub> H <sub>4</sub> Cl		1.0 (16)	86
3	R = 4 - C <sub>6</sub> H <sub>4</sub> CO <sub>2</sub> Me		1.0 (16)	85
4	R = 4 - C <sub>6</sub> H <sub>4</sub> OMe		1.0 (16)	87
5	R = Cy		2.5 (24)	89
6			1.0 (16)	85
7			5.0 (24)	86
8			2.5 (24)	87 <sup>b</sup> (1.3:1) <sup>c</sup>
9			1.0 (16)	85
10			1.0 (16)	92

**Note:** Reaction conditions: 0.25 mmol aminoalkene in 0.50 mL of 1,4-dioxane at 110 °C.

<sup>a</sup> Isolated yield unless otherwise stated.

<sup>b</sup> <sup>1</sup>H NMR yield.

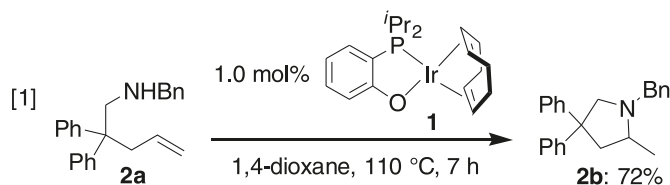
<sup>c</sup> Diastereomeric ratio (dr, <sup>1</sup>H NMR).

small number of examples in which late metal catalysts have been shown to promote the cyclization of such substrates.<sup>7</sup> As such, we became interested in identifying alternative neutral Ir complexes that function as catalysts for the intramolecular hydroamination of unactivated aminoalkenes,<sup>8</sup> especially those for which chiral variants could be developed. Encouraged by our previous observation that the phosphino-phenolate complex ( $\kappa^2$ -{2-*i*-Pr<sub>2</sub>PC<sub>6</sub>H<sub>4</sub>}O)Ir(COD) (**1**) is a highly active catalyst for the hydrogenation of substituted alkenes under mild conditions,<sup>9</sup> we viewed **1** as being an attractive candidate for use in hydroamination chemistry. We report herein that **1** is a competent catalyst at relatively low catalyst loadings for the intramolecular hydroamination of a variety of unactivated alkenes that feature pendant alkylamines. Furthermore, we report on the synthesis and crystallographic characterization of a first-generation chiral variant of **1**, and our efforts to apply this new chiral ( $\kappa^2$ -*P,O*)Ir(COD) complex in intramolecular hydroamination catalysis.<sup>10</sup>

## Results and discussion

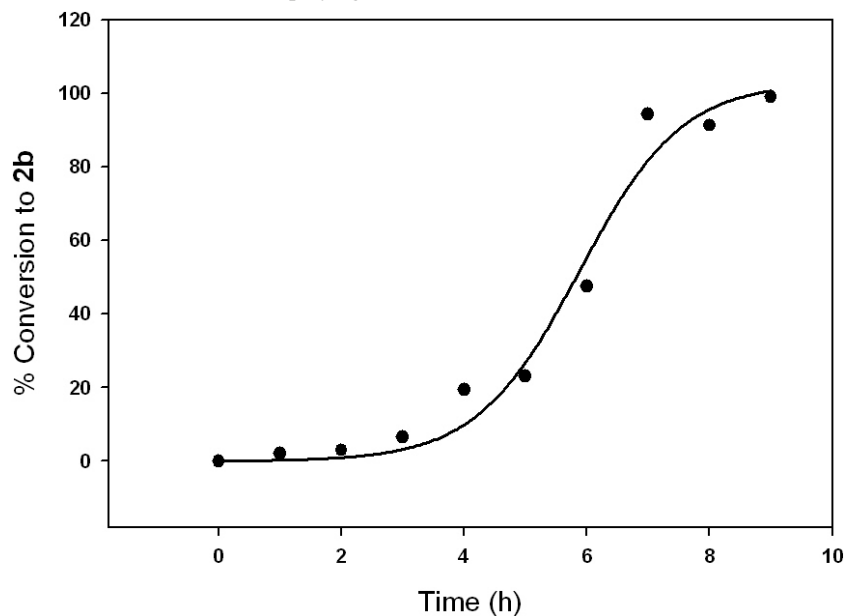
In a preliminary test experiment, the cyclization of the aminoalkene **2a** to the pyrrolidine **2b** proceeded in a 72%

yield (<sup>1</sup>H NMR) in the presence of 1.0 mol% **1** in 1,4-dioxane at 110 °C over the course of 7 h, with the balance corresponding to unreacted **2a** (eq. [1]). Under similar experimental conditions employing catalyst mixtures comprised of 0.5 mol% [Ir(COD)Cl]<sub>2</sub> and 1.0 mol% of a simple phosphine ligand including triphenylphosphine, tricyclohexylphosphine or 1,4-bis(diphenylphosphino)butane, negligible conversion to the desired cyclization product **2b** was achieved. While the use of the Rh variant of **1** under similar experimental conditions resulted in the consumption of **2a**, multiple products were formed in this reaction with the major product corresponding to alkene isomerization within the starting substrate.



The utility of **1** as a precatalyst in the hydroamination of a range of *N*-alkyl aminoalkenes was surveyed (Table 1). The cyclization of the parent *N*-benzyl substrate **2a** (Table 1,

**Fig. 1.** A plot of the conversion of **2a** to **2b** vs time employing 2.5 mol% **1** (1,4-dioxane, 110 °C).



entry 1) as well as para-substituted derivatives featuring chloride (Table 1, entry 2), methyl ester (Table 1, entry 3), or methoxy (Table 1, entry 4) substituents, was in each case achieved in high isolated yield (85%–92%) despite the use of relatively low catalyst loading (1.0 mol% **1**). The sterically hindered *N*-methylcyclohexyl aminoalkene was also cyclized (Table 1, entry 5), as were substrates that feature alternative formulations of mono- and di-substitution on the linker chain of the aminoalkene substrate (Table 1, entries 6–8). Notably, the results featured in Table 1, entries 6–8, clearly underscore the importance of the Thorpe–Ingold effect in promoting these transformations, whereby increased steric elaboration at the  $\beta$ -carbon enables more facile cyclohydroamination at lower catalyst loadings. The hydroamination of the hexenylamine substrate featured in Table 1, entry 9, was also achieved in the presence of **1** to afford the corresponding piperidine. In surveying more challenging substrates, we turned our attention to the intramolecular hydroamination of unactivated disubstituted alkenes. Whereas the efficient cyclization of a 1,1-disubstituted substrate was achieved by use of **1** (Table 1, entry 10), under our standard catalytic conditions, this catalyst proved unreactive toward aminoalkenes featuring unstrained 1,2-substituted olefins or those lacking substituents on the tethering chain that facilitate the cyclization process, as well as primary amine substrates. In comparison to the catalytic performance of  $[\text{Ir}(\text{COD})\text{Cl}]_2$ ,<sup>7a</sup> longer reaction times were needed when using **1** to achieve similar levels of conversion for the substrates featured in Table 1, entries 1–6; for **2a**, as well as the *N*-methylcyclohexyl aminoalkene substrate (Table 1, entry 5), significantly higher Ir loadings were also required when using **1**. Otherwise, the catalytic performance of **1** in the cyclization of *N*-alkyl aminoalkenes was found to be competitive with that of  $[\text{Ir}(\text{COD})\text{Cl}]_2$ , and in the case of the more challenging substrates featured in Table 1, entries 8–10, **1** proved to be superior to  $[\text{Ir}(\text{COD})\text{Cl}]_2$  on the basis of Ir loading, reaction time, and isolated yield.

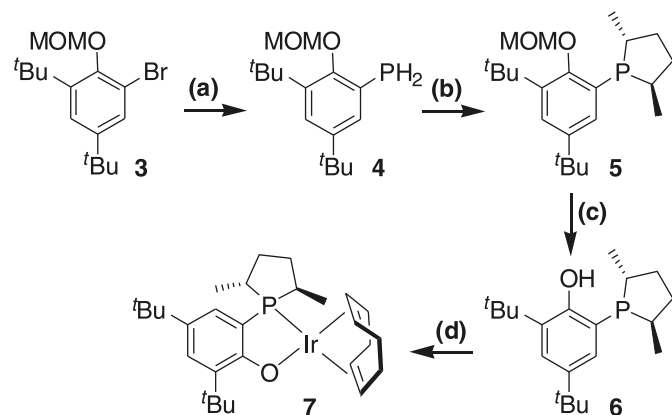
Having observed that longer reaction times and higher

catalyst loadings were needed for **1** relative to  $[\text{Ir}(\text{COD})\text{Cl}]_2$  to achieve similarly high levels of conversion in the cyclization of **2a** to **2b**, we examined the conversion versus time profile for this transformation employing **1** (2.5 mol% Ir, 1,4-dioxane, 110 °C; Fig. 1). Notably, a pronounced induction period (~3 h) was observed under these conditions; by comparison, high conversion to **2b** was achieved after 3 h by using only 0.5 mol%  $[\text{Ir}(\text{COD})\text{Cl}]_2$  under similar conditions in the absence of an induction period.<sup>7a</sup> Variable-temperature <sup>1</sup>H and <sup>31</sup>P NMR studies (25–100 °C) of an equimolar mixture of **1** and **2a**, either without preconditioning or following preconditioning for 3 h at 110 °C, revealed the presence of only **1** and **2a**, as well as small quantities of **2b** at elevated temperatures. While we are presently unable to comment definitively regarding the mechanism of hydroamination mediated by **1**, these spectroscopic observations appear to preclude a mechanism in which dissociation of the P,O ligand from Ir is responsible for the observed induction period. Mechanistic investigations regarding the cyclization of **2a** and related substrates by each of **1** and  $[\text{Ir}(\text{COD})\text{Cl}]_2$  are ongoing in our laboratory.

The late metal catalyzed enantioselective intramolecular hydroamination of unactivated alkenes featuring pendant alkylamines has yet to be reported in the literature.<sup>10</sup> Given the desirable catalytic performance of **1**, and encouraged by reports documenting the Ir-mediated enantioselective intermolecular hydroamination of activated alkenes,<sup>11</sup> we sought to construct a chiral variant of **1**. In consideration of the diisopropylphosphino present in **1**, we elected to employ a structurally similar  $\kappa^2$ -*P,O* phenylene ligand featuring the 1-aryl-2,5-dialkylphospholane scaffold.<sup>12</sup> Preparation of the target ligand precursor **6** was carried out by adapting previously published methods.<sup>12a,13</sup> As outlined in Scheme 1, the installation of the chiral phospholane fragment required initial treatment of the methoxymethyl (MOM) protected phenol **3** with *n*-BuLi and  $\text{P}(\text{NMe}_2)_2\text{Cl}$ , followed by in situ methanolysis and reduction with  $\text{LiAlH}_4$  to afford the primary phosphine **4**. Using the procedure established by Burk



**Scheme 1.** Synthesis of the new chiral ( $\kappa^2$ -*P,O*)Ir(COD) complex **7**. Reagents and conditions: (a) *n*-BuLi, Et<sub>2</sub>O, −78 °C → 25 °C, 16 h; P(NMe<sub>2</sub>)<sub>2</sub>Cl, Et<sub>2</sub>O, −78 °C → 25 °C, 3 h; MeOH, 50 °C, 3 h; LiAlH<sub>4</sub>, Et<sub>2</sub>O, 25 °C, 48 h (36% from **3**). (b) *n*-BuLi, THF, 25 °C, 1.5 h; (2*S*,5*S*)-2,5-hexanediol cyclic sulfate, THF, 25 °C, 2 h; *n*-BuLi, THF, 25 °C, 2 h, (68% from **4**). (c) 5 mol/L HCl (aq.), THF, 50 °C, 16 h; 7 mol/L NH<sub>4</sub>OH (aq.), Et<sub>2</sub>O, 25 °C, 5 h, (73% from **5**). (d) [Ir(COD)Cl]<sub>2</sub>, NEt<sub>3</sub>, THF, 25 °C, 2 h, 68%.

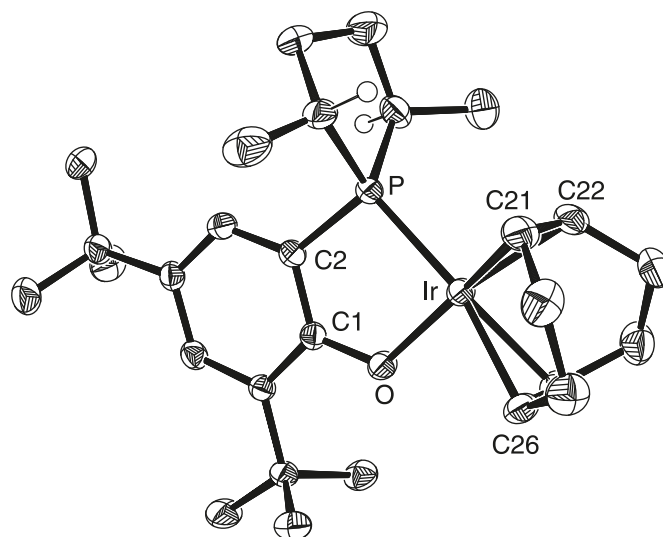


et al.<sup>12b</sup> for the construction of phospholane moieties, successive treatment of **4** with 1 equiv. *n*-BuLi, followed by 1 equiv. (2*S*,5*S*)-2,5-hexanediol cyclic sulfate, and then an additional 1 equiv. of *n*-BuLi provided the protected intermediate **5**, which was converted to the phosphinoenolate **6** upon exposure to aqueous HCl followed by workup with aqueous NH<sub>4</sub>OH. Treatment of **6** with 0.5 equiv. [Ir(COD)Cl]<sub>2</sub> and NEt<sub>3</sub> afforded **7** as an analytically pure, isolable orange solid (68% from **6**; 12% from **3**). The connectivity in **7** was established by use of NMR spectroscopic and X-ray crystallographic techniques (Fig. 2, Table 2). The structural features in **7** compare well with those found in **1**,<sup>9</sup> including the observed Ir–P and Ir–O distances (2.2797(7) and 2.0163(18) Å, respectively; cf. 2.289(1) and 2.028(3) Å in **1**, respectively), as well as the observation that in **7** the Ir–alkene distances trans to P (2.167(3) and 2.193(3) Å) are statistically longer than the Ir–alkene distances trans to O (2.114(3) and 2.131(3) Å), which is in keeping with the greater trans influence anticipated for a phosphine fragment relative to an alkoxy donor on Ir. Unfortunately, despite maintaining a catalytic activity profile similar to **1** in the hydroamination of **2a** and related substrates, the chiral complex **7** was incapable of inducing any enantioselectivity in the resulting cyclization product (e.g., **2b**) over a range of reaction conditions (1–5 mol% **7**, 80–110 °C).

## Summary and conclusion

In summary, ( $\kappa^2$ -{2-*i*-Pr<sub>2</sub>PC<sub>6</sub>H<sub>4</sub>}O)Ir(COD) (**1**) is an effective precatalyst for the intramolecular hydroamination of unactivated alkenes with pendant secondary alkylamines, providing either pyrrolidine or piperidine heterocycles in the absence of competing alkene isomerization. We have also succeeded in establishing a synthetic pathway to **7**: a chiral relative of **1** that features a 1-aryl-2,5-dialkylphospholane structure derived from (2*S*,5*S*)-2,5-hexanediol cyclic

**Fig. 2.** ORTEP diagram for **7** is shown with 50% displacement ellipsoids; selected hydrogen atoms have been removed for clarity. Selected interatomic distances (Å): Ir–P 2.2797(7), Ir–O 2.0163(18), Ir–C21 2.114(3), Ir–C22 2.131(3), Ir–C25 2.167(3), Ir–C26 2.193(3), P–C2 1.824(3), O–C1 1.343(3).



**Table 2.** Crystallographic data for **7**.

Empirical formula	C <sub>28</sub> H <sub>44</sub> IrOP
Formula weight	619.80
Crystal dimensions (mm <sup>3</sup> )	0.42 × 0.29 × 0.24
Color, habit	Orange, prism
Crystal system	Orthorhombic
Space group	<i>P</i> 2 <sub>1</sub> 2 <sub>1</sub> 2 <sub>1</sub>
<i>a</i> (Å)	10.5353 (10)
<i>b</i> (Å)	12.8694 (12)
<i>c</i> (Å)	19.3425 (18)
<i>V</i> (Å <sup>3</sup> )	2622.5 (4)
<i>Z</i>	4
Range of transmission	0.3701–0.2201
2θ limit (°)	54.96
Collection ranges	−13 ≤ <i>h</i> ≤ 13 −16 ≤ <i>k</i> ≤ 16 −24 ≤ <i>l</i> ≤ 25
Total data collected	22846
Independent reflections	5986
<i>R</i> <sub>int</sub>	0.0240
Observed reflections	5652
Data / restraints / parameters	5986 / 0 / 280
Absolute structure parameter	0.000 (5)
Goodness-of-fit	1.063
<i>R</i> <sub>1</sub> [ <i>F</i> <sub>o</sub> <sup>2</sup> ≥ 2σ( <i>F</i> <sub>o</sub> <sup>2</sup> )]	0.0190
<i>wR</i> <sub>2</sub> [ <i>F</i> <sub>o</sub> <sup>2</sup> ≥ −3σ( <i>F</i> <sub>o</sub> <sup>2</sup> )]	0.0453
Largest peak, hole (e Å <sup>−3</sup> )	1.534, −0.262

sulfate. While **7** failed to provide enantioselectivity in this hydroamination chemistry, the activity of **7** was found to be comparable to that of **1**. Future studies will focus both on preparing alternative chiral variants of **1**, as well as on exploring the mechanism of hydroamination processes mediated by ( $\kappa^2$ -*P,O*)Ir(COD) species to guide the design of increasingly effective catalysts.

## Experimental

### General considerations

All manipulations were conducted in the absence of oxygen and water under an atmosphere of dinitrogen, either by use of standard Schlenk methods or within an MBraun glovebox apparatus, utilizing glassware that was oven-dried (130 °C) and evacuated while hot prior to use. The nondeuterated solvents, tetrahydrofuran, diethyl ether, dichloromethane, benzene, hexanes, and pentane, were deoxygenated and dried by sparging with dinitrogen gas, followed by passage through a double-column solvent purification system purchased from MBraun Inc. Tetrahydrofuran, diethyl ether, and dichloromethane were purified over two alumina-packed columns, while benzene, hexanes, and pentane were purified over one alumina-packed column and one column packed with copper-Q5 reactant. 1,4-Dioxane (Sigma-Aldrich) was dried over Na/benzophenone followed by distillation under an atmosphere of dinitrogen; anhydrous 1,4-dioxane used as received from Sigma-Aldrich provided inferior results. Chloroform-*d*<sub>1</sub> (Cambridge Isotopes) was used as received. C<sub>6</sub>D<sub>6</sub> (Cambridge Isotopes Laboratories) was degassed by using three freeze-pump-thaw cycles and then dried over 3 Å molecular sieves. All solvents used within the glovebox were stored over activated 4 Å molecular sieves. Purification of NEt<sub>3</sub> was achieved by stirring over KOH for 7 d, followed by distillation; the distilled NEt<sub>3</sub> was then refluxed over CaH<sub>2</sub> for 3 d under dinitrogen, followed by distillation. Complex **1**,<sup>9</sup> P(NMe<sub>2</sub>)<sub>2</sub>Cl,<sup>14</sup> (2*S*,5*S*)-2,5-hexanediol cyclic sulfate,<sup>12b</sup> *N*-benzyl-2,2-diphenylpent-4-en-1-amine,<sup>7f</sup> *N*-(4-chlorobenzyl)-2,2-diphenylpent-4-en-1-amine,<sup>2a</sup> methyl 4-[(2,2-diphenylpent-4-enylamino)methyl]benzoate,<sup>7f</sup> *N*-(4-methoxybenzyl)-2,2-diphenylpent-4-en-1-amine,<sup>2a</sup> *N*-(cyclohexylmethyl)-2,2-diphenylpent-4-en-1-amine,<sup>7d</sup> (1-allylcyclohexyl)-*N*-benzylmethanamine,<sup>7f</sup> *N*-benzyl-2,2-dimethylpent-4-en-1-amine,<sup>7f</sup> *N*-benzyl-2-isopropylpent-4-en-1-amine,<sup>7f</sup> *N*-benzyl-2,2-diphenylhex-5-en-1-amine,<sup>7d</sup> and *N*-benzyl-4-methyl-2,2-diphenylpent-4-en-1-amine<sup>15</sup> were synthesized according to literature procedures. The synthetic route to **6** starting from **3** was carried out in accordance with previously published methods.<sup>13</sup> [Ir(COD)Cl]<sub>2</sub> (Strem) was dried in vacuo for ~24 h prior to use. All other reagents were used as received. <sup>1</sup>H, <sup>13</sup>C, and <sup>31</sup>P NMR characterization data were collected at 300 K on a Bruker AV-500 spectrometer operating at 500.1, 125.8, and 202.5 MHz (respectively) with chemical shifts reported in parts per million downfield of SiMe<sub>4</sub>. Elemental analyses were performed by Canadian Microanalytical Service Ltd., Delta, BC, Canada.

### Preparation of **4**

To a magnetically stirred solution of **3** (3.96 g, 12.0 mmol) in diethyl ether (10 mL) at -78 °C was added 4.1 mL of a 2.9 mol/L solution of *n*-BuLi in hexanes, which effected the precipitation of a white solid. The resulting mixture was magnetically stirred for 16 h followed by cooling to -78 °C and the dropwise addition of CIP(NMe<sub>2</sub>)<sub>2</sub> (1.9 mL, 12.0 mmol). The reaction mixture was warmed to ambient temperature and was magnetically stirred for 3 h. The resulting white solid was removed by filtration through a filter stick and from the remaining solution the diethyl ether was removed, which afforded a colorless oil that was

dissolved in anhydrous methanol and was heated in an oil bath at 50 °C for 3 h. Subsequent removal of the solvent afforded a colorless oil that was dissolved in diethyl ether (10 mL). The ethereal solution was added dropwise to a Schlenk tube containing LiAlH<sub>4</sub> (0.60 g, 15.6 mmol) in diethyl ether (7 mL). The resulting green solution was magnetically stirred at ambient temperature for 48 h. The reaction mixture was quenched with degassed distilled H<sub>2</sub>O followed by filtration through a filter stick to remove the solids. The diethyl ether layer was dried over Na<sub>2</sub>SO<sub>4</sub>. Subsequent filtration and removal of the solvent afforded **4** as a light brown oil, which when purified by vacuum distillation at 80–90 °C (10<sup>-3</sup> Torr) was obtained as a colorless oil that was used without further purification (1.21 g, 4.28 mmol, 36%). <sup>1</sup>H NMR (C<sub>6</sub>D<sub>6</sub>) δ: 7.46 (d, <sup>4</sup>J<sub>HH</sub> = 2.5 Hz, 1H, Ar-H), 7.41 (d of d, <sup>3</sup>J<sub>PH</sub> = 7.0 Hz, <sup>4</sup>J<sub>HH</sub> = 2.5 Hz, 1H, Ar-H), 4.96 (s, 2H, CH<sub>2</sub> (MOM)), 3.97 (d, <sup>1</sup>J<sub>PH</sub> = 202.1 Hz, 2H, -PH<sub>2</sub>), 3.40 (s, 3H, CH<sub>3</sub> (MOM)), 1.48 (s, 9H, C(CH<sub>3</sub>)<sub>3</sub>), 1.23 (s, 9H, C(CH<sub>3</sub>)<sub>3</sub>). <sup>13</sup>C{<sup>1</sup>H} NMR (C<sub>6</sub>D<sub>6</sub>) δ: 155.7 (d, J<sub>PC</sub> = 10.9 Hz, Ar-quaternary), 145.4 (d, J<sub>PC</sub> = 3.0 Hz, Ar-quaternary), 141.9 (d, J<sub>PC</sub> = 1.5 Hz, Ar-quaternary), 130.7 (d, <sup>2</sup>J<sub>PC</sub> = 7.4 Hz, Ar-CH), 124.5 (Ar-CH), 123.0 (d, J<sub>PC</sub> = 11.4 Hz, Ar-quaternary), 98.8 (d, <sup>4</sup>J<sub>PC</sub> = 7.9 Hz, CH<sub>2</sub> (MOM)), 56.2 (d, J<sub>PC</sub> = 1.5 Hz, CH<sub>3</sub> (MOM)), 34.6 (d, <sup>2</sup>J<sub>PC</sub> = 0.75 Hz, C(CH<sub>3</sub>)<sub>3</sub>), 33.5 (C(CH<sub>3</sub>)<sub>3</sub>), 30.5 (C(CH<sub>3</sub>)<sub>3</sub>), 30.3 (C(CH<sub>3</sub>)<sub>3</sub>). <sup>31</sup>P{<sup>1</sup>H} NMR (C<sub>6</sub>D<sub>6</sub>) δ: -128.6.

### Preparation of **5**

To a magnetically stirred solution of **4** (0.244 g, 0.860 mmol) in THF (5 mL) was added a 1.45 mol/L solution of *n*-BuLi in hexanes (0.600 mL, 0.860 mmol). The reaction mixture went from colorless to yellow in appearance and was magnetically stirred at ambient temperature for 1.5 h, followed by the addition of a THF (2 mL) solution of (2*S*,5*S*)-2,5-hexanediol cyclic sulfate (0.156 g, 0.860 mmol). The reaction went colorless and was magnetically stirred at ambient temperature for 2 h followed by the addition of a 1.45 mol/L solution of *n*-BuLi in hexanes (0.60 mL, 0.860 mmol). The mixture went yellow and remained that color for the subsequent 2 h of magnetic stirring. The solvent and other volatiles were removed in vacuo affording an off-white solid that was washed with pentane (2 × 3 mL) to effect the precipitation of a gelatinous white solid, which was separated by filtration through Celite. The remaining solvent was removed in vacuo affording **5** as a yellow oil that was used without further purification (0.215 g, 0.59 mmol, 68%). <sup>1</sup>H NMR (C<sub>6</sub>D<sub>6</sub>) δ: 7.53 (d, <sup>4</sup>J<sub>HH</sub> = 2.0 Hz, 1H, Ar-H), 7.39 (m, 1H, Ar-H), 5.81 (t, <sup>5</sup>J<sub>PH</sub> = 4.0 Hz, 1H, CH<sub>2</sub> (MOM)), 5.11 (d, 1H, <sup>5</sup>J<sub>PH</sub> = 3.5 Hz, 1H, CH<sub>2</sub> (MOM)), 3.56 (s, 3H, CH<sub>3</sub> (MOM)), 2.62 (m, 1H, CH (phospholane)), 2.27 (m, 1H, CH (phospholane)), 2.13 (m, 1H, CH<sub>2</sub> (phospholane)), 1.84 (m, 1H, CH<sub>2</sub> (phospholane)), 1.57 (s, 9H, C(CH<sub>3</sub>)<sub>3</sub>), 1.41 (m, 1H, CH<sub>2</sub> (phospholane)), 1.33 (d of d, <sup>3</sup>J<sub>PH</sub> = 19.0 Hz, <sup>3</sup>J<sub>HH</sub> = 6.0 Hz, 3H, CH<sub>3</sub> (phospholane)), 1.31 (s, 9H, C(CH<sub>3</sub>)<sub>3</sub>), 1.25 (m, 1H, CH<sub>2</sub> (phospholane)), 0.93 (d of d, <sup>3</sup>J<sub>PH</sub> = 9.5 Hz, <sup>3</sup>J<sub>HH</sub> = 7.0 Hz, 3H, CH<sub>3</sub> (phospholane)). <sup>13</sup>C{<sup>1</sup>H} NMR (C<sub>6</sub>D<sub>6</sub>) δ: 156.6 (d, <sup>2</sup>J<sub>PC</sub> = 18.5 Hz, Ar-quaternary), 144.4 (Ar-quaternary), 141.6 (d, J<sub>PC</sub> = 0.9 Hz, Ar-quaternary), 130.0 (d, J<sub>PC</sub> = 31.6 Hz, Ar-quaternary), 127.3 (d, <sup>2</sup>J<sub>PC</sub> = 2.3 Hz, Ar-CH), 124.4 (Ar-CH), 98.7 (d, <sup>3</sup>J<sub>PC</sub> = 21.0 Hz, CH<sub>2</sub> (MOM)), 56.2

(d,  $J_{PC} = 1.9$  Hz, CH<sub>3</sub> (MOM)), 35.9 (d,  $^2J_{PC} = 2.4$  Hz, CH<sub>2</sub> (phospholane)), 35.3 (d,  $^2J_{PC} = 2.3$  Hz, CH<sub>2</sub> (phospholane)), 34.6 (d,  $J_{PC} = 1.1$  Hz, C(CH<sub>3</sub>)<sub>3</sub>), 34.1 (d,  $^2J_{PC} = 14.7$  Hz, CH (phospholane)), 33.7 (C(CH<sub>3</sub>)<sub>3</sub>), 33.6 (d,  $^2J_{PC} = 10.9$  Hz, CH (phospholane)), 30.7 (C(CH<sub>3</sub>)<sub>3</sub>), 30.2 (C(CH<sub>3</sub>)<sub>3</sub>), 20.4 (d,  $^3J_{PC} = 35.5$  Hz, CH<sub>3</sub> (phospholane)), 15.0 (d,  $^3J_{PC} = 0.9$  Hz, CH<sub>3</sub> (phospholane)).  $^{31}\text{P}\{^1\text{H}\}$  NMR (C<sub>6</sub>D<sub>6</sub>)  $\delta$ : 2.3.

### Preparation of 6

To a magnetically stirred solution of **5** (0.382 g, 1.05 mmol) in THF (10 mL) was added 5 mol/L HCl (aq.) (5 mL) followed by heating at 50 °C in an oil bath for 16 h. Subsequent removal of the solvent afforded a white solid that was suspended in diethyl ether (10 mL) followed by the addition of 7 mol/L NH<sub>4</sub>OH (aq.) (5 mL), which caused the solution to become homogeneous. The solution was magnetically stirred for 5 h at ambient temperature followed by removal of the solvent and extraction of the residue into pentane (3 × 3 mL). Upon removal of the pentane in vacuo, **6** was obtained as a colorless oil that was used without further purification (0.246 g, 0.767 mmol, 73%).  $^1\text{H}$  NMR (C<sub>6</sub>D<sub>6</sub>)  $\delta$ : 7.72 (d,  $^4J_{PH} = 13.5$  Hz, 1H, OH), 7.52 (d,  $^4J_{HH} = 2.0$  Hz, 1H, Ar-H), 7.27 (m, 1H, Ar-H), 2.53 (m, 1H, CH (phospholane)), 2.05 (m, 2H, CH and CH<sub>2</sub> (phospholane)), 1.78 (m, 1H, CH<sub>2</sub> (phospholane)), 1.60 (s, 9H, C(CH<sub>3</sub>)<sub>3</sub>), 1.53 (m, 1H, CH<sub>2</sub> (phospholane)), 1.32 (s, 9H, C(CH<sub>3</sub>)<sub>3</sub>), 1.15 (d of d,  $^3J_{PH} = 19.5$  Hz,  $^3J_{HH} = 7.0$  Hz, 3H, CH<sub>3</sub> (phospholane)), 1.12 (m, 1H, CH<sub>2</sub> (phospholane)), 0.79 (d of d,  $^3J_{PH} = 11.5$  Hz,  $^3J_{HH} = 7.0$  Hz, 3H, CH<sub>3</sub> (phospholane)).  $^{13}\text{C}\{^1\text{H}\}$  NMR (C<sub>6</sub>D<sub>6</sub>)  $\delta$ : 156.8 (d,  $J_{PC} = 19.4$  Hz, Ar-quaternary), 140.4 (Ar-quaternary), 134.4 (Ar-quaternary), 134.3 (d,  $J_{PC} = 15.8$  Hz, Ar-quaternary), 126.9 (d,  $^2J_{PC} = 2.1$  Hz, Ar-CH), 124.9 (Ar-CH), 36.5 (d,  $^2J_{PC} = 4.2$  Hz, CH<sub>2</sub> (phospholane)), 36.4 (CH<sub>2</sub> (phospholane)), 35.8 (d,  $^1J_{PC} = 4.8$  Hz, CH (phospholane)), 34.4 (C(CH<sub>3</sub>)<sub>3</sub>), 33.5 (C(CH<sub>3</sub>)<sub>3</sub>), 33.2 (d,  $^1J_{PC} = 5.7$  Hz, CH (phospholane)), 30.8 (C(CH<sub>3</sub>)<sub>3</sub>), 28.8 (C(CH<sub>3</sub>)<sub>3</sub>), 19.6 (d,  $^2J_{PC} = 31.7$  Hz, CH<sub>3</sub> (phospholane)), 13.8 (CH<sub>3</sub> (phospholane)).  $^{31}\text{P}\{^1\text{H}\}$  NMR (C<sub>6</sub>D<sub>6</sub>)  $\delta$ : -25.6.

### Preparation of 7

To a magnetically stirred solution of [Ir(COD)Cl]<sub>2</sub> (0.14 g, 0.20 mmol) in THF (2 mL) was added a THF (2 mL) solution of **6** (0.13 g, 0.41 mmol). After 3 h of magnetic stirring, NEt<sub>3</sub> (57  $\mu\text{L}$ , 0.41 mmol) was added, which resulted in an immediate color change from yellow-orange to bright orange. After 2 h of magnetic stirring at ambient temperature,  $^{31}\text{P}$  NMR analysis of the reaction mixture confirmed the consumption of **6** and the quantitative formation of a new product (**7**). The solvent and other volatiles were removed in vacuo and the residual solid was extracted into pentane (3 × 2 mL). Subsequent removal of the solvent afforded **7** as an analytically pure orange solid (0.17 g, 0.28 mmol, 68%).  $^1\text{H}$  NMR (C<sub>6</sub>D<sub>6</sub>)  $\delta$ : 7.57 (d,  $^4J_{HH} = 2.0$  Hz, 1H, Ar-H), 7.05 (d of d,  $^3J_{PH} = 8.5$  Hz,  $^3J_{HH} = 2.5$  Hz, 1H, Ar-H), 5.36 (m, 2H, 2 × CH (COD)), 3.56 (m, 1H, CH (COD)), 3.13 (m, 1H, CH (COD)), 2.54 (m, 1H, CH (phospholane)), 2.27 (m, 3H, CH<sub>2</sub> (COD) and CH (phospholane)), 2.13 (m, 2H, CH<sub>2</sub> (COD)), 1.88 (m, 2H, CH<sub>2</sub> (COD)), 1.83 (m, 1H, CH<sub>2</sub> (phospholane)), 1.78 (m, 1H, CH<sub>2</sub> (phospholane)), 1.72 (m, 2H, CH<sub>2</sub> (COD)), 1.70 (s, 9H,

C(CH<sub>3</sub>)<sub>3</sub>), 1.39 (s, 9H, C(CH<sub>3</sub>)<sub>3</sub>), 1.35 (m, 1H, CH<sub>2</sub> (phospholane)), 1.12 (d of d,  $^3J_{PH} = 17.5$  Hz,  $^3J_{HH} = 7.5$  Hz, 3H, CH<sub>3</sub> (phospholane)), 1.03 (m, 1H, CH<sub>2</sub> (phospholane)), 0.93 (d of d,  $^3J_{PH} = 14.5$  Hz,  $^3J_{HH} = 7.0$  Hz, 3H, CH<sub>3</sub> (phospholane)).  $^{13}\text{C}\{^1\text{H}\}$  NMR (C<sub>6</sub>D<sub>6</sub>)  $\delta$ : 176.6 (d,  $J_{PC} = 18.7$  Hz, Ar-quaternary), 137.1 (d,  $J_{PC} = 6.7$  Hz, Ar-quaternary), 136.7 (d,  $J_{PC} = 8.8$  Hz, Ar-quaternary), 126.6 (d,  $J_{PC} = 2.0$  Hz, Ar-CH), 125.0 (Ar-CH), 116.8 (d,  $J_{PC} = 45.1$  (Ar-quaternary), 92.5 (d,  $^2J_{PC} = 12.7$  Hz, CH (COD)), 91.5 (d,  $^2J_{PC} = 5.4$  Hz, CH (COD)), 51.4 (CH (COD)), 45.9 (CH (COD)), 39.1 (d,  $^1J_{PC} = 43.4$  Hz, CH (phospholane)), 35.7 (CH<sub>2</sub> (phospholane)), 35.3 (d,  $^2J_{PC} = 4.9$  Hz, CH<sub>2</sub> (phospholane)), 34.0 (d,  $^3J_{PC} = 2.9$  Hz, CH<sub>2</sub> (COD)), 33.5 (d,  $^3J_{PC} = 2.8$  Hz, CH<sub>2</sub> (COD)), 33.1 (C(CH<sub>3</sub>)<sub>3</sub>), 33.0 (d,  $^1J_{PC} = 30.3$  Hz, CH (phospholane)), 31.1 (C(CH<sub>3</sub>)<sub>3</sub>), 29.0 (C(CH<sub>3</sub>)<sub>3</sub>), 28.2 (d,  $^3J_{PC} = 2.3$  Hz, CH<sub>2</sub> (COD)), 28.1 (d,  $^3J_{PC} = 2.0$  Hz, CH<sub>2</sub> (COD)), 21.7 (C(CH<sub>3</sub>)<sub>3</sub>), 16.4 (d,  $^2J_{PC} = 8.2$  Hz, CH<sub>3</sub> (phospholane)), 13.9 (d,  $^2J_{PC} = 1.6$  Hz, CH<sub>3</sub> (phospholane)).  $^{31}\text{P}\{^1\text{H}\}$  NMR (C<sub>6</sub>D<sub>6</sub>)  $\delta$ : 40.1. Anal. calcd. for C<sub>28</sub>H<sub>44</sub>IrOP: C 54.23, H 7.16, N 0.00; found: C 54.44, H 7.52, N < 0.3. Crystals suitable for X-ray crystallographic analysis were grown from a concentrated solution of **7** in pentane at -35 °C.

### Representative procedure for the intramolecular hydroamination of unactivated alkenes by secondary alkylamines catalyzed by 1

To a screw-capped vial containing **2a** (82 mg, 0.25 mmol) and a stir-bar was added 0.220 mL of a stock solution of **1** (5.8 mg in 1.000 mL of 1,4-dioxane) and 0.280 mL of 1,4-dioxane (total reaction volume = 0.5 mL). The vial was sealed under N<sub>2</sub> with a cap containing a PTFE septum and, once all the material had dissolved, was removed from the glovebox and was placed in a temperature-controlled aluminum heating block set at 110 °C. After 16 h of magnetic stirring, the vial was removed from the temperature-controlled aluminum heating block, cooled to ambient temperature, diluted with CH<sub>2</sub>Cl<sub>2</sub> (2 mL), and was washed with brine (2 × 2 mL). The organic extracts were combined, dried over Na<sub>2</sub>SO<sub>4</sub>, and concentrated. The resulting residue was purified by flash column chromatography on silica gel (hexanes/EtOAc = 20:1) to yield **2b** as a white solid (74 mg, 0.23 mmol, 92%) that afforded analytical data in agreement with data reported in the literature.<sup>7f</sup>

### 1-Benzyl-2-methyl-4,4-diphenylpyrrolidine (Table 1, entry 1)

The indicated compound was purified by flash chromatography on silica gel (EtOAc/hexanes = 20:1) in a 92% yield (74 mg) as a white solid.<sup>7f</sup>  $^1\text{H}$  NMR (CDCl<sub>3</sub>)  $\delta$ : 7.53–7.19 (m, 15H), 4.21 (d,  $J = 13.5$  Hz, 1H), 3.77 (d,  $J = 9.5$  Hz, 1H), 3.38 (d,  $J = 13.5$  Hz, 1H), 3.07–2.89 (m, 3H), 2.34 (d of d,  $J = 13.0, 8.0$  Hz, 1H), 1.29 (d,  $J = 6.5$  Hz, 3H).  $^{13}\text{C}\{^1\text{H}\}$  NMR (CDCl<sub>3</sub>)  $\delta$ : 150.6, 148.7, 140.1, 128.6, 128.2, 128.1, 127.8, 127.4, 127.2, 126.7, 125.8, 125.4, 66.4, 59.6, 58.0, 52.5, 48.0, 19.5.

### 1-(4-Chlorobenzyl)-2-methyl-4,4-diphenylpyrrolidine (Table 1, entry 2)

The indicated compound was purified by flash chromatography on silica gel (*n*-pentane/Et<sub>2</sub>O = 30:1) in an 86%



yield (78 mg) as a white solid.<sup>2a</sup> <sup>1</sup>H NMR (CDCl<sub>3</sub>)  $\delta$ : 7.43–7.17 (m, 14H), 4.12 (d,  $J$  = 13.5 Hz, 1H), 3.71 (d,  $J$  = 10.0 Hz, 1H), 3.33 (d,  $J$  = 13.5 Hz, 1H), 3.05–2.89 (m, 2H), 2.87 (d,  $J$  = 9.5 Hz, 1H), 2.33 (d of d,  $J$  = 12.5, 7.9 Hz, 1H), 1.26 (d,  $J$  = 6.5 Hz, 3H). <sup>13</sup>C{<sup>1</sup>H} NMR (CDCl<sub>3</sub>)  $\delta$ : 150.4, 148.6, 138.6, 132.4, 129.8, 128.3, 128.1, 127.8, 127.3, 127.1, 125.8, 125.5, 66.3, 59.6, 57.2, 52.5, 47.8, 19.5.

**Methyl 4-(2-methyl-4,4-diphenylpyrrolidin-1-ylmethyl)-benzoate (Table 1, entry 3)**

The indicated compound was purified by flash chromatography on silica gel (*n*-pentane/Et<sub>2</sub>O = 8:1) in a 85% yield (82 mg) as a colorless oil.<sup>7f</sup> <sup>1</sup>H NMR (CDCl<sub>3</sub>)  $\delta$ : 8.07 (d,  $J$  = 8.0 Hz, 2H), 7.50 (d,  $J$  = 8.5 Hz, 2H), 7.35–7.15 (m, 10H), 4.16 (d,  $J$  = 14.0 Hz, 1H), 3.98 (s, 3H), 3.68 (d,  $J$  = 10.0 Hz, 1H), 3.39 (d,  $J$  = 13.5 Hz, 1H), 3.02–2.88 (m, 2H), 2.86 (d,  $J$  = 10.0 Hz, 1H), 2.31 (d of d,  $J$  = 13.0, 7.5 Hz, 1H), 1.23 (d,  $J$  = 5.5 Hz, 3H). <sup>13</sup>C{<sup>1</sup>H} NMR (CDCl<sub>3</sub>)  $\delta$ : 167.1, 150.3, 148.5, 145.7, 129.6, 128.7, 128.4, 128.1, 127.8, 127.3, 127.1, 125.8, 125.5, 66.4, 59.7, 57.7, 52.6, 51.9, 47.8, 19.5.

**1-(4-Methoxybenzyl)-2-methyl-4,4-diphenylpyrrolidine (Table 1, entry 4)**

The indicated compound was purified by flash chromatography on silica gel (*n*-pentane/Et<sub>2</sub>O = 15:1) in a 87% yield (77 mg) as a colorless oil.<sup>2a</sup> <sup>1</sup>H NMR (CDCl<sub>3</sub>)  $\delta$ : 7.29 (m, 1H), 7.00–6.95 (m, 2H), 4.13 (d,  $J$  = 13.0 Hz, 1H), 3.90 (s, 3H), 3.74 (d,  $J$  = 10.0 Hz, 1H), 3.30 (d,  $J$  = 13.0 Hz, 1H), 3.02 (d of d,  $J$  = 13.0, 7.5 Hz, 1H), 2.96–2.85 (m, 2H), 2.30 (d of d,  $J$  = 13.0, 7.5 Hz, 1H), 1.27 (d,  $J$  = 6.0 Hz, 3H). <sup>13</sup>C{<sup>1</sup>H} NMR (CDCl<sub>3</sub>)  $\delta$ : 158.5, 150.6, 148.7, 132.0, 129.6, 128.1, 127.8, 127.4, 127.2, 125.7, 125.3, 113.5, 66.3, 59.5, 57.2, 55.2, 52.4, 48.0, 19.5.

**1-Cyclohexylmethyl-2-methyl-4,4-diphenylpyrrolidine (Table 1, entry 5)**

The indicated compound was purified by flash chromatography on silica gel (hexanes/EtOAc = 8:1) in a 89% yield (75 mg) as a white solid.<sup>7d</sup> <sup>1</sup>H NMR (CDCl<sub>3</sub>)  $\delta$ : 7.38–7.21 (m, 9H), 7.16 (m, 1H), 3.87 (d,  $J$  = 9.5 Hz, 1H), 2.87 (d of d,  $J$  = 13.0, 7.5 Hz, 1H), 2.82 (d,  $J$  = 10.0 Hz, 1H), 2.66 (m, 1H), 2.56 (m, 1H), 2.18–2.03 (m, 3H), 1.82–1.63 (m, 4H), 1.53 (m, 1H), 1.36–1.15 (m, 3H), 1.10 (d,  $J$  = 6.0 Hz, 3H), 1.02–0.87 (m, 2H). <sup>13</sup>C{<sup>1</sup>H} NMR (CDCl<sub>3</sub>)  $\delta$ : 151.3, 148.9, 128.1, 127.8, 127.6, 127.3, 125.7, 125.4, 67.6, 61.4, 60.3, 52.8, 48.1, 37.3, 32.2, 31.9, 26.9, 26.3, 26.1, 19.6.

**2-Benzyl-3-methyl-2-aza-spiro[4,5]decane (Table 1, entry 6)**

The indicated compound was purified by flash chromatography on silica gel (hexanes/EtOAc = 20:1) in a 85% yield (52 mg) as a colorless oil.<sup>7f</sup> <sup>1</sup>H NMR (CDCl<sub>3</sub>)  $\delta$ : 7.40–7.24 (m, 5H), 4.06 (d,  $J$  = 13.0 Hz, 1H), 3.14 (d,  $J$  = 13.5 Hz, 1H), 2.82 (d,  $J$  = 9.5 Hz, 1H), 2.54 (m, 1H), 1.91 (d,  $J$  = 9.5 Hz, 1H), 1.80 (d of d,  $J$  = 12.0, 7.0 Hz, 1H), 1.56–1.27 (m, 11H), 1.19 (d,  $J$  = 6.0 Hz, 3H). <sup>13</sup>C{<sup>1</sup>H} NMR (CDCl<sub>3</sub>)  $\delta$ : 140.0, 128.6, 128.0, 126.5, 66.6, 59.0, 58.0, 47.0, 39.3, 39.2, 38.5, 26.1, 23.6, 23.5, 19.3.

**1-Benzyl-2,4,4-trimethylpyrrolidine (Table 1, entry 7)**

The indicated compound was purified by flash chroma-

tography on silica gel (hexanes/EtOAc = 20:1) in a 86% yield (44 mg) as a colorless oil.<sup>7f</sup> <sup>1</sup>H NMR (CDCl<sub>3</sub>)  $\delta$ : 7.39–7.23 (m, 5H), 4.05 (d,  $J$  = 14.5 Hz, 1H), 3.15 (d,  $J$  = 13.5 Hz, 1H), 2.67 (d,  $J$  = 9.0 Hz, 1H), 2.59 (m, 1H), 1.98 (d,  $J$  = 9.0 Hz, 1H), 1.76 (d of d,  $J$  = 12.0, 7.5 Hz, 1H), 1.35 (d of d,  $J$  = 12.5, 9.0 Hz, 1H), 1.19 (d,  $J$  = 6.0 Hz, 3H), 1.11 (s, 3H), 1.01 (s, 3H). <sup>13</sup>C{<sup>1</sup>H} NMR (CDCl<sub>3</sub>)  $\delta$ : 140.1, 128.7, 128.0, 126.5, 68.4, 59.7, 58.0, 49.1, 35.4, 30.9, 29.2, 19.4.

**1-Benzyl-2-methyl-4-isopropylpyrrolidine (Table 1, entry 8)**

The indicated compound was obtained in 87% yield with a diastereomeric ratio of 1.3:1 on the basis of <sup>1</sup>H NMR using 1,4-bis(trifluoromethyl)benzene as an internal standard.<sup>7f</sup>

**1-Benzyl-2-methyl-5,5-diphenylpiperidine (Table 1, entry 9)**

The indicated compound was purified by flash chromatography on silica gel (hexanes/EtOAc = 20:1) in a 85% yield (73 mg) as a colorless oil.<sup>7d</sup> <sup>1</sup>H NMR (CDCl<sub>3</sub>)  $\delta$ : 7.46–7.14 (m, 15H), 4.13 (d,  $J$  = 13.5 Hz, 1H), 3.43 (d,  $J$  = 12.5 Hz, 1H), 3.21 (d,  $J$  = 13.5 Hz, 1H), 3.60–2.50 (m, 3H), 2.25 (m, 1H), 1.70 (m, 1H), 1.45 (m, 1H), 1.21 (d,  $J$  = 6.0 Hz, 3H). <sup>13</sup>C{<sup>1</sup>H} NMR (CDCl<sub>3</sub>)  $\delta$ : 148.6, 146.7, 139.4, 129.5, 128.4, 128.0, 127.9, 127.6, 127.0, 126.9, 125.6, 125.3, 61.0, 58.9, 56.1, 46.5, 34.2, 31.0, 18.6.

**1-Benzyl-2-(2-dimethyl-4,4-diphenylpyrrolidine (Table 1, entry 10)**

The indicated compound was purified by flash chromatography on silica gel (EtOAc/hexanes = 20:1) in a 92% yield (78 mg) as a white solid.<sup>15</sup> <sup>1</sup>H NMR (CDCl<sub>3</sub>)  $\delta$ : 7.52–7.20 (m, 15H), 3.73 (s, 2H), 3.41 (s, 2H), 2.74 (s, 2H), 1.26 (s, 6H). <sup>13</sup>C{<sup>1</sup>H} NMR (CDCl<sub>3</sub>)  $\delta$ : 149.7, 140.9, 128.5, 128.1, 127.8, 127.2, 126.7, 125.4, 6.1, 60.4, 54.4, 52.4, 51.6, 25.1.

**Crystallographic characterization of 7**

Crystallographic data were obtained at 193 ( $\pm$ 2) K on a Bruker PLATFORM/SMART 1000 CCD diffractometer using a graphite-monochromated Mo K $\alpha$  ( $\lambda$  = 0.71073 Å) radiation, employing a sample that was mounted in inert oil and transferred to a cold gas stream on the diffractometer. Programs for diffractometer operation, data collection, and data reduction were supplied by Bruker. SADABS was employed as the absorption correction method. The structure was solved by use of a Patterson search/structure expansion and refinement was carried out by use of full-matrix least-squares procedures (on  $F^2$ ) with  $R_1$  based on  $F_o^2 \geq 2\sigma(F_o^2)$  and  $wR_2$  based on  $F_o^2 \geq -3\sigma(F_o^2)$ . All hydrogen atoms were added at calculated positions and refined by use of a riding model employing isotropic displacement parameters based on the isotropic displacement parameter of the attached atom. The near-zero final refined value of the absolute structure parameter (0.000(5)) supported that the correct absolute structure had been chosen.<sup>16</sup> See the Supplementary data section for information on obtaining the complete supplementary crystallographic data for this paper. The thermal ellipsoid plot of 7 was generated by use of ORTEP-3 for Windows.<sup>17</sup>



## Supplementary data

Supplementary data for this article are available on the journal Web site (canjchem.nrc.ca). CCDC 744698 contains the X-ray data in CIF format for this manuscript. These data can be obtained, free of charge, via [www.ccdc.cam.ac.uk/conts/retrieving.html](http://www.ccdc.cam.ac.uk/conts/retrieving.html) (Or from the Cambridge Crystallographic Data Centre, 12 Union Road, Cambridge CB2 1EZ, UK; fax +44 1223 336033; or deposit@ccdc.cam.ac.uk).

## Acknowledgement

Acknowledgment is made to Dalhousie University (Halifax, NS) and the Natural Sciences and Engineering Research Council of Canada (including a Discovery Grant for M. S. and a Canada Graduate Scholarship for K. D. H.). We also thank Dr. Michael Lumsden (Nuclear Magnetic Resonance Research Resource (NMR-3), Dalhousie University) for assistance in the acquisition of NMR data.

## References

- (1) (a) Hartwig, J. F. *Nature* **2008**, *455* (7211), 314. doi:10.1038/nature07369. PMID:18800130.; (b) Surry, D. S.; Buchwald, S. L. *Angew. Chem. Int. Ed.* **2008**, *47* (34), 6338. doi:10.1002/anie.200800497.; (c) Hartwig, J. F. *Acc. Chem. Res.* **2008**, *41* (11), 1534. doi:10.1021/ar800098p. PMID:18681463.; (d) Müller, T. E.; Hultsch, K. C.; Yus, M.; Foubelo, F.; Tada, M. *Chem. Rev.* **2008**, *108* (9), 3795. doi:10.1021/cr0306788. PMID:18729420.
- (2) (a) Ackermann, L.; Kaspar, L. T.; Althammer, A. *Org. Biomol. Chem.* **2007**, *5* (12), 1975. doi:10.1039/b706301f. PMID:17551648.; (b) Schlummer, B.; Hartwig, J. F. *Org. Lett.* **2002**, *4* (9), 1471. doi:10.1021/ol025659j. PMID:11975606.
- (3) (a) For some recent lead references, see: Yuen, H. F.; Marks, T. J. *Organometallics* **2009**, *28* (8), 2423. doi:10.1021/om9000023.; (b) Lu, E.; Gan, W.; Chen, Y. *Organometallics* **2009**, *28* (7), 2318. doi:10.1021/om900040r.; (c) Aillaud, I.; Collin, J.; Duhayon, C.; Guillot, R.; Lyubov, D.; Schulz, E.; Trifonov, A. *Chem. Eur. J.* **2008**, *14* (7), 2189. doi:10.1002/chem.200701090.; (d) Ge, S.; Meetsma, A.; Hessen, B. *Organometallics* **2008**, *27* (20), 5339. doi:10.1021/om8005382.; (e) Stubbert, B. D.; Marks, T. J. *J. Am. Chem. Soc.* **2007**, *129* (14), 4253. doi:10.1021/ja0665444. PMID:17371022.; (f) Stubbert, B. D.; Marks, T. J. *J. Am. Chem. Soc.* **2007**, *129* (19), 6149. doi:10.1021/ja0675898. PMID:17441716.
- (4) (a) For some recent lead references, see: Zhang, W.; Werness, J. B.; Tang, W. *Tetrahedron* **2009**, *65* (16), 3090. doi:10.1016/j.tet.2008.09.045.; (b) Crimmin, M. R.; Arrow-smith, M.; Barrett, A. G. M.; Casely, I. J.; Hill, M. S.; Procopiou, P. A. *J. Am. Chem. Soc.* **2009**, *131* (28), 9670. doi:10.1021/ja9003377. PMID:19552442.; (c) Datta, S.; Gerner, M. T.; Roesky, P. W. *Organometallics* **2008**, *27* (6), 1207. doi:10.1021/om701014d.; (d) Martínez, P. H.; Hultsch, K. C.; Hampel, F. *Chem. Commun. (Camb.)* **2006**, 2221. doi:10.1039/b518360j. PMID:16718309.
- (5) (a) For some recent lead references, see: Lee, A. V.; Sajitz, M.; Schafer, L. L. *Synthesis* **2009**, 97. doi:10.1055/s-0028-1083279.; (b) Lian, B.; Spaniol, T. P.; Horrillo-Martinez, P.; Hultsch, K. C.; Okuda, J. *Eur. J. Inorg. Chem.* **2009**, 2009 (3), 429. doi:10.1002/ejic.200800977.; (c) Majumder, S.; Odom, A. L. *Organometallics* **2008**, *27* (6), 1174. doi:10.1021/om700883a.; (d) Wood, M. C.; Leitch, D. C.; Yeung, C. S.; Kozak, J. A.; Schafer, L. L. *Angew. Chem. Int. Ed.* **2007**, *46* (3), 354. doi:10.1002/anie.200603017.; (e) Lee, A. V.; Schafer, L. L. *Eur. J. Inorg. Chem.* **2007**, 2245, and refs. cited therein. doi:10.1002/ejic.200700036.
- (6) (a) For examples involving the late metal-mediated addition of secondary amides, carbamates, or ureas to unactivated olefins, see: Cochran, B. M.; Michael, F. E. *J. Am. Chem. Soc.* **2008**, *130* (9), 2786. doi:10.1021/ja0734997. PMID:18254623.; (b) Cochran, B. M.; Michael, F. E. *Org. Lett.* **2008**, *10* (2), 329. doi:10.1021/ol702891p. PMID:18154298.; (c) Komeyama, K.; Morimoto, T.; Takaki, K. *Angew. Chem. Int. Ed.* **2006**, *45* (18), 2938. doi:10.1002/anie.200503789.; (d) Michael, F. E.; Cochran, B. M. *J. Am. Chem. Soc.* **2006**, *128* (13), 4246. doi:10.1021/ja060126h. PMID:16568997.; (e) Bender, C. F.; Widenhoefer, R. A. *Chem. Commun. (Camb.)* **2006**, 4143. doi:10.1039/b608638a. PMID:17024275.; (f) Bender, C. F.; Widenhoefer, R. A. *Org. Lett.* **2006**, *8* (23), 5303. doi:10.1021/ol062107i. PMID:17078703.; (g) Zhang, J.; Yang, C.-G.; He, C. J. *Am. Chem. Soc.* **2006**, *128* (6), 1798. doi:10.1021/ja053864z. PMID:16464072.; (h) Liu, X.-Y.; Li, C.-H.; Che, C.-M. *Org. Lett.* **2006**, *8* (13), 2707. doi:10.1021/ol060719x. PMID:16774237.; (i) Han, X.; Widenhoefer, R. A. *Angew. Chem. Int. Ed.* **2006**, *45* (11), 1747. doi:10.1002/anie.200600052.
- (7) (a) The late metal-mediated addition of secondary alkyl- or aryl-amines to unactivated olefins is limited to the following reports: Hesp, K. D.; Stradiotto, M. *Org. Lett.* **2009**, *11* (6), 1449. doi:10.1021/ol900174f. PMID:19231849.; (b) Ohmiya, H.; Moriya, T.; Sawamura, M. *Org. Lett.* **2009**, *11* (10), 2145. doi:10.1021/ol9007712. PMID:19379007.; (c) Bender, C. F.; Hudson, W. B.; Widenhoefer, R. A. *Organometallics* **2008**, *27* (10), 2356. doi:10.1021/om8000982.; (d) Liu, Z.; Hartwig, J. F. *J. Am. Chem. Soc.* **2008**, *130* (5), 1570. doi:10.1021/ja710126x. PMID:18183986.; (e) Bauer, E. B.; Andavan, G. T. S.; Hollis, T. K.; Rubio, R. J.; Cho, J.; Kucheneiser, G. R.; Helgert, T. R.; Letko, C. S.; Tham, F. S. *Org. Lett.* **2008**, *10* (6), 1175. doi:10.1021/ol8000766. PMID:18293992.; (f) Bender, C. F.; Widenhoefer, R. A. *J. Am. Chem. Soc.* **2005**, *127* (4), 1070. doi:10.1021/ja043278q. PMID:15669824.
- (8) For a review documenting the use of Ir complexes as catalysts for the hydroamination of activated alkenes as well as aminoalkynes, see: Dorta, R. In *Iridium Complexes in Organic Synthesis*; Oro, L. A., Claver, C., Eds.; Wiley-VCH: Weinheim, Germany, 2009; pp 145–172.
- (9) Hesp, K. D.; Wechsler, D.; Cipot, J.; Myers, A.; McDonald, R.; Ferguson, M. J.; Schatte, G.; Stradiotto, M. *Organometallics* **2007**, *26* (22), 5430. doi:10.1021/om7006437.
- (10) Note added in proof: Following the acceptance of this manuscript, the enantioselective cyclohydroamination of unactivated alkenes in good yields with excellent enantioselectivities was reported, see: Shen, X.; Buchwald, S. L. *Angew. Chem. Int. Ed.* **2010**, *49*, 564. doi:10.1002/anie.200905402.
- (11) (a) Dorta, R.; Egli, P.; Zürcher, F.; Togni, A. *J. Am. Chem. Soc.* **1997**, *119* (44), 10857. doi:10.1021/ja972594k.; (b) Zhou, J. S.; Hartwig, J. F. *J. Am. Chem. Soc.* **2008**, *130* (37), 12220. doi:10.1021/ja803523z. PMID:18715004.
- (12) (a) 1-Aryl-2,5-dialkylphospholane chiral fragments are established motifs in asymmetric catalysis, see: Nandi, M.; Jin, J.; RajanBabu, T. V. *J. Am. Chem. Soc.* **1999**, *121* (42), 9899. doi:10.1021/ja992493h.; (b) Burk, M. J.; Feaster, J. E.; Nugent, W. A.; Harlow, R. L. *J. Am. Chem. Soc.* **1993**, *115* (22), 10125. doi:10.1021/ja00075a031.; (c) Clark, T. P.;

- Landis, C. R. *Tetrahedron Asymmetry* **2004**, *15* (14), 2123. doi:10.1016/j.tetasy.2004.06.025.
- (13) Heinicke, J.; He, M.; Kadyrov, R.; Jones, P. G. *Heteroat. Chem.* **1998**, *9* (2), 183. doi:10.1002/(SICI)1098-1071(1998)9:2<183::AID-HC14>3.0.CO;2-N.
- (14) Berens, U.; Englert, U.; Geyser, S.; Runsink, J.; Salzer, A. *Eur. J. Org. Chem.* **2006**, *2006* (9), 2100. doi:10.1002/ejoc.200500937.
- (15) Dochnahl, M.; Pissarek, J.-W.; Blechert, S.; Löhnwitz, K.; Roesky, P. W. *Chem. Commun. (Camb.)* **2006**, 3405. doi:10.1039/b607597e. PMID:16896476.
- (16) The Flack absolute structure parameter will refine to a value near zero if the structure is in the correct configuration and will refine to a value near one for the inverted configuration, see: Flack, H. D.; Bernardinelli, G. *J. Appl. Cryst.* **2000**, *33* (4), 1143. doi:10.1107/S0021889800007184.
- (17) *ORTEP-3 for Windows*, version 1.074: Farrugia, L. J. *J. Appl. Cryst.* **1997**, *30* (5), 565. doi:10.1107/S0021889897003117.

# An ab initio study of model triazene-based anticancer agents

Katherine G. Doucet, Julie F. Glistler, and Cory C. Pye

**Abstract:** A computational study of a series of model triazene-based anticancer agents based on methyl- and amidyl-substituted 5-(1-triazenyl)imidazoles has been carried out, including the drugs Dacarbazine, Temozolomide, and Mitozolomide. A number of different conformers are analyzed. The transition states for the gas-phase and water-mediated triazene tautomerization reaction are found and the barriers are determined.

**Key words:** ab initio, triazene, Dacarbazine, Temozolomide, conformational analysis.

**Résumé :** On a effectué des calculs théoriques sur une série d'agents anticancéreux modèles dérivés du triazène et à base de 5-(1-triazenyl)imidazoles substitués par des groupes méthyles et amidyles, dont les médicaments dacarbazine, témozolomide et mitozolomide. On en a analysé un certain nombre de conformères. On a pu trouver les états de transition des réactions de tautomérisation du triazène en phase gazeuse ainsi que sous la catalyse par l'eau et on en a déterminé les barrières.

**Mots-clés :** ab initio, triazène, dacarbazine, témozolomide, mitozolomide, analyse conformationnelle.

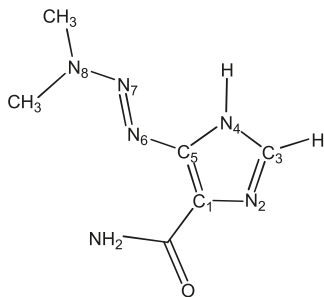
[Traduit par la Rédaction]

## Introduction

Dacarbazine, 5-(3,3-dimethyl-1-triazenyl)imidazole-4-carboxamide (Fig. 1), is the single most-reactive agent known for the treatment of malignant melanoma.<sup>1–3</sup> Dacarbazine and the closely related drug Temozolomide contain the triazene moiety, which could potentially act as an excellent leaving group if a methyltriazenes is attacked by a nucleophilic part of DNA.<sup>4,5</sup>

Our group has previously studied triazene and its mono-, di-, and tri-methyl analogues.<sup>6</sup> In addition, we have examined the S<sub>N</sub>2 reaction of mono-,<sup>7</sup> di-,<sup>8</sup> and tri-methyltriazenes<sup>9</sup> with the halide ions F<sup>–</sup>, Cl<sup>–</sup>, Br<sup>–</sup>, and I<sup>–</sup>. This work<sup>10</sup> extends the results of ref. 6 to more realistic models of this class of anticancer drugs and shall provide a basis for additional study of their S<sub>N</sub>2 reactions.

**Fig. 1.** The chemical structure of 5-(3,3-dimethyl-1-triazenyl)imidazole-4-carboxamide (Dacarbazine, DTIC®).



## Method

Gaussian 98<sup>11</sup> or Gaussian 03<sup>12</sup> were used to carry out all calculations for this computational study. Geometry optimizations were performed at the HF/STO-3G, HF/3-21G, HF/6-31G(d), HF/6-31+G(d), MP2/6-31G(d), MP2/6-31+G(d), B3LYP/6-31G(d), B3LYP/6-31+G(d), and B3LYP/6-31G(d,p) levels of theory. The role of polarization functions on hydrogen was found to be minor (footnote 2 of ref. 6). For MP2 calculations, the frozen core approximation was utilized. Harmonic vibrational frequencies and zero-point vibrational energy (ZPVE) corrections were performed at the previously mentioned levels of theory. Harmonic vibrational frequency calculations characterized the geometry optimizations. A previously determined scaling factor was used to correct the ZPVE.<sup>13</sup> Only the results at MP2/6-31+G(d) and B3LYP/6-31+G(d) will be presented, the rest are given in the Supplementary material. To allow direct comparison with our previous work,<sup>6–9</sup> we do not invoke temperature, free energy, and solvation corrections, which might affect the values given by a few kJ/mol. In addition, we do not consider the effect of intramolecular basis set superposition error<sup>14</sup> because of the difficulty of assigning interacting fragments.

## Results and discussion

### 5-(1-Triazenyl)imidazole

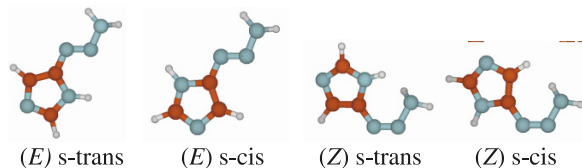
5-(1-Triazenyl)imidazole, henceforth abbreviated TI, like triazene itself, can exist as either an (*E*) or (*Z*) isomer. For

Received 11 December 2009. Accepted 9 February 2010. Published on the NRC Research Press Web site at canjchem.nrc.ca on 23 April 2010.

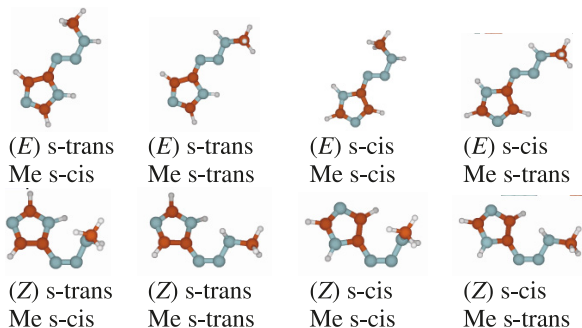
This article is part of a Special Issue dedicated to Professor R. J. Boyd.

K.G. Doucet, J.F. Glistler, and C.C. Pye.<sup>1</sup> Department of Chemistry, Saint Mary's University, Halifax, NS B3H 3C3, Canada.

<sup>1</sup>Corresponding author (e-mail: cory.pye@smu.ca).

**Fig. 2.** The four forms of 5-(1-triazenyl)imidazole.**Table 1.** Energies of TI (kJ/mol) relative to (E) s-trans.

	MP2/6-31+G(d)	B3LYP/6-31+G(d)
(E) s-cis	7.4	6.5
(Z) s-trans	43.5	47.5
(Z) s-cis	29.0	33.1

**Fig. 3.** The eight forms of 5-(3-methyl-1-triazenyl)imidazole.

each isomer, two conformations can exist, syn-periplanar (s-cis) or anti-periplanar (s-trans), which describe the relationship of the N=N and C=C double bonds about the C–N single bond between the triazene and imidazole moieties. There are thus four possibilities (Fig. 2).

The (E) s-trans form was found to be the most stable of the four minimum-energy structures (Table 1). The (E) s-cis form was slightly higher in energy. The (Z) forms, as expected, were significantly higher in energy, with the (Z) s-cis form being lower in energy than the (Z) s-trans form.

For the (E) forms, the triazene unit was found to be coplanar with the planar imidazole ring; however, for the (Z) forms, significant deviation from planarity ( $10^\circ$ – $30^\circ$ ) is noted (Supplementary material, Table S4). This suggests a significant steric interaction between the terminal amine of the triazene and the imidazole ring hydrogens, and concomitant partial breaking of conjugation between the double bonds.

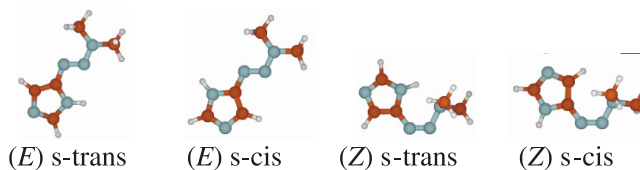
### 5-(3-Methyl-1-triazenyl)imidazole

5-(3-Methyl-1-triazenyl)imidazole (MTI), in addition to having the conformational degrees of freedom present for TI, can also have the methyl group in either an s-cis or s-trans relationship with respect to the N=N double bond, to give eight possible conformations (Fig. 3).

The (E) form with an s-trans imidazole and an s-cis methyl group ((E) s-trans Me s-cis) was found to be the most stable of the eight configurations (see Table 2). For the (E) isomers, the Me s-cis conformers are more stable than the Me s-trans, whereas for the (Z) isomers, the Me s-cis conformers are less stable than the Me s-trans conformers. These trends are the same as those of dimethyltriazene

**Table 2.** Energies of MTI (kJ/mol) relative to (E) s-trans, Me s-cis, ((E) (t,c)).

	MP2/6-31+G(d)	B3LYP/6-31+G(d)
(E) (t,t)	4.2	1.5
(E) (c,c)	7.2	5.9
(E) (c,t)	11.4	7.3
(Z) (t,c)	57.9	65.2
(Z) (t,t)	45.4	52.4
(Z) (c,c)	62.4	67.4
(Z) (c,t)	28.9	34.9

**Fig. 4.** The four forms of 5-(3,3-dimethyl-1-triazenyl)imidazole.**Table 3.** Energies of DTI (kJ/mol) relative to (E) s-trans.

	MP2/6-31+G(d)	B3LYP/6-31+G(d)
(E) s-cis	7.3	5.7
(Z) s-trans	54.7	65.3
(Z) s-cis	59.1	68.8

and can be explained similarly through a combination of hyperconjugation and steric interaction arguments.<sup>6</sup> In particular, the strong steric interaction between the methyl group and the imidazole ring in the two (Z) Me s-cis conformers causes the triazene unit to significantly distort by rotation about the N–N bond. This reduces the steric interaction in such a way that the imidazole and triazene units of the (Z) Me s-cis forms actually are more coplanar than the (Z) s-trans (i.e., the steric interaction is reduced by rotating about the N<sub>7</sub>–N<sub>8</sub> bond instead of the C<sub>5</sub>–N<sub>6</sub> bond).

### 5-(3,3-Dimethyl-1-triazenyl)imidazole

5-(3,3-Dimethyl-1-triazenyl)imidazole (DTI), like the parent TI, would be expected to have four configurations, as shown in Fig. 4.

The (E) s-trans form is the most stable configuration (see Table 3). The (E) isomers are more stable than the (Z) isomers, and the s-trans conformers are more stable than the s-cis conformers. Relative to TI, the (Z) forms are much more destabilized. An interesting observation is that the imidazole ring is nearly planar with the triazene moiety, even for the (Z) forms, in which the amine group has rotated to avoid steric congestion (Supplementary material, Table S12).

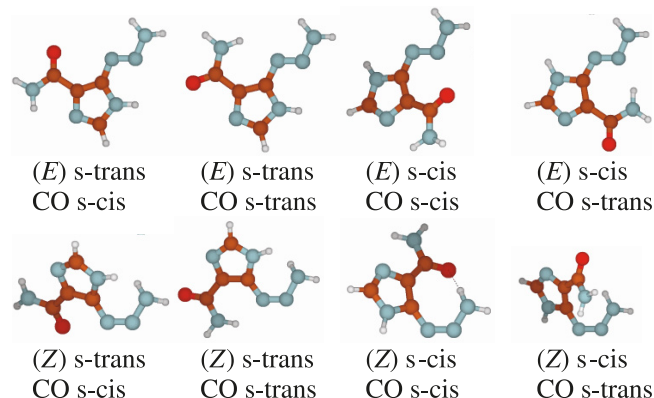
### 5-(1-Triazenyl)imidazole-4-carboxamide

5-(1-Triazenyl)imidazole-4-carboxamide (TIC), possesses the degrees of freedom of TI, and also contains a carboxamide group in which the C=O moiety may exist in either an s-cis or s-trans relation to the C=C of the imidazole ring. Eight configurations are expected (Fig. 5).

The (E) s-trans, CO s-cis conformation was the most stable configuration (Table 4). The (E) isomers are more stable



**Fig. 5.** The eight forms of 5-(1-triazenyl)imidazole-4-carboxamide. The (*Z*) (t,c) form reverts to the (c,c) form at the HF/6-31G\*, HF/6-31+G\*, MP2/6-31+G\*, and B3LYP/6-31+G\* levels.



**Table 4.** Energies of TIC (kJ/mol) relative to (*E*) s-trans, CO s-cis.

	MP2/6-31+G(d)	B3LYP/6-31+G(d)
( <i>E</i> ) (t,t)	13.0	12.0
( <i>E</i> ) (c,c)	11.8	9.4
( <i>E</i> ) (c,t)	28.4	27.4
( <i>Z</i> ) (t,c)	(c,c)	(c,c)
( <i>Z</i> ) (t,t)	52.7	58.3
( <i>Z</i> ) (c,c)	15.6	15.2
( <i>Z</i> ) (c,t)	62.4	72.7

than the (*Z*) isomers (with one exception), and the s-trans conformers are more stable than the corresponding s-cis conformers. The CO s-cis forms are more stable than the corresponding CO s-trans forms. The (*Z*) s-cis, CO s-cis conformer is unusually stable because of the internal NH...O hydrogen bond that can be formed. A short contact is also found in (*Z*) s-cis, CO s-trans (CONH...NH<sub>2</sub>N=N) for those levels with diffuse basis sets (see Supplementary material, Table S20), and the carbonyl group twists out of the plane somewhat at all levels (Supplementary material, Table S19).

### 5-(3-Methyl-1-triazenyl)imidazole-4-carboxamide

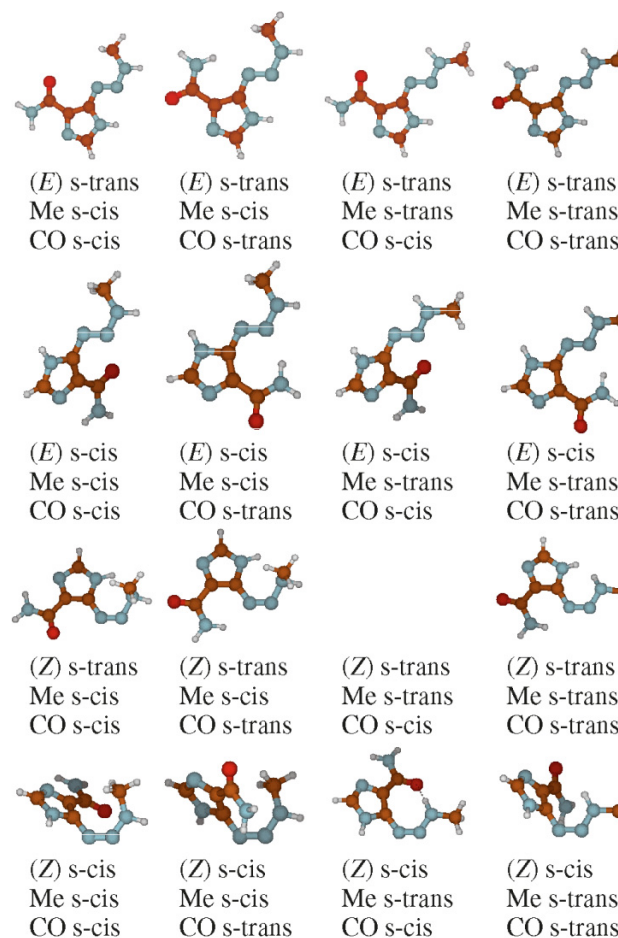
5-(3-Methyl-1-triazenyl)imidazole-4-carboxamide (MTIC) has 16 possible configurations (Fig. 6). The (*E*) s-trans (Me s-cis, CO s-cis) conformer was the most stable (Table 5). All of the (*Z*) isomers were higher in energy than the (*E*) isomers, with one exception, (*Z*) s-cis, Me s-trans, CO s-cis in which an internal hydrogen bond is formed between the amine hydrogen of the triazene and the carboxyl oxygen (Supplementary material, Table S32). The presence of the methyl group does not affect much the conformational angles. A stable (*Z*) s-trans, Me s-trans, CO s-cis structure could not be found, reverting instead to the Me s-cis form.

### 5-(3,3-Dimethyl-1-triazenyl)imidazole-4-carboxamide

5-(3,3-Dimethyl-1-triazenyl)imidazole-4-carboxamide (DTIC), also known as Dacarbazine, has eight possible configurations (Fig. 7).

The (*E*) s-trans, CO s-cis conformation was the lowest in energy (Table 6), just as for TIC itself. An interesting observation is that the (*Z*) s-cis, CO s-cis conformer is more sta-

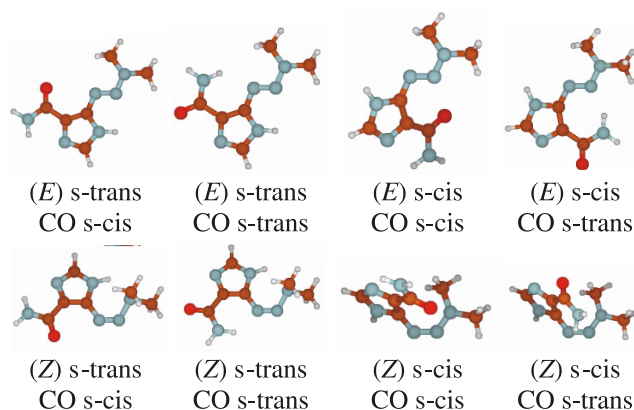
**Fig. 6.** The sixteen forms of 5-(3-methyl-1-triazenyl)imidazole-4-carboxamide.



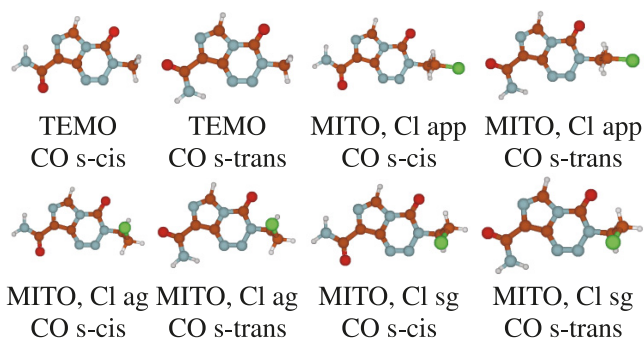
**Table 5.** Energies of MTIC (kJ/mol) relative to (*E*) s-trans, Me s-cis, CO s-cis.

	MP2/6-31+G(d)	B3LYP/6-31+G(d)
( <i>E</i> ) (t,c,t)	13.1	13.0
( <i>E</i> ) (t,t,c)	7.3	4.3
( <i>E</i> ) (t,t,t)	19.5	16.0
( <i>E</i> ) (c,t,c)	9.0	11.3
( <i>E</i> ) (c,t,t)	34.8	32.0
( <i>E</i> ) (c,c,c)	14.3	12.3
( <i>E</i> ) (c,c,t)	30.3	30.2
( <i>Z</i> ) (t,c,c)	62.3	79.5
( <i>Z</i> ) (t,c,t)	71.1	82.0
( <i>Z</i> ) (t,t,c)	(t,c,c)	(t,c,c)
( <i>Z</i> ) (t,t,t)	60.0	65.5
( <i>Z</i> ) (c,c,c)	53.8	63.9
( <i>Z</i> ) (c,c,t)	74.9	92.4
( <i>Z</i> ) (c,t,c)	19.9	19.5
( <i>Z</i> ) (c,t,t)	55.0	65.9

ble than the other (*Z*) forms, as is the case for TIC and MTIC. This was attributed solely to hydrogen bonding in TIC and MTIC, but this is not possible for this isomer. Comparison of this result to MTIC and TIC suggests that approximately 30–50 kJ/mol of the anomalous stabilization can be attributed to internal hydrogen bonding. The reason

**Fig. 7.** The eight forms of 5-(3,3-dimethyl-1-triazenyl)imidazole-4-carboxamide.**Table 6.** Energies of DTIC (kJ/mol) relative to (E) s-trans, CO s-cis.

	MP2/6-31+G(d)	B3LYP/6-31+G(d)
(E) (t,t)	12.8	13.4
(E) (c,c)	7.7	9.8
(E) (c,t)	29.8	31.1
(Z) (t,c)	68.6	81.5
(Z) (t,t)	68.5	83.2
(Z) (c,c)	49.3	62.9
(Z) (c,t)	83.2	95.0

**Fig. 8.** The two forms of Temozolomide (TEMO) and six forms of Mitozolomide (MITO).

for the other 20 kJ/mol of stabilization, although elusive, also exists for MTIC (Z) s-cis, Me s-cis, CO s-cis.

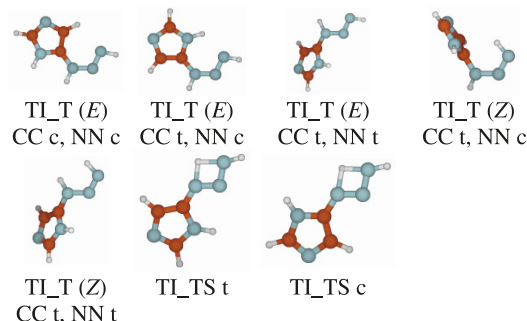
### Temozolomide and Mitozolomide

Temozolomide (3,4-dihydro-3-methyl-4-oxoimidazo-[5,1,d]-1,2,3,5-tetrazine-8-carboxamide, Temodal<sup>®</sup>, Fig. 8), which has demonstrated activity against recurrent brain cancer, is spontaneously hydrolyzed to MTIC under physiological conditions. This contrasts with the behavior of DTIC, which is poorly metabolized by the human body and is believed to require oxidative metabolism by hepatic cytochrome P450 enzymes to form MTIC.<sup>4</sup> The s-cis conformation is more stable than the s-trans form (MP2/6-31+G\*: 6.0; B3LYP/6-31+G\*: 6.2 kJ/mol). These numbers are comparable to the difference in energy between (Z) TIC s-trans, CO s-cis and (Z) TIC s-trans, CO s-trans.

Mitozolomide, which differs from Temozolomide in that a

**Table 7.** Energies of MITO (kJ/mol) relative to CO s-cis, Cl app.

	MP2/6-31+G(d)	B3LYP/6-31+G(d)
(c,ag)	-0.6	1.9
(c,sg)	0.1	2.1
(t,a)	6.5	6.9
(t,ag)	6.9	9.0
(t,sg)	6.2	7.8

**Fig. 9.** The five forms of 5-(3-triazenyl)imidazole (TI\_T) and transition states for tautomerization.**Table 8.** Energies of TI\_T (kJ/mol) relative to (E) N=N s-cis, C=C s-trans. TI\_T (t,t) and TS are relative to TI (E) (t), others are relative to TI\_T (t,t).

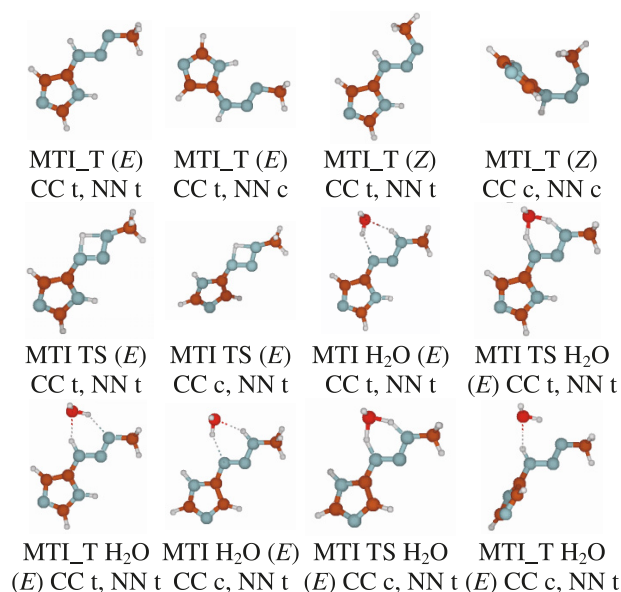
	MP2/6-31+G(d)	B3LYP/6-31+G(d)
TI_T (E) (t,t)	28.9	26.5
TI_T (E) (c,c) (t,c)		17.4
TI_T (E) (t,c)	-5.0	-4.1
TI_T (Z) (t,c)	19.0	27.5
TI_T (Z) (t,t)	28.5	26.6
TS t	172.5	175.2
TS c	175.0	178.7

methyl group is replaced with a chloroethyl group, showed some initial promise in animal testing,<sup>15</sup> but has not proven effective against human cancer and possesses some serious toxic effects. In addition to the orientation of the carboxamide group, the chloroethyl group can be either anti-periplanar (app), or in a gauche arrangement either syn to (sg) or anti to (ag) the triazene moiety, to give six configurations (Fig. 8). The CO s-cis, Cl app was the most stable conformer (Table 7). There is little difference (<2.1 kJ/mol) between the energy of the chloroethyl rotamers, but the s-trans conformers are at least 6 kJ/mol higher in energy than the s-cis conformers (cf. Temozolomide).

### Tautomerization reactions

TI can undergo tautomerization by a 1,3-hydrogen shift to form 5-(3-triazenyl)imidazole (TI\_T). In the tautomer, the N=N and C=C double bonds are no longer conjugated, so we use the designation s-cis and s-trans to refer to the arrangement of the N=N bond with the N-C single bond, or the C=C bond with the N-N bond. In most cases, the C=C s-cis arrangement is unstable and reverts to either the s-trans form or to a form in which the imidazole ring is perpendicular to the triazene moiety (Fig. 9). The TI (E) (t) would in-

**Fig. 10.** 5-(1-Methyl-3-triazenyl)imidazole (MTI\_T), transition states to tautomerization, and species involved in water-mediated tautomerization.



**Table 9.** Energies of MTI\_T (kJ/mol) relative to (E) C=C s-trans, N=N s-trans. The fourth and fifth rows are relative to MTI (E) (t,t), the sixth relative to MTI (E) (c,t). The water-mediated reactions are relative to the separated reactants ((E) MTI (t,t) or (c,t) + H<sub>2</sub>O).

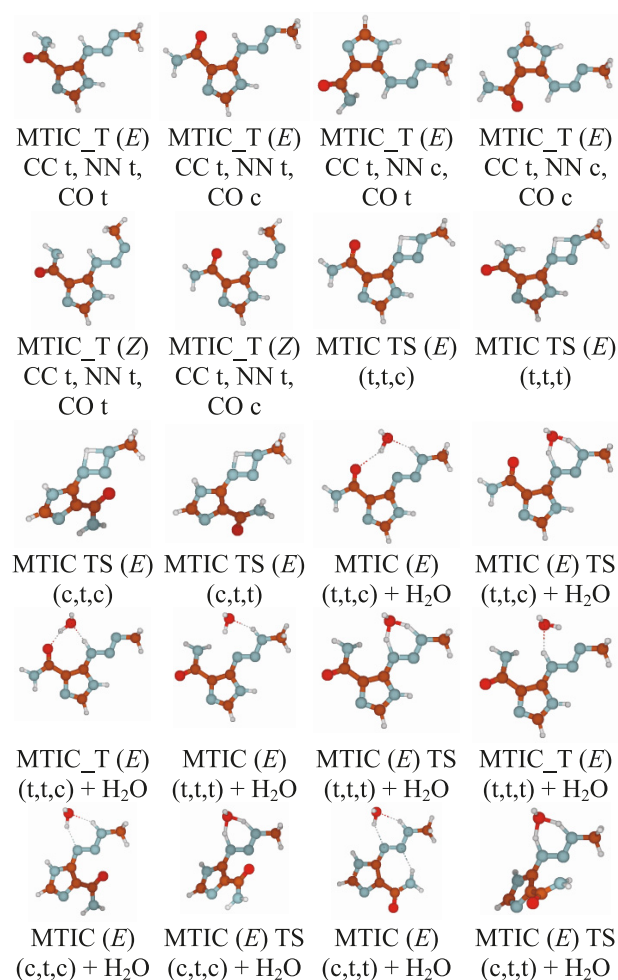
	MP2/6-31+G(d)	B3LYP/6-31+G(d)
(E) (t,c)	2.7	1.7
(Z) (c,c)	34.5	33.1
(Z) (t,t)	48.8	61.9
<b>Gas-phase tautomerization</b>		
TS (t)	157.8	166.3
(E) (t,t)	15.8	16.5
TS (c)	151.9	162.5
<b>Water mediated tautomerization</b>		
RC (t,t)	-32.3	-26.6
TS (t,t)	46.9	42.9
PC (t,t)	-16.2	-11.8
SP (t,t)	15.8	16.5
RC (c,t)	-28.1	-23.2
TS (c,t)	46.5	43.9
PC (c,t)	-21.8	-17.6

terconvert with TI\_T (E) (t,t) via the TI\_TS t transition structure. As the TI\_T (E) (c,t) form is nonexistent, the TI (E) (c) could interconvert also with TI\_T (E) (t,t) via the TI\_TS c transition structure, although conversion to TI (E) (t) is believed to be more likely.

The (scaled) zero-point corrected MP2/6-31+G\* activation energy of 172.5 kJ/mol (Table 8) may be compared to the unscaled activation energy of triazene (173.1 kJ/mol) and methyltriazene (165.5 kJ/mol).<sup>6</sup> The effect of the imidazole substituent is small.

MTI, like TI, can undergo tautomerization to form 5-(1-

**Fig. 11.** 5-(1-Methyl-3-triazenyl)imidazole-4-carboxamide tautomers (MTIC\_T), transition states to tautomerization, and species involved in water-mediated tautomerization.



methyl-3-triazenyl)imidazole (MTI\_T, Fig. 10). Only the (E) forms can interconvert. The MTI and MTI\_T (E) (t,t) forms interconvert via the (E) (t,t) transition state, whereas the MTI (E) (c,t) form might interconvert via the (E) (c,t) transition state to the MTI\_T (E) (t,t).

The MP2/6-31+G\* gas-phase tautomerization barrier of MTI (157.8 kJ/mol, Table 9) is lower than that of TI (172.5 kJ/mol) and is intermediate<sup>6</sup> between that of methyltriazene (165.5 kJ/mol) and dimethyltriazene (151.8 kJ/mol). A water molecule can mediate the proton shift and lower the effective barrier by two simultaneously acting mechanisms: by hydrating the species involved, lowering their energy, and by acting as a proton shuffle. The hydration effect lowers the barrier by approximately 30 kJ/mol by stabilizing both the reactant (RC) and product complexes (PC) (and, presumably, the TS). The barriers from RC to TS are 79.2 (t,t) and 74.6 (c,t) kJ/mol, which is about half of the barrier of the uncatalyzed reaction. These are quite comparable to the hydration energies and barriers of the water-catalyzed tautomerization of methyltriazene (-28.4, 78.0 kJ/mol) and dimethyltriazene (-30.3, 69.3 kJ/mol).<sup>6</sup>

MTIC can also undergo tautomerization to form 5-(1-methyl-3-triazenyl)imidazole-4-carboxamide (MTIC\_T, Fig. 11). The



**Table 10.** Energies of MTIC\_T (kJ/mol) relative to (*E*) C=C s-trans, N=N s-cis, C=O s-cis. The gas-phase tautomerization reactions are relative to the corresponding MTIC form. The water-mediated tautomerization reactions are relative to the separated reactants (MTIC + H<sub>2</sub>O).

	MP2/6-31+G(d)	B3LYP/6-31+G(d)
( <i>Z</i> ) (t,t,c)	31.0	30.1
( <i>Z</i> ) (t,t,t)	10.5	6.3
( <i>E</i> ) (t,t,c)	82.7	88.9
( <i>E</i> ) (t,t,t)	55.9	58.6
( <i>E</i> ) (t,c,t)	50.2	56.3
<b>Gas-phase tautomerization</b>		
( <i>E</i> ) (t,t,c) TS	147.0	151.9
( <i>E</i> ) (t,t,c) P	-17.8	-20.7
( <i>E</i> ) (t,t,t) TS	159.0	171.7
( <i>E</i> ) (t,t,t) P	15.4	19.9
( <i>E</i> ) (c,t,c) TS	144.6	156.1
( <i>E</i> ) (t,t,c) P	-24.8	-28.8
( <i>E</i> ) (c,t,t) TS	148.5	162.6
( <i>E</i> ) (t,t,t) P	0.1	3.8
<b>Water-mediated tautomerization</b>		
( <i>E</i> ) (t,t,c) RC	-57.2	-49.7
( <i>E</i> ) (t,t,c) TS	24.7	24.8
( <i>E</i> ) (t,t,c) PC	-53.3	-48.9
( <i>E</i> ) (t,t,c) SP	-17.8	-20.7
( <i>E</i> ) (t,t,t) RC	-34.8	-23.0
( <i>E</i> ) (t,t,t) TS	46.4	50.3
( <i>E</i> ) (t,t,t) PC	-17.2	-5.8
( <i>E</i> ) (t,t,t) SP	15.4	19.9
( <i>E</i> ) (c,t,c) RC	-46.2	-27.4
( <i>E</i> ) (c,t,c) TS	17.7	37.2
( <i>E</i> ) (t,t,c) PC	-60.3	-57.0
( <i>E</i> ) (t,t,c) SP	-24.8	-28.8
( <i>E</i> ) (c,t,t) RC	-48.2	-22.2
( <i>E</i> ) (c,t,t) TS	40.5	45.5
( <i>E</i> ) (t,t,t) PC	-32.6	-21.8
( <i>E</i> ) (t,t,t) SP	0.1	3.8

MTIC and MTIC\_T (*E*) (t,t,t) forms interconvert via the MTIC (t,t,t) transition state, and the MTIC and MTIC\_T(*E*) (t,t,c) forms interconvert via the MTIC (t,t,c) transition state. The MTIC (c,t,c) can interconvert with MTIC\_T (t,t,c) via the MTIC (c,t,c) transition state, and the MTIC (c,t,t) can interconvert with MTIC\_T (t,t,t) via the MTIC (c,t,t) transition state.

The MP2/6-31+G\* gas-phase tautomerization barrier of MTIC (147.0 kJ/mol, Table 10 (t,t,c)) is lower than that of MTI (157.8 kJ/mol), which suggests that the presence of the amide group stabilizes somewhat the transition state. The product complexes are stabilized by between 30–35 kJ/mol, whereas some of the reactant complexes are stabilized by as much as -60 kJ/mol. This is attributable to the existence of additional hydrogen bonds in these species. Like the hydrated MTI, the barriers from RC to TS are typically 80–85 kJ/mol.

## Conclusions

For substituted 4-(1-triazenyl)imidazoles, the (*E*) forms

are generally more stable than the (*Z*) forms. For the (*E*) forms, the s-trans imidazole conformers are more stable than the s-cis conformers. The carbonyl of a carboxamide group at the 5-position on the imidazole ring prefers to be in an s-cis arrangement. Steric interactions and hydrogen bonding modify the relative energies of the various conformers. A water molecule can catalyze the 1,3-hydrogen shift in the tautomerization reaction of the triazene moiety.

## Supplementary data

Supplementary data for this article are available on the journal Web site (canjchem.nrc.ca).

## Acknowledgements

The authors wish to thank the Saint Mary's University (SMU) Astronomy and Physics Department and the Atlantic Computational Excellence Network (ACEnet) for computer time. CCP acknowledges the support of the Natural Science and Engineering Research Council of Canada (NSERC). KGD acknowledges the support of the Faculty of Graduate Studies and Research (FGSR), SMU. KGD acknowledges helpful discussions with K. Vaughan.

## References

- (1) Vaughan, K. *The Chemistry of Antitumour Agents*; Blackie: Glasgow, 1990; Chapter 5, pp159–186.
- (2) Carter, S. K.; Friedman, M. A. *Eur. J. Cancer* **1972**, 8 (1), 85. PMID:4552317.
- (3) Godin, J. R. P.; Vaughan, K.; Renton, K. W. *Can. J. Physiol. Pharmacol.* **1981**, 59 (12), 1234. PMID:7337877.
- (4) Connors, T. A.; Goddard, P. M.; Merai, K.; Ross, W. C. J.; Wilman, D. E. V. *Biochem. Pharmacol.* **1976**, 25 (3), 241. doi:10.1016/0006-2952(76)90207-0. PMID:1267820.
- (5) Julliard, M.; Vernin, G. *Ind. Eng. Chem. Prod. Res. Dev.* **1981**, 20 (2), 287. doi:10.1021/i300002a011.
- (6) Pye, C. C.; Vaughan, K.; Glister, J. F. *Can. J. Chem.* **2002**, 80 (5), 447. doi:10.1139/v02-049.
- (7) Doucet, K. G.; Pye, C. C.; Vaughan, K.; Enright, T. G. *J. Mol. Struct. THEOCHEM* **2006**, 801 (1-3), 21. doi:10.1016/j.theochem.2006.08.059.
- (8) Doucet, K. G.; Pye, C. C.; Enright, T. G. *J. Mol. Struct. THEOCHEM* **2007**, 821 (1-3), 166. doi:10.1016/j.theochem.2007.07.001.
- (9) Doucet, K. G.; Pye, C. C.; Enright, T. G. *Can. J. Chem.* **2007**, 85 (11), 958. doi:10.1139/V07-110.
- (10) Doucet, K. G.; M. Sc. Thesis, Saint Mary's University, Halifax, NS, Canada, 2007; Chapters 3–6, pp 42–99.
- (11) Frisch, M. J.; Trucks, G. W.; Schlegel, H. B.; Scuseria, G. E.; Robb, M. A.; Cheeseman, J. R.; Zakrzewski, V. G.; Montgomery, J. A., Jr.; Stratmann, R. E.; Burant, J. C.; Dapprich, S.; Millam, J. M.; Daniels, A. D.; Kudin, K. N.; Strain, M. C.; Farkas, O.; Tomasi, J.; Barone, V.; Cossi, M.; Cammi, R.; Mennucci, B.; Pomelli, C.; Adamo, C.; Clifford, S.; Ochterski, J.; Petersson, G. A.; Ayala, P. Y.; Cui, Q.; Morokuma, K.; Malick, D. K.; Rabuck, A. D.; Raghavachari, K.; Foresman, J. B.; Cioslowski, J.; Ortiz, J. V.; Baboul, A. G.; Stefanov, B. B.; Liu, G.; Liashenko, A.; Piskorz, P.; Komaromi, I.; Gomperts, R.; Martin, R. L.; Fox, D. J.; Keith, T.; Al-Laham, M. A.; Peng, C. Y.; Nanayakkara, A.; Challacombe, M.; Gill, P. M. W.; Johnson, B.; Chen, W.; Wong, M. W.; Andres, J. L.; Gonzalez, C.; Head-Gordon, M.; Re-



- plogle, E. S.; Pople, J. A. *Gaussian 98*, Revision A.9; Gaussian Inc.: Pittsburgh, PA, 1998.
- (12) Frisch, M. J.; Trucks, G. W.; Schlegel, H. B.; Scuseria, G. E.; Robb, M. A.; Cheeseman, J. R.; Montgomery, J. A., Jr.; Vreven, T.; Kudin, K. N.; Burant, J. C.; Millam, J. M.; Iyengar, S. S.; Tomasi, J.; Barone, V.; Mennucci, B.; Cossi, M.; Scalmani, G.; Rega, N.; Petersson, G. A.; Nakatsuji, H.; Hada, M.; Ehara, M.; Toyota, K.; Fukuda, R.; Hasegawa, J.; Ishida, M.; Nakajima, T.; Honda, Y.; Kitao, O.; Nakai, H.; Klene, M.; Li, X.; Knox, J. E.; Hratchian, H. P.; Cross, J. B.; Adamo, C.; Jaramillo, J.; Gomperts, R.; Stratmann, R. E.; Yazyev, O.; Austin, A. J.; Cammi, R.; Pomelli, C.; Ochterski, J. W.; Ayala, P. Y.; Morokuma, K.; Voth, G. A.; Salvador, P.; Dannenberg, J. J.; Zakrzewski, V. G.; Dapprich, S.; Daniels, A. D.; Strain, M. C.; Farkas, O.; Malick, D. K.; Rabuck, A. D.; Raghavachari, K.; Foresman, J. B.; Ortiz, J. V.; Cui, Q.; Baboul, A. G.; Clifford, S.; Cioslowski, J.; Stefanov, B. B.; Liu, G.; Liashenko, A.; Piskorz, P.; Komaromi, I.; Martin, R. L.; Fox, D. J.; Keith, T.; Al-Laham, M. A.; Peng, C. Y.; Nanayakkara, A.; Challacombe, M.; Gill, P. M. W.; Johnson, B.; Chen, W.; Wong, M. W.; Gonzalez, C.; Pople, J. A. *Gaussian 03*, Revision B.05; Gaussian, Inc.: Pittsburgh, PA, 2003.
- (13) Scott, A. P.; Radom, L. *J. Phys. Chem.* **1996**, *100* (41), 16502. doi:10.1021/jp960976r.
- (14) Pye, C. C.; Poirier, R. A.; Yu, D.; Surjan, P. R. *J. Mol. Struct. THEOCHEM* **1994**, *307*, 239. doi:10.1016/0166-1280(94)80131-2.
- (15) Fodstad, O.; Aamdal, S.; Pihl, A.; Boyd, M. R. *Cancer Res.* **1985**, *45* (4), 1778. PMID:3978640.

# Ab initio studies of the vibrational spectra of some hydrogen-bonded complexes of fluoroacetylene

Ponnadurai Ramasami and Thomas A. Ford

**Abstract:** Ab initio molecular orbital theory has been used to compute the properties of a number of hydrogen-bonded complexes between fluoroacetylene as proton donor and ammonia, water, hydrogen fluoride, phosphine, hydrogen sulfide, and hydrogen chloride as proton acceptors. The properties considered were the vibrational spectra, the molecular structures, the hydrogen-bond energies, and the electron densities, and one of the aims of the study was to ascertain whether there was any evidence of blue-shifting hydrogen-bond character in the complexes formed. The adducts with  $\text{NH}_3$ ,  $\text{H}_2\text{O}$ ,  $\text{PH}_3$ , and  $\text{H}_2\text{S}$  were of the conventional  $\text{CH}\cdots\text{X}$  kind ( $\text{X} = \text{N}, \text{O}, \text{P}, \text{S}$ ), with hydrogen-bond energies decreasing in the order  $\text{NH}_3 > \text{H}_2\text{O} > \text{PH}_3 \approx \text{H}_2\text{S}$ . Those formed with HF and HCl showed the presence of three alternative structures; in addition to the  $\text{CH}\cdots\text{F}(\text{Cl})$  complexes, adducts of the  $\text{F}(\text{Cl})\text{H}\cdots\text{F}$  and  $\text{F}(\text{Cl})\text{H}\cdots\pi$  type were also found to be stationary points on the potential energy surfaces, with stabilities in the order  $\text{F}(\text{Cl})\text{H}\cdots\pi > \text{CH}\cdots\text{F}(\text{Cl}) > \text{F}(\text{Cl})\text{H}\cdots\text{F}$ . The hydrogen-bond energies of the  $\text{CH}\cdots\text{X}$  series correlated with the gas-phase basicities of the proton acceptors; moreover, the CH bond-length changes, the wavenumber shifts, the complex–monomer infrared intensity ratios of the CH stretching modes, and the amounts of charge transferred on complex formation were all found to track with the hydrogen-bond energies. All those properties considered here are consistent with the formation of red-shifting hydrogen bonds, to the exclusion of the blue-shifting alternatives.

**Key words:** ab initio, molecular complexes, hydrogen bonding, molecular structures, interaction energies, vibrational spectra, fluoroacetylene.

**Résumé :** On a fait appel à la théorie des orbitales moléculaires ab initio pour calculer les propriétés d'un certain nombre de complexes entre le fluoroacétylène, un donneur de proton, et l'ammoniac, l'eau, le fluorure d'hydrogène, le sulfure d'hydrogène et le chlorure d'hydrogène, des accepteurs de proton. Les propriétés considérées ont été les spectres vibrationnels, les structures moléculaires, les énergies des liaisons hydrogènes et les densités électroniques et l'un des buts de l'étude était de déterminer s'il était possible de détecter des données susceptibles de suggérer l'existence d'un déplacement vers le bleu du caractère de la liaison hydrogène dans les complexes formés. Les adduits avec les  $\text{NH}_3$ ,  $\text{H}_2\text{O}$ ,  $\text{PH}_3$  et  $\text{H}_2\text{S}$  sont du type  $\text{CH}\cdots\text{X}$  ( $\text{X} = \text{N}, \text{O}, \text{P}, \text{S}$ ) et les énergies des liaisons hydrogènes diminuent dans l'ordre  $\text{NH}_3 > \text{H}_2\text{O} > \text{PH}_3 \approx \text{H}_2\text{S}$ . Ceux qui se forment avec HF et HCl montrent la présence de trois types de structures alternatives, en plus des complexes  $\text{CH}\cdots\text{F}(\text{Cl})$ ; on a aussi observé que les adduits de types  $\text{F}(\text{Cl})\text{H}\cdots\text{F}$  et  $\text{F}(\text{Cl})\text{H}\cdots\pi$  sont des points stationnaires sur les surfaces d'énergie potentielle, avec des stabilités dans l'ordre  $\text{F}(\text{Cl})\text{H}\cdots\pi > \text{CH}\cdots\text{F}(\text{Cl}) > \text{F}(\text{Cl})\text{H}\cdots\text{F}$ . Les énergies des liaisons hydrogènes de la série  $\text{CH}\cdots\text{X}$  donnent une bonne corrélation avec les basicités en phase gazeuse des accepteurs de proton et on a aussi trouvé que les changements dans les longueurs des liaisons CH, les déplacements dans les nombres d'onde, le rapport des intensités infrarouges complexe/monomère des modes d'élongation CH ainsi que les quantités de charge transférées lors de la formation du complexe suivent les énergies des liaisons hydrogènes. Toutes les propriétés examinées dans ce travail sont en accord avec la formation de liaisons hydrogènes avec de déplacement vers le rouge, à l'exclusion des déplacements alternatifs vers le bleu.

**Mots-clés :** ab initio, complexes moléculaires, liaison hydrogène, structures moléculaires, énergies d'interaction, spectres vibrationnels, fluoroacétylène.

[Traduit par la Rédaction]

## Introduction

The intriguing phenomenon of the blue-shifting hydrogen bond has received a great deal of attention in recent years,

and a number of theories have been put forward to explain its characteristic properties.<sup>1–18</sup> In contrast to the conventional  $\text{AH}\cdots\text{B}$  hydrogen bond, which is manifested by a lengthening of the AH proton donor bond, a red shift of the

Received 24 December 2009. Accepted 16 February 2010. Published on the NRC Research Press Web site at canjchem.nrc.ca on 22 April 2010.

This article is part of a Special Issue dedicated to Professor R. J. Boyd.

**P. Ramasami.** Department of Chemistry, University of Mauritius, Réduit, Mauritius.

**T.A. Ford.**<sup>1</sup> Centre for Theoretical and Computational Chemistry, School of Chemistry, University of KwaZulu-Natal, Westville Campus, Private Bag X54001, Durban 4000, South Africa.

<sup>1</sup>Corresponding author (e-mail: ford@ukzn.ac.za).

AH stretching wavenumber, and an enhancement of the infrared intensity of the AH stretching vibration,<sup>19</sup> the blue-shifting hydrogen bond exhibits a decrease of the AH bond length, a shift of the AH stretching mode wavenumber to the blue, and a diminution of the AH stretching intensity.<sup>1</sup> For conventional hydrogen bonds, A is commonly N, O, F, or Cl and B is usually N, O, P, or S. For blue-shifting hydrogen bonds on the other hand, A can frequently be C or Si. Whereas the interpretation of the mechanism of the formation of a conventional hydrogen bond involves the overlap of a lone-pair orbital associated with the B atom (or of a  $\pi$ -orbital system) of the proton acceptor and the  $\sigma^*$  orbital of the AH bond of the proton donor, that of the blue-shifting hydrogen bond proposes donation from the lone pair or  $\pi$  orbital to a  $\sigma^*$  orbital or a lone pair of the proton donor more remote from the immediate site of interaction. Many of the early studies of this phenomenon included complexes with  $\text{CHF}_3$  or  $\text{CHCl}_3$  as the proton donor;<sup>1–13</sup> atoms-in-molecules (AIM)<sup>20</sup> calculations,<sup>10,11,15</sup> or those employing natural bond orbital (NBO)<sup>21</sup> theory<sup>1,10–12,15</sup> to characterize the electron-density changes revealed that charge typically accumulated in the  $\sigma^*(\text{CF})$  or  $\sigma^*(\text{CCl})$  orbitals and (or) in the F or Cl lone pair orbitals. Two schools of thought have emerged regarding the interpretation of these electron-density shifts: one school<sup>3,5,11,16</sup> asserts that there is no fundamental difference between blue-shifting and red-shifting hydrogen bonds, whereas the other<sup>1,2,6</sup> proposes that a two-step process is involved with blue-shifting bonds, in which electron density is first transferred from the proton acceptor lone pairs to the fluorine lone pairs, leading to an increase in the CF bond lengths, and then redistributed into the  $\sigma(\text{CH})$  orbital, resulting in a shortening of the CH bond. It was also observed that, for blue-shifting hydrogen bonding to occur, the AH stretching vibration of the proton-donor AH bond should have a negative dipole moment derivative,  $\partial\mu/\partial r(\text{AH})$ ,<sup>5</sup> and that a subtle balance exists between the effects of  $n(\text{B}) \rightarrow \sigma^*(\text{AH})$  hyperconjugation which favours AH bond lengthening, and increasing s orbital character and polarization of the AH bond (rehybridization) which have the reverse effect.<sup>7</sup>

It seems that the probability of observing the presence of a blue-shifting hydrogen bond would be enhanced in complexes in which the proton donor possessed a region of high electron density, e.g., a fluorine atom or a  $\pi$  orbital system, slightly remote from the primary site of interaction, to accommodate the electron density redistribution regarded as an essential component of the interaction. Such a proton donor is fluoroacetylene, which features a CF bond, three F lone pairs, and a  $\text{C}\equiv\text{C}$  triple bond. We have therefore studied a series of hydrogen-bonded complexes of HCCF with  $\text{NH}_3$ ,  $\text{H}_2\text{O}$ , HF,  $\text{PH}_3$ ,  $\text{H}_2\text{S}$ , and HCl, to explore the nature of the  $\text{CH}\cdots\text{B}$  hydrogen bonds in this series, and to determine the effect on the hydrogen bond properties of the position of the proton acceptor atom in the periodic table (group 15, 16, or 17, and first or second row). Complexes of HCCF with some of these proton acceptors have been studied before by other groups, e.g.,  $\text{NH}_3$ ,<sup>22,23</sup>  $\text{H}_2\text{O}$ ,<sup>3,7,23,24</sup> and HF,<sup>23,25,26</sup> but this is apparently the first attempt to carry out a systematic study on the whole range of partner molecules.

## Computational methodology

The calculations were carried out using the Gaussian 03 program,<sup>27</sup> at the second-order level of Møller–Plesset perturbation theory (MP2),<sup>28</sup> and with Dunning's aug-cc-pVTZ basis set.<sup>29–33</sup> The TIGHT convergence criterion was employed, and the vibrational properties were obtained using analytical derivatives, except for the heavier complexes, when numerical derivatives were used.<sup>27</sup> The interaction energies were corrected for basis set superposition error (BSSE)<sup>34</sup> by the Boys–Bernardi procedure,<sup>35</sup> using the COUNTERPOISE option of the program,<sup>27</sup> and for zero-point energy differences. The NBO analysis<sup>21</sup> was performed using the POP=NBO keyword.<sup>27</sup>

## Results and discussion

### Molecular structures

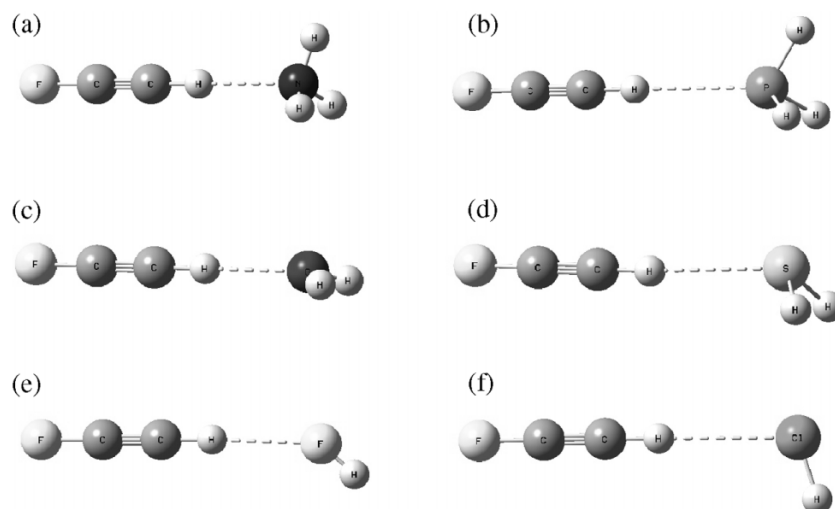
The optimized structures of the complexes of HCCF with  $\text{NH}_3$  and  $\text{PH}_3$  are of  $\text{C}_{3v}$  symmetry, with the  $\text{CH}\cdots\text{N(P)}$  angles fixed at  $180.0^\circ$ . The  $\text{H}_2\text{O}$  and  $\text{H}_2\text{S}$  complexes have  $\text{C}_s$  symmetry, with the angles between the  $\text{H}\cdots\text{O(S)}$  axis and the HOH or HSH angle bisectors being close to  $160^\circ$  and  $90^\circ$ , respectively. The HF and HCl complexes are also of  $\text{C}_s$  symmetry with  $\text{H}\cdots\text{FH}$  and  $\text{H}\cdots\text{ClH}$  angles of approximately  $137^\circ$  and  $107^\circ$ , respectively. The values of the geometrical parameters, and their changes on complexation, are presented in Table 1, and the equilibrium structures are illustrated in Fig. 1. Tables of the optimized Cartesian coordinates of the complexes are available in the Supplementary data (Table S1).

Significantly, the signs of all six  $\Delta r(\text{CH})$  are positive, indicating a lengthening of the CH bonds on hydrogen-bond formation. The increase in CH-bond length falls off in the order  $\text{NH}_3 > \text{H}_2\text{O} > \text{H}_2\text{S} > \text{PH}_3 > \text{HF} > \text{HCl}$ . The increases in the CC and CF bond lengths follow the same trend for the first row proton acceptors, but the second row acceptors are much less sensitive to complexation. The fact that the CH, CC, and CF bond lengths all increase on complexation indicates a consistent weakening of all three bonds in the HCCF sub-molecule. The HCCF fragment linearity is preserved, within  $1^\circ$ , in all six complexes. The changes in the XH bond lengths in the proton acceptor molecules are minimal and, apart from  $\text{FCCH}\cdots\text{NH}_3$  and  $\text{FCCH}\cdots\text{PH}_3$ , the HXH bond angles change by less than  $1^\circ$ . Agreement with previously reported structures<sup>3,7,22–24</sup> is variable.

In the case of the complexes with HF and HCl, two alternative equilibrium structures are possible, the “reversed”  $\text{F(Cl)H}\cdots\text{F}$  and the  $\pi$ -bonded  $\text{F(Cl)H}\cdots\pi$  species, which are also minima on the potential energy surfaces. The geometrical data for these four complexes are given in Table 2, and the plots of their structures in Fig. 2. There are significant differences between the structures of the reversed and the  $\pi$ -bonded species. The CH bond length increases are larger for  $\text{XH}\cdots\pi$  than for the  $\text{XH}\cdots\text{F}$ , the CC bond lengths increase for  $\text{XH}\cdots\pi$  and decrease for  $\text{XH}\cdots\text{F}$ , and the reverse behaviour is observed for the CF bond lengths, whereas the HF and HCl bond-length changes are substantially larger for  $\text{XH}\cdots\pi$  than for  $\text{XH}\cdots\text{F}$ . Only for the HF bond of the  $\text{FH}\cdots\text{HCCF}$   $\pi$ -bonded complex is a literature value available for comparison.<sup>26</sup> The agreement is good.

**Table 1.** Geometrical parameters, and their changes on complexation, of the CH $\cdots$ X hydrogen-bonded complexes of HCCF with NH $_3$ , H $_2$ O, HF, PH $_3$ , H $_2$ S, and HCl. Numbers in parentheses are literature values.

Parameter <sup>a</sup>	Electron donor					
	NH $_3$	H $_2$ O	HF	PH $_3$	H $_2$ S	HCl
$r(\text{CH})$ (pm)	106.98 (107.1 <sup>b</sup> , 107.2 <sup>c</sup> )	106.49 (107.16 <sup>d</sup> , 106.7 <sup>c</sup> )	106.15 (106.3 <sup>c</sup> )	106.26	106.32	106.11
$\Delta r(\text{CH})$ (pm)	1.06	0.57 (0.53 <sup>e</sup> , 0.56 <sup>d</sup> , 0.56 <sup>f</sup> )	0.23	0.34	0.40	0.19
$r(\text{CC})$ (pm)	120.73 (119.3 <sup>b</sup> )	120.65	120.59	120.62	120.63	120.59
$\Delta r(\text{CC})$ (pm)	0.20	0.11 (0.12 <sup>c</sup> )	0.05	0.08	0.10	0.06
$r(\text{CF})$ (pm)	128.46	128.37	128.23	128.21	128.21	128.14
$\Delta r(\text{CF})$ (pm)	0.42	0.33 (0.35 <sup>c</sup> )	0.18	0.17	0.16	0.09
$r(\text{XH})$ (pm)	101.27	96.16	92.29	141.12	133.68	127.57
$\Delta r(\text{XH})$ (pm)	0.06	0.03	0.11	-0.13	0.05	0.10
$\angle \text{HXH}$ ( $^\circ$ )	106.33	103.78	—	94.70	92.28	—
$\Delta \angle \text{HXH}$ ( $^\circ$ )	5.12	-0.33	—	1.07	0.05	—
$R(\text{H}\cdots\text{X})$ (pm)	223.08 (228.4 <sup>b</sup> )	216.40 (214.1 <sup>d</sup> )	222.53	290.00	277.12	271.59
$\angle \text{CH}\cdots\text{X}$ ( $^\circ$ )	180.0 <sup>g</sup> (179.8 <sup>c</sup> )	179.91 (164.9 <sup>c</sup> )	159.56 (171.9 <sup>c</sup> )	180.0 <sup>g</sup>	176.51	171.14
$\angle \text{H}\cdots\text{XH}$ ( $^\circ$ )	112.45	120.93	137.29	122.23	94.19	107.21
$\angle \text{H}\cdots\text{XY}^h$ ( $^\circ$ )	180.0 <sup>g</sup>	160.08	—	180.0 <sup>g</sup>	96.05	—

<sup>a</sup>X = N, O, F, P, S, Cl.<sup>b</sup>Reference 22 (B3LYP/6-311+G(3df,2p)).<sup>c</sup>Reference 23 (MP2/6-31G(d,p)).<sup>d</sup>Reference 7 (MP2/6-31+G(d)).<sup>e</sup>Reference 3 (MP2/6-31+G(d,p)).<sup>f</sup>Reference 24 (MP2/aug-cc-pVTZ).<sup>g</sup>Fixed.<sup>h</sup>Y is the centre of the H $\cdots$ H $\cdots$ H triangle of NH $_3$  (PH $_3$ ) or the mid-point of the H $\cdots$ H line of H $_2$ O (H $_2$ S).**Fig. 1.** Optimized structures of the (a) FCCH-NH $_3$ , (b) FCCH-PH $_3$ , (c) FCCH-OH $_2$ , (d) FCCH-SH $_2$ , (e) FCCH-FH, and (f) FCCH-ClH complexes.

### Hydrogen-bond energies

The hydrogen-bond energies, corrected for BSSE<sup>34</sup> and for zero-point energy differences, are listed in Table 3. Some other values have been reported,<sup>7,22–26</sup> but again agreement with our results is tentative, partly owing to the use of different basis sets. The absolute energies indicate that, among the complexes with HF and HCl, the  $\pi$ -bonded complex is the most stable, and is probably the global minimum, followed by the CH $\cdots$ F(Cl) and lastly the F(Cl)H $\cdots$ F, which are local minima.

The hydrogen-bond energies correlate fairly well with the gas phase basicities<sup>36</sup> of the proton acceptors, with separate

relationships for the NH $_3$ -H $_2$ O-HF and the PH $_3$ -H $_2$ S-HCl series (see Fig. 3), although there is a suggestion that the datum for FCCH-SH $_2$  may indicate some overestimation of the strength of interaction. Chan et al.<sup>37</sup> have correlated the binding energies of a range of protonated homodimers with the proton affinities of the bases, and have observed a quadratic relationship. There are insufficient data available to confirm whether the relationship between the binding energies and the gas-phase basicities for the heterodimers shown in Fig. 3 is monotonic throughout the whole range, or whether the figure represents merely a part of the whole curve. These authors have also investigated the influence of



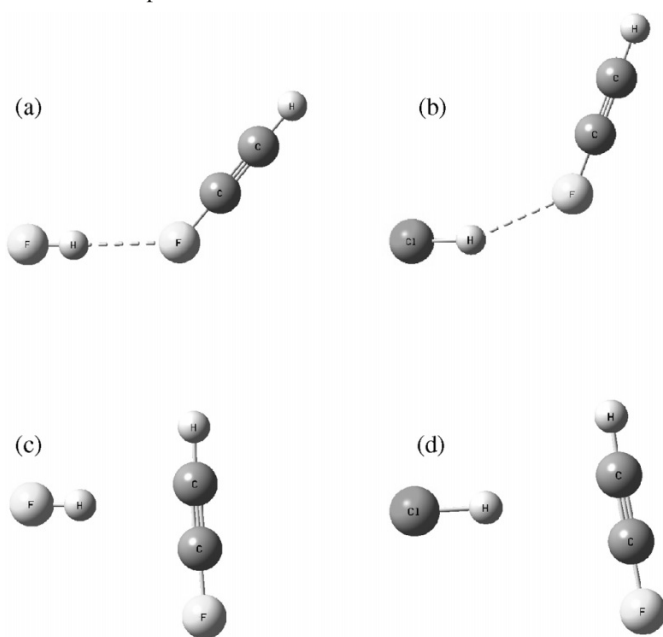
**Table 2.** Geometrical parameters, and their changes on complexation, of the  $\text{XH}\cdots\text{F}$  and  $\text{XH}\cdots\pi$  hydrogen-bonded complexes of HCCF with HF and HCl ( $\text{X} = \text{F}, \text{Cl}$ ). Value for  $r(\text{XH})$  in parentheses is a literature value.

Parameter <sup>a</sup>	Proton donor <sup>d</sup>			
	HF		HCl	
	$\text{XH}\cdots\text{F}$	$\text{XH}\cdots\pi$	$\text{XH}\cdots\text{F}$	$\text{XH}\cdots\pi$
$r(\text{CH})$ (pm)	105.97	106.11	105.95	106.07
$\Delta r(\text{CH})$ (pm)	0.05	0.19	0.04	0.15
$r(\text{CC})$ (pm)	120.41	120.75	120.47	120.72
$\Delta r(\text{CC})$ (pm)	-0.12	0.22	-0.07	0.18
$r(\text{CF})$ (pm)	128.71	127.51	128.49	127.67
$\Delta r(\text{CF})$ (pm)	0.66	-0.53	0.45	-0.38
$r(\text{XH})$ (pm)	92.31	92.96 (92.2 <sup>b</sup> )	127.56	128.27
$\Delta r(\text{XH})$ (pm)	0.13	0.78	0.08	0.80
$R(\text{H}\cdots\text{F})$ (pm)	207.11	—	227.05	—
$R(\text{H}\cdots\text{C}(\text{H}))$ (pm)	—	257.04	—	270.57
$R(\text{H}\cdots\text{C}(\text{F}))$ (pm)	—	304.91	—	314.77
$\angle\text{XH}\cdots\text{F}$ (°)	175.69	—	161.28	—
$\angle\text{H}\cdots\text{FC}$ (°)	123.93	—	113.62	—
$\angle\text{XH}\cdots\text{C}(\text{H})$ (°)	—	146.46	—	148.61
$\angle\text{XH}\cdots\text{C}(\text{F})$ (°)	—	135.95	—	137.30

<sup>a</sup> $\text{X} = \text{F}, \text{Cl}$ ; atoms H and F in parentheses distinguish between the carbon atoms bonded to H and F.

<sup>b</sup>Reference 26 (MP2/6-311++G(d,p)).

**Fig. 2.** Optimized structures of the (a) FH-FCCH reversed, (b) ClH-FCCH reversed, (c) FH-HCCF  $\pi$ -bonded, and (d) ClH-HCCF  $\pi$ -bonded complexes.



the proton affinity on whether a protonated homodimer is likely to be symmetric or not,<sup>38</sup> but this is not relevant to the present case. The order of the CH bond-length increases, shown in Table 1, virtually reflects the order of the gas phase basicities<sup>36</sup> for the first and second row proton acceptors separately, confirming the correlation between these properties.

### Vibrational spectra

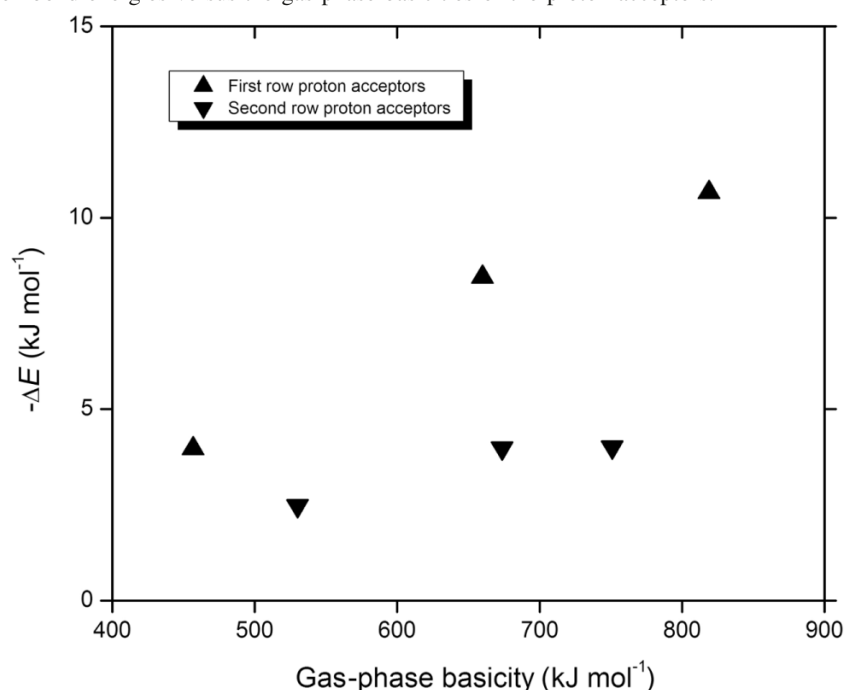
The computed wavenumbers and infrared intensities of

the  $\text{CH}\cdots\text{X}$  series of complexes are available in the Supplementary data as Table S2, together with approximate descriptions of the normal modes, for completeness. The wavenumber shifts and intensity ratios, relative to the unperturbed monomers, derived from these data are given in Table 4.

The critical mode in the analysis of the vibrational properties of the hydrogen-bonded complexes considered here is the CH stretching mode of the HCCF sub-molecule. We have shown above that the CH bond length increases in all six complexes of the  $\text{CH}\cdots\text{X}$  series, suggesting that these complexes are of the red-shifting, rather than the blue-shifting, type. Table 4 shows that the CH stretching mode is indeed consistently red-shifted by -145.8, -65.2, -18.7, -46.3, -54.5, and -21.3  $\text{cm}^{-1}$  in the sequence  $\text{NH}_3$ ,  $\text{H}_2\text{O}$ , HF,  $\text{PH}_3$ ,  $\text{H}_2\text{S}$ , and HCl. Moreover, the CH stretching-band intensity increases by factors of 4.95, 3.34, 2.15, 2.94, 3.01, and 2.22 in the same order. Thus the vibrational properties confirm the structural results that the  $\text{CH}\cdots\text{X}$  complexes behave like conventional hydrogen-bonded adducts. The wavenumber shifts are proportional to the hydrogen-bond energies, as shown in Fig. 4, and once again separate relationships are found for the first and second row bases. A similar pair of curves (not shown) was obtained for a plot of the stretching band intensity enhancements versus the binding energies. Again, it appears that the results for  $\text{FCCH}\cdot\text{SH}_2$  indicate some exaggeration of the computed interaction energy. Of the remaining modes of the HCCF sub-molecule, the CCH bending vibrations undergo a substantial regular blue shift and intensity reduction, whereas the CC and CF stretching and the CCF bending modes are red-shifted by much smaller amounts. The CC stretching and the CCH and CCF bending vibrations suffer loss of intensity, whereas the CF stretching

**Table 3.** Hydrogen-bond energies of the complexes of HCCF with NH<sub>3</sub>, H<sub>2</sub>O, HF, PH<sub>3</sub>, H<sub>2</sub>S, and HCl.

Partner molecule	Structure	$\Delta E$ (kJ mol <sup>-1</sup> )	
		This work	Literature
NH <sub>3</sub>	CH...N ( <i>C</i> <sub>3v</sub> )	-10.66	-9.8 <sup>a</sup> , -17.0 <sup>b</sup>
H <sub>2</sub> O	CH...O ( <i>C</i> <sub>s</sub> )	-8.45	-10.54 <sup>b</sup> , -24 <sup>c</sup> , -11.8 <sup>d</sup>
HF	CH...F ( <i>C</i> <sub>s</sub> )	-3.97	-5.5 <sup>b</sup>
HF	FH... $\pi$ ( <i>C</i> <sub>s</sub> )	-8.68	-3.5 <sup>e</sup> , -8.83 <sup>f</sup>
HF	FH...F ( <i>C</i> <sub>s</sub> )	-0.13	
PH <sub>3</sub>	CH...P ( <i>C</i> <sub>3v</sub> )	-4.01	
H <sub>2</sub> S	CH...S ( <i>C</i> <sub>s</sub> )	-3.99	
HCl	CH...Cl ( <i>C</i> <sub>s</sub> )	-2.48	
HCl	ClH... $\pi$ ( <i>C</i> <sub>s</sub> )	-6.76	
HCl	ClH...F ( <i>C</i> <sub>s</sub> )	-1.06	

<sup>a</sup>Reference 22.<sup>b</sup>Reference 23.<sup>c</sup>Reference 7.<sup>d</sup>Reference 24.<sup>e</sup>Reference 25.<sup>f</sup>Reference 26.**Fig. 3.** Plots of the hydrogen-bond energies versus the gas phase basicities of the proton acceptors.

intensity increases uniformly. The perturbations of the modes of the proton acceptor molecules are quite modest.

The vibrational properties of the alternative structures of the complexes with HF and HCl are given in the Supplementary data (Table S3), and the wavenumber shifts and intensity ratios in Table 5. In the case of the reversed F(Cl)H...F bonded complexes, the perturbations of the monomer spectroscopic properties are relatively insignificant, reflecting the very low energies of interaction; none of the wavenumber shifts of ClH·FCCH exceeds 10 cm<sup>-1</sup>. Those of FH·FCCH are marginally larger, the major shift being that of the hydrogen-bonded HF stretching mode (-27.7 cm<sup>-1</sup>). The corresponding hydrogen-bonded HCl stretching mode

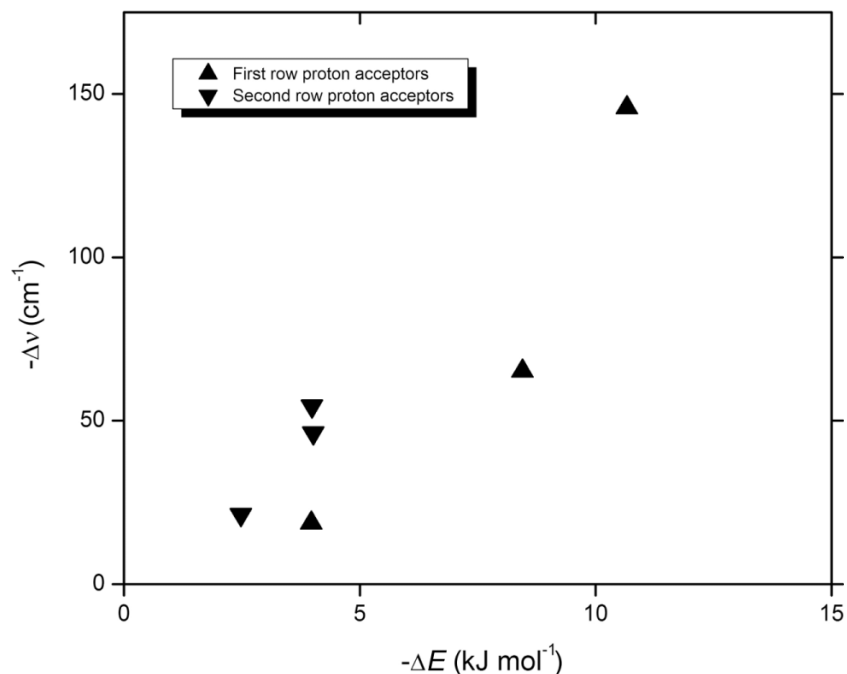
shift is only -5.8 cm<sup>-1</sup>. These results contrast with the noticeably larger changes in the spectroscopic properties of the F(Cl)H... $\pi$  complexes, in which the hydrogen-bonded HF and HCl stretching wavenumber shifts are -183.8 and -113.7 cm<sup>-1</sup> and their intensities are enhanced by factors of almost 5 and 8, respectively. These complexes represent two further examples of conventional hydrogen-bonded complexes with characteristic red-shifting behaviour.

#### Electron-density redistributions

An NBO<sup>21</sup> analysis of the various complexes indicates that for the CH...X species, in which HCCF is the proton donor, the source of the interaction is a donation of charge

**Table 4.** Wavenumber shifts and intensity ratios, relative to the unperturbed monomers, of the normal modes of the CH...X complexes of HCCF with NH<sub>3</sub>, H<sub>2</sub>O, HF, PH<sub>3</sub>, H<sub>2</sub>S, and HCl.

Symmetry	Mode	Wavenumber shift (cm <sup>-1</sup> )	Intensity ratio	Wavenumber shift (cm <sup>-1</sup> )	Intensity ratio
		FCCH·NH <sub>3</sub>		FCCH·PH <sub>3</sub>	
a <sub>1</sub>	ν <sub>1</sub>	-5.1	0.70	-46.3	2.94
	ν <sub>2</sub>	-145.8	4.95	7.2	1.11
	ν <sub>3</sub>	-23.9	0.45	-9.5	0.77
	ν <sub>4</sub>	38.9	1.10	-5.0	1.22
	ν <sub>5</sub>	-13.5	1.58	-3.4	2.24
e	ν <sub>7</sub>	-7.7	1.49	8.3	0.79
	ν <sub>8</sub>	-0.3	1.15	-1.4	0.89
	ν <sub>9</sub>	193.1	0.90	60.7	0.63
	ν <sub>10</sub>	-2.5	0.17	-3.1	0.56
		FCCH·OH <sub>2</sub>		FCCH·SH <sub>2</sub>	
a'	ν <sub>1</sub>	-2.3	1.99	-54.5	3.01
	ν <sub>2</sub>	-65.2	3.34	-3.5	9.44
	ν <sub>3</sub>	-13.1	0.61	-10.2	0.74
	ν <sub>4</sub>	1.6	0.99	-1.4	0.61
	ν <sub>5</sub>	-8.8	1.39	-5.4	1.36
	ν <sub>6</sub>	112.6	0.87	70.9	0.67
	ν <sub>7</sub>	-2.5	0.27	-2.9	0.53
a''	ν <sub>11</sub>	-4.4	1.18	-3.5	2.87
	ν <sub>12</sub>	139.4	0.99	77.6	0.65
	ν <sub>13</sub>	-2.0	0.32	-2.8	0.52
		FCCH·FH		FCCH·ClH	
a'	ν <sub>1</sub>	-15.9	1.21	-21.3	2.22
	ν <sub>2</sub>	-18.7	2.15	9.3	1.10
	ν <sub>3</sub>	-5.7	0.78	-5.2	0.84
	ν <sub>4</sub>	-4.3	1.21	-2.8	1.25
	ν <sub>5</sub>	73.6	1.00	53.5	0.74
	ν <sub>6</sub>	-0.8	0.54	-1.2	0.64
a''	ν <sub>10</sub>	66.1	0.96	44.3	0.76
	ν <sub>11</sub>	-0.9	0.51	-1.5	0.65

**Fig. 4.** Plots of the CH stretching wavenumber shifts versus the hydrogen-bond energies.

**Table 5.** Wavenumber shifts and intensity ratios, relative to the unperturbed monomers, of the normal modes of the reversed  $\text{XH}\cdots\text{F}$  and  $\text{XH}\cdots\pi$  complexes of HCCF with HF and HCl.

Symmetry	Mode	Wavenumber shift ( $\text{cm}^{-1}$ )	Intensity ratio	Wavenumber shift ( $\text{cm}^{-1}$ )	Intensity ratio
		FH-FCCH		ClH-FCCH	
$a'$	$\nu_1$	-27.7	2.47	-3.1	1.05
	$\nu_2$	-4.5	1.09	-5.8	2.24
	$\nu_3$	0.0	0.92	-1.3	0.92
	$\nu_4$	-13.7	1.15	-9.7	1.07
	$\nu_5$	14.5	0.93	8.7	0.94
	$\nu_6$	-3.8	5.47	-6.6	0.88
$a''$	$\nu_{10}$	12.5	0.97	7.8	0.97
	$\nu_{11}$	-12.9	1.40	-8.5	0.68
		FH $\cdots\pi$		ClH $\cdots\pi$	
$a'$	$\nu_1$	-183.8	4.90	-16.8	1.12
	$\nu_2$	-20.7	1.21	-113.7	7.94
	$\nu_3$	-4.6	1.02	-6.0	1.00
	$\nu_4$	8.7	1.02	5.8	0.76
	$\nu_5$	37.7	1.47	15.8	1.36
	$\nu_6$	15.9	1.95	5.4	1.91
$a''$	$\nu_{10}$	-2.8	1.45	-6.0	0.98
	$\nu_{11}$	2.5	0.31	0.1	1.61

**Table 6.** Major interorbital interactions of the complexes of HCCF with  $\text{NH}_3$ ,  $\text{H}_2\text{O}$ , HF,  $\text{PH}_3$ ,  $\text{H}_2\text{S}$ , and HCl.

Partner molecule	Structure	Electron density redistribution	
		Forward donation	Back donation
$\text{NH}_3$	$\text{CH}\cdots\text{N}$ ( $C_{3v}$ )	$n(\text{N}) \rightarrow \sigma^*(\text{CH})$	None
$\text{H}_2\text{O}$	$\text{CH}\cdots\text{O}$ ( $C_s$ )	$n(\text{O}) \rightarrow \sigma^*(\text{CH})$	None
HF	$\text{CH}\cdots\text{F}$ ( $C_s$ )	$n(\text{F}) \rightarrow \sigma^*(\text{CH})$	None
HF	$\text{FH}\cdots\pi$ ( $C_s$ )	$\pi(\text{CC}) \rightarrow \sigma^*(\text{HF})$	$n(\text{F}) \rightarrow \pi^*(\text{CC})$ , $\sigma(\text{HF}) \rightarrow \pi^*(\text{CC})$
HF	$\text{FH}\cdots\text{F}$ ( $C_s$ )	$n(\text{F}) \rightarrow \sigma^*(\text{HF})$	$\sigma(\text{HF}) \rightarrow \sigma^*(\text{CF})$
$\text{PH}_3$	$\text{CH}\cdots\text{P}$ ( $C_{3v}$ )	$n(\text{P}) \rightarrow \sigma^*(\text{CH})$	None
$\text{H}_2\text{S}$	$\text{CH}\cdots\text{S}$ ( $C_s$ )	$n(\text{S}) \rightarrow \sigma^*(\text{CH})$	None
HCl	$\text{CH}\cdots\text{Cl}$ ( $C_s$ )	$n(\text{Cl}) \rightarrow \sigma^*(\text{CH})$	None
HCl	$\text{ClH}\cdots\pi$ ( $C_s$ )	$\pi(\text{CC}) \rightarrow \sigma^*(\text{HCl})$	$n(\text{Cl}) \rightarrow \pi^*(\text{CC})$ , $\sigma(\text{HCl}) \rightarrow \pi^*(\text{CC})$
HCl	$\text{ClH}\cdots\text{F}$ ( $C_s$ )	$n(\text{F}) \rightarrow \sigma^*(\text{HCl})$	None

**Table 7.** Shifts of atomic electron density (in  $m_e$ ) on formation of the  $\text{CH}\cdots\text{X}$  complexes of HCCF with  $\text{NH}_3$ ,  $\text{H}_2\text{O}$ , HF,  $\text{PH}_3$ ,  $\text{H}_2\text{S}$ , and HCl.

Atom <sup>a</sup>	Proton acceptor					
	$\text{NH}_3$	$\text{H}_2\text{O}$	HF	$\text{PH}_3$	$\text{H}_2\text{S}$	HCl
H	34.3	27.1	16.1	12.9	12.0	7.7
C(H)	-3.9	1.4	0.5	-2.0	-2.2	-1.5
C(F)	-34.2	-28.0	-16.2	-14.8	-13.4	-8.3
F	-8.1	-6.7	-3.8	-3.5	-3.2	-2.0
Net proton donor	-11.9	-6.1	-3.3	-7.5	-6.8	-4.1
X	-5.8	-12.6	-3.8	-13.1	-4.5	-0.9
H	5.9	9.4	7.1	6.9	5.7	4.9
Net proton acceptor	11.9	6.2	3.3	7.6	6.9	4.0

<sup>a</sup>X = N, O, F, P, S, and Cl.

from a lone-pair orbital of the proton acceptor to the  $\sigma^*(\text{CH})$  orbital of HCCF, in accordance with the standard interpretation of a conventional red-shifting hydrogen bond. These results are summarized in Table 6.

For the  $\pi$ -bonded structures of the complexes with HF and HCl, the donation is from a  $\pi(\text{CC})$  orbital of HCCF to

the  $\sigma^*$  orbital of HF or HCl. In addition, there is a counter-donation from the non-bonding F or Cl orbitals and the  $\sigma$  orbitals of HF or HCl to the  $\pi^*(\text{CC})$  orbital of HCCF. In the case of the reverse  $\text{F}(\text{Cl})\text{H}\cdots\text{F}$  structures, the interaction is between a F lone pair of HCCF and the  $\sigma^*(\text{HF})$  or  $\sigma^*(\text{HCl})$  orbital and, in addition, in  $\text{FH}\cdots\text{FCCH}$ , a donation from  $\sigma(\text{HF})$  of HF to  $\sigma^*(\text{CF})$  of HCCF. In quantitative terms, the amounts of charge redistributed as a result of hydrogen bond formation are presented in Tables 7 and 8.

The net amounts of charge transferred in the  $\text{CH}\cdots\text{X}$  complexes (Table 7) correlate with the hydrogen-bond energies, again with separate relationships (not shown), for the  $\text{NH}_3$ ,  $\text{H}_2\text{O}$ , HF and the  $\text{PH}_3$ ,  $\text{H}_2\text{S}$ , HCl proton acceptors, as observed for the CH stretching wavenumber shift relationship in Fig. 4. For the alternative structures of the HF and HCl complexes, there is a considerably greater degree of charge transfer involved in the  $\text{XH}\cdots\pi$  complexes than in the  $\text{XH}\cdots\text{F}$ , and in each case this is more pronounced for the HF than for the HCl adduct (Table 8).

## Summary

These calculations have shown that the hydrogen-bonded



**Table 8.** Shifts of atomic electron density (in me) on formation of the  $\text{XH}\cdots\text{F}$  and  $\text{XH}\cdots\pi$  complexes of HCCF with HF and HCl.

Atom <sup>a</sup>	Proton donor			
	HF (reversed)	HF ( $\pi$ -bonded)	HCl (reversed)	HCl ( $\pi$ -bonded)
H	5.2	16.1	3.6	10.6
C(H)	31.3	-35.7	18.6	-22.6
C(F)	-17.6	18.1	-10.3	12.9
F	-16.3	11.1	-9.7	7.1
Net proton acceptor	2.6	9.6	2.2	8.0
X	-6.3	-21.0	-6.2	-20.4
H	3.6	11.4	3.9	12.4
Net proton donor	-2.7	-9.6	-2.3	-8.0

<sup>a</sup>X = F and Cl.

complexes formed between HCCF and  $\text{NH}_3$ ,  $\text{H}_2\text{O}$ ,  $\text{PH}_3$ , and  $\text{H}_2\text{S}$  are exclusively of the  $\text{CH}\cdots\text{X}$  type, and are of the red-shifting variety, with no evidence of shortening of the CH bonds, nor of perturbations of the CH stretching wavenumbers to higher values. The complexes with HF and HCl are of three types:  $\text{CH}\cdots\text{F}(\text{Cl})$ ,  $\text{F}(\text{Cl})\text{H}\cdots\text{F}$ , and  $\text{F}(\text{Cl})\text{H}\cdots\pi$ , with interaction energies in the sequence  $\text{F}(\text{Cl})\text{H}\cdots\pi > \text{CH}\cdots\text{F}(\text{Cl}) > \text{F}(\text{Cl})\text{H}\cdots\text{F}$ . These six complexes are also uniformly red-shifting, leading to the conclusion that, despite the presence of a fluorine atom and a  $\text{C}\equiv\text{C}$  bond, HCCF does not possess sites of sufficiently high electron density to encourage the kind of density redistribution which characterizes the blue-shifting family of hydrogen bonds. There is evidence that blue-shifting hydrogen bonding is observed only when the proton donor is rather weak. In the case of the complexes studied here, apparently the HCCF donor strength is sufficiently high to dominate the range of effects which determine the nature of the hydrogen bonds formed.

## Supplementary data

Supplementary data for this article are available on the journal Web site (canjchem.nrc.ca).

## Acknowledgements

This material is based upon work supported by the National Research Foundation of South Africa under Grant No. 2053648. Any opinion, findings, and conclusions or recommendations expressed in this material are those of the authors and do not necessarily reflect the views of the National Research Foundation. The authors also acknowledge assistance from the University of Mauritius and the University of KwaZulu-Natal Research Fund, through its support of the Centre for Theoretical and Computational Chemistry.

## References

- Hobza, P.; Havlas, Z. *Chem. Rev.* **2000**, *100* (11), 4253. doi:10.1021/cr990050q. PMID:11749346.
- van der Veken, B. J.; Herrebout, W. A.; Szostak, R.; Shchepkin, D. N.; Havlas, Z.; Hobza, P. *J. Am. Chem. Soc.* **2001**, *123* (49), 12290. doi:10.1021/ja010915t. PMID:11734029.
- Scheiner, S.; Kar, T. *J. Phys. Chem. A* **2002**, *106* (9), 1784. doi:10.1021/jp013702z.
- Li, X.; Liu, L.; Schlegel, H. B. *J. Am. Chem. Soc.* **2002**, *124* (32), 9639. doi:10.1021/ja020213j. PMID:12167060.
- Hermansson, K. *J. Phys. Chem. A* **2002**, *106* (18), 4695. doi:10.1021/jp0143948.
- Zierkiewicz, W.; Michalska, D.; Havlas, Z.; Hobza, P. *ChemPhysChem* **2002**, *3* (6), 511. doi:10.1002/1439-7641(20020617)3:6<511::AID-CPHC511>3.0.CO;2-Y. PMID:12465490.
- Alabugin, I. V.; Manoharan, M.; Peabody, S.; Weinhold, F. *J. Am. Chem. Soc.* **2003**, *125* (19), 5973. doi:10.1021/ja034656e. PMID:12733938.
- Pejov, L.; Hermansson, K. *J. Chem. Phys.* **2003**, *119* (1), 313. doi:10.1063/1.1571517.
- Rhee, S. K.; Kim, S. H.; Lee, S.; Lee, J. Y. *Chem. Phys.* **2004**, *297* (1-3), 21. doi:10.1016/j.chemphys.2003.10.003.
- Kolandaivel, P.; Nirmala, V. *J. Mol. Struct.* **2004**, *694* (1-3), 33. doi:10.1016/j.molstruc.2004.01.030.
- Barnes, A. J. *J. Mol. Struct.* **2004**, *704* (1-3), 3. doi:10.1016/j.molstruc.2004.02.040.
- Melikova, S. M.; Rutkowski, K. S.; Rodziewicz, P.; Koll, A. *J. Mol. Struct.* **2004**, *705* (1-3), 49. doi:10.1016/j.molstruc.2004.05.022.
- Feng, Y.; Zhao, S.-W.; Liu, L.; Wang, J.-T.; Li, X.-S.; Guo, Q.-X. *J. Phys. Org. Chem.* **2004**, *17* (12), 1099. doi:10.1002/poc.785.
- Karpfen, A. *J. Mol. Struct. THEOCHEM* **2004**, *710* (1-3), 85. doi:10.1016/j.theochem.2004.09.006.
- Yang, Y.; Zhang, W.; Pei, S.; Shao, J.; Huang, W.; Gao, X. *J. Mol. Struct. THEOCHEM* **2005**, *732* (1-3), 33. doi:10.1016/j.theochem.2005.07.006.
- Buckingham, A. D.; Del Bene, J. E.; McDowell, S. A. C. *Chem. Phys. Lett.* **2008**, *463* (1-3), 1. doi:10.1016/j.cplett.2008.06.060.
- Oliveira, B. G.; de Araújo, R. C. M. U.; Ramos, M. N. J. *J. Mol. Struct. THEOCHEM* **2009**, *908* (1-3), 79. doi:10.1016/j.theochem.2009.05.013.
- Kryachko, E. S. *Int. J. Quantum Chem.* **2010**, *110* (1), 104. doi:10.1002/qua.22256.
- Pimentel, G. C.; McClellan, A. L. *The Hydrogen Bond*; W. H. Freeman & Co.: San Francisco, 1960; pp. 70,71.
- Bader, R. F. W. *Atoms in Molecules: a Quantum Theory*; Clarendon Press: Oxford, 1990.
- Reed, A. E.; Curtiss, L. A.; Weinhold, F. *Chem. Rev.* **1988**, *88* (6), 899. doi:10.1021/cr00088a005.
- Wetmore, S. D.; Schofield, R.; Smith, D. M.; Radom, L. *J. Phys. Chem. A* **2001**, *105* (38), 8718. doi:10.1021/jp011087t.
- Chen, R.; Zhang, K.-C.; Liu, L.; Li, X.-S.; Guo, Q.-X. *Chem.*

- Phys. Lett.* **2001**, 338 (1), 61. doi:10.1016/S0009-2614(01)00195-6.
- (24) Scheiner, S.; Grabowski, S. J.; Kar, T. *J. Phys. Chem. A* **2001**, 105 (46), 10607. doi:10.1021/jp0131267.
- (25) Chandra, A. K.; Nguyen, M. T. *Chem. Phys.* **1998**, 232 (3), 299. doi:10.1016/S0301-0104(98)00111-6.
- (26) Wojtulewski, S.; Grabowski, S. J. *J. Mol. Struct.* **2002**, 605 (2-3), 235. doi:10.1016/S0022-2860(01)00785-2.
- (27) Gaussian 03, Revision B.03. Frisch, M. J.; Trucks, G. W.; Schlegel, H. B.; Scuseria, G. E.; Robb, M. A.; Cheeseman, J. R.; Montgomery, J. A., Jr.; Vreven, T.; Kudin, K. N.; Burant, J. C.; Millam, J. M.; Iyengar, S. S.; Tomasi, J.; Barone, V.; Mennucci, B.; Cossi, M.; Scalmani, G.; Rega, N.; Petersson, G. A.; Nakatsuji, H.; Hada, M.; Ehara, M.; Toyota, K.; Fukuda, R.; Hasegawa, J.; Ishida, M.; Nakajima, T.; Honda, Y.; Kitao, O.; Nakai, H.; Klene, M.; Li, X.; Knox, J. E.; Hratchian, H. P.; Cross, J. B.; Adamo, C.; Jaramillo, J.; Gomperts, R.; Stratmann, R. E.; Yazyev, O.; Austin, A. J.; Cammi, R.; Pomelli, C.; Ochterski, J. W.; Ayala, P. Y.; Morokuma, K.; Voth, G. A.; Salvador, P.; Dannenberg, J. J.; Zakrzewski, V. G.; Dapprich, S.; Daniels, A. D.; Strain, M. C.; Farkas, O.; Malick, D. K.; Rabuck, A. D.; Raghavachari, K.; Foresman, J. B.; Ortiz, J. V.; Cui, Q.; Baboul, A. G.; Clifford, S.; Cioslowski, J.; Stefanov, B. B.; Liu, G.; Liashenko, A.; Piskorz, P.; Komaromi, I.; Martin, R. L.; Fox, D. J.; Keith, T.; Al-Laham, M. A.; Peng, C. Y.; Nanayakkara, A.; Challacombe, M.; Gill, P. M. W.; Johnson, B.; Chen, W.; Wong, M. W.; Gonzalez, C.; Pople, J. A. Gaussian, Inc.: Pittsburgh, PA, 2003.
- (28) Møller, C.; Plesset, M. S. *Phys. Rev.* **1934**, 46 (7), 618. doi:10.1103/PhysRev.46.618.
- (29) Dunning, T. H., Jr. *J. Chem. Phys.* **1989**, 90 (2), 1007. doi:10.1063/1.456153.
- (30) Kendall, R. A.; Dunning, T. H., Jr.; Harrison, R. J. *J. Chem. Phys.* **1992**, 96 (9), 6796. doi:10.1063/1.462569.
- (31) Woon, D. E.; Dunning, T. H., Jr. *J. Chem. Phys.* **1993**, 98 (2), 1358. doi:10.1063/1.464303.
- (32) Peterson, K. A.; Woon, D. E.; Dunning, T. H., Jr. *J. Chem. Phys.* **1994**, 100 (10), 7410. doi:10.1063/1.466884.
- (33) Wilson, A.; van Mourik, T.; Dunning, T. H., Jr. *J. Mol. Struct. THEOCHEM* **1997**, 388, 339. doi:10.1016/S0166-1280(96)80048-0.
- (34) Liu, B.; McLean, A. D. *J. Chem. Phys.* **1973**, 59 (8), 4557. doi:10.1063/1.1680654.
- (35) Boys, S. F.; Bernardi, F. *Mol. Phys.* **1970**, 19 (4), 553. doi:10.1080/00268977000101561.
- (36) Hunter, E. P. L.; Lias, S. G. *J. Phys. Chem. Ref. Data* **1998**, 27, 413.
- (37) Chan, B.; Del Bene, J. E.; Radom, L. *J. Am. Chem. Soc.* **2007**, 129 (40), 12197. doi:10.1021/ja072690d. PMID: 17877345.
- (38) Chan, B.; Del Bene, J. E.; Radom, L. *Mol. Phys.* **2009**, 107 (8), 1095. doi:10.1080/00268970902740571.

# The first series of alkali dipyrinato complexes

Adeeb Al-Sheikh Ali, Judy Cipot-Wechsler, Sarah M. Crawford, Omar Selim, Rhonda L. Stoddard, T. Stanley Cameron, and Alison Thompson

**Abstract:** The first series of alkali dipyrinato complexes is reported, encompassing lithium, sodium, and potassium salts of *meso*-unsubstituted and *meso*-aryl-substituted derivatives. By varying the substituents at the *meso* position, the intermolecular distance between the two nitrogen atoms and thus the  $\kappa^2$ -*N,N*-bidentate bite angle was altered, as confirmed by comparison of crystallographic structures of dipyririn free-bases in the solid-state. The mode of bonding varies as the ionic radius of the metal ion increases: solid-state structures reveal lithium to be accommodated in the plane of the dipyrinato unit, whilst sodium is accommodated out of plane. The reactivity of analogous lithium, sodium, and potassium dipyrinato complexes increases as the ionic radius of the metal ion increases, in keeping with the concept that the complexes tend towards an increasingly ionic nature as the size of the alkali metal increases.

**Key words:** dipyririn, dipyrinato, alkali salts, monoanionic bidentate, *N,N*-chelation, pyrrolic.

**Résumé :** On rapporte la préparation de la première série de complexes dipyrinato alcalins comportant les sels de lithium, de sodium et de potassium de dérivés *més*o non substitués et *més*o substitués par des groupes aryles. En faisant varier la nature des substituants en position *més*o, on modifie la distance intermoléculaire entre les deux atomes d'azote et, en conséquence, l'angle de morsure  $\kappa^2$ -*N,N* du bidentate, tel que confirmé par une comparaison des structures cristallographiques des bases libres dipyrirines à l'état solide. Le mode de liaison varie avec une augmentation du rayon ionique de l'ion métallique; les structures à l'état solide révèlent que le lithium s'accommode dans le plan de l'unité dipyrinato alors que le sodium est accommodé hors du plan. La réactivité des complexes analogues du lithium, du sodium et du potassium augmente avec une augmentation du rayon ionique du métal ionique, en accord avec le concept que les complexes tendent vers une nature de plus en plus ionique avec une augmentation de la taille des métaux alcalins.

**Mots-clés :** dipyririne, dipyrinato, sels alcalins, bidentate monoanionique, *N,N*-chélation, pyrrolique.

[Traduit par la Rédaction]

## Introduction

The N–H hydrogen atom of dipyririns (Fig. 1), best-known for their presence in 4,4-difluoro-4-bora-3a,4a-diaza-*s*-indacenes (BODIPYs),<sup>1</sup> can be formally deprotonated to give the monoionic conjugated dipyrinato species that can act as a bidentate ligand for the synthesis of supramolecular assemblies and discrete complexes.<sup>2</sup> Crucially, dipyrinato ligands generally adopt a (*Z*)-*syn*-type arrangement and thus chelate in a  $\kappa^2$  manner.<sup>3,4</sup> Although dipyrinato metal complexes have been reported for M<sup>+</sup> species, such as thallium(I)<sup>5</sup> and rhodium(I),<sup>6</sup> alkali complexes involving the dipyrinato ligand were unknown before our recent communication involving lithium.<sup>7</sup> We showed that the monoanionic source of the ligand, rather than the corresponding free base or its protonated derivative, gave access to unprecedented reactivity and previously inaccessible heteroleptic zinc(II) complexes. Our work was followed by an example whereby a lithium dipyrinato complex was used to generate heteroleptic iron(II) and zinc(II) complexes.<sup>8</sup> Porphyrins,

which can be formed from the condensation of two appropriately substituted dipyririns, undergo deprotonation to give the di-ionic tetradentate ligand, and alkali metalloporphyrins have been well-documented,<sup>9</sup> as has the synthetic utility of such complexes in transmetallation reactions to obtain Ag(I), Zn(II), Cd(II), Hg(II), Cu(II), Sn(II), and Fe(III) complexes of porphyrins.<sup>10</sup> As lithium, sodium, and potassium complexes of porphyrins have all been reported,<sup>11</sup> we found it surprising that alkali complexes of the dipyrinato ligand were unknown before our work, apart from a single example of a lithium-cryptand-dipyrinato complex in solution:<sup>12</sup> such derivatives of related  $\beta$ -diketiminato (NacNac),<sup>13,14</sup> porphodimethene,<sup>15</sup> pyrroloimine,<sup>16,17</sup> and amino-pyrrole<sup>18,19</sup> skeletons are well-known.

Many recent advances in coordination chemistry and catalysis have been dependent upon the utility of stable *N,N*-bidentate monoanionic ligands. To this end,  $\beta$ -diketiminato ligands have attracted much attention as spectator ligands: they are isoelectronic to the cyclopentadienyl anion; they

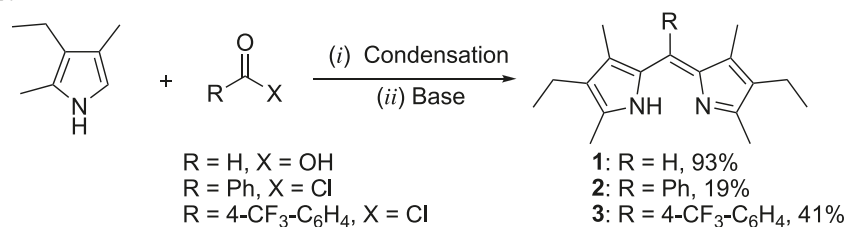
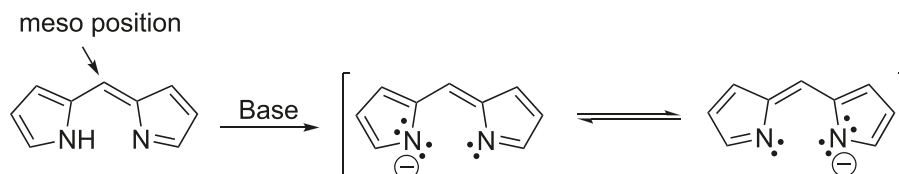
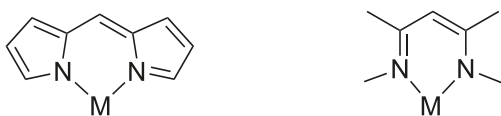
Received 25 September 2009. Accepted 23 November 2009. Published on the NRC Research Press Web site at canjchem.nrc.ca on 26 April 2010.

This article is part of a Special Issue dedicated to Professor R. J. Boyd.

A.A. Ali,<sup>1</sup> J. Cipot-Wechsler, S.M. Crawford, O. Selim, R.L. Stoddard, T.S. Cameron, and A. Thompson.<sup>2</sup> Department of Chemistry, Dalhousie University, Halifax, NS B3H 4J3, Canada.

<sup>1</sup>Present address: Chemistry Department, Taibah University, Almadinah Almunawarah, P.O. Box: 30002, Saudi Arabia.

<sup>2</sup>Corresponding author (e-mail: Alison.Thompson@dal.ca).

**Scheme 1.** Synthesis of dipyrins 1–3.**Fig. 1.** Dipyrin and the monoanionic dipyrinato skeleton.**Fig. 2.** Dipyrinato skeleton as compared to the  $\beta$ -diketimato framework.

strongly coordinate to metal centers; and the reactivities of metal centers can be tuned by changing the steric and electronic properties of the substituents at the nitrogen atoms. The  $\beta$ -diketiminato ligand<sup>20,21</sup> has a similar *N,N*-bidentate monoanionic framework to the dipyrinato ligand (Fig. 2). However, the ability of the dipyrinato unit to support catalytically active metal centers has yet to be systematically examined.<sup>2</sup> There are limited examples of dipyrins used as chelating ligands for transition-metal fragments, with no examples to date exploring the potential catalytic utility of the resulting complexes, although, in a recent report, an iron(II) dipyrinato complex was shown to undergo C–H bond amination from an organic azide, hinting towards functional possibilities.<sup>8</sup> The lack of systematic exploration is somewhat surprising given the likely useful structural features of the monoanionic dipyrinato ligand, e.g., a hard nitrogen donor pair, the formation of a six-membered ring upon metal coordination, and access to derivatives bearing variable steric and electronic substituents. Traditionally, dipyrinato complexes have been prepared using either HX salts or free-bases as the source of the ligand. Clearly, these ionization states limit the potential for the synthesis of dipyrinato complexes with a diverse array of metal fragments, and it thus follows that alkali dipyrinato complexes would be of interest.

One of the structural locations upon dipyrinato ligands that can easily be modified is the *meso* position (Fig. 1). The term “*meso*” is borrowed from the chemistry of porphyrins, and is routinely applied to dipyrins to identify the methylene position between the two pyrrolic units. By varying the substituents at the *meso* position, we hoped to alter the intermolecular distance between the two nitrogen atoms, and thus influence the C4–C5–C6 angle, and thus the bite angle, of the dipyrinato ligand. As a result, the mode of bonding and the reactivity of the alkali dipyrinato complexes would be anticipated to vary. Herein, we compare

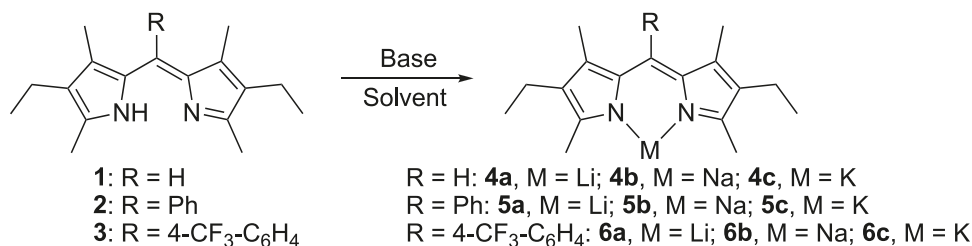
the solid-state structures of dipyrinato salts and free-bases, and report our work regarding *meso*-unsubstituted and *meso*-substituted lithium, sodium, and potassium complexes involving the dipyrinato ligand.

## Results and discussion

To investigate the stability and properties of alkali dipyrinato complexes, three free-base dipyrins were synthesized (Scheme 1); one dipyrin unsubstituted at the *meso* position and two new dipyrins bearing aryl groups at the *meso* position. We maintained the symmetrical bis(1,3-dimethyl-2-ethyl) substitution pattern across the series by using kryptopyrrole in all of our syntheses. The *meso*-unsubstituted dipyrin **1HBr**<sup>22,23</sup> was prepared by reacting kryptopyrrole with formic acid in the presence of HBr, and we then grew crystals of this salt via slow cooling of the reaction mixture. Liberation of the free-base **1** could be achieved using either lithium hydride or ammonium hydroxide.<sup>7</sup> The *meso*-phenyl and *meso*-*p*-CF<sub>3</sub>-phenyl dipyrins **2** and **3**, respectively, were prepared initially as their hydrochloride salts by reacting the corresponding acid chloride with kryptopyrrole. The salts were purified over silica gel to remove any unreacted starting materials as well as the major ketone byproduct (the structure of 4-ethyl-3,5-dimethyl-2-phenylacetylpyrrole, the intermediate en route to **2**, was confirmed using X-ray crystallography, see Experimental section). Treatment of **2HCl** and **3HCl** with satd. NaHCO<sub>3</sub> gave the requisite free-bases in analytically pure form after purification over basic alumina. The low yields of **2** and **3** were attributed to the steric and electronic factors of the persistent ketone intermediates.

Reacting a THF solution of free-base **1** with *n*BuLi gave clean conversion to the lithium dipyrinato complex **4a** (Table 1), which was crystallographically characterized as **4a** and **4a**·(THF)<sub>2</sub>.<sup>7</sup> As detailed in our previous communication, the structural features of **4a**·(THF)<sub>2</sub> are consistent with the relevant N–Li and N–C bond lengths of related lithium diketiminato complexes ( $\beta$ -diketiminato backbone substituted with either methyl<sup>24</sup> or *tert*-butyl groups<sup>25</sup>) that include at least one solvent ether molecule. However, the N–Li–O angles in **4a**·(THF)<sub>2</sub> are contracted relative to those of related lithium  $\beta$ -diketiminato structures containing only one



**Table 1.** Synthesis of *meso*-substituted alkali metal dipyrinato complexes.

Compound	R	Base	M	Solvent	Isolated yield (%)
<b>4a</b>	H	BuLi	Li	THF	95
<b>4b</b>	H	NaN(SiMe <sub>3</sub> ) <sub>2</sub>	Na	Et <sub>2</sub> O	74
<b>4c</b>	H	KCH <sub>2</sub> Ph	K	THF	66
<b>5a</b>	Ph	BuLi	Li	THF	50
<b>5b</b>	Ph	NaN(SiMe <sub>3</sub> ) <sub>2</sub>	Na	Et <sub>2</sub> O	63
<b>5c</b>	Ph	KN(SiMe <sub>3</sub> ) <sub>2</sub>	K	THF	73
<b>6a</b>	<i>p</i> -CF <sub>3</sub> -Ph	LiN(SiMe <sub>3</sub> ) <sub>2</sub>	Li	THF	81
<b>6b</b>	<i>p</i> -CF <sub>3</sub> -Ph	NaN(SiMe <sub>3</sub> ) <sub>2</sub>	Na	THF	91
<b>6c</b>	<i>p</i> -CF <sub>3</sub> -Ph	KN(SiMe <sub>3</sub> ) <sub>2</sub>	K	THF	83

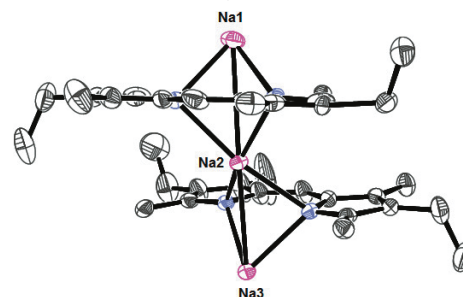
coordinated solvent molecule (average 130.8°),<sup>24,25</sup> presumably due to steric crowding.

The THF-free solid-state structure of **4a** and the THF-supported structure exhibit significant differences in bond lengths and angles, as we previously reported.<sup>7</sup> For example, the N–Li average distance is 1.39(1) Å in **4a**, compared with 1.98(1) Å in **4a**·(THF)<sub>2</sub>, akin to the Li–N bond length in related lithium diketiminato<sup>13,14,25,26</sup> and porphyrin complexes.<sup>11</sup> Furthermore, the acute C4–N1–Li and C6–N2–Li bond angles in **4a** are only 95.3(4)° and 96.4(4)°, respectively. The bond angles, the planarity of the six-membered chelate ring, and the short N–Li distances in the solid-state structure of **4a** are consistent with an otherwise uncoordinated lithium atom, which is somewhat of a rarity.<sup>24</sup>

The *meso*-unsubstituted sodium dipyrinato complex (**4b**) was prepared via the slow addition of an ethereal solution of sodium bis(trimethylsilyl)amide to an ethereal solution of the free-base **1**. An orange precipitate was immediately formed, the reaction mixture was filtered over Celite, and the residue was washed with ether to remove unreacted free-base and other byproducts. Subsequently, the product was dissolved in THF, the solution was filtered over Celite, and then the solvent was removed in vacuo.

The *meso*-unsubstituted dipyrinato sodium complex (**4b**) was crystallographically characterized after a suitable dark-red crystal was obtained from the slow evaporation of solvent from a concentrated THF solution. The X-ray structure of **4b** (Fig. 3) reveals an oligomer where complexed sodium ions are positioned within non-planar six-membered rings via *N,N'*-chelation, in contrast to the corresponding dipyrinato lithium complex<sup>7</sup> whereby the lithium atom was found to be positioned between the two nitrogen atoms in a discrete planar six-membered ring. The structure of **4b** contains three unique sodium atoms: Na(1), which is on an inversion centre, Na(2), which is in a general position, and Na(3), which is on a twofold axis. Thus, while there are three unique sodium atoms, Na(1) and Na(3) have only half occupancy. The Na(1)–Na(2) distance is 3.247(1) Å, and the Na(2)–Na(3) distance is 3.541(2) Å. Although these are

**Fig. 3.** The X-ray structure of sodium dipyrinato complex **4b**, shown with probability ellipsoids of 50% (hydrogen atoms and THF molecules omitted for clarity; the end of the oligomer and the attached side chains are disordered in two slightly different orientations; disorder not shown).



long, they are arguably just within a van der Waals radius, with the chain of sodium atoms of course propagated by the inversion centre giving a second Na(1)–Na(2) distance of 3.247(1) Å and a Na(3)–Na(2) distance of 3.541(2) Å. The coordination about Na(1) is a near-regular octahedron with two dipyrinato units and two THF molecules, obviously with pairs related by the inversion centre. The coordination about Na(3) is an approximate five-coordinate square-based pyramidal system with two dipyrinato units in the base and a THF molecule with its oxygen atom displaced just slightly off the twofold axis. The coordination about the central Na(2) atom is again five-coordinate with a very distorted square-based pyramid. The two dipyrinato units are in the base but the THF molecule and its oxygen atom are well-displaced to one side. All of the ligands (except the THF molecule coordinated to Na(3)) do double duty, coordinating and bridging between two sodium atoms. Thus, between Na(1) and Na(2) there are two dipyrinato units and the one (displaced) THF bridging the short (3.247 Å) Na(1)–Na(2) distance. However, a THF molecule is absent from the bridging position between Na(2) and Na(3), and just two dipyrinato units bridge that longer gap (3.541(2) Å). In all,

the close approach of the sodium atoms to each other is a consequence of the bridging ligands and probably has no bonding significance.

The bond angles C4–C5–C6 and C21–C22–C23 for the two dipyrinato units in the solid-state structure of **4b** were decreased to 132.9(3)° and 132.8(4)°, respectively, compared with 148.7(3)° in the free-base **1**. Although the C4–C5–C6 angles in **4b** were found to be close to those for the lithium dipyrinato complex (**4a**), the larger ionic size of the sodium ion, compared with the lithium ion, prevented a planar geometry of the complex; as a result, the sodium ion is accommodated out of the dipyrinato plane. As expected, the N–Na bond lengths of **4b** (average 2.53(4) Å) are longer than the N–Li bond lengths of **4a**·(THF)<sub>2</sub> (1.98(1) Å). Such a comparison suggests that the ionic nature of alkali dipyrinato complexes increases as the ionic radii of the metal increase. Related sodium diketiminato complexes exhibit the same trend as our dipyrinato analogues, e.g., Na–N bond length of 2.395(6) Å (cf. Li–N bond length of 1.9975(7) Å<sup>20</sup>) with the lithium ion being accommodated in plane and the sodium ion being accommodated out of plane.

The *meso*-unsubstituted potassium dipyrinato complex (**4c**) was prepared using benzyl potassium (KCH<sub>2</sub>Ph) as the base. As KCH<sub>2</sub>Ph<sup>27</sup> is insoluble in diethyl ether, THF was used as the reaction solvent. Upon the addition of a THF solution of benzyl potassium to a THF solution of the free-base **1**, the potassium dipyrinato complex (**4c**) instantly precipitated as an orange solid. The solvent was removed in vacuo and the solid was washed with ether and then hexanes. The poor solubility of **4c** hindered attempts to secure a crystal suitable for crystallographic analysis, and despite much effort, we were unsuccessful in this regard. Furthermore, we were unable to crystallize any compounds bearing *meso*-aryl substituents.

Interested in how the C4–C5–C6 bond angle and the N–N intramolecular distance affect the coordination geometry of dipyrinato complexes, we grew crystals of the three free-bases **1–3** via the slow evaporation of solvent from concentrated pentane solutions. With our hypothesis being that the nature of the *meso*-substituent would dramatically affect the C4–C5–C6 bond angle, and thus the N–N intramolecular distance and chelating bite angle, we were pleased that the X-ray crystallographic analysis revealed a dramatic decrease of the C4–C5–C6 angle from the *meso*-unsubstituted dipyrin (**1**) [C4–C5–C6 bond angle, 148.7(3)°] (Fig. 4) to the substituted dipyrins **2** [C4–C5–C6 bond angle, 124.8(2)°] (Fig. 5) and **3** [C4–C5–C6 bond angle, 124.1(2)°], respectively (Fig. 6). Moreover, as the C4–C5–C6 angle decreases across the series **1–3**, the intermolecular distance between the nitrogen atoms also decreases (2.73 Å for **1**, 2.69 Å for **2**, and 2.66 Å for **3**) and hence the bonding mode of complexation of the corresponding dipyrinato ligands would be expected to vary, in terms of bite angle and so forth.

Despite the plethora of known dipyrin salts and free-bases,<sup>2</sup> only a small number of refined crystal structures have been reported: the N–N intramolecular distances, the C4–C5–C6 angles, and the geometry across the central alkenyl bond of reported salts and free-bases are collated in Table 2, along with those for **1HBr**. Interestingly, the 148.7° C4–C5–C6 angle in the free-base **1** is much larger than in the known free-bases **7**<sup>28</sup> and **8**<sup>29</sup> (127.0° and

Fig. 4. The X-ray structure of dipyrin **1**, shown with probability ellipsoids of 50% (hydrogen atoms were omitted for clarity; the structure solves in either *Pbca* or in *Pca21*; *R* value in *Pbca* is 5.7%, and 5.1% in *Pca21*; the higher symmetry space group has been chosen; the pyrrole C and N atoms are in slightly disordered positions and the N–H hydrogen atom has not been located, since it sits on the disordered N–C bridge).

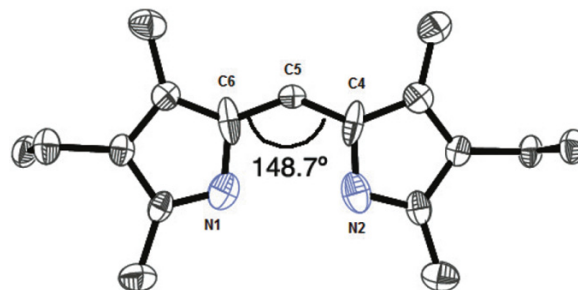


Fig. 5. The X-ray structure of dipyrin **2**, shown with probability ellipsoids of 50% (hydrogen atoms were omitted for clarity).

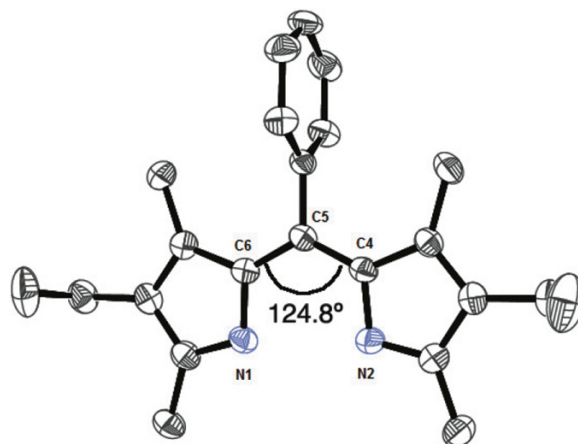
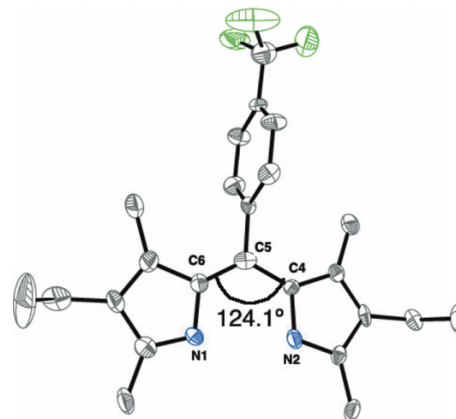
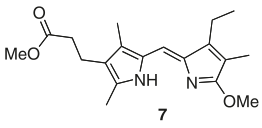
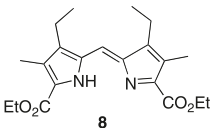
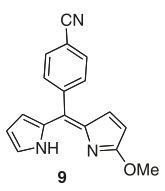
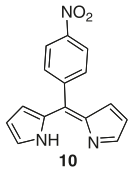
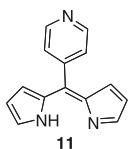
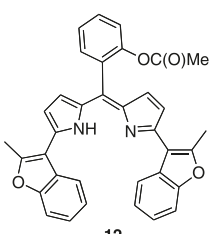
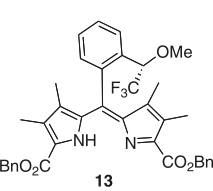
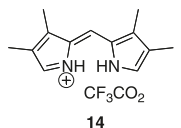


Fig. 6. The X-ray structure of dipyrin **3**, shown with probability ellipsoids of 50% (hydrogen atoms were omitted for clarity; CH<sub>2</sub>CH<sub>3</sub> disorder is not shown).

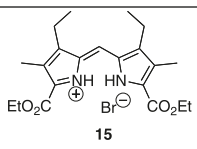
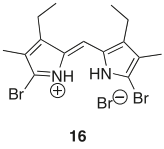
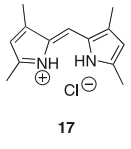
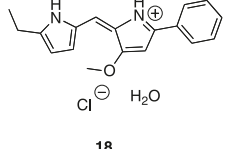
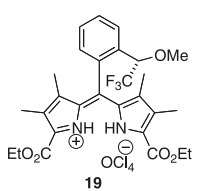
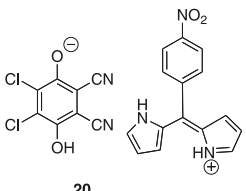
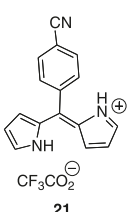
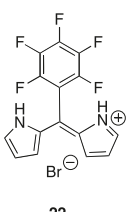


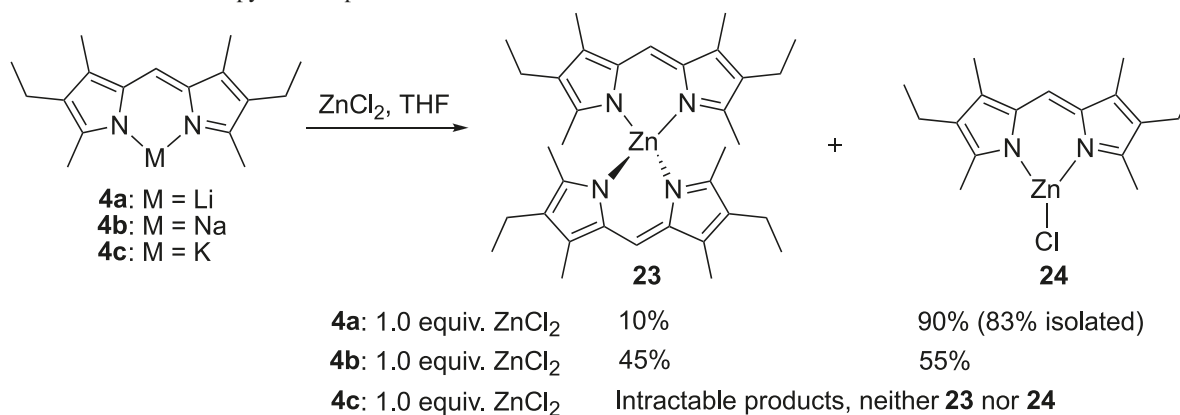
126.1°, respectively) and the salts **1HBr** (133.8°), **14**,<sup>30</sup> **15**,<sup>31</sup> **16**,<sup>32</sup> **17**,<sup>33</sup> and **18**<sup>34</sup> (within the range 132.1°–136.0°), despite the fact that all bear hydrogen atoms at the *meso* position. The significantly different sizes in the C4–C5–C6 angle are presumably a consequence of (i) the substituents that

**Table 2.** N—N distance, C4—C5—C6 angle, and configuration for solid-state dipyrins (geometric data rounded to  $\pm 0.01$  Å and  $\pm 1^\circ$ ).

Structure	N—N distance (Å)	C4—C5—C6 angle ( $^\circ$ )	Configuration
<b>1HBr</b>	3.27	134	Z
	2.72	127	Z
	2.75	126	Z
	2.74	123	Z
	2.74	124	Z
	2.76	125	Z
	2.70	123	Z
	2.64	122	Z
	3.31	136	Z

**Table 2 (Concluded).**

Structure	N—N distance (Å)	C4—C5—C6 angle ( $^\circ$ )	Configuration
	3.38	133	Z
	3.25	134	Z
	3.22	133	Z
	4.78	132	E
	2.82	122	Z
	4.40	124	Z
	4.38	125	E
	4.90	123	E

**Scheme 2.** Reactions of alkali dipyrin complexes.

flank the *meso* position, and (ii) the strength and nature of the intramolecular NH–H hydrogen bonding in which the N–H hydrogen atom(s) partake(s).

Our *meso*-aryl free-bases **2** and **3** compare well with the known *meso*-aryl dipyrin free-bases **9**,<sup>35</sup> **10**,<sup>4</sup> **11**,<sup>36</sup> **12**,<sup>37</sup> and **13**,<sup>38</sup> and the known dipyrin salt **19**:<sup>38</sup> all exhibit *Z* configuration across the alkenyl bond, all have their N atoms aligned with syn geometry (as necessary for chelated complexation), all possess an N–N intramolecular distance of around 2.7 Å (2.8 Å for the salt), and all exhibit a C4–C5–C6 angle of 123°–124° (121.7° for the salt). As shown in Table 2, the *meso*-aryl substituted dipyrin salts **20**,<sup>4</sup> **21**,<sup>39</sup> and **22**<sup>40</sup> exhibit either an *E* configuration or anti geometry, and therefore the C4–C5–C6 angles and N–N intramolecular distances cannot be usefully compared to those of **2** and **3**. All of the free-bases, whether *meso*-substituted or not, exhibit *Z* configuration across the central alkenyl bond, presumably to accommodate intramolecular NH–H hydrogen bonding. This configuration clearly predisposes the ability of such ligands to act as bidentate chelating ligands.

We previously reported<sup>7</sup> that the reaction of lithium dipyrinato complex (**4a**) with ZnCl<sub>2</sub> gives unprecedented access to heteroleptic zinc complexes (Scheme 2). To further benchmark the reactivity of alkali dipyrinato complexes as reagents in simple salt-elimination reactions, a solution of the sodium dipyrinato complex (**4b**) in THF was added dropwise to a stirring solution of a stoichiometric amount of anhydrous ZnCl<sub>2</sub> in THF. After stirring for 1 h at room temperature, the solvent was removed in vacuo and a <sup>1</sup>H NMR spectrum of the crude material revealed a mixture of the homoleptic species **23**<sup>23</sup> and the heteroleptic species **24**<sup>7</sup> in approximately equal ratios (Scheme 2). Interestingly, although **23** and **24** are the only two products observed in the reaction of the dipyrinato analogue **4a** with ZnCl<sub>2</sub>, in that instance, the formation of the heteroleptic species **24** was by far dominant.<sup>7</sup> Thus, moving from the lithium salt to the sodium salt dramatically altered the course of the reaction. A similar reaction employing the potassium dipyrinato analogue (**4c**) was also conducted, whereby a suspension of **4c** in THF was utilized, multiple and intractable products were thus generated, none of which were the known complexes **23** and **24**. This series of experiments reveals the differing reactivity of alkali dipyrinato complexes and lends further support to the notion that the ionic nature of the complexes increases as the ionic radii of the metal increase.

With alkali dipyrinato complexes of lithium, sodium, and potassium in hand, we turned our attention to the *meso*-aryl dipyrins **2** and **3** to expand the series. Lithium (**5a**), sodium (**5b**), and potassium (**5c**) *meso*-phenyl dipyrinato complexes were prepared using butyl lithium, sodium bis(trimethylsilyl)amide, and potassium bis(trimethylsilyl)amide, respectively, as the source of the metal ions. Similarly, the alkali *meso*-*p*-CF<sub>3</sub>-C<sub>6</sub>H<sub>4</sub> dipyrinato complexes **6a–6c** were prepared from the corresponding free-base **3** using the metal bis(trimethylsilyl)amide as the source of the metal ion. The yields and procedures are summarized in Table 1. Taking advantage of the phenomenon that the dipyrins **2** and **3** are soluble in pentane while the alkali complexes are not, the resultant *meso*-substituted alkali dipyrinato metal complexes **5a–5c** and **6a–6c** were repeatedly washed with pentane to remove unreacted free-base and other byproducts. Unfortunately, and despite much effort, we were unsuccessful in growing X-ray-quality crystals of any alkali dipyrinato complexes bearing *meso*-aryl substituents.

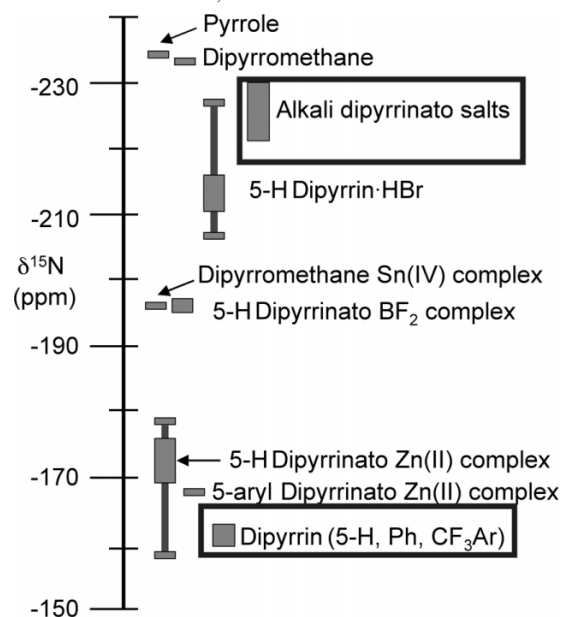
The <sup>15</sup>N NMR chemical shifts for dipyrins, their salts, and their complexes are diagnostic,<sup>23</sup> and this technique generally allows for the characterization of nitrogen-containing heterocyclic compounds, as noted by others.<sup>41–43</sup> With our current work, the published <sup>15</sup>N dipyrinato chemical-shift ranges<sup>23</sup> can now be expanded to include alkali dipyrinato complexes. As indicated in Fig. 7, the <sup>15</sup>N chemical shifts for the complexes **4–6** reported here do not overlap with their corresponding free-base dipyrins **1–3**. Indeed, the chemical shifts dramatically increase from the range of –162 to –164 ppm for the free-bases **1–3** to the range of –219 to –231 ppm for the alkali metal complexes **4–6**.

Curiously, the <sup>13</sup>C NMR spectra for the sodium and potassium dipyrinato complexes with *meso*-aryl substituents exhibited low signal/noise ratios. Indeed, many more than the expected number of scans were required to attain signals for all of the carbon atoms, and with our expectations based on concentrations of solutions and our experience with other dipyrinato complexes, we were unable to find a convincing rationale for this phenomenon but were nevertheless able to assign all signals.

## Conclusions

In summary, this work represents the first synthesis and characterization of a series of alkali dipyrinato complexes.



**Fig. 7.**  $^{15}\text{N}$  chemical shifts, relative to nitromethane at 125.41 ppm.

Three ligands bearing different substituents at the *meso* position have been utilized, along with lithium, sodium, and potassium metal ions. Variation of the substituent at the *meso* position altered the C4–C5–C6 angle of the dipyrinato unit. The alkali dipyrinato complexes were characterized on the basis of spectroscopic techniques, including  $^{15}\text{N}$  NMR spectroscopy, which was used as a diagnostic indication for these compounds. In contrast to the lithium dipyrinato complex (**4a**), which adopted  $\kappa^2$ -*N,N*-bidentate behaviour for the dipyrinato ligand with the lithium ion nestled within the plane, the analogous sodium dipyrinato complex (**4b**) showed a different mode of bonding whereby an oligomeric structure sets the sodium ions out of the  $\kappa^2$ -*N,N*-bidentate dipyrinato plane. With increasing ionic radii of the alkali metals, relative reactivity increased when reactions with  $\text{ZnCl}_2$  were investigated. Our current investigations include the use of alkali dipyrinato complexes in salt elimination strategies to generate coordination complexes not previously accessible via the use of dipyrin free-bases or their HX salts.

## Experimental section

### General procedures

Unless otherwise indicated, all manipulations were conducted in the absence of oxygen and water under an atmosphere of dinitrogen, either by using standard Schlenk methods, or within a glovebox apparatus, utilizing glassware that was oven-dried ( $130^\circ\text{C}$ ) and evacuated while hot prior to use. Celite was oven-dried ( $130^\circ\text{C}$ ) for 5 d and then evacuated for 24 h prior to use. The non-deuterated solvents: tetrahydrofuran, diethyl ether, toluene, benzene, hexanes, and pentane were deoxygenated and dried by sparging with dinitrogen gas, followed by passage through a double-column solvent-purification system. Tetrahydrofuran and diethyl ether were purified over two alumina-packed columns, while toluene, benzene, hexanes, and pentane were purified over one alumina-packed column and one column packed

with copper-Q5 reactant. Sodium benzophenone ketyl was added to the solvent to provide visual confirmation (i.e., the observed persistence of the benzophenone ketyl) that an appropriate level of purification had been achieved. The solvents used within the glovebox were stored over activated  $4\text{ \AA}$  molecular sieves. THF- $d_8$  (Aldrich) and  $\text{C}_6\text{D}_6$  (Aldrich) were degassed by using three repeated freeze–pump–thaw cycles and then dried over  $4\text{ \AA}$  molecular sieves for 24 h prior to use. HBr (48% aqueous solution),  $\text{LiN}(\text{SiMe})_2$ ,  $\text{NaN}(\text{SiMe})_2$ ,  $\text{KN}(\text{SiMe})_2$ ,  $n\text{BuLi}$  (1.6 mol/L solution in hexanes), silica gel (230–400 mesh, pH 6.5–7.5), and alumina (basic, grade 150,  $58\text{ \AA}$ ) were all used as received. All nuclear magnetic resonance experiments were conducted using 250 and 500 MHz spectrometers. All chemical shifts ( $\delta$ ) are reported in ppm. All coupling constants ( $J$ ) are reported in Hz. All  $^1\text{H}$  and  $^{13}\text{C}$  NMR chemical shifts are reported relative to solvent peaks used as internal references:  $\text{C}_6\text{D}_6$  (7.16 and 128.62 ppm, respectively), THF- $d_8$  (3.58 and 67.80 ppm, respectively), DMF- $d_7$  (8.03 and 163.15 ppm, respectively), and  $\text{CDCl}_3$  (7.26 and 77.16 ppm, respectively).  $^{15}\text{N}$  chemical shifts were obtained from two-dimensional  $^1\text{H}$  (500 MHz) –  $^{15}\text{N}$  (50.7 MHz) HMBC correlation experiments.  $^{15}\text{N}$ ,  $^7\text{Li}$ ,  $^{23}\text{Na}$ , and  $^{19}\text{F}$  shift scales were referenced as outlined in the IUPAC recommendations of 2001.<sup>44</sup> Mass spectra were obtained in ESI positive mode using a TOF instrument in both high and low resolution. All UV–vis analyses were performed using a 10 mm screw-cap cell (with Teflon tape), and solutions were prepared using glovebox techniques and dry THF. 4,4′-Diethyl-3,3′,5,5′-tetramethyldipyrin hydrobromide (**1HBr**),<sup>22</sup> benzyl potassium, 4,4′-diethyl-3,3′,5,5′-tetramethyldipyrin (**1**),<sup>7</sup> and lithium 4,4′-diethyl-3,3′,5,5′-tetramethyldipyrinato (**3a**)<sup>7</sup> were prepared according to literature procedures.

### $\kappa^2$ -(4,4′-Diethyl-3,3′,5,5′-tetramethyl-*meso*- $\text{C}_6\text{H}_5$ -dipyrin) (**2**)

To a solution of 3-ethyl-2,4-dimethylpyrrole (1.3 mL, 10 mmol) in  $\text{CHCl}_3$  (50 mL), benzoyl chloride (70 mg, 5.0 mmol) was added, and the reaction mixture was heated at reflux temperature for 3 h. The resultant pink reaction mixture was extracted with water ( $2 \times 30\text{ mL}$ ), and the organic solution was then dried over  $\text{Na}_2\text{SO}_4$ . Removal of the organic solvent in vacuo gave crude material that was purified using chromatography on silica gel. A minor byproduct was eluted with 50%  $\text{CH}_2\text{Cl}_2$  in hexane, and it was characterized to be 4-ethyl-3,5-dimethyl-2-phenyl acetylpyrrole as a pale yellow solid, mp  $159$ – $161^\circ\text{C}$ .  $\delta_{\text{H}}$  (500 MHz,  $\text{CDCl}_3$ ): 9.29 (1H, bs), 7.25–7.63 (5H, m), 2.38 (2H, q,  $J = 7.5$ ), 2.35 (3H, s), 1.89 (3H, s), 1.05 (3H, t,  $J = 7.5$ ).  $\delta_{\text{C}}$  (125 MHz,  $\text{CDCl}_3$ ): 185.7, 140.8, 133.1, 130.9, 128.9, 128.5, 128.4, 127.1, 125.5, 125.4, 123.9, 17.5, 15.3, 11.9, 11.7.  $\delta_{\text{N}}$  (50.7 MHz,  $\text{CDCl}_3$ ):  $-227.7$ .  $m/z$  (ESI<sup>+</sup>): 250.1202 ( $\text{M} + \text{Na}$ )<sup>+</sup>. A crystal of 4-ethyl-3,5-dimethyl-2-phenyl acetylpyrrole suitable for X-ray crystallographic analysis was grown via slow evaporation of a solution in hexane (structure included herein). The major band was eluted with 5%  $\text{CH}_3\text{OH}$  in  $\text{CH}_2\text{Cl}_2$ . Removal of the solvent in vacuo followed by dissolution in  $\text{CH}_2\text{Cl}_2$  (30 mL) and then washing with saturated  $\text{NaHCO}_3$  solution ( $2 \times 30\text{ mL}$ ) gave the title compound as its free-base. Drying of the solution over  $\text{Na}_2\text{SO}_4$  and removal of the organic solvent in vacuo gave

an orange solid that was purified using column chromatography on basic alumina eluting with 60%  $\text{CH}_2\text{Cl}_2$  in hexane to give the title compound as an orange solid (31 mg, 19%); mp 148–150 °C. UV–vis  $\lambda_{\text{max}}$  (nm): 515 ( $\epsilon$  45 000  $\text{mol/L}^{-1}\text{cm}^{-1}$ , MeOH).  $\delta_{\text{H}}$  (500 MHz,  $\text{CDCl}_3$ ): 7.44–7.45 (3H, m), 7.34–7.36 (2H, m), 2.31 (6H, s), 2.28 (4H, q,  $J = 7.5$ ), 1.19 (6H, s), 0.97 (6H, t,  $J = 7.5$ ).  $\delta_{\text{C}}$  (125 MHz,  $\text{CDCl}_3$ ): 150.3, 139.2, 135.7, 134.9, 131.5, 129.8, 128.6, 128.2, 124.2, 17.8, 15.1, 14.6, 11.9.  $\delta_{\text{N}}$  (50.7 MHz,  $\text{THF}-d_8$ ): –162.1.  $m/z$  HR (MH)<sup>+</sup>  $\text{C}_{23}\text{H}_{28}\text{N}_2$  calcd.: 332.2252, found: 333.2303. Anal. calcd. for  $\text{C}_{23}\text{H}_{28}\text{N}_2$ : C, 83.09; H, 8.49; N, 8.43. Found: C, 83.13; H, 8.54; N, 8.31.

**$\kappa^2$ -(4,4'-Diethyl-3,3',5,5'-tetramethyl-meso-*p*-CF<sub>3</sub>-C<sub>6</sub>H<sub>4</sub>-dipyrrin) (3)**

To a solution of 3-ethyl-2,4-dimethylpyrrole (0.34 mL, 2.50 mmol) in  $\text{CH}_2\text{Cl}_2$  (30 mL), 4-trifluoromethylbenzoylchloride (260 mg, 1.25 mmol) was added, and the reaction mixture was heated at reflux temperature for 48 h. The resultant pink reaction mixture was extracted with water (2 × 30 mL), and the organic solution was then dried over  $\text{Na}_2\text{SO}_4$ . Removal of the organic solvent in vacuo gave a crude product that was purified using chromatography on silica gel. A minor byproduct was eluted with 50%  $\text{CH}_2\text{Cl}_2$  in hexane, and it was characterized to be 4-ethyl-3,5-dimethyl-2-(trifluoromethylphenyl) acetylpyrrole as a pale yellow solid, mp 165–167 °C. UV–vis  $\lambda_{\text{max}}$  (nm): 523 ( $\epsilon$  40 000  $\text{mol/L}^{-1}\text{cm}^{-1}$ , MeOH).  $\delta_{\text{H}}$  (500 MHz,  $\text{CDCl}_3$ ): 9.20 (1H, bs), 7.65–7.71 (4H, bs), 2.38 (2H, q,  $J = 7.5$ ), 2.27 (3H, s), 1.85 (3H, s), 1.05 (3H, t,  $J = 7.5$ ).  $\delta_{\text{C}}$  (125 MHz,  $\text{CDCl}_3$ ): 183.7, 143.9, 134.0, 132.4 (q,  $J_{\text{C-F}} = 32.3$ ), 128.9, 128.4, 126.7, 125.8, 125.4, 123.9 (q,  $J_{\text{C-F}} = 270.8$ ), 17.2, 15.1, 11.7, 11.6.  $\delta_{\text{N}}$  (50.7 MHz,  $\text{CDCl}_3$ ): –228.2.  $\delta_{\text{F}}$  (243 MHz,  $\text{CDCl}_3$ ): –63.7.  $m/z$  (ESI<sup>–</sup>): 294.3 (M<sup>–</sup>). The major band was eluted with 10%  $\text{CH}_3\text{OH}$  in  $\text{CH}_2\text{Cl}_2$ . Removal of the organic solvent in vacuo followed by dissolution of the solid in  $\text{CH}_2\text{Cl}_2$  (30 mL) and then washing with satd.  $\text{NaHCO}_3$  solution (2 × 30 mL) gave **3** as its free-base. Drying of the solution over  $\text{Na}_2\text{SO}_4$  and removal of the organic solvent in vacuo gave an orange solid that was purified using column chromatography and basic alumina eluting with 50%  $\text{CH}_2\text{Cl}_2$  in hexane to give the title compound as an orange solid (226 mg, 41%), mp (dec.) > 185 °C.  $\delta_{\text{H}}$  (500 MHz,  $\text{CDCl}_3$ ): 13.22 (1H, bs), 7.69 (2H, d,  $J = 10.0$ ), 7.46 (2H, d,  $J = 10.0$ ), 2.32 (6H, s), 2.27 (4H, q,  $J = 7.5$ ), 1.15 (6H, s), 0.97 (6H, t,  $J = 7.5$ ).  $\delta_{\text{C}}$  (125 MHz,  $\text{CDCl}_3$ ): 150.7, 142.8, 135.7, 135.4, 134.3, 131.8, 130.4 (q,  $J_{\text{C-F}} = 32.3$ ), 130.2, 125.4, 124.2 (q,  $J_{\text{C-F}} = 265.0$ ), 17.6, 14.8, 14.4, 12.0.  $\delta_{\text{F}}$  (243 MHz,  $\text{CDCl}_3$ ): –63.3.  $\delta_{\text{N}}$  (50.7 MHz,  $\text{CDCl}_3$ ): –163.6.  $m/z$  (MH)<sup>+</sup> HR  $\text{C}_{24}\text{H}_{27}\text{F}_3\text{N}_2$  calcd.: 400.2126, found: 401.2187. Anal. calcd. for  $\text{C}_{24}\text{H}_{27}\text{F}_3\text{N}_2$ : C, 71.98; H, 6.80; N, 6.99. Found: C, 72.16; H, 6.82; N, 6.85.

**$\kappa^2$ -(4,4'-Diethyl-3,3',5,5'-tetramethyldipyrrinato) sodium (4b)**

In a glovebox, an  $\text{Et}_2\text{O}$  (2 mL) solution of  $\text{NaN}(\text{SiMe}_3)_2$  (40 mg, 0.22 mmol) was added dropwise over 5 min to a magnetically stirring solution of **1** (57 mg, 0.22 mmol) in  $\text{Et}_2\text{O}$  (2 mL). Upon addition of the base, a bright orange solid immediately precipitated from the reaction mixture.

After 1 h, the reaction mixture was filtered over Celite and the residue was washed with ether (4 × 2 mL) to remove any impurities and the  $\text{HN}(\text{SiMe}_3)_2$  byproduct. The product was dissolved in THF (2 mL) and filtered through Celite. Slow evaporation of the solvent from the filtrate resulted in the formation of large red plate crystals. These were isolated and dried in vacuo to leave the title compound as red crystals (46 mg, 74%).  $\delta_{\text{H}}$  (500 MHz,  $\text{THF}-d_8$ ): 6.75 (1H, s), 2.35 (4H, q,  $J = 7.5$ ), 2.16 (6H, s), 2.11 (6H, s), 1.00 (6H, t,  $J = 7.5$ ).  $\delta_{\text{C}}$  (125 MHz,  $\text{THF}-d_8$ ): 153.8, 138.2, 135.3, 128.2, 123.2, 19.4, 16.6, 16.2, 10.5.  $\delta_{\text{N}}$  (50.7 MHz,  $\text{THF}-d_8$ ): –225.4.  $\delta_{\text{Na}}$  (132.3 MHz,  $\text{THF}-d_8$ ): 10.7.

**$\kappa^2$ -(4,4'-Diethyl-3,3',5,5'-tetramethyldipyrrinato) potassium (4c)**

In a glovebox, a THF (2 mL) solution of  $\text{KCH}_2\text{Ph}^{27}$  (25 mg, 0.20 mmol) was added dropwise over 5 min to a solution of **1** (50 mg, 0.20 mmol) in THF (2 mL). Upon addition of the base, a bright orange solid precipitated from the reaction mixture. The reaction vial was sealed and the contents manually shaken for 30 s then left at room temperature. After 1 h, the solvent was removed in vacuo and the orange solid was washed with  $\text{Et}_2\text{O}$  (2 × 2 mL) and then hexanes (3 × 2 mL) to remove any impurities and byproducts. Contrary to the sodium complex, the potassium analogue was found to be insoluble in THF. Therefore, the supernatants were removed in each case by allowing the solid to settle and then carefully decanting the liquid away. The resulting orange solid was dried in vacuo to leave the title compound (37 mg, 66%).  $\delta_{\text{H}}$  (500 MHz,  $\text{DMF}-d_7$ ): 6.80 (1H, s), 2.34 (4H, q,  $J = 7.5$ ), 2.18 (6H, s), 2.13 (6H, s), 1.00 (6H, t,  $J = 7.5$ ).  $\delta_{\text{C}}$  (125 MHz,  $\text{DMF}-d_7$ ): 153.3, 137.9, 134.6, 132.0, 127.3, 19.3, 16.4, 15.9, 10.7.  $\delta_{\text{N}}$  (50.7 MHz,  $\text{DMF}-d_7$ ): –221.4.

**$\kappa^2$ -(4,4'-Diethyl-3,3',5,5'-tetramethyl-meso-C<sub>6</sub>H<sub>5</sub>-dipyrrinato) lithium (5a)**

In a glovebox,  $n\text{BuLi}$  (94  $\mu\text{L}$  of a 1.6 mol/L hexanes solution, 0.15 mmol) was added dropwise over 5 min to a solution of **2** (50 mg, 0.15 mmol) in THF (3 mL). Upon addition of the base, the colour of the solution immediately changed from orange to dark red-brown. The reaction vial was sealed and the contents were magnetically stirred for 45 min. The solvent was then removed in vacuo and the red-brown solid was washed with pentane (5 × 2 mL) to remove any impurities and byproducts. The supernatants were removed in each case by allowing the solid to settle and carefully decanting the liquid away. The resulting solid was dried in vacuo to give the title compound as a red solid (25 mg, 50%).  $\delta_{\text{H}}$  (500 MHz,  $\text{THF}-d_8$ ): 7.40–7.20 (5H, m), 2.25 (4H, q,  $J = 7.5$ ), 2.20 (6H, s), 1.08 (6H, s), 0.92 (6H, t,  $J = 7.5$ ).  $\delta_{\text{C}}$  (125 MHz,  $\text{THF}-d_8$ ): 153.3, 145.2, 138.6, 135.8, 131.9, 131.7, 130.7, 128.6, 127.8, 19.1, 16.0, 15.8, 13.3.  $\delta_{\text{N}}$  (50.7 MHz,  $\text{THF}-d_8$ ): –226.0.  $\delta_{\text{Li}}$  (194.4 MHz,  $\text{THF}-d_8$ ): 2.02.

**$\kappa^2$ -(4,4'-Diethyl-3,3',5,5'-tetramethyl-meso-C<sub>6</sub>H<sub>5</sub>-dipyrrinato) sodium (5b)**

In a glovebox, a solution of  $\text{NaN}(\text{SiMe}_3)_2$  (28 mg, 0.16 mmol) in  $\text{Et}_2\text{O}$  (2 mL) was added dropwise over 5 min to a magnetically stirring solution of **2** (51 mg, 0.16 mmol)

in Et<sub>2</sub>O (2 mL). Upon addition of the base, the colour of the solution changed from orange to red. After 1 h, the solvent was removed in vacuo and the resulting solid was triturated/washed with pentane (5 × 2 mL) to remove any impurities and any byproducts. The supernatants were removed in each case by allowing the solid to settle and carefully decanting the liquid away. The resulting orange solid was dried in vacuo to give the title compound as a red solid (35 mg, 63%).  $\delta_{\text{H}}$  (500 MHz, THF-*d*<sub>8</sub>): 7.30–7.18 (5H, m), 2.27 (4H, q, *J* = 7.4), 2.16 (6H, s), 1.14 (6H, s), 0.94 (6H, t, *J* = 7.4).  $\delta_{\text{C}}$  (125 MHz, THF-*d*<sub>8</sub>): 153.3, 146.8, 144.3, 140.3, 134.8, 132.7, 131.0, 128.25, 128.0, 19.4, 16.3, 16.0, 13.3.  $\delta_{\text{N}}$  (50.7 MHz, THF-*d*<sub>8</sub>): –221.5.  $\delta_{\text{Na}}$  (132.3 MHz, THF-*d*<sub>8</sub>): 9.9.

**$\kappa^2$ -(4,4'-Diethyl-3,3',5,5'-tetramethyl-meso-C<sub>6</sub>H<sub>5</sub>-dipyrrinato) potassium (5c)**

In a glovebox, a solution of KN(SiMe<sub>3</sub>)<sub>2</sub> (30 mg, 0.15 mmol) in THF (2 mL) was added dropwise over 5 min to a magnetically stirring solution of **2** (50 mg, 0.15 mmol) in THF (2 mL). Upon addition of the base, the colour of the solution changed from orange to dark purple. After 1 h, the solvent was removed in vacuo and the resulting solid was triturated/washed with pentane (5 × 2 mL) to remove any impurities and any byproducts. The product was dissolved in THF (2 mL) and filtered through Celite. The resulting solid was dried in vacuo to give the title compound as a red solid (41 mg, 73%).  $\delta_{\text{H}}$  (500 MHz, THF-*d*<sub>8</sub>): 7.26–7.15 (5H, m), 2.31 (4H, q, *J* = 7.5), 2.07 (6H, s), 1.39 (6H, s), 0.98 (6H, t, *J* = 7.5).  $\delta_{\text{C}}$  (125 MHz, THF-*d*<sub>8</sub>): 153.5, 146.8, 145.3, 141.5, 133.9, 133.4, 131.9, 128.2, 128.2, 19.4, 16.1, 16.0, 13.2.  $\delta_{\text{N}}$  (50.7 MHz, THF-*d*<sub>8</sub>): –211.9.

**$\kappa^2$ -(4,4'-Diethyl-3,3',5,5'-tetramethyl-meso-*p*-CF<sub>3</sub>-C<sub>6</sub>H<sub>4</sub>-dipyrrinato) lithium (6a)**

In a glovebox, a solution of LiN(SiMe<sub>3</sub>)<sub>2</sub> (41 mg, 0.25 mmol) in THF (4 mL) was added dropwise to a solution of **3** (100 mg, 0.25 mmol) in THF (2 mL). Upon addition of the base, the colour of the solution immediately changed from dark yellow-brown to dark red-brown. The reaction vial was sealed and the contents magnetically stirred for 2 h. The solvent was then removed in vacuo and the resulting red-brown solid was washed with hexane (5 × 2 mL) to remove any unreacted starting materials and byproducts. The residue was dissolved in THF and filtered over Celite. The solvent was removed in vacuo to give the title compound as a red solid (82 mg, 81%).  $\delta_{\text{H}}$  (500 MHz, THF-*d*<sub>8</sub>): 7.62 (2H, d, *J* = 8.0), 7.38 (2H, d, *J* = 8.0), 2.22 (4H, q, *J* = 7.5), 2.17 (6H, s), 1.03 (6H, s), 0.88 (6H, t, *J* = 7.5).  $\delta_{\text{C}}$  (125 MHz, THF-*d*<sub>8</sub>): 154.1, 149.3, 144.0, 138.2, 135.4, 132.5, 131.4, 130.2 (q, *J*<sub>C-F</sub> = 31.8), 125.9 (q, *J*<sub>C-F</sub> = 269.8), 125.6 (q, 2C, *J*<sub>C-F</sub> = 7.1), 19.1, 16.0, 15.5, 13.6.  $\delta_{\text{F}}$  (243 MHz, THF): –61.6.  $\delta_{\text{N}}$  (50.7 MHz, THF-*d*<sub>8</sub>): –226.9.  $\delta_{\text{Li}}$  (194.4 MHz, THF-*d*<sub>8</sub>): 2.0.

**$\kappa^2$ -(4,4'-Diethyl-3,3',5,5'-tetramethyl-meso-*p*-CF<sub>3</sub>-C<sub>6</sub>H<sub>4</sub>-dipyrrinato) sodium (6b)**

In a glovebox, a solution of NaN(SiMe<sub>3</sub>)<sub>2</sub> (46 mg, 0.25 mmol) in THF (4 mL) was added dropwise to a solution of **3** (100 mg, 0.25 mmol) in THF (2 mL). Upon addition of the base, the colour of the solution immediately changed from dark yellow-brown to dark purple. The reac-

tion vial was sealed and the contents magnetically stirred for 2 h. The solvent was then removed in vacuo and the red-brown solid was washed with hexane (5 × 2 mL) to remove any unreacted starting materials and byproducts. The residue was dissolved in THF and filtered over Celite. The solvent was removed in vacuo to leave the title compound as a dark-red solid (96 mg, 91%).  $\delta_{\text{H}}$  (500 MHz, THF-*d*<sub>8</sub>): 7.55–7.62 (2H, m), 7.19–7.41 (2H, m), 2.27 (4H, q, *J* = 7.5), 2.18 (6H, s), 1.10 (6H, s), 0.94 (6H, t, *J* = 7.5).  $\delta_{\text{C}}$  (125 MHz, THF-*d*<sub>8</sub>): 153.7, 149.0, 144.6, 139.8, 135.7, 133.2, 131.8, 130.3 (q, *J*<sub>C-F</sub> = 30.6), 125.9 (q, *J*<sub>C-F</sub> = 270.1), 125.4, 19.2, 16.0, 15.9, 13.3.  $\delta_{\text{F}}$  (243 MHz, THF): –60.1.  $\delta_{\text{N}}$  (50.7 MHz, THF-*d*<sub>8</sub>): –219.0.  $\delta_{\text{Na}}$  (132.3 MHz, THF-*d*<sub>8</sub>): 9.0.

**$\kappa^2$ -(4,4'-Diethyl-3,3',5,5'-tetramethyl-meso-*p*-CF<sub>3</sub>-C<sub>6</sub>H<sub>4</sub>-dipyrrinato) potassium (6c)**

In a glovebox, a solution of KN(SiMe<sub>3</sub>)<sub>2</sub> (50 mg, 0.25 mmol) in THF (4 mL) was added dropwise to a solution of **3** (100 mg, 0.25 mmol) in THF (2 mL). Upon addition of the base, the colour of the solution immediately changed from dark yellow-brown to dark purple. The reaction vial was sealed and the contents magnetically stirred for 2 h. The solvent was then removed in vacuo and the red-brown solid was washed with hexane (5 × 2 mL) to remove any unreacted starting materials and byproducts. The residue was dissolved in THF and filtered over Celite. The solvent was removed in vacuo to give the title compound as a red solid (93 mg, 83%).  $\delta_{\text{H}}$  (500 MHz, THF-*d*<sub>8</sub>): 7.50 (2H, d, *J* = 7.8), 7.35 (2H, d, *J* = 7.8), 2.35 (4H, q, *J* = 7.5), 2.10 (6H, s), 1.41 (6H, s), 1.01 (6H, t, *J* = 7.5).  $\delta_{\text{C}}$  (125 MHz, THF-*d*<sub>8</sub>): 153.5, 148.7, 144.4, 141.0, 133.3, 133.1, 132.0, 129.9 (q, *J*<sub>C-F</sub> = 31.9), 125.7, 125.4 (q, *J*<sub>C-F</sub> = 270), 19.3, 16.0, 15.9, 13.2.  $\delta_{\text{F}}$  (243 MHz, THF): –61.0 ppm.  $\delta_{\text{N}}$  (50.7 MHz, THF-*d*<sub>8</sub>): –226.0.

**X-ray crystallographic data**

Diffraction: Rigaku RAXIS-UNKNOWN, Mo K $\alpha$  radiation ( $\lambda$  = 0.71070 or 0.71075 Å). The structures were solved by direct methods<sup>45</sup> and expanded using Fourier techniques.<sup>46</sup> Some non-hydrogen atoms were refined anisotropically, while the rest were refined isotropically. Some hydrogen atoms were refined isotropically, the rest were included in fixed positions. The final cycle of full-matrix least-squares refinement (minimized to  $\sum w(|F_o| - |F_c|)^2$  where *w* = least squares weights on *F*) was based on 3284 observed reflections (*I* > 3.00σ(*I*)) and 271 variable parameters and converged with unweighted and weighted agreement factors of *R* =  $\sum ||F_o| - |F_c|| / \sum |F_o|$  = 0.0394; *R*<sub>w</sub> =  $[\sum w(|F_o| - |F_c|)^2 / \sum w F_o^2]^{1/2}$  = 0.0443. The standard deviation of an observation of unit weight (standard deviation of an observation of unit weight  $[\sum w(|F_o| - |F_c|)^2 / (N_o - N_v)]^{1/2}$  where *N*<sub>o</sub> = number of observations and *N*<sub>v</sub> = number of variables) was 1.06. A Robust-resistant weighting scheme was used.<sup>47</sup> Plots of  $\sum w(|F_o| - |F_c|)^2$  versus  $|F_o|$ , reflection order in data collection, sin  $\theta/\lambda$ , and various classes of indices showed no unusual trends. The maximum and minimum peaks on the final difference Fourier map corresponded to 0.78 and –0.72 e/Å<sup>3</sup>, respectively. Neutral atom scattering factors were taken from Cromer and Waber.<sup>48</sup> Anomalous dispersion effects were included in *F*<sub>calcd.</sub><sup>49</sup> the values for  $\Delta f'$  and  $\Delta f''$  were those of Creagh and McAuley.<sup>50</sup> The



values for the mass attenuation coefficients are those of Creagh and Hubbell.<sup>51</sup> All calculations were performed using the CrystalStructure<sup>52,53</sup> crystallographic software package.

**$\kappa^2$ -(4,4'-Diethyl-3,3',5,5'-tetramethyldipyrrin) hydrobromide (1HBr)**

C<sub>17</sub>H<sub>25</sub>BrN<sub>2</sub> (337.30), orange feathers, primitive monoclinic, space group *P2<sub>1</sub>/a* (No. 14), *a* = 8.7480(6) Å, *b* = 24.241(1) Å, *c* = 9.1766(6) Å,  $\beta$  = 118.248(2)°, *V* = 1714.2(2) Å<sup>3</sup>, *Z* = 4, *T* = 24 °C,  $2\theta$  = 145.3°. Residuals: *R* (*I* > 3.00σ(*I*)) = 0.0492, residuals: *R<sub>w</sub>* (*I* > 3.00σ(*I*)) = 0.0600, GoF = 1.063.

**$\kappa^2$ -(4,4'-Diethyl-3,3',5,5'-tetramethyldipyrrin) (1)**

C<sub>17</sub>H<sub>24</sub>N<sub>2</sub> (256.39), orange needles, primitive orthorhombic, space group *Pbca* (No. 61), *a* = 12.8407(4) Å, *b* = 8.3486(3) Å, *c* = 13.9647(5) Å, *V* = 1497.04(9) Å<sup>3</sup>, *Z* = 4, *T* = -150 °C,  $2\theta$  = 144.8°. Residuals: *R* (*I* > 3.00σ(*I*)) = 0.0577, residuals: *R<sub>w</sub>* (*I* > 3.00σ(*I*)) = 0.0659, GoF = 1.139.

**$\kappa^2$ -(4,4'-Diethyl-3,3',5,5'-tetramethyl-meso-C<sub>6</sub>H<sub>5</sub>-dipyrrin) (2)**

C<sub>23</sub>H<sub>28</sub>N<sub>2</sub> (332.49), yellow needle crystal, primitive monoclinic, space group *P2<sub>1</sub>/n* (No. 14), *a* = 11.1861(5) Å, *b* = 15.7267(7) Å, *c* = 11.1134(5) Å,  $\beta$  = 96.876(3)°, *V* = 1941.0(2) Å<sup>3</sup>, *Z* = 4, *T* = -150 °C,  $2\theta$  = 61.3°. Residuals: *R* (*I* > 3.00σ(*I*)) = 0.0481, residuals: *R<sub>w</sub>* (*I* > 3.00σ(*I*)) = 0.0537, GoF = 1.152.

**$\kappa^2$ -(4,4'-Diethyl-3,3',5,5'-tetramethyl-meso-p-CF<sub>3</sub>-C<sub>6</sub>H<sub>4</sub>-dipyrrin) (3)**

C<sub>24</sub>H<sub>27</sub>N<sub>2</sub>F<sub>3</sub> (400.49), golden-orange, needle-plate, primitive orthorhombic, space group *Pbca* (No. 61), *a* = 19.230(1) Å, *b* = 9.6655(5) Å, *c* = 22.594(2) Å, *V* = 4199.4(5) Å<sup>3</sup>, *Z* = 8, *T* = -173 °C,  $2\theta$  = 61.0°. Residuals: *R* (*I* > 3.00σ(*I*)) = 0.0394, residuals: *R<sub>w</sub>* (*I* > 3.00σ(*I*)) = 0.0443, GoF = 1.057.

**$\kappa^2$ -(4,4'-Diethyl-3,3',5,5'-tetramethyldipyrrinato) sodium (4b)**

C<sub>40</sub>H<sub>58</sub>O<sub>1.5</sub>Na<sub>2</sub> (664.90), dark-red prism crystal, C-centered monoclinic, space group *C2/c* (No. 15), *a* = 23.966(6) Å, *b* = 12.591(3) Å, *c* = 26.789(6) Å,  $\beta$  = 101.055(5)°, *V* = 7934(3) Å<sup>3</sup>, *Z* = 8, *T* = -173 °C,  $2\theta$  = 68.1°. Residuals: *R* (*I* > 3.00σ(*I*)) = 0.0695, residuals: *R<sub>w</sub>* (*I* > 3.00σ(*I*)) = 0.0794, GoF = 1.040.

**4-Ethyl-3,5-dimethyl-2-phenylacetylpyrrole**

C<sub>15</sub>H<sub>17</sub>NO (227.31), dark-red crystal, C-centered monoclinic, space group *C2/c* (No. 15), *a* = 27.818(1) Å, *b* = 7.3187(2) Å, *c* = 14.4726(8) Å,  $\beta$  = 119.151(2)°, *V* = 2573.3(2) Å<sup>3</sup>, *Z* = 8, *T* = -150 °C,  $2\theta$  = 144.7°. Residuals: *R* (*I* > 3.00σ(*I*)) = 0.0392, residuals: *R<sub>w</sub>* (*I* > 3.00σ(*I*)) = 0.0505, GoF = 1.033.

**Supplementary data**

Supplementary data for this article are available on the journal Web site (canjchem.nrc.ca). CCDCs 758519–758524 contain the X-ray data in CIF format for this manuscript. These data can be obtained, free of charge, via www.ccdc.cam.ac.uk/conts/retrieving.html (or from the Cambridge

Crystallographic Data Centre, 12 Union Road, Cambridge CB2 1EZ, UK; fax +44 1223 336033; or deposit@ccdc.cam.ac.uk).

**Acknowledgement**

We thank the Natural Sciences and Engineering Research Council of Canada (NSERC) for financial support, and Dr. Laura Turculet (Dalhousie University) for providing benzyl potassium.

**References**

- (1) Loudet, A.; Burgess, K. *Chem. Rev.* **2007**, *107* (11), 4891. doi:10.1021/cr078381n. PMID:17924696.
- (2) Wood, T. E.; Thompson, A. *Chem. Rev.* **2007**, *107* (5), 1831. doi:10.1021/cr050052c. PMID:17430001.
- (3) Falk, H. *The Chemistry of Linear Oligopyrroles and Bile Pigments*; Springer-Verlag: New York, 1989.
- (4) Shin, J.-Y.; Dolphin, D. *CrystEngComm* **2008**, *10* (8), 960. doi:10.1039/b800367j.
- (5) Hsieh, A. T. T.; Rogers, C. A.; West, B. O. *Aust. J. Chem.* **1976**, *29*, 49.
- (6) Roomi, M. W. *Tetrahedron Lett.* **1974**, *15* (13), 1131. doi:10.1016/S0040-4039(01)82425-4.
- (7) Cipot-Wechsler, J.; Ali, A. A.; Chapman, E. E.; Cameron, T. S.; Thompson, A. *Inorg. Chem.* **2007**, *46* (26), 10947. doi:10.1021/ic701369h. PMID:18027930.
- (8) King, E. R.; Betley, T. A. *Inorg. Chem.* **2009**, *48* (6), 2361. doi:10.1021/ic900219b.
- (9) Arnold, J. In *The Porphyrin Handbook* Kadish, K. M., Smith, K. M., Guillard, R., Eds.; Academic Press: 1999; Vol. 3.
- (10) Dorrough, G. D.; Miller, J. R.; Huennekens, F. M. *J. Am. Chem. Soc.* **1951**, *73* (9), 4315. doi:10.1021/ja01153a085.
- (11) Arnold, J.; Dawson, D. Y.; Hoffman, C. G. *J. Am. Chem. Soc.* **1993**, *115* (7), 2707. doi:10.1021/ja00060a020.
- (12) Seel, C.; Nieger, M.; Vogtle, F. *Chem. Ber.* **1992**, *125* (2), 447. doi:10.1002/cber.19921250223.
- (13) Hitchcock, P. B.; Lappert, M. F.; Layh, M. *Dalton Trans.* **2001**, 2409.
- (14) Stender, M.; Eichler, B. E.; Hardman, N. J.; Power, P. P.; Prust, J.; Noltemeyer, M.; Roesky, H. W. *Inorg. Chem.* **2001**, *40* (12), 2794. doi:10.1021/ic001311d. PMID:11375697.
- (15) Benec, J.-M.; Bonomo, L.; Solari, E.; Scopelliti, R.; Floriani, C. *Angew. Chem. Int. Ed.* **1999**, *38* (13-14), 1957. doi:10.1002/(SICI)1521-3773(19990712)38:13/14<1957::AID-ANIE1957>3.0.CO;2-1.
- (16) Liang, L.-C.; Yang, C.-W.; Chiang, M. Y.; Hung, C.-H.; Lee, P.-Y. *J. Organomet. Chem.* **2003**, *679* (1), 135. doi:10.1016/S0022-328X(03)00555-2.
- (17) Love, J. B.; Blake, A. J.; Wilson, C.; Reid, S. D.; Novak, A.; Hitchcock, P. B. *Chem. Commun. (Camb.)* **2003**, (14): 1682. doi:10.1039/b303611a.
- (18) Huang, J.-H.; Chi, L.-S.; Yu, R.-C.; Jiang, G. J.; Yang, W.-T.; Lee, G.-H.; Peng, S.-M. *Organometallics* **2001**, *20* (26), 5788. doi:10.1021/om010198b.
- (19) Klappa, J. J.; Geers, S. A.; Schmidtke, S. J.; MacManus-Spencer, L. A.; McNeill, K. *Dalton Trans.* **2004**, (6): 883. doi:10.1039/b315523d. PMID:15252473.
- (20) Bourget-Merle, L.; Lappert, M. F.; Severn, J. R. *Chem. Rev.* **2002**, *102* (9), 3031. doi:10.1021/cr010424r. PMID:12222981.



- (21) Piers, W. E.; Emslie, D. J. H. *Coord. Chem. Rev.* **2002**, 233–234, 131. doi:10.1016/S0010-8545(02)00016-4.
- (22) Tu, B.; Wang, C.; Ma, J. *Org. Prep. Proced. Int.* **1999**, 31 (3), 349. doi:10.1080/00304949909458333.
- (23) Wood, T. E.; Berno, B.; Beshara, C. S.; Thompson, A. J. *Org. Chem.* **2006**, 71 (8), 2964. doi:10.1021/jo0524932. PMID:16599589.
- (24) Stender, M.; Wright, R. J.; Eichler, B. E.; Prust, J.; Olmstead, M. M.; Roesky, H. W.; Power, P. P. *J. Chem. Soc., Dalton Trans.* **2001**, (23): 3465. doi:10.1039/b103149j.
- (25) Budzelaar, P. H. M.; Bart van Oort, A.; Orpen, A. G. *Eur. J. Inorg. Chem.* **1998**, 1485. doi:10.1002/(SICI)1099-0682(199810)1998:10<1485::AID-EJIC1485>3.0.CO;2-F.
- (26) Farwell, J. D.; Hitchcock, P. B.; Lappert, M. F. *Chem. Commun. (Camb.)* **2002**, (5): 456. doi:10.1039/b110443h. PMID:12120539.
- (27) Schlosser, M.; Hartmann, J. *Angew. Chem.* **1973**, 12, 508.
- (28) Dattagupta, J. K.; Meyer, E. F. J.; Cullen, D. L.; Falk, H.; Gergely, S., *Acta Crystallogr. Sect. C: Cryst. Struct. Commun.* **1983**, 39, 1384. doi:10.1107/S0108270183008604.
- (29) Sheldrick, W. S.; Borkenstein, A.; Stuckmeier, G.; Engel, J. *Acta Crystallogr.* **1978**, B34, 329.
- (30) Datta, S.; Lightner, D. A. *Monatsh. Chem.* **2008**, 139 (9), 1113. doi:10.1007/s00706-008-0888-2.
- (31) Struckmeier, G.; Engel, J.; Thewalt, U., *Z. Naturforsch. B: Chem. Sci.* **1978**, 33, 753.
- (32) Becker, W.; Sheldrick, W. S.; Engel, J. *Acta Crystallogr.* **1978**, B34, 1021.
- (33) Sessler, J. L.; Eller, L. R.; Cho, W.-S.; Nicolaou, S.; Aguilar, A. L., J.T.; Lynch, V. M.; Magda, D. J. *Angew. Chem. Int. Ed.* **2005**, 44, 5989. doi:10.1002/anie.200501740.
- (34) Melvin, M. S.; Tomlinson, J. T.; Park, G.; Day, C. S.; Saluta, G. R.; Kucera, G. L.; Manderville, R. A. *Chem. Res. Toxicol.* **2002**, 15 (5), 734. doi:10.1021/tx025507x. PMID:12018996.
- (35) Halper, S. R.; Stork, J. R.; Cohen, S. M. *Dalton Trans.* **2007**, (10): 1067. doi:10.1039/b615801c. PMID:17325783.
- (36) Stork, J. R.; Thoi, V. S.; Cohen, S. M. *Inorg. Chem.* **2007**, 46 (26), 11213. doi:10.1021/ic7016159. PMID:18047326.
- (37) Cavaleiro, J. A. S.; Condesso, F. P. N.; Olmstead, M. M.; Oram, D. E.; Snow, K. M.; Smith, K. M. *J. Org. Chem.* **1988**, 53 (25), 5847. doi:10.1021/jo00260a009.
- (38) Gossauer, A.; Nydegger, F.; Kiss, T.; Slezniak, R.; Stoeckli-Evans, H. *J. Am. Chem. Soc.* **2004**, 126 (6), 1772. doi:10.1021/ja030542r. PMID:14871109.
- (39) Salazar-Mendoza, D.; Baudron, S. A.; Hosseini, M. W. *Inorg. Chem.* **2008**, 47 (3), 766. doi:10.1021/ic701949k. PMID:18177038.
- (40) Shin, J.-Y.; Dolphin, D.; Patrick, B. O. *Cryst. Growth Des.* **2004**, 4 (4), 659. doi:10.1021/cg049979g.
- (41) Bonnier, C.; Piers, W. E.; Parvez, M.; Sorensen, T. S. *Chem. Commun. (Camb.)* **2008**, (38): 4593. doi:10.1039/b808739c. PMID:18815694.
- (42) Dogutan, D. K.; Zaidi, S. H. H.; Thamyonkit, P.; Lindsey, J. S. *J. Org. Chem.* **2007**, 72 (20), 7701. doi:10.1021/jo701294d. PMID:17824652.
- (43) Strong, E. T. J.; Cardile, S. A.; Brazeau, A. L.; Jennings, M. C.; McDonald, R.; Jones, N. D. *Inorg. Chem.* **2008**, 47 (22), 10575. doi:10.1021/ic8011926. PMID:18928277.
- (44) Harris, R. K.; Becker, E. D.; Cabral De Menezes, S. M.; Goodfellow, R.; Granger, P. *Pure Appl. Chem.* **2001**, 73 (11), 1795. doi:10.1351/pac200173111795.
- (45) Sheldrick, G. M. University of Gottingen, Germany, SHELXL-97, 1997.
- (46) Beurskens, P. T.; Admiraal, G.; Beurskens, G.; Bosman, W. P.; de Gelder, R.; Israel, R.; Smits, J. M. M. Technical Report of the Crystallography Laboratory: University of Nijmegen, 1999.
- (47) Carruthers, J. R.; Watkin, D. J. *Acta Crystallogr. A* **1979**, 35 (4), 698. doi:10.1107/S0567739479001613.
- (48) Cromer, D. T.; Waber, J. T. The Kynoch Press: Birmingham, 1974; Vol. IV.
- (49) Ibers, J. A.; Hamilton, W. C. *Acta Crystallogr.* **1964**, 17 (6), 781. doi:10.1107/S0365110X64002067.
- (50) Creagh, D. C.; McAuley, W. J.; Wilson, A. J. C., Ed. Kluwer Academic Publishers: Boston, 1992; Vol. C, pp 219–222.
- (51) Creagh, D. C.; Hubbell, J. H.; Wilson, A. J. C., Ed. Kluwer Academic Publishers: Boston, 1992; Vol. C, pp 200–206.
- (52) CrystalStructure; Rigaku and Rigaku Americas: 9009, New Trails Dr. The Woodlands, TX 77381, US, 2000–2007.
- (53) Carruthers, J. R.; Rollett, J. S.; Betteridge, P. W.; Kinna, D.; Pearce, L.; Larsen, A.; Gabe, E. Chemical Crystallography Laboratory: Oxford, 1999.

# Microsolvation of the formic acid dimer — $(\text{HCOOH})_2(\text{H}_2\text{O})_n$ clusters with $n = 1, \dots, 5$

Cara M. Nordstrom, Alaina J. McGrath, and Ajit J. Thakkar

**Abstract:** Density functional theory and spin-component-scaled Møller–Plesset perturbation theory calculations are used to examine the microsolvation of the formic acid dimer. The lowest energy structures with  $n$  water molecules consist of a  $n$ -water cluster, not necessarily of lowest energy, with two formic acid molecules attached to its surface by hydrogen bonds. The total number of hydrogen bonds does not correlate directly with relative stability.

**Key words:** formic acid dimer, hydration, microsolvation, clusters, hydrogen bonding.

**Résumé :** On a fait appel à des calculs basés sur la théorie de la fonctionnelle de la densité et sur la théorie de la perturbation de Møller–Plesset à composante de spin ajustée pour étudier la microsolvatation du dimère de l'acide formique. Les structures d'énergies les plus faibles comportant  $n$  molécules d'eau correspondent à un agrégat de  $n$  molécules d'eau, qui n'est pas nécessairement d'énergie la plus faible, avec deux molécules d'acide formique attachées à sa surface par des liaisons hydrogènes. Le nombre total de liaisons hydrogènes n'est pas directement relié à la stabilité relative.

**Mots-clés :** dimère de l'acide formique, hydratation, microsolvatation, agrégats, liaison hydrogène.

[Traduit par la Rédaction]

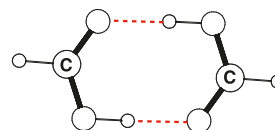
## Introduction

Formic acid is the prototypical carboxylic acid. It is present in clouds and fog, has been detected in the coma of the Hale–Bopp comet,<sup>1</sup> and may play a key role in the formation of molecules such as acetic acid and glycine in interstellar media.<sup>2</sup> Its importance and relative simplicity have made it the subject of a large number of studies. Since a significant fraction of formic acid in the atmosphere is in the aqueous phase, it is not surprising that microsolvated clusters of formic acid,  $(\text{HCOOH})(\text{H}_2\text{O})_n$  with  $n \leq 6$ , have been studied extensively.<sup>3–15</sup>

It is well-established experimentally<sup>16–19</sup> and theoretically<sup>20,21</sup> that gas-phase formic acid forms a strong, resonance-assisted, cyclic dimer with  $C_{2h}$  symmetry. As shown in Fig. 1, it consists of two formic acid monomers, both in their most stable *Z* (trans) conformation, held together by a pair of short and nearly linear  $\text{OH}\cdots\text{O}$  bonds. Since a nontrivial fraction of gaseous formic acid is dimerized, it is natural to consider the microsolvation of the formic acid dimer. One hopes to answer questions like: will the water molecules form a network connected to the dimer or will they disrupt the dimer?

Protonated forms of solvated formic acid oligomers have been observed experimentally.<sup>14</sup> However, to our knowledge, there has been only one study<sup>10</sup> on clusters of the formic acid dimer and water molecules. In that study, the interaction of the formic acid dimer with clusters of six and

Fig. 1. The formic acid dimer.



ten water molecules was considered as a model for the adsorption of the formic acid dimer on ice. They found that the dimer does not dissociate if it is adsorbed flat on the ice surface, but does dissociate otherwise. The purpose of this paper is to explore the lowest minima on the potential energy surfaces of complexes between two formic acid (f) and one to five water (w) molecules using ab initio and density functional theory (DFT) methods.

## Computational scheme

An extensive search was carried out for the low-energy structures of  $f_2w_n$  clusters with  $1 \leq n \leq 5$ . We used the multistage search-and-screen method followed in earlier work on clusters of glycolic acid with one to 16 waters,<sup>22–24</sup> and on small clusters of pure formic acid.<sup>25–28</sup> Each stage commences with higher-level optimization of the structures obtained in the previous stage. Only true minima, identified by vibrational frequency analysis, are retained. Next, single-point energy calculations in a larger basis set and higher-

Received 10 December 2009. Accepted 9 February 2010. Published on the NRC Research Press Web site at canjchem.nrc.ca on 29 April 2010.

This article is part of a Special Issue dedicated to Professor R. J. Boyd.

C.M. Nordstrom, A.J. McGrath, and A.J. Thakkar.<sup>1</sup> Department of Chemistry, University of New Brunswick, Fredericton, NB E3B 5A3, Canada.

<sup>1</sup>Corresponding author (e-mail: ajit@unb.ca).

**Table 1.** Relative energies,  $\Delta E$ , number of OH...O hydrogen bonds,  $N$ , and mean H-bond distances,  $\langle R \rangle$ , in angstroms of  $(\text{HCOOH})_2(\text{H}_2\text{O})$  clusters.

Label	$\Delta E$ (kcal/mol)				$N_{\text{fw}}$	$\langle R_{\text{fw}} \rangle$	$N_{\text{ff}}$	$\langle R_{\text{ff}} \rangle$	$N_{\text{t}}$
	MP2	SCS	MI	MIZ					
F2W101	0.00	0.00	0.00	0.00	2	1.664	1	1.699	3
F2W102	3.08	2.88	3.22	2.91	1	1.989	2	1.666	3
F2W103	3.93	3.65	4.14	3.57	1	2.108	2	1.655	3

**Note:** The reference MP2, SCS, MI, and MIZ energies for F2W101 are  $-455.4584718$ ,  $-455.4278052$ ,  $-454.7587475$ , and  $-454.6640675$  au (atomic units), respectively.

level method are carried out for the minima and an energy threshold is used to select a subset as trial structures for the next stage. A sampling of higher-energy minima that have distinct H-bonding patterns not already present in the energy-selected set are then added to the selection.

The zeroth-order step is the generation of a representative sample of guessed structures. This was done for  $f_{2w_n}$  clusters by adding a formic acid dimer to known minima of  $w_n$  clusters, adding a formic acid monomer to known minima of  $fw_n$ , and by adding a water molecule to our minima for  $f_{2w_{n-1}}$  clusters. In the first-order stage, the guessed structures were optimized using the PM3 method.<sup>29</sup> The latter leads to reasonable geometries but unreliable relative energies,<sup>22,23</sup> and hence, it is vital that screening of minima is done with single-point energies calculated using more reliable methods. In this work, we used single-point energies at the B3LYP/pc1a level. B3LYP is a hybrid DFT method.<sup>30,31</sup> The pc1a basis set of [4s3p1d/3s2p] contracted Gaussian-type functions (GTF)<sup>24,27,32</sup> is a polarized, split-valence basis set with added diffuse GTF of s- and p-type. It can be obtained from the aug-pc1 basis set,<sup>33</sup> which was specifically optimized for DFT calculations, by deletion of the diffuse d-GTF on the C and O atoms. The second stage consisted of B3LYP/pc1a geometry optimizations followed by single-point energy computations with second-order, Møller–Plesset (MP2)<sup>34</sup> perturbation theory using the aug-cc-pVDZ and aug-cc-pVTZ basis sets.<sup>35,36</sup> All electronic structure calculations were done with Gaussian 03.<sup>37</sup>

The “complete-basis-set (CBS)” limit of the MP2 correlation energy,  $E_c^{\text{MP2}} = E^{\text{MP2}} - E^{\text{HF}}$ , was found by two-point extrapolation<sup>38</sup> based on an inverse-cubic decay of basis set truncation errors with basis size. Thus,

$$[1] \quad E_c^{\text{MP2}} = (X^3 E_c^{\text{MP2}, X} - Y^3 E_c^{\text{MP2}, Y}) / (X^3 - Y^3)$$

in which  $E_c^{\text{MP2}, X}$  is the MP2 correlation energy obtained using a basis set with cardinal number  $X$ . We use  $X = 2$  and  $Y = 3$  for the MP2 energies obtained with the aug-cc-pVDZ and aug-cc-pVTZ basis sets, respectively. The MP2 correlation energy can be decomposed into contributions from electron pairs of opposite spin (os) and of the same spin (ss) as follows:

$$[2] \quad E_c^{\text{MP2}} = E_{\text{os}}^{\text{MP2}} + E_{\text{ss}}^{\text{MP2}}$$

To overcome some of the drawbacks of MP2, such as overestimation of dispersion interactions, Grimme<sup>39</sup> suggested an empirical scaling of the spin components. He recommended the spin-component-scaled (SCS) MP2 correlation energy given by

$$[3] \quad E_c^{\text{SCS-MP2}} = c_{\text{os}} E_{\text{os}}^{\text{MP2}} + c_{\text{ss}} E_{\text{ss}}^{\text{MP2}}$$

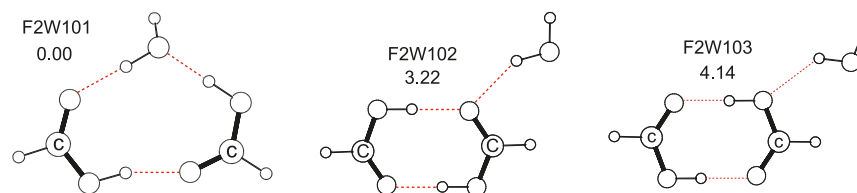
in which  $c_{\text{os}} = 6/5$  and  $c_{\text{ss}} = 1/3$ . Distasio and Head-Gordon<sup>40</sup> found that optimization of the scaling parameters for intermolecular binding energies of a diverse set of hydrogen-bonded, dispersion, and mixed complexes led to a rather different set of values, almost as if the roles of opposite- and same-spin pairs had been reversed. They recommend  $c_{\text{os}} = 0.29$  and  $c_{\text{ss}} = 1.46$  for use with cc-pVDZ and cc-pVTZ basis sets combined with CBS extrapolation schemes. The energies so obtained are designated SCS(MI)-MP2 in which MI stands for molecular interactions.<sup>40</sup> The spin components of the MP2 correlation energy we obtained with the aug-cc-pVDZ and aug-cc-pVTZ basis sets were extrapolated to the CBS limit with eq. [1] and used to obtain the extrapolated SCS-MP2 and SCS(MI)-MP2 energies from eq. [3].

## Results and discussion

The number of unique minima obtained varied between 131 and 339 at the PM3 level and ranged from 22 to 111 at the B3LYP/pc1a level for clusters with one through five water molecules. Only minima that are predicted to be the lowest lying in energy by the extrapolated MP2, SCS-MP2, and SCS(MI)-MP2 methods are considered further. We report relative energies,  $\Delta E$ , using these methods (abbreviated MP2, SCS, and MI, respectively) and also the MIZ relative energy, which is the SCS(MI)-MP2 relative energy including zero-point vibrational corrections at the B3LYP/pc1a level. The latter were calculated using harmonic frequencies and should be taken as rather approximate because some of the vibrations in the H-bonded complexes considered in this work are almost certain to be strongly anharmonic. The number of OH...O hydrogen bonds between formic acid molecules ( $N_{\text{ff}}$ ), between formic acid and water ( $N_{\text{fw}}$ ), and between water molecules ( $N_{\text{ww}}$ ) are reported together with their mean lengths denoted  $\langle R_{\text{ff}} \rangle$ ,  $\langle R_{\text{fw}} \rangle$ , and  $\langle R_{\text{ww}} \rangle$ , respectively. The total number of H bonds is denoted as  $N_{\text{t}}$ . The  $f_{2w_n}$  cluster minima obtained at the B3LYP/pc1a level are labeled as F2Wnr where  $r$  is a two-digit stability rank of the structure at the extrapolated SCS(MI)-MP2 level. Cartesian coordinates of the structures are in the Supplementary data section.

Table 1 shows that all methods predict F2W101 to be the lowest-energy structure by a margin of roughly 3 kcal/mol. Figure 2 shows that in F2W101, the water molecule has inserted itself between the formic acid molecules, breaking one of the H bonds in the formic acid dimer. In the higher-energy minima, F2W102 and F2W103, an intact formic acid

**Fig. 2.** Lowest-energy structures of  $(\text{HCOOH})_2(\text{H}_2\text{O})$ . The numbers are relative extrapolated SCS(MI)-MP2 energies. The  $\text{OH}\cdots\text{O}$  hydrogen bonds are indicated by dashed lines.

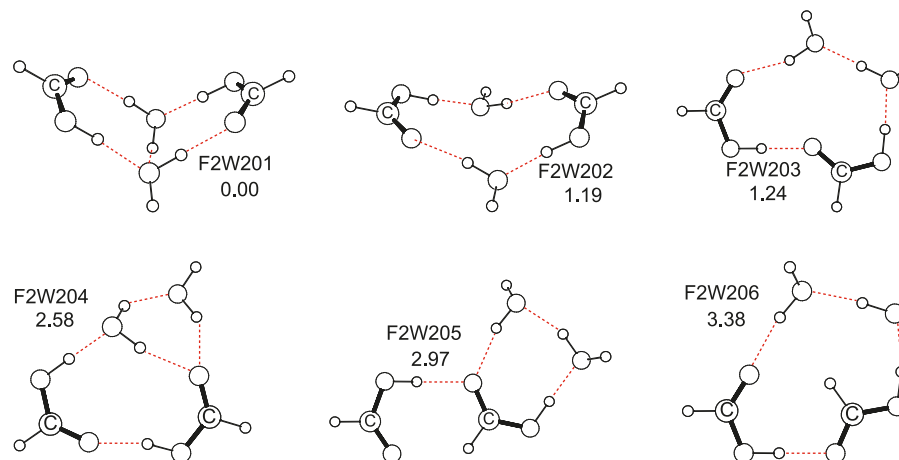


**Table 2.** Relative energies,  $\Delta E$ , number of  $\text{OH}\cdots\text{O}$  hydrogen bonds,  $N$ , and mean H-bond distances,  $\langle R \rangle$ , in angstroms of  $(\text{HCOOH})_2(\text{H}_2\text{O})_2$  clusters.

Label	$\Delta E$ (kcal/mol)				$N_{\text{ww}}$	$\langle R_{\text{ww}} \rangle$	$N_{\text{fw}}$	$\langle R_{\text{fw}} \rangle$	$N_{\text{ff}}$	$\langle R_{\text{ff}} \rangle$	$N_{\text{t}}$
	MP2	SCS	MI	MIZ							
F2W201	0.00	0.00	0.00	0.00	1	2.068	4	1.700	0	—	5
F2W202	1.76	1.40	1.19	0.41	0	—	4	1.677	0	—	4
F2W203	1.63	1.31	1.24	0.50	1	1.690	2	1.709	1	1.646	4
F2W204	3.09	2.71	2.58	1.88	1	1.981	3	1.834	1	1.671	5
F2W205	3.22	2.80	2.97	2.50	1	1.733	2	1.727	1	1.741	4
F2W206	3.56	3.26	3.38	2.85	1	1.765	2	1.773	1	1.627	4

**Note:** The reference MP2, SCS, MI, and MIZ energies for F2W201 are  $-531.8250659$ ,  $-531.7903095$ ,  $-530.9990108$ , and  $-530.8787038$  au, respectively.

**Fig. 3.** Lowest-energy minima of  $(\text{HCOOH})_2(\text{H}_2\text{O})_2$ . The numbers are relative extrapolated SCS(MI)-MP2 energies. The  $\text{OH}\cdots\text{O}$  hydrogen bonds are indicated by dashed lines.



dimer is seen held to the water molecule by an  $\text{OH}\cdots\text{O}$  hydrogen bond and a weak  $\text{CH}\cdots\text{O}$  interaction.

Table 2 shows that all methods predict F2W201 to be the global minimum. Figure 3 shows that in F2W201, the formic acid molecules have separated and H bonded to a water dimer. The primary difference between F2W202 and F2W201 is that the H bond between the water molecules is missing in F2W202. The cyclic F2W203 oligomer retains one H bond between the acid molecules, and the higher-energy F2W204 differs from it by a bridging H bond that creates a bicyclic structure. The next two minima contain higher-energy isomers of the formic acid dimer and weak  $\text{CH}\cdots\text{O}$  interactions. The F2W206 structure has one of the formic acid molecules in its E (cis) form.

Table 3 shows that the energy gap between F2W301 and F2W302 is rather small and the energy ordering of the two varies with the calculation method. There are six or seven

minima within 1 kcal/mol of F2W301. Table 3 also shows that maximizing the number of H bonds does not lead to the global minimum; in fact, the local minimum with seven H bonds lies higher in energy than nine minima with only six H bonds. The strength of the H bonds plays a role: the mean H-bond lengths in F2W310 are noticeably larger, indicating weaker bonds. Figure 4 shows that the nine lowest minima can all be described as a chain of three water molecules with a formic acid molecule attached to each side. The structures have water chains with different H-bonding topologies. The lowest-energy form of an isolated water trimer is cyclic,<sup>41</sup> but this motif is not seen among the low-energy forms of  $\text{f}_2\text{w}_3$ . In a similar vein, it was noted previously<sup>23</sup> that a cyclic water trimer is not observed in the low-energy structures of complexes consisting of one glycolic acid and three water molecules.

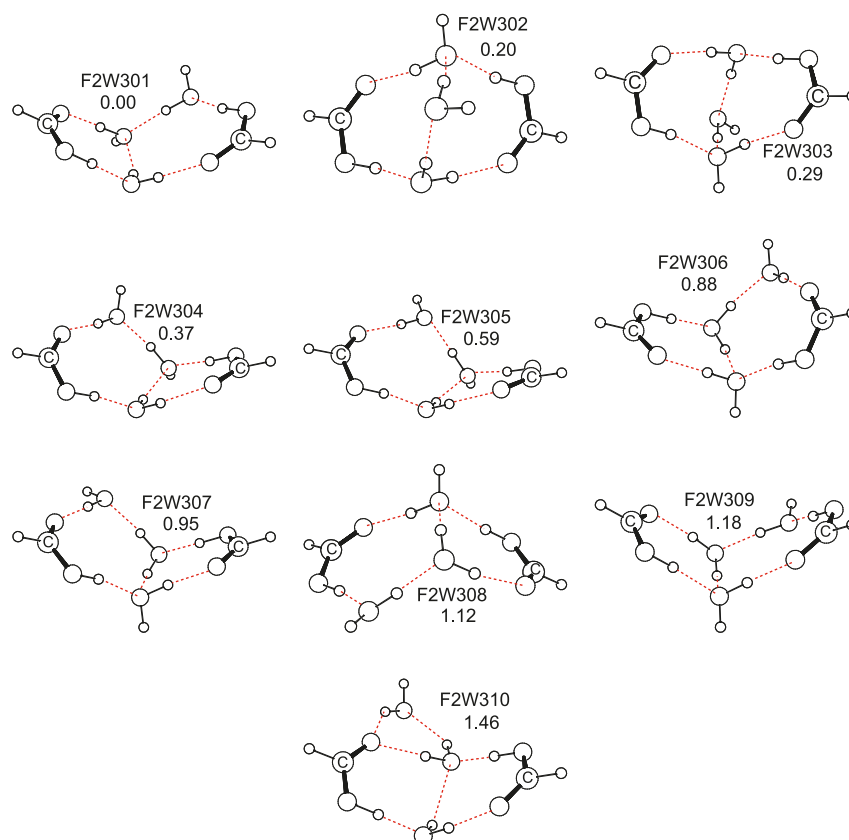
Table 4 shows that all methods predict F2W401 to be the



**Table 3.** Relative energies,  $\Delta E$ , number of OH...O hydrogen bonds,  $N$ , and mean H-bond distances,  $\langle R \rangle$ , in angstroms of  $(\text{HCOOH})_2(\text{H}_2\text{O})_3$  clusters.

Label	$\Delta E$ (kcal/mol)				$N_{\text{ww}}$	$\langle R_{\text{ww}} \rangle$	$N_{\text{fw}}$	$\langle R_{\text{fw}} \rangle$	$N_{\text{t}}$
	MP2	SCS	MI	MIZ					
F2W301	0.08	0.01	0.00	0.00	2	1.837	4	1.679	6
F2W302	0.00	0.00	0.20	0.50	2	1.849	4	1.684	6
F2W303	0.10	0.10	0.29	0.47	2	1.849	4	1.683	6
F2W304	0.41	0.24	0.37	0.39	2	1.780	4	1.721	6
F2W305	0.69	0.52	0.59	0.58	2	1.785	4	1.719	6
F2W306	0.86	0.75	0.88	0.81	2	1.853	4	1.686	6
F2W307	0.89	0.80	0.95	0.95	2	1.854	4	1.683	6
F2W308	1.18	0.93	1.12	1.10	2	1.805	4	1.724	6
F2W309	1.28	1.04	1.18	1.21	2	1.811	4	1.722	6
F2W310	1.31	1.19	1.46	1.35	2	2.110	5	1.772	7

**Note:** The reference MI and MIZ energies for F2W301 are  $-607.2383207$  and  $-607.0934227$  au, respectively. The reference MP2 and SCS energies for F2W302 are  $-608.1895303$  and  $-608.1511781$  au, respectively.

**Fig. 4.** Lowest-energy minima of  $(\text{HCOOH})_2(\text{H}_2\text{O})_3$ . The numbers are relative extrapolated SCS(MI)-MP2 energies. The OH...O hydrogen bonds are indicated by dashed lines.

global minimum. The lowest-energy structure of a water tetramer is cyclic.<sup>41</sup> Fig. 5 shows that the two lowest-energy minima consist of a cyclic water tetramer with the formic acid molecules attached by two H bonds to opposite edges. F2W404 and F2W405 consist of a cyclic water tetramer with formic acid molecules attached by two H bonds to the same edge resulting in two tetracoordinate water molecules. A plethora of other low-energy structures could be generated by varying the H-bond topology of the tetramer but this was not done because the main interest in this work is how the

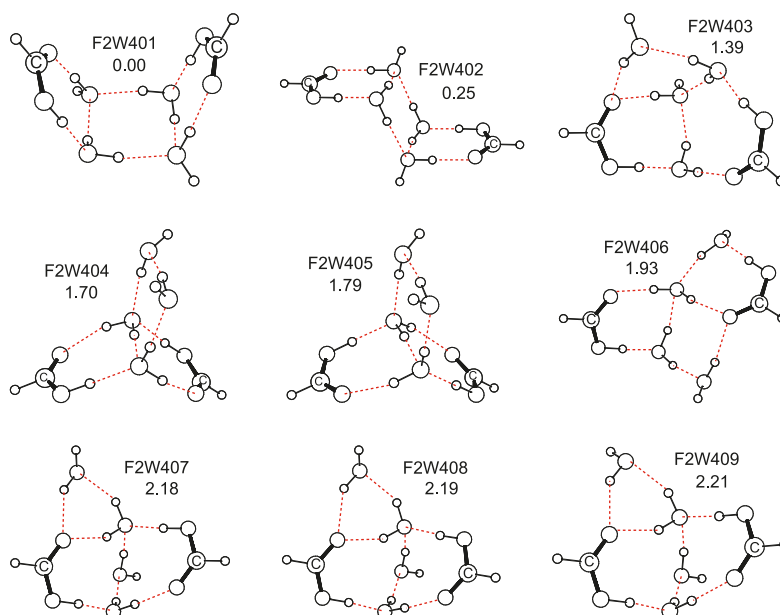
formic acid molecules attach themselves to the water tetramer. The five other isomers in Fig. 5 contain a chain form of the water tetramer with the formic acids bound to opposite sides forming various cyclic arrangements. F2W403 is bowl shaped, whereas F2W406 has three rings of similar size.

Table 5 shows that all four methods predict ten or more local minima of  $\text{f}_2\text{w}_5$  within 1 kcal/mol of the global minimum. The zero-point-energy correction changes the energy ordering of the  $\text{f}_2\text{w}_5$  clusters more than it does in the smaller

**Table 4.** Relative energies,  $\Delta E$ , number of OH...O hydrogen bonds,  $N$ , and mean H-bond distances,  $\langle R \rangle$ , in angstroms of  $(\text{HCOOH})_2(\text{H}_2\text{O})_4$  clusters.

Label	$\Delta E$ (kcal/mol)				$N_{\text{ww}}$	$\langle R_{\text{ww}} \rangle$	$N_{\text{fw}}$	$\langle R_{\text{fw}} \rangle$	$N_{\text{t}}$
	MP2	SCS	MI	MIZ					
F2W401	0.00	0.00	0.00	0.00	4	1.879	4	1.650	8
F2W402	0.31	0.27	0.25	0.14	4	1.881	4	1.651	8
F2W403	1.58	1.58	1.39	0.70	3	1.878	5	1.705	8
F2W404	1.53	1.28	1.70	1.58	4	1.770	4	1.787	8
F2W405	1.65	1.41	1.79	1.71	4	1.774	4	1.782	8
F2W406	1.93	1.84	1.93	1.67	3	1.836	5	1.740	8
F2W407	2.18	1.91	2.18	1.68	3	1.864	5	1.761	8
F2W408	2.19	1.91	2.19	1.69	3	1.863	5	1.764	8
F2W409	2.21	1.93	2.21	1.73	3	1.865	5	1.761	8

**Note:** The reference MP2, SCS, MI, and MIZ energies for F2W401 are  $-684.5581240$ ,  $-684.5156271$ ,  $-683.4809354$ , and  $-683.3099324$  au, respectively.

**Fig. 5.** Lowest-energy minima of  $(\text{HCOOH})_2(\text{H}_2\text{O})_4$ . The numbers are relative extrapolated SCS(MI)-MP2 energies. The OH...O hydrogen bonds are indicated by dashed lines.

clusters, perhaps because the harmonic frequencies are less accurate for the low-frequency modes in  $f_2w_5$ . A cyclic isomer is the lowest-energy water pentamer<sup>41</sup> and Fig. 6 shows that F2W501, F2W505, and F2W513 consist of a cyclic water pentamer with two formic acid molecules attached to it. F2W502 has a quasi-cubic structure of oxygen atoms with three of them supplied by the formic acid monomers; it has almost the same energy as F2W501. A trigonal prism of oxygen atoms with one of them supplied by a formic acid molecule is seen in F2W506. It is not a coincidence that one of the low-energy structures of a water hexamer is also a trigonal prism. A cyclic water tetramer with a fifth water attached to one of the corners can be spotted in F2W503, F2W504, F2W507, F2W508, F2W511, F2W512, F2W514, and F2W515. A cyclic water tetramer with a fifth water molecule bridging diagonally opposite corners is seen in F2W509. A tetracoordinated water is in the center of a pleasingly regular arrangement of four rings of similar size in F2W510. Table 5 shows that the number of H bonds

varies from 9 to 11 in the  $f_2w_5$  complexes. Unfortunately, we could not find a simple relationship that enables the relative energy to be predicted quantitatively from the number of H bonds and their mean lengths. As with  $f_2w_4$ , many other low-energy  $f_2w_5$  structures could be generated by varying the H-bond topology of the water network in the oligomers shown in Fig. 6.

Figure 7 shows three interesting examples of the many other local minima we found. Note that a tetracoordinated water can be found in a cluster as small as F2W105. The F2W414 structure is similar to the global minimum F2W401 but lies 2.94 kcal/mol higher in energy. Two formic acid monomers in the E conformation are present in F2W574 even though it is only 3.45 kcal/mol higher in energy than the global minimum structure.

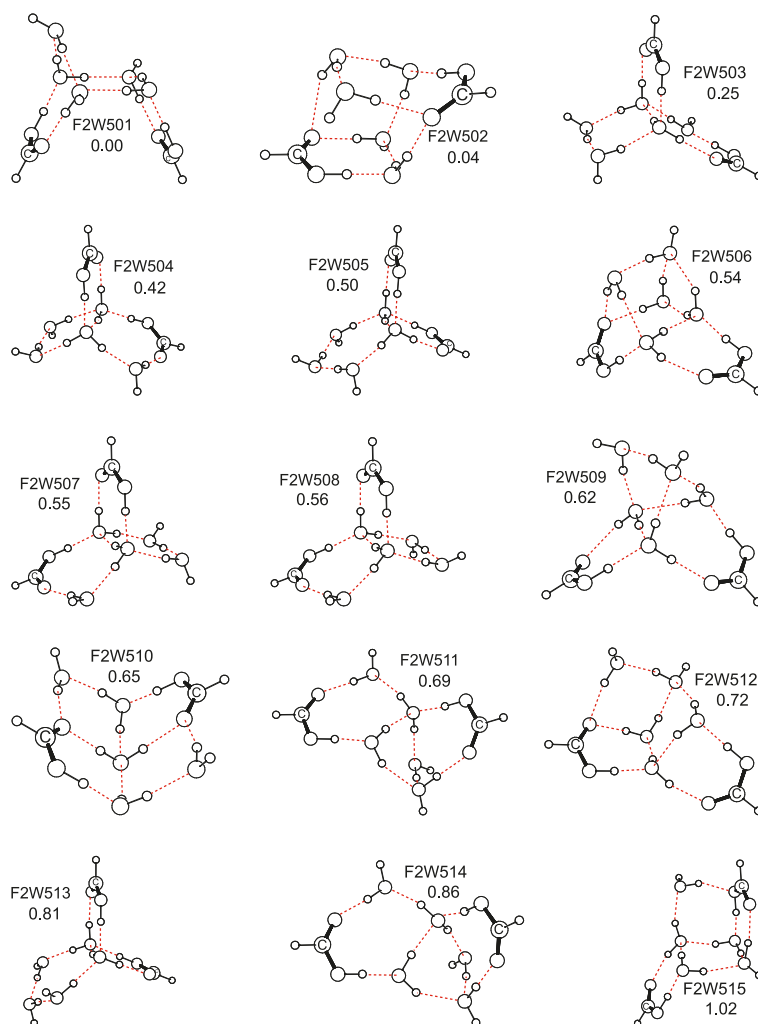
## Conclusions

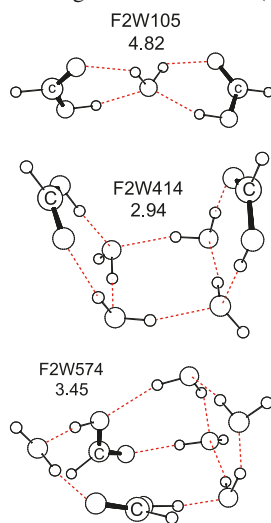
Many low-energy minima on the potential energy surfaces

**Table 5.** Relative energies,  $\Delta E$ , number of OH...O hydrogen bonds,  $N$ , and mean H-bond distances,  $\langle R \rangle$ , in angstroms of  $(\text{HCOOH})_2(\text{H}_2\text{O})_5$  clusters.

Label	$\Delta E$ (kcal/mol)				$N_{\text{ww}}$	$\langle R_{\text{ww}} \rangle$	$N_{\text{fw}}$	$\langle R_{\text{fw}} \rangle$	$N_{\text{t}}$
	MP2	SCS	MI	MIZ					
F2W501	0.38	0.00	0.00	0.24	5	1.836	4	1.630	9
F2W502	0.00	0.11	0.04	0.00	4	1.839	6	1.809	10
F2W503	0.63	0.07	0.25	0.57	5	1.762	4	1.721	9
F2W504	0.66	0.07	0.42	0.55	5	1.759	4	1.731	9
F2W505	0.65	0.14	0.50	0.94	5	1.733	4	1.751	9
F2W506	0.38	0.02	0.54	1.44	6	1.907	5	1.834	11
F2W507	0.77	0.22	0.55	0.95	5	1.762	4	1.723	9
F2W508	0.77	0.20	0.56	0.78	5	1.761	4	1.727	9
F2W509	0.70	0.13	0.62	1.35	6	1.855	4	1.798	10
F2W510	0.56	0.60	0.65	0.93	4	1.872	6	1.737	10
F2W511	1.20	0.58	0.69	0.71	5	1.826	4	1.674	9
F2W512	0.86	0.57	0.72	1.40	5	1.834	5	1.785	10
F2W513	1.01	0.47	0.81	1.15	5	1.735	4	1.752	9
F2W514	1.41	0.74	0.86	0.85	5	1.835	4	1.677	9
F2W515	0.91	0.69	1.02	1.19	5	1.864	5	1.741	10

**Note:** The reference MP2 and MIZ energies for F2W502 are  $-760.9231050$  and  $-759.5246813$  au, respectively. The reference SCS and MI energies for F2W501 are  $-760.8764241$  and  $-759.7199956$  au, respectively.

**Fig. 6.** Lowest-energy minima of  $(\text{HCOOH})_2(\text{H}_2\text{O})_5$ . The numbers are relative extrapolated SCS(MI)-MP2 energies. The OH...O hydrogen bonds are indicated by dashed lines.

**Fig. 7.** Some interesting local minima of  $(\text{HCOOH})_2(\text{H}_2\text{O})_n$ .

of the  $f_2w_n$  complexes with  $1 \leq n \leq 5$  were located. Our DFT, MP2, SCS-MP2, and SCS(MI)-MP2 calculations are not sufficiently accurate to pinpoint with certainty the lowest-energy structure of the clusters with more than two water molecules. However, they do indicate unequivocally that microsolvation dissociates the formic acid dimer. The lowest-energy  $f_2w_n$  minima consist of a  $w_n$  cluster, not necessarily of lowest energy, with two formic acid molecules attached to its surface by hydrogen bonds. As in earlier work on small microsolvated clusters of glycolic acid,<sup>23,24</sup> we find that the number of H bonds is not an adequate stand-alone criterion for determining which of two structures is more stable. Moreover, we were unable to find any quantitative correlations between relative energies and simple measures such as the number of H bonds and their average bond lengths or angles.

## Supplementary data

Supplementary data for this article are available on the journal Web site (canjchem.nrc.ca).

## Acknowledgements

AJT recalls with pleasure many enjoyable discussions with Russell Boyd over more than 30 years. The Natural Sciences and Engineering Research Council of Canada supported this work through a Discovery Grant to AJT and an Undergraduate Summer Research Award to CMN.

## References

- (1) Rodgers, S. D.; Charnley, S. B. *Mon. Not. R. Astron. Soc.* **2001**, 320 (4), L61. doi:10.1046/j.1365-8711.2001.04208.x.
- (2) Martin, I.; Skaliky, T.; Langer, J.; Abdoul-Carime, H.; Karwasz, G.; Illenberger, E.; Stano, M.; Matejcek, S. *Phys. Chem. Chem. Phys.* **2005**, 7 (10), 2212. doi:10.1039/b503517a. PMID:19791415.
- (3) Åstrand, P.-O.; Karlström, G.; Engdahl, A.; Nelander, B. *J. Chem. Phys.* **1995**, 102 (9), 3534. doi:10.1063/1.468578.
- (4) Rablen, P. R.; Lockman, J. W.; Jorgensen, W. L. *J. Phys. Chem. A* **1998**, 102 (21), 3782. doi:10.1021/jp980708o.

- (5) Priem, D.; Ha, T.-K.; Bauder, A. *J. Chem. Phys.* **2000**, 113 (1), 169. doi:10.1063/1.481817.
- (6) Wei, D.; Truchon, J.-F.; Sirois, S.; Salahub, D. *J. Chem. Phys.* **2002**, 116 (14), 6028. doi:10.1063/1.1458543.
- (7) Aloisio, S.; Hintze, P. E.; Vaida, V. *J. Phys. Chem. A* **2002**, 106 (2), 363. doi:10.1021/jp012190l.
- (8) George, L.; Sander, W. *Spectrochim. Acta A* **2004**, 60 (13), 3225. doi:10.1016/j.saa.2004.03.004.
- (9) Zhou, Z.-Y.; Shi, Y.; Zhou, X.-M. *J. Phys. Chem. A* **2004**, 108 (5), 813. doi:10.1021/jp030642j.
- (10) Allouche, A. *J. Chem. Phys.* **2005**, 122 (23), 234703. doi:10.1063/1.1929733. PMID:16008469.
- (11) Tian, Y.-C.; Fang, W.-H. *J. Phys. Chem. A* **2006**, 110 (41), 11704. doi:10.1021/jp063967j. PMID:17034164.
- (12) Chuchev, K.; BelBruno, J. J. *J. Mol. Struct. THEOCHEM* **2006**, 763 (1–3), 199. doi:10.1016/j.theochem.2006.01.033.
- (13) Marushkevich, K.; Khriachtchev, L.; Räsänen, M. *J. Phys. Chem. A* **2007**, 111 (11), 2040. doi:10.1021/jp070363m. PMID:17388271.
- (14) Heinbuch, S.; Dong, F.; Rocca, J. J.; Bernstein, E. R. *J. Chem. Phys.* **2007**, 126 (24), 244301. doi:10.1063/1.2746036. PMID:17614543.
- (15) Chen, H.-T.; Chang, J.-G.; Chen, H.-L. *J. Phys. Chem. A* **2008**, 112 (35), 8093. doi:10.1021/jp801247d. PMID:18690674.
- (16) Pauling, L.; Brockway, L. O. *Proc. Natl. Acad. Sci. U.S.A.* **1934**, 20 (6), 336. Available at www.jstor.org/stable/86584. doi:10.1073/pnas.20.6.336. PMID:16587898.
- (17) Karle, J.; Brockway, L. O. *J. Am. Chem. Soc.* **1944**, 66 (4), 574. doi:10.1021/ja01232a022.
- (18) Almenningen, A.; Bastiansen, O.; Motzfeldt, T. *Acta Chem. Scand.* **1969**, 23, 2848. doi:10.3891/acta.chem.scand.23-2848.
- (19) Almenningen, A.; Bastiansen, O.; Motzfeldt, T.; Sørensen, N. A. *Acta Chem. Scand.* **1970**, 24, 747. doi:10.3891/acta.chem.scand.24-0747.
- (20) Schuster, P.; Funck, Th. *Chem. Phys. Lett.* **1968**, 2 (8), 587. doi:10.1016/0009-2614(63)80023-8.
- (21) Turi, L. *J. Phys. Chem.* **1996**, 100 (27), 11285. doi:10.1021/jp960634l.
- (22) Thakkar, A. J.; Kassimi, N. E.-B.; Hu, S. *Chem. Phys. Lett.* **2004**, 387 (1–3), 142. doi:10.1016/j.cplett.2004.02.012.
- (23) Roy, A. K.; Hu, S.; Thakkar, A. J. *J. Chem. Phys.* **2005**, 122 (7), 074313. doi:10.1063/1.1851974. PMID:15743238.
- (24) Roy, A. K.; Hart, J. R.; Thakkar, A. J. *Chem. Phys. Lett.* **2007**, 434 (4–6), 176. doi:10.1016/j.cplett.2006.12.010.
- (25) Roy, A. K.; Thakkar, A. J. *Chem. Phys. Lett.* **2004**, 386 (1–3), 162. doi:10.1016/j.cplett.2004.01.031.
- (26) Roy, A. K.; Thakkar, A. J. *Chem. Phys. Lett.* **2004**, 393 (4–6), 347. doi:10.1016/j.cplett.2004.06.067.
- (27) Roy, A. K.; Thakkar, A. J. *Chem. Phys.* **2005**, 312 (1–3), 119. doi:10.1016/j.chemphys.2004.11.030.
- (28) Blair, S. A.; Thakkar, A. J. *Chem. Phys. Lett.* **2008**, 450 (4–6), 258. doi:10.1016/j.cplett.2007.11.050.
- (29) Stewart, J. J. P. *J. Comput. Chem.* **1989**, 10 (2), 209. doi:10.1002/jcc.540100208.
- (30) Becke, A. D. *J. Chem. Phys.* **1993**, 98 (7), 5648. doi:10.1063/1.464913.
- (31) Stephens, P. J.; Devlin, F.; Chabalowski, C.; Frisch, M. J. *J. Phys. Chem.* **1994**, 98 (45), 11623. doi:10.1021/j100096a001.
- (32) Hart, J. R.; Thakkar, A. J. *J. Mol. Struct. THEOCHEM* **2005**, 714 (2–3), 217. doi:10.1016/j.theochem.2004.11.014.



- (33) Jensen, F. *J. Chem. Phys.* **2002**, *117* (20), 9234. doi:10.1063/1.1515484.
- (34) Møller, C.; Plesset, M. S. *Phys. Rev.* **1934**, *46* (7), 618. doi:10.1103/PhysRev.46.618.
- (35) Dunning, T. H., Jr. *J. Chem. Phys.* **1989**, *90* (2), 1007. doi:10.1063/1.456153.
- (36) Kendall, R. A.; Dunning, T. H., Jr.; Harrison, R. J. *J. Chem. Phys.* **1992**, *96* (9), 6796. doi:10.1063/1.462569.
- (37) Frisch, M. J.; Trucks, G. W.; Schlegel, H. B.; Scuseria, G. E.; Robb, M. A.; Cheeseman, J. R.; Montgomery, J. A., Jr.; Vreven, T.; Kudin, K. N.; Burant, J. C.; Millam, J. M.; Iyengar, S. S.; Tomasi, J.; Barone, V.; Mennucci, B.; Cossi, M.; Scalmani, N.; Rega, N.; Petersson, G. A.; Nakatsuji, H.; Hada, M.; Ehara, M.; Toyota, K.; Fukuda, R.; Hasegawa, J.; Ishida, M.; Nakajima, T.; Honda, Y.; Kitao, O.; Nakai, H.; Klene, M.; Li, X.; Knox, J. E.; Hratchian, H. P.; Cross, J. B.; Bakken, V.; Adamo, C.; Jaramillo, J.; Gomperts, R.; Stratmann, R. E.; Yazyev, O.; Austin, A. J.; Cammi, R.; Pomelli, C.; Ochterski, J. W.; Ayala, P. Y.; Morokuma, K.; Voth, G. A.; Salvador, P.; Dannenberg, J. J.; Zakrzewski, V. G.; Dapprich, S.; Daniels, A. D.; Strain, M. C.; Farkas, O.; Malick, D. K.; Rabuck, A. D.; Raghavachari, K.; Foresman, J. B.; Ortiz, J. V.; Cui, Q.; Baboul, A. G.; Clifford, S.; Cio-slawski, J.; Stefanov, B. B.; Liu, G.; Liashenko, A.; Piskorz, P.; Komaromi, I.; Martin, R. L.; Fox, D. J.; Keith, T.; Al-La-ham, M. A.; Peng, C. Y.; Nanayakkara, A.; Challacombe, M.; Gill, P. M. W.; Johnson, B.; Chen, W.; Wong, M. W.; Gonzalez, C.; Pople, J. A. *Gaussian 03*, revision B.05; Gaussian, Inc.: Pittsburgh, PA, 2003.
- (38) Halkier, A.; Helgaker, T.; Jørgensen, P.; Klopper, W.; Koch, H.; Olsen, J.; Wilson, A. K. *Chem. Phys. Lett.* **1998**, *286* (3–4), 243. doi:10.1016/S0009-2614(98)00111-0.
- (39) Grimme, S. *J. Chem. Phys.* **2003**, *118* (20), 9095. doi:10.1063/1.1569242.
- (40) Distasio, R. A., Jr.; Head-Gordon, M. *Mol. Phys.* **2007**, *105* (8), 1073. doi:10.1080/00268970701283781.
- (41) Xantheas, S. S.; Dunning, T. H., Jr. *J. Chem. Phys.* **1993**, *99* (11), 8774. doi:10.1063/1.465599.

# Homoselenocysteine — An oxygen or selenium acid in the gas phase?

Marcela Hurtado, Otilia Mó, and Manuel Yáñez

**Abstract:** The potential energy surface of L-homoselenocysteine (HSEC) has been explored through the use of B3LYP/6-311+G(d,p) calculations. In this survey, seventy-seven different conformers have been located. These local minima can be classified in four groups, A–D. Structures A, B, and D are stabilized by intramolecular hydrogen bonds (IMHBs) with the amino group acting as the hydrogen bond (HB) donor and the carbonyl group (structures A and D) or the hydroxyl group (structure B) as HB acceptors. The structures in set C present an IMHB with the amino group acting as the HB acceptor and the hydroxyl group as the HB donor. The stability order decreases in the following order:  $A > B > C > D$ . From their relative stabilities it can be concluded that only three of these conformers, namely A1, A4, and A5, would exist in the gas phase at room temperature. The most stable deprotonated form corresponds to a Se-deprotonated species stabilized by a strong IMHB between the hydroxyl group and the Se atom. However, a direct deprotonation of the most stable neutrals lead to O-deprotonated species, which eventually isomerize to yield the global minimum. Hence, we can conclude that, quite unexpectedly, HSEC behaves as a Se acid in the gas phase, its intrinsic acidity being  $1374 \text{ kJ mol}^{-1}$  at the B3LYP/6-311++G(3df,2p) level of theory. The most stable protonated forms are systematically the N-protonated ones, the global minimum being a structure stabilized through an IMHB involving the protonated amino group as the HB donor and the SeH group as the HB acceptor. The calculated gas-phase proton affinity (PA) at the B3LYP/6-311++G(3df,2p) level of theory is  $930 \text{ kJ mol}^{-1}$ .

**Key words:** homoselenocysteine, gas-phase acidity, gas-phase basicity, density functional theory (DFT) calculations, intramolecular hydrogen bonds.

**Résumé :** On a étudié la surface d'énergie potentielle de la L-homosélénocystéine (HSEC) sur la base de calculs théoriques B3LYP/6-311+G(d,p). Dans cette revue, on a localisé soixante-dix-sept différents conformères. On peut classer ces minima locaux en quatre groupes, A–D. Les structures A, B et D sont stabilisées par des liaisons hydrogènes intramoléculaires (LHIM) dans lesquelles le groupe amino agit comme donneur de liaison hydrogène (LH) et le groupe carbonyle (structures A et D) et le groupe hydroxyle (structure B) agissent comme accepteurs de LH. Les structures de l'ensemble C présentent des LHIM dans lesquelles le groupe amino agit comme accepteur de LH et le groupe hydroxyle comme donneur de LH. L'ordre de stabilité diminue dans l'ordre suivant,  $A > B > C > D$ . Sur la base de ces stabilités, on peut conclure que seulement trois de ces conformères, sont A1, A4 et A5, pourraient exister en phase gazeuse, à la température ambiante. La forme déprotonée la plus stable correspond à une espèce Se-déprotonée, stabilisée par une forte LHIM entre le groupe hydroxyle et l'atome de Se. Toutefois, une déprotonation directe des formes neutres les plus stables conduit à des espèces O-déprotonées qui s'isomérisent éventuellement pour conduire à un minimum global. En conséquence, on peut conclure que d'une façon inattendue, en phase gazeuse, la HSEC se comporte comme un acide dérivé du sélénium et que son acidité absolue, au niveau B3LYP/6-311++G(3df,2p) de la théorie, est de  $1374 \text{ kJ mol}^{-1}$ . Les formes protonées les plus stables sont systématiquement les formes N-protonées et le minimum global d'une structure stabilisée par une LHIM implique le groupe amino protoné comme donneur de LH et le groupe SeH comme accepteur de LH. L'acidité en phase gazeuse au niveau B3LYP/6-311++G(3df,2p) de la théorie est égal à  $930 \text{ kJ mol}^{-1}$ .

**Mots-clés :** homosélénocystéine, acidité en phase gazeuse, basicité en phase gazeuse, calculs d'après la théorie de la fonctionnelle de la densité (TFD), liaisons hydrogènes intramoléculaires.

[Traduit par la Rédaction]

Received 11 December 2009. Accepted 22 January 2010. Published on the NRC Research Press Web site at canjchem.nrc.ca on 7 May 2010.

*This article is part of a Special Issue dedicated to Professor R. J. Boyd. This paper is dedicated to Professor Russell J. Boyd, a distinguished scientist.*

**M. Hurtado, O. Mó, and M. Yáñez.**<sup>1</sup> Departamento de Química, C-9, Universidad Autónoma de Madrid, Campus de Excelencia UAM-CSIC, Cantoblanco, 28049-Madrid, Spain.

<sup>1</sup>Corresponding author (e-mail: manuel.yanez@uam.es).

## Introduction

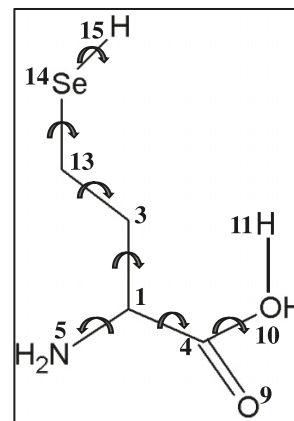
A good understanding of the chemistry of peptides requires a sound knowledge of the intrinsic reactivity of the amino acids from which the peptides are built up. This has motivated a large interest in conformational studies of amino acids, which do not only dictate their affinity for specific receptors<sup>1</sup> but also its intrinsic reactivity, in particular its basicity and acidity. Therefore, in general, the examination of the intrinsic reactivity of an amino acid requires a careful examination of its conformational characteristics, which, depending on the length of the chain attached to the amino acid moiety, can be very complicated due to the large number of possible conformers, whose structure and relative stabilities are usually obtained by means of theoretical studies. It is worth mentioning, for instance, the work by Gronert and O'Hair<sup>2</sup> about the conformers of alanine, serine, and cysteine, for which 10, 52, and 42 different conformers, respectively, were located at the HF/6-31G\* level of theory. As well, the work of Bertran and co-workers<sup>3</sup> explored several conformations of glycine, serine, and cysteine in an effort to estimate their proton affinities, and that of Kaur et al.<sup>4</sup> employed density functional theory (DFT) methods to characterize 33 stable conformers of selenocysteine in the gas phase, and investigated its proton affinity, its gas-phase acidity, and the possible implication of antioxidant activity of this selenium derivative.

Among the natural amino acids, those containing selenium are particularly important because Se is an essential trace element for humans, animals, and other living organisms.<sup>5-7</sup> Indeed, selenium amino acids have been used as supplements for cancer prevention.<sup>8</sup> Furthermore, the biological activity of selenium has been associated with several natural selenoproteins, including glutathione peroxidase, iodothyronine deiodinase, and thioredoxin reductase.<sup>5,6,9</sup> Selenocysteine has also been found to be the only essential selenoamino acid in these proteins. Special proteins are used to synthesize selenocysteinyl-tRNA and deliver it to the ribosome for incorporation at UGA codons, which normally serve to terminate translation.<sup>10,11</sup> Selenomethionine is a natural amino acid and the chemical incorporation of this amino acid, via selenohomocysteine, has been achieved.<sup>12,13</sup> The homoselenocysteine (HSEC) can facilitate efficient peptide ligation and therefore, it is important as a precursor of selenomethionine. Recently, Salon and co-workers<sup>14,15</sup> have synthesized some Se derivatives of the DNA nucleobases and studied their crystal structures, their thermostabilities, and the impact of their incorporation into oligonucleotides. In addition, specific pyrimidines in natural tRNAs have been derivatized by the incorporation of Se on the nucleobases.

Quite surprisingly, however, is that the information about the chemistry of Se compounds is not very abundant and even scarcer are the theoretical calculations on Se-containing amino acids. As a matter of fact, the first systematic assessment of different theoretical schemes for the study of organoselenium compounds was published by Boyd and co-workers<sup>16</sup> in 2005.

The aim of the present theoretical work is to explore the potential energy surface (PES) of HSEC (see Chart 1) to locate the most stable conformers in an effort to carry out a

Chart 1.



reliable estimation of its intrinsic acidity and basicity. We would like to establish whether O or Se is the most acidic site of this amino acid.

## Computational Methods

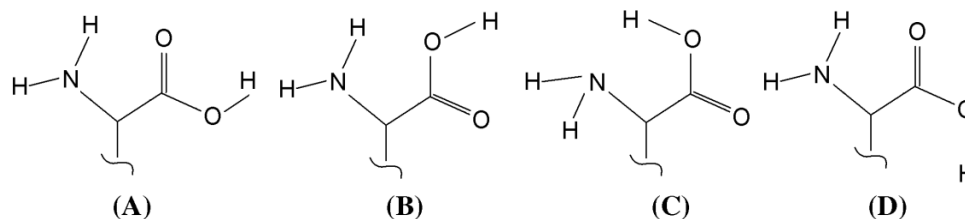
We initially carried out a systematic search of conformers at the semiempirical PM3 level using a relaxed PES scan and a wide step size. The different conformers were generated by considering all possible combinations of the rotations indicated in Chart 1.

Subsequently, the PM3 initial geometries were refined by means of B3LYP/6-311+G (d,p) calculations, and their harmonic vibrational frequencies evaluated. In this way, we were able to confirm that, from this initial set of PM3 structures, a total of 77 conformers were local minima at the B3LYP level. Some isomerization processes were also investigated for neutral, protonated, and deprotonated species. The harmonic vibrational frequencies were used to classify the different stationary points as local minima or transition states. The connectivity between local minima and transition states was ratified by means of internal reaction coordinate (ICR) calculations as implemented in the Gaussian03 suite of programs.<sup>17</sup> The B3LYP approach combines Becke's three parameter nonlocal hybrid exchange potential<sup>18</sup> with the nonlocal correlation functional of Lee et al.,<sup>19</sup> and it has been shown to provide reliable geometries for a wide variety of compounds,<sup>20-24</sup> with a rather good accuracy/cost ratio. The same functional has been shown to yield reliable gas-phase basicities and acidities,<sup>25-33</sup> provided that a flexible enough basis set is used.

For the subsequent analysis of the basicity and acidity of this amino acid, only the seven most stable conformers were considered because the energy gap between them was found to be smaller than 5.0 kJ mol<sup>-1</sup>. For this purpose, their deprotonated and protonated species were optimized and the corresponding harmonic frequencies calculated at the same level used for the neutrals. From the frequency calculations, the thermal corrections to enthalpies and Gibbs free energies were extracted at 298.2 K. Final energies were obtained by B3LYP/6-311++G(3df,2p)//B3LYP/6-311+G(d,p) single point calculations. In all cases the Gaussian03 suite of programs was used.<sup>17</sup>

The gas-phase proton affinity (PA) and the gas-phase ba-

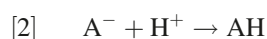
Scheme 1.



sicity (GB) of a compound A are defined as the negative of the enthalpy and the negative of the Gibbs free energy for eq. [1], respectively.



The gas-phase acidity ( $\Delta_{\text{acid}}H$ ) of a compound A is defined as the proton affinity of the corresponding anion (eq. [2]); hence, the lower the value of  $\Delta_{\text{acid}}H$ , the higher the acidity of the system.



The acidity can also be measured in terms of the corresponding Gibbs free energy,  $\Delta_{\text{acid}}G$ .

Enthalpies and Gibbs free energies were evaluated at the B3LYP/6-311+G(d) level at 298.2 K. The use of a harmonic approximation induces errors in the low-frequency torsions of the systems under investigation, which are significantly anharmonic, and therefore, in our calculated Gibbs free energies. This error can be estimated to be about 7 kJ mol<sup>-1</sup> K<sup>-1</sup> for the calculated entropies,<sup>34</sup> which lead to an error in the Gibbs free energy at 298 K of about 2 kJ mol<sup>-1</sup>. Since, as we shall discuss later, neutral, protonated, and deprotonated species are a mixture of several conformers in the gas phase, we have also included the corresponding entropy of mixing, which is evaluated as

$$[3] \quad \Delta S_{\text{mix}} = -R \sum x_i \ln x_i$$

where  $x_i$  is the mole fraction of the  $i$ th component within the mixture.

The bonding of the neutral, deprotonated, and protonated most stable forms was analyzed by means of the atoms in molecules (AIM)<sup>35</sup> and the electron localization function (ELF)<sup>36</sup> theories. By means of AIM theory we have obtained the molecular graphs showing the bond paths connecting the different bonded atoms and containing the bond critical points (BCPs), which correspond to stationary points in which the electron density is minimum along the line that connect two maxima and maximum in the other two directions.

ELF is a function, which, conveniently scaled between [0,1],<sup>37,38</sup> permits division of the physical space in regions where electron pairs are localized, either as bonding or lone pairs. These regions or basins are usually classified as monosynaptic (core or lone pairs) and disynaptic (involving two atomic valence shells), and their electron population provides useful insights into the bonding pattern of the molecule. ELF grids and basin integrations have been evaluated with the TopMod package.<sup>38</sup> For the three-dimensional plots, an ELF value of 0.8 is normally used.

## Results and discussion

A total of 77 stable conformations of HSEC have been characterized as local minima of the potential energy surface (PES). The optimized geometries of the 15 more stable conformers are given in Fig. S1 of the Supplementary data. The total and relative energies of these 77 local minima, arranged in decreasing stability order, as well as the calculated thermal corrections, are summarized in Table S1 of the Supplementary data.

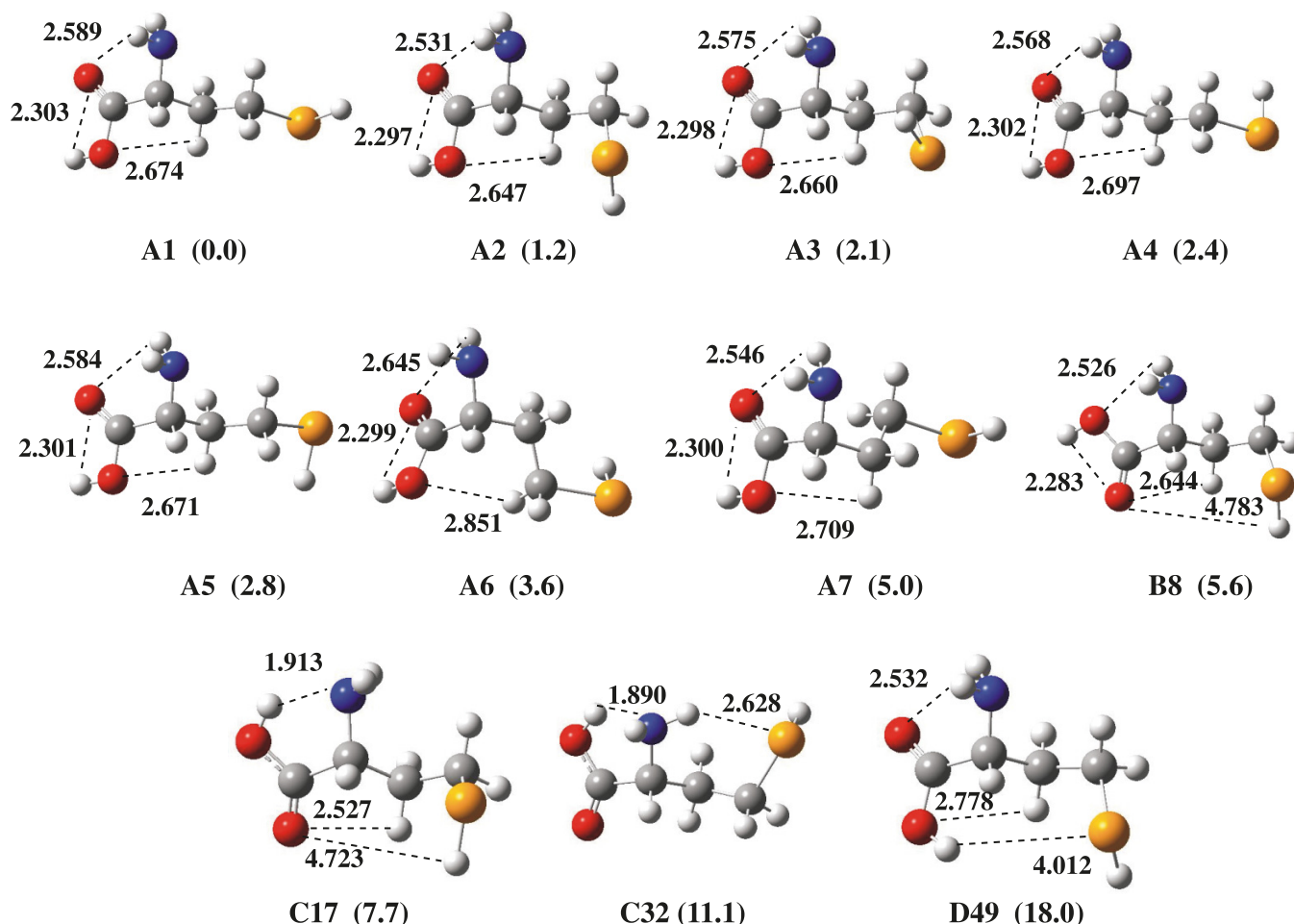
The 77 local minima of the PES can be arranged in four different groups (see Scheme 1) attending to the local conformation of the amino acid moiety. Structures A, B, and D are stabilized by an intramolecular hydrogen bond (IMHB) in which the amino group acts always as a hydrogen bond (HB) donor whereas in structures C it acts as a HB acceptor, the hydroxyl group being the HB donor. In structures A and D the HB acceptor is the carbonyl group and in structures B the hydroxyl group, the only difference between structures A and D being the relative position of the hydroxyl group. It is worth mentioning that within these four groups some structures exhibit IMHBs in which the Se-H group acts as the HB donor with respect to the amino group or the carbonyl or hydroxyl oxygen atoms as HB acceptors, but they always lie much higher in energy than the conformers shown in Fig. 1. Some of these structures are shown in Fig. S2 of the Supplementary data.

Figure 1 shows the geometries and the relative free energies of the seven lowest-energy conformations of neutral HSEC. As mentioned above, these seven structures are very close in energy, with the maximum energy gap being 5.0 kJ mol<sup>-1</sup> (see Fig. 1). It is worth noting that these seven low-lying energy conformers all belong to set A, so we have considered it of interest to include in Fig. 1 the most stable conformers of sets B, C, and D, namely structures B8, C17, and D49. It is then obvious that the relative stability decreases in the order of A > B > C > D. Actually, structures B8, C17, and D49 are predicted to be 5.6, 7.7, and 18.0 kJ mol<sup>-1</sup> higher in energy than the global minimum A1. Structures A1 and A2 are quite close in energy, with the energy gap in terms of Gibbs free energies being 1.2 kJ mol<sup>-1</sup>. It is also worth noting that the maximum energy gap, when the complete set of 77 conformers is considered, amounts to 42.7 kJ mol<sup>-1</sup>.

An inspection of Fig. 1 shows that in the seven A1–A7 conformers, the carbonyl oxygen apparently acts as a HB double-acceptor from the hydroxyl and the amino groups, with the main structural differences being associated with the local conformation of the CH<sub>2</sub>CH<sub>2</sub>SeH side chain. However, both the N–H...O and the O–H...O distances are systematically longer than 2.2 Å, and therefore, much longer than the typical bond lengths of these HBs. The correspond-



**Fig. 1.** B3LYP/6-311+G(d,p) optimized structures of the most stable A-, B-, C-, and D-type conformers of HSEC. Some significant inter-nuclear distances are given in Å. Gibbs free energies relative to A1 are given within parentheses in kJ mol<sup>-1</sup>.



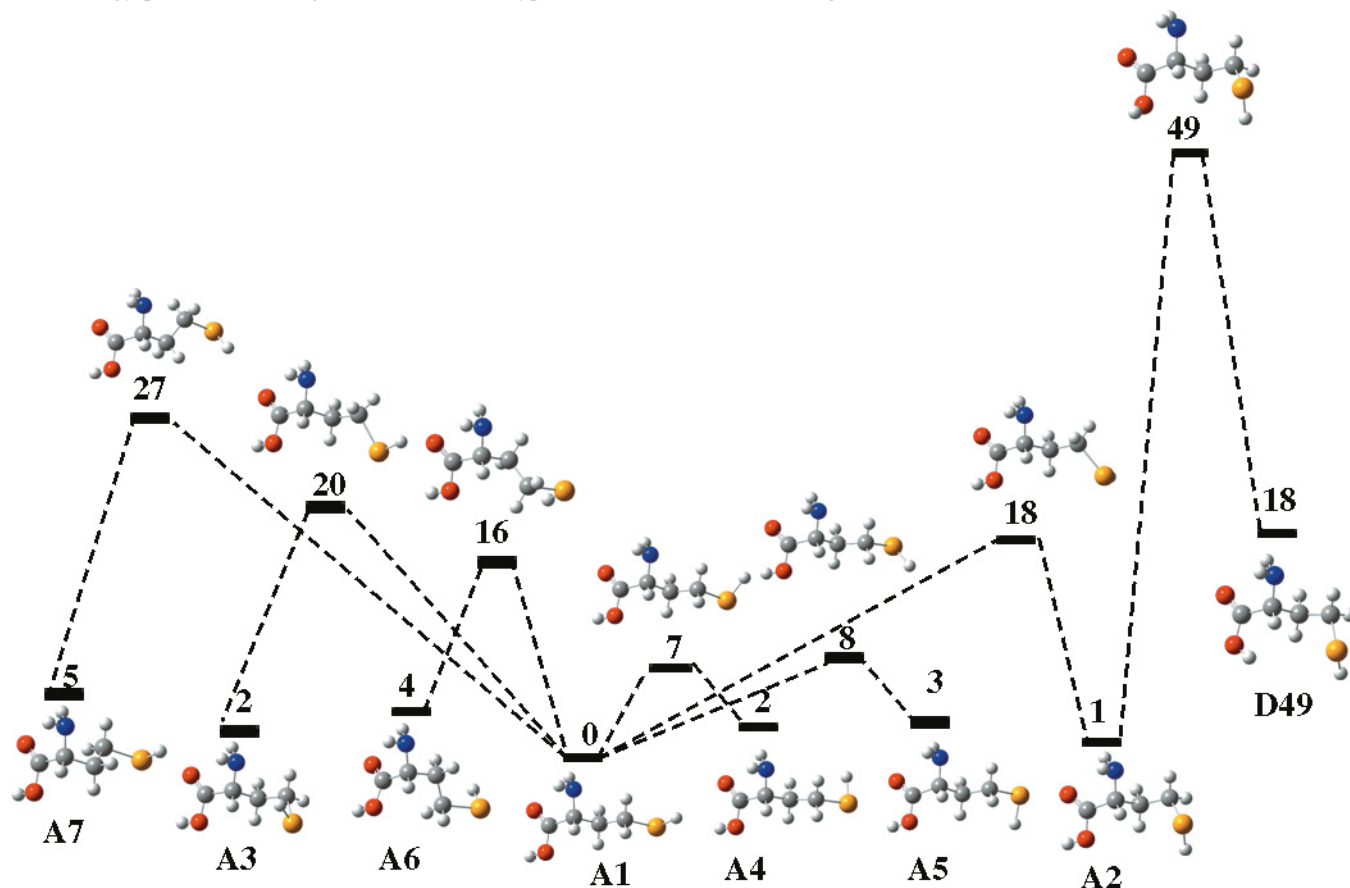
ing molecular graphs do not show the existence of a BCP along the N–H...O or the O–H...O lines, so these interactions cannot be considered, strictly speaking, as intramolecular hydrogen bonds (IMHBs). Consistently, a natural bond order (NBO) analysis does not show any second-order interaction between the carbonyl oxygen lone pair and the  $\sigma_{\text{NH}}^*$  or  $\sigma_{\text{OH}}^*$  antibonding orbitals, which would be the typical signature of the N–H...O and the O–H...O IMHBs.

If one assumes a Boltzman distribution, and using the relative Gibbs free energies summarized in Fig. 1, in the gas phase and at room temperature (298.2 K), HSEC should be an equilibrium mixture that contains 48.1%, 29.5%, 12.1%, 5.6%, 2.6%, 1.9%, and 0.2% of conformers A1, A2, A3, A4, A5, A6, and A7, respectively, and that the proportion of the most stable conformers of the series B, C, and D is null. The interconversion between these local minima involves energy barriers that range from 7 to 27 kJ mol<sup>-1</sup> (see Fig. 2). Quite importantly, the activation barrier between A1 and A2 amounts to 18 kJ mol<sup>-1</sup>, hence, structure A2 will very likely not be accessible at room temperature. The same applies to structures A3, A6, and A7, and only the connectivity between A1 and the local minima A4 and A5 involves low enough activation barriers as to expect the three of them to be accessible at room temperature. Under these circumstances, one should expect HSEC to be a mixture of these

three conformers in the following proportion: A1 (64.6%), A4 (23.9%), and A5 (11.5%). Since, as we shall discuss later, the most stable deprotonated species can be considered the result of a direct deprotonation of the form D49, we have also included in Fig. 2 the energy barrier associated with the A2 → D49 isomerization.

## Gas-phase acidities

The  $\Delta_{\text{acid}}G$  for all the species included in Fig. 1 was calculated at the B3LYP/6-311+G(d,p) level (see Table 1). The structures of the different anions have been included in Fig. S1 of the Supplementary data. However, we will only discuss in detail the deprotonation processes of the three conformers that, according to our previous analysis, should be the only ones present in a significant amount in the gas phase. In our survey of the intrinsic acidity of these systems, we have initially considered all possible acidic sites, namely the amino, the hydroxyl, and the Se–H groups. When the proton is removed from the amino group, in many of the other conformers a spontaneous proton transfer from the hydroxylic group or from the Se–H, depending on which of the two is closer, towards the deprotonated amino group takes place (see, for instance, the enhanced N acidity of A3, C17, C32, and D49 in Table 1). Finally, in practically all cases,

**Fig. 2.** Energy profile connecting the most stable A-type conformers of HSEC. Energies relative to the A1 conformer are in  $\text{kJ mol}^{-1}$ .**Table 1.**  $\Delta_{\text{acid}}G$  and GB ( $\text{kJ mol}^{-1}$ ) of HSEC calculated at the B3LYP/6-311+G(d,p) level.

Conformer	$\Delta_{\text{acid}}G$			GB		
	Acidic site			Protonated site		
	N	O	Se	N	O	Se
A1	1549.7	1367.1	1394.0	-916.1 <sup>a</sup>	-916.1 <sup>a</sup>	-827.4
A2	1555.3	1375.8	1391.3	-925.8 <sup>a</sup>	-925.8 <sup>a</sup>	-925.8 <sup>a</sup>
A3	1390.8	1374.0	1390.4	-924.9 <sup>a</sup>	-924.9 <sup>a</sup>	-924.9 <sup>a</sup>
A4	1551.2	1368.6	1396.5	-914.5 <sup>a</sup>	-914.5 <sup>a</sup>	-824.9
A5	1550.9	1366.3	1396.1	-917.5 <sup>a</sup>	-917.5 <sup>a</sup>	-825.6
A6	1550.6	1366.4	1402.8	-914.0 <sup>a</sup>	-914.0 <sup>a</sup>	-815.9
A7	1558.4	1364.9	1412.6	-919.1 <sup>a</sup>	-919.1 <sup>a</sup>	-830.3
B8	1551.8	1371.7	1390.9	-919.0	-861.3	-832.9
C17	1369.5	1372.5	1359.0	-893.6	-932.1 <sup>a</sup>	-891.8
C32	1370.8	1364.6	1348.6	-915.5	-953.0 <sup>a</sup>	-822.1
D49	1358.1	1355.2	1329.2	-907.9	-877.8	-850.5

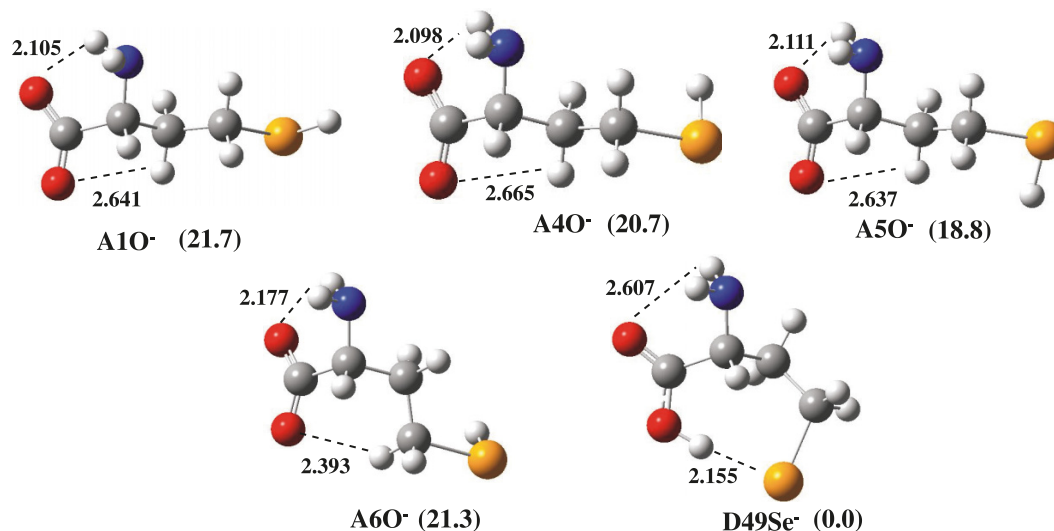
<sup>a</sup>The reported value corresponds to the protonation on the N atom because the O-protonated or Se-protonated species are not stationary points of the PES.

only oxygen and selenium deprotonated species were found to be stable. This is not the case, however, when dealing with conformers A1, A4, and A5 because in all three cases the amino group is very far apart from both the OH and the SeH group, so the aforementioned spontaneous proton transfers cannot take place. Nevertheless, the anions formed, namely A1N<sup>-</sup>, A4N<sup>-</sup>, and A5N<sup>-</sup>, are higher in energy than

the anions formed by deprotonation of the OH or the SeH groups.

The most stable anions formed by a direct deprotonation process of the three neutral conformers correspond systematically to the oxygen deprotonated species (see Fig. 3). It is very important, however, to take into account that, as for the neutrals, all anionic species exhibit many different con-

**Fig. 3.** B3LYP/6-311+G(d,p) optimized structures of the most stable anions produced by the deprotonation of the A1, A4, and A5 conformers of HSEC. The global minimum, D49Se<sup>−</sup>, corresponds to the direct deprotonation of the D49 conformer. Some significant internuclear distances are given in Å. Gibbs free energies relative to D49Se<sup>−</sup> are given in parentheses in kJ mol<sup>−1</sup>.



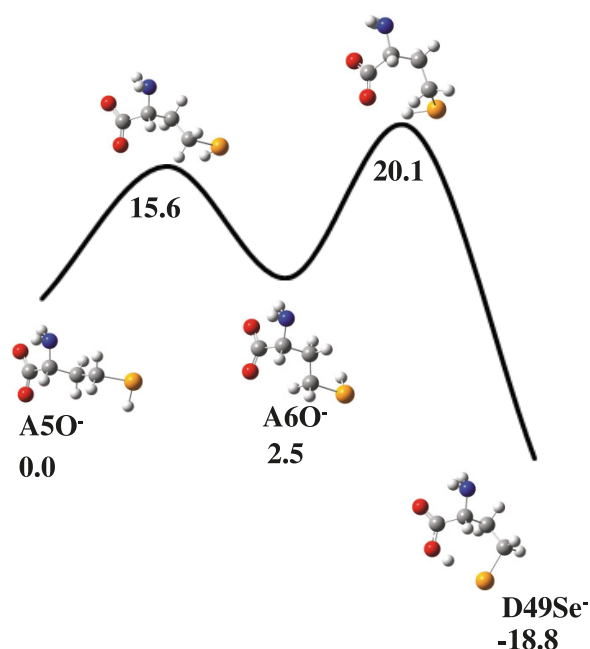
formers with quite different energies. Since the existence of different anionic conformers may play a crucial role in accurately determining the intrinsic acidity of the system, we have investigated the most stable O-deprotonated and Se-deprotonated anions, which can be generated from all the neutrals included in Fig. 1. In this survey, a total of 22 different conformers for the O-deprotonated anions and 16 for the Se-deprotonated structures have been characterized. The total free energies of all these anions have been summarized in Table S2 of the Supplementary data.

The different O-deprotonated species are rather close in energy, so that the energy gap between the most stable and the least stable one is only 14.3 kJ mol<sup>−1</sup>. For the oxygen deprotonated species, two different kind of conformers are normally found, which differ in the relative position of the amino group, with the most stable ones, namely A1O<sup>−</sup>, A4O<sup>−</sup>, A5O<sup>−</sup>, being those that exhibit the shortest O–H–N distance. Conversely, the energy gap between the most and the least stable Se-deprotonated species is much higher, 68.7 kJ mol<sup>−1</sup>. As we shall discuss later, this is a consequence of the formation of quite strong IMHBs between the Se atom, acting as a HB acceptor, and the OH group, acting as a HB donor, which significantly stabilizes some conformers.

The most important finding, however, is that the lowest-energy O-deprotonated species lies 18.8 kJ mol<sup>−1</sup> higher in energy than the lowest-energy Se-deprotonated anion, D49Se<sup>−</sup> (see Fig. 3), which would be the result of the direct deprotonation of the most stable D-type conformer (D49). Since, as we have mentioned above, a direct deprotonation of the three neutrals that likely exist in the gas phase (A1, A4, and A5) leads to the loss of the proton attached to the OH group, it is necessary to explore whether the anion so formed, namely A1O<sup>−</sup>, A4O<sup>−</sup>, and A5O<sup>−</sup>, can evolve to yield the global minimum of the PES, which is a Se-deprotonated species. In other words, we need to answer the question of whether HSEC is an O or Se acid in the gas phase.

In Fig. 4, we show the potential energy curve associated with the evolution from A5O<sup>−</sup> towards D49Se<sup>−</sup>. It should be noted that the evolution from A1O<sup>−</sup> or A4O<sup>−</sup> would imply

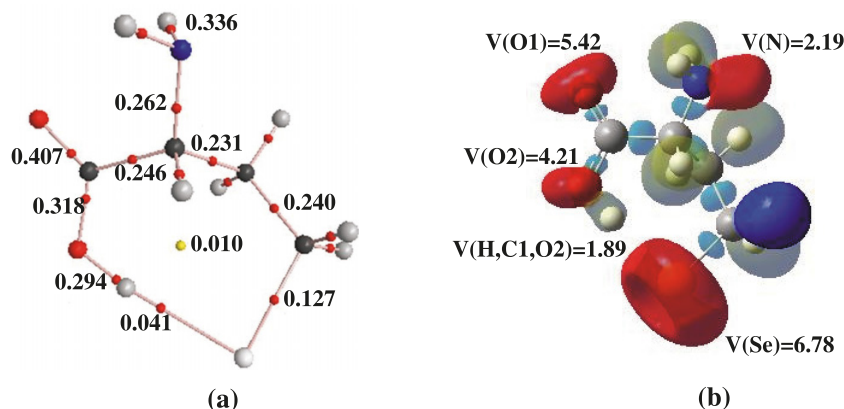
**Fig. 4.** Energy profile connecting the anion obtained by direct deprotonation of conformer A5 and the most stable deprotonated species, D49Se<sup>−</sup>. Energies relative to the A5O<sup>−</sup> anion are in kJ mol<sup>−1</sup>.



only an extra internal rotation of the SeH group, connecting these forms with A5O<sup>−</sup>, and they require rather low activation barriers (5.2 and 5.8 kJ mol<sup>−1</sup> for A1O<sup>−</sup> → A5O<sup>−</sup> and A4O<sup>−</sup> → A5O<sup>−</sup>, respectively).

As shown in Fig. 4, the first step in the A5O<sup>−</sup> → D49Se<sup>−</sup> isomerization implies an internal rotation around the C1–C3 bond (see Scheme 1), which leads to the intermediate A6O<sup>−</sup>. From here, a subsequent internal rotation around C3–C13 leads to the global minimum. This is so because as soon as the Se–H group is adequately oriented towards the deprotonated oxygen atom, a spontaneous proton transfer takes place, leading to the formation of the most stable Se-deprotonated structure. Taken into account that the activa-

**Fig. 5.** (a) The D49Se<sup>−</sup> anion molecular graph. Red and yellow dots denote the bond and ring critical points, respectively. Electron densities are given in au. (b) Three-dimensional representations of ELF isosurfaces with ELF = 0.80. The grey lobes correspond to disynaptic basins involving H atoms, red lobes to monosynaptic lone-pair basins, and green lobes to disynaptic bonding basins between nonhydrogen atoms. The population of these basins is given in e<sup>−</sup>.



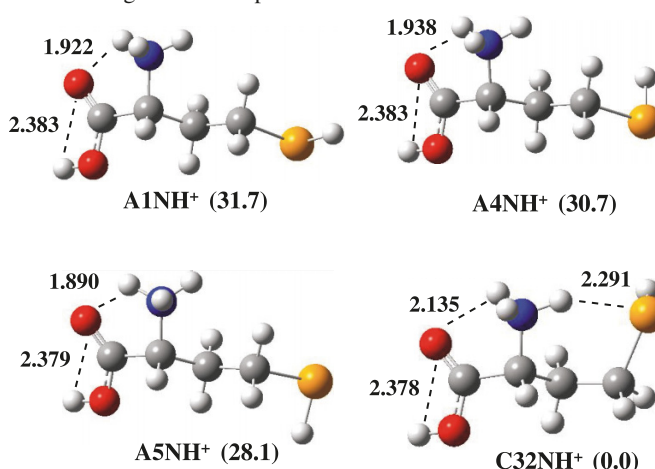
tion barriers associated with these isomerization process are systematically lower than 20 kJ mol<sup>−1</sup>, and that the energy liberated in the interaction between a neutral system and an anion, which is the typical way in which the deprotonation process takes place in an ICR experiment, is much higher,<sup>39</sup> we can safely conclude that, once the oxygen deprotonated species (either A1O<sup>−</sup>, A4O<sup>−</sup>, or A5O<sup>−</sup>) is produced by the direct deprotonation of the corresponding neutral system, the anion will have enough internal energy to isomerize to the most stable Se-deprotonated species; therefore, HSEC would behave as a Se acid in the gas phase. Since forms A2 and D49 are directly connected by a simple OH internal rotation, we have also investigated the interconversion between A2O<sup>−</sup> and D49Se<sup>−</sup> (see Fig. S3 of the Supplementary data). Although this isomerization would be possible, it must be recalled that A2 is not easily accessible and therefore, the most likely way to produce D49Se<sup>−</sup> is that shown in Fig. 4. The estimated  $\Delta_{\text{acid}}H$ , taking into account the intrinsic acidity of each of the three neutral species A1, A4, and A5 and their statistical distribution, is 1374 kJ mol<sup>−1</sup> and the corresponding  $\Delta_{\text{acid}}G$  is 1351 kJ mol<sup>−1</sup>.

The enhanced stability of the D49Se<sup>−</sup> is closely related with the existence of a O–H...Se IMHB, as corroborated by (i) the existence of a BCP with a reasonably high electron density, (ii) the existence of a ring critical point (see Fig. 5a), (iii) the large O–H bond length (1.027 Å), and (iv) the strong second-order interaction energy (177 kJ mol<sup>−1</sup>) between the lone pairs of the Se atom and the  $\sigma_{\text{OH}}^*$  antibonding orbital, pointing out a significant charge donation from the former to the latter, which is reflected in the quite large population of the  $\sigma_{\text{OH}}^*$  antibonding orbital (0.371 e<sup>−</sup>). This strong interaction is a clear consequence of the high polarizability of the Se lone pairs and to the fact that in spite of the large H...Se internuclear distance (2.155 Å), the real distance between the hydrogen and the Se lone-pairs is much shorter, as nicely shown by the ELF of the system (see Fig. 5b).

### Gas-phase basicity

As expected, for the three neutral species A1, A4, and A5, the amino nitrogen is the most favorable protonation site.

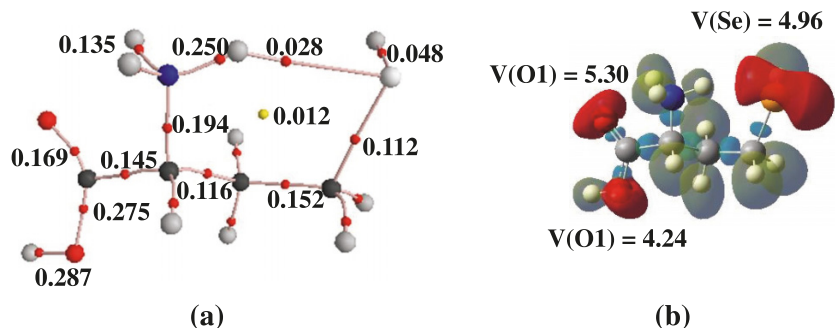
**Fig. 6.** B3LYP/6-311+G(d,p) optimized structures of the most stable cations produced by the protonation of the A1, A4, and A5 conformers of HSEC. The global minimum, C32NH<sup>+</sup>, corresponds to the direct deprotonation of the C32 conformer. Some significant internuclear distances are given in Å. Gibbs free energies relative to D49Se<sup>−</sup> are given within parentheses.



Furthermore, when these conformers are protonated at the carboxylic oxygen, a spontaneous proton transfer towards the amino group takes place, so the amino protonated species is systematically generated. Only for B8 and D49, the most stable B-type and D-type isomers, the O-protonated species was found to be stable because the carbonyl oxygen is far from the amino group and (or) because the OH group does not point towards the amino group. Interestingly, for the more stable C-type isomer, C17, the protonation at the carbonyl group triggers a spontaneous proton transfer from the hydroxyl group (not directly protonated) towards the amino group, so in this case, only the N-protonated species is found. Protonation at the SeH group is much less favorable, with the calculated proton affinities being about 90 kJ mol<sup>−1</sup> lower than those estimated for the corresponding N-protonated species. As a matter of fact, the protonation at the SeH group of species A2 and A3, where the distance between the amino group and the SeH group is not too big, is also followed by a



**Fig. 7.** (a) The C32NH<sup>+</sup> cation molecular graph. Red and yellow dots denote the bond and ring critical points, respectively. Electron densities are given in au. (b) Three-dimensional representations of ELF isosurfaces with ELF = 0.80. The grey lobes correspond to disynaptic basins involving H atoms, red lobes to monosynaptic lone-pair basins, and green lobes to disynaptic bonding basins between nonhydrogen atoms. The population of these basins is given in e<sup>-</sup>.



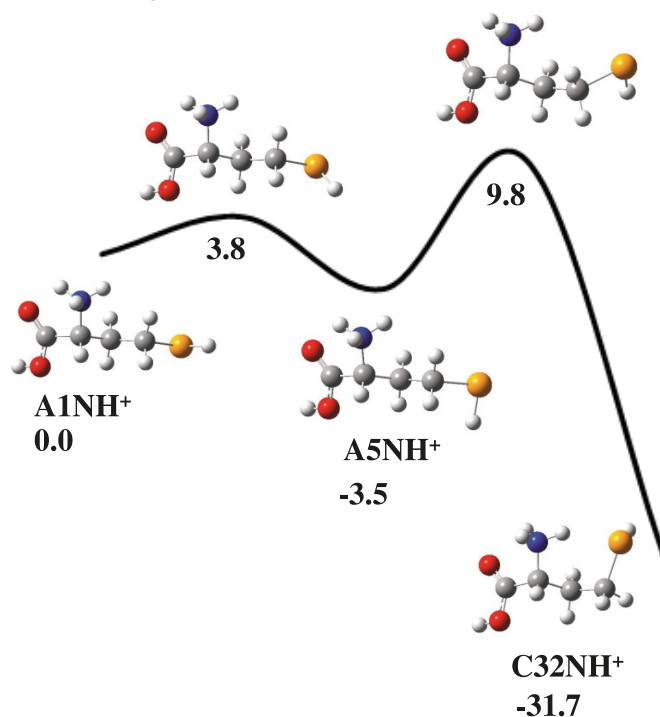
proton transfer from the latter to the former, so that only the N-protonated species exists as stationary points of the PES.

The direct protonation of species A1, A4, and A5 yield N-protonated forms, namely A1NH<sup>+</sup>, A3NH<sup>+</sup>, and A5NH<sup>+</sup>, which are rather close in energy (see Fig. 6). However, due to the flexibility of the alkyl chain, many other possible conformers are possible. To be able to obtain a reliable proton affinity for this system, it is necessary to carefully explore the PES associated with the N-protonated species. This exploration was carried out using the N-protonated forms of the 10 neutrals included in Fig. 1 as starting points. In this way, a total of 23 different stationary points could be identified, the global minimum being the C32NH<sup>+</sup> structure shown in Fig. 6. The total free energies and the optimized geometries of all these cations have been summarized in Table S2 and Fig. S1 of the Supplementary data. The enhanced stability of this form is a consequence of the formation of an IMHB between the protonated amino group, which is an excellent proton donor, and the SeH group, which acts as HB acceptor. This is reflected in the corresponding molecular graph by the existence of a BCP between one of the amino hydrogens and the Se atom, as well as by the existence of a ring critical point. (see Fig. 7) Also, a consistently significant interaction between the Se lone pairs and the  $\sigma_{\text{NH}}^*$  antibonding orbital is detected in the NBO second-order perturbation analysis, which is reflected by a sizable lengthening of the N–H bond involved in the IMHB, which is 0.03 Å longer than those not interacting with the SeH group.

The isomerization from A1NH<sup>+</sup>, A3NH<sup>+</sup>, and A5NH<sup>+</sup> towards the global minimum is the next question to be addressed to calculate the proton affinity of HSEC. In Fig. 8, we present the corresponding energy profile for the A1NH<sup>+</sup> → C32NH<sup>+</sup> isomerization. It can be observed that this isomerization is a two-step process. The first one, through an activation barrier of only 3.8 kJ mol<sup>-1</sup>, leads to the A5NH<sup>+</sup> protonated species, which finally evolves to yield the global minimum, C32NH<sup>+</sup>, through an activation barrier 13.3 kJ mol<sup>-1</sup> high.

Hence, we can conclude that although the direct protonation of the three neutrals, A1, A4, and A5, yield three different cations, these cations have enough internal energy to isomerize yielding the global minimum, C32NH<sup>+</sup>. Accordingly, the proton affinity of HSEC can be estimated to be 930 kJ mol<sup>-1</sup> by using the statistical distribution of the three

**Fig. 8.** Energy profile connecting the cation obtained by direct protonation of conformer A1 and the most stable protonated species, C32NH<sup>+</sup>. Energies relative to A1NH<sup>+</sup> cation are in kJ mol<sup>-1</sup>.



neutrals, A1, A4, and A5, and their intrinsic basicities. The corresponding gas-phase basicity will be 891 kJ mol<sup>-1</sup>.

## Conclusions

Seventy-seven different conformers for L-homoselenocysteine have been located as local minima of the PES of this amino acid by means of B3LYP/6-311+G(d,p) calculations. These local minima can be classified into four groups of conformers attending to the local conformation of the amino acid moiety. Structures A, B, and D are stabilized by an IMHB in which the amino group always acts as a HB donor, whereas, in structures A and D, the HB acceptor is the carbonyl group and in structure B the hydroxyl group. The structures in set C present an IMHB with the amino group acting as the HB acceptor and the hydroxyl group as the HB donor. The stability order decreases in the following

order: A > B > C > D, so that the seven most stable conformers belong to group A. From their relative stabilities and taking into account the barriers connecting them, it can be concluded that, very likely, only three of these conformers, namely A1, A4, and A5, would exist in the gas phase at room temperature. The PES associated with the anions formed by deprotonation of HSEC is also conformationally rich, with the global minimum being a Se-deprotonated species stabilized by a strong IMHB between the hydroxyl group and the Se atom. However, a direct deprotonation of the most stable neutrals lead to O-deprotonated species, which eventually isomerize to yield the global minimum. Hence, we can conclude that, quite unexpectedly, HSEC behaves as a Se acid in the gas phase.

The intrinsic acidity of HSEC was estimated to be 1374 kJ mol<sup>-1</sup> at the B3LYP/6-311++G(3df,2p) level of theory.

The PES associated with the protonated forms of HSEC is also conformationally rich, but the most stable protonated forms are systematically the N-protonated ones. The global minimum is again stabilized through a IMHB involving the protonated amino group as HB donor and the SeH group as HB acceptor. The calculated PA at the B3LYP/6-311++G(3df,2p) level of theory is 930 kJ mol<sup>-1</sup>.

## Supplementary data

Supplementary data for this article are available on the journal Web site (canjchem.nrc.ca).

## Acknowledgements

This work has been supported by the Dirección General de Investigación y Gestión del Plan Nacional de I+D+i (DGI) Project No. CTQ2009-13129-C02-01, by the Project MADRISOLAR2, Ref.: S-2009PPQ/1533 of the Comunidad Autónoma de Madrid, by the Consolider on Molecular Nanoscience CSD2007-00010, and by the European Cooperation in Science and Technology (COST) Action COST CM0702. A generous allocation of computing time at the Centro de computación Científica (CCC) of the Universidad Autónoma de Madrid (UAM) is also acknowledged.

## References

- (1) *Molecular and Quantum Pharmacology*; Bergman, E., Pullman, B., Eds.; Reidel D. Publishing Company Dordrecht-Holland: Boston, 1974; Vol. 7.
- (2) Gronert, S.; O'Hair, R. A. J. *J. Am. Chem. Soc.* **1995**, *117* (7), 2071. doi:10.1021/ja00112a022.
- (3) Noguera, M.; Rodríguez-Santiago, L.; Sodupe, M.; Bertran, J. *J. Mol. Struct. THEOCHEM* **2001**, *537* (1–3), 307. doi:10.1016/S0166-1280(00)00686-2.
- (4) Kaur, D.; Sharma, P.; Bharatam, P. V.; Kaur, M. *Int. J. Quantum Chem.* **2008**, *108* (5), 983. doi:10.1002/qua.21556.
- (5) Burk, R. F. *Selenium in Biology and Human Health*; Springer-Verlag: New York, 1994.
- (6) Foster, L. H.; Sumar, S. *Crit. Rev. Food Sci. Nutr.* **1997**, *37* (3), 211. doi:10.1080/10408399709527773. PMID:9143818.
- (7) Allan, C. B.; Lacourciere, G. M.; Stadtman, T. C. *Annu. Rev. Nutr.* **1999**, *19* (1), 1. doi:10.1146/annurev.nutr.19.1.1. PMID:10448514.
- (8) Clark, L. C.; Combs, G. F., Jr.; Turnbull, B. W.; Slate, E. H.; Chalker, D. K.; Chow, J.; Davis, L. S.; Glover, R. A.; Graham, G. F.; Gross, E. G.; Krongrad, A.; Lesher, J. L., Jr.; Park, H. K.; Sanders, B. B., Jr.; Smith, C. L.; Taylor, J. R. *JAMA* **1996**, *276* (24), 1957. doi:10.1001/jama.276.24.1957. PMID:8971064.
- (9) Stadtman, T. C. *J. Biol. Chem.* **1991**, *266* (25), 16257. PMID:1832153.
- (10) Müller, S.; Senn, H.; Gsell, B.; Vetter, W.; Baron, C.; Böck, A. *Biochemistry* **1994**, *33* (11), 3404. doi:10.1021/bi00177a034. PMID:8136378.
- (11) Hatfiel, D. L.; Choi, I. S.; Ohama, T.; Jung, J.-E.; Diamond, A. M. *Selenium in Biology and Human Health*; Burk, R. F., Ed.; Springer-Verlag: New York, 1994; p 221.
- (12) Roelfes, G.; Hilvert, D. *Angew. Chem. Int. Ed.* **2003**, *42* (20), 2275. doi:10.1002/anie.200250830.
- (13) Tam, J. P.; Yu, Q. *Biopolymers* **1998**, *46* (5), 319. doi:10.1002/(SICI)1097-0282(19981015)46:5<319::AID-BIP3>3.0.CO;2-S. PMID:9754028.
- (14) Salon, J.; Sheng, J.; Jiang, J. S.; Chen, G. X.; Caton-Williams, J.; Huang, Z. *J. Am. Chem. Soc.* **2007**, *129* (16), 4862. doi:10.1021/ja0680919. PMID:17388591.
- (15) Sheng, J.; Jiang, J. S.; Salon, J.; Huang, Z. *Org. Lett.* **2007**, *9* (5), 749. doi:10.1021/ol062937w. PMID:17263541.
- (16) Pearson, J. K.; Ban, F. Q.; Boyd, R. J. *J. Phys. Chem. A* **2005**, *109* (45), 10373. doi:10.1021/jp054185d. PMID:16833333.
- (17) Frisch, M. J.; Trucks, G. W.; Schlegel, H. B.; Scuseria, G. E.; Robb, M. A.; Cheeseman, J. R.; Zakrzewski, V. G.; Montgomery, J. A., Jr.; Vreven, T.; Kudin, K. N.; Burant, J. C.; Millam, J. M.; Iyengar, S. S.; Tomasi, J.; Barone, V.; Mennucci, B.; Cossi, M.; Scalmani, G.; Rega, N.; Petersson, G. A.; Nakatsuji, H.; Hada, M.; Ehara, M.; Toyota, K.; Fukuda, R.; Hasegawa, J.; Ishida, M.; Nakajima, T.; Honda, Y.; Kitao, O.; Adamo, C.; Jaramillo, J.; Gomperts, R.; Stratmann, R. E.; Yazyev, O.; Austin, J.; Cammi, R.; Pomelli, C.; Ochterski, J.; Ayala, P. Y.; Morokuma, K.; Voth, G. A.; Salvador, P.; Dannenberg, J. J.; Zakrzewski, V. G.; Dapprich, S.; Daniels, A. D.; Strain, M. C.; Farkas, O.; Malick, D. K.; Rabuck, A. D.; Raghavachari, K.; Foresman, J. B.; Ortiz, J. V.; Cui, Q.; Baboul, A. G.; Clifford, S.; Cioslowski, J.; Stefanov, B. B.; Liu, G.; Liashenko, A.; Piskorz, P.; Komaromi, I.; Martin, R. L.; Fox, D. J.; Keith, T.; Al-Laham, M. A.; Peng, C. Y.; Nanayakkara, A.; Challacombe, M.; Gill, P. M. W.; Johnson, B.; Chen, W.; Wong, M. W.; Gonzalez, C.; Pople, J. A. *Gaussian03*, revision E.01; Gaussian, Inc.: Wallingford, CT, 2003.
- (18) Becke, A. D. *J. Chem. Phys.* **1993**, *98* (2), 1372. doi:10.1063/1.464304.
- (19) Lee, C.; Yang, W.; Parr, R. G. *Phys. Rev. B* **1988**, *37* (2), 785. doi:10.1103/PhysRevB.37.785.
- (20) Mebel, A. M.; Morokuma, K.; Lin, M. C. *J. Chem. Phys.* **1995**, *103* (17), 7414. doi:10.1063/1.470313.
- (21) Ricca, A.; Bauschlicher, C. W. *Chem. Phys. Lett.* **1995**, *245* (2–3), 150. doi:10.1016/0009-2614(95)00971-6.
- (22) Llamas-Saiz, A. L.; Foces-Foces, C.; Mó, O.; Yáñez, M.; Elguero, E.; Elguero, J. *J. Comput. Chem.* **1995**, *16* (3), 263. doi:10.1002/jcc.540160302.
- (23) Montgomery, J. A., Jr.; Frisch, M. J.; Ochterski, J. W.; Petersson, G. A. *J. Chem. Phys.* **1999**, *110* (6), 2822. doi:10.1063/1.477924.
- (24) Curtiss, L. A.; Redfern, P. C.; Raghavachari, K.; Pople, J. A. *J. Chem. Phys.* **2001**, *114* (1), 108. doi:10.1063/1.1321305.
- (25) González, A. I.; Mó, O.; Yáñez, M.; León, E.; Tortajada, J.; Morizur, J. P.; Leito, I.; Maria, P.-C.; Gal, J. F. *J. Phys. Chem.* **1996**, *100* (24), 10490. doi:10.1021/jp953042w.
- (26) Lamsabhi, M.; Alcamí, M.; Mó, O.; Bouab, W.; Esseffar,

- M.; Abboud, J. L.-M.; Yáñez, M. *J. Phys. Chem. A* **2000**, *104* (21), 5122. doi:10.1021/jp000071k.
- (27) Burk, P.; Koppel, I. A.; Koppel, I.; Kurg, R.; Gal, J.-F.; Maria, P.-C.; Herreros, M.; Notario, R.; Abboud, J.-L. M.; Anvia, F.; Taft, R. W. *J. Phys. Chem. A* **2000**, *104* (12), 2824. doi:10.1021/jp9931399.
- (28) Raab, V.; Gauchenova, E.; Merkoulov, A.; Harms, K.; Sundermeyer, J.; Kovacević, B.; Maksić, Z. B. *J. Am. Chem. Soc.* **2005**, *127* (45), 15738. doi:10.1021/ja052647v. PMID: 16277515.
- (29) Kovacević, B.; Maksić, Z. B. *Chem. Commun. (Camb.)* **2006**, 1524. doi:10.1039/b517349c. PMID:16575448.
- (30) Maksić, Z. B.; Vianello, R. *Pure Appl. Chem.* **2007**, *79* (6), 1003. doi:10.1351/pac200779061003.
- (31) Despotović, I.; Maksić, Z. B.; Vianello, R. *New J. Chem.* **2007**, *31* (1), 52. doi:10.1039/b611980h.
- (32) Bouchoux, G.; Desaphy, S.; Bourcier, S.; Malosse, C.; Bim-bong, R. N. B. *J. Phys. Chem. B* **2008**, *112* (11), 3410. doi:10.1021/jp709677c. PMID:18288831.
- (33) Desaphy, S.; Malosse, C.; Bouchoux, G. *J. Mass Spectrom.* **2008**, *43* (1), 116. doi:10.1002/jms.1289. PMID:17726660.
- (34) Gal, J. F.; Maria, P. C.; Mó, O.; Yáñez, M.; Kuck, D. *Chem. Eur. J.* **2006**, *12* (29), 7676. doi:10.1002/chem.200501572.
- (35) Bader, R. F. W. *Atoms in Molecules: A Quantum Theory*; Clarendon Press: Oxford, 1990.
- (36) Becke, A. D.; Edgecombe, K. E. *J. Chem. Phys.* **1990**, *92* (9), 5397. doi:10.1063/1.458517.
- (37) Silvi, B.; Savin, A. *Nature* **1994**, *371* (6499), 683. doi:10.1038/371683a0.
- (38) Noury, S.; Krokidis, X.; Fuster, F.; Silvi, B. *Comput. Chem.* **1999**, *23* (6), 597. doi:10.1016/S0097-8485(99)00039-X.
- (39) Hurtado, M.; Yáñez, M.; Herrero, R.; Guerrero, A.; Dávalos, J. Z.; Abboud, J.-L. M.; Khater, B.; Guillemin, J.-C. *Chem. Eur. J.* **2009**, *15* (18), 4622. doi:10.1002/chem.200802307.

# Diagnostics of molecular orbital quality

Jia Deng, Andrew T.B. Gilbert, and Peter M.W. Gill

**Abstract:** We discuss several measures of the quality of a molecular orbital. Each requires only that the orbital be associated with a well-defined Fock operator and is thus applicable to both Hartree–Fock and density functional orbitals. One of the measures, the  $\gamma$  diagnostic, ranges from  $\gamma = 0$  (perfect) to  $\gamma = \pi/2$  (poor) and is conceptually simple. We illustrate its usefulness by applying it to a number of small atoms and ions.

**Key words:** molecular orbital quality, density functional theory, Hartree–Fock.

**Résumé :** On discute de plusieurs mesures de la qualité d'une orbitale moléculaire. Chacune nécessite uniquement que l'orbitale soit associée à un opérateur de Fock bien défini et qu'il soit ainsi applicable aux orbitales de Hartree–Fock ainsi qu'aux fonctionnelles de densité. L'une de ces mesures, le diagnostic, s'étend de 0 (parfait) à  $\pi/2$  (mauvais) et elle est conceptuellement simple. On illustre son utilité en l'appliquant à un certain nombre de petits atomes et de petits ions.

**Mots-clés :** qualité d'une orbitale moléculaire, théorie de la fonctionnelle de la densité, Hartree–Fock.

[Traduit par la Rédaction]

## Introduction

Some say that quantum chemistry is a branch of applied mathematics and that, by implication, quantum chemists are applied mathematicians. One can certainly mount a strong argument in favor of this. After all, quantum chemistry is primarily concerned with finding approximate solutions to a certain linear second-order partial differential equation and using those solutions to comprehend the chemical behavior of matter. However, if we are indeed applied mathematicians, we break one of the cardinal rules of our order: with few exceptions, we never check how well our “solutions” satisfy the equation!

*How well does a given wave function satisfy the Schrödinger equation?* At the conclusion of a quantum chemical calculation, any self-respecting software package ought to address this question and provide a quantitative answer that the user can interpret as a quality measure. However, it turns out that this raises a number of interesting mathematical issues, and we have therefore sought initially to address the more modest question: *How well does a given orbital satisfy its self-consistent field (SCF) equation?*

Standard practice in quantum chemistry is to gauge the quality of a molecular orbital by comparing it with the orbital obtained from a calculation with a larger basis set. However, this approach is both expensive and non-rigorous, for it is possible that the larger basis may suffer from the same deficiencies as the smaller one. Moreover, it is aesthetically unsatisfactory to judge an orbital by comparing it with another: it ought to be possible to appraise it purely on its own merits. In this paper, we propose a method for assessing the quality of a finite-basis SCF orbital in this way, without the need to perform a larger-basis calculation.

Although our approach is applicable to any orbital that is associated with a well-defined Fock operator, we will confine our numerical tests here to Hartree–Fock orbitals. The extension to density functional theory (DFT) orbitals is conceptually straightforward but requires consideration of DFT quadrature grids. We use atomic units throughout.

## Molecular orbital diagnostics

An exact orbital is an eigenfunction of its Fock operator.<sup>1</sup> However, an orbital  $\psi$  from a perfectly converged finite-basis Hartree–Fock<sup>2–4</sup> or Kohn–Sham<sup>5</sup> calculation is *not* an eigenfunction of its own Fock operator  $F$ , that is,

$$[1] \quad F\psi \neq \epsilon\psi$$

unless the basis happens to span the exact orbital.<sup>6</sup> This under-appreciated fact holds the key to our approach because the difference between the two sides of eq. [1] measures the quality of the orbital. There are several ways to exploit this. One approach is based on the local orbital energy

$$[2] \quad \epsilon(\mathbf{r}) = (F\psi)/\psi$$

If the orbital were perfect,  $\epsilon(\mathbf{r})$  would be constant everywhere; small imperfections in  $\psi$  will produce small variations in  $\epsilon(\mathbf{r})$ .

A second approach recognizes that the normalized versions of  $\psi$  and  $F\psi$  should be identical. Accordingly, the discrepancy

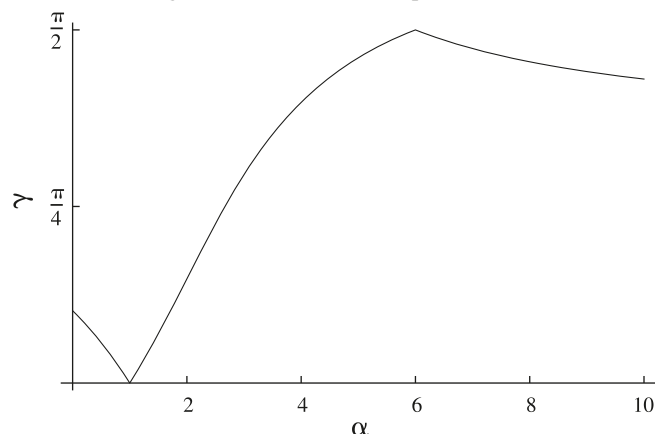
$$[3] \quad \delta(\mathbf{r}) = \frac{\psi}{\sqrt{\langle\psi|\psi\rangle}} - \frac{F\psi}{\sqrt{\langle F\psi|F\psi\rangle}}$$

Received 31 December 2009. Accepted 18 February 2010. Published on the NRC Research Press Web site at canjchem.nrc.ca on 13 May 2010.

J. Deng, A.T.B. Gilbert, and P.M.W. Gill.<sup>1</sup> Research School of Chemistry, Australian National University, ACT 0200, Australia.

<sup>1</sup>Corresponding author (e-mail: peter.gill@anu.edu.au).



**Fig. 1.** The  $\gamma$  diagnostic for the orbital  $\exp(-\alpha r)$  in the H atom.**Table 1.**  $\gamma$  values for Kellner orbitals in the He-like ions.

	H <sup>-</sup>	He	Li <sup>+</sup>	Be <sup>2+</sup>	B <sup>3+</sup>	C <sup>4+</sup>	N <sup>5+</sup>
Z	1	2	3	4	5	6	7
$\gamma$	0.488	0.063	0.033	0.023	0.017	0.014	0.012

should vanish at all points  $\mathbf{r}$  and, wherever it fails to do so, it reveals deficiencies in the orbital.

A third approach determines the angle

$$[4] \quad \gamma = \cos^{-1} \sqrt{\frac{\langle \psi | \mathbf{F} \psi \rangle^2}{\langle \psi | \psi \rangle \langle \mathbf{F} \psi | \mathbf{F} \psi \rangle}}$$

$$= \tan^{-1} \sqrt{\frac{\langle \psi | \psi \rangle \langle \mathbf{F} \psi | \mathbf{F} \psi \rangle}{\langle \psi | \mathbf{F} \psi \rangle^2} - 1}$$

between  $\psi$  and  $\mathbf{F}\psi$ . Unlike  $\epsilon(\mathbf{r})$  and  $\delta(\mathbf{r})$ , which are functions,  $\gamma$  is a number between 0 (perfect) and  $\pi/2$  (poor) and achieves the former value if, and only if,  $\psi$  is an eigenfunction of  $\mathbf{F}$ .

To calculate numerical values of  $\gamma$ , we must choose a suitable inner product  $\langle \cdot | \cdot \rangle$ . The overlap metric

$$[5] \quad \langle f | g \rangle = \int f(\mathbf{r})g(\mathbf{r})d\mathbf{r}$$

is an obvious choice but it yields poor  $\gamma$  values if the orbital fails to possess the correct nuclear cusps. This is a particularly serious problem if the orbital is expanded in a nuclear-centered Gaussian basis because, close to a nucleus, any Gaussian is flat and consequently  $\mathbf{F}\psi \sim (-Z/r)\psi$  is singular.

Because of the widespread popularity of Gaussian basis sets, we prefer an inner product that is less sensitive to such cusp violations. We have found that the Coulomb metric

$$[6] \quad \langle f | g \rangle = \iint \frac{f(\mathbf{r}_1)g(\mathbf{r}_2)}{r_{12}} d\mathbf{r}_1 d\mathbf{r}_2$$

works well and we have adopted it throughout this work. If  $\psi$  is a sum of Gaussians, all of the inner products needed for atoms can be evaluated in terms of elementary functions, using integrals such as

$$[7] \quad \left\langle \frac{e^{-b^2 r^2}}{r} \middle| \frac{e^{-d^2 r^2}}{r} \right\rangle = 4\pi^{5/2} \frac{b+d-\sqrt{b^2+d^2}}{b^2 d^2}$$

A table of such integrals is given in the Appendix.

In this preliminary exploration, we will investigate the performance of the  $\gamma$  diagnostic (eq. [4]) in very small systems. The primary question is whether or not  $\gamma$  behaves “reasonably”.

## Examples

### Hydrogen atom

This one-electron system has the Fock operator

$$[8] \quad \mathbf{F} = -\frac{\nabla^2}{2} - \frac{1}{r}$$

and its true orbital is  $\exp(-r)$ . To begin our exploration of the  $\gamma$  diagnostic, we consider an HF calculation using the single basis function  $\exp(-\alpha r)$ . The computed orbital will differ from the true orbital except, of course, when  $\alpha = 1$ .

The  $\gamma$  diagnostic (eq. [4]), using the Coulomb metric (eq. [6]), is

$$[9] \quad \gamma = \tan^{-1} \left| 2 \frac{\alpha - 1}{\alpha - 6} \right|$$

and this is plotted, for  $0 < \alpha < 10$ , in Fig. 1. As expected,  $\gamma$  vanishes for  $\alpha = 1$  and grows almost linearly as  $\alpha$  deviates from this optimal value. For  $\alpha = 6$ , it turns out that  $\psi$  and  $\mathbf{F}\psi$  are exactly orthogonal, i.e., the angle between them is  $\pi/2$ .

### Helium-like ions

These two-electron systems have the Fock operator

$$[10] \quad \mathbf{F} = -\frac{\nabla^2}{2} - \frac{Z}{r} + \int \frac{\psi(\mathbf{r}')^2}{|\mathbf{r} - \mathbf{r}'|} d\mathbf{r}'$$

where  $Z$  is the nuclear charge. The true HF orbital is unknown, but if we approximate it by the Kellner orbital<sup>7</sup>

$$[11] \quad \psi(\mathbf{r}) = \exp(-\alpha r)$$

the HF energy is minimized by choosing  $\alpha = Z - 5/16$ .

How satisfactory is this orbital? It can be shown that

$$[12] \quad \gamma = \tan^{-1} \left| \frac{a}{Z - b} \right|$$

where  $a = \sqrt{1987/388800}$  and  $b = 623/720$  and this is evaluated in Table 1 for  $Z = 1, \dots, 7$ . These results reveal that the Kellner orbital is a good approximation ( $\gamma \approx 0.01$ ) to the true orbital for large- $Z$  ions, such as  $\text{C}^{4+}$  and  $\text{N}^{5+}$ , that it is reasonable ( $\gamma \approx 0.05$ ) for the He atom itself, but that it is very poor ( $\gamma \approx 0.5$ ) for the  $\text{H}^-$  ion. This may be related to the difficulties that Cioslowski and others have encountered when seeking an accurate HF orbital for the hydride anion.<sup>8,9</sup>

### Hookium atom

This two-electron system<sup>10,11</sup> has the Fock operator

$$[13] \quad \mathbf{F} = -\frac{\nabla^2}{2} + \frac{r^2}{8} + \int \frac{\psi(\mathbf{r}')^2}{|\mathbf{r} - \mathbf{r}'|} d\mathbf{r}'$$

and its true HF orbital is unknown. However, neglecting the

**Table 2.**  $\gamma$  values for Gaussian and Ragot orbitals in hookium.

Orbital	Equation	$\alpha$	$\beta$	$\gamma$
Gaussian	[14]	0.25	—	0.0430
Gaussian	[14]	0.210 549 021	—	0.0142
Ragot	[15]	0.25	2.771 219 931	0.0007
Ragot	[15]	0.251 117 376	2.711 087 898	0.0002

**Table 3.**  $\gamma$  values for pc-*n* and aug-pc-*n* orbitals in small atoms and ions.

		pc- <i>n</i>					aug-pc- <i>n</i>				
	Orbital	0	1	2	3	4	0	1	2	3	4
H	1s	0.0436	0.0255	0.0079	0.0020	0.0007	0.0403	0.0313	0.0085	0.0015	0.0005
	2s	0.7425	0.7202	0.7131	0.7323	0.7449	0.7491	0.7573	0.7735	0.7917	0.8007
He <sup>+</sup>	1s	0.0650	0.0443	0.0133	0.0035	0.0017	0.0811	0.0495	0.0135	0.0037	0.0016
	2s	1.4198	1.3296	0.6133	0.3130	0.2424	0.1309	0.1110	0.0839	0.0563	0.0445
H <sup>-</sup>	1s	0.9572	0.7502	0.4354	0.2507	0.1873	0.1363	0.0870	0.0554	0.0348	0.0267
He	1s	0.0756	0.0389	0.0110	0.0022	0.0010	0.0620	0.0396	0.0125	0.0022	0.0009
Li <sup>+</sup>	1s	0.0297	0.0151	0.0119	0.0122	0.0042	0.0295	0.0152	0.0109	0.0124	0.0042
Be	1s	0.0349	0.0153	0.0082	0.0091	0.0034	0.0339	0.0150	0.0079	0.0093	0.0034
	2s	0.0881	0.0203	0.0123	0.0029	0.0031	0.0358	0.0147	0.0152	0.0029	0.0030

electron repulsion yields the harmonic oscillator wave function  $\exp(-r^2/4)$  and one may therefore anticipate that

$$[14] \quad \psi(\mathbf{r}) = \exp(-\alpha r^2)$$

may be a good guess. The HF energy of this orbital, using an optimized exponent, lies 1.5  $mE_h$  above the HF limit. However, Ragot has recently claimed<sup>12</sup> that the modified orbital

$$[15] \quad \psi(\mathbf{r}) = \sqrt{r^2 + \beta^2} \exp(-\alpha r^2)$$

is very much better, provided that  $\alpha$  and  $\beta$  are chosen carefully, and constructs two orbitals of this form, lying 4.5 and 0.6  $\mu E_h$  above the HF limit, respectively.

The  $\gamma$  diagnostic allows us to compare the quality of these orbitals, and though we have not been able to find  $\gamma$  in closed form for eq. [15] the required integrals can be found by quadrature. The results shown in Table 2 reveal that the Gaussian (eq. [14]) is a good approximation to the exact orbital but that the Ragot orbitals (eq. [15]) are superior by one to two orders of magnitude.

### Other small systems

Table 3 lists  $\gamma$  values for the orbitals in some small atoms and ions, using Jensen's pc-*n* basis sets.<sup>13,14</sup>

H and He<sup>+</sup> ions are one-electron species whose 1s orbitals are modeled well by the pc-*n* bases. It is not surprising that the He<sup>+</sup> orbital is slightly inferior to that of H, for the helium bases were designed to be optimal for the neutral atom, not the much more compact cation. Nevertheless, the triple-zeta pc-2 orbitals are good and the pc-3 and pc-4 orbitals are excellent.

The 2s orbitals (the LUMOs in these species) tell a very different story. In the H atom, the  $\gamma$  values are appalling, and actually deteriorate as the basis set quality improves. This arises because, in the HF picture, the virtual orbitals of the H atom experience an exponentially decaying attractive potential and therefore describe essentially free electrons.

Of course, nuclear-centered Gaussian basis sets (e.g., aug-pc-*n*) cannot capture such behavior. The situation is better in He<sup>+</sup> because the virtual orbitals experience a Coulombic attractive potential and, consequently, approximate the standard hydrogenic orbitals. Although they are too diffuse to be modelled well by pc-0, pc-1, and pc-2, the higher aug-pc-*n* bases do a better job.

H<sup>-</sup>, He, and Li<sup>+</sup> are isoelectronic but it is clear that their pc-*n* 1s orbitals vary greatly in quality. While good orbitals are provided by pc-1 (for Li<sup>+</sup>), and pc-2 (for He), a satisfactory orbital for the hydride ion is not obtained even with the septuple-zeta pc-4 basis. This arises because the second electron in H<sup>-</sup> is barely bound, and diffuse functions therefore play a crucial role in the basis. Accordingly, we find that the aug-pc-*n* orbital is consistently almost an order of magnitude better than its pc-*n* analog; indeed, even the lowly aug-pc-0 orbital exceeds the quality of the pc-4 orbital.

The last two lines in Table 3 pertain to the core and valence orbitals in the Be atom. We find that the 1s orbital is accurately modelled, even by the small pc-*n* bases, but that the 2s orbital is more challenging and benefits significantly from the addition of diffuse functions. It is surprising to find that, in passing from the pc-2 to the pc-3 basis set, the valence orbital improves dramatically but the core orbital actually becomes slightly worse. This anomaly is unaffected by the addition of diffuse functions.

### Concluding remarks

It is impossible to assess the quality of an SCF calculation from its energy alone, and as a result, quantum chemists have traditionally been compelled to perform sequences of calculations, looking for signs of convergence as the basis set is systematically improved. In contrast, the  $\gamma$  diagnostic (eq. [4]) exploits the inequality (eq. [1]) to provide a chemist with a direct measure of the quality of a computed orbital.

Using the Coulomb metric (eq. [6]), it appears empirically

that “reasonable” orbitals have  $\gamma \leq 0.05$ , “good” orbitals have  $\gamma \leq 0.01$ , and “excellent” orbitals have  $\gamma \leq 0.005$ .

In this preliminary work, we have computed  $\gamma$  for single-center systems only. To facilitate the efficient calculation of  $\gamma$  for the MOs in polyatomic molecules, the integrals in the Appendix must be generalized to the multicenter case. In large systems, straightforward evaluation of the  $\langle F\psi | F\psi \rangle$  integral becomes computationally costly, but techniques based on the resolution of the identity (RI)<sup>15–17</sup> or resolution of the Coulomb operator<sup>18–20</sup> should be helpful in this context.

In the case of Kohn–Sham orbitals, the inner products in eq. [4] involving  $F\psi$  cannot be computed in closed form, and one must resort instead to quadrature. We will discuss this elsewhere.

In this brief paper, we have proposed a diagnostic to quantify orbital quality and have studied its performance on a few very small atoms and ions. We will implement this in the Q-Chem package<sup>21</sup> and will report molecular results elsewhere. We also plan to extend these ideas to a wave function diagnostic in the near future.

## Acknowledgement

We thank Pierre-François Loos for making a number of helpful comments on this manuscript.

## References

- (1) Szabo, A.; Ostlund, N. S. *Modern Quantum Chemistry*; McGraw-Hill: New York, 1989.
- (2) Roothaan, C. C. J. *Rev. Mod. Phys.* **1951**, 23 (2), 69. doi:10.1103/RevModPhys.23.69.
- (3) Hall, G. G. *Proc. R. Soc. Lond.* **1951**, A205, 541.
- (4) Pople, J. A.; Nesbet, R. K. *J. Chem. Phys.* **1954**, 22 (3), 571. doi:10.1063/1.1740120.
- (5) Pople, J. A.; Gill, P. M. W.; Johnson, B. G. *Chem. Phys. Lett.* **1992**, 199 (6), 557. doi:10.1016/0009-2614(92)85009-Y.
- (6) Deng, J.; Gilbert, A. T. B.; Gill, P. M. W. *J. Chem. Phys.* **2009**, 130 (23), o. 231101. doi:10.1063/1.3152864.
- (7) Kellner, G. W. Z. *Phys.* **1927**, 44 (1-2), 91. doi:10.1007/BF01391720.
- (8) Cioslowski, J.; Liu, G. J. *Chem. Phys.* **1998**, 109 (19), 8225. doi:10.1063/1.477484.
- (9) Pearson, J. K.; Gill, P. M. W.; Ugalde, J.; Boyd, R. J. *Mol. Phys.* **2009**, 107 (8), 1089. doi:10.1080/00268970902740563.
- (10) Kais, S.; Herschbach, D. R.; Levine, R. D. *J. Chem. Phys.* **1989**, 91 (12), 7791. doi:10.1063/1.457247.
- (11) O'Neill, D. P.; Gill, P. M. W. *Phys. Rev. A* **2003**, 68 (2), o. 022505. doi:10.1103/PhysRevA.68.022505.
- (12) Ragot, S. *J. Chem. Phys.* **2008**, 128 (16), o. 164104. doi:10.1063/1.2904874.
- (13) Jensen, F. *J. Chem. Phys.* **2001**, 115 (20), 9113. doi:10.1063/1.1413524.
- (14) Jensen, F. *J. Phys. Chem. A* **2007**, 111 (44), 11198. doi:10.1021/jp068677h. PMID:17439196.
- (15) Baerends, E. J.; Ellis, D. E.; Ros, P. *Chem. Phys.* **1973**, 2 (1), 41. doi:10.1016/0301-0104(73)80059-X.
- (16) Dunlap, B. I.; Connolly, J.; Sabin, J. *J. Chem. Phys.* **1979**, 71 (8), 3396. doi:10.1063/1.438728.
- (17) Vahtras, O.; Almlöf, J.; Feyereisen, M. *Chem. Phys. Lett.* **1993**, 213 (5-6), 514. doi:10.1016/0009-2614(93)89151-7.
- (18) Varganov, S. A.; Gilbert, A. T. B.; Deplazes, E.; Gill, P. M. W. *J. Chem. Phys.* **2008**, 128 (20), o. 201104. doi:10.1063/1.2939239.
- (19) Gill, P. M. W.; Gilbert, A. T. B. *Chem. Phys.* **2009**, 356 (1-3), 86. doi:10.1016/j.chemphys.2008.10.047.
- (20) Limpanuparb, T.; Gill, P. M. W. *Phys. Chem. Chem. Phys.* **2009**, 11 (40), 9176. doi:10.1039/b910613h. PMID:19812838.
- (21) Shao, Y.; Molnar, L. F.; Jung, Y.; Kussmann, J.; Ochsenfeld, C.; Brown, S. T.; Gilbert, A. T. B.; Slipchenko, L. V.; Levchenko, S. V.; O'Neill, D. P.; DiStasio, R. A., Jr.; Lochan, R. C.; Wang, T.; Beran, G. J. O.; Besley, N. A.; Herbert, J. M.; Lin, C. Y.; Van Voorhis, T.; Chien, S. H.; Sodt, A.; Steele, R. P.; Rassolov, V. A.; Maslen, P. E.; Korambath, P. P.; Adamson, R. D.; Austin, B.; Baker, J.; Byrd, E. F. C.; Dachsel, H.; Doerksen, R. J.; Dreuw, A.; Dunietz, B. D.; Dutoi, A. D.; Furlani, T. R.; Gwaltney, S. R.; Heyden, A.; Hirata, S.; Hsu, C. P.; Kedziora, G.; Khalliulin, R. Z.; Klunzinger, P.; Lee, A. M.; Lee, M. S.; Liang, W. Z.; Lotan, I.; Nair, N.; Peters, B.; Proynov, E. I.; Pieniazek, P. A.; Rhee, Y. M.; Ritchie, J.; Rosta, E.; Sherrill, C. D.; Simmonett, A. C.; Subotnik, J. E.; Woodcock, H. L., III; Zhang, W.; Bell, A. T.; Chakraborty, A. K.; Chipman, D. M.; Keil, F. J.; Warshel, A.; Hehre, W. J.; Schaefer, H. F., III; Kong, J.; Krylov, A. I.; Gill, P. M. W.; Head-Gordon, M. *Phys. Chem. Chem. Phys.* **2006**, 8 (27), 3172. doi:10.1039/b517914a. PMID:16902710.

## Appendix

Table A1 contains the fundamental integrals<sup>A1</sup> (in the Coulomb metric) that are required to form  $\gamma$  in single-center systems, such as atoms.

In the final expression, the integration limits are

$$[A1] \quad X = \frac{a}{\sqrt{a^2 + b^2}} \frac{d}{\sqrt{b^2 + d^2}}$$

**Table A1.** Integrals required to form the  $\gamma$  diagnostic (eq. [4]) in atomic systems.

$\langle f   g \rangle$	$\exp(-d^2 r^2)$	$-\frac{\nabla^2}{2} \exp(-d^2 r^2)$	$\frac{\text{erf}(cr)}{r} \exp(-d^2 r^2)$
$\exp(-b^2 r^2)$	$\frac{2\pi^{5/2}}{b^2 d^2 \sqrt{b^2 + d^2}}$	$\frac{2\pi^{5/2}}{(b^2 + d^2)^{3/2}}$	$\frac{4\pi^2}{b^3 d} \tan^{-1} \left[ \frac{b}{d} \frac{c}{\sqrt{b^2 + c^2 + d^2}} \right]$
$-\frac{\nabla^2}{2} \exp(-b^2 r^2)$	$\frac{2\pi^{5/2}}{(b^2 + d^2)^{3/2}}$	$\frac{6\pi^{5/2} b^2 d^2}{(b^2 + d^2)^{3/2}}$	$\frac{4\pi^2}{b^2 + d^2} \frac{c}{\sqrt{b^2 + c^2 + d^2}}$
$\frac{\text{erf}(ar)}{r} \exp(-b^2 r^2)$	$\frac{4\pi^2}{bd^3} \tan^{-1} \left[ \frac{d}{b} \frac{a}{\sqrt{a^2 + b^2 + d^2}} \right]$	$\frac{4\pi^2}{b^2 + d^2} \frac{a}{\sqrt{a^2 + b^2 + d^2}}$	$\left( \frac{4\pi}{bd} \right)^{3/2} \sqrt{\frac{b^2 + d^2}{bd}} \int_0^X \int_0^Y \frac{dx dy}{\sqrt{1 - x^2 - y^2}}$

$$[A2] \quad Y = \frac{b}{\sqrt{b^2 + d^2}} \frac{c}{\sqrt{c^2 + d^2}}$$

The double integral is elementary and can be evaluated in terms of arctangents but the resulting expression is messy.

### Reference

- (A1) Gill, P. M. W.; Johnson, B. G.; Pople, J. A. *Int. J. Quantum Chem.* **1991**, 40 (6), 745. doi:10.1002/qua.560400604.



# Serine–Ca<sup>2+</sup> versus serine–Cu<sup>2+</sup> complexes — A theoretical perspective

Al Mokhtar Lamsabhi, Otilia Mó, and Manuel Yáñez

**Abstract:** The association of Ca<sup>2+</sup> and Cu<sup>2+</sup> to serine was investigated by means of B3LYP DFT calculations. The [serine–M]<sup>2+</sup> (M = Ca, Cu) potential energy surfaces include, as does the neutral serine, a large number of conformers, in which a drastic reorganization of the electron density of the serine moiety is observed. This leads to significant changes in the number and strength of the intramolecular hydrogen bonds existing in the neutral serine tautomers. In some cases, a proton is transferred from the carboxylic OH group to the amino group and accordingly, some of the more stable [serine–M]<sup>2+</sup> complexes can be viewed as the result of the interaction of the zwitterionic form of serine with the doubly charged metal ion. Whereas the interaction between Ca<sup>2+</sup> and serine is essentially electrostatic, that between Cu<sup>2+</sup> and serine has a non-negligible covalent character, reflected in larger electron densities at the bond critical points between the metal and the base, in the negative values of the electron density between the two interacting systems, and in much larger Cu<sup>2+</sup> than Ca<sup>2+</sup> binding energies. More importantly, the interaction with Cu<sup>2+</sup> is followed by a partial oxidation of the base, which is not observed when the metal ion is Ca<sup>2+</sup>. The main consequence is that in Cu<sup>2+</sup> complexes a significant acidity enhancement of the serine moiety takes place, which strongly favors the deprotonation of the [serine–Cu]<sup>2+</sup> complexes. This is not the case for Ca<sup>2+</sup> complexes. Thus, [serine–Ca]<sup>2+</sup> complexes, like those formed by urea, thiourea, selenourea, or glycine, should be detected in the gas phase. Conversely, the complexes with Cu<sup>2+</sup> should deprotonate spontaneously and therefore only [(serine–H)–Cu]<sup>+</sup> monocations should be experimentally accessible.

**Key words:** gas phase reactivity, transition metal, amino acids, DFT.

**Résumé :** On étudié l'association des cations Ca<sup>2+</sup> et Cu<sup>2+</sup> avec la sérine en utilisant la théorie de la fonctionnelle de la densité, B3LYP. Pour l'ion [sérine–M]<sup>2+</sup> (M = Ca, Cu), comme c'est le cas pour la sérine neutre, les surfaces d'énergie potentielle comportent un grand nombre de conformères dans lesquels on peut observer une réorganisation drastique de la densité électronique de la sérine. Ces changements conduisent à des changements significatifs dans le nombre et la force des liaisons hydrogènes intramoléculaires par rapport à celles qui existent dans les tautomères neutres de la sérine. Dans quelques cas, il se produit un transfert de proton du groupe OH de l'acide carboxylique vers le groupe amino et, en conséquence, un certain nombre des complexes les plus stables de l'ion [sérine–M]<sup>2+</sup> peuvent être considérés comme étant le résultat de l'interaction de la forme zwitterionique de la sérine avec l'ion métallique doublement chargé. Alors que l'interaction entre la Ca<sup>2+</sup> et la sérine est essentiellement électrostatique, celle entre le Cu<sup>2+</sup> et la sérine comporte un caractère covalent non négligeable qui est le reflet de densités électroniques plus grandes aux points critiques de liaison entre les deux systèmes en interaction ainsi que des énergies de liaisons beaucoup plus élevées pour le Cu<sup>2+</sup> que pour le Ca<sup>2+</sup>. Fait plus important, l'interaction avec le Cu<sup>2+</sup> est suivie d'une oxydation partielle de la base, ce qui n'est pas le cas quand l'ion métallique est le Ca<sup>2+</sup>. La conséquence principale est que dans les complexes du Cu<sup>2+</sup>, on observe une augmentation significative de l'acidité de la portion sérine qui favorise la déprotonation des complexes [sérine–Cu]<sup>2+</sup>. Ce n'est pas le cas avec les complexes Ca<sup>2+</sup>. En conséquence, il devrait être possible de détecter les complexes [sérine–Ca]<sup>2+</sup> en phase gazeuse, comme c'est le cas avec ceux formés avec l'urée, la thiourée, la sélénourée et la glycine. Inversement, les complexes qui résultent d'interactions avec le Cu<sup>2+</sup> devraient se déprotoner spontanément et seuls les monocations [(sérine–H)–Cu]<sup>+</sup> devraient être expérimentalement disponibles.

**Mots-clés :** réactivité en phase gazeuse, métal de transition, acides aminés, théorie de la fonctionnelle de la densité (TFD).

## Introduction

Serine is a chiral amino acid that can be found in proteins. It is also one of two hydroxyl amino acids and for that reason is highly hydrophilic and is commonly found in the outer regions of soluble proteins.<sup>1</sup> Serine is a good

model for studying peptide structures. Many studies have been devoted to understanding its behavior in gas phase,<sup>2–6</sup> solution,<sup>7–10</sup> and solid state.<sup>11,12</sup> One important characteristic of this molecule is the possibility of forming strong hydrogen bonds (HBs) between its HB-donor and HB-acceptor groups, which play an important role as far as the relative

Received 27 January 2010. Accepted 8 March 2010. Published on the NRC Research Press Web site at canjchem.nrc.ca on 18 May 2010.

This article is part of a Special Issue dedicated to Professor R. J. Boyd.

A.M. Lamsabhi,<sup>1</sup> O. Mó, and M. Yáñez. Departamento de Química, C-9. Universidad Autónoma de Madrid. (Campus de Excelencia UAM-CSIC). Cantoblanco, 28049-Madrid, Spain.

<sup>1</sup>Corresponding author (e-mail: mokhtar.lamsabhi@uam.es).

stability of its conformers is concerned. Serine conformers, in the gas-phase, were classified into three groups (A, B, and C) according to the main intramolecular interaction they exhibit: A ( $\text{OH}_\text{A}$ -N hydrogen bond), B ( $\text{OH}_\text{C}$ -N), and C ( $\text{OH}_\text{A}$ -O=) (the subscripts A and C stand for alcohol and carboxylic group, respectively).<sup>5,13</sup> However, more types of intramolecular hydrogen bonds (IMHBs) than those mentioned above appear in this molecule, likely playing some role on its intrinsic reactivity and its solvation, in particular when the solvent is able to form hydrogen bonds with serine. This is the case of the water molecule which, is ubiquitous in biological media. Recently, Gong et al.<sup>14</sup> have carried out an exhaustive investigation on the interaction of serine with water, exploring the specific solvation of all the reactive sites of the aminoacid. In this paper, we address the question of the intrinsic reactivity of serine with respect to  $\text{Ca}^{2+}$  and  $\text{Cu}^{2+}$  in their ground states, both doubly charged ions being also of biochemical relevance.

Calcium is also ubiquitous in biological media and is an essential actor in diverse processes such as muscle contraction, cell motility, membrane adhesion, synaptic transmission, and hormone release. While sites for calcium binding are implicit in these and other calcium-regulated processes, detailed characterization of such binding sites is very important. Copper is also omnipresent in the biological media.<sup>15-18</sup> It participates in different processes, such as enzyme regulation and stabilization of nucleic acids. Recently, we pointed out the difference between  $\text{Ca}^{2+}$  and  $\text{Cu}^{2+}$  complexes with urea and thiourea in the gas phase.<sup>19</sup> In fact, the attachment of transition metal dications to an organic base (B) is immediately followed by a deprotonation of the system, so that only  $[\text{Cu}-(\text{B}-\text{H})]^+$  singly charged species are observed in the gas phase,<sup>20</sup> because the recombination energy (the negative of the second ionization energy) of  $\text{Cu}^{2+}$  is so high that in most neutral- $\text{Cu}^{2+}$  reactions in the gas phase, the doubly charged metal ion is able to oxidize the base. This is not the case, however, when dealing with alkaline-earth dications like  $\text{Ca}^{2+}$ , whose recombination energy is almost half that of  $\text{Cu}^{2+}$ , so that the  $[\text{Ca}-\text{B}]^{2+}$  complexes are stable and easily detected. As a matter of fact, the unimolecular reactivity of complexes between  $\text{Ca}^{2+}$  and different organic bases, namely urea, glycine, thiourea, and selenourea have been reported in the literature.<sup>21-23</sup> Thus, one of the objectives of the present study is to investigate whether the behavior of serine, which presents additional basic sites and the possibility of forming different intramolecular hydrogen bonds, is similar to that exhibited by the aforementioned bases or whether it exhibits some peculiarities.

## Computational Details

All calculations were performed with the Gaussian 03 package.<sup>24</sup> The B3LYP density functional theory (DFT) approach, which combines the Becke's<sup>25</sup> three-parameter non-local hybrid exchange potential with the nonlocal correlation of Lee, Yang, and Parr,<sup>26</sup> was used in all calculations. For geometry optimizations as well as for the calculation of harmonic vibrational frequencies, a 6-311G(d,p) basis set was employed. The different stationary points of the potential energy surface (PES) were identified as local minima or transition states in terms of the number of imaginary vibra-

tional frequencies. The corresponding zero-point energy corrections (ZPE) were scaled by the empirical factor 0.9806 proposed by Scott and Radom.<sup>27</sup>

To obtain more reliable energies for the local minima, final energies were evaluated by using the same functional combined with the 6-311++G(3df,2p) basis set for all atoms except for  $\text{Cu}^{2+}$ , where the (14s9p5d/9s5p3d) basis set of Wachters<sup>28</sup> and Hay<sup>29</sup> was used, supplemented with a set of (1s2p1d) diffuse functions and with three sets of *f* and one set of *g* polarization functions. It has been shown that this approach is well-suited to the study of this kind of systems, yielding binding energies in good agreement with experimental values.<sup>30-32</sup>

The basis set superposition error (BSSE) was not considered in the present study because, as has been previously reported, for the DFT and DFT/HF hybrid methods, this error is usually small when the basis set expansion is sufficiently flexible.<sup>33</sup>

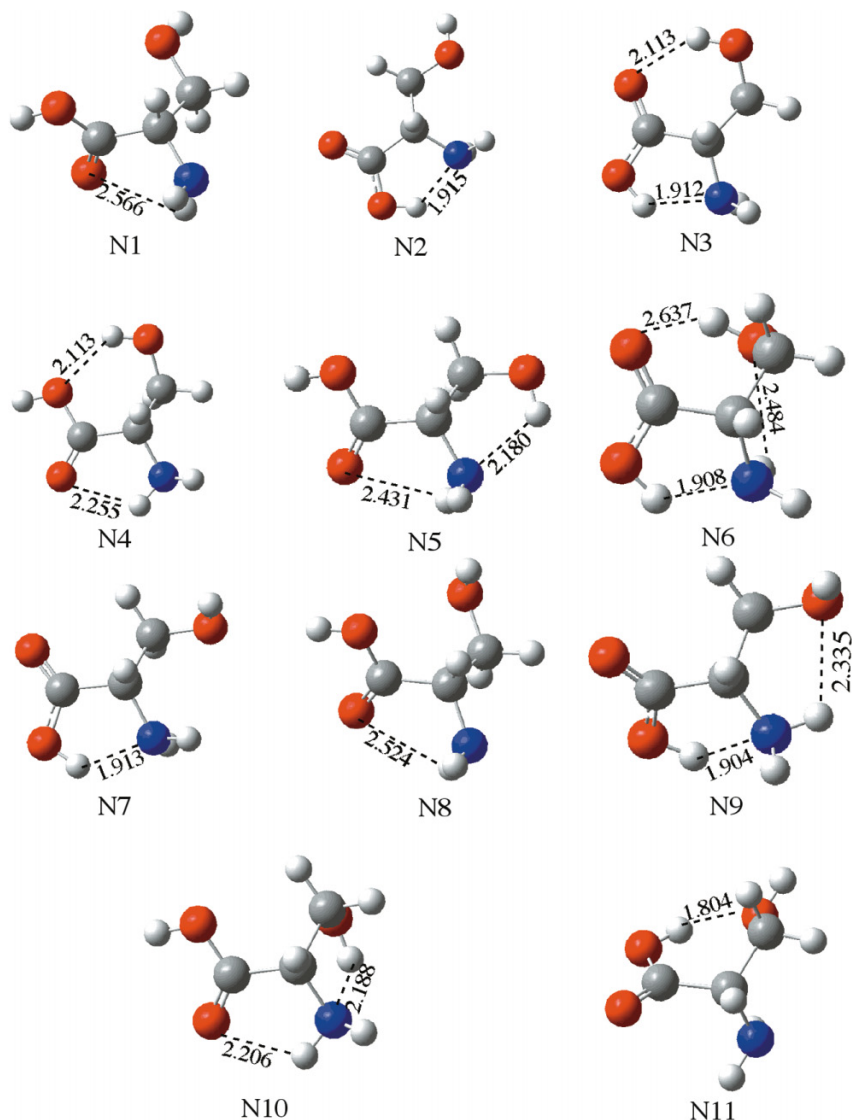
The bonding in these complexes was analyzed by means of the natural bond orbital (NBO) partitioning technique<sup>34</sup> and the quantum theory of atoms in molecules (QTAIM).<sup>35,36</sup>

## Results and Discussions

It is well known that amino acids in the gas phase or isolated in noble gas matrices adopt the nonionic form ( $\text{H}_2\text{N}-\text{CHR}-\text{COOH}$ ),<sup>4,13,37</sup> whereas in the solid state or in solution they exist in the zwitterionic form ( $\text{H}_3\text{N}^+-\text{CHR}-\text{COO}^-$ ).<sup>5,6</sup> This has been experimentally confirmed for several amino acids, including glycine,  $\alpha$ - and  $\beta$ -alanine, proline, sarcosine, *N,N*-dimethyl-glycine, and  $\gamma$ -aminobutyric acid, by studies based on electron diffraction, as well as on microwave, and matrix-isolation infrared spectroscopy techniques.<sup>37-44</sup> The stabilization of the zwitterionic form in the condensed phases is essentially due to dipolar interactions and intermolecular H-bonds. Hence, one of the major problems associated with the theoretical study of the amino acids is the abundance of different conformers.<sup>45</sup> Excluding the zwitterionic forms, the number of conformers could exceed 324 trial structures, as has been pointed out by Gronert and O'Hair.<sup>46</sup> For serine, a total of 51 conformers have been found to lie within an energy gap of 50 kJ/mol, at MP2/6-31+G\*\*/HF/6-31G\* level of theory.<sup>46</sup> Since the main aim of our study is not to explore the different conformations of serine but to look at the characteristics of its complexes with  $\text{Ca}^{2+}$  and  $\text{Cu}^{2+}$  dications, we have selected for our survey the eleven most stable ones, shown in Fig. 1. From these eleven conformations, different coordinations of the doubly charged metal ion to serine can be envisaged. The B3LYP/6-311G(d,p) optimized geometries for the most stable  $[\text{serine}-\text{Ca}]^{2+}$  and  $[\text{serine}-\text{Cu}]^{2+}$  complexes are reported in Figs. 2 and 3, respectively. Their B3LYP/6-311++G(3df,2p)//6-311G(d,p) relative energies with respect to the corresponding most stable  $[\text{serine}-\text{M}]^{2+}$  ( $\text{M} = \text{Ca}, \text{Cu}$ ) complex are listed in Table 1. Similar information for the more stable serine conformers is provided in the same table.

Serine is very rich, conformationally speaking, because a simple rotation of the hydroxyl group, or around the N-C or C-C bonds, may connect different conformers through activation barriers which are not very high. Although a detailed

**Fig. 1.** Optimized geometries of neutral conformers of serine. Some internuclear distances are shown in Å.

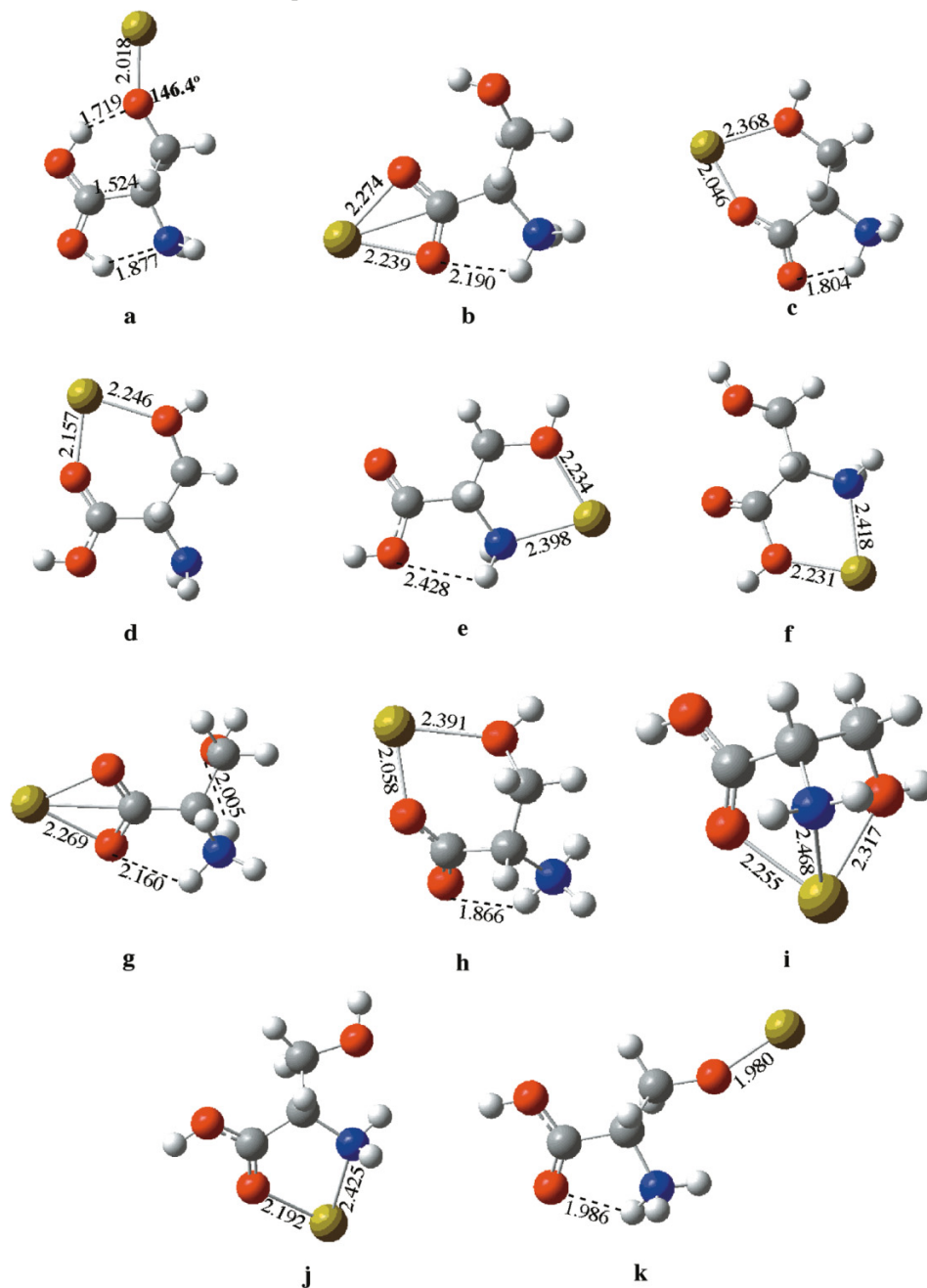


discussion of the conformations of serine is not the aim of this paper, some interesting features regarding their relative stabilities should be highlighted. Four conformers, N3, N5, N6, and N10, appear to be very close in energy, the maximum energy gap between them being about 3 kJ/mol. The least stable ones within the subset of the 15 more stable conformers are relatively close in energy, the energy gaps with respect to the global minimum varying from 6 to 19 kJ/mol. According to the work of Gong et al.,<sup>14</sup> the most stable conformer should be the structure N5 whereas from the calculations of Jarmelo et al.<sup>4</sup> N5 and N6 conformers are almost degenerate, the energy gap between them being 0.7 kJ/mol. However, it should be taken into account that Gong et al.<sup>14</sup> did not consider structure N6 in their survey and Jarmelo et al.<sup>4</sup> did not include the conformer N10 among the most stable tautomers.

The most important common characteristic of these conformers is the existence of several intramolecular hydrogen bonds (IMHB). Whereas in the conformers N3, N5, and N10 two IMHBs contribute to stabilizing these structures,

three IMHBs are responsible for the stability of the conformer N6. In the latter case, three out of the four of the serine's heteroatoms are involved in these IMHBs, either as HB-donors or as HB-acceptors (NH and OH groups). It can be also observed that the HB distances are in the range 1.90–1.92 Å when the nitrogen atom behaves as an HB-acceptor towards the OH group of the carboxylic moiety. When the HB donor is the OH alcoholic group, the bond length is longer (about 2.1 Å). The bond lengths of the IMHBs, in which the carboxylic group is the HB-acceptor, are in the range 2.113 Å (in N3) to 2.637 Å (in N6). Hence, one important question would be whether the interaction with the metal dication will affect significantly this network of IMHBs or not. Since serine presents different basic centers, many different adducts, resulting from the direct interaction with the metal dication, can be envisaged (see Figs. 2 and 3). Complexes **g** and **h** have their origin in conformer N6, complexes **j** and **k** are produced from conformer N5, the neutral form N10 yields complex **i**, and association to N3 yields complexes **a** and **b**. The other complexes are generated by the interaction of the dication with the remaining

**Fig. 2.** Optimized geometries of [serine-Ca]<sup>2+</sup> complexes. Some internuclear distances are shown in Å.



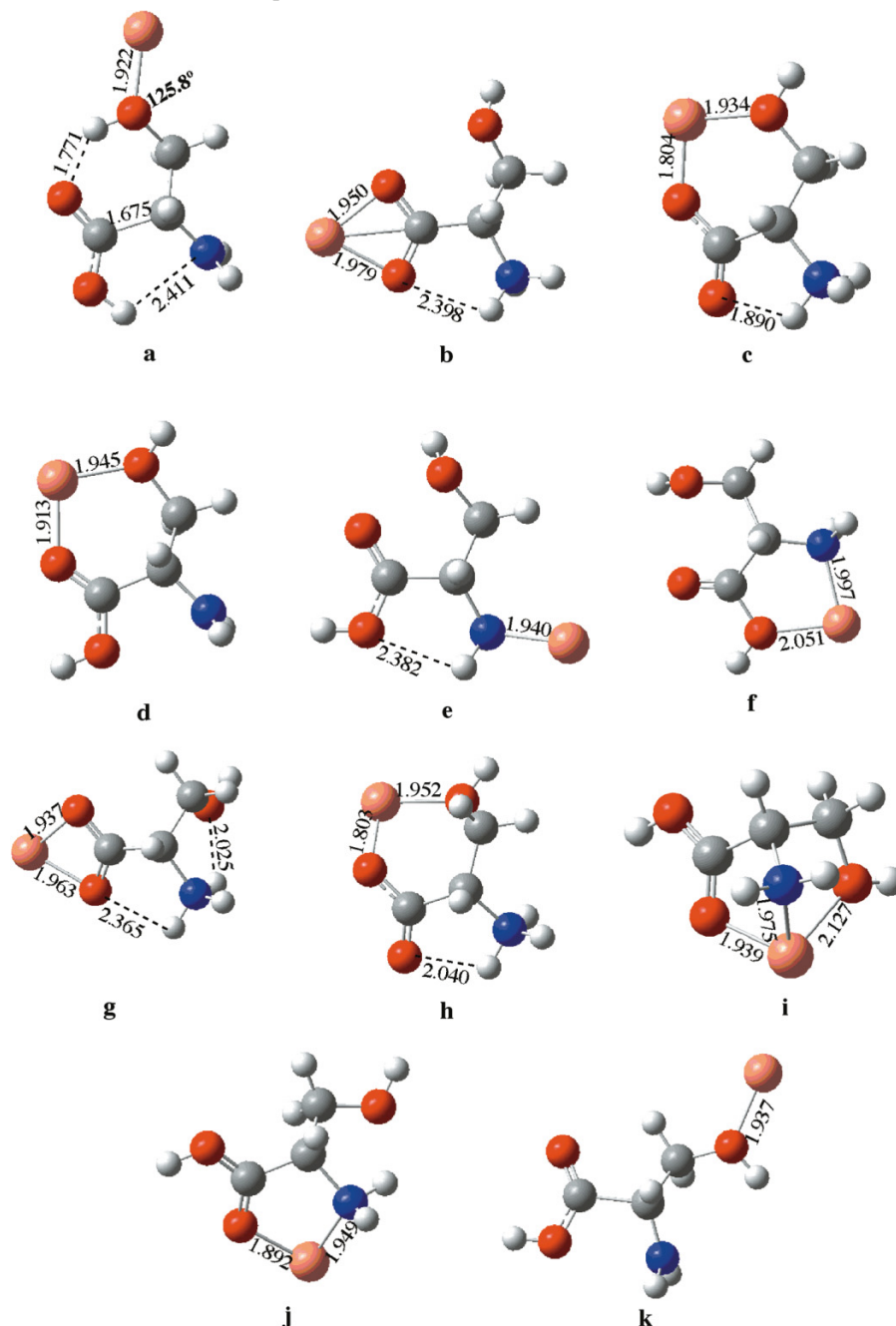
neutral conformers followed, in most of the cases, by an internal molecular reorganization.

The most stable complex (see Table 1), is structure **i** in which the metal coordinates to three of the most basic sites of the serine molecule. This interaction cleaves the intramolecular hydrogen bonds existing in the neutral form. The second most stable adduct is complex **g** where the metal is bisligated to the two oxygen atoms of the carboxylic acid moiety. Its relative energy with respect to the most stable complex **i** is about 19 and 18 kJ/mol for [serine-Ca]<sup>2+</sup> and [serine-Cu]<sup>2+</sup> complexes, respectively. It is worth noting that in complex **g** the interaction of the metal leads to a spontaneous proton transfer from the carboxylic group towards the amino group, so the complex can be considered

as the result of the association of the double charged metal ion to the zwitterionic form of serine. The same is true as far as complexes **b**, **c**, and **h** are concerned. This indicates that the association of the metal cation to serine involves a dramatic redistribution of electron density within the organic moiety, which significantly affects the strength and even the existence of the IMHBs. It is obvious, for instance, from Figs. 1–3 that the formation of the global minimum **i** implies the cleavage of the two IMHBs existing in the neutral N10 conformer. However there are some subtle differences in these electron density reorganizations when Ca<sup>2+</sup> and Cu<sup>2+</sup> complexes are compared with each other. This is apparent when the strengths of the N–H···O HBs in complexes **b**, **c**, **g**, and **h** for Ca<sup>2+</sup> containing complexes (see Fig. 2) are



**Fig. 3.** Optimized geometries of [serine-Cu]<sup>2+</sup> complexes. Some internuclear distances are shown in Å.



compared with the Cu<sup>2+</sup> analogues (see Fig. 3). The association of the metal dication to the CO<sub>2</sub> group of the zwitterionic form of serine is followed by a charge transfer, or a strong polarization, from this group towards the metal. Accordingly, the HB acceptor ability of the oxygen atom participating in the bond decreases because it is a poorer electron donor. However, this effect is clearly stronger in Cu<sup>2+</sup> than in Ca<sup>2+</sup> complexes, and the NH...O IMHBs are weaker in the former than in the latter, and therefore the bond lengths are systematically 0.2 Å longer. This is also mirrored in the topology of the electron density. As shown in Fig. 4 for the particular case of **g** complexes, whereas for the Ca<sup>2+</sup> containing system a bond critical point associated

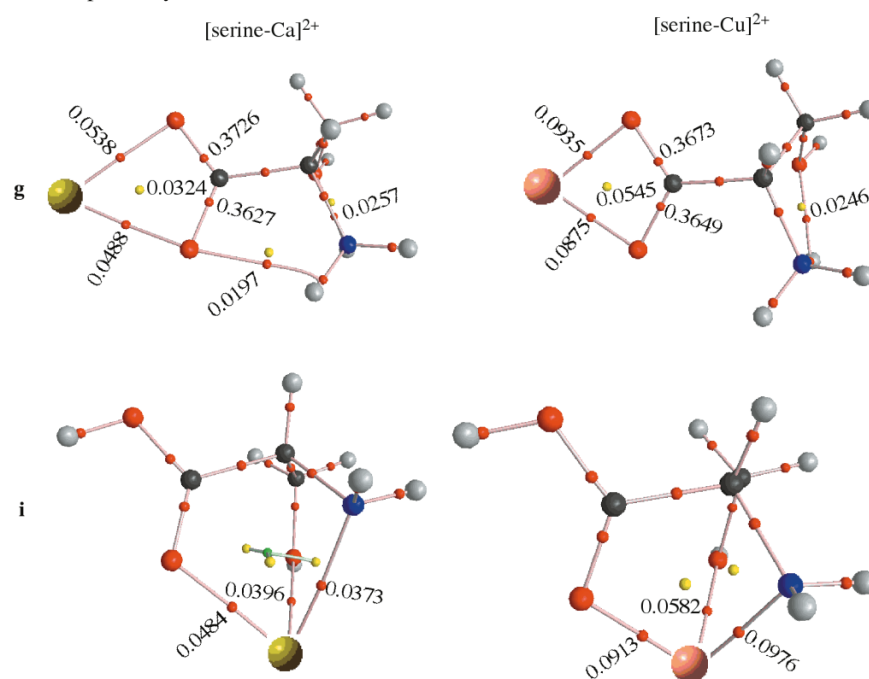
with the NH...O IMHB is found, such a BCP does not exist for the Cu<sup>2+</sup> containing analogue.

These results point to significant differences in the characteristics of the bonding depending on the nature of the metal dication. These differences are nicely reflected in the energy density maps of the global minima (see Fig. 5) which show that while the energy density between the metal and the organic moiety is positive in the case of Ca<sup>2+</sup> complexes, as it corresponds to an electrostatic interaction, for the Cu<sup>2+</sup> analogues it is negative, indicating that in this latter case the covalent character of the interaction is not at all negligible. Consistently, no covalent bonds between Ca and the serine basic centers are found in the NBO analysis, whereas the

**Table 1.** Relative energies  $\Delta E$  (kJ mol<sup>-1</sup>), enthalpies  $\Delta H(298)$  (kJ mol<sup>-1</sup>), and Gibbs energies  $\Delta G^\circ(298)$  (kJ mol<sup>-1</sup>) for neutral and complex structures included in this study.

	Neutral serine			Complex	[Serine-Ca] <sup>2+</sup>			[Serine-Cu] <sup>2+</sup>		
	$\Delta E$	$\Delta H(298)$	$\Delta G^\circ(298)$		$\Delta E$	$\Delta H(298)$	$\Delta G^\circ(298)$	$\Delta E$	$\Delta H(298)$	$\Delta G^\circ(298)$
N1	13.5	13.8	9.4	<b>a</b>	166.8	167.2	162.3	87.9	89.0	76.4
N2	6.9	7.0	5.7	<b>b</b>	67.7	68.1	57.7	50.2	50.5	40.7
N3	<b>0.8</b>	<b>0.8</b>	<b>2.5</b>	<b>c</b>	56.6	56.8	51.7	44.3	44.5	39.0
N4	10.4	10.6	9.1	<b>d</b>	86.3	86.9	79.8	27.1	27.9	19.6
N5	<b>0.1</b>	<b>0.2</b>	<b>-1.5</b>	<b>e</b>	131.2	131.5	124.2	108.6	109.6	101.4
N6	<b>0.0</b>	<b>0.0</b>	<b>0.0</b>	<b>f</b>	193.7	194.4	186.6	108.5	109.2	101.7
N7	9.6	9.8	7.9	<b>g</b>	<b>18.9</b>	<b>18.9</b>	<b>13.1</b>	<b>17.9</b>	<b>18.0</b>	<b>11.3</b>
N8	13.2	13.5	10.1	<b>h</b>	67.8	67.9	63.0	61.3	61.4	56.6
N9	6.1	6.1	6.1	<b>i</b>	<b>0.0</b>	<b>0.0</b>	<b>0.0</b>	<b>0.0</b>	<b>0.0</b>	<b>0.0</b>
N10	2.9	3.0	2.5	<b>j</b>	85.8	86.2	79.4	43.2	43.5	37.8
N11	18.9	19.0	18.8	<b>k</b>	103.3	103.5	94.0	56.8	57.8	42.8

**Fig. 4.** Molecular graphs of structures **i** and **g** of [serine-M]<sup>2+</sup> (M = Ca, Cu) complexes. Red dots and yellow dots represent bond critical points and ring critical points, respectively. Electron densities are in au.

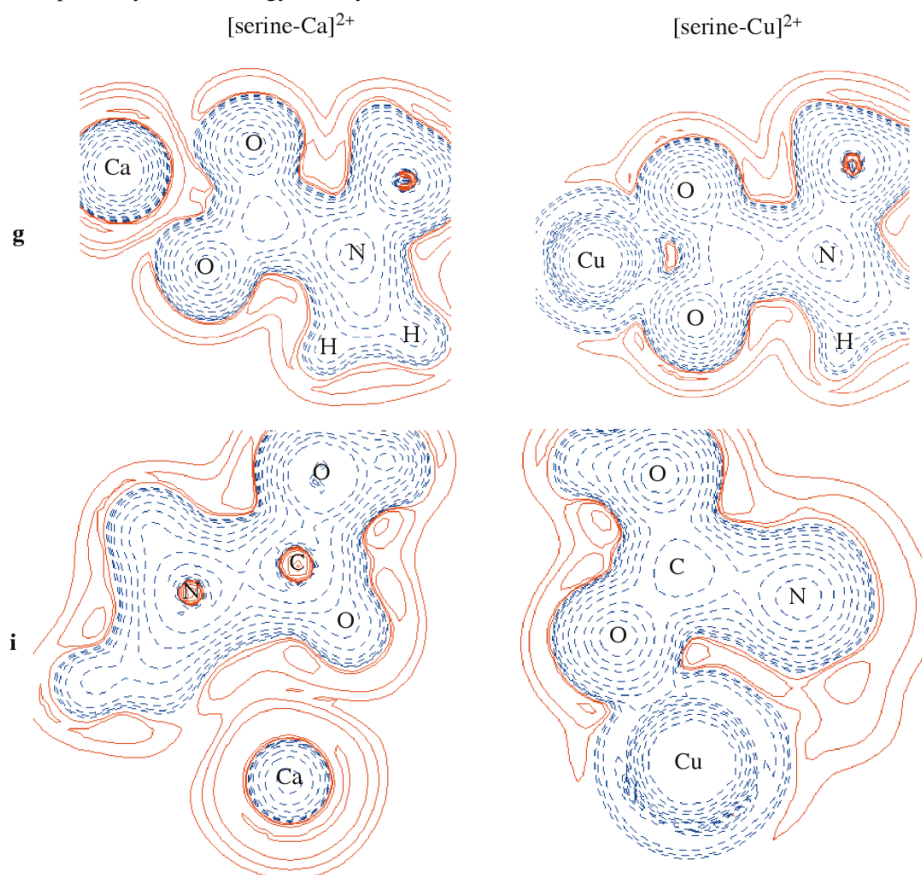


Cu-O<sub>C</sub> and N-Cu covalent bonds are found, with a very large participation of the p orbitals of O<sub>C</sub> (97%) and N (87%) and a small contribution from the 4s in Cu. Consistently, the bond order (BO) of the O<sub>C</sub>-M, O<sub>A</sub>-M, and N-M (M = Ca, Cu) linkages are much smaller for the Ca<sup>2+</sup> complex (0.0863, 0.0617, and 0.0826, respectively) than for the Cu<sup>2+</sup> containing analogue (0.091, 0.2113, and 0.2656, respectively). Besides the N-Cu and O-Cu bonds indicated above, a second-order NBO perturbation analysis shows also a strong charge donation from one of the lone pair of the alcoholic oxygen to the 4s empty orbital of copper, proving that in the global minimum, Cu is truly tricoordinated. The partially covalent character of the interactions with Cu is also reflected in the electron density at the corresponding BCPs, which are about twice as large as those calculated for the corresponding Ca<sup>2+</sup> complex. Thus, not surprisingly, the

calculated binding energy of Cu<sup>2+</sup> to serine (1054 kJ/mol) is about twice the binding energy estimated for Ca<sup>2+</sup> (567 kJ/mol).

The significant differences in the reorganization of the electron density of the serine, when interacting with Cu<sup>2+</sup> and Ca<sup>2+</sup>, have their origin in the huge difference between the recombination energy for both dications (20.29 eV for Cu<sup>2+</sup> but only 12.03 eV for Ca<sup>2+</sup>).<sup>47</sup> Hence, while the association of Cu<sup>2+</sup> with serine is followed by a partial oxidation of the amino acid as has been found in the interaction of Zn<sup>2+</sup> with thymine<sup>32</sup> and thio-oxazolidine,<sup>48</sup> no oxidation is observed upon Ca<sup>2+</sup> interaction. In fact, the NBO natural charge indicates that in complex **i** of [serine-Cu]<sup>2+</sup>, the metal bears a net positive charge of about 1.48 *e* while for the [serine-Ca]<sup>2+</sup> the net charge on the metal is about 1.88 *e*. At the same time, the spin density, which in the reactants

**Fig. 5.** Energy density contour maps for the [serine-Ca]<sup>2+</sup> and [serine-Cu]<sup>2+</sup> complexes. Dashed blue lines and solid red lines denote negative and positive values, respectively, of the energy density.



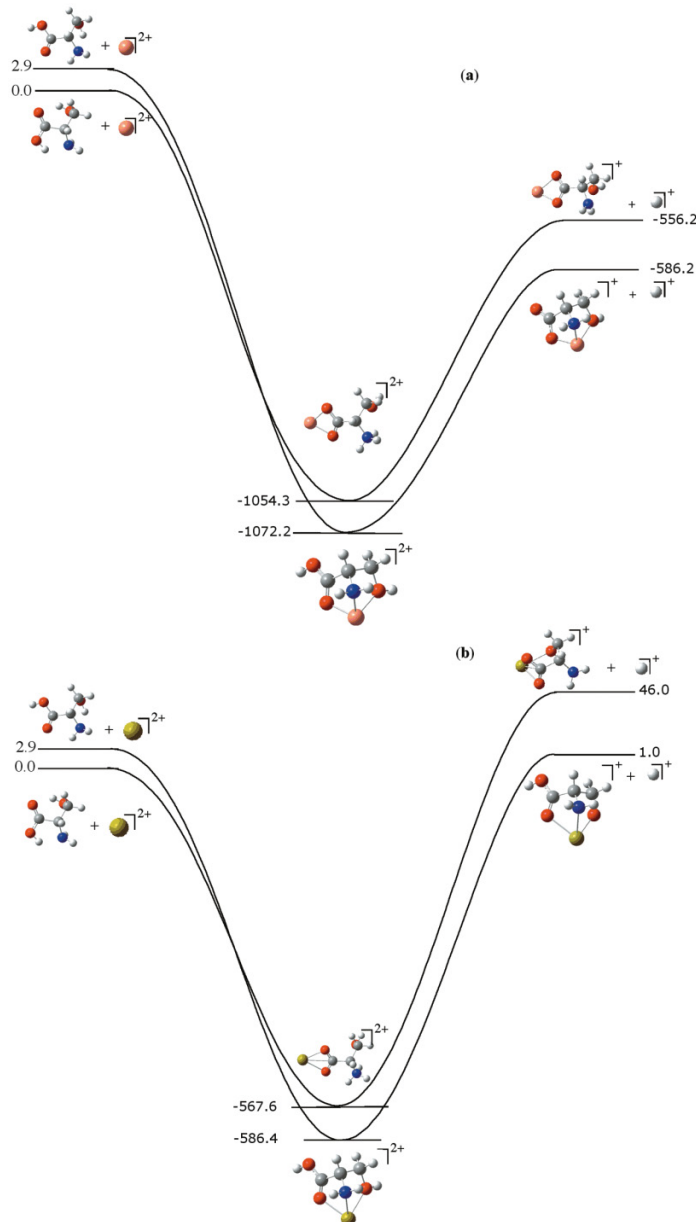
is located exclusively on Cu<sup>2+</sup> in the complex is almost equally shared by the metal (0.58) and the serine moiety (0.42). Similar results are found for complex **g**. This ability of Cu<sup>2+</sup> to oxidize the base was previously reported in the literature for some aminoacids<sup>49,50</sup> and for urea and thiourea<sup>19</sup> as well as for [uracil-Cu]<sup>2+</sup>, [thiouracil-Cu]<sup>2+</sup>, and [thymine-Cu]<sup>2+</sup> complexes.<sup>32,51</sup> However, in all these cases a complete oxidation of the base was actually found, whereas for serine only a partial oxidation seems to take place. Taking into account that the ionization energy of serine is not significantly different from that of urea or uracil, in principle a complete oxidation of the base should be expected. It is worth noting, however, that the degree of oxidation undergone by serine is different depending on the coordination of the metal. Hence, for monocoordinate complexes, such as structure **a**, the spin density on the copper atom is close to zero, indicating that the oxidation of the base has been practically complete. Conversely, in di- and tricoordinated complexes like structures **g** and **i**, the spin density is shared between the metal and serine, likely indicating that di- and tricoordination stabilize the Cu<sup>2+</sup> oxidation state more. Similar findings were reported before for the complexes between Cu<sup>2+</sup> and the oxime analogue of glycine.<sup>52</sup> Conversely, the behavior of calcium towards serine is quite similar to that exhibited towards uracil,<sup>53</sup> thiouracils,<sup>53</sup> urea, and thiourea.<sup>19</sup>

The partial oxidation of the serine upon Cu<sup>2+</sup> interaction will have an important effect on the intrinsic acidity of the

organic moiety, similar to that found when the base is uracil, and which results in a spontaneous deprotonation of the system. Hence, only [Cu-(B-H)]<sup>+</sup> singly charged species are observed in the gas phase.<sup>20,54</sup> This is not the case, however, when dealing with alkaline-earth dications like Ca<sup>2+</sup>, where [Ca-B]<sup>2+</sup> are easily detected.<sup>21,22,53</sup> In the case of serine, as shown in Fig. 6, the deprotonation of the two most stable [serine-Cu]<sup>2+</sup> complexes are thermodynamically favorable. In contrast, for the global minimum of the [serine-Ca]<sup>2+</sup> complexes, proton detachment is an almost thermoneutral process, and it becomes clearly endothermic for complex **g**.

There are two other features which should be highlighted in Figs. 6a and 6b. The first one is that, independently of the metal dication, the [serine-M]<sup>2+</sup> (M = Ca, Cu) global minimum is the result of the association of the metal dication to the second more stable tautomer of serine, whereas the most stable tautomer of serine leads to complexes which are significantly higher in energy (18.8 kJ/mol, for Ca<sup>2+</sup> and 17.9 kJ/mol for Cu<sup>2+</sup>). The second important feature is that the formation of the [serine-Ca]<sup>2+</sup> global minimum **i** implies a significant acidity enhancement of the alcoholic OH group of serine, so the proton is preferentially lost from this group, whereas in complex **g**, the most acidic site is the NH<sub>3</sub> group formed by the spontaneous proton transfer discussed in previous sections. Also interestingly, the deprotonation of complexes **i** also yields the most stable anion, although the energy gap between the deprotonated forms of complexes **i**

**Fig. 6.** Energy profile for the formation and deprotonation of the two most stable isomers of  $[\text{serine-M}]^{2+}$  ( $M = \text{Ca}, \text{Cu}$ ) complexes; (a)  $M=\text{Cu}$ ; (b)  $M=\text{Ca}$ . Values are in kJ/mol.



and **g** is slightly larger than that between the complexes **i** and **g** themselves.

## Conclusions

The association of  $\text{Ca}^{2+}$  and  $\text{Cu}^{2+}$  to serine implies a drastic electron density reorganization within the aminoacid, which leads to significant changes in the number and strength of the IMHBs present in the neutral serine tautomers, and in some particular cases to a proton transfer from the carboxylic OH group towards the amino group. Accordingly, some of the more stable  $[\text{serine-M}]^{2+}$  complexes can be viewed as the result of the interaction of the zwitterionic form of serine with the doubly charged metal ion.

Whereas the interactions between  $\text{Ca}^{2+}$  and serine are es-

entially electrostatic, those between  $\text{Cu}^{2+}$  and serine have a non-negligible covalent character, reflected in larger electron densities at the BCPs between the metal and the base, in the negative values of the electron density between the two interacting systems, and in much larger  $\text{Cu}^{2+}$  than  $\text{Ca}^{2+}$  binding energies. More importantly, the interaction with  $\text{Cu}^{2+}$  is followed by a partial oxidation of the base, which is not observed when the metal ion is  $\text{Ca}^{2+}$ .

The main consequence is that in  $\text{Cu}^{2+}$  complexes acidity of the serine moiety is significantly enhanced, thus strongly favoring the deprotonation of the  $[\text{serine-Cu}]^{2+}$  complexes. This is not the case for  $\text{Ca}^{2+}$  complexes, because the recombination energy of this metal dication is almost half that of  $\text{Cu}^{2+}$ . Thus,  $[\text{serine-Ca}]^{2+}$  complexes, like those formed by urea, thiourea, selenourea, or glycine, should be detected in



the gas phase. Conversely, the complexes with  $\text{Cu}^{2+}$  should deprotonate spontaneously and therefore only  $[(\text{serine-H})-\text{Cu}]^+$  monocations should be experimentally accessible.

## Acknowledgements

This work has been supported by the DGI Project No. CTQ2009–13129-CO2–01, by the Project MADRISOLAR, Ref.: S-0505/PPQ/0225 of the Comunidad Autónoma de Madrid, by Consolider on Molecular Nanoscience CSD2007–00010, and by the European Cooperation in Science and Technology (COST) Action COST CM0702. A generous allocation of computing time at the Centro de Computación Científica (CCC) of the Universidad Autónoma de Madrid (UAM) is also acknowledged. We thank also one of our reviewers for pointing out that the degree of oxidation of the base depends on the coordination with the metal.

## References

- (1) Lesser, G. J.; Rose, G. D. *Proteins* **1990**, *8* (1), 6. doi:10.1002/prot.340080104. PMID:2217164.
- (2) Bojesen, G.; Breindahl, T. J. *Chem. Soc., Perkin Trans. 2* **1994**, (5), 1029. doi:10.1039/p29940001029.
- (3) Maksic, Z. B.; Kovacevic, B. *Chem. Phys. Lett.* **1999**, *307* (5-6), 497. doi:10.1016/S0009-2614(99)00535-7.
- (4) Jarmelo, S.; Lapinski, L.; Nowak, M. J.; Carey, P. R.; Fausto, R. *J. Phys. Chem. A* **2005**, *109* (25), 5689. doi:10.1021/jp0511202. PMID:16833902.
- (5) Jarmelo, S.; Reva, I.; Carey, P. R.; Fausto, R. *Vib. Spectrosc.* **2007**, *43* (2), 395. doi:10.1016/j.vibspec.2006.04.025.
- (6) Jarmelo, S.; Reva, I.; Rozenberg, M.; Carey, P. R.; Fausto, R. *Vib. Spectrosc.* **2006**, *41* (1), 73. doi:10.1016/j.vibspec.2005.12.013.
- (7) Badelin, V. G.; Mezhevoi, I. N. *J. Solution Chem.* **2009**, *38* (9), 1217. doi:10.1007/s10953-009-9441-0.
- (8) Chang, J.; Lenhoff, A. M.; Sandler, S. I. *J. Phys. Chem. B* **2007**, *111* (8), 2098. doi:10.1021/jp0620163. PMID:17269814.
- (9) Mezhevoi, I. N.; Badelin, V. G. *Russ. J. Phys. Chem. A* **2009**, *83*, 388. doi:10.1134/S003602440903011X.
- (10) Upadhyay, D. M.; Rai, A. K.; Rai, D. K.; Singh, A. N.; Kumar, A. *Biomolec. Spectr.* **2007**, *66* (4-5), 909. doi:10.1016/j.saa.2006.04.030.
- (11) Frey, M. N.; Lehmann, M. S.; Koetzle, T. F.; Hamilton, W. C. *Acta Crystallogr. B* **1973**, *B29*, 876. doi:10.1107/S0567740873003481.
- (12) Kistenmacher, T. J.; Rand, G. A.; Marsh, R. E. *Acta Crystallogr. B* **1974**, *B30*, 2573. doi:10.1107/S0567740874007618.
- (13) Jarmelo, S.; Fausto, R. *J. Mol. Struct.* **2006**, *786* (2-3), 175. doi:10.1016/j.molstruc.2005.09.021.
- (14) Gong, X.; Zhou, Z.; Du, D.; Dong, X.; Liu, S. *Int. J. Quantum Chem.* **2005**, *103* (1), 105. doi:10.1002/qua.20471.
- (15) Ferreira-Cravo, M.; Ventura-Lima, J.; Sandrini, J. Z.; Amado, L. L.; Geracitano, L. A.; Rebelo, M.; Bianchini, A.; Monserrat, J. M. *Ecotoxicol. Environ. Saf.* **2009**, *72* (2), 388. doi:10.1016/j.ecoenv.2008.07.003. PMID:18692896.
- (16) Land, E. J.; Ramsden, C. A.; Riley, P. A.; Stratford, M. R. L. *Tohoku J. Exp. Med.* **2008**, *216* (3), 231. doi:10.1620/tjem.216.231. PMID:18987457.
- (17) Ozcelik, D.; Uzun, H. *Biol. Trace Elem. Res.* **2009**, *127* (1), 45. doi:10.1007/s12011-008-8219-3. PMID:18784908.
- (18) Lamsabhi, A. M.; Yáñez, M.; Salpin, J. Y.; Tortajada, J. *Gas-phase Chemistry of Organocopper Compounds*. In *The Chemistry of Functional Groups*; Rappoport, Z., Marek, I., Eds.; John Wiley & Sons, 2009.
- (19) Trujillo, C.; Lamsabhi, A. M.; Mó, O.; Yáñez, M. *Phys. Chem. Chem. Phys.* **2008**, *10* (22), 3229. doi:10.1039/b802907e. PMID:18500399.
- (20) Lamsabhi, A. M.; Alcamí, M.; Mó, O.; Yáñez, M.; Tortajada, J.; Salpin, J. Y. *ChemPhysChem* **2007**, *8* (1), 181. doi:10.1002/cphc.200600399. PMID:17154324.
- (21) Corral, I.; Mó, O.; Yáñez, M.; Salpin, J. Y.; Tortajada, J.; Moran, D.; Radom, L. *Chem. Eur. J.* **2006**, *12* (26), 6787. doi:10.1002/chem.200600127.
- (22) Corral, I.; Mó, O.; Yáñez, M.; Salpin, J. Y.; Tortajada, J.; Radom, L. *J. Phys. Chem. A* **2004**, *108* (46), 10080. doi:10.1021/jp046624z.
- (23) Trujillo, C.; Mó, O.; Yáñez, M.; Salpin, J. Y.; Tortajada, J. *ChemPhysChem* **2007**, *8* (9), 1330. doi:10.1002/cphc.200700113. PMID:17492701.
- (24) Frisch, M. J.; Trucks, G. W.; Schlegel, H. B.; Scuseria, G. E.; Robb, M. A.; Cheeseman, J. R.; Zakrzewski, V. G.; Montgomery, J. A. J.; Stratmann, R. E.; Burant, J. C.; Dapprich, S.; Millam, J. M.; Daniels, A. D.; Kudin, K. N.; Strain, M. C.; Farkas, O.; Tomasi, J.; Barone, V.; Cossi, M.; Cammi, R.; Mennucci, B.; Pomelli, C.; Adamo, C.; Clifford, S.; Ochterski, J.; Petersson, G. A.; Ayala, P. Y.; Cui, Q.; Morokuma, K.; Malick, D. K.; Rabuck, A. D.; Raghavachari, K.; Foresman, J. B.; Cioslowski, J.; Ortiz, J. V.; Stefanov, B. B.; Liu, G.; Liashenko, A.; Piskorz, P.; Komaromi, I.; Gomperts, R.; Martin, R. L.; Fox, D. J.; Keith, T.; Al-Laham, M. A.; Peng, C. Y.; Nanayakkara, A.; Gonzalez, C.; Challacombe, M.; Gill, P. M. W.; Johnson, B.; Chen, W.; Wong, M. W.; Andres, J. L.; Head-Gordon, M.; Replogle, E. S.; Pople, J. A. *Gaussian03*, Revised E.01 ed.; Gaussian, Inc.: Wallingford, CT, 2004.
- (25) Becke, A. D. *J. Chem. Phys.* **1993**, *98* (7), 5648. doi:10.1063/1.464913.
- (26) Lee, C.; Yang, W.; Parr, R. G. *Phys. Rev. B* **1988**, *37* (2), 785. doi:10.1103/PhysRevB.37.785.
- (27) Scott, A. P.; Radom, L. *J. Phys. Chem.* **1996**, *100* (41), 16502. doi:10.1021/jp960976r.
- (28) Wachters, A. J. H. *J. Chem. Phys.* **1970**, *52* (3), 1033. doi:10.1063/1.1673095.
- (29) Hay, P. J. *J. Chem. Phys.* **1977**, *66* (10), 4377. doi:10.1063/1.433731.
- (30) Luna, A.; Amekraz, B.; Morizur, J.-P.; Tortajada, J.; Mó, O.; Yáñez, M. *J. Phys. Chem. A* **1997**, *101* (33), 5931. doi:10.1021/jp9710300.
- (31) Belcastro, M.; Marino, T.; Russo, N.; Toscano, M. *J. Mass Spectrom.* **2005**, *40* (3), 300. doi:10.1002/jms.755. PMID:15685654.
- (32) Rincón, E.; Yáñez, M.; Toro-Labbé, A.; Mó, O. *Phys. Chem. Chem. Phys.* **2007**, *9* (20), 2531. doi:10.1039/b618050g. PMID:17508085.
- (33) Hertwig, R. H.; Koch, W.; Schroder, D.; Schwarz, H.; Hrusak, J.; Schwerdtfeger, P. *J. Phys. Chem.* **1996**, *100* (30), 12253. doi:10.1021/jp953064i.
- (34) Reed, A.; Weinstock, R. B.; Weinhold, F. *J. Chem. Phys.* **1985**, *83* (2), 735. doi:10.1063/1.449486.
- (35) Bader, R. F. W. *Atoms In Molecules: A Quantum Theory*; Clarendon Press, Oxford Univ.: Oxford, 1990.
- (36) Matta, C. F.; Boyd, R. J. *The Quantum Theory of Atoms in Molecules*; Wiley-VCH Verlag: Weinheim, Germany, 2007.
- (37) Stepanian, S. G.; Reva, I. D.; Radchenko, E. D.; Rosado, M.

- T. S.; Duarte, M.; Fausto, R.; Adamowicz, L. *J. Phys. Chem. A* **1998**, *102* (6), 1041. doi:10.1021/jp973397a.
- (38) Gómez-Zavaglia, A.; Fausto, R. *Vib. Spectrosc.* **2003**, *33* (1-2), 105. doi:10.1016/S0924-2031(03)00095-X.
- (39) Iijima, K.; Beagley, B. *J. Mol. Struct.* **1991**, *248* (1-2), 133. doi:10.1016/0022-2860(91)85008-Q.
- (40) Iijima, K.; Tanaka, K.; Onuma, S. *J. Mol. Struct.* **1991**, *246* (3-4), 257. doi:10.1016/0022-2860(91)80132-N.
- (41) Rosado, M. T. S.; Duarte, M. L. R. S.; Fausto, R. *J. Mol. Struct.* **1997**, *410-411*, 343. doi:10.1016/S0022-2860(96)09695-0.
- (42) Stepanian, S. G.; Reva, I. D.; Radchenko, E. D.; Adamowicz, L. *J. Phys. Chem. A* **2001**, *105* (47), 10664. doi:10.1021/jp011708i.
- (43) Suenram, R. D.; Lovas, F. J. *J. Mol. Spectrosc.* **1978**, *72* (3), 372. doi:10.1016/0022-2852(78)90137-6.
- (44) Suenram, R. D.; Lovas, F. J. *J. Am. Chem. Soc.* **1980**, *102* (24), 7180. doi:10.1021/ja00544a002.
- (45) Hurtado, M.; Mó, O.; Yáñez, M. *Can. J. Chem.* This issue. doi:10.1139/V10-034.
- (46) Gronert, S.; O'Hair, R. A. J. *J. Am. Chem. Soc.* **1995**, *117* (7), 2071. doi:10.1021/ja00112a022.
- (47) The National Institute of Standards and Technology (NIST) Chemistry Webbook. [www.nist.gov/index.html](http://www.nist.gov/index.html) (accessed December, 2009).
- (48) Safi, Z. S.; Lamsabhi, A. M. *J. Phys. Org. Chem.* **2010**, in press. doi:10.1002/poc.1648.
- (49) Bertrán, J.; Rodríguez-Santiago, L.; Sodupe, M. *J. Phys. Chem. B* **1999**, *103* (12), 2310. doi:10.1021/jp984534m.
- (50) Rimola, A.; Rodríguez-Santiago, L.; Sodupe, M. *J. Phys. Chem. B* **2006**, *110*, 24189. doi:10.1021/jp064957l.
- (51) Lamsabhi, A. M.; Alcamí, M.; Mó, O.; Yáñez, M.; Tortajada, J. *ChemPhysChem* **2004**, *5* (12), 1871. doi:10.1002/cphc.200400208. PMID:15648135.
- (52) Georgieva, I.; Trendafilova, N.; Rodríguez-Santiago, L.; Sodupe, M. *J. Phys. Chem. A* **2005**, *109* (25), 5668. doi:10.1021/jp050626h. PMID:16833899.
- (53) Trujillo, C.; Lamsabhi, A. M.; Mó, O.; Yáñez, M.; Salpin, J. Y. *Org. Biomol. Chem.* **2008**, *6* (20), 3695. doi:10.1039/b810418b. PMID:18843399.
- (54) Lamsabhi, A. M.; Alcamí, M.; Mó, O.; Yáñez, M.; Tortajada, J. *J. Phys. Chem. A* **2006**, *110* (5), 1943. doi:10.1021/jp055163u. PMID:16451028.

# Ab initio calculations on $C_6H_6 \cdots (HF)_n$ clusters — $X-H \cdots \pi$ hydrogen bond

Sławomir J. Grabowski and Jesus M. Ugalde

**Abstract:** MP2/6–311++G(d,p) calculations on  $C_6H_6 \cdots (HF)_n$  clusters were performed and full optimizations were carried out for systems containing up to four HF molecules ( $n = 4$ ) and calculations on the systems of  $C_{6v}$  symmetry were carried out for up to six HF molecules ( $n = 6$ ). Cooperativity effects were analyzed for these molecular aggregates. It was found that  $F-H \cdots \pi$  and  $F-H \cdots F$  hydrogen bonds exist for these complexes and those interactions are enhanced as the number of HF molecules increases. The cooperativity effects cause numerous changes in geometrical, energetic, and topological parameters, the latter ones derived from the quantum theory of atoms in molecules. Various correlations between the analyzed parameters are presented. There are meaningful differences between the molecular graphs for the fully optimized complexes and those for the linear complexes of  $C_{6v}$  symmetry (for the latter, the linear chain of HF molecules is attached to a benzene molecule acting as the Lewis base). For the linear complexes, unique bond paths connect the H-attractor of the HF molecule and the ring critical point of the benzene molecule.

**Key words:** hydrogen bonding, cooperativity effect, quantum theory of atoms in molecules,  $H \cdots \pi$  interaction, benzene as a proton acceptor, molecular graphs, critical points.

**Résumé :** On a effectué des calculs MP2/6–311++G(d,p) sur des agrégats de  $C_6H_6 \cdots (HF)_n$  et on a réalisé des optimisations totales pour les systèmes comportant jusqu'à quatre molécules de HF ( $n = 4$ ) alors que les calculs sur les systèmes de symétrie  $C_{6v}$  ont pu être effectués jusqu'à six molécules de HF ( $n = 6$ ). On a analysé les effets coopératifs de tels agrégats moléculaires. On a trouvé qu'il existe des liaisons hydrogènes  $F-H \cdots \pi$  et  $F-H \cdots F$  dans ces complexes et que ces interactions sont renforcées lorsque le nombre de molécules de HF augmente. Les effets coopératifs provoquent de nombreux changements dans les paramètres géométriques, énergétiques et topologiques qui ont été obtenus par la théorie quantique des atomes dans les molécules. On présente diverses corrélations entre les paramètres analysés. Il existe des différences significatives entre les graphiques moléculaires des complexes complètement optimisés et les complexes linéaires de symétrie  $C_{6v}$  (dans ces derniers cas, la chaîne linéaire de molécules HF est attachée à la molécule de benzène qui agit comme base de Lewis). Pour les complexes linéaires, il existe des voies uniques de liaison qui unissent l'attracteur-H de la molécule HF et le point critique du noyau de la molécule de benzène.

**Mots-clés :** liaison hydrogène, effet coopératif, théorie quantique des atomes dans les molécules, interaction  $H \cdots \pi$ , benzène comme accepteur de proton, graphiques moléculaires, points critiques.

## Introduction

There are numerous studies on cooperativity effects for hydrogen bonded systems.<sup>1–3</sup> There are also various definitions of this effect, each somewhat different from the other. However, the cooperativity effect is often understood as the enhancement of the hydrogen bonding between two species if a third one is attached to that system.<sup>4</sup> For most of the systems analyzed, this enhancement was observed but there are also studies where an opposite effect, the weakening of the hydrogen bond, was detected. For example, some years ago the cooperativity was investigated in  $C-H \cdots O$  and  $O-H \cdots O$  hydrogen bonds.<sup>5</sup> The authors showed that, in the case of  $O-H \cdots O$  interactions, this effect enhances the H

bond and leads to the elongation of the O–H proton-donating bond and to the red shift of the corresponding stretching mode. In the case of  $C-H \cdots O$  hydrogen bonds, the shortening of C–H bonds and the blue-shifting were detected in  $(H_2CO)_n$  and  $(HFCO)_n$  aggregates.

One can mention numerous studies on cooperativity effects. The chain of species connected by OH bonds is an example.<sup>6</sup> Another one concerns  $H_3N \cdots HF$  and  $H_3N \cdots HF \cdots HF$  complexes, which were investigated with the use of experimental microwave and theoretical ab initio techniques.<sup>7</sup> It was observed that the addition of the next HF molecule to the  $H_3N \cdots HF$  complex leads to the shortening of the  $N \cdots H$  hydrogen bond by 0.21(6) Å. Hence the cooperativity effect exists here, because the H–F molecule participates concert-

Received 14 December 2009. Accepted 18 February 2010. Published on the NRC Research Press Web site at canjchem.nrc.ca on 21 May 2010.

*This article is part of a Special Issue dedicated to Professor R. J. Boyd.*

**S.J. Grabowski.**<sup>1</sup> Kimika Fakultatea, Euskal Herriko Unibertsitatea and Donostia International Physics Center (DIPC), P.K. 1072, 20080 Donostia, Euskadi, Spain; IKERBASQUE, Basque Foundation for Science, 48011, Bilbao, Spain.

**J.M. Ugalde.** Kimika Fakultatea, Euskal Herriko Unibertsitatea and Donostia International Physics Center (DIPC), P.K. 1072, 20080 Donostia, Euskadi, Spain.

<sup>1</sup>Corresponding author (e-mail: s.grabowski@ikerbasque.org).

edly as a donor and as an acceptor. Numerous other studies on cooperativity effects may be mentioned; such effects were found in two-dimensional cyclic networks containing three-centered hydrogen bond interactions,<sup>8</sup> in amide hydrogen-bonding chains,<sup>9</sup> in intramolecular bifurcated hydrogen bonds,<sup>10</sup> and in homo (HCN)<sub>n</sub> and hetero (HCN)<sub>n</sub>...HF chains.<sup>11,12</sup>

The decomposition of the interaction energy was performed for H<sub>2</sub>C=O...(H-F)<sub>n</sub> clusters (*n* up to 9).<sup>13</sup> It was found that, for a large number of hydrogen fluoride molecules, there are shorter and stronger F-H...O hydrogen bonds and that the ratio of delocalization and electrostatic attractive interaction energy terms increases. It is worth mentioning too that the delocalization energy is often attributed to the covalency of the hydrogen bond;<sup>14,15</sup> thus, the partially covalent character is manifested for H<sub>2</sub>C=O...(H-F)<sub>n</sub> clusters for the greater number of HF molecules. Similar clusters, H<sub>2</sub>C=O...(Cl-F)<sub>n</sub> aggregates, were calculated and the cooperativity effect in F-Cl...O and F-Cl...F halogen bonds was analyzed.<sup>16</sup> One can see that cooperativity is observed not only for hydrogen bonds but also for other types of interactions. There is a very recent study on cooperativity in multiple weak bonds.<sup>17</sup> All combinations of five weak bonds: hydrogen bonds, dihydrogen bonds, hydric bonds, halogen bonds, and ion- $\pi$ -electron interactions were analyzed<sup>17</sup> using MP2/aug-cc-pVTZ level results and quantum theory of atoms in molecules (QTAIM).<sup>18</sup>

Another problem concerns the interactions often classified as hydrogen bonds where  $\pi$ -electrons act as the proton acceptor; these are usually designated as X-H... $\pi$  (or XH/ $\pi$ ).<sup>19</sup> Even the CH/ $\pi$  interactions were analyzed in crystal structures and using various methods, both theoretical as well as experimental.<sup>20,21</sup> A question arises whether or not such interactions are enhanced by cooperativity effects. The theoretical analysis of benzene-(H<sub>2</sub>O)<sub>n</sub> (*n* = 1–3) clusters is an early example.<sup>22</sup> The cooperativity phenomenon has not been considered for the latter species. However it has been found that (H<sub>2</sub>O)<sub>n</sub> clusters are “ $\pi$ -hydrogen bonded” (O-H... $\pi$  interaction) to the benzene ring, the strength of such interaction being greatest for C<sub>6</sub>H<sub>6</sub>-(H<sub>2</sub>O)<sub>2</sub>. Thus, there is enhancement of O-H... $\pi$  hydrogen bonding when the next water molecule is incorporated into the C<sub>6</sub>H<sub>6</sub>-H<sub>2</sub>O system. In the case of the C<sub>6</sub>H<sub>6</sub>-(H<sub>2</sub>O)<sub>3</sub> cluster, the O-H... $\pi$  interaction is weaker, likely owing to the strong cooperativity among the three water molecules forming the cyclic structure. The complexes of water with ethene, propene, and trans-2-butene have been studied recently.<sup>23</sup> The ab initio MP2/6-311++(2d,2p) calculations have been performed on these systems where  $\pi$ -electrons of the above-mentioned hydrocarbons act as the proton acceptor while the water molecule is the proton-donating moiety; hence, the O-H... $\pi$  interactions exist. In this study, the other O-H...O hydrogen bonds were also analyzed, since for the complexes with the O-H... $\pi$  hydrogen bond, the next water molecules were added. Additionally NBO analysis was performed to analyze intermolecular  $\pi$ (C=C)  $\rightarrow$   $\sigma^*$ (O-H) charge-transfer interactions as well as those for  $n$ (O)  $\rightarrow$   $\sigma^*$ (O-H). The other B3LYP/6-311++G(d,p) calculations for the C<sub>2</sub>H<sub>2</sub>...HF and C<sub>2</sub>H<sub>2</sub>...(HF)<sub>2</sub> complexes were performed and the F-H... $\pi$  and F-H...F interactions were characterized.<sup>24</sup> Very recently, similar systems C<sub>2</sub>H<sub>2</sub>...(HF)<sub>n</sub> and C<sub>2</sub>H<sub>4</sub>...(HF)<sub>n</sub> (*n* up to 4) were considered and MP2/6-311++G(d,p)

calculations were carried out to analyze cooperativity effects.<sup>25</sup> Thus, generally, at least a few systems were considered with the aim of showing whether cooperativity effects might enhance the X-H... $\pi$  interactions. For most of the cases mentioned here, such enhancement is observed if the number of proton-donating molecules attached to the Lewis base containing  $\pi$ -electrons increases.

The goal of this study is to analyze the cooperativity effects for the systems where the benzene molecule acts as the proton acceptor and where HF molecules are attached to benzene. Hence C<sub>6</sub>H<sub>6</sub>...(HF)<sub>n</sub> complexes (*n* up to 6) were analyzed. QTAIM<sup>18,26,27</sup> was also applied to characterize these systems. The choice of such systems was dictated by the fact that only a few studies had been performed earlier on cooperativity effects with multicenter proton acceptors, such as acetylene or ethylene molecules. Practically, except for the study on C<sub>6</sub>H<sub>6</sub>-(H<sub>2</sub>O)<sub>n</sub> clusters<sup>22</sup> and the recent study on different weak interactions,<sup>17</sup> both mentioned earlier here, no analyses on cooperativity has been performed to date for benzene as the proton acceptor. It is interesting to analyze what the interrelation is between the number of HF molecules attached to benzene and the F-H... $\pi$  interaction. Is the interaction similar in nature to the one detected for C<sub>2</sub>H<sub>2</sub> and C<sub>2</sub>H<sub>4</sub> acting as Lewis bases? In addition, the Bader theory allows one to analyze molecular graphs, especially those whose bond paths are attributed to H... $\pi$  interactions. Such QTAIM analysis was performed early on complexes of single hydrogen fluoride molecule with acetylene, ethylene, cyclopropene, cyclobutadiene, and benzene;<sup>28</sup> in these cases, a bond path with bond critical point (BCP) has been found between the H-atom attractor of hydrogen fluoride and the BCP of the CC  $\pi$ -bond. A deeper analysis of such connections for the C<sub>6</sub>H<sub>6</sub>...(HF)<sub>n</sub> clusters seems to be worth doing. On the other hand, the study of systems with multicenter proton acceptor and (or) proton donor<sup>29,30</sup> is also very interesting since this interaction very often differs in nature significantly from the typical hydrogen bonds well situated within the Pauling definition of hydrogen bonding.<sup>31</sup>

## Computational details

The calculations were carried out with the Gaussian03 set of codes.<sup>32</sup> The C<sub>6</sub>H<sub>6</sub>...(HF)<sub>n</sub> (*n* = 1,2,3,4) complexes were optimized at the MP2/6-311++G(d,p) level of approximation and these systems are in energetic minima since no imaginary frequencies were observed. Similar calculations at the same level were performed for C<sub>6</sub>H<sub>6</sub>...(HF)<sub>n</sub> complexes (*n* up to 6) with the symmetry constraints included. These complexes are known to have C<sub>6v</sub> symmetry exists because all HF molecules attached form a linear chain and are perpendicular to the benzene ring (the line of HF molecules crosses the benzene ring accurately at its geometric center).

The binding energies for the analyzed complexes were computed as the differences between the total energy of the complex and the energies of monomers. The binding energies were corrected for the basis set superposition error (BSSE) using the counterpoise method.<sup>33</sup> In this study, the term “monomer” has a special definition. Because the H... $\pi$  interaction and the influence of the number of attached HF molecules on the strength of that interaction are analyzed,



the  $C_6H_6$  is treated as one monomer and all HF molecules as another monomer. This approach is in line with the expression proposed earlier in studies on cooperative effects.<sup>34,35</sup>

$$[1] \quad E_{HBk} = E_{total} - E_{1,2,...,k} - E_{k+1,k+2,...,m}$$

$E_{HBk}$  is the  $k$ th hydrogen bond within the  $m$ -element system and two subsystems are connected through this interaction. For the systems analyzed, here the  $k$ th hydrogen bond exists between the first element (benzene) and the first hydrogen fluoride molecule (hence  $k = 1$  and  $m = n+1$  because  $n$  is the number of HF molecules).

The NBO method<sup>36,37</sup> implemented within the Gaussian03 package was applied here to calculate the atomic charges. The QTAIM theory of Bader was also applied to find the critical points<sup>26,27,38</sup> and to analyze them in terms of electron densities and their Laplacians. The molecular graphs were also analyzed to show the uniqueness of the interactions with  $\pi$ -electrons of benzene acting as the Lewis base.

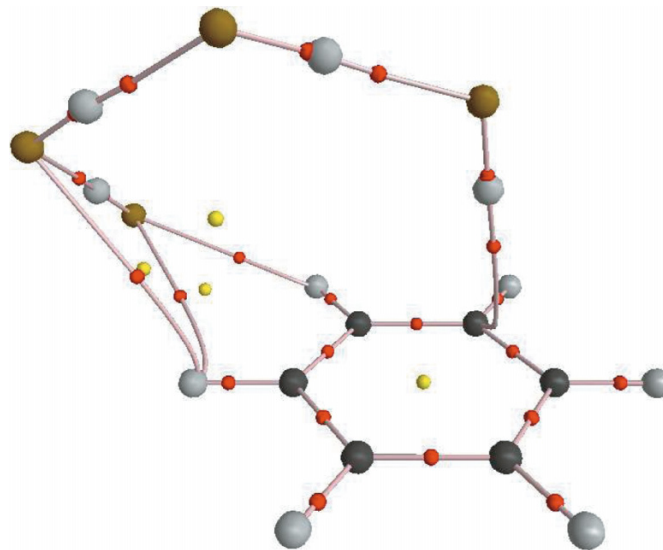
## Results and details

### Energetic and geometric parameters

Figures 1 and 2 present the molecular graphs of the  $C_6H_6 \cdots (HF)_4$  complex, the fully optimized system and the corresponding one of  $C_{6v}$  symmetry. To clarify the picture of the graph of the nonlinear complex (Fig. 1), the bond paths (BPs) of ring critical points (RCPs) are not drawn, whereas the graph of the linear system contains all BPs. Table 1 presents binding energies (corrected for BSSE) of all complexes analyzed here. The charges of the benzene ring are included in the table. It was explained in the previous section how the binding energies were calculated; the benzene molecule is one subunit and all HF molecules of the complex constitute the other subunit. Such a treatment is applied here to calculate the interaction between  $\pi$ -electrons of benzene and the remaining part of the complex, HF molecules. In other words, the energies of  $F-H \cdots \pi$  interactions are estimated by means of such a treatment.

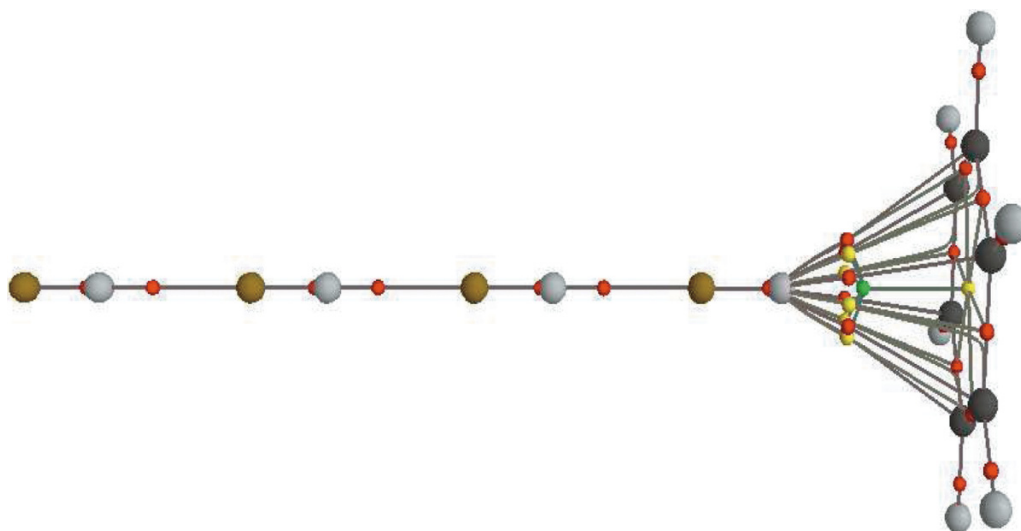
One can see that the binding energy increases (that is, it is more negative) if the number of HF molecules increases (Table 1). This is connected with the well-known effect of cooperativity (the enhancement of the H-bond strength between two interacting moieties if other additional species are attached).<sup>4</sup> Figure 3 presents this relation. For the  $C_6H_6 \cdots (HF)_2$  complex, the binding energy is about 65% greater than for the  $C_6H_6 \cdots HF$  complex if the fully optimized systems are considered. The next additional hydrogen fluoride molecules do not cause such a large increase in  $F-H \cdots \pi$  hydrogen bonding strength. If the systems containing three and four HF molecules are each compared with those possessing one fewer HF molecules then the energy increases to 38% and 11%, respectively. The changes of H-bond strength are not so significant for the linear systems, and they are practically negligible if one considers the complexes containing more than three HF molecules (Table 1, Fig. 3). The complexes of  $C_{6v}$  symmetry do not correspond to the local minima where the electron charge transfer and the corresponding electron density redistribution as an effect of complexation are most effective and lead to the most stable configurations.

**Fig. 1.** Molecular graph of the  $C_6H_6 \cdots (HF)_4$  complex, with the configuration in minimum; big circles correspond to attractors, small ones to critical points.



It is well-known that the hydrogen bonding formation is connected with the transfer of electron charge from the proton acceptor center to the proton donating system.<sup>39,40</sup> In the case of the  $H \cdots \pi$  interactions considered here, these are the benzene molecule and the system of HF molecules, respectively. Table 1 presents the benzene molecule charge for all analyzed complexes. Because an electron charge is withdrawn from benzene to the remaining parts of complexes, the benzene molecule possesses the positive charge, greater for the greater electron transfer. Table 1 shows that for the greater number of HF molecules within the complex and hence for the greater binding energy, the benzene molecule is more positive. The increase of the positive charge is greater for the fully optimized complexes. For the linear complexes, the charge changes resulting from complexation are much smaller. For example, for the  $C_6H_6 \cdots (HF)_6$  linear complex, the benzene charge is equal to 0.0065 au, whereas for the  $C_6H_6 \cdots (HF)_4$ , fully optimized complex it amounts to 0.0172 au. The positive charge for the complex in minimum is almost three times greater than for the one of  $C_{6v}$  symmetry, in spite of the greater number of HF molecules attached in the latter case. There is practically no change in the charge of benzene with the increasing number of HF molecules if the  $C_6H_6 \cdots (HF)_4$  linear complex is considered. Such negligible differences are observed for the other parameters (Table 1) for the  $C_6H_6 \cdots (HF)_n$  linear complexes ( $n = 4, 5$ , and 6). Figure 4 shows the relationship between the benzene molecule charge and the binding energy; for the linear systems, the dependence is linear ( $R^2 = 0.998$ ), whereas for the fully optimized systems the dependence seems to be nonlinear, although the number of complexes is too low to apply statistical analysis. Figure 5 presents the relationship between the benzene charge and the charge on the H-atom; the latter one concerns the HF molecule being in the closest proximity of the benzene ring. The linear and nonlinear systems belong to two subsamples; hence there are two dependencies, both of which may be described by second-order

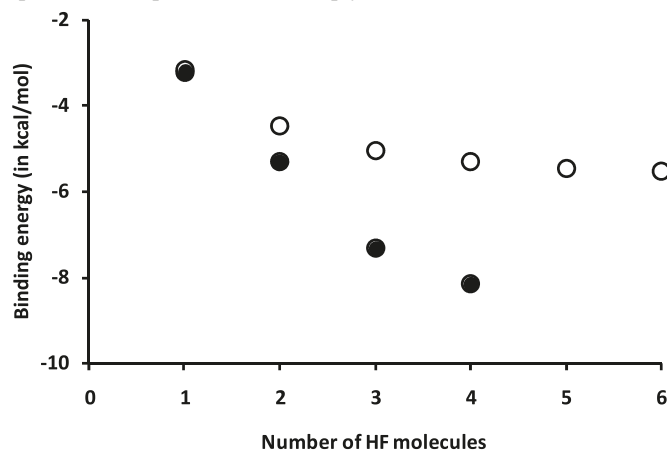
**Fig. 2.** Molecular graph of the  $C_6H_6 \cdots (HF)_4$  complex, showing the linear configuration of  $C_{6v}$  symmetry; big circles correspond to attractors, small ones to critical points.



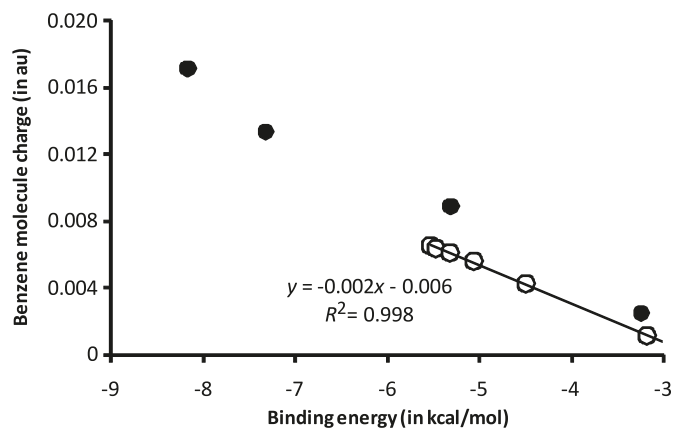
**Table 1.** Binding energies of the systems analyzed; BSSE correction is presented (both in kcal/mol), NBO charges of benzene molecule (B-charge) and H-atom of the closest to the benzene ring HF molecule (in au);  $N$  is the number of HF molecules within the complex; the shortest H $\cdots$ C intermolecular distances are given (in Å); linear systems (of  $C_{6v}$  symmetry) as well as optimized ones are shown.

$N$	$E_{\text{bin}}$	$E_{\text{BSSE}}$	B-charge	H-charge	H $\cdots$ C	C-charge
<b>Full optimization</b>						
1	-3.24	2.23	0.0025	0.5586	2.5031	-0.2245
2	-5.30	2.97	0.0089	0.5760	2.3004	-0.2509
3	-7.32	3.70	0.0134	0.5836	2.2432	-0.2504
4	-8.16	4.11	0.0172	0.5864	2.1805	-0.2557
<b>Linear systems</b>						
1	-3.17	2.27	0.0011	0.5586	2.7014	-0.2127
2	-4.49	3.14	0.0042	0.5831	2.6000	-0.2144
3	-5.06	3.42	0.0056	0.5906	2.5686	-0.2154
4	-5.32	3.47	0.0061	0.5938	2.5590	-0.2157
5	-5.46	3.49	0.0063	0.5952	2.5603	-0.2158
6	-5.53	3.51	0.0065	0.5960	2.5559	-0.2159

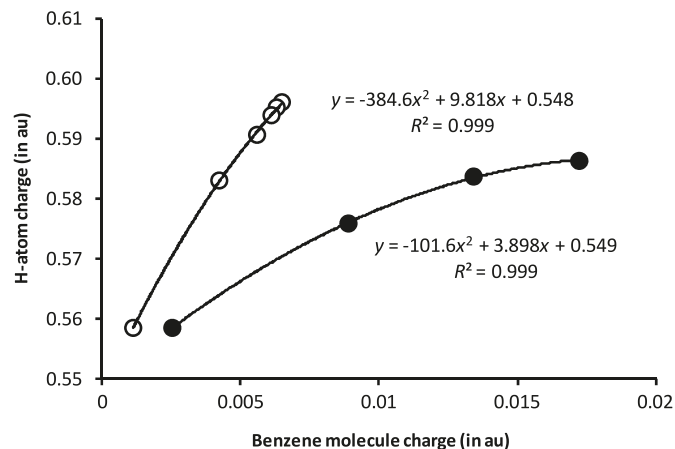
**Fig. 3.** The relationship between the number of HF molecules and the binding energy (in kcal/mol); full circles correspond to the fully optimized complexes and the empty circles to the linear ones.



**Fig. 4.** The relationship between the binding energy (in kcal/mol) and the benzene molecule charge (in au); full circles correspond to the fully optimized complexes and the empty circles to the linear ones.



**Fig. 5.** The relationship between the benzene molecule charge (in au) and the H-atom charge (in au) of the HF molecule directly connected with benzene; full circles correspond to the fully optimized complexes and the empty circles to the linear ones.

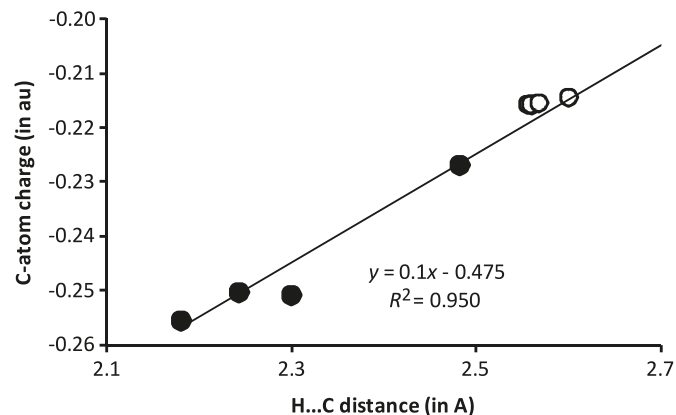


polynomials. One can see that the charges on the H-atoms are greater for linear systems, which may indicate the greater polarization of HF molecules for the  $C_{6v}$  symmetry systems than for nonlinear ones.

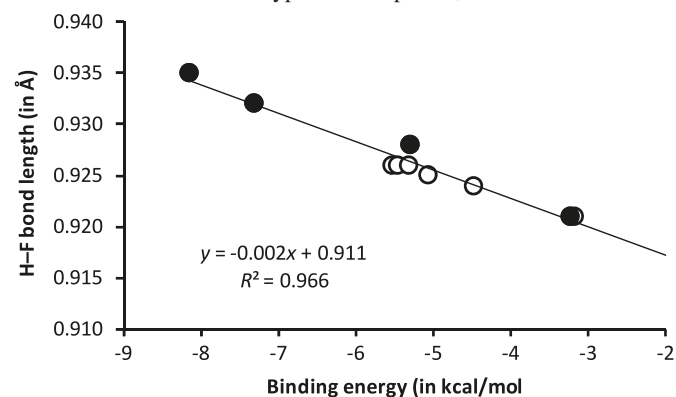
What is the reason for the systematic differences between the two subsamples, i.e., those fully optimized and those of  $C_{6v}$  symmetry? First of all, for the fully optimized systems, there is the meaningful asymmetry of the distribution of electron density. This leads to the asymmetry of numerous properties of the analyzed complexes. For example, there are differences between the charges on carbon atoms of the benzene ring. Table 1 presents the charges on the C-atoms which are the closest to the first neighboring HF molecule; the corresponding H...C distances are also included. For the complexes of  $C_{6v}$  symmetry, all such H...C distances are the same and all C-atom charges are equal. It is worth mentioning that for each fully optimized system, the charge of the C-atom nearest to an HF molecule is the most negative one of all the carbon atoms of benzene. Thus the interaction between the most negative C-atom and the HF molecule is probably the strongest of all the other such H...C interactions. This may indicate the existence of the F-H...C interaction rather than the F-H... $\pi$  one. Only for the  $C_6H_6$ -HF fully optimized complex is the situation slightly different because there are two equal shortest H...C distances. Figure 6 presents the linear dependence between the H...C distance and the charge on the corresponding C-atom; all systems, linear and nonlinear, are taken into account within this correlation. For the systems of  $C_{6v}$  symmetry; the H...C distances are longer and the negative C-charges are smaller than such values for fully optimized systems.

Figure 7 presents the relationship between the binding energy and the bond length of the first HF neighboring molecule of benzene; all systems, both linear and nonlinear, are included in the correlation and the linear correlation between energy and bond length is observed. For weaker interactions of systems with  $C_{6v}$  symmetry, the lengthening of the HF molecule is reduced as a result of complexation. This is in line with many other studies where a dependence was found between the length of the proton-donating bond

**Fig. 6.** The correlation between the H...C distance (in Å) and the C-atom charge (in au); full circles correspond to the fully optimized complexes and the empty circles to the linear ones; the correlation concerns both types of complexes, linear and nonlinear.



**Fig. 7.** The correlation between the binding energy (in kcal/mol) and the H-F bond length (in Å); full circles correspond to the fully optimized complexes and the empty circles to the linear ones; the correlation concerns both types of complexes, linear and nonlinear.



and the binding energy for the H-bonded systems.<sup>41</sup> Table 2 presents the charges of HF molecules; all systems are considered and the order of HF molecules of any complex is in line with the neighborhood of benzene molecule. This means that the HF molecule closest to benzene is given as the first one in the table. For the fully optimized  $C_6H_6$ -HF complex, the situation is as one could expect—the HF molecule has a negative charge because of the electron charge transfer from benzene. However, for the other fully optimized complexes, the HF molecules closest to benzene have positive charges. This means that there is a further transfer of electron charge to the more distant HF molecules. Usually, the last HF molecule, being the farthest from benzene, has the most negative charge. The remaining HF molecules within the chain are characterized by small and negligible negative charges. This is owing to the chain of hydrogen bonds which are created  $C_6H_6 \cdots H-F \cdots H-F \cdots$  and may be treated as a result of cooperativity. Additionally, the charge of the last HF molecule is more negative than the charge of the benzene molecule is positive. This means that, within the complexes, the negative charge is withdrawn from benzene and also from the other HF molecules to transfer it to the “tail” of the complex. A similar situation

**Table 2.** HF bond lengths (in Å) and their charges (in au),  $N$  is the number of HF molecules; the results of HF molecules are presented in the following order: the neighbor of benzene molecule is given first and next HF molecules follow it.

$N$	HF bond length	Charge
<b>Full optimization</b>		
1	0.921	-0.0025
2	0.928	0.0068
	0.925	-0.0157
3	0.932	0.0127
	0.933	-0.0080
	0.927	-0.0181
4	0.935	0.0154
	0.937	-0.0018
	0.936	-0.0109
	0.928	-0.0199
<b>Linear systems</b>		
1	0.921	-0.0011
2	0.924	0.0013
	0.921	-0.0055
3	0.925	0.0045
	0.924	-0.0042
	0.922	-0.0058
4	0.926	0.0060
	0.926	-0.0013
	0.925	-0.0047
	0.922	-0.0061
5	0.926	0.0068
	0.927	0.0001
	0.927	-0.0019
	0.925	-0.0051
	0.922	-0.0062
6	0.926	0.0071
	0.927	0.0006
	0.928	-0.0005
	0.927	-0.0021
	0.926	-0.0053
	0.922	-0.0064

occurs for the linear complexes; the charge of the first HF molecule is positive (except of the  $C_6H_6 \cdots HF$  complex). The other charges of HF molecules are usually negative although in some cases they are positive but close to zero, and the last or "tail" HF molecules are the most negative. However, for the latter ones, the modulus of negative charge is very close to the charge of the corresponding benzene molecule. This means that for the linear complexes, the enhancement of the electron charge is not so great as for the nonlinear complexes. Table 2 also shows the HF bond lengths; they are shortest for the HF molecules that are the furthest from benzene, i.e., the "tail" molecules.

### QTAIM parameters and NBO approach

Table 3 shows the parameters derived from QTAIM theory: electron density ( $\rho_{BCP}$ ), its Laplacian ( $\nabla^2 \rho_{BCP}$ ) as well as kinetic electron energy density ( $G_{BCP}$ ), and the po-

tential electron energy density ( $V_{BCP}$ ) at the H $\cdots$ C bond critical point. In other words, the characteristics of BCP corresponding to (F)H $\cdots$ C interaction are given. In the case of fully optimized complexes, there is only one bond path between the H-atom attractor and benzene, i.e., C-atom of benzene (Fig. 1) with the corresponding BCP. The  $C_6H_6 \cdots HF$  complex is the only exception since BP connects the H-atom attractor with the BCP of the CC bond (Fig. 8). For complexes of  $C_{6v}$  symmetry, there are six such bond paths. It seems that the latter situation may occur only for the complexes of benzene in the case of high  $C_{6v}$  symmetry. Any distortion from such a symmetry, as for the systems considered here (fully optimized complexes) causes the asymmetrical distribution of the electron charge. Hence, the most negatively charged carbon atom is the proton acceptor in F $\cdots$ H $\cdots$ C hydrogen bonding. It is worth mentioning that a system of  $C_{6v}$  symmetry, the benzene-acetylene complex, was analyzed by Fujii et al.<sup>42</sup> A similar high symmetry arrangement of molecules was detected for the mixed benzene-acetylene crystal.<sup>43,44</sup> Figures 1 and 2 present both of the cases mentioned above. For the linear  $C_6H_6 \cdots (HF)_4$  complex, there is the bond path which connects the H-atom attractor and the ring critical point of benzene. The cage critical point lies on such a path. It seems that in the case of benzene acting as Lewis base there are two possibilities to explain the topological evidence of X-H $\cdots$  $\pi$  interaction: (1) for the species of  $C_{6v}$  symmetry, there is the existence of BP connecting RCP and the H-atom attractor, and (2) there is BP linking the H-atom attractor and BCP of the CC  $\pi$ -bond. The second case was observed by Rozas et al.<sup>28</sup> as has been mentioned earlier. This has also been detected in this study for the fully optimized  $C_6H_6 \cdots HF$  system (Fig. 8). There are equivalent H $\cdots$ C contacts (at equal distances amounting to 2.503 Å, Table 1) and corresponding to the CC bond for this complex. Both these C-atoms of the benzene ring bear the "most negative charge", -0.2245 au (Table 1). For the remaining fully optimized complexes ( $n = 2, 3, 4$ ) there is one BP corresponding to the shortest H $\cdots$ C contact (as Fig. 1 shows for  $C_6H_6 \cdots (HF)_4$ ). The observed geometrical results nicely correspond to the bond path definition. The presence of a bond path linking a pair of atoms implies that they are bonded to one another and presents the preferable directed interactions.<sup>45,46</sup> For symmetrical systems, all six H(F) $\cdots$ C contacts are equivalent; thus, six BPs exist and also one connecting RCP with the H-attractor of hydrogen fluoride. This means that no one C-benzene atom is preferable owing to to the  $C_{6v}$  symmetry. If the symmetry of the system is broken, the BPs exist only for the shortest H $\cdots$ C contacts for which the C-atoms bear the most negative charge.

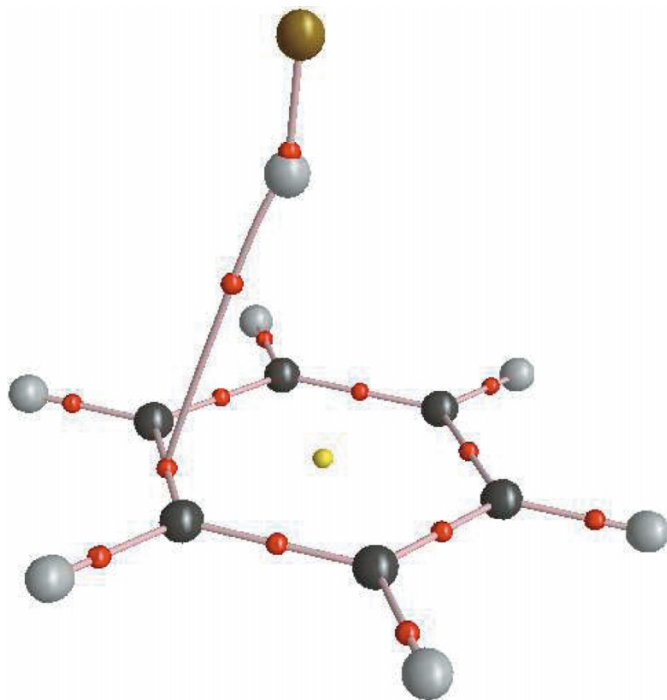
Table 3 shows the QTAIM parameters of the complexes being studied: the electron density at BCP and its Laplacian, the kinetic electron energy, and the potential electron energy. One can observe that the total electron energy density at BCP ( $H_{BCP}$ ), being the sum of kinetic ( $G_{BCP}$ ) and potential ( $V_{BCP}$ ) energies, is always positive. This means that the enhancement of the hydrogen-bond strength as an effect of cooperativity is not big enough to strengthen the interaction to be partly covalent in nature. It was proposed before that the negative  $H_{BCP}$  value for the BCP of the proton-acceptor contact is evidence for a hydrogen bond of at least partially



**Table 3.** The QTAIM parameters (in au) of the complexes analyzed; the characteristics of BCP of the C...H(F) contact are presented and in the case of linear systems the electron density at the CCP is included.

$N$	$\rho_{\text{BCP}}$	$\nabla^2 \rho_{\text{BCP}}$	$G_{\text{BCP}}$	$V_{\text{BCP}}$	$\rho_{\text{CCP}}$
<b>Full optimization</b>					
1	0.0095	0.0305	0.0058	−0.0040	No CCP
2	0.0136	0.0419	0.0082	−0.0060	No CCP
3	0.0166	0.0492	0.0099	−0.0076	No CCP
4	0.0188	0.053	0.0112	−0.0091	No CCP
<b>Linear systems</b>					
1	0.0064	0.0221	0.0043	−0.0032	0.0056
2	0.0080	0.0280	0.0054	−0.0039	0.0069
3	0.0085	0.0297	0.0058	−0.0043	0.0074
4	0.0085	0.0298	0.0058	−0.0042	0.0075
5	0.0085	0.0301	0.0059	−0.0042	0.0075
6	0.0086	0.0304	0.0059	−0.0043	0.0076

**Fig. 8.** Molecular graph of  $\text{C}_6\text{H}_6 \cdots \text{HF}$  complex, the configuration in minimum, big circles correspond to attractors, small ones to critical points.



covalent character,<sup>47–49</sup> whereas the negative value of the Laplacian ( $\nabla^2 \rho_{\text{BCP}}$ ) suggests a very strong hydrogen bond of covalent character in the latter interaction.<sup>49</sup> Sometimes for the proton–acceptor interaction, the Laplacian is positive, but  $H_{\text{BCP}}$  is negative, showing the partial covalency; this does not happen for the  $\text{H} \cdots \pi$  interactions analyzed here. However, the negative H-values were observed in the case of  $\text{H}_2\text{CO} \cdots (\text{HF})_n$  clusters for  $\text{O} \cdots \text{H}$  BCPs if the greater number of HF molecules were taken into account in the complex.<sup>13</sup> On the other hand, no negative H-values were observed for BCPs of  $\text{H} \cdots \pi$  contacts in the  $\text{C}_2\text{H}_2 \cdots (\text{HF})_n$  and  $\text{C}_2\text{H}_4 \cdots (\text{HF})_n$  complexes even for the greater number of HF molecules.<sup>25</sup> This means that cooperativity may not enhance

the  $\text{H} \cdots \pi$  interaction as significantly as for the  $\text{H} \cdots \text{O}$  interaction. However, it is worth mentioning that there are hydrogen bonds whose  $\pi$ -electrons act as a proton acceptor; such bonds may be classified as partly covalent in nature since the H-value for the BCP of the  $\text{H} \cdots \pi$  interaction is negative.<sup>50</sup>

The QTAIM parameters presented in Table 3 change monotonically if the number of HF molecules increases. This means that the electron density at  $\text{H} \cdots \text{C}$  BCP and its Laplacian increase; such dependencies for the samples of H-bonded complexes were detected very often. The other parameters also show similar tendencies: the  $G_{\text{BCP}}$  value increases while the  $V_{\text{BCP}}$  decreases (becomes more negative). Different correlations between geometrical, energetic, and QTAIM parameters were observed before. For example, numerous linear and non-linear relationships were analyzed and discussed for  $\text{N} \cdots \text{H} \cdots \text{N}$  interactions.<sup>51,52</sup> A wide range of  $\text{H} \cdots \text{F}$  interactions was also analyzed,<sup>53</sup> from short ones usually attributed to covalent bonds to longer  $\text{H} \cdots \text{F}$  distances of hydrogen bonds, or much weaker van der Waals interactions. Numerous correlations were also found there.

The above-mentioned monotonic changes are observed within subsamples of the linear and nonlinear complexes separately. For example, the largest value of the electron density at  $\text{H} \cdots \text{C}$  BCP for the  $\text{C}_6\text{H}_6 \cdots (\text{HF})_6$  complex amounts to 0.0086 au, whereas its value for the fully optimized  $\text{C}_6\text{H}_6 \cdots \text{HF}$  complex is equal to 0.0095 au. Figure 9 shows the well-known correlation between the binding energy and the electron density at  $\text{H} \cdots \text{C}$  BCP. Two subsamples mentioned above are separated. Generally, all electron densities of symmetrical systems are lower than those of fully optimized ones; however, one should remember that there are six  $\text{H} \cdots \text{C}$  bond paths for linear complexes, whereas there is only one for the nonlinear complex ( $\text{H} \cdots \text{BCP}$  in the case of the  $\text{C}_6\text{H}_6 \cdots \text{HF}$  complex, see Figs. 1, 2, and 8). The electron densities at cage critical points are also included in Table 3 and Fig. 9; one can observe the increase of this value if the number of HF molecules increases.

The Natural Bond Orbitals (NBO) results are very interesting in that they support the statement of different kinds of interactions for two subsamples analyzed here. The  $n_Y \rightarrow \sigma_{\text{XH}}^*$  interaction is connected with the maximum  $n_Y \rightarrow \sigma_{\text{XH}}^*$

overlap and, according to numerous studies, it is responsible for the existence of the X–H...Y hydrogen bond.  $n_Y$  designates the lone electron pair of the proton acceptor and  $\sigma_{XH}^*$  is an antibonding orbital of the proton-donating bond. The  $n_Y \rightarrow \sigma_{XH}^*$  interaction is calculated as the energy of the second-order perturbation theory according to the following relation (eq. [2]):

$$[2] \quad \Delta E(n_Y \rightarrow \sigma_{XH}^*) = -2\langle n_Y | F | \sigma_{XH}^* \rangle^2 / (\epsilon(\sigma_{XH}^*) - \epsilon(n_Y))$$

$\langle n_Y | F | \sigma_{XH}^* \rangle$  designates the Fock matrix element and  $(\epsilon(\sigma_{XH}^*) - \epsilon(n_Y))$  is the orbital energy difference. Such energy contributions are calculated for typical hydrogen bonds as, for example, for the F–H...F systems existing in the  $C_6H_6 \cdots (HF)_n$  complexes. However, for hydrogen bonds where  $\pi$ -electrons act as proton acceptors, the modified expression should be taken into account since the corresponding energy term is connected with the charge transfer from the  $\pi_{CC}$ -bond orbital to the  $\sigma_{XH}^*$  antibonding orbital:

$$[3] \quad \Delta E(\pi_{CC} \rightarrow \sigma_{XH}^*) = -2\langle \pi_{CC} | F | \sigma_{XH}^* \rangle^2 / (\epsilon(\sigma_{XH}^*) - \epsilon(\pi_{CC}))$$

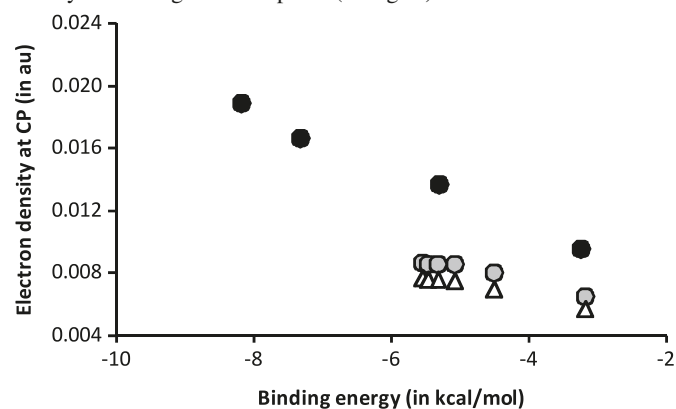
Such a situation was analyzed recently for the  $C_2H_2 \cdots (HF)_n$  and  $C_2H_4 \cdots (HF)_n$  complexes.<sup>25</sup> However, for the latter systems, QTAIM shows that the bond paths between the acetylene or ethylene molecule and the hydrogen fluoride link the approximate middle part of CC bond, i.e., the bond-critical point of the CC bond, and the attractor of the H-atom. For the benzene complexes analyzed here, the bond path concerns H...C contacts. However, the NBO approach indicates that the  $\pi_{CC} \rightarrow \sigma_{FH}^*$  charge transfer with the energy term corresponding to eq. [3].

This means that NBO indicates a situation similar to that found earlier in the case of acetylene and ethylene complexes. The  $\Delta E(\pi_{CC} \rightarrow \sigma_{FH}^*)$  energy contributions for the fully optimized complexes are greatest if the CC bond contains the carbon atom that is closest to the HF molecule. Thus it is in line with QTAIM because the latter theory shows the bond paths for the closest H...C distances. The  $\Delta E(\pi_{CC} \rightarrow \sigma_{FH}^*)$  contributions amount to 0.99, 2.49, 11.56, and 14.77 kcal/mol for increasing numbers of HF molecules, from one to four HF. The other such contributions are much lower being in the range 0.1–0.2 kcal/mol. Similarly, these contributions are much lower for linear complexes being in the range 0.1 – 0.5 kcal/mol. However, all results show that the greatest energy connected with the charge transfer to the antibonding orbital of HF molecule concern the shortest H...C intermolecular contacts.

## Summary

The results for the  $C_6H_6 \cdots (HF)_n$  complexes presented here show the enhancement of F–H...benzene interactions as the number of HF molecules increases. Different geometrical, energetic, and QTAIM parameters support this tendency. Benzene acts as the Lewis base and more specifically as the proton acceptor in hydrogen bonding. It is not clear whether the  $\pi$ -electrons of benzene, i.e., the whole aromatic electron

**Fig. 9.** The dependence between the binding energy (in kcal/mol) and the electron density at BCP (in au); full circles correspond to the fully optimized complexes and the empty circles to the linear ones; the dependence between the binding energy and the electron density at the cage critical point (triangles) is also included.



sixtet, may be treated as the proton acceptor or whether it is the CC bond proton acceptor or a single carbon atom. QTAIM reveals that, for fully optimized complexes, there is only one bond path connecting benzene with the nearest HF molecule; this is the H...C bond path with the bond critical point (see Fig. 1). The nonlinear benzene–HF complex is the only exception because the BP links the BCP of the  $\pi$ –CC bond with the H-atom attractor. This is indicative of the existence of F–H...C hydrogen bonds for some of the species considered here ( $n = 2, 3, 4$ ). The other results support such an idea because the BPs correspond to the shortest intermolecular H...C distances and the C-atoms corresponding to such paths possess the greatest negative charges when compared to the remaining carbons of benzene. The molecular graphs for the so-called linear complexes, i.e., those of  $C_{6v}$  symmetry show six symmetrical bond paths connecting the H-atom with each of the six carbon atoms of the benzene ring (see Fig. 2). Additionally, for linear complexes, there exists a bond path between the H-atom and the ring critical point of benzene with the cage critical point situated on this path.

The NBO calculations support this QTAIM analysis. Specifically, for the nonlinear complexes, the largest energy contribution for the charge transfer from benzene to the nearest HF molecule is connected with the most negative carbon atom; for linear complexes, there are six equivalent contributions involving each of the six carbon atoms of the benzene ring.

## Acknowledgment

Technical and human support provided by Informatikako Zerbitzu Orokorra – Servicio General de Informatica (IZO–SGI) SGIker (Universidad de Pais Vasco / Euskal Herriko Unibertsitate (UPV/EHU), Ministerio de Ciencia e Innovación (MICINN), Gobierno Vasco Eusko Jaurlaritza (GV/EJ), European Social Fund (ESF)) is gratefully acknowledged.

## References

- (1) Del Bene, J.; Pople, J. A. *Chem. Phys. Lett.* **1969**, *4* (7), 426. doi:10.1016/0009-2614(69)85004-9.
- (2) Kollman, P. J. *Am. Chem. Soc.* **1977**, *99* (15), 4875. doi:10.1021/ja00457a002.
- (3) Mó, O.; Yáñez, M.; Elguero, J. *J. Chem. Phys.* **1992**, *97* (9), 6628. doi:10.1063/1.463666.
- (4) Sanz, P.; Mó, O.; Yáñez, M.; Elguero, J. *ChemPhysChem* **2007**, *8* (13), 1950. doi:10.1002/cphc.200700266. PMID: 17676647.
- (5) Kar, T.; Scheiner, S. J. *Phys. Chem. A* **2004**, *108* (42), 9161. doi:10.1021/jp048546l.
- (6) Jeffrey, G. A. *An Introduction to Hydrogen Bonding*; Oxford University Press: New York, 1997.
- (7) Hunt, S. W.; Higgins, K. J.; Craddock, M. B.; Brauer, C. S.; Leopold, K. R. *J. Am. Chem. Soc.* **2003**, *125* (45), 13850. doi:10.1021/ja030435x. PMID:14599225.
- (8) Parra, R. D.; Bulusu, S.; Zeng, X. C. *J. Chem. Phys.* **2005**, *122* (18), 184325. doi:10.1063/1.1895713. PMID: 15918722.
- (9) Kobko, N.; Dannenberg, J. J. *J. Phys. Chem. A* **2003**, *107* (34), 6688. doi:10.1021/jp0345497.
- (10) Parra, R. D.; Ohlssen, J. J. *Phys. Chem. A* **2008**, *112* (15), 3492. doi:10.1021/jp711956u. PMID:18331014.
- (11) Araújo, R. C. M. U.; Soares, V. M.; Oliveira, B. G.; Lopes, K. C.; Ventura, E.; Do Monte, S. A.; Santana, O. L.; Carvalho, A. B.; Ramos, M. N. *Int. J. Quantum Chem.* **2006**, *106* (13), 2714. doi:10.1002/qua.21132.
- (12) Oliveira, B. G.; Araújo, R. C. M. U.; Soares, V. M.; Ramos, M. N. *J. Theor. Comput. Chem.* **2008**, *7* (2), 247. (JTCC). doi:10.1142/S0219633608003605.
- (13) Ziolkowski, M.; Grabowski, S. J.; Leszczynski, J. *J. Phys. Chem. A* **2006**, *110* (20), 6514. doi:10.1021/jp060537k. PMID:16706409.
- (14) Grabowski, S. J.; Sokalski, W. A.; Leszczynski, J. *J. Phys. Chem. A* **2005**, *109* (19), 4331. doi:10.1021/jp0444215. PMID:16833763.
- (15) Grabowski, S. J.; Sokalski, W. A.; Dyguda, E.; Leszczyński, J. *J. Phys. Chem. B* **2006**, *110* (13), 6444. doi:10.1021/jp0600817. PMID:16570938.
- (16) Grabowski, S. J.; Bilewicz, E. *Chem. Phys. Lett.* **2006**, *427* (1-3), 51. doi:10.1016/j.cplett.2006.06.060.
- (17) Alkorta, I.; Blanco, I.; Deyá, P. M.; Elguero, J.; Estarellas, C.; Frontera, A.; Quiñero, D. *Theor. Chem. Acc.* **2010**, *126* (1-2), 1. doi:10.1007/s00214-009-0690-1.
- (18) Matta, C.; Boyd, J. J., Eds. *Quantum Theory of Atoms in Molecules. In Recent Progress in Theory and Application*; Wiley-VCH: New York, 2007.
- (19) Desiraju, G. R.; Steiner, T. *The Weak Hydrogen Bond in Structural Chemistry and Biology*; Oxford University Press, Inc.: New York, 1999.
- (20) Nishio, M.; Hirota, M.; Umezawa, Y. *The CH/π Interaction: Evidence, Nature, and Consequences*; Wiley-VCH: New York, 1998.
- (21) Tsuzuki, S.; Fujii, A. *Phys. Chem. Chem. Phys.* **2008**, *10* (19), 2584. doi:10.1039/b718656h. PMID:18464973.
- (22) Fredericks, S. Y.; Jordan, K. D.; Zwier, T. S. *J. Phys. Chem.* **1996**, *100* (19), 7810. doi:10.1021/jp9535710.
- (23) DuPré, D. B.; Yappert, C. *J. Phys. Chem. A* **2002**, *106* (3), 567. doi:10.1021/jp013556x.
- (24) Oliveira, B. G.; Araújo, R. C. M. U.; Carvalho, A. B.; Lima, T. F.; Silva, W. L. V.; Ramos, M. N.; Tavares, A. M. *J. Mol. Struct. THEOCHEM* **2006**, *775* (1-3), 39. doi:10.1016/j.theochem.2006.06.028.
- (25) Grabowski, S. J.; Leszczynski, J. *Chem. Phys.* **2009**, *355* (2-3), 169. doi:10.1016/j.chemphys.2008.12.011.
- (26) Bader, R. F. W. *Chem. Rev.* **1991**, *91* (5), 893. doi:10.1021/cr00005a013.
- (27) Bader, R. F. W. *Atoms in Molecules: A Quantum Theory*; International Series of Monographs on Chemistry; Oxford University Press: New York, 1990; Vol. 22.
- (28) Rozas, I.; Alkorta, I.; Elguero, J. *J. Phys. Chem. A* **1997**, *101* (49), 9457. doi:10.1021/jp971893t.
- (29) Grabowski, S. J. *J. Phys. Chem. A* **2007**, *111* (17), 3387. doi:10.1021/jp070530i. PMID:17411022.
- (30) Grabowski, S. J. *J. Phys. Chem. A* **2007**, *111* (51), 13537. doi:10.1021/jp076990t. PMID:18052265.
- (31) Pauling, L. *The Nature of the Chemical Bond*, 3rd ed.; Cornell University Press: Ithaca, New York, 1960.
- (32) Frisch, M. J.; Trucks, G. W.; Schlegel, H. B.; Scuseria, G. E.; Robb, M. A.; Cheeseman, J. R.; Montgomery, J. A., Jr.; Vreven, T.; Kudin, K. N.; Burant, J. C.; Millam, J. M.; Iyengar, S. S.; Tomasi, J.; Barone, V.; Mennucci, B.; Cossi, M.; Scalmani, G.; Rega, N.; Petersson, G. A.; Nakatsuji, H.; Hada, M.; Ehara, M.; Toyota, K.; Fukuda, R.; Hasegawa, J.; Ishida, M.; Nakajima, T.; Honda, Y.; Kitao, O.; Nakai, H.; Klene, M.; Li, X.; Knox, J. E.; Hratchian, H. P.; Cross, J. B.; Adamo, C.; Jaramillo, J.; Gomperts, R.; Stratmann, R. E.; Yazyev, O.; Austin, A. J.; Cammi, R.; Pomelli, C.; Ochterski, J. W.; Ayala, P. Y.; Morokuma, K.; Voth, G. A.; Salvador, P.; Dannenberg, J. J.; Zakrzewski, V. G.; Dapprich, S.; Daniels, A. D.; Strain, M. C.; Farkas, O.; Malick, D. K.; Rabuck, A. D.; Raghavachari, K.; Foresman, J. B.; Ortiz, J. V.; Cui, Q.; Baboul, A. G.; Clifford, S.; Cioslowski, J.; Stefanov, B. B.; Liu, G.; Liashenko, A.; Piskorz, P.; Komaromi, I.; Martin, R. L.; Fox, D. J.; Keith, T.; Al-Laham, M. A.; Peng, C. Y.; Nanayakkara, A.; Challacombe, M.; Gill, P. M. W.; Johnson, B.; Chen, W.; Wong, M. W.; Gonzalez, C.; Pople, J. A. *Gaussian 03*, Revision B.03; Gaussian, Inc.: Pittsburgh PA, 2003.
- (33) Boys, S. F.; Bernardi, F. *Mol. Phys.* **1970**, *19* (4), 553. doi:10.1080/00268977000101561.
- (34) Tan, H.; Qu, W.; Chen, G.; Liu, R. *J. Phys. Chem. A* **2005**, *109* (28), 6303. doi:10.1021/jp051444q. PMID:16833972.
- (35) Li, X.; Liu, W.; Sun, K.; Wang, Y.; Tan, H.; Chen, G. *Phys. Chem. Chem. Phys.* **2008**, *10* (36), 5607. doi:10.1039/b804291h. PMID:18956096.
- (36) Reed, A. E.; Curtiss, L. A.; Weinhold, F. *Chem. Rev.* **1988**, *88* (6), 899. doi:10.1021/cr00088a005.
- (37) Weinhold, F.; Landis, C. *Valency and Bonding: a Natural Bond Orbital Donor-Acceptor Perspective*; Cambridge University Press: Cambridge, 2005.
- (38) Bader, R. F. W.; MacDougall, P. J.; Lau, C. D. H. *J. Am. Chem. Soc.* **1984**, *106* (6), 1594. doi:10.1021/ja00318a009.
- (39) Scheiner, S. *Hydrogen Bonding: A Theoretical Perspective*; Oxford University Press: Oxford, 1997.
- (40) Sobczyk, L.; Grabowski, S. J.; Krygowski, T. M. *Chem. Rev.* **2005**, *105* (10), 3513. doi:10.1021/cr030083c. PMID: 16218560.
- (41) Grabowski, S. J. *J. Phys. Org. Chem.* **2004**, *17* (1), 18. doi:10.1002/poc.685.
- (42) Fujii, A.; Morita, S.; Miyazaki, M.; Ebata, T.; Mikami, N. *J. Phys. Chem. A* **2004**, *108* (14), 2652. doi:10.1021/jp049946b.
- (43) Boese, R.; Clark, T.; Gavezzotti, A. *Helevet. Chim. Acta* **2003**, *86* (4), 1085. doi:10.1002/hlca.200390095.
- (44) Kirchner, M. T.; Bläser, D.; Boese, R. *Chem. Eur. J.* **2010**, *16* (7), 2131. doi:10.1002/chem.200901314.

- (45) Bader, R. F. W.; Nguyen-Dang, T. T.; Tal, Y. *Rep. Prog. Phys.* **1981**, *44* (8), 893. doi:10.1088/0034-4885/44/8/002.
- (46) Bader, R. F. W. *J. Phys. Chem. A* **2009**, *113* (38), 10391. doi:10.1021/jp906341r. PMID:19722600.
- (47) Cremer, D.; Kraka, E. *Croat. Chem. Acta* **1984**, *57*, 1259.
- (48) Jenkins, S.; Morrison, I. *Chem. Phys. Lett.* **2000**, *317* (1-2), 97. doi:10.1016/S0009-2614(99)01306-8.
- (49) Rozas, I.; Alkorta, I.; Elguero, J. *J. Am. Chem. Soc.* **2000**, *122* (45), 11154. doi:10.1021/ja0017864.
- (50) Grabowski, S. J.; Sokalski, W. A.; Leszczynski, J. *J. Phys. Chem. A* **2004**, *108* (10), 1806. doi:10.1021/jp036770p.
- (51) Knop, O.; Rankin, K. N.; Boyd, R. J. *J. Phys. Chem. A* **2001**, *105* (26), 6552. doi:10.1021/jp0106348.
- (52) Knop, O.; Rankin, K. N.; Boyd, R. J. *J. Phys. Chem. A* **2003**, *107* (2), 272. doi:10.1021/jp022127b.
- (53) Espinosa, E.; Alkorta, I.; Elguero, J.; Molins, E. *J. Chem. Phys.* **2002**, *117* (12), 5529. doi:10.1063/1.1501133.



# Theoretical study of the rovibrational spectrum of He<sub>2</sub>-OCS

Xiao-Gang Wang and Tucker Carrington, Jr.

**Abstract:** We report calculated microwave and infrared rovibrational transitions of the van der Waals complex He<sub>2</sub>-OCS. The calculations were done using a product basis, a Lanczos eigensolver, and potentials built from He-OCS, and He-He potential functions taken from the literature. All five of the large amplitude coordinates are treated exactly and calculations are done for  $J$  values up to five. All rovibrational levels are converged to 0.001 cm<sup>-1</sup> by using basis sets with as many as 87 million functions. Good agreement is found with previously reported experimental results. Although we assume that the dipole moment is along the OCS axis, we find transitions with appreciable intensity between different torsion states.

**Key words:** rovibrational spectroscopy, quantum dynamics, van der Waals clusters, doped helium clusters, Lanczos algorithm.

**Résumé :** Nous avons calculé des transitions rovibrationnelles du complexe de van der Waals He<sub>2</sub>-OCS. Le calcul a été fait en utilisant une base de produit, l'algorithme de Lanczos et des potentiels construits à partir de fonctions de potentiel pour He-OCS et He-He. Les cinq coordonnées qui décrivent le mouvement de grande amplitude ont été traitées de manière explicite et des niveaux d'énergie sont calculés pour des valeurs de  $J$  jusqu'à cinq. Tous les niveaux rovibrationnels ont été convergés jusqu'à 0,001 cm<sup>-1</sup> en utilisant des bases ayant jusqu'à 87 millions de fonctions. Il y a un bon accord avec les résultats expérimentaux rapportés antérieurement. Même si on fait l'hypothèse que le moment dipolaire est selon l'axe OCS, nous trouvons des transitions avec des intensités appréciables entre différents états de torsion.

**Mots-clés :** spectroscopie rovibrationnelle, dynamique quantique, agrégats de van der Waals, agrégats de hélium, algorithme de Lanczos.

## Introduction

Infrared and microwave spectra of several small molecules embedded in helium clusters have been observed<sup>1-8</sup> and calculated.<sup>9-17</sup> In this paper, we present theoretical results for He<sub>2</sub>-OCS obtained by using a product basis set, the symmetry adapted Lanczos method (SAL),<sup>18,19</sup> and a simple potential built from pairwise interactions. Similar calculations have demonstrated that three-body potential terms are small for other dopant molecules. OCS is considered an ideal probe molecule for studies of helium clusters and nanodroplets,<sup>2,20</sup> and clusters with as few as one and as many as thousands of He atoms have been investigated.<sup>1-4,21-24</sup> Calculations on small clusters are important because they confirm the accuracy of interaction potentials. The same interaction potentials can be used to study (for example with Monte Carlo methods) clusters with as many as thousands of He atoms. Experiments on such clusters are now possible.<sup>23,25</sup> Calculations are also useful because they guide experimentalists as they search for unobserved transitions, confirm and explain proposed assignments, and make new assignments possible. Because the frequency of the OCS intramolecular vibrations is much higher than the other

frequencies, an adiabatic approximation is accurate, and we have therefore computed spectra for the He<sub>2</sub>-OCS cluster by treating explicitly the two OCS-He stretch coordinates, three dopant-He bend coordinates, and the three Euler angles describing the orientation of the cluster (eight in total). Different potentials are used for different vibrational states of OCS.

He<sub>N</sub>-OCS clusters have been studied experimentally in the infrared (IR) region of the CO fundamental band and in the microwave (MW) region.<sup>1,2,21,22,24</sup> More details about the experiments, including more results for He<sub>2</sub>-OCS, in both regions were published later.<sup>3,4</sup> Theoretical calculations, using quantum Monte Carlo techniques, have successfully explained many of the observed trends as function of cluster size.<sup>26-28</sup>

## Calculations

### Kinetic energy operator and basis functions

We use the approach of ref. 14 and assume an adiabatic separation between the fast intra-dopant coordinates and the He-dopant coordinates. In atomic units, the kinetic energy operator (KEO) is<sup>14,29,30</sup>

Received 7 January 2010. Accepted 10 February 2010. Published on the NRC Research Press Web site at canjchem.nrc.ca on 21 May 2010.

*This article is part of a Special Issue dedicated to Professor R. J. Boyd.*

X.-G. Wang<sup>1</sup> and T. Carrington, Jr.<sup>2</sup> Chemistry Department, Queen's University, Kingston, ON K7L 3N6, Canada.

<sup>1</sup>Corresponding author (e-mail: Xiaogang.Wang@umontreal.ca).

<sup>2</sup>Corresponding author (e-mail: Tucker.Carrington@queensu.ca).

$$[1] \quad T = T_s + T_{b,\text{diag}} + T_{b,\text{off}} + T_{\text{Cor}}$$

with

$$[2] \quad T_s = -\frac{1}{2\mu_1} \frac{\partial^2}{\partial \mathbf{r}_1^2} - \frac{1}{2\mu_2} \frac{\partial^2}{\partial \mathbf{r}_2^2}$$

$$T_{b,\text{diag}} = -[B_L + B_1(\mathbf{r}_1)] \left[ \frac{\partial^2}{\partial \theta_1^2} + \cot \theta_1 \frac{\partial}{\partial \theta_1} - \frac{1}{\sin^2 \theta_1} (J_z - l_{2z})^2 \right] + [B_L + B_2(\mathbf{r}_2)] l_2^2 + B_L [J^2 - 2(J_z - l_{2z})^2 - 2J_z l_{2z}]$$

$$T_{b,\text{off}} = B_L [l_{2+a_1^-} + l_{2-a_1^+}]$$

$$T_{\text{Cor}} = -B_L [J_{-a_1^+} + J_{+a_1^-} + J_{-l_{2+}} + J_{+l_{2-}}]$$

where

$$[3] \quad B_i(\mathbf{r}_i) = \frac{1}{2\mu_i \mathbf{r}_i^2}, \quad l_{2\pm} = l_{2x} \pm i l_{2y},$$

$$J_{\pm} = J_x \pm i J_y, \quad a_1^{\pm} = \pm \frac{\partial}{\partial \theta_1} - \cot \theta_1 (J_z - l_{2z})$$

The vector along OCS is  $\mathbf{r}_0$ . OCS vibrational coordinates do not appear in the KEO because we assume they can be adiabatically separated.  $\mathbf{r}_1$  and  $\mathbf{r}_2$  are the lengths of Radau, or orthogonalized satellite, vectors  $\mathbf{r}_1$  and  $\mathbf{r}_2$  that are linear combinations of Jacobi (or satellite) vectors,  $\mathbf{b}_1$  and  $\mathbf{b}_2$ , from the He atoms to the centre of mass of OCS,<sup>31</sup> see Fig. 1. The polyspherical angles ( $\theta_1$ ,  $\theta_2$ , and  $\phi_2$ ) are determined by the three vectors ( $\mathbf{r}_0$ ,  $\mathbf{r}_1$ , and  $\mathbf{r}_2$ ).  $\mu_1 = \mu_2$  is the mass of the He atom. When  $\theta_1 = 0$ , He atom one is aligned with OCS as OCS–He.  $B_L$  is an OCS rotational constant; different  $B_L$  values are used for different vibrational states of OCS.  $J$  is the total angular momentum. The  $l_2$  angular momentum operator is defined in terms of the polar angles ( $\theta_2$  and  $\phi_2$ ) of the Radau vector associated with He atom 2.

For the stretch coordinates, we use discrete variable representation (DVR) functions,<sup>32–35</sup> and for the bend and rotational coordinates, we use the parity-adapted rovibrational functions<sup>36,37</sup> ( $\bar{m}_2 = -m_2$  and  $\bar{K} = -K$ )

$$[4] \quad |u_{l_1 l_2 m_2; K}^{JMP}\rangle$$

$$= N_{m_2, K} \frac{1}{\sqrt{2}} [|l_1 l_2 m_2; JKM\rangle + (-1)^{J+P} |l_1 l_2 \bar{m}_2; J\bar{K}M\rangle]$$

with

$$N_{m_2, K} = (1 + \delta_{m_2, 0} \delta_{K, 0})^{-1/2}$$

The ket in this equation is defined by

$$[5] \quad \langle \theta_1, \theta_2, \phi_2; \alpha, \beta, \gamma | l_1 l_2 m_2; JKM \rangle$$

$$= \sqrt{\frac{2J+1}{8\pi^2}} \Theta_{l_1}^{m_1}(\theta_1) Y_{l_2}^{m_2}(\theta_2, \phi_2) D_{MK}^{J*}(\alpha, \beta, \gamma)$$

with

$$[6] \quad Y_{l_2}^{m_2}(\theta_2, \phi_2) = \frac{1}{\sqrt{2\pi}} \Theta_{l_2}^{m_2}(\theta_2) e^{im_2 \phi_2}$$

$$m_1 \equiv K - m_2$$

where  $\Theta_l^m(\theta)$  is a normalized associated Legendre function with the  $(-1)^m$  Condon–Shortley phase factor.  $D_{MK}^J$  is a

Wigner function<sup>38</sup> and ( $\alpha$ ,  $\beta$ , and  $\gamma$ ) are the Euler angles. For the parity-adapted functions,  $K \geq 0$  and  $P = 0$ , and 1 correspond to even and odd parity. If  $K = 0$ , it is necessary to apply the constraint  $m_2 \geq 0$ . The combination  $m_2 = K = 0$  and  $(-1)^{J+P} = -1$  is not allowed. In our calculations,  $l_1$ ,  $l_2$ , and  $m_2$  all have the same maximum value. The parity-adapted basis makes it possible to calculate even and odd parity levels separately. The symmetry-adapted Lanczos algorithm<sup>18,19</sup> (SAL) is used within each parity block to compute states that are symmetric (*A*) and antisymmetric (*B*) with respect to exchange of the two He atoms. For more details, see ref. 14. A complete product basis function is

$$[7] \quad f_{\alpha_1}(\mathbf{r}_1) f_{\alpha_2}(\mathbf{r}_2) u_{l_1 l_2 m_2 K}^{JMP}(\theta_1, \theta_2, \phi_2; \alpha, \beta, \gamma)$$

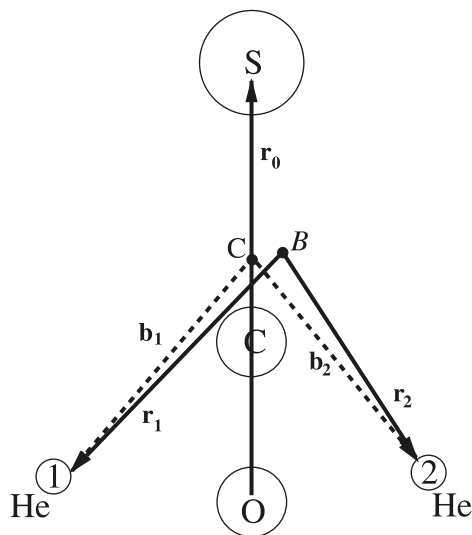
where  $f_{\alpha_k}(\mathbf{r}_k)$  is a DVR function.

### Computing rovibrational energy levels and intensities

Using the SAL algorithm, it is possible, for each parity block, to do a single calculation that yields both the symmetric and antisymmetric states with respect to permuting the two He atoms: *A*+ and *B*+ for even parity, *A*– and *B*– for odd parity. *A* and *B* label symmetries with respect to permutation of the He atoms. For <sup>4</sup>He<sub>2</sub>–OCS only, *A*+ and *A*– states are physically allowed because of the zero nuclear spin of the <sup>4</sup>He nucleus. Eigenvalues and eigenvectors are obtained by computing matrix–vector products. Matrix–vector products are evaluated by doing sums sequentially.<sup>34,39–42</sup> Similar techniques have been used to compute energy levels of many molecules.<sup>34,43–46</sup> Kinetic energy matrix elements are given in ref. 14. Potential matrix–vector products are evaluated by using quadrature and doing sums sequentially, as explained in ref. 14.

To compute intensities, we use standard equations<sup>14</sup> and assume that the dipole moment is along the OCS axis. Specifically, the line strength (*S*) and intensity (*I*) for MW and IR transitions are computed from the wave functions using eqs. [28] and [34] of ref. 14, respectively. In our previous papers on helium-doped clusters,<sup>14–16</sup> we inadvertently omitted the  $G(J, J' - J)$  factor in eq. [34] of ref. 14. The intensities in those papers are therefore off by small factors. In this pa-

**Fig. 1.**  $B$  is the canonical point for the Radau vectors.  $\mathbf{b}_1$  and  $\mathbf{b}_2$  are Jacobi vectors.  $\mathbf{r}_1$  and  $\mathbf{r}_2$  are Radau vectors.  $\phi_2$  is a dihedral angle between  $\mathbf{r}_1$  and  $\mathbf{r}_2$  around  $\mathbf{r}_0$ .  $\theta_1$  ( $\theta_2$ ) are angles between  $\mathbf{r}_0$  and  $\mathbf{r}_1$  ( $\mathbf{r}_2$ ). The angles are not shown.



per, the  $G(J, J' - J)$  factor is included correctly. Note that the line strength does not depend on the temperature. The wave functions are obtained from eigenvectors of the Hamiltonian matrix that are computed as described previously.<sup>37,47</sup>

### Details specific to He<sub>2</sub>-OCS

We use different rotational constants for  $\nu = 0$  and  $\nu = 1$ ;  $\nu$  is the quantum number associated with the normal coordinate that corresponds to the CO stretch. The OCS rotational constants are fixed to the experimental values<sup>48</sup> of 0.202856 cm<sup>-1</sup> and 0.202251 cm<sup>-1</sup> for  $\nu = 0$  and for  $\nu = 1$ , respectively, following ref. 26. The potential we use is a sum of two He-OCS potentials and a He-He potential. Different He-OCS potentials are used for the  $\nu = 0$  and  $\nu = 1$  calculations. The He-OCS potentials are the VMP4<sub>0</sub> and VMP4<sub>1</sub> potentials of ref. 26, obtained by averaging over 1D CO stretch normal-coordinate vibrational wave functions of OCS, computed for a free OCS molecule. Having the vibrationally averaged potential allows us to predict the vibrational band centre shift. See ref. 26 for an assessment of other potentials of He-OCS. The He-He potential is taken from ref. 49. The He<sub>2</sub>-OCS potential is zero when all three of the constituents of the complex are far apart. The masses are the same as those used in ref. 26.

To accelerate the convergence of the Lanczos calculation, we apply a potential ceiling value.<sup>46</sup> A ceiling of 1000 cm<sup>-1</sup> changes low-lying energy levels by less than 0.001 cm<sup>-1</sup>. For the angular basis, we use  $l_{\max} = m_{\max} = 26$  (the same  $l_{\max}$  for  $l_1$  and  $l_2$ ). We use 35 Gauss-Legendre quadrature points for  $\theta_1$  and  $\theta_2$ , and 64 equally spaced points in the range from 0 to  $2\pi$  for  $\phi_2$ . For  $r_1$  and  $r_2$ , we use 35 PODVR(potential-optimized DVR) functions.<sup>50,51</sup> The reference potential that defines the PODVR functions is obtained by minimizing the potential, for each  $r_1$  point, with respect to  $r_2$  and  $\phi_2$ .  $\theta_1$  and  $\theta_2$  are fixed at equilibrium values to ensure smoothness of the minimized potential. When minimiz-

ing, the initial values of  $r_2$  and  $\phi_2$  are equilibrium values. The minimized potential is similar to the cut potential obtained by setting  $r_2$ ,  $\phi_2$ ,  $\theta_1$ , and  $\theta_2$  to equilibrium values. For values of  $r_1$  for which the cut potential is larger than 100 cm<sup>-1</sup> (above the dissociation energy), the reference potential is set equal to the cut potential. The 1D Schrödinger equation for the reference potential is solved with 150 sinc DVR basis functions<sup>52,53</sup> in the range from 3.2 to 20 b (1 b = 5.291 77 × 10<sup>-11</sup> m). The basis size and the number of quadrature points have been chosen to ensure that the levels we report are converged to within 0.001 cm<sup>-1</sup>. The size of the product basis defined above is 8.5 million for the case of  $J = 0$ , even parity. The size grows by a factor of  $2J + 1$  if  $J > 0$ . The largest basis size is 87 million for  $J = 5$ , odd parity. We used  $T = 0.7$  K for IR spectra and MW spectra. The experimental spectra are obtained from several scans, and there is therefore no clear experimental temperature.

To compare our computed energy levels directly with experimental results, we calculate IR rovibrational transition wavenumbers from

$$[8] \quad \tilde{\nu} = \tilde{\nu}_0(\text{He}_2\text{OCS}) + E(\nu = 1) - E(\nu = 0)$$

where  $E(\nu = 0)$  and  $E(\nu = 1)$  are calculated wavenumbers measured from the  $\nu = 0$  and  $\nu = 1$  ground states and  $\tilde{\nu}_0(\text{He}_2\text{OCS})$  is the vibrational band center of He<sub>2</sub>-OCS. It can be computed from

$$[9] \quad \tilde{\nu}_0(\text{He}_2\text{OCS}) = \tilde{\nu}_0(\text{OCS}) + \Delta; \Delta = E_{\nu=1}^{\text{zpe}} - E_{\nu=0}^{\text{zpe}}$$

where  $E_{\nu=0}^{\text{zpe}}$  and  $E_{\nu=1}^{\text{zpe}}$  are zero-point energies (zpe) obtained on the adiabatic  $\nu = 0$  and  $\nu = 1$  surfaces, respectively, measured relative to the dissociation asymptote (and are therefore negative), and  $\tilde{\nu}_0(\text{OCS})$  is the vibrational frequency of the free OCS molecule. Using  $E_{\nu=0}^{\text{zpe}} = -32.2110$  cm<sup>-1</sup>,  $E_{\nu=1}^{\text{zpe}} = -32.0221$  cm<sup>-1</sup>, and  $\tilde{\nu}_0(\text{OCS}) = 2062.2012$  cm<sup>-1</sup> in eq. [9],<sup>24</sup> one finds that the band centre is  $\tilde{\nu}_0(\text{He}_2\text{OCS}) = 2062.398$  cm<sup>-1</sup>. This is very close to the experimental value (2062.426 cm<sup>-1</sup>).<sup>3</sup> The results we present are computed using the experimental value. The difference between the band centre and  $\tilde{\nu}_0(\text{OCS})$  is the frequency shift. It is 0.1968 cm<sup>-1</sup>, which is close to the frequency shift obtained from a quantum Monte Carlo calculation on the same potential.<sup>26</sup>

### Theoretical results

In Tables 1 and 2, we report  $\nu = 0$  energy levels for  $J = 0$  and  $J = 1, 2, 3$ , respectively, and give torsional and rotational assignments  $|\nu_t; JK_a K_c\rangle$ . Those for  $\nu = 1$  are very similar. Levels up to  $J = 5$  and wave functions up to  $J = 4$  have been computed. The lowest vibrational frequency of the complex is that of the He<sub>2</sub> torsion. For each  $J$ , the lowest set of  $2J + 1$  levels is assigned to the  $\nu_t = 0$  state. The next set is assigned to the  $\nu_t = 1$  levels and so on. Within each  $\nu_t$  set,  $(K_a, K_c) = (J, 0), (J, 1), \dots, (0, J)$  are assigned to levels in order of decreasing energy. In this fashion, it is possible to link irrep labels and  $\nu_t, JK_a K_c$  labels. This works remarkably well at least up to  $\nu_t = 4$ . From the permutation inversion group symmetries of the three  $J = 1$  levels, the fact that the symmetry of the  $\nu_t = 1$  torsional factor is  $B^-$ , and assuming that each state is a product of a torsional factor and a rotational factor, one can deduce the relationship between the

**Table 1.**  $J = 0$  vibrational levels (in  $\text{cm}^{-1}$ ) with the assigned torsional quantum number ( $\nu_t$ ) in the parenthesis.  $B+$  and  $B-$  levels are forbidden.

$A+$	$B+$	$A-$	$B-$
0.000(0)	8.095	9.536	0.430(1)
1.584(2)			3.540(3)
6.007(4)			8.988(5)
8.163			10.175
9.636			12.088
9.996			13.246
11.484(6)			14.068
			15.119
			16.220(7)

**Table 2.**  $J = 1, 2, 3$  rovibrational levels (in  $\text{cm}^{-1}$ ) for  $\nu = 0$  state of  $\text{He}_2\text{-OCS}$  with assignments ( $\nu_t; JK_aK_c$ ) giving the torsional ( $\nu_t$ ) and rotational ( $JK_aK_c$ ) quantum numbers.  $B+$  and  $B-$  levels are forbidden.

$A+$	$B+$	$A-$	$B-$
<b><math>J = 1</math></b>			
0.745(1; 1 <sub>11</sub> )	0.337 (0; 1 <sub>10</sub> )	0.250 (0; 1 <sub>01</sub> )	0.293 (0; 1 <sub>11</sub> )
3.827(3; 1 <sub>11</sub> )	0.668(1; 1 <sub>01</sub> )	0.751 (1; 1 <sub>10</sub> )	1.887 (2; 1 <sub>11</sub> )
	1.922 (2; 1 <sub>10</sub> )	1.836 (2; 1 <sub>01</sub> )	6.309 (4; 1 <sub>11</sub> )
	3.782 (3; 1 <sub>01</sub> )	3.856 (3; 1 <sub>10</sub> )	
	6.337 (4; 1 <sub>10</sub> )	6.246 (4; 1 <sub>01</sub> )	
<b><math>J = 2</math></b>			
0.724 (0; 2 <sub>02</sub> )	0.747 (0; 2 <sub>12</sub> )	1.000 (0; 2 <sub>21</sub> )	0.871 (0; 2 <sub>11</sub> )
1.018 (0; 2 <sub>20</sub> )	1.468 (1; 2 <sub>21</sub> )	1.219 (1; 2 <sub>12</sub> )	1.145 (1; 2 <sub>02</sub> )
1.237 (1; 2 <sub>11</sub> )	2.354 (2; 2 <sub>12</sub> )	2.602 (2; 2 <sub>21</sub> )	1.469 (1; 2 <sub>20</sub> )
2.331 (2; 2 <sub>02</sub> )	4.522 (3; 2 <sub>21</sub> )	4.285 (3; 2 <sub>12</sub> )	2.463 (2; 2 <sub>11</sub> )
2.617 (2; 2 <sub>20</sub> )	6.757 (4; 2 <sub>12</sub> )	6.975 (4; 2 <sub>21</sub> )	4.258 (3; 2 <sub>02</sub> )
4.373 (3; 2 <sub>11</sub> )			4.533 (3; 2 <sub>20</sub> )
6.718 (4; 2 <sub>02</sub> )			6.842 (4; 2 <sub>11</sub> )
6.983 (4; 2 <sub>20</sub> )			
<b><math>J = 3</math></b>			
1.730 (0; 3 <sub>22</sub> )	1.637 (0; 3 <sub>12</sub> )	1.399 (0; 3 <sub>03</sub> )	1.409 (0; 3 <sub>13</sub> )
1.932 (1; 3 <sub>13</sub> )	1.857 (0; 3 <sub>30</sub> )	1.791 (0; 3 <sub>21</sub> )	2.047(0; 3 <sub>31</sub> )
2.578 (1; 3 <sub>31</sub> )	2.050 (1; 3 <sub>03</sub> )	1.930 (0; 3 <sub>12</sub> )	2.196 (1; 3 <sub>22</sub> )
3.357 (2; 3 <sub>22</sub> )	2.198 (1; 3 <sub>21</sub> )	2.577 (1; 3 <sub>30</sub> )	3.060 (2; 3 <sub>13</sub> )
4.968 (3; 3 <sub>13</sub> )	3.280 (2; 3 <sub>12</sub> )	3.058 (2; 3 <sub>03</sub> )	3.690 (2; 3 <sub>31</sub> )
5.575 (3; 3 <sub>31</sub> )	3.696 (2; 3 <sub>30</sub> )	3.430 (2; 3 <sub>21</sub> )	5.251 (3; 3 <sub>22</sub> )
7.691 (4; 3 <sub>22</sub> )	4.954 (3; 3 <sub>03</sub> )	5.142 (3; 3 <sub>12</sub> )	7.425 (4; 3 <sub>13</sub> )
	5.300 (3; 3 <sub>21</sub> )	5.577 (3; 3 <sub>30</sub> )	8.001 (4; 3 <sub>31</sub> )
	7.593 (4; 3 <sub>12</sub> )	7.409 (4; 3 <sub>03</sub> )	
	8.003 (4; 3 <sub>30</sub> )	7.728 (4; 3 <sub>21</sub> )	

evenness or oddness of the ( $K_aK_c$ ) labels and permutation inversion group symmetries given in Table 3. This relationship holds for all the  $|\nu_t; JK_aK_c\rangle$  states we assigned. Because the symmetries associated with ( $ee$ ,  $oe$ ,  $oo$ , and  $eo$ ) are different for  $\nu_t = 0$  and  $\nu_t = 1$ , the principal axes, which, if used with

**Table 3.** The relationship between ( $\nu_t; JK_aK_c$ ) labels and permutation inversion group symmetries for two torsional states. It is derived from  $J = 0$  and 1 levels and expected to hold for higher  $J$  levels. The symmetry of  $|\nu_t = 1\rangle$  torsional state is  $B-$ . The physically allowed symmetries are in bold face.

State	$ee^a$	$oe$	$oo$	$eo$
$ \nu_t = 0\rangle$	<b><math>A+</math></b>	<b><math>B+</math></b>	<b><math>B-</math></b>	<b><math>A-</math></b>
$ \nu_t = 1\rangle$	<b><math>B-</math></b>	<b><math>A-</math></b>	<b><math>A+</math></b>	<b><math>B+</math></b>

<sup>a</sup>Evenness and oddness of  $K_aK_c$ .

the asymmetric top-symmetry rule,<sup>54</sup> would give the relation between  $J_{K_aK_c}$  and irrep labels, are different for  $\nu_t = 0$  and  $\nu_t = 1$ . Results for IR and MW transitions are reported in Tables 4 and 5. Intensities have been scaled so that the intensity of the transition (for  $\nu_t = 0$ )  $1_{01} \leftarrow 0_{00}$  equals 1.

In Fig. 2, we show the probability density computed from some of the  $\nu = 0$  and  $J = 0$  wave functions. Coupling between the torsion and other coordinates is weak enough that a clear torsional progression is evident. The probability densities are obtained by integrating over coordinates except  $\theta_2$  and  $\phi_2$ . To avoid a coordinate transformation, we use the Radau angles. It is remarkable that it is possible to identify torsional states up to  $\nu_t = 7$ . This indicates that the torsion is only weakly coupled to other coordinates.

### Comparison of theory and experiment

The dipole moment of  $\text{He}_2\text{-OCS}$  is almost parallel to the the OCS axis. In conjunction with the fact that the  $a$ -inertia axis of  $\text{He}_2\text{-OCS}$  is close to OCS, this means that the dominant transitions in the experimental (IR and MW) spectra are  $a$ -type transitions with  $\Delta K_a = 0$  and  $\Delta K_c = \pm 1$ .

In the IR study,<sup>3</sup>  $K_a = 0$   $\nu_t = 0$  lines were all assigned for  $P(3)$ ,  $P(2)$ , ...,  $R(3)$ , and  $R(4)$ . These lines are marked with an asterisk in Table 4 and also indicated on the stick spectrum of Fig. 3. According to the calculations, all of these experimental lines are correctly assigned.

Because rotational wave functions with  $K_a$  even (odd) are symmetric (antisymmetric) with respect to exchange of the He atoms, Tang and McKellar (TM), in ref. 3, argue that only states with even values of  $K_a$  are allowed for  $\nu_t = 0$  and only odd values of  $K_a$  are allowed for  $\nu_t = 1$ . This is consistent with the assignments of Table 4 derived from the assignment procedure outlined in the previous section. Table 4 contains lines that TM were unable to fully assign, but report in their Table 4.<sup>3</sup> These are  $P$  and  $R$  lines that TM assumed were either  $K_a = 1$  or  $K_a = 2$  transitions. All these lines were matched with our computed levels. Moreover,  $K_a = 1$  transitions are for  $\nu_t = 1$  state and  $K_a = 2$  transitions are for  $\nu_t = 2$  state, again confirming the TM symmetry argument.

TM do assign four  $Q$  lines close to the band centre (near  $2062.4 \text{ cm}^{-1}$ ), see Fig. 2 of ref. 3. The outer pair was assigned to  $Q_2(2)$  (the notation is  $Q_{K_a}(J)$ ) lines using the parameters fitted to the  $K_a = 0$  lines assuming that all transitions with even  $K_a$  must occur between levels with  $\nu_t = 0$ . TM propose that the inner pair may be  $Q_1(1)$  lines of the  $\nu_t = 1$  state. One



**Table 4.** Strong IR rovibrational transitions (with  $I \geq 0.10$ , except for the first four transitions and the  $\nu_t = 2$  line at  $2062.912\text{ cm}^{-1}$ , which are weaker) for  $\text{He}_2\text{-}^{16}\text{O}^{12}\text{C}^{32}\text{S}$  (in  $\text{cm}^{-1}$ ) at a temperature of 0.7 K. The experimental data are from ref. 3. Transitions marked by an asterisk were assigned as  $K_a = 0$ ; the four  $Q$  lines are marked by a dagger; the remaining experimental lines were assigned as  $K_a = 1$  or 2 by Tang and McKellar.<sup>3</sup> Their  $K_a$  assignments agree with our assignments.

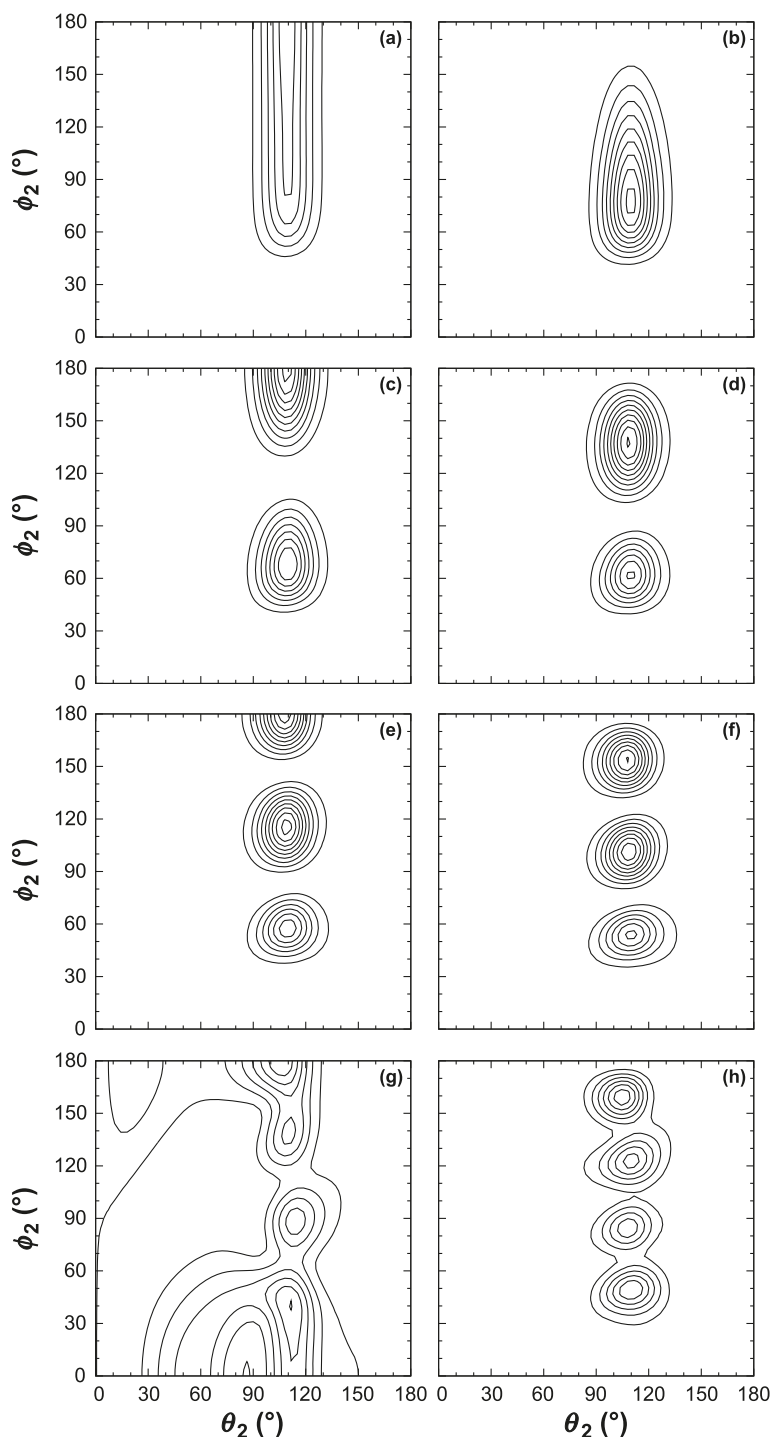
$\nu'_i; J'_{K'_a K'_c} - \nu''_i; J''_{K''_a K''_c}$	$E'_i$	$E''_i$	Calculated	Observed	Observed – Calculated	$S$	$I$
0; 2 <sub>20</sub> – 0; 3 <sub>21</sub>	1.015	1.791	2061.650	2061.633	–0.017	0.19	0.04
0; 2 <sub>21</sub> – 0; 3 <sub>22</sub>	0.997	1.730	2061.693	2061.681	–0.012	0.18	0.05
1; 2 <sub>11</sub> – 1; 3 <sub>12</sub>	1.232	1.960	2061.698	2061.681	–0.016	0.28	0.04
1; 2 <sub>12</sub> – 1; 3 <sub>13</sub>	1.215	1.932	2061.709	2061.687	–0.023	0.29	0.05
0; 2 <sub>02</sub> – 0; 3 <sub>03</sub>	0.723	1.399	2061.751	2061.744*	–0.006	0.31	0.15
1; 1 <sub>10</sub> – 1; 2 <sub>11</sub>	0.747	1.237	2061.936	2061.924	–0.013	0.16	0.11
1; 1 <sub>11</sub> – 1; 2 <sub>12</sub>	0.741	1.219	2061.947	2061.930	–0.018	0.16	0.11
0; 1 <sub>01</sub> – 0; 2 <sub>02</sub>	0.250	0.724	2061.951	2061.946*	–0.005	0.21	0.41
0; 0 <sub>00</sub> – 0; 1 <sub>01</sub>	0.000	0.250	2062.176	2062.174*	–0.002	0.11	0.60
0; 2 <sub>21</sub> – 0; 2 <sub>20</sub>	0.997	1.018	2062.406	2062.403†	–0.003	0.36	0.39
1; 1 <sub>11</sub> – 1; 1 <sub>10</sub>	0.741	0.751	2062.416	2062.413†	–0.003	0.15	0.29
1; 1 <sub>10</sub> – 1; 1 <sub>11</sub>	0.747	0.745	2062.428	2062.429†	0.000	0.15	0.29
0; 2 <sub>20</sub> – 2; 2 <sub>21</sub>	1.015	1.000	2062.441	2062.441†	0.001	0.36	0.41
0; 1 <sub>01</sub> – 0; 0 <sub>00</sub>	0.250	0.000	2062.676	2062.677*	0.003	0.11	1.00
1; 2 <sub>12</sub> – 1; 1 <sub>11</sub>	1.215	0.745	2062.896	2062.895	–0.002	0.16	0.30
0; 2 <sub>02</sub> – 0; 1 <sub>01</sub>	0.723	0.250	2062.900	2062.902*	0.002	0.21	1.10
1; 2 <sub>11</sub> – 1; 1 <sub>10</sub>	1.232	0.751	2062.907	2062.902*	–0.005	0.16	0.30
2; 2 <sub>02</sub> – 2; 1 <sub>01</sub>	2.321	1.836	2062.912			0.22	0.05
0; 3 <sub>03</sub> – 0; 2 <sub>02</sub>	1.397	0.724	2063.099	2063.100*	0.002	0.31	0.61
1; 3 <sub>13</sub> – 1; 2 <sub>12</sub>	1.927	1.219	2063.133	2063.129	–0.004	0.29	0.20
1; 3 <sub>12</sub> – 1; 2 <sub>11</sub>	1.954	1.237	2063.143	2063.145	0.002	0.29	0.20
0; 3 <sub>22</sub> – 0; 2 <sub>21</sub>	1.727	1.000	2063.152	2063.160	0.008	0.18	0.20
0; 2 <sub>20</sub> – 0; 1 <sub>01</sub>	1.015	0.250	2063.191	??		0.02	0.10
0; 3 <sub>21</sub> – 0; 2 <sub>20</sub>	1.787	1.018	2063.195	??		0.19	0.20
0; 4 <sub>04</sub> – 0; 3 <sub>03</sub>	2.260	1.399	2063.287	2063.288*	–0.001	0.42	0.21
0; 5 <sub>05</sub> – 0; 4 <sub>04</sub>	3.314	2.263	2063.477	2063.469*	–0.008	<i>a</i>	<i>a</i>

**Note:** ??: Strong and unobserved lines. *a*: Not computed.

**Table 5.** Calculated MW transitions of  $\text{He}_2\text{-OCS}$  (in  $\text{cm}^{-1}$ ) with  $I \geq 0.97$  at a temperature of 0.7 K, except for two weak  $\Delta \nu_t = 1$  transitions (marked with an asterisk) that may be observable. Transitions marked with a dagger are  $\nu_t = 1$  transitions that may be observable. Observed transitions are measured by Xu and Jäger.<sup>4</sup>

$\nu'_i; J'_{K'_a K'_c} - \nu''_i; J''_{K''_a K''_c}$	$E'_i$	$E''_i$	Calculated	Observed	Observed – Calculated	$S$	$I$
0; 1 <sub>01</sub> – 0; 0 <sub>00</sub>	0.250	0.000	0.250	0.252	0.002	0.945	1.00
0; 2 <sub>02</sub> – 0; 1 <sub>01</sub>	0.724	0.250	0.474	0.479	0.005	1.737	3.23
1; 2 <sub>12</sub> – 1; 1 <sub>11</sub>	1.219	0.745	0.475†			1.441	0.97
1; 2 <sub>11</sub> – 1; 1 <sub>10</sub>	1.237	0.751	0.485†			1.443	0.99
0; 3 <sub>03</sub> – 0; 2 <sub>02</sub>	1.399	0.724	0.675	0.679	0.004	2.527	3.04
1; 3 <sub>13</sub> – 1; 2 <sub>12</sub>	1.932	1.219	0.712†			2.568	1.21
1; 3 <sub>12</sub> – 1; 2 <sub>11</sub>	1.960	1.237	0.724†			2.585	1.20
0; 3 <sub>22</sub> – 0; 2 <sub>21</sub>	1.730	1.000	0.730			1.495	1.14
0; 3 <sub>21</sub> – 0; 2 <sub>20</sub>	1.791	1.018	0.773			1.577	1.26
0; 4 <sub>04</sub> – 0; 3 <sub>03</sub>	2.263	1.399	0.864			3.401	1.45
1; 1 <sub>10</sub> – 0; 0 <sub>00</sub>	0.751	0.000	0.751*			0.04	0.19
1; 2 <sub>11</sub> – 0; 1 <sub>01</sub>	1.237	0.250	0.987*			0.10	0.18

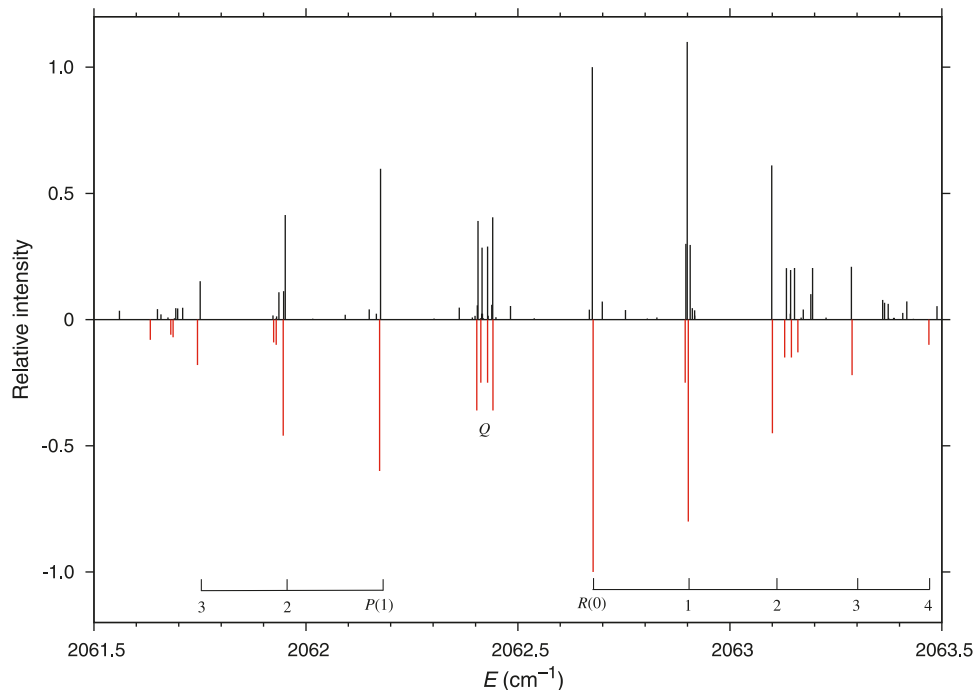
**Fig. 2.** Probability function plots for torsional states. (a), (b), (c), (d), (e), (f), (g), and (h) are the  $\nu_t = 0, 1, 2, 3, 4, 5, 6$ , and 7 torsional states, respectively. The torsional states are not strongly coupled to other modes although there are other states between them. Coupling becomes important starting at about  $\nu_t = 6$ . For (g), the contour interval is 0.05, and for all others, it is 0.1.



would normally expect the two  $Q$  a-type transitions between  $J = 2$  levels to be closer than the  $Q$  transitions between  $J = 1$  levels because, for a given  $J$ , the separation between  $J_{J,0}$  and  $J_{J,1}$  decreases as  $J$  increases. TM conjecture that  $J = 1$   $Q$  transitions are closer because the spectroscopic parameters for the  $\nu_t = 1$  differ significantly from those of the  $\nu_t = 0$  state, due to coupling. TM's assignments of the  $Q$  branches are all confirmed by our calculations, see Table 4.

None of the calculated  $\Delta\nu_t = 1$  IR transitions were strong (such transitions were found in  $\text{He}_2\text{-N}_2\text{O}^{14}$ ) and are not observed experimentally. According to the calculation, the strongest  $\nu_t = 2$  line is at  $2062.912\text{ cm}^{-1}$ . Its intensity is sensitive to the temperature. This line is not observed experimentally. Some calculated strong lines (marked by ?? in Table 4) were not observed and may have been obscured by nearby strong lines of complexes with different  $N$ .<sup>55</sup>

**Fig. 3.** Calculated (top) and observed (bottom) IR spectra of He<sub>2</sub>–OCS. The intensity of the  $R(0)$  transition is scaled to 1 for both the calculation and the experiment. The experimental data are from ref. 56. The calculated spectrum is for  $T = 0.7$  K. The  $P$  and  $R$  branches of  $K_a = 0$  lines are marked on a line below the sticks.



The agreement of the observed and calculated IR relative intensities (for  $T = 0.7$  K) in Table 4 is quite satisfactory. This is also demonstrated in Fig. 3, which shows the observed and calculated spectra in the form of a stick diagram. The intensity pattern of the four  $Q$  lines is in excellent agreement with the experiment.

Xu and Jäger observed a few  $K_a = 0$  MW transitions.<sup>4</sup> They agree well with our calculations (see Table 5). It would be interesting to attempt to detect the two transitions with  $\Delta v_t = 1$  that are marked with an asterisk in Table 5. In addition, two strong transitions with  $v_t = 1$  (marked with a dagger in Table 5) are very close to an observed transition at  $0.479 \text{ cm}^{-1}$ , shifted to the blue by only  $0.01 \text{ cm}^{-1}$  and  $0.1 \text{ cm}^{-1}$ , respectively. As MW experiments are very sensitive, it seems likely that they, and other weaker transitions between levels in Tables 1 and 2, could be detected.

## Conclusion

An understanding of small doped helium clusters facilitates the analysis of larger ones, which are used to develop a better understanding of superfluid effects. One important general conclusion is the high quality of the potential obtained by adding two-body interactions. It is remarkable that one can obtain such good agreement with experiment without including three-body interactions. The quality of the potential can only be determined by doing accurate rovibrational calculations that properly account for the interaction of the large amplitude vibrations and vibration and rotation. Several complexes with two helium atoms and a linear dopant have been studied, and in all cases, two-body potentials are excellent.

## Acknowledgements

This work has been supported by the Natural Sciences and Engineering Research Council of Canada (NSERC) and the Canada Research Chairs Program. Calculations were done on computers of the Réseau québécois de calcul de haute performance (RQCHP). We are grateful to Bob McKellar for many informative discussions and to Francesco Paesani for sending us the potentials.

## References

- (1) Xu, Y.; Jäger, W. *Chem. Phys. Lett.* **2001**, 350 (5-6), 417. doi:10.1016/S0009-2614(01)01314-8.
- (2) Tang, J.; Xu, Y.; McKellar, A. R. W.; Jäger, W. *Science* **2002**, 297 (5589), 2030. doi:10.1126/science.1073718. PMID: 12242436.
- (3) Tang, J.; McKellar, A. R. W. *J. Chem. Phys.* **2003**, 119 (11), 5467. doi:10.1063/1.1598954.
- (4) Xu, Y.; Jäger, W. *J. Chem. Phys.* **2003**, 119 (11), 5457. doi:10.1063/1.1598953.
- (5) Tang, J.; McKellar, A. R. W. *J. Chem. Phys.* **2003**, 119 (2), 754. doi:10.1063/1.1578473.
- (6) McKellar, A. R. W. *J. Chem. Phys.* **2006**, 125 (16), o. 164328. doi:10.1063/1.2363196. PMID:17092094.
- (7) Dumes, B. S.; Surin, L. A. *Physics - Uspekhi* **2006**, 49 (11), 1113. doi:10.1070/PU2006v049n11ABEH006073.
- (8) Surin, L. A.; Potapov, A. V.; Dumes, B. S.; Schlemmer, S.; Xu, Y.; Raston, P. L.; Jäger, W. *Phys. Rev. Lett.* **2008**, 101 (23), o. 233401. doi:10.1103/PhysRevLett.101.233401. PMID: 19113549.
- (9) Hernández, M. I.; Halberstadt, N.; Sands, W. D.; Janda, K. C. *J. Chem. Phys.* **2000**, 113 (17), 7252. doi:10.1063/1.1313786.

- (10) Paesani, F.; Whaley, K. B. *J. Chem. Phys.* **2004**, *121* (11), 5293. doi:10.1063/1.1782175. PMID:15352823.
- (11) Cazzato, P.; Paolini, S.; Moroni, S.; Baroni, S. *J. Chem. Phys.* **2004**, *120* (19), 9071. doi:10.1063/1.1697388. PMID:15267841.
- (12) Song, X.; Xu, Y.; Roy, P.-N.; Jäger, W. *J. Chem. Phys.* **2004**, *121* (24), 12308. doi:10.1063/1.1819875. PMID:15606249.
- (13) Topic, W.; Jäger, W.; Blinov, N.; Roy, P.-N.; Botti, M.; Moroni, S. *J. Chem. Phys.* **2006**, *125* (14), o. 144310. doi:10.1063/1.2357604. PMID:17042593.
- (14) Wang, X.-G.; Carrington, T., Jr.; Tang, J.; McKellar, A. R. W. *J. Chem. Phys.* **2005**, *123* (3), o. 034301. doi:10.1063/1.1924408.
- (15) Wang, X.-G.; Carrington, T., Jr.; McKellar, A. R. W. *J. Phys. Chem. A* **2009**, *113* (47), 13331. doi:10.1021/jp904778f. PMID:19842654.
- (16) Tang, J.; McKellar, A. R. W.; Wang, X.-G.; Carrington, T., Jr. *Can. J. Phys.* **2009**, *87* (5), 417. doi:10.1139/P08-119.
- (17) Li, H.; Blinov, N.; Roy, P.-N.; Le Roy, R. J. *J. Chem. Phys.* **2009**, *130* (14), o. 144305. doi:10.1063/1.3109897. PMID:19368443.
- (18) Wang, X.-G.; Carrington, T., Jr. *J. Chem. Phys.* **2001**, *114* (4), 1473. doi:10.1063/1.1331357.
- (19) Chen, R.; Guo, H. *J. Chem. Phys.* **2001**, *114* (4), 1467. doi:10.1063/1.1331356.
- (20) Grebenev, S.; Hartmann, M.; Havenith, M.; Sartakov, B.; Toennies, J. P.; Vilesov, A. F. *J. Chem. Phys.* **2000**, *112* (10), 4485. doi:10.1063/1.481011.
- (21) Higgins, K.; Klemperer, W. *J. Chem. Phys.* **1999**, *110* (3), 1383. doi:10.1063/1.478013.
- (22) Tang, J.; McKellar, A. R. W. *J. Chem. Phys.* **2002**, *117* (6), 2586. doi:10.1063/1.1493191.
- (23) Toennies, J. P.; Vilesov, A. F. *Annu. Rev. Phys. Chem.* **1998**, *49* (1), 1. doi:10.1146/annurev.physchem.49.1.1. PMID:15012423.
- (24) Tang, J.; McKellar, A. R. W. *J. Chem. Phys.* **2001**, *115* (7), 3053. doi:10.1063/1.1386920.
- (25) Callegari, C.; Lehmann, K. K.; Schmied, R.; Scoles, G. *J. Chem. Phys.* **2001**, *115* (22), 10090. doi:10.1063/1.1418746.
- (26) Paesani, F.; Whaley, K. B. *J. Chem. Phys.* **2004**, *121* (9), 4180. doi:10.1063/1.1768931. PMID:15332966.
- (27) Paesani, F.; Viel, A.; Gianturco, F. A.; Whaley, K. B. *Phys. Rev. Lett.* **2003**, *90* (7), o. 073401. doi:10.1103/PhysRevLett.90.073401. PMID:12633226.
- (28) Moroni, S.; Sarsa, A.; Fantoni, S.; Schmidt, K. E.; Baroni, S. *Phys. Rev. Lett.* **2003**, *90* (14), o. 143401. doi:10.1103/PhysRevLett.90.143401. PMID:12731914.
- (29) Chapuisat, X.; Iung, C. *Phys. Rev. A* **1992**, *45* (9), 6217. doi:10.1103/PhysRevA.45.6217. PMID:9907741.
- (30) Gatti, F.; Iung, C.; Menou, M.; Justum, Y.; Nauts, A.; Chapuisat, X. *J. Chem. Phys.* **1998**, *108* (21), 8804. doi:10.1063/1.476327.
- (31) Mladenović, M. *J. Chem. Phys.* **2000**, *112* (3), 1070. doi:10.1063/1.480662.
- (32) Light, J. C.; Hamilton, I. P.; Lill, J. V. *J. Chem. Phys.* **1985**, *82* (3), 1400. doi:10.1063/1.448462.
- (33) Bacic, Z.; Light, J. C. *Annu. Rev. Phys. Chem.* **1989**, *40* (1), 469. doi:10.1146/annurev.pc.40.100189.002345.
- (34) Light, J. C.; Carrington, T., Jr. *Adv. Chem. Phys.* **2000**, *114*, 263. doi:10.1002/9780470141731.ch4.
- (35) Littlejohn, R. G.; Cargo, M.; Carrington, T., Jr.; Mitchell, K. A.; Poirier, B. *J. Chem. Phys.* **2002**, *116* (20), 8691. doi:10.1063/1.1473811.
- (36) Wang, X.-G.; Carrington, T., Jr. *J. Chem. Phys.* **2004**, *121* (7), 2937. doi:10.1063/1.1767093. PMID:15291604.
- (37) Wang, X.-G.; Carrington, T., Jr. *J. Chem. Phys.* **2003**, *118* (15), 6946. doi:10.1063/1.1554735.
- (38) Zare, R. N. *Angular Momentum*; Wiley: New York, 1988.
- (39) Chen, R.; Ma, G.; Guo, H. *J. Chem. Phys.* **2001**, *114* (11), 4763. doi:10.1063/1.1348274.
- (40) Wang, X.-G.; Carrington, T., Jr. *J. Chem. Phys.* **2001**, *115* (21), 9781. doi:10.1063/1.1407277.
- (41) Bramley, M. J.; Carrington, T., Jr. *J. Chem. Phys.* **1993**, *99* (11), 8519. doi:10.1063/1.465576.
- (42) Bramley, M. J.; Carrington, T., Jr. *J. Chem. Phys.* **1994**, *101* (10), 8494. doi:10.1063/1.468110.
- (43) Carrington, T., Jr. *Encyclopedia of Computational Chemistry*; von Ragué Schleyer, P., Ed.; John Wiley & Sons, 1998; Vol. 5.
- (44) Chen, R.; Guo, H. *J. Chem. Phys.* **1998**, *108* (15), 6068. doi:10.1063/1.476017.
- (45) Wang, X.-G.; Carrington, T., Jr. *J. Chem. Phys.* **2002**, *117* (15), 6923. doi:10.1063/1.1506911.
- (46) Bramley, M. J.; Tromp, J. W.; Carrington, T., Jr.; Corey, G. C. *J. Chem. Phys.* **1994**, *100* (9), 6175. doi:10.1063/1.467273.
- (47) Wang, X.-G.; Carrington, T., Jr. *J. Chem. Phys.* **2003**, *119* (1), 101. doi:10.1063/1.1574016.
- (48) Saupe, S.; Wapperhorst, M. H.; Meyer, B.; Urban, W.; Maki, A. G. *J. Mol. Spectrosc.* **1996**, *175* (1), 190. doi:10.1006/jmsp.1996.0021.
- (49) Aziz, R. A.; McCourt, F. R. W.; Wong, C. C. K. *Mol. Phys.* **1987**, *61* (6), 1487. doi:10.1080/00268978700101941.
- (50) Wei, H.; Carrington, T., Jr. *J. Chem. Phys.* **1992**, *97* (5), 3029. doi:10.1063/1.463044.
- (51) Echave, J.; Clary, D. C. *Chem. Phys. Lett.* **1992**, *190* (3-4), 225. doi:10.1016/0009-2614(92)85330-D.
- (52) Leforestier, C. *J. Chem. Phys.* **1991**, *94* (10), 6388. doi:10.1063/1.460317.
- (53) Colbert, D. T.; Miller, W. H. *J. Chem. Phys.* **1992**, *96* (3), 1982. doi:10.1063/1.462100.
- (54) Bunker, P. R.; Jensen, P. *Molecular Symmetry and Spectroscopy*; NRC Research Press: Ottawa, 1998.
- (55) McKellar, A.R.W. Private communication.
- (56) McKellar, A.R.W. Unpublished data.



# Density functional theory study on the electron spectra of naphthalene and azulene vapours

Delano P. Chong

**Abstract:** The ionization and excitation spectra of valence and core electrons of naphthalene and azulene in the gas phase are studied with density functional theory. The results are compared with available experimental data and previous calculations. New estimates are proposed for the ionization energies of both valence and core electrons and the calculated excitation energies are consistent with experiment.

**Key words:** ionizations, photoelectron spectra (PES), excitations, UV-vis absorption, electron spectra, core-electron binding energies, naphthalene, azulene, electron spectroscopy for chemical analysis (ESCA), X-ray photoelectron spectroscopy (XPS), density functional theory (DFT).

**Résumé :** Faisant appel à la théorie de la fonctionnelle de la densité, on a étudié les spectres d'ionisation et d'excitation de valence et des électrons de cœur du naphthalène et de l'azulène en phase gazeuse. On a comparé les résultats de ces calculs avec les données expérimentales disponibles et avec les résultats de calculs antérieurs. De nouvelles évaluations sont proposées pour les énergies d'ionisation de valence ainsi que des électrons de cœur et les énergies d'excitation calculées sont en accord avec les données expérimentales.

**Mots-clés :** ionisations, spectres photoélectroniques (SPE), excitations, absorption UV-vis, spectres électroniques, énergies de liaison d'électron de cœur, naphthalène, azulène, spectroscopie électronique pour l'analyse chimique (SEAC), spectroscopie photoélectronique des rayons X (SPX), théorie de la fonctionnelle de la densité (TFD).

[Traduit par la Rédaction]

## Introduction

In the absence of the universal density functional, our efforts in density functional theory (DFT) continue to be directed towards the development of the best DFT procedure for each property of interest, such as the core-electron spectra of molecules containing heavier elements. For the ionization and excitation spectra of valence and core electrons of organic and other small molecules, we have developed reliable methods within DFT, with a limited number of test cases in benchmark databases. Naturally, more test cases are desirable and the accuracy of such additional calculations would enhance our confidence in the developed procedures and in the reliability of predictions of data not yet available experimentally.

The molecular structures and spectra of naphthalene and azulene have been the subject of many studies. Azulene has been particularly interesting to chemists as well as to the dye industry because of its absorption in the visible region, leading to its blue color. In some of the earlier investigations, the absorption spectra of azulene were studied in solutions or solid state.<sup>1–7</sup> Now, with the exception of the core-electron binding energies (CEBEs) of azulene, experimental results on ionization and excitation of both valence and core electrons of gas-phase naphthalene and azulene, including excitations to many Rydberg-like states, are available. Therefore,

we can assess the reliability of various DFT procedures by comparing calculations on single molecules to observed data of naphthalene and azulene vapours.

For the interpretation of the photoelectron spectra of valence electrons, the procedure of outer-valence Green's function (OVGF)<sup>8</sup> is usually the most reliable. However, OVGF may not be as accurate as one wishes in two situations: (i) when the basis set, usually limited by computational facilities, is not large enough and (ii) when the pole strength is small due to significant shake-up effects, in which case the method known as third-order algebraic diagrammatic construction ADC(3)<sup>9</sup> is more reliable, provided a sufficiently large basis set is used. The average absolute deviation (AAD) of OVGF and ADC(3) results from experiment can be as low as 0.2 eV or better. In some cases, however, the AAD can be greater than 0.3 eV; for example, the seven vertical ionization energies (VIEs) of *s*-triazine.<sup>10</sup> On the other hand, DFT offers alternative procedures. The meta-Koopmans' theorem (mKT) is a shortcut approximation, usually giving an AAD of 0.4 eV,<sup>11</sup> considerably better than the usual application of Koopman's theorem in Hartree-Fock calculations, but this method also performs poorly for *s*-triazine, with an AAD of 0.58 eV.<sup>10</sup> Another DFT procedure recently developed<sup>12</sup> can be abbreviated as  $\Delta$ PBE0(SAOP), which means the energy difference calculated with the parameter-free Perdew-Burke-Ernzerhof

Received 15 January 2010. Accepted 5 March 2010. Published on the NRC Research Press Web site at canjchem.nrc.ca on 26 May 2010.

This article is part of a Special Issue dedicated to Professor R. J. Boyd.

**D.P. Chong.** Department of Chemistry, 2036 Main Mall, University of British Columbia, Vancouver, BC V6T 1Z1, Canada.  
(e-mail: Chong@chem.ubc.ca).

functional (PBE0) exchange-correlation functional,  $E_{xc}$ ,<sup>13–15</sup> using the electron density obtained with the exchange-correlation potential,  $V_{xc}$ , known as the statistical average of orbital potentials (SAOP).<sup>16–18</sup> This procedure succeeded in giving an AAD of 0.21 eV for over 100 cases of nonperfluoro molecules.<sup>12</sup> For *s*-triazine, this  $\Delta$ PBE0(SAOP) was also successful, with an AAD of 0.23 eV.<sup>10</sup> It is our intention to test mKT and  $\Delta$ PBE0(SAOP) again on naphthalene and azulene.

For excitation of valence electrons, the comparison with experiment is more difficult. In the lower-energy region, the absorptions are broadened by vibrations and, in the higher-energy region, there are so many Rydberg-like states that association of calculated values with observed energies may be unreliable. On the theoretical side, some studies on naphthalene and azulene are based on semiempirical methods such as Hückel molecular orbitals (MO),<sup>19</sup> the complete neglect of differential overlap with modified parameters (CNDO/M),<sup>20</sup> and Zerner's intermediate neglect of differential overlap (ZINDO),<sup>21</sup> all using subminimal basis sets, with no hope of predicting higher energy excitations. More recent approaches include second-order multiconfigurational perturbation theory (CASPT2),<sup>22</sup> time-dependent density functional theory (TDDFT) with parameter free  $E_{xc} = \text{PBE0}$ ,<sup>23</sup> and second-order polarization propagator approximation (SOPPA).<sup>24</sup> Our own preference is time-dependent DFT using  $V_{xc} = \text{SAOP}$ , which has been shown to give reliable results.<sup>10,25</sup>

Finally, the spectroscopy of core electrons of naphthalene and azulene has not been as well-studied as that of valence electrons. The established procedure for CEBEs is relatively simple:  $\Delta E(\text{PW86-PW91})$  with localized core hole has been shown to give excellent results.<sup>26,27</sup> For inner-shell excitations, a similar procedure has been developed for small molecules,<sup>28,29</sup> but symmetric molecules such as naphthalene and azulene are more difficult and we have to resort to shifting the results for transitions between symmetry MOs by the difference between the CEBEs of symmetry and localized core holes.

The object of this work is to compare the results of DFT calculations on the ionization and excitation spectra of both valence and core electrons with experiment to gain a better overall view of the protocol developed in our continuing studies.

## Computational details

The symmetry labels for both naphthalene and azulene molecules are ambiguous. In this work, we put both molecules on the *y*-*z* plane (with the  $\pi$ -MOs being mainly linear combinations of  $p_x$  AOs). For naphthalene, atoms C9 and C10 lie on the *z* axis. This choice of symmetry axes agrees with most of the earlier studies. On the other hand, in the theoretical papers by Rubio et al.,<sup>22</sup> Adamo et al.,<sup>23</sup> and Packer et al.,<sup>24</sup> naphthalene lies on the *x*-*y* plane with *x* and *y* being the long and short molecular axes, respectively. Therefore, we need to translate their symmetry labels into our choice of axis system. For azulene, the numbering is as follows: the carbon atoms C9 and C10 shared by both rings lie on the *y* axis, with the smaller ring labeled C1–C2–C3–C10–C9 and the larger one C4–C5–C6–C7–C8–C9–C10.

All the calculations in this work are carried out at the experimental geometry of naphthalene<sup>30</sup> and azulene<sup>31</sup> with the Amsterdam density functional (ADF) program<sup>32</sup> using a large even-tempered (et) basis set of Slater-type orbitals of polarized valence quadruple-zeta (pVQZ) quality.<sup>33</sup> For the description of valence electrons, the exchange-correlation potential of  $V_{xc} = \text{SAOP}$  is our preferred choice. For example, the resulting dipole moment from SAOP/et-pVQZ is 0.923 D, compared to 0.929 D from multireference singles and doubles configuration interaction (MR-SDCI),<sup>34</sup> and the observed value of  $0.882 \pm 0.002$  D.<sup>31</sup> Both theoretical values are closer to experiment than the recent result of 1.024 D from B3LYP/6-311++G(3d,2p).<sup>35</sup>

The DFT procedures we recommend can be abbreviated as follows: (i)  $\Delta$ PBE0(SAOP)/et-pVQZ for valence ionization, (ii) TDDFT(SAOP)/et-pVQZ for valence excitations, (iii)  $\Delta$ PW86-PW91/et-pVQZ +  $C_{\text{rel}}$  for core-electron ionizations, and (iv)  $\Delta$ PW86-PW91/et-pVQZ +  $C_{\text{rel}}$  for core-electron excitation energies, with approximate *f* values obtained with truncated TDDFT(SAOP)/et-pVQZ. For core-electron spectra, a small relativistic correction,  $C_{\text{rel}}$ , in atomic form derived empirically in 1995,<sup>36</sup> is added:

$$[1] \quad C_{\text{rel}} = KX_{\text{nr}}^N$$

with  $K = 0.2198 \times 10^{-6}$ ,  $N = 2.178$ , and  $X_{\text{nr}}$  is the nonrelativistic result. For approximate *f* values, the time-saving procedure of truncated TDDFT follows the proposal of Stener et al.<sup>37</sup> and allows only excitations from core MOs.

It should be mentioned that, when there is a choice between maintaining symmetry and insisting on integral number of electrons in a cationic calculation, the latter has been found to lead to better prediction of VIEs (except for perhalo systems).

## Results and discussions

### Valence ionizations

There have been several experimental measurements of the ionization energies of gas-phase naphthalene and azulene. For naphthalene, Lindholm et al.<sup>38</sup> presented the photoelectron spectrum (PES) without giving the numerical values. Therefore, their spectrum is enlarged and the ionization energies are measured to the nearest 0.02 eV in this study. Eland<sup>39</sup> also reported the PES of naphthalene, but the spectrum recorded by Klasinc et al.<sup>40</sup> appears to have a higher resolution. We combine the various studies and give the best estimate of the VIEs in Table 1, together with the results from the DFT methods mentioned above. It is disappointing to find the poor results from the mKT/et-pVQZ approximation. We are happy to see the excellent results from  $\Delta$ PBE0(SAOP)/et-pVQZ, with an AAD of 0.15 eV for naphthalene, even surpassing the OVGf/6-311G(d,p) method with an AAD of 0.27 eV for the first 16 VIEs.<sup>42</sup> Consequently, the assignment of the VIEs to symmetry species has been partly based on the  $\Delta$ PBE0(SAOP)/et-pVQZ results.

Similarly, experimental and theoretical data for azulene are displayed in Table 2. Since some VIEs of azulene are known only to 0.1 eV accuracy, the unreliable second decimal place of the AADs are given as subscripts. Contrary to expectations, the AAD of 0.39 eV from ADC(3) in Table 2 can be greater than that from the OVGf/6-311G(d,p)

**Table 1.** Vertical ionization energies (in eV) of naphthalene vapour.

MO	Observed VIEs					This work	
	1968 <sup>a</sup>	1972 <sup>b</sup>	1972 <sup>c</sup>	1983 <sup>d</sup>	Best estimate	mKT <sup>e</sup>	ΔPBE0(SAOP) <sup>f</sup>
1a <sub>u</sub> (π)	8.13	8.18	8.12	8.09	8.13	9.57	8.00 (−0.13)
2b <sub>3u</sub> (π)		8.84	8.91	8.81	8.85	10.32	8.83 (−0.02)
1b <sub>2g</sub> (π)		10.04	10.08	9.95	10.02	11.22	9.95 (−0.07)
1b <sub>1g</sub> (π)		10.94	10.85	10.85	10.88	12.22	11.13 (+0.25)
9a <sub>g</sub>		11.28	11.05	11.03	11.12	12.10	11.26 (+0.14)
6b <sub>3g</sub>		11.60	11.35	11.36	11.44	12.09	11.30 (−0.14)
7b <sub>2u</sub>		12.46	11.90	11.86	12.07	12.98	12.23 (+0.16)
1b <sub>3u</sub> (π)		12.70	12.5	12.56	12.59	13.81	12.92 (+0.33)
7b <sub>1u</sub>		13.42	13.5		13.46	13.74	13.06 (−0.40)
6b <sub>2u</sub>		13.62	13.7	13.77	13.70	14.09	13.50 (−0.20)
5b <sub>3g</sub>		13.90			13.90	14.22	13.58 (−0.32)
8a <sub>g</sub>		14.38		14.37	14.38	14.87	14.33 (−0.05)
6b <sub>1u</sub>		14.54	14.45		14.50	15.04	14.47 (−0.03)
7a <sub>g</sub>		15.84	15.9	15.85	15.86	16.12	15.69 (−0.17)
4b <sub>3g</sub>		16.30	16.25	16.35	16.30	16.55	16.13 (−0.17)
5b <sub>2u</sub>		16.50			16.50	16.74	16.32 (−0.18)
6a <sub>g</sub>		18.72			18.72	18.87	18.70 (−0.02)
5b <sub>1u</sub>		19.04			19.04	19.16	19.04 (0.00)
4b <sub>2u</sub>		19.42			19.42	19.54	19.43 (+0.01)
AAD					(0)	0.65	0.15

<sup>a</sup>Kitagawa.<sup>41</sup>

<sup>b</sup>Lindholm et al.<sup>38</sup>

<sup>c</sup>Eland.<sup>39</sup>

<sup>d</sup>Klansinc et al.<sup>40</sup>

<sup>e</sup>meta-Koopmans' theorem = −ε(SAOP).

<sup>f</sup>Deviations from best estimates are shown in parentheses.

**Table 2.** Vertical ionization energies (in eV) of azulene vapour.

MO	Observed VIEs					ADC(3)	Present work	
	1968 <sup>a</sup>	1972 <sup>b</sup>	1974 <sup>c</sup>	1980 <sup>d</sup>	Best estimate	2002 <sup>e</sup>	mKT <sup>f</sup>	ΔPBE0(SAOP) <sup>g</sup>
2a <sub>2</sub> (π)	7.41	7.42	7.43	7.42	7.42	7.08	8.93	7.32 (−0.10)
3b <sub>1</sub> (π)		8.52	8.50	8.52	8.51	8.24	10.00	8.51 (0)
1a <sub>2</sub> (π)		10.0	10.07	10.1	10.07	10.15	11.53	10.38 (+0.31)
2b <sub>1</sub> (π)		11.0	10.85	11.1	10.85	11.00	12.21	11.19 (+0.34)
17a <sub>1</sub>		11.35			11.35	11.65	11.98	11.24 (−0.11)
12b <sub>2</sub>						12.43	12.60	11.95
16a <sub>1</sub>						12.87	13.07	12.43
11b <sub>2</sub>		12.5			12.5	12.94	13.06	12.46 (−0.04)
1b <sub>1</sub> (π)						12.52	13.66	12.83
15a <sub>1</sub>						13.47	13.56	12.97
10b <sub>2</sub>		13.2			13.2	13.87	13.79	13.25 (+0.05)
9b <sub>2</sub>		14.5			14.5	15.18	15.03	14.7 (+0.20)
14a <sub>1</sub>						15.35	15.15	14.67
13a <sub>1</sub>		15.7			15.7	16.30	16.15	15.75 (+0.05)
8b <sub>2</sub>						16.89	16.61	16.35
AAD						0.39	0.95	0.1 <sub>3</sub>

<sup>a</sup>Kitagawa.<sup>41</sup>

<sup>b</sup>Eland.<sup>39</sup>

<sup>c</sup>Boschi et al.<sup>43</sup>

<sup>d</sup>Dougherty et al.<sup>44</sup>

<sup>e</sup>Deleuze.<sup>45</sup>

<sup>f</sup>meta-Koopmans' theorem = −ε(SAOP).

<sup>g</sup>Deviations from best estimates are shown in parentheses.

**Table 3.** Vertical excitation energies for dipole-allowed transitions of naphthalene vapour (in eV) and  $f$  values in parentheses.

CASPT2	SOPPA	TDDFT (PBE0)	TDDFT(SAOP)	Observed								
1994 <sup>a</sup>	1996 <sup>b</sup>	1999 <sup>c</sup>	2010 <sup>d</sup>	1968 <sup>e</sup>	1968 <sup>f</sup>	1968 <sup>g</sup>	1971 <sup>h</sup>	1972 <sup>i</sup>	1972 <sup>j</sup>	1981 <sup>k</sup>	2003 <sup>l</sup>	2006 <sup>m</sup>
1B <sub>2u</sub> 4.03 (0.000)	1B <sub>2u</sub> 3.86 (0.000)	4.48	1B <sub>2u</sub> 4.25 (0.000)			3.97 (0.002) B <sub>2u</sub>				4.12		
1B <sub>1u</sub> 4.56 (0.050)	1B <sub>1u</sub> 4.44 (0.100)	4.58	1B <sub>1u</sub> 4.04 (0.047)			4.45 (0.102) B <sub>1u</sub>			4.45 B <sub>1u</sub>			
		5.62	1B <sub>3g</sub> 4.94				5.59			5.22		
							5.63		5.60	5.52		5.56
2B <sub>2u</sub> 5.54 (1.337)	2B <sub>2u</sub> 5.68 (1.62)	6.23	2B <sub>2u</sub> 5.57 (1.234)			5.89 (1.0) B <sub>2u</sub>	5.87 B <sub>2u</sub>	5.89 B <sub>2u</sub>	5.89 B <sub>2u</sub>			5.99
		5.50	1A <sub>u</sub> 5.74									
		7.00	2A <sub>g</sub> 5.78									
2B <sub>1u</sub> 5.93 (0.313)	2B <sub>1u</sub> 5.87 (0.304)	5.99	2B <sub>1u</sub> 5.87 (0.142)			6.14 (0.3)	6.13 B <sub>1u</sub>		6.0	6.05	6.46	
		5.84	1B <sub>2g</sub> 5.96									
		5.84	1B <sub>1g</sub> 5.97									
		6.35	2B <sub>3g</sub> 6.06									
		6.62	2B <sub>2g</sub> 6.09									
		6.24	3A <sub>g</sub> 6.16									
		0.68	2B <sub>1g</sub> 6.23									
		7.01	4A <sub>g</sub> 6.47									
1B <sub>3u</sub> 6.03 (0.003)	1B <sub>3u</sub> 5.97 (0.014)	6.29	1B <sub>3u</sub> 6.49 (0.008)		6.53	6.53 (0.1) B <sub>2u</sub>			6.52		6.57	6.58
			3B <sub>2g</sub> 6.77									
			3B <sub>1g</sub> 6.79									
			2A <sub>u</sub> 6.81									
			3B <sub>1g</sub> 6.84									
2B <sub>3u</sub> 6.50 (0.007)	2B <sub>3u</sub> 6.39 (0.009)	6.44	2B <sub>3u</sub> 6.87 (0.016)	6.91	6.78			6.78	6.78		6.79	6.80
			3B <sub>3u</sub> 6.88 (0.005)									
			4B <sub>2g</sub> 6.98	7.01							7.01	
			3B <sub>3g</sub> 7.08		7.09						7.07	7.07
			3A <sub>u</sub> 7.09		7.26						7.19	7.20
3B <sub>1u</sub> 6.34 (0.002)	3B <sub>1u</sub> 6.55 (0.003)	6.93	3B <sub>1u</sub> 7.31 (0.575)	7.31	7.37			7.37	7.36		7.35	7.35
			4A <sub>u</sub> 7.38									
			5B <sub>2g</sub> 7.39									
			4B <sub>1g</sub> 7.43									
			4B <sub>3u</sub> 7.48 (0.008)		7.50							
			6B <sub>2g</sub> 7.48									
			4B <sub>3g</sub> 7.52									
			5B <sub>3u</sub> 7.57 (0.002)		7.57			7.54				
6.58 (0.018)	6.57 (0.010)	7.23	3B <sub>2u</sub> 7.57 (0.031)	7.62	7.62			7.63	7.62			
			5A <sub>u</sub> 7.59									
			6A <sub>u</sub> 7.63									
			7A <sub>u</sub> 7.67								7.68	7.68
			8A <sub>u</sub> 7.74		7.74							
			6B <sub>3u</sub> 7.82 (0.009)	7.77	7.78			7.77	7.77			



Table 3 (concluded).

CASPT2	SOPPA	TDDFT (PBE0)	TDDFT(SAOP)	Observed	1971 <sup>h</sup>	1972 <sup>j</sup>	1981 <sup>k</sup>	2003 <sup>l</sup>	2006 <sup>m</sup>
1994 <sup>a</sup>	1996 <sup>b</sup>	1999 <sup>c</sup>	2010 <sup>d</sup>	1968 <sup>e</sup>	1968 <sup>g</sup>	1972 <sup>j</sup>	1981 <sup>k</sup>	2003 <sup>l</sup>	2006 <sup>m</sup>
			7B <sub>3u</sub> 7.88 (0.019)	7.85					
			8B <sub>3u</sub> 7.97 (0.000)	7.87					
			4B <sub>2u</sub> 8.04 (0.003)						
			7B <sub>2g</sub> 8.10						

<sup>a</sup>Rubio et al.<sup>22</sup>

<sup>b</sup>Packer et al.<sup>24</sup>

<sup>c</sup>Adamo et al.<sup>23</sup>

<sup>d</sup>This work.

<sup>e</sup>Angus et al.<sup>47</sup>

<sup>f</sup>Kitagawa.<sup>41</sup>

<sup>g</sup>George and Morris.<sup>48</sup>

<sup>h</sup>Angus and Morris.<sup>49</sup>

<sup>i</sup>Koch et al.<sup>50</sup>

<sup>j</sup>Huebner et al.<sup>51</sup>

<sup>k</sup>Dick and Hohlneicher.<sup>52</sup>

<sup>l</sup>Kuthirummal and Weber.<sup>54</sup>

<sup>m</sup>Kuthirummal and Weber.<sup>55</sup>

method with an AAD of 0.27 eV<sup>42</sup> in the case of azulene. The VIEs from the shortcut method of mKT are even poorer for azulene than for naphthalene. Again, the recommended procedure of  $\Delta$ PBE0(SAOP)/et-pVQZ does extremely well, with an AAD of 0.13 eV. For the combined results on both molecules,  $\Delta$ PBE0(SAOP)/et-pVQZ leads to an AAD of 0.14 eV for a total of 28 valence-electron ionizations.

Although valence ionization energies are often given to the nearest 0.01 eV, the probable error is more likely to be 0.05–0.10 eV due to calibration errors and vibrational effects. Therefore, our AAD of 0.14 eV, approaching experimental reliability, is a pleasant surprise but could conceivably be the result of a cancellation of errors.

The procedure we recommend is not perfect for every molecule. When the effect of shake-up satellites is significant, the single configuration used in our DFT calculation may not be able to give an accurate enough description of the cation; and we do not have intensities like the pole strengths in OVGF and ADC(3). Moreover, the same procedure did not perform as well for the limited database of 13 VIEs of perhalo molecules. Instead, choosing symmetry rather than the integer number of electrons gave a reasonable AAD of 0.25 eV.<sup>12</sup>

### Valence excitations

There have been many measurements of the excitations of valence electrons of naphthalene and azulene vapours. For a comparison of various theoretical and experimental data, we list the excitations according to the order given by our TDDFT(SAOP)/et-pVQZ calculation. Data from observed ultraviolet absorptions<sup>4,41,46–50</sup> are compared to calculated energies of singlet excitations. Electron energy loss results<sup>51</sup> are also included in Table 3, although the intensity does not strictly follow transition dipole rules. Two-photon spectroscopy<sup>52</sup> is different and may lead to dipole-forbidden excited states. Similarly, the so-called Rydberg fingerprint spectroscopy,<sup>53</sup> whether it is performed with 4-photon off-resonance ionization<sup>54</sup> or 3-photon double-resonance ionization scheme,<sup>55</sup> can also produce dipole-forbidden states. Therefore, the observed energies are placed near the closest calculated energies. The results are summarized in Table 3 for naphthalene and Table 4 for azulene. It appears that the results from our preferred procedure of TDDFT(SAOP)/et-pVQZ can be matched with most of the observed excitations. The only poor results are the first two excited singlets of naphthalene, for which the high-power method of SOPPA<sup>24</sup> is probably more reliable. For naphthalene, Table 3 shows that TDDFT(SAOP)/et-pVQZ appears to be competitive to the recent methods of CASPT2, TDDFT(PBE0), and SOPPA.

### Core-electron ionization

Little is known about the C1s ionization of naphthalene and azulene. For naphthalene, Crenshaw and Banna<sup>57</sup> reported an average CEBE of 290.12 eV. With the approach of localized core holes, we find the values of 290.33, 290.06, and 290.03 eV for C9, C2, and C1, respectively, averaging to 290.10 eV as shown in Table 5. In comparison, the CI results of Hollauer et al.<sup>58</sup> give an average CEBE(C1s) of 292.46 eV. For the purpose of determining the inner-shell excitation energies, the results from symmetry core-hole treatment are also included in Table 5.

**Table 4.** Vertical excitation energies (in eV) of azulene to singlets with *f* values in parentheses.

HMO-CI	CNDO/M	CIS(D)	TDDFT (SAOP)	Observed					
1956 <sup>a</sup>	1995 <sup>b</sup>	2005 <sup>c</sup>	2010 <sup>d</sup>	1962 <sup>e</sup>	1966 <sup>f</sup>	1987 <sup>g</sup>	1995 <sup>h</sup>	2003 <sup>i</sup>	2006 <sup>j</sup>
1.73(0.017)	2.35(0.030)	2.33	1B <sub>2</sub> 2.30(0.007)	1.76–2.36		1.77	2.32		
3.08(0.002)	3.68(0.075)	4.33	1A <sub>1</sub> 3.46(0.009)	3.54–3.57		3.57	3.67		
4.11(0.116)	4.50(0.285)	4.94	2B <sub>2</sub> 4.42(0.039)				4.50		
4.69(1.243)	5.03(1.767)	5.21	2A <sub>1</sub> 4.73(0.997)				5.07		
		7.45	1A <sub>2</sub> 5.03						
		6.51	1B <sub>1</sub> 5.23(0.000)						5.26
			2B <sub>1</sub> 5.59(0.000)						
5.60(0.365)		6.36	3B <sub>2</sub> 5.59(0.165)						
		7.39	2A <sub>2</sub> 5.72						
5.99(0.003)		6.87	3A <sub>1</sub> 5.72(0.002)						
		7.50	3A <sub>2</sub> 5.79						5.80
			4A <sub>2</sub> 5.96						
6.19(0.014)			4B <sub>2</sub> 6.02(0.081)		6.01				6.07
			3B <sub>1</sub> 6.10 (0.002)						
6.87(0.215)			4A <sub>1</sub> 6.20(0.179)					6.26	6.28
			5A <sub>2</sub> 6.23						
			6A <sub>2</sub> 6.25						
			4B <sub>1</sub> 6.31(0.000)					6.36	6.36
			5B <sub>1</sub> 6.37(0.022)		6.38				
			7A <sub>2</sub> 6.53						
7.02(0.278)			5B <sub>2</sub> 6.54(0.107)		6.62			6.46	6.47
			6B <sub>1</sub> 6.64(0.001)		6.71			6.60	6.59
			8A <sub>2</sub> 6.67						6.67
			7B <sub>1</sub> 6.80(0.000)						
			8B <sub>1</sub> 6.81(0.006)					6.84	6.84
			9A <sub>2</sub> 6.93						
			10A <sub>2</sub> 7.02						
			6B <sub>2</sub> 7.06(0.134)		6.90				
			9B <sub>1</sub> 7.08(0.001)						
			11A <sub>2</sub> 7.09						
7.02(0.199)			5A <sub>1</sub> 7.09(0.024)						
			10B <sub>1</sub> 7.12(0.000)						
			6A <sub>1</sub> 7.14(0.040)						
			7B <sub>2</sub> 7.20(0.092)		7.04				
			11B <sub>1</sub> 7.32(0.012)						

<sup>a</sup>Pariser.<sup>19</sup><sup>b</sup>Elblidi et al.<sup>20</sup><sup>c</sup>Hinchliffe and Soscún.<sup>35</sup><sup>d</sup>This work.<sup>e</sup>Hunt and Ross.<sup>4</sup><sup>f</sup>Kitagawa et al.<sup>46</sup><sup>g</sup>Suzuki and Ito.<sup>56</sup><sup>h</sup>Experimental data cited by Elblidi et al.<sup>20</sup><sup>i</sup>Kuthirummal and Weber.<sup>54</sup><sup>j</sup>Kuthirummal and Weber.<sup>55</sup>

As far as we know, the CEBE of azulene has not been determined experimentally. Hitchcock et al.<sup>59</sup> estimated the CEBE of azulene to be the same as naphthalene to calculate

the term values. We believe that our calculated value of 289.76 eV presented in Table 6 would be a more reliable estimate.

**Table 5.** Core-electron binding energies (in eV) of naphthalene vapour.

Atom	CEBE	Deviation
Observed <sup>a</sup>	290.12	(0)
<b>Localized core hole</b>		
C1=C4=C5=C8	290.03	
C2=C3=C6=C7	290.06	
C9=C10	290.33	
Average	290.10	−0.02
<b>Symmetry core hole</b>		
1a <sub>g</sub>	277.61	
1b <sub>1u</sub>	277.60	
1b <sub>2u</sub>	277.61	
1b <sub>3g</sub>	277.60	
Average	277.60	−12.52
<b>CI (2005)<sup>b</sup></b>		
C1	292.40	
C2	292.40	
C9	292.70	
Average	292.46	+2.34

<sup>a</sup>Crenshaw and Banna.<sup>57</sup><sup>b</sup>Hollaender et al.<sup>58</sup>

### Inner-shell excitations

The calculation of inner-shell excitation spectra of highly symmetric molecules, such as naphthalene and azulene, is not an easy task because we cannot use the localized core-hole approximation, which would destroy the symmetry of the excited states. Instead, we must resort to shifting the results for transitions between symmetry MOs by the difference between the CEBEs of symmetry and localized core holes. Our first step is to limit the excitation to only those from core electrons in a truncated TDDFT(SAOP)/et-pVQZ computation.<sup>35</sup> Guided by the approximate oscillator strengths from such TDDFT calculations, we compute the dipole-allowed inner-shell excited states by the method of  $\Delta E(\text{PW86-PW91})/\text{et-pVQZ} + C_{\text{rel}}$ . As shown in Tables 5 and 6, the difference between the CEBEs for localized and symmetry core holes is 12.50 eV for naphthalene and 7.02 eV for azulene. These values are used to shift the inner-shell excitation energies calculated for transitions between symmetry MOs calculated by  $\Delta \text{PW86-PW91}/\text{et-pVQZ} + C_{\text{rel}}$  and the final results are summarized in Tables 7 and 8.

Another difficulty lies in the fact that there are many core MOs in each symmetry: 1a<sub>g</sub>–3a<sub>g</sub>, 1b<sub>1u</sub> and 2b<sub>1u</sub>, 1b<sub>2u</sub>–3b<sub>2u</sub>, 1b<sub>3u</sub> and 2b<sub>3u</sub> for naphthalene, and 1a<sub>1</sub>–6a<sub>1</sub> and 1b<sub>2</sub>–4 b<sub>2</sub> for azulene. For naphthalene, the virtual MOs in increasing energies are 2b<sub>1g</sub>( $\pi$ ), 2b<sub>2g</sub>( $\pi$ ), 3b<sub>3u</sub>( $\pi$ ), 10a<sub>g</sub>, 8b<sub>2u</sub>, 8b<sub>1u</sub>, 2a<sub>u</sub>( $\pi$ ), etc. and the virtual MOs of azulene in increasing energies are 4b<sub>1</sub>( $\pi$ ), 3a<sub>2</sub>( $\pi$ ), 18a<sub>1</sub>, 5b<sub>1</sub>( $\pi$ ), 13b<sub>2</sub>, 19a<sub>1</sub>, 20a<sub>1</sub>, 14b<sub>2</sub>, 6b<sub>1</sub>( $\pi$ ), etc. With the ADF program, we cannot compute the excitation energy of 2a<sub>1</sub>–4b<sub>1</sub>( $\pi$ ) for azulene by  $\Delta \text{PW86-PW91}/\text{et-pVQZ}$ , for example. The  $f$  values obtained from truncated TDDFT(SAOP)/et-pVQZ calculations for all a<sub>1</sub> core MOs to 4b<sub>1</sub>( $\pi$ ) are therefore summed and listed as be-

**Table 6.** Core-electron binding energies (in eV) of azulene vapour.

Atom	CEBE
<b>Localized core hole</b>	
C1=C3	289.17
C2	289.53
C4=C8	290.13
C5=C7	289.75
C6	290.02
C9=C10	289.96
Average	289.76
<b>Symmetry core hole</b>	
1a <sub>1</sub>	282.74
1b <sub>2</sub>	282.74
Average	282.74

longing to 1a<sub>1</sub>–4b<sub>1</sub>( $\pi$ ) in Table 8. Similar procedure is followed for all the other transitions listed in Tables 7 and 8.

Still another difficulty is the poor resolution of the experimental spectra. This makes the comparison of theory with experiment very uncertain. One possible way to overcome this last difficulty is to average the calculated results weighted by the approximate  $f$  values. This procedure is used for Tables 7 and 8. As can be seen from Tables 7 and 8, our calculated results seem to underestimate the core-electron excitation energies by an average of 0.3 eV. Some possible causes of the underestimation are the difficulties mentioned above. If we assume that the underestimation is experiment, it is reduced to a remarkable 0.1 eV.

### Conclusions

In summary, the results of  $\Delta \text{PBE0}(\text{SAOP})/\text{et-pVQZ}$  for valence ionization of naphthalene and azulene are excellent, as can be seen from the AAD of 0.14 eV. The results from our preferred procedure of TDDFT(SAOP)/et-pVQZ can be matched with most of the observed excitations of valence electrons. Because the  $V_{\text{xc}} = \text{SAOP}$  is asymptotically correct, it is our belief that it leads to a reliable description of valence electrons and good distribution of orbital energies for both occupied and vacant MOs. Hence, the nice prediction of excitation spectra is not surprising. On the other hand, from the excellent results of VIEs, we draw the tentative conclusion that, given the electron density,  $E_{\text{xc}} = \text{PBE0}$  can provide excellent energy differences.

There is only one experimental CEBE of naphthalene at 290.12 eV with which we can compare our average calculated value of 290.10 eV from applying  $\Delta \text{PW86-PW91}/\text{et-pVQZ} + C_{\text{rel}}$  on the localized core holes. For azulene, we believe that our average CEBE(C1s) of 289.76 eV is more reliable than the estimate based on the observed 290.12 eV for naphthalene. Finally, although the difficulties in predicting core-electron excitation spectra do not allow us to make definitive conclusions on naphthalene and azulene, the results are extremely encouraging.

Such excellent performance of the recommended procedures for the ionization and excitation spectra of valence

**Table 7.** Inner-shell excitation energies (in eV) of naphthalene vapour with approximate  $f$  values in parentheses.

	From	To	$\Delta E$	Shifted <sup>a</sup>	Average <sup>b</sup>	Observed <sup>c</sup>	CI <sup>d</sup>
B <sub>3u</sub>	1b <sub>2u</sub>	2b <sub>1g</sub> ( $\pi$ )	272.40	<b>284.90</b> (0.00323)		285.0	285.1
B <sub>3u</sub>	1b <sub>1u</sub>	2b <sub>2g</sub> ( $\pi$ )	272.96	<b>285.46</b> (0.00320)		285.7	285.8
B <sub>3u</sub>	1a <sub>g</sub>	4b <sub>3u</sub> ( $\pi$ )	273.72	286.22 (0.00112)			
B <sub>1u</sub>	1b <sub>3g</sub>	10b <sub>2u</sub>	273.88	286.38 (0.00091)			
B <sub>2u</sub>	1a <sub>g</sub>	10b <sub>2u</sub>	273.89	286.39 (0.00164)			
B <sub>3u</sub>	1a <sub>g</sub>	3b <sub>3u</sub> ( $\pi$ )	274.02	286.52 (0.00330)	<b>286.42</b> (0.00697)	286.9 (sh)	286.5
B <sub>1u</sub>	1b <sub>1u</sub>	10a <sub>g</sub>	274.44	286.94 (0.00145)			
B <sub>2u</sub>	1b <sub>2u</sub>	10a <sub>g</sub>	274.45	286.95 (0.00152)			
B <sub>1u</sub>	1b <sub>3g</sub>	8b <sub>2u</sub>	274.57	287.07 (0.00029)			
B <sub>2u</sub>	1a <sub>g</sub>	8b <sub>2u</sub>	274.58	287.08 (0.00276)			
B <sub>2u</sub>	1b <sub>3g</sub>	8b <sub>1u</sub>	274.72	287.22 (0.00013)			
B <sub>1u</sub>	1a <sub>g</sub>	8b <sub>1u</sub>	274.73	287.23 (0.00367)	<b>287.10</b> (0.00982)	287.2	287.9
B <sub>2u</sub>	1b <sub>1u</sub>	7b <sub>3g</sub>	275.19	287.69 (0.00261)			
B <sub>1u</sub>	1b <sub>2u</sub>	7b <sub>3g</sub>	275.20	287.70 (0.00240)			
B <sub>1u</sub>	1b <sub>1u</sub>	11a <sub>g</sub>	275.24	287.74 (0.00137)			
B <sub>2u</sub>	1b <sub>2u</sub>	11a <sub>g</sub>	275.25	287.75 (0.00042)			
B <sub>3u</sub>	1b <sub>3g</sub>	2a <sub>u</sub>	275.38	287.88 (0.00429)			
Weighted average				287.77 (0.01109)			
B <sub>2u</sub>	1b <sub>3g</sub>	12b <sub>1u</sub>	275.69	288.19 (0.00028)			
B <sub>2u</sub>	1b <sub>3g</sub>	9b <sub>1u</sub>	275.77	288.27 (0.00297)			
B <sub>1u</sub>	1a <sub>g</sub>	9b <sub>1u</sub>	275.78	288.28 (0.00047)			
B <sub>1u</sub>	1b <sub>3g</sub>	9b <sub>2u</sub>	275.89	288.39 (0.00215)			
B <sub>2u</sub>	1a <sub>g</sub>	9b <sub>2u</sub>	275.91	288.41 (0.00089)			
B <sub>1u</sub>	1b <sub>1u</sub>	12a <sub>g</sub>	275.92	288.42 (0.00127)			
B <sub>2u</sub>	1b <sub>2u</sub>	12a <sub>g</sub>	275.93	288.43 (0.00041)			
Weighted average				288.34 (0.00844)			
B <sub>2u</sub>	1b <sub>1u</sub>	8b <sub>3g</sub>	276.22	288.72 (0.00145)			
B <sub>1u</sub>	1a <sub>g</sub>	11b <sub>1u</sub>	276.39	288.89 (0.00382)			
B <sub>2u</sub>	1b <sub>3g</sub>	11b <sub>1u</sub>	276.58	289.08 (0.00045)			
B <sub>3u</sub>	1b <sub>1u</sub>	3b <sub>2g</sub> ( $\pi$ )	276.62	289.12 (0.00087)			
B <sub>3u</sub>	1b <sub>2u</sub>	3b <sub>1g</sub> ( $\pi$ )	276.83	289.33 (0.00078)			
Weighted average					<b>288.27</b> (0.02690)	288.5	
B <sub>2u</sub>	1b <sub>1u</sub>	8b <sub>3g</sub>	276.22	288.72 (0.00145)			
B <sub>1u</sub>	1a <sub>g</sub>	11b <sub>1u</sub>	276.39	288.89 (0.00382)			
B <sub>2u</sub>	1b <sub>3g</sub>	11b <sub>1u</sub>	276.58	289.08 (0.00045)			
B <sub>3u</sub>	1b <sub>1u</sub>	3b <sub>2g</sub> ( $\pi$ )	276.62	289.12 (0.00087)			
B <sub>3u</sub>	1b <sub>2u</sub>	3b <sub>1g</sub> ( $\pi$ )	276.83	289.33 (0.00078)			
B <sub>1u</sub>	1b <sub>1u</sub>	13a <sub>g</sub>	277.29	289.79 (0.00175)			
B <sub>2u</sub>	1b <sub>2u</sub>	13a <sub>g</sub>	277.30	289.80 (0.00174)			
B <sub>1u</sub>	3b <sub>1u</sub>	14a <sub>g</sub>	277.67	290.17 (0.00115)			
B <sub>2u</sub>	1b <sub>2u</sub>	14a <sub>g</sub>	277.67	290.17 (0.00100)	<b>289.94</b> (0.00564)	290.3	290.4

<sup>a</sup>Present work: shift = CEBE (loc) – CEBE (sym) = 290.10 – 277.60 = 12.50 eV.<sup>b</sup>Average weighted by  $f$  values.<sup>c</sup>Gordon et al.<sup>60</sup><sup>d</sup>Hollauer et al.<sup>58</sup> with an empirical shift of 3.9 eV.

and core electrons of naphthalene and azulene could be due to the large basis sets employed, and (or) to the low level of charge transfer between carbon and hydrogen in

naphthalene and azulene, unlike perhalo systems. Therefore, more test cases should be investigated in future studies.



**Table 8.** Inner-shell excitation energies (in eV) of azulene vapour with approximate  $f$  values in parentheses.

	From	To	$\Delta E$	Shifted <sup>a</sup>	Average <sup>b</sup>	Observed <sup>c</sup>
B <sub>1</sub>	1a <sub>1</sub>	4b <sub>1</sub> ( $\pi$ )	276.94	<b>283.96</b> (0.0030)		284.4
B <sub>1</sub>	1b <sub>2</sub>	3a <sub>2</sub> ( $\pi$ )	277.86	<b>284.88</b> (0.0041)		285.3
A <sub>1</sub>	1a <sub>1</sub>	18a <sub>1</sub>	279.88	286.90 (0.00188)		
B <sub>2</sub>	1b <sub>2</sub>	18a <sub>1</sub>	279.88	286.90 (0.00116)		
A <sub>1</sub>	1b <sub>2</sub>	16b <sub>2</sub>	279.94	286.96 (0.00066)		
A <sub>1</sub>	1b <sub>2</sub>	13b <sub>2</sub>	280.09	287.11 (0.00057)		
B <sub>2</sub>	1a <sub>1</sub>	13b <sub>2</sub>	280.09	287.11 (0.00236)		
A <sub>1</sub>	1a <sub>1</sub>	19a <sub>1</sub>	280.39	287.41 (0.00203)		
B <sub>2</sub>	1b <sub>2</sub>	19a <sub>1</sub>	280.39	287.41 (0.00163)	<b>287.15</b> (0.0103)	287.3
A <sub>1</sub>	1a <sub>1</sub>	20a <sub>1</sub>	280.78	287.80 (0.00243)		
B <sub>2</sub>	1b <sub>2</sub>	20a <sub>1</sub>	280.79	287.81 (0.00111)		
B <sub>2</sub>	1a <sub>1</sub>	14b <sub>2</sub>	280.85	287.87 (0.00237)		
A <sub>1</sub>	1b <sub>2</sub>	14b <sub>2</sub>	280.85	287.87 (0.00088)		
B <sub>1</sub>	1a <sub>1</sub>	5b <sub>1</sub> ( $\pi$ )	280.93	287.95 (0.00321)	<b>287.87</b> (0.0100)	288.1
A <sub>1</sub>	1a <sub>1</sub>	21a <sub>1</sub>	281.34	288.36 (0.00151)		
B <sub>2</sub>	1b <sub>2</sub>	21a <sub>1</sub>	281.34	288.36 (0.00094)		
A <sub>1</sub>	1a <sub>1</sub>	22a <sub>1</sub>	281.42	288.44 (0.00168)		
B <sub>2</sub>	1b <sub>2</sub>	22a <sub>1</sub>	281.42	288.44 (0.00128)		
B <sub>1</sub>	1a <sub>1</sub>	6b <sub>1</sub> ( $\pi$ )	281.48	288.50 (0.00163)		
B <sub>2</sub>	1a <sub>1</sub>	15b <sub>2</sub>	281.52	288.54 (0.00200)		
A <sub>1</sub>	1b <sub>2</sub>	15b <sub>2</sub>	281.52	288.54 (0.00129)		
B <sub>1</sub>	1a <sub>1</sub>	7b <sub>1</sub> ( $\pi$ )	281.65	288.67 (0.00202)		
B <sub>1</sub>	1b <sub>2</sub>	4a <sub>2</sub>	281.80	288.82 (0.00239)	<b>288.55</b> (0.0147)	288.9

<sup>a</sup>Present work: shift = CEBE (loc) – CEBE (sym) = 289.76 – 282.74 = 7.02 eV.<sup>b</sup>Average weighted by  $f$  values.<sup>c</sup>Hitchcock et al.<sup>59</sup>

## Acknowledgment

The author is grateful to the Natural Sciences and Engineering Research Council of Canada (NSERC) for financial support and to Professor E. J. Baerends of Vrije University, Amsterdam, where this study was started.

## References

- (1) Mann, D. E.; Platt, J. R.; Kleven, H. B. *J. Chem. Phys.* **1949**, *17* (5), 481. doi:10.1063/1.1747292.
- (2) Clar, E. *J. Chem. Soc.* **1950**, 1823. doi:10.1039/jr9500001823.
- (3) Anderson, A. G.; Steckler, B. M. *J. Am. Chem. Soc.* **1959**, *81* (18), 4941. doi:10.1021/ja01527a046.
- (4) Hunt, G. R.; Ross, I. G. *J. Mol. Spectrosc.* **1962**, *9*, 50. doi:10.1016/0022-2852(62)90212-6.
- (5) Thulstrup, E. W.; Case, P. L.; Michel, J. *Chem. Phys.* **1974**, *6* (3), 410. doi:10.1016/0301-0104(74)85025-1.
- (6) Lewis, J. W.; Nauman, R. V.; Boulter, D. B., Jr.; McGlynn, S. P. *J. Phys. Chem.* **1983**, *87* (19), 3611. doi:10.1021/j100242a009.
- (7) Shevyakov, S. V.; Li, H.; Muthyala, R.; Asato, A. E.; Cronney, J. C.; Jameson, D. M.; Liu, R. S. H. *J. Phys. Chem. A* **2003**, *107* (18), 3295. doi:10.1021/jp021605f.
- (8) von Niessen, W.; Schirmer, J.; Cederbaum, L. S. *Comput. Phys.* **1984**, *1* (2), 57. doi:10.1016/0167-7977(84)90002-9.
- (9) Schirmer, J.; Cederbaum, L. S.; Walter, O. *Phys. Rev. A* **1983**, *28* (3), 1237. doi:10.1103/PhysRevA.28.1237.
- (10) (a) Chong, D. P. *Can. J. Chem.* **2009**, *87* (8), 1148. doi:10.1139/V09-084.; (b) Chong, D. P. *Can. J. Chem.* **2010**, *88* (6), 577. doi:10.1139/V10-065.
- (11) Chong, D. P.; Gritsenko, O. V.; Baerends, E. J. *J. Chem. Phys.* **2002**, *116* (5), 1760. doi:10.1063/1.1430255.
- (12) Segala, M.; Chong, D. P. *J. Electron Spectrosc. Relat. Phenom.* **2009**, *171* (1–3), 18. doi:10.1016/j.elspec.2008.12.006.
- (13) Perdew, J. P.; Burke, K.; Ernzerhof, M. *Phys. Rev. Lett.* **1996**, *77* (18), 3865. doi:10.1103/PhysRevLett.77.3865. PMID:10062328.
- (14) Perdew, J. P.; Burke, K.; Ernzerhof, M. *Phys. Rev. Lett.* **1997**, *78* (7), 1396. doi:10.1103/PhysRevLett.78.1396.
- (15) Adamo, C.; Barone, V. *J. Chem. Phys.* **1999**, *110* (13), 6158. doi:10.1063/1.478522.
- (16) Gritsenko, O. V.; Schipper, P. R. T.; Baerends, E. J. *Chem. Phys. Lett.* **1999**, *302* (3–4), 199. doi:10.1016/S0009-2614(99)00128-1.
- (17) Gritsenko, O. V.; Schipper, P. R. T.; Baerends, E. J. *Int. J. Quantum Chem.* **2000**, *76* (3), 407. doi:10.1002/(SICI)1097-461X(2000)76:3<407::AID-QUA9>3.0.CO;2-A.
- (18) Schipper, P. R. T.; Gritsenko, O. V.; van Gisbergen, S. J. A.; Baerends, E. J. *J. Chem. Phys.* **2000**, *112* (3), 1344. doi:10.1063/1.480688.
- (19) Pariser, R. *J. Chem. Phys.* **1956**, *25* (6), 1112. doi:10.1063/1.1743159.

- (20) Elblidi, K.; Boucetta, A.; Benali, B.; Kadiri, A.; Cazeau-Dubroca, C.; Nouchi, G.; Pesquer, M. *J. Mol. Struct. THEOCHEM* **1995**, *343*, 57. doi:10.1016/0166-1280(95)90525-1.
- (21) Patalinghug, W. C.; Chang, M.; Solis, J. *J. Chem. Educ.* **2007**, *84* (12), 1945. doi:10.1021/ed084p1945.
- (22) Rubio, M.; Merchán, M.; Orti, E.; Roos, B. O. *Chem. Phys.* **1994**, *179* (3), 395. doi:10.1016/0301-0104(94)87016-0.
- (23) Adamo, C.; Scuseria, G. E.; Barone, V. *J. Chem. Phys.* **1999**, *111* (7), 2889. doi:10.1063/1.479571.
- (24) Packer, M. J.; Dalskov, E. K.; Enevoldsen, T.; Jensen, H. J. A.; Oddershede, J. *J. Chem. Phys.* **1996**, *105* (14), 5886. doi:10.1063/1.472430.
- (25) Chong, D. P. *Mol. Phys.* **2005**, *103* (6), 749. doi:10.1080/00268970412331333618.
- (26) Takahata, Y.; Chong, D. P. *J. Electron Spectrosc. Relat. Phenom.* **2003**, *133* (1–3), 69. doi:10.1016/j.elspec.2003.08.001.
- (27) Chong, D. P. *J. Electron Spectrosc. Relat. Phenom.* **2007**, *159* (1–3), 94. doi:10.1016/j.elspec.2007.01.005.
- (28) Chong, D. P. *J. Electron Spectrosc. Relat. Phenom.* **2005**, *148* (2), 115. doi:10.1016/j.elspec.2005.04.006.
- (29) Chong, D. P. *Chem. Phys. Lett.* **2007**, *441* (4–6), 209. doi:10.1016/j.cplett.2007.05.034.
- (30) Ketkar, S. N.; Fink, M. *J. Mol. Struct.* **1981**, *77* (1–2), 139. doi:10.1016/0022-2860(81)85276-3.
- (31) Huber, S.; Grassi, G.; Bauder, A. *Mol. Phys.* **2005**, *103* (10), 1395. doi:10.1080/00268970500038451.
- (32) (a) *ADF Program System*; Release 2007.01; Scientific Computing & Modeling NV: Amsterdam, 2006. (b) For a comprehensive description of ADF, see: te Velde, G.; Bickelhaupt, F. M.; Baerends, E. J.; Fonseca Guerra, C.; van Gisbergen, S. J. A.; Snijders, J. G.; Ziegler, T. *J. Comput. Chem.* **2001**, *22* (9), 931. doi:10.1002/jcc.1056.
- (33) Chong, D. P.; van Lenthe, E.; Van Gisbergen, S.; Baerends, E. J. *J. Comput. Chem.* **2004**, *25* (8), 1030. doi:10.1002/jcc.20030. PMID:15067678.
- (34) Grimme, S. *Chem. Phys. Lett.* **1993**, *201* (1–4), 67. doi:10.1016/0009-2614(93)85035-M.
- (35) Hinchliffe, A.; Soscún, H. J. *Chem. Phys. Lett.* **2005**, *412* (4–6), 365. doi:10.1016/j.cplett.2005.07.028.
- (36) Chong, D. P. *J. Chem. Phys.* **1995**, *103* (5), 1842. doi:10.1063/1.469758.
- (37) Stener, M.; Fronzoni, G.; de Simone, M. *Chem. Phys. Lett.* **2003**, *373* (1–2), 115. doi:10.1016/S0009-2614(03)00543-8.
- (38) Lindholm, E.; Fridh, C.; Åsbrink, L. *Faraday Discuss.* **1972**, *54*, 127. doi:10.1039/dc9725400127.
- (39) Eland, J. H. D. *Int. J. Mass Spectrom. Ion Phys.* **1972**, *9* (2), 214. doi:10.1016/0020-7381(72)80047-0.
- (40) Klasinc, L.; Kovač, B.; Güsten, H. *Pure Appl. Chem.* **1983**, *55* (2), 289. doi:10.1351/pac198855020289.
- (41) Kitagawa, T. *J. Mol. Spectrosc.* **1968**, *26* (1), 1. doi:10.1016/0022-2852(68)90139-2.
- (42) Chong, D. P. Unpublished results.
- (43) Boschi, R.; Clar, E.; Schmidt, W. *J. Chem. Phys.* **1974**, *60* (11), 4406. doi:10.1063/1.1680919.
- (44) Dougherty, D.; Lewis, J.; Nauman, R. V.; McGlynn, S. P. *J. Electron Spectrosc. Relat. Phenom.* **1980**, *19* (1), 21. doi:10.1016/0368-2048(80)80032-6.
- (45) Deleuze, M. S. *J. Chem. Phys.* **2002**, *116* (16), 7012. doi:10.1063/1.1462615.
- (46) Kitagawa, T.; Harada, Y.; Inokuchi, H.; Kodaera, K. *J. Mol. Spectrosc.* **1966**, *19* (1–4), 1. doi:10.1016/0022-2852(66)90223-2.
- (47) Angus, J. G.; Christ, B. J.; Morris, G. C. *Aust. J. Chem.* **1968**, *21*, 2153. doi:10.1071/CH9682153.
- (48) George, G. A.; Morris, G. C. *J. Mol. Spectrosc.* **1968**, *26* (1), 67. doi:10.1016/0022-2852(68)90143-4.
- (49) Angus, J. G.; Morris, G. C. *Aust. J. Chem.* **1971**, *24*, 173. doi:10.1071/CH9710173.
- (50) Koch, E. E.; Otto, A.; Radler, K. *Chem. Phys. Lett.* **1972**, *16* (1), 131. doi:10.1016/0009-2614(72)80474-3.
- (51) Huebner, R. H.; Mielczark, S. R.; Kuyatt, C. E. *Chem. Phys. Lett.* **1972**, *16* (3), 464. doi:10.1016/0009-2614(72)80401-9.
- (52) Dick, B.; Hohlneicher, G. *Chem. Phys. Lett.* **1981**, *84* (3), 471. doi:10.1016/0009-2614(81)80388-0.
- (53) Gosselin, J. L.; Weber, P. M. *J. Phys. Chem. A* **2005**, *109* (22), 4899. doi:10.1021/jp0503866. PMID:16833836.
- (54) Kuthirummal, N.; Weber, P. M. *Chem. Phys. Lett.* **2003**, *378* (5–6), 647. doi:10.1016/j.cplett.2003.08.002.
- (55) Kuthirummal, N.; Weber, P. M. *J. Mol. Struct.* **2006**, *787* (1–3), 163. doi:10.1016/j.molstruc.2005.10.043.
- (56) Suzuki, T.; Ito, M. *J. Phys. Chem.* **1987**, *91* (13), 3537. doi:10.1021/j100297a015.
- (57) Crenshaw, M. L.; Banna, M. S. *J. Electron Spectrosc. Relat. Phenom.* **1989**, *48* (1), 179. doi:10.1016/0368-2048(89)80014-3.
- (58) Hollauer, E.; Prucolo, E. S.; Rocco, M. L. M.; Netto, A. D. P.; Schöll, A.; Fink, R. *J. Braz. Chem. Soc.* **2005**, *16* (1), 31. doi:10.1590/S0103-50532005000100005.
- (59) Hitchcock, A. P.; Tourillon, G.; Garrett, R.; Lazarz, N. *J. Phys. Chem.* **1989**, *93* (22), 7624. doi:10.1021/j100359a019.
- (60) Gordon, M. L.; Tulumello, D.; Cooper, G.; Hitchcock, A. P.; Glatzel, P.; Mullins, O. C.; Cramer, S. P.; Bergmann, U. *J. Phys. Chem. A* **2003**, *107* (41), 8512. doi:10.1021/jp035607r.

# Prototypical arsine–triels adducts ( $R_3AsEX_3$ for $E = B, Al, \text{ and } Ga$ )

Eamonn Conrad, Janet Pickup, Neil Burford, Robert McDonald, and Michael J. Ferguson

**Abstract:** Complexes of arsine ligands ( $R_3As$ ,  $R = Me, Et, Ph$ ) and Lewis acids of group-13 elements of the form  $EX_3$  ( $E = B$ ,  $X = Ph, C_6F_5$ ;  $E = Al$ ,  $X = Cl, Br, I$ ;  $E = Ga$ ,  $X = Cl$ ) have been isolated and characterized by X-ray crystallography, infrared spectroscopy,  $^1H$ ,  $^{13}C\{^1H\}$ ,  $^{11}B\{^1H\}$ , and  $^{27}Al$  NMR spectroscopy. The compounds are compared with rare arsine–triels adducts.

**Key words:** arsine–triels (boron, aluminum, gallium) Lewis adducts.

**Résumé :** Les complexes des ligands d'arsine ( $R_3As$ ,  $R = Me, Et, Ph$ ) et des acides de Lewis du groupe des éléments 13 de la forme  $EX_3$  ( $E = B$ ,  $X = Ph, C_6F_5$ ;  $E = Al$ ,  $X = Cl, Br, I$ ;  $E = Ga$ ,  $X = Cl$ ) ont été isolés et caractérisés par la cristallographie aux rayons-X, la spectroscopie infrarouge, et la spectroscopie RMN de  $^1H$ ,  $^{13}C\{^1H\}$ ,  $^{11}B\{^1H\}$  et  $^{27}Al$ . Les composés sont comparés aux adduits rares d'arsine–triels.

**Mots-clés :** adduits de Lewis d'arsine–triels (bore, aluminium, gallium).

[Traduit par la Rédaction]

## Introduction

Compounds involving bonds between tetracoordinate group-13 elements and tetracoordinate group-15 elements represent prototypical examples of Lewis acid–base adducts and are well-known for compounds involving nitrogen or phosphorus donors. In contrast, examples of adducts involving arsine ligands on Lewis acids of group-13 elements are rare despite the importance of arsenic in the development of semiconducting materials such as gallium arsenide.

Compounds containing a coordinatively unsaturated arsenic center bound to a coordinatively unsaturated boron center are known,<sup>1</sup> but adducts of tetracoordinate arsenic bound to tetracoordinate boron have not been reported. Moreover, although examples of complexes of arsines with alanes,<sup>2–4</sup> gallanes,<sup>5–7</sup> or indanes<sup>7,8</sup> have been spectroscopically or crystallographically characterized, there are limited data available and few acyclic complexes are known that represent prototypical examples of arsines with Lewis acids of group-13 elements and provide fundamental data for the As–E bonds.

Prompted by the recent use of arsine ligands to stabilize pnictogenium cations ( $PnR^{2+}$ )<sup>9</sup> and diphosphenium dications ( $RPPR^{2+}$ ),<sup>10</sup> we report crystallographic and NMR spectroscopic data for compounds of the form  $R_3AsEX_3$  for  $E = B, Al, \text{ and } Ga$ . Comparisons are made with the rare examples that have been previously reported.

## Results and discussion

Reaction mixtures containing an alkyl- or aryl-arsine ( $R_3As$ ,  $R = Me, Et, Ph$ ) and an arylborane ( $BX_3$ ,  $X = Ph, C_6F_5$ ) in  $CH_2Cl_2$  exhibit a single signal in the  $^{11}B\{^1H\}$  NMR spectra (Table 1). The chemical shifts are consistent with those observed for the corresponding solids that are isolated from reaction mixtures and redissolved in  $CD_2Cl_2$  (or  $CD_3CN$ ). Derivatives containing  $X = C_6F_5$  have chemical shifts in the range observed for those compounds involving  $B(C_6F_5)_3$  moieties.<sup>11</sup> Reaction mixtures of arsines ( $R_3As$ ,  $R = Me, Et, Ph$ ) with haloalanes ( $AlX_3$ ,  $X = Cl, Br, I$ ) in  $CH_2Cl_2$  show a single chemical shift in the  $^{27}Al$  NMR spectra (Table 1) with chemical shifts that are in the range of tetracoordinate aluminum centers.<sup>12</sup>

Crystalline samples of  $Me_3AsBPh_3$ ,  $Et_3AsB(C_6F_5)_3$ ,  $Ph_3AsAlCl_3$ , and  $Ph_3AsAlI_3$  have been isolated from the reaction mixtures described above and  $Ph_3AsGaCl_3$  was isolated from the reaction of  $Ph_3As$  and  $GaCl_3$ . The compounds have been crystallographically characterized as adducts of arsine ligands on group-13 Lewis acids. The structures all involve slightly distorted tetrahedral geometries at the arsenic and group-13 element centers, as illustrated in Figs. 1–5. There are no significant intermolecular interactions in any of the structures. Selected bond distances and angles are presented in Table 2 and torsional angles are available as Supplementary data.

Received 24 January 2010. Accepted 16 February 2010. Published on the NRC Research Press Web site at [canjchem.nrc.ca](http://canjchem.nrc.ca) on 27 May 2010.

This article is part of a Special Issue dedicated to Professor R. J. Boyd.

**E. Conrad, J. Pickup, and N. Burford.**<sup>1</sup> Department of Chemistry, Dalhousie University, Halifax, NS, B3H 4J3, Canada.

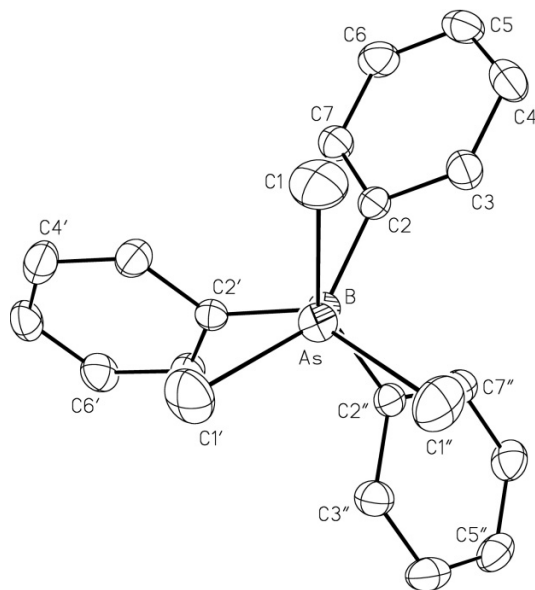
**R. McDonald and M.J. Ferguson.** X-ray Crystallography Laboratory, Department of Chemistry, University of Alberta, Edmonton, AB T6G 2G2, Canada.

<sup>1</sup>Corresponding author (e-mail: [Neil.Burford@dal.ca](mailto:Neil.Burford@dal.ca)).

**Table 1.**  $^{11}\text{B}\{^1\text{H}\}$  NMR and  $^{27}\text{Al}$  NMR chemical shifts (ppm) in reaction mixtures of  $\text{R}_3\text{As}$  with  $\text{EX}_3$  and for crystalline samples of adducts redissolved.

Compound	$^{11}\text{B}\{^1\text{H}\}$ or $^{27}\text{Al}$ ( $\delta$ , ppm)
$\text{Me}_3\text{AsBPh}_3$	53.6 (s)
$\text{Et}_3\text{AsBPh}_3$	36.3 (s)
$\text{Ph}_3\text{AsBPh}_3$	67.8 (s)
$\text{Me}_3\text{AsB}(\text{C}_6\text{F}_5)_3$	-11.0 (s)
$\text{Et}_3\text{AsB}(\text{C}_6\text{F}_5)_3$	-11.8 (s)
$\text{Ph}_3\text{AsB}(\text{C}_6\text{F}_5)_3$	-11.6 (s)
$\text{Me}_3\text{AsAlCl}_3$	104.3 (s)
$\text{Et}_3\text{AsAlCl}_3$	110.3 (s)
$\text{Ph}_3\text{AsAlCl}_3$	104.1 (s)
$\text{Me}_3\text{AsAlBr}_3$	112.9 (s)
$\text{Et}_3\text{AsAlBr}_3$	104.8 (s)
$\text{Ph}_3\text{AsAlBr}_3$	108.4 (s)
$\text{Me}_3\text{AsAlI}_3$	110.5 (s)
$\text{Et}_3\text{AsAlI}_3$	111.2 (s)
$\text{Ph}_3\text{AsAlI}_3$	103.8 (s)

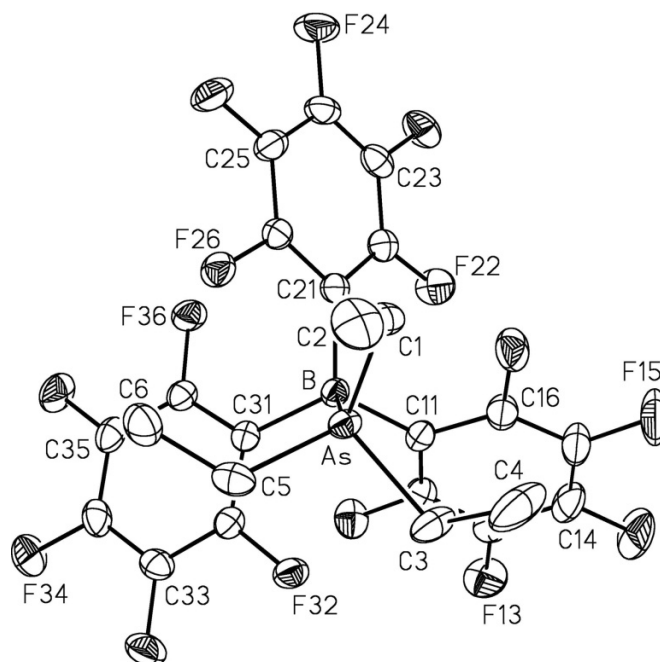
**Fig. 1.** Crystallographic view of  $\text{Me}_3\text{AsBPh}_3$ . Nonhydrogen atoms are represented by Gaussian ellipsoids at the 50% probability level.



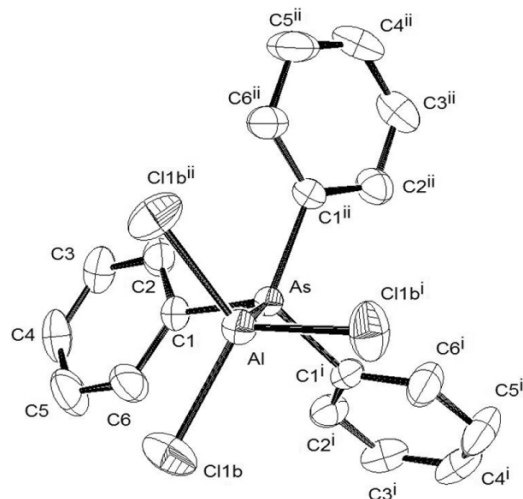
The As-B bond lengths in  $\text{Me}_3\text{AsBPh}_3$  (2.148(3) Å) and  $\text{Et}_3\text{AsB}(\text{C}_6\text{F}_5)_3$  (2.1905(18) Å) are longer than the sum of the covalent radii for arsenic and boron (2.09 Å). Both adducts adopt a close to eclipsed conformation (smallest C-As-B-C torsion angle in  $\text{Me}_3\text{AsBPh}_3$  = 24.03(8)°, in  $\text{Et}_3\text{AsB}(\text{C}_6\text{F}_5)_3$  = 9.89(13)°, which compares with the conformation observed in the phosphine-borane analogue,  $\text{Et}_3\text{PB}(\text{C}_6\text{F}_5)_3$  (smallest C-P-B-C torsion angle = 15.7(3)°).<sup>11</sup>

Adducts  $\text{Ph}_3\text{AsAlCl}_3$  and  $\text{Ph}_3\text{AsAlI}_3$  are isomorphous with both  $\text{Ph}_3\text{PGaI}_3$  and  $\text{Ph}_3\text{AsGaI}_3$ .<sup>7</sup> As for the arsine-borane adducts, the As-Al bond lengths ( $\text{Ph}_3\text{AsAlCl}_3$ , 2.5191(9) Å;  $\text{Ph}_3\text{AsAlI}_3$ , 2.517 Å) are slightly longer than the sum of the covalent radii for aluminum and arsenic (2.47 Å). Nevertheless, the As-Al bonds are shorter than those in *i*-Pr<sub>3</sub>AsAl-*t*-Bu<sub>3</sub> (2.839(1) Å) and TMS<sub>3</sub>AsAl-*t*-Bu<sub>3</sub> (2.654(2) Å),<sup>3</sup> likely due

**Fig. 2.** Crystallographic view of  $\text{Et}_3\text{AsB}(\text{C}_6\text{F}_5)_3$ . Nonhydrogen atoms are represented by Gaussian ellipsoids at the 50% probability level.



**Fig. 3.** Crystallographic view of the  $\text{Ph}_3\text{AsAlCl}_3$  molecule showing the atom labelling scheme. Nonhydrogen atoms are represented by Gaussian ellipsoids at the 50% probability level. Hydrogen atoms are shown with arbitrarily small thermal parameters.

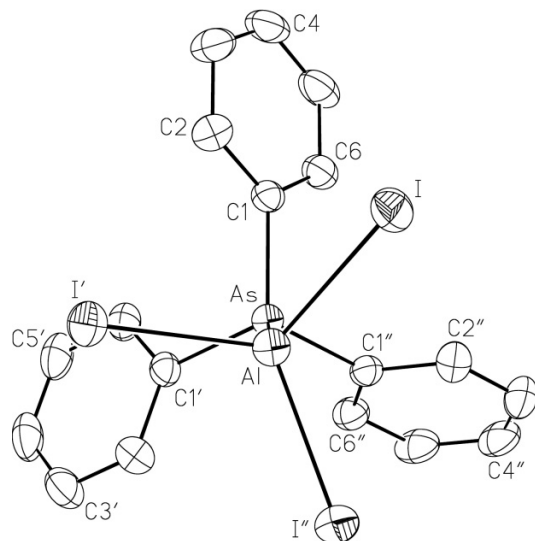


to the lower steric repulsion in the organoalane derivatives and the inductive influence of the halogens on the Lewis acidity of the alane in the haloalane. The alane adducts  $\text{Ph}_3\text{AsAlCl}_3$  and  $\text{Ph}_3\text{AsAlI}_3$  adopt a more staggered conformation about the As-Al bond axis (smallest C-As-Al-C torsion angle in  $\text{Ph}_3\text{AsAlCl}_3$  = 32.58(6)°, in  $\text{Ph}_3\text{AsAlI}_3$  = 38.83(6)°) than the borane adducts  $\text{Me}_3\text{AsBPh}_3$  and  $\text{Et}_3\text{AsB}(\text{C}_6\text{F}_5)_3$ .

Crystals of  $\text{Ph}_3\text{AsGaCl}_3$  are isomorphous with both  $\text{Ph}_3\text{PGaI}_3$  and  $\text{Ph}_3\text{AsGaI}_3$ <sup>7</sup> and there are two crystallographically independent molecules in the unit cell (Fig. 5). The As-Ga bond lengths (2.540(6) Å and 2.449(6) Å) are close to the sum of the covalent radii for arsenic and gallium



**Fig. 4.** Crystallographic views of  $\text{Ph}_3\text{AsAlI}_3$ . Nonhydrogen atoms are represented by Gaussian ellipsoids at the 50% probability level.



(2.47 Å), and to that in  $\text{Ph}_3\text{AsGaI}_3$ .<sup>7</sup> The torsion angles about the As–Ga bond (smallest C–As–Ga–Cl torsion angles for molecule A = 29.9(3)°, for molecule B = –53.4(3)°) are more staggered than in the arsine–borane adducts.

## Summary

Prototypical examples of compounds containing As → B, As → Al, and As → Ga coordinate bonds have been isolated from reaction mixtures of an arsine Lewis base with a triel Lewis acid. The compounds provide fundamental spectroscopic and structural data. While bond length trends are as expected, As → B < As → Al < As → Ga, the torsion angles are generally smaller for As → B complexes than for the As → Al and As → Ga complexes.

## Experimental procedures

Reactions were carried out in an MBraun glovebox under atmosphere of dry  $\text{N}_2$ . Solvents were dried on an MBraun solvent purification system and stored over 4 Å molecular sieves. Deuterated solvents were purchased from Sigma-Aldrich and were used as received. Experimental details relating to the single crystal X-ray diffraction studies are summarized in Table 3. X-ray diffraction data were collected on a Bruker APEX II CCD area detector/D8 diffractometer. Crystals were coated with Paratone-N oil, mounted on glass fibres, and placed in a cold stream of  $\text{N}_2$ . Structures were solved by direct methods (SHELXS-97)<sup>14</sup> or Patterson search/structure expansion (DIRDIF-2008),<sup>15</sup> and refined using full-matrix least-squares on  $F^2$  (SHELXL-97).<sup>14</sup> Hydrogen atom positions were calculated from the  $\text{sp}^2$  or  $\text{sp}^3$  hybridization geometries of their attached atoms. NMR spectra were obtained at room temperature, unless otherwise stated, on a Bruker AVANCE 500  $^1\text{H}$  (500.13 MHz, 11.7 T) and Bruker/Tecmag AC250  $^1\text{H}$  (250.06 MHz, 5.9 T).  $^{13}\text{C}\{^1\text{H}\}$  NMR (125.76 MHz) chemical shifts were referenced to  $\delta_{\text{TMS}} = 0.00$ , as were  $^{11}\text{B}\{^1\text{H}\}$  NMR (160.42 MHz) and  $^{27}\text{Al}$ -NMR (130.29 MHz). Chemical shifts ( $\delta$ ) are reported in ppm. NMR spectra of samples were obtained by

transferring an aliquot of sample in an appropriate deuterated solvent into a 5 mm sample tube. The tubes were capped and sealed with Parafilm prior to removal from the inert atmosphere. IR spectra were obtained from powdered and crystalline samples dissolved in  $\text{CH}_2\text{Cl}_2$  and spotted on CsI plates. Data collection was on a Bruker Vertex FTIR spectrometer. Peaks are reported in wavenumbers ( $\text{cm}^{-1}$ ) with ranked intensities in parenthesis beside the value, where a value of one is indicative of the most intense peak in the spectrum. Melting points were recorded on an Electrothermal melting point apparatus in sealed capillary tubes under  $\text{N}_2$ .

## Caution

All arsines are known carcinogens and must be handled using appropriate procedures.

## Preparation of $\text{Me}_3\text{AsBPh}_3$

A solution of  $\text{Me}_3\text{As}$  (52.0  $\mu\text{L}$ , 0.50 mmol) in  $\text{CH}_2\text{Cl}_2$  was added to a solution of  $\text{BPh}_3$  (121.0 mg, 0.50 mmol) in  $\text{CH}_2\text{Cl}_2$  and the mixture was stirred for 30 min. The solution was layered with hexanes and stored at  $-25^\circ\text{C}$  overnight. A white precipitate was isolated and washed with hexanes (3  $\times$  3 mL). Crystals were obtained by  $\text{CD}_3\text{CN}$ /ether diffusion at  $-25^\circ\text{C}$  over 48 h. Yield: 65%, 117 mg; mp 144–146  $^\circ\text{C}$ . FTIR (CsI plates, ranked intensities,  $\text{cm}^{-1}$ ): 3058 (1), 2917 (3), 2849 (4), 1590 (12), 1430 (13), 1261 (11), 1238 (10), 1096 (9), 1020 (8), 802 (5), 746 (6), 696 (2), 636 (7).  $^1\text{H}$  NMR ( $\text{CD}_2\text{Cl}_2$ , 273 K, 500 MHz, ppm)  $\delta$ : 1.23 (s, 9H), 7.52–7.57 (m, 6H), 7.58–7.63 (m, 3H), 7.65–7.70 (m, 6H).  $^{13}\text{C}\{^1\text{H}\}$  NMR ( $\text{CD}_2\text{Cl}_2$ , 273K, 125.76 MHz)  $\delta$ : 8.4 (s), 128.0 (s), 130.6 (s), 138.3 (s).  $^{11}\text{B}\{^1\text{H}\}$  NMR ( $\text{CD}_2\text{Cl}_2$ , 273 K, 160.42 MHz)  $\delta$ : 53.6 (s).

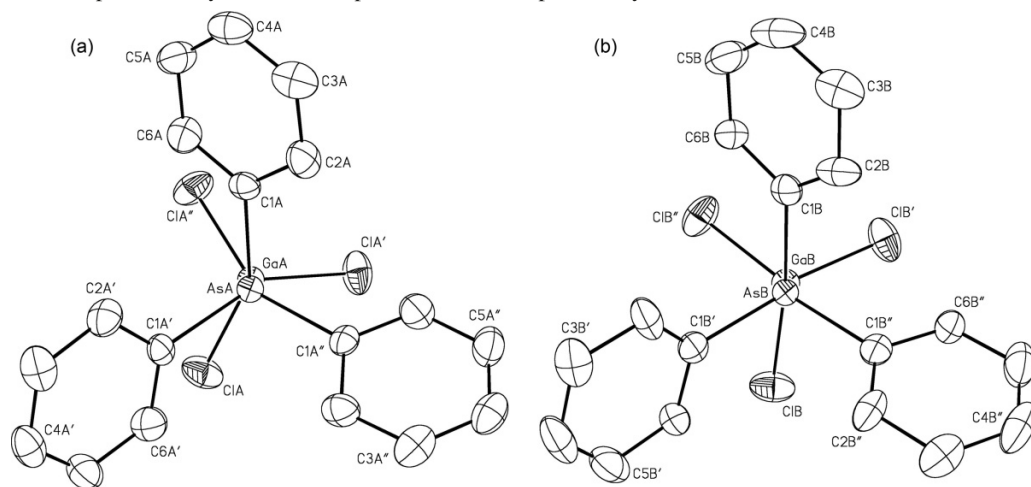
## Preparation of $\text{Me}_3\text{AsB}(\text{C}_6\text{F}_5)_3$

A solution of  $\text{Me}_3\text{As}$  (52.0  $\mu\text{L}$ , 0.50 mmol) in  $\text{CH}_2\text{Cl}_2$  was added to a solution of  $\text{B}(\text{C}_6\text{F}_5)_3$  (256.0 mg, 0.50 mmol) in  $\text{CH}_2\text{Cl}_2$  and stirred for 30 min. A white precipitate formed immediately. The solid was isolated and washed with ether (3  $\times$  3 mL) and has poor solubility. Crystals were obtained by  $\text{CD}_3\text{CN}$ /ether diffusion at  $-25^\circ\text{C}$  over 48 h. Yield: 78%, 236 mg; mp 257–259  $^\circ\text{C}$ . FTIR (CsI plates, ranked intensities,  $\text{cm}^{-1}$ ): 2917 (1), 2703 (14), 1644 (10), 1516 (4), 1446 (1), 1370 (6), 1163 (16), 1117 (15), 1087 (5), 979 (3), 960 (2), 780 (9), 770 (8), 730 (17), 667 (7), 617 (11).  $^1\text{H}$  NMR ( $\text{CD}_3\text{CN}$ , 273 K, 500 MHz, ppm)  $\delta$ : 0.96 (s, 9H).  $^{11}\text{B}\{^1\text{H}\}$  NMR ( $\text{CD}_3\text{CN}$ , 273 K, 160.42 MHz)  $\delta$ : –11.0 (s).

## Preparation of $\text{Et}_3\text{AsBPh}_3$

A solution of  $\text{Et}_3\text{As}$  (70.5  $\mu\text{L}$ , 0.50 mmol) in  $\text{CH}_2\text{Cl}_2$  was added to a solution of  $\text{BPh}_3$  (121.0 mg, 0.50 mmol) in  $\text{CH}_2\text{Cl}_2$  and stirred for 30 min. The solution was layered with ether and stored at  $-25^\circ\text{C}$  overnight. Clear colourless crystals were obtained by  $\text{CD}_3\text{CN}$ /ether diffusion at  $-25^\circ\text{C}$  over 48 h and were isolated and washed with ether (3  $\times$  3 mL). Yield: 66%, 133 mg; mp 86–88  $^\circ\text{C}$ . FTIR (CsI plates, ranked intensities,  $\text{cm}^{-1}$ ): 3666 (14), 3061 (1), 2425 (4), 1953 (13), 1642 (2), 1554 (12), 1462 (11), 1453 (10), 1260 (5), 1098 (7), 1020 (6), 847 (3), 699 (9), 613 (8).  $^1\text{H}$  NMR ( $\text{CD}_2\text{Cl}_2$ , 273 K, 500 MHz, ppm)  $\delta$ : 1.17 (t,  $^3J_{\text{HH}} = 7.0$  Hz, 9H), 1.68 (q,  $^3J_{\text{HH}} = 7.0$  Hz, 6H), 7.48–7.54 (m,

**Fig. 5.** Crystallographic views of the two crystallographically independent conformers (a and b) of the disordered structure of  $\text{Ph}_3\text{AsGaCl}_3$ . Nonhydrogen atoms are represented by Gaussian ellipsoids at the 50% probability level.



**Table 2.** Selected bond lengths (Å) and angles (°) in  $\text{Ph}_3\text{AsMe}_3$ ,  $\text{Et}_3\text{AsB}(\text{C}_6\text{F}_5)_3$ ,  $\text{Ph}_3\text{AsAlCl}_3$ ,  $\text{Ph}_3\text{AsAlI}_3$ ,  $\text{Ph}_3\text{AsGaCl}_3$ , and related compounds.

Compound	E—As (Å)	C—As—E (°)	X—E—As (°)
$\text{Me}_3\text{AsBPh}_3$	2.148(3)	115.80(6)	104.83(10)
$\text{Et}_3\text{AsB}(\text{C}_6\text{F}_5)_3$	2.1905(18)	114.70(7) 112.75(8) 117.02(7)	103.35(10) 107.52(10) 104.56(11)
$\{(t\text{-Bu})_2\text{As}\}_2\text{BPh}^1$	2.064(5)	106.9(2)	124.3(5)
$\text{Ph}_3\text{AsAlCl}_3^a$	2.5191(9)	114.17(5)	101.76(4) 108.76(4)
$\text{Ph}_3\text{AsAlI}_3$	2.5140(10)	113.78(6)	102.48(2)
$\text{Ph}_3\text{AsGaCl}_3^b$	2.540(6)	113.1(2)	106.29(16)
$\text{Ph}_3\text{AsGaI}_3^7$	2.449(6)	113.4(2)	107.40(16)
$\text{TMS}_3\text{AsGaI}_3^{13}$	2.490(1)	113.21(7)	102.97(2)
$i\text{-Pr}_3\text{AsAl-}t\text{-Bu}_3^3$	2.509	—	—
$\text{TMS}_3\text{AsAlEt}_3^3$	2.839(1)	106.3(1) 100.5(1) 105.4(1)	111.5(2) 121.8(1) 110.2(1)
$[\text{TMS}_2\text{AsAlEt}_2]_2^4$	2.654(2)	Si—As—Al 113.5(1) 113.3(1) 113.2(1)	C—Al—As 106.0(2) 102.9(2) 104.2(2)
$\text{TMS}_3\text{AsGaPh}_3^6$	2.539(2)	Si—As—Al 114.10(6) 114.79(6)	C—Al—As 112.5(2) 114.7(2) 110.3(2) 112.5(2)
	2.671(1)	Si—As—Ga 114.45(7) 110.74(7) 113.98(7)	C—Ga—As 103.3(2) 104.6(2) 105.3(2)

<sup>a</sup>Disorder in structure.

<sup>b</sup>Two crystallographically independent molecules in the asymmetric unit.

8H), 7.60–7.65 (m, 7H).  $^{13}\text{C}\{^1\text{H}\}$  NMR ( $\text{CD}_2\text{Cl}_2$ , 273 K, 125.76 MHz, ppm)  $\delta$ : 10.2 (s), 16.1 (s), 127.9 (s), 129.1 (s), 137.8 (s), 136.3 (s).  $^{11}\text{B}\{^1\text{H}\}$  NMR ( $\text{CD}_2\text{Cl}_2$ , 273 K, 160.42 MHz, ppm)  $\delta$ : 36.3 (s).

### Preparation of $\text{Et}_3\text{AsB}(\text{C}_6\text{F}_5)_3$

A solution of  $\text{Et}_3\text{As}$  (70.5  $\mu\text{L}$ , 0.50 mmol) in  $\text{CH}_2\text{Cl}_2$  was added to a solution of  $\text{B}(\text{C}_6\text{F}_5)_3$  (256.0 mg, 0.50 mmol) in  $\text{CH}_2\text{Cl}_2$  and stirred for 30 min. A white precipitate formed immediately. The solid was redissolved in  $\text{CH}_3\text{CN}$  and crystalline material was obtained by  $\text{CH}_3\text{CN}$ /ether diffusion at  $-25^\circ\text{C}$  over 48 h. Yield: 44%, 142 mg; mp 204–206  $^\circ\text{C}$ . FTIR (CsI plates, ranked intensities,  $\text{cm}^{-1}$ ): 2918 (12), 1645 (7), 1518 (4), 1460 (1), 1374 (6), 1283 (8), 1100 (5), 979 (2), 965 (3), 772 (11), 731 (10), 669 (9).  $^1\text{H}$  NMR  $\delta$ : ( $\text{CD}_3\text{CN}$ , 273 K, 500 MHz, ppm)  $\delta$ : 1.19 (t,  $^3J_{\text{HH}} = 7.5$  Hz, 9H), 1.86 (q,  $^3J_{\text{HH}} = 7.5$  Hz, 6H).  $^{11}\text{B}\{^1\text{H}\}$  NMR ( $\text{CD}_3\text{CN}$ , 273 K, 160.42 MHz, ppm)  $\delta$ :  $-11.8$  (s).

### Preparation of $\text{Ph}_3\text{AsBPh}_3$

A solution of  $\text{Ph}_3\text{As}$  (151.5 mg, 0.50 mmol) in  $\text{CH}_2\text{Cl}_2$  was added to a solution of  $\text{BPh}_3$  (121.0 mg, 0.50 mmol) in  $\text{CH}_2\text{Cl}_2$  and stirred for 30 min. The solution was layered with hexanes and stored at  $-25^\circ\text{C}$  overnight. A white powder was isolated and washed with ether (3  $\times$  3 mL). Yield: 55%, 150 mg; decomposes above 100  $^\circ\text{C}$ . FTIR (CsI plates, ranked intensities,  $\text{cm}^{-1}$ ): 3059 (1), 2429 (10), 2283 (11), 1980 (12), 1642 (2), 1260 (7), 1097 (6), 1019 (5), 910 (4), 804 (3), 734 (9), 694 (8).  $^1\text{H}$  NMR ( $\text{CD}_2\text{Cl}_2$ , 273 K, 500 MHz, ppm)  $\delta$ : 7.28–8.27 (m, 30H).  $^{13}\text{C}\{^1\text{H}\}$  NMR ( $\text{CD}_2\text{Cl}_2$ , 273 K, 125.76 MHz, ppm)  $\delta$ : 128.2 (s), 129.4 (s), 132.1 (s), 134.4 (s), 136.4 (s), 139.2 (s), 140.5 (s), 143.9 (s).  $^{11}\text{B}\{^1\text{H}\}$  NMR ( $\text{CD}_2\text{Cl}_2$ , 273 K, 160.42 MHz, ppm)  $\delta$ : 67.8 (s).

### Preparation of $\text{Ph}_3\text{AsB}(\text{C}_6\text{F}_5)_3$

A solution of  $\text{Ph}_3\text{As}$  (151.5 mg, 0.50 mmol) in  $\text{CH}_2\text{Cl}_2$  was added to a solution of  $\text{B}(\text{C}_6\text{F}_5)_3$  (256.0 mg, 0.50 mmol) in  $\text{CH}_2\text{Cl}_2$  and stirred for 30 min. A white precipitate formed immediately. The solid was redissolved in  $\text{CH}_3\text{CN}$  and then precipitated by ether diffusion at  $-25^\circ\text{C}$  over 48 h. The solid was washed with ether (3  $\times$  3 mL). Yield: 51%, 201 mg; mp 155–157  $^\circ\text{C}$ . FTIR (CsI plates, ranked intensities,  $\text{cm}^{-1}$ ): 3001 (1), 2342 (17), 1895 (16), 1645 (12), 1464 (2), 1389 (4), 1366 (3), 1260 (9), 1230 (6), 1011 (11), 1020 (10), 950 (7), 923 (8), 888 (15), 850 (14), 802 (13),

**Table 3.** Crystallographic data for Ph<sub>3</sub>BAsMe<sub>3</sub>, Et<sub>3</sub>AsB(C<sub>6</sub>F<sub>5</sub>)<sub>3</sub>, and Ph<sub>3</sub>AsEX<sub>3</sub> (E = Al and Ga; X = Cl and I).

Compound	Ph <sub>3</sub> BAsMe <sub>3</sub>	Et <sub>3</sub> AsB(C <sub>6</sub> F <sub>5</sub> ) <sub>3</sub>	Ph <sub>3</sub> AsAlCl <sub>3</sub>	Ph <sub>3</sub> AsAlI <sub>3</sub>	Ph <sub>3</sub> AsGaCl <sub>3</sub>
Formula	C <sub>21</sub> H <sub>24</sub> AsB	C <sub>24</sub> H <sub>15</sub> AsBF <sub>15</sub>	C <sub>18</sub> H <sub>15</sub> AlAsCl <sub>3</sub>	C <sub>18</sub> H <sub>15</sub> AlAsI <sub>3</sub>	C <sub>18</sub> H <sub>15</sub> AsCl <sub>3</sub> Ga
Formula weight	362.13	674.09	439.55	713.90	482.29
Crystal system	Trigonal	Monoclinic	Trigonal	Trigonal	Trigonal
Space group	$P\bar{3}$ (No. 147)	$P2_1/n$	$R\bar{3}$ (No. 148)	$R\bar{3}$ (No. 148)	$R\bar{3}$ (No. 148)
$a$ (Å)	11.3230 (6)	12.5167 (4)	13.9920 (12)	14.8705 (6)	14.0065 (7)
$b$ (Å)	11.3230 (6)	10.5712 (3)	13.9920 (12)	14.8705 (6)	14.0065 (7)
$c$ (Å)	8.1329 (4)	18.2940 (5)	16.8498 (14)	16.7263 (6)	16.8497 (9)
$\alpha$ (°)	90	90	90	90	90
$\beta$ (°)	90	90.2369 (3)	90	90	90
$\gamma$ (°)	120	90	120	120	120
Crystal size (mm <sup>3</sup> )	0.43 × 0.21 × 0.19	0.32 × 0.29 × 0.28	0.67 × 0.60 × 0.34	0.49 × 0.41 × 0.31	0.48 × 0.36 × 0.29
Reflections collected	7754	19 870	7861	9448	8386
Independent reflections ( $R_{\text{int}}$ )	1387 ( $R_{\text{int}} = 0.0219$ )	5564 ( $R_{\text{int}} = 0.0178$ )	1452 ( $R_{\text{int}} = 0.0196$ )	1644 ( $R_{\text{int}} = 0.0162$ )	1470 ( $R_{\text{int}} = 0.0152$ )
GoF <sup>a</sup>	1.106	1.046	1.072	1.119	1.158
$Z$	2	4	6	6	6
$V$ (Å <sup>3</sup> )	903.02 (8)	2420.58 (12)	2856.8 (4)	3203.2 (2)	2862.7 (3)
$\rho_{\text{calcd}}$ (mg m <sup>-3</sup> )	1.332	1.850	1.533	2.221	1.679
$R_1$	0.0199	0.0256	0.0196	0.0147	0.0171
$wR_2$	0.0534	0.0683	0.0508	0.0358	0.0509

<sup>a</sup> $S = [\sum^w (F_o^2 - F_c^2)^2 / (n - p)]^{1/2}$  ( $n$  = number of data;  $p$  = number of parameters varied;  $w = [\sigma^2(F_o^2) + (0.0259P)^2 + 0.3085P]^{-1}$ , where  $P = [\text{Max}(F_o^2, 0) + 2F_c^2]/3$ ).

729 (s).  $^1\text{H}$  NMR  $\delta$ : ( $\text{CD}_3\text{CN}$ , 273 K, 500 MHz, ppm)  $\delta$ : 7.34–7.41 (m, 15H).  $^{11}\text{B}\{^1\text{H}\}$  NMR ( $\text{CD}_3\text{CN}$ , 273 K, 160.42 MHz, ppm)  $\delta$ : –11.6 (s).

#### Preparation of $\text{Me}_3\text{AsAlCl}_3$

A solution of  $\text{Me}_3\text{As}$  (52.0  $\mu\text{L}$ , 0.50 mmol) in  $\text{CH}_2\text{Cl}_2$  was added to a solution of  $\text{AlCl}_3$  (61.5 mg, 0.50 mmol) in  $\text{CH}_2\text{Cl}_2$  and stirred for 30 min. The solution was layered with hexanes and stored at  $-25^\circ\text{C}$  overnight. A white powder formed and was isolated and washed with ether ( $3 \times 3$  mL). Yield: 70%, 89 mg; mp 143–145  $^\circ\text{C}$ . FTIR (CsI plates, ranked intensities,  $\text{cm}^{-1}$ ): 3094 (1), 2921 (2), 2850 (3), 2432 (12), 2361 (11), 1642 (5), 1462 (14), 1412 (10), 1261 (9), 1100 (13), 1018 (8), 925 (4), 848 (7), 651 (6).  $^1\text{H}$  NMR ( $\text{CD}_2\text{Cl}_2$ , 273 K, 500 MHz, ppm)  $\delta$ : 2.21 (s, 9H).  $^{13}\text{C}\{^1\text{H}\}$  NMR ( $\text{CD}_2\text{Cl}_2$ , 273 K, 125.76 MHz, ppm)  $\delta$ : 7.9 (s).  $^{27}\text{Al}$  NMR ( $\text{CD}_2\text{Cl}_2$ , 273 K, 130.29 MHz, ppm)  $\delta$ : 104.3 (s).

#### Preparation of $\text{Me}_3\text{AsAlBr}_3$

A solution of  $\text{Me}_3\text{As}$  (52.0  $\mu\text{L}$ , 0.50 mmol) in  $\text{CH}_2\text{Cl}_2$  was added to a solution of  $\text{AlBr}_3$  (133.5 mg, 0.50 mmol) in  $\text{CH}_2\text{Cl}_2$  and stirred for 30 min. The solution was layered with hexanes and stored at  $-25^\circ\text{C}$  overnight. A white powder formed and was isolated and washed with ether ( $3 \times 3$  mL). Yield: 71%, 137 mg. FTIR (CsI plates, ranked intensities,  $\text{cm}^{-1}$ ): 3016 (7), 2918 (8), 2848 (9), 1414 (4), 1269 (10), 1011 (11), 989 (12), 962 (13), 921 (1), 835 (6), 790 (2), 698 (3), 626 (5).  $^1\text{H}$  NMR ( $\text{CD}_2\text{Cl}_2$ , 273 K, 500 MHz, ppm)  $\delta$ : 1.59 (s, 9H).  $^{13}\text{C}\{^1\text{H}\}$  NMR ( $\text{CD}_2\text{Cl}_2$ , 273 K, 125.76 MHz, ppm)  $\delta$ : 6.9 (s).  $^{27}\text{Al}$  NMR ( $\text{CD}_2\text{Cl}_2$ , 273 K, 130.29 MHz, ppm)  $\delta$ : 112.9 (s).

#### Preparation of $\text{Me}_3\text{AsAlI}_3$

A solution of  $\text{Me}_3\text{As}$  (52.0  $\mu\text{L}$ , 0.50 mmol) in  $\text{CH}_2\text{Cl}_2$  was added to a solution of  $\text{AlI}_3$  (204.0 mg, 0.50 mmol) in  $\text{CH}_2\text{Cl}_2$  and stirred for 30 min. Upon completion, the solution was layered with hexanes and allowed to sit at  $-25^\circ\text{C}$  overnight. White powder was obtained and washed with ether ( $3 \times 3$  mL) and solvents removed in vacuo. Yield: 69%, 184 mg; mp 138–140  $^\circ\text{C}$ . FTIR (CsI plates, ranked intensities,  $\text{cm}^{-1}$ ): 3000 (1), 2918 (2), 2849 (3), 1641 (9), 1462 (4), 1389 (8), 1365 (7), 1261 (15), 1230 (10), 1094 (14), 1019 (11), 923 (12), 802 (13), 729 (5), 719 (6).  $^1\text{H}$  NMR ( $\text{CD}_2\text{Cl}_2$ , 273 K, 500 MHz, ppm)  $\delta$ : 1.57 (bs, 9H).  $^{13}\text{C}\{^1\text{H}\}$  NMR ( $\text{CD}_2\text{Cl}_2$ , 273 K, 125.76 MHz, ppm)  $\delta$ : 7.1 (s).  $^{27}\text{Al}$  NMR ( $\text{CD}_2\text{Cl}_2$ , 273 K, 130.29 MHz, ppm)  $\delta$ : 110.5 (s).

#### Preparation of $\text{Et}_3\text{AsAlCl}_3$

A solution of  $\text{Et}_3\text{As}$  (70.5  $\mu\text{L}$ , 0.50 mmol) in  $\text{CH}_2\text{Cl}_2$  was added to a solution of  $\text{AlCl}_3$  (61.5 mg, 0.50 mmol) in  $\text{CH}_2\text{Cl}_2$  and stirred for 30 min. The solution was layered with hexanes and stored at  $-25^\circ\text{C}$  overnight. A white powder formed and was isolated and washed with ether ( $3 \times 3$  mL). Yield: 65%, 96 mg; mp 160–162  $^\circ\text{C}$ . FTIR (CsI plates, ranked intensities,  $\text{cm}^{-1}$ ): 3341 (14), 2972 (4), 2938 (6), 2879 (7), 2304 (13), 2197 (14), 1459 (3), 1416 (9), 1387 (10), 1238 (8), 954 (2), 876 (16), 794 (12), 696 (1), 678 (5).  $^1\text{H}$  NMR ( $\text{CD}_2\text{Cl}_2$ , 273 K, 500 MHz, ppm)  $\delta$ : 1.36 (t,  $^3J_{\text{HH}} = 7.85$  Hz, 9H), 2.06 (q,  $^3J_{\text{HH}} = 7.85$  Hz, 6H).  $^{13}\text{C}\{^1\text{H}\}$  NMR ( $\text{CD}_2\text{Cl}_2$ , 273 K, 125.76 MHz, ppm)  $\delta$ : 9.3

(s), 13.6 (s).  $^{27}\text{Al}$  NMR ( $\text{CD}_2\text{Cl}_2$ , 273 K, 130.29 MHz, ppm)  $\delta$ : 110.3 (s).

#### Preparation of $\text{Et}_3\text{AsAlBr}_3$

A solution of  $\text{Et}_3\text{As}$  (70.5  $\mu\text{L}$ , 0.50 mmol) in  $\text{CH}_2\text{Cl}_2$  was added to a solution of  $\text{AlBr}_3$  (133.5 mg, 0.50 mmol) in  $\text{CH}_2\text{Cl}_2$  and stirred for 30 min. The solution was layered with hexanes and stored at  $-25^\circ\text{C}$  overnight. A white powder formed and was isolated and washed with ether ( $3 \times 3$  mL) and solvents removed in vacuo. Yield: 62%, 133 mg. FTIR (CsI plates, ranked intensities,  $\text{cm}^{-1}$ ): 2973 (1), 2940 (2), 2880 (3), 2849 (8), 2431 (16), 1640 (14), 1459 (4), 1416 (12), 1389 (13), 1240 (11), 1093 (15), 1022 (9), 923 (17), 793 (3), 744 (10), 706 (5), 678 (5).  $^1\text{H}$  NMR ( $\text{CD}_2\text{Cl}_2$ , 273 K, 500 MHz, ppm)  $\delta$ : 1.59 (t,  $^3J_{\text{HH}} = 9.0$  Hz, 9H), 3.07 (q,  $^3J_{\text{HH}} = 9.0$  Hz, 6H).  $^{13}\text{C}\{^1\text{H}\}$  NMR ( $\text{CD}_2\text{Cl}_2$ , 273 K, 125.76 MHz, ppm)  $\delta$ : 8.7 (s), 26.3 (s).  $^{27}\text{Al}$  NMR ( $\text{CD}_2\text{Cl}_2$ , 273 K, 130.29 MHz, ppm)  $\delta$ : 104.8 (s).

#### Preparation of $\text{Et}_3\text{AsAlI}_3$

A solution of  $\text{Et}_3\text{As}$  (70.5  $\mu\text{L}$ , 0.50 mmol) in  $\text{CH}_2\text{Cl}_2$  was added to a solution of  $\text{AlI}_3$  (204.0 mg, 0.50 mmol) in  $\text{CH}_2\text{Cl}_2$  and stirred for 30 min. The solution was layered with hexanes and stored at  $-25^\circ\text{C}$  overnight. A pale brown oil was obtained and washed with ether ( $3 \times 3$  mL).  $^1\text{H}$  NMR ( $\text{CD}_2\text{Cl}_2$ , 273 K, 500 MHz, ppm)  $\delta$ : 1.36 (t,  $^3J_{\text{HH}} = 7.95$  Hz, 9H), 2.06 (q,  $^3J_{\text{HH}} = 7.90$  Hz, 6H).  $^{13}\text{C}\{^1\text{H}\}$  NMR ( $\text{CD}_2\text{Cl}_2$ , 273 K, 125.76 MHz, ppm)  $\delta$ : 9.3 (s), 13.4 (s).  $^{27}\text{Al}$  NMR ( $\text{CD}_2\text{Cl}_2$ , 273 K, 130.29 MHz, ppm)  $\delta$ : 111.2 (s).

#### Preparation of $\text{Ph}_3\text{AsAlCl}_3$

A solution of  $\text{Ph}_3\text{As}$  (151.5 mg, 0.50 mmol) in  $\text{CH}_2\text{Cl}_2$  was added to a solution of  $\text{AlCl}_3$  (61.5 mg, 0.50 mmol) in  $\text{CH}_2\text{Cl}_2$  and stirred for 30 min. The solution was layered with hexanes and stored at  $-25^\circ\text{C}$  overnight. A white powder formed and was isolated and washed with ether ( $3 \times 3$  mL). Crystals were obtained by  $\text{CH}_2\text{Cl}_2$ /pentane layering at  $-25^\circ\text{C}$  over 48 h. Yield: 65%, 142 mg; mp 57–59  $^\circ\text{C}$ . FTIR (CsI plates, ranked intensities,  $\text{cm}^{-1}$ ): 3064 (1), 2432 (14), 1886 (20), 1642 (5), 1578 (11), 1480 (6), 1433 (4), 1336 (18), 1305 (16), 1261 (17), 1184 (14), 1156 (15), 1083 (8), 1074 (9), 1023 (13), 998 (11), 844 (10), 735 (2), 692 (3), 613 (2).  $^1\text{H}$  NMR ( $\text{CD}_2\text{Cl}_2$ , 273 K, 500 MHz, ppm)  $\delta$ : 7.69–7.75 (m, 6H), 7.73–7.83 (m, 6H), 7.86–7.91 (m, 3H).  $^{13}\text{C}\{^1\text{H}\}$  NMR ( $\text{CD}_2\text{Cl}_2$ , 273 K, 125.76 MHz, ppm)  $\delta$ : 131.6 (s), 133.1 (s), 133.7 (s), 135.4 (s).  $^{27}\text{Al}$  NMR ( $\text{CD}_2\text{Cl}_2$ , 273 K, 130.29 MHz, ppm)  $\delta$ : 104.1 (s).

#### Preparation of $\text{Ph}_3\text{AsAlBr}_3$

A solution of  $\text{Ph}_3\text{As}$  (151.5 mg, 0.50 mmol) in  $\text{CH}_2\text{Cl}_2$  was added to a solution of  $\text{AlBr}_3$  (133.5 mg, 0.50 mmol) in  $\text{CH}_2\text{Cl}_2$  and stirred for 30 min. The solution was layered with hexanes and stored at  $-25^\circ\text{C}$  overnight. Yellow glassy material was obtained and washed with ether ( $3 \times 3$  mL). Yield: 60%, 171 mg. FTIR (CsI plates, ranked intensities,  $\text{cm}^{-1}$ ): 3060 (1), 2905 (2), 2870 (3), 2427 (10), 1642 (4), 1515 (13), 1451 (12), 1260 (8), 1097 (7), 1019 (6), 845 (5), 730 (9), 696 (11).  $^1\text{H}$  NMR ( $\text{CD}_2\text{Cl}_2$ , 273 K, 500 MHz, ppm)  $\delta$ : 7.76–7.77 (m, 6H), 7.83–7.87 (m, 6H), 7.93–7.98 (m, 3H).  $^{13}\text{C}\{^1\text{H}\}$  NMR ( $\text{CD}_2\text{Cl}_2$ , 273 K, 125.76 MHz,



ppm)  $\delta$ : 131.8 (s), 133.3 (s), 133.5 (s), 135.8 (s).  $^{27}\text{Al}$  NMR ( $\text{CD}_2\text{Cl}_2$ , 273 K, 130.29 MHz, ppm)  $\delta$ : 108.4 (s).

### Preparation of $\text{Ph}_3\text{AsAlI}_3$

A solution of  $\text{Ph}_3\text{As}$  (151.5 mg, 0.50 mmol) in  $\text{CH}_2\text{Cl}_2$  was added to a solution of  $\text{AlI}_3$  (204.0 mg, 0.50 mmol) in  $\text{CH}_2\text{Cl}_2$  and stirred for 30 min. The solution was layered with hexanes and stored at  $-25^\circ\text{C}$  overnight. Small yellow crystals were obtained and were washed with ether ( $3 \times 3$  mL). Yield: 50%, 179 mg; mp  $86\text{--}88^\circ\text{C}$ . FTIR (CsI plates, ranked intensities,  $\text{cm}^{-1}$ ): 3052 (11), 2994 (10), 2917 (9), 2849 (8), 1578 (12), 1481 (4), 1433 (3), 1365 (17), 1261 (13), 1184 (14), 1158 (15), 1082 (5), 1022 (6), 997 (7), 799 (16), 735 (1), 694 (2).  $^1\text{H}$  NMR ( $\text{CD}_2\text{Cl}_2$ , 273 K, 500 MHz, ppm)  $\delta$ : 7.69–7.72 (m, 2H), 7.81–7.85 (m, 2H), 7.93–7.97 (m, 1H).  $^{13}\text{C}\{^1\text{H}\}$  NMR ( $\text{CD}_2\text{Cl}_2$ , 273 K, 125.76 MHz, ppm)  $\delta$ : 130.9 (s), 132.2 (s), 134.4 (s), 135.6 (s).  $^{27}\text{Al}$  NMR ( $\text{CD}_2\text{Cl}_2$ , 273 K, 130.29 MHz, ppm)  $\delta$ : 103.8 (s).

### Preparation of $\text{Ph}_3\text{AsGaCl}_3$

The procedures were described by Reid and co-workers,<sup>5a</sup> and the characterization data was consistent. Crystalline material was obtained by  $\text{CH}_2\text{Cl}_2$ /pentane layering at  $-25^\circ\text{C}$  over 48 h.

### Supplementary data

Supplementary data for this article are available on the journal Web site (canjchem.nrc.ca). CCDCs 759512–759516 contain the X-ray data in CIF format for this manuscript. These data can be obtained, free of charge, via [www.ccdc.cam.ac.uk/conts/retrieving.html](http://www.ccdc.cam.ac.uk/conts/retrieving.html) (Or from the Cambridge Crystallographic Data Centre, 12 Union Road, Cambridge CB2 1EZ, UK; fax +44 1223 336033; or [deposit@ccdc.cam.ac.uk](mailto:deposit@ccdc.cam.ac.uk)).

### Acknowledgements

We thank the Natural Sciences and Engineering Research Council of Canada (NSERC), the Canada Research Chairs Program, the Canada Foundation for Innovation (CFI), the Walter C. Sumner Foundation, and the Nova Scotia Research and Innovation Trust Fund for funding, and the Atlantic Region Magnetic Resonance Centre for use of instrumentation. We thank Sara Vickers for assistance with translations.

### References

- (1) (a) Petrie, M. A.; Olmstead, M. M.; Hope, H.; Bartlett, R. A.; Power, P. P. *J. Am. Chem. Soc.* **1993**, *115* (8), 3221.

- doi:10.1021/ja00061a021.; (b) Rivard, E.; Merrill, W. A.; Fetting, J. C.; Power, P. P. *Chem. Commun. (Camb.)* **2006**, 3800. doi:10.1039/b609748k. PMID:16969462.
- (2) (a) Atwood, A. A.; Cowley, A. H.; Harris, P. R.; Jones, R. A.; Koschmieder, S. U.; Nunn, C. M.; Atwood, J. L.; Bott, S. G. *Organometallics* **1993**, *12* (1), 24. doi:10.1021/om00025a010.; (b) Yablokov, V. A.; Dozorov, A. V.; Mitrofanova, S. V.; Yavich, B. S. *Russ. J. Gen. Chem.* **1990**, *60*, 574.
- (3) Wells, R. L.; McPhail, A. T.; Speer, T. M. *Organometallics* **1992**, *11* (2), 960. doi:10.1021/om00038a070.
- (4) Kuczkowski, A.; Schulz, S.; Nieger, M.; Schreiner, P. R. *Organometallics* **2002**, *21* (7), 1408. doi:10.1021/om0200205.
- (5) (a) Cheng, F.; Hector, A. L.; Levason, W.; Reid, G.; Webster, M.; Zhang, W. *Inorg. Chem.* **2007**, *46* (17), 7215. doi:10.1021/ic700895r. PMID:17658877.; (b) Jouet, R. J.; Wells, R. L.; Rheingold, A. L.; Incarvito, C. D. *J. Organomet. Chem.* **2000**, *601* (1), 191. doi:10.1016/S0022-328X(00)00055-3.; (c) Carty, A. J. *Can. J. Chem.* **1967**, *45* (24), 3187. doi:10.1139/v67-513.
- (6) Wells, R. L.; McPhail, A. T.; Jones, L. J., III; Self, M. F.; Butcher, R. J. *Organometallics* **1992**, *11* (7), 2694. doi:10.1021/om00043a064.
- (7) Baker, L.-J.; Kloos, L. A.; Rickard, C. E. F.; Taylor, M. J. *J. Organomet. Chem.* **1997**, *545–546* (1), 249. doi:10.1016/S0022-328X(97)00221-0.
- (8) Baker, L.-J.; Rickard, C. E. F.; Taylor, M. J. *J. Organomet. Chem.* **1994**, *464* (1), C4. doi:10.1016/0022-328X(94)87020-9.
- (9) (a) Conrad, E.; Burford, N.; McDonald, R.; Ferguson, M. J. *J. Am. Chem. Soc.* **2009**, *131* (14), 5066. doi:10.1021/ja900968j. PMID:19296681.; (b) Conrad, E.; Burford, N.; McDonald, R.; Ferguson, M. J. *Inorg. Chem.* **2008**, *47* (8), 2952. doi:10.1021/ic800287e. PMID:18345596.; (c) Kilah, N. L.; Weir, M. L.; Wild, S. B. *Dalton Trans.* **2008**, 2480. doi:10.1039/b800965a. PMID:18461204.
- (10) Conrad, E.; Burford, N.; McDonald, R.; Ferguson, M. J. *J. Am. Chem. Soc.* **2009**, *131* (46), 17000. doi:10.1021/ja907613c. PMID:19886662.
- (11) Welch, G. C.; Prieto, R.; Dureen, M. A.; Lough, A. J.; La-beodan, O. A.; Höltrichter-Rössmann, T.; Stephan, D. W. *Dalton Trans.* **2009**, 1559. doi:10.1039/b814486a. PMID:19421599.
- (12) Cowley, A. H.; Kemp, R. A. *Chem. Rev.* **1985**, *85* (5), 367. doi:10.1021/cr00069a002.
- (13) Johansen, J. D.; McPhail, A. T.; Wells, R. L. *Adv. Mater. Opt. Electron.* **1992**, *1* (1), 29. doi:10.1002/amo.860010106.
- (14) Sheldrick, G. M. *Acta Crystallogr.* **2008**, *A64*, 112. doi:10.1107/S0108767307043930.
- (15) Beurskens, P. T.; Beurskens, G.; de Gelder, R.; Smits, J. M. M.; Garcia-Granda, S.; Gould, R. O. *The DIRDIF-2008 program system*; Crystallography Laboratory, Radboud University Nijmegen: The Netherlands, 2008.

# A DFT study on the catalytic mechanism of UDP-glucose dehydrogenase

WenJuan Huang, Jorge Llano, and James W. Gauld

**Abstract:** Uridine 5'-diphosphate glucuronic acid (UDPGlcUA) is a key intermediary metabolite in many species, including pathogenic bacteria and humans. It is biosynthesized from UDP-glucose (UDPGlc) by uridine diphosphate glucose dehydrogenase (UDPGlcDH) via a twofold two-electron-one-proton oxidation that successively transforms the 6-hydroxymethyl of glucopyranose into a formyl, and the latter into the final carboxylic function. The catalytic mechanism of UDPGlcDH was investigated using a large enzyme active-site model in combination with the B3LYP method and the polarizable continuum model (IEF-PCM) self-consistent reaction field. The latter was used to correct for the long-range electrostatic effect of the protein environment. The overall mechanism consists of four catalytic steps: (i) NAD<sup>+</sup>-dependent oxidation of glucose to glucuronaldehyde, (ii) nucleophilic addition of Cys260-SH to glucuronaldehyde to form a 6-thiohemiacetal intermediate, (iii) NAD<sup>+</sup>-dependent oxidation of the 6-thiohemiacetal to form a 6-thioester intermediate, and finally, (iv) hydrolysis of the 6-thioester to give glucuronic acid. In addition, this study also provides insight into the debated roles of Lys204 and Asp264, and the most likely protonation state of a reactive Michaelis complex of UDPGlcDH.

**Key words:** density functional theory (DFT), uridine diphosphate glucose dehydrogenase (UDPGlcDH), NAD, thioester hydrolysis, acid-base, electron transfer, proton transfer.

**Résumé :** L'acide uridine-5'-diphosphate glucuronique (UDPGlcUA) est un métabolite intermédiaire clé dans plusieurs espèces incluant les humains et quelques bactéries pathogènes. L'UDPGlcUA est biosynthétisé à partir de l'uridine-diphosphate glucose (UDPGlc) par l'enzyme uridine-diphosphate glucose déshydrogénase (UDPGlcDH) au cours d'une double oxydation à deux électrons et un proton qui transforme successivement le groupe 6-hydroxyméthyle du glucopyranose en formyle, et puis, en le groupe fonctionnel carboxyle. On a étudié le mécanisme catalytique du UDPGlcDH avec un modèle de grande taille du site actif de l'enzyme et au moyen des méthodes de calcul quantique B3LYP et IEF-PCM. On a employé le champ réactionnel autocohérent IEF-PCM pour corriger l'effet électrostatique à longue distance de l'environnement de la protéine. Le mécanisme global de réaction comprend quatre étapes catalytiques : (i) oxydation du glucose en glucuronaldéhyde par le NAD<sup>+</sup>, (ii) addition nucléophile du Cys260-SH sur le glucuronaldéhyde pour donner un intermédiaire 6-thiohémiacétal, (iii) oxydation du 6-thiohémiacétal par le NAD<sup>+</sup> pour donner un intermédiaire 6-thioester, et finalement, (iv) hydrolyse du 6-thioester pour former l'acide glucuronique. Notamment, cette étude de modélisation nous a permis d'établir les rôles mécanistiques de la Lys204 et l'Asp264, ainsi que l'état le plus probable de protonation du complexe réactif de Michaelis entre l'UDPGlcDH et l'UDPGlc.

**Mots-clés :** théorie de la fonctionnelle de la densité (« DFT »), uridine-diphosphate glucose déshydrogénase (UDPGlcDH), NAD, hydrolyse de thioester, acide-base, transfert d'électron, transfert de proton.

## Introduction

Carbohydrates have key roles in cellular biochemistry including biosignalling, energy storage, membrane structural assemblage, and metabolic intermediation as nucleotides, glycolipids, and glycoproteins. In fact, several carbohydrate-containing precursors are common to unrelated metabolic pathways in different species.<sup>1,2</sup> For instance, uridine 5'-diphosphate glucuronic acid (UDPGlcUA, in Scheme 1) is an essential precursor in the syntheses of many polysaccharides. In mammalian cells, UDPGlcUA bonds to certain waste products and toxic substances, thereby increasing their water

solubility, so that they may be excreted from the body.<sup>3,4</sup> UDPGlcUA is also an essential precursor in the making of antiphagocytic capsular polysaccharides of pathogenic bacteria. In *Streptococcus pneumoniae*, for example, UDPGlcUA is a key intermediary in the synthesis of the polysaccharide capsule. This capsule acts as an antiphagocytic protector and is responsible for the toxicity and extent of the antibiotic resistance observed in many organisms.<sup>5-7</sup> UDPGlcUA is synthesized by uridine diphosphate glucose dehydrogenase (UDPGlcDH),<sup>3,8</sup> which regulates the glycoprotein biosynthesis and other pathways. Thus, UDPGlcDH is a logical target for the development of new antibacterial drugs.

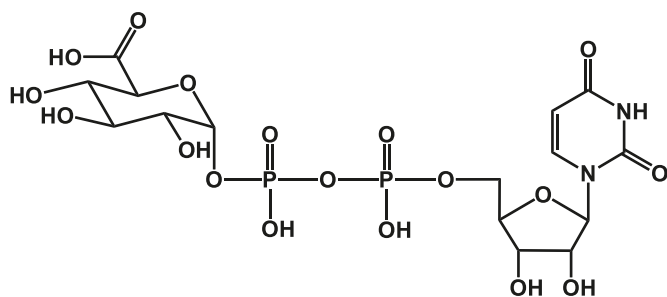
Received 14 January 2010. Accepted 13 March 2010. Published on the NRC Research Press Web site at canjchem.nrc.ca on 4 June 2010.

This article is part of a Special Issue dedicated to Professor R. J. Boyd.

**W.-J. Huang, J. Llano, and J.W. Gauld.**<sup>1</sup> Department of Chemistry and Biochemistry, University of Windsor, Windsor, ON N9B 3P4, Canada.

<sup>1</sup>Corresponding author (e-mail: gauld@uwindsor.ca).

**Scheme 1.** Uridine 5'-diphosphate glucuronic acid, abbreviated UDPGlcUA.



The catalytic performance of UDPGlcDH is unique in several aspects. First, it should be noted that the chemical oxidation of glucose is not specific, as the terminal 1-formyl and 6-hydroxymethyl groups of the open-chain form can be oxidized to carboxylic groups in the presence of moderate oxidizing agents such as transition metal ions, halogens, and warm dilute nitric acid. However, within a single active site, UDPGlcDH is able to perform an overall four-electron oxidation by successively transforming the 6-hydroxymethyl group into a formyl group, and the latter into the final carboxylic function.<sup>9,10</sup> In addition, UDPGlcDH uses two  $\text{NAD}^+$  molecules as the final electron acceptors, and this type of redox reaction path is rarely found in the enzymatic chemistry of carbohydrates.<sup>11</sup> Finally, UDPGlcDH belongs to the family of sugar nucleotide-modifying enzymes, and hence, various molecular details of the UDPGlcDH enzymatic mechanism may be common to other enzymes of the family.<sup>12,13</sup>

The first breakthrough in the elucidation of the catalytic mechanism of UDPGlcDH was obtained by Oppenheimer and Handlon<sup>8</sup> who found that the catalytic pathway was a  $\text{NAD}^+$ -dependent twofold oxidation. Thereafter, based on their X-ray crystallography, site-directed mutagenesis, and kinetic isotope effect studies, Ge et al.<sup>10</sup> proposed two possible catalytic pathways with the difference being the identity of mechanistically required acid-base active-site residues. More specifically, they proposed that either an active site aspartate or possibly a neutral lysyl residue is the mechanistic base. While the latter is directly adjacent to the substrate, the aspartate interacts indirectly via a possible  $\text{H}_2\text{O}$  bridge with substrate. Recently, studies combining gene encoding and kinetics,<sup>3,14</sup> and the crystal structures of UDPGlcDH from several species (e.g., human, cows, bacteria, and plants) have been reported.<sup>15</sup>

The proposed mechanism of UDPGlcDH involves multiple steps and is shown in Scheme 2. The first step is the oxidation of the 6-hydroxymethyl to a formyl group via hydride transfer to  $\text{NAD}^+$  with concomitant deprotonation of O6 by a general base B ( $\text{Lys204-NH}_2$  or  $\text{Asp264-COO}^-$ ). Then, Cys260 in concurrence with Glu145 attacks the carbonyl group to form a covalent thiohemiacetal adduct, while the conjugated acid HB donates the proton back to O6. In the second stage, NADH leaves to allow a new  $\text{NAD}^+$  to enter the active site. The latter, assisted by the same general base B, further oxidizes the thiohemiacetal adduct intermediate to form a thioester. In the final step, the thioester is hydrolyzed to give the final UDPGlcUA product.

While the proposed mechanism outlined in Scheme 2

shows fair agreement with the experimental evidence, there remains, unsatisfactorily, the question of the identity of the base that initiates the acid-base catalytic pathway.<sup>8,10,11,16,17</sup> This study aims to explore the potential energy surfaces of the catalytic mechanism of UDPGlcDH by applying density functional theory methods to assess the feasibility of these pathways and to clarify the role of active-site residues.

## Computational methods

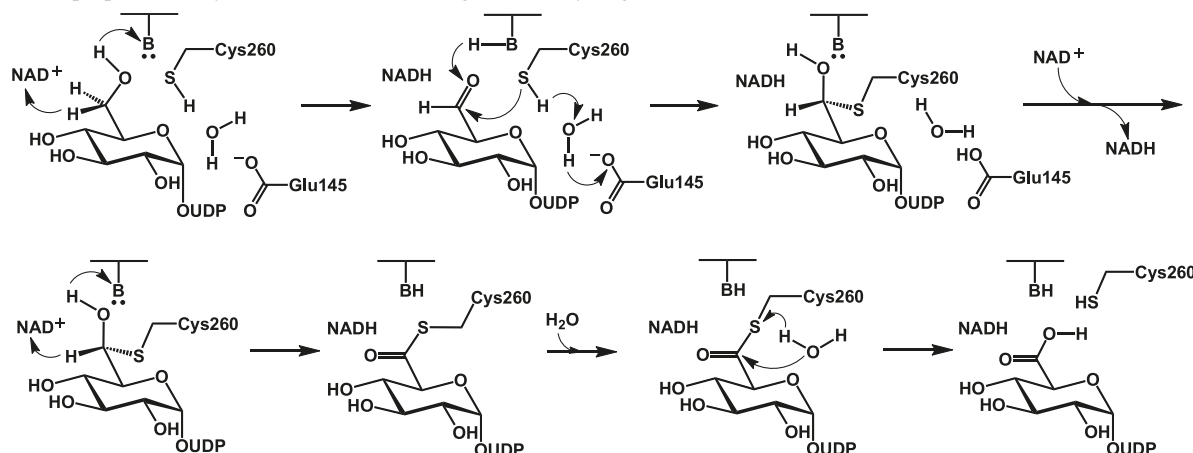
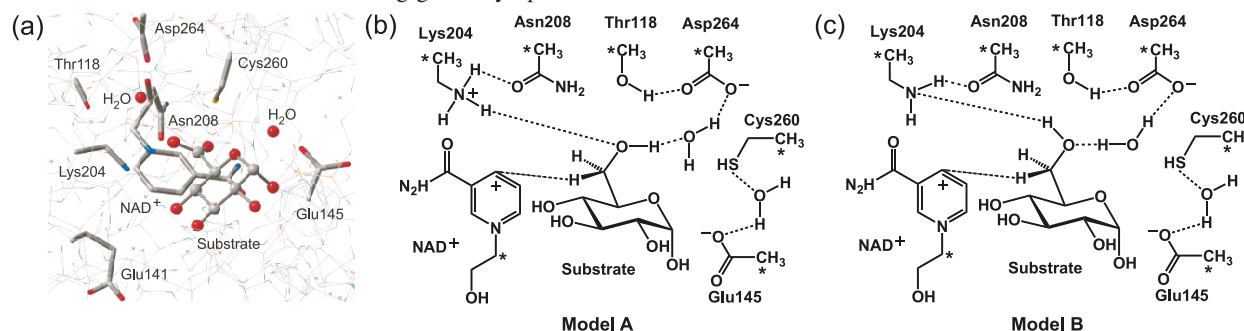
The hybrid density functional B3LYP,<sup>18–20</sup> as implemented in the Gaussian 03 program,<sup>21</sup> was used in all calculations. This functional combines Becke's<sup>18,19</sup> three-parameter hybrid exchange functional and the correlation functional of Lee et al.<sup>20</sup> The B3LYP/6-31G(d) level of theory was used for geometry optimizations, harmonic vibrational frequencies, and zero-point vibrational energy (ZPVE) corrections. Single-point calculations at the B3LYP/6-311+G(2df,p)//B3LYP/6-31G(d) level were done to compute relative total energies. In addition, the long-range dielectric effect of the protein environment that surrounds the active site was estimated by performing single-point calculations on the optimized geometries using the polarizable continuum model in the integral equation formalism (IEF-PCM) at the B3LYP/6-31G(d) level of theory. The dielectric constant,  $\epsilon$ , was set to 4.0 in these calculations.

Our active-site model was extracted from the crystallographic structure of the mutated UDPGlcDH (with Ser replacing Cys260) complexed with glucuronic acid (Protein Data Bank (PDB) accession code: 1DLJ).<sup>10</sup> Key amino acid residues were replaced as follows: Asp264 and Glu145 by acetate ions, Cys260 by ethanethiol, Asn208 by acetamide, and Thr118 by methanol. In the case of Lys204, the side chain of the residue was replaced by the ethylammonium ion in model A and by ethylamine in model B, as illustrated in Fig. 1. The substrate UDP-glucose was modelled as  $\alpha$ -D-glucopyranose, and  $\text{NAD}^+$  as an *N*-hydroxyethyl-nicotinamidium ion. The two water molecules present in the crystal structure were kept in the active-site model. One  $\text{H}_2\text{O}$  forms a hydrogen-bond bridge between Asp264 and the 6-hydroxymethyl of glucose, and the other  $\text{H}_2\text{O}$  between Glu145 and the thiol of Cys260. For both active-site models, NADH leaves the catalytic cleft during the last step, allowing Glu141 (modelled as butyrate) to approach the substrate. To keep the spatial arrangement of catalytic residues in the active site, selected atoms were held at their positions in the crystal structure (Fig. 1). The applicability of the present computational approach to the study of enzymatic reactions has been previously reviewed in detail.<sup>22–27</sup>

## Results and discussion

### Protonation state of the active site of UDPGlcDH in the Michaelis complex

The proposed catalytic mechanism of UDPGlcDH is initiated by oxidation of the 6-hydroxymethyl to a formyl group by a hydride transfer to  $\text{NAD}^+$  with concomitant deprotonation of O6 by either Lys204 or Asp264. In the case of Asp264, the experimental evidence suggests that it occurs as an aspartate rather than an aspartic group.<sup>10</sup> However, there is no unambiguous experimental evidence for the side chain of Lys204 occurring as either a neutral amine or a positively charged ammonium group.<sup>16,17</sup> As a result, we be-

**Scheme 2.** The proposed catalytic mechanism of UDP-glucose dehydrogenase (UDPGlcDH).<sup>10</sup>**Fig. 1.** Structural models of the active site: (a) Arrangement of the catalytically active residues of UDP-glucose dehydrogenase according to the crystal structure (PDB accession code: 1DLJ). (b) Catalytic groups replacing the residues and glucose replacing UDP-glucose with protonated Lys204 residue. (c) Catalytic groups replacing the residues and glucose replacing UDP-glucose with neutral Lys204 residue. Atoms marked with an asterisk were held fixed during geometry optimizations.**Table 1.** Proton affinities and basicities (in  $\text{kJ mol}^{-1}$ ) of the side chain of Lys204, modelled as ethylamine, within environments of different polarity.

$\text{B} + \text{H}^+ \rightarrow \text{BH}^+$	Proton affinity ( $\alpha = \text{vac.}$ )	Basicity ( $\alpha = \text{aq.}$ )
<b>Isolated</b>		
$\text{Lys} (\epsilon = 1) + \text{H}^+ (\alpha) \rightarrow \text{LysH}^+ (\epsilon = 1)$	941.7	-156.1
$\text{Lys} (\epsilon = 4) + \text{H}^+ (\alpha) \rightarrow \text{LysH}^+ (\epsilon = 4)$	1141.1	43.1
<b>Within the active-site model</b>		
$\text{Lys} (\epsilon = 1) + \text{H}^+ (\alpha) \rightarrow \text{LysH}^+ (\epsilon = 1)$	1280.4	182.4
$\text{Lys} (\epsilon = 4) + \text{H}^+ (\alpha) \rightarrow \text{LysH}^+ (\epsilon = 4)$	1208.2	110.5

gan our investigation by constructing the two alternate models of the active site with bound substrate and cofactor, the Michaelis complex, shown in Fig. 1. Then, we estimated the proton affinities and basicities of the side chain of Lys204 under four different electrostatic conditions to investigate the effect of the local electrostatic environment of the enzyme on the side chain of Lys204.

The proton affinities (PA) were estimated as the negative change in the internal energy of protonation of the side chain at 0 K with the proton coming from the vacuum state, i.e.,  $\text{PA} = -[E_0(\text{BH}^+) - E_0(\text{B}) - E_0(\text{H}^+)]$ , where  $E_0(\text{H}^+) = 0$ . The basicities were estimated as the negative change in the internal energy of protonation of the side chain at 0 K with the proton coming from an aqueous ideal-dilute solution at pH 7. The standard energy of bulk solvation of the proton

in aqueous solution was taken to be  $-1097.9 \text{ kJ mol}^{-1}$  because this value is the only one consistent with the Born-Haber-type cycles of both hydrogen and the electron.<sup>28,29</sup> That is,  $\text{basicity} = \text{PA} - 1097.9 \text{ kJ mol}^{-1}$ .

The proton affinities and basicities of ethylamine, the model chosen for the side chain of Lys204, within four different electrostatic environments are reported in Table 1. In a first approximation, the protonation of isolated ethylamine was considered in vacuum and in a homogeneous medium with a dielectric constant of 4. The latter value being chosen as it is typically used as an appropriate estimate of the average electrostatic dielectric constant found within a bulk protein environment.<sup>30,31</sup> The proton affinity of  $941.7 \text{ kJ mol}^{-1}$  indicates that protonation of the side chain in vacuum is thermodynamically feasible. However, the side chain in a



homogeneous medium with a dielectric constant of 1 cannot abstract a proton from the bulk of an ideal-dilute aqueous solution, according to the basicity of  $-156.1 \text{ kJ mol}^{-1}$ . However, the situation changes if the side chain of lysine is placed under conditions simulating the average effect of the bulk protein environment. In particular, the proton affinity of the lysine increases such that its estimated basicity now becomes positive at  $43.1 \text{ kJ mol}^{-1}$ . This suggests that when embedded in the average protein environment, the lysine side chain amino group is thermodynamically able to gain a proton from the bulk of an ideal-dilute aqueous solution at pH 7.

We then placed the model of lysine within our chosen active-site model and recalculated its proton affinity and basicity (Table 1). First, we only considered the anisotropic electrostatic environment generated by the first shell of residues found in the catalytic cleft with the surrounding electrostatic environment set to a dielectric constant ( $\epsilon$ ) of 1 (i.e., the vacuum state). It is found that the protonation of the side chain of Lys204 becomes even more feasible, as indicated by the now larger proton affinities and basicities of 1280.4 and  $182.4 \text{ kJ mol}^{-1}$ , respectively. In contrast to that observed for isolated lysine, however, increasing the polarity of the surrounding environment to that resembling the bulk protein (i.e., increasing  $\epsilon$  from 1 to 4) decreases the proton affinity and basicity of the lysine. Indeed, its PA decreases by approximately  $80 \text{ kJ mol}^{-1}$  to  $1208.2 \text{ kJ mol}^{-1}$  with the same decrease in basicity to  $110.5 \text{ kJ mol}^{-1}$ .

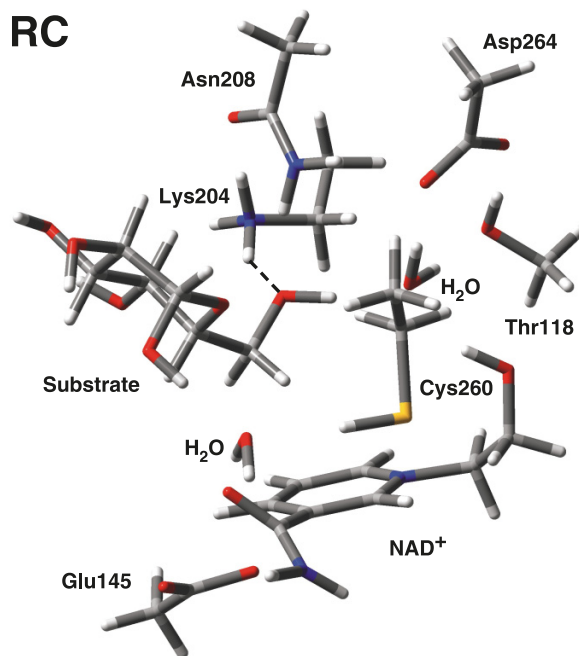
Thus, in summary, the three electrostatic conditions simulating the electrostatic environment felt by the side chain of Lys204 in the active site of UDPGlcDH unambiguously show that Lys204 is very likely to be protonated. Therefore, the protonation state of the active site of UDPGlcDH in the enzyme–substrate–cofactor complex is most likely to correspond to the structural model A (Fig. 1), with Asp264 bound to water acting as the general base in the initial step of the catalytic mechanism.

### Substrate binding the active site of UDPGlcDH

Since model A (Fig. 1) represents the most likely Michaelis complex for UDPGlcDH, it was selected as the reactant complex (RC, Fig. 2) for our mechanistic study. Model A was extracted from a crystallographic structure of the enzyme (PDB accession code: 1DLJ),<sup>16</sup> with  $\beta$ -glucopyranose as the substrate.<sup>10,16</sup> This chemical model was then carefully optimized to preserve the hydrogen-bonded network observed in the crystallographic model, as it has been suggested that this network is essential for the enzyme to carry out its catalytic mechanism.<sup>10</sup> The optimized structure of our chemical model shows that the 6-hydroxymethyl group of glucose hydrogen-bonds to the oxygen of an  $\text{H}_2\text{O}$  (1.64 Å), and this water to Asp264 and Thr118 (1.66 and 1.71 Å, respectively), forming a ring. As in the crystal structure, Lys204– $\text{NH}_3^+$  forms a hydrogen-bonded bridge to the 6-hydroxymethyl and the carbonyl group of Asn208. In addition, one of the 6-position C–H bonds points directly to the 4-position of the pyridine ring of  $\text{NAD}^+$  at a distance of 2.78 Å.

On the opposite side of the cleft, water forms hydrogen bonds that enable the bridge Glu145– $\text{COO}^- \cdots \text{H}_2\text{O} \cdots \text{HS-Cys260}$  at 1.97 and 2.08 Å, respectively. It has been debated whether Cys260 is in the thiol (Cys260–SH) or thiolate (Cys260– $\text{S}^-$ ) form in the active site.<sup>16</sup> Our computational

**Fig. 2.** Optimized structure of the reactant complex (RC): substrate and cofactor bound to the active-site model of UDPGlcDH.

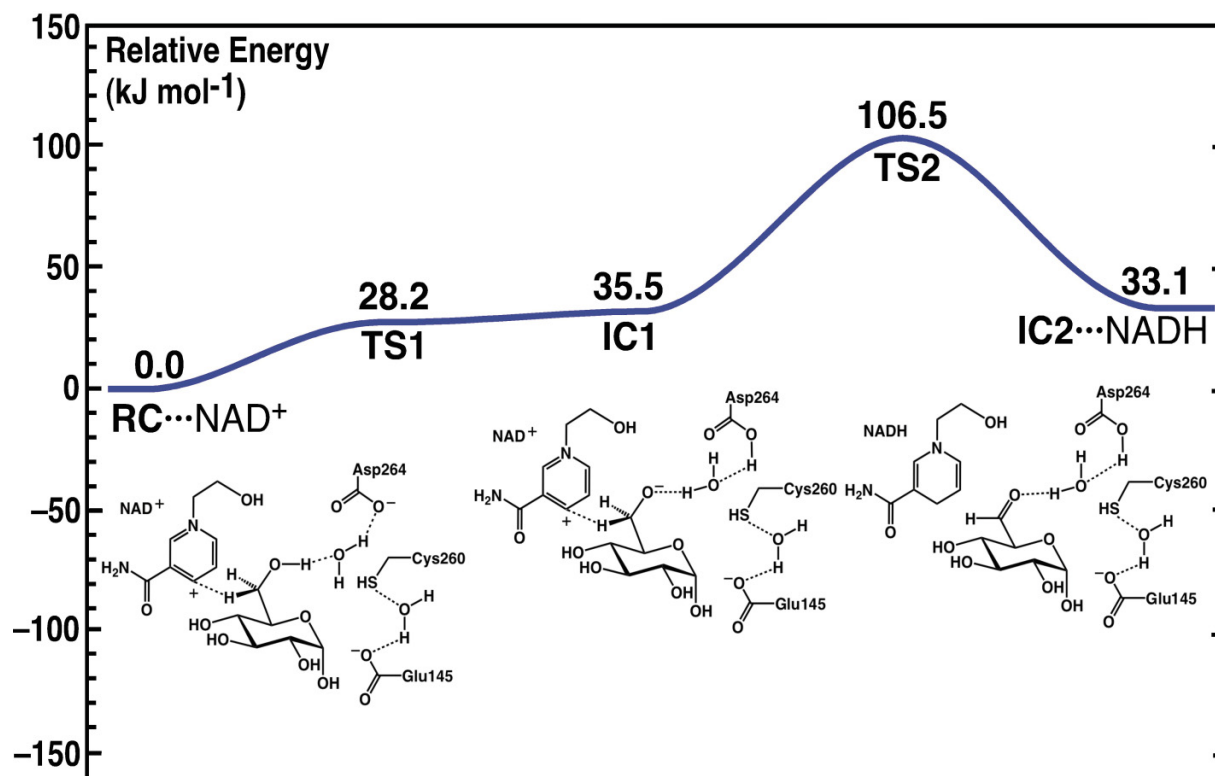


model of the enzyme–substrate complex shows that the thiolate form of Cys260 causes the orientation of Glu145 to change such that it flips into the binding region of the substrate, hydrogen bonding to glucose and  $\text{NAD}^+$ . Hence, the thiol form of Cys260 is the only alternative that makes possible a stable Glu145–water–Cys260 bridge and that is in agreement with the crystallographic structure.

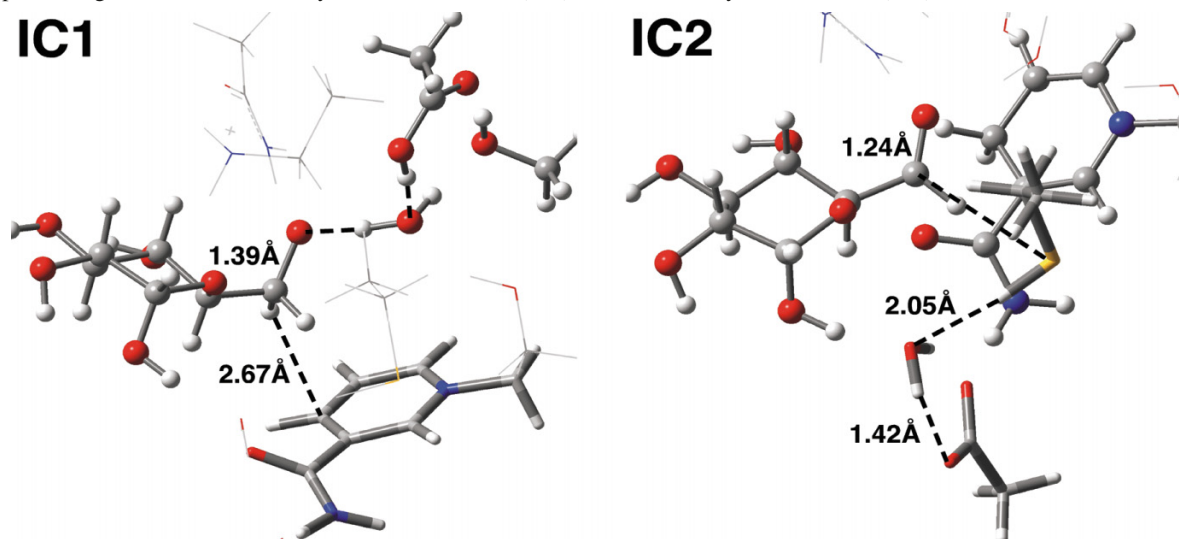
### First catalytic step: oxidation of glucose to form glucuronaldehyde

The first catalytic step of UDPGlcDH (Fig. 3) is the oxidation of the 6-hydroxymethyl group of glucopyranose to form the 6-formyl terminus. This process begins with a proton transfer from the substrate's 6-hydroxymethyl group to the  $\text{H}_2\text{O}$  bound to the carboxylate of Asp264. Concomitantly, this bridging water transfers a proton to Asp264 (RC in Fig. 2). This deprotonation has a barrier of  $28.2 \text{ kJ mol}^{-1}$ , with the resulting 6-oxymethyl anion intermediate, IC1 (Fig. 4), lying  $35.5 \text{ kJ mol}^{-1}$  above both RC and IC1 (Fig. 3). It is noted that the energy of TS1 is lower than that of IC1 due to the inclusion of ZPVE. This is a commonly occurring artifact for flat potential energy surfaces (PES) and merely indicates that the reaction proceeds without any barrier. Consequently, the deprotonation brings about a C6–O bond-length shortening from 1.43 to 1.39 Å and a disruption of the hydrogen-bonded network originally found in the Michaelis complex. More specifically, the original hydrogen-bonded chain Asp264– $\text{COO}^- \cdots \text{H}_2\text{O} \cdots \text{HO-CH}_2\text{-Glc}$  in RC changes directionality to form the Asp264– $\text{COOH} \cdots \text{OH}_2 \cdots \text{O-CH}_2\text{-Glc}$  chain in IC1, with hydrogen-bonding distances of 1.59 and 1.44 Å, respectively. In addition, the distance between the 6-position C–H bond that points to the 4-position of the pyridine ring decreases from 2.78 to 2.67 Å. (IC1 in Fig. 4). The 6-oxymethyl anion is further stabilized by accepting a hydro-

**Fig. 3.** Potential energy surface for the oxidation of the 6-hydroxymethyl group of glucopyranose (RC) to form glucuronaldehyde (IC2) through the 6-oxymethyl anion intermediate (IC1).



**Fig. 4.** Optimized geometries of the 6-oxanion intermediate (IC1) and the 6-formyl intermediate (IC2) in the active-site model.



gen bond from Lys204-NH<sub>3</sub><sup>+</sup>, which keeps bridging to the carbonyl group of Asn208.

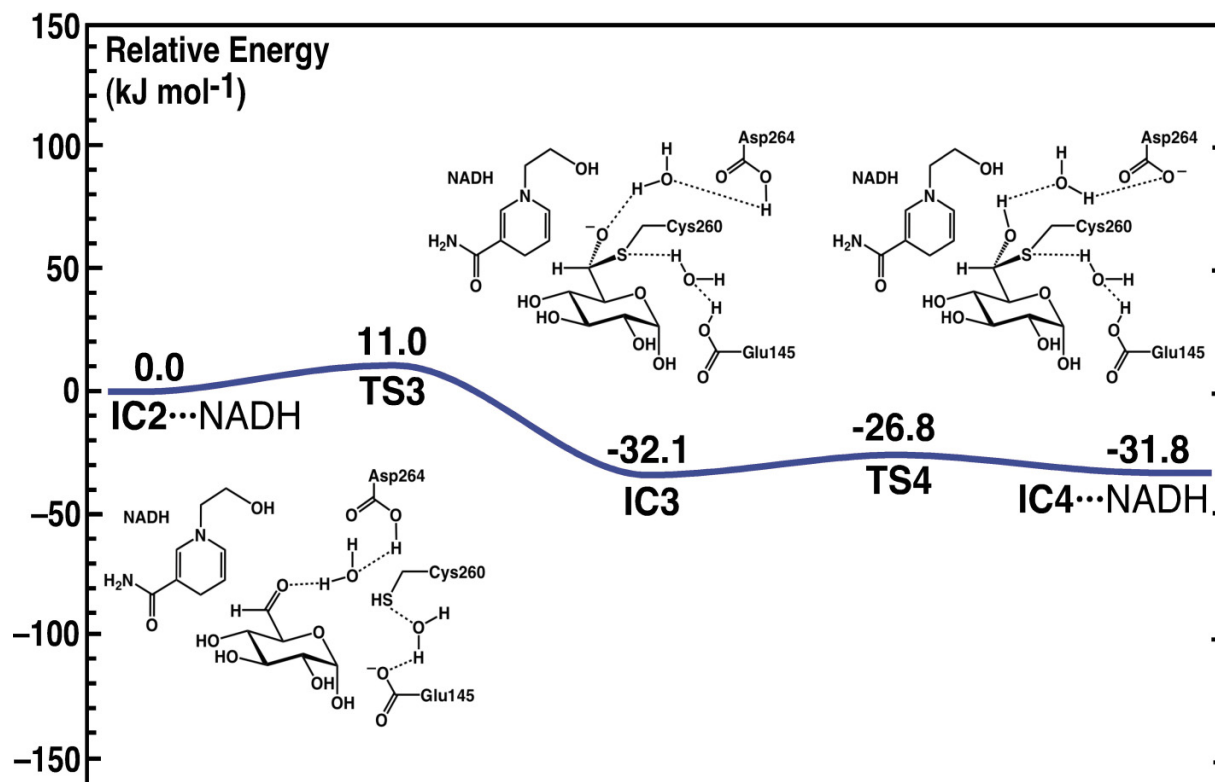
Then, the 6-oxanion undergoes a formal hydride transfer from the methyleneoxanion of IC1 to NAD<sup>+</sup> through TS2 with a barrier of 106.5 kJ mol<sup>-1</sup>, leading to formation of glucuronaldehyde, i.e., the 6-formyl intermediate, IC2 (Fig. 4). Thermodynamically, IC2 lies 33.1 kJ mol<sup>-1</sup> above RC (Fig. 3). Moreover, the C-O bond has shortened from 1.39 Å in IC1 to 1.24 Å in IC2, indicating the formation of the 6-formyl derivative. The oxidation process to give IC2 does not alter the hydrogen-bonding pattern relating to the active-

site residues, i.e., Asp264-COOH...OH<sub>2</sub>...O=CH-Glc. In addition, the formyl terminus accepts a hydrogen bond (1.65 Å) from Lys204-NH<sub>3</sub><sup>+</sup>, which keeps the bridge to the carbonyl group of Asn208 (1.90 Å).

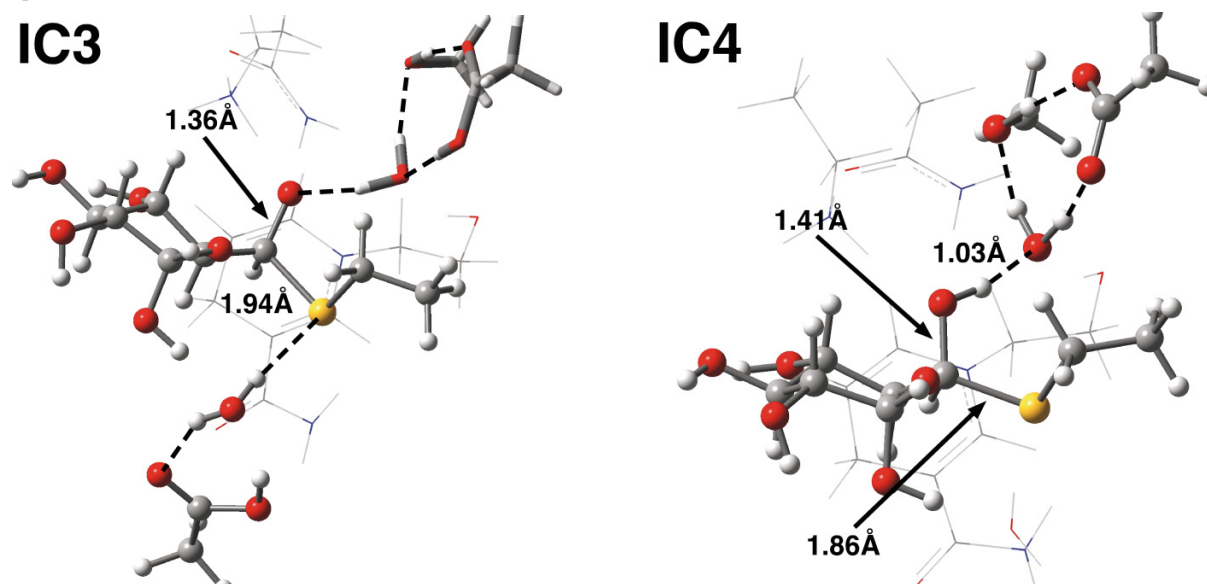
#### Second catalytic step: nucleophilic addition to form the 6-thiohemiacetal intermediate

Glucuronaldehyde, i.e., the 6-formyl intermediate, IC2, then undergoes nucleophilic addition of thiol from Cys260 to form a rather stable 6-thiohemiacetal intermediate (Fig. 5). This is achieved through the attack of the sulfur

**Fig. 5.** Potential energy surface for the nucleophilic addition of the Cys260 thiol group to the 6-formyl end of glucuronaldehyde to form a 6-thiohemiacetal intermediate (IC4).



**Fig. 6.** Optimized structures of the thiohemiacetal anion (IC3) and neutral (IC4) intermediates.



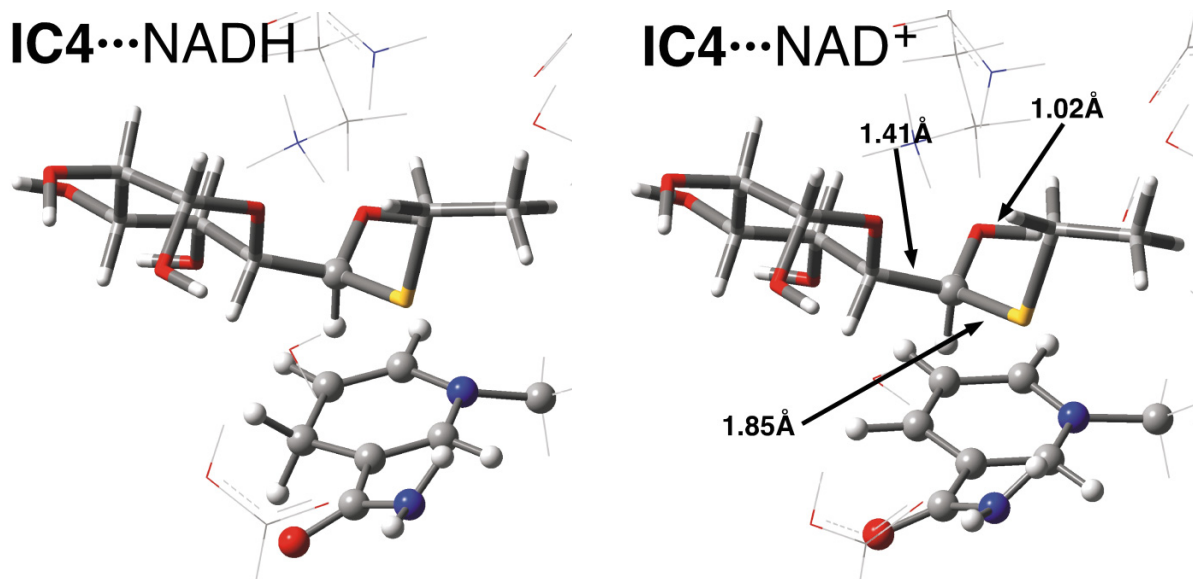
centre of Cys260 at the carbonyl carbon of IC2 with concomitant formal transfer of the thiol proton of Cys260-SH to the carboxylate of Glu145. This process occurs at a cost of just 11.0 kJ mol<sup>-1</sup> to give the thiohemiacetal anion intermediate, IC3, lying 32.1 kJ mol<sup>-1</sup> lower in energy than IC2. In fact, the formation of IC3 is essentially thermoneutral with respect to the initial active-site bound substrate complex RC...NAD<sup>+</sup>.

In IC3, the S-C bond forms at 1.94 Å, whereas the C6-O

bond lengthens to 1.36 Å (Fig. 6). Both the bond lengthening and increase of negative charge on O6 (i.e., from +0.05 in IC2 to -0.55 in IC3) indicate the formation of the highly basic oxyanion structure C6-O<sup>-</sup>. This oxyanion is further stabilized by accepting a hydrogen bond from Lys204-NH<sub>3</sub><sup>+</sup>, which has now broken the bridge to the carbonyl group of Asn208. Then, the oxyanion of IC3 abstracts a proton back from Asp264 through the bridging water molecule (at a cost of 5.3 kJ mol<sup>-1</sup>) to form the neutral thiohemiacetal



Fig. 7. Optimized structures of the 6-thiohemiacetal complex with both NADH and NAD<sup>+</sup>.



intermediate, IC4 (Glc-C6H(S-Cys260)OH), lying 31.8 kJ mol<sup>-1</sup> below IC2. Predictably, the proton transfer causes the C6-O bond to elongate to 1.41 Å and the C6-S bond to shorten to 1.86 Å in IC4 with respect to IC3. Finally, the hydrogen-bonding network around the O6-H group in IC4 (Fig. 6) is restored to the pattern found in the enzyme-substrate complex RC (Fig. 2). However, even when the C6-OH group in IC4 is stabilized by accepting a hydrogen bond from Lys204-NH<sub>3</sub><sup>+</sup>, the bridge to the carbonyl group of Asn208 remains broken in the optimized structure of this intermediate.

### Third catalytic step: second oxidation to form the 6-thioester intermediate

The first oxidation step produces an enzyme-intermediate-cofactor complex, which, for the sake of simplicity, we represent as IC2...NADH. An experiment with the Cys260 → Ala mutant complexed with labelled UDP-[6'',6''-di-<sup>2</sup>H]-D-glucose in a solution containing NAD<sup>+</sup> and excess NADH showed that the NAD<sup>2</sup>H formed in the first oxidation step did not exchange with free NADH.<sup>10</sup> Thus, according to this evidence, the reduced cofactor remains bound to the active site until the thiohemiacetal neutral intermediate, IC4...NADH, is formed. Then, the NADH can be exchanged for NAD<sup>+</sup>, which then binds and continues oxidizing the 6-position of glucose.<sup>5,10,11</sup>

The optimized geometries of the 6-thiohemiacetal complex, IC4, with the reduced and the replacing oxidized cofactor molecules (i.e., IC4...NADH and IC4...NAD<sup>+</sup>, respectively, in Fig. 7) show high structural similarity, including the hydrogen-bonding pattern to Lys204. Furthermore, it was found that the IC4...NADH complex together with an infinitely separated NAD<sup>+</sup> ion is only 4.0 kJ mol<sup>-1</sup> more stable than the IC4...NAD<sup>+</sup> complex together with an infinitely separated NADH molecule.

Once the fresh, oxidized cofactor molecule is appropriately bound to the active site, the IC4...NAD<sup>+</sup> complex is ready to proceed with the second oxidation reaction (Fig. 8). This begins with the formation of a 6-thiohemiacetal anion intermediate by way of a proton transferring from the 6-hydroxyl

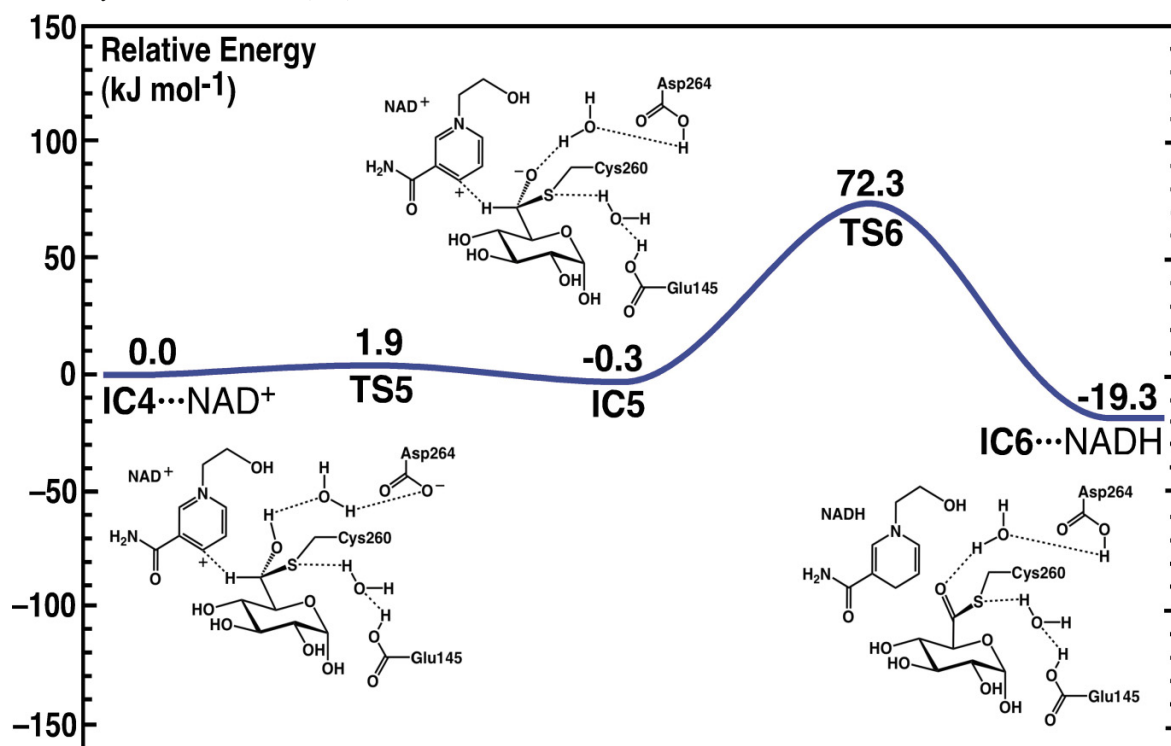
group to Asp264-COO<sup>-</sup> through the bridging water molecule. The barrier of this step is just 1.9 kJ mol<sup>-1</sup>, with the 6-thiohemiacetal oxyanion intermediate, IC5, lying 0.3 kJ mol<sup>-1</sup> lower in energy with respect to IC4...NAD<sup>+</sup>. The proton transfer reverses the directionality of the hydrogen-bonded chain from Glc-C6H(S-Cys260)OH...OH<sub>2</sub>...OOC-Asp264 in IC4 to Glc-C6H(S-Cys260)O...H<sub>2</sub>O...HOOC-Asp264 in IC5 (Fig. 9); the hydrogen-bonding distances in the latter being 1.60 and 1.65 Å. The 6-oxyanion is further stabilized by accepting a hydrogen bond from Lys204-NH<sub>3</sub><sup>+</sup>, which itself keeps the bridge to the carbonyl group of Asn208 broken. Moreover, the C6-H bond in IC5 is left directed more precisely to the reduction centre of the cofactor, with the hydrogen located 2.48 Å apart from the 4-position of the NAD<sup>+</sup> pyridine ring. In this geometrical arrangement, the two-electron one-proton transfer occurs from a C6-H group to NAD<sup>+</sup>, to give the 6-thioester intermediate, IC6. In the thioester intermediate, the C6=O link has a typical carbonyl bond distance of 1.23 Å, while the C6-S bond is shortened to 1.78 Å. This formal hydride transfer has a barrier of 72.3 kJ mol<sup>-1</sup> with respect to IC4...NAD<sup>+</sup>, and the 6-thioester intermediate, IC6...NADH, lies 19.3 kJ mol<sup>-1</sup> lower in energy than IC4...NAD<sup>+</sup>. In the IC6...NADH complex, the 6-carbonyl group accepts a hydrogen bond from Lys204-NH<sub>3</sub><sup>+</sup>, and the latter restores the bridge to the carbonyl group of Asn208.

### Fourth catalytic step: hydrolysis of the 6-thioester intermediate to form glucuronic acid

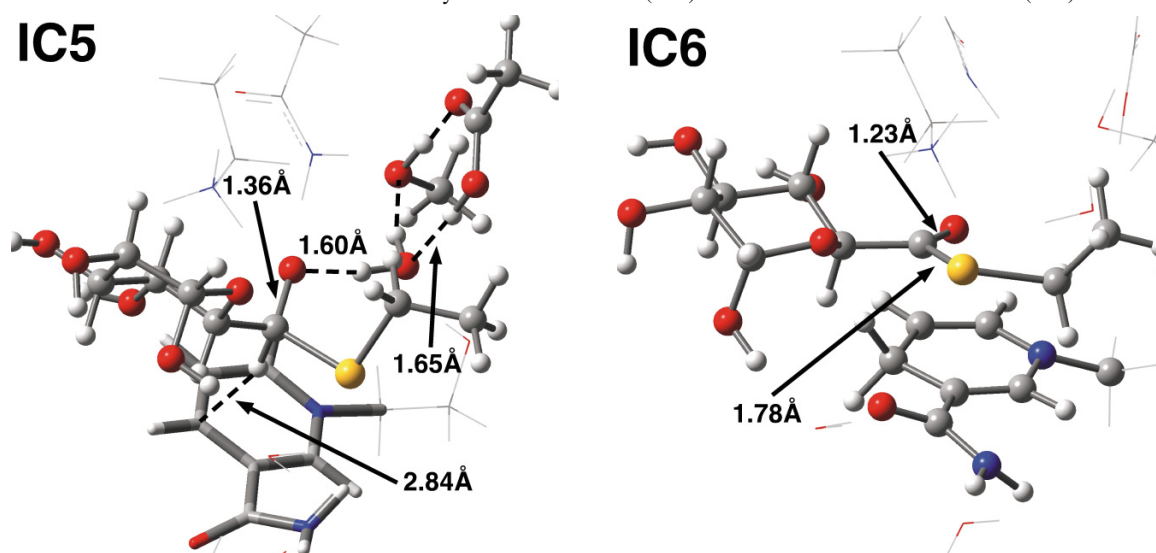
It has been proposed that hydrolysis of the 6-thioester intermediate, IC6, is catalyzed by the strictly conserved Glu141 residue.<sup>16,17</sup> However, the crystallographic structure of the UDPGlcDH Cys260 → Ser mutant with bound UDP-GlcUA and NADH shows that Glu141 lies behind the nicotinamide ring, which blocks the interaction of Glu141 with the 6-position of the thioester intermediate.<sup>16</sup> It has been hypothesized that, in the absence of NADH, Glu141 could extend into the active site and deliver an activated water molecule to the 6-position of the thioester intermediate.<sup>16</sup> In view of these ideas, we studied the hydrolysis of the thio-



**Fig. 8.** Potential energy surface for the oxidation of the 6-thiohemiacetal intermediate (IC4) to the 6-thioester intermediate (IC6) through a 6-thiohemiacetal oxyanion intermediate (IC5).



**Fig. 9.** Optimized structures of the 6-thiohemiacetal oxyanion intermediate (IC5) and the 6-thioester intermediate (IC6).



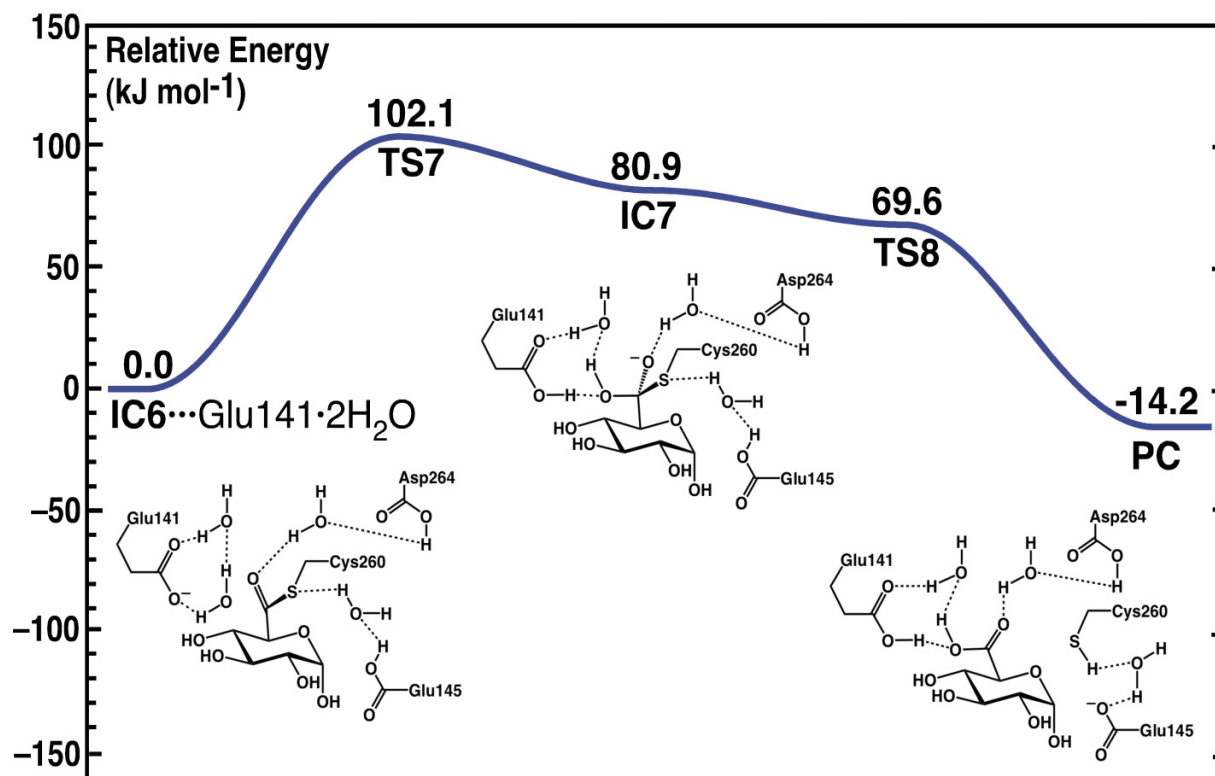
ester in both the NADH-bound active-site complex and in a complex in which NADH was exchanged by a glutamate ion bound to two water molecules.

First, we probed into the feasibility of hydrolysis of the 6-thioester within the IC6...NADH complex in the absence of nearby negatively charged groups that polarize the attacking water molecule. To this end, we devised chemical models of IC6...NADH that included one water molecule into the active site and computed 4-, 6-, and 8-membered ring transition structures. The calculated barrier heights to hydrolysis (i.e., 189.0, 197.6, and 188.2 kJ mol<sup>-1</sup>, respectively) showed a better agreement with a nonenzymatic thioester hydrolysis

reaction. For example, at the B3LYP/6-311+G(2df,p)//B3LYP/6-31G(d) level of theory, the barrier to hydrolysis of CH<sub>3</sub>(C=O)SCH<sub>3</sub> with a single water molecule is 184.7 kJ mol<sup>-1</sup>. It is noted that our barrier height is in disagreement with that of 44.3 kJ mol<sup>-1</sup> reported for the same chemical model but calculated at the HF/6-31++G\*\* level of theory.<sup>32</sup> In contrast, the MP2/6-311++G(2d,2p)//B3LYP/6-31++G(d,p) barrier to the OH<sup>-</sup> catalyzed hydrolysis of CH<sub>3</sub>(C=O)SCH<sub>3</sub>, including four explicit water molecules and the bulk solvent IPCM correction, was found to be 51.5 kJ mol<sup>-1</sup>.<sup>33</sup>

Next, our chemical model of the 6-thioester intermediate was modified by removing NADH from the IC6...NADH

**Fig. 10.** Potential energy surface for hydrolysis of the 6-thioester intermediate (IC6) assisted by Glu141 and two water molecules, and subsequent formation of a product complex containing GlcUA (PC).



complex and by incorporating glutamate and two water molecules to generate the IC6...Glu141·2H<sub>2</sub>O complex, which is illustrated in Fig. 10. The optimized structure of the IC6...Glu141-COO<sup>-</sup>·2H<sub>2</sub>O complex consists of an eight-membered hydrogen-bonded ring, in which the Glu141 carboxylate accepts one hydrogen bond from each water molecule at 1.84 and 1.99 Å, respectively. The two water molecules are hydrogen bonded to each other at 1.82 Å (Fig. 11). The displacement of NADH from the IC6...NADH complex by the eight-membered hydrogen-bonded ring complex, Glu141-COO<sup>-</sup>·2H<sub>2</sub>O, to form the IC6...Glu141-COO<sup>-</sup>·2H<sub>2</sub>O complex is highly exoergic by 122.6 kJ mol<sup>-1</sup>. In other words, the Glu141-COO<sup>-</sup>·2H<sub>2</sub>O complex binds stronger than NADH to the intermediate-active-site complex, and this provides a thermodynamic pull favoring the displacement of NADH from the active site.

In the geometric arrangement of the IC6...Glu141-COO<sup>-</sup>·2H<sub>2</sub>O complex, the 6-carbonyl group accepts a hydrogen bond from the Lys204-NH<sub>3</sub><sup>+</sup>, which itself also hydrogen-bonds to the carbonyl group of Asn208. Importantly, the nearest water oxygen is initially located 3.28 Å from C6 of the thioester intermediate. This H<sub>2</sub>O then nucleophilically adds to the carbonyl carbon of the thioester intermediate to form the 6-thioether-6,6-diol anion intermediate, IC7. The formation of IC7 is endoergic by 80.9 kJ mol<sup>-1</sup>, with a barrier of 102.1 kJ mol<sup>-1</sup> with respect to the IC6...Glu141·2H<sub>2</sub>O complex (Fig. 10). In IC7, the four-centre hydrogen-bonded ring changes slightly with the newly formed 6-hydroxyl group accepting a hydrogen bond from Glu141-COOH, while the other two hydrogen bonds remain the same as in the parent IC6...Glu141-COO<sup>-</sup>·2H<sub>2</sub>O complex. The 6-oxyan-

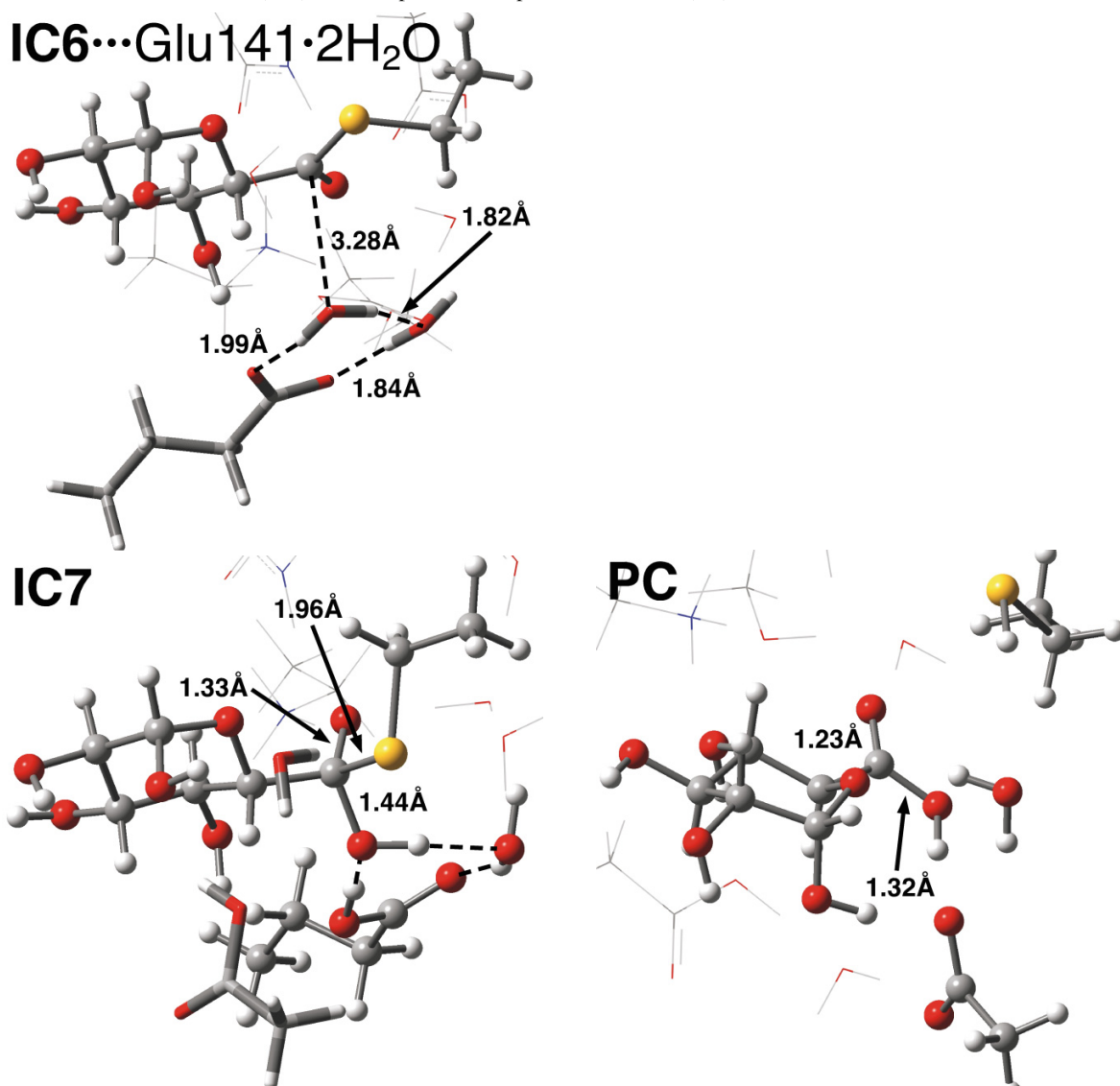
ion is further stabilized by accepting a hydrogen bond from Lys204-NH<sub>3</sub><sup>+</sup>, which has now broken the bridge to the carbonyl group of Asn208. The arrangement of the substituents around the 6-position of the 6-thioether-6,6-diol anion intermediate, IC7, is tetrahedral, with typical bond lengths of 1.44 and 1.33 Å for the C6-OH and C6-O<sup>-</sup> bonds, respectively. Predictably, the C6-S bond lengthens from 1.79 Å in IC6 to 1.96 Å in IC7 because of formation of the geminal diol intermediate (Fig. 11).

Finally, the formation of GlcUA occurs by scission of the C6-S bond in concert with two proton transfers mediated by bridging water molecules: one occurring from Asp264-COOH to the C6-O<sup>-</sup> group and the other occurring from Glu145-COOH to the S atom of Cys260 (Fig. 10). This step has a barrier of 69.6 kJ mol<sup>-1</sup> and leaves the product complex (PC) 14.2 kJ mol<sup>-1</sup> lower in energy than the IC6...Glu141·2H<sub>2</sub>O complex. In the PC, it was found that the geometry around C6 is trigonal planar with typical bond lengths for the carboxylate group of 1.23 and 1.32 Å for the C=O and C-OH bonds, respectively (Fig. 11). Lys204-NH<sub>3</sub><sup>+</sup> forms a bridge to the 6-carbonyl group of GlcUA and the carbonyl group of Asn208 in the optimized product complex. Notably, the hydrogen-bonded chain Glu145-COO<sup>-</sup>...H<sub>2</sub>O...HS-Cys260 is regenerated for the next catalytic cycle.

## Conclusions

The potential energy surface (PES) for the catalytic mechanism of UDPGlcDH was investigated for an active-site model of this enzyme and calculated with the B3LYP density functional method in conjunction with the IEF-PCM self-consistent reaction field, to correct for the long-range

**Fig. 11.** Optimized structures of the 6-thioester intermediate incorporating glutamate and two water molecules (IC6···Glu141·2H<sub>2</sub>O), the 6-thioether-6,6-diol anion intermediate (IC7), and the product complex with GlcUA (PC).



electrostatic effect of the protein environment. An overall PES for the catalytic mechanism of UDPGlcDH, with energies referenced to our active-site model of the enzyme–substrate–cofactor complex, is included in the Supplementary data for this paper (Fig. S1).

This study made it possible to give microscopic insight into the catalytic roles of the residues along the reaction path, and mainly, unravel the roles of the Lys204 and Asp264 residues. To this end, we applied three electrostatic conditions simulating the electrostatic environment felt by the side chain of Lys204 in the active site of UDPGlcDH to unambiguously show (by the calculated basicities of the side chain of lysine) that (i) Lys204 is very likely to be protonated in the active site and (ii) the reactive form of the enzyme–substrate–cofactor complex most likely contains Asp264–COO<sup>−</sup> bound to water, which acts as the general base in the initial step of the catalytic mechanism. Moreover, the stationary structures along the reaction path show that Lys204–NH<sub>3</sub><sup>+</sup> assists in decreasing the rotational free-

dom of the 6-terminus of glucopyranose and in stabilizing the 6-oxanion intermediates and transition states.

The catalytic mechanism consists of two NAD<sup>+</sup>-dependent oxidation stages. The calculations show that the first two-electron one-proton transfer from the activated 6-oxymethyl anion of glucopyranose to NAD<sup>+</sup> forming glucuronaldehyde is the rate-controlling step, with a barrier of 106.5 kJ mol<sup>−1</sup>. Within the computational error for an active-site model,<sup>27</sup> this barrier is in good agreement with the experimental activation energy of 72 kJ mol<sup>−1</sup>, which was estimated from the catalytic constant for wild-type UDPGlcDH with UDP-glucose under saturating conditions ( $k_{\text{cat}} = 1.8 \pm 0.1 \text{ s}^{-1}$ ).<sup>10</sup> Moreover, we showed that in order for the 6-thioester intermediate to be hydrolyzed and form GlcUA in the last catalytic step, hydrated Glu141–COO<sup>−</sup> has to displace the NADH molecule formed in the second oxidation step. This statement is supported by the following: (i) Calculated high barriers to hydrolysis of the 6-thioester intermediate within the NADH-bound active-site complex larger than 180 kJ mol<sup>−1</sup>, which

are unusual in enzymatic reaction mechanisms. (ii) The exoergic character ( $-122.6 \text{ kJ mol}^{-1}$ ) of displacement of NADH from the 6-thioester intermediate-active-site complex by a Glu141-COO $^{-}$ ·2H $_2$ O complex, which suggests that the Glu141-COO $^{-}$  dihydrate binds stronger than NADH to the intermediate-active-site complex. (iii) The lower barrier height ( $102.1 \text{ kJ mol}^{-1}$ ) for the hydrolysis of the activated 6-thioester intermediate within the active-site complex including the Glu141-COO $^{-}$  dihydrate residue.

## Supplementary data

Supplementary data for this article are available on the journal Web site (canjchem.nrc.ca).

## Acknowledgment

We thank the Natural Sciences and Engineering Research Council of Canada (NSERC) for funding and the Shared Hierarchical Academic Research Computing Network (SHARCNET) for a Graduate Student Fellowship (WH) and additional computational resources. We also thank Russ Boyd for his mentoring and friendship over the years.

## References

- (1) Dougherty, B. A.; van de Rijn, I. *J. Biol. Chem.* **1993**, *268* (10), 7118. PMID:8463246.
- (2) Arrecubieta, C.; García, E.; López, R. *J. Bacteriol.* **1996**, *178* (10), 2971. PMID:8631689.
- (3) Campbell, R. E.; Tanner, M. E. *J. Org. Chem.* **1999**, *64* (26), 9487. doi:10.1021/jo991092h.
- (4) Dutton, G. J. *Glucuronidation of Drug and Other Compounds*; CRC press: Boca Raton, FL, 1980.
- (5) Ge, X.; Campbell, R. E.; van de Rijn, I.; Tanner, M. E. *J. Am. Chem. Soc.* **1998**, *120* (26), 6613. doi:10.1021/ja9805977.
- (6) Dougherty, B. A.; van de Rijn, I. *J. Biol. Chem.* **1994**, *269* (1), 169. PMID:8276791.
- (7) Arrecubieta, C.; López, R.; García, E. *J. Bacteriol.* **1994**, *176* (20), 6375. PMID:7929009.
- (8) Oppenheimer, N. J.; Handlon, A. L. *Enzymes* **1992**, *20*, 453.
- (9) Feingold, D. S.; Franzen, J. S. *Trends Biochem. Sci.* **1981**, *6*, 103. doi:10.1016/0968-0004(81)90038-4.
- (10) Ge, X.; Penney, L. C.; van de Rijn, I.; Tanner, M. E. *J. Biochem.* **2004**, *271* (1), 14. doi:10.1046/j.1432-1033.2003.03876.x. PMID:14686915.
- (11) Campbell, R. E.; Sala, R. F.; van de Rijn, I.; Tanner, M. E. *J. Biol. Chem.* **1997**, *272* (6), 3416. doi:10.1074/jbc.272.6.3416. PMID:9013585.
- (12) Naught, L. E.; Gilbert, S.; Imhoff, R.; Snook, C.; Beamer, L.; Tipton, P. *Biochemistry* **2002**, *41* (30), 9637. doi:10.1021/bi025862m. PMID:12135385.
- (13) Snook, C. F.; Tipton, P. A.; Beamer, L. *J. Biochemistry* **2003**, *42* (16), 4658. doi:10.1021/bi027328k. PMID:12705829.
- (14) Moyrand, F.; Janbon, G. *Eukaryot. Cell* **2004**, *3* (6), 1601. doi:10.1128/EC.3.6.1601-1608.2004. PMID:15590833.
- (15) Sommer, B. J.; Barycki, J. J.; Simpson, M. A. *J. Biol. Chem.* **2004**, *279* (22), 23590. doi:10.1074/jbc.M401928200. PMID:15044486.
- (16) Campbell, R. E.; Mosimann, S. C.; van De Rijn, I.; Tanner, M. E.; Strynadka, N. C. *J. Biochemistry* **2000**, *39* (23), 7012. doi:10.1021/bi000181h. PMID:10841783.
- (17) Easley, K. E.; Sommer, B. J.; Boanca, G.; Barycki, J. J.; Simpson, M. A. *Biochemistry* **2007**, *46* (2), 369. doi:10.1021/bi061537d. PMID:17209547.
- (18) Becke, A. D. *J. Chem. Phys.* **1993**, *98* (2), 1372. doi:10.1063/1.464304.
- (19) Becke, A. D. *J. Chem. Phys.* **1993**, *98* (7), 5648. doi:10.1063/1.464913.
- (20) Lee, C.; Yang, W.; Parr, R. G. *Phys. Rev. B* **1988**, *37* (2), 785. doi:10.1103/PhysRevB.37.785.
- (21) Frisch, M. J.; Trucks, G. W.; Schlegel, H. B.; Scuseria, G. E.; Robb, M. A.; Cheeseman, J. R.; Zakrzewski, V. G.; Montgomery, J. A., Jr.; Vreven, T.; Kudin, K. N.; Burant, J. C.; Millam, J. M.; Iyengar, S. S.; Tomasi, J.; Barone, V.; Mennucci, B.; Cossi, M.; Scalmani, G.; Rega, N.; Petersson, G. A.; Nakatsuji, H.; Hada, M.; Ehara, M.; Toyota, K.; Fukuda, R.; Hasegawa, J.; Ishida, M.; Nakajima, T.; Honda, Y.; Kitao, O.; Adamo, C.; Jaramillo, J.; Gomperts, R.; Stratmann, R. E.; Yazyev, O.; Austin, J.; Cammi, R.; Pomelli, C.; Ochterski, J.; Ayala, P. Y.; Morokuma, K.; Voth, G. A.; Salvador, P.; Dannenberg, J. J.; Zakrzewski, V. G.; Dapprich, S.; Daniels, A. D.; Strain, M. C.; Farkas, O.; Malick, D. K.; Rabuck, A. D.; Raghavachari, K.; Foresman, J. B.; Ortiz, J. V.; Cui, Q.; Baboul, A. G.; Clifford, S.; Cioslowski, J.; Stefanov, B. B.; Liu, G.; Liashenko, A.; Piskorz, P.; Komaromi, I.; Martin, R. L.; Fox, D. J.; Keith, T.; Al-Laham, M. A.; Peng, C. Y.; Nanayakkara, A.; Challacombe, M.; Gill, P. M. W.; Johnson, B.; Chen, W.; Wong, M. W.; Gonzalez, C.; Pople, J. A. *Gaussian03*, revision E.01; Gaussian, Inc.: Wallingford, CT, 2004.
- (22) Blomberg, M. R. A.; Siegbahn, P. E. M. *J. Phys. Chem. B* **2001**, *105* (39), 9375. doi:10.1021/jp010305f.
- (23) Noodleman, L.; Lovell, T.; Han, W. G.; Li, J.; Himo, F. *Chem. Rev.* **2004**, *104* (2), 459. doi:10.1021/cr020625a. PMID:14871132.
- (24) Himo, F. *Theor. Chem. Acc.* **2006**, *116* (1–3), 232. doi:10.1007/s00214-005-0012-1.
- (25) Siegbahn, P. E. M.; Borowski, T. *Acc. Chem. Res.* **2006**, *39* (10), 729. doi:10.1021/ar050123u. PMID:17042473.
- (26) Chen, S. L.; Fang, W. H.; Himo, F. *Theor. Chem. Acc.* **2008**, *120* (4–6), 515. doi:10.1007/s00214-008-0430-y.
- (27) Llano, J.; Gauld, J. W. *Mechanistics of Enzyme Catalysis: From Small to Large Active-Site Models*. In *Quantum Biochemistry: Electronic Structure and Biological Activity*; Matta, C. F., Ed.; Wiley-VCH: Weinheim, 2010; Vol. 2, p 643.
- (28) Llano, J.; Eriksson, L. A. *J. Chem. Phys.* **2002**, *117* (22), 10193. doi:10.1063/1.1516786.
- (29) Llano, J.; Eriksson, L. A. *Phys. Chem. Chem. Phys.* **2004**, *6* (9), 2426. doi:10.1039/b400507d.
- (30) Schutz, C. N.; Warshel, A. *Proteins* **2001**, *44* (4), 400. doi:10.1002/prot.1106. PMID:11484218.
- (31) King, G.; Lee, F. S.; Warshel, A. *J. Chem. Phys.* **1991**, *95* (6), 4366. doi:10.1063/1.461760.
- (32) Deerfield, D. W.; Pedersen, L. G. *J. Mol. Struct. THEOCHEM* **1995**, *358* (1–3), 99. doi:10.1016/0166-1280(96)87754-2.
- (33) Yang, W.; Drueckhammer, D. G. *J. Am. Chem. Soc.* **2001**, *123* (44), 11004. doi:10.1021/ja010726a. PMID:11686705.



# The assessment of density functionals for DNA–protein stacked and T-shaped complexes

Lesley R. Rutledge and Stacey D. Wetmore

**Abstract:** The present work uses 129 nucleobase – amino acid CCSD(T)/CBS stacking and T-shaped interaction energies as reference data to test the ability of various density functionals with double-zeta quality basis sets, as well as some semi-empirical and molecular mechanics methods, to accurately describe noncovalent DNA–protein  $\pi$ – $\pi$  and  $\pi^+$ – $\pi$  interactions. The goal of this work is to identify methods that can be used in hybrid approaches (QM/MM, ONIOM) for large-scale modeling of enzymatic systems involving active-site (substrate)  $\pi$ – $\pi$  contacts. Our results indicate that AMBER is a more appropriate choice for the lower-level method in hybrid techniques than popular semi-empirical methods (AM1, PM3), and suggest that AMBER accurately describes the  $\pi$ – $\pi$  interactions found throughout DNA–protein complexes. The M06–2X and PBE-D density functionals were found to provide very promising descriptions of the 129 nucleobase – amino acid interaction energies, which suggests that these may be the most suitable methods for describing high-level regions. Therefore, M06–2X and PBE-D with both the 6–31G(d) and 6–31+G(d,p) basis sets were further examined through potential-energy surface scans to better understand how these techniques describe DNA–protein  $\pi$ – $\pi$  interactions in both minimum and nonminimum regions of the potential-energy surfaces, which is critical information when modeling enzymatic reaction pathways. Our results suggest that studies of stacked nucleobase – amino acid systems should implement the PBE-D/6–31+G(d,p) method. However, if T-shaped contacts are involved and (or) smaller basis sets must be considered due to limitations in computational resources, then M06–2X/6–31G(d) provides an overall excellent description of both nucleobase – amino acid stacking and T-shaped interactions for a range of DNA–protein  $\pi$ – $\pi$  and  $\pi^+$ – $\pi$  interactions.

**Key words:** DNA–protein interactions, noncovalent interactions, benchmarking, density functional theory (DFT),  $\pi$ – $\pi$  stacking interactions, T-shaped interactions.

**Résumé :** Dans ce travail, on utilise l'empilement de la nucléobase 129 – acide aminé CCSD(T)/CBS et les énergies d'interaction en forme de T comme données de référence pour vérifier l'utilité potentielle de diverses fonctionnelles de densité à ensembles de bases de qualité double-zêta ainsi que méthodes semi-empiriques de mécanique moléculaire pour décrire adéquatement les interactions  $\pi$ – $\pi$  et  $\pi^+$ – $\pi$  non covalentes entre l'ADN et une protéine. Le but de ce travail est d'identifier des méthodes qui pourraient être utilisées dans des approches hybrides (QM/MM, ONIOM) pour le modelage à grande échelle de systèmes enzymatiques impliquant des contacts  $\pi$ – $\pi$  du site actif avec un substrat. Nos résultats indiquent que la méthode AMBER serait plus appropriée que les méthodes semi-empiriques populaires (AM1, PM3) comme la méthode de faible niveau dans les techniques hybrides et ils suggèrent que la méthode AMBER décrit d'une façon correcte les interactions  $\pi$ – $\pi$  que retrouve systématiquement dans les complexes entre l'ADN et une protéine. On a trouvé que les fonctionnelles de densité M06–2X et PEB-D permettent d'obtenir des descriptions très prometteuses des énergies d'interaction de la nucléobase 129 – acide aminé, ce qui suggère qu'elles pourraient être les méthodes les plus appropriées pour décrire des régions de hauts niveaux. En conséquence, on a effectué un examen plus approfondi des fonctionnelles M06–2X et PEB-D avec les ensembles de base 6–31G(d) et 6–31+G(d,p) en faisant appel à des balayages de l'énergie potentielle de surface afin de mieux comprendre comment ces techniques décrivent les interactions  $\pi$ – $\pi$  ADN-protéine dans les régions tant minimales que non minimales des surfaces d'énergie potentielle qui est une information critique lorsqu'on effectue un modelage des voies réactionnelles des réactions enzymatiques. Nos résultats suggèrent que les études de systèmes empilés de nucléobase et d'acide aminé devraient faire appel à la méthode PBE-D/6–31+G(d,p). Toutefois, si les contacts en forme de T sont impliqués et (ou) des ensembles de bases plus simples doivent être impliqués en raisons des limitations des facilités de calcul, la méthode M06–2X/6–31G(d) fournit alors une excellente description globale à la fois de l'empilement nucléobase – acide aminé et des interactions en forme de T pour un large éventail d'interactions  $\pi$ – $\pi$  et  $\pi^+$ – $\pi$  d'ADN et de protéine.

**Mots-clés :** interactions ADN–protéine, interactions non covalentes, repérage, théorie de la fonctionnelle de la densité (« DFT »), interactions d'empilement  $\pi$ – $\pi$ , interactions en forme de T.

[Traduit par la Rédaction]

Received 14 January 2010. Accepted 13 March 2010. Published on the NRC Research Press Web site at canjchem.nrc.ca on 18 June 2010.

**L.R. Rutledge and S.D. Wetmore.**<sup>1</sup> Department of Chemistry and Biochemistry, University of Lethbridge, 4401 University Drive, Lethbridge, AB T1K 3M4, Canada.

<sup>1</sup>Corresponding author (e-mail: stacey.wetmore@uleth.ca).

## Introduction

As we strive to truly understand vital biochemical processes, it is clear that a detailed knowledge of protein function and enzymatic catalysis is essential. Experimental biochemists use many methodologies (such as protein crystallography, NMR, fluorescence, site-specific mutagenesis, and kinetic isotope effects) to understand how enzymes function under a variety of conditions. However, in recent years, computational methodologies have also become key tools for determining complete mechanisms of enzymatic reactions (see for example refs. 1–6 and references therein). Computational modeling provides a unique approach because of the capability to characterize both the structure and energetics of short-lived intermediates and transition states,<sup>4</sup> which are challenging to investigate through experimental means without interfering with the natural reaction conditions.<sup>4</sup> Nevertheless, enzymatic systems also present a unique computational challenge, where many studies have concentrated on determining how to efficiently and accurately model such large systems (for examples, see refs. 1–35 and references therein).

Promising computational approaches for studying enzymes involve hybrid techniques,<sup>26,36–38</sup> which combine two or more methods and (or) levels of theory. These approaches allow for an accurate quantum mechanical description of the chemistry in a localized (high-level) region (such as an active site), while describing the rest of the protein with a low computational method (low-level region).<sup>36</sup> These schemes can be applied in a variety of different ways. The QM/MM methodology, which combines a quantum mechanical (QM) technique with a molecular mechanics (MM) method, is the most common class of hybrid approaches.<sup>26,36</sup> For example, it was reported that over 600 QM/MM articles were published in 2007.<sup>29</sup> However, ONIOM (our Own N-layer Integrated molecular Orbital molecular Mechanics) is another promising hybrid technique that is also used to study enzymatic systems.<sup>37,38</sup> This is perhaps a more general scheme due to its ability to combine any number of molecular orbital, as well as molecular mechanics, methods.<sup>37,38</sup>

Most of the current QM/MM and ONIOM studies on enzymatic systems use density functional theory (DFT) to describe the quantum mechanical region due to its greater efficiency compared with popular wave-function-based approaches (see, for example, refs. 8, 12, 15–21, 23–25, 28, 30, and 32). The most common density functional used in hybrid methods is arguably B3LYP, where this functional has been used for a wide variety of systems.<sup>8,12,15,16,19,21,24,28,30,32,34</sup> Despite the good performance of B3LYP for a range of systems and properties, it generally underestimates barrier heights,<sup>39</sup> and does not provide an accurate description of dispersion interactions. Consequently, this functional should not be used to describe high-level regions of enzymes that rely heavily on dispersion-dominated interactions (such as  $\pi$ – $\pi$  stacking,  $X-H\cdots\pi$  ( $X = C, N, S, O$ ), lone pair ( $lp$ ) $\cdots\pi$ , and (or)  $\pi$ – $\pi$  (edge-to-face) T-shaped contacts). Therefore, until recently, studies on systems that include these types of noncovalent interactions were limited to *ab initio* electron correlation methods (such as MP2), which are relatively computationally inefficient and there-

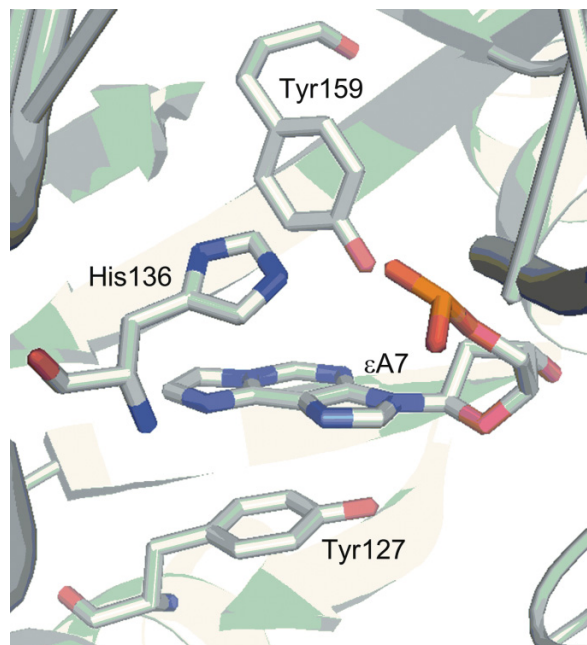
fore ultimately lead to the implementation of small model systems.

Our group is particularly interested in studying the first enzyme involved in the base excision repair (BER) mechanism,<sup>40</sup> a DNA glycosylase, which is responsible for recognizing a specific type of damaged DNA nucleobase, flipping this damaged nucleotide out of the DNA helix and into the active site, and cleaving the glycosidic bond connecting the nucleobase to the sugar-phosphate backbone.<sup>41,42</sup> There are many different DNA glycosylases, where each is responsible for repairing a particular type of DNA damage and uses specific noncovalent contacts to identify, bind, and facilitate in the excision of damaged nucleobase(s).<sup>41,42</sup> One of the enzymes of interest to our group is human alkyladenine DNA glycosylase (AAG), which removes 3-methyladenine, as well as other (cationic) alkylated purines, and the (neutral) hypoxanthine and 1,*N*<sup>6</sup>-ethenoadenine lesions.<sup>41–43</sup> Due to the wide substrate specificity of AAG, it has been proposed that nonspecific noncovalent interactions might be responsible for the unique function of this glycosylase.<sup>43</sup> Indeed, crystal structures reveal that multiple  $\pi$ – $\pi$  stacking and  $\pi$ – $\pi$  T-shaped interactions are exploited to bind substrates in the AAG active site (Fig. 1).<sup>43</sup> Although we are interested in studying the glycosidic-bond-cleavage mechanism facilitated by AAG using hybrid techniques, it is currently unclear which methods should be used to model enzymes with active sites that heavily rely on dispersion-dominated  $\pi$ – $\pi$  stacking and  $\pi$ – $\pi$  T-shaped interactions between DNA and protein components.

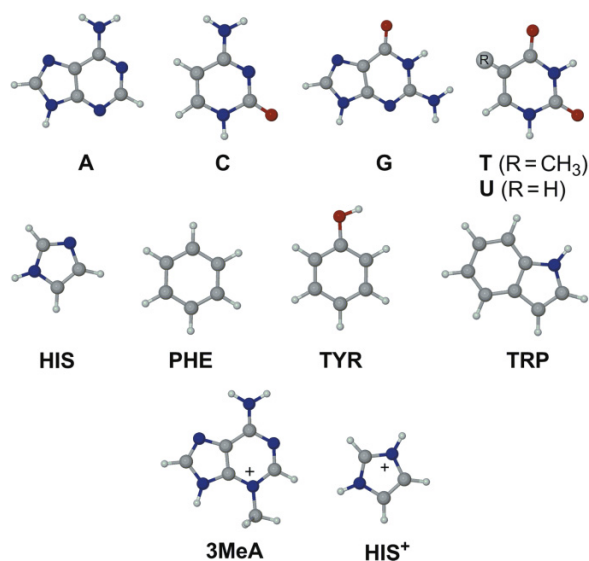
Recent work in the development of density functional techniques has concentrated on methods capable of describing dispersion interactions (see, for example, refs. 39 and 44–58). Indeed, a very recent review discusses the description of dispersion interactions by density functional theory.<sup>58</sup> Many approaches for including dispersion have emerged, and it is very important to test each functional for the specific systems of interest. As a result, an abundance of benchmarking studies have emerged in the literature (such as refs. 59–81) where many use the high-level (CCSD(T)/CBS) data sets of Hobza and co-workers<sup>82</sup> to determine the accuracy of new density functionals for noncovalent interactions (see refs. 59, 63, 65, 66, 68, 74, 76, and 79 for examples). Nevertheless, these test sets,<sup>82</sup> as well as others (such as those examined in refs. 62, 64, 70–73, 75, 77, and 80), do not include the DNA–protein interactions that can be important for enzymatic applications. Therefore, our group previously characterized the potential-energy surfaces (PESs) of  $\pi$ – $\pi$  stacking and  $\pi$ – $\pi$  (amino acid edge and nucleobase edge) T-shaped interactions between: (i) the four aromatic amino acids and the natural nucleobases<sup>83</sup>; (ii) the (cationic) alkylated damaged nucleobase, 3-methyladenine (3MeA) and the aromatic amino acids<sup>84</sup>; and (iii) the natural nucleobases and protonated histidine (HIS<sup>+</sup>, see Fig. 2).<sup>85</sup> These studies identified the (47 stacked and 82 T-shaped) most stable dimers, whose binding strengths were further characterized with CCSD(T)/CBS calculations.<sup>83–85</sup> Our test set of 129 nucleobase – amino acid interactions covers a wide variety of noncovalent (stacked, amino acid edge T-shaped, and nucleobase edge T-shaped) interactions involving both neutral ( $\pi$ – $\pi$ ) and cationic ( $\pi^+$ – $\pi$ ) systems.

The present work uses our large test set of DNA–protein

**Fig. 1.** Example of  $\pi$ - $\pi$  stacking and  $\pi$ - $\pi$  T-shaped interactions between the substrate (1,*N*<sup>6</sup>-ethenoadenine,  $\epsilon$ A7) and the aromatic amino acids (His, Tyr) in the active site of the human alkyladenine DNA glycosylase (AAG) (PDB code: 1EWN).<sup>43</sup>



**Fig. 2.** Models of the natural nucleobases (adenine (A), cytosine (C), guanine (G), thymine (T), and uracil (U)), the aromatic amino acids (histidine (HIS), phenylalanine (PHE), tyrosine (TYR), and tryptophan (TRP)), the damaged nucleobase (3-methyladenine (3MeA)), and protonated histidine (HIS<sup>+</sup>) considered in the present work.



interactions to investigate the performance of a number of density functional methods in the hopes of identifying an efficient method and basis-set combination that is currently readily available for describing the binding strengths and potential-energy surfaces of  $\pi$ - $\pi$  stacking and  $\pi$ - $\pi$  T-shaped DNA-protein interactions. This study first reports an interaction energy analysis of a variety of density functionals in the current literature for our 129 nucleobase – amino acid

dimer interactions, where our previous CCSD(T)/CBS calculations were used as the benchmark for accuracy.<sup>83–85</sup> This study also investigates how select density functional methods describe the potential-energy surfaces of three representative stacked and three representative amino acid edge T-shaped dimers. Our results are important for understanding how current density functionals describe DNA-protein  $\pi$ - $\pi$  interactions in both minimum and nonminimum regions of the potential-energy surfaces, which is rarely examined in the literature.<sup>70</sup> It is critical to understand how these methods describe both the energies and structures of  $\pi$ - $\pi$  systems to accurately model enzymatic reaction pathways.

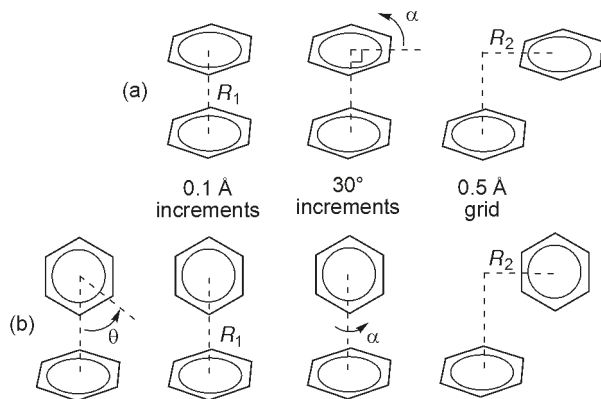
## Computational details

In our previous works,<sup>83–85</sup> a series of MP2/6–31G\*(0.25) single-point calculations were used to scan the potential-energy surfaces (PESs) for the stacked and T-shaped orientations of nucleobase – amino acid dimers according to several geometric variables (Fig. 3). This modified basis set replaces the standard d-exponent for second row atoms (0.8) with 0.25.<sup>86</sup> Initially,  $C_s$ -symmetric, MP2/6–31G(d)-optimized monomers (Fig. 2) were placed such that the truncated amino acid and nucleobase molecular planes were parallel (stacked) or perpendicular (T-shaped). In stacked dimers involving HIS, TYR and TRP, two relative orientations of the molecular planes were considered. The first was obtained by stacking the amino acid and nucleobase orientations as shown in Fig. 2, while the second conformation was obtained by mirror flipping the amino acid relative to Fig. 2 before stacking with the nucleobase (indicated using a prime (') throughout this manuscript). T-shaped dimers involving either amino acid edges or nucleobase edges were considered. To define the ring edge (monomer edge) directed towards the  $\pi$ -system (monomer face), the geometric variable  $\theta$  (Fig. 3b) was introduced, where all edges considered are shown in the Supplementary data (Figs. S1–S3). From these initial structures, three geometric variables were considered in our potential-energy surface scans using the increments defined in Fig. 3: the vertical separation ( $R_1$ ), the angle of rotation ( $\alpha$ ), and the horizontal displacement ( $R_2$ ) between monomers, where our  $R_2$  scans shift one monomer relative to the other in two directions that are perpendicular to the  $R_1$  axis. A full description of our scanning procedure is provided in our previous manuscripts.<sup>83–85</sup> Since our previous work<sup>85</sup> did not consider the interactions between uracil and protonated histidine, all data for this dimer are presented in the Supplementary data (Tables S1 and S2).

The 47 stacked and 82 T-shaped orientations (29 amino acid edge and 53 nucleobase edge dimers indicated with bold in Figs. S1–S3) with the strongest (most negative) interaction energies were further studied with CCSD(T) at the complete basis-set (CBS) limit.<sup>83–85</sup> MP2/aug-cc-pVDZ and MP2/aug-cc-pVTZ energies were used to extrapolate to MP2/CBS using the procedure of Helgaker and co-workers.<sup>87,88</sup> To account for errors in the MP2 electron correlation, the difference between the MP2/6–31G\*(0.25) and CCSD(T)/6–31G\*(0.25) energies ( $\Delta(\text{CCSD(T)} - \text{MP2})$ ) was combined with the MP2/CBS result to give an estimated CCSD(T)/CBS interaction energy. We note that recent literature denotes these extrapolated interaction energies as CBS(T)



**Fig. 3.** Definition of the geometric variables considered and increments used in our previous (a) stacking and (b) T-shaped potential-energy surface scans (angle of “edge” rotation ( $\theta$ ), vertical separation distance ( $R_1$ ), angle of rotation ( $\alpha$ ), and horizontal displacement ( $R_2$ )).



(such as in refs. 89–91); however, we refer to these values as CCSD(T)/CBS to be consistent with our previous work,<sup>83–85</sup> as well as previous stacking-interaction studies (for example, refs. 82, 92, and 93).

In the present work, a variety of density functionals that were previously shown to be promising for noncovalent interactions were tested against our 129 nucleobase – amino acid CCSD(T)/CBS dimer interaction energies. Specifically, we considered MPWB1K,<sup>94</sup> M05–2X,<sup>95</sup> M06–L,<sup>96</sup> M06–2X,<sup>96</sup> PBE–D,<sup>46</sup> BLYP–D,<sup>46</sup> TPSS–D,<sup>46</sup> and B97–D.<sup>46</sup> For comparison, we also considered PBE, BLYP, and TPSS without Grimme’s dispersion correction. We also include B3LYP due to the popularity of this approach in QM/MM and ONIOM hybrid calculations on enzymatic systems.<sup>8,12,15–16,19,21,24,28,30,32</sup> All functionals were tested with a variety of double-zeta Pople’s and Dunning’s basis sets (6–31G(d), 6–31G(d,p), 6–31+G(d,p), cc-pVDZ, and aug-cc-pVDZ).<sup>97</sup> Most benchmarking studies test the performance of these functionals using basis sets for which they were originally designed. However, since these are typically large (see, for example, refs. 61, 64, 69, 70, 72, 73, 75, 76, and 78), we focus our work on basis sets that are practical for enzymatic systems, where the intended application is full optimizations of enzyme-catalyzed reactions using hybrid methods.

To provide a greater understanding of the relative performance of the chosen DFT functionals, we include MP2 results for our 129 nucleobase – amino acid dimers. Owing to the vast literature that has studied noncovalent complexes with MP2, the shortfalls of this method are well-known, and therefore MP2 provides a good quality comparison for other methods. Additionally, we have considered the double-hybrid density functionals B2PLYP<sup>47,50</sup> and mPW2PLYP.<sup>51,74</sup> Although Grimme’s dispersion correction was originally designed for other functionals,<sup>46</sup> this empirical dispersion term has also been applied to these double-hybrid functionals.<sup>51,74</sup> Therefore, B2PLYP–D and mPW2PLYP–D were also considered in the present work. Although these methods are likely not practical for studying large enzymatic systems, these functionals will provide a worthy comparison to the other methods tested in this

manuscript due to their promise for reliably describing noncovalent  $\pi$ – $\pi$  interactions.<sup>51,74</sup>

In addition to active-site contacts, noncovalent  $\pi$ – $\pi$  interactions should be accurately described throughout the entire enzymatic model. Therefore, we considered the performance of the AMBER molecular mechanics method.<sup>98</sup> AMBER was selected, since it was originally designed to describe both DNA and protein systems,<sup>98</sup> and is commonly used in hybrid techniques (see examples in refs. 16–25). To be consistent with the original AMBER design, HF/6–31G(d) ESP charges were calculated and used to describe each monomer, which are truncated versions of those originally used to develop the force field.<sup>98</sup> AMBER atom types were assigned according to the original AMBER manuscript.<sup>98</sup> In our nucleobase models, the hydrogen atom replacing the sugar-phosphate backbone was defined as H. In the case of the amino acids, this hydrogen atom was defined as H4 for histidine (neutral and protonated) and tryptophan, and HA for phenylalanine and tyrosine. ANTECHAMBER (Version 1.0)<sup>99</sup> was used to define the atom types (Fig. S4) and parameters (Table S3) for the damaged base, 3-methyladenine. Finally, since PM3 and AM1 are frequently used to describe the lower-level regions of ONIOM calculations (for example, see refs. 7, 8, 11, 12, 14, 15, and 31), these methods were also included in our study.

All calculations were performed with Gaussian 09<sup>100</sup> with the exception of PBE, BLYP, and TPSS (with and without dispersion corrections), which were performed with GAMESS.<sup>101</sup> Despite reports that default grid sizes for various DFT methods can lead to false artifacts in the description of noncovalent interactions,<sup>102</sup> the default grids in Gaussian 09 and GAMESS were used. Additionally, all interaction energies were calculated without BSSE corrections<sup>103</sup> (with the exception of MP2). We emphasize that these choices were made due to our goal of understanding how these functionals describe noncovalent interactions in hybrid approaches, where large integration grid sizes and BSSE-free optimizations are not currently feasible.

## Results and discussion

As discussed in the Introduction, the present study focuses on identifying suitable methodologies for hybrid QM/MM or ONIOM calculations on enzyme-catalyzed reactions that involve noncovalent  $\pi$ – $\pi$  substrate – active site interactions. In this light, the ability of a variety of DFT functional and basis-set combinations, as well as some semi-empirical and molecular mechanics methods, to reproduce CCSD(T)/CBS interaction energies for our test set of 129  $\pi$ – $\pi$  stacked and T-shaped nucleobase – amino acid dimers<sup>83–85</sup> was investigated. Owing to the large number of dimers and methodologies considered, our results (Tables 1–3) are reported in terms of the mean unsigned error (MUE) and mean signed error (MSE) with respect to the CCSD(T)/CBS results. We also report the largest absolute deviation (MAX) and the largest percent difference (MAX %) from CCSD(T)/CBS observed among the dimers considered. Initially, we will separately discuss the performance of the methods for each of the two main types of  $\pi$ – $\pi$  interactions (stacking and T-shaped) considered and subsequently summarize the overall performance of these methods for both noncovalent interac-



**Table 1.** Mean unsigned error (MUE, kJ mol<sup>-1</sup>), mean signed error (MSE, kJ mol<sup>-1</sup>), maximum absolute difference (MAX, kJ mol<sup>-1</sup>), and maximum percent error (MAX %) between various methods and the CCSD(T)/CBS benchmark interaction energies for 47 nucleobase – amino acid stacked dimers.

Method	Basis set	MUE	MSE	MAX	MAX %	Method	Basis set	MUE	MSE	MAX	MAX%
MP2 <sup>a</sup>	6–31G*(0.25)	2.2	0.3	6.0	11.4	MPWB1K	6–31G(d)	10.4	10.4	15.9	–52.8
	6–31G(d)	12.7	12.7	19.4	–58.0		6–31G(d,p)	10.3	10.3	15.8	–52.5
	6–31G(d,p)	12.2	12.2	18.2	–54.8		cc-pVDZ	9.5	9.5	14.9	–46.4
	cc-pVDZ	8.8	8.8	12.8	–39.2		6–31+G(d,p)	11.3	11.3	17.2	–61.2
	6–31+G(d,p)	4.5	4.5	7.5	–22.8		aug-cc-pVDZ	10.1	10.1	15.0	–49.9
B3LYP	aug-cc-pVDZ	5.0	–5.0	10.0	35.2	M05–2X	6–31G(d)	4.5	4.4	8.8	–30.4
	6–31G(d)	26.8	26.8	39.9	–133.2		6–31G(d,p)	4.4	4.3	8.7	–29.9
	6–31G(d,p)	26.8	26.8	39.9	–132.5		cc-pVDZ	3.6	3.5	6.7	–25.4
	cc-pVDZ	27.5	27.5	42.9	–135.3		6–31+G(d,p)	4.0	3.9	8.0	–31.3
	6–31+G(d,p)	31.1	31.1	47.2	–156.2		aug-cc-pVDZ	2.5	2.3	5.5	–19.1
PBE	aug-cc-pVDZ	30.3	30.3	45.3	–149.1	M06–2X	6–31G(d)	1.9	–1.5	5.2	13.1
	6–31G(d)	20.9	20.9	30.4	–100.7		6–31G(d,p)	1.9	–1.5	5.1	13.5
	6–31G(d,p)	20.8	20.8	30.1	–99.8		cc-pVDZ	2.5	–2.5	6.2	15.1
	cc-pVDZ	20.5	20.5	31.4	–97.3		6–31+G(d,p)	2.2	–2.1	4.4	14.3
	6–31+G(d,p)	23.3	23.3	34.8	–114.6		aug-cc-pVDZ	3.3	–3.3	7.0	17.8
PBE-D	6–31G(d)	3.0	–3.0	8.4	21.5	M06–L	6–31G(d)	2.8	2.7	5.1	–17.0
	6–31G(d,p)	3.1	–3.1	8.6	21.3		6–31G(d,p)	2.6	2.6	4.9	–15.8
	cc-pVDZ	3.1	–3.1	8.6	21.3		cc-pVDZ	2.3	2.2	4.4	–12.2
	6–31+G(d,p)	0.9	–0.6	4.2	14.0		6–31+G(d,p)	2.0	1.9	4.1	–13.6
	6–31G(d)	32.3	32.3	46.7	–152.2		aug-cc-pVDZ	1.3	1.1	3.5	–12.6
BLYP	6–31G(d,p)	32.2	32.2	46.6	–151.4	B2PLYP	6–31G(d)	26.4	26.4	40.0	–135.8
	cc-pVDZ	33.1	33.1	50.0	–156.0		6–31G(d,p)	26.4	26.4	39.9	–135.2
	6–31+G(d,p)	38.1	38.1	55.9	–181.4		cc-pVDZ	27.2	27.2	43.0	–139.4
	6–31G(d)	6.0	–6.0	12.3	25.1		6–31+G(d,p)	30.8	30.8	47.4	–160.5
	6–31G(d,p)	6.1	–6.1	12.4	24.8		aug-cc-pVDZ	29.7	29.7	45.0	–151.7
BLYP-D	cc-pVDZ	5.2	–5.2	11.0	25.3	B2PLYP-D	6–31G(d)	9.3	9.3	14.7	–55.6
	6–31+G(d,p)	1.0	–0.2	3.7	9.3		6–31G(d,p)	9.3	9.3	14.5	–55.1
	6–31G(d)	26.8	26.8	38.9	–127.4		cc-pVDZ	10.2	10.2	16.3	–59.3
	6–31G(d,p)	26.7	26.7	38.8	–126.7		6–31+G(d,p)	13.7	13.7	20.6	–80.3
	cc-pVDZ	26.1	26.1	39.9	–122.2		aug-cc-pVDZ	12.6	12.6	18.6	–71.5
TPSS	6–31+G(d,p)	29.2	29.2	43.4	–141.1	mPW2PLYP	6–31G(d)	21.0	21.0	32.6	–111.5
	6–31G(d)	5.1	–5.1	11.2	23.7		6–31G(d,p)	21.0	21.0	32.5	–111.0
	6–31G(d,p)	5.2	–5.2	11.4	23.5		cc-pVDZ	22.0	22.0	35.8	–116.2
	cc-pVDZ	5.8	–5.8	11.9	25.5		6–31+G(d,p)	25.7	25.7	40.6	–138.2
	6–31+G(d,p)	2.7	–2.7	7.1	16.5		aug-cc-pVDZ	24.7	24.7	38.2	–129.7
TPSS-D	6–31G(d)	4.7	–4.7	10.1	23.8	mPW2PLYP-D	6–31G(d)	8.6	8.6	14.2	–53.3
	6–31G(d,p)	4.8	–4.8	10.2	23.6		6–31G(d,p)	8.5	8.5	14.0	–52.7
	cc-pVDZ	4.8	–4.8	9.2	24.6		cc-pVDZ	9.6	9.6	16.5	–57.9
	6–31+G(d,p)	1.1	–1.0	4.1	13.8		6–31+G(d,p)	13.2	13.2	21.1	–80.0
	aug-cc-pVDZ	2.2	–2.2	5.8	18.4		aug-cc-pVDZ	12.3	12.3	18.8	–71.4
AM1		42.3	42.3	66.1	–184.4	AMBER		3.2	2.5	12.4	–29.5
PM3		41.8	41.8	69.3	–177.1						

<sup>a</sup>MP2 interaction energies were calculated using the BSSE-corrected dimer energies.

**Table 2.** Mean unsigned error (MUE, kJ mol<sup>-1</sup>), mean signed error (MSE, kJ mol<sup>-1</sup>), maximum absolute difference (MAX, kJ mol<sup>-1</sup>), and maximum percent error (MAX %) between various methods and the CCSD(T)/CBS benchmark interaction energies for 82 nucleobase – amino acid T-shaped dimers.

Method	Basis set	MUE	MSE	MAX	MAX %	Method	Basis set	MUE	MSE	MAX	MAX%
MP2 <sup>a</sup>	6-31G*(0.25)	1.5	1.2	5.7	-19.3	MPWB1K	6-31G(d)	3.8	3.5	11.4	-57.9
	6-31G(d)	6.2	6.2	12.1	-46.1		6-31G(d,p)	3.7	3.5	10.9	-55.6
	6-31G(d,p)	6.1	6.1	11.6	-42.1		cc-pVDZ	4.0	3.8	9.8	-53.3
	cc-pVDZ	5.9	5.9	11.8	-40.3		6-31+G(d,p)	6.2	6.2	11.6	-54.6
	6-31+G(d,p)	4.4	4.4	8.4	-31.1		aug-cc-pVDZ	5.4	5.4	10.2	-45.3
B3LYP	aug-cc-pVDZ	1.0	-0.4	4.2	12.5	M05-2X	6-31G(d)	1.6	-0.6	7.5	-31.8
	6-31G(d)	9.5	9.4	19.1	-99.2		6-31G(d,p)	1.7	-0.8	8.0	-29.6
	6-31G(d,p)	9.7	9.6	19.2	-98.0		cc-pVDZ	1.7	-0.5	9.3	-27.1
	cc-pVDZ	10.5	10.4	24.0	-98.4		6-31+G(d,p)	1.4	1.1	5.0	-21.8
	6-31+G(d,p)	14.3	14.3	25.1	-112.3		aug-cc-pVDZ	1.1	-0.2	3.7	16.4
PBE	aug-cc-pVDZ	13.8	13.8	24.1	-101.6	M06-2X	6-31G(d)	1.9	-1.5	10.1	22.2
	6-31G(d)	5.9	5.5	13.7	-73.6		6-31G(d,p)	2.0	-1.6	10.4	22.1
	6-31G(d,p)	5.9	5.6	13.3	-71.8		cc-pVDZ	1.7	-1.4	11.3	15.5
	cc-pVDZ	6.4	6.0	16.1	-71.1		6-31+G(d,p)	1.2	0.4	4.9	-17.0
	6-31+G(d,p)	9.5	9.5	16.5	-75.4		aug-cc-pVDZ	1.3	-0.7	4.2	18.8
PBE-D	6-31G(d)	7.2	-7.2	12.8	47.2	M06-L	6-31G(d)	2.1	2.0	4.9	-23.0
	6-31G(d,p)	7.1	-7.1	12.9	46.9		6-31G(d,p)	1.9	1.8	4.5	-20.0
	cc-pVDZ	6.6	-6.6	13.7	42.8		cc-pVDZ	2.8	2.6	8.6	-27.5
	6-31+G(d,p)	3.2	-3.2	6.7	23.9		6-31+G(d,p)	3.1	3.1	6.0	-24.3
	6-31G(d)	12.1	12.0	24.3	-114.6		aug-cc-pVDZ	2.9	2.9	6.1	-19.8
BLYP	6-31G(d,p)	12.2	12.2	24.5	-113.6	B2PLYP	6-31G(d)	9.5	9.5	20.3	-101.8
	cc-pVDZ	13.1	13.1	29.5	-115.4		6-31G(d,p)	9.7	9.6	20.0	-100.8
	6-31+G(d,p)	18.2	18.2	31.8	-135.2		cc-pVDZ	10.4	10.4	23.3	-100.3
	6-31G(d)	8.3	-8.3	13.7	50.1		6-31+G(d,p)	13.8	13.8	24.4	-111.9
	6-31G(d,p)	8.1	-8.1	13.6	49.2		aug-cc-pVDZ	13.2	13.2	22.7	-101.0
BLYP-D	cc-pVDZ	7.3	-7.3	15.7	46.0	B2PLYP-D	6-31G(d)	1.7	0.2	7.1	-37.1
	6-31+G(d,p)	2.2	-2.1	5.1	21.5		6-31G(d,p)	1.7	0.3	7.1	-36.1
	6-31G(d)	9.4	9.3	18.2	-96.7		cc-pVDZ	2.4	1.1	7.6	-35.5
	6-31G(d,p)	9.4	9.3	17.8	-94.7		6-31+G(d,p)	4.5	4.5	8.4	-43.4
	cc-pVDZ	9.8	9.8	21.4	-93.5		aug-cc-pVDZ	3.9	3.9	6.4	-32.5
TPSS	6-31+G(d,p)	13.0	13.0	21.6	-105.0	mPW2PLYP	6-31G(d)	6.3	6.0	16.4	-81.8
	6-31G(d)	7.6	-7.6	13.0	49.7		6-31G(d,p)	6.5	6.2	16.1	-80.7
	6-31G(d,p)	7.6	-7.6	13.2	49.6		cc-pVDZ	7.3	7.0	18.5	-80.4
	cc-pVDZ	7.1	-7.1	13.5	42.3		6-31+G(d,p)	10.4	10.4	19.7	-86.4
	6-31+G(d,p)	3.9	-3.9	8.9	27.5		aug-cc-pVDZ	9.8	9.8	17.9	-76.1
TPSS-D	6-31G(d)	6.9	-6.8	11.9	44.4	mPW2PLYP-D	6-31G(d)	1.8	-0.7	8.3	-34.7
	6-31G(d,p)	6.9	-6.8	11.6	44.1		6-31G(d,p)	1.8	-0.6	8.3	-33.6
	cc-pVDZ	6.0	-6.0	11.7	45.1		cc-pVDZ	2.4	0.2	8.8	-33.4
	6-31+G(d,p)	2.7	-2.5	5.8	20.3		6-31+G(d,p)	3.7	3.6	8.1	-37.6
	aug-cc-pVDZ	3.1	-2.9	6.6	31.5		aug-cc-pVDZ	3.2	3.1	6.3	-28.0
AM1		22.5	22.5	45.4	-128.0	AMBER		4.7	2.2	18.7	-82.3
PM3		22.5	22.5	46.4	-125.6						

<sup>a</sup>MP2 interaction energies were calculated using the BSSE-corrected dimer energies.

**Table 3.** Mean unsigned error (MUE, kJ mol<sup>-1</sup>), mean signed error (MSE, kJ mol<sup>-1</sup>), maximum absolute difference (MAX, kJ mol<sup>-1</sup>), and maximum percent error (MAX %) between various methods and the CCSD(T)/CBS benchmark interaction energies for 129 nucleobase – amino acid noncovalent dimers.

Method	Basis set	MUE	MSE	MAX	MAX %	Method	Basis set	MUE	MSE	MAX	MAX %
MP2 <sup>a</sup>	6–31G*(0.25)	1.8	0.9	6.0	–19.3	MPWB1K	6–31G(d)	6.2	6.0	15.9	–57.9
	6–31G(d)	8.6	8.6	19.4	–58.0		6–31G(d,p)	6.1	6.0	15.8	–55.6
	6–31G(d,p)	8.3	8.3	18.2	–54.8		cc-pVDZ	6.0	5.9	14.9	–53.3
	cc-pVDZ	6.9	6.9	12.8	–40.3		6–31+G(d,p)	8.1	8.1	17.2	–61.2
	6–31+G(d,p)	4.5	4.5	8.4	–31.1		aug-cc-pVDZ	7.1	7.1	15.0	–49.9
	aug-cc-pVDZ	2.5	–2.1	10.0	35.2	M05–2X	6–31G(d)	2.7	1.2	8.8	–31.8
B3LYP	6–31G(d)	15.8	15.8	39.9	–133.2		6–31G(d,p)	2.7	1.1	8.7	–29.9
	6–31G(d,p)	15.9	15.8	39.9	–132.5		cc-pVDZ	2.4	1.0	9.3	–27.1
	cc-pVDZ	16.7	16.7	42.9	–135.3		6–31+G(d,p)	2.3	2.1	8.0	–31.3
	6–31+G(d,p)	20.4	20.4	47.2	–156.2		aug-cc-pVDZ	1.6	0.7	5.5	–19.1
	aug-cc-pVDZ	19.8	19.8	45.3	–149.1	M06–2X	6–31G(d)	1.9	–1.5	10.1	22.2
PBE	6–31G(d)	11.2	10.9	30.4	–100.7		6–31G(d,p)	1.9	–1.6	10.4	22.1
	6–31G(d,p)	11.1	10.9	30.1	–99.8		cc-pVDZ	2.0	–1.8	11.3	15.5
	cc-pVDZ	11.3	11.1	31.4	–97.3		6–31+G(d,p)	1.6	–0.5	4.9	–17.0
	6–31+G(d,p)	14.3	14.3	34.8	–114.6		aug-cc-pVDZ	2.0	–1.7	7.0	18.8
	6–31G(d)	5.6	–5.6	12.8	47.2	M06–L	6–31G(d)	2.3	2.2	5.1	–23.0
PBE-D	6–31G(d,p)	5.6	–5.6	12.9	46.9		6–31G(d,p)	2.2	2.1	4.9	–20.0
	cc-pVDZ	5.5	–5.5	13.7	42.8		cc-pVDZ	2.6	2.4	8.6	–27.5
	6–31+G(d,p)	2.4	–2.3	6.7	23.9		6–31+G(d,p)	2.7	2.7	6.0	–24.3
	6–31G(d)	19.1	19.1	46.7	–152.2		aug-cc-pVDZ	2.3	2.2	6.1	–19.8
	6–31G(d,p)	19.2	19.2	46.6	–151.4	B2PLYP	6–31G(d)	15.7	15.6	40.0	–135.8
BLYP	cc-pVDZ	20.0	20.0	50.0	–156.0		6–31G(d,p)	15.7	15.7	39.9	–135.2
	6–31+G(d,p)	25.1	25.1	55.9	–181.4		cc-pVDZ	16.6	16.5	43.0	–139.4
	6–31G(d)	7.4	–7.4	13.7	50.1		6–31+G(d,p)	20.0	20.0	47.4	–160.5
	6–31G(d,p)	7.3	–7.3	13.6	49.2		aug-cc-pVDZ	19.2	19.2	45.0	–151.7
	cc-pVDZ	6.5	–6.5	15.7	46.0	B2PLYP-D	6–31G(d)	4.5	3.5	14.7	–55.6
TPSS	6–31+G(d,p)	1.7	–1.4	5.1	21.5		6–31G(d,p)	4.5	3.6	14.5	–55.1
	6–31G(d)	15.4	15.4	38.9	–127.4		cc-pVDZ	5.3	4.4	16.3	–59.3
	6–31G(d,p)	15.4	15.4	38.8	–126.7		6–31+G(d,p)	7.8	7.8	20.6	–80.3
	cc-pVDZ	15.5	15.5	39.9	–122.2		aug-cc-pVDZ	7.1	7.1	18.6	–71.5
	6–31+G(d,p)	18.7	18.7	43.4	–141.1	mPW2PLYP	6–31G(d)	11.7	11.5	32.6	–111.5
TPSS-D	6–31G(d)	6.6	–6.6	13.0	49.7		6–31G(d,p)	11.7	11.6	32.5	–111.0
	6–31G(d,p)	6.7	–6.7	13.2	49.6		cc-pVDZ	12.6	12.5	35.8	–116.2
	cc-pVDZ	6.6	–6.6	13.5	42.3		6–31+G(d,p)	16.0	16.0	40.6	–138.2
	6–31+G(d,p)	3.4	–3.4	8.9	27.5		aug-cc-pVDZ	15.3	15.3	38.2	–129.7
	6–31G(d)	6.1	–6.1	11.9	44.4	mPW2PLYP-D	6–31G(d)	4.3	2.7	14.2	–53.3
B97-D	6–31G(d,p)	6.1	–6.1	11.6	44.1		6–31G(d,p)	4.2	2.7	14.0	–52.7
	cc-pVDZ	5.6	–5.6	11.7	45.1		cc-pVDZ	5.0	3.6	16.5	–57.9
	6–31+G(d,p)	2.1	–1.9	5.8	20.3		6–31+G(d,p)	7.2	7.1	21.1	–80.0
	aug-cc-pVDZ	2.8	–2.7	6.6	31.5		aug-cc-pVDZ	6.5	6.4	18.8	–71.4
AM1		29.7	29.7	66.1	–184.4	AMBER		4.1	2.3	18.7	–82.3
PM3		29.6	29.6	69.3	–177.1						

<sup>a</sup>MP2 interaction energies were calculated using the BSSE-corrected dimer energies.

tions, as well as the relative performance for dimers involving neutral and cationic monomers. Subsequently, to assess the ability of various functionals to accurately describe an extended portion of the potential-energy surface, PES scans of select dimers will be considered for the methods that best-describe the 129 dimer interaction energies with the current large-model goal in mind.

## Calculation of accurate interaction energies

### Stacking interactions

We will begin by discussing the performance of MP2 with the small basis sets considered in the present work, which will illustrate how this widely used method for stacking depends on the basis set used for our systems of interest. These data will also provide a useful reference point for discussing the basis-set dependence of other methods. As mentioned in the Computational details, we have chosen to consider two different basis-set designs of double-zeta quality, since our end goal is to use these methods to study enzyme-catalyzed reactions through full (hybrid) optimizations. As previously noted in the literature,<sup>86</sup> MP2 does not adequately recover CCSD(T)/CBS stacking energies in the absence of diffuse functions (6–31G(d), 6–31G(d,p), and cc-pVDZ), while inclusion of diffuse functions improves the quality of the results (Table 1). Nevertheless, when a modified basis set (6–31G\*(0.25)) that was designed to study stacking interactions between the DNA nucleobases is considered,<sup>86,104,105</sup> both the MUE and MSE significantly decrease, and the MAX and MAX % drastically decrease. These results emphasize that the 6–31G\*(0.25)-modified basis set provides an excellent description of DNA–protein  $\pi$ – $\pi$  stacking interactions,<sup>83–85</sup> and outperforms even the commonly used aug-cc-pVDZ basis set.

As previously shown in the literature, DFT functionals traditionally used in a variety of applications (structure, kinetics, and hydrogen-bond strengths) do not accurately describe  $\pi$ – $\pi$  stacking interactions (Table 1).<sup>58</sup> For stacking between nucleobase and amino acid monomers, this includes the widely used B3LYP functional. This result emphasizes that this functional should be cautiously used in hybrid approaches for studying enzyme-catalyzed reactions, since many high-level regions contain  $\pi$ – $\pi$  contacts. Furthermore, B3LYP should clearly not be used when stacking interactions have been proposed to have direct implications in substrate recognition or catalysis.

Although PBE, BLYP, and TPSS also fail to recover the correct CCSD(T)/CBS stacking energies, the performance of these functionals drastically improves when Grimme's dispersion correction is included (Table 1). B97-D also performs very well, which further testifies to the usefulness of empirical dispersion corrections in functional design. Other tactics have also been proposed to develop DFT functionals for noncovalent  $\pi$ – $\pi$  interactions, such as dispersion correcting potentials (DCPs).<sup>68</sup> Alternatively, more commonly used functionals (such as meta generalized gradient approximation (GGA) or hybrid-meta GGA methods MPWB1K,<sup>94</sup> M05–2X,<sup>95</sup> M06,<sup>56</sup> M06–L,<sup>96</sup> and M06–2X<sup>56</sup>) designed for these interactions were also parameterized to describe other properties (for instance, barrier heights or transition metals). Among these functional, MPWB1K does not perform as

well as PBE-D for DNA–protein  $\pi$ – $\pi$  interactions. However, newer functionals (M05–2X,<sup>95</sup> M06–L,<sup>96</sup> and M06–2X<sup>56</sup>) designed by the Truhlar group show improved performance. Indeed, the M06–L and M06–2X functionals lead to the smallest MUE and MSE among these methods.

The relative performance of the Pople's (6–31G) and Dunning's (cc-pVDZ) basis sets depends on the functional form considered. However, in most instances, the difference is minimal when the performances of basis sets containing the same types of (polarization, diffuse) functions are compared. Methods that do not perform well for stacking (B3LYP, PBE, BLYP, and TPSS) perform even worse as the basis-set size increases. Although there is not a large difference in performance as polarization functions are added to the hydrogen atoms, the description of stacking becomes much poorer when diffuse functions are included for these methods. On the contrary, drastic performance improvements are found when diffuse functions are added to the basis set used with PBE-D, BLYP-D, and TPSS-D. Interestingly, there is little change in the performance of M05–2X and M06–2X with an increase in the basis-set size, where inclusion of diffuse functions leads to a slightly poorer description of stacking. However, increasing the basis set for the M06–L functional leads to improved stacking-interaction energies, where the aug-cc-pVDZ basis sets leads to the smallest MUE and MSE for these functionals.

A potential way to further improve upon the performance of DFT methods for the calculation of  $\pi$ – $\pi$  interactions is to consider double-hybrid density functionals, such as B2PLYP and mPW2PLYP. B2PLYP, in particular, provides an extremely small absolute mean deviation for the S22 test set when Grimme's dispersion correction is included and a large triple-zeta basis set is used.<sup>74</sup> Although we find that inclusion of the dispersion correction improves the performance of both B2PLYP and mPW2PLYP, these functionals are not as accurate as the other dispersion-corrected methods considered above (Table 1). We acknowledge that this could be in part due to the fact that we do not include BSSE corrections in our reported binding energies, since these calculations would not be realistic during each optimization step when enzyme-catalyzed reactions are considered.

Although we have discussed methods suitable for the highest-level region of hybrid calculations, the performance of the method used to describe the remainder of the protein environment (low-level region) must also be carefully considered. Semi-empirical methods are sometimes employed as a highly efficient molecular orbital method for describing proteins (for examples, see refs. 7, 8, 11, 12, 14, 15, 31, and 35). For instance, these techniques can be used as the high-level method, as the mid-layer region in multi-layer approaches, or as the low-level method when truncated enzyme models are used. However, our results indicate that neither of the typically chosen semi-empirical techniques (AM1, PM3) accurately describe stacking interactions between the DNA/RNA bases and aromatic amino acids (Table 1). On the contrary, since AMBER was developed to describe the structure of both DNA and proteins,<sup>98</sup> this molecular mechanics method describes the stacking interactions between their components exceptionally well (Table 1).



### T-shaped interactions

$\pi$ - $\pi$  T-shaped interactions have been less-studied compared with the large number of stacked complexes examined in the literature. These interactions have been proposed<sup>83</sup> to be less-dependent on dispersion than stacking, and therefore more commonly used computational techniques may be able to accurately describe these contacts. This statement is confirmed in the present work where the performance of MP2 with any of our chosen basis sets is better for T-shaped (Table 2) than stacking (Table 1) interactions. Indeed, although aug-cc-pVDZ is not the optimal choice for studying stacked systems with MP2, this combination outperforms other basis sets for T-shaped interactions. However, MP2/6-31G\*(0.25), which was the best combination for the stacked orientations, also performs very well for nucleobase – amino acid T-shaped contacts. These results justify the use of MP2/6-31G\*(0.25) for  $\pi$ - $\pi$  T-shaped interactions even though this basis set was originally designed for stacked dimers.<sup>86,104,105</sup>

For all functionals, the basis-set effects on T-shaped binding strengths (Table 2) are the same as those discussed for stacking interactions (Table 1). B3LYP more accurately describes T-shaped than stacking contacts with all basis sets considered. However, B3LYP is still much less accurate than the other functionals under analysis. Therefore, we re-emphasize that B3LYP should be cautiously used in hybrid approaches for studying enzyme-catalyzed reactions when the high-level region contains  $\pi$ - $\pi$  interactions. Once again, we find that inclusion of an empirical dispersion correction greatly improves the accuracy of GGA, meta-GGA, and double-hybrid density functionals. This suggests that dispersion may play a larger role in dictating the magnitude of T-shaped interactions than initially believed. We note that although the MUE and MSE are smaller for PBE than PBE-D, the MAX and MAX % are much larger for PBE, which makes PBE a less reliable method. Nevertheless, M05-2X and M06-2X yield interaction energies closer to the CCSD(T)/CBS results, while M06-L does not perform as well as these other functionals. Indeed, M06-2X performs significantly better than PBE-D for nucleobase – amino acid T-shaped interactions.

AM1 and PM3 more accurately predict nucleobase – amino acid T-shaped interactions (Table 2) compared with the stacking binding energies (Table 1). However, the deviations from the CCSD(T)/CBS results are still very large, and therefore these methods should be used with caution for systems that include many aromatic residues. The MUE is slightly larger for AMBER T-shaped interactions (Table 2) than AMBER stacking energies (Table 1), while the MAX and MAX % are significantly larger for T-shaped contacts. However, AMBER reasonably describes both types of interactions, especially when the computational efficiency of this method is taken into account.

### Overall

We emphasize that our discussion of the performance of DFT functionals presented thus far has provided general conclusions based on the results of all dimers. However, errors for the neutral versus cationic dimers were also determined (see Supplementary data, Tables S4–S6) and fully analyzed. We found that all methods describe the binding

strengths of cationic dimers with slightly less accuracy than neutral dimers. Nevertheless, there are no drastic differences that warrant a detailed discussion of the performance of each method for cationic versus neutral systems.

Table 3 summarizes the performance of all methods for all types of (stacking and T-shaped, neutral  $\pi$ - $\pi$ , and cationic  $\pi^+$ - $\pi$ ) interactions. Over the entire data set, we conclude that AMBER is a more appropriate choice for the lower-level method in hybrid approaches than popular semi-empirical techniques. Indeed, AMBER also outperforms many of the other methods considered in the present work, especially when the low computational cost of this technique is taken into account. This suggests that MD, QM/MM, or ONIOM calculations that implement AMBER accurately describe  $\pi$ - $\pi$  interactions throughout DNA–protein systems. We find that the error in the AMBER binding strengths is greater for cationic than neutral systems (see Supplementary data), and therefore care should be taken when comparisons between systems with different charges are required.

Among the MP2 basis-set combinations considered, MP2/6-31G\*(0.25) provides the best description for a range of noncovalent  $\pi$ - $\pi$  dimer interactions (Table 3). These results further justify our use of this method for scanning the potential-energy surfaces of stacked and T-shaped nucleobase – amino acid dimers.<sup>83–85</sup> Furthermore, our findings suggest that MP2/6-31G\*(0.25) is an efficient method for use in future work of stacked or T-shaped systems when larger systems (trimers or tetramers) are considered.

As discussed previously in the literature, double-hybrid functionals yield very good performance when an empirical dispersion correction is included in the functional form.<sup>51,74</sup> Additionally, the performance reported in the present work would likely be further improved with the inclusion of BSSE corrections. However, as previously discussed, this is not a feasible approach for our intended application because of the computational scaling of these methods. Therefore, the use of these functionals for accurately determining interaction energies is currently restricted to single-point calculations with large basis sets and (or) BSSE corrections.

There is no significant difference in the results obtained with Pople's or Dunning's basis sets for any DFT method considered. Nevertheless, the Dunning's basis sets lead to a larger total number of basis functions, and therefore calculations with these basis sets require increased computational resources. Since convergence on realistic time scales is an important consideration when studying enzyme-catalyzed reactions, we recommend considering the use of Pople's basis sets in hybrid studies of large systems.

The results in Table 3 suggest that within the functionals considered in the present work, the methods that best-describe  $\pi$ - $\pi$  stacking and T-shaped interaction energies are M06-2X and PBE-D. Although BLYP-D outperforms PBE-D with the 6-31+G(d,p) basis set, PBE-D performs better with the smaller 6-31G(d) basis set. However, Table 3 suggests that M06-2X outperforms PBE-D with both the smaller 6-31G(d) and the larger 6-31+G(d,p) basis sets. We emphasize that the 6-31G(d) basis set is a more computationally efficient choice for hybrid approaches, since the inclusion of diffuse functions on heavy atoms and (or) polarization functions on hydrogen atoms during the optimization routine drastically increases the computational resour-

ces required. Thus, M06-2X/6-31G(d) may be the best choice among those considered in the present work for describing the high-level region in hybrid approaches for large-scale modeling of enzyme-catalyzed reactions that involve DNA-protein  $\pi$ - $\pi$  interactions.

### Description of potential-energy surfaces

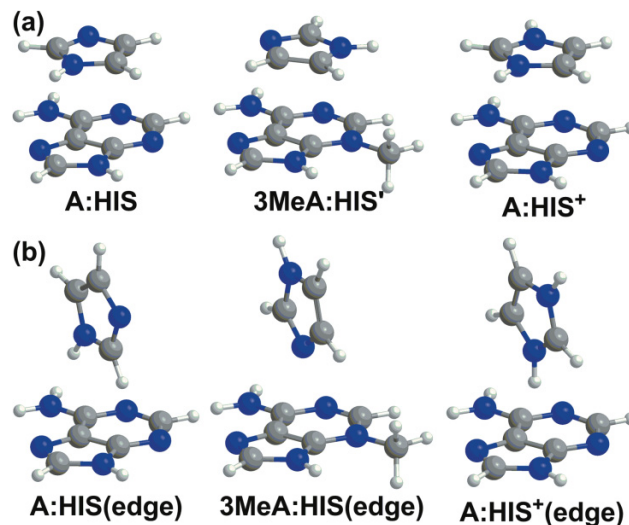
Although Tables 1–3 provide useful information about the ability of various methods to accurately predict the strength of  $\pi$ - $\pi$  interactions at minimum regions on the potential-energy surfaces of nucleobase – amino acid dimers, these data do not necessarily reflect whether the methods provide an accurate description of the entire PES. Understanding how density functionals describe both minimum and nonminimum regions of potential-energy surfaces is particularly important when applying these methods to optimize a complete reaction mechanism for DNA-protein complexes that include stacked and (or) T-shaped contacts. Therefore, as a critical first step, the functional (M06-2X, PBE-D) and basis set (6-31G(d), 6-31+G(d,p)) combinations found to best-describe nucleobase – amino acid interactions will be further scrutinized below by evaluating their ability to describe changes in both stacked and T-shaped binding strengths as a function of select geometric variables (Fig. 3). Since MP2 is widely used to study  $\pi$ - $\pi$  dimers in the literature, we have chosen to compare our results to the MP2 method that best-describes stacked (MP2/6-31G\*(0.25), Table 1) or T-shaped (MP2/aug-cc-pVDZ, Table 2) orientations. Nevertheless, both MP2 values are reported for both types of interactions to further illustrate the differences between these approaches. We focus our investigation on three dimers (adenine-histidine, 3-methyladenine-histidine, and adenine – protonated histidine) in both their optimal stacked and (amino acid edge) T-shaped orientations (Fig. 4). Our choice in molecules allows us to consider similar systems that span both  $\pi$ - $\pi$  and  $\pi^+$ - $\pi$  interactions, which have a varying dependence on the electrostatic and dispersion contributions to the interactions.

#### Stacked dimers

Deviations in the MP2-calculated curves describing dimer interaction energies as a function of the vertical separation ( $R_1$ , Fig. 3) between the monomers are not surprising (Figs. 5a–5c), since aug-cc-pVDZ is known to overestimate stacking interactions. However, both basis sets predict the same preferred MP2 vertical separation in the nucleobase – amino acid dimers considered in the present work (see Supplementary data, Tables S7–S9). Furthermore, over the  $R_1$  values investigated, the entire potential-energy surfaces calculated with both basis sets are reasonably close in both magnitude and shape for the cationic systems (Figs. 5b and 5c). Nevertheless, there are larger deviations in the calculated MP2 binding strengths for the neutral dimer (Fig. 5a), where the magnitude of the deviation depends on the vertical separation, and a better agreement is observed at larger vertical separations.

M06-2X leads to steeper potential-energy surfaces with respect to  $R_1$  than MP2 for stacked dimers. Specifically, this functional underestimates the binding strength at large vertical separations and overestimates the interaction energy at small  $R_1$  distances. The M06-2X results obtained with both

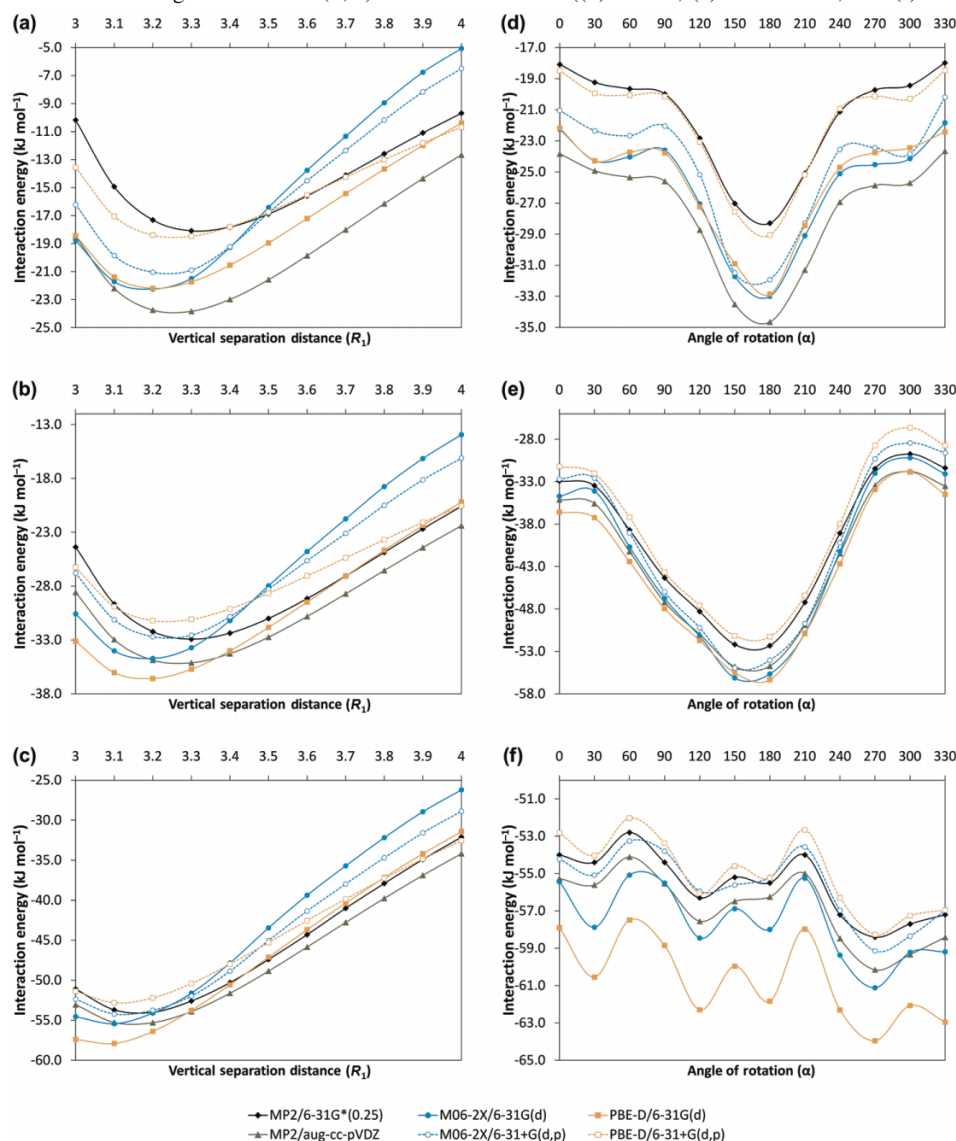
**Fig. 4.** Dimers considered in vertical separation ( $R_1$ ) and angle of rotation ( $\alpha$ ) potential-energy surface scans for (a) stacked and (b) amino acid edge T-shaped orientations.



basis sets are in good agreement with each other, which re-emphasizes that inclusion of diffuse functions does not lead to improved performance for this functional. In the absence of diffuse functions, the PES with respect to  $R_1$  is slightly steeper, which implies that deviations from MP2/6-31G\*(0.25) will be larger in non-equilibrium geometries for the M06-2X/6-31G(d) combination. For all dimers, M06-2X predicts the preferred vertical separation to be 0.1 Å smaller than MP2, which has been previously reported in the literature for the methane dimer<sup>76</sup> and the sandwiched-benzene dimer<sup>76</sup> and reflects stronger binding. However, we used an  $R_1$  scan increment of 0.1 Å (Fig. 3) and consideration of smaller increments might yield even better agreement with MP2.<sup>83</sup> Furthermore, when regions close to the preferred  $R_1$  are considered, small changes in the vertical separation lead to small changes in the interaction energy. Finally, it is interesting to note that the deviations from MP2/6-31G\*(0.25) are smaller for the M06-2X  $\pi^+$ - $\pi$  stacking interactions than the corresponding  $\pi$ - $\pi$  contacts. We note that our M06-2X surfaces are smooth despite previous reports that meta-GGA potential-energy curves for the stacked benzene dimer oscillate unless very large integration grids are used.<sup>106</sup>

PBE-D/6-31+G(d,p) provides an excellent representation of the preferred MP2 geometries, as well as the interaction energies for the entire  $R_1$  potential-energy surface of stacked dimers. Indeed, PBE-D/6-31+G(d,p) likely provides a better description of both  $\pi$ - $\pi$  and  $\pi^+$ - $\pi$  contacts than M06-2X with either basis set. However, there is a much larger basis-set effect for the PBE-D functional. Specifically, removal of diffuse functions from the basis set leads to a significant overestimation when compared with the MP2/6-31G\*(0.25) stabilization energy, which is much more pronounced at smaller  $R_1$  distances. Figure 5 also illustrates that PBE-D/6-31G(d) and MP2/6-31G\*(0.25) are in better agreement in the  $\pi^+$ - $\pi$  complexes (Figs. 5b and 5c) than the  $\pi$ - $\pi$  A:HIS dimer (Fig. 5a). Furthermore, as discussed for M06-2X, PBE-D/6-31G(d) predicts  $R_1$  to be 0.1 Å smaller than MP2,

**Fig. 5.** Interaction energy ( $\text{kJ mol}^{-1}$ ) as a function of vertical separation distance ( $R_1$ , Å) for the stacked dimers ((a) A:HIS, (b) 3MeA:HIS', and (c) A:HIS<sup>+</sup>) or as a function of angle of rotation ( $\alpha$ , °) for stacked dimers ((d) A:HIS, (e) 3MeA:HIS', and (f) A:HIS<sup>+</sup>).



but this effect is diminished when the larger basis set is used (see Supplementary data, Tables S7–S9).

Using the preferred  $R_1$  distance identified for each method, the binding strength as a function of the angle of rotation of the amino acid with respect to the nucleobase ( $\alpha$ , Fig. 3) was considered (Figs. 5d–5f). Unlike discussed for the  $R_1$  potential-energy surfaces, all methods yield the same general shape of the potential-energy surface with respect to  $\alpha$ , which is dictated by the relative orientation of the dipole moment vectors in the monomers.<sup>83</sup> Once again, we clearly see the overestimation of the interaction strength at the MP2 level with the aug-cc-pVDZ compared with the 6–31G\*(0.25) basis set.

Although M06–2X with both basis sets yields binding energies in very close agreement with one another for all  $\alpha$  values in the A:HIS and 3MeA:HIS' stacked dimers, a larger basis-set effect is seen for A:HIS<sup>+</sup> (Fig. 5f). To provide a fairer comparison by only examining the effects of  $\alpha$ , an additional  $\alpha$  scan was performed at the MP2/6–31G\*(0.25)

preferred vertical separation distance for cases where the DFT  $R_1$  distance was different (see Supplementary data, Tables S7–S9). When the same  $R_1$  value is considered, we see better agreement between the M06–2X results and the MP2/6–31G\*(0.25) results for this dimer (see Supplementary data, Table S9). In comparison, PBE-D/6–31+G(d,p) produces nearly identical potential-energy surfaces with respect to  $\alpha$  in both shape and magnitude as MP2/6–31G\*(0.25). However, PBE-D/6–31G(d) greatly overestimates the MP2 binding strength for all  $\alpha$ , especially for the A:HIS<sup>+</sup> dimer (see Fig. 5f).

In summary, PBE-D in combination with basis sets that include diffuse functions yields stacking interactions in excellent agreement with MP2 for large regions of the PES, and therefore this is the method of choice for describing DNA–protein stacking interactions in large-scale modeling. However, in instances when diffuse functions are prohibited due to the associated computational expense, PBE-D can yield acceptable  $\pi$ – $\pi$  interactions, but can lead to very large



overestimations, especially in  $\pi^+-\pi$  interactions. In comparison, M06-2X has a very small basis-set dependence and yields a reasonable description of both the dispersion and electrostatic components of the stacking interactions for both neutral and cationic systems. As a result, M06-2X is an efficient choice for modeling stacking interactions in large systems that require the use of small basis sets (without diffuse functions).

### T-shaped dimers

In contrast to the discussion of stacked systems, the MP2 potential-energy surfaces with respect to  $R_1$  calculated with aug-cc-pVDZ and 6-31G\*(0.25) for T-shaped dimers are very similar in shape, and the binding strengths are nearly identical in magnitude (within 3.3 kJ mol<sup>-1</sup>, Figs. 6a-6c). M06-2X almost always underestimates the MP2 T-shaped binding strengths regardless of the basis set used, especially when interactions with a cationic monomer are considered. On the contrary, PBE-D generally overestimates the MP2 binding strength for T-shaped dimers, where this overestimation is exaggerated when diffuse functions are omitted from the basis set (see for example, Figs. 6a and 6c). As discussed for the stacked dimers, all DFT methods predict a 0.1 Å shorter vertical separation than MP2 for A:HIS(edge) and 3MeA:HIS(edge) T-shaped dimers. However, the  $R_1$  values for A:HIS<sup>+</sup>(edge) match the MP2 results for all combinations except M06-2X/6-31+G(d,p), which predicts a 0.1 Å larger vertical separation.

Once again, all methods yield the same general shape for the curves representing the T-shaped interaction energy as a function of the angle of rotation ( $\alpha$ , Figs. 6d-6f). Furthermore, all other general conclusions discussed for the stacking interactions in regards to the method dependence for these potential-energy surfaces hold for the T-shaped interactions. However, the effects are more pronounced in the case of T-shaped contacts. Most significantly, when diffuse functions are not included in the basis set, PBE-D drastically overestimates the T-shaped interactions. These results re-emphasize our previous conclusion that PBE-D/6-31G(d) should not be used to study  $\pi-\pi$  T-shaped contacts. M06-2X, on the other hand, more consistently provides a better description for a range of  $\pi-\pi$  and  $\pi^+-\pi$  T-shaped DNA-protein interactions.

### Overall

Detailed consideration of the potential-energy surfaces of  $\pi-\pi$  and  $\pi^+-\pi$  stacked and T-shaped dimers as a function of the vertical separation ( $R_1$ ) and angle of rotation ( $\alpha$ ) between nucleobase and amino acid monomers supports our previous interaction energy analysis. Specifically, PBE-D with diffuse functions (6-31+G(d,p)) provides a very accurate description of the potential-energy surface of the stacked dimers. However, the accuracy of this combination breaks down for T-shaped complexes, where these interaction energies can be drastically overestimated. PBE-D also has a very large basis-set dependence, and therefore small basis sets with no diffuse functions should be used in conjunction with this functional with extreme caution, especially when T-shaped contacts are considered. Our results indicate that if the system of interest contains both stacked and T-shaped arrangements, then M06-2X will provide a

more reliable description of all  $\pi-\pi$  interactions in the DNA-protein complex. Nevertheless, users should be aware that M06-2X generally finds the equilibrium distances to be 0.1 Å closer than other methods, and underestimates the binding at vertical separation distances larger than the equilibrium value. Nevertheless, the description of both stacked and T-shaped interactions with M06-2X looks promising for geometry optimizations in the intended application of studying DNA-protein systems with hybrid techniques. M06-2X has minimal basis-set dependence for both stacked and T-shaped orientations and therefore can be used in conjunction with a small basis set to optimize large enzymatic systems. In fact, our results indicate that there is no advantage to including diffuse functions in attempts to improve the description of M06-2X stacking and T-shaped interactions, while the computational cost associated with implementing such basis sets for enzymatic systems is very high.

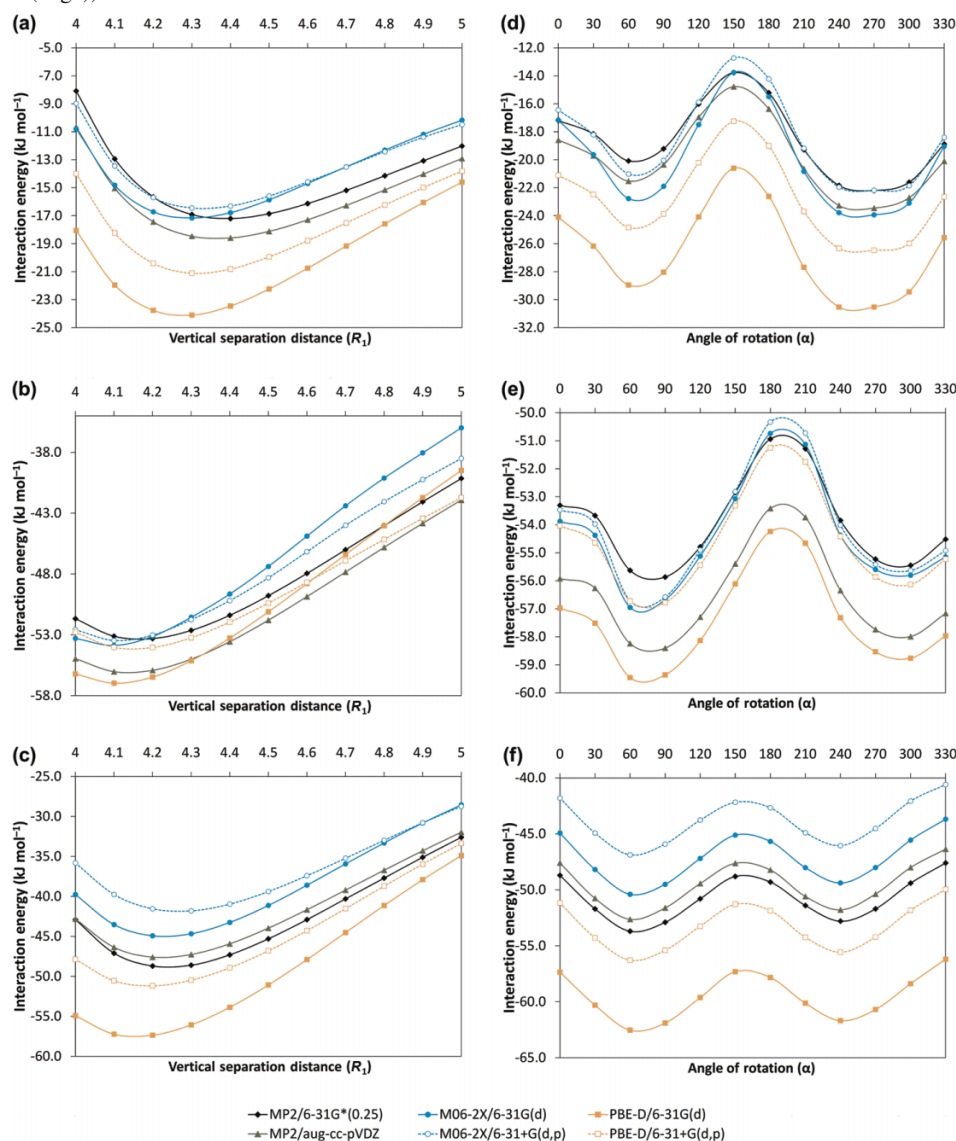
### Conclusions

The present work investigated the performance of a number of density functional methods, as well as other techniques currently used in hybrid approaches, to identify currently available method and basis-set combinations that accurately and efficiently describe the binding strengths and potential-energy surfaces of  $\pi-\pi$  stacking and  $\pi-\pi$  T-shaped DNA-protein interactions. By benchmarking against our previously reported 129 nucleobase – amino acid dimer CCSD(T)/CBS interaction energies,<sup>83-85</sup> we conclude that AMBER is a more appropriate choice for the lower-level method in hybrid approaches than popular semi-empirical techniques, and suggest that hybrid techniques that implement AMBER accurately describe  $\pi-\pi$  interactions throughout DNA-protein systems. Additionally, the M06-2X and PBE-D density functional methods were found to provide very promising descriptions of our entire 129 nucleobase – amino acid dimer test set, and therefore may be the best choice for high-level regions in hybrid approaches for studying enzyme systems that involve nucleobase – amino acid  $\pi-\pi$  interactions.

M06-2X and PBE-D, in combination with smaller (6-31G(d)) and larger (6-31+G(d,p)) double-zeta basis sets, were further examined to determine which combinations best-describe an extended portion of the potential-energy surfaces of three representative stacked and three representative (amino acid edge) T-shaped dimers. PBE-D with the larger basis set was found to provide an excellent description of stacking interactions, yet generally overestimates T-shaped interactions. However, PBE-D has a very strong basis-set dependence, where the small basis set erroneously overestimates interaction energies in both neutral and cationic systems, especially for T-shaped contacts. On the other hand, M06-2X has a small basis set dependence. Indeed, M06-2X/6-31G(d) was found to provide an excellent description of both stacked and T-shaped, as well as  $\pi-\pi$  and  $\pi^+-\pi$ , DNA-protein interactions. Therefore, we recommend using PBE-D/6-31+G(d,p) to study nucleobase – amino acid systems that rely only on stacking interactions. However, if T-shaped contacts are to be considered and (or) smaller basis sets must be used, M06-2X/6-31G(d) will provide an



**Fig. 6.** Interaction energy ( $\text{kJ mol}^{-1}$ ) as a function of vertical separation distance ( $R_1$ , Å) for the T-shaped dimers ((a) A:HIS(edge), (b) 3MeA:HIS(edge), and (c) A:HIS<sup>+</sup>(edge)) or as a function of angle of rotation ( $\alpha$ , °) for T-shaped dimers ((d) A:HIS(edge), (e) 3MeA:HI-S(edge), and (f) A:HIS<sup>+</sup>(edge)).



overall excellent description of the (stacking and T-shaped) interactions in the entire DNA–protein complex.

The present work is important for our understanding of how current density functionals describe DNA–protein  $\pi$ – $\pi$  interactions in both minimum and nonminimum regions of the potential-energy surfaces, which is critical information for our intended future application of modeling enzymatic reaction pathways using hybrid techniques. Future work should consider our 129 nucleobase – amino acid benchmark data set<sup>83–85</sup> when parameterizing new force fields and new density functionals that even more reliably account for long-range dispersion interactions. Additionally, future work should consider how the most promising techniques perform in a variety of protein and solution environments. We acknowledge that this study only examines the energies and structure–magnitude relationships in  $\pi$ – $\pi$  systems, and therefore future work should also investigate how these

functionals perform for full geometry optimizations, as well as the kinetics, of DNA–protein systems.

## Supplementary data

Supplementary data for this article (uracil – protonated histidine potential-energy surface scans and higher-level binding strengths, additional AMBER atom types and parameters, interaction energy analysis for neutral and cationic systems, and full potential-energy surface scan data for the six test dimers) are available on the journal Web site ([canjchem.nrc.ca](http://canjchem.nrc.ca)). Coordinates for all 129 nucleobase – amino acid dimers are available from the authors upon request.

## Acknowledgements

We thank the Natural Sciences and Engineering Research Council (NSERC), the Canada Research Chair program, and

the Canada Foundation for Innovation (CFI) for financial support. We acknowledge the Upscale and Robust Abacus for Chemistry In Lethbridge (URACIL) for computer resources. LRR thanks NSERC (CGS-D) and Alberta Innovates-Technology Futures for student scholarships.

## References

- (1) Claeysens, F.; Harvey, J. N.; Manby, F. R.; Mata, R. A.; Mulholland, A. J.; Ranaghan, K. E.; Schutz, M.; Thiel, S.; Thiel, W.; Werner, H.-J. *Angew. Chem. Int. Ed.* **2006**, *45* (41), 6856. doi:10.1002/anie.200602711.
- (2) Himo, F. *Theor. Chem. Acc.* **2006**, *116* (1-3), 232. doi:10.1007/s00214-005-0012-1.
- (3) Leopoldini, M.; Marino, T.; Michelini, M. C.; Rivalta, I.; Russo, N.; Sicilia, E.; Toscano, M. *Theor. Chem. Acc.* **2007**, *117* (5-6), 765. doi:10.1007/s00214-006-0199-9.
- (4) Ramos, M. J.; Fernandes, P. A. *Acc. Chem. Res.* **2008**, *41* (6), 689. doi:10.1021/ar7001045.
- (5) Siegbahn, P. E. M.; Borowski, T. *Acc. Chem. Res.* **2006**, *39* (10), 729. doi:10.1021/ar050123u. PMID:17042473.
- (6) Warshel, A.; Sharma, P. K.; Kato, M.; Xiang, Y.; Liu, H.; Olsson, M. H. M. *Chem. Rev.* **2006**, *106* (8), 3210. doi:10.1021/cr0503106. PMID:16895325.
- (7) Alzate-Morales, J. H.; Caballero, J.; Gonzalez-Nilo, F. D.; Contreras, R. *Chem. Phys. Lett.* **2009**, *479* (1-3), 149. doi:10.1016/j.cplett.2009.08.020.
- (8) Alzate-Morales, J. H.; Caballero, J.; Vergara Jague, A.; González Nilo, F. D. *J. Chem. Inf. Model.* **2009**, *49* (4), 886. doi:10.1021/ci8004034. PMID:19323453.
- (9) Barone, V.; De Rienzo, F.; Langella, E.; Menziani, M. C.; Rega, N.; Sola, M. *Proteins* **2006**, *62* (1), 262. doi:10.1002/prot.20772. PMID:16287118.
- (10) Matsubara, T.; Dupuis, M.; Aida, M. *J. Phys. Chem. B* **2007**, *111* (33), 9965. doi:10.1021/jp072732k. PMID:17661509.
- (11) O'Brien, K. A.; Salter, E. A.; Wierzbicki, A. *Int. J. Quantum Chem.* **2007**, *107* (12), 2197. doi:10.1002/qua.21332.
- (12) Pouilly, J. C.; Grégoire, G.; Schermann, J. P. *J. Phys. Chem. A* **2009**, *113* (28), 8020. doi:10.1021/jp901696d. PMID:19537745.
- (13) Salter, E. A.; O'Brien, K. A.; Edmunds, R. W.; Wierzbicki, A. *Int. J. Quantum Chem.* **2008**, *108* (6), 1189. doi:10.1002/qua.21589.
- (14) Srivab, P.; Hannongbua, S. *ChemMedChem* **2008**, *3* (5), 803. doi:10.1002/cmdc.200700181. PMID:18338369.
- (15) Yao, L. S.; Cukier, R. I.; Yan, H. G. *J. Phys. Chem. B* **2007**, *111* (16), 4200. doi:10.1021/jp0673056. PMID:17394305.
- (16) Altun, A.; Yokoyama, S.; Morokuma, K. *J. Phys. Chem. B* **2008**, *112* (22), 6814. doi:10.1021/jp709730b. PMID:18473437.
- (17) Banáš, P.; Rulíšek, L.; Hánosová, V.; Svozil, D.; Walter, N. G.; Spöner, J.; Otyepka, M. *J. Phys. Chem. B* **2008**, *112* (35), 11177. doi:10.1021/jp802592z. PMID:18686993.
- (18) Fanfrlík, J.; Brynda, J.; Rezáč, J.; Hobza, P.; Lepsík, M. *J. Phys. Chem. B* **2008**, *112* (47), 15094. doi:10.1021/jp803528w. PMID:18975888.
- (19) Inoue, T.; Shiota, Y.; Yoshizawa, K. *J. Am. Chem. Soc.* **2008**, *130* (50), 16890. doi:10.1021/ja802618s. PMID:19007228.
- (20) Li, X.; Chung, L. W.; Paneth, P.; Morokuma, K. *J. Am. Chem. Soc.* **2009**, *131* (14), 5115. doi:10.1021/ja807677z. PMID:19309090.
- (21) Lundberg, M.; Kawatsu, T.; Vreven, T.; Frisch, M. J.; Morokuma, K. *J. Chem. Theory Comput.* **2009**, *5* (1), 222. doi:10.1021/ct800457g.
- (22) Matsubara, T.; Dupuis, M.; Aida, M. *J. Comput. Chem.* **2008**, *29* (3), 458. doi:10.1002/jcc.20805.
- (23) Morgado, C. A.; Hillier, I. H.; Burton, N. A.; McDouall, J. J. W. *Phys. Chem. Chem. Phys.* **2008**, *10* (19), 2706. doi:10.1039/b715514j. PMID:18464985.
- (24) Rickard, G. A.; Bergès, J.; Houée-Levin, C.; Rauk, A. *J. Phys. Chem. B* **2008**, *112* (18), 5774. doi:10.1021/jp710917t. PMID:18447348.
- (25) Robertazzi, A.; Platts, J. A. *Chem. Eur. J.* **2006**, *12* (22), 5747. doi:10.1002/chem.200501566.
- (26) Hu, H.; Yang, W. T. *J. Mol. Struct. THEOCHEM* **2009**, *898* (1-3), 17. doi:10.1016/j.theochem.2008.12.025.
- (27) Imhof, P.; Fischer, S.; Smith, J. C. *Biochemistry* **2009**, *48* (38), 9061. doi:10.1021/bi900585m. PMID:19678693.
- (28) Kamachi, T.; Nakayama, T.; Shitamichi, O.; Jitsumori, K.; Kurihara, T.; Esaki, N.; Yoshizawa, K. *Chem. Eur. J.* **2009**, *15* (30), 7394. doi:10.1002/chem.200801813.
- (29) Kamerlin, S. C. L.; Haranczyk, M.; Warshel, A. *J. Phys. Chem. B* **2009**, *113* (5), 1253. doi:10.1021/jp8071712. PMID:19055405.
- (30) Rosta, E.; Woodcock, H. L.; Brooks, B. R.; Hummer, G. *J. Comput. Chem.* **2009**, *30* (11), 1634. doi:10.1002/jcc.21312.
- (31) de M. Seabra, G.; Walker, R. C.; Elstner, M.; Case, D. A.; Roitberg, A. E. *J. Phys. Chem. A* **2007**, *111* (26), 5655. doi:10.1021/jp0700711. PMID:17521173.
- (32) Yang, Y.; Cui, Q. *J. Phys. Chem. A* **2009**, *113* (45), 12439. doi:10.1021/jp902949f. PMID:19534504.
- (33) Yang, Y.; Yu, H. B.; Cui, Q. *J. Mol. Biol.* **2008**, *381* (5), 1407. doi:10.1016/j.jmb.2008.06.071. PMID:18619975.
- (34) Calvaresi, M.; Bottoni, A.; Garavelli, M. *J. Phys. Chem. B* **2007**, *111* (23), 6557. doi:10.1021/jp071581i. PMID:17508740.
- (35) Dinner, A. R.; Blackburn, G. M.; Karplus, M. *Nature* **2001**, *413* (6857), 752. doi:10.1038/35099587. PMID:11607036.
- (36) Lin, H.; Truhlar, D. G. *Theor. Chem. Acc.* **2007**, *117* (2), 185. doi:10.1007/s00214-006-0143-z.
- (37) Vreven, T.; Byun, K. S.; Komaromi, I.; Dapprich, S.; Montgomery, J. A.; Morokuma, K.; Frisch, M. J. *J. Chem. Theory Comput.* **2006**, *2* (3), 815. doi:10.1021/ct050289g.
- (38) Vreven, T.; Morokuma, K. *Annu. Rep. Comput. Chem.* **2006**, *2*, 35. doi:10.1016/S1574-1400(06)02003-2.
- (39) Lynch, B. J.; Fast, P. L.; Harris, M.; Truhlar, D. G. *J. Phys. Chem. A* **2000**, *104* (21), 4811. doi:10.1021/jp000497z.
- (40) Dalhus, B.; Laerdahl, J. K.; Backe, P. H.; Bjørås, M. *FEMS Microbiol. Rev.* **2009**, *33* (6), 1044. doi:10.1111/j.1574-6976.2009.00188.x. PMID:19659577.
- (41) Berti, P. J.; McCann, J. A. B. *Chem. Rev.* **2006**, *106* (2), 506. doi:10.1021/cr040461t. PMID:16464017.
- (42) Stivers, J. T.; Jiang, Y. L. *Chem. Rev.* **2003**, *103* (7), 2729. doi:10.1021/cr010219b. PMID:12848584.
- (43) Lau, A. Y.; Wyatt, M. D.; Glassner, B. J.; Samson, L. D.; Ellenberger, T. *Proc. Natl. Acad. Sci. U.S.A.* **2000**, *97* (25), 13573. doi:10.1073/pnas.97.25.13573. PMID:11106395.
- (44) Aeberhard, P. C.; Arey, J. S.; Lin, I. C.; Rothlisberger, U. *J. Chem. Theory Comput.* **2009**, *5* (1), 23. doi:10.1021/ct800299y.
- (45) Foster, M. E.; Sohlberg, K. *Phys. Chem. Chem. Phys.* **2009**, *12* (2), 307. doi:10.1039/b912859j. PMID:20023806.

- (46) Grimme, S. *J. Comput. Chem.* **2006**, 27 (15), 1787. doi:10.1002/jcc.20495. PMID:16955487.
- (47) Grimme, S. *J. Chem. Phys.* **2006**, 124.
- (48) Grimme, S.; Antony, J.; Schwabe, T.; Mück-Lichtenfeld, C. *Org. Biomol. Chem.* **2007**, 5 (5), 741. doi:10.1039/b615319b. PMID:17315059.
- (49) McNamara, J. P.; Hillier, I. H. *Phys. Chem. Chem. Phys.* **2007**, 9 (19), 2362. doi:10.1039/b701890h. PMID:17492099.
- (50) Neese, F.; Schwabe, T.; Grimme, S. *J. Chem. Phys.* **2007**, 126.
- (51) Schwabe, T.; Grimme, S. *Acc. Chem. Res.* **2008**, 41 (4), 569. doi:10.1021/ar700208h. PMID:18324790.
- (52) Sousa, S. F.; Fernandes, P. A.; Ramos, M. J. *J. Phys. Chem. A* **2007**, 111 (42), 10439. doi:10.1021/jp0734474. PMID:17718548.
- (53) Tarnopolsky, A.; Karton, A.; Sertchook, R.; Vuzman, D.; Martin, J. M. L. *J. Phys. Chem. A* **2008**, 112 (1), 3. doi:10.1021/jp710179r. PMID:18081266.
- (54) Tavernelli, I.; Lin, I. C.; Rothlisberger, U. *Phys. Rev. B* **2009**, 79.
- (55) Zhao, Y.; Truhlar, D. G. *J. Chem. Theory Comput.* **2008**, 4 (11), 1849. doi:10.1021/ct800246v.
- (56) Zhao, Y.; Truhlar, D. G. *Theor. Chem. Acc.* **2008**, 120 (1-3), 215. doi:10.1007/s00214-007-0310-x.
- (57) Zhao, Y.; Truhlar, D. G. *Acc. Chem. Res.* **2008**, 41 (2), 157. doi:10.1021/ar700111a. PMID:18186612.
- (58) Johnson, E. R.; Mackie, I. D.; DiLabio, G. A. *J. Phys. Org. Chem.* **2009**, 22 (12), 1127. doi:10.1002/poc.1606.
- (59) Antony, J.; Grimme, S. *Phys. Chem. Chem. Phys.* **2006**, 8 (45), 5287. doi:10.1039/b612585a. PMID:19810407.
- (60) Cerný, J.; Hobza, P. *Phys. Chem. Chem. Phys.* **2005**, 7 (8), 1624. doi:10.1039/b502769c. PMID:19787917.
- (61) Dey, R. C.; Seal, P.; Chakrabarti, S. *J. Phys. Chem. A* **2009**, 113 (37), 10113. doi:10.1021/jp905078p. PMID:19678694.
- (62) Gu, J. D.; Wang, J.; Leszczynski, J.; Xie, Y. M.; Schaefer, H. F., III. *Chem. Phys. Lett.* **2008**, 459 (1-6), 164. doi:10.1016/j.cplett.2008.05.049.
- (63) Hohenstein, E. G.; Chill, S. T.; Sherrill, C. D. *J. Chem. Theory Comput.* **2008**, 4 (12), 1996. doi:10.1021/ct800308k.
- (64) Kubář, T.; Jurecka, P.; Cerný, J.; Rezac, J.; Otyepka, M.; Valdés, H.; Hobza, P. *J. Phys. Chem. A* **2007**, 111 (26), 5642. doi:10.1021/jp068858j. PMID:17411021.
- (65) Nilsson Lill, S. O. *J. Phys. Chem. A* **2009**, 113 (38), 10321. doi:10.1021/jp903995e. PMID:19715288.
- (66) Lin, I. C.; Rothlisberger, U. *Phys. Chem. Chem. Phys.* **2008**, 10 (19), 2730. doi:10.1039/b718594d. PMID:18464988.
- (67) Lin, I.-C.; von Lilienfeld, O. A.; Coutinho-Neto, M. D.; Tavernelli, I.; Rothlisberger, U. *J. Phys. Chem. B* **2007**, 111 (51), 14346. doi:10.1021/jp0750102. PMID:18052270.
- (68) Mackie, I. D.; DiLabio, G. A. *J. Phys. Chem. A* **2008**, 112 (43), 10968. doi:10.1021/jp806162t. PMID:18828578.
- (69) Morgado, C.; Vincent, M. A.; Hillier, I. H.; Shan, X. *Phys. Chem. Chem. Phys.* **2007**, 9 (4), 448. doi:10.1039/b615263e. PMID:17216059.
- (70) Morgado, C. A.; Jurecka, P.; Svozil, D.; Hobza, P.; Šponer, J. *J. Chem. Theory Comput.* **2009**, 5 (6), 1524. doi:10.1021/ct9000125.
- (71) Morgado, C. A.; McNamara, J. P.; Hillier, I. H.; Burton, N. A.; Vincent, M. A. *J. Chem. Theory Comput.* **2007**, 3 (5), 1656. doi:10.1021/ct700072a.
- (72) Pitoňák, M.; Riley, K. E.; Neogrady, P.; Hobza, P. *Chem-PhysChem* **2008**, 9 (11), 1636. doi:10.1002/cphc.200800286. PMID:18574830.
- (73) Raju, R. K.; Ramraj, A.; Hillier, I. H.; Vincent, M. A.; Burton, N. A. *Phys. Chem. Chem. Phys.* **2009**, 11 (18), 3411. doi:10.1039/b822877a. PMID:19421542.
- (74) Schwabe, T.; Grimme, S. *Phys. Chem. Chem. Phys.* **2007**, 9 (26), 3397. doi:10.1039/b704725h. PMID:17664963.
- (75) Sharma, R.; McNamara, J. P.; Raju, R. K.; Vincent, M. A.; Hillier, I. H.; Morgado, C. A. *Phys. Chem. Chem. Phys.* **2008**, 10 (19), 2767. doi:10.1039/b719764k. PMID:18464992.
- (76) Sherrill, C. D.; Takatani, T.; Hohenstein, E. G. *J. Phys. Chem. A* **2009**, 113 (38), 10146. doi:10.1021/jp9034375. PMID:19689152.
- (77) Valdes, H.; Pluhackova, K.; Hobza, P. *J. Chem. Theory Comput.* **2009**, 5 (9), 2248. doi:10.1021/ct900174f.
- (78) Zhao, Y.; Ng, H. T.; Hanson, E. *J. Chem. Theory Comput.* **2009**, 5 (10), 2726. doi:10.1021/ct900333c.
- (79) Zhao, Y.; Truhlar, D. G. *J. Chem. Theory Comput.* **2007**, 3 (1), 289. doi:10.1021/ct6002719.
- (80) Bryantsev, V. S.; Diallo, M. S.; van Duin, A. C. T.; Goddard, W. A. *J. Chem. Theory Comput.* **2009**, 5 (4), 1016. doi:10.1021/ct800549f.
- (81) Fonseca Guerra, C.; Wijnst, T.; Poater, J.; Swart, M.; Bickelhaupt, F. M. *Theor. Chem. Acc.* **2010**, 125 (3-6), 245. doi:10.1007/s00214-009-0634-9.
- (82) Jurečka, P.; ponér, J.; erný, J.; Hobza, P. *Phys. Chem. Chem. Phys.* **2006**, 8 (17), 1985. doi:10.1039/b600027d. PMID:16633685.
- (83) Rutledge, L. R.; Durst, H. F.; Wetmore, S. D. *J. Chem. Theory Comput.* **2009**, 5 (5), 1400. doi:10.1021/ct800567q.
- (84) Rutledge, L. R.; Wetmore, S. D. *J. Chem. Theory Comput.* **2008**, 4 (10), 1768. doi:10.1021/ct8002332.
- (85) Churchill, C. D. M.; Wetmore, S. D. *J. Phys. Chem. B* **2009**, 113 (49), 16046. doi:10.1021/jp907887y. PMID:19904910.
- (86) Hobza, P.; Šponer, J. *Chem. Rev.* **1999**, 99 (11), 3247. doi:10.1021/cr9800255. PMID:11749516.
- (87) Halkier, A.; Helgaker, T.; Jorgensen, P.; Klopper, W.; Koch, H.; Olsen, J.; Wilson, A. K. *Chem. Phys. Lett.* **1998**, 286 (3-4), 243. doi:10.1016/S0009-2614(98)00111-0.
- (88) Halkier, A.; Helgaker, T.; Jorgensen, P.; Klopper, W.; Olsen, J. *Chem. Phys. Lett.* **1999**, 302 (5-6), 437. doi:10.1016/S0009-2614(99)00179-7.
- (89) Šponer, J.; Riley, K. E.; Hobza, P. *Phys. Chem. Chem. Phys.* **2008**, 10 (19), 2595. doi:10.1039/b719370j. PMID:18464974.
- (90) Jurečka, P.; Šponer, J.; Hobza, P. *J. Phys. Chem. B* **2004**, 108 (17), 5466. doi:10.1021/jp049956c.
- (91) Šponer, J.; Jurečka, P.; Marchan, I.; Luque, F. J.; Orozco, M.; Hobza, P. *Chem. Eur. J.* **2006**, 12 (10), 2854. doi:10.1002/chem.200501239.
- (92) Copeland, K. L.; Anderson, J. A.; Farley, A. R.; Cox, J. R.; Tschumper, G. S. *J. Phys. Chem. B* **2008**, 112 (45), 14291. doi:10.1021/jp805528v. PMID:18922031.
- (93) Pitoňák, M.; Neogrady, P.; Rezáč, J.; Jurečka, P.; Urban, M.; Hobza, P. *J. Chem. Theory Comput.* **2008**, 4 (11), 1829. doi:10.1021/ct800229h.
- (94) Zhao, Y.; Truhlar, D. G. *J. Phys. Chem. A* **2004**, 108 (33), 6908. doi:10.1021/jp048147q.
- (95) Zhao, Y.; Schultz, N. E.; Truhlar, D. G. *J. Chem. Theory Comput.* **2006**, 2 (2), 364. doi:10.1021/ct0502763.
- (96) Zhao, Y.; Truhlar, D. G. *J. Chem. Phys.* **2006**, 125.

- (97) PBE, BLYP and TPSS calculations (with and without dispersion corrections) with the aug-cc-pVDZ basis set did not converge after 120 microiterations in the SCF cycle using GAMESS. Owing to the computational efficiencies of these methods, which are currently out of reach for use in hybrid optimizations, no further attempts to obtain SCF convergence were made.
- (98) Cornell, W. D.; Cieplak, P.; Bayly, C. I.; Gould, I. R.; Merz, K. M.; Ferguson, D. M.; Spellmeyer, D. C.; Fox, T.; Caldwell, J. W.; Kollman, P. A. *J. Am. Chem. Soc.* **1995**, *117* (19), 5179. doi:10.1021/ja00124a002.
- (99) Wang, J.; Wang, W.; Kollman, P. A.; Case, D. A. *J. Mol. Graph. Model.* **2006**, *25* (2), 247. doi:10.1016/j.jmgm.2005.12.005. PMID:16458552.
- (100) Frisch, M. J.; Trucks, G. W.; Schlegel, H. B.; Scuseria, G. E.; Robb, M. A.; Cheeseman, J. R.; Scalmani, G.; Barone, V.; Mennucci, B.; Petersson, G. A.; Nakatsuji, H.; Caricato, M.; Li, X.; Hratchian, H. P.; Izmaylov, A. F.; Bloino, J.; Zheng, G.; Sonnenberg, J. L.; Hada, M.; Ehara, M.; Toyota, K.; Fukuda, R.; Hasegawa, J.; Ishida, M.; Nakajima, T.; Honda, Y.; Kitao, O.; Nakai, H.; Vreven, T.; Montgomery, J. A., Jr.; Peralta, J. E.; Ogliaro, F.; Bearpark, M.; Heyd, J. J.; Brothers, E.; Kudin, K. N.; Staroverov, V. N.; Kobayashi, R.; Normand, J.; Raghavachari, K.; Rendell, A.; Burant, J. C.; Iyengar, S. S.; Tomasi, J.; Cossi, M.; Rega, N.; Millam, N. J.; Klene, M.; Knox, J. E.; Cross, J. B.; Bakken, V.; Adamo, C.; Jaramillo, J.; Gomperts, R.; Stratmann, R. E.; Yazyev, O.; Austin, A. J.; Cammi, R.; Pomelli, C.; Ochterski, J. W.; Martin, R. L.; Morokuma, K.; Zakrzewski, V. G.; Voth, G. A.; Salvador, P.; Dannenberg, J. J.; Dapprich, S.; Daniels, A. D.; Farkas, Ö.; Foresman, J. B.; Ortiz, J. V.; Cioslowski, J.; Fox, D. J. *Gaussian 09*, Revision A.02; Gaussian, Inc.: Wallingford, CT, 2009.
- (101) Schmidt, M. W.; Baldridge, K. K.; Boatz, J. A.; Elbert, S. T.; Gordon, M. S.; Jensen, J. H.; Koseki, S.; Matsunaga, N.; Nguyen, K. A.; Su, S. J.; Windus, T. L.; Dupuis, M.; Montgomery, J. A. *J. Comput. Chem.* **1993**, *14* (11), 1347. doi:10.1002/jcc.540141112.
- (102) Johnson, E. R.; Wolkow, R. A.; DiLabio, G. A. *Chem. Phys. Lett.* **2004**, *394* (4-6), 334. doi:10.1016/j.cplett.2004.07.029.
- (103) Boys, S. F.; Bernardi, F. *Mol. Phys.* **1970**, *19* (4), 553. doi:10.1080/00268977000101561.
- (104) Šponer, J.; Leszczynski, J.; Hobza, P. *J. Mol. Struct. THEOCHEM* **2001**, *573* (1-3), 43. doi:10.1016/S0166-1280(01)00537-1.
- (105) Šponer, J.; Leszczynski, J.; Hobza, P. *Biopolymers* **2002**, *61* (1), 3. doi:10.1002/1097-0282(2001)61:1<3::AID-BIP10048>3.0.CO;2-4.
- (106) Johnson, E. R.; Becke, A. D.; Sherrill, C. D.; DiLabio, G. A. *J. Chem. Phys.* **2009**, 131.



# Concerning the conformational preferences of the 2-cyano derivatives of oxane, thiane, and selenane

Michael H. Benn, Yan Yan Huang, Frank Johanssen, Michael O'Reilly, Masood Parvez, Arvi Rauk, and Ted Sorensen

**Abstract:** This paper investigates the origin of the anomalous anomeric effect in merosinigrin, a 2-cyanothiane in which the cyano group is axial as expected for the anomeric effect, but in which bond distances are opposite to that expected from the  $n_S \rightarrow \sigma^*_{C-CN}$  orbital interaction, which underlies the classical anomeric effect. The model compounds, 2-cyano-oxane, 2-cyanothiane, and 2-cyanoselenane, were synthesized and studied both experimentally and computationally. Both the thia and seleno systems displayed an even higher preference for the axial conformation than the oxa system but also exhibited the bond length anomalies found previously in merosinigrin. Natural bond order (NBO) analysis of the B3LYP/6-311+G(3df,2p) wave functions of the axial and equatorial forms of the three systems confirmed a weakening of the  $n \rightarrow \sigma^*$  orbital interaction in the O, S, and Se series, and a strengthening of a  $\sigma-\pi^*(CN)$  interaction that explains the bond length reversals observed in the S and Se systems. It also revealed a new mechanism,  $n \rightarrow \pi^*$ , namely, a through-space interaction between the nonbonded lone pair electrons of the heteroatom and the  $\pi^*$  orbital of the cyano group, which selects for the axial conformation.

**Key words:** anomeric effect, orbital interactions, computation, conformation, oxane, thiane, selenane.

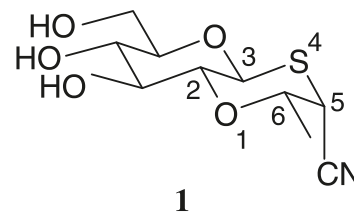
**Résumé :** Dans ce travail, on recherche l'origine de l'effet anomère anormal dans la mérosinigrine, un 2-cyanothiane dans lequel le groupe cyano est axial, tel qu'on pourrait s'y attendre en raison de l'effet anomère, mais dans lequel les longueurs des liaisons sont à l'inverse de celles attendues sur la base d'une interaction orbitalaire  $n_S \rightarrow \sigma^*_{C-CN}$  qu'on retrouve dans l'effet anomère classique. On a synthétisé les composés modèles, 2-cyano-oxane, 2-cyanothiane et 2-cyanolélénane et on les a étudiés tant d'un point de vue expérimental que théorique. Les systèmes thia et sélénia présentent tous les deux une préférence pour la conformation axiale qui est supérieure à celle du système oxa, mais ils présentent aussi les anomalies de longueurs des liaisons qui ont été observées antérieurement dans la mérosinigrine. Une analyse de l'ordre naturel de liaison (ONL) des fonctions d'onde B3LYP/6-311+G(3d,2p) des formes équatoriales et axiales des trois systèmes confirme un affaiblissement de l'interaction de l'orbitale  $n \rightarrow \sigma^*$  dans les séries O, S et Se et un affermissement de l'interaction  $\sigma-\pi^*(CN)$  qui explique les inversions des longueurs des liaisons observées dans les systèmes S et Se. Elle met aussi en évidence un nouveau mécanisme,  $n \rightarrow \pi^*$ , à savoir une interaction à travers l'espace entre la paire d'électrons non liée de l'hétéroatome et l'orbitale  $\pi^*$  du groupe cyano qui choisit la conformation axiale.

**Mots-clés :** effet anomère, interactions d'orbitales, calculs théoriques, conformation, oxane, thiane, sélénane.

[Traduit par la Rédaction]

## Introduction

Some 30 years ago, it was deduced that merosinigrin, a degradation product of the archetypical potassium allylglucosinolate (sinigrin), possessed the structure **1**.<sup>1</sup> Although there was ready base-catalyzed exchange of the proton at C-5 of the oxathiane ring, the cyano substituent remained in an axial orientation, an arrangement that recalled the anomeric effect: the preference for an electronegative substituent at the anomeric carbon of a pyranose carbohydrate to be axial.<sup>2,3</sup>



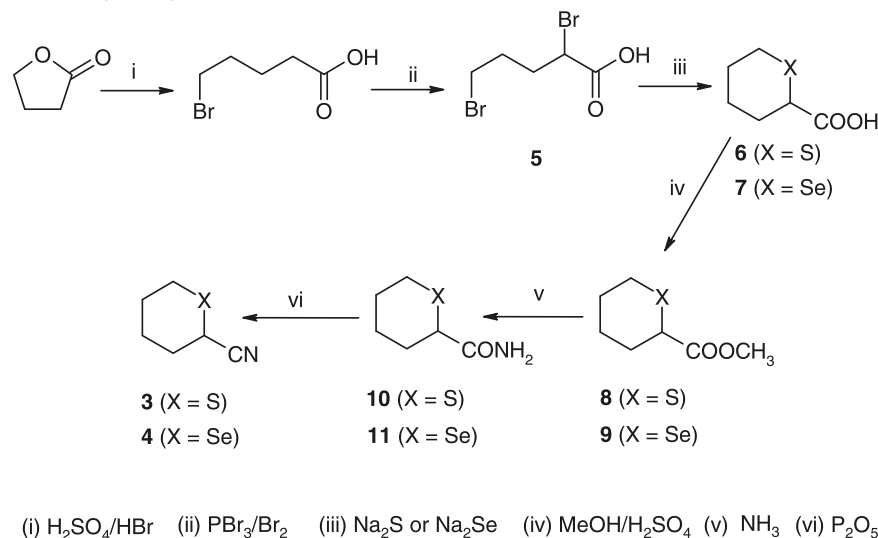
Received 1 December 2009. Accepted 10 February 2010. Published on the NRC Research Press Web site at canjchem.nrc.ca on 8 July 2010.

This article is part of a Special Issue dedicated to Professor R. J. Boyd, a good friend and colleague.

M.H. Benn,<sup>1</sup> Y.Y. Huang, F. Johanssen, M. O'Reilly, M. Parvez, A. Rauk,<sup>2</sup> and T. Sorensen. Department of Chemistry, University of Calgary, Calgary, AB, T2N 1N4, Canada.

<sup>1</sup>Corresponding author (e-mail: benn@ucalgary.ca).

<sup>2</sup>Corresponding author (e-mail: rauk@ucalgary.ca).

**Scheme 1.** Synthesis of the heterocyclic cyanides.

However, when the structure of merosinigrin was confirmed by X-ray spectroscopy,<sup>4,5</sup> the S–C(CN) bond length was found to be longer than the S–C(O) bond (1.823 vs. 1.815 Å),<sup>5</sup> i.e., the expected shortening of the S–C(CN) bond as a result of the  $n \rightarrow \sigma^*$  interaction, to which the classical anomeric effect is normally attributed,<sup>2</sup> was not observed.

While the anomeric effect is well-established for  $n_{\text{O}} \rightarrow \sigma_{\text{CX}}^*$ <sup>2,6–11</sup> and  $n_{\text{N}} \rightarrow \sigma_{\text{CX}}^*$ ,<sup>6</sup> where X is any electronegative group, including CN, its importance in the case for the donor being a second or higher row element, e.g.,  $n_{\text{S}} \rightarrow \sigma_{\text{CX}}^*$ , is less certain.<sup>10–12</sup> Cyclohexane derivatives possessing X substituents adjacent to S also preferentially adopt the C–X axial orientation.<sup>13,14</sup> A crystallographic structure determination of one such system, a 1,3 dithiane, did exhibit the expected shortening of the S–C bonds, and lengthening of the C<sub>2</sub>–X bond (X = diphenylthiophosphinoyl,  $-\text{P}(\text{S})(\text{C}_6\text{H}_5)_2$ ),<sup>15</sup> but a similar system did not (X = diphenylphosphinoyl,  $-\text{P}(\text{O})(\text{C}_6\text{H}_5)_2$ ).<sup>14</sup>

It is not our intention here to review the vast literature on anomeric effects and their various interpretations. Rather, we limit our investigation into the phenomena exhibited by **1**, namely, the clear reversal of the lengths of the S–C and C–C(N) bonds from that expected if an anomeric interaction were responsible for the axial preference of the CN group. To remove any effects due to the presence of the oxygen atoms and the ring fusion in **1**, we decided to examine the conformational preferences of 2-cyanooxane (2-cyanotetrahydropyran) (**2**), 2-cyanothiane (**3**), and 2-cyanoselenane (**4**) (see Scheme 1).

## Results and discussions

When we commenced this work, only (±)-2-cyanotetrahydropyran (**2**) had been described and we obtained it from dihydropyran according to a literature procedure.<sup>16</sup> The (±)-2-cyanothiane (**3**) and (±)-2-cyanoselenane (**4**) were prepared, as outlined in the Scheme 1, by the cyclization of (±)-2,5-dibromohexanoic acid (**5**)<sup>17,18</sup> with sodium sulfide<sup>17,18</sup> or selenide, followed by purification of the heterocyclic carboxylic acids (**6**, **7**) as their methyl esters (**8**, **9**),<sup>17,18</sup> and ammonoly-

sis of these afforded the corresponding amides (**10**, **11**), which were then dehydrated to yield the target nitriles (**3**, **4**).

In our initial investigations, examination of **2–4** by NMR (<sup>1</sup>H at 200 MHz) indicated that at room temperature, in CDCl<sub>3</sub> solution, all predominately had the cyano substituent in an axial orientation with the H-2 signals appearing as triplets with  $J \simeq 4$  Hz, i.e., as expected for a predominant conformer with a chair ring and an equatorial hydrogen at C-2 coupled to adjacent axial and equatorial hydrogens at C-3. In the case of 2-cyanooxane (**2**), dissolved in CFCl<sub>3</sub>/acetone-*d*<sub>6</sub> (1:1 v/v), a variable-temperature <sup>1</sup>H NMR study revealed that an equilibrium existed between the axial (**2-ax**) and the equatorial conformer (**2-eq**), in which the NMR signals of the two conformers were frozen out at 183 K, showing a ratio ( $K_{\text{eq/ax}}$ ) of about 0.37 as judged by the integrals for the H-2<sub>ax</sub> ( $\delta_{\text{H}}$  4.14 ppm) and H-2<sub>eq</sub> ( $\delta_{\text{H}}$  4.68 ppm). However, no such equilibrium could be detected for the 2-cyanothiane or 2-cyanoselenane, and we set the project aside.

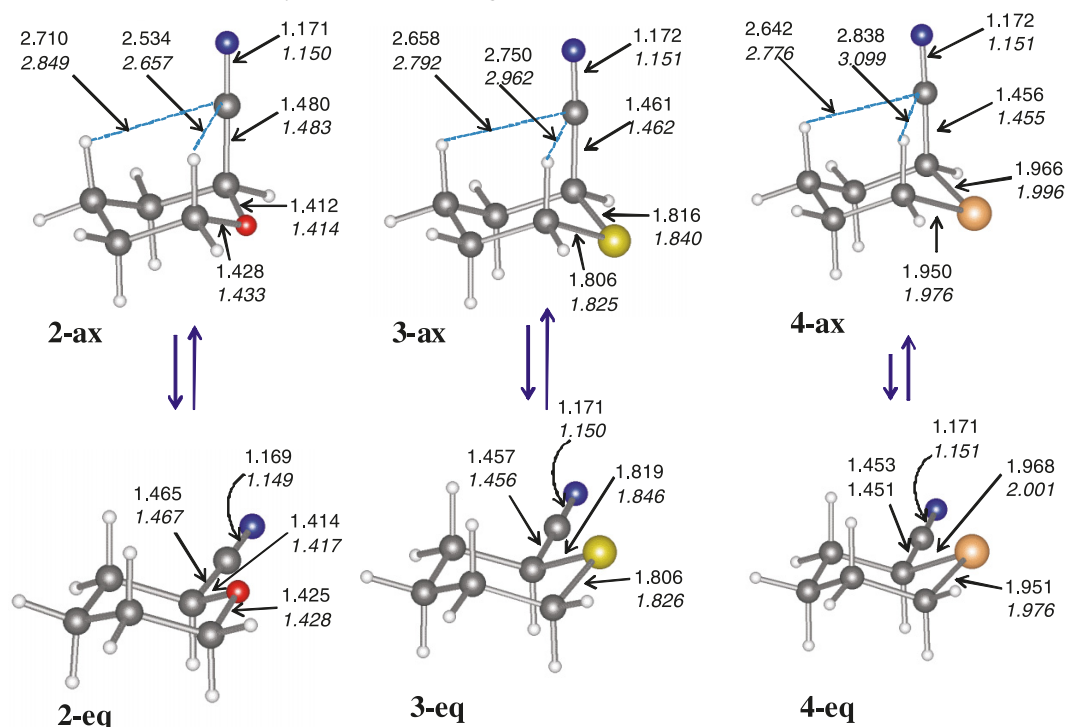
Recently, while decommissioning a laboratory, it was noticed that the samples of the (±)-2-cyanothiane (**3**) and (±)-2-cyanoselenane (**4**), which had been stored in sealed vials, had crystallized. X-ray crystallography revealed that in crystalline **3** and **4** the cyano group was indeed in the axial orientation (see Table 1). This observation, together with the advances in instrumental and computational methods induced us to return to the project, i.e., to re-examine the equilibria between the axial and equatorial conformers of the 2-cyano heterocycles in solution.

In the interim since our initial work, a variable-temperature NMR investigation of the conformational preference of (±)-2-cyanotetrahydropyran (**2**) in CDCl<sub>3</sub>/CFCl<sub>3</sub> (15:85, v/v) had been reported.<sup>6</sup> Based on the integration of <sup>13</sup>C resonances (155–180 K), and line broadenings of these at higher temperatures (190–220 K), it was deduced that the cyano substituent preferred an axial orientation, with an equilibrium constant  $K_{\text{eq/ax}}$  ranging from 0.20 at 155 K to 0.25 at 200 K. As our old observations were in accord with these results, we concentrated on re-examining the behaviour of the sulfur- and seleno-analogs (**3** and **4**, respectively), both of which had subsequently been described by other work-

**Table 1.** Selected bond lengths (Å) and angles (°) for **3** and **4** from X-ray crystallography.

3-ax		4-ax	
<b>Bond lengths</b>			
S—C(2)	1.8145(14)	Se—C(2)	1.953(4)
S—C(6)	1.8080(15)	Se—C(6)	1.937(5)
C(2)—C(3)	1.534(2)	C(2)—C(3)	1.536(6)
C(3)—C(4)	1.526(2)	C(3)—C(4)	1.522(7)
C(4)—C(5)	1.517(2)	C(4)—C(5)	1.530(7)
C(5)—C(6)	1.519(2)	C(5)—C(6)	1.515(7)
C(2)—C(7)	1.477(2)	C(2)—C(7)	1.465(6)
N—C(7)	1.138(2)	N—C(7)	1.137(6)
<b>Bond angles</b>			
C(2)—S—C(6)	98.93(7)	C(2)—Se—C(6)	95.7(2)
S—C(2)—S—C(3)	112.73(9)	C(3)—C(2)—Se	112.4(3)
C(2)—C(3)—C(4)	112.50(11)	C(4)—C(3)—C(2)	113.1(4)
C(3)—C(4)—C(5)	113.27(12)	C(3)—C(4)—C(5)	114.1(4)
C(4)—C(5)—C(6)	112.51(12)	C(4)—C(5)—C(6)	113.6(4)
C(5)—C(6)—S	112.93(10)	C(5)—C(6)—Se	113.1(3)
S—C(2)—C(7)	109.55(10)	Se—C(2)—C(7)	110.1(3)
N—C(7)—C(2)	178.81(16)	N—C(7)—C(2)	178.1(5)

**Note:** See Supplementary data section.

**Fig. 1.** MP2/6–311+G(3df,2p) and B3LYP/6–311+G(3df,2p) (in *italics*) structures of **2**, **3**, and **4**. Numbers indicate distances in Å. Spheres: C, gray; H, small white; N, blue; O, red; S, yellow; and Se, orange.

ers,<sup>19,20</sup> albeit without comment on their stereochemical preferences.

The 400 MHz <sup>1</sup>H NMR spectra of (±)-2-cyanothiane (**3**), dissolved in CD<sub>2</sub>Cl<sub>2</sub>/CFCI<sub>3</sub> (~ 1:1 v/v) containing TMS as an internal standard, were measured over the temperature range 298–163 K. This revealed line broadening of all the individual resonances but, unlike **2**, there was no clear indication at even the lowest temperatures of any signals due to

a conformer with an equatorial cyano group. However, over the same temperature range, the 100 MHz <sup>13</sup>C NMR spectra were more informative: after initial broadening of the resonances corresponding to C-4 and C-6 (a complete assignment of the <sup>13</sup>C NMR resonances had been performed via an INADEQUATE spectrum), already evident at 260 K, the signals began to sharpen at 210 K, and a second set of resonances attributable to the conformer with an equatorial cy-

**Table 2.** Computed data for **2**, **3**, and **4** at 173 K in solvent with  $\epsilon = 2.228$ .

Species	$E_{\text{MP2}}^{a,b}$	$E_{\text{CCSD(T)}}^{b,c}$	ZPE <sup>b,d</sup>	$H_0^{b,e}$	$H_{173}^b - H_0^b$	$H_{173}^b$	$S_{173}^{f,g}$	$G_{173(\text{g})}^{b,h}$	$\Delta G_{\text{soln}}^{g,i}$	$G_{173(\text{s})}^{b,j}$	$\Delta G_{173(\text{s})}^{g,k}$	$K_{\text{eq(ax)}}^l$
<b>2-ax</b>	-363.27792	-363.37081	0.14407	-363.22674	0.00339	-363.22335	268.7	-363.25385	-7.9	-363.25688	0.00	
<b>2-eq</b>	-363.28032	-363.37252	0.14437	-363.22815	0.00339	-363.22476	268.2	-363.25522	-6.7	-363.25779	2.37	<b>0.19</b>
<b>3-ax</b>	-685.88458	-685.98973	0.14078	-685.84896	0.00361	-685.84534	279.0	-685.87702	-8.2	-685.88016	0.00	
<b>3-eq</b>	-685.88766	-685.99206	0.14093	-685.85113	0.00359	-685.84754	278.0	-685.87911	-7.2	-685.88184	4.40	<b>0.047</b>
<b>4-ax</b>	-2688.12972	-2688.22640	0.13961	-2688.08679	0.00379	-2688.08300	290.6	-2688.11600	4.1	-2688.11444	0.00	
<b>4-eq</b>	-2688.13237	-2688.22834	0.13970	-2688.08864	0.00378	-2688.08486	290.0	-2688.11780	5.1	-2688.11584	3.67	<b>0.078</b>

<sup>a</sup>MP2/6-311+G(2df,2p)-optimized energy.

<sup>b</sup>In units of hartree.

<sup>c</sup>CCSD(T)/6-311G(2df,p)/MP2/6-311+G(2df,2p) energy.

<sup>d</sup>Zero-point energy at B3LYP/6-311+G(2df,2p).

<sup>e</sup>Enthalpy at 0 K (includes CCSD(T) energy and ZPE scaled by 0.9806).

<sup>f</sup>Entropy at 173 K and 1 mol/L at B3LYP/6-311+G(2df,2p).

<sup>g</sup>In units of kJ/mol.

<sup>h</sup>Gibbs free energy in gaseous phase.

<sup>i</sup>Free energy of solvation for solvent with  $\epsilon = 2.228$  (CCl<sub>4</sub>).

<sup>j</sup>Gibbs free energy in solution.

<sup>k</sup>Relative Gibbs free energy in solution.

<sup>l</sup>Equilibrium constant at 173 K.

ano group was discernable by 180 K. From the integration of the spectrum at 170 K, the equilibrium constant ( $K_{\text{eq(ax)}}$ ) at this temperature was estimated to be  $0.038 \pm 0.005$  ( $\Delta G = -4.6 \pm 0.2$  kJ/mol).

In the corresponding experiments with (±)-2-cyano-sele-nane (**4**), the <sup>13</sup>C resonances for C-4 and C-6 were also observed to undergo marked broadening, becoming noticeable at 230 K, and with resharping at 175 K; but unlike the experiences with **2** and **3**, no new resonances, which could be attributed to another conformer, appeared at low temperatures. However, it appeared that, as with **2** and **3**, the equilibrium strongly favoured the conformer with an axial cyano group.

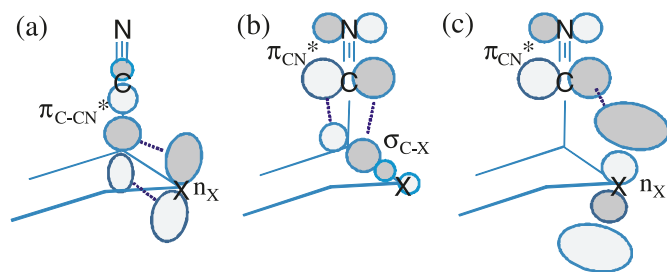
Why? The linear cyano group is a relatively sterically undemanding substituent, as reflected by the equilibrium of equatorial over axial conformers of cyanocyclohexane ( $\Delta G^0 = -0.8$  kJ/mol,  $K_{\text{eq(ax)}} \simeq 1.4$  at 298 K),<sup>21</sup> so even a small stabilization of the axial conformer by the adjacent-ring heteroatom would result in this becoming the favoured 0form. The crystallographic data for **3** and **4** reveal that the length of the bond between S or Se as the heteroatom and C2, is actually longer than that of the corresponding bond to C-6 (see Table 1), just as it was in **1**. As noted before, this is contrary to what would be expected if the stabilization of the axial cyano conformers were due to an  $n \rightarrow \sigma^*$  stereoelectronic interaction, since a direct effect of this interaction is to shorten the bond.

While equivalent crystallographic data for **2** are unavailable, several ring-substituted, carbohydrate-derived, derivatives (2,6-anhydroaldonitriles, “glycopyranosyl cyanides”) have been examined,<sup>22</sup> and these do show slight shortening of the ring oxygen–C2 bond as compared with the ring oxygen–C5 bond in accord with the conclusion that in these cases the polar cyano substituent contributed to a classical anomeric effect.

To probe the basis of the observed conformational preferences, we turned to computational investigations (see Experimental for details). The structures of axial and equatorial conformers of **2**, **3**, and **4** are shown in Fig. 1 with the computed key structural data at both MP2 and B3LYP level inserted. The B3LYP distances are systematically larger by a small amount than the MP2 values, except for the C–N separations. The same stereoelectronic effects are reflected in both sets of numbers. As the MP2 values for the C–S and C–Se distances are closer to the crystallographic values (Table 1), reference is made to the MP2 values in the discussion below. The energetic results are compiled in Table 2. Complete structural data are available in Supplementary data. At each level of theory, B3LYP, MP2, or CCSD(T), the axial conformer was more stable than the equatorial. The difference is smallest at the B3LYP level and largest at the MP2 level. The CCSD(T) values were taken as the most accurate and are used to determine the relative enthalpies at 0 K. Among the three systems, the axial preference was smallest for the oxa species (**2**), and largest for the thia species (**3**). Calculated entropies and thermochemical corrections to the enthalpies were used to derive free energies in the gaseous phase. Temperature at either 173 K or 298 K has little effect on the relative quantities (the data at 173 K are listed in Table 2). The absolute free energies of solution in CCl<sub>4</sub> were small ( $-7.5 \pm 0.8$  kJ/mol for **2** and **3**,



**Fig. 2.** Three orbital interactions responsible for geometric changes and axial preference in **2**, **3**, and **4**. X indicates O, S, or Se. (a)  $n_X \rightarrow \sigma_{C-CN}^*$  (the “anomeric” interaction); (b)  $\sigma_{C-X} \rightarrow \pi_{CN}^*$ ; and (c)  $n_X \rightarrow \pi_{CN}^*$ .



and  $+5.1 \pm 0.7$  kJ/mol for **4**), but systematically favoured the equatorial isomer by about 1 kJ/mol.

According to orbital interaction theory,<sup>23</sup> the electronic structures and geometric features of **2**, **3**, and **4** may be understood in terms of two principal orbital interactions that vary systematically in the series. These are an  $n \rightarrow \sigma^*$  interaction and a  $\sigma \rightarrow \pi^*$  interaction as illustrated in Figs. 2a and 2b. The former is usually held responsible for the anomeric effect in carbohydrate chemistry, i.e., the observed axial preference of hydroxyl or alkoxy groups at the anomeric centre. In the present context, the  $n \rightarrow \sigma^*$  interaction, or more specifically,  $n_X \rightarrow \sigma_{C-CN}^*$ , manifests itself as a preference for the axial conformer over the equatorial conformer in the usual chair–chair equilibrium of cyclohexane derivatives. The  $\sigma \rightarrow \pi^*$  interaction, or more specifically,  $\sigma_{C-X} \rightarrow \pi_{CN}^*$ , is related to a normal hyperconjugative interaction if one regards the C atom of the nitrile as having carbocation character. It is also akin to the normal stabilization of a carbanionic center by a nitrile group.

In orbital interaction theory,<sup>23</sup> the magnitude of an interaction between two orbitals is given by the perturbation theory expression (eq. [1]):

$$[1] \quad \Delta\epsilon_L \approx h_{AB}^2/(\epsilon_A - \epsilon_B)$$

where  $\Delta\epsilon_L$  is the amount of lowering of the lower energy orbital (a measure of stabilization),  $h_{AB}$  is the hamiltonian matrix element for the interaction between the higher orbital and the lower one, and  $\epsilon_A$  and  $\epsilon_B$  are their energies, respectively. The interaction energy  $h_{AB}$  is approximately proportional to the overlap between the two orbitals, and since  $\sigma$  bonds are involved, this means  $\pi$ -type overlap between the  $sp^3$  hybrid orbitals at the end(s) of the bonds closest to each other, as illustrated in Figs. 2a and 2b by the dashed lines.

In the “anomeric interaction”, the higher orbital is the empty  $\sigma_{C-CN}^*$  and the lower orbital is the occupied orbital  $n_X$ , and  $\epsilon_B$  is the bond energy, which will rise as the electronegativity of X decreases. An interaction between an empty orbital and an occupied one will always be stabilizing, bonding in character, and involve some charge transfer out of the occupied orbital. The nonbonding orbital  $n_X$  is a p-type orbital situated on X and oriented perpendicular to the C–X–C plane. In the chair conformation of cyclohexane derivatives, the axial bonds afford better overlap with the adjacent  $n_X$  than do the equatorial ones. To the extent that the “anomeric interaction” is dominant, the C–X bond involved in the conformer that has the nitrile group in the axial position will be

shortened relative to the other C–X bond or to the same C–X bond in the equatorial conformer, and the axial conformer will be favoured in the chair–chair equilibrium. From the point of view of orbital interaction theory, several consequences ensue as X changes from O to S to Se. The decreasing electronegativity of the chalcogens means that  $n_{Se}$  will be higher in energy than  $n_O$ , and  $n_S$  will be between. The decreasing energy difference in the denominator of eq. [1] implies an increasing stabilization across the series. Secondly, the  $n_X$  orbital changes from  $2p_O$  to  $3p_S$  to  $4p_{Se}$ . The increasing quantum number implies an increase in the size of the  $n$  orbital and a greater number of nodes. Both features, together with the systematic lengthening of the C–X bond imply a decrease in the overlap and consequently in the interaction matrix element  $h_{AB}$ . Because the stabilization  $\Delta\epsilon_L$  depends on the square of  $h_{AB}$ , the numerator of the rhs is expected to dominate and the overall stabilization will decrease across the series. In short, the anomeric effect should be smallest for X = Se and largest for X = O.

In the second interaction,  $\sigma \rightarrow \pi^*$ , the upper orbital is  $\pi_{CN}^*$  and the lower orbital is  $\sigma_{C-X}$ . The decreasing electronegativity of X across the series has two consequences: the energy of the bond orbital varies in the same way as the energy of  $n_X$ , namely, the lowest energy bond is C–O, the highest is C–Se, and C–S is between. This consequence implies that the  $\sigma_{C-X} \rightarrow \pi_{CN}^*$  interaction is strongest for X = Se and weakest for X = O. The geometric consequences are clear: since electron density is being removed from the C–X bond, it will be lengthened relative to the C–X bond that is not involved, and since  $\pi$ -bond character is developing in the C–CN bond, it will be shortened. However, it is not obvious from the inspection of models whether one conformer will be favoured over the other by this interaction, since the orientation of the C–X bond with respect to the CN group appears to be the same for the axial conformer as for the equatorial.

The two principal interactions have opposing effects on the C–X bond,  $n_X \rightarrow \sigma_{C-CN}^*$  tends to lengthen the bond while  $\sigma_{C-X} \rightarrow \pi_{CN}^*$  tends to shorten the bond; similarly with the C–CN bonds, the former interaction lengthens the C–CN bond while the latter shortens it. In such a case, one must resort to experiment or computation to ascertain which is dominant. From the geometric data in Fig. 1, it is evident that the lengths of the C–O bonds are consistent with dominance of the classical anomeric interaction in **2**, and that, while the effect is stronger in **2-ax** as expected, it is also operative in **2-eq**: in **2-ax**, the C–O bond to the nitrile-substituted carbon is shorter than the other C–O bond by 0.016 Å, and in **2-eq** where the anomeric interaction is weaker, the two C–O bonds differ by 0.011 Å and are intermediate in length. Similarly, the C–CN bond is longer by 0.015 Å in **2-ax** than in **2-eq**. Contrary to the case in **2**, in both the S and Se cases, **3** and **4**, respectively, the lengths of the C–X and C–CN bonds are consistent with dominance of the  $\sigma_{C-X} \rightarrow \pi_{CN}^*$  interaction. The relative lengths of the corresponding bonds to the heteroatom are reversed, and the C–CN bonds in both **3** and **4** are shorter than the C–CN bond in **2-ax** or **2-eq**.

Not resolved by the above considerations is the result that the energy difference between the axial and equatorial conformations of **3** and **4**, in which the anomeric interaction is

weaker, is *higher* than in **2**, which has a dominant anomeric interaction. It should be noted that an alternative explanation for the anomeric effect that does not depend on orbital interactions has been recently proposed.<sup>24</sup> It is supposed that an attractive interaction between the axial C–H bonds and the  $\pi_{\text{CN}}^*$  orbital is responsible for the preference for axial CN (and other unsaturated groups). This effect would be operative in all three systems, and probably does contribute to the net stabilization of the axial conformer of each system. However, it is unlikely that there will be much of a difference in the axial preference of one system over another, since the two C–H...CN distances vary in opposite directions (see Fig. 1). What then may be the reason for the greater axial preference of **3** and **4** over **2**? NBO analysis provides a quantitative version of occupied-virtual group orbital interactions and assigns a value in energy units for each. Unlike orbital interaction theory, in which the most significant interactions are isolated, NBO analysis encompasses all interactions. Often, “the baby is not seen in the bath water.” The  $n_{\text{X}} \rightarrow \sigma_{\text{C-CN}}^*$  stands out and decreases sharply in the series (in kJ/mol): **2-ax**, 35.0; **3-ax**, 20.4; and **4-ax**, 14.8. It is not significant in the equatorial conformers, (i.e., <2 kJ/mol). On the other hand, the  $\sigma_{\text{C-X}} \rightarrow \pi_{\text{CN}}^*$  interaction increases rapidly in the series and slightly favours the equatorial form (in kJ/mol): **2-ax**, 15.1; **2-eq**, 17.4; **3-ax**, 37.8. **3-eq**, 41.8; **4-ax**, 47.4; and **4-eq**, 51.0.<sup>24c</sup> However, perusal of the NBO analysis for all six systems reveals a third effect,  $n_{\text{X}} \rightarrow \pi_{\text{CN}}^*$ , illustrated in Fig. 2c, that is not significant in **2-eq**, **3-eq**, and **4-eq** (i.e., <2 kJ/mol) but is of modest strength in the axial conformers (in kJ/mol): **2-ax**, 6.6; **3-ax**, 8.0; and **4-ax**, 7.6. It must be this direct through-space interaction of the larger 3p and 4p orbitals with the empty  $\pi_{\text{CN}}^*$  orbital (3p is illustrated in Fig. 2c), and not an “anomeric effect”, that is responsible for the greater relative stability of the axial conformer in the case of **3** and **4**.

## Experimental

Unless otherwise specified, <sup>1</sup>H and <sup>13</sup>C NMR spectra were recorded on a Bruker Instruments DRX-400 spectrometer of solutions in CDCl<sub>3</sub>, with chemical shifts in ppm relative to solvent signals ( $\delta_{\text{H}}$  7.25,  $\delta_{\text{C}}$  77.0). Melting points were obtained using a Leitz hot-stage microscope and are uncorrected.

### (±)-2,6-Dibromohexanoic acid (**5**)

This acid was prepared according to a literature procedure<sup>17,18</sup> and obtained as an oil, bp 125–130 °C/0.05 mm Hg, which crystallized on storage, mp 45–47 °C. <sup>1</sup>H NMR  $\delta_{\text{H}}$  (ppm): 11.11 (1H, br s), 4.23 (1H, dd, *J* = 6.6 and 7.9 Hz) 3.37 (2H, t, *J* = 6.6 Hz), 2.05 (2H, m), 1.87 (2H, m), 1.85 (1H, m), 1.64 (1H, m). <sup>13</sup>C NMR  $\delta_{\text{C}}$  (ppm): 175.6 s, 44.8 d, 33.6 t, 32.0 t, 31.6 t, 25.7 t.

### (±)-Thiane-2-carboxylic acid (**6**)

This was prepared from (±)-2,6-dibromohexanoic acid (**5**) according to Roush et al.<sup>18</sup> and obtained as a colourless viscous oil. <sup>1</sup>H NMR  $\delta_{\text{H}}$  (ppm): 10.50 (1H, v br s), 3.53 (1H, dd, *J* = 7.6 and 3.8 Hz), 2.81 (1H, br m), 2.59 (1H, br m), 2.11 (1H, m), 2.01 (1H, m), 1.83 (3H, br m), 1.51 (1H, br

m). <sup>13</sup>C NMR  $\delta_{\text{C}}$  (ppm): 178.0 s, 42.7 d, 29.3 t, 27.8 t, 26.4 t, 23.6 t. LREIMS *m/z*: 146 (47), 101 (100).

### (±)-2-Carbomethoxythiane (**8**)

Esterification of the acid (**6**) was performed as described<sup>18</sup> to yield **8** as a colourless oil; bp 95–97 °C/15 mm Hg. <sup>1</sup>H NMR  $\delta_{\text{H}}$  (ppm): 3.60 (3H, s), 3.37 (1H, dd, *J* = 3.5 and 8.2 Hz), 2.62 (1H, m), 2.45 (1H, m), 1.96 (1H, m), 1.78 (3H, m), 1.63 (1H, m), 1.36 (1H, m). <sup>13</sup>C NMR  $\delta_{\text{C}}$  (ppm): 172.1 s, 51.9 q, 42.7 d, 29.4 t, 27.7 t, 26.2 t, 23.7 t. LREIMS *m/z*: 160 (39), 101 (100).

### (±)-Thiane-2-carboxamide (**10**)

Ammonia gas was bubbled into ice-cooled MeOH (20 mL) until about 4 g had dissolved. The ester (**8**) (5.13 g, 32 mmol) was added to this solution and the reaction mixture was allowed to warm to RT and stirred for 60 h, during which time fine white crystals separated. These were collected by filtration to afford **10** (1.96 g, 13.5 mmol), mp 163–164 °C. <sup>1</sup>H NMR  $\delta_{\text{H}}$  (ppm): 6.76 (1H, br s), 6.08 (1H, br s), 3.66 (1H, dd, *J* = 3.8 and 6.4 Hz), 2.70 (1H, m), 2.55 (1H, m), 2.25 (1H, m) 1.97 (1H, m), 1.80 (2H, m), 1.64 (1H, m) 1.57 (1H, m). <sup>13</sup>C NMR  $\delta_{\text{C}}$  (ppm): 173.7 s, 43.7 d, 28.9 t, 27.9 t, 26.5 t, 23.5 t. LREIMS *m/z*: 145 (50), 101 (100). More product (**10**) was obtained by evaporation of the mother liquors and recrystallization of the residue from MeOH (total yield 64%).

### (±)-Thiane-2-carbonitrile (**3**)

The amide (**10**) (1.7 g, 11.7 mmol) was intimately mixed with phosphorus pentoxide (1.7 g, 11.9 mmol) and subjected to dry-distillation according to a literature procedure,<sup>25</sup> but under reduced pressure, to afford the nitrile (**3**) as a colourless oil; bp 120–130 °C/25 mm Hg, which crystallized on storage at 0 °C, mp 29–30 °C (1.11 g, 8.7 mmol, 74%). FTIR  $\nu_{\text{max}}$  (cm<sup>−1</sup>): 2233. <sup>1</sup>H NMR  $\delta_{\text{H}}$  (ppm): 3.60 (1H, t, *J* = 4.1 Hz, H-2), 2.97 (1H, m, H-6A), 2.58 (1H, m, H-6B), 2.10 (1H, m, H-3A), 1.97 (2H, m, H-3B, and 5A) 1.76 (3H, m, H4 and 5B). <sup>13</sup>C NMR  $\delta_{\text{C}}$  (ppm): 119.0 s (C-7), 30.1 t (C-3), 28.0 d (C-2), 27.0 t (C-6), 26.2 t (C-5), 22.2 t (C-4). Both the <sup>1</sup>H and <sup>13</sup>C NMR data were similar to the literature.<sup>19,20</sup> In CD<sub>2</sub>Cl<sub>2</sub>/CFCl<sub>3</sub> (~ 1:1 v/v) with TMS as internal standard, at 173 K,  $\delta_{\text{C}}$  119.9, 29.5, 28.0, 26.7, 26.4, and 21.9, with a set of new minor signals due to the equatorial conformer at  $\delta_{\text{C}}$  119.5, 31.3, 28.9 25.8, and 25.0 with relative ratios 1: 0.038 ± 0.005. LREIMS *m/z*: 127.

### (±)-Selenane-2-carboxylic acid (**7**)

Mp 71–72 °C (lit.<sup>26</sup> mp 69–70 °C). <sup>1</sup>H NMR  $\delta_{\text{H}}$  (ppm): 11.40 (1H, brs), 3.66 (1H, dd, *J* = 3.7 and 9.0 Hz, H-2), 2.85 (1H, m), 2.73 (1H, m), 2.13 (1H, m), 2.07–1.77 (4H, m). 1.46 (1H, m). <sup>13</sup>C NMR  $\delta_{\text{C}}$  (ppm): 179.6 s, 32.9 d, 29.1 t, 26.8 t, 20.6 t, cf. <sup>1</sup>H and <sup>13</sup>C NMR data for **7** in D<sub>2</sub>O.<sup>26</sup>

### (±)-2-Carbomethoxyselenane (**9**)

Esterification of the acid (**7**), as for the thia-analogue, afforded **9** as a colourless oil. <sup>1</sup>H NMR  $\delta_{\text{H}}$  (ppm): 3.68 (3H, s), 3.64 (1H, dd, *J* = 3.4 and 8.7 Hz), 2.73 (2H, m), 2.11 (1H, m), 1.96 (3H, m), 1.83 (1H, m), 1.40 (1H, m). <sup>13</sup>C NMR  $\delta_{\text{C}}$  (ppm): 173.3 s, 52.1 q, 33.4 d, 29.6 t, 26.9 t, 20.6

t. Both the  $^1\text{H}$  and  $^{13}\text{C}$  NMR data were similar to the literature.<sup>19</sup>

#### (±)-Selenane-2-carboxamide (11)

Ammonolysis of the ester, as for the preparation of the thia-analogue, afforded (11) as colourless needles, mp 170.5–171.5 °C in 68% yield. FTIR  $\nu_{\text{max}}$  ( $\text{cm}^{-1}$ ): 1644.  $^1\text{H}$  NMR  $\delta_{\text{H}}$  (ppm): 6.38 (1H, br, NH), 5.78 (1H, br, NH), 3.58 (1H, dd,  $J = 3.6$  and  $7.8$  Hz, H-2), 2.75 (2H, m), 2.21 (1H, m), 2.11 (1H, m), 1.93 (2H, m), 1.78 (1H, m), 1.50 (1H, m).  $^{13}\text{C}$  NMR  $\delta_{\text{C}}$  (ppm): 174.3 s, 36.1 d, 29.9 t, 27.0 t, 25.1 t, 20.9 t. LREIMS  $m/z$ : 195 (9), 193 (60), 191 (32), 190 (7), 189 (9) ( $\text{M}^+$  with  $\text{Se}^{82}$ ,  $\text{Se}^{80}$ ,  $\text{Se}^{78}$ ,  $\text{Se}^{77}$ , and  $\text{Se}^{76}$ ), 149 (85), 147 (50), 112 (100).

#### (±)-Selenane-2-carbonitrile (5)

Dehydration of the amide (11) was performed as for the thia-analogue to afford the nitrile (5) as a colourless oil (67%), which crystallized on storage at 0 °C, mp 31–32 °C. FTIR  $\nu_{\text{max}}$  ( $\text{cm}^{-1}$ ): 2235.  $^1\text{H}$  NMR  $\delta_{\text{H}}$  (ppm): 3.45 (1H, t,  $J = 4.3$  Hz, H-2), 3.06 (1H, m, H-6A), 2.7 (1H, m, H-6B), 2.16 (1H, m, H-3A), 2.06 (2H, m, H-3B and H-5A), 1.78 (3H, br m, H-4 and 5B).  $^{13}\text{C}$  NMR  $\delta_{\text{C}}$  (ppm): 120.0 s (C-7), 30.1 t (C-3), 26.6 t (C-5), 23.2 t (C-4), 20.1 t (C-6). 14.9 d.(C-2). Both the  $^1\text{H}$  and  $^{13}\text{C}$  NMR data were similar to the literature.<sup>19</sup> LREIMS  $m/z$ : 177 (15), 175 (100), 173 (43), 172 (20), 171 (15) ( $\text{M}^+$  with  $\text{Se}^{82}$ ,  $\text{Se}^{80}$ ,  $\text{Se}^{78}$ ,  $\text{Se}^{77}$ , and  $\text{Se}^{76}$ ).

### Computational methods

Calculations have been performed using the Gaussian 03 suite of electronic structure codes.<sup>27</sup> All optimizations were performed in vacuo without using geometry or symmetry constraints using the B3LYP hybrid functional method<sup>28</sup> and second-order Møller–Plesset methodology (MP2) and the large 6–311+G(3df,2p) basis set. For all species, harmonic frequency analysis was performed at the B3LYP/6–311+G(3df,2p) level. The harmonic frequency data were used to obtain zero-point energies, entropies, and thermal corrections to enthalpies, for each structure. The zero-point energies were scaled by 0.9806.<sup>29</sup> Single-point energies were calculated by applying CCSD(T)/6–311+G(2df,2p) methodology to the optimized geometries at the MP2/6–311+G(3df,2p) level. These energies were used to provide more accurate relative enthalpies at 0 K. The IEF-PCM implicit solvation model<sup>30</sup> was used to estimate the effect of solution in the non-polar solvent used in the NMR experiments. A bulk dielectric constant of  $\epsilon = 2.228$  ( $\text{CCl}_4$ ) was assumed. Free-energy differences and axial/equatorial ratios were evaluated at two temperatures, 298 K and 173 K. The latter is approximately the lowest temperature reached in the NMR experiments. To assist in the analysis of electronic effects on the conformational equilibrium, natural bond order (NBO) analysis<sup>31</sup> was carried out on the B3LYP/6–311+G(3df,2p) wave function.

### Supplementary data

Supplementary data for this article are available on the journal Web site (canjchem.nrc.ca). CCDCs 755346 (3) and 755347 (4) contain the X-ray data in CIF format for this manuscript. These data can be obtained, free of charge, via

www.ccdc.cam.ac.uk/conts/retrieving.html (Or from the Cambridge Crystallographic Data Centre, 12 Union Road, Cambridge CB2 1EZ, UK; fax +44 1223 336033; or deposit@ccdc.cam.ac.uk).

### Acknowledgements

We thank Dr. Tom Nakashima, Chemistry Department, University of Alberta, for the INADEQUATE Spectra. The initial stages of this work were supported by an operating grant (to MHB) from the Natural Sciences and Research Council of Canada (NSERC). We also thank Westgrid for generous contributions of computer resources.

### References

- (1) Benn, M. H. *Can. J. Chem.* **1980**, *58* (17), 1892. doi:10.1139/v80-299.
- (2) Eliel, E. L.; Wilen, S. U. *Stereochemistry of Organic Compounds*; Wiley-Interscience: NY, 1994; p751; and references therein.
- (3) Graczyk, P. P.; Mikołajczyk, M. *Top. Stereochem.* **1994**, *21*, 159. doi:10.1002/9780470147306.ch2.
- (4) Nørskov-Lauritsen, L.; Jørgensen, F. S.; Jaroszewski, J. W. *Carbohydr. Res.* **1983**, *123* (1), 1. doi:10.1016/0008-6215(83)88375-X.
- (5) Richardson, J. F.; Benn, M. H. *Can. J. Chem.* **1984**, *62* (7), 1236. doi:10.1139/v84-205.
- (6) Booth, H.; Dixon, J. M.; Khedhair, K. A. *Tetrahedron* **1992**, *48*, 6161. doi:10.1016/S0040-4020(01)89862-8.
- (7) Freeman, F.; Gomarooni, F.; Hehre, W. J. *Struct. Chem.* **2002**, *13* (2), 115. doi:10.1023/A:1015700414427.
- (8) Wiberg, K. B.; Wilson, S. M.; Wang, Y.-G.; Vaccaro, P. H.; Cheeseman, J. R.; Luderer, M. R. *J. Org. Chem.* **2007**, *72* (16), 6206. doi:10.1021/jo070816j. PMID:17628107.
- (9) Wolfe, S.; Shi, Z. *Isr. J. Chem.* **2000**, *40* (3–4), 343. doi:10.1560/DY9J-0F0N-UUY5-7CLB.
- (10) Salzner, U.; Schleyer, P. v. R. *J. Am. Chem. Soc.* **1993**, *115* (22), 10231. doi:10.1021/ja00075a044.
- (11) Salzner, U.; Schleyer, P. v. R. *J. Org. Chem.* **1994**, *59* (8), 2138. doi:10.1021/jo00087a035.
- (12) Alabugin, I. V., IV. *J. Org. Chem.* **2000**, *65* (13), 3910. doi:10.1021/jo991622+. PMID:10866607.
- (13) Juaristi, E.; Ordonez, M. *Tetrahedron* **1994**, *50* (17), 4937. doi:10.1016/S0040-4020(01)90406-5.
- (14) Juaristi, E.; Valle, L.; Valenzuela, B. A.; Aguilar, M. A. *J. Am. Chem. Soc.* **1986**, *108* (8), 2000. doi:10.1021/ja00268a045.
- (15) Wieczorek, M. W.; Bujacz, G. D.; Majzner, W. R.; Graczyk, P. P.; Mikołajczyk, M. *Heteroatom Chem.* **1998**, *9*, 537. doi:10.1002/(SICI)1098-1071(1998)9:6<537::AID-HC2>3.0.CO;2-I.
- (16) Nelson, B. A.; Hodges, E. J.; Simon, J. I. *J. Org. Chem.* **1956**, *21* (7), 798. doi:10.1021/jo01113a602.
- (17) Kucsman, Á.; Kapovits, I.; Tanács, B.; Nemes, A. *Acta Chim. Acad. Sci. Hung.* **1962**, *34*, 87.
- (18) Roush, D. M.; Price, E. M.; Templeton, L. K.; Templeton, D. H.; Heathcock, C. H. *J. Am. Chem. Soc.* **1979**, *101* (11), 2971. doi:10.1021/ja00505a026.
- (19) Kataoka, T.; Iwama, T.; Tsutsumi, K.; Nakamura, Y.; Matsumoto, H.; Shimizu, H.; Hori, M. *J. Chem. Research (M)* **1992**, 3153.
- (20) Okazaki, Y.; Asai, T.; Ando, F.; Koketsu, J. *Chem. Lett.* **2006**, *35* (1), 98. doi:10.1246/cl.2006.98.
- (21) Eliel, E. L.; Wilen, S. U. *Stereochemistry of Organic Com-*



- pounds; Wiley-Interscience: NY, 1994; p. 697; and references therein.
- (22) (a) Kopf, J.; Köll, P. *Carbohydr. Res.* **1987**, *164*, 161. doi:10.1016/0008-6215(87)80128-3.; (b) see also Köll, P.; Förtsch, A. *Carbohydr. Res.* **1987**, *171* (1), 301. doi:10.1016/S0008-6215(00)90894-2.
- (23) Rauk, A. *Orbital Interaction Theory of Organic Chemistry*, 2<sup>nd</sup> ed. Wiley Interscience: NY, 2001.
- (24) (a) Takahashi, O.; Yamasaki, K.; Kohno, Y.; Ueda, K.; Suezawa, H.; Nishio, M. *Bull. Chem. Jpn* **2009**, *82* (2), 272. doi:10.1246/bcsj.82.272.; (b) Takahashi, O.; Yamasaki, K.; Kohno, Y.; Ueda, K.; Suezawa, H.; Nishio, M. *Carbohydr. Res.* **2009**, *344* (10), 1225. doi:10.1016/j.carres.2009.04.011. PMID:19467651.; (c) No significant interactions between axial C–H bonds and the cyano group are found in the NBO analysis.
- (25) Teague, P. C.; Short, W. A. In *Organic Syntheses*; Rabjohn, N., Ed.; J. Wiley and Sons: NY, 1963; collected Vol. 4; p. 706.
- (26) Iwaoka, M.; Kumakura, F. *Phosphorus, Sulfur Silicon Relat. Elem.* **2008**, *183* (4), 1009. doi:10.1080/10426500801901038.
- (27) Frisch, M. J.; Trucks, G. W.; Schlegel, H. B.; Scuseria, G. E.; Robb, M. A.; Cheeseman, J. R.; Montgomery, J. A., Jr.; Vreven, T.; Kudin, K. N.; Burant, J. C.; Millam, J. M.; Iyengar, S. S.; Tomasi, J.; Barone, V.; Mennucci, B.; Cossi, M.; Scalmani, G.; Rega, N.; Petersson, G. A.; Nakatsuji, H.; Hada, M.; Ehara, M.; Toyota, K.; Fukuda, R.; Hasegawa, J.; Ishida, M.; Nakajima, T.; Honda, Y.; Kitao, O.; Nakai, H.; Klene, M.; Li, X.; Knox, J. E.; Hratchian, H. P.; Cross, J. B.; Bakken, V.; Adamo, C.; Jaramillo, J.; Gomperts, R.; Stratmann, R. E.; Yazyev, O.; Austin, A. J.; Cammi, R.; Pomelli, C.; Ochterski, J. W.; Ayala, P. Y.; Morokuma, K.; Voth, G. A.; Salvador, P.; Dannenberg, J. J.; Zakrzewski, V. G.; Dapprich, S.; Daniels, A. D.; Strain, M. C.; Farkas, O.; Malick, D. K.; Rabuck, A. D.; Raghavachari, K.; Foresman, J. B.; Ortiz, J. V.; Cui, Q.; Baboul, A. G.; Clifford, S.; Cioslowski, J.; Stefanov, B. B.; Liu, G.; Liashenko, A.; Piskorz, P.; Komaromi, I.; Martin, R. L.; Fox, D. J.; Keith, T.; Al-Laham, M. A.; Peng, C. Y.; Nanayakkara, A.; Challacombe, M.; Gill, P. M. W.; Johnson, B.; Chen, W.; Wong, M. W.; Gonzalez, C.; Pople, J. A. *Gaussian 03*, Revision C. 02, Gaussian, Inc.: Wallingford, CT, 2004.
- (28) Becke, A. D. *J. Chem. Phys.* **1993**, *98* (7), 5648. doi:10.1063/1.464913.
- (29) Scott, A. P.; Radom, L. *J. Phys. Chem.* **1996**, *100* (41), 16502. doi:10.1021/jp960976r.
- (30) (a) Klamt, A.; Schüürmann, G. *J. Chem. Soc., Perkin Trans. 2* **1993**, 799. doi:10.1039/p29930000799.; (b) Andzelm, J.; Kolmel, C.; Klamt, A. *J. Chem. Phys.* **1995**, *103* (21), 9312. doi:10.1063/1.469990.
- (31) (a) Foster, J. P.; Weinhold, F. *J. Am. Chem. Soc.* **1980**, *102* (24), 7211. doi:10.1021/ja00544a007.; (b) Reed, A. E.; Curtiss, L. A.; Weinhold, F. *Chem. Rev.* **1988**, *88* (6), 899. doi:10.1021/cr00088a005.



# Nonequilibrium solvent effects in reaction kinetics — Steady-state solutions for the Agmon–Hopfield two-dimensional stochastic model

Paul Dance, Essex Edwards, Tsutomu Asano, Michael V. Basilevsky, and Noham Weinberg

**Abstract:** We propose an approximate localized-sink approach to the solution of the Agmon–Hopfield two-dimensional stochastic model for reactions in viscous media. The approach yields simple expressions for the sink location and the reaction rate constant, easy to use in the analysis of experimental data, and allows an intuitive phenomenological interpretation of the overall process in terms of a two-step kinetic scheme.

**Key words:** nonequilibrium solvation, dynamic effect of solvent, reactions in viscous media, Kramers theory, Agmon–Hopfield model, localized sink.

**Résumé :** On propose une approximation à l'approche du piège localisé comme solution au modèle stochastique bidimensionnel d'Agmon–Hopfield pour les réactions en milieux visqueux. Cette approche conduit à des expressions simples pour la localisation du piège et elle permet de faire une interprétation phénoménologique intuitive du processus global en termes d'un schéma cinétique en deux temps.

**Mots-clés :** solvation non équilibrée, effet dynamique du solvant, réactions dans des milieux visqueux, théorie de Kramers, modèle d'Agmon–Hopfield, piège localisé.

[Traduit par la Rédaction]

## Introduction

Nonequilibrium solvent effects can be expected and are observed<sup>1</sup> when characteristic times of chemical reactions are shorter than those of the solvent reorganization, as is the case for viscous solvents or fast reactions, where a solvent is too slow to properly adjust to the evolution of the reaction system. Although molecular dynamics and Monte Carlo simulations have increasingly become the tool of choice in studying dynamic effects of solvent on reactions and relaxation processes in solute,<sup>2</sup> in the foreseeable future, they will likely remain limited to relatively simple and fast solute systems. Much less computer-demanding stochastic models<sup>3</sup> will therefore continue to serve as a valuable instrument in describing reaction kinetics in more complex cases.

Most stochastic models follow the premise of the pioneering approach by Kramers,<sup>4</sup> further improved by Grote and Hynes<sup>5</sup> and Weidenmuller and Zhang,<sup>6</sup> in treating solvent–solute system as a fully synchronized quasi-one-dimensional dynamic object bound to undergo reaction transformations only by passing the transition-state region along a viscous reaction

coordinate. An alternative model formulated by Agmon and Hopfield<sup>7</sup> treats it as a quasi-two-dimensional desynchronized system with independent reaction and solvent coordinates. It has been shown by Berezhkovskii and Zitserman (BZ)<sup>8</sup> that both of these cases obtain from the multi-dimensional Kramers problem and correspond to different topography of the potential energy surface (PES). Our recent calculations of such PESs in solvent–solute coordinates<sup>9</sup> confirmed that, depending on the strength of the solvent–solute interactions, their topography can be either of the Kramers–Grote–Hynes (KGH) type with reactant and product valleys arranged sequentially and thus imposing strong correlation between the reaction and solvent coordinates (Fig. 1a) or of the Agmon–Hopfield (AH) type with the parallel arrangement of these valleys allowing barrier crossing by reaction system at various configurations of solvent (Fig. 1b).

In this paper, we limit ourselves to discussing solutions of the AH model, in which the overall reaction is described by an ensemble of partial reactions taking place along the solute reaction coordinate  $x$  at various solvent configurations  $y$ .

Received 9 February 2010. Accepted 24 February 2010. Published on the NRC Research Press Web site at canjchem.nrc.ca on 14 July 2010.

*This article is part of a Special Issue dedicated to Professor R. J. Boyd.*

**P. Dance and E. Edwards.** Department of Chemistry, University of the Fraser Valley, Abbotsford, BC V2S 7M8, Canada.

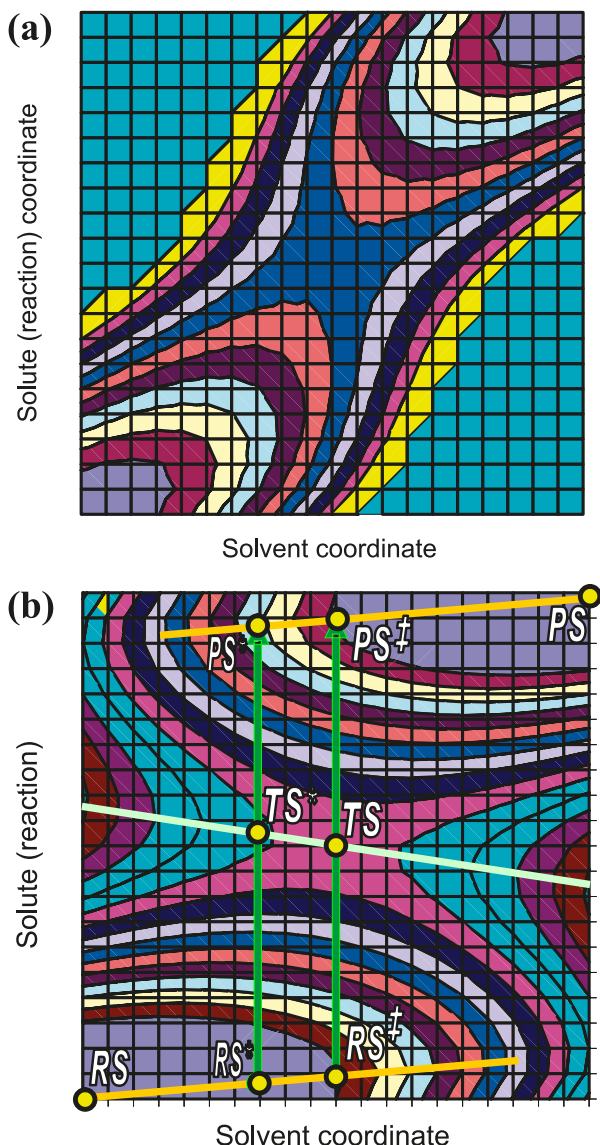
**T. Asano.** Department of Chemistry, Oita University, Oita 870-11, Japan.

**M.V. Basilevsky.** Photochemistry Center, Russian Academy of Sciences, Moscow 117421, Russia.

**N. Weinberg.**<sup>1</sup> Department of Chemistry, University of the Fraser Valley, Abbotsford, BC V2S 7M8, Canada; Department of Chemistry, Simon Fraser University, Burnaby, BC V5H 2M3, Canada.

<sup>1</sup>Corresponding author (e-mail: noham.weinberg@ufv.ca).

**Fig. 1.** Two-dimensional potential energy surface (PES) in solvent–solute coordinates: (a) KGH type for strong solvent–solute interaction; and (b) AH type for weak solvent–solute interaction. The reactant and product valleys are located in the lower left and upper right corners of the PES, respectively. **TS** is the true saddle point of the PES; **RS** and **PS** are reactant and product minima. **RS–RS\*–RS<sup>‡</sup>** is the bottom of the reactant valley; **TS\*–TS** is the ridge separating the reactant and product valleys.



In the case of a single-exponential decay, the overall rate constant  $k$  can then be found as an ensemble average

$$[1] \quad k = \int \gamma(y) P(y) dy$$

of the rate constants  $\gamma(y)$  of partial reactions, which in the simplest case are described by Arrhenius-type equation

$$[2] \quad \gamma(y) = \nu \exp(-\beta E(y))$$

with constant frequency factor  $\nu$  and solvent-configuration-dependent activation energy  $E(y)$ . The “slow” solvent is described by the normalized probability distribution  $P(y)$  that satisfies the diffusion equation

$$[3] \quad D \frac{\partial^2 P}{\partial y^2} + \beta D \frac{dV}{dy} \frac{\partial P}{\partial y} + \left( \beta D \frac{d^2 V}{dy^2} - \gamma + k \right) P = 0$$

with diffusion constant  $D$  in potential  $V(y)$  that represents a one-dimensional energy profile of the PES along the bottom of the reactant valley (Fig. 1b, line **RS–RS\*–RS<sup>‡</sup>**). Activation energy  $E(y)$  is the difference between  $V(y)$  and the one-dimensional energy profile  $U(y)$  along the ridge separating the reactant and product valleys (Fig. 1b, line **TS\*–TS**):  $E(y) = U(y) - V(y)$ .

If the reaction is relatively slow, terms  $\gamma$  and  $k$  in eq. [3] can be neglected, and the equation can be solved to give equilibrium distribution function  $P_e(y) = f_e(y)/\|f_e\|$ , ( $f_e(y) = \exp(-\beta V(y))$ ;  $\|f_e\| = \int f_e(y) dy$ ), which, substituted in eq. [1], gives transition-state-theory (TST) rate constant

$$k_e = \frac{\nu \int \exp[-\beta U(y)] dy}{\int \exp[-\beta V(y)] dy}$$

which in harmonic approximation

$$[4] \quad \begin{cases} \beta V(y) = \varepsilon y^2 \\ \beta U(y) = u_0 + \rho \varepsilon (1 - y)^2 \end{cases}$$

simplifies to

$$[5] \quad k_e = \nu \rho^{-1/2} \exp(-u_0) = \rho^{-1/2} \gamma(1) \exp(-\varepsilon)$$

The solvent coordinate  $y$  is scaled such that  $y = 0$  for the reactant minimum **RS** and  $y = 1$  for the transition state **TS**. Parameter  $\varepsilon = \beta V(1)$  is the solvent reorganization energy in the reactant state; and  $\rho$  is the ratio of the force constants of the ridge profile  $U(y)$  and the reactant valley profile  $V(y)$ :  $\rho = U'(1)/V'(0)$ .

Numerical solutions of eq. [3]<sup>10–12</sup> show a significant variation (several orders of magnitude) for the ratio  $k/k_e$  of the overall rate constant  $k$  to its equilibrium value  $k_e$  with parameters of the model  $\varepsilon$ ,  $\rho$ , and  $k_e/\omega$ . The latter characterizes the anisotropy of characteristic times of reaction and solvent and is measured by the ratio of reaction “frequency”  $k_e$  in the absence of dynamic effects of solvent to the characteristic frequency of solvent  $\omega = 2\varepsilon D$ .

BZ<sup>8</sup> were first to point out that  $\gamma(y)$  is negligible at small  $0 < y < \bar{y}$  but dominates eq. [3] at  $y$  exceeding the threshold  $\bar{y}$  determined as the largest of the three roots of the equation

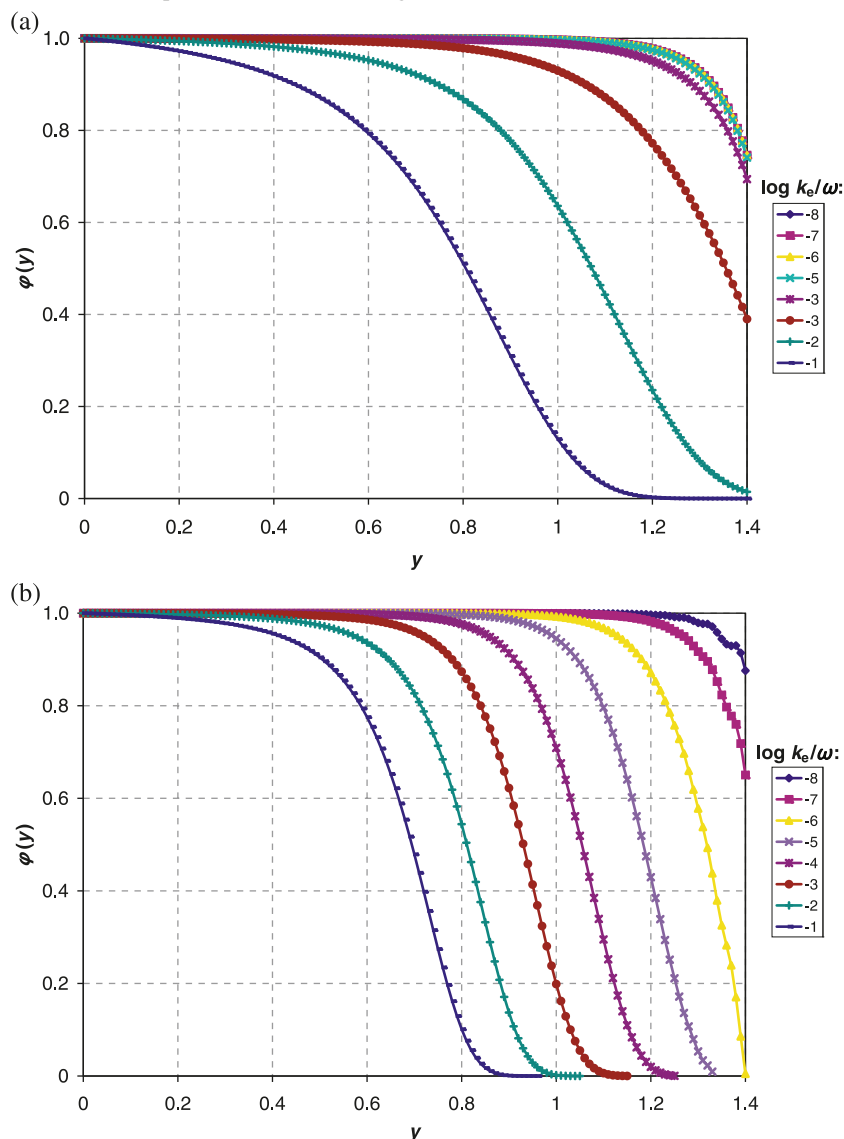
$$\frac{\beta D}{2} \left[ \left( \frac{dV}{dy} \right)^2 - \frac{d^2 V}{dy^2} \right] = \gamma(y)$$

Nonequilibrium solvent effects arise when  $\bar{y} < 1$ , and in the high viscosity limit, the overall rate constant is practically determined by the mean first passage time (MFPT) to point **RS\*** with  $y = \bar{y}$ <sup>8</sup>

$$[6] \quad k \approx k_{\text{MFPT}} = \beta D \left( \frac{d^2 V}{dy^2} \right)_{y=0} \sqrt{\frac{\beta V(\bar{y})}{\pi}} \exp(-\beta V(\bar{y}))$$

thus effectively localizing exponential sink  $\gamma(y)$  to a  $\delta$ -function centered at  $y = \bar{y}$ . BZ and co-workers also used perturbation theory to obtain interpolating solutions for the case

**Fig. 2.** Exact numerical solutions  $\varphi(y)$  of eq. [7] for  $\rho = 1.5$  and  $\log k_e/\omega$  from  $-8$  to  $-1$ : (a)  $\varepsilon = 5$ ; (b)  $\varepsilon = 10$ .



of intermediate viscosities.<sup>12</sup> A solution of eq. [3] similar to eq. [6] has also been reported by Sebastian<sup>13</sup> for a parabolic potential  $V(y)$  and a  $\delta$ -function sink, although no recipe was given for the determination of the sink location  $\bar{y}$ .

The purpose of this work is to obtain a simple approximate solution of eq. [3] suitable for the quantitative interpretation of high pressure kinetics of thermal isomerization reactions in viscous media<sup>14</sup>. For this, we use the idea of a sliding localized sink, although in a somewhat different context than BZ, and give it a simple intuitive interpretation in terms of a two-step kinetic scheme. We then compare the values of the rate constants and sink locations obtained from the approximate and exact numerical solutions.

### Exact numerical solutions

The degree of deviation of a nonequilibrium distribution function  $f(y)$  from the equilibrium distribution function  $f_e(y)$  can be conveniently described by their ratio  $\varphi(y) = f(y)/f_e(y)$ . In accordance with eq. [3],  $\varphi(y)$  must obey equation

$$[7] \quad D \frac{\partial^2 \varphi}{\partial y^2} - \beta D \frac{dV}{dy} \frac{\partial \varphi}{\partial y} + (k - \gamma) \varphi = 0$$

or, in harmonic approximation (eq. [4]), equation

$$[8] \quad \frac{\partial^2 \varphi}{\partial y^2} - 2\varepsilon y \frac{\partial \varphi}{\partial y} + 2\varepsilon \frac{k_e}{\omega} \left( \frac{k}{k_e} - \frac{\gamma}{k_e} \right) \varphi = 0$$

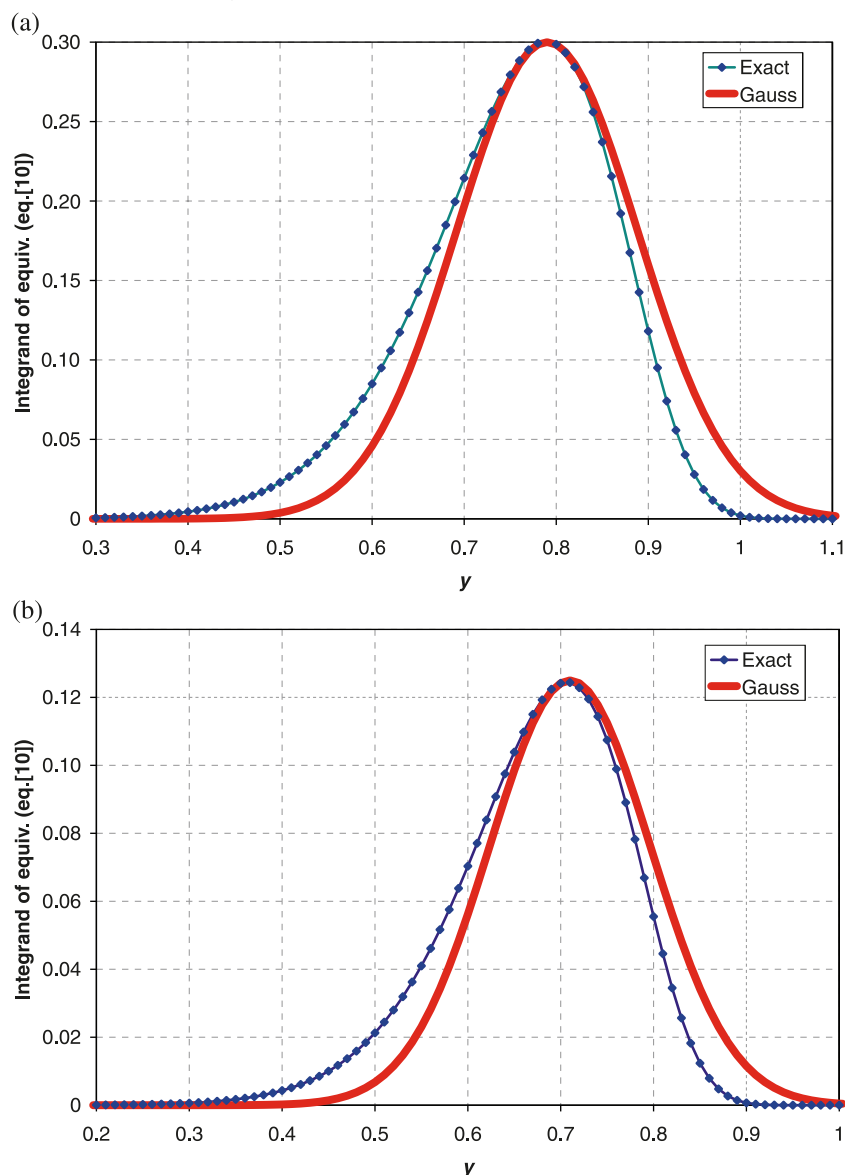
According to eqs. [2] and [5],

$$[9] \quad \frac{\gamma(y)}{k_e} = \sqrt{\rho} \exp[-\rho \varepsilon (y - 1)^2 + \varepsilon y^2]$$

i.e., for  $\rho > 1$ ,  $\gamma(y)/k_e$  is a Gaussian function that reaches its maximum value of  $\sqrt{\rho} \exp[\varepsilon \rho / (\rho - 1)]$  at  $y = \rho / (\rho - 1)$ . For  $\rho = 1$ , it degenerates into a simple exponent  $\gamma(y)/k_e = \exp[\varepsilon(2y - 1)]$ .

Typical examples of exact numerical solutions of eq. [8] obtained by its direct integration<sup>15</sup> for a range of parameters  $\rho$ ,  $\varepsilon$ , and  $\log k_e/\omega$  are shown in Fig. 2. As expected, for relatively slow reactions ( $\log k_e/\omega < -5$ ), the values of  $\varphi(y)$  are

**Fig. 3.** Integrand of eq. [10] and its Gaussian approximation for  $\rho = 1.5$  and  $\varepsilon = 10$ : (a)  $\log k_e/\omega = -2$ ; (b)  $\log k_e/\omega = -1$  (note the difference in the scales for the vertical axes in the two cases).



close to unity up to  $y = 1$  (TS), and thus  $k \approx k_e$ . As reaction becomes faster or solvent slower,  $\varphi(y)$  departs from its equilibrium value of 1 quite significantly. However, even in the most nonequilibrium cases,  $\varphi(y)$  is reasonably close to 1 for  $y < 0.6$ , i.e., the equilibrium is not perturbed at the bottom of the reactant well, where the bulk reactant resides, since both  $f(y)$  and  $f_e(y)$  exponentially decay with  $y$ . It can therefore be expected that the norms  $\|f\|$  and  $\|f_e\|$  are approximately equal and  $\varphi(y) \approx P(y)/P_e(y)$ . Accordingly,

$$[10] \quad \frac{k}{k_e} = \int F(y) dy$$

$$F(y) = \frac{\gamma(y)}{k_e} P_e(y) \varphi(y)$$

### Approximate solution: localized sink model

As a product of an exponentially increasing function  $\gamma(y)/k_e$

and an exponentially decreasing function  $P(y)$ , the integrand  $F(y)$  of eq. [10] is bell-shaped, although somewhat skewed from a perfect Gaussian curve (Fig. 3).

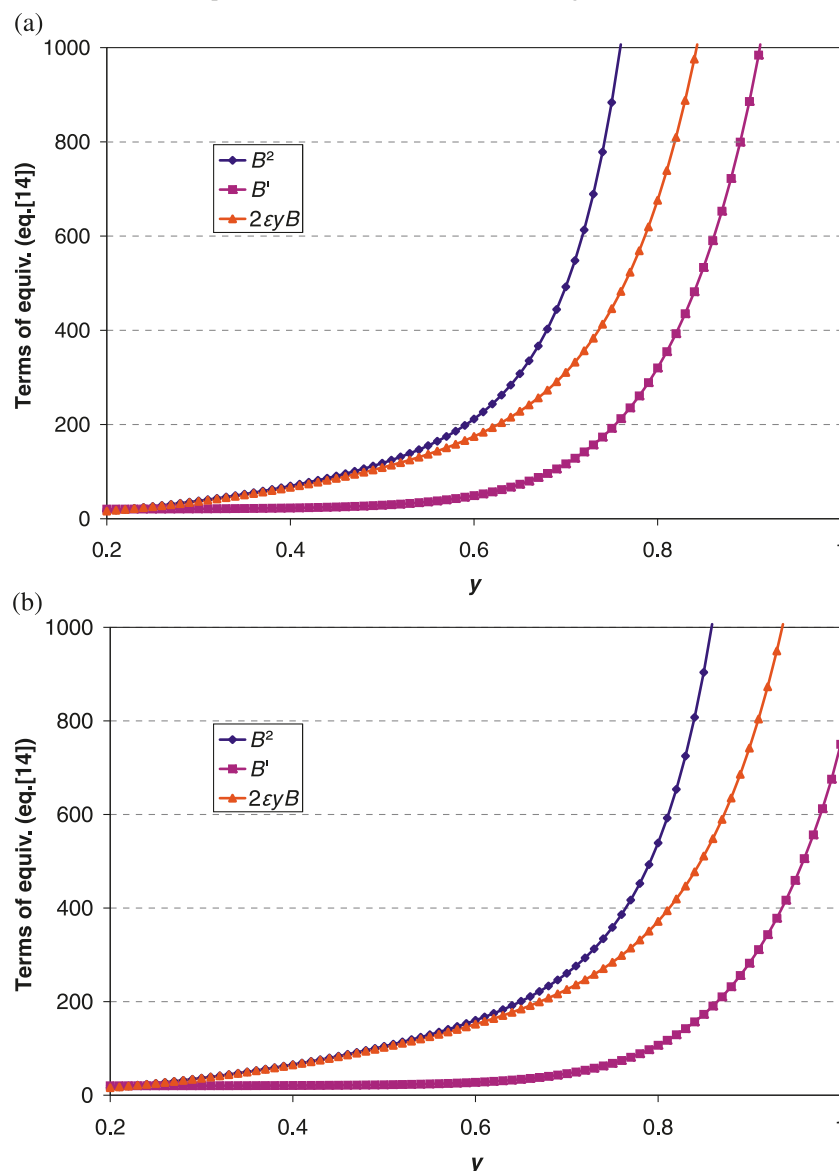
The dominant contribution to the integral of eq. [10] comes therefore from the close vicinity of the maximum of its integrand  $F(y)$ , point  $y^*$ , and thus the sink of eq. [8] is effectively localized at  $y^*$ . As solvent viscosity increases,  $y^*$  slides towards the bottom of the reactant well. Since only a close vicinity of point  $y^*$  gives notable contribution to the integral of eq. [10], the value of  $k/k_e$  can be approximated by Gaussian integral:<sup>16</sup>

$$\frac{k}{k_e} \approx \int F(y) dy \approx \int F(y^*) \exp\left(-\frac{A(y - y^*)^2}{2}\right) dy$$

$$= \sqrt{\frac{2\pi}{A}} F(y^*)$$



**Fig. 4.** Comparison of the first three terms of eq. [14] for  $\rho = 1.5$  and  $\varepsilon = 10$ : (a)  $\log k_e/\omega = -2$  ( $y^* = 0.79$ ); (b)  $\log k_e/\omega = -1$  ( $y^* = 0.71$ ).



In harmonic approximation

$$F(y) = \sqrt{\frac{\rho\varepsilon}{\pi}} \exp[-\rho\varepsilon(y-1)^2] \varphi(y)$$

and

$$A = -\left(\frac{d^2 \ln F}{dy^2}\right)_{y=y^*} = 2\rho\varepsilon + B'(y^*)$$

where

$$[11] \quad B(y) = -\left(\frac{d \ln \varphi}{dy}\right); \quad B'(y) = -\left(\frac{dB}{dy}\right)$$

thus giving

$$[12] \quad \frac{k}{k_e} \approx \sqrt{\frac{1}{1 + (B'(y^*)/2\rho\varepsilon)}} \varphi(y^*) \exp[-\rho\varepsilon(y^*-1)^2]$$

### Solution in quadratures

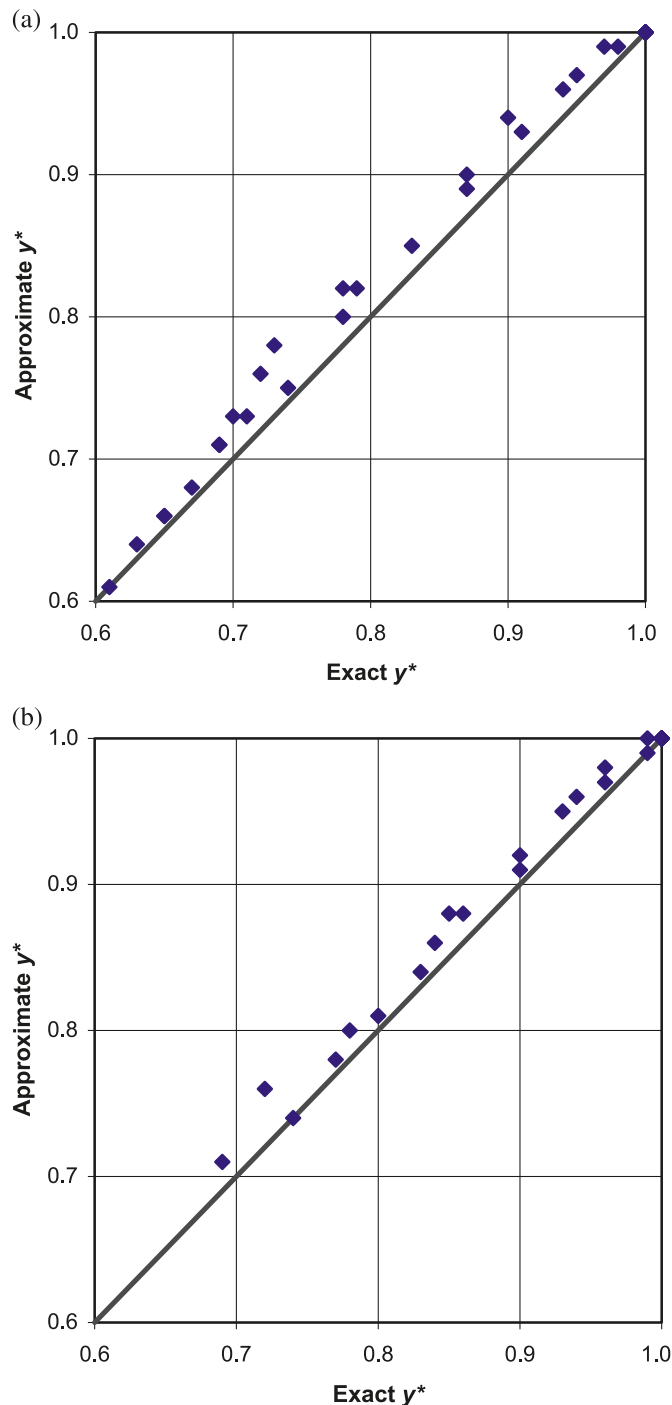
To apply eq. [12] one needs to know the sink location  $y^*$  as well as the value of function  $\varphi$  and its second logarithmic derivative  $B'$  at this point. The value of  $y^*$  can be determined from the stationary-point condition

$$[13] \quad 0 = -\left(\frac{d \ln F}{dy}\right)_{y=y^*} = 2\rho\varepsilon(y^*-1) + B(y^*)$$

if  $B(y)$  is known.

According to eq. [11],  $\varphi' = -B\varphi$  and  $\varphi'' = (B^2 - B')\varphi$ , which, substituted into eq. [8], gives

**Fig. 5.** Comparison between the exact and approximate values of  $y^*$  (eq. [16]) for  $\varepsilon$  from 5 to 40 and  $\log k_e/\omega$  from  $-8$  to  $-1$ : (a)  $\rho = 1.5$ ; (b)  $\rho = 4.0$ . The diagonal solid lines represent the ideal case of a perfect fit.



$$[14] \quad B^2 - B' + 2\varepsilon yB + 2\varepsilon \frac{k_e}{\omega} \left( \frac{k}{k_e} - \frac{\gamma}{k_e} \right) = 0$$

In the vicinity of  $y^*$ ,  $k \ll \gamma$  and thus can be neglected. In addition, as can be seen from Fig. 4 where the first three terms of eq. [14] are compared,  $B'$  can also be neglected compared to  $B^2$  and  $2\varepsilon yB$ , thus transforming differential eq. [14] into quadratic equation

$$[15] \quad B^2 + 2\varepsilon yB - 2\varepsilon \frac{k_e}{\omega} \frac{\gamma}{k_e} = 0$$

Combined with condition of eq. [13], it converts into the following transcendental equation for  $y^*$ :

$$[16] \quad 2\rho^2 \varepsilon (y^* - 1)^2 - 2\rho \varepsilon y^* (y^* - 1) - \frac{k_e}{\omega} \frac{\gamma(y^*)}{k_e} = 0$$

The values of  $y^*$  obtained from eq. [16] for various combinations of parameters  $\rho$ ,  $\varepsilon$ , and  $k_e/\omega$  are compared to the exact numerical solutions in Fig. 5. For  $\rho = 1.5$ , the deviations of the approximate  $y^*$  from the exact values do not exceed 7% and average to 2%. The results are somewhat better for  $\rho = 4.0$ , giving the maximum and average deviations of 6% and 1%, respectively.

Equation [15] can be resolved for  $B(y)$  to give

$$[17] \quad B(y) = -\varepsilon y + \sqrt{\varepsilon^2 y^2 + 2\varepsilon \sqrt{\rho} \frac{k_e}{\omega} \exp(-\rho \varepsilon (y - 1)^2 + \varepsilon y^2)}$$

from which  $\varphi(y^*)$  can be found by integration

$$[18] \quad \ln \varphi(y^*) = \int_0^{y^*} B(y) dy$$

It can then be substituted in eq. [12] to obtain  $k/k_e$ . This, however, leaves the answer in quadratures. To avoid that, we will try to find a simpler expression for  $\varphi(y)$  based on the analysis of its properties.

### Stepwise approximation for $\varphi(y)$

Function  $\varphi(y)$  quickly changes from 1 to 0 near point  $y^*$  because of the exponential rise of the sink  $\gamma(y)$ . It can therefore be presented as

$$[19] \quad \varphi(y) = \frac{\xi(y)}{\xi(y) + \gamma(y)}$$

where  $\xi(y) \gg \gamma(y)$  for  $y < y^*$  and  $\xi(y) \ll \gamma(y)$  for  $y > y^*$ . Accordingly, its logarithmic derivative (eq. [11]) takes the form of

$$B(y) = \frac{\xi'(y) + \gamma'(y)}{\xi(y) + \gamma(y)} - \frac{\xi'(y)}{\xi(y)}$$

The values of  $\xi(y^*)$  obtained from the exact numerical  $\varphi(y)$  by reversal of eq. [19] are close to  $\rho^{1/2}\omega$  (Fig. 6a). It also appears that functions  $\xi(y)$  are stationary in the vicinity of  $y^*$ :  $\xi'(y^*) \approx 0$  (Fig. 6b). The values of  $\varphi(y^*)$  and  $B(y^*)$  can therefore be approximated as

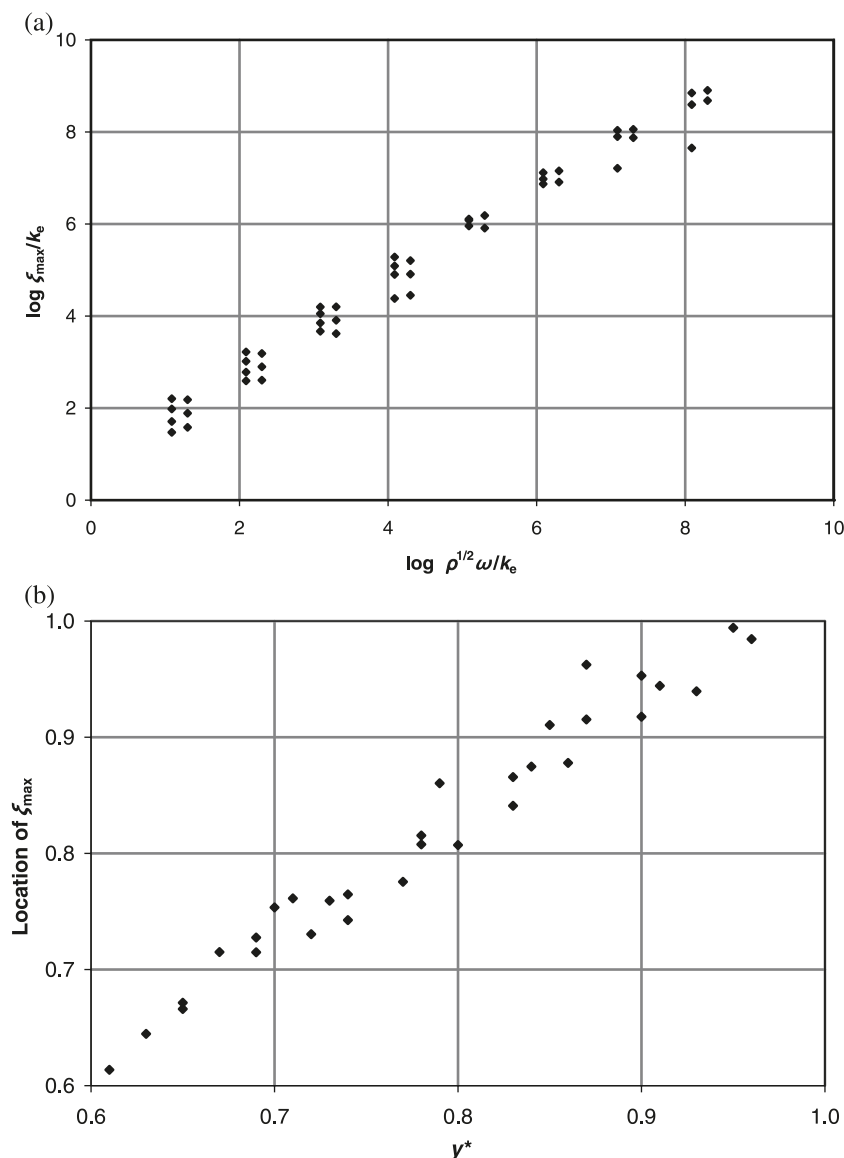
$$[20] \quad \varphi(y^*) \approx \frac{\rho^{1/2}\omega}{\rho^{1/2}\omega + \gamma(y^*)}$$

and

$$[21] \quad B(y^*) \approx \frac{\gamma'(y^*)}{\rho^{1/2}\omega + \gamma(y^*)}$$

Substituted in eqs. [12] and [13] on the assumption that

**Fig. 6.** Properties of functions  $\xi(y)$ : (a) correlation between their maximum values and the values of  $\rho^{1/2}\omega$ ; (b) correlation between locations of their stationary points and the values of  $y^*$ . The data points are for  $\varepsilon$  from 5 to 40,  $\log k_e/\omega$  from  $-8$  to  $-1$ , and  $\rho = 1.5$  and  $4.0$ .



$B'(y^*) \ll 2\rho\varepsilon$ , they give eq. [22] for the relative value of the rate constant

$$[22] \quad \frac{k}{k_e} \approx \frac{\rho^{1/2}\omega}{\rho^{1/2}\omega + \gamma(y^*)} \exp[-\rho\varepsilon(y^* - 1)^2]$$

and eq. [23] for the location of the sink  $y^*$  as the point of maximum of function  $\ln F(y)$

$$[23] \quad 2\rho\varepsilon(y^* - 1) + \frac{\gamma'(y^*)}{\rho^{1/2}\omega + \gamma(y^*)} = 0$$

Alternatively,  $y^*$  can be found as the point of minimum of the reciprocal function  $1/F(y)$ :

$$[24] \quad \frac{1}{F(y)} = \frac{k_e}{\gamma(y)P_e(y)} + \frac{k_e}{\rho^{1/2}\omega P_e(y)}$$

defined by the stationary condition  $(1/F(y))' = 0$ .

### The high viscosity limit

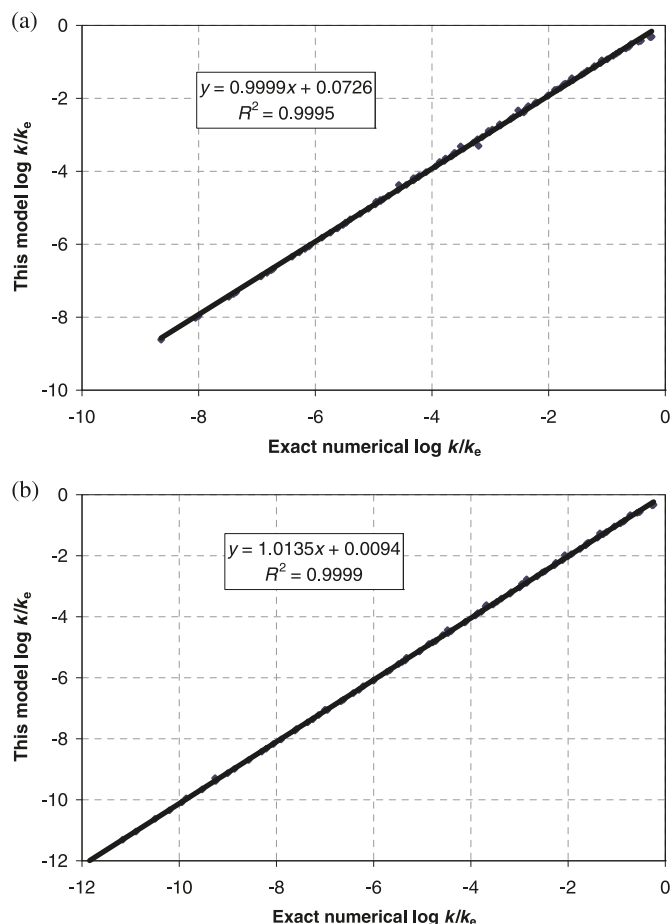
Equation [24] function represents the sum of two exponential terms, the first of which is a decreasing function of  $y$  and the second is an increasing function of  $y$  for  $0 \leq y \leq 1$ . In the high viscosity limit, these terms are comparable in the vicinity of  $y^*$ , and the exact condition  $(1/F(y))' = 0$  can be replaced by an approximate condition of the equality of the two exponential terms:

$$[25] \quad \frac{\rho^{1/2}k_e}{\gamma(y^*)} = \frac{k_e}{\omega}$$

which, by virtue of eq. [9], simplifies to the quadratic equation

$$[26] \quad \rho\varepsilon(y^* - 1)^2 - \varepsilon(y^*)^2 - \ln \frac{k_e}{\omega} = 0$$

**Fig. 7.** Comparison between the exact and approximate values of  $k/k_e$  (eq. [27]/eq. [26]) for  $\varepsilon$  from 5 to 40 and  $\log k_e/\omega$  from  $-8$  to  $-1$ : (a)  $\rho = 1.5$ ; (b)  $\rho = 4.0$ .



and, in accordance with eq. [18], it gives

$$[27] \quad \frac{k_e}{k} \cong 2 \frac{k_e}{\omega} \exp[\varepsilon(y^*)^2] = 2 \exp[\rho \varepsilon (y^* - 1)^2]$$

Approximate analytical solutions given by eq. [27]/eq. [26] are compared to the exact numerical solutions in Fig. 7 and demonstrate a good fit.

### The low viscosity limit

The validity of eqs. [25–27] is limited to nonequilibrium high viscosity cases, for which the right-hand side of eq. [24] contains comparable exponential terms. For sufficiently slow reactions in reasonably nonviscous solvents, parameter  $k_e/\omega$  is very small, and eq. [25] no longer accurately estimates the location  $y^*$  of the true minimum of function  $1/F(y)$ . The full equation  $(1/F(y))' = 0$  needs to be used instead.

When the second term of  $1/F(y)$  in eq. [24] is negligible compared with the first term owing to the smallness of  $k_e/\omega$ , eqs. [22] and [24] transform into eqs. [28] and [29], respectively:

$$[28] \quad \frac{k}{k_e} \cong \exp[-\rho \varepsilon (y^* - 1)^2]$$

$$[29] \quad \frac{1}{F(y)} \approx \frac{k_e}{\gamma(y)P_e(y)} = \rho^{-1/2} \exp[\rho \varepsilon (y - 1)^2]$$

Equation [29] function has a minimum at  $y^* = 1$ , under which condition eq. [28] gives  $k = k_e$ . Thus, eqs. [22] and [24] demonstrate proper asymptotic behavior at low viscosities.

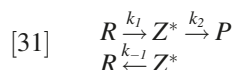
As solvent viscosity increases, so does the value of parameter  $k_e/\omega$ . As a borderline case between equilibrium (TST) and nonequilibrium kinetics, we can consider a situation where  $y^*$  is still close to 1 (as in the TST case), but the second term in eq. [24] becomes comparable to the first term, thus validating nonequilibrium eq. [27]. Combination of these conditions leads to eq. [30]

$$[30] \quad \ln \frac{k_e}{\omega} + \varepsilon \cong 0$$

that defines the boundary of the equilibrium kinetics. In accordance with eq. [27], this corresponds to the condition  $k/k_e = 0.5$ . The line of  $k/k_e = 0.5$ , obtained from the numerical solutions of eq. [3] for  $\rho$  ranging from 1.0 to 4.0, is shown in Fig. 8. It demonstrates a linear relationship between  $\varepsilon$  and  $\ln(k_e/\omega)$  with a slope close to  $-1$  independent of  $\rho$ , as predicted by eq. [30].

### Phenomenological interpretation

Despite its extreme simplicity, the solution of eqs. [26] and [27] approximates the exact numerical solutions of eq. [3] remarkably well. This makes it a useful alternative to the latter, especially in the context of the analysis of numerical results or experimental data. The following two-step-kinetics scheme<sup>14</sup> offers a simple phenomenological interpretation of eqs. [22] and [25] underlying this solution



According to this scheme, the reactant  $R$  converts reversibly into a transient intermediate  $Z^*$ , which then transforms irreversibly into product  $P$ . The scheme is similar to the one used in early formulations of the TST<sup>17</sup> with the exception that the transient species  $Z^*$  in it represents the sink (i.e., the reactant solvated by the solvent in configuration  $y = y^*$ ; Fig. 1b, point  $RS^*$ ) rather than the TS. The position of  $Z^*$  on the PES and hence the values of the step rate constants  $k_1$ ,  $k_{-1}$ , and  $k_2$  depend on  $y^*$ . In the steady-state approximation, the rate constant of the overall process described by eq. [31] is

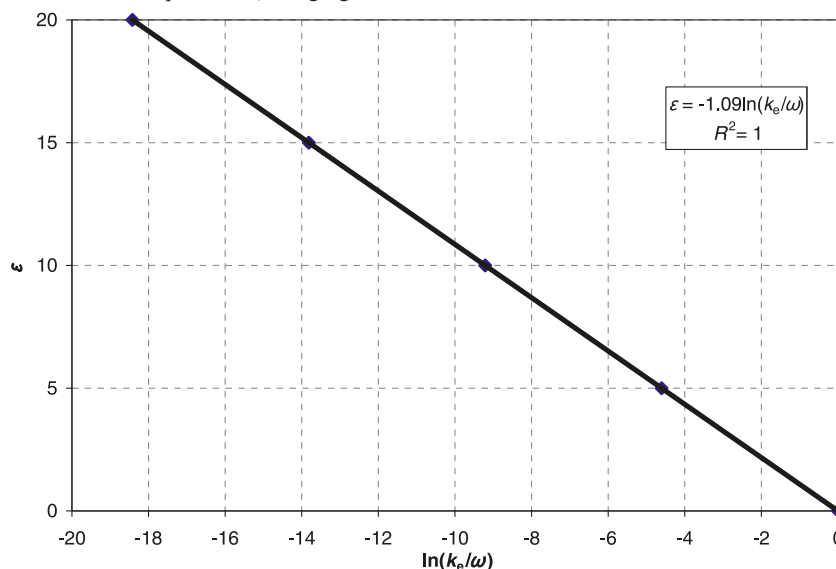
$$[32] \quad k = \frac{k_1(y^*)k_2(y^*)}{k_{-1}(y^*) + k_2(y^*)}$$

which, by virtue of eq. [9], matches eq. [22] if  $k_2 = \gamma(y^*)$ ,  $k_{-1} = \rho^{1/2}\omega$ , and  $k_1 = \omega \exp[-\varepsilon(y^*)^2]$ .

The average rate constant  $k$  given by eq. [1] can be seen as a composition of partial rate constants  $k(y)$  associated with a quasi-continuum of parallel two-step processes, similar to eq. [31], but with variable sink states  $Z(y)$  spread along the solvent coordinate  $y$ . Equation [25] condition identifies  $Z^* = Z(y^*)$  as a point for which  $k_{-1} = k_2$ . For  $y$  exceed-



**Fig. 8.** Linear relationship between  $\varepsilon$  and  $\ln(k_e/\omega)$  for the boundary of equilibrium (TST) kinetics defined by the condition  $k/k_e = 0.5$  as obtained from the numerical solutions of eq. [3] for  $\rho$  ranging from 1.0 to 4.0.



ing  $y^*$ ,  $k_{-1} \ll k_2$  and the partial rate constant  $k(y) = k_1(y) = \omega \exp[-\varepsilon y^2]$ , which is exponentially less than  $k(y^*) = (\omega/2) \exp[-\varepsilon(y^*)^2]$ . For  $y$  preceding  $y^*$ ,  $k_{-1} \gg k_2$  and  $k(y) = \rho^{-1/2} k_2(y) \exp[-\varepsilon y^2] = k_e \exp[-\rho \varepsilon (y - 1)^2]$  is again exponentially smaller than  $k(y^*) = (k_e/2) \exp[-\rho \varepsilon (y^* - 1)^2]$ . Equation [25] condition thus defines the optimum sink  $Z^*$  that gives the dominant contribution  $k(y^*)$  to the overall rate constant  $k$ , i.e., it identifies the localized sink. As the viscosity of the solvent increases, the rates  $k_1$  and  $k_{-1}$  of the diffusion step decrease, and the localized sink  $Z^*$  slides towards the bottom of the reactant valley (i.e.,  $y^*$  gets smaller) to maintain the optimum condition  $k_{-1} = k_2$ .

## Acknowledgement

Financial support by the Natural Sciences and Engineering Council of Canada (NSERC) and the University of the Fraser Valley is gratefully acknowledged.

## References

- (1) Since pressure increases solvent viscosity, these effects are not uncommon in high pressure reactions, where they manifest themselves through a significant reduction in the magnitude of the observed reaction rates, see: Drljaca, A.; Hubbard, C. D.; van Eldik, R.; Asano, T.; Basilevsky, M. V.; le Noble, W. J. *Chem. Rev.* **1998**, *98* (6), 2167; and references therein. doi:10.1021/cr970461b. PMID:11848963.
- (2) (a) Ladanyi, B. M.; Stratt, R. M. *J. Phys. Chem.* **1995**, *99* (9), 2502. doi:10.1021/j100009a007.; (b) Ladanyi, B. M.; Stratt, R. M. *J. Phys. Chem.* **1996**, *100*, 1266; (c) Stratt, R. M.; Maroncelli, M. *J. Phys. Chem.* **1996**, *100* (31), 12981. doi:10.1021/jp9608483.; (d) Fleming, G. R.; Cho, M. *Annu. Rev. Phys. Chem.* **1996**, *47* (1), 109. doi:10.1146/annurev.physchem.47.1.109.; (e) Dellago, C.; Bolhuis, P. G.; Csajka, F. S.; Chandler, D. *J. Chem. Phys.* **1998**, *108* (5), 1964. doi:10.1063/1.475562.; (f) Geissler, P. L.; Dellago, C.; Chandler, D. *J. Phys. Chem. B* **1999**, *103* (18), 3706. doi:10.1021/jp984837g.; (g) Bolhuis, P. G.; Chandler, D.; Dellago, C.; Geissler, P. L. *Annu. Rev. Phys. Chem.* **2002**, *53* (1), 291. doi:10.1146/annurev.physchem.53.082301.113146. PMID:11972010.; (h) Nandi, N.; Bhattacharyya, K.; Bagchi, B. *Chem. Rev.* **2000**, *100* (6), 2013. doi:10.1021/cr980127v. PMID:11749282.; (i) Bizzarri, A. R.; Cannistraro, S. *J. Phys. Chem. B* **2002**, *106* (26), 6617. doi:10.1021/jp020100m.;
- (2.1) (j) Ingram, J. A.; Moog, R. S.; Ito, N.; Biswas, R.; Maroncelli, M. *J. Phys. Chem. B* **2003**, *107* (24), 5926. doi:10.1021/jp034231e.; (k) Martins, L. R.; Skaf, M. S. *Chem. Phys. Lett.* **2003**, *370* (5-6), 683. doi:10.1016/S0009-2614(03)00159-3.; (l) Hummer, G. *J. Chem. Phys.* **2004**, *120* (2), 516. doi:10.1063/1.1630572. PMID:15267886.; (m) Best, R. B.; Hummer, G. *Proc. Natl. Acad. Sci. U.S.A.* **2005**, *102* (19), 6732. doi:10.1073/pnas.0408098102. PMID:15814618.; (n) Best, R. B.; Hummer, G. *Phys. Rev. Lett.* **2006**, *96* (22), 228104. doi:10.1103/PhysRevLett.96.228104. PMID:16803349.; (o) Bagchi, B. *Chem. Rev.* **2005**, *105* (9), 3197. doi:10.1021/cr020661+. PMID:16159150.; (p) Antoniou, D.; Basner, J.; Núñez, S.; Schwartz, S. D. *Chem. Rev.* **2006**, *106* (8), 3170. doi:10.1021/cr0503052. PMID:16895323.; (q) Wang, C.; Stratt, R. M. *J. Chem. Phys.* **2007**, *127* (22), 224503. doi:10.1063/1.2801994. PMID:18081402.; (r) Wang, C.; Stratt, R. M. *J. Chem. Phys.* **2007**, *127* (22), 224504. doi:10.1063/1.2801995. PMID:18081403.
- (3) (a) Hänggi, P.; Talkner, P.; Borkovec, M. *Rev. Mod. Phys.* **1990**, *62* (2), 251. doi:10.1103/RevModPhys.62.251.; (b) see also Bagchi, B. *Annu. Rev. Phys. Chem.* **1989**, *40* (1), 115. doi:10.1146/annurev.pc.40.100189.000555.; (c) Hänggi, P.; Jung, P. *Adv. Chem. Phys.* **1995**, *89*, 239; (d) Schweizer, K. S. *J. Chem. Phys.* **2005**, *123* (24), 244501. doi:10.1063/1.2137701. PMID:16396543.; (e) Pollak, E.; Talkner, P. *Chaos* **2005**, *15* (2), 026116. doi:10.1063/1.1858782.
- (4) Kramers, H. A. *Physica A* **1940**, *7* (4), 284. doi:10.1016/S0031-8914(40)90098-2.
- (5) Grote, R. F.; Hynes, J. T. *J. Chem. Phys.* **1980**, *73* (6), 2715. doi:10.1063/1.440485.
- (6) Weidenmüller, H. A.; Zhang, J.-S. *J. Stat. Phys.* **1984**, *34* (1-2), 191. doi:10.1007/BF01770354.
- (7) (a) Agmon, N.; Hopfield, J. J. *J. Chem. Phys.* **1983**, *78* (11), 6947. doi:10.1063/1.444643.; (b) Agmon, N.; Hopfield, J. J. *J. Chem. Phys.* **1983**, *79*, 2042.; (c) See also: Sumi, H.;

- Marcus, R. A. *J. Chem. Phys.* **1986**, *84* (9), 4894. doi:10.1063/1.449978.
- (8) (a) Berezhkovskii, A. M.; Zitserman, V. Yu. *Chem. Phys. Lett.* **1989**, *158* (5), 369. doi:10.1016/0009-2614(89)87353-1.; (b) Berezhkovskii, A.; Zitserman, V. *Physica A* **1990**, *166* (3), 585. doi:10.1016/0378-4371(90)90075-4.
- (9) (a) For a general definition of solvent coordinate and analysis of PESs in solvent-solute coordinates, see: Dhaliwal, M.; Basilevsky, M. V.; Weinberg, N. *J. Chem. Phys.* **2007**, *126* (23), 234505. doi:10.1063/1.2741546. PMID:17600423.; (b) Huber, L.; Edwards, E.; Basilevsky, M. V.; Weinberg, N. *Mol. Phys.* **2009**, *107* (21), 2283. doi:10.1080/00268970903272889.
- (10) Nadler, W.; Marcus, R. A. *J. Chem. Phys.* **1987**, *86* (7), 3906. doi:10.1063/1.451951.
- (11) Basilevskii, M. V.; Ryaboi, V. M.; Weinberg, N. N. *J. Phys. Chem.* **1990**, *94* (24), 8734. doi:10.1021/j100387a020.
- (12) Berezhkovskii, A. M.; D'yakov, Yu. A.; Zitserman, V. Yu. *J. Chem. Phys.* **1998**, *109* (11), 4182. doi:10.1063/1.477024.
- (13) Sebastian, K. L. *Phys. Rev. A* **1992**, *46* (4), 1732. doi:10.1103/PhysRevA.46.R1732.
- (14) (a) Asano, T.; Furuta, J. H.; Sumi, H. *J. Am. Chem. Soc.* **1994**, *116* (13), 5545. doi:10.1021/ja00092a004.; (b) For a review, see: Asano, T. *Pure Appl. Chem.* **1999**, *71* (9), 1691. doi:10.1351/pac199971091691.
- (15) Numerical solutions were highly unstable and demonstrated catastrophic behavior upon variation of the initial conditions. It was therefore easy to identify very accurately the only solution converging for a given set of parameters.
- (16) In the case of considerably nonequilibrium functions of Fig. 3, the errors in the integrals constitute only 5%.
- (17) (a) Eyring, H. *J. Chem. Phys.* **1935**, *3* (2), 107. doi:10.1063/1.1749604.; (b) Eyring, H. *Chem. Rev.* **1935**, *17* (1), 65. doi:10.1021/cr60056a006.; (c) Glasstone, S.; Laidler, K. J.; Eyring, H. *The Theory of Rate Processes*; McGraw-Hill: NY, London, 1941.

# Theoretical analysis of the (HNO)<sub>2</sub>, (HNO...HNS), and (HNS)<sub>2</sub> dimers — A case of red and blue shifts of N–H stretching frequency

Nguyen Tien Trung, Tran Thanh Hue, and Minh Tho Nguyen

**Abstract:** The hydrogen-bonded interactions in the simple (HNZ)<sub>2</sub> dimers, with Z = O and S, were investigated using quantum chemical calculations with the second-order Møller–Plesset perturbation (MP2), coupled-cluster with single, double (CCSD), and triple excitations (CCSD(T)) methods in conjunction with the 6-311++G(2d,2p), aug-cc-pVDZ, and aug-cc-pVTZ basis sets. Six-membered cyclic structures were found to be stable complexes for the dimers (HNO)<sub>2</sub>, (HNS)<sub>2</sub>, and (HNO–HNS). The pair (HNS)<sub>2</sub> has the largest complexation energy (–11 kJ/mol), and (HNO)<sub>2</sub> the smallest one (–9 kJ/mol). A bond length contraction and a frequency blue shift of the N–H bond simultaneously occur upon hydrogen bond formation of the N–H...S type, which has rarely been observed before. The stronger the intramolecular hyperconjugation and the lower the polarization of the X–H bond involved as proton donor in the hydrogen bond, the more predominant is the formation of a blue-shifting hydrogen bond.

**Key words:** blue-shifting hydrogen bond, hyperconjugative interaction, rehybridization.

**Résumé :** On a effectué des calculs de chimie quantique à l'aide des méthodes MP2, CCSD, CCSD(T) en association avec des ensembles de bases 6-311++G(2d,2p), aug-cc-pVDZ et aug-cc-pVTZ, pour étudier les interactions par liaisons hydrogènes dans des dimères simples (HNZ)<sub>2</sub> dans lesquels Z = O et S. On a trouvé que des structures cycliques à six chaînons sont des complexes stables pour les dimères (HNO)<sub>2</sub>, (HNS)<sub>2</sub> et (HNO–HNS). La paire (HNS)<sub>2</sub> donne lieu à l'énergie de complexation la plus élevée (–11 kJ/mol) alors que celle de la (HNO)<sub>2</sub> donne lieu à l'énergie de complexation la plus faible (–9 kJ/mol). On observe une contraction de la longueur de liaison et un déplacement vers le bleu pour la liaison N–H qui accompagne la formation de la liaison hydrogène de type N–H...S, ce qui n'a été observé que rarement antérieurement. Une hyperconjugaison intramoléculaire est forte et une polarisation de la liaison X–H impliquée comme donneur de proton dans la liaison hydrogène faible favorisent la formation prédominante d'une liaison hydrogène avec déplacement vers le bleu.

**Mots-clés :** liaison hydrogène avec déplacement vers le bleu, interaction par hyperconjugaison, réhybridisation.

[Traduit par la Rédaction]

## Introduction

A hydrogen bond of type X–H...Y plays an important role in many fields of chemistry and biochemistry as they determine the structures and properties of liquids, molecular crystals, and biological molecules.<sup>1–3</sup> A characteristic feature of hydrogen bond formation is a X–H bond lengthening with a concomitant red shift of the X–H stretching frequency. The origin of X–H bond lengthening and associated effects in a conventional hydrogen bond is well-understood. This is a combined effect of the electrostatic and hyperconjugative interactions, which stabilize the forming complex.<sup>4</sup> However, a large number of experimental and theoretical studies have reported in recent years the existence of a new phenomenon,

in which formation of a hydrogen bond results in a shortened X–H bond length, and a blue-shifted stretching frequency.<sup>5–16</sup> Accompanying such a frequency shift, a decrease in infrared intensity is usually predicted, even though this is not always observed. Initially, the latter complex was named “anti-hydrogen bond”,<sup>17</sup> but after vigorous discussion for a long time, the name “blue-shifting hydrogen bond” has been put forward.<sup>17</sup> There are, however, different opinions about the origin of blue shifting and red shifting in hydrogen bonds, and the origin of the blue-shifting hydrogen bond especially remains a matter of debate. A number of hypotheses and models have indeed been proposed to explain the different origin of the two kinds of hydrogen bonds.<sup>6–14,18–22</sup> However, no general explanation has been successfully applied

Received 5 December 2009. Accepted 17 March 2010. Published on the NRC Research Press Web site at canjchem.nrc.ca on 16 July 2010.

*This article is part of a Special Issue dedicated to Professor R. J. Boyd.*

**N.T. Trung.** Faculty of Chemistry, Quy Nhon University, Quy Nhon, Vietnam.

**T.T. Hue.** Faculty of Chemistry, National University of Education, Hanoi, Vietnam.

**M.T. Nguyen.**<sup>1</sup> Department of Chemistry, and Mathematical Modeling and Computational Science Center (LMCC), Katholieke Universiteit Leuven, B-3001 Leuven, Belgium.

<sup>1</sup>Corresponding author (e-mail: minh.nguyen@chem.kuleuven.be).

to all hydrogen-bonded complexes that possess the blue-shifting phenomenon.

Among the available rationalizations for the blue-shifting hydrogen bonds, five schemes have attracted more attention. Let us briefly summarize their arguments: (i) The first explanation suggests a two-step mechanism in which electron density from Y is mainly transferred to remote atoms linked to X rather than to the  $\sigma^*(X-H)$  orbital, and the contraction of the X-H bond is a result of structural reorganization of the proton donor framework.<sup>6,7,14</sup> (ii) The second model attributes the X-H bond length shortening to the short-range repulsive forces faced by H in the complex while attempting stabilization.<sup>13,19,20</sup> (iii) The main argument in the third scheme is that since an electric field is found following contraction of the X-H bond, the observed shortening is partly assigned to the effect of the electric field of Y.<sup>13,21,22</sup> (iv) The fourth explanation is based on two main factors acting in opposite directions, which are the s-character percentage of the X atom and the polarization of the X-H bond on one side and the intermolecular hyperconjugative interaction from  $n(Y)$  lone pair to the  $\sigma^*(X-H)$  orbital on another side. When the hyperconjugative interaction dominates, the X-H bond is elongated. Reversely, the X-H bond is contracted when an increase in the s-character of the X atom and the polarization of the X-H bond overcoming the weakly hyperconjugative interaction is obtained.<sup>8-11</sup> (v) Finally, the fifth scheme proposes that a transfer of electron density available at the right-hand side of the H atom involved in the X-H...Y hydrogen bond to the X-H bond, due to presence of Y, actually leads to a contraction of the X-H bond and an increase in its stretching frequency.<sup>12</sup> In general, each of the schemes mentioned above has its specific advantages and restrictions. These hypotheses rationalize the phenomenon considered on the basis of dimer properties, that is when the hydrogen-bonded complex is already formed. Another approach is to start with the inherent properties of the isolated monomer, in particular, the proton donor, to understand the dimer property. The monomer properties include the deprotonation enthalpy of the X-H bond, s-character of the X atom, electron density in the  $\sigma^*(X-H)$  orbital, and intramolecular interaction. We have recently reported some remarkable results along this direction.<sup>23,24</sup>

While numerous studies have been devoted to the C-H bond as proton donor, the blue-shifting phenomenon with N-H proton donor is less known, due to its large polarization. A few cases have recently been observed showing contraction and blue shift of a N-H bond in the N-H...O complexes.<sup>23-30</sup> Besides, N-H bond length shortening and frequency blue shift were also observed in some dihydrogen bond complexes.<sup>31-33</sup> Earlier, Hobza<sup>34</sup> and Li et al.<sup>19</sup> predicted a shift to blue of the N-H stretching frequency of type N-H...F-H at the MP2 level of calculations. However, Lu et al.<sup>35</sup> found years later an opposite trend of a red shift of the N-H stretching frequency for N-H...F-H complexes using density functional theory (DFT) computations. In an earlier study, Peters<sup>36</sup> reported on the formation of a hydrogen bond in the (HNO)<sub>2</sub> dimer, but did not pay much attention to the characteristic blue-shifting hydrogen bond. Liu et al.<sup>26</sup> recently examined the latter dimer in more detail.

We reported for the first time on the N-H blue shift in N-H...S complexes.<sup>24</sup> In the present theoretical study, we fo-

cus on the intrinsic characteristics of isolated monomers in an attempt to probe the origin of structural changes, rather than on those of the dimers. In addition, it is also established that both HNO and HNS molecules containing a N-H bond can act as either a proton donor or a proton acceptor, which is important in many processes such as pollution formation, energy release, etc.<sup>37</sup> Let us also mention that thionitrosyl hydrogen (HNS) has been generated in the gas phase,<sup>38</sup> and its molecular properties have been determined by subsequent theoretical studies.<sup>39</sup>

## Computational methods

Hydrogen-bond interactions of the (HNZ)<sub>2</sub> dimers were investigated using second-order Møller-Plesset perturbation (MP2) method in conjunction with both 6-311++G(2d,2p) and aug-cc-pVTZ basis sets. The latter basis includes higher polarization f functions on heavy atoms. Geometrical parameters of the two monomers and the three most stable complexes were also reoptimized using coupled-cluster with single and double excitations (CCSD) theory with the aug-cc-pVDZ basis set. Interaction energies were obtained using both MP2 and CCSD with triple excitations (CCSD(T)) methods, as the difference between the energies of the complexes and the respective monomers, and corrected for both zero-point energy (ZPE) and basis set superposition errors (BSSE) using the counterpoise procedure.<sup>40</sup> The ZPE corrections also included all the intermolecular frequencies. While MP2 total energies were obtained from the corresponding geometry optimizations, CCSD(T) electronic energies involved single point calculations with the aug-cc-pVTZ basis set at the CCSD/aug-cc-pVDZ geometries.

Hyperconjugation energy can be evaluated from the second-order perturbation energy of interaction.<sup>41</sup> Energy index,  $R_E$ , of the Z-X-H...Y H-bond is determined as follows:<sup>25,31</sup>

$$[1] \quad R_E = \frac{E_H^{(2)}}{E_{IM-C}^{(2)}}; \text{ in which } E_H^{(2)} = E^{(2)}[n(Y) \rightarrow \sigma^*(X-H)]$$

$$[2] \quad E_{IM-C}^{(2)} = E_{IM}^{(2)}[n(Z) \rightarrow \sigma^*(X-H)] - E_{IC}^{(2)}[n(Z) \rightarrow \sigma^*(X-H)]$$

$E_H^{(2)}$  stands for intermolecular hyperconjugation interaction energy.  $E_{IM}^{(2)}$  and  $E_{IC}^{(2)}$  denote intramolecular hyperconjugation interaction energies in the isolated proton donor and in the proton donor after complex formation, respectively.  $E_{IM-C}^{(2)}$  is symbolled for the change of intramolecular hyperconjugation interaction energy of transferring electron density from the  $n(Z)$  lone pair to the  $\sigma^*(X-H)$  antibonding orbital in the proton donor before and after complexation. The calculated vibrational frequencies were retained unscaled. To avoid vibrational coupling between the N-H stretching modes in dimers HNO...HNO and HNS...HNS, harmonic frequencies were calculated using some isotopomers. Calculations were carried out using the Gaussian 03 package.<sup>42</sup> Electron density,  $\rho(r)$ , and the Laplacian of the electron density,  $\nabla^2(\rho(r))$ , at the bond critical points (BCPs) were performed at the MP2/6-311++G(2d,2p) level using the AIM2000 program.<sup>43</sup> The natural bond orbital (NBO) analysis was also performed making use of the GenNBO 5.G<sup>44</sup>



program for all monomers and complexes at the same MP2/6-311++G(2d,2p) level.

## Results and discussion

### Geometries, frequencies, and infrared intensities

The shape of the three dimers, A, B, and C, identified on the potential energy surface (PES) at the MP2/6-311++G(2d,2p), MP2/aug-cc-pVTZ, and CCSD/aug-cc-pVDZ levels, is displayed in Fig. 1. Both dimers A and C have high point group symmetry ( $C_{2h}$ ) whereas the dimer B possesses a lower point group ( $C_s$ ). Changes of geometrical parameters following dimer formation are gathered in Table 1. Along with the changes in selected bond length, the changes in their stretching frequency and infrared intensity are tabulated in Table 2. Intermolecular distances, angles, and interaction energies upon complexation are also given in Table 3. The trends of the changes determined using the methods mentioned above are similar both qualitatively and quantitatively. In general, the changes of bond lengths of the complex relative to the respective monomer resulting from MP2 using the aug-cc-pVTZ basis set are slightly larger than those obtained by the 6-311++G(2d,2p) set. As a consequence, the changes in the relevant stretching frequencies are smaller with the 6-311++G(2d,2p) basis set than with the aug-cc-pVTZ one.

Interaction energies are similar using the MP2 method, in spite of the much larger aug-cc-pVTZ basis set (cf. Table 3). Interaction energies evaluated with both ZPE and BSSE corrections at CCSD(T)/aug-cc-pVTZ are slightly larger than those obtained at MP2/aug-cc-pVTZ for complexes A and B, but marginally smaller for C. For the purpose of comparison with previous studies using MP2 calculations, only the MP2/aug-cc-pVTZ values are given hereafter. We refer to Tables 1 and 2 for detailed comparison. We use mÅ, which denotes  $10^{-3}$  Å, as a shorthand unit for distance changes. With such a unit, the changes occurring in bond lengths are very small, but in view of the equally small effects induced by the H-bond formation, a variation of a few mÅ can already be considered to be significant.

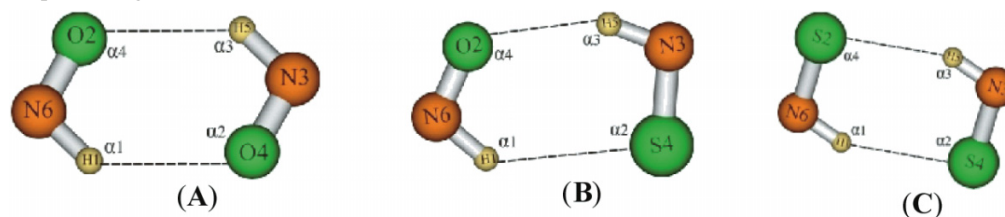
There is a contraction of 4.1 mÅ of the N3–H5 bond in A, as compared with the monomer HNO. On the other hand, elongation of N3–H5 bonds is predicted for both B and C, as compared with HNS. It is ~2.4 mÅ for the elongation of the N3–H5 bond length in C, which is larger than that in B (~0.2 mÅ). Simultaneously, the N6–H1 bond lengths are shortened upon complexation, by 4.1 and 2.4 mÅ for A and B, respectively, while a smaller elongation of 2.4 mÅ for this bond is obtained in C. Such shifts can be considered as relatively large but consistent with the expected properties of H-bonded systems. All N6=O2 and N3=O4 bonds are elongated, and a slight contraction is noted for N6=S2 and N3=S4 bonds in the dimers considered (Table 1). Therefore, it is clear that the change of the N–H bond length is inversely proportional to the change of the N=Z double bond length in HN=Z whether the Z atom is O or S. The largest contraction of the N3–H5 and N6–H1 bonds in A is associated with a significant increase of their stretching frequencies, amounting to  $80\text{ cm}^{-1}$ . On the contrary, the elongation and the decrease in stretching frequencies of the N3–H5 and N6–H1 bonds are observed in C. The

N3–H5 and N6–H1 bond lengths are both elongated by ~2.4 mÅ, leading to a decrease of  $31\text{ cm}^{-1}$  in their stretching frequencies. For the mixed dimer B, it is worth mentioning that there is an increase by  $\sim 16\text{ cm}^{-1}$  in the N3–H5 stretching frequency, although a very small elongation is predicted, by ~0.2 mÅ. As pointed out in previous papers,<sup>32,45</sup> one should be careful in classifying a hydrogen bond as being blue or red shifting on this basis, because such a small variation upon complexation strongly depends on the level of theory applied. Therefore, it is not yet conclusive to classify the N3–H5 bond in B.

As mentioned in the introduction, contraction of a covalent N–H bond has seldom been detected due to its polarity. In a few remarkable cases, N–H blue shifts with different magnitudes have recently been predicted for both dihydrogen- and hydrogen-bond complexes.<sup>23–33</sup> For a dihydrogen bond, such as in the complex pairing  $\text{BH}_3\text{NH}_3$  with  $\text{HNO}$ ,<sup>31</sup> the N–H frequency undergoes a large blue shift of  $128\text{ cm}^{-1}$ . A moderate N–H blue shift has also been obtained in complexes between  $\text{YH}_2\text{NH}_2$  (Y = B, Al) and  $\text{HNZ}$  (Z = O, S).<sup>32</sup> Significantly strong N–H blue shifts have been found in some hydrogen-bonded complexes of  $\text{HNO-HNO}$ ,<sup>26</sup>  $\text{CH}_3\text{CHO-HNO}$ ,<sup>28</sup>  $\text{HOX-HNO}$  with X = F, Cl, Br,<sup>29</sup>  $\text{CH}_3\text{X-HNO}$  with X = F, Cl, Br,<sup>30</sup>  $\text{RCHZ-HNO}$  with R = H, F, Cl, Br and Z = O, S,<sup>24</sup>  $\text{CHX}_3\text{-HNO}$  with X = F, Cl, Br,<sup>23</sup> and  $\text{HNO-HCONH}_2$ ,<sup>46</sup> which amount up to  $\sim 100\text{ cm}^{-1}$ . A comparable frequency blue shift of  $80\text{ cm}^{-1}$  along with a contraction of 4.1 mÅ of N3–H5 and N6–H1 bonds in the N–H...O type is also obtained in this work, which is significant but consistent with the values reported in ref. 23. In addition, there are a contraction and an increase in the stretching frequency of the N6–H1 bond in the N–H...S type in B. Such a blue shift of the N–H stretching frequency has only been recently revealed.<sup>24</sup> Comparing the N–H...O and N–H...S types of bonds, we found that contraction of the N–H bond length and increase of their stretching frequency are larger for the former than for the latter. This is likely due to the larger basicity at the S site in HNS with respect to that at the O site in HNO. Indeed, calculated proton affinities at O of HNO and at S of HNS amount to 528 and 688  $\text{kJ mol}^{-1}$ , respectively, at the MP2/aug-cc-pVTZ + ZPE level.

As seen from both Tables 1 and 2, the N–H bond length shortening and its blue shift are larger in HNO than in HNS. This difference is due to the larger polarity of N–H bond in HNS, which makes it more difficult to be contracted and shifted to blue. The calculated N–H deprotonation enthalpy of  $1535\text{ kJ mol}^{-1}$  in HNS is lower than that of  $1586\text{ kJ mol}^{-1}$  in HNO. This obtained result implies that the N–H bond is more polarized in HNS than in HNO.

A blue-shifting X–H...Y bond usually shortens the X–H distance and decreases the X–H stretching IR intensity. On the other hand, elongating the X–H bond and increasing its stretching IR intensity are usually observed for a red-shifting hydrogen bond. Indeed, a similar trend is obtained for all N–H bonds in the three dimers considered. Particularly, a consequent decrease in IR intensity by  $\sim 69\text{--}73\text{ km.mol}^{-1}$  is accompanied by a significant contraction of the N6–H1 and N3–H5 bonds in A, and of the N6–H1 bond in B upon, complexation (Tables 1 and 2). Likewise, an increase of  $82\text{ km mol}^{-1}$  in IR intensity is accompanied by an elongation of both the N3–H5 and N6–H1 bonds in C. However, it is

**Fig. 1.** Shape of the optimized geometries of the (HNZ)<sub>2</sub> dimers.**Table 1.** Changes of bond lengths,  $\Delta r$  (in  $10^{-3}$  Å), obtained at three levels of theory.

	$\Delta r$			
	N3–H5	N6–H1	N6=Z2	N3=Z4
<b>A</b>				
MP2/6-311++G(2d,2p)	–3.9	–3.9	3.1	3.1
MP2/aug-cc-pVTZ	–4.1	–4.1	2.8	2.8
CCSD/aug-cc-pVDZ	–5.2	–5.2	3.4	3.4
<b>B</b>				
MP2/6-311++G(2d,2p)	0.1	–2.5	3.6	–1.7
MP2/aug-cc-pVTZ	0.2	–2.4	3.3	–2.1
CCSD/aug-cc-pVDZ	0.1	–4.0	3.5	0.0
<b>C</b>				
MP2/6-311++G(2d,2p)	1.9	1.9	–1.0	–1.0
MP2/aug-cc-pVTZ	2.4	2.4	–1.5	–1.5
CCSD/aug-cc-pVDZ	1.0	1.0	–0.1	–0.1

**Table 2.** Changes of stretching frequencies,  $\Delta \nu$  ( $\text{cm}^{-1}$ ), and infrared intensities,  $\Delta I$  ( $\text{km mol}^{-1}$ ), using MP2 with two different basis sets.

Structure <sup>a</sup>	MP2/6-311++G(2d,2p)				MP2/aug-cc-pVTZ			
	$\Delta \nu$		$\Delta I$		$\Delta \nu$		$\Delta I$	
	N3–H5	N6–H1	N3–H5	N6–H1	N3–H5	N6–H1	N3–H5	N6–H1
A	80	80	–65	–65	80	80	–69	–69
B	20	51	38	–73	16	50	40	–73
C	–25	–25	84	84	–31	–31	82	82

<sup>a</sup>See Fig. 1 for the definition and atom labeling.**Table 3.** Intermolecular distances ( $R$ ; Å), angles ( $\alpha$ ; °), and interaction energies (including ZPE correction ( $\Delta E$ ), and both ZPE and BSSE corrections ( $\Delta E$ );  $\text{kJ mol}^{-1}$ ) upon formation of the dimers at two different levels of theory.

Levels	MP2/6-311++G(2d,2p)			MP2/aug-cc-pVTZ		
	A	B	C	A	B	C
Structure						
$R(\text{N6–H1} \cdots \text{Z4})$	2.36	2.80	2.65	2.34	2.76	2.63
$R(\text{N3–H5} \cdots \text{Z2})$	2.36	2.27	2.65	2.34	2.26	2.63
$\alpha 1$	132.2	135.2	153.1	131.7	134.6	151.6
$\alpha 2$	121.0	98.3	99.8	121.5	99.5	101.6
$\alpha 3$	132.2	149.8	153.1	131.7	148.5	151.6
$\alpha 4$	121.0	122.8	99.8	121.5	123.6	101.6
$\Delta E^a$	–9.5	–9.8	–12.2	–10.3	–11.5	–15.2
$\Delta E^b$	–6.0	–6.2	–7.8	–7.9 (–9.1) <sup>c</sup>	–8.8 (–9.4) <sup>c</sup>	–11.9 (–11.4) <sup>c</sup>

<sup>a</sup>Corrected only by ZPE.<sup>b</sup>Corrected by both ZPE and BSSE contributions.<sup>c</sup>The values in parentheses are the calculated interaction energies obtained at the CCSD(T)/aug-cc-pVTZ + ZPE + BSSE level.

remarkable that an increase in IR intensity of the N3–H5 vibration is also predicted in the mixed dimer B in spite of an increase of the N3–H5 stretching frequency. This amounts to 40 km mol<sup>−1</sup> with a slight increase of 16 cm<sup>−1</sup> and a negligible elongation of 0.2 mÅ. Our results, either obtained in this work or reported in previous papers,<sup>23,24,32</sup> and the data reported by other authors,<sup>47</sup> demonstrated that IR intensity can actually be increased even when an increase in stretching frequency upon complexation occurs. Hence, the change of IR intensity appears to depend on the inherent property of the monomer rather than on that of the resulting dimer.

### Complexation energies and topological analyses

Table 3 shows that the N6–H1...Z4 and N3–H5...Z2 (Z = O, S) intermolecular contacts result in quite stable six-membered cyclic structures in the examined dimers. Indeed, interaction energies with only ZPE correction are −9.5, −9.8, and −12.2 kJ mol<sup>−1</sup> at the MP2/6-311++G(2d,2p) level, and −10.3, −11.5, and −15.2 kJ mol<sup>−1</sup> at the MP2/aug-cc-pVTZ level for A via B to C, respectively. With both ZPE and BSSE corrections, they amount to −6.0, −6.2, and −7.8 kJ mol<sup>−1</sup> by MP2/6-311++G(2d,2p), −7.9, −8.8, and −11.9 kJ mol<sup>−1</sup> by MP2/aug-cc-pVTZ, and −9.1, −9.4, and −11.4 kJ mol<sup>−1</sup> at CCSD(T)/aug-cc-pVTZ in going from A, and B to C, respectively. The dimer A contains two N–H...O hydrogen bonds (cf. Fig. 1 and Table 3). After including all corrections considered, an average value of binding energy per N–H...O hydrogen bond can roughly be estimated to be from ~3.0 kJ mol<sup>−1</sup> (MP2/6-311++G(2d,2p)) to 3.9 kJ mol<sup>−1</sup> (MP2/aug-cc-pVTZ) to 4.6 kJ mol<sup>−1</sup> (CCSD(T)/aug-cc-pVTZ) in A. Similarly, an average value of binding energy per N–H...S hydrogen bond is from ~3.9 kJ mol<sup>−1</sup> (MP2/6-311++G(2d,2p)) to 6.0 kJ mol<sup>−1</sup> (MP2 and CCSD(T) with aug-cc-pVTZ) in C. Accordingly, the N–H...S hydrogen bond is somewhat stronger than the N–H...O counterpart. However, the presence of a N–H...S bond in the mixed dimer (B) causes a decrease in binding energy of the N–H...O bond as compared to that of A, by ~0.7 (MP2/6-311++G(2d,2p)) to 1.0–1.2 kJ mol<sup>−1</sup> (MP2 and CCSD(T) with aug-cc-pVTZ). Data obtained at both levels of theory, with and without BSSE corrections, all concur with each other showing that C is the strongest dimer in terms of binding energy, followed by B and then by A.

The distances of R(H...Z) are slightly longer by the MP2/6-311++G(2d,2p) calculation than those from MP2/aug-cc-pVTZ (Table 3). It is interesting that C is considerably more stable with respect to A, despite the fact that the R(H...Z) intermolecular distances in A are shorter than in C. The  $\alpha_1$  and  $\alpha_3$  bond angles in C are less bent from linearity than those in A, in particular, the  $\alpha_1$  and  $\alpha_3$  angles in C are more linear than that in A by 19°–21°. The smaller deviation from linearity results in a stronger orbital overlap, and as a consequence, the dimer C becomes more stable than A. In the same vein, A is less stable than B in terms of binding energy, which results from the smaller magnitude of  $\alpha_3$  angle, by ~15° as shown in Table 3. The stability ordering of the dimers in going from A to B to C has an intimate relationship with the increase in  $\alpha_1$  and  $\alpha_3$  angularities. Hence, it can be suggested that the strength of the complexes considered here is in part determined by the  $\alpha_1$  and  $\alpha_3$  bond

angles over the R(H...Z) intermolecular distances. Simultaneously, there is a tiny deviation of  $\alpha_2$  and  $\alpha_4$  angles in all three dimers. The R(H1...Z4) and R(H5...Z2) intermolecular distances in three optimized dimers fall within the range of 2.27–2.80 Å, from both methods. These are all shorter than the sum of the van der Waals radii of the H and S atoms (being 3.05 Å) and of the H and O atoms (being 2.60 Å).

The stability ordering of the three dimers and the properties of the H bonds in these dimers can further be understood using the maps of total electron density, which is emphasized by underlying intermolecular interactions. The 0.011 au isosurfaces of total electron density calculated at the MP2/6-311++G(2d,2p) level are plotted in Fig. 2. The relatively large intersection regions of the total electron density between intermolecular contacts such as N6–H1...Z4 and N3–H5...Z2 (Z = O, S) give an obvious indication of the electron-donating character of the lone pairs on the Z2 and Z4 atoms to the electron deficient  $\sigma^*(\text{N6–H1})$  and  $\sigma^*(\text{N3–H5})$  antibonding orbitals. As shown in Fig. 2, the largest intersection region of the total electron density is observed for the N6–H1...S4 and N3–H5...S2 intermolecular contacts in C, followed by the N6–H1...S4 and N3–H5...O2 ones in B, and then for N6–H1...O4 and N3–H5...O2 ones in A. This leads to the fact that C is the most stable dimer, and A the least stable one.

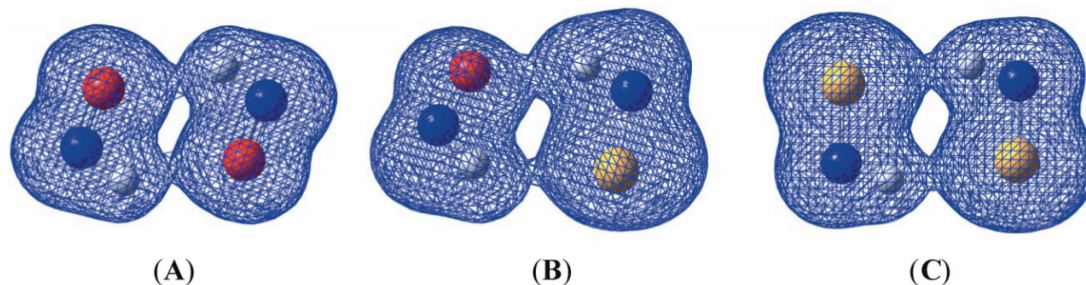
To probe further into the formation of hydrogen bonds in the studied dimers, a topological analysis was carried out by making use of atom in molecules (AIM) theory<sup>48</sup> at the MP2/6-311++G(2d,2p) level. Three of eight AIM criteria are also applied to characterize the hydrogen bond in the examined systems.<sup>49</sup> A bond path with a bond critical point between the proton and proton acceptor exists for the N6–H1...Z4 and N3–H5...Z2 intermolecular contacts (Fig. 3). The topological parameters of bond critical points (BCPs) and ring critical points (RCPs) are gathered in Table 4. There exists a RCP in one complex, which evidently indicates a ring structure in one examined dimer. The values of electron density  $\rho(r)$  (~0.011 au) and Laplacians  $\nabla^2(\rho(r))$  (~0.04 au) of BCPs also fall within the suggested ranges for a hydrogen bond,<sup>49</sup> in such a way that the N6–H1...Z4 and N3–H5...Z2 intermolecular contacts are obviously classified as hydrogen bonds. They are further confirmed on the basis of  $\nabla^2(\rho(r)) > 0$  and  $H_C > 0$  as suggested by Cremer and Kraka<sup>50</sup> and Rozas et al.,<sup>51</sup> and  $-V_C/G_C < 1$  as suggested by Grabowski et al.<sup>52</sup> for medium and weak interactions. Evaluating the contributions of the highest occupied molecular orbital (HOMO) and the innermost valence MO's to hydrogen bond interaction in three dimers are also given in Figure S4 of the Supplementary data.

### NBO analysis

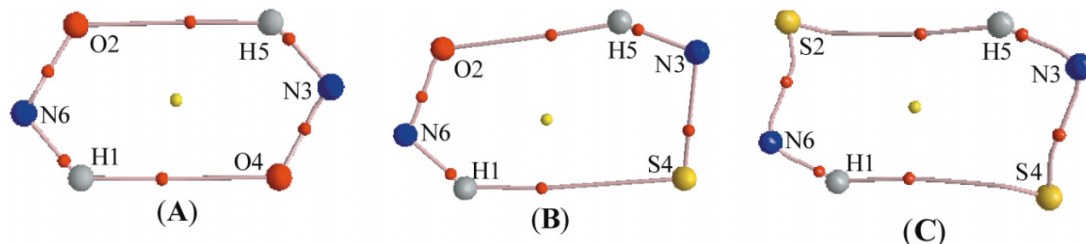
An NBO analysis was carried out at the MP2/6-311++G(2d,2p) level and the selected results are summarized in Table 5. An electron density transfer (EDT) occurs from the HNS → HNO in B (for both A and C, the EDT values are equal to zero, due to symmetry). Recently, some authors<sup>18,19,53</sup> suggested that upon complexation, a change of electron density in the  $\sigma^*(\text{X–H})$  orbital is the result of a combination of two effective factors, namely, an intermolecular hyperconjugation increases the electron density in the  $\sigma^*(\text{X–H})$  orbital, while a decrease in intramolecular hyper-



**Fig. 2.** The 0.011 au isosurface of total electron density of three optimized dimers calculated at the MP2/6-311++G(2d,2p) level.



**Fig. 3.** Topological geometry of BCPs (red small spheres) and RCPs (yellow small spheres) in the three dimers considered.



**Table 4.** AIM analysis of the dimers A, B, and C at the MP2/6-311++G(2d,2p) level.

Dimers	Critical points	$\rho(r)$ (au) <sup>a</sup>	$\nabla^2$ (au) <sup>b</sup>	$H_c$ (au) <sup>c</sup>	$-VJG_c^d$
A	N6–H1...O4	0.011	0.04	0.001	0.9
	N3–H5...O2	0.011	0.04	0.001	0.9
	RCP	0.007	0.04	0.001	0.9
B	N6–H1...S4	0.010	0.03	0.001	0.9
	N3–H5...O2	0.011	0.05	0.002	0.9
	RCP	0.006	0.03	0.001	0.8
C	N6–H1...S4	0.012	0.04	0.001	0.9
	N3–H5...S2	0.012	0.04	0.001	0.9
	RCP	0.005	0.02	0.001	0.8

<sup>a</sup>The electron density at the CP.

<sup>b</sup>The Laplacian at the CP.

<sup>c</sup>The total electron energy density at the CP.

<sup>d</sup>The electron kinetic energy density ( $G_c$ ) and the electron potential energy density ( $V_c$ ).

conjugation tends to decrease the electron density in the  $\sigma^*(X-H)$  orbital. Table 5 points out that the electron densities in both  $\sigma^*(N3-H5)$  and  $\sigma^*(N6-H1)$  orbitals of A decrease with a uniform value of 0.0019 e, implying that a strong decrease of intramolecular hyperconjugation overrides intermolecular hyperconjugation. Indeed, while the intramolecular hyperconjugation energies,  $E(n(O4) \rightarrow \sigma^*(N3-H5))$  and  $E(n(O2) \rightarrow \sigma^*(N6-H1))$ , decrease by up to 10 kJ mol<sup>-1</sup>, the intermolecular hyperconjugation energies,  $E(n(O2) \rightarrow \sigma^*(N3-H5))$  and  $E(n(O4) \rightarrow \sigma^*(N6-H1))$ , are approximately 6 kJ mol<sup>-1</sup>. Decreases of electron density in both  $\sigma^*(N3-H5)$  and  $\sigma^*(N6-H1)$  orbitals strengthen the respective N3–H5 and N6–H1 bonds, and thereby contribute to a blue shift of the corresponding stretching frequencies. On the contrary, increases of electron densities are observed in both  $\sigma^*(N3-H5)$  and  $\sigma^*(N6-H1)$  orbitals ( $\sim 0.0071$  e) in C. The strong intermolecular hyperconjugation (evaluated at  $\sim 18$  kJ mol<sup>-1</sup>) from the  $n(S2)$  lone pair to the  $\sigma^*(N3-H5)$  orbital, and from the  $n(S4)$  lone pair to the  $\sigma^*(N6-H1)$  orbital appears to exceed the smaller decrement of the intramolecular hyperconjugation energy (being  $\sim 5$  kJ mol<sup>-1</sup>). This leads to

an increase in occupation of the  $\sigma^*(N3-H5)$  and  $\sigma^*(N6-H1)$  orbitals, and results in an elongation of the N3–H5 and N6–H1 bonds along with a decrease in their stretching frequencies in C. Furthermore, very slight to moderate increases in electron densities are also observed in the  $\sigma^*(N3-H5)$  and  $\sigma^*(N6-H1)$  orbitals for B (Table 5). The larger value of intermolecular hyperconjugation interaction energy (11 kJ mol<sup>-1</sup>), which is due to a transfer from  $n(S4)$  to  $\sigma^*(N6-H1)$  with respect to a significant decrease of intramolecular  $n(O2) \rightarrow \sigma^*(N6-H1)$  hyperconjugation (10 kJ mol<sup>-1</sup>), causes a moderate increase in occupation of the  $\sigma^*(N6-H1)$  orbital. Likewise, a transfer (evaluated at 8 kJ mol<sup>-1</sup>) of electron density from  $n(O2)$  to  $\sigma^*(N3-H5)$ , despite a decrease (6 kJ mol<sup>-1</sup>) of intramolecular hyperconjugation energy, appears to play an important role in the small increase in occupation of the  $\sigma^*(N3-H5)$  orbital.

For A, electrons are basically transferred from  $n(O4)$  to  $\sigma^*(N6-H1)$ , then most electrons in  $\sigma^*(N6-H1)$  are transferred to  $n(O2)$  and then a part in  $n(O2)$  is transferred to  $\sigma^*(N3-H5)$ , and, finally, most electrons in  $\sigma^*(N3-H5)$  are transferred back to  $n(O4)$ . As a result, these transfers give



**Table 5.** NBO analysis of the dimers A, B, and C (MP2/6-311++G(2d,2p)) and hyperconjugative energies (HF/6-311++G(2d,2p)).

Structure	A	B	C
EDT ( $10^{-3}$ e)	0.0	6.9	0.0
$\Delta\sigma^*(\text{N3-H5})$ ( $10^{-3}$ e)	-1.9	0.2	7.1
$\Delta\sigma^*(\text{N6-H1})$ ( $10^{-3}$ e)	-1.9	2.8	7.1
$\Delta n(\text{Z2})$ ( $10^{-3}$ e)	2.2	1.4	-10.4
$\Delta n(\text{Z4})$ ( $10^{-3}$ e)	2.2	-6.4	-10.4
$\Delta\%s(\text{N3})$	0.94	1.13	1.59
$\Delta\%s(\text{N6})$	0.94	1.09	1.59
$\Delta q(\text{N3})$ ( $10^{-3}$ e)	16	25	16
$\Delta q(\text{N6})$ ( $10^{-3}$ e)	16	14	16
$\Delta q(\text{H5})$ ( $10^{-3}$ e)	28	26	20
$\Delta q(\text{H1})$ ( $10^{-3}$ e)	28	22	20
$E(n(\text{Z2}) \rightarrow \sigma^*(\text{N3-H5}))$ (kJ mol $^{-1}$ )	5.6	7.8	17.9
$\Delta E(n(\text{Z4}) \rightarrow \sigma^*(\text{N3-H5}))$ (kJ mol $^{-1}$ )	-10.0	-5.5	-4.9
$E(n(\text{Z4}) \rightarrow \sigma^*(\text{N6-H1}))$ (kJ mol $^{-1}$ )	5.6	11.2	17.9
$\Delta E(n(\text{Z2}) \rightarrow \sigma^*(\text{N6-H1}))$ (kJ mol $^{-1}$ )	-10.0	-10.3	-4.9
$R_E(\text{N3-H5})$ (kJ mol $^{-1}$ )	0.55	1.42	3.67
$R_E(\text{N6-H1})$ (kJ mol $^{-1}$ )	0.55	1.09	3.67
$sp^a$ (N3)	$sp^{3.75}$	$sp^{2.99}$	$sp^{2.92}$
$sp^a$ (N6)	$sp^{3.75}$	$sp^{3.72}$	$sp^{2.92}$

**Note:** The  $n$  index denotes for lone pairs on the Z atom; the positive value of EDT means that there is a transfer of electron density from HNS to HNO; the delta ( $\Delta$ ) symbolizes a change of the complex relative to the monomer.

rise to a decrease of electrons available for  $\sigma^*(\text{N6-H1})$  and  $\sigma^*(\text{N3-H5})$  orbitals, and the  $n(\text{O2})$  and  $n(\text{O4})$  lone pairs (cf. Table 5).

For C, most electrons are transferred to the  $\sigma^*(\text{N3-H5})$  and  $\sigma^*(\text{N6-H1})$  orbitals because of the weak electron density redistribution effect of HNS. This results in a large increase of occupation in both  $\sigma^*(\text{N3-H5})$  and  $\sigma^*(\text{N6-H1})$ , and a significant decrease of electron density in  $n(\text{S2})$  and  $n(\text{S4})$  (cf. Table 5).

For B, the changes of electron density in  $\sigma^*(\text{N6-H1})$  and  $\sigma^*(\text{N3-H5})$  and  $n(\text{O2})$  and  $n(\text{S4})$  can be explained as follows: Firstly, electrons are initially transferred from the  $n(\text{S4})$  to  $\sigma^*(\text{N6-H1})$  as suggested by the larger value (11 kJ mol $^{-1}$ ) of  $E(n(\text{S4}) \rightarrow \sigma^*(\text{N6-H1}))$  energy as compared to  $E(n(\text{O2}) \rightarrow \sigma^*(\text{N3-H5}))$  (8 kJ mol $^{-1}$ ), and then a small part is transferred to  $n(\text{O2})$ . As a consequence, an electron increase in the  $\sigma^*(\text{N6-H1})$ ,  $n(\text{O2})$ , and  $\sigma^*(\text{N3-H5})$  orbitals are induced, along with a strong decrease in occupancy of  $n(\text{S4})$  (cf. Table 5).

The obvious difference in electron redistribution can only be understood if one considers properties of the isolated HNO and HNS monomers. Calculated properties of the HNO and HNS monomers show that for HNO, the hyperconjugative  $E(n(\text{O}) \rightarrow \sigma^*(\text{N-H}))$  interaction amounts to up to 74 kJ mol $^{-1}$  and the electron number in the  $\sigma^*(\text{N-H})$  orbital is substantial, being 0.029 e. For HNS, the hyperconjugative  $E(n(\text{S}) \rightarrow \sigma^*(\text{N-H}))$  interaction energy is relatively small (34 kJ mol $^{-1}$ ), and the occupation in the  $\sigma^*(\text{N-H})$  orbital is only 0.015 e. Furthermore, the  $a$  index in the  $sp^a$  hybridization of the N atom in HNO (3.98) is larger than that in HNS (3.18). In addition, the polarization of the N-H bond in HNO is lower than that in HNS as NBO charges on N

(0.04 e) and H (0.26 e) atoms in HNO are sensibly different from those -0.69 e (N) and 0.33 e (H) in HNS. The remarkable difference of both HNO and HNS isolated monomers has recently been reported.<sup>28</sup> Hence, a more intensive electron redistribution is observed in the isolated monomer that possesses a lower bond polarization, higher electron occupancy in the  $\sigma^*(\text{N-H})$  orbital, larger  $a$  index, and larger intramolecular hyperconjugation.

Within a more chemical perspective, the hyperconjugation  $n(\text{Y}) \rightarrow \sigma^*(\text{X-H})$  can be balanced by an increase of the s-character and polarization of the X-H bond<sup>8</sup> to induce a difference between the blue shift and red shift of a hydrogen bond. Normally, a feature is that the X atom becomes more electronegative, and the H atom more electropositive, leading to an increase of the X-H bond polarity, when a blue-shifting hydrogen bond is formed. However, the present results show that in all dimers, A, B, and C, the H1 and H5 atoms become more positive ( $\sim 0.02$ – $0.03$  e), whereas the net charges on the N3 and N6 atoms decrease by  $\sim 0.01$ – $0.03$  e, irrespective of a blue- or red-shifting hydrogen bond. These results are similar to some previous reports on a decrease of the negative charge on the X atom.<sup>24,32,54</sup>

An increase in positive charges on H1 and H5 results in simultaneous increases in the s-character of the N3 and N5 hybrid orbitals in the N3-H5 and N6-H1 bonds, which is consistent with Bent's rule,<sup>55</sup> and contributes to the contraction of their distances. This means that the stretching frequencies of both N3-H5 and N6-H1 bonds could be expected to be shifted to blue in all three dimers examined. However, such a blue shift is only observed in A, and a red shift is found in C.

In summary, both the decrease in electron densities due to

an intensive electron redistribution and increase in s-characters (decreasing of the  $a$  index) of the N3 and N6 atoms in A tend to contribute to contractions of the N3–H5 and N6–H1 bonds, that are accompanied by blue shifts of their stretching frequencies. On the other hand, the strong intermolecular hyperconjugation, overriding the weak intramolecular hyperconjugation, leads to increases of electron densities in the  $\sigma^*(\text{N3–H5})$  and  $\sigma^*(\text{N6–H1})$  orbitals. This results in distance elongation, a stretching frequency decrease of the N3–H5 and N6–H1 bonds in C, even though there are large increases in s-characters (decreasing of the  $a$  index in  $\text{sp}^a$  hybridization) and a moderate increase of positive net charges at the H1 and H5 atoms. For the mixed dimer B, the small elongation of the N3–H5 bond length, relative to monomer, is due to a slight increase of occupation in the  $\sigma^*(\text{N3–H5})$  orbital, plus overwhelming increases of rehybridization of the N3 hybrid orbital and a positive net charge at H3. In contrast, a blue shift is observed for the N6–H1 bond even though there is a tiny increase in population of the  $\sigma^*(\text{N6–H1})$  orbital (0.003 e). Therefore, contraction of the N6–H1 length and increase of its stretching frequency are seemingly correlated with the increase of s-character at the N6 hybrid orbital of the N6–H1 bond.

According to the definition of the energy index,  $R_E$ , given in eq. [1], it can be used to describe the strength of the electron redistribution. In general, the smaller the  $R_E$  value, the stronger the density redistribution. It means that a blue shift occurs with a small  $R_E$ , and vice versa. Indeed, our calculated results coincide well with this prediction. For both N3–H5 and N6–H1 bonds, the smallest  $R_E$  value (0.55) is obtained for A and the largest  $R_E$  (3.67) is predicted in C. More moderate values of  $R_E$  are observed for these bonds in B, in particular, the larger value for N3–H5 (1.42) and the smaller one for the N6–H1 bond (1.09). Overall, the  $R_E$  parameter can be used as a convenient index to classify the hydrogen bond in these systems.

## Concluding remarks

Dimerization of HNZ leads to stable six-membered cyclic dimers whose interaction energies calculated including both ZPE and BSSE corrections are in the range of –8, –9, and –11 kJ mol<sup>–1</sup> for the dimers (HNO)<sub>2</sub> (A), (HNO–HNS) (B), and (HNS)<sub>2</sub> (C), respectively. The dimer A uniformly exhibits two blue shifts of N3–H5 and N6–H1 stretching frequencies. The red shifts are consistently observed for both the N3–H5 and N6–H1 bonds in the dimer C. Upon complexation, contraction of the N6–H1 bond length as well as increase of its stretching frequency are found in the mixed dimer B. However, the N3–H5 bond length is predicted to be elongated, and its stretching frequency and infrared intensity increase accordingly. Both the rehybridization and decrease of electron density in the  $\sigma^*(\text{N3–H5})$  and  $\sigma^*(\text{N6–H1})$  orbitals contribute to the large N–H blue shifts in A. The red shifts are observed for both N–H bonds in C, due to a large increase of electron density in the  $\sigma^*$  orbitals, exceeding rehybridization at the N3 and N6 atoms. The rehybridization at the N6 atom, which overcomes an increase of occupation in the  $\sigma^*(\text{N6–H1})$  orbital, plays an important role in the blue shift of the N6–H1 bonds in B. An electron increase in the  $\sigma^*(\text{N3–H5})$  orbital mainly determines an elongation of this

bond. It appears that whether a blue shift or red shift actually occurs in hydrogen-bonded complexes is more dependent on the proton donor partner.

## Supplementary data

Supplementary data for this article are available on the journal Web site (canjchem.nrc.ca).

## Acknowledgement

This work is supported by the Katholieke Universiteit Leuven Research Council (Flemish concerted action (GOA) program) and the Vietnamese National Foundation for Science and Technology Development (NAFOSTED) under the project 104.03.142.09.

## References

- (1) Desiraju, G. R.; Steiner, T. *The Weak Hydrogen Bond in Structural Chemistry and Biology*; Oxford University Press: New York, 1999.
- (2) Grabowski, S. J. *Hydrogen Bonding — New Insights*; Springer: Dordrecht, The Netherlands, 2006.
- (3) Buckingham, A. D.; Fowler, P. W.; Hutson, L. M. *Chem. Rev.* **1988**, 88 (6), 963. doi:10.1021/cr00088a008.
- (4) Reed, A. E.; Curtiss, L. A.; Weinhold, F. *Chem. Rev.* **1988**, 88 (6), 899. doi:10.1021/cr00088a005.
- (5) Gu, Y.; Kar, T.; Scheiner, S. *J. Am. Chem. Soc.* **1999**, 121 (40), 9411. doi:10.1021/ja991795g.
- (6) Hobza, P.; Spirko, V. *Phys. Chem. Chem. Phys.* **2003**, 5 (6), 1290. doi:10.1039/b210223d.
- (7) Hobza, P. *Phys. Chem. Chem. Phys.* **2001**, 3 (13), 2555. doi:10.1039/b103068j.
- (8) Alabugin, I. V.; Manoharan, M.; Peabody, S.; Weinhold, F. *J. Am. Chem. Soc.* **2003**, 125 (19), 5973. doi:10.1021/ja034656e. PMID:12733938.
- (9) Karpfen, A.; Kryachko, E. S. *J. Phys. Chem. A* **2007**, 111 (33), 8177. doi:10.1021/jp072717f. PMID:17661452.
- (10) Chandra, A. K.; Parveen, S.; Zeegers-Huyskens, T. *J. Phys. Chem. A* **2007**, 111 (36), 8884. doi:10.1021/jp0738715. PMID:17711270.
- (11) Karpfen, A.; Kryachko, E. S. *J. Phys. Chem. A* **2009**, 113 (17), 5217. doi:10.1021/jp9005923. PMID:19341256.
- (12) Joseph, J.; Jemmis, E. D. *J. Am. Chem. Soc.* **2007**, 129 (15), 4620. doi:10.1021/ja067545z. PMID:17375920.
- (13) Hermansson, W. *J. Phys. Chem. A* **2002**, 106 (18), 4695. doi:10.1021/jp0143948.
- (14) Hobza, P.; Havlas, Z. *Chem. Rev.* **2000**, 100 (11), 4253. doi:10.1021/cr990050q. PMID:11749346.
- (15) Hobza, P.; Spirko, V.; Havlas, Z.; Buchhold, K.; Reimann, B.; Barth, H. D.; Brutschy, B. *Chem. Phys. Lett.* **1999**, 299 (2), 180. doi:10.1016/S0009-2614(98)01264-0.
- (16) Reimann, B.; Buchhold, K.; Vaupel, S.; Brutschy, B.; Halvas, Z.; Špirko, V.; Hobza, P. *J. Phys. Chem. A* **2001**, 105 (23), 5560. doi:10.1021/jp003726q.
- (17) Hobza, P.; Špirko, V.; Selzle, H. L.; Schlag, E. W. *J. Phys. Chem. A* **1998**, 102 (15), 2501. doi:10.1021/jp973374w.
- (18) Li, A. Y. *J. Phys. Chem. A* **2006**, 110 (37), 10805. doi:10.1021/jp062291p. PMID:16970375.
- (19) Li, X.; Liu, L.; Schlegel, H. B. *J. Am. Chem. Soc.* **2002**, 124 (32), 9639. doi:10.1021/ja020213j. PMID:12167060.
- (20) Gu, Y.; Kar, T.; Scheiner, S. *J. Am. Chem. Soc.* **1999**, 121 (40), 9411. doi:10.1021/ja991795g.

- (21) Qian, W.; Krimm, S. *J. Phys. Chem. A* **2002**, *106* (28), 6628. doi:10.1021/jp020438g.
- (22) Masunov, A.; Dannenberg, J. J.; Contreras, R. H. *J. Phys. Chem. A* **2001**, *105* (19), 4737. doi:10.1021/jp0043470.
- (23) Liu, Y.; Liu, W.; Yang, Y.; Liu, J. *Int. J. Quantum Chem.* **2006**, *106* (9), 2122. doi:10.1002/qua.21000.
- (24) Liu, Y.; Liu, W.; Li, H.; Liu, J.; Yang, Y. *J. Phys. Chem. A* **2006**, *110* (41), 11760. doi:10.1021/jp060908x. PMID: 17034170.
- (25) Yang, Y.; Zhang, J. W.; Gao, X. M. *Int. J. Quantum Chem.* **2006**, *106* (5), 1199. doi:10.1002/qua.20873.
- (26) Liu, Y.; Liu, W.; Li, H.; Yang, Y.; Cheng, S. *Int. J. Quantum Chem.* **2007**, *107* (2), 396. doi:10.1002/qua.21077.
- (27) Solimannejad, M.; Scheiner, S. *J. Phys. Chem. A* **2008**, *112* (17), 4120. doi:10.1021/jp711141x. PMID:18363388.
- (28) Solimannejad, M.; Scheiner, S. *J. Phys. Chem. A* **2007**, *111* (20), 4431. doi:10.1021/jp071695u. PMID:17474730.
- (29) Trung, N. T.; Hue, T. T.; Nguyen, M. T. *Phys. Chem. Chem. Phys.* **2009**, *11* (6), 926. doi:10.1039/b816112g. PMID: 19177210.
- (30) Trung, N. T.; Hue, T. T.; Nguyen, M. T. *J. Phys. Chem. A* **2009**, *113* (13), 3245. doi:10.1021/jp810826z. PMID: 19256510.
- (31) Yang, Y.; Zhang, W. *J. Mol. Struct. THEOCHEM* **2007**, *814* (1–3), 113. doi:10.1016/j.theochem.2007.03.005.
- (32) Trung, N. T.; Hue, T. T.; Nguyen, M. T.; Zeegers-Huyskens, T. *Phys. Chem. Chem. Phys.* **2008**, *10* (33), 5105. doi:10.1039/b806346j. PMID:18701959.
- (33) Liu, Y. *Int. J. Quantum Chem.* **2008**, *108* (6), 1123. doi:10.1002/qua.21587.
- (34) Hobza, P. *Int. J. Quantum Chem.* **2002**, *90* (3), 1071. doi:10.1002/qua.10313.
- (35) Lu, P.; Liu, G. Q.; Li, J. C. *J. Mol. Struct. THEOCHEM* **2005**, *723* (1–3), 95. doi:10.1016/j.theochem.2005.01.034.
- (36) Peters, N. J. S. *J. Phys. Chem. A* **1998**, *102* (35), 7001. doi:10.1021/jp981522s.
- (37) Bunte, S. W.; Rice, B. M.; Chabalowski, C. F. *J. Phys. Chem. A* **1997**, *101* (49), 9430. doi:10.1021/jp971716s.
- (38) Nguyen, M. T.; Vanquickenbore, L. G.; Plisnier, M.; Flam-mang, R. *Mol. Phys.* **1993**, *78* (1), 111. doi:10.1080/00268979300100111.
- (39) Denis, P. A.; Ventura, O. N.; Mai, H. T.; Nguyen, M. T. *J. Phys. Chem. A* **2004**, *108* (23), 5073. doi:10.1021/jp0498466.
- (40) Boys, S. F.; Bernardi, F. *Mol. Phys.* **1970**, *19* (4), 553. doi:10.1080/00268977000101561.
- (41) Weinhold, F.; Landis, C. *Valency and Bonding*; Cambridge University Press: Cambridge, 2005.
- (42) Frisch, M. J.; Trucks, G. W.; Schlegel, H. B.; Scuseria, G. E.; Robb, M. A.; Cheeseman, J. R.; Montgomery, J. A., Jr.; Vreven, T.; Kudin, K. N.; Burant, J. C.; Millam, J. M.; Iyen-gar, S. S.; Tomasi, J.; Barone, V.; Mennucci, B.; Cossi, M.; Scalmani, G.; Rega, N.; Petersson, G. A.; Nakatsuji, H.; Hada, M.; Ehara, M.; Toyota, K.; Fukuda, R.; Hasegawa, J.; Ishida, M.; Nakajima, T.; Honda, Y.; Kitao, O.; Nakai, H.; Klene, M.; Li, X.; Knox, J. E.; Hratchian, H. P.; Cross, J. B.; Bakken, V.; Adamo, C.; Jaramillo, J.; Gomperts, R.; Stratmann, R. E.; Yazyev, O.; Austin, A. J.; Cammi, R.; Po-melli, C.; Ochterski, J. W.; Ayala, P. Y.; Morokuma, K.; Voth, G. A.; Salvador, P.; Dannenberg, J. J.; Zakrzewski, V. G.; Dapprich, S.; Daniels, A. D.; Strain, M. C.; Farkas, O.; Malick, D. K.; Rabuck, A. D.; Raghavachari, K.; Foresman, J. B.; Ortiz, J. V.; Cui, Q.; Baboul, A. G.; Clifford, S.; Cio-slowski, J.; Stefanov, B. B.; Liu, G.; Liashenko, A.; Piskorz, P.; Komaromi, I.; Martin, R. L.; Fox, D. J.; Keith, T.; Al-La-ham, M. A.; Peng, C. Y.; Nanayakkara, A.; Challacombe, M.; Gill, P. M. W.; Johnson, B.; Chen, W.; Wong, M. W.; Gonzalez, C.; Pople, J. A. *Gaussian 03*, revision D.02; Gaus-sian Inc.: Wallingford, CT, 2004.
- (43) Biegler-König, F.; Schnbohm, J. *AIM2000*, version 2.0; Uni-versity of Applied Sciences: Bielefeld, Germany, 2002.
- (44) Glendening, E. D.; Badenhoop, J.; Reed, K. A. E.; Carpen-ter, J. E.; Bohmann, J. A.; Morales, C. M.; Weinhold, F. *GenNBO 5.G*; Theoretical Chemistry Institute, University of Wisconsin: Madison, WI, 2001.
- (45) Lipkowski, P.; Grabowski, S. J.; Robinson, T. L.; Leszcz-yński, J. *J. Phys. Chem. A* **2004**, *108* (49), 10865. doi:10.1021/jp048562i.
- (46) Liu, Y.; Liu, W.; Li, H.; Yang, Y.; Cheng, S. *J. Mol. Struct. THEOCHEM* **2006**, *778* (1–3), 49. doi:10.1016/j.theochem.2006.07.023.
- (47) Keefe, C. D.; Isenor, M. *J. Phys. Chem. A* **2008**, *112* (14), 3127. doi:10.1021/jp076563f. PMID:18338874.
- (48) Bader, R. F. *Chem. Rev.* **1991**, *91* (5), 893. doi:10.1021/cr00005a013.
- (49) Koch, U.; Popelier, P. L. A. *J. Phys. Chem.* **1995**, *99* (24), 9747. doi:10.1021/j100024a016.
- (50) Cremer, D.; Kraka, E. *Angew. Chem. Int. Ed. Engl.* **1984**, *23* (8), 627. doi:10.1002/anie.198406271.
- (51) Rozas, I.; Alkorta, I.; Elguero, E. *J. Am. Chem. Soc.* **2000**, *122* (45), 11154. doi:10.1021/ja0017864.
- (52) Grabowski, S. J.; Sokalski, W. A.; Leszczynski, J. *Chem. Phys.* **2007**, *337* (1–3), 68. doi:10.1016/j.chemphys.2007.06.042.
- (53) Li, A. Y. *J. Chem. Phys.* **2007**, *126* (15), 154102. doi:10.1063/1.2715561. PMID:17461609.
- (54) Li, A. Y. *J. Mol. Struct. THEOCHEM* **2008**, *862* (1–3), 21. doi:10.1016/j.theochem.2008.04.017.
- (55) Bent, H. A. *Chem. Rev.* **1961**, *61* (3), 275. doi:10.1021/cr60211a005.

# Regaining the Woodward–Hoffmann rules for chelotropic reactions via conceptual DFT

Pablo Jaque, José V. Correa, Frank De Proft, Alejandro Toro-Labbé, and Paul Geerlings

**Abstract:** In our continuous effort to retrieve the Woodward–Hoffmann rules from conceptual density functional theory (DFT), we have examined the last type of pericyclic reactions, i.e., chelotropic reactions. Both the initial hardness response and the dual descriptor have been investigated to predict the allowed and forbidden character for the addition of SO<sub>2</sub> to butadiene ( $4n$  system) and 1,3,5-hexatriene ( $4n + 2$  system). It is shown that with both electronic descriptors, the conrotatory/disrotatory mode for the linear and nonlinear mechanisms are retrieved based on a density-only approach, free from consideration of orbital and (or) wave function symmetry. The dual descriptor moreover reveals that stabilizing interactions are presented only for the linear path, which can be considered as an overall favourable mechanism for a chelotropic reaction.

**Key words:** chelotropic reactions, Woodward–Hoffmann rules, conceptual DFT.

**Résumé :** Dans le cadre de nos travaux pour récupérer les règles de Woodward–Hoffmann à partir de la théorie de la fonctionnelle de la densité conceptuelle, on a étudié le dernier type de réactions péri-cycliques, à savoir les réactions chélotropes. On a étudié tant la réponse initiale de la dureté que le descripteur dual pour prédire le caractère permis et interdit pour l'addition du SO<sub>2</sub> sur le butadiène (système  $4n$ ) et hexa-1,3,5-triène (système  $4n + 2$ ). Il est démontré que pour les deux descripteurs électroniques, on peut retrouver le mode conrotatoire/disrotatoire pour les mécanismes linéaires et non linéaires en se basant uniquement sur une approche de densité, sans prendre en considération l'orbitale et (ou) la symétrie de la fonction d'onde. De plus, le descripteur double ne révèle l'existence d'interactions stabilisantes que pour la voie linéaire qui peut être considérée comme le mécanisme global le plus favorable pour une réaction chélotrope.

**Mots-clés :** réactions chélotrope, règles de Woodward–Hoffmann, théorie de la fonctionnelle de la densité conceptuelle (« DFT » conceptuelle).

[Traduit par la Rédaction]

## Introduction

The Woodward–Hoffmann (WH) rules<sup>1</sup> have played an unprecedented role in predicting/rationalizing the outcome of chemical reactions on the basis of a quantum chemical approach.<sup>2,3</sup> Formulated in the late sixties and based on a highly approximate, semi-empirical MO method, the extended Hückel theory,<sup>4</sup> developed by one of the two fathers of the rules, the WH rules enabled the practicing organic chemist to predict the allowedness/forbiddenness and the associated

stereochemical implications of four types of pericyclic reactions: cycloadditions, electrocyclizations, sigmatropic, and chelotropic reactions.<sup>1</sup>

Fundamental in the approaches developed by Woodward and Hoffmann is the principle of orbital conservation: an orbital, occupied or unoccupied in the reactants, retains its symmetry towards the symmetry operations associated to the geometry of the transition state (TS), when passing from the reactants, through the TS to the products. So, this approach is pervaded by the symmetry or nodal structure of

Received 6 January 2010. Accepted 18 March 2010. Published on the NRC Research Press Web site at canjchem.nrc.ca on 16 July 2010.

*This article is part of a Special Issue dedicated to Professor R. J. Boyd. The authors want to dedicate this contribution to Professor R. J. Boyd, a fine and respected colleague, whose work on electron density has been a source of inspiration for many years.*

**P. Jaque.** Universidad Andrés Bello, Facultad de Ecología y Recursos Naturales, Departamento de Ciencias Químicas, Laboratorio de Química Teórica, Av. República 275, Santiago, Chile; Eenheid Algemene Chemie (ALGC), Faculteit Wetenschappen, Vrije Universiteit Brussel (VUB), Pleinlaan 2, 1050.

**J.V. Correa.** Eenheid Algemene Chemie (ALGC), Faculteit Wetenschappen, Vrije Universiteit Brussel (VUB), Pleinlaan 2, 1050; Laboratorio de Química Teórica Computacional (QTC), Facultad de Química, Pontificia Universidad Católica de Chile, Casilla 306, Correo 22, Santiago, Chile.

**F. De Proft and P. Geerlings.**<sup>1</sup> Eenheid Algemene Chemie (ALGC), Faculteit Wetenschappen, Vrije Universiteit Brussel (VUB), Pleinlaan 2, 1050.

**A. Toro-Labbé.** Laboratorio de Química Teórica Computacional (QTC), Facultad de Química, Pontificia Universidad Católica de Chile, Casilla 306, Correo 22, Santiago, Chile.

<sup>1</sup>Corresponding author (e-mail: pgeerlin@vub.ac.be).



the orbital and (or) the symmetry of the total wave function to which they combine. These aspects and the concurrent use of correlation diagrams have also been pointed out independently in the pioneering work by Longuet-Higgins.<sup>5</sup>

In recent years, density functional theory<sup>6</sup> (DFT) gained widespread appreciation for its computational efficiency to study the properties and reaction paths for systems of varying complexity, thus entering the fields of organic, inorganic, and biochemistry, including transition-metal chemistry and catalysis. Based on the famous Hohenberg and Kohn theorems,<sup>7</sup> and when casted into the elegant Kohn–Sham formalism,<sup>8</sup> DFT nowadays plays the role of a computational workhorse used by, e.g., most practicing organic chemists when investigating reaction paths and calculating reaction and activation energies.<sup>9</sup> This highlights the role of the electron density function  $\rho(\vec{r})$  as the fundamental carrier of information of a much simpler nature than the extremely complex wave function depending on the three spatial- and single-spin coordinate of all the electrons of the system.

On the other hand, under the impetus of Parr and co-workers, DFT also paved the way for rigorous and sharp definitions of a variety of well-known but often vaguely defined concepts, such as electronegativity ( $\chi$ ), hardness ( $\eta$ ), and softness ( $S$ ), enabling their numerical evaluation. This branch of DFT, called conceptual DFT by its founding father,<sup>10</sup> has been a flourishing subfield for about 25 years, leading to the introduction of new concepts (e.g., Fukui function,<sup>11</sup> electrophilicity,<sup>12</sup> and the dual descriptor<sup>13</sup>) used as such or within the context of principles such as the electronegativity equalization principle,<sup>14</sup> the hard and soft acids and bases principle, and the maximum hardness principle.<sup>15</sup>

A true avalanche of papers have appeared since the mid 1990s presenting further extensions and applications mostly on (generalized) acid/base reactions,<sup>16</sup> including the majority of organic addition/substitution/elimination reactions. Remarkably up to a few years ago, two types of reactions remained unstudied in a conceptual DFT context: redox reactions and pericyclic reactions. Both types of reactions constituted a major line of research in our group in recent years,<sup>17</sup> leading among others to a successful interpretation of the WH rules for cycloadditions, electrocyclizations, and sigmatropic reactions.<sup>18</sup>

The aim of the present paper is to present the results on the fourth type of pericyclic reactions: the chelotropic reactions, and so this study can be seen as the final cornerstone of our endeavour to link pericyclic reactions to conceptual DFT.

Chelotropic reactions were defined by Woodward and Hoffmann as pericyclic reactions in which two  $\sigma$  bonds are formed or broken on a single atom in a concerted manner. Classical examples are the addition of sulfur dioxide ( $\text{SO}_2$ ) and carbenes ( $\text{CR}_2$ ) to a polyene forming a cyclic system due to the formation of two  $\sigma$  bonds. There are two possible mechanisms for the addition leading to different selection rules and stereochemical outcomes (see Table 1): in a linear chelotropic reaction, the attacking small molecule lies in a plane perpendicular to that of the polyene and bisects its central C–C bond, whereas in the nonlinear case, the plane of the attacking molecule no longer bisects the central C–C bond of the polyene but is rotated so that, for example in  $\text{SO}_2$ , the O–O axis parallels the C–C bond.

**Table 1.** Generalized Woodward–Hoffmann rules for chelotropic reactions.

$\pi$ -Electron number	Linear pathway	Nonlinear pathway
$4n$	Disrotatory	Conrotatory
$4n + 2$	Conrotatory	Disrotatory

## Methodology

The methodology is similar to the one adopted in our previous studies on cycloadditions, electrocyclizations and sigmatropic reactions. Two conceptual-DFT-based reactivity descriptors are used: the initial hardness response, which has been advocated by us on the basis of Zimmerman's<sup>19</sup> alternative approach to the WH rules, stressing the importance of the aromaticity of the TS as a criterion for allowedness or forbiddenness of a reaction. On this basis, the slope of the hardness vs. the reaction coordinate curve (initial hardness response) was proposed as a reactivity indicator; the higher the slope (more positive or less negative) the higher the tendency of the system to select this reaction path.<sup>18</sup> A model reaction coordinate  $R$  is thereby chosen to reduce the computational complexity of the few calculations needed for the numerical evaluation of the slope at the onset of the reaction ( $\partial\eta/\partial R$ ) (note that also and precisely at the onset or the beginning of the reaction, the replacement of the full reaction coordinate by a model coordinate is justified).

The quantity is evaluated numerically at the onset of the reaction in a finite difference approach. The hardness itself, the second derivative of the energy  $E$  with respect to the number of electrons  $N$ , at constant external (i.e., due to the nuclei) potential<sup>20</sup>

$$[1] \quad \eta = \frac{1}{2} \left( \frac{\partial^2 E}{\partial N^2} \right)_{v(\vec{r})}$$

is evaluated also in a finite difference approach as

$$[2] \quad \eta = \frac{I - A}{2}$$

where  $I$  and  $A$  are the vertical ionization energy and electron affinity, respectively.<sup>16</sup> Invoking Koopman's theorem yields

$$[3] \quad \eta \approx \frac{\varepsilon_{\text{LUMO}} - \varepsilon_{\text{HOMO}}}{2}$$

where  $\varepsilon_{\text{HOMO}}$  and  $\varepsilon_{\text{LUMO}}$  are the frontier molecular orbital energies. This approach was followed in the present version.

The hardness response is in fact a third-order derivative in the hierarchy of response functions characterizing the sensibility of a system's energy when it is perturbed in its external potential  $v(\vec{r})$  and (or) its number of electrons  $N$ , the basic variables in the so-called perturbational approach to chemical reactivity.<sup>6,16</sup>

In this approach, the change in energy upon perturbation in  $N$  and (or)  $v(\vec{r})$  can be written as

$$[4] \quad dE = \left( \frac{\partial E}{\partial N} \right)_{v(\vec{r})} dN + \int \left( \frac{\delta E}{\delta v(\vec{r})} \right)_N \delta v(\vec{r}) d\vec{r} + \left( \frac{\partial^2 E}{\partial N^2} \right)_{v(\vec{r})} dN^2 + \dots$$

where the first derivative (the electronic chemical potential,

$\mu$ )<sup>21</sup> has been identified as the negative of the electronegativity,  $\chi$ , the functional derivative  $(\delta E/\delta v(\vec{r}))_N$  has been identified as the electron density, and the second derivative  $(\partial^2 E/\partial N^2)_{v(\vec{r})}$  has been identified as the hardness (vide supra). The initial hardness response can now obviously be written as  $(\partial^3 E/\partial N^2 \partial R)$ , where  $R$  stands for the model reaction coordinate, highlighting its third-order derivative character.

An alternative approach was followed in our previous studies on pericyclic reactions<sup>18</sup> by concentrating on the following local (i.e.,  $\vec{r}$ -dependent) descriptor

$$[5] \quad f^{(2)}(\vec{r}) = \left( \frac{\partial f(\vec{r})}{\partial N} \right)_{v(\vec{r})}$$

indicating how the Fukui function changes at each position when the total number of electrons  $N$  is changing. As the Fukui function itself is defined as the first derivative of  $\rho(\vec{r})$  with respect to  $N$

$$[6] \quad f(\vec{r}) = \left( \frac{\partial \rho(\vec{r})}{\partial N} \right)_{v(\vec{r})}$$

$f^{(2)}(\vec{r})$  can be written as the following third-order derivative

$$[7] \quad f^{(2)}(\vec{r}) = \left( \frac{\partial^3 E}{\delta v(\vec{r}) \partial N^2} \right)$$

In a frozen-core approximation, it is easily seen that

$$[8] \quad f^{(2)}(\vec{r}) \approx |\phi_{\text{LUMO}}(\vec{r})|^2 - |\phi_{\text{HOMO}}(\vec{r})|^2$$

indicating that  $f^{(2)}(\vec{r})$  highlights the difference in densities between the LUMO and HOMO, giving a “one-shot” picture of nucleophilic and electrophilic regions, hence its name, the dual descriptor. It was shown that both for intra- and inter-molecular pericyclic reactions, the process proceeds along a path favouring the overlap of positive and negative regions of  $f^{(2)}(\vec{r})$ : favourable chemical reactions occur when regions that are good electron acceptors ( $f^{(2)}(\vec{r}) > 0$ ) are aligned with regions that are good electron donors ( $f^{(2)}(\vec{r}) < 0$ ).<sup>13,18b</sup> Note that it has been shown by some of the present authors that the two descriptors presented above, the initial hardness response (global in nature, i.e.,  $\vec{r}$ -independent) and the local dual descriptor are intimately related, in the sense that  $f^{(2)}(\vec{r})$  can be written as

$$[9] \quad f^{(2)}(\vec{r}) = \left( \frac{\delta \eta}{\delta v(\vec{r})} \right)_N$$

and that in the case where changes in  $v(\vec{r})$  are provoked by changes in nuclear configurations only, it can easily be seen that

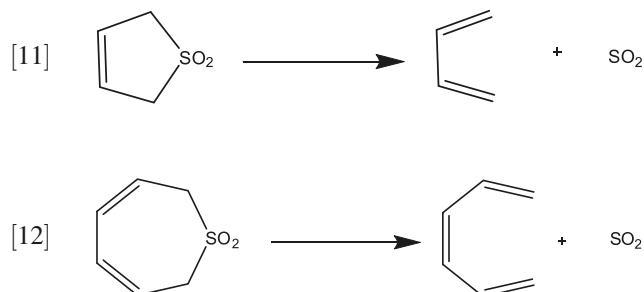
$$[10] \quad \left( \frac{\partial \eta}{\partial R} \right)_N = \int f^{(2)}(\vec{r}) \frac{\partial v(\vec{r})}{\partial R} d\vec{r}$$

This indicates that the general information in  $f^{(2)}(\vec{r})$  is refined via  $(\frac{\partial v(\vec{r})}{\partial R})_N$  to result in the initial hardness response.

As both the dual descriptor and the initial hardness response turned out to be successful in interpreting electrocyclizations, cycloadditions, and sigmatropic reactions, we

decided to apply this same “dual” approach to the remaining type of pericyclic reaction: the chelotropic reaction.

We turned to one of the prototypes of chelotropic reactions:<sup>1–3</sup> the extrusion of  $\text{SO}_2$  from sulfonene or higher sulfones yielding butadiene (a  $4n$  system) and 1,3,5-hexatriene (a  $4n + 2$  system), respectively.



For computational reasons, both reactions were considered in the reverse direction. The principle of microscopic reversibility indeed re-assures identical outcomes concerning allowedness or forbiddenness irrespective of the direction considered.

All calculations were performed at the DFT level, using the B3LYP<sup>22,23</sup> functional for geometry optimization and the PBE<sup>24</sup> functional for single-point calculations for the initial hardness response combined with a split-valence double-zeta plus polarization basis set, 6–31G(d,p).<sup>25</sup> The PBE functional is used as we prefer to work in the spirit of the Tozer–De Proft approach. As we also did in previous work in this series<sup>18c</sup> for the evaluation of hardness, pure density functionals are preferred, as in this case discontinuity problems are approximately cancelled.<sup>26,27</sup> All of these calculations were done using the Gaussian 03 program.<sup>28</sup>

## Results and discussion

### Initial hardness response

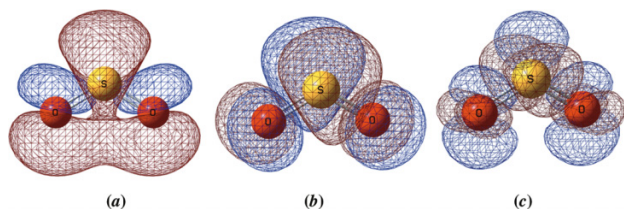
When considering the particular situation of  $\text{SO}_2$  attacking on, e.g., butadiene, it should be noticed that in a molecular orbital (MO) picture, filled and vacant frontier MOs involved in bonding to a diene (or triene) are situated on the same atom. This situation yields a picture for the dual descriptor (Fig. 1) reminiscent of that of the singlet carbenes<sup>29</sup> or silylenes<sup>30</sup> studied in depth in our group.

The geometry of the linear chelotropic reaction is shown in Fig. 2, where  $\text{SO}_2$  attacks the polyene (in case of butadiene, a  $4n$  system) lying in a plane perpendicular to the polyene plane and bisecting its central C–C bond.

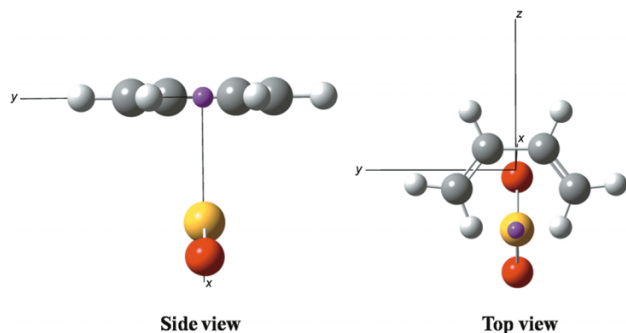
The initial hardness profile (where  $\eta$  was computed as indicated in eq. [3]) together with the energy profile (based on a model reaction coordinate involving the dihedral angle between the  $\text{CH}_2$  groups and the rest of the diene) are given in Fig. 3. It is clear that the energetically less-favoured conrotatory mode is the one that has the less negative  $(\partial \eta/\partial R)$  slope, i.e., leads to the “faster” loss of hardness upon reaction. All these observations are in line with the WH rules stating that a  $4n$  system prefers a disrotatory mode for a linear approach.

Passing now to the nonlinear case, Fig. 4 shows that the  $\text{SO}_2$  molecule approaches the diene molecule in a plane no longer bisecting the central C–C bond of the polyene. The

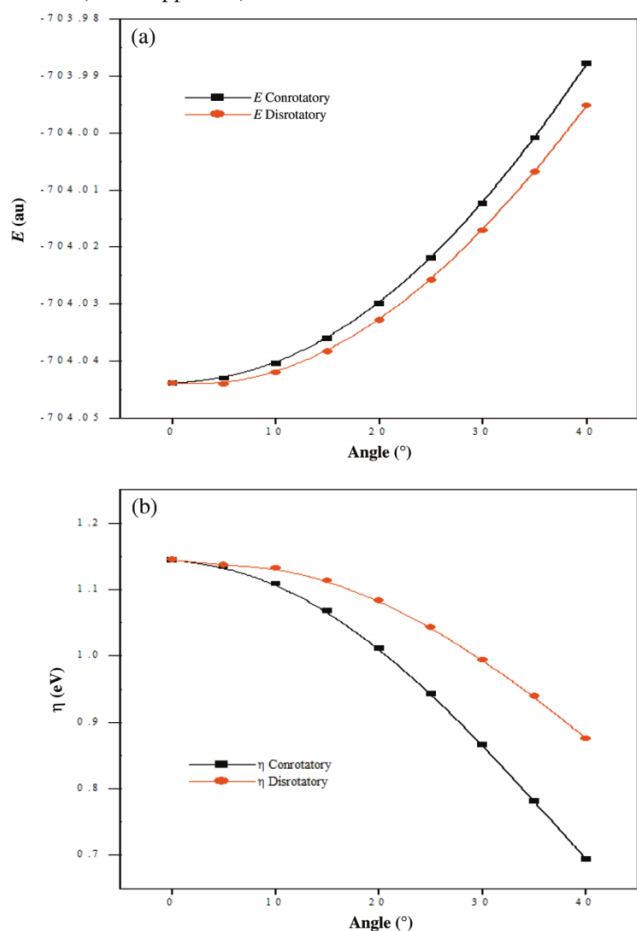
**Fig. 1.** Frontier molecular orbital maps: (a) HOMO ; (b) LUMO (where negative phases are indicated in blue and positive phases are displayed in red); and (c) the dual descriptor map for SO<sub>2</sub>; electrophilic or acidic sites ( $f^2(\vec{r}) > 0$ ) and nucleophilic or basic sites ( $f^2(\vec{r}) < 0$ ) are indicated in red and blue, respectively.



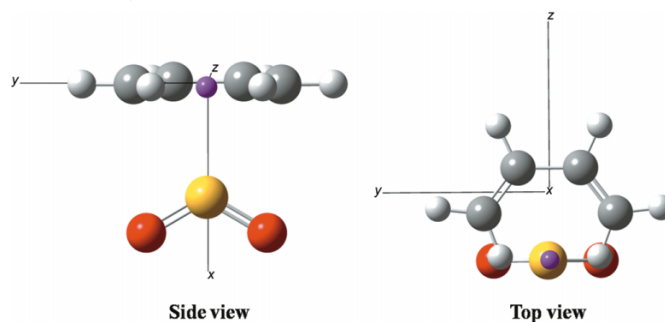
**Fig. 2.** Linear chelotropic reaction: the case of a  $4n$  system (butadiene–SO<sub>2</sub>).



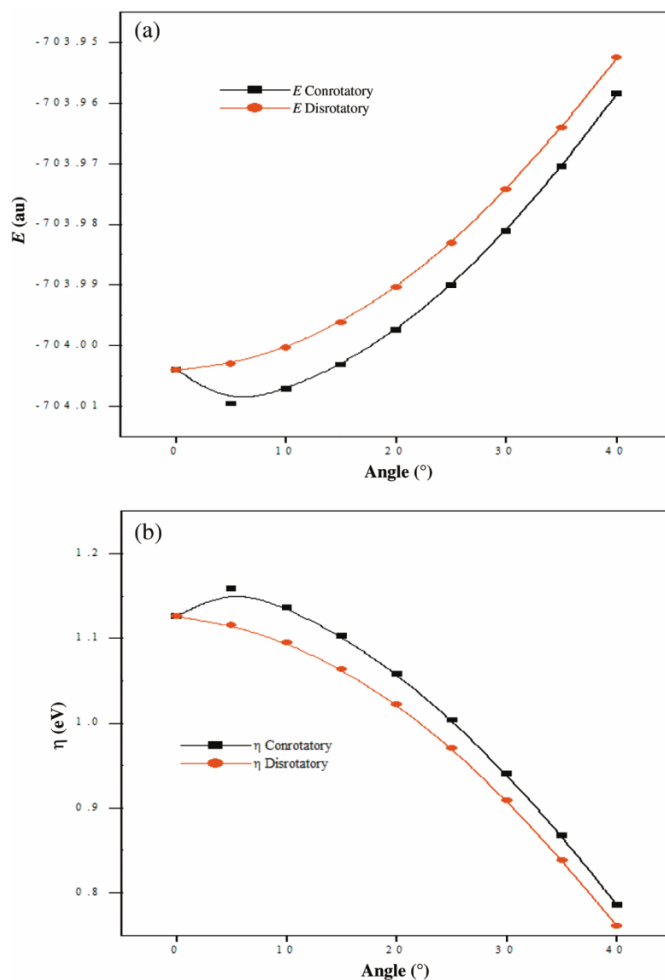
**Fig. 3.** (a) Energy and (b) hardness profiles for the butadiene–SO<sub>2</sub> reaction (linear approach).



**Fig. 4.** Nonlinear chelotropic reaction: the case of a  $4n$  system (butadiene–SO<sub>2</sub>).



**Fig. 5.** (a) Energy and (b) hardness profiles for the butadiene–SO<sub>2</sub> reaction (nonlinear approach).

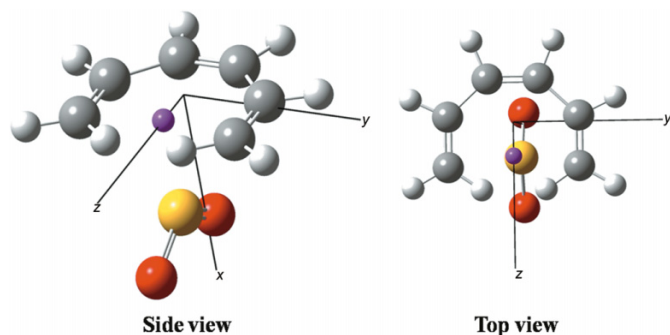


energy and hardness curves now show the inverse behaviour to the linear case (Fig. 5) with the disrotatory mode preferred on the basis of both energy and initial hardness response, in line with the inversion of the WH rules when passing from a  $4n$  to a  $4n + 2$  polyene.

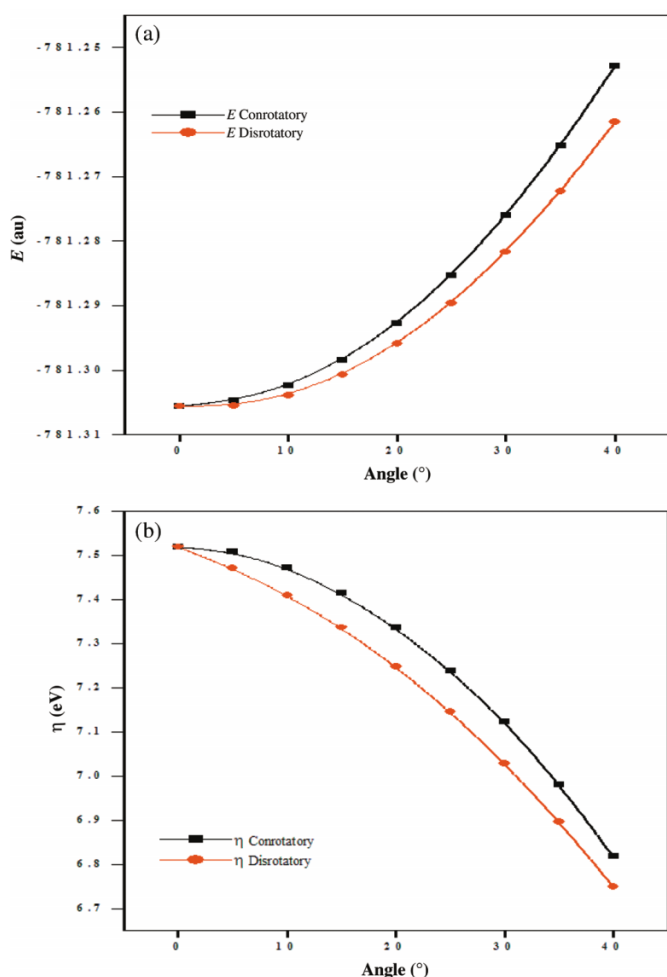
This analysis has also been carried out on the chelotropic reaction between SO<sub>2</sub> and a  $(4n + 2)$  system in both reactive attacks, linear, and nonlinear, as displayed in Figs. 6–9.

Notice that in both cases, the disrotatory mode is more favourable from the energetic point of view, whereas the

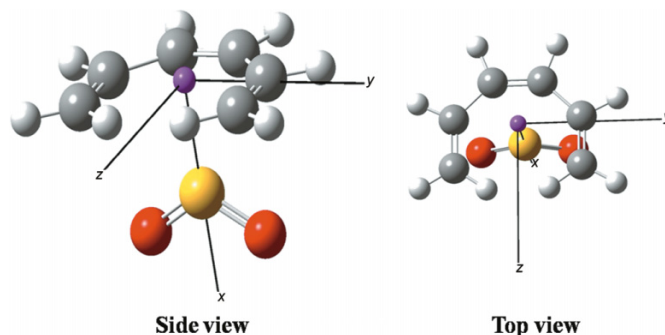
**Fig. 6.** Linear chelotropic reaction: the case of a  $(4n + 2)$  system (1,3,5-hexatriene-SO<sub>2</sub>).



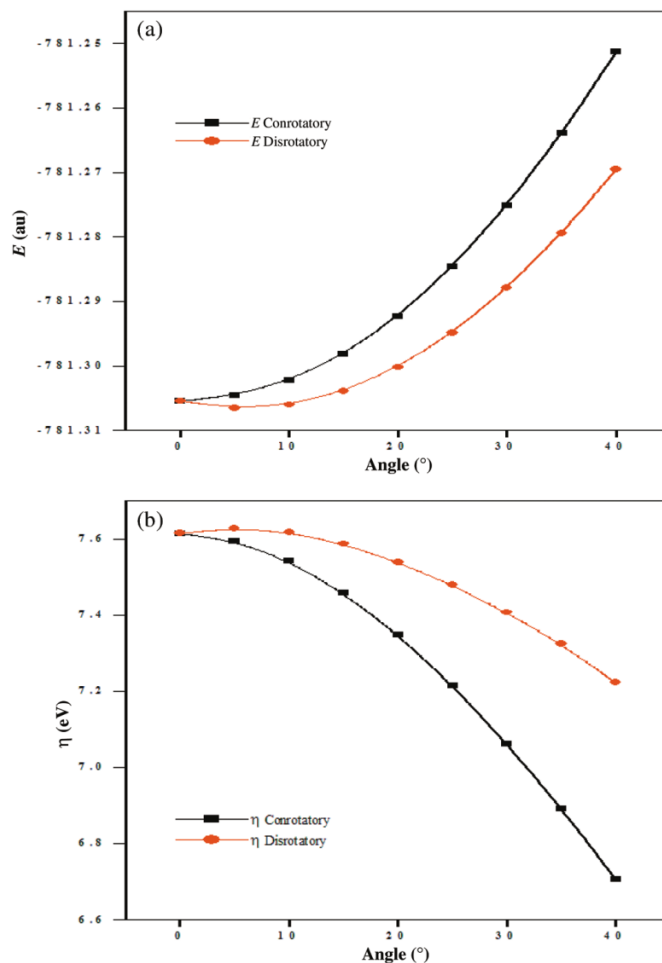
**Fig. 7.** (a) Energy and (b) hardness profiles for the 1,3,5-hexatriene-SO<sub>2</sub> reaction (linear approach).



**Fig. 8.** Nonlinear chelotropic reaction: case of a  $(4n + 2)$  system (1,3,5-hexatriene-SO<sub>2</sub>).



**Fig. 9.** (a) Energy and (b) hardness profiles for the 1,3,5-hexatriene-SO<sub>2</sub> reaction (nonlinear approach).



chemical hardness helps to discriminate between the conrotatory vs. disrotatory modes. An inverse sequence for both the linear and nonlinear mechanisms as compared with the chelotropic reaction between SO<sub>2</sub> and the  $4n$  system is found, in agreement with the WH rules.

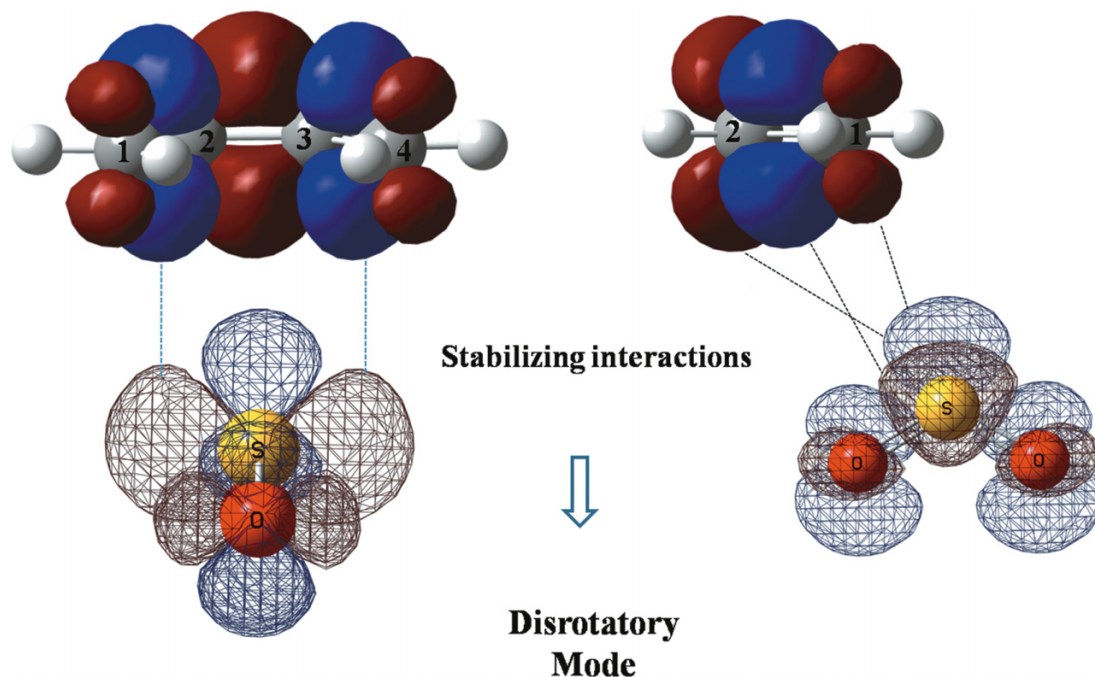
### The dual descriptor

In Fig. 10, we depict the dual descriptors of both butadiene and SO<sub>2</sub> represented as counterplots, using colour codes. Red corresponds a positive  $f^{(2)}(r)$  value and blue to a

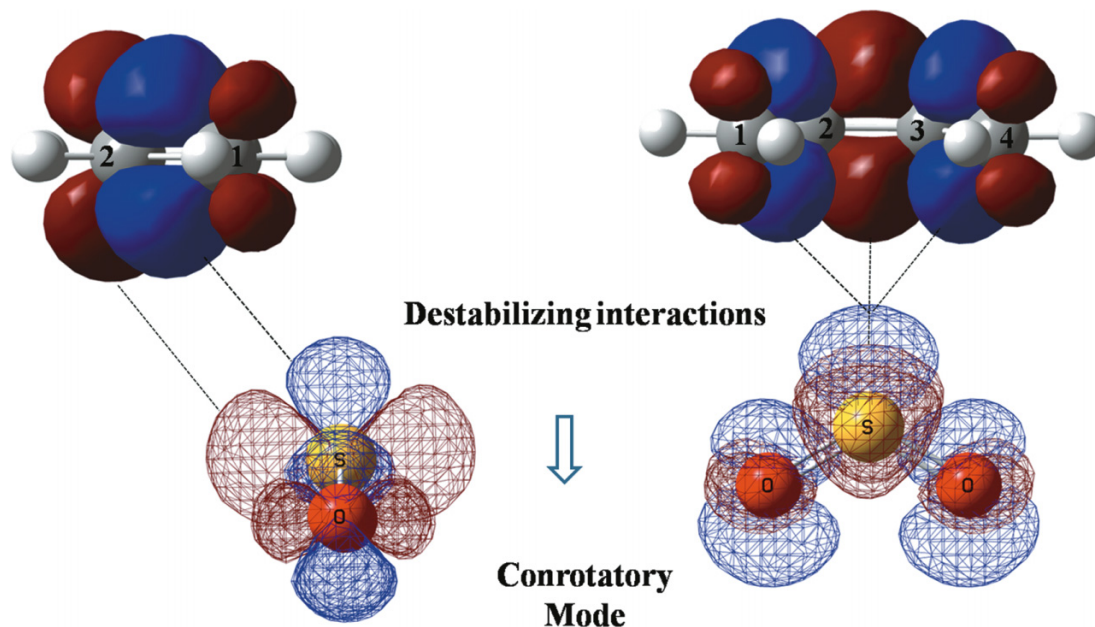
negative value, i.e., electrophilic and nucleophilic regions, respectively. In the case of the linear approach to butadiene, it is immediately seen that stabilizing interactions are at work between the central C<sub>2</sub>-C<sub>3</sub> region and the terminal C atoms with the lone pair region of SO<sub>2</sub>, and, more importantly, between the C<sub>1</sub>-C<sub>2</sub> and C<sub>3</sub>-C<sub>4</sub> regions of the diene and the empty p orbital region of SO<sub>2</sub>, further optimized by a disrotatory movement of the diene. In other words, the analysis based on the dual descriptors reveals that the linear approach is favoured by a synergism (resembling the so-called  $\sigma$ -donation/ $\pi$  back-donation phenomenon in metal-



**Fig. 10.** The dual descriptor maps for the reactants (butadiene + SO<sub>2</sub>) for the linear approach; electrophilic ( $f^{(2)}(r) > 0$ ) and nucleophilic ( $f^{(2)}(r) < 0$ ) regions are indicated in red and blue, respectively.



**Fig. 11.** The dual descriptor maps for the reactants (butadiene + SO<sub>2</sub>) for the nonlinear chelotropic approach; electrophilic ( $f^{(2)}(r) > 0$ ) and nucleophilic ( $f^{(2)}(r) < 0$ ) regions are indicated in red and blue, respectively.



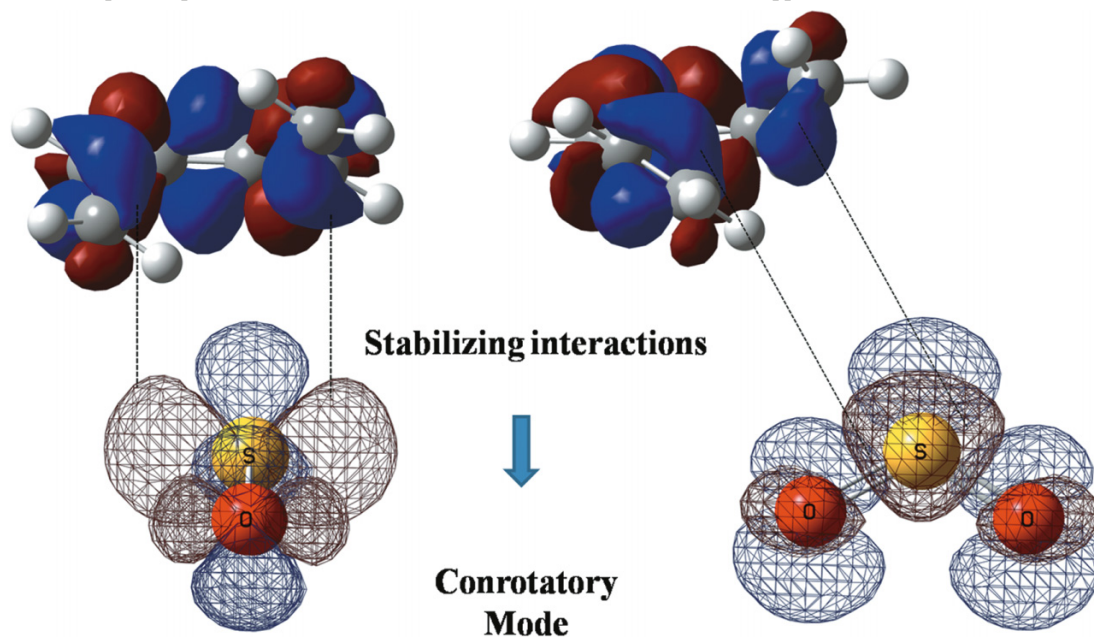
ligand bonding) driving the disrotatory movement of the CH<sub>2</sub> groups.

Turning finally to the nonlinear case, the  $4n$  system shows in fact only destabilizing interactions (see Fig. 11) between the lone pair of SO<sub>2</sub> and the C<sub>1</sub>–C<sub>2</sub> and C<sub>3</sub>–C<sub>4</sub> regions and the empty p orbital of the S atom and the C<sub>2</sub>–C<sub>3</sub> region and terminal C atoms. The system will only gain stabilization when these destabilizing interactions are reduced, for instance, through a conrotatory movement of the terminal

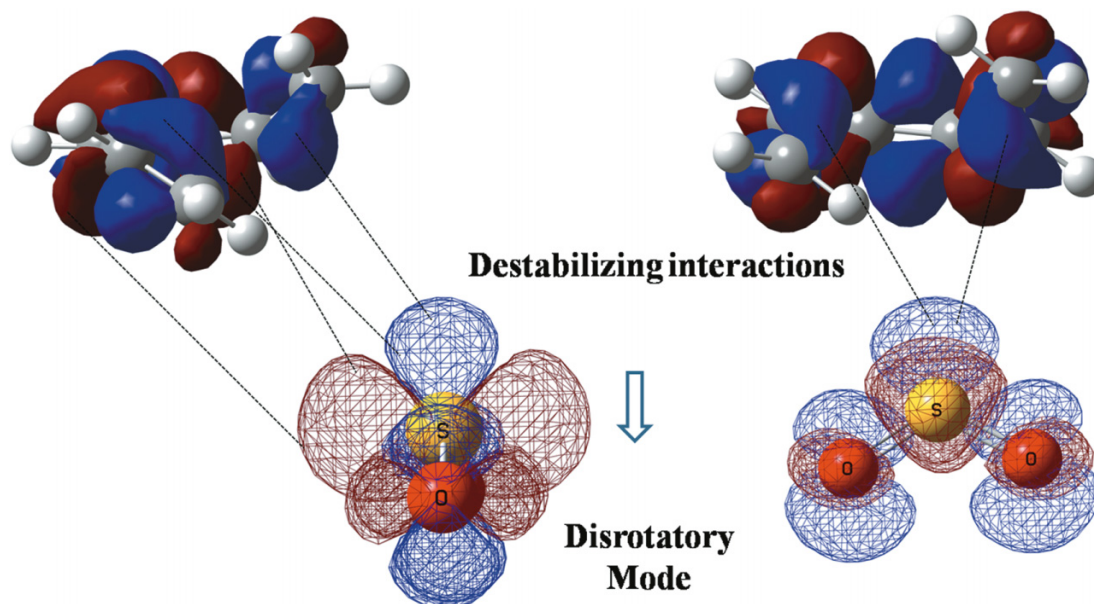
CH<sub>2</sub>, leading to the conjecture that these reactions are less favoured than their analogues in the linear case.

This is in agreement with the computational data, indicating that upon trying to locate a TS for the nonlinear approach, the system spontaneously evolves to a linear approach geometry. To our knowledge and from the experimental point of view,<sup>31</sup> no clear cut evidence has been presented for cases in which such a nonlinear approach is the preponderant mechanism.

**Fig. 12.** The dual descriptor maps for the reactants (1,3,5-hexatriene + SO<sub>2</sub>) for the linear approach; same colour codes as in Fig. 10.



**Fig. 13.** The dual descriptor maps for the reactants (1,3,5-hexatriene + SO<sub>2</sub>) for the nonlinear approach; same colour codes as in Fig. 10.



The dual descriptor maps for the reaction between SO<sub>2</sub> and 1,3,5-hexatriene are given in Figs. 12 and 13 for the linear and nonlinear path, respectively. A behaviour opposite to that of the  $4n$  system is observed.

## Conclusions

Two DFT-based reactivity descriptors, the initial hardness response and the dual descriptor turn out to be successful in predicting/interpreting the allowedness/forbiddenness of cheletropic reactions in the linear and nonlinear approaches. Combined with our earlier positive results for the three other types of pericyclic reactions (electrocyclizations, cycloadditions, and sigmatropic reactions), this study leads to the con-

clusion that the WH rules, essentially based on orbital and wave function symmetry, can be retrieved in a “density-only” context using conceptual-DFT-based descriptors. This finding highlights the basic role of the electron density, which, despite of its much simpler mathematical form (function of three variables) as compared with the wave function (function of  $4N$  variables), is shown to carry the necessary information to regain the celebrated WH rules based on the symmetry of the wave function.

## Acknowledgements

The authors would like to thank the FWO-Flanders for a Postdoctoral Fellowship to Pablo Jaque and continuous support for the Algemene Chemie (ALGC) research group.

## References

- (1) Woodward, R. B.; Hoffmann, R. *The Conservation of Orbital Symmetry*; Verlag Chemie: Weinheim, 1971.
- (2) Gilchrist, T. L.; Storr, R. C. *Organic Reactions and Orbital Symmetry*; Cambridge University Press: Cambridge, 1979.
- (3) Sankaraman, S. *Pericyclic Reactions — A Textbook*; Wiley-VCH, 2005.
- (4) Hoffmann, R. *J. Chem. Phys.* **1963**, 39 (6), 1397. doi:10.1063/1.1734456.
- (5) Longuet-Higgins, H. C.; Abrahamson, E. W. *J. Am. Chem. Soc.* **1965**, 87 (9), 2045. doi:10.1021/ja01087a033.
- (6) Parr, R.; Yang, W. T. *Density Functional Theory of Atoms and Molecules*; Oxford University Press: Oxford, UK, 1989.
- (7) Hohenberg, P.; Kohn, W. *Phys. Rev. B* **1964**, 136 (3B), B864. doi:10.1103/PhysRev.136.B864.
- (8) Kohn, W.; Sham, L. J. *Phys. Rev.* **1965**, 140 (4A), A1133. doi:10.1103/PhysRev.140.A1133.
- (9) Koch, W. *A Chemist's Guide To Density Functional Theory*; Wiley-VCH, 2001.
- (10) Parr, R. G.; Yang, W. T. *Annu. Rev. Phys. Chem.* **1995**, 46 (1), 701. doi:10.1146/annurev.pc.46.100195.003413.
- (11) Parr, R. G.; Yang, W. T. *J. Am. Chem. Soc.* **1984**, 106 (14), 4049. doi:10.1021/ja00326a036.
- (12) Parr, R. G.; von Szentpály, L.; Liu, S. *J. Am. Chem. Soc.* **1999**, 121 (9), 1922. doi:10.1021/ja983494x.
- (13) Morell, C.; Grand, A.; Toro-Labbé, A. *J. Phys. Chem. A* **2005**, 109 (1), 205. doi:10.1021/jp046577a. PMID:16839107.
- (14) Sanderson, R. T. *Science* **1951**, 114 (2973), 670. doi:10.1126/science.114.2973.670. PMID:17770191.
- (15) Pearson, R. G. *Chemical Hardness: Applications from Molecules to Solids*; Wiley-VCH, 1997.
- (16) (a) Chermette, H. *J. Comput. Chem.* **1999**, 20 (1), 129. doi:10.1002/(SICI)1096-987X(19990115)20:1<129::AID-JCC13>3.0.CO;2-A.; (b) Geerlings, P.; De Proft, F.; Langenaeker, W. *Chem. Rev.* **2003**, 103 (5), 1793. doi:10.1021/cr990029p. PMID:12744694.; (c) Ayers, P. W.; Anderson, J. S. M.; Bartolotti, J. L. *Int. J. Quantum Chem.* **2005**, 101 (5), 520. doi:10.1002/qua.20307.; (d) Geerlings, P.; De Proft, F. *Phys. Chem. Chem. Phys.* **2008**, 10 (21), 3028. doi:10.1039/b717671f. PMID:18688366.; (e) Gazquez, J. L. *J. Mex. Chem. Soc.* **2008**, 52, 1; (f) Liu, S. B. *Acta Phys.-Chim. Sin.* **2009**, 25, 590.
- (17) (a) Moens, J.; Geerlings, P.; Roos, G. *Chem. Eur. J.* **2007**, 13 (29), 8174. doi:10.1002/chem.200601896.; (b) Moens, J.; Roos, G.; Jaque, P.; De Proft, F.; Geerlings, P. *Chem. Eur. J.* **2007**, 13 (33), 9331. doi:10.1002/chem.200700547.; (c) Moens, J.; Jaque, P.; De Proft, F.; Geerlings, P. *J. Phys. Chem. A* **2008**, 112 (26), 6023. doi:10.1021/jp711652a. PMID:18543893.; (d) Moens, J.; Jaque, P.; De Proft, F.; Geerlings, P. *ChemPhysChem* **2009**, 10 (5), 847. doi:10.1002/cphc.200800864. PMID:19212963.
- (18) (a) De Proft, F.; Ayers, P. W.; Fias, S.; Geerlings, P. *J. Chem. Phys.* **2006**, 125 (21), o. 214101. doi:10.1063/1.2387953. PMID:17166009.; (b) Ayers, P. W.; Morell, C.; De Proft, F.; Geerlings, P. *Chem. Eur. J.* **2007**, 13 (29), 8240. doi:10.1002/chem.200700365.; (c) De Proft, F.; Chattaraj, P. K.; Ayers, P. W.; Torrent-Sucarrat, M.; Elango, M.; Subramanian, V.; Giri, S.; Geerlings, P. *J. Chem. Theory Comput.* **2008**, 4 (4), 595. doi:10.1021/ct700289p.; (d) Sablon, N.; De Proft, F.; Geerlings, P. *Croat. Chem. Acta* **2009**, 82, 157.
- (19) Zimmerman, H. *Acc. Chem. Res.* **1971**, 4 (8), 272. doi:10.1021/ar50044a002.
- (20) Parr, R. G.; Yang, W. *J. Am. Chem. Soc.* **1984**, 106 (14), 4049. doi:10.1021/ja00326a036.
- (21) Parr, R.; Donnelly, R.; Levy, M.; Palke, W. *J. Chem. Phys.* **1978**, 68 (8), 3801. doi:10.1063/1.436185.
- (22) Becke, A. D. *Phys. Rev. A* **1988**, 38 (6), 3098. doi:10.1103/PhysRevA.38.3098. PMID:9900728.
- (23) Lee, C.; Yang, W. T.; Parr, R. G. *Phys. Rev. B* **1988**, 37 (2), 785. doi:10.1103/PhysRevB.37.785.
- (24) Perdew, J. P.; Burke, K.; Ernzerhof, M. *Phys. Rev. Lett.* **1996**, 77 (18), 3865. doi:10.1103/PhysRevLett.77.3865. PMID:10062328.
- (25) Hariharan, P. C.; Pople, J. A. *Theor. Chim. Acta* **1973**, 28 (3), 213. doi:10.1007/BF00533485.
- (26) Tozer, D. J.; De Proft, F. *J. Phys. Chem.* **2005**, A109, 8923.
- (27) De Proft, F.; Sablon, N.; Tozer, D. J.; Geerlings, P. *Faraday Discuss.* **2007**, 135, 151, discussion 237, 503. doi:10.1039/b605302p. PMID:17328427.
- (28) Frisch, M. J.; Trucks, G. W.; Schlegel, H. B.; Scuseria, G. E.; Robb, M. A.; Cheeseman, J. R.; Montgomery, J. A.; Vreven, T.; Kudin, K. N.; Burant, J. C.; Millam, J. M.; Iyengar, S. S.; Tomasi, J.; Barone, V.; Mennucci, B.; Cossi, M.; Scalmani, G.; Rega, N.; Petersson, G. A.; Nakatsuji, H.; Hada, M.; Ehara, M.; Toyota, K.; Fukuda, R.; Hasegawa, J.; Ishida, M.; Nakajima, T.; Honda, Y.; Kitao, O.; Nakai, H.; Klene, M.; Li, X.; Knox, J. E.; Hratchian, H. P.; Cross, J. B.; Bakken, V.; Adamo, C.; Jaramillo, J.; Gomperts, R.; Stratmann, R. E.; Yazyev, O.; Austin, A. J.; Cammi, R.; Pomelli, C.; Ochterski, J. W.; Ayala, P. Y.; Morokuma, K.; Voth, G. A.; Salvador, P.; Dannenberg, J. J.; Zakrzewski, V. G.; Dapprich, S.; Daniels, A. D.; Strain, M. C.; Farkas, O.; Malick, D. K.; Rabuck, A. D.; Raghavachari, K.; Foresman, J. B.; Ortiz, J. V.; Cui, Q.; Baboul, A. G.; Clifford, S.; Cioslowski, J.; Stefanov, B. B.; Liu, G.; Liashenko, A.; Piskorz, P.; Komaromi, I.; Martin, R. L.; Fox, D. J.; Keith, T.; Laham, A.; Peng, C. Y.; Nanayakkara, A.; Challacombe, M.; Gill, P. M. W.; Johnson, B.; Chen, W.; Wong, M. W.; Gonzalez, C.; Pople, J. A. *Gaussian 03*, Revision C.02; Gaussian, Inc.: Wallingford, CT, 2003.
- (29) Olah, J.; Geerlings, P.; De Proft, F.; Geerlings, P. *J. Phys. Chem.* **2007**, 111, 10815.
- (30) Correa, J. V.; Jaque, P.; Olah, J.; Toro-Labbe, A.; Geerlings, P. *Chem. Phys. Lett.* **2009**, 470 (4-6), 180. doi:10.1016/j.cplett.2009.01.054.
- (31) (a) Monnat, F.; Vogel, P.; Sordo, J. A. *Helv. Chim. Acta* **2002**, 85 (3), 712. doi:10.1002/1522-2675(200203)85:3<712::AID-HLCA712>3.0.CO;2-5.; (b) Suárez, D.; Sordo, T. L.; Sordo, J. A. *J. Org. Chem.* **1995**, 60 (9), 2848. doi:10.1021/jo00114a039.; (c) Vogel, P.; Turks, M.; Bouchez, L.; Marković, D.; Varela-Alvarez, A.; Sordo, J. A. *Acc. Chem. Res.* **2007**, 40 (10), 931. doi:10.1021/ar700096h. PMID:17685582.



# A computational study of methanol-to-hydrocarbon conversion — Towards the design of a low-barrier process

Bun Chan and Leo Radom

**Abstract:** Computational quantum chemistry has been employed to examine the production of ethylene with methanol-to-hydrocarbon (MTH) processes via a carbon pool mechanism. We find that the M05-2X functional performs well for the types of reactions that are involved. The methylation reactions of the aromatic cocatalyst are the most energy-demanding steps in the process. For the subsequent production of C<sub>2</sub>H<sub>4</sub>, we have identified a low-energy pathway that involves multiple methyl shifts, followed by concerted deprotonation and C<sub>2</sub>H<sub>4</sub> elimination. The substitutions of the Al and Si atoms in the participating Si–OH–Al moiety of zeolite catalysts with Ga and Ge do not lead to lower barriers for the methylation reactions, nor does the use of a more electron-rich aromatic cocatalyst. However, we find that the use of two cocatalysts, a nucleophile and an aromatic carbon pool, can provide an overall low-energy pathway for the MTH process.

**Key words:** methanol-to-hydrocarbon (MTH) process, zeolite catalysis, computational chemistry.

**Résumé :** On a fait appel à des calculs de chimie quantique impliquant un mécanisme de mise en commun du carbone pour examiner la production d'éthylène par le procédé du méthanol à hydrocarbure (MAH). On a trouvé que la fonctionnelle M05-2X donne de bons résultats pour les types de réactions impliquées. Les réactions de méthylation de la portion aromatique du cocatalyseur sont les étapes qui requièrent le plus d'énergie. Pour la production subséquente du C<sub>2</sub>H<sub>4</sub>, on a identifié une voie de basse énergie qui implique de multiples déplacements de groupes méthyles, suivis d'une déprotonation concertée avec une élimination de C<sub>2</sub>H<sub>4</sub>. Les substitutions des atomes d'aluminium et de silicium de la portion Si–OH–Al participante des catalyseurs comportant du Ga et du Ge ne conduit pas à des barrières énergétiques inférieures pour les réactions de méthylation et c'est aussi le cas lorsqu'on utilise un cocatalyseur aromatique plus riche en électron. Toutefois, on a trouvé que l'utilisation de deux cocatalyseurs, un nucléophile et une mise en commun de carbones aromatiques, peut conduire à une voie de faible énergie globale pour le procédé du MAH.

**Mots-clés :** procédé du méthanol à hydrocarbure (MAH), catalyseur de zéolite, calculs de chimie quantique.

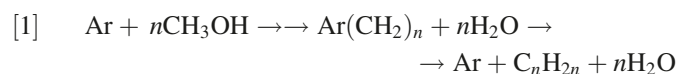
[Traduit par la Rédaction]

## Introduction

The limited supply of crude oil and the adverse environmental impact of its combustion have led to an increasing interest in alternative sources of energy. One of the most discussed alternatives is the use of hydrogen as the energy carrier.<sup>1</sup> However, there are still many obstacles to the realization of a hydrogen economy, one of which is the problem of dealing with a gas-phase fuel.<sup>2</sup> A methanol economy has been proposed as another alternative.<sup>3</sup> In this scenario, CO<sub>2</sub> is recycled and reduced to give methanol as a convenient and efficient energy carrier. We have previously used computational quantum chemistry to explore the catalytic hydrogenation of CO<sub>2</sub> to methanol by zeolites, and have found low-energy paths for such an approach to carbon fixation.<sup>4</sup>

Petroleum is not only a widely used fuel but it also pro-

vides a number of aliphatic and aromatic hydrocarbons as chemical feedstocks for a wide variety of industrial processes.<sup>5</sup> Thus, an efficient method for methanol-to-hydrocarbon (MTH) transformation would also be advantageous. Such a chemical transformation can be achieved with the use of zeolite catalysts.<sup>6</sup> The carbon pool mechanism is currently considered to be the dominant pathway for MTH processes.<sup>7</sup> According to this mechanism, an aromatic species (Ar) acts as a catalyst and is polymethylated and undergoes multiple internal rearrangements in the course of generating alkene products:



The complete catalytic process is complex but theory can

Received 4 February 2010. Accepted 13 March 2010. Published on the NRC Research Press Web site at canjchem.nrc.ca on 20 July 2010.

*This article is part of a Special Issue dedicated to Professor R. J. Boyd.*

**B. Chan<sup>1</sup> and L. Radom,<sup>2</sup>** School of Chemistry and Centre of Excellence for Free Radical Chemistry and Biotechnology, University of Sydney, Sydney NSW 2006, Australia.

<sup>1</sup>Corresponding author (e-mail: chan\_b@chem.usyd.edu.au).

<sup>2</sup>Corresponding author (e-mail: radom@chem.usyd.edu.au).



potentially provide useful insights into the mechanism. For instance, the production of isobutene from methanol via a ring contraction/expansion “paring” pathway<sup>8</sup> has been modeled.<sup>9</sup> The results show that the methylation reactions of the aromatic species are the most energy-demanding steps in the calculated catalytic cycle. There have also been computational studies<sup>10</sup> indicating that in MTH processes with an “exocyclic” mechanism,<sup>11</sup> the formation of the alkene product involves high-energy intermediates and transition structures and is rate limiting.

While these theoretical studies have identified barriers of as much as 160 kJ mol<sup>-1</sup> for some of the steps involved in MTH processes,<sup>9,10b</sup> the overall reactions are generally exothermic, driven by the formation of water. For instance, the reactions leading to the formation of ethene, propene, and isobutene from methanol ( $n = 2, 3$ , and  $4$  in eq. [1]) have reaction enthalpies of  $-21.2$ ,  $-90.1$  and  $-165.2$  kJ mol<sup>-1</sup>, respectively.<sup>12,13</sup> As a result, improvements in catalysis can potentially lead to greatly reduced energy requirements for MTH processes, and possibly include the associated benefits of achieving higher selectivities and longer lives for the catalysts under milder reaction conditions.

We have been interested for some time in studying transition-metal-free catalysis of hydrogenation processes.<sup>4,14</sup> In particular, we have investigated the zeolite-catalyzed hydrogenation of CO<sub>2</sub> to give methanol.<sup>4</sup> We find that appropriately designed zeolites can provide excellent catalysis for this conversion.

In the present study, we examine the zeolite-catalyzed MTH process that produces ethene via an exocyclic pathway. We aim to reevaluate the reaction mechanism and identify the high-barrier steps in the overall process, and then target these steps to explore the possibility of lower-energy alternatives. We hope that our work will contribute to achieving effective conversion of CO<sub>2</sub> to hydrocarbons using environmentally benign catalysts, and in turn, advance the prospects of a methanol economy.

## Computational details

Standard ab initio molecular orbital theory and density functional theory calculations<sup>15</sup> were carried out with the GAUSSIAN 03,<sup>16</sup> GAUSSIAN 09,<sup>17</sup> and MOLPRO 2006<sup>18</sup> programs. Models representing cavities of the MFI (ZSM-five: zeolite Socony Mobil-five) structure<sup>19</sup> were constructed by extracting an 8T-cluster from the literature crystal structure.<sup>20</sup> Dangling bonds were saturated with hydrogen atoms, whose locations were obtained through optimizations with the PM3 semi-empirical procedure with the heavy atoms being frozen.

For the zeolites and related complexes and transition structures, geometries were obtained at the B3-LYP/6-31+G(d,p) level of theory, with the terminal hydrogen atoms of the 8T-clusters being frozen. Improved relative energies were obtained at the B3-LYP and M05-2X<sup>21</sup> levels with the G3MP2Large<sup>22</sup> basis set. We have inspected the vibrational frequencies of the transition structures for an indication that they link the appropriate adjacent minima.

We have also briefly examined the reaction profile of smaller 2T-clusters to probe the electronic effect of cluster size on the reaction profile. The terminal OSiH<sub>3</sub> groups in

the 8T-clusters of the optimized structures for the zeolites, and related complexes and transition structures, were replaced with hydrogen atoms in these calculations. Lengths of 1.490 and 1.618 Å were used for the Si–H and Al–H bonds, respectively.<sup>23</sup> Single-point energies at the M05-2X/G3MP2Large and G3(MP2)-RAD<sup>24</sup> levels were then obtained for the resulting structures with the 2T-clusters.

Geometrical parameters within the text are B3-LYP/6-31+G(d,p) values, while relative energies correspond to vibrationless M05-2X/G3MP2Large values, unless otherwise noted. In specific cases, zero-point vibrational energies (ZPVEs), and thermal corrections to enthalpy ( $\Delta H$ ) and entropy ( $S$ ) at 298 K, derived from B3-LYP/6-31+G(d,p) frequencies, were incorporated into the relative energies. Literature scaling factors<sup>25</sup> were used in the evaluation of ZPVEs (0.9857),  $\Delta H$  (1.0062), and  $S$  (1.0099) from the calculated B3-LYP harmonic vibrational frequencies.

## Results and discussion

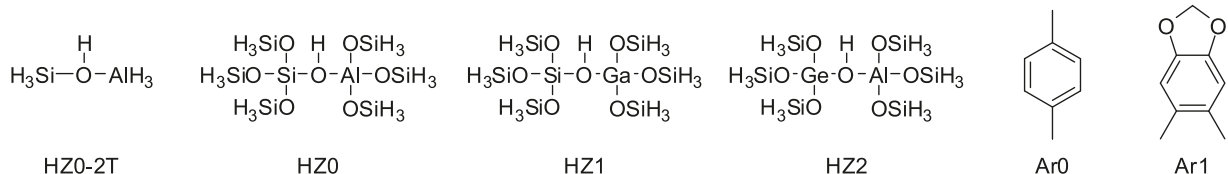
### General

The zeolite models and the aromatic cocatalysts examined in this study are listed in Fig. 1. HZ0-2T and HZ0 are 2T- and 8T-cluster models for H-ZSM-5, respectively. We have previously found that the substitution of Si atoms by Ge can somewhat lower the barrier for the zeolite-catalyzed hydrogenation of CO<sub>2</sub>.<sup>4</sup> Likewise, in the present study we explore the possibility of an improved MTH catalysis by examining the model zeolites HZ1 and HZ2. In HZ1 the Al atom that is adjacent to the acidic OH in HZ0 is substituted by Ga, while in HZ2 the Si atom that is adjacent to the acidic OH is replaced by Ge.

We use *p*-xylene (Ar0) as a prototypical model for the aromatic cocatalyst in the carbon pool mechanism for the MTH process. Since the MTH process involves carbocation intermediates, stabilization with  $\pi$ -electron-donating groups can potentially lead to a more facile set of reactions. Thus, we examine 5,6-dimethyl-1,3-benzodioxole (Ar1), which includes two  $\pi$ -electron-donating alkoxy groups, as an alternative aromatic cocatalyst. Although Ar1 serves as a convenient model for an electron-rich aromatic in our theoretical investigation, we recognize that complications might arise in its experimental usage.

The choice of cluster size for a model zeolite can have a substantial effect on the calculated properties.<sup>26</sup> While it has been demonstrated that relatively small clusters are able to capture the essential chemistry of zeolite reactions, the use of larger clusters has been found to lead to smaller calculated barriers for several types of reactions.<sup>26a,26b</sup> We, therefore, begin by investigating the effect of cluster size on the barrier for the methylation of the aromatic cocatalyst Ar0, which we find to be one of the most energy-demanding steps in the MTH process (see below).

In a recent study,<sup>9</sup> ONIOM(B3-LYP/6-31G(d):HF/6-31G(d)) calculations were employed to probe the complete catalytic cycle of an MTH process. Using a 46T-cluster model for H-ZSM-5, a barrier of 154.9 kJ mol<sup>-1</sup> was obtained for the ortho-methylation of *p*-xylene (Table 1). With the 8T-cluster HZ0, we find a barrier of 178.9 kJ mol<sup>-1</sup> for the ipso-methylation reaction at the B3-LYP/6-31G(d) level. Thus, at a comparable theoretical level and for a similar re-

**Fig. 1.** Model zeolites (HZ0-2T, HZ0, HZ1, and HZ2) and aromatic cocatalysts (Ar0 and Ar1) examined in this study.**Table 1.** Effect of cluster size and level of theory on the calculated barrier (via transition structure 1 (TS1)) for the zeolite-catalyzed ipso-methylation of *p*-xylene (Ar0) by methanol (kJ mol<sup>-1</sup>).

	HZ0-2T	HZ0 (8T)	46T
B3-LYP/6-31G(d)	212.6	178.9	154.9 <sup>a</sup>
B3-LYP/6-31+G(d,p)	210.0	175.7	
B3-LYP/G3MP2Large	201.2	175.4	
M05-2X/G3MP2Large	193.0	167.4	
G3(MP2)-RAD	195.4		

<sup>a</sup>ONIOM(B3-LYP/6-31G(d):HF/6-31G(d))/ONIOM(B3-LYP/6-31G(d):MND0) value for ortho-methylation from ref. 9.

action, our barrier obtained using the 8T-cluster model is 24.0 kJ mol<sup>-1</sup> higher than the value obtained with a 46T-cluster. The use of an even smaller 2T-cluster, HZ0-2T, leads to a further increase in the calculated barrier (to 212.6 kJ mol<sup>-1</sup>). Thus, our results are consistent with the previous findings that increasing cluster size leads to lower calculated barriers.<sup>26a,26b</sup>

Turning our attention to the effect of level of theory on the calculated barrier, we find that the use of the larger 6-31+G(d,p) and G3MP2Large basis sets with B3-LYP lead to somewhat lower barriers than that obtained with the 6-31G(d) basis set (Table 1), with the basis set effect being reduced for the larger 8T cluster. Of the four DFT levels examined, M05-2X/G3MP2Large gives the best agreement with our benchmark G3(MP2)-RAD value for the HZ0-2T-catalyzed process.

We have also compared the energy profile for the complete MTH process with the HZ0-2T cluster, as obtained at the three DFT levels, with that of the G3(MP2)-RAD benchmark (Table 2). We find that M05-2X/G3MP2Large gives the closest agreement for the barriers and reaction energies with the G3(MP2)-RAD values, with a mean absolute deviation (MAD) of 11.2 kJ mol<sup>-1</sup>, compared with 38.0 and 43.4 kJ mol<sup>-1</sup> for B3-LYP/G3MP2Large and B3-LYP/6-31+G(d,p), respectively. The large MADs for B3-LYP can be partly attributed to the poorer description of complexation. For instance, if one uses C1 + MeOH for the reference energy, the MADs for B3-LYP/6-31+G(d,p), B3-LYP/G3MP2Large, and M05-2X/G3MP2Large become 26.8, 18.3, and 12.4 kJ mol<sup>-1</sup>, respectively. Nonetheless, M05-2X/G3MP2Large provides a better compromise between accuracy and computational cost for this study.

### Mechanism of the MTH process catalyzed by HZ0 and *p*-xylene

The reaction profile for the HZ0-Ar0-catalyzed HTH process is shown in Fig. 2, and the transition structures (TS1–TS7) in the reaction scheme are displayed in Fig. 3.

The process begins with the HZ0-catalyzed methylation

of Ar0 by methanol (via TS1), giving the trimethyl-cyclohexadienyl cation intermediate (in the complex C2), followed by elimination of water. Abstraction of a proton from this cation by Z0<sup>-</sup> gives dimethyl-methylene-cyclohexadiene (C3 → C4 via TS2). A second catalytic methylation leads to the formation of the ethyl-dimethyl-cyclohexadienyl cation intermediate (C5 → C6 via TS3), followed again by elimination of water to give C7.

There are many feasible pathways for the elimination of the alkene product, i.e., C<sub>2</sub>H<sub>4</sub>, starting from C7.<sup>10,27</sup> These pathways often involve higher-energy cationic intermediates, associated with high barriers for their formation.<sup>10</sup> On the other hand, a concerted mechanism has been proposed (Fig. 4),<sup>27a</sup> in which the elimination of C<sub>2</sub>H<sub>4</sub> and the regeneration of Ar0 and HZ0 occur concurrently, without the participation of higher-energy cations. However, this pathway has not previously been examined in detail. Because it can potentially provide a lower-energy route to product formation, we have explored this possibility in the present investigation.

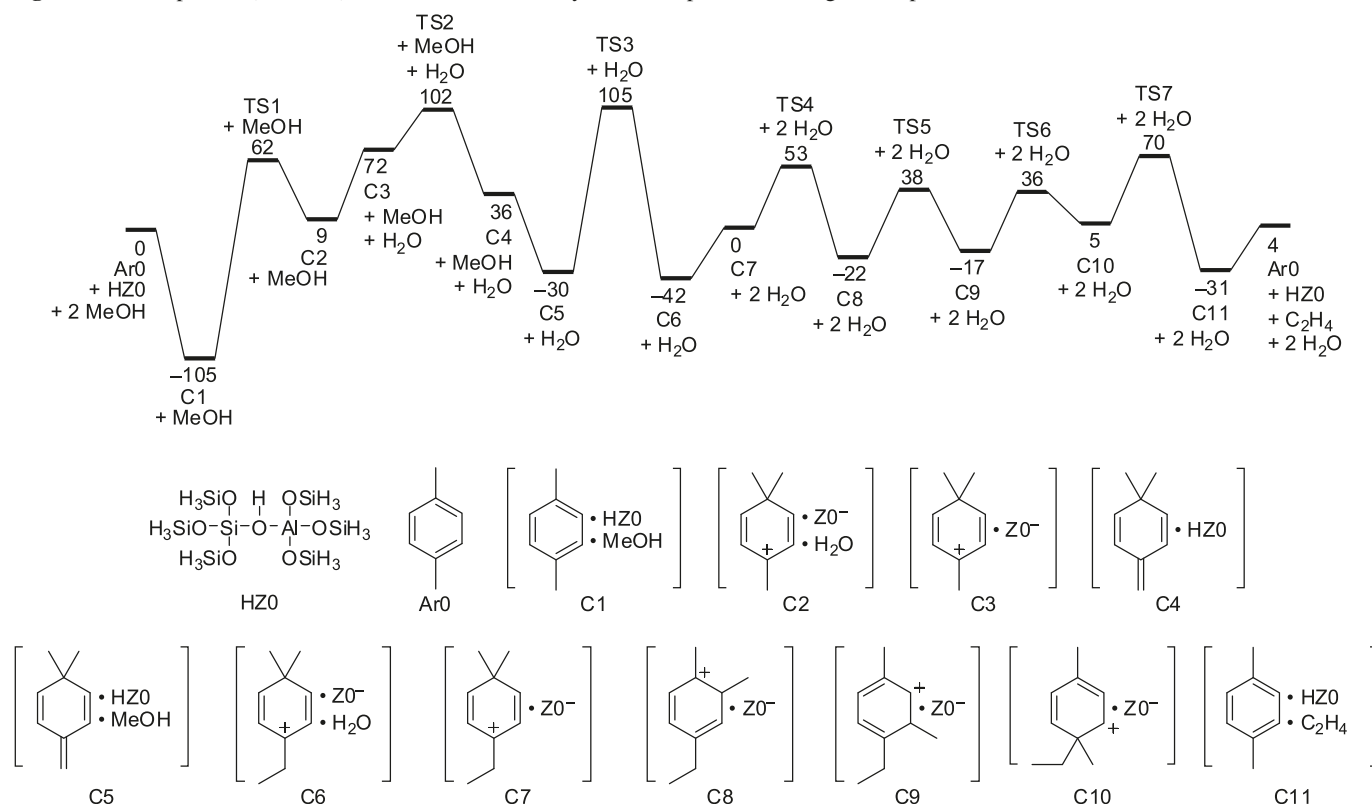
For the process shown in Fig. 2, the ethyl-dimethyl-cyclohexadienyl cation in C10 is required in the proposed concerted mechanism. The formation of this cation can be accomplished by multiple methyl migrations, starting from the cation in C7 (C7 → C8 → C9 → C10 via TS4, TS5, and TS6, respectively). The concerted deprotonation and elimination of C<sub>2</sub>H<sub>4</sub> to regenerate Ar0 and HZ0 via TS7 completes the catalytic cycle.

The calculated energy profile for the HZ0-Ar0-catalyzed MTH process and the barriers for the various steps, evaluated from the preceding minima, are shown in Table 3, which also includes free energies at 298 K. We realize that species that involve the zeolite models (HZ0 and Z0<sup>-</sup>) are optimized with structural constraints and, therefore, are not true minima on the potential energy surface. As a result, the inclusion of ZPVEs and thermal corrections for enthalpy and entropy, obtained from calculated harmonic frequencies, is not strictly correct from a theoretical point of view. However, as the same structural constraints are employed for the entire reaction profile, we anticipate substantial cancellation of errors, and that the free energies listed in the table can thus serve as reasonable estimates for the effect of thermal energies and entropies in the zeolite system.

The energies of the various points along the reaction profile span a range of 209.8 kJ mol<sup>-1</sup>, from the lowest point of -105.3 kJ mol<sup>-1</sup> for C1 + MeOH (Fig. 2) to the highest point of 104.5 kJ mol<sup>-1</sup> for TS3 + H<sub>2</sub>O (Fig. 3). We find that the two methylation reactions are the most energy demanding, with barriers of 167.4 and 134.3 kJ mol<sup>-1</sup> for the first (via TS1) and second (via TS3) methylation reactions, respectively. These are substantially higher than the next largest barrier of 64.6 kJ mol<sup>-1</sup> for the elimination of C<sub>2</sub>H<sub>4</sub> from C10 (via TS7), while the methyl shifts that precede

**Table 2.** Energy profile for the HZ0-2T-Ar0-catalyzed MTH process calculated with G3(MP2)-RAD and various DFT procedures (kJ mol<sup>-1</sup>).

		G3(MP2)-RAD	B3-LYP/6-31+G(d,p)	B3-LYP/G3MP2Large	M05-2X/G3MP2Large
1	Ar0 + HZ0 + 2MeOH	0.0	0.0	0.0	0.0
2	C1 + MeOH	-86.3	-67.4	-62.5	-87.0
3	TS1 + MeOH	109.1	142.6	138.7	106.0
4	C2 + MeOH	56.4	95.4	92.2	58.2
5	C3 + MeOH + H <sub>2</sub> O	102.6	127.2	120.4	107.2
6	TS2 + MeOH + H <sub>2</sub> O	105.8	127.5	129.3	113.2
7	C4 + MeOH + H <sub>2</sub> O	17.3	67.2	69.3	40.9
8	C5 + H <sub>2</sub> O	-32.7	24.4	29.9	-11.5
9	TS3 + H <sub>2</sub> O	135.0	185.0	178.7	145.7
10	C6 + H <sub>2</sub> O	-2.4	53.4	50.0	6.5
11	C7 + 2H <sub>2</sub> O	30.7	87.0	78.8	42.5
12	TS4 + 2H <sub>2</sub> O	84.3	155.3	142.9	95.7
13	C8 + 2H <sub>2</sub> O	-6.0	39.1	34.1	10.8
14	TS5 + 2H <sub>2</sub> O	70.8	137.5	127.8	81.7
15	C9 + 2H <sub>2</sub> O	11.6	64.5	55.1	26.2
16	TS6 + 2H <sub>2</sub> O	66.1	136.3	125.2	76.4
17	C10 + 2H <sub>2</sub> O	30.0	83.9	72.8	44.3
18	TS7 + 2H <sub>2</sub> O	94.9	136.0	124.3	105.1
19	C11 + 2H <sub>2</sub> O	-52.5	-13.2	-22.2	-30.7
20	Ar0 + HZ0 + C <sub>2</sub> H <sub>4</sub> + 2H <sub>2</sub> O	-16.5	5.3	-5.8	4.0
MAD <sup>a</sup>		—	43.4	38.0	11.2
LD <sup>b</sup>		—	+71.0	+62.5	+23.6

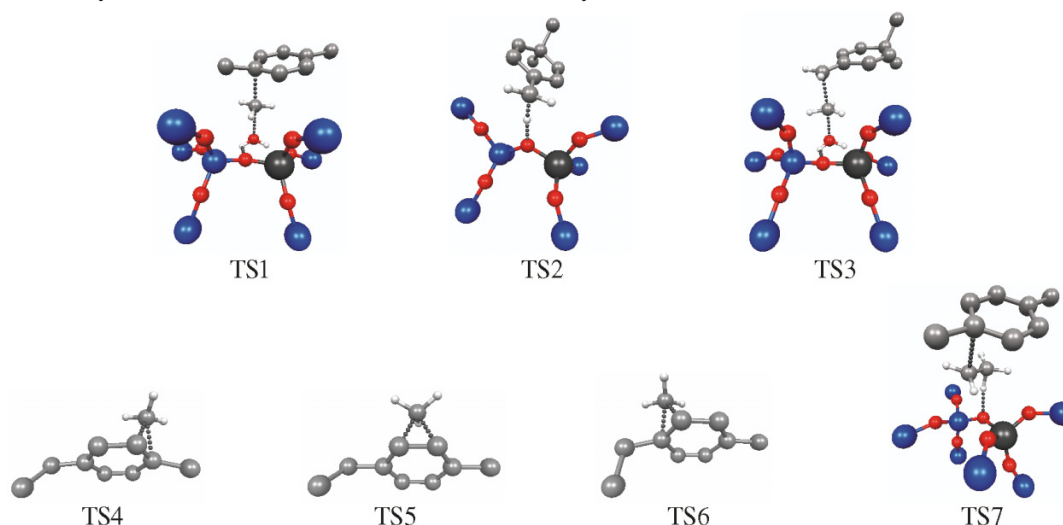
<sup>a</sup>Mean absolute deviation.<sup>b</sup>Largest deviation.**Fig. 2.** Reaction profile (kJ mol<sup>-1</sup>) for the HZ0-Ar0-catalyzed MTH process leading to the production of C<sub>2</sub>H<sub>4</sub> from MeOH.

this final step of the process have somewhat lower barriers of 50–60 kJ mol<sup>-1</sup>.

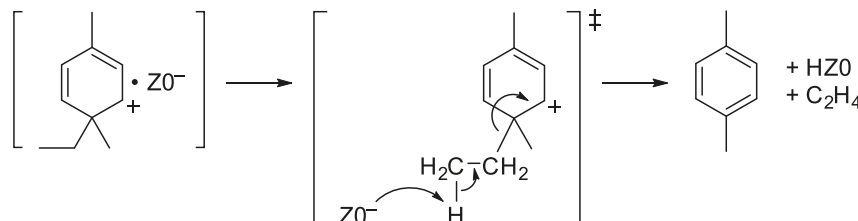
Thermal enthalpy and entropy contributions lead to an in-

crease in the free energy values for the complexes and transition structures relative to the separated reactants, a widened range of 272.1 kJ mol<sup>-1</sup> for the free energy profile,

**Fig. 3.** Optimized transition structures (TS1–TS7) for the HZ0-Ar0-catalyzed MTH process (see Fig. 2). Selected hydrogen atoms in TS1–TS7 and the zeolite catalyst in TS4–TS6 are omitted for the sake of clarity.



**Fig. 4.** The  $ZO^-$ -catalyzed concerted deprotonation and  $C_2H_4$  elimination from 6-ethyl-3,6-dimethylcyclohexadienyl cation.



**Table 3.** Calculated energy profile ( $\text{kJ mol}^{-1}$ ) for the HZ0-Ar0-catalyzed MTH process.

		$\Delta E$	$\Delta G$ (298 K)
1	Ar0 + HZ0 + 2MeOH	0.0	0.0
2	C1 + MeOH	-105.3	-5.7
3	TS1 + MeOH	62.1	175.1
4	C2 + MeOH	9.4	118.9
5	C3 + MeOH + $H_2O$	72.1	139.5
6	TS2 + MeOH + $H_2O$	102.3	159.5
7	C4 + MeOH + $H_2O$	36.0	96.3
8	C5 + $H_2O$	-29.8	84.0
9	TS3 + $H_2O$	104.5	223.4
10	C6 + $H_2O$	-41.5	77.1
11	C7 + 2 $H_2O$	-0.3	72.1
12	TS4 + 2 $H_2O$	52.5	117.4
13	C8 + 2 $H_2O$	-21.8	48.7
14	TS5 + 2 $H_2O$	37.8	107.6
15	C9 + 2 $H_2O$	-17.1	51.2
16	TS6 + 2 $H_2O$	35.5	105.7
17	C10 + 2 $H_2O$	5.3	76.0
18	TS7 + 2 $H_2O$	69.9	121.6
19	C11 + 2 $H_2O$	-31.1	16.8
20	Ar0 + HZ0 + $C_2H_4$ + 2 $H_2O$	4.0	-48.7
$\Delta E_1^\ddagger, \Delta G_1^\ddagger$ (2 $\rightarrow$ 4)		167.4	180.8
$\Delta E_2^\ddagger, \Delta G_2^\ddagger$ (5 $\rightarrow$ 7)		30.2	20.1
$\Delta E_3^\ddagger, \Delta G_3^\ddagger$ (8 $\rightarrow$ 10)		134.3	139.3
$\Delta E_4^\ddagger, \Delta G_4^\ddagger$ (11 $\rightarrow$ 13)		52.8	45.3
$\Delta E_5^\ddagger, \Delta G_5^\ddagger$ (13 $\rightarrow$ 15)		59.6	58.9
$\Delta E_6^\ddagger, \Delta G_6^\ddagger$ (15 $\rightarrow$ 17)		52.6	54.5
$\Delta E_7^\ddagger, \Delta G_7^\ddagger$ (17 $\rightarrow$ 19)		64.6	45.6

and somewhat higher barriers for most of the reactions (e.g.,  $180.8 \text{ kJ mol}^{-1}$  for  $\Delta G_1^\ddagger$ ). However, the general features for the process remain the same, with the methylation reactions being substantially more energy-demanding than the other reactions.

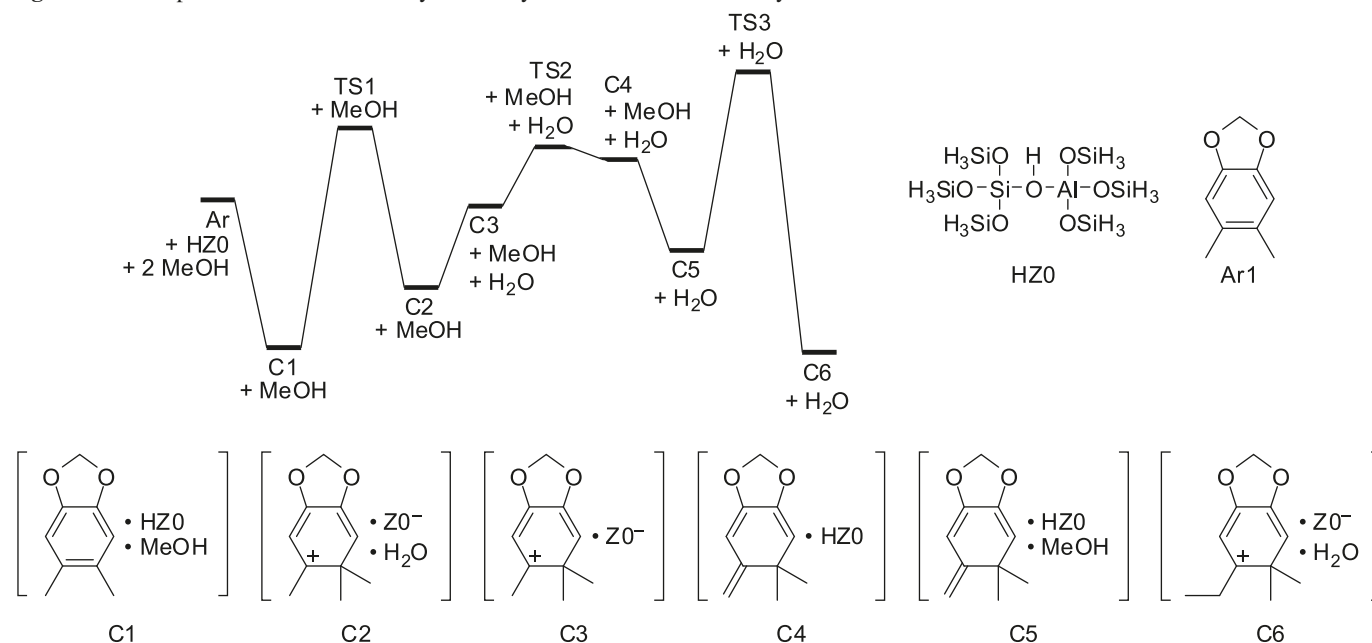
Thus, our results suggest that, upon methylation of the aromatic cocatalyst, internal methyl shifts, followed by concerted deprotonation and  $C_2H_4$  elimination, can provide a low-energy pathway for completing the catalytic cycle. The methylation reactions that generate the cationic intermediates and the deprotonated zeolite are rate limiting. We will explore various means to reduce the energy requirements for this reaction type in the next two sections.

### Effect of alternative zeolites and cocatalysts on the methylation barriers

In this section, we explore three alternatives to the prototypical HZ0-Ar0-catalyzed MTH process. Our focus is on the methylation reactions of the aromatic cocatalyst (i.e., for the steps up to C6 +  $H_2O$  in Fig. 2), since these represent the most energy-demanding steps.

The first two alternatives involve modified zeolite catalysts HZ1 and HZ2 (Fig. 1), whereby the Al and Si atoms in the Si–O–Al moiety in HZ0 are replaced, respectively, by Ga and Ge, in HZ1 and HZ2. The reaction profiles in these two cases are very similar to that for the HZ0-catalyzed process (Fig. 2). For the third alternative process considered in this section, a modified aromatic cocatalyst (Ar1) is employed. This leads to intermediates that are considerably different from those for the Ar0 process. The intermediates involved in the Ar1 process are shown in Fig. 5.



**Fig. 5.** Reaction profile for the HZ0-catalyzed methylation reactions of Ar1 by methanol.**Table 4.** Calculated energy profiles (kJ mol<sup>-1</sup>) for the methylation reactions of aromatic substrates Ar0 and Ar1, catalyzed by zeolites HZ0–HZ2.

		HZ0-Ar0	HZ1-Ar0	HZ2-Ar0	HZ0-Ar1
1	Ar + HZ0 + 2MeOH	0.0	0.0	0.0	0.0
2	C1 + MeOH	-105.3	-104.3	-110.3	-108.5
3	TS1 + MeOH	62.1	66.5	67.1	52.1
4	C2 + MeOH	9.4	17.7	6.2	-66.5
5	C3 + MeOH + H <sub>2</sub> O	72.1	78.4	71.1	-3.9
6	TS2 + MeOH + H <sub>2</sub> O	102.3	105.6	105.0	37.7
7	C4 + MeOH + H <sub>2</sub> O	36.0	33.5	35.8	29.8
8	C5 + H <sub>2</sub> O	-29.8	-30.5	-23.6	-35.7
9	TS3 + H <sub>2</sub> O	104.5	105.8	103.5	96.2
10	C6 + H <sub>2</sub> O	-41.5	-40.3	-48.2	-111.8
	$\Delta E_1^\ddagger$ (2 → 4)	167.4	170.9	177.3	160.7
	$\Delta E_2^\ddagger$ (5 → 7)	30.2	27.2	33.9	41.6
	$\Delta E_3^\ddagger$ (8 → 10)	134.3	136.3	127.2	131.9

The calculated energy profiles and the barriers for the HZ0-catalyzed methylation of Ar0, and for the three alternatives, are shown in Table 4. We find that neither HZ1 nor HZ2 improve the energies for the methylation reactions. In fact, either the substitution of Al by Ga (HZ1) or Si by Ge (HZ2) generally lead to higher methylation barriers for Ar0. This is in contrast to the results from our previous investigation on zeolite-catalyzed hydrogenation of CO<sub>2</sub>,<sup>4</sup> in which we found that substitution of an Si atom by Ge can lead to a lower barrier. On the other hand, the methylation reactions with Ar1 have somewhat lower barriers than those with Ar0.

Interestingly, the use of Ar1 leads to much greater stabilization for the cationic intermediates than for the transition structures. By comparing the energies for C2 + MeOH (Table 4, entry 4) for the two substrates, as well as those for C6 + H<sub>2</sub>O (Table 4, entry 10), we can see that the cationic intermediates derived from Ar1 are relatively more stable compared with those from Ar0 by more than 70 kJ

mol<sup>-1</sup>. In contrast, the greatest decrease in the methylation barriers is just 6.7 kJ mol<sup>-1</sup> for  $\Delta E_1^\ddagger$ .

In general, electron-donating groups can stabilize a cation by delocalizing the positive charge. Similarly, for reactions that lead to the formation of a cation, electron-donating groups generally stabilize the transition structure, as cationic character develops. Why do the additional electron-donating substituents in this case give rise to substantial stabilization for the cation but do not significantly lower the methylation barriers? To answer this question, we have examined the geometries of the transition structures for the methylation reactions. Figure 6 shows selected reactive sections of the transition structures (TS1) for the first methylation of Ar0 and Ar1, as prototypical examples for the HZ0-catalyzed methylation reactions. An intriguing feature for both transition structures is the long O...C distances for the breaking C–O bond of MeOH (2.273 and 2.181 Å for Ar0 and Ar1, respectively), as well as the long C...C distances for the C–

C bond that is being formed (2.066 and 2.114 Å for Ar0 and Ar1, respectively). In addition, the CH<sub>3</sub> moiety is almost planar in both transition structures.

Essentially, the transition structure in both cases is very loose, including a nearly fully-formed CH<sub>3</sub><sup>+</sup> cation. As a result, while the cationic intermediate produced from Ar1 is much more stable than the intermediate produced from Ar0, the transition structure for its formation benefits little from this additional stability. This provides a simple rationalization for the high energy requirements for the methylation reactions.

### Designing an improved MTH process with a second cocatalyst

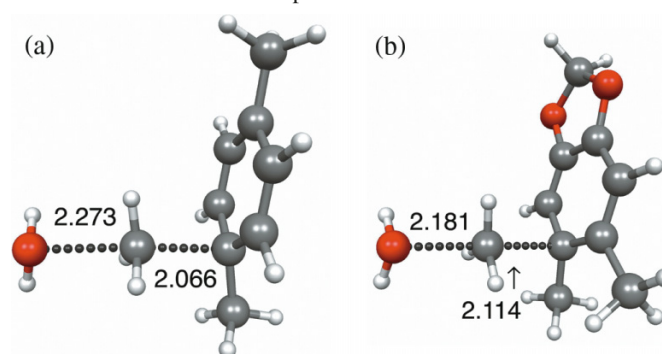
With the knowledge that the high energy requirements for the methylation reactions are the consequence of kinetic rather than thermodynamic effects, can we design an improved process? We consider the use of a stronger nucleophile, THF in this case, in which the oxygen atom has a more concentrated electron density than the  $\pi$ -electrons in Ar0 and Ar1. The aim is that the higher nucleophilicity of THF might better stabilize the almost naked CH<sub>3</sub><sup>+</sup> cation in the transition structure, and give rise to a lower methylation barrier. While the practical use of THF in zeolite catalysis might involve complications such as the potential for its dehydration, THF serves as a convenient oxygen base for the theoretical testing of the above hypothesis.

Ideally, the base cocatalyst should be able to undergo multiple methylation, and it should be possible to eliminate the product alkene from the methylated intermediate. However, such processes are not possible with THF beyond the initial methylation. Thus, we have also examined the subsequent transfer of a CH<sub>3</sub><sup>+</sup> group from THFMe<sup>+</sup> to Ar0 and Ar1 and their monomethylated intermediates, so that the MTH process may follow through to completion. Thus, THF acts as a second cocatalyst in this mechanism.

The reaction profiles for the process leading up to the formation of the dimethylated intermediates are shown in Fig. 7. The initial methylation of THF (via TS8) gives the methylated THF cation (in the complex C13). The CH<sub>3</sub><sup>+</sup> group is then transferred to the aromatic cocatalyst (via TS9), and this is followed by deprotonation of the resulting cationic intermediate (via TS2) to give C4. The sequence of reactions, THF methylation and CH<sub>3</sub><sup>+</sup> transfer (this time via TS10), is then repeated to give the dimethylated aromatic intermediate (C17).

Table 5 shows the calculated energy profiles for the HZO-THF-catalyzed methylation processes of Ar0 and Ar1. It also shows the energy profile for the HZO-catalyzed methylation of Ar0 for comparison. The species in the HZO-THF-catalyzed processes span energy ranges of 220.6 and 215.7 kJ mol<sup>-1</sup>, for Ar0 and Ar1, respectively. The lowest-energy point on the energy profiles is Ar + C12 + MeOH (Table 5, entry 22) for both cases, where C12 is the HZO-MeOH-THF complex, while the highest energy point is TS10 + 2H<sub>2</sub>O (Table 5, entry 35), where TS10 is the transition structure for the second CH<sub>3</sub><sup>+</sup> transfer from THFMe<sup>+</sup> to Ar'. The energy ranges for these two processes, and the energies of the lowest and highest points along the pathways, are similar to those for the HZO-catalyzed process in the absence of THF. However, we find that the high barriers are eliminated when

**Fig. 6.** Selected bond distances (Å) in the transition structures (TS1) for the HZO-catalyzed methylation of (a) Ar0 and (b) Ar1. The zeolite moieties in the optimized structures are not shown.

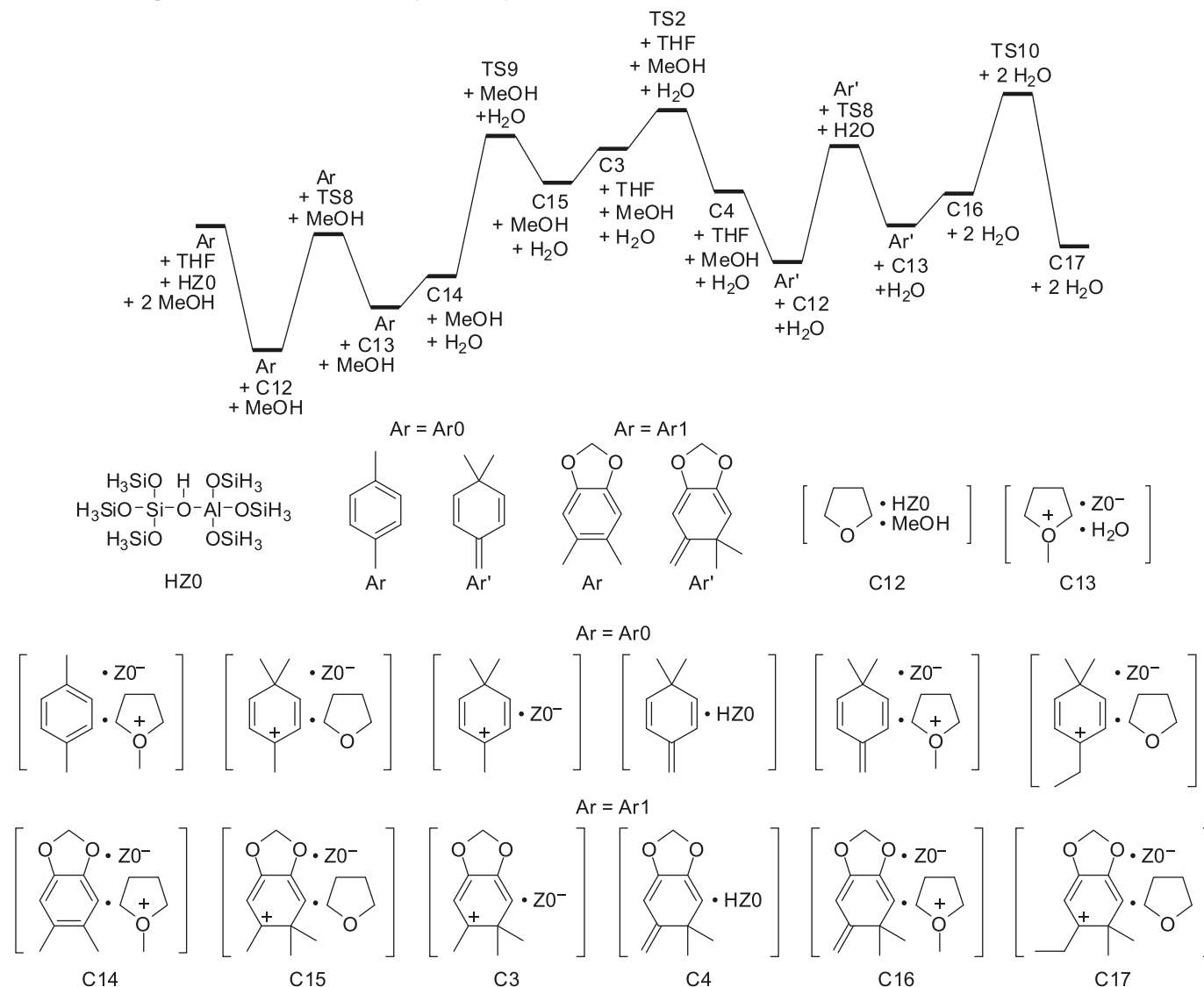


THF is involved. Thus, the highest barriers for the HZO-THF-Ar0 and HZO-THF-Ar1 processes are 123.4 and 118.6 kJ mol<sup>-1</sup>, respectively, which are considerably lower than the highest barrier of 167.4 kJ mol<sup>-1</sup> for the HZO-Ar0 process.

While the highest barrier in the HZO-Ar0 process is found for the HZO-catalyzed methylation of Ar0, we find that the corresponding HZO-catalyzed methylation of THF has a much lower barrier of 99.3 kJ mol<sup>-1</sup>. This is consistent with our hypothesis that a more nucleophilic oxygen base favors the methylation reaction compared with  $\pi$ -electron nucleophiles. Instead, the highest barriers in the THF-catalyzed processes correspond to the transfer of CH<sub>3</sub><sup>+</sup> from the methylated THF cation to the aromatic substrates Ar0 and Ar1. Nonetheless, the barriers for the transfer reactions of CH<sub>3</sub><sup>+</sup> are still considerably lower than those for the HZO-catalyzed methylation of the aromatic substrates.

The reactive segments in the transition structures for the HZO-catalyzed methylation reactions of Ar0 and THF, and for the CH<sub>3</sub><sup>+</sup> transfer from THFMe<sup>+</sup> to Ar0 (in the presence of ZO<sup>-</sup>), are shown in Fig. 8. An intriguing observation in comparing the three transition structures is the short C...O distance between the CH<sub>3</sub><sup>+</sup> moiety and THF for the methylation of THF (Fig. 8b). This short distance, along with the nucleophilicity of the O atom, facilitates the stabilization of the CH<sub>3</sub><sup>+</sup> and the lowering of the barrier. We can see that the O...C distance in the ZO<sup>-</sup>-THFMe<sup>+</sup>-Ar0 reaction (Fig. 8c) is comparable to the corresponding distance in the HZO-MeOH-Ar0 reaction (Fig. 8a), and the C...C distance in the former is noticeably longer than that in the latter. The barrier for the CH<sub>3</sub><sup>+</sup> transfer (Fig. 8c) is nevertheless markedly lower. Presumably, this is due to ZO<sup>-</sup>-THFMe<sup>+</sup> being a better donor of CH<sub>3</sub><sup>+</sup> than HZO-MeOH.

Our results show that the use of THF as a "CH<sub>3</sub><sup>+</sup> sink" might lead to facilitation of the methylation of the aromatic cocatalyst, which is likely to be the most energy-intensive reaction in the MTH process. From a practical point of view, it would be more desirable to design a single aromatic cocatalyst that can be easily methylated. In this connection, we have briefly examined the thermodynamics for the various intermediates involved for methylation at oxygen in Ar1 (Fig. 9). Our results show that methylation at the oxygen atom of Ar1 is much less favorable than methylating the aromatic ring. This may be attributed to the delocalization of

**Fig. 7.** Reaction profile for the HZ0-THF-catalyzed methylation of Ar0 and Ar1.

the oxygen lone pair over the  $\pi$ -system, making it substantially less nucleophilic. Thus, among the processes examined in this study, the use of THF as an additional and more nucleophilic cocatalyst appears to provide the least energy intensive path for the MTH conversion.

### Concluding remarks

We have employed computational quantum chemistry to examine the production of  $\text{C}_2\text{H}_4$  in methanol-to-hydrocarbon (MTH) processes via an exocyclic carbon pool mechanism. The following principal findings have emerged from the present study.

The M05-2X functional performs well for the investigation of these reactions, with an MAD of  $11.2 \text{ kJ mol}^{-1}$ , compared with G3(MP2)-RAD, for the species involved in the MTH process. The use of 8T-clusters as models for zeolites appears to provide a good qualitative picture of the catalysis, but tends to overestimate the barriers in the MTH process.

In contrast to previous studies, we find that the methyla-

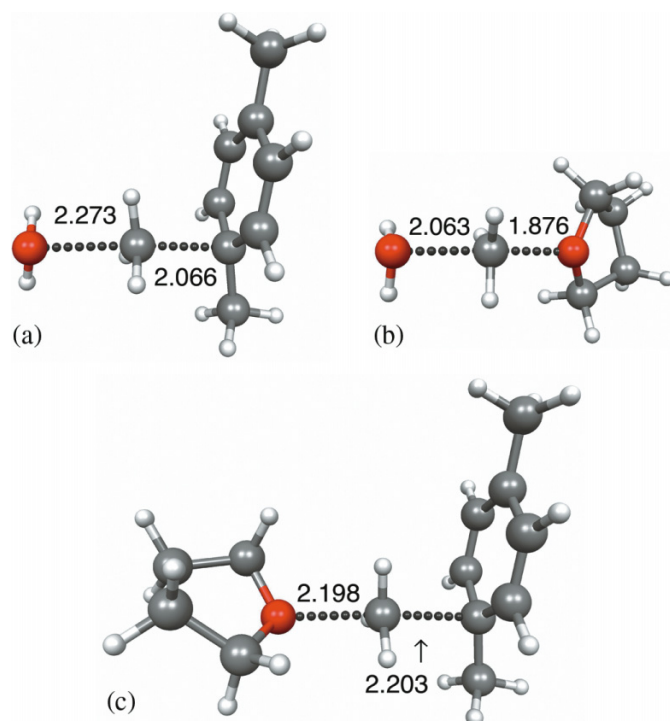
tion reactions of the aromatic cocatalyst are the most energy-demanding steps in the MTH process. We have identified a low-energy pathway to the production of  $\text{C}_2\text{H}_4$  from the methylated intermediates, which involves multiple methyl shifts, followed by concerted zeolite-catalyzed deprotonation and  $\text{C}_2\text{H}_4$  formation.

We find that the substitution of the SiOH group in our zeolite model with GeOH, or of AlOH with GaOH, does not lead to lower barriers for the methylation reactions. While the use of a more electron-rich aromatic cocatalyst greatly stabilizes the cationic intermediates, it does not provide significant benefit to the transition structures that lead to the formation of these intermediates. This can be attributed to the formation of an almost naked  $\text{CH}_3^+$  in the transition structure, regardless of the aromatic cocatalyst.

The use of a more nucleophilic substrate, such as THF, in the methylation reaction reduces the barrier significantly. We find that the resulting  $\text{THFMe}^+$  cation can also methylate an aromatic molecule with a significantly reduced barrier. Thus,

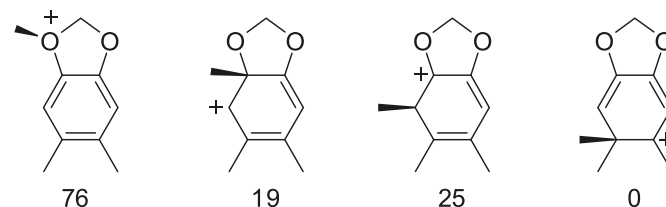
**Table 5.** Calculated energy profiles (kJ mol<sup>-1</sup>) for the HZO-catalyzed methylation of Ar0 and the HZO-THF-catalyzed methylation of Ar0 and Ar1.

		HZO-Ar0 <sup>a</sup>	HZO-THF-Ar0	HZO-THF-Ar1
21	Ar + HZO + THF + 2MeOH	0.0	0.0	0.0
22	Ar + C12 + MeOH	-105.3	-103.7	-103.7
23	Ar + TS8 + MeOH	62.1	-4.4	-4.4
24	Ar + C13 + MeOH	9.4	-70.9	-70.9
25	C14 + MeOH + H <sub>2</sub> O	—	-44.4	-47.7
26	TS9 + MeOH + H <sub>2</sub> O	—	78.9	71.0
27	C15 + MeOH + H <sub>2</sub> O	—	39.7	3.7
28	C3 + THF + MeOH + H <sub>2</sub> O	72.1	72.1	-3.9
29	TS2 + THF + MeOH + H <sub>2</sub> O	102.3	102.3	37.7
30	C4 + THF + MeOH + H <sub>2</sub> O	36.0	36.0	29.8
31	Ar' + C12 + H <sub>2</sub> O	—	-31.8	-34.9
32	Ar' + TS8 + H <sub>2</sub> O	—	67.5	64.4
33	Ar' + C13 + H <sub>2</sub> O	—	1.1	-2.1
34	C16 + 2H <sub>2</sub> O	-29.8	32.4	26.7
35	TS10 + 2H <sub>2</sub> O	104.5	116.9	111.9
36	C17 + 2H <sub>2</sub> O	-41.5	-14.0	-60.7
$\Delta E_8^\ddagger$	(22 → 24)	167.4	99.3	99.3
$\Delta E_9^\ddagger$	(25 → 27)	—	123.4	118.6
$\Delta E_{10}^\ddagger$	(28 → 30)	30.2	30.2	41.6
$\Delta E_{11}^\ddagger$	(31 → 33)	—	99.3	99.3
$\Delta E_{12}^\ddagger$	(34 → 36)	134.3	84.5	85.2

<sup>a</sup>Values correspond sequentially to those of entries 1–10 in Table 4.**Fig. 8.** Selected bond distances (Å) in the HZO-catalyzed methylation of (a) Ar0 and (b) THF, and (c) methyl transfer from THFMe<sup>+</sup> to Ar0 in the presence of HZO. The zeolite moieties in the optimized structures are not shown.

the combination of two cocatalysts, namely a nucleophile and an aromatic carbon pool, can potentially provide a low-energy pathway for the MTH process.

It would be advantageous to combine the nucleophile and

**Fig. 9.** Relative energies (kJ mol<sup>-1</sup>) for the methylation of Ar1 at various positions.

the aromatic carbon pool in a single molecule. However, our preliminary studies indicate that this is not entirely straightforward. We are currently undertaking further investigations, aiming to design an effective cocatalyst for the MTH process.

### Supplementary data

Supplementary data for this article (GAUSSIAN 03 archive entries for B3-LYP/6-31+G(d,p)-optimized geometries of relevant equilibrium structures and transition structures (Table S1), and M05-2X/G3MP2Large electronic energies (Table S2)) are available on the journal Web site (canjchem.nrc.ca).

### Acknowledgements

We gratefully acknowledge generous allocations of computing time from the National Computational Infrastructure (NCI) National Facility and the Australian Center for Advanced Computing and Communications (AC3), the award (to LR) of an Australian Research Council (ARC) Discovery Grant, and support from the ARC Centre of Excellence for Free Radical Chemistry and Biotechnology.



## References

- (1) (a) Bockris, J. O. M. *Int. J. Hydrogen Energy* **1999**, *24* (1), 1. doi:10.1016/S0360-3199(98)00115-3.; (b) Midilli, A.; Ay, M.; Dincer, I.; Rosen, M. A. *Renew. Sustain. Energy Rev.* **2005**, *9* (3), 255. doi:10.1016/j.rser.2004.05.003.; (c) Muradov, N. Z.; Veziroglu, T. N. *Int. J. Hydrogen Energy* **2008**, *33* (23), 6804. doi:10.1016/j.ijhydene.2008.08.054.
- (2) (a) Coontz, R.; Hanson, B. *Science* **2004**, *305* (5686), 957. doi:10.1126/science.305.5686.957.; (b) Rimm, J. J. *The Hype About Hydrogen*; Island Press: Washington, D.C., 2004.
- (3) Olah, G. A.; Prakash, G. K. S. *Beyond Oil and Gas: The Methanol Economy*; Wiley-VCH: Weinheim, Germany, 2006.
- (4) (a) Chan, B.; Radom, L. *J. Am. Chem. Soc.* **2006**, *128* (16), 5322. doi:10.1021/ja0602492. PMID:16620086.; (b) Chan, B.; Radom, L. *J. Am. Chem. Soc.* **2008**, *130* (30), 9790. doi:10.1021/ja800840q. PMID:18593117.
- (5) (a) Meyers, R. A. *Handbook of Petrochemicals Production Processes*; McGraw-Hill: New York, 2004; (b) Speight, J. G. *The Chemistry and Technology of Petroleum*, 4th ed.; CRC Press: Boca Raton, FL, 2006.
- (6) Stöcker, M. *Microporous Mesoporous Mater.* **1999**, *29* (1–2), 3. doi:10.1016/S1387-1811(98)00319-9.
- (7) (a) Haw, J. F.; Song, W.; Marcus, D. M.; Nicholas, J. B. *Acc. Chem. Res.* **2003**, *36* (5), 317. doi:10.1021/ar020006o. PMID:12755641.; (b) Olsbye, U.; Bjørgen, M.; Svelle, S.; Lillerud, K.-P.; Kolboe, S. *Catal. Today* **2005**, *106* (1–4), 108. doi:10.1016/j.cattod.2005.07.135.
- (8) Sullivan, R. F.; Egan, C. J.; Langlois, G. E.; Sieg, R. P. *J. Am. Chem. Soc.* **1961**, *83* (5), 1156. doi:10.1021/ja01466a036.
- (9) McCann, D. M.; Lesthaeghe, D.; Kletnieks, P. W.; Guenther, D. R.; Hayman, M. J.; Van Speybroeck, V.; Waroquier, M.; Haw, J. F. *Angew. Chem. Int. Ed.* **2008**, *47* (28), 5179. doi:10.1002/anie.200705453.
- (10) (a) Arstad, B.; Nicholas, J. B.; Haw, J. F. *J. Am. Chem. Soc.* **2004**, *126* (9), 2991. doi:10.1021/ja035923j. PMID:14995217.; (b) Wang, C.-M.; Wang, Y.-D.; Xie, A.-K.; Liu, Z.-P. *J. Phys. Chem. C* **2009**, *113* (11), 4584. doi:10.1021/jp810350x.
- (11) Mole, T.; Bett, G.; Seddon, D. J. *J. Catal.* **1983**, *84* (2), 435. doi:10.1016/0021-9517(83)90014-3.
- (12) Calculated from experimental heats of formation at 298 K of methanol (–205.0 kJ mol<sup>–1</sup>), water (–241.8 kJ mol<sup>–1</sup>), ethene (52.5 kJ mol<sup>–1</sup>), propene (20.4 kJ mol<sup>–1</sup>), and isobutene (–17.9 kJ mol<sup>–1</sup>) obtained from ref. 13.
- (13) Linstrom, P. J.; Mallard, W. G., Eds. *NIST Chemistry Web-Book, NIST Standard Reference Database Number 69*; National Institute of Standards and Technology: Gaithersburg, MD, 2009.
- (14) (a) Chan, B.; Radom, L. *Aust. J. Chem.* **2004**, *57* (7), 659. doi:10.1071/CH04031.; (b) Chan, B.; Radom, L. *J. Am. Chem. Soc.* **2005**, *127* (8), 2443. doi:10.1021/ja0450253. PMID:15724999.; (c) Miller, D. J.; Smith, D. M.; Chan, B.; Radom, L. *Mol. Phys.* **2006**, *104* (5–7), 777. doi:10.1080/00268970500417093.; (d) Zhong, G.; Chan, B.; Radom, L. *J. Am. Chem. Soc.* **2007**, *129* (4), 924. doi:10.1021/ja066251a. PMID:17243829.; (e) Zhong, G.; Chan, B.; Radom, L. *J. Mol. Struct. THEOCHEM* **2007**, *811* (1–3), 13. doi:10.1016/j.theochem.2007.02.030.; (f) Chan, B.; Radom, L. *J. Phys. Chem. A* **2007**, *111* (28), 6456. doi:10.1021/jp072837n. PMID:17585851.; (g) Zhong, G.; Chan, B.; Radom, L. *Org. Lett.* **2009**, *11* (3), 749. doi:10.1021/ol802826h. PMID:19140697.
- (15) (a) Hehre, W. J.; Radom, L.; Schleyer, P. v. R.; Pople, J. A. *Ab Initio Molecular Orbital Theory*; Wiley: New York, 1986; (b) Jensen, F. *Introduction to Computational Chemistry*, 2nd ed.; Wiley: Chichester, UK, 2007; (c) Koch, W.; Holthausen, M. C. *A Chemist's Guide to Density Functional Theory*, 2nd ed.; Wiley: New York, 2001.
- (16) Frisch, M. J.; Trucks, G. W.; Schlegel, H. B.; Scuseria, G. E.; Robb, M. A.; Cheeseman, J. R.; Montgomery, J. A., Jr.; Vreven, T.; Kudin, K. N.; Burant, J. C.; Millam, J. M.; Iyengar, S. S.; Tomasi, J.; Barone, V.; Mennucci, B.; Cossi, M.; Scalmani, G.; Rega, N.; Petersson, G. A.; Nakatsuji, H.; Hada, M.; Ehara, M.; Toyota, K.; Fukuda, R.; Hasegawa, J.; Ishida, M.; Nakajima, T.; Honda, Y.; Kitao, O.; Nakai, H.; Klene, M.; Li, X.; Knox, J. E.; Hratchian, H. P.; Cross, J. B.; Bakken, V.; Adamo, C.; Jaramillo, J.; Gomperts, R.; Stratmann, R. E.; Yazyev, O.; Austin, A. J.; Cammi, R.; Pomelli, C.; Ochterski, J. W.; Ayala, P. Y.; Morokuma, K.; Voth, G. A.; Salvador, P.; Dannenberg, J. J.; Zakrzewski, V. G.; Dapprich, S.; Daniels, A. D.; Strain, M. C.; Farkas, O.; Malick, D. K.; Rabuck, A. D.; Raghavachari, K.; Foresman, J. B.; Ortiz, J. V.; Cui, Q.; Baboul, A. G.; Clifford, S.; Cio-slowski, J.; Stefanov, B. B.; Liu, G.; Liashenko, A.; Piskorz, P.; Komaromi, I.; Martin, R. L.; Fox, D. J.; Keith, T.; Al-Laham, M. A.; Peng, C. Y.; Nanayakkara, A.; Challacombe, M.; Gill, P. M. W.; Johnson, B.; Chen, W.; Wong, M. W.; Gonzalez, C.; Pople, J. A. *Gaussian 03*, revision D.02; Gaussian, Inc.: Wallingford, CT, 2004.
- (17) Frisch, M. J.; Trucks, G. W.; Schlegel, H. B.; Scuseria, G. E.; Robb, M. A.; Cheeseman, J. R.; Scalmani, G.; Barone, V.; Mennucci, B.; Petersson, G. A.; Nakatsuji, H.; Caricato, M.; Li, X.; Hratchian, H. P.; Izmaylov, A. F.; Bloino, J.; Zheng, G.; Sonnenberg, J. L.; Hada, M.; Ehara, M.; Toyota, K.; Fukuda, R.; Hasegawa, J.; Ishida, M.; Nakajima, T.; Honda, Y.; Kitao, O.; Nakai, H.; Vreven, T.; Montgomery, J. A., Jr.; Peralta, J. E.; Ogliaro, F.; Bearpark, M.; Heyd, J. J.; Brothers, E.; Kudin, K. N.; Staroverov, V. N.; Kobayashi, R.; Normand, J.; Raghavachari, K.; Rendell, A.; Burant, J. C.; Iyengar, S. S.; Tomasi, J.; Cossi, M.; Rega, N.; Millam, N. J.; Klene, M.; Knox, J. E.; Cross, J. B.; Bakken, V.; Adamo, C.; Jaramillo, J.; Gomperts, R. E.; Stratmann, O.; Yazyev, A. J.; Austin, R.; Cammi, C.; Pomelli, J. W.; Ochterski, R.; Martin, R. L.; Morokuma, K.; Zakrzewski, V. G.; Voth, G. A.; Salvador, P.; Dannenberg, J. J.; Dapprich, S.; Daniels, A. D.; Farkas, O.; Foresman, J. B.; Ortiz, J. V.; Cio-slowski, J.; Fox, D. J. *Gaussian 09*, revision A.02; Gaussian, Inc.: Wallingford, CT, 2009.
- (18) Werner, H.-J.; Knowles, P. J.; Lindh, R.; Manby, F. R.; Schütz, M.; Celani, P.; Korona, T.; Mitrushenkov, A.; Rauhut, G.; Adler, T. B.; Amos, R. D.; Bernhardsson, A.; Berning, A.; Cooper, D. L.; Deegan, M. J. O.; Dobbyn, A. J.; Eckert, F.; Goll, E.; Hampel, C.; Hetzer, G.; Hrenar, T.; Knizia, G.; Köppl, C.; Liu, Y.; Lloyd, A. W.; Mata, R. A.; May, A. J.; McNicholas, S. J.; Meyer, W.; Mura, M. E.; Nicklaß, A.; Palmieri, P.; Pflüger, K.; Pitzer, R.; Reiher, M.; Schumann, U.; Stoll, H.; Stone, A. J.; Tarroni, R.; Thorsteinsson, T.; Wang, M.; Wolf, A. *MOLPRO 2006.1*; University of Birmingham: Birmingham, UK, 2006.
- (19) (a) Flanigen, E. M.; Bennett, J. M.; Grose, R. W.; Cohen, J. P.; Patton, R. L.; Kirchner, R. M.; Smith, J. V. *Nature* **1978**, *271* (5645), 512. doi:10.1038/271512a0.; (b) Kokotailo, G. T.; Lawton, S. L.; Olson, D. H.; Meier, W. M. *Nature* **1978**, *272* (5652), 437. doi:10.1038/272437a0.
- (20) The ZSM-5 crystal structure was obtained from the Inorganic Crystal Structure Database (ICSD) and was originally published in Olson, D. H.; Kokotailo, G. T.; Lawton, S. L.; Meier, W. M. *J. Phys. Chem.* **1981**, *85* (15), 2238. doi:10.

- 1021/j150615a020. The 8T-cluster is extracted from the crystal structure according to the International Zeolite Association (IZA) MFI building scheme. Two Al atoms are located in two equivalent sites within this 8T-cluster. For simplicity, one of the Al atoms is replaced by an Si atom, such that there is only one acidic proton in the cluster.
- (21) Zhao, Y.; Schultz, N. E.; Truhlar, D. G. *J. Chem. Theory Comput.* **2006**, 2 (2), 364. doi:10.1021/ct0502763.
- (22) (a) Curtiss, L. A.; Raghavachari, K.; Redfern, P. C.; Rassolov, V.; Pople, J. A. *J. Chem. Phys.* **1998**, 109 (18), 7764. doi:10.1063/1.477422.; (b) Curtiss, L. A.; Redfern, P. C.; Raghavachari, K.; Rassolov, V.; Pople, J. A. *J. Chem. Phys.* **1999**, 110 (10), 4703. doi:10.1063/1.478385.
- (23) The Si-H and Al-H distances were obtained as averages of the Si-H and Al-H bond lengths in the B3-LYP/6-31+G(d,p) optimized geometries for  $\text{H}_3\text{Si-OH-AlH}_3$  and  $[\text{H}_3\text{Si-O-AlH}_3]^-$ .
- (24) Henry, D. J.; Sullivan, M. B.; Radom, L. *J. Chem. Phys.* **2003**, 118 (11), 4849. doi:10.1063/1.1544731.
- (25) Merrick, J. P.; Moran, D.; Radom, L. *J. Phys. Chem. A* **2007**, 111 (45), 11683. doi:10.1021/jp073974n. PMID:17948971.
- (26) (a) Zheng, X.; Blowers, P. *J. Mol. Catal. Chem.* **2005**, 229 (1-2), 77. doi:10.1016/j.molcata.2004.11.009.; (b) van Santen, R. A. *Catal. Today* **1997**, 38 (3), 377. doi:10.1016/S0920-5861(97)81505-0.; (c) Brand, H. V.; Curtiss, L. A.; Iton, L. E. *J. Phys. Chem.* **1993**, 97 (49), 12773. doi:10.1021/j100151a024.
- (27) (a) Arstad, B.; Kolboe, S.; Swang, O. *J. Phys. Chem. B* **2004**, 108 (7), 2300. doi:10.1021/jp0307147.; (b) Arstad, B.; Kolboe, S.; Swang, O. *J. Phys. Chem. A* **2005**, 109 (39), 8914. doi:10.1021/jp058166f. PMID:16834295.; (c) Kolboe, S.; Svelle, S.; Arstad, B. *J. Phys. Chem. A* **2009**, 113 (5), 917. doi:10.1021/jp8070234. PMID:19099448.

## TRIBUTE

Russell Jaye Boyd was born in 1945 in Kelowna, the centre of British Columbia's wine-producing and fruit-growing Okanagan Valley. His early years were devoted to hockey, basketball, baseball, golf, and water-related activities. Just before his fifteenth birthday, his family moved to New Westminster, where he attended Lester Pearson High School and began to show some interest in science and mathematics.

Russ enrolled in the Science program at the University of British Columbia in 1963 and graduated in 1967 with First-Class Honours in Chemistry and the Lefevre Gold Medal for highest standing in the Honours Chemistry program. His Honours thesis focused on the new technique of photoelectron spectroscopy. At the time, there were no commercial instruments and UBC had the only photoelectron spectrometers in Canada. With enthusiastic encouragement from his thesis supervisor, David C. Frost, Russ attempted to carry out the first study of the angular dependence of photoelectron emission. Despite the best efforts of the strong technical support team in the machine shop, two different designs failed to produce meaningful results. To obtain some positive results, Russ rounded up supplies of some boron trihalides and recorded their spectra.

As one of the first recipients of a 1967 Science Scholarship (introduced in 1967 by the National Research Council (NRC) of Canada to celebrate Canada's centennial), he went east to pursue his Ph.D. in Theoretical Chemistry at McGill University under the supervision of M.A. (Tony) Whitehead. As a consequence of the fact that he had recorded the photoelectron spectra of some boron trihalides (and some siloxanes) as an undergraduate, Russ realized that there was no theoretical framework for interpreting such spectra in the absence of electronic structure calculations. In 1967, reliable *ab initio* calculations were restricted to small molecules. In fact, the largest molecule in the 1967 compendium of *ab initio* calculations compiled by Morris Kraus is HCCN for which A.D. McLean and M. Yoshimine reported a single-point SCF calculation with a small basis set. In his first few months as a graduate student, Russ completed some semi-empirical molecular orbital calculations on the boron trihalides and sent the results to David Frost, which led to his first paper entitled "The Ionization Potentials of  $\text{BF}_3$ ,  $\text{BCl}_3$  and  $\text{BBr}_3$ ", in April 1968 in the first volume of *Chemical Physics Letters*.

The existing semi-empirical molecular orbital methods in 1967 were not capable of predicting the equilibrium geometries of molecules. All calculations were carried out at the experimental geometries or using assumed bond lengths and angles. Russ realized that this situation was unsatisfactory for studying reaction mechanisms and set out to develop a method that would yield molecular potential-energy surfaces and properties that agree with the experimental data. He developed a method based on the complete neglect of differential overlap approximation that had been introduced in 1965 by John Pople and his co-workers. He focused on equilibrium geometries, bond energies, and force constants (vibrational frequencies), the three chemically interesting properties associated with the minima of molecular potential-energy surfaces. This was an improvement over any other method that existed and was ultimately superseded by the work of Michael Dewar and his colleagues who used a slightly higher and chemically more reliable level of semi-empirical molecular orbital theory.

After defending his Ph.D. in 1971, Russ joined the group of

Charles A. Coulson in the Mathematical Institute at Oxford University as an NRC Postdoctoral Fellow. He had become disillusioned with semi-empirical approaches by the time he completed his thesis and saw more future in the *ab initio* approaches that John A. Pople and his group were developing within their Gaussian code. Russ turned his attention to electron correlation and published two papers with Coulson, including a description of the Coulomb hole in the first two excited states of the helium atom, his best-known paper from Oxford.

With encouragement from Charles A. McDowell, Russ returned to the University of British Columbia where he held a Killam Postdoctoral Fellowship in the Department of Chemistry from 1973 to 1975, where he renewed his interest in photoelectron spectroscopy. He published a single author letter in *Nature* in 1974 in which he pointed out that contrary to the usual interpretation of structural studies of porphyrin complexes, the lowest lying high-spin state of an atom (ion) in a given configuration is smaller than any state of lower spin. His prediction was verified two years later by scattering experiments on the first two excited states of the helium atom.

Russ joined Dalhousie University as an Assistant Professor of Chemistry in 1975 and rose through the ranks to become a Professor in 1985. He was named a Faculty of Science Killam Professor in 1997, and in 2001 he became the seventh Alexander McLeod Chair of Chemistry. The McLeod Chair, one of the oldest named professorships in chemistry in Canada, was created in 1884 in accordance with a bequest from Alexander McLeod. Russ served as Chair of Chemistry from 1992 to 2005. During this time, 11 new faculty members, including four outstanding senior chemists, were recruited, the graduate program expanded significantly, and an addition to the Chemistry Building was approved. The Department gained four Tier I Canada Research Chairs (Neil Burford, Jeff Dahn, Don Weaver, and Joe Zwanziger) between 2001 and 2003.

His research interests span a range of topics in computational and theoretical chemistry with an emphasis on problems relevant to biological systems. He has published about 240 research papers and 10 review chapters and he co-edited *The Quantum Theory of Atoms in Molecules* with Chérif Matta in 2007. With over 5000 citations of his papers and an H-index of 42, Russ is one of Canada's best-known computational chemists. He has supervised the research of 20 Ph.D. students, more than 25 postdoctoral fellows and senior visitors, and a comparable number of undergraduate students. His former students have successful careers in academic institutions, government laboratories, and the industry. Fourteen former members of his group hold academic appointments in Canadian universities and another eight hold similar appointments abroad. He is especially proud of the number of excellent young scientists who received a significant part of their training in his group.

Russ received the 1983 APICS/Fraser Medal. He was the first and only chemist to receive this prize, which was awarded in the 1970s and 1980s to recognize outstanding research work carried out in the Atlantic Provinces by a young scientist or engineer. His other awards include the Fellowship of The Chemical Institute of Canada (1983), the CNC-IUPAC Award (1986), Dalhousie University Senior Killam Fellowship (1989), and the 2009 Montreal Medal of The Chemical Institute of Canada.

Russ took on leading roles in organizing the Canadian Society for Chemistry Conferences in Halifax in 1981, 1990, and 2006. He was the principal organizer of the 8th Canadian Symposium on Theoretical Chemistry in 1983 and the 7th Canadian Computational Chemistry Conference in 2009. He is a member of the College of Reviewers of the Canada Research Chairs Program, and he has served on many committees of the Natural Sciences and Engineering Research Council of Canada (NSERC). He has served on selection panels for the National Science Foundation (NSF) of the USA and the Canada–US Fulbright Program. He has served on many boards, including the Canadian Society for Chemistry, the *Canadian Journal of Chemistry*, the Dalhousie University Foundation, the Atlantic Provinces Council on the Sciences, and the World Association of Theoretical and Computational Chemists. He was an editor of the *Canadian Journal of Chemistry* from 1988 to 1998 and served as President of the Canadian Society for Chemistry in 2007–2008. His many other

activities include Judge-in-Chief for the 1984 Canada-Wide Science Fair. He is currently the Principal Investigator (Research Director) for the Atlantic Computational Excellence Network (ACEnet), a consortium of nine universities in Atlantic Canada that provides high-performance computing facilities by means of funding from the Canada Foundation for Innovation (CFI).

The number, quality, and countries of origin of the papers submitted to this dedicated issue of the *Canadian Journal of Chemistry* attest to breadth and reach of Russ Boyd's influence in the computational and theoretical chemistry community in Canada and abroad, as well as his contributions to the broader chemical community.

**Neil Burford**  
*Halifax, Nova Scotia*



## HOMMAGE

Russell Jaye Boyd naît en 1945 à Kelowna, située au centre de la région viticole et fruitière de la vallée de l'Okanagan (Colombie-Britannique). Il consacre les premières années de sa vie au hockey, au basketball, au baseball, au golf et aux activités aquatiques. Peu de temps avant son quinzième anniversaire, sa famille déménage à New Westminster où il fréquente l'école secondaire Lester Pearson et commence à manifester un intérêt pour les sciences et les mathématiques.

En 1963, Russ s'inscrit au programme de sciences de l'Université de la Colombie-Britannique (UBC) et en 1967, il obtient son diplôme en chimie avec très grande distinction et la Lefevre Gold Medal pour avoir obtenu les meilleurs résultats dans le programme spécialisé en chimie. Sa thèse de spécialisation porte principalement sur la nouvelle technique de spectroscopie photoélectronique. À ce moment-là, il n'existe aucun spectromètre photoélectronique vendu sur le marché et l'UBC est seule à en posséder au Canada. Fort de l'encouragement enthousiaste de son directeur de thèse, David C. Frost, Russ tente de mener la première étude sur la dépendance angulaire de l'émission de photoélectrons. Malgré tous les efforts déployés par la solide équipe de soutien technique de l'atelier de mécanique, deux concepts différents ne parviennent pas à produire des résultats significatifs. Afin d'obtenir des résultats positifs, Russ rassemble des réserves de trihalogénures de bore et enregistre leur spectre.

Lauréat de l'une des premières bourses 1967 en sciences (instaurée en 1967 par le Conseil national de recherches du Canada pour souligner le centenaire de la Confédération), il se dirige vers l'est pour poursuivre un doctorat en chimie théorique à l'Université McGill sous la direction de M. A. (Tony) Whitehead. En raison du fait qu'au cours de ses études de premier cycle, il a eu à enregistrer les spectres photoélectroniques de trihalogénures de bore (et de siloxanes), Russ se rend compte qu'il n'existe aucun cadre théorique pour interpréter de tels spectres en l'absence de calculs de structures électroniques. En 1967, les seuls calculs ab initio fiables se limitent aux petites molécules. En fait, la plus grosse molécule répertoriée dans le recueil des calculs ab initio de 1967 (Morris Kraus) est le cyanoacétylène (HCCCN) pour laquelle A.D. McLean et M. Yoshimine ont fait état d'un calcul SCF en un seul point avec un petit ensemble de base. Au cours de ses premiers mois comme étudiant diplômé, Russ effectue des calculs semi-empiriques d'orbitales moléculaires sur des trihalogénures de bore et il fait parvenir ses résultats à David Frost, ce qui mène la publication, en avril 1968, de son premier article intitulé « The Ionization Potentials of  $\text{BF}_3$ ,  $\text{BCl}_3$  and  $\text{BBr}_3$  » dans le premier volume de la revue *Chemical Physics Letters*.

En 1967, les méthodes semi-empiriques d'orbitales moléculaires utilisées ne permettent pas de prévoir les géométries d'équilibre des molécules. Tous les calculs sont effectués sur des géométries expérimentales ou au moyen de longueurs et d'angles de liaison présumés. Russ se rend compte que cette situation est peu satisfaisante pour étudier les mécanismes de réaction et entreprend de mettre au point une méthode qui permettrait de produire des surfaces et des propriétés d'énergie potentielle moléculaire qui cadrent avec des données expérimentales. Il met au point une méthode fondée sur l'approximation du recouvrement différentiel nul, introduite en 1965 par John Pople et ses collègues. Il concentre ses efforts

sur les géométries d'équilibre, les énergies de liaison et les constantes de force (fréquences vibrationnelles), trois propriétés revêtant un intérêt certain sur le plan de la chimie et associées aux minima des surfaces d'énergie potentielle. Il s'agit d'une amélioration par rapport à toutes les autres méthodes existantes. Mais finalement, elle sera détrônée par les travaux de Michael Dewar et de ses collègues, qui utilisent un niveau légèrement plus élevé et plus fiable chimiquement de la théorie semi-empirique des orbitales moléculaires.

Après avoir défendu sa thèse de doctorat en 1971, Russ se joint à l'équipe de Charles A. Coulson à l'Institut de mathématiques de l'Université d'Oxford à titre de boursier postdoctoral du CNRC. Désenchanté des méthodes semi-empiriques et avant même qu'il ne termine sa thèse, il se tourne vers les méthodes ab initio plus prometteuses que John A. Pople et son équipe sont à mettre au point dans un cadre gaussien. Russ se penche donc sur la corrélation électronique et publie deux articles avec Coulson, dont une description du trou de Coulomb dans les deux premiers états d'excitation de l'atome d'hélium, son article le mieux connu issu d'Oxford.

Encouragé par Charles A. McDowell, Russ retourne à l'Université de la Colombie-Britannique où il est titulaire d'une bourse postdoctorale Killam au Département de chimie de 1973 à 1975. C'est là qu'il s'intéresse de nouveau à la spectroscopie photoélectronique. En 1974, dans un texte publié dans la revue *Nature*, il fait valoir que contrairement à l'interprétation courante des études structurales des complexes de porphyrine, le plus faible état de spin élevé d'un atome (ion) dans une configuration donnée est plus petit que tout état de spin plus faible. Sa prédiction sera vérifiée deux ans plus tard par des expériences de diffusion menées sur les deux premiers états excités de l'atome d'hélium.

Russ est embauché par l'Université Dalhousie à titre de professeur adjoint de chimie en 1975 et grimpe les échelons pour devenir professeur en 1985. En 1997, on le nomme professeur Killam de la Faculté des sciences, et en 2001, il devient le septième titulaire de la chaire de chimie Alexander McLeod. La chaire McLeod, l'une des plus anciennes chaires dénommées en chimie au Canada, a été créée en 1884 conformément à un legs d'Alexander McLeod. Russ occupe les fonctions de directeur du Département de chimie de 1992 à 2005. Au cours de cette période, onze nouveaux membres du corps professoral sont recrutés (dont quatre éminents chimistes chevronnés), le programme d'études supérieures prend de l'expansion de façon importante et on approuve la construction d'une adjonction à l'édifice de la Faculté de chimie. Entre 2001 et 2003, le Département recrute quatre chercheurs inscrits au Programme des chaires de recherche du Canada de niveau I (Neil Burford, Jeff Dahn, Don Weaver et Joe Zwanziger).

Les travaux de recherche de Russ englobent divers sujets dans les domaines de la chimie théorique et numérique tout en portant une attention particulière aux problèmes liés aux systèmes biologiques. Il a publié jusqu'à maintenant environ 240 articles de recherche et dix chapitres de synthèse et a corédigé, en 2007, l'ouvrage « *The Quantum Theory of Atoms in Molecules* » avec Chérif Matta. Plus de 5000 citations de ses articles et un indice h de 42 font de Russ l'un des chimistes-informaticiens canadiens les plus connus. Au cours de sa carrière, il dirige les travaux de 20 étudiants au doctorat, de plus de 25 boursiers postdoctoraux et de visiteurs

de haut niveau et d'un nombre comparable d'étudiants de premier cycle. Ses anciens étudiants poursuivent des carrières florissantes dans des établissements universitaires, des laboratoires gouvernementaux ou l'industrie. Quatorze anciens membres de son équipe occupent des postes de professeur dans des universités canadiennes et huit autres font de même à l'étranger. Il est particulièrement fier du nombre d'excellents jeunes scientifiques qui ont reçu une partie importante de leur formation au sein de son équipe.

Russ reçoit l'APICS/Fraser Medal en 1983. Il est le premier et le seul chimiste à recevoir ce prix, remis dans les années 1970 et 1980 pour souligner les travaux de recherche remarquables menés par de jeunes scientifiques ou ingénieurs dans les provinces de l'Atlantique. Il compte également parmi ses récompenses la bourse de recherche de l'Institut de chimie du Canada (1983), le prix CNC-UICPA (1986), la bourse de chercheur chevronné Killam de l'Université Dalhousie (1989) et la Médaille de Montréal de l'Institut de chimie du Canada (2009).

Russ assume des rôles de premier plan dans l'organisation des congrès de la Société canadienne de chimie de 1981, de 1990 et de 2006. Il est le principal organisateur du 8<sup>e</sup> symposium canadien de chimie théorique (1983) et du 7<sup>e</sup> congrès canadien de chimie numérique (2009). Il fait partie du Collège d'examineurs du Programme de chaires de recherche du Canada et siège à de nombreux comités au Conseil de recherches en sciences naturelles et en génie du Canada. Il

siège à des jurys de sélection pour la National Science Foundation des États-Unis et le Programme Fulbright Canada-États-Unis. Il fait également partie de nombreux conseils d'administration, dont ceux de la Société canadienne de chimie, de la *Revue canadienne de chimie*, de la Fondation de l'Université Dalhousie, du Conseil des provinces atlantiques pour les sciences et de la World Association of Theoretical and Computational Chemists. Il est l'un des rédacteurs en chef de la *Revue canadienne de chimie* de 1988 à 1998 et il siège à titre de président de la Société canadienne de chimie en 2007-2008. De plus, le rôle de juge en chef à l'occasion de l'Expo-sciences pancanadienne de 1984 constitue une autre de ses nombreuses activités. Il est actuellement le chercheur principal (directeur de la recherche) de l'Atlantic Computational Excellence Network (ACEnet), un consortium de neuf universités du Canada atlantique qui fournit des infrastructures informatiques de haute performance grâce aux fonds provenant de la Fondation canadienne pour l'innovation.

Le nombre, la qualité et les pays d'origine des articles soumis au présent numéro spécial de la *Revue canadienne de chimie* témoignent aussi bien de l'ampleur et du rayonnement de l'influence de Russ Boyd dans les milieux de la chimie théorique et numérique tant au Canada qu'à l'étranger que de son apport au milieu de la chimie en général.

**Neil Burford**  
*Halifax (Nouvelle-Écosse)*

# Equilibrium studies of triphenyltin(IV) complexes with glycine, glycyl-glycine, and glycyl-glycyl-glycine in different aqueous solutions of ethanol

Morteza Jabbari and Farrokh Gharib

**Abstract:** The protonation equilibria of glycine (gly), glycyl-glycine (gly-gly), and glycyl-glycyl-glycine (gly-gly-gly) and their formation constants with triphenyltin(IV) chloride were studied over a wide pH range (pH 1–11), using a combination of spectrophotometric and potentiometric methods at constant temperature (25 °C), different ethanol–water mixtures (50%–80%, v/v), and constant ionic strength (0.1 mol dm<sup>-3</sup> NaClO<sub>4</sub>). Least-squares regression calculations are consistent with the formation of  $\text{ph}_3\text{SnHL}^+$ ,  $\text{ph}_3\text{SnL}$ , and  $\text{ph}_3\text{SnHL}_2\text{L}^-$  complex species, where  $\text{L}^-$  represents the fully dissociated form of each ligand. The stability constant of the formed complexes in different media were analyzed in terms of Kamlet, Abboud, and Taft (KAT) parameters. Single-parameter correlations of the stability constants versus  $\alpha$  (hydrogen-bond donor acidity),  $\beta$  (hydrogen-bond acceptor basicity), and for  $\pi^*$  (dipolarity/polarizability) are relatively poor in all solutions, but multi-parameter correlations represent significant improvements with regard to the single- and dual-parameter models. Linear correlation is observed when the experimental  $\log\beta_{\text{xyz}}$  values are plotted versus the calculated ones, while all the KAT parameters are considered. Also, the stability constant values of the formed complexes are determined in zero percent of organic solvent using the Yasuda–Shedlovsky extrapolation approach. Finally, the results are discussed in terms of the effect of solvent on complexation.

**Key words:** triphenyltin(IV), glycine, glycyl-glycine, glycyl-glycyl-glycine, formation constant, solvent effect.

**Résumé :** Faisant appel à une combinaison de méthodes spectrophotométrique et potentiométrique et opérant à température constante (25 °C), dans divers mélanges d'éthanol–eau (50 % à 80 %, v/v) et à force ionique constante (0,1 mol dm<sup>-3</sup> NaClO<sub>4</sub>), on a étudié l'équilibre de protonation de la glycine (gly), de la glycyl-glycine (gly-gly) et de la glycyl-glycyl-glycine (gly-gly-gly) ainsi que des leurs constantes de formation avec le chlorure de triphénylétain(IV) sur la plage de pH allant de 1 à 11. Les calculs de régression par la méthode des moindres carrés sont en accord avec la formation d'espèces complexes  $\text{ph}_3\text{SnHL}^+$ ,  $\text{ph}_3\text{SnL}$  et  $\text{ph}_3\text{SnHL}_2\text{L}^-$  dans lesquelles  $\text{L}^-$  représente chaque ligand complètement dissocié. On a analysé les constantes de stabilité des complexes formés dans les divers média en fonction des paramètres de Kamlet, Abboud et Taft (KAT). Dans chacune des solutions, les corrélations de paramètres uniques des constantes de stabilité en fonction de  $\alpha$  (acidité comme donneur de liaison hydrogène),  $\beta$  (basicité comme accepteur de basicité) et  $\pi^*$  (dipolarité/polarisabilité) ne sont pas bonnes, mais les corrélations de paramètres multiples représentent des améliorations significatives par rapport aux modèles à un ou deux paramètres. On observe une corrélation linéaire avec les valeurs expérimentales  $\log\beta_{\text{xyz}}$  en fonction des valeurs calculées en considérant tous les paramètres KAT. De plus, les valeurs des constantes de stabilité des complexes formés ont aussi été déterminées pour un solvant contenant zéro pourcent de solvant organique en utilisant l'approche de l'extrapolation de Yasuda–Shedlovsky. Enfin, on discute des résultats en fonction de l'effet de solvant sur la complexation.

**Mots-clés :** triphénylétain(IV), glycine, glycyl-glycine, glycyl-glycyl-glycine, constante de formation, effet de solvant.

[Traduit par la Rédaction]

## Introduction

Organotin compounds have a wide variety of industrial applications, including pesticides, fire-retardants, anti-fouling paints, anti-mold agents, production of poly(vinyl chloride) stabilizers, industrial catalyst, timber preservatives, and so forth,<sup>1,2</sup> and so they are widespread in the environment. The consumption of organotin(IV) compounds during the last 50 years has led to their accumulation in the environment and finally in biological systems. These compounds

interact with living organisms by affecting various biochemical processes.<sup>3–5</sup> Organotin(IV) compounds are generally toxic (specially triorganotins), even at low concentration, and believed to possess anticancer effects on different tumour cells.<sup>6–15</sup> The moiety  $\text{R}_n\text{Sn(IV)}$  can bond to proteins and glycoproteins of the cell membranes, and also to cellular proteins and DNA.<sup>16</sup> This fact has led to considerable efforts to characterize organotin(IV) complexes with variety of biological ligands containing oxygen, nitrogen, or

Received 2 September 2009. Accepted 12 January 2010. Published on the NRC Research Press Web site at canjchem.nrc.ca on 27 July 2010.

M. Jabbari and F. Gharib,<sup>1</sup> Chemistry Department, Shahid Beheshti University, G. C., Tehran, Evin, Iran.

<sup>1</sup>Corresponding author (e-mail: f-gharib@cc.sbu.ac.ir).

sulfur donor atoms.<sup>6–15</sup> Today, a number of organotin(IV) derivatives are known to have an efficient anticancer activity, and their structures are well-characterized in the solid state.<sup>17–20</sup>

Accepting the hypothesis that  $R_2Sn^{2+}$  and  $R_3Sn^+$  are the usual active species for antitumour action of organotin(IV) derivatives, a good antitumour agent should be easily dissociable following administration to animals. This requires weak bonds between tin and the donor atom of the coordinated ligands, which are readily hydrolyzable. If the compound is hydrolytically unstable, the  $R_2Sn^{2+}$  and  $R_3Sn^+$  moieties will be released too soon, and if it is too stable, it may be released too slowly, and consequently lower activity will be observed. Therefore, there is a relationship between the stability of the organotin compounds and their antitumour activity.

This work deals with the study of complexation of triphenyltin(IV) chloride with glycine, glycyl-glycine, and glycyl-glycyl-glycine. Triphenyltin(IV) chloride is not soluble in water, but it is soluble in aqueous-organic mixed solvent with higher percent of the organic solvent. So, the study is performed in different solutions of water-ethanol systems to show how the solvents and their mixtures with various dielectric constants affect the formation reactions of the triorganotin(IV).

In addition, there has been increasing interest during the past decade in the determination of many chemical and biochemical equilibria in aqueous mixed-solvent systems. However, in the literature, it has been shown that water is not an ideal model for *in vivo* reactions. In enzymes, membranes, and other biologically important media, the formation-constant values are different from those in water, as these media tend to be lipophilic rather than hydrophilic.<sup>21,22</sup> Usually, it has been suggested that non-aqueous media, such as ethanol, could provide a better model for *in vivo* reactions.<sup>23,24</sup> Hence, studies in media other than water should provide some understanding of the reactions in living systems. Besides, the knowledge obtained from the mixed-solvent systems could complement the majority of the knowledge collected from the studies in aqueous media of the chemistry and biochemistry of the reactions. However, water and some organic solvents, such as methanol, ethanol, and so forth, are believed to be completely miscible together. These mixtures are macroscopically homogeneous, but it has been reported that water and organic-solvent molecules are not homogeneously dispersed microscopically,<sup>25</sup> owing to the hydrogen-bonding network formation and hydrophobic interactions. Consequently, the molecular composition of the solvation layer around a solute molecule is not the same as that of the bulk mixing ratio of water and organic solvent. The hydrophobic and hydrophilic properties of a solute may be reflected by preferential solvation in such mixed solvents. Therefore, the influence of which solvent exerts on the formation equilibria constant values depends upon the extent and nature of the solute-solvent interactions.

## Experimental section

### Chemicals

Sodium perchlorate was obtained from Merck as analytical reagent-grade material and was dried under vacuum at room temperature at least 72 h before use. The NaOH solu-

tion was prepared from a titrisol solution (Merck). Perchloric acid and ethanol (absolute) were obtained from Merck as analytical reagent-grade materials and were used as supplied. Glycine, gly-gly, gly-gly-gly, and triphenyltin(IV) chloride were obtained from Fluka as reagent-grade materials and were used as received. All dilute solutions were prepared from double-distilled water with specific conductance equal to  $1.2 \pm 0.1 \mu\Omega^{-1} \text{ cm}^{-1}$ . Aqueous stock solutions of the ligands were freshly prepared daily, and their concentrations were determined each time by titration with a NaOH solution.

### Measurements

pH measurements were performed with a Jenway research pH meter, model 3520. All measurements were carried out at 25 °C and constant ionic strength of 0.1 mol dm<sup>-3</sup> sodium perchlorate. The pH meter was calibrated for the relevant  $H^+$  concentration with a solution of 0.01 mol dm<sup>-3</sup> of HClO<sub>4</sub> solution containing 0.09 mol dm<sup>-3</sup> sodium perchlorate (for adjusting the ionic strength to 0.1 mol dm<sup>-3</sup>). For this standard solution, we set  $-\log[H^+]$  to 2.0,<sup>26</sup> assuming the acid is dissociated 100%. The junction potential corrections were calculated from eq. [1]

$$[1] \quad -\log[H^+]_{\text{real}} = -\log[H^+]_{\text{measured}} + a + b[H^+]_{\text{measured}}$$

where  $a$  and  $b$  were determined by measuring the hydrogen ion concentration for two different solutions of perchloric acid or sodium hydroxide with sufficient sodium perchlorate to adjust the ionic strength.

The determination of the hydrogen-ion concentration was performed with a combination electrode (Jenway). The term pH has significance only in aqueous media. The glass electrode potential in an aqueous solution differs from that in a solution of mixed solvents, and a liquid-junction potential of uncertain magnitude may affect the results. To overcome this difficulty, it was necessary to calibrate the glass electrode in different solvent mixtures. The experimental method outlined by van Uitert and Hass<sup>27</sup> was employed for this purpose. The pH meter reading  $B$  in ethanol-water media was converted into  $[H^+]$  using the equation

$$[2] \quad p_c H = B + \log_{10} \mu_H$$

where the concentration factor  $\log_{10} \mu_H$  was obtained for the ionic strength 0.1 mol dm<sup>-3</sup> NaClO<sub>4</sub> from the expression  $\log_{10} \mu_H = \log_{10} \mu_H^\circ + \log_{10} \gamma_{\pm}$ . The value of  $\mu_H^\circ$  is independent of ionic concentration but is dependent on solvent composition, and  $\gamma_{\pm}$  is the mean activity coefficient of perchloric acid in the solvent mixtures. In this work, the values of  $B$  were recorded in various solvent mixtures containing known concentrations of perchloric acid and sufficient sodium perchlorate to give a constant ionic strength of 0.1 mol dm<sup>-3</sup>. The differences between the logarithm of known hydrogen ion concentrations and the corresponding values of  $B$  were used to calculate values of the correction term  $\log_{10} \mu_H = \log_{10}(\mu_H^\circ \gamma_{\pm})$ .

The following species of the ligands may exist in solution at different pH values:  $L^-$ ,  $HL$ , and  $H_2L^+$ , where  $L^-$  represents the fully dissociated ligand anion. The protonation constants of the ligands have been studied previously in different kinds of background electrolytes, and the results are



**Table 1.** Protonation constants of carboxylic,  $K_1$ , and the amino,  $K_2$ , groups of glycine, gly-gly, and gly-gly-gly at 25 °C in different aqueous solutions of ethanol, and at constant ionic strength, 0.1 mol dm<sup>-3</sup> NaClO<sub>4</sub>, together with the values reported in the literature for comparison.

Ethanol % (v/v)	Glycine		gly-gly		gly-gly-gly		Reference
	$\log_{10}K_1$	$\log_{10}K_2$	$\log_{10}K_1$	$\log_{10}K_2$	$\log_{10}K_1$	$\log_{10}K_2$	
50	3.11±0.01	9.51±0.02	3.18±0.01	8.39±0.02	3.19±0.01	8.14±0.01	This work
55	3.10±0.02	9.48±0.02	3.11±0.01	8.37±0.04	3.11±0.01	8.12±0.02	This work
60	3.08±0.02	9.45±0.01	2.92±0.02	8.34±0.03	2.92±0.02	8.09±0.04	This work
65	3.05±0.03	9.41±0.03	2.83±0.03	8.29±0.02	2.89±0.03	8.07±0.03	This work
70	3.01±0.04	9.38±0.02	2.65±0.03	8.26±0.04	2.86±0.04	8.06±0.03	This work
75	2.86±0.01	9.27±0.04	2.64±0.02	8.18±0.01	2.74±0.04	7.99±0.02	This work
80	2.64±0.02	9.19±0.03	2.64±0.03	8.11±0.03	2.67±0.03	7.93±0.01	This work
0	2.32	9.58					28
50	2.90	9.35					29
50% Acetonitrile			4.28	8.50	4.24	8.32	30

**Table 2.** The hydrolysis-constant values of triphenyltin(IV) species in different aqueous solutions of ethanol at 25 °C and ionic strength of 0.1 mol dm<sup>-3</sup> (NaClO<sub>4</sub>).

Ethanol (% v/v)	p <i>K</i> <sub>11</sub>	p <i>K</i> <sub>12</sub>
50	0.84±0.02	5.53±0.04
55	0.68±0.03	5.25±0.05
60	0.57±0.03	5.07±0.05
65	0.73±0.02	5.20±0.06
70	0.98±0.04	5.49±0.05
80	1.10±0.03	5.95±0.04

reported in the literature.<sup>28–30</sup> The protonation constant values of the ligands have been determined using the potentiometric technique under the same conditions of temperature, ionic strength, and mole fraction of ethanol and calculated using a suitable computer program (Microsoft Excel Solver<sup>®</sup>), which employs a nonlinear least-squares method.<sup>31</sup> The protonation constant values, expressed in log units, are collected in Table 1 together with the values reported in the literature for comparison.<sup>28–30</sup>

UV-vis spectra were recorded using a Shimadzu 2100 spectrophotometer with a Pentium-4 computer and using thermostated matched 10 mm quartz cells. The measurement cell was of flow type. A Masterflex pump allowed circulation of the solution under study from the potentiometric cell to the spectrophotometric cell. So, the absorbance and pH of the solution could be measured simultaneously.

A 50 mL acidic solution (0.1 mol dm<sup>-3</sup>) of triphenyltin(IV) chloride (0.6 × 10<sup>-3</sup> to 1.0 × 10<sup>-3</sup> mol dm<sup>-3</sup>), for UV-vis studies, was titrated with an alkali solution (0.1 mol dm<sup>-3</sup> NaOH) of the ligands (1.0 × 10<sup>-3</sup> to 2.2 × 10<sup>-3</sup> mol dm<sup>-3</sup>) both in the same ionic strength and mole fraction of ethanol. The p<sub>c</sub>H (–log[H<sup>+</sup>]) and absorbance were measured after addition of 0.05 mL of titrant, and this procedure extended up to the required p<sub>c</sub>H. To exclude carbon dioxide from the system, a stream of purified nitrogen was passed through a sodium hydroxide solution and then bubbled slowly through the reaction solution. In all cases, the procedure was repeated at least three times, and the resulting average values and corresponding standard deviation are shown in the text and Tables.

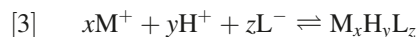
### Results and discussion

Organotin(IV) generally hydrolyze to form a series of mono- and poly-nuclear hydroxo complexes. Previously, we performed spectrophotometric titrations to obtain these data in various aqueous solutions of ethanol (50%–80% ethanol, v/v).<sup>32,33</sup> Two hydrolytic species [ph<sub>3</sub>Sn(OH) and ph<sub>3</sub>Sn(OH)<sub>2</sub><sup>–</sup>] were found, and their formation-constant values in different aqueous ethanol solutions are listed in Table 2.

The protonation-constant values of the ligands, expressed in log units (Table 1), are in good agreement with those reported earlier in pure water.<sup>28–30</sup> A comparison between the protonation constants of glycine and gly-gly show the presence of a nucleophilic amide group close to the α-carbon in the peptide decreases the basicity of the amino and increases the acidity of the carboxyl groups. The same rule is governed to gly-gly-gly, and hence causes a smaller protonation

constant for the amino and a greater one for the carboxyl groups in gly-gly and gly-gly-gly with respect to glycine.

The formed complex species  $M_xH_yL_z^{(x+y-z)}$  is characterized by its stoichiometry ( $x:y:z$ ), where  $M$  represents the metal ion. To determine the stability constant of complexation, eq. [4] is defined by  $\beta_{xyz}$ :



$$[4] \quad \beta_{xyz} = [M_xH_yL_z^{x+y-z}] / ([M^+]^x [H^+]^y [L^-]^z)$$

The method of determination of the formation constant was employed using the method mentioned before.<sup>34,35</sup> Absorbance,  $A$ , and  $pH$  were measured by successive addition of an alkali solution of the ligand to the acidic metal ion solution in the UV range of 250 to 280 nm (with an interval of 1 nm). The UV spectral data correlated with  $[H^+]$  were processed using the same computer program, which allows calculation of formation constants for different stoichiometric models.

Considering the protonation constants of the ligands, in acidic  $pH$ , the predominant species for complexation is  $H_2L^+$ . In this case, the spectrophotometric titration data were analyzed by using the absorbance of  $Sn(IV)$  + each ligand at wavelengths in the UV range that is given by

$$[5] \quad A = \varepsilon_M[Sn(IV)] + \varepsilon_C[complex] + A_{ligand}$$

where  $\varepsilon_M$  and  $\varepsilon_C$  are the molar absorptivities of  $Sn(IV)$  and the formed complex species, respectively. The mass balance can be expressed as

$$[6] \quad [Sn(IV)] = C_M - [complex]$$

$$[7] \quad [H_2L^+] = C_L - [complex] - [free\ ligand]$$

where  $C_M$  and  $C_L$  are the total concentrations of  $Sn(IV)$  and each ligand, respectively. Substituting eqs. [5], [6], and [7] into eq. [4] gives the final equation for fitting. Using the same computer program, the data were fitted to the final equation for estimating the formation constant of eq. [3]. The Gauss-Newton nonlinear least-squares method was used in the computer program to refine the absorbance by minimizing the error squares sum from eq. [8]

$$[8] \quad S = \Sigma(A_{exptl.} - A_{calcd.})^2$$

where  $A_{exptl.}$  is the experimental absorbance and  $A_{calcd.}$  is the calculated one. The computer program consisted of two different kinds of fitting: (i) graphical and (ii) numerical. The final selection of the species was based on both graphical and numerical methods, considering in addition, the various statistical criteria, i.e., sums of squared residuals and differences of  $C_M(exptl.)$  and  $C_L(exptl.)$  values from the calculated ones.

As expected, polynuclear complexes and  $MH_2L$ ,  $MH_2L_2$ , and  $MHL_2$  species were rejected by the computer program (the charges are omitted for simplicity). The models finally chosen were  $MHL$ ,  $ML$ , and  $MH_{-1}L$  resulting in a satisfactory numerical and graphical fitting. The correlation between the average values of these parameters for the wavelengths range used in this study and the  $\log_{10}\beta$  is listed in Table 3.

In Fig. 1, the equilibrium distribution of various species of  $Sn(IV)$  + gly system, as a typical example, is shown as a function of  $pH$  at 60% ethanol (by v/v). The calculations are based on the stability-constant values given in Table 3. The curves clearly demonstrate that increasing the  $pH$  is accompanied by an increase in the formation of deprotonated complex species, and so the stability of the species quite depends upon the  $pH$ . The most stable complex species at  $pH$  2–2.5, 4.5–5.5, and  $>9$  are  $Sn(IV)HL$ ,  $Sn(IV)L$ , and  $Sn(IV)H_{-1}L$ , respectively.

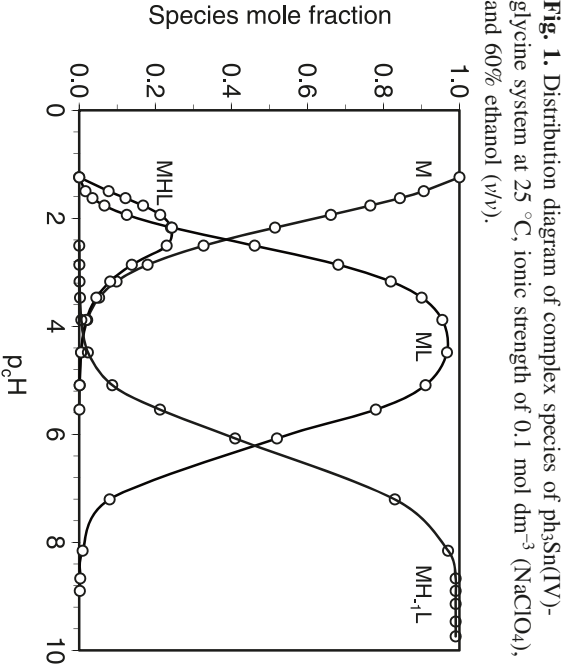
### Solvent effect

The stability constants of the formed complexes in water-ethanol mixed solvents have different behavior, Table 3.  $\beta_{MHL}$  and  $\beta_{MH_{-1}L}$  values increased as the solvent became enriched in the organic component, but  $\beta_{ML}$  decreased as ethanol increased in the mixtures. It is very difficult to interpret the variation of the stability-constant values of the complexes with respect to the percentage of ethanol in the mixtures using the dielectric constant of the solutions as a single parameter. In general, the standard free energy of complexation equilibria consists of two terms: an electrostatic term, which can be estimated by the Born equation,<sup>37,38</sup> and a non-electrostatic term, which includes specific solute-solvent interaction. When the electrostatic effects predominate, then in accordance with the Born equation, eq. [9], the plot of  $\log_{10}\beta$  versus the reciprocal of dielectric constant,  $\varepsilon$ , of the media should be linear.

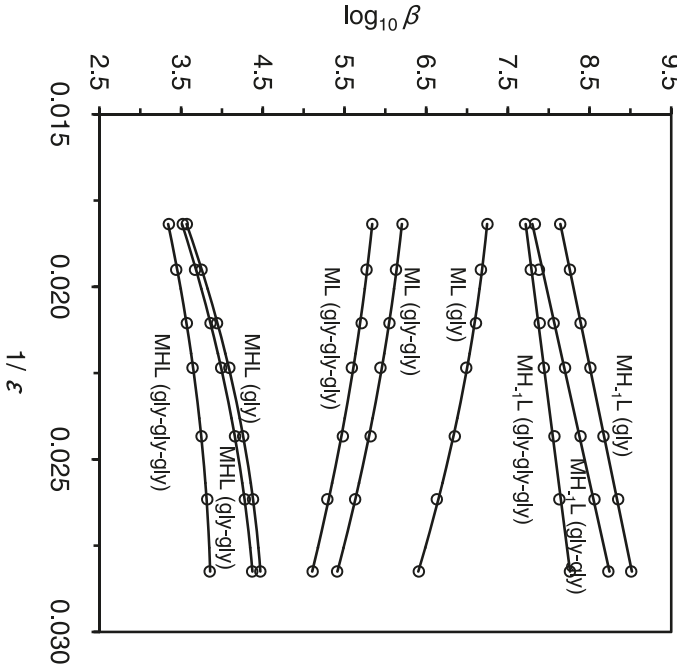
$$[9] \quad \Delta \log_{10}\beta = (121.6n/r)(1/\varepsilon - 0.0128)$$

where  $r$  is the common radius of the ions, and  $n$  is the square summation of the charges involved in the complexation equilibria. For example,  $n = 0$  for the charge type  $M^+ \rightleftharpoons MHL^+$  or  $MHL^+ \rightleftharpoons ML$ , and  $n = 2$  for the charge type  $ML \rightleftharpoons MH_{-1}L^-$ . So, the correlation between  $\log_{10}\beta_{MH_{-1}L}$  and the reciprocal of the dielectric constant of ethanol-water mixtures is linear, with correlation coefficient  $> 0.99$  (Fig. 2). However, there is no change in the number of charges involved in the complexation equilibria when  $n = 0$ , and so, their stability constants deviate from the Born equation. In this case, the correlation between  $\log_{10}\beta_{MHL}$  and  $\log_{10}\beta_{ML}$  values and  $1/\varepsilon$  are poor, Fig. 2, and the complexation possibly depends on the solute-solvent interaction of the different species in the mixed solvents. Therefore, it seems essential to elucidate the nature of solute-solvent interactions for a better understanding of solvent effects.

To obtain a quantitative method for evaluation of the solute-solvent interaction on protonation or the formation constants, we have used the method introduced by Kamlet, Abboud, and Taft.<sup>39,40</sup> The KAT equation contains non-specific as well as specific solute-solvent interactions separately, and that the latter could be subdivided into solvent Lewis acidity interactions (hydrogen-bond acceptor, HBA solute, and hydrogen-bond donor, HBD solvent) and solvent Lewis basicity interactions (HBD solute – HBA solvent). In general, all of these parameters constitute more comprehensive measures of solvent polarity than the dielectric constant or any other single physical characteristic alone, because they reflect more reliably the complete picture of all intermolecular forces acting between solute and solvent molecules. This approach has been widely and successfully applied in the



**Fig. 2.** Plots of the experimental values of  $\log_{10}\beta_{\text{ML}}$ ,  $\log_{10}\beta_{\text{ML}}$ , and  $\log_{10}\beta_{\text{MH}_{1,\text{L}}}$  versus the reciprocal of the dielectric constants of different mixed solvents at 25 °C and ionic strength of 0.1 mol dm<sup>-3</sup> (NaClO<sub>4</sub>).



correlation analysis of all kinds of solvent-dependent processes.<sup>41</sup> The multiparametric equation, eq. [10], has been proposed, using the solvatochromic solvent parameters,  $\alpha$ ,  $\beta$ , and  $\pi^*$ , which have been introduced in previous reports.<sup>42,43</sup>

[10]  $\log_{10}K = A_0 + \alpha\alpha + b\beta + p\pi^*$

where  $A_0$  represents the regression value, and  $\pi^*$  is the index of the solvent dipolarity/polarizability, which is a measure of the ability of a solvent to stabilize a charge or a dipole by its own dielectric effects. The  $\pi^*$  scale was selected to run from 0.0 for cyclohexanone to 1.0 for di-

**Table 3.** Experimental values of the stability constants of  $\text{ph}_3\text{Sn(IV)}$  + glycine, gly-gly, and gly-gly-gly systems at 25 °C, in different aqueous solutions of ethanol, and at constant ionic strength, 0.1 mol dm<sup>-3</sup> NaClO<sub>4</sub>.

Ethanol % (v/v)	Glycine			gly-gly			gly-gly-gly		
	$\log\beta_{\text{MHL}}$	$\log\beta_{\text{ML}}$	$\log\beta_{\text{MH}_{1,\text{L}}}$	$\log\beta_{\text{MHL}}$	$\log\beta_{\text{ML}}$	$\log\beta_{\text{MH}_{1,\text{L}}}$	$\log\beta_{\text{MHL}}$	$\log\beta_{\text{ML}}$	$\log\beta_{\text{MH}_{1,\text{L}}}$
50	3.57±0.02	7.25±0.05	8.14±0.04	3.52±0.05	6.21±0.06	7.83±0.04	3.35±0.06	5.84±0.05	7.71±0.04
55	3.75±0.02	7.17±0.06	8.26±0.03	3.67±0.07	6.13±0.04	7.88±0.04	3.44±0.08	5.77±0.07	7.78±0.05
60	3.94±0.04	7.11±0.04	8.39±0.06	3.86±0.06	6.05±0.05	8.06±0.06	3.57±0.07	5.71±0.06	7.89±0.05
65	4.09±0.03	6.99±0.06	8.51±0.07	3.99±0.06	5.94±0.06	8.20±0.07	3.64±0.05	5.59±0.05	7.94±0.04
70	4.26±0.05	6.85±0.03	8.67±0.06	4.16±0.05	5.82±0.07	8.39±0.06	3.75±0.06	5.48±0.04	8.07±0.06
75	4.38±0.02	6.63±0.04	8.85±0.05	4.28±0.04	5.63±0.07	8.56±0.07	3.82±0.04	5.29±0.04	8.13±0.07
80	4.47±0.05	6.41±0.06	9.01±0.04	4.37±0.07	5.41±0.05	8.73±0.05	3.85±0.04	5.11±0.06	8.26±0.05
75% Dioxan		6.75 <sup>a</sup>							

<sup>a</sup>Taken from ref. 36.

**Table 4.** KAT solvatochromic parameters and the dielectric constants of different ethanol–water mixtures at 25 °C.

Ethanol % (v/v)	$\alpha$	$\beta$	$\pi^*$	$\epsilon$
50	0.87	0.70	0.97	55.01
55	0.86	0.72	0.93	51.27
60	0.87	0.74	0.89	47.50
65	0.88	0.76	0.85	44.75
70	0.89	0.77	0.81	41.10
75	0.90	0.79	0.77	38.23
80	0.91	0.80	0.74	35.40

methylsulfoxide. The  $\alpha$  coefficient represents the solvent HBD acidity; in other words, it describes the ability of a solvent to donate a proton in a solvent to the hydrogen bond of a solute. The  $\alpha$  scale extends from 0.0 for non-HBD solvents to about 1.0 for methanol. The  $\beta$  coefficient is a measure of solvent HBA basicity, and describes the ability of a solvent to accept a proton from a solute to form a hydrogen bond. The  $\beta$  scale was selected to extend from 0.0 for non-HBA solvents to about 1.0 for hexamethylphosphoric triamide.

The regression coefficients  $a$ ,  $b$  and  $p$  measure the relative susceptibilities of the solvent dependence of  $\log_{10}\beta$  to the indicated solvent parameters. To explain the obtained  $\log_{10}\beta$  values through the KAT solvent parameters, the stability constants were correlated with solvent properties by means of single-, dual-, and multi-parameters regression analysis with the same computer program. We used the Gauss–Newton nonlinear least-squares method in the computer program to refine the  $\log_{10}\beta$  values by minimizing the error squares sum from eq. [11].

$$[11] \quad S = \sum (\log_{10}\beta_{\text{exptl.}} - \log_{10}\beta_{\text{calcd.}})^2$$

The procedure used in the regression analysis involves a rigorous statistical treatment to find out which parameter in eq. [10] is best-suited to the water–organic mixed solvents. The KAT parameters for all the water – organic solvent mixtures used in this work were obtained from the plots of each property versus the mole fraction of the organic solvent of the values that have been reported in the literature for some other percentages of aqueous solutions of ethanol used in this study,<sup>44</sup> and the dielectric constant values have been taken from the literature.<sup>45</sup> The calculated KAT-parameter values are listed in Table 4. A stepwise procedure and least-squares analysis were applied to select the significant solvent properties to be influenced in the model and to obtain the final expression for the formation constants. Therefore, the KAT equation, eq. [10], was reduced to single-, dual-, and finally multi-parameters for the correlation analysis of  $\log_{10}\beta$  in various solvent mixtures. The computer program used can produce the values of  $A_0$ ,  $a$ ,  $b$ ,  $p$ , and some statistical parameters including  $r^2$  coefficients.

Although the solvent polarity is identified as the main reason of the variation of  $\log_{10}\beta$  values in water – organic solvent mixtures, but the results show that any single-parameter correlations of  $\log_{10}\beta$  values individually with  $\pi^*$ , as well with  $\alpha$ , and  $\beta$  did not give good results in all cases with  $r^2$  values in the range of 0.88 to 0.97. However, the correlation analysis of  $\log_{10}\beta$  values with dual-parameter equations, indicate significant improvement with regard to

the single-parameter, but finally the multi-parameter equations show the best results and yield the lowest standard deviation and possessing an acceptable correlation coefficients.

The expressions of the KAT equation obtained for multi-parameters are shown by eqs. [12a–12i].

$$[12a] \quad \log_{10}\beta_{\text{MHL}}(\text{glycerine}) = 6.95 - 2.76\alpha + 3.02\beta - 3.22\pi^*$$

$$[12b] \quad \log_{10}\beta_{\text{ML}}(\text{glycine}) = 2.15 - 7.27\alpha + 8.21\beta - 5.86\pi^*$$

$$[12c] \quad \log_{10}\beta_{\text{MH-L}}(\text{glycine}) = 14.54 - 2.37\alpha + 4.59\beta - 5.43\pi^*$$

$$[12d] \quad \log_{10}\beta_{\text{MHL}}(\text{gly-gly}) = 7.76 - 1.83\alpha + 1.24\beta - 3.65\pi^*$$

$$[12e] \quad \log_{10}\beta_{\text{ML}}(\text{gly-gly}) = 1.30 - 5.64\alpha + 6.70\beta - 5.29\pi^*$$

$$[12f] \quad \log_{10}\beta_{\text{MH-L}}(\text{gly-gly}) = 10.99 - 5.97\alpha - 4.86\beta - 5.11\pi^*$$

$$[12g] \quad \log_{10}\beta_{\text{MHL}}(\text{gly-gly-gly}) = 7.65 - 2.18\alpha + 0.21\beta - 2.66\pi^*$$

$$[12h] \quad \log_{10}\beta_{\text{ML}}(\text{gly-gly-gly}) = 4.03 - 5.01\alpha + 6.54\beta - 4.11\pi^*$$

$$[12i] \quad \log_{10}\beta_{\text{MH-L}}(\text{gly-gly-gly}) = 14.83 - 0.22\alpha + 4.44\beta - 4.36\pi^*$$

( $N = 7$ ,  $r^2 > 0.99$  in different cases).

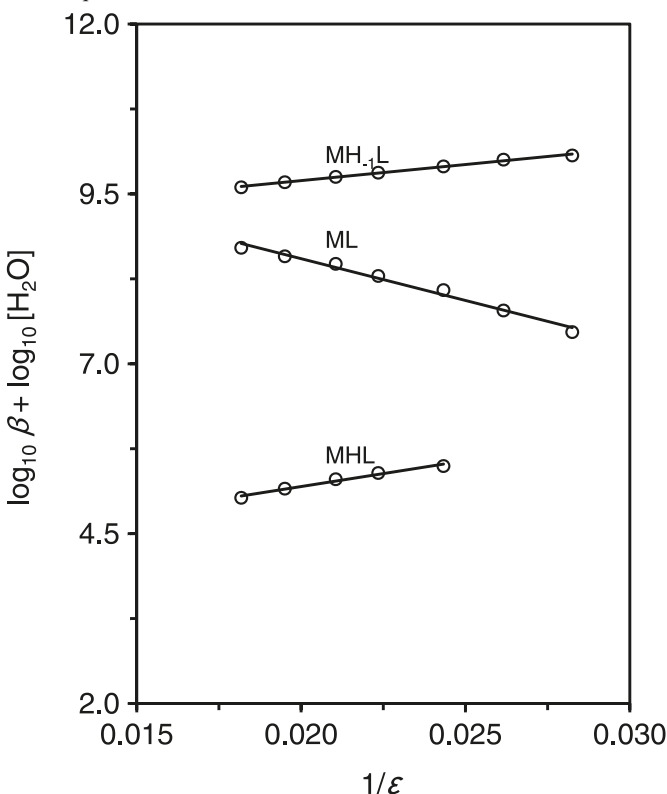
In all cases, the solvent polarity parameter of the media,  $\pi^*$ , has a major role and increases with increasing the mole fraction of water in aqueous solutions of ethanol, Table 4. If the  $\pi^*$  of the media was the only factor for describing the solvent effect on complexation, it may be expected that the  $\log_{10}\beta$  in water should be greater than those of all the other aqueous solutions of ethanol. However,  $\log_{10}\beta_{\text{MHL}}$  values of the complex species increase with an increase in the solvent HBA-basicity parameter,  $\beta$ , and decrease with increasing the solvent polarity  $\pi^*$ . They also increase with increasing the HBD-acidity parameter,  $\alpha$ , of the solvents. In this case, a de-



**Table 5.** Calculated values of the stability constants of  $\text{ph}_3\text{Sn(IV)} + \text{glycine}$ ,  $\text{gly-gly}$ , and  $\text{gly-gly-gly}$  systems (from eq. [12] at 25 °C, in different aqueous solutions of ethanol, and at constant ionic strength, 0.1 mol  $\text{dm}^{-3}$   $\text{NaClO}_4$ .

Ethanol % (v/v)	Glycine			gly-gly			gly-gly-gly		
	$\log\beta_{\text{MHL}}$	$\log\beta_{\text{ML}}$	$\log\beta_{\text{MH}_{-1}\text{L}}$	$\log\beta_{\text{MHL}}$	$\log\beta_{\text{ML}}$	$\log\beta_{\text{MH}_{-1}\text{L}}$	$\log\beta_{\text{MHL}}$	$\log\beta_{\text{ML}}$	$\log\beta_{\text{MH}_{-1}\text{L}}$
50	3.57±0.03	7.24±0.04	8.15±0.02	3.52±0.06	6.20±0.06	7.83±0.05	3.35±0.03	5.83±0.03	7.71±0.02
55	3.76±0.04	7.25±0.05	8.22±0.05	3.69±0.04	6.19±0.04	7.87±0.03	3.46±0.04	5.83±0.08	7.77±0.03
60	3.94±0.05	7.08±0.06	8.40±0.03	3.85±0.06	6.03±0.05	8.06±0.02	3.56±0.02	5.69±0.07	7.88±0.04
65	4.09±0.02	6.97±0.04	8.52±0.06	3.99±0.06	5.92±0.04	8.21±0.04	3.64±0.03	5.57±0.06	7.95±0.02
70	4.24±0.06	6.78±0.04	8.70±0.05	4.14±0.05	5.75±0.02	8.40±0.03	3.73±0.04	5.42±0.06	8.07±0.04
75	4.38±0.01	6.60±0.03	8.87±0.06	4.28±0.04	5.59±0.05	8.59±0.05	3.81±0.05	5.27±0.07	8.17±0.03
80	4.48±0.04	6.50±0.03	8.97±0.05	4.38±0.07	5.50±0.06	8.70±0.02	3.87±0.05	5.18±0.07	8.23±0.02

**Fig. 3.** The Yasuda–Shedlovsky plots for  $\text{ph}_3\text{Sn(IV)}$ -glycine in different aqueous solutions of ethanol.



crease in the polarity of the mixed solvents increases the solvation of the complex species, which has a positive charge and therefore makes formation equilibrium more likely. The  $\log_{10}\beta_{\text{ML}}$  values decrease with decreasing  $\pi^*$  and increasing  $\alpha$  and  $\beta$  parameters. In this case, the formed complex species has no charge, so HBA-basicity parameter of the mixed solvents,  $\beta$ , possibly has a major role in the correlation analysis of  $\log_{10}\beta_{\text{ML}}$ . However,  $\log_{10}\beta_{\text{MH}_{-1}\text{L}}$  of the complexes increases with increasing  $\alpha$  and  $\beta$  and decreasing  $\pi^*$  values. This could be explained as solvation by decreasing the polarity of the mixed solvents affects the formed complex species with a negative charge. Consequently,  $\log_{10}\beta_{\text{MH}_{-1}\text{L}}$  values increase with decreasing  $\pi^*$  parameters.

To show the efficiency of the suggested multi-parameter correlations, the stability constants were calculated by eq. [12] and are listed in Table 5 for comparison. It can be seen that the experimental values of  $\log_{10}\beta$  and the calculated ones are in good agreement.

To obtain  $\log_{10}\beta$  values of the complexation in pure water, a correlation method has been used between the experimental formation-constant values that are introduced by extrapolation of Yasuda–Shedlovsky approach in different aqueous solutions of ethanol.<sup>46,47</sup> This approach was successfully applied to determine the protonation constant of many weak acids or weak bases in pure water as solvent from the protonation-constant values in different water–methanol mixtures.<sup>48</sup> It is claimed that Yasuda–Shedlovsky extrapolation procedure is generally more accurate than the conventional method ( $\log_{10}\beta$  versus weight percent of an or-

**Table 6.**  $\log_{10} \beta_{\text{MHL}}$ ,  $\log_{10} \beta_{\text{ML}}$ , and  $\log_{10} \beta_{\text{MH-L}}$  values of the studied systems by extrapolation of Yasuda–Shedlovsky equation to pure water in different ranges of ethanol% (v/v) used,  $R$ , the regression values,  $r^2$ , are also given in each case.

Species	$\log \beta_{\text{MHL}}$	$R$	$r^2$	$\log \beta_{\text{ML}}$	$R$	$r^2$	$\log \beta_{\text{MH-L}}$	$R$	$r^2$
Glycine	1.92	50–70	0.98	9.26	50–80	0.99	7.01	50–80	0.99
gly-gly	2.01	50–70	0.98	8.11	50–80	0.99	6.54	50–80	0.98
gly-gly-gly	2.54	50–70	0.95	7.65	50–80	0.99	7.03	50–70	0.94

ganic solvent) for the determination of  $\log_{10} \beta$  of a broad range of insoluble or sparingly water-soluble drug compounds.<sup>48,49</sup> We have applied the Yasuda–Shedlovsky approach to determine  $\log_{10} \beta$  of the formed complexes studied in this work in pure water. On the basis of Born electrostatic model and Bjerrum's theory of ion association, Yasuda<sup>46</sup> and Shedlovsky<sup>47</sup> derived eq. [13]. The plot of  $\log_{10} \beta + \log_{10} [\text{H}_2\text{O}]$  versus  $1/\epsilon$  should produce a straight line in different aqueous – organic solvents mixtures, where  $\beta$  represents the stability constant of the complex species formed,  $[\text{H}_2\text{O}]$  is the molar concentration of water and  $\epsilon$  shows the dielectric constant of the medium.

$$[13] \quad \log_{10} \beta + \log_{10} [\text{H}_2\text{O}] = a\epsilon^{-1} + b$$

where  $a$  and  $b$  are two constants that should be determined for the various ethanol–water mixtures used in this work. Figure 3 shows the Yasuda–Shedlovsky plots for the Sn(IV)–glycine system, and the  $\log_{10} \beta$  values were determined by extrapolation to 0% ethanol and are summarized in Table 6.

## Acknowledgement

M.J. gratefully acknowledges a research grant from the Research Council of Shahid Beheshti University.

## References

- (1) Davies, A. G.; Smith, P. M. In *Comprehensive Organometallic Chemistry*; Pergamon Press: Oxford, 1982.
- (2) Molloy, K. C. *The Chemistry of Tin*; Blackie: Glasgow, 1989.
- (3) Momparler, R. L.; Bovenzi, V. *J. Cell. Physiol.* **2000**, *183* (2), 145. doi:10.1002/(SICI)1097-4652(200005)183:2<145::AID-JCP1>3.0.CO;2-V. PMID:10737890.
- (4) Demertzis, M. A.; Hadjikakou, S. K.; Kovala-Demertzi, D.; Koutsodimou, A.; Kubicki, M. *Helv. Chim. Acta* **2000**, *83* (10), 2787. doi:10.1002/1522-2675(20001004)83:10<2787::AID-HLCA2787>3.0.CO;2-6.
- (5) Pellerito, C.; Scopelliti, M.; Fiore, T.; Nagy, L.; Barone, G.; Abbate, M.; Stocco, G. C.; Pellerito, L. *J. Organomet. Chem.* **2006**, *691* (8), 1573. doi:10.1016/j.jorgchem.2005.12.012.
- (6) Gharib, F.; Jaber, F.; Zandevakili, M. *Appl. Organomet. Chem.* **2008**, *22* (4), 215. doi:10.1002/aoc.1374.
- (7) Gharib, F.; Farzad, E.; Amini, M. M. *Can. J. Chem.* **2006**, *84* (11), 1534. doi:10.1139/V06-152.
- (8) Yang, Z.; Bakas, T.; Sanchez-Diaz, A.; Charalampopoulos, C.; Tsangaris, J.; Hadjiliadis, N. *J. Inorg. Biochem.* **1998**, *72* (3-4), 133. doi:10.1016/S0162-0134(98)10073-9. PMID:10065532.
- (9) Mohamed, M. M. A.; Abd-Alla, E. M.; El-Badawy, A. S. *J. Organomet. Chem.* **2007**, *692* (8), 1735. doi:10.1016/j.jorgchem.2006.12.035.
- (10) Di Stefano, R.; Scopelliti, M.; Pellerito, C.; Casella, G.; Fiore, T.; Stocco, G. C.; Vitturi, R.; Colomba, M.; Ronconi, L.; Sciacca, I. D.; Pellerito, L. *J. Inorg. Biochem.* **2004**, *98* (3), 534. doi:10.1016/j.jinorgbio.2003.12.013. PMID:14987855.
- (11) Ghys, L.; Biesemans, M.; Gielen, M.; Garoufis, A.; Hadjiliadis, N.; Willem, R.; Martins, J. *Eur. J. Inorg. Chem.* **2000**, *2000* (3), 513. doi:10.1002/(SICI)1099-0682(200003)2000:3<513::AID-EJIC513>3.0.CO;2-M.
- (12) Gajda-Schranz, K.; Jancso, A.; Pettinari, C.; Gajda, T. *J. Chem. Soc., Dalton Trans.* **2003**, 2912.
- (13) Yang, P.; Guo, M. *Coord. Chem. Rev.* **1999**, *185–186* (1), 189. doi:10.1016/S0010-8545(98)00268-9.
- (14) Nath, M.; Pokharia, S.; Song, X.; Eng, G.; Gielen, M.; Kemmer, M.; Biesemans, M.; Willem, R.; De Vos, D. *Appl. Organomet. Chem.* **2003**, *17* (5), 305. doi:10.1002/aoc.451.
- (15) Pellerito, L.; Nagy, L. *Coord. Chem. Rev.* **2002**, *224* (1-2), 111. doi:10.1016/S0010-8545(01)00399-X.
- (16) Ali, A. A.; Upreti, R. K.; Kidway, A. M. *Toxicol. Appl. Pharmacol.* **1987**, *38*, 13.
- (17) Jankovics, H.; Nagy, L.; Buzás, N.; Pellerito, L.; Barbieri, R. *J. Inorg. Biochem.* **2002**, *92* (1), 55. doi:10.1016/S0162-0134(02)00470-1. PMID:12230988.
- (18) Sexena, A. K.; Huber, F. *Coord. Chem. Rev.* **1989**, *95* (1), 109. doi:10.1016/0010-8545(89)80003-7.
- (19) Gielen, M. *Coord. Chem. Rev.* **1996**, *151*, 41.
- (20) Barbieri, R.; Silvestri, A.; Giuliani, A. M.; Piro, V.; Di Simone, F.; Madonia, G. *J. Chem. Soc., Dalton Trans.* **1992**, (4): 585. doi:10.1039/dt9920000585.
- (21) Fiol, S.; Brandariz, I.; Sastre de Vicente, M. *Talanta* **1995**, *42* (6), 797. doi:10.1016/0039-9140(95)01484-S. PMID:18966294.
- (22) Partanen, I. *J. Phys. Chem.* **1998**, *102*, 855.
- (23) Hughes, D. L.; Bergan, I. J.; Grabowski, E. J. J. *J. Org. Chem.* **1986**, *51* (13), 2579. doi:10.1021/jo00363a033.
- (24) Crosby, J.; Stone, R.; Lienhard, G. E. *J. Am. Chem. Soc.* **1970**, *92* (9), 2891. doi:10.1021/ja00712a048. PMID:5439974.
- (25) Nishi, N.; Takahashi, S.; Matsumoto, M.; Tanaka, A.; Muraya, K.; Takamuku, T.; Yamaguchi, T. *J. Phys. Chem.* **1995**, *99* (1), 462. doi:10.1021/j100001a068.
- (26) Lagrange, Ph.; Schneider, M.; Zare, K.; Lagrange, J. *Polyhedron* **1994**, *13* (6-7), 861. doi:10.1016/S0277-5387(00)83001-6.
- (27) van Uitert, L. G.; Hass, G. G. *J. Am. Chem. Soc.* **1953**, *75* (2), 451. doi:10.1021/ja01098a057.
- (28) Köseoglu, F.; Kiliç, E.; Dogan, A. *Anal. Biochem.* **2000**, *277* (2), 243. doi:10.1006/abio.1999.4371. PMID:10625513.
- (29) Dogan, A.; Köseoglu, F.; Kiliç, E. *Anal. Biochem.* **2002**, *309* (1), 75. doi:10.1016/S0003-2697(02)00254-3. PMID:12381364.
- (30) Barbosa, J.; Fonrodona, G.; Marques, I.; Sanz-Nebot, V.; Toro, I. *Anal. Chim. Acta* **1997**, *351* (1-3), 397. doi:10.1016/S0003-2670(97)00234-1.

- (31) Maleki, N.; Haghighi, B.; Safavi, A. *Microchem. J.* **1999**, 62 (2), 229. doi:10.1006/mchj.1998.1665.
- (32) Mehdizadeh, S.; Jabbari, M.; Shakibazadeh, R.; Gharib, F. *Heteroatom Chem.* **2008**, 19 (7), 654. doi:10.1002/hc.20484.
- (33) Jabbari, M.; Gharib, F.; Amini, M. M.; Azadmehr, A. *Can. J. Chem.* **2008**, 86 (8), 751. doi:10.1139/V08-079.
- (34) Gharib, F.; Jabbari, M.; Farajtabar, A.; Shamel, A. *J. Chem. Eng. Data* **2008**, 53 (8), 1772. doi:10.1021/je800106j.
- (35) Gharib, F.; Shamel, A. *J. Chem. Eng. Data* **2009**, 54 (3), 933. doi:10.1021/je800712x.
- (36) Shoukry, M. M.; Mohamed, M. M. H. *J. Coord. Chem.* **1998**, 43 (2), 217. doi:10.1080/00958979808022670.
- (37) Barbosa, J.; Barrón, D.; Beltrán, J. L.; Butí, S. *Talanta* **1998**, 45 (5), 817. doi:10.1016/S0039-9140(97)00167-7. PMID: 18967066.
- (38) Barbosa, J.; Toro, I.; Sanz-Nebot, V. *Anal. Chim. Acta* **1997**, 347 (3), 295. doi:10.1016/S0003-2670(97)00163-3.
- (39) Taft, R. W.; Abboud, J.-L. M.; Kamlet, M. J. *J. Org. Chem.* **1984**, 49, 2001. doi:10.1021/jo00185a034.
- (40) Kamlet, M. J.; Abboud, J.-L. M.; Abraham, M. H.; Taft, R. W. *J. Org. Chem.* **1983**, 48 (17), 2877. doi:10.1021/jo00165a018.
- (41) Reichardt, C. *Solvents and Solvent Effects in Organic Chemistry*, 3rd ed; VCH: New York, 2004.
- (42) Gharib, F.; Sadeghi, F. *Appl. Organomet. Chem.* **2007**, 21 (4), 218. doi:10.1002/aoc.1211.
- (43) Gharib, F. *J. Chem. Eng. Data* **2005**, 50 (1), 196. doi:10.1021/je049737k.
- (44) Buhvestov, U.; Rived, F.; Ràfols, C.; Bosch, E.; Rosés, M. *J. Phys. Org. Chem.* **1998**, 11 (3), 185. doi:10.1002/(SICI)1099-1395(199803)11:3<185::AID-POC993>3.0.CO;2-5.
- (45) Deb, N.; Shannigrahi, M.; Bagchi, S. *J. Phys. Chem. B* **2008**, 112 (10), 2868. doi:10.1021/jp710299t. PMID:18278903.
- (46) Yasuda, M. *Bull. Chem. Soc. Jpn.* **1959**, 32 (5), 429. doi:10.1246/bcsj.32.429.
- (47) Shedlovsky, T. In *Electrolytes*; B. Peasce, Ed.; Pergamon: New York, 1962.
- (48) Ruiz, R.; Ràfols, C.; Rosés, M.; Bosch, E. *J. Pharm. Sci.* **2003**, 92 (7), 1473. doi:10.1002/jps.10415. PMID:12820151.
- (49) Avdeef, A.; Box, K. J.; Comer, J. E. A.; Gilges, M.; Hadley, M.; Hibbert, C.; Patterson, W.; Tam, K. Y. *J. Pharm. Biomed. Anal.* **1999**, 20 (4), 631. doi:10.1016/S0731-7085(98)00235-0. PMID:10704132.

# Syntheses of ruthenium(II)-4,4'-biimidazole complexes and their potential anti-tumour activity

David C. Kennedy and Brian R. James

**Abstract:** Synthesis and characterization of the Ru<sup>II</sup> complexes, [Ru(N-N)<sub>3</sub>][CF<sub>3</sub>SO<sub>3</sub>]<sub>2</sub>, where N-N is 4,4'-biimidazole (complex **1a**) or 2,2'-dimethyl-4,4'-biimidazole (**1b**), and the dimethylsulfoxide complexes RuCl<sub>2</sub>(DMSO)<sub>2</sub>(N-N) are reported. The air-stable, water-soluble complexes were characterized by elemental analysis, <sup>1</sup>H NMR and IR spectroscopies, mass spectrometry, and solution conductivity. Evidence is presented also for the existence of the diruthenium complexes Ru<sub>2</sub>Cl<sub>4</sub>(DMSO)<sub>4</sub>(N-N), but there are insufficient data for elucidation of their structure. The complexes (and cisplatin) were tested against human breast-cancer cells (MDA-MB-435S) using an in vitro MTT assay, a colorimetric determination of cell viability: **1a** and **1b** exhibit the lowest IC<sub>50</sub> values of 18 ± 5 and 36 ± 5 µmol/L, respectively, with cisplatin exhibiting an IC<sub>50</sub> value of 35 ± 5 µmol/L. Isolation of DNA from cells treated with a solution of the Ru species showed no evidence of DNA-binding to the metal, although examination of the cells indicated that Ru was being taken up into the cells.

**Key words:** ruthenium complexes, 4,4'-biimidazoles, anti-proliferatory.

**Résumé :** On rapporte la synthèse et la caractérisation de complexes de ruthénium(II), [Ru(N-N)][CF<sub>3</sub>SO<sub>3</sub>]<sub>2</sub>, dans lesquels N-N est un 4,4'-biimidazole (complexe **1a**) ou 2,2'-diméthyl-4,4'-biimidazole (**1b**) ainsi que les complexes du diméthylsulfoxyde RuCl<sub>2</sub>(DMSO)<sub>2</sub>(N-N). On a caractérisé ces complexes stables à l'air et solubles dans l'eau par analyse chimique, spectroscopies IR et RMN du <sup>1</sup>H, spectrométrie de masse et par conductivité de leurs solutions. On présente aussi des données suggérant l'existence des complexes de diruthénium Ru<sub>2</sub>Cl<sub>4</sub>(DMSO)<sub>4</sub>(N-N), mais les données ne sont pas suffisantes pour élucider leurs structures. On a évalué ces complexes, ainsi que le cisplatine, contre des cellules cancéreuses de seins humains (MDA-MB-435S) en faisant appel à un essai MTT in vitro, une détermination colorimétrique de la viabilité de la cellule; les composés **1a** et **1b** présentent les valeurs IC<sub>50</sub> les plus faibles de 18 ± 5 et 36 ± 5 µmol/L respectivement alors que le cisplatine présente une valeur IC<sub>50</sub> de 35 ± 5 µmol/L. L'ADN isolé des cellules traitées avec une solution d'espèces contenant du ruthénium ne présente aucune évidence de liaison de l'ADN au métal, même si l'examen des cellules indique que le ruthénium est absorbé par les cellules.

**Mots-clés :** complexes du ruthénium, 4,4'-biimidazoles, antiprolifération.

## Introduction

The use of cisplatin for the treatment of more than 70% of all cancer patients, coupled with the understanding of its mechanism of action, represents the most widely known, metal-based anti-cancer agent, and the topic has been exhaustively reviewed.<sup>1</sup> Amongst other metal-based anti-cancer agents, the most promising appear to be based on ruthenium. Often quoted complexes showing activity include both Ru<sup>II</sup> and Ru<sup>III</sup> species, exemplified by *cis*-Ru<sup>II</sup>Cl<sub>2</sub>(DMSO)<sub>4</sub>,<sup>1c,2</sup> [HIm][*trans*-Ru<sup>III</sup>Cl<sub>4</sub>(Im)(*S*-DMSO)] (Im = imidazole, a complex called NAMI-A),<sup>1b,1d,1e</sup> [HL][*trans*-Ru<sup>III</sup>Cl<sub>4</sub>L<sub>2</sub>] (L = indazole or Im, called KP1019 and KP418, respectively),<sup>3</sup> and a wide range of arene complexes.<sup>4</sup> The arene derivatives include Ru<sup>III</sup>L<sub>2</sub>(arene)(PTA), where PTA = 1,3,5-triaza-7-phosphaadamantane, so-called RAPTA type complexes, and in place of PTA a related P-N chelating ligand (PTN) has been used; when L is Cl, the formula represents a cationic monochloro complex, while for example, if L<sub>2</sub> is a

chelating O-O dianion, a neutral complex is formed. Many other monocationic and neutral Ru<sup>II</sup>-(arene) and Ru<sup>II</sup>-(half-sandwich) complexes, containing mono- and bi-dentate ancillary ligands and incorporating PTA, PTN, or other P-, N-, O-, and S-donor ligands, have been studied.<sup>4</sup> KP1019 and NAMI-A have both recently completed successful clinical trials, and their mechanisms of action are being hotly pursued, particularly for the NAMI-A system, which exhibits significant anti-metastatic activity.<sup>3,5</sup> More generally, the medicinal chemistry of Ru is an area of intense current interest, and the rapidly expanding literature can be traced through recent reviews<sup>1b,1d,1e</sup> and publications,<sup>3,4</sup> while earlier reviews by Clarke et al. provide excellent background material.<sup>6</sup>

Our group has previously published on the synthesis and anti-proliferatory activity of Ru<sup>III</sup>(O-O)<sub>3</sub> where O-O<sup>-</sup> is maltolato (the monoanion of 3-OH-2-Me-4-pyrone),<sup>7</sup> mixed-ligand Ru<sup>III</sup>(maltolato)(nitroimidazole) systems,<sup>8</sup> Ru<sup>II</sup>(sulfoxide) species with or without ancillary maltolato, acetylaceto-

Received 8 March 2010. Accepted 11 June 2010. Published on the NRC Research Press Web site at canjchem.nrc.ca on 29 July 2010.

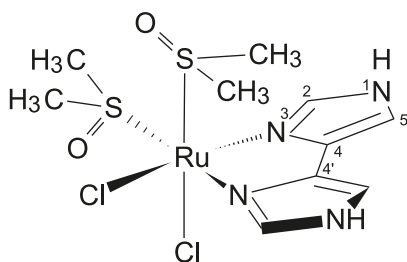
Adapted from the Ph.D. thesis of D.C. Kennedy (see ref. 29).

**D.C. Kennedy and B.R. James.**<sup>1</sup> Department of Chemistry, The University of British Columbia, Vancouver, BC V6T 1Z1, Canada.

<sup>1</sup>Corresponding author (e-mail: brj@chem.ubc.ca).



**Fig. 1.** Proposed solid-state structure for  $\text{RuCl}_2(\text{DMSO})_2(4,4'\text{-biim})$  (**2a**).



nato, or nitroimidazole ligands,<sup>9</sup> and  $\text{Ru}^{\text{II}}(\text{arene})(\text{sulfoxide})$  species.<sup>10</sup>

In terms of metal-biimidazole complexes (the relevant topic here), 2,2'-biimidazole (2,2'-biim) has been widely used, including reports on  $\text{Ru}^{\text{II}}$  species,<sup>11,12</sup> some of which have the dianionic form of this ligand bridging in  $\text{Ru}_2^{\text{II}}$  complexes.<sup>12</sup> Metal complexes of 4,4'-biim (see Fig. 1 for numbering) are rare, and we have found references to only Cu and Pd species,<sup>13</sup> even though the syntheses of this biimidazole and the 2,2'-Me<sub>2</sub> derivative (as the diprotonated trifluoroacetate salts) were first published in 1994.<sup>14</sup> This present paper describes the first studies of  $\text{Ru}^{\text{II}}$  complexes containing 4,4'-biim and its 2,2'-dimethyl derivative (Me<sub>2</sub>biim). The anti-proliferative properties of the complexes are examined using a standard MTT assay to test for cell viability,<sup>9a</sup> and Ru-uptake and DNA-binding assays are used to further probe their biological activity. The measured IC<sub>50</sub> values against human breast-cancer cells (MDA-MB-435S) reveal high activity for the  $[\text{Ru}(\text{N}-\text{N})_3][\text{CF}_3\text{SO}_3]_2$  complexes, where N-N is 4,4'-biim or Me<sub>2</sub>biim. To the best of our knowledge, there are no previous reports of studies on the anti-proliferative properties of metal-4,4'-biimidazole complexes.

## Experimental section

### Materials for synthesis

Reagent-grade solvents (Fisher Scientific) were dried using standard procedures under N<sub>2</sub> before use,<sup>15</sup> and deuterated solvents (Cambridge Isotope Laboratories) were used as received.  $\text{RuCl}_3 \cdot 3\text{H}_2\text{O}$  (Colonial Metals) and cisplatin (Aldrich) were used as received; *cis*- $\text{RuCl}_2(\text{DMSO})_4$  and  $[\text{Ru}(\text{DMF})_6][\text{CF}_3\text{SO}_3]_3$  were prepared by literature methods.<sup>16</sup> The 4,4'-biim and Me<sub>2</sub>biim compounds were prepared as the respective biimidazolium trifluoroacetate salts  $[\text{H}_2(\text{biim})][\text{CF}_3\text{CO}_2]_2$  and  $[\text{H}_2(\text{Me}_2\text{biim})][\text{CF}_3\text{CO}_2]_2$  by a literature method.<sup>14</sup> Standard Schlenk techniques using N<sub>2</sub> atmosphere were used for synthesis of the complexes, although these were found to be air-stable.

### Physical techniques and instrumentation

<sup>1</sup>H NMR spectra were recorded at room temperature (RT, ~20 °C) on a Bruker AV300 instrument (s = singlet, br = broad) with chemical shifts being calibrated using residual proton resonances from deuterated solvents. Elemental analyses were performed on a Carlo Erba EA 1108 CHN-O instrument. Mass spectral data (reported as *m/z* values) were acquired on a Bruker Esquire ES spectrometer; M<sup>+</sup> refers to the solid-state formulation plus a proton acquired in the ion-

ization process. IR spectra (KBr pellets, s = strong, m = medium) were recorded on ATI Mattson Genesis or Bomem-Michelson MB-100 FTIR spectrometers; selected  $\nu$  values (cm<sup>-1</sup>) are given with assigned functional groups.<sup>17</sup> Conductivity measurements were carried out on a RCM151B Serfass conductance bridge (A. H. Thomas Co. Ltd.) with a 3403 cell (Yellow Springs Instrument Company) calibrated using 0.01000 mol/L aq. KCl solution ( $\Lambda_{\text{M}} = 141.3 \Omega^{-1} \text{cm}^2 \text{mol}^{-1}$  at 25 °C, cell constant = 1.016 cm<sup>-1</sup>), and data are given in units of  $\Omega^{-1} \text{cm}^2 \text{mol}^{-1}$ .<sup>18</sup>

### Biological assays

All reagents and cell-handling techniques, as well as experimental procedures for the the MTT assay, the Ru-uptake assay into cells, and DNA-binding to Ru have been described in detail in our previous publications.<sup>7-9</sup> For the MTT assay, complexes were dissolved in PBS (phosphate-buffered saline solution), and were tested against MDA-MB-435S cells in Leibovitz's L-15 medium with L-glutamine after incubation at 37 °C for 70 h; Ru-uptake was studied with a Chinese hamster ovary (CHO) cell line.

### $[\text{Ru}(\text{biim})_3][\text{CF}_3\text{SO}_3]_2$ (**1a**)

To a yellow solution of  $[\text{Ru}(\text{DMF})_6][\text{CF}_3\text{SO}_3]_3$  (83 mg, 0.085 mmol) in MeOH (5 mL) was added  $[\text{H}_2\text{biim}][\text{CF}_3\text{CO}_2]_2$  (120 mg, 0.34 mmol). On being refluxed over 24 h, the solution became dark green. The solvent was then removed under vacuum, and acetone (10 mL) was added to the green residue; the resulting mixture was filtered through Celite, and the filtrate was then reduced in volume to ~1 mL. Addition of hexanes (8 mL) yielded a green precipitate that was collected, washed with hexanes (2 × 5 mL), and dried under vacuum at 78 °C for 24 h. Yield: 34 mg (60%). <sup>1</sup>H NMR (CD<sub>3</sub>OD):  $\delta$  8.37 (s, 6H, *H*<sub>2,2'</sub>), 7.62 (s, 6H, *H*<sub>5,5'</sub>). ESI-MS (MeOH): 652 (M<sup>+</sup> – CF<sub>3</sub>SO<sub>3</sub>), 502 (M<sup>+</sup> – 2 CF<sub>3</sub>SO<sub>3</sub>), 369 (M<sup>+</sup> – 2 CF<sub>3</sub>SO<sub>3</sub> – biim).  $\Lambda_{\text{M}}$  (MeOH) = 243. Anal. calcd. for C<sub>20</sub>H<sub>18</sub>F<sub>6</sub>N<sub>12</sub>O<sub>6</sub>S<sub>2</sub>Ru: C, 29.97; H, 2.26; N, 20.97. Found: C, 29.75; H, 2.31; N, 20.64.

### $[\text{Ru}(\text{Me}_2\text{biim})_3][\text{CF}_3\text{SO}_3]_2$ (**1b**)

To a solution of  $[\text{Ru}(\text{DMF})_6][\text{CF}_3\text{SO}_3]_3$  (74 mg, 0.075 mmol) in MeOH (5 mL) was added  $[\text{H}_2(\text{Me}_2\text{biim})][\text{CF}_3\text{CO}_2]_2$  (120 mg, 0.30 mmol). On being refluxed for 16 h, the solution became brown and then dark blue, when the solvent was removed under vacuum, and acetone (10 mL) was added to the black residue; the resulting mixture was filtered through Celite, and the filtrate was reduced in volume to ~1 mL. Addition of hexanes (8 mL) yielded a blue precipitate that was collected and dried under vacuum at 78 °C for 24 h. Yield: 42 mg (63%). <sup>1</sup>H NMR (CD<sub>3</sub>OD):  $\delta$  7.43 (s, 6H, *H*<sub>5,5'</sub>), 2.54 (s, 18H, *CH*<sub>3</sub>). ESI-MS (MeOH): 736 (M<sup>+</sup> – CF<sub>3</sub>SO<sub>3</sub>), 587 (M<sup>+</sup> – 2 CF<sub>3</sub>SO<sub>3</sub>), 575 (M<sup>+</sup> – CF<sub>3</sub>SO<sub>3</sub> – Me<sub>2</sub>biim), 425 (M<sup>+</sup> – 2 CF<sub>3</sub>SO<sub>3</sub> – Me<sub>2</sub>biim).  $\Lambda_{\text{M}}$  (MeOH) = 228. Anal. calcd. for C<sub>26</sub>H<sub>30</sub>F<sub>6</sub>N<sub>12</sub>O<sub>6</sub>S<sub>2</sub>Ru: C, 35.26; H, 3.41; N, 18.98. Found: C, 35.16; H, 3.32; N, 18.44.

### *cis*- $\text{RuCl}_2(\text{DMSO})_2(\text{biim})$ (**2a**)

To a yellow solution of *cis*- $\text{RuCl}_2(\text{DMSO})_4$  (70 mg, 0.15 mmol) in MeOH (10 mL) was added  $[\text{H}_2\text{biim}][\text{CF}_3\text{CO}_2]_2$  (54 mg, 0.15 mmol), and the mixture was refluxed for 4 h. The solvent was then reduced in volume to ~1 mL, when

addition of acetone (10 mL) yielded a yellow precipitate that was collected, washed with acetone ( $2 \times 5$  mL), and dried in vacuo at 78 °C for 24 h. Yield: 59 mg (88%).  $^1\text{H}$  NMR ( $\text{CD}_3\text{OD}$ ):  $\delta$  8.39, 8.37 (s, 2H,  $\text{H}_{2,2'}$ ), 7.72, 7.67 (s, 2H,  $\text{H}_{5,5'}$ ), 3.49 (s, 3H,  $\text{CH}_3$ ), 3.23 (s, 3H,  $\text{CH}_3$ ), 3.01 (s, 3H,  $\text{CH}_3$ ), 2.29 (s, 3H,  $\text{CH}_3$ ). IR: 3451 (s,  $\nu_{\text{N-H}}$ ), 1071 (s,  $\nu_{\text{S=O}}$ ), 1067 (s,  $\nu_{\text{S=O}}$ ), 1020 (m). ESI-MS (MeOH): 463 ( $\text{M}^+$ ), 427 ( $\text{M}^+ - \text{Cl}$ ), 349 ( $\text{M}^+ - \text{Cl} - \text{DMSO}$ ).  $\Lambda_{\text{M}}$  (MeOH) = 127. Anal. calcd. for  $\text{C}_{10}\text{H}_{18}\text{Cl}_2\text{N}_4\text{O}_2\text{S}_2\text{Ru}$ : C, 25.77; H, 3.93; N, 12.12. Found: C, 25.67; H, 3.98; N, 11.99.

#### $\text{RuCl}_2(\text{DMSO})_2(\text{Me}_2\text{biim})$ (**2b**)

This complex was synthesized using the procedure given for **2a**, but using  $[\text{H}_2(\text{Me}_2\text{biim})][\text{CF}_3\text{CO}_2]_2$  (58 mg, 0.15 mmol). Yield: 64 mg (90%).  $^1\text{H}$  NMR ( $\text{CD}_3\text{OD}$ ):  $\delta$  7.65, 7.47, 7.25 (s, 2H,  $\text{H}_{5,5'}$ ), 3.54–3.32, 3.25–2.73, 2.32 (br s, 12H,  $\text{CH}_3$ -S), 1.66, 1.59, 1.58 (s, 6H,  $\text{CH}_3$ - $\text{Me}_2\text{biim}$ ). IR: 3455 (s,  $\nu_{\text{N-H}}$ ), 1420 (s), 1099 (s,  $\nu_{\text{S=O}}$ ), 1091 (s,  $\nu_{\text{S=O}}$ ), 1014 (m). ESI-MS (MeOH): 491 ( $\text{M}^+$ ), 455 ( $\text{M}^+ - \text{Cl}$ ), 377 ( $\text{M}^+ - \text{Cl} - \text{DMSO}$ ).  $\Lambda_{\text{M}}$  (MeOH) = 132. Anal. calcd. for  $\text{C}_{12}\text{H}_{22}\text{Cl}_2\text{N}_4\text{O}_2\text{S}_2\text{Ru}$ : C, 29.39; H, 4.52; N, 11.42. Found: C, 29.58; H, 4.64; N, 11.82.

#### $\text{Ru}_2\text{Cl}_4(\text{DMSO})_4(\text{biim})$ (**3a**)

This complex was synthesized using the procedure given for **2a**, but using  $[\text{H}_2\text{biim}][\text{CF}_3\text{CO}_2]_2$  (26 mg, 0.074 mmol). Yield: 42 mg (73%).  $^1\text{H}$  NMR ( $\text{CD}_3\text{OD}$ ): see Results and discussion. IR: 3449 (br s,  $\nu_{\text{N-H}}$ ), 1086 (s,  $\nu_{\text{S=O}}$ ), 1081 (s,  $\nu_{\text{S=O}}$ ), 1013 (m). ESI-MS (MeOH): 757 ( $\text{M}^+ - \text{Cl}$ ), 679 ( $\text{M}^+ - \text{Cl} - \text{DMSO}$ ).  $\Lambda_{\text{M}}$  (MeOH)  $\approx$  110. Anal. calcd. for  $\text{C}_{14}\text{H}_{30}\text{Cl}_4\text{N}_4\text{O}_4\text{S}_4\text{Ru}_2$ : C, 21.27; H, 3.82; N, 7.09. Found: C, 21.36; H, 4.00; N, 7.51.

#### $\text{Ru}_2\text{Cl}_4(\text{DMSO})_4(\text{Me}_2\text{biim})$ (**3b**)

This complex was synthesized using the procedure given for **2a**, but using  $[\text{H}_2(\text{Me}_2\text{biim})][\text{CF}_3\text{CO}_2]_2$  (29 mg, 0.074 mmol). Yield: 49 mg (81%).  $^1\text{H}$  NMR ( $\text{CD}_3\text{OD}$ ): see Results and discussion. IR: 3457 (s,  $\nu_{\text{N-H}}$ ), 1090 (s,  $\nu_{\text{S=O}}$ ), 1085 (s,  $\nu_{\text{S=O}}$ ). ESI-MS (MeOH): 785 ( $\text{M}^+ - \text{Cl}$ ), 707 ( $\text{M}^+ - \text{Cl} - \text{DMSO}$ ), 629 ( $\text{M}^+ - \text{Cl} - 2 \text{ DMSO}$ ), 551 ( $\text{M}^+ - \text{Cl} - 3 \text{ DMSO}$ ).  $\Lambda_{\text{M}}$  (MeOH)  $\approx$  100. Anal. calcd. for  $\text{C}_{16}\text{H}_{34}\text{Cl}_4\text{N}_4\text{O}_4\text{S}_4\text{Ru}_2$ : C, 23.47; H, 4.19; N, 6.84. Found: C, 23.58; H, 4.19; N, 6.65.

#### In situ experiments on the syntheses

The biimidazole (0.005–0.05 mmol) was added to the Ru precursor ( $\sim 5$  mg, 0.01 mmol) dissolved in 1 mL  $\text{CD}_3\text{OD}$  in an NMR tube, fitted with a septum with a pin-hole for pressure release. The bottom of the tube was immersed in a water bath at 65 °C, so that the tube worked like an effective condenser. After selected times, the tube was cooled to RT, and the  $^1\text{H}$  NMR spectra were recorded.

## Results and discussion

### Ru complexes

Our group has previously used  $[\text{Ru}(\text{DMF})_6][\text{CF}_3\text{SO}_3]_3$ , an air-stable  $\text{Ru}^{\text{III}}$  complex, as a precursor for the synthesis of  $\text{Ru}^{\text{II}}$ -homoleptic complexes of the type  $[\text{RuL}_6][\text{CF}_3\text{SO}_3]_2$ , where L is a range of imidazoles. The syntheses were carried out in MeOH, but it was unclear whether the solvent or the imidazole was reducing the metal.<sup>19</sup> In this current work,

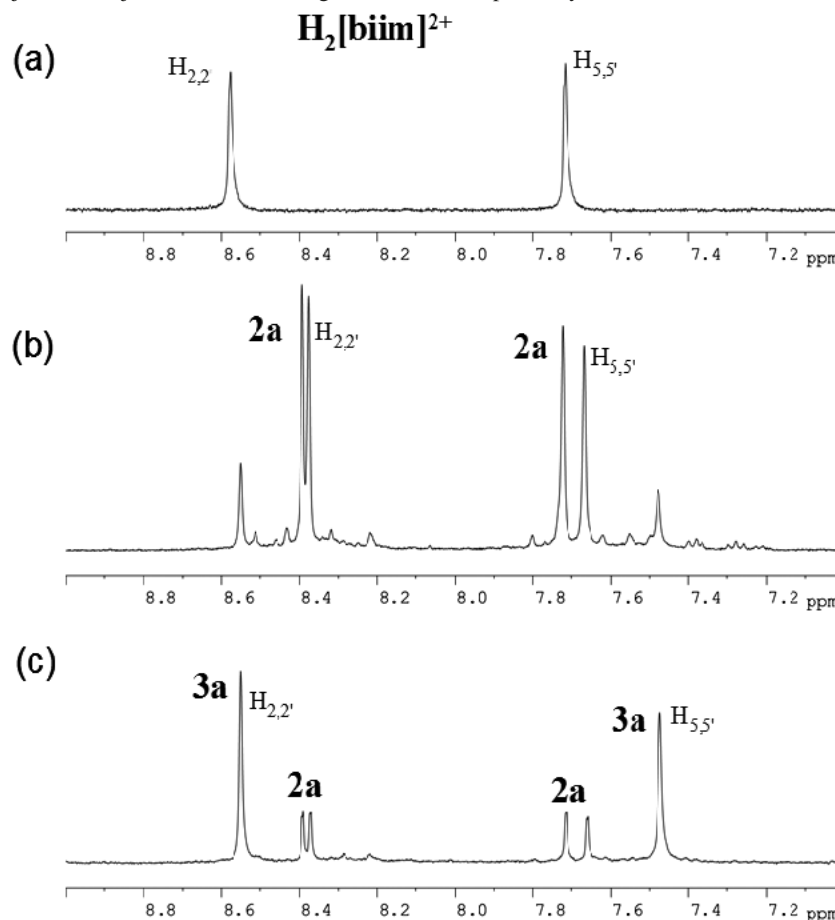
the same general procedure has been used for syntheses of  $[\text{Ru}(\text{N-N})_3][\text{CF}_3\text{SO}_3]_2$  complexes, where N–N is biim (complex **1a**) or  $\text{Me}_2\text{biim}$  (complex **1b**). Qualitative data from in situ experiments using biim:Ru ratios of 3:1 and 4:1 in  $\text{CD}_3\text{OD}$  suggest that biim acts as the reductant. At the 3:1 ratio, the in situ  $^1\text{H}$  spectrum after 12 h showed no trace of free  $[\text{H}_2\text{biim}]^{2+}$  (Fig. 2a),  $\sim 20\%$  formation of **1a** ( $\delta$  8.37 and 7.62; see below), and several other singlets in this same region including two at  $\delta$  8.92 and 7.84. At the 4:1 ratio after the same reaction time, formation of **1a** was close to completion and the other singlets except for those at  $\delta$  8.92 and 7.84 had decreased significantly in intensity. The retained  $\delta$  8.92 and 7.84 singlets are tentatively attributed to a biim oxidation product, while the “several other singlets” are attributed to  $\text{Ru}^{\text{II}}$ -mixed DMF/biim species. Such redox chemistry has been observed previously within  $\text{Ru}^{\text{III}}$ -imidazole systems<sup>20</sup>; the imidazole oxidation product was not identified, but chemistry involving loss of an H-atom to generate a radical that subsequently dimerizes seems feasible.<sup>21</sup>

With use of a biim:Ru reactant ratio of 4:1, **1a** and **1b** are isolated in reasonable yields ( $\sim 60\%$ ), and are well-characterized in the solid state and in solution by elemental analysis,  $^1\text{H}$  NMR spectroscopy, mass spectrometry, and conductivity data, while unfortunately X-ray quality crystals could not be isolated for any of the complexes reported in this paper. The  $^1\text{H}$  NMR spectrum of **1a** displays equal-intensity singlets at  $\delta$  8.37 and 7.62 for the  $\text{H}_{2,2'}$  and  $\text{H}_{5,5'}$  protons, respectively (cf. Fig. 2); the corresponding spectrum of **1b** consists of resonances at  $\delta$  7.43 and 2.54 (in a 1:3 integration ratio) for the  $\text{H}_{5,5'}$  and Me protons, respectively. The mass spectra of **1a** and **1b** do not show the peaks for the parent ionic compound, but peaks for species with the loss of one and two triflate anions, as well as a further loss of one N–N ligand, are evident. The molar conductivity values are consistent with the ionic formulations.<sup>18</sup>

The 1:1 reactions of the biimidazolium salts with *cis*- $\text{RuCl}_2(\text{DMSO})_4$  resulted in replacement of two DMSO ligands by the biimidazole with the isolation of **2a** and **2b** in  $\sim 90\%$  yield, the complexes being characterized by the methods given for **1a** and **1b**. The mass spectra of **2a** and **2b** show the  $\text{M}^+$  species, as well as fragments corresponding to the loss of one  $\text{Cl}^-$  and the subsequent loss of one DMSO ligand, and are consistent with the proposed solid-state formulations. The immediately measured and constant conductivities of **2a** and **2b** in MeOH ( $\sim 130 \Omega^{-1} \text{ cm}^2 \text{ mol}^{-1}$ ) are consistent with dissociation of a chlorido ligand,<sup>18</sup> and thus the ionic species  $[\text{RuCl}(\text{DMSO})_2(\text{MeOH})(\text{N-N})]\text{Cl}$  are considered to be present in solution.

The time-independent solution  $^1\text{H}$  NMR spectra in  $\text{CD}_3\text{OD}$  of **2a** (Fig. 2b) are consistent with this formulation: the four resonances seen for the biim protons show that the two rings are magnetically inequivalent, while four different, equal-intensity resonances seen for the Me groups of the DMSO indicate their inequivalence. Both DMSO ligands are considered to be S-bonded, mainly because of the strong  $\nu_{\text{SO}}$  IR bands seen in the solid state at 1071 and 1067  $\text{cm}^{-1}$ ; IR bands for O-DMSO are typically  $<1000 \text{ cm}^{-1}$  for  $\text{Ru}^{\text{II}}$  complexes.<sup>22</sup> Of the  $^1\text{H}$  NMR shifts for the Me protons of DMSO, the three at  $\delta$  3.49, 3.23, and 3.01 are consistent with S-bound DMSO, while the  $\delta$  2.29 resonance is unique in being upfield-shifted from that of free DMSO ( $\delta$  2.65)

**Fig. 2.**  $^1\text{H}$  NMR spectra (300 MHz,  $\sim 20^\circ\text{C}$ ) in  $\text{CD}_3\text{OD}$  showing the imidazole protons of: (a) free  $[\text{H}_2\text{biim}]^{2+}$ , (b) an in situ, 1:1  $\text{H}_2\text{biim}:\text{RuCl}_2(\text{DMSO})_4$  system after 4 h at  $65^\circ\text{C}$ , and (c) an in situ, 1:2  $\text{H}_2\text{biim}:\text{RuCl}_2(\text{DMSO})_4$  system after 4 h at  $65^\circ\text{C}$ . The spectra for isolated **2a** and **3a** in  $\text{CD}_3\text{OD}$  show just the major resonances of Figs. 2b and 2c, respectively.



but must also be due to an *S*-DMSO ligand. The upfield shift must arise from an interaction of this *S*-DMSO (*cis* to biim) with the  $\pi$ -system of an imidazole ring; similar upfield shifts have been noted by others.<sup>4f</sup> No signal at  $\delta$  2.65 was seen for free DMSO. The  $^1\text{H}$ - $^1\text{H}$  COSY NMR spectrum of **2a** (Fig. S1 of the Supplementary data) shows correlation between the two DMSO singlets at  $\delta$  2.29 and 3.01 and between those at  $\delta$  3.23 and 3.49, each pair corresponding to the two Me groups within one DMSO ligand. Similarly, the imidazole proton resonances correlate to reveal that the signals at  $\delta$  8.39 and 7.67 belong to the  $\text{H}_2$  and  $\text{H}_5$  of one ring, and those at  $\delta$  8.37 and 7.72 are associated with the  $\text{H}_{2'}$  and  $\text{H}_{5'}$  protons of the other ring.

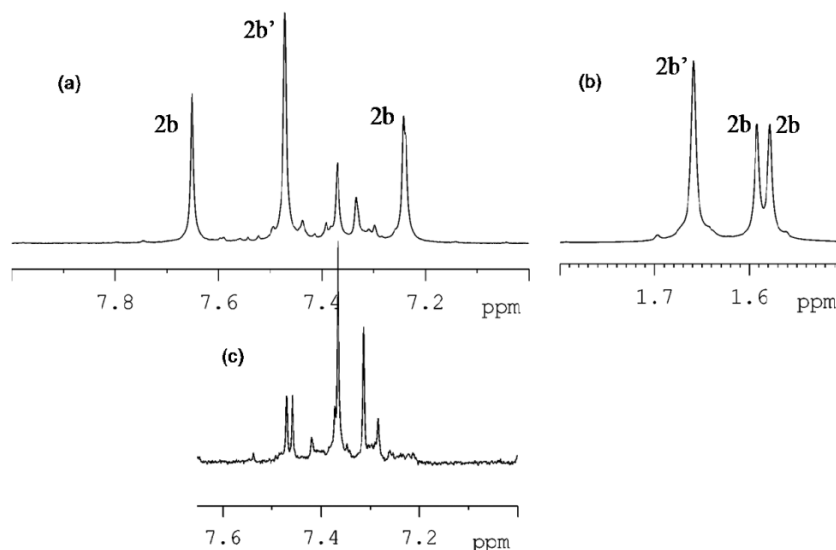
Assuming that no immediate isomerization of **2a** occurs on its dissolution in MeOH, an all-*cis* isomer for the solid-state structure seems reasonable (Fig. 1); replacement of one of the chlorides by MeOH (likely the one *trans* to the DMSO) would give a solution species consistent with the NMR data. Of note, the all-*cis* structure has been demonstrated crystallographically for the similar complex  $\text{RuCl}_2(\text{DMSO})_2(1,2\text{-dimethylimidazole})_2$ <sup>23</sup>; however, a complex of the type  $\text{RuCl}_2(\text{S-S})\text{L}_2$ , where S-S is a bidentate *S*-bonded sulfoxide and L is a nitro-substituted imidazole, has *trans* chlorides in the solid state, although in aqueous solution *cis*- and *trans*-isomers are present.<sup>9a</sup>

Use of an increased 5:1 reactant ratio ( $[\text{H}_2\text{biim}]^{2+}:\text{cis-RuCl}_2(\text{DMSO})_4$ ) was anticipated to form  $\text{RuCl}_2(\text{biim})_2$ , analogous to the production of  $\text{RuCl}_2(\text{pyridine})_4$  when the sulfoxide complex was reacted with pyridine,<sup>24</sup> but only **2a** was isolated.

Complex **2b** is considered to be analogous to **2a**, the IR data (1099, 1091, and 1014  $\text{cm}^{-1}$ ) and the  $^1\text{H}$  NMR data (overlapping signals between  $\delta$  3.51–2.23) are again considered consistent with solely *S*-bonded DMSO; again no free DMSO was detected. However, the  $^1\text{H}$  NMR spectrum of **2b** in  $\text{CD}_3\text{OD}$  (Fig. 3a) is more complicated than that of **2a**, in that three resonances are observed for the  $\text{H}_5$  protons: two equal intensity signals at  $\delta$  7.65 and 7.25, and a more intense signal at  $\delta$  7.47. Further, there are three resonances for the Me protons of the  $\text{Me}_2\text{biim}$ :  $\delta$  1.66, 1.59, and 1.58 (Fig. 3b), the equal intensities of two higher-field ones being three times the intensity of the  $\delta$  7.65 and 7.25 signals. These four resonances correspond to a single isomer (labelled **2b**) in which the two halves of  $\text{Me}_2\text{biim}$  ligand are inequivalent, while the remaining two 1:3 intensity  $\delta$  7.47 and 1.66 signals correspond to a second isomer (**2b'**) containing equivalent Me groups in the  $\text{Me}_2\text{biim}$  ligand. The 1:1 electrolyte conductivity of **2b** in MeOH implies that an average of one  $\text{Cl}^-$  is dissociated, probably from each isomer. In the absence of any rapid isomerization processes,



**Fig. 3.**  $^1\text{H}$  NMR data (300 MHz, 298 K) for  $\text{Me}_2\text{biim}$  complexes in  $\text{CD}_3\text{OD}$ . (a) In situ spectrum shows  $\text{H}_{5,5'}$  protons of **2b** and **2b'**, and the side-product **3b**. (b) Me signals for the  $\text{Me}_2\text{biim}$  of **2b** and **2b'**. (c)  $\text{H}_{5,5'}$  protons for isomers of **3b** (see text). The intensity scales in (a), (b), and (c) are different.



the solution **2b'** species could be generated from a solid-state *trans*-,*cis*- $\text{RuCl}_2(\text{DMSO})_2(\text{N}-\text{N})$  isomer via replacement of a  $\text{Cl}^-$  by  $\text{MeOH}$ . Similarly, the two solid-state “precursor structures” *cis*-,*trans*- $\text{RuCl}_2(\text{DMSO})_2(\text{N}-\text{N})$  and *cis*-,*cis*- $\text{RuCl}_2(\text{DMSO})_2(\text{N}-\text{N})$  could generate the **2b** isomer in solution. The latter is preferred because  $^1\text{H}$  NMR data (in  $\text{CDCl}_3$ ) of  $\text{RuCl}_2(\text{DMSO})_2(2\text{Me-imidazole})_2$ ,<sup>25</sup> and analogous complexes with other substituted imidazoles,<sup>22,23</sup> are consistent with an all-*cis* structure; and further, the same geometry seems likely for **2a**.

The reactions of the biimidazolium salts with *cis*- $\text{RuCl}_2(\text{DMSO})_4$ , but using a  $\text{Ru}:[\text{H}_2(\text{N}-\text{N})]^{2+}$  ratio of 2:1, generate the diruthenium complexes  $\text{Ru}_2\text{Cl}_4(\text{DMSO})_4(\text{N}-\text{N})$ , where (N-N) is biim (complex **3a**) or  $\text{Me}_2\text{biim}$  (complex **3b**). Elemental analyses support this formulation, as well as  $[\text{M}^+ - \text{Cl} - n \times \text{DMSO}]$  fragments in the mass spectra ( $n = 0$  and 1 for **3a**, and 0–3 for **3b**), with isotopic distribution patterns different from those of **2a** and **2b**, and consistent with the presence of two Ru atoms (Figs. S2 and S3). The IR  $\nu_{\text{SO}}$  data for **3a** and **3b** show strong bands in the  $1080\text{ cm}^{-1}$  region that are again consistent with *S*-bonded DMSO.

The immediately measured molar conductivities of a  $\text{MeOH}$  solution of the isolated **3a** and **3b** ( $\sim 100\text{ }\Omega^{-1}\text{ cm}^2\text{ mol}^{-1}$ ) are in the range for a 1:1 electrolyte,<sup>18</sup> again consistent with loss of a chlorido ligand. The immediately measured  $^1\text{H}$  NMR spectrum of **3a** dissolved in  $\text{CD}_3\text{OD}$  reveals two singlets for the  $\text{H}_{2,2'}$  and  $\text{H}_{5,5'}$  protons (Fig. 2), indicating a species with equivalent imidazole rings; this could be formed from a solid-state structure with a  $\text{Ru}^{\text{II}}(\mu\text{-Cl})_n\text{Ru}^{\text{II}}$  core ( $n = 2, 3$ ), but even species with  $\mu\text{-SO}$  cannot be ruled out.<sup>26</sup> In the DMSO region of the  $^1\text{H}$  NMR spectrum, there are signals in the  $\delta\text{ } 3.45\text{--}3.25$  and  $2.65$  regions (Fig. S4), which correspond to *S*-DMSO and free DMSO, but the spectra change with time, and this could be due to solvation and (or) monomer formation. Further studies are needed to determine the true nature of this “dimer”. Loss of  $\text{Cl}^-$  and DMSO ligands from  $\text{Ru}^{\text{II}}$ -chloro(DMSO) complexes in solu-

tion is well-documented, with *S*-DMSO exchanging slower than *O*-DMSO.<sup>27</sup> The **3b** system is more complex because the immediate  $^1\text{H}$  NMR spectrum of **3b** dissolved in  $\text{CD}_3\text{OD}$  shows major resonances for the  $\text{H}_{5,5'}$  protons at  $\delta\text{ } 7.38$  and  $7.33$  with a respective intensity ratio of  $\sim 2:1$  (Fig. 3c), these being attributed to two isomers, each with equivalent imidazole rings; there is also a pair of less intense, 1:1 singlets at  $\delta\text{ } 7.47$  and  $7.46$ , implying the presence of a third isomer with inequivalent imidazoles. The methyl region is complex because of numerous overlapping and unresolved resonances attributed to the Me resonances of DMSO (coordinated and free) and  $\text{Me}_2\text{biim}$  ligands.

### Biological data

The new complexes were tested against MDA-MB-435S human breast-cancer cells for anti-proliferatory activity using the MTT assay (Table 1). Complexes **1a** and **1b** exhibit  $\text{IC}_{50}$  values of 18 and  $36\text{ }\mu\text{mol/L}$ , respectively (Fig. S5), which indicates significant activity better than, or equal to, that of cisplatin ( $35\text{ }\mu\text{mol/L}$ ). No MTT studies have been reported on the analogous  $[\text{Ru}(\text{imidazole})_6][\text{CF}_3\text{SO}_3]_2$  or other similar homoleptic imidazole complexes,<sup>19</sup> and so the toxicity effect of the bidentate versus the corresponding monodentate imidazole ligands cannot be compared. Our group has shown that incubation of mouse squamous-cell carcinoma cells (SCCVII) with  $[\text{Ru}(\text{imidazole})_6][\text{CF}_3\text{SO}_3]_2$  for 3 h did lead to Ru-uptake of about  $15\text{ ng per } 10^6\text{ cells}$ .<sup>28</sup> In the current work, Ru-uptakes of **1a** and **1b** in Chinese hamster ovary (CHO) cells were 26 and  $20\text{ ng per } 10^6\text{ cells}$ , respectively, but the DNA isolated from these cells contained no detectable Ru, implying that the uptake is not associated with DNA-binding at the metal, in contrast to the behaviour of cisplatin.<sup>1</sup> There is considerable evidence elsewhere that biologically active Ru species might react with protein targets other than DNA.<sup>1–3</sup> Although our data are for different cell lines, the respective  $\text{IC}_{50}$  values for **1a** and **1b** possibly correlate with the degree of Ru accumulation, rather than resulting, for example, from a difference in activity of the



**Table 1.** IC<sub>50</sub> values for complexes.

Complex	IC <sub>50</sub> (μmol/L)
[Ru(biim) <sub>3</sub> ][CF <sub>3</sub> SO <sub>3</sub> ] <sub>2</sub> ( <b>1a</b> )	18
[Ru(Me <sub>2</sub> biim) <sub>3</sub> ][CF <sub>3</sub> SO <sub>3</sub> ] <sub>2</sub> ( <b>1b</b> )	36
RuCl <sub>2</sub> (DMSO) <sub>2</sub> (biim) ( <b>2a</b> )	800
RuCl <sub>2</sub> (DMSO) <sub>2</sub> (Me <sub>2</sub> biim) ( <b>2b</b> )	400
Ru <sub>2</sub> Cl <sub>4</sub> (DMSO) <sub>4</sub> (biim) ( <b>3a</b> )	>1000
Ru <sub>2</sub> Cl <sub>4</sub> (DMSO) <sub>4</sub> (Me <sub>2</sub> biim) ( <b>3b</b> )	>1000
Cisplatin	35

**Note:** Error limits are ± 10%; tested against MDA-MB-435S cells in Leibovitz's L-15 medium with L-glutamine after incubation at 37 °C for 70 h (ref. 9a).

complexes inside the cell. Further MTT, Ru-uptake, and DNA-binding studies on the Ru<sup>II</sup>-imidazole and (or) the Ru-biimidazole systems with the use of the same cell line are needed for a more direct comparison between the two systems. The promising activities of **1a** and **1b** are the highest of the Ru<sup>II</sup> complexes that our group has studied with the same cell line (see the Introduction)<sup>7–10</sup> and, of note, the Ru<sup>III</sup> complexes [Ru(O–O)<sub>2</sub>(N–N)]CF<sub>3</sub>SO<sub>3</sub>, where O–O<sup>–</sup> is maltolato (see the Introduction) and N–N is biim or Me<sub>2</sub>-Biim, have respective IC<sub>50</sub> values of 50 and 15 μmol/L against the same cell line,<sup>29</sup> close to the values for **1a** and **1b**; this finding indirectly supports the early premise that Ru<sup>III</sup> complexes are likely activated via in vivo reduction to Ru<sup>II</sup>.<sup>6</sup> To contribute constructively to this aspect, more systematic studies are required on the Ru<sup>III</sup>/Ru<sup>II</sup> reduction potentials of the complexes studied in our group.<sup>7–10,29</sup>

The mixed biimidazole/DMSO complexes **2a** and **2b** exhibit IC<sub>50</sub> values of 800 and 400 μmol/L, respectively, which are close to values measured for the respective free biimidazoles (800 and 650 μmol/L for H<sub>2</sub>biim and Me<sub>2</sub>-biim). IC<sub>50</sub> values for **3a** and **3b** were >1000 μmol/L.

The conclusions on the nature of the new complexes presented here would certainly be strengthened by X-ray data, particularly for type-2 and -3 complexes, but many attempts at growing suitable crystals were unsuccessful. Nevertheless, the findings perhaps suggest that the presence of labile chlorido or DMSO ligands is detrimental for anti-proliferative activity.

## Supplementary data

Supplementary data for this article are available on the journal Web site (<http://canjchem.nrc.ca>).

## Acknowledgments

We thank Dr. Elena Polishchuk of the Biological Services in this department for assistance with the MTT assay, the Natural Sciences and Engineering Research Council of Canada (NSERC) for financial support, and Colonial Metals Inc. for the RuCl<sub>3</sub>·3H<sub>2</sub>O.

## References

- (1) (a) Reedijk, J. *Eur. J. Inorg. Chem.* **2009**, (10), 1303; and refs. cited therein. doi:10.1002/ejic.200900054.; (b) Jakupc, M. A.; Galanski, M.; Arion, V. B.; Hartinger, C. G.; Keppler, B. K. *Dalton Trans.* **2008**, (2): 183; and refs. cited therein. doi:10.1039/b712656p. PMID:18097483.; (c) Grif-

- fith, D.; Cecco, S.; Zangrando, E.; Bergamo, A.; Sava, G.; Marmion, C. J. *J. Biol. Inorg. Chem.* **2008**, *13* (4), 511; and refs. cited therein. doi:10.1007/s00775-007-0337-4. PMID: 18183430.; (d) Hannon, M. J. *Pure Appl. Chem.* **2007**, *79* (12), 2243; and refs. cited therein. doi:10.1351/pac200779122243.; (e) Dyson, P. J.; Sava, G. *Dalton Trans.* **2006**, (16): 1929; and refs. cited therein. doi:10.1039/b601840h. PMID:16609762.
- (2) (a) Tian, Y.; Yang, P.; Li, Q.; Guo, M.; Zhao, M. *Polyhedron* **1997**, *16* (12), 1993. doi:10.1016/S0277-5387(96)00526-8.; (b) Sava, G.; Zorzet, S.; Giralaldi, T.; Mestroni, G.; Zassinovich, G. *Eur. J. Cancer Clin. Oncol.* **1984**, *20* (6), 841. doi:10.1016/0277-5379(84)90223-2. PMID:6540184.
- (3) (a) Cetinbas, N.; Webb, M. I.; Dubland, J. A.; Walsby, C. J. *J. Biol. Inorg. Chem.* **2010**, *15* (2), 131; and refs. cited therein. doi:10.1007/s00775-009-0578-5. PMID:19707803.; (b) Hartinger, C. G.; Jakupc, M. A.; Zorbas-Seifried, S.; Groessl, M.; Egger, A.; Berger, W.; Zorbas, H.; Dyson, P. J.; Keppler, B. K. *Chem. Biodivers.* **2008**, *5* (10), 2140; and refs. cited therein. doi:10.1002/cbdv.200890195. PMID: 18972504.
- (4) (a) Bergamo, A.; Masi, A.; Peacock, A. F. A.; Habtemariam, A.; Sadler, P. J.; Sava, G. *J. Inorg. Biochem.* **2010**, *104* (1), 79; and refs. cited therein. doi:10.1016/j.jinorgbio.2009.10.005. PMID:19906432.; (b) Süß-Fink, G. *Dalton Trans.* **2010**, *39* (7), 1673; and refs. cited therein. doi:10.1039/b916860p. PMID:20449402.; (c) Kandoll, W.; Hartinger, C. G.; Nazarov, A. A.; Bartel, C.; Skocic, M.; Jakupc, M. A.; Arion, V. B.; Keppler, B. K. *Chem. Eur. J.* **2009**, *15* (45), 12283; and refs. cited therein. doi:10.1002/chem.200901939.; (d) Kandoll, W.; Hartinger, C. G.; Nazarov, A. A.; Kuznetsov, M. L.; John, R. O.; Bartel, C.; Jakupc, M. A.; Arion, V. B.; Keppler, B. K. *Organometallics* **2009**, *28* (15), 4249; and refs. cited therein. doi:10.1021/om900483t.; (e) Renfrew, A. K.; Phillips, A. D.; Egger, A. E.; Hartinger, C. G.; Bosquain, S. S.; Nazarov, A. A.; Keppler, B. K.; Gonsalvi, L.; Peruzzini, M.; Dyson, P. J. *Organometallics* **2009**, *28* (4), 1165; and refs. cited therein. doi:10.1021/om800899e.; (f) Bratsos, I.; Jedner, S.; Bergamo, A.; Sava, G.; Gianferrara, T.; Zangrando, E.; Alessio, E. *J. Inorg. Biochem.* **2008**, *102* (5-6), 1120; and refs. cited therein. doi:10.1016/j.jinorgbio.2008.01.005. PMID: 18279961.; (g) Ronconi, L.; Sadler, P. J. *Coord. Chem. Rev.* **2007**, *251* (13-14), 1633; and refs. cited therein. doi:10.1016/j.ccr.2006.11.017.
- (5) Lentz, F.; Drescher, A.; Lindauer, A.; Henke, M.; Hilger, R. A.; Hartinger, C. G.; Scheulen, M. E.; Dittich, C.; Keppler, B. K.; Jaehde, U. *Anticancer Drugs* **2009**, *20* (2), 97. doi:10.1097/CAD.0b013e328322fbc5. PMID:19209025.
- (6) (a) Clarke, M. J. *Coord. Chem. Rev.* **2003**, *236* (1-2), 209. doi:10.1016/S0010-8545(02)00312-0.; (b) Clarke, M. J.; Zhu, F.; Frasca, D. R. *Chem. Rev.* **1999**, *99* (9), 2511. doi:10.1021/cr9804238. PMID:11749489.
- (7) Kennedy, D. C.; Wu, A.; Patrick, B. O.; James, B. R. *Inorg. Chem.* **2005**, *44* (19), 6529. doi:10.1021/ic050034d. PMID: 16156610.
- (8) Kennedy, D. C.; Wu, A.; Patrick, B. O.; James, B. R. *J. Inorg. Biochem.* **2006**, *100* (12), 1974. doi:10.1016/j.jinorgbio.2006.07.001. PMID:16938347.
- (9) (a) Wu, A.; Kennedy, D. C.; Patrick, B. O.; James, B. R. *Inorg. Chem.* **2003**, *42* (23), 7579. doi:10.1021/ic030119j. PMID:14606854.; (b) Wu, A.; Kennedy, D. C.; Patrick, B. O.; James, B. R. *Inorg. Chem. Commun.* **2003**, *6* (8), 996.

- doi:10.1016/S1387-7003(03)00164-3.; (c) Yapp, D. T. T.; Rettig, S. J.; James, B. R.; Skov, K. A. *Inorg. Chem.* **1997**, 36 (24), 5635. doi:10.1021/ic9606486.
- (10) Huxham, L. A.; Cheu, E. L. S.; Patrick, B. O.; James, B. R. *Inorg. Chim. Acta* **2003**, 352, 238. doi:10.1016/S0020-1693(03)00155-5.
- (11) (a) Goulle, V.; Thummel, R. *Inorg. Chem.* **1990**, 29 (9), 1767. doi:10.1021/ic00334a034.; (b) Rau, S.; Büttner, T.; Temme, C.; Ruben, M.; Görls, H.; Walther, D.; Duati, M.; Fanni, S.; Vos, J. G. *Inorg. Chem.* **2000**, 39 (7), 1621. doi:10.1021/ic991225h. PMID:12526478.; (c) Rillema, D. P.; Sahai, R.; Matthews, P.; Edwards, A. K.; Shaver, R. J.; Morgan, L. *Inorg. Chem.* **1990**, 29 (2), 167. doi:10.1021/ic00327a006.; (d) Panda, B. K.; Sengupta, S.; Chakravorty, A. *Eur. J. Inorg. Chem.* **2004**, (1), 178. doi:10.1002/ejic.200300293.
- (12) Majumdar, P.; Peng, S.-M.; Goswami, S. *J. Chem. Soc., Dalton Trans.* **1998**, (10): 1569. doi:10.1039/a801071d.
- (13) (a) Burns, C. T.; Jordan, R. F. *Organometallics* **2007**, 26 (27), 6726. doi:10.1021/om700767r.; (b) Morita, Y.; Murata, T.; Fukui, K.; Tadokoro, M.; Sato, K.; Shiomi, D.; Takui, T.; Nakasujii, K. *Chem. Lett.* **2004**, 33 (2), 188. doi:10.1246/cl.2004.188.; (c) Zhang, W.; Landee, C. P.; Willett, R. D.; Turnbull, M. M. *Tetrahedron* **2003**, 59 (32), 6027. doi:10.1016/S0040-4020(03)00987-6.; (d) Aromí, G.; Gamez, P.; Kooijman, H.; Spek, A. L.; Driessen, W. L.; Reedijk, J. *Eur. J. Inorg. Chem.* **2003**, (7), 1394. doi:10.1002/ejic.200390181.
- (14) Cliff, M. D.; Pyne, S. G. *Synthesis* **1994**, 1994 (07), 681. doi:10.1055/s-1994-25544.
- (15) Gordon, A. J.; Ford, R. A. *The Chemist's Companion: A Handbook of Practical Data, Techniques, and References*; John Wiley & Sons, Inc.: New York, 1972.
- (16) (a) Evans, I. P.; Spencer, A.; Wilkinson, G. J. *J. Chem. Soc., Dalton Trans.* **1973**, (2): 204. doi:10.1039/dt9730000204.; (b) Judd, R. J.; Cao, R.; Biner, M.; Armbruster, T.; Buergi, H.; Merbach, A. E.; Ludi, A. *Inorg. Chem.* **1995**, 34 (20), 5080. doi:10.1021/ic00124a026.
- (17) Pavia, D. L.; Lampman, G. M.; Kriz, G. S. *Introduction to Spectroscopy*, 2nd ed.; Harcourt Brace & Company: Orlando, 1996.
- (18) Geary, W. J. *Coord. Chem. Rev.* **1971**, 7 (1), 81. doi:10.1016/S0010-8545(00)80009-0.
- (19) Baird, I. R.; Rettig, S. J.; James, B. R.; Skov, K. A. *Can. J. Chem.* **1998**, 76 (10), 1379. doi:10.1139/cjc-76-10-1379.
- (20) Anderson, C.; Beauchamp, A. *Inorg. Chem.* **1995**, 34 (24), 6065. doi:10.1021/ic00128a017.
- (21) Eaton, D. R.; Wilson, K. M. *J. Inorg. Biochem.* **1979**, 10 (3), 195. doi:10.1016/S0162-0134(00)80279-2.
- (22) Alessio, E. *Chem. Rev.* **2004**, 104 (9), 4203. doi:10.1021/cr0307291. PMID:15352790.; (b) Chan, P. K. L.; James, B. R.; Frost, D. C.; Chan, P. K. H.; Hu, H.-L.; Skov, K. A. *Can. J. Chem.* **1989**, 67, 508.
- (23) Iwamoto, M.; Alessio, E.; Marzilli, L. G. *Inorg. Chem.* **1996**, 35 (8), 2384. doi:10.1021/ic951063z. PMID:11666440.
- (24) Evans, I. P.; Spencer, A.; Wilkinson, G. J. *J. Chem. Soc., Dalton Trans.* **1972**, 204.
- (25) Chan, P. K. L. Ph.D. Thesis, Department of Chemistry, The University of British Columbia, Vancouver, BC, 1988.
- (26) (a) Lessing, S. F.; Lotz, S.; Roos, H. M.; van Rooyen, P. H. J. *Chem. Soc., Dalton Trans.* **1999**, (9): 1499. doi:10.1039/a901393h.; (b) Tanase, T.; Aiko, T.; Yamamoto, Y. *Chem. Commun. (Camb.)* **1996**, (20): 2341. doi:10.1039/cc9960002341.
- (27) (a) Alessio, E.; Mestroni, G.; Nardin, G.; Attia, W. M.; Calligaris, M.; Sava, G.; Zorzet, S. *Inorg. Chem.* **1988**, 27 (23), 4099. doi:10.1021/ic00296a006.; (b) Davies, A. R.; Einstein, F. W. B.; Farrell, N. P.; James, B. R.; McMillan, R. S. *Inorg. Chem.* **1978**, 17 (7), 1965. doi:10.1021/ic50185a054.
- (28) Baird, I. R. Ph.D. Thesis, Department of Chemistry, The University of British Columbia, Vancouver, BC, 1999.
- (29) Kennedy, D. C. Ph.D. Thesis, Department of Chemistry, The University of British Columbia, Vancouver, BC, 2003.

# A quasi-classical trajectory (QCT) study of the H + OF reaction stereodynamics

Dan Zhao, Tian Yu Zhang, and Tian Shu Chu

**Abstract:** Based on the global three-dimensional adiabatic potential surface of the  $1^3A'$  excited electronic state (*J. Chem. Phys.* 2005, **123**, 114310) of the OHF system, we investigated the  $H + OF \rightarrow OH + F/HF + O$  reaction stereodynamics by using the quasi-classical trajectory (QCT) method. The four polarization-dependent differential cross sections (PDDCSs) and the three angular distributions  $P(\theta_r)$ ,  $P(\varphi_r)$ ,  $P(\theta_r, \varphi_r)$  were calculated at a low collision energy of 0.48 eV for both product channels. The results indicated that the products are backward-scattering on the triplet state, and the product rotational angular momenta are aligned or oriented. Moreover, there is a remarkable difference between the polarization behaviors of the two product channels. Product orientation exhibited by the  $OH + F$  channel is found to be absent in the  $HF + O$  channel at this collision energy albeit the latter shows stronger alignment along the direction perpendicular to the reagent relative velocity  $k$  than  $OH + F$ .

**Key words:** chemical stereodynamics, product alignment, product orientation, quasi-classical trajectory (QCT).

**Résumé :** En se basant sur la surface de potentiel adiabatique tridimensionnel global de l'état excité électronique excité  $1^3A'$  (*J. Chem. Phys.* 2005, **123**, 114310) du système OHF, on a étudié la stéréodynamique de la réaction  $H + OF \rightarrow OH + F/HF + O$  à l'aide de la méthode de la trajectoire quasi-classique (TQC). On a calculé les quatre sections droites différentielles dépendantes de la polarisation (SDDDP) et les trois distributions angulaires  $P(\theta_r)$ ,  $P(\varphi_r)$  et  $P(\theta_r, \varphi_r)$  à une faible énergie de collision, 0,48 eV, pour chacune des deux voies conduisant au produit. Les résultats indiquent que les produits correspondent à une rétrodiffusion sur l'état triplet et que les moments angulaires rotationnels du produit sont alignés ou orientés. De plus, il existe une différence remarquable entre les comportements de polarisation des deux voies conduisant aux produits. On a trouvé que, à ce niveau d'énergie de collision, l'orientation du produit présentée par la voie  $OH + F$  est absente de la voie  $HF + O$  même si cette dernière présente un alignement plus important le long de la direction perpendiculaire à la vitesse relative du réactif,  $k$ , que celui observé pour la voie  $OH + F$ .

**Mots-clés :** stéréodynamique chimique, alignement du produit, orientation du produit, méthode de la trajectoire quasi-classique (TQC).

[Traduit par la Rédaction]

## Introduction

The HOF system is one of the most elementary trimolecular systems and can be considered as a model system for HOX (X = F, Cl, Br, and so forth). Recently, Gómez-Carrasco et al. have studied the global three-dimensional potential energy surfaces (PESs) for the OHF system at a high ab initio level<sup>1</sup> and obtained the adiabatic PESs of OHF for the ground  $1^1A'$  singlet state and the excited  $2^3A''$  and  $1^3A'$  triplet states.<sup>2</sup> The reaction dynamics of  $F + OH \rightarrow HF + O$  has been studied by a quantum wave packet method within a centrifugal sudden (CS) approximation on the two excited triplet electronic states.<sup>2</sup> A comparative study of the full channels of the  $H + OF$  reaction by quantum mechanical (QM) and quasi-classical trajectory (QCT) methods,<sup>3</sup> as well as the QCT calculations for the reaction  $H + OF \rightarrow OH + F$ <sup>4,5</sup> have also been reported recently using the  $2^3A''$  PES.

In this article, by performing the QCT calculation on the  $1^3A'$  triplet state,<sup>6</sup> we explored the stereodynamics of the ti-

tle reaction at a fixed collision energy of 0.48 eV by means of depicting the polarization-dependent differential cross sections (PDDCSs) and the three angular distributions of  $P(\theta_r)$ ,  $P(\varphi_r)$ , and  $P(\theta_r, \varphi_r)$  for the two product channels. The validity of applying QCT method to the title reaction has been tested and proved in a previous study<sup>3</sup> showing a fairly good agreement between the QM and QCT calculations with the  $2^3A''$  electronic state being involved.

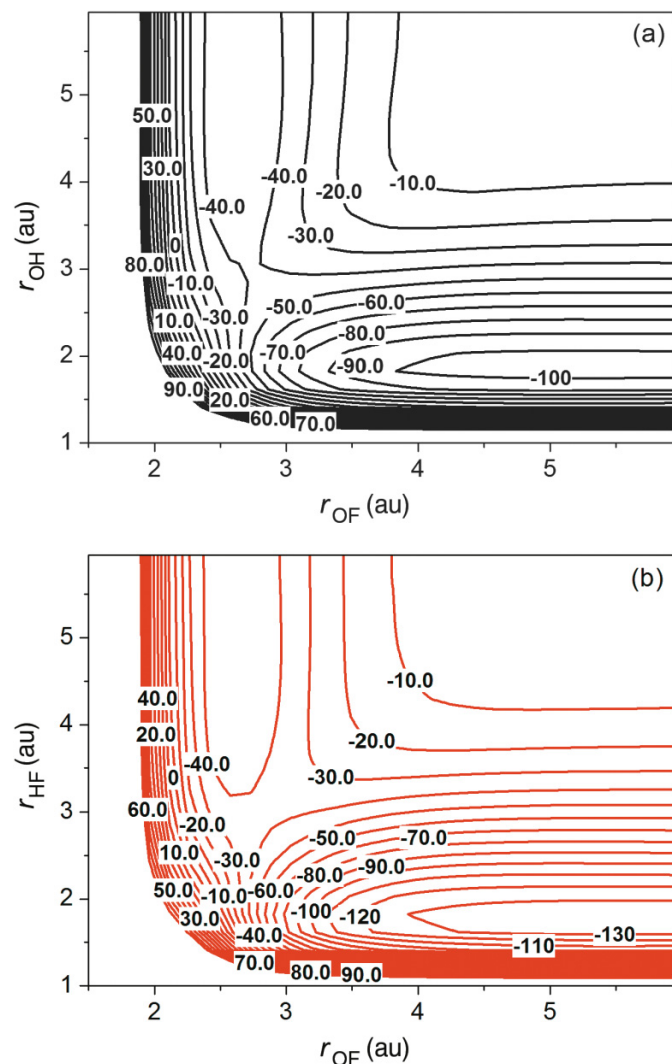
The present study employed the benchmark QCT code<sup>7–18</sup> developed initially to simulate and explain the polarization behaviors of the products in laser-induced molecular beam experiments. Furthermore, an innovative theoretical work came up in 1997 describing the optical preparation of oriented and aligned reagents in weak laser field.<sup>19</sup> Despite the QCT code we employed here, there are many other developed theoretical methods and computational codes,<sup>20–25</sup> which can be used in the stereodynamics exploration of a chemical reaction. In the following section, we briefly de-

Received 11 February 2010. Accepted 20 April 2010. Published on the NRC Research Press Web site at canjchem.nrc.ca on 28 July 2010.

**D. Zhao and T.Y. Zhang.** School of Chemical Engineering, Dalian University of Technology, Dalian 116023, China.  
**T.S. Chu.**<sup>1</sup> Institute for Computational Sciences and Engineering, Qingdao University, Qingdao 266071, China.

<sup>1</sup>Corresponding author (e-mail: tschu008@163.com).

**Fig. 1.** The contour plots of the  $1^3A'$  PES for (a)  $H + OF \rightarrow OH + F$  and (b)  $H + OF \rightarrow HF + O$  with collinear geometry. Potential energy in kcal/mol.



scribe the present QCT calculation method together with relevant details of the calculation. Results and discussion are presented in a later section. Finally, the last section is the conclusions.

### Calculation aspects

The calculation method we used here is the same as the one described in refs. 8–18. The QCT calculation is performed within a center of mass frame in which the reagent relative velocity vector  $k$  is parallel to the  $z$  axis, and  $x$ – $z$  plane is the scattering plane containing the initial and final relative velocity vectors,  $k$  and  $k'$ . The scattering angle between the reagent relative velocity and product relative velocity is  $\theta_r$ . The polar and azimuthal angles of the product rotational angular momentum  $j'$  are  $\theta_r$  and  $\varphi_r$ , respectively.

The fully correlated center-of-mass angular distribution is written as the sum,

$$[1] \quad P(\omega_t, \omega_r) = \sum_{kq} \frac{[k]}{4\pi} \frac{1}{\sigma} \frac{d\sigma_{kq}}{d\omega_t} C_{kq}(\theta_r, \varphi_r)^*$$

where  $[k] = 2k + 1$ ,  $\frac{1}{\sigma} \frac{d\sigma_{kq}}{d\omega_t}$  is a generalized polarization-dependent differential cross section, and  $C_{kq}(\theta_r, \varphi_r)$  are modified spherical harmonics.

The PDDCS can be further written as follows:

$$[2] \quad \frac{1}{\sigma} \frac{d\sigma_{kq}}{d\omega_t} = \sum_{k_1} \frac{[k_1]}{4\pi} S_{kq\pm}^{k_1} C_{k_1-q}(\theta_r, 0)$$

where  $S_{kq\pm}^{k_1} = \langle c_{k_1q}(\theta_r, 0) c_{kq}(\theta_r, 0) [(-1)^q e^{iq\varphi_r} \pm e^{-iq\varphi_r}] \rangle$ , which is evaluated using the expected value expression.

The angular distribution function  $P(\theta_r)$  describing the  $k - j'$  correlation can be expanded in a series of Legendre polynomials

$$[3] \quad P(\theta_r) = 1/2 \sum_k (2k + 1) a_0^k P_k(\cos \theta_r)$$

The coefficients  $a_0^k = \langle P_k(\cos \theta_r) \rangle$  are called orientation ( $k$  is odd) or alignment ( $k$  is even) parameters.

The dihedral angle distribution function  $P(\varphi_r)$  describing  $k - k' - j$  correlation can be expanded in Fourier series

$$[4] \quad P(\varphi_r) = \frac{1}{2\pi} \left[ 1 + \sum_{n(\text{even} \geq 2)} a_n \cos(n\varphi_r) + \sum_{n(\text{odd} \geq 1)} b_n \sin(n\varphi_r) \right]$$

where  $a_n = 2\langle \cos n\varphi_r \rangle$  and  $b_n = 2\langle \sin n\varphi_r \rangle$ .

The following expansion is used to obtain the  $P(\theta_r, \varphi_r)$  distribution,

$$[5] \quad P(\theta_r, \varphi_r) = \frac{1}{4\pi} \sum_k \sum_{q \geq 0} (a_{q\pm}^k \cos q\varphi_r - a_{q\mp}^k \sin q\varphi_r) C_{kq}(\theta_r, 0)$$

with  $a_{q\pm}^k = 2\langle C_{kq}(\theta_r, 0) \cos q\varphi_r \rangle$  ( $k$  is even) and  $a_{q\pm}^k = 2i\langle C_{kq}(\theta_r, 0) \sin q\varphi_r \rangle$  ( $k$  is odd).

In this study, the initial distance from the H atom to the center of mass of OF is 10 Å. The batches of 250 000 trajectories were sampled at the collision energy of 0.48 eV (the lowest collision energy to ensure the reaction takes place via both channels), while setting the initial rovibrational conditions of the OF reagent to be  $v = 0$ ,  $j = 0$ . An integration step of 1 fs is found sufficient to ensure the convergence of the calculated stereodynamics quantities we presented here. The optimized maximum impact parameter  $b_{\text{max}}$  at 0.48 eV is 1.2 Å and 0.35 Å for the OH + F and HF + O product channels, respectively.

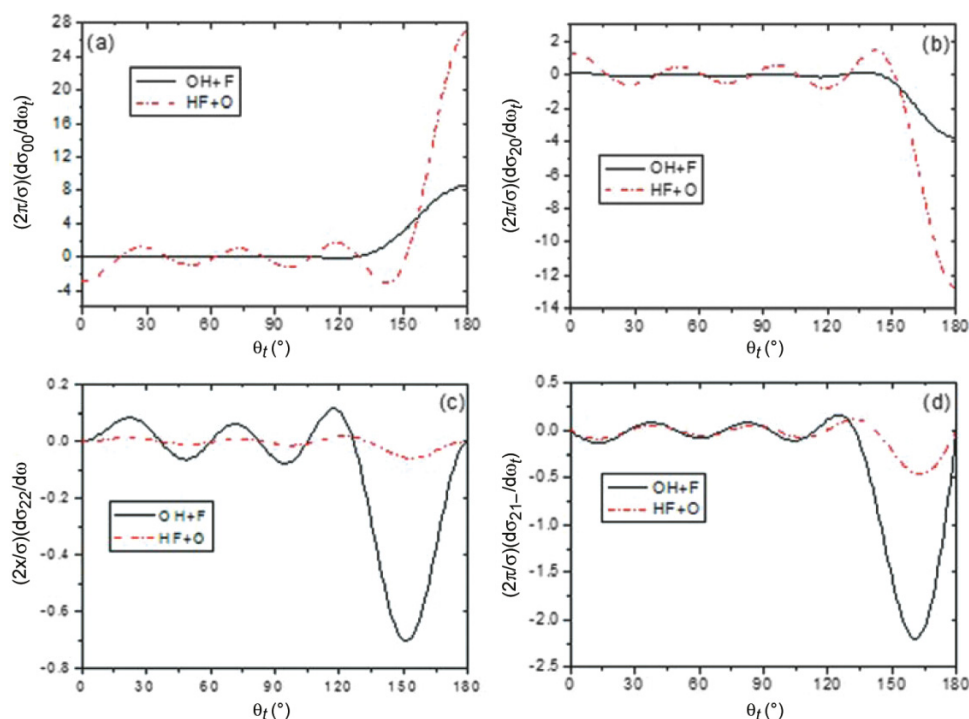
### Results and discussion

It is known that PES plays a critical role in chemical stereodynamics. Shown in Fig. 1 are the contour plots of the  $1^3A'$  PES for the reactions of  $H + OF \rightarrow OH + F$  and  $H + OF \rightarrow HF + O$  with collinear geometry. The topographic features of the PES reflect that both reactive channels are dominated by abstraction mechanism due to the barrier in reactant region.

Figure 2 shows the calculated four PDDCSs for  $H + OF \rightarrow OH + F$  and  $H + OF \rightarrow HF + O$ . The  $(2\pi/\sigma)(d\sigma_{00}/d\omega_t)$  is proportional to the usual differential cross section and displays the scattering direction of the products. From



**Fig. 2.** The polarization-dependent differential cross sections  $(2\pi/\sigma)(d\sigma_{kl}/d\omega_l)$  for  $\text{H} + \text{OF} \rightarrow \text{OH} + \text{F}$  (solid line) and  $\text{H} + \text{OF} \rightarrow \text{HF} + \text{O}$  (dash-dotted line) at the collision energy of 0.48 eV. (a)  $(2\pi/\sigma)(d\sigma_{00}/d\omega_l)$ , (b)  $(2\pi/\sigma)(d\sigma_{20}/d\omega_l)$ , (c)  $(2\pi/\sigma)(d\sigma_{22+}/d\omega_l)$ , and (d)  $(2\pi/\sigma)(d\sigma_{21-}/d\omega_l)$ .



**Fig. 3.** The distribution of  $P(\theta_r)$  reflecting  $k - j'$  correlation for  $\text{H} + \text{OF} \rightarrow \text{OH} + \text{F}$  (solid line) and  $\text{H} + \text{OF} \rightarrow \text{HF} + \text{O}$  (dashed-dotted line) at the collision energy of 0.48 eV.

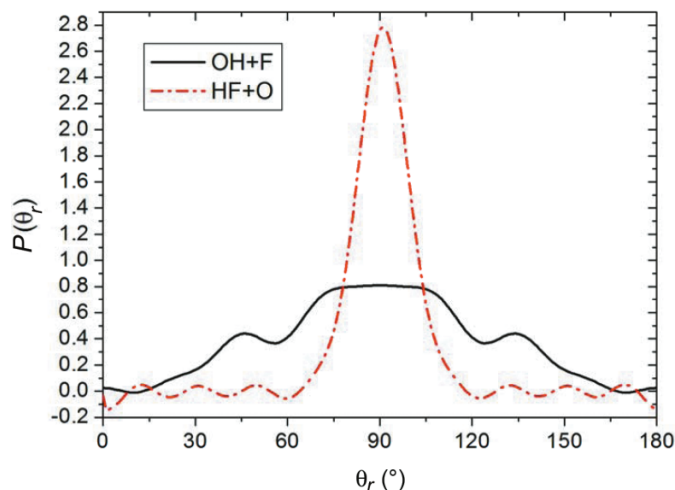
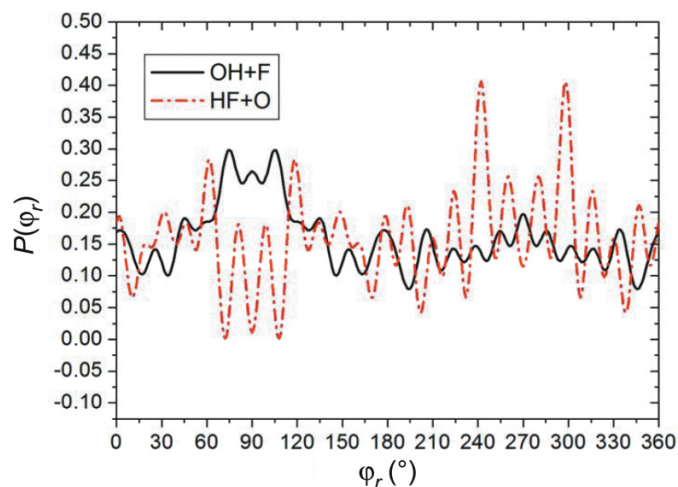


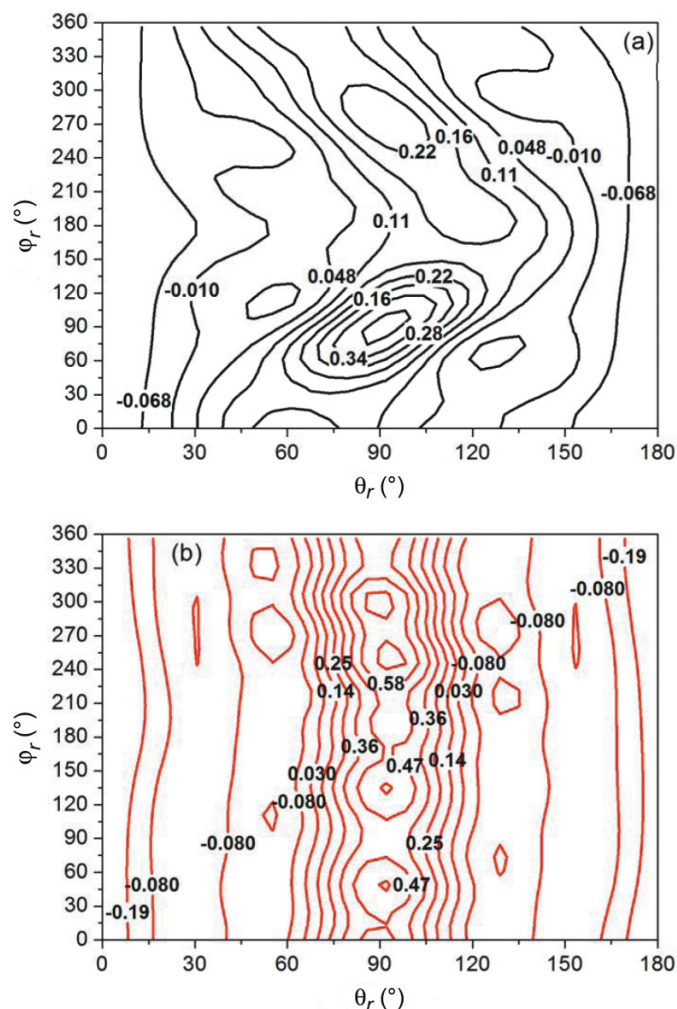
Fig. 2a, it can be seen that the two product channels are obviously backward-scattering and the degree of the backward scattering is much larger in the  $\text{HF} + \text{O}$  product channel. Such backward scattering shown here is in consistence with the abstraction mechanism of the title reaction that occurred on the  $1^3\text{A}'$  electronic state. Figure 2b plotted the  $(2\pi/\sigma)(d\sigma_{20}/d\omega_l)$ , which is found to be opposite to the  $(2\pi/\sigma)(d\sigma_{00}/d\omega_l)$  over the whole range of the scattering angle and for both product channels. This opposite trend suggests that product angular momentum is strongly aligned perpendicular to the reagent relative velocity  $k$ . Figure 2c shows the  $(2\pi/\sigma)(d\sigma_{22+}/d\omega_l)$  of the two product channels. Comparing the two channels, it

**Fig. 4.** The dihedral angle distribution of  $P(\varphi_r)$  with respect to the  $k - k'$  and  $k - j'$  planes for  $\text{H} + \text{OF} \rightarrow \text{OH} + \text{F}$  (solid line) and  $\text{H} + \text{OF} \rightarrow \text{HF} + \text{O}$  (dashed-dotted line) at the collision energy of 0.48 eV.



can be seen that the  $(2\pi/\sigma)(d\sigma_{22+}/d\omega_l)$  of the  $\text{HF} + \text{O}$  product channel is completely different from that of  $\text{OH} + \text{F}$ . That is, the  $(2\pi/\sigma)(d\sigma_{22+}/d\omega_l)$  of the  $\text{HF} + \text{O}$  product channel is almost zero while that of the  $\text{OH} + \text{F}$  product channel is fluctuant with the scattering angle. As indicated by the present calculation, around the two scattering angles of  $145^\circ$  and  $158^\circ$ , the value of  $(2\pi/\sigma)(d\sigma_{22+}/d\omega_l)$  in Fig. 2c is approximately  $-0.6124$  for the  $\text{OH} + \text{F}$  product channel. According to the classical limiting value of the alignment parameters, this value of  $-0.6124$  gives the information that the azimuthal angles ( $\theta_r$  and  $\varphi_r$ ) of  $j'$  are  $(45^\circ, \text{ and } 90^\circ, \text{ respectively})$ . Therefore, around these two scattering angles,

**Fig. 5.** Polar plots of  $P(\theta_r, \varphi_r)$  distribution averaged over all scattering angles for (a)  $\text{H} + \text{OF} \rightarrow \text{OH} + \text{F}$  and (b)  $\text{H} + \text{OF} \rightarrow \text{HF} + \text{O}$ .



the  $\text{OH} + \text{F}$  products tend to align along the direction of the vector addition of  $y$  and  $z$ . In turn, the value of  $(2\pi/\sigma)(d\sigma_{21}/d\omega_r)$  of the  $\text{OH} + \text{F}$  product channel in Fig. 2d is found to be  $-1.2247$  with the scattering angles around  $147^\circ$  and  $173^\circ$ . In these cases, the azimuthal angles ( $\theta_r$  and  $\varphi_r$ ) of  $j'$  are ( $45^\circ$  and  $0^\circ$ , respectively), which means that the product alignment in the  $\text{OH} + \text{F}$  channel is along the direction of the vector addition of  $z$  and  $x$ .

The distribution of  $P(\theta_r)$  reflected the  $k - j'$  correlation of the products. Seen from Fig. 3, the  $P(\theta_r)$  distributions of the two product channels all peaked at  $90^\circ$  and are symmetric with respect to  $90^\circ$ . This symmetric phenomenon observed in the two  $P(\theta_r)$  distributions implies that the product rotational angular momentum is strongly aligned along the perpendicular direction to the reagent relative velocity. Moreover, the  $P(\theta_r)$  peak position in  $\text{H} + \text{OF} \rightarrow \text{HF} + \text{O}$  is much higher than in  $\text{H} + \text{OF} \rightarrow \text{OH} + \text{F}$ , and the  $P(\theta_r)$  distribution in the latter is much broader than the former. As a result, we can say that of the two product channels, there is much stronger product alignment perpendicular to  $k$  in  $\text{H} + \text{OF} \rightarrow \text{HF} + \text{O}$ .

The distribution of  $P(\varphi_r)$  reflected the  $k - k' - j'$  correla-

tion of the products. Figure 4 plotted the  $P(\varphi_r)$  distributions for  $\text{H} + \text{OF} \rightarrow \text{OH} + \text{F}$  and  $\text{H} + \text{OF} \rightarrow \text{HF} + \text{O}$ , respectively. The  $P(\varphi_r)$  distribution can reflect the alignment and orientation of the product rotational angular momentum  $j'$ . In contrast to the distribution of  $P(\theta_r)$ , this kind of distribution is asymmetric with respect to  $\varphi_r = 180^\circ$ . Clearly, in  $\text{H} + \text{OF} \rightarrow \text{OH} + \text{F}$ ,  $P(\varphi_r)$  peaked around  $90^\circ$  and at  $270^\circ$ , reflecting that the  $\text{OH}$  product tends to align along the  $y$  axis or along the direction perpendicular to the scattering  $k - k'$  plane. In addition, the fact that the value of  $P(\varphi_r)$  around  $90^\circ$  is larger than that at  $270^\circ$  has also demonstrated that the orientation of  $j'$  of the product  $\text{OH}$  tends to point to the positive direction of the  $y$  axis. While in  $\text{H} + \text{OF} \rightarrow \text{HF} + \text{O}$ , we see that the corresponding  $P(\varphi_r)$  distribution exhibits rather isotropic behavior with lots of oscillations. This means that as compared with  $\text{OH} + \text{F}$ , the  $k - k' - j'$  correlation is not very remarkable for the  $\text{HF} + \text{O}$  products. The rather isotropic feature of the  $P(\varphi_r)$  distribution observed in the reaction  $\text{H} + \text{FO} \rightarrow \text{HF} + \text{O}$  has nonetheless suggested that, at such a low collision energy, the  $\text{HF} + \text{O}$  products have very weak or almost no polarization (alignment and orientation) behaviors that are indicated by the  $P(\varphi_r)$  distribution. It is notable here that although the  $\text{HF} + \text{O}$  product channel lacked the obvious product alignment along the direction perpendicular to the scattering  $k - k'$  plane as informed by the  $P(\varphi_r)$  distribution, it does illustrate stronger product alignment that is perpendicular to the reagent relative velocity  $k$  as indicated by the  $P(\theta_r)$  distribution in Fig. 3.

The  $P(\theta_r, \varphi_r)$  distribution further supported the above-observed polarization behaviors of both products. Figure 5 plotted the  $P(\theta_r, \varphi_r)$  distribution averaged over all scattering angles for  $\text{H} + \text{OF} \rightarrow \text{HF} + \text{O}$  and  $\text{H} + \text{OF} \rightarrow \text{HO} + \text{F}$ . We can see that the distributions of  $P(\theta_r, \varphi_r)$  are consistent with the distributions of  $P(\theta_r)$  and  $P(\varphi_r)$  in Figs. 3 and 4. Again, these distributions indicated a rather stronger product polarization in  $\text{OH} + \text{F}$  than  $\text{HF} + \text{O}$ , as described by the  $P(\varphi_r)$  distribution. This polar plot also supported a stronger product alignment in  $\text{HF} + \text{O}$  than  $\text{OH} + \text{F}$ , as indicated by the  $P(\theta_r)$  distribution.

## Conclusions

By running a batch of 250 000 trajectories on the excited  $1^3\text{A}'$  electronic state, this paper presented a stereodynamical picture for the title reaction at a low collision energy of 0.48 eV. The calculated PDDCS results revealed that the products in  $\text{H} + \text{OF} \rightarrow \text{OH} + \text{F}$  and  $\text{H} + \text{OF} \rightarrow \text{HF} + \text{O}$  are both backward scattering, with much stronger backward scattering being found in the  $\text{HF} + \text{O}$  product channel. Both channels show the product alignment along the direction perpendicular to the reagent relative velocity  $k$ , and such product alignment is found to be more pronounced in the  $\text{HF} + \text{O}$  product channel. With respect to the  $P(\varphi_r)$  distribution, however, the  $\text{OH} + \text{F}$  product channel is found to have much stronger polarizations, and the product tends to align along the direction perpendicular to the scattering  $k - k'$  plane and orient to the positive direction of the  $y$  axis. Such polarization behaviors are absent in the  $\text{HF} + \text{O}$  product channel. The stereodynamics information is further validated with the calculated results of the  $P(\theta_r, \varphi_r)$  distribution.

## Acknowledgements

This work is supported by the National Natural Science Foundation of China (NSFC) (10874096) and Qingdao University Foundation (QDUF) (063–06300510). The authors thank Professor Keli Han for providing the benchmark stereodynamics code to do the present calculation.

## References

- (1) Gómez-Carrasco, S.; González-Sánchez, L.; Aguado, A.; Paniagua, M.; Roncero, O.; Hernández, M. L.; Alvarino, J. M. *Chem. Phys. Lett.* **2004**, *383* (1-2), 25. doi:10.1016/j.cplett.2003.10.142.
- (2) Gómez-Carrasco, S.; Roncero, O.; González-Sánchez, L.; Hernández, M. L.; Alvarino, J. M.; Paniagua, M.; Aguado, A. *J. Chem. Phys.* **2005**, *123* (11), 114310. doi:10.1063/1.2046669.
- (3) Chu, T. S.; Zhang, H.; Yuan, S. P.; Fu, A. P.; Si, H. Z.; Tian, F. H.; Duan, Y. B. *J. Phys. Chem. A* **2009**, *113* (15), 3470. doi:10.1021/jp9003505. PMID:19317412.
- (4) Zhao, J.; Xu, Y.; Yue, D. G.; Meng, Q. T. *Chem. Phys. Lett.* **2009**, *471* (1-3), 160. doi:10.1016/j.cplett.2009.02.007.
- (5) Meng, Q. T.; Zhao, J.; Xu, Y.; Yue, D. *Chem. Phys.* **2009**, *362* (1-2), 65. doi:10.1016/j.chemphys.2009.06.009.
- (6) Gómez-Carrasco, S.; Aguado, A.; Paniagua, M.; Roncero, O. *J. Chem. Phys.* **2006**, *125* (16), 164321. doi:10.1063/1.2363988. PMID:17092087.
- (7) Han, K. L.; Zheng, X. G.; Sun, B. F.; He, G. Z.; Zhang, R. Q. *Chem. Phys. Lett.* **1991**, *181* (5), 474. doi:10.1016/0009-2614(91)90383-K.
- (8) Han, K. L.; He, G. Z.; Lou, N. Q. *J. Chem. Phys.* **1996**, *105* (19), 8699. doi:10.1063/1.472651.
- (9) Wang, M. L.; Han, K. L.; Zhan, J. P.; Wu, V. W. K.; He, G. Z.; Lou, N. Q. *Chem. Phys. Lett.* **1997**, *278* (4-6), 307. doi:10.1016/S0009-2614(97)01063-4.
- (10) Wang, M. L.; Han, K. L.; He, G. Z. *J. Phys. Chem. A* **1998**, *102* (50), 10204. doi:10.1021/jp981738u.
- (11) Wang, M. L.; Han, K. L.; He, G. Z. *J. Chem. Phys.* **1998**, *109* (13), 5446. doi:10.1063/1.476522.
- (12) Han, K. L.; Zhang, L.; Xu, D. L.; He, G. Z.; Lou, N. Q. *J. Phys. Chem. A* **2001**, *105* (13), 2956. doi:10.1021/jp002181x.
- (13) Zhan, J. P.; Yang, H. P.; Han, K. L.; Deng, W. Q.; He, G. Z.; Lou, N. Q. *J. Phys. Chem. A* **1997**, *101* (41), 7486. doi:10.1021/jp970535n.
- (14) Zhang, L.; Chen, M. D.; Wang, M. L.; Han, K. L. *J. Chem. Phys.* **2000**, *112* (8), 3710. doi:10.1063/1.480523.
- (15) Ju, L. P.; Han, K. L.; Zhang, J. Z. H. *J. Comput. Chem.* **2009**, *30* (2), 305. doi:10.1002/jcc.21032. PMID:18615407.
- (16) Li, R. J.; Han, K. L.; Li, F. E.; Lu, R. C.; He, G. Z.; Lou, N. Q. *Chem. Phys. Lett.* **1994**, *220* (3-5), 281. doi:10.1016/0009-2614(94)00174-X.
- (17) Zhang, X.; Han, K. L. *Int. J. Quantum Chem.* **2006**, *106* (8), 1815. doi:10.1002/qua.20929.
- (18) Wang, M. L.; Han, K. L.; Cong, S. L.; He, G. Z.; Lou, N. Q. *Chem. Phys.* **1998**, *238* (3), 481. doi:10.1016/S0301-0104(98)00326-7.
- (19) Han, K. L. *Phys. Rev. A* **1997**, *56* (6), 4992. doi:10.1103/PhysRevA.56.4992.
- (20) Case, D. A.; Herschbach, D. R. *Mol. Phys.* **1975**, *30* (5), 1537. doi:10.1080/00268977500103061.
- (21) Shafer-Ray, N. E.; Orr-Ewing, A. J.; Zare, R. N. *J. Phys. Chem.* **1995**, *99* (19), 7591. doi:10.1021/j100019a045.
- (22) Brouard, M.; Lambert, H. M.; Rayner, S. P.; Simons, J. P. *Mol. Phys.* **1996**, *89*, 403.
- (23) Aoiz, F. J.; Brouard, M.; Enriquez, P. A. *J. Chem. Phys.* **1996**, *105* (12), 4964. doi:10.1063/1.472346.
- (24) de Miranda, M. P.; Clary, D. C. *J. Chem. Phys.* **1997**, *106* (11), 4509. doi:10.1063/1.473483.
- (25) Aoiz, F. J.; Martínez, M. T.; Sáez Rábanos, V. *J. Chem. Phys.* **2001**, *114* (20), 8880. doi:10.1063/1.1350916.



# Direct ultrasound-assisted methylation of fatty acids in serum for free fatty acid determinations

Liyan Liu, Ying Li, Rennan Feng, and Changhao Sun

**Abstract:** A method for simultaneous determination of 16 free fatty acids (FFAs) in serum is described. The method involves conversion of FFAs to fatty acid methyl esters (FAMES) using the heat of ultrasonic waves followed by gas chromatography and mass spectrometry (GC–MS) analysis. Optimum levels of the variables affecting the yield of FAMES were investigated. The results indicate that the optimal levels are 55 °C, 60 W, 10% H<sub>2</sub>SO<sub>4</sub>/CH<sub>3</sub>OH, and 50 min. Recoveries ranged from 85.32% to 112.11%, with a detection limit ranging from 0.03 to 0.08 µg mL<sup>-1</sup>. The linearity, using the linear correlation coefficient, was higher than 0.9914.

**Key words:** ultrasound-assisted methylation, fatty acid, gas chromatography and mass spectrometry (GC–MS), serum.

**Résumé :** On décrit une méthode de détermination simultanée de seize acides gras libres (AGL) dans le sérum. La méthode implique la conversion de ces acides gras en esters méthyliques d'acides gras (EMAG) par un chauffage à l'aide d'ondes ultrasoniques, suivi d'une analyse par spectrométrie de masse couplée à une chromatographie gazeuse (SM–CG). On a étudié les niveaux optimum des variables affectant le rendement en esters méthyliques (EMAG). Les résultats indiquent que le niveau optimal est de 55 °C, 60 W, 10 % de H<sub>2</sub>SO<sub>4</sub> dans le méthanol et 50 min. Les taux de récupération varient de 85,32 % à 112,11 %, avec des limites de détection allant de 0,03 à 0,08 µg mL<sup>-1</sup>. La linéarité en fonction du coefficient de corrélation est supérieure à 0,9914.

**Mots-clés :** méthylation assistée par des ultrasons, acide gras, spectrométrie de masse couplée à une chromatographie gazeuse, sérum.

## Introduction

Free fatty acids (FFAs) are one kind of active molecule in the body. They not only play an important role in energy generation and storage, but also act as a critical role in cell, tissue, and organ physiology.<sup>1–3</sup> For example, long-chain fatty acids contribute to the synthesis of phospholipids, molecules necessary for the structure, integrity, and function of plasma membranes, and are precursors for prostaglandins. The n-3 polyunsaturated fatty acids (PUFA), specifically docosahexaenoic acid (22:6n-3, DHA) and eicosapentaenoic acid (20:5n-3, EPA), have beneficial impact on mitochondrial biogenesis, intrinsic antioxidant enzyme expression, and efficiency in oxygen consumption.<sup>4</sup> Some studies have shown that free fatty acids in serum were closely related to many diseases, such as diabetes and cardiovascular disease; they are biomarkers of identifying these diseases and health controls.<sup>5,6</sup> It has been proposed that FFAs measures in serum could be developed into a risk factor for diabetes and cardiovascular disease. Large-scale clinical intervention and population-based studies are needed to support the use of serum measures of FFAs as a risk factor for diabetes and cardiovascular disease.

At present, the common analyses for fatty acids include the enzyme method, spectrophotometry, high performance liquid chromatography (HPLC),<sup>7–9</sup> and gas chromatography (GC).<sup>10–12</sup> Enzyme methods, which are simple and fast, are

widely used in the clinic for the analysis of FFAs, but this method can only obtain the total free fatty acids level, leading to the unknown concentration of each fatty acid.

These disadvantages are avoided by gas chromatography (GC). Present-day GC methods using high quality capillary columns allow sensitive and reproducible fatty acid analysis. When coupled with mass spectrometry (MS), this technique has shown more powerful abilities in fatty acids profiling analysis.<sup>13</sup>

Although GC is the technique most widely used in the determination of fatty acids, they must be converted to convenient volatile derivatives previous to their analysis. There are many derivatization agents for GC, such as trimethylsilyl derivatives, diazomethane, and sulfuric acid–methanol. Trimethylsilyl derivatives are less used for determining the long fatty acids (from 12 to 24 carbon atoms).<sup>14</sup> Reactions of diazomethane in a plasma–methanol medium should not only lead to a higher pH due to the consumption of acids<sup>15</sup> but also by reaction with negative ions like chloride.<sup>16</sup> However, the sulfuric acid – methanol reagent preparing fatty acids methyl esters (FAMES) performed well in terms of cost, speed, safety, and GC response, which is the most suitable for determination of fatty acids in serum.<sup>17,18</sup> Therefore, the conventional methylation of free fatty acids in serum was performed with the batch heat method using sulfuric acid – methanol reagent.

Received 18 January 2010. Accepted 25 May 2010. Published on the NRC Research Press Web site at canjchem.nrc.ca on 30 July 2010.

**L. Liu, Y. Li, R. Feng, and C. Sun.**<sup>1</sup> Department of Nutrition and Food Hygiene, Public Health College, Harbin Medical University, 157 Baojian Road, Nangang District, Harbin 150086, P. R. China.

<sup>1</sup>Corresponding author (e-mail: Sun2002changhao@yahoo.com).

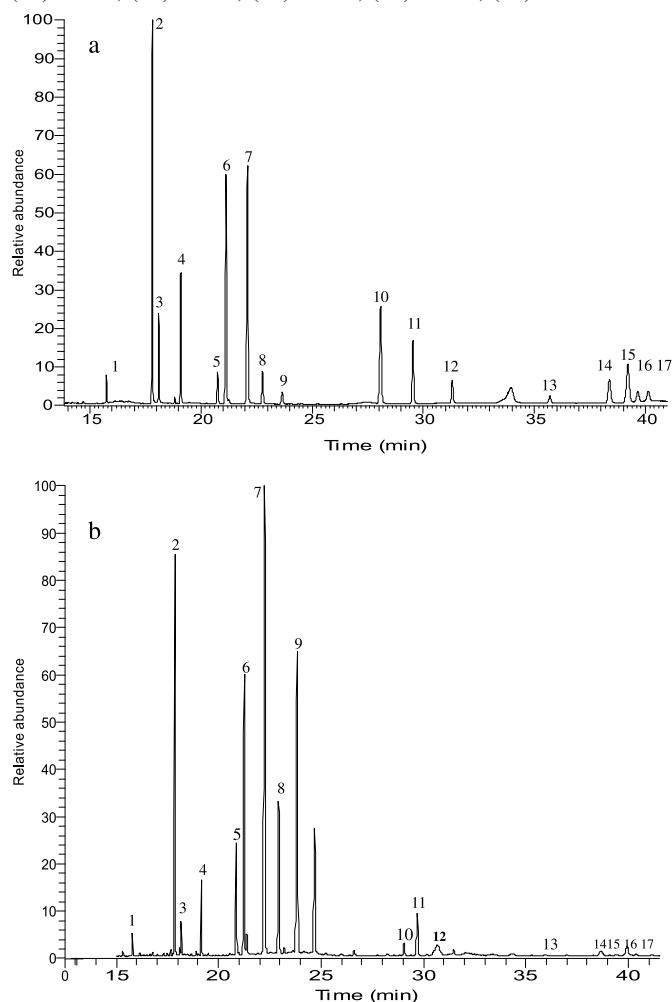


**Table 1.** Intraday and interday instrument assays of C18:0 methyl ester ( $n = 6$ ).

The true concentration	Intraday ( $n = 6$ )			Interday ( $n = 6$ )		
	Measured concentration	CV%	Bias%	Measured concentration	CV%	Bias%
<b>C18:0 methyl ester</b>						
15.00	15.36 $\pm$ 1.07	6.97	102.4	16.78 $\pm$ 1.27	7.57	111.8
150.00	142.38 $\pm$ 8.29	5.82	94.9	139.87 $\pm$ 12.26	8.77	93.2
1500.00	1534.67 $\pm$ 102.08	6.65	102.3	1540.57 $\pm$ 145.08	9.42	102.7

**Note:** Values shown are mean  $\pm$  standard deviation (SD) for FAME concentration ( $\mu\text{g mL}^{-1}$ ).

**Fig. 1.** Total-ion chromatogram of a mixture of 17 fatty acid methyl esters with the (a) standard and (b) serum sample. (1) C14:0, (2) C16:0, (3) C16:1, (4) C17:0, (5) C18:0, (6) C18:1, (7) C18:2, (8)  $\gamma$ -C18:3, (9) C18:3, (10) C20:2, (11) C20:4, (12) C20:5, (13) C22:4, (14) C22:5, (15) C22:6, (16) C24:0, (17) C24:1.



The conventional method is a multistep process that requires highly trained manual labor. Although it has also been demonstrated that FAMES can be prepared by direct methylation without prior extraction,<sup>19</sup> the preparation of FAMES remains time consuming with conventional methylation, often requiring 2 h with convectional heat to catalyze the reaction.<sup>20</sup> However, ultrasonic mixing had a significant effect on fatty acids transesterification. Ultrasound-assisted transesterification reactions of fatty acids showed higher (faster) transesterification rates without changing the charac-

teristics of the reaction. The method has been studied for many vegetable oils and biodiesel,<sup>21,22</sup> but this technique has not been widely applied for the determination of fatty acids in serum or tested exhaustively. The yield of FAMES in the process of methylation is affected by several process parameters and variables. The most important variables affecting the yield of FAMES from methylation are the reaction time, ultrasound power level, concentration of the catalyst, and reaction temperature. Therefore, it is necessary to systematically investigate which factors influence methylation and establish an efficient analytical method of free fatty acids in serum.

In the present study, we describe a simple and stable method to methylate free fatty acids with the help of ultrasonic waves. To achieve the optimum reaction conditions, parameters affecting the yield of FAMES, such as the reaction time, power of ultrasonic waves, concentration of the catalyst (sulfuric acid), and reaction temperature, were investigated by using the ultrasound-assisted methylation method. Moreover, the use of ultrasound-assisted methylation was compared to the traditional use of convectional heat for the preparation of FAMES. Gas chromatography and mass spectrometry (GC-MS) were used to isolate and identify the detected fatty acids and the method was applied to establish stable fatty acid metabolic profiles of type 2 diabetic patients (T2DM) and health controls.

## Experimental section

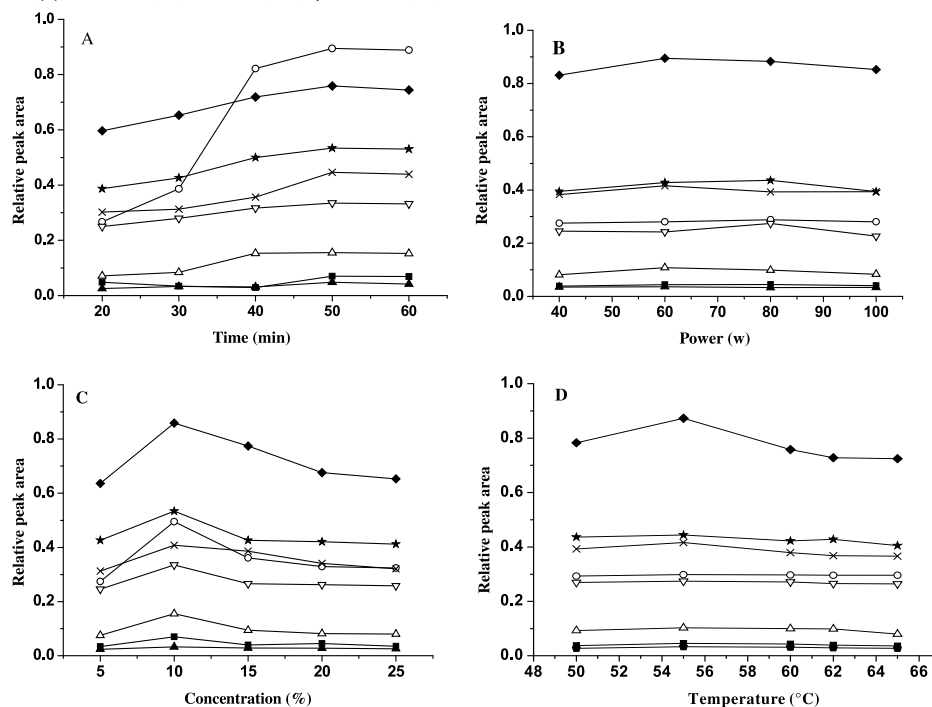
### Chemicals and reagents

Fatty acid standards were purchased from Sigma-Aldrich (St Louis, MO, USA,  $\geq 99\%$  purity): myristic acid (C14:0), palmitic acid (C16:0), palmitoleic acid (C16:1n-7), heptadecanoic acid (C17:0), stearic acid (C18:0), oleic acid (C18:1n-9), linoleic acid (C18:2n-6), linolenic acid (C18:3n-3),  $\gamma$ -linolenic acid (C18:3n-6), *cis*-11,14-eicosadienoic acid (C20:2n-6), arachidonic acid (C20:4n-6), *cis*-5,8,11,14,17-eicosapentaenoic acid (C20:5n-3), *cis*-7,10,13,16,19-docosapentaenoic acid (C22:5n-6), *cis*-4,7,10,13,16,19-docosahexaenoic acid (C22:6n-3), tetracosanoic acid (C24:0), and selacholeic acid (C24:1n-9). The solution of 10%  $\text{H}_2\text{SO}_4/\text{CH}_3\text{OH}$  was freshly prepared with diluting  $\text{H}_2\text{SO}_4$  (purity  $\geq 98.0\%$ ) in chromatographic grade methanol. *n*-Hexane (chromatographic grade), ethyl acetate (analytical reagent), and sodium chloride (analytical reagent) were purchased from Tianjin Guangfu Chemical Reagent Co. (Tianjin, China).

### Preparation of standard solutions and quality-control samples

Stock solutions of the 16 FAs and an internal standard

**Fig. 2.** Effects of the parameters on the results of transesterification: (A) reaction time, (B) power, (C) the concentration of catalyst, and (D) reaction temperature. The relative peak area is the peak area of the fatty acid/peak area of the internal standard. (■) C14:0, (○) C16:0, (△) C16:1, (▽) C18:0, (★) C18:1, (×) C18:2, (◆)  $\gamma$ -C18:3, (▲) C18:3.



**Table 2.** Linear calibration of 16 fatty acids.

Fatty acid	Calibration equation <sup>a</sup>	Linearity <sup>b</sup>	Calibration range ( $\mu\text{g mL}^{-1}$ )	Detection limit ( $\mu\text{g mL}^{-1}$ )
C14:0	$y = 0.0238x + 0.0532$	0.9962	2.97 ~ 14.85	0.05
C16:0	$y = 0.0159x + 0.8506$	0.9978	200.00 ~ 600.00	0.03
C16:1	$y = 0.0576x - 0.2029$	0.9998	20.25 ~ 59.85	0.08
C18:0	$y = 0.0107x + 0.233$	0.9974	50.50 ~ 400.00	0.03
C18:1	$y = 0.019x + 0.9099$	0.9991	300.00 ~ 800.00	0.04
C18:2	$y = 0.0234x + 0.3494$	0.9998	300.00 ~ 800.00	0.05
$\gamma$ -C18:3	$y = 0.0458x - 0.0249$	0.9972	5.25 ~ 25.00	0.08
C18:3	$y = 0.0232x + 0.0615$	0.9914	3.40 ~ 25.00	0.08
C20:2	$y = 0.0197x + 0.0038$	0.9972	5.10 ~ 25.00	0.08
C20:4	$y = 0.024x - 0.005$	0.9990	50.00 ~ 250.00	0.05
C20:5	$y = 0.1727x - 0.0759$	0.9961	1.25 ~ 15.50	0.05
C22:4	$y = 0.017x - 0.0064$	0.9998	1.00 ~ 20.00	0.03
C22:5	$y = 0.0146x + 0.0182$	0.9941	5.00 ~ 50.00	0.06
C22:6	$y = 0.0085x + 0.0202$	0.9987	20.00 ~ 100.00	0.07
C24:0	$y = 0.0084x + 0.034$	0.9964	20.00 ~ 60.00	0.08
C24:1	$y = 0.0416x - 0.0124$	0.9964	2.30 ~ 15.00	0.05

<sup>a</sup> $x$  is the quality of fatty acids and  $y$  is the relative peak area, which is the peak area of the fatty acid/peak area of the internal standard C17:0.

<sup>b</sup>Linearity is described using the linear correlation coefficients of calibration curves.

(heptadecanoic acid) were prepared at  $1000 \mu\text{g mL}^{-1}$  in methanol. Working solutions were prepared with methanol at concentrations of  $1.25\text{--}800.00 \mu\text{g mL}^{-1}$ . All standard solutions were stored at  $-20^\circ\text{C}$  until required.

To evaluate the recovery of the method, quality-control (QC) samples of FFAs studied came from two fasting male subjects, 28 years of age, for initial quantitative analysis.

#### The choice of the optimal methylated condition

An ultrasonic processor (KQ-250B, Kunshan Ultrasonic In-

strument Co., Kunshan, China) was used to perform the methylation reaction. The processor operated at 25 kHz frequency. The power and the temperature for the reaction were adjustable from 40 to 100 W and from 25 to  $100^\circ\text{C}$ . A series of 200  $\mu\text{L}$  aliquots of serum, which came from one healthy person, were spiked with internal standard (I.S.) working solution (200  $\mu\text{L}$  heptadecanoic acid,  $\text{C17:0}$ ,  $200 \mu\text{g mL}^{-1}$ ) and transferred to the reaction chamber to be subjected to ultrasound waves. Then the solution of  $\text{H}_2\text{SO}_4/\text{CH}_3\text{OH}$  (2 mL) was added to the chamber. The reaction

**Table 3.** Intraday and interday assays of serum spiked with known amounts of fatty acids.

Fatty acids	Background value ( $\mu\text{g mL}^{-1}$ )	Intraday ( $n = 3$ )				Interday ( $n = 3$ )			
		Added ( $\mu\text{g mL}^{-1}$ )	Found ( $\mu\text{g mL}^{-1}$ )	CV%	Bias%	Added ( $\mu\text{g mL}^{-1}$ )	Found ( $\mu\text{g mL}^{-1}$ )	CV%	Bias%
C14:0	3.02	2.00	4.73 $\pm$ 0.47	9.94	85.52	2.15	5.43 $\pm$ 0.57	10.50	112.11
	3.02	3.00	5.99 $\pm$ 0.58	9.68	98.90	3.25	6.04 $\pm$ 0.47	7.86	92.79
	3.02	5.00	7.93 $\pm$ 0.41	5.17	98.31	5.00	8.53 $\pm$ 0.69	8.09	110.27
C16:0	222.54	200.00	440.39 $\pm$ 45.06	10.23	108.94	200.00	420.17 $\pm$ 24.91	5.93	98.82
	222.54	300.00	542.51 $\pm$ 38.84	7.16	106.73	300.00	539.15 $\pm$ 40.60	7.53	105.54
	222.54	400.00	658.00 $\pm$ 23.62	3.59	108.90	400.00	649.28 $\pm$ 43.69	6.73	106.69
C16:1	22.77	20.00	43.79 $\pm$ 1.85	4.23	105.16	20.00	44.08 $\pm$ 2.86	6.49	106.55
	22.77	30.00	52.10 $\pm$ 5.21	10.00	97.82	30.00	51.99 $\pm$ 1.64	3.15	97.41
	22.77	40.00	64.37 $\pm$ 3.80	5.91	104.03	40.00	63.59 $\pm$ 4.76	7.49	102.05
C18:0	231.74	250.00	472.89 $\pm$ 20.00	4.23	96.57	250.00	485.36 $\pm$ 38.35	7.90	101.45
	231.74	350.00	543.24 $\pm$ 41.01	7.55	89.08	350.00	546.87 $\pm$ 31.29	5.72	90.04
	231.74	450.00	674.93 $\pm$ 19.10	2.83	98.57	450.00	701.48 $\pm$ 52.85	7.53	104.39
C18:1	206.38	150.00	364.06 $\pm$ 21.34	5.86	105.14	150.00	370.16 $\pm$ 21.32	5.76	109.19
	206.38	250.00	453.55 $\pm$ 17.37	3.83	98.98	250.00	450.21 $\pm$ 37.24	8.27	97.53
	206.38	350.00	540.01 $\pm$ 28.94	5.36	95.36	350.00	526.47 $\pm$ 28.22	5.36	91.45
C18:2	448.52	500.00	955.92 $\pm$ 59.36	6.21	101.48	500.00	1001.16 $\pm$ 62.17	6.21	110.53
	448.52	600.00	1040.19 $\pm$ 73.75	7.09	98.61	600.00	1020.34 $\pm$ 72.34	7.09	95.30
	448.52	700.00	1140.92 $\pm$ 95.50	8.37	98.91	700.00	1069.21 $\pm$ 89.49	8.37	88.67
$\gamma$ -C18:3	10.61	5.00	15.05 $\pm$ 1.24	8.24	88.73	5.00	14.93 $\pm$ 1.15	7.70	86.40
	10.61	10.00	19.14 $\pm$ 0.66	3.47	85.32	10.00	21.34 $\pm$ 2.01	9.42	86.40
	10.61	15.00	24.63 $\pm$ 0.53	2.16	93.47	15.00	26.87 $\pm$ 2.58	9.60	107.32
C18:3	7.33	5.00	12.32 $\pm$ 1.08	8.77	99.78	5.00	11.65 $\pm$ 1.04	8.93	108.40
	7.33	10.00	18.01 $\pm$ 1.17	6.51	106.89	10.00	18.01 $\pm$ 1.17	6.51	86.40
	7.33	15.00	22.63 $\pm$ 1.84	8.14	102.01	15.00	21.46 $\pm$ 1.75	8.14	106.89
C20:2	10.23	10.00	19.85 $\pm$ 1.87	9.42	96.21	10.00	20.15 $\pm$ 1.56	7.74	99.23
	10.23	20.00	29.15 $\pm$ 2.57	8.82	94.64	20.00	31.23 $\pm$ 2.45	7.85	105.04
	10.23	30.00	41.23 $\pm$ 3.45	8.37	103.32	30.00	40.87 $\pm$ 2.91	7.12	102.14
C20:4	91.34	50.00	140.56 $\pm$ 7.12	5.07	98.41	50.00	138.23 $\pm$ 12.14	8.78	93.83
	91.34	100.00	189.12 $\pm$ 5.03	2.66	97.87	100.00	190.15 $\pm$ 7.36	3.87	98.84
	91.34	150.00	243.02 $\pm$ 4.25	1.75	101.14	150.00	236.42 $\pm$ 10.27	4.34	96.72
C20:5	4.43	3.00	7.05 $\pm$ 0.59	8.37	87.36	3.00	7.18 $\pm$ 0.56	7.80	91.74
	4.43	5.00	9.02 $\pm$ 0.78	8.65	91.81	5.00	9.69 $\pm$ 0.64	6.60	105.21
	4.43	8.00	11.98 $\pm$ 1.08	9.02	94.47	8.00	12.08 $\pm$ 0.95	7.86	95.61
C22:4	9.16	5.00	14.56 $\pm$ 1.28	8.79	108.08	5.00	14.12 $\pm$ 1.26	8.92	99.24
	9.16	10.00	19.89 $\pm$ 1.37	6.89	107.34	10.00	18.67 $\pm$ 1.14	6.11	95.16
	9.16	15.00	24.79 $\pm$ 2.14	8.63	104.24	15.00	25.08 $\pm$ 1.39	5.54	106.17
C22:5	12.21	10.00	21.45 $\pm$ 1.95	9.09	92.43	10.00	21.87 $\pm$ 1.63	7.45	96.61
	12.21	15.00	27.89 $\pm$ 2.57	9.21	104.62	15.00	28.09 $\pm$ 1.57	5.59	105.90
	12.21	20.00	32.67 $\pm$ 2.65	8.11	102.34	20.00	33.17 $\pm$ 2.04	6.15	104.84
C22:6	27.97	20.00	48.25 $\pm$ 3.17	6.57	101.43	20.00	47.95 $\pm$ 2.59	5.40	99.91
	27.97	30.00	58.26 $\pm$ 5.24	8.99	101.04	30.00	59.37 $\pm$ 3.82	6.43	104.76
	27.97	40.00	69.01 $\pm$ 4.19	6.07	102.60	40.00	70.12 $\pm$ 4.23	6.03	105.44
C24:0	21.41	10.00	30.89 $\pm$ 2.54	8.22	94.84	10.00	31.04 $\pm$ 1.57	5.06	96.37
	21.41	20.00	40.68 $\pm$ 3.71	9.12	96.32	20.00	39.95 $\pm$ 2.18	5.46	92.71
	21.41	30.00	52.09 $\pm$ 2.99	5.74	102.37	30.00	51.78 $\pm$ 2.14	4.13	101.20
C24:1	4.15	3.00	6.98 $\pm$ 0.58	8.31	94.34	3.00	7.25 $\pm$ 0.61	8.41	103.38
	4.15	5.00	8.99 $\pm$ 0.69	7.68	96.86	5.00	9.01 $\pm$ 0.58	6.44	97.24
	4.15	8.00	12.98 $\pm$ 1.07	8.24	110.42	8.00	11.97 $\pm$ 0.91	7.60	97.80

time, ultrasound power level, concentration of catalyst, and reaction temperature were the influencing parameters. At the same time, the effects of these parameters on the methylation yield were investigated and observed: (i) with 20, 30, 40, 50, and 60 min of reaction duration under the condition of 10%  $\text{H}_2\text{SO}_4$  catalysts, 80 W, and 62 °C; (ii) with 40, 60,

80, and 100 W of power under the condition of 10%  $\text{H}_2\text{SO}_4$  catalysts, 50 min, and 62 °C; (iii) with 5%, 10%, 15%, 20%, and 25%  $\text{H}_2\text{SO}_4$  catalysts under the condition of 50 min, 60 W, and 62 °C; (iv) at 50, 55, 60, 62, and 65 °C reaction temperatures under the condition of 10%  $\text{H}_2\text{SO}_4$  catalysts, 50 min, and 60 W. After completion of the reaction, the sol-

**Table 4.** Quantitative determinations after methylation of serum using convectional heat and direct ultrasonic wave heat.

Fatty acids ( $\mu\text{g mL}^{-1}$ )	Convectional ( $n = 6$ )	Convectional CV%	Ultrasonic wave ( $n = 6$ )	Ultrasonic wave CV%	$p$
C14:0	3.31 $\pm$ 0.08	2.42	3.30 $\pm$ 0.35	10.60	0.967
C16:0	306.69 $\pm$ 5.79	19.16	313.61 $\pm$ 13.79	4.39	0.431
C16:1	28.11 $\pm$ 1.49	5.30	32.31 $\pm$ 4.25	13.15	0.223
C18:0	347.50 $\pm$ 26.15	7.52	379.53 $\pm$ 37.26	9.82	0.686
C18:1	261.83 $\pm$ 7.03	2.68	314.92 $\pm$ 20.76	6.59	0.210
C18:2	608.44 $\pm$ 21.08	3.46	562.26 $\pm$ 33.92	6.03	0.397
$\gamma$ -C18:3	11.03 $\pm$ 0.33	2.99	11.39 $\pm$ 0.66	5.79	0.456
C18:3	10.61 $\pm$ 0.46	4.33	11.70 $\pm$ 1.88	16.07	0.418
C20:2	9.41 $\pm$ 0.33	3.51	9.94 $\pm$ 0.59	5.93	0.265
C20:4	134.34 $\pm$ 8.58	6.38	136.93 $\pm$ 6.05	4.42	0.694
C20:5	6.95 $\pm$ 0.16	2.30	6.61 $\pm$ 0.40	6.05	0.270
C22:4	10.23 $\pm$ 0.57	5.57	9.11 $\pm$ 1.08	11.85	0.208
C22:5	22.63 $\pm$ 1.16	5.12	22.49 $\pm$ 1.16	5.16	0.925
C22:6	28.76 $\pm$ 0.42	1.46	28.91 $\pm$ 1.68	5.81	0.888
C24:0	38.74 $\pm$ 1.78	4.59	37.27 $\pm$ 3.75	1.01	0.584
C24:1	4.68 $\pm$ 0.38	8.11	4.91 $\pm$ 0.80	16.29	0.682

**Table 5.** Quantitative analysis of FFAs of health controls and T2DM patients.

Fatty acid ( $\mu\text{g mL}^{-1}$ )	Health controls ( $n = 31$ )	T2DM patients ( $n = 30$ )	$t$ -test
C14:0	2.92 $\pm$ 0.15	3.30 $\pm$ 0.41	1
C16:0	215.38 $\pm$ 63.67	439.03 $\pm$ 189.29	1
C16:1	29.34 $\pm$ 3.27	34.18 $\pm$ 6.29	1
C18:0	195.37 $\pm$ 65.20	334.77 $\pm$ 143.11	1
C18:1	193.57 $\pm$ 35.84	291.81 $\pm$ 101.60	1
C18:2	718.25 $\pm$ 105.68	947.71 $\pm$ 111.62	1
$\gamma$ -C18:3	5.44 $\pm$ 1.53	7.21 $\pm$ 2.88	1
C18:3	6.34 $\pm$ 2.56	9.76 $\pm$ 3.84	1
C20:2	7.81 $\pm$ 2.84	10.41 $\pm$ 2.88	1
C20:4	141.57 $\pm$ 38.91	218.55 $\pm$ 69.05	1
C20:5	4.05 $\pm$ 1.40	4.65 $\pm$ 1.36	0
C22:4	6.24 $\pm$ 1.89	8.86 $\pm$ 3.51	1
C22:5	7.57 $\pm$ 4.13	13.62 $\pm$ 8.83	1
C22:6	28.65 $\pm$ 0.91	28.80 $\pm$ 0.50	0
C24:0	61.21 $\pm$ 17.87	114.98 $\pm$ 37.56	1
C24:1	2.07 $\pm$ 0.33	2.00 $\pm$ 0.26	0
Total	1625.80 $\pm$ 272.36	2469.64 $\pm$ 524.12	1

**Note:** FFA values of type 2 diabetic patients and health controls were compared using  $t$ -tests. A  $p$  value of  $<0.05$  was considered statistically significant and assigned 1, therefore, 0 indicates statistical insignificance.

ution was treated with saturated sodium chloride and then was extracted with 2 mL of hexane. The product, a mixture of FAMES, was analyzed by GC-MS.

## Sample preparation

### Conventional heat methylation

Each collected fasting blood sample was immediately centrifuged at 3000g for 10 min and the serum was transferred into a clean Eppendorf tube. The serum samples were stored at  $-80^\circ\text{C}$  until analysis. Samples were randomly selected for free fatty acids extract and GC-MS acquisition. Briefly, aliquots (200  $\mu\text{L}$ ) of serum were spiked

with internal standard (IS) working solution (200  $\mu\text{L}$  heptadecanoic acid C17:0, 200  $\mu\text{g mL}^{-1}$ ) and 2 mL 10%  $\text{H}_2\text{SO}_4/\text{CH}_3\text{OH}$  was added, vortex-mixed for 30 s, reacted at  $62^\circ\text{C}$ , and had a water bath for 2 h. This was followed by adding 2 mL of saturated sodium chloride solution, then it was extracted with 2 mL of hexane using a vortex mixer for 60 s, and FAMES were obtained. The samples were evaporated to dryness under  $\text{N}_2$  gas and hexane (100  $\mu\text{L}$ ) was then added prior to analysis.

### Ultrasonic wave methylation

Aliquots (200  $\mu\text{L}$ ) of serum were spiked with IS working solution (200  $\mu\text{L}$  heptadecanoic acid, C17:0, 200  $\mu\text{g mL}^{-1}$ ).  $\text{H}_2\text{SO}_4/\text{CH}_3\text{OH}$  (2 mL) was added to the serum and reacted at the optimal reaction condition. After that, 2 mL of saturated sodium chloride solution were added, then it was extracted with 2 mL of hexane using a vortex mixer for 60 s, and FAMES were obtained. The samples were evaporated to dryness under  $\text{N}_2$  gas and hexane (100  $\mu\text{L}$ ) was then added prior to analysis.

### Gas chromatography and mass spectrometry

GC-MS analysis was performed on a gas chromatograph coupled to an ion trap mass spectrometer (TRACE GC/PolarisQ MS, Thermo Finnigan, USA). Separation was accomplished on a J&W DB-WAX capillary column (30 m  $\times$  0.25 mm I.D, 0.25  $\mu\text{m}$  film thickness). Helium was used as the carrier gas with a flow rate of 1.0  $\text{mL min}^{-1}$ . The temperature of the injector was  $230^\circ\text{C}$ , and the sample (1.0  $\mu\text{L}$ ) was injected, with the split ratio of the injector being 1:10. FAMES were separated at a constant flow with the following oven program: (i)  $50^\circ\text{C}$  for 2 min, (ii) increased at a rate of  $10^\circ\text{C/min}$  up to  $200^\circ\text{C}$ , (iii) held at  $200^\circ\text{C}$  for 10 min, (iv) increased at a rate of  $10^\circ\text{C/min}$  up to  $220^\circ\text{C}$ , and (v) held at  $220^\circ\text{C}$  for 15 min. The transfer line was maintained  $230^\circ\text{C}$ . The ion trap mass spectrometer was operated in electron ionization (EI) mode and full scan monitoring mode ( $m/z$  30–450). The source temperature was at  $230^\circ\text{C}$  and electron energy at 70 eV.



## Method validation

Calibration samples were prepared using serum from healthy human subjects, which were spiked at increasing amounts (2.0–700.0  $\mu\text{g mL}^{-1}$ ) with 16 fatty acid standards. The limit of detection (LOD) was defined as the lowest concentrations with signal-to-noise (S/N) ratios of 10. Precisions and accuracies of QC samples were determined using intraday and interday assays that had three different concentrations including a low, medium, and high point of the calibration range (see Table 1), which were expressed as coefficients of variation (CV%) and percentage biases (bias%), respectively.

## Application to the human serum samples

Human serum samples were collected from 31 healthy adults (the age range was 35–69) and 30 patients with type 2 diabetes mellitus (the age range was 35–71). All type 2 diabetic patients were from the Second Affiliated Hospital of Harbin Medical University of China with a fasting plasma glucose concentration above 7.0  $\text{mmol L}^{-1}$ . The study was approved by the Ethical Committee of the Harbin Medical University and an informed consent was obtained from all subjects.

## Statistical analysis

For quantitative analysis in this study, all of the peaks exceeding a signal-to-noise (S/N) of 10 were selected and the internal standard method was used. Statistical analysis was performed using the statistical package of social sciences (SPSS) 13.0 (SPSS Inc., Chicago, USA). Results are presented as mean  $\pm$  standard deviation (SD). Data that were not normally distributed were logarithmically transformed to obtain near normality before analysis. Statistical evaluations of continuous variables were performed by using *t*-tests. All *p* values are two-tailed and a *p* value of  $<0.05$  was considered statistically significant.

## Results and discussion

### GC–MS analysis

First of all, it is important to find a suitable GC–MS condition to establish a stable quantitative metabolite profile with good separation, since there are tens of fatty acids in human serum. Column selection is one of the focuses in the process of optimizing chromatographic conditions. Because many long chain FAMES with high boiling points will be assayed, the highest analytical temperature was set at 220 °C. DB-WAX, which is a polar capillary column, was chosen because of its longer life than other columns at the high temperature.<sup>19</sup> Furthermore, other chromatographic conditions were modified, such as temperature process, split ratio, and injection temperature. Seventeen fatty acid methyl esters in human serum were baseline isolated within 40 min under those final chromatographic conditions, as depicted in the total-ion chromatogram (Fig. 1).

Analytical accuracy and precision data are shown in Table 1. Intraday and interday accuracy and precision (each  $n = 6$ ) were evaluated by analysis of QC samples (15, 150, and 1500  $\mu\text{g mL}^{-1}$  of C18:0 methyl ester). The range of coefficients of variation was 5.82%~9.42%. The results show

that the developed GC–MS method has good precision and accuracy.

### Effect of the parameters on the results of methylation

In this study, optimum levels of the variables affecting the yield of FAMES are obtained. For comparison, the reaction time was established at 20, 30, 40, 50, and 60 min; the powers of ultrasonic waves were taken at 40, 60, 80, and 100 W; and the reaction temperatures were chosen at 50, 55, 60, 62, and 65 °C. Effects of the concentration of catalyst on the yield of FAMES were investigated for 5, 10, 15, 20, and 25% sulfuric acid levels. The analysis results are given in Fig. 2. The reaction time is important for maximizing the yield of FAMES during the methylation process. Figure 2A shows the effects of the reaction time on the yield of FAMES. It was observed that the yield of methylation gradually increased before 50 min and the yield of most fatty acid methyl esters maximized at 50 min. After 50 min, the yield of methylation was approximately invariable. This indicated that the balance of the reaction was obtained at 50 min. The reaction time was, therefore, chosen to be 50 min.

Figure 2B shows that the ultrasound power influenced the yield of methylation. According to Fig. 2B, it is evident that as the power increased, the FAMES yield increased, reached a maximum, and then kept to similar levels. Higher power tends to decrease yields. This was attributed to cracking, which was followed by oxidation of FAMES to aldehydes, ketones, and lower-chained organic fractions under high-power conditions.<sup>23</sup> Accordingly, for the power less than 60 W, most of the FAMES yields were relatively maximized. The power for the methylation should be maintained at 60 W to obtain maximal yields and save energy.

Sulfuric acid is often used as the catalyst in the methylation and transesterification process for fatty acids.<sup>24,25</sup> The concentration of sulfuric acid is another important factor influencing the FAMES yields. Figure 2C summarized the experimental results of the effect of variations in the catalyst concentrations from 5%–25% on the reaction conversion. Figure 2C shows that as the catalyst concentration increased, the FAMES yields also increased. However, at higher catalyst concentrations (15%–25%), this effect became minimal. The upper limit to the catalyst effectiveness was reached at a much lower catalyst concentration for larger methanol excess levels. A higher catalyst concentration increased the solubility of methyl esters in the methanol phase. As a result, the optimal concentration of catalyst was 10%.

Temperature is one of important factors in a methylation reaction. From Fig. 2D, as the temperature increased, the yield of FAMES increased. However, the maximum value of yield was obtained at 55 °C. When the temperature was higher than 55 °C, the yield of FAMES decreased. As is well-known, the reaction rate is raised with the temperature, but high temperature (60–65 °C) makes methanol volatilize. The results indicate that FAMES decomposed to remedy the decrease of methanol. Therefore, high temperature (60–65 °C) was not in favor of the increase of methylation yield and the optimal reaction temperature was 55 °C.

### Method validation

Method validation was conducted by evaluating the linearity, limit of detection (LOD), precision, and accuracy of

the present method using spiked samples prepared from free fatty acids and human serum. The sample was methylated under the optimum condition. The devised method had excellent linearity (correlation coefficient,  $r$ : 0.9914–0.9998). LODs ranged from 0.03 to 0.08  $\mu\text{g mL}^{-1}$  (Table 2). Accuracies and precisions were determined by analyzing three QC samples at three different concentration levels for the 16 FFAs. Intraday ( $n = 3$ ) precisions ranged from 1.75% to 10.23%, whereas accuracies ranged from 85.32% to 108.94%. Interday ( $n = 3$ ) precisions and accuracies were 3.15%–10.50% and 86.40%–112.11%, respectively (Table 3).

### Comparison between conventional and ultrasonic wave heat

Two methylation methods using convectional heat and ultrasonic wave heat were compared. Under the same concentration of catalyst, a single serum sample was analyzed by both methods. The results demonstrated there were no significant differences in fatty acid compositions (Table 4). The concentration of seven FFAs with direct ultrasonic wave methylation was a little higher than the convectional heat's, but there was no significant difference. Moreover, compared with the conventional method, there was higher precision with the ultrasonic method. This suggested that direct methylation of serum by ultrasonic wave heat was much better than the conventional method to a degree. The reason may be that prior FFA extraction from serum followed by conventional heat methylation resulted in values a little lower than those obtained by methylation mediated by ultrasonic wave heat. Moreover, ultrasonication is able to reveal subtle interactions and particular effects of entropic and enthalpic origin. The cavitation and collapse of the cavitation bubble, where transient hot spots with local extremely harsh conditions occur, are generally accepted as the origin of the chemical effects.<sup>26,27</sup> Another beneficial effect of ultrasonication compared to the corresponding convectional heat reaction is the efficient removal of bubbles from the bulk solution. The presence of bubbles is detrimental to the methylation process as they can attach to the drop, thus minimizing the surface available to extraction and facilitating its dislodgement. Furthermore, it was more troublesome with the convectional heat method than direct ultrasonic wave methylation.

### Analysis of human serum samples

According to the optimum ultrasonic wave method, serum FFAs of type 2 diabetic patients (T2DM) and health controls were detected (shown in Table 5). The kinds of FFA in T2DM patients and health controls were almost the same, while the concentrations were different. Sixteen fatty acids were detected including four saturated fatty acids, three monounsaturated fatty acids, and nine polyunsaturated fatty acids. Serum levels of these FFAs were all increased from health controls to T2DM patients. After adjusting for some confounding factors, including age, sex, alcohol consumption, smoking habits, physical activity, blood pressure, and blood lipids, the differences in free fatty acids concentration between groups were evaluated by analyses of  $t$ -test. The  $t$ -test results showed that there were 13 components having distinct differences between T2DM patients and health con-

trols. Moreover, in the clinic, total free fatty acid levels are a very important index for diagnosis of T2DM. Here, total FFA levels (the sum of the sixteen detected FFAs) were also evaluated. Total FFA levels had distinct differences between T2DM patients and health controls. From the above, there are different free fatty acids profiles among human beings. There could be formation of more biologically potent molecules from the fatty acids. Therefore, it seems that metabolic network research of fatty acids is very important for pathogenesis research of diabetes and it will help with our further study of diabetes.

### Conclusion

Initially, the aim of the study was to search for a method for the determination of free fatty acids (FFAs) in serum using ultrasonic waves. In this study, the optimal reaction conditions were observed. The heat from ultrasonic waves produced high FAME yields at significantly short times in comparison to those using the convectional batch heat method. This method was successfully applied to construct quantitative free fatty acid metabolic profiles in human serum. We suggest that the present method is suitable for the analysis of FFAs in metabolic studies of fatty acids.

### Acknowledgement

This work was supported by the Natural Science Foundation of China (No. 30671756) and China's 11th Five-Year Scientific and Technical Plan (No. 2006BAD27B05).

### References

- (1) Charles, M. A.; Eschwège, E.; Thibault, N.; Claude, J.-R.; Warnet, J.-M.; Rosselin, G. E.; Girard, J.; Balkau, B. *Diabetologia* **1997**, *40* (9), 1101. doi:10.1007/s001250050793. PMID:9300248.
- (2) Bergman, R. N.; Ader, M. *Trends Endocrinol. Metab.* **2000**, *11* (9), 351. doi:10.1016/S1043-2760(00)00323-4. PMID:11042464.
- (3) Wyne, K. L. *Am. J. Med.* **2003**, *115* (8), 29. doi:10.1016/j.amjmed.2003.09.004.
- (4) Leaf, A. K.; Kang, J. X.; Xiao, Y.-F.; Billman, G. E. *Circulation* **2003**, *107* (21), 2646. doi:10.1161/01.CIR.0000069566.78305.33.
- (5) Yang, J.; Xu, G. W.; Hong, Q.; Liebig, H. M.; Lutz, K.; Schmülling, R. M.; Wahl, H. G. *J. Chromatogr. B Analyt. Technol. Biomed. Life Sci.* **2004**, *813* (1–2), 53. doi:10.1016/j.jchromb.2004.09.023. PMID:15556515.
- (6) Zheng, X. T.; Shen, J.; Liu, Q.; Wang, S.; Cheng, Y.; Qu, H. *J. Pharm. Biomed. Anal.* **2009**, *49* (2), 481. doi:10.1016/j.jpba.2008.10.018. PMID:19058943.
- (7) You, J.; Zhao, X.; Suo, Y.; Li, Y.; Wang, H.; Chen, G. *J. Chromatogr. B Analyt. Technol. Biomed. Life Sci.* **2007**, *848* (2), 283. doi:10.1016/j.jchromb.2006.10.025. PMID:17097358.
- (8) Bravi, E.; Perretti, G.; Montanari, L. *J. Chromatogr. A* **2006**, *1134* (1–2), 210. doi:10.1016/j.chroma.2006.09.007. PMID:17007865.
- (9) Hvattum, E.; Uran, S.; Sandbaek, A. G.; Karlsson, A. A.; Skotland, T. *J. Pharm. Biomed. Anal.* **2006**, *42* (4), 506. doi:10.1016/j.jpba.2006.04.027. PMID:16762523.
- (10) Masukawa, Y.; Tsujimura, H.; Imokawa, G. *J. Chromatogr. B Analyt. Technol. Biomed. Life Sci.* **2005**, *823* (2), 131. doi:10.1016/j.jchromb.2005.06.014. PMID:16006202.

- (11) Hajimahmoodi, M.; Vander Heyden, Y.; Sadeghi, N.; Jannat, B.; Oveisi, M. R.; Shahbazian, S. *Talanta* **2005**, *66* (5), 1108. doi:10.1016/j.talanta.2005.01.011. PMID:18970097.
- (12) Patterson, B. W.; Zhao, G. H.; Elias, N.; Hachey, D. L.; Klein, S. *J. Lipid Res.* **1999**, *40* (11), 2118. PMID:10553015.
- (13) Seppänen-Laakso, T.; Laakso, I.; Hiltunen, R. *Anal. Chim. Acta* **2002**, *465* (1–2), 39. doi:10.1016/S0003-2670(02)00397-5.
- (14) Aoyama, T.; Yashiro, T. *J. Chromatogr. A* **1983**, *265*, 57. doi:10.1016/S0021-9673(01)96698-1.
- (15) Schmid, P. C.; Schmid, H. H. O. *Lipids* **1994**, *29* (12), 883. doi:10.1007/BF02536257. PMID:7854015.
- (16) Valenteković, S.; Keglević, D. *Carbohydr. Res.* **1976**, *47* (1), 35. doi:10.1016/S0008-6215(00)83546-6. PMID:1268875.
- (17) Chetty, N.; Naran, N. H.; Walker, A. R. P.; Seftel, H. C.; Joffe, B. I.; Raal, F. J. *Clin. Chim. Acta* **1997**, *258* (1), 31. doi:10.1016/S0009-8981(96)06426-1. PMID:9049441.
- (18) Conquer, J. A.; Martin, J. B.; Tummon, I.; Watson, L.; Tekpetey, F. *Lipids* **1999**, *34* (8), 793. doi:10.1007/s11745-999-0425-1. PMID:10529089.
- (19) Yi, L. Z.; He, J.; Liang, Y. Z.; Yuan, D.; Gao, H.; Zhou, H. *Chem. Phys. Lipids* **2007**, *150* (2), 204. doi:10.1016/j.chemphyslip.2007.08.002. PMID:17880934.
- (20) Xie, M. X.; Liu, J.; Kang, Y.; Li, M.; Guo, M.; Lue, M. *Chinese J. Anal. Chem.* **2001**, *29* (12), 1389.
- (21) Stavarache, C.; Vinatoru, M.; Maeda, Y. *Ultrason. Sonochem.* **2007**, *14* (3), 380. doi:10.1016/j.ultsonch.2006.08.004. PMID:17079181.
- (22) Kalva, A.; Sivasankar, T. S.; Moholkar, V. S. *Ind. Eng. Chem. Res.* **2009**, *48* (1), 534. doi:10.1021/ie800269g.
- (23) Singh, A. K.; Fernando, S. D.; Hernandez, R. *Energy Fuels* **2007**, *21* (2), 1161. doi:10.1021/ef060507g.
- (24) Goff, M. J.; Bauer, N. S.; Lopes, S.; Sutterlin, W. R.; Suppes, G. J. *J. Am. Oil Chem. Soc.* **2004**, *81* (4), 415. doi:10.1007/s11746-004-0915-6.
- (25) Yi, L. Z.; He, J.; Liang, Y. Z.; Yuan, D. L.; Chau, F. T. *FEBS Lett.* **2006**, *580* (30), 6837. doi:10.1016/j.febslet.2006.11.043. PMID:17141227.
- (26) Tuulmets, A.; Salmar, S.; Hagu, H. *J. Phys. Chem. B* **2003**, *107* (46), 12891. doi:10.1021/jp035714l.
- (27) Beckett, M. A.; Hua, I. *J. Phys. Chem. A* **2001**, *105* (15), 3796. doi:10.1021/jp003226x.

# Aqueous sodium hypochlorite mediated chemoselective oxidation of chalcogenides to monoxides and dioxides by microwave exposure

Jitender M. Khurana and Bhaskara Nand

**Abstract:** A solvent-free, rapid, and highly selective oxidation of sulfides, selenides, and tellurides (chalcogenides) to the corresponding monoxides (sulfoxides, selenoxides, and telluroxides) or the corresponding dioxides (sulfones, selenones, and tellurones) has been developed using aqueous sodium hypochlorite on solid supports by exposure to microwave. Chemoselectivity and quantitative yields have been attained in most cases.

**Key words:** chalcogenides, selective oxidation, sodium hypochlorite, microwave, solid support, solvent-free.

**Résumé :** On a mis au point une méthode rapide et n'impliquant aucun solvant pour l'oxydation hautement sélective des sulfures, de séléniures et des tellurures (chalcogénures) en monoxydes correspondants (sulfoxydes, sélénoxydes et telluroxydes) ou en dioxydes correspondants (sulfones, sélénones et tellurénones) à l'aide d'hypochlorite de sodium aqueux sur des supports solides exposés à des microondes. Dans la plupart des cas, on a atteint la chimiosélectivité accompagnée de rendements pratiquement quantitatifs.

**Mots-clés :** chalcogénures, oxydation sélective, hypochlorite de sodium, microonde, support solide, sans solvant.

[Traduit par la Rédaction]

## Introduction

Oxidation of sulfur, selenium, and tellurium compounds has significant importance in organic chemistry, medicinal chemistry, and drug metabolism.<sup>1</sup> Sulfoxides, sulfones, organoselenium, and tellurium compounds are valuable synthons for carbon-carbon bond formation<sup>2</sup> as chiral auxiliaries<sup>3</sup> and for metal-centered catalysis.<sup>4</sup> The chemistry of selenium and tellurium oxides is of particular interest owing to their thermal instability<sup>5</sup> and their ability to stabilize adjacent anionic centers.<sup>6</sup> These transformations have been accomplished in a variety of ways.<sup>7</sup> Many of the reported methods suffer from poor yields, lack of generality, use of expensive reagents/catalysts, complex catalysts, toxic metallic compounds, or rare oxidizing reagents. On the other hand, selective oxidation of chalcogenides to their corresponding monoxides and dioxides with the same reagent system under adjusted reaction conditions is an important process, and only a few reports are available.<sup>8</sup> Diaryl and dialkyl telluroxides and tellurones are not well-explored compounds and have not received significant attention. Recently, microwave-enhanced chemical reactions on inorganic solid supports under solvent-free conditions<sup>9</sup> have attracted attention for various reasons. In view of the importance of these compounds, we decided to investigate the use of inexpensive aq. sodium hypochlorite for the selective oxidation of chalcogenides under microwave irradiation.

## Experimental

All the products were known and were identified by comparison of the spectral and physical data with the literature.<sup>7,8,10</sup> Melting points were recorded on Tropical Labequip apparatus and are uncorrected. IR spectra were recorded on PerkinElmer FTIR spectrum-2000. <sup>1</sup>H NMR spectra were recorded on FTNMR model R-600 Hitachi (60 MHz) with TMS as internal standard. The products were identified by co-TLC, melting point determination (mp), superimposable IR, and NMR spectra with authentic samples. Silica gel (100–200 mesh, for column chromatography) and neutral alumina (S.D. Fine) were used as inorganic solid supports. Sodium hypochlorite was used after estimation by the reported procedure.<sup>11</sup> Sulfides, selenides, and tellurides were prepared by the literature-reported methods.<sup>12–17</sup>

## General procedure

### General procedure for the oxidation of chalcogenides to dioxides

In a typical experiment, diphenyl sulfide (0.2 g, 1.074 mmol) was dissolved in dichloromethane (3 mL) and adsorbed over silica gel (100–200 mesh, 1.2 g). Aqueous sodium hypochlorite (0.65 mol/L, 3 mL) was added and mixed uniformly in a beaker. The reaction mixture was inserted in a silica bath (20 g of silica gel) and placed in a microwave oven (Model No.OM-9925-E, 800 W, 2450 MHz) and irradiated at 100 W

Received 25 January 2010. Accepted 21 April 2010. Published on the NRC Research Press Web site at canjchem.nrc.ca on 4 August 2010.

J.M. Khurana<sup>1</sup> and B. Nand. Department of Chemistry, University of Delhi, Delhi 110007, India.

<sup>1</sup>Corresponding author (e-mail: jmkhurana@chemistry.du.ac.in).



**Table 1.** Oxidation of sulfides, selenides, and tellurides with aq. sodium hypochlorite to dioxides, supported on silica gel, under microwave exposure.

Entry	Substrate	Product	Time (min)	Yield (%)
1	Diphenyl sulfide	Diphenyl sulfone <sup>8,10b,10c,10e</sup>	10	93
2	Dibenzyl sulfide	Dibenzyl sulfone <sup>8,10b,10e</sup>	10	80
3	Di( <i>n</i> -dodecyl) sulfide	Di( <i>n</i> -dodecyl)sulfone <sup>8,10b,10e</sup>	9	82
4	Benzyl phenyl sulfide	Benzyl phenyl sulfone <sup>8,10b,10e</sup>	9	87
5	Phenyl <i>n</i> -propyl sulfide	Phenyl <i>n</i> -propyl sulfone <sup>8,10b,10e</sup>	10	82
6	<i>n</i> -Dodecyl phenyl sulfide	<i>n</i> -Dodecyl phenyl sulfone <sup>8,10b,10e</sup>	10	83
7	<i>p</i> -Chlorophenyl phenyl sulfide	<i>p</i> -Chlorophenyl phenyl sulfone <sup>8,10b,10e</sup>	10	84
8	<i>p</i> -Bromophenyl phenyl sulfide	<i>p</i> -Bromophenyl phenyl sulfone <sup>8,10b,10e</sup>	10	81
9	<i>m</i> -Chlorophenyl phenyl sulfide	<i>m</i> -Chlorophenyl phenyl sulfone <sup>8,10b,10e</sup>	10	80
10	Diphenyl selenide	Diphenyl selenone <sup>7g,10b,10d,10e</sup>	5	91
11	Dibenzyl selenide	Dibenzyl selenone <sup>7g,10b,10d,10e</sup>	6	88
12	Di( <i>p</i> -bromophenyl) selenide	Di( <i>p</i> -bromophenyl) selenone <sup>7g,10b,10d,10e</sup>	6	86
13	Di( <i>p</i> -methylphenyl) selenide	Di( <i>p</i> -methylphenyl) selenone <sup>7g,10b,10d,10e</sup>	6	86
14	Di( <i>p</i> -methoxyphenyl) selenide	Di( <i>p</i> -methoxyphenyl) selenone <sup>7g,10b,10d,10e</sup>	7	89
15	Di( <i>p</i> -methylphenyl) telluride	Di( <i>p</i> -methylphenyl) tellurone <sup>7g,10b,10d,10e</sup>	5	80
16	Di( <i>p</i> -methoxyphenyl) telluride	Di( <i>p</i> -methoxyphenyl) tellurone <sup>7g,10b,10d,10e</sup>	7	79
17	Di( <i>p</i> -bromophenyl) telluride	Di( <i>p</i> -bromophenyl) tellurone <sup>7g,10b,10d,10e</sup>	6	76
18	Methyl phenyl telluride	Methyl phenyl tellurone <sup>7g,10b,10d,10e</sup>	6	77

**Note:** Reactions were carried out using 3 mL of aq. NaOCl (0.65 mol/L) per mmol of substrate.

for 10 min. The progress of the reaction was monitored by TLC using petroleum ether as eluent, which showed complete disappearance of starting material after 10 min and formation of a new product having lower  $R_f$  (eluent: ethyl acetate), which was believed to be diphenyl sulfone by co-TLC. The reaction mixture was cooled to room temperature and the product was extracted with dichloromethane (2 × 5 mL). The combined dichloromethane extract was dried over anhyd.  $\text{Na}_2\text{SO}_4$ , filtered, and concentrated to afford 0.22 g (93%) of pure diphenyl sulfone as white solid identified by its mp 126 °C (lit.<sup>10b</sup> mp 128 °C), superimposable IR, and  $^1\text{H}$  NMR spectra.

#### General procedure for the oxidation of chalcogenides to monoxides

In a typical experiment, diphenyl sulfide (0.2 g, 1.074 mmol) is dissolved in dichloromethane (3 mL) and adsorbed over neutral alumina (1.2 g). Aqueous sodium hypochlorite (1 mL, 0.65 mol/L) was added and mixed thoroughly in a beaker. The reaction mixture was inserted in an alumina bath (20 g of neutral alumina) and placed in a microwave oven (Model No.OM-9925-E, 800 W, 2450 MHz) and irradiated at 100 W for 3 min. After cooling for 1 min, another 1 mL of aq. sodium hypochlorite solution (0.65 mol/L) was added, and the mixture was stirred with a glass rod and irradiated again for 3 min. The progress of the reaction was monitored by TLC using petroleum ether as eluent. TLC showed complete disappearance of the starting material after 6 min and formation of a product having lower  $R_f$  (eluent: ethyl acetate), which was believed to be diphenyl sulfoxide by co-TLC. The reaction mixture was cooled to room temperature and the product was extracted with dichloromethane (2 × 5 mL). The combined dichloromethane extract was dried over anhyd.  $\text{Na}_2\text{SO}_4$ , filtered, and concentrated. The product was purified by column chromatography on silica gel using petroleum ether/ethyl acetate as eluent. The

white solid obtained was identified to be diphenyl sulfoxide (0.18 g, 82%) by mp 70 °C (lit.<sup>10e</sup> mp 71 °C), superimposable IR, and  $^1\text{H}$  NMR spectra. Oxidation of selenides and tellurides was carried out in a similar fashion using 0.36 mol/L aq. NaOCl solution.

## Results and discussion

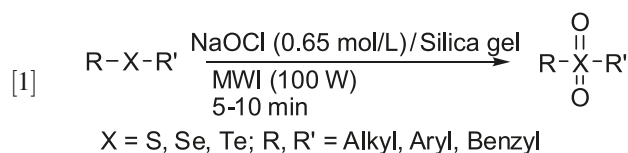
We report herein an efficient, mild, and rapid method for the selective oxidation of chalcogenides (sulfides, selenides, and tellurides) to the corresponding monoxides (sulfoxides, selenoxides, and telluroxides) or the corresponding dioxides (sulfone, selenone, and tellurone) with inexpensive aq. sodium hypochlorite under microwave irradiation. Diphenyl sulfide was chosen as a model substrate for optimization. Oxidation of diphenyl sulfide was attempted with aq. NaOCl (0.65 mol/L) on different inorganic solid supports, e.g., neutral, acidic, and basic alumina; silica gel and montmorillonite K10 by adsorbing the substrate; and aq. sodium hypochlorite on solid support followed by exposing the reaction mixture to microwave irradiation (100 W). Oxidations on silica gel gave diphenyl sulfone in high yields (93%) in shorter time unlike other supports, which required longer reaction times and (or) gave reaction mixtures. Diphenyl selenide and di(*p*-methylphenyl) telluride also underwent oxidation to diphenyl selenone and di(*p*-methylphenyl) tellurone, respectively, under the same reaction conditions but required even shorter exposure to microwaves. Oxidation in the absence of solid support was incomplete, and a mixture of monoxide and dioxide was obtained. Subsequently, oxidation of various substituted aromatic and aliphatic sulfides, selenides, and tellurides was carried out with aq. sodium hypochlorite on silica gel solid support after exposure to microwaves to give the corresponding sulfones, selenones, and tellurones in high yields (eq. [1], Table 1).

**Table 2.** Oxidation of sulfides, selenides, and tellurides with aq. sodium hypochlorite to monoxides under microwave exposure, supported on neutral alumina.

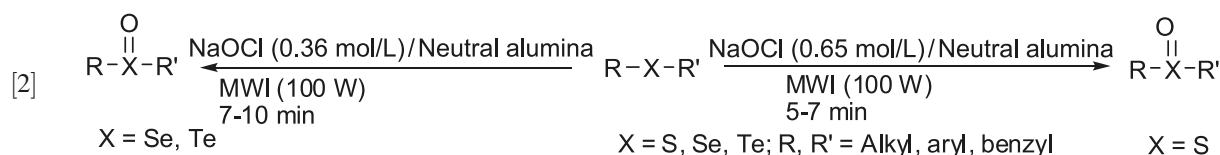
Entry	Substrate	Product	Time (min) <sup>a</sup>	Yield (%)
1	Diphenyl sulfide	Diphenyl sulfoxide <sup>8,10a-10c,10e</sup>	6 (3+3)	82
2	Di( <i>n</i> -butyl) sulfide	Di( <i>n</i> -butyl) sulfoxide <sup>8,10a,10b,10e</sup>	5 (3+2)	87
3	Benzyl phenyl sulfide	Benzyl phenyl sulfoxide <sup>8,10a,10b,10e</sup>	5 (3+2)	83
4	Phenyl <i>n</i> -propyl sulfide	Phenyl- <i>n</i> -propyl sulfoxide <sup>8,10a,10b,10e</sup>	5 (3+2)	84
5	Di( <i>n</i> -dodecyl) sulfide	Di( <i>n</i> -dodecyl) sulfoxide <sup>8,10a,10b,10e</sup>	6 (3+3)	81
6	Methyl phenyl sulfide	Methyl phenyl sulfoxide <sup>8,10a,10b,10e</sup>	6 (3+3)	80
7	Dibenzyl sulfide	Dibenzyl sulfoxide <sup>8,10a,10b,10e</sup>	6 (3+3)	91
8	<i>n</i> -Dodecyl phenyl sulfide	<i>n</i> -Dodecyl phenyl sulfoxide <sup>8,10a,10b,10e</sup>	6 (3+3)	83
9	<i>n</i> -Butyl phenyl sulfide	<i>n</i> -Butyl phenyl sulfoxide <sup>8,10a</sup>	6 (3+3)	84
10	<i>p</i> -Chlorophenyl phenyl sulfide	<i>p</i> -Chlorophenyl phenyl sulfoxide <sup>10b,10e</sup>	7 (3+4)	77
11	<i>p</i> -Bromophenyl phenyl sulfide	<i>p</i> -Bromophenyl phenyl sulfoxide <sup>10b,10e</sup>	7 (3+4)	78
12	Diphenyl selenide	Diphenyl selenoxide <sup>10b,10e</sup>	7 (3+4)	89
13	Di( <i>p</i> -methylphenyl) selenide	Di( <i>p</i> -methylphenyl) selenoxide <sup>10b,10e</sup>	8 (4+4)	87
14	Di( <i>p</i> -chlorophenyl) selenide	Di( <i>p</i> -chlorophenyl) selenoxide <sup>10b,10e</sup>	8 (4+4)	84
15	Di( <i>p</i> -methylphenyl) telluride	Di( <i>p</i> -methylphenyl) telluroxide <sup>10b,10e</sup>	10 (5+5)	88
16	Di( <i>p</i> -methoxyphenyl) telluride	Di( <i>p</i> -methoxyphenyl) telluroxid <sup>10b,10e</sup>	9 (5+4)	86
17	Di( <i>p</i> -bromophenyl) telluride	Di( <i>p</i> -bromophenyl) telluroxide <sup>10b,10e</sup>	10 (5+5)	87

**Note:** Reactions were carried out using 2 mL of aq. NaOCl per mmol of substrate. Aqueous NaOCl solution (0.65 mol/L) was used for the oxidation of sulfides, and aq. NaOCl (0.36 mol/L) was used for the oxidation of selenides and tellurides.

<sup>a</sup>Sodium hypochlorite used in two lots and the reaction mixture was irradiated in two intervals after a time gap of 1 min.



The applicability of the reagent under microwave irradiation was then investigated for the selective oxidation of different chalcogenides to their monoxides. During our exploratory experiments on diphenyl sulfide, we had observed that higher amount of diphenyl sulfoxide was formed when neutral alumina was used as the solid support. Subsequently, we have found that neutral alumina is the best solid support for selective oxidation to diphenyl sulfoxide using aq. sodium hypochlorite (0.65 mol/L) under microwave irradiation (100 W) only when sodium hypochlorite was added in two portions and the reaction mixture was irradiated twice with a 1 min time interval. No over oxidation to the sulfone was observed.



We conclude that chalcogenides can be selectively oxidized to their monoxides or dioxides in high yields by an environmentally benign and safe protocol using aq. sodium hypochlorite under microwave irradiation. Synergism of microwave methodology, use of aqueous reagent, and solvent-

However, diphenyl selenide and di(*p*-methylphenyl) telluride gave mixtures of corresponding monoxides and dioxides under similar experimental conditions. Reaction conditions for the selective oxidation of selenides and tellurides were achieved with 0.36 mol/L aq. NaOCl solution. Diphenyl selenide and di(*p*-methylphenyl) telluride underwent selective oxidation with 0.36 mol/L aq. NaOCl solution under otherwise identical conditions. Thereafter, selective oxidation of a variety of sulfides was carried out with 0.65 mol/L aq. NaOCl solution, and oxidation of different selenides and tellurides was achieved with 0.36 mol/L aq. NaOCl solution supported on neutral alumina to give the corresponding monoxides in high yields in 5–10 min under microwave exposure (eq. [2], Table 2). The addition of sodium hypochlorite was done in two portions, and microwave exposure was done in two intervals with a gap of 1 min for the addition of reagent and cooling.

free conditions make this oxidation an attractive and facile synthetic protocol.

## Acknowledgement

BN thanks the Council of Scientific and Industrial Re-

search (CSIR), New Delhi, India, for the grant of Junior Research Fellowship.

## References

- (1) Patai, S.; Rappoport, Z. C. J. M., Eds. Stirling. *The Chemistry of Sulphones and Sulphoxides*; John Wiley, 1988; Vol. 3.
- (2) Kumar, A.; Akanksha. *Tetrahedron Lett.* **2007**, 48 (44), 7857; and references cited therein. doi:10.1016/j.tetlet.2007.08.128.
- (3) Fernández, I.; Khiar, N. *Chem. Rev.* **2003**, 103 (9), 3651. doi:10.1021/cr990372u. PMID:12964880.
- (4) (a) Hiroi, K.; Watanabe, K.; Abe, I.; Koseki, M. *Tetrahedron Lett.* **2001**, 42 (43), 7617. doi:10.1016/S0040-4039(01)01646-X.; (b) Priego, J.; Mancheño, O. G.; Cabrera, S.; Carretero, J. C. *J. Org. Chem.* **2002**, 67 (4), 1346. doi:10.1021/jo016271p. PMID:11846685.
- (5) (a) Sharpless, K. B.; Lauer, R. F.; Teranishi, A. Y. *J. Am. Chem. Soc.* **1973**, 95 (18), 6137. doi:10.1021/ja00799a062.; (b) Reich, H. J.; Renga, G. M.; Reich, I. L. *J. Am. Chem. Soc.* **1975**, 97 (19), 5434. doi:10.1021/ja00852a019.; (c) Shimizu, M.; Ando, R.; Kuwajima, I. *J. Org. Chem.* **1984**, 49 (7), 1230. doi:10.1021/jo00181a020.; (d) Uemura, S.; Fukuzawa, S. *J. Am. Chem. Soc.* **1983**, 105 (9), 2748. doi:10.1021/ja00347a039.
- (6) Reich, H. J.; Shah, S. K. *J. Am. Chem. Soc.* **1975**, 97 (11), 3250. doi:10.1021/ja00844a072.
- (7) (a) Khurana, J. M.; Panda, A.; Ray, A.; Gogia, A. *Org. Prep. Proced. Int.* **1996**, 28 (2), 234. doi:10.1080/00304949609356529.; (b) Noguchi, T.; Hirai, Y.; Kirihaara, M. *Chem. Commun. (Camb.)* **2008**, (26): 3040. doi:10.1039/b802502a. PMID:18688341.; (c) Bordoloi, A.; Vinu, A.; Halligudi, S. B. *Chem. Commun. (Camb.)* **2007**, 4806. doi:10.1039/b709459k. PMID:18004448.; (d) Fraile, J. M.; Lázaro, B.; Mayoral, J. A. *Chem. Commun. (Camb.)* **1998**, 10 (17), 1807. doi:10.1039/a804180f.; (e) Pordea, A.; Creus, M.; Panek, J.; Duboc, C.; Mathis, D.; Novic, M.; Ward, T. R. *J. Am. Chem. Soc.* **2008**, 130 (25), 8085. doi:10.1021/ja8017219. PMID:18507383.; (f) Zen, J. M.; Liou, S. L.; Kumar, A. S.; Hsia, M. S. *Angew. Chem. Int. Ed.* **2003**, 42 (5), 577. doi:10.1002/anie.200390166.; (g) Khurana, J. M.; Kandpal, B. M.; Chauhan, Y. K. *Phosphorus Sulfur Silicon Relat. Elem.* **2003**, 178 (6), 1369; and references cited therein. doi:10.1080/10426500307909.
- (8) Bahrami, K. *Tetrahedron Lett.* **2006**, 47 (12), 2009; and references cited therein. doi:10.1016/j.tetlet.2006.01.051.
- (9) (a) de la Hoz, A.; Díaz-Ortiz, Á.; Moreno, A. *Chem. Soc. Rev.* **2005**, 34 (2), 164. doi:10.1039/b411438h. PMID:15672180.; (b) Loupy, A., Ed. *Microwaves in Organic Synthesis*; Wiley-VCH: Weinheim, 2006.
- (10) (a) Surendra, K.; Krishnaveni, N. S.; Kumar, V. P.; Sridhar, R.; Rao, K. R. *Tetrahedron Lett.* **2005**, 46 (27), 4581; and references cited therein. doi:10.1016/j.tetlet.2005.05.011.; (b) Belstein, F. K. *Beilstein Handbuch Der Organischen Chemie*; Springer: Berlin, 1883; (c) Leandri, G.; Mangini, A.; Passerini, R. *J. Chem. Soc.* **1957**, 1386. doi:10.1039/jr9570001386.; (d) Khurana, J. M.; Agrawal, A.; Kumar, S. *J. Braz. Chem. Soc.* **2009**, 20 (7), 1256. doi:10.1590/S0103-50532009000700009.; (e) Bucking, J., Ed. *Dictionary of Organic Compounds*, Vth ed.; Chapman and Hall: New York, 1982;
- (11) Vogel, A. I. *Inorganic Quantitative Analysis*, 5th ed.; Wiley Interscience Longman Group: UK, 1989; p. 396.
- (12) (a) Rábai, J. *Synthesis* **1989**, 1989 (07), 523. doi:10.1055/s-1989-27305.; (b) Petrillo, G.; Novi, M.; Gabrarianso, G.; Del-lieberba, C. *Tetrahedron* **1986**, 42 (14), 4007. doi:10.1016/S0040-4020(01)87556-6.
- (13) Khurana, J. M.; Sahoo, P. K. *Synth. Commun.* **1992**, 22 (12), 1691. doi:10.1080/00397919208020489.
- (14) Vogel, A. I. *Textbook of Practical Organic Chemistry*, 4th ed.; ELBS/Longman, 1978; p. 584.
- (15) Leicester, H. M.; Bergstrom, F. W. *J. Am. Chem. Soc.* **1931**, 53 (12), 4428. doi:10.1021/ja01363a024.
- (16) Klayman, D. L.; Griffin, T. S. *J. Am. Chem. Soc.* **1973**, 95 (1), 197. doi:10.1021/ja00782a034.
- (17) Li, J.; Lue, P.; Zhou, X.-J. *Synthesis* **1992**, (3), 281. doi:10.1055/s-1992-26091.

# Synthesis and characterization of low-molecular-weight azo-acetoxystyrene and azo-naphthalene oligomers via stable free radical polymerization (SFRP)

Dildar Ali, Zaheer Ahmed, Peter M. Kazmaier, and Erwin Buncel

**Abstract:** As an approach toward controlled molecular architecture through stable free radical polymerization (SFRP), we have prepared a series of oligomers of controlled molecular weights ( $M_n$ ) and low polydispersities (structures **2** and **3**, with  $n$  values ranging from 2 to 52). Definitive evidence of structure was obtained through MALDI/MS (inter-peak interval of 162  $m/z$  in azo-acetoxystyrene oligomers **2** and 260  $m/z$  in azo-naphthalene oligomers **3**, which correspond to the acetoxystyrene (AS) and naphthalenic (Np) repeating units, with corroborative evidence from NMR and GPC. Two synthetic pathways were explored. Pathway 1 yields azo-acetoxystyrene oligomer **2** via SFR addition of a TEMPO-capped unimer **1** to acetoxystyrene. Subsequent reactions would convert **2** into **3**. In an alternative pathway 2, SFR addition of **1** to 4-(1-methoxynaphthyl)styrene gives azo-naphthalene oligomer **3** directly. Thus, the present reported methodology for controlled architecture has achieved synthesis of oligomers from low  $M_n$  (chlorobenzene, PhCl, solvent) to relatively high  $M_n$  (bulk), with incorporation of naphthyl (donor) and azobenzene (acceptor) moieties, as well as spacer moieties, in a controlled manner.

**Key words:** azo-acetoxystyrene oligomers, azo-naphthalene oligomers, stable (controlled) free radical polymerization.

**Résumé :** Comme approche à une architecture moléculaire contrôlée par le biais d'une polymérisation à l'aide de radicaux libres stables (PRLS), on a préparé une série d'oligomères de masses moléculaires ( $M_n$ ) contrôlées et de faibles polydispersités (structures **2** et **3**, avec des valeurs de  $n$  allant de 2 à 52). Les données définitives permettant de déterminer les structures ont été obtenues par spectrométrie de masse avec ionisation laser assistée par une matrice de désorption (SM-ILAMD) [intervalle entre pics de 162  $m/z$  dans les oligomères azo-acétoxystyrène **2** et de 260  $m/z$  dans les oligomères azo-naphtalène **3** qui correspondent aux motifs constitutifs de l'acétoxystyrène (AS) et naphtalénique (Np)] et corroborées par RMN et par chromatographie par perméation de gel (CPG). On a exploré deux voies de synthèse. La voie 1 conduit à l'oligomère azo-acétoxystyrène **2** par le biais d'une addition à l'aide de radicaux libres stables (RLS) de l'unimère **1** couvert d'un groupe tétraméthylpipéridine oxyde (TEMPO) à l'acétoxystyrène. Des réactions subséquentes devraient permettre de transformer le produit **2** en **3**. Dans une voie alternative 2, une addition à l'aide de radicaux libres stables aux 4-(1-méthoxynaphtyl)styrène conduit directement à l'oligomère azo-naphtalène **3**. La méthodologie rapportée ici pour obtenir une architecture contrôlée a permis de réaliser la synthèse d'oligomères à partir de produits de masses moléculaires basses (chlorobenzène, PhCl, solvant) à des masses moléculaires relativement élevées (en bloc), avec l'incorporation de portions naphtyles (donneur) et azobenzène (accepteur) ainsi que de portions agissant comme d'espacement d'une façon contrôlée.

**Mots-clés :** oligomères de l'azo-acétoxystyrène, oligomères de l'azo-naphtalène, stable (contrôlée), polymérisation par radicaux libres.

## Introduction

As part of a research program in materials science, we have been engaged in studies of light harvesting (LH) systems and underlying energy transfer (ET) processes.<sup>1-4</sup> Energy transfer and (or) electron transfer are basic to the process of light harvesting and processes such as photosynthesis.<sup>5-10</sup> In turn, the efficiency of ET has been shown to

require specific architecture that, typically, incorporates energy donor (**D**) and energy acceptor (**A**) moieties, as shown in Scheme 1. The donor group(s) absorb light energy, which is then transferred from the excited **D** group (**D\***), with varying degrees of efficiency, to the acceptors. In principle, electron transfer could also occur, depending upon **D** and **A** groups incorporated in the LH system.

Considerable effort has gone into understanding the pho-

Received 22 January 2010. Accepted 3 May 2010. Published on the NRC Research Press Web site at canjchem.nrc.ca on 6 August 2010.

**D. Ali.** Department of Chemistry, Queen's University, Kingston, ON K7L 3N6, Canada; H.E.J. Research Institute of Chemistry, University of Karachi, Karachi 75270, Pakistan.

**Z. Ahmed.** H.E.J. Research Institute of Chemistry, University of Karachi, Karachi 75270, Pakistan.

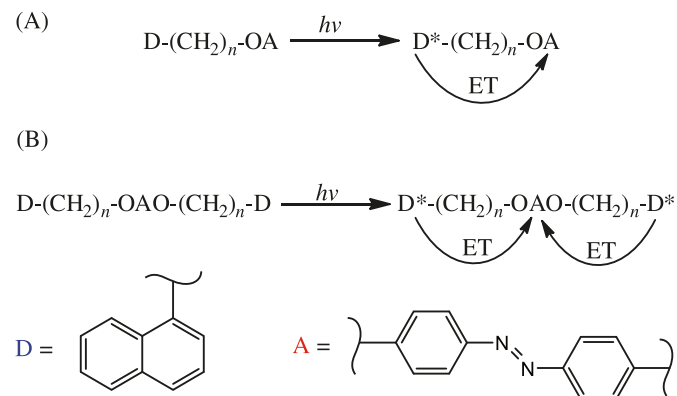
**P.M. Kazmaier.** Xerox Research Centre of Canada, 2660 Speakman Drive, Mississauga ON L5K 2L1, Canada.

**E. Buncel.**<sup>1</sup> Department of Chemistry, Queen's University, Kingston, ON K7L 3N6, Canada.

<sup>1</sup>Corresponding author (e-mail: buncel@chem.queensu.ca).



Scheme 1.



tochemical and photophysical processes involved in light harvesting and this effort is, partly, reflected in the range of authoritative reviews that have appeared lately.<sup>11–16</sup>

We have taken a two-pronged approach to probing LH systems. First and in common with a number of research groups,<sup>5,6,17,18</sup> we have prepared a range of dendrimer and starburst polymeric LH model systems, including azobenzene moieties as **A** groups and naphthalenes as **D** moieties.<sup>1–4</sup> Second, we have prepared two LH model systems (Scheme 1) using naphthalene **D** and azobenzene **A** groups tethered by methoxy linkages: **A**–(OCH<sub>2</sub>)–**D** and **D**–(CH<sub>2</sub>O)–**A**–(OCH<sub>2</sub>)–**D**. Our study of the photophysical/chemical properties of two models (Scheme 1) revealed a new criterion for efficiency of energy transfer, involving ratios of rate constants for cis–trans isomerization and ratios of light energy absorption; the LH models were each compared to relevant benchmark molecules. According to this new criterion, energy transfer was virtually complete for both model systems. Electron transfer, under the conditions studied, was not found to be feasible. However, a need for a greater loading of light harvesting donor groups was also identified, as a pre-requisite to the preparation of more practical LH systems.<sup>4</sup> To this end, we have now prepared a series of oligomers **3** containing an azobenzene acceptor group at one end of the chain and a progressively larger number of donor naphthalenic repeating units, as shown in Scheme 2. The long-term goal is to study the LH **3** to **4** interconversion and the photophysics involved (Scheme 2).

Herein, we describe our synthetic strategy, which is based on stable free radical polymerization (SFRP, also termed nitroxide-mediated polymerization, NMP)<sup>19–27</sup> to yield LH oligomers in a controlled manner. SFRP has proven to be particularly valuable in the preparation of polymers with controlled architecture. The Georges,<sup>21,23</sup> Hawker,<sup>20,22,25</sup> Fischer,<sup>19</sup> and Matyjaszewski<sup>26</sup> groups, among others, have pioneered and elaborated on this approach to the preparation of high-molecular-weight polymers. Our aim here, however, is the preparation of low-molecular-weight oligomers for the purpose of preparation of controlled oligomeric structures. The starting point in two different synthetic approaches is the same: the azobenzene-containing unimer, **1**, which is capped reversibly with the persistent nitroxyl radical TEMPO. Reaction of the **1** with 4-acetoxystyrene, **5**, was expected to give low-molecular-weight oligomers **2** (Scheme 2, pathway 1) incorporating the acetoxystyrene repeating unit, *n*,

for subsequent conversion of acetoxy functions to naphthyl methoxy donor groups, i.e., formation of **3**. In an alternative preparation (Scheme 2, pathway 2), the SFRP process involved addition oligomerization of 4(1-methoxynaphthyl)styrene, **6**, with the unimer **1** to give **3**. The results of preparation of the LH models containing 4(1-methoxynaphthyl)styrene donor repeating units and their characterization (MALDI-TOF/MS and GPC analyses), as well as corroborative NMR analyses, will be discussed in terms of optimization of reaction time and the use of a suitable solvent to control the molecular weight.

## Results and discussion

### Synthetic strategy

Two synthetic approaches (Scheme 2, pathways 1 and 2), which differed in the structure of the arylvinyl monomer oligomerized with unimer **1**, were examined as routes to the target oligomers, **3**. Addition under SFRP conditions of the benzylic radical derived from **1** (arising from facile scission of the C–O bond of the TEMPO cap) to 4-acetoxystyrene, **5**, should yield oligomers, **2**, with a range of acetoxystyrene repeating units, *n*. Hydrolysis of **2** followed by functionalization with a naphthyl moiety yields the azonaphthyl oligomer **3**.

The alternative route (Scheme 2, pathway 2) consists of SFRP-style addition of the benzylic radical of **1** (formed as before) to the 4-(1-methoxynaphthyl)styrene, **6**, should again give models, **3**.

The difference in the two routes lies, then, in whether the naphthyl donor group is incorporated into the product **3** after oligomerization (pathway 1) or, alternatively, preparation of a suitable arylvinyl monomer, **6**, leads to direct oligomerization to give **3** (pathway 2).

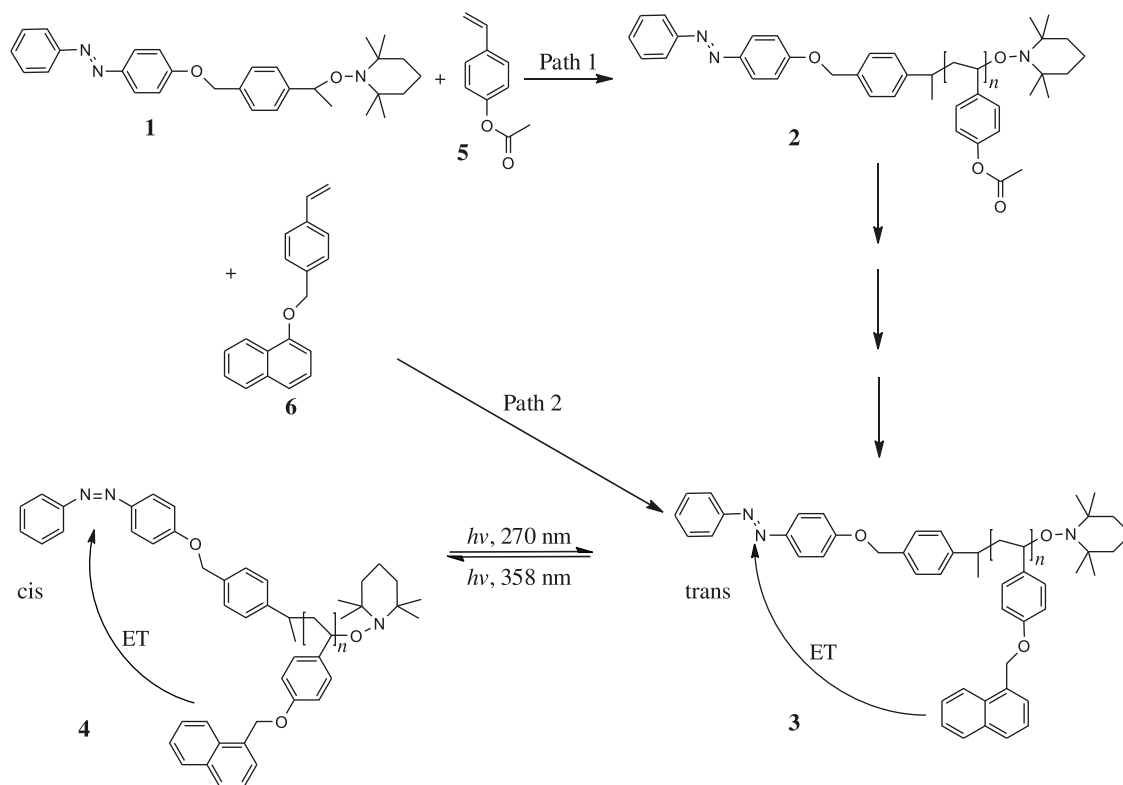
In the preparation of model **3**, controlled low-molecular-weight oligomers were desired. To this end, both the reaction medium and the reaction times were empirically optimized. For the azo-acetoxystyrene oligomerization to yield **2**, bulk (at 130 °C) and solution media (at 120 °C) were studied, where varying amounts, i.e., 1:1 to 1:5 w/w ratios of the arylvinyl monomer to chlorobenzene (PhCl) solvent,<sup>20,22,25,28</sup> were used. Reaction times were varied from 1 min to 5 h in a given set of solvent conditions by quenching a reaction run by pouring the reaction mixture into excess cold methanol (~10 mL). For the azo-naphthalene oligomerizations to yield **3** directly, only the solution conditions (i.e., dilution with PhCl at 120 °C) were studied, as a consequence of the information gleaned from the results in the azo-acetoxystyrene systems, **2**. Reaction times were varied from 10 min to 1 h, again as prompted by the results in the related oligomerization system.

The results of these two preparatory routes are listed in Tables 1 and 2 and will be discussed below.

### Azo-acetoxystyrene oligomers, **2**

The results of the SFRP between the unimer **1** and 4-acetoxystyrene, **5**, as the arylvinyl monomer, are summarized in Table 1. Specifically, the reaction conditions including reaction times, the analysis of the maximum number of acetoxystyrene repeating units (*n*) as determined by MALDI-TOF/MS,<sup>29–31</sup> the number average molecular weight of the

Scheme 2.

**Table 1.** Characterization of azo-acetoxystyrene (AS) oligomers, **2**, as a function of reaction conditions: MALDI-TOF/MS and GPC results.

Conditions (w/w ratio AS:PhCl)	Reaction time (min) <sup>a</sup>	MALDI/MS repeating units $n^b$	GPC ( $M_n$ , <sup>c</sup> kDa (PD)) <sup>d</sup>
<b>A = Bulk</b>			
A-1, A-2, A-3, A-4	1, 3, 5, 10	0, <sup>e</sup> 37, 50, 52	0, <sup>e</sup> 6.7(1.6), 7.8(1.4), 8.2(1.3)
<b>B = 1:1</b>			
B-1, B-2, B-3	5, 30, 240	25, 30, 39	4.6(1.4), 5.3(1.3), 9.7(1.3)
<b>C = 1:2</b>			
C-1, C-2, C-3	5, 20, 90	0, <sup>e</sup> 5, 10	NA <sup>f</sup>
<b>D = 1:3</b>			
D-1, D-2, D-3	5, 20, 114	0, <sup>e</sup> 20, 24	0, <sup>e</sup> 5.1(1.2), 8.49(1.1)
<b>E = 1:4</b>			
E-1, E-2, E-3	5, 20, 90	0, <sup>e</sup> 7, 17	NA
<b>F = 1:9</b>			
F-1, F-2, F-3	5, 20, 300	0, <sup>e</sup> 0, <sup>e</sup> 0 <sup>e</sup>	0, <sup>e</sup> 0, <sup>e</sup> 0 <sup>e</sup>

<sup>a</sup>Bulk reactions were carried out at 130 °C. Solution reactions with PhCl diluent were carried out at 120 °C. Both were quenched by addition to cold MeOH accompanied by precipitation of oligomeric product(s) at times cited.

<sup>b</sup> $n$  is the maximum number of repeating acetoxystyrene (AS) units in **2** observed ( $\pm 5\%$ –10% error).

<sup>c</sup>Number average molecular weight (kDa) from GPC, calibrated with polystyrene standards.

<sup>d</sup>Polydispersity,  $M_w/M_n$ .

<sup>e</sup>Peaks ( $m/z$ ) corresponding to oligomer formation were not observed; the only major peak recorded is ascribed to the parent molecular ion for protonated azobenzene unimer at  $[M + H]^+ = 472$ . Oligomer formation was not observed in GPC traces.

<sup>f</sup>NA: not applicable.

oligomers ( $M_n$ ) as determined by GPC, as well as the polydispersity ( $PD = M_w/M_n$ ) are listed in the Table.

#### Mechanistic effects on oligomerization

As can readily be seen in Table 1, even at short reaction times, bulk conditions (experiment series A) yield relatively

long chain oligomers, **2**. For example, a 3 min reaction time produces **2** with  $M_n$  of 6.7 kDa, corresponding to about a maximum of 37 acetoxystyrene repeating units ( $n = 37$ ), and a relatively broad molecular weight distribution ( $PD = M_w/M_n = 1.4$ ). In fact, repetition of the oligomerization at a somewhat lower temperature (120 °C here versus 130 °C in

**Table 2.** Characterization of azo-naphthalene oligomers, **3**, as a function of reaction conditions: MALDI-TOF/MS and GPC results.

Conditions (w/w ratio AS:PhCl)	Reaction time (min) <sup>a</sup>	MALDI/MS repeating units $n^b$	GPC ( $M_n$ , <sup>c</sup> kDa (PD)) <sup>d</sup>
<b>Q = 1:3</b>			
Q-1, Q-2	15, 40	2, 12	0.75 (1.2), 3.8 (1.3)
<b>R = 1:4</b>			
	10	2	0.69 (1.1)
<b>S = 1:5</b>			
	30	10	2.5 (1.2)
<b>T = 1:49</b>			
	60	5	1.8 (1.1)

<sup>a</sup>Solution reactions (PhCl diluent) were carried out at 120 °C and were quenched by addition to cold MeOH accompanied by precipitation of oligomeric product(s) at times cited.

<sup>b</sup> $n$  is the maximum number of repeating 4-(1-methoxynaphthyl)styrene (Np) units in **3** observed ( $\pm 5\%$ – $10\%$  error).

<sup>c</sup>Number average molecular weight (kDa) from GPC, calibrated with polystyrene standards.

<sup>d</sup>Polydispersity,  $M_w/M_n$ .

the bulk system) and with an equal weight of chlorobenzene (experiment series B) requires 240 min (B-3) to yield **2** with approximately the same number of repeating units (according to MALDI/MS), i.e.,  $n = 39$ . Representative MALDI/MS spectra for experimental series C-1 to C-3 are shown in Fig. 1 and illustrate the number of repeating units,  $n$ , analyzed via this method.

These results are consistent with the mechanism of SFRP, where at the temperature of the reaction the TEMPO-capped unimer **1** dissociates to give persistent TEMPO nitroxyl radical and a resonance-stabilized benzylic radical.<sup>32</sup> The benzylic radical concentration is partitioned between recombination with the TEMPO radical and addition to 4-acetoxystyrene, **5**. Under bulk conditions, the TEMPO-benzylic radical pair is effectively caged by **5**, the arylvinyl monomer. Addition of the benzylic radical to the vinyl functional group of the surrounding acetoxystyrenes should be facile, and relatively high  $M_n$  oligomer, **2**, arises in accord with the results listed in Table 1. Recombination of TEMPO with the growing benzylic radical end of the chain provides a termination step in the chain mechanism, and through potential further dissociation, provides an avenue for conversion to a “living” chain mechanism.

#### Chlorobenzene solvent effects on oligomerization

In principle, addition of chlorobenzene solvent could have two effects.<sup>20,22,25,28</sup> The first and presumably smaller effect is a solvent effect on the dissociation of the unimer. Preferential solvation of the dissociated radicals (e.g., via  $\pi$ – $\pi$  stacking) relative to the bulky TEMPO-capped unimer could favour dissociation of the unimer. On the other hand, the concentration of acetoxystyrene in the cage surrounding the radical pair would be reduced as a function of increasing added PhCl and the probability of addition to the vinyl group reduced. At short reaction times, the number of repeating groups incorporated in the oligomer would be reduced, as is observed (Table 1).

Generally, then, increasing dilution (Table 1, experiment series C through F) leads to lower-molecular-weight oligomer at comparable reaction times. At 5 min, a 1:1 dilution (AS:PhCl, B-1) gives an oligomer, **2**, incorporating 25 repeating units according to MALDI/MS analysis, while

with all other series, a 5 min reaction time yields no oligomer detectable by MALDI/MS or GPC. The results at 20 min appear anomalous; a 1:2 dilution (AS:PhCl; Table 1, C-2) yields an oligomer with five repeating units, while 1:3 dilution (D-2) gives 20 repeating unit oligomer and 1:4 dilution gives seven repeating-unit oligomer, but 1:9 dilution (F-2) yields no detectable oligomer, **2**.

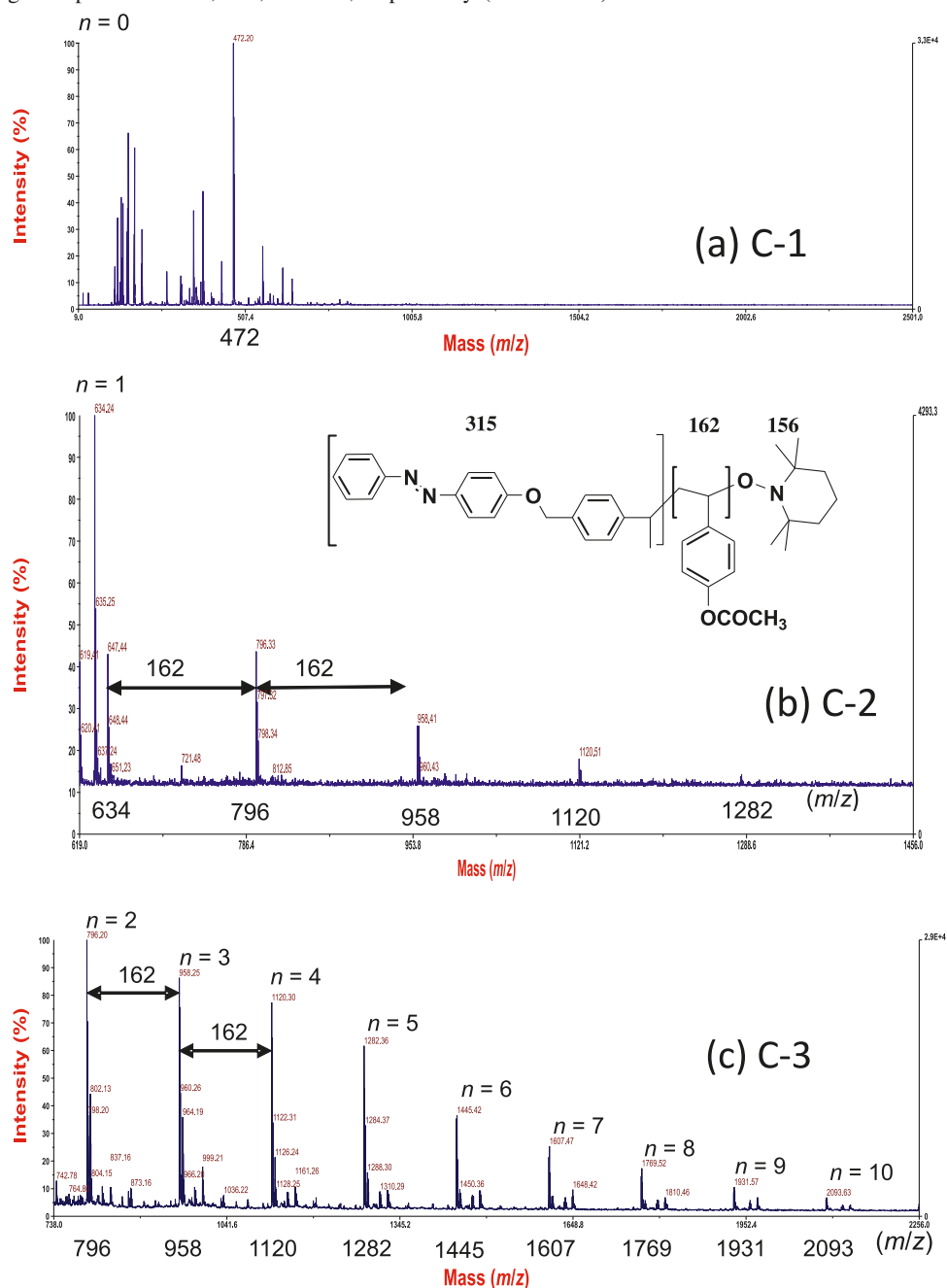
One possibility that accounts for the observed behaviour, namely, an increase in number of repeating units for D-2, as compared to the C-2 and E-2 experiments (Table 1), is that the solvent effect of dilution (i.e., preferential stabilization of the dissociated radicals that would favour dissociation) opposes the concentration effect, that would reduce the probability of radical addition to the arylvinyl monomer. In short, dilution favours dissociation freeing the benzylic radical derived from **1** to add to the vinyl function of **5**, but the decreased concentration of the styrene counteracts this effect partly. The interplay of these factors could lead to the behaviour observed.

At extreme dilution (series F), none of the reaction times studied (5 to 300 min) were sufficient to lead to any oligomer formation. The radicals derived from **1** are effectively free in solution but the concentration of AS is too low to lead to oligomerization.

Also in accord with the foregoing interpretation are the polydispersities determined by GPC (Table 1). In Fig. 2, the GPC traces for experimental series B, D, and F (Table 1) are shown. The bulk run even at 3 min reaction time (Table 1, A-1) gives a PD of 1.6, and modest dilution (B-1, 5 min) yields only a somewhat narrower molecular-weight distribution (PD = 1.4). In living polymerizations, an effective equilibrium is established between dormant or dead polymer (oligomer). This arises from recombination of the benzylic radical end of the growing chain and the TEMPO radical, on the one hand, and propagation of the chain by addition of the benzylic radical to the arylvinyl monomer, on the other. The closer the PD value is to 1 (i.e., monodispersity), the more nearly the polymerization is considered a living process. With a 1:3 dilution with PhCl (D-2, 20 min), the PD drops to 1.3.

The relatively low overall mass recovery found for the acetoxystyrene oligomer **2** indicated that additional steps

**Fig. 1.** MALDI/MS spectra of azo-acetoxystyrene oligomers with varying acetoxystyrene repeating unit ( $n$ ) values: (a),  $n = 0$ ; (b),  $n = 5$ ; (c),  $n = 10$ , corresponding to experiments C-1, C-2, and C-3, respectively (see Table 1).



leading to the desired LH-model oligomer, **3**, could result in little final product. The time-consuming nature of the necessary oligomer characterization at each subsequent step was another consideration that prompted us to consider direct incorporation of the naphthalenic donors (Np) in the SFRP step (Scheme 2). However, the results of the preparation of oligomer **2** indicated that dilutions of 1:3 to 1:5 could yield the appropriate LH oligomer **3** comprising a controlled range of repeating donor units.

### Azo-naphthalene oligomers, **3**

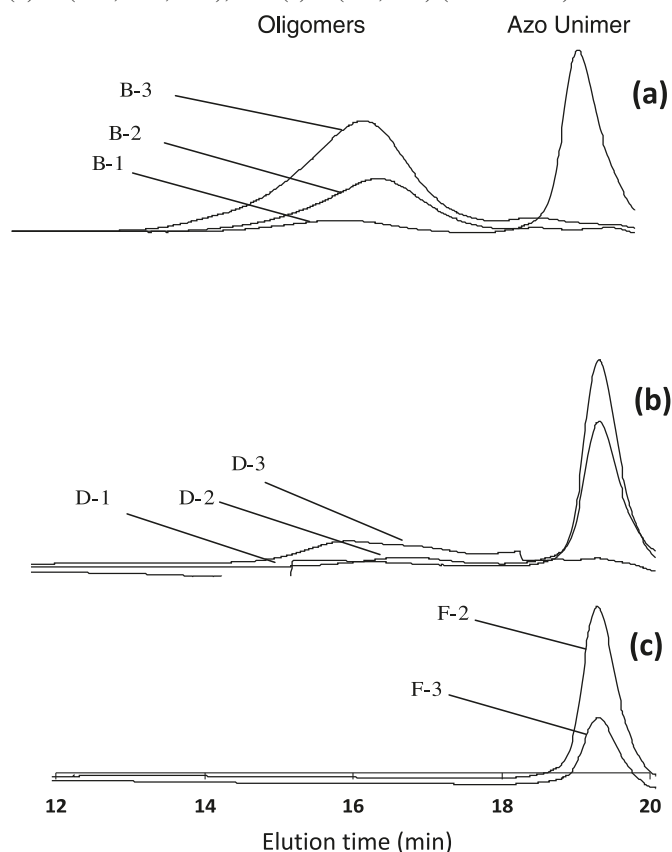
SFRP using unimer **1** and 4-(1-methoxynaphthyl)styrene,

**6**, under the range of conditions identified as favouring formation of low-molecular-weight oligomer **2**, was undertaken to prepare **3** directly (Scheme 2). Table 2 summarizes the MALDI-TOF/MS and GPC characterization of **3**.

With a ratio of 1:3 of the arylvinyl monomer, **6**, to PhCl solvent ( $120\text{ }^{\circ}\text{C}$ ; experiment Q, comparable to the D series of experiments in Table 1), SFRP yields low average molecular weight oligomer ( $M_n = 0.75$  kDa) with low polydispersity ( $PD = 1.2$ ). MALDI/MS analysis shows the expected inter-peak  $m/z$  interval of 260 that corresponds to the naphthalenic repeating unit (Np) as shown in Fig. 3 for experiment R. At 15 min reaction time (experiment Q-1), the



**Fig. 2.** GPC chromatograms for experiments (a) B (B-1, B-2, B-3); (b) D (D-1, D-2, D-3); and (c) F (F-2, F-3) (see Table 1).



maximum number of repeating units found was two; the “oligomer” here consists solely of unimer and dimer. An increase in reaction time to 40 min (Q-2) gives higher-molecular-weight oligomer ( $M_n = 3.9$  kDa; 12 repeating units by MALDI/MS analysis) with only a slight broadening of the molecular weight distribution (PD = 1.3 by GPC). Note, for comparison, that at 20 min reaction time in the acetoxystyrene series (Table 1, D-2), MALDI/MS analysis gave oligomer **2** containing a maximum of 20 repeating units and GPC traces indicated a number average molecular weight of 5.1 kDa for the oligomer with a PD of 1.2, all similar to the results obtained here for experiment Q-2 with a reaction time of 40 min. Clearly, the experimental conditions optimized for the acetoxystyrene SFR oligomerizations (Scheme 2, pathway 1) extend reasonably to the 4-(1-methoxynaphthyl)styrene additions, i.e., formation of **3** directly via pathway 2 in Scheme 2.

Reasonably, the considerations of solvent enhancement of the dissociation of the unimer **1** and the opposing influence of dilution on the addition step apply consistently to pathway 2 to give **3**. It follows that experiments R (1:4, 6:PhCl solvent) through T (1:49, 6:PhCl; Table 2) mimic the trend in degree of oligomerization and polydispersity found for the comparable experimental series D through F (Table 1) found for pathway 1. The number average molecular weight of the oligomer increases, according to GPC, in going from R (1:3) to T (1:4), i.e., from 0.69 kDa to 2.5 kDa with similar PD values and in a maximum number of repeating units of two rising to 10 in the latter run. Experiment T gives an

oligomer with a lower maximum number of repeating units ( $n = 5$ ) and a lower number average molecular weight (1.8 kDa). This parallelism, namely, first increase and then decrease in molecular weight and maximum number of repeating units, which was found in the acetoxystyrene oligomerization runs to give **2**, is consistent with the behaviour found in the oligomerization to give **3**. The same reasons appear to apply: compensatory interplay of solvent and dilution effects on the SFRP chain mechanism.

## Highlights of characterization and fractionation

### MALDI-TOF/MS

Figure 1 shows the MALDI-TOF/MS analysis<sup>29–31</sup> for three experimental runs (Figs. 1a to 1c, C-1 to C-3, Scheme 2, pathway 1). As can be seen in run C-1, no acetoxystyrene oligomer **2** formed (i.e.,  $n = 0$ ); the major MS peak corresponds to unmodified unimer **1** ( $M - H^+ = 472$   $m/z$ ) while in the subsequent runs, C-2 and C-3, the major peaks correspond to the oligomers with  $n = 5$  and  $n = 10$ , repeating units, respectively. Significantly, for C-2 and C-3, the main fragmentation route involves sequential scission of the acetoxystyrene repeating units. Accordingly, in Fig. 1b, main peaks are seen at  $n = 5$  ( $m/z = 1282$ ) and at consecutively smaller  $m/z$  values with intervals of 162  $m/z$  for  $n = 4, 3, 2$ , and 1. This pattern applies equally to C-3 and all experimental runs summarized in Table 1.

An additional feature of these MALDI/MS spectra is the presence of minor peaks at  $m/z$  values significantly greater than that of the main peak. Representative is C-2 (Fig. 1b). Arising from the presence of TEMPO radical in the system and multiple benzylic sites for H-abstraction and coupling, the possibility exists for incorporation of *multiple* TEMPO moieties at the oligomeric end groups. This accounts for these higher  $m/z$  peaks.

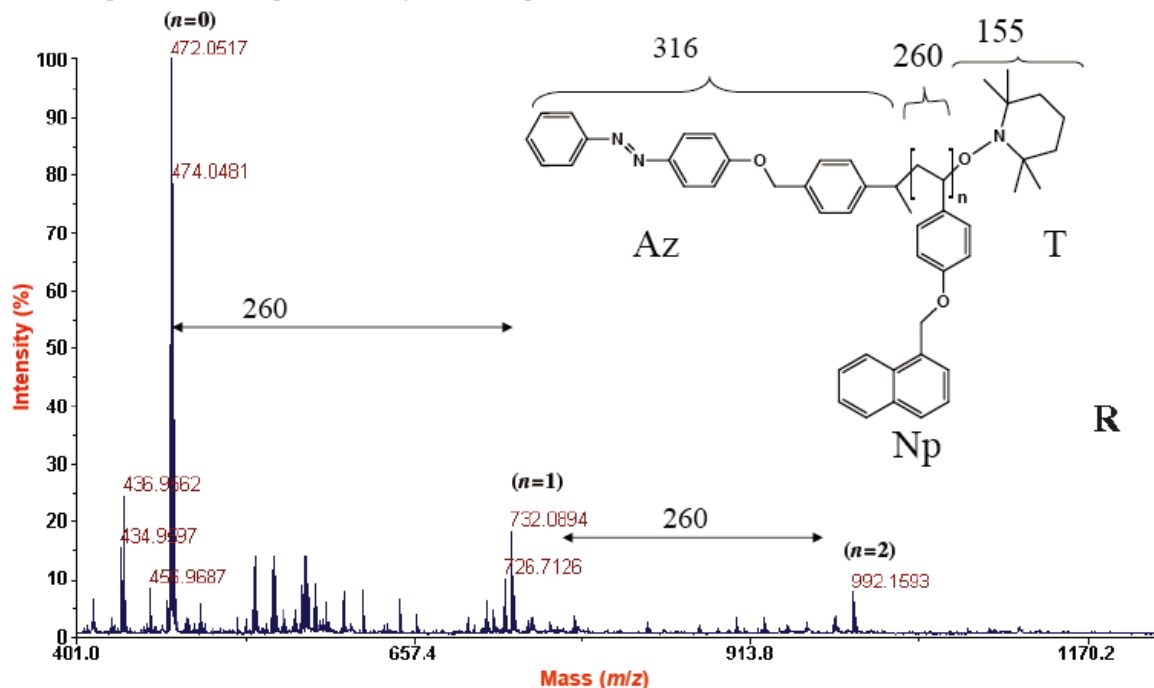
Beyond the major sequential splitting off of repeating units, small fragmentation peaks are evident between the 162  $m/z$  intervals, e.g., between  $n = 5$  and  $n = 4$  in C-3 (Fig. 1c). These small peaks may result from minor defects in the oligomer structure.

Turning to pathway 2 (Scheme 2), the direct preparation of oligomer **3**, representative MALDI/MS spectra are shown in Fig. 3 for experiment R; reaction conditions are given in Table 2. Once again major peaks result from the oligomer molecular ions with the main fragmentation route involving sequential repeating-unit scission with intervals now of 260  $m/z$ . Minor fragmentation routes for **3** are accounted for as previously outlined for **2** (Scheme 2).

Importantly, the dominant features of the MALDI/MS analysis of **2**, which apply equally to **3**, are the observation of the  $M - H^+$  molecular ions corresponding to the maximum number of repeating units in the respective oligomers. Further, the sequential loss of the repeating moiety emphasizes the source of these oligomers: a living SFRP process. Thus, the nature of any minor peaks, arising from impurities or defects, was not investigated in detail, but their presence cannot affect the conclusions or impact the main theme of this study.

### GPC

Oligomers **2** and **3** were analyzed by GPC<sup>30</sup> (UV-vis de-

**Fig. 3.** MALDI/MS spectra for azo-naphthalene oligomer, **3**, experiment R ( $n = 2$ ).

tector; see Experimental). The results of molecular weight determination (polystyrene calibration) and polydispersity (PD) are summarized in Tables 1 and 2 and discussed earlier in the text (see Fig. 2). Typical GPC traces for 4-(1-methoxynaphthyl)styrene monomer **6** (Fig. 4, experiments R, T, and S) show the separation of oligomeric fractions **3** with elution time, as well as the presence/absence of residual monomer.

### $^1\text{H}$ NMR

$^1\text{H}$  NMR spectra (Supplementary data, Figs. S2 and S3) for the acetoxystyrene oligomerizations (Scheme 2, pathway 1) are in accord with the MALDI/MS and GPC analyses summarized in Table 1. Specifically, the spectra for oligomer **2** contain a diagnostic signal at 2.27 ppm for the acetoxy methyl of the repeating unit. This signal increases in relative intensity with increasing  $n$  values for **2**. Similarly, for samples A-2 to A-4, B-1 to B-3, C-2, and C-3 (Fig. S3), increasingly broad signals are centred at 6.2 and 6.9 ppm and are ascribed to the aromatic protons of the acetoxystyrene residues. These NMR peaks for the acetoxystyrene repeating unit of **2** are absent in those runs (e.g., A-1) where oligomerization was deemed to be absent, on the basis of MALDI/MS and GPC determinations.

Considering formation of **3** (Scheme 2, pathway 2),  $^1\text{H}$  NMR spectroscopic analysis agrees with the results given in Table 2 in that higher degrees of oligomerization are accompanied with more intense signals attributable to the Np repeating units and overall broadening of all signals in the relevant spectrum. This is shown in Fig. 5 for experiments T and S.

### Fractionation of azo-naphthalene oligomers **3** via flash chromatography

Reaction of a scaled up quantity of **1** and 1-[(4-vinylphenoxy)methyl]naphthalene (20 min; 1:4, monomer:PhCl)

yielded a mixture of oligomers containing an oligomer **3** with a maximum of 14 Np repeating units. Flash column chromatography (dichloromethane eluant) gave, after recombination based on TLC, five fractions. The first (H-1) consisted only of unmodified arylvinyl monomer, **6**.

The remaining fractions contained mixtures of oligomers **3**; the longest chain oligomers eluted first. Hence, fraction H-2 contained oligomers with a maximum of 14 Np repeating units according to MALDI/MS. The next in order had  $n = 8$  (H-3),  $n = 2$  (H-4), and  $n = 1$  (H-5).

GPC analysis of the crude reaction product (H) prior to fractionation gave a number average molecular weight of 0.73 kDa with a relatively broad molecular weight distribution (PD = 1.5). Fractions H-2 and H-3 gave GPC peaks corresponding to lower-molecular-weight oligomer ( $M_n = 0.57$  kDa) and narrower distribution (PD = 1.4), while fraction H-4 was found to have  $M_n = 1.1$  kDa with a PD of 1.2. Figure 6 shows an ESI-MS spectrum for oligomer **3** where  $n = 1$  (fraction H-5).

The results show that the number of Np repeating units,  $n$ , in the oligomer **3** (via pathway 2 in Scheme 2) and the corresponding molecular weight with low polydispersity (Table 2) may be achieved through careful control of the SFRP reaction conditions (temperature and dilution with PhCl). The oligomeric mixture may be further fractionated by standard flash chromatography.

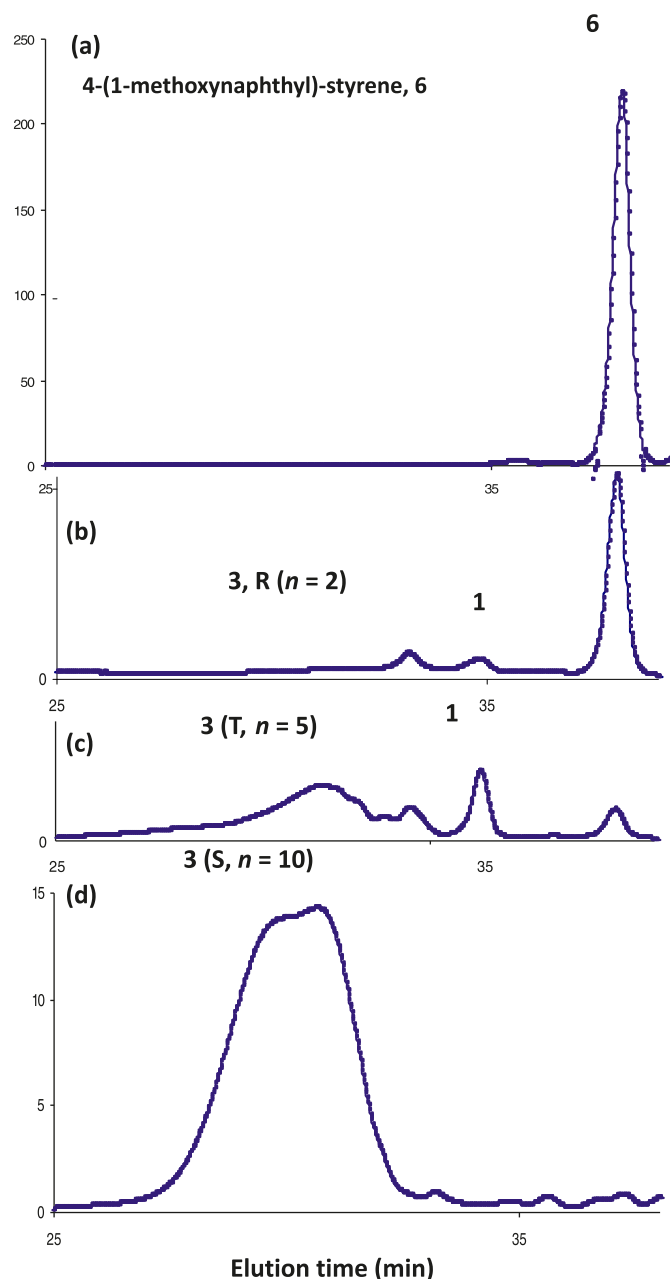
In conclusion, it can be envisaged that the described methodology will lead to a controlled range of oligomers, varying in the numbers of naphthalenic donor units.

## Experimental

### Instruments and materials

$^1\text{H}$  NMR spectra were recorded using a Bruker Avance-

**Fig. 4.** GPC chromatograms showing the increasing molecular weights of **3** and peaks for **1**, **3**, and **6** (Scheme 2), experiments R, T, and S.



400 spectrometer operating at 400.1 MHz, broad band probe, auto-tuned. All chemical shifts are reported as  $\delta$  in parts per million (ppm) relative to residual  $\text{CHCl}_3$  ( $\delta = 7.28$  ppm) and  $\text{CH}_2\text{Cl}_2$  ( $\delta = 5.30$  ppm) in  $\text{CDCl}_3$  (source: CDN) and  $\text{CD}_2\text{Cl}_2$  (CDN) solvents, respectively. Coupling constants ( $J$ ) are reported in Hz. IR samples were recorded using a Bomem MB-120 FTIR spectrophotometer. Dilute samples dissolved in a suitable volatile solvent were allowed to evaporate to provide a film on a KBr plate. Melting points were measured using a Fisher-Johns melting point apparatus and are reported as uncorrected. Gel permeation chromatography (GPC) was performed using Waters 2695 HPLC (Waters 410 differential refractometer detector,

40 °C) with a separation module consisting of four Waters Ultrastaygel® (HR5.0, HR3.0, HR1.0, and HR0.5) in series. Distilled THF was used as eluant with a flow rate of  $1.0 \text{ mL min}^{-1}$ . The GPC system was calibrated with standard polystyrenes up to an elution time of 35 min. MALDI-TOF/MS traces were recorded using an Applied Biosystems Voyager DE-STR MALDI-time of flight/mass spectrometer with a nitrogen laser (337 nm), delayed extraction and reflectors. An accelerating potential of 20 kV was used in the MS detector in both linear and reflector modes. The optimum matrix used for oligomer characterization was 2,5-dihydroxybenzoic acid (DHB) containing no added salt. Typically, oligomeric samples were prepared by mixing a THF solution of the oligomer(s) ( $1 \text{ mg mL}^{-1}$ ) with a solution of DHB ( $20 \text{ mg mL}^{-1}$  in 1:1 MeCN:MeOH) in 1:1 (v/v) proportions to give the analytical matrix. A  $1 \mu\text{L}$  aliquot of the analytical matrix was placed onto a sample plate and the solvent was evaporated at room temperature to give the MALDI-TOF/MS sample for characterization.

All common solvents (acetone, THF, and so forth) used in the preparations outlined below were purchased commercially in HPLC-grade or better and, where necessary, were further purified by standard methods.<sup>33</sup> 4-Hydroxyazobenzene (Aldrich) was recrystallized from ethanol and THF (VWR) was dried over and distilled from sodium metal/benzophenone. All inorganics (e.g.,  $\text{NaBH}_4$ ) and the remaining requisite chemicals and organic reagents were purchased commercially and used without further purification. 4-Acetoxy styrene (96%, Aldrich), di-*t*-butyl peroxide (3.5 mol/L in decane, Aldrich), 18-crown-6 (98%, Aldrich), 4-ethylbenzaldehyde (98%, Aldrich), oxalyl chloride (95%, Aldrich), and 2,2,6,6-tetramethyl-1-piperidinoxyl (TEMPO, gift of Xerox Research Canada) were used as received.

The azo unimer **1** was prepared in a five-step procedure as previously described<sup>1,27</sup> starting from 4-ethylbenzaldehyde that was reduced with  $\text{NaBH}_4$  to 4-ethylbenzyl alcohol, converted to the bromide, and capped with 2,2,6,6-tetramethyl-1-piperidinoxyl using TEMPO and di-*t*-butylperoxyoxalate. Further reaction with NaI in acetone converted the bromide to the iodide, which, in a final step, was reacted with 4-hydroxyazobenzene in the presence of  $\text{K}_2\text{CO}_3$  and 18-crown-6 in acetone to give **1**. The overall yield of this five-step procedure was 24%. All physical and spectroscopic properties were in good agreement with those previously published.<sup>1</sup> The MALDI/MS of **1** contained small extraneous peaks at greater  $m/z$  values than the protonated molecular ion for **1** (i.e.,  $M - \text{H}^+$  at  $472.28 \text{ m/z}$ ). The minor impurity was not removed by column chromatography (60 mesh silica gel; dichloromethane eluent), and **1** was used as is in the following syntheses.

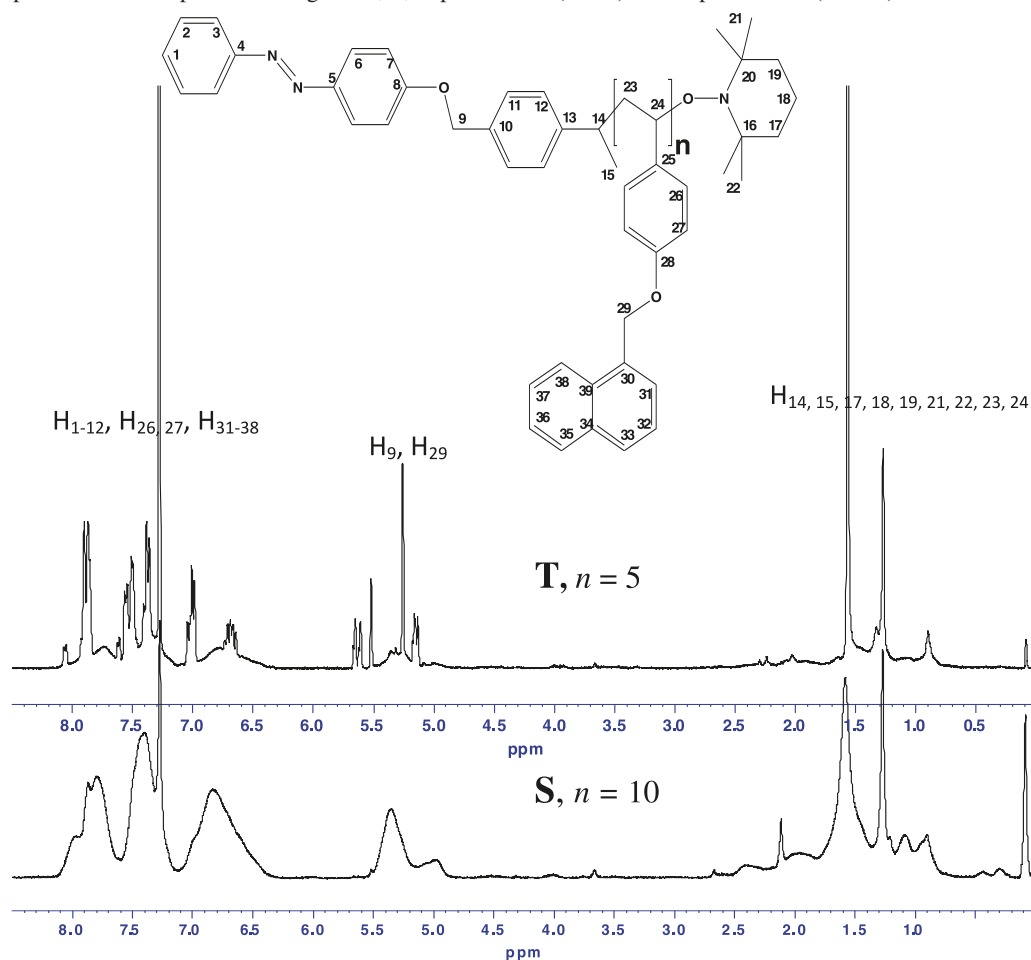
### Preparation of azo-acetoxystyrene oligomers, **2**

Azo-acetoxystyrene oligomers, **2**, capped with TEMPO were prepared under SFRP reaction conditions via addition of **1** to acetoxystyrene, AS, under bulk and chlorobenzene (PhCl) solvent conditions.

### General bulk procedure

Mixtures of **1** and AS were introduced into silicone-septum-capped ampoules (10 mL), swept with  $\text{N}_2$ , and these were immersed in an oil bath thermostatted to 130 °C. After the

**Fig. 5.**  $^1\text{H}$  NMR spectra for azo-naphthalene oligomers, **3**, experiment T ( $n = 5$ ) and experiment S ( $n = 10$ ).



set reaction times, each mixture was poured into excess cold MeOH (10 mL) to quench the reaction and the precipitate, in each case, was collected by filtration. The precipitates were dried in vacuo (<1 torr, 50 °C) (1 torr = 133.322 Pa) overnight to give yellow coloured powders.

#### General solvent procedure

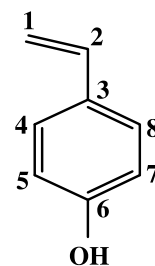
Experimental series B–F (cf. Table 1) were carried out at 120 °C. Mixtures of the reagents and PhCl solvent were prepared in ampoules, as given above, and the temperature maintained by immersion of the vials in the thermostatted oil bath. The mass ratios of AS to PhCl are listed in Table 1. Three aliquots were withdrawn via gas-tight syringe from each experimental series at different time intervals to yield a range of oligomeric mixtures, **2**, that were analyzed by MALDI-TOF/MS,  $^1\text{H}$  NMR spectrometry, IR spectrophotometry, and GPC (UV–vis detector), as outlined in the previous text and in the Results and discussion section.

Table 3 shows molar ratios and amount of PhCl solvent used in each experimental run.

#### Preparation of azo-naphthalene oligomers, **3**

Saponification of 4-acetoxystyrene (10 g, 0.061 mol in 2.5 g MeOH) with KOH (0.25 g, 0.0045 mol), under  $\text{N}_2$  atmosphere, followed by acidification (glacial AcOH) and addition of toluene to precipitate any poly(4-hydroxystyrene)

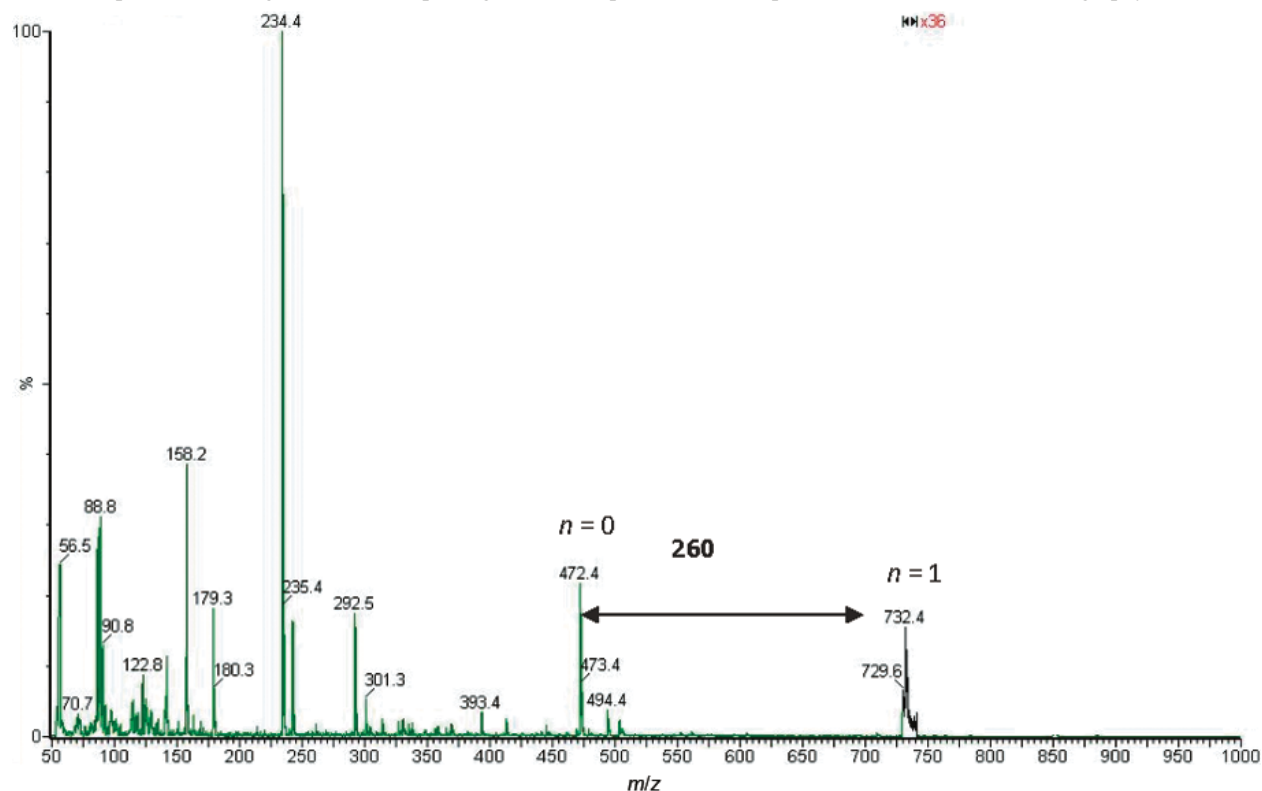
gave a colourless solution, after filtration. This filtrate was cooled ( $\sim -70$  °C) from which 4-vinylphenol (4-hydroxystyrene) crystallized as colourless crystals (4.5 g, 45%); mp 59–60 °C (lit. 68–69 °C,<sup>34</sup> 73.5 °C<sup>35</sup>). IR (KBr,  $\text{cm}^{-1}$ )  $\nu$ : 3249, 2977, 1656, 1541, 1410, 1110, 992, 834, 647.  $^1\text{H}$  NMR ( $[\text{CD}_3]_2\text{CO}$ , 400 MHz)  $\delta$ : 8.45 (1H, s, OH), 7.34 (2H, d,  $J = 6.8$ , H-4,8), 6.98 (2H, d,  $J = 6.8$ , H-5,7), 6.67 (1H, d, d, 17.6, 10.4, H-2), 5.60 (1H, d,  $J_{\text{trans}} = 17.6$ , H-1), 5.01 (1H, d,  $J_{\text{cis}} = 10.4$ , H-1).  $^{13}\text{C}$  NMR ( $\text{CD}_3\text{OD}$ , 100 MHz)  $\delta$ : 157.0, C-6; 136.4, C-5,7; 129.4, C-3; 127.0, C-4,8; 114.9, C-1; 109.4, C-2. EI-MS ( $\text{M} + \text{H}^+$ )  $m/z$ : 120.0532 (calcd. for  $\text{C}_8\text{H}_8\text{O}$ : 120.0531 g/mol).



#### 4-(1-methoxynaphthyl)styrene

Weighed quantities of 4-vinylphenol (1.04 g, 8.6 mmol), 1-chloromethylnaphthalene (1.2 g, 6.8 mmol),  $\text{K}_2\text{CO}_3$  (2.05 g, 14.7 mmol), and 18-crown-6 polyether (0.29 g,



**Fig. 6.** ESI-MS spectrum for oligomer **3** with repeating unit “*n*” equal to 1 after separation with column chromatography (fraction H-5).**Table 3.** Reaction conditions for azo-acetoxystyrene oligomers **2**.

Experimental series	Azo unimer, 1 mg (mmol)	Acetoxystyrene, 5 mg (mmol)	Chlorobenzene (PhCl) mg (mmol)
A-1 <sup>a</sup>	10 (0.02)	251 (1.54)	Bulk (monomer solvent)
A-2	10 (0.02)	230 (1.41)	Bulk (monomer solvent)
A-3	10 (0.02)	267 (1.65)	Bulk (monomer solvent)
A-4	10 (0.02)	250 (1.54)	Bulk (monomer solvent)
B	28 (0.06)	170 (1.05)	170 (1.51)
C	31 (0.06)	162 (1.05)	324 (2.90)
D	30 (0.06)	162 (1.05)	487 (4.34)
E	31 (0.06)	162 (1.05)	648 (5.78)
F	31 (0.06)	162 (1.05)	1600 (14.2)

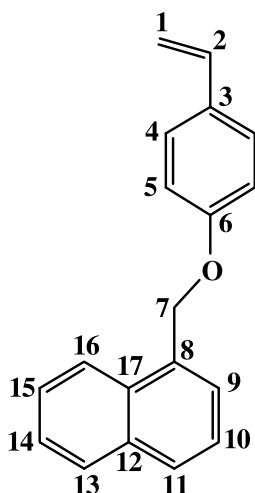
<sup>a</sup>Experiments A-1 through A-4 were performed at 130 °C. All other runs were performed at 120 °C.

**Table 4.** Azo-naphthalene oligomers **3**. Reaction conditions: 120 °C.

Experiment	1 mg (mol)	6 mg (mmol)	PhCl mg (mmol)	Ratio 6:PhCl (w/w)	Time (min)
Q-1	12 (0.027)	500 (1.92)	1500 (13.3)	1:3	15
Q-2	12 (0.027)	500 (1.92)	1500 (13.3)	1:3	40
R	13 (0.025)	50 (0.20)	288 (2.57)	1:4	10
S	13 (0.028)	110 (0.42)	600 (5.30)	1:5	30
T	11 (0.024)	50 (0.20)	1 mL	1:49	60

1.1 mmol) were mixed with acetone (25 mL) in a round-bottom flask and the reaction mixture was brought to reflux for 36 h. The acetone was removed under reduced pressure (rotary evaporator) and the residue added to water and dichloromethane. Separation, drying, and evaporation of the organic layer yielded crude product as an oil. This product was purified by column chromatography (CH<sub>2</sub>Cl<sub>2</sub>/hexane,

1:1 v/v) to yield after evaporation of solvent colourless crystals of 4-(1-methoxynaphthyl)styrene (1.7 g, 75%); mp 48–50 °C. <sup>1</sup>H NMR (CD<sub>2</sub>Cl<sub>2</sub>, 400 Mz) δ: 8.23 (1H, d, *J* = 7.6, H-16), 7.99 (1H, d, *J* = 8.8, H-13), 7.95 (1H, d, *J* = 8.0, H-11), 7.66 (1H, m, H-15), 7.61 (2H, m overlapping signals, H-10,14), 7.56 (1H, d, *J* = 8.4, H-9), 7.45 (2H, d, *J* = 8.0, H-4,4').



### Oligomerization to give 3

Mixtures of **1**, **6**, and PhCl were placed in a 25 mL round-bottomed flask sealed with Teflon rubber septum and purged with N<sub>2</sub> for 5 min prior to immersion in an oil bath stabilized at 120 °C. After selected reaction times (Table 4), the reaction was quenched by addition of copious cold MeOH to give a gummy material that was dissolved upon addition of THF (2 mL). Precipitation of **3** with MeOH and evaporation of solvent in vacuo yielded **3** after filtration; the product was dried under high vacuum (<1 torr) overnight.

Table 4 lists reaction conditions including mole ratios of reagents and reaction times for the preparation of **3**.

### Supplementary data

Supplementary data (MALDI-MS traces, <sup>1</sup>H NMR spectra, GPC profiles for oligomers) for this article are available on the journal Web site (canjchem.nrc.ca).

### Acknowledgements

We thank the Natural Sciences and Engineering Research Council of Canada (NSERC) for funding of this research (E.B.) and the Higher Education Commission of Pakistan (HECP) for support (D.A.). Dildar Ali especially thanks HECP for a Fellowship under the Split Ph.D. Program. The authors thank Thomas M. Kraft for editorial assistance and Dr. Julian M. Dust for discussion.

### References

- (1) Abdallah, D.; Ghani, M. A. A.; Cunningham, M. F.; Kazmaier, P. M.; Keoshkerian, B.; Buncel, E. *Can. J. Chem.* **2004**, *82* (9), 1393. doi:10.1139/v04-107.
- (2) Cheon, K. S.; Kazmaier, P. M.; Keum, S. R.; Park, K. T.; Buncel, E. *Can. J. Chem.* **2004**, *82* (4), 551. doi:10.1139/v04-009.
- (3) Ghani, M. A. A.; Abdallah, D.; Kazmaier, P. M.; Keoshkerian, B.; Buncel, E. *Can. J. Chem.* **2004**, *82* (9), 1403. doi:10.1139/v04-106.
- (4) Abdallah, D.; Whelan, J.; Dust, J. M.; Hoz, S.; Buncel, E. *J. Phys. Chem. A* **2009**, *113* (24), 6640. doi:10.1021/jp901596t. PMID:19456113.
- (5) Adronov, A.; Gilat, S. L.; Fréchet, J. M. J.; Ohta, K.; Neu-

- wahl, F. V. R.; Fleming, G. R. *J. Am. Chem. Soc.* **2000**, *122* (6), 1175. doi:10.1021/ja993272e.
- (6) Sapsford, K. E.; Berti, L.; Medintz, I. L. *Angew. Chem. Int. Ed.* **2006**, *45* (28), 4562. doi:10.1002/anie.200503873.
- (7) Ishi-i, T.; Murakami, K. I.; Imai, Y.; Mataka, S. *J. Org. Chem.* **2006**, *71* (15), 5752. doi:10.1021/jo060768n. PMID:16839159.
- (8) Ding, L.; Russell, T. P. *Macromolecules* **2007**, *40* (6), 2267. doi:10.1021/ma062653r.
- (9) Aida, T.; Jiang, D. L.; Yashima, E.; Okamoto, Y. *Thin Solid Films* **1998**, *331* (1-2), 254. doi:10.1016/S0040-6090(98)00927-4.
- (10) Vögtle, F.; Gorka, M.; Hesse, R.; Ceroni, P.; Maestri, M.; Balzani, V. *Photochem. Photobiol. Sci.* **2002**, *1* (1), 45. doi:10.1039/b106813j. PMID:12659148.
- (11) Pieroni, O.; Fissi, A.; Angelini, N.; Lenci, F. *Acc. Chem. Res.* **2001**, *34* (1), 9. doi:10.1021/ar990141+. PMID:11170352.
- (12) Balzani, V.; Credi, A.; Venturi, M. *ChemSusChem* **2008**, *1* (1-2), 26. doi:10.1002/cssc.200700087. PMID:18605661.
- (13) Chu, C. C.; Bassani, D. M. *Photochem. Photobiol. Sci.* **2008**, *7* (5), 521. doi:10.1039/b800113h. PMID:18465006.
- (14) Armaroli, N.; Balzani, V. *Angew. Chem. Int. Ed.* **2007**, *46* (1-2), 52. doi:10.1002/anie.200602373.
- (15) Brédas, J. L.; Beljonne, D.; Coropceanu, V.; Cornil, J. *Chem. Rev.* **2004**, *104* (11), 4971. doi:10.1021/cr040084k. PMID:15535639.
- (16) Borisov, A. *Photosynth. Res.* **2003**, *76* (1-3), 413. doi:10.1023/A:1024962531792. PMID:16228597.
- (17) Nantalaksakul, A.; Reddy, D. R.; Bardeen, C. J.; Thayumanavan, S. *Photosynth. Res.* **2006**, *87* (1), 133. doi:10.1007/s11120-005-8387-3. PMID:16408144.
- (18) Kurihara, S.; Sakamoto, A.; Nonaka, T. *Macromolecules* **1998**, *31* (14), 4648. doi:10.1021/ma980074j.
- (19) Fischer, H. *Chem. Rev.* **2001**, *101* (12), 3581. doi:10.1021/cr990124y. PMID:11740916.
- (20) Hawker, C. J. *Acc. Chem. Res.* **1997**, *30* (9), 373. doi:10.1021/ar960248m.
- (21) Georges, M. K.; Veregin, R. P. N.; Kazmaier, P. M.; Hamer, G. K. *Macromolecules* **1993**, *26* (11), 2987. doi:10.1021/ma00063a054.
- (22) Hawker, C. J.; Barclay, G. G.; Orellana, A.; Dao, J.; Devonport, W. *Macromolecules* **1996**, *29* (16), 5245. doi:10.1021/ma951905d.
- (23) Kazmaier, P. M.; Daimon, K.; Georges, M. K.; Hamer, G. K. *Polymer Prepr.* **1996**, *37*, 485.
- (24) Turro, N. J.; Lem, G.; Zavarine, I. S. *Macromolecules* **2000**, *33* (26), 9782. doi:10.1021/ma001327n.
- (25) Hawker, C. J.; Bosman, A. W.; Harth, E. *Chem. Rev.* **2001**, *101* (12), 3661. doi:10.1021/cr990119u. PMID:11740918.
- (26) Tsarevsky, N. V.; Matyjaszewski, K. *Chem. Rev.* **2001**, *101*, 2270.
- (27) Ali, D. Ph.D. thesis, University of Karachi, Pakistan, 2008; pp 67-74.
- (28) Harth, E.; Hawker, C. J.; Fan, W.; Waymouth, R. M. *Macromolecules* **2001**, *34* (12), 3856. doi:10.1021/ma0019297.
- (29) Dourges, M.-A.; Charleux, B.; Vairon, J.-P.; Blais, J.-C.; Bolbach, G.; Tabet, J.-C. *Macromolecules* **1999**, *32* (8), 2495. doi:10.1021/ma981513h.
- (30) Montaudo, G.; Garozzo, D.; Montaudo, M. S.; Puglisi, C.; Samperi, F. *Macromolecules* **1995**, *28* (24), 7983. doi:10.1021/ma00128a003.
- (31) Guittard, J.; Tessier, M.; Blais, J. C.; Bolbach, G.; Rozes, L.; Maréchal, E.; Tabet, J. C. *J. Mass Spectrom.* **1996**, *31* (12), 1409.

- doi:10.1002/(SICI)1096-9888(199612)31:12<1409::AID-JMS440>3.0.CO;2-T.
- (32) Dust, J. M.; Arnold, D. R. *J. Am. Chem. Soc.* **1983**, *105* (5), 1221. doi:10.1021/ja00343a024.
- (33) Perrin, D. D.; Armarego, W. L. F. *Purification of Laboratory Chemicals*, 3rd ed.; Pergamon Press: Toronto, 1988.
- (34) Corson, B. B.; Heintzelman, W. J.; Schwartzman, L. H.; Tie-fenthal, H. E.; Lokken, R. J.; Nickels, J. E.; Atwood, G. R.; Pavlik, F. J. *J. Org. Chem.* **1958**, *23* (4), 544. doi:10.1021/jo01098a012.
- (35) Miller, W.; Kinkelin, F. *Ber.* **1889**, *22*, 1705.

# Naphthalene derivatives from *Diospyros wallichii*

Abdul-Wahab Salae, Chatchanok Karalai, Chanita Ponglimanont, Akkharawit Kanjana-Opas, and Supreeya Yuenyongsawad

**Abstract:** Three new naphthalene derivatives, 2-hydroxymethyl-1,5-dimethoxynaphthalen-4-ol (**1**), 2,2'-bis-hydroxymethyl-1,1',5,5'-tetramethoxy-3,3'-binaphthalen-4,4'-diol (**2**), and 5,5'-dihydroxy-2,2'-dimethyl-7,7'-binaphthalen-1,1',4,4'-tetraone (**3**), were isolated from the hexane and CH<sub>2</sub>Cl<sub>2</sub> extracts of the roots and fruits of *Diospyros wallichii*, along with sixteen known compounds comprising nine naphthoquinones (**4–12**), a coumarin (**13**), and six triterpenes (**14–19**). The structures of these compounds were established on the basis of spectroscopic data and comparison with reported values. The antibacterial, antifungal, and cytotoxic activities of naphthalene derivatives were also reported.

**Key words:** *Diospyros wallichii*, Ebenaceae, naphthoquinones, triterpenoids, antibacterial activity, cytotoxicity.

**Résumé :** L'extraction à l'aide d'hexane et de CH<sub>2</sub>Cl<sub>2</sub> des racines et des fruits de *Diospyros wallichii* a permis d'isoler trois nouveaux dérivés du naphthalène, le 2-hydroxyméthyl-1,5-diméthoxynaphthalène-4-ol (**1**), le 2,2'-bis-hydroxyméthyl-1,1',5,5'-tétraméthoxy-3,3'-binaphthalène-4,4'-diol (**2**) et le 5,5'-dihydroxy-2,2'-diméthyl-7,7'-binaphthalène-1,1',4,4'-tétraone (**3**), ainsi que seize composés connus, dont neuf naphthoquinones (**4–12**), une coumarine (**13**) et six triterpènes (**14–19**). Les structures de ces produits ont été établies sur la base de données spectroscopiques et par comparaison avec des données rapportées antérieurement. On rapporte aussi les résultats d'études sur les activités antibactériennes, antifongiques et cytotoxiques des dérivés naphthaléniques.

**Mots-clés :** *Diospyros wallichii*, Ebenaceae, naphthoquinones, triterpénoïdes, activité antibactérienne, cytotoxicité.

## Introduction

The genus *Diospyros* (family Ebenaceae) is found in most part of the tropics and subtropics and many of the species have been used in traditional medicines, e.g., the fruit of *D. montana* is used to treat hiccups, ulcers, urinary diseases, and dysentery. The fruit of *D. decandra* and *D. malabarica* is used as an emmenagogue in Vietnam and leukorrhea in India, respectively.<sup>1</sup> Several workers have isolated triterpenoids and naphthoquinones from some species of *Diospyros*, including the stem bark of *D. decandra*<sup>2</sup> and fruits of *D. ehereitoides*.<sup>3</sup> In our ongoing search for bioactive compounds, we have studied *D. wallichii*, which is known in Thailand as “damtako”.<sup>4</sup> This plant grows to about 10–20 m in height, whose round fruits are poisonous and used for fishing. We report herein the isolation of three new naphthoquinone derivatives (**1–3**), together with sixteen known compounds comprising nine naphthoquinones (**4–12**), a coumarin (**13**), and six triterpenes (**14–19**) from the roots and fruits of *D. wallichii* (Fig. 1). The new compounds were determined to be 2-hydroxymethyl-1,5-dimethoxynaphthalen-4-ol (**1**), 2,2'-bis-hydroxymethyl-1,1',5,5'-tetramethoxy-3,3'-

binaphthalen-4,4'-diol (**2**), and 5,5'-dihydroxy-2,2'-dimethyl-7,7'-binaphthalen-1,1',4,4'-tetraone (**3**).

## Results and discussion

The crude hexane and methylene chloride extracts from the roots and fruits of *D. wallichii* were subjected to a succession of chromatographic procedures to afford three new compounds (**1–3**), together with sixteen known compounds (**4–19**). Characterization of the known compounds was carried out by direct comparison of their physicochemical data with those reported in the literature. The structures of the new compounds were established as follows.

Compound **1** was obtained as a white amorphous powder with a molecular formula of C<sub>13</sub>H<sub>14</sub>O<sub>4</sub>, on the basis of [M]<sup>+</sup> at *m/z* 234.0920 in the HR-EI-MS, which suggested seven unsaturations. The UV spectrum exhibited absorption bands at 231 and 291 nm, while IR spectrum showed absorption bands for a hydroxyl (3400 cm<sup>-1</sup>) and aromatic ring (1613 cm<sup>-1</sup>). The <sup>1</sup>H and <sup>13</sup>C NMR spectral data, together with COSY, DEPT, HMQC, HMBC, and NOESY experiments allowed full assignment of the NMR data.

Received 13 March 2010. Accepted 7 June 2010. Published on the NRC Research Press Web site at canjchem.nrc.ca on 12 August 2010.

**A. Salae and C. Ponglimanont.** Department of Chemistry and Center for Innovation in Chemistry, Faculty of Science, Prince of Songkla University, Hat-Yai, Songkhla 90112, Thailand.

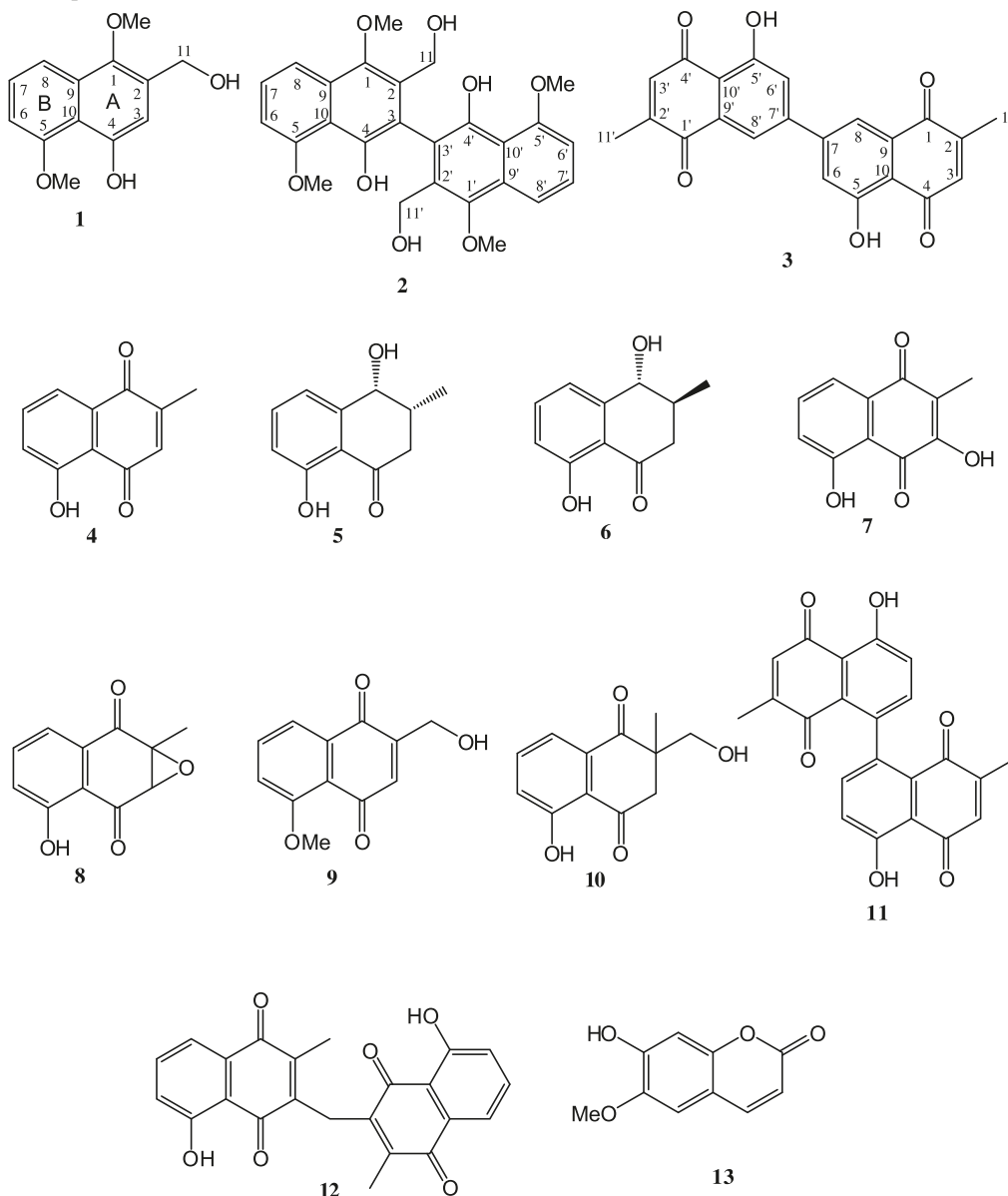
**C. Karalai.**<sup>1</sup> Department of Chemistry and Center for Innovation in Chemistry, Faculty of Science, Prince of Songkla University, Hat-Yai, Songkhla 90112, Thailand; Crystal Materials Research Unit and Department of Chemistry, Faculty of Science, Prince of Songkla University, Hat-Yai, Songkhla 90112, Thailand.

**A. Kanjana-Opas.** Department of Industrial Biotechnology, Faculty of Agro-Industry, Prince of Songkla University, Hat-Yai, Songkhla 90112, Thailand.

**S. Yuenyongsawad.** Department of Pharmacognosy and Pharmaceutical Botany, Faculty of Pharmaceutical Sciences, Prince of Songkla University, Hat-Yai, Songkhla 90112, Thailand.

<sup>1</sup>Corresponding author (e-mail: chatchanok.k@psu.ac.th).



**Fig. 1.** Structures of compounds **1–13**.

The analysis of the  $^{13}\text{C}$  NMR spectral data of **1** (Table 1) through DEPT revealed 13 carbons among which are two methoxys ( $\delta_{\text{C}}$  56.1 and 62.3), an oxymethylene ( $\delta_{\text{C}}$  60.3), four  $\text{sp}^2$  methine, and six  $\text{sp}^2$  quaternary carbons. Of the six  $\text{sp}^2$  quaternary carbons, three were linked to oxygen atoms in view of their deshielded chemical shifts at  $\delta_{\text{C}}$  145.5, 150.7, and 156.3. Since two methoxyl groups are present, the third oxygenated quaternary carbon should link to a hydroxyl group. These data, together with seven unsaturations, suggested a naphthalene skeleton.

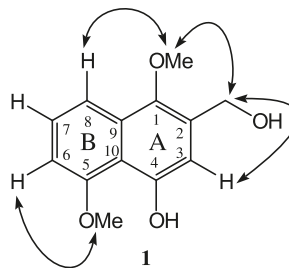
The  $^1\text{H}$  NMR data (Table 1) showed four aromatic proton signals. The first three signals appeared at  $\delta_{\text{H}}$  6.72 (1H, d,  $J$  = 8.4 Hz, H-6), 7.30 (1H, t,  $J$  = 8.4 Hz, H-7), and 7.60 (1H, d,  $J$  = 8.4 Hz, H-8). The fourth aromatic proton signal appeared as a broad singlet at  $\delta_{\text{H}}$  6.86 (1H, H-3), suggesting a substituent group in ring B and three substituent groups in ring A of a naphthalene skeleton. The two methoxyl protons, a hydroxyl proton and oxymethylene protons, appeared at  $\delta_{\text{H}}$

3.81, 3.98, 9.13, and 4.78 ppm, respectively. The HMBC experiment allowed the assignment of the structure as follows: the methyl singlet of O-CH<sub>3</sub> at  $\delta$  3.81 showed a correlation with C-1 ( $\delta$  145.5), whereas that at  $\delta$  3.98 showed a correlation with C-5 ( $\delta$  156.3), indicating the locations of the two O-CH<sub>3</sub> groups at C-1 and C-5, respectively. A methine proton H-3 ( $\delta$  6.86) showed clear  $^3J$  correlations with oxymethylene carbon C-11 ( $\delta$  60.3), the oxyquaternary carbon C-1 ( $\delta$  145.5), and C-10 ( $\delta$  115.1), and a  $^2J$  correlation with an oxyquaternary carbon C-4 ( $\delta$  150.7), in turn, oxymethylene protons H<sub>2</sub>-11 ( $\delta$  4.78) showed correlations with C-1 ( $\delta$  145.5), C-2 ( $\delta$  131.1), and C-3 ( $\delta$  109.8), hence, the hydroxymethyl group was located at C-2 and a hydroxyl group at C-4 of ring A. The NOESY experiment revealed interactions between 1-OCH<sub>3</sub>-H<sub>2</sub>-11, H<sub>2</sub>-11-H-3, 1-OCH<sub>3</sub>-H-8, and 5-OCH<sub>3</sub>-H-6, thus supporting the assigned structure (Fig. 2). Compound **1** was therefore characterized as 2-hydroxy-

**Table 1.**  $^1\text{H}$  NMR and  $^{13}\text{C}$  NMR spectral data of compounds **1** (400 MHz) and **2–4** (300 MHz) in  $\text{CDCl}_3$ .

	<b>1</b>			<b>2</b>			<b>3</b>			<b>4</b>		
Position	$\delta_{\text{H}}$ (mult., $J$ in Hz)	$\delta_{\text{C}}$		$\delta_{\text{H}}$ (mult., $J$ in Hz)	$\delta_{\text{C}}$		$\delta_{\text{H}}$ (mult., $J$ in Hz)	$\delta_{\text{C}}$		$\delta_{\text{H}}$ (mult., $J$ in Hz)	$\delta_{\text{C}}$	
1		145.5			147.8			183.1			183.9	
2		131.1			131.1			149.8			149.2	
3	6.86, br s	109.8			118.1		6.85, q, 1.5	135.5		6.63, brq, 1.5	134.9	
4		150.7			147.2			190.4			189.7	
5		156.3			156.3			158.9			160.7	
6	6.72, d, 8.4	104.3		6.84, d, 8.4	105.0		7.73, br s	118.7		7.06, dd, 8.4, 1.2	123.7	
7	7.30, t, 8.4	126.1		7.40, d, 8.4	126.1			131.2		7.46, t, 8.4	135.7	
8	7.60, d, 8.4	115.7		7.80, d, 8.4	116.5		7.73, br s	137.6		7.35, dd, 8.4, 1.2	118.7	
9		130.3			130.5			131.9			131.5	
10		115.1			115.6			115.3			114.5	
11	4.78, br s	60.3		4.50, d, 11.1	58.2		2.22, d, 1.5	16.4		2.01, d, 1.5	16.1	
11'				4.56, d, 11.1								
1-OCH <sub>3</sub>	3.81, s	62.3		4.01, s	63.4							
5-OCH <sub>3</sub>	3.98, s	56.1		3.98, s	56.2							
4-OH	9.13, s			9.58, s								
5-OH							12.50, s			11.79, s		

**Fig. 2.** NOESY correlations of compound **1**.



methyl-1,5-dimethoxynaphthalen-4-ol, a reduced and 1-*O*-methylated derivative of compound **9**.

Compound **2** was obtained as a white amorphous powder. The HR-EI-MS spectrum showed a molecular ion peak  $[\text{M}]^+$  at  $m/z$  466.1622, suggesting a molecular formula of  $\text{C}_{26}\text{H}_{26}\text{O}_8$ . A comparison of the NMR and mass spectral data between compounds **1** and **2** suggested that **2** was a dimer of **1** with  $\text{C}_2$  symmetry (see Table 1). A broad singlet signal of H-3 at  $\delta$  6.86 as shown in **1** was absent in **2**, suggesting the dimeric linkage between C-3 and C-3'. In addition, the methylene protons  $\text{H}_2$ -11 and  $\text{H}_2$ -11' were shown as two sets of doublets ( $\delta$  4.50 and 4.56, each  $J = 11.1$  Hz) implying a biaryl axis with four ortho substituents, which led to a restricted rotation. On the basis of this evidence, compound **2** was identified as 2,2'-bis-hydroxymethyl-1,1',5,5'-tetramethoxy-3,3'-binaphthalen-4,4'-diol.

Compound **3** was obtained as a red solid. The HR-EI-MS spectrum showed a molecular ion peak  $[\text{M}]^+$  at  $m/z$  374.0812, corresponding to the molecular formula of  $\text{C}_{22}\text{H}_{14}\text{O}_6$ . The UV spectrum exhibited bands at 210, 270, and 415 nm, typical of the general pattern observed for plumbagin.<sup>5</sup> The IR spectrum showed absorption bands for a hydroxyl ( $3473\text{ cm}^{-1}$ ), carbonyl ( $1664\text{ cm}^{-1}$ ), and aromatic ring ( $1600\text{ cm}^{-1}$ ). The  $^{13}\text{C}$  and  $^1\text{H}$  NMR spectral data revealed only 11 carbon signals and proton signals similar to a plumbagin, but the mass spectrum and the molecular formula revealed 22 carbons, thus suggesting that **3** is a symmetrical dimer of plumbagin. The  $^1\text{H}$  NMR spectrum (see Table 1) of **3** was comparable to that of plumbagin (**4**) except that there were no clear signals for the ortho- and meta-coupled protons, but there was the presence of a broad singlet aromatic proton at  $\delta_{\text{H}}$  7.73 (2H, H-6 and H-8). The triplet proton signal of H-7 at  $\delta$  7.46, as was present in **4**, was absent in **3**, thus suggesting the linkage to be at the 7 to 7' positions. The structure of **3** was thus established to be 5,5'-dihydroxy-2,2'-dimethyl-7,7'-binaphthalen-1,1',4,4'-tetraone, a 7-7'-plumbagin dimer.

In addition, sixteen other compounds of known structures were isolated from *D. wallichii*, viz., plumbagin (**4**),<sup>6</sup> isoshinanolone (**5**), epi-isoshinanolone (**6**),<sup>7</sup> droserone (**7**),<sup>5</sup> 2,3-epoxyplumbagin (**8**),<sup>8</sup> 2-hydroxymethyl-5-methoxy-1,4-naphthoquinone (**9**),<sup>9</sup> diomuscione (**10**),<sup>10</sup> maritnone (**11**),<sup>6</sup> methylene-3,3'-biplumbagin (**12**),<sup>8</sup> scopoletin (**13**),<sup>11</sup> lupeone (**14**), lupeol (**15**), betulin (**16**), betulinaldehyde (**17**), betulinic acid (**18**),<sup>12</sup> and queretaroic acid (**19**).<sup>13</sup> All of the isolates were first reported from this species.

The antibacterial activity of naphthalene derivatives **1–5** and **7–11** are reported in Table 2. Compound **4** showed significant antibacterial activities against *Bacillus subtilis* and *En-*

**Table 2.** Antibacterial and cytotoxic activities of compounds **1–5** and **7–12**

Compounds	Antibacterial activity (MIC, µg/mL)								Cytotoxic activity MCF-7 (IC <sub>50</sub> , µg/mL) <sup>c</sup>
	Gram-positive bacteria <sup>a</sup>					Gram-negative bacteria <sup>b</sup>			
	<i>B. subtilis</i>	<i>S. aureus</i>	<i>E. faecalis</i>	MRSA	VRE	<i>S. typhi</i>	<i>S. sonei</i>	<i>P. aeruginosa</i>	
<b>1</b>	75	300	150	150	150	300	150	>300	0.78
<b>2</b>	>300	>300	>300	>300	>300	>300	>300	300	0.51
<b>3</b>	150	>300	300	150	300	>300	150	>300	0.09
<b>4</b>	4.68	37.5	4.68	9.37	9.37	37.5	9.37	150	0.46
<b>5</b>	300	>300	300	>300	>300	>300	300	>300	9.57
<b>7</b>	150	>300	300	>300	150	>300	150	>300	0.29
<b>8</b>	75	150	75	18.75	75	300	75	300	0.35
<b>9</b>	9.37	37.5	9.37	9.37	37.5	37.5	9.37	>300	0.80
<b>10</b>	9.37	75	18.75	18.75	37.5	75	9.37	300	0.86
<b>11</b>	150	>300	150	>300	>300	>300	>300	>300	0.06
<b>12</b>	—	—	—	—	—	—	—	—	0.31
Camptothecin									<0.024
Vancomycin	<2.34	<2.34	<2.34	<2.34	<2.34	<2.34	<2.34	<2.34	

<sup>a</sup>*Bacillus subtilis*, *Staphylococcus aureus* TISTR 517, *Enterococcus faecalis* TISTR 459, methicillin-resistant *S. aureus* (MRSA) ATCC 43300, and vancomycin-resistant *E. faecalis* (VRE) ATCC 51299.  
<sup>b</sup>*Salmonella typhi*, *Shigella sonei*, and *Pseudomonas aeruginosa*.  
<sup>c</sup>Human breast adenocarcinoma cell line.

*terococcus faecalis*, but moderate activity against methicillin-resistant *Staphylococcus aureus* (MRSA), vancomycin-resistant *E. faecalis* (VRE), and *Shigella sonei*. Compounds **9** and **10** exhibited moderate antibacterial activities against *B. subtilis* and *S. sonei*, while compound **9** also exhibited moderate antibacterial activities against *E. faecalis* and MRSA. Anti-fungal activity against *Candida albicans* was inactive for all compounds. In addition, the cytotoxicity against MCF-7 (human breast adenocarcinoma) cell line of compounds **1–5** and **7–12** was also evaluated. All compounds except compound **5** were active. Compounds **3** and **11** exhibited better activity than the rest of the tested compounds with IC<sub>50</sub> values of 0.09 and 0.06 µg/mL, respectively.

Experimental

General experimental procedures

Melting points were determined on the Fisher–Johns melting-point apparatus. The optical rotation [α]<sub>D</sub> was measured in chloroform solution with sodium D line (590 nm) on a JASCO P-1020 digital polarimeter. UV and IR spectra were recorded on a SPECORD S100 (Analytikjena) and PerkinElmer FTS FTIR spectrophotometer, respectively. NMR spectra were recorded using 300 and 400 MHz Bruker FTNMR Ultra Shield spectrometers in CDCl<sub>3</sub> with TMS as the internal standard. Chemical shifts are reported in δ (ppm) and coupling constants (*J*) are expressed in hertz. EI and HR-EI mass spectra were measured on a Kratos MS 25 RFA spectrometer. Solvents for extraction and chromatography were distilled at their boiling point ranges prior to use except chloroform was an analytical grade reagent. Quick column chromatography (QCC) and column chromatography (CC) were carried out on silica gel 60H (Merck) and silica gel 100 (Merck), respectively.

Plant material

The roots and fruits of *D. wallichii* were collected in De-

cember 2008 from Satun Province in the southern part of Thailand. This plant was identified by Professor Puangpen Siriruga and a voucher specimen (No. PSU 0013410) has been deposited at the Herbarium of the Department of Biology, Faculty of Science, Prince of Songkla University (PSU), Thailand.

Extraction and isolation

The dried roots of *D. wallichii* (2.5 kg) were extracted with hexane and CH<sub>2</sub>Cl<sub>2</sub> successively (2 × 10 L for each solvent for one week) at room temperature and evaporated under reduced pressure to provide crude hexane (30.7 g) and CH<sub>2</sub>Cl<sub>2</sub> (20.2 g) extracts.  
The crude hexane extract (30.7 g) was subjected to quick column chromatography (QCC) using hexane as eluent and increasing the polarity with EtOAc to give nine fractions (F1–F9). Fraction F2 (8.8 g) was recrystallized from methylene chloride to give **4** (4.3 g). Fraction F4 (3.5 g) was separated by QCC using EtOAc–hexane (1:9, v/v) as the eluting solvent to afford five subfractions (F4a–F4e). Subfraction F4d (762.3 mg) was purified by QCC with EtOAc–hexane (0.5:9.5, v/v) to afford **6** (117.2 mg). Fraction F6 (1.5 g) was separated by QCC using CH<sub>2</sub>Cl<sub>2</sub>–hexane (4:6, v/v) as the eluting solvent to afford three subfractions (F6a–F6c). Subfraction F6c (428.6 mg) was purified by QCC with EtOAc–hexane (2:8, v/v) to give **5** (47.7 mg). Fraction F7 (6.4 g) was separated by QCC with EtOAc–hexane (3:7, v/v) to afford **15** (3.9 g) and **17** (509.2 mg). Fraction F9 (1.3 g) was separated by QCC with EtOAc–CH<sub>2</sub>Cl<sub>2</sub> (1:9, v/v) to give **3** (156.4 mg).  
The CH<sub>2</sub>Cl<sub>2</sub> extract (20.2 g) was separated by QCC using hexane as eluent and increasing the polarity with EtOAc to give six fractions (F1–F6). Fraction F2 (3.6 g) was separated by QCC with EtOAc–hexane (2:8, v/v) to afford **13** (35.4 mg), **14** (3.7 g), and **16** (25.6 mg). Fraction F3 (1.2 g) was separated by QCC using acetone–hexane (2:9, v/v) as

the eluting solvent to afford six subfractions (F3a–F3f). Subfraction F3d (352.8 mg) was purified by QCC with EtOAc–hexane (1:9, v/v) to give **7** (33.6 mg). Fraction F4 (612.8 mg) was separated by QCC with acetone–hexane (1:9, v/v) to afford **10** (18.4 mg). Fraction F5 (2.3 g) was separated by QCC using EtOAc–hexane (3:7, v/v) as the eluting solvent to afford four subfractions (F5a–F5d). Subfraction F5c (1.5 g) was separated by QCC using acetone–hexane (2:8, v/v) as the eluting solvent to afford five subfractions (F5c1–F5c5). Subfraction F5c3 (527.2 mg) was purified by QCC with CH<sub>2</sub>Cl<sub>2</sub>–hexane (4:6, v/v) to give **1** (40.4 mg). Subfraction F5c5 (752.3 mg) was purified by QCC with EtOAc–hexane (3:7, v/v) to give **2** (32.4 mg).

The fresh fruits of *D. wallichii* (0.5 kg) were extracted with MeOH successively (2 × 2 L for each solvent for one week) at room temperature. The extract was evaporated to dryness and the residue was partitioned between CH<sub>2</sub>Cl<sub>2</sub> and H<sub>2</sub>O. The CH<sub>2</sub>Cl<sub>2</sub> layer was evaporated and the residue (9.2 g) was subjected to QCC using hexane as eluent and increasing the polarity with EtOAc to give five fractions (F1–F5). Fraction F2 (1.3 g) was separated by QCC using EtOAc–hexane (1:9, v/v) as the eluting solvent to afford five subfractions (F2a–F2e). Subfraction F2d (452.2 mg) was purified by QCC with EtOAc–hexane (0.5:9.5, v/v) to give **8** (19.5 mg) and **19** (11.7 mg). Subfraction F2e (552.3 mg) was separated by QCC using EtOAc–hexane (0.5:9.5, v/v) as the eluting solvent to afford two subfractions (F2e1 and F2e2). Subfraction F2e2 (359.3 mg) was purified by QCC with CH<sub>2</sub>Cl<sub>2</sub>–hexane (3:7, v/v) to afford **11** (14.7 mg). Fraction F3 (3.3 g) was separated by QCC using acetone–hexane (2:8, v/v) as the eluting solvent to afford five subfractions (F3a–F4e). Subfraction F3a (528.1 mg) was purified by QCC with EtOAc–hexane (3:7, v/v) to give **9** (10.5 mg) and **12** (13.4 mg). Fraction F4 (1.5 g) was separated by QCC with EtOAc–hexane (5:5, v/v) to afford **18** (18.9 mg).

### 2-Hydroxymethyl-1,5-dimethoxynaphthalen-4-ol (**1**)

White amorphous powder; mp 63–65 °C. UV (MeOH, nm)  $\lambda_{\text{max}}$ : 231 and 291. IR (neat, cm<sup>-1</sup>)  $\nu_{\text{max}}$ : 3400, 1633, 1613, 1445, 1387, 1262, 1239, 1072, 996, 755. <sup>1</sup>H NMR (CDCl<sub>3</sub>, 300 MHz) and <sup>13</sup>C NMR (CDCl<sub>3</sub>, 75 MHz), see Table 1. HR-EI-MS *m/z* [M]<sup>+</sup>: 234.0920 (calcd. for C<sub>13</sub>H<sub>14</sub>O<sub>4</sub>: 233.9992).

### 2,2'-Bis-hydroxymethyl-1,1',5,5'-tetramethoxy-3,3'-binaphthalen-4,4'-diol (**2**)

White amorphous powder; mp 115–117 °C. [ $\alpha$ ]<sub>D</sub><sup>27</sup> +5.64 (c 0.36, CHCl<sub>3</sub>). UV (MeOH, nm)  $\lambda_{\text{max}}$ : 228 and 295. IR (neat, cm<sup>-1</sup>)  $\nu_{\text{max}}$ : 3389, 1632, 1605, 1455, 1382, 1357, 1244, 1069, 998, 762. <sup>1</sup>H NMR (CDCl<sub>3</sub>, 400 MHz) and <sup>13</sup>C NMR (CDCl<sub>3</sub>, 100 MHz), see Table 1. HR-EI-MS *m/z* [M]<sup>+</sup>: 466.1622 (calcd. for C<sub>26</sub>H<sub>26</sub>O<sub>8</sub>: 466.1627).

### 5,5'-dihydroxy-2,2'-dimethyl-7,7'-binaphthalen-1,1',4,4'-tetraone (**3**)

Red solid; mp 250 °C (decomposed). UV (MeOH, nm)  $\lambda_{\text{max}}$ : 210, 270, and 415. IR (neat, cm<sup>-1</sup>)  $\nu_{\text{max}}$ : 3473, 1664, 1641, 1600, 1418, 1367, 1353, 1261, 774. <sup>1</sup>H NMR (CDCl<sub>3</sub>, 300 MHz) and <sup>13</sup>C NMR (CDCl<sub>3</sub>, 75 MHz), see Table 1.

HR-EI-MS *m/z* [M]<sup>+</sup>: 374.0812 (calcd. for C<sub>22</sub>H<sub>14</sub>O<sub>6</sub>: 347.0790).

## Bioassays

### Antibacterial assay

The isolated compounds from the roots and fresh fruits of *D. wallichii* were tested against both Gram-positive and Gram-negative bacteria: *B. subtilis*, *S. aureus* TISTR 517, *E. faecalis* TISTR 459, methicillin-resistant *S. aureus* (MRSA) ATCC43300, vancomycin-resistant *E. faecalis* (VRE) ATCC 51299, *Streptococcus faecalis*, *Salmonella typhi*, *S. sonnei*, and *Pseudomonas aeruginosa*. The microorganisms were obtained from the culture collections from the Department of Industrial Biotechnology and Department of Pharmacognosy and Botany, PSU, Thailand, except for the TISTR and ATCC strains, which were obtained from the Microbial Research Center (MIRCEN), Bangkok, Thailand. The antibacterial assay employed was the same as described in Boonsri et al.<sup>14</sup> Vancomycin, which was used as a standard, showed antibacterial activity against vancomycin-resistant *E. faecalis* (VRE) ATCC 51299 at <2.34 µg/mL.

### Cytotoxic assay

The cancer cell lines MCF-7 (human breast adenocarcinoma) were grown in Dulbecco's modified eagle medium: nutrient mixture F12 (D-MEM/F12) supplemented with 10% fetal bovine serum (FBS). Cells were seeded in 96 wells (3000 cell/well) and allowed to adhere for 24 h at 37 °C with 5% CO<sub>2</sub> in a fully humidified incubator. Then 100 µL of 25 µg/mL crude extract or fivefold diluted pure compound in medium (final concentration 0.008, 0.04, 0.2, 1, and 5 µg/mL) were dispensed into wells of the cell plates and incubated further for 72 h. After removal of the sample medium, the cells were topped up with 200 µL D-MEM/F12 medium and incubated. After 72 h, cells were fixed with cold 40% trichloroacetic acid and kept at 4 °C for 1 h and washed with tap water. The cells were determined by a sulphorhodamine assay. The absorbance was measured at 492 nm using a microplate reader. The results were based on the ability of the extracts to inhibit cell growth compared to control (cells in media without extract) and calculated for IC<sub>50</sub> using probit analysis. Camptothecin, which was used as a standard, showed cytotoxic activity at <0.024 µg/mL.

## Acknowledgements

We are grateful to the Center for Innovation in Chemistry (PERCH-CIC), Commission on Higher Education, Ministry of Education, and the Prince of Songkla University through the Crystal Materials Research Unit and the Graduate School for financial support. AWS thanks Associate Professor Dr. Uma Prawat for her helpful suggestion, Mr. T. Anantapong for the bioactivity tests, and Dr. Yaowapa Sukpondma and Miss Nareerat Thongtip for the NMR measurements.

## References

- (1) Utsunomiya, N.; Subhadrabandhu, S.; Yonemori, K.; Oshida, M.; Kanzaki, S.; Nakatsubo, F.; Sugiura, A. *Econ. Bot.* **1998**, 52, 343.



- (2) Nareeboon, P.; Kraus, W.; Beifuss, U.; Conrad, J.; Klaiber, I.; Sutthivaiyakit, S. *Tetrahedron* **2006**, *62* (23), 5519. doi:10.1016/j.tet.2006.03.034.
- (3) Prajoubklang, A.; Sirithunyalug, B.; Charoenchai, P.; Suvannakad, R.; Sriubolmas, N.; Piyamongkol, S.; Kongsaree, P.; Kittakoo, P. *Chem. Biodivers.* **2005**, *2* (10), 1358. doi:10.1002/cbdv.200590108. PMID:17191937.
- (4) Smitinand, T. *Thai Plant Names*; Prachachon: Bangkok, 2001; p. 94.
- (5) Gunaherath, G. M. K. B.; Gunatilaka, A. A. L.; Sultanbawa, M. U. S.; Balasubramaniam, S. *Phytochemistry* **1983**, *22* (5), 1245. doi:10.1016/0031-9422(83)80232-5.
- (6) Gu, J. Q.; Graf, T. N.; Lee, D.; Chai, H. B.; Mi, Q.; Kardono, L. B. S.; Setyowati, F. M.; Ismail, R.; Riswan, S.; Farnsworth, N. R.; Cordell, G. A.; Pezzuto, J. M.; Swanson, S. M.; Kroll, D. J.; Falkinham, J. O., III; Wall, M. E.; Wani, M. C.; Kinghorn, A. D.; Oberlies, N. H. *J. Nat. Prod.* **2004**, *67* (7), 1156. doi:10.1021/np040027m. PMID:15270571.
- (7) Bringmann, G.; Munchbach, M.; Messer, K.; Koppler, D.; Michel, M.; Schupp, O.; Wenzel, M.; Louis, A. M. *Phytochemistry* **1999**, *51* (5), 693. doi:10.1016/S0031-9422(99)00080-1.
- (8) Higa, M.; Noha, N.; Yokaryo, H.; Ogihara, K.; Yogi, S. *Chem. Pharm. Bull. (Tokyo)* **2002**, *50* (5), 590. doi:10.1248/cpb.50.590. PMID:12036010.
- (9) Wurm, G.; Geres, U.; Schmidt, H. *Arch. Pharm. (Weinheim)* **1981**, *314* (12), 1055. doi:10.1002/ardp.19813141214.
- (10) Miyoshi, E.; Shizuri, Y.; Yamamura, S. *Phytochemistry* **1984**, *23* (10), 2385. doi:10.1016/S0031-9422(00)80563-4.
- (11) Razdan, T. K.; Qadri, B.; Harkar, S.; Waight, E. S. *Phytochemistry* **1987**, *26* (7), 2063. doi:10.1016/S0031-9422(00)81759-8.
- (12) Mahato, S. B.; Kundu, A. P. *Phytochemistry* **1994**, *37* (6), 1517. doi:10.1016/S0031-9422(00)89569-2.
- (13) Ye, Y.; Kinoshita, K.; Koyama, K.; Takahashi, K.; Kondo, N.; Yuasa, H. *J. Nat. Prod.* **1998**, *61* (4), 456. doi:10.1021/np970364d.
- (14) Boonsri, S.; Karalai, C.; Ponglimanont, C.; Kanjana-opas, A.; Chantrapromma, K. *Phytochemistry* **2006**, *67* (7), 723. doi:10.1016/j.phytochem.2006.01.007. PMID:16494905.

# Electrochemical oxidation of sulfide ion in synthetic sour brines using periodic polarity reversal at Ebonex<sup>®</sup> electrodes

Shaimaa El-Sherif, Dorin Bejan, and Nigel J. Bunce

**Abstract:** The Magneli phase Ti<sub>4</sub>O<sub>7</sub> (Ebonex<sup>®</sup>) was used as both anode and cathode in the electrochemical oxidation of sulfide ion in alkaline solution in the absence and presence of chloride and naphthenate ions. Ebonex anodes gradually lost their activity through the formation of an over-oxidized surface layer, but their activity could be maintained by periodic polarity reversal. In the context of the current paradigm for the mechanistic behaviour of oxide-based anodes, Ti<sub>4</sub>O<sub>7</sub> has properties that combine those of “inactive” anodes (formation of hydroxyl radicals) and “active” anodes (formation of a higher oxide at the surface), with the exception that the higher oxide in the case of Ti<sub>4</sub>O<sub>7</sub> is TiO<sub>2</sub>, which is incapable of substrate oxidation. Sulfate is the major oxidation product, especially in the presence of chloride, an ubiquitous component of sour brines, via mediated electro-oxidation to hypochlorite. Unlike at boron-doped diamond anodes, at which sulfide is oxidized with near-quantitative current efficiency, significant parasitic oxidation of water to O<sub>2</sub> occurs at Ebonex, and oxidation of sulfide requires ~16 F mol<sup>-1</sup>, corresponding to a 50% current efficiency.

**Key words:** geothermal sour brines, electrochemical oxidation of sulfide, Magneli phase Ti<sub>4</sub>O<sub>7</sub>, hydroxyl radicals.

**Résumé :** La phase Magneli du Ti<sub>4</sub>O<sub>7</sub> (Ebonex<sup>®</sup>) a été utilisée tant comme anode que comme cathode dans l'oxydation électrochimique de l'ion sulfure en solution alcaline, en l'absence et en présence d'ions chlorure et naphténate. Les anodes d'Ebonex perdent graduellement leur activité en raison de la formation d'une couche superficielle suroxydée; toutefois, leur activité peut être maintenue par un renversement périodique de polarité. Dans le contexte du paradigme actuel pour le comportement mécanistique des anodes à base d'oxydes, le Ti<sub>4</sub>O<sub>7</sub> possède des propriétés qui combinent celles des anodes « inactives » (formation de radicaux hydroxyles) et celles des anodes « actives » (formation à la surface d'un oxyde plus élevé); toutefois, dans le cas du Ti<sub>4</sub>O<sub>7</sub>, l'oxyde plus élevé est le TiO<sub>2</sub> qui est incapable de donner lieu à une oxydation du substrat. Le sulfate est le produit d'oxydation majeur, particulièrement en présence de l'ion chlorure, un composant normal de toutes les saumures acides obtenu par l'électrooxydation en hypochlorite. Contrairement aux anodes de diamant dopées au bore avec lesquelles le sulfure est oxydé avec une efficacité de courant pratiquement quantitative, l'Ebonex donne lieu à une oxydation parasite importante de l'eau en O<sub>2</sub> et l'oxydation du sulfure requiert environ 16 F mol<sup>-1</sup>, ce qui correspond à une efficacité de courant d'environ 50 %.

**Mots-clés :** saumures acides géothermiques, oxydation électrochimique du sulfure, phase Magneli du Ti<sub>4</sub>O<sub>7</sub>, radicaux hydroxyles.

## Introduction

Geothermal “sour brines” that accompany natural-gas extraction contain inorganic sulfide at concentrations up to ~60 mmol L<sup>-1</sup> and have pH ~8.<sup>1</sup> Volatilization of hydrogen sulfide (pK<sub>a1</sub> = 6.88, pK<sub>a2</sub> = 14.15)<sup>2</sup> from sour brines is problematic in terms of odour and toxicity, and the brine itself causes corrosion of metal pipes.<sup>3–6</sup> Electrolysis is of interest for their remediation because sulfide ion is readily oxidizable, and because geothermal brines contain sufficient electrolytes that no additional supporting electrolyte is required. Advantages of electrochemical oxidation include the low cost of electrons per mol compared with chemical reagents, and avoiding the cost of disposal of toxic sludge when metal-based oxidants or precipitants are used.<sup>7,8</sup> Major anionic species present in sour brines include chloride (up to

5% NaCl) and naphthenates (up to 6%); the latter are polycyclic aliphatic carboxylates ubiquitously associated with hydrocarbon resources.

Our research into the electrochemical oxidation of sulfide in geothermal brines has the goal of finding cheap, rugged, and long-lasting anode materials that oxidize sulfide efficiently. The experimental approach involves studying the kinetics and products of sulfide oxidation in synthetic solutions in the absence and presence of chloride and naphthenate ions. To date, no anode material satisfies all the above conditions. Boron-doped diamond (BDD) anodes gave exceptional (near quantitative) chemical and current efficiencies for the oxidation of sulfide to sulfate in both the absence and presence of chloride ion,<sup>9</sup> but are not available inexpensively in large format. Carbon anodes (graphite,

Received 2 March 2010. Accepted 11 May 2010. Published on the NRC Research Press Web site at canjchem.nrc.ca on 6 August 2010.

S. El-Sherif, D. Bejan, and N.J. Bunce.<sup>1</sup> Electrochemical Technology Centre, Chemistry Department, University of Guelph, 50 Stone Road East, Guelph, ON N1G 2W1, Canada.

<sup>1</sup>Corresponding author (e-mail: nbunce@uoguelph.ca).

**Table 1.** Repeated use of the same Ebonex anode in the electrolysis of sulfide; cathode: stainless steel; supporting electrolyte: 0.25 mol L<sup>-1</sup> NaOH; current, 100 mA; experiments 6 and 7 with 1% sodium chloride. All  $\pm$  values represent one standard deviation.

Experiment No.	Sulfide loss		Sulfate formation		
	Rate (slope) (mmol L <sup>-1</sup> min <sup>-1</sup> )	Intercept	Rate (mmol L <sup>-1</sup> min <sup>-1</sup> )	Intercept	Sulfate yield (%)
1	0.073 ( $\pm 0.004$ )	56.0 ( $\pm 0.3$ )	0.017 ( $\pm 0.007$ )	1.4 ( $\pm 0.5$ )	39
2	0.033 ( $\pm 0.004$ )	40.9 ( $\pm 0.5$ )	0.006 ( $\pm 0.006$ )	6.1 ( $\pm 0.8$ )	9
3	0.024 ( $\pm 0.001$ )	30.2 ( $\pm 0.2$ )	0.005 ( $\pm 0.005$ )	2.6 ( $\pm 0.3$ )	21
4	0.020 ( $\pm 0.001$ )	17.3 ( $\pm 0.3$ )	0.015 ( $\pm 0.002$ )	-0.9 ( $\pm 0.5$ )	76
5	0.029 ( $\pm 0.002$ )	30.6 ( $\pm 0.4$ )	0.009 ( $\pm 0.002$ )	0.7 ( $\pm 0.2$ )	38
6	0.011 ( $\pm 0.002$ )	31.4 ( $\pm 0.4$ )	0.011 ( $\pm 0.001$ )	0.4 ( $\pm 0.2$ )	104
7	0.004 ( $\pm 0.001$ )	32.6 ( $\pm 0.1$ )	0.001 ( $\pm 0.001$ )	0.5 ( $\pm 0.2$ )	69

granulated activated carbon, and industrial coke) behaved sacrificially, giving preponderantly organosulfonate species as products.<sup>10,11</sup> Dimensionally stable anodes based on Ti/IrO<sub>2</sub>-Ta<sub>2</sub>O<sub>5</sub> were gradually poisoned by sulfide,<sup>12</sup> as previously observed with other noble metal anodes.<sup>13-16</sup>

Ebonex<sup>®</sup> is the registered trademark for an electrically conductive and corrosion-resistant ceramic “sub-oxide” of TiO<sub>2</sub> having the approximate composition Ti<sub>4</sub>O<sub>7</sub>.<sup>17</sup> Ebonex is structurally a Magneli phase, with interleaved layers averaging one TiO unit for every three TiO<sub>2</sub> units. Ebonex is like BDD with respect to its wide stability range vs. water decomposition under both anodic (>2 V vs. SCE) and cathodic (-1.4 V vs. SCE) polarization.<sup>18-21</sup> To date, the chief commercial application of Ebonex is cathodic protection of the reinforcing bars in structural concrete, to inhibit corrosion through exposure to road salt<sup>17</sup> and as coated electrodes in bipolar lead-acid batteries.<sup>22,23</sup>

Our interest in the use of Ebonex as an anode for environmental remediation<sup>24</sup> was stimulated by a report of the mineralization of trichloroethylene at an Ebonex anode.<sup>25</sup> The present investigation was undertaken to evaluate the performance of Ebonex for the remediation of sour brines.

## Materials and methods

### Materials

Sodium sulfide nonahydrate (ACS reagent, 98%) and barium chloride dihydrate were provided by Sigma-Aldrich (St. Louis, MO). Sodium chloride and sodium hydroxide were supplied by Fisher Scientific (Fair Lawn, NJ) and naphthenic acids were supplied by Fluka (Sigma-Aldrich, Oakville, ON). Bleach “No Name” was bought from Zehrs, Guelph. Sodium thiosulfate and starch indicator used in iodometric titrations, magnesium chloride, potassium nitrate, anhydrous sodium acetate, hydrochloric acid, and glacial acetic acid were provided by Fisher Scientific (Fair Lawn, NJ). Iodine, potassium iodide, and sodium sulfate (anhydrous, 99%) were provided by Caledon Laboratories, Georgetown, ON. Solutions were prepared using distilled water and reagent-grade chemicals.

Cylindrical Ebonex electrodes (length 7.5 cm and diameter 1.8 cm) were supplied by Vector Corrosion, Stoney Creek, ON, and were cut lengthwise for use as semicylindrical electrodes. The immersed area was 10 cm<sup>2</sup>. In initial experiments, stainless steel plates (machine shop, University of Guelph) were used as cathodes.

### Apparatus

Batch electrolyses were performed at constant current in a 100 mL Pyrex beaker with 80 mL of solution under stirring using a magnetic stir bar. Power was supplied by an EG&G Model 363 potentiostat/galvanostat. The electrode material was cut into pieces of 7.5  $\times$  1.8 cm and the immersed area was 10 cm<sup>2</sup>. Electrical connections were made to the electrodes with alligator clips. The electrodes were positioned vertically to allow the escape of gases evolved during electrolysis. Most experiments were done by switching polarity between two Ebonex electrodes using a Siemens Logo! 12/24 RC device. A multimeter (Wavetek DM5XL) was used to monitor the voltage as well as the anode potential, against a Hg/HgSO<sub>4</sub> reference electrode, in some experiments.

Electrolysis in flow mode of operation utilized a rectangular Plexiglas cell (internal dimensions: 2.9  $\times$  2.9  $\times$  7.5 cm) whose lid (also Plexiglas) held four cylindrical Ebonex electrodes (7.5 cm length and 1 cm diameter, external dimensions) and immersed 6 cm length in 40 mL of solution. A single-pass upward flow was provided by a Masterflex C/L peristaltic pump with adjustable flow. The electrodes were connected in diagonal pairs and operated with periodically reversed polarity.

### Experimental procedures

The solutions contained sodium sulfide (5–60 mmol L<sup>-1</sup>) with 0.25 mmol L<sup>-1</sup> sodium hydroxide supporting electrolyte. Experiments were also conducted in the presence of sodium chloride (1%–5% w/v) and (or) naphthenic acids (1% w/v). Concentrations of sulfide and tetrathionate were determined iodometrically.<sup>26,27</sup> The concentration of sulfate was determined by turbidimetry at 420 nm using a Pharmacia LKB Novaspec II UV-vis spectrophotometer. Throughout the paper, including in Tables 1–4, the “rate of sulfate formation” is based on the fit to a linear model (where appropriate), but “sulfate yield” is calculated as mol sulfate formed per mol sulfide consumed, based on the final data point in the experiment. For samples containing naphthenic acids, a 1 mL sample was acidified with two drops of concentrated HCl, and the naphthenic acids were extracted with 1 mL of chloroform prior to analyzing for sulfate turbidimetrically. Hypochlorite was determined iodometrically.<sup>26</sup>

X-ray photoelectron spectroscopy was carried out using a Kratos Axis Ultra X-ray photoelectron spectrometer at the Surface Science Western laboratories of the University of Western Ontario, London, ON. Survey scan analyses were carried out with an analysis area of 300  $\times$  700 microns (1

**Table 2.** Repeated use of the same Ebonex pair of electrodes in the electrolysis of sulfide with reverse polarity every 60 min; supporting electrolyte: 0.25 mol L<sup>-1</sup> NaOH; current: 100 mA; experiments 4, 5, and 6 with 1%, 3%, and 5% sodium chloride, respectively. All  $\pm$  values represent one standard deviation.

Experiment No.	Sulfide loss		Sulfate formation		Sulfate yield (%)
	Rate (slope) (mmol L <sup>-1</sup> min <sup>-1</sup> )	Intercept	Rate (mmol L <sup>-1</sup> min <sup>-1</sup> )	Intercept	
1	0.052 ( $\pm 0.004$ )	30.1 ( $\pm 0.7$ )	0.038 ( $\pm 0.002$ )	0.4 ( $\pm 0.2$ )	72
2	0.042 ( $\pm 0.003$ )	27.9 ( $\pm 0.3$ )	0.032 ( $\pm 0.002$ )	0.6 ( $\pm 0.2$ )	85
3	0.049 ( $\pm 0.002$ )	30.6 ( $\pm 0.3$ )	0.030 ( $\pm 0.003$ )	0.6 ( $\pm 0.5$ )	71
4	0.046 ( $\pm 0.000$ )	30.4 ( $\pm 0.1$ )	0.031 ( $\pm 0.002$ )	0.8 ( $\pm 0.2$ )	78
5	0.061 ( $\pm 0.003$ )	31.3 ( $\pm 0.4$ )	0.033 ( $\pm 0.002$ )	0.1 ( $\pm 0.1$ )	57
6	0.058 ( $\pm 0.003$ )	30.1 ( $\pm 0.4$ )	0.045 (0.004)	0.0 ( $\pm 0.6$ )	82
7	0.043 ( $\pm 0.001$ )	30.0 ( $\pm 0.2$ )	0.024 ( $\pm 0.005$ )	0.0 ( $\pm 0.6$ )	56

**Table 3.** Sulfide reaction rate and sulfate yield in the electrolysis of 30 mmol L<sup>-1</sup> sulfide with different concentrations of NaCl; supporting electrolyte: 0.25 mol L<sup>-1</sup> NaOH; current: 100 mA; reversed polarity every 60 min.

Chloride concentration (%)	Sulfide		Sulfate yield (%)
	Rate (mmol L <sup>-1</sup> min <sup>-1</sup> )	Intercept	
0	0.042 ( $\pm 0.003$ )	27.9 ( $\pm 0.3$ )	85
1	0.046 ( $\pm 0.000$ )	30.4 ( $\pm 0.1$ )	78
3	0.061 ( $\pm 0.003$ )	31.3 ( $\pm 0.4$ )	57
5	0.058 ( $\pm 0.003$ )	30.1 ( $\pm 0.4$ )	82

**Table 4.** Sulfide reaction rate and sulfate yield in the electrolysis of 30 mmol L<sup>-1</sup> sulfide with 1% NaCl at different switching polarity times; supporting electrolyte: 0.25 mol L<sup>-1</sup> NaOH; current: 100 mA.

Polarity switching time (min)	Sulfide		Sulfate yield (%)
	Rate (mmol L <sup>-1</sup> min <sup>-1</sup> )	Intercept	
60	0.046 ( $\pm 0.000$ )	30.4 ( $\pm 0.1$ )	78
30	0.064 ( $\pm 0.003$ )	29.3 ( $\pm 0.3$ )	88
<b>15</b>	<b>0.072 (<math>\pm 0.004</math>)</b>	<b>29.7 (<math>\pm 0.4</math>)</b>	<b>91</b>
5	0.060 ( $\pm 0.002$ )	28.1 ( $\pm 0.3$ )	100

micron = 1  $\mu$ m) and pass energy of 160 eV. High-resolution analyses were carried out with an analysis area of 300  $\times$  700 microns and pass energy of 20 eV.

## Results and discussion

### Batch cell experiments in the absence of naphthenic acids

Initial experiments were carried out in the undivided cell with an Ebonex anode and stainless steel cathode, using Na<sub>2</sub>S in the presence of 0.25 mol L<sup>-1</sup> NaOH as supporting electrolyte at constant current of 100 mA (10 mA cm<sup>-2</sup>). The loss of sulfide was current-controlled (linear with time/charge). The formation of sulfate ion was also linear with time, and corresponded to a yield of 79% based on moles of sulfide reacted (Fig. 1). The anode lost its activity upon repeated use, as shown in Table 1, which shows the trends for loss of sulfide and formation of sulfate (in mmol L<sup>-1</sup> min<sup>-1</sup>).

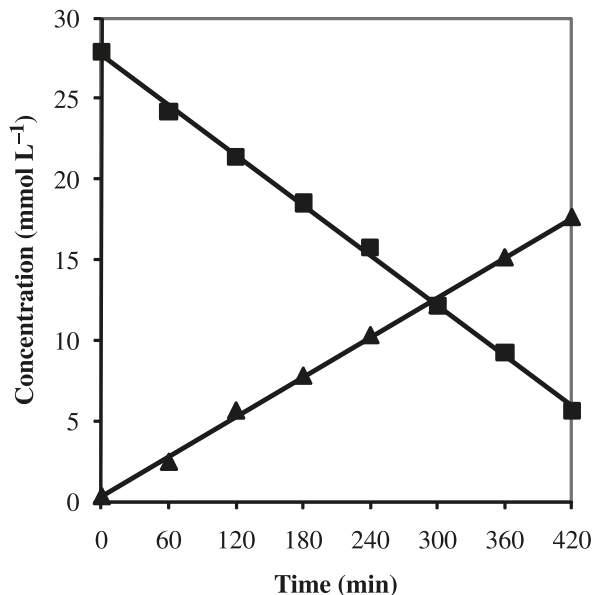
The Ebonex anode was regenerated after 10 experiments by sandblasting its surface to remove the presumed surface oxide layer. When it was then used for the oxidation of 30 mmol L<sup>-1</sup> sulfide, the activity was greater than that of an unused and untreated anode in the first hour of use (rate of

oxidation of sulfide: 0.087 mmol L<sup>-1</sup> min<sup>-1</sup>) but then decreased to 0.034 mmol L<sup>-1</sup> min<sup>-1</sup> (see Fig. 1 in the Supplementary data).

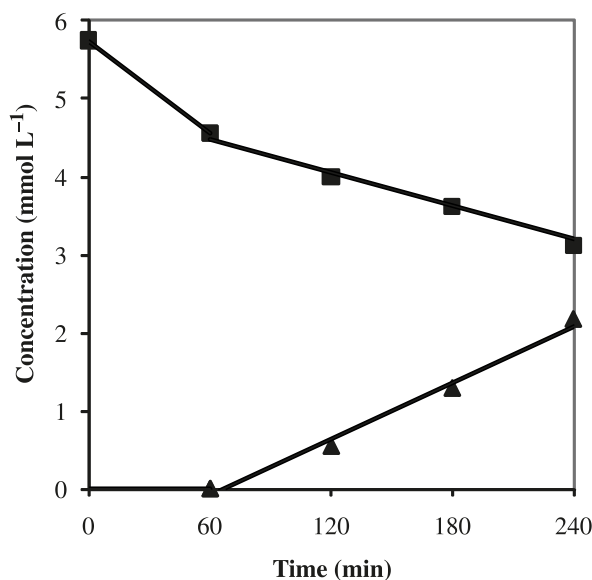
In previous work, a galvanic cell was produced when Ebonex anode and Ebonex cathode were used in an electrolytic cell. This indicated that the surface of the former anode had been oxidized to a composition Ti<sub>4</sub>O<sub>7</sub> and that of the former cathode had been reduced to Ti<sub>4</sub>O<sub><7</sub>.<sup>28</sup> In that work, Ebonex gradually lost its anodic activity towards the oxidation of the organic substrates *p*-nitrosodimethylaniline and acetaminophen upon repeated use, but could be partly reactivated by a single reversal of the polarity. This technique was also used in the present work, but a more successful method was to use Ebonex as both anode and cathode, and to reactivate the anode by reversing the polarity periodically. When a pair of Ebonex electrodes was used for the oxidation of sulfide under the same conditions as before, but with polarity reversal every 60 min, the efficiency of sulfide oxidation was maintained (Table 2) (the apparent anomaly that the activity was highest on the first use of the electrodes will be discussed below). Polarity reversal was used in all subsequent experiments except as noted. Unlike at BDD,<sup>9</sup>



**Fig. 1.** Loss of sulfide (■) and formation of sulfate (▲) in the electrolysis of a 28 mmol L<sup>-1</sup> sulfide solution at an unused Ebonex anode; cathode: stainless steel; supporting electrolyte: 0.25 mol L<sup>-1</sup> NaOH; current: 100 mA.



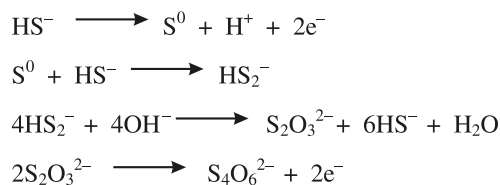
**Fig. 2.** Electrolysis of sulfide using an Ebonex pair of electrodes with polarity reversal every 60 min; supporting electrolyte: 0.25 mol L<sup>-1</sup> NaOH; current: 100 mA; sulfide (■); sulfate (▲).



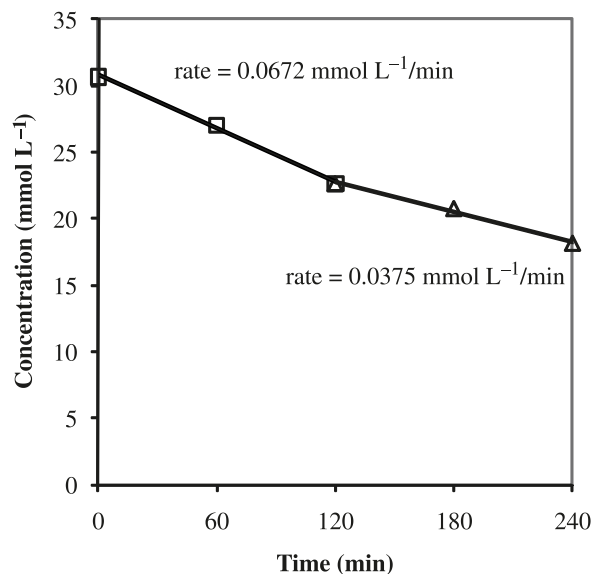
the oxidation of sulfide at Ebonex was accompanied by significant evolution of O<sub>2</sub> at the anode, showing that the current efficiency for oxidation of sulfide was not quantitative.

Tables 1 and 2 show that sulfate was not formed quantitatively when sulfide ion was oxidized at an Ebonex anode. Missing material was identified as tetrathionate ion;<sup>27</sup> one such experiment (still in the absence of chloride), starting with 32 mmol L<sup>-1</sup> sulfide, produced 88% sulfate and 8% tetrathionate, leaving only 4% unaccounted for. Tetrathionate is formed by a sequence involving formation and disproportionation of polysulfide (written here as HS<sub>2</sub><sup>-</sup>), yielding thiosulfate ion, which is further oxidized (Scheme 1).<sup>14</sup>

**Scheme 1.**



**Fig. 3.** Electrolysis of sulfide using a sandblasted Ebonex pair of electrodes with polarity reversal every 60 min; supporting electrolyte: 0.25 mol L<sup>-1</sup> NaOH; current: 100 mA.



Kinetically, the rate of oxidation of 30–60 mmol L<sup>-1</sup> sulfide was independent of the initial substrate concentration, and proportional to the applied current (50 and 100 mA). In a current-controlled process such as this, there is always an abundance of substrate at the anode. In a series of experiments beginning with a low concentration of sulfide (5 mmol L<sup>-1</sup>), the kinetics tended towards mass-transport control.<sup>29</sup> We noted that the relationship between [sulfate] and absorbance was nonlinear in this low concentration range (for the calibration curve, see Fig. 2 in the Supplementary data). A typical experiment is shown in Fig. 2.

Possible mechanisms for sulfide oxidation include direct oxidation of HS<sup>-</sup> at the anode and chemical oxidation of sulfide by electrolytically produced hydroxyl radicals. We attempted to resolve this question by voltammetry. Previously, Lawrence et al.,<sup>30</sup> had reported that the overpotential for the two-electron oxidation of sulfide at pH 10 was anode-dependent: *E* values (vs. SCE) were +1.30, +0.76, +0.45, and +0.36 V at BDD, gold, glassy carbon, and platinum, respectively. The thermodynamic value for oxidation of sulfide to elemental sulfur is +0.44 V vs. SHE.<sup>31</sup>

To avoid the reproducibility problems encountered in previous voltammetry experiments with Ebonex anodes<sup>28</sup>, the microelectrodes in this work were prepared by cutting a slice (~1 mm) of Ebonex, making an electrical contact, and then encasing the assembly in epoxy resin in a small polypropylene test tube. Once cured, the bottom of the test tube was sawn off, and the rigidity of the assembly allowed fresh anode surfaces (~3 mm<sup>2</sup>) to be obtained by abrasion. No ox-

**Table 5.** Survey XPS spectra of Ebonex samples (area percent); sample 1: unused Ebonex; sample 2: Ebonex used as an anode for electrolysis of 0.25 mol L<sup>-1</sup> NaOH; sample 3: Ebonex used as a cathode for electrolysis of 0.25 mol L<sup>-1</sup> NaOH; sample 4: Ebonex used as an anode for electrolysis of 0.25 mol L<sup>-1</sup> NaOH with 30 mmol L<sup>-1</sup> Na<sub>2</sub>S; sample 5: Ebonex used as a cathode for electrolysis of 0.25 mol L<sup>-1</sup> NaOH with 30 mmol L<sup>-1</sup> Na<sub>2</sub>S.

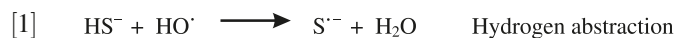
Sample No.	Electrode function	Electrolyte solution	C	O	S	Ti	Na
1	unused	—	44.1	35.8	0.3	4.8	6.5
2	anode	NaOH	26.6	44.4	0.4	5.3	14.3
3	cathode	NaOH	28.0	38.1	0.2	3.7	18.7
4	anode	NaOH/ Na <sub>2</sub> S	23.5	51.1	7.6	3.0	6.8
5	cathode	NaOH/ Na <sub>2</sub> S	24.3	32.6	0.4	3.3	27.1

idation current for sulfide was seen independent of the oxidation of water, consistent with a high overpotential for oxidation of sulfide at this material.<sup>32</sup>

We interpreted the behaviour of Ebonex anodes in the context of the paradigm developed by Kapalka et al.<sup>33</sup> to explain the oxidation chemistry of substrates at oxide-based anodes. At “inactive” anodes such as Ti/SnO<sub>2</sub>, β-PbO<sub>2</sub>, and BDD, the substrate undergoes a series of one-electron oxidations with hydroxyl radicals sorbed to the anode surface A, i.e., A~OH•. By contrast, at “active” anodes based on noble metals (e.g., Ti/IrO<sub>2</sub>, Ti/RuO<sub>2</sub>), the initially formed A~OH• is further oxidized to A=O, and substrate oxidation is a two-electron reaction. Panizza and Cerisola<sup>34</sup> have recently suggested that not all anodes necessarily fall neatly into active and inactive classifications; there may be some overlap in properties.

In this work, significant evolution of O<sub>2</sub> at the anode, combined with the high overpotential for sulfide oxidation, indicated the intermediacy of hydroxyl radicals by partial oxidation of water. The wide anodic range of water stability<sup>18–21</sup> indicates that Ebonex probably behaves as an inactive (BDD-like) anode, acting as a source of sorbed hydroxyl radicals A~OH•.<sup>35</sup> This conclusion is consistent with our previous observation that ethanol quenched the oxidation of *p*-nitrosodimethylaniline at an Ebonex anode.<sup>28</sup>

HS<sup>-</sup>(aq) and HO•(aq) react together at nearly the rate of diffusion ( $k = 5.4 \times 10^9 \text{ M}^{-1} \text{ s}^{-1}$ ),<sup>36</sup> so it is likely that the reaction between HS<sup>-</sup>(aq) and anode-sorbed HO• is also fast. However, the products of this reaction are unknown. Equations [1–3] show three possibilities, although we cannot unequivocally rule out direct electron transfer between sulfide ion and the anode, because the kinetics of current-controlled oxidation indicates that there is always a ready supply of substrate at the anode.



In terms of the paradigm of Kapalka et al.,<sup>33</sup> we propose that Ti<sub>4</sub>O<sub>7</sub> initially oxidizes water to form Ti<sub>4</sub>O<sub>7</sub>OH•. Unlike at BDD, for which “BDD-OH•” does not oxidize further, the fate of Ti<sub>4</sub>O<sub>7</sub>OH• is a three-way competition: reaction with an oxidizable substrate, oxidation of the sorbed HO• to O<sub>2</sub>, and oxidation of Ti<sub>4</sub>O<sub>7</sub>OH• to Ti<sub>4</sub>O<sub>8</sub> (= TiO<sub>2</sub>) on

the surface. To the extent that hydroxyl radical chemistry competes with surface oxidation, Ebonex exhibits properties characteristic of active and inactive anodes, as suggested by Panizza and Cerisola.<sup>34</sup> Unlike at active anodes based on Ti/IrO<sub>2</sub> or Ti/RuO<sub>2</sub>, the oxidized surface layer cannot initiate substrate oxidation and serves only to inactivate the anode. We hypothesized that polarity reversal during electrolysis served to regenerate the less oxidized surface; confirmation was obtained when sandblasted electrodes were used for the oxidation of 30 mmol L<sup>-1</sup> sulfide with polarity reversal (Fig. 3). For the first 2 × 60 min, each anode was “new”; at subsequent time points, each anode had been previously used and then regenerated. The reaction rate accordingly fell after the first 2 h (compare the rates shown on Fig. 3 with those recorded in Table 1).

Investigation of the surface of Ebonex was carried out by X-ray photoelectron spectroscopy (XPS), with unused Ebonex and with samples used as anode or cathode ± sulfide ion (without polarity reversal). Sulfur was present at levels greater than background only in sample No. 4, which had been used as an anode for the oxidation of sulfide (Table 5), and was shown to be present as sulfate (binding energy: 168.7/169.9 eV) in the high resolution scans (see Figs. 3–7 in the Supplementary data).

We were unable to observe a change in the ratio Ti:O in cathodic vs. anodic Ebonex samples, even though the Ti(2p) binding energies of TiO and TiO<sub>2</sub> are readily distinguishable.<sup>37</sup> All samples showed only TiO<sub>2</sub>-like titanium on account of air oxidation of the surface prior to XPS analysis. The O(1s) spectra showed the presence of both metal oxide and metal hydroxide at the surface, with the hydroxide predominating in electrolyzed samples.

A high level of carbon was detected on the surface of Ebonex, as previously observed by Pouilleau et al.<sup>38</sup> The predominant peak had binding energy of 284.9 eV, corresponding to C–C and C–H bonded carbon. Sources of surface carbon include its use as a desiccant in the hydrogenation of TiO<sub>2</sub> to Ebonex,<sup>39</sup> and sorption of atmospheric hydrocarbon material, as routinely found in non-ablated samples. All electrolyzed samples (anodes and cathodes) showed increased carbon intensities at higher binding energies, corresponding to C=O functional groups, but still with a high intensity of C–C and C–H bonded carbon because of contamination. Elemental analysis showed that the overall mass percentage of carbon in finely ground Ebonex is small (0.04%); correspondingly, Ebonex anodes released only a little organic carbon into solution during

electrolysis in 0.25 mol L<sup>-1</sup> NaOH (first use, 5.2 ppm; second use, 3.3 ppm).

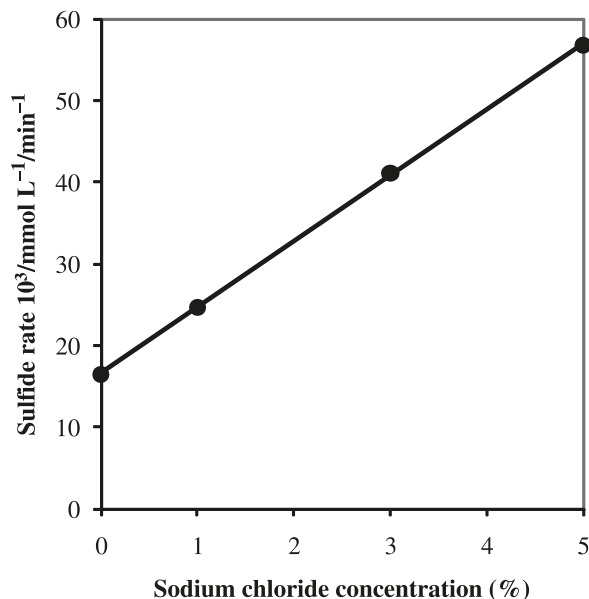
In both the absence and presence of chloride, Ebonex anodes gradually lost their ability to oxidize sulfide on repeated use, unless polarity switching was employed. Returning to Tables 1 and 2, we make three observations. First, in Table 1, entries 6 and 7 (1% NaCl) show pronounced anode inactivation compared with the earlier entries. Second, no inhibiting effect of chloride was seen when using polarity reversal (Table 2, entries 4–6). Third, the activity of an Ebonex anode was greatly diminished by the presence of hypochlorite as shown by the following experiment, carried out without polarity reversal. This experiment had three parts. First, sulfide was oxidized in the absence of chloride with an Ebonex anode and stainless steel cathode without polarity reversal at 100 mA (rate of oxidation, 0.025 mmol min<sup>-1</sup>). Second, 5% NaCl/0.25 mol L<sup>-1</sup> NaOH was electrolyzed with the same electrodes in the absence of sodium sulfide, producing hypochlorite at the anode. Third, the first electrolysis was repeated, again using the same electrodes; the rate of sulfide oxidation was now only 0.009 mmol min<sup>-1</sup>. Our interpretation is that hypochlorite oxidized the surface of Ebonex to the inactive, oxidized form. Using polarity reversal, however, the active form can be regenerated under cathodic polarization even when chloride is present.

In the oxidation of high (30 mmol L<sup>-1</sup>) concentrations of sulfide in the presence of NaCl, the disappearance of sulfide and the formation of sulfate were both linear with time (see Fig. 8 in the Supplementary data), and the rate of oxidation was directly proportional to the applied current (50 and 100 mA). The rate of oxidation and the chemical yield of sulfate increased only slightly at higher concentrations of NaCl (Table 3). In this system (30 mmol L<sup>-1</sup> Na<sub>2</sub>S, 1% NaCl), the influence of the rate of polarity reversal was also investigated over the range 5–60 min; the optimum switching time was 15 min, but the effect was small (Table 4). The kinetic response to chloride was significantly different at a low (5 mmol L<sup>-1</sup>) initial concentration of sulfide; chloride ion had a strong accelerating effect (Fig. 4), and gave a quantitative yield of sulfate. The isoelectronic species Cl<sup>-</sup> and S<sup>2-</sup> have very similar mass transport coefficients, and the range 1%–5% w/v NaCl corresponds to 0.17–0.85 mol L<sup>-1</sup>, about two orders of magnitude more than that of 5 mmol L<sup>-1</sup> sulfide. Under these conditions, conversion of chloride to hypochlorite is the major electro-oxidation process, making sulfide oxidation a mediated reaction that occurs in the bulk solution. Control experiments in our previous work<sup>9</sup> showed that hypochlorite ion oxidizes sulfide to sulfate quantitatively.

#### Batch cell experiments in the presence of naphthenic acids with or without chloride

Naphthenic acids (NAs) have pK<sub>a</sub> ~5 and are present as carboxylates at pH ~8, typical of sour brines. Previous work at BDD in the presence of NAs showed that over-oxidation of sulfide solutions produced an oily film on the anode, which inhibited further oxidation of sulfide.<sup>40</sup> This was explained by parasitic Kolbe decarboxylation of the naphthenate anions.<sup>41,42</sup> At Ti/IrO<sub>2</sub>–Ta<sub>2</sub>O<sub>5</sub>, the rate of oxidation of sulfide at 100 mA was independent of the presence of 3%

**Fig. 4.** Acceleration of the sulfide oxidation rate with sodium chloride concentration; initial sulfide concentration: 5 mmol L<sup>-1</sup>; supporting electrolyte: 0.25 mol L<sup>-1</sup> NaOH; current: 100 mA; polarity reversal every 60 min.



NAs, but at higher current (and correspondingly higher anode potential), the NAs inhibited sulfide oxidation because of the competing Kolbe reaction.<sup>12</sup> In the present work, the applied current was limited to 100 mA (at which the anode potential was +2.8 V) to minimize the Kolbe reaction.

In the oxidation of 30 mmol L<sup>-1</sup> sulfide with 1% NA, the disappearance of sulfide was again linear with time, with rate (0.040 mmol L<sup>-1</sup> min<sup>-1</sup>) similar to that in the absence of NAs at the same current (100 mA). In contrast with experiments in the absence of NAs, sulfate did not form in appreciable quantities till late in the reaction, and its yield always remained low (Fig. 5). To analyze sulfate in this system, precipitation of NAs was required prior to turbidimetric analysis; this was done by acidifying the solution to pH ~2 with HCl.<sup>12</sup> The delay in the appearance of sulfate was more pronounced starting with the low (5 mmol L<sup>-1</sup>) concentration of sulfide and the loss of sulfide was less regular with time (see Supplementary data, Fig. 9).

In the presence of NAs, a yellow colour developed in the partly electrolyzed solutions. Visible absorption spectroscopy failed to show whether this was due to the presence of polysulfide, because of the inherent color of the NAs. Polysulfide would form if the surfactant effect of NAs removed sulfur from the anode surface before it could be oxidized further. Under this hypothesis, sulfate would only form when the remaining sulfide concentration was too low to support the concentration of polysulfide. In support of this hypothesis, an experiment in the presence of NAs gave 74% sulfate and 16% tetrathionate at high conversion of sulfide, according to Scheme 1, leaving 10% sulfide unaccounted for. However, an alternative explanation for the delay in forming sulfate in the presence of NAs might be trapping of sulfur species by alkyl radical intermediates from Kolbe oxidation of the NAs, followed by hydroxyl rad-

**Table 6.** Comparison of the reaction rate and charge per mol for the electrolysis of 30 mmol L<sup>-1</sup> sulfide at different anodes: supporting electrolyte, 0.25 mol L<sup>-1</sup> NaOH; current, 100 mA. Data at BDD were obtained from ref. 9, data at IrO<sub>2</sub>/Ti were obtained from ref. 10, and data at coke were obtained from ref. 39.

Electrode	Rate (mmol L <sup>-1</sup> min <sup>-1</sup> ) <sup>a</sup>	Charge per mol (F/mol)	Rate (mmol L <sup>-1</sup> min <sup>-1</sup> ) Cl <sup>-</sup>	Charge per mol (F/mol)	Rate (mmol L <sup>-1</sup> min <sup>-1</sup> ) Cl <sup>-</sup> + NA <sup>c</sup>	Charge per mol (F/mol)
BDD/Si	0.094	8.3	0.098	7.9	N/A	—
IrO <sub>2</sub> /Ti	0.086	9.0	0.074	10.5	0.104	7.5
Coke <sup>d</sup>	0.237	3.3	0.155	5.0	0.136	5.7
Coke <sup>e</sup>	0.099	7.8	0.089	8.7	0.074	10.5
Ebonex	0.073	10.7 <sup>f</sup>	N/A	—	N/A	—
Ebonex	0.048 <sup>g</sup>	16.2 <sup>h</sup>	0.046 <sup>i</sup>	16.9 <sup>j</sup>	0.057 <sup>j</sup>	13.7 <sup>k</sup>

<sup>a</sup>No added solutes.

<sup>b</sup>+1% NaCl.

<sup>c</sup>+1% NaCl with 3% NA (IrO<sub>2</sub>/Ti); with 5% NA (coke); with 1% NA (Ebonex).

<sup>d</sup>Low conversion of sulfide.

<sup>e</sup>High conversion of sulfide.

<sup>f</sup>Cell voltage increased gradually from 4.8 V at time zero to 6.5 V at 120 min.

<sup>g</sup>Polarity reversal every 60 min; all others in this column without polarity reversal.

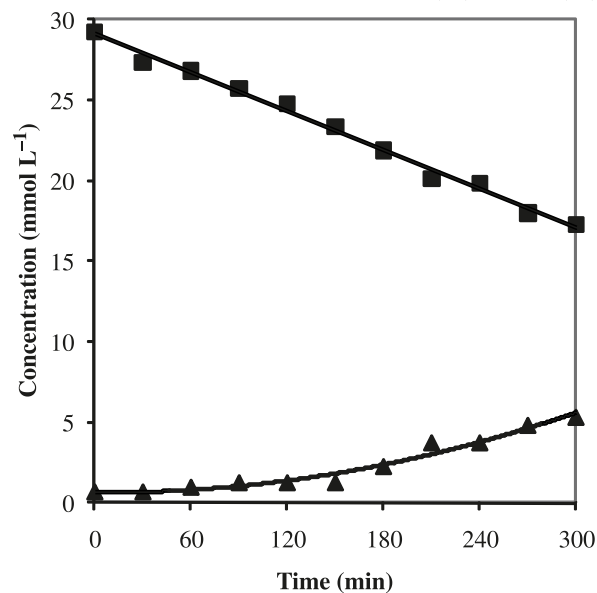
<sup>h</sup>Cell voltage increased gradually from 4.4 V at time zero to 5.1 V at 180 min.

<sup>i</sup>Cell voltage increased gradually from 4.9 V at time zero to 5.4 V at 240 min.

<sup>j</sup>Polarity reversal every 15 min; all others in this column without polarity reversal.

<sup>k</sup>Cell voltage increased gradually from 5.0 V at time zero to 5.9 V at 180 min.

**Fig. 5.** Electrolysis of sulfide in the presence of 1% w/v naphthenic acids and in the absence of chloride using an Ebonex pair of electrodes with polarity reversal every 60 min; supporting electrolyte: 0.25 mol L<sup>-1</sup> NaOH; current: 100 mA; sulfide (■); sulfate (▲).



ical-mediated release of sulfate. This has been observed previously when the products of sulfide electrooxidation at a coke anode were reoxidized at BDD.<sup>10</sup> We do not have experimental information to distinguish these possibilities.

The oxidation of sulfide was modestly inhibited by the presence of 1% NAs when chloride was added to the medium (rate 0.017 mmol L<sup>-1</sup> min<sup>-1</sup> compared with 0.025 mmol L<sup>-1</sup> min<sup>-1</sup>) and the yield of sulfate was nearly quantitative by the end of the reaction. This indicates that the course of the chloride-assisted reaction again involves mainly hypochlorination (Fig. 6).

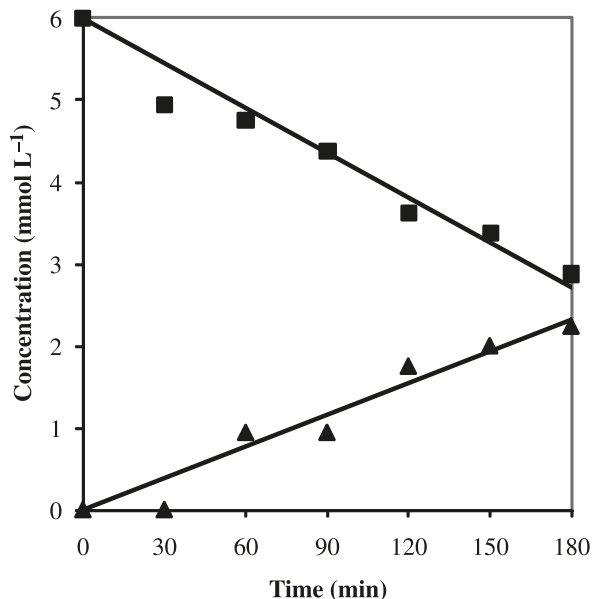
### Flow cell experiments

The flow cell had a rectangular cross section and contained two Ebonex anodes and two Ebonex cathodes, arranged diagonally. The solution volume was 40 mL. Ports set near the bottom (in) and top (out) allowed flow through the cell, with stirring provided by a magnetic stir bar, as well as by gas evolution. Experiments were carried out only in the absence of chloride and NAs, to show proof of concept in the flow mode of operation with polarity reversal every 60 min. No attempt was made to achieve “complete” remediation. Steady-state concentrations of sulfide and sulfate were established within 80 min at a flow rate of 0.5 mL min<sup>-1</sup>.

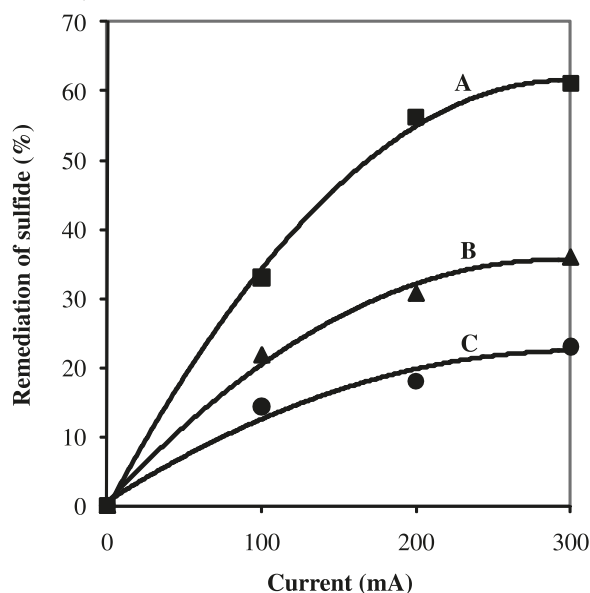
In the absence of flow, the rate of sulfide loss at 100 mA in this reactor was similar ( $8.7 \times 10^{-6}$  mol min<sup>-1</sup>) to that in the open batch reactor ( $7.5 \times 10^{-6}$  mol min<sup>-1</sup>); under flow conditions at the same current, remediation rates were  $4.0 \times 10^{-6}$  mol min<sup>-1</sup>,  $3.1 \times 10^{-6}$  mol min<sup>-1</sup>, and  $2.3 \times 10^{-6}$  mol min<sup>-1</sup> at flow rates 1.0, 0.5, and 0.25 mL min<sup>-1</sup>, respectively. Fig. 7 shows that the extent of remediation did not increase proportionately with current at constant flow rate, nor did it increase reciprocally with flow rate at constant current. This indicates that the reactor was operating



**Fig. 6.** Electrolysis of sulfide in the presence of 1% w/v naphthenic acids and 1% chloride using an Ebonex pair of electrodes with polarity reversal every 60 min; supporting electrolyte: 0.25 mol L<sup>-1</sup> NaOH; current: 100 mA; sulfide (■); sulfate (▲).



**Fig. 7.** Electrolysis of 30 mmol L<sup>-1</sup> sulfide in an electrochemical CSTR using Ebonex electrodes with polarity reversal every 60 min; supporting electrolyte: 0.25 mol L<sup>-1</sup> NaOH; A: 0.25 mL/min; B: 0.5 mL/min; C: 1 mL/min.



under conditions intermediate between current and mass transport control.

## Conclusions

According to the paradigm of Kapałka et al.,<sup>33</sup> Ebonex has the characteristic properties of both “active” and “inactive” anodes. As an inactive anode, the oxidation of water affords anode-sorbed hydroxyl radicals, which can be described as Ti<sub>4</sub>O<sub>7</sub>-OH•. These are the proximate species for substrate oxidation. However, Ti<sub>4</sub>O<sub>7</sub>-OH• is also oxidizable,

leading to a surface layer of TiO<sub>2</sub>. Unlike active anodes such as Ti/RuO<sub>2</sub>, this surface layer is incapable of substrate oxidation, and causes anode passivation. A significant innovation in this work has been to introduce periodic polarity reversal to overcome the problem of over-oxidation of the Ebonex surface that causes the inactivation and the irreproducible behaviour of Ebonex electrodes observed by us<sup>28</sup> and others.<sup>17,43</sup>

We introduced this work with the comment that no anode material is ideal in all respects for the oxidation of sulfide ion. Table 6 presents comparative data for the oxidation of 30 mmol L<sup>-1</sup> sulfide under common conditions of 100 mA current in batch cells of 80 mL capacity at several anodes (except as noted in the Table footnotes). As the “base case”, we consider oxidation at BDD, which affords sulfate ion with near 100% chemical and current yields.<sup>9</sup> This reaction has a value of ~8 F per mol sulfide remediated. Similar values are seen for Ti/IrO<sub>2</sub>-Ta<sub>2</sub>O<sub>5</sub>,<sup>12</sup> with the proviso that because this anode is gradually poisoned by sulfide, the data refer to a relatively new anode. Coke electrodes are exceptional because they show two regimes of sulfide oxidation:<sup>10</sup> sulfur is the major product at low conversion (2 F mol S<sup>-1</sup>); subsequently, sulfate and organosulfate formation become predominant (~8 F mol S<sup>-1</sup>).

For Ebonex, the current efficiency per mol of the oxidized sulfide is about half that at BDD; part of the inefficiency arises from the irreversible passivation of the Ebonex surface, which can be reactivated by polarity reversal, the remainder by extensive parasitic formation of O<sub>2</sub>. Despite the lower current efficiency, this work demonstrates the prospective value of Ebonex for the remediation of sulfide in synthetic geothermal brines. Even at ~50% of current efficiency, the method is viable, based on the low cost of electrons per mol. Although Ebonex (the trademarked material) is available from only a single manufacturer, the original patent has long since expired,<sup>17</sup> and the raw materials for the Magneli phase Ti<sub>4</sub>O<sub>7</sub> are TiO<sub>2</sub> and hydrogen, both of which are inexpensively and readily available.

## Supplementary data

Supplementary data for this article are available on the journal Web site ([canjchem.nrc.ca](http://canjchem.nrc.ca)).

## Acknowledgements

We thank Imperial Oil Ltd. and the Strategic Grants program of the Natural Sciences and Engineering Research Council of Canada (NSERC) for financial support.

## References

- (1) Ateya, B. G.; Al-Kharafi, F. M. *Electrochem. Commun.* **2002**, 4 (3), 231. doi:10.1016/S1388-2481(02)00254-0.
- (2) Greenwood, N. N.; Earnshaw, A. *Chemistry of the Elements*; Pergamon Press: Oxford, 1986, p. 807.
- (3) Galvan-Martinez, R.; Mendoza-Flores, J.; Duran-Romero, R.; Genesca, J. *Mater. Corros.* **2007**, 58 (7), 514. doi:10.1002/maco.200604038.
- (4) Sosa, E.; Cabrera-Sierra, R.; Rincon, M. E.; Oropeza, M. T.; Gonzalez, I. *Electrochim. Acta* **2002**, 47 (8), 1197. doi:10.1016/S0013-4686(01)00851-9.

- (5) Radkevych, O. I.; Chumalo, H. V. *Mater. Sci.* **2003**, 39 (4), 596. doi:10.1023/B:MASC.0000010938.39343.ed.
- (6) Krutsan, H.; Radkevych, O.; Melekhov, R.; Yurkevych, R. *Mater. Sci.* **2005**, 41 (6), 833. doi:10.1007/s11003-006-0049-x.
- (7) Scott, P. *Oil Gas J.* **1994**, 92 (21), 72.
- (8) Murugananthan, M.; Raju, G. B.; Prabhakar, S. *J. Hazard. Mater.* **2004**, 109 (1-3), 37. doi:10.1016/j.jhazmat.2003.12.009. PMID:15177743.
- (9) Waterston, K.; Bejan, D.; Bunce, N. J. *J. Appl. Electrochem.* **2007**, 37 (3), 367. doi:10.1007/s10800-006-9267-z.
- (10) Rankin, K.; Bejan, D.; Bunce, N. J. *Ind. Eng. Chem. Res.* **2010**, 49 (14), 6261. doi:10.1021/ie901511a.
- (11) Hastie, J. University of Guelph, ON. Unpublished observations, 2010.
- (12) Haner, J.; Bejan, D.; Bunce, N. J. *J. Appl. Electrochem.* **2009**, 39 (10), 1733. doi:10.1007/s10800-009-9873-7.
- (13) Ramasubramanian, N. *J. Electroanal. Chem.* **1975**, 64 (1), 21. doi:10.1016/S0022-0728(75)80276-2.
- (14) Behm, M.; Simonsson, D. *J. Appl. Electrochem.* **1997**, 27 (5), 507. doi:10.1023/A:1018486309601.
- (15) Helms, H.; Schloemer, E.; Jansen, W. *Monatsh. Chem.* **1998**, 129 (6/7), 617.
- (16) Buckley, A. N.; Hamilton, I. C.; Woods, R. *J. Electroanal. Chem.* **1987**, 216 (1-2), 213. doi:10.1016/0022-0728(87)80208-5.
- (17) Hayfield, P. C. S. *Development of a New Material, Monolithic Ti<sub>4</sub>O<sub>7</sub> Ebonex Ceramic*; Royal Society of Chemistry: Cambridge, UK, 2002, Chap. 1 and 2.
- (18) Graves, J. E.; Pletcher, D.; Clarke, R. L.; Walsh, F. C. *J. Appl. Electrochem.* **1991**, 21 (10), 848. doi:10.1007/BF01042450.
- (19) Miller-Folk, R. R.; Nofle, R. E.; Pletcher, D. *J. Electroanal. Chem. Interfacial Electrochem.* **1989**, 274 (1-2), 257. doi:10.1016/0022-0728(89)87047-0.
- (20) Pollock, R. J.; Houlihan, J. F.; Bain, A. N.; Coryea, B. S. *Mater. Res. Bull.* **1984**, 19 (1), 17. doi:10.1016/0025-5408(84)90005-9.
- (21) Scott, K.; Cheng, H. *J. Appl. Electrochem.* **2002**, 32 (6), 583. doi:10.1023/A:1020107631326.
- (22) Ellis, K.; Hill, A.; Hill, J.; Loyns, A.; Partington, T. *J. Power Sources* **2004**, 136 (2), 366. doi:10.1016/j.jpowsour.2004.03.025.
- (23) Loyns, A. C.; Hill, A.; Ellis, K. G.; Partington, T. J.; Hill, J. M. *J. Power Sources* **2005**, 144 (2), 329. doi:10.1016/j.jpowsour.2004.11.048.
- (24) Bejan, D.; Rabson, L. M.; Bunce, N. J. *Can. J. Chem. Eng.* **2007**, 85 (6), 929.
- (25) Chen, G.; Betterton, E. A.; Arnold, R. G. *J. Appl. Electrochem.* **1999**, 29 (8), 961. doi:10.1023/A:1003541706456.
- (26) WEF *Standard Methods for the Examination of Water and Wastewater*, 19th ed. American Public Health Association, American Water Works Association, and Water Environment Federation: Washington, DC, 1995.
- (27) Ciesielski, W.; Zlobinska, U.; Krenc, A. *Chem. Anal. (Warsaw, Poland)* **2001**, 46 (3), 397.
- (28) Bejan, D.; Malcolm, J. D.; Morrison, L.; Bunce, N. J. *Electrochim. Acta* **2009**, 54 (23), 5548. doi:10.1016/j.electacta.2009.04.057.
- (29) Li, S.; Bejan, D.; McDowell, M. S.; Bunce, N. J. *J. Appl. Electrochem.* **2008**, 38 (2), 151. doi:10.1007/s10800-007-9413-2.
- (30) Lawrence, N. S.; Thompson, M.; Prado, C.; Jiang, L.; Jones, T. G. J.; Compton, R. G. *Electroanal.* **2002**, 14 (7-8), 499. doi:10.1002/1521-4109(200204)14:7/8<499::AID-ELAN499>3.0.CO;2-P.
- (31) Weast, R. C., Ed. *Handbook of Chemistry and Physics*, 64th ed.; CRC Press: , 1984, pp D52-D93.
- (32) Caution: unless the epoxy resin is cured for several weeks, one sees an oxidation peak that (i) appears in a potential range that can be mistaken for sulfide, (ii) diminishes upon repeated voltammetric scans, and (iii) can be restored in intensity by abrasion to generate a new surface. Control experiments showed that this peak is actually attributable to residual traces of the amine component of the epoxy resin.
- (33) Kapačka, A.; Fóti, G.; Comninellis, C. *J. Appl. Electrochem.* **2007**, 38 (1), 7. doi:10.1007/s10800-007-9365-6.
- (34) Panizza, M.; Cerisola, G. *Chem. Rev.* **2009**, 109 (12), 6541. doi:10.1021/cr9001319. PMID:19658401.
- (35) Ongoing work in our laboratory has shown that the oxidation of coumarin at an Ebonex anode produces a low yield of 7-hydroxycoumarin, a product that has been taken as evidence for the intermediacy of hydroxyl radicals: Guinea, E. Unpublished observations.
- (36) Karmann, W.; Meissner, G.; Henglein, A. *Z. Naturforsch. [B]* **1967**, 22 (3), 273.
- (37) Chastain, J., Ed. *Handbook of X-ray Photoelectron Spectroscopy*; PerkinElmer Corporation: Eden Prairie, Minnesota, 1992.
- (38) Pouilleau, J.; Devilliers, D.; Groult, H.; Marcus, P. *J. Mater. Sci.* **1997**, 32 (21), 5645. doi:10.1023/A:1018645112465.
- (39) Simpson, A.; Carter, P. UK Pat. Appl. No. 061 896 1.7, 2008.
- (40) Waterston, K. University of Guelph, ON. Unpublished data, 2007.
- (41) Gibson, R. E. *J. Chem. Soc. Trans.* **1925**, 127, 475. doi:10.1039/ct9252700475.
- (42) Utley, J. *Chem. Soc. Rev.* **1997**, 26 (3), 157. doi:10.1039/cs9972600157.
- (43) Scialdone, O.; Galia, A.; Filardo, G. *Electrochim. Acta* **2008**, 53 (24), 7220. doi:10.1016/j.electacta.2008.05.004.

# Terpenoid constituents and antifungal activity of *Aglaia forbesii* seed against phytopathogens

Nantiya Joycharat, Patimaporn Plodpai, Kanda Panthong,  
Boon-ek Yingyongnarongkul, and Supayang Piyawan Voravuthikunchai

**Abstract:** Two new trisnortriterpenoids possessing a  $\gamma$ -lactone ring linked to the D-ring of a 3,4-secodammarane skeleton in a 20*R* configuration, named isoeichlerialactone (**1**) and methyl isoeichlerialactone (**2**), were isolated from the seed of *Aglaia forbesii*, along with the three dammarane triterpenes, isocabralealactone (**3**), isoeichlerianic acid (**4**), and aglinin A (**5**), the sesquiterpene spathulenol (**6**), and the widespread sterols  $\beta$ -sitosterol and stigmasterol. Their structures were established based on detailed spectroscopic analysis. Antifungal activity of *A. forbesii* seed against three phytopathogens, *Phytophthora botryosa*, *P. palmivora*, and *Rigidoporus microporus*, was carried out using the mycelium inhibition test and broth microdilution technique. Superior activity was exhibited by hexane and dichloromethane fractions containing the compounds **1**, **4**, and **5** as the main components. Subsequent antiphytopathogenic fungi tests proved that compounds **1**, **4**, and **5** possessed good antifungal activity.

**Key words:** *Aglaia forbesii*, Meliaceae, dammarane, triterpenes, antifungal, *Phytophthora botryosa*, *Phytophthora palmivora*, *Rigidoporus microporus*.

**Résumé :** L'extraction des graines d'*Aglaia forbesii* a permis d'isoler deux nouveaux trisnortriterpénoïdes possédant une  $\gamma$ -lactone attachée au cycle D au squelette du 3,4-sécodammarane dans la configuration 20*R*, l'isoeichlériallactone (**1**) et l'ester méthylique de la isoeichlériallactone (**2**), ainsi que trois triterpènes de la famille du dammarane, l'isocabraléallactone (**3**), l'acide isoeichlérianique (**4**) et l'aglinine A (**5**), le sesquiterpène spathuléol (**6**) et les stérols très répandus  $\beta$ -sitostérol et stigmasterol. On a établi leur structure sur la base d'analyses spectroscopiques détaillées. Faisant appel au test d'inhibition du mycélium et à la technique de microdilution du bouillon, on a étudié l'activité antifongique des graines d'*A. Forbesii* contre trois phytopathogènes, *Phytophthora botryosa*, *Phytophthora palmivora* et *Rigidoporus microporus*. Des solutions contenant les composés **1**, **4** et **5** comme composants principaux dans de l'hexane et du dichlorométhane présentent une activité supérieure. Un test de champignon antiphytopathogène subséquent a permis de démontrer que les composés **1**, **4** et **5** possèdent une bonne activité antifongique.

**Mots-clés :** *Aglaia forbesii*, Meliaceae, dammarane, triterpènes, antifongique, *Phytophthora botryosa*, *Phytophthora palmivora*, *Rigidoporus microporus*.

## Introduction

The genus *Aglaia*, consisting of over 100 species, forms an important component of the moist tropical forest in the Indo-Malaysian region.<sup>1</sup> Previous phytochemical investigations of plants in this genus have revealed the presence of a variety of compounds including several flavaglines (cyclopenta[*b*]benzofurans, cyclopenta[*bc*]benzopyrans, and benzo[*b*]oxepines),<sup>2,3</sup> bisamides,<sup>4</sup> triterpenoids (baccharane, cycloartane, dammarane, glabretal, lupane, and tirucallane types),<sup>5</sup> steroids (cholestane, ergostane, pregnane, and stigmasterane types),<sup>6,7</sup> limonoids,<sup>8</sup> sesquiterpenes,<sup>9</sup> lignans,<sup>10</sup> and flavonoids.<sup>11</sup> Some of these known isolates were shown to

possess high insecticidal activity,<sup>4,11</sup> antifungal activity,<sup>12</sup> antiviral activity,<sup>13</sup> anti-inflammatory activity,<sup>14</sup> as well as significant antiproliferative activity.<sup>2</sup>

*Aglaia forbesii*, a large tree of up to 35 m, is widely distributed in the southern region of Thailand. So far, phytochemical studies on the bark and leaf extracts of this plant have been documented.<sup>3,9</sup> In our previous work, we described several new compounds including benzopyran flavaglines desacetylpyramidaglains A, C, and D and the triterpene 23,24,25-trihydroxycycloartan-3-one from the leaf extract of this plant, some of which showed antituberculosis and antiviral activities.<sup>9</sup> However, no information on the chemical profiles and the biological activities from the seed

Received 11 March 2010. Accepted 13 May 2010. Published on the NRC Research Press Web site at canjchem.nrc.ca on 10 August 2010.

**N. Joycharat.** Faculty of Traditional Thai Medicine and Natural Products Research Center, Faculty of Science, Prince of Songkla University, Songkhla 90112, Thailand.

**P. Plodpai.** Department of Microbiology, Faculty of Science, Prince of Songkla University, Songkhla 90112, Thailand.

**K. Panthong.** Department of Chemistry, Faculty of Science, Prince of Songkla University, Songkhla 90112, Thailand.

**B. Yingyongnarongkul.** Department of Chemistry, Faculty of Science, Ramkhamhaeng University, Bangkok 10240, Thailand.

**S.P. Voravuthikunchai.**<sup>1</sup> Department of Microbiology and Natural Products Research Center, Faculty of Science, Prince of Songkla University, Songkhla 90112, Thailand.

<sup>1</sup>Corresponding author (e-mail: supayang.v@psu.ac.th).

of this plant species is currently available. Regarding the available data of bioactivities of plants in the genus *Aglaiia*, less is known about the antifungal activity. To date, only a few studies have been performed on the antifungal activities of some members of this genus, including *A. elaeagnoides*,<sup>8,12</sup> *A. leptantha*,<sup>10</sup> *A. edulis*,<sup>12</sup> and *A. odorata*.<sup>12</sup>

Our preliminary test for antifungal activity against the three plant pathogens *Phytophthora botryosa*, *P. palmivora*, and *Rigidoporus microporus*, based on the mycelium inhibition test, demonstrated that the ethanolic extract from the seed of this plant species exhibited more pronounced activity against phytopathogenic fungi tested than those from the leaves and pericarp, as well as some other medicinal plants previously documented for their good antibacterial activities in our laboratory, including *Rhodomyrtus tomentosa* and *Quercus infectoria*.<sup>15</sup>

*P. botryosa*, *P. palmivora*, and *R. microporus* have been frequently isolated as the important phytopathogens in many economically important agricultural crops, especially rubber. *P. botryosa* and *P. palmivora* cause various diseases on rubber, of which black stripe is the most severe,<sup>16</sup> while *R. microporus* is the causative pathogen of white root disease in rubber plantations.<sup>17</sup> Interestingly, plants produce a wide variety of physiologically active chemicals, which often serve as alternative sources for the control of fungal diseases in plants.<sup>18</sup>

Phytochemical investigation of the *A. forbesii* seed has led to the isolation of two new trisnortriterpenoids linking the  $\gamma$ -lactone system of the side chain to the D-ring of the 3,4-secodammarane skeleton in a 20*R* configuration (**1**) and the corresponding methyl ester (**2**), along with four known terpenoids (**3–6**) and the common phytosterols  $\beta$ -sitosterol and stigmasterol. We described herein the isolation and structure elucidation of the two newly isolated trisnortriterpenoids, as well as the antifungal activity of the crude ethanolic extract, fractions, and some isolated compounds from the seed of *A. forbesii* against the three phytopathogens *P. botryosa*, *P. palmivora*, and *R. microporus*.

## Results and discussion

Chromatographic separation of the *n*-hexane fraction of the ethanolic seed extract of *A. forbesii* yielded a new trisnortriterpenoid (**1**), named isoeichlerialactone, together with six known compounds including the three known dammaranes, isocabralealactone (**3**), isoeichlerianic acid (**4**), and aglinin A (**5**), the sesquiterpene spathulenol (**6**), and the common phytosterols  $\beta$ -sitosterol and stigmasterol. Similarly, repeated silica gel chromatography of the  $\text{CH}_2\text{Cl}_2$  fraction also afforded the newly isolated compound **1** and the three known dammarane triterpenes (**3–5**), as well as another new compound, named methyl isoeichlerialactone (**2**). The known compounds, isocabralealactone (**3**),<sup>19</sup> isoeichlerianic acid (**4**),<sup>20</sup> aglinin A (**5**),<sup>21</sup> spathulenol (**6**),<sup>22</sup> and the mixture of  $\beta$ -sitosterol and stigmasterol<sup>23</sup> were identified by comparison of their spectroscopic data with those previously reported in the literature.

Compound **1** was isolated as colourless needles. The molecular formula was deduced as  $\text{C}_{27}\text{H}_{42}\text{O}_4$  based on a molecular ion peak at  $m/z$  430.3086  $[\text{M}]^+$  (calcd.: 430.3083) in the HR-EI-MS. The important fragment ion peak visible at  $m/z$

99 ( $\text{C}_5\text{H}_7\text{O}_2$ ) indicative of a  $\gamma$ -butyrolactone was observed in the EI-MS. The IR spectrum showed the absorption bands due to carboxylic acid (3500–2500, 1707  $\text{cm}^{-1}$ ), olefinic (3073, 1636, 1455, 936, 892  $\text{cm}^{-1}$ ), and a  $\gamma$ -lactone (1763  $\text{cm}^{-1}$ ). The  $^1\text{H}$  NMR (Table 1) spectrum revealed the presence of four shielded methyl singlets ( $\delta$  1.32, 0.99, 0.88, 0.84), one methyl singlet on a double bond ( $\delta$  1.71), and two singlets of olefinic methylene protons ( $\delta$  4.86, 4.65). The  $^{13}\text{C}$  NMR spectrum (Table 1) in combination with DEPT-135 experiments indicated 27 signals: five signals for tertiary methyl groups ( $\delta$  23.18, 22.44, 20.11, 16.11, 15.31), an ester carbonyl ( $\delta$  176.91), a carboxylic carbon ( $\delta$  178.18), eleven methylenes in which one of them is an olefinic methylene ( $\delta$  113.52), four methines, five quaternary carbons including a carbon bearing an oxygen atom ( $\delta$  89.86), and an olefinic quaternary carbon ( $\delta$  147.39). Further inspection of the  $^{13}\text{C}$  NMR spectrum of **1** revealed resonance signals similar to those of isoeichlerianic acid (**4**),<sup>20</sup> but instead of an isopropanol group, it showed an extra carbonyl carbon ( $\delta$  176.91). According to previous literature, the trinor- $\gamma$ -lactone derivatives, obtained by Jones oxidation of the corresponding triterpenoid precursors possessing a tetrahydrofurylpropanol side chain, showed no evidence of epimerization at C-20 during the oxidation reaction.<sup>24,25</sup> Similarly, the co-occurrence of compound **4**, the C-20*R* isomer of eichlerianic acid, suggested that this compound should be considered an intermediate in a biosynthetic pathway to the further oxidation of product **1** with the configuration at C-20 remaining unchanged.

Based on the data mentioned above, compound **1** was suggested to be a trisnor- $\gamma$ -lactone derivative of **4** and its configuration at C-20 could be assumed to be 20*R*, followed from that of **4**. The  $^{13}\text{C}$  chemical shift values of compound **1**, especially C-21 of the  $\gamma$ -lactone ring, significantly differed from the corresponding data of eichlerialactone. The  $^{13}\text{C}$  chemical shift of C-21 for eichlerialactone appeared at 25.0 ppm in  $\text{CDCl}_3$ ,<sup>26</sup> whereas that of compound **1** was 22.44 ppm, which differs by about 3 ppm. In addition, according to recent literature, the 20*R* and 20*S* isomers of dammarane-type triterpenoids with a tetrahydrofuryl side chain can be easily distinguished by the resonances of C-21, which resonated at about  $\delta$  23.6–27.2 ppm and at about  $\delta$  21.7–22.0 ppm for the 20*S* isomer and 20*R* isomer, respectively.<sup>20</sup> Consequently, this fact was used to assign either 20*S* or 20*R* configuration of triterpenes accumulated in the genus *Aglaiia*.<sup>27</sup> In our case, the shift value of C-21 for **1** appeared at  $\delta$  22.44 ppm, which was almost identical to that of the 20*R* isomer; therefore, the configuration could be assigned unambiguously as 20*R*.<sup>20</sup> Regarding the trisnor- $\gamma$ -lactone (**1**), only its 20*S* isomer (eichlerialactone) was reported earlier;<sup>26</sup> therefore, the 20*R* compound **1**, namely, isoeichlerialactone, is new.

The structure elucidation of **1** was accomplished by complete spectral analyses ( $^1\text{H}$ – $^1\text{H}$  COSY, HMQC, HMBC, and ROESY). The observed COSY (Table 1) coupling between  $\text{H}_2$ -1 ( $\delta$  1.62, m) and  $\text{H}_2$ -2 ( $\delta$  2.35, ddd,  $J = 9.1, 8.3, 3.2$  Hz, H-2a;  $\delta$  2.16, ddd,  $J = 15.6, 9.1, 6.4$  Hz, H-2b), as well as the HMBC cross peaks from  $\text{H}_2$ -2 to C-3 ( $\delta$  178.18, s) and from  $\text{H}_2$ -28 ( $\delta$  4.86, 4.65, br s each) to C-5 ( $\delta$  50.79, d) and C-29 ( $\delta$  16.11, q) confirmed the assignments of ring A-*seco*-3 acid moiety. The HMBC data (Table 1), especially



**Table 1.** NMR spectroscopic data (400 MHz, CDCl<sub>3</sub>) for isoeichlerialactone (**1**).

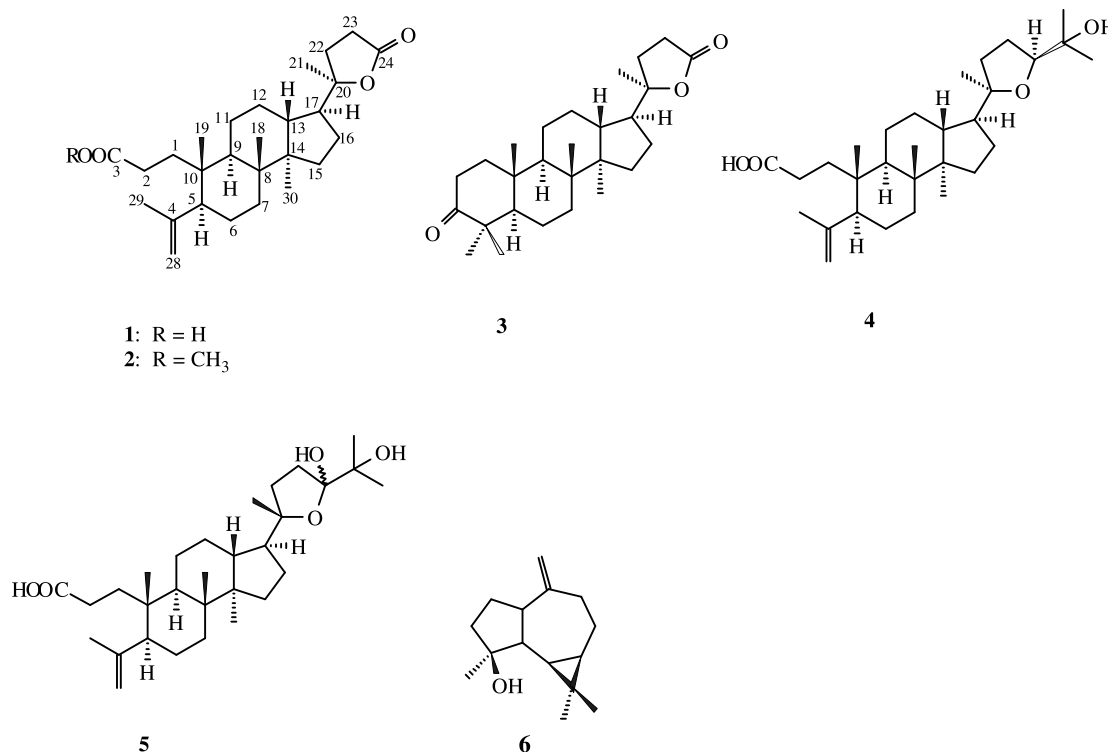
Position	$\delta$ C	$\delta$ H (mult., <i>J</i> in Hz)	<sup>1</sup> H– <sup>1</sup> H COSY	HMBC
1	34.19 t	1.62 m	H-2a, H-2b	C-2, C-5, C-19
2	27.97 t	a 2.35 (ddd, 9.1, 8.3, 3.2) b 2.16 (ddd, 15.6, 9.1, 6.4)	H <sub>2</sub> -1, H-2b H <sub>2</sub> -1, H-2a	C-1, C-3
3	178.18 s			
4	147.39 s			
5	50.79 d	1.97 m		
6	24.53 t	a 1.95 m b 1.28 m		
7	33.86 t	a 1.54 m b 1.20 m		
8	40.09 s			
9	41.04 d	1.52 m	H-11a, H-11b	
10	39.08 s			
11	21.82 t	a 1.43 m b 1.26 m	H-11b, H-12a, H-12b H-11a, H-12a, H-12b	
12	26.36 t	a 1.76 m b 1.28 m		
13	42.67 d	1.61 m	H-12a, H-12b, H-17	
14	50.39 s			
15	31.04 t	a 1.47 m b 1.16 m		
16	24.97 t	a 1.85 m b 1.19 m		C-21
17	49.41 d	1.94 m	H-13, H-16a, H-16b	C-13, C-16, C-20, C-21, C-22, C-23
18	15.31 q	0.99 s		C-7, C-8, C-9, C-19
19	20.11 q	0.84 s		C-1, C-2, C-5, C-9, C-10
20	89.86 s			
21	22.44 q	1.32 s		C-17, C-20, C-22
22	32.92 t	$\alpha$ 2.03 m $\beta$ 1.90 m		C-20, C-21, C-23, C-24
23	28.66 t	a 2.57 (dt, 18.1, 9.0) b 2.49 (ddd, 18.1, 10.1, 5.1)		C-20, C-22, C-24
24	176.91 s			
28	113.52 t	a 4.86 br s b 4.65 br s		C-5, C-29
29	23.18 q	1.71 s		C-5, C-2, C-8
30	16.11 q	0.88 s		C-8, C-13, C-15

the long range correlations of five methyl groups, proved to be very valuable in assigning the resonances of the rings A–D of the 3,4-secodammarane skeleton. The HMBC correlations from Me-18 to C-7, C-8, C-9, and C-19, from Me-19 to C-1, C-2, C-5, C-9, and C-10, from Me-21 to C-17, C-20, and C-22, from Me-29 to C-5 and C-28, and from Me-30 to C-8, C-13, and C-15 supported the estimated structures. This is also in accordance with the extensive NMR data described for other related compounds recently reported.<sup>20</sup> The 20*R* configuration of **1** was confirmed by the diagnostic ROESY cross peaks from Me-21 to H-22 $\alpha$  and from H-17 to Me-21, H-22 $\alpha$ , and Me-30. The absence of ROESY correlation between Me-21 and H-13 was observed in compound **1** and further supported the 20*R* configuration in which the Me-21 was in the  $\alpha$ -position (Fig. 1).

Compound **2** was obtained as colourless needles. It has almost identical <sup>1</sup>H and <sup>13</sup>C NMR spectral data to those of **1**, suggesting that they have the same core structure of the 3,4-secodammarane triterpenoids with the  $\gamma$ -lactone side chain.

The additional characteristic features of an ester carbonyl and a methyl ester with their respective resonances at  $\delta$  174.4 and 51.59 ppm, as well as a corresponding singlet integrated for three protons visible at  $\delta$  3.64 ppm in the <sup>1</sup>H NMR spectrum, indicated that compound **2** was a corresponding ester of **1**. This was supported by the [M]<sup>+</sup> peak in the HR-EI-MS at *m/z* 444.3240 (calcd.: 444.3240) corresponding to the molecular formula of C<sub>28</sub>H<sub>44</sub>O<sub>4</sub>. The 20*R* configuration of **2** was determined by comparison of the typical <sup>13</sup>C resonance of C-21 (22.41) with those of **1** and other relevant compounds,<sup>20</sup> and they completely agree with the proposed structure. The synthetical 20*S* isomer of **2** has already been published.<sup>24</sup> However, the trisnortriterpene possessing the 20*R* configuration of **2** has not been documented yet. Therefore, the new compound was designated as methyl isoeichlerialactone (**2**). Its <sup>1</sup>H and <sup>13</sup>C NMR spectral data are summarized in Table 2.

Compound **3** has a molecular formula of C<sub>27</sub>H<sub>42</sub>O<sub>3</sub>, which was assigned from its mass spectrum ([M]<sup>+</sup> at *m/z* 414) in

**Fig. 1.** Structures of compounds 1–6.

combination with the  $^1\text{H}$  and  $^{13}\text{C}$  NMR spectra and its IR spectrum, which indicated the presence of carbonyl function ( $1705\text{ cm}^{-1}$ ) and a  $\gamma$ -lactone system ( $1767\text{ cm}^{-1}$ ). Further comparison of the  $^1\text{H}$  and  $^{13}\text{C}$  spectra of **3** with the corresponding data of **1** revealed that the two compounds have very similar resonances except for the signals in the A-ring region. The former did not show the resonances of a carboxylic carbon ( $\delta\ 178.18$ ), an olefinic methylene ( $\delta\ 113.52$ ), and an olefinic quaternary carbon ( $\delta\ 147.39$ ), instead, a keto carbonyl ( $\delta\ 217.95$ ) was evident in the  $^{13}\text{C}$  spectrum. This indicated that compound **3** possessed a  $\gamma$ -lactone ring attached to the D-ring of a dammaran-3-one skeleton. The  $^{13}\text{C}$  chemical shift of C-21, visible at  $22.13\text{ ppm}$ , was indicative of a  $20R$  configuration in comparison to **1** and the other  $20R$  isomers.<sup>20</sup> Up until now, within the Meliaceae, only the  $20S$  isomer (cabralealactone) of compound **3** has been published.<sup>25</sup> Whereas the  $20R$  isomer of cabralealactone, named isocabralealactone, has been previously mentioned in some literature,<sup>28</sup> its  $^{13}\text{C}$  NMR (Table 2) spectral data are documented here for a first time.

Antifungal activity screening against the three phytopathogens *P. botryosa*, *P. palmivora*, and *R. microporus* revealed that the ethanolic extracts from the seed and pericarp of *A. forbesii* exhibited higher activity than the leaf ethanolic extracts of *R. tomentosa* and *Q. infectoria*. In the mycelium inhibition test, the percentage of inhibition of mycelial growth from the seed, pericarp, and leaf extracts of *A. forbesii* are in the range of 39%–68%, 38%–65%, and 0%–12%, respectively, whereas those of *R. tomentosa* and *Q. infectoria* are in the range of 11%–41% and 0%–18%, respectively. *R. microporus* was more susceptible to all extracts of *A. forbesii* than *P. botryosa* and *P. palmivora*, of

which the ethanolic seed extract, with 68% mycelial growth inhibition, is the most active extract.

The crude ethanolic extract, fractions, and pure compounds from *A. forbesii* seed were further evaluated for their minimum inhibitory concentration (MIC) and minimum fungicidal concentration (MFC) values against the plant pathogens using broth microdilution method. The MIC and MFC values of *A. forbesii* seed extract ranged from 500 to 1000  $\mu\text{g mL}^{-1}$  and 1000 to 2000  $\mu\text{g mL}^{-1}$ , respectively (Table 3).

**3**). All the fractions, except for that of buthanol, showed a higher and broader spectrum of antifungal activity as compared to that of the unfractionated ethanolic extract. Although almost of the active extract and fractions demonstrated stronger inhibitory effect against *R. microporus* with MICs and MFCs better than those of the other organisms, both the hexane and dichloromethane fractions in which the 3,4-secodammarane triterpenes (**1**, **4**, and **5**) were observed to be the major components displayed similar antifungal effect against all the plant pathogens tested, with their respective MIC and MFC values ranging from 250 to 500  $\mu\text{g mL}^{-1}$  and 250 to 1000  $\mu\text{g mL}^{-1}$ .

The 3,4-secodammarane triterpenes, isoeichlerialactone (**1**), isoeichlerianic acid (**4**), and aglinin A (**5**), showed a broad antifungal spectrum against all phytopathogens tested, whereas the dammaran-3-one derivative (**3**) and the sesquiterpene (**6**) were only active against *R. microporus*. Among the compounds tested, isoeichlerialactone (**1**) was found to be the most effective derivative against *R. microporus* with the identical MIC and MFC values of  $62.5\text{ }\mu\text{g mL}^{-1}$ , better than a positive control carboxin with the MIC and MFC values of 125 and 250  $\mu\text{g mL}^{-1}$ , respectively. Compounds **1**, **4**, and **5** showed a very similar effect against *P. botryosa* and *P. palmivora*. However, aglinin A (**5**) was more active

**Table 2.**  $^1\text{H}$  (400 MHz) and  $^{13}\text{C}$  NMR (100 MHz) data for methyl isoeichlerialactone (**2**) and  $^{13}\text{C}$  NMR (100 MHz) data for isocabralealactone (**3**) in  $\text{CDCl}_3$ .

Position	<b>2</b>		<b>3</b>
	$\delta$ H (mult.)	$\delta$ C	$\delta$ C
1	1.63 m	34.42 t	39.85 t
2	a 2.32 m b 2.16 m	28.39 t	34.07 t
3		174.4 s	217.95 s
4		147.45 s	47.39 s
5	1.95 m	50.74 d	55.34 d
6	a 1.26 m b 1.95 m	24.58 t	19.62 t
7	a 1.22 m b 1.54 m	33.89 t	34.58 t
8		40.09 s	40.34 s
9	1.53 m	41.00 d	50.0 d
10		39.12 s	36.85 s
11	a 1.42 m b 1.23 m	21.83 t	21.78 t
12	a 1.76 m b 1.26 m	26.39 t	30.99 t
13	1.61 m	42.69 d	42.77 d
14		50.40 s	50.0 s
15	a 1.46 m b 1.16 m	31.05 t	33.15 t
16	a 1.82 m b 1.18 m	24.98 t	26.43 t
17	1.93 m	49.44 d	49.47 d
18	0.99 s	15.32 q	15.19 q
19	0.83 s	20.11 q	15.99 q
20		89.81 s	89.88 s
21	1.32 s	22.41 q	22.13 q
22	a 2.03 m b 1.88 m	32.96 t	33.15 t
23	a 2.52 m b 2.48 m	28.65 t	28.62 t
24		176.81 s	176.8 s
28	a 4.83 br s b 4.64 br s	113.45 t	26.72 q
29	1.71 s	23.25 q	21.01 q
30	0.87 s	16.09 q	16.1 q
–COOCH <sub>3</sub>	3.64 s	51.59 q	

against *P. botryosa* with the MIC and MFC values of 125 and 250  $\mu\text{g mL}^{-1}$ , respectively, comparable to the activity of a positive control metalaxyl.

A number of plant-derived *seco*-A-triterpenoids have been described to be highly antimicrobial.<sup>29</sup> Similarly, among the closely related dammarane compounds, **1**, **3**, **4**, and **5**, the 3,4-*seco*-3 acid derivatives, **1**, **4**, and **5**, exhibited higher activity than the dammaran-3-one derivative (**3**), suggesting that the 3,4-*seco*-3 acid skeleton could account for some of the antifungal properties. In recent work, antimycobacterial activity of the related dammarane-type triterpenoids has been published.<sup>30</sup> Antifungal activity of the other *Aglaia* spp. has been previously reported against a few organisms causing rice blast disease<sup>12</sup> and two other fungal plant pathogens in the genus *Cladosporium*.<sup>8,10</sup> With respect to the increasing negative effects of synthetic fungicides to hu-

mans and the environment, as well as the improved resistance of phytopathogenic fungi against conventional fungicides, our finding suggests possible benefits of bioactive compounds from *A. forbesii* seed for effective control of fungal plant pathogens.

## Experimental

### General

The following instrumentation was used: Mps, Electrothermal 9100; Optical rotation, Jasco P-1020 polarimeter; IR, EQUINOX 55, Bruker FTIR; 1D- and 2D-NMR, FT-NMR Bruker Advance 400 MHz; EI-MS and HR-EI-MS, MAT 95 XL mass spectrometer (ThermoFinnigan). Column chromatography (CC) was performed using silica gel (Merck, 70–230 mesh ASTM) and Sephadex LH20 (Pharmacia). Thin-layer chromatography (TLC) was carried out on precoated sheets of silica gel 60 F<sub>254</sub>. Compounds were monitored by TLC sprayed with an anisaldehyde–sulfuric acid solution or 10% sulfuric acid. Fungal culture media, the Standard Roswell Park Memorial Institute (RPMI) 1640 powder, as well as potato dextrose agar (PDA) and V8 juice agar (VA), were purchased from Sigma-Aldrich (St. Louis, MO) and Difco (Detroit, MI). Dimethyl sulfoxide (DMSO) was purchased from Merck (Darmstadt, Germany).

### Plant material

The seed of *A. forbesii* was collected in March 2009 from Nakhon Sri Thammarat, Thailand. Identification was made by comparison with authentic specimens (ES-0403) previously established.<sup>9</sup> A voucher specimen (NJ-0309) was deposited at the Herbarium of the Department of Biology, Faculty of Science, Prince of Songkla University, Thailand.

### Extraction and isolation

The seed of *A. forbesii* (48 g) was dried, ground, and exhaustively extracted with EtOH at room temperature three times, filtered, and concentrated. The EtOH extract (5.7 g) was resuspended in a mixture of MeOH and water and then extracted with hexane,  $\text{CH}_2\text{Cl}_2$ , and BuOH, successively. Each filtrate was pooled and evaporated to dryness under reduced pressure at 40 °C to yield the hexane fraction (2.42 g, 5.04%),  $\text{CH}_2\text{Cl}_2$  fraction (1.87 g, 3.89%), and BuOH fraction (1 g, 2.08%).

The hexane fraction (2.42 g) was subjected to CC using silica gel as adsorbent and eluted with a gradient system of EtOAc–hexane, then washed down with MeOH. The fractions were then combined, on the basis of their TLC profiles, to give seven fractions (I<sub>H</sub>–VII<sub>H</sub>). Fraction II<sub>H</sub> (94 mg) was rechromatographed on silica gel, eluting with 20%  $\text{CH}_2\text{Cl}_2$  in hexane affording compound **6** (7 mg). Fraction III<sub>H</sub> (97.2 mg), yielding a white precipitate during the concentration process, was further recrystallized from acetone to give a mixture (9.1 mg) of  $\beta$ -sitosterol and stigmasterol. Fraction IV<sub>H</sub> (150 mg) was purified on a silica gel column with 20% acetone in hexane as the eluent and further by a Sephadex LH20 column with  $\text{CH}_2\text{Cl}_2$ –MeOH (1:1) as the eluent to yield compound **1** (4.7 mg). Fraction V<sub>H</sub> (500 mg) was further separated by a silica gel CC, eluting with 40% acetone in hexane and then by crystallization in EtOH to give compound **4** (10.2 mg). Fraction VII<sub>H</sub> (93.7 mg) was

**Table 3.** The minimum inhibitory concentrations and minimum fungicidal concentrations of extract, fractions, and compounds from *Aglaia forbesii* seed against *Phytophthora botryosa*, *P. palmivora*, and *Rigidoporus microporus*.

Sample tested	MIC/MFC ( $\mu\text{g mL}^{-1}$ )		
	<i>P. botryosa</i>	<i>P. palmivora</i>	<i>R. microporus</i>
EtOH extract	1 000/2 000	1 000/1 000	500/1 000
Hexane fraction	500/500	250/250	250/500
CH <sub>2</sub> Cl <sub>2</sub> fraction	500/1 000	500/500	250/500
BuOH fraction	1 000/2 000	1 000/1 000	2 000/>2 000
Isoeichlerialactone ( <b>1</b> )	250/>250	250/250	62.5/62.5
Isocabralealactone ( <b>3</b> )	>250	>250	125/250
Isoeichlerianic acid ( <b>4</b> )	250/>250	250/250	125/250
Aglinin A ( <b>5</b> )	125/250	250/250	62.5/125
Spathulenol ( <b>6</b> )	>250	>250	125/125
Metalaxyl	125/125	125/125	NA <sup>a</sup>
Carboxin	NA <sup>a</sup>	NA <sup>a</sup>	125/250

<sup>a</sup>Not applicable.

loaded to a Sephadex LH20 column, eluting with CH<sub>2</sub>Cl<sub>2</sub>–MeOH (1:1), and further purified by recrystallization from EtOH to afford compound **5** (8.4 mg).

The dichloromethane fraction (1.87 g) was applied to CC over silica gel using gradient elution with acetone–CH<sub>2</sub>Cl<sub>2</sub>, and finally washed down with MeOH. The fractions were then combined according to their TLC patterns, to give seven fractions (I<sub>D</sub>–VII<sub>D</sub>). Fraction II<sub>D</sub> (48 mg) was rechromatographed on silica gel, eluting with a gradient system of acetone–hexane, and followed by crystallization in EtOH to yield compound **3** (4.1 mg). Fraction IV<sub>D</sub> (136 mg) was loaded on a silica gel column, eluting with 8% acetone in CH<sub>2</sub>Cl<sub>2</sub> and then by crystallization in EtOH gave compound **1** (10.7 mg). Fraction V<sub>D</sub> (243 mg) was subjected to silica gel CC using gradient elution with acetone–hexane. Column fractions eluted with 15% and 40% acetone in hexane afforded compound **2** (3 mg) and compound **4** (14.2 mg), respectively. Fraction VII<sub>D</sub> (218 mg) was further purified on a silica gel column with 20% acetone in hexane as the eluent and then on a Sephadex LH20 column eluting with CH<sub>2</sub>Cl<sub>2</sub>–MeOH (1:1) to yield compound **5** (26 mg).

#### Isoeichlerialactone (**1**)

Colourless needles (EtOH); mp 166–167 °C.  $[\alpha]_D^{20} +19.2$  (*c* 0.33 g/100 mL EtOH). IR (neat, cm<sup>-1</sup>)  $\nu_{\text{max}}$ : 3500–2500, 3073, 2945, 2872, 1763, 1707, 1636, 1455, 1383, 1294, 1195, 1126, 936, 892, 756. <sup>1</sup>H NMR (400 MHz, CDCl<sub>3</sub>) and <sup>13</sup>C NMR (100 MHz, CDCl<sub>3</sub>) data: see Table 1. EI-MS *m/z* (% rel. int.): 430 ([M]<sup>+</sup>, 3), 357 (9), 331 (8), 290 (1), 235 (9), 221 (11), 180 (16), 107 (35), 99 (100), 95 (42), 81 (33), 71 (11), 67 (12). HR-EI-MS *m/z*: 430.3086 [M]<sup>+</sup>; calcd. for C<sub>27</sub>H<sub>42</sub>O<sub>4</sub>: 430.3083.

#### Methyl isoeichlerialactone (**2**)

Colourless needles (EtOH); mp 141–143 °C.  $[\alpha]_D^{20} +19.8$  (*c* 0.19 g/100 mL EtOH). <sup>1</sup>H NMR (400 MHz, CDCl<sub>3</sub>) and <sup>13</sup>C NMR (100 MHz, CDCl<sub>3</sub>) data: see Table 2. EI-MS *m/z* (% rel. int.): 444 ([M]<sup>+</sup>, 9), 363 (89), 357 (37), 345 (6), 154 (14), 121 (36), 115 (11), 109 (27), 99 (100), 95 (43), 81 (35), 71 (13), 67 (16). HR-EI-MS *m/z*: 444.3240 [M]<sup>+</sup>; calcd. for C<sub>28</sub>H<sub>44</sub>O<sub>4</sub>: 444.3240.

#### Isocabralealactone (**3**)

White solid (CH<sub>2</sub>Cl<sub>2</sub>); mp 180–182 °C. IR (neat, cm<sup>-1</sup>)  $\nu_{\text{max}}$ : 2952, 2869, 1767, 1705, 1461, 1382, 1255, 1193, 1152, 936, 755. <sup>1</sup>H NMR (400 MHz, CDCl<sub>3</sub>)  $\delta$ : 0.87 (3H, s, H-30), 0.92 (3H, s, H-19), 0.98 (3H, s, H-18), 1.02 (3H, s, H-29), 1.06 (3H, s, H-28), 1.32 (3H, s, H-21). <sup>13</sup>C NMR (100 MHz, CDCl<sub>3</sub>) data: see Table 2. EI-MS *m/z* (% rel. int.): 414 ([M]<sup>+</sup>, 52), 399 (12), 315 (28), 205 (72), 195 (23), 147 (26), 107 (44), 99 (100), 95 (64), 81 (51).

#### Antifungal activity evaluation

Phytopathogenic fungi including *P. botryosa*, *P. palmivora*, and *R. microporus*, as well as fungicides, metalaxyl, and carboxin, were obtained from the Department of Pest Management, Faculty of Natural Resources, Prince of Songkla University, Thailand. Preliminary screening for antifungal activity was employed based on the mycelium inhibition test.<sup>31</sup> The MIC and MFC were evaluated using the broth microdilution method.<sup>32</sup>

#### Mycelium inhibition test

The ethanolic extracts from the leaves, pericarp, and seed of *A. forbesii* were tested. The ethanolic leaf extracts of *R. tomentosa* and *Q. infectoria* from the Natural Products Research Center, Faculty of Science, Prince of Songkla University, Thailand were included. The mycelial growth inhibition of phytopathogenic fungi tested was determined as previously described.<sup>32</sup> Briefly, each extract was dissolved in 10% DMSO and added on PDA at concentrations of 200  $\mu\text{g mL}^{-1}$ . A mycelial plug of phytopathogenic fungi from a three day old culture was placed in the center of the PDA plate and incubated at 28 °C. After seven days, percentage inhibition of mycelial growth was recorded and calculated by a formula,  $100 - [(R^2/r^2) \times 100]$ , where *R* and *r* represent the radius of the fungus colony in the treated and control plates, respectively. There were four replications in each treatment and the experiment was designed as a completely randomized design. DMSO (10%) was included as control.

#### Inoculum preparation

Sporangiospore suspensions of *Phytophthora* spp. and a



mycelial suspension of *R. microporus* were prepared from 10 day old cultures incubated at 35 °C on VA and PDA, respectively. The colonies were covered with 1 mL of sterile 0.85% saline and the surface scraped with a sterile loop. The mixture of zoospore and hyphal fragments were transferred to sterile tubes. After heavy particles were allowed to settle for 15 min, the upper homogenous suspensions were transferred to sterile tubes. Turbidity of the inocula was adjusted to  $0.4 \times 10^6$  to  $5 \times 10^6$  cfu mL<sup>-1</sup> at a wavelength of 520 nm and transmission was adjusted to 68%–70% in a spectrophotometer. The inocula were diluted (1:50) in RPMI 1640 to a final concentration of  $0.4 \times 10^4$  to  $5 \times 10^4$  cfu mL<sup>-1</sup>. The inocula were quantified by plating 0.01 mL of a 1:100 dilution of the adjusted inoculum on PDA plates to determine the viable number of colony-forming units (cfu) per milliliter. The plates were incubated at 28 °C and observed daily for the presence of growth.<sup>32</sup>

### Broth microdilution method

The crude extract, fractions, and pure compounds from *A. forbesii* seed and fungicides were evaluated. The broth microdilution method was performed according to the guidelines of the Clinical and Laboratory Standards Institute document M38-A.<sup>32</sup> The tests were performed in polystyrene microtitre plates with 96 flat-bottomed wells. Stock solutions of the crude extract, their fractions, pure compounds, metalaxyl, and carboxin were prepared in DMSO to a 100-fold the final concentration needed and followed by further dilution in RPMI 1640 to yield twice the final strength required for the test. Aliquots of 100 µL of samples tested were inoculated into the wells with a multichannel pipette. Each microplate was inoculated with 100 µL of the diluted inoculum suspensions to bring the dilutions of the inoculum to  $0.4 \times 10^4$  to  $5 \times 10^4$  cfu mL<sup>-1</sup>. Sample solutions were subsequently serially diluted twofold in the plates with the broth, starting with the final concentration of 2000 µg mL<sup>-1</sup> for the extract and fractions and 250 µg mL<sup>-1</sup> for the pure compounds and fungicides. The microplates were incubated at 35 °C for 24 h. All the tests were performed in triplicate. The MIC was defined as the lowest concentration that completely inhibited growth. The MIC of samples was detected following the addition of resazurin (10 µL/well) and incubated at 37 °C for 30 min. Viable microorganisms reduced the blue dye to a pink colour. To obtain the MFCs, 100 µL volumes were taken from every well showing inhibition and were spread on PDA. Colony forming units were counted after incubating the plates at 35 °C until growth of the subcultures from the growth control well was apparent. The MFC was defined as the lowest drug concentration at which 99% of the inoculum was killed.

### Supplementary data

Supplementary data for this article are available on the journal Web site (canjchem.nrc.ca).

### Acknowledgements

This work was financially supported by the Office of the Higher Education Commission (CHE-RES-PD).

### References

- (1) Pannell, C. M. *Taxonomic Monograph of the Genus Aglaia Lour. (Meliaceae)*; Her Majesty's Stationary Office (HMSO): London, 1999.
- (2) Proksch, P.; Edrada, R. A.; Ebel, R.; Bohnenstengel, F. I.; Nugroho, B. W. *Curr. Org. Chem.* **2001**, 5 (9), 923. doi:10.2174/1385272013375049.
- (3) Dumontet, V.; Thoison, O.; Omobuwajo, R.; Martin, M. T.; Perromat, G.; Chiaroni, A.; Riche, C.; Païs, M.; Sevenet, T. *Tetrahedron* **1996**, 52 (20), 6931. doi:10.1016/0040-4020(96)00322-5.
- (4) Brader, G.; Vajrodaya, S.; Greger, H.; Bacher, M.; Kalchhauser, H.; Hofer, O. *J. Nat. Prod.* **1998**, 61 (12), 1482. doi:10.1021/np9801965. PMID:9868148.
- (5) Joycharat, N.; Greger, H.; Hofer, O.; Saifah, E. *Biochem. Syst. Ecol.* **2008**, 36 (7), 584. doi:10.1016/j.bse.2008.03.009.
- (6) Rivero-Cruz, J. F.; Chai, H. B.; Kardono, L. B. S.; Setyowati, F. M.; Afriatini, J. J.; Riswan, S.; Farnsworth, N. R.; Cordell, G. A.; Pezzuto, J. M.; Swanson, S. M.; Kinghorn, A. D. *J. Nat. Prod.* **2004**, 67 (3), 343. doi:10.1021/np0304417. PMID:15043407.
- (7) Mohamad, K.; Martin, M. T.; Najdar, H.; Gaspard, C.; Sévenet, T.; Awang, K.; Hadi, H.; Païs, M. *J. Nat. Prod.* **1999**, 62 (6), 868. doi:10.1021/np990013u. PMID:10395505.
- (8) Fuzzati, N.; Dyatmiko, W.; Rahman, A.; Achmad, F.; Hostettmann, K. *Phytochemistry* **1996**, 42 (5), 1395. doi:10.1016/0031-9422(96)00130-6.
- (9) Joycharat, N.; Greger, H.; Hofer, O.; Saifah, E. *Phytochemistry* **2008**, 69 (1), 206. doi:10.1016/j.phytochem.2007.06.016. PMID:17707871.
- (10) Greger, H.; Pacher, T.; Vajrodaya, S.; Bacher, M.; Hofer, O. *J. Nat. Prod.* **2000**, 63 (5), 616. doi:10.1021/np990542y. PMID:10843571.
- (11) Greger, H.; Pacher, T.; Brem, B.; Bacher, M.; Hofer, O. *Phytochemistry* **2001**, 57 (1), 57. doi:10.1016/S0031-9422(00)00471-4. PMID:11336261.
- (12) Engelmeier, D.; Hadacek, F.; Pacher, T.; Vajrodaya, S.; Greger, H. *J. Agric. Food Chem.* **2000**, 48 (4), 1400. doi:10.1021/jf990509h. PMID:10775404.
- (13) Esimone, C. O.; Eck, G.; Duong, T. N.; Überla, K.; Proksch, P.; Grunwald, T. *Pharmazie* **2008**, 63 (10), 768. doi:10.1016/j.phymed.2009.10.015. PMID:18972843.
- (14) Proksch, P.; Giaisi, M.; Treiber, M. K.; Palfi, K.; Merling, A.; Spring, H.; Krammer, P. H.; Li-Weber, M. *J. Immunol.* **2005**, 174 (11), 7075. doi:10.1074/jbc.M208003200. PMID:15905551.
- (15) Limsuwan, S.; Subhadhirasakul, S.; Voravuthikunchai, S. P. *Pharm. Biol.* **2009**, 47 (8), 683.
- (16) Chowana, C.; Templeton, J. K. *Kasetsart J. (Nat. Sci.)* **1974**, 8 (2), 93. Available at: <http://kucon.lib.ku.ac.th/Fulltext/KC1301002.pdf>
- (17) Jayasuriya, K. E.; Thennakoon, B. I. *Cey. J. Sci. (Bio. Sci.)* **2007**, 36 (1), 9. Available at: <http://www.pdn.ac.lk/cjsbs/text/text36.1.2.pdf>
- (18) Slusarenko, A. J.; Patel, A.; Portz, D. *Eur. J. Plant Pathol.* **2008**, 121 (3), 313. doi:10.1007/s10658-007-9232-7.
- (19) Ahmad, V. U.; Alvi, K. A. *Phytochemistry* **1986**, 26 (1), 315. doi:10.1016/S0031-9422(00)81537-X.
- (20) Seger, C.; Pointinger, S.; Greger, H.; Hofer, O. *Tetrahedron Lett.* **2008**, 49 (27), 4313. doi:10.1016/j.tetlet.2008.04.109.
- (21) Luo, X. D.; Wu, S. H.; Ma, Y. B.; Wu, D. G. *Heterocycles* **2000**, 53 (12), 2795. doi:10.3987/COM-00-9045.
- (22) Brochinia, C. B.; Roque, N. F. *J. Braz. Chem. Soc.* **2000**, 11 (4), 361. doi:10.1590/S0103-50532000000400006.

- (23) Rubinstein, I.; Goad, L. J.; Chague, A. D. H.; Mulhein, L. J. *Phytochemistry* **1976**, *15* (1), 195. doi:10.1016/S0031-9422(00)89083-4.
- (24) Rao, M. M.; Meshulam, H.; Zelnik, R.; Lavie, D. *Tetrahedron* **1975**, *31* (4), 333. doi:10.1016/0040-4020(75)80042-1.
- (25) Cascon, S. C.; Brown, K. S. *Tetrahedron* **1972**, *28* (2), 315. doi:10.1016/0040-4020(72)80138-8.
- (26) Singh, Y.; Aalbersberg, W. *Phytochemistry* **1992**, *31* (11), 4033. doi:10.1016/S0031-9422(00)97581-2.
- (27) Pointinger, S.; Promdang, S.; Vajrodaya, S.; Pannell, C. M.; Hofer, O.; Mereiter, K.; Greger, H. *Phytochemistry* **2008**, *69* (15), 2696. doi:10.1016/j.phytochem.2008.08.025. PMID: 18930298.
- (28) Hirose, Y.; Yanagawa, T.; Nakatsuka, T. *Mokuzai Gakkaishi* **1968**, *14* (1), 59.
- (29) Kuroyanagi, M.; Sugiyama, K.; Kanazawa, M.; Kawahara, N. *Chem. Pharm. Bull. (Tokyo)* **2000**, *48* (12), 1917. PMID: 11145144.
- (30) Phongmaykin, J.; Kumamoto, T.; Ishikawa, T.; Suttisri, R.; Saifah, E. *Arch. Pharm. Res.* **2008**, *31* (1), 21. doi:10.1007/s12272-008-1115-8. PMID:18277603.
- (31) Gamliel, A.; Kantan, J.; Cohen, E. *Phytoparasitica* **1989**, *17* (2), 101. doi:10.1007/BF02979517.
- (32) Clinical and Laboratory Standards Institute. *Reference Method for Broth Dilution Antifungal Susceptibility Testing of Filamentous Fungi, Approved Standard*; CLSI document M38-A; Clinical and Laboratory Standards Institute: Wayne, PA, 2002.

# Understanding the reversible anodic behaviour and fluorescence properties of fluorenylazomethines — A structure–property study

Satyananda Barik, Sayuri Friedland, and W.G. Skene

**Abstract:** A series of fluorenylazomethine dyads and triads were prepared by simple condensation between the corresponding amine and aldehyde fluorene derivatives. These compounds were prepared as model compounds for investigating the effects of substitution and electronic groups on both the electrochemical properties and fluorescence quantum yields. It was found that the oxidation potential could be decreased by both incorporating electron donating groups and increasing the degree of conjugation. It was further found that alkylation in the fluorene's 9-position increased the azomethine degree of conjugation by forcing all the fluorene moieties to be coplanar with the azomethine bonds to which they are attached. Meanwhile, reversible radical cation behaviour was possible by substituting the terminal 2,2'-positions with atoms other than hydrogen. The radical cation was theoretically found to be distributed evenly across the fluorene, corroborating the reversible anodic behaviour with 2,2'-substitution. The fluorescence quantum yields of the azomethines were not found to be dependent on substitution. This was because the azomethine fluorescence was found to be quenched relative to their precursors regardless of substitution. The fluorescence could be restored at both low temperature and by acid protonation.

**Key words:** fluorenylimines, reversible oxidation, cyclic voltammetry, azomethines, Schiff base, radical ions.

**Résumé :** On a préparé une série de dyades et de triades de la fluorénylazométhine par simple condensation entre des dérivés de l'amine et de l'aldéhyde du fluorène. On a préparé ces composés comme modèles pour des études sur les effets de substitution et des groupes électroniques tant sur les propriétés électrochimiques que sur les rendements quantiques de fluorescence. On a trouvé que le potentiel d'oxydation peut être réduit tant par l'incorporation de groupes électrodonneurs que par une augmentation du degré de conjugaison. On a aussi trouvé que l'alkylation en position 9 des fluorènes augmente le degré de conjugaison des azométhines en forçant toutes les entités fluorènes à être coplanaires avec les liaisons azométhines auxquelles sont attachées. Par ailleurs, un comportement de cation radical réversible est possible si l'on substitue les positions terminales en 2,2' par des atomes autres que l'hydrogène. On a trouvé sur une base théorique que le cation radical peut être distribué d'une façon uniforme sur l'ensemble de la portion fluorène, ce qui confirme le comportement anodique réversible avec une substitution 2,2'. Les résultats obtenus suggèrent que les rendements quantiques de fluorescence des azométhines ne dépendent pas de la substitution. Cette conclusion repose sur le fait que la fluorescence de l'azométhine est désactivée par rapport à celles de leurs précurseurs quelle que soit la substitution. La fluorescence peut être restaurée aussi bien par une basse température que par une protonation acide.

**Mots-clés :** fluorénylimines, oxydation réversible, voltampérométrie cyclique, azométhines, base de Schiff, ions radicaux.

## Introduction

Conjugated polymers are of great interest in part due to their electrochemical and optoelectronic properties that are well-suited for use in plastic devices such as organic field effect transistors (OFET), light emitting diodes (OLED), and organic photovoltaics (OPVD), to name but a few.<sup>1–4</sup> Polyfluorenes are particularly interesting because of their inherent fluorescence making them appropriate emitting materials for OLED usage.<sup>5</sup> Many polyfluorene derivatives have been prepared and investigated to afford materials with improved device efficiency and color purity for addressing the performance requirements for the next generation of plastic electronics and consumer demands.<sup>5–7</sup> Desired property improvements are possible by connecting the fluorene segments

with vinylene linkages.<sup>7–9</sup> Their preparation uses Gilch and Horner–Emmons protocols, requiring rigorous reaction conditions such as anhydrous solvents and inert atmospheres. These coupling methods, unfortunately, produce significant byproducts requiring product purification in order not to compromise the material's colour emission and device performance.

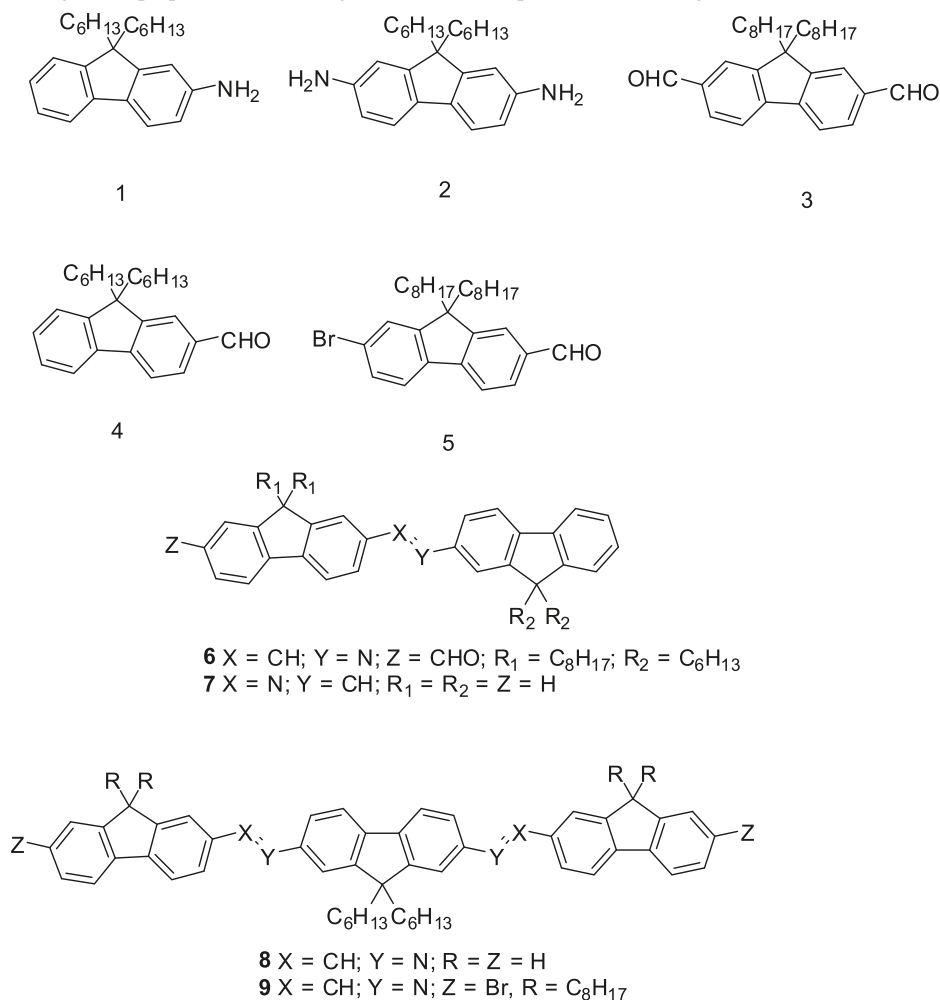
Azomethines ( $-N=C-$ ) are highly attractive alternatives to vinylene linkages owing to their easy preparation not requiring stringent reaction conditions.<sup>10</sup> They are further advantageous because their preparation is environmentally friendly with water being the unique byproduct produced. The preparation of azomethines, therefore, requires little or no purification. Moreover, the azomethine bond is isoelectronic to its all-carbon counterpart, making it ideally suited for func-

Received 5 May 2010. Accepted 6 June 2010. Published on the NRC Research Press Web site at canjchem.nrc.ca on 18 August 2010.

S. Barik, S. Friedland,<sup>1</sup> and W. Skene,<sup>2</sup> Centre of Self-Assembled Chemical Structures, Département de Chimie, Université de Montréal, CP 6128, succ. Centre-ville, Montréal, QC H3C 3J7, Canada.

<sup>1</sup>Present address: Department of Chemistry, McGill University, Montreal, QC, Canada.

<sup>2</sup>Corresponding author (e-mail: w.skene@umontreal.ca).

**Chart 1.** Monomers and oligomers prepared and investigated and some representative analogues.

tional materials usage, but with the advantage of simple preparation and little purification.<sup>11–13</sup>

Despite these advantages, azomethine fluorenes have not been fully exploited as functional materials in emitting devices. This is a result of previously investigated fluorenylazomethine derivatives that were irreversibly oxidized and were nonfluorescent.<sup>14,15</sup> Such properties, unfortunately, preclude their use in functioning devices, and as a result, have attracted little attention for property improvement. It is therefore important to understand the reasons for irreversible oxidation to design and prepare new azomethine derivatives with functional materials properties. For this reason, we investigated the effect of fluorenylazomethine structure on the electrochemical properties to achieve reversible oxidation. We were further enticed to undertake such structure–property studies to bring to light the potential uses of fluorenylazomethines as functional materials. This is in part because azomethines are dismissed as useful functional materials owing to the limited properties of previously examined compounds. We therefore examined the electrochemical properties of a series of model fluorenylazomethines complemented with theoretical studies to better understand the oxidation process. The knowledge gained from such studies is not only pivotal for demonstrating the suitability of azomethines as functional materials, but also for designing and preparing future genera-

tions of fluorenyl compounds with tailored properties for specific applications. Herein, we present the preparation and electrochemical studies of a series of fluorenylazomethines, represented in Chart 1, for understanding the structure–reversible oxidation relationship.

## Experimental

### Materials and general experimental procedures

All reagents were commercially available from Sigma-Aldrich and were used as received unless otherwise stated. Anhydrous and deaerated solvents were obtained via a Glass Contour Solvent Purification System. <sup>1</sup>H NMR and <sup>13</sup>C NMR spectra were recorded on a Bruker 400 MHz spectrometer with the appropriate deuterated solvents.

### Spectroscopic measurements

Absorption measurements were performed on a Cary-500 spectrometer and fluorescence studies were done on an Edinburgh Instruments FLS-920 fluorimeter after deaerating the samples thoroughly with nitrogen for 20 min. Relative fluorescence quantum yields were measured at 10<sup>–5</sup> mol/L by exciting the corresponding compounds at its maximum absorption in spectroscopic grade dichloromethane relative to itself at 77 K under the same conditions.



### Electrochemical measurements

Cyclic voltammetric measurements were performed on a Bio Analytical Systems EC Epsilon potentiostat at scan rates of 100 mV/s. Compounds were dissolved in anhydrous and deaerated dichloromethane at  $10^{-4}$  mol/L with 0.5 mol/L  $\text{Bu}_4\text{NPF}_6$ . A platinum electrode and a saturated Ag/AgCl electrode were employed as auxiliary and reference electrodes, respectively, and ferrocene was added at the end of the electrochemical measurements to serve as an internal reference.

The highest occupied molecular orbital (HOMO) and lowest unoccupied molecular orbital (LUMO) energy levels and spin densities were calculated using density functional theory (DFT) calculation methods available in Spartan 06 (Wavefunction, Inc.) with the 6-31g\* basis set.<sup>16</sup> The bond angles, distances, torsions, and other parameters were experimentally derived from the X-ray data for an analogous compound. The crystallographic data were used as the optimized geometry from which the single point energy was calculated to semiempirically calculate the molecular orbitals and spin densities. The rotational barriers were semiempirically calculated using the AM1 method.<sup>17</sup> The desired dihedral angle was varied from  $0^\circ$  to  $360^\circ$  and constrained at a given angle. The heat of formation ( $\Delta H_f$ ) for the given angle was subsequently calculated without additional structural optimization.

### Synthetic procedures

The syntheses of **3**, **4**, **7**, and **8** were prepared according to reported procedures.<sup>18</sup>

#### 9,9-Dihexylfluorene

Fluorene (5 g, 30.8 mmol) was dissolved in DMSO (50 mL) and triethylbenzyl ammonium bromide (0.1 g, 1.5 mol) was added under  $\text{N}_2$ .<sup>19</sup> A 50% aqueous NaOH (15 mL) solution was added while stirring at room temperature. After 0.5 h, 1-bromohexane (12.41 g, 75.2 mmol) was added dropwise for 15 min. The reaction mixture was then stirred at room temperature for 4 d. The reaction mixture was diluted with an excess of diethyl ether and the aqueous layer was removed. The organic layer was washed with water, 2 mol/L HCl, and brine and then dried over  $\text{MgSO}_4$ . The solvent was removed under vacuum and the residue was purified by column chromatography over silica gel with hexanes as eluent to give the product as a white solid at  $-40^\circ\text{C}$  (7.8 g, 90%).  $^1\text{H}$  NMR (400 MHz,  $\text{CDCl}_3$ )  $\delta$ : 7.73 (d, 2H), 7.31–7.38 (m, 6H), 1.99 (dd, 4H), 1.07–1.33 (m, 12H), 0.77 (t, 4H), 0.63 (t, 6H).  $^{13}\text{C}$  NMR (100 MHz,  $\text{CDCl}_3$ )  $\delta$ : 151.1, 141.5, 127.4, 121.1, 123.2, 120.0, 55.4, 40.8, 31.9, 30.1, 24.1, 23.0, 14.2.

#### 2,7-Dinitro-9,9-dihexylfluorene

The nitration was done similarly to published procedures.<sup>20</sup> A solution of 9,9-dihexylfluorene (2.12 g, 6.33 mmol) in 20 mL of  $\text{HNO}_3$  in a 100 mL roundbottom flask was heated to reflux for 2 h under  $\text{N}_2$  atmosphere. The reaction mixture was then cooled to room temperature and poured onto ice and the product was extracted with dichloromethane. The organic layer was washed with water three times, saturated  $\text{NaHCO}_3$ , and brine solution and then finally dried over  $\text{MgSO}_4$ . The solvent was evaporated and

the crude product was purified by column chromatography with hexanes/ethyl acetate (7:3) to give a mixture of 2-nitro-9,9-dihexylfluorene and 2,7-dinitro-9,9-dihexylfluorene. The products were further recrystallized from EtOH to separate the two products, which were isolated as yellow solids.

#### 2,7-Dinitro-9,9-dihexylfluorene

Isolated yield of 66% (1.94 g).  $^1\text{H}$  NMR (400 MHz,  $\text{CDCl}_3$ )  $\delta$ : 8.33 (dd, 2H), 8.28 (d, 2H), 7.93 (d, 2H), 2.09 (dd, 4H), 1.02–1.13 (m, 12H), 0.76 (t, 4H), 0.55 (t, 6H).  $^{13}\text{C}$  NMR (100 MHz,  $\text{CDCl}_3$ )  $\delta$ : 152.7, 147.5, 127.7, 123.6, 121.6, 120.1, 56.0, 40.4, 31.8, 29.9, 24.1, 22.9, 14.3.

#### 2-Nitro-9,9-dihexylfluorene

$^1\text{H}$  NMR (400 MHz,  $\text{CDCl}_3$ )  $\delta$ : 8.27 (d, 1H), 8.23 (d, 1H), 7.82 (dd, 2H), 7.41–7.44 (m, 3H), 2.03 (dd, 4H), 1.05–1.13 (m, 12H), 0.76 (t, 4H), 0.60 (t, 6H).  $^{13}\text{C}$  NMR (100 MHz,  $\text{CDCl}_3$ )  $\delta$ : 152.7, 152.3, 148.0, 147.5, 129.6, 127.8, 123.6, 123.5, 121.6, 120.1, 118.6, 56.0, 40.5, 31.8, 29.9, 24.1, 22.9, 14.3.

#### 2-Amino-9,9-dihexylfluorene (1)

2-Nitro-9,9-dihexylfluorene (0.84 g, 2.21 mmol) was dissolved in 10 mL of EtOH and stirred at room temperature under  $\text{N}_2$ . A catalytic amount of 10% Pd/C (0.2 g) was added followed by the addition of hydrazine monohydrate (1.6 g, 11.05 mmol) and the mixture was refluxed for 2 h. The reaction mixture was filtered to remove the Pd/C and the product was extracted with dichloromethane. The organic layer was washed with water ( $3 \times 50$  mL) and brine solution and then dried over  $\text{MgSO}_4$ . The solvent was evaporated and the crude product was purified by column chromatography with hexanes/ethyl acetate (1:1) as eluent to give the product as a brown sticky liquid with an isolated yield of 78%. The product was unstable and was kept under  $\text{N}_2$  atmosphere and used immediately for subsequent reactions.  $^1\text{H}$  NMR (400 MHz,  $\text{CDCl}_3$ )  $\delta$ : 7.57 (d, 1H), 7.48 (d, 1H), 7.26 (m, 3H), 7.19 (dd, 2H), 6.68 (d, 2H), 1.90 (dd, 4H), 1.04 (m, 12H), 0.78 (t, 6H), 0.64 (d, 4H).  $^{13}\text{C}$  NMR (100 MHz,  $\text{CDCl}_3$ )  $\delta$ : 153.0, 150.1, 148.2, 128.9, 125.7, 122.9, 120.9, 118.7, 114.3, 110.2, 55.1, 41.0, 31.9, 30.2, 24.1, 23.0, 14.4. MS  $m/z$ : 350.54 ( $\text{M}^+$ ).

#### 2,7-Diamino-9,9-dihexylfluorene (2)

The solution of 2,7-dinitro-9,9-dihexylfluorene (1.2 g, 2.8 mmol) in 20 mL of EtOH was stirred at room temperature under  $\text{N}_2$ . To the above solution, a catalytic amount of 10% Pd/C (0.1 g) was added followed by hydrazine monohydrate (1.02 g, 20.18 mmol) and the mixture was refluxed for 2 h. The reaction mixture was filtered and the product was extracted with dichloromethane. The organic layer was washed with water ( $3 \times 50$  mL) and brine solution and then dried over  $\text{MgSO}_4$ . The solvent was evaporated and the crude product was purified by column chromatography with hexanes/ethyl acetate (1:1) to afford the title compound as a brown liquid with an isolated yield of 72%. The product was unstable and was stored under  $\text{N}_2$  until used.  $^1\text{H}$  NMR (400 MHz,  $\text{CDCl}_3$ )  $\delta$ : 7.35 (d, 2H), 6.66 (d, 4H), 3.94 (br,  $\text{NH}_2$ ), 1.83 (dd, 4H), 1.06 (m, 12H), 0.78 (t, 6H), 0.66 (d, 4H).  $^{13}\text{C}$  NMR (100 MHz,  $\text{CDCl}_3$ )  $\delta$ : 152.1, 144.3, 133.8, 119.5, 114.6, 110.7, 55.0, 41.3, 32.0, 30.2, 24.1, 23.1, 14.4. MS  $m/z$ : 356.3 ( $\text{M}^+$ ).

### 9,9-Dioctylfluorene-2,7-dicarboxaldehyde (3)

A 250 mL two-necked flask containing 9,9-dioctyl-2,7-dibromofluorene (2.2 g, 4.01 mmol) in anhydrous THF (40 mL) was stirred under N<sub>2</sub> at -78 °C in an acetone-dry ice bath.<sup>21</sup> *n*-Butyl lithium (7.6 mL, 16.0 mmol) was added under vigorous stirring and stirred for 1.5 h. A deaerated mixture of DMF (5 mL) and anhydrous THF (3 mL) was added dropwise to the reaction mixture at -78 °C and allowed to stir for 1 h at room temperature. The reaction mixture was cooled to 0 °C and 10% HCl was added until the solution was acidic (tested by litmus paper). After stirring for 30 min, the mixture was partitioned between dichloromethane and water and the organic layer was isolated. The aqueous layer was washed with dichloromethane and the combined organic extracts were dried over Na<sub>2</sub>SO<sub>4</sub>. The crude product was purified by column chromatography using hexanes/dichloromethane (1:1) as eluent. The product was obtained as colourless crystals (58%, 1.05 g). <sup>1</sup>H NMR (400 MHz, CDCl<sub>3</sub>) δ: 10.1 (s, 2H, CHO), 7.91–7.96 (m, 6H), 2.0 (dd, 4H), 1.02 (m, 20H), 0.78 (t, 6H), 0.56 (d, 4H). <sup>13</sup>C NMR (100 MHz, CDCl<sub>3</sub>) δ: 192.5, 153.2, 146.0, 136.8, 130.7, 123.8, 121.7, 56.0, 40.4, 32.1, 30.2, 29.5, 24.2, 22.9, 14.4. MS *m/z*: 446.4 (M<sup>+</sup>).

### 9,9-Dihexylfluorene-2-carboxaldehyde (4)

The synthesis was followed according to known methods.<sup>17</sup> The solution of 2-bromo-9,9-dihexylfluorene (4.0 g, 9.67 mmol) in anhydrous THF (50 mL) was purged with N<sub>2</sub> at -78 °C in an acetone-dry ice bath. To the above solution, *n*-butyl lithium (9.21 mL, 19.35 mmol) was added dropwise and stirred for 1.5 h. A degassed solution of DMF (2 mL) and anhydrous THF (3 mL) was added dropwise while maintaining the reaction mixture at -78 °C, after which the temperature was raised to room temperature and stirred for 1 h. The reaction mixture was cooled to 0 °C and 10% HCl was added until the solution was acidic as verified by litmus paper. After stirring for 30 min, the mixture was partitioned between dichloromethane and water. The organic layer was extracted and the aqueous layer was washed again with dichloromethane. The combined organic fractions were dried over Na<sub>2</sub>SO<sub>4</sub>. After solvent removal, the crude product was purified by column chromatography with hexanes/dichloromethane (1:1). The product was obtained as a colourless liquid (2.15 g, 48%). <sup>1</sup>H NMR (400 MHz, CDCl<sub>3</sub>) δ: 10.09 (s, 1H, CHO), 7.91 (s, 1H), 7.86 (dd, 2H), 7.97 (dd, 1H), 7.41 (m, 3H), 2.02 (dd, 4H), 1.04 (m, 12H), 0.75 (t, 6H), 0.569 (d, 4H). <sup>13</sup>C NMR (100 MHz, CDCl<sub>3</sub>) δ: 192.7, 152.5, 147.9, 139.9, 135.7, 130.9, 129.2, 127.5, 123.5, 123.4, 121.3, 120.3, 55.8, 40.64, 31.8, 30.0, 29.5, 24.1, 22.9, 14.4. MS *m/z*: 363.24 (M<sup>+</sup>).

### 2-Bromo-9,9-dioctylfluorene-7-carboxaldehyde (5)

To the solution containing 9,9-dioctyl-2,7-dibromofluorene (3.0 g, 5.47 mmol) in anhydrous THF (60 mL) purged with N<sub>2</sub> at -78 °C was added *n*-butyl lithium (2.84 mL, 7.11 mmol) and the reaction was allowed to stir for another 1.5 h. Afterwards, deaerated DMF (1 mL) diluted in anhydrous THF (1 mL) was added dropwise to the reaction mixture at -78 °C, after which the temperature was allowed to warm to room temperature and then stirred for 1 h. The reaction mixture was cooled to 0 °C and 10% HCl was added

until the solution was acidic. The solution was stirred for 30 min then the product was extracted in dichloromethane. The organic layer was isolated while the aqueous layer was washed with dichloromethane once more and the combined organic extracts were dried over Na<sub>2</sub>SO<sub>4</sub>. The crude product was purified by column chromatography with hexanes/dichloromethane (1:1) to afford the title product as colorless crystals (0.9 g, 58%). <sup>1</sup>H NMR (400 MHz, CDCl<sub>3</sub>) δ: 10.08 (s, 1H, CHO), 7.83–7.88 (m, 3H), 7.64 (d, 1H), 7.51 (d, 2H), 2.01 (dd, 4H), 1.05 (m, 20H), 0.81 (t, 6H), 0.57 (d, 4H). <sup>13</sup>C NMR (100 MHz, CDCl<sub>3</sub>) δ: 192.5, 154.6, 151.5, 146.7, 138.9, 136.0, 130.9, 130.8, 126.8, 123.5, 122.6, 120.5, 56.0, 40.4, 32.1, 32.0, 30.2, 29.5, 24.1, 22.9, 14.4. MS *m/z*: 497.0 (M<sup>+</sup>).

### 7-[(9,9'-Dihexylfluorene-2'-ylimino)-methyl]-9,9-dioctylfluorene-2-carboxaldehyde (6)

Both **3** (100 mg, 0.22 mmol) and **1** (180.1 mg, 0.514 mmol) were dissolved in absolute ethanol under N<sub>2</sub>. A catalytic amount of TFA (60 μL of 1% in absolute ethanol) was added and the reaction mixture was stirred overnight at room temperature. The solvent was evaporated to afford a dark oil that was extracted with dichloromethane (25 mL). The organic layer was washed with water and brine solution and then dried over MgSO<sub>4</sub>. The crude product was chromatographed on activated basic alumina with ethyl acetate/hexanes (1:1 v/v) to yield the product as a yellow oil (80 mg, 60%). <sup>1</sup>H NMR (400 MHz, CDCl<sub>3</sub>) δ: 10.08 (s, 1H), 8.65 (s, 1H), 8.00 (s, 1H), 7.89 (m, 4H), 7.86 (m, 3H), 7.74 (d, 1H, *J* = 7.3 Hz), 7.41 (s, 1H), 7.4 (t, 1H, *J* = 7.3 Hz), 7.31 (m, 2H), 2.01 (m, 8H), 1.08 (m, 30 H), 0.79 (t, 12H, *J* = 7.0 Hz), 0.61 (m, 8H). <sup>13</sup>C NMR (100 MHz, CDCl<sub>3</sub>) δ: 192.8, 160.7, 152.5, 152.4, 151.9, 151.2, 147.9, 139.9, 135.7, 130.9, 129.2, 127.5, 127.3, 127.1, 123.5, 123.4, 121.3, 120.3, 119.8, 116.5, 55.6, 40.6, 32.0, 31.9, 31.8, 30.1, 30.0, 24.2, 24.1, 23.1, 23.0, 22.9, 14.4, 14.3. MS *m/z*: 778.49.

### 2',7'-[(9,9',9'')-Tetraoctylfluorene-7,7''-diylimino)-methyl]-9,9'-dihexyl-2,2''-dibromotrifluorene (9)

Both **6** (0.511 g, 1.02 mmol) and **4** (0.150 g, 0.411 mmol) were dissolved in absolute ethanol (5 mL) under N<sub>2</sub>. TFA (60 μL of 1% in ethanol) was added to the reaction mixture and then it was stirred for 1 h at room temperature. The solvent was evaporated to afford a brown oil that was extracted with dichloromethane (25 mL). The organic layer was washed with water (2 × 50 mL) and brine solution (2 × 50 mL) and then dried over MgSO<sub>4</sub>. The product was isolated as a yellow solid (44%) after flash column chromatography with basic activated alumina with hexanes/ethyl acetate (7:3). <sup>1</sup>H NMR (400 MHz, CDCl<sub>3</sub>) δ: 8.64 (d, 2H), 7.9 (d, 4H), 7.62 (dd, 4H), 7.52 (d, 4H), 7.31 (d, 2H), 6.65 (4H), 2.06 (dd, 12H), 1.08 (m, 50H), 0.81 (m, 18H), 0.63 (m, 12H). <sup>13</sup>C NMR (100 MHz, CDCl<sub>3</sub>) δ: 160.3, 154.1, 153.2, 152.6, 151.4, 146.2, 143.8, 140.5, 139.8, 139.7, 136.2, 136.0, 132.5, 130.5, 129.3, 126.7, 122.8, 122.0, 120.7, 120.3, 119.6, 119.2, 116.4, 114.4, 110.2, 56.0, 55.3, 41.2, 40.6, 32.0, 30.4, 30.3, 30.2, 29.6, 24.1, 24.0, 23.0, 22.9, 14.4. MS *m/z*: 1323.6 (M<sup>+</sup>).

## Results and discussion

### Synthesis

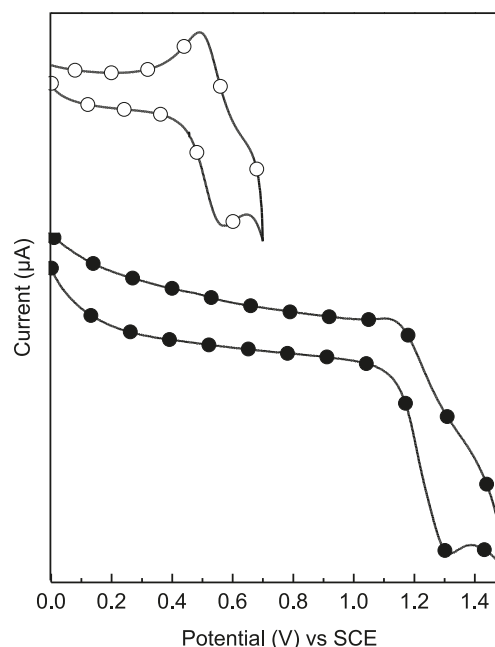
Compounds **6–9** were prepared and investigated to provide insight into the fluorescence and electrochemical behaviour of fluorenylazomethines. The compounds were chosen as model compounds for such studies given the complexity of absolute characterization of their polymeric counterparts. The advantage of investigating these model compounds is that precise structure–property relationships can be accurately obtained. The compounds were judiciously selected because the effect of the imine bond, 9-fluorenyl alkylation, degree of conjugation, and substitution of the fluorene's 2,7-positions on both the electrochemical and photophysical properties could be investigated. The required fluorenyl aldehyde precursors were prepared from 9,9-dioctyl 2,7-dibromofluorene by standard metal–halogen exchange with *n*-butyl lithium and quenching with DMF.<sup>22</sup> The various aldehyde derivatives were obtained by varying the *n*-BuLi/dibromofluorene ratio. The complementary aminofluorene derivatives were obtained by nitrating 9,9-dihexyl-fluorene, prepared from fluorene by known methods, followed by reduction with activated Pd/C (10%).<sup>23</sup> The resulting amino fluorenes were extremely sensitive to ambient conditions and underwent spontaneous decomposition. Consequently, they were used immediately once synthesized for preparing the targeted azomethines. The desired azomethines were prepared using mild coupling conditions by refluxing the complementary fluorenes in absolute ethanol in the presence of a catalytic amount of TFA. The desired products were readily purified by column chromatography without any decomposition and were obtained in sufficient purity for electrochemical and spectroscopic characterization. The extended degree of conjugation of **6–9** make these compounds stable and less sensitive to acid hydrolysis to their aliphatic counter parts.

### Electrochemical studies

The electrochemical behaviour is an important property for functional materials. Given that the exciton in an emitting device is produced by the recombination of an electron and hole, it is desired that the emitting layer be able to repeatedly sustain the harsh oxidation and reduction environment found in the device environment for ensuring device longevity. The redox properties of the fluorenylazomethines were therefore investigated and the structure-redox potentials examined. The effects of substitution in the 2, 2'-positions, degree of conjugation, and alkylation on the electrochemical properties are possible with the compounds in Chart 1.

The effect of the single heteroatomic bond on the  $E_{\text{pa}}$  is evident by comparing **6** with **4**. The oxidation potential of the fluorenylazomethine is increased by 130 mV. Although the  $E_{\text{pa}}$  of **6** is expected to be reduced significantly compared to **4** as a result of the increased degree conjugation arising from the azomethine bond, the heteroconjugated bond is a good electron-withdrawing group and counterbalances some of the energetic gain from the increased conjugation. The  $E_{\text{pa}}$  of **7** is increased relative to **6** owing to the absence of the electron-withdrawing aldehyde group. Meanwhile, the  $E_{\text{pa}}$  of **8** is 120 mV lower than **7** because of its

**Fig. 1.** Cyclic voltammogram of **6** (●) and **9** (○) measured at 100 mV/s.

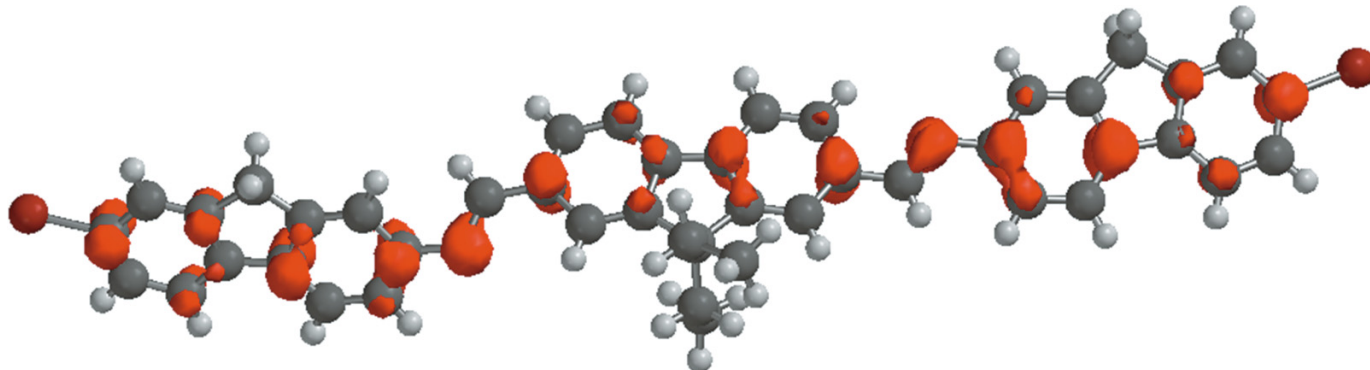


increased degree of conjugation. A significantly larger decrease in the oxidation is expected for **8** as a result of the increased degree of conjugation; however, previous crystallographic studies showed that the terminal fluorenes are highly twisted with respect to the central axis.<sup>24</sup> Therefore, it has a limited degree of conjugation, located predominantly on the =N–fluorene–N= central moiety. Conversely, **9** is highly conjugated according to the extremely low  $E_{\text{pa}}$  measured. The difference in conjugation between **8** and **9** is most likely a result of the alkyl substitution that forces coplanarization of the fluorene and azomethine units to minimize interchain interactions. Although unequivocal confirmation of the extended conjugation can be had from the crystal structure, repeated attempts to crystallize **9** were, unfortunately, unsuccessful. The optimized geometry was subsequently calculated via DFT for examining the structure of **9**. We first tested this method for accurately calculating the optimized azomethine geometries by comparing calculated structures with those measured experimentally from known crystal structure data. The calculated optimized geometries were consistent with those obtained by X-ray diffraction (XRD). The resulting structure calculated for **9** showed the terminal fluorenes to be twisted by 12° from the plane described by the central fluorene and the azomethines. This is in contrast to **8**, whose terminal fluorenes are twisted by 26.7° and 65.3° from the central fluorene plane.<sup>18,25</sup> The low  $E_{\text{pa}}$  of **9** relative to the other azomethines is therefore a result of both its extended degree of conjugation and the weak electron-donating terminal bromines.

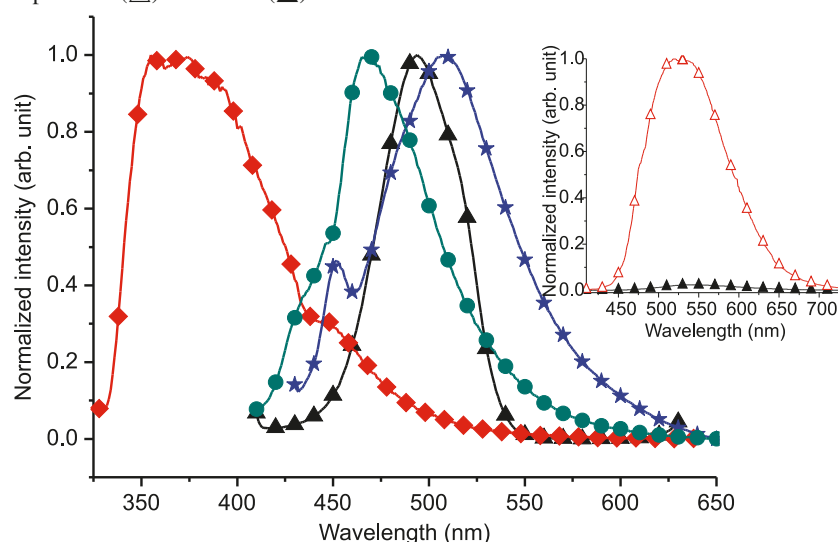
As seen in Fig. 1, the first oxidation process of **9** is reversible. This is in contrast to the other fluorenylazomethines, such as **6**, that undergo irreversible oxidation. The electrochemical sample of **9** was thoroughly deaerated to ensure that the observed reversible process was not from the reduction of residual oxygen. The peak persisted despite persistent nitrogen purging. The anodic process corresponds to a one-



**Fig. 2.** Calculated spin densities shown in red for the radical cation **9**. The alkyl groups in the 9-positions are omitted for clarity.



**Fig. 3.** Normalized fluorescence spectra of **2** (▲), **3** (◆), **6** (★), and **9** (●) excited at their respective maximum. Inset: normalized emission spectra of **9** at room temperature (△) and 77 K (▲).



electron transfer process while oxygen reduction is a two-electron process. The radical cation produced from the one-electron oxidation of **9** is therefore stable, based on the observed reversible oxidation, while similar intermediates for the other azomethines are unstable, evidenced by the irreversible anodic processes.

The spin densities of the radical cation of **9** were investigated to understand the reversible anodic behaviour. As seen in Fig. 2, the calculated spin densities is evenly distributed over most of the carbons of **9**. The 2,2'-positions are substituted with bromine for **9** while for the other azomethines, such as **6–8**, these positions are unsubstituted. Therefore, the resulting radical cation undergoes homocross-coupling according to known means when it is located in the terminal position.<sup>26</sup> This leads to the irreversible oxidation, as observed for **6–8**.<sup>27,28</sup> The terminal halogens of **9** effectively prevent radical cross-coupling and make the one-electron transfer process reversible. Alkylation in the 9-position is also important for reversible radical cation formation, according to Fig. 2. Azomethine structure and substitution play important roles in determining both the oxidation potentials at which the radical cation is produced and its reversible formation. The fluorenylazomethine oxidation potentials and the reversibility of these

processes can thus be tuned courtesy of substitution in the 2,2'-positions. It is therefore expected that polymers derived from **2** and **3** should sustain reversible oxidation.

### Fluorescence studies

Fluorescence investigations involving previously studied azomethines have exclusively used relative actinometry. The challenge with this approach is the lack of universal reference whose emission yield is accurately known and is both wavelength and solvent independent. Also, there is no general actinometer that consistently absorbs across the entire visible spectrum for measuring the emission yields of highly conjugated compounds regardless of the degree of conjugation. As a result of these limitations, large variations of fluorescence quantum yields are reported and cannot be accurately known. The absolute quantum yields of the fluorenylazomethine model compounds and their precursors were therefore measured using an integrating sphere because of their variable absorbance and fluorescence, evident in Fig. 3. As seen in Table 1, the fluorescence yields of the precursors **1–5** are all quenched. This is not surprising given that the fluorescence of fluorene is highly dependent on substitution.<sup>29,30</sup> The addition of the azomethine bond to the flu-



**Table 1.** Photophysical and electrochemical properties of fluorenylazomethine derivatives and their precursors.

Compound	$\lambda_{\text{abs}}$ (nm)	$\lambda_{\text{em}}$ (nm)	$\Phi_{\text{fl}}$ (77 K) <sup>a</sup>	$E_{\text{g}}$ (eV) <sup>b</sup>	$E_{\text{pa}}$ (V) <sup>c</sup>	$E_{\text{pc}}$ (V) <sup>d</sup>	HOMO (eV) <sup>e</sup>	LUMO (eV) <sup>e</sup>	$E_{\text{g}}$ (eV) <sup>f</sup>
Fluorene <sup>g</sup>	261	302	0.72	3.9	1.36	−1.31	5.2	3.3	1.9
<b>1</b> <sup>h</sup>	292	389	0	3.5	—	—	—	—	—
<b>2</b> <sup>h</sup>	398	494	0.01	2.5	—	—	—	—	—
<b>3</b>	339	383	0	3.4	1.00	−1.02	5.4	3.4	2.0
<b>4</b>	326	366	0.01	3.5	1.15	−1.06	5.8	3.3	2.5
<b>5</b>	330	425	0.02	3.4	0.86	−1.90	5.26	2.5	2.76
<b>6</b>	384	509	0.02 (0.32)	2.6	1.30	−1.64	5.7	2.8	2.9
<b>7</b> <sup>i</sup>	361	445	0.01 (0.05)	2.9	1.53	−1.12	5.6	3.5	2.1
<b>8</b> <sup>i</sup>	396	472	0.01 (0.31)	2.8	1.41	−1.52	5.6	3.4	2.2
<b>9</b>	410	470	0.02 (0.38)	2.6	0.56	—	4.9	2.3	2.6

<sup>a</sup>Fluorescence quantum yield at room temperature. Values in parentheses are the emission yields measured at 77 K and calculated relative to the absolute room temperature fluorescence yields.

<sup>b</sup>Spectroscopically determined energy gap taken from the absorption onset.

<sup>c</sup>Oxidation potential relative to saturated Ag/Ag<sup>+</sup> electrode.

<sup>d</sup>Reduction potential relative to Ag/Ag<sup>+</sup>.

<sup>e</sup>Relative to the vacuum level.

<sup>f</sup>Electrochemical energy gap.

<sup>g</sup>Reference 25.

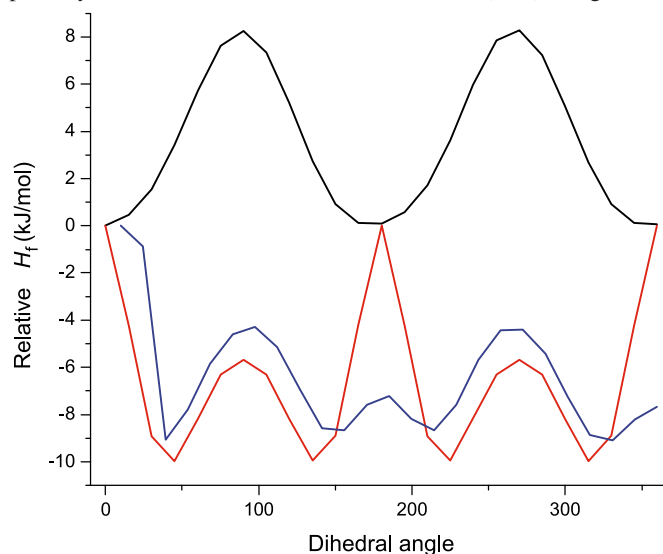
<sup>h</sup>Reliable electrochemical data for **1** and **2** could not be obtained as a result of their instability under our experimental conditions.

<sup>i</sup>Reference 18.

orene moiety does not increase the fluorescence. In all cases, the fluorenylazomethine fluorescence is quenched regardless of degree of oligomerization.

With increasing oligomerization, the number of degrees of freedom increases, representing additional modes of fluorescence deactivation. Fluorescence deactivation by aryl–azomethine bond rotation was subsequently investigated to determine whether this deactivation mode was responsible for the quenched azomethine fluorescence. This was done by examining the fluorescence emission at 77 K, at which temperature all non-radiative fluorescence deactivation modes by bond rotation are suppressed. Therefore, fluorescence increase is expected at 77 K if deactivation by nonradiative means occurs. The oligofluorenes **6–9** all exhibited significant increases in fluorescence yields at this reduced temperature as seen in the inset of Fig. 3. Unfortunately, accurate quantitative measurements of the emission yields at 77 K cannot be obtained because they are reliant on the weak room temperature fluorescence signals. Nonetheless, the fluorescence quantum yields of the oligofluorenylazomethines at low 77 K surpass those of their precursors at room temperature and reach the same order of magnitude as native fluorene.

To provide further insight into the origins of the temperature dependent fluorescence of the azomethines, the rotational barrier around the =N–fluorenyl and =CH–fluorenyl bonds were semiempirically calculated. A simple alkylated dyad analogue of **7** was used as a model compound because its crystal structure data is known, which were used for inputting the correct optimized ground state geometry. The heats of formation ( $\Delta H_f$ ) of each torsion around the fluorene–N= and =CH–fluorene bonds were calculated. Although absolute  $\Delta H_f$  values are not possible as a result of scaling errors, the relative values can, however, be accurately calculated. The semiempirically calculated bond rotation energies for an analogous fluorene–fluorene dyad were also calculated. 2,2'-Bifluorene was used as a benchmark

**Fig. 4.** Rotational bond energies of the fluorene–N= (black) and =CH–fluorene (blue) bonds for **6** and 2,2'-bifluorene (red) semiempirically calculated from the heats of formation ( $\Delta H_f$ ) using AM1.

since its fluorescence yields are reduced relative to native fluorene as a result of nonradiative deactivation around the fluorene–fluorene bond.<sup>24</sup> As seen in Fig. 4, the bond rotation energies for both the azomethine and fluorene dyads are similar. This suggests that fluorescence quenching by nonradiative bond rotation is a possible deactivation mode for azomethines. The absolute fluorescence yield of **9** was subsequently examined in thin films, where bond rotation deactivation processes cannot occur. A fluorescence quantum yield of 0.08 was measured in the solid state, confirming that deactivation by means other than simple fluorene–N= and =CH–fluorene bond rotation as responsible for azomethine fluorescence quenching. Meanwhile, the fluores-

cence of both **6** and **9** could, however, be significantly restored by protonating the azomethine bond with TFA. The measured absolute fluorescence yield for these two compounds was 0.4 and 0.11, respectively. The fluorescence on/off switching by acid protonation corroborates previous studies that the major deactivation mode is by intramolecular photoinduced electron transfer.<sup>31</sup> Fluorenylazomethines are therefore interesting because their fluorescence can be tuned by both temperature and acid doping.

## Conclusion

A series of dyad and triad fluorenylazomethines were prepared with different electronic groups and substitution. The oxidation potential was contingent on both substitution and degree of conjugation. Although homoaryl groups are normally twisted by up to 65° from the azomethines to which they are linked, increased planarity and hence increased degree of conjugation was possible by alkylating the fluorene's 9-position. Substitution in the 2,2'-position was also found to play an important role in determining the reversibility of the electrochemically generated radical cation. Meanwhile, the fluorescence of the azomethines remained quenched similar to their precursors. The fluorescence could be restored at low temperature and by acid protonation. The fluorenylazomethines therefore have sensor properties. The collective knowledge gained from the combined electrochemical and fluorimetric studies is pivotal for the design and preparation for the future generation of azomethines for emitting applications and will lead to highly fluorescent materials with desired reversible oxidation. The results further suggest that polymers derived from **2** and **3** will exhibit desired reversible oxidation, making them suitable materials for emitting applications.

## Supplementary data

Supplementary data for this article are available on the journal Web site (canjchem.nrc.ca).

## Acknowledgements

The Natural Sciences and Engineering Research Council of Canada (NSERC) is thanked for a Discovery Grant (DG) and a Research Tools and Instruments (RTI) Grant, and the Centre for Self-Assembled Chemical Structures (CSACS) for a Strategic Research Grant (SRG), which allowed this work to be performed. In addition, the Canada Foundation for Innovation (CFI) is thanked for additional equipment funding. WGS also thanks both the Alexander von Humboldt Foundation and the Royal Society of Chemistry (RSC) for a J. W. T. Jones Travelling Fellowship, allowing this manuscript to be completed. SF thanks NSERC and the Reactive Intermediate Student Exchange Program (RISE) program for an undergraduate scholarship.

## References

- (1) Brédas, J.-L.; Norton, J. E.; Cornil, J.; Coropceanu, V. *Acc. Chem. Res.* **2009**, *42* (11), 1691. doi:10.1021/ar900099h. PMID:19653630.
- (2) Brédas, J.-L.; Durrant, J. R. *Acc. Chem. Res.* **2009**, *42* (11), 1689. doi:10.1021/ar900238j. PMID:19916562.

- (3) Kamtekar, K. T.; Monkman, A. P.; Bryce, M. R. *Adv. Mater.* **2010**, *22* (5), 572. doi:10.1002/adma.200902148. PMID:20217752.
- (4) Lee, K.; Nair, P. R.; Scott, A.; Alam, M. A.; Janes, D. B. *J. Appl. Phys.* **2009**, *105* (10), 102046. doi:10.1063/1.3116630.
- (5) Simas, E. R.; Gehlen, M. H.; Glogauer, A.; Akcelrud, L. *J. Phys. Chem. A* **2008**, *112* (23), 5054. doi:10.1021/jp711934d. PMID:18481838.
- (6) Zhang, K.; Chen, Z.; Yang, C.; Zou, Y.; Gong, S.; Qin, J.; Cao, Y. *J. Phys. Chem. C* **2008**, *112* (10), 3907. doi:10.1021/jp077433+.
- (7) Mikroyannidis, J. A.; Gibbons, K. M.; Kulkarni, A. P.; Jenekhe, S. A. *Macromolecules* **2008**, *41* (3), 663. doi:10.1021/ma071504l.
- (8) Sun, M.; Zhong, C.; Li, F.; Cao, Y.; Pei, Q. *Macromolecules* **2010**, *43* (4), 1714. doi:10.1021/ma9024762. PMID:17343421.
- (9) Bezgin, B.; Yagan, A.; Onal, A. M. *J. Electroanal. Chem.* **2009**, *632* (1–2), 143. doi:10.1016/j.jelechem.2009.04.011.
- (10) Guarin, S. A.; Bourdeaux, M.; Dufresne, S.; Skene, W. G. *J. Org. Chem.* **2007**, *72* (7), 2631. doi:10.1021/jo070100o. PMID:17343421.
- (11) Wang, C.; Shieh, S.; LeGoff, E.; Kanatzidis, M. G. *Macromolecules* **1996**, *29* (9), 3147. doi:10.1021/ma9514131.
- (12) Yang, C.-J.; Jenekhe, S. A. *Chem. Mater.* **1991**, *3* (5), 878. doi:10.1021/cm00017a025.
- (13) Kuder, J. E.; Gibson, H. W.; Wychick, D. *J. Org. Chem.* **1975**, *40* (7), 875. doi:10.1021/jo00895a013.
- (14) Tsai, F.-C.; Chang, C.-C.; Liu, C.-L.; Chen, W.-C.; Jenekhe, S. A. *Macromolecules* **2005**, *38* (5), 1958. doi:10.1021/ma048112o.
- (15) Liu, C.-L.; Chen, W.-C. *Macromol. Chem. Phys.* **2005**, *206* (21), 2212. doi:10.1002/macp.200500236.
- (16) Sherrill, C. D. *J. Chem. Phys.* **2010**, *132* (11), 110902. doi:10.1063/1.3369628.
- (17) Thiel, W. In *Theory and Applications of Computational Chemistry: The First Forty Years*; Dykstra, C. E., Kim, K. S., Frenking, G., Scuseria, G. E., Eds.; Elsevier: Amsterdam, 2005; pp 559–580.
- (18) Guarin, S. A. P.; Dufresne, S.; Tsang, D.; Sylla, A.; Skene, W. G. *J. Mater. Chem.* **2007**, *17* (27), 2801. doi:10.1039/b618098a.
- (19) Chen, Q.-Q.; Liu, F.; Ma, Z.; Peng, B.; Wei, W.; Huang, W. *Chem. Lett.* **2008**, *37* (2), 178. doi:10.1246/cl.2008.178.
- (20) Dudek, S. P.; Pouderoijen, M.; Abbel, R.; Schenning, A. P. H. J.; Meijer, E. W. *J. Am. Chem. Soc.* **2005**, *127* (33), 11763. doi:10.1021/ja052054k. PMID:16104754.
- (21) Giuseppe, N.; Fuks, G.; Lehn, J.-M. *Chem. Eur. J.* **2006**, *12* (6), 1723. doi:10.1002/chem.200501037.
- (22) Belfield, K. D.; Morales, A. R.; Kang, B.-S.; Hales, J. M.; Hagan, D. J.; Van Stryland, E. W.; Chapela, V. M.; Percino, J. *Chem. Mater.* **2004**, *16* (23), 4634. doi:10.1021/cm049872g.
- (23) Dudek, S. P.; Pouderoijen, M.; Abbel, R.; Schenning, A. P. H. J.; Meijer, E. W. *J. Am. Chem. Soc.* **2005**, *127* (33), 11763. doi:10.1021/ja052054k. PMID:16104754.
- (24) Guarin, S. A. P.; Dufresne, S.; Tsang, D.; Sylla, A.; Skene, W. G. *Polymeric Materials: Science and Engineering (PMSE) Preprints*; American Chemical Society: Washington, DC, 2007; Vol. 96, p 244.
- (25) Dufresne, S.; Pérez Guarin, S. A.; Bolduc, A.; Bourque, A. N.; Skene, W. G. *Photochem. Photobiol. Sci.* **2009**, *8* (6), 796. doi:10.1039/b819735k. PMID:19492107.
- (26) Roncali, J. *Chem. Rev.* **1992**, *92* (4), 711. doi:10.1021/cr00012a009.
- (27) Roncali, J.; Blanchard, P.; Frère, P. *J. Mater. Chem.* **2005**, *15* (16), 1589. doi:10.1039/b415481a.

- (28) Hapiot, P.; Lagrost, C.; LeFloch, F.; Raoult, E.; Rault-Berthelot, J. *Chem. Mater.* **2005**, *17* (8), 2003. doi:10.1021/cm048331o.
- (29) Turro, N. J.; Ramamurthy, V.; Scaiano, J. C. *Principles of Molecular Photochemistry: An Introduction*; University Science Books: Sausalito, CA, 2009.
- (30) Murphy, R. S.; Moorlag, C. P.; Green, W. H.; Bohne, C. J. *Photochem. Photobiol. A* **1997**, *110* (2), 123. doi:10.1016/S1010-6030(97)00191-3.
- (31) Dufresne, S.; Callaghan, L.; Skene, W. G. *J. Phys. Chem. B* **2009**, *113* (47), 15541. doi:10.1021/jp907391y.

# Iron(II) complexes containing thiophene-substituted “bispicen” ligands — Spin-crossover, ligand rearrangements, and ferromagnetic interactions

Haojin Cheng, Brandon Djukic, Hilary A. Jenkins, Serge I. Gorelsky, and Martin T. Lemaire

**Abstract:** The synthesis and characterization of three new tetradentate “bispicen-type” ligands containing a substituted thiophene heterocycle are described [2,5-thienyl substituents = H (**7**), Ph (**8**), or 2-thienyl (**9**)]. Iron(II) bis(thiocyanate) coordination complexes containing **7–9** were prepared, and the electronic and variable-temperature magnetic properties of complexes containing **7** (**10**) and **9** (**12**) are described. Complex **10** features a gradual and incomplete spin crossover in the solid state, and **12** remains high-spin over the entire temperature range. Complex **11** is extremely unstable and rearranges to another iron(II) complex (**13**), which was structurally characterized. The temperature-dependent magnetic properties of **13** are described as a one-dimensional ferromagnetic chain, with interchain antiferromagnetic interactions and (or) zero-field splitting dominant at low temperatures. The magnetic analysis is corroborated by the molecular packing and density functional theory calculations, which suggest intermolecular interactions between coordinated thiocyanate ligands bearing a significant spin density.

**Key words:** spin crossover, iron(II), thiophene, ferromagnetic interactions.

**Résumé :** On décrit la synthèse et la caractérisation de trois nouveaux ligands tétradentates de type bispicène contenant un hétérocycle thiophène substitué [substituants 2,5-thiényle = H (**7**), Ph (**8**) ou 2-thiényle (**9**)]. On a préparé les complexes de coordination bis(thiocyanate) de fer(II) contenant les ligands **7–9** et on décrit les propriétés magnétiques en fonction de la température des complexes contenant le ligand **7** (**10**) et le ligand **9** (**12**). Le complexe **10** par une inversion graduelle et incomplète de spin à l'état solide alors que le complexe **12** garde un spin élevé sur toute la plage de température. Le complexe **11** est extrêmement instable et il se réarrange en un autre complexe du fer(II) (**13**) dont on a caractérisé la structure. On décrit les propriétés magnétiques du complexe **13** en fonction de la température comme une chaîne ferromagnétique unidimensionnelle avec des interactions antiferromagnétiques interchaînes et (ou) un dédoublement de champ dominant nul à basses températures. L'analyse magnétique est corroborée par des calculs d'empilement moléculaire et par la théorie de la fonctionnelle de la densité, ce qui suggère qu'il existe des interactions intermoléculaires entre les ligands thiocyanates porteurs d'une densité de spin significative.

**Mots-clés :** inversion de spin, fer(II), thiophène, interactions ferromagnétiques.

## Introduction

Spin-crossover (SCO) in iron(II) coordination complexes provides the best example of molecular bistability.<sup>1</sup> There are many examples of iron(II) complexes exhibiting abrupt spin state transitions and concomitant thermal hysteresis, conferring true bistability on these materials.<sup>2</sup> Exploration of new avenues for research with SCO complexes is underway, including coupling SCO with other properties in single-component materials (so-called multifunctional materials).<sup>3</sup> SCO complexes also exhibiting magnetic exchange coupling, liquid crystalline behaviour, porosity, and photo-

chromism have all now been reported. A number of research groups have also reported single-component ionic-coordination complexes containing SCO cations and electrically conducting anions as fascinating SCO conductors.<sup>4</sup> We are also interested in SCO conducting materials and our approach is focused on combining SCO properties with electrical conductivity in novel metallopolymer materials.<sup>5</sup> To date, all reported SCO conductors have contained iron(III), and we thought it would be interesting to produce SCO conductors instead containing iron(II).

As an initial foray into this research, we have designed

Received 3 March 2010. Accepted 14 June 2010. Published on the NRC Research Press Web site at [canjchem.nrc.ca](http://canjchem.nrc.ca) on 18 August 2010.

**H. Cheng, B. Djukic, and M.T. Lemaire.**<sup>1</sup> Department of Chemistry, Brock University, 500 Glenridge Avenue, St. Catharines, ON L2S 3A1, Canada.

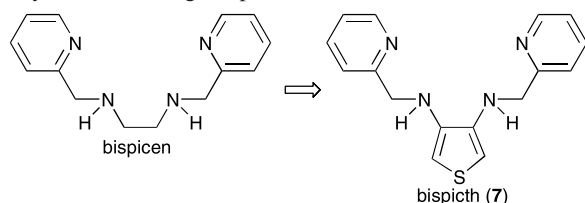
**H.A. Jenkins.** Department of Chemistry, McMaster University, 1280 Main Street West, Hamilton, ON L8S 4M1, Canada.

**S.I. Gorelsky.** Centre for Catalysis Research and Innovation, Department of Chemistry, University of Ottawa, 10 Marie Curie, Ottawa, ON K1N 6N5, Canada.

<sup>1</sup>Corresponding author (e-mail: [mlemaire@brocku.ca](mailto:mlemaire@brocku.ca)).



**Fig. 1.** Structural relationship between known bispicen ligands and a thienyl-substituted ligand produced herein.



**Table 1.** Crystallographic data and structure refinement for **13**.

Empirical formula	C <sub>58</sub> H <sub>40</sub> FeN <sub>10</sub> S <sub>4</sub>
Formula mass	1061.09
Habit	Rod
Color	Orange
Crystal size (mm)	0.37 × 0.13 × 0.10
Crystal system	Monoclinic
Space group	C2/c
Z	4
<i>a</i> (Å)	17.343(4)
<i>b</i> (Å)	17.136(4)
<i>c</i> (Å)	17.227(4)
$\alpha$ (°)	90
$\beta$ (°)	108.315(5)
$\gamma$ (°)	90
Collection ranges	–16 ≤ <i>h</i> ≤ 21 –16 ≤ <i>k</i> ≤ 21 –21 ≤ <i>l</i> ≤ 20
<i>V</i> (Å <sup>3</sup> )	4860(2)
<i>D</i> <sub>calcd.</sub> (Mg m <sup>–3</sup> )	1.450
$\mu$ (mm <sup>–1</sup> )	0.535
<i>F</i> (000)	2192
$\theta$ range for data collection (°)	1.88–26.00
Observed reflections	26762
Independent reflections	4768 ( <i>R</i> <sub>int</sub> = 0.0713)
Data/restraints/parameters	4768/3/335
GOF on <i>F</i> <sup>2</sup>	1.326
Final <i>R</i> <sub>1</sub> indices [ <i>I</i> > 2σ( <i>I</i> )]	0.0670, 0.1791
<i>wR</i> <sub>2</sub> indices (all data)	0.1162, 0.2037
Largest diff. peak and hole (e Å <sup>–3</sup> )	0.816 and –0.524

new tetradentate ligands with structural features that could enable electropolymerization of the precursor iron(II) coordination complexes. We also wanted the ligand to coordinate the metal ion close to the polymer backbone to facilitate stronger interactions among the coordinated SCO unit and the conducting polymer. Inspection of the SCO literature led us to the bis(2-pyridylmethyl)-diamine type (bispicen) reported by Toftlund and co-workers in the 1980s (Fig. 1).<sup>6</sup> These tetradentate ligands feature an ethyl or propyl spacer between the 2-pyridylmethylamine substituents, which could easily be replaced with a polymerizable thiophene heterocycle substituted at the 3,4-ring positions (bispicth **7**). Also, *cis*-iron(II) complexes containing bispicen (or other derivatives) and two equivalents of thiocyanate have been observed to exhibit SCO, including abrupt transitions with small thermal hysteresis cycles.

Herein, we describe the multistep syntheses of three new bis-(2-pyridylmethyl) ligands containing thienyl substituents

and the preparation, electronic, and variable-temperature magnetic properties of mononuclear iron(II) coordination complexes containing these ligands, including the observation of SCO. We also report an unusual ligand-centered structural rearrangement in solutions containing these coordination complexes, which produces new iron complexes. One of these complexes features significant intermolecular ferromagnetic interactions.

## Experimental

### General procedures

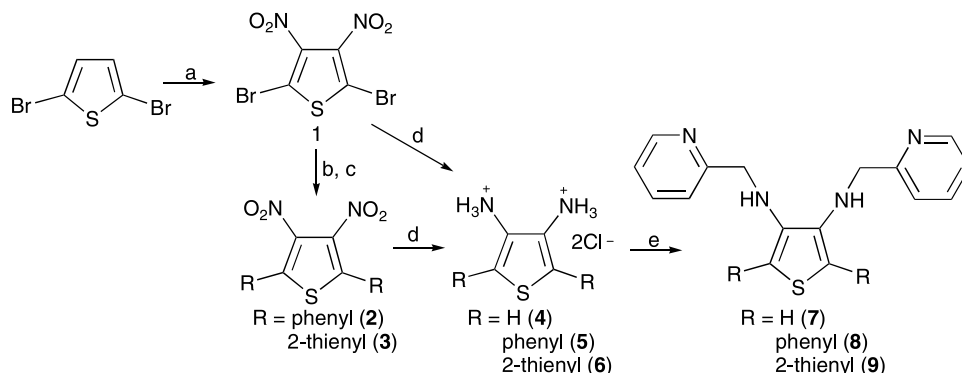
All reagents were commercially available and used as received unless otherwise stated. Deaerated and anhydrous solvents were obtained from a Puresolve PS MD-4 solvent-purification system, and all air- and (or) moisture-sensitive reactions were carried out using standard Schlenk techniques, unless otherwise stated. <sup>1</sup>H/<sup>13</sup>C NMR spectra were recorded on a Bruker Advance 300 (or 600) MHz spectrometer (as indicated) with a 7.05 (or 14.1) T Ultra-shield magnet using deuterated solvents. FTIR spectra were recorded on a Shimadzu IR/Affinity spectrometer as KBr discs or thin films on KBr plates. EI and FAB mass spectra were obtained using a Kratos Concept 1S High Resolution E/B mass spectrometer, and ESI mass spectra were obtained using a Bruker HCT Plus Proteineer LC–MS. Room temperature vis–NIR spectra were recorded on a Shimadzu 3600 UV–vis–NIR spectrophotometer as solutions in appropriate solvents. Spectra at 77 K were obtained as frozen ethanol glasses in 5 mm NMR tubes immersed in a liquid N<sub>2</sub> Dewar. Elemental analyses were carried out by Guelph Chemical Laboratories LTD, Guelph, ON, Canada.

### X-ray crystallography

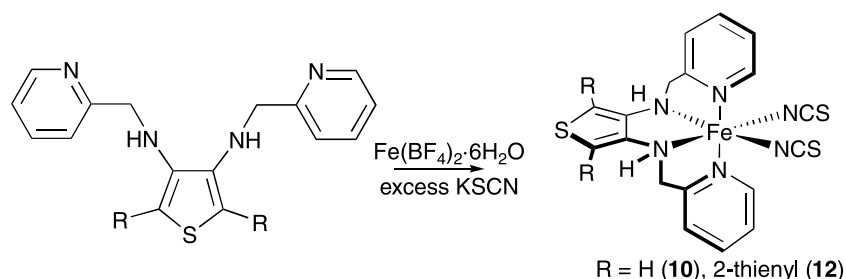
An orange rod was mounted on a MiTeGen mount, and placed in the cold stream at 100 K. Data were collected on a SMART APEX II diffractometer with Mo K $\alpha$  radiation ( $\lambda$  = 0.71073 Å) located at the McMaster Analytical X-ray Diffraction Facility (MAX). Data were collected using omega and phi scans, integrated, and a numerical face-indexed absorption correction was applied with a secondary absorption correction using redundant data (SADABS). The space group chosen was C2/c, based on systematic absences. Data were solved using direct methods (SHELXS-97), and refined using least-squares techniques. All non-hydrogen atoms were refined anisotropically; hydrogen atoms were located and then treated as riding on their constituent atoms and updated after each cycle of refinement. The NCS ligand showed a 73:27 disorder over two positions, which were symmetry-related to each other due to the twofold axis at Fe1. The non-bonded pyridine also showed disorder between N5 and C13/C17, which was similar in magnitude to the NCS disorder, and due to some intermolecular interactions between these moieties, we chose to couple the C/N disorder in the pyridine ring to the NCS disorder.

The possibility of choosing a lower-symmetry space group to solve the structure was investigated, with the expectation that the disorder would be resolved; however, solving the data in *Cc* (the *c*-glide is obvious in the reciprocal lattice) gave a highly correlated structure, with the same

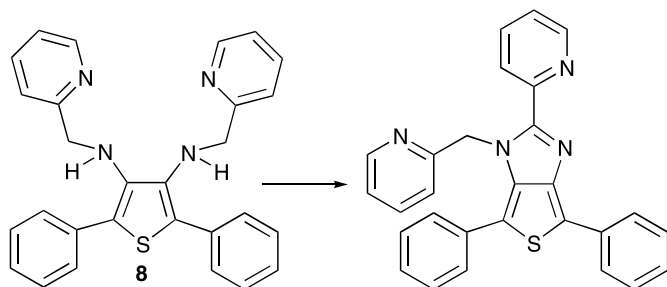
**Scheme 1.** Preparation of ligands. Reagents and conditions: (a) concentrated  $\text{H}_2\text{SO}_4/\text{HNO}_3$ . (b) Phenylboronic acid, 6 mol%  $\text{Pd}(\text{PPh}_3)_4$ ,  $\text{K}_2\text{CO}_3(\text{aq})$ , dimethoxyethane, 13 h reflux. (c) 2-Thienylboronic acid, 6 mol%  $\text{Pd}(\text{PPh}_3)_4$ ,  $\text{K}_2\text{CO}_3(\text{aq})$ , dimethoxyethane, 8 h reflux. (d)  $\text{Sn}$ ,  $\text{HCl}/\text{EtOH}$ . (e)  $\text{KOH}(\text{aq})$ , 2-pyridinecarboxaldehyde,  $\text{NaBH}_4$ ,  $\text{MeOH}$ , 1 h reflux.



**Scheme 2.** Preparation of *cis*-iron(II) complexes **10** and **12**.



**Scheme 3.** Ligand structural rearrangement in solutions of complex **11**.

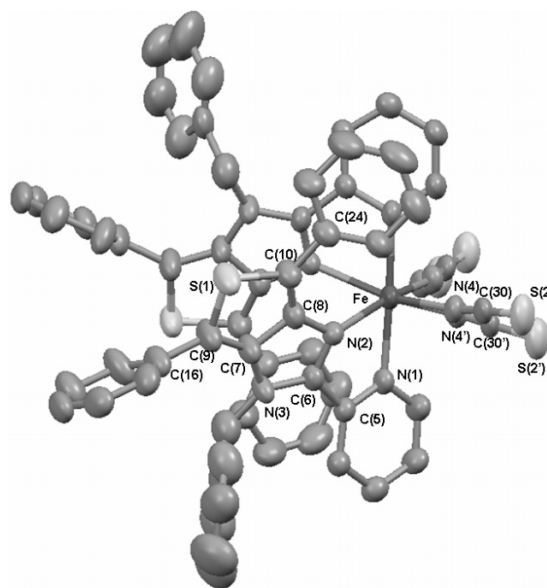


disorder of the NCS ligand. Twin refinement indicated the presence of the twofold rotation axis in the molecule, and in the end, it was decided that  $C2/c$  was the correct space group. In the final cycles of refinement,  $R_1 = 6.70\%$ ,  $wR_2 = 20.37\%$  (Table 1).

### Electrochemical measurements

Cyclic voltammetry (CV) experiments were performed with a Bioanalytical Systems Inc. Epsilon electrochemical workstation. Compounds were dissolved in anhydrous solvent ( $\text{CH}_3\text{CN}$ ) and deaerated by sparging with  $\text{N}_2$  gas for 20 min. Solution concentrations were approximately  $10^{-3}$  mol/L in analyte containing 0.1 mol/L supporting electrolyte ( $\text{Bu}_4\text{NPF}_6$ ). A typical three-electrode setup was used including a platinum working electrode, Ag-wire pseudo-reference electrode, and a platinum-wire auxiliary electrode. Ferrocene was used in all cases as an internal standard and was oxidized at a potential of +0.51 V in our setup; all potentials quoted are versus the ferrocene redox potential. Scan rates for CV experiments were, generally, 100 mV/s.

**Fig. 2.** ORTEP view of **13**. Thermal ellipsoids are drawn at the 50% probability level.



### Variable-temperature magnetic susceptibility measurements

Variable-temperature magnetic susceptibility measurements were recorded on a superconducting quantum interference device (SQUID) magnetometer (Quantum Design MPMS) with a 5.5 T magnet (temperature range: 1.8 to 400 K) in an external field of 5000 Oe. Samples were carefully weighed into gelatin capsules, with empty gelatin capsules above and below to eliminate background contribu-

**Table 2.** Selected bond lengths (Å) and angles (°) for **13**.

Bond lengths (Å)	
Fe—N(1)	2.203(3)
Fe—N(2)	2.293(3)
Fe—N(4)	2.127(5)
Fe—N(4')	1.983(10)
C(9)—C(18)	1.502(6)
C(10)—C(24)	1.469(6)
C(5)—C(6)	1.474(5)
C(30)—S(2)	1.642(7)
C(30')—S(2')	1.642(8)
N(2)—C(6)	1.338(5)
N(2)—C(8)	1.404(5)
N(3)—C(6)	1.375(5)
N(3)—C(7)	1.388(5)
N(4)—C(30)	1.163(7)
N(4')—C(30')	1.163(8)
Bond angles (°)	
N(1)—Fe—N(2)	73.46(11)
N(1)—Fe—N(4)	92.9(4)
N(1)—Fe—N(4')	87.2(12)
N(2)—Fe—N(4)	91.0(3)
N(2)—Fe—N(4')	100.2(10)
Fe—N(1)—C(5)	118.1(2)
Fe—N(2)—C(6)	108.7(2)
Fe—N(2)—C(8)	136.5(3)
Fe—N(4)—C(30)	166.3(6)
Fe—N(4')—C(30')	163(3)
N(4)—C(30)—S(2)	177.4(10)
N(4')—C(30')—S(2')	178(2)

tions from the gelatin, which were loaded into plastic straws, and attached to the sample transport rod. Diamagnetic corrections were made using Pascal's constants.

### Computational details

All density functional theory (DFT) calculations were performed using the Gaussian 03 package using the B3LYP hybrid functional and the DZVP basis set for all atoms.<sup>7</sup> Tight SCF convergence criteria were used for all calculations. The converged wave functions were tested to confirm that they correspond to the ground-state surface. The evaluation of atomic charges and spin densities was performed using the natural population analysis (NPA).<sup>8</sup> The analysis of molecular orbitals in terms of fragment orbital contributions were carried out using the AOMix program.<sup>9</sup> Time-dependent DFT (TD-DFT) calculations at the B3LYP/DZVP level were performed to calculate the absorption spectra as previously described.<sup>9b</sup>

### Synthesis

#### 2,5-Dibromo-3,4-dinitrothiophene (1)

H<sub>2</sub>SO<sub>4</sub> (18 mol/L, 40 mL) was added to a three-neck round-bottom flask then purged with N<sub>2</sub> for 30 min and cooled in an ice-water bath. Under N<sub>2</sub>, 2,5-dibromothiophene (10.74 g, 5.00 mL, 44.37 mmol) was added slowly to maintain a temperature below 20 °C. HNO<sub>3</sub> (16 mol/L,

7.00 mL) was then added dropwise, maintaining a temperature under 30 °C. Once the addition was complete, the reaction mixture was allowed to react for an additional 3 h and then poured over ~160 g of ice. Upon melting of the ice, the solid residue was recovered by vacuum filtration and washed with water to produce a light yellow powder. Recrystallization from methanol afforded 7.64 g (52%) of pure material. Mp 135–136 °C. The FTIR spectrum of **1** is identical to that previously reported.<sup>10</sup> <sup>13</sup>C NMR (75.5 MHz, CDCl<sub>3</sub>): δ 140.3, 113.4 ppm. MS (EI+): *m/z* 332 (M<sup>+</sup>, 100%).

#### 3,4-Dinitro-2,5-diphenylthiophene (2)

Phenylboronic acid (0.20 g, 1.66 mmol) was added to a Schlenk flask and flushed with N<sub>2</sub> gas. Then, 1.8 mL of H<sub>2</sub>O and 5 mL of 1,2-dimethoxyethane were added to the reaction flask, which was sparged with N<sub>2</sub> for 30 min. After that, K<sub>2</sub>CO<sub>3</sub> (0.50 g, 3.62 mmol), **1** (0.10 g, 0.60 mmol), 6 mol% Pd(PPh<sub>3</sub>)<sub>4</sub> (0.04 g, 0.04 mmol) were added to the flask, respectively, and the mixture was refluxed at 65 °C under nitrogen for 13 h. The reaction mixture was washed with water and extracted into CH<sub>2</sub>Cl<sub>2</sub>. The combined organic layers were dried over MgSO<sub>4</sub> and concentrated to dryness. The crude product was chromatographed over silica gel using 1:3 CH<sub>2</sub>Cl<sub>2</sub>:hexane as eluent to yield 0.16 g (80%) of bright yellow crystal. Mp 145–147 °C. FTIR (KBr): 3448 (m, br), 3059 (w), 1963 (w), 1542 (s), 1524 (s), 1448 (m), 1395 (s), 1327 (s), 1261 (m), 1079 (m), 902 (m), 748 (s), 691 (s) cm<sup>-1</sup>. <sup>1</sup>H NMR (300 MHz, CDCl<sub>3</sub>): δ 7.54 (m, 10H) ppm. <sup>13</sup>C NMR (75.5 MHz, CDCl<sub>3</sub>): δ 140.8, 136.8, 130.9, 129.3, 129.1, 128.1 ppm. MS (EI+): *m/z* 326 (M<sup>+</sup>, 100%). HR-MS (EI+) calculated for [C<sub>16</sub>H<sub>10</sub>N<sub>2</sub>O<sub>4</sub>S]<sup>+</sup>: 326.03613; found: 326.03557.

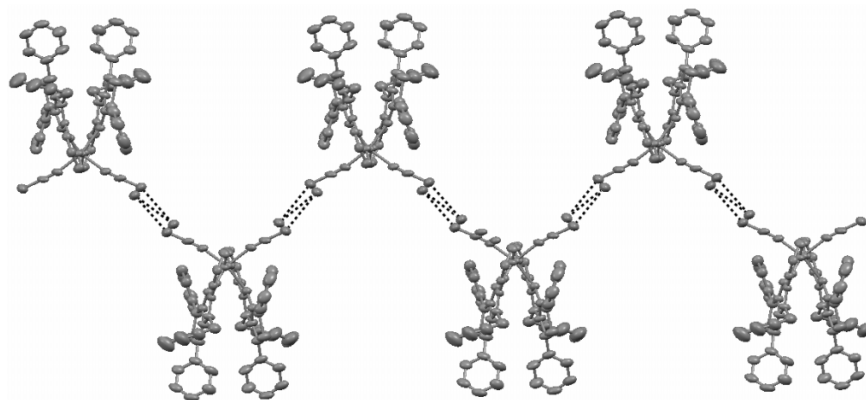
#### 3',4'-Dinitro-2,2':5',2''-terthiophene (3)

Thiophene-2-boronic acid (3.29 g, 25.68 mmol) was added to a Schlenk flask and flushed with N<sub>2</sub>. Then, 1.8 mL of H<sub>2</sub>O and 5 mL of 1,2-dimethoxyethane were added to the reaction flask, which was sparged with N<sub>2</sub> for 0.5 h. After that, K<sub>2</sub>CO<sub>3</sub> (0.25 g, 1.81 mmol), **1** (3.1 g, 9.34 mmol), 6 mol% Pd(PPh<sub>3</sub>)<sub>4</sub> (0.65 g, 0.56 mmol) were added to the flask, respectively, and the mixture was refluxed at 100 °C for 8 h. The reaction mixture was washed with water and extracted into CH<sub>2</sub>Cl<sub>2</sub>. The combined organic layers were dried over MgSO<sub>4</sub> and concentrated to dryness. The crude product was chromatographed over silica gel using 1:3 CH<sub>2</sub>Cl<sub>2</sub>:hexane as eluent to yield 0.05 g (48%) of yellow solid. <sup>1</sup>H NMR (300 MHz, CDCl<sub>3</sub>): δ 7.20 (m, 2H), 7.57 (m, 2H), 7.62 (m, 2H) ppm. <sup>13</sup>C NMR (75.5 MHz, CDCl<sub>3</sub>): δ 133.8, 131.3, 131.2, 128.4, 128.1, 96.13 ppm. MS (FAB+): *m/z* 338 [M<sup>+</sup>, 100%]. HR-MS (EI+) calculated for [C<sub>12</sub>H<sub>6</sub>N<sub>2</sub>O<sub>4</sub>S<sub>3</sub>]<sup>+</sup>: 337.94897; found: 337.94872.

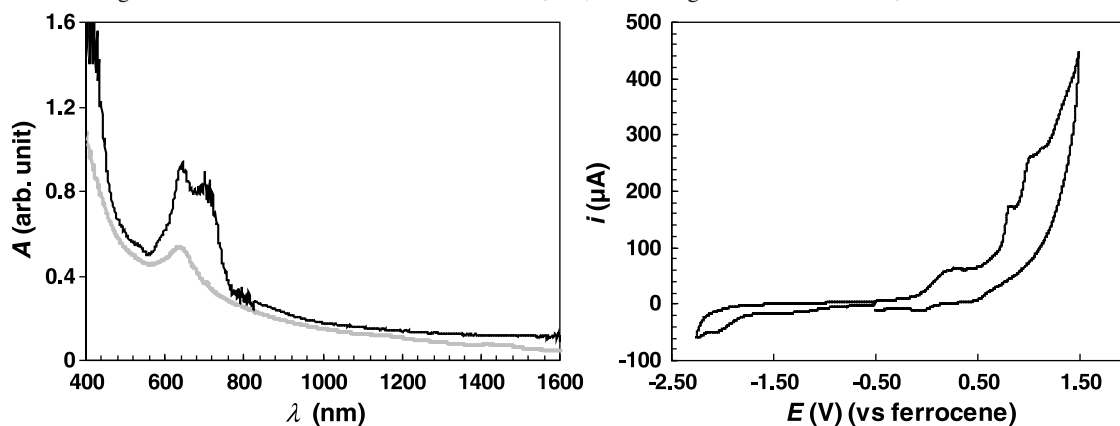
#### 3,4-Diaminothiophene·2HCl (4)

Concentrated HCl (25 mL) was added to a three-neck round-bottom flask and sparged with N<sub>2</sub> for 0.5 h. Then, **1** (1.28 g, 3.80 mmol) was carefully combined with the HCl, cooled in an ice-water bath. Tin (mossy) metal (3.19 g, 26.89 mmol) was added slowly to maintain a temperature

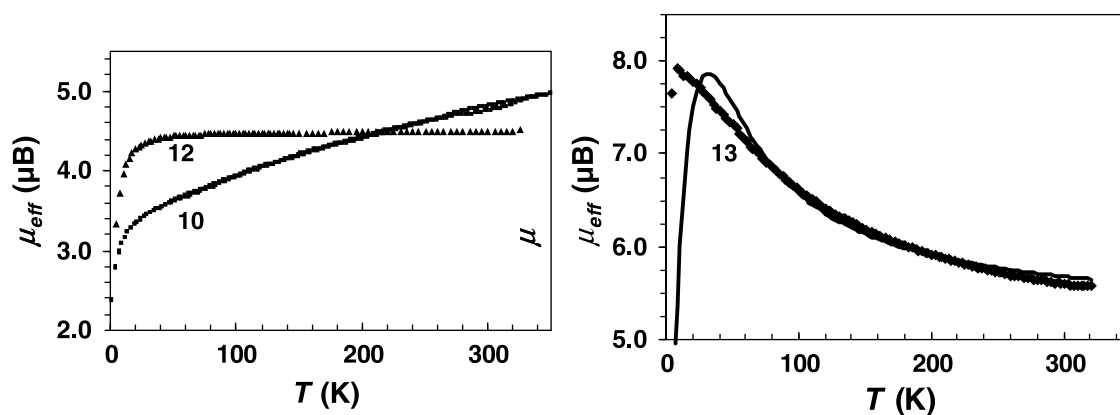
**Fig. 3.** Molecular packing of **13** with a view down the *ac* diagonal. Intermolecular S2...S2' and S2'...S2' contacts are indicated by dashed lines.



**Fig. 4.** Left: Visible–NIR spectrum of **10** in ethanol solution at 298 K (grey curve) and as a frozen ethanol glass at 77 K (black curve). Right: Cyclic voltammogram of a  $10^{-3}$  mol/L solution of **12** in  $\text{CH}_3\text{CN}$ , containing 0.1 mol/L  $\text{Bu}_4\text{NPF}_6$ .



**Fig. 5.** Variable-temperature magnetic properties of **10** (■), **12** (▲) (left) and **13** (◆) (right). External magnetic field of 5000 Oe was applied in all experiments. Magnetic data was acquired between 2–350 K for **10** and between 5–325 K for **12** and **13**. The best fit to a 1-D Bonner–Fisher chain model is indicated as a solid line.



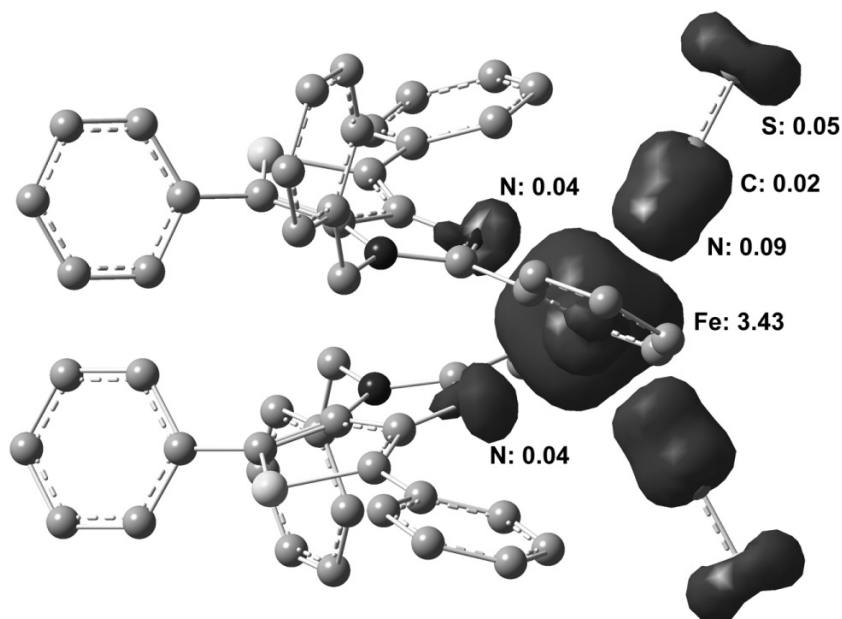
between 25–30 °C. After stabilizing at 25 °C, the reaction continued until all the tin metal was consumed and then placed in a refrigerator overnight. The solid precipitate was recovered by vacuum filtration and washed with diethyl ether and acetonitrile until the wash was colorless to afford 0.64 g (83%) of white solid.  $^1\text{H}$  and  $^{13}\text{C}$  NMR spectra and the FTIR spectrum of **4** are identical to those previously reported.<sup>11</sup> MS (EI+):  $m/z$  114 [(M – 2HCl)<sup>+</sup>, 100%].

### 3,4-Diamino-2,5-diphenylthiophene·2HCl (**5**)

To a mixture of **2** (0.33 g, 1.00 mmol) in absolute ethanol (30 mL) and concentrated HCl (60 mL) was added tin (mossy) metal (3.63 g, 30.58 mmol) in small portions. The resulting mixture was stirred at room temperature for 15 h in air. A pale yellow solid was obtained, which was collected by vacuum filtration and washed with  $\text{H}_2\text{O}$  to afford 0.24 g (71%) of product. Mp 205–207 °C. FTIR (KBr):



**Fig. 6.** Calculated spin density distribution in **13**. NPA-derived atomic spin density is shown for most important contributors. H atoms are not shown for clarity.



3330 (m, d), 3047 (w), 2920 (w), 2848 (w), 1616 (m), 1595 (m), 1523 (m), 1489 (m), 1429 (s), 1313 (w), 970 (m), 754 (s), 703 (m), 621 (w), 573 (w)  $\text{cm}^{-1}$ .  $^1\text{H}$  NMR (300 MHz,  $\text{CDCl}_3$ ):  $\delta$  3.67 (br, s, 4H), 7.30 (m, 2H), 7.45 (m, 4H), 7.56 (m, 4H) ppm.  $^{13}\text{C}$  NMR (75.5 MHz,  $\text{CDCl}_3$ ):  $\delta$  134.4, 133.2, 129.1, 127.6, 126.7, 116.5 ppm. MS (FAB+):  $m/z$  266 [(M – 2HCl) $^+$ , 100%]. HR-MS (EI+) calculated for  $[\text{C}_{16}\text{H}_{14}\text{N}_4\text{S}]^+$ : 266.08777; found: 266.08880.

#### **3',4'-Diamino-2,2':5',2''-terthiophene-2HCl (6)**

To a mixture of **3** (0.27 g, 0.80 mmol) in absolute ethanol (30 mL) and concentrated HCl (60 mL) was added tin (mossy) metal (2.84 g, 23.96 mmol) in small portions. The resulting mixture was stirred at room temperature for 15 h in air. A deep yellow solid was collected by vacuum filtration and washed with  $\text{H}_2\text{O}$  to afford 0.28 g (88%) of the product. Melting point and FTIR spectrum (KBr) are identical to those previously report.<sup>11</sup>  $^1\text{H}$  NMR (300 MHz,  $\text{CDCl}_3$ ):  $\delta$  3.76 (br, s, 4H), 7.11 (m, 4H), 7.30 (m, 2H) ppm.  $^{13}\text{C}$  NMR (150.9 MHz,  $\text{CDCl}_3$ ):  $\delta$  135.9, 133.6, 127.8, 124.0, 123.9, 110.13 ppm. MS (FAB+):  $m/z$  278 [(M – 2HCl) $^+$ , 100%].

#### **N,N'-Bis(2-pyridylmethyl)-3,4-diaminothiophene (7)**

Compound **4** (0.20 g, 1.07 mmol) was added to an oven-dried three-neck round-bottom flask fitted with a reflux condenser. The apparatus was then flushed with  $\text{N}_2$  for 5 min. NaOH (0.086 g, 2.15 mmol) was dissolved in methanol (20 mL), the solution was sparged with  $\text{N}_2$  for 0.5 h and transferred by syringe into the three-neck flask. The mixture was stirred for 0.5 h, and then 2-pyridinecarboxaldehyde (0.24 g, 0.20 mL, 2.25 mmol) was added. The reaction mixture was refluxed for 1.5 h and protected from light by covering with foil.  $\text{NaBH}_4$  (0.21 g, 5.67 mmol) was added in small portions followed by a reflux for 14 h under  $\text{N}_2$ . The solvent was removed by rotary evaporation. The residue was extracted into  $\text{CH}_2\text{Cl}_2$ , washed with water and dried over

$\text{MgSO}_4$ . The solution was filtered by passing through a Celite pad. The filtrate was concentrated by rotary evaporation, and pentane was used to precipitate impurities, which were removed by gravity filtration. The filtrate was then concentrated to dryness and chromatographed over neutral alumina using 2:1 hexane:EtOAc, followed by 1:2 hexane:EtOAc as eluent to yield 0.053 g (17%) of a bright yellow viscous oil. FTIR (KBr): 3447 (s, br), 3105 (m), 2960 (w), 2923 (m), 2851 (w), 1594 (s), 15.7 (m), 1436 (m), 1261 (w), 1097 (w, br), 801 (w), 757 (m)  $\text{cm}^{-1}$ .  $^1\text{H}$  NMR (300 MHz,  $\text{CDCl}_3$ ):  $\delta$  4.45 (m, 6H), 6.01 (s, 2H), 7.21 (dd, 2H,  $J = 5.2, 1.8$  Hz), 7.39 (d, 2H,  $J = 7.8$  Hz), 7.67 (td, 2H,  $J = 7.5, 1.8$  Hz), 8.60 (d, 2H,  $J = 4.5$  Hz) ppm.  $^{13}\text{C}$  NMR (75.5 MHz,  $\text{CDCl}_3$ ):  $\delta$  158.5, 149.3, 139.5, 136.7, 122.2, 121.8, 97.6, 51.4 ppm. MS (FAB+):  $m/z$  297 [(M $^+$ , 100%)], 93 [(M –  $\text{C}_{10}\text{H}_{10}\text{N}_3\text{S}$ ) $^+$ , 62%]. HR-MS (EI+) calculated for  $[\text{C}_{16}\text{H}_{16}\text{N}_4\text{S}]^+$ : 296.10951; found: 296.10957.

#### **N,N'-Bis(2-pyridylmethyl)-3,4-diamino-2,5-diphenylthiophene (8)**

Compound **5** (0.12 g, 0.35 mmol) was added to an oven-dried three-neck round-bottom flask fitted with a reflux condenser. The apparatus was then flushed with  $\text{N}_2$ . Then, KOH (0.04 g, 0.69 mmol) was dissolved in methanol (20 mL) in a round-bottom flask, the solution was sparged with  $\text{N}_2$  for 0.5 h, and transferred by syringe into the three-neck round-bottom flask. The mixture was stirred for 0.5 h followed by the addition of 2-pyridinecarboxaldehyde (0.22 g, 0.20 mL, 2.07 mmol). The reaction mixture was refluxed for 1 h while protected from light by covering with foil. The reaction was cooled to RT followed by adding  $\text{NaBH}_4$  (0.26 g, 6.90 mmol), and the mixture was again refluxed at 75  $^\circ\text{C}$  for 1 h. The reaction mixture was diluted into  $\text{Na}_2\text{CO}_3$  solution (pH 9.5) and extracted into diethyl ether. The organic extracts were combined and dried over  $\text{MgSO}_4$ . Concentration by rotary evaporation and chromatography over neutral alumina using  $\text{CH}_2\text{Cl}_2$  as eluent provided 0.12 g of a vibrant

orange oil, which is very unstable.  $^1\text{H}$  NMR (300 MHz,  $\text{CDCl}_3$ ):  $\delta$  4.35 (br s, 6H), 7.59–7.13 (m, 16H), 8.49 (dd, 2H) ppm. HR-MS (FAB+) calculated for  $[\text{C}_{28}\text{H}_{25}\text{N}_4\text{S}]^+$ : 449.17999; found: 449.17897.

***N,N'*-Bis(2-pyridylmethyl)-3',4'-diamino-2,2':5,2''-terthiophene (9)**

Compound **6** (0.10 g, 0.28 mmol) was added to an oven-dried three-neck round-bottom flask fitted with a reflux condenser. The apparatus was then flushed with  $\text{N}_2$  for 5 min. Then, KOH (0.032 g, 0.57 mmol) was dissolved in methanol (20 mL) and the solution was sparged with  $\text{N}_2$  for 0.5 h. The solution was transferred by syringe into the three-neck round-bottom flask. The mixture was stirred for 0.5 h followed by the addition of 2-pyridinecarboxaldehyde (0.18 g, 0.16 mL, 1.71 mmol). The reaction mixture was refluxed for 1 h while protected from light by covering with foil. The reaction was cooled to RT, and  $\text{NaBH}_4$  (0.22 g, 5.70 mmol) was carefully added and the mixture was again refluxed for 1 h under  $\text{N}_2$ . The reaction mixture was diluted into  $\text{NaHCO}_3$  solution (pH 9.5) and extracted into diethyl ether. The organic extracts were combined and dried over  $\text{MgSO}_4$ . Concentration by rotary evaporation provided 0.10 g (76%) of a brown-yellow oil, which required no further purification. FTIR (KBr): 3428 (s), 2922 (s), 2853 (m), 1593 (m), 1466 (m, br), 1431 (m), 1402 (m), 1219 (w, br), 1148 (m), 1045 (m, br), 691 (s)  $\text{cm}^{-1}$ .  $^1\text{H}$  NMR (300 MHz,  $\text{CDCl}_3$ ):  $\delta$  4.38 (s, 4H), 4.92 (br, 2H), 7.04 (m, 2H), 7.16 (m, 4H), 7.25 (m, 4H), 7.61 (m, 2H), 8.50 (d, 2H,  $J = 4.8$  Hz) ppm.  $^{13}\text{C}$  NMR (150.9 MHz,  $\text{CDCl}_3$ ):  $\delta$  159.0, 149.1, 138.7, 136.5, 135.7, 127.2, 125.2, 124.9, 122.1, 116.1, 52.6 ppm. MS (FAB+):  $m/z$  461  $[(\text{M}^+, 52\%)]$ , 369  $[(\text{M} - \text{C}_6\text{H}_6\text{N})^+, 100\%]$ . HR-MS (FAB+) calculated for  $[\text{C}_{24}\text{H}_{21}\text{N}_4\text{S}_3]^+$ : 461.09284; found: 461.09655.

***[Fe<sup>II</sup>(7)(NCS)<sub>2</sub>]* (10)**

A 25 mL Schlenk flask was charged with **7** (0.025 g, 0.08 mmol) and flushed with  $\text{N}_2$ . Methanol (8 mL) was then added to the flask, which was sparged with  $\text{N}_2$  for 0.5 h.  $\text{Fe}(\text{BF}_4)_2 \cdot 6\text{H}_2\text{O}$  (0.028 g, 0.08 mmol) was added to the solution and the mixture was stirred for 0.5 h under  $\text{N}_2$ . KSCN (0.033 g, 0.338 mmol) was dissolved in 10 mL of  $\text{H}_2\text{O}$  and was added to the mixture noted above. Gradually, a green precipitate was observed, which was isolated by vacuum filtration to afford 0.032 g (80%) of green powder. UV-vis (MeOH):  $\lambda_{\text{max}}$  ( $\epsilon$ ) = 640 nm (400  $\text{mol/L}^{-1} \text{cm}^{-1}$ ). FTIR (KBr): 3448 (s, br), 3159 (m, br), 2920 (m), 2060 (s, br), 1603 (m), 1425 (m), 787 (m), 762 (m)  $\text{cm}^{-1}$ . MS (FAB+):  $m/z$  468  $[(\text{M}^+, 17\%)]$ , 410  $[(\text{M} - \text{SCN})^+, 100\%]$ , 351  $[(\text{M} - 2\text{SCN})^+, 99\%]$ . HR-MS (FAB+) calculated for  $[\text{C}_{18}\text{H}_{16}\text{N}_6\text{S}_3\text{Fe}]^+$ : 467.98843; found: 467.99476.

***[Fe<sup>II</sup>(8)(NCS)<sub>2</sub>]* (11)**

A solution of **8** (0.10 g, 0.22 mmol) in 10 mL of MeOH was degassed by sparging with  $\text{N}_2$  gas for 0.5 h.  $\text{Fe}(\text{BF}_4)_2 \cdot 6\text{H}_2\text{O}$  (0.08 g, 0.22 mmol) was added to generate a yellow-green solution. A solution of KSCN (0.09 g, 0.89 mmol) in 10 mL of water was added under  $\text{N}_2$ , followed by the addition of 10 mL of diethyl ether to instantly produce a green precipitate. The solid residue was isolated by vacuum filtration to afford 0.069 g (50%) of bright green

solid. UV-vis (MeOH):  $\lambda_{\text{max}}$  = 650 nm. FTIR (KBr): 3424 (m, br), 3194 (w, br), 2921 (m), 2851 (w), 2071 (s), 1602 (w), 1508 (w), 1261 (w), 1102 (m), 1018 (m), 802 (m), 757 (m), 698 (m)  $\text{cm}^{-1}$ . MS (FAB+):  $m/z$  620  $[(\text{M}^+, 3\%)]$ , 562  $[(\text{M} - \text{SCN})^+, 18\%]$ , 503  $[(\text{M} - 2\text{SCN})^+, 17\%]$ . Anal. calcd. for  $\text{C}_{30}\text{H}_{24}\text{N}_6\text{S}_3\text{Fe} \cdot 2\text{C}_2\text{H}_6\text{O}$  (found %): C 59.21 (59.21), H 5.54 (4.97), N 11.21 (11.00)

***[Fe<sup>II</sup>(9)(NCS)<sub>2</sub>]* (12)**

Compound **9** (0.12 g, 0.25 mmol) was added to a Schlenk flask and flushed with  $\text{N}_2$ . Then, methanol (8 mL) was added to the flask, which was sparged with  $\text{N}_2$  for 0.5 h.  $\text{Fe}(\text{BF}_4)_2 \cdot 6\text{H}_2\text{O}$  (0.085 g, 0.25 mmol) was added to the solution, and the mixture was stirred for 0.5 h under  $\text{N}_2$ . KSCN (0.10 g, 1.00 mmol) was dissolved in 10 mL of  $\text{H}_2\text{O}$ , and this solution was added to the reaction. A dark green precipitate was observed, which was isolated by vacuum filtration to afford 0.09 g (57%) of dark green solid. UV-vis (MeOH):  $\lambda_{\text{max}}$  ( $\epsilon$ ) = 656 nm (400  $\text{mol/L}^{-1} \text{cm}^{-1}$ ). FTIR (KBr): 3425 (m, br), 3222 (w), 3107 (w), 3075 (w), 2921 (w), 2851 (w), 2081 (s), 2063 (s), 1602 (m), 1572 (w), 1484 (w), 1440 (w), 1411 (m), 1232 (w), 1101 (w), 899 (w), 760 (w), 697 (m)  $\text{cm}^{-1}$ . MS (FAB+):  $m/z$  632  $[(\text{M}^+, 20\%)]$ , 574  $[(\text{M} - \text{SCN})^+, 95\%]$ . Anal. calcd. for  $\text{C}_{26}\text{H}_{20}\text{N}_6\text{S}_3\text{Fe}$  (found %): C 49.38 (49.30), H 3.19 (2.96), N 13.30 (12.86).

***C<sub>58</sub>H<sub>40</sub>N<sub>10</sub>S<sub>4</sub>Fe* (13)**

Complex **11** (20 mg) was recrystallized in 1:1 MeOH: $\text{CH}_2\text{Cl}_2$  (4 mL) to produce orange rod-shaped crystals over a period of two weeks. FTIR (KBr): 2961 (m), 2922 (m), 2855 (m), 2060 (s), 1628 (m), 1597 (w), 1470 (w), 1437 (w), 1261 (m), 1096 (s), 1024 (s), 802 (s), 754 (m), 694 (m)  $\text{cm}^{-1}$ . MS (FAB+):  $m/z$  1002  $[(\text{M} - \text{NCS})^+, 8\%]$ , 445  $[(\text{C}_{28}\text{H}_{21}\text{N}_4\text{S})^+, 100\%]$ , 353  $[(\text{C}_{22}\text{H}_{15}\text{N}_3\text{S})^+, 52\%]$ . Anal. calcd. for  $\text{C}_{58}\text{H}_{40}\text{N}_{10}\text{S}_4\text{Fe} \cdot 0.5\text{CH}_2\text{Cl}_2$  (found %): C 63.86 (63.90), H 3.73 (2.84), N 12.63 (12.13).

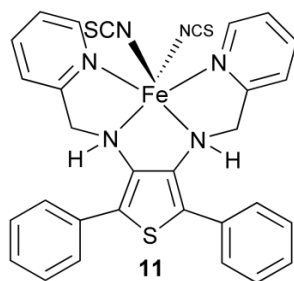
## Results and discussion

### Ligand synthesis and coordination chemistry

Ligand preparation is outlined in Scheme 1. 2,5-Dibromo-3,4-dinitrothiophene (**1**) was prepared by nitration of commercially available 2,5-dibromothiophene in a modified literature procedure.<sup>10</sup> We chose to use non-fuming concentrated acids and generated **1** in reasonably good yield. To generate the 2,5-disubstituted ligands (where the substituents are phenyl or 2-thienyl), we performed Suzuki–Miyaura cross-coupling reactions between **1** and phenylboronic acid or 2-thienylboronic acid. 3,4-Dinitro-substituted thiophenes (**1–3**) were reduced with a 30-fold excess of mossy tin and the 3,4-diamino-substituted thiophenes, as dihydrochloride salts, precipitated out in each case.<sup>11</sup> Tetradentate ligands were prepared in one pot by neutralization of the dihydrochloride salts with KOH, followed by condensation reactions in methanol with 2-pyridinecarboxaldehyde to generate the imine intermediates and subsequent imine reduction with  $\text{NaBH}_4$ . Ligands **7–9** are very unstable oils (particularly ligand **8**, which is so unstable we could not generate a quality  $^{13}\text{C}$  NMR spectrum prior to decomposition) and had to be purified quickly and used directly in coordination reactions. To our knowledge, these instability

issues are not observed with similar reported tetradentate ligands that do not feature thiophene substitution, which could in all cases be purified by short-path vacuum distillation.<sup>6</sup> Our attempts to purify **7–9** in this manner in all cases resulted in decomposition. We speculate that the observed instability likely arises from oligomerization or polymerization of the thiophene heterocycle, and (or) from nucleophilic reaction of the amino N atoms at the 3,4 thiophene ring positions. Unfortunately, our spectral data does not allow us to unambiguously identify the products of the decomposition. We have some mass spectral evidence that would seem to suggest that ligands **8–9**, in solution and over time, undergo a similar rearrangement that is observed in complexes **11** and **12** (*vide infra*).

Iron(II) complexes were prepared by coordination of **7–9** with iron(II) tetrafluoroborate in deaerated methanol solution, followed by addition of excess aqueous KSCN to generate green precipitates of complexes **10** or **12** (Scheme 2). Complexes **10** and **12** are analytically pure powders, stable to air in the solid state, but very unstable in solution, including deaerated solutions. It is likely that oligomerization or polymerization of the thienyl substituents is at least one destabilizing factor in these materials, but we are not exactly sure what the pathway(s) for decomposition in these complexes is (are). Mass spectral data suggests that decomposition leads to a complex mixture of products. Although X-ray diffraction data could not be obtained from samples of **10** or **12** because of solution instability issues, we could use FTIR spectroscopy ( $\nu_{C\equiv N}$ ) to identify the stereochemistry about the metal centre. Complexes **10** or **12** feature a strong “doublet” between 2060–2080  $\text{cm}^{-1}$ , indicating a *cis* stereochemistry, which has been observed in other similar reported complexes. In fact, the energy of this band has been previously correlated to the electronic ground state of the complex and the energies observed for complexes **10** or **12** suggest a significant population of the high spin (HS)  $^5T_2$  state at room temperature.



Complex **11**, which was prepared under identical conditions to **10** or **12**, is unstable in the solid state and solution, making characterization difficult; however, based on our spectroscopic data, we are confident in the purported structure. As opposed to **10** or **12**, complex **11** features a single sharp strong band at 2070  $\text{cm}^{-1}$ , which strongly suggests an unusual *trans* disposition of the thiocyanate ligands (and a HS ground state).

Attempts to recrystallize deaerated solutions of **10–12** consistently resulted in solution color changes, from green to red over a period of days, which we anticipated was the result of iron(II) oxidation. Red solutions of **11** deposited

X-ray quality crystals and, to our surprise, a structurally rearranged material was indicated. Complex **13** contains two coordinated molecules of rearranged **8**. For clarity, the ligand rearrangement is indicated in Scheme 3.

An Oakridge thermal ellipsoid plot (ORTEP) of the molecular structure of **13** is shown in Figure 2. The metal center falls on a twofold axis, rendering each coordinated ligand equivalent. Coordinate bond lengths (Table 2) are consistent with an oxidation state assignment of +2 for the metal ion. Each molecule of rearranged **8** is coordinated through N1 and N2 of a bidentate pyridine–imidazole-type fragment of the molecule. The other imidazole-type ring atom N3 features a covalently bound and uncoordinated 2-pyridylmethylene substituent. Crystallographically equivalent thiocyanate ligands are coordinated *cis* to the iron center, and are disordered over two positions.

Along the *ac* diagonal, molecules of **13** pack in a one-dimensional chain structure, with intermolecular S...S contacts between coordinated and disordered thiocyanate ligands among adjacent molecules along the chain (Fig. 3). As noted in the Experimental section, the NCS ligand exhibits a 73:27 disorder over two positions. The S...S contacts vary from shorter [3.54(1) Å] than the sum of the van der Waals radii for the interaction between S2'–S2' to longer (3.85 and 4.40 Å) than the sum of the van der Waals radii for the interaction between S2–S2' and S2–S2, respectively. This packing structure is possibly implicated in the unusual variable-temperature magnetic properties of **13** because no other close intermolecular contacts were found in the X-ray structure between sites carrying a significant amount of spin density (*vide infra*).

Red solutions of **12** deposit a dark red powder from which FTIR and mass spectrometric data indicate a similar structural rearrangement occurs. Unfortunately, we could not obtain X-ray quality crystals from solutions containing **12**. Solutions of **10** decompose to a mixture of products over time. To our knowledge, similar structural rearrangements have not been reported for other iron(II) bis(thiocyanate) complexes containing tetradentate bis(2-pyridylmethyl)-type ligands, suggesting that the thienyl substituent or the electronic effect of this substituent is possibly involved in the mechanism for this rearrangement.

## Electrochemistry

The electrochemical properties of complexes **10** and **12** were investigated with cyclic voltammetry, and as an example, the CV of **12** is presented in Fig. 4 (right). Each voltammogram features a number of broad and irreversible processes versus ferrocene. Cathodic scans are unremarkable and each complex exhibits irreversible waves at potentials greater than –1.5 V, which are attributed to pyridine ring reductions. Over anodic potentials, an irreversible oxidation process centered at +0.4 V is observed in the voltammograms of **10** and **12**. A similar wave at approximately +0.4 V is observed in the voltammogram of uncoordinated **7** and is likely a ligand-centered oxidation (dehydrogenation of NH bond). Beyond +0.4 V, **10** exhibits a very broad irreversible oxidation at +1.3 V and **12** features irreversible processes at +0.8, +1.0, and +1.3 V, which we attribute to a combination of terthienyl and iron(II) oxidation processes. We attempted to electropolymerize complex **12** by repeated



scans over the terthienyl oxidation potential; however, we observed no indication for any successful electropolymerization reactions.

### Visible–NIR spectroscopy

Ethanol solutions of complexes **11** and **12** exhibit absorption maxima at 650 nm ( $\epsilon = 400 \text{ mol/L}^{-1} \text{ cm}^{-1}$ ), with absorption intensities that are not temperature-dependent. To help provide the assignments of the absorption bands in **11** and **12**, the absorption spectrum of **13** was calculated using TD-DFT at the B3LYP/DZVP level. The calculated spectrum of **13** in the visible region contains a main band at 638 nm with the oscillator strength ( $\phi$ ) of 0.0040 and a weaker band at 629 nm ( $\phi = 0.0011$ ). The 638 nm band originates from the  $\beta$ -spin HOMO  $\rightarrow$  LUMO excitation with the  $\beta$ -spin HOMO being the Fe  $d\pi - \text{NCS } \pi$  orbital (35% Fe and 65% NCS contributions) and the  $\beta$ -spin LUMO being the Fe  $d\sigma - \text{pyridine-imidazole } \pi^*$  orbital (12% Fe and 85% L). As a result, this absorption band has a mixed metal-to-ligand and ligand-to-ligand charge transfer (MLCT/LLCT) character. The 629 nm band originates from a mixture of several electron excitations (the two principal components are the  $\alpha$ -spin HOMO-4  $\rightarrow$  LUMO and  $\beta$ -spin HOMO-4  $\rightarrow$  LUMO excitations). The room-temperature spectrum of **10** in ethanol also features a weak absorption at 640 nm; however, upon cooling to 77 K, a large increase in absorption intensity is observed concomitant with the growth of a shoulder on the low-energy side of the 640 nm absorption. The color of the solution becomes intensely dark green from the pale green/yellow color observed at room temperature (Fig. 4, left). These observations suggest an electronic change, likely spin-crossover is occurring in solutions containing **10**. The new absorption feature centered at 700 nm is likely the band of the low-spin state of **10**.

### Variable-temperature magnetic properties

The variable-temperature magnetic properties of **10**, **12**, and **13** were probed via SQUID magnetometry and the data are presented as plots of the effective magnetic moment ( $\mu_{\text{eff}}$ ) versus temperature (Fig. 5). The magnetic properties of **12** feature very little temperature dependence and the observed magnetic moment values suggest a high-spin ground state for this complex. The magnetic moment of **12** decreases rapidly below 40 K, which likely results from a combination of zero-field splitting (ZFS) and intermolecular antiferromagnetic interactions.

Data from variable-temperature visible–NIR spectroscopy indicated spin-crossover was operative in solutions of **10**. In the solid state, variable-temperature magnetic susceptibility data indicates a gradual and incomplete spin-crossover without thermal hysteresis in powder samples of **10**. The magnetic moment of **10** at the highest measured temperature (350 K) is 4.95  $\mu_B$  and a gradual decrease is observed with decreasing temperature to 2 K, where the observed magnetic moment is 2.4  $\mu_B$ , which is higher than anticipated for a complete crossover to the low-spin (LS) state (theoretical value is 0 BM). However, the profile of the data, including the higher than expected moments at very low temperature, is very similar to that observed by Toftlund for structurally similar iron(II) complexes (without thienyl substituents) and

points toward an incomplete spin-crossover in these materials.<sup>6</sup>

The variable-temperature magnetic properties of **13** are completely different. At room temperature, the magnetic moment is significantly higher than anticipated for a magnetically isolated mononuclear iron(II) complex (Fig. 5, right). With decreasing temperature, we see a gradual increase in magnetic moment, indicating intermolecular ferromagnetic interactions are operative. The magnetic moment reaches a plateau of 8.1 BM at approximately 8 K, and then slightly decreases. Low-temperature (5 K) magnetization versus field experiments provided no indication of ferromagnetic ordering, with a saturation magnetization of 4.6 NB at 3.5 T, which is a typical value for HS iron(II) (see Supplementary data). In the molecular packing of **13**, close intermolecular S...S contacts were observed between coordinated thiocyanate ligands from adjacent molecules, suggesting a possible pathway for magnetic exchange coupling. We used DFT at the B3LYP/DZVP level to calculate the structure and spin density of complex **13**, and found significant spin delocalization onto the coordinated thiocyanate ligands (0.16 on each NCS, Fig. 6), suggesting that the magnetic exchange pathway in **13** is possibly that of a 1-D  $S = 2$  ferromagnetic chain. The fit to a Bonner–Fisher 1-D chain model<sup>12</sup> (eq. [1],  $g = 2.13$  and  $J/k = +7.5 \text{ K}$ ) containing a correction for interchain magnetic interactions (eq. [2]  $zJ'/k = -2.2 \text{ K}$ ) is good between 320 and 30 K, and then deviates at low temperature.

$$[1] \quad \chi_{\text{chain}} T = \frac{Ng^2\beta_e^2 S(S+1)}{3kT} \left( \frac{1+u}{1-u} \right)$$

$$[2] \quad \chi_m T = \left( \frac{1}{\chi_{\text{chain}} T} - \frac{zJ'}{kT} \right)$$

where

$$u = \coth \frac{2JS(S+1)}{kT} - \frac{kT}{2JS(S+1)}$$

Since there are no other significant intermolecular magnetic exchange pathways between atoms/fragments with high spin density in the molecular packing of **13**, which would suggest that another competing antiferromagnetic interchain coupling is dominant at lower temperatures, it is also reasonable to assume that the deviation from 1-D chain behaviour at lower temperatures is a result of ZFS of the iron(II)  $S = 2$  ground state. The relatively large value of  $J/k$  is surprising, especially considering that this exchange pathway is *intermolecular*. Typically, weak magnetic interactions are mediated in an intramolecular fashion through ambidentate N and S coordinated and bridging thiocyanate between metal ions within bimetallic complexes or coordination polymers.<sup>13</sup> We could find no other reported examples of intermolecular ferromagnetic coupling mediated by coordinated thiocyanate ligands.

### Conclusions

We have described the synthesis of three new thiophene-containing “Toftlund-like” bispicen ligands (**7–9**). In apparent contrast to the bispicen family of ligands, **7–9** are unsta-



ble oils, which we could isolate and characterize, but must be coordinated quickly, or else suffer decomposition. Coordination of **7** and **9** with iron(II) bis(thiocyanate) resulted in the anticipated cis-pseudo-octahedral complexes (**10** and **12**), which were characterized and featured incomplete spin-crossover (**10**), or HS iron(II) (**12**). Coordination of **8** with iron(II) bis(thiocyanate) produced a very unstable complex (**11**), which in solution undergoes a ligand-centered structural rearrangement to produce a stable complex **13**, featuring intriguing variable-temperature magnetic properties. Our analysis indicates that the temperature-dependent magnetic behaviour of **13** is best-described as a one-dimensional ferromagnetic chain with interchain antiferromagnetic interactions and (or) ZFS at low temperatures, which reduces the magnetization. We are currently exploring the synthesis of derivatives of **13**, including other iron(II) complexes with different ligand structures as precursors to novel iron(II) containing spin-crossover conductors.

## Supplementary data

Supplementary data for this article are available on the journal Web site (canjchem.nrc.ca). CCDC 758104 contains the X-ray data in CIF format for this manuscript. These data can be obtained, free of charge, via [www.ccdc.cam.ac.uk/conts/retrieving.html](http://www.ccdc.cam.ac.uk/conts/retrieving.html) (or from the Cambridge Crystallographic Data Centre, 12 Union Road, Cambridge CB2 1EZ, UK; fax +44 1223 336033; or [deposit@ccdc.cam.ac.uk](mailto:deposit@ccdc.cam.ac.uk)).

## Acknowledgement

MTL acknowledges the Natural Sciences and Engineering Research Council of Canada (NSERC) and the Canadian Foundation for Innovation (CFI) for support of this research.

## References

- (1) Kahn, O.; Martinez, C. J. *Science* **1998**, 279 (5347), 44. doi:10.1126/science.279.5347.44.
- (2) Halcrow, M. A. *Polyhedron* **2007**, 26 (14), 3523. doi:10.1016/j.poly.2007.03.033.
- (3) (a) Gaspar, A. B.; Ksenofontov, V.; Seredyuk, M.; Güetlich, P. *Coord. Chem. Rev.* **2005**, 249 (23), 2661. doi:10.1016/j.ccr.2005.04.028.; (b) Gamez, P.; Costa, J. S.; Quesada, M.; Aromí, G. *Dalton Trans.* **2009**, (38), 7845. doi:10.1039/b908208e. PMID:19771343.
- (4) (a) Takahashi, K.; Cui, H.-B.; Okano, Y.; Kobayashi, H.; Einaga, Y.; Sato, O. *Inorg. Chem.* **2006**, 45, 5739. doi:10.1021/ic060852l.; (b) Faulmann, C.; Jacob, K.; Dorbes, S.; Lampert, S.; Malfant, I.; Doublet, M.-L.; Valade, L.; Real, J. A. *Inorg. Chem.* **2007**, 46 (21), 8548. doi:10.1021/ic062461c. PMID:17850071.; (c) Takahashi, K.; Cui, H.-B.; Okano, Y.; Kobayashi, H.; Mori, H.; Tajima, H.; Einaga, Y.; Sato, O. *J. Am. Chem. Soc.* **2008**, 130 (21), 6688. doi:10.1021/ja801585r. PMID:18452289.
- (5) (a) Djukic, B.; Dube, P. A.; Razavi, F.; Seda, T.; Jenkins, H. A.; Britten, J. F.; Lemaire, M. T. *Inorg. Chem.* **2009**, 48 (2), 699. doi:10.1021/ic801233x. PMID:19053331.; (b) Djukic, B.; Lemaire, M. T. *Inorg. Chem.* **2009**, 48 (22), 10489. doi:10.1021/ic9015542. PMID:19831361.
- (6) Toftlund, H.; Pedersen, E.; Yde-Andersen, S.; Westdahl, M. *Acta Chem. Scand. A* **1984**, 38, 693. doi:10.3891/acta.chem.scand.38a-0693.
- (7) (a) Frisch, M. J.; Trucks, G. W.; Schlegel, H. B.; Scuseria, G. E.; Robb, M. A.; Cheeseman, J. R.; Montgomery, J. A.; Vreven, T.; Kudin, K. N.; Burant, J. C.; Millam, J. M.; Lyengar, S. S.; Tomasi, J.; Barone, V.; Mennucci, B.; Cossi, M.; Scalmani, G.; Rega, N.; Petersson, G. A.; Nakatsuji, H.; Hada, M.; Ehara, M.; Toyota, K.; Fukuda, R.; Hasegawa, J.; Ishida, M.; Nakajima, T.; Honda, Y.; Kitao, O.; Nakai, H.; Klene, M.; Li, X.; Knox, J. E.; Hratchian, H. P.; Cross, J. B.; Adamo, C.; Jaramillo, J.; Gomperts, R.; Stratmann, R. E.; Yazyev, O.; Austin, A. J.; Cammi, R.; Pomelli, C.; Ochterski, J. W.; Ayala, P. Y.; Morokuma, K.; Voth, G. A.; Salvador, P.; Dannenberg, J. J.; Zakrzewski, V. G.; Dapprich, S.; Daniels, A. D.; Strain, M. C.; Farkas, O.; Malick, D. K.; Rabuck, A. D.; Raghavachari, K.; Foresman, J. B.; Ortiz, J. V.; Cui, Q.; Baboul, A. G.; Clifford, S.; Cioslowski, J.; Stefanov, B. B.; Liu, G.; Liashenko, A.; Piskorz, P.; Komaromi, I.; Martin, R. L.; Fox, D. J.; Keith, T.; Al-Laham, M. A.; Peng, C. Y.; Nanayakkara, A.; Challacombe, M.; Gill, P. M. W.; Johnson, B.; Chen, W.; Wong, M. W.; Gonzalez, C.; Pople, J. A. *Gaussian 03*; Gaussian, Inc.: Wallingford, CT, 2003;(b) Becke, A. D. *J. Chem. Phys.* **1993**, 98 (7), 5648. doi:10.1063/1.464913.; (c) Lee, C.; Yang, W.; Parr, R. G. *Phys. Rev. B* **1988**, 37 (2), 785. doi:10.1103/PhysRevB.37.785.
- (8) (a) Godbout, N.; Salahub, D. R.; Andzelm, J.; Wimmer, E. *Can. J. Chem.* **1992**, 70 (2), 560. doi:10.1139/v92-079.; (b) Reed, A. E.; Curtiss, L. A.; Weinhold, F. *Chem. Rev.* **1988**, 88 (6), 899. doi:10.1021/cr00088a005.
- (9) (a) Gorelsky, S. I. *AOMix*, version 6.46 ed.; University of Ottawa: Ottawa, Canada, 2010; (b) Gorelsky, S. I.; Lever, A. B. P. *J. Organomet. Chem.* **2001**, 635 (1-2), 187. doi:10.1016/S0022-328X(01)01079-8.
- (10) Kenning, D. D.; Mitchell, K. A.; Calhoun, T. R.; Funfar, M. R.; Sattler, D. J.; Rasmussen, S. C. *J. Org. Chem.* **2002**, 67 (25), 9073. doi:10.1021/jo0262255. PMID:12467431.
- (11) (a) Outurquin, F.; Paulmier, C. *Bull. Soc. Chim. Fr.* **1983**, 2, 153; (b) Kitamura, C.; Tanaka, S.; Yamashita, Y. *Chem. Mater.* **1996**, 8 (2), 570. doi:10.1021/cm950467m.; (c) Reddinger, J. L.; Reynolds, J. R. *Chem. Mater.* **1998**, 10 (5), 1236. doi:10.1021/cm970574b.
- (12) (a) Bonner, J. C.; Fisher, M. E. *Phys. Rev.* **1964**, 135 (3A), A640. doi:10.1103/PhysRev.135.A640.; (b) Gerstein, B. C.; Gehring, F. D.; Willet, R. D. *J. Appl. Phys.* **1972**, 43 (4), 1932. doi:10.1063/1.1661419.
- (13) (a) Dockum, B. W.; Reiff, W. M. *Inorg. Chem.* **1982**, 21 (1), 391. doi:10.1021/ic00131a070.; (b) Escuer, A.; Kumar, S. B.; Mautner, F.; Vicente, R. *Inorg. Chim. Acta* **1998**, 269 (2), 313. doi:10.1016/S0020-1693(97)05801-5.

# Preparation of aromatic amines by copper-catalyzed coupling of boronic acids with aqueous ammonia

Zhaoqiong Jiang, Zhiqing Wu, Lixia Wang, Di Wu, and Xiangge Zhou

**Abstract:** A simple, highly efficient, and environmentally friendly protocol for the synthesis of primary aromatic amines by catalytic coupling of aromatic boronic acids with aqueous ammonia has been developed by using commercial and inexpensive  $\text{CuSO}_4 \cdot 5\text{H}_2\text{O}$  as catalyst without addition of other solvents under mild reaction conditions.

**Key words:** ammonia, primary aromatic amine, aromatic boronic acid, water.

**Résumé :** Opérant dans des conditions de réactions douces et utilisant le  $\text{CuSO}_4 \cdot 5\text{H}_2\text{O}$  peu coûteux et commercialement disponible comme catalyseur, on a développé une méthode simple, hautement efficace et écologique pour synthétiser des amines primaires aromatiques par couplage catalytique d'acide boroniques aromatiques avec l'ammoniaque en solution aqueuse et n'impliquant aucun autre solvant.

**Mots-clés :** ammoniac, amine primaire aromatique, acide boronique aromatique, eau.

## Introduction

Preparation of primary aromatic amines has attracted increasing attention because they are valuable compounds widely employed in the manufacture of natural products, agrochemicals, pharmaceuticals, biological compounds, dyes, pigments, and rubber.<sup>1</sup> Ammonia is one of the most abundant, inexpensive, and attractive nitrogen sources in chemical synthesis, but the direct consumption of it in catalytic reactions is less reported.<sup>2</sup> In general, the difficulties in the use of ammonia for metal-catalyzed processes may result from two facts: (i) many kinds of transition metals are bonded with ammonia to form catalytically unreactive complexes, and (ii) the primary amine product formed during catalysis is usually more reactive than ammonia itself and easily converted to a secondary amine.<sup>2g,3</sup> Thus, the synthesis of primary aryl amines generally relies on the use of ammonia surrogates such as allyl,<sup>4</sup> benzyl<sup>5</sup> and silyl amines,<sup>6</sup> imines,<sup>7</sup> amides,<sup>8</sup> and others.<sup>9</sup> However, the products of these reactions need an additional deprotection step, which makes those methodologies less attractive. Hence, the use of ammonia as a nitrogen source is still by far one of the most desired approaches.<sup>2</sup> A few copper-catalyzed protocols for the preparation of primary arylamines have been recently developed by the coupling of aryl halides with ammonia. However, these catalyses were usually performed under high pressure using liquid ammonia.<sup>10</sup> More recently, palladium-catalyzed cross-coupling reactions between simple aryl halides and ammonia would allow the direct synthesis of valuable primary aromatic amines with good yields in solvents of 1,2-dimethoxyethane or 1,4-dioxane.<sup>2g,11</sup> Instead of

palladium, Cu-catalyzed amination of aryl halides using aqueous ammonia was first reported by Kim and Chang.<sup>12</sup> Following these pioneering works, several Cu-catalyzed preparation of primary arylamines have been efficiently carried out with excellent yields by using DMF, *N*-methyl pyrrolidinone, alcohol, or 1,4-dioxane as reaction medium.<sup>13</sup> Although these methods mentioned above have led to remarkable advancement in the synthesis of primary arylamines, it is worth noting that they were all performed in organic solvents.<sup>14</sup>

From the standpoint of green chemistry, the development of a more environmentally benign reaction media would be highly desirable.<sup>15</sup> Obviously, water, which is an ideal non-toxic, extremely abundant, and readily available green substance, is the most inexpensive and environmentally benign solvent. In continuation of our endeavors in aqueous catalysis,<sup>16</sup> herein is reported the synthesis of primary arylamines by cross-coupling reactions between aromatic boronic acids and aqueous ammonia catalyzed by  $\text{CuSO}_4 \cdot 5\text{H}_2\text{O}$  at room temperature (RT) without the addition of other solvents.

## Results and discussion

Initially, we chose phenylboronic acid as the model substrate in the optimization of reaction conditions. The preliminary survey was carried out by using 28% aqueous ammonia as the nitrogen source,  $\text{CuSO}_4 \cdot 5\text{H}_2\text{O}$  as catalyst, and NaOH as base. The results were listed in Table 1.

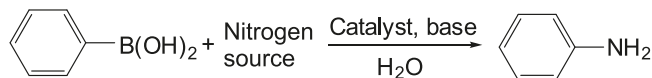
Unlike most of the other coupling reactions, as shown in Table 1, the yields decreased sharply from 70% and 69% to 51% when the reaction temperature increased from room

Received 21 April 2010. Accepted 30 June 2010. Published on the NRC Research Press Web site at canjchem.nrc.ca on 20 August 2010.

**Z. Jiang, Z. Wu, and L. Wang.** Institute of Homogeneous Catalysis, College of Chemistry, Sichuan University, Chengdu 610064, China.

**D. Wu<sup>1</sup> and X. Zhou.** State Key Laboratory of Coordination Chemistry, Nanjing University, Nanjing 210093, China.

<sup>1</sup>Corresponding author (e-mail: wood@scu.edu.cn).

**Table 1.** Copper-catalyzed synthesis of aniline from phenylboronic acid in water.

Entry	Nitrogen source	Catalyst	Base	<i>T</i> (°C)	Yield (%) <sup>a</sup>
1	NH <sub>3</sub> ·H <sub>2</sub> O	CuSO <sub>4</sub> ·5H <sub>2</sub> O	NaOH	90	51
2	NH <sub>3</sub> ·H <sub>2</sub> O	CuSO <sub>4</sub> ·5H <sub>2</sub> O	NaOH	60	69
3	NH <sub>3</sub> ·H <sub>2</sub> O	CuSO <sub>4</sub> ·5H <sub>2</sub> O	NaOH	RT	70
4	NH <sub>3</sub> ·H <sub>2</sub> O	CuSO <sub>4</sub> ·5H <sub>2</sub> O	Cs <sub>2</sub> CO <sub>3</sub>	RT	33
5	NH <sub>3</sub> ·H <sub>2</sub> O	CuSO <sub>4</sub> ·5H <sub>2</sub> O	K <sub>2</sub> CO <sub>3</sub>	RT	24
6	NH <sub>3</sub> ·H <sub>2</sub> O	CuSO <sub>4</sub> ·5H <sub>2</sub> O	Na <sub>2</sub> CO <sub>3</sub>	RT	28
7	NH <sub>3</sub> ·H <sub>2</sub> O	CuSO <sub>4</sub> ·5H <sub>2</sub> O	CH <sub>3</sub> COONa	RT	39
8	NH <sub>3</sub> ·H <sub>2</sub> O	CuSO <sub>4</sub> ·5H <sub>2</sub> O	K <sub>3</sub> PO <sub>4</sub>	RT	39
9	NH <sub>3</sub> ·H <sub>2</sub> O	CuSO <sub>4</sub> ·5H <sub>2</sub> O	Na <sub>2</sub> HPO <sub>4</sub>	RT	19
10	NH <sub>3</sub> ·H <sub>2</sub> O	CuSO <sub>4</sub> ·5H <sub>2</sub> O	KOH	RT	50
11	NH <sub>3</sub> ·H <sub>2</sub> O	CuSO <sub>4</sub> ·5H <sub>2</sub> O	NaHCO <sub>3</sub>	RT	30
12	NH <sub>3</sub> ·H <sub>2</sub> O	CuSO <sub>4</sub> ·5H <sub>2</sub> O	EtONa	RT	50
13	NH <sub>3</sub> ·H <sub>2</sub> O	CuSO <sub>4</sub> ·5H <sub>2</sub> O	—	RT	18
14	NH <sub>3</sub> ·H <sub>2</sub> O <sup>b</sup>	CuSO <sub>4</sub> ·5H <sub>2</sub> O	NaOH	RT	78
15	NH <sub>3</sub> ·H <sub>2</sub> O <sup>c</sup>	CuSO <sub>4</sub> ·5H <sub>2</sub> O	NaOH	RT	90
16	NH <sub>3</sub> ·H <sub>2</sub> O <sup>d</sup>	CuSO <sub>4</sub> ·5H <sub>2</sub> O	NaOH	RT	91
17	NH <sub>3</sub> ·H <sub>2</sub> O <sup>d</sup>	Cu(OAc) <sub>2</sub> ·H <sub>2</sub> O	NaOH	RT	89
18	NH <sub>3</sub> ·H <sub>2</sub> O <sup>d</sup>	CuCl <sub>2</sub> ·2H <sub>2</sub> O	NaOH	RT	79
19	NH <sub>3</sub> ·H <sub>2</sub> O <sup>d</sup>	Cu <sub>2</sub> O	NaOH	RT	65
20	NH <sub>3</sub> ·H <sub>2</sub> O <sup>d</sup>	CuClO <sub>4</sub>	NaOH	RT	82
21	NH <sub>3</sub> ·H <sub>2</sub> O <sup>d</sup>	CuI	NaOH	RT	87
22	NH <sub>3</sub> ·H <sub>2</sub> O <sup>d</sup>	—	NaOH	RT	Trace
23	(NH <sub>4</sub> ) <sub>2</sub> CO <sub>3</sub>	CuSO <sub>4</sub> ·5H <sub>2</sub> O	NaOH	RT	5
24	NH <sub>4</sub> HCO <sub>3</sub>	CuSO <sub>4</sub> ·5H <sub>2</sub> O	NaOH	RT	3
25	NH <sub>4</sub> Cl	CuSO <sub>4</sub> ·5H <sub>2</sub> O	NaOH	RT	5
26	(NH <sub>4</sub> ) <sub>2</sub> SO <sub>4</sub>	CuSO <sub>4</sub> ·5H <sub>2</sub> O	NaOH	RT	4

**Note:** Unless otherwise noted, the reaction was carried out with phenylboronic acid (0.2 mmol), nitrogen sources (2 mmol), catalyst (0.02 mmol), and base (0.4 mmol) in 2 mL water.

<sup>a</sup>Determined by GC–MS using 1,4-dichlorobenzene as internal standard.

<sup>b</sup>Aqueous ammonia (28%, 4 mmol) in 2 mL water.

<sup>c</sup>Aqueous ammonia (28%, 4 mmol) in 1 mL water.

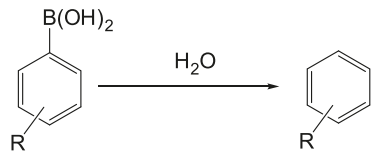
<sup>d</sup>Aqueous ammonia (28%, 1 mL).

temperature and 60 °C to 90 °C, respectively (Table 1, entries 1–3). The formation of the byproduct phenol, which resulted from the hydrolysis of phenylboronic acid at high temperature in water, might be attributed to the decrease of yields. Control experiment proved that more than 50% phenylboronic acid was found to convert into phenol at 100 °C. Comparison of a variety of bases indicated NaOH to be a proper candidate with a yield of 70% (Table 1, entries 3–13). Considering phenol as the main side product, we increased the concentration of ammonia to inhibit the competition of water; the yield was sharply improved from 70% to 91% when the concentration of ammonia was increased from 2% to 28% (Table 1, entries 3, 14–16). Thus, the addition of other solvents, including water, was unnecessary in this case. Other different copper sources such as Cu(OAc)<sub>2</sub>, CuCl<sub>2</sub>, Cu<sub>2</sub>O, CuClO<sub>4</sub>, and CuI have also been examined, and CuSO<sub>4</sub> gave the best result with a 91% GC–MS yield (Table 1, entries 16–21) and there was only trace product without catalyst (Table 1, entry 22). Several inorganic nitrogen sources were also tried with poor results (Table 1, entries 23–26). In summary, the optimal conditions for the

synthesis of primary aromatic amines are as follows: 28% aqueous ammonia (3 mL, when 0.6 mmol aromatic boronic acid was used) as the nitrogen source, CuSO<sub>4</sub> (10 mol%) as the catalyst, NaOH (2 equiv.) as the base, and the reaction was carried out at room temperature in a sealed tube without inert gas protection.

The scope of aromatic boronic acids was then investigated by using this catalytic system under the optimized reaction conditions. The results are listed in Table 2.

In general, the catalytic cross-coupling reactions between aqueous ammonia and aromatic boronic acids containing electron-withdrawing substituents were efficiently promoted with excellent yields within 3–5 h. For instance, *p*-fluorophenylboronic acid and *p*-cyanophenylboronic acid afforded 91% and 92% of the desired aminated products, respectively (Table 2, entries 3 and 5, respectively). Lower yields were obtained with *p*-methoxyphenyl boronic acid, *o*-methoxyphenyl boronic acid, and  $\alpha$ -naphthyl boronic acid, due to the formation of protodeboronation byproducts as shown in Scheme 1 (Table 2, entries 6, 8, and 11, respectively).<sup>17</sup> Normally, protodeboronation occurs by the reported A-SE<sub>2</sub>

**Scheme 1.** Protodeboronation of aromatic boronic acids.**Table 2.** Synthesis of primary aromatic amines catalyzed by  $\text{CuSO}_4 \cdot 5\text{H}_2\text{O}$  in water.

Entry	Ar-B(OH) <sub>2</sub>	ArNH <sub>2</sub>	Time (h)	Yield (%) <sup>a</sup>
1			4	88
2			5	87
3			5	91
4			5	90
5			5	92
6			5	66
7			4	84
8			4	55
9			4	59
10			4	58
11			3	50

**Note:** Reaction conditions: aromatic boronic acids (0.6 mmol), 28% aqueous ammonia (3 mL),  $\text{CuSO}_4 \cdot 5\text{H}_2\text{O}$  (0.06 mmol), NaOH (1.2 mmol), room temperature.

<sup>a</sup>Isolated yields.

mechanism, in which proton transfer is the rate-determining step, and is followed by a rapid ionic cleavage of the boron-carbon bond.<sup>18</sup> The rate sequence of protodeboronation of substituted phenylboronic acids was reported to be  $p\text{-OCH}_3 > p\text{-CH}_3 > p\text{-F} > \text{H} > p\text{-Br} > m\text{-Cl} > m\text{-F}$ .<sup>18c,18d,19</sup> Meanwhile, electron-withdrawing groups, especially those located at the *m*-position of phenylboronic acids, retarded the rate of protodeboronation.<sup>18d</sup> Furthermore, the protodeboronation process was reported to be easier for  $\alpha$ -naphthyl boronic acid than *p*-methoxyphenyl boronic acid.<sup>17b,20</sup> Thus, in this experiment, *p*-methoxyphenyl boronic acid, *o*-methoxyphenyl boronic acid, and  $\alpha$ -naphthyl boronic acid afforded moderate yields ranging from 50% to 66%, while a much higher yield (84%) was obtained in the case of *m*-methoxyphenyl boronic acid (Table 2, entries 6–8). On the other hand, steric hindrance was another important factor affecting the results.

For example, only a 58% yield of the aminated product was obtained when 2,6-dimethylphenylboronic acid was employed (Table 2, entry 10).

## Conclusion

In summary, we have developed a simple, highly efficient, economical, and environmentally friendly protocol for the synthesis of primary aromatic amines by coupling of aromatic boronic acids with aqueous ammonia without the addition of other solvents under mild reaction conditions. This method has the following advantages: commercial and inexpensive  $\text{CuSO}_4 \cdot 5\text{H}_2\text{O}$  as catalyst, the use of aqueous ammonia as reactant as well as solvent, and NaOH as base at room temperature under atmospheric pressure without ligand and any other additive. This method avoids the use of stringent inert conditions and organic solvents, and the operation is very simple. Overall, we believe that this method could provide an avenue toward the Cu-catalyzed methods that have scarcely been adopted in the aqueous phase.

## Experimental

All reagents were purchased from commercial suppliers and used without further purification. Column chromatography was carried out with silica gel (200–300 mesh). Thin layer chromatography was carried out using Merck silica gel GF254 plates. <sup>1</sup>H NMR and <sup>13</sup>C NMR (400 and 100 MHz, respectively) spectra were recorded in  $\text{CDCl}_3$ . Chemical shifts are reported in ppm using TMS as the internal standard. Gas chromatography/mass spectra (GC–MS) were recorded on an Agilent Technologies 6890N instrument with an Agilent 5973N mass detector (EI) and a HP5-MS 30 m  $\times$  0.25 mm capillary apolar column (stationary phase: 5% diphenyldimethylpolysiloxane film, 0.25  $\mu\text{m}$ ).

### General procedure for the synthesis of primary aromatic amines

Aromatic boronic acid (0.6 mmol),  $\text{CuSO}_4 \cdot 5\text{H}_2\text{O}$  (0.06 mmol), NaOH (1.2 mmol), and aqueous ammonia (3 mL) were added to a sealed tube. The reaction mixture was stirred at room temperature for 3–5 h as shown in Table 2. After completion of the reaction, the mixture was extracted with ethyl acetate. The organic layer was then dried over anhydrous  $\text{Na}_2\text{SO}_4$  and the solvent was removed under reduced pressure. The residue was finally purified by column chromatography on silica gel using a hexane–ethyl acetate mixture as eluent.

#### Aniline<sup>13c</sup>

Purification by flash chromatography (petroleum ether/ethyl acetate 9:1). Yellow oil. <sup>1</sup>H NMR ( $\text{CDCl}_3$ , 400 MHz)  $\delta$ : 7.15 (t, 2H, *J* = 8.0 Hz), 6.76 (t, 1H, *J* = 7.4 Hz), 6.69 (d, 2H, *J* = 7.6 Hz), 3.52 (s, br, 2H). <sup>13</sup>C NMR ( $\text{CDCl}_3$ , 100 MHz)  $\delta$ : 145.9, 128.5, 117.6, 114.4. EI-MS *m/z*: 93 [*M*<sup>+</sup>].

#### *p*-Toluidine<sup>13c</sup>

Purification by flash chromatography (petroleum ether/ethyl acetate 9:1). Slight yellow solid. <sup>1</sup>H NMR ( $\text{CDCl}_3$ , 400 MHz)  $\delta$ : 6.96 (d, 2H, *J* = 8.4 Hz), 6.61 (d, 2H, *J* = 8.4 Hz), 3.42 (s, br, 2H), 2.24 (s, 3H). <sup>13</sup>C NMR ( $\text{CDCl}_3$ ,



100 MHz)  $\delta$ : 143.8, 129.7, 127.7, 115.3, 20.4. EI-MS  $m/z$ : 107 [ $M^+$ ].

### **p-Anisidine**<sup>13c</sup>

Purification by flash chromatography (petroleum ether/ethyl acetate 6:1). Slight brown solid. <sup>1</sup>H NMR (CDCl<sub>3</sub>, 400 MHz)  $\delta$ : 6.75 (d, 2H,  $J$  = 8.8 Hz), 6.66 (d, 2H,  $J$  = 8.8 Hz), 3.75 (s, 3H), 3.32 (s, br, 2H). <sup>13</sup>C NMR (CDCl<sub>3</sub>, 100 MHz)  $\delta$ : 152.8, 134.0, 116.5, 114.8, 56.0. EI-MS  $m/z$ : 123 [ $M^+$ ].

### **m-Anisidine**<sup>13c</sup>

Purification by flash chromatography (petroleum ether/ethyl acetate 6:1). Yellow oil. <sup>1</sup>H NMR (CDCl<sub>3</sub>, 400 MHz)  $\delta$ : 7.06 (t, 1H,  $J$  = 8.0 Hz), 6.34–6.29 (m, 2H), 6.25 (t, 1H), 3.76 (s, 3H), 3.55 (s, br, 2H). <sup>13</sup>C NMR (CDCl<sub>3</sub>, 100 MHz)  $\delta$ : 159.7, 146.7, 129.1, 106.9, 103.0, 100.1, 54.0. EI-MS  $m/z$ : 123 [ $M^+$ ].

### **o-Anisidine**<sup>13f</sup>

Purification by flash chromatography (petroleum ether/ethyl acetate 6:1). Yellow oil. <sup>1</sup>H NMR (CDCl<sub>3</sub>, 400 MHz)  $\delta$ : 6.81–6.78 (m, 2H), 6.75–6.71 (m, 2H), 3.84 (s, 3H), 3.60 (s, br, 2H). <sup>13</sup>C NMR (CDCl<sub>3</sub>, 100 MHz)  $\delta$ : 146.3, 135.1, 120.1, 117.5, 114.0, 109.4, 54.4. EI-MS  $m/z$ : 123 [ $M^+$ ].

### **o-Toluidine**<sup>13c</sup>

Purification by flash chromatography (petroleum ether/ethyl acetate 9:1). Pale yellow oil. <sup>1</sup>H NMR (CDCl<sub>3</sub>, 400 MHz)  $\delta$ : 7.07–7.03 (m, 2H), 6.76–6.72 (m, 2H), 4.02 (s, br, 2H), 2.20 (s, 3H). <sup>13</sup>C NMR (CDCl<sub>3</sub>, 100 MHz)  $\delta$ : 143.0, 129.5, 126.0, 121.7, 118.0, 114.2, 16.3. EI-MS  $m/z$ : 107 [ $M^+$ ].

### **2,6-Dimethylaniline**<sup>13b</sup>

Purification by flash chromatography (petroleum ether/ethyl acetate 9:1). Yellow oil. <sup>1</sup>H NMR (CDCl<sub>3</sub>, 400 MHz)  $\delta$ : 6.95 (d, 2H,  $J$  = 7.6 Hz), 6.66 (t, 1H,  $J$  = 7.6 Hz), 3.83 (s, br, 2H), 2.20 (s, 6H). <sup>13</sup>C NMR (CDCl<sub>3</sub>, 100 MHz)  $\delta$ : 142.5, 128.3, 121.9, 118.2, 17.7. EI-MS  $m/z$ : 121 [ $M^+$ ].

### **$\alpha$ -Aminonaphthalene**<sup>13c</sup>

Purification by flash chromatography (petroleum ether/ethyl acetate 9:1). White solid. <sup>1</sup>H NMR (CDCl<sub>3</sub>, 400 MHz)  $\delta$ : 7.85–7.78 (m, 2H), 7.46–7.43 (m, 2H), 7.33–7.24 (m, 2H), 6.79–6.76 (m, 1H), 4.13 (s, br, 2H). <sup>13</sup>C NMR (CDCl<sub>3</sub>, 100 MHz)  $\delta$ : 142.1, 134.3, 128.5, 126.3, 125.8, 124.7, 123.6, 120.8, 118.8, 109.6. EI-MS  $m/z$ : 143 [ $M^+$ ].

### **p-Chloroaniline**<sup>13f</sup>

Purification by flash chromatography (petroleum ether/ethyl acetate 6:1). White solid. <sup>1</sup>H NMR (CDCl<sub>3</sub>, 400 MHz)  $\delta$ : 7.10 (d, 2H,  $J$  = 8.0 Hz), 6.61 (d, 2H,  $J$  = 8.4 Hz), 3.63 (s, br, 2H). <sup>13</sup>C NMR (CDCl<sub>3</sub>, 100 MHz)  $\delta$ : 145.0, 129.1, 123.2, 116.2. EI-MS  $m/z$ : 127 [ $M^+$ ].

### **p-Fluoroaniline**<sup>21</sup>

Purification by flash chromatography (petroleum ether/ethyl acetate 6:1). Yellow oil. <sup>1</sup>H NMR (CDCl<sub>3</sub>, 400 MHz)  $\delta$ : 6.88–6.82 (m, 2H), 6.64–6.60 (m, 2H), 3.53 (s, br, 2H). <sup>13</sup>C NMR (CDCl<sub>3</sub>, 100 MHz)  $\delta$ : 157.6, 155.3, 142.4, 116.1, 116.0, 115.8, 115.6. EI-MS  $m/z$ : 111 [ $M^+$ ].

### **p-Aminobenzonitrile**<sup>13c</sup>

Purification by flash chromatography (petroleum ether/ethyl acetate 6:1). Yellow solid. <sup>1</sup>H NMR (CDCl<sub>3</sub>, 400 MHz)  $\delta$ : 7.42 (d, 2H,  $J$  = 8.4 Hz), 6.65 (d, 2H,  $J$  = 8.4 Hz), 4.18 (s, br, 2H). <sup>13</sup>C NMR (CDCl<sub>3</sub>, 100 MHz)  $\delta$ : 150.5, 133.8, 120.2, 114.4, 100.1. EI-MS  $m/z$ : 118 [ $M^+$ ].

## **Supplementary data**

Supplementary data for this article (<sup>1</sup>H NMR and <sup>13</sup>C NMR spectra for all products) are available on the journal Web site (canjchem.nrc.ca).

## **Acknowledgement**

This project was sponsored by the Natural Science Foundation of China (No. 20672075, 20771076, and 20901052) and the Sichuan Provincial Foundation (08ZQ026-041). We also thank the Analytic and Testing Centre of Sichuan University for the NMR spectral determination.

## **References**

- (1) (a) Weissmehl, K.; Arpe, H. J. *Industrial Organic Chemistry*; Wiley-VCH: Weinheim, 1997; (b) Lawrence, S. A. *Amines: Synthesis, Properties and Applications*; Cambridge University Press: Cambridge, 2004; (c) Suwanprasop, S.; Nhujak, T.; Roengsumran, S.; Petsom, A. *Ind. Eng. Chem. Res.* **2004**, *43* (17), 4973. doi:10.1021/ie030739s.
- (2) (a) For the application of ammonia as a reagent in catalytic amination processes, see: Roundhill, D. M. *Chem. Rev.* **1992**, *92* (1), 1. doi:10.1021/cr00009a001.; (b) Prinz, T.; Keim, W.; Driessen-Holscher, B. *Angew. Chem. Int. Ed. Engl.* **1996**, *35* (15), 1708. doi:10.1002/anie.199617081.; (c) Zimmermann, B.; Herwig, J.; Beller, M. *Angew. Chem. Int. Ed.* **1999**, *38* (16), 2372. doi:10.1002/(SICI)1521-3773(19990816)38:16<2372::AID-ANIE2372>3.0.CO;2-H.; (d) Prinz, T.; Driessen-Holscher, B. *Chem. Eur. J.* **1999**, *5* (7), 2069. doi:10.1002/(SICI)1521-3765(19990702)5:7<2069::AID-CHEM2069>3.0.CO;2-K.; (e) Gross, T.; Seayad, A. M.; Ahmad, M.; Beller, M. *Org. Lett.* **2002**, *4* (12), 2055. doi:10.1021/ol0200605. PMID:12049516.; (f) Ogo, S.; Uehara, K.; Abura, T.; Fukuzumi, S. *J. Am. Chem. Soc.* **2004**, *126* (10), 3020. doi:10.1021/ja031633r. PMID:15012110.; (g) Shen, Q.; Hartwig, J. F. *J. Am. Chem. Soc.* **2006**, *128* (31), 10028. doi:10.1021/ja064005t. PMID:16881628.; (h) Kim, J.; Lee, S. Y.; Lee, J.; Do, Y.; Chang, S. *J. Org. Chem.* **2008**, *73* (23), 9454. doi:10.1021/jo802014g. PMID:18956843.
- (3) (a) Widenhoefer, R. A.; Buchwald, S. L. *Organometallics* **1996**, *15* (12), 2755. doi:10.1021/om9509608.; (b) Widenhoefer, R. A.; Buchwald, S. L. *Organometallics* **1996**, *15* (16), 3534. doi:10.1021/om9603169.; (c) Paul, F.; Patt, J.; Hartwig, J. F. *Organometallics* **1995**, *14* (6), 3030. doi:10.1021/om00006a053.; (d) Nagano, T.; Kobayashi, S. *J. Am. Chem. Soc.* **2009**, *131* (12), 4200. doi:10.1021/ja900328x. PMID:19265379.
- (4) Jaime-Figueroa, S.; Liu, Y.; Muchowski, J. M.; Putman, D. G. *Tetrahedron Lett.* **1998**, *39* (11), 1313. doi:10.1016/S0040-4039(97)10877-2.
- (5) Wolfe, J. P.; Tomori, H.; Sadighi, J. P.; Yin, J.; Buchwald, S. L. *J. Org. Chem.* **2000**, *65* (4), 1158. doi:10.1021/jo991699y. PMID:10814067.
- (6) (a) Hori, K.; Mori, M. *J. Am. Chem. Soc.* **1998**, *120* (30), 7651. doi:10.1021/ja981465g.; (b) Lee, S.; Jørgensen, M.;

- Hartwig, J. F. *Org. Lett.* **2001**, 3 (17), 2729. doi:10.1021/ol016333y. PMID:11506620.; (c) Huang, X. H.; Buchwald, S. L. *Org. Lett.* **2001**, 3 (21), 3417. doi:10.1021/ol0166808. PMID:11594848.; (d) Barluenga, J.; Aznar, F.; Valdes, C. *Angew. Chem. Int. Ed.* **2004**, 43 (3), 343. doi:10.1002/anie.200352808.; (e) Lee, D. Y.; Hartwig, J. F. *Org. Lett.* **2005**, 7 (6), 1169. doi:10.1021/ol050141b. PMID:15760166.
- (7) (a) Wolfe, J. P.; Ahman, J.; Sadighi, J. P.; Singer, R. A.; Buchwald, S. L. *Tetrahedron Lett.* **1997**, 38 (36), 6367. doi:10.1016/S0040-4039(97)01465-2.; (b) Mann, G.; Hartwig, J. F.; Driver, M. S.; Fernandez-Rivas, C. *J. Am. Chem. Soc.* **1998**, 120 (4), 827. doi:10.1021/ja973524g.; (c) Grasa, G. A.; Viciu, M. S.; Huang, J.; Nolan, S. P. *J. Org. Chem.* **2001**, 66 (23), 7729. doi:10.1021/jo010613+. PMID:11701028.
- (8) (a) Ikawa, T.; Barder, T. E.; Biscoe, M. R.; Buchwald, S. L. *J. Am. Chem. Soc.* **2007**, 129 (43), 13001. doi:10.1021/ja0717414. PMID:17918833.; (b) Tao, C.-Z.; Li, J.; Fu, Y.; Liu, L.; Guo, Q.-X. *Tetrahedron Lett.* **2008**, 49 (1), 70. doi:10.1016/j.tetlet.2007.11.012.
- (9) (a) Trabanco, A. A.; Vega, J. A.; Fernandez, M. A. *J. Org. Chem.* **2007**, 72 (21), 8146. doi:10.1021/jo701573w. PMID:17877407.; (b) Liu, X.; Barry, M.; Tsou, H.-R. *Tetrahedron Lett.* **2007**, 48 (48), 8409. doi:10.1016/j.tetlet.2007.09.177.; (c) Huang, X. H.; Anderson, K. W.; Zim, D.; Jiang, L.; Klarpars, A.; Buchwald, S. L. *J. Am. Chem. Soc.* **2003**, 125 (22), 6653. doi:10.1021/ja035483w. PMID:12769573.; (d) Gao, X.; Fu, H.; Qiao, R.; Jiang, Y.; Zhao, Y. *J. Org. Chem.* **2008**, 73 (17), 6864. doi:10.1021/jo800818e. PMID:18662031.
- (10) (a) Lang, F.; Zewge, D.; Houpi, I. N.; Volante, R. P. *Tetrahedron Lett.* **2001**, 42 (19), 3251. doi:10.1016/S0040-4039(01)00458-0.; (b) Gaillard, S.; Elmkaddem, M. K.; Fischmeister, C.; Thomas, C. M.; Renaud, J.-L. *Tetrahedron Lett.* **2008**, 49 (21), 3471. doi:10.1016/j.tetlet.2008.03.096.
- (11) (a) Surry, D. S.; Buchwald, S. L. *J. Am. Chem. Soc.* **2007**, 129 (34), 10354. doi:10.1021/ja074681a. PMID:17672469.; (b) Willis, M. C. *Angew. Chem. Int. Ed.* **2007**, 46 (19), 3402. doi:10.1002/anie.200605071.; (c) Schulz, T.; Torborg, C.; Enthaler, S.; Schäffner, B.; Dumrath, A.; Spannenberg, A.; Neumann, H.; Börner, A.; Beller, M. *Chem. Eur. J.* **2009**, 15 (18), 4528. doi:10.1002/chem.200802678.; (d) Vo, G. D.; Hartwig, J. F. *J. Am. Chem. Soc.* **2009**, 131 (31), 11049. doi:10.1021/ja903049z. PMID:19591470.
- (12) Kim, J.; Chang, S. *Chem. Commun. (Camb.)* **2008**, 44 (26), 3052. doi:10.1039/b804637a.
- (13) (a) Xia, N.; Taillefer, M. *Angew. Chem. Int. Ed.* **2009**, 48 (2), 337. doi:10.1002/anie.200802569.; (b) Rao, H.; Fu, H.; Jiang, Y.; Zhao, Y. *Angew. Chem. Int. Ed.* **2009**, 48 (6), 1114. doi:10.1002/anie.200805424.; (c) Xu, H.; Wolf, C. *Chem. Commun. (Camb.)* **2009**, 45 (21), 3035. doi:10.1039/b904188e.; (d) Wu, X. F.; Darcel, C. *Eur. J. Org. Chem.* **2009**, 4753. doi:10.1002/ejoc.200900588.; (e) Yang, C.-T.; Fu, Y.; Huang, Y.-B.; Yi, J.; Guo, Q.-X.; Liu, L. *Angew. Chem. Int. Ed.* **2009**, 48 (40), 7398. doi:10.1002/anie.200903158.; (f) Wang, D.; Cai, Q.; Ding, K. *Adv. Synth. Catal.* **2009**, 351 (11–12), 1722. doi:10.1002/adsc.200900327.
- (14) During the making of this manuscript, our group reported the coupling of aryl halides with ammonia in water for the synthesis of primary amines: Wu, Z.; Jiang, Z.; Wu, D.; Xiang, H.; Zhou, X. *Eur. J. Org. Chem.* **2010**, 1854. doi:10.1002/ejoc.201000060.
- (15) (a) Siskin, M.; Katritzky, A. R. *Chem. Rev.* **2001**, 101 (4), 825. doi:10.1021/cr000088z. PMID:11709859.; (b) Lindström, U. M. *Chem. Rev.* **2002**, 102 (8), 2751. doi:10.1021/cr010122p. PMID:12175267.; (c) DeSimone, J. M. *Science* **2002**, 297 (5582), 799. doi:10.1126/science.1069622. PMID:12161645.; (d) Poliakoff, M.; Fitzpatrick, J. M.; Farren, T. R.; Anastas, P. T. *Science* **2002**, 297 (5582), 807. doi:10.1126/science.297.5582.807. PMID:12161647.; (e) Li, C.-J. *Chem. Rev.* **2005**, 105 (8), 3095. doi:10.1021/cr030009u. PMID:16092827.; (f) Blackmond, D. G.; Armstrong, A.; Coombe, V.; Wells, A. *Angew. Chem. Int. Ed.* **2007**, 46 (21), 3798. doi:10.1002/anie.200604952.; (g) Teo, Y.-C.; Chua, G.-L. *Chem. Eur. J.* **2009**, 15 (13), 3072. doi:10.1002/chem.200802483.; (h) Teo, Y.-C. *Adv. Synth. Catal.* **2009**, 351 (5), 720. doi:10.1002/adsc.200800746.
- (16) (a) Wang, Y.; Wu, Z.; Wang, L.; Li, Z.; Zhou, X. *Chem. Eur. J.* **2009**, 15 (36), 8971. doi:10.1002/chem.200901232.; (b) Liang, L.; Li, Z.; Zhou, X. *Org. Lett.* **2009**, 11 (15), 3294. doi:10.1021/ol9010773. PMID:19572739.
- (17) (a) Protodeboronation of aromatic boronic acid usually occurs under drastic hydrolytic conditions. For base-promoted protodeboronation of aromatic boronic acid, see: Ainley, A. D.; Challenger, F. *J. Chem. Soc.* **1930**, 2171. doi:10.1039/jr9300002171.; (b) Pourbaix, C.; Carreaux, F.; Carboni, B.; Deleuze, H. *Chem. Commun. (Camb.)* **2000**, (14): 1275. doi:10.1039/b003487h.
- (18) (a) Kuivila, H. G.; Nahabedian, K. V. *J. Am. Chem. Soc.* **1961**, 83 (9), 2159. doi:10.1021/ja01470a028.; (b) Kuivila, H. G.; Nahabedian, K. V. *J. Am. Chem. Soc.* **1961**, 83 (9), 2164. doi:10.1021/ja01470a029.; (c) Nahabedian, K. V.; Kuivila, H. G. *J. Am. Chem. Soc.* **1961**, 83 (9), 2167. doi:10.1021/ja01470a030.; (d) Klingensmith, L. M.; Bio, M. M.; Moniz, G. A. *Tetrahedron Lett.* **2007**, 48 (46), 8242. doi:10.1016/j.tetlet.2007.09.060.
- (19) Cerichelli, G.; Floris, B.; Illuminati, G.; Ortaggi, G. *J. Org. Chem.* **1974**, 39 (26), 3948. doi:10.1021/jo00940a037.
- (20) Smith, K. A.; Campi, E. M.; Jackson, W. R.; Marcuccio, S.; Naeslund, C. G. M.; Deacon, G. B. *Synlett* **1997**, 131. doi:10.1055/s-1997-710.
- (21) Rahaim, R. J., Jr.; Maleczka, R. E., Jr. *Org. Lett.* **2005**, 7 (22), 5087. doi:10.1021/ol052120n. PMID:16235964.

# Novel $\beta$ -galactosidase-specific O<sup>2</sup>-glycosylated diazeniumdiolate probes

Barry J. Bedell, D. Scott Bohle, Zhijie Chua, Alexander Czerniewski, Alan C. Evans, and Shadreck Mzengeza

**Abstract:** Three  $\beta$ -galactosidase-specific nitric-oxide-releasing diazeniumdiolate conjugated probes were prepared as a prelude to studies of new potential molecular MRI imaging agents. A glycosylated derivative, **2e**, designed to be trafficked across cell membranes, was also prepared. We report, in detail, the synthesis and characterization of these probes. In addition, the release of diazeniumdiolate from the probes by  $\beta$ -galactosidase-catalyzed hydrolysis was used to estimate their efficacy as serum-stable, specific NO donors.

**Key words:** nitric oxide, diazeniumdiolate, glycosylated, galactosidase.

**Résumé :** Comme prélude à des études de nouveaux produits pouvant éventuellement être utilisés comme agents moléculaires en imagerie de résonance magnétique (IRM), on a préparé trois nouvelles sondes spécifiques pour les  $\beta$ -galactosidase et conjuguées à un diazéniumdiolate qui libère de l'oxyde nitrique. On a aussi préparé un dérivé glycosylé, **2e**, qui devrait pouvoir pénétrer à l'intérieur des membranes des cellules. On rapporte, en détail, la synthèse et la caractérisation de ces sondes. De plus, on utilise le fait que l'hydrolyse catalysée par le  $\beta$ -galoactosidase libère le diazéniumdiolate des sondes pour évaluer leur efficacité comme donneurs spécifiques de NO, stables dans le sérum.

**Mots-clés :** oxyde nitrique, diazéniumdiolate, glycosylé, galactosidase.

## Introduction

With the numerous biological roles of nitric oxide (NO), there is now great interest in developing NO-releasing compounds capable of providing required quantities of NO to specific biological tissues without disturbing other NO-sensitive physiology.<sup>1–19</sup> Because of their NO-releasing ability, diazeniumdiolates have become especially attractive for their potential use in novel drug therapies.<sup>13,20–22</sup> However, to design site-specific diazeniumdiolates, careful functionalization of these compounds is required. This strategy has been successfully achieved by derivatizing the terminal oxygen (O<sup>2</sup>) of the diazeniumdiolate functionality.<sup>6</sup> To date, several O<sup>2</sup>-protected diazeniumdiolates that only release NO in targeted biological tissues have been prepared, Scheme 1.<sup>3,6,19,23–29</sup> For example, Keefer and co-workers have reported O<sup>2</sup>-vinyl diazeniumdiolates and their ability for liver-selectivity and activation by hepatic cytochrome P450.<sup>6</sup> They have also shown that O<sup>2</sup>-acetoxymethyl diazeniumdiolates were esterase-sensitive and exhibited considerable anti-leukemia activity.<sup>30</sup> A number of peptide-diazeniumdiolate conjugates were recently prepared by

Tang and Wang and found to be activated by  $\alpha$ -chymotrypsin or prostate-specific antigens.<sup>31</sup>

Related efforts have led to the development of glycosylated derivatives of diazeniumdiolates, Scheme 2.<sup>19,32–34</sup> Such compounds constitute a novel series of tissue-specific diazeniumdiolates. For example, a library of pyranosyl derivatives of diazeniumdiolates was recently prepared by Valdez et al.,<sup>19</sup> and these derivatives have the ability to pharmacologically target NO to pathogen-infected macrophages.

These recent examples of glycosylated diazeniumdiolate derivatives were not the first to be synthesized. Almost 25 years ago, Vasella and co-workers reported two sugar derivatives containing the diazeniumdiolate functionality and prepared them by a route involving oxidation of sugar oximes or sugar hydroxylamines<sup>35</sup> (see Scheme 3).

Analogous with the initial Valdez or Tang and Wang carbohydrate-substituted diazeniumdiolates, Vasella and co-workers' compounds are O<sup>2</sup>-substituted diazeniumdiolates. Unlike the recent N-bound diazeniumdiolates, those two products are C-bound diazeniumdiolates. Jochims and co-workers have recently prepared a number of C-bound glycosylated diazeniumdiolates, Scheme 4, via nitrosation of

Received 17 February 2010. Accepted 2 June 2010. Published on the NRC Research Press Web site at canjchem.nrc.ca on 23 August 2010.

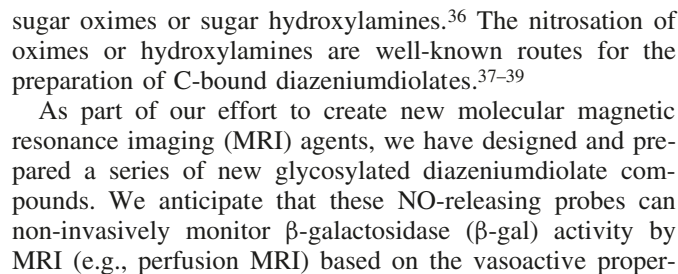
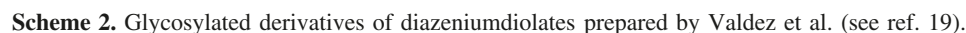
**B.J. Bedell and A.C. Evans.** McConnell Brain Imaging Centre, Montreal Neurological Institute, McGill University, Montreal, QC H3A 3B4, Canada.

**D.S. Bohle,<sup>1</sup> Z. Chua, and A. Czerniewski.** Department of Chemistry, McGill University, 801 Sherbrooke St. W, Montreal, QC H3A 2K6, Canada.

**S. Mzengeza.** The Great-West Life PET Imaging Centre, University of Manitoba, 715-751 McDermot Avenue, Winnipeg, R3E 3P4, Canada.

<sup>1</sup>Corresponding author (e-mail: scott.bohle@mcgill.ca).

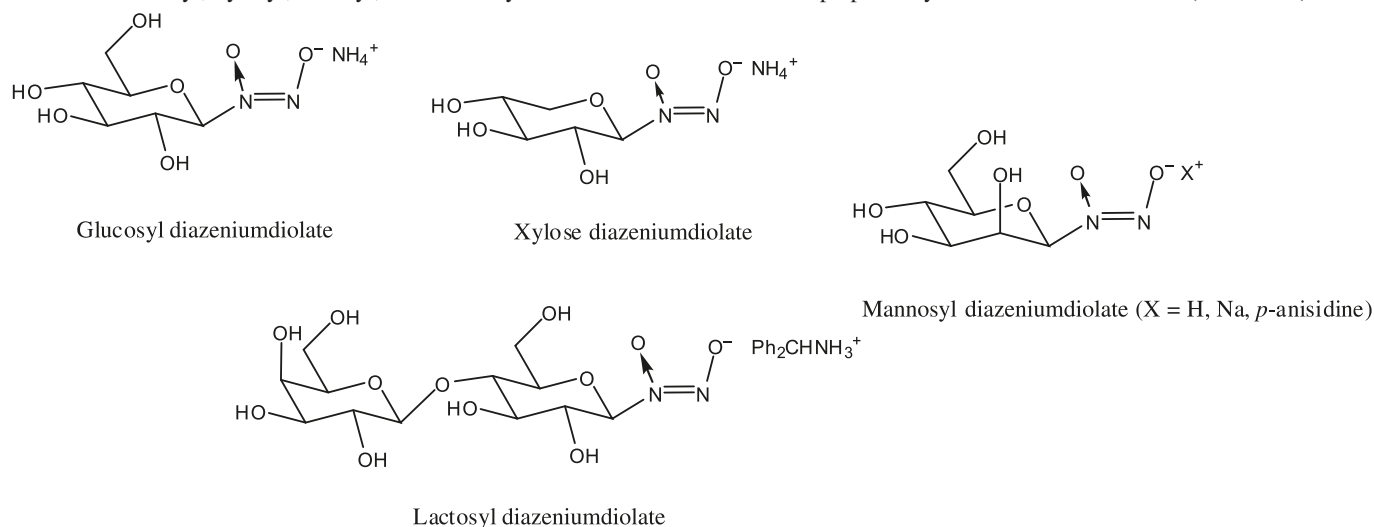
sugar oximes or sugar hydroxylamines.<sup>36</sup> The nitrosation of oximes or hydroxylamines are well-known routes for the preparation of C-bound diazeniumdiolates.<sup>37–39</sup>



ties of NO. As proof-of-principle, our monosaccharide-diazoniumdiolate derivatives are designed to target cells expressing a high level of  $\beta$ -gal, since the lacZ gene is commonly used as a reporter of gene expression. Specificity is proposed to arise from the coupling of a  $\beta$ -gal active component, namely a galactose molecule, with an amine-bound diazoniumdiolate salt via the glycosidic bond of the sugar.

In addition, we further explored the idea of tissue-specific glycosylated diazeniumdiolates by designing a diazeniumdio-



**Scheme 4.** Glucosyl, xylosyl, lactosyl, and mannosyl diazeniumdiolate derivatives prepared by Jochims and co-workers (see ref. 36).

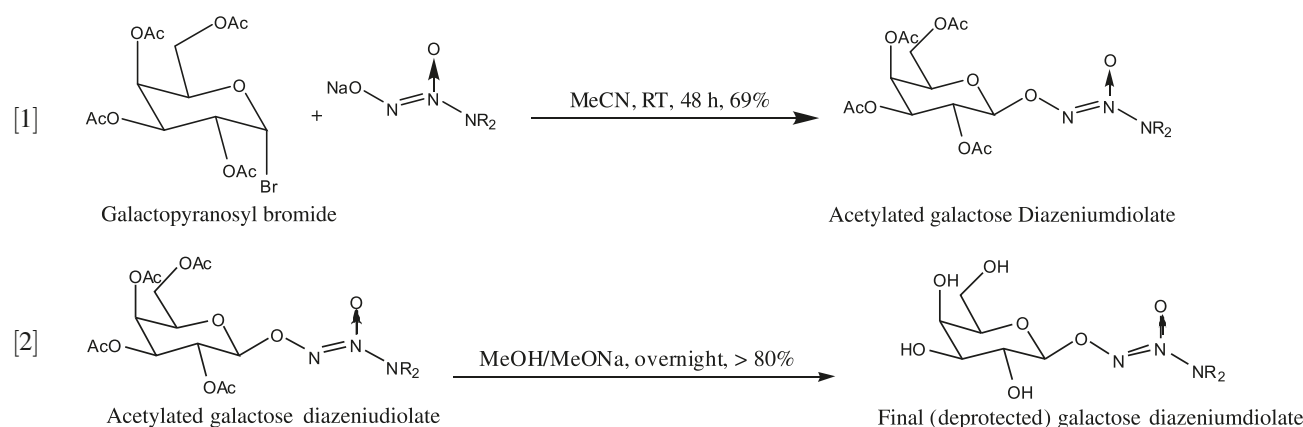
late glycoside derivative capable of crossing cell membranes. Our strategy was accomplished by appending the galactose-diazeniumdiolate derivative to another moiety that traffics the glycoside across plasma membranes (Scheme 5).<sup>40–43</sup> The ester conjugates of glucose, substituted at the pyranose C6-position, have high affinities for glucose transporters, such as GLUT-1.<sup>7</sup> Thus, a “bifunctional” NO-releasing probe was prepared with glucose coupled via its C-6 linkage, for trafficking via a GLUT-1 transporter, and galactose coupled via a glycosidic bond to a diazeniumdiolate core, for the probe’s  $\beta$ -gal activation, Scheme 6.

We thus prepared “bifunctional” NO-releasing probes de-

signed to be potentially activated by  $\beta$ -gal-expressing cells. Herein, the preparation and characterization of these new probes are described in detail.

## Results

The synthetic scheme employed to design our probes is based on a halide-displacement reaction.<sup>19,32,34,44</sup> The diazeniumdiolate sodium salt was coupled with an acetylated pyranosyl bromide, eq. [1]. Base-catalyzed hydrolysis of the acetyl protecting groups then afforded the deprotected glycosylated diazeniumdiolate, eq. [2].

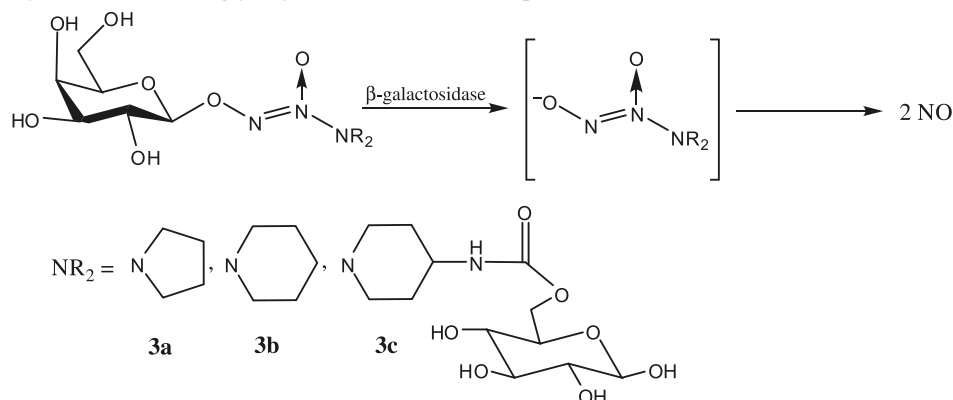
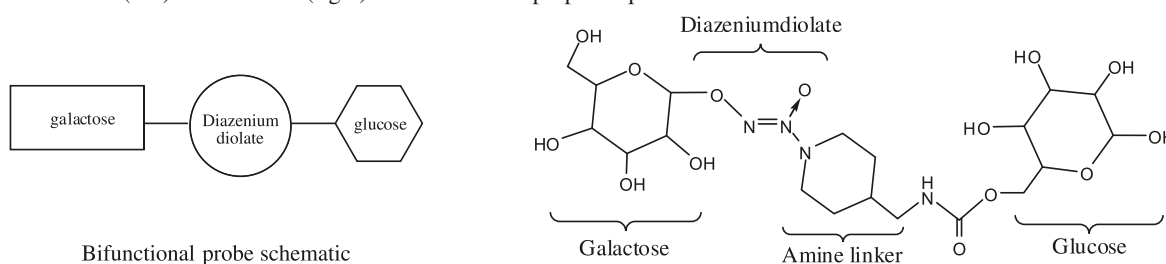


The presence of acetyl protecting groups on all of the pyranose C-2 to C-6 hydroxyl functionalities ensure that it is the diazeniumdiolate oxygen, and not the hydroxyl groups, which adds to the pyranose anomeric position. The acetyl protecting groups also aid in the purification and isolation of the glycosylated probe.

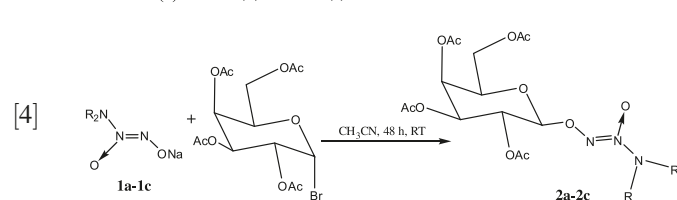
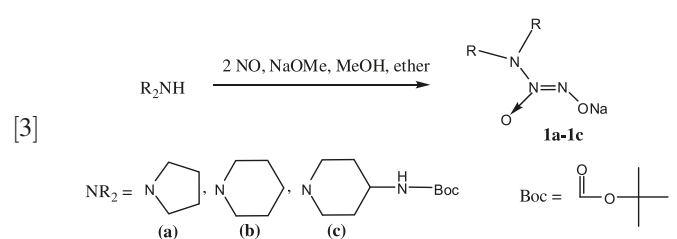
The “bifunctional” probes are comprised of three integral components as shown in Scheme 6. These three components

include (i) a glucose moiety, coupled via its C-6 linkage and (ii) a galactose entity, coupled via a glycosidic bond to (iii) a piperidine-bound diazeniumdiolate core. Synthesis of the bifunctional probes involved the use of a *tert*-butyloxycarbonyl (Boc)-protected secondary amine, representing the precursor of the secondary amine linker.

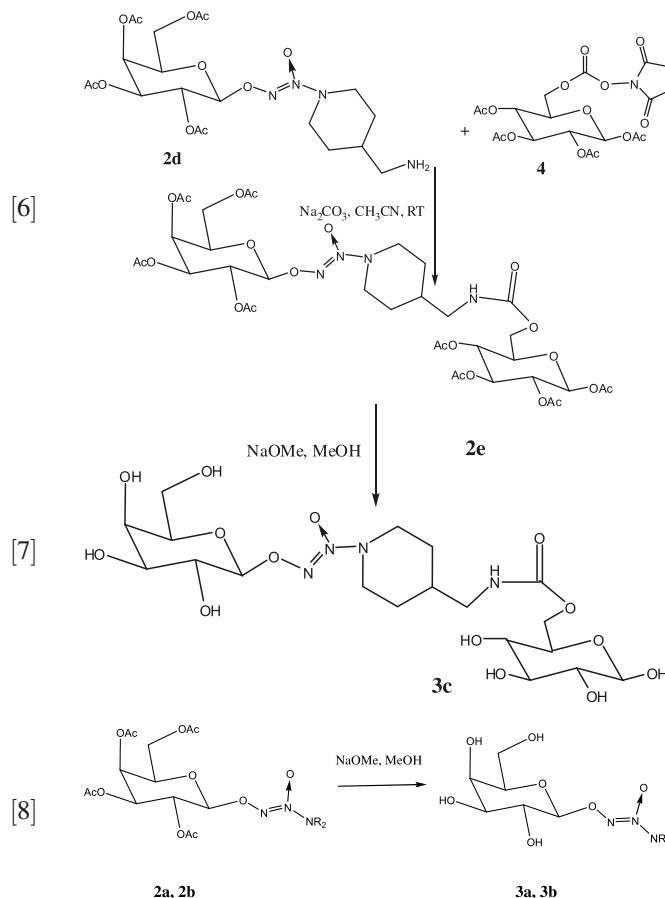
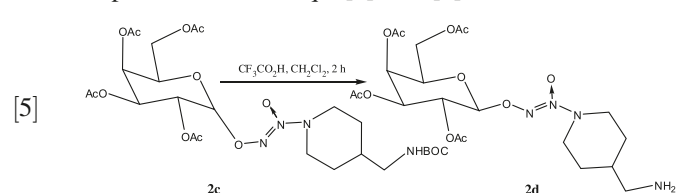
The diazeniumdiolate **1c** was prepared from the Boc-protected secondary amine, eq. [3], with typical conditions for

**Scheme 5.**  $\beta$ -gal hydrolysis of constructed glycosylated diazeniumdiolate probes.**Scheme 6.** Schematic (left) and detailed (right) structure of the proposed probes construction.

generating secondary-amine-bound diazeniumdiolates.<sup>45,46</sup> The diazeniumdiolates were then coupled with galactosyl bromide, eq. [4], to give the O<sup>2</sup>-protected adducts **2a–2c** in good yields. The presence of a Boc protecting group in **1c** prevented any competitive coupling to galactosyl bromide by the protected primary amine.

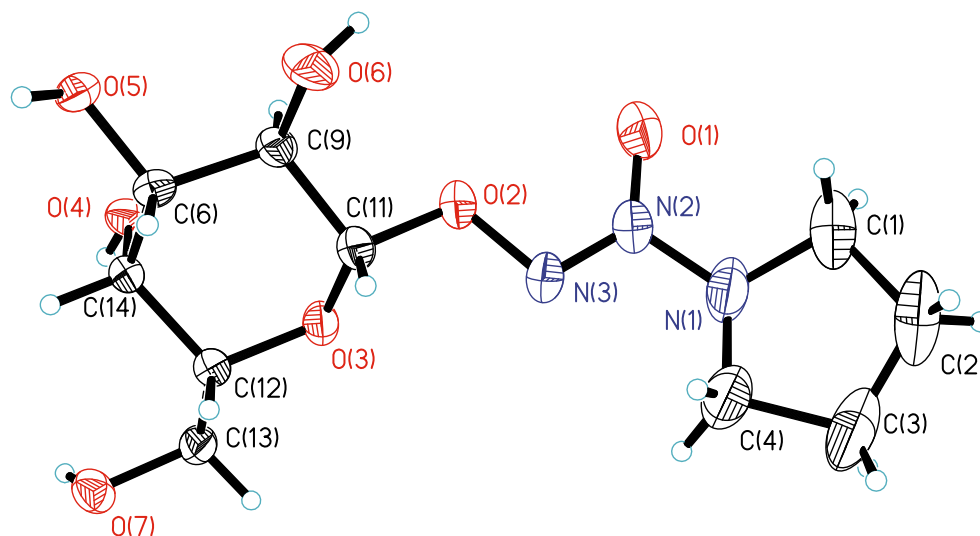


Removal of the Boc protecting group was then readily effected under acidic conditions,<sup>47,48</sup> eq. [5], and lead to the generation of the free primary amine in **2d**, which was then coupled with an activated glucose ester to give **2e**, eq. [6]. Removal of all protecting groups using NaOMe generated the final products **3a–3c**, eqs. [7] and [8].



To verify the final product stereochemistry and linkage, a single-crystal X-ray diffraction structure for **3a** was determined, Fig. 1. Crystals for this adduct adopt the monoclinic

**Fig. 1.** X-ray crystal structure of **3a**. Important metric parameters (bond lengths, Å) and (angles, °): N(2)—N(1) 1.384(3), N(2)—N(3) 1.265(3), N(2)—O(1) 1.246(3), N(3)—O(2) 1.395(3), N(1)—C(4) 1.475(4), N(1)—C(1) 1.469(5), O(2)—N(3)—N(2) 106.7(2), O(1)—N(2)—N(3) 127.0(2), O(1)—N(2)—N(1) 117.3(2), N(3)—N(2)—N(1) 115.4(2). Hydrogen atoms are omitted for clarity.



non-centrosymmetric space group  $P2_1$  with  $Z = 2$ . Complete details of the structure and refinement are provided in the Experimental and Supplementary data sections.

### Enzymatic hydrolysis by $\beta$ -galactosidase of compounds **3a–3c**

Glycosylation of the diazeniumdiolate oxygen protects the diazeniumdiolate from its rapid reversion to two nitric oxides and the secondary amine, that is, the reverse of eq. [3] at neutral pH. The strong  $n-\pi^*$  transition at  $\sim 260$  nm in diazeniumdiolates allows for the facile monitoring of its hydrolytic breakdown. Since the half-life of the deprotected diazeniumdiolate under these conditions is less than 2 s, the loss of extinction at 256 nm corresponds to the limiting slow enzymatic cleavage of the C–O bond by galactosidase. As shown in the Supplementary data in that buffer and ion concentration, the half-life for **3a** at pH = 7.3, 37 °C, and  $[\beta\text{-gal}] = 8$  nmol/L, is less than 120 s, which corresponds to at least a five orders of magnitude enhancement in the decomposition of these compounds over background degradation. Similar results are observed for **3b** and **3c** and for related glycosylated diazeniumdiolates.<sup>32</sup> Under physiological levels of cation concentration, these  $\beta$ -gal-promoted hydrolysis rates are likely to be faster and thus these half-lives and the resulting enhancement described earlier in the text is likely to be an underestimate of their activity in vivo.

### Discussion

Diazeniumdiolate glycosylation not only confers probe specificity, but it is also a useful protecting-group strategy. In general, diazeniumdiolate anions are susceptible to acid-promoted thermal and photolytic decomposition with their  $O^2$ -alkyl and coordinated complexes being much more stable under all of these conditions.<sup>28,49</sup> For example, **3a** in phosphate buffer solution (PBS, 0.1 mol/L, pH 7.4) at 37 °C has a half-life of several days ( $>10$  days), whereas the corresponding pyrrolidine diazeniumdiolate **1a**, under the same conditions, has a half-life of 1.8–2.8 s.<sup>28</sup> Compound **3a** can

be stored as a solid at  $-20$  °C with a minimum shelf-life of six months and can remain in PBS at room temperature for at least 10 days. Consequently, glycosylation of diazeniumdiolate ions not only offers a convenient route to deliver NO tissue-specifically, but it has the added advantage of significantly increasing the stability of the diazeniumdiolate in a physiological milieu.

Moreover, the probe's durability in physiological media may be enhanced by increasing the half-life of the diazeniumdiolate itself. This half-life depends on the nature of the substituent directly attached to the first nitrogen atom of the diazeniumdiolate functionality (i.e.,  $-\text{N}(\text{O})=\text{NO}^-$ ). For example, the piperidine diazeniumdiolate, **1b**, has a half-life of  $\sim 11$  s in phosphate buffer solution (PBS, 0.1 mol/L, pH 7.4) at 37 °C, thus nearly an order of magnitude greater than the pyrrolidine substituent in **1a** with its half-life of ( $\sim 1.8$  s) under the same conditions. However, to ensure an instantaneous release of NO by the probes upon enzymatic hydrolysis, a diazeniumdiolate salt with a half-life that is not significantly longer either must be selected. Since the rate of  $\beta$ -galactosidase hydrolysis of the glycosylated diazeniumdiolate derivatives was monitored via the degradation of their corresponding diazeniumdiolate salts (generated upon enzyme hydrolysis) using UV spectroscopy, selecting a very slow NO-releasing diazeniumdiolate for the probe construction has the disadvantage of masking the kinetic parameters associated with enzyme hydrolysis. Furthermore, extensive structural modification of the diazeniumdiolate component in a given probe may lead to lowered rates of the probe's enzyme hydrolysis, and thus complicate the probe's NO release upon activation due to poorer enzyme recognition of the modified substrate. What was thus sought in the probe's design was a balance between the probe durability under physiological conditions and instantaneous NO release upon the probe's activation.

Overall, three glycosylated diazeniumdiolate probes (**3a–3c**) and their intermediates were generated. Their preparation employed a halide displacement reaction between an acetylated glycoside halide (gal–Br) and a diazeniumdiolate salt.

NMR spectroscopy confirmed that a single  $\beta$ -anomer was produced as has been found in related coupling products.<sup>32</sup> The coupling reactions usually took 2–3 days to proceed to completion. The slow pace of the reaction could be, at least partially, explained by the fact that the sodium diazeniumdiolate salts dissolve very slowly in MeCN. Yields for the coupling reactions averaged  $\sim 60\%$  after chromatographic purification. A slight excess of diazeniumdiolate salt was used during these reactions to maximize the yields. An optimal ratio consisted of 5.8 equiv. diazeniumdiolate salt for every 5.5 equiv. of gal-Br. Exceeding this ratio did not significantly affect the reaction rate or yield. The use of rigorously dry conditions, that is doubly distilled acetonitrile stored in an inert-atmosphere box, led to reproducible and higher yields. The coupling reactions were undertaken in the glovebox as well. Despite these measures, TLC comparisons using solutions of degraded diazeniumdiolate salts in wet MeCN, along with  $^1\text{H}$  NMR evaluations of the reaction mixtures, showed that the most important impurities that appeared during the reaction were mainly nitrosamines generated by diazeniumdiolate salt degradation. These degradation products made up roughly about 20%–30% (by weight) of the reaction material. Some unidentified sugar impurities during these coupling reactions were also detected by NMR, but they were not further examined. As described in the Supplementary data, chromatographic purification is critical to obtain pure final products.

## Conclusion

The three  $\beta$ -galactosidase-specific probes described here release NO upon  $\beta$ -gal hydrolysis. Glycosylation of the diazeniumdiolate core leads to both probe stability and specificity. These novel probes are currently being evaluated for their potential to detect  $\beta$ -gal in vivo using MRI.

## Experimental

General methods and materials used in these preparations and for the characterization of new compounds are described in recent papers.<sup>50</sup> Where required, the probes were characterized by  $^1\text{H}$  NMR in 0.01 mol/L NaOD in  $\text{D}_2\text{O}$ .

### Sodium 1-(pyrrolidin-1-yl)diazene-1-ium-1,2-diolate (1a)

This salt was prepared by the method of Saavedra<sup>6</sup> et al. in 61% yield and has the following characteristic data: UV (10 mmol/L NaOH, RT)  $\lambda_{\text{max}}$  ( $\epsilon$ ): 252 nm (7.4 mmol/L $^{-1}$  cm $^{-1}$ ). UV<sub>kinetics</sub> (in 75% excess PBS (0.1 mol/L, pH 7.36)) half-lives: 3.20 s and 1.82 s at RT and 37 °C, respectively. FTIR  $\nu$  (cm $^{-1}$ ): 3455 (br), 3378 (br), 2970 (m), 2880 (m), 1664 (w), 1608 (m), 1463 (w), 1393 (m), 1359 (m), 1266 (m), 1226 (s), 1184 (s), 984 (m), 972 (m), 905 (m).  $^1\text{H}$  NMR (270 MHz,  $\text{D}_2\text{O}/\text{NaOD}$ )  $\delta$ : 3.21 (m, 4H,  $J = 5.9$  Hz), 1.90 (m, 4H,  $J = 5.3$  Hz).  $^{13}\text{C}$  NMR (67.5 MHz,  $\text{D}_2\text{O}/\text{NaOD}$ )  $\delta$ : 51.38 (2C, C-1 and C-4), 22.40 (2C, C-2 and C-3). DSC onset temperature at 169.5 °C, decomposition temperature at 176.7 °C,  $\Delta H = +151.1$  kJ mol $^{-1}$ . MS (MALDI-TOF)  $m/z$ : 153.1 [M] $^{+}$ .

### Sodium 1-(piperidin-1-yl)diazene-1-ium-1,2-diolate (1b)

A solution of piperidine (5.00 g, 58.0 mmols) in acetonitrile (20 mL), ether (20 mL), and 25% sodium methoxide in methanol (11.9 mL, 1 equiv.) was prepared. A white powder

was ultimately obtained (8.3 g; 85% yield). UV (10 mmol/L NaOH, RT)  $\lambda_{\text{max}}$  ( $\epsilon$ ): 250 nm (8.8 mmol/L $^{-1}$  cm $^{-1}$ ). UV<sub>kinetics</sub> (in 75% excess PBS (0.1 mol/L, pH 7.36)) half-lives: 26 s and 11 s at RT and 37 °C, respectively. FTIR  $\nu$  (cm $^{-1}$ ): 3450 (br), 3364 (br), 2969 (m), 2964 (m), 2951 (m), 2942 (s), 2926 (m), 2233 (br, w), 2170 (w), 1676 (m), 1654 (m), 1538 (w), 1473 (m), 1453 (m), 1442 (m), 1435 (m), 1381 (m), 1356 (s), 1291 (m), 1270 (m), 1216 and 1183 (s), 1137 (m), 1096 (m), 1064 (m), 1031 (m), 944 (s), 913 (m), 884 (m), 863 (w), 828 (m), 726 (s).  $^1\text{H}$  NMR (400 MHz,  $\text{D}_2\text{O}/\text{NaOD}$ )  $\delta$ : 2.70 (t, 4H,  $J = 5.6$  Hz), 1.38 (t, 4H,  $J = 5.6$  Hz), 1.12 (t, 2H,  $J = 5.6$  Hz).  $^{13}\text{C}$  NMR (75 MHz,  $\text{D}_2\text{O}/\text{NaOD}$ )  $\delta$ : 52.77 (C-1 and C-5), 24.34 (C-2 and C-4), 22.11 (C-3). DSC onset temperature at 195.9 °C, decomposition temperature at 197.4 °C,  $\Delta H = +46.1$  kJ mol $^{-1}$ . MS (EI)  $m/z$ : 167.1 [M] $^{+}$ , 114 [M – NO] $^{+}$ , 84 [M – 2NO] $^{+}$ , 56 [M – 2NO – 2CH $_2$ ] $^{+}$ , 42 [M – 2NO – 3CH $_2$ ] $^{+}$ . MS (MALDI-TOF)  $m/z$ : 168.5 [M + H] $^{+}$ . The key characteristic data concur with those briefly reported elsewhere.<sup>45</sup>

### Sodium 1-(4-Boc-4-aminomethylpiperidin-1-yl)diazene-1-ium-1,2-diolate (1c)

A solution of Boc-protected 4-aminomethylpiperidine (2.50 g, 11.7 mmols) in methanol (2.00 mL) and ether (40 mL) and 25% sodium methoxide in methanol (8.00 mL, 39.1 mmol) was prepared. A white powder was ultimately derived (2.97 g; 97% yield). Alternatively, the same reaction conditions were undertaken, but this time without ether and stirred at room temperature for 2–3 days. During this time period, the flask was periodically recharged with NO gas (up to 60 psi) until no significant gas consumption was noted over the course of several hours. No precipitate appeared during this time period, but upon pressure release and removal of solvent in vacuo, a yellowish oil was isolated. The product was obtained by performing a trituration on this yellow oil by dissolving it initially in hot ethanol and allowing the product to precipitate as a snow-white powder with the ensuing addition of excess cold hexane or ether. This powder was collected by filtration, rinsed with ether, and dried in a vacuum at room temperature (58% yield). UV (10 mmol/L NaOH, RT)  $\lambda_{\text{max}}$  ( $\epsilon$ ): 250 nm (7.8 mmol/L $^{-1}$  cm $^{-1}$ ), 326 nm (2.88 mmol/L $^{-1}$  cm $^{-1}$ ). UV<sub>kinetics</sub> (in 75% excess PBS (0.1 mol/L, pH 7.36)) half-lives: 33 s and 24 s at RT and 37 °C, respectively. FTIR  $\nu$  (cm $^{-1}$ ): 3359 (s), 2978 (m), 2967 (m), 2951 (m), 2931 (m), 2858 (m), 2254 (m), 1686 (s), 1527 (s), 1473 (m), 1446 (m), 1386 (m), 1364 (s), 1268 (s), 1247 (s), 1177 (s), 1140 (m), 1088 (w), 1043 (w), 1014 (w), 996 (w), 964 (s), 955 (w), 916 (w), 880 (w), 868 (w), 779 (w), 623 (w), 583 (w).  $^1\text{H}$  NMR (400 MHz,  $\text{CD}_3\text{OD}-\text{NaOH}$  (0.1 mol/L))  $\delta$ : 3.20 (d, 2H,  $J = 10.8$  Hz, H-1 and H-5), 3.00 (m, 3H, H-1', H-5' and H-3), 1.81 (m, 2H, H-2 and H-4), 1.50 (m, 2H, partly overlapped by *t*-butyl peak, methylene Hs), 1.43 (s, 9H, *t*-butyl H), 1.40 (m, 2H, partly overlapped by *t*-butyl peak, H-2' and H-4').  $^{13}\text{C}$  NMR (75 MHz,  $\text{CD}_3\text{OD}-\text{NaOH}$  (0.1 mol/L))  $\delta$ : 157.46 (Boc's C=O), 78.65 (Boc's tertiary carbon), 52.24 (piperidine's C-1 and C-5), 45.25 (4-amino methylene carbon), 35.77 (piperidine's C-3), 28.95 (piperidine's C-2 and C-4), 27.67 (Boc's methyl carbons). DSC onset temperature at 172.3 °C, decomposition temperature at 173.3 °C,  $\Delta H = +50.4$  kJ mol $^{-1}$ . MS (ESI, + c)  $m/z$ : 318.9 [M + H] $^{+}$ ,



266.0 [M – Na – NO + H]<sup>+</sup>, 237.1 [M – Na – 2NO + 2H]<sup>+</sup>. MS (ESI, – c) *m/z*: 295.0 [M – Na]<sup>–</sup>, 235.2 [M – Na – 2NO]<sup>–</sup>. MS/MS (ESI) *m/z*: 318.9 [M + H]<sup>+</sup>, 289 [M – NO + H]<sup>+</sup>. MS (MALDI-TOF): *m/z*: 318.0 [M]<sup>+</sup>. HR-MS (ESI) calcd. for Na<sub>2</sub>C<sub>11</sub>H<sub>21</sub>N<sub>4</sub>O<sub>4</sub> [M + H]<sup>+</sup>: 319.1358. Found: 319.1351. Anal. calcd. for Na<sub>2</sub>C<sub>11</sub>H<sub>20</sub>N<sub>4</sub>O<sub>4</sub>: C, 41.51; H, 6.33; N, 17.60. Found: C, 41.27; H, 6.57; N, 17.68.

### General procedure for the synthesis of O<sup>2</sup>-glycosylated diazeniumdiolates

To a solution of 2,3,4,6-tetra-*O*-acetyl- $\alpha$ -D-galactopyranosyl bromide (5.5 equiv.) in anhydrous acetonitrile (20 mL), the desired solid diazeniumdiolate salt (5.8 equiv.) was added and stirred until all the galactopyranosyl bromide had reacted (2–3 days) as monitored by TLC (ethyl acetate:hexane, 2:3). Upon filtration, the solvent was removed under vacuum and the product was dissolved in ethyl acetate (25.0 mL). The organic layer was washed with distilled water (3  $\times$  15 mL/wash), dried over Na<sub>2</sub>SO<sub>4</sub> (2 g), filtered, and its solvent removed under vacuum. The isolated material was purified by column chromatography (silica gel, ethyl acetate:hexane, 1:3) to yield a clear colorless oil. To generate the deacetylated version of the O<sup>2</sup>-glycosylated diazeniumdiolate, a few drops of sodium methoxide (25% in methanol) were added to a solution of the protected/acetylated glycosylated diazeniumdiolate in anhydrous methanol (20.0 mL), and the solution was stirred at RT overnight. TLC (methanol:ethyl acetate, 3:7) showed the presence of a new product. The deacetylated product is precipitated in (~97%) by allowing its solution in ethanol, which was diluted with ether, to stand in an ice bath overnight. An alternative synthetic procedure to prepare the deacetylated product involved bypassing the column chromatography step during the synthesis of acetylated glycosylated diazeniumdiolate and carrying out the deprotection step right after the workup of the acetylated glycosylated diazeniumdiolate synthesis. A solid hygroscopic white product was generated (~65% overall). Spectroscopic results were identical whichever methodology was employed.

### O<sup>2</sup>-(2,3,4,6-tetra-*O*-acetyl- $\beta$ -D-galactopyranosyl) 1-(pyrrolidin-1-yl)diazen-1-ium-1,2-diolate (2a)

To a solution of 2,3,4,6-tetra-*O*-acetyl- $\alpha$ -D-galactopyranosyl bromide (400 mg, 0.976 mmol, 5.5 equiv.) in anhydrous acetonitrile (20.0 mL), **1a** (158 mg, 1.03 mmol, 5.8 equiv.) was added and stirred until all the galactopyranosyl bromide had reacted (2–3 days, as determined by TLC on silica ethyl acetate:hexane, 2:3, *R*<sub>f</sub> = 0.24). A clear colorless oil (280 mg, 0.607 mmol, 62% yield) was obtained after purification by column chromatography (silica gel, ethyl acetate:hexane, 1:3). UV (MeOH, RT)  $\lambda_{\text{max}}$  ( $\epsilon$ ): 251 nm (2.05 mmol/L<sup>–1</sup> cm<sup>–1</sup>). FTIR  $\nu$  (cm<sup>–1</sup>): 3475 (mbr), 2981 (m), 2886 (w), 1751 (s), 1652 (w), 1489 (w), 1436 (w), 1373 (s), 1233 (sbr), 1156 (w), 1127 (w), 1079 (s), 1059 (s), 989 (w), 956 (w), 917 (w), 902 (w), 883 (w), 851 (w), 823 (w), 777 (w), 713 (w), 676 (w), 655 (w), 627 (w), 601 (w), 557 (w), 525 (w), 493 (w), 461 (w), 432 (w), 415 (w). <sup>1</sup>H NMR (400 MHz, CD<sub>3</sub>OD)  $\delta$ : 5.40 (m, 3H, overlapped, H-1, H-2, and H-4), 5.22 (dd, 1H, *J* = 9.8, 3.4 Hz, H-3), 4.15 (m, 3H, overlapped, H-5, H-6, and H-7), 3.57 (t, 4H, *J* = 6.6 Hz, H-1' and H-4'), 2.13 (s, 3H, CH<sub>3</sub>), 2.06 (s, 3H, CH<sub>3</sub>),

2.03 (s, 3H, CH<sub>3</sub>), 1.96 (s, 3H, overlapped, CH<sub>3</sub>), 1.97 (m, 4H, overlapped, H-2' and H-3'). <sup>13</sup>C NMR (75 MHz, CD<sub>3</sub>OD)  $\delta$ : 170.53 (C=O), 170.39 (C=O), 170.23 (C=O), 169.83 (C=O), 100.76 (C-1), 71.34 (C-5), 71.27 (C-3), 67.43 (C-2), 67.25 (C-4), 61.36 (C-6), 50.64 (C-1' and C-4'), 22.76 (C-2' and C-3'), 19.52, 19.51, 19.44, 19.40 (acetyl CH<sub>3</sub>). MS (ESI) *m/z*: 484.1 [M + Na]<sup>+</sup>. MS/MS (ESI) *m/z*: 484.0 [M + Na]<sup>+</sup>, 371.0 [M + Na – pyrrolidine (NC<sub>4</sub>H<sub>8</sub>) – acetyl (C(=O)CH<sub>3</sub>)]<sup>+</sup>, 311.0 [M + Na – pyrrolidine (NC<sub>4</sub>H<sub>8</sub>) – 2NO – acetyl (C(=O)CH<sub>3</sub>)]<sup>+</sup>. MS/MS (ESI) *m/z*: 479.0 [M + NH<sub>4</sub>]<sup>+</sup>, 331.1 [M – pyrrolidine diazeniumdiolate (C<sub>4</sub>H<sub>8</sub>N–NONO)]<sup>+</sup>. HR-MS (ESI) calcd. for C<sub>18</sub>H<sub>31</sub>N<sub>4</sub>O<sub>11</sub> [M + NH<sub>4</sub>]<sup>+</sup>: 479.1989. Found: 479.1979. HR-MS (ESI) calcd. for NaC<sub>18</sub>H<sub>27</sub>N<sub>3</sub>O<sub>11</sub> [M + Na]<sup>+</sup>: 484.1543. Found: 484.1535. DSC onset temperature at 154.2 °C, decomposition temperature at 175.5 °C,  $\Delta H$  = +53.0 kJ mol<sup>–1</sup>. Anal. calcd. for C<sub>18</sub>H<sub>27</sub>N<sub>3</sub>O<sub>11</sub>: C, 46.85; H, 5.90; N, 9.11. Found: 47.05; H, 5.76; N, 9.05.

### O<sup>2</sup>-(2,3,4,6-tetra-*O*-acetyl- $\beta$ -D-galactopyranosyl) 1-(piperidin-1-yl)diazen-1-ium-1,2-diolate (2b)

To a solution of 2,3,4,6-tetra-*O*-acetyl- $\alpha$ -D-galactopyranosyl bromide (400 mg, 0.976 mmol, 5.5 equiv.) in anhydrous acetonitrile (20 mL), PipNONO **1b** (180 mg, 1.08 mmol, 5.8 equiv.) was added and stirred until all the galactopyranosyl bromide had reacted (2–3 days, TLC monitored, ethyl acetate:hexane, 2:3, *R*<sub>f</sub> = 0.27). A clear colorless oil (282 mg, 0.593 mmol, 61% yield) was obtained after purification by column chromatography (silica gel, ethyl acetate:hexane, 1:3). UV (MeOH, RT)  $\lambda_{\text{max}}$  ( $\epsilon$ ) 227 nm (5.40 mmol/L<sup>–1</sup> cm<sup>–1</sup>). FTIR  $\nu$  (cm<sup>–1</sup>): 3480 (wbr), 2943 (m), 2860 (m), 1754 (s), 1508 (w), 1476 (w), 1447 (w), 1371 (m), 1228 (s), 1170 (w), 1129 (w), 1083 (m), 1062 (m), 1000 (w), 954 (w), 913 (w), 898 (w), 864 (w), 851 (w), 821 (w), 797 (w), 767 (w), 738 (w), 708 (w), 684 (w), 651 (w), 602 (w), 565 (w), 528 (w). <sup>1</sup>H NMR (400 MHz, CD<sub>3</sub>OD)  $\delta$ : 5.40 (m, 3H, overlapped, H-1, H-2, and H-4), 5.23 (dt, 1H, *J* = 7.2, 2.6 Hz, H-3), 4.18 (m, overlapped, 3H, H-5, H-6, and H-7), 3.43 (m, 4H, H-1' and H-5'), 2.15 (s, 3H, CH<sub>3</sub>), 2.03 (s, 3H, CH<sub>3</sub>), 2.02 (s, 3H, CH<sub>3</sub>), 1.95 (s, 3H, CH<sub>3</sub>), 1.74 (quint, 4H, *J* = 5.6, H-2' and H-4'), 1.55 (quint, 2H, *J* = 5.6, H-3'). <sup>13</sup>C NMR (75 MHz, CD<sub>3</sub>OD)  $\delta$ : 170.82 (C=O), 170.71 (C=O), 170.19 (C=O), 169.78 (C=O), 100.81 (C-1), 71.43 (C-5), 71.21 (C-3), 67.35 (C-2), 67.25 (C-4), 61.30 (C-6), 51.92 (C-1' and C-5'), 24.38 (C-3'), 23.25 (C-2' and C-4'), 19.45, 19.39, 19.31 (acetyl CH<sub>3</sub>). MS (ESI) *m/z*: 498.0 [M + Na]<sup>+</sup>. MS/MS (ESI) *m/z*: 498.0 [M + Na]<sup>+</sup>, 310.9 [M + Na – piperidine diazeniumdiolate (C<sub>5</sub>H<sub>10</sub>N–N(O)=NO) – acetyl (C(=O)CH<sub>3</sub>)]<sup>+</sup>, 294.9 [M + Na – piperidine diazeniumdiolate (C<sub>5</sub>H<sub>10</sub>N–N(O)=NO) – *O*-acetyl (O–C(=O)CH<sub>3</sub>)]<sup>+</sup>. HR-MS (ESI) calcd. for NaC<sub>19</sub>H<sub>29</sub>N<sub>3</sub>O<sub>11</sub> [M + Na]<sup>+</sup>: 498.1700. Found: 498.1688. HR-MS (ESI) calcd. for C<sub>19</sub>H<sub>33</sub>N<sub>4</sub>O<sub>11</sub> [M + NH<sub>4</sub>]<sup>+</sup>: 493.2146. Found: 493.2138. DSC onset temperature at 213.8 °C, decomposition temperature at 221.0 °C,  $\Delta H$  = + 103.9 kJ mol<sup>–1</sup>. Anal. calcd. for C<sub>19</sub>H<sub>29</sub>N<sub>3</sub>O<sub>11</sub>: C, 48.00; H, 6.15; N, 8.84. Found: C, 48.24; H, 6.31; N, 8.40.

### O<sup>2</sup>-(2,3,4,6-tetra-*O*-acetyl- $\beta$ -D-galactopyranosyl) 1-(4-Boc-4-aminomethylpiperidin-1-yl)diazen-1-ium-1,2-diolate (2c)

To a solution of 2,3,4,6-tetra-*O*-acetyl- $\alpha$ -D-galactopyranosyl bromide (400 mg, 0.976 mmol, 5.5 equiv.) in anhydrous

acetonitrile (20 mL), **1c** (330 mg, 1.04 mmol, 5.8 equiv.) was added and stirred until all the galactopyranosyl bromide had reacted (2–3 days, TLC monitored, ethyl acetate:hexane, 2:3,  $R_f$  = 0.13). A clear colorless oil (389 mg, 0.644 mmol, 66% yield) was isolated after purification by column chromatography (silica gel, ethyl acetate:hexane, 1:3). UV (MeOH, RT)  $\lambda_{\max}$  ( $\epsilon$ ): 229 nm (5.10 mmol/L<sup>-1</sup> cm<sup>-1</sup>). FTIR  $\nu$  (cm<sup>-1</sup>): 3411 (wbr), 2980 (w), 2930 (w), 2850 (w), 1752 (s), 1513 (w), 1458 (w), 1438 (w), 1370 (m), 1224 (sbr), 1171 (w), 1137 (w), 1081 (m), 1063 (m), 1010 (w), 950 (w), 914 (w), 902 (w), 868 (w), 840 (w), 780 (w), 766 (w), 750 (w), 721 (w), 603 (w), 496 (w), 410 (w). <sup>1</sup>H NMR (400 MHz, CD<sub>3</sub>OD)  $\delta$ : 5.40 (m, 3H, overlapped, H-1, H-2, and H-4), 5.23 (dt, 1H,  $J$  = 7.2, 2.6 Hz, H-3), 4.18 (m, 3H, overlapped, H-5, H-6, and H-7), 4.01 (m, 2H, H-1' and H-5'), 2.95 (m, 3H, overlapped, H-1', H-3', and H-5'), 2.15 (s, 3H, CH<sub>3</sub>), 2.03 (s, 3H, CH<sub>3</sub>), 2.02 (s, 3H, CH<sub>3</sub>), 1.96 (s, 3H, CH<sub>3</sub>), 1.82 (m, 2H, H-2' and H-4'), 1.60 (m, 2H, methylene Hs), 1.43 (s, 9H, *t*-butyl H), 1.38 (m, 2H, partly overlapped by *t*-butyl peak, H-2' and H-4'). <sup>13</sup>C NMR (75 MHz, CD<sub>3</sub>OD)  $\delta$ : 170.81 (C=O), 170.70 (C=O), 170.18 (C=O), 169.78 (C=O), 157.46 (Boc's C=O), 100.81 (C-1), 78.79 (Boc's tertiary carbon), 71.42 (C-5), 71.20 (C-3), 67.32 (C-2), 67.22 (C-4), 61.26 (C-6), 50.91, 50.74 (C1' and C-5'), 45.03 (4-aminomethyl carbon), 35.84 (C-3'), 28.11, 28.05 (C-2' and C-4'), 27.58 (Boc CH<sub>3</sub>), 19.38, 19.30 (acetyl CH<sub>3</sub>). MS (ESI)  $m/z$ : 627.2 [M + Na]<sup>+</sup>, 1230.7 [2M + Na]<sup>+</sup>. MS/MS (ESI)  $m/z$ : 627.3 [M + Na]<sup>+</sup>, 583.0 [M + Na - CO<sub>2</sub>]<sup>+</sup>, 567.5, 522.9, 441.5, 365.7, 217.9. HR-MS (ESI) calcd. for NaC<sub>25</sub>H<sub>40</sub>N<sub>4</sub>O<sub>13</sub> [M + Na]<sup>+</sup>: 627.2490. Found: 627.2474. DSC onset temperature at 192.6 °C, decomposition temperature at 220.2 °C,  $\Delta H$  = +62.0 kJ mol<sup>-1</sup>. Anal. calcd. for C<sub>25</sub>H<sub>40</sub>N<sub>4</sub>O<sub>13</sub>: C, 49.66; H, 6.67; N, 9.27. Found: C, 49.98; H, 6.54; N, 9.06.

#### O<sup>2</sup>-(2,3,4,6-tetra-*O*-acetyl- $\beta$ -D-galactopyranosyl) 1-(4-aminomethylpiperidin-1-yl)diazene-1-ium-1,2-diolate (**2d**)

A solution of compound **2c** (389 mg, 0.644 mmol, 1 equiv.) in distilled dichloromethane (DCM, 20.0 mL), and trifluoroacetic acid (TFA, 10.0 mL) was prepared initially at around 0 °C and then stirred under N<sub>2</sub> at RT for 2–3 h. NMR studies in deuterated DCM/TFA solutions demonstrated the complete absence of the Boc methyl peak after this time period with near 100% conversion. Prolonged exposure of this product under such acidic conditions, however, led to deterioration of the product. The acid was subsequently removed from solution via a vacuum line with successive dilutions using DCM (100 mL). The residue was dissolved with aqueous NaCO<sub>3</sub> (1.0 mol/L solution) and extracted thrice with DCM (30 mL/extraction). The combined extracts were dried over Na<sub>2</sub>SO<sub>4</sub> (2 g), filtered, and the solvent removed using a vacuum line to yield a sticky yellow oil (310 mg). The product turned out to be reactive with silica gel, and hence was not further purified by column chromatography. The yield for the ensuing intermediate of this product (see synthesis of protected (**2e**)) was 79% assuming the 310 mg isolated in this synthesis is essentially compound **2d**. On the other hand, during another trial of these syntheses, compound **2e** was isolated with an 81% yield relative to **2c**. This result suggests that the yield of compound **2d** obtained between these two synthetic steps is

very high. UV (MeOH, RT)  $\lambda_{\max}$  ( $\epsilon$ ): 230 nm (3.86 mmol/L<sup>-1</sup> cm<sup>-1</sup>). FTIR  $\nu$  (cm<sup>-1</sup>): 3431 (mbr), 2960 (w), 2926 (w), 2860 (w), 1752 (s), 1681 (s), 1508 (w), 1432 (w), 1384 (m), 1373 (m), 1232 (sbr), 1182 (m), 1134 (m), 1080 (m), 1062 (s), 992 (w), 955 (w), 915 (w), 837 (m), 801 (m), 780 (w), 723 (m), 601 (w), 519 (w), 495 (w), 462 (w), 409 (w). <sup>1</sup>H NMR (400 MHz, CD<sub>3</sub>OD)  $\delta$ : 5.40 (m, 3H, overlapped, H-1, H-2, and H-4), 5.23 (dt, 1H,  $J$  = 7.2, 2.6 Hz, H-3), 4.12 (m, 3H, overlapped, H-5, H-6, and H-7), 4.06 (m, 2H, H-1' and H-5'), 3.00 (dd, 2H,  $J$  = 22.4, 10 Hz, H-1' and H-5'), 2.88 (t, 1H,  $J$  = 6.8 Hz, H-3'), 2.15 (s, 3H, CH<sub>3</sub>), 2.03 (s, 3H, CH<sub>3</sub>), 2.02 (s, 3H, CH<sub>3</sub>), 1.95 (s, 3H, CH<sub>3</sub>), 1.90 (m, 2H, H-2' and H-4'), 1.81 (m, 2H, methylene Hs), 1.49 (m, 2H, H-2' and H-4'). <sup>13</sup>C NMR (75 MHz, CD<sub>3</sub>OD)  $\delta$ : 170.80 (C=O), 170.63 (C=O), 170.14 (C=O), 169.83 (C=O), 100.78 (C-1), 71.47 (C-5), 71.13 (C-3), 67.29 (C-2), 67.19 (C-4), 61.21 (C-6), 53.63 (DCM solvent), 50.36, 50.17 (C1' and C-5'), 43.86 (4-aminomethyl carbon), 33.61 (C-3'), 27.58, 27.48 (C-2' and C-4'), 19.37, 19.28 (acetyl CH<sub>3</sub>). MS (ESI)  $m/z$ : 527.1 [M + Na]<sup>+</sup>, 505.0 [M + H]<sup>+</sup>, 1008.8 [2M + H]<sup>+</sup>, 1030.7 [2M + Na]<sup>+</sup>. MS/MS (ESI)  $m/z$ : 505.0 [M + H]<sup>+</sup>, 390.8 [M - 4-aminomethylpiperidine (NC<sub>5</sub>H<sub>9</sub>-CH<sub>2</sub>NH<sub>2</sub>)]<sup>+</sup>. MS/MS (ESI)  $m/z$ : 527.0 [M + Na]<sup>+</sup>, 399.9 [M + Na - 4-aminomethylpiperidine (NC<sub>5</sub>H<sub>9</sub>-CH<sub>2</sub>NH<sub>2</sub>) - nitrogen]<sup>+</sup>, 371.0, 353.0, 341.1, 310.9, 295.0. HR-MS (ESI) calcd. for C<sub>20</sub>H<sub>33</sub>N<sub>4</sub>O<sub>11</sub> [M + H]<sup>+</sup>: 505.2146. Found: 505.2134. DSC onset temperature at 150.4 °C, decomposition temperature at 174.5 °C,  $\Delta H$  = +52.5 kJ mol<sup>-1</sup>.

#### O<sup>2</sup>-(2,3,4,6-tetra-*O*-acetyl- $\beta$ -D-galactopyranosyl) 1-(4-[1,2,3,4-tetra-*O*-acetyl- $\beta$ -D-glucopyranosyl]-4-aminomethylpiperidin-1-yl)diazene-1-ium-1,2-diolate (**2e**)

To a solution of **2d** (310 mg, 0.615 mmol, 1 equiv.) in anhydrous acetonitrile (20 mL), Na<sub>2</sub>CO<sub>3</sub> (80.0 mg, 0.755 mmol, 1.2 equiv.) was added followed by a solution of GluDSC (345 mg, 0.705 mmol, 1.15 equiv.) in anhydrous acetonitrile (10 mL). The solution was stirred under N<sub>2</sub> at RT overnight. The solution was passed through a fine frit filter, and the solvent was removed in vacuo. The residue was dissolved in dichloromethane (DCM, 10 mL). This organic layer was washed thrice with distilled water (15 mL/wash), dried over Na<sub>2</sub>SO<sub>4</sub> (2 g), filtered, and its solvent removed in vacuo. TLC demonstrated the appearance of a single new spot (ethyl acetate:hexane, 7:3, with  $R_f$  = 0.34). Interestingly, over time, two new spots appeared on the TLC plate above the initial new spot ( $R_f$  = 0.66, 0.76). NMR and MS studies however show that the TLC spot with  $R_f$  = 0.34 corresponds to the desired compound. The isolated material was purified by column chromatography (silica gel, ethyl acetate:hexane, 7:3) to yield a clear, colorless oil (427 mg, 0.486 mmol, 79%). UV (MeOH, RT)  $\lambda_{\max}$  ( $\epsilon$ ): 229 nm (4.33 mmol/L<sup>-1</sup> cm<sup>-1</sup>). FTIR  $\nu$  (cm<sup>-1</sup>): 3391 (wbr), 2942 (w), 2872 (w), 1756 (s), 1652 (w), 1520 (w), 1436 (w), 1371 (m), 1221 (sbr), 1153 (w), 1079 (m), 1039 (m), 952 (w), 912 (w), 902 (w), 847 (w), 775 (w), 743 (w), 702 (w), 647 (w), 601 (w), 558 (w), 496 (w), 410 (w). <sup>1</sup>H NMR (400 MHz, CD<sub>3</sub>OD)  $\delta$ : 5.82 (d, 1H,  $J$  = 8.4 Hz, glucopyranosyl H-1), 5.40 (m, 3H, overlapped, H-1, H-2, and H-4), 5.33 (t, 1H,  $J$  = 9.6 Hz, glucopyranosyl H-3), 5.23 (dt 1H,  $J$  = 6.8, 2.4 Hz, galactopyranosyl H-3), 5.06 (t, 1H,  $J$  = 9.8 Hz, dd overlapping, 1H,  $J$  = 29.2, 9.6 Hz, glucopyranosyl H-2

and H-4), 4.24 (m, 1H, galactopyranosyl H-7) 4.14 (m, 4H, overlap of glucopyranosyl H-5 and H-6 as well as galactopyranosyl H-5 and H-6), 4.03 (m, 3H, overlap of glucopyranosyl H-7 and piperidinyl H-1' and H-5''), 2.98 (m, 2H, overlap of piperidinyl H-1', H-5', and H-3'), 2.16 (s, 3H, CH<sub>3</sub>), 2.07 (s, 3H, CH<sub>3</sub>), 2.03 (s, 3H, CH<sub>3</sub>), 2.02 (s, 6H, CH<sub>3</sub>), 2.01 (s, 3H, CH<sub>3</sub>), 1.97 (s, 3H, CH<sub>3</sub>), 1.96 (s, 3H, CH<sub>3</sub>), 1.85 (m, 2H, piperidinyl H-2' and H-4'), 1.58 (m, 2H, piperidinyl methylene Hs), 1.36 (m, 2H, piperidinyl H-2'' and H-4''). <sup>13</sup>C NMR (75 MHz, CD<sub>3</sub>OD) δ: 170.87, 170.75, 170.39, 170.22, 170.02, 169.83, 169.26 (acetyl C=O), 157.46 (amide's C=O), 100.82 (C-1), 91.72 (C-1'), 73.05 (C-3''), 72.92 (C-5''), 71.46 (C-5), 71.21 (C-3), 70.50 (C-2''), 68.10 (C-4''), 67.37 (C-2), 67.25 (C-4), 61.93 (C-6''), 61.34 (C-6), 50.96, 50.76 (C1' and C-5'), 45.63, 45.50 (4-aminomethyl carbon), 35.60 (C-3'), 28.02, 27.97 (C-2' and C-4'), 19.47, 19.36, 19.32 (acetyl CH<sub>3</sub>). MS (ESI) *m/z*: 901.1 [M + Na]<sup>+</sup>. MS/MS (ESI) *m/z*: 901.0 [M + Na]<sup>+</sup>, 841.0 [M + Na - O-acetyl (O-C(=O)CH<sub>3</sub>) - H]<sup>+</sup>, 715.1, 540.0 [M + Na - acetylated pyranose (C<sub>14</sub>H<sub>19</sub>O<sub>9</sub>) - 2NO]<sup>+</sup>, 509.1, 449.0. HR-MS (ESI) calcd. for NaC<sub>35</sub>H<sub>50</sub>N<sub>4</sub>O<sub>22</sub> [M + Na]<sup>+</sup>: 901.2814. Found: 901.2788. DSC onset temperature at 164.9 °C, decomposition temperature at 188.7 °C, Δ*H* = +58.5 kJ mol<sup>-1</sup>. Anal. calcd. for C<sub>35</sub>H<sub>50</sub>N<sub>4</sub>O<sub>22</sub>: C, 47.84; H, 5.73; N, 6.38. Found: C, 47.94; H, 6.00; N, 6.19.

#### O<sup>2</sup>-β-D-galactopyranosyl 1-(pyrrolidin-1-yl)diazene-1-ium-1,2-diolate (3a)

A few drops of NaOMe (25% in methanol) were added to a solution of **2a** (163 mg, 0.353 mmol) in anhydrous methanol (20.0 mL), and the mixture was stirred at RT overnight. TLC (methanol:ethyl acetate, 3:7, *R<sub>f</sub>* = 0.32) showed presence of a new product, which was isolated as a white powder (77.7 mg, 0.265 mmol, 75%) after purification by column chromatography (silica gel, methanol:ethyl acetate, 1:4). The product was also obtained in better yield (97%) by allowing it to precipitate in solution. NMR studies confirmed that the material obtained in this manner is identical to the product obtained after chromatography. Alternatively, bypassing the column chromatography step during the synthesis of **2a** and carrying out the deprotection step right after the **2a** workup generated an overall yield of 67%. Spectroscopic results were identical whichever methodology was employed. UV (Tris Buffer (0.1 mol/L, pH 7.4) + (NH<sub>4</sub>)SO<sub>4</sub> (1.7 mol/L) + MgCl<sub>2</sub> (10 mmol/L), RT) λ<sub>max</sub> (ε): 256 nm (6.86 mmol/L<sup>-1</sup> cm<sup>-1</sup>). FTIR ν (cm<sup>-1</sup>): 3528 (m), 3434 (br), 3210(sbr), 2979 (m), 2968 (m), 2916 (m), 2883 (m), 2866 (m), 1752 (w), 1642 (m), 1472 (s), 1384 (s), 1347 (m), 1285 (m), 1249 (m), 1211 (w), 1196 (w), 1150 (s), 1124 (w), 1102 (s), 1086 (s), 1067 (s), 1044 (s), 1003 (s), 985 (m), 976 (w), 929 (w), 907 (w), 887 (w), 849 (w), 761 (w), 673 (w), 654 (w), 620 (w), 562 (w), 502 (w), 488 (w), 449 (w). <sup>1</sup>H NMR (400 MHz, CD<sub>3</sub>OD) δ: 4.91 (d, 1H, *J* = 8.0 Hz, H-1), 3.86 (d, 1H, *J* = 3.2 Hz, H-4), 3.77 (d, 1H, *J* = 9.6 Hz, H-2), 3.73 (m, 2H, H-6 and H-7), 3.62 (t, 1H, *J* = 6.0 Hz, H-5), 3.56 (quintet, 4H, *J* = 6 Hz, H-1' and H-4'), 3.53 (m, 1H, overlapped, H-6), 1.97 (m, 4H, H-2' and H-3'). <sup>13</sup>C NMR (75 MHz, CD<sub>3</sub>OD) δ: 104.21 (C-1), 76.14 (C-3), 73.64 (C-5), 69.29 (C-2), 68.85 (C-4), 61.12 (C-6), 50.70 (pyrrolidine's C-1' and C-4'), 22.64 (pyrrolidine's C-2 and C-3'). MS (ESI) *m/z*: 316.1 [M + Na]<sup>+</sup>, 609.0 [2M + Na]<sup>+</sup>.

MS/MS (ESI) *m/z*: 316.0 [M + Na]<sup>+</sup>, 246.9 [M + Na - pyrrolidine (C<sub>4</sub>H<sub>8</sub>)]<sup>+</sup>, 203.1, 185.9 [M + Na - pyrrolidine diazeniumdiolate (C<sub>4</sub>H<sub>8</sub>N-N(O)=NO)]<sup>+</sup>, 157.9, 155.8. HR-MS (ESI) calcd. for NaC<sub>10</sub>H<sub>19</sub>N<sub>3</sub>O<sub>7</sub> [M + Na]<sup>+</sup>: 316.1121. Found: 316.1112. DSC onset temperature at 145.5 °C, decomposition temperature at 171.0 °C, Δ*H* = +37.05 kJ mol<sup>-1</sup>. Anal. calcd. for C<sub>10</sub>H<sub>19</sub>N<sub>3</sub>O<sub>7</sub>: C, 40.95; H, 6.53; N, 14.33. Found: C, 40.45; H, 6.86; N, 14.04.

#### O<sup>2</sup>-β-D-galactopyranosyl 1-(piperidin-1-yl)diazene-1-ium-1,2-diolate (3b)

A few drops of sodium methoxide (25% in methanol) were added to a solution of **2c** (190 mg, 0.400 mmol) in anhydrous methanol (20 mL) and stirred at RT overnight. TLC (methanol:ethyl acetate, 3:7, *R<sub>f</sub>* = 0.36) showed the presence of a new product, which was isolated as a white powder (88.4 g, 0.288 mmol, 72%) after purification by column chromatography (silica gel, methanol:ethyl acetate, 1:4). The product was also obtained in better yield (94%) by allowing it to precipitate in solution. NMR studies confirmed that the material obtained in this manner is identical to the product obtained after chromatography. Alternatively, bypassing the column chromatography step during the synthesis of **2c** and carrying out the deprotection step right after the **2c** workup generated an overall yield of 65%. Spectroscopic results were identical whichever methodology was employed. UV (Tris Buffer (0.1 mol/L, pH 7.4) + (NH<sub>4</sub>)SO<sub>4</sub> (1.7 mol/L) + MgCl<sub>2</sub> (10 mmol/L), RT) λ<sub>max</sub> (ε): 224 nm (9.44 mmol/L<sup>-1</sup> cm<sup>-1</sup>). FTIR ν (cm<sup>-1</sup>): 3418 (sbr), 3015 (w), 2965 (m), 2928 (m), 2886 (m), 2857 (m), 2705 (m), 2530 (m), 2408 (m), 1645 (m), 1483 (s), 1456 (w), 1384 (s), 1348 (w), 1297 (w), 1230 (m), 1151 (m), 1104 (s), 1085 (s), 1048 (s), 1004 (s), 962 (w), 923 (w), 898 (w), 875 (w), 864 (w), 854 (w), 823 (w), 758 (w), 694 (w), 660 (w), 614 (w), 558 (w), 489 (w). <sup>1</sup>H NMR (400 MHz, CD<sub>3</sub>OD) δ: 4.96 (d, 1H, *J* = 8.0 Hz, H-1), 3.86 (d, 1H, *J* = 2.8 Hz, H-4), 3.80 (d, 1H, *J* = 9.6 Hz, H-2), 3.74 (m, 2H, H-6 and H-7), 3.63 (t, 1H, *J* = 6.0 Hz, H-5), 3.56 (dd, 1H, *J* = 9.6, 3.6 Hz, H-3), 3.41 (m, 4H, H-1' and H-5'), 1.73 (quintet, 4H, *J* = 5.6 Hz, H-2' and H-4'), 1.53 (quintet, 2H, *J* = 5.6 Hz, H-3'). <sup>13</sup>C NMR (75 MHz, CD<sub>3</sub>OD) δ: 104.39 (C-1), 76.25 (C-3), 73.65 (C-5), 69.26 (C-2), 68.85 (C-4), 61.13 (C-6), 52.10 (C-1' and C-5'), 24.51 (C-3'), 23.27 (C-2' and C-4'). MS (ESI) *m/z*: 330.1 [M + Na]<sup>+</sup>, 637.0 [2M + Na]<sup>+</sup>, 944 [3M + Na]<sup>+</sup>. MS/MS (ESI) *m/z*: 330.0 [M + Na]<sup>+</sup>, 216.0 [M + Na - piperidine nitrosamine (i.e., - C<sub>5</sub>H<sub>10</sub>N-N=O)]<sup>+</sup>, 203.1, 186.0 [M + Na - piperidine diazeniumdiolate (C<sub>5</sub>H<sub>10</sub>N-N(O)=NO)]<sup>+</sup>, 158.1, 141.0, 128.0 [piperidine diazeniumdiolate - oxygen (C<sub>5</sub>H<sub>10</sub>N-N(O)=N)], 125.0, 113.9 [piperidine nitrosamine (C<sub>5</sub>H<sub>10</sub>N-N=O)]<sup>+</sup>. HR-MS (ESI) calcd. for NaC<sub>11</sub>H<sub>21</sub>N<sub>3</sub>O<sub>7</sub> [M + Na]<sup>+</sup>: 330.1277. Found: 330.1267. DSC onset temperature at 153.9 °C, decomposition temperature at 164.1 °C, Δ*H* = +18.3 kJ mol<sup>-1</sup>.

#### O<sup>2</sup>-β-D-galactopyranosyl 1-(4-β-D-glucopyranosyl-4-aminomethylpiperidin-1-yl)diazene-1-ium-1,2-diolate (3c)

To a solution of **2e** (427 mg, 0.486 mmol) in anhydrous methanol (20 mL), a few drops of sodium methoxide (25% by weight in methanol) were added, and the solution was stirred at RT overnight. TLC (ethyl acetate:hexane, 7:3) showed absence of starting material. The solvent volume



was reduced to 5 mL under vacuum and upon addition of ether (20 mL), the product precipitated out of solution as an expected white solid. Because of its hygroscopic nature, it was collected by filtration under  $N_2$  and dried under reduced pressure overnight (250 mg, 95%). While the product could not be purified by column chromatography, it was nevertheless quite pure by NMR standards. UV (Tris Buffer (0.1 mol/L, pH 7.4) +  $(NH_4)SO_4$  (1.7 mol/L) +  $MgCl_2$  (10 mmol/L), RT)  $\lambda_{max}$  ( $\epsilon$ ): 229 nm (7.44 mmol/L $^{-1}$  cm $^{-1}$ ). FTIR  $\nu$  (cm $^{-1}$ ): 3407 (sbr), 2926 (w), 1699 (w), 1652 (w), 1579 (w), 1451 (w), 1384 (s), 1270 (w), 1222 (w), 1151 (w), 1080 (m), 1020 (w), 957 (w), 888 (w), 836 (m), 763 (w), 685 (w), 610 (w), 553 (w), 481 (w), 469 (w).  $^1H$  NMR (400 MHz,  $CD_3OD$ )  $\delta$ : 4.97 (d, 1H,  $J$  = 7.6 Hz, galactopyranosyl H-1), 4.44 (m, 1H, glucopyranosyl H-4), 4.32 (m, 1H, glucopyranosyl H-1), 4.22 (m, H, glucopyranosyl H-2), 4.00 (m, 2H, piperidiny H-1'' and H-5''), 3.87 (m, 1H, galactopyranosyl H-3), 3.75 (m, 1H, partly overlapped, galactopyranosyl H-2), 3.61 (2 dds, 4H, partly overlapped, galactopyranosyl H-4, H-5, H-6 and H-7), 3.48 (m, 1H, glucopyranosyl H-3) 3.12 (m, 1H, glucopyranosyl H-5), 3.03 (m, 2H, piperidiny methylene Hs), 2.93 (t, 2H,  $J$  = 10.8 piperidiny H-1' and H-5'), 2.45 (m, 2H, glucopyranosyl H-6 and H-7), 1.86 (m, 2H, piperidiny H-2' and H-4'), 1.63 (m, 1H, piperidiny H-3'), 1.37 (m, 2H, piperidiny H-2'' and H-4'').  $^{13}C$  NMR (75 MHz,  $CD_3OD$ )  $\delta$ : 157.46 (amide's C=O), 100.86 (C-1), 91.76 (C-1''), 73.08 (C-3''), 72.93 (C-5''), 71.48 (C-5), 71.21 (C-3), 70.49 (C-2''), 68.13 (C-4''), 67.38 (C-2), 67.23 (C-4), 61.92 (C-6''), 61.33 (C-6), 50.93, 50.73 (C1' and C-5'), 45.65, 45.48 (4-aminomethyl carbon), 35.58 (C-3'), 28.06, 27.87 (C-2' and C-4'). MS (ESI)  $m/z$ : 565.2 [M + Na] $^+$ . MS/MS (ESI)  $m/z$ : 565.1 [M + Na] $^+$ , 372.1 [M + Na - pyranose ( $C_6H_{11}O_5$ ) - NO] $^+$ , 341.1 [M + Na - pyranose ( $C_6H_{11}O_5$ ) - 2NO - H] $^+$ . HR-MS (ESI) calcd. for  $NaC_{19}H_{34}N_4O_{14}$  [M + Na] $^+$ : 565.1969. Found: 565.1966. DSC onset temperature at 146.5  $^{\circ}C$ , decomposition temperature at 176.7  $^{\circ}C$ ,  $\Delta H$  = +102 kJ mol $^{-1}$ .

#### 1,2,3,4-Tetra-*O*-acetyl- $\beta$ -D-glucopyranosyl succinimidyl carbonate (GluDSC) (4)

To a solution of 1,2,3,4-tetra-*O*-acetyl- $\beta$ -D-glucopyranose (200 mg, 0.575 mmol, 1 equiv.) in anhydrous acetonitrile (25 mL), *N,N'*-disuccinimidyl carbonate (DSC, 221 mg, 0.863 mmol, 1.5 equiv.) and triethylamine (TEA, 240  $\mu$ L, 1.73 mmol, 3 equiv.) were added, and the mixture was stirred until all the glucopyranose had reacted (overnight, TLC monitored, ethyl acetate:hexane, 3:1). The solvent was removed under vacuum and the residue was dissolved with aqueous  $NaHCO_3$  (1.0 mol/L solution) and extracted with ethyl acetate (3  $\times$  30 mL). The combined extracts were washed with brine (20 mL) and dried over  $Na_2SO_4$  (2.0 g), filtered, and the solvent was removed under vacuum. The isolated material turned out as a yellow sticky paste (265 mg, 0.542 mmol, 94%). The product turned out to be reactive with silica gel and hence was not further purified by column chromatography. NMR studies have demonstrated nonetheless rather high purity (yield by NMR: 96%). UV (DCM, RT)  $\lambda_{max}$  ( $\epsilon$ ): 229 nm (0.509 mmol/L $^{-1}$  cm $^{-1}$ ). FTIR  $\nu$  (cm $^{-1}$ ): 3487 (wbr), 2950 (w), 1817 (m), 1791 (m), 1743 (s), 1636 (w), 1432 (w), 1370 (m), 1222 (sbr), 1166 (w), 1078 (m), 1040 (m), 915 (w), 899 (w), 853 (w), 838 (w),

817 (w), 794 (w), 779 (w), 762 (w), 645 (w), 602 (w), 555 (w), 492 (w).  $^1H$  NMR (300 MHz,  $CD_2Cl_2$ )  $\delta$ : 5.77 (d, 1H,  $J$  = 10.8 Hz, H-1), 5.30 (t, 1H,  $J$  = 12.4 Hz, H-3), 5.11 (dd, 1H,  $J$  = 9.3, 11.7 Hz, H-2), 5.08 (dd, 1H,  $J$  = 9.3, 13.8 Hz, H-4), 4.43 (dd, 1H,  $J$  = 16.0, 3.6 Hz, H-6), 4.35 (dd, 1H,  $J$  = 16.0, 7.0 Hz, H-7), 3.99 (ddd, 1H,  $J$  = 3.6 Hz, H-5), 2.83 (s, 4H, succinimide Hs), 2.13 (s, 3H,  $CH_3$ ), 2.06 (s, 3H,  $CH_3$ ), 2.03 (s, 3H,  $CH_3$ ), 2.01 (s, 3H,  $CH_3$ ).  $^{13}C$  NMR (75 MHz,  $CD_3OD$ )  $\delta$ : 170.06, 169.74, 169.34, 169.11 (acetyl C=O), 168.82 (succinimide C=O), 151.45 (activated ester C=O), 91.61 (C-1), 72.48 (C-5), 72.14 (C-2), 70.13 (C-4), 68.58 (C-3), 68.17 (C-6), 25.83, 25.71 (succinimide  $CH_2$ ), 20.81, 20.61, 20.58 (acetyl  $CH_3$ ). MS (ESI)  $m/z$ : 512.1 [M + Na] $^+$ . MS/MS (ESI)  $m/z$ : 512.0 [M + Na] $^+$ , 452.0 [M + Na - *O*-acetyl ( $O-C(=O)CH_3$ ) - H] $^+$ . HR-MS (ESI) calcd. for  $NaC_{19}H_{23}N_1O_{14}$  [M + Na] $^+$ : 512.1016. Found: 512.1007.

#### X-ray diffraction crystal structure of 3a

Crystals of **3a** suitable for single-crystal X-ray diffraction were grown from water/methanol and crystallized in the monoclinic noncentrosymmetric space group  $P2_1$   $Z$  = 2, with unit cell dimensions of  $a$  = 4.8350(18),  $b$  = 9.435(3), and  $c$  = 15.552(6)  $\text{\AA}$ ;  $\beta$  = 92.423(5) $^{\circ}$ ,  $\alpha$  =  $\gamma$  = 90 $^{\circ}$ ;  $V$  = 708.8(4)  $\text{\AA}^3$ ; The structure was solved by direct methods, and the refined chirality was based upon that of the starting carbohydrate. Other key crystallographic data include  $\rho_c$  = 1.459 Mg m $^{-3}$ ; crystal size = 1.0  $\times$  0.05  $\times$  0.01 mm $^3$ . Data: 2882 independent data with  $I > 2\sigma(I)$ ,  $S_{\text{go}}$  = 1.039;  $R_1$  = 4.02%,  $wR_2$  = 10.52%. For further details, see the Supplementary data section.

#### Investigation of the stability of compounds 3a–3c

The solid deprotected glycosylated diazeniumdiolates are quite hygroscopic and have a tendency to turn brown over the course of a few hours if exposed to warm moist air. However, NMR examination of these brown materials reveals that there is only slight degradation (<5%) of the products. Under  $N_2$ , the same materials do not change in consistency over the course of two weeks at room temperature. Again, NMR examination showed negligible degradation of these materials when stored at room temperature under  $N_2$ . The optimal conditions for these compounds are as dried solids at  $-20$   $^{\circ}C$  under  $N_2$  in the dark. Under these conditions, the compounds have been stored for up to six months without significant degradation. Probe stability in aqueous and alcoholic media was also determined at room temperature over 2–3 weeks using NMR ( $D_2O$ ,  $CH_3OD$ ) and by UV ( $H_2O$ , Tris buffer (0.1 mol/L, pH 7.4),  $CH_3OH$ ). Degradation over this time period was in general minor (<10%) as revealed by either spectroscopic technique. The acetylated intermediate sugar diazeniumdiolates also presented similar stability. These oils were generally clear and colorless after purification (except for compound **3**) and slowly yellowed over 2–3 weeks when exposed to air at room temperature. NMR examination of these yellow oils show some signs of degradation (<2%). The optimal storage conditions for these oils were the same as for the deprotected sugar diazeniumdiolates degraded considerably (~40%) when exposed continually to UV light for prolonged periods of time (4–5 h).



## Supplementary data

Supplementary data for this article (general methods, instrumentation, preparation, and diffraction data) are available on the journal Web site (canjchem.nrc.ca). CCDC 740859 contains the X-ray data in CIF format for this manuscript. These data can be obtained, free of charge, via [www.ccdc.cam.ac.uk/conts/retrieving.html](http://www.ccdc.cam.ac.uk/conts/retrieving.html) (or from the Cambridge Crystallographic Data Centre, 12 Union Road, Cambridge CB2 1EZ, UK; fax +44 1223 336033; or [deposit@ccdc.cam.ac.uk](mailto:deposit@ccdc.cam.ac.uk)).

## Acknowledgements

The authors thank the National Institutes of Health (NIH) (grant No. 5R33CA109965), Quebec Transgenic Research Network (QTRN), and Canada Research Chair (CRC) for financial support of this research, and the Canadian Institutes of Health Research (CIHR) for Trainee fellowship to AC.

## References

- (1) Del Carlo, M., Jr.; Loeser, R. F. *ARTH. RHEUM* **2002**, *46*, 394.
- (2) Rauli, R. J. *Pharm. Pharmac.* **1998**, *50*, 75.
- (3) Ruane, P. H.; Toscano, J. P. (Johns Hopkins University, USA). Preparation of O<sup>2</sup>-substituted diazeniumdiolate compounds as prodrugs releasing nitric oxide at controlled rates upon photolysis. PCT Int. Appl. 2003/006427, 2003; p. 53.
- (4) Saavedra, J. E.; Bonifant, C. L.; Fitzhugh, A. L.; Keefer, L. K.; Citro, M. L. *Book of Abstracts*, 219th National Meeting of the American Chemical Society, San Francisco, CA, March 26–30, 2000; American Chemical Society: Washington, DC, 2000; 2000TOXI-113.
- (5) Saavedra, J. E.; Bohle, D. S.; Smith, K. N.; George, C.; Deschamps, J. R.; Parrish, D.; Ivanic, J.; Wang, Y.-N.; Citro, M. L.; Keefer, L. K. *J. Am. Chem. Soc.* **2004**, *126* (40), 12880. doi:10.1021/ja031538i.
- (6) Saavedra, J. E.; Billiar, T. R.; Williams, D. L.; Kim, Y.-M.; Watkins, S. C.; Keefer, L. K. *J. Med. Chem.* **1997**, *40* (13), 1947. doi:10.1021/jm9701031.
- (7) Saavedra, J.; Keefer, L. *Chem. Br.* **2000**, *36*, 30.
- (8) Saavedra, J. E.; Booth, M. N.; Keefer, L. K. *Book of Abstracts*, 212th National Meeting of the American Chemical Society, Orlando, FL, August 25–29, 1996; American Chemical Society: Washington, DC, 1996; TOXI-100.
- (9) Ricciardi, R.; Foley, D. P.; Quarfordt, S. H.; Saavedra, J. E.; Keefer, L. K.; Wheeler, S. M.; Donohue, S. E.; Callery, M. P.; Meyers, W. C. *Transplantation* **2001**, *71* (2), 193. doi:10.1097/00007890-200101270-00004. PMID:11213058.
- (10) Rehse, K.; Schleifer, K.-J.; Ludtke, E.; Böhme, E. *Archiv der Pharmazie (Weinheim, Germany)* **1994**, *327* (6), 359. doi:10.1002/ardp.19943270603.
- (11) Rehse, K.; Schleifer, K. J.; Ciborski, T.; Bohn, H. *Archiv der Pharmazie (Weinheim, Germany)* **1993**, *326* (10), 791. doi:10.1002/ardp.19933261005.
- (12) Lehmann, J. *Expert Opinion on Therapeutic Patents* **2000**, *10* (5), 559. doi:10.1517/13543776.10.5.559.
- (13) Lam, C.-F.; Sviri, S.; Ilett, K. F.; van Heerden, P. V. *Expert Opin. Investig. Drugs* **2002**, *11* (7), 897. doi:10.1517/13543784.11.7.897. PMID:12084001.
- (14) Keefer, L. K.; Smith, D. J.; Pulfer, S.; Hanson, S. R.; Saavedra, J. E.; Billiar, T. R.; Roller, P. P. *Portland Press Proceedings* **1996**, *10*, 335.
- (15) Keefer, L. K. *Book of Abstracts*, 215th National Meeting of the American Chemical Society, Dallas, March 29–April 2, 1998; American Chemical Society: Washington, DC, 1998; CHED-641.
- (16) Homer, K. L.; Wanstall, J. C. *Br. J. Pharmacol.* **2000**, *131* (4), 673. doi:10.1038/sj.bjp.0703613. PMID:11030715.
- (17) Hanson, S. R.; Hutsell, T. C.; Keefer, L. K.; Mooradian, D. L.; Smith, D. J. *Adv. Pharmacol. (San Diego)* **1995**, *34*, 383. doi:10.1016/S1054-3589(08)61099-6.
- (18) Sogo, N.; Magid, K. S.; Shaw, C. A.; Webb, D. J.; Megson, I. L. *Biochem. Biophys. Res. Commun.* **2000**, *279* (2), 412. doi:10.1006/bbrc.2000.3976. PMID:11118301.
- (19) Valdez, C. A.; Saavedra, J. E.; Showalter, B. M.; Davies, K. M.; Wilde, T. C.; Citro, M. L.; Barchi, J. J., Jr.; Deschamps, J. R.; Parrish, D.; El-Gayar, S.; Schleicher, U.; Bogdan, C.; Keefer, L. K. *J. Med. Chem.* **2008**, *51* (13), 3961. doi:10.1021/jm8000482.
- (20) Keefer, L. K. *Chemtech* **1998**, *28*, 30.
- (21) McGrowder, D.; Ragoobirsingh, D.; Brown, P. *Int. J. Pharmacol.* **2006**, *2* (4), 366. doi:10.3923/ijp.2006.366.373.
- (22) Pulfer, S. K.; Ott, D.; Smith, D. J. *J. Biomed. Mat. Res.* **1997**, *37* (2), 182. doi:10.1002/(SICI)1097-4636(199711)37:2<182::AID-JBM6>3.0.CO;2-N.
- (23) Velázquez, C. A.; Praveen Rao, P. N.; Citro, M. L.; Keefer, L. K.; Knaus, E. E. *Bioorg. Med. Chem.* **2007**, *15* (14), 4767. doi:10.1016/j.bmc.2007.05.009. PMID:17509888.
- (24) Showalter, B. M.; Reynolds, M. M.; Valdez, C. A.; Saavedra, J. E.; Davies, K. M.; Klose, J. R.; Chmurny, G. N.; Citro, M. L.; Barchi, J. J., Jr.; Merz, S. I.; Meyerhoff, M. E.; Keefer, L. K. *J. Am. Chem. Soc.* **2005**, *127* (41), 14188. doi:10.1021/ja054510a.
- (25) Pavlos, C. M.; Xu, H.; Toscano, J. P. *Free Radic. Biol. Med.* **2004**, *37* (6), 745. doi:10.1016/j.freeradbiomed.2004.06.010. PMID:15304250.
- (26) Ruane, P. H.; Bushan, K. M.; Pavlos, C. M.; D'Sa, R. A.; Toscano, J. P. *J. Am. Chem. Soc.* **2002**, *124* (33), 9806. doi:10.1021/ja026900s.
- (27) Bushan, K. M.; Xu, H.; Ruane, P. H.; D'Sa, R. A.; Pavlos, C. M.; Smith, J. A.; Celius, T. C.; Toscano, J. P. *J. Am. Chem. Soc.* **2002**, *124* (43), 12640. doi:10.1021/ja027957h. PMID:12392393.
- (28) Saavedra, J. E.; Shami, P. J.; Wang, L. Y.; Davies, K. M.; Booth, M. N.; Citro, M. L.; Keefer, L. K. *J. Med. Chem.* **2000**, *43* (2), 261. doi:10.1021/jm9903850.
- (29) Tang, X.; Xian, M.; Trikha, M.; Honn, K. V.; Wang, P. G. *Tetrahedron Lett.* **2001**, *42* (14), 2625. doi:10.1016/S0040-4039(01)00263-5.
- (30) Saavedra, J. E.; Mooradian, D. L.; Mowery, K. A.; Schoenfish, M. H.; Citro, M. L.; Davies, K. M.; Meyerhoff, M. E.; Keefer, L. K. *Bioorg. Med. Chem. Lett.* **2000**, *10* (8), 751. doi:10.1016/S0960-894X(00)00086-X. PMID:10782678.
- (31) Tang, X.; Wang, P. G. *Abstracts of Papers*, 222nd National Meeting of the American Chemical Society, Chicago, IL, United States, August 26–30, 2001; American Chemical Society: Washington, DC, 2001; MEDI-092.
- (32) Wu, X.; Tang, X.; Xian, M.; Wang, P. G. *Tetrahedron Lett.* **2001**, *42* (23), 3779. doi:10.1016/S0040-4039(01)00614-1.
- (33) Cai, T. B.; Lu, D.; Landerholm, M.; Wang, P. G. *Org. Lett.* **2004**, *6* (23), 4203. doi:10.1021/ol048397p. PMID:15524443.
- (34) Saavedra, J. E.; Keefer, L. K.; Srinivasan, A.; Bogdan, C.; Rice, W. G.; Ji, X. (United States Dept. of Health and Human Services, USA). Preparation of O<sup>2</sup>-arylated or O<sup>2</sup>-glycosylated 1-substituted diazen-1-ium-1,2-diols and O<sup>2</sup>-substituted 1-[(2-carboxylato)pyrrolidin-1-yl]diazen-1-ium-

- 1,2-diols as virucides. PCT Int. Appl. 9 811 121, 1998; 100 pp.
- (35) Aebischer, B. M.; Hanssen, H. W.; Vasella, A. T.; Schweizer, W. B. *Perkin Trans.* **1982**, 2139.
- (36) Brand, J.; Huhn, T.; Groth, U.; Jochims, J. C. *Chem. Eur. J.* **2006**, 12 (2), 499. doi:10.1002/chem.200500325.
- (37) Shiino, M.; Watanabe, Y.; Umezawa, K. *Bioorg. Med. Chem.* **2001**, 9 (5), 1233. doi:10.1016/S0968-0896(01)00003-7. PMID:11377181.
- (38) Southan, G. J.; Srinivasan, A.; Keefer, L. K.; George, C.; Fales, H. M. *Chem. Commun. (Camb.)* **1998**, (11): 1191. doi:10.1039/a801543k.
- (39) Hrabie, J. A.; Keefer, L. K. *Chem. Rev.* **2002**, 102 (4), 1135. doi:10.1021/cr000028t. PMID:11942789.
- (40) Cantuaria, G.; Magalhaes, A.; Angioli, R.; Mendez, L.; Mirhashemi, R.; Wang, J.; Wang, P.; Penalver, M.; Averette, H.; Braunschweiler, P. *Cancer* **2000**, 88 (2), 381. doi:10.1002/(SICI)1097-0142(20000115)88:2<381::AID-CNCR20>3.0.CO;2-M. PMID:10640972.
- (41) Battaglia, G.; La Russa, M.; Bruno, V.; Arenare, L.; Ippolito, R.; Copani, A.; Bonina, F.; Nicoletti, F. *Brain Res.* **2000**, 860 (1-2), 149. doi:10.1016/S0006-8993(00)01962-4. PMID:10727634.
- (42) Zhang, M.; Zhang, Z.; Blessington, D.; Li, H.; Busch, T. M.; Madrak, V.; Miles, J.; Chance, B.; Glickson, J. D.; Zheng, G. *Bioconj. Chem.* **2003**, 14 (4), 709. doi:10.1021/bc034038n. PMID:12862422.
- (43) Fernández, C.; Nieto, O.; Fontenla, J. A.; Rivas, E.; de Ceballos, M. L.; Fernández-Mayoralas, A. *Org. Biomol. Chem.* **2003**, 1 (5), 767. doi:10.1039/b212066f. PMID:12929357.
- (44) Koenigs, W.; Knorr, E. *Ber. Dtsch. Chem. Ges.* **1901**, 34 (1), 957. doi:10.1002/cber.190103401162.
- (45) Drago, R. S.; Paulik, F. E. *J. Am. Chem. Soc.* **1960**, 82 (1), 96. doi:10.1021/ja01486a021.
- (46) Drago, R. S.; Paulik, F. E. *J. Am. Chem. Soc.* **1960**, 82 (1), 96. doi:10.1021/ja01486a021.
- (47) Shendage, D. M.; Fröhlich, R.; Haufe, G. *Org. Lett.* **2004**, 6 (21), 3675. doi:10.1021/ol048771l. PMID:15469321.
- (48) Englund, E. A.; Gopi, H. N.; Appella, D. H. *Org. Lett.* **2004**, 6 (2), 213. doi:10.1021/ol0361599. PMID:14723531.
- (49) Saavedra, J. E.; Southan, G. D.; Davies, K. M.; Lundell, A.; Markou, C.; Hanson, S. R.; Adrie, C.; Hurford, W. E.; Zapol, W. M.; Keefer, L. K. *J. Med. Chem.* **1996**, 39 (22), 4361. doi:10.1021/jm960616s.
- (50) Bohle, D. S.; Perepichka, I. *J. Org. Chem.* **2009**, 74 (4), 1621. doi:10.1021/jo802343k.

# Bisoxazoline–copper(I)-catalyzed aziridination of diazoacetate with imines — A DFT study

Qingxi Meng, Fen Wang, and Ming Li

**Abstract:** Density functional theory (DFT) has been used to study bisoxazoline–copper(I)-catalyzed aziridination of diazoacetate with *syn*-imines or *anti*-imines. All the intermediates and transition states were optimized completely at the B3LYP/6-31G(d) level. Calculation results confirm that Cu(I)-catalyzed aziridination goes mainly through the catalyst–diazoacetate complex (**M1**), the copper(I)–carbene intermediate (**M2**), the copper–carbene–imine complex (**M3**), and the catalyst–aziridine carboxylate complex (**M4**). For *syn*-imines, the reaction mode I (C3–N5 bond attacking the Cu–C1 bond of **M2**) is more dominant than the reaction mode II (C3–N5 bond attacking the carbene–carbon C1 of **M2**), and the attack from the *si*-surface of **M2** is prior to the *re*-surface. For *anti*-imines, the reaction modes and attacks from the *si*- or *re*-surface coexist. The reactivity of *syn*-imines is stronger than *anti*-imines. The favorable reaction channel is **CA2** → **M1b** → **TS1b** → **M2** → *syn*-**TS2b** → *syn*-**M3b** → *syn*-**TS3b** → *syn*-**M4b** → *syn*-**P2**. The dominant product theoretically predicted is of (S,S)-chirality. On the whole, the solvent effect decreases the free energies of the species.

**Key words:** bisoxazoline–copper(I) complex, aziridination, imines, reaction mechanism, density functional theory (DFT).

**Résumé :** On a fait appel à la théorie de la fonctionnelle de la densité pour étudier l'aziridination catalysée par le bisoxazoline-cuivre(I) du diazoacétate avec des imines *syn*- ou *anti*-. On a complètement optimisé tous les intermédiaires et les états de transition au niveau B3LYP/6-31G(d). Les résultats de ces calculs confirment que l'aziridination catalysée par le cuivre(I) se produit principalement par le biais du complexe catalyseur-diazoacétate, **M1**, de l'intermédiaire cuivre(I)-carbone, **M2**, du complexe cuivre(I)-carbone-imine, **M3** et du complexe catalyseur-aziridinecarboxylate, **M4**. Pour les imines *syn*, le mode de réaction I (attaque de la liaison C3-N5 sur la liaison Cu-C1 de **M2**) est plus dominant que le mode II (attaque de la liaison C3-N5 sur le carbone C1 du carbone de **M2**); l'attaque sur la surface *si* de **M2** se fait avant celle sur la surface *re*. Toutefois, pour les imines *anti*, elles coexistent. La réactivité des imines *syn* est plus grande que celle des imines *anti*. La voie réactionnelle la plus favorable est **CA2** → **M1b** → **TS1b** → **M2** → *syn*-**TS2b** → *syn*-**M3b** → *syn*-**TS3b** → *syn*-**M4b** → *syn*-**P2**. Sur la base des calculs théoriques, il est prédit que la chiralité du produit dominant devrait être (S,S). Dans l'ensemble, l'effet de solvant diminue les énergies libres des espèces.

**Mots-clés :** complexe bisoxazoline-cuivre(I), aziridination, imines, mécanisme de réaction, théorie de la fonctionnelle de la densité (« DFT »).

## Introduction

Aziridines have been attractive organic molecules due to their great synthetic utilities.<sup>1–3</sup> Aziridines have been used as intermediates in the preparation of amino acids,<sup>4,5</sup>  $\beta$ -lactams,<sup>6</sup> polymers,<sup>7</sup> and pyrrolidines.<sup>8</sup> A number of synthetic aziridines have found biological applications as antitumor agents, antibiotics, and as enzyme inhibitors.<sup>9</sup> Many noncatalytic pathways to aziridines have been developed.<sup>10,11</sup> Recently, however, the development of the asymmetric catalytic aziridinations has received the most attention.<sup>2</sup> A variety of methods has been developed for the synthesis of aziridines,<sup>9,12,13</sup> including a ring closure reaction of 1,2-amino alcohols or their derivatives,<sup>14,15</sup> ring opening of epoxides with metal azides,<sup>16,17</sup> the addition of  $\alpha$ -haloester enolates to imines,<sup>18</sup> a transfer of a nitrene group to an alkene,<sup>19,20</sup> and the reactions between diazo esters and imines

mediated by either carbene transfer catalysts<sup>21–23</sup> or Lewis acid catalysts.<sup>24–29</sup>

The aziridination catalyzed by transition metals, which is defined as a [2+1] cycloaddition between a carbene-type species and imines (Scheme 1), is an important synthetic method to obtain aziridine rings. Transition metals such as rhodium and copper are found to be able to catalyze the aziridination.<sup>30,31</sup>

As illustrated in Scheme 2, it is also generally accepted that the copper-catalyzed aziridination proceeds via a copper–carbene complex (**E**), which is formed by the association of the diazoimido compound (**D**) and the active catalyst (**B**) with concomitant extrusion of nitrogen, and then the attack of imines (**F**) on the copper–carbene intermediate (**E**) leads to the asymmetric aziridine (**G**). In copper-catalyzed asymmetric aziridination, the copper–carbene in-

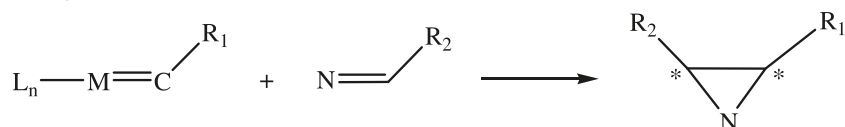
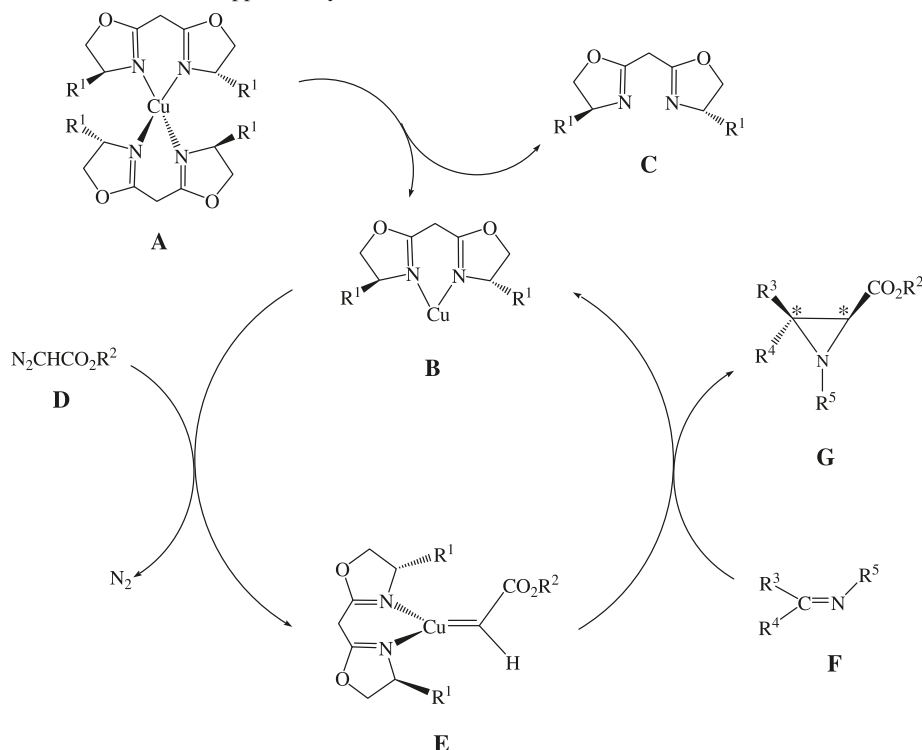
Received 12 February 2010. Accepted 11 June 2010. Published on the NRC Research Press Web site at canjchem.nrc.ca on 1 September 2010.

**Q. Meng**,<sup>1</sup> Department of Chemistry and Material Science, Shandong Agricultural University, Taian, Shandong, 271018, People's Republic of China.

**F. Wang**, Department of Chemistry, Taishan University, Taian, Shandong, 271021, People's Republic of China.

**M. Li**, Department of Chemistry, Southwest University, Chongqing 400715, People's Republic of China.

<sup>1</sup>Corresponding author (e-mail: qingxim@sdau.edu.cn).

**Scheme 1.** Transition-metal-catalyzed aziridination of diazoacetate with imines.**Scheme 2.** Possible reaction mechanism of copper-catalyzed aziridination of diazoacetate with imines.

intermediate plays an important role. The copper-carbene complex has a better stabilization and enantioselectivity, compared with a free carbene, and has been detected as the reaction intermediate in experiment.<sup>32</sup>

Ikeno et al.<sup>33</sup> have studied some transition metal-carbene complexes such as Co-, Cu-, and Ru-carbenes at the B3LYP/6-31G(d) and B3LYP/LANL2DZ levels. The formation of a copper-carbene intermediate has been studied by Salvatella and co-workers<sup>34</sup> at the B3LYP/6-31G(d) level. Comba et al.<sup>35</sup> have studied the mechanism of the (bispidine)copper(II)-catalyzed aziridination of styrene, both experimentally and theoretically. We have studied the copper(I)-carbene complexes<sup>36</sup> at the B3LYP/631G(d,p) level and the copper(I)-catalyzed asymmetric cyclopropanation of diazoacetate with alkene<sup>37</sup> at the B3LYP/631G level. The theoretical data available for the mechanism of the aziridination of diazoacetate with imines are rather limited. Therefore, to understand the reaction mechanism of the aziridination catalyzed by the copper complex in detail, chiral bisoxazoline-copper(I)-catalyzed aziridination of diazoacetate with *syn*-imines or *anti*-imines is studied in the present work. Herein, a theoretical study with the B3LYP density functional was carried out to elucidate the following issues in details: (i) the reactivity of *syn*-imines or *anti*-imines, (ii) the two reaction modes, I (imines attacking the Cu-C<sub>carbene</sub> bond of the copper-carbene complex) and II (imines attacking the carbene carbon), (iii) the imines attacking the copper-carbene

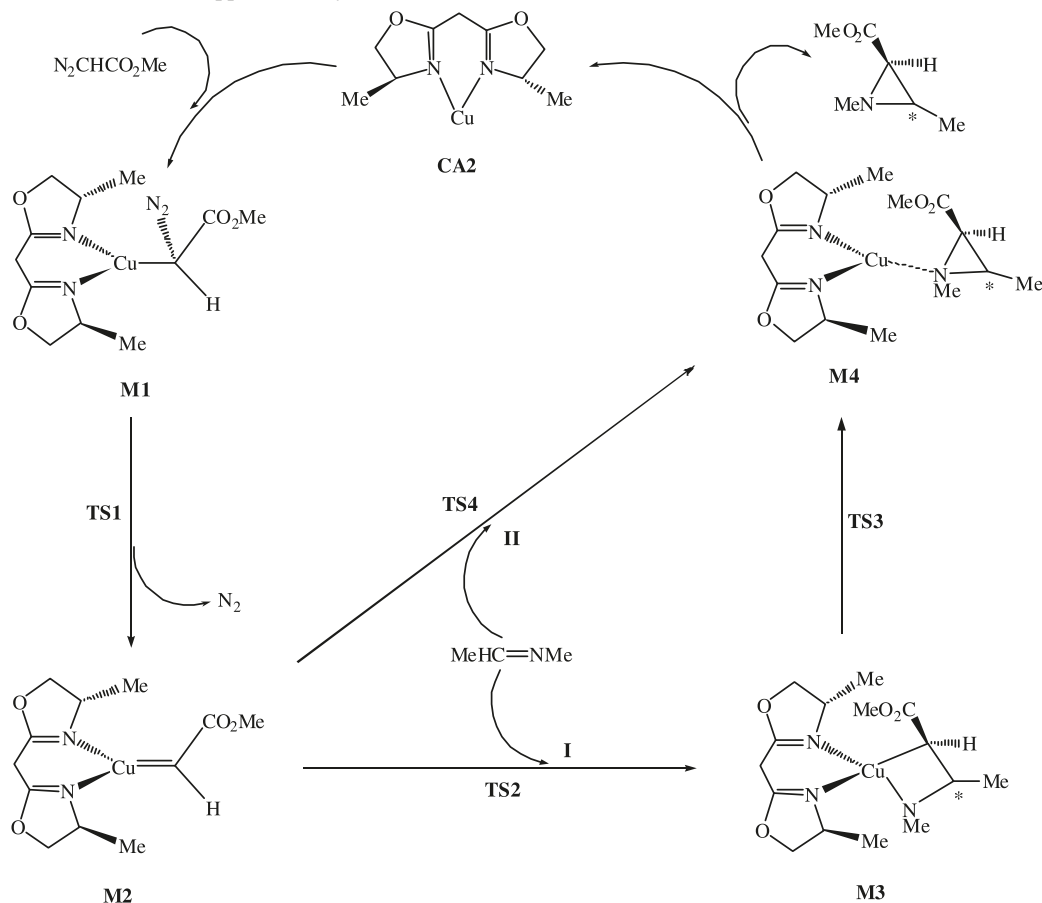
complex from the *re*-surface or *si*-surface, and (iv) the most favorable channel and dominant product. The possible reaction mechanism is outlined in Scheme 3.

## Computational details

All computations were carried out by using the Gaussian03 program package.<sup>38</sup> Density functional theory (DFT) methods<sup>39</sup> have now been widely applied to various molecular systems with great success because of their efficiency and accuracy,<sup>40–42</sup> especially the B3LYP method,<sup>43–45</sup> which includes Becke's three-parameter-exchange functionals and nonlocal Lee, Yang, and Parr correlation functional that generally provides better results. The 6-31G(d) basis set is used for all the atoms. All the species are positively identified for local minima with zero of the number of imaginary frequencies and for transition states with the sole imaginary frequency. The transition states were verified by intrinsic reaction coordinate (IRC)<sup>46</sup> calculations and by animating the negative eigenvector coordinates with a visualization program (Molekel 4.3).<sup>47,48</sup> In addition, based on the gas phase optimized geometry for each species, the solvent effects of CH<sub>2</sub>Cl<sub>2</sub> were studied by performing the self-consistent reaction field (SCRF) of polarizable continuum model (PCM)<sup>49</sup> approach at the same computational level.

Furthermore, the bonding characteristics were analyzed by using the "atoms in molecules" (AIM) theory,<sup>50</sup> which is



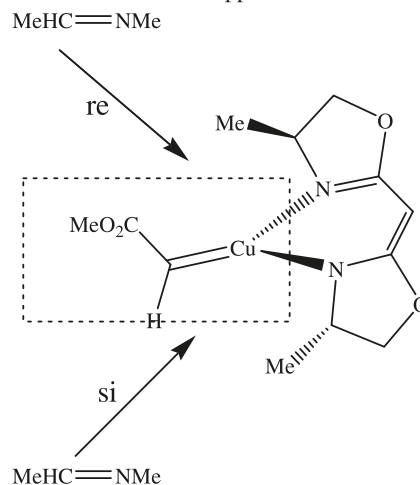
**Scheme 3.** Proposed mechanism of copper(I)-catalyzed aziridination.

based on a topological analysis of the electron charge density and its Laplacian. The magnitude of the electron density,  $\rho(r)$ , at the bond critical points (BCPs) depends on the interatomic distance and the degree of coordination of the atoms, and it is often used as a measure of the bond strength or similar types of bonds.<sup>51</sup> The analysis went further with those obtained by means of the natural bond orbital (NBO) theory.<sup>52–55</sup> AIM analysis was carried out by employing the AIM2000 code<sup>56</sup> with the B3LYP/6-31G(d) wave functions as input. NBO analysis was performed by utilizing NBO5.0code<sup>57</sup> with the optimized structures.

Molecular orbital (MO) compositions and the overlap populations were calculated by employing the AOMix program.<sup>58,59</sup> The analysis of the MO compositions in terms of occupied and unoccupied fragment molecular orbitals (OFOs and UFOs, respectively), the charge decomposition analysis (CDA), and the construction of orbital interaction diagrams were performed by using AOMix-CDA.<sup>60</sup>

## Results and discussion

As illustrated in Scheme 3, copper(I)-catalyzed aziridination is suggested as the following: the decomposition of the catalyst, the bisoxazoline-copper(I) complex (CA), leading to oxazoline and an active oxazoline-copper(I) catalyst (CA2); the reaction of diazoacetate with CA2 generating the catalyst-diazoacetate complex (M1); the decomposition of N<sub>2</sub> in M1 leading to the copper(I)-carbene intermediate (M2); the reaction of M2 with imines resulting in the cop-

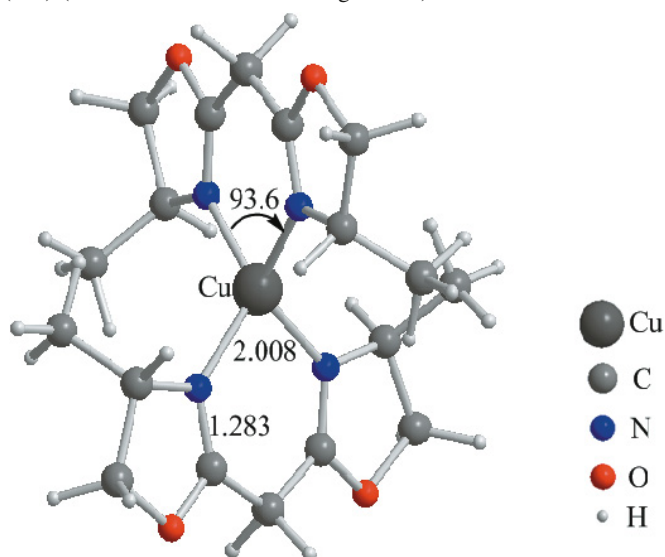
**Scheme 4.** Attack of imines on copper-carbene intermediate M2.

per(I)-carbene-imine complex (M3); the formation of the catalyst-aziridine carboxylate complex (M4); the decomposition of M4 leading to the aziridine carboxylate and regenerating the active catalyst CA2. Scheme 3 also shows that the attack of *syn*-imines or *anti*-imines on M2 has two reaction modes, I and II, where the C3–N5 bond attacks the Cu–C1 bond or C1 (carbene-carbon) of M2, respectively. As shown in Scheme 4, *syn*-imines or *anti*-imines can attack M2 from the *re*-surface or the *si*-surface. In the following discussion, the attack of imines from the *re*-surface of M2

**Table 1.** Solvent effect energies,  $\Delta G_{\text{solv}}$  (kJ mol<sup>-1</sup>), relative free energies,  $\Delta G(\text{sol})$  (in solvent) and  $\Delta G$  (kJ mol<sup>-1</sup>) (in gas phase), relative enthalpies,  $\Delta H$  (kJ mol<sup>-1</sup>), relative energies including zero-point vibrational energy correlation,  $\Delta E$  (kJ mol<sup>-1</sup>) and absolute entropies,  $S$  (kJ mol<sup>-1</sup> K<sup>-1</sup>), and the first two frequencies,  $\nu_1$  and  $\nu_2$  (cm<sup>-1</sup>), for stationary points.

Stationary points	In CH <sub>2</sub> Cl <sub>2</sub>		In gas phase				Frequencies	
	$\Delta G(\text{sol})$	$\Delta G_{\text{solv}}$	$\Delta G$	$\Delta H$	$\Delta E$	$S$	$\nu_1$	$\nu_2$
CA2 + R1 + R2-N <sub>2</sub>	0.0	—	0.0	0.0	0.0	—	—	—
M1a + R2-N <sub>2</sub>	-97.5	—	-74.9	-125.9	-127.5	—	—	—
M1b + R2-N <sub>2</sub>	-95.5	—	-73.7	-124.4	-125.6	—	—	—
TS1a + R2-N <sub>2</sub>	-55.8	—	-39.7	-89.3	-91.0	—	—	—
TS1b + R2-N <sub>2</sub>	-57.0	—	-41.9	-93.8	-95.2	—	—	—
M2 + R2	-117.3	—	-145.4	-153.2	-157.3	—	—	—
anti-TS2a	-69.0	-91.5	-50.9	-119.1	-121.0	178.06	311.2i	17.2
anti-TS2b	-72.3	-98.6	-51.1	-116.5	-119.2	180.33	348.8i	21.3
anti-M3a	-244.5	-90.7	-212.5	-285.4	-285.6	174.27	19.2	29.6
anti-M3b	-243.3	-93.6	-202.9	-279.8	-278.8	171.08	20.3	27.0
anti-TS3a	-213.7	-90.3	-187.9	-258.6	-259.1	176.08	229.3i	25.2
anti-TS3b	-200.2	-81.5	-180.5	-251.9	-252.3	175.48	307.4i	48.7
anti-M4a	-298.5	-81.5	-275.6	-345.7	-347.0	176.51	17.2	26.9
anti-M4b	-274.6	-89.0	-253.4	-314.5	-316.8	183.69	11.3	15.6
anti-P1 + CA2	-151.3	—	-139.5	-152.2	-152.4	—	—	—
anti-P2 + CA2	-153.2	—	-141.3	-154.1	-154.3	—	—	—
anti-TS4a	-70.1	-91.1	-53.3	-119.6	-121.6	179.61	226.1i	23.7
anti-TS4b	-65.9	-92.0	-48.7	-114.5	-116.8	180.00	263.2i	16.2
syn-TS2a	-75.1	-85.7	-61.7	-129.7	-131.6	178.19	299.5i	17.7
syn-TS2b	-84.9	-105.8	-53.5	-121.7	-123.7	178.04	303.6i	15.8
syn-M3a	-241.1	-89.5	-208.5	-282.4	-282.4	173.47	18.1	26.0
syn-M3b	-233.0	-101.6	-182.5	-261.7	-260.3	169.28	20.3	27.0
syn-TS3a	-207.6	-85.7	-185.7	-256.4	-257.2	176.01	231.1i	16.0
syn-TS3b	-158.5	-96.1	-120.6	-204.1	-202.8	165.74	261.4i	17.2
syn-M4a	-289.1	-75.2	-276.4	-342.2	-344.2	179.94	18.9	36.6
syn-M4b	-261.2	-90.7	-239.6	-299.5	-301.7	184.77	14.3	20.8
syn-P1 + CA2	-144.6	—	-131.2	-143.1	-143.4	—	—	—
syn-P2 + CA2	-137.4	—	-125.9	-139.4	-139.4	—	—	—
syn-TS4a	-63.3	-89.9	-50.1	-113.3	-116.1	182.01	242.9i	25.0
syn-TS4b	-59.8	-97.8	-34.7	-101.2	-103.4	179.43	233.1i	15.9

**Fig. 1.** Optimized structure of the bisoxazoline–copper(I) complex (CA) (bond distances in Å and angles in °).



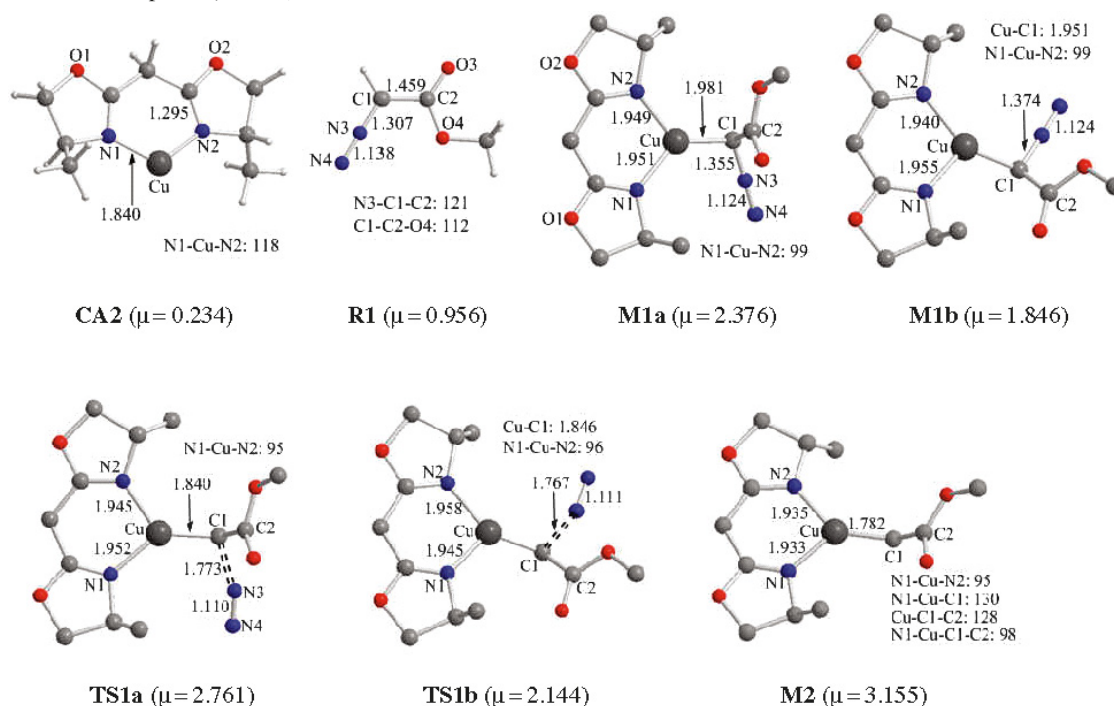
is marked by an “a” and its attack from the *si*-surface is marked by a “b”.

The relative free energies,  $\Delta G(\text{sol})$ , including solvent energies, and the relative gas phase free energies,  $\Delta G$ , enthalpies,  $\Delta H$ , and zero-point energy (ZPE) corrected electronic energies,  $\Delta E$ , are provided in Table 1. Unless otherwise noted, the discussed energies are relative free energies,  $\Delta G(\text{sol})$ , in the following discussions.

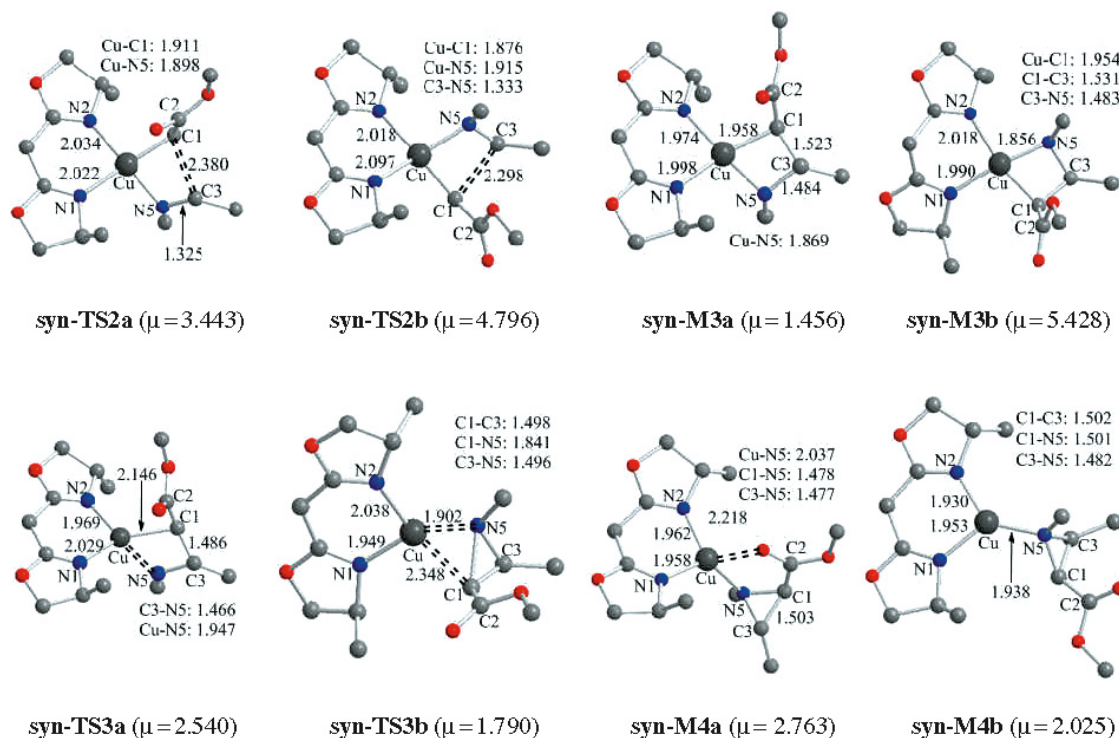
### Catalyst

The optimized structure of the catalyst, chiral bisoxazoline–copper(I) complex (CA), is illustrated in Fig. 1. It is a  $C_2$ -symmetry complex. There is a Cu–N–C–C–C–N six-membered ring in the catalyst CA and the six atoms are nearly coplanar. (As shown, most of the intermediates and transition states have this character.) The Cu–N and C–N bonds are 2.008 and 1.283 Å, respectively. The Cu–N and C–N bonds are 1.841 and 1.295 Å in the active catalyst CA2, which is also a  $C_2$ -symmetry complex (Fig. 2). The highest occupied molecular orbital (HOMO) and lowest unoccupied molecular orbital (LUMO) of CA2 are shown in Fig. S1 of the Supplementary data.

**Fig. 2.** The intermediates and transition states of the formation of the copper–carbene complex (**M2**) (bond distances in Å, angles and dihedral angles in °, moment dipoles,  $\mu$ , in D).



**Fig. 3.** The intermediates and transition states of the reaction of **M2** and *syn*-imines (bond distances in Å, angles and dihedral angles in °, moment dipoles,  $\mu$ , in D).



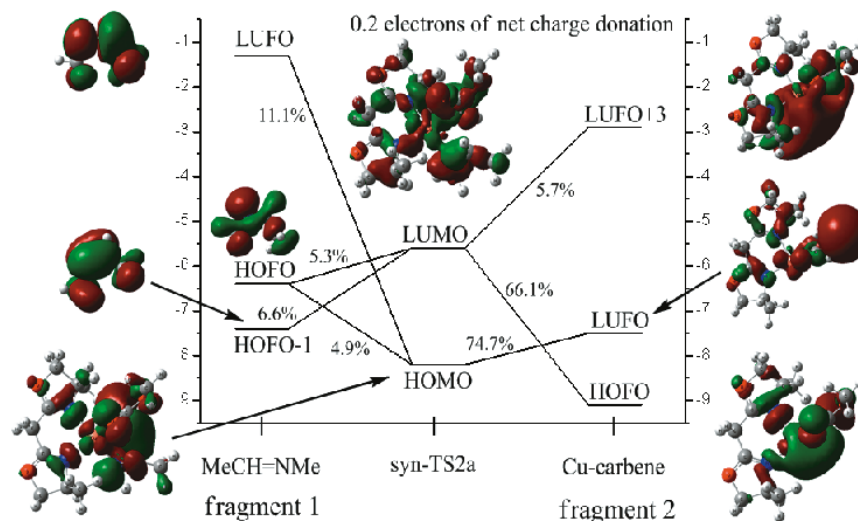
#### Formation of the copper(I)–carbene intermediate

As illustrated in Scheme 3, the reaction of diazoacetate (**R1**) with the active catalyst **CA2** leads to the catalyst–diazoacetate complex (**M1**), and then the decomposition of  $N_2$  in

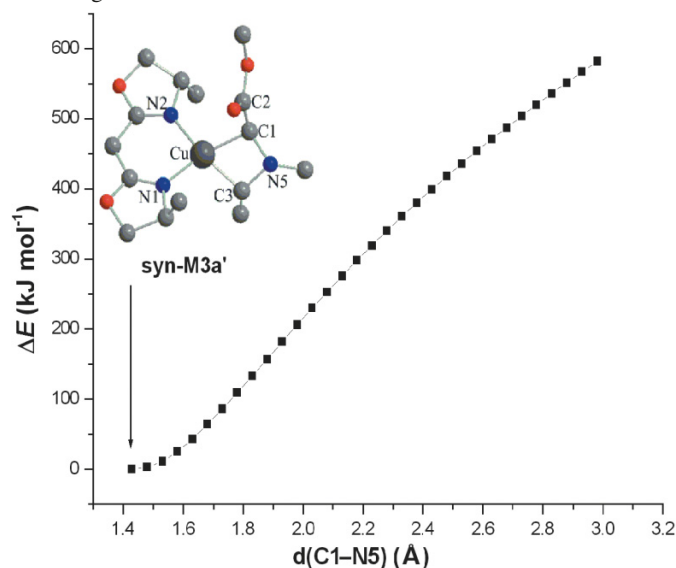
**M1** generates the copper(I)–carbene intermediate (**M2**) via the transition state **TS1**.

Figure 2 shows that the Cu–C1 and C1–N3 bonds are 1.981 and 1.355 Å in **M1a** and 1.951 and 1.374 Å in **M1b**,

**Fig. 4.** Orbital interaction diagram for *syn*-TS2a, which is formed by imines (*syn*) and the copper-carbene fragment (the AOMix-CDA calculation, based on B3LYP/6-31G\*; the net charge donation, CT(1 → 2) – CT(2 → 1), is 0.2 e).



**Fig. 5.** A loose scan profile of **M2** with imine to *syn*-M3a' along the C1–N5 distance increased with the electronic state of the close shell singlet.



respectively. Compared to diazoacetate, C1–N3 bonds become longer by about 0.06 Å, which possibly results from the formation of Cu–C1 bonds. The N1–Cu–C1–C2 and N1–Cu–C1–N3 torsion angles are, respectively, 87.4° and 19.0° for **M1a** and 140.2° and 15.6° for **M1b**. In the transition states **TS1a** and **TS1b**, the C1–N3 bonds are stretched considerably and the Cu–C1 bonds shortened compared with those of **M1** (**M1** → **TS1**: C1–N3 bond: 1.4 → 1.8 Å, Wiberg bond order,  $P_{ij}$ : 0.98 → 0.48, the electron densities,  $\rho$ , of the bond critical points (BCPs): 0.26 → 0.10 e Å<sup>-3</sup>; Cu–C1 bond: 2.0 → 1.8 Å,  $P_{ij}$ : 0.25 → 0.38,  $\rho$ : 0.10 → 0.14 e Å<sup>-3</sup>; Table S1 in the Supplementary data). The high stabilization energies of about 160 kJ/mol for the (2p)<sub>N1</sub> →  $\sigma^*_{\text{Cu–C1}}$  and (2p)<sub>N2</sub> →  $\sigma^*_{\text{Cu–C1}}$  in **TS1a** and **TS1b** (Table S6 in the Supplementary data), which is obtained from the second-order perturbation analysis of donor–acceptor interactions

in the NBO analysis and used to estimate the strengths of the donor–acceptor interactions of the NBOs, reveals the strong interaction between (2p)<sub>N1</sub> and (2p)<sub>N2</sub> and  $\sigma^*_{\text{Cu–C1}}$  orbitals and the electron transfer tendency from (2p)<sub>N1</sub> and (2p)<sub>N2</sub> to  $\sigma^*_{\text{Cu–C1}}$ . The copper(I)–carbene intermediate (**M2**) has only one geometry, which is in agreement with our previous study,<sup>37</sup> and the N1–Cu–C1–H and N1–Cu–C1–C2 torsion angles are 90.0° and 100.8°, respectively. In **M2**, the Cu–C1 bond is 1.782 Å, which is shorter than **M1**. As illustrated in NBO analysis, the Cu–C1 bond shows a strong single-bonded character, and the NBO energy is –1102.16 kJ/mol. The atomic polar tensor (APT) charges of copper and carbon atoms of the Cu–C1 bond are +0.397 and +0.019, respectively (Table S5 in the Supplementary data).

### M2 reaction with *syn*-imines

Scheme 3 shows that the attack of *syn*-imines on **M2** has two reaction modes: I (C3–N5 bond attacking the Cu–C1 bond of **M2**) and II (C3–N5 bond attacking the carbene-carbon C1 of **M2**).

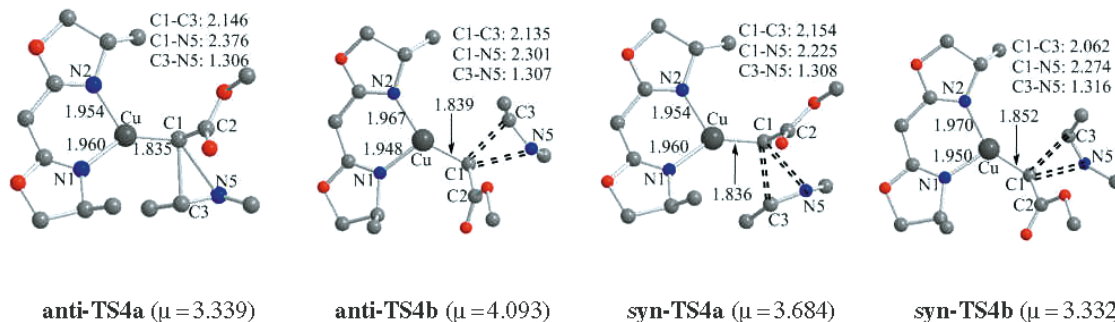
#### Reaction mode I — The C3–N5 bond attacking the Cu–C1 bond

##### Formation of the copper(I)–carbene–imine complex

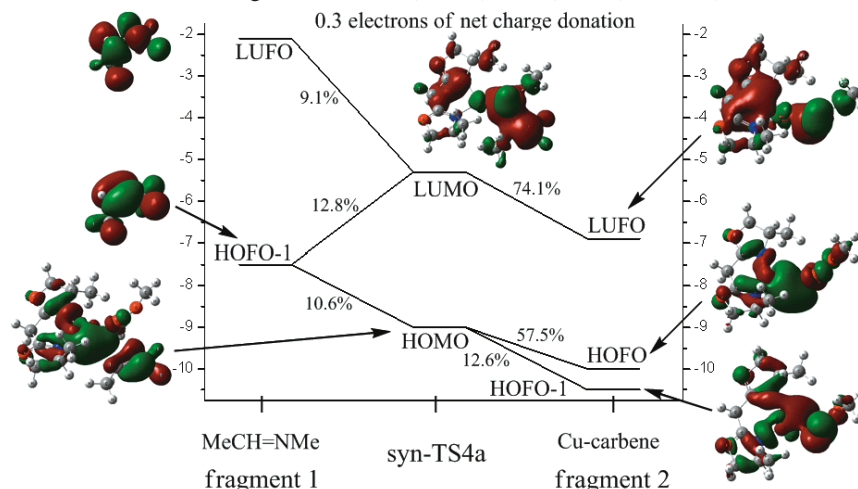
Scheme 4 shows that the attack of imines on **M2** has two reaction channels: from the *re*-surface or *si*-surface of **M2**. Transition states *syn*-TS2a and *syn*-TS2b have sole imaginary frequencies, in correspondence with the stretching vibrations of Cu–N5 and C1–C3 bonds. The Cu–N5 and C1–C3 bonds are about 1.9 and 2.4 Å. Obviously, Cu–N5 and C1–C3 bonds are strengthened markedly. It is shown by these results that Cu–N5 and C1–C3 bonds could be formed at the same time. Compared with imines and **M2**, the C3–N5 and Cu–C1 bonds are weakened and lengthened by 0.06 and 0.13 Å, respectively. There is a strong interaction between the  $\pi$  orbital of the C3–N5 bond and the  $\sigma^*$  antibond orbital of the Cu–C1 bond, which makes the electrons in the  $\pi$  orbital transfer easily to the  $\sigma^*$  antibond orbital of the Cu–C1 bond, so the  $\pi$  orbital of the C3–N5 bond has a ten-



**Fig. 6.** The transition states of the reaction mode II (bond distances in Å, angles and dihedral angles in °, moment dipoles,  $\mu$ , in D).



**Fig. 7.** Orbital interaction diagram for *syn-TS4a*, which is formed by imines (*syn*) and the copper-carbene fragment (the AOMix-CDA calculation, based on B3LYP/6-31G\*; the net charge donation,  $CT(1 \rightarrow 2) - CT(2 \rightarrow 1)$ , is 0.3 e).



dency to be fractured. As demonstrated in Fig. 3, the transition states involve a Cu–C1–C3–N5 four-membered ring, and the electron densities,  $\rho$ , of the ring critical points (RCPs) are about  $0.04 \text{ e } \text{\AA}^{-3}$ .

As illustrated in Fig. 4, the HOMO (including the orbital interaction between imines and copper-carbene) for *syn-TS2a* is a mixture of 11.1% LUFO (the LUMO of fragment orbitals), 4.9% HOFO for imines (Fig. 4, fragment 1), and 74.7% LUFO for the copper-carbene fragment (Fig. 4, fragment 2). And the LUMO for *syn-TS2a* is a mixture of 6.6% LUFO+1, 5.3% HOFO for imines, 66.1% HOFO, and 5.7% LUFO+3 for the copper-carbene fragment. It is clear that the reaction between imines and the Cu-carbene complex occurs dominantly between LUFO, HOFO, and HOFO-1 of fragment 1 and HOFO and LUFO of fragment 2 (Fig. 4). The net charge donation, which includes both charge donation and electronic polarization contributions, is 0.20 e.

In the copper-carbene-imine complex (**M3**), four atoms, Cu, C1, C3, and N5, are nearly coplanar and there is a ring critical point, with  $0.06 \text{ e } \text{\AA}^{-3}$  of electron density, inside the area encircled by the four atoms. There is a little angle between the Cu–C1–C3–N5 four-membered ring and the N1–Cu–N2 plane. NBO analysis of **M3** shows that the Cu–C1 bond shows a strong single-bonded character, and NBO energies are  $-1300 \text{ kJ/mol}$ , which are lower than those of **TS2** by  $200 \text{ kJ/mol}$ .

In addition, we tried to compute another four transition states (**TS2'**): when the C3–N5 bond attacks the Cu–C1

bond of **M2** leading to four complexes (**M3'**) (Figure S2 in the Supplementary data), N5 attacks the carbene carbon, and thus C3 attacks the copper. Unfortunately, all of our efforts failed. A loose scan from **M3'** to **M2** along the  $\sigma_{(C1-N5)}$  formation is calculated and illustrated in Fig. 5. Obviously, no first-saddle point is found in this energy curve and this fact implies that the transition states **TS2'** are not in existence.

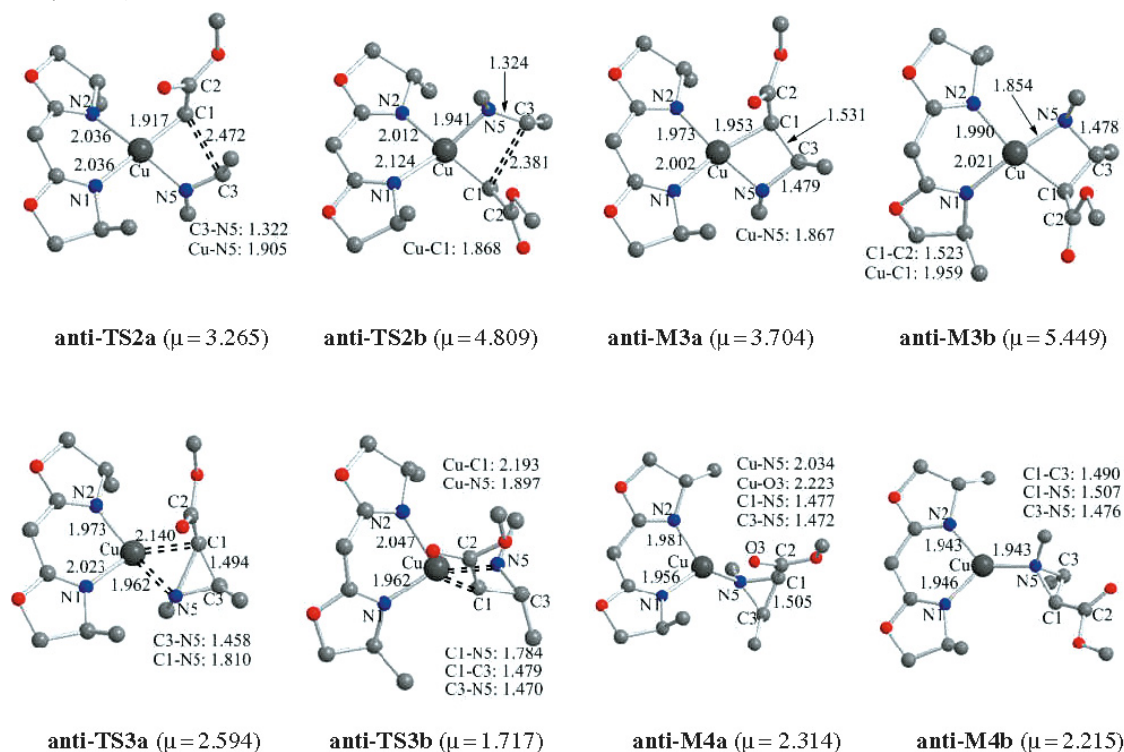
#### The elimination — Formation of aziridine carboxylate

As shown in Scheme 3, the elimination of **M3** leads, via the transition state **TS3**, to the catalyst-aziridine carboxylate complex (**M4**); the decomposition of **M4** results in the aziridine carboxylate and regenerates the active catalyst **CA2**. In the transition states *syn-TS3a* and *syn-TS3b*, the Cu–C1, Cu–N5, and C1–N5 bonds are about 2.2, 1.9, and 1.8 Å, respectively. Compared with **M3**, the Cu–C1 and Cu–N5 bonds are stretched, and the C1–N5 bonds are shortened. The transition states involve a Cu–C1–C3–N5 four-membered ring and the electron densities,  $\rho$ , of the RCPs are about  $0.07 \text{ e } \text{\AA}^{-3}$ . In *syn-M4a*, there is a Cu–N5–C1–C2–O five-membered ring, and the Cu–N5 and Cu–O bonds are 2.0 and 2.2 Å. But in the complex *syn-M4b*, there is no five-membered ring; only the Cu–N5 bond is formatted, and the distance is 1.9 Å.

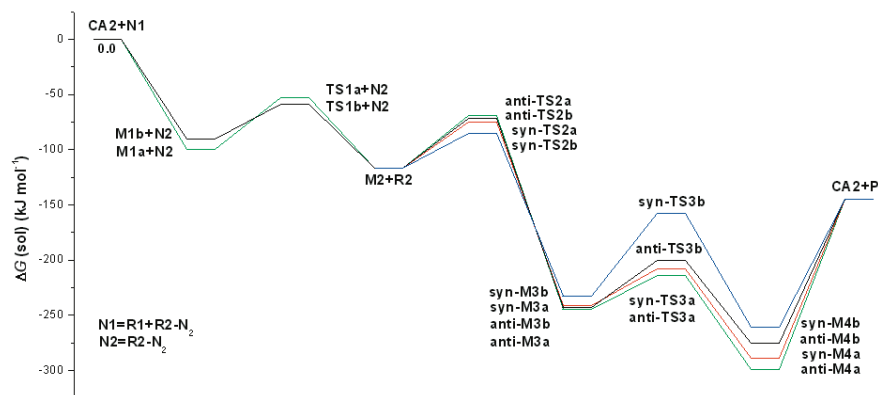
#### Reaction mode II — The C3–N5 bond attacking the carbene-carbon C1

The double bonds  $\pi_{C3-N5}$  of imines attack directly on the

**Fig. 8.** The intermediates and transition states of the reaction of **M2** and *anti*-imines (bond distances in Å, angles and dihedral angles in °, moment dipoles,  $\mu$ , in D).



**Fig. 9.** The schematic reaction profiles of copper(I)-catalyzed aziridination.



carbene-carbon of **M2**, leading to the complex *syn*-**M4**, via the transition state **TS4** (Fig. 6). As illustrated in Fig. 7, the HOMO for *syn*-**TS4a** is a mixture of 10.6% HOFO-1 for imines (Fig. 7, fragment 1), 57.5% HOFO, and 12.6% HOFO-1 for the copper-carbene fragment (Fig. 7, fragment 2). The LUMO for *syn*-**TS4a** is a mixture of 9.1% LUFO, 12.8% HOFO-1 for imines, and 74.1% LUFO for the copper-carbene fragment. It is clear that the reaction between imines and the Cu-carbene complex occurs dominantly between LUFO and HOFO-1 of fragment 1 and HOFO and LUFO of fragment 2 (Fig. 7), which is different from *syn*-**TS2a** illustrated in Fig. 4. The net charge donation, which includes both charge donation and electronic polarization contributions, is 0.30 e. The high stabilization energies of 400 kJ/mol for the  $\pi_{(N3-N5)} \rightarrow (2p)_{C1}$  in *syn*-**TS4a** and *syn*-**TS4b** reveals the strong interaction between  $\pi_{(N3-N5)}$  and

$(2p)_{C1}$  and the electron transfer tendency from  $\pi_{(N3-N5)}$  to  $(2p)_{C1}$ , which results in the formation of C1-C3 and C1-N5 bonds.

As discussed above, the reaction of **M2** with *syn*-imines has two attacking modes, I and II. Table 1 shows that the free energies of activation of *syn*-**TS2a** and *syn*-**TS2b** are lower than those of *syn*-**TS4a** and *syn*-**TS4b** by 12~24 kJ/mol. Therefore, the reaction mode I is more dominant than the reaction mode II. Therefore, in the reaction of **M2** with *syn*-imines, the attack of the C3-N5 bond on the Cu-C1 bond of **M2** is easier than that on the carbene-carbon C1 of **M2**.

#### **M2 reaction with *anti*-imines**

Similar to *syn*-imines, the attack of *anti*-imines on the copper-carbene intermediate (**M2**) also has two reaction modes, I and II. All the optimized structures on the saddle

points of this reaction profile of *anti*-imines and **M2** are similar to those of *syn*-imines and **M2**, and are shown in Fig. 6 and Fig. 8. Table 1 shows that the free energies of activation of *anti*-**TS2a** and *anti*-**TS2b** are almost equivalent to those of *anti*-**TS4a** and *anti*-**TS4b** with a difference of 1~6 kJ/mol. So, in the reaction of **M2** with *anti*-imines, the two reaction modes I and II coexist, and the attack of *anti*-imines on **M2** from the *re*-surface or the *si*-surface also coexist.

### Copper(I)-catalyzed aziridination

The copper(I)-catalyzed aziridination goes mainly through the catalyst-diazoacetate complex (**M1**), the copper(I)-carbene intermediate (**M2**), the copper-carbene-imine complex (**M3**), and the catalyst-aziridine carboxylate complex (**M4**). Table 1 and Fig. 9 show that the formation of these complexes, **M1**, **M2**, **M3**, and **M4**, are exothermic, and the released free energies are about 100, 120, 240, and 300 kJ/mol, respectively. Furthermore, calculation results indicate that copper(I)-catalyzed aziridination is exergonic by 140 kJ/mol in free energy.

As discussed above, the attack of imines on **M2** has two reaction modes: I (C3–N5 bond attacking the Cu–C1 bond of **M2**) and II (C3–N5 bond attacking the carbene–carbon C1 of **M2**). For *syn*-imines, the reaction mode I is more dominant; but for *anti*-imines, the two reaction modes coexist. Because the free energies of activation of *anti*-**TS2a** and *anti*-**TS2b** are higher than those of *syn*-**TS2a** and *syn*-**TS2b** (Table 1), the reactivity of *syn*-imines is stronger than that of *anti*-imines. Hence, *syn*-imines are the more active reactant in the copper-catalyzed aziridination.

In the reaction of **M2** with *syn*-imines, the free energy of activation of *syn*-**TS2a** is higher than *syn*-**TS2b** by 10 kJ/mol, which indicates the attack of *syn*-imines from the *si*-surface of **M2** occurs prior to that from the *re*-surface. Therefore, the reaction channel **CA2** → **M1b** → **TS1b** → **M2** → *syn*-**TS2b** → *syn*-**M3b** → *syn*-**TS3b** → *syn*-**M4b** → *syn*-**P2** is the most favorable one. The dominant product obtained from this reaction channel is of (*S,S*)-chirality.

### Conclusion

In this study, we have investigated chiral bisoxazoline–copper(I)-catalyzed aziridination of diazoacetate with *syn*-imines or *anti*-imines using density functional theory. All the intermediates and transition states were optimized completely at the B3LYP/6-31G(d) level. Calculation results confirm that Cu(I)-catalyzed aziridination goes mainly through the catalyst-diazoacetate complex (**M1**), the copper(I)-carbene intermediate (**M2**), the copper-carbene-imine complex (**M3**), and the catalyst-aziridine carboxylate complex (**M4**). For *syn*-imines, the reaction mode I (C3–N5 bond attacking the Cu–C1 bond of **M2**) is more dominant than the reaction mode II (C3–N5 bond attacking the carbene–carbon C1 of **M2**), and the attack from the *si*-surface of **M2** occurs prior to that from the *re*-surface; however, for the *anti*-imines, the reaction modes and attacks from the *si*- or *re*-surface coexist. *Syn*-imines are a more active reactant than *anti*-imines in the copper-catalyzed aziridination. The reaction channel **CA2** → **M1b** → **TS1b** → **M2** → *syn*-**TS2b** → *syn*-**M3b** → *syn*-**TS3b** → *syn*-**M4b** → *syn*-**P2** is

the most favorable one. The dominant product obtained from this reaction channel is of (*S,S*)-chirality. The solvent effect is remarkable, and it decreases the free energy of intermediates and transition states.

### Supplementary data

Supplementary data for this article are available on the journal Web site (canjchem.nrc.ca).

### References

- (1) Tanner, D. *Pure Appl. Chem.* **1993**, 65 (6), 1319. doi:10.1351/pac199365061319.
- (2) Tanner, D. *Angew. Chem. Int. Ed. Engl.* **1994**, 33 (6), 599. doi:10.1002/anie.199405991.
- (3) McCoull, W.; Davis, F. A. *Synthesis* **2000**, 2000 (10), 1347. doi:10.1055/s-2000-7097.
- (4) Dubois, L.; Dodd, R. H. *Tetrahedron* **1993**, 49 (47), 901. doi:10.1016/S0040-4020(01)80332-X.
- (5) Tanner, D.; Birgersson, C.; Dhaliwal, H. K. *Tetrahedron Lett.* **1990**, 31 (13), 1903. doi:10.1016/S0040-4039(00)98816-6.
- (6) Piotti, M. E.; Alper, H. *J. Am. Chem. Soc.* **1996**, 118 (1), 111. doi:10.1021/ja9531586.
- (7) Tsuboyama, K.; Tsuboyama, S.; Yanagita, M. *Bull. Chem. Soc. Jpn.* **1967**, 40 (12), 2954. doi:10.1246/bcsj.40.2954.
- (8) Gaebert, C.; Mattay, M. *Tetrahedron* **1997**, 53 (42), 14297. doi:10.1016/S0040-4020(97)00951-4.
- (9) Osborn, H. M. I.; Sweeney, J. *Tetrahedron Asymmetry* **1997**, 8 (11), 1693. doi:10.1016/S0957-4166(97)00177-8.
- (10) Padwa, A.; Woolhouse, A. D.; Katritzky, A. R.; Rees, C. W. In *Comprehensive Heterocyclic Chemistry*; Lwowski, W., Ed.; Pergamon: Oxford, 1984; Vol. 7, p 47.
- (11) Dermer, O. C.; Ham, G. E. *Ethylenimine and Other Aziridines*; Academic Press: New York, 1969.
- (12) Jacobsen, E. N. In *Comprehensive Asymmetric Catalysis*; Jacobsen, E. N., Pfaltz, A., Yamamoto, H., Eds.; Springer-Verlag: New York, 1999. Vol. 2, p 607.
- (13) Atkinson, R. S. *Tetrahedron* **1999**, 55 (6), 1519. doi:10.1016/S0040-4020(98)01199-5.
- (14) Kelly, J. W.; Anderson, N. L.; Evans, S. A. *J. Org. Chem.* **1986**, 51 (1), 95. doi:10.1021/jo00351a020.
- (15) Kuyil-Yeheskiely, E.; Lodder, M.; van der Marel, G. A.; van Boom, J. H. *Tetrahedron Lett.* **1992**, 33 (21), 3013. doi:10.1016/S0040-4039(00)79586-4.
- (16) Legters, J.; Thijs, L.; Zwanenburg, B. *Tetrahedron Lett.* **1989**, 30 (36), 4881. doi:10.1016/S0040-4039(01)80534-7.
- (17) Tanner, D.; Somfai, P. *Tetrahedron Lett.* **1987**, 28 (11), 1211. doi:10.1016/S0040-4039(00)95328-0.
- (18) Cainelli, G.; Panunzio, M.; Giacomoni, D. *Tetrahedron Lett.* **1991**, 32 (1), 121. doi:10.1016/S0040-4039(00)71234-2.
- (19) Evans, D. A.; Faul, M. M.; Bilodeau, M. T.; Anderson, B. A.; Barnes, D. M. *J. Am. Chem. Soc.* **1993**, 115 (12), 5328. doi:10.1021/ja00065a068.
- (20) Halfen, J. A.; Hallman, J. K.; Schultz, J. A.; Emerson, J. P. *Organometallics* **1999**, 18 (26), 5435. doi:10.1021/om9908579.
- (21) Hansen, K. B.; Finney, N. S.; Jacobsen, E. N. *Angew. Chem. Int. Ed. Engl.* **1995**, 34 (6), 676. doi:10.1002/anie.199506761.
- (22) Rasmussen, K. G.; Jørgensen, K. A. *J. Chem. Soc. Chem. Commun.* **1995**, 1401. doi:10.1039/c39950001401.
- (23) Gunnoe, T. B.; White, P. S.; Templeton, J. L.; Casarrubios,



- L. *J. Am. Chem. Soc.* **1997**, *119* (13), 3171. doi:10.1021/ja9640206.
- (24) Ha, H.-J.; Kang, K.-H.; Suh, J.-M.; Ahn, Y.-G. *Tetrahedron Lett.* **1996**, *37* (39), 7069. doi:10.1016/0040-4039(96)01554-7.
- (25) Casarrubios, L.; Perez, J. A.; Brookhart, M.; Templeton, J. L. *J. Org. Chem.* **1996**, *61* (24), 8358. doi:10.1021/jo961391w.
- (26) Rasmussen, K. G.; Jørgensen, K. A. *J. Chem. Soc. Perkin Trans. 1* **1997**, 1287. doi:10.1039/a608098g.
- (27) Xie, W.; Fang, J.; Li, J.; Wang, P. G. *Tetrahedron* **1999**, *55* (45), 12929. doi:10.1016/S0040-4020(99)00791-7.
- (28) Antilla, J. C.; Wulff, W. D. *J. Am. Chem. Soc.* **1999**, *121* (21), 5099. doi:10.1021/ja9905187.
- (29) Juhl, K.; Hazell, R. G.; Jørgensen, K. A. *J. Chem. Soc. Perkin Trans. 1* **1999**, 2293. doi:10.1039/a903521d.
- (30) Li, A.-H.; Dai, L.-X.; Aggarwal, V. K. *Chem. Rev.* **1997**, *97* (6), 2341. doi:10.1021/cr960411r. PMID:11848902.
- (31) Lee, S.-H.; Han, T.-D.; Yu, K.; Ahn, K.-H. *Bull. Korean Chem. Soc.* **2001**, *22*, 449.
- (32) Straub, B. F.; Hofmann, P. *Angew. Chem. Int. Ed. Engl.* **2001**, *40* (7), 1288. doi:10.1002/1521-3773(20010401)40:7<1288::AID-ANIE1288>3.0.CO;2-6. PMID:11301454.
- (33) Ikeno, T.; Iwakura, I.; Yamada, T. *J. Am. Chem. Soc.* **2002**, *124* (51), 15152. doi:10.1021/ja027713x. PMID:12487572.
- (34) Fraile, J. M.; García, J. I.; Martínez-Merino, V.; Mayoral, J. A.; Salvatella, L. *J. Am. Chem. Soc.* **2001**, *123* (31), 7616. doi:10.1021/ja003695c. PMID:11480983.
- (35) Comba, P.; Lang, C.; de Laorden, C. L.; Muruganatham, A.; Rajaraman, G.; Wadepohl, H.; Zajaczkowski, M. *Chem. Eur. J.* **2008**, *14* (17), 5313. doi:10.1002/chem.200701910.
- (36) Meng, Q.; Li, M. *J. Mol. Struct. THEOCHEM* **2006**, *765* (1–3), 13. doi:10.1016/j.theochem.2006.02.026.
- (37) Meng, Q.; Li, M.; Tang, D.; Shen, W.; Zhang, J. *J. Mol. Struct. THEOCHEM* **2004**, *711* (1–3), 193. doi:10.1016/j.theochem.2004.06.050.
- (38) Frisch, M. J.; Trucks, G. W.; Schlegel, H. B.; Scuseria, G. E.; Robb, M. A.; Cheeseman, J. R.; Montgomery, J. A., Jr.; Vreven, T.; Kudin, K. N.; Burant, J. C.; Millam, J. M.; Iyengar, S. S.; Tomasi, J.; Barone, V.; Mennucci, B.; Cossi, M.; Scalmani, G.; Rega, N.; Petersson, G. A.; Nakatsuji, H.; Hada, M.; Ehara, M.; Toyota, K.; Fukuda, R.; Hasegawa, J.; Ishida, M.; Nakajima, T.; Honda, Y.; Kitao, O.; Nakai, H.; Klene, M.; Li, X.; Knox, J. E.; Hratchian, H. P.; Cross, J. B.; Adamo, C.; Jaramillo, J.; Gomperts, R.; Stratmann, R. E.; Yazyev, O.; Austin, A. J.; Cammi, R.; Pomelli, C.; Ochterski, J. W.; Ayala, P. Y.; Morokuma, K.; Voth, G. A.; Salvador, P.; Dannenberg, J. J.; Zakrzewski, V. G.; Dapprich, S.; Daniels, A. D.; Strain, M. C.; Farkas, O.; Malick, D. K.; Rabuck, A. D.; Raghavachari, K.; Foresman, J. B.; Ortiz, J. V.; Cui, Q.; Baboul, A. G.; Clifford, S.; Cioslowski, J.; Stefanov, B. B.; Liu, G.; Liashenko, A.; Piskorz, P.; Komaromi, I.; Martin, R. L.; Fox, D. J.; Keith, T.; Al-Laham, M. A.; Peng, C. Y.; Nanayakkara, A.; Challacombe, M.; Gill, P. M. W.; Johnson, B.; Chen, W.; Wong, M. W.; Gonzalez, C.; Pople, J. A. *Gaussian 03*, revision B.03; Gaussian, Inc.: Pittsburgh, PA, 2003.
- (39) Parr, R. G.; Yang, W. *Density-functional Theory of Atoms and Molecules*; Oxford University Press: New York, 1989.
- (40) Pisano, L.; Farriol, M.; Asensio, X.; Gallardo, I.; González-Lafont, A.; Lluch, J. M.; Marquet, J. *J. Am. Chem. Soc.* **2002**, *124* (17), 4708. doi:10.1021/ja012444g. PMID:11971720.
- (41) Pierini, A. B.; Vera, D. M. A. *J. Org. Chem.* **2003**, *68* (24), 9191. doi:10.1021/jo035087w. PMID:14629135.
- (42) Pratt, D. A.; de Heer, M. I.; Mulder, P.; Ingold, K. U. *J. Am. Chem. Soc.* **2001**, *123* (23), 5518. doi:10.1021/ja004081a. PMID:11389634.
- (43) Becke, A. D. *Phys. Rev. A* **1988**, *38* (6), 3098. doi:10.1103/PhysRevA.38.3098. PMID:9900728.
- (44) Becke, A. D. *J. Chem. Phys.* **1993**, *98* (7), 5648. doi:10.1063/1.464913.
- (45) Lee, C.; Yang, W.; Parr, R. G. *Phys. Rev. B* **1988**, *37* (2), 785. doi:10.1103/PhysRevB.37.785.
- (46) Gonzalez, C.; Schlegel, H. B. *J. Phys. Chem.* **1990**, *94* (14), 5523. doi:10.1021/j100377a021.
- (47) Flükiger, P.; Lüthi, H. P.; Portmann, S.; Weber, J. *MOLEKEL 4.3*; Swiss Center for Scientific Computing: Manno, Switzerland, 2000–2002.
- (48) Portmann, S.; Lüthi, H. P. *Chimia (Aarau)* **2000**, *54*, 766.
- (49) Miertus, S.; Tomasi, J. *Chem. Phys.* **1982**, *65* (2), 239. doi:10.1016/0301-0104(82)85072-6.
- (50) Bader, R. F. W. *Atoms in Molecules. In A Quantum Theory: International Series of Monographs in Chemistry*; Oxford University Press: Oxford, UK, 1990.
- (51) Bader, R. F. W.; Popelier, P. L. A.; Keith, T. A. *Angew. Chem. Int. Ed. Engl.* **1994**, *33* (6), 620. doi:10.1002/anie.199406201.
- (52) Carpenter, J. E.; Weinhold, F. *J. Mol. Struct. THEOCHEM* **1988**, *169* (1), 41. doi:10.1016/0166-1280(88)80248-3.
- (53) Foster, J. P.; Weinhold, F. *J. Am. Chem. Soc.* **1980**, *102* (24), 7211. doi:10.1021/ja00544a007.
- (54) Reed, A. E.; Weinstock, R. B.; Weinhold, F. *J. Chem. Phys.* **1985**, *83* (2), 735. doi:10.1063/1.449486.
- (55) Reed, A. E.; Curtiss, L. A.; Weinhold, F. *Chem. Rev.* **1988**, *88* (6), 899. doi:10.1021/cr00088a005.
- (56) Biegler-König, F.; Schönbohm, J.; Derdau, R.; Bayles, D.; Bader, R. F. W. *AIM 2000*, version 2.0; McMaster University: Hamilton, ON, 2002.
- (57) Glendening, E. D.; Badenhoop, J. K.; Reed, A. E.; Carpenter, J. E.; Bohmann, J. A.; Morales, C. M.; Weinhold, F. *NBO 5.0*; Theoretical Chemistry Institute, University of Wisconsin: Madison, WI, 2001.
- (58) Gorelsky, S. I.; Lever, A. B. P. *J. Organomet. Chem.* **2001**, *635* (1–2), 187. doi:10.1016/S0022-328X(01)01079-8.
- (59) Gorelsky, S. I. *AOMix: Program for Molecular Orbital Analysis*; York University: Toronto, ON, 1997; Available from <http://www.sg-chem.net/aomix>.
- (60) Gorelsky, S. I.; Ghosh, S.; Solomon, E. I. *J. Am. Chem. Soc.* **2006**, *128* (1), 278. doi:10.1021/ja055856o. PMID:16390158.



# Synthesis of metallocarbonyl substituted 1,2,3-triazole complexes via copper(I)-catalyzed azide-alkyne cycloaddition

Bogna Rudolf

**Abstract:**  $(\eta^5\text{-C}_5\text{H}_5)\text{M}(\text{CO})_x(\eta^1\text{-}N\text{-maleimidato})$  ( $\text{M} = \text{Fe}$ ,  $x = 2$ ;  $\text{M} = \text{W}$ ,  $x = 3$ ) complexes react with propargylamine and propargyl alcohol giving products from the Michael addition to the  $\eta^1\text{-}N\text{-maleimidato}$  ligand. Metallocarbonyl compounds bearing a terminal alkyne group were reacted with organic azides affording corresponding 1,2,3-triazoles in high yields. One of these metallocarbonyl 1,2,3-triazoles ( $\text{M} = \text{Fe}$ ,  $x = 2$ ) was characterized by X-ray diffraction.

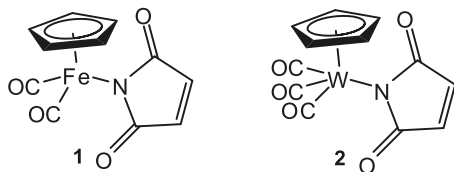
**Key words:** copper(I)-catalyzed azide-alkyne cycloaddition, click chemistry, metallocarbonyl complexes, X-ray structure.

**Résumé :** Les complexes  $(\eta^5\text{-C}_5\text{H}_5)\text{M}(\text{CO})_x(\eta^1\text{-}N\text{-maléimidato})$  ( $\text{M} = \text{Fe}$ ,  $x = 2$ ;  $\text{M} = \text{W}$ ,  $x = 3$ ) réagissent avec la propargylamine et l'alcool propargylique pour conduire à la formation de produits d'addition de Michael sur le ligand  $\eta^1\text{-}N\text{-maléimidato}$ . La réaction de composés métallcarbonyles portant un groupe alcyne terminal avec des azotures organiques conduit à la formation des 1,2,3-triazoles correspondants avec des rendements élevés. Faisant appel à la diffraction des rayons-X, on a caractérisé le métallcarbonyl-1,2,3-triazole dans lequel  $\text{M} = \text{Fe}$  et  $x = 2$ .

**Mots-clés :** cycloaddition azoture-alcyne catalysée par le cuivre(I), chimie de cliquage, complexes métallcarbonyles, structure, diffraction des rayons X.

## Introduction

The copper(I) catalyzed, regioselective synthesis of 1,4-disubstituted-1,2,3-triazoles, from azides and terminal alkynes, which was developed by Sharpless et al., has been shown to be amongst the most popular reactions recently studied, known as "click chemistry"<sup>1-3</sup>. There have been numerous applications of this reaction in the fields of bioconjugation, materials science, and drug discovery.<sup>4-7</sup> Copper(I)-catalyzed azide-alkyne cycloaddition (CuAAC) has been used to obtain conjugates which possess numerous functional subunits with fluorescent or electrochemical properties.<sup>8,9</sup> However, this methodology has not yet been applied to connecting metallocarbonyl complexes with organic ligands. In view of this situation, I became interested in exploring the CuAAC reaction as a synthetic method for preparing 1,4-disubstituted-1,2,3-triazoles bearing IR-detectable metallocarbonyl complexes.<sup>10</sup> Over the past years we have explored the chemistry of the metallocarbonyl  $(\eta^5\text{-C}_5\text{H}_5)\text{M}(\text{CO})_x(\eta^1\text{-}N\text{-maleimidato})$  complexes of Fe, **1**, and W, **2**,<sup>11,12</sup> which were applied as labels of peptides and proteins, with potential applications in immunoassay analysis.<sup>12-16</sup>



It appeared of interest to introduce a terminal alkyne group to compounds **1** or **2** to form metallocarbonyl complexes that would be able to react with organic azides. Such a process could be an entry to new selective labeling of biomolecules, using the CuAAC reaction. In this paper, I report the synthesis of two new metallocarbonyl complexes bearing terminal alkyne ligands, **3** and **4**, and a preliminary study of their reactions with organic azide derivatives in the presence of a Cu(I) catalyst. The structure of the 1,3-cycloaddition product, **5**, has been established by a single crystal X-ray analysis.

## Results and discussion

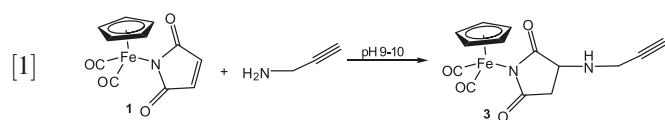
The Huisgen 1,3-cycloaddition of organic azides and alkynes has been shown to be the most direct route to obtaining 1,2,3-triazoles. The use of Cu(I) complexes in this process led to the formation of one regioisomer, a 1,4-disubstituted 1,2,3-triazole derivative. Cu(I) halide salts can also be used, or, alternatively, the Cu(I) complex could be generated in situ by the reduction of Cu(II) salts.<sup>1-3</sup> The reaction could be performed in various solvents or mixtures of organic solvents, or in water. Owing to the high regioselectivity, high yields, and an exceptional tolerance towards a wide range of functional groups and reaction conditions, the copper(I)-catalyzed azide-alkyne cycloaddition has been found to have numerous applications in biochemistry research, allowing the regioselective incorporation of various labels to biomolecules.<sup>17-20</sup>

Received 21 May 2010. Accepted 29 June 2010. Published on the NRC Research Press Web site at canjchem.nrc.ca on 8 September 2010.

**B. Rudolf.** Department of Organic Chemistry, University of Łódź, Tamka 12, Łódź 91-403, Poland.  
(e-mail: brudolf@chemia.uni.lodz.pl).

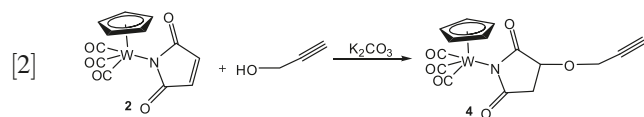
There has been no reported research concerning the Huisgen 1,3-cycloaddition of metallocarbonyl complexes in the literature, to my knowledge; however, there were several published examples of ferrocene compounds bearing azide or alkyne groups, which underwent the CuAAC reactions leading to the expected triazole products.<sup>21–25</sup> To investigate the CuAAC reaction of metallocarbonyl complexes with azides, it was first necessary to synthesize such complexes, bearing an alkyne group.

Because complex **1** reacted with primary amines at pH 9–10 providing aza-Michael addition products,<sup>13</sup> the reaction with propargylamine seemed a straightforward synthetic approach for the introduction of the terminal alkyne function to this complex (eq. [1])



The reaction was carried out at room temperature in MeOH–H<sub>2</sub>O, and afforded a yellow crystalline product. The <sup>1</sup>H NMR spectrum confirmed the structure of **3**, with the signal at 6.68 ppm, characteristic of the ethylenic protons in **1**, being absent, while the complex signals attributed to the succinimide ring and the propargyl protons were observed at 2.42, 3.33, and 3.83, including the acetylene proton signal, which appeared at 2.09 ppm, as a triplet.

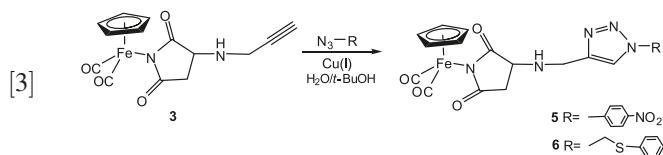
Since it was reported that maleimide derivatives undergo an oxa-Michael addition reaction with alcohols in the presence of K<sub>2</sub>CO<sub>3</sub> under mild reaction conditions,<sup>26</sup> I decided to react **2** with propargyl alcohol, to give **4** (eq. [2]). This reaction resulted in the isolation of a yellow crystalline complex, whose <sup>1</sup>H NMR spectrum confirmed the structure as **4** (Yield 42%)



The <sup>1</sup>H NMR spectrum showed a triplet at 2.48 ppm, which was expected for the alkyne proton, with an absence of the singlet at ~6.7 ppm, characteristic for the olefinic protons in the substrate, **2**. Further evidence of the oxa-Michael addition to the maleimide double bond were the signals of the succinimide protons at 2.66, 3.03, and 4.48 ppm.

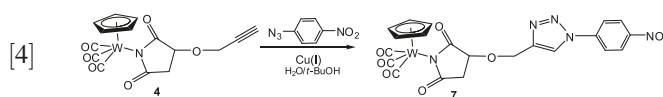
Metallocarbonyl complexes, **3** and **4**, displayed the characteristic strong absorption bands in their IR spectra, the ν<sub>C≡O</sub> appearing in the 1950–2060 cm<sup>–1</sup> spectral region, which is usually free of any absorption of biomolecules or biological matrices.

With the successful synthesis of complexes **3** and **4**, their reactivity towards organic azides in the presence of a CuCl–Cu catalyst were investigated. Both compounds were allowed to react with *p*-nitrophenyl azide, and complex **3** was also reacted with (phenylthio)methyl azide. In all cases, the cycloaddition reaction took place, and the expected triazoles, **5–7**, were isolated in 81%–88% yields (eqs. [3] and [4]).



The yellow products, **5** and **6**, were isolated by flash chromatography and crystallized from CH<sub>2</sub>Cl<sub>2</sub>–heptane. The identity and purity of these compounds were confirmed by spectroscopic methods and elemental analyses. The singlets in the <sup>1</sup>H NMR spectra of **5** and **6** (δ 8.06 and 7.51 ppm, respectively) were attributed to the triazole ring protons, and provided evidence of the formation of this heterocyclic ring. The structure of 1,2,3-triazole **5** was also confirmed by single crystal X-ray diffraction (vide infra).

The 1,2,3-triazole, **7**, was synthesized in the same manner from alkyne complex **4** and *p*-nitrophenyl azide in the presence of the CuCl–Cu catalyst (eq. [4]). The expected product was isolated in 81% yield, as an orange oil. The lack of an alkyne proton signal and the appearance of a singlet at δ 8.19 ppm in its <sup>1</sup>H NMR spectrum provided evidence of the formation of a 1,2,3-triazole derivative.



### The X-ray crystal structure of **5**

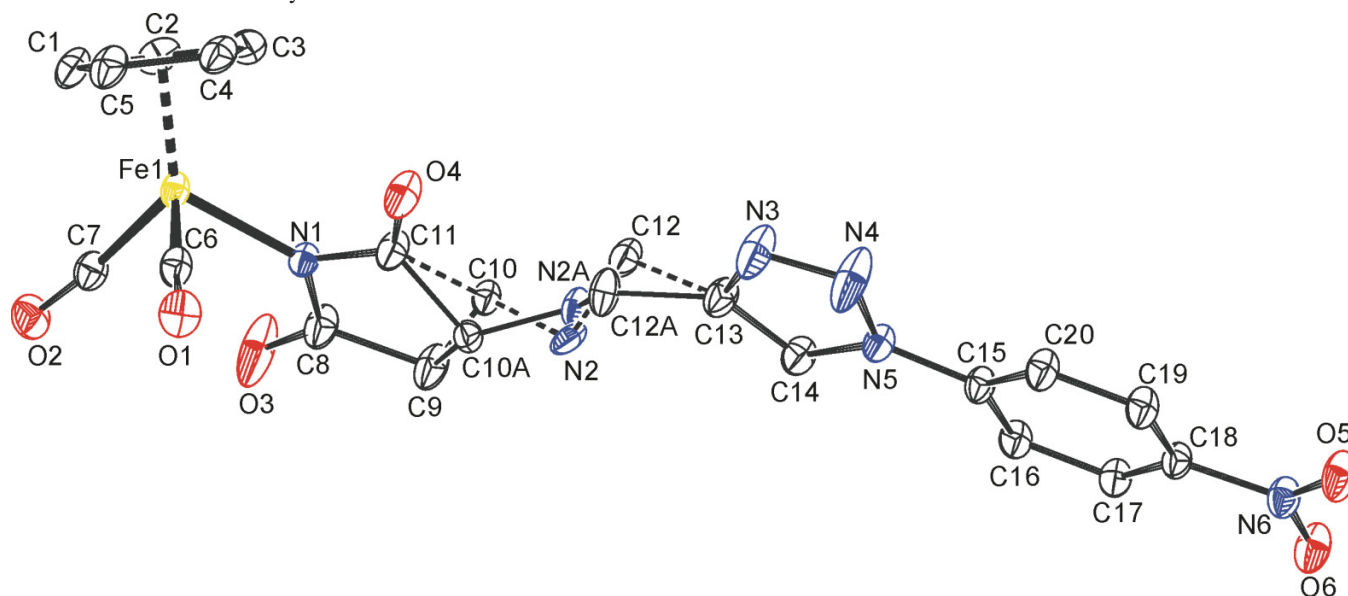
Crystals of **5** suitable for X-ray structure determination were grown from CH<sub>2</sub>Cl<sub>2</sub>–heptane. Compound **5** crystallized in the triclinic *P*1 space group (see Fig. 1 for the graphical representation). The selected crystal data and structure refinement details are shown in Table 1. The triazole *p*-nitrophenyl substituent was shown to be attached to the succinimide ring in a position opposite to the Fp moiety. The best plane of the succinimide ring forms an angle of 44.02(19)° with the best plane of the Cp ring. The succinimide ring was nearly coplanar with the triazole and *p*-nitrophenyl rings. This was shown by the relatively small values of the dihedral angles, being 9.00(19)° and 15.87(18)° for the triazole and phenyl rings, respectively. The triazole and phenyl rings were found to be coplanar, with the dihedral angle being 8.61(12)°. No classical hydrogen bonds were found for this compound; however, the crystal structure of **5** was stabilized by several weak intermolecular, non-covalent interactions of the C–H...O type.

Selected bond lengths (Å) and angles (°) are gathered in Table 2.

### Conclusions

The metallocarbonyl complexes **3** and **4**, with terminal alkyne bonds, have been synthesized, and found to be effective CuAAC reaction substrates. Under the Sharpless conditions, the alkynes **3** and **4** effectively reacted with selected organic azides, affording the corresponding 1,2,3-triazoles in high yields. We plan to use this technique to develop new bioprobes for Carbonyl Metallo Immuno Assay (CMIA).

**Fig. 1.** ORTEP drawing of compound **5** with the atom-labelling scheme. Displacements ellipsoids are drawn at the 50% probability level. H atoms are omitted for clarity.



**Table 1.** Crystallographic data and structure refinement of **5**.

Chemical formula	C <sub>20</sub> H <sub>16</sub> FeN <sub>6</sub> O <sub>6</sub>
Measurement temperature	293 K
Beam length $\lambda$ (Å)	0.71073
Space group	<i>P</i> 1
<i>a</i> (Å)	6.6833(3)
<i>b</i> (Å)	11.9347(7)
<i>c</i> (Å)	12.4586(6)
$\alpha$ (°)	79.417(3)
$\beta$ (°)	84.442(3)
$\gamma$ (°)	85.386(3)
<i>V</i> (Å <sup>3</sup> )	970.25(9)
<i>Z</i>	2
Absorption coefficient (mm <sup>-1</sup> )	0.83
Independent reflections	5794, 4644
<i>T</i> <sub>min</sub> , <i>T</i> <sub>max</sub>	0.6914, 0.7461
( <i>sin</i> $\theta$ / $\lambda$ ) <sub>max</sub> (Å <sup>-1</sup> )	0.70
<i>R</i> <sub>(int)</sub> , <i>R</i> <sub>(sigma)</sub>	0.0000, 0.0362
<i>R</i> <sub>1</sub> [ <i>I</i> > 2σ ( <i>I</i> )], <i>R</i> <sub>1</sub> all	0.0426, 0.0568
<i>wR</i> <sub>2</sub> all	0.1122
Goodness-of-fit	1.060

**Table 2.** Bond lengths (Å) and angles (°) for **5**.

Bond lengths (Å)	
Fe(1)—C(6)	1.781(2)
Fe(1)—C(7)	1.783 (2)
Fe(1)—N(1)	1.9773(15)
Fe(1)—C(1)	2.083(2)
C(8)—O(3)	1.212(3)
C(10)—N(2)	1.450(12)
C(10a)—N(2a)	1.451(9)
C(11)—O(4)	1.209(2)
C(12A)—N(2A)	1.450(9)
C(12A)—C(13)	1.523(5)
N(1)—C(8)	1.363(2)
N(3)—N(4)	1.302(3)
N(4)—N(5)	1.349(2)
N(5)—C(15)	1.417(2)
O(2)—C(7)	1.134(3)
Bond angles (°)	
C(7)—Fe(1)—C(1)	88.96(9)
C(7)—Fe(1)—N(1)	95.55(8)
C(11)—N(1)—Fe(1)	120.72(13)
C(20)—C(15)—N(5)	118.31(17)
N(2)—C(12)—C(13)	112.5(6)
N(2A)—C(10A)—C(11)	113.3(5)
N(4)—N(5)—C(15)	118.88(16)
O(2)—C(7)—Fe(1)	174.19(18)
O(4)—C(11)—C(10)	123.6(2)
O(5)—N(6)—C(18)	118.28(17)
O(5)—N(6)—O(6)	123.84(17)

## Experimental section

### General remarks

The <sup>1</sup>H NMR spectra were recorded in CDCl<sub>3</sub> on a Varian Gemini 200BB (200 MHz for <sup>1</sup>H) spectrometer and referenced to internal tetramethylsilane. The IR spectra were recorded in CHCl<sub>3</sub> on a FTIR NEXUS (Thermo Nicolet) spectrometer. Elemental analyses were performed by the Analytical Services of the Center of Molecular and Macromolecular Studies of the Polish Academy of the Sciences (Łódź). All solvents were purified according to standard procedures. Chromatographic separations were performed on Silica gel Merck 60 (230–400 mesh ASTM). All reactions were carried out under argon.

### Materials

Complexes **1** and **2** were synthesized as previously described.<sup>11,12</sup> Propargylamine, propargyl alcohol, and (phenylthio)methyl azide were purchased from Sigma-Aldrich. Propargyl alcohol and propargylamine were distilled before

use. *p*-Nitrophenyl azide was synthesized according to Meudtner and al.<sup>27</sup>

### Synthesis of 3

Propargylamine (20  $\mu$ L, 0.37 mmol) and aqueous solution of  $K_2CO_3$  pH 9–10 (2 mL) were added to an argon-saturated solution of complex **1** (100 mg, 0.37 mmol) in MeOH (3 mL) and the reaction mixture was stirred overnight at rt. After this time the mixture was diluted with water (15 mL) and extracted with  $CH_2Cl_2$  ( $3 \times 15$  mL). The organic phases were combined, dried over  $MgSO_4$ , and concentrated under reduced pressure. The residue was subjected to column chromatography; a yellow band containing the starting material **1** was eluted with dichloromethane, followed by a yellow band containing product **3** eluted with chloroform–MeOH (9:1). Crystallization from  $CH_2Cl_2$ –heptane (3:1) gave an analytically pure sample; yield: 57 mg (47%). IR  $\nu$  ( $cm^{-1}$ ): 3290 (CH alkyne), 2103 ( $C\equiv C$ ), 2056, 2009 ( $C\equiv O$ ), 1639 (CO imide).  $^1H$  NMR (200 MHz,  $CDCl_3$ )  $\delta$  (ppm): 2.09 (t,  $J = 1.4$  Hz, H, CH, alkyne), 2.42 (dd,  $J = 5.1$  Hz,  $J = 16$  Hz, H, succinimide), 2.83 (dd,  $J = 7.9$  Hz,  $J = 16$  Hz, H, succinimide), 3.33 (d,  $J = 17$  Hz, H,  $CH_2$ ), 3.58 (d,  $J = 17$  Hz, H,  $CH_2$ ), 3.83 (dd,  $J = 5.1$  Hz,  $J = 16$  Hz, H, succinimide), 5.04 (s, 5H, Cp). Anal. calcd. for  $C_{14}H_{12}FeN_2O_4$ : C 54.24, H 3.66, N 8.54; found C 51.42, H 3.61, N 8.49.

### Synthesis of 4

Tungsten complex **2** (120 mg, 0.29 mmol) was dissolved in propargyl alcohol (3 mL) and a saturated aqueous solution of  $K_2CO_3$  (2 mL) was added. Then the reaction mixture was stirred overnight at rt. After this time, the mixture was diluted with water (15 mL) and extracted with  $CH_2Cl_2$  ( $3 \times 15$  mL). The organic phases were combined, dried over  $MgSO_4$ , and concentrated at reduced pressure. The residue was subjected to column chromatography; an orange band containing the starting material **2** was eluted with hexane–dichloromethane (1:4), followed by a yellow band containing product **4** eluted by the mixture of dichloromethane–MeOH 19:1. Crystallization from  $CH_2Cl_2$ –heptane (3:1) gave an analytically pure sample; yield: 59 mg (42%). IR  $\nu$  ( $cm^{-1}$ ): 3307 (CH alkyne), 2100 ( $C\equiv C$ ), 2056, 2046, 1959 ( $C\equiv O$ ), 1655 (CO imide).  $^1H$  NMR (200 MHz,  $CDCl_3$ )  $\delta$  (ppm): 2.48 (t,  $J = 2.4$  Hz, H, CH alkyne), 2.66 (dd,  $J = 4.6$  Hz,  $J = 20$  Hz, H, succinimide), 3.03 (dd,  $J = 9.2$  Hz,  $J = 16$  Hz, H, succinimide), 4.48 (dd,  $J = 4.6$  Hz,  $J = 20$  Hz, H, succinimide), 4.53 (t, 2H,  $CH_2$ ,  $J = 4$  Hz, H,  $CH_2$ ), 5.64 (s, 5H, Cp). Anal. calcd. for  $C_{15}H_{11}NO_6W$ : C 37.14, H 2.29, N 2.89; found C 37.25, H 2.47, N 2.89.

### Synthesis of metallocarbonyl 1,2,3-triazoles 5–7

A typical procedure for the 1,3-dipolar cycloaddition of organic azides to metallocarbonyl alkynes was as follows: azide (0.11 mmol),  $CuCl$  (2 mg), and  $Cu$  (50 mg as thin wire) were added to a solution of **3** or **4** (0.11 mmol) in the mixture of  $H_2O$ –*tert*-butanol (1:1). Then the reaction mixture was stirred overnight. The resulting solution was filtered and concentrated under reduced pressure. The residue was diluted in  $CH_2Cl_2$  and crude product was chromatographed on silica gel, using the mixture of  $MeOH$ – $CH_2Cl_2$  (1:19) as eluent to obtain compounds **5**–**7**. Crystallization

from  $CH_2Cl_2$ –heptane (2:1) gave an analytically pure sample.

**5** Yield: 45 mg (84%). IR  $\nu$  ( $cm^{-1}$ ): 2045, 1999 ( $C\equiv O$ ), 1636 (CO imide), 1525, 1343 ( $NO_2$ ).  $^1H$  NMR (200 MHz,  $CDCl_3$ )  $\delta$  (ppm): 2.45 (dd,  $J = 5$  Hz,  $J = 16$  Hz, H, succinimide), 2.85 (dd,  $J = 8.2$  Hz,  $J = 16$  Hz, H, succinimide), 3.72 (dd,  $J = 5$  Hz,  $J = 8$  Hz, H, succinimide), 4.06 (s, 2H,  $CH_2$ ), 5.04 (s, 5H, Cp), 7.97 (d,  $J = 9.1$  Hz, 2H), 8.06 (s, triazole H), 8.41 (d,  $J = 9.1$  Hz, 2H). Anal. calcd. for  $C_{20}H_{16}FeN_6O_6$ : C 48.80, H 3.28, N 17.07; found: C 48.69, H 3.41, N 16.89.

**6** Yield: 47 mg (88%). IR  $\nu$  ( $cm^{-1}$ ): 2044, 1993 ( $C\equiv O$ ), 1636 (CO imide).  $^1H$  NMR (200 MHz,  $CDCl_3$ )  $\delta$  (ppm): 2.38 (dd,  $J = 5$  Hz,  $J = 18$  Hz, H, succinimide), 2.79 (dd,  $J = 8$  Hz,  $J = 16$  Hz, H, succinimide), 3.60 (dd,  $J = 5$  Hz,  $J = 8$  Hz, H, succinimide), 3.91 (s, 2H,  $CH_2$ ), 5.03 (s, 5H, Cp), 5.61 (s,  $CH_2$ , H), 7.31 (s, 5H), 7.51 (s, triazole H). Anal. calcd. for  $C_{21}H_{19}FeN_5O_4$ : C 51.13, H 3.88, N 14.20; found C 50.98, H 4.17, N 14.23.

**7** Yield: 58 mg 81%. IR  $\nu$  ( $cm^{-1}$ ): 2037, 1932 ( $C\equiv O$ ), 1636 (CO imide).  $^1H$  NMR (200 MHz,  $CDCl_3$ )  $\delta$  (ppm): 2.66 (dd,  $J = 4.8$  Hz,  $J = 18$  Hz, H, succinimide), 3.04 (dd,  $J = 8.3$  Hz,  $J = 20$  Hz, H, succinimide), 4.44 (dd,  $J = 4.8$  Hz,  $J = 8$  Hz, H, succinimide), 5.07 (dd,  $J = 12.5$  Hz, 2H,  $CH_2$ ), 5.64 (s, 5H, Cp), 7.98 (d,  $J = 9$  Hz, 2H), 8.19 (s, H, =CH), 8.43 (d,  $J = 9$  Hz, 2H), 8.06 (s, triazole H). ESI-MS ( $M+Na$ )  $m/z = 672$ . Anal. calcd. for  $C_{21}H_{15}N_5O_8W$ : C 38.85, H 2.33, N 10.79; found C 39.05, H 2.28.

### X-ray structure determination of 5

Single-crystal X-ray measurement of **5** was performed on a BRUKER APEX II ULTRAK-axis diffractometer with a TXS rotating anode using  $MoK\alpha$  radiation at 293 K. The data were collected using the omega scan measurement method, with 0.5 degrees scan width and 30s maximal counting time. The  $\theta$  angle for data collection was varied in the range of 5.00–20.00°. The data were corrected with respect to Lorentz and polarization effects. An analytical absorption correction was applied using SADABS.<sup>28</sup> Indexing, integration, and scaling were performed with original Bruker Apex II software.<sup>29</sup> The structure was solved using direct methods and refined using SHELXL.<sup>30</sup> The refinement was based on  $F^2$  for all reflections. Weighted  $R$  factors  $wR$  and all goodness-of-fit  $S$  values were based on  $F^2$ . All non-hydrogen atoms were refined anisotropically. Hydrogen atoms were refined on idealized positions using a riding model.

### Supplementary data

Supplementary data for this article are available on the journal Web site (canjchem.nrc.ca). CCDC 763118 contains the X-ray data in CIF format for this manuscript. These data can be obtained, free of charge, via [www.ccdc.cam.ac.uk/conts/retrieving.html](http://www.ccdc.cam.ac.uk/conts/retrieving.html) (or from the Cambridge Crystallographic Data Centre, 12 Union Road, Cambridge CB2 1EZ, UK; fax +44 1223 336033; or [deposit@ccdc.cam.ac.uk](mailto:deposit@ccdc.cam.ac.uk)).

### Acknowledgements

Dr. Damian Plazuk is gratefully acknowledged for the synthesis of *p*-nitrophenylazide. The Polish Ministry of Sci-



ence and Education is gratefully acknowledged for financial support (Grant PBZ-KBN 118/T09/12).

## References

- (1) Rostovtsev, V. V.; Green, L. G.; Fokin, V. V.; Sharpless, K. B. *Angew. Chem. Int. Ed.* **2002**, *41* (14), 2596. doi:10.1002/1521-3773(20020715)41:14<2596::AID-ANIE2596>3.0.CO;2-4.
- (2) Tornøe, C. W.; Christensen, C.; Meldal, M. *J. Org. Chem.* **2002**, *67* (9), 3057. doi:10.1021/jo011148j. PMID:11975567.
- (3) Gil, M. V.; Arévalo, M. J.; López, O. *Synthesis* **2007**, 2007 (11), 1589. doi:10.1055/s-2007-966071.
- (4) Dyson, P. J.; Sava, G. *Dalton Trans.* **2006**, (16), 1929. doi:10.1039/b601840h. PMID:16609762.
- (5) Ming, L.-J. *Med. Res. Rev.* **2003**, *23* (6), 697. doi:10.1002/med.10052. PMID:12939790.
- (6) Top, S.; Tang, J.; Vessièrès, A.; Carrez, D.; Provot, C.; Jaouen, G. *Chem. Commun. (Cambridge)* **1996**, (8), 955. doi:10.1039/cc9960000955.
- (7) Top, S.; Vessièrès, A.; Cabestaing, C.; Laios, I.; Leclercq, G.; Provot, C.; Jaouen, G. *J. Organomet. Chem.* **2001**, *637*–*639* (1–2), 500. doi:10.1016/S0022-328X(01)00953-6.
- (8) Kosiova, I.; Kovackova, S.; Kois, P. *Tetrahedron* **2007**, *63* (2), 312. doi:10.1016/j.tet.2006.10.075.
- (9) Hüsken, N.; Gasser, G.; Koster, S. D.; Metzler-Nolte, N. *Bioconjug. Chem.* **2009**, *20* (8), 1578. doi:10.1021/bc9001272.
- (10) Stephenson, G. R. "Organometallic Bioprobes". In *Bioorganometallics: Biomolecules, Labeling, Medicine*; G. Jaouen, Ed.; Wiley-VCH, 2006; pp. 215–262.
- (11) Rudolf, B.; Zakrzewski, J. *Tetrahedron Lett.* **1994**, *35* (51), 9611. doi:10.1016/0040-4039(94)88524-9.
- (12) Rudolf, B.; Palusiak, M.; Zakrzewski, J.; Salmain, M.; Jaouen, G. *Bioconjug. Chem.* **2005**, *16* (5), 1218. doi:10.1021/bc050073d. PMID:16173801.
- (13) Rudolf, B.; Zakrzewski, J.; Salmain, M.; Jaouen, G. *New J. Chem.* **1998**, *22* (8), 813. doi:10.1039/a709263f.
- (14) Fischer-Durand, N.; Salmain, M.; Rudolf, B.; Vessièrès, A.; Zakrzewski, J.; Jaouen, G. *ChemBioChem* **2004**, *5* (4), 519. doi:10.1002/cbic.200300800. PMID:15185376.
- (15) Fischer-Durand, N.; Salmain, M.; Rudolf, B.; Jugé, L.; Guérineau, V.; Laprèvote, O.; Vessièrès, A.; Jaouen, G. *Macromolecules* **2007**, *40* (24), 8568. doi:10.1021/ma071621g.
- (16) Haquette, P.; Salmain, M.; Svedlung, K.; Martel, A.; Rudolf, B.; Zakrzewski, J.; Cordier, S.; Roisnel, T.; Fosse, C.; Jaouen, G. *ChemBioChem* **2007**, *8* (2), 224. doi:10.1002/cbic.200600387. PMID:17167808.
- (17) Tron, G. C.; Pirali, T.; Billington, R. A.; Canonico, P. L.; Sorba, G.; Genazzani, A. A. *Med. Res. Rev.* **2008**, *28* (2), 278. doi:10.1002/med.20107.
- (18) Moses, J. E.; Moorhouse, A. D. *Chem. Soc. Rev.* **2007**, *36* (8), 1249. doi:10.1039/b613014n. PMID:17619685.
- (19) Moorhouse, A. D.; Moses, J. E. *ChemMedChem* **2008**, *3* (5), 715. doi:10.1002/cmdc.200700334. PMID:18214878.
- (20) Nwe, K.; Brechbiel, M. W. *Cancer Biother. Radiopharm.* **2009**, *24* (3), 289. doi:10.1089/cbr.2008.0626. PMID:19538051.
- (21) Collman, J. P.; Devaraj, N. K.; Chidsey, C. E. D. *Langmuir* **2004**, *20* (4), 1051. doi:10.1021/la0362977. PMID:15803676.
- (22) Salmon, A. J.; Williams, M. L.; Innocenti, A.; Vullo, D.; Supuran, C. T.; Poulsen, S. A. *Bioorg. Med. Chem. Lett.* **2007**, *17* (18), 5032. doi:10.1016/j.bmcl.2007.07.024. PMID:17681760.
- (23) Sai Sudhir, V.; Phani Kumar, N. Y.; Chandrasekaran, S. *Tetrahedron* **2010**, *66* (6), 1327. doi:10.1016/j.tet.2009.12.011.
- (24) Plažuk, D.; Zakrzewski, J. *J. Organomet. Chem.* **2009**, *694* (12), 1802. doi:10.1016/j.jorganchem.2009.01.007.
- (25) Gasser, G.; Hüsken, N.; Köster, S. D.; Metzler-Nolte, N. *Chem. Commun. (Camb.)* **2008**, *31* (31), 3675. doi:10.1039/b805369c. PMID:18665296.
- (26) Mhaske, S. B.; Agrade, N. P. *Synthesis* **2003**, *6*, 859.
- (27) Meudtner, R. M.; Ostermeier, M.; Goddard, R.; Limberg, C.; Hecht, S. *Chem. Eur. J.* **2007**, *13* (35), 9834. doi:10.1002/chem.200701240.
- (28) Sheldrick, G. M. *SADABS*; University of Göttingen: Germany, 1996.
- (29) Bruker Nonius. *SAINT V7.34A*; Madison, Wisconsin, USA, 2007.
- (30) Sheldrick, G. M. *SHELXL 97*; University of Göttingen: Germany, 1997.

# Reactions of toluquinone–cyclopentadiene Diels–Alder epoxide adducts with nucleophiles under heterogeneous conditions

Andreas A. von Richthofen, José E. P. Cardoso Filho, Liliana Marzorati, Julio Zukerman-Schpector, Edward R.T. Tiepink, and Claudio Di Vitta

**Abstract:** Toluquinone–cyclopentadiene Diels–Alder epoxide adducts react with sulfur and oxygen nucleophiles under heterogeneous conditions, leading to products resulting from the epoxide ring opening and from skeletal rearrangement, respectively. Pyrolysis of the sulfanyl adducts gave the new 3-sulfanyltoluquinones (**1**).

**Key words:** toluquinone, phase-transfer catalysis (PTC) conditions, thiolation, epoxide, Diels–Alder.

**Résumé :** Les époxydes des adduits de Diels–Alder de la toluquinone et du cyclopentadiène réagissent avec des nucléophiles sulfurés et oxygénés, dans des conditions hétérogènes pour conduire respectivement à des produits résultats d'une ouverture de l'époxyde et d'une transposition du squelette. La pyrolyse des adduits sulfanyles conduit aux nouvelles 3-sulfanyltoluquinones (**1**).

**Mots-clés :** toluquinone, conditions de transfert catalytique de phase (TCP), époxyde, Diels–Alder.

[Traduit par la Rédaction]

## Introduction

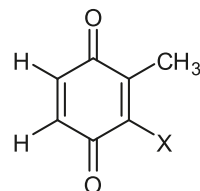
Quinones occur widely in nature as important components of organisms.<sup>1</sup> Natural and synthetic quinone-based compounds are frequently used for therapeutic purposes such as antitumor and anti-infection agents.<sup>2</sup> In particular, benzoquinone thioethers possess a variety of biological and toxicological activities.<sup>3</sup> In the case of 3-sulfanyltoluquinones (**1**) (Fig. 1), it should be mentioned that, although Karrer and Dutta<sup>4</sup> had described the synthesis of the methylsulfanyl derivative **1** (X = SCH<sub>3</sub>), by reacting *p*-toluquinone with methanethiol in water, McHale et al.,<sup>5</sup> after trying to reproduce Karrer and Dutta's work, concluded that the product formed under these conditions was 6-methylsulfanyltoluquinone instead of **1** (X = SCH<sub>3</sub>).

Therefore, we decided to synthesize **1** (X = SR or SAr) according to the route depicted in Scheme 1, which is based on the pyrolysis of adducts **2**.<sup>6</sup> Such adducts could be prepared by selective cycloaddition at the unsubstituted C=C double bond of **3**, followed by bromine/SR exchange.

However, in view of the described low yields of 3-bromo-toluquinone (**3**),<sup>7</sup> we considered an alternative route for adducts **2**, based on the ring opening of epoxides **4** (Scheme 2).

Although the successful ring opening of epoxides **4** (R = R' = H) was described<sup>8</sup> for 1-phenyl-5-mercaptopotetrazole (HPMT) as nucleophile in the presence of catalytic amounts

Fig. 1. 2-Alkylsulfanyl- and arylsulfanyl-toluquinones (**1**).



**1**; X = SR or SAr

of Et<sub>3</sub>N, leading to adduct **2** (R = R' = H; X = PMT), the use of a stoichiometric mixture of Et<sub>3</sub>N and thiols like HPMT, 2-mercaptobenzothiazole (HMBT), and *p*-toluenethiol (HPTT) gave the aromatized substituted adducts **5** in yields ranging from 41% to 50% (Scheme 3) as the result of the action of the base on the  $\alpha$ -carbonyl hydrogens of **2** (R = R' = H; X = SAr). Aromatization was also observed when the epoxide **4** (R = R' = H) was treated with sodium ethylsulfide in EtOH.<sup>9</sup>

Considering the successful use of phase-transfer catalysis (PTC) conditions in suppressing the aromatization reaction, as described by Ferreira et al.,<sup>10</sup> for the substitution of the chlorine atoms of **6** by methylsulfide anion (Scheme 4), we

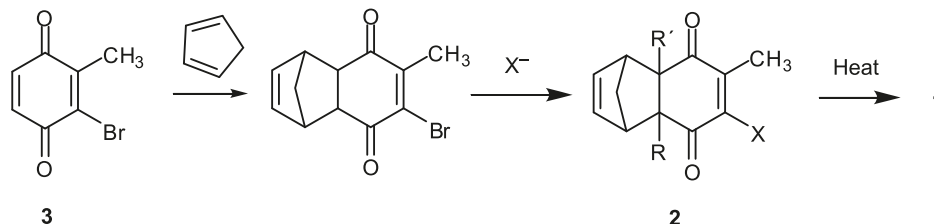
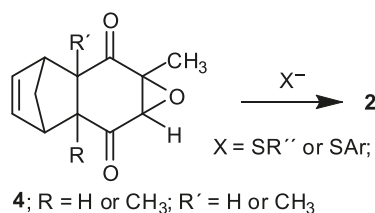
Received 24 February 2010. Accepted 2 June 2010. Published on the NRC Research Press Web site at canjchem.nrc.ca on 15 September 2010.

A.A. von Richthofen, J.E.P. Cardoso Filho, L. Marzorati, and C. Di Vitta.<sup>1</sup> Chemistry Institute of the University of São Paulo, Av. Prof. Lineu Prestes 748, 05508-000 São Paulo, SP, Brazil.

J. Zukerman-Schpector. Departamento de Química, Universidade Federal de São Carlos-CP 676-13565-905 São Carlos, SP, Brazil.

E.R.T. Tiepink. Department of Chemistry, University of Malaya, Kuala Lumpur 50603, Malaysia.

<sup>1</sup>Corresponding author (e-mail: cldvitta@iq.usp.br).

**Scheme 1.** Proposed synthesis of **1**.**Scheme 2.** Proposed alternative synthesis of adducts **2**.

reasoned that we could successfully apply this methodology to the route depicted in Scheme 2 to avoid the aromatization of **2**.

## Results and discussion

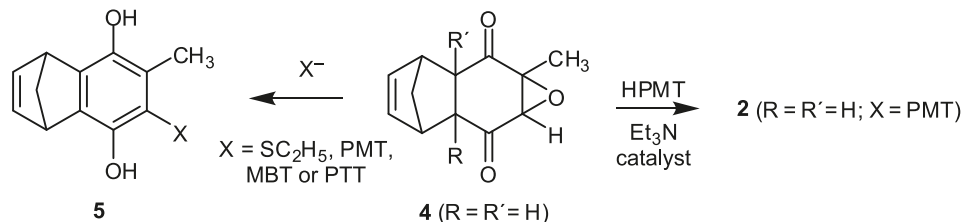
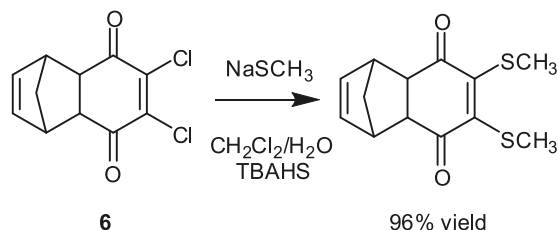
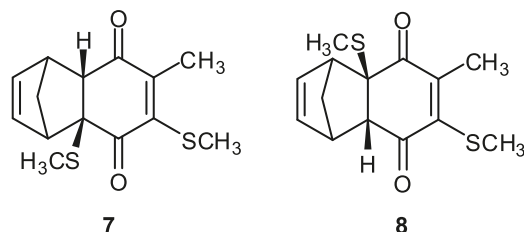
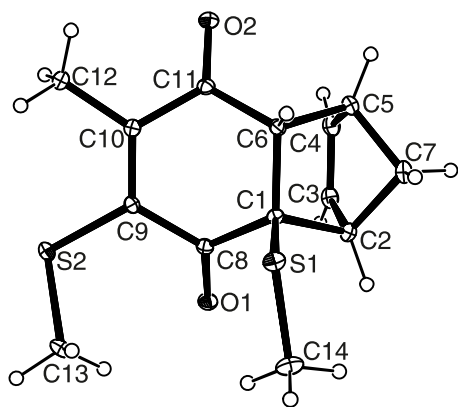
Accordingly, epoxide **4** ( $R = R' = H$ ) was dissolved in benzene and submitted to the reaction with an aqueous solution of methanethiol and sodium hydroxide, using tetrabutylammonium hydrogensulfate (TBAHS) as catalyst.<sup>11</sup> By monitoring the reaction by TLC, and after complete consumption of the starting epoxide **4** ( $R = R' = H$ ), three products were formed, two of them had similar retention factors. All these products were easily isolated by chromatography. The minor product (10% yield) was identified by NMR spectroscopy as the desired sulfurated adduct **2** ( $R = R' = H$ ;  $X = SCH_3$ ). The  $^1H$  NMR spectra of the two major products were consistent with the isomeric bis-sulfanylated adducts **7** (30% yield) and **8** (15% yield) (Fig. 2). In the case of the major product, a single crystal was also obtained,<sup>12</sup> allowing for the unequivocal determination of the cis-endo structure **7** for this compound (Fig. 3). Owing to the similarity of the spectroscopic data for compounds **7** and **8**, the same kind of cis-endo structure can be proposed for the latter adduct.

Although under PTC conditions the aromatization side reaction could be completely suppressed, the selective formation of the sulfanylated product **2** could not be achieved. However, by using  $HSCH_3$  and a less basic PTC condition ( $K_2CO_3$ /benzene/TBAHS), the formation of bis-sulfanylated products was completely avoided and the desired mono-sulfanylated adduct **2** ( $R = R' = H$ ;  $X = SCH_3$ ) was isolated in 21% yield. Unfortunately, a considerable amount of **5** ( $X = SCH_3$ ; 24% yield) was also obtained.<sup>13</sup> As for other thiols, when benzenethiol was employed as nucleophile in the benzene/NaOH/ $H_2O$  system, the mono-sulfanylated adduct **2** ( $R = R' = H$ ;  $X = SC_6H_5$ ) was the sole product and could be isolated in 81% yield. Under such conditions, the  $C_6H_5S^-$  nucleophile was also selective in the oxirane ring opening of other similar epoxides **4** ( $R = H$ ;  $R' = CH_3$  or  $R = CH_3$ ;  $R' = H$ ), leading exclusively to the mono-sulfanylated adducts **2** ( $R = H$ ;  $R' = CH_3$ ;  $X = SC_6H_5$  in 61% yield, and  $R = CH_3$ ;  $R' = H$ ;  $X = SC_6H_5$  in 40% yield).

Considering that the formation of the bis-sulfanylated adducts **7** and **8**, obtained by using the  $HSCH_3$ /benzene/NaOH/ $H_2O$  system, could arise from the sulfanylation of the two possible enolic forms of adduct **2**<sup>14</sup> ( $R = R' = H$ ;  $X = SCH_3$ ), we performed the same reaction under more controlled conditions, avoiding the presence of oxygen to minimize the oxidation of methanethiol to methyl disulfide, which could act as electrophile in the sulfanylation reaction<sup>15</sup> of **2** ( $R = R' = H$ ;  $X = SCH_3$ ). However, even after careful degassing of the employed solvents and the reaction apparatus, adducts **7** and **8** were still produced in comparable yields. Thus, due to the low concentration of the sulfanylation agent ( $CH_3SSCH_3$ , as electrophile) present in the reaction medium,<sup>16</sup> the formation of compounds **7** and **8** via the mechanism depicted in Scheme 5, involving the thiolation process of the intermediate benzoquinone **9**, was suggested. To test this hypothesis, **9** was prepared in 94% yield by oxidation of **5** ( $X = SCH_3$ ) using  $Fe^{3+}$ .<sup>17</sup> Under the heterogeneous conditions used for the thiolation of epoxides **2**, quinone **9** reacted rapidly yielding compounds **7** and **8**, although in a 1:1 ratio, in contrast to the observed 2:1 ratio for the same reaction performed with **2** or **4**.<sup>18</sup>

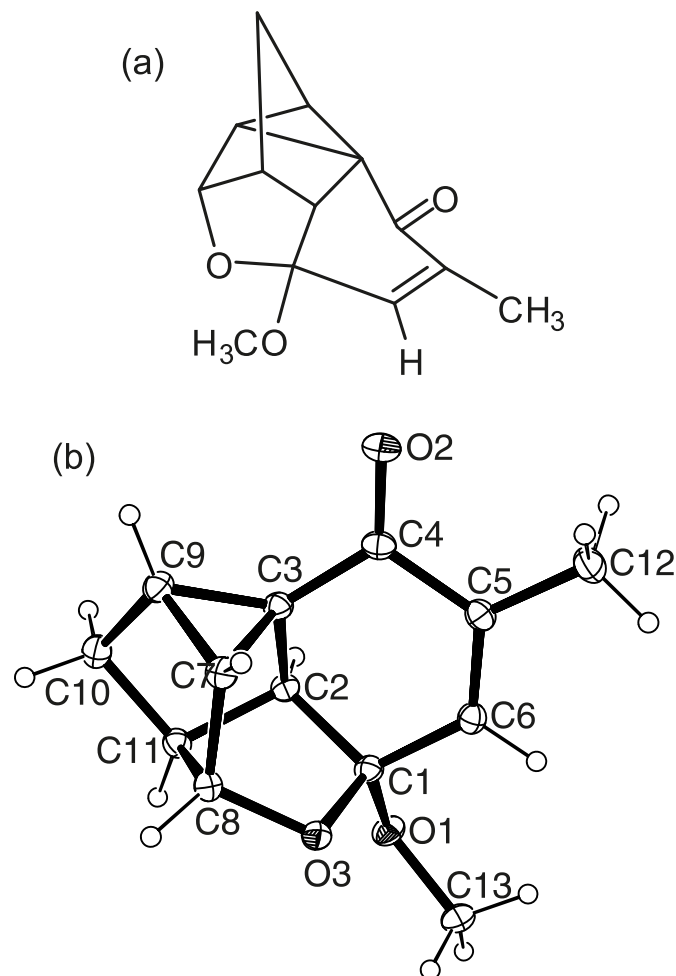
Having in hands the mono-sulfanylated adducts **2** ( $R = R' = H$ ;  $X = SCH_3$  or  $SC_6H_5$ ), they were heated under vacuum, yielding the corresponding new toluquinones **1** ( $X = SCH_3$  in 80% yield;  $SC_6H_5$  in 25% yield).

In an attempt to explore the use of the heterogeneous condition for the reaction of **4** ( $R = R' = H$ ) with other nucleophiles, this compound was submitted to the reaction with methoxide ion in the biphasic system (benzene/ $H_2O$ ). A colourless solid was obtained in 51% yield for which the presence of a methoxy group incorporated to the structure of the product was evidenced by a singlet at 3.41 ppm in the  $^1H$  NMR spectrum. However, the lack of signals corresponding to the norbornene hydrogens led us to the conclusion that the reaction promoted a structural change also at that moiety of **4** ( $R = R' = H$ ). The absence of the characteristic pale yellow colour of toluquinone–cyclopentadiene Diels–Alder adducts indicated the lack of conjugation between the carbonyl groups and the  $C=C$  double bond, suggesting that one of the carbonyl groups was no longer present. Accordingly, the  $^{13}C$  NMR spectrum for the product revealed the presence of only one  $C=O$  group and two olefinic carbons, thus confirming the absence of the norbornene system. On the other hand, the counting of 13 carbons was consistent with a product resulting from the incorporation of a methoxy group to the epoxide **4** ( $R = R' = H$ ). Additionally, the summing of 14 hydrogens by integration of the  $^1H$  NMR spectrum was in agreement with this addition of a methoxide anion, and the same conclusion emerged from the elemental composition of the product for which the minimal formulae

**Scheme 3.** Reactions of epoxides **4** with nucleophiles under homogeneous conditions.**Scheme 4.** Substitution of chlorine atoms of **6** under PTC conditions.**Fig. 2.** Bis-sulfanylated products formed by reaction of **4** ( $R=R'=H$ ) with  $HSCH_3$ /benzene/ $NaOH/H_2O$ .**Fig. 3.** X-ray crystal structure of compound **7** showing atom labeling and displacement ellipsoids at the 50% probability level (arbitrary spheres for the H atoms).

$C_{13}H_{14}O_3$  could be determined. For this compound, structure **10** (Fig. 4) emerged after a single-crystal X-ray analysis. Crystallographic data are summarized in Table 1.

At this point, it is worth mentioning the remarkable capability of the heterogeneous conditions in changing the reactivity of the methoxide ion in comparison to the homogeneous system. In this sense, in contrast to our result for the reaction between **4** ( $R=R'=H$ ) and sodium ethoxide in ethanol, a Favorskii-type ring contraction was described by Herz et al.<sup>19</sup> Our proposal for the formation of **10** is depicted in Scheme 6. The initial step is in accordance

**Fig. 4.** Molecular structure and X-ray crystal structure of compound **10** showing atom labeling and displacement ellipsoids at the 50% probability level (arbitrary spheres for the H atoms).

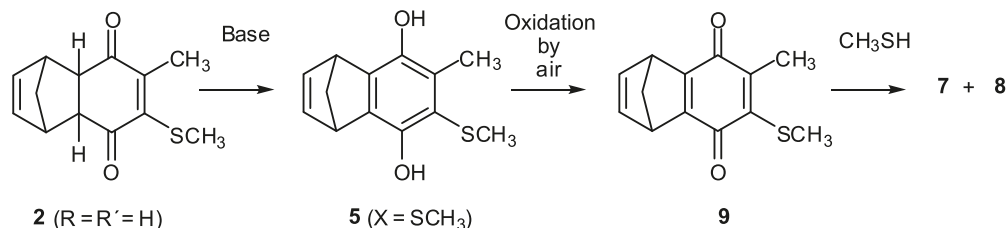
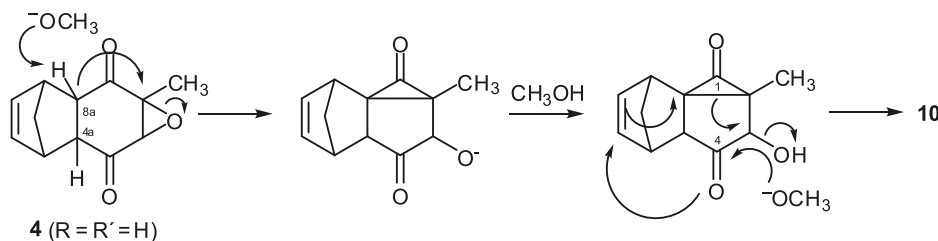
with the Loftfield mechanism for the Favorskii rearrangement,<sup>20</sup> giving an intermediate resulting from displacement of an oxirane bond by the enolate of C8a. However, in the second step under heterogeneous conditions, attack of methoxide ion occurs on C4 of the protonated intermediate, leading to compound **10** instead of the cyclopropanone ring opening by attack at C1.

It should be mentioned that no reaction was observed employing nitrogen nucleophiles like  $H_2NCH_3$ ,  $HN(CH_3)_2$ , or aniline under the same heterogeneous conditions.

## Conclusion

For the reactions of **4** with  $^-SCH_3$ , the two-phase system



**Scheme 5.** Proposed mechanism for the formation of **7** and **8** under heterogeneous condition.**Scheme 6.** Proposed mechanism for the formation of **10** under heterogeneous condition.

can suppress the aromatization process. The use of sodium methoxide as nucleophile under similar conditions led to the product with the conspicuous strained structure **10**, with complete suppression of the Favorskii-type ring contraction reaction.

The present work reports also the first unequivocal synthesis of 3-sulfanyltoluquinones (**1**; X = SCH<sub>3</sub> or SC<sub>6</sub>H<sub>5</sub>).

## Experimental

### Methods and materials

Melting points were determined on a Koffler micro hot stage and are uncorrected. NMR spectra were recorded with a Bruker AC 200 or a Varian INOVA 300 spectrometers against Me<sub>4</sub>Si (for <sup>1</sup>H NMR) or the central line of the solvent signal (CDCl<sub>3</sub> triplet at 77.0 ppm, for <sup>13</sup>C NMR). TLC and dry-flash chromatography were carried out on Merck silica gel. All reagents and solvents were used as received from commercial suppliers. Epoxides **4** (R = R' = H or R = H; R' = CH<sub>3</sub> or R = CH<sub>3</sub>; R' = H) were prepared according to literature procedures.<sup>21</sup>

### X-ray crystallography for compound **10**

A single crystal suitable for X-ray crystallographic analysis was obtained from a slow evaporation of a methanol solution (see Supplementary data section). Intensity data were measured at 153 K on a Rigaku AFC12κ/SATURN724 diffractometer fitted with Mo Kα radiation (λ = 0.71073 Å). Data processing and absorption corrections were accomplished with CrystalClear and ABSCOR,<sup>22</sup> respectively. Details of cell data, X-ray data collection, and structure refinement are given in Table 1. The structures were solved by direct-methods.<sup>23</sup> Full-matrix least-squares refinement on F<sup>2</sup> with anisotropic thermal parameters for all non-hydrogen atoms was performed.<sup>24</sup> H atoms were placed on stereochemical grounds and refined with fixed geometry, each riding on a carrier atom with an isotropic displacement parameter amounting to 1.2 times (1.5 for methyl-H) the value of the equivalent isotropic displacement parameter of the respective carrier atom. A weighing scheme of the form

$$w = 1/[\sigma^2(F_o^2) + (0.0429P)^2 + 0.534P] \text{ where } P = (F_o^2 + 2F_c^2)/3 \text{ was introduced in each case.}^{24}$$

### Reaction of **4** with nucleophiles

#### Using thiols in a liquid–liquid system — General procedure

A mixture of epoxide **4** (1.0 mmol), benzene (14 mL), aqueous sodium hydroxide (0.35 mol/L; 14 mL), and thiol (10 mmol) was vigorously stirred at room temperature until complete consumption of the epoxide, as indicated by TLC. For CH<sub>3</sub>SH, the reaction flask was equipped with a dry-ice cold finger, and the mixture was saturated with the thiol. The organic layer was separated and the aqueous layer was extracted with CH<sub>2</sub>Cl<sub>2</sub>. The combined organic extracts were washed twice with water, dried over anhydrous MgSO<sub>4</sub>, and concentrated under vacuum. The crude product was submitted to dry-flash chromatography using a gradient of *n*-hexane/ethyl acetate as eluant.

**Adduct 2 (R = R' = H; X = SCH<sub>3</sub>)** was isolated as a yellow solid. Mp 75–76 °C. δ<sub>H</sub> (200 MHz, CDCl<sub>3</sub>, Me<sub>4</sub>Si): 1.42 (d, 1H, *J* = 8.8 Hz), 1.54 (d, 1H, *J* = 8.8 Hz), 2.02 (s, 3H), 2.46 (s, 3H), 3.27 (m, 2H), 3.50 (m, 2H), 6.05 (m, 2H). δ<sub>C</sub> (75 MHz, CDCl<sub>3</sub>, Me<sub>4</sub>Si): 13.59, 16.03, 36.77, 42.77, 40.85, 59.74, 77.45, 96.40, 82.99, 87.02, 91.00, 110.21, 112.77. Elemental analysis (%) (C<sub>13</sub>H<sub>14</sub>SO<sub>2</sub>) calcd.: C 66.6, H 6.0; found: C 66.4, H 6.1.

**Adduct 2 (R = R' = H; X = SC<sub>6</sub>H<sub>5</sub>)** was isolated as a yellow solid. Mp 82–83 °C. δ<sub>H</sub> (200 MHz, CDCl<sub>3</sub>, Me<sub>4</sub>Si): 1.42 (d, 1H; *J* = 6.5 Hz), 1.52 (d, 1H; *J* = 6.5 Hz), 2.05 (s, 3H), 3.23 (dd, 1H, *J*<sub>1</sub> = 9.0 Hz; *J*<sub>2</sub> = 3.6 Hz), 3.30 (dd, 1H, *J*<sub>1</sub> = 9.0 Hz; *J*<sub>2</sub> = 3.6 Hz), 3.45 (m, 1H), 3.53 (m, 1H), 6.06 (m, 2H), 7.30 (m, 5H). δ<sub>C</sub> (75 MHz, CDCl<sub>3</sub>, Me<sub>4</sub>Si): 15.69, 48.00, 48.16, 48.54, 48.77, 49.48, 127.72, 129.09, 131.32, 133.03, 135.38, 135.99, 150.47, 150.76, 193.73, 196.30. Elemental analysis (%) (C<sub>18</sub>H<sub>16</sub>SO<sub>2</sub>) calcd.: C 72.9, H 5.4; found: C 72.8, H 5.3.

**Adduct 2 (R = H; R' = CH<sub>3</sub>; X = SC<sub>6</sub>H<sub>5</sub>)** was isolated as a yellow solid. Mp 61–62 °C. δ<sub>H</sub> (200 MHz, CDCl<sub>3</sub>, Me<sub>4</sub>Si): 1.36 (s, 3H), 1.51 (dt, 1H, *J*<sub>1</sub> = 10 Hz, *J*<sub>2</sub> = 1.6 Hz), 1.63 (br

**Table 1.** Crystallographic data and refinement details for compound **10**.

Empirical formula	C <sub>13</sub> H <sub>14</sub> O <sub>3</sub>
Formula mass	218.24
Colour, habit	Colourless, plate
Crystal dimensions (mm)	0.25 × 0.25 × 0.05
Crystal system	Monoclinic
Space group	<i>P</i> 2 <sub>1</sub> / <i>c</i>
<i>a</i> (Å)	6.0728(10)
<i>b</i> (Å)	16.256(3)
<i>c</i> (Å)	10.474(2)
$\beta$ (°)	102.119(6)
<i>V</i> (Å <sup>3</sup> )	1010.9(3)
<i>D</i> <sub>calcd.</sub> (Mg m <sup>-3</sup> )	1.434
<i>Z</i>	4
Absorption coeff. ( $\mu$ ) (mm <sup>-1</sup> )	0.101
<i>F</i> (000)	464
$\theta$ range for data collection (°)	3.43–26.50
Collected/Independent/observed refls. [ <i>I</i> > 2 $\sigma$ ( <i>I</i> )]	5506 ( <i>R</i> <sub>sigma</sub> = 0.0286)/2085/1941 ( <i>R</i> <sub>int</sub> = 0.0296)
Data/restraint/parameters	2085/0/146
Goodnes-of-fit on <i>F</i> <sup>2</sup>	1.088
Final <i>R</i> indices [ <i>I</i> > 2 $\sigma$ ( <i>I</i> )]	<i>R</i> = 0.0480, <i>wR</i> = 0.1090
<i>R</i> indices (all data)	<i>R</i> = 0.0515, <i>wR</i> = 0.1116
Largest diff. peak and hole (e Å <sup>-3</sup> )	0.220, –0.195

d, 1H, *J* = 10 Hz), 2.08 (s, 3H), 2.84 (d, 1H, *J* = 4 Hz), 2.98 (br s, 1H), 3.44 (br s, 1H), 5.99 (dd, 1H, *J*<sub>1</sub> = 4.0 Hz; *J*<sub>2</sub> = 2.0 Hz), 6.11 (dd, 1H, *J*<sub>1</sub> = 4.0 Hz; *J*<sub>2</sub> = 2.0 Hz), 7.20–7.42 (m, 5H).  $\delta_{\text{C}}$  (75 MHz, CDCl<sub>3</sub>, Me<sub>4</sub>Si): 15.3, 26.3, 45.7, 47.9, 52.2, 53.8, 57.2, 127.9, 129.0, 131.8, 132.7, 134.8, 139.2, 149.0, 151.0, 196.1, 196.8. Elemental analysis (%) (C<sub>19</sub>H<sub>18</sub>SO<sub>2</sub>) calcd.: C 73.5, H 5.8; found: C 73.4, H 6.1.

**Adduct 2** (**R** = CH<sub>3</sub>; **R'** = H; **X** = SC<sub>6</sub>H<sub>5</sub>) was isolated as a yellow solid. Mp 76–77 °C.  $\delta_{\text{H}}$  (200 MHz, CDCl<sub>3</sub>, Me<sub>4</sub>Si): 1.50 (s, 3H), 1.52 (m, 1H), 1.62 (br d, 1H, *J* = 9.6 Hz), 2.07 (s, 3H), 2.82 (d, 1H, *J* = 4.0 Hz), 3.08 (br s, 1H), 3.37 (br s, 1H), 6.00 (dd, 1H, *J*<sub>1</sub> = 6.5 Hz, *J*<sub>2</sub> = 3.3 Hz), 6.15 (dd, 1H, *J*<sub>1</sub> = 6.5 Hz, *J*<sub>2</sub> = 3.3 Hz), 7.20–7.35 (m, 5H).  $\delta_{\text{C}}$  (75 MHz, CDCl<sub>3</sub>, Me<sub>4</sub>Si): 15.9, 27.3, 46.1, 48.1, 53.0, 58.1, 127.7, 129.1, 131.1, 133.1, 135.3, 138.3, 149.8, 149.9, 193.9, 200.1. Elemental analysis (%) (C<sub>19</sub>H<sub>18</sub>SO<sub>2</sub>) calcd.: C 73.5, H 5.8; found: C 73.8, H 6.2.

**Adduct 7** was isolated as a yellow solid. Mp 69–72 °C.  $\delta_{\text{H}}$  (300 MHz, CDCl<sub>3</sub>, Me<sub>4</sub>Si): 1.62 (dt, 1H, *J*<sub>1</sub> = 8.9 Hz; *J*<sub>2</sub> = 1.7 Hz), 1.97 (s, 3H), 2.01–2.06 (m, 1H), 2.11 (s, 3H), 2.46 (s, 3H), 2.86 (d, 1H, *J* = 3.9 Hz), 3.37 (br s, 1H), 3.51 (br s, 1H), 6.08–6.17 (m, 2H).  $\delta_{\text{C}}$  (75 MHz, CDCl<sub>3</sub>, Me<sub>4</sub>Si): 12.8, 14.0, 14.9, 15.2, 45.0, 45.8, 46.0, 46.2, 57.7, 59.6, 134.4, 137.5 (2C), 142.9, 154.2, 184.8, 193.0. Elemental analysis (%) (C<sub>14</sub>H<sub>16</sub>S<sub>2</sub>O<sub>2</sub>) calcd.: C 60.0, H 5.7; found: C 60.7; H 6.0.

**Adduct 8** was isolated as a yellow solid. Mp 75–76 °C.  $\delta_{\text{H}}$  (300 MHz, CDCl<sub>3</sub>, Me<sub>4</sub>Si): 1.63 (dt, 1H, *J*<sub>1</sub> = 9.0 Hz; *J*<sub>2</sub> = 1.9 Hz), 2.04 (br d, 1H, *J* = 9.1 Hz), 2.07 (s, 3H), 2.11 (s, 3H), 2.43 (s, 3H), 2.89 (d, 1H, *J* = 3.9 Hz), 3.35 (br s, 1H), 3.50 (br s, 1H), 6.05 (dd, 1H, *J*<sub>1</sub> = 6.0 Hz; *J*<sub>2</sub> = 3.0 Hz), 6.15 (dd, 1H, *J*<sub>1</sub> = 6.0 Hz; *J*<sub>2</sub> = 3.0 Hz).

#### Using CH<sub>3</sub>SH in a solid–liquid system

A mixture of epoxide **4** (**R** = **R'** = H; 1.0 mmol), benzene

(15 mL), TBAHS (0.030 mmol), and solid anhydrous potassium carbonate (10 mmol) was saturated with methanethiol in a reaction flask equipped with a dry-ice cold finger. The mixture was vigorously stirred at room temperature for 2 h.<sup>12</sup> Water (15 mL) was added and the organic layer was separated. The aqueous phase was extracted with CH<sub>2</sub>Cl<sub>2</sub> (3 × 15 mL), and the combined organic extracts were dried over anhydrous MgSO<sub>4</sub> and concentrated under vacuum. The crude product was submitted to dry-flash chromatography.

Aromatic **5** (**X** = SCH<sub>3</sub>) was isolated as a white solid. Mp 121–123 °C after dry-flash chromatography separation using, as eluant, a gradient of *n*-hexane/acetone.  $\delta_{\text{H}}$  (200 MHz, CDCl<sub>3</sub>, Me<sub>4</sub>Si): 2.12–2.26 (m, 2H), 2.15 (s, 3H), 2.41 (s, 3H), 4.06 (br s, 1H), 4.17 (br s, 1H), 6.73 (dd, 1H, *J*<sub>1</sub> = 5.1 Hz; *J*<sub>2</sub> = 2.9 Hz), 6.84 (dd, 1H, *J*<sub>1</sub> = 5.1 Hz; *J*<sub>2</sub> = 2.9 Hz).  $\delta_{\text{C}}$  (75 MHz, CDCl<sub>3</sub>, Me<sub>4</sub>Si): 14.1, 18.7, 46.7, 47.2, 69.2, 117.7, 126.3, 133.2, 139.6, 141.6, 142.0, 143.2, 144.8. Elemental analysis (%) (C<sub>13</sub>H<sub>14</sub>O<sub>2</sub>S) calcd.: C 66.6, H 6.0; found: C 66.9, H 6.1.

#### Using CH<sub>3</sub>OH in a liquid–liquid system

A mixture of epoxide **4** (**R** = **R'** = H; 0.75 mmol), benzene (10 mL), water (11 mL), and sodium methoxide (8.3 mmol) was vigorously stirred at room temperature until complete consumption of the epoxide, as indicated by TLC. The organic layer was separated and the aqueous layer was extracted with CH<sub>2</sub>Cl<sub>2</sub>. The combined organic extracts were washed twice with water, dried over anhydrous MgSO<sub>4</sub>, and concentrated under vacuum. The crude product was submitted to dry-flash chromatography separation using a gradient of *n*-hexane/ethyl acetate as eluant. Compound **10** was isolated as white crystals. Mp 105–107 °C.  $\delta_{\text{H}}$  (300 MHz, CDCl<sub>3</sub>, Me<sub>4</sub>Si): 1.38 (dd, 1H, *J*<sub>1</sub> = 4.5 Hz; *J*<sub>2</sub> = 1.2 Hz), 1.72 (d, 1H, *J* = 11.9 Hz), 1.78 (d, 1H, *J* = 11.9 Hz), 1.82 (d, 3H, *J* = 1.8 Hz), 2.54 (br d, 1H, *J* = 4.5 Hz), 2.65 (br s,

1H), 2.86 (d, 1H,  $J = 2.1$  Hz), 3.41 (s, 3H), 4.63 (br s, 1H), 6.60 (br s, 1H).  $\delta_C$  (75 MHz,  $CDCl_3$ ,  $Me_4Si$ ): 15.2, 23.5, 27.0, 29.2, 33.3, 40.7, 49.7, 53.3, 85.8, 102.9, 136.7, 140.6, 195.1. Elemental analysis (%) ( $C_{13}H_{14}O_3$ ) calcd.: C 71.5, H 6.5; found: C 71.3, H 6.2.

### Pyrolysis of adduct **2** ( $R = R' = H$ ; $X = SCH_3$ )

Adduct **2** ( $R = R' = H$ ;  $X = SCH_3$ ; 0.25 mmol) was heated under vacuum (0.1 mm Hg) at 200 °C in a Kugelrohr, and 3-methylsulfanyltoluquinone (**1**;  $X = SCH_3$ ; 0.20 mmol) was collected as a red oil.  $\delta_H$  (200 MHz,  $CDCl_3$ ,  $Me_4Si$ ): 2.19 (s, 3H), 2.59 (s, 3H), 6.74 (d, 2H,  $J = 1.2$  Hz).  $\delta_C$  (75 MHz,  $CDCl_3$ ,  $Me_4Si$ ): 14.09, 17.22, 136.31, 137.15, 142.75, 145.02, 183.03, 184.03. Elemental analysis (%) ( $C_8H_8SO_2$ ) calcd.: C 57.1, H 4.8; found: C 56.8, H 4.8.

3-Phenylsulfanyltoluquinone (**1**;  $X = SC_6H_5$ ; 0.070 mmol) was obtained by a process similar to the above described as a red oil, starting from adduct **2** ( $R = R' = H$ ;  $X = SC_6H_5$ ; 0.28 mmol).  $\delta_H$  (200 MHz,  $CDCl_3$ ,  $Me_4Si$ ): 2.21 (s, 3H), 6.78 (s, 2H), 7.29 (m, 5H).  $\delta_C$  (75 MHz,  $CDCl_3$ ,  $Me_4Si$ ): 15.08, 127.44, 129.17, 130.70, 133.56, 136.52, 137.10, 142.98, 146.96, 182.34, 185.18. Elemental analysis (%) ( $C_{13}H_{10}SO_2$ ) calcd.: C 67.8, H 4.4; found: C 67.6, H 4.4.

### Supplementary data

Supplementary data for this article (general methods, instrumentation, preparation, and diffraction data) are available on the journal Web site (canjchem.nrc.ca). CCDC 766956 contains the X-ray data in CIF format for this manuscript. These data can be obtained, free of charge, via www.ccdc.cam.ac.uk/conts/retrieving.html (or from the Cambridge Crystallographic Data Centre, 12 Union Road, Cambridge CB2 1EZ, UK; fax +44 1223 336033; or deposit@ccdc.cam.ac.uk).

### Acknowledgements

This work was supported by Fundação de Amparo à Pesquisa do Estado de São Paulo (FAPESP), Coordenação de Aperfeiçoamento de Pessoal de Nível Superior (CAPES), and Conselho Nacional de Desenvolvimento Científico e Tecnológico (CNPq).

### References

- (1) (a) Morton, R. A. *Biochemistry of Quinones*; Academic Press: London, 1965; (b) Patai, S.; Rappoport, Z. *The Chemistry of the Functional Groups. The Chemistry of the Quinonoid Compounds*; John Wiley & Sons: New York, 1988; (c) Thomson, R. H. *Naturally Occurring Quinones IV*; Blackie Academic & Professional: London, 1997.
- (2) (a) Oostveen, E. A.; Speckamp, W. N. *Tetrahedron* **1987**, 43 (1), 255. doi:10.1016/S0040-4020(01)89952-X.; (b) Hargreaves, R. H. J.; Hartley, J. A.; Butler, J. *Front. Biosci.* **2000**, 5 (1), e172. doi:10.2741/hargreav.; (c) Colucci, M. A.; Couch, G. D.; Moody, C. J. *Org. Biomol. Chem.* **2008**, 6 (4), 637. doi:10.1039/b715270a. PMID:18264564.; (d) Koyama, J. *Recent Patents Anti-Infect. Drug Disc.* **2006**, 1 (1), 113. doi:10.2174/157489106775244073.
- (3) (a) Monks, T. J.; Hanzlik, R. P.; Cohen, G. M.; Ross, D.; Graham, D. G. *Toxicol. Appl. Pharmacol.* **1992**, 112 (1), 2. doi:10.1016/0041-008X(92)90273-U. PMID:1733045.; (b) Valderrama, J. A.; Zamorano, C.; González, M. F.; Prina,

- E.; Fournet, A. *Bioorg. Med. Chem.* **2005**, 13 (13), 4153. doi:10.1016/j.bmc.2005.04.041. PMID:15876538.
- (4) Karrer, P.; Dutta, P. C. *Helv. Chim. Acta* **1948**, 31 (7), 2080. doi:10.1002/hlca.19480310724. PMID:18100036.
- (5) McHale, D.; Mamalis, P.; Marcinkiewicz, S.; Green, J. J. *Chem. Soc.* **1959**, 3358. doi:10.1039/jr9590003358.
- (6) Wladislaw, B.; Marzorati, L.; Di Vitta, C. *Synthesis* **1983**, (06), 464. doi:10.1055/s-1983-30382.
- (7) According to Sato and co-workers (Inoue, S.; Saito, K.; Kato, K.; Nozaki, S.; Sato, K. *J. Chem. Soc. Perkin Trans.1* **1974**, 2097), toluquinone (**3**) was obtained in 1.5% yield starting from the commercially available 2-bromo-3-nitrotoluene. Hewson et al. (Hewson, A. T.; Sharpe, D. A.; Wadsworth, A. H. *Synthetic Commun.* **1989**, 19, 2095) obtained **3** in 26% yield by oxidation of *N*-2-methyl-3-bromophenylphenylsulfonamide; however, no data on yield was reported by the authors for the preparation of the starting sulfonamide.
- (8) (a) O'Brien, D. F.; Gates, J. W., Jr. *J. Org. Chem.* **1965**, 30 (8), 2593. doi:10.1021/jo01019a022.; (b) Wilgus, H. S., III; Frauenglass, E.; Chiesa, P. P.; Nawn, G. H.; Evans, F. J.; Gates, J. W., Jr. *Can. J. Chem.* **1966**, 44 (5), 603. doi:10.1139/v66-081.; (c) Youngquist, M. J.; O'Brien, D. F.; Gates, J. W., Jr. *J. Am. Chem. Soc.* **1966**, 88 (21), 4960. doi:10.1021/ja00973a032.; (d) O'Brien, D. F. *J. Org. Chem.* **1968**, 33 (1), 262. doi:10.1021/jo01265a052.
- (9) Wladislaw, B. Chemistry Institute of University of São Paulo, São Paulo, SP, Brazil; unpublished results.
- (10) Ferreira, V. F.; Park, A.; Schmitz, F. J.; Valeriotte, F. A. *Tetrahedron* **2003**, 59 (8), 1349. doi:10.1016/S0040-4020(02)01591-0.
- (11) In the presence or absence of the catalyst, the reaction proceeds at similar rates, and it probably occurs at the benzene/water interface.
- (12) von Richthofen, A. A.; Cardoso Filho, J. E. P.; Marzorati, L.; Zukerman-Schpector, J.; Tiekink, E. R. T.; Di Vitta, C. *Acta Cryst.* **2010**, E66, o1259. doi:10.1107/S1600536810015710.
- (13) The reaction was quenched after 2 h, although without complete consumption of starting epoxide to avoid further aromatization.
- (14) Adduct **2** ( $R = R' = H$ ;  $X = SCH_3$ ) is the precursor of **7** and **8**, as proved by the formation of the latter compounds in a 2:1 ratio by treatment of **2** ( $R = R' = H$ ;  $X = SCH_3$ ) with benzene/ $H_2O$ / $NaOH$ / $HSCH_3$ .
- (15) Wladislaw, B.; Marzorati, L.; Di Vitta, C. *Org. Prep. Proced. Int.* **2007**, 39 (5), 447. doi:10.1080/00304940709458600.
- (16) After 24 h of stirring, only 2% of  $CH_3SSCH_3$  was detected by GLC in the benzene layer of the heterogeneous system (benzene/ $H_2O$ / $NaOH$ / $HSCH_3$ ).
- (17) Aromatic **5** ( $X = SCH_3$ ; 0.080 g; 0.34 mmol) was dissolved in acetone (2 mL) and to the stirred solution at RT, an aqueous saturated solution of  $Fe(NO_3)_3$  was dropwise until complete consumption of the starting material by TLC (Hexane:EtOAc, 6:1). The reaction mixture was poured into water (10 mL) and extracted with  $Et_2O$ . After drying ( $MgSO_4$ ), concentration and purification by dry-flash chromatography (Hexane:EtOAc, 20:1), quinone **9**, a red oil, was obtained (0.074 g; 3.2 mmol; 94% yield).  $\delta_H$  (200 MHz,  $CDCl_3$ ,  $Me_4Si$ ): 2.16 (s, 3H), 2.27 (dt, 2H;  $J_1 = 7.0$  Hz;  $J_2 = 1.6$  Hz), 2.30 (dt, 2H;  $J_1 = 7.0$  Hz;  $J_2 = 1.6$  Hz), 2.55 (s, 3H), 4.09 (m, 2H), 6.84 (m, 1H).  $\delta_C$  (75 MHz;  $CDCl_3$ ,  $Me_4Si$ ): 14.4, 17.7, 48.6, 48.9, 73.2, 142.4 (2C), 142.5, 143.4, 160.6, 161.0, 180.0, 181.4. Elemental

analysis (%) ( $C_{13}H_{12}O_2S$ ) calcd.: C 67.2, H 5.2; found: C 67.0, H 5.4.

- (18) Compound **9** is rapidly formed by bubbling air into a solution of **5** ( $X = SCH_3$ ) in a mixture of benzene/ $H_2O$ / $NaOH$ . Therefore, although working in the absence of oxygen, the possibility of an in situ oxidation of **5** ( $X = SCH_3$ ) to quinone **9** by residual oxygen cannot be excluded under the heterogeneous conditions. It should be noted that when compound **5** ( $X = SCH_3$ ) was submitted to the reaction with benzene/ $H_2O$ / $NaOH$ / $HSCl_3$ , **7** and **8** were quantitatively formed in a 2:1 ratio after 24 h of stirring.
- (19) Herz, W.; Iyer, V. S.; Nair, M. G. *J. Org. Chem.* **1975**, 40 (24), 3519. doi:10.1021/jo00912a011.
- (20) (a) Loftfield, R. B. *J. Am. Chem. Soc.* **1951**, 73 (10), 4707. doi:10.1021/ja01154a066.; (b) Chenier, P. J. *J. Chem. Educ.* **1978**, 55 (5), 286. doi:10.1021/ed055p286.
- (21) Alder, K.; Flock, F. H.; Beumling, H. *Chem. Ber.* **1960**, 93 (8), 1896. doi:10.1002/cber.19600930830.
- (22) (a) CrystalClear. *User Manual*; Rigaku/MSI Inc., Rigaku Corporation: The Woodlands, TX, 2005; (b) Higashi, T. *AB-SCOR*; Rigaku Corporation: Tokyo, Japan, 1995.
- (23) Altomare, A.; Cascarano, G.; Giacovazzo, C.; Guagliardi, A. *J. Appl. Cryst.* **1993**, 26 (3), 343. doi:10.1107/S0021889892010331.
- (24) Sheldrick, G. M. *SHELXL97. Program for Crystal Structure Analysis*, release 97-2; University of Göttingen: Germany, 1997.



# Deoxygenation of diarylmethanols with dilute mineral acid

Kyle A. Hope-Ross and John F. Kadla

**Abstract:** A new mild and efficient method for the deoxygenation of diarylmethanols is reported. The reaction employs catalytic hydrochloric acid in ethanol at reflux for 48 h. This reaction works on a variety of diarylmethanol substrates and mitigates the need for expensive and toxic reagents such as stannanes and silanes used in alternative procedures. In addition, this reaction can be used in tandem with the deprotection of acid-sensitive silyl ether protecting groups in a one-pot procedure.

**Key words:** deoxygenation, diarylmethanols, reduction, silyl ether deprotection.

**Résumé :** On rapporte une nouvelle méthode douce et efficace de désoxygénation des diarylméthanol. La réaction fait appel à une quantité catalytique d'acide chlorhydrique, dans l'éthanol au reflux, pendant 48 h. La réaction donne de bons résultats avec une variété de substrats diarylméthanol et elle atténue le besoin pour des réactifs toxiques et dispendieux, tels les stannanes et les silanes utilisés dans des méthodes alternatives. De plus, cette réaction peut être utilisée en tandem avec la déprotection d'éthers silylés sensibles aux acides utilisés comme groupes protecteurs dans des méthodes monotonos.

**Mots-clés :** désoxygénation, diarylméthanol, réduction, déprotection d'éther silylé.

## Introduction

Diarylmethane is a reoccurring structural motif in numerous natural products, including alangifolioside,<sup>1</sup> itoside K,<sup>2</sup> mastigophorene C,<sup>3</sup> and terrestrols F–H<sup>4</sup> (2–4, 5a–5c, Fig. 1).

A possible synthetic route towards these natural products is the deoxygenation of diarylmethanols, which could be achieved in a number of ways, including the Grignard reaction.<sup>5</sup> As such, the deoxygenation of secondary alcohols is an important transformation in synthetic organic chemistry. Unfortunately, few conditions for this transformation, which are both mild and widely applicable, have been reported.

Perhaps the most well-known example is the Barton–McCombie reaction, developed in 1975.<sup>6</sup> In this reaction the alcohol is converted to a thiocarbonyl derivative that, upon treatment with tributylstannane and the radical initiator AIBN (azobisisobutyronitrile), affords the corresponding hydrocarbon.<sup>7</sup> Unfortunately, this reaction involves the homolytic cleavage of the C–O bond, and because of the radical nature of the reaction, this somewhat limits the substrate scope. Additionally, the use of stoichiometric amounts of toxic heavy metals such as tin limits the industrial applications of such reactions.

More recently, variants of this reaction have been reported using silanes<sup>8</sup> or dialkyl phosphites<sup>9</sup> as hydrogen donors, and trialkyl boron–oxygen or peroxides as radical initiators.<sup>10</sup>

For the specific case of diarylmethanols (benzhydrols),

one reported deoxygenation involves treatment of the alcohol with triflic acid followed by triethyl silane.<sup>11</sup>

Herein, we report a new mild and efficient deoxygenation of diaryl methanols to their corresponding diaryl methanes. This method uses dilute mineral acid in ethanol and proceeds without the use of silanes or toxic heavy metals. A variety of substrates were examined, and it was found that the reaction proceeds exclusively for diarylmethanols, but not for the other secondary alcohols examined.

## Experimental

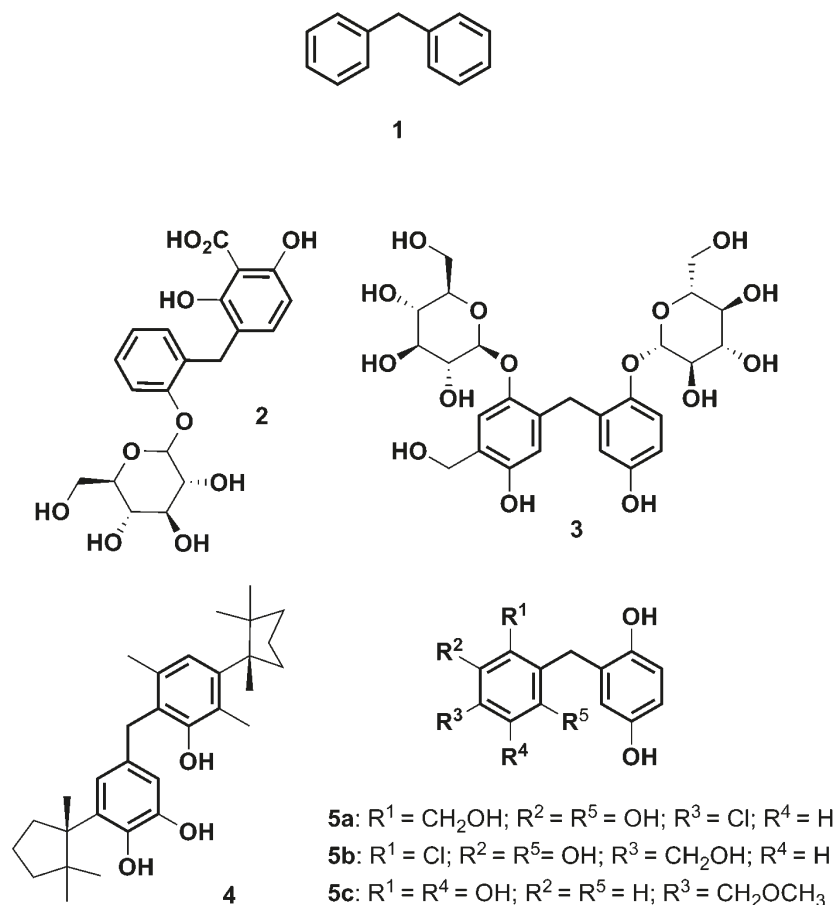
All chemicals were purchased from Sigma-Aldrich and used without further purification unless otherwise noted. Solvents were purchased from Fisher Scientific and used as received. All reactions were monitored by TLC, which was performed on Merck Alumafol 60 Å TLC plates with an UV indicator. Flash chromatography was performed on 60 Å, 70–230 mesh silica gel purchased from Fisher Scientific. <sup>1</sup>H and <sup>13</sup>C NMR spectra were recorded using a 300 MHz Bruker Avance Ultrashield NMR spectrometer (300.13 and 75.03 MHz, respectively) and referenced to CDCl<sub>3</sub> (7.28 ppm). IR spectra were recorded using a PerkinElmer Spectrum One FT-IR spectrometer. Melting points were determined using a Mel-Temp melting point apparatus and are uncorrected. Boiling points were determined using differential scanning calorimetry (DSC) (TA Instruments Q1000) at 101.1 kPa according to ASTM E1782.<sup>12</sup>

Received 24 September 2009. Accepted 14 June 2010. Published on the NRC Research Press Web site at canjchem.nrc.ca on 20 September 2010.

**K.A. Hope-Ross and J.F. Kadla.**<sup>1</sup> Advanced Biomaterials Chemistry Laboratory, Department of Wood Science, University of British Columbia, Vancouver, BC V6T 1Z4, Canada.

<sup>1</sup>Corresponding author (e-mail: john.kadla@ubc.ca).

**Fig. 1.** Natural products containing the diarylmethane (**1**) moiety: alangifolioside (**2**), itoside K (**3**), mastigophorene C (**4**), and terrestrols F–H (**5a–5c**).



#### General procedure for the attempted deoxygenation of aryl methanols **6**, **7**, and **8**

To a solution of aryl methanol (0.50 g) in ethanol (50 mL) at 0 °C was added concentrated HCl (1.0 mL) as a solution in ethanol. The solutions were heated to reflux for 48–120 h, and the reactions were monitored by TLC (hexanes/ethyl acetate, 3:1). After cooling to room temperature, the reaction mixture was poured into a saturated solution of  $\text{NaHCO}_3$  (25 mL), mixed well, and extracted with  $\text{CH}_2\text{Cl}_2$  ( $2 \times 100$  mL). The combined organics were washed with water (200 mL), dried over  $\text{MgSO}_4$ , filtered, and solvent removed in vacuo to afford the starting materials quantitatively.

1-[4-(*tert*-Butyl-dimethylsiloxy)phenyl]ethanol (**7**) was prepared according to the literature.<sup>13</sup> Yield: 1.38 g, 91%.  $^1\text{H}$  NMR (300 MHz,  $\text{CDCl}_3$ )  $\delta$ : 7.22 (d,  $J = 8.20$  Hz, 2H), 6.80 (d,  $J = 8.20$  Hz, 2H), 4.82 (m, 1H), 1.76 (s, 1H), 1.47 (d,  $J = 6.28$ , 3H), 0.98 (s, 9H), 0.21 (s, 6H).  $^{13}\text{C}$  NMR (75 MHz,  $\text{CDCl}_3$ )  $\delta$ : 158.82, 138.35, 126.43, 119.86, 70.07, 25.81, 25.11, –4.21.  $^1\text{H}$  NMR and  $^{13}\text{C}$  NMR spectra are in agreement with those previously reported.<sup>13</sup>

#### 4-(1-Hydroxyethyl)phenol (**8**)

To a solution of 1-[4-(*tert*-butyl-dimethylsiloxy)phenyl]ethanol (**7**, 0.50 g, 1.98 mmol) in ethanol (50 mL) at 0 °C was added concd. HCl (1.0 mL) as a solution in ethanol (9.0 mL). The reaction was heated to reflux for 48 h. After

cooling to room temperature, the reaction mixture was poured into a saturated solution of  $\text{NaHCO}_3$  (25 mL), added to water (150 mL), and extracted with  $\text{CH}_2\text{Cl}_2$  ( $3 \times 100$  mL). The combined organics were washed with water (200 mL), dried over  $\text{MgSO}_4$ , filtered, and the solvent removed in vacuo. Crystallization from hexanes afforded **8** as a white powdery solid. Yield: 0.24 g, 90%; mp 136–139 °C (hexanes) (lit.<sup>13</sup> 134–138 °C).  $^1\text{H}$  NMR (300 MHz,  $\text{CDCl}_3$ )  $\delta$ : 7.27 (d,  $J = 8.28$  Hz, 2H), 6.82 (d,  $J = 8.79$  Hz, 2H), 4.86 (q,  $J = 6.37$  Hz, 1H), 4.82 (s, 1H), 1.72 (s, 1H), 1.53 (d,  $J = 6.38$  Hz, 3H).  $^1\text{H}$  NMR spectrum is in agreement with that previously reported.<sup>13</sup>

#### Diphenylmethanol (**10**)

To a solution of benzophenone (2.50 g, 13.72 mmol) in freshly distilled THF (50 mL) was added sodium borohydride (1.00 g, 27.44 mmol). The solution was heated to reflux for 18 h. After cooling to room temperature, the reaction mixture was poured into water (125 mL) and extracted with  $\text{CH}_2\text{Cl}_2$  ( $2 \times 200$  mL). The combined organics were washed with water (200 mL), dried over  $\text{MgSO}_4$ , filtered, and the solvent removed in vacuo to afford **10** as a white crystalline solid. Yield: 2.23 g, 88%; mp 65–68 °C ( $\text{CH}_2\text{Cl}_2$ ) (lit.<sup>14</sup> 65–66 °C).  $^1\text{H}$  NMR (300 MHz,  $\text{CDCl}_3$ )  $\delta$ : 7.43–7.26 (m, 10H), 5.87 (d,  $J = 3.41$  Hz, 1H), 2.25 (d,  $J = 3.49$  Hz, 1H).  $^{13}\text{C}$  NMR (75 MHz,  $\text{CDCl}_3$ )  $\delta$ : 143.81,

128.51, 127.59, 126.55, 76.29.  $^1\text{H}$  NMR and  $^{13}\text{C}$  NMR spectra are in agreement with those previously reported.<sup>14</sup>

### Diphenylmethane (11)

To a solution of diphenylmethanol (**10**, 1.00 g, 5.43 mmol) in ethanol (50 mL) at 0 °C was added concd. HCl (1.0 mL) as a solution in ethanol (9.0 mL). The solution was heated to reflux for 72 h. After cooling to room temperature, the reaction mixture was poured into a saturated solution of  $\text{NaHCO}_3$  (25 mL) and water (100 mL) was added. The material was extracted with  $\text{CH}_2\text{Cl}_2$  (2  $\times$  100 mL), washed with water (200 mL), dried over  $\text{MgSO}_4$ , filtered, and the solvent removed in vacuo to afford a clear, colourless oil that crystallized on standing. Yield: 0.64 g, 72%; mp 24–26 °C ( $\text{CH}_2\text{Cl}_2$ ) lit.<sup>15</sup> 25–26 °C.  $^1\text{H}$  NMR (300 MHz,  $\text{CDCl}_3$ )  $\delta$ : 7.26–7.30 (m, 4H), 7.18–7.21 (m, 6H), 3.98 (s, 2H).  $^{13}\text{C}$  NMR (75 MHz,  $\text{CDCl}_3$ )  $\delta$ : 141.31, 129.07, 128.66, 126.29, 42.11.  $^1\text{H}$  NMR and  $^{13}\text{C}$  NMR spectra are in agreement with those previously reported.<sup>15</sup>

### [4-(*tert*-Butyl-dimethylsilanoxy)phenyl]-4-(octyloxy)phenylmethanol (**12a**)

To a solution of 1-bromo-4-(octyloxy)benzene (1.46 g, 5.12 mmol) in freshly distilled THF (60 mL) at –78 °C under an Ar atmosphere was added *tert*-butyl lithium (6.02 mL of a 1.7 mol/L solution in pentane, 10.24 mmol) dropwise. After the mixture was allowed to stir for 1 h, a solution of 4-(*tert*-butyl-dimethylsilanoxy)benzaldehyde (1.21 g, 5.12 mmol) in freshly distilled THF (10 mL) was added dropwise. The solution was warmed to room temperature and stirred for 20 h. The reaction mixture was quenched with brine (10 mL) and extracted with a 50:50 mixture of ether/petroleum ether (3  $\times$  80 mL). The combined organic fractions were washed with water (3  $\times$  100 mL), dried over  $\text{MgSO}_4$ , filtered, and the solvent removed in vacuo. Flash chromatography (ether/petroleum ether, 10:1) afforded **12a** as a clear, light orange oil. Yield: 1.33 g, 59%; bp 435 °C (determined from DSC).  $^1\text{H}$  NMR (300 MHz,  $\text{CDCl}_3$ )  $\delta$ : 7.28 (d,  $J$  = 8.34 Hz, 2H), 7.23 (d,  $J$  = 8.43 Hz, 2H), 6.87 (d,  $J$  = 8.63 Hz, 2H), 6.81 (d,  $J$  = 8.51 Hz, 2H), 5.77 (s, 1H); 3.96 (t,  $J$  = 6.51 Hz, 2H), 1.79 (quin.,  $J$  = 6.80 Hz, 2H), 1.53–1.20 (m, 10H), 1.00 (s, 9H), 0.91 (m, 3H), 0.20 (s, 6H).  $^{13}\text{C}$  NMR (75 MHz,  $\text{CDCl}_3$ )  $\delta$ : 158.57, 155.01, 136.88, 136.10, 127.77, 127.70, 119.92, 114.37, 75.50, 68.03, 31.92, 29.66, 29.63, 29.60, 29.58, 29.40, 29.34, 29.28, 26.05, 25.67, 22.69, 18.18, 14.12, –4.42. Anal. calcd. for  $\text{C}_{31}\text{H}_{50}\text{O}_3\text{Si}$ : C, 74.73; H, 10.10. Found: C, 74.71; H, 9.96.

[4-(*tert*-Butyl-dimethylsilanoxy)phenyl]-4-(dodecyloxy)phenylmethanol (**12b**) was prepared in a method analogous to **12a**. Yield: 3.53 g, 56%; bp 443 °C (determined from DSC).  $^1\text{H}$  NMR (300 MHz,  $\text{CDCl}_3$ )  $\delta$ : 7.27 (m, 2H), 7.23 (d,  $J$  = 10.04 Hz, 2H), 6.87 (d,  $J$  = 8.16 Hz, 2H), 6.81 (d,  $J$  = 7.98 Hz, 2H), 5.77 (s, 1H), 3.95 (t,  $J$  = 6.33 Hz, 2H), 2.07 (s, 1H), 1.78 (quin.,  $J$  = 7.02 Hz, 2H), 1.51–1.21 (m, 18H), 0.99 (s, 9H), 0.90 (t,  $J$  = 6.42 Hz, 3H), 0.20 (s, 6H).  $^{13}\text{C}$  NMR (75 MHz,  $\text{CDCl}_3$ )  $\delta$ : 158.57, 155.01, 136.88, 136.10, 127.77, 127.70, 119.92, 114.37, 75.50, 68.03, 31.92, 29.68, 29.64, 29.60, 29.58, 29.40, 29.35, 29.29, 26.05, 25.67, 22.70, 18.18, 14.12, –4.42. Anal. calcd. for  $\text{C}_{27}\text{H}_{42}\text{O}_3\text{Si}$ : C, 73.25; H, 9.56. Found: C, 73.21; H, 9.46.

[4-(*tert*-Butyl-dimethylsilanoxy)phenyl]-4-(hexadecyloxy)phenylmethanol (**12c**) was prepared in a method analogous to **12a**. Yield: 3.54 g, 50%; bp 450 °C (determined from DSC).  $^1\text{H}$  NMR (300 MHz,  $\text{CDCl}_3$ )  $\delta$ : 7.27 (d,  $J$  = 8.21 Hz, 2H), 7.23 (d,  $J$  = 8.48 Hz, 2H), 6.87 (d,  $J$  = 8.67 Hz, 2H), 6.81 (d,  $J$  = 8.53 Hz, 2H), 5.77 (d,  $J$  = 3.39 Hz, 1H), 3.95 (t,  $J$  = 6.55 Hz, 2H), 2.07 (d,  $J$  = 3.58 Hz, 1H), 1.78 (quin.,  $J$  = 6.89 Hz, 2H), 1.54–1.23 (m, 26H), 0.99 (s, 9H), 0.94–0.87 (m, 3H), 0.20 (s, 6H).  $^{13}\text{C}$  NMR (75 MHz,  $\text{CDCl}_3$ )  $\delta$ : 158.57, 155.01, 136.88, 136.10, 127.77, 127.70, 119.92, 114.37, 75.50, 68.03, 31.93, 29.69, 29.66, 29.60, 29.58, 29.40, 29.36, 29.29, 26.05, 25.67, 22.70, 18.19, 14.12, –4.42. Anal. calcd. for  $\text{C}_{35}\text{H}_{58}\text{O}_3\text{Si}$ : C, 75.75; H, 10.53. Found: C, 75.71; H, 10.46.

### 4-(4-(Octyloxy)benzyl)phenol (**13a**)

To a solution of [4-(*tert*-butyl-dimethylsilanoxy)phenyl]-4-(octyloxy)phenylmethanol (**12a**, 1.00 g, 2.26 mmol) in ethanol (50 mL) at 0 °C was added concd. HCl (1.0 mL) as a solution in ethanol (10 mL). The solution was heated to reflux for 48 h. After cooling to room temperature, the reaction mixture was poured into a saturated solution of  $\text{NaHCO}_3$  (25 mL), mixed well, and extracted with hexanes (3  $\times$  50 mL) and ether (50 mL). The combined organics were washed with water (200 mL), dried over  $\text{MgSO}_4$ , filtered, and the solvent removed in vacuo. Crystallization from 5% ether in petroleum ether afforded **13a** as a white, powdery solid. Yield: 0.56 g, 79%; mp 70–73 °C (5% ether in petroleum ether).  $^1\text{H}$  NMR (300 MHz,  $\text{CDCl}_3$ )  $\delta$ : 7.07 (t,  $J$  = 8.22 Hz, 4H), 6.83 (d,  $J$  = 8.52 Hz, 2H), 6.76 (d,  $J$  = 8.42 Hz, 2H), 3.94 (t,  $J$  = 6.60 Hz, 2H), 3.86 (s, 2H), 1.78 (quin.,  $J$  = 6.93 Hz, 2H), 1.52–1.21 (m, 10 H), 0.90 (t,  $J$  = 5.97 Hz, 3H).  $^{13}\text{C}$  NMR (75 MHz,  $\text{CDCl}_3$ )  $\delta$ : 157.48, 153.75, 133.93, 133.45, 129.94, 129.70, 115.24, 114.50, 68.07, 40.13, 31.83, 29.37, 29.33, 29.25, 26.07, 22.66, 14.10. Anal. calcd. for  $\text{C}_{21}\text{H}_{28}\text{O}_2$ : C, 80.73; H, 9.03; O, 10.24. Found: C, 80.31; H, 9.02; O, 10.67.

4-(4-(Dodecyloxy)benzyl)phenol (**13b**) was prepared in a method analogous to **13a**. Yield: 0.50 g, 68%; mp 80–83 °C (5% ether in petroleum ether).  $^1\text{H}$  NMR (300 MHz,  $\text{CDCl}_3$ )  $\delta$ : 7.07 (t,  $J$  = 8.20 Hz, 4H), 6.83 (d,  $J$  = 8.59 Hz, 2H), 6.76 (d,  $J$  = 8.48 Hz, 2H), 3.94 (t,  $J$  = 6.54 Hz, 2H), 3.86 (s, 2H), 1.78 (quin.,  $J$  = 6.52 Hz, 2H), 1.51–1.21 (m, 14 H), 0.90 (t,  $J$  = 6.51 Hz, 3H).  $^{13}\text{C}$  NMR (75 MHz,  $\text{CDCl}_3$ )  $\delta$ : 157.48, 153.73, 133.95, 133.46, 129.94, 129.70, 115.25, 114.52, 68.09, 40.14, 31.93, 29.67, 29.64, 29.61, 29.59, 29.42, 29.35, 29.34, 26.07, 22.70, 14.12. Anal. calcd. for  $\text{C}_{25}\text{H}_{36}\text{O}_2$ : C, 81.47; H, 9.85; O, 8.68. Found: C, 81.40; H, 9.81; O, 8.79.

4-(4-(Hexadecyloxy)benzyl)phenol (**13c**) was prepared in a method analogous to **13a**. Yield: 0.60 g, 78%; mp 83–90 °C (5% ether in petroleum ether).  $^1\text{H}$  NMR (300 MHz,  $\text{CDCl}_3$ )  $\delta$ : 7.07 (t,  $J$  = 8.20 Hz, 4H), 6.80 (dd,  $J_1$  = 8.66 Hz,  $J_2$  = 2.00 Hz, 4H), 4.56 (s, 1H), 3.94 (t,  $J$  = 6.58 Hz, 2H), 3.86 (s, 2H), 1.78 (quin.,  $J$  = 6.58 Hz, 2H), 1.37 (m, 26H); 0.90 (t,  $J$  = 6.58 Hz, 3H).  $^{13}\text{C}$  NMR (75 MHz,  $\text{CDCl}_3$ )  $\delta$ : 157.5, 153.7, 134.0, 133.4, 129.9, 129.7, 115.2, 114.5, 68.0, 40.1, 31.9, 29.7 (3), 29.6 (4), 29.4 (3), 29.3, 26.1, 22.7, 14.1. Anal. calcd. for  $\text{C}_{29}\text{H}_{44}\text{O}_2$ : C, 82.02; H, 10.44; O, 7.53. Found: C, 82.05; H, 10.48; O, 7.47.



#### 4-[Hydroxyl(4-(octyloxy)phenyl)methyl]phenol (**14a**)

To a solution of [4-(*tert*-butyl-dimethylsiloxy)phenyl]-(4-(octyloxy)phenyl)methanol (**12a**, 2.50 g, 5.65 mmol) in freshly distilled THF (20 mL) at 0 °C was added a solution of tributyl ammonium fluoride trihydrate (TBAF, 3.57 g, 11.30 mmol) in freshly distilled THF (20 mL). The solution was allowed to stir for 1 h, warmed to room temperature, and then stirred for 2 h. The reaction mixture was poured into water (50 mL), mixed well, and then separated. The aqueous phase was extracted with a 50:50 mixture of ether/petroleum ether (2 × 100 mL), and the combined organics were washed with water (250 mL), dried over MgSO<sub>4</sub>, filtered, and the solvent removed in vacuo. Crystallization from 5% ether in petroleum ether afforded **14a** as a white, powdery solid. Yield: 1.02 g, 55%; mp 81–86 °C (5% ether in petroleum ether). <sup>1</sup>H NMR (300 MHz, CDCl<sub>3</sub>) δ: 7.27 (d, *J* = 8.44 Hz, 2H), 7.25 (d, *J* = 8.37 Hz, 2H), 6.87 (d, *J* = 8.71 Hz, 2H), 6.81 (d, *J* = 8.62 Hz, 2H), 5.78 (s, 1H), 4.77 (s, 1H), 3.95 (t, *J* = 6.57 Hz, 2H), 1.78 (quin., *J* = 6.57 Hz, 2H), 1.52–1.24 (m, 10H), 0.90 (t, *J* = 6.72 Hz, 3H). <sup>13</sup>C NMR (75 MHz, CDCl<sub>3</sub>) δ: 158.60, 154.86, 136.58, 136.05, 127.99, 127.72, 115.22, 114.42, 75.41, 68.05, 31.81, 29.35, 29.27, 29.23, 26.05, 22.65, 14.09. Anal. calcd. for C<sub>21</sub>H<sub>28</sub>O<sub>3</sub>: C, 76.79; H, 8.59; O, 14.61. Found: C, 77.38; H, 7.80; O, 14.82.

4-[Hydroxy(4-(hexadecyloxy)phenyl)methyl]phenol (**14c**) was prepared in a method analogous to **14a**. Yield: 0.53 g, 50%; mp 95–101 °C (5% ether in petroleum ether). <sup>1</sup>H NMR (300 MHz, CDCl<sub>3</sub>) δ: 7.28 (d, *J* = 8.11 Hz, 2H), 7.26 (d, *J* = 8.66 Hz, 2H), 6.87 (d, *J* = 8.49 Hz, 2H), 6.81 (d, *J* = 8.32 Hz, 2H), 5.78 (s, 1H), 4.69 (s, 1H), 3.95 (t, *J* = 6.51 Hz, 2H), 1.78 (quin., *J* = 6.53 Hz, 2H), 1.54–1.20 (m, 26H), 0.90 (t, *J* = 6.57 Hz, 3H). <sup>13</sup>C NMR (75 MHz, CDCl<sub>3</sub>) δ: 158.59, 154.84, 136.58, 136.05, 128.39, 127.92, 115.22, 114.46, 75.41, 68.07, 31.81, 29.35, 29.29, 29.25, 26.06, 22.66, 14.10. Anal. calcd. for C<sub>29</sub>H<sub>44</sub>O<sub>3</sub>: C, 79.04; H, 10.06; O, 10.89. Found: C, 78.43; H, 10.47; O, 11.10.

#### 4-(4-(Octyloxy)benzyl)phenol (**13a**)

To a solution of 4-[hydroxyl(4-(octyloxy)phenyl)methyl]phenol (**14a**, 0.20 g, 0.61 mmol) in ethanol (50 mL) °C was added concd. HCl (0.5 mL) as a solution in ethanol (9.5 mL). The solution was allowed to stir for 1 h and then heated to reflux for 48 h. After cooling to room temperature, the reaction mixture was poured into a saturated solution of NaHCO<sub>3</sub> (25 mL), mixed well, and then extracted with petroleum ether (3 × 50 mL) and ether (50 mL). The combined organics were washed with water (200 mL), dried over MgSO<sub>4</sub>, filtered, and the solvent removed in vacuo to afford 4-(4-(octyloxy)benzyl)phenol as a white powdery solid. Yield: 0.17 g, 90%; mp 70–73 °C (ether/petroleum ether). <sup>1</sup>H NMR (300 MHz, CDCl<sub>3</sub>) δ: 7.07 (t, *J* = 8.22 Hz, 4H), 6.83 (d, *J* = 8.52 Hz, 2H), 6.76 (d, *J* = 8.42 Hz, 2H), 3.94 (t, *J* = 6.60 Hz, 2H), 3.86 (s, 2H), 1.78 (quin., *J* = 6.93 Hz, 2H), 1.52–1.21 (m, 10 H), 0.90 (t, *J* = 5.97 Hz, 3H). <sup>13</sup>C NMR (75 MHz, CDCl<sub>3</sub>) δ: 157.48, 153.75, 133.93, 133.45, 129.94, 129.70, 115.24, 114.50, 68.07, 40.13, 31.83, 29.37, 29.33, 29.25, 26.07, 22.66, 14.10. Anal. calcd. for C<sub>21</sub>H<sub>28</sub>O<sub>2</sub>: C, 80.73; H, 9.03; O, 10.24. Found: C, 80.01; H, 9.46; O, 10.53.

4-(4-(Hexadecyloxy)benzyl)phenol (**13c**) was prepared in

a method analogous to 4-(4-(octyloxy)benzyl)phenol. Yield: 0.18 g, 79%; mp 83–90 °C (ether/petroleum ether). <sup>1</sup>H NMR (300 MHz, CDCl<sub>3</sub>) δ: 7.07 (t, *J* = 8.20 Hz, 4H), 6.80 (dd, *J*<sub>1</sub> = 8.66 Hz, *J*<sub>2</sub> = 2.00 Hz, 4H), 4.56 (s, 1H), 3.94 (t, *J* = 6.58 Hz, 2H), 3.86 (s, 2H), 1.78 (quin., *J* = 6.58 Hz, 2H), 1.37 (m, 26H), 0.90 (t, *J* = 6.58 Hz, 3H). <sup>13</sup>C NMR (75 MHz, CDCl<sub>3</sub>) δ: 157.5, 153.7, 134.0, 133.4, 129.9, 129.7, 115.2, 114.5, 68.0, 40.1, 31.9, 29.7 (3), 29.6 (4), 29.4 (3), 29.3, 26.1, 22.7, 14.1. Anal. calcd. for C<sub>29</sub>H<sub>44</sub>O<sub>2</sub>: C, 82.02; H, 10.44; O, 7.53. Found: C, 82.05; H, 10.48; O, 7.47.

#### Bis(4-(dodecyloxy)phenyl)methanol (**15**)

A solution of 4,4'-bis(dodecyloxy)benzophenone (0.30 g, 0.55 mmol) and sodium borohydride (0.046 g, 1.20 mmol) in ethanol (40 mL) was allowed to reflux for 1 h. After cooling to room temperature, the reaction mixture was poured into water (100 mL) and extracted with CH<sub>2</sub>Cl<sub>2</sub> (2 × 100 mL). The combined organics were washed with water (2 × 200 mL), dried over MgSO<sub>4</sub>, filtered, and the solvent removed in vacuo. Crystallization from hexanes afforded **15** as a white powdery solid. Yield: 0.23 g, 76%; mp 37–39 °C (hexanes). <sup>1</sup>H NMR (300 MHz, CDCl<sub>3</sub>) δ: 7.28 (d, *J* = 8.55 Hz, 4H), 6.88 (d, *J* = 8.55 Hz, 4H), 5.78 (d, *J* = 3.40 Hz, 1H), 3.95 (t, *J* = 6.58 Hz, 4H), 2.06 (d, *J* = 3.40 Hz, 1H), 1.78 (quin. *J* = 6.58 Hz, 4H), 1.52–1.19 (m, 36 H); 0.90 (t, *J* = 6.58 Hz, 6H). <sup>13</sup>C NMR (75 MHz, CDCl<sub>3</sub>) δ: 158.55, 136.16, 127.71, 114.39, 75.46, 68.04, 31.92, 29.66, 29.63, 29.60, 29.58, 29.40, 29.35, 29.28, 26.05, 22.69, 14.12. Anal. calcd. for C<sub>37</sub>H<sub>61</sub>O<sub>3</sub>: C, 80.23; H, 11.10; O, 8.67. Found: C, 80.31; H, 11.03; O, 8.66.

#### Bis(4-(dodecyloxy)phenyl)methane (**16**)

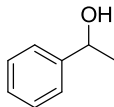
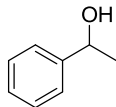
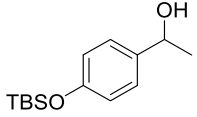
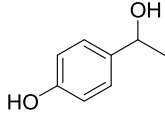
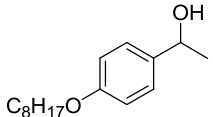
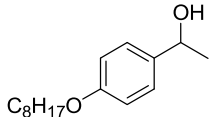
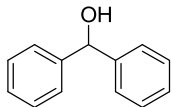
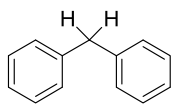
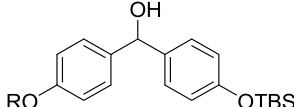
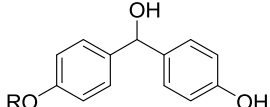
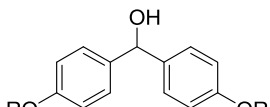
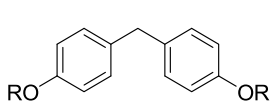
To a solution of bis(4-(dodecyloxy)phenyl)methanol (**15**, 0.25 g, 0.45 mmol) in ethanol (50 mL) at reflux was added a solution of concd. HCl (0.5 mL) in ethanol (9.5 mL). The solution was allowed to reflux for 48 h. After cooling to room temperature, the reaction mixture was poured into a saturated solution of NaHCO<sub>3</sub> (25 mL) and mixed well. Water (100 mL) was added and the mixture was extracted with petroleum ether (150 mL) and ether (100 mL). The combined organics were washed with water (200 mL), dried over MgSO<sub>4</sub>, filtered, and the solvent removed in vacuo to afford bis(4-(dodecyloxy)phenyl)methane as a waxy white solid. Yield: 0.20 g, 83%; mp 30–33 °C (petroleum ether/ether). <sup>1</sup>H NMR (300 MHz, CDCl<sub>3</sub>) δ: 7.08 (d, *J* = 8.59 Hz, 4H), 6.83 (d, *J* = 8.59 Hz, 4H), 3.94 (t, *J* = 6.57 Hz, 4H), 3.87 (s, 2H), 1.78 (quin., *J* = 6.56 Hz, 4H), 1.51–1.22 (m, 36H), 0.91 (t, *J* = 6.57 Hz, 6H). <sup>13</sup>C NMR (75 MHz, CDCl<sub>3</sub>) δ: 157.46, 133.54, 129.68, 114.44, 68.02, 40.14, 31.92, 29.66, 29.63, 29.60, 29.59, 29.41, 29.34, 29.33, 26.07, 22.69, 14.12. Anal. calcd. for C<sub>37</sub>H<sub>61</sub>O<sub>2</sub>: C, 82.62; H, 11.43; O, 5.95. Found: C, 82.65; H, 11.48; O, 5.87.

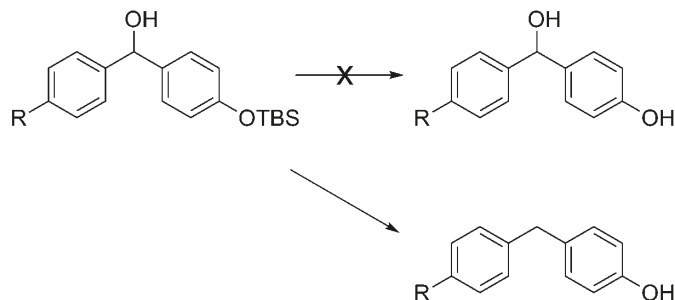
## Results and discussion

In our efforts towards the acidic hydrolysis of silyl ether protecting groups,<sup>16</sup> we discovered an unexpected result: in addition to cleavage of the silicon–oxygen bond, we also observed deoxygenation of the diarylmethanol (Scheme 1).



**Table 1.** Deoxygenation of secondary alcohols using HCl/EtOH.

Entry	Reactant	Time (h)	Yield (%)	Product	
6		96	NR <sup>a</sup>	6 	
7		48	90	8 	
9		120	NR	9 	
10		48	72	11 	
12a		R = C <sub>8</sub> H <sub>17</sub>	48	79	13a
12b		R = C <sub>12</sub> H <sub>25</sub>	48	68	13b
12c		R = C <sub>16</sub> H <sub>33</sub>	48	78	13c
14a		R = C <sub>8</sub> H <sub>17</sub>	48	90	13a
14c		R = C <sub>16</sub> H <sub>33</sub>	48	79	13c
15		R = C <sub>12</sub> H <sub>25</sub>	48	83	16 

<sup>a</sup> NR: no reaction**Scheme 1.** Attempted acidic hydrolysis of silyl ether protecting groups. Reagents and conditions: HCl, EtOH, reflux 48 h.

To further probe the generality of this reaction, we tested a number of substrates including secondary alcohols and diarylmethanols with different substitution patterns, with and without silyl ether protecting groups. Table 1 outlines the substrates examined and the results, including reaction time and yield. It was found that the reaction does not proceed for primary alcohols or secondary alcohols not bearing two aryl functionalities, nor was the presence of the silyl protect-

ing group required. The reaction proceeds in good yields (68%–90%) for substrates displaying a variety of substitution patterns.

## Conclusions

A new mild and efficient method for the deoxygenation of diarylmethanols has been developed. This reaction mitigates

the need to use radical conditions or toxic heavy metals employed in the Barton–McCombie deoxygenation.

## Acknowledgements

We thank the Natural Sciences and Engineering Research Council of Canada (NSERC) for financial support.

## References

- (1) Otsuka, H.; Yamasaki, K.; Yamauchi, T. *Phytochemistry* **1989**, 28 (11), 3197. doi:10.1016/0031-9422(89)80306-1.
- (2) Chai, X. Y.; Song, Y. L.; Xu, Z. R.; Shi, H. M.; Bai, C. C.; Bi, D.; Wen, J.; Li, F. F.; Tu, P. F. *J. Nat. Prod.* **2008**, 71 (5), 814. doi:10.1021/np800014s. PMID:18412396.
- (3) Bringmann, G.; Pabst, T.; Henschel, P.; Hubland, A. *Tetrahedron* **2001**, 57 (7), 1269. doi:10.1016/S0040-4020(00)01131-5.
- (4) Chen, L.; Fang, Y.; Zhu, T.; Gu, Q.; Zhu, W. *J. Nat. Prod.* **2008**, 71 (1), 66. doi:10.1021/np070421v. PMID:18163588.
- (5) Grignard, V. *C. R. Hebd. Seances Acad. Sci.* **1900**, 130, 1322.
- (6) Barton, D. H. R.; McCombie, S. W. *J. Chem. Soc., Perkin Trans. 1* **1975**, (16): 1574. doi:10.1039/p19750001574.
- (7) Gimisis, T.; Ballestri, M.; Ferreri, C.; Chatgililoglu, C.; Boukherroub, R.; Manuel, G. *Tetrahedron Lett.* **1995**, 36 (22), 3897. doi:10.1016/0040-4039(95)00593-2.
- (8) Barton, D. H. R.; Jang, D. O.; Jaszberenyi, J. C. *Tetrahedron Lett.* **1990**, 31 (33), 4681. doi:10.1016/S0040-4039(00)97705-0.
- (9) Barton, D. H. R.; Jang, D. O.; Jaszberenyi, J. C. *Tetrahedron Lett.* **1991**, 32 (49), 7187. doi:10.1016/0040-4039(91)80472-I.
- (10) Barton, D. H. R.; Jang, D. O.; Jaszberenyi, J. C. *Tetrahedron Lett.* **1992**, 33 (17), 2311. doi:10.1016/S0040-4039(00)74198-0.
- (11) Waterlot, C.; Coutourier, D.; De Backer, M.; Rigo, B. *Can. J. Chem.* **2000**, 78 (9), 1242. doi:10.1139/cjc-78-9-1242.
- (12) *Standard Test Method for Determining Vapor Pressure by Thermal Analysis*; ASTM Standard E1782 [Online]; ASTM International: West Conshohocken, PA, 2008. doi:10.1520/E1782-08. Available from www.astm.org.
- (13) Noji, M.; Ohno, T.; Fuji, K.; Futaba, N.; Tajima, H.; Ishii, K. *J. Org. Chem.* **2003**, 68 (24), 9340. doi:10.1021/jo034255h. PMID:14629155.
- (14) Kuriyama, M.; Shimazawa, R.; Shirai, R. *J. Org. Chem.* **2008**, 73 (4), 1597. doi:10.1021/jo7020983. PMID:18186645.
- (15) Gilman, H.; Diehl, J. *J. Org. Chem.* **1961**, 26 (12), 4817. doi:10.1021/jo01070a010.
- (16) (a) Cunico, R. F.; Bedell, L. *J. Org. Chem.* **1980**, 45 (23), 4797. doi:10.1021/jo01311a058.; (b) Wetter, H.; Oertle, K. *Tetrahedron Lett.* **1985**, 26 (45), 5515. doi:10.1016/S0040-4039(01)80874-1.; (c) Kawahara, S.; Wada, T.; Sekine, M. *J. Am. Chem. Soc.* **1996**, 118 (40), 9461. doi:10.1021/ja961959i.; (d) Nimmagadda, R. D.; McRae, C. *Tetrahedron Lett.* **2006**, 47 (32), 5755. doi:10.1016/j.tetlet.2006.06.007.

# Modular incorporation of 1-benzyltryptophan into dipeptide hosts that bind acetylcholine in pure water

Cory S. Beshara and Fraser Hof

**Abstract:** Proteins that recognize and bind quaternary ammonium ions depend on “aromatic-cage” structural motifs that use multiple aromatic residues to engage the side chain’s ammonium cation. We introduce herein the use of 1-benzyltryptophan (Trp(Bn)) residues as synthetic, unnatural partial analogues of natural aromatic cages. We demonstrate the modular incorporation of these building blocks into simple dipeptide hosts and show that they are capable of binding quaternary ammonium ions in buffered water and in chloroform.

**Key words:** molecular recognition, tryptophan, peptides, cation– $\pi$  interaction, hydrophobic effect.

**Résumé :** Les protéines qui reconnaissent et qui se lient à des ions ammonium quaternaires dépendent sur des motifs structuraux « cage aromatique » qui font appel à de multiples résidus aromatiques pour s’engager avec le cation ammonium de la chaîne latérale. Dans ce travail, on introduit l’utilisation des résidus 1-benzyltryptophane (Trp(Bn)) comme analogues partiels de synthèse, non naturels, des cages aromatiques naturelles. On démontre que l’incorporation modulaire des ces blocs dans des hôtes dipeptidiques et on montre qu’ils sont capables de se lier à des ions ammonium quaternaires dans l’eau tamponnée et dans le chloroforme.

**Mots-clés :** reconnaissance moléculaire, tryptophane, peptides, interaction cation– $\pi$ , effet hydrophobe.

## Introduction

The cation– $\pi$  interaction is implicated in many recognition events in biology.<sup>1–5</sup> Its importance for the recognition of cholinergic agents by their receptors<sup>3,6,7</sup> has long been understood. Its role in the recognition of post-translationally methylated lysine residues has more recently come to light,<sup>4,8–10</sup> and the protein data bank (PDB) now contains many examples of trimethyllysine-containing quaternary ammonium complexes.<sup>11</sup> In these structures, the binding of the quaternary ammonium ion is accomplished by motifs referred to as “aromatic cages” in which clusters of three to four aromatic side chains make close cation– $\pi$  contacts with the RNMe<sub>3</sub><sup>+</sup> portion of the side chain (Fig. 1). The most electron-rich aromatic side chain, tryptophan (Trp), is present as at least one of the binding partners in all trimethyllysine-binding aromatic cage motifs currently reported in the PDB, where it is accompanied by additional phenylalanine (Phe) and (or) tyrosine (Tyr) residues.

Inspired by the use of multiple aromatic rings in the protein domains that bind quaternary ammonium ions, we considered the unnatural modified amino acid 1-benzyltryptophan (Trp(Bn), **1**, Fig. 1) as a building block that could be easily incorporated into peptide-based hosts. A prior report of the dipeptide Boc-Trp-Trp-OMe (**2**) as a simple receptor for ammonium ions in organic solvents<sup>12</sup> led us to wonder if it

could be adapted to achieve the far more difficult task of binding cations in pure water by the incorporation of Trp(Bn) residues. We report here, the synthesis of 1-benzyltryptophan based reagents and their rapid and modular incorporation into quaternary ammonium ion binding dipeptide hosts related to the parent Trp-Trp dipeptide (**2**).

## Results and discussion

We were surprised to find very few reports of the apparently simple 1-benzyltryptophan (**1**) in the literature. Only six literature references were found in a Scifinder structure-based search,<sup>13–18</sup> and none of these references report the appended 1-benzyl group being used as a functional element. The obvious routes for the synthesis of **1** start with simple tryptophan analogs and involve deprotonation and alkylation of the side chain nitrogen atom. We first targeted the treatment of tryptophan methyl ester with 1 equiv. of NaH followed by treatment with a benzyl halide. Reactions were attempted in THF and DMF using a variety of temperatures and reaction times. While selective benzylation of the side chain nitrogen could be achieved, we found significant racemization of the  $\alpha$ -carbon under all conditions that we tested (racemization is most easily detected by the observation of diastereomeric  $\alpha$ -CH <sup>1</sup>H NMR resonances once dipeptides are made from a Trp(Bn) precursor). We next attempted to

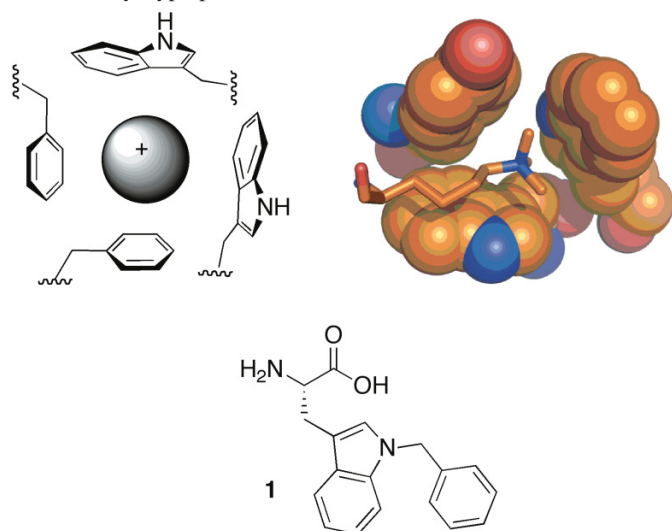
Received 9 April 2010. Accepted 27 June 2010. Published on the NRC Research Press Web site at canjchem.nrc.ca on 23 September 2010.

*In memory of Michael Pollard.*

C.S. Beshara and F. Hof.<sup>1</sup> University of Victoria, Department of Chemistry, PO Box 3065, STN CSC, Victoria, BC V8W 3V6, Canada.

<sup>1</sup>Corresponding author (e-mail: fhof@uvic.ca).

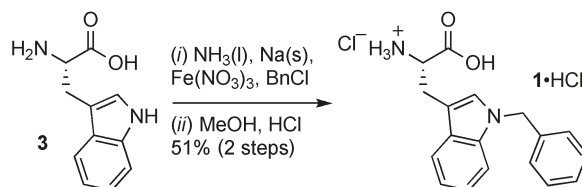
**Fig. 1.** Top: aromatic cage binding motifs that are used by proteins that recognize biologically important ammonium ions of the form  $\text{RNMe}_3^+$ . The structure on the right is an example of an aromatic cage taken from the PDB entry 1PDQ. Bottom: the unnatural amino acid 1-benzyltryptophan.



treat the free-acid Trp (**3**) with two or more equivalents of NaH to generate the doubly deprotonated carboxylate-indole dianion, with the idea that the more reactive indole anion could be reacted selectively with 1 equiv. of benzyl halide. These efforts effectively prevented racemization, but generated intractable mixtures and low yields arising from mixtures of O- and N-benylation products. We subsequently adapted a reported deprotonation of unprotected Trp under dissolving metal conditions ( $\text{Na-NH}_3$ ) and subsequent treatment with BnCl in liquid  $\text{NH}_3$  (Scheme 1).<sup>14</sup> We found that this method was successful only when performed on  $\geq 5$  g of **3**, and crude yields of **1**, uncontaminated by O-benzyl or racemized by-products, reached a high of 70% when the reaction was carried out on a 40 g scale. We found an efficient purification for **1** by first dissolving the crude in a mixture of MeOH and concentrated aqueous HCl; precipitation by the addition of  $\text{Et}_2\text{O}$  gave the pure product as the HCl salt (**1**·HCl) in a 51% overall yield.

Scheme 2 depicts the synthesis of Boc-Trp(Bn)-OH (**4**) and  $\text{H}_2\text{N-Trp(Bn)-OMe}$  (**5**) that were used in the subsequent synthesis of a family of organic- and water-soluble host dipeptides. Treatment of **1**·HCl with thionyl chloride in methanol gives methyl ester **5** in a 87% yield, whereas treatment of **1**·HCl with NaOH in the presence of  $(\text{Boc})_2\text{O}$  under mixed aqueous-organic conditions gives the Boc-protected compound **4** in a 78% yield. Compound **5** was coupled with commercially available Boc-Trp-OH (**6**) to form the monobenzylated dipeptide host (Boc-Trp-Trp(Bn)-OMe, **7**) in a 49% yield. Compound **4** was combined with **5** under standard solution-phase HBTU coupling conditions to yield the dibenzylated dipeptide host (Boc-Trp(Bn)-Trp(Bn)-OMe, **8**) in a 61% yield. To complete the series, **4** was coupled with commercially available  $\text{H}_2\text{N-Trp-OMe}$  (**9**) to afford Boc-Trp-Trp-OMe (**2**) with free indole side chains in a 76% yield. Unlike the prior synthesis of host **2**,<sup>12</sup> all transformations reported herein were optimized to allow purification without resorting to flash chromatography.

**Scheme 1.** Selective 1-benylation of Trp and isolation as the HCl salt.



To create water-soluble analogs that retained an overall anionic charge, we doubly deprotected compounds **2**, **7**, and **8** and created simple N-terminal acetylated derivatives of the form Ac-Trp-Trp-OH (not shown). Unfortunately, dipeptides of this form were insoluble in phosphate-buffered  $\text{D}_2\text{O}$  ( $\text{pD} = 7.4$ ). In an effort to increase water solubility while leaving the Trp(Bn) binding motifs unchanged, we targeted structures with N-terminal succinyl groups. Thus, compounds **2**, **7**, and **8** were Boc-deprotected in HCl-AcOH to give the dipeptide hydrochloride salts **10**, **11**, and **12**, respectively, as pure white solids after filtration and washing with  $\text{Et}_2\text{O}$ . The suspension of **10–12** in  $\text{CH}_2\text{Cl}_2$ , neutralization with  $i\text{-Pr}_2\text{EtN}$ , and treatment with succinic anhydride gave the succinyl (Suc) derived Suc-Trp-Trp-OMe dipeptides, which were directly saponified in methanol-water to yield, after acidification of the aqueous work-up layer, dipeptides **13–15** (40%–56% overall yield over four synthetic steps; Scheme 2). Compounds **13–15** are all soluble in phosphate-buffered  $\text{D}_2\text{O}$  ( $\text{pD} = 7.4$ ) at concentrations up to 10 mmol/L.

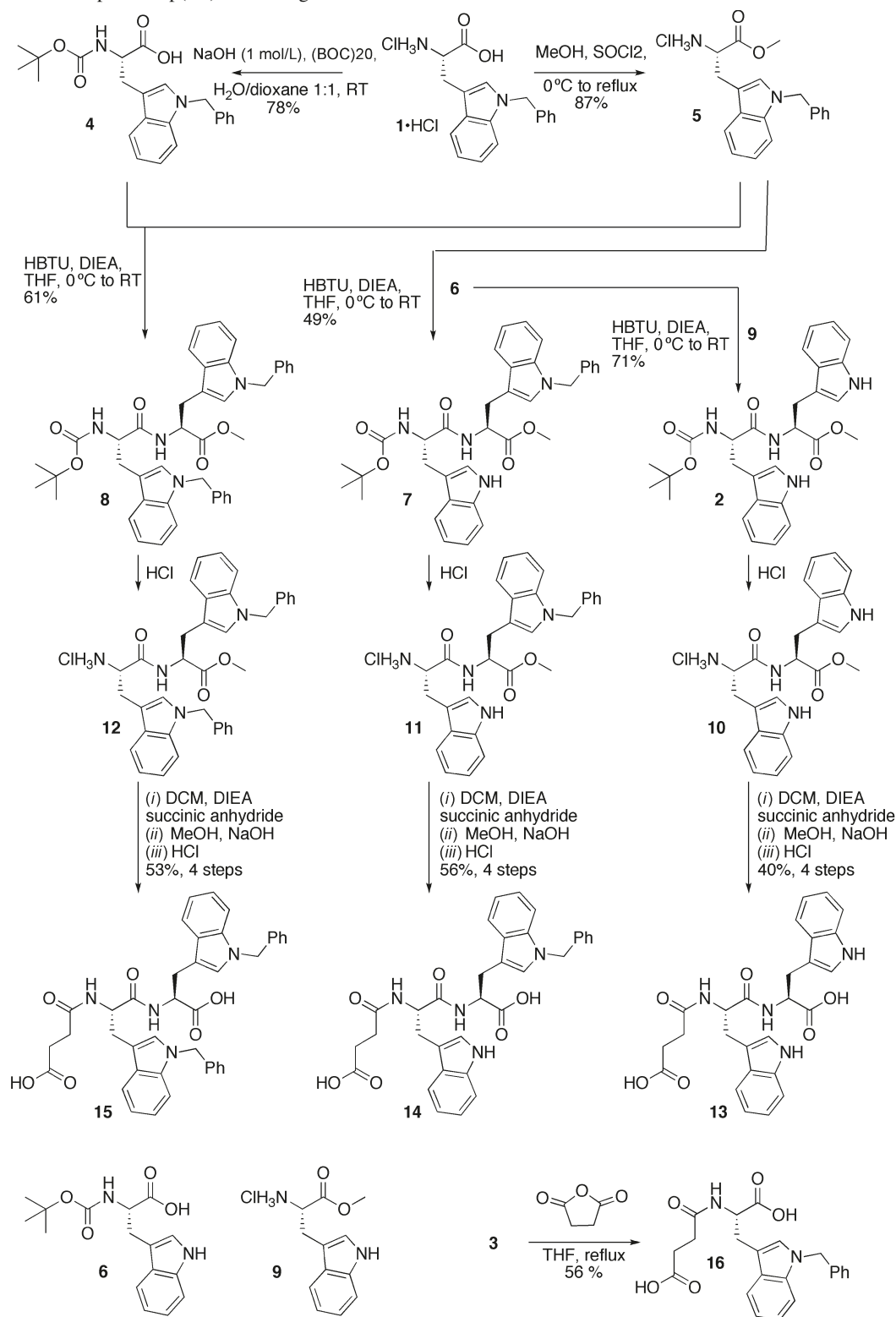
Acetylcholine chloride ( $\text{AcCh}^+ \text{Cl}^-$ ) was used as a prototypical  $\text{RNMe}_3^+$  guest because of its high solubility in both water and chloroform, which is a critical feature that we did not find in halide or BArF salts of other guest candidates trimethyllysine, tetramethylammonium, or benzyltrimethylammonium. Titration of  $\text{AcCh}^+ \text{Cl}^-$  into the dipeptide hosts **13–15** in phosphate-buffered  $\text{D}_2\text{O}$  (10 mmol/L  $\text{Na}_2\text{HPO}_4$ – $\text{NaH}_2\text{PO}_4$ ,  $\text{pD} = 7.4$ ) revealed guest-induced chemical shifts that fit to 1:1 binding isotherms to provide  $K_{\text{assoc}}$  values (Fig. 2 and Table 1). Even at the highest host and guest concentrations tested (10 and 930 mmol/L, respectively), the unbzylated host **13**, which is most closely related to the literature host **2** that can bind  $\text{AcCh}^+$  in  $\text{CDCl}_3$ ,<sup>12</sup> showed no detectable binding of  $\text{AcCh}^+$  under these competitive solvent conditions.

The monobenzylated host **14** and dibenzylated host **15** both showed evidence of binding that, while weak, was reproducibly observed over many determinations with the highest affinity arising from dibenzylated **15**. Direct evidence for the interaction of benzyl groups with the bound cation was given by the large chemical shift changes among the benzylic methylenes of dipeptide **15** (Fig. 2B), while the shifts of both benzyl and indolyl resonances in the aromatic regions (Fig. 2A) further support the participation of both types of aromatic rings in binding.

To examine the role of solvent effects in these hosts, we carried out binding studies of the chloroform-soluble analogs **2**, **7**, and **8** using the same titration methodology. In this solvent, the unbzylated host **2** bound  $\text{AcCh}^+ \text{Cl}^-$  with a  $K_{\text{assoc}}$  of  $85 (\text{mol/L})^{-1}$ , which is in agreement with the value previously reported.<sup>12</sup> Surprisingly, our new benzylated hosts **7** and **8** bound  $\text{AcCh}^+$  more weakly than did the unbzylated



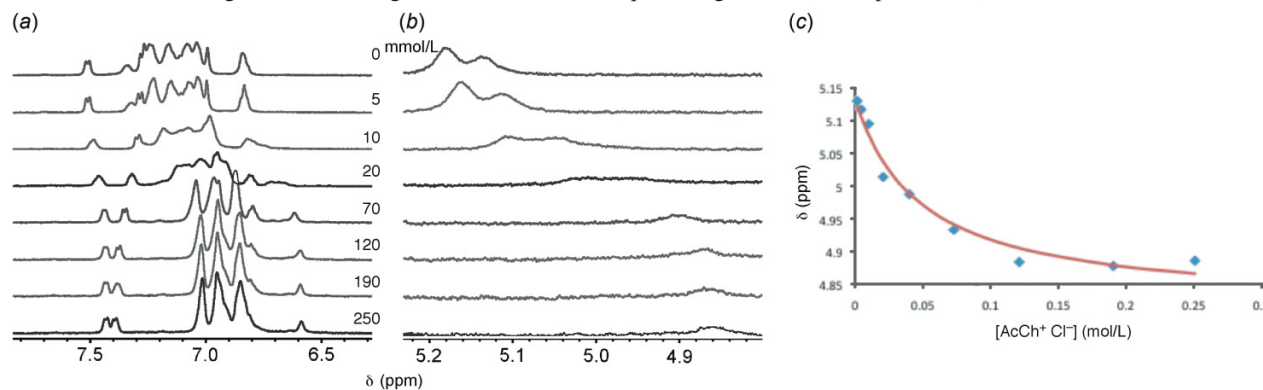
**Scheme 2.** Synthesis of Trp and Trp(Bn)-containing hosts.



parent (Table 1), despite the presence of additional aromatic binding surfaces. We also found that host **2** is also the most potent host for the binding of the the noncoordinating  $\text{BnNMe}_3^+ \text{BARF}^-$ , suggesting that this result is not an artifact arising from counterion effects in chloroform.<sup>19</sup> The cation- $\pi$  interaction is an electrostatic attraction that should be

stronger in nonpolar media; the fact that we see the opposite trend in  $\text{CDCl}_3$  suggests that it is not a major contributor to interactions between the benzyl groups and cationic guests. Instead, it is likely the increase in hydrophobic surface area provided by the benzyl groups that leads to the higher cation affinities observed for benzylated hosts in  $\text{D}_2\text{O}$ .

**Fig. 2.** Concentration-dependent chemical shift changes displayed by the host **15** (10 mmol/L) in its (a) aromatic and (b) methylene regions upon addition of AcCh<sup>+</sup> Cl<sup>−</sup> in D<sub>2</sub>O (phosphate buffer, pD 7.4, 10 mmol/L). Concentrations of AcCh<sup>+</sup> Cl<sup>−</sup> are indicated. (c) A plot of titration data and the 1:1 binding isotherm arising from nonlinear least-squares regression (see Experimental).



**Table 1.**  $K_{\text{assoc}}$  values for cations with hosts **13**–**16** in D<sub>2</sub>O and **2**, **7**, and **8** in CDCl<sub>3</sub>.

Host	Guest	Solvent	$K_{\text{assoc}}$ ((mol/L) <sup>−1</sup> )
<b>13</b> (Trp–Trp)	AcCh <sup>+</sup> Cl <sup>−a</sup>	D <sub>2</sub> O	≤1 <sup>b</sup>
<b>14</b> (Trp–Trp(Bn))	AcCh <sup>+</sup> Cl <sup>−a</sup>	D <sub>2</sub> O	3±1
<b>15</b> (Trp(Bn)–Trp(Bn))	AcCh <sup>+</sup> Cl <sup>−a</sup>	D <sub>2</sub> O	14±6
<b>16</b> (Trp(Bn))	AcCh <sup>+</sup> Cl <sup>−a</sup>	D <sub>2</sub> O	≤1 <sup>b</sup>
<b>2</b> (Trp–Trp)	AcCh <sup>+</sup> Cl <sup>−a</sup>	CDCl <sub>3</sub>	85±17
<b>7</b> (Trp–Trp(Bn))	AcCh <sup>+</sup> Cl <sup>−a</sup>	CDCl <sub>3</sub>	22±4
<b>8</b> (Trp(Bn)–Trp(Bn))	AcCh <sup>+</sup> Cl <sup>−a</sup>	CDCl <sub>3</sub>	1±0.5
<b>2</b> (Trp–Trp)	BnNMe <sub>3</sub> <sup>+</sup> BArF <sup>−c</sup>	CDCl <sub>3</sub>	63±12
<b>7</b> (Trp–Trp(Bn))	BnNMe <sub>3</sub> <sup>+</sup> BArF <sup>−c</sup>	CDCl <sub>3</sub>	27±5
<b>8</b> (Trp(Bn)–Trp(Bn))	BnNMe <sub>3</sub> <sup>+</sup> BArF <sup>−c</sup>	CDCl <sub>3</sub>	47±3

**Note:**  $K_{\text{assoc}}$  was determined using at least three replicate titrations, tracking two to three proton resonances during each titration. Errors represent the upper and lower limits of replicate titrations. “D<sub>2</sub>O” also contained 10 mmol/L NaH<sub>2</sub>PO<sub>4</sub>–Na<sub>2</sub>HPO<sub>4</sub> adjusted to pD 7.4.

<sup>a</sup>Guest solution (ranging from 80 to 930 mmol/L) was titrated into a solution of the host (10 mmol/L).

<sup>b</sup>Titration resulted in insignificant  $\Delta\delta$  values.

<sup>c</sup>A concentrated solution of the host (80–250 mmol/L) was titrated into the guest (2 mmol/L) due to low solubility of the BnNMe<sub>3</sub><sup>+</sup> BArF<sup>−</sup> salt in CDCl<sub>3</sub>.

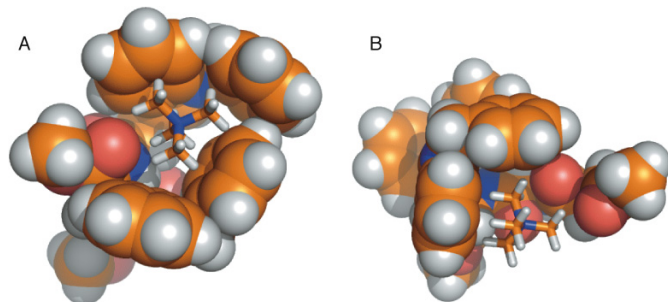
To gain some insight into the possible structures of these host–guest complexes, we carried out Monte Carlo conformational searches using a representative dibenzylated dipeptide host (the methyl ester analog of **15**) and the truncated guest Me<sub>4</sub>N<sup>+</sup>. These gas-phase calculations are limited in scope and capabilities; they are subject to unrealistic overemphasis of electrostatic attractions (hence our use of the methyl ester host analog) and they are incapable of representing the hydrophobic driving forces that are critical in aqueous solution. However, they are very good at determining energetically reasonable bond angles and intra- and intermolecular contacts, and are therefore useful for gaining a qualitative sense of what types of structures might be allowable for the host–guest complex. The two most common types of structures among low-energy conformations obtained from our Monte Carlo calculation involve (i) the interaction of the cation with both benzyl indole moieties in a pocket-like geometry (“pocket”, Fig. 3A) or (ii) the interaction of the cation with only a single Trp(Bn) side chain (“cleft”, Fig. 3B). The cleft structure in Fig. 3B suggests

that only one benzyl indole group and a neighboring carbonyl might be needed to engage the cationic guest. To test this hypothesis, we designed compound **16** (Suc-Trp(Bn)-OH) to see if this monomeric host fragment was a competent cation binder in water. Compound **16** was synthesized in a 56% yield by the reaction of succinic anhydride with precursor **3** (Scheme 2). NMR titrations of **16** with AcCh<sup>+</sup> Cl<sup>−</sup> in buffered D<sub>2</sub>O, carried out as for the other hosts, gave no observable sign of binding, proving that two Trp residues are required for cation binding in water by these dipeptides.

## Conclusions

These studies with simple dipeptide hosts introduce the readily synthesized Trp(Bn) building block as a new quaternary ammonium ion binding motif that can function in pure, buffered water. The weakness of the observed binding by these dipeptides in either medium almost certainly arises from their lack of preorganization relative to more rigid

**Fig. 3.** Representative structures, (A) “pocket” and (B) “cleft”, arising from Monte Carlo conformation searches at the PM3 level of theory. Structures like that shown in Fig. 3A are consistent with both of our key experimental observations in water: the *N*-benzyl substituents play a significant role in binding, and both amino acid side chains are required for cation binding in water.



macrocyclic systems.<sup>9,10</sup> We are curious to see if rigidification of these building blocks by incorporation into small, folded peptide scaffolds increases the potency of Trp(Bn) building blocks as cation binders.

## Experimental

### General procedure

All solvents and reagents were used as purchased from Sigma-Aldrich and used without further purification, except solvents that were dried using an MBraun solvent purification system. NMR spectra and NMR titration data were obtained on a Bruker Avance 500 MHz NMR spectrometer with the exception of <sup>19</sup>F NMR, which was obtained on a Bruker Avance 300 MHz spectrometer. Coupling constants are reported in Hertz. <sup>1</sup>H and <sup>13</sup>C spectra were referenced to residual solvent signals, and the <sup>19</sup>F spectrum was externally referenced to FCCL<sub>3</sub>. HR-MS were acquired on a Waters/Micromass LCT TOF instrument. Melting points were determined with the use of a Gallenkamp melting point apparatus. Specific rotations (*c* = g/100 mL) were acquired with a Rodolf Research Analytical Autopol I instrument and are given in units of 10<sup>-1</sup> deg cm<sup>2</sup> g<sup>-1</sup>.

The typical titration procedure is as follows: The molecule of interest was dissolved in the appropriate solvent (dispensed with a micropipette) to make a solution (4 mL) of a predetermined concentration (2–10 mmol/L). The stock (600 μL) was then introduced into an NMR tube and to the remaining stock solution was added an excess of host or guest. The NMR spectrum of the stock solution was used as a reference for unbound host or guest and the solution titrated with predetermined volumes (micropipette) of titrant, followed by the collection of new NMR spectra. This method ensures that the concentration of the host remains constant throughout the titration. The Δδs were recorded and the data worked-up and fitted to the 1:1 binding isotherm using the spreadsheet made freely available by Sanderson.<sup>20</sup> Initial guesses for host or guest concentrations during the course of the experiments were obtained by the method discussed by Hirose.<sup>21</sup>

Calculations were carried out at the PM3 level of theory using the conformational search routine in Spartan'04.<sup>22</sup> Structures within 5 kcal/mol (1 cal = 4.1868 J) of the global

minimum were retained, and examination revealed that all such low-energy structures could be sorted into two groups by considering the number of aryl side chains making contact with the quaternary ammonium ion (pocket = two Trp(Bn) side chains in contact, Fig. 3A; cleft = one Trp(Bn) residue in contact, Fig. 3B).

### 1-Benzyltryptophan hydrochloride (1·HCl)

Liquid ammonia (1000 mL) was condensed into a 2 L flask containing Na(s) (10.4 g, 452 mmol) and Fe(NO<sub>3</sub>)<sub>3</sub> (0.6 g, 0.01 mmol) under argon. To facilitate the addition of ammonia, the flask was cooled in a dry ice–acetone bath and equipped with a cold finger (dry ice–acetone) via a Claisen adapter. The resultant mixture turns blue immediately and slowly fades to a grey color. Tryptophan (40 g, 196 mmol) was introduced to the grey solution as a slurry in ether, and benzyl chloride (22.5 mL, 196 mmol) was added immediately thereafter via syringe through the septum. The reaction refluxed on an ice bath for 1 h, and evaporated overnight. The crude product dissolved in hot water and a small amount of solid residue was removed by filtration. Acetic acid was added until the product precipitated, and filtration yielded the 1-benzyltryptophan as an off-white solid (41 g, 71%). A portion of this product (24 g, 81 mmol) was suspended in methanol (200 mL) at room temperature and concentrated aqueous hydrochloric acid was added dropwise until the starting material was completely dissolved. The reaction was stirred for 5 min, and was then concentrated to half volume. The solution was then poured into 1.6 L of ether and the resultant slurry was filtered to yield 1·HCl as a white solid that was left to air-dry overnight (19 g, 72%); mp 204–206 °C. [α]<sub>D</sub><sup>25</sup> +5.0° (*c* 0.08 in MeOH). <sup>1</sup>H NMR (300 MHz, DMSO-*d*<sub>6</sub>) δ: 3.32 (2H, *J* = 6.3, d), 4.12 (1H, bs), 5.38 (2H, s), 7.03 (1H *J* = 7 and 1, td), 7.10 (1H, *J* = 8 and 1, td), 7.18–7.33 (5H, m), 7.37 (1H, *J* = 8, d), 7.39 (1H, s), 7.63 (1H, *J*<sub>HH</sub> = 7, d), 8.31 (3H, bs), 13.77 (1H, bs). <sup>13</sup>C NMR (75.5 MHz, DMSO-*d*<sub>6</sub>) δ: 26.0, 49.1, 52.6, 106.8, 110.2, 118.7, 118.9, 121.4, 127.0, 127.3, 127.7, 128.5, 128.7, 136.1, 138.1, 170.7. ESI (accurate mass) *m/z*: 295.1452 (M<sup>+</sup> C<sub>18</sub>H<sub>19</sub>N<sub>2</sub>O<sub>2</sub> requires 295.1447).

### *N*-(tert-Butoxycarbonyl)-1-benzyltryptophan (4)

**3** (1.0 g, 3.0 mmol) was suspended in 1:1 dioxane–water (12 mL) at room temperature. NaOH (aq, 1 mol/L, 6 mL, 6 mmol) was added, followed by the addition of (Boc)<sub>2</sub>O (0.84 mL, 3.6 mmol), and this mixture was stirred for 18 h. The reaction was acidified to pH 2.5 with HCl (2 mol/L), and diluted further with water (50 mL). Ethyl acetate was then used to extract the mostly aqueous mixture. The organic layers were combined, dried, and concentrated to yield a white solid (0.928 g, 78%); mp 181–182 °C (EtOAc). [α]<sub>D</sub><sup>25</sup> +9.1° (*c* 0.08 in MeOH). <sup>1</sup>H NMR (300 MHz, DMSO-*d*<sub>6</sub>) δ: 1.13 (9H, s), 2.99 (1H, *J* = 15 and 9, dd), 3.14 (1H, *J* = 14 and 5, dd), 4.16 (1H, *J* = 9 and 5, td), 5.36 (2H, s), 6.97–7.1 (3H, m), 7.13–7.16 (2H, m), 7.19–7.31 (4H, m), 7.37 (1H, *J* = 8, d), 7.55 (1H, *J* = 7, d), 12.55 (1H, bs). <sup>13</sup>C NMR (75.5 MHz, DMSO-*d*<sub>6</sub>) δ: 26.7, 28.1, 48.9, 54.4, 77.9, 110.0, 110.3, 118.6, 121.2, 126.9, 127.2, 127.4, 127.8, 128.4, 135.9, 138.3, 155.3, 173.8. ESI (accurate mass) *m/z* calcd.: 417.1790; found: 417.1789.

**Methyl 1-benzyltryptophanate hydrochloride (5)**

**3** (5.0 g, 15.1 mmol) was dissolved in methanol (300 mL) and cooled to 0 °C. Thionyl chloride (1.1 mL, 15.1 mmol) was added dropwise and the mixture was then allowed to warm to room temperature before being brought to reflux. After overnight stirring at reflux, the reaction was cooled and concentrated. Trituration with diethyl ether provided a white powder with no further purification needed (4.55 g, 87%); mp 115–117 °C (ether).  $[\alpha]_{\text{D}}^{25} +11.3^\circ$  (*c* 0.15 in MeOH). <sup>1</sup>H NMR (300 MHz, DMSO-*d*<sub>6</sub>)  $\delta$ : 3.26 (1H, *J* = 15 and 7, dd), 3.38 (1H, *J* = 15 and 5, dd), 3.60 (3H, s), 4.19 (1H, *J* = 7 and 5, dd), 5.38 (2H, s), 7.04 (1H, *J* = 7 and 1, td), 7.11 (1H, *J* = 8 and 1, td), 7.18–7.33 (5H, m), 7.37 (1H, s), 7.41 (1H, *J* = 8, d), 7.59 (1H, *J* = 7, d), 8.71 (3H, bs). <sup>13</sup>C NMR (75.5 MHz, DMSO-*d*<sub>6</sub>)  $\delta$ : 26.1, 49.0, 52.5, 52.7, 106.6, 110.2, 118.5, 119.0, 121.5, 127.0, 127.3, 127.5, 128.4, 128.5, 136.0, 138.1, 169.7. ESI (accurate mass) *m/z* calcd.: 309.1603; found: 309.1603.

**Dipeptide coupling general procedure**

N-terminally protected (Boc) amino acid (2.0 mmol) and HBTU (0.78 g, 2 mmol) were added to a flask containing THF (70 mL). The mixture was cooled to 0 °C and 1 equiv. of DIEA (0.35 mL, 2.03 mmol) was added. The mixture was stirred for 10 min. C-terminally protected (methyl ester) amino acid (2 mmol) and 1.2 more equiv. of DIEA (0.42 mL, 2.4 mmol) were added to the reaction, which was then warmed to room temperature and stirred for 2 h, regardless of completeness. Once complete, the reaction was concentrated, taken up in ethyl acetate, and washed with 1 mol/L HCl (×2), satd. NaHCO<sub>3</sub> (×2), water, and brine. The organic layer was dried with Na<sub>2</sub>SO<sub>4</sub> and concentrated to produce a white powder (or foam) after exposure of the residue to high vacuum overnight.

**Methyl N-[N-(tert-butoxycarbonyltryptophyl)]-tryptophanate (2)**

After initial concentration, the product was precipitated from a minimum volume of CH<sub>2</sub>Cl<sub>2</sub> at –20 °C as a white solid (1.51 g, 71%); mp 162–164 °C (CH<sub>2</sub>Cl<sub>2</sub>).  $[\alpha]_{\text{D}}^{25} -7.0^\circ$  (*c* 0.08 in MeOH). <sup>1</sup>H NMR (500 MHz, DMSO-*d*<sub>6</sub>)  $\delta$ : 1.26 (9H, s), 2.84 (1H, *J* = 15 and 9, dd), 3.00 (1H, *J* = 15 and 4, dd), 3.06 (1H, *J* = 15 and 7, dd), 3.13 (1H, *J* = 15 and 6, dd), 3.52 (3H, s), 4.21 (1H, *J* = 9 and 4, td), 4.53 (1H, *J* = 7.0 and 6, td), 6.69 (1H, *J* = 8, d), 6.92–6.97 (2H, m), 7.00–7.06 (3H, m), 7.14 (1H, *J* = 2, d), 7.28–7.33 (2H, m), 7.44 (1H, *J*<sub>HH</sub> = 8, d), 7.55 (1H, *J* = 8, d), 8.23 (1H, *J* = 8, d), 10.77 (1H, s), 10.86 (1H, s). <sup>13</sup>C NMR (126 MHz, DMSO-*d*<sub>6</sub>)  $\delta$ : 27.1, 27.7, 28.1, 51.8, 53.1, 55.0, 78.1, 109.2, 110.1, 111.3, 111.5, 118.0, 118.2, 118.46, 118.51, 118.9, 120.8, 121.0, 123.7, 127.1, 127.4, 136.06, 136.10, 155.1, 172.1, 172.2. ESI (accurate mass) *m/z* calcd.: 527.2270; found: 527.2271.

**Methyl N-[N-(tert-butoxycarbonyl)tryptophyl]-1-benzyltryptophanate (7)**

A white powder was isolated (1.16 g, 49%); mp 76–78 °C then 99–100 °C (EtOAc).  $[\alpha]_{\text{D}}^{25} -15.6^\circ$  (*c* 0.09 in MeOH). <sup>1</sup>H NMR (500 MHz)  $\delta$ : 1.26 (9H, s), 2.89 (1H, *J* = 15 and 9, dd), 3.06 (1H, *J* = 15 and 4, dd), 3.10 (1H, *J* = 15 and 7, dd), 3.18 (1H, *J* = 15 and 6, dd), 3.54 (3H, s), 4.26 (1H,

*J* = 9 and 4, td), 4.60 (1H, *J* = 7 and 6, td), 5.35 (2H, s), 6.72 (1H, *J* = 8, d), 6.97 (1H, *J* = 7, t), 7.00–7.10 (3H, m), 7.12–7.21 (3H, m), 7.25–7.27 (2H, m), 7.31–7.33 (2H, m), 7.38 (1H, *J* = 8, d), 7.51 (1H, *J* = 8, d), 7.60 (1H, *J* = 8, d), 8.38 (1H, *J* = 7, d), 10.81 (1H, s). <sup>13</sup>C NMR (126 MHz, DMSO-*d*<sub>6</sub>)  $\delta$ : 27.0, 27.7, 28.1, 49.0, 51.8, 53.0, 55.0, 78.0, 109.3, 110.07, 110.12, 111.2, 118.1, 118.4, 118.5, 118.8, 120.8, 121.3, 123.7, 126.9, 127.2, 127.4, 127.5, 127.7, 128.5, 135.8, 136.0, 138.2, 155.1, 172.1, 172.2. ESI (accurate mass) *m/z* calcd.: 617.2740; found: 617.2754.

**Methyl N-[N-(tert-butoxycarbonyl)-1-benzyltryptophyl]-1-benzyltryptophanate (8)**

A white powder was isolated (0.83 g, 61%); mp 149–151 °C (EtOAc).  $[\alpha]_{\text{D}}^{25} +4.0^\circ$  (*c* 0.08 in MeOH). <sup>1</sup>H NMR (500 MHz, DMSO-*d*<sub>6</sub>)  $\delta$ : 1.28 (9H, s), 2.91 (1H, *J* = 15 and 9, dd), 3.05 (1H, *J* = 15 and 4, dd), 3.09 (1H, *J* = 15 and 7, dd), 3.18 (1H, *J* = 15 and 6, dd), 3.52 (3H, s), 4.27 (1H, *J* = 9 and 4, td), 4.58 (1H, *J* = 7 and 6, td), 5.32 (2H, s), 5.35 (2H, s), 6.74 (1H, *J* = 8, d), 6.98–7.03 (1H, m), 7.05–7.09 (2H, m), 7.12–7.28 (11H, m), 7.32–7.38 (2H, m), 7.51 (1H, *J* = 8, d), 7.61 (1H, *J* = 8, d), 8.31 (1H, *J* = 7, d). <sup>13</sup>C NMR (126 MHz, DMSO-*d*<sub>6</sub>)  $\delta$ : 27.0, 27.6, 28.1, 48.90, 48.94, 51.8, 53.0, 55.0, 78.0, 109.3, 109.9, 110.1, 110.2, 118.4, 118.5, 118.8, 118.9, 121.1, 121.3, 126.8, 126.9, 127.2, 127.5, 127.7, 128.0, 128.4, 135.8, 135.9, 138.2, 138.3, 155.1, 171.9, 172.2. ESI (accurate mass) *m/z* calcd.: 707.3209; found: 707.3201.

**General procedure for BOC deprotection**

Starting material (0.6 mmol) was suspended in acetic acid at room temperature. In a separate flask, HCl (concd) was diluted with acetic acid to form a 1.5 mol/L solution of HCl in acetic acid. The resultant HCl in acetic acid solution (9.4 mL, 14 mmol HCl) was added in one portion to the starting material suspension. The suspension was dispersed upon addition of the HCl solution, followed by the appearance of another precipitate 1 h postaddition. The reaction was stirred overnight, filtered, and the cake washed with ether to yield a white solid that needs no further purification.

**Methyl N-tryptophyl-tryptophanate hydrochloride (10)**

The work-up differed as the product was soluble in acetic acid. The acetic acid was concentrated and diluted with ether. A light brown solid resulted, was filtered, and isolated (0.23 g, 90%); mp (foams) 162–170 °C, mp (melts) 178–180 °C (ether).  $[\alpha]_{\text{D}}^{25} -4.2^\circ$  (*c* 0.08 in MeOH). <sup>1</sup>H NMR (500 MHz, DMSO-*d*<sub>6</sub>)  $\delta$ : 3.05–3.30 (4H, m), 3.58 (3H, s), 4.03 (1H, *J* = 8 and 6, dd), 4.62 (1H, *J* = 7, q), 6.98–7.01 (2H, m), 7.08 (2H, *J* = 8, q), 7.21 (1H, s), 7.22 (1H, s), 7.35 (2H, *J* = 8, t), 7.50 (1H, *J* = 8, d), 7.71 (1H, *J* = 8, d), 8.1 (3H, bs), 9.11 (1H, *J* = 7.0, d), 10.96 (1H, s), 11.04 (1H, s). <sup>13</sup>C NMR (126 MHz, DMSO-*d*<sub>6</sub>)  $\delta$ : 27.2, 27.3, 52.0, 52.5, 53.3, 106.8, 108.9, 111.4, 111.5, 117.9, 118.4, 118.47, 118.52, 121.0, 121.1, 124.0, 125.0, 127.0, 127.1, 136.1, 136.3, 168.8, 171.6. ESI (accurate mass) *m/z* calcd.: 405.1927; found: 405.1927.

**Methyl N-tryptophyl-1-benzyltryptophanate hydrochloride (11)**

A white solid was isolated (0.112 g, 69%); mp 222–



224 °C (AcOH).  $[\alpha]_D^{25} +2.3^\circ$  (*c* 0.08 in MeOH).  $^1\text{H}$  NMR (500 MHz, DMSO- $d_6$ )  $\delta$ : 3.08–3.29 (4H, m), 3.55 (3H, s), 4.04 (1H, *J* = 6, t), 4.62 (1H, *J* = 7, q), 5.37 (2H, s), 5.37 (2H, s), 7.00 (1H, *J* = 7, t), 7.03 (1H, *J* = 7, t), 7.09 (2H, *J* = 7, t), 7.16 (2H, *J* = 7, d), 7.21 (2H, *J* = 7, t), 7.27 (2H, *J* = 7, t), 7.35 (1H, s), 7.36 (1H, *J* = 11, d), 7.41 (1H, *J* = 8, d), 7.53 (1H, *J* = 8, d), 7.70 (1H, *J* = 8, d), 8.16 (3H, bs), 9.15 (1H, *J* = 6, d) 11.00 (1H, s).  $^{13}\text{C}$  NMR (126 MHz, DMSO- $d_6$ )  $\delta$ : 27.1, 27.3, 48.9, 51.9, 52.4, 53.4, 106.7, 108.9, 110.2, 111.4, 118.4, 118.5, 118.8, 121.1, 121.3, 125.0, 126.9, 127.1, 127.3, 127.6, 127.8, 128.5, 135.9, 136.3, 138.3, 168.6, 171.5. ESI (accurate mass) *m/z* calcd.: 495.2396; found: 495.2397.

#### **Methyl N-(1-benzyltryptophyl)-1-benzyltryptophanate hydrochloride (12)**

A white solid was isolated (0.30 g, 83%); mp 219–220 °C (AcOH).  $[\alpha]_D^{25} +6.2^\circ$  (*c* 0.08 in MeOH).  $^1\text{H}$  NMR (500 MHz, DMSO- $d_6$ )  $\delta$ : 3.12–3.28 (4H, m), 3.51 (3H, s), 4.09 (1H, bs), 4.61 (1H, *J* = 7, q), 5.35 (2H, s), 5.37 (2H, s), 7.03 (2H, *J* = 7, t), 7.08–7.12 (2H, m), 7.16–7.31 (10H, m), 7.33 (1H, s), 7.37 (1H, *J* = 8, d), 7.39 (1H, s), 7.41 (1H, *J* = 8, d), 7.53 (1H, *J* = 8, d), 7.75 (1H, *J* = 8, d), 8.31 (3H, bs), 9.2 (1H, *J* = 7, d).  $^{13}\text{C}$  NMR (126 MHz, DMSO- $d_6$ )  $\delta$ : 27.7, 27.8, 49.6, 49.8, 52.5, 53.2, 54.1, 107.5, 109.5, 110.7, 110.8, 119.0, 119.4, 119.5, 119.6, 121.97, 122.02, 127.6, 127.7, 127.89, 127.93, 128.2, 128.4, 128.5, 129.1 ( $\times 2$ ), 129.4, 136.6, 136.8, 138.7, 138.9, 169.2, 172.2. ESI (accurate mass) *m/z* calcd.: 585.2866; found: 585.2875.

#### **General method for the sequential installation of the succinyl group on N-terminal amines and saponification of C-terminal methyl esters**

Starting material **10**, **11**, or **12** (0.25 mmol) was suspended in  $\text{CH}_2\text{Cl}_2$  (10 mL) at room temperature. Succinic anhydride (0.036 g, 0.36 mmol) was added to the reaction, followed by DIEA (0.095 mL, 0.55 mmol), and the mixture stirred overnight. Dilution of the reaction with  $\text{CH}_2\text{Cl}_2$  (50 mL), followed by extraction with HCl (1 mol/L,  $2 \times 50$  mL), followed by back extraction of the aqueous with  $\text{CH}_2\text{Cl}_2$  was sufficient to isolate the methyl ester of the desired product. The combined organic layers were washed with brine (1  $\times$  50 mL) and dried over  $\text{Na}_2\text{SO}_4$  before concentration. The sticky residue was used without further purification to produce the de-esterified product. Dissolution in methanol (3 mL), followed by the addition of NaOH (1 mol/L, 0.75 mL) furnished the final product after 2 h of stirring. The reaction was diluted with water (5 mL) and acidified with HCl (1 mol/L) to pH 2. The suspension was extracted with ethyl acetate and the organic layer was washed with brine and dried over  $\text{Na}_2\text{SO}_4$  before concentration.

#### **N-[N-(3-Carboxypropanoyl)-tryptophyl]-tryptophan (13)**

Isolated as a light brown powder (0.055 g, 44%); mp (turns dark brown) 88 °C, mp (melts) 154–156 °C (EtOAc).  $[\alpha]_D^{25} -11.6^\circ$  (*c* 0.09 in MeOH).  $^1\text{H}$  NMR (500 MHz, DMSO- $d_6$ )  $\delta$ : 2.25–2.34 (4H, m), 2.88 (1H, *J* = 15 and 9, dd), 3.08 (1H, *J* = 15 and 8, dd), 3.12 (1H, *J* = 15 and 4, dd), 3.19 (1H, *J* = 15 and 5, dd), 4.50 (1H, *J* = 8 and 5, td), 4.58 (1H, *J* = 9.0 and 4, td), 6.97 (1H, *J* = 8, t), 6.98 (1H, *J* = 8,

t), 7.05 (1H, *J* = 8, t), 7.06 (1H, *J* = 8, t), 7.11 (1H, *J* = 2.0, d), 7.16 (1H, *J* = 2.0, d), 7.31 (1H, *J* = 8, d), 7.33 (1H, *J* = 8, d), 7.53 (1H, *J* = 8, d), 7.58 (1H, *J* = 8, d), 8.01 (1H, *J* = 8, d), 8.17 (1H, *J* = 8, d), 10.77 (1H, bs), 10.85 (1H, bs), 12.36 (2H, bs), 12.7 (bs, 1H).  $^{13}\text{C}$  NMR (126 MHz)  $\delta$ : 27.0, 27.6, 29.2, 30.0, 53.0, 53.2, 109.7, 110.2, 111.2, 111.4, 118.2, 118.40, 118.44, 120.8, 120.9, 123.5, 123.6, 127.3, 127.4, 136.0, 136.1, 170.9, 171.6, 173.2, 173.9. ESI (accurate mass) *m/z* calcd.: 489.1774; found: 489.1773.

#### **N-[N-(3-Carboxypropanoyl)-tryptophyl]-1-benzyltryptophan (14)**

Isolated as a white powder (0.074 g, 88%); mp 180 °C dec (EtOAc).  $[\alpha]_D^{25} -11.9^\circ$  (*c* 0.09 in MeOH).  $^1\text{H}$  NMR (500 MHz, DMSO- $d_6$ )  $\delta$ : 2.25–2.32 (4H, m), 2.89 (1H, *J* = 15 and 9, dd), 3.06 (1H, *J* = 15 and 8, dd), 3.11 (1H, *J* = 15 and 4, dd), 3.21 (1H, *J* = 15 and 5, dd), 4.50 (1H, *J* = 8.0 and 5, td), 4.58 (1H, *J* = 9.0 and 4, td), 5.35 (2H, s), 6.96 (1H, *J* = 7, t), 7.01 (1H, *J* = 7, t), 7.04 (1H, *J* = 7, t), 7.07 (1H, *J* = 7, t), 7.12 (1H, *J* = 2, d), 7.16–7.27 (5H, m), 7.31 (1H, *J* = 8, d), 7.32 (1H, s), 7.35 (1H, *J* = 8, d), 7.55 (1H, *J* = 8, d), 7.58 (1H, *J* = 8, d), 8.01 (1H, *J* = 8, d), 8.28 (1H, *J* = 8, d), 10.78 (1H, *J* = 2, d), 12.3 (1H, bs), 12.7 (1H, bs).  $^{13}\text{C}$  NMR (126 MHz, DMSO- $d_6$ )  $\delta$ : 26.8, 27.6, 29.1, 30.0, 49.0, 52.9, 53.3, 109.7, 110.1, 110.2, 111.2, 118.1, 118.4, 118.5, 118.7, 120.8, 121.2, 123.6, 126.9, 127.2, 127.4, 127.6, 127.9, 128.5, 135.8, 136.0, 138.3, 170.9, 171.7, 173.1, 173.8. ESI (accurate mass) *m/z* calcd.: 579.2244; found: 579.2231.

#### **N-[N-(3-Carboxypropanoyl)-1-benzyltryptophyl]-1-benzyltryptophan (15)**

A white solid was isolated (0.106 g, 64%); mp (turns brown) 180 °C, mp (melts) 190–192 °C (EtOAc).  $[\alpha]_D^{25} -1.1^\circ$  (*c* 0.09 in MeOH).  $^1\text{H}$  NMR (500 MHz, DMSO- $d_6$ )  $\delta$ : 2.24–2.32 (4H, m), 2.88 (1H, *J* = 15 and 9, dd), 3.07 (1H, *J* = 15 and 8, dd), 3.12 (1H, *J* = 15 and 4, dd), 3.21 (1H, *J* = 15 and 5, dd), 4.49 (1H, *J* = 8.0 and 5, td), 4.59 (1H, *J* = 9.0 and 4, td), 5.32 (2H, s), 5.34 (2H, s), 6.99 (1H, *J* = 7, q), 7.05–7.08 (2H, m), 7.14–7.29 (10H, m), 7.34 (2H, *J* = 9, d), 7.35 (2H, *J* = 8, d), 7.56 (1H, *J* = 8, d), 7.60 (1H, *J* = 8, d), 8.05 (1H, *J* = 8, d), 8.31 (1H, *J* = 8, d), 12.7 (2H, bs).  $^{13}\text{C}$  NMR (126 MHz, DMSO- $d_6$ )  $\delta$ : 26.8, 27.5, 29.1, 29.9, 48.9, 49.0, 53.0, 53.2, 109.7, 109.9, 110.0, 110.2, 118.5, 118.6, 118.7, 118.9, 121.1, 121.2, 126.9, 127.2, 127.4, 127.6, 127.9, 128.0, 128.4, 135.8, 138.3, 138.4, 170.8, 171.5, 173.1, 173.8. ESI (accurate mass) *m/z* calcd.: 669.2724; found: 669.2713.

#### **Benzyltrimethylammonium tetrakis[3,5-bis(trifluoromethyl)phenyl]borate ( $\text{BnNMe}_3^+ \text{BArF}^-$ )**

Benzyltrimethylammonium chloride (0.107 g, 0.57 mmol) and  $\text{NaBArF}$  (0.510 g, 0.57 mmol) were stirred overnight in  $\text{CH}_2\text{Cl}_2$  (40 mL). The resulting suspension was filtered through a syringe filter with a pore size of 0.45  $\mu\text{m}$  and the filtrate was concentrated to produce a white solid. The solid was rinsed with pentane and dried in vacuo for 3 h (0.499 g, 86%); mp 136–137 °C ( $\text{CH}_2\text{Cl}_2$ ).  $^1\text{H}$  NMR (500 MHz,  $\text{CDCl}_3$ )  $\delta$ : 2.82 (9H, s), 4.12 (2H, s), 7.22 (2H, *J* = 10, d), 7.47 (2H, *J* = 10, t), 7.51 (4H, bs), 7.57 (1H, *J* = 10, t), 7.67–7.68 (8H, m).  $^{13}\text{C}$  NMR (126 MHz, DMSO- $d_6$ )  $\delta$ : 53.2

( $J_{\text{CN}} = 4$ , t), 71.9, 117.8, 124.7 ( $J_{\text{CF}} = 273$ , q), 124.8, 129.2 ( $J_{\text{CF}} = 29$ , q), 130.4, 132.3, 132.7, 134.9, 161.9 ( $J_{\text{CB}} = 50$ , q).  $^{19}\text{F}$  NMR (282 MHz)  $\delta$ : -62.3.  $^{11}\text{B}$  NMR (160 MHz)  $\delta$ : -6.8. ESI (accurate mass)  $m/z$  calcd. (anion): 862.0685; found: 862.0700; calcd. (cation): 150.1283; found: 150.1281.

### N-(3-Carboxypropanoyl)-1-benzyltryptophan (16)

**5** (0.926 g, 2.8 mmol) was suspended in dry THF and stirred at room temperature. Succinic anhydride (0.28 g, 2.8 mmol) and DIEA (0.49 mL, 2.8 mmol) were then added and the mixture refluxed overnight. The volume was reduced until a thick syrup formed. Ethyl acetate was added (300 mL) and the organic was extracted three times with NaOH (aq, 0.5 mol/L,  $3 \times 75$  mL). The aqueous extracts were combined and acidified to pH 2 with HCl (1 mol/L). The brown oil was extracted with ethyl acetate. Upon drying ( $\text{Na}_2\text{SO}_4$ ) and concentrating the residue solidifies on exposure to vacuum overnight. Purification with column chromatography ( $\text{CHCl}_3$ , AcOH, MeOH) with gradient elution from 94:5:1 to 93:5:2 was used to elute pure product. Trituration of the combined and concentrated fractions with ether yielded a white crystalline solid (0.634 g, 56%); mp 148–150 °C (ether).  $[\alpha]_{\text{D}}^{25} +30^\circ$  ( $c$  0.09 in MeOH).  $^1\text{H}$  NMR (500 MHz,  $\text{DMSO}-d_6$ )  $\delta$ : 2.25–2.34 (4H, m), 3.00 (1H,  $J = 15$  and 9, dd), 3.17 (1H,  $J = 15$  and 5, dd), 4.88 (1H, m), 7.01 (1H,  $J = 8$ , t), 5.35 (2H, s), 7.07 (1H,  $J = 8$ , t), 7.15–7.16 (2H, m), 7.21–7.23 (1H, m), 7.27–7.30 (3H, m), 7.37 (1H,  $J = 8$ , d), 7.56 (1H,  $J = 8$ , d), 8.19 (1H,  $J = 8$ , d), 12.37 (2H, bs).  $^{13}\text{C}$  NMR (126 MHz,  $\text{DMSO}-d_6$ )  $\delta$ : 27.1, 29.0, 29.8, 48.9, 52.9, 109.9, 110.0, 118.6, 118.7, 121.2, 126.9, 127.2, 127.5, 127.8, 128.4, 135.9, 138.3, 170.9, 173.3, 173.8. ESI (accurate mass)  $m/z$  calcd.: 393.1456; found: 393.1450.

### Supplementary data

Supplementary data for this article are available on the journal Web site (canjchem.nrc.ca).

### Acknowledgements

This work was funded by the Michael Smith Foundation for Health Research (MSFHR). FH is a MSFHR Career Scholar and Canadian Institutes of Health Research (CIHR) New Investigator.

### References

- (1) Dougherty, D. A.; Stauffer, D. A. *Science* **1990**, 250 (4987), 1558. doi:10.1126/science.2274786. PMID:2274786.
- (2) Dougherty, D. A. *Science* **1996**, 271 (5246), 163. doi:10.1126/science.271.5246.163. PMID:8539615.
- (3) Beene, D. L.; Brandt, G. S.; Zhong, W.; Zacharias, N. M.; Lester, H. A.; Dougherty, D. A. *Biochemistry* **2002**, 41 (32), 10262. doi:10.1021/bi020266d. PMID:12162741.
- (4) Hughes, R. M.; Benshoff, M. L.; Waters, M. L. *Chem. Eur. J.* **2007**, 13 (20), 5753. doi:10.1002/chem.200601753.
- (5) Hughes, R. M.; Wiggins, K. R.; Khorasanizadeh, S.; Waters, M. L. *Proc. Natl. Acad. Sci. U.S.A.* **2007**, 104 (27), 11184. doi:10.1073/pnas.0610850104. PMID:17581885.
- (6) Beene, D. L.; Brandt, G. S.; Zhong, W.; Zacharias, N. M.; Lester, H. A.; Dougherty, D. A. *Biochemistry* **2002**, 41 (32), 10262. doi:10.1021/bi020266d. PMID:12162741.
- (7) Schmitt, J. D.; Sharples, C. G. V.; Caldwell, W. S. *J. Med. Chem.* **1999**, 42 (16), 3066. doi:10.1021/jm990093z. PMID:10447950.
- (8) Taverna, S. D.; Li, H.; Ruthenburg, A. J.; Allis, C. D.; Patel, D. J. *Nat. Struct. Mol. Biol.* **2007**, 14 (11), 1025. doi:10.1038/nsmb1338. PMID:17984965.
- (9) (a) Beshara, C. S.; Jones, C. E.; Daze, K. D.; Lilgert, B. J.; Hof, F. *ChemBioChem* **2010**, 11 (1), 63. doi:10.1002/cbic.200900633. PMID:19937593; (b) Whiting, A. L.; Neufeld, N. M.; Hof, F. *Tetrahedron Lett.* **2009**, 50 (50), 7035. doi:10.1016/j.tetlet.2009.09.161.
- (10) Ingerman, L. A.; Cuellar, M. E.; Waters, M. L. *Chem. Commun. (Camb.)* **2010**, 46 (11), 1839. doi:10.1039/c000255k. PMID:20198226.
- (11) (a) Shi, X.; Kachirskia, I.; Walter, K. L.; Kuo, J.-H. A.; Lake, A.; Davrazou, F.; Chan, S. M.; Martin, D. G. E.; Fingerman, I. M.; Briggs, S. D.; Howe, L.; Utz, P. J.; Kutateladze, T. G.; Lugovskoy, A. A.; Bedford, M. T.; Gozani, O. *J. Biol. Chem.* **2007**, 282 (4), 2450. doi:10.1074/jbc.C600286200. PMID:17142463; (b) Jacobs, S. A.; Khorasanizadeh, S. *Science* **2002**, 295 (5562), 2080. doi:10.1126/science.1069473. PMID:11859155; (c) Flanagan, J. F.; Mi, L.-Z.; Chruszcz, M.; Cymborowski, M.; Clines, K. L.; Kim, Y.; Minor, W.; Rastinejad, F.; Khorasanizadeh, S. *Nature* **2005**, 438 (7071), 1181. doi:10.1038/nature04290. PMID:16372014; (d) Huang, Y.; Fang, J.; Bedford, M. T.; Zhang, Y.; Xu, R.-M. *Science* **2006**, 312 (5774), 748. doi:10.1126/science.1125162. PMID:16601153.
- (12) Ito, K.; Nagase, K.; Morohashi, N.; Ohba, Y. *Chem. Pharm. Bull. (Tokyo)* **2005**, 53 (1), 90. doi:10.1248/cpb.53.90. PMID:15635237.
- (13) Powers, J. C. *Tetrahedron Lett.* **1965**, 6 (11), 655. doi:10.1016/S0040-4039(00)90013-3.
- (14) Yamada, S.; Shioiri, T.; Itaya, T.; Hara, T.; Matsueda, R. *Chem. Pharm. Bull. (Tokyo)* **1965**, 13 (1), 88. PMID:5864290.
- (15) Magnus, P.; Mugrage, B.; DeLuca, M. R.; Cain, G. A. *J. Am. Chem. Soc.* **1990**, 112 (13), 5220. doi:10.1021/ja00169a033.
- (16) Cornforth, J. W.; Cornforth, R. H.; Dalglish, C. E.; Neuberger, A. *Biochem. J.* **1951**, 48 (5), 591. PMID:14838907.
- (17) Chen, Y.; Bilban, M.; Foster, C. A.; Boger, D. L. *J. Am. Chem. Soc.* **2002**, 124 (19), 5431. doi:10.1021/ja020166v. PMID:11996584.
- (18) Kumaraswamy, G.; Pitchaiah, A.; Ramakrishna, G.; Ramakrishna, D. S.; Sadaiah, K. *Tetrahedron Lett.* **2006**, 47 (12), 2013. doi:10.1016/j.tetlet.2006.01.050.
- (19) Ito et al.<sup>12</sup> previously reported that the Trp-Trp dipeptide **2** bound  $\text{BnNMe}_3^+ \text{Cl}^-$  with  $K_{\text{assoc}}$  of  $69 (\text{mol/L})^{-1}$  in chloroform, and they attributed the relative strength to  $\text{NH}-\text{Cl}^-$  hydrogen bonding effects. Our observation that the binding of the  $\text{BnNMe}_3^+$  salt of the nonhydrogen-bonding  $\text{BARF}^-$  anion is essentially equal to their reported value indicates that the role of  $\text{Cl}^-$  may not be as important as previously described.
- (20) Sanderson, J. M. *Excel Workbooks for Curve-fitting NMR Titration Data*; The Centre for Bioactive Chemistry, Department of Chemistry University Science Laboratories, Durham University; Durham, UK; Available from <http://www.dur.ac.uk/j.m.sanderson/science/downloads.html>.
- (21) Hirose, K. *J. Incl. Phenom. Macrocycl. Chem.* **2001**, 39 (3–4), 193. doi:10.1023/A:1011117412693.
- (22) *Spartan'04*; Wavefunction, Inc.: Irvine, CA, 2004.

# An atmospheric pressure static reactor – ion trap mass spectrometer for studying gas-phase reactions

Fadel Wedian and Dean B. Atkinson

**Abstract:** The design and operation of an atmospheric pressure static reactor coupled to an ion trap mass spectrometer is described. The reactor is designed for studying gas-phase reactions that are important in atmospheric chemistry. The system provides a simple and robust method for identifying the products of gas-phase reactions. Results for the reaction of O<sub>3</sub> with 2,3-dimethyl-2-butene (tetramethylethylene, TME) are demonstrated as a proof of the principle for the performance of the static reactor. All of the previously reported major primary products of the reaction were observed, and the yields of two compounds (acetone and hydroxyacetone) were quantified, in excellent agreement with previous work. Several minor species were also observed, demonstrating the potential for this method to investigate the product channels for less well-studied atmospherically relevant reactions.

**Key words:** atmospheric pressure reactor, ozone, tetramethylethylene (TME), ion trap mass spectrometer, gas-phase reaction.

**Résumé :** On décrit la fabrication et l'opération d'un réacteur statique à pression atmosphérique couplée à un spectromètre de masse avec trappe ionique. Le réacteur a été construit de façon à pouvoir étudier les réactions en phase gazeuse importantes en chimie de l'atmosphère. Le système fournit une méthode simple et robuste pour identifier les produits des réactions en phase gazeuse. On a utilisé les résultats de la réaction de l'ozone, O<sub>3</sub>, avec le 2,3-diméthylbut-2-ène (tétraméthyléthylène, TME) comme preuve du principe de la performance du réacteur statique. Tous les produits primaires majeurs de la réaction rapportés antérieurement ont été observés et les rendements de deux composés (acétone et hydroxyacétone) ont été quantifiés, en excellent accord avec les résultats obtenus antérieurement. On a aussi observé plusieurs espèces mineures, ce qui démontre le potentiel de cette méthode pour étudier les voies réactionnelles de réactions intéressantes d'un point de vue atmosphérique, mais moins bien étudiées.

**Mots-clés :** réacteur à pression atmosphérique, ozone, tétraméthyléthylène (TME), spectromètre de masse à piège ionique, réaction en phase gazeuse.

[Traduit par la Rédaction]

## Introduction

There are numerous approaches available to investigate the kinetics and mechanisms of gas-phase reactions; these include FTIR spectroscopy,<sup>1–3</sup> fast flow tube mass spectrometers (FF-MS),<sup>4,5</sup> turbulent flow tube high-pressure chemical ionization mass spectrometry,<sup>6–8</sup> and atmospheric chambers coupled with GC-FID,<sup>9</sup> atmospheric pressure ionization mass spectrometry (API-MS),<sup>10–12</sup> and atmospheric pressure chemical ionization ion trap (APCI-IT) mass spectrometry.<sup>13,14</sup> In this article we introduce a method where an atmospheric pressure reactor is coupled to an ion trap mass spectrometer (IT-MS). The IT-MS is potentially valuable as a detector for gas-phase reaction experiments since it provides various clean chemical ionization modes and MS–MS experiments, which can be performed for structure determination. In addition, the IT-MS is an inexpensive bench top instrument.

Alkenes are an important class of volatile organic compounds that have natural and industrial sources.<sup>15</sup> In the atmosphere, the main sinks for alkenes are chemical reactions with ozone, OH, and NO<sub>3</sub>.<sup>15,16</sup> The mechanism of gas-phase reactions of ozone with alkenes in the troposphere has been studied over the last few decades.<sup>16–18</sup> Major overall features of ozone–alkene reactions have been established for simple alkenes, for example, 1-butene, 1-pentene, 3-methyl-1-pentene, and 3,3-dimethyl-1-butene, while little verifiable information is available for reactions with large alkenes (either open-chain or ring compounds), especially regarding the nature and yields of their products, for example, 1-methylcyclohexene, camphene, limonene, and β-pinene.<sup>16–18</sup>

The accepted mechanism of the gas-phase reaction of ozone with alkenes proceeds via the addition of O<sub>3</sub> to the double bond to yield an energy rich ozonide, which rapidly dissociates to a carbonyl product and a biradical “Criegee”

Received 17 May 2010. Accepted 26 July 2010. Published on the NRC Research Press Web site at canjchem.nrc.ca on 30 September 2010.

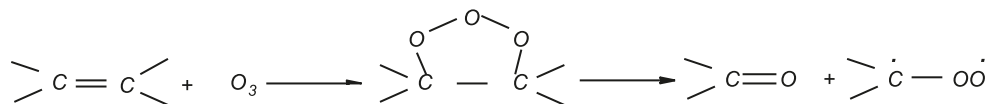
**F. Wedian.**<sup>1</sup> Department of Chemistry, Faculty of Science, Tafila Technical University, P.O. Box 179, Tafila 66110, Jordan.

**D.B. Atkinson.** Department of Chemistry, Portland State University, Portland, OR 97207, USA.

<sup>1</sup>Corresponding author (e-mail: alwedfad@yahoo.com).



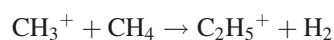
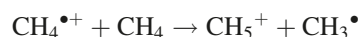
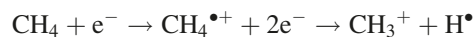
intermediate:<sup>1,16,19</sup>



The biradical intermediate is an energy-rich species, which rapidly undergoes complex bimolecular and unimolecular rearrangement and (or) fragmentation to yield a set of secondary products, including hydroxyl radicals (OH).<sup>16</sup> The carbonyl compounds formed in the decomposition of the ozonide will be denoted as the primary products. Typical OH-alkene reaction rate coefficients are several orders of magnitude larger than those for the corresponding O<sub>3</sub>-alkene reaction; therefore, OH reacts rapidly with the alkene to produce a secondary set of gas-phase products in laboratory studies. The reactivity of OH causes problems for studying the primary products of ozonolysis, so OH-scavengers such as cyclohexane<sup>20</sup> and 2-butanol<sup>21</sup> are commonly used in previous works to suppress the OH formed from the reactions of O<sub>3</sub> with alkenes.

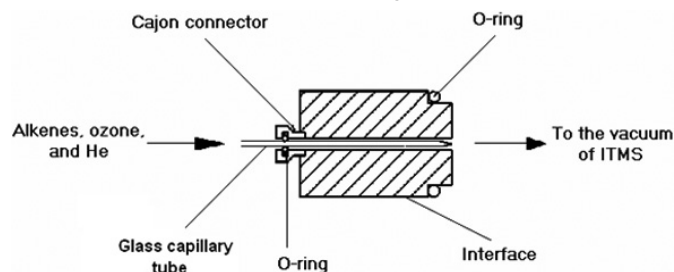
In this paper, 2,3-dimethyl-2-butene (tetramethylethylene, TME) was used as a reagent because the TME-O<sub>3</sub> reaction has been studied intensively<sup>1,19</sup> and the major features of the reaction's kinetics and products are well-established.<sup>1,15,17,18,22-29</sup> The reaction is one of the fastest ozonolyses with a room temperature rate coefficient of  $k \approx 1 \times 10^{-15} \text{ cm}^3 \text{ molec}^{-1} \text{ s}^{-1}$ . The known primary stable products of the TME-O<sub>3</sub> reaction are acetone, (CH<sub>3</sub>)<sub>2</sub>CO, methylglyoxal, CH<sub>3</sub>C(=O)CHO, and hydroxyacetone or acetol, CH<sub>3</sub>C(=O)CH<sub>2</sub>OH.<sup>1,19</sup>

A problem in these types of studies is that a multicomponent mass spectrum is obtained from the mixture of reactants and products. The approach investigated here to mitigate this problem is to replace the electron impact ionization (EI) mode with a "softer" chemical ionization (CI) mode. Soft ionization refers to the ability to produce molecular ions or ions related to the original compound (e.g., protonated ions) from analytes with little or no fragmentation. Since the major products of the ozonolysis are easily protonated oxygenated compounds, methane was used as a proton exchange chemical ionization reagent. In methane positive chemical ionization mode, CH<sub>3</sub><sup>+</sup>, CH<sub>5</sub><sup>+</sup>, and C<sub>2</sub>H<sub>5</sub><sup>+</sup> are the proton donor species, which are produced in the ion source of the ion trap mass spectrometer mainly through the following reactions:



The mechanisms of methane chemical ionization are (i) the proton transfer in which the CH<sub>3</sub><sup>+</sup>, CH<sub>5</sub><sup>+</sup>, and C<sub>2</sub>H<sub>5</sub><sup>+</sup> react with gaseous compounds leading to the formation of "molecular ions", (MH)<sup>+</sup>, which dominates the mass spectrum of oxygenated compounds, and (ii) the ion-molecule adduct formation, which leads to the formation of adduct ions

Fig. 1. Schematic view of the static-bag interface.



[M + CH<sub>3</sub>]<sup>+</sup> and [M + C<sub>2</sub>H<sub>5</sub>]<sup>+</sup>.<sup>30</sup> Because of the clean chemical ionization mode of the IT-MS, all ions observed came from the ion-molecule reaction.

This paper describes the external reactor design for the atmospheric pressure static reactor and its operational procedure. The interface between the reactor and the low pressure mass spectrometer is discussed. The experimental results for the TME-O<sub>3</sub> reactions are used to demonstrate the strengths and weaknesses of the reactor. The future outlook for this reactor design is discussed.

## Experimental method

### The ion trap mass spectrometer

The reactor was coupled to an ion trap mass spectrometer (Varian, Inc. Saturn 2000 GC-MS) via 1.4 in. (1 in. = 25.4 mm) outer diameter (o.d.) direct insertion probe interfaces (the Saturn was originally coupled to a GC through a transfer line, which was removed for all studies described here). The reactor interface was inserted into the vacuum adaptor installed in the GC transfer line inlet port.

The ion trap usually operates at a pressure of a few millitorr (1 Torr = 133.32 Pa) of He (buffer gas). High-energy ions in the trap collide with He as the radio frequency potential increases, allowing the ions to lose some energy and remain in the center of the ion trap, improving the mass resolution. Therefore, the reactor interface described here was designed to admit a small flow of He (~2 mL/min) to help transfer analytes into the ion trap and to supply the ion trap buffer gas requirement.

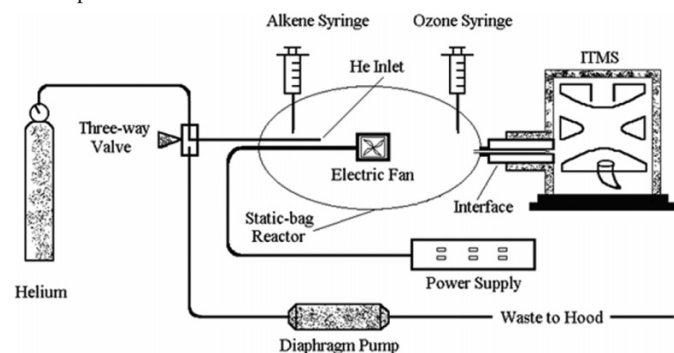
All experiments reported here were conducted using methane chemical ionization. The mass spectra (50–200 *m/z*) were collected using the Varian Saturn 2000 ion trap control software in the GC (repetitive mass scan vs time) mode. An aftermarket mass spectral data reduction program (WSearchPro) was used to convert the data to a useful form (i.e., ASCII text) for further analysis.

### Static reactor design

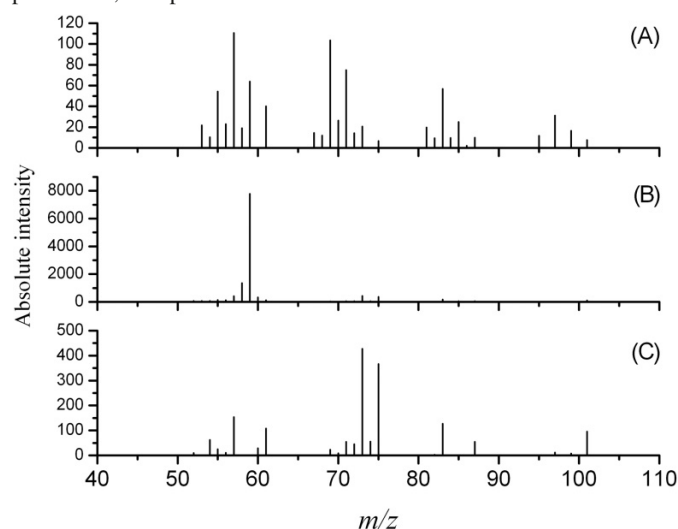
A vacuum interface was used to sample the static reactor



**Fig. 2.** Schematic of the static-bag reactor coupled with the ion trap mass spectrometer.



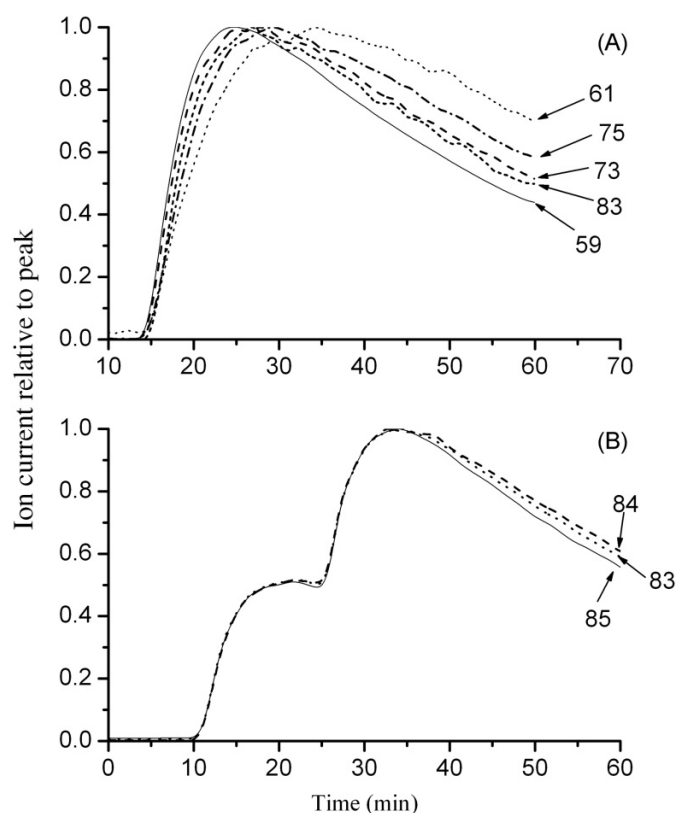
**Fig. 3.** (A) The mass spectrum of ozone background in the absence of added TME. (B) The mass spectrum of the TME–ozone reaction mixture after subtraction of the ozone background. The spectrum is dominated by acetone. (C) The net mass spectrum of the TME–ozone reaction mixture after subtracting contributions of ozone, pure TME, and pure acetone.



as shown in Fig. 1. The interface to the IT-MS consisted of a 8 cm glass capillary tube mounted in a brass plug with O-ring seals, allowing substitution for the standard GC interface of the mass spectrometer. The flow-restricting inlet in this design was a 1/16 in. o.d. glass capillary, which was heated and pulled to make a long thin tube that gave a measured flow of 2 cm<sup>3</sup>/min of helium at the atmospheric pressure differential. The capillary was held in a Cajon Swagelok connector using an O-ring seal that extended through the brass interface.

The static reactor was a 12 L Teflon bag where reactions were carried out. One side of the bag was connected to the mass spectrometer interface while the other side was connected to a three-way valve. In one position, the valve admitted a He flow sufficient to supply the mass-spectrometer interface, while maintaining the bag shape. Helium served as the gas medium for reactions as well as the carrier gas that delivered the reactants and products into the mass spectrometer and the ion trap buffer gas source, as described above. In the other valve position, the bag was connected to a diaphragm pump (Environmental Monitoring Systems) to evac-

**Fig. 4.** Ion profiles of reactant and product masses (10 ppm of TME reacting with an excess amount of purified ozone) in the static reactor, without fan, using methane as a chemical ionization reagent. (A) Ion profiles of products of the TME–O<sub>3</sub> reaction ( $m/z$  59, 61, 73, 75, and 83) that show differences in rise and decay rates among the products. (B) Ion profiles of two successive injections of pure TME ( $m/z$  83, 84, and 85) that show good reproducibility and show no observable differences among the rise times ( $t_{10\%–90\%}$ ) of these three ions associated with TME.



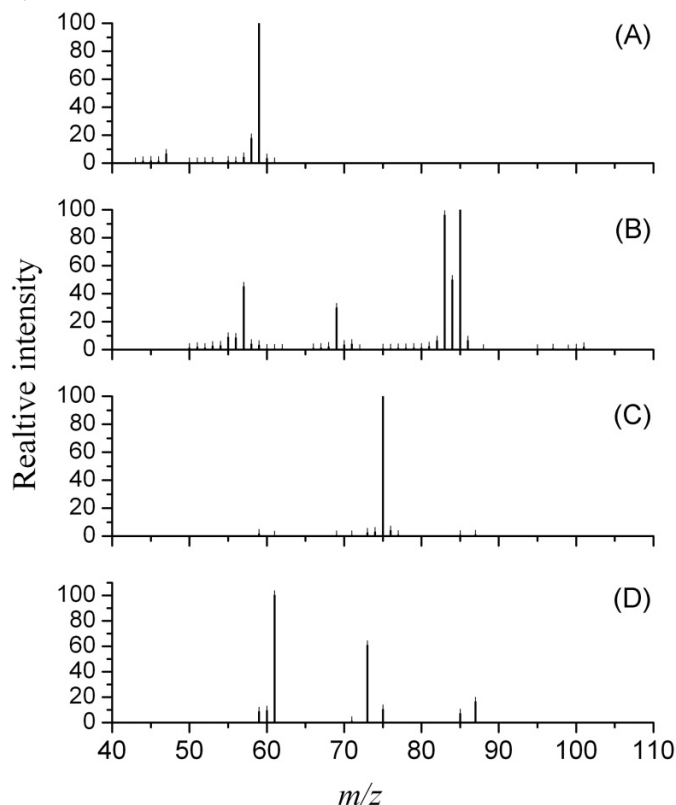
uate the bag's contents between successive experiments. Vapor phase reagent alkenes and ozone were injected with a syringe through a hole in the side of the bag, which was then covered with Teflon tape. A small electric fan inside the bag stirred the gas mixture if needed during the experiment (Fig. 2).

### Static reactor operation

In preparation for a reaction sequence, the reactor bag was filled with helium. Purified ozone in nitrogen (see below) was then injected into the bag using a 50 mL syringe. A sufficient time was given to ensure a uniform distribution of ozone throughout the bag. Then vapor-phase samples (head space air above liquids) of selected organic compounds were directly injected into the bag using a 25 mL syringe. Following the observation of the products of the ozone–TME reaction (typically several minutes), the bag was flushed and filled several times with He to remove the contents from the previous experiment, which was confirmed by low ion signals for masses of interest.

Ozone was trapped on cold silica gel via the standard procedure.<sup>31</sup> In brief, pure oxygen was photolyzed by the ozonator, and the resulting ozone–oxygen flow was allowed to

**Fig. 5.** (A) The CI mass spectrum of pure acetone (dominated by  $m/z$  59). (B) The CI mass spectrum of pure TME (dominated by  $m/z$  57, 69, 83, 84, and 85). The relative ratio of  $m/z$  83–85 is 0.98. (C) The CI mass spectrum of pure hydroxyacetone (dominated by  $m/z$  75). (D) The CI mass spectrum of pure methylglyoxal (dominated by  $m/z$  61 and 73).



pass over the cold surface of silica gel (dry ice–isobutyl alcohol temperature) where the ozone was trapped. After an hour of trapping, the ozone–oxygen flow was replaced by an ultrahigh purity nitrogen flow that was used to deliver the trapped ozone to a 5 L Tedlar bag (Alltech Associates, Inc.). The ozone–nitrogen mixture was observed to be stable in the Tedlar bags for several hours. Aliquots of the mixture were transferred to the 12 L bag reactor with a syringe and released at room temperature. The ozone concentration in the reactor was determined in separate experiments by exhausting the reactor through a Dasibi ozone instrument (Dasibi, Inc., model X).

### Chemicals

Pressurized mixtures of TME in  $N_2$ , acetone in  $N_2$ , and hydroxyacetone in  $N_2$  were prepared using a gas manifold system. Chemicals and gases used in these experiments were: TME (Sigma-Aldrich, 99%), acetone (Sigma-Aldrich, 99%), hydroxyacetone (Sigma-Aldrich, 90%), pyruvic aldehyde (Sigma-Aldrich, 40 wt%), He (commercial grade 99.998, Airgas Inc.), methane (UHP 99.9995, Airgas Inc.),  $N_2$  (UHP 99.9995, Airgas Inc.),  $O_2$  (UHP 99.9995, Airgas Inc.), and isobutane (commercial grade 99.9, Airgas Inc.).

### Results and discussion

Figures 3 and 4 show results for the ozone–TME reaction,

**Table 1.** Major ions observed by ion trap mass spectrometry using  $CH_4$  chemical ionization, sampling from 1 atm (1 atm = 101.325 kPa) static reactor (without stirring), after ozone–TME reaction, listed in order of decreasing rise rates.

$m/z$	Rise coefficient ( $s^{-1}$ ) <sup>a</sup>	Tentative assignment of neutral parent	bp (°C)
59	0.004 06	Acetone	56
73	0.003 48	Methylglyoxal	72
83	0.002 86	(Not TME)	
75	0.002 34	Hydroxyacetone <sup>b</sup>	145 <sup>c</sup>
101	0.002 33	TME oxirane	
87	0.001 84	$C_5H_{10}O$	
61	0.001 75	Acetic acid	118

<sup>a</sup>Obtained by fitting  $(1 - \exp(-a_1 t))a_2$  to measured signals vs time after the injection of TME into the unstirred reactor containing excess  $O_3$  (with  $O_2$ ) in He.

<sup>b</sup>Intermediate species with  $m/z$  74 may contribute.

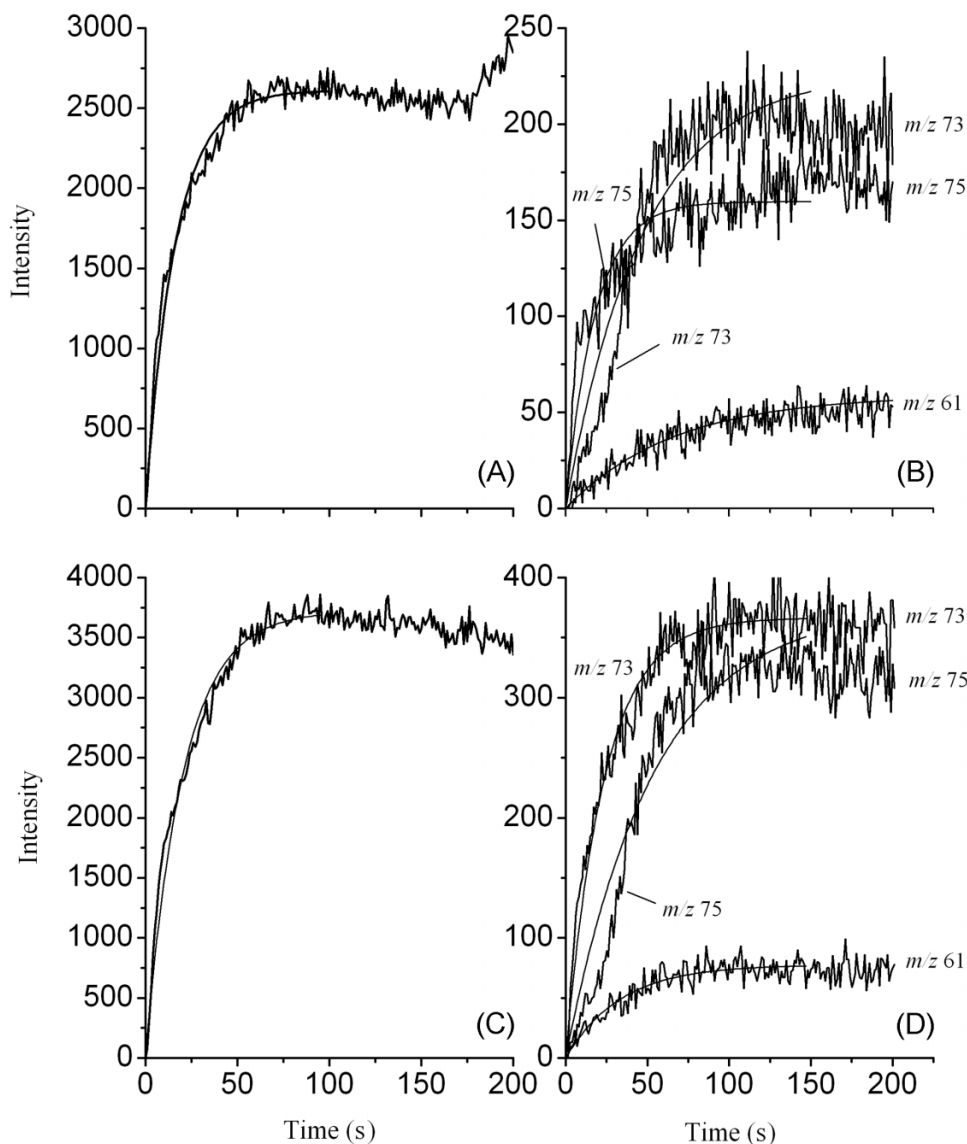
<sup>c</sup>Decomposes.

monitored using methane as the CI reagent. Figure 3A shows the mass spectrum of the reactor contents when ozone is the only added reagent; it shows significant fragmentations and severe overlapping of ions in at least three regions,  $m/z$  50–60, 65–75, and 80–90. These low intensity ions may correspond to impurities associated with the injected ozone into the reactor. Figure 3B shows the reaction mixture at a long reaction time in the static reactor, after subtraction of the prereaction background, much of which comes from the ozone injection. The mass spectrum is dominated by acetone, which produces a strong peak at  $m/z$  59 ( $[M + 1]^+$ ) and a few weaker fragments and isotopic variant peaks. The CI mass spectra of pure acetone, TME, methylglyoxal, and hydroxyacetone were obtained in separate experiments (Fig. 5). Multiplying the pure acetone spectrum by an appropriate weighting factor, and then subtracting this from the ozone–TME reaction mixture allows the contribution of acetone to be removed. A similar procedure is used to remove the small contribution of unreacted TME, and Fig. 3C shows the resulting mass spectrum. The other products of the ozone–TME reaction are now visible at mass peaks  $m/z$  57, 60, 61, 73, 75, 83, and 101. The following paragraphs will try to distinguish which of those ions are due to single products from multiple ion fragments of those products.

Figure 4A shows data obtained in the static reactor without stirring. These data help to distinguish ions due to single products of the ozonolysis of the TME reaction from multiple ion fragments of those products. The experimental sequence in this case was injection of ozone, equilibration, and then injection of TME at concentrations where nearly all the TME is consumed. Figure 4 shows the rise and decay of net ion signals, normalized to the maximum observed for each ion ( $m/z$  59, 61, 73, 75, and 83). Since the products of the reaction are continuously diluted by the helium inflow and (or) lost by adsorption to the bag wall, all stable compounds show a long-time decline. The peak at  $m/z$  83 arises here almost entirely from an unidentified product in the bag reactor, since the other TME fragment ions ( $m/z$  57, 69, 84, and 85) are absent (Fig. 5B).

The primary and secondary reactions in the ozone–TME system run to near-completion (99%) within a few seconds,

**Fig. 6.** The function  $(1 - \exp(-a_1 t))a_2$ , with adjustable coefficients, was used to fit the initial growth of product ions of TME- $O_3$  in the stirred bag reactor. (A) The growth ion profile of  $m/z$  59 in the absence of isobutane. (B) The growth ion profiles of  $m/z$  61, 73, and 75 in the absence of isobutane. (C) The growth ion profile of  $m/z$  59 in the presence of isobutane. (D) The growth ion profiles of  $m/z$  61, 73, and 75 in the presence of isobutane.



and they occur in a relatively small volume of the bag reactor at a considerable distance from the IT-MS sampling interface. As the fully-reacted mixture mixes with helium at atmospheric pressure in the bag, we might expect similar dilution and transport of all products at  $m/z$  59, 61, 73, 75, and 83. Thus, we would expect all peaks to diffuse with an identical time behavior, which is not what we find. The individual ion signals' time dependences were fitted to an exponential growth expression to obtain coefficients for comparison (Table 1). There are observable differences in the rise rates among those five products at  $m/z$  59, 61, 73, 75, and 83. Figure 6 shows the growth ion profile of  $m/z$  59, 61, 73, and 75 in the absence and presence of isobutane.

We ascribe the differences in rates observed in Fig. 6 to substance-dependent differential absorption and desorption at the walls of the reactor bag, and in the atmospheric-pressure portion of the glass capillary of the IT-MS interface. Re-

gardless of the mechanism, we conclude that each of the displayed ion curves corresponds to a distinct protonated neutral species in the atmospheric-pressure reactor. This means that no pair of the curves belongs to a pair of fragments produced in the IT-MS by low-pressure chemical ionization of a single species entering from the reactor.

In contrast, Fig. 4B shows the behavior of ions ascribed to a single neutral parent; in this case, TME in the absence of ozone, where two equal TME injections were performed, separated by about 15 min. The small irreproducible differences between the ion profiles represent the relative intensity measurement uncertainty for the ion trap mass spectrometer over very long times. These differences indicate the reliability of distinct neutral parent identifications such as those in Fig. 4A.

We used the logistic growth function  $(1 - \exp(-a_1 t))a_2$ , with adjustable coefficients  $a_1$  (rise coefficient,  $s^{-1}$ ) and  $a_2$

**Table 2.** Reported primary and secondary products for the TME–O<sub>3</sub> reaction (see refs. 1 and 16).

Compound name	Molecular weight (g/mol)	Chemical formula
Carbon monoxide	28	CO
Formaldehyde	30	HCOH
Methanol	32	CH <sub>3</sub> OH
Carbon dioxide	40	CO <sub>2</sub>
Methyl hydroperoxide	48	CH <sub>3</sub> OOH
Ozone	48	O <sub>3</sub>
Acetone	58	CH <sub>3</sub> COCH <sub>3</sub>
Acetic acid	60	CH <sub>3</sub> COOH
Methylglyoxal (pyruvic aldehyde)	72	CH <sub>3</sub> COCHO
Methyl acetate	74	CH <sub>3</sub> COOCH <sub>3</sub>
Hydroxyacetone	74	CH <sub>3</sub> COCH <sub>2</sub> OH
Peroxyacetic acid	76	CH <sub>3</sub> COOOH
TME	84	(CH <sub>3</sub> ) <sub>2</sub> C=C(CH <sub>3</sub> ) <sub>2</sub>

(the upper limit of the growth), to fit the initial growth of product ions versus time after injection of excess ozone into the stirred reactor. This experiment was carried out by injecting excess ozone into the stirred reactor containing TME to monitor the unreacted TME and the products of the TME–ozone reaction (Fig. 6). The measured growth time of any ion may help in identifying that ion as a primary product showing a short rising time or as a secondary product showing a relatively long rising time. The growth of  $m/z$  59 was associated with acetone. The growth of  $m/z$  73, associated with methylglyoxal, was satisfactorily fitted with rise times ( $t_{10\%–90\%}$ ) of  $20 \pm 4$  s. In contrast, the growth of  $m/z$  75, associated with hydroxyacetone (or other neutrals yielding  $m/z$  75 on protonation) was poorly fitted by the above function. This conclusion was reached based on the chemical ionization mass spectra of pure acetone (dominated by the protonated molecular ion  $m/z$  59), methylglyoxal (dominated by  $m/z$  61 and the protonated molecular ion at  $m/z$  73), and hydroxyacetone (dominated by the protonated molecular ion  $m/z$  75) (Fig. 3).

The stirred-reactor data at  $m/z$  75 indicated the presence of both an immediate component and another component with an induction delay of approximately 30 s. The ion at  $m/z$  61, presumably protonated acetic acid, grew with a rise time ( $t_{10\%–90\%}$ ) of  $50 \pm 17$  s, consistent with its identification as a secondary product. Ions at  $m/z$  87 and 101 also showed slow rise times of approximately  $63 \pm 17$  and  $50 \pm 16$  s, respectively, in the stirred reactor, diagnostic for secondary products.

Unfortunately, the static reactor will not be effective for gas-phase kinetic measurements of reactant decay and product growth at atmospheric pressure for reaction times in the range of 0.2–2 s. However, the stirred bag reactor provides kinetic measurements in the range of 10–200 s, as well as calibrated product yield measurements where the products have been identified and are separately available in pure form for response calibration. Without stirring, the bag reactor assists in the identification of ions arising from distinct gas-phase neutral species, as opposed to multiple low-pressure ion fragments from single neutral parents.

Table 2 lists all primary and secondary products of the

**Table 3.** The initial concentration of all starting materials for the TME–ozone reaction in the static-bag reactor.

Chemical	Static-bag reactor
TME	10 ppm
Ozone	Excess
Isobutane	0.04%

ozone–TME reaction identified in the literature.<sup>1</sup> All products that have a molar mass less than 50 (the first six in Table 2) were not observed by the IT-MS, so they were not measured in our experiments. We did not observe any detectable signal at  $m/z$  76 or 77 that might indicate the presence of peroxyacetic acid.

Niki et al.<sup>1</sup> performed FTIR observations on the ozonolysis of TME, with positive spectral identification of 11 products (Table 2). Their additional experiments with <sup>18</sup>O<sub>3</sub> in the presence of <sup>16</sup>O<sub>2</sub> established that several of the observed products incorporated only <sup>16</sup>O and thus were products only of free-radical reactions. Other evidence pointed to free-radical reactions as the source of several observed products. Niki et al.<sup>1</sup> concluded that there were only three primary products: acetone, methylglyoxal, and hydroxyacetone. Among the hypothesized species with mass 74, only hydroxyacetone was available to provide a reference FTIR spectrum, so precursors of the same mass whose reference spectra were not available, if present in the reaction mixture, would be contained in the residual FTIR spectrum reported in that work, and thus not reported as measured products.

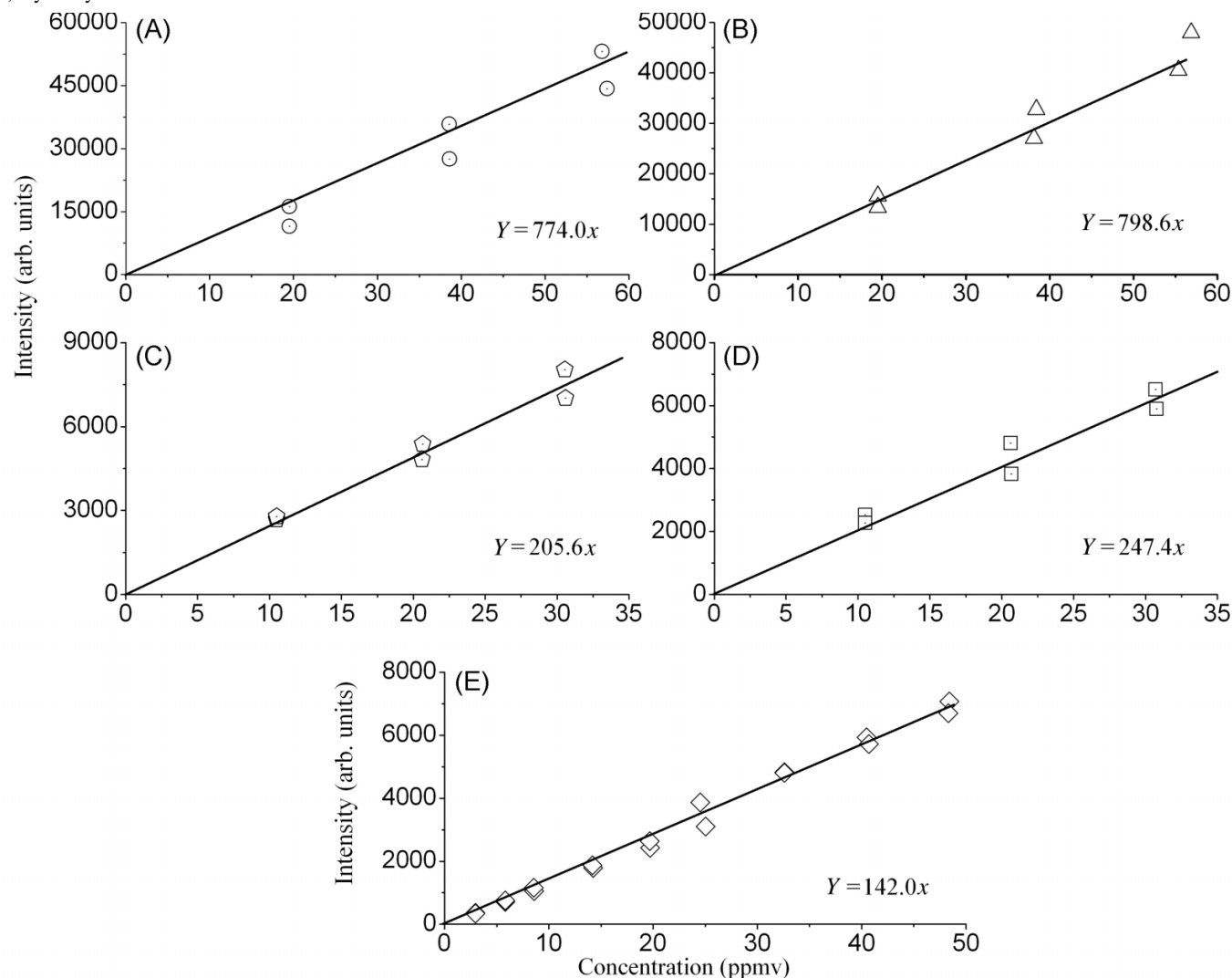
In our system, the observed peaks at  $m/z$  59, 73, and 75 probably correspond to protonation of the three primary products identified by Niki et al.:<sup>1</sup> acetone, methylglyoxal, and hydroxyacetone. These three peaks also correspond to those reported at  $m/z$  58, 72, and 74 by Martinez and Heron,<sup>19</sup> who used electron-impact ionization to observe products from ozonolysis of TME in a stopped-flow reactor at a total pressure of 4 Torr. In the case of  $m/z$  75, our experimental results do not exclude possible contributions from protonation of thermalized neutral intermediates of mass 74, such as 2-hydroperoxypropene or dimethylcarbonyl oxide. However, quantum thermochemical calculations by Olzmann et al.<sup>22</sup> predict very rapid dissociation of the hydroperoxide and persistence of the thermalized carbonyl oxide for times on the order of only 0.1 μs. From their theoretical results, one would predict an inability to detect either the carbonyl oxide or the hydroperoxide in the time range accessible to our experiments.

### Calibrations and calculation of yields

As discussed previously, acetone, methylglyoxal, and hydroxyacetone are identified as primary products of TME ozonolysis. For the purpose of quantitation of those products, we calibrated the response of the IT-MS (in CH<sub>4</sub> chemical ionization mode) to TME ( $P_{\text{vap}} = 99.665$  Torr at 20 °C from ref. 32), acetone ( $P_{\text{vap}} = 185.45$  Torr at 20 °C from ref. 32), and hydroxyacetone ( $P_{\text{vap}} = 5.6$  Torr at 20 °C from ref. 32; 7.6 mbar (1 bar = 100 kPa) in the MSDS) at their respective dominant mass numbers. Using the internal fan to stir the contents of the static reactor, we performed calibrations with and without added isobutane, which is used in some reaction experiments to scavenge OH, and found less



**Fig. 7.** Static-bag reactor calibration curves of TME, acetone, and hydroxyacetone. The responses were corrected for dilution decay: (A) acetone without isobutane, (B) acetone in the presence of isobutane, (C) TME without isobutane, (D) TME in the presence of isobutane, and (E) hydroxyacetone without isobutane.



**Table 4.** The responses and relative responses of TME, acetone, and hydroxyacetone for the static-bag reactor.

Compound	Response without isobutane	Response with isobutane	Relative response without isobutane <sup>a</sup>	Relative response with isobutane <sup>a</sup>
TME ( <i>m/z</i> 84, 85)	205.6±7.7	247.4±7.0		
Acetone ( <i>m/z</i> 59)	774.0±41.0	798.6±68.5	0.266±0.017	0.310±0.027
Hydroxyacetone ( <i>m/z</i> 75)	142.0±2.0		1.42±0.058	(1.42±0.058) <sup>b</sup>

<sup>a</sup>The relative responses were calculated with respect to TME.

<sup>b</sup>It was concluded that the presence of isobutane does not affect the performance of the ion trap, therefore, this calibration was not carried out. Based on the data shown in Fig. 7.

than 10% differences in the responses at the isobutane concentrations used. We were unable to calibrate the response to methylglyoxal due to difficulties in obtaining the pure compound. The initial typical ozone, TME, oxygen, and isobutane concentrations for the bag reactor are listed in Table 3. Since unstirred-bag experiments had indicated that the signal at *m/z* 83 may correspond to an intermediate or a product of the ozone reaction, we used only the sum of the signals at *m/z* 84 and 85 to calibrate and measure TME in the bag reactor experiments.

We measured the yields of the products of the ozone–TME reaction in the stirred bag, relative to consumption of TME. To calibrate the IT-MS response to TME, acetone, and hydroxyacetone with the bag reactor interface, we used a syringe to obtain known small volumes of air in vapor–pressure equilibrium with the analyte liquid at a known temperature, and injected them through the resealable hole in the bag wall.

A series of experiments were carried out to measure the response factor and relative response of the ion trap mass

**Table 5.** Yields of products from the reaction of ozone with TME.

	This work: stirred static bag reactor <sup>a</sup>	Niki et al. (1987) <sup>1,b</sup>	Grosjean et al. (1996) <sup>29</sup>	Tuazon et al. (1997) <sup>17</sup>
Acetone	0.98±0.05	1.0±0.13	1.006±0.049	1.14±0.19 <sup>c</sup>
Methylglyoxal	Not calibrated	0.09	0.314±0.071 <sup>d</sup>	Not observed
Hydroxyacetone	0.18±0.1	0.07±0.01		Not observed

<sup>a</sup>Stirred static bag: yields relative to TME consumed in the presence of isobutane. The total theoretical yields of all products are expected to be 200%.

<sup>b</sup>Absolute yields with FTIR absorption spectroscopy as reported in Calvert et al.<sup>33</sup> The analyses were based on monitoring selected absorption bands for reactants and products.

<sup>c</sup>Absolute yield with FTIR absorption spectroscopy.

<sup>d</sup>Combined absolute yields of methylglyoxal and hydroxyacetone. The yield was calculated as  $\Delta$  product formed /  $\Delta$  reacted ozone (ppb).

spectrometer for the compounds. Under similar conditions and isobutane concentrations as in the TME–O<sub>3</sub> reaction, the responses of the ion trap mass spectrometer for TME, acetone, and hydroxyacetone were plotted against the standard concentrations. Best-fit regression lines were determined from the data, the mathematical equations of the line were then used to determine the response factors (*R*), and then to determine the relative response factors (RR). The relative responses were calculated with respect to TME as follows: relative response = response of TME/response of a product. Then, a number of experiments were performed to obtain the product yield, which is given as yield =  $\Delta$ product/ $\Delta$ TME  $\times$  RR, where RR is the relative response of acetone or hydroxyacetone with respect to TME,  $\Delta$  is the change of concentrations of compounds formed or the change in concentration of reacted TME. The  $\Delta$  could be calculated as the difference between the final concentrations (at the completion of the reaction) and the initial (starting) concentration.

The calibration results are given in Fig. 7; the slope of the regression lines was used as the response (*R*) of the IT-MS for each compound. The responses and the relative responses of TME, acetone, and hydroxyacetone for the static bag in the absence and presence of the OH scavenger (isobutane) are given in Table 4. The results in Fig. 7 show the dependence of responses of compounds on the presence of isobutane, which apparently behaves as another source to protonate the compounds and by altering the IT-MS signal responses for polar compounds over nonpolar compounds under the chemical ionization mechanism mode (see Supplementary data).

In all cases, we calibrated the interface–IT-MS with and without isobutane added. We used the appropriate response calibration factor (with or without isobutane) in the calculation of product yields. The measured acetone yield (per molecule TME consumed) was nearly independent of the presence of isobutane. This is expected since acetone is also a major primary product of the reaction of O<sub>3</sub> with TME.<sup>33</sup> Though uncalibrated, the methylglyoxal yield relative to the acetone yield increased by a factor of 1.7 with the addition of isobutane, sufficient to compete equally (same reaction half-life) with TME for reaction with OH. This is consistent with earlier work that found that methylglyoxal is not a product of the reaction of OH with TME,<sup>33</sup> but that it is a primary product of ozone plus TME.<sup>1</sup> Table 5 shows a comparison of this work and other previous TME–ozone studies.

## Conclusion

It was demonstrated that a static atmospheric pressure reactor coupled with an ion trap mass spectrometer can be used to study gas-phase reactions. The TME–ozone reaction was a sample case for the application of the new design. The unstirred static reactor can be used to distinguish between different reaction products, while the stirred reactor and the flow tube described in a companion paper can be used to study the kinetics of the reaction and to follow the product formation in different time ranges, as well as to measure the product yields. This new design is convenient to use because it permits continuous, sensitive, and specific monitoring by the IT-MS.

Future work will seek to study short-lived intermediate product behavior, for example, the as yet unconfirmed products we detect at *m/z* 75 and 83. The method can also be used to investigate less well-studied biogenic alkene–ozone reactions. Furthermore, future work will seek to test a newly designed flow tube reactor, which will be coupled with the same IT-MS detector system. This flow tube reactor will be used to study the kinetics of the products as well as the product yields. In principle, those instruments may be used to study other oxidation reactions of hydrocarbons (e.g., reactions with OH and with NO<sub>3</sub>) relevant to atmospheric chemistry at realistic pressures and temperatures.

## Supplementary data

Supplementary data for this article are available on the journal Web site (canjchem.nrc.ca).

## Acknowledgments

The authors would like to acknowledge the support of the Portland State University (PSU) College of Liberal Arts and Sciences and the PSU Atmospheric Research Group.

## References

- (1) Niki, H.; Maker, P. D.; Savage, C. M.; Breitenbach, L. P.; Hurley, M. D. *J. Phys. Chem.* **1987**, *91* (4), 941. doi:10.1021/j100288a035.
- (2) Koch, S.; Winterhalter, R.; Uhrek, E.; Kolloff, A.; Neeb, P.; Moortgat, G. K. *Atmos. Environ.* **2000**, *34* (23), 4031. doi:10.1016/S1352-2310(00)00133-3.
- (3) Winterhalter, R.; Neeb, P.; Grossmann, D.; Kolloff, A.; Horie, O.; Moortgat, G. *J. Atmos. Chem.* **2000**, *35* (2), 165. doi:10.1023/A:1006257800929.

- (4) Li, Z.; Wuebbles, R. D.; Pylawka, N. J. *Chem. Phys. Lett.* **2002**, *354* (5–6), 491. doi:10.1016/S0009-2614(02)00181-1.
- (5) Thornberry, T.; Abbatt, J. P. D. *Phys. Chem. Chem. Phys.* **2004**, *6* (1), 84. doi:10.1039/b310149e.
- (6) Seeley, J. V.; Meads, R. F.; Elrod, M. J.; Molina, M. J. *J. Phys. Chem. A* **1996**, *100*, 4026.
- (7) Scholtens, K. W.; Messer, B. M.; Cappa, C. D.; Elrod, M. J. *J. Phys. Chem. A* **1999**, *103* (22), 4378. doi:10.1021/jp990469k.
- (8) Patchen, A. K.; Pennino, M. J.; Kiep, A. C.; Elrod, M. J. *Int. J. Chem. Kinet.* **2007**, *39* (6), 353. doi:10.1002/kin.20248.
- (9) Xu, Y.; Jia, L.; Ge, M.; Du, L.; Wang, G.; Wang, D. *Chin. Sci. Bull.* **2006**, *51* (23), 2839. doi:10.1007/s11434-006-2180-3.
- (10) Arey, J.; Aschmann, S. M.; Kwok, E. S. C.; Atkinson, R. J. *Phys. Chem. A* **2001**, *105* (6), 1020. doi:10.1021/jp003292z.
- (11) Foster, K. L.; Caldwell, T. E.; Benter, T.; Langer, S.; Hemminger, J. C.; Finlayson-Pitts, B. J. *Phys. Chem. Chem. Phys.* **1999**, *1* (24), 5615. doi:10.1039/a907362k.
- (12) Wang, L.; Atkinson, R.; Arey, J. *Atmos. Environ.* **2007**, *41* (10), 2025. doi:10.1016/j.atmosenv.2006.11.008.
- (13) Reinnig, M.-C.; Warnke, J.; Hoffmann, T. *Rapid Commun. Mass Spectrom.* **2009**, *23* (11), 1735. doi:10.1002/rcm.4065. PMID:19412924.
- (14) Warscheid, B.; Kückelmann, U.; Hoffmann, T. *Anal. Chem.* **2003**, *75* (6), 1410. doi:10.1021/ac025788d. PMID:12659203.
- (15) Seinfeld, J. H.; Pandis, S. N. *Atmospheric Chemistry and Physics: From Air Pollution to Climate Change*, 2nd ed.; Wiley: New York, 1998.
- (16) Atkinson, R. *J. Phys. Chem. Ref. Data* **1997**, *26* (2), 215. doi:10.1063/1.556012.
- (17) Tuazon, E. C.; Aschmann, S. M.; Arey, J.; Atkinson, R. *Environ. Sci. Technol.* **1998**, *32* (14), 2106. doi:10.1021/es980153a.
- (18) Hasson, A. S.; Orzechowska, G.; Paulson, S. E. *J. Geophys. Res.* **2001**, *106* (D24), 34131. doi:10.1029/2001JD000597.
- (19) Martinez, R. I.; Herron, J. T. *J. Phys. Chem. A* **1987**, *91* (4), 946.
- (20) Shu, Y.; Atkinson, R. *Int. J. Chem. Kinet.* **1994**, *26* (12), 1193. doi:10.1002/kin.550261207.
- (21) Chew, A. A.; Atkinson, R. *J. Geophys. Res.* **1996**, *101* (D22), 28649. doi:10.1029/96JD02722.
- (22) Olzmann, M.; Kraka, E.; Cremer, D.; Gutbrod, R.; Andersson, S. *J. Phys. Chem. A* **1997**, *101* (49), 9421. doi:10.1021/jp971663e.
- (23) Kroll, J. H.; Hanisco, T. F.; Donahue, N. M.; Demerjian, K. L.; Anderson, J. G. *Geophys. Res. Lett.* **2001**, *28* (20), 3863. doi:10.1029/2001GL013406.
- (24) Johnson, D.; Rickard, A. R.; Marston, G.; Fish, D. J. In *Mechanism of OH Formation in The Gas-Phase Ozonolysis of Alkenes*, Proceedings of the 6th EUROTRAC Symposium, Garmisch-Partenkirchen, Germany, 27–31 March 2000; Midgley, P.M., Reuther, M., Williams, M., Eds.; Springer-Verlag: Berlin, 2001; pp 405–409.
- (25) Greene, C. R.; Atkinson, R. *Int. J. Chem. Kinet.* **1992**, *24* (9), 803. doi:10.1002/kin.550240905.
- (26) Schäfer, C.; Horie, O.; Crowley, J. N.; Moortgat, G. K. *Geophys. Res. Lett.* **1997**, *24* (13), 1611. doi:10.1029/97GL01545.
- (27) Rickard, A. R.; Johnson, D.; McGill, C. D.; Marston, G. J. *Phys. Chem. A* **1999**, *103* (38), 7656. doi:10.1021/jp9916992.
- (28) Siese, M.; Becker, K. H.; Brockmann, K. J.; Geiger, H.; Hofzumahaus, A.; Holland, F.; Mihelcic, D.; Wirtz, K. *Environ. Sci. Technol.* **2001**, *35* (23), 4660. doi:10.1021/es010150p. PMID:11770768.
- (29) Grosjean, E.; de Andrade, J. B.; Grosjean, D. *Environ. Sci. Technol.* **1996**, *30* (3), 975. doi:10.1021/es950442o.
- (30) de Hoffmann, E.; Stroobant, V. *Mass Spectrometry: Principles and Applications*; John Wiley and Sons, Ltd.: New York, 2002.
- (31) Cook, R. G.; Kiffer, A. D.; Klumpp, C. V.; Malik, A. H.; Spence, L. A. *Adv. Chem. Ser.* **1959**, *21*, 44. doi:10.1021/ba-1959-0021.ch007.
- (32) Dean, J. A., Ed. *Lange's Handbook of Chemistry*, 15th ed.; McGraw-Hill: New York, 1999.
- (33) Calvert, J. G.; Atkinson, R.; Kerr, J. A.; Madronich, S.; Moortgat, G. K.; Wallington, T. J.; Yarwood, G. *The Mechanisms of Atmospheric Oxidation of the Alkenes*; Oxford University Press: New York, 2000.

# Temperature and density effects on the absorption maximum of solvated electrons in sub- and super-critical methanol

Y. Yan, M. Lin, Y. Katsumura, Y. Muroya, S. Yamashita, K. Hata, J. Meesungnoen, and J.-P. Jay-Gerin

**Abstract:** The optical absorption spectra of the solvated electron ( $e_{\text{sol}}^-$ ) in sub- and super-critical methanol are measured by both electron pulse radiolysis and laser photolysis techniques, at temperatures in the range 220–270 °C. Over the density range studied (~0.45–0.59 g/cm<sup>3</sup>), the position of the absorption maximum ( $E_{A_{\text{max}}}$ ) of  $e_{\text{sol}}^-$  is found to shift only slightly to the red with decreasing density. In agreement with our previous work in water, at a fixed pressure,  $E_{A_{\text{max}}}$  decreases monotonically with increasing temperature in passing through the phase transition at  $T_c$  (239.5 °C). By contrast, at a fixed density,  $E_{A_{\text{max}}}$  exhibits a minimum as the solvent passes above the critical point into the supercritical state. These behaviors are discussed in terms of microscopic arguments based on the changes that occur in the methanol properties and methanol structure in the sub- and super-critical regimes. The effect of the addition of a small amount of water to the alcohol on the optical absorption energy of  $e_{\text{sol}}^-$  is also investigated.

**Key words:** methanol, methanol–water mixtures, supercritical fluid, solvated electron, absorption spectrum, density fluctuations, critical phenomena.

**Résumé :** En utilisant les techniques de radiolyse pulsée et de photolyse éclair, nous avons mesuré les spectres d'absorption optique de l'électron solvate ( $e_{\text{sol}}^-$ ) dans le méthanol à l'état sous- et supercritique, à des températures entre 220 et 270 °C. Dans la gamme de densité étudiée (~0,45–0,59 g/cm<sup>3</sup>), nous observons un léger déplacement du maximum d'absorption ( $E_{A_{\text{max}}}$ ) de  $e_{\text{sol}}^-$  vers le rouge (soit vers des énergies plus faibles) lorsque la densité diminue. De façon similaire à ce que nous avons observé précédemment dans l'eau, à pression fixée,  $E_{A_{\text{max}}}$  diminue de façon monotone lorsque la température augmente en passant la transition de phase à  $T_c$  (239,5 °C). En revanche, à une densité fixée,  $E_{A_{\text{max}}}$  présente un minimum lorsque le solvant passe au-dessus du point critique dans l'état supercritique. Ces comportements sont discutés en termes d'arguments microscopiques basés sur les changements qui interviennent dans les propriétés du méthanol et la structure de celui-ci dans les régimes sous-critique et supercritique. L'effet de l'addition d'une faible quantité d'eau à l'alcool sur  $E_{A_{\text{max}}}$  au voisinage du point critique a aussi été étudié.

**Mots-clés :** méthanol, mélanges méthanol–eau, fluide supercritique, électron solvate, spectre d'absorption, fluctuations de densité, phénomène critique.

## Introduction

In the last two decades, there has been an increased interest in various applications of supercritical fluids (SCFs).<sup>1,2</sup>

Besides their importance from the standpoint of fundamental chemistry, and especially the question of their unique physicochemical properties, SCFs have drawn interest because of their innovative role in a variety of chemical processes and

Received 15 April 2010. Accepted 9 July 2010. Published on the NRC Research Press Web site at canjchem.nrc.ca on 30 September 2010.

**Y. Yan and K. Hata.** Department of Nuclear Engineering and Management, Graduate School of Engineering, University of Tokyo, 7-3-1 Hongo, Bunkyo, Tokyo 113-8656, Japan.

**M. Lin.** Nuclear Science and Engineering Directorate, Japan Atomic Energy Agency, 2-4 Sirakata-shirane, Tokai, Naka, Ibaraki 319-1195, Japan.

**Y. Katsumura.**<sup>1</sup> Department of Nuclear Engineering and Management, Graduate School of Engineering, University of Tokyo, 7-3-1 Hongo, Bunkyo, Tokyo 113-8656, Japan; Nuclear Professional School, Graduate School of Engineering, University of Tokyo, 2-22 Shirakata-shirane, Tokai, Naka, Ibaraki 319-1188, Japan.

**Y. Muroya.** Nuclear Professional School, Graduate School of Engineering, University of Tokyo, 2-22 Shirakata-shirane, Tokai, Naka, Ibaraki 319-1188, Japan.

**S. Yamashita.** Advanced Science Research Center, Japan Atomic Energy Agency, 2-4 Shirakata-shirane, Tokai, Naka, Ibaraki 319-1195, Japan.

**J. Meesungnoen and J.-P. Jay-Gerin.**<sup>2</sup> Département de Médecine Nucléaire et de Radiobiologie, Faculté de Médecine et des Sciences de la Santé, Université de Sherbrooke, Sherbrooke, QC J1H 5N4, Canada.

<sup>1</sup>Corresponding author (e-mail: katsu@n.t.u-tokyo.ac.jp).

<sup>2</sup>Corresponding author (e-mail: jean-paul.jay-gerin@USherbrooke.ca).



technological applications. Among the most attractive applications used or being considered in this area are the possibility of using SCFs as alternative single-phase environment-friendly “green” reaction media for the synthesis of new materials and the destruction of hazardous waste compounds.<sup>3–9</sup> Underlying this growing attention to SCFs is the fact that many of their properties are distinctly different from those of ambient liquid fluids. In particular, it is possible to sensitively control the reaction rate and the selectivity by varying the density continuously at constant temperature over a wide range from liquid- to gas-like values using only small changes in the applied pressure.

To investigate the reaction mechanisms up to supercritical conditions, one possible measurement is to establish an *in situ* method to infer time-resolved information on transient species at high temperatures and pressures. The solvated electron ( $e_{\text{sol}}^-$ ) is ubiquitous and one of the most important species in radiolysis and photolysis. Since its original identification in aqueous solution in the early 1960s,<sup>10,11</sup> the studies of the properties of solvated electrons in various solvents, as well as under different conditions, have attracted much attention in many diverse research areas. The optical absorption spectra of solvated electrons in polar liquids are broad, asymmetrical, and featureless bands with a long tail on the high-energy side of the spectrum. The investigation of the absorption spectrum of  $e_{\text{sol}}^-$  is not only significant for our understanding of how the solvent molecules play a central role in solvation processes and in the mechanism of reactions involving the solvated electron, but is also helpful for revealing the microscopic structure of solvent-cluster anions.

Recently, spectroscopic techniques implementing a high-temperature, high-pressure optical cell coupled with an electron accelerator or a short-pulsed laser have been developed by several groups<sup>12–14</sup> for the study of SCFs. Our group also has developed spectroscopic systems applicable to pulse radiolysis–laser photolysis experiments on supercritical water (SCW) and alcohols. Two high-temperature, high-pressure optical cells have successively been designed and used.<sup>15–19</sup>

In our previous work,<sup>20</sup> we measured, using electron pulse radiolysis experiments, the absorption spectra of the hydrated electron ( $e_{\text{aq}}^-$ ) in sub- and super-critical water ( $\text{D}_2\text{O}$ ) at different temperatures and densities. A most remarkable result was that at a fixed pressure (25 MPa),  $E_{\text{A,max}}$  decreases (the position of the maximum absorption shifts to the red) monotonically with increasing temperature in passing through the liquid–SCW phase transition at  $T_c$  (370.74 °C), but exhibits a minimum at a fixed density (0.2 and 0.65 g/cm<sup>3</sup>) as the water passes above  $T_c$  into SCW. Also, over the density range studied (~0.2–0.65 g/cm<sup>3</sup>), the position of the maximum of the  $e_{\text{aq}}^-$  absorption spectra was found to move only *slightly* (~5.5%) toward the red when the density decreased, in marked contrast with computer simulation studies<sup>21</sup> that predicted an ~46% decrease of  $E_{\text{A,max}}$  for the same range of density. These behaviors were explained in terms of simple microscopic arguments based on the changes that occur in the water properties and the water structure in the subcritical water and SCW regimes. Most importantly, the role played by local density and molecular configurational fluctuations (associated with criticality) in providing pre-

existing polymeric clusters, which act as trapping sites for the excess electron, was a pivotal point in the interpretation of the data. For example, we estimated that in SCW at 400 °C, the *average* size of a water cluster anion ( $(\text{H}_2\text{O})_n^-$ ) was  $n \sim 26$ –32 water molecules in the investigated density range. Such cluster size values are consistent with reported experimental clustering data for  $(\text{H}_2\text{O})_n^-$  ions, indicating that interior-bound excess electron states are energetically favored (compared with surface states) in these sub- and super-critical regions. Electrons “internalized” in such clusters can, alternatively, be viewed as microscopic probes of the local structure of their host environment.

Alcohols form an interesting class of liquids that can be used to investigate the factors influencing the formation and stabilization of electrons in fluids. Considering that the structure of methanol is very like that of water (methanol, the simplest alcohol, may be considered as “methylated water”), just one methyl group replacing one H• atom, it is reasonable to assume that density-dependent behaviors similar to those observed for water also exist in sub- and super-critical methanol (SCM). In this work, we report our measurements of the temperature and density (pressure) dependences of the absorption band maximum of  $e_{\text{sol}}^-$  in sub- and super-critical methanol at temperatures from 220 to 270 °C, using electron pulse radiolysis and laser photolysis experiments. The effect of the addition of a small amount of water to the alcohol on the optical absorption energy of  $e_{\text{sol}}^-$  is also investigated.

## Experimental

Two different high-temperature, high-pressure cells (Taiatsu Techno) were used in pulse radiolysis and laser photolysis experiments, coupled with a linear electron accelerator or a KrF excimer laser (Lambda Physik, Compex 102; pulse duration, 20 ns;  $\lambda = 248$  nm), respectively, at the Nuclear Professional School of the University of Tokyo.

As guaranteed by the manufacturer, the corrosion-resistant Hastelloy HC22 irradiation cells, equipped with sapphire windows, can withstand maximum temperatures of ~400 °C and maximum pressures of ~40 MPa. The optical path length was 15 mm for both cells. Compared with the optical cell for pulse radiolysis experiments, which has only two sapphire windows, the cell for laser photolysis experiments consists of three windows, one for the incidence of laser and the other two for analyzing light. Other details of these cells were described previously.<sup>17,18,22,23</sup>

For the pulse radiolysis experiment, the electron beam had an energy of 35 MeV and its width was ~50 ns with a dose (in water at room temperature) of ~45 Gy/pulse. The laser photolysis experiments were generally carried out using a 248 nm (5 eV) KrF excimer laser, with a pulse duration of 20 ns and an energy of 100 mJ/pulse. The UV photons were used to generate solvated electrons via the photodetachment of  $\text{I}^-$  ions dissolved in the alcoholic solution (the energy of the lowest CTTS band of the iodide ion in methanol at 25 °C is known to be centered at ~5.6 eV above the ground state).<sup>19,24</sup>

In both the pulse radiolysis and laser photolysis experiments, a flow system, which was composed of a high-performance liquid chromatography (HPLC) pump and a back pressure regulator, was used. The solution was loaded

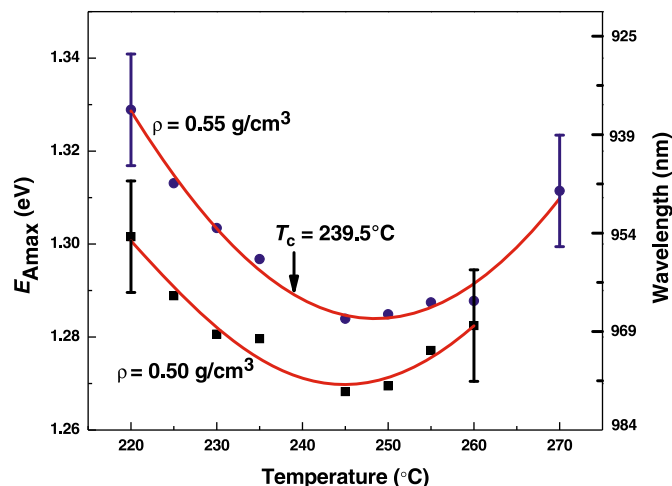
into the cell by the HPLC pump, and the pressure was adjusted with the back pressure regulator. Four thermocouples were used to monitor temperatures at the preheater and the heater of the cell; one of these thermocouples was placed inside the solution for monitoring the temperature of irradiated samples. The trigger to the linear accelerator or laser, the pulsed xenon lamp and the monochromator (Shimadzu SPG-120S for the UV–vis spectral region and SPG-120IR for the near-IR region), as well as data accumulation and transfer were all controlled by a computer.

For the UV–vis region (400–900 nm), a silicon photodiode was used as a detector. Because the light intensity was strong enough in this region, no preamp was necessary. An InGaAs *p-i-n* photodiode detector was used for the near-IR region (800–1250 nm). The signals were amplified 3–100 times by a variable gain 200 MHz wideband voltage amplifier DHPVA-200 (FEMTO, Germany) before being sent to a digital oscilloscope that was connected to a PC through a GPIB interface. A blocking filter of 750 nm was employed to cut the scattered and multiple order light for the measurements ranging from 800 to 1250 nm. In our experimental conditions, the errors on the positions of the absorption maxima ( $E_{A_{\max}}$ ) were estimated to be  $\pm 0.012$  eV (i.e.,  $\sim 2\%$ ).

In the laser flash photolysis experiment, the solvated electron generated by the resonant one-photon photodetachment of  $I^-$  pumped directly into its charge-transfer-to-solvent band, was not the only species absorbing light in the energy range of 0.7 to 4.0 eV. Thus, at room temperature we could not directly obtain a “pure” absorption spectrum of  $e_{\text{sol}}^-$  in laser photolysis (unlike in pulse radiolysis), but a mixed spectrum (recorded at the end of laser pulse) of  $e_{\text{sol}}^-$  and the  $I_2^-$  anion radical. However,  $I_2^-$ , with its absorption bands at 1.67 and  $\sim 3.2$  eV (i.e.,  $\sim 740$  and  $380$  nm), has a much longer lifetime than  $e_{\text{sol}}^-$ . Therefore, the overlapping spectra of  $e_{\text{sol}}^-$  and  $I_2^-$  can easily be separated.<sup>19,25</sup> In this study, since only high temperatures (in the range from 220 to 270 °C) were used, the peak positions of the  $e_{\text{sol}}^-$  spectrum were always lower than 1.33 eV; therefore, it was not necessary to consider the effect owing to the absorption of the  $I_2^-$  anion radical. As the extinction coefficient at 248 nm of  $I^-$  is known to increase with increasing temperature in methanol, more solvated electrons were produced at higher temperature in the solution for a given concentration of KI. In the present experiment, a concentration of 0.1 mmol/L KI in methanol was used.

Dehydrated methanol ( $\text{CH}_3\text{OH}$ ) with a purity  $>99.8\%$  (containing  $<50$  ppm water), methanol with a purity of  $99.8\%$  (G.R. grade) (assuming that the remainder is water, this would correspond to a mole fraction for  $\text{H}_2\text{O}$  of  $0.36\%$ ), and high-purity potassium iodide (KI) were purchased from Wako Pure Chemical Industries Ltd. and used as received. The pure alcohols or dilute (0.1 mmol/L) KI–methanol solutions were deaerated by bubbling with high-purity argon gas before being pumped into the irradiation cell. Methanol densities at the various temperatures and pressures used in this study were taken from the NIST Chemistry WebBook.<sup>26</sup>

**Fig. 1.** Energy of the maximum absorption ( $E_{A_{\max}}$ ) for the solvated electron ( $e_{\text{sol}}^-$ ) in sub- and super-critical methanol (SCM) ( $\text{CH}_3\text{OH}$ ) as a function of temperature at two different densities: 0.5 and  $0.55 \text{ g/cm}^3$ . A minimum of  $E_{A_{\max}}$  versus temperature is observed at both densities as the methanol passes above  $T_c$  (239.5 °C) into SCM. Smooth lines are polynomial fits to the experimental data. Error bars for  $E_{A_{\max}}$  are shown at the ends of the curves.

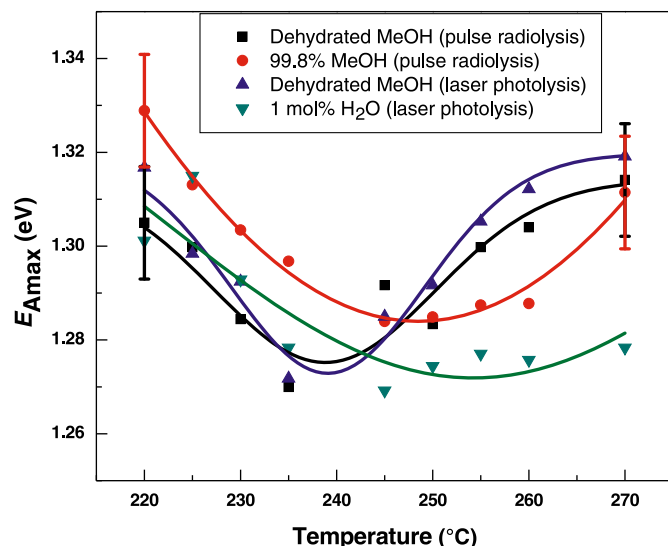


## Results and discussion

After irradiation of methanol (99.8%) with a high-energy electron pulse, the absorption of solvated electrons could clearly be detected by spectrophotometry even up to 270 °C. Figure 1 shows the temperature dependence of  $E_{A_{\max}}$  near the critical point of methanol ( $T_c = 239.5$  °C,  $P_c = 8.10$  MPa, and  $\rho_c = 0.280 \text{ g/cm}^3$ )<sup>26</sup> at our two limiting bulk methanol densities (namely, 0.50 and  $0.55 \text{ g/cm}^3$ ). These data suggest that at constant density (at least over the density range studied here),  $E_{A_{\max}}$  first decreases (the maximum absorption shifts to the red) as temperature increases in the subcritical region up to the critical point, reaches a (well-defined) minimum near this point, and then rises (the absorption spectrum shifts to the blue) as the temperature is increased further in the supercritical region. Interestingly, similar behavior was observed for the temperature dependence of  $E_{A_{\max}}$  of the hydrated electron as the water ( $\text{D}_2\text{O}$ ) passes above  $T_c$  into SCW.<sup>20</sup> Here, however, the minimum value of  $E_{A_{\max}}$  ( $\sim 245$ – $250$  °C, slightly depending on the density) does not occur exactly at the critical point. As our study below makes clear, this slight change in  $E_{A_{\max}}$  can be attributed to the presence of a small amount of water in the methanol used in the experiments.

Figure 2 shows the effects caused by the presence of water in methanol on the minimum value of  $E_{A_{\max}}$  versus temperature. Using pulse radiolysis and laser photolysis, experiments were carried out for dehydrated methanol, methanol (99.8%), and a 1 mol% water–methanol mixed solution at several temperatures in the range of 220 to 270 °C, at a fixed density of  $\rho = 0.55 \text{ g/cm}^3$ . As seen in Fig. 2, the shapes of the curves and the positions of the minima of  $E_{A_{\max}}$  found for dehydrated methanol by both nanosecond pulse radiolysis and laser photolysis are practically the same, indicating that these two methods are reliable for methanol. For dehydrated methanol and methanol (99.8%), we ignored the water effect on the density and assumed that

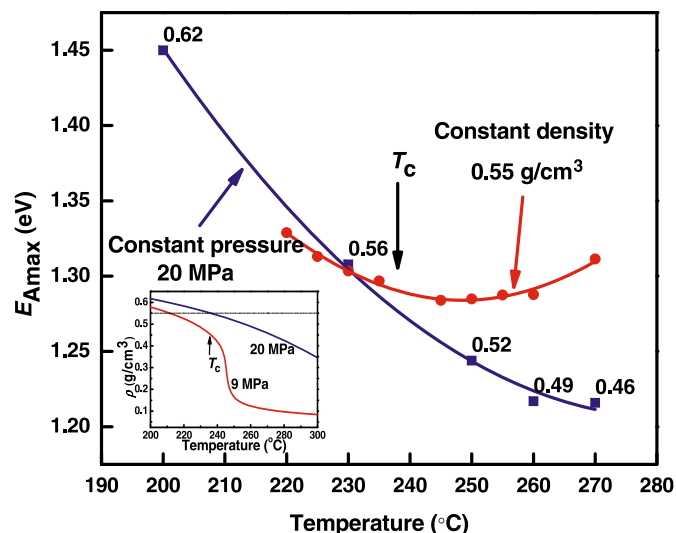
**Fig. 2.** Energy of the maximum absorption ( $E_{A_{\max}}$ ) for the solvated electron ( $e_{\text{sol}}^-$ ) in sub- and super-critical methanol ( $\text{CH}_3\text{OH}$ ) as a function of temperature at a fixed density ( $0.55 \text{ g/cm}^3$ ) for dehydrated methanol (containing <50 ppm water) using electron pulse radiolysis (■) and laser photolysis (▲), for methanol (99.8%) using electron pulse radiolysis (●), and for a 1 mol% water–methanol mixed solution using laser photolysis (▼). As demonstrated for dehydrated methanol, the minimum for  $E_{A_{\max}}$  is precisely located at the critical point of methanol ( $239.5^\circ\text{C}$ ). Error bars for  $E_{A_{\max}}$  are shown at the ends of the curves.



at the same temperature and pressure, the densities of these two kinds of methanol were also the same. Since there is no density data available for the mixtures of methanol and water, we just used the same conditions of temperature and pressure as for the other two kinds of methanol studied. The results show that, for dehydrated methanol, the minimum of  $E_{A_{\max}}$  is precisely located at the critical point of methanol ( $239.5^\circ\text{C}$ ), as was the case with  $\text{D}_2\text{O}$ .<sup>20</sup> For methanol (99.8%) containing a little water, the shape of the  $E_{A_{\max}}$ –temperature curve is roughly similar (in particular, its width is increased) to what we observe for methanol without water, but the position of the minimum of  $E_{A_{\max}}$  is clearly shifted from  $T_c$  to higher temperatures ( $\sim 248^\circ\text{C}$ ). This shift is even larger for methanol containing 1 mol% of water. For this latter case, although  $E_{A_{\max}}$  first decreases with increasing temperature, there is no obvious tendency for it to increase after passing through the minimum point (near  $255^\circ\text{C}$ ). In addition, with the addition of 1 mol% of water to the methanol, the width of the curve of  $E_{A_{\max}}$  versus temperature increases significantly.

In a series of papers, Gordon Freeman and co-workers<sup>27</sup> investigated in considerable detail the effect of water content on  $E_{A_{\max}}$  (and also on the yield of solvated electrons at  $1 \mu\text{s}$ ) at room temperature in several alcohols. These authors indicated that addition of up to 30 mol% of water causes the  $E_{A_{\max}}$  in methanol to decrease gradually. At around 30 mol% water  $E_{A_{\max}}$  remains approximately constant until 80 mol%, and then decreases again to the value of  $E_{A_{\max}}$  in pure water. Figure 2 shows that below the critical temperature, the difference between the values of  $E_{A_{\max}}$  in dehydrated methanol and in methanol containing 1 mol% water

**Fig. 3.** Energy of the maximum absorption ( $E_{A_{\max}}$ ) for  $e_{\text{sol}}^-$  in sub- and super-critical methanol (SCM) ( $\text{CH}_3\text{OH}$ ) as a function of temperature for two different thermodynamic conditions: at a constant density ( $0.55 \text{ g/cm}^3$ ) and at a fixed pressure (20 MPa). The inset shows the temperature dependence of the methanol density at 9 and 20 MPa. The (liquid–SCM) phase transition is indicated by an arrow at  $T_c$  ( $239.5^\circ\text{C}$ ). Smooth lines are polynomial fits to the experimental data.



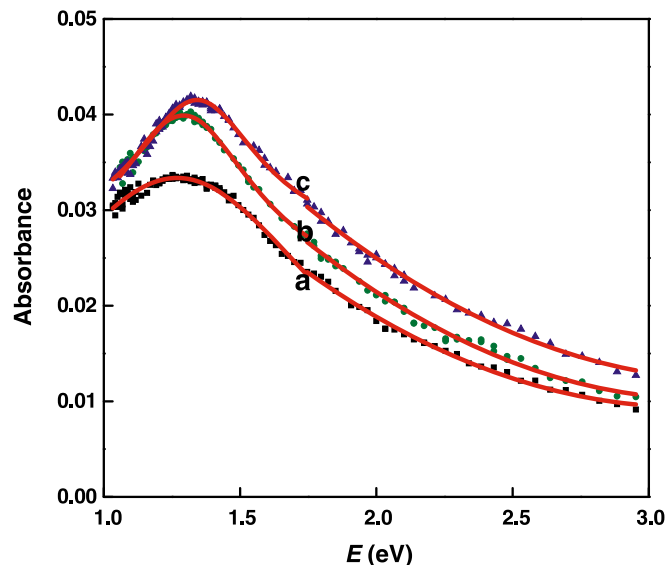
is in the range of experimental error. However, above the critical temperature the values of  $E_{A_{\max}}$  in dehydrated methanol are clearly higher than those in 1 mol% water–methanol solutions. As changes in  $E_{A_{\max}}$  imply that the energy of the bound state for the solvated electron is changed,<sup>27,28</sup> this indicates that in the supercritical state there is a change in the *intermolecular structure of the solvent* (which in fact corresponds to a decrease in the degree of local order) at the excess electron site caused by the addition of a small amount of water to the alcohol.

The temperature dependence of  $E_{A_{\max}}$  in methanol (99.8%) is further displayed in Fig. 3 under two different experimental conditions, namely, at constant density ( $0.55 \text{ g/cm}^3$ ) and *along an isobar* (20 MPa). As we can see, at temperatures higher than  $\sim 230$ – $235^\circ\text{C}$ , the two  $E_{A_{\max}}$ –temperature curves move away from each other. Whereas  $E_{A_{\max}}$  exhibits a minimum around  $245^\circ\text{C}$  (as shown in Fig. 1), we observe on the contrary, at fixed pressure, a smooth *monotonic* red-shift of the  $e_{\text{sol}}^-$  absorption maximum in passing through the liquid–SCM phase transition. These behaviors bear a striking similarity to those previously observed for sub- and super-critical water ( $\text{D}_2\text{O}$ ).<sup>20</sup>

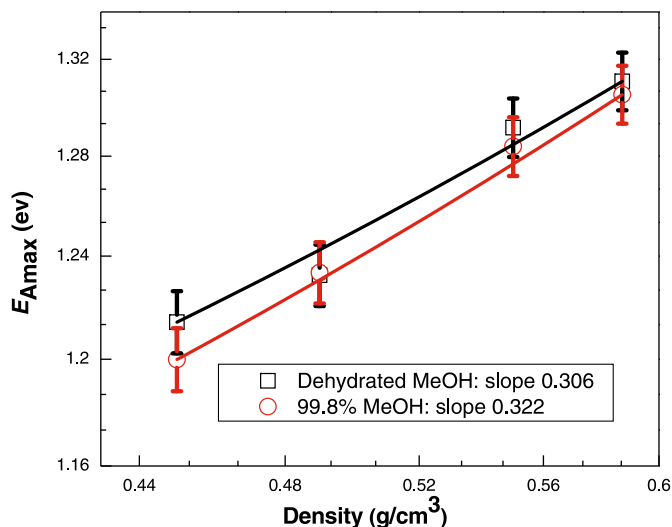
Figure 4 shows the absorption spectra of the solvated electron obtained after an  $\sim 50 \text{ ns}$  pulse at a constant temperature of  $245^\circ\text{C}$  in SCM at three different pressures: 15, 24, and 35 MPa for which the corresponding methanol (bulk) densities are 0.495, 0.549, and  $0.587 \text{ g/cm}^3$ , respectively. Although methanol itself has strong absorbance below  $\sim 1 \text{ eV}$  (or above  $\sim 1240 \text{ nm}$ ), we can clearly see the position of the maximum of the  $e_{\text{sol}}^-$  spectra, which is found to shift *slightly* to lower energies (or longer wavelengths) with decreasing density. In fact, the  $E_{A_{\max}}$  (obtained by Lorentzian fitting) of the  $e_{\text{sol}}^-$  spectra in Fig. 4 changes from 1.34 eV at



**Fig. 4.** Optical absorption spectra of the solvated electron  $e_{\text{sol}}^-$  in supercritical methanol (dehydrated  $\text{CH}_3\text{OH}$ ) at 245 °C obtained by electron pulse radiolysis at various pressures (densities): (a) 15 MPa (0.495  $\text{g}/\text{cm}^3$ ,  $\blacksquare$ ), (b) 24 MPa (0.549  $\text{g}/\text{cm}^3$ ,  $\bullet$ ), and (c) 35 MPa (0.587  $\text{g}/\text{cm}^3$ ,  $\blacktriangle$ ). The data are recorded just at the end of the electron pulse ( $\sim 50$  ns). The end-of-pulse absorbance decreases with decreasing density, reflecting the fact that the deposited dose decreases as the density decreases. As for the hydrated electron spectrum in supercritical  $\text{D}_2\text{O}$  (ref. 20), a broadening of the maximum of the  $e_{\text{sol}}^-$  absorption spectrum is observed at lower density (curve (a)), which is attributed to an increasing randomness of the supercritical phase  $e_{\text{sol}}^-$  trap configurations. The experimental points within the 1.0–1.7 eV energy range are fitted by Lorentzian functions (smooth lines) to read out  $E_{\text{Amax}}$ . Dose per pulse, 45 Gy; optical path length, 1.5 cm.



**Fig. 5.** Double logarithmic plots of the energy absorption maximum ( $E_{\text{Amax}}$ , in eV) for  $e_{\text{sol}}^-$  against bulk methanol density ( $\rho$ , in  $\text{g}/\text{cm}^3$ ) in supercritical  $\text{CH}_3\text{OH}$  at 245 °C: in methanol (99.8%,  $\square$ ) and in dehydrated methanol (containing  $<50$  ppm water,  $\circ$ ). Straight lines are fits to the experimental data. The errors in our  $E_{\text{Amax}}$  values are  $\sim 2\%$ .



0.587  $\text{g}/\text{cm}^3$  to 1.27 eV at 0.495  $\text{g}/\text{cm}^3$ , a decrease of 0.07 eV ( $\sim 5.2\%$ ). Similar behavior was also observed for the density dependence of  $E_{\text{Amax}}$  of solvated electrons in supercritical  $\text{D}_2\text{O}$ <sup>20</sup> as well as in supercritical ammonia<sup>29</sup> and deuterioammonia.<sup>30</sup>

In Fig. 5 we show  $E_{\text{Amax}}$  as a function of density in a double logarithmic plot for the temperature of 245 °C in dehydrated methanol and in methanol (99.8%). As can be seen, there is a good linear relationship of  $E_{\text{Amax}}$  with density, very similar to what we observed in the case of heavy water,<sup>20</sup> and the two resulting lines (calculated by least-squares fits to the data) are *almost superposed*. Therefore, this indicates that above the critical temperature and for the  $\sim 0.45$ – $0.59$   $\text{g}/\text{cm}^3$  density range studied, the variation of  $E_{\text{Amax}}$  (in eV) with bulk methanol density ( $\rho$ , in  $\text{g}/\text{cm}^3$ ) can be well represented by the empirical equation

$$[1] \quad E_{\text{Amax}} = A(T)\rho^p$$

where the exponent  $p \approx 0.306$  ( $\pm 0.01$ ) for dehydrated methanol and  $p \approx 0.322$  ( $\pm 0.01$ ) for methanol (99.8%), is the slope of the lines, and  $A$  is a proportionality coefficient, which, according to our results for SCW ( $\text{D}_2\text{O}$ ),<sup>20</sup> varies little with temperature (fitted values of  $A$  are, respectively, 1.208 for dehydrated methanol and 1.210 for methanol (99.8%)). Considering the experimental error, the difference regarding the effects of density on  $E_{\text{Amax}}$  in methanol (99.8%) and dehydrated methanol at a *fixed* temperature can simply be ignored.

Some simple microscopic arguments, based on the large density fluctuations (or inhomogeneities) and the highly disrupted hydrogen bond network associated with criticality, can be employed to better understand, at the molecular level, the mechanisms of localization and solvation of excess electrons in near-critical methanol and SCM. As discussed in our previous work on  $e_{\text{aq}}^-$  in SCW,<sup>20</sup> these arguments rely on the pioneering work of Jortner and Gaathon<sup>31</sup> who proposed that *local density fluctuations can be viewed as pre-existing clusters that act as electron traps*. As for water, this proposition is particularly relevant for SCM where structural investigations<sup>32</sup> have clearly shown the existence of significant methanol “clustering” and the formation of hydrogen-bonded molecular clusters whose number decreases with increasing temperature and decreasing density. However, whereas many studies have focused on the electronic structure, spectroscopy, and dynamics of  $(\text{H}_2\text{O})_n^-$ , similar investigations for methanol cluster anions  $((\text{CH}_3\text{OH})_n^-)$  have so far received little attention.<sup>33–37</sup> Indeed, since the first detection of  $(\text{H}_2\text{O})_n^-$  ions mass spectroscopically in 1981,<sup>38</sup> significant experimental and theoretical efforts have been devoted to exploring how excess electrons are bound to water clusters (over a very wide range of cluster sizes) and, more recently, the key issue of the existence of both surface and internal states of hydrated electron clusters in relation to the bulk hydrated electron as  $n \rightarrow \infty$  (see refs. 20, 37, 39, 40, and refs. therein). Much of this work has centered on the photoelectron and absorption spectroscopic studies of  $(\text{H}_2\text{O})_n^-$  clusters as a function of size ( $n$ ), providing a wealth of information about the nature of the excess electron–water interactions in these clusters. One most important result is that the parameters that govern the



whole line shapes of both the  $(\text{H}_2\text{O})_n^-$  cluster photoelectron and absorption spectra (namely, peak energy position, Gaussian peak width to the low-energy side, and Lorentzian peak width to the high-energy side) can be fitted linearly in  $n^{-1/3}$  (which derives from the reciprocal of cluster radius).<sup>40</sup> For example, the fit of the peak centres of the *photoelectron spectra* (PES) (or “vertical detachment energies” (VDEs), representing the energy required to remove an electron with no change in nuclear geometry) gives<sup>39,40</sup>

$$[2] \quad E_{\text{max,PES,H}_2\text{O}}(n) = \text{VDE}(n) = -5.65n^{-1/3} + 3.25$$

where  $n$  is the number of water molecules and  $E_{\text{max}}$  is in eV. A similar linear relationship is obtained between the peak centres of the *absorption spectra* (ABS) and  $n^{-1/3}$ , namely,<sup>20,39,41</sup>

$$[3] \quad E_{\text{max,ABS,H}_2\text{O}}(n) = E_{\text{Amax}} = -2.403n^{-1/3} + 1.783$$

Equation [3] builds a bridge, connecting  $E_{\text{Amax}}$  to the  $(\text{H}_2\text{O})_n^-$  cluster size or, alternatively, the electronic absorption maxima to the local molecular microstructures accommodating the excess charge. Notably, much of the absorption spectrum of the *bulk* hydrated electron (which is inherently an “internal” state) is immediately evident from the fitted cluster value of  $E_{\text{max}}$  when  $n \rightarrow \infty$ . Indeed, as we can see from eq. [3],  $E_{\text{max}}$  extrapolates to the bulk  $e_{\text{aq}}^-$  absorption value in ambient water ( $\lambda_{\text{Amax}} = 715 \text{ nm}$  or  $E_{\text{Amax}} = 1.73 \text{ eV}$  in  $\text{H}_2\text{O}$  at  $25^\circ\text{C}$ ),<sup>42</sup> which is consistent with water cluster anions characterized by internalized excess electron states.

Unfortunately, for methanol, while the photoelectron spectra of  $(\text{CH}_3\text{OH})_n^-$  ( $n \sim 70\text{--}460$ ) are known, their absorption spectra are not. Nevertheless, as far as the  $(\text{CH}_3\text{OH})_n^-$  cluster photoelectron spectra are concerned, there are clear analogies with the anionic water cluster spectra. In particular, there is evidence for two isomeric classes of methanol cluster anion excess electron states (evolving smoothly with cluster size),<sup>43</sup> namely, an internally localized, bulklike electron state (methanol I) and a weakly dipole-bound surface state (methanol II).<sup>35,37</sup> Just as in  $(\text{H}_2\text{O})_n^-$  clusters, the measured photoelectron peak centres  $E_{\text{max}}$  (in eV) have been fitted linearly in  $n^{-1/3}$ , giving for methanol I,<sup>35</sup>

$$[4] \quad E_{\text{max,PES,CH}_3\text{OH}}(n) = -2.25n^{-1/3} + 2.51$$

Analogies also exist between the most stable (higher electron binding) isomer I clusters for methanol and water cluster anions (assigned both with an internally solvated electron); for example, their formation is favored under similar ion source conditions, their VDEs are similar for comparably sized clusters, and their ultrafast excited-state relaxation dynamics exhibit similar trends.<sup>37</sup> Moreover, the solvation of an electron in bulk methanol is similar to that in water in that the electron resides in a roughly spherical s-type ground state of  $\sim 2.5 \text{ \AA}$  radius surrounded by approximately six methanol molecules in the first solvent shell with mostly O–H bond orientation and followed by three localized, nondegenerate p-like excited states.<sup>44</sup> As in normal bulk liquid water, the absorption spectrum is dominated by three bound-bound  $s \rightarrow p$  transitions resulting in a single, broad, asymmetric, and structureless band centered at

$E_{\text{Amax}} = 1.97 \text{ eV}$  ( $630 \text{ nm}$ ) at  $25^\circ\text{C}$ .<sup>25,44,45</sup> Since measurements of the electronic absorption spectra of size-selected methanol anion clusters have not yet been reported, it is not unreasonable, in view of the close relationship between the spectroscopy and dynamics of excess electrons in clusters and bulk solvated electrons in water and methanol, to propose that the linear scaling of  $E_{\text{Amax}}$  with  $n^{-1/3}$  observed for  $(\text{H}_2\text{O})_n^-$ <sup>20,39,41</sup> also applies for  $(\text{CH}_3\text{OH})_n^-$ . Under this assumption,  $E_{\text{Amax}}(n)$  may then simply be written in the same functional form as eq. [3] as follows:

$$[5] \quad E_{\text{Amax}} = -B(T)n^{-1/3} + C(T)$$

where the coefficients  $B$  and  $C$  depend on the temperature. Obviously, as  $n \rightarrow \infty$ ,  $(\text{CH}_3\text{OH})_n^-$  clusters accommodating internal electron states (methanol I) will grow into bulk solvated electrons as a constraint on the properties of  $e_{\text{sol}}^-$ . In other words, the  $n^{-1/3}$  plot of  $E_{\text{Amax}}$  for those clusters should extrapolate meaningfully to the bulk solvated electron absorption value,<sup>25,44,45</sup> implying that in ambient methanol  $C(25^\circ\text{C}) \sim 1.97 \text{ eV}$ . Combining eqs. [1] and [5] would offer a potentially useful method (see eq. [4] of ref. 20) for predicting the *average* size of a methanol anion cluster at a given temperature for any value of the density. Since  $B(T)$  is unknown at this stage for  $(\text{CH}_3\text{OH})_n^-$ , we are left to speculate that the cluster size values in SCM are comparable to those estimated<sup>20</sup> in supercritical  $\text{D}_2\text{O}$  (at  $400^\circ\text{C}$ , we estimated that  $n$  decreases from  $\sim 32$  to  $26$  for a change in density from  $\sim 0.65$  to  $0.2 \text{ g/cm}^3$ ). These values are not inconsistent with the most recent molecular dynamics simulations of Krishtal et al.,<sup>32</sup> who found  $n \sim 15\text{--}20$  for near-critical methanol at  $\sim 212^\circ\text{C}$  and  $\rho = 0.65 \text{ g/cm}^3$ . Overall, one can assume that just as in water, the amplitudes of density fluctuations (or sizes of existing clusters) in subcritical methanol and SCM are *sufficiently large* to ensure internalized electron capture and solvation.

Some discussion, based on the above microscopic arguments, should be added here with regard to the temperature and density dependences of  $E_{\text{Amax}}$  in the vicinity of the critical point. As demonstrated in Fig. 3, at fixed pressure  $E_{\text{Amax}}$  decreases with increasing temperature, which means that the excess electron is less solvated or, in other words, that the average cluster size of  $(\text{CH}_3\text{OH})_n^-$  decreases. On the other hand, Fig. 5 indicates that at a fixed temperature  $E_{\text{Amax}}$  shifts (slightly) to higher energies as the pressure increases, implying the formation of larger cluster anions. These results can be used to explain, at least partly, the behavior of  $E_{\text{Amax}}$  as a function of temperature at two constant bulk densities as shown in Fig. 1. In fact, the observed decrease in  $E_{\text{Amax}}$  when the temperature is raised in the subcritical region can readily be attributed to a (gradual) decrease in hydrogen bonding with increasing temperature,<sup>32</sup> which results in a decrease of the average size of the existing clusters. Therefore, in these conditions, the “structure-breaking” effect of the temperature (i.e., the higher temperature causes the cluster size to decrease) dominates the “structure-making” effect of the pressure (i.e., the higher pressure required to keep the density constant while increasing the temperature works toward an increase in the cluster size). However, above the critical point, the competition between the structure-breaking and -making effects (in other words, the decrease and increase in the cluster size) of the temperature

and pressure appears to be inverted. In fact, on the basis of our experimental results, we are led to conclude that the structure-making effect of the pressure is larger above  $T_c$ . These findings are interesting in the sense that they can shed some light on the size of clusters as temperature increases at constant bulk density (actually, we know of no published work on this subject). As originally proposed by Jortner and Gaathon,<sup>31</sup> a “snowball effect” could explain the variation of  $E_{A_{\max}}$  vs temperature at constant bulk density in SCM (just as in SCW). In this regard, such an effect would likely induce an increased pressure-dependent *local* clustering around the initially formed charged cluster, leading to cluster growth. Obviously, the existence of this effect, and especially its dependence on the thermodynamic (temperature and pressure) conditions and its time scale, would certainly deserve further investigation. Quantum-classical molecular dynamics simulations of the excess electron-binding structures at play in SCM (and SCW) would likely be of great help to better understand the detailed atomistic picture underlying these findings. Finally, as seen in Fig. 2, holding density constant, the presence of a small amount of water in methanol affects the spectral peak positions  $E_{A_{\max}}$ , which indicates that the density of the *bulk* methanol is *not* the most important variable in determining the position of the  $e_{\text{sol}}^-$  absorption maximum at temperatures that are near-critical or higher. What, in fact, plays a crucial role in the determination of  $E_{A_{\max}}$  in the sub- and super-critical regions is the *extension* of the microscopic changes in the fluid structure (i.e., the amplitude of density fluctuations or, alternatively, the size of pre-existing methanol clusters to which the electron is confined).<sup>20</sup>

## Conclusion

In this study, we measured the absorption spectra of the solvated electron in sub- and super-critical methanol at different temperatures (in the range of ~220 to 270 °C) and densities (or pressures) using electron pulse radiolysis and laser photolysis techniques. Over the density range studied (~0.45–0.59 g/cm<sup>3</sup>), the  $e_{\text{sol}}^-$  absorption maximum is found to shift only slightly to the red with decreasing density, in agreement with our previous work in water. The data show that  $E_{A_{\max}}$  varies linearly (in a double logarithmic plot) with density for the temperature investigated (namely, 245 °C) and that the resulting lines are nearly the same for methanol (99.8%) and dehydrated methanol (within the experimental uncertainties). It is also shown that above the critical temperature, the values of  $E_{A_{\max}}$  in dehydrated methanol are higher than those in 1 mol% water–methanol solutions, indicating that in the supercritical state there is a change in the intermolecular structure of the solvent at the excess electron site caused by the addition of a small amount of water to the alcohol. The temperature dependence of  $E_{A_{\max}}$  in sub- and super-critical methanol further reveals that at a fixed pressure (20 MPa),  $E_{A_{\max}}$  decreases monotonically with increasing temperature while passing through the liquid-supercritical phase transition at  $T_c$ , but exhibits a minimum at fixed densities (0.50 and 0.55 g/cm<sup>3</sup>) as the methanol passes above  $T_c$  into SCM. These behaviors can be understood by means of simple microscopic arguments based on the changes that occur in the methanol properties and methanol structure in the

sub- and super-critical regimes. Most importantly, the role of local density and molecular configurational fluctuations (associated with criticality) in providing pre-existing polymeric clusters, which act as trapping sites for the excess electron, is a pivotal point in the interpretation of the data.

## Acknowledgments

We thank the Linac Division staff for their help during the pulse radiolysis experiments. We gratefully acknowledge the support of the Ministry of Education, Culture, Sports, Science, and Technology (MEXT) of Japan, and the Japan Atomic Energy Agency. J.-P. J.-G. also thanks the Natural Sciences and Engineering Research Council of Canada (NSERC), Natural Resources Canada, and Atomic Energy of Canada Limited for financial support.

## References

- (1) Parsons, E. J. *CHEMTECH* **1996**, 26, 30.
- (2) Randall, L. G. *Sep. Sci. Technol.* **1982**, 17 (1), 1. doi:10.1080/01496398208058142.
- (3) Akiya, N.; Savage, P. E. *Chem. Rev.* **2002**, 102 (8), 2725. doi:10.1021/cr000668w. PMID:12175266.
- (4) Tester, J. W.; Holgate, H. R.; Armellini, F. J.; Webley, P. A.; Killilea, W. R.; Hong, G. T.; Barner, H. E. In *Emerging Technologies in Hazardous Waste Management III*; Tedder, D. W., Pohland, F. G., Eds.; ACS Symposium Series No. 518; American Chemical Society, Washington, DC, 1993; p 35.
- (5) Jessop, P. G.; Ikariya, T.; Noyori, R. *Nature* **1994**, 368 (6468), 231. doi:10.1038/368231a0.
- (6) Eckert, C. A.; Knutson, B. L.; Debenedetti, P. G. *Nature* **1996**, 383 (6598), 313. doi:10.1038/383313a0.
- (7) Darr, J. A.; Poliakoff, M. *Chem. Rev.* **1999**, 99 (2), 495. doi:10.1021/cr970036i. PMID:11848991.
- (8) Savage, P. E. *Chem. Rev.* **1999**, 99 (2), 603. doi:10.1021/cr9700989. PMID:11848994.
- (9) Savage, P. E.; Gopalan, S.; Mizan, T. I.; Martino, C. J.; Brock, E. E. *AIChE J.* **1995**, 41 (7), 1723. doi:10.1002/aic.690410712.
- (10) (a) Hart, E. J.; Boag, J. W. *J. Am. Chem. Soc.* **1962**, 84 (21), 4090. doi:10.1021/ja00880a025.; (b) Boag, J. W.; Hart, E. J. *Nature* **1963**, 197 (4862), 45. doi:10.1038/197045a0.
- (11) Keene, J. P. *Nature* **1963**, 197 (4862), 47. doi:10.1038/197047a0.
- (12) Ferry, J. L.; Fox, M. A. *J. Phys. Chem. A* **1998**, 102 (21), 3705. doi:10.1021/jp973471p.
- (13) Takahashi, K.; Cline, J. A.; Bartels, D. M.; Jonah, C. D. *Rev. Sci. Instrum.* **2000**, 71 (9), 3345. doi:10.1063/1.1288258.
- (14) Amita, F.; Okada, K.; Oka, H.; Kajimoto, O. *Rev. Sci. Instrum.* **2001**, 72 (9), 3605. doi:10.1063/1.1389494.
- (15) Han, Z.; Katsumura, Y.; Lin, M.; He, H.; Muroya, Y.; Kudo, H. *Chem. Phys. Lett.* **2005**, 404 (4–6), 267. doi:10.1016/j.cplett.2005.01.095.
- (16) Mostafavi, M.; Lin, M.; He, H.; Muroya, Y.; Katsumura, Y. *Chem. Phys. Lett.* **2004**, 384 (1–3), 52. doi:10.1016/j.cplett.2003.12.012.
- (17) Mostafavi, M.; Lin, M.; Wu, G.; Katsumura, Y.; Muroya, Y. *J. Phys. Chem. A* **2002**, 106 (13), 3123. doi:10.1021/jp012853z.
- (18) Wu, G.; Katsumura, Y.; Muroya, Y.; Li, X.; Terada, Y. *Chem. Phys. Lett.* **2000**, 325 (5–6), 531. doi:10.1016/S0009-2614(00)00688-6.
- (19) Han, Z.; Katsumura, Y.; Lin, M.; He, H.; Muroya, Y.; Kudo,

- H. *Radiat. Phys. Chem.* **2008**, *77* (4), 409. doi:10.1016/j.radphyschem.2007.05.015.
- (20) Jay-Gerin, J.-P.; Lin, M.; Katsumura, Y.; He, H.; Muroya, Y.; Meesungnoen, J. *J. Chem. Phys.* **2008**, *129* (11), 114511. doi:10.1063/1.2978955. PMID:19044973.
- (21) Boutin, A.; Spezia, R.; Coudert, F.-X.; Mostafavi, M. *Chem. Phys. Lett.* **2005**, *409* (4-6), 219. doi:10.1016/j.cplett.2005.05.012.
- (22) Lin, M.; Kumagai, Y.; Lampre, I.; Coudert, F.-X.; Muroya, Y.; Boutin, A.; Mostafavi, M.; Katsumura, Y. *J. Phys. Chem. A* **2007**, *111* (18), 3548. doi:10.1021/jp070615j. PMID:17429955.
- (23) Lin, M.; Katsumura, Y.; Muroya, Y.; He, H. *Indian J. Radiat. Res.* **2006**, *3*, 69.
- (24) Fox, M. F.; Hayon, E. *J. Chem. Soc., Faraday Trans. I* **1977**, *73*, 1003. doi:10.1039/f19777301003.
- (25) Herrmann, V.; Krebs, P. *J. Phys. Chem.* **1995**, *99* (18), 6794. doi:10.1021/j100018a007.
- (26) Linstrom, P. J.; Mallard, W. G., Eds. *NIST Chemistry Web-Book*; NIST Standard Reference Database No. 69; National Institute of Standards and Technology, Gaithersburg, MD, 2005. Available from <http://webbook.nist.gov>.
- (27) (a) Leu, A.-D.; Jha, K. N.; Freeman, G. R. *Can. J. Chem.* **1982**, *60* (18), 2342. doi:10.1139/v82-334.; (b) Leu, A.-D.; Jha, K. N.; Freeman, G. R. *Can. J. Chem.* **1983**, *61* (6), 1115. doi:10.1139/v83-199.
- (28) Bernas, A.; Ferradini, C.; Jay-Gerin, J.-P. *Can. J. Chem.* **1996**, *74* (1), 1. doi:10.1139/v96-001.
- (29) Olinger, R.; Schindewolf, U.; Gaathon, A.; Jortner, J. *Ber. Bunsenges. Phys. Chem.* **1971**, *75*, 690.
- (30) Olinger, R.; Hahne, S.; Schindewolf, U. *Ber. Bunsenges. Phys. Chem.* **1972**, *76*, 349.
- (31) Jortner, J.; Gaathon, A. *Can. J. Chem.* **1977**, *55* (11), 1801. doi:10.1139/v77-253.
- (32) The structure of SCM and the details of hydrogen bonding at the molecular level have been investigated by various methods, including computer simulations. These investigations, however, are much less complete than for water. See, for example: (a) Asahi, N.; Nakamura, Y. *J. Chem. Phys.* **1998**, *109*, 9879. doi:10.1063/1.477656.; (b) Hoffmann, M. M.; Conradi, M. S. *J. Phys. Chem. B* **1998**, *102* (1), 263. doi:10.1021/jp9726706.; (c) Chalaris, M.; Samios, J. *J. Phys. Chem. B* **1999**, *103* (7), 1161. doi:10.1021/jp982559f.; (d) Yamaguchi, T.; Benmore, C. J.; Soper, A. K. *J. Chem. Phys.* **2000**, *112* (20), 8976. doi:10.1063/1.481530.; (e) Andanson, J.-M.; Bopp, Ph. A.; Soetens, J.-C. *J. Mol. Liq.* **2006**, *129* (1-2), 101. doi:10.1016/j.molliq.2006.08.019.; (f) Krishtal, S.; Kiselev, M.; Kolker, A.; Idrissi, A. *Theor. Chem. Acc.* **2007**, *117* (2), 297. doi:10.1007/s00214-006-0140-2.
- (33) Desfrancois, C.; Abdoul-Carime, H.; Khelifa, N.; Schermann, J. P.; Brenner, V.; Millie, P. *J. Chem. Phys.* **1995**, *102* (12), 4952. doi:10.1063/1.469543.
- (34) Turi, L. *J. Chem. Phys.* **1999**, *110* (21), 10364. doi:10.1063/1.478969.
- (35) Kammrath, A.; Verlet, J. R. R.; Griffin, G. B.; Neumark, D. M. *J. Chem. Phys.* **2006**, *125* (17), 171102. doi:10.1063/1.2355484. PMID:17100420.
- (36) Kammrath, A.; Griffin, G. B.; Verlet, J. R. R.; Young, R. M.; Neumark, D. M. *J. Chem. Phys.* **2007**, *126* (24), 244306. doi:10.1063/1.2747618. PMID:17614548.
- (37) Neumark, D. M. *Mol. Phys.* **2008**, *106* (16), 2183. doi:10.1080/00268970802279555.
- (38) Armbruster, M.; Haberland, H.; Schindler, H.-G. *Phys. Rev. Lett.* **1981**, *47* (5), 323. doi:10.1103/PhysRevLett.47.323.
- (39) Coe, J. V. *Int. Rev. Phys. Chem.* **2001**, *20* (1), 33. doi:10.1080/01442350010008589.
- (40) Coe, J. V.; Williams, S. M.; Bowen, K. H. *Int. Rev. Phys. Chem.* **2008**, *27* (1), 27. doi:10.1080/01442350701783543.
- (41) Ayotte, P.; Johnson, M. A. *J. Chem. Phys.* **1997**, *106* (2), 811. doi:10.1063/1.473167.
- (42) Hart, E. J.; Anbar, M. *The Hydrated Electron*; Wiley: New York, 1970; p 39.
- (43) Recall here that PES of  $(\text{H}_2\text{O})_n^-$  identified (at least) three different water-cluster anion isomers over a large range of cluster sizes, namely, an internally hydrated electron isomer and two kinds of surface-localized electron isomers (differing primarily in the molecular nature of the electron-binding site). See, for example: (a) Coe, J. V.; Arnold, S. T.; Eaton, J. G.; Lee, G. H.; Bowen, K. H. *J. Chem. Phys.* **2006**, *125* (1), 014315. doi:10.1063/1.2212415. PMID:16863306.; (b) Verlet, J. R. R.; Bragg, A. E.; Kammrath, A.; Cheshnovsky, O.; Neumark, D. M. *Science* **2005**, *307* (5706), 93. doi:10.1126/science.1106719. PMID:15604360.; (c) Kim, J.; Becker, I.; Cheshnovsky, O.; Johnson, M. A. *Chem. Phys. Lett.* **1998**, *297* (1-2), 90. doi:10.1016/S0009-2614(98)01109-9.
- (44) (a) Turi, L.; Mosyak, A.; Rossy, P. J. *J. Chem. Phys.* **1997**, *107* (6), 1970. doi:10.1063/1.474549.; (b) Zhu, J.; Cukier, R. I. *J. Chem. Phys.* **1993**, *98* (7), 5679. doi:10.1063/1.464883.; (c) Feng, D.-F.; Kevan, L. *Chem. Rev.* **1980**, *80* (1), 1. doi:10.1021/cr60323a001.; (d) Kevan, L. *Radiat. Phys. Chem.* **1981**, *17*, 413.
- (45) Jay-Gerin, J.-P.; Ferradini, C. *J. Chim. Phys.* **1994**, *91*, 173 and references therein.



# Surface-mediated synthesis of organophosphorus-based hydrazides using basic alumina

Kavita, P. Joshi, N. Sharma, and Y.C. Joshi

**Abstract:** The surface-mediated synthesis of *O*-alkyl alkylphosphorohydrazides and *N,N*-dialkylamino alkylphosphorohydrazides from phosphoryl chlorides is described. The effect of the presence of chromatographic-grade  $\text{Al}_2\text{O}_3$  (basic) on the hydrazinolysis of a series of *O*-alkyl alkylphosphonic chlorides and *N,N*-dialkylamino alkylphosphonic chlorides has also been investigated. It was observed that higher yields of the less-hindered hydrazides were obtained

**Key words:** *O*-alkyl alkylphosphonic chlorides, *N,N*-dialkylamino alkylphosphoric chlorides, phosphorohydrazides, surface mediated,  $\text{Al}_2\text{O}_3$  (basic).

**Résumé :** On décrit une méthode de synthèse catalysée par la surface de *O*-alkylphosphorohydrazides et de *N,N*-dialkylaminoalkylphosphorohydrazides à partir de chlorures du phosphoryle. On a aussi étudié l'effet de la présence d'alumine,  $\text{Al}_2\text{O}_3$  (basique), de qualité chromatographique sur l'hydrazinolysé d'une série de chlorures d'acides *O*-alkyl alkylphosphoniques et d'acides *N,N*-dialkylamino alkylphosphoniques. Il a été observé que les rendements obtenus sont plus élevés avec les hydrazides les moins encombrées.

**Mots-clés :** chlorures d'acides *O*-alkyl alkylphosphoniques, chlorures d'acides *N,N*-dialkylamino alkylphosphoniques,  $\text{Al}_2\text{O}_3$  (basique).

## Introduction

The chemistry of organophosphorus compounds is a rapidly developing area of research because of their importance in industrial, agricultural, biochemical, and medicinal applications.<sup>1</sup> It is interesting to note that the variation in their physical, chemical, and biological properties is governed by the selection of the group attached to the phosphorus atom. Although phosphorous compounds containing the P–C bond are not abundant in nature, they have diverse range of biological activity and have attracted considerable synthetic and pharmacological interest.<sup>2</sup>

Hydrazides are versatile intermediates for the synthesis of hydrazones,<sup>3</sup> pyrazoles,<sup>4</sup> and various heterocyclic compounds.<sup>5</sup> It is well known that hydrazides play an important role in antimicrobial activity. Furthermore, a number of hydrazide derivatives have been reported to possess interesting antibacterial, antifungal,<sup>6–8</sup> anticonvulsant,<sup>9,10</sup> anti-inflammatory,<sup>11,12</sup> antimalarial,<sup>13</sup> and antituberculosis activities.<sup>3,14–18</sup>

Several methods have been reported in the literature for the synthesis of hydrazides.<sup>19</sup> However, the synthesis of phosphorohydrazides has not been fully explored. There have been only a few reports on the synthesis of phosphorohydrazides, and these have several drawbacks such as the use of carcinogenic solvents, long reaction times, and formation of several by-products.

Surface-mediated solid-phase reactions are of growing interest<sup>20</sup> in the synthesis of hydrazides because of their ease

of execution and work-ups, mild reaction conditions, fast rate of reactions, selectivity, higher yields, solvent-less reaction conditions, and low cost in comparison with their homogeneous counterparts.<sup>21–23</sup> Chromatographic grade  $\text{Al}_2\text{O}_3$  (basic) has many applications as a heterogeneous catalyst either by itself or, more commonly, as a support for other reagents.<sup>20</sup> There have been only a few reports, however, on the use of  $\text{Al}_2\text{O}_3$  as a support for substrates, despite the fact that novel, synthetically useful, reactions have been observed under these conditions. Symmetrical functional substrates adsorb to the surface of  $\text{Al}_2\text{O}_3$  via a functional group. The other reactant selectively attaches to the alumina surface by reaction with the free functional group. This prompted us to explore the utility of a surface-mediated reaction for the synthesis of title compounds, in continuation of our ongoing research program to develop new synthetic methods for antibacterial compounds.<sup>24</sup> We have synthesized various *O*-alkyl alkylphosphorohydrazides and *N,N*-dialkylaminophosphonohydrazides **3a–3p**.

## Results and discussion

To test the above proposition, we have carried out the reaction of alkyl phosphonic dichloride **1**<sup>25</sup> with various alcohols and amines in the presence of triethylamine at 0 °C followed by heating at 50 °C. This reaction gave *O*-alkyl- and *N,N*-dialkylamino alkylphosphonic chlorides **2a–2p**.<sup>26</sup>

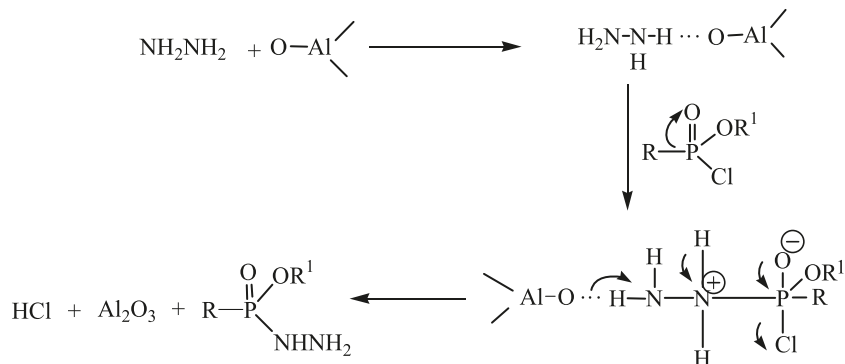
After obtaining the intermediates **2a–2p**, we optimized the

Received 3 March 2010. Accepted 20 July 2010. Published on the NRC Research Press Web site at canjchem.nrc.ca on 2 October 2010.

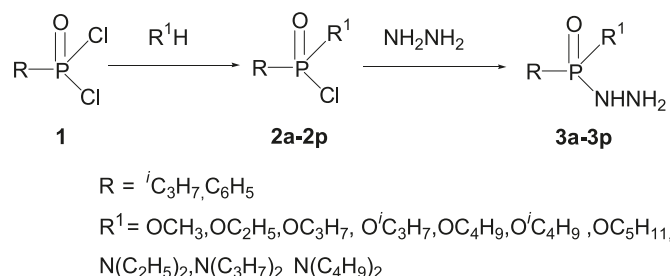
Kavita,<sup>1</sup> N. Sharma, and Y.C. Joshi. Department of Chemistry, University of Rajasthan, Jaipur 302004, India.  
P. Joshi. S.S. Jain Subodh P.G. College, Jaipur, India.

<sup>1</sup>Corresponding author (e-mail: drkavitaraj@rediffmail.com).



**Scheme 1.** Proposed mechanism for the synthesis of phosphonohydrazides on alumina.

reaction conditions to obtain phosphorohydrazides. In this regard, several reactions of *O*-methyl isopropylphosphonic chloride with various reagents such as neutral  $\text{Al}_2\text{O}_3$ , basic  $\text{Al}_2\text{O}_3$ , acidic  $\text{Al}_2\text{O}_3$ ,  $\text{SiO}_2$ ,  $\text{ZnO}$ , and  $\text{ZnO-SiO}_2$  were performed as model reactions. Maximum yield was obtained when basic  $\text{Al}_2\text{O}_3$  was used. Further, to optimize the molar ratio of basic  $\text{Al}_2\text{O}_3$ , various reactions of *O*-methyl isopropylphosphonic chloride were also performed by changing the mole ratio of basic  $\text{Al}_2\text{O}_3$ , reaction time, and temperature. These reactions were monitored through TLC and  $^{31}\text{P}$  NMR. Best results were obtained when the model reaction was performed with basic  $\text{Al}_2\text{O}_3$  and *O*-methyl isopropylphosphonic chloride in the mole ratio of 1:1 at  $60^\circ\text{C}$  for 30 min.



After optimization, the general applicability of the method was applied with diversity in structures **2a–2p** and results of the reactions are summarized in Table 1. All the compounds **3a–3p** were characterized by spectroscopic techniques such as FTIR,  $^{31}\text{P}$  NMR, LC–MS, and elemental analysis. The FTIR spectra showed the presence of NH bands at 3320, 3260 ( $\text{NH}_2$ ), and 3140 (*sec*-amine). It is worth noticing that the  $^{31}\text{P}$  NMR signal of *O*-alkyl alkylphosphonochloridates **2a–2p** disappeared and a new signal appeared in the range of 19–42 ppm for **3a–3p**. The results of other analysis **3a–3p** are compiled in the Experimental section.

## Experimental

### General

Melting points were determined on a hot stage microscope and are uncorrected. IR spectra were recorded on FTIR spectrometer model Jasco 610 on KBr pellets.  $^1\text{H}$ ,  $^{13}\text{C}$ , and  $^{31}\text{P}$  NMR spectra were recorded in  $\text{CDCl}_3$  on Bruker FTNMR at 400, 100, and 162 MHz, respectively, using tetramethylsilane as an internal standard for  $^1\text{H}$  and 85%

$\text{H}_3\text{PO}_4$  as an external standard for  $^{31}\text{P}$  NMR. Mass spectra were performed on a LCMS. Satisfactory C, H, N analyses were obtained for all the compounds.

### General procedure for the preparation of *O*-methyl isopropylphosphorohydrazide 3a

In a typical experimental procedure, basic activated alumina (1.0 g, 0.01 mol/L) was mixed with hydrazine hydrate 99% (0.32 g, 0.01 mol/L) in a mortar and pestle. It was ground for 5 min. at room temperature. The mixture was transferred into a single-necked flask and sealed with rubber septum, and then *O*-methyl isopropylphosphonic chloride (1.55 g, 0.01 mol/L) was added through a syringe at  $0^\circ\text{C}$ . The resultant dispersion was shaken occasionally at room temperature followed by heating at  $60^\circ\text{C}$  for 30 min. The reaction mixture was monitored using TLC and GC by drawing a few milligrams of the mixture and suspending it in 1 mL of diethyl ether. After completion of the reaction, the reaction mixture was extracted in dichloromethane and filtered. The solvent was removed and the residue was crystallized with diethyl ether.

### *O*-Methyl isopropylphosphorohydrazide 3a

IR  $\nu_{\text{max}}$  ( $\text{cm}^{-1}$ ): 3320, 3265 (N–H), 3140 (N–H), 2890 (C–H), 1235 (P=O), 1090 (P–O–C), 695 (P–C).  $^1\text{H}$  NMR  $\delta$ : 1.10 (dd,  $^3J(\text{PH}) = 21.4$  Hz, 6H,  $\text{CH}_3$ ), 2.05 (m,  $^2J(\text{PH}) = 17.3$  Hz, 1H, CH), 2.92 (br s, 2H,  $\text{NH}_2$ ), 3.95 (s,  $^3J(\text{PH}) = 19.4$  Hz, 3H,  $\text{CH}_3$ ), 4.22 (d,  $^2J(\text{PH}) = 18.5$  Hz, 1H, NH).  $^{13}\text{C}$  NMR  $\delta$ : 15.85 ( $\text{CH}_3$ ), 26.78 (CH), 62.58 ( $\text{CH}_3$ ). LCMS (EI)  $m/z$ : 153 ( $\text{M} + \text{H}^+$ ). Anal. calcd. for  $\text{C}_4\text{H}_{13}\text{N}_2\text{O}_2\text{P}$ : C 31.58, H 8.61, N 18.41; found: C 31.50, H 8.58, N 18.35.

### *O*-Ethyl isopropylphosphorohydrazide 3b

IR  $\nu_{\text{max}}$  ( $\text{cm}^{-1}$ ): 3325, 3260 (N–H), 3145 (N–H), 2885 (C–H), 1230 (P=O), 1090 (P–O–C), 697 (P–C).  $^1\text{H}$  NMR  $\delta$ : 1.05 (dd,  $^3J(\text{PH}) = 21.4$  Hz, 6H,  $\text{CH}_3$ ), 1.15 (t,  $J = 7.8$  Hz, 3H,  $\text{CH}_3$ ), 2.05 (m,  $^2J(\text{PH}) = 17.5$  Hz, 1H, CH), 2.95 (br s, 2H,  $\text{NH}_2$ ), 3.90 (q,  $^3J(\text{PH}) = 19.7$  Hz, 2H,  $\text{CH}_2$ ), 4.20 (d,  $^2J(\text{PH}) = 18.5$  Hz, 1H, NH).  $^{13}\text{C}$  NMR  $\delta$ : 15.85 ( $\text{CH}_3$ ), 17.25 ( $\text{CH}_3$ ), 26.78 (CH), 62.58 ( $\text{CH}_2$ ). LCMS (EI)  $m/z$ : 167 ( $\text{M} + \text{H}^+$ ). Anal. calcd. for  $\text{C}_5\text{H}_{15}\text{N}_2\text{O}_2\text{P}$ : C 36.14, H 9.10, N 16.86; found: C 36.15, H 9.05, N 16.83.

### *O*-Propyl isopropylphosphorohydrazide 3c

IR  $\nu_{\text{max}}$  ( $\text{cm}^{-1}$ ): 3320, 3270 (N–H), 3150 (N–H), 2905 (C–H), 1240 (P=O), 1085 (P–O–C), 705 (P–C).  $^1\text{H}$  NMR  $\delta$ : 0.95

**Table 1.** Synthesis of *O*-alkyl alkylphosphoro- and *N,N*-dialkylaminophosphonohydrazides (**3a–3p**).

Entry	Product	Reaction time (min)	Yield (%) <sup>a</sup>	Mp (°C)	<sup>31</sup> P NMR (δ ppm) <sup>b</sup>
<b>3a</b>		30	80.5	45	39.04
<b>3b</b>		30	81.7	52	38.18
<b>3c</b>		30	82.6	63	40.79
<b>3d</b>		35	82.4	66	40.83
<b>3e</b>		40	85.5	70	39.65
<b>3f</b>		35	70.7	59	19.74
<b>3g</b>		35	71.8	63	23.41
<b>3h</b>		40	72.6	62	22.28
<b>3i</b>		40	75.4	69	23.52
<b>3j</b>		40	81.3	76	23.28
<b>3k</b>		30	81.5	56	41.19
<b>3l</b>		35	75.7	65	40.41
<b>3m</b>		40	82.9	72	40.51
<b>3n</b>		35	70.5	67	23.37
<b>3o</b>		40	81.8	81	23.81
<b>3p</b>		45	78.7	83	25.76

<sup>a</sup> Isolated yield.<sup>b</sup> <sup>31</sup>P NMR spectra were recorded in CDCl<sub>3</sub> at 162 MHz.

(t,  $J = 7.8$  Hz, 3H, CH<sub>3</sub>), 1.10 (dd,  $^3J(\text{PH}) = 21.5$  Hz, 6H, CH<sub>3</sub>), 1.15 (m,  $J = 7.9$  Hz, 3H, CH<sub>2</sub>), 2.05 (m,  $^2J(\text{PH}) = 17.5$  Hz, 1H, CH), 3.07 (br s, 2H, NH<sub>2</sub>), 3.95 (q,  $^3J(\text{PH}) = 19.4$  Hz, 2H, CH<sub>2</sub>), 4.25 (d,  $^2J(\text{PH}) = 18.7$  Hz, 1H, NH). <sup>13</sup>C NMR  $\delta$ : 15.93 (CH<sub>3</sub>), 17.23 (CH<sub>3</sub>), 22.58 (CH<sub>2</sub>), 26.80 (CH), 62.70 (CH<sub>2</sub>). LCMS (EI)  $m/z$ : 181 (M + H<sup>+</sup>). Anal. calcd. for C<sub>6</sub>H<sub>17</sub>N<sub>2</sub>O<sub>2</sub>P: C 39.99, H 9.15, N 15.55; found: C 39.95, H 9.17, N 15.53.

#### ***O*-Butyl isopropyl phosphorohydrazide 3d**

IR  $\nu_{\text{max}}$  (cm<sup>-1</sup>): 3315, 3240 (N–H), 3160 (N–H), 2897 (C–H), 1239 (P=O), 1090 (P–O–C), 697 (P–C). <sup>1</sup>H NMR  $\delta$ : 0.95 (t,  $J = 8.2$  Hz, 3H, CH<sub>3</sub>), 1.07 (dd,  $^3J(\text{PH}) = 22.3$  Hz, 6H, CH<sub>3</sub>), 1.15 (m,  $J = 7.9$  Hz, 3H, CH<sub>2</sub>), 1.28 (m,  $J = 7.6$  Hz, 3H, CH<sub>2</sub>), 2.05 (m,  $^2J(\text{PH}) = 17.3$  Hz, 1H, CH), 2.92 (br s, 2H, NH<sub>2</sub>), 4.05 (q,  $^3J(\text{PH}) = 19.4$  Hz, 2H, CH<sub>2</sub>), 4.27 (d,  $^2J(\text{PH}) = 18.5$  Hz, 1H, NH). <sup>13</sup>C NMR  $\delta$ : 15.80 (CH<sub>3</sub>), 17.23 (CH<sub>3</sub>), 23.60 (CH<sub>2</sub>), 25.85 (CH<sub>2</sub>), 26.98 (CH), 62.45 (CH<sub>2</sub>). LCMS (EI)  $m/z$ : 195 (M + H<sup>+</sup>). Anal. calcd. for C<sub>7</sub>H<sub>19</sub>N<sub>2</sub>O<sub>2</sub>P: C 43.29, H 9.86, N 14.42; found: C 43.30, H 9.81, N 14.43.

#### ***O*-Pentyl isopropylphosphorohydrazide 3e**

IR  $\nu_{\text{max}}$  (cm<sup>-1</sup>): 3325, 3260 (N–H), 3170 (N–H), 2907 (C–H), 1245 (P=O), 1095 (P–O–C), 705 (P–C). <sup>1</sup>H NMR  $\delta$ : 0.95 (t,  $J = 7.9$  Hz, 3H, CH<sub>3</sub>), 1.07 (dd,  $^3J(\text{PH}) = 21.4$  Hz, 6H, CH<sub>3</sub>), 1.18 (m,  $J = 7.3$  Hz, 3H, CH<sub>2</sub>), 1.25 (m,  $J = 8.5$  Hz, 3H, CH<sub>2</sub>), 1.35 (m,  $J = 8.3$  Hz, 3H, CH<sub>2</sub>), 2.05 (m,  $^2J(\text{PH}) = 17.6$  Hz, 1H, CH), 2.92 (br s, 2H, NH<sub>2</sub>), 3.95 (q,  $^3J(\text{PH}) = 19.5$  Hz, 2H, CH<sub>2</sub>), 4.15 (d,  $^2J(\text{PH}) = 18.2$  Hz, 1H, NH). <sup>13</sup>C NMR  $\delta$ : 15.90 (CH<sub>3</sub>), 17.20 (CH<sub>3</sub>), 21.89 (CH<sub>2</sub>), 22.26 (CH<sub>2</sub>), 25.85 (CH<sub>2</sub>), 26.58 (CH), 62.54 (CH<sub>2</sub>). LCMS (EI)  $m/z$ : 209 (M + H<sup>+</sup>). Anal. calcd. for C<sub>8</sub>H<sub>21</sub>N<sub>2</sub>O<sub>2</sub>P: C 46.14, H 10.16, N 13.45; found: C 46.15, H 10.15, N 13.43.

#### ***O*-Ethyl phenylphosphorohydrazide 3f**

IR  $\nu_{\text{max}}$  (cm<sup>-1</sup>): 3320, 3260 (N–H), 3140 (N–H), 2890 (C–H), 1235 (P=O), 1090 (P–O–C), 695 (P–C). <sup>1</sup>H NMR  $\delta$ : 1.15 (t,  $^3J(\text{PH}) = 21.4$  Hz, 3H, CH<sub>3</sub>), 2.85 (br s, 2H, NH<sub>2</sub>), 4.15 (q,  $^3J(\text{PH}) = 19.4$  Hz, 2H, CH<sub>2</sub>), 4.22 (d,  $^3J(\text{PH}) = 18.5$  Hz, 1H, NH), 7.25–7.50 (m, 5H, C<sub>6</sub>H<sub>5</sub>). <sup>13</sup>C NMR  $\delta$ : 15.85 (CH<sub>3</sub>), 62.58 (CH<sub>2</sub>), 172–178 (Ar–C). LCMS (EI)  $m/z$ : 201 (M + H<sup>+</sup>). Anal. calcd. for C<sub>8</sub>H<sub>13</sub>N<sub>2</sub>O<sub>2</sub>P: C 48.00, H 6.55, N 13.99; found: C 48.05, H 6.51, N 13.95.

#### ***O*-Propyl phenylphosphorohydrazide 3g**

IR  $\nu_{\text{max}}$  (cm<sup>-1</sup>): 3320, 3260 (N–H), 3140 (N–H), 2890 (C–H), 1235 (P=O), 1090 (P–O–C), 695 (P–C). <sup>1</sup>H NMR  $\delta$ : 1.15 (t,  $J = 6.5$  Hz, 3H, CH<sub>3</sub>), 1.35 (q,  $J = 7.4$  Hz, 2H, CH<sub>2</sub>), 2.85 (br s, 2H, NH<sub>2</sub>), 4.15 (q,  $^3J(\text{PH}) = 19.4$  Hz, 2H, CH<sub>2</sub>), 4.22 (d,  $^3J(\text{PH}) = 18.5$  Hz, 1H, NH), 7.25–7.50 (m, 5H, C<sub>6</sub>H<sub>5</sub>). <sup>13</sup>C NMR  $\delta$ : 15.85 (CH<sub>3</sub>), 22.53 (CH<sub>2</sub>), 62.58 (CH<sub>2</sub>), 172–178 (Ar–C). LCMS (EI)  $m/z$ : 215 (M + H<sup>+</sup>). Anal. calcd. for C<sub>9</sub>H<sub>15</sub>N<sub>2</sub>O<sub>2</sub>P: C 50.46, H 7.06, N 13.08; found: C 50.45, H 7.10, N 13.05.

#### ***O*-Isopropyl phenylphosphorohydrazide 3h**

IR  $\nu_{\text{max}}$  (cm<sup>-1</sup>): 3320, 3260 (N–H), 3140 (N–H), 2890 (C–H), 1235 (P=O), 1090 (P–O–C), 695 (P–C). <sup>1</sup>H NMR  $\delta$ : 1.15 (d,  $J = 6.5$  Hz, 6H, CH<sub>3</sub>), 2.85 (br s, 2H, NH<sub>2</sub>), 4.15 (sextet,  $^3J(\text{PH}) = 19.4$  Hz, 2H, CH), 4.22 (d,  $^3J(\text{PH}) = 18.5$  Hz, 1H,

NH), 7.25–7.50 (m, 5H, C<sub>6</sub>H<sub>5</sub>). <sup>13</sup>C NMR  $\delta$ : 15.85 (CH<sub>3</sub>), 62.58 (CH), 172–178 (Ar–C). LCMS (EI)  $m/z$ : 215 (M + H<sup>+</sup>). Anal. calcd. for C<sub>9</sub>H<sub>15</sub>N<sub>2</sub>O<sub>2</sub>P: C 50.46, H 7.06, N 13.08; found: C 50.45, H 7.10, N 13.05.

#### ***O*-Isobutyl phenylphosphorohydrazide 3i**

IR  $\nu_{\text{max}}$  (cm<sup>-1</sup>): 3320, 3260 (N–H), 3140 (N–H), 2890 (C–H), 1235 (P=O), 1090 (P–O–C), 695 (P–C). <sup>1</sup>H NMR  $\delta$ : 1.15 (d,  $J = 6.5$  Hz, 6H, CH<sub>3</sub>), 1.20 (sextet,  $J = 6.5$  Hz, 1H, CH), 2.85 (br s, 2H, NH<sub>2</sub>), 4.15 (sextet,  $^3J(\text{PH}) = 19.4$  Hz, 2H, CH<sub>2</sub>), 4.22 (d,  $^3J(\text{PH}) = 18.5$  Hz, 1H, NH), 7.25–7.88 (m, 5H, C<sub>6</sub>H<sub>5</sub>). <sup>13</sup>C NMR  $\delta$ : 15.68 (CH<sub>3</sub>), 22.50 (CH), 62.58 (CH<sub>2</sub>), 172–178 (Ar–C). LCMS (EI)  $m/z$ : 229 (M + H<sup>+</sup>). Anal. calcd. for C<sub>10</sub>H<sub>17</sub>N<sub>2</sub>O<sub>2</sub>P: C 52.63, H 7.51, N 12.27; found: C 52.65, H 7.50, N 12.28.

#### ***O*-Pentyl phenylphosphorohydrazide 3j**

IR  $\nu_{\text{max}}$  (cm<sup>-1</sup>): 3309, 3256 (N–H), 3143 (N–H), 2908 (C–H), 1255 (P=O), 1070 (P–O–C), 693 (P–C). <sup>1</sup>H NMR  $\delta$ : 0.95 (t,  $J = 7.8$  Hz, 3H, CH<sub>3</sub>), 1.15 (m,  $J = 8.6$  Hz, 3H, CH<sub>2</sub>), 1.23 (m,  $J = 8.1$  Hz, 3H, CH<sub>2</sub>), 1.37 (m,  $J = 7.4$  Hz, 3H, CH<sub>2</sub>), 2.92 (br s, 2H, NH<sub>2</sub>), 3.97 (q,  $^3J(\text{PH}) = 19.4$  Hz, 2H, CH<sub>2</sub>), 4.56 (d,  $^2J(\text{PH}) = 18.9$  Hz, 1H, NH), 7.25–7.50 (m, 5H, C<sub>6</sub>H<sub>5</sub>). <sup>13</sup>C NMR  $\delta$ : 15.83 (CH<sub>3</sub>), 21.89 (CH<sub>2</sub>), 22.38 (CH<sub>2</sub>), 25.75 (CH<sub>2</sub>), 63.03 (CH<sub>2</sub>), 172–178 (Ar–C). LCMS (EI)  $m/z$ : 243 (M + H<sup>+</sup>). Anal. calcd. for C<sub>8</sub>H<sub>21</sub>N<sub>2</sub>O<sub>2</sub>P: requires C 54.54, H 7.91, N 11.56; found: C 54.52, H 7.93, N 11.55.

#### ***N,N*-Diethylamino isopropylphosphonohydrazide 3k**

IR  $\nu_{\text{max}}$  (cm<sup>-1</sup>): 3340, 3265 (N–H), 3150 (N–H), 2910 (C–H), 1460 (C–N), 1245 (P=O), 1070, 1155 (P–N–C), 705 (P–C). <sup>1</sup>H NMR  $\delta$ : 1.03 (t,  $J = 8.4$  Hz, 6H, CH<sub>3</sub>), 1.15 (dd,  $^3J(\text{PH}) = 22.5$  Hz, 6H, CH<sub>3</sub>), 1.85 (m,  $^2J(\text{PH}) = 16.7$  Hz, 1H, CH), 2.60 (br s, 2H, NH<sub>2</sub>), 3.65 (q,  $^3J(\text{PH}) = 19.4$  Hz, 4H, CH<sub>2</sub>), 4.25 (d,  $^2J(\text{PH}) = 17.9$  Hz, 1H, NH). <sup>13</sup>C NMR  $\delta$ : 16.88 (CH<sub>3</sub>), 17.37 (CH<sub>3</sub>), 26.98 (CH), 42.58 (CH<sub>2</sub>). LCMS (EI)  $m/z$ : 194 (M + H<sup>+</sup>). Anal. calcd. for C<sub>7</sub>H<sub>20</sub>N<sub>3</sub>OP: C 45.51, H 10.43, N 21.75; found: C 45.50, H 10.45, N 21.73.

#### ***N,N*-Dipropylamino isopropylphosphonohydrazide 3l**

IR  $\nu_{\text{max}}$  (cm<sup>-1</sup>): 3327, 3265 (N–H), 3146 (N–H), 2920 (C–H), 1435 (C–N), 1235 (P=O), 1080, 1150 (P–N–C), 703 (P–C). <sup>1</sup>H NMR  $\delta$ : 0.75 (t,  $J = 8.4$  Hz, 6H, CH<sub>3</sub>), 1.15 (dd,  $^3J(\text{PH}) = 21.9$  Hz, 6H, CH<sub>3</sub>), 1.45 (m, 4H, CH<sub>2</sub>), 1.95 (m,  $^2J(\text{PH}) = 17.3$  Hz, 1H, CH), 3.15 (br s, 2H, NH<sub>2</sub>), 3.85 (q,  $^3J(\text{PH}) = 19.8$  Hz, 4H, CH<sub>2</sub>), 3.98 (d,  $^2J(\text{PH}) = 16.5$  Hz, 1H, NH). <sup>13</sup>C NMR  $\delta$ : 15.67 (CH<sub>3</sub>), 17.20 (CH<sub>3</sub>), 22.45 (CH<sub>2</sub>), 27.03 (CH), 41.37 (CH<sub>2</sub>). LCMS (EI)  $m/z$ : 222 (M + H<sup>+</sup>). Anal. calcd. for C<sub>7</sub>H<sub>20</sub>N<sub>3</sub>OP: C 48.85, H 10.93, N 18.99; found: C 48.86, H 10.95, N 18.96.

#### ***N,N*-Dibutylamino isopropylphosphonohydrazide 3m**

IR  $\nu_{\text{max}}$  (cm<sup>-1</sup>): 3320, 3260 (N–H), 3150 (N–H), 2920 (C–H), 1447 (C–N), 1230 (P=O), 1070, 1150 (P–N–C), 693 (P–C). <sup>1</sup>H NMR  $\delta$ : 0.75 (t,  $J = 8.4$  Hz, 6H, CH<sub>3</sub>), 1.10 (dd,  $^3J(\text{PH}) = 21.8$  Hz, 6H, CH<sub>3</sub>), 1.40 (m, 4H, CH<sub>2</sub>), 1.55 (m, 4H, CH<sub>2</sub>), 1.97 (m,  $^2J(\text{PH}) = 16.9$  Hz, 1H, CH), 2.92 (bd s, 2H, NH<sub>2</sub>), 3.15 (q,  $^3J(\text{PH}) = 18.4$  Hz, 4H, CH<sub>2</sub>), 4.20 (d,  $^2J(\text{PH}) = 17.5$  Hz, 1H, NH). <sup>13</sup>C NMR  $\delta$ : 15.85 (CH<sub>3</sub>), 17.23 (CH<sub>3</sub>), 20.45 (CH<sub>2</sub>), 22.45 (CH<sub>2</sub>), 26.78 (CH), 42.58 (CH<sub>2</sub>). LCMS (EI)  $m/z$ : 250 (M + H<sup>+</sup>). Anal. calcd. for

C<sub>7</sub>H<sub>20</sub>N<sub>3</sub>OP: C 52.99, H 11.32, N 16.85; found: C 52.95, H 11.33, N 16.86.

### *N,N*-Diethylamino phenylphosphonohydrazide **3n**

IR  $\nu_{\max}$  (cm<sup>-1</sup>): 3320, 3260 (N–H), 3140 (N–H), 2890 (C–H), 1457 (C–N), 1239 (P=O), 1070, 1150 (P–N–C), 695 (P–C). <sup>1</sup>H NMR  $\delta$ : 1.03 (t,  $J$  = 8.4 Hz, 6H, CH<sub>3</sub>), 2.92 (br s, 2H, NH<sub>2</sub>), 3.95 (q, <sup>3</sup> $J$ (PH) = 17.3 Hz, 4H, CH<sub>2</sub>), 4.15 (d, <sup>2</sup> $J$ (PH) = 17.6 Hz, 1H, NH), 7.25–7.58 (m, 5H, C<sub>6</sub>H<sub>5</sub>). <sup>13</sup>C NMR  $\delta$ : 17.23 (CH<sub>3</sub>), 42.58 (CH<sub>2</sub>), 172–178.27 (Ar–C). LCMS (EI)  $m/z$ : 228 (M + H<sup>+</sup>). Anal. calcd. for C<sub>10</sub>H<sub>18</sub>N<sub>3</sub>OP: C 52.85, H 7.98, N 18.49; found: C 52.87, H 7.96, N 18.47.

### *N,N*-Dipropylamino phenylphosphonohydrazide **3o**

IR  $\nu_{\max}$  (cm<sup>-1</sup>): 3320, 3260 (N–H), 3140 (N–H), 2890 (C–H), 1450 (C–N), 1235 (P=O), 1070, 1150 (P–N–C), 695 (P–C). <sup>1</sup>H NMR  $\delta$ : 0.75 (t,  $J$  = 8.4 Hz, 6H, CH<sub>3</sub>), 1.45 (m, 4H, CH<sub>2</sub>), 2.92 (br s, 2H, NH<sub>2</sub>), 3.95 (q, <sup>3</sup> $J$ (PH) = 19.4 Hz, 4H, CH<sub>2</sub>), 4.22 (d, <sup>2</sup> $J$ (PH) = 18.5 Hz, 1H, NH), 7.25–7.50 (m, 5H, C<sub>6</sub>H<sub>5</sub>). <sup>13</sup>C NMR  $\delta$ : 17.23 (CH<sub>3</sub>), 22.45 (CH<sub>2</sub>), 42.15 (CH<sub>2</sub>), 172–178 (Ar–C). LCMS (EI)  $m/z$ : 256 (M + H<sup>+</sup>). Anal. calcd. for C<sub>12</sub>H<sub>22</sub>N<sub>3</sub>OP: C 56.46, H 8.69, N 16.46; found: C 56.48, H 8.67, N 16.44.

### *N,N*-Dibutylamino phenylphosphonohydrazide **3p**

IR  $\nu_{\max}$  (cm<sup>-1</sup>): 3315, 3250 (N–H), 3135 (N–H), 2895 (C–H), 1450 (C–N), 1235 (P=O), 1070, 1150 (P–N–C), 695 (P–C). <sup>1</sup>H NMR  $\delta$ : 0.75 (t,  $J$  = 8.4 Hz, 6H, CH<sub>3</sub>), 1.45 (m, 4H, CH<sub>2</sub>), 1.55 (m, 4H, CH<sub>2</sub>), 3.10 (br s, 2H, NH<sub>2</sub>), 2.95 (q, <sup>3</sup> $J$ (PH) = 18.6 Hz, 4H, CH<sub>2</sub>), 4.10 (d, <sup>2</sup> $J$ (PH) = 17.5 Hz, 1H, NH), 7.25–7.50 (m, 5H, C<sub>6</sub>H<sub>5</sub>). <sup>13</sup>C NMR  $\delta$ : 15.85 (CH<sub>3</sub>), 17.28 (CH<sub>3</sub>), 20.49 (CH<sub>2</sub>), 22.47 (CH<sub>2</sub>), 26.78 (CH), 42.58 (CH<sub>2</sub>), 172–178 (Ar–C). LCMS (EI)  $m/z$ : 284 (M + H<sup>+</sup>). Anal. calcd. for C<sub>14</sub>H<sub>26</sub>N<sub>3</sub>OP: C 59.34, H 9.25, N 14.83; found: C 59.35, H 9.23, N 14.80.

## Conclusion

In conclusion, we have developed a rapid and efficient method for the synthesis of *O*-alkyl alkylphosphorohydrazides and *N,N*-dialkyl aminophosphonohydrazides **3a–3p** with excellent yields.

## References

- (1) (a) Majoral, J. P. *New Aspects in Phosphorus Chemistry I & II*; Berlin: Heidelberg, 2000; (b) Wilson, B. W.; Walker, C. R. *Proc. Natl. Acad. Sci. U.S.A.* **1974**, *71* (8), 3194. doi:10.1073/pnas.71.8.3194. PMID:4528709; (c) Eto, M. *Organophosphorus Pesticides: Organic and Biological Chemistry*; CRC Press: Cleveland, OH, 1974; (d) Kosolapoff, G. M. *Organic Phosphorus Compounds*; Wiley-Interscience: NY, 1950; 6, 319; (e) De Frank, J. J. *Applications of Enzyme Biotechnology*; Kelly, J. W., Baldwin, T. O., Eds.; Plenum: New York, 1991; pp. 165–180.
- (2) (a) Sikorski, J. A.; Logusch, E. W. *Aliphatic carbon-phosphorous compounds as herbicides*; In *Handbook of Organophosphorus Chemistry*; Engel, R., Ed.; Marshel Dekker: New York, 1992; 739; (b) Van Wazer, J. R. *Phosphorus and its Compounds*; Interscience Publishers Inc.: New York, 1961; Vol. II; (c) Hildebrand, R. *The Role of Phosphonates in Living Systems*; CRC Press: Boca Raton, 1983.

- (3) Küçükgülzel, S. G.; Rollas, S.; Küçükgülzel, I.; Kiraz, M. *Eur. J. Med. Chem.* **1999**, *34* (12), 1093. doi:10.1016/S0223-5234(99)00129-4.
- (4) Tumah, H.; Tashtoush, B.; Tashtoush, H.; Ababneh, K.; Mahmoud, A.-T. *Acta Pharmaceutica Turcica* **2005**, *47*, 189.
- (5) Prakash, O.; Kumar, R.; Kumar, R.; Tyagi, P.; Kuhad, R. C. *Eur. J. Med. Chem.* **2007**, *42* (6), 868. doi:10.1016/j.ejmech.2006.11.019. PMID:17222483.
- (6) Loncle, C.; Brunel, J. M.; Vidal, N.; Dherbomez, M.; Letourneux, Y. *Eur. J. Med. Chem.* **2004**, *39*, 1067. doi:10.1016/j.ejmech.2004.07.005.
- (7) Papakonstantinou-Garoufalas, S.; Pouli, N.; Marakos, P.; Chytiroglou-Ladas, A. *Farmaco* **2002**, *57* (12), 973. doi:10.1016/S0014-827X(02)01227-2. PMID:12564470.
- (8) Vicini, P.; Zani, F.; Cozzini, P.; Doytchinova, I. *Eur. J. Med. Chem.* **2002**, *37* (7), 553. doi:10.1016/S0223-5234(02)01378-8. PMID:12126774.
- (9) Sridhar, S. K.; Pandeya, S. N.; Stables, J. P.; Atmakuru, R. *Eur. J. Pharm. Sci.* **2002**, *16*, 129. doi:10.1016/S0928-0987(02)00077-5.
- (10) Küçükgülzel, S. G.; Mazi, A.; Sahin, F.; Oztürk, S.; Stables, J. P. *Eur. J. Med. Chem.* **2003**, *38* (11–12), 1005. doi:10.1016/j.ejmech.2003.08.004. PMID:14642333.
- (11) Todeschini, A. R.; de Miranda, A. L. P.; da Silva, K. C. M.; Parrini, S. C.; Barreiro, E. J. *Eur. J. Med. Chem.* **1998**, *33* (3), 189. doi:10.1016/S0223-5234(98)80008-1.
- (12) Gaston, M. A.; Dias, L. R. S.; Freitas, A. C. C.; Miranda AIP.; Barrerio, E. J. *Pharm. Acta Helv.* **1996**, *71* (3), 213. doi:10.1016/0031-6865(96)00012-X. PMID:9036388.
- (13) Melnyk, P.; Leroux, V.; Sergheraert, C.; Grellier, P. *Bioorg. Med. Chem. Lett.* **2006**, *16* (1), 31. doi:10.1016/j.bmcl.2005.09.058. PMID:16263280.
- (14) Patole, J.; Sandbhor, U.; Padhye, S.; Deobagkar, D. N.; Anson, C. E.; Powell, A. *Bioorg. Med. Chem. Lett.* **2003**, *13* (1), 51. doi:10.1016/S0960-894X(02)00855-7. PMID:12467615.
- (15) Maccari, R.; Ottanà, R.; Vigorita, M. G. *Bioorg. Med. Chem. Lett.* **2005**, *15* (10), 2509. doi:10.1016/j.bmcl.2005.03.065. PMID:15863306.
- (16) Cocco, M. T.; Congiu, C.; Onnis, V.; Pusceddu, M. C.; Schivo, M. L.; Logu, A. *Eur. J. Med. Chem.* **1999**, *34* (12), 1071. doi:10.1016/S0223-5234(99)00124-5.
- (17) Karalı, N.; Kocabalkanlı, A.; Gürsoy, A.; Ateş, O. *Farmaco* **2002**, *57* (7), 589. doi:10.1016/S0014-827X(02)01254-5. PMID:12164220.
- (18) Rando, D. G.; Sato, D. N.; Siqueira, L.; Malvezzi, A.; Leite, C. Q. F.; do Amaral, A. T.; Ferreira, E. I.; Tavares, L. C. *Bioorg. Med. Chem.* **2002**, *10* (3), 557. doi:10.1016/S0968-0896(01)00313-3. PMID:11814842.
- (19) (a) Wagner, R. B.; Zook, H. D. *Synthetic Organic Chemistry*; John Wiley & Sons: New York, 1953. pp. 569; (b) Khan, K. M.; Rasheed, M.; Zia-Ullah, H. S.; Hayat, S.; Kaukab, F.; Choudhary, M. I.; Atta-ur-Rahman.; Perveen, S. *Bioorg. Med. Chem.* **2003**, *11* (7), 1381. doi:10.1016/S0968-0896(02)00611-9. PMID:12628664.
- (20) (a) Fadel, A.; Yefsah, R.; Salaün, J. *Synthesis* **1987**, 1987 (01), 37. doi:10.1055/s-1987-27833; (b) Rosini, G.; Galarini, R.; Marotta, E.; Righi, R. *J. Org. Chem.* **1990**, *55* (3), 781. doi:10.1021/jo00290a001; (c) Patney, H. K. *Tetrahedron Lett.* **1991**, *32* (20), 2259. doi:10.1016/S0040-4039(00)79696-1; (d) Pautet, F.; Daudon, M. *Tetrahedron Lett.* **1991**, *32* (11), 1457. doi:10.1016/0040-4039(91)80357-C.
- (21) Sardarian, A. R.; Kaboudin, B. *Synth. Commun.* **1997**, *27* (4), 543. doi:10.1080/00397919708003324.



- (22) Sardarian, A. R.; Kaboudin, B. *Tetrahedron Lett.* **1997**, 38 (14), 2543. doi:10.1016/S0040-4039(97)00396-1.
- (23) Kaboudin, B. J. *Chem. Res.* **1999**, 1999, 402. doi:10.1039/a900183b.
- (24) (a) Kumar, R.; Joshi, Y. C. *Indian J. Chem.* **2007**, 46B, 2021; (b) Kumar, R.; Joshi, Y. C. *Arkivoc* **2007**, xiii, 142; (c) Kumar, R.; Joshi, Y. C. *J. Chem. Sci.* **2009**, 121 (4), 497. doi:10.1007/s12039-009-0059-y.
- (25) Kinnear, A. M.; Perren, E. A. *J. Chem. Soc.* **1952**, 3437. doi:10.1039/jr9520003437.
- (26) Semon, W. W.; Damerll, V. R. *Org. Synth. Coll. Vol.* 2 **1943**, 11, 204.

# One-pot synthesis of $\beta$ -diketimine ligands

Ibrahim El-Zoghbi, Aysha Ased, Paul O. Oguadinma, Ekou Tchirioua, and Frank Schaper

**Abstract:** Symmetric  $N,N'$ -dialkyl-2-amino-4-imino-pent-2-enes (nacnac<sup>R</sup>H) can be prepared in high yields in a simple one-pot reaction from acetylacetone and 2 equiv. of amine. Optimized conditions require the azeotropic removal of water, use of a minimum amount of solvent, and of 1 equiv. of acid. Either *para*-toluenesulfonic acid, hydrochloric acid, or a mixture of both can be employed, with the latter being most advantageous. Symmetric nacnac<sup>R</sup>H are thus obtained in higher than 95% purity and with 65% yield for R = Me and 80%–95% yields for R = *n*-Pr, *i*-Pr, *i*-Bu, Bn, Cy, and (+)-CH(Me)Ph.

**Key words:** diketimines, one-pot synthesis.

**Résumé :** On peut préparer les  $N,N'$ -dialkyl-2-amino-4-iminopent-2-ènes (nacnac<sup>R</sup>H) avec des rendements élevés en réalisant la réaction monotope de l'acétylacétone avec deux équivalents d'amine. Les conditions optimisées nécessitent l'élimination azéotropique de l'eau, l'utilisation d'une quantité minimale de solvant et un équivalent d'acide qui peut être l'acide *para*-toluènesulfonique, l'acide chlorhydrique ou un mélange des deux; ce dernier est le plus avantageux. Des nacnac<sup>R</sup>H symétriques peuvent ainsi être obtenus avec une pureté de plus de 95 % et un rendement de 65 % lorsque R = Me et des rendements allant de 80 à 95 % lorsque le groupe R = *n*-Pr, *i*-Pr, *i*-Bu, Bu, Cy et (+)-CH(Me)Ph.

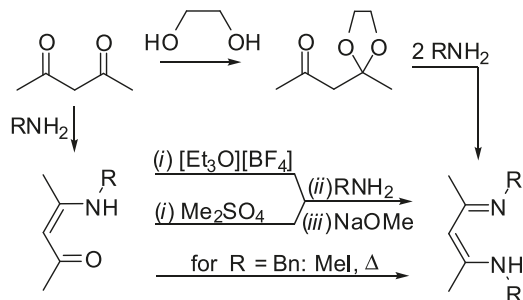
**Mots-clés :** dicétimines, synthèse monotope.

## Introduction

Preparation of  $\beta$ -diketimines ("nacnac" ligands), based on diimine analogues of acetylacetone, was described already in 1950,<sup>1</sup> and their first metal complexes in 1968.<sup>2,3</sup> They played only a marginal role in coordination chemistry until the introduction of nacnac<sup>dipp</sup> (dipp = 2,6-diisopropylphenyl) as a spectator ligand in the late 1990s.<sup>4</sup> Since then,  $\beta$ -diketiminate ligands have become some of the most widely used bidentate N-donor ligands in coordination chemistry.<sup>5</sup> Interest in diketiminate ligands concentrated mostly on their N-aryl derivatives, and N-alkyl substituted diketimines were used only sparingly, mostly as low-molecular-weight ligands for chemical vapour deposition and atomic layer deposition applications.<sup>6</sup> We recently started to investigate the coordination chemistry of diketiminate ligands with aliphatic N-substituents.<sup>7–11</sup> For these investigations, we required a simple, efficient, and economic access to these compounds.

The most efficient and versatile preparation of 2-amino-4-imino-pent-2-enes is condensation of acetylacetone with amines. While condensation of the first amine proceeds readily, the resulting enaminoketone has to be activated for the second condensation.<sup>2,5</sup> This might be achieved by transformation into the ketal, and the ethylene glycol monoketal has been used successfully as starting material for the synthesis of nacnac<sup>Bn</sup>H and some macrocyclic diketimines (Scheme 1).<sup>12,13</sup> Alternatively, in the case of aryl N-substituents, reaction in ethanolic HCl yielded the desired dicondensation product, probably by intermediate formation of the diethoxyketal.<sup>3</sup> For the diketimines with N-alkyl substituents of in-

Scheme 1.



terest here, alkylation of the enaminoketone obtained after the first condensation with Meerwein salt and subsequent reaction with a second equivalent of amine is the most commonly employed method.<sup>2</sup> In an isolated report, nacnac<sup>Bn</sup>H, **1**, has been obtained by refluxing the monocondensation product acnac<sup>Bn</sup>H, **1b**, in methyl iodide.<sup>14</sup> The mechanism of this reaction (no second equivalent of amine was added) remains unclear. Recently, Bradley et al. showed that Meerwein salt can be replaced by the less toxic and more economic methyl sulfate as alkylating agent (Scheme 1).<sup>15</sup> The latter, to our knowledge, is the most efficient synthesis described, and diketimines were obtained in yields of 46%–87% starting from the enaminoketone intermediate after distillation. Diketimines with aliphatic substituents are thus accessible, but their synthesis still requires a two-step reaction, often distillation of the obtained product for purification, ex-

Received 8 July 2010. Accepted 14 July 2010. Published on the NRC Research Press Web site at canjchem.nrc.ca on 5 October 2010.

I. El-Zoghbi, A. Ased, P.O. Oguadinma, E. Tchirioua, and F. Schaper.<sup>1</sup> Département de chimie, Université de Montréal, Montréal, QC H3C 3J7, Canada.

<sup>1</sup>Corresponding author (e-mail: Frank.Schaper@umontreal.ca).

clusion of moisture, and the use of toxic alkylating reagents. In the following, we describe a one-step preparation of these compounds, which avoids these drawbacks.

## Results and discussion

### Initial explorations

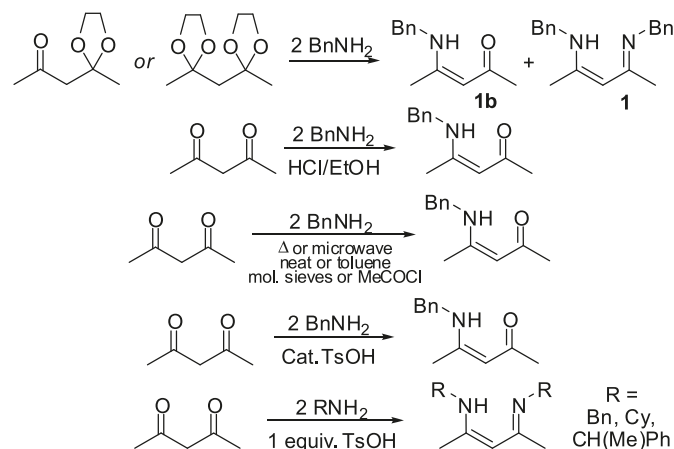
We repeated the preparation of  $\text{nacnac}^{\text{Bn}}\text{H}$ , **1**, described by Dorman<sup>12</sup> using either acetylacetone ethylene glycol mono- or di-ketal as starting material. We found, however, the reaction to give varying yields of diketimine product and to be highly dependent on reaction conditions (Scheme 2). If the reaction is carried out in diluted toluene solution, only the monocondensation product **1b** was obtained. Reaction of acetylacetone with 2 equiv. benzylamine in ethanolic HCl, following the procedure described by Parks and Holm<sup>3</sup> and Feldman et al.<sup>16</sup> for N-aryl substituted diketimines, also yielded only **1b**. Direct condensation of acetylacetone and benzylamine (no solvent,  $T > 100^\circ\text{C}$ , in the presence of molecular sieves or thionyl chloride), under microwave heating (neat or in toluene solution, without or with addition of molecular sieves or acetyl chloride), or under azeotropic removal of water (toluene solution, catalytic quantities of *para*-toluenesulfonic acid, several days) yielded either **1b** or decomposition products and at best traces (<10%) of the desired **1**.

While aryl-substituted diketimines have been sometimes obtained under typical “Dean–Stark conditions”, i.e., catalytic amounts of acid and azeotropic removal of water, yields have been generally low-to-moderate. Budzelaar et al. reported the synthesis of  $\text{nacnac}^{\text{Xyl}}\text{H}$ , **2**, (Xyl = 2,6-dimethylphenyl) in 75% yield in the presence of stoichiometric amounts of acid. Applying this protocol, we had previously obtained  $\text{nacnac}^{\text{Bn}}\text{H}$ ,<sup>8</sup>  $\text{nacnac}^{\text{Cy}}\text{H}$ ,<sup>10</sup> and  $\text{nacnac}^{\text{CH(Me)Ph}}\text{H}$ <sup>7</sup> in 67%–82% yield. The initially obtained tosylate salt can be neutralized using a variety of bases of which aqueous potassium hydroxide proved to be the most convenient (aqueous  $\text{NaHCO}_3$  failed in some cases to deprotonate the tosylate salt). Azeotropic water removal is required and reaction of  $\text{BnNH}_2$  (or *i*- $\text{BuNH}_2$ ), acetylacetone, and 1 equiv. TsOH either in toluene or without solvent only yielded the monocondensation product **1b**.

### Optimization of the reaction conditions

Attempts to widen the synthesis described above to diketimines with simple alkyl substituents such as Me, *i*-Pr, *n*-Pr, and *i*-Bu yielded even after prolonged heating only mixtures of bis- and mono-condensation products with less than 60% of the desired diketimine according to NMR analysis. Use of more than 1 equiv. of TsOH showed no or only detrimental influence on product yields. While it has never been clarified why reactions proceed differently when catalytic or stoichiometric amounts of acid are used, we find it reasonable to assume that alkylation of the intermediate enaminketone is replaced by its (reversible) protonation and that the latter requires amounts of acid, which are equal or slightly higher than those of the amine. In agreement with this putative mechanism, presence of excess amine reduced the yield of diketimine when not compensated with excess TsOH (Table 1). Since the presence of excess amine and TsOH in equimolar amounts did not increase the yield when com-

Scheme 2.



pared to the stoichiometric reaction (Table 1), loss of the low-boiling amine seems not to be responsible for the low yields obtained.

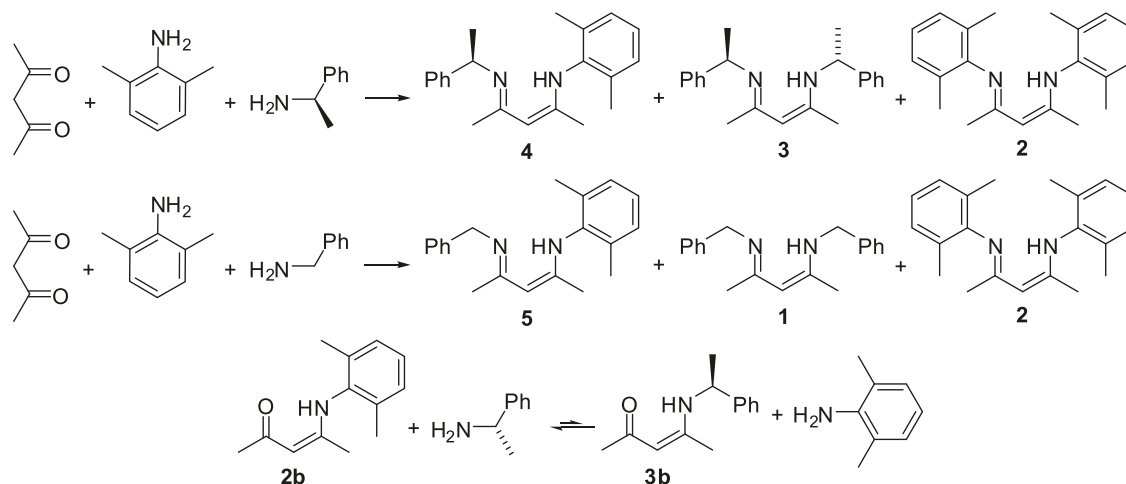
Inspired by the decrease in yields in the reaction of acetylacetone ketal with amines on dilution, we found that concentration of the reaction mixture reduced drastically the amounts of monocondensation product and impurities formed (Table 2). Best results were obtained when the minimum amount of toluene necessary to operate the Dean–Stark apparatus was employed.

Reactions with other primary and secondary amines showed that concentration of the solution in general improved product yields and in most cases shortened reaction times to less than one day (Table 3). The low isolated yields for  $\text{nacnac}^{\text{Me}}\text{H}$  are related to its high volatility and its high sensitivity towards hydrolysis.<sup>15</sup> Reactions with isopropyl amine and isobutyl amine, however, did not show conversions above 30% even under these conditions. Substituting *p*-toluenesulfonic acid with sulfuric acid led to strongly decreased yields. The use of concentrated hydrochloric acid, on the other hand, increased the yields to 85%–95% for R = *i*-Pr and *i*-Bu, respectively. In addition, use of concentrated HCl prevented the formation of impurities observed in reactions with TsOH, and diketimines were obtained analytically pure for R = *i*-Bu, *i*-Pr, and *n*-Pr without the need for further purification. Diketimines with R = Bn or CH(Me)Ph were obtained with >90% purity according to NMR (the main contamination being the monocondensation product), which is in most cases sufficient for their use in subsequent reactions. Analytically pure compounds were obtained by recrystallization from ethanol. For methylamine and cyclohexylamine, yields were drastically reduced by replacing *para*-toluenesulfonic acid with HCl. In both cases, the formation of an insoluble precipitate even at reflux temperature indicated that this might be related to the insolubility of the respective ammonium chloride salt. Consequently, use of an equimolar mixture of HCl/TsOH restored the yields observed for TsOH in these two cases, but did not otherwise affect reactions for other amines (Table 3).

### Non-symmetric diketimines

Synthesis of non-symmetrically substituted diketimines with different substituents on N and N' is a challenge and

Scheme 3.

**Table 1.** Influence of excess base in the preparation of  $\text{nacnac}^{i\text{-Bu}}\text{H}$ .

$i\text{-BuNH}_2/\text{acacH}$	$\text{TsOH}/\text{acacH}$	Reaction time (h)	$\text{nacnac}^{i\text{-Bu}}\text{H}$ (%) <sup>a</sup>	$\text{acnac}^{i\text{-Bu}}\text{H}$ (%) <sup>a</sup>
2	1.1	24	60	30
3	1.1	24	5	70
3	1.5	20	15	30
3	2.2	18–54	60	30

<sup>a</sup>Determined by  $^1\text{H}$  NMR from the crude product after basic workup.**Table 2.** Influence of concentration in the preparation of  $\text{nacnac}^{n\text{Pr}}\text{H}$ .

$[\text{acacH}]$ (mol/L)	Reaction time (h)	$\text{nacnac}^{i\text{-Bu}}\text{H}$ (%) <sup>a</sup>	$\text{acnac}^{i\text{-Bu}}\text{H}$ (%) <sup>a</sup>
0.048	68	62	18
1.2	68	80	Traces
4.0	16	90	Traces

**Note:**  $\text{acacH}/n\text{-PrNH}_2/\text{TsOH} = 1:2:1$ ; toluene solution; azeotropic removal of water.<sup>a</sup>Determined via  $^1\text{H}$  NMR from the crude product after washing with aqueous KOH.

stepwise reaction using alkylating reagents such as Meerwein salt led to product mixtures.<sup>17,18</sup> We thus explored if non-symmetric diketimines can be obtained using the one-pot procedure established above. Reactions of acetylacetone with 1 equiv. 2,6-dimethylaniline and 1 equiv. of either (+)-methylbenzylamine or benzylamine yielded product mixtures containing the non-symmetric diketimines **4** or **5** in higher than statistical amounts, but always accompanied by the two symmetric diketimines (Scheme 3).

The preferred formation of the non-symmetric diketimine can be rationalized by the trapping of the more reactive 2,6-dimethylaniline in the monocondensation product, which diminishes its concentration in solution. Following reactions between  $\text{acnac}^{\text{Xyl}}\text{H}$ , **2b**, with methylbenzylamine, and vice versa of  $\text{acnac}^{\text{CH(Me)Ph}}\text{H}$ , **3b**, with 2,6-dimethylaniline by NMR showed that scrambling between the monocondensation products and free amines was observed already before significant amounts of diketimine were obtained (Scheme 3). In all cases,  $\text{acnac}^{\text{Xyl}}\text{H}$  was obtained preferentially. In particular at the beginning of the reaction, diketimines were thus

formed from the two species present in the highest concentrations, i.e.,  $\text{acnac}^{\text{Xyl}}\text{H}$  and either methylbenzylamine or benzylamine. As was previously observed by others, separation of non-symmetrical substituted diketimines from their symmetric counterparts is nearly impossible.<sup>18</sup> Despite their disproportionally high amount in the obtained product mixtures, **4** and **5** were not separated from the symmetric diketimines **1–3** by recrystallization, sublimation, or column chromatography (extensive hydrolysis in the latter case). For **5**, diketimine **1** could be separated by recrystallization and **5** was obtained in 30% yield and 90% purity, still contaminated by 10% of **2**.

## Summary and conclusions

$\beta$ -Diketimines with aliphatic substituents on nitrogen can be obtained in simple one-pot condensation reactions between acetylacetone and primary or secondary amine, provided that water is removed azeotropically and that one equivalent of acid is present. Under optimized reaction conditions, we employed an equimolar mixture of hydrochloric and *para*-toluenesulfonic acids, and the amount of solvent was kept to the minimum required for water removal. Symmetric diketimines can thus be obtained very economically, without the need of toxic alkylating reagents or moisture-free conditions.

For non-symmetric diketimines, the fast scrambling between free amine and monocondensation products makes the proposed protocol less efficient. Although they are obtained in higher than statistic ratio, their separation from the symmetric diketimines, invariably formed as side products, was not possible and the synthetically more demanding routes proposed by Park et al.<sup>18,19</sup> are still more advantageous.



**Table 3.** Yields in diketimine synthesis for different combinations of amines and acids (purity is given in parentheses).

R	TsOH ( $c_{\text{acacH}} < 1$ mol/L)	TsOH	HCl	HCl/TsOH	Reaction time
<i>n</i> -Pr	50% (EA)	80% (90%)	90% (EA)		72 h
Bn	82% (EA) <sup>a</sup>	80% (>95%)	75% (>95%)		24 h
CH(Me)Ph	70% (EA) <sup>b</sup>	80% (90%)	80% (90%)	80% (90%)	5 d
<i>i</i> -Bu	35% (EA)	30%	95% (EA)		18 h
<i>i</i> -Pr	23% (90%) <sup>c</sup>	30% (>95%)	85% (EA)	95% (EA)	24 h
Cy	69% (EA) <sup>d</sup>	90% (>95%)	0%	90% (90%)	72 h
Me	60% (50%)	50% (95%)	5%	65% (>95%)	18 h

**Note:** Purity was estimated by  $^1\text{H}$  NMR, EA indicates correct elemental analysis. Reaction conditions:  $\text{acacH}/\text{RNH}_2/\text{acid} = 1:2:1$ ; minimum amount of toluene used with exception of the first column.

<sup>a</sup> $c_{\text{acacH}} = 0.5$  mol/L.<sup>8</sup>

<sup>b</sup> $c_{\text{acacH}} = 0.1$  mol/L, 5 d.<sup>7</sup>

<sup>c</sup> $c_{\text{acacH}} = 0.2$  mol/L, 3 d.<sup>9</sup>

<sup>d</sup> $c_{\text{acacH}} = 0.1$  mol/L, 3 d.<sup>10</sup>

## Experimental section

All chemicals were obtained from commercial suppliers and used as received. Elemental analyses were performed at the Laboratoire d'Analyse Élémentaire (Université de Montréal). NMR spectra were recorded on a Bruker ARX 400 MHz spectrometer and referenced to residual solvent ( $\text{CHCl}_3$ ;  $\delta$  7.26).

### General procedure for the synthesis of symmetric diketimines

Acetylacetone and 1 equiv. of the desired acid or acid mixture (see Table 3) were combined in a minimum volume of toluene, usually equal to the combined volumes of all reactants. The mixture was stirred for 10 min and 2 equiv. of the desired amine were added to give a white suspension, which was allowed to stir for approximately 20 min. The reaction mixture was then refluxed for the required time (Table 3) with azeotropic removal of water (Dean–Stark apparatus). The brown precipitate formed after cooling to room temperature and standing for 3–4 h was isolated by decantation. Ether (50 mL) and aqueous KOH (11.2 g, 0.2 mol, 50 mL) were added and the mixture stirred for 15 min. The ether phase was separated, dried over  $\text{Na}_2\text{SO}_4$ , and the solvent evaporated. Yields and purities of the obtained products, estimated from  $^1\text{H}$  NMR, are given in Table 3. Characterization data and quantities are given below for selected experiments.

#### $\text{nacnac}^{\text{Bn}}\text{H}$ , **1**

Acetylacetone (2.00 g, 20 mmol), HCl (12.1 mol/L, 1.65 mL, 20 mmol), and benzylamine (4.28 g, 40 mmol) in toluene (7 mL) gave a red brown solid (2.90 g, 75%, >95% purity).  $^1\text{H}$  NMR ( $\text{CDCl}_3$ , 400 MHz):  $\delta$  11.49 (bs, 1H, NH), 7.22–7.30 (m, 10H, Ph), 4.64 (s, 1H,  $\text{CH}(\text{C}=\text{N})_2$ ), 4.46 (s, 4H,  $\text{CH}_2$ ), 1.95 (s, 6H, Me). Recrystallization from a saturated ethanol solution at  $-20^\circ\text{C}$  gave the following: Anal. calcd. for  $\text{C}_{21}\text{H}_{26}\text{N}_2$ : C, 81.97; H, 7.97; N, 10.06. Found: C, 81.75; H, 8.19; N, 10.05.<sup>2,14,15</sup>

#### $\text{nacnac}^{\text{CH(Me)Ph}}\text{H}$ , **3**

Acetylacetone (1.00 g, 10 mmol), HCl (12.1 mol/L, 0.82 mL, 10 mmol), and (+)-phenylethylamine (2.42 g, 20 mmol) in toluene (6 mL) gave a red brown oil (2.45 g,

80%, 92% purity).  $^1\text{H}$  NMR ( $\text{CDCl}_3$ , 400 MHz):  $\delta$  11.89 (bs, 1H, NH), 7.20–7.35 (m, 10H, Ph), 4.68 (q, 2H,  $J = 7$  Hz,  $\text{CH}(\text{Me})\text{Ph}$ ), 4.48 (s, 1H,  $\text{CH}(\text{C}=\text{N})_2$ ), 1.82 (s, 6H,  $\text{Me}(\text{C}=\text{N})$ ), 1.49 (d, 6H,  $J = 7$  Hz  $\text{CH}(\text{Me})\text{Ph}$ ). Recrystallization from a saturated ethanol solution at  $-20^\circ\text{C}$  gave the following: Anal. calcd. for  $\text{C}_{21}\text{H}_{26}\text{N}_2$ : C, 82.31; H, 8.55; N, 9.15. Found: C, 81.75; H, 8.52; N, 9.06.<sup>7,20</sup>

#### $\text{nacnac}^{\text{n-Pr}}\text{H}$

Acetylacetone (2.00 g, 20 mmol), HCl (12.1 mol/L, 1.65 mL, 20 mmol), and *n*-propylamine (2.36 g, 40 mmol) in toluene (5 mL) gave a dark brown oil (3.3 g, 90%).  $^1\text{H}$  NMR ( $\text{CDCl}_3$ , 400 MHz):  $\delta$  10.04 (bs, 1H, NH), 4.47 (s, 1H,  $\text{CH}(\text{C}=\text{N})_2$ ), 3.17 (t,  $J = 9$  Hz, 4H,  $\text{NCH}_2$ ), 1.87 (s, 6H,  $\text{Me}(\text{C}=\text{N})$ ), 1.61 (m, 4H,  $\text{CH}_2\text{CH}_2\text{CH}_3$ ), 0.97 (t,  $J = 9$  Hz, 6H,  $\text{CH}_2\text{CH}_3$ ). Anal. calcd. for  $\text{C}_{11}\text{H}_{22}\text{N}_2$ : C, 72.47; H, 12.16; N, 15.37. Found C, 72.41; H, 11.81; N, 15.39.<sup>15</sup>

#### $\text{nacnac}^{\text{i-Pr}}\text{H}$

Obtained from acetylacetone (2.00 g, 20 mmol), HCl (12.1 mol/L, 1.65 mL, 20 mmol), and isopropylamine (2.36 g, 40 mmol) in toluene (5 mL). To eliminate monocondensation product, the oil obtained after decantation of toluene was treated with excess saturated aqueous  $\text{NaHCO}_3$  and ether (20 mL). Ether and water phases were decanted from the remaining oil. Ether (50 mL) and aqueous KOH (11.2 g, 0.2 mol, 50 mL) were added and the mixture stirred. The ether phase was separated, dried over  $\text{Na}_2\text{SO}_4$ , and evaporated to dryness to give a dark-red oil (3.4 g, 85%).  $^1\text{H}$  NMR ( $\text{CDCl}_3$ , 400 MHz):  $\delta$  11.43 (bs, 1H, NH), 4.38 (s, 1H,  $\text{CH}(\text{C}=\text{N})_2$ ), 3.06 (hept.,  $J = 6$  Hz, 2H,  $\text{CH}(\text{CH}_3)_2$ ), 1.89 (s, 6H,  $\text{CH}_3(\text{C}=\text{N})$ ), 1.16 (d,  $J = 6$  Hz, 12H,  $\text{CH}(\text{CH}_3)_2$ ). Anal. calcd. for  $\text{C}_{11}\text{H}_{22}\text{N}_2$ : C, 72.47; H, 12.16; N, 15.37. Found C, 72.06; H, 12.08; N, 15.15.<sup>2</sup>

#### $\text{nacnac}^{\text{i-Bu}}\text{H}$

Acetylacetone (2.00 g, 20 mmol), HCl (12.1 mol/L, 1.65 mL, 20 mmol), and isobutylamine (2.92 g, 40 mmol) in toluene (5 mL) gave a brown oil (4.3 g, 95%).  $^1\text{H}$  NMR ( $\text{CDCl}_3$ , 400 MHz):  $\delta$  11.07 (bs, 1H, NH), 4.48 (s, 1H,  $\text{CH}(\text{C}=\text{N})_2$ ), 3.05 (d,  $J = 9$  Hz, 4H,  $\text{CH}_2$ ), 1.88 (m, 2H,  $\text{CH}(\text{CH}_3)_2$ ), 1.86 (s, 6H,  $\text{CH}_3(\text{C}=\text{N})$ ), 0.96 (d,  $J = 9$  Hz, 12H,  $\text{CH}(\text{CH}_3)_2$ ). Anal. calcd. for  $\text{C}_{13}\text{H}_{26}\text{N}_2$ : C, 74.23; H, 12.46; N, 13.32. Found C, 74.06; H, 13.03; N, 12.99.<sup>15,21</sup>

**nacnac<sup>Cy</sup>H**

Acetylacetone (2.00 g, 20 mmol), HCl (12.1 mol/L, 0.82 mL, 10 mmol), *p*-toluenesulfonic acid monohydrate (2.00 g, 11 mmol), and cyclohexylamine (3.98 g, 40 mmol) in toluene (15 mL) gave a colorless oil that crystallizes into colorless crystals upon standing for 2–3 h (4.75 g, 90%). <sup>1</sup>H NMR (CDCl<sub>3</sub>, 400 MHz): δ 11.72 (bs, 1H, NH), 4.44 (s, 1H, CH(C=N)<sub>2</sub>), 3.32–3.35 (m, 2H, Cy CH), 1.90 (s, 6H, Me(C=N)), 1.80–1.35 (m, 20H, Cy). Anal. calcd. for C<sub>13</sub>H<sub>26</sub>N<sub>2</sub>: C, 77.80; H, 11.52; N, 10.64. Found C, 77.44; H, 11.57; N, 10.67.<sup>22</sup>

**nacnac<sup>Me</sup>H**

Acetylacetone (3.00 g, 30 mmol), HCl (12.1 mol/L, 1.24 mL, 15 mmol), *p*-toluenesulfonic acid monohydrate (2.99 g, 16 mmol), and methylamine (40%, 4.65 g, 0.06 mol) in toluene (6 mL). The aqueous phase was re-extracted with ether (3 × 300 mL), and the combined organic phases were dried over Na<sub>2</sub>SO<sub>4</sub> and evaporated to dryness. The dark-yellow oil obtained solidifies to an orange precipitate that darkens upon standing to room temperature (2.5 g, 65%). <sup>1</sup>H NMR (CDCl<sub>3</sub>, 400 MHz): δ 10.04 (bs, 1H, NH), 5.2 (s, 1H, CH(C=N)<sub>2</sub>), 2.99 (s, 6H, NMe), 1.86 (s, 6H, CH<sub>3</sub>(C=N)). <sup>13</sup>C{<sup>1</sup>H} NMR (CDCl<sub>3</sub>, 400 MHz): δ 162.1 (C=N), 93.9 (CH(C=N)<sub>2</sub>), 33.3 (Me), 19.0 (CH<sub>3</sub>(C=N)). Elemental analysis data were unsatisfactory due to easy decomposition.<sup>2,15</sup>

**nacnac<sup>Xyl,Bn</sup>H**

Acetylacetone (3.00 g, 30 mmol), HCl (12.1 mol/L, 2.5 mL, 30 mmol), and 2,6-dimethylaniline (3.63 g, 30 mmol) in toluene (12 mL) were refluxed for approximately 2 h. To the obtained yellow suspension, benzylamine (3.27 g, 30 mmol) was added and allowed to reflux for 3 days under azeotropic removal of water in a Dean–Stark apparatus. After cooling to room temperature and decantation of toluene, the brown oil obtained was treated with ether (50 mL) and aqueous KOH (16.8 g, 0.3 mol, 50 mL). The ether phase was separated and evaporated to dryness. The obtained red-brown oil was dissolved in a minimum amount of ethanol and kept at –20 °C for several days. Crystals of nacnac<sup>Bn</sup>H formed were removed by filtration, and the remaining ethanol solution was evaporated to dryness to yield a brown oil (2.62 g, 30%, in 90% purity containing 10% of **2**). Further recrystallizations in MeOH or in EtOH as well as sublimation still yielded product mixtures. <sup>1</sup>H NMR (CDCl<sub>3</sub>, 400 MHz): δ 11.18 (bs, 1H, NH), 7.22–7.30 (m, 8H, Ph), 4.45 (s, 1H, CH(C=N)<sub>2</sub>), 4.43 (s, 2H, CH<sub>2</sub>), 2.07 (s, 6H, Ar Me), 1.90 (s, 3H, Me(C=N)), 1.63 (s, 3H, Me(C=N)). <sup>13</sup>C{<sup>1</sup>H} NMR (CDCl<sub>3</sub>, 400 MHz): δ 160.1 (C=N), 140.1 (C=N), 128.4, 128.3, 127.6, 127.5, 127.2, 127.0, 126.7, 126.3 (all Ph), 93.9 (CH(C=N)<sub>2</sub>), 46.5 (CH<sub>2</sub>), 21.2 (Me(C=N)), 19.1 (Me(C=N)), 18.3 (Me<sub>2</sub>Ph). EI-HR-MS (*m/z*): calcd. for C<sub>20</sub>H<sub>25</sub>N<sub>2</sub> [M + H]<sup>+</sup>: 293.2012; found: 293.2013.<sup>5</sup>

**Acknowledgements**

Financial support from the Natural Sciences and Engineering Research Council of Canada (NSERC) and the Université de Montréal is gratefully acknowledged. Boris Vabre, Marie Teillard, and Sébastien Guillard contributed during

their research internships to initial explorations of this subject.

**References**

- (1) Julia, M. *Ann. Chim.* **1950**, *5*, 595.
- (2) McGeachin, S. G. *Can. J. Chem.* **1968**, *46* (11), 1903. doi:10.1139/v68-315.
- (3) Parks, J. E.; Holm, R. H. *Inorg. Chem.* **1968**, *7* (7), 1408. doi:10.1021/ic50065a029.
- (4) (a) Johnson, L. K.; Killian, C. M.; Arthur, S. D.; Feldman, J.; McCord, E. F.; McLain, S. J.; Kreutzer, K. A.; Bennett, M. A.; Coughlin, E. B.; Ittel, S. D.; Parthasarathy, A.; Tempel, D. J.; Brookhart, M. *α-Olefins and Olefin Polymers and Processes Therefore*. WO 9623 010; E. I. Du Pont de Nemours & Co. and University of North Carolina At Chapel Hill: USA, 1996; (b) Clegg, W.; Cope, E. K.; Edwards, A. J.; Mair, F. S. *Inorg. Chem.* **1998**, *37* (9), 2317. doi:10.1021/ic970956j. PMID:11670390.
- (5) Bourget-Merle, L.; Lappert, M. F.; Severn, J. R. *Chem. Rev.* **2002**, *102* (9), 3031. doi:10.1021/cr010424r. PMID:12222981.
- (6) (a) For a recent review and selected examples, see: Fahlman, B. D. *Curr. Org. Chem.* **2006**, *10* (9), 1021. doi:10.2174/138527206777435481.; (b) Thompson, D. M.; Geary, J.; Lavoie, A. R.; Dominguez, J. E. Praxair Technology, Inc.: USA; WO 2009094263, 2009; (c) Sedai, B.; Heeg, M. J.; Winter, C. H. *Organometallics* **2009**, *28* (4), 1032. doi:10.1021/om8006739.; (d) Dussarrat, C.; Feist, B. J. US 2009197411, 2009; (e) Thompson, J. S. E. I. Du Pont De Nemours and Company: USA; WO 2007019437, 2007; (f) Park, K.-H.; Bradley, A. Z.; Thompson, J. S.; Marshall, W. J. *Inorg. Chem.* **2006**, *45* (21), 8480. doi:10.1021/ic061016e. PMID:17029355.; (g) Morozova, N. B.; Gelfond, N. V.; Liskovskaya, T. I.; Stabnikov, P. A.; Semyannikov, P. P.; Trubin, S. V.; Mischenko, A. V.; Igumenov, I. K.; Norman, J. A. *Proc. Electrochem. Soc.* **2005**, 2005–09, 667; (h) Franceschini, P. L.; Morstein, M.; Berke, H.; Schmalle, H. W. *Inorg. Chem.* **2003**, *42* (22), 7273. doi:10.1021/ic034328f. PMID:14577797.
- (7) Oguadinma, P. O.; Schaper, F. *Organometallics* **2009**, *28* (14), 4089. doi:10.1021/om9002279.
- (8) Oguadinma, P. O.; Schaper, F. *Organometallics* **2009**, *28* (23), 6721. doi:10.1021/om900840f.
- (9) Oguadinma, P. O.; Schaper, F. *Can. J. Chem.* **2010**, *88* (5), 472. doi:10.1139/V10-013.
- (10) El-Zoghbi, I.; Latreche, S.; Schaper, F. *Organometallics* **2010**, *29* (7), 1551. doi:10.1021/om900852y.
- (11) El-Zoghbi, I.; Verguet, E.; Oguadinma, P. O.; Schaper, F. *Inorg. Chem. Commun.* **2010**, *13* (4), 529. doi:10.1016/j.inoche.2010.01.029.
- (12) Dorman, L. C. *Tetrahedron Lett.* **1966**, *7* (44), 459. doi:10.1016/S0040-4039(00)72963-7.
- (13) Vela, J.; Zhu, L.; Flaschenriem, C. J.; Brennessel, W. W.; Lachicotte, R. J.; Holland, P. L. *Organometallics* **2007**, *26* (14), 3416. doi:10.1021/om0700258. PMID:19132137.
- (14) Böhme, H.; Tränka, M. *Arch. Pharm. (Weinheim)* **1985**, *318* (10), 911. doi:10.1002/ardp.19853181009.
- (15) Bradley, A. Z.; Thorn, D. L.; Glover, G. V. *J. Org. Chem.* **2008**, *73* (21), 8673. doi:10.1021/jo801691m. PMID:18844410.
- (16) Feldman, J.; McLain, S. J.; Parthasarathy, A.; Marshall, W. J.; Calabrese, J. C.; Arthur, S. D. *Organometallics* **1997**, *16* (8), 1514. doi:10.1021/om960968x.
- (17) Park, K.-H.; Marshall, W. J. *J. Am. Chem. Soc.* **2005**, *127* (26), 9330. doi:10.1021/ja051158s. PMID:15984835.

- (18) Park, K.-H.; Marshall, W. J. *J. Org. Chem.* **2005**, *70* (6), 2075. doi:10.1021/jo047798f. PMID:15760190.
- (19) Park, K.-H. US 2007 191 638; E. I. Du Pont de Nemours and Company: USA, 2007.
- (20) Buch, F.; Harder, S. Z. *Naturforsch. B Chem. Sci.* **2008**, *63*, 169.
- (21) Bradley, A. Z.; Thompson, J. S. WO 2004 094 689; E. I. Du Pont de Nemours and Company: USA, 2004.
- (22) Clegg, W.; Coles, S. J.; Cope, E. K.; Mair, F. S. *Angew. Chem. Int. Ed.* **1998**, *37* (6), 796. doi:10.1002/(SICI)1521-3773(19980403)37:6<796::AID-ANIE796>3.0.CO;2-B.

# A convenient route to distannanes, oligostannanes, and polystannanes

Aman Khan, Robert A. Gossage, and Daniel A. Foucher

**Abstract:** The quantitative conversion of the tertiary stannane (*n*-Bu)<sub>3</sub>SnH (**2**) into (*n*-Bu)<sub>6</sub>Sn<sub>2</sub> (**4**) was achieved by heating the neat hydride material under low pressure or under closed inert atmosphere conditions. A 31% conversion of Ph<sub>3</sub>SnH (**3**) to Ph<sub>6</sub>Sn<sub>2</sub> (**5**) was also observed under low pressure; however, under closed inert atmosphere conditions afforded Ph<sub>4</sub>Sn (**6**) as the major product. A mixed distannane, (*n*-Bu)<sub>3</sub>SnSnPh<sub>3</sub> (**7**), can also be prepared in good yield utilizing an equal molar ratio of **2** and **3** and the same reaction conditions used to prepare **4**. This solvent-free, catalyst-free route to distannanes was extended to a secondary stannane, (*n*-Bu)<sub>2</sub>SnH<sub>2</sub> (**8**), which yielded evidence (NMR) for hydride terminated distannane H(*n*-Bu)<sub>2</sub>SnSn(*n*-Bu)<sub>2</sub>H (**9**), the polystannane [(*n*-Bu)<sub>2</sub>Sn]<sub>*n*</sub> (**10**), and various cyclic stannanes [(*n*-Bu)<sub>2</sub>Sn]<sub>*n=5,6*</sub> (**11**, **12**). Further evidence for **10** was afforded by gel permeation chromatography (GPC) where a broad, moderate molecular weight, but highly dispersed polymer, was obtained (*M*<sub>w</sub> = 1.8 × 10<sup>4</sup> Da, polydispersity index (PDI) = 6.9) and a characteristic UV–vis absorbance (λ<sub>max</sub>) of ≈ 370 nm observed.

**Key words:** solvent free, catalyst free, dehydrogenation, stannanes, polystannanes.

**Résumé :** On a effectué la conversion quantitative du stannane tertiaire (*n*-Bu)<sub>3</sub>SnH (**2**) en (*n*-Bu)<sub>6</sub>Sn<sub>2</sub> (**4**) par chauffage de l'hydruire net, à basse pression ou dans des conditions atmosphériques inertes, sans contact avec l'extérieur. On a aussi observé une conversion de 31 % du Ph<sub>3</sub>SnH (**3**) en Ph<sub>6</sub>Sn<sub>2</sub> (**5**) dans des conditions de basse pression; toutefois, dans des conditions atmosphériques inertes sans contact avec l'extérieur, le produit majeur est le Ph<sub>4</sub>Sn (**6**). Un distannane mixte (*n*-Bu)<sub>3</sub>SnSnPh<sub>3</sub> (**7**) peut aussi être préparé avec un bon rendement en utilisant un rapport molaire égal à l'unité des composés **2** et **3** dans les mêmes conditions que celles utilisées pour préparer le composé **4**. On a étendu cette nouvelle voie de préparation des distannanes, sans solvant et sans catalyseur, pour obtenir un distannane secondaire, le (*n*-Bu)<sub>2</sub>SnH<sub>2</sub> (**8**) qui, sur la base de données de RMN, contient aussi un distannane à hydruire terminal, H(*n*-Bu)<sub>2</sub>SnSn(*n*-Bu)<sub>2</sub>H (**9**), du polystannane, [(*n*-Bu)<sub>2</sub>Sn]<sub>*n*</sub> (**10**), et divers stannanes cycliques [(*n*-Bu)<sub>2</sub>Sn]<sub>*n=5,6*</sub> (**11**, **12**) dans lesquels *n* = 5 et 6. La chromatographie par perméation de gel (CPG) a aussi permis d'obtenir des données mettant en évidence la présence d'un polymère de poids moléculaire modéré, mais hautement dispersé (*M*<sub>w</sub> = 1,8 × 10<sup>4</sup> Da, indice de polydispersion (IPD) = 6,9) et d'observer une absorbance caractéristique dans le spectre UV–vis avec un λ<sub>max</sub> ≈ 370 nm.

**Mots-clés :** sans solvant, sans catalyseur, déshydrogénation, stannanes, polystannanes.

[Traduit par la Rédaction]

## Introduction

Hexaorganodistannanes are a convenient source of stannyl radicals and have found applications in organic chemistry in a variety of reduction reactions,<sup>1</sup> in addition to their utility in palladium-catalyzed cross-coupling processes.<sup>2</sup> Distannanes also serve as useful models for polystannanes.<sup>3</sup> Industrially, distannanes show considerable antibacterial and fungicidal activity and were previously used as wood preservatives.<sup>4</sup> The distannane class of compounds are the tin analogues of ethanes but possess a Sn–Sn bond that is comparatively weaker (154 vs 356 kJ/mol) and longer (2.80 vs 1.54 Å) than typical C–C bonds.<sup>5,6</sup> Organodistannanes are generally thermally stable but are chemically sensitive to the presence of oxygen (more so than that of water, mild acids, or alkalis) and can readily decompose to form stannoxanes (i.e., R<sub>3</sub>Sn–O–SnR<sub>3</sub>) such as **1** (Fig. 1).<sup>7</sup>

Distannanes can be synthesized directly from the dehydrogenative dimerization of tin hydrides (e.g., **2** and **3**) with either amines or alkoxides acting as the catalyst.<sup>8</sup> Organotin hydrides can also be dehydrogenatively coupled using transition metal catalysts such as Pd(PPh<sub>3</sub>)<sub>4</sub>, PdCl<sub>2</sub>(NCMe)<sub>2</sub>,<sup>9</sup> or ruthenium–allenylidene complexes.<sup>10</sup> Electrochemical preparations of R<sub>3</sub>SnSnR<sub>3</sub> (e.g., R = *n*-C<sub>4</sub>H<sub>9</sub> (**4**), C<sub>6</sub>H<sub>5</sub> (**5**), *p*-CH<sub>3</sub>C<sub>6</sub>H<sub>4</sub>–, or C<sub>6</sub>H<sub>5</sub>CH<sub>2</sub>–) compounds involving the reduction of R<sub>3</sub>SnX (X = Cl, NO<sub>3</sub>, H, SPh, OCHO, OCOCH<sub>3</sub>, etc.) have also been reported.<sup>11,12</sup> Stoichiometrically, **5** can be prepared via the reductive coupling of triphenyltin derivatives (Ph<sub>3</sub>SnX, where X = Cl, I, or OH) in a THF/aq NH<sub>4</sub>Cl solution containing Zn metal.<sup>13,14</sup> The first high yield synthesis of **4** was reported by Sawyer<sup>15</sup> from the treatment of distannoxane **1** with **2** at 100 °C for several days (Scheme 1).

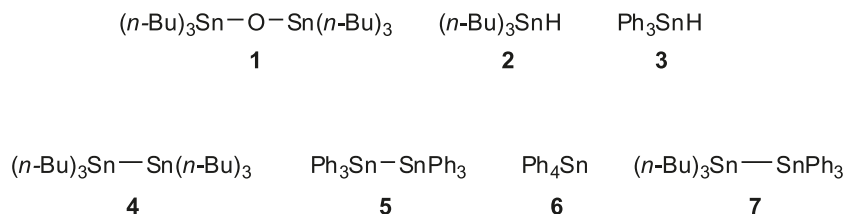
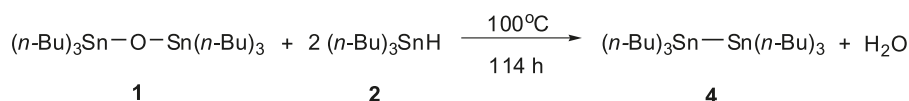
Alternative methods for the synthesis of **4** from **1** include

Received 22 June 2010. Accepted 29 July 2010. Published on the NRC Research Press Web site at canjchem.nrc.ca on 7 October 2010.

A. Khan, R.A. Gossage, and D.A. Foucher.<sup>1</sup> Department of Chemistry and Biology, Ryerson University, 350 Victoria Street, Toronto, ON M5B 2K3, Canada.

<sup>1</sup>Corresponding author (e-mail: daniel.foucher@ryerson.ca).



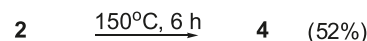
**Fig. 1.** Various stannanes.**Scheme 1.**

reactions with formic acid,<sup>16</sup> or reductions utilizing Mg, Na, or K metal in THF<sup>17</sup> solution; NaBH<sub>4</sub><sup>18</sup> or SmI<sub>2</sub><sup>19</sup> in hexamethylphosphoramide (HMPA) has also been used. Recently, an improvement in the synthesis of **4**<sup>20</sup> was reported, which involves a high temperature (200 °C), catalyst-free protocol using **1** and **2** at a molar ratio of 1:2.2. This method gives **4** in a quantitative yield. Interestingly, these same authors also reported a lower yield (52%) of **4** by simply heating **2** at a lower temperature (150 °C) for 6 h under vacuum (Scheme 2).

In this study, we reinvestigate the solvent and catalyst-free dehydrocoupling of **2** to produce **4** in an effort to identify the optimum reaction conditions for a variety of distannanes. This direct approach was thus extended to the aryl tin hydride (**3**) to obtain Ph<sub>3</sub>SnSnPh<sub>3</sub> (**5**). We also report on the catalyst-free reactions involving equimolar ratios of alkyl (**2**) and aryl (**3**) tin hydrides. Finally, we present evidence that this approach can be extended to alkyl dihydrostannanes for the production of both oligostannanes and polystannanes.

## Results and discussion

The reaction conditions for both **2** and **3** to produce distannanes **4** and **5** are listed in Table 1. An attempt to distill **2** (200 °C, in vacuo) using a long path distillation condenser was initiated with the intention to further purify **2**. Surprisingly, the product of this distillation was not **2**, but a nearly quantitative conversion (<sup>1</sup>H and <sup>119</sup>Sn NMR, yield: 97%) to distannane **4**. We investigated the impact of heating **2** to reflux temperature (200 °C) under reduced pressure using a long path reflux condenser. After 6 h, analysis by <sup>1</sup>H and <sup>119</sup>Sn NMR indicated a 75% conversion of **2** into **4**. The sample was further heated (6 h) under these conditions, but NMR analysis showed virtually no change in the proportions of the product and starting material. A plausible reason for this observation is that the more volatile hydride is retained by the cool portion of the reflux condenser rather than in close proximity to the heat source. To improve this conversion, **2** was heated (200 °C) under static vacuum conditions in a sealed Schlenk flask. An analysis (<sup>119</sup>Sn NMR) of a small aliquot of the reaction mixture taken every hour revealed that after 5 h, **2** had completely converted to the distannane **4**. A single <sup>119</sup>Sn resonance (δ = −83.6 ppm) was observed for **4**, with characteristic Sn satellites (*J*<sub>119Sn–117Sn</sub> = 1280 Hz), which is in agreement with reported literature values.<sup>20</sup> The reaction was also carried out in a sealed flask

**Scheme 2.**

under a nitrogen atmosphere. Analysis by <sup>119</sup>Sn NMR showed a small peak for **2** after 5 h, which was completely consumed after heating for an additional 1 h (Fig. 2). There was no evidence of redistribution products, which were reported when **2** was thermally dehydrocoupled in the presence of group 4 or 6 transition metal complexes.<sup>21</sup>

Similar dehydrocoupling conditions were used for hydride **3**. After 6 h at reflux (200 °C) under reduced pressure, analysis by NMR showed that approximately 31% of the starting material had converted to distannane **5**, with most of the remainder represented by the starting material **3** in addition to a significant fraction of the redistribution product (24%) Ph<sub>4</sub>Sn (**6**). Product **5** precipitated from the reaction mixture as a crystalline solid as it cooled and could be easily recovered from the starting material by recrystallization. The reaction was also repeated in a heated (200 °C) and sealed Schlenk flask under static vacuum. The <sup>119</sup>Sn NMR spectrum showed evidence of a thermal redistribution reaction with the bulk of the material converted (87%) to **6** and a considerably lower fraction of **5** (10%), in addition to a trace of grayish sediment, which was attributed to elemental tin (3%).

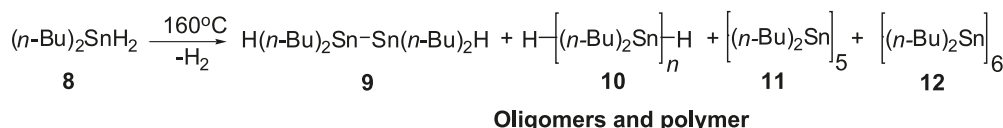
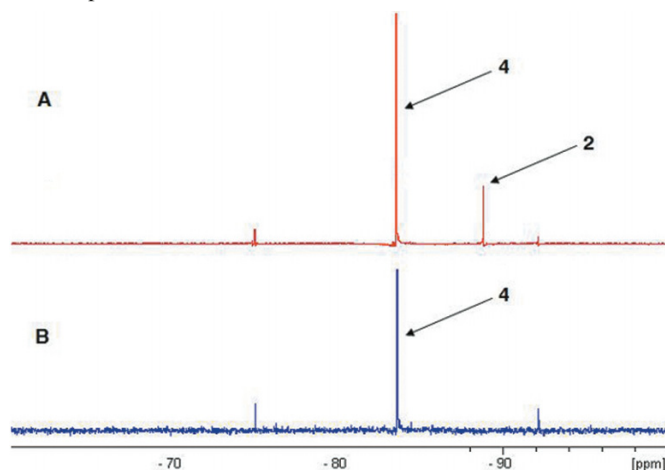
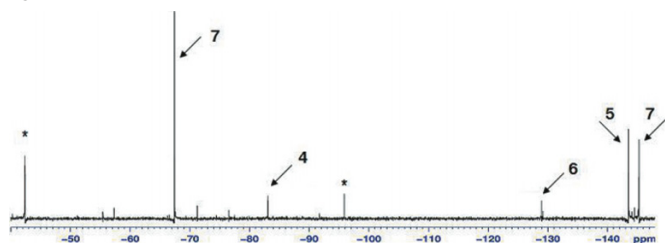
Utilizing closed, reduced-pressure reaction conditions, an equimolar mixture reaction of **2** and **3** was heated (200 °C) for 5 h. Analysis by <sup>119</sup>Sn NMR spectroscopy (Fig. 3) revealed resonances at δ = −145.8 and −67 ppm consistent with the formation of **7**.<sup>22</sup> The NMR evaluation of the reaction mixture also indicated that compound **7** was present in a 36.6% yield. Traces of the starting materials, along with **4** (11.9%) and **5** (37.6%), the redistribution product **6** (12.9%), recovered tin metal (1.2%), and two unassigned peaks were also noted. These unidentified materials may be other higher molecular weight redistribution products.

The solvent-free, catalyst-free reaction N<sub>2</sub>(g) conditions were also employed with the secondary stannane, (*n*-Bu)<sub>2</sub>SnH<sub>2</sub> (**8**; Scheme 3). After 6 h of heating (160 °C), <sup>119</sup>Sn NMR spectroscopic analysis of the bright yellow oily solid material revealed a multitude of resonances.

Clearly identifiable in this spectrum, however, was a resonance at δ ≈ −208 ppm, which is attributed to the hydride terminated distannane (*n*-Bu<sub>2</sub>SnH)<sub>2</sub> (**9**).<sup>23</sup> Additionally, a resonance at δ ≈ −189 ppm can be assigned to linear dibutyl-

**Table 1.** Catalyst- and solvent-free thermal couplings of tin hydrides.

Starting material	Reaction conditions	Reaction time (h)	Product	Yield (%)
<b>2</b>	200 °C, N <sub>2</sub>	6	<b>4</b>	97
	200 °C, reflux/reduced pressure	12	<b>4</b>	75
	200 °C, static/reduced pressure	5	<b>4</b>	95
<b>3</b>	200 °C, reflux/reduced pressure	6	<b>5, 6</b>	31, 24
	200 °C, static/reduced pressure	4	<b>5, 6</b>	10, 87
<b>2 and 3</b>	200 °C, static/reduced pressure	5	<b>4</b>	12
			<b>5</b>	37
			<b>6</b>	13
			<b>7</b>	37

**Scheme 3.****Fig. 2.** <sup>119</sup>Sn NMR spectra of the products from the dehydrocoupling of **2** at (A) 4 h at 200 °C and (B) 5 h at 200 °C under static reduced pressure.**Fig. 3.** <sup>119</sup>Sn NMR spectrum of the products from the dehydrocoupling of **2** and **3** at 200 °C for 5 h. Peaks with an asterisk are unassigned.

polystannane (**10**).<sup>24</sup> Two cyclic species (**11** and **12**) were identified by comparison with the literature <sup>119</sup>Sn chemical shift values.<sup>25,26</sup> The assignments of the rest of the minor signals has not yet been made but these are likely due to the presence of higher molecular weight hydride terminated oligomers (e.g., *n*-Bu<sub>2</sub>SnH(*n*-Bu<sub>2</sub>Sn)<sub>*n*</sub>SnH*n*-Bu<sub>2</sub>). Analysis of this material by gel permeation chromatography (GPC) showed a broad polymer distribution and a modest molecu-

lar weight polystannane (*M<sub>w</sub>* = 1.8 × 10<sup>4</sup> Da, polydispersity index (PDI) = 6.9), along with a considerable fraction of lower molecular weight linear and cyclic products. A UV-vis spectrum (Fig. 4) of the mixture containing the polymer **10** displayed a broad absorbance with a λ<sub>max</sub> centered at ≈ 370 nm. This absorbance can be attributed to the σ-σ\* of the polystannane, which is in good agreement with reported values.<sup>24</sup>

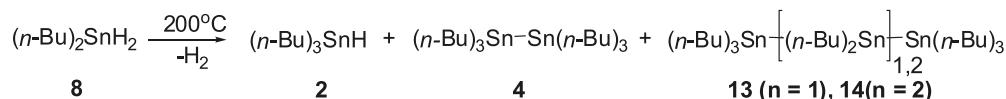
When the dehydrocoupling of **8** was attempted at a higher temperature (200 °C, 6 h), evidence of multitude of alkyl redistribution products was found (Scheme 4). Analysis by <sup>119</sup>Sn NMR spectroscopy showed resonances attributed to **2**, as well as to dimeric **4** and higher tributylstannane terminated oligomers (i.e., **13** and **14**), which were identified by comparison to literature values.<sup>16</sup> A large unassigned resonance was observed at +156 ppm. This downfield shift is characteristic of a four-coordinate dialkyl tin alkoxide species, e.g., R<sub>2</sub>Sn(OR)<sub>2</sub>, which typically have resonances in the range of +90 to +200 ppm.<sup>27</sup> There is no evidence of cyclic products nor hydride terminated oligomers.

## Mechanistic considerations

The catalyst- and solvent-free, presumably radically driven, dehydrocoupling reactions described herein (Scheme 5) are apparently activated through the thermolysis of the relatively weak Sn-H bonds of R<sub>3</sub>SnH (R = *n*-Bu<sub>3</sub>, Ph). The small differences between the ground state bond dissociation energies for known stannanes (e.g., Me<sub>3</sub>SnH = 305 ± 17 kJ/mol, Me<sub>3</sub>SnEt = 284 ± 17 kJ/mol, Me<sub>3</sub>SnPh = 339 ± 21 kJ/mol, and Me<sub>3</sub>SnSnMe<sub>3</sub> = 317 ± 25 kJ/mol) provides little insight to identifying clear redistribution trends with these systems.<sup>28</sup>

In the case of **3**, additional redistribution reactions to yield products such as **6** also occur. The Sn-aryl bonds also appear to be thermally labile at 200 °C and redistribution chemistry is competitive with dehydrogenation. In contrast, trialkyl stannanes seem less active towards such redistribution at this temperature. To maximize yields of distannanes and reduce the potential of unwanted redistribution products, it is essential to identify the optimum reaction conditions

Scheme 4.



(e.g., temperature and duration of the reaction). Closed reaction vessels under slight reduced pressure produce the highest yields for all products (**4**, **5**, and **7**). A likely driving force in these reactions is the liberation of  $\text{H}_2(\text{g})$  along with the formation of the persistent tin alkyl and aryl radicals that later combine to form distannanes. Attempts to carry out dehydrocoupling reactions at higher temperatures ( $>200^\circ\text{C}$ ) resulted in the decomposition of the starting materials and (or) lower product yields. Reaction of the secondary stannane **8** at lower temperatures ( $160^\circ\text{C}$ ) resulted in the formation of linear and cyclic polystannane species including a modest molecular weight polymer (**10**). The broad polydispersity found for this sample is typical of other radical polymers prepared from an uncontrolled polymerization process. The mechanism of propagation for this species is unclear, but may occur through the coupling of two growing oligomeric species that contain active radical end groups. When **8** is heated at  $200^\circ\text{C}$ , redistribution to tributylstannyl terminated species are dominant but no evidence for cyclics or polymers was noted.

## Conclusion

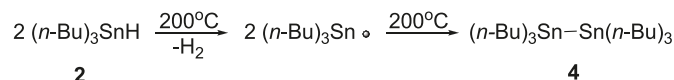
Compound **4** was successfully synthesized in a high yield from the thermally driven dehydrocoupling of the tertiary stannane **2** under a variety of catalyst- and solvent-free conditions. Compound **5** was also obtained in a similar way with lower conversion from the tertiary stannane **3**. A mixed distannane **7** was also prepared from the equimolar reaction of **2** and **3** under similar conditions. Evidence for the redistribution product **6** was found when aryl stannane (**3**) was used. Solvent- and catalyst-free dehydrogenative coupling of the secondary distannane **8** at  $160^\circ\text{C}$  resulted in the formation of a modest molecular weight polystannane (**10**) and other linear and cyclic stannanes, but favours only redistribution products at  $200^\circ\text{C}$ . This work has demonstrated that dehydrocoupling of stannanes in the absence of a catalyst under a variety of conditions may provide a viable route to valuable organic radical sources. Future efforts will be directed to the coupling of tertiary and secondary stannanes using other metal-free routes, including the use of light and microwave mediated coupling processes.

## Experimental methods

### Equipment and procedures

$^1\text{H}$ ,  $^{13}\text{C}\{^1\text{H}\}$ , and  $^{119}\text{Sn}\{^1\text{H}\}$  NMR spectra were recorded on a Bruker Avance 400 MHz NMR spectrometer.  $^1\text{H}$  spectra were referenced to the residual solvent peaks in the deuterated solvents, whereas the  $^{13}\text{C}$  spectra are referenced internally to the deuterated solvent resonances, which are in turn referenced to  $\text{SiMe}_4$  ( $\delta$  0 ppm), whereas  $^{119}\text{Sn}$  was referenced to  $\text{SnMe}_4$  ( $\delta$  0 ppm). UV-vis measurements were carried out in THF solutions using a PerkinElmer Lambda 40 spectrometer. Molecular weights of polymers were deter-

Scheme 5.



mined by gel permeation chromatography (GPC) using a Viscotek Triple Model 302 detector system equipped with a refractive index detector (RI), a four capillary differential viscometer (VISC), a right angle ( $90^\circ$ ) laser light scattering detector ( $\lambda_0 = 670 \text{ nm}$ ), and a low angle ( $7^\circ$ ) laser light scattering detector. GPC columns were calibrated versus polystyrene standards (American Polymer Standards). A flow rate of  $1.0 \text{ mL/min}$  was used with ACS grade THF as the eluent. GPC samples were prepared using 3–10 mg of polymers per mL THF, and filtered using a  $0.45 \mu\text{m}$  filter. All samples were run with and without ultraviolet absorbers (UVA; concn  $\approx 0.001 \text{ mol/L}$ ) for comparison. All reactions were carried out under a nitrogen atmosphere using Schlenk techniques unless otherwise described. Thermally driven dehydrocoupling reactions were performed under a variety of conditions in Schlenk flasks, including in an inert  $\text{N}_2$  atmosphere, or in a sealed Schlenk flask placed under a static reduced pressure (closed), or finally in a Schlenk flask exposed to dynamic reduced pressure (open). Pressures were measured using a mercury manometer attached to the Schlenk line.

### Materials

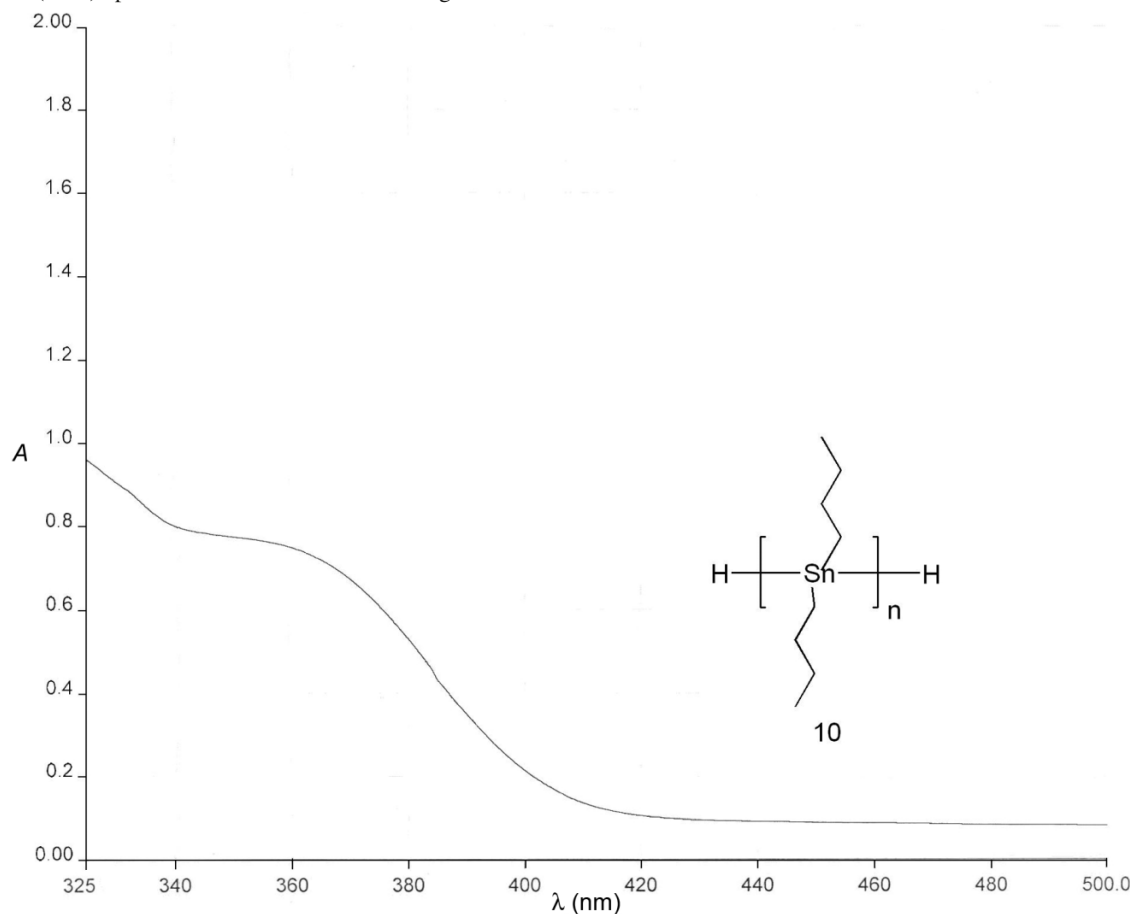
$(n\text{-Bu})_3\text{SnH}$  (**2**, 99%),  $\text{Ph}_3\text{SnH}$  (**3**, 97%),  $(n\text{-Bu})_2\text{SnCl}_2$  (97%),  $\text{LiAlH}_4$  (1.0 mol/L in ether), and anhydrous  $\text{CaCl}_2$  were purchased commercially and used without further purification.  $(n\text{-Bu})_6\text{Sn}_2$  (**4**) and  $\text{Ph}_6\text{Sn}_2$  (**5**) were purchased from Strem and used as reference samples.  $(n\text{-Bu})_2\text{SnH}_2$  (**8**) was prepared from  $(n\text{-Bu})_2\text{SnCl}_2$  and  $\text{LiAlH}_4$  according to literature preparation.<sup>24,25</sup> Solvents were dried by standard procedures prior to use.

### Large-scale thermal dehydrocoupling of **2** under reduced pressure (open system)

The tin hydride **2** (50 g, 0.17 mol) was added to a 100 mL round-bottom flask connected to a long path distillation condenser (13 cm) and the volatile components distilled at  $200^\circ\text{C}$  under reduced pressure ( $\approx 1 \times 10^{-2} \text{ mm Hg}$ ;  $1 \text{ mm Hg} = 133.32 \text{ Pa}$ ). The product of this distillation was then analyzed by NMR spectroscopy. The  $^1\text{H}$  and  $^{119}\text{Sn}$  NMR spectra revealed that **2** had been consumed and converted (recovered yield: 97%) into **4**. The NMR data provided here are in good agreement with literature values.<sup>18,20,22</sup>

### Small-scale thermal dehydrocoupling of **2** under reduced pressure (open system)

To a 25 mL round-bottom flask equipped with long path reflux condenser (20 cm), was added tin hydride **2** (1.0 g,

**Fig. 4.** UV-vis (THF) spectrum of the mixture containing **10**.

3.44 mmol). The sample was heated to reflux temperature (200 °C) under reduced pressure ( $\approx 2 \times 10^{-2}$  mm Hg) for 6 h. Analysis ( $^1\text{H}$  and  $^{119}\text{Sn}$  NMR spectroscopy) of a small aliquot of the reaction mixture revealed 75% conversion of **2** into **4**, while the remainder was unreacted **2**. Additional heating for 6 h under these conditions showed no further reactant conversion (NMR).

#### Small-scale thermal dehydrocoupling of **2** under reduced pressure (closed system)

To a 25 mL Schlenk flask equipped with a glass stopper was added **2** (530 mg, 1.82 mmol). The neat hydride was placed under static reduced pressure ( $\approx 5 \times 10^{-1}$  mm Hg), the vessel was then sealed and subsequently heated (200 °C) for 5 h. Analysis ( $^1\text{H}$  and  $^{119}\text{Sn}$  NMR spectroscopy) showed that the majority of **2** had been consumed and was converted to **4** (recovered yield: 95%).

#### Small-scale thermal dehydrocoupling of **2** under inert atmosphere (open system)

Compound **2** (530 mg, 1.82 mmol) was added to a 25 mL Schlenk flask equipped with a long path (20 cm) reflux condenser that was open to a  $\text{N}_2(\text{g})$  atmosphere. The flask was then heated (200 °C) for 6 h. Analysis ( $^1\text{H}$  and  $^{119}\text{Sn}$  NMR spectroscopy) of the reaction mixture indicated that **2** had been consumed and was converted to **4** (recovered yield: 97%).  $^1\text{H}$  NMR ( $\text{C}_6\text{D}_6$ , ppm)  $\delta$ : 0.97 (3H, t,  $\text{CH}_3\text{CH}_2\text{CH}_2\text{CH}_2\text{-Sn}$ ), 1.16 (2H, m,  $\text{CH}_3\text{CH}_2\text{CH}_2\text{CH}_2\text{-Sn}$ ), 1.42 (2H, m,

$\text{CH}_3\text{CH}_2\text{CH}_2\text{CH}_2\text{-Sn}$ ), 1.66 (2H, m,  $\text{CH}_3\text{CH}_2\text{CH}_2\text{CH}_2\text{-Sn}$ ).  $^{13}\text{C}\{^1\text{H}\}$  NMR ( $\text{C}_6\text{D}_6$ , ppm)  $\delta$ : 10.49 ( $^1J_{\text{C-Sn}}$  ( $\text{CH}_3\text{CH}_2\text{CH}_2\text{CH}_2\text{-Sn}$ ) = 120.3 Hz and  $^2J_{\text{C-Sn}}$  ( $\text{CH}_3\text{CH}_2\text{CH}_2\text{CH}_2\text{-Sn-Sn}$ ) = 19.6 Hz), 14.01 ( $\text{CH}_3\text{CH}_2\text{CH}_2\text{CH}_2\text{-Sn}$ ), 27.98 ( $^3J_{\text{C-Sn}}$  ( $\text{CH}_3\text{CH}_2\text{CH}_2\text{CH}_2\text{-Sn}$ ) = 26.5 Hz), 31.23 ( $^2J_{\text{C-Sn}}$  ( $\text{CH}_3\text{CH}_2\text{CH}_2\text{CH}_2\text{-Sn}$ ) = 8.1 Hz).  $^{119}\text{Sn}\{^1\text{H}\}$  NMR ( $\text{C}_6\text{D}_6$ , ppm)  $\nu$ : -83.6 ( $J_{^{119}\text{Sn}-^{117}\text{Sn}}$  = 1280 Hz).

#### Small-scale thermal dehydrocoupling of **3** under reduced pressure (open system)

Compound **3** (471 mg, 1.34 mmol) was added to a 25 mL round-bottom flask equipped with a long path reflux condenser (20 cm). The sample was heated (200 °C) under reduced dynamic pressure ( $\approx 1 \times 10^{-3}$  mm Hg) for 6 h. During this time period, clear and colourless crystals formed on the sides of the reaction flask that were then collected and analyzed ( $^1\text{H}$  and  $^{119}\text{Sn}$  NMR spectroscopy). These data indicated that a considerable fraction of **3** (41%) was unreacted. Approximately 59% of **3** was consumed and was converted to both **5** (31%),<sup>29</sup> **6** (24%),<sup>30</sup> and Sn metal (4%). Major product **5**:  $^1\text{H}$  NMR ( $\text{CDCl}_3$ , ppm)  $\delta$ : 7.28–7.36 (12H, m), 7.39–7.52 (12H, m), 7.60–7.63 (6H, m).  $^{13}\text{C}\{^1\text{H}\}$  NMR ( $\text{CDCl}_3$ , ppm)  $\delta$ : 139.24 (C1), 137.61 (C2, C6), 128.82 (C3, C5), 128.94 (C4).  $^{119}\text{Sn}\{^1\text{H}\}$  ( $\text{CDCl}_3$ , ppm)  $\delta$ : -143.7.

#### Small-scale thermal dehydrocoupling of **3** under reduced pressure (closed system)

To a 50 mL Schlenk flask equipped with a glass stopper



was added **3** (394 mg, 1.12 mmol). The neat hydride was kept under static reduced pressure ( $\approx 5 \times 10^{-1}$  mm Hg), the flask sealed, and heated (200 °C) for 4 h. Analysis ( $^1\text{H}$  and  $^{119}\text{Sn}$  NMR) of the reaction mixture indicated that **3** had been consumed and was converted to both **6** (yield: 87%),<sup>30</sup> **5** (yield: 10%),<sup>29</sup> and Sn metal (3%). Major product **6**:  $^{13}\text{C}\{^1\text{H}\}$  NMR ( $\text{CDCl}_3$ , ppm)  $\delta$ : 138.04 (C1), 137.39 (C2, C6), 128.79 (C3, C5), 128.28 (C4).  $^{119}\text{Sn}\{^1\text{H}\}$  NMR ( $\text{CDCl}_3$ , ppm)  $\delta$ : -129.6.

#### Small-scale thermal dehydrocoupling of **2** and **3** under reduced pressure (closed system)

To a 50 mL Schlenk flask equipped with a glass stopper was added **2** (291 mg, 1.00 mmol) and **3** (351 mg, 1.00 mmol). Neat tin hydrides were then placed under static reduced pressure ( $\approx 5 \times 10^{-1}$  mm Hg), sealed, and heated (200 °C) for 5 h. Analysis ( $^1\text{H}$  and  $^{119}\text{Sn}$  NMR) of the reaction products indicated the conversion of **2** and **3** into a mixture containing **4** (12%), **5** (37%), **6** (13%), **7** (37%), and trace of elemental tin (1%).

#### Small-scale thermal dehydrocoupling of **8** under nitrogen (open system)

To a 50 mL Schlenk flask equipped with a glass stopper was added **8** (428 mg, 1.82 mmol). The flask containing **8** was then placed under an atmosphere of  $\text{N}_2$  and heated (160 °C) for 6 h. Analysis ( $^1\text{H}$  and  $^{119}\text{Sn}$  NMR spectroscopy) of a small aliquot of the reaction mixture indicated the conversion of **8** to a mixture containing **9**, **10**, **11**, and **12** along with unassigned oligomers. UV-vis  $\lambda_{\text{max}}$  (nm): 370.  $^{119}\text{Sn}\{^1\text{H}\}$  NMR ( $\text{C}_6\text{D}_6$ , ppm)  $\delta$ : **10**: -189.3; **12**: -202.1; **8**: -203.2; **9**: -207.9; others: -195.6, -209.5, -220.1. Analysis by GPC revealed a molecular weight of  $M_w = 1.8 \times 10^4$  Da, PDI = 6.9.

#### Small-scale thermal dehydrocoupling of **8** under reduced pressure (open system)

To a 50 mL Schlenk flask equipped with a glass stopper was added **8** (500 mg, 2.12 mmol). The flask containing **8** was then placed under an atmosphere of  $\text{N}_2$  and heated (200 °C) for 6 h. Analysis ( $^1\text{H}$  and  $^{119}\text{Sn}$  NMR spectroscopy) of a small aliquot of the reaction mixture indicated the conversion of **8** to a mixture containing **2**, **4**, **13**, and **14** along with other unassigned peaks.  $^{119}\text{Sn}\{^1\text{H}\}$  NMR ( $\text{C}_6\text{D}_6$ , ppm)  $\delta$ : **14**: -75.3, -213.4; **13**: -76.2, -227.0; **4**: -83.2; **2**: -87.3; others: +155.9, -57.7, -66.6, -210.2.

#### Supplementary data

Supplementary data of  $^1\text{H}$  and  $^{119}\text{Sn}\{^1\text{H}\}$  NMR spectra for compounds **4**, **5**, **6**, and the products of the dehydrocoupling of **8** at two different temperatures are provided.

#### Acknowledgment

Drs. Foucher and Gossage would like to thank the Natural Sciences and Engineering Research Council of Canada (NSERC) Discovery Grants program and the Ryerson Dean's startup fund program for support of this research. A. Khan would like to thank the Molecular Sciences Program at Ryerson University for a graduate student award.

#### References

- (1) (a) Chabaud, L.; Landais, Y.; Renaud, P. *Org. Lett.* **2002**, *4* (24), 4257. doi:10.1021/ol026824y. PMID:12443072.; (b) Harendza, M.; Leßmann, K.; Neumann, W. P. *Synlett* **1993**, 283. doi:10.1055/s-1993-22433.; (c) Verlhac, J. B.; Chanson, E.; Jousseau, B.; Quintard, J. P. *Tetrahedron Lett.* **1985**, *26* (49), 6075. doi:10.1016/S0040-4039(00)95129-3.
- (2) (a) McIntee, J. W.; Sundararajan, C.; Donovan, A. C.; Kovacs, M. S.; Capretta, A.; Valliant, J. F. *J. Org. Chem.* **2008**, *73* (21), 8236. doi:10.1021/jo8013287. PMID:18826327.; (b) Ha, Y.-H.; Kang, S. K. *Org. Lett.* **2002**, *4* (7), 1143. doi:10.1021/ol025557t. PMID:11922803.
- (3) Adams, S.; Dräger, M. *Angew. Chem. Int. Ed. Engl.* **1987**, *26* (12), 1255. doi:10.1002/anie.198712551.
- (4) Crowe, A. J.; Hill, R.; Smith, P. J.; Cox, T. R. G. *Int. J. Wood. Preserv.* **1979**, *1*, 119.
- (5) Windus, T. L.; Gordon, M. S. *J. Am. Chem. Soc.* **1992**, *114* (24), 9559. doi:10.1021/ja00050a040.
- (6) Jacobsen, H.; Ziegler, T. *J. Am. Chem. Soc.* **1994**, *116* (9), 3667. doi:10.1021/ja00088a001.
- (7) See, for example: Podlech, J. Compounds of Group 14 (Ge, Sn, Pb); In *Science of Synthesis: Houben-Weyl Methods of Molecular Transformation — Category 1: Organometallics*; Moloney, M. G., Thieme, G., Eds.; Verlag: Stuttgart, 2003; Vol. 5, pp 273–283.
- (8) Smith, P. J. In *Comprehensive Organometallic Chemistry*; Abel, E. W., Ed.; Pergamon Press: Oxford, 1982; Vol. 2, Chapter 11, p 591.
- (9) Bumagin, N. A.; Gulevich, Y. V.; Beletskaya, I. P. *Bull. Acad. Sci. USSR Div. Chem. Sci. (Engl. Transl.)* **1984**, *33* (5), 1044. doi:10.1007/BF01141722.
- (10) Maddock, S. M.; Finn, M. G. *Angew. Chem. Int. Ed.* **2001**, *40* (11), 2138. doi:10.1002/1521-3773(20010601)40:11<2138::AID-ANIE2138>3.0.CO;2-6.
- (11) Nokami, J.; Nose, H.; Okawara, R. *J. Organomet. Chem.* **1981**, *212* (3), 325. doi:10.1016/S0022-328X(00)85658-2.
- (12) Savall, A.; Lacoste, G.; Mazerolles, P. *J. Appl. Electrochem.* **1981**, *11* (1), 61. doi:10.1007/BF00615323.
- (13) von Gyldenfeldt, F.; Marton, D.; Tagliavini, G. *Organometallics* **1994**, *13* (3), 906. doi:10.1021/om00015a025.
- (14) Makosza, M.; Grela, K. *Synth. Commun.* **1998**, *28* (14), 2697. doi:10.1080/00397919808004840.
- (15) Sawyer, A. K. *J. Am. Chem. Soc.* **1965**, *87* (3), 537. doi:10.1021/ja01081a025.
- (16) Jousseau, B.; Chanson, E.; Bevilacqua, M.; Saux, A.; Pereyre, M.; Barbe, B.; Petraud, M. *J. Organomet. Chem.* **1985**, *294* (3), C41. doi:10.1016/0022-328X(85)87458-1.
- (17) Jousseau, B.; Chanson, E.; Pereyre, M. *Organometallics* **1986**, *5* (6), 1271. doi:10.1021/om00137a042.
- (18) McAlonan, H.; Stevenson, P. J. *Organometallics* **1995**, *14* (8), 4021. doi:10.1021/om00008a058.
- (19) Handa, Y.; Inanaga, J.; Yamaguchi, M. *J. Chem. Soc. Chem. Commun.* **1989**, 298. doi:10.1039/C39890000298.
- (20) Darwish, A.; Chong, J. M. *Synth. Commun.* **2004**, *34* (10), 1885. doi:10.1081/SCC-120034172.
- (21) Woo, H.-G.; Song, S.-J.; Kim, B.-K. *Bull. Korean Chem. Soc.* **1998**, *19*, 1161.
- (22) Lee, A. S.-Y.; Zhang, S.-L.; Pan, O.-G. *J. Chin. Chem. Soc.* **1997**, *44*, 625.
- (23) Sharma, H. K.; Arias-Ugarte, R.; Metta-Magana, A. J.; Pannell, K. H. *Angew. Chem. Int. Ed.* **2009**, *48* (34), 6309. doi:10.1002/anie.200902327.
- (24) Imori, T.; Tilley, T. D. *J. Chem. Soc. Chem. Commun.* **1993**, 1607. doi:10.1039/c39930001607.

- (25) Imori, T.; Lu, V.; Cai, H.; Tilley, T. D. *J. Am. Chem. Soc.* **1995**, *117* (40), 9931. doi:10.1021/ja00145a001.
- (26) Pannell, K. H. In *Tin Chemistry: Fundamentals, Frontiers and Applications*; Davies, A. G., Tickink, E. R. T., Eds.; Wiley: New York, 2008; pp 371–387, and refs. cited therein.
- (27) Yergey, A. L.; Lampe, F. W. *J. Am. Chem. Soc.* **1965**, *87* (18), 4204. doi:10.1021/ja01096a046.
- (28) Davies, A. G. *Organotin Chemistry*, 2nd ed.; Davis, A. G., Ed.; Wiley-VCH: Weinheim, 2004; p 426.
- (29) King, B.; Eckert, H.; Denney, D. Z.; Herber, R. H. *Inorg. Chim. Acta* **1986**, *122* (1), 45. doi:10.1016/S0020-1693(00)81265-7.
- (30) Wharf, I.; Simard, M. G. *J. Organomet. Chem.* **1997**, *532* (1–2), 1. doi:10.1016/S0022-328X(96)06782-4.

# Is the oxygen “side-on”, or “end-on” and fluctional, in peroxy radicals with magnetically equivalent oxygen atoms?

K.U. Ingold and Gino A. DiLabio

**Abstract:** The  $g$  values that have been measured for the group-14 peroxy radicals are sufficiently similar to suggest that they all have very similar structures. However, the  $^{17}\text{O}$  hyperfine splittings seem to indicate that tin peroxy radicals have structures that differ from their lighter group-14 analogs. We hypothesize that the oxygen atoms in tin peroxy radicals are magnetically equivalent because they undergo a rapid 1,2-shift. Density-functional and wave-function theory calculations support this view.

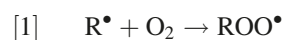
**Key words:** electron paramagnetic resonance spectroscopy, density-functional theory, group-14 peroxy radicals.

**Résumé :** Les valeurs  $g$  qui ont été mesurées pour les groupes hydroxyles du groupe 14 sont suffisamment semblables pour suggérer qu'ils ont tous des structures très semblables. Toutefois, les dédoublements hyperfins du  $^{17}\text{O}$  semblent indiquer que les peroxydes de l'étain possèdent des structures qui diffèrent de celles de leurs analogues plus légers du groupe 14. On croit que les atomes d'oxygène des peroxydes de l'étain sont magnétiquement équivalents parce qu'ils subissent un rapide déplacement 1,2. La théorie de la fonctionnelle de la densité et celle de la fonction d'onde supportent toutes les deux cette hypothèse.

**Mots-clés :** spectroscopie de résonance paramagnétique électronique, théorie de la fonctionnelle de la densité, radicaux peroxydes du groupe 14.

[Traduit par la Rédaction]

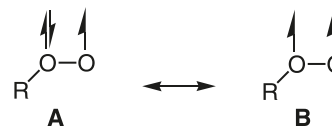
The oxidative degradation of organic materials, such as lubricating oils, plastics, edible fats, and even lipids in living organisms, are free-radical, two-step, chain processes (see reactions. [1] and [2]).



The economic costs of such degradation have led to exhaustive research on the kinetics, thermodynamics, and reaction mechanisms of these autoxidation processes and on methods for their retardation (inhibition). There has also been extensive research on the structures of the chain-propagating alkylperoxy radicals,  $\text{ROO}^\bullet$ , primarily by electron paramagnetic resonance (EPR) spectroscopy. Most organic radicals have  $g$  values near that of the free electron (2.0023) as a consequence of the almost complete quenching of orbital angular momentum. In contrast, alkylperoxy radicals have much higher  $g$  values (range: 2.014–2.017)<sup>1</sup> because their orbital angular momentum is incompletely quenched.<sup>2</sup>

The use of  $^{17}\text{O}$ -labelled dioxygen to trap carbon-centered radicals has revealed that alkylperoxy radicals have two magnetically

inequivalent oxygen atoms.<sup>1,3–6</sup> This is readily understood by consideration of the two canonical structures, **A** and **B**.



In  $\text{Me}_3\text{COO}^\bullet$ , inductive electron donation by the *tert*-butyl group and conjugative electron delocalization stabilize **B**, with  $^{17}\text{O}$  labelling indicating that **A** and **B** make contributions of approximately 60% and 40%, respectively.<sup>3,4</sup> The relative importance of **A** increases as the inductive electron-donating ability of R declines and, with the electron-withdrawing trichloromethyl group, the unpaired spin density on the outer oxygen atom reaches 70%.<sup>6,7–9</sup>

Other triorgano group-14 peroxy radicals have been prepared and examined by EPR spectroscopy.<sup>1</sup> Relevant EPR data are given in Table 1. Table 1 contains the isotropic  $g$  values measured in cyclopropane solution<sup>10</sup> and the two  $^{17}\text{O}$  hyperfine splittings (hfs) for triorgano-silylperoxy radicals,<sup>11</sup> -germylperoxy radicals,<sup>12</sup> and -stannylperoxy radicals.<sup>11,13</sup> These hfs have not been measured for plumbylperoxy radicals. The  $g$  values of these peroxy

Received 25 January 2010. Accepted 31 March 2010. Published on the NRC Research Press Web site at canjchem.nrc.ca on 19 August 2010.

This article is part of a Special Issue dedicated to Professor R. J. Boyd.

**K.U. Ingold.** National Research Council, 100 Sussex Drive, Ottawa, ON K1A 0R6, Canada.

**G.A. DiLabio.**<sup>1</sup> National Institute for Nanotechnology, National Research Council, 11421 SK Drive, Edmonton, AB T6G 2M9, Canada.

<sup>1</sup>Corresponding author (e-mail: gino.dilabio@nrc.ca).

**Table 1.** EPR parameters for some triorgano group-14 peroxy radicals.

Peroxy radical	<i>g</i> value	<i>a</i> <sub>17O</sub> (inner) (G)	<i>a</i> <sub>17O</sub> (outer) (G)	<i>a</i> <sub>17O</sub> ref.
Me <sub>3</sub> COO•	2.0154 <sup>a</sup>	17.6 <sup>b</sup>	23.45	4
Ph <sub>3</sub> COO•	2.014 <sup>c</sup>	14.3 <sub>av</sub> <sup>c,d</sup>	24.3 <sub>av</sub> <sup>c,d</sup>	5
Cl <sub>3</sub> COO•	2.0153 <sup>e</sup>	10.4 <sub>av</sub> <sup>e,f</sup>	28.2 <sub>av</sub> <sup>e,f</sup>	6
(Me <sub>3</sub> C) <sub>3</sub> SiOO•	2.0294 <sup>g</sup>	14.6	25.4	11
Me <sub>3</sub> GeOO•	2.024 <sup>h</sup>	~15 <sup>i</sup>	~25 <sup>i</sup>	12
( <i>n</i> -Bu) <sub>3</sub> SnOO•	2.024 <sup>j</sup>	25	25	13
Me <sub>3</sub> PbOO•	2.034	NA <sup>k</sup>	NA <sup>k</sup>	NA <sup>k</sup>

**Note:** Isotropic parameters measured in cyclopropane solution are from ref. 10 unless otherwise noted.

<sup>a</sup>In C<sub>6</sub>D<sub>6</sub>, ref. 10.

<sup>b</sup>The value of 16.4 G from ref. 3 has been corrected for sweep width error by a factor of 23.45/21.8 = 1.076, see footnote 2 in ref. 4.

<sup>c</sup>At 123 K in polycrystalline triphenylacetic acid.

<sup>d</sup>Based on <sup>17</sup>O hfs of 61 and 91 G and the suggestion<sup>5</sup> that the other principal values of the <sup>17</sup>O tensors are both approximately –8 G.

<sup>e</sup>At 93 K in a methanol glass.

<sup>f</sup>Based on <sup>17</sup>O hfs of 49.2 and 102.6 G at 93 K and the suggestion<sup>5</sup> that the other principal values of the <sup>17</sup>O tensors are both approximately –8 G.

<sup>g</sup>Values for Me<sub>3</sub>SiOO• and Ph<sub>3</sub>SiOO• are 2.0277 and 2.0271, respectively.<sup>11</sup>

<sup>h</sup>Ph<sub>3</sub>GeOO• has the same *g*.<sup>12</sup>

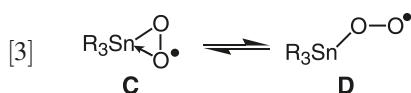
<sup>i</sup>From the text of ref. 13.

<sup>j</sup>Given as 2.025 in ref. 11. This reference includes Me<sub>3</sub>SnOO• (*g* = 2.024) and Ph<sub>3</sub>SnOO• (*g* = 2.020).

<sup>k</sup>NA: not available.

yls are somewhat greater than those of triorgano carbon centered radicals (as might be expected from the presence of heavier atoms attached to the O–O moiety). However, the *g* values of all the group-14 peroxy radicals are sufficiently similar to suggest that they all have very similar structures.

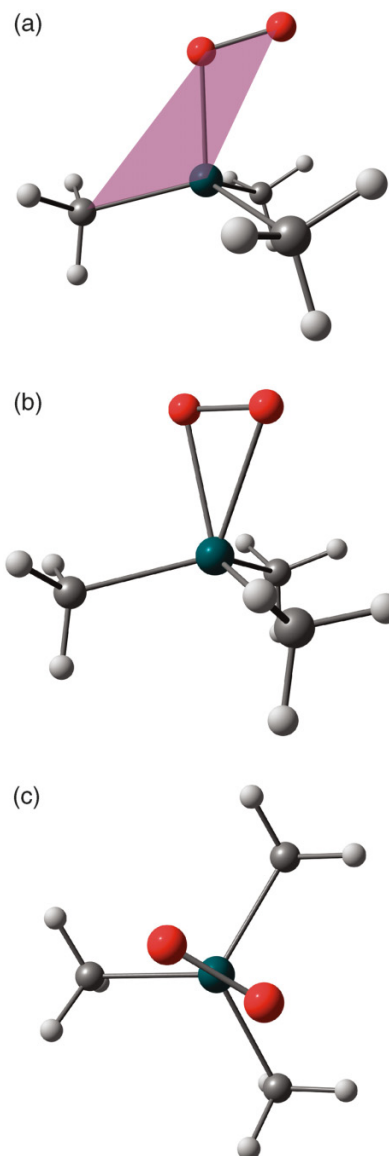
On the other hand, the <sup>17</sup>O hyperfine splittings (hfs) appear to tell a different story. For *tert*-butylperoxy radical it has been established that the larger <sup>17</sup>O hfs comes from the terminal (outer) O atom.<sup>4</sup> The same is presumed to be true for all other alkylperoxy radicals and also for the silyl- and germylperoxy radicals.<sup>14</sup> However, the tri-*n*-butylstannylperoxy radical was found to have two magnetically equivalent O atoms,<sup>11,13</sup> and it was hypothesized to have “a pentacoordinate, trigonal bipyramidal structure in which the vacant Sn 5d orbitals are used to form a dative bond with the lone pair of electrons on the terminal oxygen of the peroxy function”<sup>10,12</sup> (structure **C**). Later,<sup>13</sup> it was found that stannylperoxy radicals reacted rather like alkylperoxy radicals,<sup>15</sup> which led to the suggestion that structure **C** might be in equilibrium with the “usual structure for a peroxy radical” (**D**).<sup>13</sup>



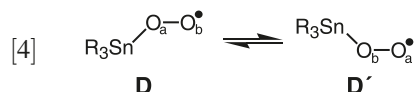
The possibility that **C** was simply the transition state structure for a rapid 1,2 shift of the trialkylstannyl group between the two oxygen atoms, appears not to have been considered.<sup>11,13</sup>

In view of the foregoing, we hypothesized that the oxygen atoms in *n*-Bu<sub>3</sub>SnOO• were magnetically equivalent because of a fast 1,2-shift of the *n*-Bu<sub>3</sub>Sn group, **D** ↔ **D'**, rather than

**Fig. 1.** Perspective images representing (a) the minimum energy structure for Me<sub>3</sub>XOO• and the (b) side and (c) top-down views of the transition state structure interconverting two equivalent structures of the type in (a). Atoms are represented as follows: H = white, C = gray, X = blue (X = C, Si, Ge, Sn, and Pb), and O = red. Atoms in the shaded area are coplanar.



because this radical had the symmetric structure, **C**. To check this hypothesis we turned to theory.



Using a density functional theory (DFT) approach,<sup>16</sup> we computed the lowest energy structures for Me<sub>3</sub>XOO• (X = C, Si, Ge, Sn, and Pb) radicals and subsequently verified the structures as minima by obtaining all positive vibration frequencies. We chose to use methyl-substituted group-14 peroxy radicals for simplicity, recognizing that more elaborate substituents (e.g., butyl groups) will not change our general conclusions. In all cases, the lowest energy structure was



**Table 2.** Zero-point corrected energies of  $\text{Me}_3\text{XCOO}^\bullet$  “side-on” structures relative to “end-on” structures ( $\Delta E$ ),<sup>24</sup> calculated rate constants for  $[\text{Me}_3\text{XOO}^\bullet]^\ddagger = [\text{Me}_3\text{XO}^\bullet\text{O}]^\ddagger$ , and calculated EPR parameters for lowest energy, i.e., “end-on”, structures.

X	$\Delta E$ (kcal/mol)	$k$ ( $\text{s}^{-1}$ ) <sup>a</sup>	$a_{17\text{O}}$ (inner) (G)	$a_{17\text{O}}$ (outer) (G)	Calcd. (exptl.) ratio <sup>b</sup>
C	59.7	$8 \times 10^{-52}$	16.9	23.2	1.37 (1.33)
Si	12.8	$2 \times 10^{-1}$	13.1	23.2	1.77 (1.74)
Ge	15.0	$1 \times 10^{-3}$	14.8	23.3	1.57 (1.67)
Sn	4.5	$5 \times 10^8$	15.7	23.1	1.47 (1)
Pb	5.6	$3 \times 10^7$	16.7	23.1	NA <sup>c</sup>

<sup>a</sup>Thermochemical corrections obtained at 200 K.

<sup>b</sup>Obtained as  $a_{17\text{O}}(\text{outer})/a_{17\text{O}}(\text{inner})$ .

<sup>c</sup>NA: not available.

found to be “end-on”, as illustrated in Fig. 1a. Are “side-on” structures also minima? Calculations show that structures of this type represent transition states (TS) connecting equivalent end-on structures.<sup>23</sup> The energies of these TS structures, relative to their corresponding ground-state end-on radicals, are given in Table 2. Two views of a representative TS structure are shown in Figs. 1b and 1c.

The relative energies in Table 2 reveal a nonmonotonic decrease in the barrier to interconversion between equivalent end-on structures, through the side-on TS structure, with increasing atomic mass of the group-14 atom. Using the barrier heights associated with  $\text{Me}_3\text{COO}^\bullet$ ,<sup>25–28</sup>  $\text{Me}_3\text{SiOO}^\bullet$ , and  $\text{Me}_3\text{GeOO}^\bullet$ , together with conventional transition state theory gives rate constants at “EPR” temperatures, viz., 200 K, for interconversion between end-on structures that are too small for interconversion to be observed on the EPR time scale. However, the calculated rate constants associated with interconversion of  $\text{Me}_3\text{SnOO}^\bullet$  and  $\text{Me}_3\text{PbOO}^\bullet$  are very large, viz.,  $>10^7 \text{ s}^{-1}$ , which lends support to the mechanism implied by reaction [4]. We note that our calculations indicate that the energy required to dissociate  $\text{O}_2$  from the  $\text{Me}_3\text{Sn}$  moiety is  $\sim 33$  kcal/mol, indicating that the interconversion is a concerted process. In contrast, the computed energy required to dissociate  $\text{O}_2$  from  $\text{Me}_3\text{COO}^\bullet$  is  $\sim 31.4$  kcal/mol, indicating that the concerted process will never compete with dissociation.

To provide additional support for the interconversion via the reaction in reaction [4], we sought to calculate the  $a_{17\text{O}}$  values of the group-14 trimethyl peroxy radicals. Our initial calculations were performed using “EPR-III” basis sets,<sup>29</sup> which are specifically designed to give reasonable hyperfine coupling constants. However, we found these basis sets to be inadequate for the systems investigated in the present work. Using  $\text{Me}_3\text{COO}^\bullet$  as a single example,  $a_{17\text{O}}$  values computed with EPR-III bases using a variety of computational methods were in very poor agreement with experiment, e.g., values (in G) obtained from the following methods for  $a_{17\text{O}}$  (inner) and  $a_{17\text{O}}$  (outer) were HF 23.6 and 48.3, BHandH<sup>30</sup>LYP<sup>31</sup> 19.3 and 28.5, B3<sup>17</sup>LYP<sup>31</sup> 12.7 and 16.8, B3<sup>2</sup>LYP<sup>31</sup> 8.6 and 10.9, B97<sup>133</sup> 13.3 and 20.0, HCTH407<sup>34</sup> 6.4 and 12.2, MP2 18.9 and 21.9, respectively; experiment 17.6 and 23.5, see Table 1. Similarly poor results were obtained for  $\text{Me}_3\text{SiOO}^\bullet$ . We therefore resorted to the use of diffusion augmented, correlation-consistent polarized core/valence triple-zeta polarization (aug-cc-CVpVTZ)<sup>35</sup> basis sets. Additional testing revealed

that various methods with the aug-cc-CVpVTZ bases produced  $a_{17\text{O}}$  values that are in better agreement with experiment, compared to those obtained with the EPR-III bases, but were still not satisfactorily accurate. Once again using the example of  $\text{Me}_3\text{COO}^\bullet$ , we obtained the following  $a_{17\text{O}}$  (inner) and  $a_{17\text{O}}$  (outer) values (all in G): BHandHLYP 18.4 and 27.0, MP2 17.9 and 21.0, respectively. It was clear that it was necessary to perform the calculations at a higher level of electronic correlation. We chose to use the coupled-cluster approach with single and double electronic excitation (CCSD) with all electrons (core and valence) correlated. The large size of the basis set and extent of correlation required that we use a local dense basis set (LDBS) approach,<sup>36</sup> in which we apply the aug-cc-CVpTZ basis set to the O atoms, and the remaining atoms were treated with smaller basis sets and (or) effective core potentials.<sup>21,22</sup> Additional tests showed that  $a_{17\text{O}}$  values obtained using the LDBS approach described above are within  $\sim 0.5\%$  of those obtained using balanced basis sets (i.e., aug-cc-CVpTZ basis sets on all atoms).

Table 2 shows the  $a_{17\text{O}}$  values obtained using the CCSD/LDBS approach described above. The values for  $\text{Me}_3\text{COO}^\bullet$ ,  $\text{Me}_3\text{SiOO}^\bullet$ , and  $\text{Me}_3\text{GeOO}^\bullet$  are within  $\sim 8.4\%$  of the measured values presented in Table 1, an agreement that can be considered reasonable. For these three peroxy radicals, the calculated ratio of  $a_{17\text{O}}$  (inner)/ $a_{17\text{O}}$  (outer) show excellent agreement with the experimentally determined ratios, and provide us with considerable confidence in the results of the calculations.

For  $\text{Me}_3\text{SnOO}^\bullet$ , theory predicts a large difference in inner (15.7 G) and outer (23.1 G)  $a_{17\text{O}}$  values with a ratio of 1.49, whereas EPR measurements on  $^{17}\text{O}$ -labelled  $(n\text{-Bu})_3\text{SnOO}^\bullet$  indicate that both oxygen atoms are magnetically equivalent (25 G). Clearly, the equivalent measured  $a_{17\text{O}}$  values result because of the low (calculated) barrier to interconversion between end-on structures. Calculations show similar results and would be observed for analogous lead peroxy radicals.

## References

- (1) (a) Howard, J. A. In *Magnetic Properties of Free Radicals*; Fischer, H., Ed.; Landolt-Börnstein, New Series, Springer-Verlag: Berlin, 1979; Vol. 9, Part c2; 1988; Vol. 17, Part e; 2004; Vol. 26, Part c.
- (2) Thomas, J. R. *J. Am. Chem. Soc.* **1966**, 88 (9), 2064. doi:10.1021/ja00961a050.

- (3) Adamic, K.; Ingold, K. U.; Morton, J. R. *J. Am. Chem. Soc.* **1970**, 92 (4), 922. doi:10.1021/ja00707a031.
- (4) Howard, J. A. *Can. J. Chem.* **1972**, 50 (12), 1981. doi:10.1139/v72-318.
- (5) Melamud, E.; Silver, B. L. *J. Magn. Reson.* **1974**, 14, 112.
- (6) Sevilla, M. D.; Becker, D.; Yan, M. *J. Chem. Soc., Faraday Trans.* **1990**, 86 (19), 3279. doi:10.1039/ft9908603279.
- (7) The more localized unpaired electron in  $\text{Cl}_3\text{COO}^\bullet$  makes this radical much more reactive than  $\text{Me}_3\text{COO}^\bullet$ , e.g.,  $k(\text{Cl}_3\text{COO}^\bullet + c\text{-C}_6\text{H}_{12}) = 1 \times 10^3 \text{ (mol/L)}^{-1} \text{ s}^{-1}$ ,<sup>8</sup>  $k(\text{Me}_3\text{COO}^\bullet + c\text{-C}_6\text{H}_{12}) = 3 \times 10^{-3} \text{ (mol/L)}^{-1} \text{ s}^{-1}$ .<sup>9</sup>
- (8) Mosseri, S.; Alfassi, Z. B.; Neta, P. *Int. J. Chem. Kinet.* **1987**, 19 (4), 309. doi:10.1002/kin.550190405.
- (9) Howard, J. A. *Isr. J. Chem.* **1984**, 24, 33.
- (10) Bennett, J. E.; Howard, J. A. *J. Am. Chem. Soc.* **1972**, 94 (23), 8244. doi:10.1021/ja00778a058.
- (11) Howard, J. A.; Tait, J. C.; Tong, S. B. *Can. J. Chem.* **1979**, 57 (20), 2761. doi:10.1139/v79-446.
- (12) Howard, J. A.; Tait, J. C. *Can. J. Chem.* **1976**, 54 (16), 2669. doi:10.1139/v76-376.
- (13) Howard, J. A.; Tait, J. C. *J. Am. Chem. Soc.* **1977**, 99 (25), 8349. doi:10.1021/ja00467a053.
- (14) Quite a number of peroxy radicals on heteroatoms,  $\text{Y}_n\text{XOO}^\bullet$ , are also known to have magnetically inequivalent  $^{17}\text{O}$  atoms,<sup>1</sup> including X = N, O, F, P, S, As, Mn, Co, and Cu. Presumably, all these radicals have more or less the same linear, nonfluctuating, structure as alkylperoxy radicals. They will not be considered further in this paper.
- (15) Like alkylperoxy radicals, the stannylperoxy radicals decay with second-order kinetics. Values of  $\log(A)$  and  $E_a$  for the reactions of  $n\text{-Bu}_3\text{SnOO}^\bullet$  with 2,6-di-*tert*-butyl-4-methylphenol and Co(II) acetylacetonate are 7.5 and 7  $\text{(mol/L)}^{-1} \text{ s}^{-1}$  and 12 and 11.5 kcal/mol, respectively, while the corresponding values for  $\text{Me}_3\text{COO}^\bullet$  are 4.6 and 0.8  $\text{(mol/L)}^{-1} \text{ s}^{-1}$  and 8.9 and 4.7 kcal/mol, respectively.<sup>11</sup>
- (16) Structures were optimized at the  $\text{B3}^{17}\text{P86}^{18}$  level of theory using 6-311+G(2d,2p) basis sets for C, H, O, Si, and Ge atoms. This approach has been shown to predict fairly accurate bond dissociation enthalpies in a broad range of compounds.<sup>19</sup> Small-core, averaged relativistic effective potentials (AREPs) and accompanying (uncontracted) basis sets were used for the Sn<sup>20</sup> and Pb<sup>21</sup> atoms. All calculations used the Gaussian 03 program package.<sup>22</sup>
- (17) Becke, A. D. *J. Chem. Phys.* **1993**, 98 (7), 5648. doi:10.1063/1.464913.
- (18) Perdew, J. P. *Phys. Rev. B* **1986**, 33 (12), 8822. doi:10.1103/PhysRevB.33.8822.
- (19) Johnson, E. R.; Clarkin, O. J.; DiLabio, G. A. *J. Phys. Chem. A* **2003**, 107 (46), 9953. doi:10.1021/jp035315q.
- (20) LaJohn, L. A.; Christiansen, P. A.; Ross, R. B.; Atashroo, T.; Ernler, W. C. *J. Chem. Phys.* **1987**, 87 (5), 2812. doi:10.1063/1.453069.
- (21) Wildman, S. A.; DiLabio, G. A.; Christiansen, P. A. *J. Chem. Phys.* **1997**, 107 (23), 9975. doi:10.1063/1.475301.
- (22) Frisch, M. J.; Trucks, G. W.; Schlegel, H. B.; Scuseria, G. E.; Robb, M. A.; Cheeseman, J. R.; Montgomery, J. A., Jr.; Vreven, T.; Kudin, K. N.; Burant, J. C.; Millam, J. M.; Iyengar, S. S.; Tomasi, J.; Barone, V.; Mennucci, B.; Cossi, M.; Scalmani, G.; Rega, N.; Petersson, G. A.; Nakatsuji, H.; Hada, M.; Ehara, M.; Toyota, K.; Fukuda, R.; Hasegawa, J.; Ishida, M.; Nakajima, T.; Honda, Y.; Kitao, O.; Nakai, H.; Klene, M.; Li, X.; Knox, J. E.; Hratchian, H. P.; Cross, J. B.; Adamo, C.; Jaramillo, J.; Gomperts, R.; Stratmann, R. E.; Yazyev, O.; Austin, A. J.; Cammi, R.; Pomelli, C.; Ochterski, J. W.; Ayala, P. Y.; Morokuma, K.; Voth, G. A.; Salvador, P.; Dannenberg, J. J.; Zakrzewski, V. G.; Dapprich, S.; Daniels, A. D.; Strain, M. C.; Farkas, O.; Malick, D. K.; Rabuck, A. D.; Raghavachari, K.; Foresman, J. B.; Ortiz, J. V.; Cui, Q.; Baboul, A. G.; Clifford, S.; Cioslowski, J.; Stefanov, B. B.; Liu, G.; Liashenko, A.; Piskorz, P.; Komaromi, I.; Martin, R. L.; Fox, D. J.; Keith, T.; Al-Laham, M. A.; Peng, C. Y.; Nanayakkara, A.; Challacombe, M.; Gill, P. M. W.; Johnson, B.; Chen, W.; Wong, M. W.; Gonzalez, C.; Pople, J. A. *Gaussian 03*, revision D.01; Gaussian, Inc.: Pittsburgh, PA, 2004.
- (23) All "side-on" structures were found to have a single imaginary vibration frequency. Displacement along this vibration mode generates structures that have "end-on" character.
- (24) The general trend in  $\Delta E$  as a function of group-14 atomic mass was verified by performing QCISD(T) single-point energy calculations.
- (25) At the suggestion of a reviewer, we computed<sup>16</sup> the zero-point corrected barrier associated with the interconversion of the phenylperoxy radical ( $\text{C}_6\text{H}_5\text{OO}^\bullet$ ). As in the case of the 1,1-diphenylethoxy radical<sup>26,27</sup> and triphenylmethoxy radical,<sup>28</sup> the phenylperoxy radical is predicted to have a stable spiro-type intermediate that is 20.4 kcal/mol higher in energy than the open form of the radical. The barrier to the formation of the intermediate is predicted to be 26.9 kcal/mol.
- (26) Smeu, M.; DiLabio, G. A. *J. Org. Chem.* **2007**, 72 (12), 4520. doi:10.1021/jo070126f. PMID:17488039.
- (27) Bietti, M.; Ercolani, G.; Salamone, M. *J. Org. Chem.* **2007**, 72 (12), 4515. doi:10.1021/jo070125n. PMID:17488038.
- (28) DiLabio, G. A.; Ingold, K. U.; Lin, S.; Litwinienko, G.; Mozenon, O.; Mulder, P.; Tidwell, T. T. *Angew. Chem. Int. Ed.* **2010**, in press. doi:10.1002/anie.201001008.
- (29) Barone, V. In *Recent Advances in Density Functional Theory*; Chong, D. P., Ed.; World Scientific Publishing Co.: Singapore, 1996.
- (30) Becke, A. D. *J. Chem. Phys.* **1993**, 98 (2), 1372. doi:10.1063/1.464304.
- (31) Lee, C.; Yang, W.; Parr, R. G. *Phys. Rev. B* **1988**, 37 (2), 785. doi:10.1103/PhysRevB.37.785.
- (32) Becke, A. D. *Phys. Rev. A* **1988**, 38 (6), 3098. doi:10.1103/PhysRevA.38.3098. PMID:9900728.
- (33) Hamprecht, F. A.; Cohen, A. J.; Tozer, D. J.; Handy, N. C. *J. Chem. Phys.* **1998**, 109 (15), 6264. doi:10.1063/1.477267.
- (34) Boese, A. D.; Handy, N. C. *J. Chem. Phys.* **2001**, 114 (13), 5497. doi:10.1063/1.1347371.
- (35) (a) Dunning, T. H., Jr. *J. Chem. Phys.* **1989**, 90 (2), 1007. doi:10.1063/1.456153.; (b) Kendall, R. A.; Dunning, T. H., Jr.; Harrison, R. J. *J. Chem. Phys.* **1992**, 96 (9), 6796. doi:10.1063/1.462569.; (c) Basis sets were obtained from the "basis set exchange" library: Feller, D. *J. Comput. Chem.* **1996**, 17 (13), 1571. doi:10.1002/(SICI)1096-987X(199610)17:13<1571::AID-JCC9>3.0.CO;2-P.; (d) Schuchardt, K. L.; Didier, B. T.; Elsethagen, T.; Sun, L.; Gurumoorthi, V.; Chase, J.; Li, J.; Windus, T. L. *J. Chem. Inf. Model.* **2007**, 47 (3), 1045. doi:10.1021/ci600510j. PMID:17428029.
- (36) DiLabio, G. A. *J. Phys. Chem. A* **1999**, 103 (51), 11414. doi:10.1021/jp992492b.

# Nonempirical density-functional theory for van der Waals interactions

Axel D. Becke, Alya A. Arabi, and Felix O. Kannemann

**Abstract:** In previous work, Kannemann and Becke [*J. Chem. Theory Comput.* **5**, 719 (2009) and *J. Chem. Theory Comput.* **6**, 1081 (2010)] have demonstrated that the generalized gradient approximations (GGAs) of Perdew and Wang for exchange [*Phys. Rev. B* **33**, 8800 (1986)] and Perdew, Burke, and Ernzerhof for correlation [*Phys. Rev. Lett.* **77**, 3865 (1996)], plus the dispersion density functional of Becke and Johnson [*J. Chem. Phys.* **127**, 154108 (2007)], comprise a nonempirical density-functional theory of high accuracy for thermochemistry and van der Waals complexes. The theory is nonempirical except for two universal cutoff parameters in the dispersion energy. Our calculations so far have been grid-based and have employed the local density approximation (LDA) for the orbitals. In this work, we employ orbitals from self-consistent GGA calculations using Gaussian basis sets. The results, on a benchmark set of 65 van der Waals complexes, are similar to our grid-based post-LDA results. This work sets the stage for van der Waals force computations and geometry optimizations.

**Key words:** density-functional theory, van der Waals interactions, dispersion interactions.

**Résumé :** Dans un travail antérieur, Kannemann et Becke [*J. Chem. Theory Comput.* **5**, 719 (2009) and *J. Chem. Theory Comput.* **6**, 1081 (2010)], il a été démontré que les approximations généralisées du gradient (AGG) de Perdew et Wang pour l'échange [*Phys. Rev. B* **33**, 8800 (1986)] et Perdew, Burke et Ernzerhof [*Phys. Rev. Lett.* **77**, 3865 (1996)] pour la corrélation combinées à la fonctionnelle de la densité de dispersion de Becke et Johnson [*J. Chem. Phys.* **127**, 154108 (2007)] s'avère être une théorie de la fonctionnelle de densité non empirique d'une grande exactitude pour la thermochemie et les complexes de van der Waals. La théorie est non empirique, à l'exception de deux paramètres universels de coupure de l'énergie de dispersion. Les calculs effectués jusqu'à présent ont été faits sur la base d'une grille et ils ont fait appel à l'approximation de la densité locale (ADL) pour les orbitales. Dans le présent travail, on utilise des orbitales obtenus par calculs autocohérents d'approximation généralisée du gradient utilisant des ensembles de base gaussiens. Les résultats obtenus sur un ensemble de référence de 65 complexes de van der Waals sont semblables à ceux obtenus avec nos résultats obtenus sur la base d'une grille post-ADL. Ce travail permet de faire des calculs de force de van der Waals et d'optimisation de géométrie.

**Mots-clés :** théorie de la fonctionnelle de la densité, interactions de van der Waals, interactions de dispersion.

## Introduction

The treatment of weak chemical interactions in density-functional theory (DFT) is fraught with difficulties. The weakest interaction, dispersion, is the result of long-range correlations which are impossible to model with standard local or semilocal density-functional approximations<sup>1</sup> such as the local density approximation (LDA) or generalized gradient approximations (GGAs). To make matters worse, the exchange part alone of the LDA or standard GGAs gives anything from massive over-binding to massive over-repulsion in dispersion-bound complexes, depending on the choice of functional.<sup>2</sup> Compared to the purely repulsive curves given by Hartree–Fock theory, the performance of the various

standard exchange GGAs in the DFT literature is unacceptably erratic (see Fig. 1 in ref. 2).

The latter of these problems, reproducing Hartree–Fock repulsion in closed-shell interactions, has been addressed by Lacks and Gordon<sup>3</sup> and, more recently, by Kannemann and Becke,<sup>2</sup> and Murray, Lee, and Langreth.<sup>4</sup> It has been discovered that, among the many available exchange GGAs in the literature, the nonempirical exchange GGA of Perdew and Wang<sup>5</sup> (PW86) reproduces Hartree–Fock repulsions remarkably well. For the ten pair interactions between the rare-gas atoms He, Ne, Ar, and Kr, self-consistent PW86 repulsion energies have a mean absolute percent error with respect to Hartree–Fock of only 10%.<sup>2</sup> Considering that the model underlying PW86 is not explicitly designed to capture weak interatomic interactions, this agreement is perhaps fortuitous. It has been pointed out by Zhang, Pan, and Yang<sup>6</sup> that weak interactions are extremely sensitive to the behaviour of exchange GGAs in the limit of large reduced density gradient

$$[1] \quad \chi = \frac{|\nabla \rho|}{\rho^{4/3}}$$

Fortuitous or not, the large- $\chi$  behaviour of PW86 is ideal for reproducing closed-shell Hartree–Fock repulsions. The

Received 2 February 2010. Accepted 2 May 2010. Published on the NRC Research Press Web site at [canjchem.nrc.ca](http://canjchem.nrc.ca) on 25 August 2010.

This article is part of a Special Issue dedicated to Professor R. J. Boyd.

A.D. Becke,<sup>1</sup> A.A. Arabi, and F.O. Kannemann. Department of Chemistry, Dalhousie University, Halifax, NS B3H 4J3, Canada.

<sup>1</sup>Corresponding author (e-mail: [axel.becke@dal.ca](mailto:axel.becke@dal.ca)).



**Table 1.** Repulsion energies in rare-gas diatomics ( $\mu\text{H}$ ).

	HF <sup>a</sup>	PW86 <sup>b</sup>	PW86 <sup>c</sup>	PW86 <sup>d</sup>
	Numerical	aug-cc-pV5Z	aug-cc-pVTZ	aug-cc-pVDZ
He2	28	29	34	28
He–Ne	47	52	41	13
He–Ar	85	87	96	76
He–Kr	103	98	104	88
Ne2	96	117	114	19
Ne–Ar	190	198	196	117
Ne–Kr	227	219	206	136
Ar2	435	503	519	482
Ar–Kr	538	626	632	621
Kr2	674	796	786	807
MPE <sup>e</sup>		8	9	–21
MAPE <sup>f</sup>		10	13	30
MaxAPE <sup>g</sup>		22	20	81

<sup>a</sup>Exact numerical Hartree–Fock.<sup>b</sup>PW86: CP-corrected aug-cc-pV5Z from ref. 2.<sup>c</sup>PW86: aug-cc-pVTZ (without CP correction).<sup>d</sup>PW86: aug-cc-pVDZ (without CP correction).<sup>e</sup>MPE: Mean percent error.<sup>f</sup>MAPE: Mean absolute percent error.<sup>g</sup>MaxAPE: Maximum absolute percent error.

“B86b” exchange GGA of Becke<sup>7</sup> also performs well at this task, and has nearly the same asymptotic behaviour as PW86 (Fig. 1 in ref. 6).

The long-range London dispersion interaction responsible for binding in van der Waals (vdW) complexes cannot be obtained from local or semilocal density functionals, as first argued by Kristyán and Pulay.<sup>1</sup> Explicit models incorporating the necessary long-range physics are known,<sup>8–13</sup> but are complicated. Models of the *asymptotic* dispersion interaction (i.e., dispersion coefficients) of relatively simple form have been proposed by several groups.<sup>14–17</sup> We use in our work the model of Becke and Johnson,<sup>14,15</sup> which exploits non-sphericity of the exchange hole around its reference point to generate  $C_6$ ,  $C_8$ , and  $C_{10}$  interatomic dispersion coefficients in a nonempirical density-functional manner. We will refer to this model as the exchange-hole dipole moment (XDM) dispersion model. Although XDM generates asymptotic dispersion coefficients without empirical fit parameters, two (universal) fit parameters are required to damp the dispersion energy at small internuclear separations.

We have reported in refs. 2 and 18 that the PW86 exchange GGA, combined with the nonempirical correlation GGA of Perdew, Burke, and Ernzerhof<sup>19</sup> (PBE) and the XDM dispersion model, yields excellent binding-energy curves in rare-gas diatomics<sup>2</sup> and excellent binding energies in a wide variety of intermolecular complexes.<sup>18</sup> Our work thus far has been grid-based fully numerical, using LDA orbitals computed by the basis-set-free NUMOL program<sup>20,21</sup> (i.e., “post-LDA”). In the present work, we instead use self-consistent PW86+PBE orbitals (i.e., “post-GGA”) computed with the Gaussian09 program.<sup>22</sup> The objective is to obtain PW86+PBE+XDM forces suitable for geometry optimization of intermolecular complexes. Forces cannot be obtained from our NUMOL post-LDA approach, and self-consistent NUMOL GGA calculations are not yet feasible.<sup>23</sup>

We therefore explore a post-Gaussian09-GGA approach in this work.

In the following section, we discuss the suitability for our purposes of the Dunning<sup>24</sup> aug-cc-pVDZ and aug-cc-pVTZ basis sets by considering rare-gas Hartree–Fock repulsion energies. In a later section, the two dispersion damping parameters in our PW86+PBE+XDM functional are fit to benchmark binding energies of 65 intermolecular complexes compiled in ref. 18. The results are of excellent quality, similar in quality to our NUMOL post-LDA results.<sup>18</sup> Future directions are discussed in the final section.

## Hartree–Fock repulsion in rare-gas diatomics: basis-set considerations

In ref. 2, the ability of the PW86 exchange GGA to reproduce Hartree–Fock repulsion energies in rare-gas systems was carefully studied. Our test set consisted of the ten pair interactions between the atoms He, Ne, Ar, and Kr. Post-Hartree–Fock, post-exchange-only-LDA, and self-consistent PW86 repulsion energies, computed at experimental Tang–Toennies internuclear separations,<sup>25</sup> were compared to exact Hartree–Fock repulsion energies from fully numerical NUMOL calculations. In Table 1, the Hartree–Fock and the self-consistent PW86 repulsion energies are listed. The deviation of the PW86 from the Hartree–Fock results is remarkably small. The mean absolute error of PW86 is only 10%, and the maximum error is 20%.

The PW86 benchmarks in Table 1 were obtained with Gaussian09 and the Dunning aug-cc-pV5Z basis set, including counterpoise (CP) corrections for basis-set superposition error.<sup>26</sup> This basis set is much too large, however, for practical applications. CP corrections are impractical as well, especially for the computation of intra-molecular dispersion energies. In this work we therefore undertake additional PW86 calculations with small Dunning basis sets, and *with-*



**Table 2.** Binding energies of intermolecular complexes (kcal/mol).

Complex	Data set <sup>a</sup>	Reference <sup>b</sup>	Numerical <sup>c</sup>	TZ <sup>d</sup>	DZ <sup>e</sup>
			(Post-LDA)	(Post-GGA)	
He–He	TT	0.022	0.018	0.021	0.015
He–Ne	TT	0.041	0.048	0.051	0.050
He–Ar	TT	0.059	0.059	0.058	0.052
He–Kr	TT	0.063	0.065	0.064	0.055
Ne–Ne	TT	0.084	0.100	0.088	0.097
Ne–Ar	TT	0.132	0.143	0.133	0.132
Ne–Kr	TT	0.141	0.164	0.154	0.148
Ar–Ar	TT	0.285	0.255	0.245	0.217
Ar–Kr	TT	0.333	0.311	0.302	0.256
Kr–Kr	TT	0.400	0.381	0.378	0.311
He–N <sub>2</sub> L-shaped	JB	0.053	0.040	0.046	0.035
He–N <sub>2</sub> T-shaped	JB	0.066	0.062	0.066	0.082
He–FCl	JB	0.097	0.077	0.080	0.096
FCl–He	JB	0.182	0.157	0.181	0.191
CH <sub>4</sub> –C <sub>2</sub> H <sub>4</sub>	JB	0.50	0.67	0.67	0.75
CF <sub>4</sub> –CF <sub>4</sub>	JB	0.78	0.70	0.76	0.82
SiH <sub>4</sub> –CH <sub>4</sub>	JB	0.81	0.88	0.90	1.13
CO <sub>2</sub> –CO <sub>2</sub>	JB	1.37	1.15	1.19	1.07
OCS–OCS	JB	1.40	1.38	1.35	1.19
C <sub>10</sub> H <sub>8</sub> –C <sub>10</sub> H <sub>8</sub> parallel	JB	3.78	4.50	4.55	3.98
C <sub>10</sub> H <sub>8</sub> –C <sub>10</sub> H <sub>8</sub> parallel crossed	JB	5.28	5.85	5.92	5.28
C <sub>10</sub> H <sub>8</sub> –C <sub>10</sub> H <sub>8</sub> T shaped	JB	4.34	4.46	4.62	4.68
C <sub>10</sub> H <sub>8</sub> –C <sub>10</sub> H <sub>8</sub> T shaped crossed	JB	3.09	3.50	3.59	3.63
CH <sub>4</sub> –NH <sub>3</sub>	JB	0.73	0.97	0.96	1.12
SiH <sub>4</sub> –HF	JB	0.73	0.62	0.62	0.91
CH <sub>4</sub> –HF	JB	1.65	1.76	1.79	1.94
C <sub>2</sub> H <sub>4</sub> –HF	JB	4.47	5.16	5.21	5.27
CH <sub>3</sub> F–CH <sub>3</sub> F	JB	2.33	2.16	2.16	2.17
H <sub>2</sub> CO–H <sub>2</sub> CO	JB	3.37	2.99	3.00	3.09
CH <sub>3</sub> CN–CH <sub>3</sub> CN	JB	6.16	6.13	6.18	6.20
HCN–HF	JB	7.3	7.71	7.83	7.91
(NH <sub>3</sub> ) <sub>2</sub> [C <sub>2h</sub> ]	S22	3.17	3.24	3.23	3.29
(H <sub>2</sub> O) <sub>2</sub> [C <sub>s</sub> ]	S22	5.02	5.23	5.22	5.25
Formic acid dimer [C <sub>2h</sub> ]	S22	18.61	19.13	19.14	18.99
Formamide dimer [C <sub>2h</sub> ]	S22	15.96	16.09	16.08	16.20
Uracil dimer [C <sub>2h</sub> ]	S22	20.65	20.28	20.45	20.70
2-Pyridoxine–2-aminopyridine [C <sub>1</sub> ]	S22	16.71	17.44	17.53	17.89
Adenine–thymine WC [C <sub>1</sub> ]	S22	16.37	16.68	16.89	17.17
(CH <sub>4</sub> ) <sub>2</sub> [D <sub>3d</sub> ]	S22	0.53	0.54	0.53	0.77
(C <sub>2</sub> H <sub>4</sub> ) <sub>2</sub> [D <sub>2d</sub> ]	S22	1.51	1.36	1.38	1.55
Benzene–CH <sub>4</sub> [C <sub>3</sub> ]	S22	1.50	1.48	1.48	1.50
Benzene dimer parallel displaced [C <sub>2h</sub> ]	S22	2.73	2.63	2.64	2.63
Pyrazine dimer [C <sub>s</sub> ]	S22	4.42	3.69	3.62	3.64
Uracil dimer stack [C <sub>2</sub> ]	S22	10.12	8.78	8.71	8.47
Indole–benzene stack [C <sub>1</sub> ]	S22	5.22	4.27	4.23	4.16
Adenine–thymine stack [C <sub>1</sub> ]	S22	12.23	10.07	9.96	9.82
Ethene–ethyne [C <sub>2v</sub> ]	S22	1.53	1.71	1.76	1.92
Benzene–H <sub>2</sub> O [C <sub>s</sub> ]	S22	3.28	3.17	3.19	3.12
Benzene–NH <sub>3</sub> [C <sub>s</sub> ]	S22	2.35	2.22	2.24	2.24
Benzene–HCN [C <sub>s</sub> ]	S22	4.46	4.15	4.30	4.26
Benzene dimer T-shaped [C <sub>2v</sub> ]	S22	2.74	2.40	2.52	2.79
Indole–benzene T-shaped [C <sub>1</sub> ]	S22	5.73	4.95	5.16	5.42
Phenol dimer [C <sub>1</sub> ]	S22	7.05	6.52	6.55	6.65
HF–HF	ZT	4.57	4.91	4.86	4.90
NH <sub>3</sub> –H <sub>2</sub> O	ZT	6.41	7.12	7.17	7.45

Table 2 (concluded).

Complex	Data set <sup>a</sup>	Reference <sup>b</sup>	Numerical <sup>c</sup>	TZ <sup>d</sup>	DZ <sup>e</sup>
			(Post-LDA)	(Post-GGA)	
H <sub>2</sub> S–H <sub>2</sub> S	ZT	1.66	2.02	2.25	2.35
HCl–HCl	ZT	2.01	2.43	2.45	2.50
H <sub>2</sub> S–HCl	ZT	3.35	4.43	4.53	4.76
CH <sub>3</sub> Cl–HCl	ZT	3.55	4.06	4.08	4.16
HCN–CH <sub>3</sub> SH	ZT	3.59	4.20	4.21	4.44
CH <sub>3</sub> SH–HCl	ZT	4.16	6.14	6.22	6.59
CH <sub>4</sub> –Ne	ZT	0.22	0.14	0.17	0.24
C <sub>6</sub> H <sub>6</sub> –Ne	ZT	0.47	0.35	0.35	0.37
C <sub>2</sub> H <sub>2</sub> –C <sub>2</sub> H <sub>2</sub>	ZT	1.34	1.64	1.49	1.57
C <sub>6</sub> H <sub>6</sub> –C <sub>6</sub> H <sub>6</sub> parallel	ZT	1.81	1.49	1.50	0.56
Mean percent error			—	2.1	4.1
Mean absolute percent error			12.6	11.5	16.6
Maximum absolute percent error			—	49.5	69.3

<sup>a</sup>Tang–Toennies<sup>25</sup> (TT), Johnson–Becke<sup>27</sup> (JB), S22,<sup>28</sup> Zhao–Truhlar<sup>29,30</sup> (ZT).

<sup>b</sup>Reference binding energy from respective data set.

<sup>c</sup>Numerical post-LDA binding energy from ref. 18.

<sup>d</sup>Present aug-cc-pVTZ post-GGA binding energy.

<sup>e</sup>Present aug-cc-pVDZ post-GGA binding energy.

out CP corrections, in search of a practical PW86 scheme able to mimic Hartree–Fock repulsions in rare-gas systems.

We consider the Dunning basis sets aug-cc-pVDZ and aug-cc-pVTZ to be of practical size for general applications and have therefore assessed them, without CP correction, on our repulsion-energy test set. Integration grids of 200 radial  $\times$  590 angular points (unpruned) were used throughout. The results are reported in the last two columns of Table 1. Both the DZ and the TZ basis sets give repulsion for all ten systems considered. However, the triple-zeta results are clearly superior to the double-zeta results. Indeed the triple-zeta data is similar in quality to the CP-corrected quintuple-zeta data. The worst cases for aug-cc-pVDZ noticeably involve the Ne atom, but this doesn't necessarily rule out the utility of aug-cc-pVDZ in general.

We are therefore encouraged to adopt aug-cc-pVTZ, without CP corrections, as a viable and practical basis set for GGA computations of weak chemical interactions. The viability of non-CP-corrected aug-cc-pVDZ remains to be seen. We apply both to the computation of vdW binding energies in the next section.

## Binding energies of intermolecular complexes

A comprehensive binding-energy (BE) test set of 65 intermolecular complexes, spanning three orders of binding-energy strength from 0.022 kcal/mol (He<sub>2</sub>) to 20.65 kcal/mol (uracil dimer), has been assembled in ref. 18 for the assessment of vdW computational methods. The set includes the ten rare-gas diatomics in Table 1 with experimentally derived BEs from Tang and Toennies,<sup>25</sup> 21 complexes from the test set of Johnson and Becke<sup>27</sup> with CCSD(T)-computed BEs, the 22 complexes of the “S22” biochemical benchmark set of Jurečka et al.<sup>28</sup> also with CCSD(T)-computed BEs, and 12 complexes from Zhao and Truhlar<sup>29,30</sup> with BEs computed by W1 theory. These 65 complexes are listed in Table 2

along with their reference binding energies. Cartesian coordinate files of all the complexes and their monomers are available as supplementary data to ref. 18.

We assess the exchange-correlation functional

$$[2] \quad E_{XC} = E_X^{\text{PW86}} + E_C^{\text{PBE}} + E_{\text{disp}}^{\text{XDM}}$$

on our 65 benchmark complexes and report the results in Table 2. The PW86 exchange GGA is given in ref. 5 and the PBE correlation GGA in ref. 19. The XDM dispersion energy is given by<sup>27</sup>

$$[3] \quad E_{\text{disp}}^{\text{XDM}} = -\frac{1}{2} \sum_{i \neq j} \left( \frac{C_{6,ij}}{R_{\text{vdW},ij}^6 + R_{ij}^6} + \frac{C_{8,ij}}{R_{\text{vdW},ij}^8 + R_{ij}^8} + \frac{C_{10,ij}}{R_{\text{vdW},ij}^{10} + R_{ij}^{10}} \right)$$

with dispersion coefficients  $C_{6,ij}$ ,  $C_{8,ij}$ , and  $C_{10,ij}$  computed as in refs. 15 and 31. The effective vdW interatomic separations  $R_{\text{vdW},ij}$  are linearly related to “critical” interatomic separations  $R_{c,ij}$  by

$$[4] \quad R_{\text{vdW},ij} = a_1 R_{c,ij} + a_2$$

with the critical separation  $R_{c,ij}$  given by the average of  $(C_{8,ij}/C_{6,ij})^{1/2}$ ,  $(C_{10,ij}/C_{6,ij})^{1/4}$ , and  $(C_{10,ij}/C_{8,ij})^{1/2}$ .

We use the “BR” variant of XDM,<sup>31</sup> since the BR variant was found to be superior to the “XX” variant in ref. 18. XDM-BR is based on a density-functional approximation of the exchange hole, whereas XDM-XX uses the exact orbital-based exchange hole. That the former outperforms the latter in intermolecular complexes is rationalized in ref. 18.

Self-consistent PW86+PBE orbitals were computed with Gaussian09 using the aug-cc-pVDZ and aug-cc-pVTZ basis sets, without CP corrections, as motivated in the previous section. The XDM dispersion energy was then computed by an interface program<sup>32</sup> that reads Gaussian09 orbital infor-

mation from “wfn” files. These calculations are therefore not fully self-consistent, rather “post-GGA”. Since the dispersion energy is a very small fraction of the total energy, however, we expect that ignoring self-consistency in the  $E_{\text{disp}}^{\text{XDM}}$  term is of negligible consequence. Investigations of the XDM dispersion model by Kong et al.<sup>33</sup> support this expectation.

The binding energies in Table 2 of the present methods are quite similar to those of our previous numerical post-LDA method.<sup>18</sup> The present mean absolute percent error (MAPE) with the aug-cc-pVDZ basis is 16.6, and with the aug-cc-pVTZ basis is 11.5, compared to our previous 12.6%. Best-fit values (minimum RMS percent error) of the damping parameters are

$$a_1 = 0.80, \quad a_2 = 1.49 \text{ \AA} \quad (\text{SCF aug-cc-pVDZ})$$

$$a_1 = 0.79, \quad a_2 = 1.36 \text{ \AA} \quad (\text{SCF aug-cc-pVTZ})$$

$$a_1 = 0.82, \quad a_2 = 1.16 \text{ \AA} \quad (\text{numerical post-LDA}^{18})$$

Here, we also see similarity between the basis-set and our previous numerical results, especially for the  $a_1$  parameter.

The quality of the double-zeta results, though not as good overall as triple-zeta, is pleasantly surprising. Even the rare-gas diatomic binding energies involving Ne are in good agreement with reference data, despite the notably poor repulsion energies seen above. The under-repulsive tendency of the DZ basis set compared to TZ (see Table 1) is apparently compensated by a slightly larger best-fit  $a_2$  parameter. The only significant qualitative failure of the double-zeta method is the parallel benzene dimer (the last entry in Table 2), for which only one third of the reference binding energy is obtained. This failure is not seen in our numerical or triple-zeta results.

## Conclusions and outlook

The nonempirical (except for two universal dispersion damping parameters) exchange-correlation density functional of eq. [2] was found in refs. 2 and 18 to be an excellent model for van der Waals interactions in chemistry. The GGA exchange and nondynamical correlation parts, PW86+PBE, are a very good model for intra-molecular chemistry as well, as are most standard GGAs. On the atomization energies of the 222 molecules of the G3/99 thermochemical test set of Curtiss et al.<sup>34</sup> the mean absolute error of PW86+PBE+XDM is 10.0 kcal/mol<sup>2</sup>. This is similar to the mean absolute error of 9.3 kcal/mol<sup>34</sup> for the popular BLYP<sup>35,36</sup> GGA. Thus, PW86+PBE+XDM is a promising GGA-DFT for simultaneous optimization of intra- and inter-molecular geometries in complex chemical systems. Our previous post-LDA approach,<sup>2,18</sup> while useful for assessing the performance of density functionals on energetics, cannot provide forces for optimization of geometries. Here we have tested a methodology with the promise to provide energies, and forces, at reasonable computational cost. This PW86+PBE/aug-cc-pVnZ scheme, with  $n = 2$  or 3 and XDM dispersion added post-GGA, will provide useful forces (and Hessians) if orbital self-consistency can be ignored in the XDM part, and if changes in the XDM dispersion coefficients  $C_{6,ij}$ ,  $C_{8,ij}$ , and  $C_{10,ij}$  with molecular geometry can be ignored in the energy derivatives. Preliminary tests of these

suppositions by Kong et al.<sup>33</sup> are encouraging. We will undertake our own independent tests in future work. Also in future work, we will refit the dispersion damping parameters  $a_1$  and  $a_2$  for inclusion of exact Hartree–Fock exchange (i.e., “hybrid” functionals plus XDM dispersion) for even better accuracy in the intra-molecular energetics.

## Acknowledgements

The authors gratefully acknowledge the support of the Killam Trust of Dalhousie University through a Killam Chair to ADB, the Natural Sciences and Engineering Research Council of Canada (NSERC), and the Atlantic Computational Excellence Network (ACEnet).

## References

- (1) Kristyán, S.; Pulay, P. *Chem. Phys. Lett.* **1994**, 229 (3), 175. doi:10.1016/0009-2614(94)01027-7.
- (2) Kannemann, F. O.; Becke, A. D. *J. Chem. Theory Comput.* **2009**, 5 (4), 719. doi:10.1021/ct800522r.
- (3) Lacks, D. J.; Gordon, R. G. *Phys. Rev. A* **1993**, 47 (6), 4681. doi:10.1103/PhysRevA.47.4681. PMID:9909494.
- (4) Murray, E. D.; Lee, K.; Langreth, D. C. *J. Chem. Theory Comput.* **2009**, 5 (10), 2754. doi:10.1021/ct900365q.
- (5) Perdew, J. P.; Wang, Y. *Phys. Rev. B* **1986**, 33 (12), 8800. doi:10.1103/PhysRevB.33.8800.
- (6) Zhang, Y.; Pan, W.; Yang, W. *J. Chem. Phys.* **1997**, 107 (19), 7921. doi:10.1063/1.475105.
- (7) Becke, A. D. *J. Chem. Phys.* **1986**, 85 (12), 7184. doi:10.1063/1.451353.
- (8) Andersson, Y.; Langreth, D. C.; Lundqvist, B. I. *Phys. Rev. Lett.* **1996**, 76 (1), 102. doi:10.1103/PhysRevLett.76.102. PMID:10060444.
- (9) Dobson, J. F.; Dinte, B. P. *Phys. Rev. Lett.* **1996**, 76 (11), 1780. doi:10.1103/PhysRevLett.76.1780. PMID:10060519.
- (10) Kamiya, M.; Tsuneda, T.; Hirao, K. *J. Chem. Phys.* **2002**, 117 (13), 6010. doi:10.1063/1.1501132.
- (11) Sato, T.; Tsuneda, T.; Hirao, K. *J. Chem. Phys.* **2007**, 126 (23), o. 234114. doi:10.1063/1.2747243. PMID:17600411.
- (12) Dion, M.; Rydberg, H.; Schröder, E.; Langreth, D. C.; Lundqvist, B. I. *Phys. Rev. Lett.* **2004**, 92 (24), o. 246401. doi:10.1103/PhysRevLett.92.246401. PMID:15245113.
- (13) Thonhauser, T.; Cooper, V. R.; Li, S.; Puzder, A.; Hyldgaard, P.; Langreth, D. C. *Phys. Rev. B* **2007**, 76 (12), o. 125112. doi:10.1103/PhysRevB.76.125112.
- (14) Becke, A. D.; Johnson, E. R. *J. Chem. Phys.* **2005**, 122 (15), o. 154104. doi:10.1063/1.1884601. PMID:15945622.
- (15) Becke, A. D.; Johnson, E. R. *J. Chem. Phys.* **2007**, 127 (15), o. 154108. doi:10.1063/1.2795701. PMID:17949133.
- (16) Tkatchenko, A.; Scheffler, M. *Phys. Rev. Lett.* **2009**, 102 (7), o. 073005. doi:10.1103/PhysRevLett.102.073005. PMID:19257665.
- (17) Sato, T.; Nakai, H. *J. Chem. Phys.* **2009**, 131 (22), o. 224104. doi:10.1063/1.3269802. PMID:20001021.
- (18) Kannemann, F. O.; Becke, A. D. *J. Chem. Theory Comput.* **2010**, 6 (4), 1081. doi:10.1021/ct900699r.
- (19) Perdew, J. P.; Burke, K.; Ernzerhof, M. *Phys. Rev. Lett.* **1996**, 77 (18), 3865. doi:10.1103/PhysRevLett.77.3865. PMID:10062328.
- (20) Becke, A. D. *Int. J. Quantum Chem.* **1989**, 36 (S23), 599. doi:10.1002/qua.560360862.
- (21) Becke, A. D.; Dickson, R. M. *J. Chem. Phys.* **1990**, 92 (6), 3610. doi:10.1063/1.457869.

- (22) Frisch, M. J.; Trucks, G. W.; Schlegel, H. B.; Scuseria, G. E.; Robb, M. A.; Cheeseman, J. R.; Scalmani, G.; Barone, V.; Mennucci, B.; Petersson, G. A.; Nakatsuji, H.; Caricato, M.; Li, X.; Hratchian, H. P.; Izmaylov, A. F.; Bloino, J.; Zheng, G.; Sonnenberg, J. L.; Hada, M.; Ehara, M.; Toyota, K.; Fukuda, R.; Hasegawa, J.; Ishida, M.; Nakajima, T.; Honda, Y.; Kitao, O.; Nakai, H.; Vreven, T.; Montgomery, J. A., Jr.; Peralta, J. E.; Ogliaro, F.; Bearpark, M.; Heyd, J. J.; Brothers, E.; Kudin, K. N.; Staroverov, V. N.; Kobayashi, R.; Normand, J.; Raghavachari, K.; Rendell, A.; Burant, J. C.; Iyengar, S. S.; Tomasi, J.; Cossi, M.; Rega, N.; Millam, J. M.; Klene, M.; Knox, J. E.; Cross, J. B.; Bakken, V.; Adamo, C.; Jaramillo, J.; Gomperts, R.; Stratmann, R. E.; Yazyev, O.; Austin, A. J.; Cammi, R.; Pomelli, C.; Ochterski, J. W.; Martin, R. L.; Morokuma, K.; Zakrzewski, V. G.; Voth, G. A.; Salvador, P.; Dannenberg, J. J.; Dapprich, S.; Daniels, A. D.; Farkas, O.; Foresman, J. B.; Ortiz, J. V.; Cioslowski, J.; Fox, D. J. *Gaussian 09*; Gaussian, Inc.: Wallingford, CT, 2009.
- (23) NUMOL numerical grid noise in the GGA exchange-correlation potential is too large for application to dispersion-bound systems.
- (24) Dunning, T. H. *J. Chem. Phys.* **1989**, *90* (2), 1007. doi:10.1063/1.456153.
- (25) Tang, K. T.; Toennies, J. P. *J. Chem. Phys.* **2003**, *118* (11), 4976. doi:10.1063/1.1543944.
- (26) Boys, S. F.; Bernardi, F. *Mol. Phys.* **1970**, *19* (4), 553. doi:10.1080/00268977000101561.
- (27) Johnson, E. R.; Becke, A. D. *J. Chem. Phys.* **2006**, *124* (17), o. 174104. doi:10.1063/1.2190220. PMID:16689564.
- (28) Jurečka, P.; Šponer, J.; Černý, J.; Hobza, P. *Phys. Chem. Chem. Phys.* **2006**, *8* (17), 1985. doi:10.1039/b600027d. PMID:16633685.
- (29) Zhao, Y.; Truhlar, D. G. *J. Chem. Theory Comput.* **2005**, *1* (3), 415. doi:10.1021/ct049851d.
- (30) Zhao, Y.; Truhlar, D. G. *J. Phys. Chem. A* **2005**, *109* (25), 5656. doi:10.1021/jp050536c. PMID:16833898.
- (31) Becke, A. D.; Johnson, E. R. *J. Chem. Phys.* **2005**, *123* (15), o. 154101. doi:10.1063/1.2065267. PMID:16252936.
- (32) H.L. Schmider, E.R. Johnson, and A.D. Becke, unpublished code.
- (33) Kong, J.; Gan, Z.; Proynov, E.; Freindorf, M.; Furlani, T. R. *Phys. Rev. A* **2009**, *79* (4), o. 042510. doi:10.1103/PhysRevA.79.042510.
- (34) Curtiss, L. A.; Raghavachari, K.; Redfern, P. C.; Pople, J. A. *J. Chem. Phys.* **2000**, *112* (17), 7374. doi:10.1063/1.481336.
- (35) Becke, A. D. *Phys. Rev. A* **1988**, *38* (6), 3098. doi:10.1103/PhysRevA.38.3098. PMID:9900728.
- (36) Lee, C.; Yang, W.; Parr, R. G. *Phys. Rev. B* **1988**, *37* (2), 785. doi:10.1103/PhysRevB.37.785.



# New insights concerning the mechanism of reversible thermochromic mixtures

Hong Tang, Douglas C. MacLaren, and Mary Anne White

**Abstract:** Three-component organic thermochromic materials, consisting of a leuco dye, a weak acid acting as the colour developer, and a low-melting organic solvent, can change their colour in response to temperature changes. Although widely used in applications, their detailed thermochromic mechanism is not fully understood. The present study delineates the role of subtle changes in the solvent's molecular structure and concentration in the crystal violet lactone (CVL, dye)/lauryl gallate (LG, developer)/1-alcohol (dodecanol (DD), tetradecanol (TD), hexadecanol (HD), or octadecanol (OD); solvent) system. Through inkjet printing of the components directly onto a substrate, combinatorial approaches reveal differences when the alkyl chain length of the alcohol solvent is changed slightly. During the process of heating to the melt, followed by cooling to room temperature, CVL/LG/DD showed no colour change. On the other hand, CVL/LG/TD exhibited reversible thermochromism with colour forming in the molten state and colour loss in the solid state. In the composition range investigated, the CVL/LG/HD system showed no colour change during heating, but on cooling from the molten state, at first a blue colour appeared just below the freezing point, and this was followed by a slow colour fading on further cooling. A significant new finding is that the orientationally disordered  $\alpha$ -phase of the solvent is required to support the dye-developer complex that provides colour. Furthermore, there is an optimal solvent chain length for thermochromism: if too short, there is no disordered phase and no colour; if too long, the formation of the coloured developer-dye complex is prevented in the melt.

**Key words:** thermochromism, polymorphism, dynamical disorder.

**Résumé :** Des matériaux thermochromiques organiques à trois composants formés d'un colorant leuco, d'un acide faible agissant comme agent de développement de la couleur et d'un solvant organique de faible point de fusion peuvent changer de couleur en réponse à des changements de température. Le présent travail permet de délimiter le rôle de changements subtils dans la structure moléculaire du solvant et les concentrations dans le système formé par le colorant, la lactone du cristal violet (LCV), l'acide faible agissant comme agent de développement de la couleur (gallate de lauryle, GL) et les divers solvants [dodécane-1-ol (DD); tétradécane-1-ol (TD); hexadécane-1-ol (HD); octadécane-1-ol (OC)]. En procédant à une impression à jet d'encre directement sur un substrat, des approches combinatoires permettent d'identifier les différences résultant d'un faible changement dans la longueur des chaînes alkyles de l'alcool agissant comme solvant. Durant le processus de chauffage conduisant au liquide suivi d'un refroidissement à la température ambiante, on n'observe aucun changement de couleur pour le système LCV/GL/DD. Par ailleurs, pour le système LCV/GL/TD, on observe une thermochromie réversible avec une formation de couleur dans l'état liquide et une perte de couleur à l'état solide. Pour le système LCV/GL/HD, il n'y a pas de changement de couleur durant le chauffage mais, lorsqu'on refroidit à partir de l'état fondu, il y a d'abord apparition d'une couleur bleue juste en dessous du point de fusion et ceci est suivi d'une disparition lente de la couleur par refroidissement subséquent. Une observation significative a trait au fait que la phase  $\alpha$  du solvant, désordonnée d'un point de vue de l'orientation, a besoin du support du complexe colorant/agent de développement de la couleur pour conduire au développement d'une couleur. De plus, l'apparition d'une thermochromie ne se produit qu'avec un solvant comportant une chaîne carbonée de longueur optimale : si la chaîne est trop courte, il n'y a pas de phase désordonnée et il n'y a pas de couleur; si elle est trop longue, le complexe colorant/agent de développement de la couleur ne peut se produire.

**Mots-clés :** thermochromie, polymorphie, désordre dynamique.

## Introduction

Thermochromism, i.e., temperature-induced colour changes, can be the basis of functional materials such as sensors,

thermometers, or thermal printing. Some thermochromic processes, such as chemical degradation, are irreversible, while others are reversible. The mechanisms of thermo-

Received 18 January 2010. Accepted 25 May 2010. Published on the NRC Research Press Web site at [canjchem.nrc.ca](http://canjchem.nrc.ca) on 25 August 2010.

*This article is part of a Special Issue dedicated to Professor R. J. Boyd. We dedicate this manuscript to our colleague, Professor Russ Boyd, on the occasion of his 65th birthday.*

**H. Tang, D.C. MacLaren, and M.A. White.**<sup>1</sup> Department of Chemistry and Institute for Research in Materials, Dalhousie University, Halifax, NS B4H 4J3, Canada.

<sup>1</sup>Corresponding author (e-mail: [mawhite@dal.ca](mailto:mawhite@dal.ca)).

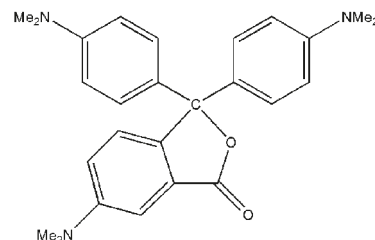
chromism are varied, including phase-transition induced changes in the crystal field and a change in wavelength of constructively interfered light due to thermal expansion of layered structures such as liquid crystals,<sup>1,2</sup> and changes in luminescence in sol-gel films,<sup>3</sup> or polymer structures,<sup>4</sup> or the shape of gold or silver nanorods,<sup>5</sup> or isomer distribution.<sup>6</sup> Spiropyrans are known to have potential for thermochromism, whether they are adsorbed on a surface,<sup>7,8</sup> embedded in a polymer,<sup>9</sup> part of a polymer backbone,<sup>10</sup> or a component in an organic thermochromic mixture. In current materials applications, the latter is most common; thermochromism arises from the change in interaction of a spiro-pyran leuco dye with a developer in the presence of a low-melting solvent.<sup>1,11–13</sup> Often, heating results in colour loss and such mixtures are particularly promising as components of thermally erasable toner for printers, allowing the same paper to be used, thermally erased, and then used again.<sup>14</sup> A recent development is thermochromic fibers, with polymeric shells and thermoresponsive cores based on such mixtures.<sup>15</sup> Such materials have recently been proposed as the basis for low-cost (<\$0.10/m<sup>2</sup>) displays.<sup>16</sup>

Although we now have some insights into the molecular processes involved in thermochromic organic mixtures, important issues remain unresolved, such as control of the contrast between the coloured and uncoloured states, the kinetics of decolourization, and the long-term stability of the coloured state.<sup>17</sup>

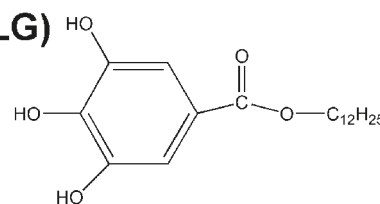
Early mechanistic studies of ternary organic thermochromic mixtures outlined the main features of the mechanism,<sup>18</sup> but left open important questions. More detailed studies showed the importance of interactions of spiropyran with the developer,<sup>19–21</sup> and how the competition between the developer–dye complex (metastable, coloured state) and the developer–solvent complex (equilibrium, uncoloured state) leads to thermochromism.<sup>22–24</sup> However, considering the range of possible compositions in the ternary system and the many possible dyes, developers, and solvents, the generality of the mechanism has not been tested. Combinatorial approaches are known to lead to rapid advances when there are many compositional variables; a relevant example is colorimetric differentiation of polydiacetylene sensors.<sup>25</sup> To advance understanding of thermochromism mechanisms, we have embarked on combinatorial investigations of three-component thermochromic mixtures, delivered directly on paper by an inkjet printer. The dye was crystal violet lactone (CVL), the developer was lauryl gallate (LG), and the solvent was a long-chain alcohol. In the present studies we explore the question: *How does the solvent's molecular structure influence reversible, rewritable thermochromism?* Although the solvent was initially thought to be most important for its thermochromism-initiating melting point, or as a decolourization acceleration agent in which the solvent provides nucleation sites for the phase separation of developer molecules,<sup>26,27</sup> detailed studies have revealed that the nature of the solvent controls decolourization, through formation of a solvent–developer complex.<sup>23</sup> We now show that the role of the solvent is more subtle and complex, and is important for both colour formation and thermal erasure. Although the present system usually shows colour formation on heating

rather than the more usual colour loss, the conclusions presented here apply to both types of thermochromic systems.

## CVL



## Lauryl gallate (LG)



## Experimental methods

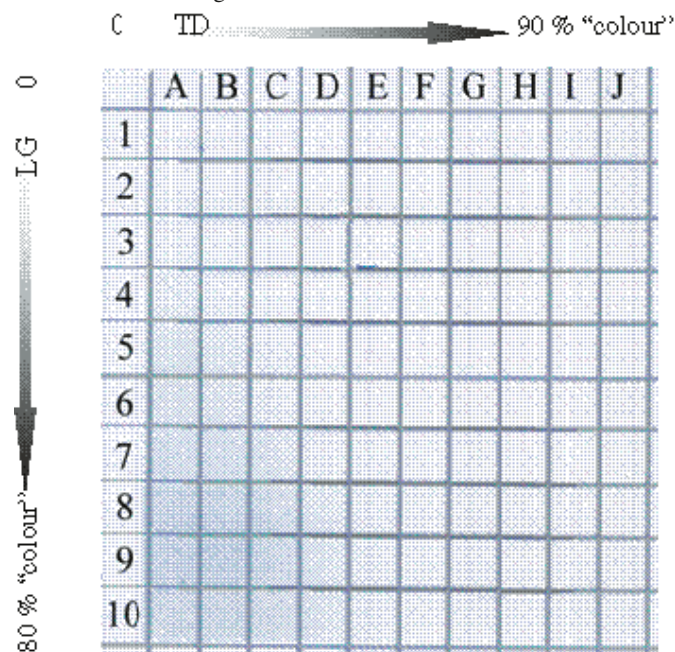
### Chemicals

Crystal violet lactone (3,3-bis(*p*-*N,N*-dimethylamino-phenyl)-6-*N,N*-dimethyl-aminophthalide, CVL, 97%), lauryl gallate (dodecyl(3,4,5-trihydroxy)benzoate, LG, 97%), 1-dodecanol (DD, 96%), 1-tetradecanol (TD, 96%), 1-hexadecanol (HD, 99%), and 1-octadecanol (OD, 99%) were obtained from Sigma-Aldrich. All compounds were used without further purification.

### Combinatorial sample preparation

Small quantities of the dye (CVL), developer (LG), and solvent (DD, TD, HD, or OD) were delivered onto paper via a combinatorial inkjet printing technique. In brief, the dye (0.025 mol/L), developer (0.3 mol/L), and solvent (0.5 mol/L), each in an ethyl acetate/1-butanol (16:9 volume ratio) were placed in the cleaned “ink” cartridges of a drop-on-demand thermal roof-shooter inkjet printer (HP 5940c). The mixed solvent system of ethyl acetate (EMD, 99.5%) and 1-butanol (ACP, 99.4%) was selected as the volatile solvent system to deliver the thermochromic components to the paper (ordinary printer paper) and allow mixing before its evaporation. (Note that we refer here to ethyl acetate/1-butanol as the *volatile* solvent, to distinguish it from the solvent required for the thermochromic mixture.) The ratio in the mixed volatile solvent system was optimized to give rheological properties in the same range as the commercial ink for which the printer was designed. In particular, it should not be so viscous that it cannot flow, or so low in viscosity that leakage is a problem, yet it needs appropriate spreading (no splashing). The Ohnesorge number<sup>28</sup> for this system was about 12. Quantitative delivery of the components (dye, developer, and solvent) to the various regions of the paper was handled through the software (Adobe Photoshop 5.0) controlling the printer. Optimal parameters included using <90% “colour” density and 10–30 passes per location. (Fewer passes led to too little deposition; more passes increased the

**Fig. 1.** The combinatorial dye–developer–solvent library as deposited directly on a 7.5 cm × 7.5 cm area on ordinary printer paper. The dye (CVL) was deposited evenly (0.025 mol/L printed at 60% colour density in Adobe Photoshop 5.0), the developer (0.3 mol/L LG) was gradually increasing from top to bottom (up to 80% colour density in Adobe Photoshop 5.0), and the solvent (0.5 mol/L TD) was gradually increasing from left to right (up to 80% colour density). Each of the 100 cells shown represents a certain smoothly changing mole range of the three components. A faint blue colour is more intense at high LG and low TD concentration.



probability of wipe-off.) Typical sample preparations consisted of a uniform deposition of CVL dye, a vertically graduated deposition of LG developer, and a horizontally graduated deposition of solvent, with the deposition repeated 10–30 times. Deposited amounts (excluding volatile solvent) were quantified by simultaneous deposition on pre-cut round weighing paper (12.7 mm diameter) adhered to the paper by low-residue double-sided tape (3M). The deposited thermochromic mixtures (after evaporation of the volatile solvent) were in the range of 0.2–8  $\mu\text{g mm}^{-2}$ . Further details of the combinatorial delivery of thermochromic components via inkjet printing are given elsewhere.<sup>29,30</sup>

### Bulk sample preparation

Although most of the results reported herein are for inkjet delivered combinatorial samples, in a few key experiments, bulk quantities of thermochromic mixtures were prepared as previously described.<sup>24</sup>

### Characterization

An Ocean Optics USB4000 spectrometer was used to measure diffuse reflectance. The light was sent to the probe via six 200  $\mu\text{m}$  diameter optical fibers, and reflected light was detected through a parallel fiber. All diffuse reflectance measurements were taken for light with a  $\lambda = 620$  nm, the wavelength of maximum absorbance of CVL in its (blue) zwitterionic state.<sup>31</sup> The probe was used at a 90° angle to the surface to eliminate spurious results from any gap be-

tween the probe and sample during heating and cooling, including any moisture influence. For the normal cooling process for ternary mixtures (after heating to a molten state at  $\sim 60^\circ\text{C}$ , samples were quenched to room temperature), kinetic reflectance measurements were taken after they cooled from the molten state. For rapid cooling (after heating to a molten state at  $\sim 60^\circ\text{C}$ , samples were quenched in liquid nitrogen), the kinetic reflectance measurements were taken after the rapidly quenched samples were placed at room temperature. Diffuse reflection was typically measured at 100 locations (10 across, 10 down) on the 7.5 cm × 7.5 cm deposition area.

Bulk samples were examined by Raman spectroscopy using a Bruker RFS 100 Raman spectrometer (excitation by the 1064.5 nm line of a Nd:YAG laser with an incident power of 447 mW). Typical spectra consisted of 25–200 scans. Rapid (30 s) scans for kinetic studies typically had a 4  $\text{cm}^{-1}$  resolution, while longer scans had a 2  $\text{cm}^{-1}$  resolution.

## Results and discussion

### Combinatorial library

A typical library of mixtures, printed directly on a 7.5 cm × 7.5 cm area on printer paper, is shown in Fig. 1.

### Combinatorial approaches represent bulk

Diffuse reflectance for a 10 × 10 matrix of CVL/LG/TD of varying composition immediately after cooling from 60  $^\circ\text{C}$  to room temperature is shown in Fig. 2. The quantity of CVL is constant in this deposition, and TD increases from left to right, while LG increases from top to bottom. Of particular interest is the cell labeled D8, which corresponds to the same components and composition as the system previously studied in bulk.<sup>24</sup> The thermochromic properties (kinetics of colour loss on cooling) are the same for both, despite a reduction in sample mass density by a factor of  $\sim 100$  in the present studies, validating the inkjet combinatorial approach.

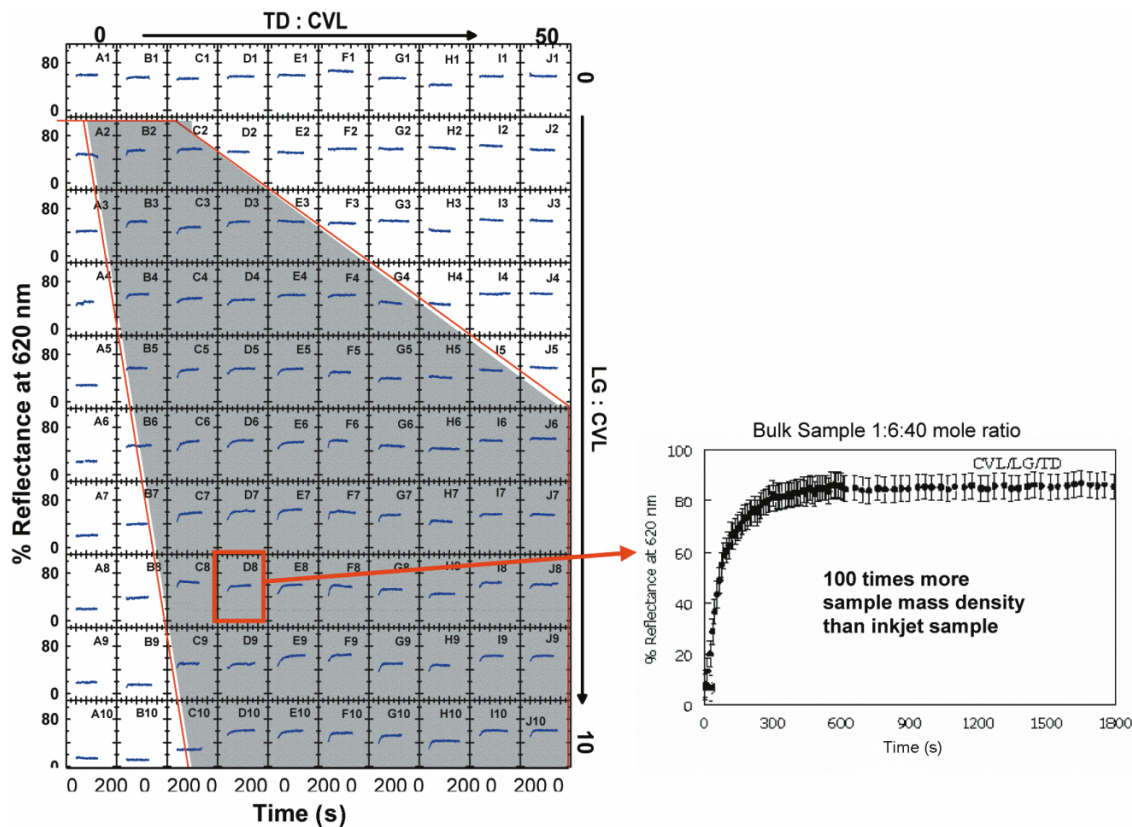
### Different thermochromic behaviours of CVL/LG/alcohols

From Fig. 2 and knowledge of the composition at each point in the matrix, a ternary thermochromism phase diagram for the system CVL/LD/TD has been constructed (Fig. 3a). From this diagram, the compositional limits of thermochromism are apparent. When the mole fraction of LG is high and there is less TD, the system exhibits long-lived (essentially permanent) colour due to the limited ability to decolourize (too little TD to interact with LG). By contrast, when the mole fraction of LG is low and TD is high, no colour was observed because TD separates the CVL and LG species completely, preventing formation of the CVL–LG coloured complex.

Results for parallel studies in which the alkyl chain length for the alcohol solvent has been increased by two carbons, i.e. CVL/LG/HD, are shown in Fig. 3b. This slight change in solvent has a dramatic effect on the thermochromic properties of the mixture. In particular, thermochromism exists for a much smaller range of compositions in CVL/LG/HD, while CVL/LG/TD can show thermochromism when less solvent is present. From thermodynamic studies, it has been



**Fig. 2.** The diffuse reflection intensity at  $\lambda = 620$  nm as a function of time for lauryl gallate/tetradecanol/crystal violet lactone thermochromic mixtures cooled from 60 °C to room temperature. Low reflectance corresponds to high colour density. The left side shows 100 elements of the combinatorial library varying in tetradecanol to crystal violet lactone mole ratio (TD:CVL ranges from 0 to 50) across the rows, and lauryl gallate to crystal violet lactone mole ratio (LG:CVL ranges from 0 to 10) down the columns. The shaded region inside the red lines corresponds to thermochromic behaviour. The red box corresponds to CVL/LG/TD in the mole ratio 1:6:40. This composition has been investigated earlier for bulk samples<sup>24</sup> and the resulting evolution of diffuse thermal reflection for the thicker sample is shown on the right.



shown that the HD–LG interaction is less attractive than TD–LG,<sup>23</sup> so more HD is required to achieve thermochromism. Another distinction from the CVL/LG/TD system is that for CVL/LG/HD no colour development was observed on heating. However, on cooling from 60 °C to room temperature, the blue colour appeared and then decolourized, albeit with slower kinetics than for CVL/LG/TD.

When the alkyl chain of the alcohol solvent was shortened to dodecanol (DD), no thermochromism was observed in the explored composition range, mole ratios of DD:CVL from 0 to 35 and LG:CVL from 0 to 10. In CVL/LG/DD, high LG and low DD concentrations gave a temperature-independent pale blue colour because of the dominance of the CVL–LG coloured complex. However, in other compositional regions, no colour appeared during either heating or cooling. On the basis that the solvent–developer interaction becomes stronger as the solvent chain length decreases,<sup>23</sup> we conclude that when DD is present, there are essentially no free LG developer molecules available to interact with CVL and give the coloured complex.

These three long-chain alcohol solvents, dodecanol, tetradecanol, and hexadecanol, only differ by a total of four carbons in their alkyl chains, yet the behaviour in thermochromic mixtures is markedly different. Not only are the thermochromic compositional ranges different (Fig. 3), but the overall behaviour, as summarized in Fig. 4, is funda-

mentally different. During the process of heating to the melt followed by cooling to room temperature, CVL/LG/DD showed no colour change. On the other hand, CVL/LG/TD exhibited reversible thermochromism with colour forming in the molten state and colour loss in the solid state. The CVL/LG/HD system showed no colour change during heating, but on cooling from the molten state, at first a blue colour appeared just below the freezing point, and this was followed by a slow colour fading on further cooling.

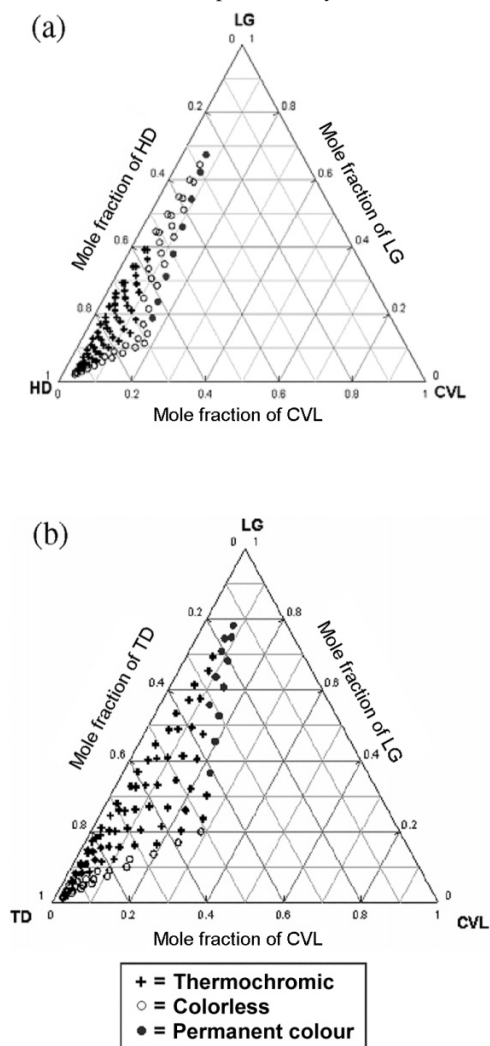
Burkinshaw et al.<sup>18</sup> studied the solubility of the alkyl phenol developer in stearic acid solvent in both liquid and solid state. Their results support a phase-separation mechanism and they proposed that a good reversible thermochromic mixture should have a solvent with good solubility for the developer in the liquid state and poor solubility in the solid state. But this phase separation mechanism alone cannot explain why CVL/LG/TD exhibits colour in the molten state while CVL/LG/HD does not.

### Thermochromism and polymorphism of the long-chain alcohol solvents

The polymorphism of long-chain 1-alcohols is well-established.<sup>32–38</sup> Three phases, called  $\alpha$ ,  $\beta$ , and  $\gamma$ , are observed in the solid state in 1-alcohols with long alkyl chains. The  $\alpha$ -phase, a disordered rotator phase sometimes called the  $R'_{IV}$  phase,<sup>38</sup> appears immediately below the melting



**Fig. 3.** The thermochromism ternary phase diagram for the systems (a) lauryl gallate/tetradecanol/crystal violet lactone (LG/TD/CVL) and (b) lauryl gallate/hexadecanol/crystal violet lactone (LG/HD/CVL). Symbols indicate investigated compositions, categorized as thermochromic, colourless, or permanently coloured.



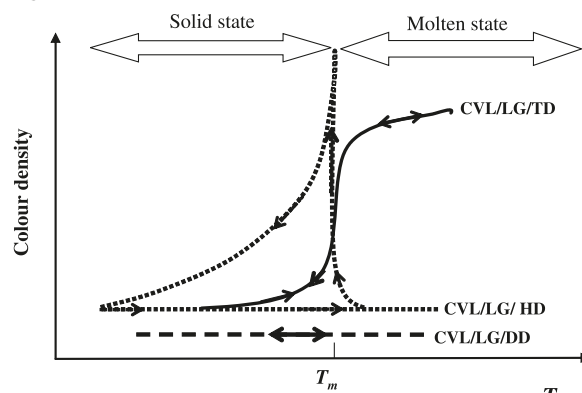
point. The  $\beta$ - and  $\gamma$ -phases have the chains ordered, and are both monoclinic but with different tilt angles. They have head-to-head forms and are both thermodynamically stable at temperatures below the stability range of the  $\alpha$ -phase. The entropy of the various alcohol phases increases as  $S_\gamma \sim S_\beta < S_\alpha < S_{\text{liquid}}$ .<sup>39,40</sup> The shortest alcohol studied here, 1-dodecanol, only exists in an ordered phase.<sup>35</sup> However, both disordered ( $\alpha$ ) and ordered ( $\beta$  and  $\gamma$ ) phases have been reported for 1-tetradecanol and 1-hexadecanol,<sup>34,35</sup> and for 1-octadecanol.<sup>38</sup>

When long-chain alcohols are present in the thermochromic mixtures, different polymorphs of the alcohol could influence the coloured species. From the experimental results discussed here, we propose a thermochromic mechanism influenced by the phase and chain length of the solvent component, as follows.

#### Colour in the solid state

There seems to be a strong correlation between the exist-

**Fig. 4.** A schematic view of the colour as a function of temperature for thermochromic mixtures composed of crystal violet lactone (dye), lauryl gallate (developer), and various different alcohols (solvent). The colour density is shown as a function of temperature, relative to the melting point of the mixture,  $T_m$ , highlighting the dependence on the solvent. The mixture with dodecanol (DD) does not show colour development. Tetradecanol (TD) solvent leads to reversible thermochromism with little hysteresis. The mixture with hexadecanol (HD) as the solvent was colourless on initial heating above the melting point and then exhibited colour when it was cooled to the solid state, followed by loss of colour on further cooling.



tence of the coloured complex and the presence of the disordered  $\alpha$ -phase of the alcohol. Direct evidence comes from Raman studies of bulk samples of CVL/LG/TD (1:6:40 mole ratio) quenched in liquid nitrogen and then equilibrated at 25 °C, showing the peak at 1710  $\text{cm}^{-1}$  that is associated with the  $\alpha$ -phase of the alcohol, decreasing into the baseline within about 3 min (Fig. 5a), with the same kinetic profile as the formation of the (uncoloured) LG–TD complex (Fig. 5b). We conclude that on first cooling from the melt, the coloured LG–CVL complex stays (TD) or forms (HD) when the alcohol solidifies to the dynamically disordered  $\alpha$ -phase, providing colour.

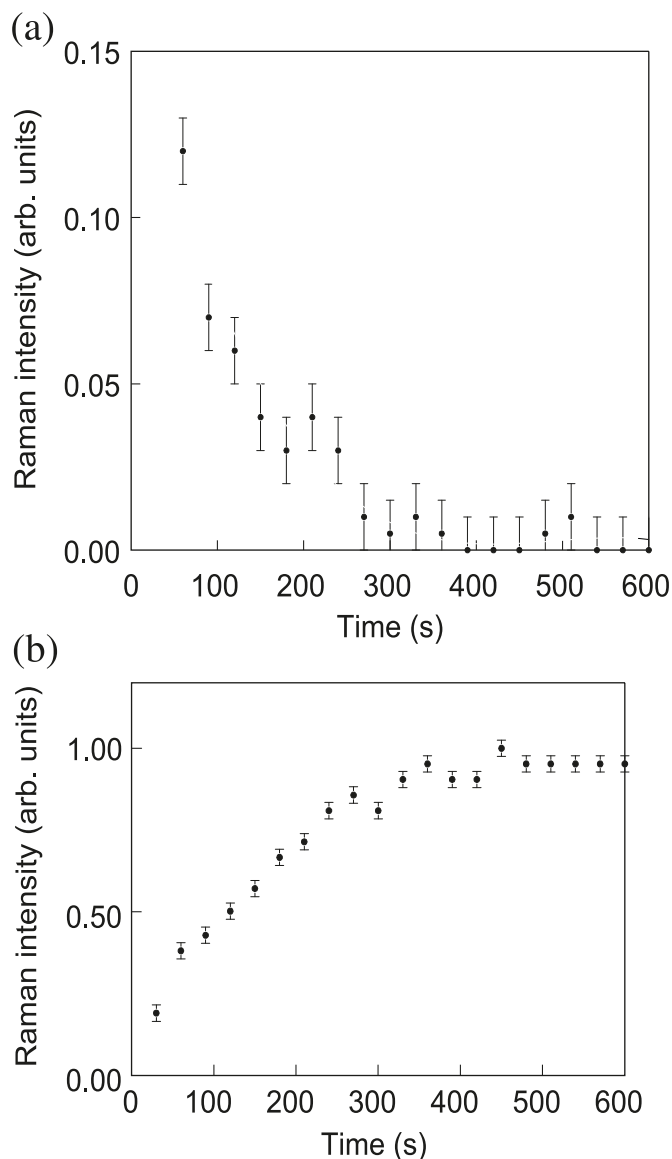
In the case of CVL/LG/DD, no disordered phase is observed for the 1-dodecanol solvent on either heating or cooling, which correlates with the absence of colour in the solid phase. On the other hand, TD, HD, and also octadecanol (OD) all experience a significant  $\alpha$ -phase range when cooled from the molten state and colour is observed on solidifying the melt.

At lower temperature, longer-chain alcohols transform to an ordered  $\beta$ - (or  $\gamma$ -) phase. The colour loss rate corresponds to the loss of the  $\alpha$ -phase, indicating that the disordered  $\alpha$ -phase of the alcohols favors the formation of coloured developer–dye complexes, while the more rigid  $\beta$ - and  $\gamma$ -phases destroy the colour complex, presumably in favor of the formation of developer–solvent complexes. Although the mechanism is different, the stability of a mesophase also leads to thermochromism in poly(3-alkylthiophene)s.<sup>4</sup>

#### Colour in the molten state

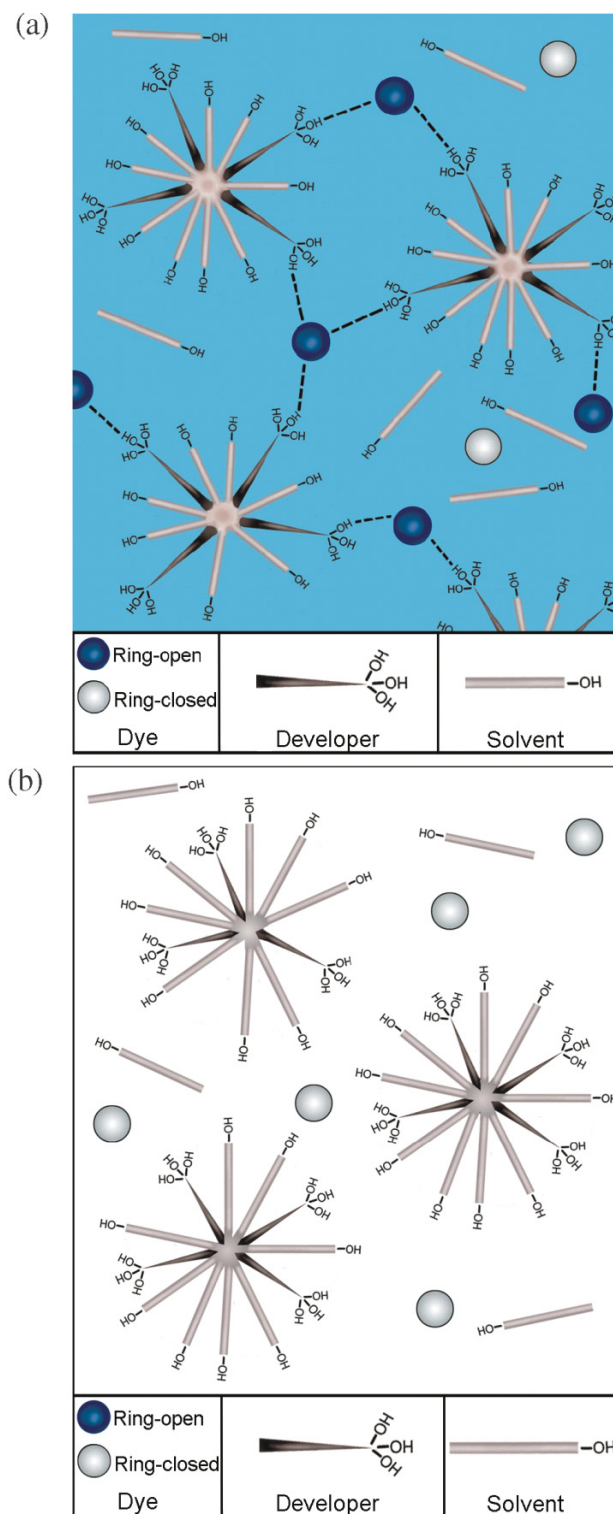
From previous work on this system<sup>22</sup> and studies of a related system,<sup>41</sup> it is known that the colour arises from dye–developer complexes. Solvent components in the ther-

**Fig. 5.** (a) Raman intensity of a bulk sample of crystal violet lactone/lauryl gallate/tetradecanol (CVL/LG/TD in a 1:6:40 mole ratio) quenched in liquid nitrogen and then equilibrated at 25 °C, showing the peak at 1710  $\text{cm}^{-1}$  that is associated with the  $\alpha$ -phase of the alcohol, decreasing into the baseline within about 3 min. (b) Raman intensity of the peak at 1683  $\text{cm}^{-1}$  that is associated with the formation of the LG–TD complex, for the same sample taken at the same time as the data shown in (a), showing the same kinetic profile for LG–TD complex formation as for the loss of the  $\alpha$ -phase of the alcohol.



mochromic mixtures have been mostly considered as phase separators, although it has been proven that the polarity of the organic solvent will affect the colour development.<sup>42</sup> This also agrees with the fact that the CVL–LG complex will lose its colour in polar solvents such as ethanol or butanol. When the three-component mixtures are heated to the molten state, if the solubility of the developer in the solvent is low, or if there is insufficient solvent to separate the dye and developer, colour will appear, which correlates with our observation that CVL/LG/HD exhibited colour in the molten

**Fig. 6.** Schematic view of possible dynamic structures in the melt for (a) crystal violet lactone (dye)/lauryl gallate (developer)/tetradecanol (solvent), showing developer–solvent complexation that allows the developer to interact with the dye, bringing it to its ring-open state, and imparting colour to the mixture. (b) The solvent is changed to hexadecanol, and now the longer alcohol (solvent rods shown schematically here are longer than in (a)) prevents the developer from interacting with the dye, leaving it in its ring-closed colourless state.



state when there was not enough HD present (mole ratio of HD/LG < 1).

In the melt, shorter alcohols are superior at dissolving the developer molecules. For example, DD can dissolve LG, thereby isolating the developer from the dye molecules and preventing colour formation. Longer alcohols (14 or more carbons) at a sufficiently high concentration give a different separation mechanism. We propose that in the molten state, the long-chain alcohol molecules form dynamic structures in which the long alkyl chains interact. A possibility is shown in Fig. 6a. In this schematic view, meant to advance our understanding of the thermochromic mechanism, the –OH group of LG in CVL/LG/TD is exposed. Therefore, CVL is able to interact with the –OH group(s) of LG in CVL/LG/TD to develop colour. In contrast, the longer carbon chain of HD (Fig. 6b) envelops the polar group on the developer, and CVL and LG are separated, resulting in a lack of colour.

To test the hypothesis that the longer-chain alcohol carbon “hides” the developer and prevents it from interacting with the dye, an additional system was examined, namely crystal violet lactone/lauryl gallate/1-octadecanol (CVL/LG/OD), in the mole ratio of 1:10:40 on the same substrate. This showed the same colour change phenomenon as CVL/LG/HD. Colour loss occurred at the molten state, consistent with the separation of CVL and LG by OD solvent molecules due to the long chains of OD.

## Conclusions

Through combinatorial studies of the thermochromic system containing crystal violet lactone (dye), lauryl gallate (developer), and long-chain alcohols (solvent), we found that subtle changes in the solvent can lead to substantial changes in both the compositional range in which thermochromism is supported and differences in thermochromic behaviour. Colour development in the solid is correlated with the presence of the dynamically disordered  $\alpha$ -phase of the alcohol on cooling. In cases where there is colour, it fades when cooled below the  $\alpha$ -phase. If the alcohol carbon chain length is too short to allow the rotator phase, as in dodecanol, no colour is observed. On the other hand, if the alcohol's carbon chain exceeds a critical length, the developer is hidden from the dye in the melt, preventing colour formation at high temperatures.

## Acknowledgements

We gratefully acknowledge financial support from the Natural Sciences and Engineering Research Council of Canada (NSERC) and the Killam Trusts, Kim Miller's assistance, and helpful discussions with Professor Jeff Dahn and Alex Bourque.

## References

- (1) Day, J. H. *Chem. Rev.* **1963**, 63 (1), 65. doi:10.1021/cr60221a005.
- (2) White, M. A.; LeBlanc, M. J. *Chem. Educ.* **1999**, 76 (9), 1201. doi:10.1021/ed076p1201.
- (3) Tard, C.; Perruchas, S.; Maron, S.; Le Goff, X. F.; Guillen, F.; Garcia, A.; Vigneron, J.; Etcheberry, A.; Gacoin, T.; Boilot, J.-P. *Chem. Mater.* **2008**, 20 (22), 7010. doi:10.1021/cm801780g.

- (4) Wang, Y.; Archambault, A.; Belcher, A. M.; Busse, D.; Damon, D. B.; Mills, A.; Riddle, A. E.; Samardjiev, I. J.; Lucht, B. L.; Euler, W. B. *Macromolecules* **2008**, 41 (19), 7115. doi:10.1021/ma801352f.
- (5) Tollan, C. M.; Marcilla, R.; Pomposo, J. A.; Rodriguez, J.; Aizpurua, J.; Molina, J.; Mecerreyes, D. *ACS Appl. Mater. Interfaces* **2009**, 1 (2), 348. doi:10.1021/am800058x. PMID: 20353222.
- (6) Morita, Y.; Suzuki, S.; Fukui, K.; Nakazawa, S.; Kitagawa, H.; Kishida, H.; Okamoto, H.; Naito, A.; Sekine, A.; Ohashi, Y.; Shiro, M.; Sasaki, K.; Shiomi, D.; Sato, K.; Takui, T.; Nakasuji, K. *Nat. Mater.* **2008**, 7 (1), 48. doi:10.1038/nmat2067. PMID:18059277.
- (7) Ichimura, K.; Funabiki, A.; Aoki, K.; Akiyama, H. *Langmuir* **2008**, 24 (13), 6470. doi:10.1021/la8002178. PMID:18537277.
- (8) Scarmagnani, S.; Walsh, Z.; Slater, C.; Alhashimy, N.; Paull, B.; Macka, M.; Diamond, D. J. *Mater. Chem.* **2008**, 18 (42), 5063. doi:10.1039/b810080b.
- (9) Seeboth, A.; Löttsch, D.; Potchius, E.; Vetter, R. *Chin J. Polymer Sci.* **2006**, 24 (4), 363. doi:10.1142/S0256767906001400.
- (10) Shiraishi, Y.; Miyamoto, R.; Hirai, T. *Org. Lett.* **2009**, 11 (7), 1571. doi:10.1021/ol900188m. PMID:19254006.
- (11) Aitken, D.; Burkinshaw, S. M.; Griffiths, J.; Towns, A. D. *Rev. Prog. Color.* **1996**, 26, 1.
- (12) Christie, R. M. *Colour Chemistry*; RSC: Cambridge, 2001.
- (13) Zhu, C. F.; Wu, A. B. *Thermochim. Acta* **2005**, 425 (1–2), 7. doi:10.1016/j.tca.2003.08.001.
- (14) Takayama, S.; Gotanda, T.; Ikeda, N.; Sano, K. *J. Imaging Sci. Technol.* **2006**, 50 (5), 489. doi:10.2352/J.ImagingSci.Technol.(2006)50:5(489).
- (15) Li, F.; Zhao, Y.; Wang, S.; Han, D.; Jiang, L.; Song, Y. J. *Appl. Polym. Sci.* **2009**, 112 (1), 269. doi:10.1002/app.29384.
- (16) Siegel, A. C.; Phillips, S. T.; Wiley, B. J.; Whitesides, G. M. *Lab Chip* **2009**, 9 (19), 2775. doi:10.1039/b905832j. PMID: 19967113.
- (17) Mather, R. R. *Rev. Prog. Color.* **2001**, 31, 36.
- (18) Burkinshaw, S. M.; Griffiths, J.; Towns, A. D. *J. Mater. Chem.* **1998**, 8 (12), 2677. doi:10.1039/a805994b.
- (19) Luthern, J.; Peredes, A. J. *Mater. Sci. Lett.* **2000**, 19 (3), 185. doi:10.1023/A:1006790104175.
- (20) Luthern, J.; Peredes, A. J. *Mater. Sci. Lett.* **2003**, 22 (12), 881. doi:10.1023/A:1024410703372.
- (21) Yamamoto, S.; Furuya, H.; Tsutsui, K.; Ueno, S.; Sato, K. *Cryst. Growth Des.* **2008**, 8 (7), 2256. doi:10.1021/cg7009034.
- (22) MacLaren, D. C.; White, M. A. *J. Mater. Chem.* **2003**, 13 (7), 1695. doi:10.1039/b302249h.
- (23) MacLaren, D. C.; White, M. A. *J. Mater. Chem.* **2003**, 13 (7), 1701. doi:10.1039/b302250a.
- (24) MacLaren, D. C.; White, M. A. *J. Mater. Sci.* **2005**, 40 (3), 669. doi:10.1007/s10853-005-6305-x.
- (25) Yoon, J.; Jung, Y.-S.; Kim, J.-M. *Adv. Funct. Mater.* **2009**, 19 (2), 209. doi:10.1002/adfm.200800963.
- (26) Shimada, M.; Goto, H.; Kaawamura, E.; Maruyama, S.; Kubo, K.; Tsutsui, K. U.S. Patent 5,521,138, 1996.
- (27) Sano, K.; Naito, K.; Takayama, K. S.; Fujioka, S.; Okuyama, T. U.S. Patent 5,922,115, 1999.
- (28) Fromm, J. E. *IBM J. Res. Dev.* **1984**, 28 (3), 322. doi:10.1147/rd.283.0322.
- (29) Tang, H.; M.Sc. Thesis, Dalhousie University, Halifax, NS, 2007.
- (30) White, M. A.; Tang, H. In *High-Throughput Synthesis and Measurement Methods for Rapid Optimization and Discovery of Advanced Materials*; Green, M. L., Takeuchi, I.,

- Chiang, T., Paul, J., Eds.; Mater. Res. Soc. Symp. Proc.: Warrendale, PA, 2009; Vol. 1159E, Paper No. 1159-G06-10. doi:10.1557/PROC-1159-G06-10.
- (31) Allen, N. S.; Hughes, N.; Mahon, P. J. *Photochem.* **1987**, *37* (2), 379. doi:10.1016/0047-2670(87)85017-7.
- (32) Parsonage, N. G.; Staveley, L. A. K. *Disorder in Crystals*; Oxford University Press: Oxford, 1978.
- (33) Baker, W. O.; Smyth, C. P. *J. Am. Chem. Soc.* **1938**, *60* (5), 1229. doi:10.1021/ja01272a064.
- (34) Pradhan, S. D.; Katti, S. S.; Kulkarni, S. B. *Int. J. Chem.* **1970**, *8*, 632.
- (35) Hoffman, J. D.; Smyth, C. P. *J. Am. Chem. Soc.* **1949**, *71* (2), 431. doi:10.1021/ja01170a018.
- (36) Kuchhal, Y. K.; Shukla, R. N.; Biswas, A. B. *Thermochim. Acta* **1979**, *31* (1), 61. doi:10.1016/0040-6031(79)80008-8.
- (37) van Miltenburg, J. C.; Oonk, H. A. J.; Ventola, L. *J. Chem. Eng. Data* **2001**, *46* (1), 90. doi:10.1021/je000048s.
- (38) Ventolà, L.; Ramírez, M.; Calvet, T.; Solans, X.; Cuevas-Diarte, M. A.; Negrier, P.; Mondieig, D.; Van Miltenburg, J. C.; Oonk, H. A. J. *Chem. Mater.* **2002**, *14* (2), 508. doi:10.1021/cm011010h.
- (39) Tanaka, K.; Sato, T.; Hayashida, T. *Bull. Inst. Chem. Res. Kyoto Univ.* **1957**, *35*, 123.
- (40) Tanaka, K.; Sato, T.; Watanabe, A.; Hayashida, T. *Bull. Inst. Chem. Res. Kyoto Univ.* **1959**, *39*, 281.
- (41) Sekiguchi, Y.; Takayama, S.; Gotanda, T.; Sano, K. *Chem. Lett.* **2007**, *36* (8), 1010. doi:10.1246/cl.2007.1010.
- (42) Sekiguchi, Y.; Takayama, S.; Gotanda, T.; Sano, K. *Chem. Lett.* **2006**, *35* (4), 458. doi:10.1246/cl.2006.458.



# Density-functional and global optimization study of copper–tin core-shell clusters

René Fournier

**Abstract:** We obtained minimum-energy structures for 13  $\text{Cu}_p\text{Sn}_q^+$  ( $p = 1-4$ ) species by a combined taboo search and density functional theory (DFT) approach. The putative global minima are all  $\text{Cu}_p@\text{Sn}_q^+$  core-shell structures. There is a stabilization energy on the order of 0.5 to 1.0 eV associated with completion of the outer shell of Sn atoms. The stabilization associated with electronic shell closing is also on the order of 0.5 to 1.0 eV.  $\text{CuSn}_{10}^+$  has both a closed atomic shell and a closed electronic shell, and it is extrastable. We found two or more isomers within 0.6 eV of the global minimum for all 13 species except  $\text{CuSn}_{10}^+$ .

**Key words:** bimetallic clusters, nanostructured materials, global energy minima, segregation.

**Résumé :** Nous avons obtenu des structures d'énergie minimum pour 13 espèces d'agrégats  $\text{Cu}_p\text{Sn}_q^+$  ( $p = 1-4$ ) par une combinaison de recherche taboo et de théorie de la fonctionnelle de la densité. Les minimas globaux présumés possèdent tous une structure en couches avec un coeur de cuivre,  $\text{Cu}_p@\text{Sn}_q^+$ . On observe une stabilisation d'environ 0,5 à 1,0 eV quand la couche externe d'atomes d'étain devient complète. L'agrégat  $\text{CuSn}_{10}^+$  est particulièrement stable dû au fait qu'il a une structure de couche fermée pour les atomes et aussi pour les électrons. Nous avons trouvé deux isomères ou plus en-deçà de 0,6 eV du minimum global pour chacune des 13 espèces sauf  $\text{CuSn}_{10}^+$ .

**Mots-clés :** agrégats bimétalliques, matériaux nanostructurés, minima d'énergie globale, ségrégation.

## Introduction

Bimetallic clusters  $\text{A}_p\text{B}_q$  received a lot of attention lately.<sup>1</sup> They obviously form a much bigger class of compounds than elemental clusters  $\text{A}_n$ , since one can independently vary A, B, size ( $p + q$ ), and composition  $p/q$ . Furthermore, one can sometimes achieve kinetic control over the A–B ordering<sup>2–4</sup> or particle shape<sup>5,6</sup> in a given  $\text{A}_p\text{B}_q$  species. So, bimetallic clusters offer more opportunities than elemental clusters for observing new phenomena, or unusual properties, or for design of materials.<sup>7</sup> Yet, their complexity is still manageable. A number of bimetallic clusters have been made with rather well-defined size, composition, and structure.<sup>1</sup> Applications are mainly in catalysis,<sup>8</sup> magnetic-recording media,<sup>9</sup> and biondiagnostics.<sup>10</sup>

Generally speaking, the geometric structures of small bimetallic clusters fall into three broad categories: mixed (alloyed), segregated (or, “left–right segregated”, LRS), and core-shell structures (CSS). A fourth category, onion-layered, can be seen as a special case of CSS. The CSS clusters receive special attention because they have no equivalent in the bulk. Upon coalescence, mixed clusters will likely produce a bulk alloy. LRS clusters, on the other hand, would likely produce poorly defined materials with A and B domains having large size distributions. But well-defined (in size and composition)  $\text{A}_p\text{B}_q$  CSS clusters could coalesce into a metastable material having several identical  $\text{A}_p$  cores embedded in a B matrix, with the  $\text{A}_p$  cores roughly equidis-

tant from each other. By controlling  $p$  and  $q$ , one can, in principle, control the size of the  $\text{A}_p$  cluster cores and their separation inside the B matrix and this would open up interesting possibilities for nanomaterials. The special case where  $p = 1$  and B is Sn, that is, a  $\text{Sn}_q$  cluster doped with a single endohedral A atom, has received a lot of attention theoretically<sup>11</sup> and experimentally.<sup>12–14</sup> Many of these endohedral  $\text{M}@\text{Sn}_q$  clusters (neutral or charged) have large HOMO–LUMO gaps and appear to be stable.

Breaux et al. found, by thermal annealing in the gas phase, that  $\text{Cu}_p\text{Sn}_q$  cluster cations are stable over a fairly narrow range of compositions and suggested that these clusters may have a CSS.<sup>15</sup> The main goal of our study was to determine, by theory, the detailed geometric structures of a few  $\text{Cu}_p\text{Sn}_q^+$  species in or near the composition range observed by Breaux et al.,  $p = 1-4$  and  $q \approx (9 + 2p) \pm 2$ , and offer a rationale for the enhanced stability of these clusters.

## Methods and computational details

All energies were calculated by density functional theory (DFT) with the Perdew–Burke–Ernzerhof (PBE)<sup>16</sup> generalized gradient approximation to exchange–correlation and a LANL2 double-zeta (LANL2DZ) basis set as implemented in the Gaussian 03 software package.<sup>17</sup> Global optimization was performed by taboo search in descriptor space (TSDS)<sup>18</sup> for singlet or doublet states. We set the number of DFT energy evaluations in the global optimization stage to  $3N^2 +$

Received 16 December 2009. Accepted 22 March 2010. Published on the NRC Research Press Web site at canjchem.nrc.ca on 10 September 2010.

*This article is part of a Special Issue dedicated to Professor R. J. Boyd on the occasion of his 65th birthday.*

**R. Fournier.** Department of Chemistry, York University, Toronto, ON M3J 1P3, Canada. (e-mail: renef@yorku.ca).

30, where  $N = p + q$  is the number of atoms, except for  $\text{Cu}_4\text{Sn}_{19}$  where we did 1410 energy evaluations. Ten to twenty distinct structures among the lowest energy ones were selected from the  $3N^2 + 30$  in the dataset generated by TSDS. Local optimization was performed on those 10 to 20 structures with a standard method (Gaussian keyword BFGS). Local optimizations typically required 50 to 100 DFT energy evaluations, so, overall, the computational effort was divided roughly equally between global and local optimization.

The number of possible isomers (local minima) for  $\text{A}_p\text{B}_q$  clusters is quite large. For an  $\text{X}_n$  cluster ( $n > 9$ ),  $3^{n-6.5}$  gives a rough estimate of the number of distinct isomers. Ignoring symmetry there would be  $(p+q)!/(p!q!)$   $\text{A}_p\text{B}_q$  homotops for every  $\text{X}_{p+q}$  parent structure. Then, for instance, we would estimate that  $\text{Cu}_4\text{Sn}_{19}$  has roughly  $3^{16.5} \times 23!/(4!19!) \approx 10^{11}$  distinct local minima. But this optimization problem is not as difficult as it seems because the vast majority of isomers are very high in energy, and the low-energy isomers fall into one or a few categories that share common geometric characteristics. The TSDS algorithm exploits resemblances among low-energy structures to quickly narrow down the search to structures that have favorable characteristics. For instance, in this study, one of the descriptors quantifies Cu–Sn mixing: after a few hundred energy evaluations on quasi-random  $\text{Cu}_4\text{Sn}_{19}$  structures, the TSDS algorithm “learns” that all mixed structures have much higher energies than segregated ones, and TSDS begins to search preferentially among segregated structures.

Some of the most relevant descriptors for our discussion will now be described. We define the number of interior atoms  $N_i$  as follows. First, we calculate the asphericity  $\zeta_j$  around each atom  $j$  by

$$[1] \quad \zeta_j = \frac{(I_a - I_b)^2 + (I_b - I_c)^2 + (I_c - I_a)^2}{I_a^2 + I_b^2 + I_c^2}$$

where  $I_a$ ,  $I_b$ , and  $I_c$  are the moments of inertia of the neighbours of atom  $j$  calculated after assigning a unit mass to every atom. We assign to atom  $j$  a number  $n_j = \exp(-(\zeta_j/\zeta_0))^2$ , which tends toward one for interior atoms and zero for surface atoms, and get an effective number of interior atoms,  $N_i$ , by adding up the  $n_j$ s.

$$[2] \quad N_i = \sum_j n_j = \sum_j \exp(-(\zeta_j/\zeta_0)^2)$$

With these definitions and  $\zeta_0 = 0.0601$ , we almost always get  $n_j > 0.9$  for atoms that we would have classified as “interior atoms” upon visual inspection and  $n_j < 10^{-5}$  for typical surface atoms. Another descriptor of geometry that we use is  $F_{90}$ , the number of  $90^\circ$  angles per atom. It is defined by

$$[3] \quad F_{90} = \frac{1}{n} \sum_j \sum_{k>\ell} \cos(\theta_{kj\ell} - 90^\circ)^{100}$$

where  $k$  and  $\ell$  index the neighbours of atom  $j$ . The exponent 100 in the formula is arbitrary but produces an intuitively correct count of the number of right angles. Finally, we describe the overall shape of clusters by the variable  $\eta = (2I_b - I_a - I_c)/I_a$ , where  $I_a \geq I_b \geq I_c$  are the moments of inertia of

the clusters when we assign a unit mass to each atom. Note that  $\eta < 0$  for oblate clusters and  $\eta > 0$  for prolate clusters.

## Results and discussion

We studied 13  $\text{Cu}_p\text{Sn}_q^+$  species  $(p,q)$ : (1,9), (1,10), (1,11), (1,15), (2,11), (2,12), (2,13), (2,18), (3,14), (3,15), (3,16), (4,17), and (4,19). TSDS followed by local optimization yielded a total of 210 structures, out of which 134 were distinct (76 were repeats): 105 of those 134 were within 1 eV of the putative global minimum (GM). Table 1 shows the relative energies (RE) of those 105 isomers and the number of isomers with  $\text{RE} < 1$  eV for each species. The notation we will use to identify structures will be  $p\text{--}q.n$ , where  $n$  is the energy rank of the isomer. So, for instance, the RE of **1–11.2** is 0.13 eV, the RE of **3–14.8** is 0.60 eV, and  $p\text{--}q.1$  is the GM of  $\text{Cu}_p\text{Sn}_q^+$ . Figures 1 and 2 show the structures of the 13 GM, and Fig. 3 shows the structures of all isomers (15 of them) found within 0.2 eV of the GM.

It is immediately clear that there are many isomers within a small energy range for most species, **1–10**, **1–11**, and **2–13** being exceptions. Assuming that we found the actual GM, the mean energy separation between isomers is typically on the order of 0.1 eV and maybe even smaller considering the likelihood that we may have missed several low-energy isomers. The uncertainty on calculated relative energies (due to inexact functional, basis sets, and other numerical approximations) is probably on the order of 0.1 eV, and no global optimization method can guarantee finding the GM. So, the precise GM and isomer structures reported here may not all be correct predictions of actual cluster geometries, but they can be used for predicting trends and general structural features.

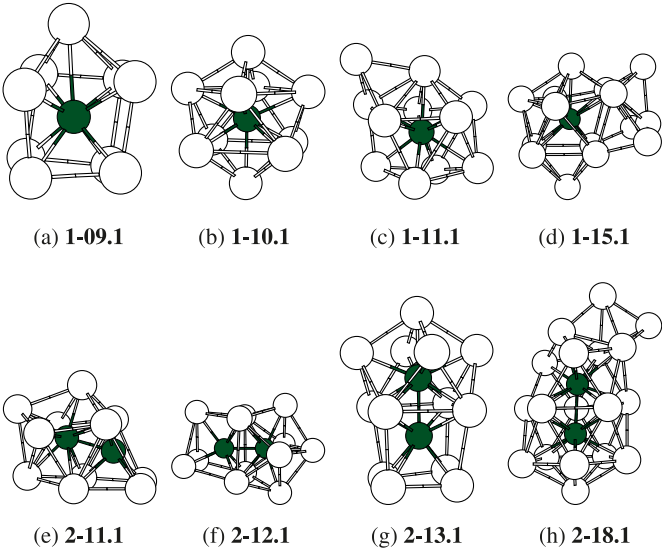
One thing is clear from Figs. 1 and 2: all global minima have the Cu atoms closer to the center of mass of the cluster. This unambiguously confirms what Breau et al. suggested:  $\text{Cu}_p\text{Sn}_q^+$  clusters adopt CSS. This is not a trivial result because, in the bulk, copper and tin form alloys. This trend can be rationalized from the higher surface energy of Cu compared with Sn. In metals, the surface energy is roughly proportional to the ratio of the cohesive energy and the square of the bulk nearest-neighbour distance<sup>19</sup>: this is  $3.49/2.56^2 = 0.53$  eV/Å<sup>2</sup> for Cu, and  $3.14/2.81^2 = 0.40$  eV/Å<sup>2</sup> for Sn. Clearly, Cu atoms have a propensity to go in the interior of mixed Cu–Sn clusters, or, equivalently, Sn atoms tend to arrange themselves in a compact way around Cu atoms to minimize the surface energy term associated with Cu. Another rationale for bimetallic CSS is that putting the smaller atoms in the interior decreases the strain.<sup>20</sup>

In principle, two things could oppose the surface energy driven formation of CSS: (i) ionic energy terms favor A–B ordering (mixing),<sup>21</sup> and (ii) there are many more possible structures (i.e., local minima) having one or more surface Cu atoms than there are CSS structures, so, everything else being equal, one expects a high probability that the GM will not be a CSS. However: (i) the ionic contributions to energy in Cu–Sn mixed clusters are negligible because these two elements have almost the same electronegativity; and (ii) as shown in the Cohesive energies section, the stabilization associated with atomic shell closing (CSS formation) is on the order of 0.5 to 1 eV, and this is apparently bigger than en-

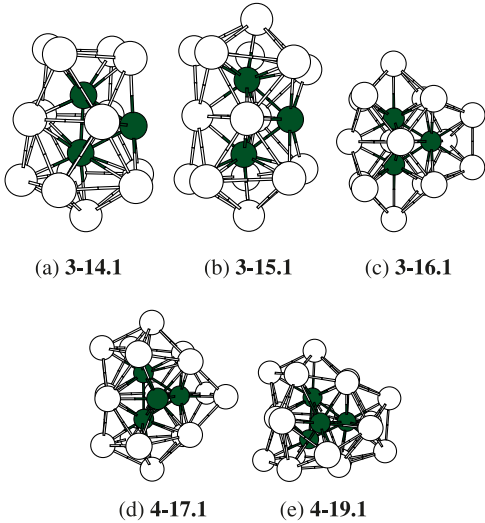
**Table 1.** Number of isomers of  $\text{Cu}_p\text{Sn}_q^+$  found and their calculated relative energies (eV).

	No. of isomers with RE < 1 eV	Relative energies (eV)
<b>1–09</b> = $\text{CuSn}_9^+$	6	0.00, 0.07, 0.28, 0.29, 0.42, 0.97
<b>1–10</b> = $\text{CuSn}_{10}^+$	2	0.00, 0.89
<b>1–11</b> = $\text{CuSn}_{11}^+$	4	0.00, 0.13, 0.54, 0.93
<b>1–15</b> = $\text{CuSn}_{15}^+$	13	0.00, 0.14, 0.23, 0.35, 0.39, 0.39, 0.55, 0.69, 0.70, 0.72, 0.78, 0.82, 0.89
<b>2–11</b> = $\text{CuSn}_{11}^+$	7	0.00, 0.05, 0.05, 0.11, 0.18, 0.33, 0.39
<b>2–12</b> = $\text{CuSn}_{12}^+$	12	0.00, 0.06, 0.19, 0.23, 0.24, 0.31, 0.39, 0.41, 0.42, 0.44, 0.50, 0.93
<b>2–13</b> = $\text{CuSn}_{13}^+$	3	0.00, 0.18, 0.53
<b>2–18</b> = $\text{Cu}_2\text{Sn}_{18}^+$	12	0.00, 0.05, 0.07, 0.41, 0.46, 0.48, 0.52, 0.53, 0.43, 0.75, 0.93, 0.99
<b>3–14</b> = $\text{Cu}_3\text{Sn}_{14}^+$	14	0.00, 0.10, 0.42, 0.44, 0.44, 0.45, 0.54, 0.60, 0.63, 0.64, 0.70, 0.71, 0.77, 0.80
<b>3–15</b> = $\text{Cu}_3\text{Sn}_{15}^+$	8	0.00, 0.3, 0.38, 0.46, 0.51, 0.65, 0.67, 0.77
<b>3–16</b> = $\text{Cu}_3\text{Sn}_{16}^+$	7	0.00, 0.22, 0.26, 0.27, 0.37, 0.54, 0.69
<b>4–17</b> = $\text{Cu}_4\text{Sn}_{17}^+$	10	0.00, 0.09, 0.25, 0.32, 0.38, 0.38, 0.41, 0.66, 0.76, 0.82
<b>4–19</b> = $\text{Cu}_4\text{Sn}_{19}^+$	5	0.00, 0.15, 0.28, 0.34, 0.46

**Fig. 1.** The eight computed global minima of  $\text{Cu}_p\text{Sn}_q^+$  cluster cations,  $p = 1, 2$ .



**Fig. 2.** The five computer global minima of  $\text{Cu}_p\text{Sn}_q^+$  cluster cations,  $p = 3, 4$ .



ergy differences caused by arbitrary small changes in cluster topology.

It is also apparent from Figs. 1 and 2 that Cu-centered square antiprisms and Cu-centered icosahedra are common fragments, and that the clusters are generally very compact. The geometries with centered square antiprisms resemble some of the GM we found in lithium clusters.<sup>22</sup> These are characterized by a bimodal distribution of nearest-neighbor interatomic distances that is feasible only for clusters of highly compressible atoms (e.g., Li) or, as here, mixed clusters where the smaller atoms are in the interior. We will now describe the lowest-energy structures of each species.

**Geometric structures**

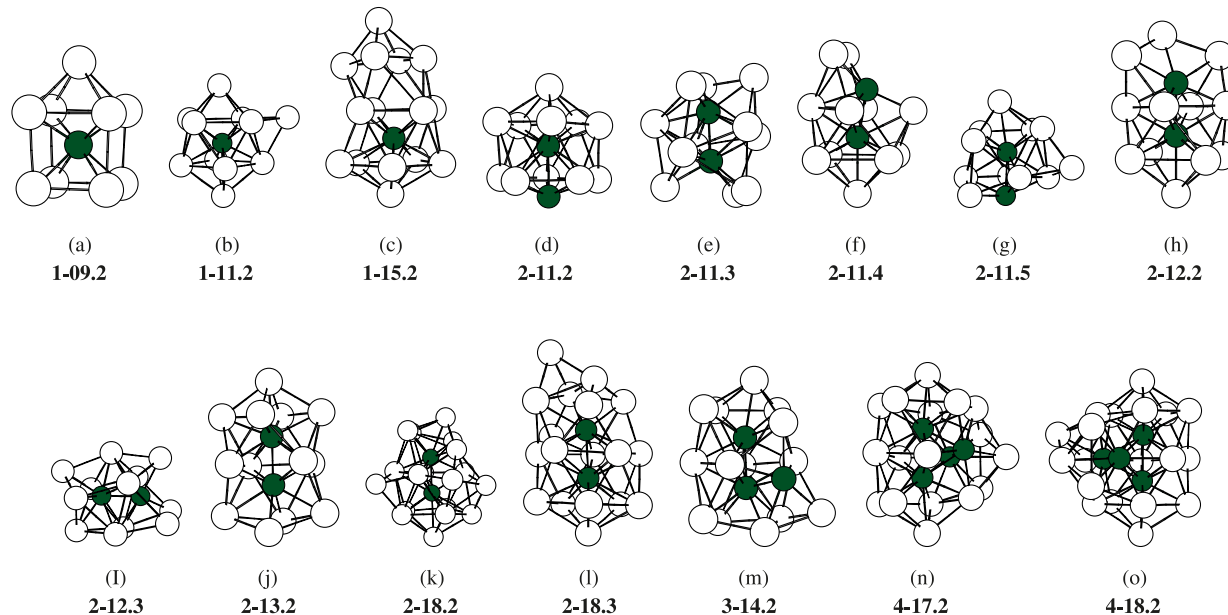
The GM of **1–9** is a distorted Cu-centered  $\text{Sn}_8$  cube with a face-capping Sn atom. Its undistorted  $C_{4v}$  version, **1–09.2** (Fig. 3), lies 0.07 eV higher. The lowest-energy isomer with a low coordinated (four-coordinated) Cu atom is much higher, 1.04 eV above the GM.

The GM for **1–10** is a  $D_{4d}$  Cu-centered bicapped square antiprism, which is the fourfold analog of a centered icosahedron.

The same structure was found, by DFT, for  $\text{NiSn}_{10}$ .<sup>23</sup> The center-to-surface interatomic distance in **1–10.1** is 9% shorter than the shortest surface interatomic distance, compared with 5% for a centered icosahedron. Such a short center-to-surface distance is favorable in  $\text{CuSn}_{10}$  (neutral or charged) owing to the small atomic radius of Cu (1.28 Å) compared with Sn (1.41 Å). The high symmetry and compact nature of **1–10.1**, coupled with the fact that the next lowest isomer found is almost a full eV higher, suggest that **1–10.1** is the only form of  $\text{CuSn}_{10}^+$  observed experimentally and that it has special stability. Arguments in the next section also suggest that **1–10.1** is particularly stable.

The GM of **1–11** resembles **1–10.1** but with a five-member ring and one capping Sn atom. **1–11.2** (RE = 0.13 eV) is **1–10.1** plus a triangular capping Sn atom. There is one Sn atom far away from the Cu atom in both **1–11.1** and **1–11.2**. Isomer **1–11.3** is a  $C_{5v}$  Cu-centered icosahedron with a missing Sn atom: it is unstable (RE = 0.54 eV) even though all Sn atoms are near the central Cu atom. In that sense, we can say that, for  $p = 1$ , the CSS is complete at 10 Sn atoms.

The low-energy structures of  $\text{CuSn}_{15}^+$  all have a Cu atoms

**Fig. 3.** The fifteen isomers found within 0.2 eV of the global minima.**Table 2.** Atomization energies of the GM clusters (AE, eV), cohesive energy divided by the bulk value ( $\varepsilon$ , dimensionless), and excess energy ( $E_{\text{excess}}$ , eV).

Cluster	AE	$\varepsilon$	$E_{\text{excess}}$
1-09.1	27.82	0.876	+0.45
1-10.1	31.91	0.915	-0.77
1-11.1	34.41	0.905	-0.40
1-15.1	45.25	0.894	+0.30
2-11.1	37.09	0.893	+0.52
2-12.1	40.18	0.900	+0.31
2-13.1	43.69	0.914	-0.32
2-18.1	57.10	0.899	+0.74
3-14.1	49.96	0.918	-0.10
3-15.1	53.08	0.922	-0.33
3-16.1	56.12	0.924	-0.48
4-17.1	62.30	0.925	-0.16
4-19.1	67.70	0.920	+0.24

with high coordination (between 8 and 11). The presence of Sn atoms not bonded to Cu leads to multiple low-energy structures that generally look amorphous, except for the GM and 1-15.2, which have a plane of symmetry. 1-15.1 has the highest Cu coordination (10) and there generally is a correlation among isomers between higher Cu coordination and lower energy.

In  $\text{Cu}_2\text{Sn}_{11}^+$ , it is not possible to have a geometric structure where both Cu atoms achieve full coordination (10 or higher), but many structures with two relatively high-coordination Cu atoms compete and are close in energy. The RE (in eV) and coordinations of the two Cu atoms in the best isomers are as follows: 2-11.1, 0.00, 10, and 7; 2-11.2 (a  $C_{5v}$  Cu-centered icosahedron analog), 0.05, 12, and 6; 2-11.3, 0.05, 8, and 8; 2-11.4, 0.11, 10, and 7; 2-11.5, 0.18, 10, and 6. The GM has a plane of symmetry that contains the two Cu atoms. The Sn-centered icosahedron analog is 1.93 eV above the GM.

The GM of  $\text{Cu}_2\text{Sn}_{12}^+$  has a plane of symmetry that con-

tains the two Cu atoms. The Cu atoms are more or less evenly surrounded by Sn atoms but are not fully coordinated (the coordinations are 10 and 8). 2-12.1 lacks symmetry and, as was the case for  $\text{Cu}_2\text{Sn}_{11}^+$ , there are many other imperfect ways of surrounding Cu. This gives six isomers in a 0.3 eV range. Many of these isomers contain a Cu-centered square antiprism motif. 2-12.11 (RE = 0.50 eV) is the lowest-energy isomer containing a Cu-centered  $\text{Sn}_8$  cubic fragment.

Curiously, the GM of  $\text{Cu}_2\text{Sn}_{13}^+$  has one Cu atom surrounded by a distorted cube of Sn atoms and the other one at the center of a  $\text{Sn}_8$  antiprism. The next lowest-energy isomer (RE = 0.18 eV) has both Cu atoms in square antiprism environments. Isomers 2-13.1 and 2-13.2 both have approximate  $C_{4v}$  symmetry and Cu atom coordinations of 10 and 9. The next isomer, 2-13.3, also has Cu atom coordinations of 10 and 9, but it lacks symmetry and is found at a significantly higher energy (RE = 0.53 eV).

Isomer 2-18.1, like 1-15.1, has more Sn atoms than needed to fully surround the Cu atoms. Two of its Sn atoms have no contact with Cu. One Cu atom is in a distorted icosahedral environment (and 12-coordinated), the other is 11-coordinated.

The basic shape of 3-14.1 is a Cu-centered icosahedron with four capping Sn atoms on one side. The Cu atoms are bonded to each other and have coordinations equal to 12, 10, and 7. Isomer 3-14.3 has a prolate structure resembling a double icosahedron, with four atoms (Sn, Cu, Cu, and Sn) aligned along  $z$  alternating with three layers (perpendicular to  $z$ ) of 5, 4, and 4 atoms. The Cu atoms have coordinations of 11, 10, and 5 in 3-14.3.

Isomer 3-15.1 resembles 3-14.3, with Sn-Cu-Cu-Sn down the  $z$  axis, but with layers of 5, 4, and 5 atoms. The two axial Cu atoms are 10-coordinated. The third Cu atom is in the central four-atom layer and has a coordination of 8 (atoms in the other two layers are six-coordinated). This structure was discovered many times by TSDS, and the next isomer, 3-15.2, has an RE of 0.36 eV. This suggests that no



**Table 3.** Descriptors  $N_i$ ,  $F_{90}$ , and  $\eta$  (see text) for the GM structures, and HOMO–LUMO gaps (eV) and average atomic charge on Cu,  $Q_{\text{Cu}}$ .

	$N_i$	$F_{90}$	$\eta$	$E_{\text{gap}}$	$Q_{\text{Cu}}$
<b>1–09.1</b>	1.0	1.4	0.16	1.27	+0.11
<b>1–10.1</b>	1.0	0.3	0.01	1.26	+0.08
<b>1–11.1</b>	1.0	0.4	0.19	1.06	+0.12
<b>1–15.1</b>	1.0	0.6	0.24	1.27	+0.16
<b>2–11.1</b>	1.6	1.1	0.15	0.67	+0.18
<b>2–12.1</b>	2.0	0.9	0.33	0.83	+0.16
<b>2–13.1</b>	2.0	0.9	0.35	0.84	+0.21
<b>2–18.1</b>	2.0	0.4	0.49	0.58	+0.31
<b>3–14.1</b>	2.0	1.2	0.27	0.89	+0.30
<b>3–15.1</b>	2.0	0.9	0.40	1.10	+0.31
<b>3–16.1</b>	3.0	0.8	–0.16	0.99	+0.24
<b>4–17.1</b>	3.3	1.0	–0.02	0.61	+0.27
<b>4–19.1</b>	3.9	0.5	0.08	0.30	+0.33

isomer would be seen experimentally. Isomer **3–15.5** is like the GM but with layers of 5, 5, and 4 atoms instead of 5, 4, and 5. Isomer **3–15.2** is quite different from the GM and **3–15.5**: it has a central triangle of Cu atoms, with coordination 10, 9, and 9, fully surrounded by Sn atoms and has an oblate shape.

Isomer **3–16.1** is oblate and has efficient packing of Sn atoms around a central triangle of Cu atoms that have coordinations 11, 10, and 10. It is very regular, with a 1–4–1–4–1–4–1 centered square antiprism motif running in the vertical direction in Fig. 2. An additional capping atom next to the 11-coordinated Cu atom would complete its shell to something resembling a distorted fcc environment and would give overall  $C_{2v}$  symmetry, so we speculate that this is the GM of **3–17**. The next isomer of  $\text{Cu}_3\text{Sn}_{16}^+$  is relatively high in energy (0.22 eV). The double icosahedron is the most compact 19-atom structure and is a minor shell closing in the Lennard–Jones clusters sequence, but it (**3–16.3**) lies 0.26 eV above the GM of  $\text{Cu}_3\text{Sn}_{16}^+$ . Note that the Cu atoms coordinations in **3–16.3**, 12, 12, and 8, add up to 32, compared to 31 in **3–16.1**. This is just one of many examples among  $\text{Cu}_p\text{Sn}_q^+$  isomers where it seems energetically favorable to not only maximize atomic coordinations, but also equalize them. This tendency has been noted in other types of clusters.<sup>24–26</sup>

Isomer **4–17.1** is a distorted double icosahedron with two capping atoms on its side. The four Cu atoms occupy the highest possible coordination sites and form a tetrahedron. Isomer **4–17.2** differs from **4–17.1** by the position of one Sn atom. The following isomers in energy, up to **4–17.7** (RE = 0.41 eV), are all variations of the double icosahedron with highly coordinated  $\text{Cu}_4$  tetrahedral fragments. The Cu atoms coordinations are 11, 11, 10, and 8 in both **4–17.1** and **4–17.2**.

Isomer **4–19.1** is an incomplete multiple icosahedron where the four Cu atoms form a tetrahedron and have coordinations equal to 12, 11, 11, and 11. Three more Sn atoms would be needed to complete the icosahedral shell around each Cu atom, so it seems that  $\text{Cu}_4\text{Sn}_{22}^+$  might have special stability and properties. Isomer **4–19.2** is another multiple icosahedron that would also require three more Sn atoms to fully coordinate the Cu atoms.

### Cohesive energies

The calculated ionization energies of Sn and Cu are 7.458 eV and 7.838 eV, respectively, in very good agreement with the experimental values of Brown et al. (7.3439 eV)<sup>27</sup> (Sn) and Look et al. (7.7264 eV)<sup>28</sup> (Cu). We calculated the atomization energy (AE) of  $\text{Cu}_p\text{Sn}_q^+$  as

$$[4] \quad \text{AE}(p, q) = pE(\text{Cu}) + (q - 1)E(\text{Sn}) + E(\text{Sn}^+) - E(\text{Cu}_p\text{Sn}_q^+)$$

To compare the energy of different  $(p, q)$  species, we fitted a function of  $p$  and  $q$  to the set of thirteen AEs:

$$[5] \quad f(p, q) = pE_c(\text{Cu}) + qE_c(\text{Sn}) - q^{2/3}E_s(\text{Sn}) - q^{1/3}E_r(\text{Sn})$$

The four parameters have the following physical interpretation:  $E_c(\text{Cu})$  and  $E_c(\text{Sn})$  are effective cohesive energies (eV/atom),  $E_s(\text{Sn})$  relates to the surface energy of tin, and  $E_r(\text{Sn})$  comes from the fact that the clusters' surfaces have a finite radius of curvature. This function form implicitly assumes that Cu atoms make no contribution to the surface energy of the cluster. The best fit is obtained with  $E_c(\text{Cu}) = 3.601$ ,  $E_c(\text{Sn}) = 2.994$ ,  $E_s(\text{Sn}) = 0.092$ , and  $E_r(\text{Sn}) = 0.174$ . It reproduces PBE atomization energies with a mean error of 1.1%. The most interesting quantities derived from this fit are the *energy differences*  $E_{\text{excess}}(p, q) = f(p, q) - \text{AE}(p, q)$ . A negative value of  $E_{\text{excess}}$  means that the cluster is stable relative to the 12 other clusters, a positive value means that it is unstable. By the criterion of  $E_{\text{excess}}(p, q)$  (Table 2), **1–10.1** is the most stable and **2–18.1** is the least stable. It is easy to see why: **2–18.1** has two extra Sn atoms not bonded to Cu, whereas **1–10.1** has a full shell of Sn atoms around Cu but no extra Sn. Further, **1–10.1** has 40 valence electrons, which matches a closed electronic shell of the jellium model. The other relatively stable clusters (**1–11.1**, **2–13.1**, **3–16.1**) are all at, or slightly above, the lower  $q$  limit for completing a CSS. The least stable clusters do not have a CSS: they either have too few or too many Sn atoms to form a monolayer around the  $\text{Cu}_p$  core. On the whole, the calculated  $E_{\text{excess}}$  indicate that for Cu–Sn clusters: (i) there is a stabilization associated with completing a Sn shell and

forming a CSS; and (ii) the energies associated with this geometric effect are on the order of  $\pm 0.5$  eV.

### Trends in geometry and electronic structure

Table 3 shows three geometric descriptors ( $N_i$ ,  $F_{90}$ , and  $\eta$ ) and two electronic descriptors (HOMO–LUMO gap, and average of Cu atomic charges). The  $N_i$ s indicate that the smallest numbers of Sn atoms required to achieve a  $\text{Cu}_p\text{@Sn}_q^+$  CSS structure,  $q^*$ , are 9 (for  $p = 1$ ), 12 ( $p = 2$ ), 16 ( $p = 3$ ), and roughly 18 ( $p = 4$ ). The  $E_{\text{excess}}$  numbers, however, suggest that  $q^* = 10, 13, 16$ , and 18 may be more appropriate:  $\text{Cu}_p\text{Sn}_q^+$  are stable if all their Cu atoms are interior atoms, no Sn atom is without a Cu neighbour, and all Cu atoms have a sufficiently high coordination.

The  $F_{90}$  values are small compared with other metal clusters<sup>26</sup> except in **1–09.1** and, to a lesser degree, **2–11.1** and **3–14.1**. The small  $F_{90}$  reflect the fact that square antiprisms are generally favored over cubes.

The  $\eta$  parameters are relevant for interpreting cluster ion mobility experiments because mobility is a function of shape and gets higher as  $\eta$  approaches zero. Not too surprisingly, CSS have shapes consistent with that of the Cu inner core: roughly spherical for  $p = 1, 4$  ( $\eta = 0.16, 0.01, 0.19$ , and  $0.08$ ), prolate for  $p = 2$  ( $\eta = 0.33, 0.35$ ), and oblate for  $p = 3$  ( $\eta = -0.16$ ). The non-CSS clusters, on the other hand, often have  $\eta$  that deviate from those shapes, or extreme values of  $\eta$  (for example,  $0.49$  for **2–18.1**). If the Cu inner core of bigger  $\text{Cu}_p\text{Sn}_q^+$  CSS follows the polytetrahedral (icosahedral) packing sequence,<sup>29,30</sup> as expected, the CSS  $\text{Cu}_p\text{Sn}_q^+$  clusters should be prolate at  $p = 5$ , spherical or prolate at  $p = 6$ , oblate at  $p = 7$ , prolate from  $p = 8$  to  $p = 11$  (strongly prolate at  $p = 10$ ), and quasi-spherical at  $p = 12, 13$ .

The HOMO–LUMO gaps of odd electron species were calculated by taking the smaller of the  $\alpha$  spin value and the  $\beta$  spin value. The gaps in Table 3 are unremarkable: fairly large for metal clusters, but this is expected of GM, and largest for even electron species. One somewhat surprising finding is that the gap of **1–10.1** is not particularly large, compared with other  $p = 1$  species, despite its large negative  $E_{\text{excess}}$  and the fact that **1–10.1** has 40 valence electrons (the only jellium closed electronic shell number among the thirteen species).

Atomic charges calculated by Mulliken population analysis are not meaningful for metal clusters: the central atoms always have a very large unphysical negative charge, even in cluster cations. Atomic charges calculated by natural bond orbitals (NBO)<sup>31</sup> analysis are much more meaningful. The NBO charges on individual Cu atoms vary between  $+0.1$  and  $+0.4$ , and the average of Cu atomic charges is given in Table 3 for each cluster. One can see that the net  $+1$  charge is delocalized in  $\text{Cu@Sn}_q^+$ , but that it is localized on the Cu atoms of  $\text{Cu}_p\text{@Sn}_q^+$  ( $p = 3, 4$ ), and that  $\text{Cu}_2\text{@Sn}_q^+$  clusters represent an intermediate case. The electron population for Cu Rydberg states is appreciable: it generally varies between  $0.30$  and  $0.50$ , and reaches a maximum ( $0.57$ ) for the Cu atom of  $\text{Cu@Sn}_{10}^+$ . By comparison, the Rydberg populations on Sn atoms are always around  $0.02$ . The Cu atomic charges could be more positive than shown in Table 3 if one used a different basis set or a different way of analyzing

the electron density associated with the NBO Cu Rydberg population.

### Stability criteria

The most stable clusters within a sequence often have a closed atomic shell<sup>30,32</sup> or a closed electronic shell.<sup>33,34</sup> The former usually have a compact geometry and high symmetry. The latter have an electron count that corresponds to having filled shells in some simple model of electronic structure, for instance, the jellium model for metal clusters, which predicts favorable electron counts of 2, 8, 18, 20, 34, 40, and so forth. Clusters that simultaneously satisfy geometric and electronic criteria, the so-called “doubly magic clusters” (DMC), are expected to be extra stable. An example of a DMC is  $\text{Al}_{13}$ ,<sup>35</sup> with its closed quasi-spherical atomic structure and 40 valence electrons. A number of stable metal cluster compounds have been synthesized, which can be viewed as DMCs to which are attached an outer layer of ligands that lowers their surface energy.<sup>36–38</sup> In this section, we try to identify possible  $\text{Cu}_p\text{Sn}_q^{+m}$  DMC cations because they might give stable compounds after passivation with ligands such as  $\text{CO}$ <sup>39</sup> or chloride ions. The geometric structures and  $E_{\text{excess}}$  we obtained suggest that stability is associated with CSS formation at certain values of  $q$  ( $q^* = 10, 13, 16$ , and  $18$  for  $p = 1$  to  $4$ , respectively). We now describe a simple model that reproduces these  $q^*$  values.

Experimentally, the nearest-neighbor distance for bulk Cu is  $R_{\text{Cu}} = 2.56$  Å and the atomic volume is  $V_{\text{Cu}} = 11.86$  Å<sup>3</sup>. For Sn, we have  $R_{\text{Sn}} = 2.81$  Å and  $V_{\text{Sn}} = 27.1$  Å<sup>3</sup>. First, we calculate the radius  $R_i$  of a hypothetical spherical inner core of  $p$  Cu atoms:  $R_i = (3pV_{\text{Cu}}/4\pi)^{1/3}$ . The outer radius  $R_o$  of a spherical  $\text{Cu}_p\text{@Sn}_q$  cluster can then be approximated by  $R_o = R_i + c \times R_{\text{Sn}}$  where  $c$  is an adjustable parameter. As it turns out,  $c = 1.00$  gives  $q^*$  values that agree reasonably well with the most stable compositions in Table 2, so we simply set  $c = 1$ . We estimate the number  $q^*$  of Sn atoms needed to form a quasi-spherical monolayer around a  $\text{Cu}_p$  core like this:  $q^* = (4\pi R_o^3/R - pV_{\text{Cu}})/V_{\text{Sn}}$ . With this, the predicted compositions ( $p, q^*$ ) of  $\text{Cu}_p\text{Sn}_q$  CSS clusters are (1,11), (2,14), (3,16), (4,18), (5,20), (6,21), (7,23), (8,24), and ( $p, p + 17$ ) for  $8 < p < 22$ . These ( $p, q^*$ ), and nearby combinations, are where we expect to find extra stability on account of atomic shell closing (CSS formation). This could be combined with the closed-shell electron counts of the jellium model ( $N_e = 2, 8, 18, 20, 34, 40, 58, 92, 138, \dots$ ) to estimate the composition and charge state of stable  $\text{Cu}_p\text{@Sn}_q^{+m}$  DMC cations. For instance, some of the species that look promising as central units for stable DMC compounds would include  $(\text{CuSn}_{11})^{5+}$ ,  $(\text{CuSn}_{11})^{11+}$ ,  $(\text{Cu}_3\text{Sn}_{16})^{9+}$ ,  $(\text{Cu}_4\text{Sn}_{18})^{18+}$ , and so forth. Note that high formal positive charges on the DMC part of ligand-passivated cluster compounds have been proposed before,<sup>36–38</sup> and are entirely possible if ligands are very electronegative or bind covalently to the outer layer atoms of the DMC.

We believe that the tendency of some binary clusters  $\text{M}_p\text{B}_q$  ( $\text{M}$  is a metal) to adopt structures where the  $\text{M}_p$  unit is encapsulated by a shell of B atoms can be rationalized most simply from surface-energy considerations. The parameter  $E_c/R_{\text{NN}}^2$ , where  $E_c$  is the cohesive energy of an element and  $R_{\text{NN}}$  is its atomic radius, is particularly helpful. Gener-

ally, atoms of M are encapsulated by clusters of B if B has a smaller  $E_c/R_{NN}^2$  than M. For instance, some values of  $E_c/R_{NN}^2$  (in eV/Å<sup>2</sup>) are 0.84 (Si), 0.40 (Sn), 0.53 (Cu), 0.35 (Ag), 0.58 (Mn), and 0.66 (Cr): experiments and calculations indicate that Si clusters do *not* encapsulate atoms of Cu and Ag,<sup>40</sup> Sn clusters encapsulate Cu (this work and ref. 15) and Mn,<sup>11,14</sup> and that Si clusters may be able to encapsulate Cr.<sup>40</sup> The SiCr case (and SiMo also)<sup>40</sup> suggest that  $(E_c + P)/R_{NN}^2$ , where  $P$  is the promotion energy from the atom's ground state to the effective electronic state of an atom in a solid, could be a more appropriate parameter than  $E_c/R_{NN}^2$ . For instance, the ground states of Cr (septet d<sup>5</sup>s<sup>1</sup>) and Mn (d<sup>5</sup>s<sup>2</sup>) are usually *not* appropriate references for assessing the strengths of interatomic interactions, and  $(E_c + P)/R_{NN}^2$  ( $P > 0$ ) would indicate a stronger tendency for Cr and Mn to be encapsulated in Si cages.

## Conclusion

Here is what we can conclude from our DFT and global optimization study of  $Cu_pSn_q^+$ . First,  $Cu_pSn_q^+$  do form CSS. Second, the stabilization associated with completion of a monolayer outer-shell of Sn atoms is 0.5 to 1.0 eV. Third, most of the  $Cu_pSn_q^+$  species (even those with good core-shell structures) have many low-lying isomers, within a few tenths of eV from the GM and from each other. Fourth,  $CuSn_{10}^+$  has a large negative  $E_{excess}$  and no low-lying isomer: it stands out as particularly stable among the species investigated here. A similar conclusion was reached by Breau et al.<sup>15</sup> based on their observed fragmentation patterns. We ascribe the stability of  $CuSn_{10}^+$  to its doubly magic nature; atomic shell closing (10 Sn atoms in a square antiprism geometry) and electronic shell closing (40 electrons). Fifth, the moments of inertia of  $Cu_p@Sn_q^+$  mirror those of the inner Cu core when  $q$  is close to an atomic shell closing value,  $q^*$ . This, together with the observation that the  $Cu_p$  cores appear to favor the same polytetrahedral structures as Lennard-Jones clusters, could facilitate the interpretation of cluster ion mobility experiments.

We fitted a simple atomic-shells model to our DFT results and used it to predict the likely values of  $p$ ,  $q$ , and  $m$  of  $Cu_pSn_q^{m+}$  species that would satisfy two stability criteria and might, with adequate ligand passivation, make stable metal cluster compounds. We think that  $(E_c + P)/R_{NN}^2$  (where  $(E_c + P)$  is an element's cohesive energy calculated relative to a relevant dissociated atoms state) can be a useful parameter for predicting which binary cluster systems could lead to CSS formation.

## Supplementary data

Supplementary data for this article are available on the journal Web site (canjchem.nrc.ca).

## Acknowledgements

RF thanks the Natural Sciences and Engineering Research Council (NSERC) of Canada for funding.

## References

- (1) Ferrando, R.; Jellinek, J.; Johnston, R. L. *Chem. Rev.* **2008**, *108* (3), 845. doi:10.1021/cr040090g. PMID:18335972.
- (2) Goia, D. V.; Matijevic, E. *N. J. Chem.* **1998**, *22* (11), 1203. doi:10.1039/a709236i.
- (3) Park, J. I.; Kim, M. G.; Jun, Y. W.; Lee, J. S.; Lee, W. R.; Cheon, J. *J. Am. Chem. Soc.* **2004**, *126* (29), 9072. doi:10.1021/ja049649k. PMID:15264840.
- (4) Bente, W.; Nilius, N.; Ernst, N.; Freund, H.-J. *Phys. Rev. B* **2005**, *72* (4), 045403. doi:10.1103/PhysRevB.72.045403.
- (5) Doudna, C. M.; Bertino, M. F.; Blum, F. D.; Tokuhito, A. T.; Lahiri-Dey, D.; Chattopadhyay, S.; Terry, J. *J. Phys. Chem. B* **2003**, *107* (13), 2966. doi:10.1021/jp0273124.
- (6) Mizukoshi, Y.; Fujimoto, T.; Nagata, Y.; Oshima, R.; Maeda, Y. *J. Phys. Chem. B* **2000**, *104* (25), 6028. doi:10.1021/jp994255e.
- (7) Kumar, V. *Comput. Mater. Sci.* **2006**, *36* (1-2), 1. doi:10.1016/j.commatsci.2005.06.004.
- (8) Sinfelt, J. H. *Catal. Today* **1999**, *53* (3), 305. doi:10.1016/S0920-5861(99)00124-8.
- (9) Tournus, F.; Tamion, A.; Blanc, N.; Hannour, A.; Bardotti, L.; Prével, B.; Ohresser, P.; Bonet, E.; Épicier, T.; Dupuis, V. *Phys. Rev. B* **2008**, *77* (14), 144411. doi:10.1103/PhysRevB.77.144411.
- (10) Rosi, N. L.; Mirkin, C. A. *Chem. Rev.* **2005**, *105* (4), 1547. doi:10.1021/cr030067f. PMID:15826019.
- (11) Kumar, V.; Kawazoe, Y. *Appl. Phys. Lett.* **2003**, *83* (13), 2677. doi:10.1063/1.1609661.
- (12) Neukermans, S.; Wang, X.; Veldeman, N.; Janssens, E.; Silverans, R. E.; Lievens, P. *Int. J. Mass Spectrom.* **2006**, *252* (2), 145. doi:10.1016/j.ijms.2005.12.056.
- (13) Cui, L.-F.; Huang, X.; Wang, L.-M.; Li, J.; Wang, L.-S. *Angew. Chem. Int. Ed.* **2007**, *46* (5), 742. doi:10.1002/anie.200603226.
- (14) Rohrmann, U.; Schäfer, S.; Schäfer, R. *J. Phys. Chem. A* **2009**, *113* (44), 12115. doi:10.1021/jp906140b. PMID:19863131.
- (15) Breau, G. A.; Hillman, D. A.; Neal, C. M.; Jarrold, M. F. *J. Phys. Chem. A* **2005**, *109* (39), 8755. doi:10.1021/jp0501650. PMID:16834277.
- (16) (a) Perdew, J. P.; Burke, K.; Ernzerhof, M. *Phys. Rev. Lett.* **1996**, *77* (18), 3865. doi:10.1103/PhysRevLett.77.3865. PMID:10062328; (b) Perdew, J. P.; Burke, K.; Ernzerhof, M. *Phys. Rev. Lett.* **1997**, *78* (7), 1396. (E). doi:10.1103/PhysRevLett.78.1396.
- (17) Frisch, M. J.; Trucks, G. W.; Schlegel, H. B.; Scuseria, G. E.; Robb, M. A.; Cheeseman, J. R.; Montgomery, J. A., Jr.; Vreven, T.; Kudin, K. N.; Burant, J. C.; Millam, J. M.; Iyengar, S. S.; Tomasi, J.; Barone, V.; Mennucci, B.; Cossi, M.; Scalmani, G.; Rega, N.; Petersson, G. A.; Nakatsuji, H.; Hada, M.; Ehara, M.; Toyota, K.; Fukuda, R.; Hasegawa, J.; Ishida, M.; Nakajima, T.; Honda, Y.; Kitao, O.; Nakai, H.; Klene, M.; Li, X.; Knox, J. E.; Hratchian, H. P.; Cross, J. B.; Bakken, V.; Adamo, C.; Jaramillo, J.; Gomperts, R.; Stratmann, R. E.; Yazyev, O.; Austin, A. J.; Cammi, R.; Pomelli, C.; Ochterski, J. W.; Ayala, P. Y.; Morokuma, K.; Voth, G. A.; Salvador, P.; Dannenberg, J. J.; Zakrzewski, V. G.; Dapprich, S.; Daniels, A. D.; Strain, M. C.; Farkas, O.; Malick, D. K.; Rabuck, A. D.; Raghavachari, K.; Foresman, J. B.; Ortiz, J. V.; Cui, Q.; Baboul, A. G.; Clifford, S.; Cio-slawski, J.; Stefanov, B. B.; Liu, G.; Liashenko, A.; Piskorz, P.; Komaromi, I.; Martin, R. L.; Fox, D. J.; Keith, T.; Al-Laham, M. A.; Peng, C. Y.; Nanayakkara, A.; Challacombe, M.; Gill, P. M. W.; Johnson, B.; Chen, W.; Wong, M. W.;

- Gonzalez, C.; Pople, J. A. *Gaussian 03*, Revision C.02; Gaussian, Inc.: Wallingford, CT, 2004.
- (18) Cheng, J.; Fournier, R. *Theor. Chem. Acc.* **2004**, *112*, 7.
- (19) Somorjai, G. A. *Introduction to Surface Chemistry and Catalysis*; Wiley: New York, 1994.
- (20) Rapallo, A.; Rossi, G.; Ferrando, R.; Fortunelli, A.; Curley, B. C.; Lloyd, L. D.; Tarbuck, G. M.; Johnston, R. L. *J. Chem. Phys.* **2005**, *122* (19), 194308. doi:10.1063/1.1898223. PMID:16161574.
- (21) Fournier, R.; Zamiruddin, S.; Zhang, M. *Can. J. Chem.* **2009**, *87* (7), 1013. doi:10.1139/V09-065.
- (22) Fournier, R.; Cheng, J. B. Y.; Wong, A. *J. Chem. Phys.* **2003**, *119* (18), 9444. doi:10.1063/1.1615237.
- (23) Kumar, V.; Singh, A. K.; Kawazoe, Y. *Nano Lett.* **2004**, *4* (4), 677. doi:10.1021/nl0498076.
- (24) Fournier, R. *J. Chem. Phys.* **2001**, *115* (5), 2165. doi:10.1063/1.1383288.
- (25) Sun, Y.; Fournier, R.; *Comput. Lett.* **2005**, *1* (4), 210. doi:10.1163/157404005776611448.
- (26) Sun, Y.; Zhang, M.; Fournier, R.; *Phys. Rev. B* **2008**, (77), 075435.
- (27) Brown, C. M.; Tilford, S. G.; Ginter, M. L. *J. Opt. Soc. Am.* **1977**, *67* (5), 607. doi:10.1364/JOSA.67.000607.
- (28) Loock, H.-P.; Beaty, L. M.; Simard, B. *Phys. Rev. A* **1999**, *59* (1), 873. doi:10.1103/PhysRevA.59.873.
- (29) Echt, O.; Sattler, K.; Recknagel, E. *Phys. Rev. Lett.* **1981**, *47* (16), 1121. doi:10.1103/PhysRevLett.47.1121.
- (30) Martin, T. P. *Phys. Rep.* **1996**, *273* (4), 199. doi:10.1016/0370-1573(95)00083-6.
- (31) Reed, A. E.; Curtiss, L. A.; Weinhold, F. *Chem. Rev.* **1988**, *88* (6), 899. doi:10.1021/cr00088a005.
- (32) Alonso, J. A. *Structure and Properties of Atomic Nanoclusters*; Imperial College Press: London, 2005.
- (33) (a) de Heer, W. A. *Rev. Mod. Phys.* **1993**, *65* (3), 611. doi:10.1103/RevModPhys.65.611.; (b) Brack, M. *Rev. Mod. Phys.* **1993**, *65* (3), 677. doi:10.1103/RevModPhys.65.677.
- (34) Knight, W. D.; Clemenger, K.; DeHeer, W. A.; Saunders, W. A.; Chou, Y. M.; Cohen, M. L. *Phys. Rev. Lett.* **1984**, *52* (24), 2141. doi:10.1103/PhysRevLett.52.2141.
- (35) Castleman, A. W., Jr.; Khanna, S. N. *J. Phys. Chem. C* **2009**, *113* (7), 2664. doi:10.1021/jp806850h.
- (36) Heaven, M. W.; Dass, A.; White, P. S.; Holt, K. M.; Murray, R. W. *J. Am. Chem. Soc.* **2008**, *130* (12), 3754. doi:10.1021/ja800561b. PMID:18321116.
- (37) Akola, J.; Walter, M.; Whetten, R. L.; Häkkinen, H.; Grönbeck, H. *J. Am. Chem. Soc.* **2008**, *130* (12), 3756. doi:10.1021/ja800594p. PMID:18321117.
- (38) Walter, M.; Akola, J.; Lopez-Acevedo, O.; Jadzinsky, P. D.; Calero, G.; Ackerson, C. J.; Whetten, R. L.; Grönbeck, H.; Häkkinen, H. *Proc. Natl. Acad. Sci. U.S.A.* **2008**, *105* (27), 9157. doi:10.1073/pnas.0801001105. PMID:18599443.
- (39) Femoni, C.; Iapalucci, M. C.; Longoni, G.; Svensson, P. H. *Chem. Commun. (Camb.)* **2001**, (18): 1776. doi:10.1039/b103610f. PMID:12240310.
- (40) Jaeger, J. B.; Jaeger, T. D.; Duncan, M. A. *J. Phys. Chem. A* **2006**, *110* (30), 9310. doi:10.1021/jp0629947. PMID:16869677.



# On the nature of homo- and hetero-dinuclear metal–metal quadruple bonds — Analysis of the bonding situation and benchmarking DFT against wave function methods

Nozomi Takagi, Andreas Krapp, and Gernot Frenking

**Abstract:** Homo- and hetero-dimetallic (d–d)<sup>8</sup> analogues of the formally quadruply bonded [Re<sub>2</sub>Cl<sub>8</sub>]<sup>2–</sup> system with the general formula [MM'Cl<sub>8</sub>]<sup>x</sup> (M, M' = Tc, Re, Ru, Os, Rh, Ir and x = –2, –1, 0, +1, +2) have been calculated with the density functional theory (DFT) functionals SVWN, BLYP, BP86, PBE, OLYP, OPBE, HCTH, B3LYP, O3LYP, X3LYP, BH&HLYP, TPSS, VSXC, TPPSh, and ab initio methods (CASPT2, CCSD(T)) using basis sets of triple-ζ quality. The performance of the functionals for the description of the metal–metal bond distance and the bond dissociation energy as well as the singlet–triplet gap was evaluated with respect to ab initio data at the CASPT2 level. Generally, the generalized gradient approximation (GGA) functionals, BLYP, BP86, and PBE, show good performance in the description of the metal–metal bond distance and for the dissociation energy. Hybrid functionals are not to be used for compounds of the type discussed here as they lead to increasingly too short and too weak bonds with the amount of exact exchange included. All functionals underestimate the singlet–triplet gap, with the GGA functionals BLYP, BP86, PBE being the closest to the CASPT2 values. The bonding situations of the [MM'Cl<sub>8</sub>]<sup>x</sup> compounds were analyzed at the DFT level (BP86) using the natural bond orbital (NBO) method and the energy decomposition analysis. The M–M bond in homodimetallic compounds, [MMCl<sub>8</sub>]<sup>x</sup>, becomes weaker from group 7 to group 8 to group 9 metals and the bond is weaker for 4d metal systems than for 5d transition metal compounds. The M–M bonds have approximately 50% covalent and 50% electrostatic character and the covalent contribution is dominated by the π orbitals, whereas the δ orbitals do not contribute significantly to the covalent bonding. Heterodimetallic systems, [MM'Cl<sub>8</sub>]<sup>x</sup>, have significantly stronger metal–metal bonds than the homodimetallic compounds. This comes from weaker Pauli repulsion and stronger electrostatic attraction. The most stable heterodimetallic bonds are observed for 5d–5d metal pairs.

**Key words:** metal–metal bond, metal–metal quadruple bond, heterodimetallic compounds, homodimetallic compounds, dissociation energy, bonding analysis.

**Résumé :** On a effectué des calculs théoriques sur des analogues homo- et hétéro-dimétalliques (d–d)<sup>8</sup> du système [Re<sub>2</sub>Cl<sub>8</sub>]<sup>2–</sup> formellement à quadruple liaison et de formule générale [MM'Cl<sub>8</sub>]<sup>x</sup> (M, M' = Tc, Re, Ru, Os, Rh et Ir et x = –2, –1, 0, 1 et +2) en faisant appel à la théorie de la fonctionnelle de la densité (« DFT »), des fonctionnelles SVWN, BLYP, BP86, PBE, OLYP, OPBE, HCTH, B3LYP, O3LYP, BH&HLYP, TPSS, VSXC, TPPSh et des méthodes ab initio [CASPT2 et CCSD(T)] à base d'ensembles de qualité triple ζ. On a évalué la performance des fonctionnelles pour la description de la longueur de la liaison métal–métal et de l'énergie de dissociation de la liaison ainsi que l'intervalle singulet–triplet par rapport aux données ab initio au niveau CASPT2. En général, les fonctionnelles GGA BLYP, BP86 et PBE donnent une bonne performance dans la description de la longueur de la liaison métal–métal et pour l'énergie de dissociation. Il ne faut pas utiliser les fonctionnelles hybrides pour le type de composés discutés ici parce qu'elles conduisent à des longueurs de liaison qui sont de plus en plus trop courtes et des énergies de liaison trop faibles pour les quantités exactes d'échange incluses. Toutes les fonctionnelles sous estiment l'intervalle singulet–triplet avec les fonctionnelles GGA BLYP, BP86 et PBE conduisant aux valeurs les plus près de valeurs CASPT2. On a examiné les situations de liaison des composés [MM'Cl<sub>8</sub>]<sup>x</sup> à l'aide de la « DFT » au niveau BP86, en utilisant la méthode NBO et l'analyse de la décomposition de l'énergie. La liaison M–M des composés homodimétalliques [MMCl<sub>8</sub>]<sup>x</sup> devient de plus en plus faible lorsqu'on passe des éléments du groupe 7, à ceux des groupes 8 et 9 et la liaison est plus faible pour les systèmes métalliques 4d que pour les composés métalliques de transition 5d. Les liaisons M–M comportent des quantités approximativement égales 50/50, de caractère covalent et électrostatique; la contribution covalente est dominée par les orbitales π alors que les orbi-

Received 18 February 2010. Accepted 5 May 2010. Published on the NRC Research Press Web site at [canjchem.nrc.ca](http://canjchem.nrc.ca) on 10 September 2010.

*This article is part of a Special Issue dedicated to Professor R. J. Boyd.*

**N. Takagi and G. Frenking,**<sup>1</sup> Fachbereich Chemie, Philipps-Universität, Hans-Meerwein-Strasse, D-35039 Marburg, Germany.

**A. Krapp,** Fachbereich Chemie, Philipps-Universität, Hans-Meerwein-Strasse, D-35039 Marburg, Germany; Senter for teoretisk og beregningsorientert kjemi, Kjemisk institutt, Universitetet i Oslo, Postboks 1033 Blindern, 0315 Oslo, Norway.

<sup>1</sup>Corresponding author (e-mail: [frenking@chemie.uni-marburg.de](mailto:frenking@chemie.uni-marburg.de)).

tales  $\delta$  ne contribuent pas d'une façon significative à la liaison covalente. Les systèmes hétérodimmétalliques  $[\text{MM}'\text{Cl}_8]^x$  comportent des liaisons métal-métal qui sont beaucoup plus fortes que celles des composés homodimétalliques. Cette situation résulte de la répulsion de Pauli et d'une attraction électrostatique plus forte. Les liaisons hétérodimmétalliques les plus stables sont observées pour les paires métalliques 5d–5d.

**Mots-clés :** liaison métal-métal, liaison quadruple métal-métal, composés hétérodimmétalliques, composés homodimétalliques, énergie de dissociation, analyse des liaisons.

[Traduit par la Rédaction]

## Introduction

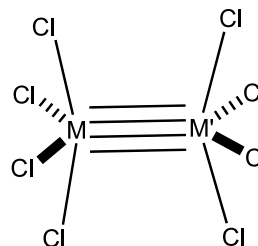
The exploration of the chemistry of metal–metal multiple bonds started in 1965 when Cotton and Harris<sup>1</sup> isolated the anion  $[\text{Re}_2\text{Cl}_8]^{2-}$  in the complex  $\text{K}_2[\text{Re}_2\text{Cl}_8] \cdot 2\text{H}_2\text{O}$ . This compound with a formal Re–Re quadruple bond has since become the prototype of a metal–metal multiple bonded species. Its electronic structure is known in detail and a gas-phase photoelectron spectrum has been collected.<sup>2</sup> Following this initial discovery, the field expanded considerably and a wealth of knowledge has been gained as reflected in the prominent book by Cotton, Murillo, and Walton,<sup>3</sup> which covers the literature up to 2004. In recent years, the field came into general focus again, as exemplified by the isolation of the formally quintuply bonded compound  $\text{RCr}=\text{CrR}$  ( $\text{R} = \text{C}_6\text{H}_3-2,6(-\text{C}_6\text{H}_3-2,6-i\text{-Pr}_3)_2$ ) by the group of Power<sup>4</sup> and by a number of recent quantum chemical studies about molecules with high bond orders between metal atoms.<sup>5–7</sup>

In the last 20 years, heterodinuclear compounds between different metal atoms  $\text{M}=\text{M}'$  were studied experimentally due to their potential as catalysts in metal-mediated reactions, as exemplified by the “early–late” complexes, which mainly contain metal–metal single bonds.<sup>8–11</sup> Much less is known about polar metal–metal bonds of higher bond multiplicity.<sup>3,12</sup> Collmann and Boulatov<sup>12</sup> reported in a series of studies about the structures and intriguing spectral properties of systems with polar metal–metal multiple bonds with the general formula  $\text{PorM}=\text{M}'\text{Por}$  ( $\text{Por}$  = substituted porphyrins).

Little is known about the bonding situation and the stability of these polar metal–metal multiple bonds from a theoretical point of view. As a first step towards the description of the experimentally known systems and the systematic exploration of the bonding possibilities in polar metal–metal multiple bonding, we set out a systematic study of heterodinuclear analogues of  $[\text{Re}_2\text{Cl}_8]^{2-}$ . The results of the work are reported in this paper. We focused on the formally quadruply bonded (d–d)<sup>8</sup> systems with the general formula  $[\text{Cl}_4\text{MM}'\text{Cl}_4]^x$  ( $\text{M}, \text{M}' = \text{Tc}, \text{Re}, \text{Ru}, \text{Os}, \text{Rh}, \text{Ir}; x = -2, -1, 0, +1, +2$ ). We did not include the analogues of the first row transition metals ( $\text{Mn}, \text{Fe}, \text{Co}$ ) in our study, since explorative calculations on the systems  $[\text{M}_2\text{Cl}_8]^x$  showed that they are unbound and because of the highly multideterminantal character inherent in these species, demand far too large active spaces to be tractable. Since our intention was to shed light onto the metal–metal quadruple bond, we restricted ourselves to geometrical arrangements, which enable two  $\text{MCl}_4^x$  fragments to form a metal–metal quadruple bond. This is the  $D_{4h}$  ( $C_{4v}$  for heterodinuclear systems) symmetric structure (see Scheme 1), which might not be the global minimum for all species studied.

Metal–metal bonded systems are typical examples of mul-

Scheme 1.



tideterminant problems. We therefore tested the performance of a variety of density functional theory (DFT) functionals in comparison to theoretical results at the CASPT2 and CCSD(T) levels of theory. The bonding situation of the formally metal–metal bonded systems was studied in detail, making use of the energy decomposition analysis (EDA) and the natural bond orbital method (NBO).

## Computational methods

For benchmarking the performance of DFT we tested the following functionals: (i) local density approximation (LDA): SVWN;<sup>13,14</sup> (ii) generalized gradient approximation (GGA): BP86,<sup>15,16</sup> BLYP,<sup>15,17</sup> OLYP,<sup>17,18</sup> OPBE,<sup>18,19</sup> PBE (also called PBE-PBE),<sup>19</sup> and HCTH (also called HCTH407);<sup>20</sup> (iii) hybrid GGA: B3LYP,<sup>15,17,21</sup> BH&HLYP,<sup>15,17,22</sup> O3LYP,<sup>15,17,23</sup> and X3LYP;<sup>17,24</sup> (iv) meta-GGA: TPSS (also called TPSS-TPSS)<sup>25</sup> and VSXC;<sup>26</sup> and (v) hybrid meta-GGA: TPSSH.<sup>25</sup>

We used split-valence basis sets of doubly polarized triple- $\zeta$  quality developed by Weigend<sup>27</sup> and Ahlrichs,<sup>28</sup> which are denoted as def2-TZVPP. For the metal atoms we used valence basis sets in conjunction with small-core quasi-relativistic effective core potentials.<sup>29</sup> The DFT calculations were performed with the Gaussian03 program package<sup>22</sup> using standard settings for the DFT integration (fine grids) and for the convergence criteria. Care has been taken to obtain the correct electronic states, e.g.,  $^1A_{1g}$  states for the  $D_{4h}$  symmetry  $[\text{M}_2\text{Cl}_8]^x$  molecules and  $^1A_1$  states for the  $C_{4v}$  symmetric  $[\text{MM}'\text{Cl}_8]^x$  systems.

Single point energy calculations using coupled cluster theory<sup>30</sup> at the CCSD(T) level<sup>31–35</sup> in conjunction with the def2-TZVPP basis set were performed on BP86/TZ2P geometries (the TZ2P basis set will be specified below) with the program MolPro2006.<sup>36</sup> To account for static and dynamic correlation effects by wave function methodology, we performed complete active space (CAS) SCF<sup>37</sup> calculations with the dynamic correlation added by multiconfigurational second-order perturbation theory (CASPT2).<sup>38–40</sup> Scalar relativistic effects were included via a Douglas–Kroll Hamiltonian.<sup>41,42</sup> Large ANO-RCC basis sets of Roos and

**Table 1.** Optimized metal–metal distances in Å of  $[MM'Cl_8]^x$  in the lowest totally symmetric closed-shell singlet state (for  $M = M'$ :  $D_{4h}$  symmetry,  $^1A_{1g}$  state; for  $M \neq M'$ :  $C_{4v}$  symmetry,  $^1A_1$  state). All DFT results were obtained using the def2-TZVPP basis set. For the CASPT2 calculations, the large ANO-RCC basis was employed (see Computational methods).

Functional	$[Re_2Cl_8]^{2-}$	$[Tc_2Cl_8]^{2-}$	$[Os_2Cl_8]^0$	$[Ru_2Cl_8]^0$	$[Ir_2Cl_8]^{2+}$	$[Rh_2Cl_8]^{2+}$	$[ReTeCl_8]^{2-}$	$[ReOsCl_8]^{1-}$	$[ReIrCl_8]^0$	$[OsIrCl_8]^{1+}$
SVWN	2.202	2.106	2.156	2.246	2.217	2.360	2.400	2.217	2.273	2.325
BP86	2.226	2.132	2.181	2.270	2.245	2.394	2.464	2.241	2.299	2.351
BLYP	2.244	2.152	2.200	2.294	2.271	2.422	2.508	2.263	2.325	2.381
HCTH	2.208	2.108	2.161	2.256	2.227	2.378	2.393	2.226	2.286	2.333
OLYP	2.213	2.116	2.167	2.258	2.227	2.379	2.391	2.230	2.287	2.332
OPBE	2.195	2.096	2.147	2.232	2.198	2.350	2.353	2.209	2.260	2.301
PBE	2.224	2.131	2.179	2.267	2.242	2.391	2.462	2.239	2.296	2.347
B3LYP	2.201	2.096	2.151	2.240	2.201	2.413	2.472	2.218	2.279	2.330
BH&HLYP	2.153	2.034	2.115	2.180	2.117	2.415	2.439	2.192	2.232	2.287
O3LYP	2.194	2.090	2.145	2.233	2.194	2.380	2.452	2.209	2.266	2.309
X3LYP	2.198	2.092	2.147	2.236	2.196	2.413	2.468	2.215	2.274	2.327
TPSS	2.222	2.128	2.177	2.263	2.237	2.391	2.457	2.236	2.292	2.344
VXC	2.200	2.110	2.157	2.260	2.229	2.401	2.487	2.225	2.289	2.344
TPSSH	2.203	2.103	2.155	2.241	2.207	2.388	2.443	2.217	2.273	2.324
CASPT2(12,12)	2.252									

co-workers,<sup>43</sup> as implemented in the program package MOLCAS, were used in the following contractions: (17s12p5d4f2g)  $\rightarrow$  [5s4p3d1f] for Cl, (24s21p15d11f4g2h)  $\rightarrow$  [8s7p5d3f1g] for Re, Os, Ir, and (21s18p13d6f4g2h)  $\rightarrow$  [7s6p4d2f1g] for Tc, Ru, Rh. These calculations were performed with the program MOLCAS6.<sup>43</sup> The CASPT2 calculations were performed on BP86/TZ2P geometries except for the data presented in Table 1, which are results of geometry optimizations at the CASPT2 level.

In the CASSCF calculations of the  $[MM'Cl_8]^x$  systems, we chose active spaces consisting of either eight electrons in eight orbitals, CAS(8,8), or 12 electrons in 12 orbitals, CAS(12,12). The smaller active space formally comprises the  $nd\sigma$ , two  $nd\pi$ , and one  $nd\delta$  metal–metal bonding and antibonding orbitals, whereas the larger active space also includes a metal–ligand  $\sigma$  bonding and antibonding orbital pair. These active spaces can cover static electron correlation effects connected to the metal–metal bond.

To give a balanced description of correlation effects in the calculation of the dissociation of  $[MM'Cl_8]^x$  into the  $D_{4h}$  symmetric  $MCl_4^y$  fragments, the  $MCl_4^y$  systems in their  $^5A_{1g}$  state were calculated using (4/4) and (6/6) active spaces in the CASSCF. It is, however, important to notice that for systems in which the metal and ligand orbitals interact strongly, e.g., in the case of the cationic system  $[Ir_2Cl_8]^{2+}$ , the active space has to be considerably larger than (12/12) if one is to calculate dissociation energies, since it is necessary to include the chlorine lone pair orbitals in the active space. As will be discussed later, some of the calculated dissociation energies must therefore be considered with care.

The electronic structure of the  $[MM'Cl_8]^x$  molecules was analyzed with various methods. For the charge analysis, we used the natural bond orbital method (NBO) of Weinhold and co-workers<sup>44</sup> as implemented in the Gaussian program.<sup>22</sup> The energy decomposition analysis (EDA)<sup>45–49</sup> calculations have been performed at the BP86 level using uncontracted Slater-type orbitals (STOs), which have TZ2P quality, on geometries optimized at the BP86/TZ2P level.<sup>50</sup> Scalar relativistic effects have been considered using the zero-order regular approximation (ZORA).<sup>51–55</sup> The latter calculations were carried out with the program package ADF.<sup>56,57</sup>

The focus of the EDA<sup>47</sup> is the instantaneous interaction energy,  $\Delta E_{\text{int}}$ , which is the energy difference between the molecule and the fragments with the frozen geometry of the complex. The interaction energy is divided into three main components:

$$\Delta E_{\text{int}} = \Delta E_{\text{elstat}} + \Delta E_{\text{Pauli}} + \Delta E_{\text{orb}}$$

The term  $\Delta E_{\text{elstat}}$  gives the electrostatic interaction energy between the fragments, which are calculated with a frozen density distribution in the geometry of the complex. The Pauli repulsion ( $\Delta E_{\text{Pauli}}$ ) arises as the energy change associated with the transformation from the superposition of the unperturbed electron densities of fragments  $\rho_A + \rho_B$  to the wave function  $\Psi^0 = N\hat{A}\{\Psi_A \times \Psi_B\}$ , which properly obeys the Pauli principle through explicit antisymmetrization ( $\hat{A}$ ) and renormalization ( $N$ ) of the product wave function. It comprises the destabilizing interactions between electrons on either fragment with the same spin. The stabilizing orbital interaction term,  $\Delta E_{\text{orb}}$ , is calculated in the final step of

the analysis when the orbitals relax to their final form. The latter can be decomposed into contributions from each irreducible representation of the point group of the interacting system. This is very helpful because it directly gives the stabilization, which comes from orbitals having different symmetry. To obtain the bond dissociation energy,  $D_e$ , one has to consider the preparation energy,  $\Delta E_{\text{prep}}$ , which is the energy difference of the fragments between their equilibrium geometry and the geometry that they have in the molecule:

$$\Delta E (= -D_e) = \Delta E_{\text{int}} + \Delta E_{\text{prep}}$$

## Performance of DFT functionals

To estimate the performance of the DFT functionals in the description of M–M' formal quadruple bonds, the species  $[\text{Cl}_4\text{MM}'\text{Cl}_4]^x$  (M, M' = Tc, Re, Ru, Os, Rh, Ir;  $x = -2, 0, +2$ ) were completely optimized under  $D_{4h}$  ( $C_{4v}$  in the case of  $M \neq M'$ ) symmetry constraint in the  $^1A_{1g}$  ( $^1A_1$ ) state at the DFT level using the def2-TZVPP basis set. The optimized metal–metal bond lengths are listed in Table 1.

For the parent compound,  $[\text{Re}_2\text{Cl}_8]^{2-}$ , the optimized Re–Re bond length varies considerably between 2.153 Å (BH&HLYP) and 2.244 Å (BLYP), with the experimental value being 2.237(2) Å<sup>3</sup>, which is in good agreement with the CASPT2(12,12) result of 2.252 Å and comparable to recently reported DFT values<sup>58</sup> of 2.29, 2.27, and 2.24 Å at the BLYP, PBE, and OPBE level of theory, respectively. In comparison to experiment, the BLYP functional performs best (2.244 Å), followed by BP86 (2.226 Å), PBE (2.224 Å), and TPSS (2.222 Å). This observation also holds for  $[\text{Tc}_2\text{Cl}_8]^{2-}$ , where the BLYP value of 2.152 Å is in excellent agreement with the experimental values of 2.147(4) Å<sup>59</sup> and 2.17(1) Å.<sup>60</sup> The BP86 (2.132 Å), PBE (2.131 Å), and TPSS (2.128 Å) results are again very close.

For the other test systems, the M–M' bond length variation lies between 0.071 and 0.155 Å. BH&HLYP always results in the shortest M–M contacts except for  $[\text{Rh}_2\text{Cl}_8]^{2+}$  and  $[\text{ReTcCl}_8]^{2-}$ , whereas BLYP in all cases gives the longest bonds.

Among the five different types of functionals (LDA, GGA, hybrid-GGA, meta-GGA, hybrid-meta-GGA) there is no clear trend of the accuracy of the calculated bond length. LDA delivers, in all cases, shorter bonds than all GGA functionals, except for OPBE. The GGA functionals are best grouped into two classes: the first one giving longer bonds with the trend  $\text{PBE} < \text{BP86} < \text{BLYP}$  and the second one resulting in shorter bonds with the trend  $\text{OPBE} < \text{HTCH} \approx \text{OLYP}$ . The latter class gives only slightly longer bonds than the hybrid-GGA functionals with a mixing of exact exchange (B3LYP, X3LYP, O3LYP). The general observation that higher amounts of exact exchange lead to shorter bonds also holds in the case of metal–metal bonds as exemplified in the series  $\text{BLYP} > \text{B3LYP} > \text{BH\&HLYP}$ . The two meta-GGA functionals, TPSS and VSXC, lead to longer bonds than hybrid-GGA functionals, with TPSS being close to the GGA functionals of the first class. Mixing of exact exchange admixture to TPSS, which gives the hybrid-meta-GGA TPSSh, leads to a shortening of the M–M bonds, with the consequence that the performance of TPSSh is comparable to SVWN.

Overall, we conclude that the GGA functionals, BLYP, BP86, PBE, and the meta-GGA functional TPSS deliver acceptable metal–metal bond lengths for the systems under study, irrespective of the metal–metal bond being polar or unpolar, or whether 4d or 5d transition metal atoms are involved. This observation adds to the increasing evidence that GGA functionals perform especially well in the study of transition metal species, as, for example, is summarized in the recent review by Cramer and Truhlar.<sup>61</sup> Also, Cavigliasso and Kaltsoyannis<sup>58</sup> observed that GGAs perform well in the description of structural features of  $[\text{M}_2\text{Cl}_8]^{2-}$  systems. In general, hybrid functionals with more than 5%–15% Hartree–Fock exchange are not capable to describe systems with significant multireference character, as, e.g., is shown by Zhao et al.,<sup>62</sup> and are therefore not suited in the study of systems like the  $[\text{MM}'\text{Cl}_8]^x$  species we are dealing with in this study.

Our main concern, however, is not so much the bond length but the bond dissociation energy (BDE) of the metal–metal formal quadruple bonds. We therefore compared the dissociation energies of the  $[\text{MM}'\text{Cl}_8]^x$  species (M, M' = Tc, Re, Ru, Os, Rh, Ir;  $x = -2, 0, +2$ ) for the dissociation in two square planar  $D_{4h}$  symmetric  $\text{MCl}_4^{x/2}$  species in the  $(^5A_{1g})$  quintet state. To reduce the influence of structural effects, we based all calculations for a given species on the same geometries, which were optimized at the BP86/TZ2P level. Table 2 gives the results and the following discussion will be based on this. For completeness, Table S1 in the Supplementary data gives the dissociation energies for completely optimized structures at the respective level whose inspection reveals that the geometrical relaxation has no impact on the conclusion presented in the following.

For the parent compound,  $[\text{Re}_2\text{Cl}_8]^{2-}$ , we calculate a dissociation energy of  $D_e = 15.6$  kcal/mol at the CASPT2(12,12) level of theory. The comparison with the CASPT2(8,8) result of 17.2 kcal/mol demonstrates that the result can be considered stable with respect to the active space and should thus be a reliable ab initio estimate of the dissociation energy. To the best of our knowledge, there are no reliable experimental values to compare with. The experimental estimate of  $152.7 \pm 19$  kcal/mol is considered “very unreliable”.<sup>63</sup> The ab initio, single reference CCSD(T) method underestimates the stability of the Re–Re bond, giving a value of 5.5 kcal/mol. The calculated value at CCSD is  $D_e = -36.4$  kcal/mol (Table 2). The very large contribution from the quasi-perturbative treatment of the connected triple excitations when going from CCSD to CCSD(T) shows that a single configuration wave function method is not appropriate for calculating the bond energy of  $[\text{Re}_2\text{Cl}_8]^{2-}$ . Single configuration DFT methods could perform better because of fortuitous error cancellation. However, the DFT results clearly show that the functionals assign stabilities in the wide range from 17.6 kcal/mol (VSXC) to  $-77.4$  kcal/mol (BH&HLYP). There are eight functionals that give negative values for the BDE of  $[\text{Re}_2\text{Cl}_8]^{2-}$ . Thus, a careful choice of functional is important for even a qualitatively correct description. Concerning the different types of functionals (LDA, GGA, meta-GGA, meta-hybrid-GGA), one can observe clear trends. The LDA functional SVWN overestimates the stability of the Re–Re



**Table 2.** Dissociation energy,  $D_e$ , in kcal/mol for the dissociation of  $[MM'Cl_8]^+$  in the lowest totally symmetric closed-shell singlet state (for  $M = M'$ :  $D_{4h}$  symmetry,  $^1A_{1g}$  state; for  $M \neq M'$ :  $C_{4v}$  symmetry,  $^1A_1$  state) in two square planar quintet states of  $D_{4h}$  symmetry ( $^5A_{1g}$ ). All DFT and coupled cluster results were obtained using the def2-TZVPP basis set. For the CASPT2 calculations, a large ANO-RCC basis was employed (see Computational methods). All geometries were optimized at the BP86/TZ2P level.

Functional	$[Re_2Cl_8]^{2-}$	$[Tc_2Cl_8]^{2-}$	$[Os_2Cl_8]^0$	$[Ru_2Cl_8]^0$	$[Ir_2Cl_8]^{2+}$	$[Rh_2Cl_8]^{2+}$	$[ReTcCl_8]^{2-}$	$[ReOsCl_8]^{1-}$	$[ReIrCl_8]^0$	$[OsIrCl_8]^{1+}$	$\Delta E^a$
SVWN	63.6	38.1	116.2	89.1	3.4	23.5	51.2	147.9	272.7	130.0	45.8
BP86	10.2	-14.3	64.9	39.2	-46.1	-25.7	-1.9	94.7	218.6	78.4	8.4
BLYP	8.9	-17.4	55.7	29.9	-54.7	-38.6	-4.2	90.0	211.3	69.5	12.4
HCTH	-14.0	-38.1	43.9	13.9	-71.0	-60.0	-25.9	72.7	196.9	56.2	29.6
OLYP	-6.7	-34.0	46.1	14.9	-71.0	-60.3	-20.3	77.3	200.1	57.2	26.0
OPBE	-7.4	-34.6	50.3	20.3	-66.9	-55.1	-20.3	79.7	204.8	62.5	23.4
PBE	15.7	-9.2	69.6	43.3	-42.7	-21.9	3.5	99.1	223.9	82.9	6.1
B3LYP	-20.4	-56.9	25.7	-11.1	-69.4	-69.1	-38.3	61.4	190.7	39.7	44.0
BH&HLYP	-77.4	-132.4	-38.4	-92.2	-102.9	-132.6	-105.1	13.7	150.8	-12.6	104.5
O3LYP	-21.4	-54.0	29.2	-5.3	-76.6	-68.2	-37.5	62.7	189.8	41.8	42.2
X3LYP	-21.9	-59.4	23.9	-13.9	-69.3	-69.7	-40.3	60.6	190.3	38.4	45.6
TPSS	6.7	-20.1	59.9	32.4	-49.9	-30.5	-6.4	91.1	215.3	73.4	12.3
VSXC	17.6	-6.7	66.4	41.7	-43.9	-23.3	5.9	95.7	224.5	79.6	8.5
TPPSh	-9.5	-41.6	42.3	10.1	-59.3	-48.3	-25.2	75.8	203.5	56.6	28.8
CCSD	-36.4	-218.6	0.7	-87.9	-74.1	-84.4	-97.7	— <sup>b</sup>	— <sup>b</sup>	— <sup>b</sup>	117.6
CCSD(T)	5.5	-165.3	56.0	— <sup>b</sup>	-3.6	-7.0	-69.3	— <sup>b</sup>	— <sup>b</sup>	— <sup>b</sup>	64.0
CASPT2(8,8)	17.2	-10.0	83.7	75.7	— <sup>c</sup>	— <sup>c</sup>	4.1	102.7	220.1	96.0	5.9
CASPT2(12,12)	15.6	-13.7	77.9	65.4	— <sup>c</sup>	— <sup>c</sup>	3.0	99.6	211.4	83.5	

<sup>a</sup>Average deviation with respect to the CASPT2(12,12) value.

<sup>b</sup>No convergence.

<sup>c</sup>Active space not large enough for the calculation of dissociation energies.

**Table 3.** Energy lowering of the closed-shell singlet  $^1A_{1g}$  ( $^1A_1$  for  $M \neq M'$ ) state in  $D_{4h}$  ( $C_{4v}$  for  $M \neq M'$ ) symmetry of  $[MM'Cl_8]^x$  due to the symmetry breaking unpairing of two electrons leading to open-shell  $^1A_1$  biradicals in  $C_{4v}$  symmetry. All energies are in kcal/mol and geometries are optimized at BP86/TZ2P.

Functional	$[Re_2Cl_8]^{2-}$	$[Tc_2Cl_8]^{2-}$	$[Os_2Cl_8]^0$	$[Ru_2Cl_8]^0$	$[Rh_2Cl_8]^{2+}$	$[ReTcCl_8]^{2-}$
SVWN	+2.0	+2.3	+2.1	0.0	+2.4	0.0
BP86	-1.4	-2.4	-2.0	-3.3	-0.9	-2.4
BLYP	-1.9	-2.6	-4.2	-4.0	-3.2	-1.7
HCTH	-1.7	-2.3	-2.3	-5.5	-9.1	-3.0
OLYP	-1.1	-2.0	-1.8	-3.9	-8.4	-2.4
OPBE	-1.3	-2.6	-1.2	-1.4	-8.9	-2.7
PBE	-1.1	-2.1	-1.7	-3.1	-0.7	-1.9
B3LYP	-10.5	-13.4	-11.2	-14.5	-10.7	-12.2
BH&HLYP	-29.6	-35.5	-38.7	-39.4	-35.3	-24.6
O3LYP	-6.4	-8.3	-6.7	-9.6	-6.1	-8.3
X3LYP	-11.4	-14.6	-12.6	-17.2	-11.8	-13.4
TPSS	-3.3	-4.7	-3.2	-5.2	-1.9	-4.2
VSXC	-6.9	-7.7	-5.8	-7.4	-3.7	-7.1
TPPSh	-7.7	-10.3	-7.6	-10.9	-6.6	-9.5

bond considerably ( $D_e = 63.6$  kcal/mol), whereas GGA functionals of the first class (PBE, BP86, BLYP) assign values of 15.7, 10.2, and 8.9 kcal/mol, respectively, which are close to the CASPT2(12,12) value. The second class of GGA functionals (HCTH, OLYP, OPBE) underestimates the Re–Re bond stability and leads to even qualitative incorrect  $D_e$  values of -14.0, -7.4, and -6.7 kcal/mol, respectively. All hybrid-GGA functionals underestimate the stability considerably with  $D_e$  values of -20.4, -21.4, -21.9, and -77.4 kcal/mol for B3LYP, O3LYP, X3LYP, and BH&HLYP, respectively. The meta-GGA functionals, TPSS and VSXC, are comparable to the first class of GGA functionals in their description of the stability of the Re–Re bond, leading to  $D_e$  values of 6.7 and 17.6 kcal/mol, respectively. The admixture of exact exchange leads to a decreasing bond stability as exemplified in the series BLYP > B3LYP > BH&HLYP. The same holds for the comparison of the meta-GGA functional TPSS ( $D_e = 6.7$  kcal/mol) with its hybrid congener TPPSh ( $D_e = -9.5$  kcal/mol).

The resulting overall picture for the Re–Re BDE of  $[Re_2Cl_8]^{2-}$  is that the first class of GGA functionals (PBE, BP86, BLYP) and the meta-GGA functionals (TPSS and VSXC) give values that are in a reasonably good agreement with the CASPT2(12,12) value, while the other functionals give very poor results.

This conclusion also holds when the remaining  $[MM'Cl_8]^x$  systems in our study are considered. For  $[Tc_2Cl_8]^{2-}$ , e.g., the CASPT2(12,12)  $D_e$  value of -13.7 kcal/mol is matched by the GGA functionals BP86 (-14.3 kcal/mol), BLYP (-17.4 kcal/mol), and PBE (-9.2 kcal/mol). The meta-GGA functionals, VSXC and TPSS, are still in reasonable agreement with -6.7 and -20.1 kcal/mol, respectively, whereas all hybrid-GGA functionals, the hybrid-meta-GGA functional, and the second class of GGA functionals underestimate and the LDA overestimates the metal–metal BDE considerably. The CCSD and CCSD(T) values for the BDE of  $[Tc_2Cl_8]^{2-}$  are dramatically wrong.

In  $[Os_2Cl_8]^0$ , we notice a larger difference between the CASPT2(8,8) and the CASPT2(12,12) results, underlining that the metal centered orbitals interact more heavily with

the chlorine lone pair orbitals, as discussed above, which leads to a slight imbalance in the correlation energy, which is covered by the active spaces in  $[M_2Cl_8]^x$  and the  $MCl_4^{x/2}$  fragments. The same holds for  $[Ru_2Cl_8]^0$ ,  $[ReIrCl_8]^0$ , and  $[OsIrCl_8]^{1+}$ . We therefore have to assign a larger error bar to the CASPT2(12,12) values of these compounds. For  $[Ir_2Cl_8]^{2+}$  and  $[Rh_2Cl_8]^{2+}$ , it was not possible to design an active space large enough to include all the orbital pairs describing the metal–metal and metal–ligand interactions, so as to obtain a reliable and balanced dissociation energy. This is due to the fact that in these positively charged systems, the metal orbitals contract and lie much deeper than the chlorine lone pair orbitals.

The conclusion is that GGA functionals are able to describe the BDE of metal–metal quadruple bonds with an estimated uncertainty of  $\pm 5$  kcal/mol, whereas hybrid functionals are not even reliable for qualitative discussions. This observation is in line with the conclusions of numerous DFT validation studies on transition metal compounds as summarized recently by Cramer and Truhlar.<sup>61</sup> The performance of DFT functionals in the studies of M–M bond dissociation energies is normally tested on transition metal dimers, as for these systems experimental data are available. It is therefore interesting to see that the conclusion put forward for such systems, e.g., in refs. 64 and 65, can be carried over to larger systems in which direct, unbridged metal–metal multiple bonds are present. Ab initio calculations must be carried out using multideterminantal methods, as single reference methods, even at CCSD(T), give large errors for  $D_e$ .

The natural orbital occupation numbers of the CASSCF wave function for the  $\delta/\delta^*$  orbital pair are a measure for the biradical character of the metal–metal bond. The occupation numbers are 1.56/0.44, 1.48/0.52, 1.47/0.53, 1.30/0.70, 1.51/0.49, 1.61/0.39, 1.97/0.03, and 1.95/0.05 in  $[Re_2Cl_8]^{2-}$ ,  $[Tc_2Cl_8]^{2-}$ ,  $[Os_2Cl_8]^0$ ,  $[Ru_2Cl_8]^0$ ,  $[ReTcCl_8]^{2-}$ ,  $[ReOsCl_8]^{1-}$ ,  $[ReIrCl_8]^0$ , and  $[OsIrCl_8]^{1-}$ , respectively. This indicates that, except for  $[Ru_2Cl_8]^0$ , the biradical character of the metal–metal bond is moderate and, thus, closed-shell DFT calculations of singlet species should allow for a qualitative correct

**Table 4.** Singlet–triplet gap ( $^3A_{2u} \leftarrow ^1A_{1g}$  for  $M = M'$  and  $^3A_1 \leftarrow ^1A_1$  for  $M \neq M'$ ) in kcal/mol for  $[MM'Cl_8]^x$  in the  $D_{4h}$  ( $C_{4v}$  for  $M \neq M'$ ) symmetric geometry. All DFT results were obtained using the def2-TZVPP basis set. For the CASPT2 calculations, a large ANO-RCC basis was employed (see Computational methods). All geometries were optimized at BP86/TZ2P.

Functional	$[Re_2Cl_8]^{2-}$	$[Tc_2Cl_8]^{2-}$	$[Os_2Cl_8]^0$	$[Ru_2Cl_8]^0$	$[Ir_2Cl_8]^{2+}$	$[Rh_2Cl_8]^{2+}$	$[ReTcCl_8]^{2-}$	$[ReOsCl_8]^{1-}$	$[ReIrCl_8]^0$	$[OsIrCl_8]^{1-}$	$\Delta E^a$
SVWN	8.8	7.8	5.2	3.5	−11.0	6.3	8.4	9.9	16.2	7.6	2.1
BP86	2.8	1.9	0.8	−1.1	−18.8	1.7	2.4	4.6	10.7	2.8	5.9
BLYP	2.9	1.7	0.5	−1.5	−20.5	0.8	2.3	4.4	9.9	2.2	6.0
HCTH	2.9	2.8	1.0	−0.7	−24.1	5.7	2.8	4.8	10.1	2.4	5.6
OLYP	3.5	2.5	1.2	−0.9	−21.7	8.0	3.0	5.2	10.5	2.5	5.6
OPBE	3.8	3.1	1.7	−0.4	−18.1	13.8	3.5	5.7	11.4	3.3	5.2
PBE	3.2	2.3	1.1	−0.8	−18.7	1.9	2.8	5.0	11.0	3.1	5.7
B3LYP	−6.6	−9.0	−8.6	−12.2	−6.9	−9.6	−7.7	−3.6	4.7	−5.2	14.8
BH&HLYP	−23.3	−28.1	−25.3	−32.1	15.1	−39.0	−24.8	−13.8	−3.6	−12.1	29.2
O3LYP	−1.9	−3.5	−3.9	−6.9	−13.1	−4.2	−2.7	0.5	7.3	−1.8	10.4
X3LYP	−7.5	−10.0	−9.5	−13.3	−5.5	−10.7	−8.7	−4.1	4.3	−5.8	15.6
TPSS	1.1	−0.5	−0.8	−3.1	−17.6	0.1	0.3	3.1	9.8	1.6	7.4
VSXC	−2.1	−1.7	−2.7	−3.9	−23.0	−0.9	−1.9	0.7	8.2	0.2	9.2
TPPSh	−3.6	−5.8	−5.4	−8.5	−11.4	−5.1	−4.7	−1.0	7.0	−2.4	11.8
CASPT2(8,8)	9.5	9.1	6.6	6.4	— <sup>b</sup>	— <sup>b</sup>	9.3	9.0	9.5	9.1	0.2
CASPT2(12,12)	9.6	9.1	6.8	6.7	— <sup>b</sup>	— <sup>b</sup>	9.9	9.3	9.6	9.1	

<sup>a</sup>Average deviation with respect to the CASPT2(12,12) value.  
<sup>b</sup>Active space is not large enough for the correct description of M–M orbital manifold.

**Table 5.** Excitation energy from the square planar  $D_{4h}$  quintet ( $^5A_{1g}$ ) to the tetrahedral  $T_d$  singlet ( $^1A_1$ ) for  $[MCl_4]^x$  in kcal/mol. All results were obtained using the def2-TZVPP basis set. All DFT geometries were optimized at the respective level; for the coupled cluster calculations, BP86/TZ2P geometries were used.

Functional	$[ReCl_4]^-$	$[TcCl_4]^-$	$[OsCl_4]^0$	$[RuCl_4]^0$	$[IrCl_4]^+$	$[RhCl_4]^+$	$\Delta E^a$
SVWN	15.9	9.9	-13.9	-19.8	-37.8	-40.9	7.9
BP86	25.3	18.3	-6.0	-12.5	-29.9	-32.9	5.3
BLYP	19.2	13.1	-9.2	-14.7	-30.8	-32.6	7.3
HCTH	29.7	22.9	-4.2	-10.2	-29.1	-30.8	4.8
OLYP	22.8	16.5	-8.0	-13.5	-30.8	-32.4	6.1
OPBE	27.4	20.4	-5.8	-12.2	-30.3	-32.9	4.5
PBE	24.3	17.5	-6.7	-12.9	-30.4	-33.1	5.5
B3LYP	23.7	18.2	-6.6	-12.5	-30.7	-33.1	5.5
BH&HLYP	31.2	27.2	-0.4	-6.4	-29.0	-31.4	5.8
O3LYP	25.2	19.3	-6.6	-12.4	-30.7	-32.8	5.1
X3LYP	23.9	18.9	-6.1	-12.0	-30.4	-32.9	5.4
TPSS	24.7	17.3	-5.2	-12.0	-28.3	-31.3	6.1
VSXC	36.4	30.4	5.2	-1.0	-20.3	-23.0	11.9
TPPSh	27.2	20.2	-3.6	-10.5	-27.8	-31.0	5.9
CCSD	34.0	29.4	-2.2	-10.8	-38.7	-45.6	3.2
CCSD(T)	30.5	25.5	-5.5	-14.4	-36.7	-42.9	

<sup>a</sup>Average deviation with respect to the CCSD(T)/def2-TZVPP value.

description. However, as near degeneracy problems may be better modeled by broken-symmetry DFT approaches, we tested the stability of the closed-shell singlet states towards unpairing of the electron pair in the M–M  $\delta$ -bonding orbital leading to singlet biradicals with localized, singly occupied  $d_{xy}$  metal orbitals. We observed broken-symmetry states for  $[Re_2Cl_8]^{2-}$ ,  $[Tc_2Cl_8]^{2-}$ ,  $[Os_2Cl_8]^0$ ,  $[Ru_2Cl_8]^0$ ,  $[Rh_2Cl_8]^{2+}$ , and  $[ReTcCl_8]^{2-}$ , whereas the other systems collapsed to the closed-shell singlet solution. The energy lowering due to the symmetry breaking is given in Table 3. It becomes obvious that, except for SVWN, all functionals predict the biradical state to be energetically favorable. GGA functionals point to a modest stabilization of the biradical state, whereas hybrid functionals give a clear preference for the open-shell singlet states reflecting the general trend that hybrid functionals tend to be favored toward open-shell states. Meta-GGA functionals are between GGA and hybrid functionals.

Related to the stability of the closed singlet state towards the broken-symmetry singlet solution is the question of whether the triplet state, with both the metal–metal  $\delta$  bonding and antibonding orbitals being singly occupied ( $^3A_{2u}$  state in  $D_{4h}$  symmetry and  $^3A_1$  state in  $C_{4v}$  symmetry), is energetically favored over the closed-shell singlet state. In Table 4, we give the  $^3A_{2u} \leftarrow ^1A_{1g}$  adiabatic excitation energy ( $^3A_1 \leftarrow ^1A_1$  in  $C_{4v}$  symmetry) for the selected DFT functionals and the CASPT2 model chemistry. The reported splitting for  $[Re_2Cl_8]^{2-}$  of 9.6 kcal/mol at the CASPT2 level is in good agreement with former ab initio results, e.g., at the CASPT2 level (9.9 kcal/mol)<sup>66</sup> and at the MRMP2 level (12.0 kcal/mol).<sup>67</sup> For all systems, the singlet–triplet gap is underestimated compared to CASPT2(12,12) by all DFT functionals but SVWN. An exception is  $[ReIrCl_8]^0$ , where the GGA functionals are in good agreement with the correlated ab initio results. In general, only GGA and LDA functionals give a qualitative correct ordering of states, the singlet state being the ground state.  $[ReIrCl_8]^0$  is again an exception. For a quantitative assessment of the electronic

states in question, it is clear that no DFT functional provides sufficient reliability.

The above results suggest that (i) the conclusion about the performance of the DFT functionals to describe the BDE of metal–metal formal quadruple bonds remains essentially unchanged when considering broken-symmetry states, (ii) the natural orbital occupation numbers in the CASSCF point towards small biradical character, and (iii) the singlet state is qualitatively correctly assigned to be lower than the triplet state for a chosen subset of functionals. Therefore, it is justified to discuss the bonding situation in the later section on closed-shell singlet calculations with GGA functionals. Furthermore, as both geometries and stabilities of the  $[M_2Cl_8]^x$  model systems are reasonably well-described by the GGA functionals, BLYP, PBE, and BP86, these functionals are appropriate for an analysis of the bonding situation.

### Comments on the ground state of the $MCl_4$ fragments

For the  $d^4$ - $MCl_4^x$  fragments ( $M = Tc, Re, Ru, Os, Rh, Ir$ ;  $x = -1, 0, +1$ ), two states must be considered in the quest for the ground state: the square planar quintet state ( $^5A_{1g}$  in  $D_{4h}$  symmetry) and the tetrahedral singlet state ( $^1A_1$  in  $T_d$  symmetry). In Table 5, we give the excitation energy  $^1A_1 \leftarrow ^5A_{1g}$  at DFT for a number of functionals and at the CCSD(T) level of theory. The latter is an adequate ab initio method, since the  $MCl_4^x$  systems do not exhibit multideterminantal character. Qualitatively, all functionals give the correct ground state compared to CCSD(T) except for VSXC, which wrongly predicts that the quintet state is the ground state for  $[OsCl_4]^0$ . In general, VSXC gives too positive excitation energies, which is probably the consequence of a destabilization of the singlet state. On the other hand, SVWN always gives too negative values, which can be traced back to SVWN underestimating the stability of the quintet state. BH&HLYP, as a third extreme, overestimates the singlet–



triplet gap, probably due to an over stabilization of the quintet state.

Conceptually, two  $[\text{MCl}_4]^x$  fragments have to be in a quintet state to form a metal–metal quadruple bond. It thus comes as no surprise that the  $[\text{ReCl}_4]^-$  fragment building the prominent metal–metal quadruple bond  $[\text{Re}_2\text{Cl}_8]^{2-}$  has the largest quintet  $\rightarrow$  singlet gap (30.5 kcal/mol) and is thus ideally suited for the quadruple metal–metal bond. Except for the Re and Tc species, all  $\text{MCl}_4^x$  fragments have singlet ground states and rather large singlet  $\rightarrow$  quintet gaps. Only if the metal–metal bond strength overcomes this excitation energy, stable compounds with metal–metal quadruple bonds may be expected.

### Analysis of the metal–metal bonding situation

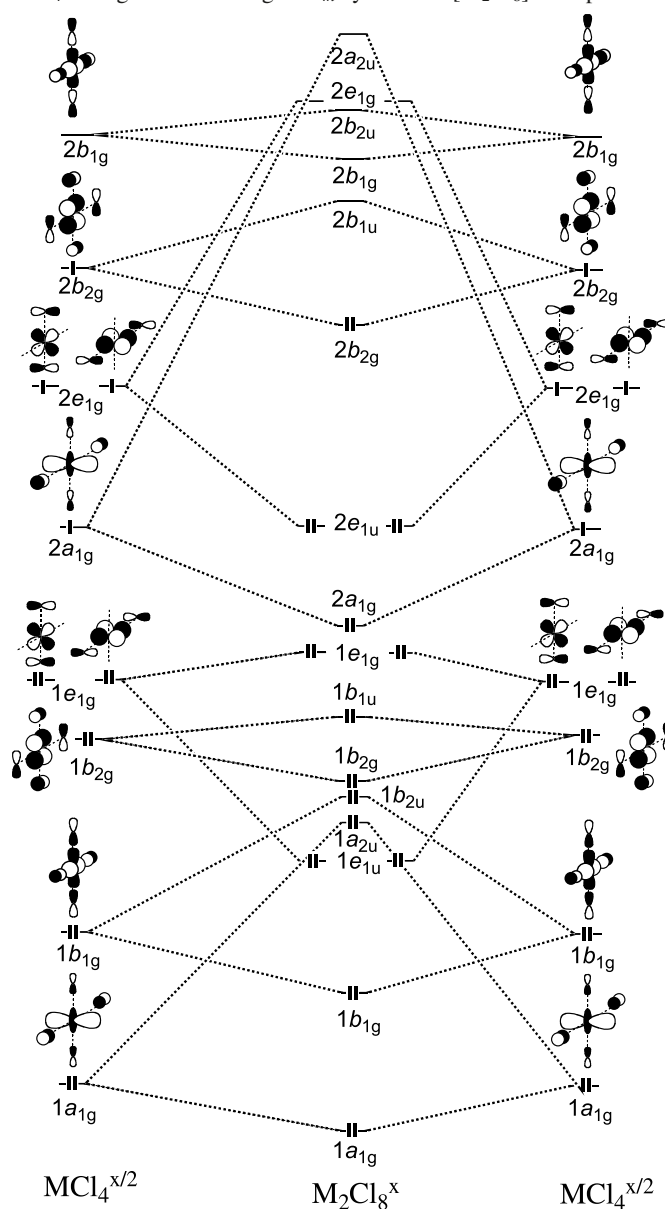
To obtain a thorough understanding of the metal–metal quadruple bond in the  $(\text{d}-\text{d})^8$  systems  $[\text{MM}'\text{Cl}_8]^x$ , we start with a qualitative discussion of the orbitals involved in this bonding. Figure 1 serves as an illustration for this purpose.

For each  $\text{M}-\text{M}'$  bond in question one must, in principle, consider four orbitals of different character. Depending on whether it is metal–metal bonding or antibonding and whether it is metal–ligand bonding or antibonding, one obtains (a) one metal–ligand bonding/metal–metal bonding orbital, (b) one metal–ligand bonding/metal–metal antibonding orbital, (c) one metal–ligand antibonding/metal–metal bonding orbital, and (d) one metal–ligand antibonding/metal–metal antibonding orbital.

In the case of the metal–metal  $\delta$  bond in  $[\text{MM}'\text{Cl}_8]^x$ , these four orbitals are (Fig. 1) the  $1b_{2g}$  orbital as component (a), the  $1b_{1u}$  orbital as component (b), the  $2b_{2g}$  orbital as component (c), and the  $2b_{1u}$  orbital as component (d).

The discussion of the metal–metal bond usually considers only the pair of the metal–ligand antibonding orbitals (c) and (d). This is reasonable in cases where the metal orbitals lie considerably higher in energy than the ligand orbitals or where the metal–ligand overlap is poor. For the metal–metal  $\delta$  bond in the  $[\text{Re}_2\text{Cl}_8]^{2-}$  system, the orbitals of type (c) and (d) are basically metal orbitals (65% metal character)<sup>68</sup> with small contributions from the chlorine atoms, whereas the fully occupied and energetically much lower lying orbitals of type (a) and (b) are mainly ligand orbitals with only 33% and 24% contribution of the Re atomic orbitals, respectively. If, however, the size of the metal atom decreases and the metal orbitals are energetically more stabilized as in  $[\text{Os}_2\text{Cl}_8]^0$  and  $[\text{Ir}_2\text{Cl}_8]^{2+}$ , the metal atom contribution of the completely occupied orbitals (a) and (b) increases; for the metal–metal  $\delta$  bond in  $[\text{Os}_2\text{Cl}_8]^0$  to 50% and 44%, for (a) and (b), respectively, and for  $[\text{Ir}_2\text{Cl}_8]^{2+}$  to 59% and 58% for (a) and (b), respectively. The metal contribution to the occupied metal–metal bonding orbital of type (c) decreases once the metal orbitals contract and become energetically stabilized. Since orbitals (a) and (c) are metal–metal bonding and orbital (b) is metal–metal antibonding, the net metal–metal bond order is thus smaller if the metal orbitals contract and become energetically stabilized, as is the case for  $[\text{Os}_2\text{Cl}_8]^0$  and  $[\text{Ir}_2\text{Cl}_8]^{2+}$ . This qualitative insight is corroborated by numerical results. The Wiberg bond order at BP86/def2-TZVPP//BP86/TZ2P for the metal–metal bond de-

**Fig. 1.** Schematic molecular orbital interaction diagram for two  $\text{d}^4\text{-MCl}_4^{x/2}$  fragments building a  $D_{4h}$  symmetric  $[\text{M}_2\text{Cl}_8]^x$  complex.



creases in the order of 2.41, 1.55, and 0.77 for  $[\text{Re}_2\text{Cl}_8]^{2-}$ ,  $[\text{Os}_2\text{Cl}_8]^0$ , and  $[\text{Ir}_2\text{Cl}_8]^{2+}$ , respectively. Likewise, the occupation of the metal- $\text{d}_{xy}$  orbital, as given by the natural population analysis at BP86/def2-TZVPP//BP86/TZ2P, increases in the order of 1.30, 1.51, and 1.65 e for  $[\text{Re}_2\text{Cl}_8]^{2-}$ ,  $[\text{Os}_2\text{Cl}_8]^0$ , and  $[\text{Ir}_2\text{Cl}_8]^{2+}$ , respectively, reflecting the higher metal character of the two low lying, occupied metal–metal bonding and antibonding orbitals of type (a) and (b), respectively.

Tables 6–9 give the results of the energy decomposition analysis (EDA) and the population analysis data (partial charges,  $q$ , orbital occupation numbers,  $n$ , and Wiberg bond indices,  $P$ ) for  $[\text{MM}'\text{Cl}_8]^x$  ( $\text{M}, \text{M}' = \text{Tc}, \text{Re}, \text{Ru}, \text{Os}, \text{Rh}, \text{Ir}; x = -2, -1, 0, +1, +2$ ). For the EDA, we chose  $C_{4v}$  symmetric  $\text{MCl}_4^x$  species in the  $^5\text{A}_1$  state as interacting fragments, which corresponds to a formal d-electron distribution of  $\text{d}_{z^2}^1, \text{d}_{xz}^1, \text{d}_{yz}^1, \text{d}_{xy}^1$ , and  $\text{d}_{x^2-y^2}^0$  at the metal atoms.

**Table 6.** Energy decomposition analysis for the  $D_{4h}$  symmetric  $M_2Cl_8^x$  ( $M = \text{Tc, Re, Ru, Os, Rh, Ir}$ ;  $x = -2, 0, +2$ ) under  $C_{4v}$  symmetry at BP86/TZ2P.  $MCl_4^y$  ( $y = -1, 0, +1$ ) in the quintet  $^5A_1$  state were used as fragments. Optimized metal–metal distances ( $R$ , in Å), NBO partial charge of the metal atom and of the  $MCl_4^{y/2}$  fragment ( $q$ ), occupation of the  $d_{xy}$  orbital of the metal atom ( $n$ ), as well as the Wiberg bond index of the M–M pair ( $P$ ) are also given. The latter population analysis data are given at BP86/def2-TZVPP//BP86/TZ2P.

	$[\text{Re}_2\text{Cl}_8]^{2-}$	$[\text{Tc}_2\text{Cl}_8]^{2-}$	$[\text{Os}_2\text{Cl}_8]^0$	$[\text{Ru}_2\text{Cl}_8]^0$	$[\text{Ir}_2\text{Cl}_8]^{2+}$	$[\text{Rh}_2\text{Cl}_8]^{2+}$
$\Delta E_{\text{int}}$	−54.2	−22.2	−92.8	−56.2	3.5	19.0
$\Delta E_{\text{Pauli}}$	404.9	338.3	256.7	187.6	162.4	161.3
$\Delta E_{\text{elstat}}^a$	−244.1 (53.2%)	−162.9 (45.2%)	−151.7 (43.4%)	−88.7 (36.4%)	30.5 (<0.0%)	41.3 (<0.0%)
$\Delta E_{\text{orb}}^a$	−214.9 (46.8%)	−197.6 (54.8%)	−197.8 (56.6%)	−155.1 (63.6%)	−189.5 (100.0%)	−183.6 (100.0%)
$\Delta a_1(\sigma, \delta)^b$	−84.4 (39.3%)	−78.6 (39.8%)	−97.6 (49.3%)	−81.6 (52.6%)	−102.6 (54.1%)	−88.1 (48.0%)
$\Delta a_2^b$	−0.1 (0.1%)	−0.1 (0.1%)	−0.1 (<0.1%)	−0.1 (0.1%)	−0.6 (0.3%)	−0.8 (0.5%)
$\Delta b_1^b$	−1.4 (0.7%)	−2.1 (1.0%)	−2.9 (1.5%)	−2.8 (1.8%)	−4.1 (2.1%)	−4.1 (2.2%)
$\Delta b_2(\delta)^b$	−0.5 (0.2%)	2.4 (<0.0%)	0.9 (<0.0%)	4.1 (<0.0%)	−0.6 (0.3%)	−1.2 (0.6%)
$\Delta e(\pi)^b$	−128.5 (59.8%)	−119.2 (60.3%)	−98.2 (49.6%)	−74.6 (48.1%)	−81.7 (43.1%)	−89.4 (48.7%)
$\Delta E_{\text{prep}}^c$	36.7	38.7	33.0	33.1	37.7	40.2
$D_e$	17.5	−16.5	59.8	23.1	−41.2	−59.2
$n(M[d_{xy}])$	1.30	1.33	1.51	1.53	1.65	1.66
$q(M)$	0.55	0.45	0.56	0.39	0.59	0.45
$q(MCl_4)$	−1.0	−1.0	0.00	0.00	1.00	1.00
$P(M-M)$	2.41	2.30	1.55	1.30	0.77	0.58
$R(M-M)$	2.231	2.152	2.273	2.263	2.438	2.464

<sup>a</sup>Values in parentheses give the percentage contribution to the total attractive interactions,  $\Delta E_{\text{elstat}} + \Delta E_{\text{orb}}$ .

<sup>b</sup>Values in parentheses give the percentage contribution to the total orbital interactions,  $\Delta E_{\text{orb}}$ .

<sup>c</sup>Fragments relax into a tetrahedrally distorted square planar quintet of  $D_{2d}$  symmetry.

Table 6 shows that, in the parent compound  $[\text{Re}_2\text{Cl}_8]^{2-}$ , the major stabilizing contribution to the total interaction energy,  $\Delta E_{\text{int}} = -54.2$  kcal/mol, is due to the classical electrostatic contribution (53.2% of the stabilizing terms), whereas the orbital (covalent) interaction contributes 46.8%.<sup>69</sup> This observation is somewhat surprising, given the fact that two negatively charged moieties,  $\text{ReCl}_4^-$ , interact. One would intuitively assume to observe a net electrostatic repulsion. Such an assumption is not justified because the charge distribution in the atomic basins is highly anisotropic. The rhenium atoms carry a positive charge of +0.55 e but the attraction of the singly occupied metal  $d_{z^2}$  orbital of one Re atom by the nucleus of the other Re atom yields a strong electrostatic attraction.<sup>70</sup> Note that even nonpolar bonds are, in most cases, stabilized by classical electrostatic contributions.<sup>71,72</sup> The very large Pauli repulsion between the two fragments of 404.9 kcal/mol compensates to a large extent for the stabilizing electrostatic and orbital contributions. The attractive orbital contributions result mainly from orbitals of  $e(\pi)$  symmetry (59.8% of the total orbital interaction), followed by orbitals of  $a_1(\sigma)$  symmetry with 39.3%. Interestingly, the  $\delta$  bonding orbitals in  $b_2$  symmetry do not seem to be of importance for the covalent stabilization, as they contribute only 0.2% to the total  $\Delta E_{\text{orb}}$ .

Comparing the former results with the 4d transition metal congener  $[\text{Tc}_2\text{Cl}_8]^{2-}$ , one notices some similarities but also a significant difference. A steep decrease in the electrostatic attraction is responsible for the overall instability of  $[\text{Tc}_2\text{Cl}_8]^{2-}$ . The drop in the  $\Delta E_{\text{elstat}}$  contribution can be explained by two factors. On the one hand, the Tc orbitals are more compact than the Re orbitals, leading to a reduced net attraction of the electrons in this orbital by the opposing metal nucleus. On the other hand, the Tc atom has a lower positive charge (+0.45 e) than the Re atom (+0.55 e), mean-

ing that the positive charge of the nucleus is screened more effectively in the Tc compound. The increased electron density on Tc can be rationalized based on the qualitative bonding picture developed above and noticing that the Tc atomic orbitals are more compact and lie energetically below the Re atomic orbitals (see, e.g., the discussion in ref. 73). The details of the covalent contributions to the bond energy remain unchanged compared to the Re compound, with the  $e(\pi)$  term (60.3%) exceeding the  $a_1(\sigma)$  contribution (39.8%). The similarity in the covalent bonding contribution is also reflected in the comparable Wiberg bond indices of 2.41 and 2.30 for the Re and the Tc complexes, respectively. It is interesting to notice that the intrinsic bond strength, as measured by the interaction energy,  $\Delta E_{\text{int}}$ , is still stabilizing (−22.2 kcal/mol). This, however, is not sufficient to overcompensate the preparation energy of  $\Delta E_{\text{prep}} = 38.7$  kcal/mol, which is needed for the deformation of the  $[\text{TcCl}_4]^-$  fragments from their relaxed geometry to the structure that they adopt to interact.

The M–M bond in  $[\text{Os}_2\text{Cl}_8]^0$  is considerably stronger than in its group 7 isoelectronic congener,  $[\text{Re}_2\text{Cl}_8]^{2-}$ . This is indicated by the interaction energy, which amounts to −92.8 kcal/mol in the former compared to −54.2 kcal/mol in the latter. The absolute values of the individual contributions to  $\Delta E_{\text{int}}$ , however, are smaller. The main reason for the higher stability of  $[\text{Os}_2\text{Cl}_8]^0$  is the steep decrease of the Pauli repulsion, an effect that is clearly related to the reduced net charge of the complex. A similar behavior was observed and discussed in ref. 69 for  $[\text{Re}_2\text{Cl}_8]^{2-}$  and  $[\text{Re}_2\text{Cl}_8]^0$ . Interestingly, the absolute values of the electrostatic and the orbital contributions are very similar for the  $[\text{Os}_2\text{Cl}_8]^0$  and the  $[\text{Tc}_2\text{Cl}_8]^{2-}$  complexes, suggesting a very similar bonding picture. This is misleading though, since the  $\pi$  orbital contributions are reduced to 49.6% and the  $\sigma$  orbital contributions are enhanced

**Table 7.** Energy decomposition analysis for the  $C_{4v}$  symmetric  $[MM'Cl_8]^x$  ( $M, M' = \text{Tc, Re, Ru, Os, Rh, Ir}; x = -1, 0, +1$ ) at BP86/TZ2P.  $MCl_4^y$  ( $y = -1, 0, +1$ ) in the quintet  $^5A_1$  state were used as fragments. Optimized metal–metal distances ( $R$ ) in Å, the Wiberg bond index of the  $M-M'$  pair ( $P$ ), the change in the orbital occupation ( $\Delta n$ ), and the change in partial charge ( $\Delta q$ ) relative to the homodimetallic systems are also given. The population analysis data are given at BP86/def2-TZVPP//BP86/TZ2P.

	$[ReOsCl_8]^{1-}$		$[ReIrCl_8]^0$		$[OsIrCl_8]^{1+}$		$[TcRuCl_8]^{-1}$		$[TcRhCl_8]^0$		$[RuRhCl_8]^{1+}$	
$\Delta E_{\text{int}}$	−132.0		−247.4		−95.3		−95.4		−207.9		−66.8	
$\Delta E_{\text{Pauli}}$	335.8		270.8		196.5		261.2		196.3		159.8	
$\Delta E_{\text{elstat}}^a$	−239.6 (51.2%)		−255.1 (49.2%)		−93.4 (32.0%)		−162.7 (45.6%)		−188.7 (46.7%)		−58.7 (25.9%)	
$\Delta E_{\text{orb}}^a$	−228.2 (48.8%)		−263.1 (50.8%)		−198.4 (67.8%)		−193.9 (54.4%)		−215.5 (53.3%)		−167.9 (74.1%)	
$\Delta a_1 (\sigma, \delta)^b$	−92.4 (40.5%)		−98.6 (37.5%)		−100.4 (50.6%)		−80.7 (41.7%)		−82.0 (38.0%)		−82.3 (49.0%)	
$\Delta a_2^b$	−0.1 (<0.1%)		−0.3 (0.1%)		−0.3 (0.1%)		−0.1 (0.1%)		−0.3 (0.1%)		−0.4 (0.2%)	
$\Delta b_1^b$	−2.5 (1.1%)		−4.1 (1.6%)		−3.7 (1.9%)		−2.9 (1.5%)		−4.1 (1.9%)		−3.4 (2.1%)	
$\Delta b_2 (\delta)^b$	−10.4 (4.6%)		−41.1 (15.6%)		−10.1 (5.1%)		−6.8 (3.5%)		−37.5 (17.4%)		−8.1 (4.9%)	
$\Delta e (\pi)^b$	−122.8 (53.8%)		−119.1 (45.3%)		−83.9 (42.3%)		−103.3 (53.3%)		−91.7 (42.6%)		−73.7 (43.9%)	
$\Delta E_{\text{prep}}^c$	37.3		41.9		33.7		38.7		39.9		33.9	
$D_e$	94.7		205.5		61.6		56.7		168.0		32.9	
M	Re	Os	Re	Ir	Os	Ir	Tc	Ru	Tc	Rh	Ru	Rh
$\Delta n(d_{xy})$	−0.09	0.08	−0.19	0.20	−0.11	0.11	−0.09	0.10	−0.19	0.20	−0.13	0.11
$\Delta q(M)$	0.02	0.01	0.02	0.02	−0.04	0.04	−0.02	0.03	−0.11	0.06	−0.08	0.03
$\Delta q(MCl_4)$	0.61	−0.61	1.30	−1.30	0.64	−0.64	0.65	−0.65	1.25	−1.25	0.61	−0.61
$P(M-M')$	1.94		1.36		1.08		1.74		1.11		0.82	
$R(M-M')$	2.245		2.300		2.352		2.195		2.299		2.395	

<sup>a</sup>Values in parentheses give the percentage contribution to the total attractive interactions,  $\Delta E_{\text{elstat}} + \Delta E_{\text{orb}}$ .

<sup>b</sup>Values in parentheses give the percentage contribution to the total orbital interactions,  $\Delta E_{\text{orb}}$ .

<sup>c</sup>Fragments relax into a tetrahedrally distorted square planar quintet of  $D_{2d}$  symmetry.

**Table 8.** Energy decomposition analysis for the  $C_{4v}$  symmetric  $[MM'Cl_8]^x$  ( $M, M' = \text{Tc, Re, Ru, Os, Rh, Ir}; x = -1, 0, +1$ ) at BP86/TZ2P.  $MCl_4^y$  ( $y = -1, 0, +1$ ) in the quintet  $^5A_1$  state were used as fragments. Optimized metal–metal distances ( $R$ ) in Å, the Wiberg bond index of the  $M-M'$  pair ( $P$ ), the change in the orbital occupation ( $\Delta n$ ), and the change in partial charge ( $\Delta q$ ) relative to the homodimetallic systems are also given. The population analysis data are given at BP86/def2-TZVPP//BP86/TZ2P.

	$[ReRuCl_8]^{1-}$		$[ReRhCl_8]^0$		$[OsRhCl_8]^{1+}$		$[TcOsCl_8]^{-1}$		$[TcIrCl_8]^0$		$[RuIrCl_8]^{1+}$	
$\Delta E_{\text{int}}$	−119.9		−238.0		−84.3		−106.9		−216.2		−75.0	
$\Delta E_{\text{Pauli}}$	290.9		221.3		168.0		299.1		236.5		172.7	
$\Delta E_{\text{elstat}}^a$	−194.2 (47.3%)		−213.0 (46.4%)		−69.0 (27.3%)		−199.9 (49.2%)		−221.5 (48.9%)		−70.8 (28.6%)	
$\Delta E_{\text{orb}}^a$	−216.6 (52.7%)		−246.4 (53.6%)		−183.3 (72.7%)		−206.0 (50.8%)		−231.2 (51.1%)		−176.8 (71.4%)	
$\Delta a_1 (\sigma, \delta)^b$	−85.4 (39.4%)		−86.0 (34.9%)		−88.0 (48.0%)		−87.6 (42.5%)		−93.9 (40.6%)		−93.2 (52.7%)	
$\Delta a_2^b$	−0.1 (0.1%)		−0.3 (0.1%)		−0.3 (0.2%)		−0.1 (0.0%)		−0.3 (0.1%)		−0.3 (0.2%)	
$\Delta b_1^b$	−2.6 (1.2%)		−3.9 (1.6%)		−3.4 (1.9%)		−2.8 (1.4%)		−4.3 (1.9%)		−3.6 (2.0%)	
$\Delta b_2 (\delta)^b$	−13.2 (6.1%)		−48.6 (19.7%)		−15.6 (8.5%)		−4.6 (2.2%)		−30.2 (13.1%)		−3.5 (2.0%)	
$\Delta e (\pi)^b$	−115.3 (53.2%)		−107.6 (43.7%)		−75.9 (41.4%)		−111.0 (53.9%)		−102.6 (44.4%)		−76.2 (43.1%)	
$\Delta E_{\text{prep}}^c$	38.8		41.5		33.1		36.9		40.4		33.8	
$D_e$	81.1		196.5		51.2		70.0		175.8		41.2	
M	Re	Ru	Re	Rh	Os	Rh	Tc	Os	Tc	Ir	Ru	Ir
$\Delta n(d_{xy})$	−0.13	0.13	−0.21	0.22	−0.17	0.15	−0.07	0.07	−0.15	0.17	−0.07	0.06
$\Delta q(M)$	0.12	−0.06	0.03	0.02	−0.04	0.01	−0.08	0.06	−0.13	0.08	−0.09	0.06
$\Delta q(MCl_4)$	0.86	−0.86	1.43	−1.43	0.77	−0.77	0.46	−0.46	1.11	−1.11	0.46	−0.46
$P(M-M)$	1.79		1.18		0.91		1.86		1.29		0.97	
$R(M-M)$	2.219		2.297		2.275		2.222		2.296		2.371	

<sup>a</sup>Values in parentheses give the percentage contribution to the total attractive interactions,  $\Delta E_{\text{elstat}} + \Delta E_{\text{orb}}$ .

<sup>b</sup>Values in parentheses give the percentage contribution to the total orbital interactions,  $\Delta E_{\text{orb}}$ .

<sup>c</sup>Fragments relax into a tetrahedrally distorted square planar quintet of  $D_{2d}$  symmetry.

to 49.3% of the total  $\Delta E_{\text{orb}}$  in the Os compound. The reduced  $\pi$  contribution can be explained by the reduced overlap between the fragment  $\pi$  orbitals with overlap integrals of 0.21, 0.18, and 0.14 in the Re, Tc, and Os compounds, respectively. This is a consequence of the decreasing size of

the metal orbitals with decreasing negative charge and (or) decreasing row in the periodic system.

The nonclassical interaction between the fragments building the group 8 compound  $[\text{Ir}_2\text{Cl}_8]^{2+}$  is not strong enough to compensate for their electrostatic repulsion of 30.5 kcal/mol

**Table 9.** Energy decomposition analysis for the  $C_{4v}$  symmetric  $[MM'Cl_8]^x$  ( $M, M' = \text{Tc, Re, Ru, Os, Rh, Ir}; x = -2, 0, +2$ ) at BP86/TZ2P.  $MCl_4^y$  ( $y = -1, 0, +1$ ) in the quintet  $^5A_1$  state were used as fragments. Optimized metal–metal distances ( $R$ ) in Å, the Wiberg bond index of the  $M-M'$  pair ( $P$ ), the change in the orbital occupation ( $\Delta n$ ), and the change in partial charge ( $\Delta q$ ) relative to the homodimetallic systems are also given. The population analysis data are given at BP86/def2-TZVPP/BP86/TZ2P.

	$[\text{ReTcCl}_8]^{2-}$		$[\text{OsRuCl}_8]^0$		$[\text{IrRhCl}_8]^{2+}$	
$\Delta E_{\text{int}}$	-37.9		-73.9		12.0	
$\Delta E_{\text{Pauli}}$	367.8		217.3		156.7	
$\Delta E_{\text{elstat}}^a$	-199.3 (49.1%)		-115.2 (39.6%)		40.0 (0.0%)	
$\Delta E_{\text{orb}}^a$	-206.4 (50.9%)		-176.0 (60.4%)		-184.7 (100.0%)	
$\Delta a_1 (\sigma, \delta)^b$	-81.4 (39.5%)		-89.4 (50.1%)		-94.5 (51.2%)	
$\Delta a_2^b$	-0.1 (0.1%)		-0.1 (0.1%)		-0.7 (0.4%)	
$\Delta b_1^b$	-1.7 (0.8%)		-2.9 (1.6%)		-4.0 (2.2%)	
$\Delta b_2 (\delta)^b$	0.7 (<0.0%)		2.0 (<0.0%)		-1.5 (0.1%)	
$\Delta e (\pi)^b$	-123.9 (60.0%)		-85.7 (48.7%)		-84.0 (45.5%)	
$\Delta E_{\text{prep}}^c$	38.7		33.0		39.0	
$D_e$	0.4		40.9		-51.0	
M	Re	Tc	Os	Ru	Ir	Rh
$\Delta n(d_{xy})$	-0.03	0.03	-0.04	0.03	-0.06	0.05
$\Delta q(M)$	0.12	-0.10	0.04	-0.04	0.00	-0.02
$\Delta q(MCl_4)$	0.20	-0.20	0.17	-0.17	0.13	-0.13
$P(M-M)$	2.35		1.42		0.66	
$R(M-M)$	2.193		2.265		2.454	

<sup>a</sup>Values in parentheses give the percentage contribution to the total attractive interactions,  $\Delta E_{\text{elstat}} + \Delta E_{\text{orb}}$ .

<sup>b</sup>Values in parentheses give the percentage contribution to the total orbital interactions,  $\Delta E_{\text{orb}}$ .

<sup>c</sup>Fragments relax into a tetrahedrally distorted square planar quintet of  $D_{2d}$  symmetry.

and the Pauli repulsion of 162.4 kcal/mol. The resulting total interaction energy of 3.5 kcal/mol is destabilizing. The size of the orbital interaction term should be regarded with some care, as the singly occupied fragment orbitals, whose coupling is mainly responsible for this energy lowering, have some ligand character in the case of  $[\text{Ir}_2\text{Cl}_8]^{2+}$ , as was discussed in the beginning of the section in connection with Fig. 1. The  $\Delta E_{\text{orb}}$  term should thus not be identified with the pure  $M-M$  interaction, but contains a mixture of metal–metal, metal–ligand, and eventually also ligand–ligand interactions. This argument is supported by the considerably smaller Wiberg bond index of 0.77 for  $[\text{Ir}_2\text{Cl}_8]^{2+}$  compared to 1.55 for  $[\text{Os}_2\text{Cl}_8]^0$ , whereas the difference between the  $\Delta E_{\text{orb}}$  values of the Os compound (–197.8 kcal/mol) and the Ir species (–189.5 kcal/mol) is relatively low and blurs, to a certain degree, the difference in the bonding pattern.

The difference between  $[\text{Os}_2\text{Cl}_8]^0$  and its lighter analogue  $[\text{Ru}_2\text{Cl}_8]^0$  is comparable to the difference between  $[\text{Re}_2\text{Cl}_8]^{2-}$  and  $[\text{Tc}_2\text{Cl}_8]^{2-}$ . The change from a 5d to a 4d metal weakens the metal–metal interaction considerably, due to the reduction in size of the metal orbitals. This reduction leads to a decreased overlap between the metal orbitals, to which the system can answer by a decrease in the central metal–metal bond length, but only to a limited degree, since an increased ligand–ligand repulsion counterbalances this process. The strong decrease in the electrostatic contribution in the 4d

systems can also be attributed to the more compact orbitals of the 4d metal atoms.

Comparing the analysis results for  $[\text{M}_2\text{Cl}_8]^{2-}$  with the ones for  $[\text{M}_2\text{Cl}_8]^0$  and for  $[\text{M}_2\text{Cl}_8]^{2+}$  shows that the uncharged species are the most stable, followed by the negatively charged ones, with the positively charged systems being unstable. The lower bond strength of  $[\text{M}_2\text{Cl}_8]^{2-}$  is due to a very high Pauli repulsion, whereas the positively charged species are destabilized by classical electrostatic repulsion. In all cases, the  $\delta$  bonding orbitals are of no importance for the bond strength, whereas the  $\pi$  orbitals dominate the covalent contribution for the negatively charged species and the  $\sigma$  contribution is more important for the remaining compounds.

The EDA results for some heteronuclear compounds,  $[\text{MM}'\text{Cl}_8]^x$  ( $M = \text{Tc, Re, Ru, Os, Rh, Ir}; x = -2, 0, +2$ ), are given in Table 9. These compounds are species in which two metal atoms of the same group, but of different rows in the periodic table, interact with each other. The comparison with the corresponding homodinuclear systems reveals that all bond energy contributions are halfway between the homonuclear values. The bonding situation does thus not change from the homo- to the hetero-dinuclear systems and thus, the polarity of the metal–metal bond appears to be low. The partial charges support this finding as the charge transfer between the two different  $\text{MCl}_4^x$  units is small ( $|\Delta q(\text{MCl}_4^x)|$  between 0.13–0.20 e) with the charge of the metal atoms being essentially unchanged. The picture does change for the heterodimetallic systems with metal atoms of the same row but of different groups in the periodic table (Table 7). In this case, the intrinsic bond strength is considerably enhanced compared to the corresponding nonpolar compounds. For example,  $[\text{ReOsCl}_8]^{1-}$  has an intrinsic bond strength of –132.0 kcal/mol, while for  $[\text{Re}_2\text{Cl}_8]^{2-}$   $\Delta E_{\text{int}}$  amounts to –54.2 kcal/mol and for  $[\text{Os}_2\text{Cl}_8]^0$  to –92.8 kcal/mol. The main reason for this observation is that the Pauli repulsion is considerably weaker compared to the dianionic Re system, while the classical electrostatic interaction in the monoanionic system is increased compared to the neutral Os system. The covalent bonding does not dramatically change; the  $\pi$  bonding remains the dominating contribution to  $\Delta E_{\text{orb}}$  (53.8%). There is, however, an increase in the contribution due to the  $b_2 (\delta)$  orbitals of 4.6%. We attribute a part of this energy gain to a charge transfer from the  $\delta$  orbitals of  $\text{ReCl}_4^-$  to the  $\delta$  orbitals of the  $\text{OsCl}_4^0$  fragment, since the  $d_{xy}$  orbital of Re loses 0.1 e to the Os  $d_{xy}$  orbital (Table 7). The overall charge transfer from the  $\text{ReCl}_4^-$  onto the  $\text{OsCl}_4^0$  moiety is considerable with 0.61 e, but the partial charge of the metal atoms remains virtually constant. A similar interpretation can be given to the  $[\text{ReIrCl}_8]^0$  system, where the two oppositely charged fragments,  $\text{ReCl}_4^-$  and  $\text{IrCl}_4^+$ , interact, which leads to an exceptionally large electrostatic contribution of –255.1 kcal/mol. The charge transfer in this system is large with 1.30 e, while the metal atom partial charge changes very little. As in the former case, charge transfer between the  $d_{xy}$  orbitals of the two metal atoms of 0.2 e leads to a large energy contribution in the  $\Delta b_2$  term. The combination of the group 8 metal Os with the group 9 metal Ir leads to the cationic  $[\text{OsIrCl}_8]^+$  system, which also has an increased stability compared to both homodimetallic analogues, which is interesting as  $[\text{Ir}_2\text{Cl}_8]^{2+}$  is unstable. The



much more favorable electrostatic interaction between a neutral and a cationic system compared to the one between two cations is the main reason for this observation.

For the combination of two 4d metals of different rows in the periodic table (Table 7), the same bonding picture emerges as for the 5d metals. The polar metal–metal bonds show an increased stability compared to the homodinuclear counterparts, mainly due to a reduced Pauli repulsion, more favorable electrostatic interactions, and charge transfer.

Table 8 shows the analysis results for heterodinuclear compounds with metal atoms of different groups and different rows in the periodic table. Also in this case, the stability of the metal–metal bond increases compared to the unpolar situation, but the bonding situation of the two systems is very similar. However, the charge transfer contribution as measured by  $|\Delta q(\text{MCl}_4)|$  increases whenever the 5d moiety is more negatively charged than the 4d moiety, compared to the 5d–5d analogues. On the other hand, a 4d  $\text{MCl}_4^x$  fragment that is more negatively charged than the 5d fragment interacts and loses fewer electrons than it would when combined with a 4d fragment. This is exemplified by the systems  $[\text{TcOsCl}_8]^{1-}$  with  $|\Delta q(\text{MCl}_4)| = 0.47$  and  $[\text{TcRuCl}_8]^{1-}$  with  $|\Delta q(\text{MCl}_4)| = 0.65$ . This means that there is a better “match” if the M–M bond is built between a 4d metal of a lower group number than the 5d metal (“early 4d–late 5d”). We note that the charge transfer trends are reflected in the trends of the  $\Delta b_2$  ( $\delta$ ) contributions to the orbital interaction energy in the EDA. Furthermore, the size of the bond order as measured by the Wiberg bond index also follows this matching rule.

## Summary

The study of the bonding situation in the formally quadruply bonded (d–d)<sup>8</sup>  $[\text{MM}'\text{Cl}_8]^x$  compounds and the test of the performance of DFT functionals can be summarized as follows: (i) The GGA functionals BLYP, BP86, and PBE, show the best performance when it comes to structure prediction and in the description of the dissociation energies. We estimate these functionals to deliver dissociation energies within  $\pm 5$  kcal/mol from the CASPT2 results. (ii) Hybrid functionals are not to be used for compounds of the type discussed here as they lead to increasingly too short and too weak bonds with the amount of exact exchange included. (iii) The ground state of the  $\text{MCl}_4^x$  fragments can either be a  $D_{4h}$  symmetric quintet or a  $T_d$  symmetric singlet state. Most of the studied fragments have a singlet ground state with the exception of  $\text{ReCl}_4^-$  and  $\text{TcCl}_4^-$ . Since the quintet state is the valence state for building a metal–metal quadruple bond, this finding can serve as an explanation for the difficulties to isolate more metal–metal multiply bonded systems. (iv) The strength of unpolar metal–metal bonds is reduced in going from group 7 metals to group 8 metals and to group 9 metals. 4d transition metal atoms form weaker metal–metal bonds than 5d species. (v) The intrinsic bond strength in the unpolar systems is in approximately equal parts due to orbital interactions and classical electrostatic contributions. The  $\pi$  orbitals dominate the orbital interaction, while  $\delta$  orbitals are of minor importance. (vi) Polar metal–metal bonds show enhanced bond strength compared to unpolar bonds due to a reduced Pauli repulsion,

more favorable classical electrostatics interactions, and charge transfer. 5d–5d metal atom pairs form the most stable polar metal–metal bonds. The charge transfer is small in a heterodinuclear system with two metal atoms of the same group and it is large if the two metal atoms have considerably different size as, e.g., in a system in which a more negatively charged 5d metal fragment interacts with a more positively charged 4d metal fragment.

The knowledge on the performance of the DFT functionals will be useful in the study of more complex systems, e.g., the Por–M–M'–Por systems of Collmann, which will be the subject of further studies. The insight into the bonding situation of metal–metal bonded systems should be helpful in the design of new polar metal–metal bonded systems.

## Supplementary data

Supplementary data for this article are available on the journal Web site ([canjchem.nrc.ca](http://canjchem.nrc.ca)).

## Acknowledgment

This work was supported by the Deutsche Forschungsgemeinschaft.

## References

- (1) (a) Cotton, F. A.; Harris, C. B. *Inorg. Chem.* **1965**, *4* (3), 330. doi:10.1021/ic50025a015.; (b) Cotton, F. A. *Inorg. Chem.* **1965**, *4* (3), 334. doi:10.1021/ic50025a016.
- (2) (a) Poineau, F.; Gagliardi, L.; Forster, P. M.; Sattelberger, A. P.; Czerwinski, K. R. *Dalton Trans.* **2009**, 5954. doi:10.1039/b902106j. PMID:19623396.; (b) Wang, X.-B.; Wang, L.-S. *J. Am. Chem. Soc.* **2000**, *122* (9), 2096. doi:10.1021/ja994200q.
- (3) Cotton, F. A.; Murillo, C. A.; Walton, R. A. *Multiple Bonds Between Metal Atoms*, 3rd ed.; Springer Science and Business Media, Inc.: New York, 2005.
- (4) Nguyen, T.; Sutton, A. D.; Brynda, M.; Fetting, J. C.; Long, G. J.; Power, P. P. *Science* **2005**, *310* (5749), 844. doi:10.1126/science.1116789. PMID:16179432.
- (5) (a) Gagliardi, L.; Roos, B. O. *Nature* **2005**, *433* (7028), 848. doi:10.1038/nature03249. PMID:15729337.; (b) Roos, B. O.; Borin, A. C.; Gagliardi, L. *Angew. Chem. Int. Ed.* **2007**, *46* (9), 1469. doi:10.1002/anie.200603600.; (c) Roos, B. O.; Malmqvist, P.-Å.; Gagliardi, L. *J. Am. Chem. Soc.* **2006**, *128* (51), 17000. doi:10.1021/ja066615z. PMID:17177451.
- (6) (a) Kreisel, K. A.; Yap, G. P. A.; Dmitrenko, O.; Landis, C. R.; Theopold, K. H. *J. Am. Chem. Soc.* **2007**, *129* (46), 14162. doi:10.1021/ja076356t. PMID:17967028.; (b) Noor, A.; Wagner, F. R.; Kempe, R. *Angew. Chem. Int. Ed.* **2008**, *47* (38), 7246. doi:10.1002/anie.200801160.; (c) Tsai, Y.-C.; Hsu, C.-W.; Yu, J.-S. K.; Lee, G.-H.; Wang, Y.; Kuo, T.-S. *Angew. Chem. Int. Ed.* **2008**, *47* (38), 7250. doi:10.1002/anie.200801286.; (d) Horvath, S.; Gorelsky, S. I.; Gambarotta, S.; Korobkov, I. *Angew. Chem. Int. Ed.* **2008**, *47* (51), 9937. doi:10.1002/anie.200804048.
- (7) (a) Kurokawa, Y. I.; Nakao, Y.; Sakaki, S. *J. Phys. Chem. A* **2009**, *113* (13), 3202. doi:10.1021/jp809597m. PMID:19271722.; (b) Saito, K.; Nakao, Y.; Sato, H.; Sakaki, S. *J. Phys. Chem. A* **2006**, *110* (31), 9710. doi:10.1021/jp057558j. PMID:16884203.
- (8) Braunstein, P.; Rose, J. In *Comprehensive Organometallic Chemistry II: A Review of the Literature 1982–1994*; Abel,

- E. W., Stone, F. G. A., Wilkinson, G., Eds.; Pergamon: New York, 1995; Vol. 10.
- (9) Chetcuti, M. J. In *Comprehensive Organometallic Chemistry II: A Review of the Literature 1982–1994*; Abel, E. W., Stone, F. G. A., Wilkinson, G., Eds.; Pergamon: New York, 1995; Vol. 10.
  - (10) Gade, L. H. *Angew. Chem.* **2000**, *112* (15), 2768. doi:10.1002/1521-3757(20000804)112:15<2768::AID-ANGE2768>3.0.CO;2-O.
  - (11) Wheatley, N.; Kalk, P. *Chem. Rev.* **1999**, *99* (12), 3379. doi:10.1021/cr980325m. PMID:11849025.
  - (12) Collman, J. P.; Boulakov, R. *Angew. Chem.* **2002**, *114* (21), 4120. doi:10.1002/1521-3757(20021104)114:21<4120::AID-ANGE4120>3.0.CO;2-N.
  - (13) Slater, J. C. *Quantum Theory of Molecules and Solids*; McGraw-Hill: New York, 1974; Vol. 4.
  - (14) Vosko, S. H.; Wilk, L.; Nusair, M. *Can. J. Phys.* **1980**, *58* (8), 1200. doi:10.1139/p80-159.
  - (15) Becke, A. D. *Phys. Rev. A* **1988**, *38* (6), 3098. doi:10.1103/PhysRevA.38.3098. PMID:9900728.
  - (16) Perdew, J. P. *Phys. Rev. B* **1986**, *33* (12), 8822. doi:10.1103/PhysRevB.33.8822.
  - (17) Lee, C.; Yang, W.; Parr, R. G. *Phys. Rev. B* **1988**, *37* (2), 785. doi:10.1103/PhysRevB.37.785.
  - (18) Handy, N. C.; Cohen, A. J. *Mol. Phys.* **2001**, *99* (5), 403. doi:10.1080/00268970010018431.
  - (19) Perdew, J. P.; Burke, K.; Ernzerhof, M. *Phys. Rev. Lett.* **1996**, *77* (18), 3865. doi:10.1103/PhysRevLett.77.3865. PMID:10062328.
  - (20) Hamprecht, F. A.; Cohen, A. J.; Tozer, D. J.; Handy, N. C. *J. Chem. Phys.* **1998**, *109* (15), 6264. doi:10.1063/1.477267.
  - (21) Stephens, P. J.; Devlin, F. J.; Chabalowski, C. F.; Frisch, M. J. *J. Phys. Chem.* **1994**, *98* (45), 11623. doi:10.1021/j100096a001.
  - (22) Frisch, M. J.; Trucks, G. W.; Schlegel, H. B.; Scuseria, G. E.; Robb, M. A.; Cheeseman, J. R.; Montgomery, J. A., Jr.; Vreven, T.; Kudin, K. N.; Burant, J. C.; Millam, J. M.; Iyengar, S. S.; Tomasi, J.; Barone, V.; Mennucci, B.; Cossi, M.; Scalmani, G.; Rega, N.; Petersson, G. A.; Nakatsuji, H.; Hada, M.; Ehara, M.; Toyota, K.; Fukuda, R.; Hasegawa, J.; Ishida, M.; Nakajima, T.; Honda, Y.; Kitao, O.; Nakai, H.; Klene, M.; Li, X.; Knox, J. E.; Hratchian, H. P.; Cross, J. B.; Bakken, V.; Adamo, C.; Jaramillo, J.; Gomperts, R.; Stratmann, R. E.; Yazyev, O.; Austin, A. J.; Cammi, R.; Pomelli, C.; Ochterski, J. W.; Ayala, P. Y.; Morokuma, K.; Voth, G. A.; Salvador, P.; Dannenberg, J. J.; Zakrzewski, V. G.; Dapprich, S.; Daniels, A. D.; Strain, M. C.; Farkas, O.; Malick, D. K.; Rabuck, A. D.; Raghavachari, K.; Foresman, J. B.; Ortiz, J. V.; Cui, Q.; Baboul, A. G.; Clifford, S.; Cioslowski, J.; Stefanov, B. B.; Liu, G.; Liashenko, A.; Piskorz, P.; Komaromi, I.; Martin, R. L.; Fox, D. J.; Keith, T.; Al-Laham, M. A.; Peng, C. Y.; Nanayakkara, A.; Challacombe, M.; Gill, P. M. W.; Johnson, B.; Chen, W.; Wong, M. W.; Gonzalez, C.; Pople, J. A. *Gaussian03*, revision D01; Gaussian, Inc.: Wallingford, CT, 2004.
  - (23) Hoe, W.-M.; Cohen, A. J.; Handy, N. C. *Chem. Phys. Lett.* **2001**, *341* (3–4), 319. doi:10.1016/S0009-2614(01)00581-4.
  - (24) Xu, X.; Goddard, W. A., III. *Proc. Natl. Acad. Sci. U.S.A.* **2004**, *101* (9), 2673. doi:10.1073/pnas.0308730100. PMID:14981235.
  - (25) Tao, J.; Perdew, J. P.; Staroverov, V. N.; Scuseria, G. E. *Phys. Rev. Lett.* **2003**, *91* (14), 146401. doi:10.1103/PhysRevLett.91.146401. PMID:14611541.
  - (26) Van Voorhis, T.; Scuseria, G. E. *J. Chem. Phys.* **1998**, *109* (2), 400. doi:10.1063/1.476577.
  - (27) Weigend, F. *Phys. Chem. Chem. Phys.* **2006**, *8* (9), 1057. doi:10.1039/b515623h. PMID:16633586.
  - (28) Weigend, F.; Ahlrichs, R. *Phys. Chem. Chem. Phys.* **2005**, *7* (18), 3297. doi:10.1039/b508541a. PMID:16240044.
  - (29) Andrae, D.; Häußermann, U.; Dolg, M.; Stoll, H.; Preuß, H. *Theor. Chim. Acta* **1990**, *77* (2), 123. doi:10.1007/BF01114537.
  - (30) Čížek, J. *J. Chem. Phys.* **1966**, *45* (11), 4256. doi:10.1063/1.1727484.
  - (31) Bartlett, R. J.; Purvis, G. D. *Int. J. Quantum Chem.* **1978**, *14* (5), 561. doi:10.1002/qua.560140504.
  - (32) Hampel, C.; Peterson, K.; Werner, H.-J. *Chem. Phys. Lett.* **1992**, *190* (1–2), 1. doi:10.1016/0009-2614(92)86093-W.
  - (33) Pople, J. A.; Head-Gordon, M.; Raghavachari, K. *J. Chem. Phys.* **1987**, *87* (10), 5968. doi:10.1063/1.453520.
  - (34) Pople, J. A.; Krishnan, R.; Schlegel, H. B.; Binkley, J. S. *Int. J. Quantum Chem.* **1978**, *14* (5), 545. doi:10.1002/qua.560140503.
  - (35) Purvis, G. D.; Bartlett, R. J. *J. Chem. Phys.* **1982**, *76* (4), 1910. doi:10.1063/1.443164.
  - (36) Werner, H.-J.; Knowles, P. J.; Lindh, R.; Manby, F. R.; Schütz, M.; Celani, P.; Korona, T.; Rauhut, G.; Amos, R. D.; Bernhardsson, A.; Berning, A.; Cooper, D. L.; Deegan, M. J. O.; Dobbyn, A. J.; Eckert, F.; Hampel, C.; Hertzner, G.; Lloyd, A. W.; McNicholas, S. J.; Meyer, W.; Mura, M. E.; Nicklass, A.; Palmieri, P.; Pitzer, R.; Schumann, U.; Stoll, H.; Stone, A. J.; Tarroni, R.; Thorsteinsson, T. *MOL-PRO*, version 2006.1; a package of ab initio programs; 2006. Available from <http://www.molpro.net>.
  - (37) Roos, B. O. In *Advances in Chemical Physics: Ab initio Methods in Quantum Chemistry*; Lawley, K. P., Ed.; John Wiley & Sons Ltd.: Chichester, UK, 1987; Vol. II, p 399.
  - (38) Andersson, K.; Malmqvist, P.-Å.; Roos, B. O.; Sadlej, A. J.; Wolinski, K. *J. Phys. Chem.* **1990**, *94* (14), 5483. doi:10.1021/j100377a012.
  - (39) Andersson, K.; Malmqvist, P.-Å.; Roos, B. O. *J. Chem. Phys.* **1992**, *96* (2), 1218. doi:10.1063/1.462209.
  - (40) Roos, B. O.; Andersson, K.; Fülcher, M. P.; Malmqvist, P.-Å.; Serrano-Andrés, L.; Pierloot, K.; Merchán, M. In *Advances in Chemical Physics: New Methods in Computational Quantum Mechanics*; Prigogine, I., Rice, S. A., Eds.; John Wiley & Sons Ltd.: Chichester, UK, 1996; Vol. XCIII; p 219.
  - (41) Douglas, N.; Kroll, N. M. *Ann. Phys.* **1974**, *82* (1), 89. doi:10.1016/0003-4916(74)90333-9.
  - (42) Hess, B. *Phys. Rev. A* **1986**, *33* (6), 3742. doi:10.1103/PhysRevA.33.3742.
  - (43) Karlström, G.; Lindh, R.; Malmqvist, P.-Å.; Roos, B. O.; Ryde, U.; Veryazov, V.; Widmark, P.-O.; Cossi, M.; Schimelpfennig, B.; Neogrady, P.; Seijo, L. *Comput. Mater. Sci.* **2003**, *28* (2), 222. doi:10.1016/S0927-0256(03)00109-5.
  - (44) Reed, A. E.; Curtiss, L. A.; Weinhold, F. *Chem. Rev.* **1988**, *88* (6), 899. doi:10.1021/cr00088a005.
  - (45) Morokuma, K. *J. Chem. Phys.* **1971**, *55* (3), 1236. doi:10.1063/1.1676210.
  - (46) Kitaura, K.; Morokuma, K. *Int. J. Quantum Chem.* **1976**, *10* (2), 325. doi:10.1002/qua.560100211.
  - (47) Bickelhaupt, F. M.; Baerends, E. J. In *Reviews in Computational Chemistry*; Lipkowitz, K. B., Boyd, D. B., Eds.; Wiley-VCH: New York, 2000; Vol. 15, p 1.
  - (48) Ziegler, T.; Rauk, A. *Theor. Chim. Acta* **1977**, *46* (1), 1. doi:10.1007/BF02401406.

- (49) Ziegler, T.; Rauk, A. *Inorg. Chem.* **1979**, *18* (7), 1755. doi:10.1021/ic50197a006.
- (50) Snijders, J. G.; Baerends, E. J.; Vernooijs, P. *At. Data Nucl. Data Tables (N.Y.)* **1981**, *26* (6), 483. doi:10.1016/0092-640X(81)90004-8.
- (51) Chang, C.; Pelissier, M.; Durand, P. *Phys. Scr.* **1986**, *34* (5), 394. doi:10.1088/0031-8949/34/5/007.
- (52) Heully, J.-L.; Lindgren, I.; Lindroth, E.; Lundqvist, S.; Martensson-Pendrill, A.-M. *J. Phys. B* **1986**, *19* (18), 2799. doi:10.1088/0022-3700/19/18/011.
- (53) van Lenthe, E.; Baerends, E. J.; Snijders, J. G. *J. Chem. Phys.* **1993**, *99* (6), 4597. doi:10.1063/1.466059.
- (54) van Lenthe, E.; van Leeuwen, R.; Baerends, E. J.; Snijders, J. G. *Int. J. Quantum Chem.* **1996**, *57* (3), 281. doi:10.1002/(SICI)1097-461X(1996)57:3<281::AID-QUA2>3.0.CO;2-U.
- (55) van Lenthe, E.; Snijders, J. G.; Baerends, E. J. *J. Chem. Phys.* **1996**, *105* (15), 6505. doi:10.1063/1.472460.
- (56) te Velde, G.; Bickelhaupt, F. M.; Baerends, E. J.; Van Fonseca Guerra, C.; van Gisbergen, S. J. A.; Snijders, J. G.; Ziegler, T. *J. Comput. Chem.* **2001**, *22* (9), 931. doi:10.1002/jcc.1056.
- (57) Scientific Computing & Modelling (SCM). *ADF2005.01*; SCM, Theoretical Chemistry, Vrije Universiteit: Amsterdam, The Netherlands. Available from <http://www.scm.com>.
- (58) Cavagliasso, G.; Kaltsoyannis, N. *Dalton Trans.* **2006**, 5476. doi:10.1039/b613446g. PMID:17117217.
- (59) Cotton, F. A.; Daniels, L.; Davison, A.; Orvig, C. *Inorg. Chem.* **1981**, *20* (9), 3051. doi:10.1021/ic50223a058.
- (60) Poineau, F.; Sattelberger, A. P.; Conradson, S. D.; Czerwinski, K. R. *Inorg. Chem.* **2008**, *47* (6), 1991. doi:10.1021/ic701453k. PMID:18290609.
- (61) Cramer, C. J.; Truhlar, D. G. *Phys. Chem. Chem. Phys.* **2009**, *11* (46), 10757. doi:10.1039/b907148b. PMID:19924312.
- (62) Zhao, Y.; Schultz, N. E.; Truhlar, D. G. *J. Chem. Theory Comput.* **2006**, *2* (2), 364. doi:10.1021/ct0502763.
- (63) Cotton, F. A.; Murillo, C. A.; Walton, R. A. *Multiple Bonds Between Metal Atoms*, 3rd ed.; Springer Science and Business Media, Inc.: New York, 2005; p 724.
- (64) Furche, F.; Perdew, J. P. *J. Chem. Phys.* **2006**, *124* (4), 044103. doi:10.1063/1.2162161. PMID:16460145.
- (65) Schultz, N. E.; Zhao, Y.; Truhlar, D. G. *J. Phys. Chem. A* **2005**, *109* (19), 4388. doi:10.1021/jp0504468. PMID:16833770.
- (66) Gagliardi, L.; Roos, B. O. *Inorg. Chem.* **2003**, *42* (5), 1599. doi:10.1021/ic0261068. PMID:12611528.
- (67) Saito, K.; Nakao, Y.; Sato, H.; Sakaki, S. *J. Phys. Chem. A* **2006**, *110* (31), 9710. doi:10.1021/jp057558j. PMID:16884203.
- (68) All orbital contributions presented in this section are based on the MO coefficients at the BP86/TZ2P level.
- (69) This result has been discussed in detail in Krapp, A.; Lein, M.; Frenking, G. *Theor. Chem. Acc.* **2008**, *120* (1–3), 313. doi:10.1007/s00214-007-0294-6.
- (70) (a) Diefenbach, A.; Bickelhaupt, F. M.; Frenking, G. *J. Am. Chem. Soc.* **2000**, *122* (27), 6449. doi:10.1021/ja000663g.; (b) Boehme, C.; Uddin, J.; Frenking, G. *Coord. Chem. Rev.* **2000**, *197* (1), 249. doi:10.1016/S0010-8545(99)00227-1.; (c) Uddin, J.; Frenking, G. *J. Am. Chem. Soc.* **2001**, *123* (8), 1683. doi:10.1021/ja002845g. PMID:11456768.
- (71) Spackman, M. A.; Maslen, E. N. *J. Phys. Chem.* **1986**, *90* (10), 2020. doi:10.1021/j100401a010.
- (72) (a) Krapp, A.; Bickelhaupt, F. M.; Frenking, G. *Chem. Eur. J.* **2006**, *12* (36), 9196. doi:10.1002/chem.200600564.; (b) Kovács, A.; Esterhuysen, C.; Frenking, G. *Chem. Eur. J.* **2005**, *11* (6), 1813. doi:10.1002/chem.200400525.; (c) Esterhuysen, C.; Frenking, G. *Theor. Chem. Acc.* **2004**, *111* (2–6), 381. doi:10.1007/s00214-003-0535-2.
- (73) Frenking, G.; Fröhlich, N. *Chem. Rev.* **2000**, *100* (2), 717. doi:10.1021/cr9804011.

# Ring-chain equilibria of R-but-3-enoate esters — A quantum mechanical study of direct and indirect ring-closing reactions

Michael B. Burt, Angela K. Crane, Ning Su, Nicole Rice, and Raymond A. Poirier

**Abstract:** Macrocyclic structures can be synthesized through two simultaneous olefin metathesis reactions: either directly through ring-closing metathesis (RCM) or indirectly through an intermediate formed by acyclic diene metathesis (ADMET). The proclivity of a homologous series of 16 R-but-3-enoate esters to form lactones through one of these two processes is studied at the HF/6–31G(d), B3LYP/6–31G(d), and MP2(full)/6–31G(d) levels of theory. Computed Gibbs free energies are used to determine  $\Delta G_{\text{RCM}}$ ,  $\Delta G_{\text{ADMET}}$ , and  $\Delta\Delta G$  ( $\Delta G_{\text{RCM}} - \Delta G_{\text{ADMET}}$ ).  $\Delta\Delta G$  is evaluated to compare the relative favourability of the RCM and ADMET reactions for the various R-but-3-enoate esters, where each system is differentiated by the number of methylene groups ( $n$ ) added to the ester chain. When  $n = 0, 1, 10$ , or  $13$ , cyclic lactone formation by direct RCM is predicted to be thermodynamically favoured, and the indirect synthesis is preferred for all other heterocyclic structures. The same trend holds between 298.15 and 333.15 K, therefore, the gas-phase model is a reasonable approximation of the experimental reaction conditions. The theoretical model is sufficient for smaller systems, but molecules larger than the  $n = 6$  case do not follow experimental results for similar saturated structures. Hence, the assumptions pertaining to straight-chain and cis-ring conformations need to be re-evaluated. In particular, chain flexibility should be further examined.

**Key words:** olefin metathesis, ring-chain equilibria, ring-closing metathesis, acyclic diene metathesis.

**Résumé :** On a réalisé des synthèses de structures macrocycliques par le biais de réactions de métathèse simultanées d'oléfines, soit directement par une métathèse avec fermeture de cycle (MFC) ou indirectement par un intermédiaire formé par une métathèse de diène acyclique (METDA). On a étudié d'un point de vue théorique la proclivité d'une série homologue de seize esters de l'acide R-but-3-énoïque à former des lactones par un de ces deux processus aux niveaux HF/6–31G(d), B3LYP/6–31G(d) et MP2(complet)/6–31G(d) de la théorie. On a utilisé les énergies libres de Gibbs calculées pour déterminer les valeurs de  $\Delta G_{\text{MFC}}$ ,  $\Delta G_{\text{METDA}}$  et  $\Delta\Delta G$  ( $\Delta G_{\text{MFC}} - \Delta G_{\text{METDA}}$ ). La valeur de  $\Delta\Delta G$  a été évaluée afin de comparer le caractère favorable relatif des réactions de MFC et de METDA des divers esters de l'acide R-but-3-énoïque dans lesquels chaque système se distingue par le nombre de groupes méthylènes ( $n$ ) ajouté à la chaîne de l'ester. Quand  $n = 0, 1, 10$  ou  $13$ , il est prédit que la formation de la lactone cyclique par une MFC est thermodynamiquement favorisée alors que la synthèse indirecte est la réaction préférée pour toutes les autres structures hétérocycliques. La même tendance est observée pour 298,15 et 333,15 K; le modèle en phase gazeuse est donc une approximation raisonnable des conditions réactionnelles expérimentales. Le modèle théorique est suffisant pour les systèmes les plus petits, toutefois les molécules dans lesquelles est supérieure à 6 ne reproduisent pas les résultats expérimentaux pour des structures saturées similaires. Il est donc impératif de réévaluer les hypothèses concernant les chaînes droites et les conformations cis du cycle. On devrait réexaminer en particulier la question de la flexibilité de la chaîne.

**Mots-clés :** métathèse d'oléfine, équilibre cycle-chaîne, métathèse avec fermeture de cycle.

## Introduction

The development of olefin metathesis, a transalkylidenation reaction involving the redistribution of alkene bonds, has opened a variety of novel pathways to challenging or previously impossible syntheses.<sup>1–16</sup> In particular, ring-closing metathesis (RCM) has been used for decades to create functionalized macrocycles because of its excellent functional group tolerance and neutral reaction conditions. Since these

cyclic products are found in many synthetic targets, it is not surprising that RCM has become a popular methodology among synthetic chemists. Furthermore, the advent of Grubbs' highly reactive ruthenium catalyst has made RCM reactions quick and easily accessible; especially when the catalyst is modified by N-heterocyclic carbene derivatives.<sup>17</sup>

Unfortunately, RCM is still impractical at the commercial level owing to the high dilution conditions ( $1 \times 10^{-3}$  mol/L)

Received 27 January 2010. Accepted 20 April 2010. Published on the NRC Research Press Web site at canjchem.nrc.ca on 22 October 2010.

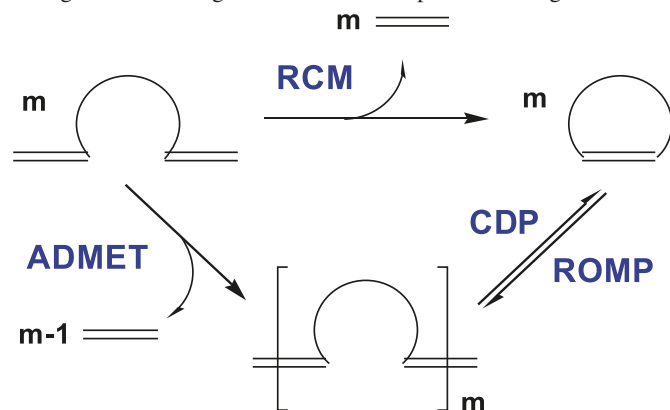
This article is part of a Special Issue dedicated to Professor R. J. Boyd.

M.B. Burt,<sup>1</sup> A.K. Crane, N. Su, N. Rice, and R.A. Poirier. Department of Chemistry, Memorial University of Newfoundland, St. John's, NL A1B 3X7, Canada.

<sup>1</sup>Corresponding author (e-mail: mburt@mun.ca).



**Scheme 1.** An  $\alpha,\omega$ -unsaturated diene can form either a polymer or a macrocycle by following the ADMET or RCM pathways, respectively ( $m$  is the number of substrates used). Each reaction is irreversible because of the loss of ethylene. The polymer product can further undergo a CDP reaction to form the macrocycle. Hence, there are two routes to the cyclic product: the direct RCM approach and the indirect two-step approach where the polymer produced through ADMET ring-closes to form the product through CDP.



required.<sup>11–13</sup> This restriction comes from a well-known equilibrium between the RCM pathway and a step growth polymerization reaction known as acyclic diene metathesis (ADMET). Hence, the distribution of products will be dependent on the relative rates of these two reactions. When the reactant monomer is present in high concentrations, the polymer is favoured. Conversely, the cyclic products dominate under dilute conditions. Scheme 1 illustrates the simultaneous RCM and ADMET reactions and demonstrates that the polymer product can further undergo a cyclodepolymerisation (CDP) reaction to ring close and form the cyclic product.<sup>5,7</sup> Therefore, in addition to the competition between RCM and ADMET, the yield of the cyclic product also depends on the equilibrium between the “backbiting” CDP reaction and the macrocycles proclivity towards ring-opening metathesis polymerization (ROMP).<sup>12–14</sup>

ADMET has previously been considered to impede RCM, however, Fogg and co-workers<sup>5,7</sup> recently used a series of typical  $\alpha,\omega$ -unsaturated dienes to demonstrate that oligomeric products were being quantitatively converted to macrocycles despite the volatilization of ethylene during ADMET. Because the loss of ethylene makes the RCM and ADMET pathways irreversible, the conversion of polymers to cyclic products implies that the ADMET polymers are actually key intermediates for the RCM of conformationally flexible dienes. Macrocylic products can therefore be produced either through the direct RCM pathway or by a two-step indirect pathway, which involves ADMET followed by CDP, implying that ADMET is actually intrinsic to macrocycle production rather than an impediment.

Because the formation of cyclic products from diene monomers follows two separate pathways, it would be useful to have some way of quickly predicting the product distribution for different systems. If the direct RCM pathway was uniquely followed, the product mixture would contain only the macrocycle and any unreacted diene; however, if the indirect pathway were contributing, then the intermedi-

ary oligomers produced through ADMET would also be present; although, this would be dependent on the rate of CDP. The preference for a homologous series of R-but-3-enoate ester substrates to follow the direct or indirect pathways will be examined by observing the inclination of these  $\alpha,\omega$ -diene monomers to form either cyclic or acyclic products. These substrates were chosen because they are similar to experimental products reported previously by Mandolini and co-workers,<sup>18–20</sup> and because they were already known to yield cyclic products through both direct and indirect ring-closing methods.<sup>5</sup> The ring-chain equilibrium between the RCM and ADMET reactions will be evaluated using a computational approach to determine the relative stabilities of the direct RCM lactone product and the oligomer produced through ADMET. Density functional theory (DFT) and ab initio approaches have already been successfully used to examine the mechanism of the RCM reaction with different catalysts,<sup>21–26</sup> and similar approaches to the one used here have been reported for the ring-chain product distribution for the ROMP of cycloolefins;<sup>27</sup> the equilibrium distribution for the metathesis of linear olefins;<sup>28</sup> and for the ring-chain equilibria in the cross-metathesis of cyclohexanone and *cis,cis*-cycloocta-1,5-diene.<sup>29</sup>

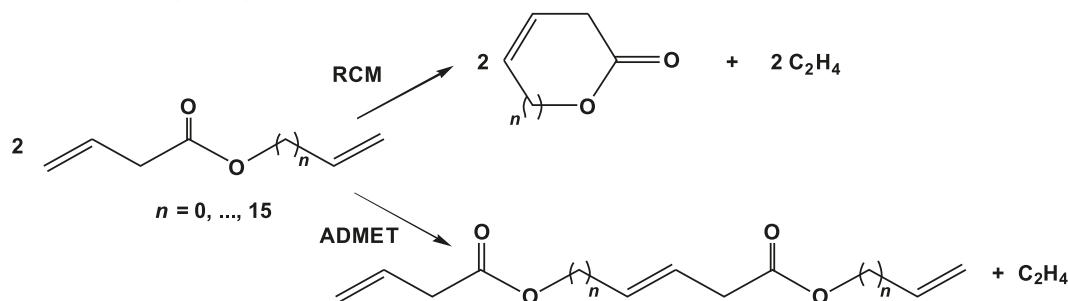
The competition between polymerization and ring-closing pathways has already been well-characterized:<sup>10,17</sup> the bifunctional nature of the  $\alpha,\omega$ -diene substrate leads to the two pathways, and further complications arise from head-to-head condensation reactions as opposed to head-to-tail. Mandolini and co-workers<sup>18–20</sup> used kinetic data to express the favourability of the two reactions by constructing reactivity profiles of ring size against the effective molarity or the rate of the intramolecular pathway. Our computational approach will investigate the thermochemistry involved in the ring-chain equilibrium instead of the kinetics. Thermochemical data will be used to determine  $\Delta G_{\text{RCM}}$ , the free energy change associated with the direct RCM reaction, and  $\Delta G_{\text{ADMET}}$ , the free energy change associated with the first step (ADMET) of the indirect ring-closing reaction. The difference between these two values,  $\Delta\Delta G$  ( $\Delta G_{\text{RCM}} - \Delta G_{\text{ADMET}}$ ), will then be examined as a function of ring size to assess the behaviour of the ring-chain equilibria for the R-but-3-enoate esters. A negative  $\Delta\Delta G$  means direct RCM is thermodynamically favoured, and a positive  $\Delta\Delta G$  implies lactone formation will occur through the indirect route. Hence, by comparing the  $\Delta\Delta G$  to ring size, the preference of a substrate to follow the direct or indirect RCM pathways can be determined. The theoretical predictions will be compared with Mandolini and co-workers’<sup>18–20</sup> experimentally determined trends to see whether or not the thermochemical approach can adequately approximate reactions, which are known to display a kinetic bias.

## Methods

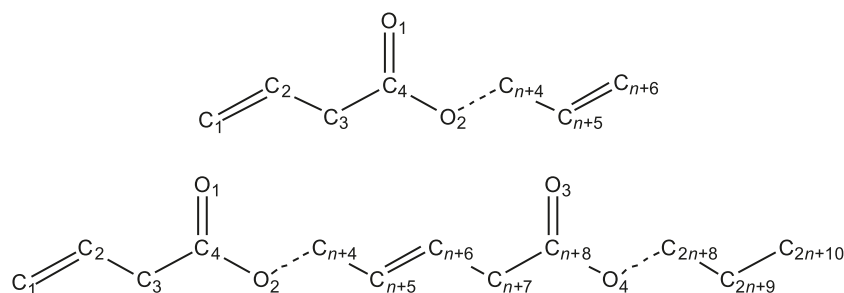
The R-but-3-enoate esters were chosen for their versatility in forming unsaturated lactones of various sizes (Scheme 2). This system is experimentally relevant, and has been well-documented with respect to RCM.<sup>4,5,30–32</sup>

In analyzing the reactions, several assumptions were made for computational convenience: it was assumed that polymerization did not produce any structures larger than the

**Scheme 2.** The R-but-3-enoate reaction system, where “ $n$ ” is the number of additional methylene groups added to a substrate. For example, the largest monomer considered ( $n = 15$ ) has 22 constituent atoms in its chain.



**Fig. 1.** The numbering system for dihedral angle assignments. The values of  $n$ , which describe the monomers, dimers, and lactones seen in Scheme 2, are given in Table 1. The broken line represents any methylene units ignored in the diagram. For example, in the  $n = 3$  case, the broken line includes C5 and C6. In the  $n = 0$  case,  $C_{n+4}$  and  $C_{2n+8}$  must both be ignored to avoid numbering duplication.



**Table 1.** The legend for the monomer and dimer systems studied, including the number of constituent atoms in each monomer or dimer chain, as well as the ring size for each lactone.

System ( $n$ )	Monomer length (no. of atoms in chain)	Dimer length (no. of atoms in chain)	Ring size (no. of atoms in ring)
0	7	12	5
1	8	14	6
2	9	16	7
3	10	18	8
4	11	20	9
5	12	22	10
6	13	24	11
7	14	26	12
8	15	28	13
9	16	30	14
10	17	32	15
11	18	34	16
12	19	36	17
13	20	38	18
14	21	40	19
15	22	42	20

dimer, that head-to-tail monomer linkages were ubiquitous, and that each dimer was expected to be a straight chain since straight-chain monomers were used to produce them. The second assumption is likely valid, but the first and third assumptions are less realistic and could lead to deviation from experimental data. Furthermore, calculations were made for the gas-phase reaction at 298.15 K, whereas the reaction itself is carried out in solution (e.g., dichloromethane) with various concentrations and at elevated tempera-

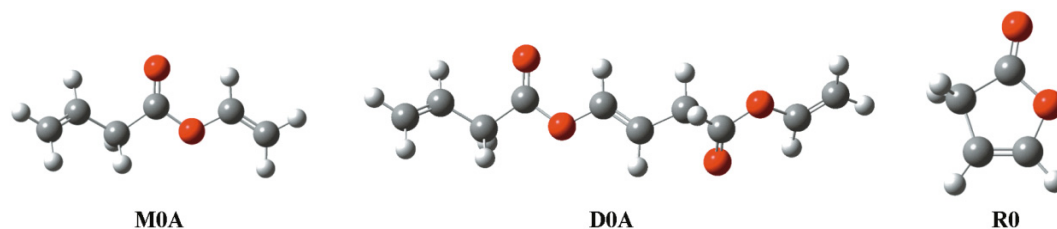
tures.<sup>4,5,10</sup> The temperature dependence of the ring-chain equilibrium will therefore also be examined for the reactions standard conditions (333.15 K).

Calculations were performed at the HF/6-31G(d), B3LYP/6-31G(d), and MP2(full)/6-31G(d) levels of theory as implemented in the Gaussian 03 suite of programs.<sup>33</sup> Sixteen R-but-3-enoate esters were considered (Scheme 2), with each system containing between 0 and 15 methylene units ( $n$ ) added to the ester chain of the  $\alpha,\omega$ -unsaturated ethyl butyrate. In each system, optimized geometries and vibrational frequencies were determined for the monomer, the dimer, and the cyclic lactone. Geometry optimizations were initially performed using HF/STO-3G. Optimized conformer structures with the lowest energies were then further refined using the methods described above. For all optimized structures, no imaginary frequencies were found.

The 16 systems were split into two groups. For the first group, consisting of the  $n = 0-7$  systems, many conformers were considered for each molecule. In general, the straight-chain conformers of the monomer and dimers appeared to be favoured. For the lactones, the *cis* configuration emerged as the preferred conformation. In the second group, which consisted of the  $n = 8-15$  systems, the structures became very large, so an assumption was made that the structures would follow the trend previously observed for the smaller  $n = 0-7$  systems; thus, only one to two conformers were considered for each straight-chained monomer and dimer, and only the *cis* rings were considered.

The determination of the lowest energy conformers for the monomer, dimer, and ring forms of each system allowed the reaction thermochemistry to be determined from the  $\Delta H$ ,  $\Delta S$ , and  $\Delta G$  values extracted from the *ab initio* and DFT data. It should also be noted that since the ADMET reaction

**Fig. 2.** The B3LYP/6–31G(d) optimized structures for the  $n = 0$  system: the monomer (M0A), the dimer (D0A), and the five-membered lactone (R0). The structures for other systems can be found in the Supplementary data.



**Table 2.** Thermochemical data calculated at HF/6–31G(d) for the lowest energy structures defined in the Supplementary data.  $\Delta\Delta G = \Delta G_{\text{RCM}} - \Delta G_{\text{ADMET}}$ ;  $\Delta\Delta H$  and  $\Delta\Delta S$  are similarly defined.

Ring size	$\Delta H_{\text{RCM}}$ (kJ/mol)	$\Delta H_{\text{ADMET}}$ (kJ/mol)	$\Delta S_{\text{RCM}}$ (J/(mol K))	$\Delta S_{\text{ADMET}}$ (J/(mol K))	$\Delta G_{\text{RCM}}$ (kJ/mol)	$\Delta G_{\text{ADMET}}$ (kJ/mol)	$\Delta\Delta H$ (kJ/mol)	$\Delta\Delta S$ (J/(mol K))	$\Delta\Delta G$ (kJ/mol)
5	27.8	3.6	128.7	–18.8	–10.6	9.2	24.2	147.5	–19.8
6	28.0	–4.2	142.9	–15.7	–14.6	0.5	32.2	158.6	–15.1
7	43.6	0.5	112.9	–18.6	10.0	6.1	43.1	131.5	3.9
8	65.7	0.5	103.1	–18.6	34.9	6.1	65.2	121.7	28.8
9	52.2	0.7	92.5	–18.3	24.6	6.2	51.5	110.8	18.4
10	50.3	9.6	82.6	–21.6	25.7	16.0	40.7	104.2	9.7
11	51.1	–2.3	83.0	–18.6	26.3	3.3	53.4	101.6	23.0
12	35.5	0.8	74.3	–18.3	13.3	6.3	34.7	92.6	7.0
13	65.1	0.8	68.8	–18.0	44.6	6.2	64.3	86.8	38.4
14	87.9	0.8	71.2	–18.1	66.6	6.2	87.1	89.3	60.4
15	56.8	51.5	66.9	–21.6	36.9	57.9	5.3	88.5	–21.0
16	121.3	0.6	54.7	–18.4	105.0	6.1	120.7	73.1	98.9
17	56.5	0.8	67.0	–17.8	36.6	6.1	55.7	84.8	30.5
18	54.6	51.2	57.0	–31.0	37.6	60.5	3.4	88.0	–22.9
19	59.9	0.8	59.6	–18.1	42.1	6.2	59.1	77.7	35.9
20	82.2	0.6	32.4	–18.4	72.5	6.1	81.6	50.8	66.4

**Table 3.** Thermochemical data calculated at B3LYP/6–31G(d) for the lowest energy structures defined in the Supplementary data.  $\Delta\Delta G = \Delta G_{\text{RCM}} - \Delta G_{\text{ADMET}}$ ;  $\Delta\Delta H$  and  $\Delta\Delta S$  are similarly defined.

Ring size	$\Delta H_{\text{RCM}}$ (kJ/mol)	$\Delta H_{\text{ADMET}}$ (kJ/mol)	$\Delta S_{\text{RCM}}$ (J/(mol K))	$\Delta S_{\text{ADMET}}$ (J/(mol K))	$\Delta G_{\text{RCM}}$ (kJ/mol)	$\Delta G_{\text{ADMET}}$ (kJ/mol)	$\Delta\Delta H$ (kJ/mol)	$\Delta\Delta S$ (J/(mol K))	$\Delta\Delta G$ (kJ/mol)
5	27.7	3.9	123.9	–25.7	–9.3	11.6	23.8	149.6	–20.9
6	26.8	–3.1	135.3	–20.4	–13.5	3.0	29.9	155.7	–16.5
7	38.8	0.6	106.0	–15.2	7.2	5.1	38.2	121.2	2.1
8	56.6	0.8	96.7	–10.8	27.7	4.0	55.8	107.5	23.7
9	46.6	1.0	85.4	–19.1	21.1	6.7	45.6	104.5	14.4
10	43.3	7.0	78.6	–30.0	19.9	16.0	36.3	108.6	3.9
11	43.3	–2.0	79.1	–26.6	19.7	5.9	45.3	105.7	13.8
12	27.6	0.9	73.5	–20.6	5.7	7.0	26.7	94.1	–1.3
13	52.5	1.1	66.8	–41.0	32.5	13.3	51.4	107.8	19.2
14	71.7	0.7	68.1	–23.5	51.4	7.7	71.0	91.6	43.7
15	45.9	42.4	57.4	–55.7	28.8	59.0	3.5	113.1	–30.2
16	97.1	0.8	55.5	–6.8	80.5	2.8	96.3	62.3	77.7
17	46.5	0.9	62.6	–46.4	27.8	14.7	45.6	109.0	13.1
18	45.8	38.8	65.2	–38.8	26.3	50.4	7.0	104.0	–24.1
19	45.8	1.1	50.8	–61.9	30.7	19.6	44.7	112.7	11.1
20	65.4	1.3	40.0	–40.5	53.5	13.4	64.1	80.5	40.1

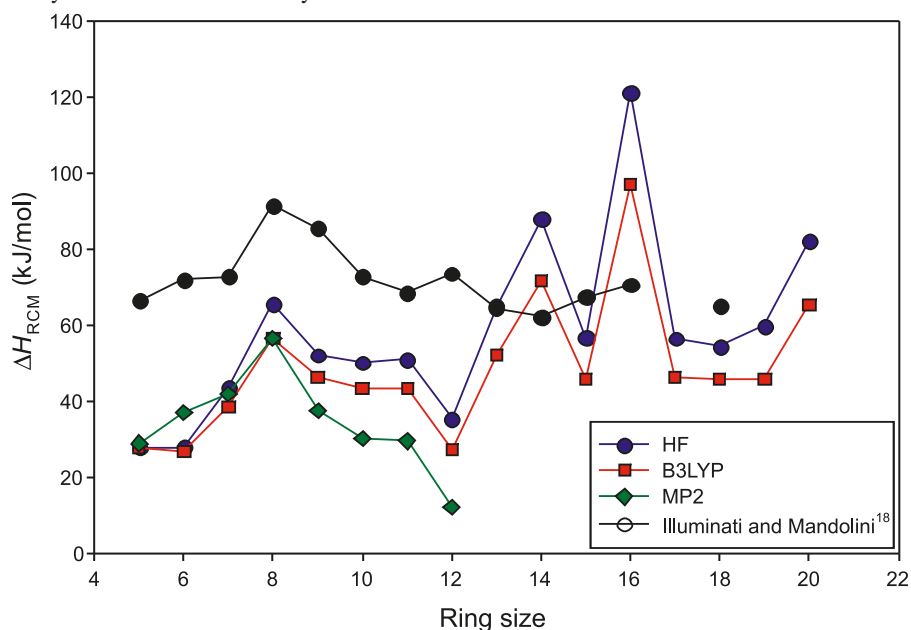
is irreversible due to the volatilization of ethylene, the CDP reaction was not examined in great detail since the formation of the dimer is sufficient to show that the indirect ring-closure pathway is preferred in the cases where  $\Delta\Delta G$

( $\Delta G_{\text{RCM}} - \Delta G_{\text{ADMET}}$ ) is positive. A plot of  $\Delta\Delta G$  against ring size was then used to determine the predicted preference of lactone (negative  $\Delta\Delta G$ ) or dimer (positive  $\Delta\Delta G$ ) formation.

**Table 4.** Thermochemical data calculated at MP2(full)/6–31G(d) for the lowest energy structures defined in the Supplementary data.  $\Delta\Delta G = \Delta G_{\text{RCM}} - \Delta G_{\text{ADMET}}$ ;  $\Delta\Delta H$  and  $\Delta\Delta S$  are similarly defined.

Ring size	$\Delta H_{\text{RCM}}$ (kJ/mol)	$\Delta H_{\text{ADMET}}$ (kJ/mol)	$\Delta S_{\text{RCM}}$ (J/(mol K))	$\Delta S_{\text{ADMET}}$ (J/(mol K))	$\Delta G_{\text{RCM}}$ (kJ/mol)	$\Delta G_{\text{ADMET}}$ (kJ/mol)	$\Delta\Delta H$ (kJ/mol)	$\Delta\Delta S$ (J/(mol K))	$\Delta\Delta G$ (kJ/mol)
5	29.0	2.0	126.4	–19.8	–8.6	7.9	27.0	146.2	–16.5
6	37.2	–1.6	124.0	–7.8	0.2	0.7	38.8	131.8	–0.5
7	42.2	–1.9	106.2	–18.1	10.5	3.5	44.1	124.3	7.0
8	56.4	–2.0	95.9	–17.3	27.8	3.2	58.4	113.2	24.6
9	37.5	–1.8	85.1	–17.8	12.1	3.5	39.3	102.9	8.6
10	30.4	—	73.8	—	8.4	—	—	—	—
11	29.6	—	74.0	—	7.5	—	—	—	—
12	12.3	—	66.9	—	–7.7	—	—	—	—

**Fig. 3.**  $\Delta H_{\text{RCM}}$  vs ring size for the HF/6–31G(d) (blue), B3LYP/6–31G(d) (red), and MP2(full)/6–31G(d) (green) levels of theory. The 5- to 11-membered ( $n = 0$ –6) ring cases agree very well with the  $\Delta H_{\text{RCM}}^{\#}$  values (black) determined experimentally by Illuminati and Mandolini<sup>18</sup> for the saturated analogues of the R-but-3-enoate esters considered here. The gap between  $\Delta H_{\text{RCM}}^{\#}$  and  $\Delta H_{\text{RCM}}$  remains roughly consistent for the smaller systems, hence, thermodynamics can be used to model the kinetically controlled reaction. However, for systems larger than the 11-membered ring ( $n > 6$ ), the agreement becomes much poorer, implying that the reaction has a stronger kinetic bias and that the predictive ability of thermodynamic data becomes very limited.



## Results

### Conformer geometries

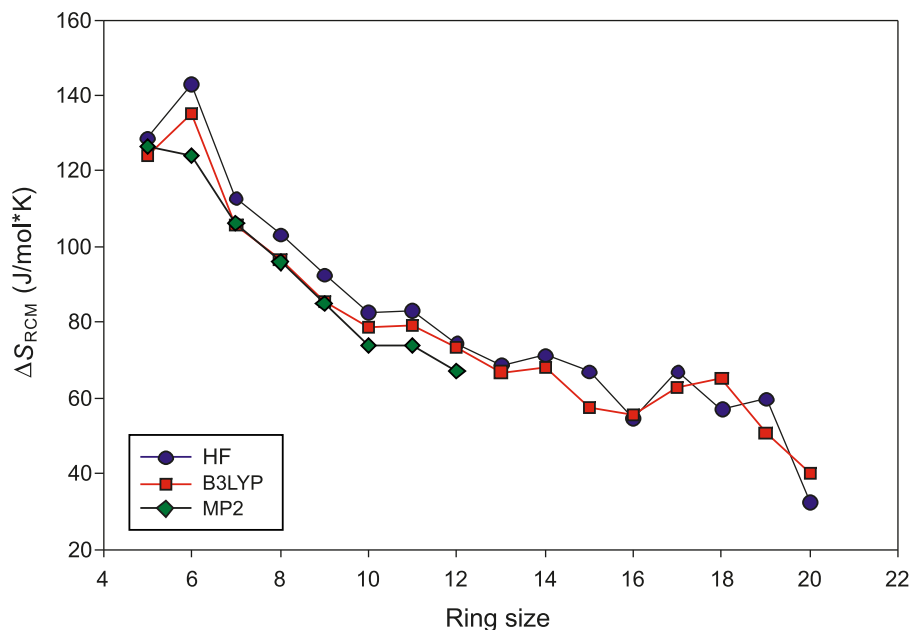
The lowest energy geometries of the monomer, dimer, and lactone compounds for the 16 R-but-3-enoate ester systems were initially determined at the HF/STO–3G level of theory. The method used to distinguish each structure is given in Fig. 1, and a legend summarizing the systems of interest is given in Table 1. The geometries (defined by dihedral angles) and relative energies of each conformer can be found in the Supplementary data. The lowest energy HF/STO–3G structures were then further refined at the B3LYP/6–31G(d) and MP2(full)/6–31G(d) levels of theory. The B3LYP/6–31G(d) theoretical structures for the  $n = 0$  case are shown in Fig. 2, whereas the remaining B3LYP/6–31G(d) lowest energy geometries are also available in the Supplementary data.

The computational data appears to agree with the assump-

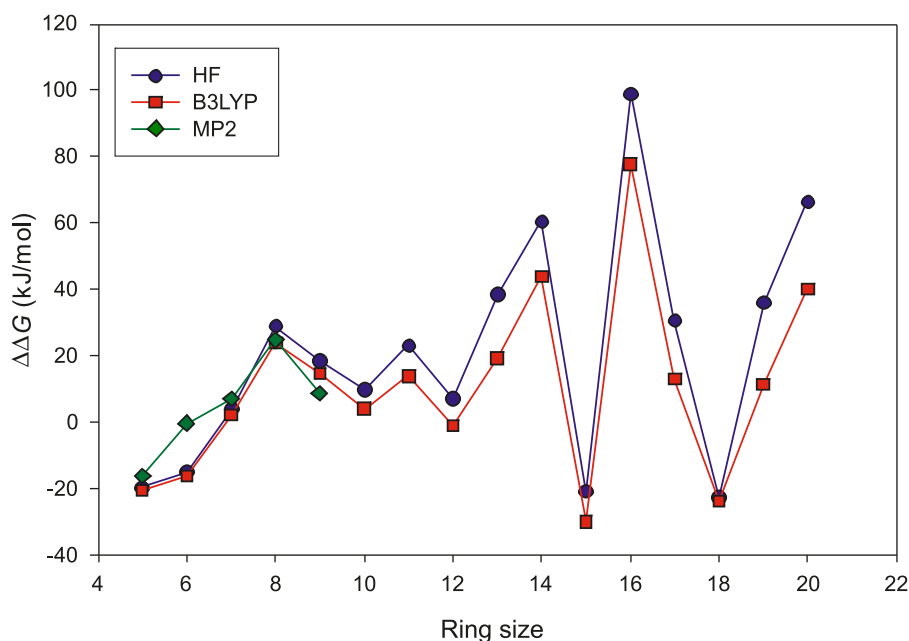
tion that the smaller monomers and dimers ( $n = 0 - 7$ ) will prefer straight-chain conformations; and this behaviour is consistent across all levels of theory. In the larger substrates ( $n = 8 - 15$ ), all monomers were also linear, however the lowest energy dimer geometries for the  $n = 8, 9, 12$ , and 14 cases exhibited a small bend around the ester moiety at the center of the dimer. The increased availability of conformational space in these larger dimers likely allows for more flexibility, hence the straight-chain assumption becomes less realistic as the substrate chain length increases. For each lactone, the cis-ring conformer was determined to be the most stable. This trend carried through all the systems considered except the 12-membered ring in the  $n = 7$  case, where the trans conformer appeared to be far more stable. This result is not entirely unexpected, as it has been shown experimentally that macrocyclic ring closures prefer to form the trans-conformer.<sup>4</sup>



**Fig. 4.**  $\Delta S_{\text{RCM}}$  vs ring size for the HF/6–31G(d) (blue), B3LYP/6–31G(d) (red), and MP2(full)/6–31G(d) (green) levels of theory. The overall trend is for  $\Delta S_{\text{RCM}}$  to decrease as ring size increases. See Fig. 3 for colour legend.



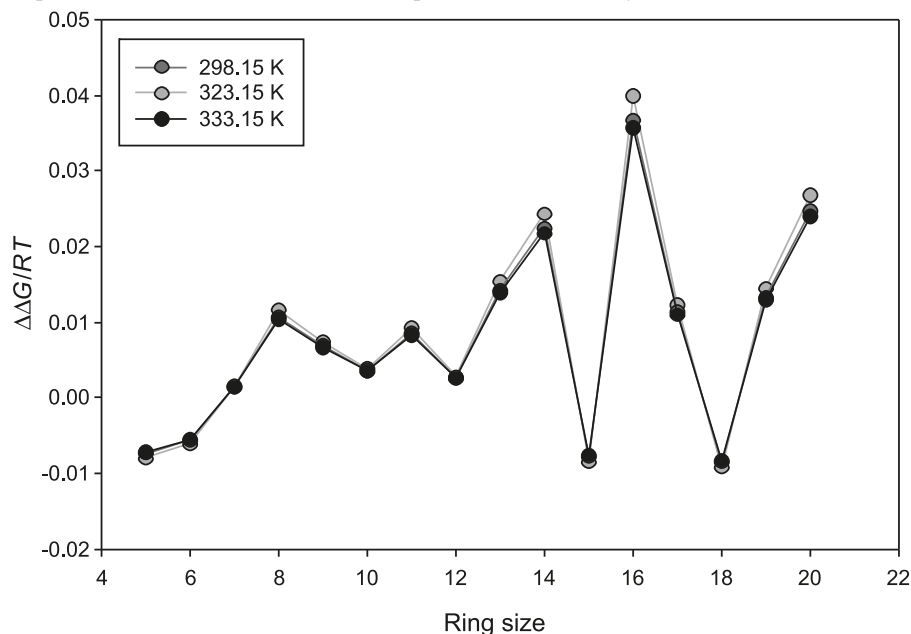
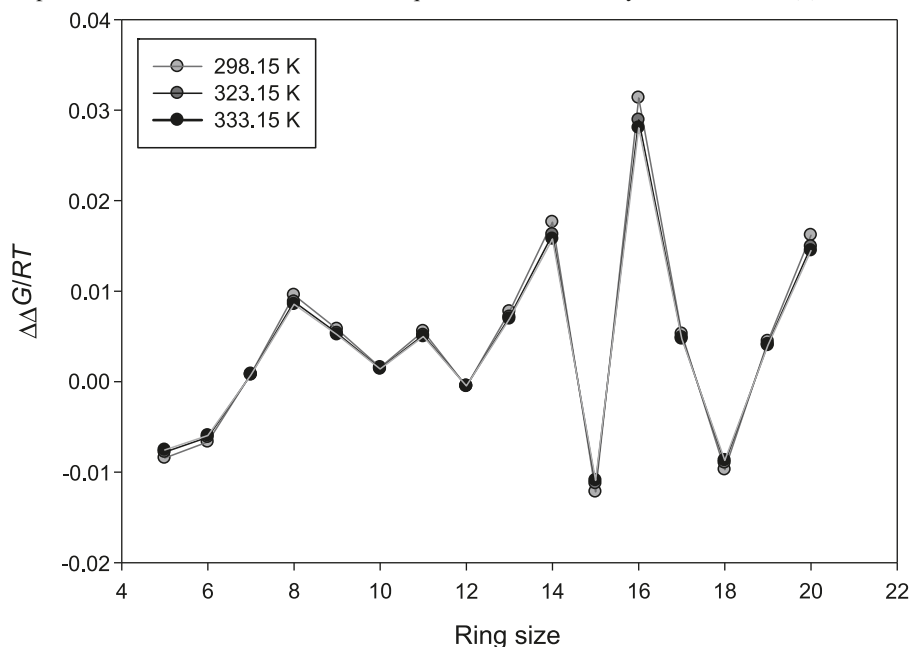
**Fig. 5.**  $\Delta\Delta G$  ( $\Delta G_{\text{RCM}} - \Delta G_{\text{ADMET}}$ ) (kJ/mol) vs ring size at the HF/6–31G(d) (blue), B3LYP/6–31G(d) (red), and MP2(full)/6–31G(d) (green) levels of theory.  $\Delta\Delta G$  data can be found in Tables 2–4. The indirect pathway is followed for the majority of systems, however, direct RCM predominates in the formation of the 5-, 6-, 15-, and 18-membered lactones ( $n = 0, 1, 10,$  and  $13,$  respectively). See Fig. 3 for colour legend.



### Thermochemistry

The results for the RCM and ADMET reaction enthalpies, entropies, and free energies for the HF/6–31G(d), B3LYP/6–31G(d), and MP2(full)/6–31G(d) levels of theory are given in Tables 2–4, respectively. There are no significant deviations between the HF, B3LYP, and MP2 results; each theory predicts the same trend. In general, MP2 predicts the lowest values for  $\Delta H_{\text{RCM}}$  and  $\Delta S_{\text{RCM}}$ , while B3LYP and HF return slightly higher energy differences. The data in Tables 2–4 is

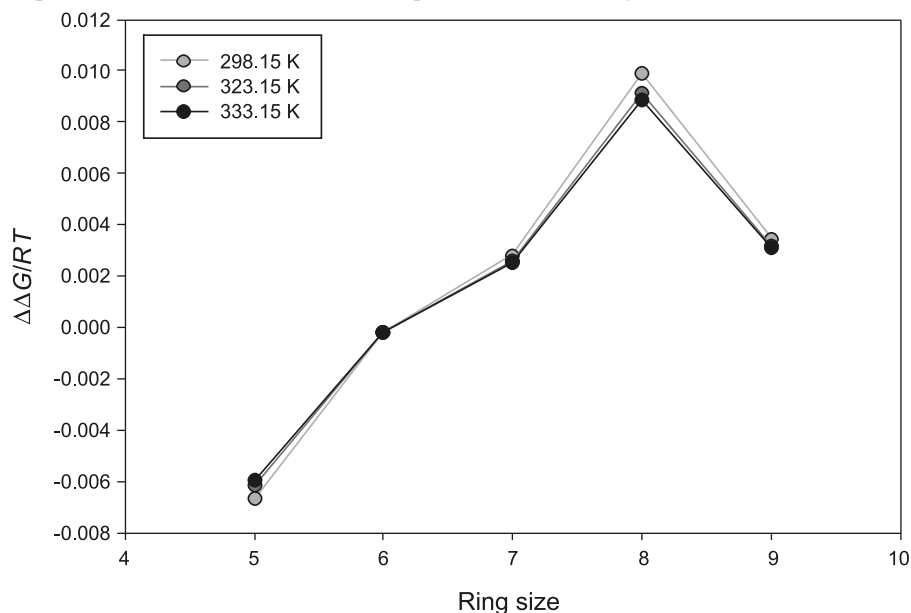
best seen as a function of lactone size (Figs. 3 and 4). It can be seen that the formation of 5- and 6-membered rings ( $n = 0$  and  $1$ , respectively) is more enthalpically favourable than the formation of larger lactones, whereas the 8-, 14-, and 16-membered rings ( $n = 3, 9,$  and  $11$ , respectively) are particularly unfavourable. The 8-membered lactone was predicted to be more stable than the 14- and 16-membered rings; however, it should be noted that to the best of the authors' knowledge, this cyclic product has never been experimen-

**Fig. 6.** The temperature dependence of the RCM and ADMET equilibria determined by HF/6–31G(d).**Fig. 7.** The temperature dependence of the RCM and ADMET equilibria determined by B3LYP/6–31G(d).

tally produced, whereas larger macrocycles are known to be accessible.<sup>1–3,18</sup> As was mentioned in the discussion of the conformer geometries, the discrepancy in the  $n = 9$  and 11 cases likely arises from the assumption that the larger monomer substrates prefer linear orientations. Hence, conformer flexibility should be more extensively examined to further refine the predictive power of this methodology.

The predicted dependence of  $\Delta H_{\text{RCM}}$  (Fig. 3) and  $\Delta S_{\text{RCM}}$  (Fig. 4) on ring size resembles trends characterized by Illuminati and Mandolini<sup>18</sup> for a saturated analogue of the system reported here. The formation of lactones is computed to be endothermic in all cases; lactone formation for the 5-, 6-, and 12-membered systems ( $n = 0, 1$ , and 7, respectively) re-

quires the lowest enthalpy cost, whereas the 8-membered lactone ( $n = 3$ ) and systems greater than  $n = 8$  are the least enthalpically favoured out of all the ring structures. Interestingly, computed  $\Delta H_{\text{RCM}}$  values have a comparable trend to the  $\Delta H_{\text{RCM}}^{\ddagger}$  behaviour reported by Illuminati and Mandolini<sup>18</sup> for a homologous series of saturated R-but-3-enoate esters. The agreement is only noticeable for small systems ( $n = 0–6$ ), implying that in these reactions experimental products were likely thermodynamic rather than kinetic. The consistent energy gap between the predicted  $\Delta H_{\text{RCM}}$  and experimental  $\Delta H_{\text{RCM}}^{\ddagger}$  values for the 5- to 11-membered rings further suggests that thermochemistry can adequately be used to approximate the kinetically controlled RCM reac-

**Fig. 8.** The temperature dependence of the RCM and ADMET equilibria determined by MP2(full)/6–31G(d).

tion for smaller substrates. However, at larger ring sizes, experimental agreement is much poorer, reflecting both that large systems have a strong kinetic bias and that the assumption of the conformers existing as straight chains is invalid for longer chains, which have more available conformational degrees of freedom. Encouragingly, despite the discrepancies at larger ring sizes, the positions of relative maxima (the 8- and 16-membered ring systems) and minima (the 5-membered ring system) in the  $\Delta H_{\text{RCM}}$  profile correspond reasonably well with the experimental results.

In analyzing the entropy results (Fig. 4), we can see that except for small increases in the 6- and 11-membered lactones ( $n = 1$  and 6, respectively), entropy change generally decreases as ring size increases. The maximum  $\Delta S_{\text{RCM}}$  occurs in the 6-membered lactone, and then steadily decreases with increasing ring size. This makes sense considering 5-membered lactones are subject to more ring strain and because it would be more difficult for longer chains to orient themselves in an appropriate way for ring closure to occur. In every case, the largest contribution to the reported entropies is vibrational. The  $\Delta S_{\text{RCM}}$  trend is very similar to the  $\Delta S_{\text{RCM}}^{\ddagger}$  behaviour reported by Illuminati and Mandolini;<sup>18</sup> both data series generally decrease as ring size increases, and the energy gap between the two sets of data is consistently about 0.3 kJ/(mol K).

For smaller substrates, the predictive ability of thermochemical data is clear. However, for larger systems ( $n > 6$ ), deviations from experimental kinetic data become more noticeable, implying that our assumptions need to be further refined; particularly the one pertaining to chain flexibility.

### Thermodynamic evaluation of the ADMET and RCM competition

$\Delta G_{\text{RCM}}$  and  $\Delta G_{\text{ADMET}}$  were determined from computed data and used to construct a thermodynamic profile of  $\Delta\Delta G$  against ring size (Fig. 5). This data indicates that ring formation by direct RCM only predominates in the 5-, 6-, 15-, and 18-membered lactones ( $n = 0, 1, 10$ , and 13, re-

spectively). In all other cases, indirect ring closure is the preferred pathway; although in the  $n = 7$  case, the HF and B3LYP theories disagree as to which pathway is preferred. HF/6–31G(d) predicts that the dimer will form preferentially while B3LYP/6–31G(d) suggests the opposite (+7.0 kJ/mol compared with –1.3 kJ/mol, respectively). The predictions taken from the thermodynamic profile correspond to similar experimental kinetic results,<sup>18</sup> although there are significant deviations for systems larger than  $n = 6$ , in particular for the  $n = 10, 11$ , and 13 cases. This implies that the predictive ability of computed thermodynamic data towards competing metathesis reactions is limited to at best small systems. We have not directly considered the CDP step, yet have found evidence that this pathway should be commonly involved in macrocycle formation because of the strong preference seen by these ester substrates to polymerize instead of ring close by RCM.

### Temperature dependence

The thermodynamic properties of the monomer, dimer, and ring structures were further explored by altering their temperature. The ab initio results accounted for a temperature of 298.15 K, but Illuminati and Mandolini's<sup>18</sup> experimental results were carried out at 323.15 K and contemporary RCM reactions are normally promoted at 333.15 K.<sup>6</sup> Therefore, the temperatures of these latter cases were considered at the different levels of theory used to see if agreement between experiment and computation improved (Figs. 6–8). Clearly, over the experimental temperature ranges considered, the ring-chain equilibrium should only be marginally affected. However, this conflicts with recent work by Danishefsky and co-workers,<sup>8</sup> which noted that increasing the reaction temperature yields more macrocycles. This discrepancy with the thermodynamic approach is not surprising, since the olefin metathesis pathways display a strong kinetic bias. Hence, although this thermodynamic approach is sufficient to determine the proclivity of a R-but-3-enoate ester to follow the direct or indirect ring-closure

pathways, it does not adequately predict the temperature dependence of the product distribution.

## Conclusions

Thermochemical data for the simultaneous RCM and ADMET processes were determined using electronic structural calculations and used to assess the relative product formation by analyzing  $\Delta\Delta G$ . In the homologous series of R-but-3-enoate esters, direct RCM is only preferential for the 5-, 6-, 15-, and 18-membered cases ( $n = 0, 1, 10$ , and 13, respectively); in every other system, indirect ring closure was favoured. Polymerization was especially dominant in the cases where  $n = 3, 6, 9, 11$ , or 15. Our methodology assumed the following: that the polymer formation never extended to trimers or oligomers and that the lowest energy structures were always cis-conformer rings or straight-chain monomers and dimers. Whereas the first assumption makes sense from a computational perspective, clearly our predictions will not correspond totally with reality, since we are entirely ignoring oligomer formations. Furthermore, as a consequence of assuming linearity in the monomers and dimers, substantial deviation from reported behaviour was noted for the larger systems;<sup>18</sup> bent conformers may be lower in energy, especially structures where the olefinic bond is capable of interacting with the chain. In ring systems containing more than 11 members ( $n > 6$ ), the data appears to vary markedly in its preference for direct or indirect ring closure. However, it is also possible that the metathesis reactions involving large substrates are kinetically controlled, and hence the predictive power of thermodynamics will be limited to the smaller substrates. Therefore, if our model were improved to account for greater chain flexibility in the larger oligomer systems, there appears to be no great obstacle in using thermodynamic data derived from lowest energy geometries as a predictive tool for predicting whether or not ring closure will occur by the direct RCM or indirect ADMET routes, so long as the reaction system considered is governed primarily by thermodynamic considerations rather than kinetics. However, it should be stressed that predicting the temperature dependence of this ring-chain product distribution is unfeasible. The temperature dependence of the competing metathesis reactions was shown to be thermodynamically negligible over the range of temperatures suitable for laboratory work with RCM and ADMET processes; however, this conflicts with experimental reports due to the kinetic bias of this system.<sup>8</sup> Therefore, the overall predictive power of this approach is limited to reactions where the product distribution is not strictly controlled by kinetic effects.

## Supplementary data

Supplementary data for this article are available on the journal Web site (canjchem.nrc.ca).

## Acknowledgements

The authors would like to acknowledge both the Atlantic Computational Excellence Network (ACENet) and Westgrid for providing excellent computational resources. M. Staveley and L. Thompson are recognized for their instruction and suggestions.

## References

- (1) Nicolaou, K. C.; Bulger, P. G.; Sarlah, D. *Angew. Chem. Int. Ed.* **2005**, 44 (29), 4490. doi:10.1002/anie.200500369.
- (2) Fürstner, A. *Angew. Chem. Int. Ed.* **2000**, 39 (17), 3012. doi:10.1002/(SICI)1521-3773(20000403)39:7<1234::AID-ANIE1234>3.0.CO;2-V.
- (3) Gradillas, A.; Pérez-Castells, J. *Angew. Chem. Int. Ed.* **2006**, 45 (37), 6086. doi:10.1002/anie.200600641.
- (4) Lee, C. W.; Grubbs, R. H. *Org. Lett.* **2000**, 2 (14), 2145. doi:10.1021/ol006059s. PMID:10891252.
- (5) Conrad, J. C.; Eelman, M. D.; Silva, J. A. D.; Monfette, S.; Parnas, H. H.; Snelgrove, J. L.; Fogg, D. E. *J. Am. Chem. Soc.* **2007**, 129 (5), 1024. doi:10.1021/ja067531t. PMID:17263371.
- (6) Correa, A.; Cavallo, L. *J. Am. Chem. Soc.* **2006**, 128 (41), 13352. doi:10.1021/ja064924j. PMID:17031936.
- (7) Monfette, S.; Crane, A. K.; Duarte Silva, J. A.; Facey, G. A.; dos Santos, E. N.; Araujo, M. H.; Fogg, D. E. *Inorg. Chim. Acta* **2010**, 363 (3), 481. doi:10.1016/j.ica.2009.09.030.
- (8) Yamamoto, K.; Biswas, K.; Gaul, C.; Danishefsky, S. J. *Tetrahedron Lett.* **2003**, 44 (16), 3297. doi:10.1016/S0040-4039(03)00618-X.
- (9) Kirkland, T. A.; Grubbs, R. H. *J. Org. Chem.* **1997**, 62 (21), 7310. doi:10.1021/jo970877p. PMID:11671845.
- (10) Ghosh, S.; Ghosh, S.; Sarkar, N. J. *Chem. Sci.* **2006**, 118 (3), 223. doi:10.1007/BF02708281.
- (11) Shu, C.; Zeng, X.; Hao, M. H.; Wei, X.; Yee, N. K.; Busacca, C. A.; Han, Z.; Farina, V.; Senanayake, C. H. *Org. Lett.* **2008**, 10 (6), 1303. doi:10.1021/ol800183x. PMID:18293994.
- (12) Kamau, S. D.; Hodge, P.; Hall, A. J.; Dad, S.; Ben-Haida, A. *Polymer (Guildf.)* **2007**, 48 (23), 6808. doi:10.1016/j.polymer.2007.09.014.
- (13) Tastard, C. Y.; Hodge, P.; Ben-Haida, A.; Dobinson, M. *React. Funct. Polym.* **2006**, 66 (1), 93. doi:10.1016/j.reactfunctpolym.2005.07.010.
- (14) Hodge, P.; Kamau, S. D. *Angew. Chem. Int. Ed.* **2003**, 42 (21), 2412. doi:10.1002/anie.200250842.
- (15) Zuercher, W. J.; Hashimoto, M.; Grubbs, R. H. *J. Am. Chem. Soc.* **1996**, 118 (28), 6634. doi:10.1021/ja9606743.
- (16) Prunet, J. *Angew. Chem. Int. Ed.* **2003**, 42 (25), 2826. doi:10.1002/anie.200301628.
- (17) Grubbs, R. H. *Handbook of Metathesis*; Wiley-VCH: Weinheim, Germany, 2003.
- (18) Illuminati, G.; Mandolini, L. *Acc. Chem. Res.* **1981**, 14 (4), 95. doi:10.1021/ar00064a001.
- (19) Illuminati, G.; Mandolini, L.; Masci, B. *J. Am. Chem. Soc.* **1977**, 99 (19), 6308. doi:10.1021/ja00461a021.
- (20) Galli, C.; Mandolini, L. *Eur. J. Org. Chem.* **2000**, 3117. doi:10.1002/1099-0690(200009)2000:18<3117::AID-EJOC3117>3.0.CO;2-5.
- (21) Musaev, D. G.; Mebel, A. M.; Morokuma, K. *J. Am. Chem. Soc.* **1994**, 116 (23), 10693. doi:10.1021/ja00102a039.
- (22) Handzlik, J. J. *PhysChemComm* **2007**, 111, 9337.
- (23) Cundari, T. R.; Gordon, M. S. *Organometallics* **1992**, 11 (1), 55. doi:10.1021/om00037a017.
- (24) Benitez, D.; Goddard, W. A., III. *J. Am. Chem. Soc.* **2005**, 127 (35), 12218. doi:10.1021/ja051796a. PMID:16131188.
- (25) Rappé, A. K.; Goddard, W. A. *J. Am. Chem. Soc.* **1982**, 104 (2), 448. doi:10.1021/ja00366a013.
- (26) Ercolani, G.; Mencarelli, P. J. *Chem. Soc., Perkin Trans. 2* **1989**, 187. doi:10.1039/P29890000187.
- (27) Chen, Z.-R.; Claverie, J. P.; Grubbs, R. H.; Kornfield, J. A.



- Macromolecules* **1995**, 28 (7), 2147. doi:10.1021/ma00111a007.
- (28) Kapteijn, F.; Homburg, E.; Mol, J. C. *J. Chem. Thermodyn.* **1983**, 15 (2), 147. doi:10.1016/0021-9614(83)90153-2.
- (29) Gutierrez, S.; Fulgencio, A.; Tlenkopatchev, M. A. *J. Chem. Thermodyn.* **2006**, 38 (4), 383. doi:10.1016/j.jct.2005.06.004.
- (30) Litinas, K. E.; Salteris, B. E. *J. Chem. Soc., Perkin Trans. I* **1997**, 2869. doi:10.1039/a702353g.
- (31) Goldring, W. P. D.; Hodder, A. S.; Weiler, L. *Tetrahedron Lett.* **1998**, 39 (28), 4955. doi:10.1016/S0040-4039(98)00966-6.
- (32) Pentzer, E. B.; Gadzikwa, T.; Nguyen, S. T. *Org. Lett.* **2008**, 10 (24), 5613. doi:10.1021/ol8022227. PMID:19053741.
- (33) Frisch, M. J.; Trucks, G. W.; Schlegel, H. B.; Scuseria, G. E.; Robb, M. A.; Cheeseman, J. R.; Montgomery, J. A., Jr.; Vreven, T.; Kudin, K. N.; Burant, J. C.; Millam, J. M.; Iyengar, S. S.; Tomasi, J.; Barone, V.; Mennucci, B.; Cossi, M.; Scalmani, G.; Rega, N.; Petersson, G. A.; Nakatsuji, H.; Hada, M.; Ehara, M.; Toyota, K.; Fukuda, R.; Hasegawa, J.; Ishida, M.; Nakajima, T.; Honda, Y.; Kitao, O.; Nakai, H.; Klene, M.; Li, X.; Knox, J. E.; Hratchian, H. P.; Cross, J. B.; Bakken, V.; Adamo, C.; Jaramillo, J.; Gomperts, R.; Stratmann, R. E.; Yazyev, O.; Austin, A. J.; Cammi, R.; Pomelli, C.; Ochterski, J. W.; Ayala, P. Y.; Morokuma, K.; Voth, G. A.; Salvador, P.; Dannenberg, J. J.; Zakrzewski, V. G.; Dapprich, S.; Daniels, A. D.; Strain, M. C.; Farkas, O.; Malick, D. K.; Rabuck, A. D.; Raghavachari, K.; Foresman, J. B.; Ortiz, J. V.; Cui, Q.; Baboul, A. G.; Clifford, S.; Cioslowski, J.; Stefanov, B. B.; Liu, G.; Liashenko, A.; Piskorz, P.; Komaromi, I.; Martin, R. L.; Fox, D. J.; Keith, T.; Al-Laham, M. A.; Peng, C. Y.; Nanayakkara, A.; Challacombe, M.; Gill, P. M. W.; Johnson, B.; Chen, W.; Wong, M. W.; Gonzalez, C.; Pople, J. A. *Gaussian 03*, revision D.02; Gaussian, Inc.: Wallingford, CT, 2004.

# A water potential based on multipole moments trained by machine learning — Reducing maximum energy errors

Glenn I. Hawe and Paul L.A. Popelier

**Abstract:** A potential that strives to represent the Coulomb interaction realistically must include polarization. In our approach, three decisions were made to accomplish this: (i) define an atom according to quantum chemical topology (QCT), (ii) express the interaction between atoms via their multipole moments, and (iii) use machine learning to capture the response of an atomic multipole moment to a change in this atom's environment. This approach avoids explicit (distributed) polarizabilities and eliminates the problem of polarization catastrophe. Previously, we showed (*Phys. Chem. Chem. Phys.* **2009**, *11*, 6365) that a machine learning method called kriging predicted atomic multipole moments more accurately than competing machine learning methods. This was established for the atoms of a central water molecule in water clusters, from the dimer to the hexamer. The prediction errors in all multipole moments were collectively assessed by errors in total interaction energy, for thousands of clusters configurations. Here, we target the maximum errors, with an eye on reducing the worst predictions that the potential may return. We demonstrate proof-of-principle for the water dimer using local kriging.

**Key words:** quantum chemical topology (QCT), atoms in molecules, kriging, water dimer, polarization, machine learning, force field.

**Résumé :** Un potentiel qui tend à représenter d'une façon réaliste l'interaction de Coulomb doit inclure une polarisation. Dans l'approche présentée ici, on prend trois décisions pour y arriver : (i) on définit un atome suivant la topologie de la chimie quantique (TCQ), (ii) on exprime l'interaction entre les atomes par le biais de leurs moments multipolaires et (iii) et on utilise une machine qui apprend à capturer la réponse d'un moment multipolaire atomique à un changement dans l'environnement de cet atome. Cette approche évite les polarisabilités distribuées d'une façon explicite et élimine le problème de la catastrophe de polarisation. On a démontré antérieurement (*Phys. Chem. Chem. Phys.* **2009**, *11*, 6365) qu'une méthode à base d'une machine qui apprend à capturer une réponse, appelée kriging, permet de prédire les moments multipolaires atomiques d'une façon plus précise que les méthodes faisant appel à d'autres machines qui apprennent à capturer une réponse. Cette conclusion a été établie pour les atomes d'une molécule d'eau centrale d'agrégats d'eau allant du dimère à l'hexamère. Les erreurs de prédictions dans tous les moments multipolaires ont été évalués collectivement par les erreurs dans l'énergie d'interaction totale pour des milliers de configurations d'agrégats. Dans le présent travail, on s'adresse aux erreurs maximales dans le but de réduire les plus mauvaises prédictions qui peuvent être faites pour le potentiel. On établit le principe de preuve pour le dimère de l'eau à l'aide de la machine kriging locale.

**Mots-clés :** topologie de chimie quantique (TCQ), atomes dans les molécules, kriging, dimère de l'eau, polarisation, machine à apprendre, champ de force.

[Traduit par la Rédaction]

## Introduction

Unless computing power surges by a dramatic and unexpected technological leap, using force fields will be the only option to run long simulations of sizeable molecular systems for many years to come. Many systems, even non-biological ones, involve water and therefore water force fields are very important. Several popular water force fields have been developed over the decades, such as the transfer-

able interaction potential (TIPnP;  $n = 3, 4, 5$ ) series<sup>1–3</sup> or the simple point charge (SPC) series of models.<sup>4</sup> The simplest water models represent the electron density of water via atomic point charges, one charge per nuclear site. A more realistic description warrants extra point charges, this time not centered on the nuclear position. This is why potentials with as many as three off-nuclear charges on oxygen have been constructed. Such potential was shown<sup>5</sup> to be much more suitable than the TIP4P and TIP5P models for the sim-

Received 2 January 2010. Accepted 20 April 2010. Published on the NRC Research Press Web site at [canjchem.nrc.ca](http://canjchem.nrc.ca) on 27 October 2010.

This article is part of a Special Issue dedicated to Professor R. J. Boyd.

**G.I. Hawe and P.L. Popelier.**<sup>1</sup> Manchester Interdisciplinary Biocentre (MIB), 131 Princess Street, Manchester M1 7DN, UK; School of Chemistry, University of Manchester, Oxford Road, Manchester M13 9PL, UK.

<sup>1</sup>Corresponding author (e-mail: [pla@manchester.ac.uk](mailto:pla@manchester.ac.uk)).

ulations of ice and water near melting point. An alternative path to represent electron density more realistically is through multipole moments.<sup>6</sup> Dipole, quadrupole, and higher-rank moments, while all centered on the nucleus, capture important nonspherical features of the electron density. The formulae<sup>7,8</sup> expressing interactions between atomic multipole moments are more complicated than the formula for interaction between atomic point charges. This complexity leads to an increase in floating point operations that a computer must carry out to evaluate the electrostatic energy between two atoms. However, this increase is more pronounced the shorter the range of atomic interaction. High-rank multipolar interaction is known to decrease quickly with interatomic distance,  $R$ , because it obeys a high inverse-power law. For example, interaction energy between two quadrupole moments drops off as  $R^{-5}$ . Hence, the increase in computational cost due to multipole moments is only local. In contrast, the cost of evaluating interaction energies between point charges perpetuates as the system grows in size. This is because charge–charge interactions are long-range. The proliferation of point charges introduced by more accurate point charge models therefore causes a substantial increase in computational cost.

There are various ways in which atomic multipole moments can be defined and used.<sup>9–11</sup> A popular and influential method is called distributed multipole analysis (DMA).<sup>7</sup> The Anisotropic site potential or Anthony Stone potential (ASP) water potential,<sup>12</sup> the atomic multipole optimized energetics for biomolecular applications (AMOEBA)<sup>13</sup> water model, and the effective fragment potential (EFP) method,<sup>14</sup> for example, all use DMA. However, the sum of interactions between fragments *ab initio* (SIBFA)<sup>15,16</sup> potential has its multipole moments determined by the partitioning method of Vigné-Maeder and Claverie.<sup>17</sup>

A further enhancement of realism in potential design comes from the inclusion of polarization. There is a vast literature on this topic and water has received probably more attention than any other molecule. As recently as 2007, a whole issue<sup>18</sup> of the *Journal of Chemical Theory and Computation* was dedicated to polarization. A simple way to account for the polarization of a water molecule in liquid water is to artificially enhance its dipole moment beyond its gas phase value of 1.85 D. The exact value to which the enhanced dipole moment should be fixed remains a topic of debate<sup>19–22</sup> and can vary between 2.3 and 3.1 D. This debate is fuelled by the uncertainty surrounding an answer to the question of how to define a water molecule inside the condensed phase that is a liquid. If one allows quantum chemical topology (QCT)<sup>23,24</sup> to answer this question then one obtains<sup>25</sup> about 2.3 D. This is actually a dipole moment averaged over the order of a hundred water clusters. The actual value depends on the level of theory at which the *ab initio* electron densities were obtained and the number of water molecules in the cluster. Water on surfaces, at interfaces or in very polar environments, however, needs a non-averaged treatment. To account for the response of water in such heterogeneous conditions, an anisotropic polarization needs to be modelled. This makes nonpolarizable models with implicit polarization, such as SPC/E and TIP4P, only accurate for bulk water and unfit for water in heterogeneous conditions. It is generally agreed that polarization needs to

be modelled *explicitly* for more accurate, transferable, potentials. Polarization can also be modelled by polarizable point dipoles but this method can suffer from the “polarization catastrophe”. In that case, the dipoles respond in such a way that the interaction energy becomes infinite. Damping functions, artificial corrections that limit the response of the dipole moments,<sup>26,27</sup> can prevent this catastrophe. A number of force fields<sup>13,15,28–31</sup> have adopted the popular point dipole method. A final method is the charge-on-spring method.<sup>32–35</sup> Here, polarization is modelled by a negative point charge connected by a harmonic spring to another site that bears a positive charge.

Within the context of multipole moments of arbitrarily high rank, one could proceed with distributed polarizabilities, either in the DMA framework<sup>36</sup> or the QCT framework,<sup>37</sup> as applied to the water dimer before.<sup>38</sup> In this paper, however, we pursue a radically alternative route, and focus directly on an atom’s response to its local environment. Machine learning is invoked to establish a link between the nuclear positions of the atoms surrounding a given (central) atom and this atom’s multipole moments. This approach does not yield polarizabilities; instead, polarization is embedded in the mapping of nuclear positions (input) and atomic multipole moments (output), delivered by the machine learning solution. Preliminary work on the hydrogen fluoride dimer<sup>39</sup> led to a more refined methodology able to construct a polarizable water potential.<sup>40</sup> Intramolecular polarization was tackled along similar lines in subsequent work,<sup>41</sup> demonstrating proof-of-concept with glycine and *N*-methylacetamide, the smallest molecule realistically representing a peptide bond. The water potential, constructed using multilayer perceptrons, was then revisited<sup>42</sup> using a more accurate machine learning method called kriging. Kriging<sup>43</sup> (also known as Gaussian process regression<sup>44</sup>) models observations as realizations of an underlying probabilistic model. A typical kriging model predicts an error in total interaction energy of less than 0.4 kJ/mol for 50% of about a thousand water dimer configurations. Although 90% of the configurations are predicted with an error of less than 1 kJ/mol, the maximum error encountered can be as large as 4 kJ/mol, albeit for a handful of configurations. This paper tackles the latter problem by introducing local kriging.<sup>45</sup>

## Background

### Quantum chemical topology and electrostatics

The molecular electron density, denoted by  $\tilde{n}$ , is partitioned according to its gradient vector field, as prescribed by the quantum chemical topology (QCT) approach.<sup>23,24,46</sup> A justification for the relatively new name QCT was first given in ref. 47 and amplified in a book chapter,<sup>48</sup> the Appendix of ref. 49, and the Introduction of ref. 50. QCT defines topological atoms as 3D volumes, whose shape is determined by the gradient paths in  $\tilde{n}$ . A gradient path follows the direction of steepest ascent in  $\tilde{n}$ , typically terminating at a nuclear position, where  $\tilde{n}$  is a maximum. A 2D bundle of gradient paths form an interatomic surface that marks the boundary between two atoms. An important characteristic of topological atoms is that they collectively take up all space, without leaving gaps between them. Integration

of property densities over an atomic volume yields the atomic properties. An atomic multipole moment is obtained from a volume integral over  $\tilde{n}$  multiplied by a regular spherical harmonic. Note that we do not use Cartesian tensors because they lead to an excess of redundant components.

Equation [1] expresses the electrostatic interaction energy between two topological atoms:<sup>51</sup>

$$[1] \quad E^{AB} = \sum_{l_A=0}^{\infty} \sum_{l_B=0}^{\infty} \sum_{m_A=-l_A}^{l_A} \sum_{m_B=-l_B}^{l_B} T_{l_A m_A l_B m_B}(\mathbf{R}) Q_{l_A m_A}(\Omega_A) \times Q_{l_B m_B}(\Omega_B)$$

where the multipole moments of atom A,  $Q_{l_A m_A}(\Omega_A)$ , and atom B,  $Q_{l_B m_B}(\Omega_B)$ , interact through the tensor  $\mathbf{T}(\mathbf{R})$ .  $\mathbf{R}$  is the vector from nucleus A to nucleus B, which are the origins of the local frames of atoms A and B. It is convenient to collect the terms of eq. [1] by their power of  $R = |\mathbf{R}|$ , gathering terms of the same (overall) rank. This rank, denoted by  $L$ , is defined as  $\ell_A + \ell_B + 1$ , where  $\ell$  is the rank of the multipole moment. For example, multipolar interaction of  $R^{-5}$  dependence consists of interactions between a monopole moment ( $\ell = 0$ ) and an hexadecapole moment ( $\ell = 4$ ), a dipole moment ( $\ell = 1$ ) and an octupole moment ( $\ell = 3$ ) and two quadrupole moments ( $\ell = 2$ ). The convergence of the multipole expansion can be examined<sup>52</sup> as a function of  $L$ .

### Kriging

Here, we only summarize the salient features of the kriging approach and more details can be found in ref. 42. In our case, the observations that the kriging method models are values of a particular multipole moment. A *probability density function* (PDF) returns the probability of observing a set of values of a particular multipole moment. The following general equation is used for making predictions:

$$[2] \quad y(\mathbf{x}) = \sum_{i=1}^m \beta_i f_i(\mathbf{x}) + z(\mathbf{x})$$

where the vector  $\mathbf{x} = [x_1, x_2, \dots, x_d]^T$  and where T designates the transpose and  $d$  the number of features. In this work, the features are geometrical coordinates of the nuclei surrounding the central atom of interest, whose multipole moments are being predicted. The right hand side of eq. [2] consists of two parts. The first part is a “global term”, which is a sum of  $m$  basis functions,  $f_i$  ( $i = 1, \dots, m$ ), which are typically polynomials of the form  $x_1^{g_1} x_2^{g_2} \dots x_d^{g_d}$  with  $g_1 + g_2 + \dots + g_d \leq G$  ( $G$  being the order of the polynomial). The number of features in the problem,  $d$ , determines the exact value of  $m$ . The second part of eq. [2],  $z(\mathbf{x})$ , can be regarded as an “error term”. This term compensates for the inadequacy of the global term to model observed data exactly. This term is modelled as a Gaussian process with a zero mean and some unknown variance,  $\sigma^2$ . The error terms for two different molecules are modelled as being correlated in a way that may be expressed through the difference in the values of their features. A familiar correlation function is given in eq. [3]

$$[3] \quad \text{Cor}[z(\mathbf{x}^i), z(\mathbf{x}^j)] = \exp\left(-\sum_{h=1}^d \theta_h |x_h^i - x_h^j|^{p_h}\right)$$

where  $\theta_h > 0$  and  $0 < p_h \leq 2$ . The indices  $i$  and  $j$  refer to

individuals of the training set, which are water dimer configurations. Both indices run from 1 to  $n$ , where  $n$  is the number of water dimers in the training set, typically of the order of a thousand. It is convenient to introduce the (symmetric)  $n \times n$  matrix  $\mathbf{R}$  whose  $i$ th- $j$ th entry is given by eq. [3], which gives the correlation between the  $i$ th and  $j$ th training set examples. Note that the correlation is expressed at the level of the atomic multipole moments (the dependent variable) rather than the geometrical coordinates of the water dimers (the independent variable). The unknown parameters of the kriging model are thus  $\beta_j$ ,  $\sigma^2$ ,  $\theta_i$ , and  $p_i$ . The  $\beta_j$  parameters are found by fitting to the data, using the generalized least-squares method:

$$[4] \quad \boldsymbol{\beta} = (\mathbf{F}^T \mathbf{R}^{-1} \mathbf{F})^{-1} \mathbf{F}^T \mathbf{R}^{-1} \mathbf{y}$$

where  $\mathbf{y}$  is a  $n \times 1$  vector containing the  $n$  observed data.  $\mathbf{F}$  is the  $n \times m$  matrix whose  $i$ th- $j$ th entry is  $f_j(\mathbf{x}^i)$ . The values of  $\sigma^2$ ,  $\theta_i$ , and  $p_i$  are found by maximizing the likelihood  $L$  of the observations, as given by

$$[5] \quad L(\boldsymbol{\theta}, \mathbf{p}, \sigma^2 | \mathbf{y}^i, i = 1, 2, \dots, n) = \frac{1}{(2\pi)^{n/2}} (\sigma^2)^{n/2} |\mathbf{R}|^{1/2} \exp \left[ \frac{-(\mathbf{y} - \mathbf{F}\boldsymbol{\beta})^T \mathbf{R}^{-1} (\mathbf{y} - \mathbf{F}\boldsymbol{\beta})}{2\sigma^2} \right]$$

It is actually the logarithm of the likelihood,  $\log(L)$ , that is maximized. By setting the derivative of  $\log(L)$  with respect to  $\sigma^2$  equal to zero and solving this new equation, the optimal value of  $\sigma^2$  can be written in terms of  $\boldsymbol{\theta}$  and  $\mathbf{p}$ . Hence,  $L$  only needs to be optimized with respect to  $\boldsymbol{\theta}$  and  $\mathbf{p}$ , which amounts to optimizing  $2d$  parameters.

Two comments are in place. First, we extend the model in eq. [2] to tackle noisy data, as in ref. 53 and 54:

$$[6] \quad y(\mathbf{x}) = \sum_{i=1}^m \beta_i f_i(\mathbf{x}) + z(\mathbf{x}) + \varepsilon(\mathbf{x})$$

This leads to the addition of an extra parameter to the diagonal of the correlation matrix  $\mathbf{R}$ , which has to be fitted during the maximization of  $\log(L)$ . Note that noisy kriging<sup>53</sup> does not necessarily reproduce the training data exactly but has the flexibility to generate the best possible fit without the constraint of reproducing these data. Secondly, we make use of the fact that the kriging parameters,  $\theta_h$ , may be examined to determine which features are most important for making predictions.<sup>55</sup> This procedure is called *feature selection*.

### Feature representation and feature selection

The inputs for the machine learning methods are generated using a transformation from the Cartesian coordinates of the cluster to a set of nonredundant coordinates following the method laid out by Stone.<sup>7</sup> For systems of rigid and nonlinear molecules, only  $6(N - 1)$  coordinates are needed, where  $N$  is the number of molecules. Hence, the water dimer is described by only  $6(2 - 1) = 6$  coordinates. These six coordinates consist of three polar coordinates and three Euler angles. Imagine that the oxygen atom of the central molecule lies at the origin. The position of the second oxygen in the water dimer is then fully described by three polar coordinates ( $R_{OO}$ ,  $\theta$ , and  $\phi$ ). The polar coordinates are the distance,  $R_{OO}$ , between the two oxygen atoms, the angle,  $\theta$ ,



spanning the vector  $\mathbf{R}_{OO}$  and the  $z$  axis, and the angle,  $\phi$ , spanning the (positive)  $x$  axis and the projection of the vector  $\mathbf{R}_{OO}$  onto the  $xy$  plane. The three Euler angles,  $\alpha$ ,  $\beta$ , and  $\gamma$ , describe the water neighbouring the central water molecule as follows: Position the neighbouring water in the axis system of the central water such that the HOH plane lies in the  $xz$  plane, with the hydrogen atoms in the negative  $z$  direction. Then a succession of three rigid body rotations corresponding to the three Euler angles is applied. Finally, this water is translated by  $\mathbf{R}_{OO}$ .

After defining the coordinates of each configuration (for a given cluster size), the data are normalized, that is, transformed to lie between 0 and 1, for subsequent exploitation by kriging. Training operates on these transformed input and output data. As explained above, training is an optimization problem with  $2d$  variables. Therefore, constructing a kriging model for a water dimer ( $N = 2$ ) becomes an optimization problem with  $2d \times 6(N - 1) = 12d$  variables. The optimization consists of a hybrid in which a particle swarm<sup>56</sup> is followed by the algorithm of Nelder and Mead.<sup>57</sup>

### Targeting maximum errors—Procedure and results

A main point of concern about the performance of the kriging water potential, as published before,<sup>42</sup> are the high maximum errors between the true and predicted intermolecular interaction energy. Table 1 shows the maximum errors of the kriging models targeted in this work for the water dimer, trimer, and tetramer.

In this work, we approach the problem of reducing the maximum energy errors by implementing a feedback loop in EREBUS. EREBUS is an in-house software package central to the force field design implemented in our lab. It contains all machine learning and optimization code, alongside user-friendly interfaces to make atom type construction automatic. This loop, shown in Fig. 1, involves the following five stages:

(i) The “\*.gjf generator” generates an initial set of water dimer configurations sampled from a molecular dynamics (MD) simulation of liquid water at ambient conditions, using a high-rank multipolar potential without polarization.<sup>58</sup> The \*.gjf files are Gaussian job files, which contain the geometries of the water clusters and the level of theory at which the ab initio electron density needs to be computed. Since the water molecules are rigid bodies, only single point calculations were performed at the B3LYP/aug-cc-pVTZ level. This level of theory is an adequate compromise between accuracy and CPU time<sup>25</sup> given that an order of a thousand configurations are required. This stage is labelled stage 1 in Fig. 1.

(ii) The EREBUS *pre-processor* generates scripts for constructing training data for the kriging models (stage 2a in Fig. 1). These scripts run the programs Gaussian<sup>59</sup> and MORPHY,<sup>60</sup> generating multipole moments for the central water molecule in each of the water dimer configurations, produced by the \*.gjf generator (stage 2b in Fig. 1). The geometric features describing a water dimer configuration (input), along with the multipole moments on the atoms of the central water

**Table 1.** The maximum total interaction energy errors (in kJ/mol) for kriging models used in previous work.<sup>42</sup>

Water cluster	Maximum error
Dimer	3.6
Trimer	20.5
Tetramer	41.4

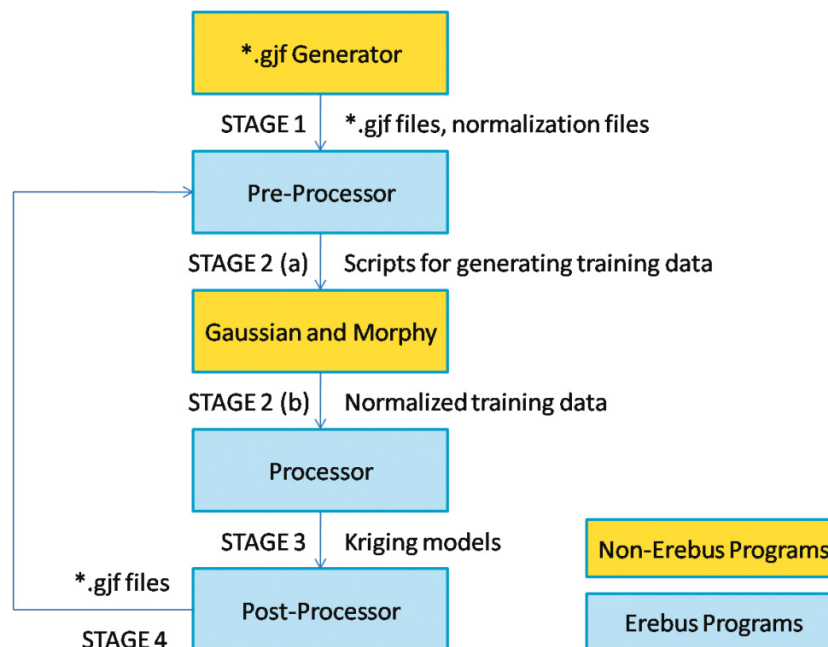
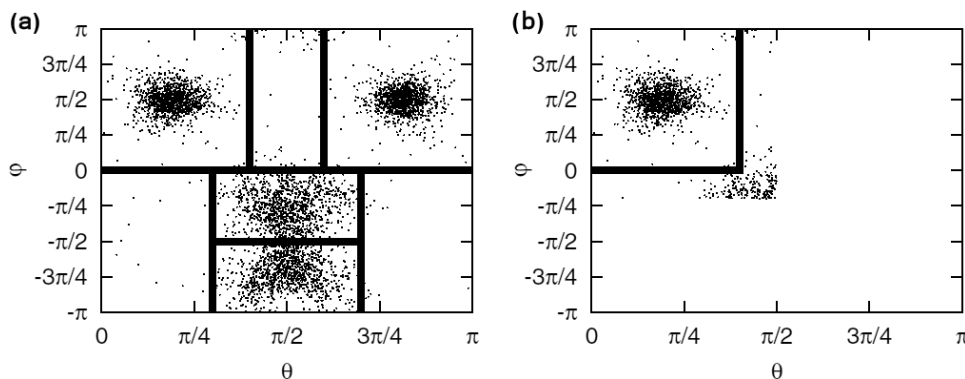
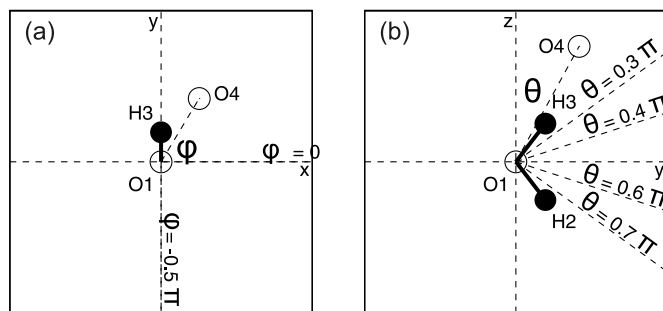
molecule (output), constitute one training example. Several thousand examples are evaluated to make up the training data for use by the EREBUS processor.

(iii) The EREBUS *processor* uses a subset of the training data to build kriging models for each of the multipole moments, for each atom in the central water molecule (stage 3 in Fig. 1). Each individual kriging model predicts a particular multipole moment, on a particular atom in the central water molecule. Rather than use all the available training data, a method of sequential selection<sup>61</sup> is used to construct a training set for each model, as described in ref. 42. An upper limit of 1000 is applied to the training set size. Consequently, each moment has multiple models built for it, one at each iteration of the sequential building of the training sets. Each of these models is tested by making predictions for the values of the multipole moments of the configurations not used. The model that minimizes the median error is the one selected for use. All 25 multipole moments, from monopole ( $\ell = 0$ ) to hexadecapole ( $\ell = 4$ ), were trained for.

(iv) The EREBUS *post-processor* uses the kriging models to make energy predictions for an external set of (~1000) water configurations. Extra configurations (\*.gjf files) are generated that are similar to those configurations with an energy error above a certain threshold. (stage 4 in Fig. 1). In this work, a threshold error of 0.75 kJ/mol is used. Suppose a dimer configuration, represented by the normalized features  $r^*$ ,  $\theta^*$ ,  $\phi^*$ ,  $\alpha^*$ ,  $\beta^*$ , and  $\gamma^*$ , gives an energy error above this threshold. Then extra configurations are generated at random in the range ( $r^* \pm \delta$ ,  $\theta^* \pm \delta$ ,  $\phi^* \pm \delta$ ,  $\alpha^* \pm \delta$ ,  $\beta^* \pm \delta$ ,  $\gamma^* \pm \delta$ ), where  $\delta$  is a small tolerance set to 0.1. If a particular feature value is generated to be  $<0$ , it is set to 0, and if it is generated to be  $>1$ , then it is set to 1. The total number of extra configurations generated is set to 1500. These are divided equally over the configurations that gave energy errors above the error threshold of 0.75 kJ/mol.

(v) (Feedback stage). The EREBUS pre-processor then generates scripts that run the programs Gaussian and MORPHY for each of the extra water configurations. These extra training data are subsequently used along with the original training data (from the \*.gjf generator) in the EREBUS processor. The new “targeted” kriging models are then tested in the EREBUS post-processor. This stage is really a repetition of stages 2 and 3 in Fig. 1, with extra training data.

The targeted kriging models use extra training data, focusing on water configurations that give high energy errors (for the original kriging models use training data coming from the MD simulation only). Hence, it is reasonable to ex-

**Fig. 1.** Feedback loop in EREBUS.**Fig. 2.** Splitting of feature space: (a) Projection of feature space for the water dimer configurations (from simulation) onto the  $\theta$ - $\phi$  plane. (b) Dimer configurations considered as training data for the top left region.**Fig. 3.** Two projections of the positioning of the noncentral oxygen atom, relative to the central oxygen atom, for the regions in Fig. 2; xy (left), yz (right).

pect that these models will produce lower maximum energy errors than the original kriging models. However, improving a single (global) kriging model to predict a multipole moment well for unusual configurations could come at the expense of predicting the moment less well for more “normal” configurations. To alleviate this potential problem, we split

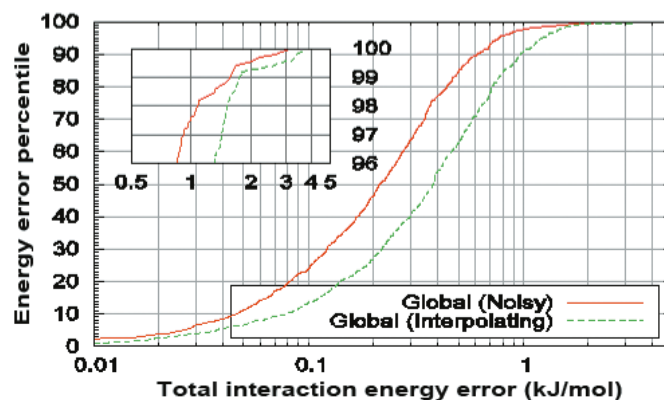
**Fig. 4.** The energy error percentiles for the water dimer, using the noisy global kriging model trained only on data sampled from a MD simulation and using the interpolating global kriging model as described in previous work.<sup>42</sup>

Fig. 5. The energy error percentiles using targeted global kriging models for the water dimer.

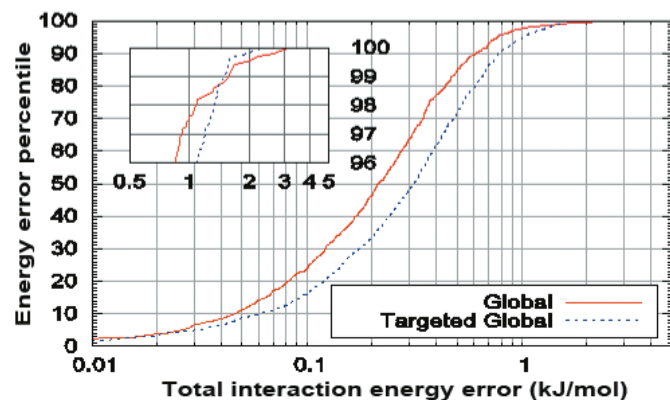


Fig. 6. The energy error percentiles using targeted local kriging models for the water dimer.

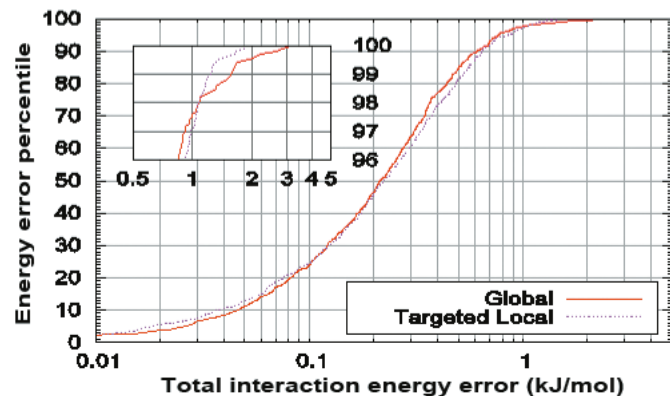
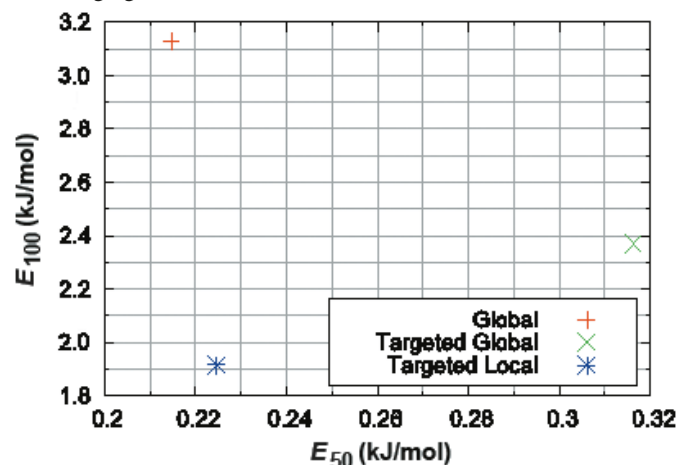


Fig. 7. The trade-off between median energy error ( $E_{50}$ ) and maximum energy error ( $E_{100}$ ) for global, targeted global, and targeted local kriging models for the water dimer.



up feature space into several subspaces based on the two most significant features,  $\theta$  and  $\phi$ . Figure 2 shows how this is achieved. Each dot in Fig. 2 represents a particular water configuration. This is in fact a projection onto  $(\theta, \phi)$ -space since the four remaining coordinates ( $R_{OO}$  and the three Euler angles) remain unspecified. The clusters in Fig. 2a naturally fall apart in easily perceptible clusters, or feature

subspaces. Using multiple local kriging models to predict each multipole moment has the consequence that the unusual structures are only used in the training set if they are relevant to the prediction being made. A corollary of this is that unusual configurations are not used in kriging models for predictions they are not relevant for, and so should not adversely affect the quality of predictions for normal configurations.

Figure 3 explicitly shows the two features of Fig. 2, in terms of the molecular geometry of the water dimer. To see how Fig. 3 helps interpreting the feature subspaces in Fig. 2, we focus on the two vertical divisions of the lower half of Fig. 2a; these divisions correspond to  $\theta = 0.3\pi$  (left) and  $\theta = 0.7\pi$  (right). The geometrical meaning of these divisions can be seen in the right panel of Fig. 3. Similarly, there are two vertical divisions in the upper half of Fig. 2a, which correspond to  $\theta = 0.4\pi$  (left) and  $\theta = 0.6\pi$  (right), again marked in Fig. 3.

A “local” kriging model is trained on each of these seven distinct regions, for each multipole moment on each atom of the central water molecule. For each region, configurations slightly outside the region boundary are included as (potential) training set points. By including points outside the region that a model will be making predictions for, the risk of needing to extrapolate to make predictions is reduced. For example, Fig. 2b shows the points considered as training data points for the top left region in the  $\theta$ - $\phi$  plot.

In summary, by employing multiple local kriging models for predicting each multipole moment, we should be able to use unusual configurations in the training sets, thus targeting maximum errors, with minimal impact on the quality of the predictions for the more normal configurations. In the next section, we test this hypothesis by comparing the trade-off between maximum interaction energy error and median energy error for both global targeted kriging models and local targeted kriging models.

One final point to note is that the global kriging models used in this paper are not exactly the same as the global kriging models used before.<sup>42</sup> The models in this paper differ in that they have the flexibility to not interpolate the data, but to find a best fit instead. In other words, the so-called *noisy kriging* models generated here do not exactly reproduce the training data, but the kriging models in the previous paper<sup>42</sup> did reproduce data. The original kriging models, published in ref. 42, will be referred to as *interpolating kriging*.

It is convenient to assess the accuracy of the kriging models through a statistical measure of the total interaction energies arising from predicted multipole moments. For example, we define the 90th energy error percentile,  $E_{90}$ , as the error in energy that 90% of predictions are within, as determined over a set of predictions of  $\sim 1000$  configurations. All such percentiles can be shown in one plot, which is typically S-shaped.  $E_{100}$ , the energy error that all predictions fall within, coincides with the maximum error. The difference in energy error percentiles between interpolating kriging models used in previous work and the non-interpolating (“noisy”) kriging models is given in Fig. 4 for the water dimer. By using noisy kriging models, the median energy error ( $E_{50}$ ) is reduced from 0.38 to 0.21 kJ/mol, and the maximum energy error is reduced from 3.62 to 3.13 kJ/mol.



Noisy kriging is also used for the targeted global and targeted local kriging models. We call global kriging models *targeted global kriging* if they have been trained with extra configurations similar to those that gave high energy errors. Local kriging models that have been trained with such configurations are called *targeted local kriging*.

The energy error percentiles of targeted global kriging models are shown in Fig. 5. Compared with the global kriging model (trained using data sampled from simulation only), a 24% reduction in maximum energy error is achieved, that is, 2.37 kJ/mol compared with 3.13 kJ/mol. However, this reduction comes at the expense of all energy error percentiles below  $E_{98}$ . For example,  $E_{50}$  rises by 52%, from 0.21 to 0.32 kJ/mol. Clearly, adding unusual configurations to the training set of a single global kriging model deteriorates the quality of the model as a whole, albeit with an improvement in maximum errors. This trade-off does not seem acceptable, which is why local kriging is invoked.

The energy error percentiles of targeted local kriging models are shown in Fig. 6. Compared with the global kriging model, a 39% reduction in maximum energy error is achieved, from 3.13 to 1.92 kJ/mol. This time, however, lower energy error percentiles are barely affected. For example, the median energy error rises by <5%, from 0.21 to 0.22 kJ/mol. The trade-off using local targeted is much more acceptable.

The trade-offs between  $E_{100}$  and  $E_{50}$  are summarized in Fig. 7. The targeted local dominates the targeted global, i.e., it is better in both median energy error and maximum energy error. Comparing the targeted local and global reveals that neither is better than the other in both median energy error and maximum energy error. Nevertheless, the targeted local is arguably more attractive as it offers a large improvement in maximum energy error at a small cost to median energy error.

Previous work<sup>42</sup> showed that kriging is the most accurate machine learning model compared with multilayer perceptrons and radial basis function neural networks in terms of average performance as well as maximum errors. This work has delivered the proof-of-principle that the maximum errors can be substantially reduced by cutting feature space into subspaces and training for each subspace separately. Generalizing this accomplishment to higher dimensional feature spaces will require a (semi-)automatic procedure able to partition features space.

## Conclusions

By splitting feature space up into natural regions for the water dimer, a 39% reduction in maximum energy error was achieved at a small cost (4.5%) to the median energy. Without splitting up feature space, a 24% reduction in maximum energy error is achieved, at the cost of a 52% increase in the median energy error. Thus, splitting feature space up is useful when targeting maximum errors, without causing a loss in accuracy for normal configurations.

## Acknowledgments

We thank the University of Manchester Intellectual Property Limited (UMIP) for financial support of one of us (GIH).

## References

- (1) Jorgensen, W. L. *J. Am. Chem. Soc.* **1981**, *103* (2), 335. doi:10.1021/ja00392a016.
- (2) Jorgensen, W. L.; Chandrasekhar, J.; Madura, J. D.; Impey, R. W.; Klein, M. L. *J. Chem. Phys.* **1983**, *79* (2), 926. doi:10.1063/1.445869.
- (3) Mahoney, M. W.; Jorgensen, W. L. *J. Chem. Phys.* **2000**, *112* (20), 8910. doi:10.1063/1.481505.
- (4) Berendsen, H. J. C.; Grigera, J. R.; Straatsma, T. P. *J. Phys. Chem.* **1987**, *91* (24), 6269. doi:10.1021/j100308a038.
- (5) Nada, H.; van der Eerden, J. P. J. M. *J. Chem. Phys.* **2003**, *118* (16), 7401. doi:10.1063/1.1562610.
- (6) Stone, A. J.; Price, S. L. *J. Phys. Chem.* **1988**, *92* (12), 3325. doi:10.1021/j100323a006.
- (7) Stone, A. J. *The Theory of Intermolecular Forces*; Clarendon: Oxford, 1996.
- (8) Popelier, P. L. A.; Stone, A. J. *Mol. Phys.* **1994**, *82* (2), 411. doi:10.1080/00268979400100314.
- (9) Gresh, N.; Kafafi, S. A.; Truchon, J.-F.; Salahub, D. R. *J. Comput. Chem.* **2004**, *25* (6), 823. doi:10.1002/jcc.20012. PMID:15011254.
- (10) Kaminský, J.; Jensen, F. *J. Chem. Theory Comput.* **2007**, *3* (5), 1774. doi:10.1021/ct700082f.
- (11) Rasmussen, T. D.; Ren, P.; Ponder, J. W.; Jensen, F. *Int. J. Quantum Chem.* **2007**, *107* (6), 1390. doi:10.1002/qua.21278.
- (12) Millot, C.; Stone, A. J. *Mol. Phys.* **1992**, *77* (3), 439. doi:10.1080/00268979200102541.
- (13) Ren, P.; Ponder, J. W. *J. Phys. Chem. B* **2003**, *107* (24), 5933. doi:10.1021/jp027815+.
- (14) Gordon, M. S.; Slipchenko, L.; Hui, L.; Jensen, J. H. *Annu. Rep. Comput. Chem.* **2007**, *3*, 177. doi:10.1016/S1574-1400(07)03010-1.
- (15) Gresh, N. *J. Comput. Chem.* **1995**, *16* (7), 856. doi:10.1002/jcc.540160705.
- (16) Piquemal, J.-P.; Williams-Hubbard, B.; Fey, N.; Deeth, R. J.; Gresh, N.; Giessner-Prettre, C. *Comput. Chem.* **2003**, *24* (16), 1963. doi:10.1002/jcc.10354.
- (17) Vigné-Maeder, F.; Claverie, P. *J. Chem. Phys.* **1988**, *88* (8), 4934. doi:10.1063/1.454705.
- (18) Jorgensen, W. L. *J. Chem. Theory Comput.* **2007**, *3* (6), 1877. doi:10.1021/ct700252g.
- (19) Coulson, C. A.; Eisenberg, D. *Proc. R. Soc. Lond. A Math. Phys. Sci.* **1966**, *291* (1427), 445. doi:10.1098/rspa.1966.0105.
- (20) Silvestrelli, P. L.; Parrinello, M. *Phys. Rev. Lett.* **1999**, *82* (16), 3308. doi:10.1103/PhysRevLett.82.3308.
- (21) Gregory, J. K.; Clary, D. C.; Liu, K.; Brown, M. G.; Saykally, R. J. *Science* **1997**, *275* (5301), 814. doi:10.1126/science.275.5301.814. PMID:9012344.
- (22) Gubskaya, A. V.; Kusalik, P. G. *J. Chem. Phys.* **2002**, *117* (11), 5290. doi:10.1063/1.1501122.
- (23) Popelier, P. L. A. *Atoms in Molecules: An Introduction*; Pearson Education: London, 2000.
- (24) Bader, R. F. W. *Atoms in Molecules: A Quantum Theory*; Oxford University Press: Oxford, 1990.
- (25) Handley, C. M.; Popelier, P. L. A. *Synth. React. Inorg. Met.-Org. Nano-Met. Chem.* **2008**, *38*, 91.
- (26) Thole, B. T. *Chem. Phys.* **1981**, *59* (3), 341. doi:10.1016/0301-0104(81)85176-2.
- (27) Soteras, I.; Curutchet, C.; Bidon-Chanal, A.; Dehez, F.; Ángyán, J. G.; Orozco, M.; Chipot, C.; Luque, F. J. *J. Chem. Theory Comput.* **2007**, *3* (6), 1901. doi:10.1021/ct7001122.



- (28) Piquemal, J.-P.; Gresh, N.; Giessner-Prettre, C. *J. Phys. Chem. A* **2003**, *107* (48), 10353. doi:10.1021/jp035748t.
- (29) Piquemal, J.-P.; Chelli, R.; Procacci, P.; Gresh, N. *J. Phys. Chem. A* **2007**, *111* (33), 8170. doi:10.1021/jp072687g.
- (30) Ledecq, M.; Lebon, F.; Durant, F.; Giessner-Prettre, C.; Marquez, A.; Gresh, N. *J. Phys. Chem. B* **2003**, *107* (38), 10640. doi:10.1021/jp0354604.
- (31) Chen, W.; Gordon, M. S. *J. Chem. Phys.* **1996**, *105* (24), 11081. doi:10.1063/1.472909.
- (32) Harder, E.; Anisimov, V. M.; Vorobyov, I. V.; Lopes, P. E. M.; Noskov, S. Y.; MacKerell, A. D., Jr.; Roux, B. *J. Chem. Theory Comput.* **2006**, *2* (6), 1587. doi:10.1021/ct600180x.
- (33) Yu, H.; van Gunsteren, W. F. *J. Chem. Phys.* **2004**, *121* (19), 9549. doi:10.1063/1.1805516. PMID:15538877.
- (34) Yang, M.; Senet, P.; Van Alsenoy, C. *Int. J. Quantum Chem.* **2005**, *101* (5), 535. doi:10.1002/qua.20308.
- (35) Yu, H.; Geerke, D. P.; Liu, H.; van Gunsteren, W. F. *J. Comput. Chem.* **2006**, *27* (13), 1494. doi:10.1002/jcc.20429. PMID:16838298.
- (36) Stone, A. J. *Mol. Phys.* **1985**, *56* (5), 1065. doi:10.1080/00268978500102901.
- (37) Ángyán, J. G.; Jansen, G.; Loss, M.; Hättig, C.; Heß, B. A. *Chem. Phys. Lett.* **1994**, *219* (3–4), 267. doi:10.1016/0009-2614(94)87056-X.
- (38) in het Panhuis, M.; Popelier, P. L. A.; Munn, R. W.; Angyan, J. G. *J. Chem. Phys.* **2001**, *114* (18), 7951. doi:10.1063/1.1361247.
- (39) Houlding, S.; Liem, S. Y.; Popelier, P. L. A. *Int. J. Quantum Chem.* **2007**, *107* (14), 2817. doi:10.1002/qua.21507.
- (40) Handley, C. M.; Popelier, P. L. A. *J. Chem. Theory Comput.* **2009**, *5* (6), 1474. doi:10.1021/ct800468h.
- (41) Darley, M. G.; Handley, C. M.; Popelier, P. L. A. *J. Chem. Theory Comput.* **2008**, *4* (9), 1435. doi:10.1021/ct800166r.
- (42) Handley, C. M.; Hawe, G. I.; Kell, D. B.; Popelier, P. L. A. *Phys. Chem. Chem. Phys.* **2009**, *11* (30), 6365. doi:10.1039/b905748j. PMID:19809668.
- (43) Cressie, N. *Statistics for Spatial Data*; Wiley: New York, 1993.
- (44) Rasmussen, C. E.; Williams, C. K. I. *Gaussian Processes for Machine Learning*; The M. I. T. Press: Cambridge, 2006.
- (45) Haas, T. C. *J. Am. Stat. Assoc.* **1990**, *85* (412), 950. doi:10.2307/2289592.
- (46) Matta, C. F.; Boyd, R. J. *The Quantum Theory of Atoms in Molecules: From Solid State to DNA and Drug Design*; Wiley-VCH: Weinheim, Germany, 2007.
- (47) Popelier, P. L. A.; Aicken, F. M. *ChemPhysChem* **2003**, *4* (8), 824. doi:10.1002/cphc.200300737. PMID:12961979.
- (48) Popelier, P. L. A. Quantum Chemical Topology: On Bonds and Potentials. In *Structure and Bonding: Intermolecular Forces and Clusters*; Wales, D. J., Ed.; Springer: Heidelberg, Germany, 2005; Vol. 115, p 1.
- (49) Devereux, M.; Popelier, P. L. A.; McLay, I. M. *J. Comput. Chem.* **2009**, *30* (8), 1300. doi:10.1002/jcc.21146. PMID:19003976.
- (50) Popelier, P. L. A.; Bremond, E. A. G. *Int. J. Quantum Chem.* **2009**, *109* (11), 2542. doi:10.1002/qua.22215.
- (51) Popelier, P. L. A.; Joubert, L.; Kosov, D. S. *J. Phys. Chem. A* **2001**, *105* (35), 8254. doi:10.1021/jp011511q.
- (52) Rafat, M.; Popelier, P. L. A. *J. Comput. Chem.* **2007**, *28* (4), 832. doi:10.1002/jcc.20610. PMID:17226840.
- (53) Yin, H.; Li, R.; Fang, K.-T.; Liang, Y.-Z. *J. Chemometr.* **2007**, *21* (1–2), 43. doi:10.1002/cem.1033.
- (54) Obrezanova, O.; Csanyi, G.; Gola, J. M. R.; Segall, M. D. *J. Chem. Inf. Model.* **2007**, *47* (5), 1847. doi:10.1021/ci7000633. PMID:17602549.
- (55) Welch, W. J.; Buck, R. J.; Sacks, J.; Wynn, H. P.; Mitchell, T. J.; Morris, M. D. *Technometrics* **1992**, *34* (1), 15. doi:10.2307/1269548.
- (56) Kennedy, J.; Eberhart, R. Particle Swarm Optimization. In *Proceedings of the IEEE International Conference on Neural Networks*; IEEE Press: Piscataway, NJ, 1995; pp 1942–1948.
- (57) Nelder, J. A.; Mead, R. *Comput. J.* **1965**, *7* (4), 308. doi:10.1093/comjnl/7.4.308.
- (58) Liem, S. Y.; Popelier, P. L. A. *J. Chem. Theory Comput.* **2008**, *4* (2), 353. doi:10.1021/ct700266n.
- (59) Frisch, M. J.; Trucks, G. W.; Schlegel, H. B.; Scuseria, G. E.; Robb, M. A.; Cheeseman, J. R.; Montgomery, J. A. J.; Vreven, J. T.; Kudin, K. N.; Burant, J. C.; Millam, J. M.; Iyengar, S. S.; Tomasi, J.; Barone, V.; Mennucci, B.; Cossi, M.; Scalmani, G.; Rega, N.; Petersson, G. A.; Nakatsuji, H.; Hada, M.; Ehara, M.; Toyota, K.; Fukuda, R.; Hasegawa, J.; Ishida, M.; Nakajima, T.; Honda, Y.; Kitao, O.; Nakai, H.; Klene, M.; Li, X.; Knox, J. E.; Hratchian, H. P.; Cross, J. B.; Adamo, C.; Jaramillo, J.; Gomperts, R.; Stratmann, R. E.; Yazyev, O.; Austin, A. J.; Cammi, R.; Pomelli, C.; Ochterski, J. W.; Ayala, P. Y.; Morokuma, K.; Voth, G. A.; Salvador, P.; Dannenberg, J. J.; Zakrzewski, V. G.; Dapprich, S.; Daniels, A. D.; Strain, M. C.; Farkas, O.; Malick, D. K.; Rabuck, A. D.; Raghavachari, K.; Foresman, J. B.; Ortiz, J. V.; Cui, Q.; Baboul, A. G.; Clifford, S.; Cioslowski, J.; Stefanov, B. B.; Liu, G.; Liashenko, A.; Piskorz, P.; Komaromi, I.; Martin, R. L.; Fox, D. J.; Keith, T.; Al-Laham, M. A.; Peng, C. Y.; Nanayakkara, A.; Challacombe, M.; Gill, P. M. W.; Johnson, B.; Chen, W.; Wong, M. W.; Gonzalez, C.; Pople, J. A. *Gaussian 03*; Gaussian, Inc.: Pittsburgh PA, 2003.
- (60) Popelier, P. L. A. *Comput. Phys. Commun.* **1998**, *108* (2–3), 180. doi:10.1016/S0010-4655(97)00121-5.
- (61) Rennen, G. *Struct. Multidisc. Optim.* **2009**, *38* (6), 545. doi:10.1007/s00158-008-0306-8.

# A computational study of the threshold energies of the 1,2-FCl interchange reaction of chlorofluoroethanes

William C. Everett, Bert E. Holmes, and George L. Heard

**Abstract:** The 1,2-FCl rearrangement reaction of a series of haloethanes is investigated by comparisons of the optimized ground- and transition-state geometries. Investigation of the effect of level of theory and basis set shows that the trends in threshold energies for rearrangement are reproduced across all levels of theory and basis set, and hence that a moderate level of theory and basis set is adequate for investigating the important trends in this reaction. Threshold barriers increase when a large number of fluorine atoms are attached to the carbon atom bearing the interchanging fluorine, suggesting that the C–F bonds prove difficult to distort to the transition geometry; the increase is smaller for fluorine substitution on the carbon atom bearing the interchanging hydrogen atom. By considering sets of isomeric reactions, the barrier height is shown to closely follow the thermodynamic stability of the alkane undergoing rearrangement; however there is a secondary effect owing to the relative stability of the transition geometry. This relative stability can be related to the thermodynamic stability of a series of isomeric alkenes that resemble the transition geometry without the rearranging atoms. This series of molecules constitute an unusual set owing to the ability to consider these three contributions to the activation barrier separately.

**Key words:** transition-state geometries, atmospheric chemistry, reaction kinetics, computational chemistry.

**Résumé :** Faisant appel à des calculs théoriques, on a étudié la réaction de réarrangement 1,2-FCl d'une série de haloéthane en procédant à une comparaison de l'état fondamental et de géométries d'état de transition optimisés. Une étude de l'effet du niveau de la théorie et des ensembles de base montre que les tendances dans les énergies de seuil des réarrangements sont reproduites par tous les niveaux de la théorie et tous les ensembles de base et que, en conséquence, un niveau modéré de la théorie et d'ensemble de base est adéquat pour étudier les tendances les plus importantes de cette réaction. Les barrières de seuil augmentent quand un grand nombre d'atomes de fluor sont liés à l'atome de carbone portant l'atome de fluor qui s'échange et ceci suggère que les liaisons C–F s'avèrent difficiles à déformer vers l'état de transition; l'augmentation est moins grande pour une substitution par du fluor sur l'atome de carbone portant l'atome d'hydrogène qui s'échange. Par considération d'ensembles de réactions isomères, on peut démontrer que la hauteur de la barrière suit assez bien la stabilité thermodynamique de l'alcane qui subit le réarrangement; toutefois, on observe un effet secondaire dû à la stabilité relative de l'état de transition. Cette stabilité relative peut être reliée à la stabilité thermodynamique d'une série d'alcènes isomères qui ressemblent à l'état de transition sans les atomes qui donnent lieu au réarrangement. Cette série de molécule constitue un ensemble inhabituel en raison de l'habilité à considérer ces trois contributions à la barrière d'activation séparément.

**Mots-clés :** géométries de l'état de transition, chimie de l'atmosphère, cinétique d'une réaction, chimie quantique.

## Introduction

Our group first proposed a 1,2-FCl interchange reaction to explain the loss of HCl from chemically activated  $\text{CF}_2\text{ClCF}_2\text{CH}_3$ . The mechanism involved the interchange of  $\text{CF}_2\text{ClCF}_2\text{CH}_3$  to  $\text{CF}_3\text{CFCICH}_3$ , which subsequently underwent a 2,3-ClH elimination giving  $\text{CF}_3\text{CF}=\text{CH}_2$  as the observed product. The same process was observed for chemically activated  $\text{CF}_2\text{ClCF}_2\text{CD}_3$ .<sup>1</sup> Computed kinetic H–D isotope effects for this reaction pathway closely matched the experimental values. The threshold energy barrier height,

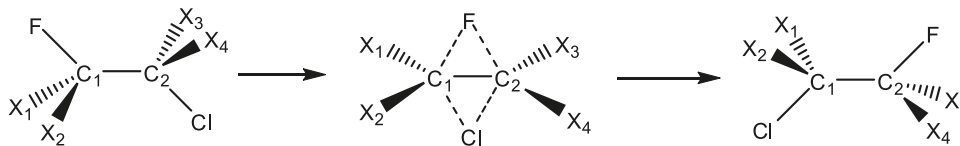
$E_0$ , for that reaction was calculated to be 62.5 kcal/mol (1 cal = 4.184 J) using a B3PW91/6–31G(d',p') level of theory. The 1,2-FCl interchange reaction has subsequently been shown to explain the ratio of product yields in the thermal decomposition of  $\text{CF}_2\text{HCH}_2\text{Cl}$ ,<sup>2,3</sup>  $\text{CF}_2\text{ClCHFCH}_3$ ,<sup>4</sup> and  $\text{CF}_2\text{ClCHFCH}_2\text{CH}_3$ .<sup>5</sup> Calculations on these systems were performed at the B3PW91/6–31G(d',p') and B3PW91/6–311+G(2d,p) levels of theory based on the ability of the B3PW91 functional to reproduce the kinetic parameters for 1,2-HF elimination from  $\text{CH}_3\text{CF}_3$ .<sup>6</sup> Because this reaction ap-

Received 31 December 2009. Accepted 11 June 2010. Published on the NRC Research Press Web site at canjchem.nrc.ca on 27 October 2010.

*This article is part of a Special Issue dedicated to Professor R. J. Boyd.*

**W.C. Everett, B.E. Holmes, and G.L. Heard.**<sup>1</sup> Department of Chemistry, The University of North Carolina at Asheville, One University Heights, Asheville NC 28804, USA.

<sup>1</sup>Corresponding author (e-mail: gheard@unca.edu).

**Fig. 1.** 1,2-FCl interchange mechanism.  $X_{1-4} = \text{H, F, or Cl}$ .

pears to be an important step in energized hydrofluorochlorocarbon (HCFC) reactions, this paper seeks to address whether these levels of theory are appropriate by providing a rigorous theoretical treatment using a wide range of theories and basis sets, as well as to examine the effects of different substituents on the transition-state geometry and energy. Understanding the best theoretical method for these reactions and a knowledge of the factors that favor the rearrangement would allow for accurate prediction of which systems are likely to undergo a 1,2-FCl rearrangement and which systems would likely allow detection of the rearranged HCFC prior to subsequent HX ( $X = \text{Cl or F}$ ) elimination.

The transition-state geometry for 1,2-FCl interchange involves an exchanging fluorine and chlorine atom, each formally bonded to separate carbons, as shown in Fig. 1. This leaves four positions for substituents, which we have labeled  $X_1$ ,  $X_2$ ,  $X_3$ , and  $X_4$ , where  $X_1$  and  $X_2$  are attached to the carbon with the migrating fluorine atom (hereafter referred to as  $C_1$ ), and  $X_3$  and  $X_4$  are attached to the carbon with the migrating chlorine atom (hereafter referred to as  $C_2$ ). All possible combinations of H, F, and Cl in these positions give a complete set of chlorofluoroethanes and hydrofluorochloroethanes. This will lead to some redundancies in the reactant and product molecules because each transition geometry can describe a forward and a reverse reaction that are both 1,2-FCl interchanges. Since this leads to a large number of rearrangements (45), we have selected three molecules to be test cases for the level of theory:  $\text{CH}_2\text{FCH}_2\text{Cl}$ , the simplest molecule for which a 1,2-FCl interchange is possible, and  $\text{CHF}_2\text{CH}_2\text{Cl}$ , and  $\text{CH}_2\text{FCHCl}_2$ , representing the substitution of one chlorine atom and one fluorine atom to the  $\text{CH}_2\text{FCH}_2\text{Cl}$  molecule. These test case molecules were studied using a number of basis sets (using the B3PW91 level of theory) and levels of theory including ab initio, density functional theory, and model chemistries.

## Computational methods

Standard ab initio and density functional theory calculations have been performed using the *Gaussian 03* program.<sup>7</sup> The following basis sets have been used: 6-31G(d',p'),<sup>8</sup> 6-311+G(2d,p),<sup>9</sup> Dunning's cc-PVTZ, aug-cc-PVTZ cc-PVQZ,<sup>10</sup> and the Truhlar-modified 6-311+G(2df,2p) and 6-311++G(2df,2p).<sup>11</sup> Density functional methods considered were B3PW91,<sup>12,13</sup> B3LYP,<sup>14,15</sup> MPWB1K,<sup>15,16</sup> and MPWB95,<sup>15,17</sup> and ab initio levels of theory were MP2, CCSD, and QCISD, as well as the model chemistries G2MP2, G2MP2B3,<sup>18</sup> and CBS-QB3.<sup>19</sup> All geometries were characterized as local minima or transition states by vibrational frequency calculations; unscaled frequencies were used to determine the zero-point energy contribution to all local minima and transition-state energies.

## Results and discussion

Transition-state geometries were successfully characterized for 1,2-FCl interchanges of  $\text{CH}_2\text{FCH}_2\text{Cl}$ ,  $\text{CHF}_2\text{CH}_2\text{Cl}$ , and  $\text{CH}_2\text{FCHCl}_2$  using a wide range of levels of theory. There is very little variation in the bond lengths and angles with level of theory. The carbon-carbon bond distances are all between 1.40 and 1.42 Å, indicating a contraction from the bond distance in the ground-state geometries. The carbon-fluorine distance for the interchanging fluorine atom varies between 1.77 and 1.88 Å across the levels of theory, and the carbon-chlorine distance varies from 2.24 to 2.31 Å. The angle made between the carbon-carbon bond and the interchanging chlorine atom is  $71^\circ$ – $72^\circ$ , and there is only slightly more variation in the angle between the carbon-carbon bond and the interchanging fluorine bond of  $67^\circ$ – $70^\circ$ . The four atoms involved in the transition are very close to planar, with a maximum deviation of  $6^\circ$ . The four atoms not involved in the transition geometry are close to planar, within  $15^\circ$  of planarity in all cases, and hence the transition state resembles a substituted ethylene bonded to a fluorine atom above the plane of the molecule and a chlorine atom bonded below the plane of the molecule. We conclude from this that the choice of level of theory is not important in obtaining an accurate geometry for this transition-state geometry.

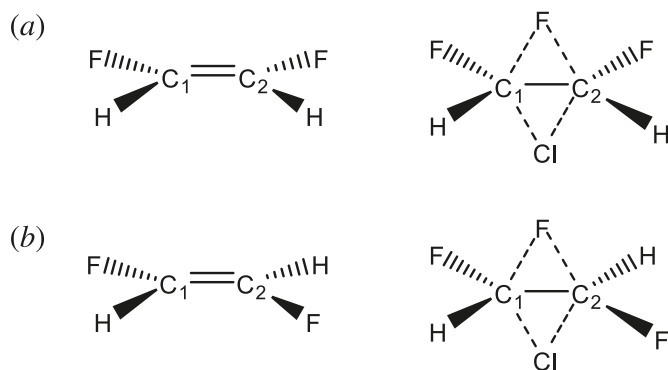
Table 1 presents the threshold energy,  $E_0$ , for the 1,2-FCl interchange reaction of the three model systems chosen as a function of level of theory and basis set. The level of theory was changed while keeping the basis set the same, using the 6-31G(d',p') basis set previously used in studies of this reaction. With the exception of the model chemistries (G2MP2, G3MP2B3, and CBS-QB3, where the trends are relatively greater in magnitude), the trends in energy are duplicated across the three molecules—the threshold energies for rearrangement of  $\text{CH}_2\text{FCH}_2\text{Cl}$  and  $\text{CH}_2\text{FCHCl}_2$  are very close (though  $\text{CH}_2\text{FCH}_2\text{Cl}$  is consistently slightly higher in energy), and the barrier height for rearrangement of  $\text{CHF}_2\text{CH}_2\text{Cl}$  is consistently slightly  $>5$  kcal/mol higher in energy than that of  $\text{CH}_2\text{FCH}_2\text{Cl}$ . There is a consistency in the percent change in energy; in comparing  $\text{CH}_2\text{FCH}_2\text{Cl}$  with  $\text{CHF}_2\text{CH}_2\text{Cl}$ , there is a 9%–10% increase in the barrier height, and in comparing  $\text{CH}_2\text{FCH}_2\text{Cl}$  with  $\text{CH}_2\text{FCHCl}_2$ , there is a 1%–2% increase in the barrier height with all computational methods. MP2, CCSD, and QCISD consistently give the greatest barrier heights, and the MPW levels consistently give the lowest barrier heights. There is an interesting question in comparing the effects of level of theory on reaction barrier heights—the answer is an unbound number, and hence there is no guarantee that a lower energy means a more appropriate level of theory. While the energy of the initial geometry will behave variationally, there is no lower bound to the energy of the transition-state geometry, and a low barrier height may be an indication that a level

**Table 1.** 1,2-FCl interchange barrier height ( $E_0$ ), in kcal/mol (1 cal = 4.184 J) for  $\text{CH}_2\text{FCH}_2\text{Cl}$ ,  $\text{CHF}_2\text{CH}_2\text{Cl}$ , and  $\text{CH}_2\text{FCHCl}_2$ , calculated using a range of basis sets and levels of theory.

Theory/basis set	$E_0$ (kcal/mol)		
	$\text{CH}_2\text{FCH}_2\text{Cl}$	$\text{CHF}_2\text{CH}_2\text{Cl}$	$\text{CH}_2\text{FCHCl}_2$
B3PW91/6-31g(d',p')	60.0	65.6	60.9
B3LYP/6-31g(d',p')	57.5	63.2	58.7
MPWB1K/6-31g(d',p')	49.1	54.0	49.4
MPWB95/6-31g(d',p')	48.9	53.7	49.2
MP2/6-31g(d',p')	72.6	78.2	73.6
CCSD/6-31g(d',p')	73.8	80.5	75.4
QCISD/6-31g(d',p')	71.4	78.2	72.9
G2MP2	62.0	69.2	63.2
G3MP2B3	57.8	63.8	58.9
CBS-QB3	62.3	69.4	— <sup>a</sup>
B3PW91/6-311+g(2d,p)	56.4	61.8	56.8
B3PW91/6-311+g(2df,2p)	58.0	63.3	58.2
B3PW91/6-311++g(2d,p)	58.0	63.3	58.2
B3PW91/cc-pvtz	58.4	63.7	58.8
B3PW91/aug-cc-pvtz	57.4	62.7	57.9
B3PW91/cc-pvqz	58.3	63.6	58.7

<sup>a</sup>CBS-QB3 calculations on this molecule could not be performed owing to the size of the molecule.

**Fig. 2.** (a) The *Z* isomer of  $\text{CHFCHF}$  and the corresponding *Z*-transition geometry for 1,2-FCl interchange of  $\text{CF}_2\text{HCHFCl}$ . (b) The *E* isomer and corresponding *E*-transition geometry.



of theory is not correctly treating the stretched bonds of a transition state. The model chemistries predict values within the range of the other levels of theory used in this study, likely by virtue of the geometry staying constant at varying levels of theory, because the model chemistries use thermal calculations of one level of theory applied to a geometry calculated at a different level of theory.

In comparing the result of changing the basis set at the B3PW91 level of theory, there is a consistently small effect across each of the three molecules. Going from a doubly split valence basis set to a triply split valence basis set in all cases lowers the activation energy slightly; the only quadruple-zeta basis set we used led to a lowering of the  $E_0$  by 0.1 kcal/mol for each interchange.

There is no experimental data on the true value of the energy of these interchanges. In two similar systems,  $\text{CF}_2\text{ClCF}_2\text{CH}_2\text{Cl}$ <sup>20</sup> and  $\text{CF}_3\text{CFClCH}_2\text{Cl}$ ,<sup>21</sup> the barrier heights have been estimated as  $66 \pm 2$  and  $67 \pm 2$  kcal/mol, respectively, from matching the ratio of products formed to

RRKM calculations of rate constants as a function of energy. From these results, we conclude that of the DFT levels, the one that provides the most reasonable energies is B3PW91. The choice of basis set is a little more problematic, as the 6-31G(d',p') gives the highest energy barrier (and thus the closest correlation with the estimated experimental energies); however, this basis set is generally considered small, and questions may be raised about the ability of a basis set lacking diffuse functions in obtaining transition-state geometries. Because the trends in energy are reproduced across the set of basis sets, we have chosen the 6-311+G(2d,p) basis set as convenient and accurate enough to use for calculations on a wide series of molecules.

There are 36 unique combinations of the form  $\text{X}_1\text{X}_2\text{FCCCIX}_3\text{X}_4$ , where  $\text{X}_1\text{--X}_4$  are hydrogen, fluorine, or chlorine atoms, which are capable of a 1,2-FCl interchange. Of these, nine have two possible interchanges—we label these *E*- and *Z*- in the transition geometry because of the similarity of the transition state to a substituted ethene. A scheme for these interchanges is given in Fig. 1, and an explanation of the *E*- and *Z*- labels is given in Fig. 2. The  $E_0$  values for these 45 interchanges are presented in Table 2, and from this table several general trends can be seen. The replacement of a hydrogen atom with a fluorine atom on  $\text{C}_1$  increases the barrier height in all cases; this effect is similar for a second fluorine substitution. The effect of fluorine substitution on the second carbon is less consistent than on the first carbon—substitution of one fluorine in most cases leads to a slight increase in threshold energy, but in some cases (such as going from  $\text{CH}_2\text{FCH}_2\text{Cl}$  to  $\text{CH}_2\text{FCHCl}_2$ ), there is a small decrease in threshold energy. Overall, there is a consistently upward trend in the barrier height with the number of fluorine atoms; complete replacement of  $\text{X} = \text{H}$  with  $\text{X} = \text{F}$  leads to an increase in the value of  $E_0$  from 56.4 kcal/mol in  $\text{CH}_2\text{FCH}_2\text{Cl}$  to 74.3 kcal/mol in  $\text{CF}_3\text{CF}_2\text{Cl}$ .

Substitution of a hydrogen by a chlorine on the first car-



**Table 2.** 1,2-FCl interchange barrier heights ( $E_0$  values) in kcal/mol (1 cal = 4.184 J), calculated at B3PW91/6–311+G(2d,p) for all possible combinations of  $X_1X_2CFCClX_3X_4$ , where X = H, F, or Cl.

Substituent	$E_0$ (kcal/mol)					
	–CH <sub>2</sub> Cl	–CHCl <sub>2</sub>	–CCl <sub>3</sub>	–CHFCl	–CFCl <sub>2</sub>	–CF <sub>2</sub> Cl
CH <sub>2</sub> F–	56.4	56.8	55.3	55.4	56	56.6
CHClF–	60.5	60.7/63.7 <sup>a</sup>	62.1	59.5/61.8 <sup>a</sup>	62.3/63.0 <sup>a</sup>	63.2
CHF <sub>2</sub> –	61.8	63.9/63.0 <sup>a</sup>	63.2	61.4/63.3 <sup>a</sup>	63.9/64.4 <sup>a</sup>	65.2
CCl <sub>2</sub> F–	62.1	65.4	66.8	63.4	67.1	67.3
CF <sub>2</sub> Cl–	65.1	67.8/68.5 <sup>a</sup>	69.3	66.5/67.0 <sup>a</sup>	69.9/70.1 <sup>a</sup>	70.9
CF <sub>3</sub> –	67.9	70.8	71.6	70	72.9	74.3

<sup>a</sup>When there are two possible interchanges, the *Z* interchange is listed first, followed by the *E* interchange (see Fig. 2).**Table 3.**  $E_0$  values (in kcal/mol; (1 cal = 4.184 J)) for 1,2-FCl rearrangements divided into a series of isomers, and corresponding relative energies of alkanes and alkenes, all calculated at the B3PW91/6–311+G(2d,p) level of theory.

Isomers and rearrangements	$E_0$ (kcal/mol)	Relative energy of alkane	Relative energy of alkene
C <sub>2</sub> F <sub>3</sub> H <sub>2</sub> Cl			
CF <sub>2</sub> HCHFCl ( <i>Z</i> )	61.4	13.7	10.3
CF <sub>2</sub> HCHFCl ( <i>E</i> )	63.3	12.5	9.6
CF <sub>3</sub> CH <sub>2</sub> Cl	67.9	0	0
C <sub>2</sub> Cl <sub>2</sub> F <sub>2</sub> H <sub>2</sub>			
CF <sub>2</sub> HCHCl <sub>2</sub> ( <i>Z</i> )	63.9	5.3	2.7
CF <sub>2</sub> HCHCl <sub>2</sub> ( <i>E</i> )	63.0	4.6	0.6
CF <sub>2</sub> ClCH <sub>2</sub> Cl	65.1	0	0
C <sub>2</sub> Cl <sub>3</sub> H <sub>2</sub> F			
CHFCICHCl <sub>2</sub> ( <i>Z</i> )	63.7	2.0	1.1
CHFCICHCl <sub>2</sub> ( <i>E</i> )	60.7	1.5	0
CFCl <sub>2</sub> CH <sub>2</sub> Cl	62.1	0	1.2
C <sub>2</sub> F <sub>3</sub> Cl <sub>3</sub>			
CF <sub>2</sub> ClCFCl <sub>2</sub> ( <i>Z</i> )	70.1	4.3	0
CF <sub>2</sub> ClCFCl <sub>2</sub> ( <i>E</i> )	69.9	4.2	2.4
CF <sub>3</sub> CCl <sub>3</sub>	74.3	0	2.6
C <sub>2</sub> F <sub>3</sub> Cl <sub>2</sub> H			
CF <sub>2</sub> ClCHFCl ( <i>Z</i> )	66.5	7.3	5.9
CF <sub>2</sub> ClCHFCl ( <i>E</i> )	67.0	7.6	5.9
CF <sub>3</sub> CCl <sub>2</sub> H	70.8	0	0

bon leads to an increase in the  $E_0$  value; in general, the first chlorine substitution has a greater effect than a second chlorine substitution. Substitution of a hydrogen atom by a chlorine atom on the second carbon produces a smaller increase in energy than does substitution on the first carbon atom, and a second chlorine substitution on the second carbon atom produces an inconsistent effect, sometimes raising the energy barrier, sometimes lowering it, all to a slight extent. The effect of chlorine substitution is consistently smaller than that of fluorine substitution, and in all comparisons, the chlorine-substituted molecules have a lower barrier height than the fluorine-substituted molecules. In all cases where there are the *E* and *Z* pathways, the *Z* pathway is slightly lower (between 0.9 and 3.0 kcal/mol) in energy.

We can investigate the trends in barrier heights by systematically looking at a number of selected results. The threshold energy for rearrangement depends on the relative thermodynamic stabilities of the reactant geometry and the transition geometry—a reactant geometry that is low in energy would lead to a large value of  $E_0$ ; however, a transition

geometry that is low in energy would lead to a small value of  $E_0$ . As these are all rearrangements, the relative energies of the two alkanes have an effect on the barrier height, the more thermodynamically stable leading to the higher barrier height. Because five of these systems are self-exchanges, we can identify the effects of the transition geometry energy alone. In two of the molecules capable of self-exchange there are two transition geometries—the *E* transition geometry is the self-exchange, the *Z* transition geometry leads to a molecule that resembles a rotated form of the opposite stereoisomer. The barrier height for CH<sub>2</sub>FCH<sub>2</sub>Cl is 56.4 kcal/mol, for the *E* interchange of CHF<sub>2</sub>CHFCl it is 61.4 kcal/mol, for the *E* interchange of CHFCICHCl<sub>2</sub> it is 60.7 kcal/mol, for CCl<sub>2</sub>FCCL<sub>3</sub> it is 69.3 kcal/mol, and for CF<sub>3</sub>CF<sub>2</sub>Cl it is 74.3 kcal/mol. These show a clear increase in the barrier height with the replacement of hydrogen atoms by chlorine and fluorine atoms. Because there is no appreciable change in the bond lengths and angles in the transition geometries, this is attributed to the strengths of the C–F and C–Cl bonds, and the difficulty in bending those to the near-

planar transition geometry. If we consider the carbon atoms of the transition geometry to be five-coordinate, the large chlorine atoms are going to have a significant steric effect. These results seem to indicate that the strength of the carbon–fluorine bonds make it more difficult to bend them to a more highly coordinated geometry, similar to findings of the Lewis acidity of  $\text{BF}_3$  and  $\text{BCl}_3$ .<sup>22</sup> This could also explain the larger increase in barrier height owing to fluorines on  $\text{C}_1$  as there are more carbon–fluorine bonds on the one center that need to distort to rearrange.

We can identify individual trends in the energies of the starting geometries and the transition-state geometries by considering the rearrangements in groups of isomeric reactions, as detailed in Table 3, which lists the barrier heights along with the relative energies of the alkanes that are undergoing rearrangement, calculated at the B3PW91/6–311+G(2d,p) level of theory. In all cases except for  $\text{C}_2\text{Cl}_3\text{H}_2\text{F}$ , the alkane with the lowest energy corresponds to the rearrangement with the highest energy barrier. This explains why substitution of a fluorine on  $\text{C}_1$  leads to a larger barrier height than substitution of a fluorine on  $\text{C}_2$ , because in all the haloethanes there is a significant increase in energy when there is both a chlorine and a fluorine on the same carbon (the 2-carbon having the chlorine in the position to rearrange). It is a general trend that the barrier height decreases with the increasing energy of the alkanes; however, the decrease in energy of the threshold barrier is smaller than the increase in energy of the alkanes. This is an indication that the relative energy of the transition geometry is increasing as well as the relative energy of the alkanes; moreover, it is generally a smaller increase in energy.

As pointed out earlier in the results, these transition-state geometries resemble substituted ethylenes loosely coordinated to a fluorine atom and a chlorine atom. This presents an opportunity to divide the transition geometries into families related by the isomers of the substituted ethylenes, allowing us to make some comparisons of the transition geometries alone. Optimizations of the three isomeric alkenes corresponding to the transition geometries have been performed, and their relative energies are included in Table 3. With the exception of  $\text{C}_2\text{F}_2\text{Cl}_2$  (the alkene corresponding to isomers of  $\text{C}_2\text{F}_3\text{Cl}_3$ ), the lowest energy alkene corresponds to the rearrangement with the largest barrier height. It is satisfying to note that the trends in energy of these alkenes can account for many of the variations in barrier height. The increase in energy of the alkenes is not as large in magnitude as the change in energy of the alkanes; hence, the overall barrier height increases slightly. When there is a large increase in the energy of the alkane, but only a small increase in the barrier height (such as in  $\text{CF}_2\text{HCCl}_2\text{F}$ ), there is a substantial increase in the energy of the alkene corresponding to the transition geometry. These alkenes share some common factors—the *Z* isomer is always lower in energy than the *E* isomer, and in most cases this is also seen in the rearrangement.

## Conclusions

We have established that the transition-state geometry for the 1,2-FCl rearrangement of halogenated ethanes is reproduced with a wide range of levels of theory. Despite there

being considerable variation in the value of the barrier heights, a problem when there is no lower bound to the energy, the relative trends in barrier height for the reaction are reproduced with almost any level of theory, so we propose the B3PW91/6–311+G(2d,p) level of theory to be computationally adequate for our study of the factors affecting this rearrangement.

Investigation of the barrier heights for all possible F- and Cl-substituted ethanes show that there is a significant increase in the barrier height if there are fluorines on the same carbon as the fluorine that is undergoing rearrangement, owing to the increased thermodynamic stability of the alkane. There is a smaller, but consistent increase in barrier height when chlorines are substituted, interpreted as a steric effect of having to bring the chlorines into close proximity in the quasi-pentavalent carbon involved in the transition geometry. There is also an effect on the interchange energy dependent upon the transition geometry—a transition geometry that resembles a low-energy alkene is likely to have a large barrier height, and increased energy of the alkene leads to a smaller barrier height. Rearrangement is most likely when there are a number of hydrogen atoms on the alkane; however, that can make the interchange less likely to be observed, as it will be in competition with 1,2-HF and 1,2-HCl eliminations.

## References

- (1) Burgin, M. O.; Heard, G. L.; Martell, J. M.; Holmes, B. E. *J. Phys. Chem. A* **2001**, *105* (9), 1615. doi:10.1021/jp002511d.
- (2) Dolbier, W. R., Jr.; Romelaer, R.; Baker, J. M. *Tetrahedron Lett.* **2002**, *43* (45), 8075. doi:10.1016/S0040-4039(02)01952-4.
- (3) Beaver, M. R.; Heard, G. L.; Holmes, B. E. *Tetrahedron Lett.* **2003**, *44* (39), 7265. doi:10.1016/S0040-4039(03)01883-5.
- (4) Burgin, M. O.; Simmons, J. G., Jr.; Heard, G. L.; Setser, D. W.; Holmes, B. E. *J. Phys. Chem. A* **2007**, *111* (12), 2283. doi:10.1021/jp066722f. PMID:17388315.
- (5) Beaver, M. R.; Simmons, J. G., Jr.; Heard, G. L.; Setser, D. W.; Holmes, B. E. *J. Phys. Chem. A* **2007**, *111* (34), 8445. doi:10.1021/jp071837k. PMID:17685496.
- (6) Martell, J. M.; Beaton, P. T.; Holmes, B. E. *J. Phys. Chem. A* **2002**, *106* (36), 8471. doi:10.1021/jp020931s.
- (7) Frisch, M. J.; Trucks, G. W.; Schlegel, H. B.; Scuseria, G. E.; Robb, M. A.; Cheeseman, J. R.; Montgomery, J. A., Jr.; Vreven, T.; Kudin, K. N.; Burant, J. C.; Millam, J. M.; Iyengar, S. S.; Tomasi, J.; Barone, V.; Mennucci, B.; Cossi, M.; Scalmani, G.; Rega, N.; Petersson, G. A.; Nakatsuji, H.; Hada, M.; Ehara, M.; Toyota, K.; Fukuda, R.; Hasegawa, J.; Ishida, M.; Nakajima, T.; Honda, Y.; Kitao, O.; Nakai, H.; Klene, M.; Li, X.; Knox, J. E.; Hratchian, H. P.; Cross, J. B.; Adamo, C.; Jaramillo, J.; Gomperts, R.; Stratmann, R. E.; Yazyev, O.; Austin, A. J.; Cammi, R.; Pomelli, C.; Ochterski, J. W.; Ayala, P. Y.; Morokuma, K.; Voth, G. A.; Salvador, P.; Dannenberg, J. J.; Zakrzewski, V. G.; Dapprich, S.; Daniels, A. D.; Strain, M. C.; Farkas, O.; Malick, D. K.; Rabuck, A. D.; Raghavachari, K.; Foresman, J. B.; Ortiz, J. V.; Cui, Q.; Baboul, A. G.; Clifford, S.; Cioslowski, J.; Stefanov, B. B.; Liu, G.; Liashenko, A.; Piskorz, P.; Komaromi, I.; Martin, R. L.; Fox, D. J.; Keith, T.; Al-Laham, M. A.; Peng, C. Y.; Nanayakkara, A.; Challacombe, M.; Gill, P. M. W.; Johnson, B.; Chen, W.; Wong, M. W.;

- Gonzalez, C.; Pople, J. A. *Gaussian 03*, revision B.04; Gaussian, Inc.: Wallingford, CT, 2004.
- (8) Petersson, G. A.; Al-Laham, M. A. *J. Chem. Phys.* **1991**, *94* (9), 6081. doi:10.1063/1.460447.
  - (9) McLean, A. D.; Chandler, G. S. *J. Chem. Phys.* **1980**, *72* (10), 5639. doi:10.1063/1.438980.
  - (10) Woon, D. E.; Dunning, T. H., Jr. *J. Chem. Phys.* **1993**, *98* (2), 1358. doi:10.1063/1.464303.
  - (11) Lynch, B. J.; Zhao, Y.; Truhlar, D. G. *J. Phys. Chem. A* **2003**, *107* (9), 1384. doi:10.1021/jp021590l.
  - (12) Becke, A. D. *J. Chem. Phys.* **1993**, *98* (7), 5648. doi:10.1063/1.464913.
  - (13) Perdew, J. P.; Burke, K.; Wang, Y. *Phys. Rev. B* **1996**, *54* (23), 16533. doi:10.1103/PhysRevB.54.16533.
  - (14) Lee, C.; Yang, W.; Parr, R. G. *Phys. Rev. B* **1988**, *37* (2), 785. doi:10.1103/PhysRevB.37.785.
  - (15) Adamo, C.; Barone, V. *J. Chem. Phys.* **1998**, *108* (2), 664. doi:10.1063/1.475428.
  - (16) Zhao, Y.; Truhlar, D. G. *J. Phys. Chem. A* **2004**, *108* (33), 6908. doi:10.1021/jp048147q.
  - (17) Becke, A. D. *J. Chem. Phys.* **1996**, *104* (3), 1040. doi:10.1063/1.470829.
  - (18) Curtiss, L. A.; Raghavachari, K.; Pople, J. A. *J. Chem. Phys.* **1993**, *98* (2), 1293. doi:10.1063/1.464297.
  - (19) Montgomery, J. A., Jr.; Frisch, M. J.; Ochterski, J. W.; Petersson, G. A. *J. Chem. Phys.* **2000**, *112* (15), 6532. doi:10.1063/1.481224.
  - (20) Zaluzhna, O.; Simmons, J. G., Jr.; Setser, D. W.; Holmes, B. E. *J. Phys. Chem. A* **2008**, *112* (47), 12117. doi:10.1021/jp806732e. PMID:18983135.
  - (21) Zaluzhna, O.; Simmons, J. G., Jr.; Heard, G. L.; Setser, D. W.; Holmes, B. E. *J. Phys. Chem. A* **2008**, *112* (27), 6090. doi:10.1021/jp800488q. PMID:18553952.
  - (22) Rowsell, B. D.; Gillespie, R. J.; Heard, G. L. *Inorg. Chem.* **1999**, *38* (21), 4659. doi:10.1021/ic990713m. PMID:11671188.

# Geminal acylation of $\alpha$ -heterosubstituted cyclohexanones and their ketals

Ian R. Pottie, Sheldon N. Crane, Anna Lee Gosse, David O. Miller, and D. Jean Burnell

**Abstract:** Geminal acylation of derivatives of cyclohexanone with Br, Cl, F, and OCH<sub>3</sub> in the  $\alpha$  position, and of their corresponding dimethyl ketals, could not be accomplished to a significant extent following published procedures. The transformation was accomplished in two steps. The initial BF<sub>3</sub>·Et<sub>2</sub>O-mediated reaction with 1,2-bis(trimethylsilyloxy)cyclobutene gave a cyclobutanone product as a mixture of diastereomers. Only with 2-chlorocyclohexanone did this occur with good diastereoselectivity. Then, pinacol rearrangement of the diastereomeric mixture mediated by Amberlyst-15 in benzene provided the heterosubstituted spirocyclic diketone.

**Key words:** diastereoselectivity, Mukaiyama aldol, geminal acylation, spirocyclic diketone.

**Résumé :** L'acylation géminal de dérivés de la cyclohexanone portant des substituants Br, Cl, F et OCH<sub>3</sub> en position  $\alpha$  ainsi que celle des diméthylcétales correspondants ne peut pas être réalisée avec des rendements significatifs par les méthodes rapportées jusqu'à maintenant. On a réussi à effectuer cette transformation en deux étapes. La réaction initiale catalysée par le BF<sub>3</sub>·Et<sub>2</sub>O avec le 1,2-bis(triméthylsilyloxy)cyclobutène conduit à un produit à base de cyclobutanone, sous la forme de mélange de diastéréoisomères. Cette transformation ne s'est effectuée avec une bonne diastéréosélectivité qu'avec la 2-chlorocyclohexanone. La transposition pinacolique du mélange diastéréoisomère catalysée par l'Amberlyst-15 dans le benzène conduit alors à une dicétone spirocyclique hétérosubstituée.

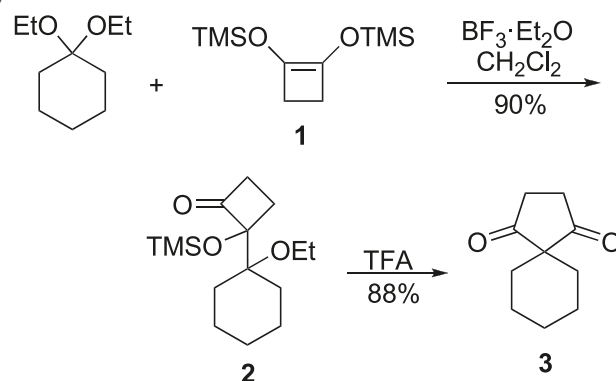
**Mots-clés :** diastéréosélectivité, aldol de Mukaiyama, acylation géminal, dicétone spirocyclique.

## Introduction

The geminal acylation of ketones and their ketals with 1,2-bis(trimethylsilyloxy)cyclobutene (**1**) is a powerful method for generating 2,2-disubstituted 1,3-cyclopentanedione systems in high yield. Kuwajima and co-workers<sup>1</sup> introduced this transformation as a two-step procedure (Scheme 1). First, a BF<sub>3</sub>·Et<sub>2</sub>O-mediated Mukaiyama aldol between a ketal and **1**<sup>2,3</sup> affords a cyclobutanone, e.g., **2**. Then, pinacol rearrangement of **2** is effected by treatment with trifluoroacetic acid (TFA), generating a 1,3-diketone such as **3**.

The process can be carried out, generally in excellent yield, in one pot by the use of a large excess of BF<sub>3</sub>·Et<sub>2</sub>O.<sup>4–7</sup> Geminal acylation of ketones is facilitated by the addition of a small amount of water to the reaction medium after formation of the cyclobutanone intermediate.<sup>8</sup> Methyl-substituted versions of **1** can also be used for this reaction.<sup>9,10</sup> Geminal acylation has appeared as a key process in many synthetic and methodological endeavors.<sup>11–13</sup> Substitution by alkyl groups  $\alpha$  to the ketone, or ketal, reduces the yield of the geminal acylation. For instance, the ethylene ketal of cyclo-

**Scheme 1.** Geminal acylation in two steps with the diethyl ketal of cyclohexanone.<sup>1</sup>



hexanone was geminally acylated in 96% yield using the one-pot procedure,<sup>13</sup> but the ketal of 2-methylcyclohexanone gave only a 30% yield of the geminal acylation product.<sup>7</sup> In a similar way, yields with ketones were lower when the  $\alpha$  position was more substituted. The geminal acylation of cyclohexanone gave the diketone product in 94% yield, but

Received 8 January 2010. Accepted 9 February 2010. Published on the NRC Research Press Web site at canjchem.nrc.ca on 28 October 2010.

This article is part of a Special Issue dedicated to Professor R. J. Boyd.

**I.R. Pottie.** Department of Chemistry and Physics, Mount Saint Vincent University, Halifax, NS B3M 2J6, Canada.

**S.N. Crane, A.L. Gosse, and D.O. Miller.** Department of Chemistry, Memorial University of Newfoundland, St. John's, NL A1B 3X7, Canada.

**D.J. Burnell.**<sup>1</sup> Department of Chemistry, Dalhousie University, Halifax, NS B3H 4J3, Canada.

<sup>1</sup>Corresponding author (e-mail: jean.burnell@dal.ca).



under very similar conditions 2-methylcyclohexanone provided the diketone in only 62% yield.<sup>8</sup> Differing degrees of  $\alpha$  substitution has allowed selective geminal acylation to take place.<sup>8,13</sup> The reason for the attenuation of the yields has been presumed to be steric hindrance.

It was thought that  $\alpha$  substitution by a heteroatom might be better tolerated than  $\alpha$  substitution by an alkyl group because the former might have a smaller steric effect. The products of geminal acylations with  $\alpha$ -substituted ketones or ketals would possess functionality that might be useful for further synthetic manipulation. The results of our experiments with  $\alpha$ -substituted cyclohexanones and their corresponding dimethyl ketals are presented here.

## Results and discussion

The dimethyl ketals of 2-bromo-, 2-chloro-, 2-fluoro-, and 2-methoxycyclohexanone were subjected to the conditions previously used by Kuwajima and co-workers<sup>1</sup> for the two-step geminal acylation of the ketal of cyclohexanone. Geminally acylated product was not detected from any of these ketals. The same ketals were treated with an excess of **1** and a large excess of  $\text{BF}_3 \cdot \text{Et}_2\text{O}$ . These conditions would have geminally acylated the ketal of cyclohexanone in high yield,<sup>4,7</sup> but, once again, no geminally acylated product was obtained.

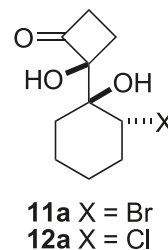
The procedure developed by Kuwajima and co-workers was used with the four  $\alpha$ -substituted ketones, but only two gave geminally acylated products: **4** in 7% yield from the 2-bromocyclohexanone and **5** in 10% yield from the 2-methoxycyclohexanone. Conditions had been developed specifically for the geminal acylation of ketones in one pot.<sup>8</sup> When these conditions were applied to the four  $\alpha$ -substituted ketones, only two yielded a detectable amount of a geminally acylated product: **4** in 24% yield from the 2-bromocyclohexanone and **6** in 4% yield from the 2-chlorocyclohexanone.

TLC analysis of the reactions of the ketals and of the ketones indicated that the starting compounds were consumed fairly rapidly.  $^{13}\text{C}$  NMR spectra of the resulting material included clusters of resonances between  $\delta$  90 and 100 ppm. Chemical shifts in this region have been seen for the carbinolic carbon of a cyclobutane intermediate,<sup>1,8,9</sup> and it was surmised that as a result of these attempted geminal acylations, the Mukaiyama aldol reactions had taken place to give cyclobutanone derivatives (**7–14**), but the pinacol rearrangements had failed. The products from the ketals **7–10** were mixtures with silylated alcohol functions, but product ratios could not be determined owing to partial desilylation. The products from the ketones **11–14** were obtained with alcohol functions only. NMR signals were discerned for at least three of the four possible diastereomers of **11–14**, and the proportions of these diastereomers (Table 1) were estimated by integration of the NMR spectra of the crude mixtures of diastereomers.

Only 2-chlorocyclohexanone showed good stereoselectivity (80% of one diastereomer by NMR), and a tiny amount of the major diastereomer **12a** was isolated by repeated flash chromatography. 2-Bromocyclohexanone had reacted with modest stereoselectivity (the ratio of diastereomers was only 3:1:1:1), and a very small amount of the major diaste-

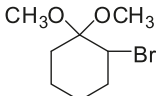
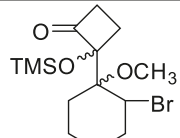
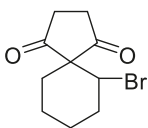
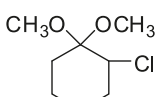
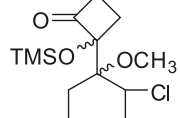
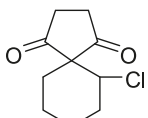
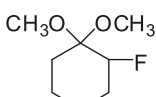
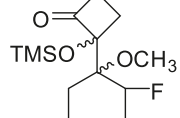
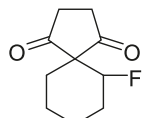
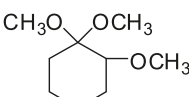
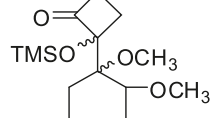
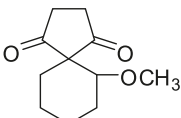
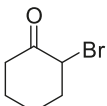
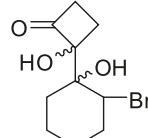
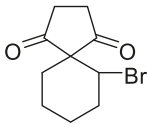
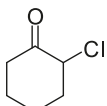
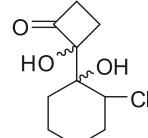
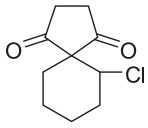
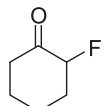
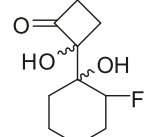
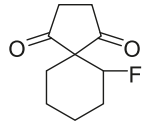
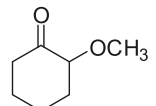
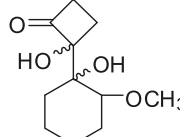
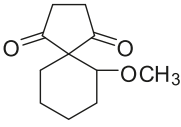
reomer **11a** separated from the others during chromatography. (The diastereomeric mixtures **9**, **10**, **13**, and **14** could not be separated by flash chromatography.) It was fortuitous that both **11a** and **12a** provided crystals that allowed analysis by X-ray crystallography. This analysis revealed that these major diastereomers had the same basic structure (Figs. 1 and 2).

Diastereoselective additions of nucleophiles, such as hydride, organomagnesium reagents, and organolithium reagents, to  $\alpha$ -heterosubstituted cyclohexanones have been noted a number of times.<sup>14–16</sup> The selectivity has been rationalized in terms of Felkin–Anh control<sup>15</sup> and electrostatic interactions.<sup>14,17</sup> Previous studies involved products that were predominantly the result of addition to the face of the carbonyl anti to the heteroatom. However, in both **11a** and **12a**, the position of the cyclobutanone moiety relative to the halogen was *cis* with respect to the cyclohexane ring, which implied that the Mukaiyama aldol reaction preferentially occurred on the face of the ketone *syn* to the halogen. Previous work with conformationally locked cyclohexanones indicated that addition of hydride was predominantly axial, and the rate of anti addition to the carbonyl was faster when the  $\alpha$ -heteroatom was axial.<sup>14</sup> In other words, the diastereoselectivity of additions of smaller nucleophiles to  $\alpha$ -substituted cyclohexanones arises from axial addition to the carbonyl when the  $\alpha$ -substituent is axial and anti to the incoming nucleophile. NMR studies have shown that the cyclohexanone conformer with the  $\alpha$ -halogen in an axial position is either the major conformer or at least similar in energy to the conformer with an equatorial halogen.<sup>15,18</sup>

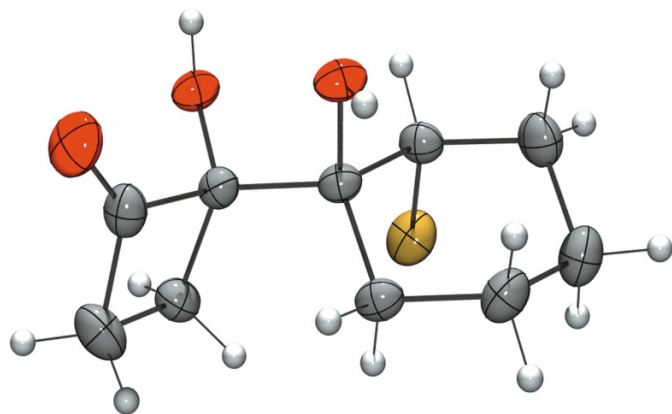
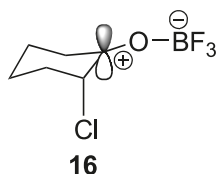
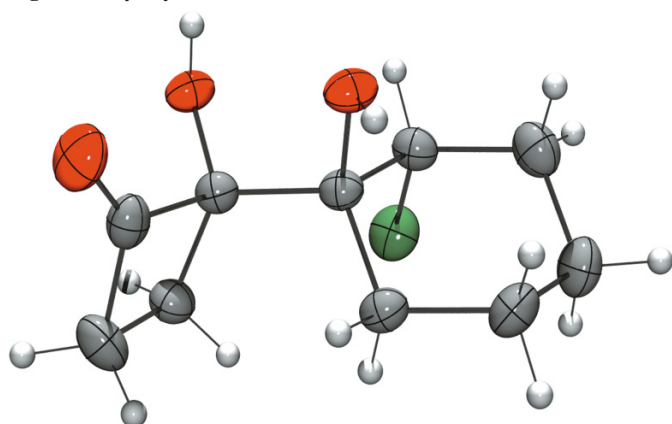


In contrast with the reactions of hydride and many organometallics, the initial step of the geminal acylation of cyclohexanone or its ketal gives mainly the product of equatorial addition.<sup>1,8</sup> If that mode of addition is still the case with the  $\alpha$ -heterosubstituted cyclohexanones, what is intriguing is that the relative stereochemistry observed with **11a** and **12a** must have arisen by addition of **1** *syn* to the  $\alpha$ -heteroatom, but with the conformation of the cyclohexanone having the heteroatom in an axial position. It has been accepted for a long time that equatorial additions to cyclohexanones by larger nucleophiles are due to larger steric interactions in the transition state for axial addition.<sup>19</sup> On the other hand, the axial disposition of the heteroatom is likely due to stabilization of the intermediate carbocation (e.g., **16**). Thus, a plausible reason for the generally low stereoselectivity of the addition reactions summarized in Table 1, relative to additions of smaller nucleophiles,<sup>13–15</sup> would be that the axial heteroatom would retard attack by **1**, since this larger nucleophile would be adding equatorially, which would be *syn* to the heteroatom, making other modes of reaction competitive in rate.

**Table 1.** Results of the two-step geminal acylation of  $\alpha$ -heterosubstituted cyclohexanones and their ketals.

Substrate	Cyclobutanone	Yield (%)	1, 3-Diketone	Yield (%)
	 <b>7</b>	46	 <b>4</b>	62
	 <b>8</b>	48	 <b>6</b>	42
	 <b>9</b>	80	 <b>15</b>	80
	 <b>10</b>	90	 <b>5</b>	0
	 <b>11</b> (dr 3:1:1:1)	56	 <b>4</b>	80
	 <b>12</b> (dr 12:2:2:1)	77	 <b>6</b>	95
	 <b>13</b> (dr 2:1:1:0)	54	 <b>15</b>	92
	 <b>14</b> (dr 2:1:1:0)	83	 <b>5</b>	51

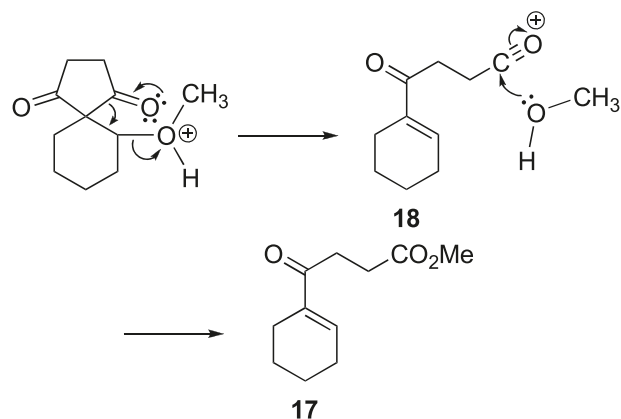
<sup>a</sup> The initial reaction involved **1** with  $\text{BF}_3 \cdot \text{Et}_2\text{O}$  in  $\text{CH}_2\text{Cl}_2$  at  $-78^\circ\text{C}$ , and the rearrangement step was with Amberlyst-15 in benzene under reflux.

Fig. 1. X-ray crystal structure of **11a**.Fig. 2. X-ray crystal structure of **12a**.

When some cyclobutanone compounds were maintained in warm TFA, very little, if any, rearrangement took place, but the starting compound was steadily consumed, and some material that was insoluble in common organic solvents was produced. The formation of a spirocyclic 1,3-diketone from the cyclobutanone might take place in a step-wise fashion, by initial generation of an intermediate tertiary carbocation followed by rearrangement, or by a concerted mechanism in which carbon–carbon bond reorganization accompanies the loss of the oxygen. TFA, being a polar medium, should stabilize a discrete carbocation. However, calculations by Nakamura and Osamura<sup>20</sup> suggested that as a carbocation is stabilized, the energy required for carbon–carbon bond reorganization increases. This would likely make other reaction pathways (leading to decomposition) more competitive. It was hypothesized that performing the rearrangement in a nonpolar medium would create a more favorable situation for a concerted process to occur instead of other more destructive reaction pathways.

To this end, benzene was chosen as the solvent and

Scheme 2.



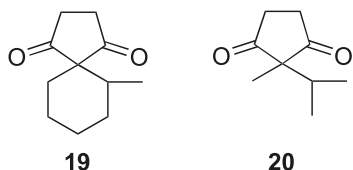
Amberlyst-15, which is a resin with sulfonic acid sites, was chosen as the acid. Amberlyst-15 had proven to be an excellent catalyst for the rearrangement of cyclobutanone intermediates generated from aldehydes.<sup>21</sup> It was gratifying that the desired spirocyclic 1,3-diketone (**6**) was obtained in 95% yield. The use of *p*-TsOH in the place of Amberlyst-15 gave no rearranged product, just intractable material. This dramatic difference in the result was evidence that the macroreticular structure of the resin, and not just its acidity, plays an important role in promoting the rearrangement of the cyclobutanone. This may be related to pinacol rearrangements mediated by acidic agents in other porous structures, e.g., iron(III)-substituted molecular sieves.<sup>22</sup>

The procedure using Amberlyst-15 was carried out with all of the cyclobutanone derivatives in Table 1. The cyclobutanones derived from ketones (**11–14**) rearranged within an hour in benzene under reflux. The halogenated compounds **11–13** provided the 1,3-diketones **4**, **6**, and **15** in excellent yield. The methoxy derivative **5** was obtained in modest yield from **14**. Diketone **5** was accompanied by a significant amount of by-product, which was difficult to separate. It appeared by <sup>1</sup>H NMR spectroscopic analysis to be **17**. (Its diagnostic NMR signals were a multiplet at  $\delta$  6.98 ppm, a singlet at  $\delta$  3.71 ppm, and triplets at  $\delta$  3.00 and 2.64 ppm.) It was likely that **17** was produced from **5** (Scheme 2). Acid-catalyzed elimination of methanol might be accompanied by ring-opening and generation of the acylium ion **18**, which would then capture the evolved methanol to provide **17**.

The reactions of the cyclobutanones derived from the ketals (**7–10**) were sluggish, requiring 48 h to consume the starting materials in benzene under reflux. The 1,3-diketones **4**, **6**, and **15** were isolated in poorer yield than from **11–13**, and the methoxycyclobutanone **10** gave none of the 1,3-diketone **5**. The reason for the slower reaction was the presence of the TMS group, because desilylation of **8** with TBAF followed immediately by treatment with Amberlyst-15 in benzene gave **6** in 88% yield.

The success of the two-step process from ketones prompted us to re-examine the reactions of two  $\alpha$ -substituted substrates that had given only modest yields of 1,3-diketones previously. 2-Methylcyclohexanone and 3-methylbutanone had given **19** and **20** in yields of 62% and 52%, respectively, using the one-pot, two-step method using excess  $\text{BF}_3 \cdot \text{Et}_2\text{O}$  to effect the rearrangement.<sup>8</sup> In contrast, using the

same two-step procedure involving Amberlyst-15 that was used to produce the spirocyclic 1,3-diketones in Table 1, **19** and **20** were prepared in 84% and 80% yield, respectively, from the ketones.



In summary, a two-step procedure has been developed for the geminal acylation of an  $\alpha$ -heterosubstituted cyclohexanone. The first step is the  $\text{BF}_3 \cdot \text{Et}_2\text{O}$ -mediated addition of **1** to the ketone to give a cyclobutanone intermediate, and the second is the rearrangement of the cyclobutanone in benzene with Amberlyst-15. The process works less well with the corresponding ketal. Following the same procedure, yields of geminally acylated products from ketones substituted in the  $\alpha$  position with alkyl groups are improved over the older one-pot, two-step procedure. It is expected that the procedure will be widely applicable for the geminal acylation of other cyclic and acyclic ketones with  $\alpha$  substitution.

## Experimental

### General

All reactions were performed under  $\text{N}_2$ .  $\text{BF}_3 \cdot \text{Et}_2\text{O}$  was distilled before use.  $\text{CH}_2\text{Cl}_2$  and benzene were distilled from calcium hydride before use. Flash chromatography used 230–400 mesh silica gel, starting with 20% ethyl acetate–hexane mixtures with an increasing portion of ethyl acetate as the eluting solvent.  $^1\text{H}$  NMR spectra were recorded in  $\text{CDCl}_3$ . Chemical shifts are relative to internal TMS.  $^{13}\text{C}$  NMR chemical shifts are relative to the  $\text{CDCl}_3$  solvent ( $\delta$  77.0 ppm). Each  $^{13}\text{C}$  NMR chemical shift is followed by a number in parentheses that represents the number of attached protons as determined by DEPT experiments. Compound **1** was prepared by the method of Bloomfield and Nelke.<sup>3</sup> 2-Chloro-, 2-methoxy-, and 2-methyl-cyclohexanone and 3-methylbutanone were purchased (Sigma-Aldrich). 2-Bromo- and 2-fluorocyclohexanone were prepared by oxidation of the corresponding alcohols<sup>23</sup> with pyridinium chlorochromate. Ketals<sup>24</sup> were formed by treatment of the ketones with methanol–trimethyl-orthoformate (1:1) with some *p*-TsOH.

### General procedure for geminal acylation

To a solution of the ketone or ketal (1.0 mmol) in  $\text{CH}_2\text{Cl}_2$  (8 mL) at  $-78^\circ\text{C}$  was added  $\text{BF}_3 \cdot \text{Et}_2\text{O}$  (1.5 mmol) and then **1** (3.0 mmol) dropwise. The mixture was warmed slowly to room temperature (rt) and then stirred until TLC indicated that the starting ketone or ketal was consumed. The mixture was concentrated under reduced pressure. Flash chromatography was used to remove unreacted and decomposed **1** from the mixture of cyclobutanone products. The cyclobutanone mixture was dissolved in benzene (25 mL). Amberlyst-15 (0.25 g) was added to this solution, and the resulting mixture was heated under reflux. When TLC indicated that the cyclobutanones had been consumed, the mixture was

cooled to rt, and the Amberlyst-15 was removed by gravity filtration. The filtrate was concentrated under reduced pressure, and flash chromatography afforded the 1,3-diketone. Characterization data for the 1,3-diketones **4**, **5**, **6**, and **15** and the cyclobutanone intermediates **11a** and **12a** are given in the following. Data for **19** and **20** were consistent with published data.<sup>7</sup>

### 6-Bromospiro[4.5]decane-1,4-dione (**4**)

Solid, mp  $56\text{--}58^\circ\text{C}$ . IR (Nujol,  $\text{cm}^{-1}$ ): 1728, 1460, 1377, 1311, 1178, 986, 696.  $^1\text{H}$  NMR (500 MHz)  $\delta$ : 4.12 (dd,  $J = 12.7, 4.7$  Hz, 1H), 2.81–2.73 (m, 4H), 2.54 (dq,  $J = 13.1, 4.1$  Hz, 1H), 2.13 (m, 1H), 1.86 (m, 1H), 1.80–1.73 (m, 2H), 1.59 (m, 1H), 1.51 (m, 1H), 1.40 (m, 1H).  $^{13}\text{C}$  NMR (125 MHz)  $\delta$ : 214.2 (0), 213.1 (0), 59.3 (0), 49.4 (1), 35.5 (2), 34.8 (2), 32.9 (2), 31.7 (2), 26.7 (2), 18.9 (2). GC–MS: 246 ( $\text{M}^{+2}$ , 2), 244 ( $\text{M}^{+}$ , 2), 166 (11), 165 (100), 164 (8), 147 (4), 123 (15), 109 (14), 95 (7). HRMS (EI) calcd. for  $\text{C}_{10}\text{H}_{13}\text{BrO}_2$ : 244.0099; found: 244.0098.

### 6-Methoxyspiro[4.5]decane-1,4-dione (**5**)

Yellow oil.  $^1\text{H}$  NMR (500 MHz)  $\delta$ : 3.44 (dd,  $J = 11.7, 4.5$  Hz, 1H), 3.20 (s, 3H), 2.73–2.63 (m, 4H), 1.97 (m, 1H), 1.88 (m, 1H), 1.83–1.75 (m, 2H), 1.59 (m, 1H), 1.50–1.44 (m, 2H), 1.30–1.24 (m, 2H).  $^{13}\text{C}$  NMR (125 MHz)  $\delta$ : 217.8 (0), 215.9 (0), 83.8 (1), 59.4 (0), 56.9 (3), 36.5 (2), 35.9 (2), 30.1 (2), 24.9 (2), 23.8 (2), 19.9 (2). GC–MS: 196 ( $\text{M}^{+}$ , 64), 182 (25), 181 (100), 165 (53), 164 (80), 163 (54), 141 (51), 138 (58), 136 (58), 125 (68), 112 (96). HRMS (EI) calcd. for  $\text{C}_{11}\text{H}_{16}\text{O}_3$ : 196.1099; found: 196.1092.

### 6-Chlorospiro[4.5]decane-1,4-dione (**6**)

Solid, mp  $42\text{--}46^\circ\text{C}$ .  $^1\text{H}$  NMR (500 MHz)  $\delta$ : 4.08 (dd,  $J = 12.5, 4.7$  Hz, 1H), 2.82–2.72 (m, 4H), 2.38 (m, 1H), 2.01 (m, 1H), 1.91 (m, 1H), 1.78–1.71 (m, 2H), 1.56–1.46 (m, 2H), 1.38 (m, 1H).  $^{13}\text{C}$  NMR (125 MHz)  $\delta$ : 214.4 (0), 213.1 (0), 59.4 (0), 59.1 (1), 35.9 (2), 35.2 (2), 32.2 (2), 31.0 (2), 25.6 (2), 18.9 (2). GC–MS: 202 ( $\text{M}^{+2}$ , 2), 200 ( $\text{M}^{+}$ , 5), 166 (11), 165 (100), 164 (28), 147 (9), 137 (6), 123 (24), 109 (34). HRMS (EI) calcd. for  $\text{C}_{10}\text{H}_{13}\text{ClO}_2$ : 200.0604; found: 200.0598.

### 6-Fluorospiro[4.5]decane-1,4-dione (**15**)

Solid, mp  $62\text{--}63^\circ\text{C}$ . IR (Nujol,  $\text{cm}^{-1}$ ): 1721, 1456, 1377, 1307, 1182, 1020, 963.  $^1\text{H}$  NMR (500 MHz)  $\delta$ : 4.70 (ddd,  $J = 4.8, 11.8, 47.4$  Hz, 1H), 2.80–2.70 (m, 4H), 2.15 (m, 1H), 1.97–1.89 (m, 2H), 1.78–1.65 (m, 2H), 1.51–1.45 (m, 2H), 1.32 (m, 1H).  $^{13}\text{C}$  NMR (125 MHz)  $\delta$ : 215.0 (0), 213.4 (0), 94.2 (1, d,  $J = 175.4$  Hz), 58.9 (0, d,  $J = 20.0$  Hz), 35.8 (2, d,  $J = 70.7$  Hz), 30.2 (2, d,  $J = 5.7$  Hz), 26.8 (2, d,  $J = 18.0$  Hz), 23.1 (2, d,  $J = 11.5$  Hz), 19.2 (2). GC–MS: 184 ( $\text{M}^{+}$ , 80), 164 (49), 155 (18), 129 (18), 109 (96), 103 (23), 81 (100). HRMS (EI) calcd. for  $\text{C}_{10}\text{H}_{13}\text{FO}_2$ : 184.0900; found: 184.0904.

### (1'*R*\*,2'*R*\*,2'*S*\*)-2-(2-Bromo-1-hydroxycyclohexyl)-2-hydroxycyclobutanone (**11a**)

Solid. IR (Nujol,  $\text{cm}^{-1}$ ): 3389 (sharp), 1776, 1737, 1462, 1377.  $^1\text{H}$  NMR (300 MHz)  $\delta$ : 4.40 (narrow m, 1H), 3.25 (ddd,  $J = 8.6, 12.4, 17.4$  Hz, 1H), 3.23 (s, OH), 2.93 (ddd,  $J = 6.9, 10.8, 17.4$  Hz, 1H), 2.70 (m, 1H), 2.45 (s, OH),



**Table 2.** X-ray crystallographic data for **11a** and **12a**.

Data	Crystal	
	<b>11a</b>	<b>12a</b>
Empirical formula	C <sub>10</sub> H <sub>15</sub> BrO <sub>3</sub>	C <sub>10</sub> H <sub>15</sub> ClO <sub>3</sub>
Formula mass	263.13	218.68
Color, habit	Colorless, irregular	Colorless, irregular
Dimensions (mm)	0.40×0.25×0.25	0.40×0.30×0.10
Crystal system	Orthorhombic	Orthorhombic
Space group	<i>Pbca</i> (No. 61)	<i>Pbca</i> (No. 61)
<i>Z</i>	8	8
<i>a</i> (Å)	11.490(2)	11.440(5)
<i>b</i> (Å)	22.733(5)	22.389(6)
<i>c</i> (Å)	8.156(2)	8.122(7)
Collection ranges	−12≤ <i>h</i> ≤12; −25≤ <i>k</i> ≤25; −9≤ <i>l</i> ≤9	0≤ <i>h</i> ≤12; 0≤ <i>k</i> ≤25; 0≤ <i>l</i> ≤9
Temperature (K)	299(2)	299(2)
<i>V</i> (Å <sup>3</sup> )	2130.1(8)	2080.4(20)
Calcd. density (g cm <sup>−3</sup> )	1.641	1.396
Absorption coefficient $\mu$ (Cu K $\alpha$ ) (cm <sup>−1</sup> )	51.15	31.02
<i>F</i> (000)	1072	928
$\theta$ range for data collection (°)	3.89–59.97	3.95–59.99
No. of reflections	3278	1612
No. of unique reflections	1583 ( <i>R</i> <sub>int</sub> = 0.0177)	1545 ( <i>R</i> <sub>int</sub> = 0.0215)
Reflection parameter	12.37	11.98
Maximum shift –error	0.001	0.001
Goodness-of-fit on <i>F</i> <sup>2</sup>	1.037	1.099
<i>R</i> <sub>1</sub> , [ <i>I</i> > $\sigma$ ( <i>I</i> )]	0.0399	0.0365
<i>R</i> indices (all reflections)	<i>R</i> = 0.0529, <i>wR</i> <sub>2</sub> = 0.1153	<i>R</i> = 0.0572, <i>wR</i> <sub>2</sub> = 0.1126
Largest diff. peak and hole (e Å <sup>−3</sup> )	0.32 and −0.83	0.22 and −0.34

2.37–2.14 (m, 4H), 1.91 (d of narrow m, *J* = 15.0 Hz, 1H), 1.81–1.55 (m, 4H), 1.41 (br d, *J* = 13.8 Hz, 1H). <sup>13</sup>C NMR (75 MHz)  $\delta$ : 212.7 (0), 95.5 (0), 74.6 (0), 51.4 (1), 44.4 (2), 30.5 (2), 27.6 (2), 26.0 (2), 20.1 (2), 20.0 (2). GC–MS: no M<sup>+</sup>, 182 (2), 164 (46), 139 (53), 125 (43), 112 (59), 111 (60), 81 (68), 79 (57), 55 (100).

#### (1'*R*\*,2*R*\*,2'*S*\*)-2-(2-Chloro-1-hydroxycyclohexyl)-2-hydroxycyclobutanone (**12a**)

Solid, mp 126–128 °C. <sup>1</sup>H NMR (300 MHz)  $\delta$ : 4.29 (br s, 1H), 3.42 (s, OH), 3.24 (m, 1H), 2.90 (m, 1H), 2.67 (m, 1H), 2.44 (s, OH), 2.35–1.94 (m, 4H), 1.82 (d of narrow m, *J* = 17 Hz, 1H), 1.81–1.55 (m, 4H), 1.41 (br d, *J* = 12 Hz, 1H). <sup>13</sup>C NMR (75 MHz)  $\delta$ : 211.8 (0), 94.2 (0), 74.6 (0), 60.2 (1), 46.1 (2), 31.7 (2), 29.1 (2), 27.2 (2), 21.9 (2), 21.0 (2). GC–MS: no M<sup>+</sup>, 183 (3), 165 (56), 133 (45), 109 (77), 81 (100), 79 (64), 55 (80), 43 (99).

#### X-ray crystallography

Table 2 summarizes the crystallographic data for **11a** and **12a**. Diffraction data were acquired using a Rigaku AFC6S diffractometer with graphite-monochromated Cu K $\alpha$  radiation ( $\lambda$  = 1.54178 Å). An empirical absorption correction was applied. The data were corrected for Lorentz and polarization effects. The structures were solved by direct methods and expanded using Fourier techniques. The non-hydrogen atoms were refined anisotropically. Hydrogen atoms were refined using the riding model. Final cycles of full-matrix least-squares refinement were applied. All calculations were performed using the CrystalStructure<sup>25</sup> crystallographic soft-

ware package except for refinement, which was performed using SHELXL-97.<sup>26</sup>

#### Supplementary data

Supplementary data for this article are available on the journal Web site (canjchem.nrc.ca). CCDC 760849 and 760850 contain the X-ray data in CIF format for this manuscript. These data can be obtained, free of charge, via [www.ccdc.cam.ac.uk/conts/retrieving.html](http://www.ccdc.cam.ac.uk/conts/retrieving.html) (or from the Cambridge Crystallographic Data Centre, 12 Union Road, Cambridge CB2 1EZ, UK; fax +44 1223 336033; or [deposit@ccdc.cam.ac.uk](mailto:deposit@ccdc.cam.ac.uk)).

#### Acknowledgement

We thank the Natural Sciences and Engineering Research Council of Canada (NSERC) for financial support.

#### References

- (1) Shimada, J.; Hashimoto, K.; Kim, B. H.; Nakamura, E.; Kuwajima, I. *J. Am. Chem. Soc.* **1984**, *106* (6), 1759. doi:10.1021/ja00318a035.
- (2) Rühlmann, K. *Synthesis* **1971**, 1971 (05), 236. doi:10.1055/s-1971-21707.
- (3) Nelke, J. M. *Organic Syntheses*; Wiley: New York, 1988; Collect. Vol. VI, pp 167–172.
- (4) Wu, Y.-J.; Burnell, D. J. *Tetrahedron Lett.* **1988**, *29* (35), 4369. doi:10.1016/S0040-4039(00)80497-9.
- (5) Wu, Y.-J.; Burnell, D. J. *Tetrahedron Lett.* **1989**, *30* (9), 1021. doi:10.1016/S0040-4039(01)80348-8.

- (6) Pandey, B.; Khire, U. R.; Ayyangar, N. R. *Synth. Commun.* **1989**, *19* (15), 2741. doi:10.1080/00397918908053069.
- (7) Wu, Y.-J.; Strickland, D. W.; Jenkins, T. J.; Liu, P.-Y.; Burnell, D. J. *Can. J. Chem.* **1993**, *71* (9), 1311. doi:10.1139/v93-169.
- (8) Jenkins, T. J.; Burnell, D. J. *J. Org. Chem.* **1994**, *59* (6), 1485. doi:10.1021/jo00085a041.
- (9) Crane, S. N.; Jenkins, T. J.; Burnell, D. J. *J. Org. Chem.* **1997**, *62* (25), 8722. doi:10.1021/jo971055v.
- (10) (a) Crane, S. N.; Burnell, D. J. *J. Org. Chem.* **1998**, *63* (4), 1352. doi:10.1021/jo971867r.; (b) Crane, S. N.; Burnell, D. J. *J. Org. Chem.* **1998**, *63* (16), 5708. doi:10.1021/jo9806308.
- (11) (a) Parker, K. A.; Breault, G. A. *Tetrahedron Lett.* **1986**, *27* (33), 3835. doi:10.1016/S0040-4039(00)83892-7.; (b) Saint-Jalmes, L.; Lila, C.; Xu, J. Z.; Moreau, L.; Pfeiffer, B.; Eck, G.; Pelsez, L.; Rolando, C.; Julia, M. *Bull. Soc. Chim. Fr.* **1993**, *130*, 447; (c) Wendt, J. A.; Gauvreau, P. J.; Bach, R. D. *J. Am. Chem. Soc.* **1994**, *116* (22), 9921. doi:10.1021/ja00101a013.; (d) Balog, A.; Curran, D. P. *J. Org. Chem.* **1995**, *60* (2), 337. doi:10.1021/jo00107a011.; (e) Balog, A.; Geib, S. J.; Curran, D. P. *J. Org. Chem.* **1995**, *60* (2), 345. doi:10.1021/jo00107a012.; (f) Lin, X.; Kavash, R. W.; Mariano, P. S. *J. Org. Chem.* **1996**, *61* (21), 7335. doi:10.1021/jo961179s. PMID:11667659.; (g) Kanada, R. M.; Taniguchi, T.; Ogasawara, K. *J. Chem. Soc. Chem. Commun.* **1998**, 1755; (h) Chavan, S. P.; Kharul, R. K.; Kale, R. R.; Khobragade, D. A. *Tetrahedron* **2003**, *59* (15), 2737. doi:10.1016/S0040-4020(03)00236-9.
- (12) (a) Burnell, D. J.; Wu, Y.-J. *Can. J. Chem.* **1989**, *67* (5), 816. doi:10.1139/v89-125.; (b) Wu, Y.-J.; Zhu, Y.-Y.; Burnell, D. J. *J. Org. Chem.* **1994**, *59* (1), 104. doi:10.1021/jo00080a018.; (c) Liu, P.-Y.; Burnell, D. J. *J. Chem. Soc. Chem. Commun.* **1994**, (10): 1183. doi:10.1039/c39940001183.; (d) Zhu, Y.-Y.; Burnell, D. J. *Tetrahedron Asymmetry* **1996**, *7* (11), 3295. doi:10.1016/0957-4166(96)00430-2.; (e) Liu, P.-Y.; Wu, Y.-J.; Burnell, D. J. *Can. J. Chem.* **1997**, *75* (6), 656. doi:10.1139/v97-080.; (f) Blanchard, A. N.; Burnell, D. J. *Tetrahedron Lett.* **2001**, *42* (29), 4779. doi:10.1016/S0040-4039(01)00852-8.; (g) Elliott, C. E.; Miller, D. O.; Burnell, D. J. *J. Chem. Soc., Perkin Trans. 1* **2002**, 217; (h) Thornton, P. D.; Burnell, D. J. *Org. Lett.* **2006**, *8* (15), 3195. doi:10.1021/ol0609715. PMID: 16836364.; (i) Gao, F.; Burnell, D. J. *Tetrahedron Lett.* **2007**, *48* (46), 8185. doi:10.1016/j.tetlet.2007.09.089.; (j) Morrison, C. F.; Stamp, C. T. M.; Burnell, D. J. *Tetrahedron Lett.* **2009**, *50* (50), 7021. doi:10.1016/j.tetlet.2009.09.162.
- (13) Burnell, D. J.; Wu, Y.-J. *Can. J. Chem.* **1990**, *68* (6), 804. doi:10.1139/v90-128.
- (14) Rosenberg, R. E.; Abel, R. L.; Drake, M. D.; Fox, D. J.; Ignatz, A. K.; Kwiat, D. M.; Schaal, K. M.; Virkler, P. R. *J. Org. Chem.* **2001**, *66* (5), 1694. doi:10.1021/jo0011787. PMID:11262115.
- (15) Billings, S. B.; Woerpel, K. A. *J. Org. Chem.* **2006**, *71* (14), 5171. doi:10.1021/jo060077r. PMID:16808503.
- (16) (a) Additional examples: Cherest, M. *Tetrahedron* **1980**, *36* (11), 1593. doi:10.1016/S0040-4020(01)83127-6.; (b) Angoh, A. G.; Clive, D. L. J. *J. Chem. Soc. Chem. Commun.* **1985**, (14): 980 doi:10.1039/c39850000980.; (c) Chu, Y.; Colclough, D.; Hotchkin, D.; Tuazon, M.; White, J. B. *Tetrahedron* **1997**, *53* (42), 14235. doi:10.1016/S0040-4020(97)00952-6.; (d) Dunet, G.; Mayer, P.; Knochel, P. *Org. Lett.* **2008**, *10* (1), 117. doi:10.1021/ol702607t. PMID:18067308.
- (17) Wipf, P.; Kim, Y. *J. Am. Chem. Soc.* **1994**, *116* (26), 11678. doi:10.1021/ja00105a009.
- (18) Yoshinaga, F.; Tormena, C. F.; Freitas, M. P.; Rittner, R.; Abraham, R. J. *J. Chem. Soc., Perkin Trans. 2* **2002**, (9): 1494. doi:10.1039/b204635k.
- (19) Gung, B. W. *Chem. Rev.* **1999**, *99* (5), 1377. doi:10.1021/cr980365q. PMID:11749449.
- (20) (a) Nakamura, K.; Osamura, Y. *J. Am. Chem. Soc.* **1993**, *115* (20), 9112. doi:10.1021/ja00073a029.; (b) See also: Helal, M. R.; Abbas, K. A. *Jordan J. Chem.* **2009**, *4*, 251.
- (21) Gao, F.; Burnell, D. J. *J. Org. Chem.* **2006**, *71* (1), 356. doi:10.1021/jo051683+. PMID:16388658.
- (22) Hsien, M.; Sheu, H.-T.; Lee, T.; Cheng, S.; Lee, J.-F. *J. Mol. Catal. Chem.* **2002**, *181* (1-2), 189. doi:10.1016/S1381-1169(01)00382-X.
- (23) Wölker, D.; Haufe, G. *J. Org. Chem.* **2002**, *67* (9), 3015. doi:10.1021/jo016331r. PMID:11975561.
- (24) (a) Mursakulov, I. G.; Guseinov, M. M.; Kasumov, N. K.; Zefirov, N. S.; Samoshin, V. V.; Chalenko, E. G. *Tetrahedron* **1982**, *38* (14), 2213. doi:10.1016/0040-4020(82)85169-7.; (b) Mursakulov, I. G.; Samoshin, V. V.; Binnatov, R. V.; Kasumov, N. K.; Povolotskii, M. I.; Zefirov, N. S. *Zh. Organich. Khim.* **1983**, *19*, 2527.
- (25) (a) *CrystalStructure 3.7.0* (Crystal Structure Analysis Package); Rigaku and Rigaku/MS: The Woodlands, TX, 2000–2005.; (b) Watkin, D. J.; Prout, C. K.; Carruthers, J. R.; Betteridge, P. W. *CRYSTALS Issue 10*; Chemical Crystallography Laboratory, Oxford, UK, 1996.
- (26) Sheldrick, G. M. *SHELX97*; University of Göttingen, Göttingen, Germany, 1997.

# On the stabilization of the carbonate dianion by sulfur dioxide

Friedrich Grein, Justin K. Chan, and Idlir Liko

**Abstract:** The stabilization in the gas phase of the carbonate dianion  $\text{CO}_3^{2-}$  by  $\text{SO}_2$  molecules is being investigated. The geometries of various isomers of  $\text{CO}_3^{2-}(\text{SO}_2)_n$  and  $\text{CO}_3^{1-}(\text{SO}_2)_n$ , for  $n = 1-4$ , have been optimized by the B3PW91/6-311+G(3df) method. Single-point CCSD and CCSD(T) energies at the DFT-optimized geometries were obtained for  $n = 1-3$ , using the 6-311+G(d) basis set. For  $n = 1$  and 2, the monoanionic clusters are adiabatically more stable than the dianionic ones. However, starting at  $n = 3$ , they become less stable. The CCSD adiabatic electron detachment energy of the dianionic cluster switches from  $-0.39$  eV for  $n = 2$  to  $+0.20$  eV for  $n = 3$ . The vertical electron detachment energy turns positive at  $n = 2$ , with a CCSD value of  $1.35$  eV. Several of the less stable dianionic, and most of the monoanionic clusters, are characterized by the transfer of an oxygen atom from  $\text{CO}_3$  to  $\text{SO}_2$ , forming  $\text{SO}_3^{2-}$  or  $\text{SO}_3^{1-}$  units, owing to  $\text{SO}_3^{2-/1-} + \text{CO}_2$  being more stable than  $\text{CO}_3^{2-/1-} + \text{SO}_2$ . For the stabilization of the sulfate dianion by stepwise hydration, studied both experimentally and theoretically by other groups, a minimum of three water molecules was required.

**Key words:** dianion stabilization, carbonate dianion, stabilization with  $\text{SO}_2$ , adiabatic electron detachment energy, vertical electron detachment energy, density functional calculations, coupled cluster calculations, structure of carbonate–sulfur dioxide clusters,  $\text{SO}_3$  formation.

**Résumé :** On a étudié la stabilisation en phase gazeuse du dianion carbonate,  $\text{CO}_3^{2-}$ , par des molécules de  $\text{SO}_2$ . Les géométries des divers isomères de  $\text{CO}_3^{2-}(\text{SO}_2)_n$  et de  $\text{CO}_3^{1-}(\text{SO}_2)_n$ , pour  $n = 1$  à 4, ont été optimisées par la méthode B3PW91/6-311+G(3df). On a obtenu des énergies ponctuelles d'agrégats couplés avec des excitations simple et double (ACSD) et d'agrégats couplés avec des excitations simple et double et perturbatrices triples (ACSD(T)) pour les géométries optimisées par des calculs basés sur la théorie de fonctionnelle de la densité (TFD) pour  $n = 1$  à 3, en utilisant un ensemble de base 6-311+G(d). Pour  $n = 1$  et 2, les agrégats monoanioniques sont adiabatiquement plus stables que les diatomiques. Toutefois, commençant avec  $n = 3$ , ils deviennent moins stables. L'énergie d'arrachement adiabatique d'un électron d'un agrégat dianionique (ACSD) passe de  $-0,39$  eV pour  $n = 2$  à  $+0,20$  eV pour  $n = 3$ . L'énergie d'arrachement vertical d'un électron devient positive à  $n = 2$ , avec une valeur d'ACSD de  $1,35$  eV. Plusieurs agrégats dianioniques moins stables et la plupart des monoanioniques sont caractérisés par le transfert d'un atome d'oxygène du  $\text{CO}_3$  au  $\text{SO}_2$ , conduisant à la formation d'unités  $\text{SO}_3^{2-}$  ou  $\text{SO}_3^{1-}$  en raison du fait que  $\text{SO}_3^{2-/1-} + \text{CO}_2$  est plus stable que  $\text{CO}_3^{2-/1-} + \text{SO}_2$ . Pour la stabilisation du dianion sulfate par hydratation par étape, étudiée tant d'un point de vue expérimental que théorique par d'autres groupes, un minimum de trois molécules d'eau est requis.

**Mots-clés :** stabilisation de dianion, dianion carbonate, stabilisation par du  $\text{SO}_2$ , énergie d'arrachement adiabatique d'électron, énergie d'arrachement vertical d'électron, calculs d'après la théorie de la fonctionnelle de la densité, calculs de couplages d'agrégats, structure d'agrégats carbonate–dioxyde de soufre, formation de  $\text{SO}_3$ .

## Introduction

It is well known that the “textbook” dianions  $\text{CO}_3^{2-}$ ,  $\text{SO}_4^{2-}$ , and other multiply charged anions (MCA), like  $\text{PO}_4^{3-}$ , are not electronically stable in the gas phase, and decay by auto electron detachment to the corresponding lower charge anions.<sup>1</sup> However, these polyanions are stabilized in solution and through counterions in the solid state. Stefanovich et al.<sup>2</sup> performed quantum chemical studies on dianions in the isolated state and solvated in water. For  $\text{CO}_3^{2-}$ , the vertical electron detachment energy (VDE) changed from  $-3.4$  eV

in the gas phase ( $\text{CO}_3^{2-}$  less stable than  $\text{CO}_3^{1-}$ ) to  $+9.9$  eV in water ( $\text{CO}_3^{2-}(\text{aq})$  more stable than  $\text{CO}_3^{1-}(\text{aq})$ ). For the sulfate dianion  $\text{SO}_4^{2-}$ , VDE changed from  $-1.6$  to  $+9.6$  eV. Indeed, the changes in stability are substantial.

Experimental studies led to a better understanding of MCAs. Hydrated sulfate clusters  $\text{SO}_4^{2-}(\text{H}_2\text{O})_n$ , dithionate clusters  $\text{S}_2\text{O}_6^{2-}(\text{H}_2\text{O})_n$ , and peroxydisulfate clusters  $\text{S}_2\text{O}_8^{2-}(\text{H}_2\text{O})_n$  in the gas phase were discovered by Blades and Kebarle.<sup>3</sup> The smallest number of  $\text{H}_2\text{O}$  molecules needed to stabilize the sulfate dianion was three. Wang et

Received 08 February 2010. Accepted 14 June 2010. Published on the NRC Research Press Web site at canjchem.nrc.ca on 29 October 2010.

This article is part of a Special Issue dedicated to Professor R. J. Boyd.

F. Grein,<sup>1</sup> J.K. Chan, and I. Liko. Department of Chemistry, University of New Brunswick, PO Box 4400, Fredericton, NB E3B 5A3, Canada.

<sup>1</sup>Corresponding author (e-mail: fritz@unb.ca).

al.<sup>4</sup> performed photoelectron spectroscopy of gas-phase  $\text{SO}_4^{2-}(\text{H}_2\text{O})_n$  clusters. In agreement with Blades and Kebarle, they found the minimum number of water molecules required to stabilize  $\text{SO}_4^{2-}$  in the gas phase to be three. Smaller clusters were not stable. The experimental findings were supported by DFT/B3LYP geometry optimizations on clusters of the dianions  $\text{SO}_4^{2-}(\text{H}_2\text{O})_n$  and corresponding monoanions  $\text{SO}_4^{1-}(\text{H}_2\text{O})_n$  for  $n = 1$ –6, using the TZVP basis set augmented with diffuse functions on all atoms. Single-point B3LYP calculations were added using the aug-cc-pVTZ basis set for S and O, and cc-pVTZ for H. In agreement with experimental results, the calculated adiabatic electron detachment energies (ADE) were negative (unstable dianionic clusters) for  $n = 1$  and  $n = 2$ , but turned positive starting with  $n = 3$ . For  $n = 3$ , ADE was calculated as 0.32 eV, compared with  $0.4 \pm 0.2$  eV experimental. For  $n = 4$ , a calculated ADE of 0.90 eV is to be compared with an experimental value of  $1.00 \pm 0.1$  eV. All calculated ADEs were found to lie within the error bars of the experimental values. In a more recent paper, temperature-dependent isomer populations of gas-phase  $\text{SO}_4^{2-}(\text{H}_2\text{O})_n$  clusters were studied by performing measurements also at low temperature.<sup>5</sup> In another case of interest to the present work, photoelectron spectra of oxalate dianion clusters  $\text{C}_2\text{O}_4^{2-}(\text{H}_2\text{O})_n$  in the gas phase were investigated.<sup>6</sup> The smallest observable cluster was  $n = 3$ , with an experimental ADE of 0.00 eV and a VDE of 0.50 eV. B3LYP calculations were performed up to  $n = 6$ . The calculated VDE for  $n = 3$  was 0.48 eV, in excellent agreement with the experimental value. VDE for the highest calculated cluster,  $n = 6$ , was 1.75 eV vs 1.84 eV experimental. Again, all calculated VDEs were found to lie within 0.1 eV of the experimental values.

Whereas the stabilization of dianions by water has been relatively well studied, it can be argued that dianions may also be stabilized in atmospheres of oxygen, carbon dioxide, sulfur dioxide, other oxides, and by other gases. The driving force of MCA stabilization by cluster formation with molecules like carbon dioxide and sulfur dioxide is seen in the delocalization of negative charge, owing to bond formation and the increase in volume available for charge distribution.

The stabilization of dianions and more highly charged anions by common gases is considered to be of interest. For this purpose, we have embarked on a project to theoretically study the stabilization of  $\text{CO}_3^{2-}$ ,  $\text{SO}_4^{2-}$ , and  $\text{PO}_4^{3-}$  by the dioxides  $\text{CO}_2$ ,  $\text{SO}_2$ , and  $\text{NO}_2$ . Obviously, the program can be extended to other MCAs and to many other gas molecules.

In the present first paper in this series, the stabilization of the carbonate dianion by sulfur dioxide will be investigated. Geometries of the clusters  $\text{CO}_3^{1-}(\text{SO}_2)_n$  and  $\text{CO}_3^{2-}(\text{SO}_2)_n$  are to be optimized by DFT methods. From these studies, it is predicted that carbonate requires a minimum of three sulfur dioxide molecules to be adiabatically stabilized in the gas phase. For vertical stabilization, only two  $\text{SO}_2$  molecules are required. A search of the literature on carbonate monoanion and dianion clusters showed studies on  $\text{CO}_3^{2-}(\text{H}_2\text{O})_n$ ,  $\text{CO}_3^{1-}(\text{H}_2\text{O})_n$ ,  $\text{CO}_3^{1-}(\text{CO}_2)$ , and  $\text{CO}_3^{1-}(\text{CO})_n$ .<sup>7–11</sup> However, to the best of our knowledge, the question of stabilization of  $\text{CO}_3^{2-}$  by water molecules or any other molecules has not been addressed. Rudolph et al.<sup>7</sup> obtained Raman spectra of hydrated carbonate in aq  $\text{K}_2\text{CO}_3$  solutions. The vibrational

frequencies were compared with DFT values calculated for  $\text{CO}_3^{2-}$  and  $\text{CO}_3^{2-}(\text{H}_2\text{O})_n$ , with  $n = 1$  and 2. In a theoretical paper by Pathak et al.,<sup>8</sup> geometries and energies of  $\text{CO}_3^{2-}(\text{H}_2\text{O})_n$  ( $n = 1$ –6) clusters were obtained for the purpose of studying the changes to the IR spectra by sequential hydration of the carbonate dianion. Large shifts in the stretching mode of  $\text{H}_2\text{O}$  were found, whereas the bending mode of  $\text{H}_2\text{O}$  and the normal modes of  $\text{CO}_3^{2-}$  were little affected. Hydration energies were calculated as the difference between the energy of  $\text{CO}_3^{2-}(\text{H}_2\text{O})_n$  and the energy of  $\text{CO}_3^{2-}$  plus  $n$  water molecules in the gas phase. In a recent paper by Pathak and Maity,<sup>9</sup> IR spectra of the monoanionic hydrated clusters  $\text{CO}_3^{1-}(\text{H}_2\text{O})_n$  were calculated. Shkrob<sup>10</sup> investigated several possible structures of  $\text{CO}_3^{1-}(\text{H}_2\text{O})$  and  $\text{CO}_3^{1-}(\text{CO}_2)$ . Hiraoka et al.<sup>11</sup> performed experimental and theoretical studies on  $\text{CO}_3^{1-}(\text{CO})_n$ , for  $n = 0$ –4.

## Methods

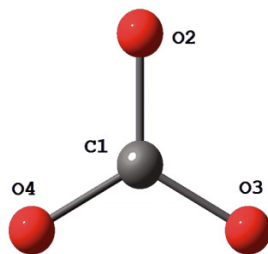
DFT calculations on  $\text{CO}_3^{1-}(\text{SO}_2)_n$  and  $\text{CO}_3^{2-}(\text{SO}_2)_n$ , from  $n = 0$ –4, were performed with the Gaussian03 programs,<sup>12</sup> using the B3PW91 functional<sup>13,14</sup> with the 6–311+G(3df) basis set.

The  $D_{3h}$  structure of  $\text{CO}_3^{2-}$  is shown in Fig. 1. Starting structures for geometry optimizations of the  $\text{CO}_3^{1-}(\text{SO}_2)_n$  and  $\text{CO}_3^{2-}(\text{SO}_2)_n$  clusters were chosen such as to cover all possible bonding arrangements. A summary is provided in Table 1. The structures are labelled **1A**, **2A**, **2B**, **2C**, **3A**, etc., where the number indicates the total number of  $\text{SO}_2$  groups, and the letters differentiate between the different structures for the given  $n$ . One to three  $\text{SO}_2$ s are O–S bound to the  $\text{CO}_3$  oxygens O2, O3, and O4 (Fig. 1, primary  $\text{SO}_2$ s). Clusters having only primary  $\text{SO}_2$ s are **1A**, **2B**, and **3C**.  $\text{SO}_2$  groups attached to prior  $\text{SO}_2$  can be S–S or O–S bound. Both possibilities have been taken into account. S–S clusters are **2C**, **3D**, **3E**, and **4F**–**4I**. For those,  $C_s$  symmetry is possible. Clusters that have O–S bonds in addition to the primary bonds (**2A**, **3A**, **3B**, **4A**, **4B**, **4C**, **4D**, and **4E**) do not have any symmetry. The same starting structures were used for monoanionic and dianionic clusters. Optimized structures fitting these basic types will be shown in the forthcoming figures. In cases where no symmetry was imposed, the final optimized structure did not necessarily retain the type of bonding imposed in the starting structure. For example, S–S bonds have in several cases changed to O–S bonds. Overall, Table 1 contains 18 different structures. Structures that allow for  $C_s$  symmetry, 10 of 18, were initially calculated without symmetry, and thereafter with  $C_s$  symmetry. In total, 28 starting structures were used for geometry optimizations, both for the monoanionic and dianionic clusters.

Convergence was usually fast for the dianionic clusters, but often very slow and difficult for the monoanionic ones. Full convergence, or convergence to at least  $1 \times 10^{-6}$  au, has been accomplished in all cases listed in the tables. The reason for the poor convergence characteristics of the monoanions will be explained later.

Single-point calculations with the 6–311+G(d) basis set were performed using the coupled cluster method with single and double excitations (CCSD) for  $n = 0, 1, 2$ , and 3, and with noniterative triple excitations (CCSD(T)) for  $n =$



**Fig. 1.** Structure of  $\text{CO}_3^{2-}$ .

0, 1, and 2 at the B3PW91/6–311+G(3df) optimized geometries.

## Results

### $\text{CO}_3^{2-}$ and $\text{CO}_3^{1-}$

The literature is unanimous on  $\text{CO}_3^{2-}$  having  $D_{3h}$  symmetry. The situation is not so clear for  $\text{CO}_3^{1-}$ , which in some calculations shows  $D_{3h}$  and in others  $C_{2v}$  symmetry. In Table 2, DFT/B3PW91 and CCSD(T) results are listed for  $\text{CO}_3^{1-}$  and  $\text{CO}_3^{2-}$ , always using the 6–311+G(3df) basis set. CCSD(T) results for  $\text{CO}_3^{1-}$  have been obtained in both  $C_{2v}$  and  $D_{3h}$  symmetry. In CCSD(T), the  $C_{2v}$  structure is 1.11 eV lower in energy than the  $D_{3h}$  structure. The  $C_{2v}$  structure for  $\text{CO}_3^{1-}$  is in agreement with experimental results.<sup>15</sup> The opposite is the case in DFT. Here, a geometry optimization of  $\text{CO}_3^{1-}$  starting in  $C_{2v}$  leads to  $D_{3h}$  symmetry. Table 2 shows that the DFT geometry for the dianion is close to the CCSD(T) values. CCSD(T) and DFT ADEs and VDEs of  $\text{CO}_3^{2-}$ , also given in Table 2, differ by about 0.2 eV.

While there is agreement on the need for diffuse functions for *stable* negative ions, such is not the case for *unstable* or *metastable* anions, like  $\text{CO}_3^{1-}$ . Indeed, energies like ADE depend much on the amount of diffuse character in the basis set. For example, using the 6–311G(3df) basis set, differing from the standard basis set by the omission of diffuse functions, the DFT ADE for  $\text{CO}_3^{2-}$  is –5.34 eV, compared with –3.69 eV using 6–311+G(3df), a difference of 1.65 eV. Obviously, with more diffuse functions, the ADE will become lower (less negative), as the energy of the dianion approaches that of the monoanion. On the other hand, comparing the energies of dianions with those of the corresponding monoanions, a task that is required for the present work, demands a common basis set. One cannot use a diffuse basis set for the monoanions, and a nondiffuse set for the dianions. This is especially important, as with increased additions of  $\text{SO}_2$ , the dianionic structures eventually become more stable than the monoanionic ones. Of the two possibilities, a basis set with no diffuse functions or one with, the latter has been chosen. This choice is supported by the fact that excellent results were obtained for the  $\text{SO}_4^{2-}(\text{H}_2\text{O})_n$  clusters using diffuse functions.<sup>4</sup> Also,  $\text{VDE}(\text{CO}_3^{2-})$  calculated here with the diffuse basis set (–3.56 eV for DFT and –3.34 eV for CCSD(T)) is close to the result obtained by Stefanovich et al.<sup>2</sup> (3.4 eV, see Introduction).

### Binding and stabilization energies of clusters

In Table 3, calculated B3PW91 energies of the

$\text{CO}_3^{1-}(\text{SO}_2)_n$  and  $\text{CO}_3^{2-}(\text{SO}_2)_n$  clusters are listed for each bonding type, as detailed in Table 1. The lowest energy structures (bold in Table 3) for the monoanions/dianions are **2C/2B** for  $n = 2$ , **3E/3C** for  $n = 3$ , and **4H/4H** for  $n = 4$ . A discussion of these structures will be deferred until later. Also included in Table 3 are the binding energies. The binding energies  $\Delta E_n(-1)$  and  $\Delta E_n(-2)$  express the stabilization of monoanionic or dianionic complexes relative to the fragments  $\text{CO}_3^{1-} + n\text{SO}_2$  or  $\text{CO}_3^{2-} + n\text{SO}_2$ .

$$[1] \quad \Delta E_n(-1) = -E[\text{CO}_3^{1-}(\text{SO}_2)_n] + E(\text{CO}_3^{1-}) + nE(\text{SO}_2)$$

$$[2] \quad \Delta E_n(-2) = -E[\text{CO}_3^{2-}(\text{SO}_2)_n] + E(\text{CO}_3^{2-}) + nE(\text{SO}_2)$$

Table 3 shows that the binding energies for the monoanionic clusters increase from 1.67 eV for  $n = 1$ , to 2.44 eV for  $n = 2$ , to 2.77 eV for  $n = 3$ , and to 3.00 eV for  $n = 4$ . As expected, the dianionic clusters have much larger binding energies, ranging from 3.39 eV for  $n = 1$  to 7.18 eV for  $n = 4$ .

The incremental binding energies for the lowest energy clusters of each  $n$ , calculated by B3PW91, CCSD, and CCSD(T), are shown in Table 4. They are defined as

$$[3] \quad \Delta E_{n-1,n}(-1) = \Delta E_n(-1) - \Delta E_{n-1}(-1)$$

$$[4] \quad \Delta E_{n-1,n}(-2) = \Delta E_n(-2) - \Delta E_{n-1}(-2)$$

The B3PW91 values decrease from 1.67 to 0.23 eV for  $\text{CO}_3^{1-}(\text{SO}_2)_n$ ,  $n = 1-4$ , and from 3.39 to 0.75 eV for  $\text{CO}_3^{2-}(\text{SO}_2)_n$ ,  $n = 1-4$ . The CCSD and CCSD(T) values, as far as available, follow a similar pattern. Most lie within 0.2 eV of the DFT numbers.

In Table 5, B3PW91, CCSD and CCSD(T) ADEs and VDEs for the lowest energy structures are listed. The ADE is given by

$$[5] \quad \text{ADE} = E_0[\text{CO}_3^{1-}(\text{SO}_2)_n] - E_0[\text{CO}_3^{2-}(\text{SO}_2)_n]$$

for the lowest energy structure of the mono- and di-anion. The VDE is defined as

$$[6] \quad \text{VDE} = E_{\text{vert}}[\text{CO}_3^{1-}(\text{SO}_2)_n] - E_0[\text{CO}_3^{2-}(\text{SO}_2)_n]$$

where the energy of the anionic cluster  $\text{CO}_3^{1-}(\text{SO}_2)_n$  is calculated at the optimized geometry of the lowest energy dianion  $\text{CO}_3^{2-}(\text{SO}_2)_n$  for the given  $n$ . As defined, ADE and VDE are negative if the dianion is less stable than the monoanion, and positive otherwise.

As seen from Table 5, the B3PW91 values for ADE are negative for  $n = 0-2$ . The ADE for  $n = 3$  is –0.03 eV, an energy small enough to fall within the error range of the calculations. However, at  $n = 4$  the ADE has turned positive, with a value of +0.50 eV. ADE values obtained by the CCSD and CCSD(T) methods are very close to the DFT numbers for  $n = 0$ , ~0.2 eV less negative for  $n = 1$ , and ~0.5 eV less negative for  $n = 2$ . For  $n = 3$ , the ADE calculated by CCSD has become positive, with a value of 0.20 eV. It is expected that the CCSD(T) value for  $n = 3$  is very close. Using the CCSD result, it can be concluded that with the addition of *three*  $\text{SO}_2$  molecules the dianionic clusters have turned from being less to being more stable than

**Table 1.** Schematics for the starting structures of  $\text{CO}_3(\text{SO}_2)_n$ .

Structure	Oxygen		
	O2	O3	O4
<b>1A</b> ( $C_s$ )	–SO <sub>2</sub>		
<b>2A</b>	–SOO–SO <sub>2</sub>		
<b>2B</b> ( $C_s$ )	–SO <sub>2</sub>	–SO <sub>2</sub>	
<b>2C</b> ( $C_s$ )	–S(O <sub>2</sub> )–SO <sub>2</sub>		
<b>3A</b>	–SOO–SOO–SO <sub>2</sub>		
<b>3B</b>	–SOO–SO <sub>2</sub>	–SO <sub>2</sub>	
<b>3C</b> ( $C_s$ )	–SO <sub>2</sub>	–SO <sub>2</sub>	–SO <sub>2</sub>
<b>3D</b> ( $C_s$ )	–S(O <sub>2</sub> )–S(O <sub>2</sub> )–SO <sub>2</sub>		
<b>3E</b> ( $C_s$ )	–S(O <sub>2</sub> )–SO <sub>2</sub>	–SO <sub>2</sub>	
<b>4A</b>	–SOO–SOO–SOO–SO <sub>2</sub>		
<b>4B</b>	–SOO–SOO–SO <sub>2</sub>	–SO <sub>2</sub>	
<b>4C</b>	–SOO–SO <sub>2</sub>	–SO <sub>2</sub>	–SO <sub>2</sub>
<b>4D</b>	–SOO–SO <sub>2</sub>	–SOO–SO <sub>2</sub>	
<b>4E</b>	–SOO–SOO(–SO <sub>2</sub> )–SO <sub>2</sub>		
<b>4F</b> ( $C_s$ )	–S(O <sub>2</sub> )–S(O <sub>2</sub> )–S(O <sub>2</sub> )–SO <sub>2</sub>		
<b>4G</b> ( $C_s$ )	–S(O <sub>2</sub> )–S(O <sub>2</sub> )–SO <sub>2</sub>	–SO <sub>2</sub>	
<b>4H</b> ( $C_s$ )	–S(O <sub>2</sub> )–SO <sub>2</sub>	–SO <sub>2</sub>	–SO <sub>2</sub>
<b>4I</b> ( $C_s$ )	–S(O <sub>2</sub> )–SO <sub>2</sub>	–S(O <sub>2</sub> )–SO <sub>2</sub>	

**Note:** The SO<sub>2</sub> groups are bonded to the CO<sub>3</sub> oxygens O2 to O4, and chainlike to previously added SO<sub>2</sub>s. –SOO–SO<sub>2</sub> represents O–S bonding, –S(O<sub>2</sub>)–SO<sub>2</sub> represents S–S bonding. 4E is a branched structure.

**Table 2.** Comparison of B3PW91/6–311+G(3df) (DFT) with CCSD(T)/6–311+G(3df) (CC) results for  $\text{CO}_3^{1-}$  and  $\text{CO}_3^{2-}$ .

Parameter	$\text{CO}_3^{1-}$			$\text{CO}_3^{2-}$	
	Method			Method	
	DFT	CC ( $D_{3h}$ )	CC ( $C_{2v}$ )	DFT	CC ( $D_{3h}$ )
$R$ (C–O2)	1.2667	1.2716	1.2480	1.3011	1.3057
$R$ (C–O3/C–O4)	—	—	1.2863	—	—
$\alpha$ (O–C–O)	120	120	124.07	120	120
ADE	—	—	—	–3.69	–3.43
VDE	—	—	—	–3.56	–3.34

**Note:** Distances ( $R$ ) are in Å, angles ( $\alpha$ ) are in °. Adiabatic (ADE) and vertical (VDE) electron detachment energies are in eV. The  $C_{2v}$  structure is 1.11 eV lower in energy than the  $D_{3h}$  structure.

the monoanionic ones. All methods agree on the VDEs being negative for  $n = 0$  and 1, but turning positive for  $n = 2$ . VDE differences between DFT and CCSD(T) values are 0.2 eV or less. The CCSD value for  $n = 3$  is 2.12 eV, compared with 2.02 eV for DFT.

### Geometries of clusters

A selection of optimized structures for the dianions  $\text{CO}_3^{2-}(\text{SO}_2)_n$  is shown in Fig. 2, and for the monoanions  $\text{CO}_3^{1-}(\text{SO}_2)_n$  in Fig. 3. The labels refer to the starting structures. In most, but not all, cases the geometry optimization retained the bonding arrangements of the starting structures. Looking first at the dianionic structures in Fig. 2, one recognizes that in all structures C1–O–S is bent, with an angle of  $\sim 120^\circ$ . In **1A** the O2–S5 bond distance is 1.740 Å. The lowest energy structure for  $n = 2$  is **2B**, with  $C_s$  symmetry. Both O–S bonds are about 1.90 Å long. Apparently, attaching the second SO<sub>2</sub> group to a second CO<sub>3</sub> oxygen is energetically more favorable than a chainlike attachment, such as seen in **2A** (O–S) or **2C** (S–S). This trend continues for  $n = 3$ . Here,

**3C**, with three SO<sub>2</sub> groups attached to the three CO<sub>3</sub> oxygens, is the lowest energy structure. **3C** has a “paddle-wheel” shape, with an O–S bond length of 2.049 Å. It actually has the higher symmetry  $C_{3h}$ . The energies of **3B** and **3E**, with two SO<sub>2</sub> groups attached to CO<sub>3</sub>, are closest to **3C**, whereas the chainlike structure **3D** is highest in energy. For  $n = 4$ , eight structures are shown. The lowest energy one is **4H**. Here, as expected, three SO<sub>2</sub> groups are attached to CO<sub>3</sub>, as in **3C**, and the fourth group is attached to one of the primary SO<sub>2</sub>s. The only question here refers to the type of bonding for the fourth SO<sub>2</sub>. Somewhat to our surprise, the S–S bonded symmetric structure **4H**( $C_s$ ) lies 0.41 eV higher in energy than the nonsymmetrical structure **4H**, the latter having S–O bonding. In **4H**, the O2–S5 bond is 1.834 Å, whereas the O3–S11 and O4–S14 bonds are 2.15 and 2.16 Å, respectively, in length. The O7–S8 bond length is 2.261 Å. A S–S bond length of 2.716 Å in **4H**( $C_s$ ) indicates very weak S–S bonding. The **4H** structure was designed to give S–S bonding, but without symmetry restriction it converted to O–S bonding. As such, it is the equivalent of **4C**.

**Table 3.** Calculated B3PW91/6–311+G(3df) energies of  $\text{CO}_3^{1-}(\text{SO}_2)_n$  and  $\text{CO}_3^{2-}(\text{SO}_2)_n$ ,  $E(-1)$  and  $E(-2)$ , respectively, in atomic units.

Structure	Calculated B3PW91/6–311+G(3df) energy		Binding energy	
	$E(-1)$	$E(-2)$	$\Delta E_n(-1)$	$\Delta E_n(-2)$
<b>0</b>	<b>–263.805 799</b>	<b>–263.670 269</b>	—	—
<b>1A</b>	<b>–812.469 863</b> ( $C_s$ )	<b>–812.397 830</b> ( $C_s$ )	<b>1.67</b>	<b>3.39</b>
<b>2A</b>	–1361.101 128	–1361.057 597	2.44	4.94
<b>2B</b>	–1361.086 910 ( $C_s$ )	<b>–1361.068 646</b> ( $C_s$ )	2.05	<b>5.25</b>
<b>2C</b>	<b>–1361.101 146</b>	–1361.049 932	<b>2.44</b>	4.74
<b>3A</b>	–1909.663 066	–1909.698 821	1.33	5.99
<b>3B</b>	–1909.679 486	–1909.700 259	1.78	6.03
<b>3C</b>	–1909.684 457 ( $C_s$ )	<b>–1909.714 963</b> ( $C_s$ )	1.91	<b>6.43</b>
<b>3D</b>	–1909.711 485 ( $C_s$ )	–1909.699 007	2.65	6.00
<b>3E</b>	<b>–1909.716 062</b>	–1909.700 636	<b>2.77</b>	6.04
<b>4A</b>	–2458.318 112	–2458.334 160	2.75	6.88
<b>4B</b>	–2458.323 810	–2458.327 984	2.91	6.71
<b>4C</b>	–2458.326 406	–2458.335 024	2.98	6.90
<b>4D</b>	–2458.322 398	–2458.335 753	2.87	6.92
<b>4E</b>	–2458.323 934	–2458.336 237	2.91	6.93
<b>4F</b>	–2458.323 908	–2458.331 613	2.91	6.81
<b>4G</b>	–2458.323 318 ( $C_s$ )	–2458.326 667	2.89	6.67
<b>4H</b>	<b>–2458.327 115</b>	<b>–2458.345 496</b>	<b>3.00</b>	<b>7.18</b>
<b>4I</b>	–2458.323 816	–2458.323 056	2.91	6.57

**Note:** Binding energies  $\Delta E_n(-1)$  and  $\Delta E_n(-2)$  are in eV. The structure labels refer to the starting structure used for geometry optimizations (Table 1). The energy of  $\text{SO}_2$  is –548.602792 au.

**Table 4.** Incremental binding energies (eV) for the lowest energy structures, obtained by B3PW91, CCSD, and CCSD(T) methods. Binding energy  $\Delta E(-1) \equiv \Delta E_{n,n-1}(-1)$  for  $\text{CO}_3^{1-}(\text{SO}_2)_n$  and  $\Delta E(-2) \equiv \Delta E_{n,n-1}(-2)$  for  $\text{CO}_3^{2-}(\text{SO}_2)_n$ .

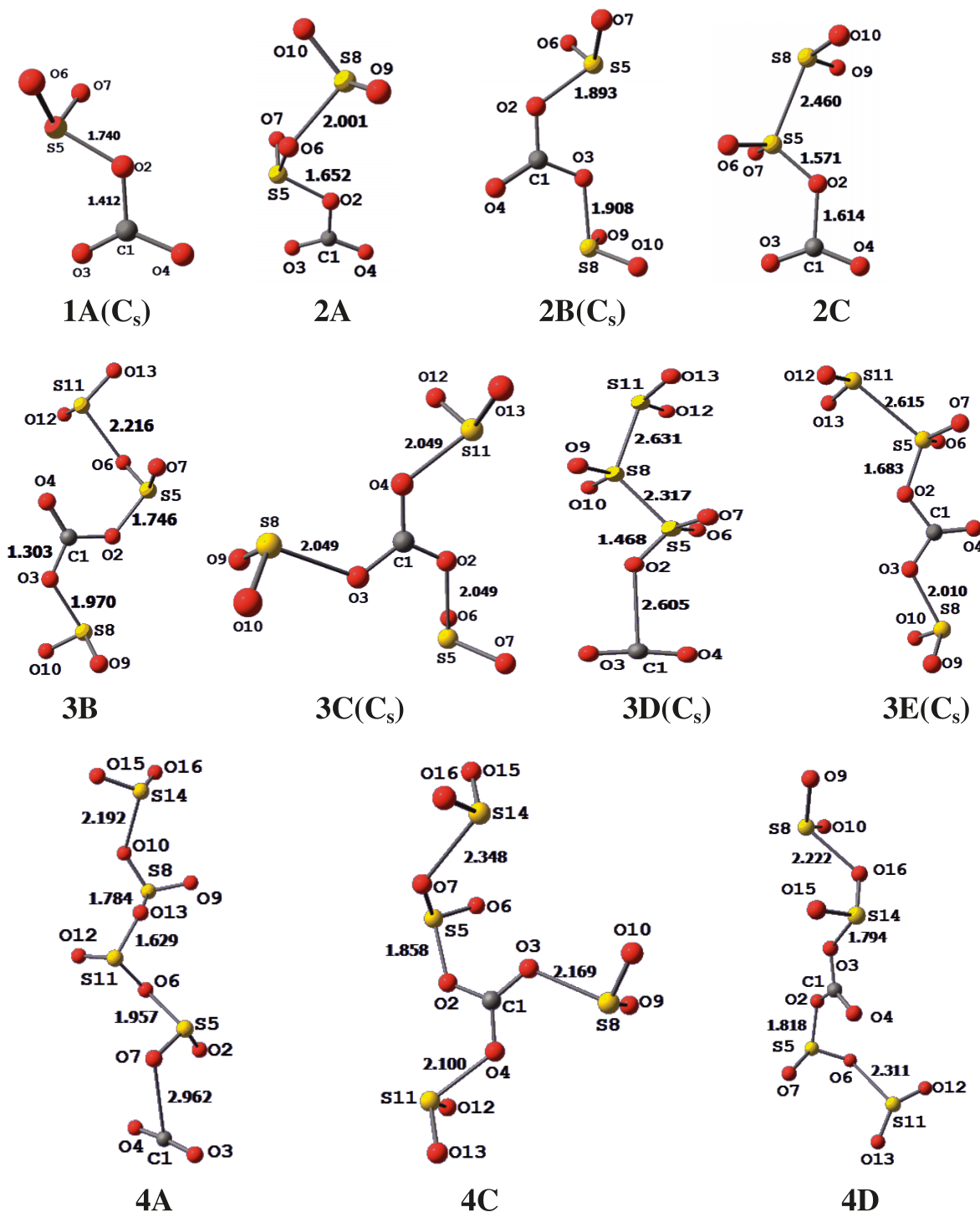
Cluster	Method					
	B3PW91		CCSD		CCSD(T)	
	Binding energy (eV)					
	$\Delta E(-1)$	$\Delta E(-2)$	$\Delta E(-1)$	$\Delta E(-2)$	$\Delta E(-1)$	$\Delta E(-2)$
$\text{CO}_3^{1-/2-}(\text{SO}_2)_1$	1.67	3.39	1.45	3.23	1.27	3.11
$\text{CO}_3^{1-/2-}(\text{SO}_2)_2$	0.77	1.86	0.25	1.67	0.56	1.67
$\text{CO}_3^{1-/2-}(\text{SO}_2)_3$	0.33	1.18	0.55	1.14	—	1.15
$\text{CO}_3^{1-/2-}(\text{SO}_2)_4$	0.23	0.75	—	—	—	—

**Table 5.** Adiabatic (ADE) and vertical (VDE) electron detachment energies (eV) for  $\text{CO}_3^{2-}(\text{SO}_2)_n$ , obtained by B3PW91, CCSD, and CCSD(T) methods.

Cluster	Method					
	B3PW91		CCSD		CCSD(T)	
	ADE	VDE	ADE	VDE	ADE	VDE
$\text{CO}_3^{1-/2-}$	–3.69	–3.56	–3.59	–3.38	–3.64	–3.55
$\text{CO}_3^{1-/2-}(\text{SO}_2)_1$	–1.96	–0.55	–1.82	–0.31	–1.79	–0.43
$\text{CO}_3^{1-/2-}(\text{SO}_2)_2$	–0.88	+0.84	–0.39	+1.35	–0.39	+1.04
$\text{CO}_3^{1-/2-}(\text{SO}_2)_3$	–0.03	+2.02	+0.20	+2.12	—	—
$\text{CO}_3^{1-/2-}(\text{SO}_2)_4$	+0.50	+2.45	—	—	—	—

The latter structure has a slightly higher energy (by 0.02 eV), caused by the different orientation of the secondary  $\text{SO}_2$  group. In **3D**, **4A**, **4E**, and **4F**, the C1–O2 bond is very long, ranging from 2.60 to 2.98 Å. Here, an oxygen has been pulled off the carbonate dianion to form  $\text{CO}_2$  +

$\text{SO}_3^{2-}(\text{SO}_2)_{n-1}$ . In these structures, only one of the  $\text{SO}_2$ s is bonded directly to  $\text{CO}_3^{2-}$ , whereas the other  $\text{SO}_2$  groups have chainlike attachments. Calculations show that  $\text{SO}_3^{2-} + \text{CO}_2$  is lower in energy than  $\text{CO}_3^{2-} + \text{SO}_2$  by 1.47 eV. In  $C_{3v}$  symmetry, the calculated S–O bond distance of  $\text{SO}_3^{2-}$  is

**Fig. 2.** Optimized structures of the dianionic clusters  $\text{CO}_3^{2-}(\text{SO}_2)_n$ .

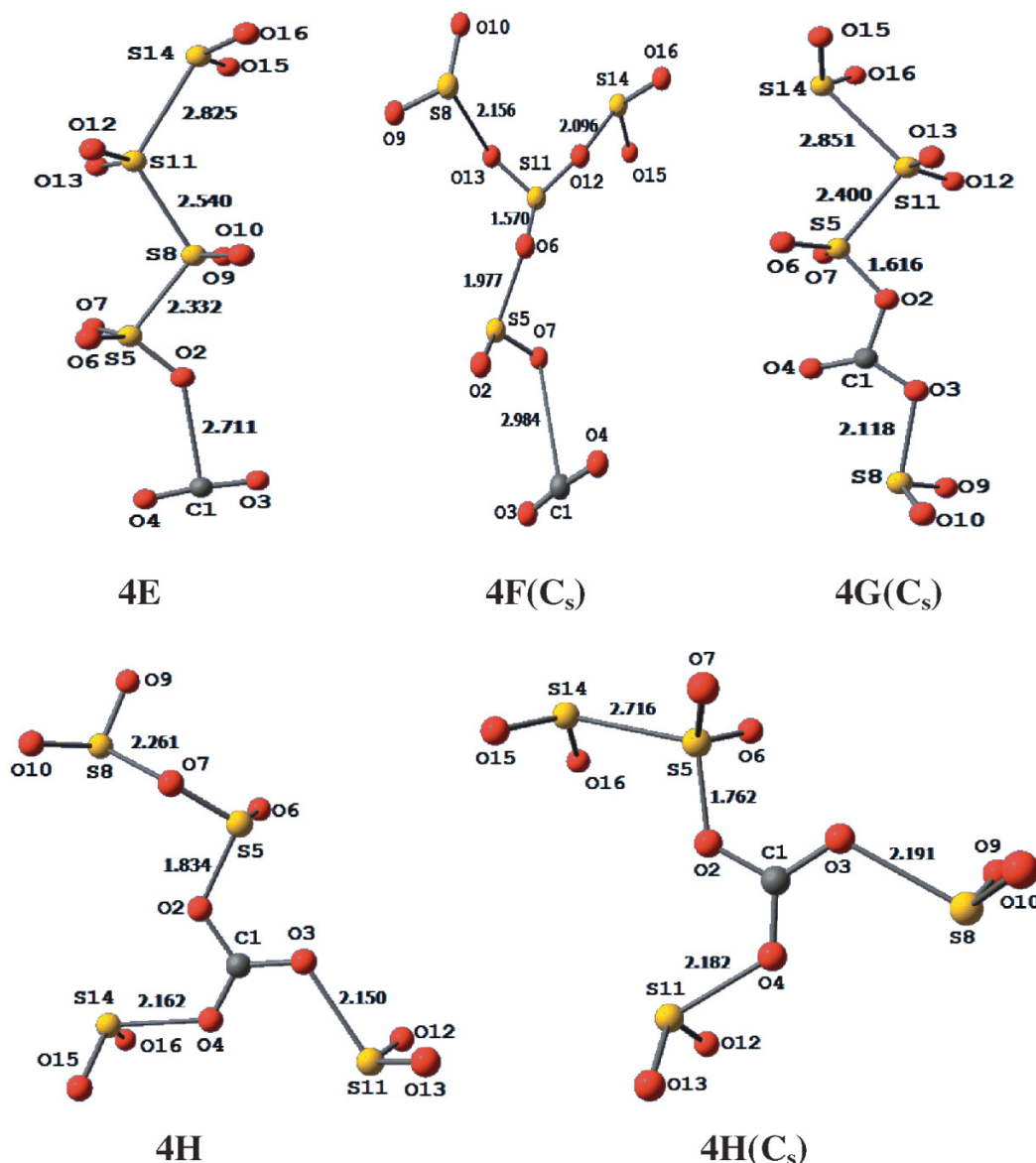
1.530 Å, and the O–S–O angle is 107.8°. The total energy of  $\text{SO}_3^{2-}$  is –623.744988 au (B3PW91/6–311+G(3df) optimization). Both for  $n = 3$  and  $n = 4$ , the lowest energy dianionic clusters retain the  $\text{CO}_3^{2-}$  moiety, having three primary  $\text{SO}_2$  bonds, with an energy gain by far exceeding that of  $\text{SO}_3^{2-}$  formation.

Most of the optimized monoanionic structures (Fig. 3) are much changed from their initial input shapes, explaining the difficulties encountered in the geometry optimizations. In all

cases of single substitution on  $\text{CO}_3^{1-}$ , and in several cases of multiple substitutions, one of the C–O bonds is very long. In **1A**, C1–O2 is 2.689 Å; in **2A** and **2C** it becomes 3.175 and 2.895 Å, respectively. Further examples are **3D**, **3E**, **4A**, **4C**, **4G**, **4H**, and **4I**. Similar to the dianionic case, the reason is the lower stability of  $\text{CO}_3^{1-}$  relative to  $\text{SO}_3^{1-}$ , causing the formation of the  $\text{SO}_3^{1-}$  anion. The reaction  $\text{CO}_3^{1-} + \text{SO}_2 \rightarrow \text{SO}_3^{1-} + \text{CO}_2$  is exothermic, with a calculated  $\Delta E$  (no zero-point energy corrections) of 1.50 eV (only slightly larger



Fig. 2. concluded.



than in the dianionic case).  $\text{SO}_3^{1-}$  has  $C_{3v}$  symmetry, which can be seen, for example, in **1A**. The calculated S–O bond distance of  $\text{SO}_3^{1-}$  is 1.476 Å (1.481 Å in **1A**), and the O–S–O angle is 114.1°. The total energy of  $\text{SO}_3^{1-}$  is –623.881416 au (B3PW91/6–311+G(3df) optimization). Such long C1–O bonds occur much more frequently in cases of monoanionic than in dianionic clusters, and are seen even for  $n = 1$  and  $n = 2$ . The reason is seen in the energy gain being higher by bonding to a dianion than to a monoanion, owing to the stronger desire for charge dissipation.

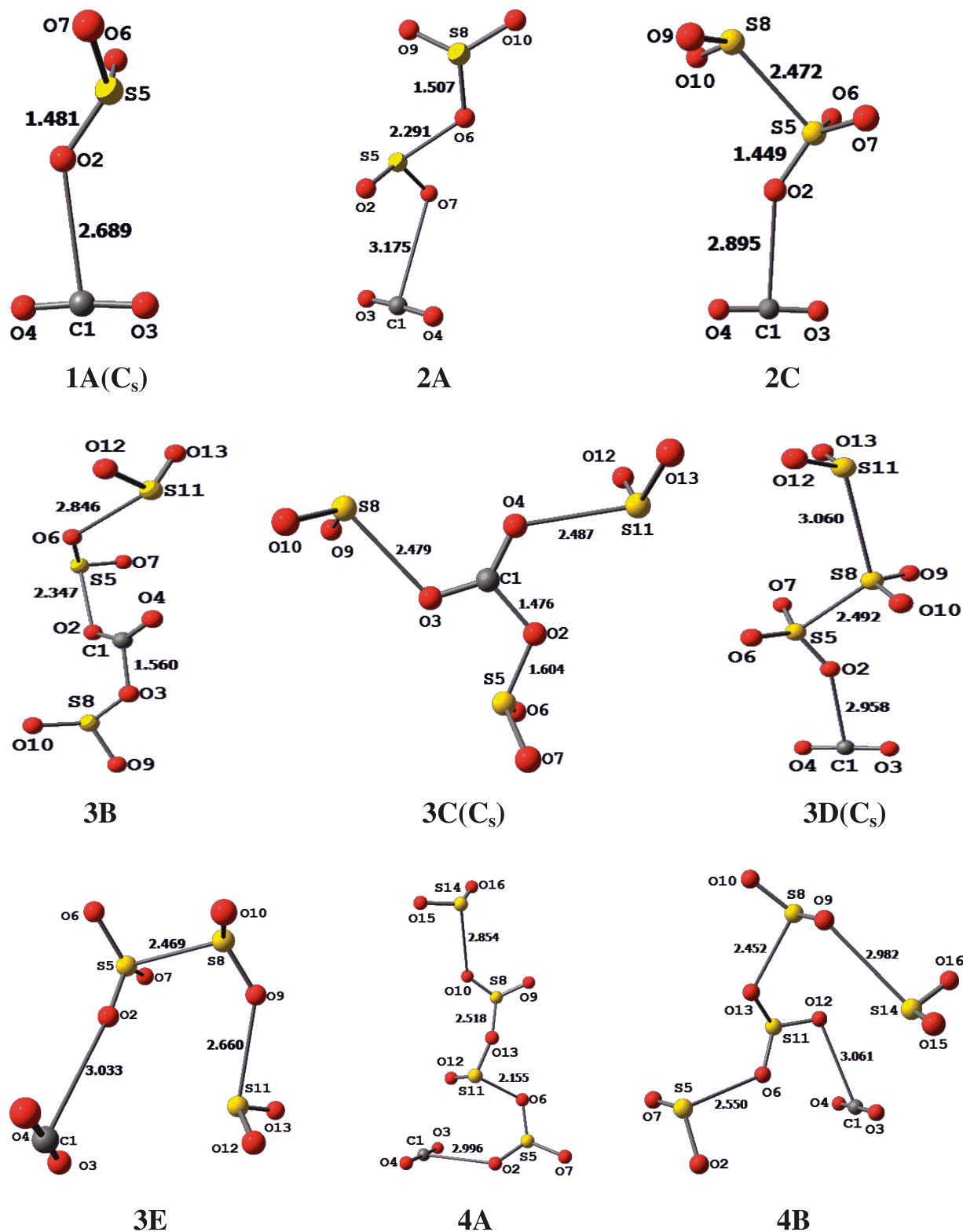
The  $\text{CO}_3^{1-}(\text{SO}_2)_1$  structure **1A** (C<sub>s</sub>) has a large C–O distance, as mentioned before. For  $n = 2$ , **2C** has the lowest energy. It again has a large C–O distance, and also a large S5–S8 distance of 2.472 Å. In structures **3B** and **3C**, the  $\text{CO}_3^{1-}$  moiety is retained. **3C** has the paddle-wheel structure, just like **3C** of the dianion. However, owing to the lack of  $\text{CO}_3^{1-} \rightarrow \text{SO}_3^{1-}$  stabilization, caused by the imposed symmetry, **3C** is not the lowest energy structure for  $n = 3$ . This dis-

tingction goes to **3E**, an awkward looking structure, with a very large C–O distance, followed by a  $\text{SO}_3^{1-}$  unit, with further S–S and O–S bonds. The lowest energy structure for  $n = 4$  is **4H**, which superficially looks like a paddle wheel, but the carbon atom is not at the centre of the wheel. Instead S5, the centre of the  $\text{SO}_3^{1-}$  unit, takes such a position. The three oxygens of  $\text{SO}_3^{1-}$ , O2, O6 and O7, are (weakly) bonded to three  $\text{SO}_2$ s.

## Discussion

The structures of the stable monoanionic clusters are characterized by  $\text{SO}_2$  pulling one oxygen from  $\text{CO}_3^{1-}$ , thereby forming the  $\text{SO}_3^{1-}$  anion. Structures where  $\text{CO}_3^{1-}$  has been retained had little chance of competing for the lowest energy. The  $\text{CO}_2$  left from this reaction is weakly bonded to the nearest oxygen from  $\text{SO}_3^{1-}$ . Without this reionizing effect, the monoanionic clusters would have higher energies,

Fig. 3. Optimized structures of the monoanionic clusters  $\text{CO}_3^{1-}(\text{SO}_2)_n$ .



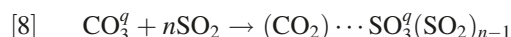
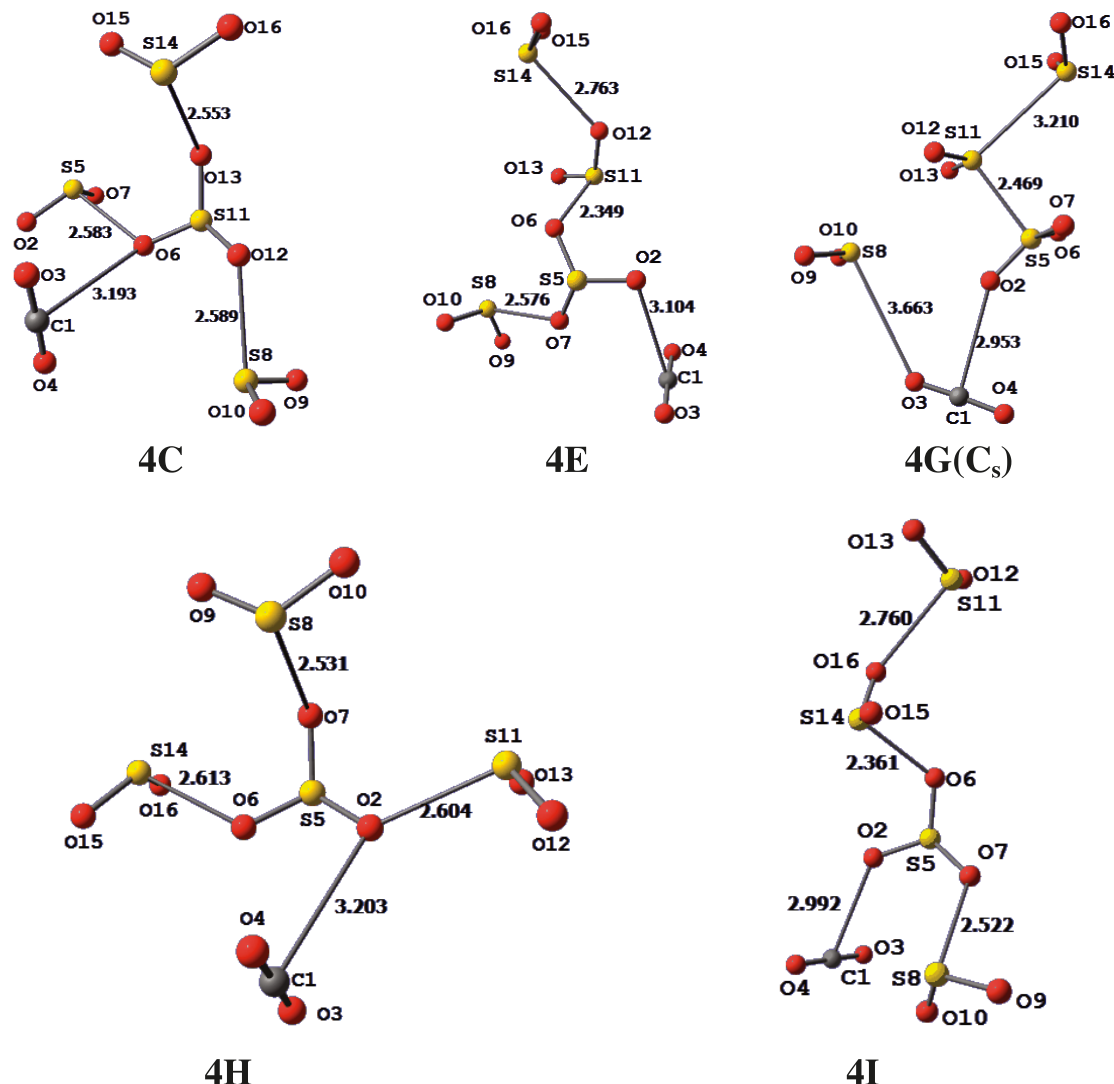
and even fewer  $\text{SO}_2$  molecules would be required for the stabilization of  $\text{CO}_3^{2-}$ . In contrast, only the less stable dianionic clusters have long C1–O2 bonds, leading to the formation of  $\text{SO}_3^{2-}$ .

The two possible outcomes of adding  $\text{SO}_2$  molecules to

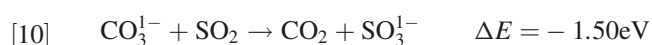
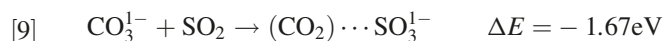
the carbonate mono- or di-anion can be described by eqs. [7] and [8]. In eq. [7] the carbonate remains, whereas in eq. [8] the charge is transferred from  $\text{CO}_3$  to  $\text{SO}_3$ .



Fig. 3. concluded.

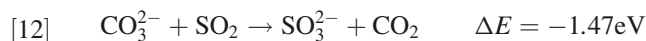
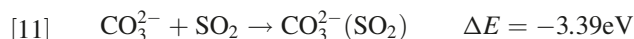


Here,  $(\text{CO}_2) \cdots \text{SO}_3^q(\text{SO}_2)_{n-1}$  indicates a  $\text{CO}_2$  loosely bound to  $\text{SO}_3^q$ , with a large O–S distance. For  $q = -1$ , the lowest energy structure for each  $n$  follows eq. [8], whereas for  $q = -2$  it follows eq. [7]. However, (less stable) structures of the other type are also encountered. Energetic data for  $n = 1$  illustrate the two cases. For  $q = -1$ , one has



The calculated energies of eqs. [9] and [10] show that the optimized structure with the large O–S distance still has a small amount of  $\text{CO}_2$  bonding to  $\text{SO}_3^{1-}$  (0.17 eV). The energy gain for  $\text{CO}_3^{1-} + \text{SO}_2 \rightarrow \text{CO}_3^{1-}(\text{SO}_2)$  cannot be calculated. It is less than 1.67 eV.

For  $q = -2$ , we have



Here, bonding of  $\text{SO}_2$  to  $\text{CO}_3^{2-}$  is almost 2 eV more favorable than a charge transfer from  $\text{CO}_3^{2-}$  to  $\text{SO}_3^{2-}$ . In the case of  $q = -2$ , the energy gain of  $\text{CO}_3^{2-} + \text{SO}_2 \rightarrow (\text{CO}_2) \cdots \text{SO}_3^{2-}$  is estimated to be in the order of 1.5 eV, certainly much less than 3.39 eV.

According to Table 5, three  $\text{SO}_2$  molecules are required to adiabatically stabilize the carbonate dianion. There is no literature on the stabilization of  $\text{CO}_3^{2-}$  by  $\text{H}_2\text{O}$  or any other molecule. The only comparison we have is the stabilization of the sulfate dianion and the oxalate dianion by  $\text{H}_2\text{O}$  molecules.<sup>4,6</sup> In both cases, three water molecules are required for stabilization. Stabilization by  $\text{SO}_2$  molecules occurs through the formation of chemical bonds, and the associated delocalization of the negative charge. On the other hand, stabilization by  $\text{H}_2\text{O}$  is accomplished mainly via hydrogen bonds, causing neutralization of charges via electrostatic ef-

fects. A direct comparison of the two processes is therefore not possible. All one may conclude is that stabilization of small dianions is relatively easy and can be accomplished by the addition of very few solvent molecules. Vertical stabilization of the carbonate dianion can be accomplished by the addition of just two SO<sub>2</sub> molecules. Therefore, the  $n = 2$  dianionic cluster is stable with respect to auto ionization.

Binding energies (DFT values) reported for CO<sub>3</sub><sup>2-</sup>(H<sub>2</sub>O)<sub>*n*</sub> are 1.85 eV for  $n = 1$ , 3.51 eV for  $n = 2$ , 5.00 eV for  $n = 3$ , and 6.16 eV for  $n = 4$ .<sup>8</sup> Binding energies for CO<sub>3</sub><sup>2-</sup>(SO<sub>2</sub>)<sub>*n*</sub> are substantially higher, with DFT values of 3.39, 5.25, 6.43, and 7.18 eV for  $n = 1$ –4.

The lowest-energy structures for the dianionic clusters have a maximum number of SO<sub>2</sub> groups attached to the carbonate dianion. This is understandable as such bonding facilitates the dissemination of the excess negative charge of the dianion. Chainlike arrangements of SO<sub>2</sub> molecules have higher energies. The fourth SO<sub>2</sub> in the lowest energy isomer of  $n = 4$  prefers O–S over S–S bonding, with a rather large energy difference of 0.41 eV. The O2–S or O3–S bond distances of the dianionic clusters increase from 1.740 Å in **1A** to 1.893 Å in **2B** to 2.049 Å in **3C** and to 2.191 Å in **4H**.

According to Table 3, the binding energy (DFT value) at  $n = 4$  is 7.18 eV for the dianionic cluster and 3.00 eV for the monoanionic ones. Using the PCM model (without geometry reoptimization), the solvation energy for CO<sub>3</sub><sup>2-</sup> dissolved in SO<sub>2</sub> (dielectric constant  $\epsilon = 15.4$ ) is calculated to be 10.3 eV and that of CO<sub>3</sub><sup>1-</sup> is 2.6 eV. Therefore, at  $n = 4$  ~70% of the  $n = \infty$  solvation energy of CO<sub>3</sub><sup>2-</sup> was obtained. For CO<sub>3</sub><sup>1-</sup>, however, the solvation energy calculated at  $n = 4$ , 3.0 eV, exceeds the PCM value of 2.6 eV. The reason can be seen in the charge transfer from CO<sub>3</sub><sup>1-</sup> to SO<sub>3</sub><sup>1-</sup>, leading to a lower energy of the monoanionic cluster, a process that cannot be captured by the solvation model. If the  $n = 4$  solvation energy for CO<sub>3</sub><sup>1-</sup> were 70% of the PCM value, it would be 1.8 eV, so the difference of 1.2 eV with the  $n = 4$  binding energy can be attributed to the formation of SO<sub>3</sub><sup>1-</sup>.

Whereas in the gas phase small dianions are less stable than corresponding monoanions, solvation of dianions occurs with larger energy gain than solvation of monoanions. This can already be seen from the Born equation, according to which the solvation energy is proportional to the square of the ionic charge.<sup>16</sup> (This is nicely demonstrated by the approximate 4:1 ratio calculated for the solvation energies of the dianion CO<sub>3</sub><sup>2-</sup> and the monoanion CO<sub>3</sub><sup>1-</sup>.) It is therefore obvious that in a step-by-step solvation, as done here by adding one SO<sub>2</sub> molecule at a time, and in other cases as well, the dianionic clusters have to eventually become more stable than the monoanionic ones.

## Concluding remarks

It has been shown that the unstable dianion CO<sub>3</sub><sup>2-</sup> can be stabilized in the gas phase by bonding to at least three SO<sub>2</sub> molecules. For  $n = 3$ , the calculated energy of the dianionic cluster is 0.20 eV (CCSD value) lower than that of the monoanionic one. For higher  $n$ , larger positive stabilization energies are expected. The VDE turned positive for  $n = 2$ , with a CCSD(T) value of 1.04 eV. In several of the optimized structures, SO<sub>3</sub><sup>2-</sup> or SO<sub>3</sub><sup>1-</sup> units could be recognized.

Calculations show that CO<sub>3</sub><sup>2-/1-</sup> + SO<sub>2</sub> is less stable than SO<sub>3</sub><sup>2-/1-</sup> + CO<sub>2</sub>.

Work on the stabilization of the carbonate dianion by CO<sub>2</sub> and of the sulfate dianion by CO<sub>2</sub> and SO<sub>2</sub> is in progress.

## Acknowledgments

F.G. would like to thank Dr. J. Passmore for introducing him to the wonderful and somewhat mysterious world of dianions. We would like to thank Drs. Passmore and P. Bruna, and S. Burrill, for reading the manuscript and for valuable comments. Financial support by the Natural Sciences and Engineering Research Council of Canada (NSERC) is gratefully acknowledged. Thanks to members of the Atlantic Computational Excellence network (ACEnet) computer network for providing support and ample computing times.

## References

- (1) Boldyrev, A. I.; Gutowski, M.; Simons, J. *Acc. Chem. Res.* **1996**, 29 (10), 497 and references therein. doi:10.1021/ar960147o.
- (2) Stefanovich, E. V.; Boldyrev, A. I.; Truong, T. N.; Simons, J. *J. Phys. Chem. B* **1998**, 102 (21), 4205. doi:10.1021/jp980766+.
- (3) Blades, A. T.; Kebarle, P. *J. Am. Chem. Soc.* **1994**, 116 (23), 10761. doi:10.1021/ja00102a046.
- (4) Wang, X.; Nicholas, J. B.; Wang, L. *J. Chem. Phys.* **2000**, 113 (24), 10837. doi:10.1063/1.1333703.
- (5) Wang, X. B.; Sergeeva, A. P.; Yang, J.; Xing, X. P.; Boldyrev, A. I.; Wang, L. *J. Phys. Chem. A* **2009**, 113 (19), 5567. doi:10.1021/jp900682g. PMID:19419223.
- (6) Wang, X.; Yang, X.; Nicholas, J. B.; Wang, L. *J. Chem. Phys.* **2003**, 119 (7), 3631. doi:10.1063/1.1590641.
- (7) Rudolph, W. W.; Fischer, D.; Irmer, G. *Appl. Spectrosc.* **2006**, 60 (2), 130. doi:10.1366/000370206776023421. PMID:16542564.
- (8) Pathak, A. K.; Mukherjee, T.; Maity, D. K. *Synth. React. Inorg., Met.-Org., Nano-Met. Chem.* **2008**, 38, 76. doi:10.1080/15533170701854148.
- (9) Pathak, A. K.; Maity, D. K. *J. Phys. Chem. A* **2009**, 113 (48), 13443. doi:10.1021/jp907577j. PMID:19886648.
- (10) Shkrob, I. A. *J. Phys. Chem. A* **2002**, 106 (49), 11871. doi:10.1021/jp0214918.
- (11) Hiraoka, K.; Katsuragawa, J.; Sugiyama, T.; Fujimaki, S.; Kojima, T.; Yamabe, S. *J. Phys. Chem. A* **2003**, 107 (24), 4817. doi:10.1021/jp022337o.
- (12) Frisch, M. J.; Trucks, G. W.; Schlegel, H. B.; Scuseria, G. E.; Robb, M. A.; Cheeseman, J. R.; Zakrzewski, V. G.; Montgomery, J. A., Jr.; Stratmann, R. E.; Burant, J. C.; Dapprich, S.; Millam, J. M.; Daniels, A. D.; Kudin, K. N.; Strain, M. C.; Farkas, O.; Tomasi, J.; Barone, V.; Cossi, M.; Cammi, R.; Mennucci, B.; Pomelli, C.; Adamo, C.; Clifford, S.; Ochterski, J.; Petersson, G. A.; Ayala, P. Y.; Cui, Q.; Morokuma, K.; Malick, D. K.; Rabuck, A. D.; Raghavachari, K.; Foresman, J. B.; Cioslowski, J.; Ortiz, J. V.; Stefanov, B. B.; Liu, G.; Liashenko, A.; Piskorz, P.; Komaromi, I.; Gomperts, R.; Martin, R. L.; Fox, D. J.; Keith, T.; Al-Laham, M. A.; Peng, C. Y.; Nanayakkara, A.; Gonzalez, C.; Challacombe, M.; Gill, P. M. W.; Johnson, B. G.; Chen, W.; Wong, M. W.; Andres, J. L.; Head-Gordon, M.; Replogle, E. S.; Pople, J. A. *Gaussian 03*; Gaussian, Inc.; Pittsburgh, PA.



- (13) Becke, A. D. *J. Chem. Phys.* **1993**, 98 (7), 5648. doi:10.1063/1.464913.
- (14) Perdew, J. P.; Burke, K.; Wang, Y. *Phys. Rev. B* **1992**, 96, 6796.
- (15) Jacox, M. E.; Milligan, D. E. *J. Mol. Spectrosc.* **1974**, 52 (3), 363. doi:10.1016/0022-2852(74)90186-6.
- (16) Born, M. Z. *Phys.* **1920**, 1 (1), 45. doi:10.1007/BF01881023.

# A theoretical analysis of the kinetics of the reaction of atomic bromine with tetrahydrofuran

John M.H. Lo, Robert A. Marriott, Binod R. Giri, John M. Roscoe, and Mariusz Klobukowski

**Abstract:** The kinetic behaviour for the reaction of atomic bromine with tetrahydrofuran has been analysed using the information from quantum chemical calculations. Structures and energy profiles were first obtained using density functional theory (DFT) employing the Dunning's basis sets of triple-zeta quality, and then for an accurate energetic description, single-point calculations were carried out at the coupled-cluster with single and double excitations (CCSD) and the fourth-order Møller–Plesset (MP4(SDQ)) levels of theory. The rate coefficients and the equilibrium constants for the potential reaction channels were obtained from the statistical rate theories and statistical thermodynamics, respectively, using the results of quantum chemical calculations; and the results were compared with our recently published experimental data. In terms of reaction mechanism, this reaction was found to be analogous to the reactions of the Br atom with 1,4-dioxane and with methanol, where the reaction proceeds via an addition–elimination mechanism. The dominant reaction channel involved coordination of the approaching Br atom to one of the hydrogen atoms adjacent to the ether oxygen atom, i.e.,  $\beta$ -hydrogen abstraction is uncompetitive. Although the complexes formed by direct coordination of the Br atom to the ether oxygen atom appeared in the reaction mechanism, we were not able to link them specifically to any reaction. The density functional theory predicted an activation energy and enthalpy of reaction that were much smaller than the experimental values, which led to an overestimation of the theoretical rate coefficients. The source of this discrepancy could be attributed to the overbinding of the transition states and of the tetrahydrofuran radical by DFT. Single-point calculations at the DFT structures using the CCSD and MP4(SDQ) methods yielded an accurate energetic description of the reaction of tetrahydrofuran with bromine, resulting in rate coefficients that showed excellent agreement with the experimental values.

**Key words:** gas-phase chemical kinetics, complex forming reactions, atmospheric chemistry, density functional theory (DFT), statistical rate theory, potential energy surfaces.

**Résumé :** Le comportement cinétique pour la réaction du brome atomique dans le tétrahydrofurane a été analysé à l'aide d'informations obtenues par calculs de chimie quantique. Les structures et les profils d'énergie ont été obtenues dans un premier temps à l'aide de la théorie de la fonctionnelle de la densité (TFD) en utilisant les ensembles de base de Dunning de qualité triple zêta et, ensuite pour une description précise des énergies, on a effectué des calculs ponctuels aux niveaux de l'agrégat couplé (« CCSD ») et du quatrième ordre de Møller–Plesset (« MP4(SDQ) »). Les coefficients de vitesse et les constantes d'équilibre des voies réactionnelles potentielles ont été à partir de résultats de chimie quantique en faisant appel aux théories statistiques standard des vitesses et à des calculs de thermodynamique statistique et on a comparé les résultats de ces calculs avec des données expérimentales publiées récemment. En termes de mécanisme réactionnel, on a trouvé que cette réaction est analogue aux réactions de l'atome de brome dans le 1,4-dioxane et le méthanol dans lesquels elle se produit par le biais d'un mécanisme d'addition–élimination. La voie réactionnelle principale implique une coordination de l'atome de brome qui approche à des atomes d'hydrogène adjacents de l'atome d'oxygène de l'éther, c'est-à-dire que l'enlèvement d'un atome d'hydrogène  $\beta$  n'est pas compétitif. Même si les complexes qui se forment par coordination directe de l'atome de brome sur l'atome d'oxygène de l'éther apparaissent dans le mécanisme réactionnel, il n'a pas été possible de les relier à aucune réaction. La théorie de la fonctionnelle de la densité prédit une énergie d'activation et une enthalpie de réaction qui sont beaucoup plus faibles que les valeurs expérimentales qui ont conduit à une surévaluation des coefficients théoriques de vitesse. La source de cette différence pourrait être attribuée à une sur-fixation des états de transition et du radical tétrahydrofuranylle par la TFD. Des calculs ponctuels des structures obtenues par la TFD, utilisant des méthodes « CCSD » et « MP4(SDQ) » conduisent à une description correcte des énergies impliquées dans la réaction du tétrahydrofurane avec le brome, ce qui conduit à des coefficients de vitesse présentant un excellent accord avec les valeurs expérimentales.

Received 11 January 2010. Accepted 17 June 2010. Published on the NRC Research Press Web site at canjchem.nrc.ca on 3 November 2010.

*This article is part of a Special Issue dedicated to Professor R. J. Boyd.*

**J.M.H. Lo, R.A. Marriott, and B.R. Giri.**<sup>1</sup> Alberta Sulphur Research Ltd., Centre for Applied Catalysis and Industrial Sulphur Chemistry, University Research Centre, 3535 Research Road NW, Calgary, AB T2L 2K8, Canada.

**J.M. Roscoe.** Department of Chemistry, Acadia University, Wolfville, NS B4P 2R6, Canada.

**M. Klobukowski.** Department of Chemistry, University of Alberta, Edmonton, AB T6G 2G2, Canada.

<sup>1</sup>Corresponding author (e-mail: brgiri@ucalgary.ca).

*Mots-clés* : cinétique chimique en phase gazeuse, réactions formant des complexes, chimie de l'atmosphère, théorie de la fonctionnelle de la densité, théorie statistique des vitesses, surfaces d'énergie potentielle.

## Introduction

The importance of halogen atoms reactions with organic compounds for understanding atmospheric chemistry has been recognized for some time.<sup>1–3</sup> Atomic bromine can initiate atmospheric oxidation of volatile organic compounds (VOCs) by producing organic-free radicals, which are then able to react rapidly with atmospheric oxygen. However, the rate coefficients for hydrogen abstraction from VOCs by Br are typically one to two orders of magnitude smaller than those for the corresponding reactions of Cl. This makes them less important than Cl as sinks for VOCs. On the other hand, the rate coefficient for the reaction of Br with O<sub>3</sub> is larger than that for the corresponding reaction of Cl, so the ability of VOCs to act as sinks for Br is relevant to the potential for Br to remove ozone. This would be of greatest importance in the marine boundary layer where the concentration of Br<sub>2</sub> is particularly large. Reactions of Br with organic compounds are also important in the incineration of halogen-containing waste.<sup>4–6</sup> A considerable body of data exists for the rates of reactions of atomic chlorine with organic compounds at both ambient and elevated temperatures, however, the kinetics of reactions of atomic bromine with organics has received much less attention. We have recently reported rate coefficients over a temperature range of ~290–380 K for several reactions of atomic bromine with ethers<sup>7–9</sup> in an effort to address this deficiency.

In our most recent work,<sup>9</sup> the kinetic behaviour for the reaction of bromine with 1,4-dioxane deviated markedly from that expected on the basis of our measurements for the reactions of bromine with other cyclic ethers.<sup>8</sup> We were able to understand the origins of these differences by a theoretical analysis of the potential energy surface for the reaction. The theoretical analysis showed that the bromine atom first forms a comparatively stable complex with the chair conformer of the dioxane molecule. This complex has too large an activation energy for the loss of HBr to account for the observed reactivity. The rate-limiting step was predicted to be the conversion of the chair conformer of the complex to the less stable boat conformer. Loss of HBr then occurs from the boat conformer, moderated by a weak van der Waals interaction between the departing HBr molecule and one of the ether oxygen atoms of the incipient dioxanyl radical.

The deduction of this complex reaction mechanism involving a number of elementary steps for the reaction of dioxane with atomic bromine would not have been possible without a detailed theoretical analysis. Indeed, even the formation of a complex between the ether oxygen atom and the approaching bromine atom would not be evident solely from the experimental kinetic measurements. The question then arises whether the potential energy surfaces (PES) for the reactions of atomic bromine with other cyclic ethers might require both complex formation and conformational change. In this work, we have computed a detailed picture of the PES, which has enabled us to evaluate the effects of complex for-

mation and of their conformational change for the reaction of atomic bromine with tetrahydrofuran (THF). Furthermore, this study will provide an opportunity to discriminate among the various possible reaction channels for the H abstraction as THF offers four different types of H atoms; each carbon atom at  $\alpha$  and  $\beta$  positions has two types of H atoms at the axial and equatorial positions, respectively. It is widely accepted that the H abstraction in ethers by the Br atom takes place from an  $\alpha$ -carbon atom because the ether oxygen provides a reduction in enthalpy of activation, offering a preferential H abstraction from the adjacent carbon atom; see ref. 8 and the refs. cited therein. A detailed kinetic analysis will help to verify the postulate that  $\beta$ -hydrogen abstraction reactions in ethers are unimportant.

## Calculations

### Structures and energies

A number of computational approaches were employed to obtain the energy profiles pertaining to the hydrogen-abstraction reaction of THF by atomic bromine. Initially, the geometries of the reactants, intermediates, and products were optimized using density functional theory with the hybrid Becke-3-Lee-Yang-Parr (B3LYP) functional.<sup>10</sup> For C, H, and O, the all-electron Dunning's correlation-consistent polarized valence triple-zeta basis sets (cc-pVTZ) were used,<sup>11</sup> whereas for Br, a small-core relativistic pseudopotential, which includes 4s, 4p, 4d, 5s, and 5p shells in the valence space, in conjunction with an energy-consistent valence triple-zeta basis set (cc-pVTZ-PP) was utilized.<sup>12</sup> Harmonic frequencies were computed on the optimized geometries using numerical Hessians with a step size of 0.01 bohr. The computed frequencies were scaled by a factor of 0.9648, which was obtained from the Computational Chemistry Comparison and Benchmark Database (CCCBDB).<sup>13</sup>

B3LYP in conjunction with a triple-zeta type basis is found to yield reasonably good results for geometries (in the order of 0.005 Å). However, on occasion it shows inadequacy in predicting the energetics of the reactions. Usually the discrepancy is between 8 and 10 kJ/mol.<sup>14</sup> For reliable rate coefficients, an accurate knowledge of the computed potential energy surface is required. To improve the energetic description, additional single-point calculations using coupled cluster with single and double excitations (CCSD)<sup>15</sup> and the fourth-order Møller-Plesset (MP4(SDQ))<sup>16</sup> level of theory were performed at the DFT-optimized geometries. In these calculations, all-electron cc-pVTZ basis sets for all atoms were used. These calculations applied the frozen core approximation for the computational efficiency, and for the radical species, the restricted open-shell scheme was employed to obtain the Hartree-Fock reference wave functions.

All the B3LYP calculations were performed with the GAMESS-US suite,<sup>17</sup> whereas the GAUSSIAN 09 package<sup>18</sup> was used for the CCSD and MP4(SDQ) calculations. The

molecular graphics presented in this work were created by the MacMolPlt<sup>19</sup> and GaussView programs (Gaussian, Inc.).

### Equilibrium constants and rate coefficients

Based on the molecular and transition state parameters from the results of quantum chemical calculations, equilibrium constants,  $K(T)$ , and high pressure rate coefficients,  $k_\infty(T)$ , for various channels were calculated using standard equations from statistical thermodynamics<sup>20</sup> and statistical rate theories,<sup>21–25</sup> respectively:

$$[1] \quad K(T) = \frac{\prod_{\text{products}} (Q_i/V)}{\prod_{\text{reactants}} (Q_i/V)} \exp\left(\frac{-\Delta H_0}{k_B T}\right)$$

$$[2] \quad k_\infty(T) = \frac{k_B T}{h} \frac{(Q_i^*/V)}{\prod_{\text{reactants}} (Q_i/V)} \exp\left(\frac{-E_0}{k_B T}\right)$$

Here,  $Q_i$  denotes the molecular partition function of the species  $i$  and an asterisk signifies the activated complex;  $E_0$  and  $\Delta H_0$  are the threshold energy and enthalpy of reaction at  $T = 0$  K, respectively;  $V$  is the volume;  $k_B$  is Boltzmann's constant; and  $h$  is Planck's constant. The rotational and vibrational partition functions were calculated using the rigid rotor–harmonic oscillator approximation, whereas the electronic partition functions were set equal to 2 for the radical species and 4 for the Br atom. The external symmetry numbers are included in the rotational partition function. For a simple bond fission reaction where no potential barrier exists along the reaction coordinate, the partition function ( $Q_i^*$ ) should be understood as the pseudopartition function within the framework of the statistical adiabatic channel model (SACM). The pseudo-partition function of the threshold energies  $E_{0,i}$  for all individual channel states  $i$  is given<sup>23–25</sup> by

$$[3] \quad Q_i^* = \sum_i \exp\left(-\frac{E_{0,i} - E_0}{k_B T}\right)$$

## Results and discussion

### The B3LYP calculations

We first begin our discussion on the results of our calculations at the B3LYP/cc-pVTZ/cc-pVTZ-PP level of theory. The optimized geometries and selected structural parameters of the reactants, intermediate species, and products obtained at this level of theory are displayed in Figs. 1 and 2. The rotational constants and harmonic wave numbers for the species used in the kinetic analyses are compiled in Table 1. Several stationary points within the potential energy surface describing the hydrogen abstraction reactions of THF by the Br atom were computed.

The calculations predicted the conformation with  $C_2$  symmetry as the most stable form of THF. The nearly energetically degenerate bent conformer with  $C_s$  symmetry was also found to exist. The  $C_2$  and  $C_s$  species differed in energy by only 0.3 kJ/mol. The planar form of THF with  $C_{2v}$  symmetry represents the transition state that lies 12.4 kJ/mol above the

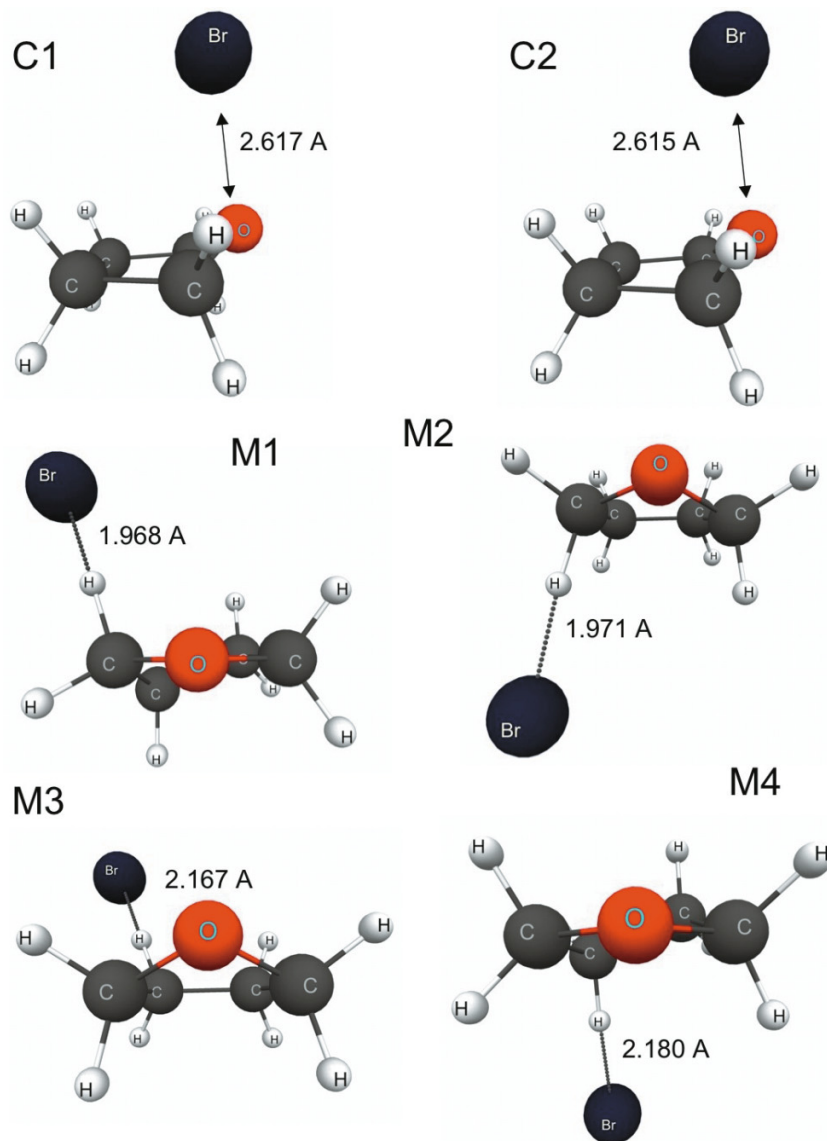
bent conformer. As for the reaction of THF and the Br atom, the H abstraction does not occur directly. Instead, it occurs via an addition–elimination mechanism in a similar fashion to that seen in the reactions of dioxane<sup>9</sup> and methanol<sup>26</sup> with the Br atom. The lack of mirror plane of symmetry within the ground state of THF results in the nonequivalence of the four hydrogen atoms. As a consequence, the Br-atom attack on H atoms of THF results in four possible adducts, M1–M4 (see Fig. 1), which can eventually eliminate HBr leading to the products,  $C_4H_7O^\bullet$  and HBr. Among the complexes, M1 and M2 are formed by the interaction of the approaching Br atom with the  $\alpha$ -hydrogen atoms, whereas M3 and M4 result from the attack of the Br atom on the H atoms that are not adjacent to the ether oxygen, i.e.,  $\beta$ -hydrogen atoms. The most stable complex (M1) is located 40.8 kJ/mol below the reactant, whereas M3 is found to be the least stable complex with the exothermicity of 14.2 kJ/mol. The thermal stability of M2 and M4 with respect to the reactant is calculated to be 27.7 and 14.2 kJ/mol, respectively. Constrained potential energy surface scans were performed along the reaction coordinates (C–H bond distance), but no maximum-energy configurations for further dissociation of M3 and M4 leading to the products were detected. The direct HBr elimination via these complexes is endothermic by 20.3 kJ/mol and occurs without an intramolecular hydrogen-transfer step. In contrast, M1 and M2 undergo conformational change into predissociative complexes, I1 and I2, respectively, before they can get rid of HBr. The latter species lie at energies of 12.4 and 12.2 kJ/mol, respectively, below the reactants. The barrier heights for the transition states (T1 and T2) for the conversions of M1 to I1 and M2 to I2 are found to be 32.2 and 24.5 kJ/mol, respectively.

In addition to the direct Br atom association with the hydrogen atoms of THF, the calculations also revealed two additional stable configurations where the Br atom is coordinated either solely to the oxygen atom (C1) or simultaneously to the oxygen and hydrogen atoms (C2). This binding mode has also been previously observed in the reaction of Br with methanol.<sup>26</sup> These conformers (C1 and C2) are less stable than M1 by 5.9 and 15.8 kJ/mol, respectively.

Subsequent kinetic analyses showed that the reaction of THF with the Br atom proceeds via the reaction sequence  $\text{THF} + \text{Br} \rightleftharpoons \text{M1} \rightleftharpoons \text{I1} \rightarrow \text{C}_4\text{H}_7\text{O}^\bullet + \text{HBr}$ . The calculated overall rate coefficients were overestimated by at least 70 times larger than our experimental rate coefficients (see Fig. 3). The calculated overall reaction enthalpy was 1.93 kJ/mol at 0 K, whereas the experimental reaction enthalpy was  $19 \pm 6$  kJ/mol.<sup>8</sup> This is an indication that the B3LYP level of theory is inadequate to accurately describe the energetics of this type of reaction system; and it is often found to underestimate it by an average deviation of  $\sim 13.0$  kJ/mol.<sup>27,28</sup> The deviation is even larger for non-hydrogen systems ( $\sim 22.4$  kJ/mol).<sup>27</sup> This severe disagreement between the theory and the experiments suggests that the B3LYP functional only provides a qualitative picture of energetics for the title reaction. Therefore, a more suitable methodology is required for a better description of the energetics of this type of reaction.



**Fig. 1.** B3LYP/cc-pVTZ/cc-pVTZ-PP structures of C1–C2 and M1–M4, and selected geometric parameters.



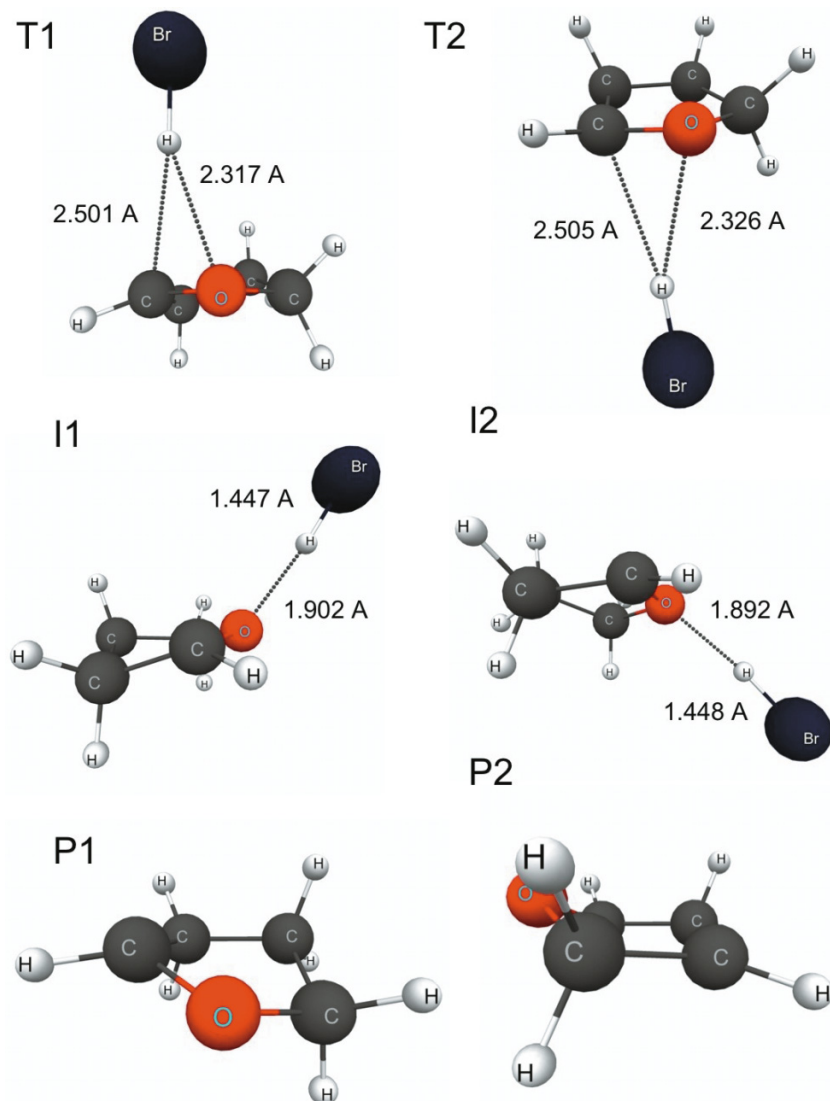
### The CCSD and MP4(SDQ) calculations

In an effort to more accurately understand the energetics of the title reaction, we further performed a series of single-point calculations at the CCSD and MP4(SDQ) levels of theory. The computed energies are illustrated in Figs. 4 and 5. Interestingly, the order of relative stability of molecular complexes (M1–M4) remains unchanged at the CCSD and MP4(SDQ) levels of theory when compared to that computed at B3LYP. However, in contrast with B3LYP, both CCSD and MP4(SDQ) predicted the molecular complexes M3 and M4 to be unstable. Both theories predicted a higher total energy of about 1.5 kJ/mol than the reactants for M3, whereas for the formation of M4, it was found to be almost thermoneutral. The reaction enthalpy for the  $\beta$ -hydrogen abstraction from THF by the Br atom via M3 and M4 is calculated to be  $\sim 31$  kJ/mol at both levels of theory (Figs. 4 and 5). Owing to its high threshold energy, the  $\beta$ -hydrogen abstraction channel may be considered to be unimportant.

At first, we note here that our experiments<sup>8</sup> indicated no discernible pressure dependence. This lack of pressure de-

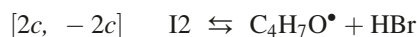
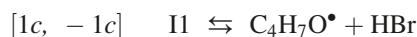
pendence and also the low temperature of our experiments suggest that the rate coefficients of all elementary steps involved in the title reaction are at their high pressure limits. Here, the pressure activation effects are not required to be considered in which case eqs. [1] and [2] can be used for kinetic analyses. Before ignoring the reaction channels via M3 or M4, we calculated the equilibrium constant for the reaction  $\text{THF} + \text{Br} \rightleftharpoons \text{P2} + \text{HBr}$  ( $K = 2.38 \times 10^{-5}$  at  $T = 293$  K) using eq. [1] with  $\Delta H_0 = 30.7$  kJ/mol, which was then combined with the rate coefficients (barrierless collision limit ( $k_{\text{coll}} = \bar{v}\sigma \approx 10^{-10} \text{ cm}^3 \text{ s}^{-1}$  with a typical molecular velocity ( $\bar{v}$ ) of  $5 \times 10^4 \text{ cm s}^{-1}$  and molecular cross section ( $\sigma$ ) of  $5 \times 10^{-15} \text{ cm}^2$ )<sup>22</sup> for the reverse reaction to estimate the rate coefficient for the forward reaction. The rate coefficient calculated this way was found to be  $\sim 1 \times 10^{-15} \text{ s}^{-1}$  at  $T = 293$  K, which is more than two orders of magnitude smaller than the experimental value. Even at  $T = 363$  K, it is calculated to be slower by  $\sim 28$  times. This clearly shows that the  $\beta$ -hydrogen abstraction reaction via M3 or M4 plays no role in the reaction kinetics, though

**Fig. 2.** B3LYP/cc-pVTZ/cc-pVTZ-PP structures of T1–T2, I1–I2, and P1–P2, as well as selected geometric parameters.



they appear in the potential energy surface for the reaction of THF with Br. Thus,  $\alpha$ -hydrogen abstraction appears to be more favourable than  $\beta$ -hydrogen abstraction from THF. This site preference is due to the fact that the Br-atom interaction with the H atom at the  $\alpha$  position is stabilized by hyperconjugation with the oxygen lone pair of electrons. This stabilization effect is, however, absent when Br is coordinated to the  $\beta$  hydrogen. Among the complexes, the addition complex (C1 or C2) is interestingly predicted to be the most stable complex. However, we failed to connect these species to any reaction. Hence, our calculation supports the postulate that the only significant channel for hydrogen abstraction from ethers by a Br atom is the removal of a hydrogen atom adjacent to the ether oxygen (see ref. 8 and the refs. cited therein).

The analysis to this point suggests that the reaction of THF with Br is governed by the addition complexes M1 and M2, which are linked to the reaction products via intermediates, I1 and I2, respectively:



As evident from Figs. 4 and 5, the hydrogen abstraction does not occur directly from these addition complexes, but requires H-atom transfer from the  $\alpha$  carbon to the ether oxygen to form a predissociative complex,  $\text{C}_4\text{H}_7\text{O}^\bullet \cdots \text{HBr}$ . Here, HBr is coordinated to the oxygen atom at either the axial (I1) or equatorial (I2) position. We were able to locate the transition states (T1 and T2) for the conversions of M1 to I1 and M2 to I2, respectively. These transition states are product-like, with the HBr molecule simultaneously weakly

**Table 1.** Rotational constants (*A*, *B*, and *C*) and harmonic wave numbers ( $\nu_i$ ) of stationary points calculated at the B3LYP level of theory used for kinetic analyses.

Species	<i>A</i> , <i>B</i> , <i>C</i> (cm <sup>-1</sup> )	$\nu_i$ (cm <sup>-1</sup> )
THF	0.237 52, 0.230 99, 0.132 55	2994, 2981, 2978, 2967, 2951, 2942, 2857, 2852, 1473, 1457, 1454, 1439, 1347, 1309, 1275, 1262, 1220 (2), 1186, 1172, 1109, 1056, 1010, 924, 907, 901, 870, 836, 773, 631, 623, 260, 25
HBr	8.320 1, 8.320 1	2501
M1	0.152 56, 0.028 63, 0.027 83	3005, 2998, 2974, 2971, 2952, 2924, 2922, 1999, 1466, 1447, 1431, 1340, 1313, 1297, 1274, 1266, 1206, 1167, 1150, 1126, 1095, 1076, 997, 919, 893, 892, 868, 837, 799, 664, 575, 304, 161, 137, 73, 46
M2	0.151 79, 0.028 66, 0.027 84	3009, 3001, 2990, 2983, 2959, 2949, 2905, 2011, 1465, 1450, 1436, 1339, 1314, 1296, 1272, 1251, 1204, 1198, 1173, 1119, 1094, 1072, 1004, 922, 910, 892, 873, 816, 767, 664, 620, 304, 166, 92, 67, 21
M3	0.173 86, 0.023 51, 0.022 56	2995, 2987, 2985, 2976, 2950, 2866, 2830, 2524, 1466, 1442, 1440, 1342, 1327, 1299, 1268, 1240, 1215, 1182, 1175, 1121, 1096, 1052, 1004, 919, 901, 898, 873, 825, 761, 636, 623, 258, 113, 66, 43, 24
M4	0.155 41, 0.024 95, 0.024 29	2990, 2988, 2961, 2939, 2922, 2892, 2861, 2515, 1476, 1453, 1432, 1346, 1331, 1309, 1276, 1238, 1204, 1178, 1144, 1124, 1107, 1051, 995, 925, 892, 882, 867, 838, 798, 650, 567, 243, 96, 56, 43, 28
T1	0.150 25, 0.024 01, 0.023 68	3078, 2996, 2984, 2956, 2945, 2916, 2835, 2409, 1468, 1444, 1429, 1352, 1299, 1269, 1262, 1206, 1163, 1143, 1128, 1035, 997, 920, 906, 888, 848, 823, 719, 600, 505, 313, 229, 194, 72, 62, 22, 224i
T2	0.163 50, 0.022 66, 0.022 00	3072, 2999, 2976, 2959, 2932, 2930, 2863, 2415, 1474, 1456, 1434, 1359, 1297, 1270, 1213, 1217, 1196, 1155, 1137, 1035, 1009, 929, 903, 877, 868, 759, 738, 678, 549, 315, 199, 125, 78, 63, 23, 212i
I1	0.203 07, 0.022 07, 0.021 03	3093, 2999, 2987, 2955, 2945, 2922, 2831, 2263, 1469, 1444, 1430, 1352, 1302, 1271, 1263, 1209, 1163, 1143, 1120, 1033, 997, 921, 902, 887, 850, 823, 714, 594, 479, 450, 402, 224, 189, 81, 40, 20
I2	0.212 50, 0.021 92, 0.020 78	3091, 2999, 2988, 2957, 2944, 2923, 2833, 2248, 1470, 1445, 1430, 1354, 1302, 1272, 1263, 1208, 1165, 1141, 1120, 1035, 998, 921, 902, 887, 851, 821, 718, 599, 490, 464, 414, 226, 184, 81, 41, 21
P1	0.254 31, 0.239 95, 0.136 09	3081, 2990, 2974, 2951, 2940, 2905, 2820, 1469, 1443, 1431, 1355, 1297, 1268, 1261, 1205, 1165, 1144, 1131, 1033, 995, 921, 912, 889, 850, 826, 716, 598, 469, 227, 169
P2	0.255 21, 0.239 18, 0.135 91	3102, 2978, 2923, 2891, 2864, 2843, 2789, 1466, 1440, 1417, 1347, 1302, 1274, 1239, 1205, 1149, 1140, 1055, 1006, 984, 931, 905, 892, 882, 829, 702, 622, 286, 213, 159

**Note:** The wavenumbers are scaled by 0.9648.

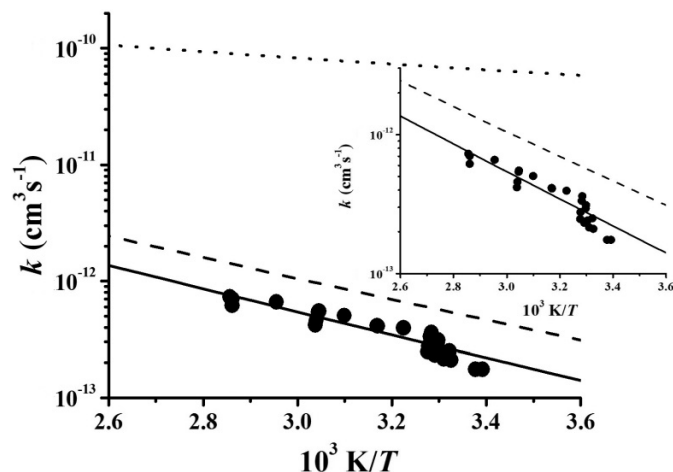
bound to the  $\alpha$  carbon and the oxygen via the abstracted hydrogen. Their structures are depicted in Fig. 2. As the relative energies of all species computed at the CCSD and MP4(SDQ) levels of theory concur well within the uncertainty of the calculations, we focus below on the results of our kinetic analysis based on the CCSD energies depicted in Fig. 4 to avoid confusion. However, one would reach to the same conclusion with the MP4(SDQ) potential energy surface displayed in Fig. 5.

The thermal stability of the complexes M1 and M2, with respect to the reactants, is calculated to be 4.5 and 2.1 kJ/mol, respectively. The formation of M2 at MP4(SDQ) is almost thermoneutral. For the elementary step M1  $\rightarrow$  I1, T1 is located 4.2 kJ/mol above M1 and 2.2 kJ/mol above I1, whereas for the M2  $\rightarrow$  I2 step, T2 lies 9.0 and 8.9 kJ/mol

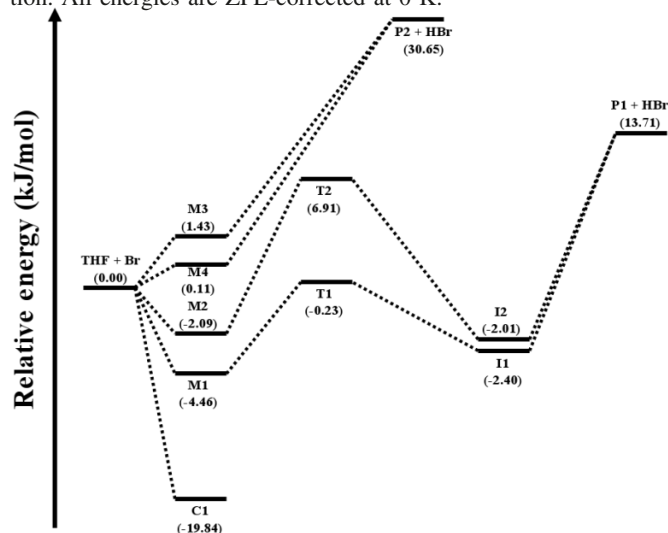
above M2 and I2, respectively. It is interesting to note here that the two predissociative adducts I1 and I2 are of similar stability with respect to the reactants. This phenomenon can be accounted for by the fact that the C<sub>4</sub>H<sub>7</sub>O<sup>•</sup> fragments of I1 and I2 are almost identical and HBr is only loosely bound to the oxygen atom through long-range interaction. The computed O $\cdots$ H distances are 1.902 and 1.892 Å for I1 and I2, respectively, and the H–Br bond is only marginally stretched by 0.02 Å. The unimolecular dissociation of these loose complexes to release HBr proceeds without a distinct energy barrier and these loose dissociation pathways are endothermic by 16.1 kJ/mol.

The formation of M2 is less exothermic than it is for M1 and it has a more pronounced energy barrier for H migration to the ether oxygen to form a predissociative complex (I2).

**Fig. 3.** Arrhenius plot for the reaction of Br atoms with THF. (●) Experimental data from our previous work.<sup>8</sup> (· · ·), (---), and (—) are the results of eq. [6] using the energies at the B3LYP, CCSD, and MP4(SDQ) level of theory, respectively. The inset figure magnifies a portion of the Arrhenius plot to show the agreement between the theoretical and experimental results.



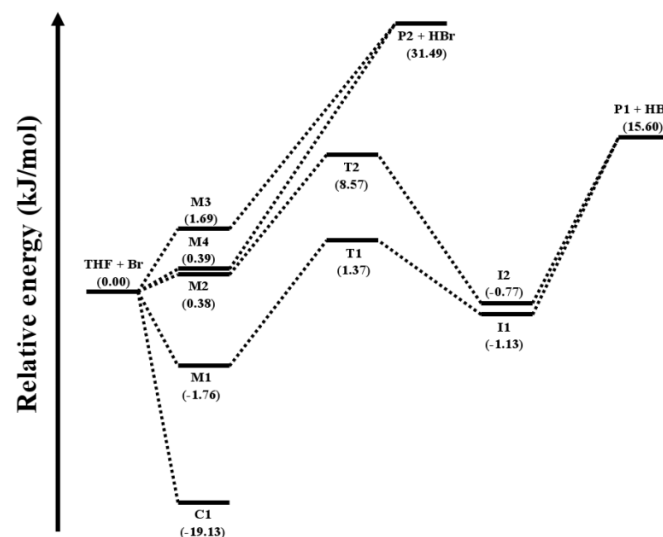
**Fig. 4.** CCSD/cc-pVTZ energy diagram for the THF and Br reaction. All energies are ZPE-corrected at 0 K.



At  $T = 293$  K, we calculated the rate coefficient for the step [2b],  $k_{2b}$ , to be  $4.0 \times 10^{11} \text{ s}^{-1}$ , which is 16 times smaller than  $k_{1b}$ . The ratio ( $k_{1b}/k_{2b}$ ) = 11.7 even at  $T = 353$  K, the highest temperature of our experiments.<sup>8</sup> Accordingly, the H-abstraction reaction via M2 is unimportant and therefore will not be considered for further kinetic analyses. Therefore, the reaction of THF with Br appears to proceed only via M1 with the reaction sequence [1a]–[1c].

It is evident from Fig. 4 that the reaction [–1b] has a lower threshold energy than the reaction [1c]. Despite the fact that the reaction [1c] is a loose dissociation pathway and an entropically favoured path, the reaction [–1b] appeared to be at least 10 times faster than reaction [1c], even at  $T = 353$  K. This was verified by comparing the rate coefficients for reaction [–1b],  $k_{-1b} = k_{1b}/K_{1b}$  with the rate coefficient for reaction [1c], see Table 2. The simplified

**Fig. 5.** MP4(SDQ)/cc-pVTZ energy diagram for the THF and Br reaction. All energies are ZPE-corrected at 0 K.



statistical adiabatic channel model (s-SACM)<sup>23–25</sup> was employed to calculate the high pressure rate coefficients for reaction [1c]. In these calculations, I1 was treated as a quasi-triatomic prolate symmetric top, whereas the fragments P1 and HBr were considered as spherical top and linear, respectively. Within the s-SACM model, the evaluation of two empirical parameters, namely the looseness parameter ( $\alpha$ ) and the Morse parameter ( $\beta$ ), is required. The choice of the ratio,  $\alpha/\beta$  (anisotropy parameter), is crucial as it determines the quality of the predicted high pressure rate coefficients. The Morse parameter ( $\beta$ ) is calculated from the following expression:

$$[4] \quad \beta = \sqrt{\frac{2\pi^2\mu}{Dh^2}} \varepsilon_{RC}$$

where  $\varepsilon_{RC}$  is the energy of the vibrational mode describing the motion along the reaction coordinate,  $\mu$  is the reduced mass of the fragments, and  $D$  is the Morse dissociation energy, which can be calculated from the zero-point energies,  $E_{zn}$  and  $E_{zp}$  for the reactant and fragments, respectively:

$$[5] \quad D = \Delta H_0 + E_{zn} - E_{zp}$$

Generally,  $\alpha$  is considered as the fitting parameter, the value of which is chosen to get the best fit with the experimental data. However, after a rigorous study for a number of reaction systems, Cobos and Troe<sup>29</sup> found a standard value of  $0.46 \pm 0.07$  for the anisotropy parameter,  $\alpha/\beta$ . For our calculations, we set this ratio equal to 0.46. All the other internal parameters are taken from our quantum chemical calculations and there is no other adjustable parameter. The results are compiled in Table 2. As the reaction [1c] has the highest threshold energy in the reaction sequence [1a]–[1c], it represents the rate-determining step for the overall reaction of the Br atom with THF. This is obvious when the rate coefficients compiled in Table 2 are compared. Therefore, it follows that M1 is in equilibrium with I1 and the reactants, which is rapidly established and virtually not affected by the reaction [1c]. Accordingly, this allows the overall rate



**Table 2.** Calculated rate constants for the reaction of the Br atom with tetrahydrofuran based on the CCSD energies.

<i>T</i> (K)	$K_{1a} \times 10^{24}$ (cm <sup>3</sup> )	$K_{1b} \times 10^{24}$ (cm <sup>3</sup> )	$k_{1b} \times 10^{-12}$ (s <sup>-1</sup> )	$k_{-1b} \times 10^{-12}$ (s <sup>-1</sup> )	$k_{1c} \times 10^{-12}$ (s <sup>-1</sup> )	$k_{1c} \times 10^{-10}$ (s <sup>-1</sup> )	$k_{ov,calcd} \times 10^{13}$ (cm <sup>3</sup> s <sup>-1</sup> )	$k_{ov,expt} \times 10^{13}$ (cm <sup>3</sup> s <sup>-1</sup> )	$k_{ov,calcd}/k_{ov,expt}$
273	1.61	3.35	4.98	1.49	5.09	2.74	1.17	1.17	2.3
283	1.53	3.59	5.67	1.58	6.46	3.55	1.56	1.56	2.3
293	1.47	3.83	6.41	1.67	8.06	4.53	2.03	2.03	2.2
303	1.41	4.08	7.21	1.77	9.90	5.68	2.60	2.60	2.2
313	1.36	4.33	8.06	1.86	12.0	7.04	3.28	3.28	2.1
323	1.32	4.59	8.97	1.95	14.3	8.63	4.08	4.08	2.1
333	1.28	4.86	9.94	2.05	16.8	10.4	5.00	5.00	2.1
343	1.24	5.13	11.0	2.14	19.6	12.5	6.06	6.06	2.1
353	1.22	5.41	12.0	2.23	22.7	14.9	7.27	7.27	2.1
363	1.19	5.69	13.2	2.31	25.9	17.6	8.63	8.63	2.0

coefficient ( $k_{ov}$ ) for the title reaction to be approximated reasonably well with the following expression:

$$[6] \quad k_{ov,calcd}(T) = K_{1a}(T)K_{1b}(T)k_{1c}(T)$$

The values of  $k_{ov,calcd}(T)$  obtained in this way at CCSD energies are higher by a factor of 2 at all temperatures when compared with the experimental ones. However, the calculated overall rate coefficients using the energy profile from MP4(SDQ) calculations are in excellent agreement with our experimental values,<sup>8</sup> which is demonstrated in Fig. 3. The rate coefficients calculated on the basis of the MP4(SDQ) PES for the reaction sequence [1a]–[1c] are summarized in Table 3. It is further encouraging to notice here the agreement between the calculated overall endothermicity of 16.7 kJ/mol and the experimentally determined activation energy of  $(18.6 \pm 1.8)$  kJ/mol for this reaction. This agreement further supports our earlier assumption that the H-abstraction reaction of THF by the Br atom is, indeed, at the high pressure limit. The calculated rate coefficients using MP4(SDQ) energies and eq. [6] in the temperature range of 273–363 K for the reaction of Br atoms with THF can be given by the following Arrhenius expression:

$$[7] \quad k_{ov,calcd}(T) = 5.03 \times 10^{-10} \exp[-18.9/(RT)]$$

## Conclusion

The reaction mechanism for abstraction of a hydrogen atom from THF by atomic bromine was found to be analogous to the reactions of the Br atom with dioxane<sup>9</sup> and methanol,<sup>26</sup> where the reaction proceeds via an addition–elimination mechanism. Our quantum chemical calculations show that the attack by Br on an H atom of THF results in four stable associative complexes, M1–M4, whereas the addition of Br to the ether oxygen yields two more adducts, namely C1 and C2. The latter complexes are not found to link to any reactions. Hence, they are believed to play no role in the reaction kinetics of the Br atom with THF, though they appear in the reaction mechanism. Subsequent calculations showed that the only channel responsible for the overall rate coefficient of the reaction is the one that exits through M1. Before M1 can decompose into the products, it has to undergo an intramolecular H abstraction to yield I1 (reaction [1b]), which eventually liberates HBr via a loose dissociation pathway. The B3LYP level of theory was found to be inadequate to describe the energetics of this system. This is evident when the calculated overall endothermicity of 1.9 kJ/mol at 0 K (almost a thermoneutral reaction) is compared with the experimental value of  $19 \pm 6$  kJ/mol. In an effort to better understand the energetics of this reaction, we further employed single-point calculations at the CCSD and MP4(SDQ) levels of theory to recompute the potential energy surfaces. This approach predicted an overall reaction enthalpy at 0 K of about 16.5 kJ/mol, which matched very well with the experimental value. As the final step, reaction [1c], has the highest threshold energy, it is calculated to be the rate-determining step. Whereas the rate coefficient calculations at CCSD energies overpredicted the experimental rate coefficients by a factor of two at all tem-

**Table 3.** Calculated rate constants for the reaction of the Br atom with tetrahydrofuran based on the MP4(SDQ) energies.

T (K)	$K_{1a} \times 10^{25} \text{ (cm}^3\text{)}$	$K_{1b} \times 10^{25} \text{ (cm}^3\text{)}$	$K_{1b} \times 10^{-13} \text{ (s}^{-1}\text{)}$	$k_{-1b} \times 10^{-12} \text{ (s}^{-1}\text{)}$	$k_{1c} \times 10^{-10} \text{ (s}^{-1}\text{)}$	$k_{\text{ov,calcd}} \times 10^{13} \text{ (cm}^3 \text{ s}^{-1}\text{)}$	$k_{\text{ov,expt}} \times 10^{13} \text{ (cm}^3 \text{ s}^{-1}\text{)}$	$k_{\text{ov,calcd}}/k_{\text{ov,expt}}$
273	4.90	6.40	0.82	1.28	3.91	1.23	1.17	1.1
283	4.86	6.70	0.92	1.37	5.01	1.63	1.56	1.0
293	4.84	7.00	1.02	1.46	6.31	2.14	2.03	1.1
303	4.82	7.31	1.13	1.55	7.80	2.75	2.60	1.1
313	4.81	7.62	1.25	1.64	9.50	3.48	3.28	1.1
323	4.81	7.94	1.37	1.73	11.4	4.36	4.08	1.1
333	4.82	8.27	1.50	1.82	13.5	5.38	5.00	1.1
343	4.83	8.59	1.63	1.90	15.9	6.58	6.06	1.1
353	4.84	8.93	1.78	1.99	18.4	7.96	7.27	1.1
363	4.87	9.27	1.92	2.07	21.2	9.54	8.63	1.1

peratures, the best agreement with the experimental data was obtained from the energetic description at MP4(SDQ) level of theory.

## Acknowledgments

The computations described in this work were performed on the computing facilities of the Department of Academic Information and Communication Technologies (AICT) and the Department of Chemistry, University of Alberta (Edmonton, Alberta), as well as the High-Performance Computing (HPC) facilities within the Research Computing Services of the University of Calgary (Calgary, Alberta) and the Western Canada Research Grid. The authors are grateful to Drs. M. Olzmann and N. González-García of the Institut für Physikalische Chemie, Karlsruher Institut für Technologie (KIT; Karlsruhe, Germany) for numerous helpful discussions and also for providing the program script for SACM calculations.

## References

- (1) Bedjanian, Y.; Poulet, G. *Chem. Rev.* **2003**, *103* (12), 4639. doi:10.1021/cr0205210. PMID:14664627.
- (2) Finlayson-Pitts, B. J. *Chem. Rev.* **2003**, *103* (12), 4801. doi:10.1021/cr020653t. PMID:14664634.
- (3) Finlayson-Pitts, B. J.; Pitts, J. N., Jr. *Chemistry of the Upper and Lower Atmosphere Theory, Experiments, and Applications*; Academic Press: New York, 2000.
- (4) Moltó, J.; Font, R.; Gálvez, A.; Conesa, J. A. *J. Anal. Appl. Pyrolysis* **2009**, *84* (1), 68. doi:10.1016/j.jaap.2008.10.023.
- (5) Miskolczi, N.; Hall, W. J.; Angyal, A.; Bartha, L.; Williams, P. T. *J. Anal. Appl. Pyrolysis* **2008**, *83* (1), 115. doi:10.1016/j.jaap.2008.06.010.
- (6) Zhu, H. M.; Jiang, X. G.; Yan, J. H.; Chi, Y.; Cen, K. F. *J. Anal. Appl. Pyrolysis* **2008**, *82* (1), 1. doi:10.1016/j.jaap.2007.11.011.
- (7) Wheeler, M.; Mills, R.; Roscoe, J. M. *J. Phys. Chem. A* **2008**, *112* (5), 858. doi:10.1021/jp077420w. PMID:18186619.
- (8) Giri, B. R.; Roscoe, J. M. *J. Phys. Chem. A* **2009**, *113* (28), 8001. doi:10.1021/jp903293y. PMID:19555110.
- (9) Giri, B. R.; Roscoe, J. M.; González-García, N.; Olzmann, M. *J. Phys. Chem. A* **2010**, *114* (1), 291. doi:10.1021/jp908168u. PMID:19848396.
- (10) (a) Becke, A. D. *J. Chem. Phys.* **1992**, *97* (12), 9173. doi:10.1063/1.463343.; (b) Becke, A. D. *J. Chem. Phys.* **1993**, *98* (7), 5648. doi:10.1063/1.464913.; (c) Lee, C.; Yang, W.; Parr, R. G. *Phys. Rev.* **1988**, *B37* (2), 785. doi:10.1103/PhysRevB.37.785.
- (11) Dunning, T. H., Jr. *J. Chem. Phys.* **1989**, *90* (2), 1007. doi:10.1063/1.456153.
- (12) Peterson, K. A.; Figgen, D.; Goll, E.; Stoll, H.; Dolg, M. *J. Chem. Phys.* **2003**, *119* (21), 11113. doi:10.1063/1.1622924.
- (13) Computational Chemistry Comparison and Benchmark Database (CCCBDB), Release 15a [Online]. <http://cccbdb.nist.gov> (accessed April 2010).
- (14) Cramer, C. J. *Essentials of Computational Chemistry: Theories and Models*, 2nd ed.; Wiley: New York, 2004; Chapter 8.
- (15) (a) Čížek, J. *Adv. Chem. Phys.* **1969**, *14*, 35. doi:10.1002/9780470143599.ch2.; (b) Purvis, G. D.; Bartlett, R. J. *J. Chem. Phys.* **1982**, *76* (4), 1910. doi:10.1063/1.443164.; (c) Scuseria, G. E.; Janssen, C. L.; Schaefer, H. F., III. *J.*

- Chem. Phys.* **1988**, 89 (12), 7382. doi:10.1063/1.455269.; (d) Scuseria, G. E.; Schaefer, H. F., III. *J. Chem. Phys.* **1989**, 90 (7), 3700. doi:10.1063/1.455827.
- (16) (a) Trucks, G. W.; Salter, E. A.; Sosa, C.; Bartlett, R. J. *Chem. Phys. Lett.* **1988**, 147 (4), 359. doi:10.1016/0009-2614(88)80249-5.; (b) Trucks, G. W.; Watts, J. D.; Salter, E. A.; Bartlett, R. J. *Chem. Phys. Lett.* **1988**, 153 (6), 490. doi:10.1016/0009-2614(88)85248-5.
- (17) Schmidt, M. W.; Baldridge, K. K.; Boatz, J. A.; Elbert, S. T.; Gordon, M. S.; Jensen, J. H.; Koseki, S.; Matsunaga, N.; Nguyen, K. A.; Su, S. J.; Windus, T. L.; Dupuis, M.; Montgomery, J. A. *J. Comput. Chem.* **1993**, 14 (11), 1347. doi:10.1002/jcc.540141112.
- (18) Frisch, M. J.; Trucks, G. W.; Schlegel, H. B.; Scuseria, G. E.; Robb, M. A.; Cheeseman, J. R.; Montgomery, J. A., Jr.; Vreven, T.; Kudin, K. N.; Burant, J. C.; Millam, J. M.; Iyengar, S. S.; Tomasi, J.; Barone, V.; Mennucci, B.; Cossi, M.; Scalmani, G.; Rega, N.; Petersson, G. A.; Nakatsuji, H.; Hada, M.; Ehara, M.; Toyota, K.; Fukuda, R.; Hasegawa, J.; Ishida, M.; Nakajima, T.; Honda, Y.; Kitao, O.; Nakai, H.; Klene, M.; Li, X.; Knox, J. E.; Hratchian, H. P.; Cross, J. B.; Adamo, C.; Jaramillo, J.; Gomperts, R.; Stratmann, R. E.; Yazyev, O.; Austin, A. J.; Cammi, R.; Pomelli, C.; Ochterski, J. W.; Ayala, P. Y.; Morokuma, K.; Voth, G. A.; Salvador, P.; Dannenberg, J. J.; Zakrzewski, V. G.; Dapprich, S.; Daniels, A. D.; Strain, M. C.; Farkas, O.; Malick, D. K.; Rabuck, A. D.; Raghavachari, K.; Foresman, J. B.; Ortiz, J. V.; Cui, Q.; Baboul, A. G.; Clifford, S.; Cioslowski, J.; Stefanov, B. B.; Liu, G.; Liashenko, A.; Piskorz, P.; Komaromi, I.; Martin, R. L.; Fox, D. J.; Keith, T.; Al-Laham, M. A.; Peng, C. Y.; Nanayakkara, A.; Challacombe, M.; Gill, P. M. W.; Johnson, B.; Chen, W.; Wong, M. W.; Gonzalez, C.; Pople, J. A. *Gaussian 09*, Revision A.02; Gaussian, Inc.: Wallingford, CT, 2009.
- (19) Bode, B. M.; Gordon, M. S. *J. Mol. Graph. Model.* **1998**, 16 (3), 133, 164. doi:10.1016/S1093-3263(99)00002-9. PMID: 10434252.
- (20) McQuarrie, D. A. *Statistical Thermodynamics*; University Science Books: Mill Valley, CA, 1973.
- (21) Glasstone, S.; Laidler, K. J.; Eyring, H. *The Theory of Rate Processes*; McGraw-Hill: New York, 1941.
- (22) Steinfeld, J. I.; Francisco, J. S.; Hase, W. L. *Chemical Kinetics and Dynamics*; Prentice Hall: Englewood Cliffs, NJ, 1989.
- (23) Troe, J. *J. Chem. Phys.* **1981**, 75 (1), 226. doi:10.1063/1.441829.
- (24) Quack, M.; Troe, J. *Ber. Bunsenges. Phys. Chem* **1974**, 78, 240.
- (25) Quack, M.; Troe, J. In *Encyclopedia of Computational Chemistry*; von Ragué Schleyer, P.; Allinger, N.; Clark, T.; Gasteiger, J.; Kollmann, P. A.; Schaefer, H. F., Eds.; Wiley: New York, 1998; p 2708.
- (26) Jodkowski, J. T.; Rayez, M.-T.; Rayez, J.-C.; Berces, T.; Dobe, S. *J. Phys. Chem. A* **1998**, 102 (46), 9230. doi:10.1021/jp980846d.
- (27) Curtiss, L. A.; Raghavachari, K.; Redfern, P. C.; Pople, J. A. *J. Chem. Phys.* **1997**, 106 (3), 1063. doi:10.1063/1.473182.
- (28) Jensen, F. *Introduction to Computational Chemistry*; 2nd ed.; Wiley: New York, 2007; Chapters 5 and 6.
- (29) Cobos, C. J.; Troe, J. *J. Chem. Phys.* **1985**, 83 (3), 1010. doi:10.1063/1.449464.

# Theoretical study of the microwave spectrum of isotopologues of OCS–(He)<sub>2</sub>

Hui Li, Yongdong Liu, Wolfgang Jäger, Robert J. Le Roy, and Pierre-Nicholas Roy

**Abstract:** The rovibrational energy levels ( $J = 0-3$ ) and rotational spectra of seven isotopologues of the OCS–(He)<sub>2</sub> complex have been determined by numerically exact basis set calculations. The interaction energy is represented as a sum of two-body terms consisting of the OCS–He potential, which Howson and Hutson (*J. Chem. Phys.* **2001**, *115*, 5059) obtained at the CCSD(T)/aug-cc-pVTZ level of theory, and the He–He potential that Jeziorska et al. (*J. Chem. Phys.* **2007**, *127*, 124303) obtained with SAPT theory. Three-body effects and the quality of the potential are discussed. Comparison with experiment shows that microwave transitions can be predicted by this additive approach with an accuracy equal or better than 0.7% for all the observed spectral lines. A method for the three-dimensional representation of the helium density in the body-fixed frame is presented that highlights the highly delocalized nature of the helium subsystem.

**Key words:** weakly bound clusters, quantum clusters, exact bound state calculations, microwave spectroscopy, rotational dynamics.

**Résumé :** Utilisant des ensembles de base numériquement exacts, on a calculé les niveaux d'énergie rovibrationnels ( $J = 0-3$ ) et les spectres rotationnels de sept isotopologues du complexe OCS–(He)<sub>2</sub>. L'énergie d'interaction est représentée par la somme de termes à deux corps formée du potentiel OCS–He que Howson et Hutson (*J. Chem. Phys.* **2001**, *115*, 5059) ont déterminé au niveau CCSD(T)/aug-cc-pVTZ de la théorie et du potentiel He–He que Jeziorska et al. (*J. Chem. Phys.* **2007**, *127*, 124303) ont déterminé à l'aide de la théorie des perturbations adaptée pour la symétrie (TPAS). On discute aussi des effets de trois corps et de la qualité du potentiel. Une comparaison des résultats des calculs avec des résultats expérimentaux montre que les transitions de microondes peuvent être mieux prédites par cette approche additive, avec une précision égale ou meilleure à 0,7 % pour toutes les raies spectrales observées. On présente une méthode de représentation tridimensionnelle de la densité de l'hélium dans un squelette à corps fixes qui est caractérisé par la nature hautement délocalisée du sous-système de l'hélium.

**Mots-clés :** agrégats faiblement liés, agrégats quantiques, calculs exacts de l'état lié, spectroscopie de microondes, dynamique rotationnelle.

[Traduit par la Rédaction]

## Introduction

Doped helium clusters offer a unique opportunity to understand quantum solvation and microscopic superfluidity, and this topic has been the subject of several studies in recent years.<sup>1–13</sup> Helium clusters doped with carbonyl sulfide (OCS) are of particular interest, because the OCS chromophore was the dopant used to provide the first evidence of microscopic superfluidity in helium nanodroplets.<sup>1</sup> In that seminal work, it was found that the OCS molecule undergoes nearly free rotational motion with a renormalization of its moment of inertia owing to its coupling to the helium environment, and the nearly free nature of that rotational motion was attributed to superfluidity. Since that time, helium clusters doped with OCS have become the focus of numer-

ous experimental and theoretical studies.<sup>4,7,11,14–18</sup> In particular, Xu and Jäger<sup>3,6</sup> and Tang and McKellar<sup>4,7</sup> have gone beyond the traditional binary or ternary complex limit to obtain infrared and microwave spectra of OCS–(He)<sub>N</sub> clusters for  $N = 2-8$ . In addition to being a technical breakthrough, that work hinted at the onset of superfluidity and provided benchmark challenges for theoretical studies.

To fully understand the experimental spectra on the atomic scale, computer simulation studies are important and necessary,<sup>19,20</sup> and a number of theoretical studies of OCS–(He)<sub>N</sub> clusters based on quantum Monte Carlo techniques have been reported.<sup>14–18,21</sup> Such techniques have also been applied to He clusters containing other dopants such as N<sub>2</sub>O,<sup>22,23</sup> CO<sub>2</sub>,<sup>20,24,25</sup> and HCCCN,<sup>26</sup> yielding excellent agreement with experiment. To date, however, exact quan-

Received 1 March 2010. Accepted 11 June 2010. Published on the NRC Research Press Web site at canjchem.nrc.ca on 4 November 2010.

This article is part of a Special Issue dedicated to Professor R. J. Boyd.

**H. Li.** Department of Chemistry, University of Waterloo, Waterloo, ON N2L 3G1, Canada; Institute of Theoretical Chemistry, State Key Laboratory of Theoretical and Computational Chemistry, Jilin University, 2519 Jiefang Road, Changchun 130023, P.R. China.

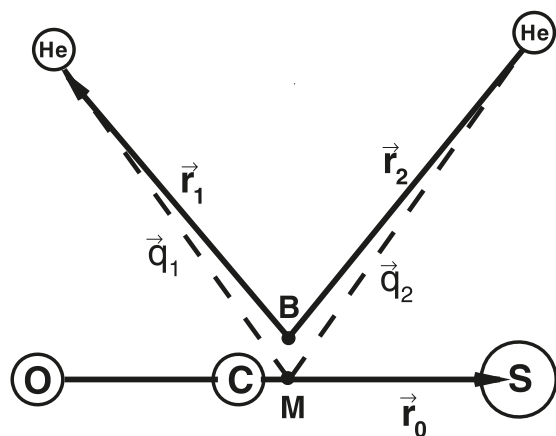
**Y. Liu and W. Jäger.** Department of Chemistry, University of Alberta, Edmonton, AB T6G 2G2, Canada.

**R.J. LeRoy and P.-N. Roy.**<sup>1</sup> Department of Chemistry, University of Waterloo, Waterloo, ON N2L 3G1, Canada.

<sup>1</sup>Corresponding author (e-mail: pnroy@uwaterloo.ca).



**Fig. 1.** Illustration of the coordinate system used in the bound-state calculations: M is the centre of mass of OCS and B is the canonical point for the Radau vectors  $\mathbf{r}_1$  and  $\mathbf{r}_2$ , and  $\mathbf{q}_1$  and  $\mathbf{q}_2$  are the Jacobi vectors and  $\mathbf{r}_0$  is a vector defining the axis of the OCS molecule;  $\phi$  is a dihedral angle between  $\mathbf{r}_1 \times \mathbf{r}_0$  and  $\mathbf{r}_2 \times \mathbf{r}_0$ , and  $\theta_1$  and  $\theta_2$  are angles between  $\mathbf{r}_0$  and  $\mathbf{r}_1$  and  $\mathbf{r}_2$ , respectively.



tum calculations on  $\text{OCS}-(\text{He})_N$  clusters have been restricted to the  $\text{He}-\text{OCS}$  dimer.<sup>18,27</sup> The present paper extends this work to the case of two helium atoms with OCS. In the remainder of this paper, details of the theory and computational procedure are given in the Theory and methods section, results are presented and discussed in the Results

and discussion section, and concluding remarks appear in last section.

## Theory and methods

### General

The methodology used in this work is based mainly on the work of Wang, Carrington, and co-workers<sup>28</sup> and on fundamental ideas presented by Mladenovic.<sup>29</sup> The Wang and Carrington group applied their approach to the  $\text{N}_2\text{O}-(\text{He})_2$  system and were able to reproduce experimentally observable rovibrational transitions quite accurately. Recently, they also applied their approach to  $\text{CO}_2-(\text{He})_2$  and to  $\text{CO}-(\text{He})_2$ , again with great success.<sup>30,31</sup> The method is briefly reviewed here, and the reader is referred to ref. 28 for further details.

The rovibrational Hamiltonian of the  $\text{OCS}-(\text{He})_2$  complex in the body-fixed frame has the following form (in au):<sup>28,29,32,33</sup>

$$[1] \quad \hat{H} = \hat{T}_{\text{str}} + \hat{T}_{\text{diag}} + \hat{T}_{\text{off}} + \hat{T}_{\text{Cor}} + \bar{V}(r_1, r_2, \theta_1, \theta_2, \phi)$$

with

$$[2] \quad \hat{T}_{\text{str}} = -\frac{1}{2m_{\text{He}}} \frac{\partial^2}{\partial r_1^2} - \frac{1}{2m_{\text{He}}} \frac{\partial^2}{\partial r_2^2}$$

$$[3] \quad \hat{T}_{\text{diag}} = -\left(\frac{1}{2m_{\text{He}}r_1^2} + B_{\text{OCS}}\right) \left[ \frac{\partial^2}{\partial \theta_1^2} + \cot \theta_1 \frac{\partial}{\partial \theta_1} - \frac{1}{\sin^2 \theta_1} (\hat{J}_z - \hat{l}_{2z})^2 \right] + \left(\frac{1}{2m_{\text{He}}r_2^2} + B_{\text{OCS}}\right) \hat{l}_2^2 + B_{\text{OCS}} [\hat{J}^2 - 2(\hat{J}_z - \hat{l}_{2z})^2 - 2\hat{J}_z \hat{l}_{2z}]$$

$$[4] \quad \hat{T}_{\text{off}} = B_{\text{OCS}} (\hat{l}_{2+} \hat{a}_1^- + \hat{l}_{2-} \hat{a}_1^+)$$

$$[5] \quad \hat{T}_{\text{Cor}} = -B_{\text{OCS}} (\hat{J}_- \hat{a}_1^+ + \hat{J}_+ \hat{a}_1^- + \hat{J}_- \hat{l}_{2+} + \hat{J}_+ \hat{l}_{2-})$$

in which

$$[6] \quad \hat{J}_{\pm} = \hat{J}_x \pm i\hat{J}_y, \quad \hat{l}_{2\pm} = \hat{l}_{2x} \pm i\hat{l}_{2y}$$

$$[7] \quad \hat{a}_1^{\pm} = \pm \frac{\partial}{\partial \theta_1} - \cot \theta_1 (\hat{J}_z - \hat{l}_{2z})$$

Details of the coordinate system are presented in Fig. 1, where  $r_1$  and  $r_2$  are the lengths of Radau (or orthogonalized satellite) vectors  $\mathbf{r}_1$  and  $\mathbf{r}_2$ , which are linear combinations of the Jacobi (or satellite) vectors  $\mathbf{q}_1$  and  $\mathbf{q}_2$  from the centre of mass of OCS to the He atoms.<sup>29</sup> The polyspherical angles ( $\theta_1$ ,  $\theta_2$ , and  $\phi$ ) are determined by the three vectors ( $\mathbf{r}_0$ ,  $\mathbf{r}_1$ , and  $\mathbf{r}_2$ ), where  $\mathbf{r}_0$  is a vector along the axis of OCS,  $m_{\text{He}}$  is the mass of the He atom, and  $B_{\text{OCS}}$  is the inertial rotation constant of OCS. The operators  $\hat{J}_x$ ,  $\hat{J}_y$ , and  $\hat{J}_z$  are the components of the total angular momentum operator  $\hat{J}$  in the body-fixed frame, the  $z$  axis of the body-fixed frame lies along the Jacobi radial vector  $\mathbf{r}_0$ , and its  $x$  axis is in the plane that contains the vector  $\mathbf{r}_0$  and one He atom.  $\bar{V}(r_1, r_2, \theta_1, \theta_2, \phi)$  is the total potential represented as a sum of two He-OCS poten-

tials plus the He-He intermolecular potential. The above Hamiltonian contains full vibration-rotation coupling.

### Basis function and matrix elements

A discrete variable representation (DVR) grid<sup>34</sup> is used for the radial degree of freedom, while parity-adapted rovibrational basis functions are used for the angular part. The latter are linear combinations of the functions

$$[8] \quad \langle \theta_1, \theta_2, \phi; \alpha, \beta, \gamma | l_1, l_2, m_2; J, K, M \rangle = \sqrt{\frac{2J+1}{8\pi^2}} \Theta_{l_1}^{K-m_2}(\theta_1) Y_{l_2}^{m_2}(\theta_2, \phi) D_{M,K}^{J*}(\alpha, \beta, \gamma)$$

with

$$[9] \quad Y_{l_2}^{m_2}(\theta_2, \phi) = \frac{1}{\sqrt{2\pi}} \Theta_{l_2}^{m_2}(\theta_2) e^{im_2\phi}$$

where  $\Theta_l^{m_2}$ ,  $Y_l^{m_2}$ , and  $D_{M,K}^J$  are, respectively, the normalized associated Legendre function with the  $(-1)^{m_2}$  Condon-Shortley phase factor,<sup>35</sup> spherical harmonic functions, and Wigner functions.<sup>35</sup> The body-fixed frame is related to the space-fixed frame via a rotation in the three Euler angles ( $\alpha$ ,  $\beta$ ,  $\gamma$ ). The projection of the total angular momentum  $J$  onto the space-fixed or body-fixed frame is given by  $M$  or  $K$ . Applying the parity operator  $\hat{E}^*$  to the rovibrational function has the effect

$$[10] \quad \hat{E}^* |l_1, l_2, m_2, K; J, M\rangle = (-1)^J |l_1, l_2, -m_2, -K; J, M\rangle$$

Parity-adapted basis functions may be written as

$$[11] \quad |l_1, l_2, m_2, K; J, M, P\rangle = \frac{1}{\sqrt{2(1 + \delta_{m_2,0}\delta_{K,0})}} |l_1, l_2, m_2, K; J, M\rangle + (-1)^{J+P} |l_1, l_2, -m_2, -K; J, M\rangle$$

where  $K \geq 0$  and  $P = 0$  or  $1$  correspond to even or odd parities, respectively. When  $K = 0$  the constraint  $m_2 \geq 0$  holds and the combination  $m_2 = K = 0$  and  $(-1)^{J+P} = -1$  is not allowed.

In the parity-adapted angular finite basis representation (FBR), the kinetic energy terms have simple matrix elements. The diagonal matrix elements are

$$[12] \quad \langle l_1, l_2, m_2, K; J, M, P | \hat{T}_{\text{diag}} | l_1, l_2, m_2, K; J, M, P \rangle = \frac{1}{2m_{\text{He}}r_1^2} l_1(l_1 + 1) + \frac{1}{2m_{\text{He}}r_2^2} l_2(l_2 + 1) + B_{\text{OCS}} l_1(l_1 + 1) + B_{\text{OCS}} [J(J + 1) + l_1(l_1 + 1) + l_2(l_2 + 1) - 2K^2 + 2m_2(K - m_2)]$$

and the three types of off-diagonal matrix elements are

$$[13] \quad \langle l_1, l_2, m_2 + 1, K; J, M, P | \hat{T}_{\text{off}} | l_1, l_2, m_2, K; J, M, P \rangle = \sqrt{1 + \delta_{m_2,0}\delta_{K,0}} B_{\text{OCS}} \lambda_{l_1, K-m_2}^- \lambda_{l_2, m_2}^+$$

$$[14] \quad \langle l_1, l_2, m_2, K + 1; J, M, P | \hat{T}_{\text{Cor}} | l_1, l_2, m_2, K; J, M, P \rangle = -\sqrt{1 + \delta_{m_2,0}\delta_{K,0}} B_{\text{OCS}} \lambda_{l_1, K-m_2}^+ \lambda_{l_2, K}^+$$

$$[15] \quad \langle l_1, l_2, m_2 + 1, K + 1; J, M, P | \hat{T}_{\text{Cor}} | l_1, l_2, m_2, K; J, M, P \rangle = -\sqrt{1 + \delta_{m_2,0}\delta_{K,0}} B_{\text{OCS}} \lambda_{l_2, m_2}^+ \lambda_{l_1, K}^+$$

with two special cases

$$[16] \quad \langle l_1, l_2, -m_2, 1; J, M, P | \hat{T}_{\text{Cor}} | l_1, l_2, m_2, 0; J, M, P \rangle = -(-1)^{J+P} B_{\text{OCS}} \lambda_{l_1, K-m_2}^- \lambda_{J,0}^- \quad (m_2 > 0)$$

$$[17] \quad \langle l_1, l_2, -m_2 + 1, 1; J, M, P | \hat{T}_{\text{Cor}} | l_1, l_2, m_2, 0; J, M, P \rangle = -(-1)^{J+P} B_{\text{OCS}} \lambda_{l_2, m_2}^- \lambda_{J,0}^- \quad (m_2 > 0)$$

where

$$\lambda_{l,m}^\pm = \sqrt{l(l+1) - m(m \pm 1)}$$

While the potential is not diagonal in the angular FBR, its matrix element integrals can be calculated in a grid representation via a three-dimensional transformation<sup>36</sup> for the  $\theta_1$ ,  $\theta_2$ , and  $\phi$  angles.<sup>28,36</sup> A Gauss–Legendre quadrature was used for the  $\theta_1$  and  $\theta_2$  angles, and Gauss–Chebyshev quadratures of the first and second kind were used to integrate  $\phi$  for even and odd parity cases, respectively. For  $J > 0$ , a Fourier transform method has been used for potential matrix–vector products.<sup>28,37</sup> The Lanczos algorithm was then used to calculate the rovibrational energy levels by recursively diagonalizing the discretized Hamiltonian matrix.<sup>38–40</sup> Projection operator techniques were used in combination with the Lanczos iteration method to compute symmetric states upon identical helium exchanges to properly account for the bosonic nature of the  $^4\text{He}$  atoms. This corresponds to a version of the symmetry-adapted Lanczos (SAL) algorithm<sup>41,42</sup> previously used for atomic trimers containing two or more bosonic atoms.<sup>28,43,44</sup> Eigenvectors were obtained using a second Lanczos recursion to avoid the storage of Lanczos vectors as previously done in ref. 43.

### Helium density in the body-fixed frame

To develop some intuitive feeling regarding the nature of these species, it is very useful to develop a three-dimensional representation of the helium part of the wave function in the body-fixed frame. In terms of the basis functions and Radau coordinate system, the wave function for the  $n$ th energy level for a given set of  $J$ ,  $M$ , and  $P$  quantum numbers is

$$[18] \quad \Psi_n^{J,M,P}(r_1, r_2, \theta_1, \theta_2, \phi; \alpha, \beta, \gamma) = \sum_{\alpha_1, \alpha_2, l_1, l_2, m_2, K} \langle \theta_1, \theta_2, \phi; \alpha, \beta, \gamma | l_1, l_2, m_2, ; J, K, M, P \rangle \langle r_1 | \alpha_1 \rangle \langle r_2 | \alpha_2 \rangle \times \langle \alpha_1, \alpha_2, l_1, l_2, m_2; J, K, M, P | \Psi_n^{J,M,P} \rangle$$

in which  $\langle r_j | \alpha_j \rangle$  is a localized DVR basis function for helium atom  $j$ , and the coefficient  $\langle \alpha_1, \alpha_2, l_1, l_2, m_2; J, K, M, P | \Psi_n^{J,M,P} \rangle$  is an eigenvector obtained via Lanczos diagonalization.

The three-dimensional density of the  $j$ th helium atom associated with  $\Psi_n^{J,M,P}$  is defined as

$$[19] \quad \rho_j^{J,M,P,n}(\mathbf{R}) = \int dr_1 dr_2 \sin \theta_1 d\theta_1 \sin \theta_2 d\theta_2 d\phi |\Psi_n^{J,M,P}(r_1, r_2, \theta_1, \theta_2, \phi; \alpha, \beta, \gamma)|^2 \delta(\mathbf{R} - \mathbf{R}_j[r_1, r_2, \theta_1, \theta_2, \phi])$$

in which  $\mathbf{R}_j[r_1, r_2, \theta_1, \theta_2, \phi]$  is the vector function that maps the Radau coordinates to the body-fixed Cartesian coordinates

**Table 1.** Calculated energies (in cm<sup>-1</sup>) for the lowest rotational sublevels of the ground vibrational level for seven OCS–He<sub>2</sub> isotopologues.

Isotopologues	Calculated energy (cm <sup>-1</sup> )			
	Level ( <i>J</i> , <i>P</i> , <i>n</i> )			
	0 (0, 0, 0)	1 (1, 1, 0)	2 (2, 0, 0)	3 (3, 1, 0)
<sup>16</sup> O <sup>12</sup> C <sup>32</sup> S	–37.9505	–37.6994	–37.2200	–36.5363
<sup>16</sup> O <sup>13</sup> C <sup>32</sup> S	–37.9780	–37.7277	–37.2495	–36.5674
<sup>16</sup> O <sup>12</sup> C <sup>34</sup> S	–38.0512	–37.8047	–37.3327	–36.6585
<sup>16</sup> O <sup>13</sup> C <sup>34</sup> S	–38.0821	–37.8362	–37.3649	–36.6914
<sup>16</sup> O <sup>12</sup> C <sup>33</sup> S	–38.0021	–37.7534	–37.2778	–36.5989
<sup>18</sup> O <sup>12</sup> C <sup>32</sup> S	–38.1526	–37.9125	–37.4508	–36.7893
<sup>17</sup> O <sup>12</sup> C <sup>32</sup> S	–38.0556	–37.8103	–37.3400	–36.6677

**Note:** *J*, total angular momentum; *P*, parity; and *n*, vibrational quantum number.

**Table 2.** Comparison of predicted and observed rotational transitions energies of OCS–He<sub>2</sub> isotopologues (in cm<sup>-1</sup>).

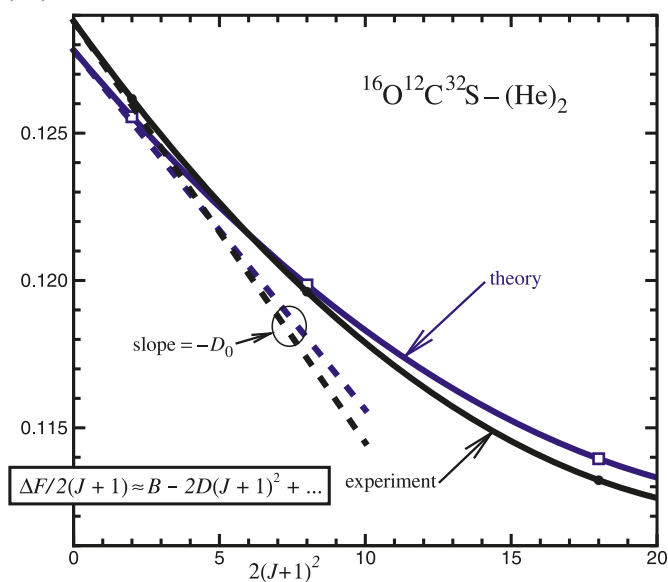
Isotopologue	<i>J'</i> ← <i>J</i>	Rotational transition energy (cm <sup>-1</sup> )		Theory – Expt.	
		Theory	Expt. <sup>3,6</sup>	cm <sup>-1</sup>	% Diff.
<sup>16</sup> O <sup>12</sup> C <sup>32</sup> S	1 ← 0	0.2511	0.252 329	–0.0013	–0.5
	2 ← 1	0.4794	0.478 473	0.0010	0.2
	3 ← 2	0.6837	0.679 346	0.0044	0.6
	Δ <i>v</i> <sub>t</sub>	0.4510	—		
<sup>16</sup> O <sup>13</sup> C <sup>32</sup> S	1 ← 0	0.2503	0.25 2064	–0.0017	–0.7
	2 ← 1	0.4782	0.478 130	0.0001	0.0
	3 ← 2	0.6821	0.678 995	0.0031	0.5
	Δ <i>v</i> <sub>t</sub>	0.4486	—		
<sup>16</sup> O <sup>12</sup> C <sup>34</sup> S	1 ← 0	0.2465	0.246 883	–0.0004	–0.2
	2 ← 1	0.4720	0.470 301	0.0017	0.4
	3 ← 2	0.6742			
	Δ <i>v</i> <sub>t</sub>	0.4412	—		
<sup>16</sup> O <sup>13</sup> C <sup>34</sup> S	1 ← 0	0.2460	0.246 584	–0.0006	–0.3
	2 ← 1	0.4713	0.469 894	0.0013	0.3
	3 ← 2	0.6735	—		
	Δ <i>v</i> <sub>t</sub>	0.4417	—		
<sup>16</sup> O <sup>12</sup> C <sup>33</sup> S	1 ← 0	0.2487	0.249 531	–0.0008	–0.3
	2 ← 1	0.4756	—		
	3 ← 2	0.6789	—		
	Δ <i>v</i> <sub>t</sub>	0.4459	—		
<sup>18</sup> O <sup>12</sup> C <sup>32</sup> S	1 ← 0	0.2401	—		
	2 ← 1	0.4617	—		
	3 ← 2	0.6615	—		
	Δ <i>v</i> <sub>t</sub>	0.4328	—		
<sup>17</sup> O <sup>12</sup> C <sup>32</sup> S	1 ← 0	0.2453	—		
	2 ← 1	0.4703	—		
	3 ← 2	0.6723	—		
	Δ <i>v</i> <sub>t</sub>	0.4413	—		

**Note:** All of the observed transitions were *a*-type between levels within the *K*<sub>a</sub> = 0 stack. Δ*v*<sub>t</sub> is the transition energy between the first excited and ground torsion states of He<sub>2</sub> in OCS–He<sub>2</sub> complexes. *J*, total angular momentum.

(**R***j* = {*x*<sub>*j*</sub>, *y*<sub>*j*</sub>, *z*<sub>*j*</sub>}). The above integral can be evaluated on the same grid as the potential integral. However, because of the discrete nature of the Gaussian quadrature grid used for the integration, the density may not appear to be smooth. To obtain a smooth representation of the density, we use a Gaussian representation of the three-dimensional delta function that appears in eq. [19]

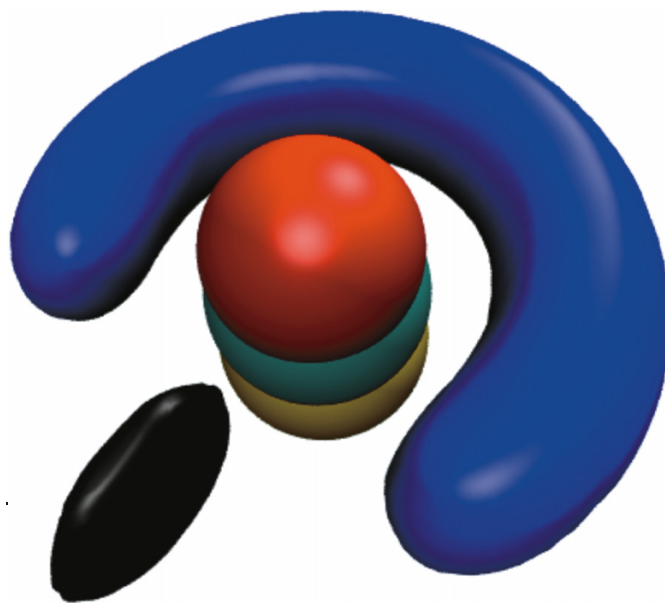
**Table 3.** Comparison of predicted and observed spectroscopic constants (in MHz) of OCS–He<sub>2</sub> isotopologues.

Isotopologue	Rotational constants	Spectroscopic constant		Theory – Expt.	
		Theory	Expt. <sup>6</sup>	MHz	% Diff.
<sup>16</sup> O <sup>12</sup> C <sup>32</sup> S	A	5104.99(14)	5169.6746	–64.6846	–1.25
	B	4308.556(17)	4385.6366	–77.0806	–1.76
	C	3235.885(18)	3195.6404	40.2446	1.26
<sup>16</sup> O <sup>13</sup> C <sup>32</sup> S	A	5107.05(35)	5741.2483	–634.1983	–11.05
	B	4293.006(42)	4522.5175	–229.5115	–05.08
	C	3227.451(45)	3035.8419	191.6091	06.31
<sup>16</sup> O <sup>12</sup> C <sup>34</sup> S	A	5018.0(10)	—	—	—
	B	4208.66(12)	—	—	—
	C	3197.88(13)	—	—	—
<sup>16</sup> O <sup>13</sup> C <sup>34</sup> S	A	5007.1(15)	—	—	—
	B	4194.38(16)	—	—	—
	C	3195.86(18)	—	—	—
<sup>16</sup> O <sup>12</sup> C <sup>33</sup> S	A	5069.81(59)	—	—	—
	B	4257.462(69)	—	—	—
	C	3215.390(74)	—	—	—
<sup>18</sup> O <sup>12</sup> C <sup>32</sup> S	A	4873.6(61)	—	—	—
	B	4062.90(64)	—	—	—
	C	3150.95(74)	—	—	—
<sup>17</sup> O <sup>12</sup> C <sup>32</sup> S	A	4997.7(19)	—	—	—
	B	4180.55(21)	—	—	—
	C	3190.89(24)	—	—	—

**Fig. 2.** Reduced rotational transition energy plot for <sup>16</sup>O<sup>12</sup>C<sup>32</sup>S–(He)<sub>2</sub>.

$$[20] \quad \delta(\mathbf{R} - \mathbf{R}_j[r_1, r_2, \theta_1, \theta_2, \phi]) \\ \approx \frac{1}{(2\pi)^{3/2} \sigma_x \sigma_y \sigma_z} e^{-(x-x_i)^2/2\sigma_x^2} e^{-(y-y_i)^2/2\sigma_y^2} e^{-(z-z_i)^2/2\sigma_z^2}$$

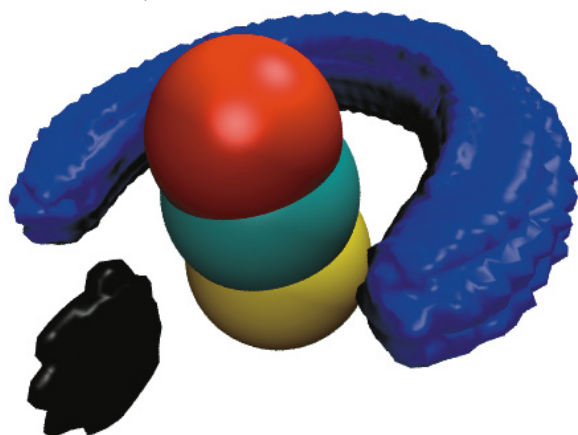
This expression reduces to an exact delta function in the limit where  $(\sigma_x, \sigma_y, \sigma_z) \rightarrow (0, 0, 0)$ . Using such a representa-

**Fig. 3.** Three-dimensional representation of the helium-atom density in the body-fixed frame. The position of the first helium defines the location of the *zx* plane, and its density is shown in black, whereas the density of the second He atom is shown in blue. These results were obtained with the values of the Gaussian standard deviations defining the densities set at  $\sigma_x = \sigma_z = 0.25$  Å and  $\sigma_y = 0.1$  Å for atom-1 and  $\sigma_x = \sigma_y = \sigma_z = 0.25$  Å for atom-2.

tion of the delta function amounts to performing a Gaussian binning of the density and leads to a smooth representation of the density, as will be illustrated in the following.



**Fig. 4.** As in Fig. 3, but with  $\sigma_x = \sigma_z = 0.1$  Å and  $\sigma_y = 0.05$  Å for atom-1 and  $\sigma_x = \sigma_y = \sigma_z = 0.1$  Å for atom-2.



## Results and discussion

### Bound-state energies and microwave spectrum

The rovibrational energy levels of seven isotopologues of the OCS-(He)<sub>2</sub> complex were calculated using the radial DVR and parity-adapted angular FBR methods described in the Theory and methods section. The inertial rotational constants  $B_{\text{OCS}}$  required for these calculations were fixed at the experimental values of 0.202 856 741 cm<sup>-1</sup> for <sup>16</sup>O<sup>12</sup>C<sup>32</sup>S, 0.202 204 019 cm<sup>-1</sup> for <sup>16</sup>O<sup>13</sup>C<sup>32</sup>S, 0.197 898 033 cm<sup>-1</sup> for <sup>16</sup>O<sup>12</sup>C<sup>34</sup>S, 0.197 194 087 cm<sup>-1</sup> for <sup>16</sup>O<sup>13</sup>C<sup>34</sup>S, 0.200 302 07 cm<sup>-1</sup> for <sup>16</sup>O<sup>12</sup>C<sup>33</sup>S, 0.190 293 341 cm<sup>-1</sup> for <sup>18</sup>O<sup>12</sup>C<sup>32</sup>S, and 0.196 258 106 cm<sup>-1</sup> for <sup>17</sup>O<sup>12</sup>C<sup>32</sup>S<sup>45–47</sup> and the masses were set at 4.002 603 24 u for <sup>4</sup>He, 15.994 914 635 u for <sup>16</sup>O, 16.999 131 5 u for <sup>17</sup>O, 17.999 160 3 u for <sup>18</sup>O, 12 u for <sup>12</sup>C, 13.003 354 826 u for <sup>13</sup>C, 31.972 070 70 u for <sup>32</sup>S, 32.971 458 43 u for <sup>33</sup>S, and 33.967 866 65 u for <sup>34</sup>S. The He-OCS and He-He potentials were taken from refs. 27 and 48, respectively. For  $r_1$  and  $r_2$ , 35 sine DVR basis functions were used on the domain 3.0–19.0 b. For the angular basis,  $l_{\text{max}} = m_{\text{max}} = 25$ , and 30 Gauss-Legendre quadrature points were used for each of  $\theta_1$  and  $\theta_2$ , while 64 equally spaced points on the range  $[0, 2\pi]$  were used for  $\phi$ . To accelerate the convergence of the Lanczos calculation, an energy ceiling of 1000 cm<sup>-1</sup> was imposed. This energy cutoff affected the low-lying levels by less than 0.001 cm<sup>-1</sup>.

The energies of the  $J = 0, 1, 2$ , and 3 rotational sublevels of the ground vibrational level for seven OCS-(He)<sub>2</sub> isotopologues are listed in Table 1, where  $P$  is the total parity. As shown there, the binding energy of the ground vibrational level of <sup>16</sup>O<sup>12</sup>C<sup>32</sup>S-(He)<sub>2</sub> is 37.9505 cm<sup>-1</sup>, which is approximately one-third of the total three-body well depth of 108.0896 cm<sup>-1</sup>. Because of our additive model, this well depth is exactly twice the 50.22 cm<sup>-1</sup> well depth<sup>27</sup> of He-OCS plus the 7.6496 cm<sup>-1</sup> depth of the He-He potential.<sup>48</sup> However, this ground-state level is bound by 0.6993 cm<sup>-1</sup> more than the twice the binding energy of the He-OCS dimer (18.625 cm<sup>-1</sup>)<sup>27</sup> plus the binding energy of the helium dimer (0.0012 cm<sup>-1</sup>),<sup>48</sup> which add up to 37.2512 cm<sup>-1</sup>. That additive value is expected to be approximate because it neglects the effect of correlation associated with the mixing of the two He-atom wave functions.

**Fig. 5.** He-atom density as a function of the azimuthal angle  $\phi$ .

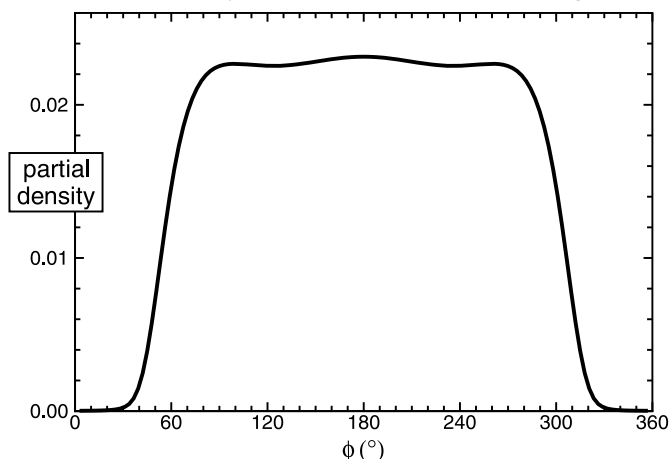


Table 2 compares our calculated microwave transition energies with the experimental results of refs. 3 and 6. As shown there, the agreement is quite good, as the relative errors are never larger than 0.7%. The  $\Delta\nu_t$  torsional frequency values are also presented in Table 2. For additional comparison, the calculated microwave transitions were fitted to Watson's S-reduction Hamiltonian as an asymmetric top molecule and compared to the experimental results of ref. 6. All resulting spectroscopic constants are listed in Table 3. As shown in Table 3 for <sup>16</sup>O<sup>12</sup>C<sup>32</sup>S-(He)<sub>2</sub>, the fitted A, B, and C rotational constants agree well with experimental results, as the relative errors are less than 2%. However, for <sup>16</sup>O<sup>13</sup>C<sup>32</sup>S-(He)<sub>2</sub>, the errors are relatively larger than those of <sup>16</sup>O<sup>12</sup>C<sup>32</sup>S-(He)<sub>2</sub> isotopomer. This is in part due to the fact that the centrifugal distortion constants for all isotopologues were fixed to the same infrared value<sup>7</sup> of <sup>16</sup>O<sup>12</sup>C<sup>32</sup>S-(He)<sub>2</sub>. Another explanation for the discrepancy is the neglect of three-body terms in the interaction potential used in the calculations as discussed below.

It is evident that the  $J$  dependence of the residual discrepancies in Table 2 has the same systematic behaviour for all isotopologues: the theoretical  $1 \leftarrow 0$  transition frequencies are smaller than the experimental ones, whereas the experimental transition frequencies are larger in the  $3 \leftarrow 2$  and  $2 \leftarrow 1$  cases. This behaviour can be understood if we use a basic spectroscopic analysis to determine estimates of the leading rotational constants implied by these results. In particular, according to a standard spectroscopic analysis in which rotational energies are written as  $F(J) = B_v[J(J+1)] - D_v[J(J+1)]^2 + \dots$ , the expression for the rotational transition energies  $\Delta F(J) \equiv F(J+1) - F(J)$  may be rearranged into the form

$$[21] \quad \frac{\Delta F(J)}{2(J+1)} = B_v - 2D_v(J+1)^2 + 3H_v[(J+1)^2(J^2+2J+2)] \dots$$

Plots of the experimental and theoretical results for <sup>16</sup>O<sup>12</sup>C<sup>32</sup>S-He in the manner suggested by eq. [21] are presented in Fig. 2; the intercepts of these plots indicate the values of the inertial rotational constants  $B_v$  and the slopes the values of the leading centrifugal distortion constant  $D_v$ . The 0.77% difference between the experimental and theoretical  $B_v$  values and 17% difference between the corresponding

$D_v$  values are orders of magnitude larger than the discrepancies implied by the differences between the experimental and theoretical results for He–OCS obtained by Howson and Hutson.<sup>27</sup> Since our calculations are based on their He–OCS pair potential, and given that the He–He pair potential<sup>48</sup> is believed to be very reliable, we interpret these differences as being due to our neglect of nonadditive contributions to the overall interaction potential of our three-body system. The fact that the experimental values are larger than those obtained from our additive model would be consistent with the existence of an attractive three-body interaction.

### Helium density

Figures 3 and 4 present the three-dimensional density for the two helium atoms in the body-fixed frame as calculated for the ground state of OCS–(He)<sub>2</sub> using the procedure described in the Helium density in the body-fixed frame section. Iso-surfaces are used to represent the three-dimensional densities, and the  $z$  axis is defined to lie on the OCS molecular axis. The density of helium atom–1 is represented in black and that of helium atom–2 is shown in blue. Two sets of standard deviation parameters have been chosen to illustrate the smearing effect of the Gaussian binning. Larger values of  $\sigma_x = \sigma_z = 0.25$  Å and  $\sigma_y = 0.1$  Å for atom–1 and  $\sigma_x = \sigma_y = \sigma_z = 0.25$  Å for atom–2 are used in Fig. 3, whereas smaller values of  $\sigma_x = \sigma_z = 0.1$  Å and  $\sigma_y = 0.05$  Å for atom–1 and  $\sigma_x = \sigma_y = \sigma_z = 0.1$  Å for atom–2 are used in Fig. 4. We first observe that a smoother density is obtained with the larger standard deviation parameters, although the general features of the helium density are the same in both Figs. 3 and 4. The density will be accurately represented as long as the standard deviations are smaller than the characteristic length scale of the features of the wave function. The values chosen above obey this criterion.

One significant feature of these representations is the fact that the two helium atoms appear to have very different density distributions. This is an artifact of the fact that the position of helium atom–1 is used to define the  $xz$  plane of the body-fixed frame, and its density is therefore completely localized with respect to the  $y$  direction. Indeed, the only reason that its density distribution appears to have nonzero width in the  $y$  direction (the thickness of the black “disk”) is the use of a finite bin size ( $\sigma_y > 0$ ) in the calculation. The density of helium atom–1 is of course somewhat delocalized in the  $xz$  plane, but it is centred at the minimum of the potential energy surface.

The second helium atom is clearly highly delocalized relative to the first, being distributed on a “sausage”-shaped incomplete ring about the OCS molecule axis. In Figs. 3 and 4 it appears to have a uniform density as a function of the azimuthal angle  $\phi$ , apart from the region near atom–1 whence it is excluded by the short-range repulsive wall of the He–He potential. However, Fig. 5 shows that the “partial density” obtained by integrating the density of He atom–2 with respect to  $R$  and  $z$  at each value of  $\phi$  has interesting substructure. In particular, in addition to the expected excluded volume near  $\phi = 0^\circ$  and  $360^\circ$ , there are small but distinct local maxima at  $\phi = 101^\circ$  and  $259^\circ$  corresponding to the two He atoms lying  $\sim 5.4$  Å apart. This distance is almost double the He–He potential equilibrium distance of  $r_e =$

$2.968$  Å, but is much smaller than the  $45.6$  Å expectation value of the internuclear distance in the ground state of an isolated He<sub>2</sub> molecule, since the relatively strong He–OCS potential constrains the two He atoms to lie within a ring about the axis of the OCS. However, the weakness of the He–He potential means that over a  $\phi$  range of almost  $180^\circ$  the two He atoms move almost freely relative to one another. Note that the present structural analysis is consistent with Fig. 2 of ref. 49, and the findings of Wang and Carrington and co-workers for the related He<sub>2</sub>–N<sub>2</sub>O.<sup>28</sup>

### Concluding remarks

Calculated rovibrational energy levels and microwave transitions for seven OCS–(He)<sub>2</sub> isotopologues have been obtained from using a global potential energy surface defined as a sum of accurate He–OCS and He–He pair potentials. The predicted microwave transitions are in fairly good agreement with experiment, but small systematic residual differences are attributed to our neglect of three-body contributions to the interaction. A new approach for visualizing the helium density in the body-fixed frame is introduced that shows that for the ground state, relative to the first, the second helium atom lies in a sausage-shaped incomplete ring about the OCS axis, with a region of excluded density owing to the helium–helium repulsion. This study is complementary to one by Wang and Carrington,<sup>49</sup> for this same OCS–(He)<sub>2</sub> system in the August 2010 issue of this journal—they focus more on the infrared spectra and the intramolecular vibrational structure and consider only the most abundant isotopologues. Although they use different interaction potentials, their results are in general agreement with ours.

### Acknowledgments

The authors thank Professor T. Carrington, Jr. and Dr. X.-G. Wang for helpful discussions. Drs. H.-G. Yu and N. Blinov are also gratefully acknowledged for useful suggestions. This research has been supported by the Natural Sciences and Engineering Research Council of Canada (NSERC), the Canada Foundation for Innovation (CFI), and the University of Waterloo. We thank the Shared Hierarchical Academic Research Computing Network (SHARCNET) for computing time.

### References

- (1) Grebenev, S.; Toennies, J. P.; Vilesov, A. F. *Science* **1998**, 279 (5359), 2083. doi:10.1126/science.279.5359.2083. PMID:9516103.
- (2) Toennies, J. P.; Vilesov, A. F. *Annu. Rev. Phys. Chem.* **1998**, 49 (1), 1. doi:10.1146/annurev.physchem.49.1.1. PMID:15012423.
- (3) Xu, Y.; Jäger, W. *Chem. Phys. Lett.* **2001**, 350 (5-6), 417. doi:10.1016/S0009-2614(01)01314-8.
- (4) Tang, J.; Xu, Y.; McKellar, A. R. W.; Jäger, W. *Science* **2002**, 297 (5589), 2030. doi:10.1126/science.1073718. PMID:12242436.
- (5) Tang, J.; McKellar, A. R. W. *J. Chem. Phys.* **2003**, 119 (2), 754. doi:10.1063/1.1578473.
- (6) Xu, Y.; Jäger, W. *J. Chem. Phys.* **2003**, 119 (11), 5457. doi:10.1063/1.1598953.

- (7) Tang, J.; McKellar, A. R. W. *J. Chem. Phys.* **2003**, *119* (11), 5467. doi:10.1063/1.1598954.
- (8) Tang, J.; McKellar, A. R.; Mezzacapo, F.; Moroni, S. *Phys. Rev. Lett.* **2004**, *92* (14), 145503. doi:10.1103/PhysRevLett.92.145503. PMID:15089550.
- (9) Tang, J.; McKellar, A. R. W. *J. Chem. Phys.* **2004**, *121* (1), 181. doi:10.1063/1.1758701. PMID:15260536.
- (10) McKellar, A. R. *J. Chem. Phys.* **2007**, *127* (4), 044315. doi:10.1063/1.2756537. PMID:17672698.
- (11) McKellar, A. R.; Xu, Y.; Jäger, W. *J. Phys. Chem. A* **2007**, *111* (31), 7329. doi:10.1021/jp070618w. PMID:17455923.
- (12) McKellar, A. R. W. *J. Chem. Phys.* **2008**, *128* (4), 044308. doi:10.1063/1.2822903. PMID:18247950.
- (13) Surin, L. A.; Potapov, A. V.; Dumes, B. S.; Schlemmer, S.; Xu, Y.; Raston, P. L.; Jäger, W. *Phys. Rev. Lett.* **2008**, *101* (23), 233401. doi:10.1103/PhysRevLett.101.233401. PMID:19113549.
- (14) Paesani, F.; Gianturco, F. A.; Whaley, K. B. *J. Chem. Phys.* **2001**, *115* (22), 10225. doi:10.1063/1.1412873.
- (15) Paesani, F.; Viel, A.; Gianturco, F. A.; Whaley, K. B. *Phys. Rev. Lett.* **2003**, *90* (7), 073401. doi:10.1103/PhysRevLett.90.073401.
- (16) Paesani, F.; Whaley, K. B. *J. Chem. Phys.* **2004**, *121* (9), 4180. doi:10.1063/1.1768931. PMID:15332966.
- (17) Moroni, S.; Sarsa, A.; Fantoni, S.; Schmidt, K. E.; Baroni, S. *Phys. Rev. Lett.* **2003**, *90* (14), 143401. doi:10.1103/PhysRevLett.90.143401. PMID:12731914.
- (18) Blinov, N.; Song, X.-G.; Roy, P.-N. *J. Chem. Phys.* **2004**, *120* (13), 5916. doi:10.1063/1.1650301. PMID:15267473.
- (19) Paolini, S.; Fantoni, S.; Moroni, S.; Baroni, S. *J. Chem. Phys.* **2005**, *123* (11), 114306. doi:10.1063/1.2032969. PMID:16392558.
- (20) Li, H.; Blinov, N.; Roy, P.-N.; Le Roy, R. J. *J. Chem. Phys.* **2009**, *130* (14), 144305. doi:10.1063/1.3109897. PMID:19368443.
- (21) Blinov, N.; Roy, P.-N. *ACS Symp. Ser.* **2007**, *953*, 165. doi:10.1021/bk-2007-0953.ch012.
- (22) Moroni, S.; Blinov, N.; Roy, P.-N. *J. Chem. Phys.* **2004**, *121* (8), 3577. doi:10.1063/1.1774160. PMID:15303924.
- (23) Xu, Y. J.; Blinov, N.; Jäger, W.; Roy, P. N. *J. Chem. Phys.* **2006**, *124* (8), 081101. doi:10.1063/1.2173640. PMID:16512695.
- (24) Blinov, N.; Roy, P.-N. *J. Low Temp. Phys.* **2005**, *140* (3–4), 253. doi:10.1007/s10909-005-6312-y.
- (25) Paesani, F.; Kwon, Y.; Whaley, K. B. *Phys. Rev. Lett.* **2005**, *94* (15), 153401. doi:10.1103/PhysRevLett.94.153401. PMID:15904142.
- (26) Topic, W.; Jäger, W.; Blinov, N.; Roy, P. N.; Botti, M.; Moroni, S. *J. Chem. Phys.* **2006**, *125* (14), 144310. doi:10.1063/1.2357604. PMID:17042593.
- (27) Howson, J. M. M.; Hutson, J. M. *J. Chem. Phys.* **2001**, *115* (11), 5059. doi:10.1063/1.1394940.
- (28) Wang, X.-G.; Carrington, T., Jr.; Tang, J.; McKellar, A. R. *J. Chem. Phys.* **2005**, *123* (3), 034301. doi:10.1063/1.1924408. PMID:16080731.
- (29) Mladenović, M. *J. Chem. Phys.* **2000**, *112* (3), 1070. doi:10.1063/1.480662.
- (30) Tang, J.; McKellar, A. R. W.; Wang, X. G.; Carrington, T., Jr. *Can. J. Phys.* **2009**, *87* (5), 417. doi:10.1139/P08-119.
- (31) Wang, X.-G.; Carrington, T., Jr.; McKellar, A. R. W. *J. Phys. Chem. A* **2009**, *113* (47), 13331. doi:10.1021/jp904778f. PMID:19842654.
- (32) Gatti, F.; Iung, C.; Menou, M.; Justum, Y.; Nauts, A.; Chapuisat, X. *J. Chem. Phys.* **1998**, *108* (21), 8804. doi:10.1063/1.476327.
- (33) Yu, H.-G. *Chem. Phys. Lett.* **2002**, *365*, 189. doi:10.1016/S0009-2614(02)01453-7.
- (34) Light, J. C.; Hamilton, I. P.; Lill, J. V. *J. Chem. Phys.* **1985**, *82* (3), 1400. doi:10.1063/1.448462.
- (35) Zare, R. N. *Angular Momentum*; Wiley: New York, 1988.
- (36) Ying Lin, S.; Guo, H. *J. Chem. Phys.* **2002**, *117* (11), 5183. doi:10.1063/1.1500731.
- (37) Wang, X.-G.; Carrington, T., Jr. *J. Chem. Phys.* **2005**, *123* (15), 154303. doi:10.1063/1.2043148. PMID:16252944.
- (38) Lanczos, C. *J. Res. Natl. Bur. Stand.* **1950**, *45*, 255.
- (39) Golub, G. H.; van Loan, C. F. *Matrix Computations*; Johns Hopkins University Press: Baltimore, 1989.
- (40) Cullum, J. K.; Willoughby, R. A. *Lanczos Algorithms for Large Symmetric Eigenvalue Computations*; Birkhäuser: Boston, 1985.
- (41) Wang, X.-G.; Carrington, T., Jr. *J. Chem. Phys.* **2001**, *114* (4), 1473. doi:10.1063/1.1331357.
- (42) Chen, R.; Guo, H. *J. Chem. Phys.* **2001**, *114* (4), 1467. doi:10.1063/1.1331356.
- (43) Roy, P.-N. *J. Chem. Phys.* **2003**, *119* (11), 5437. doi:10.1063/1.1599348.
- (44) Liu, Y. D.; Roy, P.-N. *J. Chem. Phys.* **2004**, *121* (13), 6282. doi:10.1063/1.1787488. PMID:15446922.
- (45) Saupe, S.; Wappelhorst, M. H.; Meyer, B.; Urban, W.; Maki, A. G. *J. Mol. Spectrosc.* **1996**, *175* (1), 190. doi:10.1006/jmsp.1996.0021.
- (46) Lahaye, J. G.; Vandenhaute, R.; Fayt, A. *J. Mol. Spectrosc.* **1987**, *123* (1), 48. doi:10.1016/0022-2852(87)90262-1.
- (47) Townes, C. H.; Schawlow, A. L. *Microwave Spectroscopy*; McGraw-Hill: New York, 1955.
- (48) Jeziorska, M.; Cencek, W.; Patkowski, K.; Jeziorski, B.; Szalewicz, K. *J. Chem. Phys.* **2007**, *127* (12), 124303. doi:10.1063/1.2770721. PMID:17902899.
- (49) Wang, X.-G.; Carrington, T., Jr. *Can. J. Chem.* **2010**, *88*, 779. doi:10.1139/v10-030.

# Configurations and conformations of glycosyl sulfoxides

Hong Liang, Micheline MacKay, T. Bruce Grindley, Katherine N. Robertson, and T. Stanley Cameron

**Abstract:** X-ray crystallographic studies of two axial glycosyl sulfoxides having  $R_S$  configurations (derivatives of phenyl 2-azido-2-deoxy-1-thio- $\alpha$ -D-galactopyranoside *S*-oxide) show that they adopt anti conformations in the solid state, in contrast to previous observations and assumptions. Density functional theory (DFT) calculations at the B3LYP6-311G+(d,p)/6-31G(d) level confirm that anti conformations of both phenyl and methyl  $R_S$  glycosyl sulfoxides of 2-azido-2-deoxy- $\alpha$ -D-pyranosides are more stable than exo-anomeric conformations in the gas phase. 1D NOE measurements indicate that the more polar exo-anomeric conformers are only populated to a slight extent in solution. The anti conformations are distorted so that the glycosyl substituents are closer to being eclipsed with H1. This distortion allows S  $n \rightarrow \sigma^*$  overlap if the sulfur lone pair is a p-type lone pair. Evidence for this overlap comes from short C1–S bond distances, as short as the comparable bond distances in the X-ray crystal structure and in the results from DFT calculations for the  $S_S$  glycoside, which does adopt the expected exo-anomeric conformation, both in the solid state and in solution, and has normal  $n \rightarrow \sigma^*$  overlap. For 2-deoxy derivatives not bearing a 2-azido group, gas-phase DFT calculations at the same level indicate that the anti- and exo-anomeric conformers have comparable stabilities. Comparison of the results of the two series shows that electro-negative substituents in equatorial orientations at C2 destabilize conformations with parallel S–O arrangements, the conformation favored by having an endocyclic C–O dipole antiparallel to the S–O dipole, by about 2.5 kcal mol<sup>−1</sup> (1 cal = 4.184 J). An equatorial glycosyl sulfoxide, ( $S_S$ ) phenyl 3,4,6-tri-*O*-acetyl-2-deoxy-2-phthalimido-1-thio- $\beta$ -D-glucopyranoside *S*-oxide, also adopts an anti conformation in the solid state as shown by X-ray diffraction. It also adopts this conformation in solution, in contrast to studies of other equatorial glycosyl sulfoxides.

**Key words:** sulfoxide configurations, glycosyl sulfoxides, conformational analysis, density functional theory (DFT) calculations, 1D NOE measurements, X-ray crystallography.

**Résumé :** Des études de cristallographie par diffraction des rayons-X de deux glycosyles sulfoxydes axiaux de configurations  $R_S$ , des dérivés du *S*-oxyde de 2-azido-2-désoxy-1-thio- $\alpha$ -galactopyranoside de phényle, montrent qu'ils adoptent des conformations anti à l'état solide, contrairement aux observations antérieures et aux hypothèses. Des calculs selon la théorie de la fonctionnelle de la densité (TFD) au niveau B3LYP6-311G+(d,p)/6-31G(d) confirment que les conformations anti que, en phase gazeuse, chacun des  $R_S$  glycosyles sulfoxydes, 2-azido-2-désoxy-1-thio- $\alpha$ -galactopyranoside tant de méthyle que de phényle sont plus stable dans les conformations anomères exo. Des mesures d'effet Overhauser nucléaire (eOn) 1D indiquent que, en solution, les conformères anomères les plus polaires ne forment qu'une faible partie de la population. Les conformations anti sont déformées de façon à ce que les substituants glycolyses soient dans une position pratiquement éclipse avec le H1. Cette distorsion permet un recouvrement S  $n \rightarrow \sigma^*$  sur la paire libre du soufre est une paire libre de type p. Un support pour ce recouvrement vient des courtes longueurs de liaison C1–S, pratiquement aussi courtes que les longueurs mesurées par diffraction des rayons-X dans la structure cristalline et en accord avec les résultats des calculs TFD pour le  $S_S$  glycoside qui adopte la conformation anomère exo attendue, tant à l'état solide qu'en solution, et pour le recouvrement  $n \rightarrow \sigma^*$  normal. Pour les dérivés 2-désoxy ne portant pas de groupe azido, les calculs de TFD en phase gazeuse, au même niveau, indiquent que les conformères anomères anti et exo ont des stabilités comparables. Une comparaison des résultats des deux séries montre que les substituants électronégatifs en orientations équatoriales en C2 déstabilisent les conformations avec des arrangements S–O parallèles, la conformation favorisée par un dipôle C–O endocyclique antiparallèle au dipôle S–O par environ 2,5 kcal mol<sup>−1</sup> (1 cal = 4.184 J). La diffraction des rayons-X montre aussi que, à l'état solide, un glycosyle sulfoxyde équatorial, le *S*-oxyde du  $S_S$  3,4,6-tri-*O*-acétyl-2-désoxy-2-phthalimido-1-thio- $\beta$ -D-glucopyranoside de phényle, adopte aussi une conformation anti. Il adopte aussi cette conformation en solution, en opposition à ce qui a été observé dans les études sur glycosyles sulfoxydes équatoriaux.

**Mots-clés :** configurations de sulfoxydes, glycosyles sulfoxydes, analyse conformationnelle, calculs selon la théorie de la fonctionnelle de la densité (TFD), mesures d'effet Overhauser nucléaire (eOn) 1D, cristallographie.

Received 3 January 2010. Accepted 11 June 2010. Published on the NRC Research Press Web site at canjchem.nrc.ca on 5 November 2010.

*This article is part of a Special Issue dedicated to Professor R. J. Boyd.*

H. Liang, M. MacKay, T.B. Grindley,<sup>1</sup> K.N. Robertson, and T.S. Cameron. Department of Chemistry, Dalhousie University, Halifax, NS B3H 4J3, Canada.

<sup>1</sup>Corresponding author (e-mail: Bruce.Grindley@Dal.ca).



## Introduction

One of the most important techniques for the formation of glycosides employs glycosyl sulfoxides activated by electrophiles as leaving groups.<sup>1</sup> This method has been used to form glycosides that have widely varying structures for both the glycosyl donors and aglycones.<sup>2–14</sup> The activated sulfoxide is sufficiently reactive that reactions in solution can be conducted at  $-78^{\circ}\text{C}$  and it can also be used in solid-phase reactions.<sup>15</sup> The configuration of the sulfoxide does not influence the stereochemistry of glycosylation reactions but does affect the rate of glycosylation reactions<sup>16</sup> and the rates of competing elimination and hydrolysis reactions.<sup>17,18</sup> The stabilities of the different sulfoxide diastereomers and the physical properties of the diastereomers are inherently linked to the conformations that they adopt. The conformations are termed *exo* if the aglycone is *gauche* to both the ring oxygen atom and H1 and *anti* if the aglycone is *anti* to the ring oxygen as shown in Figs. 1 and 2. The staggered conformations where the aglycone is *gauche* to both the ring oxygen and C2 are much less stable and will not be considered here.

It has been assumed that these conformations are influenced primarily by the tendency of the aglycones to adopt *exo* conformations, the *exo*-anomeric effect,<sup>19–22</sup> with contributions from repulsion between C–O and S–O dipoles.<sup>23</sup> The *exo*-anomeric effect is a result of several factors:<sup>24,25</sup>  $n \rightarrow \sigma^*$  donation,<sup>26</sup> dipole dipole repulsion, reduced steric interactions, and electrostatic attraction.<sup>27</sup> Glycosyl sulfoxides provide platforms that allow the examination of the geometrical effects of the contributions of  $n \rightarrow \sigma^*$  donation on conformer stability because the availability of two diastereomers allows the contributions of the two lone pairs to be evaluated individually, albeit with the complication of an additional polar S–O bond. We will show herein that the *exo*-anomeric effect is much less dominant in controlling the conformations of glycosyl sulfoxides than that of glycosyl sulfides or of normal glycosides and that C–O S–O dipole repulsion is less important than previously thought. We will also show that the conformer stabilities are consistent with the sulfoxide lone pair being a *p*-type lone pair, rather than an *sp*<sup>3</sup> lone pair.

Crich et al.<sup>23,28</sup> observed that oxidation of axial thioglycosides on pyranose rings gave one stereoisomer predominantly, the *R*<sub>S</sub> isomer for  $\alpha$ -D-pyranosides. Stereoselectivity is particularly high if the pyranoside rings are made rigid by fusion to 4,6-*O*-benzylidene acetals.<sup>29,30</sup> The stereoselectivity attained is consistent<sup>23</sup> with kinetically controlled oxidation of the accessible face of the sulfur atom in the most stable conformer of the thioglycoside, the conformer favored by the *exo*-anomeric effect. This group<sup>23</sup> and others<sup>31</sup> observed that oxidation of equatorial sulfoxides was unselective. Khiar et al.<sup>17,26</sup> also found that oxidation of O2-protected equatorial thioglycosides was normally unselective but noted that oxidation of O2-unprotected equatorial thioglycosides is highly diastereoselective. A few O2-substituted equatorial thioglycosides were also found to exhibit highly selective oxidations; peresters of  $\beta$ -thiophenyl or  $\beta$ -ethyl 2-tetrachlorophthalimido-2-deoxy-D-glucopyranosides gave diastereomeric ratios  $>9:1$ .<sup>17</sup>

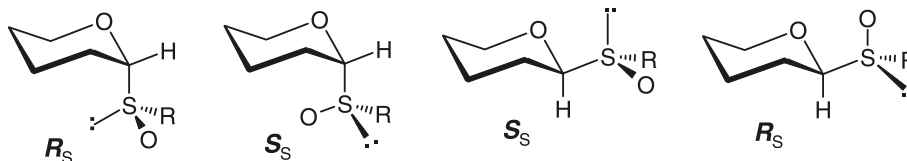
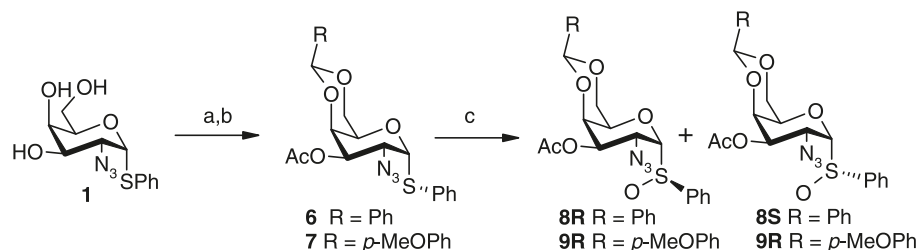
The assignment of configuration of the product sulfoxides has been based on results from X-ray crystallogra-

phy,<sup>16,17,23,28,32–34</sup> augmented by empirical rules developed from NMR measurements<sup>26</sup> and from the use of chiral shift reagents.<sup>33,35</sup> Khiar<sup>26</sup> proposed two methods for making assignments directly based on NMR results. For ethyl sulfoxides, the methylene protons of the ethyl group are diastereotopic. For equatorial sulfoxides of D-pyranosides, the chemical shift differences between the <sup>1</sup>H NMR signals of these diastereotopic protons are considerably larger for the *R*<sub>S</sub> isomer than the *S*<sub>S</sub> isomer.<sup>17,26</sup> This observation has been rationalized in terms of the assumption that the major conformations present for the *R*<sub>S</sub> sulfoxides are those in which the ethyl group adopts the *exo* orientation,<sup>26</sup> which agreed with results from semiempirical (AM1) calculations.<sup>33</sup> This conformation of the *R*<sub>S</sub> sulfoxides has the sulfoxide sulfur lone pair *anti* to the C1–O5 bond, aligned so that  $n \rightarrow \sigma^*$  overlap can occur (see Figs. 1 and 2). Crich et al.<sup>23</sup> commented in a footnote that they have observed several exceptions to the tendency for the methylene protons of ethyl sulfoxides to have larger chemical shift differences in particular diastereomers.

The second method proposed for assigning sulfoxide configurations from NMR spectral measurements was based on the <sup>13</sup>C NMR chemical shifts of anomeric carbons; those for *R*<sub>S</sub> sulfoxides of equatorial D-pyranosides are more shielded by  $>2$  ppm for both aryl and alkyl sulfoxides.<sup>17,26</sup> For axial sulfoxides of D-pyranosides, the minor *S*<sub>S</sub> isomer exhibits the more shielded anomeric carbon and the larger chemical shift difference between the diastereotopic protons of ethyl sulfoxides.<sup>17</sup> The larger shielding was attributed to the  $n \rightarrow \sigma^*$  overlap mentioned above.<sup>26</sup> If it is assumed that the contribution of conformers with the aglycone *gauche* to both the ring oxygen and C2 are negligible, this arrangement only occurs in the *exo* conformation of the equatorial *R*<sub>S</sub> sulfoxide of D-sugars and in the *exo* conformation of the minor *S*<sub>S</sub> isomer of axial sulfoxides (see Figs. 1 and 2).

Crich et al.<sup>23</sup> have suggested that S–O C1–O5 dipole repulsion is very important in determining the conformations of axial sulfoxides. For  $\alpha$ -D-pyranosides, the *R*<sub>S</sub> sulfoxide, which is the major product of oxidation, has the S–O group *anti* to the ring C1–O5 bond if the conformation adopted is that favored by the *exo*-anomeric effect. This group has interpreted equilibration results on glycosyl allyl sulfoxides in terms of the importance of dipole–dipole repulsion.<sup>23</sup>

Most of the conclusions about sulfoxide conformation and configuration have been based on X-ray crystallography,<sup>16,17,23,28,32–34</sup> supported by AM1 calculations.<sup>33</sup> With one exception,<sup>23</sup> the ten glycosyl sulfoxides previously studied adopted conformations in the solid state with the sulfoxide alkyl or aryl group in the *exo*-anomeric conformation. This paper was prompted by our studies of three glycosyl phenyl sulfoxides, all of which adopt conformations in the solid state with the phenyl group *anti* to the ring C–O bond. We report these crystallographic studies here. In addition, NMR studies have been performed in which NOE buildup rates have been used to determine the preferred conformations of these apparently anomalous sulfoxides in solution. Extensive molecular orbital calculations using density functional theory at the B3LYP6–311+(d,p) level have now provided improved understanding of the factors that determine the relative stabilities of the conformations of the two sulfoxide configurations. These calculations suggest that the

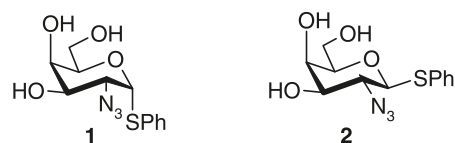
**Fig. 1.** Exo conformations of the glycosyl sulfoxides of D-sugars in  ${}^4C_1$  chair conformations.**Fig. 2.** Anti conformations of the glycosyl sulfoxides of D-sugars in  ${}^4C_1$  chair conformation.**Scheme 1.** (a) PhCHO or *p*-MeOPhCHO, *p*-methoxybenzoic acid in DMF–benzene, reflux; (b) Ac<sub>2</sub>O/Py; (c) MCPBA, DCM, –78 °C.

configuration of the glycosyl sulfoxide determines which conformations are populated; a glycosyl sulfoxide, which can adopt a conformation with the aglycone exo and the sulfur lone pair anti, will favor that conformation (the  $S_S$  configuration for  $\beta$ -D-pyranosides, the  $R_S$  configuration for  $\alpha$ -D-pyranosides); for the other diastereomer, the conformer with the aglycone anti is more stable or comparable in stability with the exo conformer.

## Results

### Axial glycosyl sulfoxides

As previously reported,<sup>36</sup> the treatment of 2-azido-2-deoxy-1,3,4,6-tetra-*O*-acetyl- $\alpha$ -D-galactopyranoside<sup>37</sup> with thiophenol and boron trifluoride etherate in chloroform gave close to a 1:1 mixture of the  $\alpha$ - and  $\beta$ -isomers. Deacetylation gave a mixture of compounds **1** and **2** that were separated by column chromatography. As shown in Scheme 1, the  $\alpha$ -isomer was converted using standard methods into the 4,6-*O*-benzylidene acetal (**3**) and the 4,6-*O*-*p*-methoxybenzylidene acetal (**5**) that were acetylated to give compounds **6** and **7**, respectively. Compound **3** had been made previously by a different route but was not fully characterized.<sup>38</sup> Oxidation with *m*-chloroperbenzoic acid (MCPBA) in dichloromethane (DCM) at –76 °C yielded two isomeric sulfoxides for the 4,6-benzylidene derivative (**8R** and **8S**) and for the 4,6-*O*-*p*-methoxybenzylidene derivative (**9R** and **9S**). In both cases, the sulfoxide diastereomers were separated by column chromatography. The preferences for the oxidation reactions to yield the  $R_S$  isomer were much less than noted for gluco<sup>34,39</sup> and manno<sup>5,29</sup> analogues, being 3/1 for compound **3** and 7/2 for compound **5**.



X-ray crystal structure determinations were performed on compounds **6**, **8R**, **8S**, and **9R**. The phenyl thioglycoside, **6**, adopted the exo conformation (Fig. 3). A compilation of all 22 structures previously published that contain axial thioglycosides was assembled from the Cambridge Data File and data from this compilation is listed in the Supplementary data as Table S1. In all previous 22 structures, as well as in the one determined here, the conformation adopted was exo.

The X-ray crystal structure determinations of the kinetically favored sulfoxides **8R** and **9R** show that both adopt anti conformations, different from the exo conformations present in the five previous determinations of axial glycosyl sulfoxides. Two  $R_S$  ethyl 1-thio- $\alpha$ -D-mannopyranoside *S*-oxides adopted exo conformations,<sup>28</sup> as did an  $R_S$  2-cyanoethyl 1-thio- $\alpha$ -D-glucopyranoside *S*-oxide,<sup>34</sup> and two 1-thio- $\beta$ -D-galactofuranoside *S*-oxides with the sulfur atom in pseudo-axial positions also adopt exo-like conformations.<sup>16</sup> ORTEP diagrams for **8R** and **9R** are shown in Figs. 4 and 5. The minor diastereomer, **8S**, adopts an exo conformation in the solid state. Its ORTEP diagram is shown in Fig. 6.

The geometries about the anomeric centre deviate from perfect staggering to different extents in the three axial sulfoxide X-ray crystal structure determinations. The torsional angles are shown in Fig. 7. In the crystal of the parent phenyl thioglycoside, **6**, the quaternary phenyl carbon atom is perfectly staggered between the ring O and H1. In the crys-

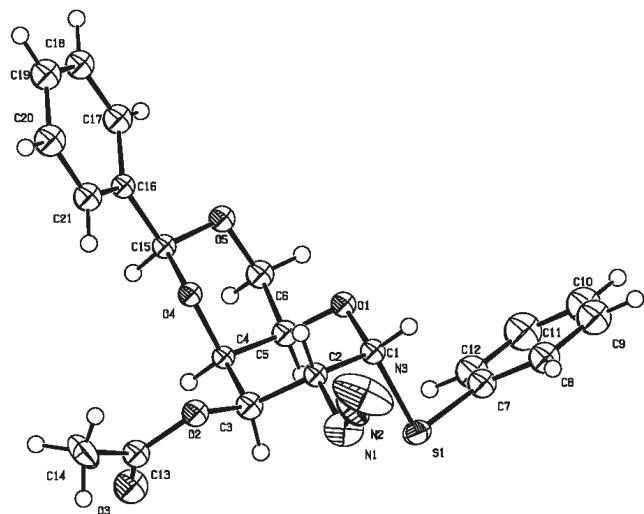
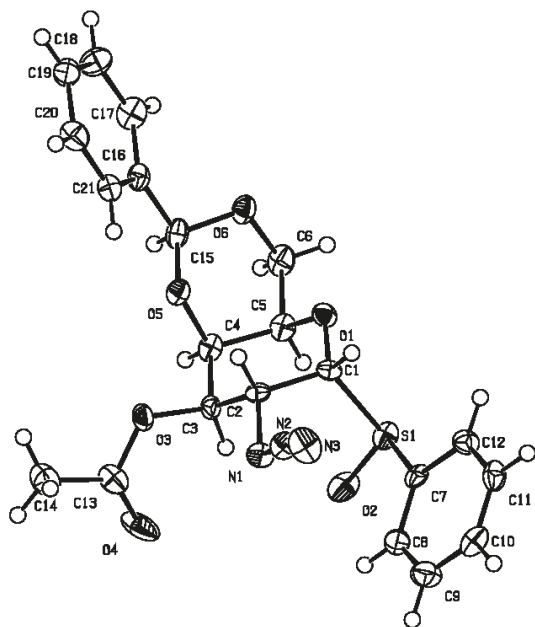
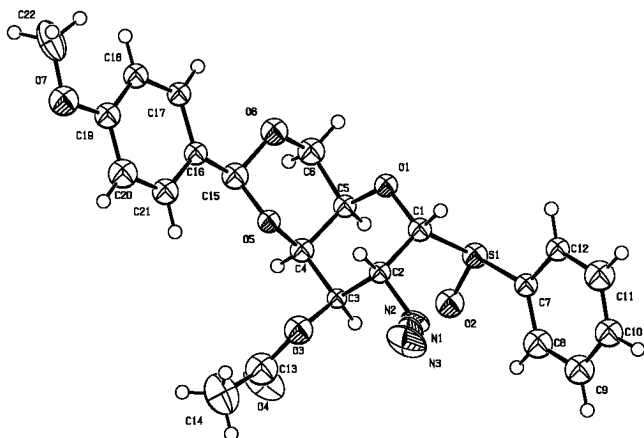
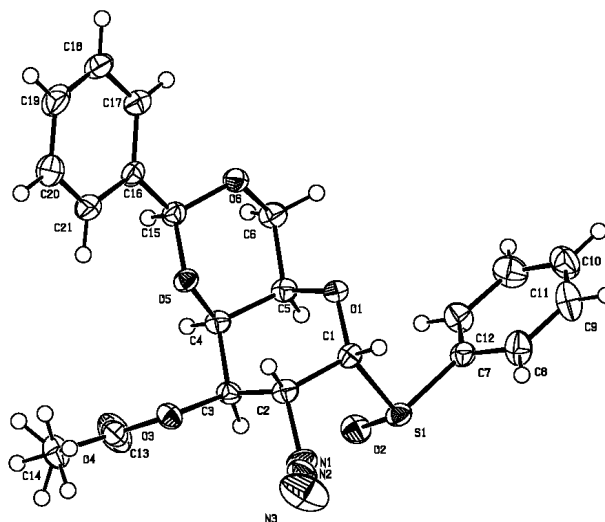
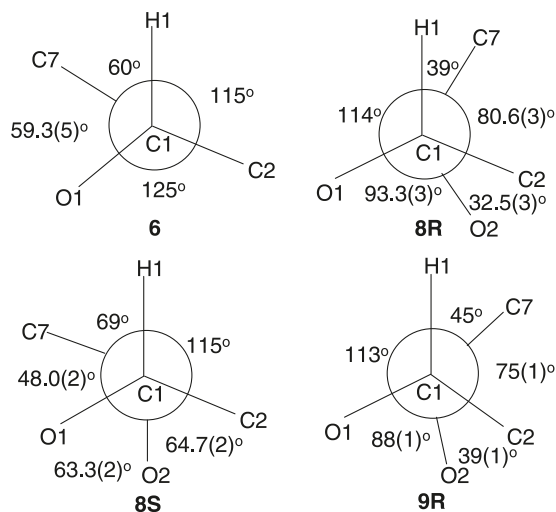
Fig. 3. ORTEP diagram of **6**.Fig. 4. ORTEP diagram of **8R**.Fig. 5. ORTEP diagram of **9R**.Fig. 6. ORTEP diagram of **8S**.

Fig. 7. Newman diagrams from C1 to S indicating torsional angles about the anomeric centres of **6**, **8R**, **8S**, and **9R** calculated for bond angles using the program PLATON.<sup>40</sup> The top two structures have the azide groups in gauche minus conformations, whereas the bottom two are in gauche plus conformations (see the following for further discussion).



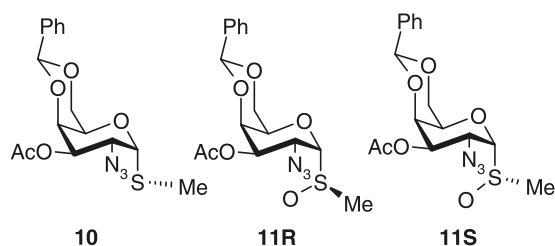
tals of the two sulfoxides that adopt anti conformations, **8R** and **9R**, the quaternary phenyl carbon atom is much further away from C2 than expected for a staggered conformation, having C2-C1-S-C7 torsional angles of 80.6(3)° and 75(1)°, for **8R** and **9R**, respectively. In contrast, in the crystal of the sulfoxide that adopts an exo conformation, **8S**, the quaternary phenyl carbon atom is closer to the ring oxygen (O-C1-S-C7 torsional angle of 48.0(2)°) than expected for a staggered conformation.

Full geometry optimizations were carried out at the B3LYP/6-31G(d) level of theory on the parent phenyl thio-glycoside, **6**, its oxides **8R** and **8S**, and their SMe analogs (**10**, **11R**, and **11S**) in the gas phase. Frequency calculations confirmed that all structures identified as conformers were minima on the potential energy surfaces. In these cases, single-point calculations were performed for all conformers



at the B3LYP/6-311G+(d,p) level of theory. The conformational situation is more complicated for these compounds. Rotamer geometries and energies about two torsional angles were evaluated, the glycosidic torsional angle, O5-C1-S-C, and the torsional angle to the azide group, H2-C2-N-N. All other torsional angles were allowed to rotate freely to minimum energy values.

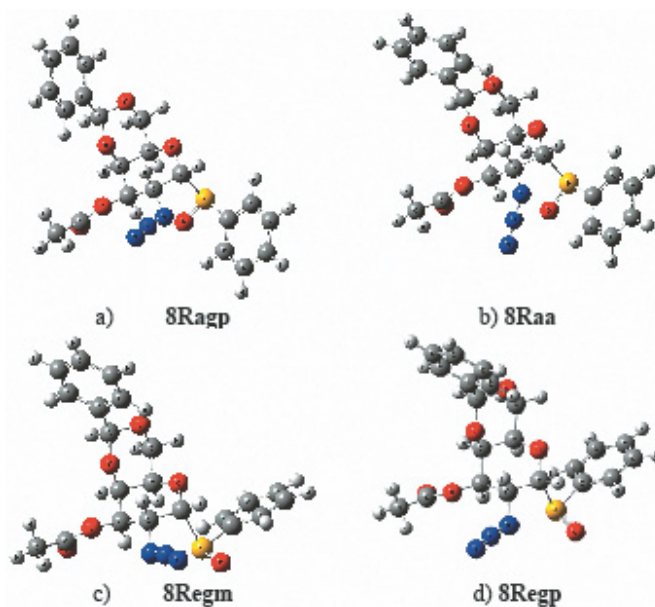
Anti conformations about the C1-S bond of the phenyl thioglycoside, **6**, were not minima on this potential energy surface; initial geometries obtained from a variety of strategies always rotated smoothly back to the exo conformer on minimization. The anti conformer of the methyl analogue **10** was a minimum, 2.30 kcal mol<sup>-1</sup> (1 cal = 4.184 J) less stable than the exo conformer at the B3LYP/6-311G(d) + ZPVE and 1.70 kcal mol<sup>-1</sup> less at the B3LYP/6-311G+(d,p) + ZPVE level of theory. Initial geometries for the two additional rotamers about the C2-N bond were obtained by starting from the minimized geometry for each C1-S rotamer and rotating about this bond. Several of these C-N rotamers minimized to previously minimized structures, but two sets of exo and anti minima were obtained for **8R** and **11R**, and one set of two for the exo conformer of **6**. Only one azide rotamer was found for each of the exo and anti conformers of **8S** and **11S**.



The conformers obtained for **8R** are illustrated in Fig. 8. These are named with the compound number, followed by **e** or **a** to indicate the anomeric conformation (exo or anti, respectively), which is then followed by **a**, **gp**, or **gm**, to indicate whether the azide N-N-C2-H2 torsional angle is anti, gauche plus, or gauche minus, respectively. Conformer stabilities are listed in Table 1.

For the conformers arising because of rotation about the C2-N bond, the gauche plus (**gp**) and gauche minus (**gm**) conformers are calculated to be more stable than the anti (**a**) conformer. The **gp** conformer is always a minimum on the potential energy surface. In the three cases where the **a** conformation is a minimum (**6**, **8R**, **11R**), it is less stable than the **gp** conformer by 1.0 ± 0.2 kcal mol<sup>-1</sup>. The gauche minus (**gm**) conformer was calculated to be a minimum only for **Re** sulfoxide conformers, **8Re** and **11Re**, but in those two cases, it was calculated to be more stable than the **gp** conformer by 0.7 and 0.9 kcal mol<sup>-1</sup>, respectively. The azides in the crystal structures of **6** (exo conformer) and **8R** (anti conformer) are present in **gm** conformations, while those in **8S** (exo conformer) and **9R** (anti conformer) are present in **gp** conformations, consistent with the small energy differences between the latter two conformations and probably small barriers between these two minima. The absence of anti conformations for azides in these crystal structures are consistent with the larger energetic destabilizations

Fig. 8. Diagrams indicating the conformations calculated to be adopted by the minima of compound **8R**.



calculated for the **a** conformations with respect to the **gp** conformations. H2-C2-N-N torsional angles were calculated to be small, having absolute values of 38°–46° in all **gp** and **gm** conformers. In the three C-N anti conformers, the H2-C2-N-N torsional angles were between 127° and 147° with the N close to being eclipsed by C3.

The relative energies calculated for the anomeric conformers of these axial glycosyl sulfoxides (Table 1) were unexpected in view of all previous discussion.<sup>17,23,33</sup> The anti conformers of the kinetically favored *R<sub>S</sub>* sulfoxides were calculated to be more stable than the exo conformers by 2.0 and 1.4 kcal mol<sup>-1</sup> at the B3LYP/6-311G+(d,p) + ZPVE level of theory for the phenyl and methyl sulfoxides, respectively. For the minor sulfoxides, the *S<sub>S</sub>* diastereomers, the exo conformer is calculated to be more stable by 1.1 kcal mol<sup>-1</sup> for the phenyl glycoside and 2.0 kcal mol<sup>-1</sup> for the methyl glycoside.

The interesting variations in geometry from perfect staggering around the C1-S bond observed in the X-ray results were evident here for all conformers (see Fig. 9). In particular, the quaternary phenyl carbon atom in the anti conformer of **8R** (**gp**) is calculated to be about as far away from C2 as observed in the crystal, having a C2-C1-S-C7 torsional angle of 81°. In the methyl sulfoxide (**11Ragp**), this angle is calculated to be slightly smaller, 76°. The exo conformers of **8R** are calculated to deviate more from perfect staggering in the unexpected direction than observed in the X-ray structure of **8S**; the O1-C1-S-C7 angle was calculated to be 31° in the most stable **gp** conformer. In the two previously determined X-ray structures of α-D-mannopyranosyl ethyl sulfoxides, the comparable angles observed were larger, 50.7°–56.8°.<sup>28</sup>

In view of the distance determinations obtained from NOE measurements (vide infra) and the difference between calculated and X-ray geometries mentioned earlier, the variations in energy as a function of two different torsional angles were evaluated for compound **8R**. Rotation about the



**Table 1.** Calculated conformational energies and dipole moments for axial glycosyl sulfoxides.

Conformer	$\Delta E$ (6-31G(d)) (kcal mol <sup>-1</sup> ) <sup>a</sup>	$\Delta E$ (6-31G(d)) (kcal mol <sup>-1</sup> ) <sup>b</sup>	$\Delta E$ (6-31G(d)) + ZPVE (kcal mol <sup>-1</sup> ) <sup>a</sup>	$\Delta E$ (6-31G(d)) + ZPVE (kcal mol <sup>-1</sup> ) <sup>b</sup>	$\Delta E$ (6-311+G(d,p)) + ZPVE (kcal mol <sup>-1</sup> ) <sup>a</sup>	$\Delta E$ (6-311+G(d,p)) + ZPVE (kcal mol <sup>-1</sup> ) <sup>b</sup>	Dipole moment (D) <sup>c</sup>
<b>6egp</b> <sup>d</sup>	0.0	0.0	0.0	0.0	0.0	0.0	1.84
<b>6ea</b>	1.21	1.21	1.28	1.28	1.08	1.08	1.96
<b>10egp</b>	0.0	0.0	0.0	0.0	0.0	0.0	2.24
<b>10agp</b>	2.30	2.30	2.33	2.33	1.70	1.70	0.57
<b>8Ragp</b>	2.03	0.0	2.00	0.0	2.25	0.0	2.54
<b>8Raa</b>	3.04	1.01	3.08	1.07	3.08	0.83	3.31
<b>8Regm</b>	5.36	3.33	5.12	3.12	4.27	2.02	5.55
<b>8Regp</b>	5.97	3.94	5.63	3.62	5.18	2.92	5.73
<b>11Ragp</b>	2.36	0.0	2.42	0.0	2.61	0.0	2.54
<b>11Raa</b>	3.47	1.11	3.58	1.16	3.67	1.05	3.17
<b>11Regm</b>	5.62	3.26	5.29	2.86	4.04	1.42	5.64
<b>11Regp</b>	6.08	3.72	5.62	3.35	5.16	2.54	5.75
<b>8Segp</b>	0.0	0.0	0.0	0.0	0.0	0.0	3.49
<b>8Sagp</b>	1.39	1.39	1.41	1.41	1.08	1.08	2.62
<b>11Segp</b>	0.0	0.0	0.0	0.0	0.0	0.0	3.33
<b>11Sagp</b>	2.45	2.45	2.46	2.46	1.96	1.96	2.99

<sup>a</sup>Relative to the most stable conformer of all diastereomers of this compound.

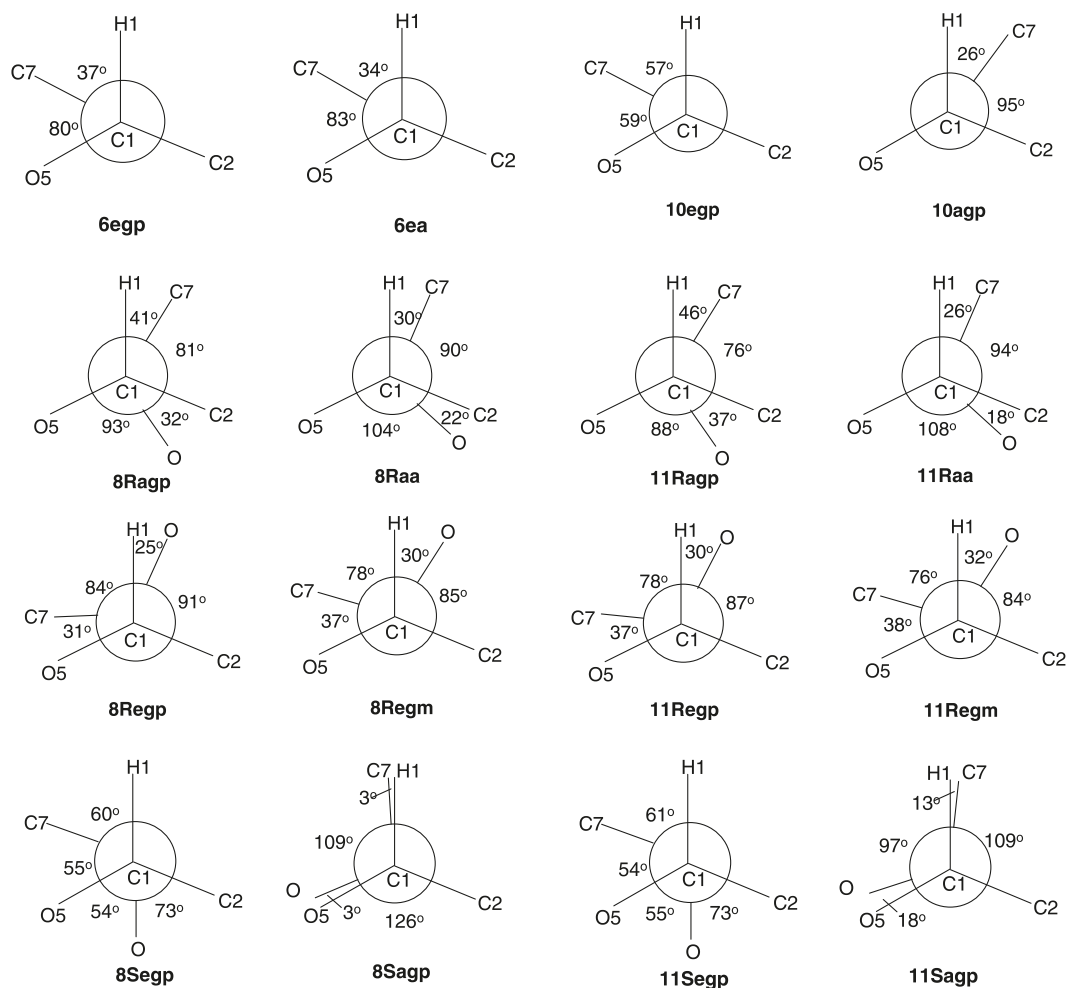
<sup>b</sup>Relative to the most stable conformer of this diastereomer.

<sup>c</sup>Calculated at the 6-311G+(d,p) level of theory.

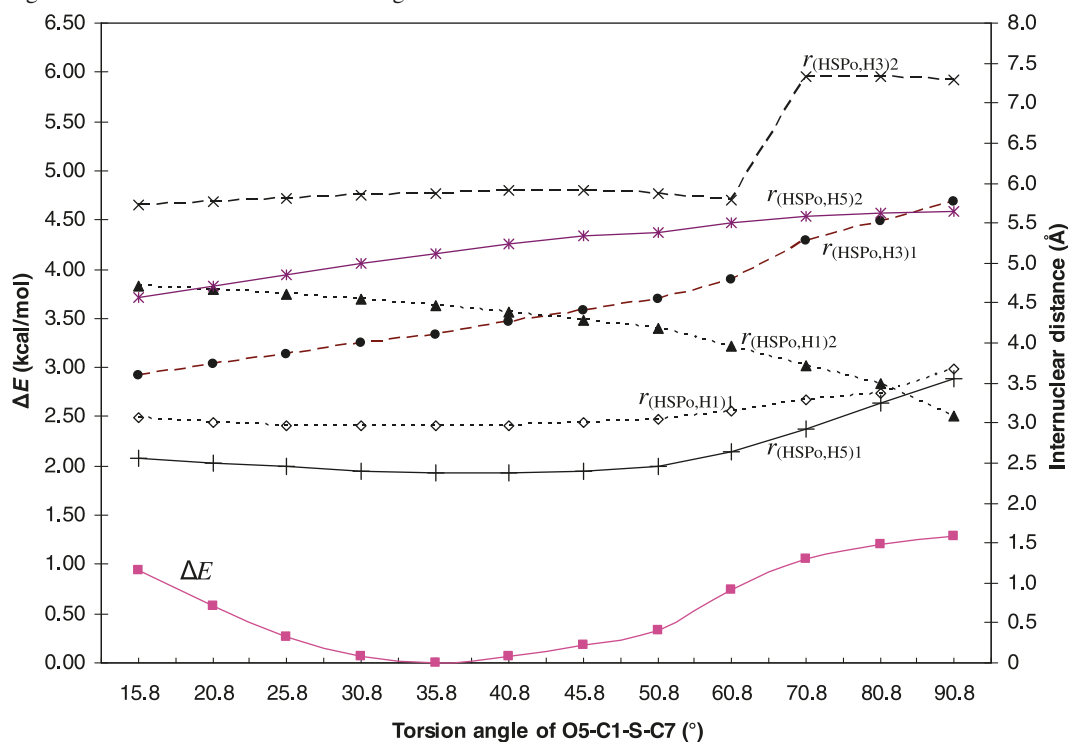
<sup>d</sup>No anti conformation of compound **6** was calculated to be a minimum.

**Table 2.** Comparison of results obtained by different methods.

Compound	Method	Internuclear distance (Å) <sup>a</sup>			Relative energy (kcal mol <sup>-1</sup> ) <sup>b</sup>
		<i>r</i> (HSPo,H1)	<i>r</i> (HSPo,H3)	<i>r</i> (HSPo,H5)	
<b>6</b>	NOE	3.0	NO <sup>c</sup>	3.4	NA <sup>d</sup>
	DFT ( <b>egp</b> )	2.64	5.09	3.40	0.00
	DFT ( <b>ea</b> )	2.64	5.59	3.46	1.08
	X-ray ( <b>egm</b> )	2.84	4.78	2.67	NA <sup>d</sup>
<b>8R</b>	NOE	3.0	4.7	3.6	NA <sup>d</sup>
	DFT ( <b>agp</b> )	2.55	3.84	5.15	0.00
	DFT ( <b>aa</b> )	2.51	4.17	5.11	0.83
	DFT ( <b>egm</b> )	2.96	4.12	2.38	2.02
	DFT ( <b>egp</b> )	2.93	3.96	2.38	2.92
	X-ray ( <b>agm</b> )	2.68	3.92	5.18	NA <sup>d</sup>
	X-ray ( <b>agp</b> )	2.53	3.86	5.07	NA <sup>d</sup>
	X-ray ( <b>egp</b> )	2.95	4.58	2.55	NA <sup>d</sup>

<sup>a</sup>The distance to the closest ortho H (HSPo).<sup>b</sup>From 6-311G+(d,p) + ZPVE/6-31G(d) calculations.<sup>c</sup>NO = not observed.<sup>d</sup>NA = not applicable.**Fig. 9.** Newman projections from C1 to S showing torsional angles about the anomeric centre calculated for the various conformers of compounds **6**, **10**, **8R**, **11R**, **8S**, and **11S**.

**Fig. 10.** Variation in energy and internuclear distances calculated using B3LYP6–31G(d) as a function of O5–C1–S–C7 torsional angle for compound **8R**. Right: internuclear distances. Left: energies.



axis of the glycosyl phenyl ring was evaluated first. The torsion angle C1–S–C7–C8 was held constant at fixed values in  $10^\circ$  intervals from the value found at the minimum for the conformer **8Regp**. The energy change as a function of torsional angle is fairly symmetrical about the minima indicating that the measured NOE should represent the minimum well (Fig. S1 in the Supplementary data). Then the torsion angle O1–C1–S–C7 was held constant at values ranging from  $5^\circ$  to  $10^\circ$  increments about the value found at the minimum for the conformer **8Regp**. Figure 10 shows how the energy and the internuclear distances vary as a function of this angle. For torsional angles  $>90^\circ$ , the energy decreased in a nonsymmetric way because the azide conformation minimized from the **gm** arrangement was most stable in **8Re** and to the **gp** conformation was most stable for **8Ra**. The variation in energy is not symmetric about this angle, being much flatter towards values of the torsional angle that are larger than that of the minimum. Hence, the time-averaged O1–C1–S–C7 torsional angle will be significantly larger than that present in the geometry of the minimum and the NOEs observed for this conformer and will yield longer H1–HSPo and H5–HSPo distances than calculated for the minimum.

To determine the cause of the method of assignment of sulfoxide configuration based on  $^{13}\text{C}$  NMR chemical shifts,<sup>26</sup> the Gauge invariant atomic orbital (GIAO) method<sup>41,42</sup> was used to calculate  $^{13}\text{C}$  shieldings for all carbons of the **8R** and **8S** conformers using the 6–311+G(d,p) basis set and 6–31G(d) geometries. TMS was used as the chemical shift reference. The chemical shifts obtained are listed in Table S5 in the Supplementary data and all calculated values were slightly larger than the experimental values. Plots of experimental chemical shifts against the chemical shifts calculated for all nonaromatic carbons gave

good straight lines with correlation constants of 0.989–0.996 and slopes ranging from 0.947 to 0.982 (not shown). The anomeric chemical shifts of the carbons consistently deviated from the lines, having calculated values that were larger than the experimental values by greater amounts than those of carbons with similar shifts. According to the method proposed by Khier,<sup>26</sup> to assign glycosyl sulfoxide stereochemistry from anomeric carbon chemical shifts, C1 of the  $S_S$  sulfoxide should be more shielded than that of the  $R_S$  sulfoxide. This was observed experimentally: the C1 chemical shifts were 92.5, 96.4, 89.9, and 96.5 ppm for **8S**, **8R**, **9S**, and **9R**, respectively. The values calculated for the four **8R** conformers were 108.9, 112.6, 114.8, and 114.8 ppm for **8Ragp**, **8Raa**, **8Regp**, and **8Regm**, respectively, and those for **8Segp** and **8Sagp** were 106.1 and 105.7 ppm, respectively. Thus, all values for **8S** conformers were less than those for **8R** conformers, which is in agreement with both experiment and prediction. A value for **8R** in between that of **8Ragp** and those of the exo conformers and one for **8S** of the exo conformer would give a difference very similar to those observed in solution for the **8** and **9** diastereomers. Khier<sup>26</sup> ascribed the shielding of the  $S_S$  isomers to  $n \rightarrow \sigma^*$  overlap. The value calculated for C1 of **8Sagp**, which cannot have  $n \rightarrow \sigma^*$  overlap, is the lowest of all, indicating that  $n \rightarrow \sigma^*$  overlap does not cause this shielding effect.

The conformation adopted in solution was investigated by measuring initial NOE buildup rates using both selective 1D NOE measurements with the double pulsed field gradient spin echo (DPFGSE) sequence<sup>43</sup> and 2D NOESY experiments using a variety of mixing times. The initial rates are directly proportional to the internuclear distances ( $r_{\text{IS}}$ ) and were calibrated using a known internuclear distance ( $r_{\text{ref}}$ ) as follows:

$$r_{\text{IS}} = r_{\text{ref}} \left( \frac{\text{NOE}_{\text{ref}}}{\text{NOE}_{\text{IS}}} \right)^{1/6}$$

The distance between ortho phenyl protons (HSPo; 2.8 Å) was used as the reference distance ( $r_{\text{ref}}$ ).<sup>44</sup> The results are given in Table 2 along with the results obtained by the previous methods.

For the parent compound **6**, the NOE results fit the geometry calculated for the exo conformer well. The distances from HSPo obtained to H1 and to H5 are within 0.4 Å of those calculated and no NOE was observed for the interaction with H3, as expected. However, the H5–HSPo distance obtained from the NOE measurement was much longer than that measured from the X-ray results. As discussed previously, the potential surface is fairly flat with respect to changes in the O1–C1–S–C7 torsional angle from the 80° value calculated for the gas phase. Crystal packing presumably causes this value to be altered from that calculated for the minimum to the 59.4(5)° value observed in the solid state. The average of all 23 O1–C1–S–C7 torsional angles from the crystal structures in the Cambridge data file (Table S1 in the Supplementary data) was 61.5°.

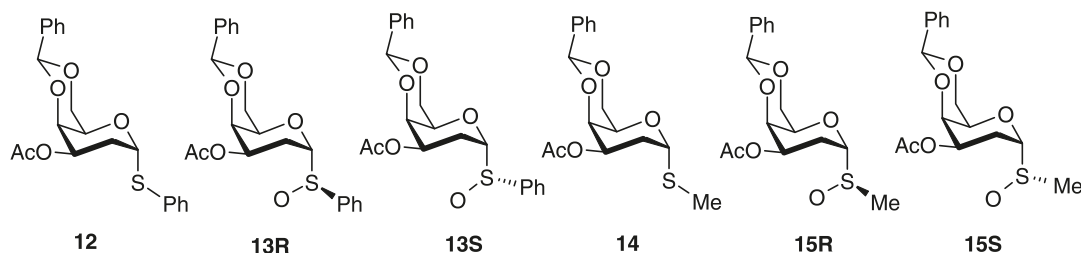
For the  $R_S$  sulfoxide, the distances obtained from the NOE measurements do not match the pattern obtained from the X-ray results or from the geometries calculated for the two lowest energy minima, the global minimum, the **8Ragg** conformer, and the other anti conformer (see Table 2). In both anti conformers, the H5–HSPo distance is calculated by DFT to be >5 Å, too large to give an NOE. However, an H5–HSPo NOE was observed and the distance calculated from it was 3.62 Å. For both exo conformers, the H5–HSPo distances are calculated by DFT to be 2.38 Å, much shorter than the dis-

tance obtained from the NOE. The H1–HSPo distance, obtained from the NOE, was 3.05 Å. The average of DFT calculated values in the two exo conformers is 2.95 Å and is 2.53 Å in the two anti conformers. These results indicate that a mixture of the exo and anti conformers is present in solution.

A very approximate estimate of the amount of the exo conformer present can be obtained from the H5–HSPo distances calculated for exo and anti conformers and the value obtained from the NOE measurement using  $r^6$  averaging. The use of 3.6 Å for the average, 5.15 Å for the anti conformer, and 2.38 Å for the exo conformer yields 7% of the exo conformer. This amount corresponds to a  $\Delta G^\circ$  value of 1.5 kcal mol<sup>-1</sup> for the equilibrium between conformers, which is on the same order as that calculated.

### Evaluation of the effect of the 2-azido group

To examine whether the above results were influenced by the 2-azido group, calculations were performed on the 2-deoxy analogs shown below at the same level of theory, except that conformations were also minimized at the B3LYP/6-311+G(d,p) level. As previously, calculations were performed on two conformations of each of these, the anti (**a**) and exo (**e**) conformers. In addition, calculations were performed on the endo conformers of the methyl glycosyl sulfoxides, **15Sen** and **15Ren**, to check whether the earlier assumption that this class of conformer was too energetic to contribute to the mixture present was valid. The anti conformers of both  $S_8$  diastereomers, that is, **13Sa** and **15Sa**, were not minima on their potential energy surfaces and neither was one of the endo conformers, **15Ren**. The results are given in Table 3 and Newman projections showing the relationships among groups at the anomeric centres are shown in Fig. 11.



The exo conformer of the methyl 2-deoxythioglycoside (**14**) was calculated to be somewhat more stable with respect to the anti conformer than its 2-azido-2-deoxy analogue (**10**) (3.2 vs 2.3 kcal mol<sup>-1</sup>). For this series, the anti conformer of the phenyl thioglycoside was also a minimum, 2.3 kcal mol<sup>-1</sup> less stable than the exo conformer. For the  $R_S$  sulfoxide of the 2-deoxy analogue, **15**, the exo conformer (**15e**) was more stable than the anti conformer (**15a**) by 1.5 kcal mol<sup>-1</sup>. The two conformers of the  $R_S$  phenyl 2-deoxy sulfoxides (**13**) were calculated to be almost equally stable at the B3LYP 6-311+G(d,p) level of theory, the exo conformer being 0.1 kcal mol<sup>-1</sup> more stable. Neither of the anti conformers of the  $S_8$  sulfoxides of the 2-deoxy derivatives (**13Sa** and **15Sa**) were minima at this level of theory.

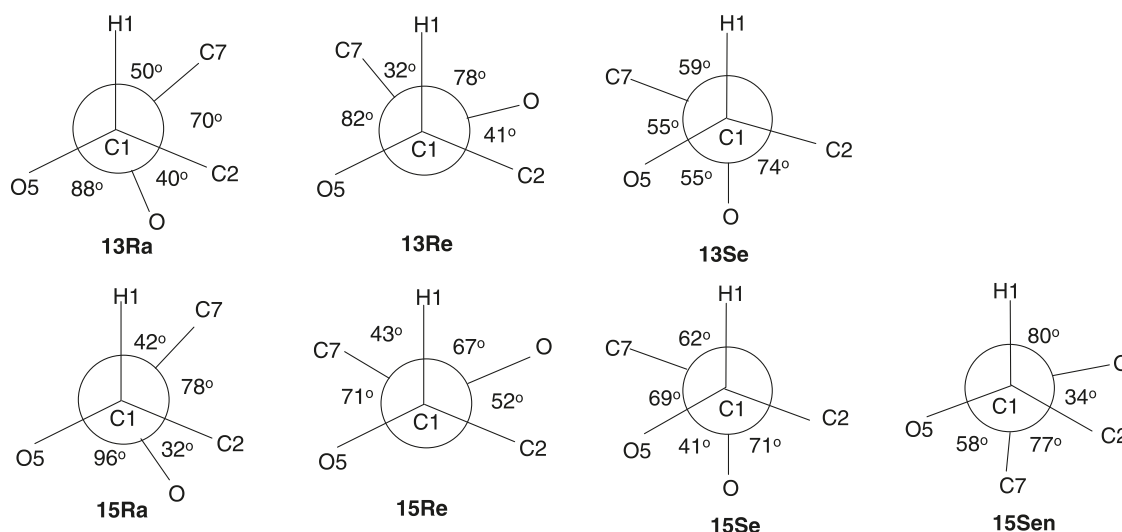
As shown in Fig. 11, the C2–C1–S–C7 torsional angles in the anti conformers of the  $R_S$  sulfoxides are similar to those of their 2-azido analogues; the values are greater than those

expected for perfect staggering, being 70° for **R13a** and 78° for **R15a**. In contrast, the exo conformers of **R13** and **R15** deviate from perfect staggering in the opposite direction from their 2-azido analogues. In the latter derivatives (see Fig. 9), the O5–C1–S–C7 torsional angle had values in the 31°–38° range, whereas the O–S–C1–C2 angle was in the 84°–91° range. For **13Re** and **15Re**, the values of the O5–C1–S–C7 torsional angles are 82° and 71°, respectively, whereas those of the O–S–C1–C2 angles are 41° and 52°, respectively. These changes are consistent with relief of dipole–dipole repulsion between the potentially parallel C–N and S–O dipoles of the 2-azido derivatives. When the 2-azido group was removed, the conformational minima have O–S–C1–C2 angles <60° and the O5–C1–S–C7 values are >60°, relieving steric strain from the interaction of the aglycone with the pyranose ring.



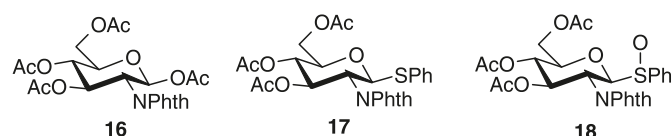
**Table 3.** Calculated conformational energies and dipole moments for axial 2-deoxyglycosyl sulfoxides.

Conformer	$\Delta E$ (6-31G(d)) + ZPVE (kcal mol <sup>-1</sup> ) <sup>a</sup>	$\Delta E$ (6-311+G(d,p)) + ZPVE (kcal mol <sup>-1</sup> ) <sup>a</sup>	Dipole moment (D) <sup>b</sup>
<b>12e</b>	0.0	0.0	0.98
<b>12a</b>	2.45	2.26	2.55
<b>13Re</b>	0.29	0.0	2.96
<b>13Ra</b>	0.0	0.08	3.76
<b>13Se</b>	0.84	0.45	3.29
<b>14e</b>	0.0	0.0	0.78
<b>14a</b>	3.22	3.16	2.24
<b>15Re</b>	0.37	0.0	3.18
<b>15Ra</b>	1.34	1.54	3.33
<b>15Se</b>	0.0	0.14	3.32
<b>15Sen</b>	5.82	5.25	3.75

<sup>a</sup>Relative to the most stable conformer of all diastereomers of this compound.<sup>b</sup>Calculated at the 6-311G+(d,p) level of theory.**Fig. 11.** Newman projections from C1 to S showing torsional angles about the anomeric centre calculated for the conformers of compounds **12R**, **12S**, **13R**, **13S**, **14R**, **14S**, **15R**, and **15S**.

### An equatorial glycosyl sulfoxide

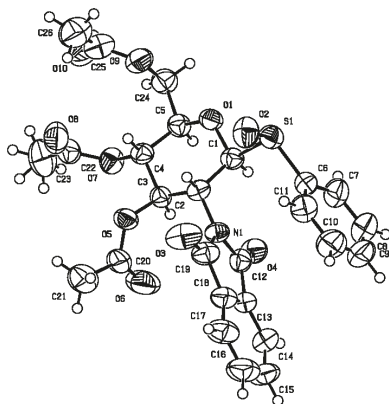
Treatment of 1,3,4,6-tetra-*O*-acetyl-2-deoxy-2-phthalimido- $\beta$ -D-glucopyranoside<sup>45–47</sup> (**16**) with thiophenol and boron trifluoride etherate gave phenyl 3,4,6-tri-*O*-acetyl-2-deoxy-2-phthalimido-1-thio- $\beta$ -D-glucopyranoside (**17**), previously prepared by another method,<sup>48</sup> in an 81% yield. Oxidation with 1 equiv of *m*-chloroperbenzoic acid in dichloromethane at  $-78^\circ\text{C}$  yielded 92% of a 2.1:1 mixture (**18**) of the *S<sub>S</sub>* (**18S**) and *R<sub>S</sub>* (**18R**) isomers. It had previously been reported that oxidation under similar conditions gave a 3:1 ratio of the same isomers.<sup>17</sup> The isomers were separated using flash chromatography on silica gel with 5% acetone in dichloromethane as eluent.



The major isomer (**18S**), the *S<sub>S</sub>* isomer, was recrystallized

from a solution of 1% ethanol in hexanes. Its crystal structure (Fig. 12) establishes the *S<sub>S</sub>* configuration. Interestingly, the compound adopts the conformation with the phenyl group anti to the C1–O5 bond, in contrast to the results from all previous X-ray determinations of equatorial glycosyl sulfoxides except one<sup>23</sup> (see Table S1 in the Supplementary data for data on previous X-ray determinations of glycosyl sulfoxides). In this conformation, the phenyl and phthalimido groups lie roughly parallel to each other and perpendicular to the plane of the tetrahydropyran ring, in an arrangement typical of  $\pi$  stacking.

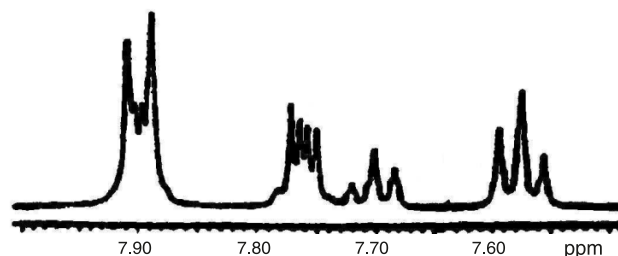
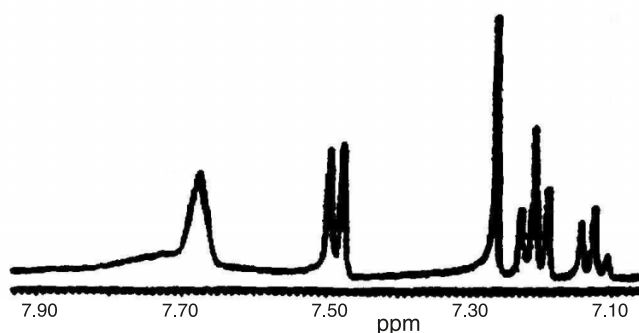
This conformation of **18S** persists in solution in chloroform-*d*. The nearly parallel alignment of the aryl groups is evident in both the chemical shifts of the phenyl protons and of the phthalimido protons, which are affected by the anisotropic chemical shift effects of these aryl groups (for recent summaries of these effects, see papers by Lazzeretti and co-workers<sup>49,50</sup>). In the <sup>1</sup>H NMR spectrum of the starting material (**17**), the phenyl ortho Hs appear at 7.45 ppm, whereas the meta and para Hs appear as a complex multiplet from 7.2 to 7.3 ppm. Similar shifts have been reported for cyclo-

Fig. 12. ORTEP diagram of **18S**.

hexyl phenyl sulfide, 7.38 (ortho), 7.25 (meta), and 7.17 (para) ppm.<sup>51</sup> Conversion to the sulfoxide results in deshielding, e.g., in the spectrum of cyclohexyl phenyl sulfoxide, 7.54 (ortho), 7.45 (meta), and 7.45 (para) ppm,<sup>51</sup> and also in that of compound **18R**, 7.90 (ortho), 7.58 (meta), and 7.70 (para) ppm (see Fig. 13). In contrast, in the <sup>1</sup>H NMR spectrum of **18S**, these signals appear at 7.49 (ortho), 7.21 (meta), and 7.13 (para) ppm (Fig. 14). All signals are shielded in comparison with those of the *R<sub>S</sub>* isomer,  $\Delta\delta$  0.41 (ortho), 0.37 (meta), and 0.57 (para) ppm, which are consistent with the effects of a nearly parallel phthalimido group.

The effects on the phthalimido protons are more dramatic. AA'BB' patterns typical of disubstituted benzenes with identical ortho substituents are observed for the parent compound with chemical shifts of 7.76 and 7.87 ppm and for **18R** with chemical shifts of 7.77 and 7.90 ppm (Fig. 13). In contrast, the phthalimido proton signals in the spectrum of **18S** are exchange broadened (Fig. 14). A broad singlet at 7.67 ppm is superimposed on a much broader smooth low band centered at about 7.73 ppm. Rotation of the phthalimido group is hindered by the favorable interactions associated with the near parallel arrangement of the phenyl and phthalimido groups. If there was a rapid equilibrium between anti and exo conformations, the phthalimido group would be able to rotate freely when the phenyl group was exo. Thus, the observation of a single pattern exhibiting hindered rotation indicates that the anti conformation is essentially the only conformation populated in solution and that rotation about the C1–S bond to the exo conformation is slow, as are rotation about both the phenyl C–S bond and the C2–N bond.

Quantum mechanical calculations were performed with density functional theory as implemented in Gaussian 03<sup>52</sup> with Becke's three parameter exchange functional and Lee–Yang–Parr correlational functionals.<sup>53,54</sup> The X-ray structure of compound **18S** provided the initial geometry of the glycosyl sulfoxide. The initial geometries for the second staggered rotamer were generated by rotating about the C1–S bond and those for the other sulfoxide diastereomer were generated by inverting at sulfur. The third staggered rotamer, with the aglycone gauche to both C2 and the ring oxygen, was not used as a starting point for geometry minimization. Initial geometries for the SMe analog and its sulfoxides were obtained from the minimized thiophenyl conformers. Initial geometries for **17** and its methyl ana-

Fig. 13. Part of the 400 MHz <sup>1</sup>H NMR spectrum of compound **18R**. PDFFig. 14. Part of the 400 MHz <sup>1</sup>H NMR spectrum of compound **18S**. PDF

logue, **17Me**, were obtained by removing an oxygen atom from the minimized sulfoxide conformers. Full geometry optimizations were carried out at the B3LYP/6–31G(d) level of theory on **17**, **18S**, and **18R**, and their SMe analogs (**17Me**, **18SMe**, and **18RMe**). However, neither Hartree–Fock molecular orbital theory nor current implementations of density functional theory, which use local approximations of the density, are capable of accurately describing the dispersion forces, which are the major interaction causing  $\pi$  stacking.<sup>55</sup> Theoretical methods that could provide accurate measures of the dispersion forces are too time-consuming for molecules of the size of compound **18S**. Thus, the stabilities of conformers with geometries in which two arene rings are close to parallel will be underestimated.

All starting conformations, that is, both anti and exo conformations, of the parent thioglycosides, **17** and **17Me**, smoothly changed geometry on optimization to that of the exo conformers. On this potential energy surface, the anti conformations are not minima. The results for the glycosyl sulfoxides are shown in Table 4. The most stable conformer of the *S<sub>S</sub>* diastereomer is calculated to be more stable than that of the *R<sub>S</sub>* diastereomer by 1.85 and 1.36 kcal mol<sup>–1</sup> for the phenyl and methyl glycosyl sulfoxides, respectively. For all compounds, the exo conformers are calculated to be more stable than the anti conformers. For **18S**, which was observed to adopt the anti conformer both in the solid state and in solution, the exo conformer was calculated to be the more stable conformer by 1.57 kcal mol<sup>–1</sup>, although the anti conformer is calculated to have the larger dipole moment, 5.63 vs 1.40 D. For **18R**, which is present as the exo conformer in solution, the calculated difference is 3.03 kcal mol<sup>–1</sup>.

**Table 4.** Calculated conformational energies and dipole moments for the equatorial glycosyl sulfoxides.

Conformer	$\Delta E$ (6-31G(d)) (kcal mol <sup>-1</sup> ) <sup>a</sup>	$\Delta E$ (6-31G(d)) (kcal mol <sup>-1</sup> ) <sup>b</sup>	Torsional angle O5-C1-S-C (°)	Torsional angle O5-C1-S-O (°)	Dipole moment (D) <sup>c</sup>
<b>18Santi</b>	1.57	1.57	-157.7	91.4	5.63
<b>18Sexo</b>	0.0	0.0	-67.6	-177.1	1.41
<b>18Ranti</b>	3.03	4.88	-176.1	-66.5	6.60
<b>18Rexo</b>	0.0	1.85	-54.2	56.7	4.00
<b>18SMeanti</b>	2.31	2.31	-145.1	103.7	4.61
<b>18SMeexo</b>	0.0	0.0	-65.5	-175.3	0.86
<b>18RMeanti</b>	3.48	4.83	-168.4	-59.4	6.46
<b>18RMeexo</b>	0.0	1.36	-44.9	66.4	3.85

<sup>a</sup>Relative to the most stable conformer of all diastereomers of this compound.<sup>b</sup>Relative to the most stable conformer of this diastereomer.<sup>c</sup>Calculated at the 6-31G(d) level of theory.

## Discussion

### Axial glycosyl sulfoxides

The gas phase DFT calculations indicate that axial glycosyl sulfides favor the exo-anomeric conformers over anti conformers by substantial amounts, 1.7 kcal mol<sup>-1</sup> for the methyl 2-azido-2-deoxythioglycoside (**10**) and 3.2 kcal mol<sup>-1</sup> for the methyl 2-deoxythioglycoside (**14**). For the phenyl 2-azido-2-deoxythioglycosides, the anti conformations were not minima on the potential energy surfaces. The fact that in all 23 X-ray structure determinations of axial glycosyl sulfides, the conformation observed was the exo conformation (Table S3 in the Supplementary data) confirms these calculated results.

Of the two diastereomers of the glycosyl sulfoxides, **8** and **11**, the most stable conformer of the minor diastereomers, **8S** and **11S**, are calculated to be more stable than that of the major diastereomers by 2.3 and 2.6 kcal mol<sup>-1</sup>, respectively. Because the diastereomers obtained to a greater extent from the oxidation are calculated to be less stable than the diastereomers obtained in lesser amounts, this result strongly supports the conclusion that the stereoselectivity of oxidation is kinetically controlled and results from the preferred exo conformation of the sulfide.<sup>23,28</sup>

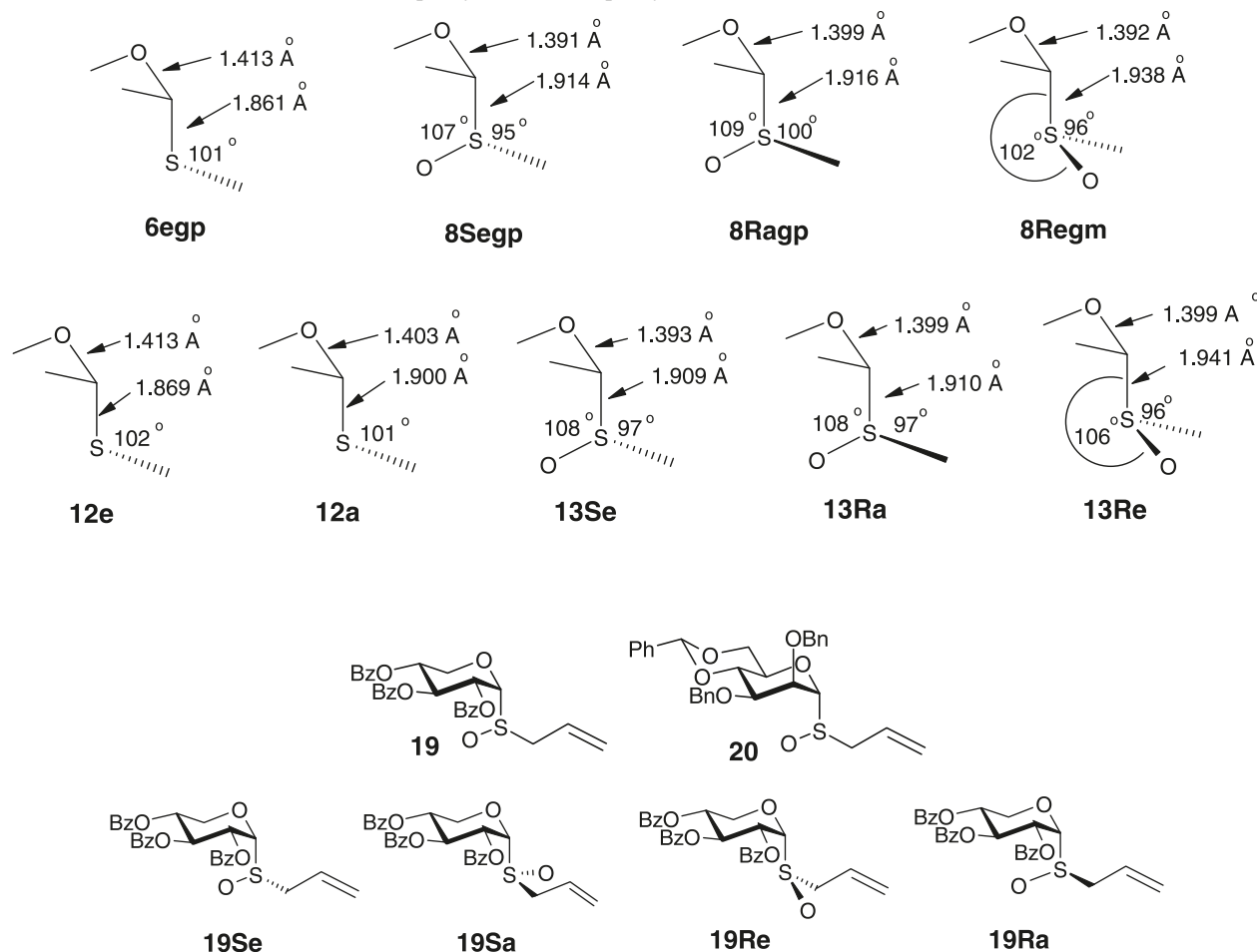
The 2-azido-2-deoxy *S<sub>S</sub>* sulfoxides (**8S** and **11S**), which retain the sulfur lone pair anti to the C1-O5 bond in the exo conformers, were calculated to have about the same conformational preferences for these exo conformers as the parent sulfides. One factor favoring this conformer must be *n* →  $\sigma^*$  donation from the sulfur lone pair into the C1-O5 antibonding orbital. This conformer is calculated to have the shortest C1-S bonds of all conformers of **8** and **13** (see Fig. 15), which is consistent with this overlap. Thus, the exo arrangement of the aglycone plus the *n* →  $\sigma^*$  overlap helps explain the greater stability of this conformer of the kinetically disfavored diastereomer.

However, for the *R<sub>S</sub>* sulfoxide (**11Ragp**), which does not have an anti lone pair in the exo conformation, the conformational preference is calculated to shift from being in favor of the exo conformer for the parent methyl sulfide (**10egp**) by 1.7 kcal mol<sup>-1</sup> to being in favor of the anti conformer by 1.4 kcal mol<sup>-1</sup>, a change of 3.1 kcal mol<sup>-1</sup> (3.7 kcal mol<sup>-1</sup> for the phenyl glycoside, if it is assumed that the sulfide preference is the same as for the methyl glycoside). For the *R<sub>S</sub>* sulf-

oxide of the 2-deoxy analogue, **15**, the exo conformer (**15e**) was more stable than the anti conformer (**15a**) by 1.5 kcal mol<sup>-1</sup>. Therefore, the extent to which the anti conformer of the methyl thioglycoside was stabilized on oxidation to the *R<sub>S</sub>* diastereomer was smaller for the 2-deoxy derivative, 1.5 kcal mol<sup>-1</sup>, but was still substantial. For the phenyl thioglycoside (**12**), the corresponding stabilization of the anti conformer of the *R<sub>S</sub>* sulfoxide was calculated to be 2.2 kcal mol<sup>-1</sup>, again at the B3LYP 6-311+G(d,p) level of theory.

Comparison of the geometries of the *R<sub>S</sub>* exo conformers of the 2-deoxy derivatives with the 2-azido-2-deoxy derivatives shows that the 2-azido substituent has a significant effect. The O5-C1-S-O torsional angles calculated for **8Regp**, **8Regm**, **11Regp**, **11Regm**, **13Re**, and **15Re** are 139.3°, 144.4°, 145.0°, 146.2°, 168.5°, and 179.5°, respectively. The latter two values are consistent with minimization of steric interactions for the R group and dipole-dipole repulsion due to interaction of the endocyclic C-O bond and the sulfoxide S-O bond. When the 2-azido group is present, dipole-dipole repulsion between the parallel C2-N bond and the S-O bond causes rotation about the C1-S bond resulting in much smaller O5-C1-S-O torsional angles. This is a significant effect because it is at the expense of increased R pyranose ring steric interactions and increased dipole-dipole repulsion due to interaction of the endocyclic C-O bond and the sulfoxide S-O bond. The small effect of the latter type of dipole-dipole repulsion suggests that it is not as important as other factors in determining conformational preferences for glycosyl sulfoxides.

In terms of energies, the most stable azide conformers of the anti *R<sub>S</sub>* 2-azido-2-deoxy derivatives are calculated to be more stable than the most stable azide conformers of the exo *R<sub>S</sub>* 2-azido-2-deoxy derivatives by 2.0 and 1.4 kcal mol<sup>-1</sup> for the phenyl and methyl sulfoxides, respectively, at the B3LYP6-311+G(d,p) level of theory. For the 2-deoxy derivatives, without the parallel C-N dipole, the exo conformers are now more stable by 0.1 and 1.5 kcal mol<sup>-1</sup> for the phenyl and methyl sulfoxides, respectively. This represents changes of 2.1 and 2.9 kcal mol<sup>-1</sup> for the phenyl and methyl sulfoxides, respectively, and represents the costs of having these dipoles parallel.

**Fig. 15.** Calculated structural features for axial phenyl sulfide and phenyl sulfoxide conformers.

Crich et al.<sup>23</sup> equilibrated the two sulfoxide diastereomers of allyl 2,3,4-tri-*O*-benzoyl-1-thio- $\alpha$ -D-xylopyranoside oxide (**19**) and allyl 2,3-di-*O*-benzyl-4,6-*O*-benzylidene-1-thio- $\alpha$ -D-mannopyranoside oxide (**20**) in both benzene-*d*<sub>6</sub> and methanol-*d*<sub>4</sub> at 60 °C. The former compound is most analogous to those studied here because in its <sup>4</sup>C<sub>1</sub> conformation it bears an equatorial substituent at C2. For **19**, the *S<sub>S</sub>* diastereomer was favored by 2 to 1 in benzene but the other diastereomer was favored by 2.5 to 1 in methanol. The results here indicate that **19S** will prefer the exo conformation, **19Se**, rather than the anti conformation, **19Sa**, because this allows the allyl group to assume the sterically preferred exo orientation and because the sulfur lone pair is correctly oriented for  $n \rightarrow \sigma^*$  overlap. Crich et al.'s<sup>23</sup> results do not provide a direct estimate of the preference for the *S<sub>S</sub>* diastereomer because the *R<sub>S</sub>* diastereomer ring inverts completely (as determined from <sup>3</sup>*J*<sub>H,H</sub> values) to the <sup>1</sup>C<sub>4</sub> chair. To compare relative stabilities of particular conformers of the *S<sub>S</sub>* and *R<sub>S</sub>* diastereomers, the same ring conformations must be employed. If the conformational preference for <sup>1</sup>C<sub>4</sub> over <sup>4</sup>C<sub>1</sub> is estimated at >9/1, the equilibration results for **19** correspond to  $\Delta G^\circ$  values of >1.9 and >0.8 kcal mol<sup>-1</sup> at 60 °C in benzene and methanol, respectively, in favor of the *S<sub>S</sub>* diastereomer in the <sup>4</sup>C<sub>1</sub> conformation. The value in benzene is in the same range as that calculated by DFT methods here (**11Segp** is calcu-

lated to be 2.4 kcal mol<sup>-1</sup> more stable than **11Ragp**), even though the C2 substituent is very different. Since the *S<sub>S</sub>* diastereomers are calculated to have somewhat larger dipole moments (3.3 vs 2.5 D for **18**, 3.5 vs 2.5 D for **11**), the decreased preference for this diastereomer in methanol is unexpected and may be due to specific solvation of the *R<sub>S</sub>* diastereomer as suggested by Crich et al.<sup>23</sup>

For compound **20**, the preferences for the *R<sub>S</sub>* diastereomer are 0.7 and 0.6 mol<sup>-1</sup> at 60 °C in benzene and methanol, respectively. Using the value estimated previously, this result indicates that the *R<sub>S</sub>* diastereomer is stabilized by >2.6 kcal mol<sup>-1</sup> when the equatorial 2-*O*-benzoyl group is converted to axial. Comparison of the calculated relative stabilities of the analogous 2-azido-2-deoxy diastereomers (**11**) with their 2-deoxy analogs (**15**) shows a similar 2.5 kcal mol<sup>-1</sup> relative stabilization of the *R<sub>S</sub>* diastereomer on removal of the equatorial 2-azido group. From these results, it is clear that the C2 configuration has a large effect on diastereomer stability.

It remains to be considered why the anti conformers of the *R<sub>S</sub>* sulfoxides are more stable relative to the exo conformers than expected based on normal<sup>23</sup> conformational arguments. It is very well established that glycosides and thioglycosides prefer exo-anomeric conformations. Several factors influence this preference:  $n \rightarrow \sigma^*$  overlap, dipole–



dipole repulsion, and reduced steric interactions and electrostatic attraction. Changing from a sulfide in the exo-anomeric conformation to the  $R_S$  sulfoxide results in the loss of the  $n \rightarrow \sigma^*$  overlap but adds a dipole in its most favorable arrangement with respect to the endocyclic C1–O5 dipole, namely, antiparallel. However, in **8Re** and **11Re**, it also adds a parallel dipole–dipole repulsive interaction between the S–O dipole and the C2–N dipole. As noted previously, the anti conformers have C2–C1–S–C7 torsional angles that are considerably greater than staggered, both in the presence and absence of electronegative substituents on C2. This deviation from perfect staggering has the effect of minimizing steric interactions at the expense of increasing dipole–dipole repulsion between the S–O bond and the endocyclic C–O bond. Clearly, the latter factor is less important than the former and any other interactions. It is interesting that the C7–S–O units in the anti conformers are close to being eclipsed by the H1–C1–C2 unit (see Fig. 13, **8Ra** and **11Ra**, and Fig. 12, **13Ra** and **15Ra**). If they were eclipsed, the sulfur lone pair would be syn to the C1–O5 bond. The C1–S bonds in the most stable **Ra** conformers, **8Ragp** and **13a**, are calculated to be almost as short as they are in the conformers having  $n \rightarrow \sigma^*$  overlap, **8Sepg** and **13Se**, which is consistent with an extra stabilizing interaction. This interaction is between orbitals of correct symmetry if the S lone pair that overlaps with the C1–O5  $\sigma^*$  orbital is a p-type lone pair. All of the other conformers are calculated to have C1–S bond lengths that are 0.02–0.05 Å longer (see Fig. 15). Based on a perturbation molecular orbital (MO) approach for dimethoxymethane,<sup>56</sup> Tvaroška and Bleha<sup>21</sup> have concluded that both the  $\sigma$  and  $\pi$  lone pairs on oxygen can overlap with the C–O  $\sigma^*$  orbital and both overlaps provide similar stabilization. The overlap advocated here is similar to the oxygen atom  $\pi \rightarrow \sigma^*$  overlap of that view.<sup>21</sup>

Comparison of the **Re** and **Se** conformers of the 2-deoxy derivatives allows an evaluation of the relative strengths of  $n \rightarrow \sigma^*$  overlap and adoption of antiparallel endocyclic C–O and S–O dipoles (see Fig. 12 for Newman projections of the relevant relationships). The **Re** conformers have antiparallel endocyclic C–O and S–O dipoles. The **Se** conformers adopt shapes with ideal geometries for  $n \rightarrow \sigma^*$  overlap but are presumably destabilized by gauche interactions between endocyclic C–O and S–O dipoles. For both the phenyl and methyl sulfoxides, the **Re** conformers are calculated to be slightly more stable, by 0.45 and 0.14 kcal mol<sup>−1</sup>, respectively, suggesting that the two interactions are comparable in magnitude.

### Equatorial glycosyl sulfoxides

Equatorial alkyl and aryl thioglycosides overwhelmingly adopt exo-anomeric conformations in the solid state (22 out of 25, see Table S1 in the Supplementary data), indicating that there is a strong thermodynamic preference for this conformation. The results of DFT (6–31G(d) B3LYP) calculations support this conclusion, since the anti conformations of both the thiophenyl and thiomethyl glycosides smoothly change geometry on minimization to the exo conformer, although this level of theory underestimates<sup>55</sup> the stabilizing effect of  $\pi$  stacking.

In contrast, ( $S_S$ ) phenyl 3,4,6-tri-*O*-acetyl-2-deoxy-2-phthalimido-1-thio- $\beta$ -D-glucopyranoside *S*-oxide (**18S**)

adopts the anti conformation about the glycosidic linkage in the solid state and the NMR evidence described in the Results section demonstrated conclusively that this conformation is the predominant one in solution. The near parallel alignment of the SPh and phthalimido groups suggests that  $\pi$  stacking contributes to the stabilization of this conformation.  $\pi$  Stacking was recently shown to influence the conformation about the glycosidic bond in a disaccharide.<sup>57</sup> Such interactions provide stabilizations on the order of 2.8 kcal mol<sup>−1</sup> for the most favorable displaced parallel geometries.<sup>55,58–61</sup> This factor is presumably very important in causing compound **18S** to adopt the anti conformation. It is notable that compound **18R**, which could also adopt a  $\pi$ -stacked conformation, clearly adopts the conformation favored by the exo-anomeric effect (as shown by its NMR spectra data) with the phenyl group exo and the lone pair on sulfur correctly aligned for  $n \rightarrow \sigma^*$  overlap with the C1–O5 antibonding orbital.

The DFT calculations for the glycosyl sulfoxides indicate that the exo conformers of both diastereomers are more stable in the gas phase. For the phenyl glycosyl sulfoxides, the differences are calculated to be 1.57 and 3.03 kcal mol<sup>−1</sup> for **18S** and **18R**, respectively. The **18R** exo conformer is stabilized by having the S lone pair anti to the ring C–O bond, which is geometry suitable for  $n \rightarrow \sigma^*$  overlap. This conformer is calculated to have the shortest C1–S bond length, 1.878 vs 1.885 Å for the **18S** exo conformer and >1.89 Å for the anti conformers, which is in agreement that this overlap is significant.

Even though the conformation adopted by the  $S_S$  diastereomer is not that predicted on the basis of the exo-anomeric effect, the <sup>13</sup>C NMR chemical shift of its carbon atom (89.1 ppm) was greater than that of the corresponding carbon atom of the  $R_S$  diastereomer (86.1 ppm), which is in agreement with the method for assignment of sulfoxide configuration proposed by Khair.<sup>26</sup>

### Conclusions

The evidence presented here shows that the most stable configurations of glycosyl sulfoxides are those that can adopt conformations with the aglycone exo and the lone pair on sulfur anti to the C1–O5 bond, because of the  $n \rightarrow \sigma^*$  overlap possible in this orientation. For D-pyranosides, these are the  $S_S$  configurations of the  $\alpha$ -anomers and the  $R_S$  configurations of the  $\beta$ -anomers. Equilibration studies by Crich et al.<sup>23</sup> are in agreement with the conclusions drawn here for glycosyl sulfoxides with substituents at C2 equatorial but indicate that the configuration at C2 has a major effect on glycosyl sulfoxide conformer stability. Electronegative substituents in equatorial orientations at C2 destabilize the conformation with the sulfoxide oxygen atom anti by about 2.5 kcal mol<sup>−1</sup>. The calculations indicate that  $n \rightarrow \sigma^*$  overlap and the preference for the endocyclic C–O dipole and the S–O to adopt antiparallel conformations have effects that are about equal in size in determining glycosyl sulfoxide conformations in the gas phase or nonpolar solvents. For the less stable but kinetically favoured  $R_S$  diastereomers of the  $\beta$ -anomers, anti conformers are comparable in stability to the exo conformers because of the  $n \rightarrow \sigma^*$  overlap possible if the sulfur lone pair is a p-type lone pair.

The method for assignment of glycosyl sulfoxide configurations by comparing the  $^{13}\text{C}$  NMR chemical shifts of C1 for the two diastereomers proposed by Khair<sup>26</sup> was supported by the chemical shifts calculated by the Gauge invariant atomic orbital (GIAO) method. However, the explanation advanced for the rule that C1 from the  $S_S$  sulfoxide is more shielded than that of the  $R_S$  sulfoxide, because of  $n \rightarrow \sigma^*$  overlap in the  $S_S$  sulfoxide, does not appear to be correct.

## Experimental section

### General methods

Melting points were determined with a Fisher-Johns melting point apparatus and are uncorrected.  $^1\text{H}$  and  $^{13}\text{C}$  NMR spectra were recorded at 300 K in 5 mm NMR tubes on Bruker NMR spectrometers (AC-250, AMX-400, or Avance-500) operating at 250.13, 400.13, or 500.13 MHz for proton spectra and 62.9, 100.08, or 125.77 MHz for carbon spectra, respectively, on solutions in chloroform- $d$ , unless otherwise indicated. Chemical shifts are given in parts per million (ppm;  $\pm 0.01$  ppm) relative to that of tetramethylsilane (TMS; 0.00 ppm) in the case of  $^1\text{H}$  NMR spectra and to the central line of chloroform- $d$  ( $\delta$  77.16) for the  $^{13}\text{C}$  NMR spectra. All assignments were confirmed by COSY, HETCOR, HMQC, HSQC, or HMBC experiments. Exact masses measured using electron ionization (EI; 70 eV) were done on a CEC 21-110B mass spectrometer. Electrospray mass spectra were recorded on a Fisons Quattro mass spectrometer with a Quattro source (cone voltage, 55 V; flow rate, 5  $\mu\text{L}/\text{min}$ ; complexing agent, potassium acetate; solvent, 75:25  $v/v$  acetonitrile/water). Optical rotations were determined with a Rudolph Instruments Digipol 781 automatic polarimeter or with a PerkinElmer model 141 polarimeter. Thin layer chromatography (TLC) was performed on aluminum-backed plates bearing 200  $\mu\text{m}$  silica gel 60 F<sub>254</sub> (Merck or Silicycle). The ratio of the solvents used in TLC and column chromatography was a volume ratio. Compounds were visualized by UV where applicable and (or) were located by spraying with a solution of 2% ceric sulfate in 1 mol/L sulfuric acid followed by heating on a hot plate until colour developed. Compounds were purified on silica gel (TLC standard grade, 230–400 mesh) by flash chromatography using specified eluents. Elemental analyses were performed by the Canadian Microanalytical Service, Delta, British Columbia.

Pyridine was dried by refluxing over calcium hydride followed by distillation and stored over molecular sieves. Amberlite IR-120 ( $\text{H}^+$ ) resin was washed with a 10% hydrochloric acid solution and distilled water, and then dried under vacuum at 50  $^\circ\text{C}$  overnight. Ammonium cerium (IV) nitrate and sodium azide were ground to powders and dried in vacuo for 2 days. Boron trifluoride diethyl etherate was distilled before use.

### X-ray crystallography

Crystals for X-ray structural determinations were mounted on glass fibers. All measurements were made on a Rigaku AFC5R diffractometer equipped with graphite-monochromated Mo  $K\alpha$  radiation (**6**, **8R**, **8S**, and **9R**) or Cu  $K\alpha$  radiation (**18S**) and a rotating anode generator. Cell constants and an orientation matrix for data collection were obtained from a

least-squares refinement using the setting angles of a minimum of 24 reflections (with the exception of **12R** where only 10 reflections were obtained). The data were collected at temperatures of 23  $^\circ\text{C}$  (**8S** and **18S**),  $-100$   $^\circ\text{C}$  (**6** and **9R**), or  $-130$   $^\circ\text{C}$  (**8R**) using the  $\omega$ - $2\theta$  scan technique. The intensities of three representative reflections were measured after every 150 reflections; no decay corrections were applied. An empirical absorption correction<sup>62</sup> based on azimuthal scans of several reflections was applied for every structure except **9R**. The data were corrected for Lorentz and polarization effects. Data reduction was carried out using the TEXSAN software package.<sup>63</sup> The structures were solved by direct methods using SIR-92.<sup>64,65</sup> Full-matrix least-squares refinement was carried out on  $F^2$  data using SHELXL-97.<sup>66</sup> Secondary extinction was refined for **18S**. In all cases, the non-hydrogen atoms were refined anisotropically. Hydrogen atoms were included but not refined. They were placed in geometrically calculated positions and allowed to ride on the heavy atom to which they were bonded with isotropic temperature factors ( $U_{\text{iso}}$ ) equal to 1.2 times  $U_{\text{eq}}$  of the heavy atom (1.5 times  $U_{\text{eq}}$  for methyl hydrogens).

### NMR experiments

Experiments were performed on 0.04 mol/L solutions in acetone- $d_6$  unless otherwise specified. NOESY spectra were recorded on the Bruker Avance 500 MHz NMR spectrometer using different mixing times. Spectra were processed with Bruker's XWIN-NMR package. The matrices were transformed to a final size of 8192 and 2048 points in F2 and F1 dimensions, respectively. The signal was multiplied by a shifted qsin bell window in both dimensions prior to Fourier transformation, then phase and baseline corrections on both dimensions were applied. The numbers of contour layers were set at 18. For compound **6**, spectra were recorded with a relaxation delay of 1 s with mixing times of 0.3, 0.5, 0.7, 1, and 1.5 s. For **8R**, spectra were recorded with a relaxation delay of 2.5 s and mixing times of 0.5, 0.7, 0.9, 1.1, and 1.3 s. For compound **9R**, spectra were recorded with a relaxation delay of 1 s and mixing times of 0.3, 0.5, 0.7, 1, and 1.5 s.

Relaxation times were determined for compounds **6** and **8R** by the inversion recovery method to set the relaxation delays for the 1D NOE experiments. The t1ir pulse program on the 500 MHz NMR spectrometer was used to acquire data and the proc\_t1 program was used to process data. The results are shown in Table S4 in the Supplementary data. Based on these results, the delay time used for 1D gradient NOE experiments was set at 10 s. The selnpg pulse sequence was used for 1D gradient NOE experiments. For compounds **6**, **8R**, and **8S**, the signals of H-SPo were irradiated and mixing times of 0.3, 0.5, 0.75, 0.9, 1, 1.1, and 1.25 s; 0.3, 0.9, 1.25, 1.5, 1.75, and 2.25 s; and 0.5, 0.75, 1, 1.25, 1.5, 1.75, 2, 2.25, 2.5, and 3 s, respectively, were used.

The distance between ortho phenyl protons ( $r = 2.8$  Å) was used as the reference distance to calculate internuclear distances using the equation

$$r_{\text{IS}} = r_{\text{ref}} \left( \frac{\text{NOE}_{\text{ref}}}{\text{NOE}_{\text{IS}}} \right)^{1/6}$$

## Computational methods

Most geometry optimizations were carried out at the B3LYP hybrid density functional in conjunction with the B3LYP/6–31G(d) basis set using the Gaussian 03 suite of programs.<sup>52</sup> The B3LYP functional is a combination of Becke's three-parameter hybrid exchange functional and Lee–Yang–Parr correlational functional.<sup>53,54</sup> Harmonic vibrational frequencies and zero-point vibrational energies (ZPVEs) were obtained at the same level of theory. Relative energies were obtained by performing single-point calculations at the B3LYP level of theory with the 6–311G+(d,p) basis set using the above optimized geometries and by including the zero-point vibrational energy, i.e., B3LYP/6–311G+(d,p)/B3LYP/6–31G(d) + ZPVE. Compounds **12–15** were also optimized at the 6–311G+(d,p) level of theory. The GIAO method was used for <sup>13</sup>C shielding calculations using the 6–311+G(d,p) basis set.

## Synthetic procedures

### Phenyl 2-azido-2-deoxy-1-thio- $\alpha$ -D-galactopyranoside (**1**) and phenyl 2-azido-2-deoxy-1-thio- $\beta$ -D-galactopyranoside (**2**)

Freshly distilled boron trifluoride diethyl etherate (19 mL, 151.3 mmol, 5.6 equiv) was added dropwise to a stirred clear colorless solution of thiophenol (14 mL, 136.0 mmol, 5 equiv) and 2-azido-2-deoxy-1,3,4,6-tetra-*O*-acetyl- $\alpha$ -D-galactopyranoside<sup>37</sup> (10.07 g, 27.0 mmol) in chloroform (175 mL) at 0 °C. The reaction mixture was stirred at room temperature (RT) for 24 h. The clear orange solution was washed with saturated sodium bicarbonate aqueous solution (3 × 30 mL) and distilled water (3 × 30 mL), dried (anhydrous sodium sulphate), filtered, and concentrated to give a yellow syrup, phenyl 3,4,6-tetra-*O*-acetyl-2-azido-2-deoxy-1-thio-*O*-acetyl-D-galactopyranoside.

The yellow syrup was taken up in methanol (100 mL) and a solution of sodium methoxide in methanol (100 mL, 1.2 mol/L) was added. The basic solution was stirred for 1 h, neutralized by Amberlite IR-120 (H<sup>+</sup>), filtered, and concentrated to a yellow syrup, phenyl 2-azido-2-deoxy-1-thio-D-galactopyranoside. The  $\alpha$ - $\beta$  mixture was separated by column chromatography (ethyl acetate–hexanes, 10:1). The pure anomers were crystallized from ethanol–hexanes.

#### $\alpha$ -Isomer (**1**)

Colorless needles; yield: 3.21 g (40%); mp 130.0–133.0 °C.  $[\alpha]_{\text{D}}^{25} +252.2^\circ$  (*c* 1.3, ethanol).  $R_f = 0.34$ . <sup>1</sup>H NMR (acetone-*d*<sub>6</sub>)  $\delta$ : 7.58–7.29 (m, 5H, Ph), 5.67 (d, 1H,  $J_{1,2} = 5.4$  Hz, H-1), 4.47 (d, 1H,  $J_{3,\text{OH}} = 7.1$  Hz, OH-3), 4.31 (t, 1H, H-5), 4.17 (dd, 1H,  $J_{2,3} = 10.5$  Hz, H-2), 4.15 (d, 1H,  $J_{4,\text{OH}} = 3.7$  Hz, OH-4), 4.09 (ddd, 1H,  $J_{3,4} = 3.4$  Hz,  $J_{4,5} = 1.3$  Hz, H-4), 3.84 (ddd, 1H, H-3), 3.79–3.69 (m, 3H, 2 × H-6, OH-6). <sup>13</sup>C NMR (acetone-*d*<sub>6</sub>)  $\delta$ : 135.4, 133.1, 129.9, 128.2 (Ph), 88.8 (C-1), 73.2 (C-5), 71.1 (C-3), 70.0 (C-4), 62.1 (C-6), 62.0 (C-2). HR-MS (EI, *m/z*) calcd. for [C<sub>12</sub>H<sub>15</sub>N<sub>3</sub>O<sub>4</sub>S]<sup>+</sup>: 297.0783; found: 297.0793.

#### $\beta$ -Isomer (**2**)

Colorless needles; yield: 3.09 g (39%); mp 149.0–149.5 °C.  $[\alpha]_{\text{D}}^{25} +24.0^\circ$  (*c* 0.3, ethanol).  $R_f = 0.26$ . <sup>1</sup>H NMR (acetone-*d*<sub>6</sub>)  $\delta$ : 7.58–7.29 (m, 5H, aromatic protons), 4.60 (d,

1H,  $J_{1,2} = 10.0$  Hz, H-1), 4.53 (d, 1H,  $J_{3,\text{OH}} = 7.3$  Hz, OH-3), 4.05 (d, 1H,  $J_{4,\text{OH}} = 4.1$  Hz, OH-4), 3.98 (dd, 1H,  $J_{3,4} = 3.2$  Hz,  $J_{4,5} < 1$  Hz, H-4), 3.90 (dd, 1H,  $J_{6,\text{OH}} = 6.8$  Hz,  $J_{6',\text{OH}} = 6.6$  Hz, OH-6), 3.79 (m, 2H, H6 and H6'), 3.68 (ddd, 1H,  $J_{2,3} = 10.5$  Hz, H-3), 3.65 (dd, 1H,  $J_{5,6} = 6.6$  Hz,  $J_{5,6'} = 3.9$  Hz, H-5), 3.57 (dd, 1H, H-2). <sup>13</sup>C NMR (acetone-*d*<sub>6</sub>)  $\delta$ : 132.5, 129.8, 128.3 (Ph), 86.8 (C-1), 80.1 (C-5), 74.9 (C-3), 69.3 (C-4), 64.2 (C-2), 62.2 (C-6). HR-MS (EI, *m/z*) calcd. for [C<sub>12</sub>H<sub>15</sub>N<sub>3</sub>O<sub>4</sub>S]<sup>+</sup>: 297.0783; found: 297.0794.

### Phenyl 2-azido-4,6-*O*-benzylidene-2-deoxy-1-thio- $\alpha$ -D-galactopyranoside (**3**)

A solution of compound **1** (2.98 g, 10.0 mmol), *p*-methoxybenzoic acid (0.10 g), and benzaldehyde (5 mL, 50.0 mmol, 5 equiv) in DMF–benzene (100 mL, 3:2 v/v) was refluxed in an apparatus for the azeotropic removal of water for 15 h. After TLC showed complete disappearance of the starting material, the reaction mixture was cooled to RT, neutralized with anhydrous potassium carbonate (1.00 g), filtered, and concentrated to yield an orange syrup, which was purified by flash column chromatography. Crystallization from ethanol–hexanes gave the title compound (**3**) as colorless needles; yield: 3.50 g (91%); mp 114.5–115.5 °C.  $[\alpha]_{\text{D}}^{23} +157.7^\circ$  (*c* 0.8, CHCl<sub>3</sub>); lit. value<sup>38</sup>  $[\alpha]_{\text{D}} +134.9^\circ$  (*c* 0.5, CHCl<sub>3</sub>).  $R_f = 0.35$  (ethyl acetate–hexanes 1:3). <sup>1</sup>H NMR  $\delta$ : 7.48–7.28 (m, 10H, Ph), 5.76 (d, 1H,  $J_{1,2} = 5.3$  Hz, H-1), 5.62 (s, 1H, CHPh), 4.34 (dd, 1H,  $J_{3,4} = 3.4$  Hz,  $J_{4,5} = 0.8$  Hz, H-4), 4.27 (bs, 1H, H-5), 4.26 (dd, 1H,  $J_{5,6a} = 1.6$  Hz,  $J_{6a,6e} = 12.5$  Hz, H-6a), 4.21 (dd, 1H,  $J_{2,3} = 10.5$  Hz, H-2), 4.16 (dd, 1H,  $J_{5,6e} = 1.5$  Hz, H-6e), 4.03 (ddd, 1H,  $J_{3,\text{OH}} = 10.4$  Hz, H-3), 2.54 (d, 1H, 3-OH). <sup>13</sup>C NMR  $\delta$ : 137.2, 137.7, 131.2, 129.5, 129.2, 128.4, 127.5, 126.2 (Ph), 101.4 (CHPh), 87.4 (C-1), 75.2 (C-4), 69.6 (C-3), 69.2 (C-6), 63.7 (C-5), 61.5 (C-2). HR-MS (EI, *m/z*) calcd. for [C<sub>19</sub>H<sub>19</sub>N<sub>3</sub>O<sub>4</sub>S]<sup>+</sup>: 385.1096; found: 385.1107.

### Phenyl 2-azido-4,6-*O*-benzylidene-2-deoxy-1-thio- $\beta$ -D-galactopyranoside (**4**)

Following the same procedure as in the preparation of compound **3**, compound **4** (3.21 g, 10.8 mmol) gave the title compound as colorless needles; yield: 3.70 g (89%); mp 79.0–80.0 °C.  $[\alpha]_{\text{D}}^{20} -23.0^\circ$  (*c* 0.5, CHCl<sub>3</sub>).  $R_f = 0.4$  (ethyl acetate–hexanes, 1:1). <sup>1</sup>H NMR (500 MHz)  $\delta$ : 7.79–7.33 (m, 10H, Ph), 5.58 (s, 1H, CHPh), 4.47 (d, 1H,  $J_{1,2} = 9.8$  Hz, H-1), 4.46 (dd, 1H,  $J_{5,6a} = 1.2$  Hz, H-6a), 4.24 (d, 1H,  $J_{3,4} = 3.5$  Hz, 1H, H-4), 4.09 (dd, 1H,  $J_{5,6e} = 1.4$  Hz,  $J_{6a,6e} = 12.5$  Hz, H-6e), 3.70 (ddd, 1H,  $J_{2,3} = 9.7$  Hz,  $J_{\text{OH},3} = 9.8$  Hz, H-3), 3.58 (dd, 1H, H-2), 3.57 (bs, 1H, H-5), 2.55 (d, 1H, 3-OH). <sup>1</sup>H NMR (acetone-*d*<sub>6</sub>, 500 MHz)  $\delta$ : 7.74–7.31 (m, 10H, Ph), 5.68 (s, CHPh), 4.68 (d, 1H,  $J_{1,2} = 9.9$  Hz, H-1), 4.58 (d, 1H,  $J_{\text{OH},3} = 8.8$  Hz, 3-OH), 4.33 (d, 1H,  $J_{3,4} = 2.7$  Hz, 1H, H-4), 4.27 (dd, 1H,  $J_{5,6a} = 1.4$  Hz,  $J_{6a,6e} = 12.2$  Hz, H-6a), 4.18 (dd, 1H,  $J_{5,6e} = 1.6$  Hz, H-6e), 3.81 (ddd, 1H,  $J_{2,3} = 9.7$  Hz, H-3), 3.79 (bs, 1H, H-5), 3.69 (d, 1H, H-2). <sup>13</sup>C NMR  $\delta$ : 137.4, 134.3, 130.4, 129.5, 129.0, 128.5, 128.3, 126.5 (Ph), 101.5 (CHPh), 85.2 (C-1), 74.5 (C-4), 73.3 (C-3), 69.9 (C-5), 69.3 (C-6), 62.2 (C-2). <sup>13</sup>C NMR (acetone-*d*<sub>6</sub>)  $\delta$ : 139.0, 133.1, 132.1, 129.0, 128.8, 128.0, 127.9, 126.7 (Ph), 100.9 (CHPh), 84.9 (C-1), 75.5 (C-4),



73.0 (C-3), 70.1 (C-5), 69.1 (C-6), 62.5 (C-2). HR-MS (EI,  $m/z$ ) calcd. for  $[C_{19}H_{19}N_3O_4S]^+$ : 385.1096; found: 385.1088.

**Phenyl 2-azido-2-deoxy-4,6-O-(*p*-methoxybenzylidene)-1-thio- $\alpha$ -D-galactopyranoside (5)**

A solution of compound **1** (0.97 g, 3.26 mmol), *p*-anisaldehyde (3.2 mL), and *p*-toluenesulfonic acid (80.0 mg) in DMF–benzene (65 mL, 3:2) was refluxed for 45 h in an apparatus for the azeotropic removal of water. After TLC showed that the starting material had disappeared, the reaction mixture was cooled to RT, neutralized by anhydrous potassium carbonate (1.00 g), filtered, and concentrated to a brown syrup. Purification by column chromatography (ethyl acetate–hexanes, 1:3) gave a colorless solid that crystallized from ethanol–hexanes as colorless needles; yield: 1.18 g (87%); mp 133.5–134.0 °C.  $[\alpha]_D^{23} +89.1^\circ$  (*c* 0.5, chloroform).  $R_f = 0.43$  (ethyl acetate–hexanes, 1:2).  $^1H$  NMR  $\delta$ : 7.48–7.26 (m, 8H, Ph), 6.91 (d, 1H, Ph), 5.76 (d, 1H,  $J_{1,2} = 5.3$  Hz, H-1), 5.58 (s, 1H, CHPh), 4.32 (bd, 1H,  $J_{3,4} = 3.5$  Hz, H-4), 4.26 (bs, 1H, H-5), 4.24 (bd, 1H, H-6a), 4.20 (dd, 1H,  $J_{2,3} = 10.6$  Hz, H-2), 4.12 (dd, 1H,  $J_{5,6a} = 1.5$  Hz,  $J_{6a,6b} = 12.3$  Hz, H-6b), 4.03 (ddd, 1H,  $J_{3,OH} = 10.4$  Hz, H-3), 2.55 (d, 1H, 3-OH).  $^{13}C$  NMR  $\delta$ : 160.5, 133.7, 129.7 (tertiary aromatic carbons), 131.2, 129.2, 127.7, 127.5, 113.7 (Ph), 101.4 (CHPh), 87.3 (C-1), 75.1 (C-4), 69.6 (C-3), 69.2 (C-6), 63.7 (C-5), 61.5 (C-2), 55.4 (OCH<sub>3</sub>).

**Phenyl 3-O-acetyl-2-azido-4,6-O-benzylidene-2-deoxy-1-thio- $\alpha$ -D-galactopyranoside (6)**

Acetic anhydride (1.5 mL, 97%, 15.0 mmol, 5 equiv) was added to a solution of compound **3** (1.15 g, 2.98 mmol) in dry pyridine (10 mL). The reaction mixture was stirred at RT for 24 h, and then concentrated under vacuum to give a colorless syrup. The syrup was dissolved in chloroform (15 mL). The solution was washed with saturated sodium bicarbonate aqueous solution (3 mL) and distilled water (3 mL), dried over sodium sulphate anhydrous, filtered, and concentrated to yield a colorless syrup. The syrup was crystallized from diethyl ether to give a colorless solid and recrystallized from ethanol–chloroform as colorless needles; yield: 1.20 g (94%); mp 154.5–155.5 °C.  $[\alpha] +198.9^\circ$  (*c* 0.6, CHCl<sub>3</sub>).  $^1H$  NMR  $\delta$ : 7.50–7.24 (m, 10H, Ph), 5.81 (d, 1H,  $J_{1,2} = 5.3$  Hz, H-1), 5.56 (s, 1H, CHPh), 5.13 (dd, 1H,  $J_{2,3} = 11.0$  Hz,  $J_{3,4} = 3.4$  Hz, H-3), 4.57 (dd, 1H, H-2), 4.53 (d, 1H, H-4), 4.26 (bs, 1H, H-5), 4.22 (dd, 1H,  $J_{5,6a} = 1.4$  Hz,  $J_{6a,6e} = 12.6$  Hz, H-6a), 4.09 (dd, 1H,  $J_{5,6e} = 1.7$  Hz, H-6e), 2.16 (s, 3H, COCH<sub>3</sub>).  $^{13}C$  NMR (acetone-*d*<sub>6</sub>)  $\delta$ : 170.6 (C=O), 139.5, 134.5, 132.9, 129.3, 128.9, 128.5, 127.3 (Ph), 101.4 (CHPh), 88.3 (C-1), 74.2 (C-4), 71.5 (C-3), 69.6 (C-6), 64.7 (C-5), 59.0 (C-2), 20.8 (COCH<sub>3</sub>). HR-MS (EI,  $m/z$ ) calcd. for  $[C_{21}H_{21}N_3O_5S]^+$ : 427.1202; found: 427.1202.

**Phenyl 3-O-acetyl-2-azido-2-deoxy-4,6-O-(*p*-methoxybenzylidene)-1-thio- $\alpha$ -D-galactopyranoside (7)**

Acetic anhydride (2 mL, 97%, 20.0 mmol) was added to a solution of compound **5** (1.18 g, 2.84 mmol) in dry pyridine (10 mL) and the reaction mixture was stirred at RT for 16 h, and was then concentrated under vacuum to give a orange syrup that was azeotroped with toluene (3  $\times$  4 mL) to give a yellow solid that on crystallization from ethanol, appeared

as colorless needles; yield: 1.26 g (97%); mp 138.5–140.0 °C.  $[\alpha] +206.2^\circ$  (*c* 0.6, CHCl<sub>3</sub>).  $R_f = 0.33$  (ethyl acetate–hexanes, 1:3).  $^1H$  NMR  $\delta$ : 7.50–6.88 (m, 9H, Ph), 5.80 (d, 1H,  $J_{1,2} = 5.5$  Hz, H-1), 5.51 (s, 1H, CHPh), 5.12 (dd, 1H,  $J_{2,3} = 11.0$  Hz,  $J_{3,4} = 3.1$  Hz, H-3), 4.57 (dd, 1H, H-2), 4.50 (d, 1H, H-4), 4.24 (bs, 1H, H-5), 4.20 (dd, 1H,  $J_{5,6a} = 1.4$  Hz,  $J_{6a,6b} = 12.8$  Hz, H-6a), 4.07 (dd, 1H,  $J_{5,6b} = 1.5$  Hz, H-6b), 3.81 (s, 3H, OCH<sub>3</sub>), 2.16 (s, 3H, COCH<sub>3</sub>).  $^{13}C$  NMR  $\delta$ : 170.3 (C=O), 160.2, 133.4, 130.0 (tertiary aromatic carbons), 131.3, 129.1, 127.5, 113.6 (Ph), 100.9 (CHPh), 87.3 (C-1), 73.1 (C-4), 71.4 (C-3), 69.1 (C-6), 63.4 (C-5), 57.8 (C-2), 55.3 (OCH<sub>3</sub>), 20.95 (COCH<sub>3</sub>).

**(*R*<sub>S</sub>) Phenyl 2-azido-4,6-O-benzylidene-2-deoxy-1-thio- $\alpha$ -D-galactopyranoside S-oxide (8*R*) and (*S*<sub>S</sub>) phenyl 2-azido-4,6-O-benzylidene-2-deoxy-1-thio- $\alpha$ -D-galactopyranoside S-oxide (8*S*)**

A solution of *m*-chloroperbenzoic acid (0.22 g, 77%, 1.02 mmol, 1.1 equiv) in dichloromethane (2 mL) was added to a mixture of compound **6** (0.40 g, 0.93 mmol) and sodium bicarbonate (0.10 g, 1.21 mmol, 1.3 equiv) in dichloromethane (8 mL) at –76 °C. The reaction mixture was stirred at –76 °C for 16 h. The reaction mixture was allowed to warm to RT and then diluted with dichloromethane (10 mL). The mixture was washed with 20% sodium thiosulfate (5 mL), saturated aqueous sodium bicarbonate solution (5 mL), and distilled water (5 mL), and then dried (sodium sulphate), filtered, and concentrated to give a colorless solid. Fractionation by column chromatography (ethyl acetate–hexanes, 1:2) yielded three compounds.

Compound **8*R*** was crystallized from ethanol–chloroform; yield: 247.5 mg (60%); mp 191.5–192.5 °C.  $[\alpha]_D^{22} +34.6^\circ$  (*c* 0.4, CHCl<sub>3</sub>).  $R_f = 0.20$ .  $^1H$  NMR (500 MHz)  $\delta$ : 7.54 (m, 2H, Ho-SPh), 7.45 (m, 3H, Hp-SPh and Hm-SPh), 7.36 (m, 5H, Ho-CHPh, Hm-CHPh, and Hp-CHPh), 5.78 (dd, 1H,  $J_{2,3} = 10.8$  Hz,  $J_{3,4} = 3.4$  Hz, H-3), 5.53 (s, 1H, CHPh), 4.95 (s, 1H,  $J_{1,2} = 5.7$  Hz, H-1), 4.65 (dd, 1H, H-2), 4.62 (d, 1H, H-4), 4.11 (bs, 1H, H-5), 4.14 (dd, 1H,  $J_{5,6e} = 1.5$  Hz, H-6e), 4.02 (dd, 1H,  $J_{5,6a} = 2.2$  Hz,  $J_{6a,6e} = 12.3$  Hz, H-6a), 2.16 (s, 3H, COCH<sub>3</sub>).  $^1H$  NMR (acetone-*d*<sub>6</sub>, 500 MHz)  $\delta$ : 7.86 (d, 2H, Ho-SPh), 7.65 (t, 2H, Hm-SPh), 7.60 (t, 2H, Hp-SPh), 7.51 (m, 2H, Ho-CHPh), 7.39 (m, 3H, Hm-CHPh and Hp-CHPh), 5.85 (dd, 1H,  $J_{2,3} = 11.0$  Hz,  $J_{3,4} = 3.5$  Hz, H-3), 5.69 (s, 1H, CHPh), 5.15 (d, 1H,  $J_{1,2} = 6.6$  Hz, H-1), 4.78 (dd, 1H, H-2), 4.66 (d, 1H, H-4), 4.32 (bs, 1H, H-5), 4.21 (dd, 1H,  $J_{5,6a} = 1.5$  Hz,  $J_{6a,6e} = 12.7$  Hz, H-6a), 4.09 (dd, 1H,  $J_{5,6e} = 1.5$  Hz, H-6a), 2.12 (s, 3H, COCH<sub>3</sub>).  $^1H$  NMR (CD<sub>2</sub>Cl<sub>2</sub>, 500 MHz)  $\delta$ : 7.77 (m, 2H, Ho-SPh), 7.63 (m, 2H, Hm-SPh), 7.61 (t, 2H, Hp-SPh), 7.50 (m, 2H, Ho-CHPh), 7.43 (m, 3H, Hm-CHPh and Hp-CHPh), 5.86 (dd, 1H,  $J_{2,3} = 10.8$  Hz,  $J_{3,4} = 3.5$  Hz, H-3), 5.58 (s, 1H, CHPh), 5.01 (d, 1H,  $J_{1,2} = 5.6$  Hz, H-1), 4.67 (dd, 1H, H-2), 4.61 (d, 1H, H-4), 4.20 (bs, 1H, H-5), 4.15 (dd, 1H,  $J_{5,6a} = 1.6$  Hz,  $J_{6a,6e} = 12.8$  Hz, H-6a), 4.07 (dd, 1H,  $J_{5,6e} = 1.6$  Hz, H-6a), 2.19 (s, 3H, COCH<sub>3</sub>).  $^1H$  NMR (CD<sub>3</sub>CN, 500 MHz)  $\delta$ : 7.80 (m, 2H, Ho-SPh), 7.63 (m, 3H, Hm-SPh and Hp-SPh), 7.48 (m, 2H, Ho-CHPh), 7.42 (m, 3H, Hm-CHPh and Hp-CHPh), 5.78 (dd, 1H,  $J_{2,3} = 11.0$  Hz,  $J_{3,4} = 3.4$  Hz, H-3), 5.61 (s, 1H, CHPh), 5.07 (d, 1H,  $J_{1,2} = 5.6$  Hz, H-1), 4.70 (dd, 1H, H-2),



4.54 (d, 1H, H-4), 4.14 (bs, 1H, H-5), 4.05 (dd, 1H,  $J_{5,6a} = 1.4$  Hz,  $J_{6a,6e} = 12.9$  Hz, H-6a), 3.95 (dd, 1H,  $J_{5,6e} = 1.4$  Hz, H-6a), 2.17 (s, 3H, COCH<sub>3</sub>). <sup>13</sup>C NMR  $\delta$ : 170.1 (C=O), 141.3, 137.2, 131.3, 129.2, 129.2, 128.3, 126.0, 124.8 (Ph), 100.7 (CHPh), 96.3 (C-1), 72.7 (C-4), 70.2 (C-3), 68.9 (C-6), 67.6 (C-5), 57.9 (C-2), 20.9 (COCH<sub>3</sub>). HR-MS (EI,  $m/z$ ) calcd. for [C<sub>21</sub>H<sub>21</sub>N<sub>3</sub>O<sub>6</sub>S - N<sub>2</sub>]<sup>+</sup>: 415.1089; found: 415.1096.

Compound **8S** was crystallized from ethanol–chloroform; yield: 82.1 mg (20%); mp 197.5–198.5 °C.  $[\alpha]_D^{23} +367.7^\circ$  (c 0.6, CHCl<sub>3</sub>).  $R_f = 0.45$ . <sup>1</sup>H NMR (500 MHz)  $\delta$ : 7.63 (d, 2H, *Ho*-SPh), 7.55 (t, 1H, *Hp*-SPh), 7.52 (t, 2H, *Hm*-SPh), 7.43 (m, 2H, *Ho*-CHPh), 7.35 (m, 3H, *Hm*-CHPh and *Hp*-CHPh), 5.94 (dd, 1H,  $J_{2,3} = 10.9$  Hz,  $J_{3,4} = 3.3$  Hz, H-3), 5.49 (s, 1H, CHPh), 4.90 (s, 1H, H-5), 4.76 (dd, 1H,  $J_{1,2} = 6.6$  Hz, H-2), 4.61 (d, 1H, H-4), 4.56 (d, 1H, H-1), 4.01 (dd, 1H,  $J_{5,6e} = 1.4$  Hz,  $J_{6a,6e} = 12.9$  Hz, H-6e), 3.90 (dd, 1H,  $J_{5,6a} = 1.3$  Hz, H-6a), 2.12 (s, 3H, COCH<sub>3</sub>). <sup>1</sup>H NMR (acetone-*d*<sub>6</sub>, 500 MHz)  $\delta$ : 7.78 (d, 2H, *Ho*-SPh), 7.67 (t, 2H, *Hm*-SPh), 7.62 (t, 2H, *Hp*-SPh), 7.48 (m, 2H, *Ho*-CHPh), 7.37 (t, 3H, *Hm*-CHPh and *Hp*-CHPh), 6.02 (m, 1H, H-3), 5.64 (s, 1H, CHPh), 4.92–4.89 (m, 3H, H-1, H-2, H-5), 4.63 (d, 1H,  $J_{3,4} = 2.5$  Hz, H-4), 4.07 (dd, 1H,  $J_{5,6e} = 1.3$  Hz,  $J_{6a,6e} = 12.8$  Hz, H-6e), 3.85 (dd, 1H,  $J_{5,6a} = 1.4$  Hz, H-6a), 2.12 (s, 3H COCH<sub>3</sub>). <sup>13</sup>C NMR  $\delta$ : 170.0 (C=O), 140.5, 137.3, 131.1, 129.2, 129.1, 128.2, 126.0, 124.7 (Ph), 100.7 (CHPh), 92.5 (C-1), 73.0 (C-4), 71.2 (C-3), 68.8 (C-4), 68.7 (C-6), 57.3 (C-2), 21.0 (COCH<sub>3</sub>). <sup>13</sup>C NMR (acetone-*d*<sub>6</sub>)  $\delta$ : 169.6 (C=O), 141.4, 138.7, 130.9, 129.8, 128.8, 128.0, 126.4, 125.0 (Ph), 100.4 (CHPh), 92.4 (C-1), 73.2 (C-4), 70.4 (C-3), 69.1 (C-5), 68.4 (C-6), 58.2 (C-2), 20.1 (COCH<sub>3</sub>). MS (ESI,  $m/z$ ) calcd. for [C<sub>21</sub>H<sub>21</sub>N<sub>3</sub>O<sub>6</sub>S + Na]<sup>+</sup>: 466.0; found: 466.0. HR-MS (EI,  $m/z$ ) calcd. for [C<sub>21</sub>H<sub>21</sub>N<sub>3</sub>O<sub>6</sub>S - C<sub>6</sub>H<sub>5</sub>OS]<sup>+</sup>: 318.1090; found: 318.1098.

The third fraction was phenyl 2-azido-4,6-*O*-benzylidene-2-deoxy-1-thio- $\alpha$ -D-galactopyranoside dioxide; yield: 46.8 mg (11%); mp 183.0–184.0 °C.  $[\alpha]_D^{23} +131.4^\circ$  (c 0.4, CHCl<sub>3</sub>).  $R_f = 0.42$ . <sup>1</sup>H NMR (acetone-*d*<sub>6</sub>, 500 MHz)  $\delta$ : 8.04 (d, 2H, *o*-SPh), 7.82 (t, 1H, *p*-SPh), 7.73 (t, 2H, *m*-SPh), 7.41 (d, 2H,  $J = 7.1$  Hz, *o*-Ph), 6.92 (d, 2H, *m*-Ph), 5.85 (dd, 1H,  $J_{2,3} = 11.3$  Hz,  $J_{3,4} = 3.4$  Hz, H-3), 5.63 (s, 1H, CHPh), 5.55 (d, 1H,  $J_{1,2} = 6.0$  Hz, H-1), 4.83 (dd, 1H, H-2), 4.64 (bs, 1H, H-4), 4.41 (bs, 1H, H-5), 4.16 (d, 1H,  $J_{6a,6e} = 12.4$  Hz, H-6a), 3.89 (d, 1H, H-6e), 3.82 (s, 3H, OCH<sub>3</sub>), 2.83 (s, 3H, COCH<sub>3</sub>). <sup>1</sup>H NMR (500 MHz)  $\delta$ : 7.92 (d, 2H, *o*-SPh), 7.68 (t, 1H, *p*-SPh), 7.58 (t, 2H, *m*-SPh), 7.44–7.35 (m, 4H, Ph), 5.87 (dd, 1H,  $J_{2,3} = 11.1$  Hz,  $J_{3,4} = 3.4$  Hz, H-3), 5.52 (s, 1H, CHPh), 5.13 (d, 1H,  $J_{1,2} = 6.3$  Hz, H-1), 4.66 (dd, 1H, H-2), 4.64 (bs, 1H, H-4), 4.35 (bs, 1H, H-5), 4.06 (d, 1H,  $J_{5,6a} = 1.3$  Hz,  $J_{6a,6e} = 12.8$  Hz, H-6a), 3.99 (d, 1H,  $J_{5,6e} = 1.2$  Hz, H-6e), 3.82 (s, 3H, OCH<sub>3</sub>), 2.17 (s, 3H, COCH<sub>3</sub>). <sup>13</sup>C NMR  $\delta$ : 170.1 (C=O), 138.8, 137.3, 134.4, 129.4, 128.9, 128.4, 126.1 (Ph), 100.9 (CHPh), 89.9 (C-1), 72.7 (C-4), 69.9 (C-3), 68.9 (C-6), 67.1 (C-5), 56.3 (C-2), 21.1 (COCH<sub>3</sub>). MS (ESI,  $m/z$ ) calcd. for [C<sub>21</sub>H<sub>21</sub>N<sub>3</sub>O<sub>7</sub>S + Na]<sup>+</sup>: 482.0; found: 482.0. HR-MS (EI,  $m/z$ ) calcd. for [C<sub>21</sub>H<sub>21</sub>N<sub>3</sub>O<sub>7</sub>S - C<sub>6</sub>H<sub>5</sub>O<sub>2</sub>S]<sup>+</sup>: 318.1090; found: 318.1092.

**(R<sub>S</sub>) Phenyl 3-*O*-acetyl-2-azido-2-deoxy-4,6-*O*-(*p*-methoxybenzylidene)-1-thio- $\alpha$ -D-galactopyranoside S-oxide (9R) and (S<sub>S</sub>) phenyl 3-*O*-acetyl-2-azido-2-deoxy-4,6-*O*-(*p*-methoxybenzylidene)-1-thio- $\alpha$ -D-galactopyranoside S-oxide (9S)**

Following the same procedure as for compound **6**, compounds **9R** and **9S** were obtained from compound **8** (0.30 g), *m*-chloroperbenzoic acid (0.13 g), and sodium hydrogen carbonate (0.07 g), followed by separation by column chromatography on silica gel using the same solvent system.

Compound **9R** was crystallized from ethanol–chloroform to give colorless needles; yield: 0.22 g (70%); mp 161.5–163.0 °C.  $[\alpha]_D^{23} +44.4^\circ$  (c 0.3, chloroform).  $R_f = 0.17$  (ethyl acetate–hexanes, 1:2). <sup>1</sup>H NMR  $\delta$ : 7.71–6.89 (m, 9H, aromatic protons), 5.76 (dd, 1H,  $J_{2,3} = 11.0$  Hz,  $J_{3,4} = 3.7$  Hz, H-3), 5.48 (s, 1H, CHPh), 4.95 (d, 1H,  $J_{1,2} = 5.5$  Hz, H-1), 4.64 (dd, 1H, H-2), 4.60 (bd, 1H,  $J_{4,5} < 1$  Hz, H-4), 4.08 (bs, 1H, H-5), 4.10, 3.98 (2H, AB part of ABX pattern,  $J_{5,6a} = 1.2$  Hz,  $J_{5,6b} = 2.4$  Hz,  $J_{6a,6b} = 12.5$  Hz, H-6a, H-6b), 3.80 (s, 3H, OCH<sub>3</sub>), 2.16 (s, 3H, COCH<sub>3</sub>). <sup>13</sup>C NMR  $\delta$ : 170.2 (C=O), 160.3, 141.4, 131.4, 129.7, 129.2, 127.4, 124.9, 113.7 (Ph), 100.8 (CHPh), 96.3 (C-1), 72.7 (C-4), 70.4 (C-3), 68.9 (C-6), 67.6 (C-5), 57.9 (C-2), 55.3 (OCH<sub>3</sub>), 20.9 (COCH<sub>3</sub>). HR-MS (EI,  $m/z$ ) calcd. for [C<sub>22</sub>H<sub>23</sub>N<sub>3</sub>O<sub>7</sub>S - C<sub>6</sub>H<sub>5</sub>OS]<sup>+</sup>: 348.1195; found: 348.1188.

Compound **9S** was crystallized from ethanol–chloroform to give colorless needles; yield: 56 mg (19%); mp 224.0–224.5 °C.  $[\alpha] +153.8^\circ$  (c 0.3, chloroform).  $R_f = 0.30$  (ethyl acetate–hexanes, 1:2). <sup>1</sup>H NMR  $\delta$ : 7.65–7.54 (m, 5H, PhH), 7.36, 6.87 (2d, 4H, PhH), 5.86 (dd, 1H,  $J_{2,3} = 11.0$  Hz,  $J_{3,4} = 3.4$  Hz, H-3), 5.47 (s, 1H, CHPh), 5.14 (d, 1H,  $J_{1,2} = 6.3$  Hz, H-1), 4.65 (dd, 1H, H-2), 4.61 (bd, 1H,  $J_{4,5} < 1$  Hz, H-4), 4.43 (bs, 1H, H-5), 4.02, 3.98 (2H, AB part of ABX pattern,  $J_{5,6a} = 1.5$  Hz,  $J_{5,6b} = 1.6$  Hz,  $J_{6a,6b} = 12.8$  Hz, H-6a, H-6b), 3.79 (s, 3H, OCH<sub>3</sub>), 2.16 (s, 3H, COCH<sub>3</sub>). <sup>13</sup>C NMR  $\delta$ : 170.3 (C=O), 160.4, 138.7, 134.4, 129.8, 129.4, 128.9, 127.6, 113.8 (Ph), 100.9 (CHPh), 89.9 (C-1), 72.7 (C-4), 69.9 (C-3), 68.8 (C-6), 67.1 (C-5), 56.2 (C-2), 55.5 (OCH<sub>3</sub>), 21.1 (COCH<sub>3</sub>).

**Phenyl 3,4,6-tri-*O*-acetyl-2-deoxy-2-phthalimido-1-thio- $\beta$ -D-glucopyranoside (17)**

1,3,4,6-Tetra-*O*-acetyl-2-deoxy-2-phthalimido- $\beta$ -D-glucopyranose<sup>45–47</sup> (72.2 g, 0.15 mol) was treated with thiophenol and boron trifluoride etherate to give the title compound as a solid that was crystallized from 15% ethyl acetate in hexanes; yield: 64.4 g (81%); mp 140–141 °C, lit. value<sup>48</sup> mp 145–146 °C.  $[\alpha]_D^{25} 49.4^\circ$  (c 0.88, chloroform); lit. value<sup>48</sup>  $[\alpha]_D^{25} 53.0^\circ$ .

**(S<sub>S</sub>) Phenyl 3,4,6-tri-*O*-acetyl-2-deoxy-2-phthalimido-1-thio- $\beta$ -D-glucopyranoside S-oxide (18S)**

A solution of *m*-chloroperbenzoic acid (0.60 g, 70%, 3.4 mmol, 1.0 equiv) in dry dichloromethane (7 mL) was added to a precooled solution of compound **17** (1.22 g, 2.31 mmol) in dichloromethane (18 mL) at –78 °C. The reaction mixture was stirred at –78 °C for 26 h and then allowed to warm to RT over 12 h. The mixture was washed with saturated sodium bicarbonate solutions (3  $\times$  25 mL) and water (25 mL), and then dried (sodium sulphate), fil-

tered, and concentrated to give a bright yellowish solid. Separation by flash column chromatography (ethyl acetate–hexanes, 1:1) gave the starting material (0.22 g) and colorless crystals of the product (0.95 g, 92% based on starting material consumed). Further fractionation using flash column chromatography (5% acetone in chloroform) gave **18S** as fluffy crystals that were recrystallized from 1% ethanol in hexanes to give clear colorless needles; mp 124–126 °C.  $[\alpha]_D^{25} +113^\circ$  (*c* 0.6, chloroform).  $R_f = 0.68$  (5% acetone in chloroform).  $^1\text{H}$  NMR (400 MHz)  $\delta$ : 7.68 (bd s, 2H, Phth-H), 7.84–7.60 (very bd s, 2H, Phth-H), 7.49 (d, 2H,  $J = 7.5$  Hz, *o*-Ar H), 7.21 (t, 2H,  $J = 7.5$  Hz, *m*-Ar H), 7.13 (t, 1H,  $J = 7.3$  Hz, *p*-Ar H), 5.77 (t, 1H,  $J_{2,3} = J_{3,4} = 9.7$  Hz, H-3), 5.40 (d, 1H,  $J_{1,2} = 10.1$  Hz, H-1), 5.16 (t, 1H,  $J_{3,4} = J_{4,5} = 9.7$  Hz, H-4), 4.89 (t, 1H, H-2), 4.20 and 4.28 (AB part of ABX pattern, 2H,  $J_{6a,6b} = 12.3$  Hz,  $J_{5,6a} = J_{5,6b} = 4.9$  Hz, 2 H-6), 3.91 (m, 1H, H-5), 2.09, 2.05, 1.85 (3s, 9H, 3 Ac).  $^{13}\text{C}$  NMR (100 MHz)  $\delta$ : 170.1, 169.8, 168.9 (3 Ac C=O), 167.6 (2 phth C=O), 138.8, 130.2, 128.4, 123.0 (S-Ph C), 133.9, 130.8, 123.9 (Phth C), 89.1 (C-1), 76.0 (C-5), 71.1 (C-3), 67.6 (C-4), 61.4 (C-6), 47.4 (C-2), 20.4, 20.2, 20.0 (Ac Me).

The second fraction was obtained as colorless fluffy crystals that decomposed on standing or on attempted recrystallization,  $R_f = 0.54$  (5% acetone in chloroform).  $^1\text{H}$  NMR (400 MHz)  $\delta$ : 7.90 (half of AA'BB' pattern, 2H, *o*-Phth-H), 7.90 (d, 2H, *o*-Ph H), 7.76 (half of AA'BB' pattern, 2H, Phth-H), 7.70 (t, 1H,  $J = 7.5$  Hz, *p*-Ar H), 7.58 (t, 2H,  $J = 7.7$  Hz, *m*-Ar H), 5.81 (t, 1H,  $J_{2,3} = J_{3,4} = 9.7$  Hz, H-3), 5.51 (d, 1H,  $J_{1,2} = 10.6$  Hz, H-1), 5.02 (t, 1H,  $J_{3,4} = J_{4,5} = 9.7$  Hz, H-4), 4.62 (t, 1H, H-2), 4.13 and 4.21 (AB part of ABX pattern, 2H,  $J_{6a,6b} = 12.8$  Hz,  $J_{5,6a} = J_{5,6b} = 4.8$  Hz, 2 H-6), 3.88 (m, 1H, H-5), 2.01, 2.00, 1.99 (3s, 9H, 3 Ac).  $^{13}\text{C}$  NMR (100 MHz)  $\delta$ : 170.0, 169.8, 168.9 (3 Ac C=O), 167.9 (2 phth C=O), 137.9, 130.1, 128.6, 123.4 (S-Ph C), 134.2, 131.3, 124.4 (Phth C), 86.1 (C-1), 76.3 (C-5), 71.2 (C-3), 67.8 (C-4), 61.4 (C-6), 49.4 (C-2), 20.3, 20.2, 20.0 (Ac Me).

This compound decomposed on standing into a compound ( $R_f = 0.82$ , 5% acetone in chloroform) that was purified by flash chromatography on silica gel (3% acetone in dichloromethane) as a syrup, identified as 3,4,6-tri-*O*-acetyl-2-deoxy-2-phthalimido-D-glucal;  $[\alpha]_D^{25} - 15.7^\circ$  (*c* 5.1, chloroform), lit.<sup>67</sup>  $[\alpha]_D - 15.0^\circ$ .  $^1\text{H}$  NMR (250.13 MHz)  $\delta$ : 7.96–7.74 (AA'BB' pattern, 4H, Phth-H), 6.78 (s, 1H, H-1), 5.61 (d, 1H,  $J_{3,4} = 4.0$  Hz, H-1), 5.33 (t, 1H,  $J_{4,5} = 4.4$  Hz, H-4), 4.54 (m, 2H, H-5, H-6a), 4.40 (m, 1H, H-6b), 2.16, 2.14, 1.94 (3s, 9H, 3 Ac).  $^{13}\text{C}$  NMR (100 MHz)  $\delta$ : 170.1, 169.9, 168.9 (3 Ac C=O), 167.9 (2 phth C=O), 148.2 (C-1), 134.3, 131.6, 123.7 (Phth C), 105.6 (C-2), 74.6 (C-5), 67.3 (C-3), 65.7 (C-4), 61.1 (C-6), 20.8, 20.6, 20.2 (Ac Me). HR-MS (EI)  $m/z$  calcd. for  $\text{C}_{20}\text{H}_{19}\text{NO}_9$ : 417.1059; found: 417.1045.

## Supplementary data

Supplementary data for this article are available on the journal Web site (canjchem.nrc.ca). CCDC 782358–782362 contain the X-ray data in CIF format for this manuscript. These data can be obtained, free of charge, via [www.ccdc.cam.ac.uk/conts/retrieving.html](http://www.ccdc.cam.ac.uk/conts/retrieving.html) (or from the Cambridge Crystallographic Data Centre, 12 Union Road, Cambridge CB2 1EZ, UK; fax +44 1223 336033; or [deposit@ccdc.cam.ac.uk](mailto:deposit@ccdc.cam.ac.uk)).

Supplementary data for this article are available on the journal Web site (canjchem.nrc.ca).

## Acknowledgements

We thank the Natural Sciences and Engineering Research Council of Canada (NSERC) for financial support and the Atlantic Region Magnetic Resonance Centre (ARMRC) for NMR time. We thank Dr. B.M. Pinto for discussions and a referee for a suggestion. Some of the computational facilities were provided by the Atlantic Computational Excellence network (ACEnet), the regional high-performance computing consortium for universities in Atlantic Canada. ACEnet is funded by the Canada Foundation for Innovation (CFI), the Atlantic Canada Opportunities Agency (ACOA), and the provinces of Newfoundland and Labrador, Nova Scotia, and New Brunswick.

## References

- (1) Kahne, D.; Walker, S.; Cheng, Y.; van Engen, D. *J. Am. Chem. Soc.* **1989**, *111* (17), 6881. doi:10.1021/ja00199a081.
- (2) Aversa, M. C.; Barattucci, A.; Bonaccorsi, P. *Tetrahedron* **2008**, *64* (33), 7659. doi:10.1016/j.tet.2008.05.051.
- (3) Yan, L.; Kahne, D. *J. Am. Chem. Soc.* **1996**, *118* (39), 9239. doi:10.1021/ja9608555.
- (4) Nicolaou, K. C.; Mitchell, H. J.; Rodriguez, R. M.; Fylaktakidou, K. C.; Suzuki, H.; Conley, S. R. *Chem. Eur. J.* **2000**, *6* (17), 3149. doi:10.1002/1521-3765(20000901)6:17<3149::AID-CHEM3149>3.0.CO;2-L.
- (5) Crich, D.; Dai, Z. M. *Tetrahedron* **1999**, *55* (6), 1569. doi:10.1016/S0040-4020(98)01202-2.
- (6) Gadikota, R. R.; Callam, C. S.; Wagner, T.; Del Fraino, B.; Lowary, T. L. *J. Am. Chem. Soc.* **2003**, *125* (14), 4155. doi:10.1021/ja029302m. PMID:12670238.
- (7) Houseknecht, J. B.; Lowary, T. L. *J. Org. Chem.* **2002**, *67* (12), 4150. doi:10.1021/jo011127p. PMID:12054950.
- (8) Dudkin, V. Y.; Miller, J. S.; Danishefsky, S. J. *Tetrahedron Lett.* **2003**, *44* (9), 1791. doi:10.1016/S0040-4039(03)00101-1.
- (9) Zhang, H.; Wang, Y. L.; Thurmer, R.; Meisenbach, M.; Voelter, W. *Liebigs Ann./Recl.* **1997**, 1871. doi:10.1002/jlac.199719970910.
- (10) Wipf, P.; Reeves, J. T. *J. Org. Chem.* **2001**, *66* (23), 7910. doi:10.1021/jo015952h. PMID:11701059.
- (11) Crich, D.; Banerjee, A.; Yao, Q. J. *J. Am. Chem. Soc.* **2004**, *126* (45), 14930. doi:10.1021/ja047194t. PMID:15535720.
- (12) Crich, D.; Pedersen, C. M.; Bowers, A. A.; Wink, D. J. *J. Org. Chem.* **2007**, *72* (5), 1553. doi:10.1021/jo061440x. PMID:17286432.
- (13) Taylor, J. G.; Li, X. C.; Oberthür, M.; Zhu, W. J.; Kahne, D. E. *J. Am. Chem. Soc.* **2006**, *128* (47), 15084. doi:10.1021/ja065907x. PMID:17117848.
- (14) Bai, Y.; Lowary, T. L. *J. Org. Chem.* **2006**, *71* (26), 9658. doi:10.1021/jo061713o. PMID:17168583.
- (15) Yan, L.; Taylor, C. M.; Goodnow, R., Jr.; Kahne, D. *J. Am. Chem. Soc.* **1994**, *116* (15), 6953. doi:10.1021/ja00094a067.
- (16) Ferrières, V.; Joutel, J.; Boulch, R.; Roussel, M.; Toupet, L.; Plusquellec, D. *Tetrahedron Lett.* **2000**, *41* (29), 5515. doi:10.1016/S0040-4039(00)00887-X.
- (17) Khair, N.; Fernández, I.; Araújo, C. S.; Rodríguez, J.-A.; Suárez, B.; Álvarez, E. *J. Org. Chem.* **2003**, *68* (4), 1433. doi:10.1021/jo026519q. PMID:12585884.

- (18) Safatli, M. *MSc. Thesis*; Dalhousie University: Halifax, NS, 1998.
- (19) Lemieux, R. U.; Koto, S.; Voisin, D. The Exoanomeric Effect. In *Anomeric Effect: Origin and Consequences*; Szarek, W. A., Horton, D., Eds.; American Chemical Society: Washington, DC, 1979; p 17.
- (20) Kirby, A. J. *The Anomeric Effect and Related Stereoelectronic Effects at Oxygen*; Springer-Verlag: New York, 1983.
- (21) Tvaroška, I.; Bleha, T. *Adv. Carbohydr. Chem. Biochem.* **1989**, 47, 45. doi:10.1016/S0065-2318(08)60412-6.
- (22) Juaristi, E.; Cuevas, G. *The Anomeric Effect*; CRC Press: Boca Raton, FL, 1994.
- (23) Crich, D.; Mataka, J.; Zakharov, L. N.; Rheingold, A. L.; Wink, D. J. *J. Am. Chem. Soc.* **2002**, 124 (21), 6028. doi:10.1021/ja0122694. PMID:12022836.
- (24) Cramer, C. J.; Truhlar, D. G.; French, A. D. *Carbohydr. Res.* **1997**, 298 (1–2), 1. doi:10.1016/S0008-6215(96)00297-2.
- (25) Tvaroška, I.; Carver, J. P. *Carbohydr. Res.* **1998**, 309 (1), 1. doi:10.1016/S0008-6215(98)00114-1.
- (26) Khair, N. *Tetrahedron Lett.* **2000**, 41 (47), 9059. doi:10.1016/S0040-4039(00)01651-8.
- (27) Houk, K. N.; Eksterowicz, J. E.; Wu, Y.-D.; Fuglesang, C. D.; Mitchell, D. B. *J. Am. Chem. Soc.* **1993**, 115 (10), 4170. doi:10.1021/ja00063a040.
- (28) Crich, D.; Mataka, J.; Sun, S.; Wink, D. J.; Lam, K.-C.; Rheingold, A. L.; Wink, D. *J. Chem. Commun. (Camb.)* **1998**, 2763. doi:10.1039/a804126a.
- (29) Crich, D.; Sun, S. X. *Tetrahedron* **1998**, 54 (29), 8321. doi:10.1016/S0040-4020(98)00426-8.
- (30) Crich, D.; Cai, W. L.; Dai, Z. M. *J. Org. Chem.* **2000**, 65 (5), 1291. doi:10.1021/jo9910482.
- (31) Misbahi, K.; Lardic, M.; Ferrières, V.; Noiret, N.; Kerbal, A.; Plusquellec, D. *Tetrahedron: Asymmetry* **2001**, 12 (17), 2389. doi:10.1016/S0957-4166(01)00437-2.
- (32) Khair, N.; Alonso, I.; Rodriguez, N.; Fernandez-Mayoralas, A.; Jimenez-Barbero, J.; Nieto, O.; Cano, F.; Foces-Foces, C.; Martin-Lomas, M. *Tetrahedron Lett.* **1997**, 38 (47), 8267. doi:10.1016/S0040-4039(97)10164-2.
- (33) Buist, P. H.; Behrouzian, B.; MacIsaac, K. D.; Cassel, S.; Rollin, P.; Imbert, A.; Gautier, C.; Pérez, S.; Genix, P. *Tetrahedron: Asymmetry* **1999**, 10 (15), 2881. doi:10.1016/S0957-4166(99)00294-3.
- (34) Aversa, M. C.; Barattucci, A.; Bonaccorsi, P.; Bruno, G.; Giannetto, P.; Rollin, P. *Lett. Org. Chem.* **2004**, 1 (4), 376. doi:10.2174/1570178043400631.
- (35) Buist, P. H.; Behrouzian, B.; Cassel, S.; Lorin, C.; Rollin, P.; Imbert, A.; Pérez, S. *Tetrahedron: Asymmetry* **1997**, 8 (12), 1959. doi:10.1016/S0957-4166(97)00207-3.
- (36) Miyajima, K.; Nekado, T.; Ikeda, K.; Achiwa, K. *Chem. Pharm. Bull. (Tokyo)* **1998**, 46 (11), 1676. PMID:9845951.
- (37) Lemieux, R. U.; Ratcliffe, R. M. *Can. J. Chem.* **1979**, 57 (10), 1244. doi:10.1139/v79-203.
- (38) Cheshev, P. E.; Kononov, L. O.; Tsvetkov, Y. E.; Shashkov, A. S.; Nifantiev, N. E. *Russ. J. Bioorganic Chem.* **2002**, 28 (5), 419. doi:10.1023/A:1020428329743.
- (39) Crich, D.; Cai, W. L. *J. Org. Chem.* **1999**, 64 (13), 4926. doi:10.1021/jo990243d. PMID:11674572.
- (40) Spek, A. L. *PLATON*; a multipurpose crystallographic tool; Utrecht University: Utrecht, The Netherlands, 2003.
- (41) Wolinski, K.; Hinton, J. F.; Pulay, P. *J. Am. Chem. Soc.* **1990**, 112 (23), 8251. doi:10.1021/ja00179a005.
- (42) Forsyth, D. A.; Sebag, A. B. *J. Am. Chem. Soc.* **1997**, 119 (40), 9483. doi:10.1021/ja970112z.
- (43) Stott, K.; Stonehouse, J.; Keeler, J.; Hwang, T. L.; Shaka, A. *J. J. Am. Chem. Soc.* **1995**, 117 (14), 4199. doi:10.1021/ja00119a048.
- (44) Neuhaus, D.; Williamson, M. P. *The Nuclear Overhauser Effect in Structural and Conformational Analysis*; Wiley-VCH, Inc.: New York, 2000.
- (45) Lemieux, R. U.; Takeda, T.; Chung, B. Y. Synthesis of 2-Amino-2-deoxy- $\beta$ -D-glucopyranosides. In *Synthetic Methods for Carbohydrates*; El Khadem, H. S., Ed.; American Chemical Society: Washington, DC, 1976; p 90.
- (46) Dasgupta, F.; Garegg, P. J. *J. Carbohydr. Chem.* **1988**, 7 (3), 701. doi:10.1080/07328308808057560.
- (47) Medgyes, A.; Farkas, E.; Lipták, A.; Pozsgay, V. *Tetrahedron* **1997**, 53 (12), 4159. doi:10.1016/S0040-4020(97)00145-2.
- (48) Jain, R. K.; Matta, K. L. *Carbohydr. Res.* **1992**, 226 (1), 91. doi:10.1016/0008-6215(92)84057-Y. PMID:1499025.
- (49) Cuesta, I. G.; De Merás, A. S.; Pelloni, S.; Lazzeretti, P. *J. Comput. Chem.* **2009**, 30 (4), 551. doi:10.1002/jcc.21083. PMID:18711723.
- (50) Lazzeretti, P. *Prog. Nucl. Magn. Reson. Spectrosc.* **2000**, 36 (1), 1. doi:10.1016/S0079-6565(99)00021-7.
- (51) Duddeck, H.; Korek, U.; Rosenbaum, D.; Drabowicz, J. *Magn. Reson. Chem.* **1986**, 24 (9), 792. doi:10.1002/mrc.1260240911.
- (52) Frisch, M. J.; Trucks, G. W.; Schlegel, H. B.; Scuseria, G. E.; Robb, M. A.; Cheeseman, J. R.; Montgomery, J. A., Jr.; Vreven, T.; Kudin, K. N.; Burant, J. C.; Millam, J. M.; Iyengar, S. S.; Tomasi, J.; Barnone, V.; Mennucci, B.; Cossi, M.; Scalmani, G.; Nega, N.; Petersson, G. A.; Nakatsuji, H.; Haha, M.; Ehara, M.; Toyota, K.; Fukuda, R.; Hasegawa, J.; Ishida, M.; Nakajima, T.; Honda, Y.; Kitao, O.; Nakai, H.; Klene, M.; Li, X.; Knox, J. E.; Hratchian, H. P.; Cross, J. B.; Adamo, C.; Jaramillo, J.; Gomperts, R.; Stratmann, R. E.; Yazyev, O.; Austin, J.; Cammi, R.; Pomelli, C.; Ochterski, J. W.; Ayala, P. Y.; Morokuma, K.; Voth, G. A.; Salvador, P.; Dannenberg, J. J.; Zakrzewski, V. G.; Dapprich, S.; Daniels, A. D.; Strain, M. C.; Farkas, O.; Malick, D. K.; Rabuck, A. D.; Raghavachari, K.; Foresman, J. B.; Ortiz, J. V.; Cui, Q.; Baboul, A. G.; Clifford, S.; Cioslowski, J.; Stefanov, B. B.; Liu, G.; Liashenko, A.; Piskorz, P.; Peng, C. Y.; Nanayakkara, A.; Challacombe, M.; Gill, P. M. W.; Johnson, B.; Chen, W.; Wong, M. W.; Gonzales, C.; Pople, J. A. *Gaussian 03*; Gaussian, Inc.: Wallingford, CT, 2003.
- (53) Becke, A. D. *J. Chem. Phys.* **1993**, 98 (7), 5648. doi:10.1063/1.464913.
- (54) Becke, A. D. *J. Chem. Phys.* **1993**, 98 (2), 1372. doi:10.1063/1.464304.
- (55) Sinnokrot, M. O.; Valeev, E. F.; Sherrill, C. D. *J. Am. Chem. Soc.* **2002**, 124 (36), 10887. doi:10.1021/ja025896h. PMID:12207544.
- (56) Tvaroška, I.; Bleha, T. *Can. J. Chem.* **1979**, 57 (4), 424. doi:10.1139/v79-069.
- (57) Watts, J.; Jiménez-Barbero, J.; Poveda, A.; Grindley, T. B. *Can. J. Chem.* **2003**, 81 (5), 364. doi:10.1139/v03-062.
- (58) Hunter, C. A.; Sanders, J. K. M. *J. Am. Chem. Soc.* **1990**, 112 (14), 5525. doi:10.1021/ja00170a016.
- (59) Grover, J. R.; Walters, E. A.; Hui, E. T. *J. Phys. Chem.* **1987**, 91 (12), 3233. doi:10.1021/j100296a026.
- (60) Sinnokrot, M. O.; Sherrill, C. D. *J. Am. Chem. Soc.* **2004**, 126 (24), 7690. doi:10.1021/ja049434a. PMID:15198617.
- (61) Krause, H.; Ernstberger, B.; Neusser, H. *J. Chem. Phys. Lett.* **1991**, 184 (5–6), 411. doi:10.1016/0009-2614(91)80010-U.
- (62) North, A. C. T.; Phillips, D. C.; Mathews, F. S. *Acta Crystallogr.* **1968**, A24, 351.

- (63) Molecular Structure Corporation. *TEXSAN for Windows*, version 1.06; single crystal structure analysis software; Molecular Structure Corporation: The Woodlands, TX, 1999.
- (64) Altomare, A.; Cascarano, M.; Giacovazzo, C.; Guagliardi, A.; Burla, M. C.; Polidori, G.; Camalli, M. *J. Appl. Cryst.* **1994**, 27 (3), 435. doi:10.1107/ÖS002188989400021X.
- (65) Altomare, A.; Cascarano, G.; Giacovazzo, C.; Guagliardi, A. *J. Appl. Cryst.* **1993**, 26 (3), 343. doi:10.1107/S0021889892010331.
- (66) Sheldrick, G. M. *SHELXL-97*, release 97-2; programs for crystal structure analysis; Institute für Anorganische Chemie, Universität Göttingen, Germany, 1998.
- (67) Ogawa, T.; Nakabayashi, S.; Sasajima, K. *Carbohydr. Res.* **1981**, 95 (2), 308. doi:10.1016/S0008-6215(00)85587-1.



# A general measure of conjugation in biphenyls and their radical cations

Lei Zhang, Gilles H. Peslherbe, and Heidi M. Muchall

**Abstract:** Changes in the amount of conjugation in the biphenyl system upon torsion have been investigated with quantum chemistry computations. For the unsubstituted biphenyl and its radical cation, the change in the energy for the first electronic transition as determined from time-dependent density functional theory, specifically TD-B3LYP, upon an imposed change in torsion angle appears to provide a good general measure of the delocalization of the  $\pi$ -electrons. Upon substitution, though, a relationship could not be established between the excitation energy and the twist across the C–C bond connecting the two phenyl rings. In contrast, the  $\pi$ -interaction energy, i.e., the  $\pi$ – $\pi$  interaction across the central C–C bond, determined from a natural bond orbital analysis, provides a uniform description of conjugation in the electronically different systems, for an imposed twist as well as upon substitution. Substituent effects are found to be larger and more varied for the biphenyl radical cations. Of particular interest is the introduction of the oxidizable substituents OCH<sub>3</sub> (methoxyl) and SCH<sub>3</sub> (methylthio), as this leads to the smallest changes in torsion angle in the biphenyl unit upon removal of an electron from the molecule. The findings of this work could ultimately prove useful for the rational design of conductive polymer materials.

**Key words:** biphenyl, conjugation, substituent effect, electronic excitation,  $\pi$ -interaction energy.

**Résumé :** Des calculs de chimie quantique, utilisant la théorie de la fonctionnelle de la densité dépendante du temps, spécifiquement TD-B3LYP, ont été effectués afin d'évaluer les variations de conjugaison dans le système biphenyle en fonction de sa torsion. Pour le biphenyle non substitué et son cation radicalaire, l'énergie correspondant à la première transition électronique suivant la torsion imposée semble fournir une mesure adéquate de la délocalisation des électrons  $\pi$ . Par contre, pour les biphenyles substitués, il n'est pas possible d'établir une relation entre l'énergie d'excitation et l'angle de torsion au niveau de la liaison C–C qui relie les deux phényles. Toutefois, l'énergie d'interaction  $\pi$ , c'est-à-dire l'interaction  $\pi$ – $\pi$  le long de la liaison C–C centrale, telle que déterminée par une analyse des orbitales naturelles de liaison, fournit une description uniforme de la conjugaison dans des systèmes électroniquement différents, que ce soit par torsion imposée ou par substitution. De plus, les effets de substitution sur la conjugaison sont plus prononcés et plus variés pour les cations radicalaires des biphenyles. Il est particulièrement intéressant de noter que l'introduction de substituants oxydables, tels que OCH<sub>3</sub> (méthoxyle) ou SCH<sub>3</sub> (méthylthio), entraîne la plus faible variation de l'angle de torsion de l'unité biphenyle lorsqu'elle perd un électron. Les résultats de ces travaux pourraient éventuellement aider à mieux prédire les propriétés de nouveaux matériaux à base de polymères conducteurs.

**Mots-clés :** biphenyle, conjugaison, effet de substituant, excitation électronique, énergie d'interaction  $\pi$ .

## Introduction

Conjugation, the delocalization of  $\pi$ -electrons, is related to important chemical and physical phenomena, such as aromaticity, spectral shifts, and electronic conductivity. Conductive polymers, especially oligo- and poly-*para*-phenylenes, have found widespread attention as active materials in light-emitting diodes and polymer lasers.<sup>1–5</sup> The properties of a conducting polymer are usually modified by manipulating their chemical structures, for example through substitution, to allow improved application in a particular optoelectronic device.<sup>6–8</sup> Whereas conjugation results in stabilization of a system through  $\pi$ -electron delocalization,

which is usually associated with the planarity of the system which guarantees maximum overlap between p-orbitals, steric effects<sup>9</sup> from substituents often induce a twist away from the planar conformation. The rational design of conductive polymers therefore requires a general measure of conjugation for an understanding of the structure–property relationships in both neutral (all-electron) and charged (radical cation) species.

The biphenyl unit (C<sub>6</sub>H<sub>5</sub>–C<sub>6</sub>H<sub>5</sub>) is ubiquitous in nature, and in the above context constitutes the smallest oligo-*para*-phenylene. Its planar geometry has been observed experimentally in the crystalline phase,<sup>13–10</sup> whereas a nonplanar

Received 28 April 2010. Accepted 29 July 2010. Published on the NRC Research Press Web site at [canjchem.nrc.ca](http://canjchem.nrc.ca) on 5 November 2010.

*This article is part of a Special Issue dedicated to Professor R. J. Boyd.*

**L. Zhang, G.H. Peslherbe,<sup>1</sup> and H.M. Muchall.<sup>2</sup>** Centre for Research in Molecular Modeling and Department of Chemistry and Biochemistry, Concordia University, Montreal, QC, H4B 1R6, Canada.

<sup>1</sup>Corresponding author (e-mail: [gilles.peslherbe@concordia.ca](mailto:gilles.peslherbe@concordia.ca)).

<sup>2</sup>Corresponding author (e-mail: [muchall@alcor.concordia.ca](mailto:muchall@alcor.concordia.ca)).

geometry has been observed in solutions<sup>14–16</sup> and in liquid<sup>17</sup> and gaseous<sup>14,18–20</sup> phases. A relationship between geometry and electronic structure has been established for the all-electron biphenyls.<sup>21,22</sup> In addition, experimental and theoretical studies have been carried out on halogenated biphenyl radical cations to determine how the type and position of substituents influence the geometry, optical absorption characteristics, ionization potentials, electron affinities, and decay kinetics of these radical cations.<sup>23–27</sup> Vibrational frequencies of the biphenyl radical cation have been calculated<sup>28,29</sup> and compared with those measured by Raman spectroscopy<sup>30–32</sup> to address geometrical changes upon ionization.

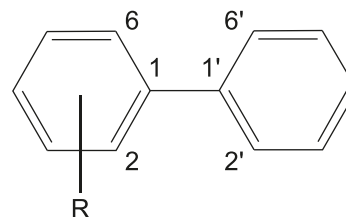
Whereas the geometry of an all-electron system is readily determined experimentally from diffraction studies, spectroscopic properties have to be employed to unveil information on the geometry and electronic structure of charged and radical species. Even for all-electron systems, though, electronic spectra are often consulted to determine an increase in conjugation. Yet, for subtle changes in geometry, as can be expected upon substitution in the biphenyl system, it might be difficult to distinguish between a shift in the appropriate absorption maximum owing to a change in conjugation between the two rings versus a shift from a simple change in chromophore upon substitution. Alternative parameters that have been traditionally considered to evaluate the  $\pi$ -electron delocalization in conjugated systems are the bond length, the electron density, and the ellipticity at its bond critical point (as determined within the quantum theory of atoms in molecules<sup>33</sup>). None of these is suitable as a general measure of  $\pi$ -electron delocalization, as will be shown below.

In this work, we establish that the  $\pi$ -interaction energy, given by the  $\pi$ - $\pi$  interaction across the central C–C bond and evaluated with the natural bond orbital approach, yields consistent results for forced twists of the unsubstituted biphenyl and its radical cation, as well as for a variety of monosubstituted biphenyls and their radical cations (Chart 1), which exhibit inherent twists over a wide range of torsion angles. This should prove of particular value with respect to the need for the rational design of materials.

## Computational details

Our previous benchmark calculations on substituted phenols suggest that time-dependent density functional theory (TD-DFT)<sup>34</sup> gives accurate results for excitation energies associated with electronic transitions from the ground state to the first two low-lying excited states, which correspond to absorption in the UV spectral region.<sup>35</sup> The same method has been used to accurately reproduce the absorption spectra of methoxyl- and methyl-substituted phenol radical cations<sup>36</sup> and phenoxyl radicals,<sup>37</sup> and to identify the source of substituent effects that cause significant band shifts in their experimental spectra. TD-DFT has also been used successfully to predict the electronic transition energies of polycyclic aromatic hydrocarbons,<sup>38</sup> and is therefore employed for the calculation of the excitation energies of biphenyl systems in this work. For comparison and further validation, excitation energies for the biphenyl radical cation were also determined with the multi-configuration complete active space

Chart 1.



second-order perturbation theory (CASPT2),<sup>39</sup> using the MOLPRO quantum chemistry package.<sup>40</sup>

All TD-DFT calculations were performed with the Gaussian 03 quantum chemistry package.<sup>41</sup> Ground-state equilibrium geometries were located by full optimization with Becke's three-parameter hybrid exchange functional and the Lee, Yang, and Parr correlation functional, commonly referred to as B3LYP,<sup>42–44</sup> with the 6–31G(d) basis set.<sup>45,46</sup> This method and basis set have been shown to produce results with an accuracy close to that of calculations with the quadratic configuration interaction with single, double, and perturbative triple excitations (QCISD(T)) level of theory in the forced torsion of the 1,3-butadiene radical cation.<sup>47</sup> Vibrational frequency calculations using the same model chemistry were performed to confirm that all stationary points are minima on the potential energy surface. Torsional profiles were obtained by constraining the torsion angle between the two phenyl rings and relaxing all other geometrical parameters. More specifically, both C2–C1–C1'–C2' and C6–C1–C1'–C6' torsion angles (see Chart 1 for atom numbers) were constrained to the same value to avoid the pyramidalization of C1 and C1' that has been observed earlier in the torsion of the 1,3-butadiene radical cation.<sup>47</sup> Vertical excitation energies were calculated for ground-state geometries using TD-B3LYP and CASPT2 (with an active space consisting of nine ring electrons distributed into five occupied and two virtual  $\pi$ -type orbitals) with the 6–311++G(d,p) basis set.<sup>48,49</sup>

A topological analysis of the electron density was performed for all substituted biphenyls and their radical cations with the quantum theory of atoms in molecules.<sup>33,50</sup> The electron density and ellipticity at the bond critical point (the point between two nuclei where the gradient vector field of the electron density is zero with two negative and one positive curvature) of the central C–C bond were obtained from the B3LYP/6–31G(d) electron density using the AIM2000 package.<sup>51</sup>

The  $\pi$ -interaction energies were estimated from the orbital energy difference between the “filled” (donor) Lewis-type natural bond orbital (NBO) corresponding to the  $\pi$ -orbital of one C=C bond in one ring and the “empty” (acceptor) non-Lewis NBO corresponding to the  $\pi^*$ -orbital of its conjugated C=C bond in the other ring, the electron occupancy of the donor Lewis-type NBO and the off-diagonal Fock (or Kohn–Sham) matrix element by natural bond orbital (NBO) analysis,<sup>52–57</sup> using the NBO version 3.1 program embedded in the Gaussian 03 package. Because the NBO procedure localizes  $\pi$ -bonds in the aromatic ring, artificially distinct  $s$ -cis and  $s$ -trans interactions across the central C–C bond can

**Table 1.** Total energies ( $E_{\text{total}}$ , hartree; not zero-point energy corrected),  $\pi$ -interaction energies ( $E_{\text{inter}}$ , kcal/mol), and torsion angles ( $\varphi$ ,  $^{\circ}$ ) of equilibrium geometries of biphenyls ( $\text{C}_6\text{H}_5\text{--C}_6\text{H}_4\text{R}$ ) and their radical cations.

Biphenyls						Biphenyl radical cations					
R	$E_{\text{total}}$	$\varphi$	$E_{\text{inter}}$			$E_{\text{total}}$	$\varphi$	$E_{\text{inter}}$			$\Delta\varphi$
			<i>s-trans</i>	<i>s-cis</i>	Avg.			<i>s-trans</i>	<i>s-cis</i>	Avg.	
H	−463.306 078	38.4	10.0 <sup>a</sup>	9.6	9.8	−463.026 794	19.5	7.9	7.0	7.5	18.9
<i>o</i> -CN	−555.546 725	46.6	7.7 <sup>a</sup>	7.6	7.7	−555.251 042	31.6	6.7	6.2	6.4	15.0
<i>o</i> -Me	−502.619 912	55.3	5.1	5.8 <sup>a</sup>	5.4	−502.341 401	34.1	6.2	5.9	6.1	21.2
<i>o</i> -Et	−541.930 967	56.4	4.7	5.5 <sup>a</sup>	5.1	−541.653 563	35.3	6.0	5.8	5.9	21.1
<i>o</i> -Cl	−922.897 329	54.6	5.2	6.0 <sup>a</sup>	5.6	−922.610 806	36.5	5.7	5.6	5.6	18.1
<i>o</i> -OMe	−577.825 170	45.6	7.6	8.0 <sup>a</sup>	7.8	−577.561 730	32.2	6.3	6.1	6.2	13.4
<i>o</i> -SMe	−900.801 899	58.7	4.3 <sup>a</sup>	5.0	4.6	−900.540 032	44.6	4.4	4.4	4.4	14.1
<i>o</i> - <i>t</i> -Bu	−620.546 539	86.3	0.0	0.0 <sup>a</sup>	0.0	−620.266 370	41.3	4.7	5.0	4.9	45.0
<i>o</i> -Adamantyl	−852.818 301	62.6	3.1 <sup>a</sup>	3.9	3.5						
<i>m</i> -CN	−555.549 339	38.4	9.9 <sup>a</sup>	9.5	9.7	−555.252 953	19.7	7.9	7.0	7.4	18.6
<i>m</i> -Me	−502.624 061	38.4	9.9 <sup>a</sup>	9.7 <sup>a</sup>	9.8	−502.349 188	20.2	7.8 <sup>a</sup>	7.0	7.4	18.2
<i>m</i> -Et <sup>b</sup>	−541.935 838	38.3	9.8	9.5	9.7	—					
	−541.935 806	38.5	9.7	9.5	9.6	−541.663 232	20.4	7.8	6.9	7.3	18.1
<i>m</i> -Cl	−922.902 199	38.3	9.8	9.6	9.7	−922.615 920	20.4	7.7	6.8	7.3	17.8
<i>m</i> -CF <sub>3</sub> <sup>b</sup>	−800.343 800	38.0	10.0 <sup>a</sup>	9.8 <sup>a</sup>	9.9	−800.053 770	19.1	8.0	7.1 <sup>a</sup>	7.6	18.9
	−800.343 640	38.1	9.9	9.7 <sup>a</sup>	9.8	—					
<i>m</i> -OMe <sup>b</sup>	−577.828 675	38.4	9.7	9.5 <sup>a</sup>	9.6	−577.560 730	25.6	7.1	6.4 <sup>a</sup>	6.7	12.7
	−577.828 617	37.9	9.7	9.6 <sup>a</sup>	9.6	—					
<i>m</i> -SMe <sup>b</sup>	−900.806 752	39.0	9.6	9.5 <sup>a</sup>	9.5	−900.541 752	28.9	6.6	6.2	6.4	10.1
	−900.806 676	38.6	9.7 <sup>a</sup>	9.4	9.6	—					
<i>m</i> - <i>t</i> -Bu <sup>b</sup>	−620.560 970	38.4	9.9 <sup>a</sup>	9.7 <sup>a</sup>	9.8	−620.288 898	21.0	7.8	6.9	7.3	17.4
	−620.560 910	38.4	9.7	9.6 <sup>a</sup>	9.7	—					
<i>p</i> -CN	−555.550 019	37.7	10.1	9.8	9.9	−555.255 605	19.9	8.0	7.1	7.5	17.7
<i>p</i> -Me	−502.624 177	37.8	10.0	9.9 <sup>a</sup>	9.9	−502.353 162	18.9	8.0	7.1	7.5	18.9
<i>p</i> -Et	−541.936 041	37.6	10.0	9.9 <sup>a</sup>	10.0	−541.666 785	19.0	8.0	7.1	7.5	18.6
<i>p</i> -Cl	−922.902 269	38.2	9.9	9.7	9.8	−922.621 961	19.6	7.9	7.0	7.5	18.5
<i>p</i> -CF <sub>3</sub>	−800.344 027	38.1	9.9	9.7	9.8	−800.052 650	19.3	8.0	7.1	7.5	18.8
<i>p</i> -OMe	−577.828 802	37.5	10.1	10.0 <sup>a</sup>	10.0	−577.570 798	20.3	7.8	6.9	7.4	17.2
<i>p</i> -SMe	−900.807 057	37.0	10.3	10.0 <sup>a</sup>	10.2	−900.551 358	22.5	7.5	6.7	7.1	14.5
<i>p</i> - <i>t</i> -Bu	−620.561 232	37.3	10.1	9.9 <sup>a</sup>	10.0	−620.292 925	18.8	8.0	7.1	7.6	18.5

<sup>a</sup>From NBO 4.M.

<sup>b</sup>Two equally populated biphenyl rotamers are found as minima, differing in the orientation of the substituent. A unique global minimum is found for their corresponding radical cations.

be characterized. As these carry different energy values, a phenomenon reflective of the differences in the electronic excitation for cisoid and transoid dienes, both energies were evaluated. When NBO 3.1 would not provide a given  $\pi$ -interaction energy (*s*-cis or *s*-trans) by default for the mono-substituted biphenyls included in this study (Chart 1), that particular Lewis structure (indicated in the footnote of Table 1) was analyzed with the stand-alone NBO 4.M program.<sup>58</sup>

## Results and discussion

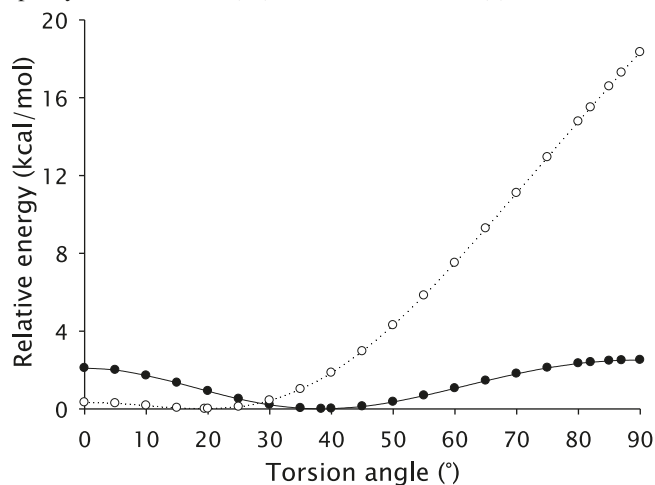
### Biphenyl and its radical cation

The energy barrier for torsion in biphenyl was determined to be about 1–2 kcal/mol (1 cal = 4.184 J) by nuclear magnetic resonance (NMR) and Raman spectroscopic techniques.<sup>18,19,59,60</sup> Such a small torsional energy barrier has been a challenge for molecular mechanics owing to the improper parameterization of the torsional term in force fields,<sup>61,62</sup> and characterizing the torsional potential energy profile of biphenyl from quantum chemistry calculations has been the central topic of many reports.<sup>63–66</sup>

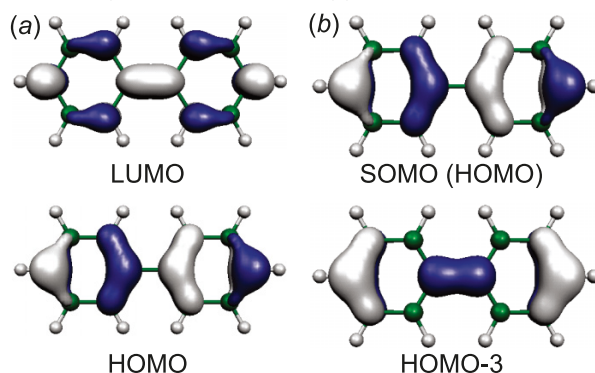
The torsional potential energy profiles for biphenyl and its radical cation in the range 0° to 90° are shown superimposed in Fig. 1. For biphenyl, the calculated energy barriers of 2.1 kcal/mol (0°) and 2.5 kcal/mol (90°) are comparable to the experimental values of  $\Delta E_0 = 1.4 \pm 0.5$  kcal/mol and  $\Delta E_{90} = 1.6 \pm 0.5$  kcal/mol,<sup>18</sup> and to the calculated values of 2.0–3.9 kcal/mol for  $\Delta E_0$  and 1.2–2.4 kcal/mol for  $\Delta E_{90}$  in previous reports.<sup>22,64,67–70</sup> In contrast to these small barriers, the calculated torsional potential energy profile for the biphenyl radical cation exhibits an energy barrier as high as 18.3 kcal/mol, corresponding to the 90° conformation. Although there is a lack of direct experimental evidence for the size of the barrier in the biphenyl radical cation itself, a similarly high torsional energy barrier (>10 kcal/mol) has been reported for the related 3,3'-dimethyl-4,4'-dihydroxybiphenyl radical cation from the temperature dependence of the electron spin resonance (ESR) signal.<sup>71</sup> The torsional potential energy profile for the biphenyl radical cation beyond 90° (up to 180°) was also evaluated; it was found to be smooth and symmetric about the 90° mark without evidence for a jump to a higher energy surface beyond 90°, as had been a concern for the related 1,3-butadiene radical cation.<sup>47</sup>

The torsion angle of the equilibrium geometry changes from 38.4° in biphenyl to 19.5° in its radical cation. Such a partial planarization upon removal of one electron has also been found for 4,4'-dihydroxybiphenyl and for halogenated biphenyls.<sup>23–25,72,73</sup> Accordingly, for the unsubstituted biphenyl radical cation, the planar conformation is only 0.3 kcal/mol (1.1 kcal/mol if corrected for zero-point vibrational energies) higher in energy than the equilibrium geometry. This very small barrier to planarity is an indication of the importance of increased conjugation in the stabilization of the biphenyl radical cation. Given the very small energy difference, and in view of computational accuracy, although the calculated equilibrium geometry is nonplanar, a planar structure might well be found experimentally. In fact, the ESR spectrum of the biphenyl radical cation in solution does not provide any evidence for nonplanarity.<sup>74</sup>

**Fig. 1.** Torsional potential energy profiles for biphenyl (●) and the biphenyl radical cation (○) from B3LYP/6–31G(d) calculations.



**Chart 2.** Molecular orbitals for the lowest energy electronic transition for (a) biphenyl and (b) the biphenyl radical cation (planar conformations) from B3LYP/6–31G(d) calculations.



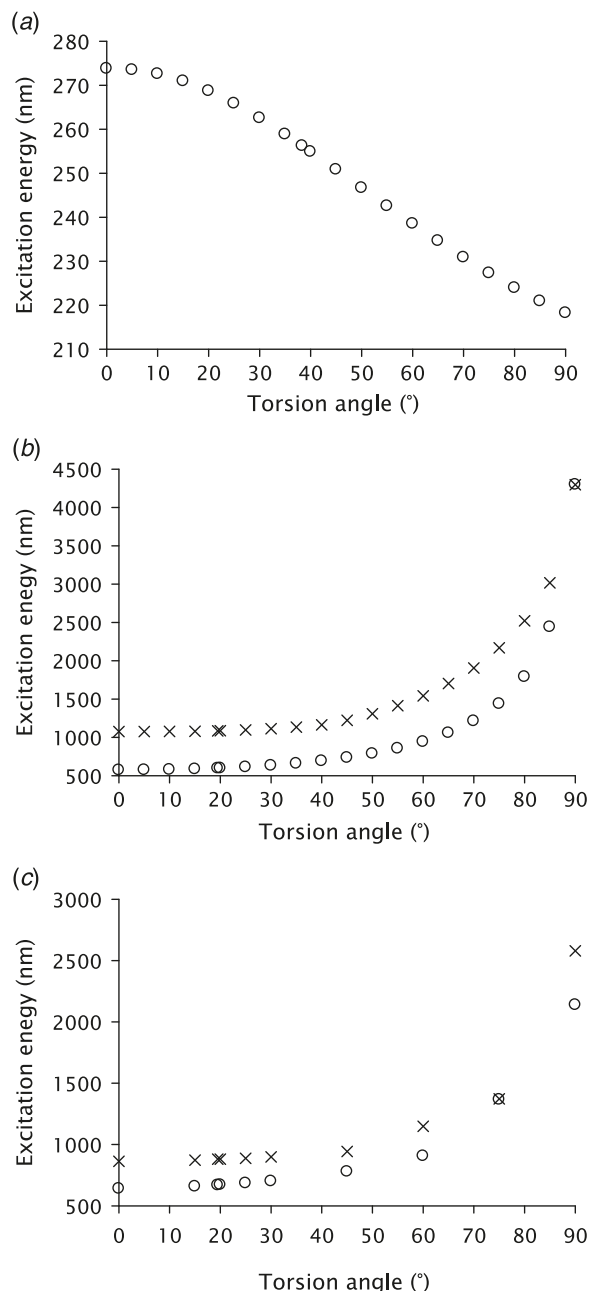
### Energy of the first electronic transition

It is generally accepted that an increase in conjugation leads to an energetic destabilization of the highest occupied molecular orbital (HOMO) and stabilization of the lowest unoccupied molecular orbital (LUMO). The resulting decrease in the HOMO–LUMO gap can be probed spectroscopically, and a shift of the corresponding absorption maximum ( $\lambda_{\max}$ ) to longer wavelengths is indeed observed for more highly conjugated systems.<sup>75,76</sup> The energy of the first electronic transition, expressed in nm, is plotted as a function of torsion angle in Fig. 2. Numerical data are provided in Table S1 of the Supplementary data. Figure 2a shows the expected shift to longer wavelengths (bathochromic or red shift) for the corresponding absorption wavelength,  $\lambda_{\max}$  for the all-electron biphenyl system upon planarization. As expected, this absorption band results from a transition from the HOMO to the LUMO. These orbitals, obtained from B3LYP/6–31G(d) calculations for the planar conformation, are shown in Chart 2.

In contrast, an increase in conjugation in the biphenyl radical cation leads to a shift of the first electronic excitation to shorter wavelengths (hypsochromic or blue shift) for the corresponding  $\lambda_{\max}$ , Fig. 2b). This fundamentally different behaviour of the excitation energy upon torsion from that in biphenyl takes its roots from the molecular orbitals (MOs)



**Fig. 2.** Excitation energy versus torsion angle for (a) biphenyl and (b) and (c) the biphenyl radical cation. In (b) and (c), the energies are given for the first observable electronic excitation (○) and for the electronic excitation from HOMO-1 to SOMO (×); (a) and (b) are from TD-B3LYP/6-311++G(d,p) calculations and (c) from CASPT2/6-311++G(d,p) calculations.



implicated in the electronic transition. In contrast to biphenyl, where the absorption maximum corresponds to the HOMO–LUMO transition, for the biphenyl radical cation, the absorption involves a transition from a lower lying doubly occupied molecular orbital to the singly occupied molecular orbital (SOMO, which is still the highest occupied MO). The SOMO and the third lower-lying doubly occupied MO (HOMO-3) are shown in Chart 2b for the planar confor-

mation of the biphenyl radical cation. Because the SOMO of the radical cation has the same character as the HOMO of biphenyl, it is also destabilized upon planarization, whereas the favourable interaction between the two rings in the HOMO-3 is facilitated, leading to a stabilization of this orbital. As a result, the largest HOMO-3–SOMO gap, and therefore the largest excitation energy or the shortest wavelength of excitation, is found for the planar conformation. The character of the lower-lying doubly occupied MO implicated in the electronic transition remains upon torsion, but the orbital energy ordering changes smoothly with the torsion angle, as the MO shifts from HOMO-3 at 0° to HOMO-1 at 90°. Yet, even if the HOMO-1 to SOMO electronic excitation is considered throughout the torsion, increasing planarity still leads to this blue shift (Fig. 2b). High-accuracy CASPT2 calculations (Fig. 2c) confirm that the excitation energies for the more highly-twisted conformations lie in the near-IR spectral region and that these are not long-wavelength artifacts of the TD-B3LYP method. Finally, the calculated excitation energy, expressed in nm, for the minimum geometry resembles the experimental  $\lambda_{\text{max}}$  value of 670 nm.<sup>77</sup>

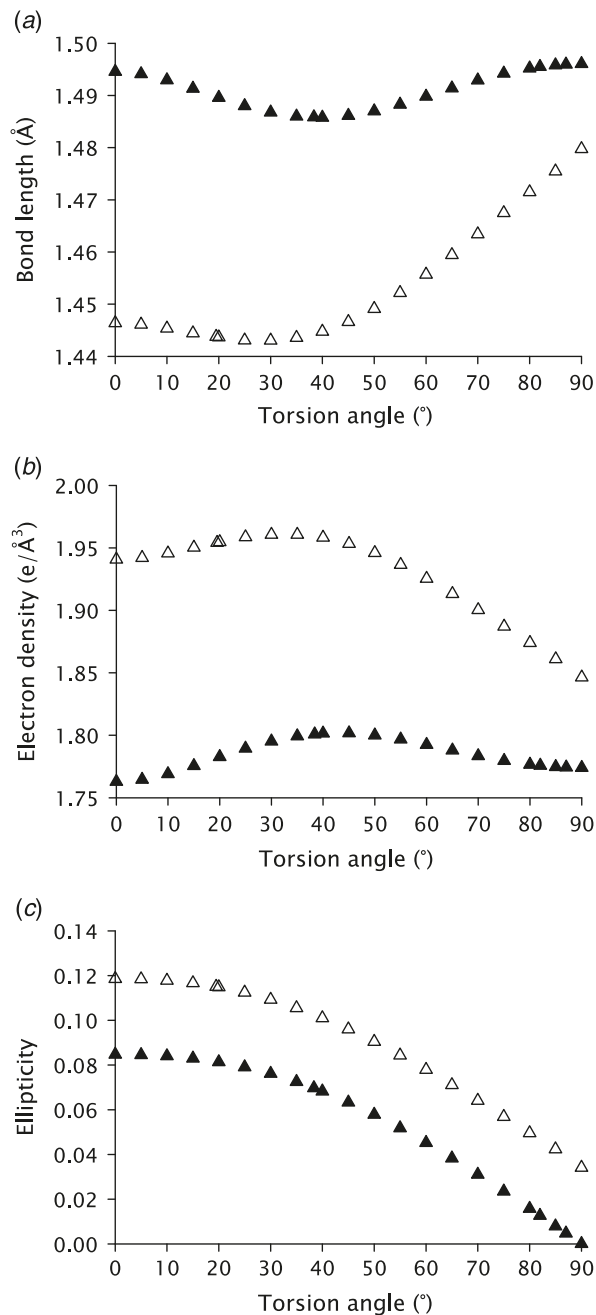
According to the monotonic behaviour of the torsional plots determined above in the range of 0° to 90° for biphenyl and its radical cation, the energy of the first electronic transition appears to reflect the extent of the delocalization of  $\pi$ -electrons, at least for these unsubstituted, electronically different systems.

#### **Bond length, electron density, and ellipticity of the central C–C bond**

Planarization in the biphenyl system favors a maximum overlap between the p-orbitals, leading to a shorter central C–C bond with more double-bond character owing to increased delocalization of  $\pi$ -electrons between the two rings. In general, changes in  $\pi$ -character can be probed conveniently by the quantum theory of atoms in molecules<sup>33,50</sup> through the values of the electron density and ellipticity at the bond critical point.<sup>54</sup> The relationships involving bond length, bond-critical-point electron density, and ellipticity are shown in Fig. 3, while the numerical data are provided in Table S2 of the Supplementary data. For biphenyl and its radical cation, the bond length and bond-critical-point electron density (Figs. 3a and 3b) do not vary monotonically in the twist range of 0° (planar) to 90° (perpendicular), so neither can provide a reasonable measure of conjugation in biphenyl systems.

Derived from the two negative curvatures of the electron density at the bond critical point, the ellipticity quantifies the deviation from cylindrical symmetry of a bond.<sup>54</sup> Figure 3c shows a good correlation between the ellipticity and the torsion angle for both the all-electron and radical cationic biphenyls. Figure 3c also clearly shows that the  $\pi$ -bond character of the central C–C bond increases along with the conjugation and upon removal of an electron, in agreement with earlier reports on halogenated and hydroxyl-substituted biphenyls.<sup>67,76</sup> The ellipticity thus also proves to provide a general measure of delocalization for the unsubstituted biphenyl and its radical cation.

**Fig. 3.** Properties of the central C–C bond. (a) Bond length, (b) electron density, and (c) ellipticity at the bond critical point versus torsion angle for biphenyl ( $\blacktriangle$ ) and the biphenyl radical cation ( $\triangle$ ) from B3LYP/6–31G(d) calculations.

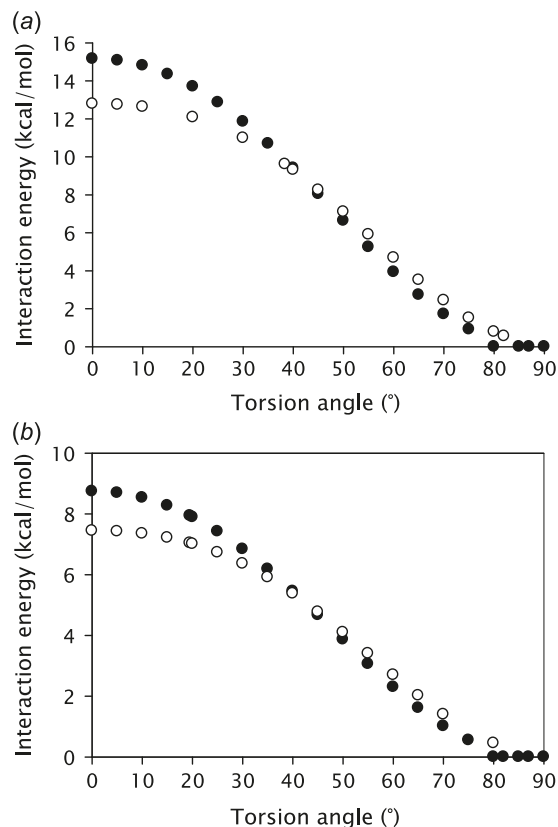


### $\pi$ -Interaction energy

The  $\pi$ -interaction energy for the  $\pi$ – $\pi$  interaction across the central C–C bond connecting the two phenyl rings is plotted as a function of torsion angle in Fig. 4, and numerical data are provided in Table S1 of the Supplementary data. As one might expect, for both biphenyl and its radical cation, the  $\pi$ -interaction energy decreases monotonically with an increase in torsion angle from 0° to 90°. The  $\pi$ -interaction energy therefore also captures changes in the delocalization of  $\pi$ -electrons in these electronically different systems.

As noted above, since the NBO treatment localizes  $\pi$ -

**Fig. 4.**  $\pi$ -Interaction energy versus torsion angle for (a) biphenyl and (b) the biphenyl radical cation ( $\circ$ , *s*-cis, and  $\bullet$ , *s*-trans  $\pi$ -interaction, across the central C–C bond) from B3LYP/6–31G(d) calculations.

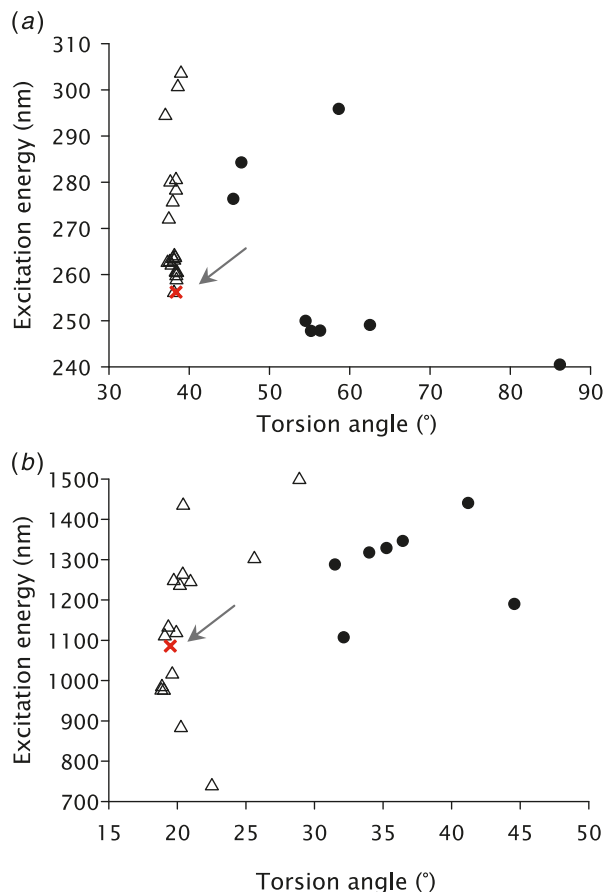


bonds in the phenyl rings, both artificial *s*-cis and *s*-trans interactions are possible across the central C–C bond. For the planar conformation of biphenyl, the *s*-trans  $\pi$ -interaction energy is 2.4 kcal/mol larger than the *s*-cis  $\pi$ -interaction energy (the difference is only 1.3 kcal/mol in the planar biphenyl radical cation), which is comparable to the size of the largest change in the  $\pi$ -interaction energy upon a 10° twist in the region of 45° (Fig. 4). A crossover occurs at a torsion angle of about 40°, and the *s*-cis  $\pi$ -interaction energy becomes slightly larger than the *s*-trans  $\pi$ -interaction energy for torsion angles in the range 45–90° (numerical data are given in Table S1 of the Supplementary data). In view of the fact that *s*-trans and *s*-cis  $\pi$ -interactions contribute almost equally to the stability of biphenyl systems, the average value of the  $\pi$ -interaction energy is adopted in the following discussion to characterize monosubstituted biphenyl systems, while both *s*-cis and *s*-trans numerical data are reported in Table 1 and provided in Fig. S1 of the Supplementary data.

### Substituted biphenyls and their radical cation

The calculated torsion angle at the equilibrium geometry of gas-phase biphenyl is 38.4°. The twist is more or less controlled by the steric effect of the *ortho*-hydrogen atoms.<sup>78–80</sup> In the monosubstituted biphenyls included in this study (Chart 1), one hydrogen atom is replaced by a substituent, differing in size and electronic property. While its size might be of principal importance in the *ortho* posi-

**Fig. 5.** Excitation energy versus torsion angle for (a) monosubstituted biphenyls (first observable electronic excitation) and (b) monosubstituted biphenyl radical cations (electronic excitation from HOMO-1 to SOMO) from TD-B3LYP/6-311++G(d,p) calculations. The unsubstituted species are included for reference and pointed out by the arrows (●, ortho-substituted; △, meta- or para-substituted; and ×, unsubstituted).



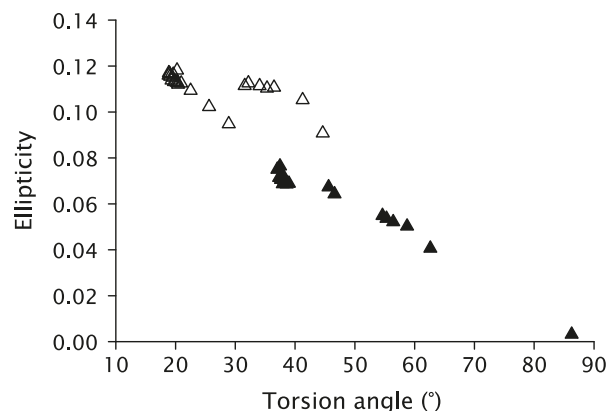
tion, its electronic properties might be expected to surface in meta and para positions, thus leading to a different torsion angle for the respective equilibrium geometry. It is therefore desirable to identify a suitable parameter that can describe changes in conjugation in the presence of these factors.

#### Energy of the first electronic transition

In UV-vis spectroscopy, for a variety of parent chromophores, it is well established that, and how,  $\lambda_{\max}$  for the lowest energy  $\pi \rightarrow \pi^*$  transition varies with substitution. Conversely, for substituted phenoxyl radicals and phenol radical cations,  $\lambda_{\max}$  can vary in a seemingly unpredictable way.<sup>13</sup> Thus, for a molecular system in which conjugation can be removed or increased through torsion, such as in the biphenyls, substitution constitutes a second, independent factor affecting the energy of absorption. An experimentally observed  $\lambda_{\max}$  or a corresponding calculated excitation energy consequently might not be a suitable measure for the change in conjugation.

The energy of the first electronic excitation is plotted as a function of torsion angle in Fig. 5, and the numerical data are provided in Table S3 of the Supplementary data. It is

**Fig. 6.** Ellipticity at the bond critical point of the central C–C bond versus torsion angle for substituted biphenyls (▲) and substituted biphenyl radical cations (△) from B3LYP/6-31G(d) calculations.



evident from Fig. 5 that a correlation between the lowest excitation energy for a  $\pi \rightarrow \pi^*$  transition and the size of the torsion angle does not exist for substituted biphenyls or their radical cations.

#### Ellipticity at the bond critical point of the central C–C bond

The relationship between the ellipticity at the bond critical point of the central C–C bond and the torsion angle is shown in Fig. 6, and the numerical data are provided in Table S3 of the Supplementary data. Figure 6 exhibits a small set of data points that could have been considered outliers to an otherwise good correlation between the ellipticity and the torsion angle. However, those data points stem entirely from the ortho-substituted biphenyl radical cations, and therefore the ellipticity fails to provide a general measure of delocalization for both substituted all-electron and radical cationic biphenyls.

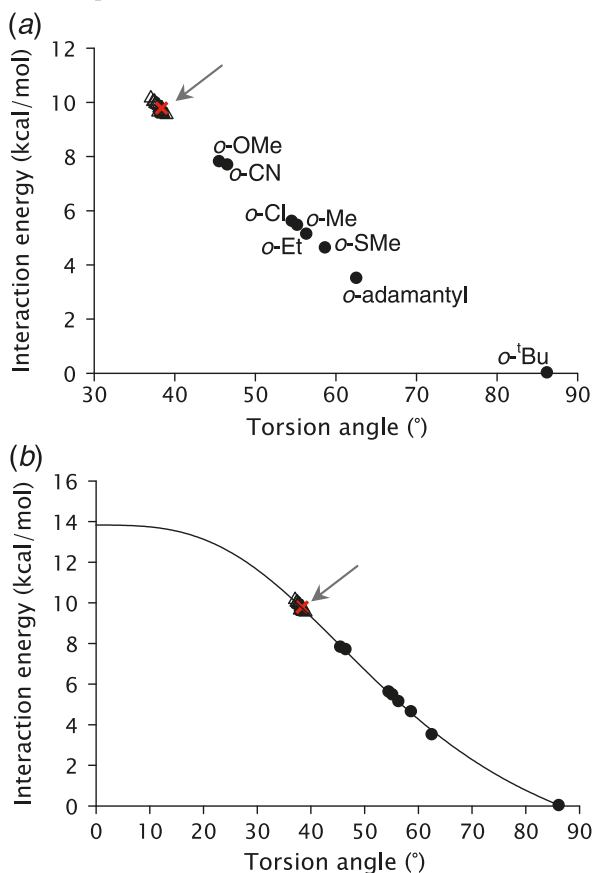
#### $\pi$ -Interaction energy

##### Substituted biphenyls

The equilibrium-geometry torsion angles and  $\pi$ -interaction energies for substituted biphenyls are provided in Table 1, and the  $\pi$ -interaction energies are plotted as a function of torsion angle in Fig. 7. In general, the relationship between the  $\pi$ -interaction energy and the torsion angle at the equilibrium geometry for the substituted biphenyls (Fig. 7a) is similar to that for torsion of the unsubstituted biphenyl (Fig. 4a). As expected, the steric effect at the ortho position is pronounced and results in torsion angles of around 45° for a small substituent, around 55° for medium-sized substituents, and up to 86° for the bulky *tert*-butyl substituent. Qualitatively, the similar-size chloro- and methyl-substituents lead to comparable torsion angles, as does the ethyl group, which exercises a steric hindrance comparable to that of the methyl group.<sup>81</sup> This assessment fits well with the results from a recent attempt at quantifying steric effects in the biphenyl system.<sup>82</sup>

Any steric effect for meta-substitution has to be transmitted through a change in bond angle on the adjacent ortho-carbon atom. Figure 7a shows that, if present, the increased hindrance between ortho-H atoms in meta-substituted bi-

**Fig. 7.** (a) Average  $\pi$ -interaction energy versus torsion angle for monosubstituted biphenyls from B3LYP/6–31G(d) calculations. (b) Superposition of the data from (a) with the trend line obtained from the biphenyl torsion profile. The unsubstituted biphenyl is included for reference and is pointed out by the arrow (●, ortho-substituted;  $\Delta$ , meta- or para-substituted; and  $\times$ , unsubstituted).

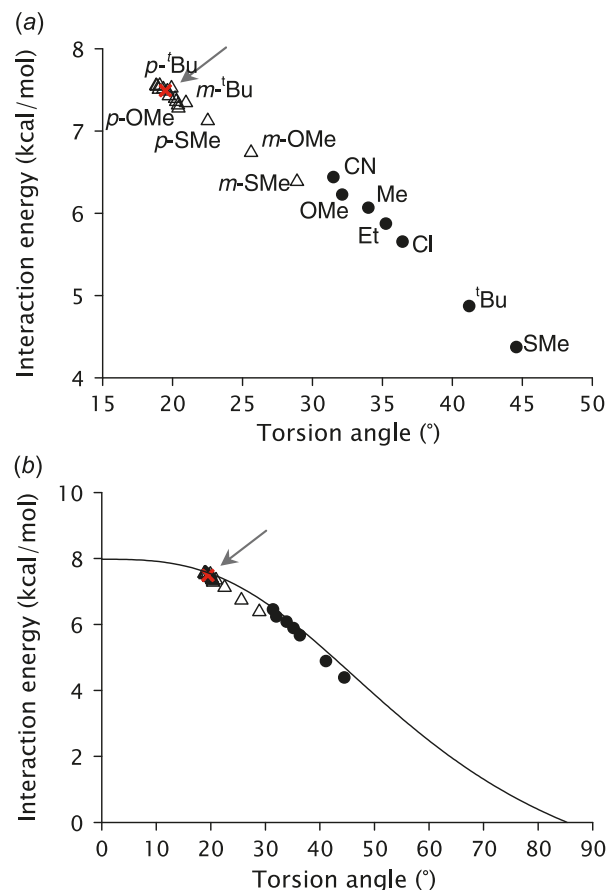


phenyls is negligible, as their torsion angles fall into the narrow range of 37.9 to 39.0° (Table 1), which is close to the torsion angle in the unsubstituted biphenyl. All torsion angles of para-substituted biphenyls also fall into this general range (37.0–38.2°). The values are somewhat smaller than those found for meta-substitution, which is a reflection of the small electronic effect the para-substituents exercise. In fact, Fig. 7b shows that the equilibrium data for the substituted biphenyls from Fig. 7a are superimposed with the corresponding data for the unsubstituted biphenyl torsion (Fig. 4a), which further confirms that the steric effect, controlled by the size of the ortho-substituent, dominates over any electronic effect.

#### Substituted biphenyl radical cations

The equilibrium-geometry torsion angles and  $\pi$ -interaction energies for the substituted biphenyl radical cations are provided in Table 1, and the  $\pi$ -interaction energies are plotted as a function of torsion angle in Fig. 8. Similarly to what was observed for the unsubstituted biphenyl and its radical cation, the  $\pi$ -interaction energy decreases, as expected, with an increase in torsion angle (Fig. 8a), and all substituted radical cations are more planar than their corresponding all-electron counterparts. The changes in torsion angle between substituted all-electron biphenyls and their radical cations,

**Fig. 8.** (a) Average  $\pi$ -interaction energy versus torsion angle for monosubstituted biphenyl radical cations from B3LYP/6–31G(d) calculations. (b) Superposition of the data from (a) with the trend line obtained from the biphenyl radical cation torsion profile. The unsubstituted biphenyl radical cation is included for reference and is pointed out by the arrow (●, ortho-substituted;  $\Delta$ , meta- or para-substituted; and  $\times$ , unsubstituted).

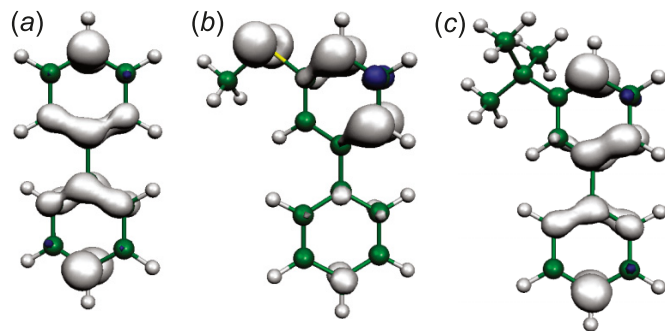


given in Table 1, are consistent with the differences in the electronic properties of the substituents. The decrease in torsion angle ( $\Delta\phi$ ) upon ionization is in the range 10.1 to 21.2° for all substituted biphenyls, except for the *tert*-butyl substituted system with a sizeable  $\Delta\phi$  of 45.0°. As a consequence, and in contrast to the all-electron system, the *ortho-tert*-butyl biphenyl radical cation does not exhibit the largest torsion angle in the series. In fact, a marginally larger torsion angle is found for *ortho*-methylthio (SMe) substitution (Table 1). One important difference between these two substituents is clearly the fact that the sulfur atom possesses electron lone pairs and can thus be easily oxidized, whereas low-energy ionization for the *tert*-butyl system can only be achieved by removal of electrons from the aromatic rings. Because the *tert*-butyl group is electronically simply an observer in the oxidation, the biphenyl unit experiences an increased need for  $\pi$ -electron delocalization, similar to that in the unsubstituted biphenyl radical cation itself, which is counteracted by the size of the *tert*-butyl group. In short, for ortho-substituted biphenyl radical cations, although steric effects still control the equilibrium-geometry torsion angle, electronic effects become apparent.

For the meta- and para-substituted biphenyl radical cations,



**Chart 3.** Spin density plots for (a) unsubstituted, (b) *meta*-methylthio, and (c) *meta-tert*-butyl biphenyl radical cations from B3LYP/6–31G(d) calculations.



ons, a much wider range of torsion angles is found when compared with their all-electron counterparts (a range of  $10^\circ$  versus  $2^\circ$  for the biphenyls), and this can be ascribed to electronic effects. As was observed for the substituted biphenyls, all torsion angles for the para-substituted radical cations are similar to or only slightly smaller than those found for meta-substitution, with two notable exceptions. For methoxyl (OMe) substitution the difference is  $5.3^\circ$  and for methylthio (SMe) substitution it is  $6.4^\circ$ . The  $\Delta\varphi$  values in Table 1 suggest that the two meta-substituted species are not planarized to the same extent as most other biphenyl radical cations. In other words, delocalization across the two aromatic rings is less important in these two cases because of the role of the substituent. Overall, for meta- and para-substitution, electronic effects govern the control of the geometry, and deviations from the torsional profile of the unsubstituted biphenyl radical cation are observed (Fig. 8b). The data show that substitution with electron-donating groups leads to less planarization upon removal of one electron from the molecule. These radical cations remain in more highly twisted equilibrium geometries, with the methylthio-substituted biphenyl radical cations exhibiting the largest torsion angles in their respective series (Table 1). Upon ionization of these biphenyls, in contrast to alkyl-substituted biphenyls, the electron can be removed mainly from the substituent electron lone pairs. As a consequence, the aromaticity of the phenyl rings is less disrupted, and the propensity for planarization in the radical cation is decreased. This is particularly pronounced in the meta-substituted series, where methylthio substitution results in a torsion angle that is larger than that for *tert*-butyl substitution by  $8^\circ$  (Table 1). The spin density plots from B3LYP/6–31G(d) calculations in Chart 3 confirm that the electron is mainly removed from the electron lone-pairs of sulfur for *meta*-methylthio substitution, while it is mainly removed from the phenyl rings for the *meta-tert*-butyl biphenyl radical cation.

## Conclusions

Although at times the spectroscopic behaviour in the UV and visible spectral regions can be used to evaluate the extent of conjugation in organic molecules, the dependence of the energy of the first electronic excitation on the torsion appears to provide a general measure of conjugation only for the unsubstituted biphenyl and its radical cation. General correlations between the excitation energy and the amount

of twist in substituted biphenyls and their radical cations are absent. Equally unsuitable as general measures of conjugation are the bond length and the bond-critical-point electron density of the central C–C bond. The ellipticity at the bond critical point of the central C–C bond only provides a good measure of conjugation for unsubstituted biphenyl species, not for substituted ones.

In contrast, the  $\pi$ -interaction energy, calculated from the  $\pi$ – $\pi^*$  orbital interaction across the central C–C bond connecting the two phenyl rings, provides a good general measure of the delocalization of the  $\pi$ -electrons, as increased  $\pi$ -interaction energies are obtained upon planarization of both the biphenyls and their radical cations. Whereas steric effects controlled by the size of the substituent at the ortho-position prevail over electronic effects for the biphenyls, in the radical cations, electronic effects play an increased role in dictating the twist.

This work suggests that, where traditional indicators fail, the calculated  $\pi$ -interaction energy can be used as a measure of conjugation. Assessing the amount of conjugation is indeed important given the relationship between conjugation and propensity for radical cation formation within systems containing biphenyl templates, such as conducting polymers or natural polymers like lignin.

## Supplementary data

Supplementary data for this article are available on the journal Web site (canjchem.nrc.ca) (tables of vertical excitation energies, absorption wavelengths, and  $\pi$ -interaction energies of biphenyl and its radical cation upon forced torsion; electron densities and ellipticities at the bond critical point of the central C–C bond, and C–C bond lengths for substituted biphenyls and their radical cations; and correlation diagrams for *s*-cis and *s*-trans  $\pi$ -interaction energies of monosubstituted biphenyls and their radical cations).

## Acknowledgements

The authors would like to thank R. Gaudreault for stimulating discussions and an anonymous reviewer for excellent suggestions. This work was funded by the Natural Sciences and Engineering Research Council of Canada (NSERC). Calculations were performed at the Centre for Research in Molecular Modeling (CERMM), which was established with the financial support of the Concordia University Faculty of Arts and Science, the Ministère de l'Éducation du Québec (MEQ), and the Canada Foundation for Innovation (CFI). G.H.P. holds a Concordia University Research Chair.

## References

- (1) Kraft, A.; Grimsdale, A. C.; Holmes, A. B. *Angew. Chem., Int. Ed.* **1998**, 37 (4), 402. doi:10.1002/(SICI)1521-3773(19980302)37:4<402::AID-ANIE402>3.0.CO;2-9.
- (2) Mitschke, U.; Bauerle, P. *J. Mater. Chem.* **2000**, 10 (7), 1471. doi:10.1039/a908713c.
- (3) McGehee, M. D.; Heeger, A. J. *Advanced Materials (Weinheim, Germany)* **2000**, 12 (22), 1655. doi:10.1002/1521-4095(200011)12:22<1655::AID-ADMA1655>3.0.CO;2-2.
- (4) Grimsdale, A. C.; Lupton, J. M. In *Electronic and Optical Properties of Conjugated Molecular Systems in Condensed*

- Phases*; Hotta, S., Ed.; Research Signpost: Kerala, India, 2003; pp 355–375.
- (5) Grimsdale, A. C.; Muellen, K. *Adv. Polym. Sci.* **2006**, *199*, 1–82.
  - (6) Grimsdale, A. C.; Muellen, K. *Adv. Polym. Sci.* **2008**, *212*, 1–48.
  - (7) Pan, J.-F.; Chua, S.-J.; Huang, W. *Thin Solid Films* **2000**, *363*, 1. doi:10.1016/S0040-6090(99)00969-4ym.
  - (8) Schlüter, A.-D.; Wegner, G. *Acta Polym.* **1993**, *44* (2), 59. doi:10.1002/actp.1993.010440201.
  - (9) Park, K. C.; Dodd, L. R.; Levon, K.; Kwei, T. K. *Macromolecules* **1996**, *29* (22), 7149. doi:10.1021/ma960607t.
  - (10) Trotter, J. *Acta Crystallogr.* **1961**, *14* (11), 1135. doi:10.1107/S0365110X6100334X.
  - (11) Hargreaves, A.; Rizvi, S. H. *Acta Crystallogr.* **1962**, *15* (4), 365. doi:10.1107/S0365110X62000894.
  - (12) Charbonneau, G. P.; Delugeard, Y. *Acta Crystallogr. B* **1977**, *B33* (5), 1586. doi:10.1107/S0567740877006566.
  - (13) Charbonneau, G. P.; Delugeard, Y. *Acta Crystallogr. B* **1976**, *B32* (5), 1420. doi:10.1107/S0567740876005487.
  - (14) Suzuki, H. *Bull. Chem. Soc. Jpn.* **1959**, *32* (12), 1340. doi:10.1246/bcsj.32.1340.
  - (15) Eaton, V. J.; Steele, D. *J. Chem. Soc., Faraday Trans. II* **1973**, *69* (11), 1601. doi:10.1039/f29736901601.
  - (16) Schmid, E. D.; Brosa, B. *J. Chem. Phys.* **1972**, *56* (12), 6267. doi:10.1063/1.1677191.
  - (17) Barrett, R. M.; Steele, D. *J. Mol. Struct.* **1972**, *11* (1), 105. doi:10.1016/0022-2860(72)85224-4.
  - (18) Almenningen, A.; Bastiansen, O.; Fernholt, L.; Cyvin, B. N.; Cyvin, S. J.; Samdal, S. *J. Mol. Struct.* **1985**, *128* (1–3), 59. doi:10.1016/0022-2860(85)85041-9.
  - (19) Bastiansen, O.; Samdal, S. *J. Mol. Struct.* **1985**, *128* (1–3), 115. doi:10.1016/0022-2860(85)85044-4.
  - (20) Bastiansen, O.; Borgiel, H.; Saluste, E. *Acta Chem. Scand.* **1949**, *3*, 408. doi:10.3891/acta.chem.scand.03-0408.
  - (21) Häfelinger, G.; Regelman, C. *J. Comput. Chem.* **1987**, *8* (7), 1057. doi:10.1002/jcc.540080714.
  - (22) Grein, F. *J. Phys. Chem. A* **2002**, *106* (15), 3823. doi:10.1021/jp0122124.
  - (23) Lee, C. W.; Pan, D.; Shoute, L. C. T.; Phillips, D. L. *Res. Chem. Intermed.* **2001**, *27* (4–5), 485. doi:10.1163/156856701104202138.
  - (24) Anklam, E.; Asmus, K. D.; Robertson, L. W. *J. Chem. Soc., Perkin Trans. 2* **1989**, (10): 1569. doi:10.1039/p29890001569.
  - (25) Anklam, E.; Asmus, K. D.; Robertson, L. W. *J. Chem. Soc., Perkin Trans. 2* **1989**, (10): 1573. doi:10.1039/p29890001573.
  - (26) Maier, J. P.; Turner, D. W. *Faraday Discuss. Chem. Soc.* **1972**, *54*, 149. doi:10.1039/dc9725400149.
  - (27) Pan, D.; Shoute, L. C. T.; Phillips, D. L. *Chem. Phys. Lett.* **2000**, *316*, 395. doi:10.1016/S0009-2614(99)01359-7.
  - (28) Furuya, K.; Torii, H.; Furukawa, Y.; Tasumi, M. *Chem. Lett.* **1996**, *25* (10), 913. doi:10.1246/cl.1996.913.
  - (29) Furuya, K.; Torii, H.; Furukawa, Y.; Tasumi, M. *THEOCHEM* **1998**, *424* (3), 225. doi:10.1016/S0166-1280(97)00153-X.
  - (30) Kato, C.; Hamaguchi, H.; Tasumi, M. *Chem. Phys. Lett.* **1985**, *120* (2), 183. doi:10.1016/0009-2614(85)87037-8.
  - (31) Buntinx, G.; Poizat, O. *J. Chem. Phys.* **1989**, *91* (4), 2153. doi:10.1063/1.457023.
  - (32) Sasaki, Y.; Hamaguchi, H. *Spectrochim. Acta Part A*, **1994**, *50A* (8–9), 1475. doi:10.1016/0584-8539(94)E0058-1.
  - (33) Bader, R. F. W. *Atoms in Molecules: A Quantum Theory*; Oxford University Press: Oxford, UK, 1990.
  - (34) Casida, M. E.; Jamorski, C.; Casida, K. C.; Salahub, D. R. *J. Chem. Phys.* **1998**, *108* (11), 4439. doi:10.1063/1.475855.
  - (35) Zhang, L.; Peslherbe, G. H.; Muchall, H. M. *Photochem. Photobiol.* **2006**, *82* (1), 324. doi:10.1562/2005-07-08-RA-605. PMID:16313201.
  - (36) Zhang, L.; Muchall, H. M.; Peslherbe, G. H. In *Absorption Spectra of Substituted Phenols and Phenol Radical Cations: Possible Models for Lignin Photochemistry*, Proceedings of the First Applied Pulp and Paper Molecular Modeling Symposium, McGill University, Montreal, QC, Canada, August 24–26, 2005; Gaudreault, R., Whitehead, M. A. T., Ven, T. V. D., Eds.; Cascades Inc.: Montreal, 2006.
  - (37) Zhang, L.; Peslherbe, G. H.; Muchall, H. M. Unpublished data.
  - (38) Hirata, S.; Head-Gordon, M.; Szczepanski, J.; Vala, M. *J. Phys. Chem. A* **2003**, *107* (24), 4940. doi:10.1021/jp0301913.
  - (39) Andersson, K.; Malmqvist, P.-A.; Roos, B. O. *J. Chem. Phys.* **1992**, *96* (2), 1218. doi:10.1063/1.462209.
  - (40) MOLPRO is a package of ab initio programs written by H.-J. Werner, P. J. Knowles, R. Lindh, F. R. Manby, M. Schütz, P. Celani, T. Korona, A. Mitrushenkov, G. Rauhut, T. B. Adler, R. D. Amos, A. Bernhardsson, A. Berning, D. L. Cooper, M. J. O. Deegan, A. J. Dobbyn, F. Eckert, E. Goll, C. Hampel, G. Hetzer, T. Hrenar, G. Knizia, C. Köppl, Y. Liu, A. W. Lloyd, R. A. Mata, A. J. May, S. J. McNicholas, W. Meyer, M. E. Mura, A. Nicklaß, P. Palmieri, K. Pflüger, R. Pitzer, M. Reiher, U. Schumann, H. Stoll, A. J. Stone, R. Tarroni, T. Thorsteinsson, M. Wang, A. Wolf.
  - (41) Frisch, M. J.; Trucks, G. W.; Schlegel, H. B.; Scuseria, G. E.; Robb, M. A.; Cheeseman, J. R.; Montgomery, Jr., J. A.; Vreven, T.; Kudin, K. N.; Burant, J. C.; Millam, J. M.; Iyengar, S. S.; Tomasi, J.; Barone, V.; Mennucci, B.; Cossi, M.; Scalmani, G.; Rega, N.; Petersson, G. A.; Nakatsuji, H.; Hada, M.; Ehara, M.; Toyota, K.; Fukuda, R.; Hasegawa, J.; Ishida, M.; Nakajima, T.; Honda, Y.; Kitao, O.; Nakai, H.; Klene, M.; Li, X.; Knox, J. E.; Hratchian, H. P.; Cross, J. B.; Bakken, V.; Adamo, C.; Jaramillo, J.; Gomperts, R.; Stratmann, R. E.; Yazyev, O.; Austin, A. J.; Cammi, R.; Pomelli, C.; Ochterski, J. W.; Ayala, P. Y.; Morokuma, K.; Voth, G. A.; Salvador, P.; Dannenberg, J. J.; Zakrzewski, V. G.; Dapprich, S.; Daniels, A. D.; Strain, M. C.; Farkas, O.; Malick, D. K.; Rabuck, A. D.; Raghavachari, K.; Foresman, J. B.; Ortiz, J. V.; Cui, Q.; Baboul, A. G.; Clifford, S.; Cioslowski, J.; Stefanov, B. B.; Liu, G.; Liashenko, A.; Piskorz, P.; Komaromi, I.; Martin, R. L.; Fox, D. J.; Keith, T.; Al-Laham, M. A.; Peng, C. Y.; Nanayakkara, A.; Challacombe, M.; Gill, P. M. W.; Johnson, B.; Chen, W.; Wong, M. W.; Gonzalez, C.; Pople, J. A. *Gaussian 03*, Revision C.02; Gaussian, Inc.: Wallingford CT, 2004.
  - (42) Becke, A. D. *Phys. Rev. A* **1988**, *38* (6), 3098. doi:10.1103/PhysRevA.38.3098. PMID:9900728.
  - (43) Lee, C.; Yang, W.; Parr, R. G. *Phys. Rev. B* **1988**, *37* (2), 785. doi:10.1103/PhysRevB.37.785.
  - (44) Stephens, P. J.; Devlin, F. J.; Chabalowski, C. F.; Frisch, M. J. *J. Phys. Chem.* **1994**, *98* (45), 11623. doi:10.1021/j100096a001.
  - (45) Petersson, G. A.; Bennett, A.; Tensfeldt, T. G.; Al-Laham, M. A.; Shirley, W. A.; Mantzaris, J. *J. Chem. Phys.* **1988**, *89* (4), 2193. doi:10.1063/1.455064.
  - (46) Petersson, G. A.; Al-Laham, M. A. *J. Chem. Phys.* **1991**, *94* (9), 6081. doi:10.1063/1.460447.

- (47) Oxgaard, J.; Wiest, O. *J. Phys. Chem. A* **2002**, *106* (15), 3967. doi:10.1021/jp020041c.
- (48) Krishnan, R.; Binkley, J. S.; Seeger, R.; Pople, J. A. *J. Chem. Phys.* **1980**, *72* (1), 650. doi:10.1063/1.438955.
- (49) McLean, A. D.; Chandler, G. S. *J. Chem. Phys.* **1980**, *72* (10), 5639. doi:10.1063/1.438980.
- (50) Koch, U.; Popelier, P. L. A. *J. Phys. Chem.* **1995**, *99* (24), 9747. doi:10.1021/j100024a016.
- (51) Biegler-König, F. *J. Comput. Chem.* **2000**, *21* (12), 1040. doi:10.1002/1096-987X(200009)21:12<1040::AID-JCC2>3.0.CO;2-8.
- (52) Carpenter, J. E.; Weinhold, F. *THEOCHEM* **1988**, *169* (1), 41. doi:10.1016/0166-1280(88)80248-3.
- (53) Foster, J. P.; Weinhold, F. *J. Am. Chem. Soc.* **1980**, *102* (24), 7211. doi:10.1021/ja00544a007.
- (54) Reed, A. E.; Weinhold, F. *J. Chem. Phys.* **1983**, *78* (6 Pt. 2), 4066. doi:10.1063/1.445134.
- (55) Reed, A. E.; Weinhold, F. *J. Chem. Phys.* **1985**, *83* (4), 1736. doi:10.1063/1.449360.
- (56) Reed, A. E.; Weinstock, R. B.; Weinhold, F. *J. Chem. Phys.* **1985**, *83* (2), 735. doi:10.1063/1.449486.
- (57) Reed, A. E.; Curtiss, L. A.; Weinhold, F. *Chem. Rev.* **1988**, *88* (6), 899. doi:10.1021/cr00088a005.
- (58) Glendening, E. D.; Badenhop, J. K.; Reed, A. E.; Carpenter, J. E.; Weinhold, F. *NBO 4.0 M.* [computer program]; Theoretical Chemistry Institute, University of Wisconsin: Madison, WI, 1999.
- (59) Kurland, R. J.; Wise, W. B. *J. Am. Chem. Soc.* **1964**, *86* (9), 1877. doi:10.1021/ja01063a062.
- (60) Carreira, L. A.; Towns, T. G. *J. Mol. Struct.* **1977**, *41* (1), 1. doi:10.1016/0022-2860(77)80034-3.
- (61) Jaime, C.; Font, J. *J. Mol. Struct.* **1989**, *195* (1–2), 103. doi:10.1016/0022-2860(89)80162-0.
- (62) Cheung, D. L.; Clark, S. J.; Wilson, M. R. *Phys. Rev. E* **2002**, *65* (5–1), 051709/1. doi:10.1103/PhysRevE.65.051709.
- (63) Baranyai, A.; Welberry, T. R. *Mol. Phys.* **1991**, *73* (6), 1317. doi:10.1080/00268979100101941.
- (64) Tsuzuki, S.; Tanabe, K. *J. Phys. Chem.* **1991**, *95* (1), 139. doi:10.1021/j100154a030.
- (65) Baranyai, A.; Welberry, T. R. *Mol. Phys.* **1992**, *75* (4), 867. doi:10.1080/00268979200100661.
- (66) Goller, A.; Grummt, U.-W. *Chem. Phys. Lett.* **2000**, *321* (5,6), 399. doi:10.1016/S0009-2614(00)00352-3.
- (67) Karpfen, A.; Choi, C. H.; Kertesz, M. *J. Phys. Chem. A* **1997**, *101* (40), 7426. doi:10.1021/jp971606l.
- (68) Sancho-García, J. C.; Cornil, J. *J. Chem. Theory Comput.* **2005**, *1* (4), 581. doi:10.1021/ct0500242.
- (69) Rubio, M.; Merchan, M.; Orti, E. *Theor. Chim. Acta* **1995**, *91* (1/2), 17.
- (70) Tsuzuki, S.; Uchimaru, T.; Matsumura, K.; Mikami, M.; Tanabe, K. *J. Chem. Phys.* **1999**, *110* (6), 2858. doi:10.1063/1.477928.
- (71) Sullivan, P. D.; Fong, J. Y. *J. Phys. Chem.* **1977**, *81* (1), 71. doi:10.1021/j100516a017.
- (72) Sullivan, P. D.; Fong, J. Y. *Chem. Phys. Lett.* **1976**, *38* (3), 555. doi:10.1016/0009-2614(76)80038-3.
- (73) Arulmozhiraja, S.; Fujii, T.; Morita, M. *J. Phys. Chem. A* **2002**, *106* (44), 10590. doi:10.1021/jp021014p.
- (74) Courtneidge, J. L.; Davies, A. G.; Clark, T.; Wilhelm, D. *J. Chem. Soc., Perkin Trans. 2* **1984**, (7): 1197. doi:10.1039/p29840001197.
- (75) Salaneck, W. R.; Inganas, O.; Nilsson, J. O.; Osterholm, J. E.; Themans, B.; Bredas, J. L. *Synth. Met.* **1989**, *28* (1–2), 451. doi:10.1016/0379-6779(89)90558-4.
- (76) Zhang, H.; Yang, B.; Zheng, Y.; Yang, G.; Ye, L.; Ma, Y.; Chen, X.; Cheng, G.; Liu, S. *J. Phys. Chem. B* **2004**, *108* (28), 9571. doi:10.1021/jp048600y.
- (77) Gadosy, T. A.; Shukla, D.; Johnston, L. J. *J. Phys. Chem. A* **1999**, *103* (44), 8834. doi:10.1021/jp992216x.
- (78) Matta, C. F.; Hernandez-Trujillo, J.; Tang, T.-H.; Bader, R. F. W. *Chem. Eur. J.* **2003**, *9* (9), 1940. doi:10.1002/chem.200204626.
- (79) Poater, J.; Sola, M.; Bickelhaupt, F. M. *Chem. Eur. J.* **2006**, *12* (10), 2889. doi:10.1002/chem.200500850.
- (80) Bader, R. F. W. *Chem. Eur. J.* **2006**, *12* (10), 2896. doi:10.1002/chem.200501589.
- (81) Eliel, E. L.; Wilen, S. H.; Mander, L. N. *Stereochemistry of Organic Compounds*; Wiley: New York, NY, 1994.
- (82) Ruzziconi, R.; Spizzichino, S.; Lunazzi, L.; Mazzanti, A.; Schlosser, M. *Chem. Eur. J.* **2009**, *15* (11), 2645. doi:10.1002/chem.200801963.



# Nonlinear time-dependent density functional theory investigation and visualization of ionizations in CO<sub>2</sub>—Effects of laser intensities and molecular orientations

Emmanuel Penka Fowe and André Dieter Bandrauk

**Abstract:** Time-dependent density functional theory (TDDFT) studies of the ionization of CO<sub>2</sub> by intense laser pulses  $I_0 \geq 1 \times 10^{14}$  W/cm<sup>2</sup>, at 800 nm are presented using the LB94 and the LDA potentials. Results reveal that for lower laser peak intensity,  $I_0 = 3.5 \times 10^{14}$  W/cm<sup>2</sup>, the highest occupied molecular orbital (HOMO) contributes significantly to ionization owing to its lower ionization potential (IP), whereas the inner orbitals play the important role for higher laser peak intensities. Even though such lower orbitals have higher IP, the ionization process occurs when orbital densities are maximum along the direction of the laser field polarization. These findings are confirmed through the analysis of the images from the time-dependent electron localization function (TDELf) and the spectra of higher order harmonic generation (HOHG). Additionally, in spite of the IP difference between Kohn–Sham orbitals from LDA and LB94 potentials, our results show almost the same trend for both.

**Key words:** TDDFT, orbital ionization, TDELf, HOHG.

**Résumé :** On rapporte les résultats d'études faites en utilisant le potentiel LB94 et LDA et la théorie de la densité fonctionnelle dépendante du temps (TDFDT) sur l'ionisation du CO<sub>2</sub> en champ laser intense,  $I_0 \geq 1 \times 10^{14}$  W/cm<sup>2</sup>, à 800 nm. Les résultats démontrent que, pour une intensité plus faible du pic laser, intensités  $I_0 = 3,5 \times 10^{14}$  W/cm<sup>2</sup>, à 800 nm, l'orbitale moléculaire hautement occupée (OMHO), contribue d'une façon significative à l'ionisation en raison de son potentiel d'ionisation (PI) plus faible, alors que pour les intensités de pics laser plus élevées, ce sont les orbitales internes qui jouent le rôle principal. Bien que les orbitales inférieures soient caractérisées par des potentiels d'ionisation, PI, plus élevés, le processus d'ionisation se produit quand les densités d'orbitales sont maximal dans la direction du champ de polarisation du laser. Ces observations sont confirmées par une analyse des images obtenues à partir de la fonction de localisation de l'électron dépendante du temps (FLEDt) et des spectres de génération d'harmonique d'ordre élevé (GHOE). De plus, malgré la différence de potentiels d'ionisation entre les orbitales Kohn Sham obtenues à l'aide des potentiels LB94 et LDA, les résultats présentés dans ce travail montrent la même tendance pour les deux.

**Mots-clés :** théorie de la densité fonctionnelle dépendante du temps (TDFDT), ionisation d'orbitale, fonction de localisation de l'électron dépendante du temps (FLEDt), génération d'harmonique d'ordre élevé (GHOE).

## Introduction

In recent years, the interaction of atoms and molecules with intense laser pulses has attracted widespread research. One of the reasons is that laser fields induce interesting nonlinear electron dynamics such as multiphoton ionization<sup>1</sup> (MPI), above threshold ionization<sup>2</sup> (ATI), and tunnelling ionization<sup>3</sup> (TI). Numerous experiments on molecular ionization have been performed<sup>4</sup> thanks to the refinement of the techniques<sup>5</sup> of molecular orientation and alignment. While experimental efforts for better understanding of the ionization processes are growing, theoretical investigations are still limited, even though computational power is increasing rapidly. The first step for a one-electron system is

accurate numerical solution of the time-dependent multidimensional Schrödinger equation (TDSE), followed by propagation of pulses in molecular media through Maxwell's equations.<sup>6</sup> The major difficulties in the theoretical study of molecular systems in a laser field reside on the multi-centre nature of the molecule including the treatment of the electron–electron interactions.<sup>7–9</sup> In the present work, we focus on time-dependent density functional theory (TDDFT) methods as one tool for studying the nonlinear nonperturbative response of molecules to intense ultrashort laser pulses.<sup>10</sup> As an example, simple TDDFT functionals have been used to characterize pulses interacting with metal surfaces.<sup>11</sup> Density functional theory (DFT) has become an ubiquitous method

Received 13 July 2010. Accepted 20 April 2010. Published on the NRC Research Press Web site at canjchem.nrc.ca on 5 November 2010.

*This article is part of a Special Issue dedicated to Professor R. J. Boyd.*

**E.P. Fowe and A.D. Bandrauk.**<sup>1</sup> Laboratoire de Chimie Théorique, Faculté des Sciences, Université de Sherbrooke, Sherbrooke, QC J1K 2R1, Canada.

<sup>1</sup>Corresponding author (e-mail: Andre.Dieter.Bandrauk@USherbrooke.ca).



of solving ground-state electronic problems in atoms and molecules.<sup>12</sup>

For the visual understanding of the electron motion in CO<sub>2</sub> during the time propagation under strong laser pulses, we used the time-dependent approach of the electron localization function (ELF).<sup>13</sup> Conceptually, the physical idea is based on the fact that a highly localized electron repels other electrons more strongly. Then the ELF makes use of the probability to find a second like-spin electron in the vicinity of the first one as a measure for electronic localization. Numerical values of the probability are conveniently mapped on the interval [0,1] facilitating analysis and interpretation. So, in areas where two electrons of the same spin have a high probability to be found (with respect to the homogeneous gas) the function should tend to 0 by construction. It follows that, in areas where the probability of finding two electrons of opposite spin (when present) is smaller than the one of finding two electrons of same spin, the function tends to 1. As such, a region of the space with a high value of ELF corresponds to a region where it is more likely to localize an electron or a pair of electrons in relation to the original Lewis original definition of bonding. When applied to molecules, the advantage of ELF is to show a clear separation between the core and valence electrons, and thus, it shows covalent bonds and lone pairs, in the spirit of valence shell electron pair repulsion theory (VSEPR).<sup>14</sup> Here, our goal is to shed light onto the effect of different laser intensities on the molecular regions (bond, lone pair).

## Methods

### Nonperturbative TDDFT Kohn–Sham formalism

The TDDFT method provides the most detailed and feasible ab initio approach for tackling many-body problems. DFT as first introduced by Hohenberg and Kohn<sup>15</sup> and extended by Kohn and Sham<sup>16</sup> (KS) is based on the existence of an exact mapping between one-particle density and external potentials. This leads to the density of the interacting system being obtained from the density of an auxiliary system of noninteracting particles moving in an effective local single-particle potential. A time-dependent generalization of DFT was provided by Runge and Gross,<sup>17</sup> showing that there is a one-to-one correspondence between the external (time-dependent) potential ( $v_{\text{ext}}(r, t)$ ) and the time-dependent one-electron density ( $n(r, t)$ ) for many-body systems evolving from a fixed initial state. The time-dependent electronic density is written as:<sup>18</sup>

$$[1] \quad n(r, t) = \sum_{\sigma=\uparrow, \downarrow} n_{\sigma}(r, t) = \sum_{\sigma=\uparrow, \downarrow} \sum_i^{N_{\sigma}} |\psi_{i\sigma}(r, t)|^2$$

where  $N_{\sigma}$  is the number of the occupied KS orbital in the spin state  $\sigma$  and  $\psi_{i\sigma}(r, t)$  is the orbital obtained through the time-dependent KS equations (in au):

$$[2] \quad i \frac{\partial}{\partial t} \psi_{i\sigma}(r, t) = \left[ -\frac{1}{2} \nabla^2 + v_{\text{eff}}(r, t) \right] \psi_{i\sigma}(r, t)$$

where

$$[3] \quad v_{\text{eff}}(r, t) = v_{\text{ext}}(r, t) + v_h(r, t) + v_{xc,\sigma}(r, t)$$

the first term is the external potential owing to the interaction of the electron with an external laser field and the nuclei, the second term accounts for the classical Hartree electrostatic interaction between electrons, and the third term is the exchange correlation (xc) potential that includes all non-trivial many body effects, and has an extremely complex (and essentially unknown) functional<sup>16,19</sup> dependence on the density. When an intense electric with a low frequency field is applied to a molecule, electrons tend to be displaced out by ionization; thus, the higher the ionization potential (IP) or barriers, the more this electronic displacement will be hindered. Therefore, the choice of an approach that accurately reproduces the experimental IP is useful for our analysis. For this work, we have used the local density approximation (LDA), which has been widely used in strong fields<sup>10</sup> owing to its simplicity and applicability to various systems with relatively lower computational cost. However, LDA is constructed from homogenous gas systems and suffers from the wrong asymptotic behavior originating from the incomplete cancellation of the self-interactions. For these reasons, we have also used the Van Leeuwen and Baerends<sup>20</sup> potential (LB94) for comparison, which introduces a gradient correction to the LDA exchange correlation so as to reproduce the Coulomb asymptotic behavior of the potential. A convenience of the LB94 potential lies in its explicit dependency on the local density and its gradient. This potential yields good estimates of the IP for atoms and small molecules, especially in the framework of the linear response TDDFT excitation energy.<sup>21</sup> This model potential significantly corrects the higher moments of the density, notably for diffuse outer orbitals involved in excitations and in our case in ionization. The LB94 also includes partial and considerable self-interaction correction (SIC), resulting from an interaction of an electron with itself, of importance to electronic transport.<sup>22</sup> Such corrections are known to produce spurious oscillations in photoionization calculations,<sup>23</sup> but little is known about the corrections for strong fields in the nonperturbative regime. Our results show that the LB94 potential offers accurate IPs for all orbitals; an essential starting point for accurate ionization.

### Time-dependent electron localization function (TDELf)

The ELF is a method for the mapping of electron pair probability in multi-electron systems. It was first introduced by Becke and Edgecombe<sup>24</sup> as a descriptor of electronic localization, using arguments based on the conditional same-spin pair probability function. Here, we briefly recall the definitions of the extension of the ELF for time-dependent processes.<sup>13</sup> The time-dependent ELF or TDELf ( $\eta(r, t)$ ) is given as

$$[4a] \quad \eta(r, t) = \frac{1}{1 + \left[ \frac{C(r, t)}{C_h(r, t)} \right]^2}$$

where

$$[4b] \quad C(r, t) = \sum_{\sigma} \left\{ \sum_{i=1}^{N_{\sigma}} |\nabla \psi_{i\sigma}(r, t)|^2 - \frac{1}{4} \frac{[\nabla n_{\sigma}(r, t)]^2}{n_{\sigma}(r, t)} - \frac{j_{\sigma}^2(r, t)}{n_{\sigma}(r, t)} \right\}$$

$$[4c] \quad C_h(r, t) = \frac{3}{5} (6\pi^2)^{2/3} n_\sigma(r, t)^{5/3}$$

where  $j_\sigma^2$  is the squared modulus of the current density and  $C(r, t)$  measures the probability of finding one electron in the near vicinity of a reference like-spin electron at position  $r$  and time  $t$ . Thus, the Pauli repulsion between two like-spin electrons, described by the smallness of  $C(r, t)$ , is taken as a measure of the electron localization.  $C_h(r, t)$  is the corresponding factor found for uniform electron gas, i.e., a homogeneous electron gas whose density is the same as that of the real system. Equation [4b] is valid only for one-determinantal wave functions, and therefore lends itself to be used within the context of HF or DFT. The TDELf will be used for the time-resolved observation of the molecular ionization and can thus provide a visual understanding of the particle dynamic (most notably lone pair and bond electrons) under strong laser pulses.

## Computational details

In the present work, the TDDFT KS equation (eq. [2]) was discretized in space using finite-difference (FD) grid techniques. For numerical reasons we represent the electron-ion interaction by the norm conserving nonlocal Troullier-Martins pseudopotential,<sup>25</sup> which allows explicit treatment of many fewer electrons and avoidance of the fast oscillations produced by the core electrons. The pseudopotentials are generated such that the pseudo-wave functions imitate the all-electron atomic wave functions. The C–O bond length is set to its experimental<sup>26</sup> value, CO = 0.1162 nm, and the CO<sub>2</sub> molecule is placed in a large three-dimensional (3D) cubic grid cell (atomic units (au) are used) of dimension  $|z_{\max}| = 40$  au (1 au = 0.0529 nm). The uniform FD grid spacing ( $\Delta z = 0.28$  au) was used and the convergence of the calculations was checked against results making use of a smaller grid spacing. The size of the grid is determined by the maximum radius  $\alpha = E_0/m\omega^2$  of an electron in a time-dependent electric field of maximum amplitude  $E_0$ . Thus, at  $E_0 = 0.1$  au corresponding to an intensity  $I_0 = 3.50 \times 10^{14}$  W/cm<sup>2</sup> (1 au:  $I_0 = 3.50 \times 10^{16}$  W/cm<sup>2</sup>,  $E_0 = 5 \times 10^9$  V/cm),  $\alpha = 30$  au at  $\lambda = 800$  nm,  $\omega = 0.057$  au. The external potential created by an intense laser field is assumed to arise from an oscillating electric field with a cosine envelope. When the laser is polarized parallel to the molecular axis  $z$ ,  $v_{\text{ext}}(r, t)$  is given by

$$[5] \quad v_{\text{ext}}(r, t) = zE_0 \cos^2\left(\frac{\pi t}{T}\right) \sin(\omega t) \quad (0 \prec t \prec T)$$

where  $T$  determines the laser pulse duration. The laser intensity is related to the field strength by  $I = \frac{1}{2} \epsilon_0 c E_0^2$ , where  $\epsilon_0$  is the permittivity of free space and  $c$  is the speed of the light. The angle ( $\theta$ ) between the linear polarized laser and the main molecular axis varies from 0° to 90°. The total area condition  $\int_{-\infty}^{+\infty} E(t) dt = 0$  is verified to ensure that there are no spurious static effects.<sup>3,9</sup> The time-dependent equation (eq. [2]) are solved using the Crank–Nicholson scheme<sup>27</sup> with  $\Delta t = 0.02$  au (1 au =  $24 \times 10^{-18}$  s) as the time step. All calculations use an eight optical cycle pulse duration.

## Orbital ionization

To absorb the ionized charge density and avoid reflections at the boundary of the box owing to ionization during the propagation, we employed a mask function. By using this technique, the KS wave function is multiplied in each time step by a function  $M(z)$ , which is 1 in the inner simulation region and gradually goes to 0 at the borders. The masking function in one dimension is defined as

$$[6] \quad M(z) = \begin{cases} \sin^4\left(\frac{z_{\max} - |z|}{2a}\pi\right) & (z_{\max} - |z| \prec a) \\ 1 & (\text{otherwise}) \end{cases}$$

where  $z_{\max} = 40$  au is the extension of the box in the  $z$  direction and  $a = 6$  au is the width of the mask function. It is assumed that the electrons in the  $z_{\max} \succ |z|$  domain are completely ionized and cannot return to the nuclei. A different approach to remove outgoing flux density consists of an addition of an imaginary potential<sup>28</sup> that causes an exponential decay of the wave function or in using the exterior complex scaling coordinate transformation as the absorbing boundary.<sup>29</sup> The time-dependent ionization probability ( $P_{i,\sigma}(t)$ ) of an individual spin-orbital population is calculated as<sup>10</sup>

$$[7] \quad P_{i,\sigma}(t) = 1 - N_{i,\sigma}(t)$$

where  $N_{i,\sigma}(t) = \langle \psi_{i,\sigma}(r, t) | \psi_{i,\sigma}(r, t) \rangle$  is the time-dependent population (survival probability) of the  $i, \sigma$ -th spin population.

## Higher order harmonic generation

Molecular high order harmonic generation<sup>9</sup> (MHOHG) is a highly nonlinear nonperturbative effect resulting from two essential steps: (i) ionization at the peaks of an electromagnetic pulse  $E(t)$  of maximum amplitude  $E_0$  (eq. [4]), followed by (ii) laser-induced recollision after 2/3 of a cycle with maximum energy of harmonics of order  $N_m$ ,  $N_m\omega = \text{IP} + 3.17U_p$  where  $N_m$  is the order of the harmonics and  $U_p = I_0/4m\omega^2$  is the ponderomotive energy.<sup>30</sup> Calculations of MHOHG with ultrashort (a few cycles) intense  $I_0 \geq 10^{14}$  W/cm<sup>2</sup> requires special attention to grid sizes and gauges as mentioned in recent works.<sup>31</sup> In the present work, the MHOHG is calculated during the dynamical propagation as follows.<sup>10</sup> The time-dependent dipole  $\vec{d}(t) = e^n(\vec{r}, t) \vec{r} d^3r$  is recorded at time intervals  $\Delta t = 0.02$  au. Recent works have shown that the most accurate method for generating the MHOHG spectra when dealing with molecular systems<sup>9,31</sup> is to calculate the dipole acceleration ( $\ddot{d}_z(t)$ ), according to Ehrenfest's theorem.<sup>8</sup> The power spectrum of  $\ddot{d}_z(t)$  in a given direction yields to the predicted High order harmonic generation (HHG) spectra.<sup>31</sup>

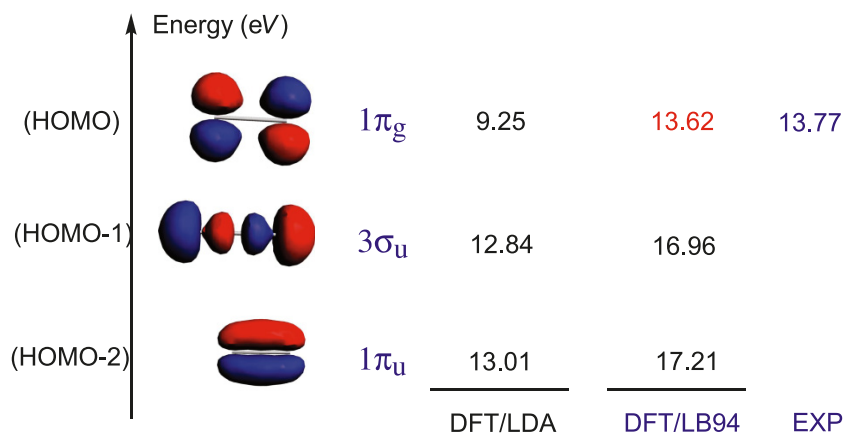
$$[8] \quad S_z(\omega) \propto |a(\omega)|^2 = \left| \int \left[ \frac{d^2}{dt^2} d_z(t) \right] e^{i\omega t} dt \right|^2$$

## Results and discussion

### Electronic analysis and IP

The relevant information about the ground-state geometry of CO<sub>2</sub> is that the molecule is linear with an equilibrium C–O bond length  $R = 0.1162$  nm. The analysis of the electronic

**Fig. 1.** DFT images of the molecular orbitals of CO<sub>2</sub>. Only the three highest relevant occupied molecular orbitals (HOMO, HOMO-1, and HOMO-2) are shown.



structure from the DFT-KS calculation is depicted in Fig. 1, where the three highest occupied KS molecular orbitals (HOMO, HOMO-1, and HOMO-2), with their phases, are presented. The nodal properties that correctly reflect the  $g$  and  $u$  symmetry character of the orbitals are visible. One finds that the HOMO is the antibonding ( $1\pi_g$ ) formed of  $\pi$  lobes lying perpendicular to the internuclear axis and located on the oxygen atoms. The computed eigenvalue of the relevant HOMO, HOMO-1, and HOMO-2 are 9.25, 12.84, and 13.01 eV, respectively, for LDA and 13.62, 16.96, and 17.21 eV, respectively, for the LB94 potential. Comparison with the experimental values of 13.8, 18.1, and 17.6 eV reveals<sup>32</sup> the expected underestimation of the HOMO eigenvalue by the LDA, the computed value being ~43% lower when compared with the experimental data. The origin of this large discrepancy lies in the wrong asymptotic behaviour of the LDA. The LB94 potential, on the other hand, performs much better, the global agreement with the experiment being within 5%. We note a near constant (~4 eV) difference between the LDA and LB94 IPs.

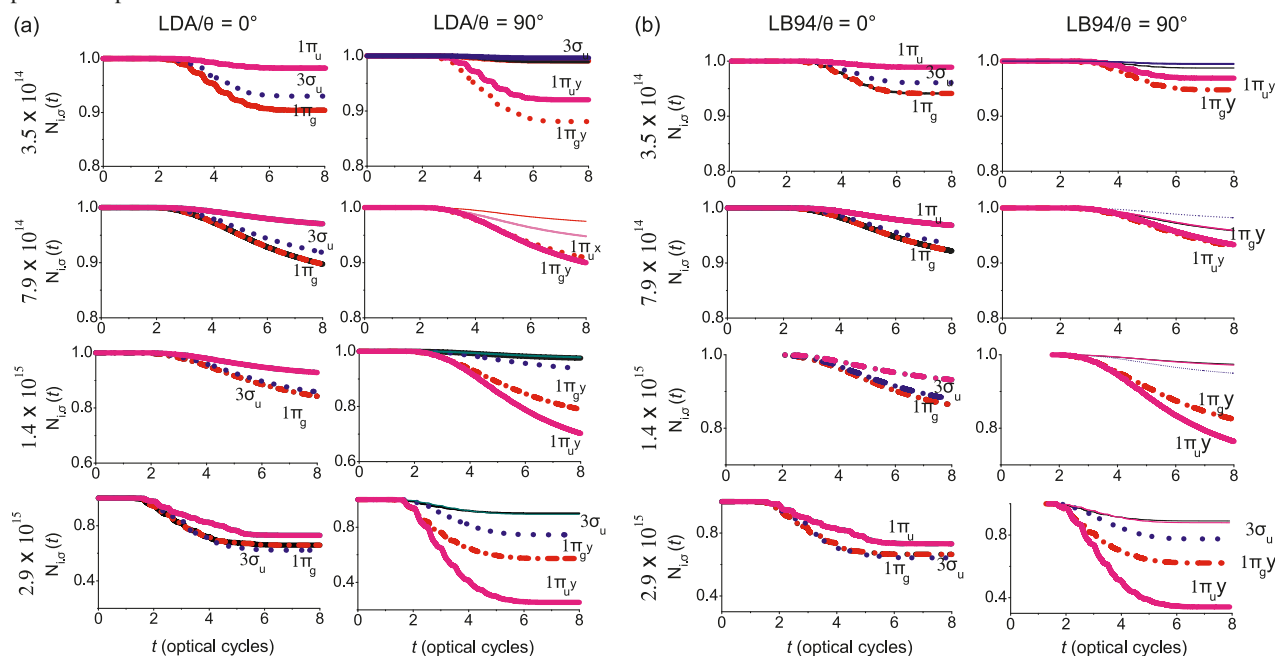
### KS orbital ionization

Our time-dependent calculation allows a detailed analysis of the ionization process as it evolves with time. From the initial ground state, we have propagated in time the KS orbitals with different laser peak intensities ( $3.50 \times 10^{14}$ ,  $7.90 \times 10^{14}$ ,  $1.40 \times 10^{15}$ , and  $2.99 \times 10^{15}$  W/cm<sup>2</sup>) at the 800 nm wavelength. The calculations used eight optical cycle pulse duration. Two molecular orientations have been considered,  $\theta = 0^\circ$  and  $90^\circ$ . Figures 2a and 2b show the results with the LDA and the LB94 potentials, respectively, for the selected KS orbitals. For  $\theta = 0^\circ$ , the two degenerate components of each  $\pi$  orbital have the same behaviour, whereas the symmetry is broken for the other orientations.

We have renamed those KS orbitals as  $1\pi_{gx}$  and  $1\pi_{gy}$  for  $1\pi_g$  and we did the same for the  $1\pi_u$  components. From the figures, one clearly notes a strong dependence of the orbital electron population ( $N_{i,\sigma}(t)$ ), with the laser intensities. Therefore, the higher the laser intensity, the lower the remaining electron population. One also finds that the ionization is sensitive to the orientation ( $\theta$ ) of the molecule with respect to the laser field. Similar results have been observed in H<sub>2</sub><sup>+</sup> from exact TDSE calculations.<sup>7,8</sup> It also emerges, as ex-

pected, that the KS orbital ionization yield computed using the LDA functional is larger than what was obtained from the LB94 potential because of its lower IP. A close look at these figures reveals that for the lowest laser intensity ( $3.50 \times 10^{14}$  W/cm<sup>2</sup>) independent of the potential used and the orientation  $\theta$ , the HOMO,  $1\pi_g$ , molecular orbital shows the dominant response to the laser field. It is followed by the inner  $3\sigma_u$ , HOMO-1 when  $\theta = 0^\circ$  and by the  $1\pi_u$  KS orbital when  $\theta = 90^\circ$ . By increasing the laser peak intensity to  $7.90 \times 10^{14}$  W/cm<sup>2</sup>, the result is almost the same as the previous peak intensity when  $\theta = 0^\circ$ , but with  $\theta = 90^\circ$  the HOMO  $1\pi_g$  shows the dominant response to the laser field followed by the HOMO-2  $1\pi_u$  with the LB94, whereas the opposite trend is observed with the LDA potential. This behaviour is related to the lower IP of the HOMO-2 for the LDA potential 13.01 eV compared with 17.21 eV for the LB94 potential. For the  $1.40 \times 10^{15}$  laser peak intensity, one notices the KS molecular orbital ionization enhancement with both potentials, the bonding  $1\pi_g$  and the  $3\sigma_u$  ( $3\sigma_u$  is still more pronounced) when  $\theta = 0^\circ$ , whereas the HOMO-2  $1\pi_u$  shows the dominant response to the field for  $\theta = 90^\circ$ . Finally, with the  $2.99 \times 10^{15}$  W/cm<sup>2</sup> laser intensity, our results reveal that the inner  $3\sigma_u$  molecular orbital presents the dominant response to the field, whereas the effect of the valence  $1\pi_g$  orbital on the ionization process decreases and is getting closer to that of the  $1\pi_u$  orbital for  $\theta = 0^\circ$ . This is related to the symmetry of the  $3\sigma_u$  whose electron density is along the molecular axis; this gives rise to a high ionization yield when aligned parallel to the laser electric field. When  $\theta = 90^\circ$ , the HOMO-2  $1\pi_u$  shows the dominant response to the laser field, this comes from the bonding character (ionization enhancement) of the HOMO-2  $1\pi_u$ , which possesses the right symmetry and maximum density to interact more properly with the laser polarized perpendicularly to the molecular axis. Although this orbital has a larger IP than the HOMO  $1\pi_g$ , its density dominates at  $90^\circ$ , whereas the HOMO,  $1\pi_g$  has a node (zero density) at  $90^\circ$  in the centre of the molecule. In general, one finds that the main difference between the results for the LDA and LB94 potentials comes only from the ionization slope that lies only in their IP difference. We conclude that for the two potentials, orbitals that have maximum density in the direction of laser polarization will influence or dominate in ionization. This will

**Fig. 2.** (a) Time-dependent Kohn–Sham orbital population,  $N_{i,\sigma}(t)$ , using Local density approximation (LDA) potential at  $I_0 = 3.50 \times 10^{14}$ ,  $7.90 \times 10^{14}$ ,  $1.40 \times 10^{15}$ , and  $2.99 \times 10^{15}$  W/cm<sup>2</sup> laser peak intensities for  $\theta = 0^\circ$  and  $90^\circ$ . (b) Time-dependent Kohn–Sham orbital population,  $N_{i,\sigma}(t)$ , using LB94 potential at  $I_0 = 3.50 \times 10^{14}$ ,  $7.90 \times 10^{14}$ ,  $1.40 \times 10^{15}$ , and  $2.99 \times 10^{15}$  W/cm<sup>2</sup> laser peak intensities for  $\theta = 0^\circ$  and  $90^\circ$ .  $\theta$  is the angle between the molecular axis and the laser polarization direction. Only the relevant Kohn–Sham orbitals that possess an important response to the laser field are shown with their labels.



be checked in the TDEL processes and in the MHOHG spectrum as follows.

### TDEL analysis

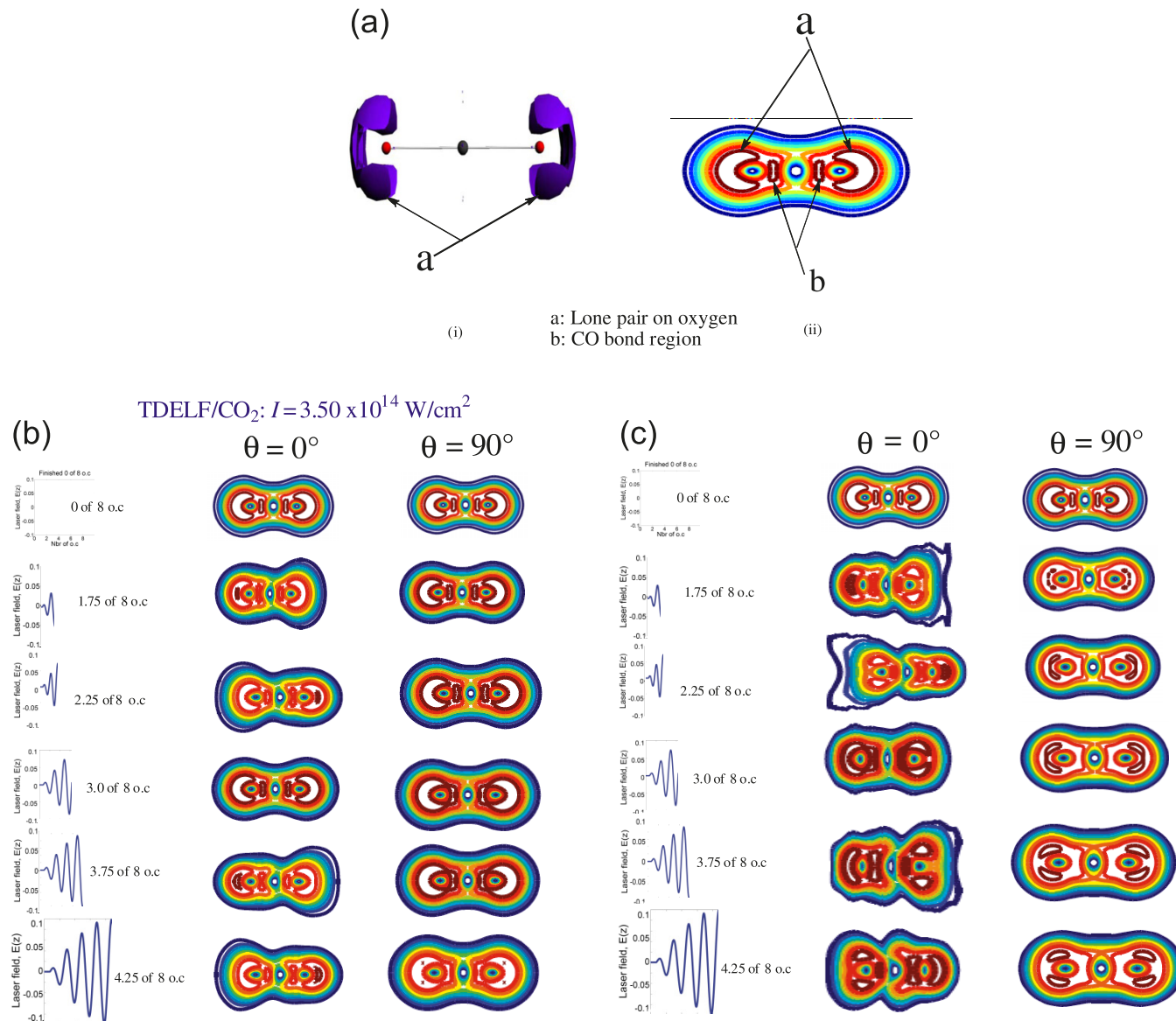
The ground-state ELF pictures are shown in Fig. 3a for  $\eta = 0.8$  (left) and the two-dimensional representation of the ELF isosurfaces in the plane containing the three atoms of the molecule (right). At  $\eta = 0.8$  (left), the image exhibits only the lone pair (noted a) of the oxygen atom, whereas the C–O bond localization is absent; this is because the lone pair electron on the oxygen is the most localized in the CO<sub>2</sub> molecule. By representing the ELF from the plane containing the three atoms (right), one can easily identify the C–O chemical bond region (note b). From the electronic structure analysis (Fig. 1), it is evident that the HOMO,  $1\pi_g$  is essentially located in region (a), whereas the HOMO-1,  $3\sigma_u$ , and the HOMO-2,  $1\pi_u$  are essentially located in region (b). Such clear separation between HOMO and relevant inner orbitals (shape and IP) of the KS ionization process as described in the KS orbital ionization section). Figures 3b and 3c represent the TDEL images for  $\theta = 0^\circ$  and  $90^\circ$  using two different laser peak intensities,  $3.50 \times 10^{14}$  and  $2.99 \times 10^{15}$  W/cm<sup>2</sup> with the LB94 potential; the corresponding time propagation is also shown.

For the  $3.50 \times 10^{14}$  W/cm<sup>2</sup> laser peak intensity, when  $\theta = 0^\circ$ , the first major perturbation occurs after 1.75 optical cycles (oc). Note that the dissymmetric distribution of the electron density on the two oxygen atom shows that the two atoms do not simultaneously experience the same laser field strength, and that depending on the sign of the electric field, the perturbation successively affects each of the oxygen atoms (Fig. 3 shows that at 1.75 oc, the oxygen atom at the

left-hand side is the most affected, whereas at 2.25 oc, the oxygen atom of the right-hand side shows the dominant response to the field). As expected from the previous KS ionization analysis, the figure shows that the major part of the perturbation is located in the region corresponding to the lone pair region ( $1\pi_g$ ). As our propagation evolves the intensity of the perturbation on the lone pair domain increases as well, reaching a maximum for the extrema (minimum, 3.75 oc, or maximum, 4.25 oc) of the external electric field and seeming to disappear around zero values of the external field (e.g., at 3.0 oc). The weak deformation on the C–O bond domain reflects the contribution of the inner orbital into the molecular ionization process in agreement with the previous KS ionization finding. For  $\theta = 90^\circ$ , the first noticeable perturbation occurs after 1.75 oc and corresponds to the lengthening of the lone pair region on the oxygen atoms of CO<sub>2</sub>. The perturbation is symmetrically distributed on the system; this effect reflects the fact that the two oxygen atoms simultaneously feel the same effect of the perpendicular laser field. As the time propagation evolves (3.75 and 4.25 oc), one also sees that the dominant response comes from the lone pair region. Most notably, one observes that during the propagation, the electronic perturbation is mainly characterized by an interaction between the lone pair and the bonding C–O region. This may be regarded as the manifestation of the enhancement of the ionization of the bonding  $1\pi_u$  molecular orbital located on the C–O bond region. Evidence of the laser field intensity is noticeable, the stronger the intensity peak value and the higher the perturbation. One remarks that the electron density perturbation does not disappear around the zero values of the laser field. Results using the  $2.99 \times 10^{15}$  W/cm<sup>2</sup> laser peak intensity are depicted in Fig. 3c.



**Fig. 3.** (a) DFT/LB94 representation of the electron localization function ground state of the CO<sub>2</sub> molecule. (b) Snapshot of the isosurface of the time-dependent electron localization function (TDELf) images for  $I_0 = 3.5 \times 10^{14}$  W/cm<sup>2</sup> as the CO<sub>2</sub> molecule evolves in the laser field. (c) Snapshot of the isosurface of the TDELf images for  $I_0 = 2.99 \times 10^{15}$  W/cm<sup>2</sup> as the CO<sub>2</sub> molecule evolves in the laser field. Calculations are done for  $\theta = 0^\circ$  and  $90^\circ$ .



For  $\theta = 0^\circ$ , one finds that the first major perturbation starts closer to the beginning of the propagation and it is mostly localized on one of the lone pair regions of the molecule. Thereafter, the disymmetric perturbation appears instantaneously on the C–O bond and the lone pair domain (1.75 o.c), its effect increasing with the duration of the propagation. Therefore, it is difficult to identify which part of the system presents the dominant response to the field; this reflects the contribution of both the HOMO KS orbital (owing to its lower IP) and the inner  $3\sigma_u$  MO (owing to its shape or its electron density, which is maximal along the polarization of the electric field). These results corroborate our finding in the previous section concerning the KS ionization. When  $\theta = 90^\circ$ , at the beginning of the propagation, the electron depletion occurs on the lone pair region and is characterized by lengthening of this region. The image shows that at 1.75 o.c,

the interaction between the lone pair density and that of the C–O bond is visible, and an amount of electron depletion is noticeable in the lone pair region. The symmetric distribution of the electron density perturbation in the two oxygen atoms is clearly evident. As the propagation evolves, the bi-partition of the perturbation domain of the lone pair orbital of each oxygen atom is observable and tends to enhance the overlap between the lone pair and the C–O bonding region. This can be seen as the strong perturbation (ionization) of the inner  $1\pi_u$  KS orbital. These observations are consistent with our results in Figs. 2a and 2b, which show that the IP and the shape of the KS orbital are the main factors that define its ionization. At lower laser peak intensity, the IP is the main factor, whereas at higher laser peak intensity, the ionization of the KS orbital is influenced by its shape.

### Higher order harmonic generation

In Figs. 4a and 4b, we present the MHOHG power spectra, eq. [8] emitted by CO<sub>2</sub> computed with the LB94 potential. Two angular orientations of the molecule ( $\theta = 0^\circ$  and  $90^\circ$ ) with respect to the laser field polarization axis are considered. Calculations are done at the lower  $3.50 \times 10^{14}$  and the higher  $1.40 \times 10^{15}$  W/cm<sup>2</sup> laser intensities to observe the effect of inner orbitals. An overview of these pictures shows that in general, the overall shapes of the power spectra for these two laser intensities are similar.

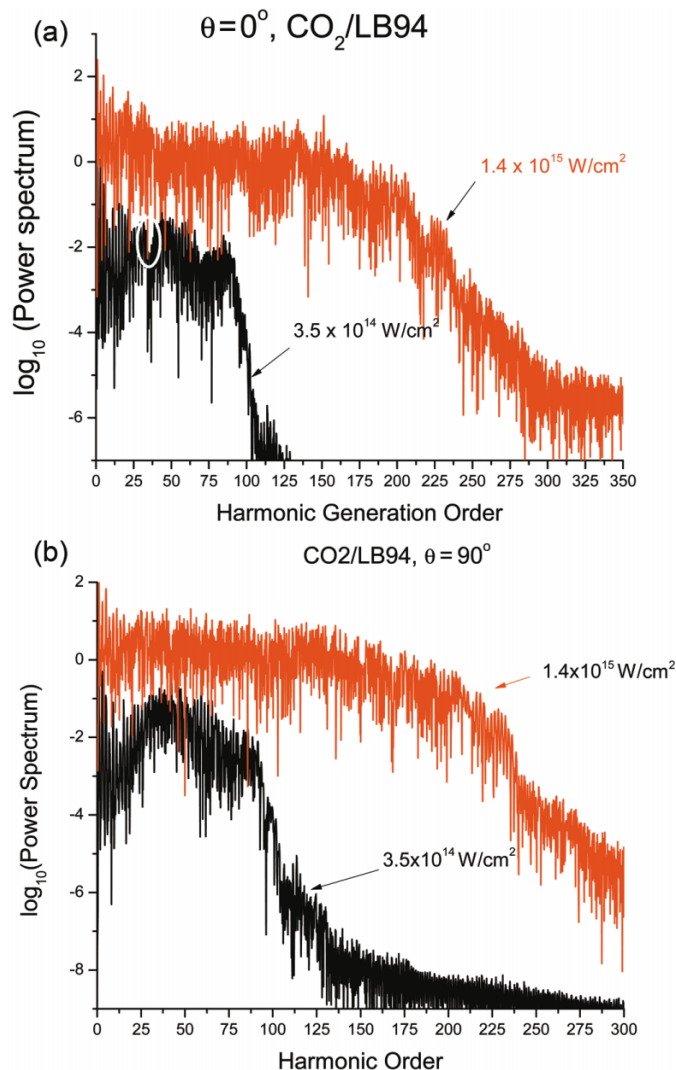
For the two orientations, features of these spectra strongly resemble those of harmonic spectra from atoms: a sharp decrease after the first few harmonics, followed by a "plateau," and ending with a "cut-off" that usually determines the highest harmonic order achievable. One also notes that the cut-off is independent of the molecular orientation and is located approximately at the 91st harmonic for the  $3.50 \times 10^{14}$  W/cm<sup>2</sup> laser peak intensity and around the 237th harmonic order for  $1.40 \times 10^{15}$  W/cm<sup>2</sup>. For the latter, one observes that the cut-off domain is not abrupt like that of  $3.50 \times 10^{14}$  W/cm<sup>2</sup>. This is most probably related to the size of our box, which is not large enough to allow the ionized electron to acquire a maximum velocity in the continuum. The figure shows that the power spectrum amplitude is sensitive to the laser peak intensity. For  $\theta = 0^\circ$  (Fig. 4a), a close look at the plateau region shows the presence of pronounced minima (encircled in the graph) at the 27th and 67th harmonic order when  $I_0 = 3.50 \times 10^{14}$  W/cm<sup>2</sup>, whereas such minima are not clearly visible with  $1.40 \times 10^{15}$  W/cm<sup>2</sup>. This minimum is due to a destructive resonance between the recolliding electron wavepacket and the orbital; this phenomenon has been observed experimentally.<sup>33</sup> This has been interpreted in terms of two centre interferences between the contributions from the two atomic centres.<sup>34</sup> In fact, with the  $3.50 \times 10^{14}$  W/cm<sup>2</sup> laser peak intensity, owing to the dominant effect of the HOMO,  $1\pi_g$  on the molecular ionization, the CO<sub>2</sub> molecule can be regarded as an elongated diatomic molecule where the point emitters are located on the two O nuclei. This phenomenon is less pronounced with the  $1.40 \times 10^{15}$  W/cm<sup>2</sup> laser peak intensity owing to the contribution of the  $3\sigma_u$  inner orbital. For  $\theta = 90^\circ$  (Fig. 4b), in comparison with  $\theta = 0^\circ$ , the absence of minima is evident and instead one finds as expected that the HHG intensity increases with the laser peak intensity.

One of the main observable differences among the two plots is that the spectrum for  $1.40 \times 10^{15}$  W/cm<sup>2</sup> laser peak intensity is flatter than the one for a peak laser intensity of  $3.50 \times 10^{14}$  W/cm<sup>2</sup> in the plateau region. This difference is most probably related to the constructive interference between the contributions from the two atomic oxygen centres (HOMO) at the  $3.50 \times 10^{14}$  W/cm<sup>2</sup>. This process is more complicated at high laser peak intensity owing to the contribution of inner orbitals.

### Conclusion

In this work, KS time-dependent orbital populations,  $N_{i,\sigma}(r,t)$ , and ionizations have been computed for the CO<sub>2</sub> molecule with different laser intensities from a nonlinear nonperturbative TDDFT approach.<sup>18,19</sup> In view of all the results, we conclude that both the shape of the KS orbitals

**Fig. 4.** (a) Comparative TDDFT/LB94 harmonic spectra study for  $\theta = 0^\circ$  using two laser peak intensities,  $I_0 = 3.50 \times 10^{14}$  and  $1.40 \times 10^{15}$  W/cm<sup>2</sup>. (b) Comparative TDDFT/LB94 harmonic spectra study for  $\theta = 90^\circ$  using two laser peak intensities,  $I_0 = 3.50 \times 10^{14}$  and  $1.40 \times 10^{15}$  W/cm<sup>2</sup>.



and the laser intensities play a key role in the ionization process. We showed that for  $3.5 \times 10^{14}$  W/cm<sup>2</sup>, the HOMO provides the dominant response in the presence of the external laser field owing to its lower IP, whereas for higher laser peak intensities, the shape and the orientation of the KS orbitals vs the laser field polarization are the main factors in their ionization. This has been confirmed by time-dependent electron localization function images, which have shown that the electronic perturbation is symmetric when the laser electric is perpendicular to the molecular axis and disymmetric when it is aligned along the molecular axis. As a consequence of these perturbations, for  $3.5 \times 10^{14}$  W/cm<sup>2</sup>, minima are found on the harmonic generation spectrum as a function of harmonic order when the laser is aligned with the molecular axis, whereas the harmonic generation spectrum exhibits higher intensities over a longer range of harmonic orders when the laser is perpendicular to the molecular axis.

## Acknowledgements

The authors would like to express their thanks to the Natural Sciences and Engineering Research Council of Canada (NSERC) and to the Canadian Institute for Photonic Innovations (CIPI) for funding this research on the theory of the intense laser-molecule interaction, and to Réseau Québécois de Calcul de Haute Performance (RQCHP), for parallel computer time. The authors are also thankful to C. Lefebvre, M. Ziou, and Y. Kaijun for the plots and their helpful discussions.

## References

- (1) (a) Lin, S. H.; Fujimura, Y.; Neusser, H. J.; Schlag, E. W. *Multiphoton Spectroscopy of Molecules*; Academic Press: London, 1984; (b) Bandrauk, A. *Molecules in Laser Fields*; M. Dekker, New York, 1994.
- (2) (a) Gavrilin, M. *Atoms in Intense Fields*; Academic Press: New York, 1992; (b) Lewenstein, M.; Kulander, K. C.; Schafer, K. J.; Bucksbaum, P. H. *Phys. Rev. A* **1995**, *51*, 1495. doi:10.1103/PhysRevA.51.1495.
- (3) Brabec, T.; Krausz, F. *Rev. Mod. Phys.* **2000**, *72* (2), 545. doi:10.1103/RevModPhys.72.545.
- (4) (a) l'Huillier, A.; Lompre, L. A.; Mainfray, G.; Manus, C. *Phys. Rev. A* **1983**, *27* (5), 2503. doi:10.1103/PhysRevA.27.2503.; (b) Perry, M. D.; Landen, O. L.; Szöke, A.; Campbell, E. M. *Phys. Rev. A* **1988**, *37* (3), 747. doi:10.1103/PhysRevA.37.747. PMID:9899717.; (c) Chin, S. L.; Rolland, C.; Corkum, P. B.; Kelly, P. *Phys. Rev. Lett.* **1988**, *61*, 153.; (d) Mainfray, G.; Manus, C. *Rep. Prog. Phys.* **1991**, *54* (10), 1333. doi:10.1088/0034-4885/54/10/002.; (e) Larochelle, S.; Talebpour, A.; Chin, S. L. *J. Phys. At. Mol. Opt. Phys.* **1988**, *31* (6), 1201. doi:10.1088/0953-4075/31/6/008.; (f) Alnaser, A. S.; Maharjan, C. M.; Tong, X. M.; Ulrich, B.; Ranitovic, P.; Shan, B.; Chang, Z.; Lin, C. D.; Cocke, C. L.; Litvinyuk, I. V. *Phys. Rev. A* **2005**, *71* (3), 031403. doi:10.1103/PhysRevA.71.031403.; (g) Pavičić, D.; Lee, K. F.; Rayner, D. M.; Corkum, P. B.; Villeneuve, D. M. *Phys. Rev. Lett.* **2007**, *98* (24), 243001. doi:10.1103/PhysRevLett.98.243001. PMID:17677961.; (h) Litvinyuk, I. V.; Lee, K. F.; Dooley, P. W.; Rayner, D. M.; Villeneuve, D. M.; Corkum, P. B. *Phys. Rev. Lett.* **2003**, *90* (23), 233003. doi:10.1103/PhysRevLett.90.233003. PMID:12857255.
- (5) Stapelfeldt, H.; Seideman, T. *Rev. Mod. Phys.* **2003**, *75* (2), 543. doi:10.1103/RevModPhys.75.543.
- (6) Lorin, E.; Chelkowski, S.; Bandrauk, A. D. *N. J. Phys.* **2008**, *10* (2), 025033. doi:10.1088/1367-2630/10/2/025033.
- (7) (a) Kamta, G. L.; Bandrauk, A. D. *Phys. Rev. A* **2004**, *70* (1), 011404. doi:10.1103/PhysRevA.70.011404.; (b) Kamta, G. L.; Bandrauk, A. D. *Laser Phys.* **2005**, *15*, 502.
- (8) Kamta, G. L.; Bandrauk, A. D. *Phys. Rev. A* **2005**, *71* (5), 053407. doi:10.1103/PhysRevA.71.053407.
- (9) (a) Bandrauk, A. D.; Barmaki, S.; Lagmago Kamta, G. In *Progress in Ultrafast Intense Laser Science*; Yamanouchi, K., Chin, S. L., Agostini, P., Ferrante, G., Eds.; Springer: New York, 2007; Vol. III; (b) Bandrauk, A. D.; Barmaki, S.; Kamta, G. L. *Phys. Rev. Lett.* **2007**, *98*, 013001. doi:10.1103/PhysRevLett.98.013001.
- (10) Ullrich, C. A.; Bandrauk, A. D. In *Time-Dependent Density Functional Theory*; Marques, M. A. L., Ed.; Springer: Berlin, 2006; pp. 357.
- (11) Lemell, C.; Tong, X. M.; Krausz, F.; Burgdörfer, J. *Phys. Rev. Lett.* **2003**, *90* (7), 076403. doi:10.1103/PhysRevLett.90.076403. PMID:12633255.
- (12) (a) Kohn, W. *Rev. Mod. Phys.* **1999**, *71* (5), 1253. doi:10.1103/RevModPhys.71.1253.; (b) Pearson, J. K.; Boyd, R. J. *J. Phys. Chem. A* **2007**, *111* (16), 3152. doi:10.1021/jp071499n. PMID:17407273.; (c) Wang, J.; Shi, Z.; Boyd, R. J.; Gonzalez, C. A. *J. Phys. Chem.* **1994**, *98* (28), 6988. doi:10.1021/j100079a017.
- (13) (a) Erdmann, M.; Gross, E. K. U.; Engel, V. *J. Chem. Phys.* **2004**, *121* (19), 9666. doi:10.1063/1.1806812. PMID:15538889.; (b) Burnus, T.; Marques, M. A. L.; Gross, E. K. U. *Phys. Rev. A* **2005**, *71* (1), 010501. doi:10.1103/PhysRevA.71.010501.
- (14) (a) Chaquin, P.; Chevreau, H. *Int. J. Quantum Chem.* **2007**, *107* (1), 72. doi:10.1002/qua.21020.; (b) Santos, J. C.; Andres, J.; Aizman, A.; Fuentealba, P.; Polo, V. *J. Phys. Chem. A* **2005**, *109* (16), 3687. doi:10.1021/jp0441947. PMID:16839035.; (c) Wagner, F. R.; Bezugly, V.; Kohout, M.; Grin, Y. *Chem. Eur. J.* **2007**, *13* (20), 5724. doi:10.1002/chem.200700013.
- (15) Hohenberg, P.; Kohn, W. *Phys. Rev.* **1964**, *136* (3B), B864. doi:10.1103/PhysRev.136.B864.
- (16) Kohn, W.; Sham, L. J. *Phys. Rev.* **1965**, *140* (4A), A1133. doi:10.1103/PhysRev.140.A1133.
- (17) Runge, E.; Gross, E. K. U. *Phys. Rev. Lett.* **1984**, *52* (12), 997. doi:10.1103/PhysRevLett.52.997.
- (18) Nguyen, H. S.; Bandrauk, A. D.; Ullrich, C. A. *Phys. Rev. A* **2004**, *69* (6), 063415. doi:10.1103/PhysRevA.69.063415.
- (19) Ullrich, C. A.; Bandrauk, A. D. In *Time-Dependent Density Functional Theory*; Burke, K., Marques, M., Eds.; Springer: New York, 2006; pp. 357.
- (20) van Leeuwen, R.; Baerends, E. J. *Phys. Rev. A* **1994**, *49* (4), 2421. doi:10.1103/PhysRevA.49.2421. PMID:9910514.
- (21) Banerjee, A.; Harbola, M. K. *Phys. Rev. A* **1999**, *60* (5), 3599. doi:10.1103/PhysRevA.60.3599.
- (22) Toher, C.; Filippetti, A.; Sanvito, S.; Burke, K. *Phys. Rev. Lett.* **2005**, *95* (14), 146402. doi:10.1103/PhysRevLett.95.146402. PMID:16241675.
- (23) Madjet, M. E.; Chakraborty, H. S.; Rost, J.-M. *J. Phys. B* **2001**, *34* (10), L345. doi:10.1088/0953-4075/34/10/106.
- (24) Becke, A. D.; Edgecombe, K. E. *J. Chem. Phys.* **1990**, *92* (9), 5397. doi:10.1063/1.458517.
- (25) Troullier, N.; Martins, J. L. *Phys. Rev. B* **1991**, *43* (3), 1993. doi:10.1103/PhysRevB.43.1993.
- (26) Jiang, H.; Novak, I. J. *Mol. Struct.* **2003**, *645* (2-3), 177. doi:10.1016/S0022-2860(02)00545-8.
- (27) Bandrauk, A. D.; Lu, H. Z. *Phys. Rev. A* **2005**, *72* (2), 023408. doi:10.1103/PhysRevA.72.023408.
- (28) Hussain, A. N.; Roberts, G. *Phys. Rev. A* **2000**, *63* (1), 012703. doi:10.1103/PhysRevA.63.012703.
- (29) He, F.; Ruiz, C.; Becker, A. *Phys. Rev. A* **2007**, *75* (5), 053407. doi:10.1103/PhysRevA.75.053407.
- (30) Lewenstein, M.; Balcou, P.; Ivanov, M. Y.; l'Huillier, A.; Corkum, P. B. *Phys. Rev. A* **1994**, *49* (3), 2117. doi:10.1103/PhysRevA.49.2117. PMID:9910464.
- (31) Bandrauk, A. D.; Chelkowski, S.; Diestler, D.; Manz, J.; Yuan, K.-J. *Phys. Rev. A* **2009**, *79* (2), 023403. doi:10.1103/PhysRevA.79.023403.
- (32) (a) Lias, S. G. In *Ionization Energy Evaluation in NIST Chemistry WebBook* [Online]; Linstrom, P. J., Ed.; National Institute of Standards and Technology: Gaithersburg, MD, June 2005. <http://webbook.nist.gov>. (b) Turner, D. W.; Baker, C.; Baker, A. D.; Brundle, C. R. *Molecular Photoelectron Spectroscopy*; J. Wiley and Sons: London, 1970.

- (33) Mairesse, Y.; Dudovich, N.; Levesque, J.; Yu Ivanov, M.; Corkum, P. B.; Villeneuve, D. M. *N. J. Phys.* **2008**, *10* (2), 025015. doi:10.1088/1367-2630/10/2/025015.
- (34) Lein, M.; Hay, N.; Velotta, R.; Marangos, J.; Knight, P. *Phys. Rev. A* **2002**, *66* (2), 023805. doi:10.1103/PhysRevA.66.023805.



# The 9-barbaralyl and related $C_9H_9^+$ carbocations — A QTAIM-DI-VISAB computational study

Nick H. Werstiuk

**Abstract:** QTAIM-DI-VISAB analyses were used to characterize the bonding of the 9-barbaralyl cation, related  $C_9H_9^+$  cations, and rearrangement transition states. These analyses involved obtaining quantum theory of an atom in a molecule (QTAIM) molecular graphs and delocalization indexes (DIs) that were correlated with visualization of the proximities of atomic basins (VISAB). This study provides new insights into the bonding of these species and cements the QTAIM-DI-VISAB analysis as a method of choice for establishing the nature of the bonding in so-called nonclassical carbocations, while obviating the need for dashed-line representations of bonding.

**Key words:** 9-barbaralyl and related  $C_9H_9^+$  carbocations, couple-clustered method with single and double excitations (CCSD) and density functional theory (DFT) calculations, molecular structure, QTAIM-DI-VISAB analyses.

**Résumé :** On a fait appel à des analyses faisant appel à la théorie quantique des atomes dans les molécules (TQADM), aux indices de délocalisation (ID) et à la visualisation de la proximité des bassins atomiques (VISBA) pour caractériser la liaison du cation 9-barbaralyle, apparenté aux cations  $C_9H_9^+$ , et les états de transition de son réarrangement. Les analyses impliquent l'obtention de graphiques moléculaires suivant la théorie quantique des atomes dans les molécules (TQADM) et d'indices de délocalisation (ID) pour lesquels il a été établi une corrélation avec la visualisation des proximités des bassins atomiques (VISBA). Cette étude a permis d'obtenir de nouvelles connaissances concernant les liaisons dans ces espèces et confirme que l'approche TQADM-ID-VISBA est une méthode de choix pour établir la nature des liaisons dans les carbocations dit non classiques tout en permettant d'éviter l'utilisation de représentations de liaisons par des lignes à traits tiretés.

**Mots-clés :** carbocations 9-barbaralyle et autres carbocations  $C_9H_9^+$  apparentés, calculs selon la théorie de la fonctionnelle de la densité (TFD) et de l'agrégat couplé avec des excitations simple et double (ACSD), analyses par une combinaison de la théorie quantique des atomes dans les molécules, des indices de délocalisation et de la visualisation des proximités des bassins atomiques (TQADM-ID-VISBA).

[Traduit par la Rédaction]

## Introduction

The structure and bonding of the 9-barbaralyl cation shown as **2** and related species on the  $C_9H_9^+$  potential energy surface were the focus of many experimental<sup>1</sup> and theoretical<sup>2</sup> studies over several decades. The most recent computational studies were carried out in 1993 by Cremer et al.,<sup>3a,3b</sup> with the latter publication dealing exclusively with the 1,4-bishomotropylium cation **4-C<sub>s</sub>**. This flurry of activity followed the experimental work in the late 1960s including NMR studies, which were carried out to detail its structure and rearrangements. Four possible minima on the  $C_9H_9^+$  potential energy surface are displayed as “localized” structures **1**, **2**, **3**, and **4**, along with their ring-system labels. A very complex array of dashed-line structures were used in attempts to describe the bonding in these species and the transition states for their rearrangements are seen in the first 1993 computational paper.<sup>3a</sup> Whereas two dashed-line structures shown as **3a-D<sub>3h</sub>** and **3b-D<sub>3h</sub>**<sup>2a</sup> have been used to describe the bonding of the so-called nonclassical  $D_{3h}$

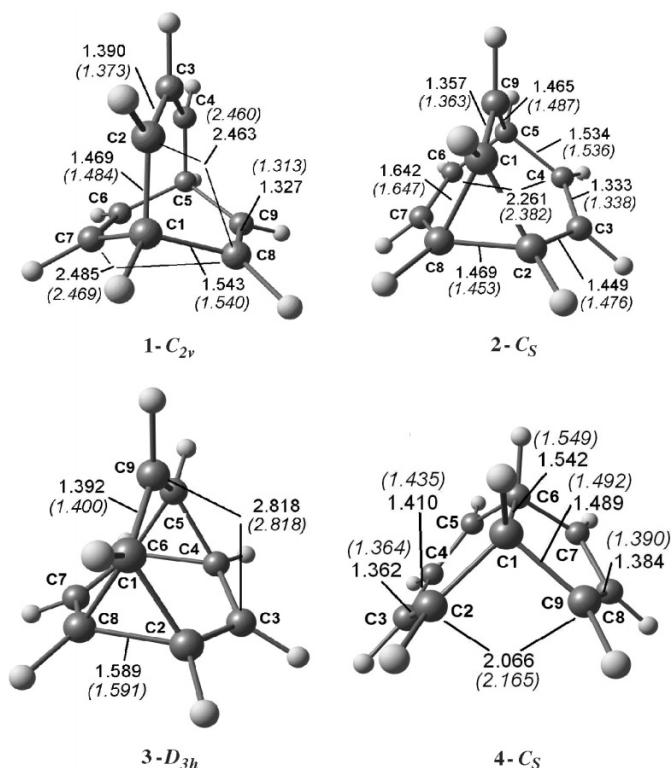
[3.3.1.0.0] cation, no dashed lines were used to describe the bonding of **2-C<sub>s</sub>**. Dashed lines have also been used for the [4.3.0] cation considered to be a bishomoaromatic species; it is shown as **4-C<sub>s</sub>** in its usual dashed-line representation. The computational studies by Cremer et al.<sup>3a,3b</sup> demonstrated that defining the  $C_9H_9^+$  potential energy surface is a very challenging computational problem. It was established that **2-C<sub>s</sub>** was a minimum at the HF, MP3, and MP4 levels of theory, but not at MP2; at this level, **2-C<sub>s</sub>** optimized to the lower energy species **3-D<sub>3h</sub>**. MP3 and MP4 energies were obtained from single-point calculations on geometries obtained from MP2 geometry searches. In the latter 1993 paper,<sup>3b</sup> optimized geometries of **4-C<sub>s</sub>** were obtained at the HF/6–31G(d) and MP2/6–31G(d) levels of theory: the former and latter are known to underestimate and overestimate homoaromaticity, respectively. Our recent computational studies<sup>4</sup> on a number of intermediates, including the 2-norbornyl, 7-norbornyl, and bicyclobutonium cations, established that coordination based on the number of bond paths,

Received 09 February 2010. Accepted 13 August 2010. Published on the NRC Research Press Web site at canjchem.nrc.ca on 5 November 2010.

This article is part of a Special Issue dedicated to Professor R. J. Boyd.

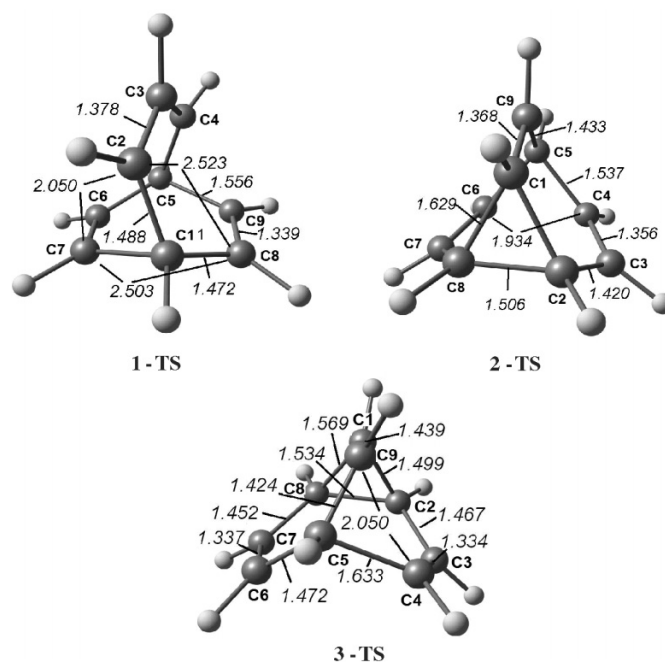
N.H. Werstiuk. Department of Chemistry, McMaster University Hamilton, ON L8S 4M1, Canada (e-mail: werstiuk@mcmaster.ca).

**Fig. 1.** Selected internuclear distances (Å) of cations at CCSD(full)/6-31+G(d,p) and B3PW91/aug-cc-pVTZ in parentheses.

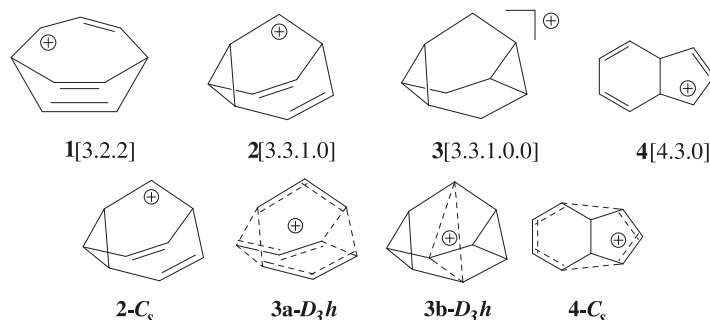


as defined in a quantum theory of an atom in a molecule (QTAIM)<sup>5</sup> molecular graph, terminating at a nucleus in any species (cation, carbanion, radical, or carbene) should be used as the criterion of hypercoordination and hypervalency. We argued that this approach should be used regardless of the nature of the intermediate to obviate the confusion and inaccuracies associated with arbitrarily using indicators such as dashed lines, dotted lines, cross-hatched lines, hollow tubes, and solid tubes in structural formulas, which have been used extensively in publications to this point. In fact, we recently

**Fig. 2.** Selected internuclear distances (Å) of transition states at B3PW91/aug-cc-pVTZ.



showed that a QTAIM-DI-VISAB analysis is the method of choice for characterizing the bonding of intermediates, molecules at their equilibrium geometries, and Diels–Alder transition states.<sup>6–9</sup> In such an analysis, in addition to using molecular graphs to define *molecular structure* and examining the properties at extrema (bond critical points (CPs), ring CPs, and cage CPs) in the topology of the density in a normal QTAIM analysis, delocalization indexes (DIs) are evaluated for pairs of atoms and correlated with a visualization of the closeness of atomic basins (VISAB). Homoconjugative and homoaromatic interactions between pairs of atoms are easily quantified on the basis of DIs without resorting to complex studies involving the nature of geometries, relative energies of hypothetical species, and NMR chemical shifts.



Results of a QTAIM-DI-VISAB study on **2-*C<sub>s</sub>***, **3-*D<sub>3h</sub>***, and **4-*C<sub>s</sub>*** and selected transition states, **1-*C<sub>2v</sub>***, **TS-1**, **TS-2**, and **TS-3**, for their rearrangements at couple-clustered method with single and double excitations (CCSD) and density functional theory (DFT) levels of theory are presented and discussed in this paper.

## Computational details

Our previous experiences with DFT calculations on carbo-cations clearly showed that the B3PW91 hybrid functional is superior to B3LYP in computing the geometries of delocalized, so-called nonclassical species.<sup>4,8</sup> Additional support for

**Table 1.** Total and relative energies and thermochemical data of cations at B3PW91/aug-cc-pVTZ and CCSD(full)/6-31+G(d,p).

Thermochemical data	Cation		
	2-C <sub>s</sub>	3-D <sub>3h</sub>	4-C <sub>s</sub>
$E_{\text{elec}}^a$	-348.009 345 (0.00)	-348.011 248 ( $\Delta E_{\text{elec}} = -1.19$ ) <sup>b</sup>	-348.029 748 ( $\Delta E_{\text{elec}} = -12.80$ ) <sup>b</sup>
$E_{\text{elec}}$ CCSD <sup>c</sup>	-347.045 022 (0.00)	-347.032 864 ( $\Delta E_{\text{elec}} = 7.63$ ) <sup>b</sup>	-347.059 782 ( $\Delta E_{\text{elec}} = -9.26$ ) <sup>b</sup>
$E_0^d$	-347.858 527 (0.00)	-347.860 414 ( $\Delta E_0 = -1.18$ )	-347.877 661 ( $\Delta E_0 = -12.01$ )
$E^e$	-347.851 937	-347.854 238	-347.870 990
$H_{298}^f$	-347.850 992 (0.00)	-347.853 293 ( $\Delta H_{298} = -1.44$ )	-347.870 045 ( $\Delta H_{298} = -11.95$ )
$G_{298}^g$	-347.888 693 (0.00)	-347.888 375 ( $\Delta G_{298} = 0.20$ )	-347.908 334 ( $\Delta G_{298} = -12.32$ )

**Note:** ZPE, zero-point energy. 1 cal = 4.184 J.

<sup>a</sup> $E_{\text{elec}}$  is the uncorrected total energy in hartrees.

<sup>b</sup>Energies relative to 2-C<sub>s</sub> in kcal mol<sup>-1</sup>.

<sup>c</sup> $E_{\text{elec}}$  CCSD is the uncorrected total CCSD energy in hartrees.

<sup>d</sup> $E_0 = E_{\text{elec}} + \text{ZPE}$ .

<sup>e</sup> $E = E_0 + E_{\text{vib}} + E_{\text{rot}} + E_{\text{trans}}$ .

<sup>f</sup> $H = E + RT$ .

<sup>g</sup> $G = H + TS$ .

**Table 2.** Total and relative energies and thermochemical data of transition states at B3PW91/aug-cc-pVTZ.

Thermochemical data	Cation			
	1-C <sub>2v</sub>	TS-1	TS-2	TS-3
$E_{\text{elec}}^a$	-347.997 782 (264.0i) <sup>b</sup> ( $\Delta E_{\text{elec}}^\ddagger = 5.06$ ) <sup>c</sup>	-348.005 853 (208.0i) <sup>b</sup> ( $\Delta E_{\text{elec}}^\ddagger = 2.19$ ) <sup>d</sup>	-348.007 537 (272.1i) <sup>b</sup> (1.13) <sup>d</sup>	-347.993 822 (397.8i) <sup>b</sup> (9.74) <sup>d</sup>
$E_{\text{elec}}$ CCSD	-347.038 13 (158.4i) <sup>b</sup>			
$E_0^e$	-347.847 496 ( $\Delta E_0^\ddagger = 5.16$ ) <sup>c</sup>	-347.855 725 ( $\Delta E_0^\ddagger = 1.76$ ) <sup>d</sup>	-347.857 380 (0.72) <sup>d</sup>	-347.843 004 (9.74) <sup>d</sup>
$E^f$	-347.841 251	-347.849 482	-347.851 433	-347.837 108
$H_{298}^g$	-347.840 307 ( $\Delta H_{298}^\ddagger = 5.16$ ) <sup>c</sup>	-347.848 538 ( $\Delta H_{298}^\ddagger = 1.53$ ) <sup>d</sup>	-347.850 489 (0.31) <sup>d</sup>	-347.836 164 (9.30) <sup>d</sup>
$G_{298}^h$	-347.876 791 ( $\Delta G_{298}^\ddagger = 2.65$ ) <sup>c</sup>	-347.885 213 ( $\Delta G_{298}^\ddagger = 2.18$ ) <sup>d</sup>	-347.887 022 (1.05) <sup>d</sup>	-347.872 668 (10.05) <sup>d</sup>

**Note:** ZPE, zero-point energy. 1 cal = 4.184 J.

<sup>a</sup> $E_{\text{elec}}$  is the uncorrected total energy in hartrees.

<sup>b</sup>The imaginary frequency in cm<sup>-1</sup>.

<sup>c</sup>Energy relative to TS-1 in kcal mol<sup>-1</sup>.

<sup>d</sup>Energy relative to 2-C<sub>s</sub> in kcal mol<sup>-1</sup>.

<sup>e</sup> $E_0 = E_{\text{elec}} + \text{ZPE}$ .

<sup>f</sup> $E = E_0 + E_{\text{vib}} + E_{\text{rot}} + E_{\text{trans}}$ .

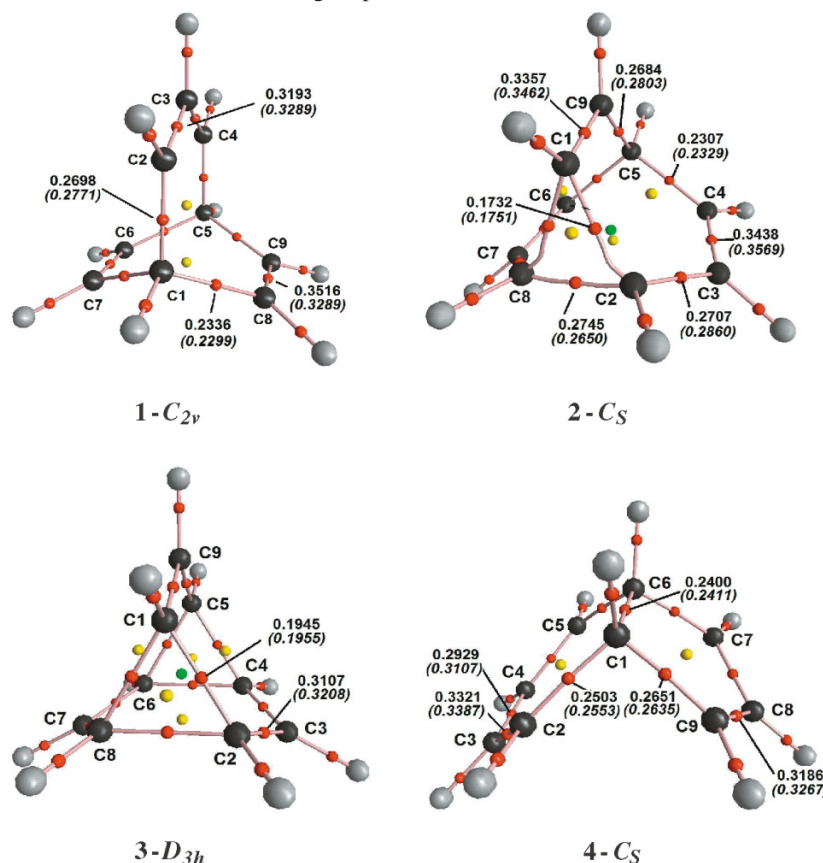
<sup>g</sup> $H = E + RT$ .

<sup>h</sup> $G = H + TS$ .

this finding was obtained as part of a previous study. Calculations were carried out on O-protonated 2,2-dimethyloxirane, which was studied recently by Carrier et al.<sup>10</sup> and described as a particularly challenging computational problem, to compare results from B3LYP, B3PW91, PBE1PBE, and CCSD calculations at the 6-311G(d,p) level as implemented in Gaussian 03.<sup>11</sup> The results clearly showed that B3PW91 and PBE1PBE are expected to be superior to B3LYP in cases where relatively weak polar bonds are involved. Cation geometries were optimized at B3PW91/aug-cc-pVTZ, MP2(full)/6-311+G(2d,p), and CCSD(full)/6-31+G(d,p) levels with Chemcraft<sup>12</sup> and GaussView<sup>13</sup> being used to fix symmetries where necessary. As found by Cremer et al.,<sup>3a</sup> all optimizations of 2-C<sub>s</sub> at the MP2 level yielded 3-D<sub>3h</sub>. They also suggested that CCSD calculations would be required to accurately define the C<sub>9</sub>H<sub>9</sub><sup>+</sup> surface.

Consequently, the MP2 results were discounted and calculations were carried out on 2-C<sub>s</sub>, 3-D<sub>3h</sub>, and 4-C<sub>s</sub> at CCSD(full)/6-31+G(d,p). Calculations were also carried out at B3PW91/aug-cc-pVTZ on 2-C<sub>s</sub>, 3-D<sub>3h</sub>, and 4-C<sub>s</sub> so a comparison could be made with the CCSD results. Calculations on the transition state (TS) for the degenerate rearrangement of 2-C<sub>s</sub> (TS-1) and the TSs for the rearrangements of 2-C<sub>s</sub> to 3-D<sub>3h</sub> (TS-2) and 4-C<sub>s</sub> (TS-3) were only carried out at B3PW91/aug-cc-pVTZ because the CCSD(full)/6-31+G(d,p) calculations were expected to be prohibitively long. Selected internuclear distances of 2-C<sub>s</sub>, 3-D<sub>3h</sub>, and 4-C<sub>s</sub> given in angstroms are collected in Fig. 1; for TS-1, TS-2, and TS-3, selected values are given in Fig. 2. Cartesian coordinates of all geometrical structures are collected in Tables 1S–11S in the Supplementary data. Frequency calculations were carried out at B3PW91/aug-cc-

**Fig. 3.** Molecular graphs of cations at CCSD(full)/6-31+G(d,p), along with values of the electron density ( $\rho(\mathbf{r})$ ) at selected bond critical points. Values in parentheses were obtained at B3PW91/aug-cc-pVTZ.



pVTZ; CCSD(full)/6-31+G(d,p) calculations were expected to be prohibitively long for all the species on the stationary points to confirm them as energy minima or transition states. CCSD(full)/6-31+G(d,p) frequency calculations were only carried out in the case of **1-C<sub>2v</sub>** to confirm that it is a TS. Total energies and thermochemical data ( $\Delta E_{\text{elec}}$ ,  $\Delta E_0$ ,  $\Delta H_{298}$ , and  $\Delta G_{298}$ ) for **2-C<sub>s</sub>**, **3-D<sub>3h</sub>**, and **4-C<sub>s</sub>** are collected in Table 1. Total energies and thermochemical data ( $\Delta E_{\text{elec}}^\ddagger$ ,  $\Delta E_0^\ddagger$ ,  $\Delta H_{298}^\ddagger$ , and  $\Delta G_{298}^\ddagger$ ) for **1-C<sub>2v</sub>**, **TS-1**, **TS-2**, and **TS-3** are collected in Table 2. QTAIM analyses of the wave functions to investigate the topologies of the electron densities were carried out with AIM 2000<sup>14</sup> and values of  $\rho(\mathbf{r})$  at selected bond critical points (bcps) given in atomic units ( $1 \text{ au} = e/a_0^3 = 6.7483 \text{ e/\AA}^3$ ) are collected in Fig. 3. AIMALL<sup>15</sup> was used to integrate atomic basins, to obtain atomic populations, and total charges, as well as atomic overlap matrices required for DI calculations. That the total charges of **1-C<sub>2v</sub>**, **2-C<sub>s</sub>**, **3-D<sub>3h</sub>**, **4-C<sub>s</sub>**, **TS-1**, **TS-2**, and **TS-3** obtained at the various levels of theory (data not included) deviated by <1% from the expected value of +1.0 confirmed the quality and validity of the QTAIM data. The program LIDICALC<sup>16</sup> was used to obtain DIs; selected values for pairs of atoms are listed in Table 3. Atomic basins were obtained with AIM 2000<sup>14</sup> at a contour value of 0.005, which includes >95% of the electrons, using a mesh grid size of 0.125 and plotted.

**Table 3.** Selected delocalization indexes for pairs of atoms at CCSD(full)/6-31+G(d,p) and B3PW91/aug-cc-pVTZ.

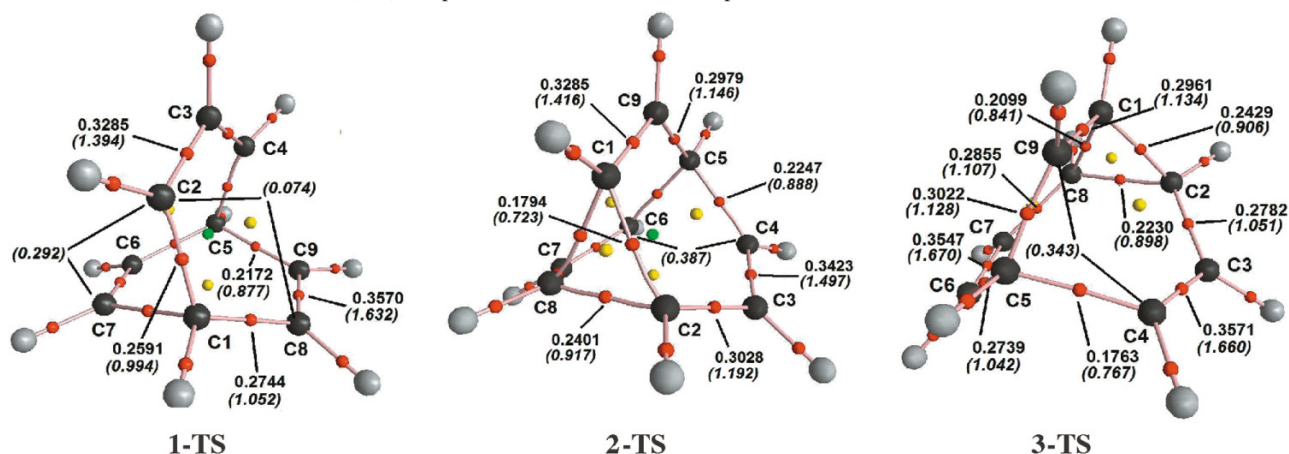
Atom pairs ( $\Omega$ and $\Omega'$ )	Cation		
	<b>2-C<sub>s</sub></b>	<b>3-D<sub>3h</sub></b>	<b>4-C<sub>s</sub></b>
C1–C2	0.587 (0.702) <sup>a</sup>	0.658 (0.775) <sup>a</sup>	0.836 (0.979) <sup>a</sup>
C2–C3	0.904 (1.103)	1.091 (1.300)	1.291 (1.480)
C3–C4	1.398 (1.676)	— <sup>a</sup>	1.012 (1.256)
C4–C5	0.806 (0.930)	— <sup>a</sup>	— <sup>a</sup>
C4–C6	0.073 (0.150)	— <sup>a</sup>	— <sup>a</sup>
C1–C9	1.240 (1.472)	— <sup>a</sup>	0.849 (0.989)
C2–C8	0.889 (1.005)	— <sup>a</sup>	—
C5–C9	0.879 (1.068)	— <sup>a</sup>	—
C7–C9	0.024 (0.048)	0.040 (0.104)	0.109 (0.308)
C2–C9	—	—	0.182 (0.308)

**Note:** The values are at CCSD(full)/6-31+G(d,p) and those values in parentheses are at B3PW91/aug-cc-pVTZ.

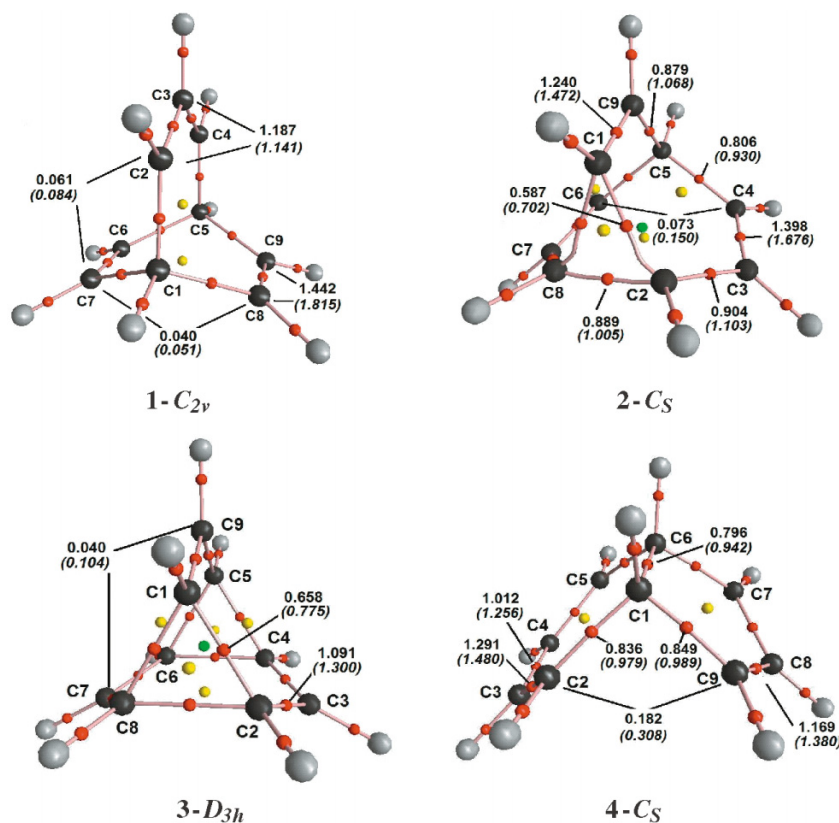
<sup>a</sup>Data for atom pairs related by symmetry not included.



**Fig. 4.** Molecular graphs of cations at B3PW91/aug-cc-pVTZ along with values of the electron density ( $\rho(r)$ ) at selected bond critical points. Selected delocalization indexes (DIs) for pairs of atoms are shown in parentheses in italics.



**Fig. 5.** Molecular graphs of cations at CCSD(full)/6-31+G(d,p) including selected delocalization indexes (DIs). The DI values in parentheses are obtained at B3PW91/aug-cc-pVTZ.



## Results and discussion

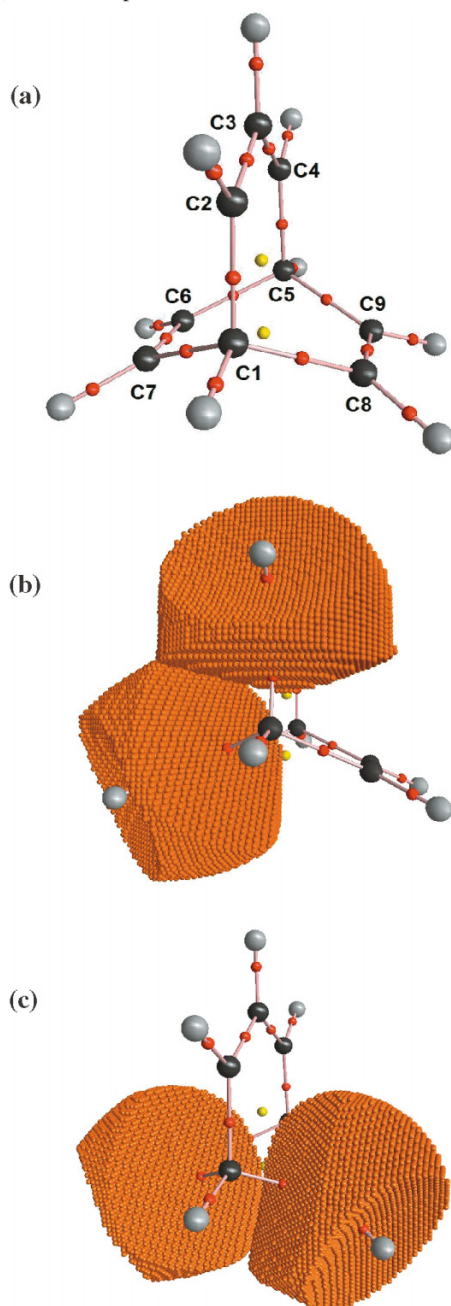
### Thermochemistry

At both levels of theory, **1-C<sub>2v</sub>** is a transition state (B3PW91/aug-cc-pVTZ imaginary frequency: 264.0i cm<sup>-1</sup>; Table 2) on the bifurcation path on the C<sub>9</sub>H<sub>9</sub><sup>+</sup> PE surface. Based on intrinsic reaction coordinate (IRC) calculations carried out in this study at B3PW91/aug-cc-pVTZ (data not included), **1-C<sub>2v</sub>** connects **TS-1s** exactly as concluded by Cremer et al.<sup>3a</sup> Given the prohibitive length of the CCSD calculations frequency, calculations were carried out only

on **1-C<sub>2v</sub>** confirming that it is a transition state exhibiting an imaginary frequency of 158.4i cm<sup>-1</sup> (Table 2). Based on the thermodynamic parameters,  $E_{\text{elec}}$ ,  $E_0$ , and  $H_{298}$ , collected in Table 2, **1-C<sub>2v</sub>** is in the region of 5 kcal mol<sup>-1</sup> (1 cal = 4.184 J) higher in energy than **TS-1** at B3PW91/aug-cc-pVTZ; based on  $G_{298}$ , **1-C<sub>2v</sub>** is only 2.65 kcal mol<sup>-1</sup> higher in energy than **TS-1**.

Whereas **3-D<sub>3h</sub>** is found to be marginally lower in energy than **2-C<sub>s</sub>** based on  $\Delta E_{\text{elec}}$  (-1.19),  $\Delta E_0$  (-1.18), and  $\Delta H_{298}$  (-1.44) at B3PW91/aug-cc-pVTZ, it is marginally higher in energy (+0.20) based on  $\Delta G_{298}$ . At CCSD(full)/6-

**Fig. 6.** Molecular graph and selected atom basins of **1-C<sub>2v</sub>** at CCSD(full)/6-31+G(d,p).



31+G(d,p), **3-D<sub>3h</sub>** is significantly higher in energy (+7.63 kcal mol<sup>-1</sup>) than **2-C<sub>s</sub>**, in keeping with the MP4(SDQ) results reported by Cremer et al.<sup>3a</sup> **4-C<sub>s</sub>** is the potential well at both levels of theory (Table 1), in keeping with experimental results. IRC calculations on **TS-1** (imaginary frequency: 208.0i cm<sup>-1</sup>) that exhibits C<sub>2</sub> symmetry confirmed that it is the TS for the degenerate rearrangement of **2-C<sub>s</sub>**. At B3PW91/aug-cc-pVTZ,  $\Delta G_{298}^\ddagger$  is 2.18 kcal mol<sup>-1</sup>, in line with a value of 3.6 kcal mol<sup>-1</sup> for  $\Delta E_{\text{elec}}^\ddagger$  at MP4(SDQ) based on HF/6-31G(d) geometries. That **TS-2** (imaginary frequency: 272.1i cm<sup>-1</sup>) is the TS for the rearrangement of **2-C<sub>s</sub>** to **3-D<sub>3h</sub>** was established by an IRC calculation at B3PW91/aug-cc-pVTZ; the barrier,  $\Delta E_{\text{elec}}^\ddagger =$

1.13 kcal mol<sup>-1</sup>, at this level of theory was significantly lower than the MP4(SDQ) value of 8.1 kcal mol<sup>-1</sup> obtained from the MP2(FC)/6-31G(d) geometries. This is undoubtedly due to the fact that B3PW91 overestimates the stability of **3-D<sub>3h</sub>**. **TS-3**, which was confirmed with an IRC calculation and an imaginary frequency of 397.8i cm<sup>-1</sup>, was located as the transition state for the rearrangement of **2-C<sub>s</sub>** to **4-C<sub>s</sub>**. At B3PW91/aug-cc-pVTZ,  $\Delta G_{298}^\ddagger$  was 10.05 kcal mol<sup>-1</sup>.

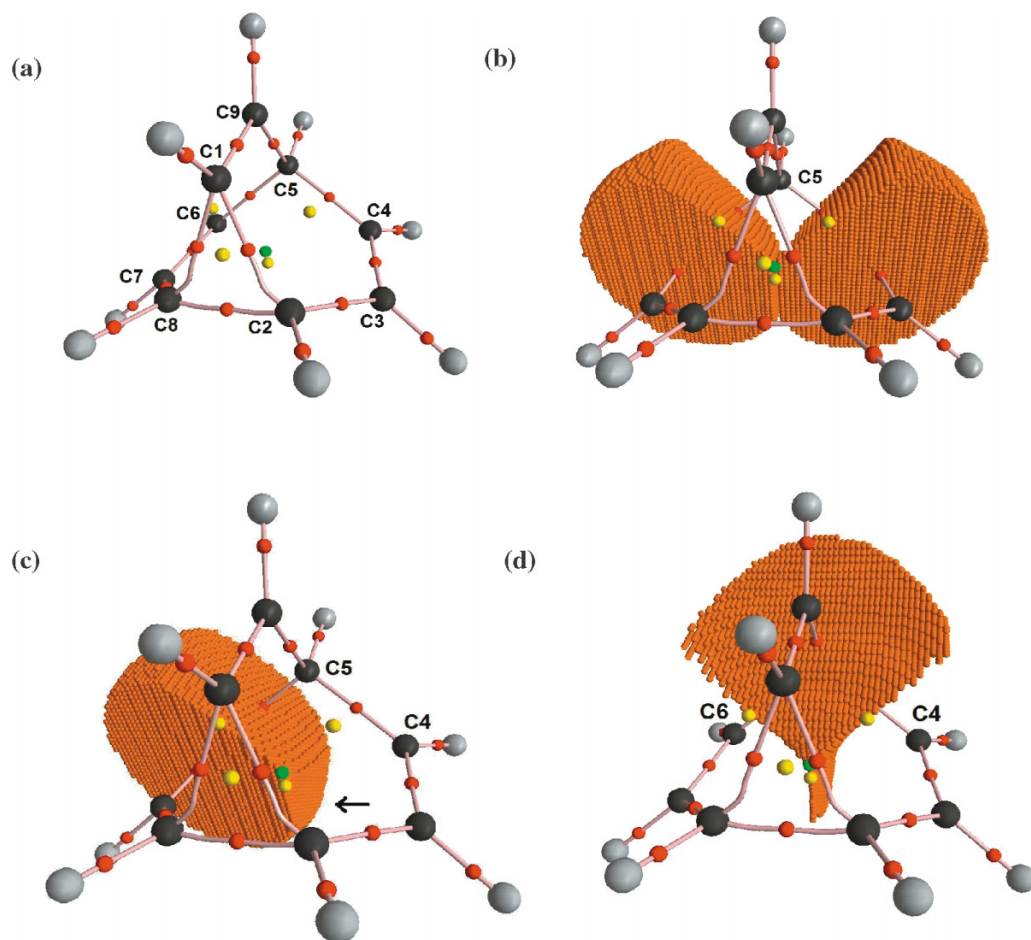
#### Molecular geometries of cations and transition states

Selected CCSD and B3PW91 (in *italics*) computed internuclear distances of **1-C<sub>2v</sub>**, **2-C<sub>s</sub>**, **3-D<sub>3h</sub>**, and **4-C<sub>s</sub>** are collected in Fig. 1. B3PW91 (in *italics*) computed internuclear distances of **TS-1**, **TS-2**, and **TS-3** are displayed in Fig. 2. On the whole, the CCSD and B3PW91 internuclear distances are similar except where through-space interactions are involved: C7–C8 of **1-C<sub>2v</sub>**, and C4–C6 of **2-C<sub>s</sub>**. It is interesting to note that the geometries of **4-C<sub>s</sub>** obtained at CCSD and B3PW91 are similar to the geometry obtained by Cremer et al.<sup>3b</sup> at MP2(FC)/6-31G(d) by fixing the folding angle at the value estimated from limited scanning (the C2–C9 distance was fixed) of the potential energy surface at MP4(SDQ)/6-31G(d), even though MP2 is considered to overestimate homoaromaticity. Surprisingly, the C2–C9 distance of **4-C<sub>s</sub>** is shorter at CCSD than at B3PW91, presumably because the C1–C2 and C1–C9 distances are shorter in the case of CCSD than B3PW91. The C2–C7 (C4–C9) distances of **TS-1** are shorter (2.050 Å) than the C2–C7 (C4–C9) distances of **1-C<sub>2v</sub>** (2.469 Å). On the other hand, the C7–C8 (C6–C9) distances (2.469 Å) increase slightly (2.503 Å) in going from **1-C<sub>2v</sub>** to **TS-1**. In the case of **TS-2** that is the TS for the rearrangement of **2-C<sub>s</sub>** to **3-D<sub>3h</sub>**, the C4–C6 distance decreases from 2.382 to 1.934 Å and the C2–C8 distance increases marginally from 1.453 to 1.506 Å. That **TS-3** is the transition state for the rearrangement of **2-C<sub>s</sub>** to **4-C<sub>s</sub>** (this was a new finding) was confirmed with an IRC calculation where optimization of the final forward and reverse end-points yielded **2-C<sub>s</sub>** to **4-C<sub>s</sub>**, respectively, and animation of the nuclear motion associated with the imaginary frequency clearly showed that **TS-3** connects **2-C<sub>s</sub>** to **4-C<sub>s</sub>**; rearrangement of **2-C<sub>s</sub>** to **4-C<sub>s</sub>** involves shifting the C6–C5 (or C4–C5) bond (the C6–C9 or C4–C5 distance decreases from 2.472 to 2.050 Å in the TS) of **2-C<sub>s</sub>** to C9 and cleaving the C2–C8 bond, which lengthens from 1.453 to 1.534 Å in the TS.

#### QTAIM-DI-VISAB analyses

The molecular graphs of **1-C<sub>2v</sub>**, **2-C<sub>s</sub>**, **3-D<sub>3h</sub>**, and **4-C<sub>s</sub>** along with bcps (red spheres), ring critical points (rcps, yellow spheres), and cage critical points (ccps, green spheres) obtained at the CCSD(full)/6-31+G(d,p) level are displayed in Fig. 3, along with the values of the density ( $\rho(\mathbf{r})$ ) at selected bcps; for comparison purposes, the B3PW91/aug-cc-pVTZ values are shown in parentheses in *italics*. All the molecular structures obey the Poincaré–Hopf equation ( $n$  (nuclei) –  $b$  (bcps) +  $r$  (rcps) –  $c$  (ccps) = 1).<sup>5</sup> On the whole, the values of  $\rho(\mathbf{r})$  at the bcps are similar at both levels of theory. As expected, the C1–C2 and C1–C8 bonds of **2-C<sub>s</sub>** are significantly weaker than the C2–C8 bond given that **2-C<sub>s</sub>** cation includes the cyclopropyl carbinyl cation fragment. The key point is that there are *no* bond paths between C4–

**Fig. 7.** (a) Molecular graph of **2-C<sub>s</sub>** at CCSD(full)/6-31+G(d,p). (b) C4–C6 basins of **2-C<sub>s</sub>**. (c) C6 atom basin of **2-C<sub>s</sub>**. (d) C5 atom basin of **2-C<sub>s</sub>**.



C6 of **2-C<sub>s</sub>** or C3–C9, C3–C7, or C7–C9 of **3-D<sub>3h</sub>**. This is even the case for **4-C<sub>s</sub>**, which is considered to be a bishomoaromatic species that is usually represented with dashed lines connecting C2–C9 and C5–C7.

Figure 4 displays the molecular graphs of **TS-1**, **TS-2**, and **TS-3**, along with the bcps, rcps, and ccps obtained at the B3PW91/aug-cc-pVTZ level. All these molecular structures also obey the Poincaré–Hopf equation.<sup>5</sup> Also included in Fig. 4 are the values of  $\rho(\mathbf{r})$  at selected bcps and the delocalization indexes (DIs) for selected pairs of atoms in parentheses in italics. Whereas **TS-2**, which is the transition state for the rearrangement of **2-C<sub>s</sub>** to **3-D<sub>3h</sub>**, does not exhibit a bond path between C4–C6, it possesses a significant DI (0.387) between the atoms showing that there is substantial homoconjugative interaction between the atoms. The DI is a measure of the number of electron pairs delocalized between atomic basins; for a “full single” bond, DI = 1.0 and for a “full double” bond it is 2.0.

Figure 5 displays the DIs for selected pairs of atoms obtained at CCSD(full)/6-31+G(d,p) and in italics at B3PW91/aug-cc-pVTZ. In the case of **1-C<sub>2v</sub>**, there is no significant through-space interaction between C7–C8 (C6–C9) based on a DI cutoff of 0.05.<sup>8</sup> However, there is a marginal degree of delocalization above the threshold between C2–C7 (C4–C6), or C2–C8 (C4–C9). These conclusions are in keeping with the displays of the C2–C8 (Fig. 6b) and C7–C8 (Fig. 6c) ba-

sins, which show that the basins do not significantly impinge on each other.

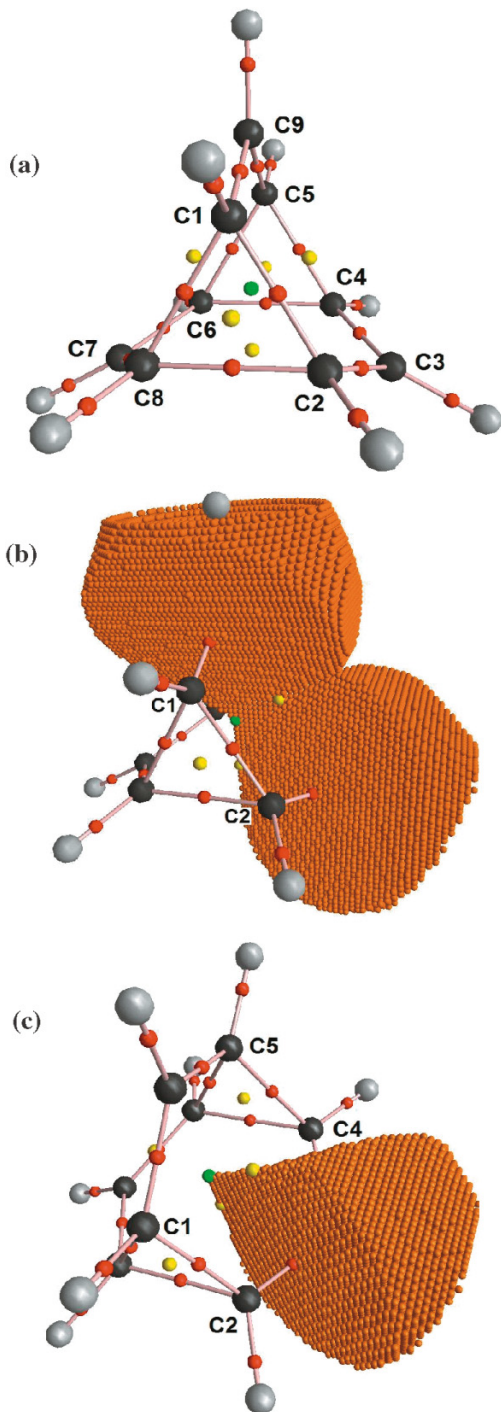
As far as **2-C<sub>s</sub>** is concerned, based on the DI there is a homoconjugative interaction above the threshold between C4–C6 showing that **2-C<sub>s</sub>** is a homoaromatic species. This contrasts with the conclusion reached by Cremer et al.<sup>3b</sup> that **2-C<sub>s</sub>**, the 9-barbaralyl cation, was not homoaromatic. Figure 7a displays its CCSD molecular graph. Figure 7b shows the C4–C6 basins that are in close proximity to each other and Fig. 7c shows the C6 basin with an arrow pointing to the surface that is distorted by the closeness of the C4 basin. These results are in accord with the fact that there is an above-threshold homoconjugative interaction between C4 and C6; Fig. 7d shows how the C5 basin intrudes between the C4–C6 basins and precludes bond path formation.

Figure 8a shows the molecular graph of **3-D<sub>3h</sub>** at CCSD; Fig. 8b shows the C3–C9 basins that do not impinge on each other; Fig. 8c shows the C3 basin. These displays are in accord with the fact that C3–C9 CCSD DI is 0.04, which is below the threshold of 0.05; at B3PW91, the DI is 0.104. That the DI is below the threshold at CCSD means that there is no need to use dashed lines to connect C3–C7, C3–C9, and C7–C9 as seen in **3b-D<sub>3h</sub>**.

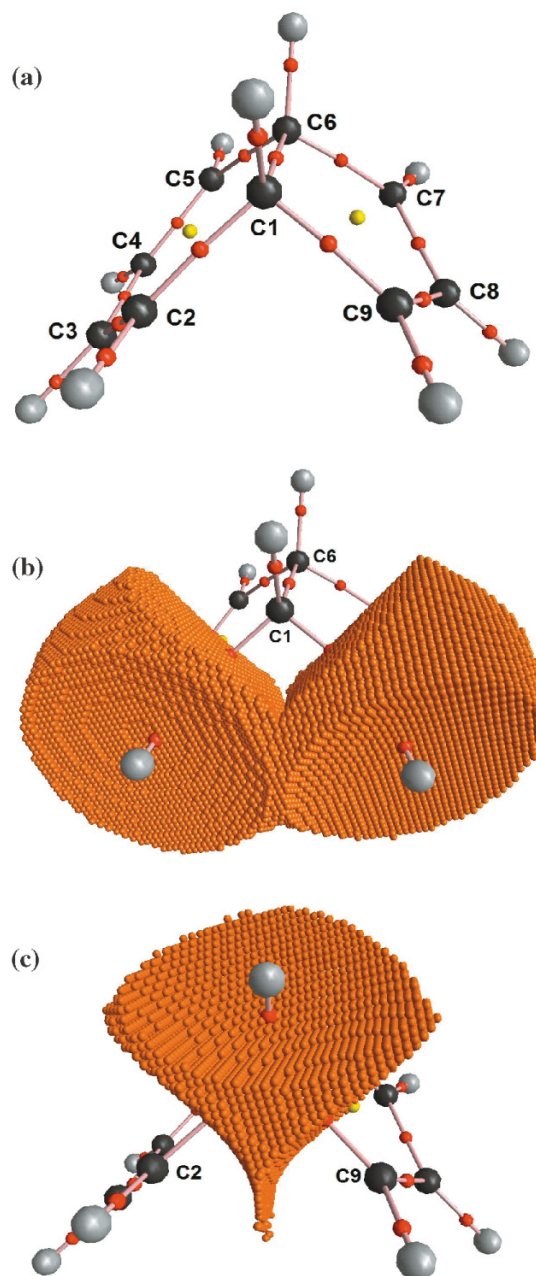
Figure 9a displays the CCSD molecular graph of **4-C<sub>s</sub>**, and while a relief plot of the Laplacian obtained at the MP2(FC)/6-31G(d) level was included in the 1993 publica-



**Fig. 8.** (a) Molecular graph of **3- $D_{3h}$**  at CCSD(full)/6-31+G(d,p). (b) C3–C9 basins of **3- $D_{3h}$** . (c) C3 atom basin of **3- $D_{3h}$** .



**Fig. 9.** (a) Molecular graph of **4- $C_s$**  at CCSD(full)/6-31+G(d,p). (b) C2–C9 basins of **4- $C_s$** . (c) C1 atom basin of **4- $C_s$** .



tion,<sup>3b</sup> the molecular graph was not; Fig. 9b shows the C2–C9 basins that impinge on each other. This display is in accord with the fact that the C2–C9 (C5–C7) DI (0.180 at CCSD, 0.308 at B3PW91) is well above the threshold, clearly confirming that **4- $C_s$**  is a bishomoaromatic species; Fig. 9c shows how the C1 basin intrudes between the C2–C9 basins and thereby precludes bond path formation between C2–C9. That **4- $C_s$**  exhibits a low DI of 0.180 at CCSD supports the conclusion reached by Cremer et al.<sup>3b</sup> that its homoaromaticity is low.

Figure 1Sa (see the Supplementary data) displays the B3PW91 molecular graph of **TS-1** and Fig. 1Sb shows the C2–C7 basins that impinge on each other; Fig. 1Sc shows how the face of the C7 basin labeled with an arrow is distorted by C2, in keeping with the fact that the C2–C7 DI (0.292) is well above the threshold value of 0.05; Fig. 1Sd shows the C1 basin, which clearly intrudes between C2–C7 and thereby precludes bond path formation even though the DI is 0.292; Fig. 1Se shows the C7–C8 basins that marginally impinge on each other in keeping with the DI of 0.058 that is marginally above the threshold of 0.050.

Figure 2Sa (see the Supplementary data) displays the B3PW91 molecular graph of **TS-2** and Fig. 2Sb shows the C4–C8 basins impinging on each other; Fig. 2Sc shows how



C8 is flattened (labeled with an arrow) by C4, in keeping with the fact that the DI (0.387) is large and well above the threshold value of 0.05. There is no doubt that **TS-2** is a homoaromatic species. The C5 basin (not shown) intrudes between C4–C8 and precludes bp formation.

Figure 3Sa (see the Supplementary data) is a display of the the B3PW91 molecular graph of **TS-3**. In going from **TS-3** to the [4.3.0] cation **4-C<sub>s</sub>**, it is interesting to note that whereas bond path formation is being achieved between C4 and C9, which demands that a new bcp replaces the one between C4 and C5, the bond between C2–C8 is cleaved by the coalescence of the C2–C8 bcp and the three-membered rcp. It is seen that the C1–C8 bond ( $\rho(\mathbf{r})_{\text{bcp}} = 0.2099$ , DI = 0.841) is slightly weaker than the C2–C8 bond ( $\rho(\mathbf{r})_{\text{bcp}} = 0.2230$ , DI = 0.898) of the nominal three-membered ring even though it is the C2–C8 bond that is cleaved in achieving **4-C<sub>s</sub>**; Fig. 3Sb shows the C4–C9 basins that are in close proximity to each other and Fig. 3Sc shows how the face of the C4 basin labeled with an arrow is distorted by C9, in keeping with the fact that the C4–C9 B3PW91 DI (0.343) is well above the threshold value of 0.05; Fig. 3Sd shows how the C5 basin intrudes between the C4–C9 basins and thereby precludes bond path formation between C4–C9.

## Conclusions

A QTAIM-DI-VISAB computational study on the 9-barbaralyl and related  $\text{C}_9\text{H}_9^+$  carbocations has been used to unambiguously define the bonding and homoaromaticity of these species in keeping with our view that it is the method of choice for establishing the nature of the bonding in hypercoordinated so-called nonclassical carbocations. This approach, which in our view is the most computationally economical method, obviates the need for arbitrary dotted-line representations of bonding. It is possible to quantify homoconjugation and homoaromaticity without relying on the nature of geometries, relative energies of hypothetical species, and NMR chemical shifts.

## Supplementary data

Supplementary data for this article are available on the journal Web site (canjchem.nrc.ca).

## Acknowledgement

Financial support by the Natural Sciences and Engineering Research Council of Canada (NSERC) is gratefully acknowledged. Computing resources of the McMaster node of SHARCnet (Shared Hierarchical Academic Research Computing Network (of Ontario)) were used in this study.

## References

- (1) (a) Ahlberg, P.; Harris, D. L.; Winstein, S. *J. Am. Chem. Soc.* **1970**, *92* (7), 2146. doi:10.1021/ja00710a065.; (b) Ahlberg, P.; Harris, D. L.; Winstein, S. *J. Am. Chem. Soc.* **1970**, *92* (14), 4454. doi:10.1021/ja00717a053.; (c) Ahlberg, P.; Harris, D. L.; Roberts, M.; Warner, P.; Seidl, P.; Sakai, M.; Cook, D.; Diaz, A.; Diriam, J. P.; Hamberger, H.; Winstein, S. *J. Am. Chem. Soc.* **1972**, *94* (20), 7063. doi:10.1021/ja00775a033.; (d) Engdahl, C.; Jönsäll, G.; Ahlberg, P. *J. Chem. Soc. Chem. Commun.* **1979**, 626. doi:10.1039/c39790000626.; (e) Ahlberg, P.; Engdahl, C.; Jönsäll, G. *J.*

- Am. Chem. Soc.* **1981**, *103* (6), 1583. doi:10.1021/ja00396a059.; (f) Engdahl, C.; Jönsäll, G.; Ahlberg, P. *J. Am. Chem. Soc.* **1983**, *105* (4), 891. doi:10.1021/ja00342a042.
- (2) (a) Hoffman, R.; Stohrer, W.-D.; Goldstein, M. *J. Bull. Chem. Soc. Jpn.* **1972**, *45* (8), 2513. doi:10.1246/bcsj.45.2513.; (b) Goldstein, M. J.; Hoffmann, R. *J. Am. Chem. Soc.* **1971**, *93* (23), 6193. doi:10.1021/ja00752a034.; (c) Goldstein, M. J. *J. Am. Chem. Soc.* **1967**, *89* (24), 6357. doi:10.1021/ja01000a069.; (d) Goldstein, M. J.; Odell, B. J. *J. Am. Chem. Soc.* **1967**, *89* (24), 6356. doi:10.1021/ja01000a068.; (e) Yoneda, S.; Winstein, S.; Yoshida, Z. *Bull. Chem. Soc. Jpn.* **1972**, *45* (8), 2510. doi:10.1246/bcsj.45.2510.; (f) Huang, M. B.; Goscinski, O.; Jönsäll, G.; Ahlberg, P. *J. Chem. Soc. Perkin Trans. 2* **1983**, 305. doi:10.1039/P29830000305.; (g) Huang, M. B.; Jönsäll, G. *Tetrahedron* **1985**, *41* (24), 6055. doi:10.1016/S0040-4020(01)91448-6.; (h) Jørgensen, K. A.; Linderberg, J.; Swanström, P. *Collect. Czech. Chem. Commun.* **1988**, *53* (9), 2055. doi:10.1135/cccc19882055.; (i) Bella, J.; Poblet, J. M.; Demoullins, A.; Volatron, F. J. *J. Chem. Soc. Perkin Trans. 2* **1989**, 37. doi:10.1039/P29890000037.; (j) Bouman, T. D.; Trindle, C. *Theor. Chim. Acta* **1975**, *37* (3), 217. doi:10.1007/BF00548091.
- (3) (a) Cremer, D.; Svensson, P.; Kraka, E.; Ahlberg, P. *J. Am. Chem. Soc.* **1993**, *115* (16), 7445. doi:10.1021/ja00069a051.; (b) Cremer, D.; Svensson, P.; Kraka, E.; Konkoli, Z.; Ahlberg, P. *J. Am. Chem. Soc.* **1993**, *115* (16), 7457. doi:10.1021/ja00069a052.
- (4) (a) Werstiuk, N. H.; Muchall, H. M. *J. Mol. Struct. THEOCHEM* **1999**, *463* (3), 225. doi:10.1016/S0166-1280(98)00625-3.; (b) Muchall, H. M.; Werstiuk, N. H. *J. Phys. Chem. A* **1999**, *103* (33), 6599. doi:10.1021/jp9912298.; (c) Werstiuk, N. H.; Muchall, H. *J. Phys. Chem. A* **2000**, *104* (10), 2054. doi:10.1021/jp992043b.; (d) Werstiuk, N. H.; Muchall, H. M.; Noury, S. *J. Phys. Chem. A* **2000**, *104* (49), 11601. doi:10.1021/jp0019781.; (e) Werstiuk, N. H.; Poulsen, D. A. *Arkivoc* **2009**, 5, 38.
- (5) Bader, R. F. W. *Atoms in Molecules — A Quantum Theory*; Oxford University Press: Oxford, UK, 1990.
- (6) Bajorek, T.; Werstiuk, N. H. *Can. J. Chem.* **2005**, *83* (9), 1352. doi:10.1139/v05-145.
- (7) Brown, E. C.; Bader, R. F. W.; Werstiuk, N. H. *J. Phys. Chem. A* **2009**, *113* (13), 3254. doi:10.1021/jp8109385. PMID:19275139.
- (8) Poulsen, D. A.; Werstiuk, N. H. *J. Chem. Theory Comput.* **2006**, *2* (1), 75. doi:10.1021/ct0501654.
- (9) Werstiuk, N. H.; Sokol, W. *Can. J. Chem.* **2008**, *86* (7), 737. doi:10.1139/V08-070.
- (10) Carlier, P. R.; Deora, N.; Crawford, T. D. *J. Org. Chem.* **2006**, *71* (4), 1592. doi:10.1021/jo052303n. PMID:16468811.
- (11) Frisch, M. J.; Trucks, G. W.; Schlegel, H. B.; Scuseria, G. E.; Robb, M. A.; Cheeseman, J. R.; Montgomery, J. A., Jr.; Vreven, T.; Kudin, K. N.; Burant, J. C.; Millam, J. M.; Iyengar, S. S.; Tomasi, J.; Barone, V.; Mennucci, B.; Cossi, M.; Scalmani, G.; Rega, N.; Petersson, G. A.; Nakatsuji, H.; Hada, M.; Ehara, M.; Toyota, K.; Fukuda, R.; Hasegawa, J.; Ishida, M.; Nakajima, T.; Honda, Y.; Kitao, O.; Nakai, H.; Klene, M.; Li, X.; Knox, J. E.; Hratchian, H. P.; Cross, J. B.; Bakken, V.; Adamo, C.; Jaramillo, J.; Gomperts, R.; Stratmann, R. E.; Yazyev, O.; Austin, A. J.; Cammi, R.; Pomelli, C.; Ochterski, J. W.; Ayala, P. Y.; Morokuma, K.; Voth, G. A.; Salvador, P.; Dannenberg, J. J.; Zakrzewski, V.

- G.; Dapprich, S.; Daniels, A. D.; Strain, M. C.; Farkas, O.; Malick, D. K.; Rabuck, A. D.; Raghavachari, K.; Foresman, J. B.; Ortiz, J. V.; Cui, Q.; Baboul, A. G.; Clifford, S.; Cioslowski, J.; Stefanov, B. B.; Liu, G.; Liashenko, A.; Piskorz, P.; Komaromi, I.; Martin, R. L.; Fox, D. J.; Keith, T.; Al-Laham, M. A.; Peng, C. Y.; Nanayakkara, A.; Challacombe, M.; Gill, P. M. W.; Johnson, B.; Chen, W.; Wong, M. W.; Gonzalez, C.; Pople, J. A. *Gaussian 03*, revisions B.02 and C.02; Gaussian, Inc.: Wallingford, CT, 2004.
- (12) *Chemcraft*, version 1.5. Available from <http://www.chemcraftprog.com>.
- (13) Dennington, R., II; Keith, T.; Millam, J.; Eppinnett, K.; Hovell, W. L.; Gilliland, R. *GaussView*, version 3.09; Semi-chem, Inc.: Shawnee Mission, KS, 2003.
- (14) Biegler-König, F. *AIM 2000*; University of Applied Science: Bielefeld, Germany, 2000.
- (15) Keith, T. A. *AIMALL97*, Package (B3) for Windows. Available from [aim@tkgristmill.com](mailto:aim@tkgristmill.com).
- (16) (a) Wang, Y.-G.; Matta, C. F.; Werstiuk, N. H. *J. Comput. Chem.* **2003**, *24* (14), 1720. doi:10.1002/jcc.10435. PMID: 12964190.; (b) Wang, Y.-G.; Werstiuk, N. H. *J. Comput. Chem.* **2003**, *24* (3), 379. doi:10.1002/jcc.10188.; (c) Wang, Y.-G.; Wiberg, K. B.; Werstiuk, N. H. *J. Phys. Chem. A* **2007**, *111* (18), 3592. doi:10.1021/jp067579t. PMID: 17441698.

## TRIBUTE

Russell Jaye Boyd was born in 1945 in Kelowna, the centre of British Columbia's wine-producing and fruit-growing Okanagan Valley. His early years were devoted to hockey, basketball, baseball, golf, and water-related activities. Just before his fifteenth birthday, his family moved to New Westminster, where he attended Lester Pearson High School and began to show some interest in science and mathematics.

Russ enrolled in the Science program at the University of British Columbia in 1963 and graduated in 1967 with First-Class Honours in Chemistry and the Lefevre Gold Medal for highest standing in the Honours Chemistry program. His Honours thesis focused on the new technique of photoelectron spectroscopy. At the time, there were no commercial instruments and UBC had the only photoelectron spectrometers in Canada. With enthusiastic encouragement from his thesis supervisor, David C. Frost, Russ attempted to carry out the first study of the angular dependence of photoelectron emission. Despite the best efforts of the strong technical support team in the machine shop, two different designs failed to produce meaningful results. To obtain some positive results, Russ rounded up supplies of some boron trihalides and recorded their spectra.

As one of the first recipients of a 1967 Science Scholarship (introduced in 1967 by the National Research Council (NRC) of Canada to celebrate Canada's centennial), he went east to pursue his Ph.D. in Theoretical Chemistry at McGill University under the supervision of M.A. (Tony) Whitehead. As a consequence of the fact that he had recorded the photoelectron spectra of some boron trihalides (and some siloxanes) as an undergraduate, Russ realized that there was no theoretical framework for interpreting such spectra in the absence of electronic structure calculations. In 1967, reliable *ab initio* calculations were restricted to small molecules. In fact, the largest molecule in the 1967 compendium of *ab initio* calculations compiled by Morris Kraus is HCCCN for which A.D. McLean and M. Yoshimine reported a single-point SCF calculation with a small basis set. In his first few months as a graduate student, Russ completed some semi-empirical molecular orbital calculations on the boron trihalides and sent the results to David Frost, which led to his first paper entitled "The Ionization Potentials of  $\text{BF}_3$ ,  $\text{BCl}_3$  and  $\text{BBr}_3$ ", in April 1968 in the first volume of *Chemical Physics Letters*.

The existing semi-empirical molecular orbital methods in 1967 were not capable of predicting the equilibrium geometries of molecules. All calculations were carried out at the experimental geometries or using assumed bond lengths and angles. Russ realized that this situation was unsatisfactory for studying reaction mechanisms and set out to develop a method that would yield molecular potential-energy surfaces and properties that agree with the experimental data. He developed a method based on the complete neglect of differential overlap approximation that had been introduced in 1965 by John Pople and his co-workers. He focused on equilibrium geometries, bond energies, and force constants (vibrational frequencies), the three chemically interesting properties associated with the minima of molecular potential-energy surfaces. This was an improvement over any other method that existed and was ultimately superseded by the work of Michael Dewar and his colleagues who used a slightly higher and chemically more reliable level of semi-empirical molecular orbital theory.

After defending his Ph.D. in 1971, Russ joined the group of

Charles A. Coulson in the Mathematical Institute at Oxford University as an NRC Postdoctoral Fellow. He had become disillusioned with semi-empirical approaches by the time he completed his thesis and saw more future in the *ab initio* approaches that John A. Pople and his group were developing within their Gaussian code. Russ turned his attention to electron correlation and published two papers with Coulson, including a description of the Coulomb hole in the first two excited states of the helium atom, his best-known paper from Oxford.

With encouragement from Charles A. McDowell, Russ returned to the University of British Columbia where he held a Killam Postdoctoral Fellowship in the Department of Chemistry from 1973 to 1975, where he renewed his interest in photoelectron spectroscopy. He published a single author letter in *Nature* in 1974 in which he pointed out that contrary to the usual interpretation of structural studies of porphyrin complexes, the lowest lying high-spin state of an atom (ion) in a given configuration is smaller than any state of lower spin. His prediction was verified two years later by scattering experiments on the first two excited states of the helium atom.

Russ joined Dalhousie University as an Assistant Professor of Chemistry in 1975 and rose through the ranks to become a Professor in 1985. He was named a Faculty of Science Killam Professor in 1997, and in 2001 he became the seventh Alexander McLeod Chair of Chemistry. The McLeod Chair, one of the oldest named professorships in chemistry in Canada, was created in 1884 in accordance with a bequest from Alexander McLeod. Russ served as Chair of Chemistry from 1992 to 2005. During this time, 11 new faculty members, including four outstanding senior chemists, were recruited, the graduate program expanded significantly, and an addition to the Chemistry Building was approved. The Department gained four Tier I Canada Research Chairs (Neil Burford, Jeff Dahn, Don Weaver, and Joe Zwanziger) between 2001 and 2003.

His research interests span a range of topics in computational and theoretical chemistry with an emphasis on problems relevant to biological systems. He has published about 240 research papers and 10 review chapters and he co-edited *The Quantum Theory of Atoms in Molecules* with Chérif Matta in 2007. With over 5000 citations of his papers and an H-index of 42, Russ is one of Canada's best-known computational chemists. He has supervised the research of 20 Ph.D. students, more than 25 postdoctoral fellows and senior visitors, and a comparable number of undergraduate students. His former students have successful careers in academic institutions, government laboratories, and the industry. Fourteen former members of his group hold academic appointments in Canadian universities and another eight hold similar appointments abroad. He is especially proud of the number of excellent young scientists who received a significant part of their training in his group.

Russ received the 1983 APICS/Fraser Medal. He was the first and only chemist to receive this prize, which was awarded in the 1970s and 1980s to recognize outstanding research work carried out in the Atlantic Provinces by a young scientist or engineer. His other awards include the Fellowship of The Chemical Institute of Canada (1983), the CNC-IUPAC Award (1986), Dalhousie University Senior Killam Fellowship (1989), and the 2009 Montreal Medal of The Chemical Institute of Canada.

Russ took on leading roles in organizing the Canadian Society for Chemistry Conferences in Halifax in 1981, 1990, and 2006. He was the principal organizer of the 8th Canadian Symposium on Theoretical Chemistry in 1983 and the 7th Canadian Computational Chemistry Conference in 2009. He is a member of the College of Reviewers of the Canada Research Chairs Program, and he has served on many committees of the Natural Sciences and Engineering Research Council of Canada (NSERC). He has served on selection panels for the National Science Foundation (NSF) of the USA and the Canada–US Fulbright Program. He has served on many boards, including the Canadian Society for Chemistry, the *Canadian Journal of Chemistry*, the Dalhousie University Foundation, the Atlantic Provinces Council on the Sciences, and the World Association of Theoretical and Computational Chemists. He was an editor of the *Canadian Journal of Chemistry* from 1988 to 1998 and served as President of the Canadian Society for Chemistry in 2007–2008. His many other

activities include Judge-in-Chief for the 1984 Canada-Wide Science Fair. He is currently the Principal Investigator (Research Director) for the Atlantic Computational Excellence Network (ACEnet), a consortium of nine universities in Atlantic Canada that provides high-performance computing facilities by means of funding from the Canada Foundation for Innovation (CFI).

The number, quality, and countries of origin of the papers submitted to this dedicated issue of the *Canadian Journal of Chemistry* attest to breadth and reach of Russ Boyd's influence in the computational and theoretical chemistry community in Canada and abroad, as well as his contributions to the broader chemical community.

**Neil Burford**

*Halifax, Nova Scotia*



## HOMMAGE

Russell Jaye Boyd naît en 1945 à Kelowna, située au centre de la région viticole et fruitière de la vallée de l'Okanagan (Colombie-Britannique). Il consacre les premières années de sa vie au hockey, au basketball, au baseball, au golf et aux activités aquatiques. Peu de temps avant son quinzième anniversaire, sa famille déménage à New Westminster où il fréquente l'école secondaire Lester Pearson et commence à manifester un intérêt pour les sciences et les mathématiques.

En 1963, Russ s'inscrit au programme de sciences de l'Université de la Colombie-Britannique (UBC) et en 1967, il obtient son diplôme en chimie avec très grande distinction et la Lefevre Gold Medal pour avoir obtenu les meilleurs résultats dans le programme spécialisé en chimie. Sa thèse de spécialisation porte principalement sur la nouvelle technique de spectroscopie photoélectronique. À ce moment-là, il n'existe aucun spectromètre photoélectronique vendu sur le marché et l'UBC est seule à en posséder au Canada. Fort de l'encouragement enthousiaste de son directeur de thèse, David C. Frost, Russ tente de mener la première étude sur la dépendance angulaire de l'émission de photoélectrons. Malgré tous les efforts déployés par la solide équipe de soutien technique de l'atelier de mécanique, deux concepts différents ne parviennent pas à produire des résultats significatifs. Afin d'obtenir des résultats positifs, Russ rassemble des réserves de trihalogénures de bore et enregistre leur spectre.

Lauréat de l'une des premières bourses 1967 en sciences (instaurée en 1967 par le Conseil national de recherches du Canada pour souligner le centenaire de la Confédération), il se dirige vers l'est pour poursuivre un doctorat en chimie théorique à l'Université McGill sous la direction de M. A. (Tony) Whitehead. En raison du fait qu'au cours de ses études de premier cycle, il a eu à enregistrer les spectres photoélectroniques de trihalogénures de bore (et de siloxanes), Russ se rend compte qu'il n'existe aucun cadre théorique pour interpréter de tels spectres en l'absence de calculs de structures électroniques. En 1967, les seuls calculs ab initio fiables se limitent aux petites molécules. En fait, la plus grosse molécule répertoriée dans le recueil des calculs ab initio de 1967 (Morris Kraus) est le cyanoacétylène (HCCCN) pour laquelle A.D. McLean et M. Yoshimine ont fait état d'un calcul SCF en un seul point avec un petit ensemble de base. Au cours de ses premiers mois comme étudiant diplômé, Russ effectue des calculs semi-empiriques d'orbitales moléculaires sur des trihalogénures de bore et il fait parvenir ses résultats à David Frost, ce qui mène la publication, en avril 1968, de son premier article intitulé « The Ionization Potentials of  $\text{BF}_3$ ,  $\text{BCl}_3$  and  $\text{BBr}_3$  » dans le premier volume de la revue *Chemical Physics Letters*.

En 1967, les méthodes semi-empiriques d'orbitales moléculaires utilisées ne permettent pas de prévoir les géométries d'équilibre des molécules. Tous les calculs sont effectués sur des géométries expérimentales ou au moyen de longueurs et d'angles de liaison présumés. Russ se rend compte que cette situation est peu satisfaisante pour étudier les mécanismes de réaction et entreprend de mettre au point une méthode qui permettrait de produire des surfaces et des propriétés d'énergie potentielle moléculaire qui cadrent avec des données expérimentales. Il met au point une méthode fondée sur l'approximation du recouvrement différentiel nul, introduite en 1965 par John Pople et ses collègues. Il concentre ses efforts

sur les géométries d'équilibre, les énergies de liaison et les constantes de force (fréquences vibrationnelles), trois propriétés revêtant un intérêt certain sur le plan de la chimie et associées aux minima des surfaces d'énergie potentielle. Il s'agit d'une amélioration par rapport à toutes les autres méthodes existantes. Mais finalement, elle sera détrônée par les travaux de Michael Dewar et de ses collègues, qui utilisent un niveau légèrement plus élevé et plus fiable chimiquement de la théorie semi-empirique des orbitales moléculaires.

Après avoir défendu sa thèse de doctorat en 1971, Russ se joint à l'équipe de Charles A. Coulson à l'Institut de mathématiques de l'Université d'Oxford à titre de boursier postdoctoral du CNRC. Désenchanté des méthodes semi-empiriques et avant même qu'il ne termine sa thèse, il se tourne vers les méthodes ab initio plus prometteuses que John A. Pople et son équipe sont à mettre au point dans un cadre gaussien. Russ se penche donc sur la corrélation électronique et publie deux articles avec Coulson, dont une description du trou de Coulomb dans les deux premiers états d'excitation de l'atome d'hélium, son article le mieux connu issu d'Oxford.

Encouragé par Charles A. McDowell, Russ retourne à l'Université de la Colombie-Britannique où il est titulaire d'une bourse postdoctorale Killam au Département de chimie de 1973 à 1975. C'est là qu'il s'intéresse de nouveau à la spectroscopie photoélectronique. En 1974, dans un texte publié dans la revue *Nature*, il fait valoir que contrairement à l'interprétation courante des études structurales des complexes de porphyrine, le plus faible état de spin élevé d'un atome (ion) dans une configuration donnée est plus petit que tout état de spin plus faible. Sa prédiction sera vérifiée deux ans plus tard par des expériences de diffusion menées sur les deux premiers états excités de l'atome d'hélium.

Russ est embauché par l'Université Dalhousie à titre de professeur adjoint de chimie en 1975 et grimpe les échelons pour devenir professeur en 1985. En 1997, on le nomme professeur Killam de la Faculté des sciences, et en 2001, il devient le septième titulaire de la chaire de chimie Alexander McLeod. La chaire McLeod, l'une des plus anciennes chaires dénommées en chimie au Canada, a été créée en 1884 conformément à un legs d'Alexander McLeod. Russ occupe les fonctions de directeur du Département de chimie de 1992 à 2005. Au cours de cette période, onze nouveaux membres du corps professoral sont recrutés (dont quatre éminents chimistes chevronnés), le programme d'études supérieures prend de l'expansion de façon importante et on approuve la construction d'une adjonction à l'édifice de la Faculté de chimie. Entre 2001 et 2003, le Département recrute quatre chercheurs inscrits au Programme des chaires de recherche du Canada de niveau I (Neil Burford, Jeff Dahn, Don Weaver et Joe Zwanziger).

Les travaux de recherche de Russ englobent divers sujets dans les domaines de la chimie théorique et numérique tout en portant une attention particulière aux problèmes liés aux systèmes biologiques. Il a publié jusqu'à maintenant environ 240 articles de recherche et dix chapitres de synthèse et a corédigé, en 2007, l'ouvrage « *The Quantum Theory of Atoms in Molecules* » avec Chérif Matta. Plus de 5000 citations de ses articles et un indice h de 42 font de Russ l'un des chimistes-informaticiens canadiens les plus connus. Au cours de sa carrière, il dirige les travaux de 20 étudiants au doctorat, de plus de 25 boursiers postdoctoraux et de visiteurs

de haut niveau et d'un nombre comparable d'étudiants de premier cycle. Ses anciens étudiants poursuivent des carrières florissantes dans des établissements universitaires, des laboratoires gouvernementaux ou l'industrie. Quatorze anciens membres de son équipe occupent des postes de professeur dans des universités canadiennes et huit autres font de même à l'étranger. Il est particulièrement fier du nombre d'excellents jeunes scientifiques qui ont reçu une partie importante de leur formation au sein de son équipe.

Russ reçoit l'APICS/Fraser Medal en 1983. Il est le premier et le seul chimiste à recevoir ce prix, remis dans les années 1970 et 1980 pour souligner les travaux de recherche remarquables menés par de jeunes scientifiques ou ingénieurs dans les provinces de l'Atlantique. Il compte également parmi ses récompenses la bourse de recherche de l'Institut de chimie du Canada (1983), le prix CNC-UICPA (1986), la bourse de chercheur chevronné Killam de l'Université Dalhousie (1989) et la Médaille de Montréal de l'Institut de chimie du Canada (2009).

Russ assume des rôles de premier plan dans l'organisation des congrès de la Société canadienne de chimie de 1981, de 1990 et de 2006. Il est le principal organisateur du 8<sup>e</sup> symposium canadien de chimie théorique (1983) et du 7<sup>e</sup> congrès canadien de chimie numérique (2009). Il fait partie du Collège d'examineurs du Programme de chaires de recherche du Canada et siège à de nombreux comités au Conseil de recherches en sciences naturelles et en génie du Canada. Il

siège à des jurys de sélection pour la National Science Foundation des États-Unis et le Programme Fulbright Canada-États-Unis. Il fait également partie de nombreux conseils d'administration, dont ceux de la Société canadienne de chimie, de la *Revue canadienne de chimie*, de la Fondation de l'Université Dalhousie, du Conseil des provinces atlantiques pour les sciences et de la World Association of Theoretical and Computational Chemists. Il est l'un des rédacteurs en chef de la *Revue canadienne de chimie* de 1988 à 1998 et il siège à titre de président de la Société canadienne de chimie en 2007-2008. De plus, le rôle de juge en chef à l'occasion de l'Expo-sciences pancanadienne de 1984 constitue une autre de ses nombreuses activités. Il est actuellement le chercheur principal (directeur de la recherche) de l'Atlantic Computational Excellence Network (ACEnet), un consortium de neuf universités du Canada atlantique qui fournit des infrastructures informatiques de haute performance grâce aux fonds provenant de la Fondation canadienne pour l'innovation.

Le nombre, la qualité et les pays d'origine des articles soumis au présent numéro spécial de la *Revue canadienne de chimie* témoignent aussi bien de l'ampleur et du rayonnement de l'influence de Russ Boyd dans les milieux de la chimie théorique et numérique tant au Canada qu'à l'étranger que de son apport au milieu de la chimie en général.

**Neil Burford**  
*Halifax (Nouvelle-Écosse)*

# Spectrophotometric study of the selective binding behavior of aliphatic oligopeptides by bridged bis( $\beta$ -cyclodextrin) linked by a 4,4'-diaminodiphenyl disulfide tether

Yang Yong-Cun, Chi Shao-Ming, Liu Ming-Hua, Huang Rong, Wang Yu-Fei, Jing Bi, and Zhao Yan

**Abstract:** The conformation and binding behavior of 4,4'-diaminodiphenyl disulfide bridged bis( $\beta$ -cyclodextrin) (**1**) towards representative aliphatic oligopeptides, i.e., Leu-Gly, Gly-Leu, Glu-Glu, Met-Met, Gly-Gly, Gly-Gly-Gly, and Gly-Pro, were investigated by circular dichroism, fluorescence, and  $^1\text{H}$  and 2D NMR spectroscopy at 25 °C in phosphate buffer (pH 7.20). The results indicated that **1** acts as an efficient fluorescent sensor and displays remarkable fluorescence enhancement upon addition of optically inert oligopeptides. Owing to the cooperative host-linker-guest binding mode in which the linker and guest are coincluded in the two cyclodextrin cavities, the bis( $\beta$ -cyclodextrin) **1** gives high binding constants of up to  $10^3$ – $10^4$  (mol/L) $^{-1}$  for oligopeptides. The bis( $\beta$ -cyclodextrin) **1** can recognize not only the size and shape of oligopeptides but also the hydrophobicity, giving an exciting residue selectivity of up to 61.3 for the Gly-Leu/Glu-Glu pair. These phenomena are discussed from the viewpoints of multiple recognition and induce-fit interactions between host and guest.

**Key words:** bridged bis( $\beta$ -cyclodextrin)s, aliphatic oligopeptides, fluorescence spectroscopy, binding behavior, inclusion phenomena.

**Résumé :** Faisant appel au dichroïsme circulaire, à la fluorescence, à la spectroscopie RMN  $^1\text{H}$  et 2D, à 25 °C dans un tampon de phosphate (pH de 7,20), on a étudié la conformation et le comportement de fixation du disulfure de 4,4'-diaminodiphényle lié à la  $\beta$ -cyclodextrine, **1**, avec des oligopeptides aliphatiques représentatifs, tels Leu-Gly, Gly-Leu, Glu-Glu, Met-Met, Gly-Gly, Gly-Gly-Gly et Gly-Pro. Les résultats obtenus indiquent que le composé **1** agit comme un capteur de fluorescence efficace et qu'il donne lieu à une augmentation de fluorescence remarquable lors de l'addition d'oligopeptides inertes. En raison du mode de fixation coopératif hôte-coupleur-invité dans lequel le coupleur et l'invité sont co-inclus dans les deux cavités de la cyclodextrine, les constantes de fixation de la bis( $\beta$ -cyclodextrine), **1**, avec les oligopeptides sont élevées, soit de  $10^3$  à  $10^4$  (mol/L) $^{-1}$ . En plus de reconnaître la taille et la forme des oligopeptides, la bis( $\beta$ -cyclodextrine), **1**, reconnaît aussi le caractère hydrophobe qui lui permet d'avoir une excitante sélectivité de résidu allant jusqu'à 61,3 pour la paire Gly-Leu/Glu-Glu. On discute de ces phénomènes du point de vue de la reconnaissance multiple et des interactions à arrimage induit entre hôte et invité.

**Mots-clés :** bis( $\beta$ -cyclodextrines) pontées, oligopeptides aliphatiques, spectroscopie de fluorescence, comportement de fixation, phénomène d'inclusion.

[Traduit par la Rédaction]

## Introduction

Native and chemically modified cyclodextrins (CDs), which act as synthetic receptors (hosts) of supramolecular systems, display dramatically different binding behavior toward guest molecules.<sup>1–6</sup> As a new family of CD derivatives, the bridged CD dimers are known to greatly enhance the original binding ability and molecular selectivity of native CD by the cooperative interaction of its two nearly lo-

cated hydrophobic cavities.<sup>7–10</sup> Hence, the molecular recognition of substrate (guest) by bridged CDs linked with a functional tether group becomes one of the most crucial current topics in supramolecular chemistry and biochemistry.<sup>11–14</sup> Among the various families of organic and biological guests for these studies, aliphatic oligopeptides have attracted considerable interest because they represent an intermediate step toward the recognition of protein surfaces, and the short peptide sequences are themselves worthwhile

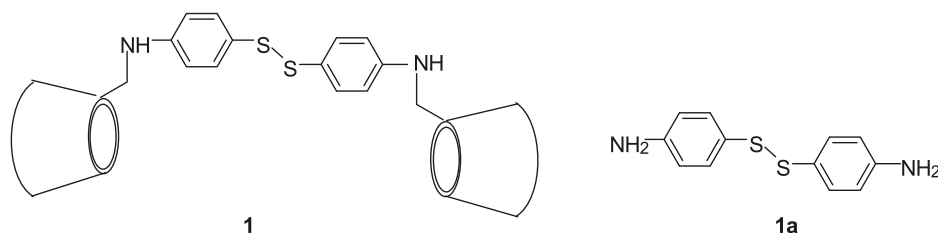
Received 3 July 2010. Accepted 24 September 2010. Published on the NRC Research Press Web site at canjchem.nrc.ca on 16 November 2010.

**Y. Yong-Cun, C. Shao-Ming, L. Ming-Hua, W. Yu-Fei, J. Bi, and Z. Yan.**<sup>1</sup> College of Chemistry and Chemical Engineering, Yunnan Normal University, Kunming 650092, P.R. China.

**H. Rong.** Experimental Center, Yunnan University, Kunming 650091, P.R. China.

<sup>1</sup>Corresponding author (e-mail: zhaooyann@163.com).

Scheme 1.



targets for recognition owing to their potential applications in separation, diagnostic, or biological areas.<sup>15–18</sup> However, the work on molecular recognition by bis( $\beta$ -CD)s has been concentrated mostly on the complexation of rather simple organic guests, and practically no attempt has been made to study the recognition of aliphatic oligopeptides by bis( $\beta$ -CD)s.<sup>19–23</sup> To elucidate the detailed recognition mechanism of bridged bis( $\beta$ -CD)s toward oligopeptides, we investigate the conformation of 4,4'-diaminodiphenyl disulfide bridged bis( $\beta$ -CD) (**1**, Scheme 1) as well as its selective binding behavior with a series of aliphatic oligopeptides (Scheme 2) by circular dichroism, fluorescence, and  $^1\text{H}$  and 2D NMR spectroscopy in a phosphate buffer solution of pH 7.20. It is our special interest to explore how the bridge group affects the cooperative binding of bis( $\beta$ -CD)s and further understand the factors governing the molecular multiple recognition mechanism.

## Experimental

### Instruments

Circular dichroism and UV-vis spectra were recorded in a conventional quartz cell (light path 10 mm) on a JASCO 810 spectropolarimeter and a Shimadzu UV2401 PC spectrometer, respectively.  $^1\text{H}$  NMR spectra were recorded on a Bruker AV DRX5 instrument operated at 500 MHz. Fluorescence spectra were measured in a conventional quartz cell (10 mm  $\times$  10 mm  $\times$  45 mm) at 25  $^\circ\text{C}$  on a Hitachi F-4500 spectrometer equipped with a constant-temperature water bath, with excitation and emission slits 10 nm in width at an excitation wavelength of 310 nm.

### Materials

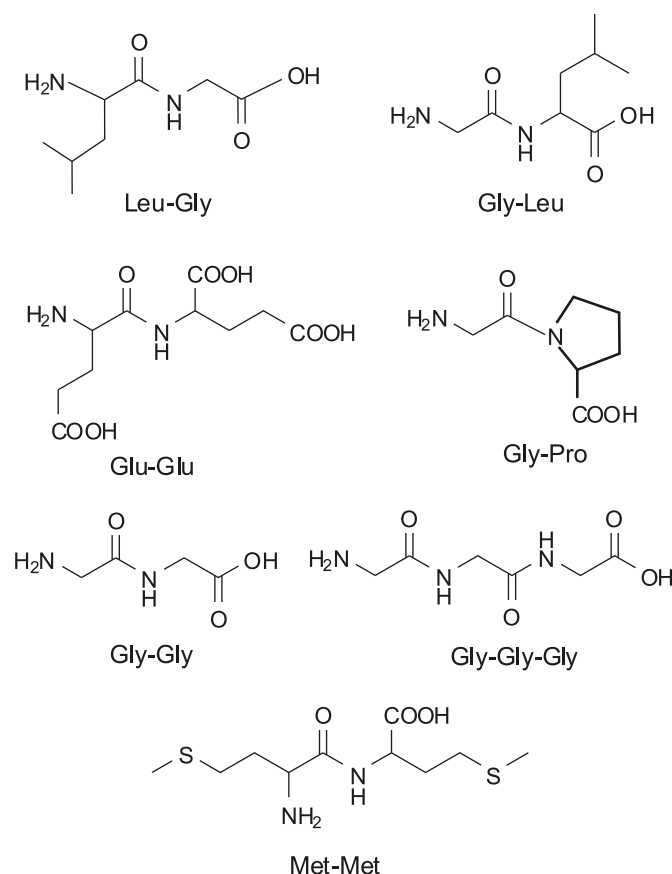
All guest aliphatic oligopeptides, i.e., Leu-Gly, Gly-Leu, Glu-Glu, Met-Met, Gly-Gly, Gly-Gly-Gly, and Gly-Pro, were purchased from Sigma-Aldrich and used as received. Disodium hydrogen phosphate and sodium dihydrogen phosphate were dissolved in distilled, deionized water to make a 0.10 mol/L phosphate buffer solution of pH 7.20 for spectral measurements. 4,4'-Diaminodiphenyl disulfide bridged bis( $\beta$ -CD) (**1**) was prepared according to our previous report.<sup>24</sup>

## Results and discussion

### Circular dichroism

Circular dichroism spectra have been widely employed to elucidate the absolute conformation of chiral compounds. The achiral compounds located in a chiral environment produce induced circular dichroism (ICD) signal(s) in the corresponding transition band(s).<sup>25</sup> Therefore, to examine the

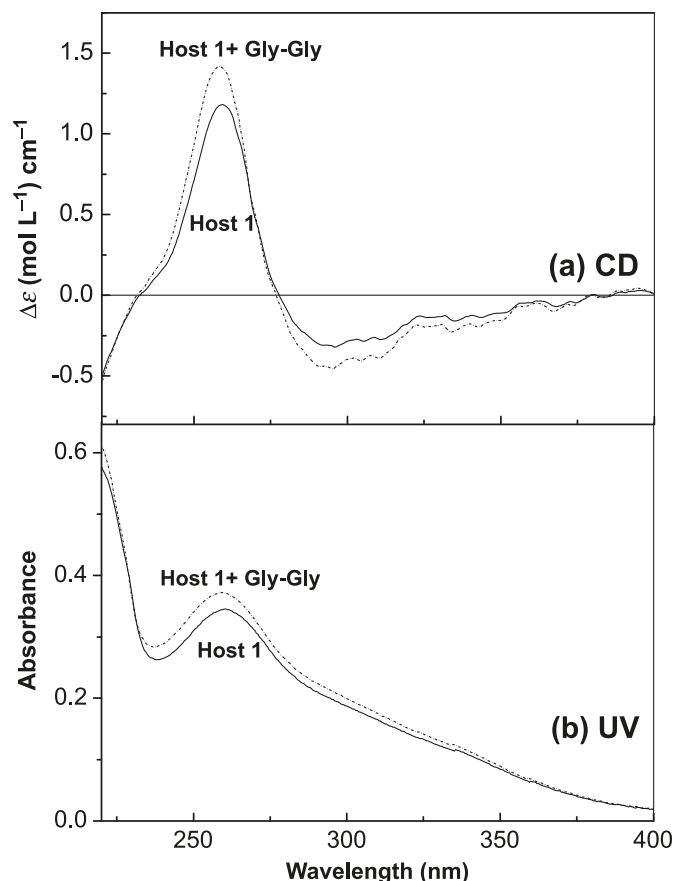
Scheme 2.



conformation of host **1**, its circular dichroism spectrum was measured at 25  $^\circ\text{C}$  in phosphate buffer solution (pH 7.20). As shown in Fig. 1, the circular dichroism spectrum of **1** displays a relatively strong positive Cotton effect peak around 259 nm ( $\Delta\epsilon = +1.18 \text{ (mol/L)}^{-1} \text{ cm}^{-1}$ ) for the  $^1\text{L}_a$  transition and a weak negative Cotton effect peak around 296 nm ( $\Delta\epsilon = -0.32 \text{ (mol/L)}^{-1} \text{ cm}^{-1}$ ) for the  $^1\text{L}_b$  transition of phenyl moieties in the linker group. According to the empirical rule proposed by Kajtar et al.<sup>26</sup> and Harata and Uedaira,<sup>27</sup> the sign of the ICD signal depends on the orientation of the transition dipole moment of the chromophore with respect to the dipole moment of CD. The chromophore located inside the CD axis gives a positive ICD signal, whereas the perpendicular transitions give a negative signal, but this situation is reversed for the chromophore located outside the CD cavity. Therefore, we can deduce that the phenyl chromophore in the diaminodiphenyl disulfide linker of host **1** shallowly penetrates into the CD cavity to



**Fig. 1.** (a) Circular dichroism and (b) absorption spectra of the bis( $\beta$ -CD) **1** ( $1.0 \times 10^{-4}$  mol/L) in the absence and presence of Gly-Gly ( $9.96 \times 10^{-3}$  mol/L) in phosphate buffer (pH 7.20) at 25 °C.



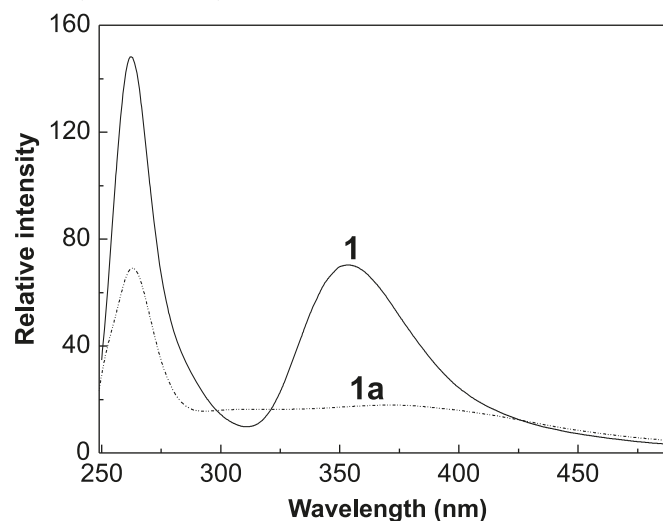
form the self-included complexes, which is in good agreement with the 2D NMR spectral study.<sup>24</sup>

### Fluorescence titrations

The emission intensity of a fluorophore attached to the CD rim is usually stronger than that of the parent fluorophore because of the increased microenvironmental hydrophobicity introduced by self-inclusion. As can be seen from Fig. 2, the fluorescence intensity of host **1** is much larger than that of the reference compound **1a** under the same conditions. Since the fluorescence intensity of the phenyl moiety is sensitive to changes in its microenvironment and is greater in a hydrophobic microenvironment than in a hydrophilic one, the above results suggest that the phenyl moiety of **1** is included into the cavity of the CD. This outcome is consistent with the ICD result described above.

The binding ability of a fluorescently labeled CD can be quantitatively assessed by analysis of the spectral changes induced by guest inclusion. Fluorescence titrations of the bis( $\beta$ -CD) **1** with optically inert oligopeptides were performed at 25 °C in phosphate buffer solution (pH 7.20) to quantitatively assess the inclusion complexation behavior of host **1**. As shown in Fig. 3, the fluorescence intensity of the bis( $\beta$ -CD) **1** presents a continuous enhancement upon the addition of Gly-Gly and Gly-Pro. The enhanced fluorescence of **1** upon addition of oligopeptides may be due to

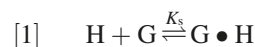
**Fig. 2.** Fluorescence spectra of **1a** and the bis( $\beta$ -CD) **1** at the same concentration of  $9.6 \times 10^{-5}$  mol/L in phosphate buffer (pH 7.20) at 25 °C ( $\lambda_{\text{ex}} = 270$  nm).



the increased microenvironmental hydrophobicity and (or) steric shielding around the phenyl fluorophore arising from the cooperative host-linker-guest interactions. This hypothesis is supported by the 2D NMR measurements. The unique fluorescence behavior may enable **1** to be efficient fluorescence sensors for optically inserted molecules.

The stoichiometries for the inclusion complexation of host **1** with representative guests were determined by Job's experiments by fluorescence spectroscopy. Within the examined concentration range, each of Job's plots for the inclusion complexation of the bis( $\beta$ -CD) **1** with oligopeptides shows a maximum at a host **1** molar fraction of 0.5, confirming the 1:1 binding stoichiometry between host and guest (Fig. 4).

With the 1:1 stoichiometry for the inclusion complexation of oligopeptide guests (G) with CDs (H), where the two CD moieties in bis( $\beta$ -CD)s are treated as a single unit, the inclusion complexation is expressed by eq. [1] and the complex stability constant ( $K_s$ ) is given by eq. [2]:

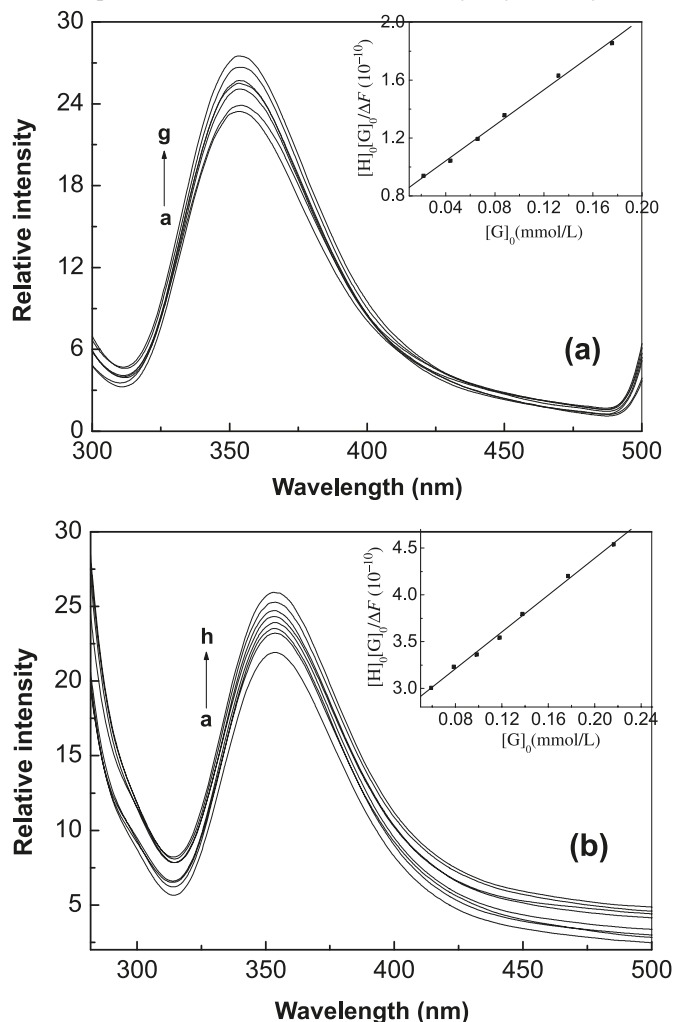


$$[2] \quad K_s = \frac{[\text{H} \bullet \text{G}]}{[\text{H}][\text{G}]}$$

$$[3] \quad \Delta F = \Delta \varepsilon [\text{H} \bullet \text{G}]$$

where  $\Delta F$  and  $\Delta \varepsilon$  denote the sequential changes of fluorescence intensity and the differential molar extinction coefficient of host  $\beta$ -CDs in the absence and presence of the guest molecule. Under the conditions employed, the initial concentration of guest molecules is much larger than that of the host  $\beta$ -CD, i.e.,  $[\text{G}]_0 \gg [\text{H}]_0$ . Therefore, the combination of eqs. [2] and [3] leads to the extended Benesi-Hildebrand equation (eq. [4]),<sup>28</sup> which is used to calculate the  $K_s$  (eq. [2]) from the slope and intercept of  $[\text{H}]_0[\text{G}]_0/\Delta F$  versus  $[\text{G}]_0$  plots.

**Fig. 3.** Fluorescence spectral changes of (a) the bis( $\beta$ -CD) **1** ( $6.4 \times 10^{-6}$  mol/L) upon addition of Gly-Gly (from a to g = 0, 22, 44, 66, 88, 132, and 176  $\mu$ mol/L) and (b) the bis( $\beta$ -CD) **1** ( $5.0 \times 10^{-6}$  mol/L) upon addition of Gly-Pro (from a to h = 0, 60, 80, 100, 120, 140, 180, and 220  $\mu$ mol/L) in phosphate buffer (pH 7.20) at 25  $^{\circ}$ C;  $\lambda_{\text{ex}}$  = 270 nm. Insets: typical plots of  $[H]_0[G]_0/\Delta F$  vs  $[G]_0$  for the inclusion complexation of the bis( $\beta$ -CD) **1** with Gly-Gly and Gly-Pro.



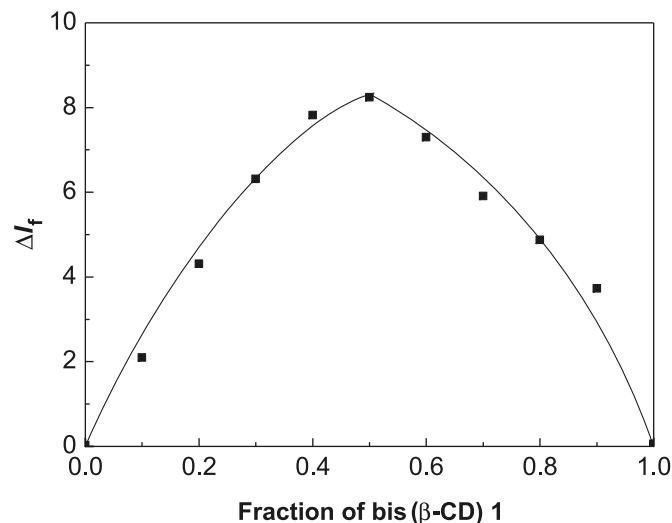
$$[4] \quad \frac{[H]_0[G]_0}{\Delta F} = \frac{1}{K_s \Delta \varepsilon} + \frac{[G]_0}{\Delta \varepsilon}$$

Figure 3 (insets) illustrates the result of such a treatment for the inclusion complexation of the bis( $\beta$ -CD) **1** with Gly-Gly and Gly-Pro, where the calculated  $[H]_0[G]_0/\Delta F$  values were plotted against the  $[G]_0$  to give an excellent linear relationship. The complex stability constants ( $K_s$ ) and the free energy changes ( $-\Delta G^{\circ}$ ) calculated from the slope and intercept are listed in Table 1.

### NMR analysis

$^1\text{H}$  NMR spectrometry is one of the most important techniques used for the characterization of inclusion complexes.<sup>29,30</sup> It is well known that CD possesses outer-surface (H2 and H4) and inner-surface (H3 and H5) protons, and the H6 protons are situated at the primary side of the CD cavity. The inclusion complexation of a guest molecule into the CD

**Fig. 4.** Continuous variation plot of the bis( $\beta$ -CD) **1** / Gly-Gly system ( $[\text{bis}(\beta\text{-CD}) \text{ unit}] + [\text{Gly-Gly}] = 2.0 \times 10^{-5}$  mol/L).

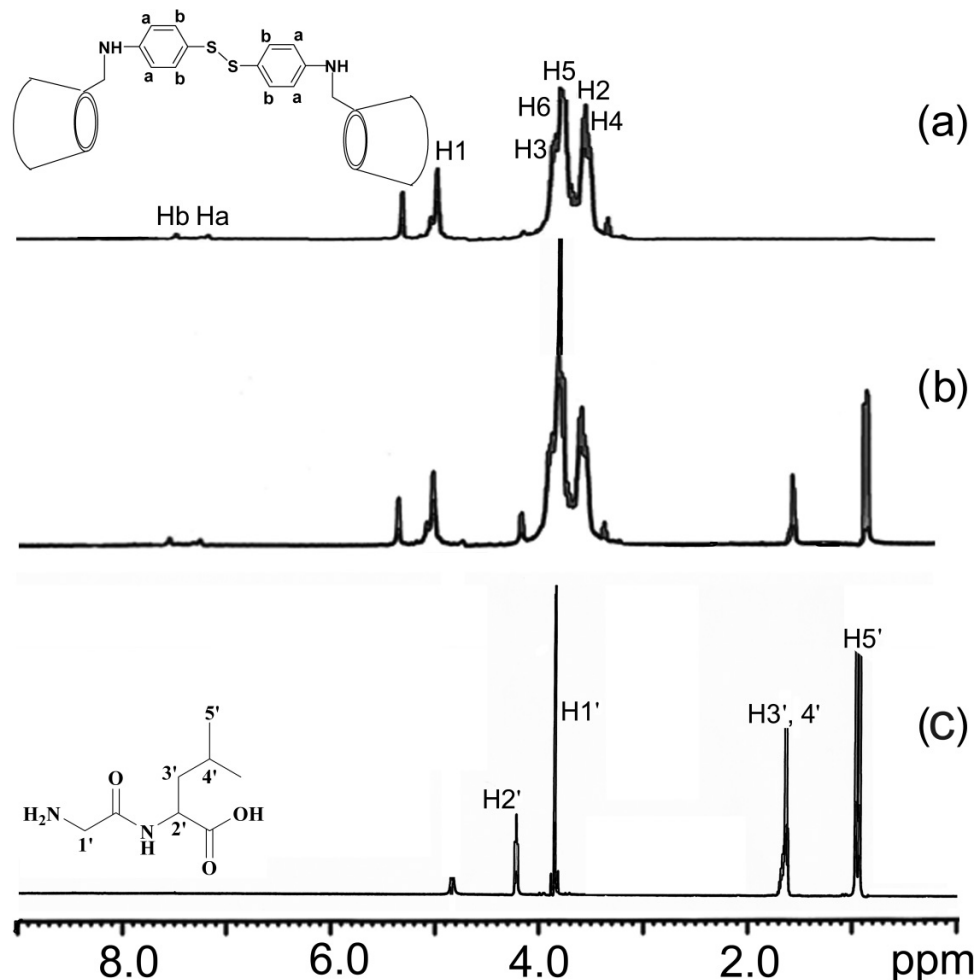


**Table 1.** Complex stability constants ( $K_s$ ) and Gibbs free energy changes ( $-\Delta G^{\circ}$ ) for the inclusion complexation of the bis( $\beta$ -CD) **1** with aliphatic oligopeptides in phosphate buffer (pH 7.20) at 25  $^{\circ}$ C.

Host	Guest	$K_s$ ((mol/L) $^{-1}$ )	Log $K_s$	$-\Delta G^{\circ}$ (kJ/mol)
<b>1</b>	Leu-Gly	$3220 \pm 100$	3.5	20.0
<b>1</b>	Gly-Leu	$14700 \pm 700$	4.2	23.8
<b>1</b>	Glu-Glu	$240 \pm 10$	2.4	13.6
<b>1</b>	Met-Met	$12900 \pm 600$	4.1	23.5
<b>1</b>	Gly-Gly	$7050 \pm 300$	3.8	22.0
<b>1</b>	Gly-Gly-Gly	$11700 \pm 600$	4.1	23.2
<b>1</b>	Gly-Pro	$4030 \pm 200$	3.6	20.6

cavity will result in changes of the chemical shifts of guest protons, and these changes of the protons inside and (or) outside the CD cavity can be used to analyze the formation of the inclusion complex between the CD and the guest. For the sake of comparison, the spectra of the bis( $\beta$ -CD) **1** and Gly-Leu as well as their mixture at the same concentration are shown in Fig. 5, while the spectral characteristics of the bis( $\beta$ -CD) **1** and Gly-Leu are shown in Table 2. The reason for choosing Gly-Leu as the guest molecule to examine the binding behavior of the bis( $\beta$ -CD) **1** with the oligopeptides is that the chemical shifts of the isopropyl protons in the Leu fragment are distant from those of the protons in **1** and can be easily recognized in NMR spectra. As can be seen from Table 2, in the presence of Gly-Leu, a negligible effect is observed on the CD protons H1, H2, and H4. In contrast, protons H3, H5, and H6 exhibit substantial changes, and they undergo relatively strong shielding exceeding 0.06 ppm. Moreover, the changes in the  $^1\text{H}$  NMR chemical shifts of the guest Gly-Leu are also observed in the presence of the bis( $\beta$ -CD) **1** (Table 2). In the presence of the bis( $\beta$ -CD) **1**, the protons of 1', 3', 4', and 5' positions in the Gly-Leu show appreciable upfield shifts ( $\Delta\delta = -0.05$  ppm), whereas the proton of 2' exhibits relatively weak changes ( $\Delta\delta = -0.03$  ppm). These shifts in the  $^1\text{H}$  NMR spectra indicate complex formation between the bis( $\beta$ -CD) **1** and the guest Gly-Leu.

**Fig. 5.**  $^1\text{H}$  NMR spectra of (a) the bis( $\beta$ -CD) **1** ( $5.0 \times 10^{-3}$  mol/L), (b) the bis( $\beta$ -CD) **1** ( $5.0 \times 10^{-3}$  mol/L) in the presence of Gly-Leu ( $5.0 \times 10^{-3}$  mol/L), and (c) Gly-Leu ( $5.0 \times 10^{-3}$  mol/L) in  $\text{D}_2\text{O}$  at  $25^\circ\text{C}$ .



**Table 2.** The chemical shifts ( $\delta$ ) of the bis( $\beta$ -CD) **1**, Gly-Leu, and their mixture at the same concentration and the corresponding changes ( $\Delta\delta$ ).

	Host <b>1</b> ( $\delta$ )	Host <b>1</b> + Gly-Leu		Gly-Leu ( $\delta$ )
		$\delta$	$\Delta\delta$	
H-1	4.98	5.01	0.02	
H-2	3.58	3.60	0.02	
H-3	3.82	3.88	0.06	
H-4	3.51	3.54	0.03	
H-5	3.72	3.79	0.07	
H-6	3.81	3.88	0.07	
H-1'		3.81	0.05	3.86
H-2'		4.18	0.03	4.21
H-3'		1.62	0.08	1.70
H-4'		1.53	0.09	1.62
H-5'		0.85	0.07	0.92

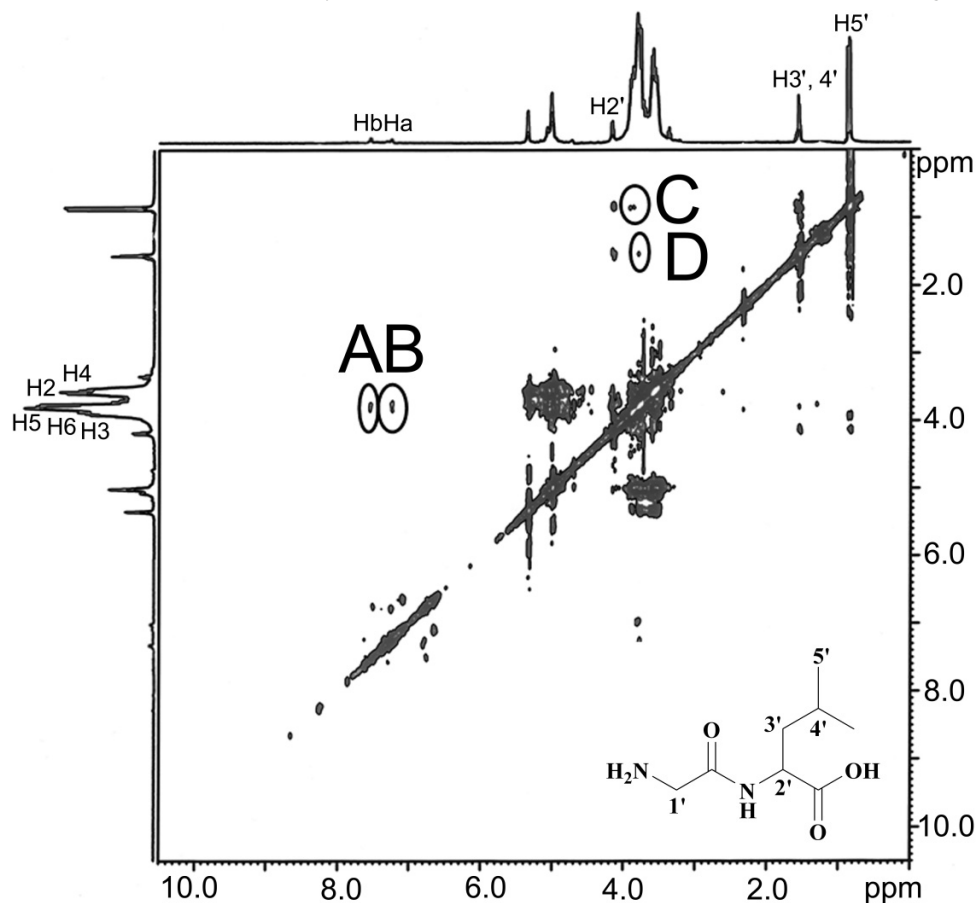
### Binding mode

We examined the circular dichroism spectrum of the bis( $\beta$ -CD) **1** in the presence of Gly-Gly (Fig. 1). The Gly-Gly guest displays no appreciable ICD signal in the range of 200–400 nm. However, the intensity of the absorption bands of the bis( $\beta$ -CD) **1** increased upon addition of the

Gly-Gly guest, giving a relatively strong positive Cotton effect peak ( $\Delta\epsilon = +1.42$  (mol/L) $^{-1}$  cm $^{-1}$ ) at 258 nm for the  $^1\text{L}_a$  band, and a weak negative Cotton effect peak ( $\Delta\epsilon = -0.46$  (mol/L) $^{-1}$  cm $^{-1}$ ) at 295 nm for the  $^1\text{L}_b$  band. The circular dichroism spectral pattern of the bis( $\beta$ -CD) **1** is almost the same as the spectrum without guests, except for an increase in intensity, which indicates **1** almost maintains its original conformation during the addition of Gly-Gly. However, the circular dichroism spectra do not provide further information about the binding mode, which prompted us to perform more detailed conformation analysis by 2D NMR.

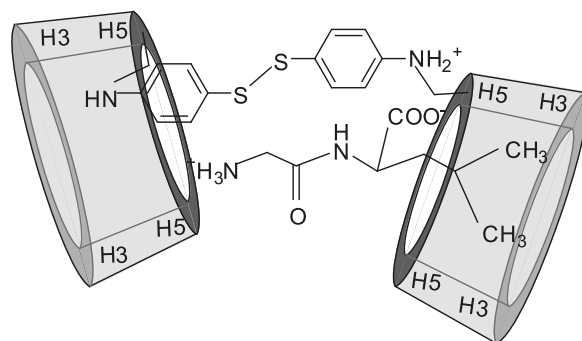
2D NMR spectroscopy has recently become an essential method for the study of the structures of CDs and their complexes, since one can conclude that two protons are closely located in space if an NOE cross peak is detected between the relevant proton signals in the NOESY or ROESY spectrum.<sup>31</sup> As illustrated in Fig. 6, the NOESY spectrum of an equimolar mixture of the bis( $\beta$ -CD) **1** with Gly-Leu (0.5 mmol/L each) displays the correlations (Fig. 6, peaks C and D) between the isobutyl protons of Gly-Leu and H3/H5/H6 of the CD cavity, while no other NOE correlations between host and guest can be found. Moreover, it can be seen from these peaks that the methenyl proton (H5') of Gly-Leu correlates with the H3 protons of CD (Fig. 6, peak

**Fig. 6.** ROESY spectrum of the bis( $\beta$ -CD) **1** with Gly-Leu ( $5.0 \times 10^{-3}$  mol/L each) in D<sub>2</sub>O at 25 °C with a mixing time of 400 ms.



C), whereas the methine proton (H4') of Gly-Leu correlates with the H5/H6 protons of CD (Fig. 6, peak D). In addition, the correlations (Fig. 6, peaks A and B) between the aromatic protons in the linker group and H5/H6 protons of CD are also observed, indicating that the phenyl moiety is not driven out of the CD cavity by guest inclusion. Since H3 protons are located near the wide side of the CD cavity, while H5 protons are near the narrow side, we can deduce that the phenyl unit in the linker group is self-included in another CD cavity from the narrow side. These results, together with the 1:1 host-guest inclusion complexation stoichiometry indicated by Job's experiment, indicate that a cooperative host-linker-guest binding mode is operative in the association of the bis( $\beta$ -CD) **1** with a guest molecule. That is, upon complexation with the bis( $\beta$ -CD) **1**, the guest Gly-Leu is embedded into one hydrophobic CD cavity from the primary side, while the linker group is partly self-included in the other cavity (Fig. 7). According to this binding mode, several interactions will simultaneously work between host and guest. Under our experimental conditions, the carboxylate group in the Gly-Leu is not protonated and should exist as a carboxylate anion, and the  $-NH-$  group in the linker of the bis( $\beta$ -CD) **1** should be partly protonated. Therefore, besides the van der Waals and hydrophobic interactions between the CD cavity and guest oligopeptides, the electrostatic interactions between the protonated amino groups ( $-NH_2^+$ ) in the linker and the carboxylate anion of the oligopeptide may to some extent favor the inclusion

**Fig. 7.** Possible binding mode of the bis( $\beta$ -CD) **1** with Gly-Leu.



complexations of **1** with Gly-Leu. Moreover, the hydrogen bonding interactions between the protonated amino groups ( $-NH_2^+$ ) in the linker and guest oligopeptide also contribute to the strong binding of the bis( $\beta$ -CD) **1**.

The binding mode consequently rationalizes the enhanced fluorescence of **1** in the presence of the guest oligopeptides. Firstly, the inclusion of an oligopeptide can extrude water from the CD cavity and thus increase the microenvironmental hydrophobicity around the fluorophore. In addition, the phenyl chromophore may be efficiently protected from the deactivating water attack by steric shielding by the close oligopeptide guests. As a joint result of these two factors, **1** gives enhanced fluorescence upon inclusion complexation with the oligopeptide.



### Binding ability and molecular selectivity

Many investigations have demonstrated that several weak noncovalent forces, including van der Waals forces, hydrophobic interactions, hydrogen bonding, and electrostatic interactions, contribute cooperatively to inclusion complexation by CDs, and a good match of the size and shape of the host to those of the guest should greatly favor host–guest inclusion complexation, since the strength of these interactions is closely related to the distance and contact surface area between the host and guest.<sup>15</sup> The complex formation constants ( $K_s$ ) for the inclusion complexation of host **1** with oligopeptides decreased in the following order: Gly-Leu > Met-Met > Gly-Gly-Gly > Gly-Gly > Gly-Pro > Leu-Gly > Glu-Glu. It seems reasonable that the bis( $\beta$ -CD) **1** shows the strongest binding ability toward Gly-Leu and Met-Met, since both possess a carboxyl group located in the middle of the peptide chain, which greatly promotes inclusion by the electrostatic and hydrogen bonding interactions between the protonated amino groups ( $-\text{NH}_2^+$ ) in the linker of **1** and the anionic carboxylate of Gly-Leu and Met-Met. On the other hand, although Glu-Glu has a similar structure to Met-Met, its poor hydrophobicity arising from the presence of three hydrophilic carboxyl groups in the molecule reduces the hydrophobic interactions upon complexation with the CD cavity and thus results in the smallest  $K_s$  value with the bis( $\beta$ -CD) **1**. Furthermore, bis( $\beta$ -CD) **1** exhibits a higher  $K_s$  value for the longer Gly-Gly-Gly than for the shorter Gly-Gly ( $K_s$  Gly-Gly-Gly /  $K_s$  Gly-Gly = 1.7). This may be attributed to the strict size and shape between the host and guest. Possessing a relatively long skeleton and less branched chains, Gly-Gly-Gly is able to fully enjoy the cooperative multi-point binding of the long-tethered bis( $\beta$ -CD) **1** as compared with the Gly-Gly guest. Moreover, the hydrogen bonding interactions between one of the carbonyl groups in Gly-Gly-Gly and the amino groups ( $-\text{NH}_2^+$ ) in the linker of the bis( $\beta$ -CD) **1** further promotes the host–guest inclusion complexation. As a joint result of these two factors, the bis( $\beta$ -CD) **1** toward Gly-Gly-Gly gives a stronger binding ability. Another intriguing phenomenon is that the bis( $\beta$ -CD) **1** shows higher binding ability upon complexation with Gly-Leu ( $K_s = 14\,700$  (mol/L)<sup>-1</sup>) as compared with Leu-Gly ( $K_s = 3220$  (mol/L)<sup>-1</sup>). This result seems reasonable, since the guest Gly-Leu and diamino group in **1** are closely located, and the electrostatic and hydrogen bonding interactions between the protonated linker ( $-\text{NH}_2^+$ ) and Leu  $\text{COO}^-$  will provide the additional binding interactions between the host and guest, which consequently favors the host–guest inclusion complexation to some extent. In contrast, the inclusion of the Leu-Gly guest inevitably causes electrostatic repulsion between the linker  $\text{NH}_2^+$  of the bis( $\beta$ -CD) **1** and Leu  $\text{NH}_3^+$  groups of Leu-Gly, resulting in poor host–guest inclusion. Owing to the multiple recognition mechanism involving size and shape fit, hydrophobic electrostatic, and hydrogen bonding interactions, the  $K_s$  values for the bis( $\beta$ -CD) **1** with oligopeptides are variable according to the guest structures from 240 to 14 700 (mol/L)<sup>-1</sup>. The host **1** gives an exciting residue selectivity of up to 61.3 for the Gly-Leu/Glu-Glu pair, and a relatively higher sequence selectivity of up to 4.6 for the Gly-Leu/Leu-Gly pair.

### Conclusions

In summary, the conformation and binding behavior of 4,4'-diaminodiphenyl disulfide bridged bis( $\beta$ -CD) (**1**) with aliphatic oligopeptides has been investigated. The guest-induced fluorescence enhancement of the bis( $\beta$ -CD) **1** opens a new channel for the design of materials. Owing to the multiple recognition mechanism, the bis( $\beta$ -CD) **1** not only affords the highest binding constants of 14 700 (mol/L)<sup>-1</sup> for Gly-Leu, but can also recognize the size and hydrophobicity of oligopeptides, exhibiting dramatically high residue selectivity. These results provide a convenient and powerful method for controlling the binding behavior of dimeric receptors in aqueous solution, which should be useful for the design and synthesis of new supramolecular systems and further improve the understanding of the molecular multiple recognition mechanism in supramolecular systems.

### Acknowledgments

This work was supported by the National Natural Science Foundation (No. 21062030) and the Yunnan Province Natural Science Foundation (No. 2008ZC040M), which are gratefully acknowledged.

### References

- (1) Douhal, A. *Chem. Rev.* **2004**, *104* (4), 1955. doi:10.1021/cr020669j.
- (2) Murphy, R. S.; Barros, T. C.; Mayer, B.; Marconi, G.; Bohne, C. *Langmuir* **2000**, *16* (23), 8780. doi:10.1021/la0005311.
- (3) Wenz, G.; Han, B. H.; Muller, A. *Chem. Rev.* **2006**, *106* (3), 782. doi:10.1021/cr970027+.
- (4) Chen, Y.; Liu, Y. *Chem. Soc. Rev.* **2010**, *39* (2), 495. doi:10.1039/b816354p.
- (5) Churchill, D.; Cheung, J. C. F.; Park, Y. S.; Smith, V. H.; vanLoon, G.; Buncel, E. *Can. J. Chem.* **2006**, *84* (4), 702. doi:10.1139/V06-053.
- (6) Li, L.; Cui, G. H.; Zhao, M.; Wang, Y. J.; Wang, H.; Li, W.; Peng, S. Q. *J. Phys. Chem. B* **2008**, *112* (38), 12139. doi:10.1021/jp8025495.
- (7) Michels, J. J.; Huskens, J.; Reinhoudt, D. N. *J. Am. Chem. Soc.* **2002**, *124* (9), 2056. doi:10.1021/ja017025y.
- (8) Liu, Y.; Zhao, Y. L.; Chen, Y.; Ding, F.; Chen, G. S. *Bioconjug. Chem.* **2004**, *15* (6), 1236. doi:10.1021/bc049870m.
- (9) Baugh, S. D. P.; Yang, Z.; Leung, D. K.; Wilson, D. M.; Breslow, R. *J. Am. Chem. Soc.* **2001**, *123* (50), 12488. doi:10.1021/ja011709o.
- (10) Mulder, A.; Jukovic, A.; van Leeuwen, F. W. B.; Kooijman, H.; Spek, A. L.; Huskens, J.; Reinhoudt, D. N. *Chem. Eur. J.* **2004**, *10* (5), 1114. doi:10.1002/chem.200305567.
- (11) Filippone, S.; Heimann, F.; Rassat, A. *Chem. Commun. (Camb.)* **2002**, 1508. doi:10.1039/b202410a.
- (12) Liu, Y.; Chen, G. S.; Chen, Y.; Ding, F.; Liu, T.; Zhao, Y. L. *Bioconjug. Chem.* **2004**, *15* (2), 300. doi:10.1021/bc034230p.
- (13) Dong, Z.; Liu, J.; Mao, S.; Huang, X.; Yang, B.; Ren, X.; Luo, G.; Shen, J. *J. Am. Chem. Soc.* **2004**, *126* (50), 16395. doi:10.1021/ja045964v.
- (14) Mulder, A.; Juković, A.; Huskens, J.; Reinhoudt, D. N. *Org. Biomol. Chem.* **2004**, *2* (12), 1748. doi:10.1039/b402146k.
- (15) Liu, Y.; Yang, Y. W.; Chen, Y.; Ding, F. *Bioorg. Med. Chem.* **2005**, *13* (4), 963. doi:10.1016/j.bmc.2004.11.042.
- (16) Pecuh, M. W.; Hamilton, A. D. *Chem. Rev.* **2000**, *100* (7), 2479. doi:10.1021/cr9900026.

- (17) Tsubaki, K.; Kusumoto, T.; Hayashi, N.; Nuruzzaman, M.; Fuji, K. *Org. Lett.* **2002**, *4* (14), 2313. doi:10.1021/ol026191n.
- (18) Liu, Y.; Kang, S.; Chen, Y.; Shi, J.; Ke, C. F. *Comb. Chem. High Throughput Screen.* **2007**, *10* (6), 451.
- (19) Zhao, Y.; Liu, X. Q.; Gu, J.; Wang, L. Q.; Zhu, H. Y.; Huang, R.; Wang, Y. F.; Yang, Z. M. *J. Phys. Org. Chem.* **2008**, *21* (6), 440. doi:10.1002/poc.1345.
- (20) Zhao, Y.; Yang, Z. M.; Chi, S. M.; Gu, J.; Yang, Y. C.; Huang, R.; Wang, B. J.; Zhu, H. Y. *Bull. Korean Chem. Soc.* **2008**, *29* (5), 953. doi:10.5012/bkcs.2008.29.5.953.
- (21) Zhao, Y.; Yang, Y. C.; Shi, H.; Zhu, H. Y.; Huang, R.; Chi, S. M.; Zhao, Y. *Helv. Chim. Acta* **2010**, *93* (6), 1136. doi:10.1002/hlca.200900345.
- (22) Zhang, X. Y.; Gramlich, G.; Wang, X. J.; Nau, W. M. *J. Am. Chem. Soc.* **2002**, *124* (2), 254. doi:10.1021/ja011866n.
- (23) Liu, Y.; Song, Y.; Chen, Y.; Yang, Z. X.; Ding, F. *J. Phys. Chem. B* **2005**, *109* (21), 10717. doi:10.1021/jp0504017.
- (24) Yang, Y. C.; Chi, S. M.; Shi, H.; Zhao, Y.; Huang, R.; Zhu, H. Y.; Zhao, Y. *Phys. Chem. Liq.*, in press.
- (25) Park, J. W.; Song, H. E.; Lee, S. Y. *J. Phys. Chem. B* **2002**, *106* (20), 5177. doi:10.1021/jp014191j.
- (26) Kajtar, M.; Horvath-Toro, C.; Kuthi, E.; Szejtli, J. *Acta Chim. Acad. Sci. Hung.* **1982**, *110*, 327.
- (27) Harata, K.; Uedaira, H. *Bull. Chem. Soc. Jpn.* **1975**, *48* (2), 375. doi:10.1246/bcsj.48.375.
- (28) Benesi, H. A.; Hildebrand, J. H. *J. Am. Chem. Soc.* **1949**, *71* (8), 2703. doi:10.1021/ja01176a030.
- (29) Shukla, A. D.; Bajaj, H. C.; Das, A. *Angew. Chem. Int. Ed.* **2001**, *40* (2), 446. doi:10.1002/1521-3773(20010119)40:2<446::AID-ANIE446>3.0.CO;2-N.
- (30) Kawaguchi, Y.; Harada, A. *Org. Lett.* **2000**, *2* (10), 1353. doi:10.1021/ol0055667.
- (31) Schneider, H. J.; Hackett, F.; Rudiger, V.; Ikeda, H. *Chem. Rev.* **1998**, *98* (5), 1755. doi:10.1021/cr970019t.

# Synthesis and reactivity of bis-alkynyl appended metallocenes of Ti, Fe, and Co

Preeti Chadha, Jason L. Dutton, and Paul J. Ragogna

**Abstract:** (Dimethyl)(phenylethynyl)silyl-substituted cyclopentadiene  $C_5H_5SiMe_2C_2Ph$  (**1**) was synthesized by the reaction of in situ generated  $C_5H_5SiMe_2Cl$  with  $LiC_2Ph$ . Metallation of **1** with  $^nBuLi$  or  $KN(SiMe_3)_2$  gave the corresponding Li (**2**) and K (**3**) salts. Transmetalation of **2** with transition metal halides  $MCl_2$  ( $M = TiCl_2$ , Fe, and Co) generated the corresponding early and late transition metal metallocenes (**4**, **5**, and **6**) with pendant alkynyl substituents. Compounds **4** and **6** are the first examples of bis alkyne appended Ti and Co metallocenes. Complexes **5** and **6** undergo alkyne dimerization in the presence of  $CpCo(CO)_2$  generating metallocenophanes **7** and **8** incorporating two metal atoms. Compounds **3**, **4** $Cl_2$ , **6**, and **[8][OTf]** have been characterized by single crystal X-ray structure analysis.

**Key words:** cyclopentadiene, alkyne, titanium, cobalt, heterometallic, metallocenophane.

**Résumé :** On a réalisé la synthèse du (diméthyl)(phényléthynyl)silylcyclopentadiène,  $C_5H_5SiMe_2C_2Ph$  (**1**) par réaction du chlorure de (diméthyl)(phényléthynyl)silyle,  $C_5H_5SiMe_2Cl$  avec le  $LiC_2Ph$ . La métallation du produit **1** avec  $^nBuLi$  ou le  $KN(SiMe_3)_2$  conduit aux sels correspondants du lithium (**2**) ou du potassium (**3**). La transmétallation du produit **2** avec des halogénures de métaux de transitions,  $MCl_2$  ( $M = TiCl_2$ , Fe et Co) conduit aux métallocènes correspondants (**4**, **5** et **6**) de métaux de transition du début et de la fin de cette série portant des substituants alcynyles. Les composés **4** et **6** sont les premiers exemples de métallocènes du titane et du cobalt portant deux appendices bisalcyne. Les complexes **5** et **6**, mis en présence de  $CpCo(CO)_3$ , donnent lieu à une dimérisation de l'alcyne qui conduit aux métallocénophanes **7** et **8** incorporant deux atomes métalliques. On a caractérisé les composés **3**, **4** $Cl_2$ , **6** et **[8][OTf]** par diffraction des rayons-X par un cristal unique.

**Mots-clés :** cyclopentadiène, alcyne, titane, cobalt, hétérométallique, métallocénophane.

[Traduit par la Rédaction]

## Introduction

Cyclopentadienyl (Cp) ligands are one of the most common ligands used in organometallic chemistry as they form complexes with most of the transition metals. Various functional groups have been attached to the Cp ring such as phosphines,<sup>1</sup> amines,<sup>2</sup> and carboxylates,<sup>3</sup> as well as directly linked hetero atoms including numerous p-block elements<sup>4</sup> and transition metals.<sup>5</sup> In many of these cases, the substituents are attached to the  $\pi$ -ligand framework early on during the ligand synthesis, prior to complexation of the central metal. The attachment of various types of alkenyl substituents continues to be of considerable interest, since it allows for the development of organic functional group chemistry at the framework of the preassembled metallocene systems. This includes addition reactions,<sup>6</sup> carbon-carbon coupling reactions at the metallocene backbone resulting in the formation of ansa-metallocenes by intramolecular olefin metathesis (RCM),<sup>7</sup> photochemical [2 + 2] cycloaddition reactions,<sup>8</sup> or by a Mannich type reaction.<sup>9</sup> However, there are few examples of metallocenes with alkyne-appended Cp ligands except for the group 8 metals, which are easily accessible owing to their high stability under various condi-

tions.<sup>10</sup> The bis-alkynyl substituted ferrocenes have been primarily prepared by the coupling of alkynes with diiodo ferrocene.<sup>11a,11b</sup> To make these alkyne substituents more accessible for other transition metals, we have developed a preassembled alkyne-appended Cp ligand (**1**), which can then be attached to various metals such as Ti, Co, and Fe to generate the corresponding metallocenes.

In this context, we describe the synthesis of an alkyne-appended Cp ligand where the alkyne is bridged to the Cp ring by the heteroatom silicon. Various metallocenes have been synthesized using the ligand, and dimerization of the alkyne substituent has been carried out yielding metallocenophanes **7** and **8** incorporating two metal atoms.

## Results and discussion

### Synthesis

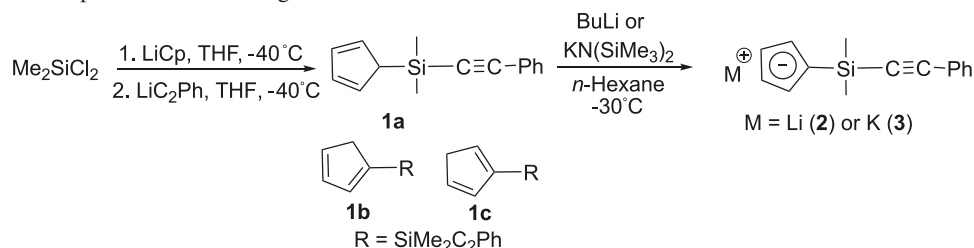
#### Ligand synthesis

The 1:1 stoichiometric reaction of  $LiCp$  with  $Me_2SiCl_2$  at  $-40\text{ }^\circ\text{C}$  in THF resulted in a pale yellow solution. The reaction mixture was allowed to stir for 3–4 h, warming

Received 6 June 2010. Accepted 28 July 2010. Published on the NRC Research Press Web site at [canjchem.nrc.ca](http://canjchem.nrc.ca) on 18 November 2010.

P. Chadha, J.L. Dutton, and P.J. Ragogna.<sup>1</sup> Department of Chemistry, The University of Western Ontario, 1151 Richmond St, London, ON N6A 5B7, Canada.

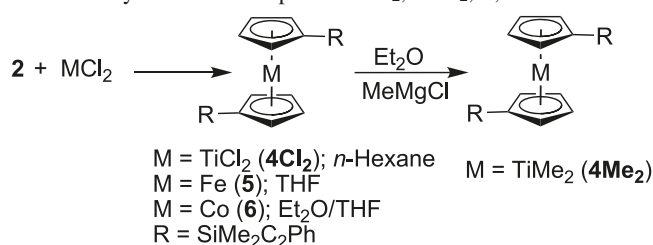
<sup>1</sup>Corresponding author (e-mail: [pragogna@uwo.ca](mailto:pragogna@uwo.ca)).

**Scheme 1.** Synthesis and deprotonation of the ligand.

slowly to room temperature. The reaction mixture was cooled again to  $-40^\circ\text{C}$  and 1 stoichiometric equiv of lithium phenyl acetylide was added (Scheme 1). The solvent was removed in vacuo and the solids washed with *n*-pentane and filtered. The filtrate was concentrated resulting in the formation of a yellow-orange oil. Proton NMR spectroscopy of the crude oil revealed signals consistent with one major product; however, one broad signal was observed for the Cp protons at room temperature. Upon lowering the temperature to  $-20^\circ\text{C}$ , the Cp protons became resolved within the NMR spectra and the three expected isomers (**1a–1c**) were detected. The ratio of the three isomers **1a** (84%), **1b** (13%), and **1c** (3%) were obtained by  $^1\text{H}$  NMR spectroscopy at  $-20^\circ\text{C}$ .<sup>11</sup> The presence of the three isomers were confirmed by  $^{29}\text{Si}$  NMR spectroscopy ( $^1\text{H}$ - $^{29}\text{Si}$  gHMBC) and were observed at  $\delta_{\text{Si}} = -18.6$  for **1a** and  $\delta_{\text{Si}} = -25$  ppm for **1b** and **1c**. The intermediate  $\text{CpSiMe}_2\text{Cl}$ <sup>11a</sup> generated during the initial reaction of LiCp and  $\text{Me}_2\text{SiCl}_2$  was not isolated as it has a very low boiling point,<sup>12</sup> which hinders its isolation in good yields. The in situ generation of  $\text{CpSiMe}_2\text{Cl}$  in a one-pot procedure results in higher yields of **1**. In an independent recent report by Roewer and co-workers,<sup>13</sup> where the  $\text{CpSiMe}_2\text{Cl}$  was isolated, the yield was 30%, whereas our approach gives a 50% yield. Reverse addition of  $\text{Me}_2\text{SiCl}_2$  to the LiCp solution leads to the formation of other unwanted side products, namely  $\text{Cp}_2\text{SiMe}_2$ . Traces of  $\text{Cp}_2\text{SiMe}_2$  and  $(\text{PhC}_2)_2\text{SiMe}_2$  were identified in the crude mixture resulting from slight variations in the stoichiometry. Further purification was carried out by fractional distillation to give the ligand (**1**) in 50% overall yield. The ligand must be pure before attempting the subsequent deprotonation to generate the lithium salt (**2**) cleanly. Freshly prepared **1** was either stored at  $-30^\circ\text{C}$  or converted to its stable Li or K salt (**2**<sup>13</sup> and **3**, respectively) by deprotonation with either  $n\text{-BuLi}$  or  $\text{KN}(\text{SiMe}_3)_2$ . Single crystals were obtained for the potassium salt (**3**) by slow diffusion of *n*-pentane into a THF solution of the ligand and X-ray diffraction studies confirmed the expected connectivity (Fig. 1).

#### Metallation of the ligand — Formation of cyclopentadienyl sandwich complexes

To probe the reactivity and utility of the ligand, metal–Cp complexes were synthesized. The general scheme for the synthesis of the  $(\text{RC}_5\text{H}_4)_2\text{M}$  complexes ( $\text{M} = \text{TiCl}_2$ , Fe, Co;  $\text{R} = \text{SiMe}_2\text{C}_2\text{Ph}$ ) involved transmetallation of the lithium salt (**2**) with the corresponding transition metal halide. Reaction of 2.4 stoichiometric equiv of **2** with  $\text{TiCl}_4$  in *n*-hexane resulted in a colour change from white to yellow and finally to red over a period of 4 h. Proton NMR spectra obtained from the yellow solution showed two sets of Cp pseudo triplets and when the reaction mixture turned red, only one set of Cp protons remained. An excess of the ligand **2** (2.4 stoichiometric equiv instead of 2) was used to ensure complete conversion.

**Scheme 2.** Synthesis of compounds **4Cl<sub>2</sub>**, **4Me<sub>2</sub>**, **5**, and **6**.

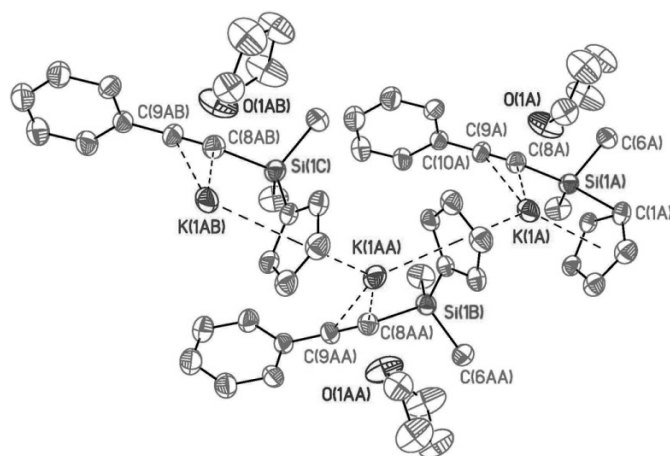
chometric equiv instead of 2) was used to ensure complete conversion. The red solution was filtered, cooled to  $-30^\circ\text{C}$  for complete precipitation of LiCl, filtered again, then concentrated and left at  $-30^\circ\text{C}$  allowing red crystals of **4Cl<sub>2</sub>** to form. X-ray quality crystals of **4Cl<sub>2</sub>** were obtained from a concentrated *n*-hexane solution (see X-ray crystallography, see Fig. 2). Compound **4Cl<sub>2</sub>** was treated with 3 stoichiometric equiv of  $\text{MeMgCl}$  in an  $\text{Et}_2\text{O}/n\text{-hexane}$  mixture resulting in a colour change from red to yellow-orange (Scheme 2). The  $^1\text{H}$  NMR spectrum of an aliquot of the reaction mixture showed a significant shift of the Cp protons ( $\Delta\delta = 0.59$  in **4Cl<sub>2</sub>** to  $\Delta\delta = 0.09$  in **4Me<sub>2</sub>**) and an upfield shift of 0.3 ppm in the methyl groups attached to the silicon atom (Table 1). An upfield shift of  $\sim 6$  ppm is observed in the  $^{29}\text{Si}$  NMR spectrum of **4Cl<sub>2</sub>** and **4Me<sub>2</sub>** when compared with the free ligand (**1**).

Treatment of **2** with 0.5 stoichiometric equiv of anhydrous  $\text{FeCl}_2$  or  $\text{CoCl}_2$  in THF at room temperature resulted in the formation of a yellow-orange or red solution, respectively, over a period of 3–4 h (Scheme 2). The solvent was removed in vacuo, the residue washed with *n*-pentane, and centrifuged. The *n*-pentane was then removed to give orange or red-maroon solids, respectively. The orange solid was identified as compound **5** by comparison with the literature.<sup>14</sup> However, the literature procedure involves the reaction between dilithio-ferrocene and chloro(dimethyl)(phenylethynyl) silane, which is not readily accessible. Compound **5** was further purified by sublimation or recrystallization from *n*-hexane. The  $^1\text{H}$  NMR spectrum of the redissolved red-maroon powder showed a singlet at 3.62 ppm integrating to six protons ( $\text{SiMe}_2$ ), a doublet and two triplets in the aryl region integrating in a 2:2:1 ratio. The Cp protons were not observed owing to the paramagnetic nature of compound **6**. Single crystals were obtained from a concentrated  $\text{Et}_2\text{O}$  solution of the red-maroon powder and X-ray diffraction studies showed the expected connectivity (Fig. 3).

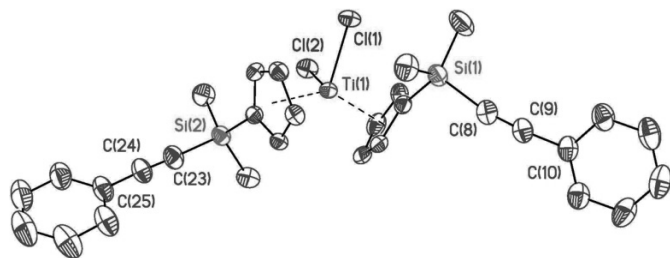
Compound **6** was purified by recrystallization from  $\text{Et}_2\text{O}/n\text{-pentane}$  and was then oxidized with  $\text{AgOTf}$  to form compound **[6][OTf]**, allowing full NMR spectroscopic characterization.



**Fig. 1.** Extended solid-state structure of **3**. Thermal ellipsoids are drawn to the 50% probability level and hydrogen atoms are removed for clarity. The THF molecule is disordered with the four carbon atoms occupying two different positions of 50% occupancy each. Only one set of carbon atoms is shown for THF.



**Fig. 2.** Solid-state structure of  $(RC_5H_4)_2TiCl_2$  (**4Cl<sub>2</sub>**), R = Si-Me<sub>2</sub>C<sub>2</sub>Ph. Thermal ellipsoids are drawn to the 50% probability level and hydrogen atoms are removed for clarity.



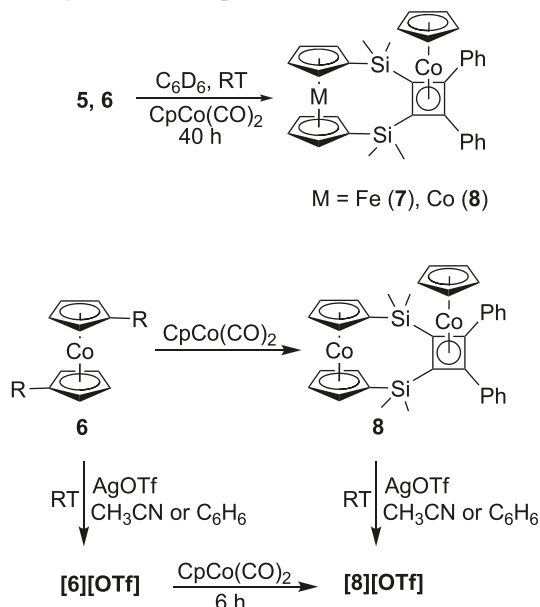
### Cyclization of the alkyne moiety

Compounds **5**, **6**, and **[6][OTf]** were photolyzed with  $CpCo(CO)_2$  to study if the alkynes undergo inter- or intramolecular cyclization. The reactions were performed in benzene-*d*<sub>6</sub> and monitored by <sup>1</sup>H NMR spectroscopy. The reaction proceeded to completion over a period of 40 h (Scheme 3). Some decomposition was observed, resulting in the formation of a brown solid, which was filtered off, the volatiles removed, and the residue washed with *n*-pentane to give orange (**7**) and brown solids (**8** and **[8][OTf]**), respectively. The <sup>1</sup>H NMR spectra of the solids revealed a lowering of symmetry resulting in four different signals for the cyclopentadienyl rings and two different methyl signals in **7** and **[8][OTf]** for the silicon-bound methyl groups.

Carbon-13 NMR spectra of **7** and **[8][OTf]** revealed an upfield shift in the alkyne carbon signals ( $\delta = 93$  and 106 ppm in **5** to  $\delta = 66$  and 88 ppm in **7**; see Table 1), which is typical of  $CbCoCp$  complexes<sup>15</sup>, giving evidence for the formation of a cyclobutadiene ring. A similar effect was observed for **[8][OTf]**. Silicon-29 NMR spectrum showed a downfield shift of about 12 ppm in both **7** and **[8][OTf]**.

Compound **[8][OTf]** can be prepared either by the alkyne cyclization of **[6][OTf]** or by the cyclization of **6** first to form **8** and then oxidation of **8** with AgOTf to yield **[8][OTf]** (Scheme 3).

**Scheme 3.** Synthesis of compounds **7–8**.



### X-ray crystallography

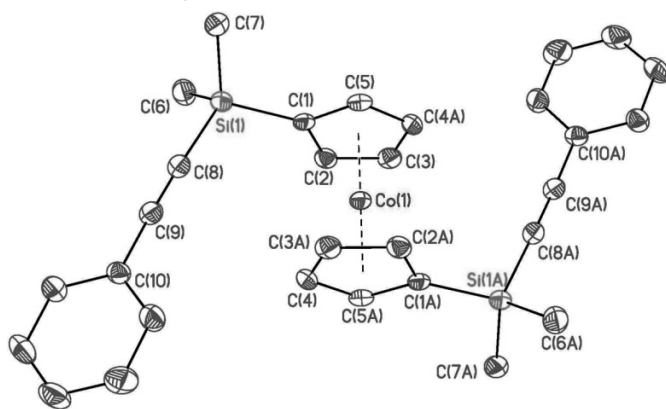
The solid-state structure of the potassium salt of the ligand (**3**) shows that the K atom is sandwiched between two Cp rings and is coordinated by a THF molecule. The interaction between the K and the Cp rings gives rise to extended zigzag chain structure (Fig. 1), reminiscent of group 1 metallocenes.<sup>1a,16,17</sup> The K–Cp<sub>centroid</sub> distances are 2.81 Å and 2.82 Å; the Cp<sub>centroid</sub>–K–Cp<sub>centroid</sub> angle is 138.0°; the K–K–K angle is 138.5°; and the K–Cp<sub>centroid</sub>–K angle is 173.2°, which are indicative of a formal coordination number of 8 for each K atom.<sup>17</sup> This suggests an interaction with the alkyne filling the eighth coordination site (K–C8 = 3.406(3) Å). Similar interaction was observed for an appended alkene moiety; however, the interaction was slightly weaker (3.58(3) Å).<sup>17</sup>

The molecular structure of **4Cl<sub>2</sub>** reveals the anticipated connectivity (Fig. 2).<sup>18</sup> Selected bond lengths and angles are given in Table 2. The alkyne fragments are oriented away from each other and away from the metal centre, and there is no interaction observed between the metal and the alkyne.

In the solid-state structure of **6** (Fig. 3), the two alkynes are oriented away from each other in a trans fashion, the two Cp rings being completely staggered, with the alkynes bent towards the metal centre as opposed to **4Cl<sub>2</sub>**. However, for the cyclization to take place, the alkynes are forced to rotate to obtain a cis geometry. As reported earlier for various [2 + 2] cyclization reactions at the cobalt centre,<sup>19</sup> initial complexation of one of the alkynes with the cobalt centre, probably drives the formation of the cyclized products **7**, **8**, and **[8][OTf]**. In this case, the formation of only one isomer (cis isomer) was observed where the two phenyl groups are cis to each other, as seen from the solid-state structure of **[8][OTf]** (Fig. 4) and from NMR spectroscopy. There is no indication of intermolecular cyclization. The change from sp to sp<sup>2</sup> hybridization is clearly evident on comparison of the C–alkyne bond lengths in **8** and **[10][OTf]**, which changes from 1.20 Å (avg.) in **6** to 1.48 Å (avg.) in **[8][OTf]**, typical of other  $CbCoCp$  compounds (Table 2). The Si–CC<sub>alkyne</sub>

**Table 1.** Selected spectral data for compounds 1–8.

Compound	$^{29}\text{Si}$ (ppm)	$^{13}\text{C}$ (Si–CC–Ph) (ppm)	$^1\text{H}$ NMR shifts (ppm)		
			Cp	$\Delta\delta_{\text{Cp}}$	SiMe <sub>2</sub>
<b>1</b>			6.59, 6.67	0.08	0.10
<b>4Cl<sub>2</sub></b>	–25.0	93.51, 107.96	6.20, 6.79	0.59	0.65
<b>4Me<sub>2</sub></b>	–25.8	93.29, 107.57	6.35, 6.44	0.09	0.35, 0.39
<b>5</b>	–21.5	93.40, 106.00	4.35, 4.51	0.16	0.52
<b>7</b>	–9.3	66.42, 88.11 (Cb)	4.16, 4.27, 4.46		0.40, 0.60
<b>[6][OTf]</b>	–22.5	92.71, 109.34	5.73, 5.93	0.20	0.47
<b>[8][OTf]</b>	–9.8	61.35, 88.77 (Cb)	4.96, 5.78, 6.09, 6.48		0.08, 0.41

**Fig. 3.** Solid-state structure of compound **6**. Thermal ellipsoids are drawn to the 50% probability level and hydrogen atoms are removed for clarity.

bond length is slightly elongated in **[8][OTf]** (1.858(5) and 1.856(6) Å) compared with that in **6** (1.848(3) Å). The Cb–Co–Cp angle remains almost linear (179.6°), indicating that the structure is not strained and is in accordance to what is expected for a [4]cobaltocenophane.<sup>20</sup> However, there are no other known structures of [4]cobaltocenophanes. The crystallographic data for **3**, **4Cl<sub>2</sub>**, **6**, and **[8][OTf]** are found in Table 3.

Similar [2 + 2] cyclization reactions of the appended alkynes in compound **4Me<sub>2</sub>** were, however, unsuccessful and lead to the formation of multiple products as seen from the  $^1\text{H}$  NMR spectrum of the crude sample.

## Conclusion

Early and late transition metal metallocenes (**4Cl<sub>2</sub>**, **4Me<sub>2</sub>**, **6**, and **7**) with a cyclopentadienyl ligand bearing an appended alkyne moiety have been synthesized following a general metathesis route with the preassembled ligand system. Compounds **4** and **6** are the first examples of bis(alkyne)-appended Ti and Co metallocenes. This shows the potential of this ligand to form complexes with a wide variety of transition metals. Alkyne dimerization of the appended alkynes gave rise to metallocenophanes **7** and **8** incorporating two metal atoms. Compound **8** is the first example of a [4]cobaltocenophane with a single Si<sub>2</sub>C<sub>2</sub> bridge.

## Experimental section

Manipulations were performed in an N<sub>2</sub>-filled MBraun

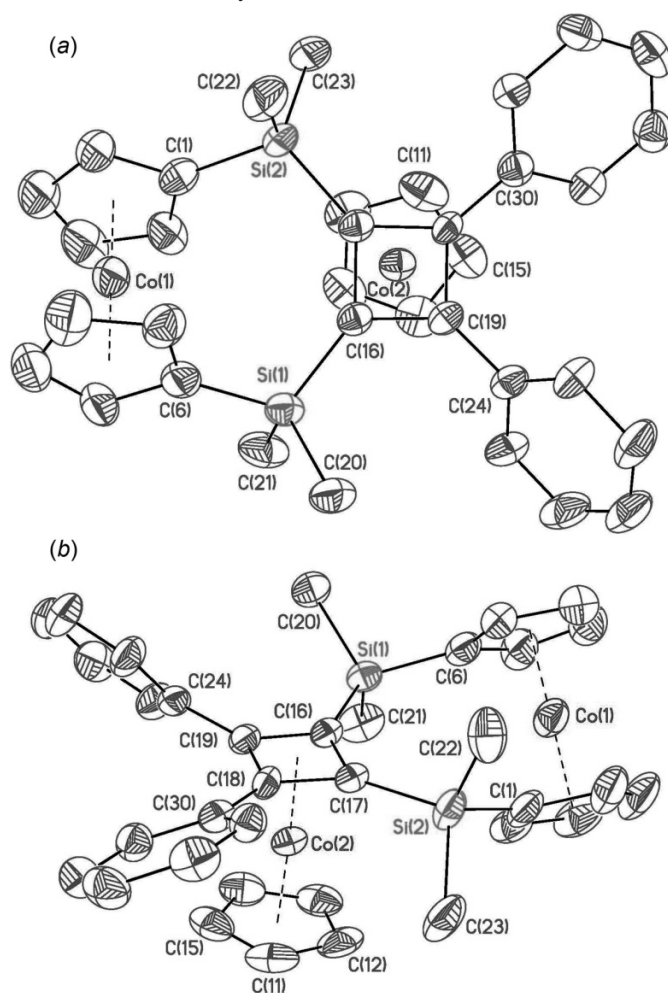
Labmaster 130 glovebox in 4 dram vials (1 dram = 3.552 cm<sup>3</sup>) affixed with Teflon-lined screw caps or using standard Schlenk techniques. Dichloromethane, THF, MeCN, Et<sub>2</sub>O, *n*-pentane, and *n*-hexane were obtained from Caledon Laboratories and dried using the MBraun solvent purification system that utilizes appropriate drying agents. The dried solvents were stored in Straus flasks under a N<sub>2</sub> atmosphere or over 4 Å molecular sieves in the glovebox. Solvents for NMR spectroscopy (CDCl<sub>3</sub>, C<sub>6</sub>D<sub>6</sub>, CD<sub>3</sub>CN, and C<sub>5</sub>D<sub>5</sub>N) were purchased from Cambridge Isotope Laboratories and dried by stirring overnight over CaH<sub>2</sub>, distilled prior to use, and stored in the glovebox over 4 Å molecular sieves.

Dicyclopentadiene and phenyl acetylene were purchased from Sigma-Aldrich and distilled prior to use. Lithium cyclopentadienide<sup>21a</sup> and lithium phenylacetylide<sup>21b</sup> were prepared using literature methods. <sup>*n*</sup>BuLi (1.6 mol/L solution in *n*-hexane), MeMgCl (2 mol/L solution in THF), KN(SiMe<sub>3</sub>)<sub>2</sub>, and PPh<sub>3</sub> were purchased from Sigma-Aldrich and used as received. Cobalt chloride, FeCl<sub>2</sub>, and CpCo(CO)<sub>2</sub> were purchased from Strem Chemicals. Dichlorodimethylsilane was purchased from the Fluka Chemical Company, dried over CaH<sub>2</sub>, distilled prior to use, and stored in the glovebox. Titanium tetrachloride (TiCl<sub>4</sub>) and AgOTf were purchased from Alfa Aesar and used as received (OTf = triflate; trifluoromethanesulphonate).

NMR spectra were recorded using a Varian INOVA 400 MHz spectrometer ( $^3\text{P}$  = 161.83 MHz,  $^{29}\text{Si}$  = 19.86 MHz, and  $^{13}\text{C}$  = 100.52 MHz). Phosphorus-31 NMR spectra was externally referenced to 85% H<sub>3</sub>PO<sub>4</sub> ( $\delta$  = 0.00 ppm). Proton and  $^{13}\text{C}\{^1\text{H}\}$  NMR spectra were referenced relative to Me<sub>4</sub>Si using the NMR solvent ( $^1\text{H}$ –CHCl<sub>3</sub>,  $\delta$  = 7.26 ppm; C<sub>6</sub>HD<sub>5</sub>,  $\delta$  = 7.16 ppm; CHD<sub>2</sub>CN,  $\delta$  = 1.96 ppm; C<sub>5</sub>HD<sub>4</sub>N,  $\delta$  = 8.74, 7.58, or 7.22 ppm;  $^{13}\text{C}\{^1\text{H}\}$ –CDCl<sub>3</sub>,  $\delta$  = 77.2 ppm; C<sub>6</sub>D<sub>6</sub>,  $\delta$  = 128.4 ppm; CD<sub>3</sub>CN,  $\delta$  = 1.3 or 118.3 ppm; C<sub>5</sub>D<sub>5</sub>N,  $\delta$  = 150.2, 135.9, or 123.9 ppm). Fluorine-19 NMR spectra were referenced relative to CFCl<sub>3</sub> ( $\delta$  = 0.00 ppm) using neat Ph–CF<sub>3</sub> ( $\delta$  = –63.7 ppm) as an external standard. Silicon-29 NMR chemical shifts were determined by gradient heteronuclear multiple bond coherence (gHMBC) experiments. FT-IR spectra were collected on samples as thin films on KBr plates or as a KBr disk using a Bruker Tensor 27 spectrometer, with a resolution of 4 cm<sup>–1</sup>. Decomposition and (or) melting points were recorded in flame-sealed capillary tubes using a Gallenkamp variable heater. Suitable single crystals for X-ray diffraction studies were individually selected under Paratone-N oil and

**Table 2.** Selected bond lengths and angles for compounds **3**, **4Cl<sub>2</sub>**, **6**, and **[8][OTf]**.

	Compound			
	<b>3</b>	<b>4Cl<sub>2</sub></b>	<b>6</b>	<b>[8][OTf]</b>
<b>Bond length (Å)</b>				
M—C <sub>pcentroid</sub>	2.81(±0.01)	2.06(±0.01)	1.72(±0.01)	1.64(±0.01)
C—C <sub>alkyne</sub>	1.200(4)	1.200(4), 1.203(4)	1.207(3)	1.475(7), 1.477(7), 1.488(7), 1.506(7) (Cb)
<b>Bond angles (°)</b>				
C <sub>pcentroid</sub> —M—C <sub>pcentroid</sub>	138(±1)	132(±1)	180(±1)	179(±1)
(Cp)C—Si—C <sub>alkyne</sub>	107.5(1)	107.0(1), 101.6(1)	111.2(1)	109.3(2), 109.4(3)
Si—C—C <sub>alkyne</sub>	173.0(3)	168.3(3), 176.5(3)	175.1(2)	—
Ph—C—C <sub>alkyne</sub>	179.4(3)	175.0(4), 177.6(4)	177.8(3)	—

**Fig. 4.** Solid-state structure of compound **[8][OTf]**. Thermal ellipsoids are drawn to the 50% probability level and hydrogen atoms are removed for clarity. The triflate anion is disordered and has been removed for clarity.

mounted on nylon loops and immediately placed in a cold stream of N<sub>2</sub> (150 K). Data were collected on a Bruker Nonius Kappa CCD X-ray diffractometer using graphite-monochromated Mo K $\alpha$  radiation ( $\lambda = 0.71073$  Å). The solution and subsequent refinement of the data were performed using the SHELXTL suite of programs. Elemental analyses were performed by Columbia Analytical Services, Tucson, Arizona. Mass spectra were recorded using an electron ion-

ization Finnigan MAT 8200 mass spectrometer. Photolysis experiments were performed using an Ace Glass medium pressure 450 Watt mercury vapour lamp.

Elemental analysis was performed on compounds **7** and **8**, but the results obtained were not satisfactory. HRMS data is provided for samples that do not decompose in the mass spectrometer. Proton NMR data is provided in the supporting information as a proof of purity of the samples.

#### Synthesis of ligand (1a–1c)

A solution of LiCp (6.25 g, 87 mmol; 100 mL THF) was added to a solution of Me<sub>2</sub>SiCl<sub>2</sub> (10.5 mL, 87 mmol; 30 mL THF) at  $-40$  °C, at which time the solution turned yellow. The reaction mixture was allowed to slowly warm to  $0$  °C, then the cold bath was removed and the reaction mixture was stirred for a further 3–4 h at room temperature (RT). The flask was then cooled to  $-40$  °C and PhC<sub>2</sub>Li (9.39 g, 87 mmol; 40 mL THF) was added, generating an orange solution. The reaction mixture was stirred for 15 h. The volatiles were removed under vacuum, and the resulting mixture taken up in *n*-hexane or *n*-pentane, filtered to remove LiCl, and the volatiles removed in vacuo to yield a yellow-orange liquid. The liquid was then distilled under vacuum (0.1 Torr; 1 Torr = 133.3224 Pa) and the required fraction was obtained at  $100$  °C. Yield: 9.74 g, 50%. <sup>1</sup>H NMR (CDCl<sub>3</sub>,  $-20$  °C)  $\delta$ : major isomer **1a** (84%): 0.10 (s, 6H, Me), 3.59 (m, 1H, Cp), 6.59 (m, 2H, Cp), 6.67 (m, 2H, Cp), 7.32 (m, 3H, Ph), 7.49 (m, 2H, Ph); isomer **1b** (13%): 0.40 (s, 6H, Me), 3.16 (m, 2H, Cp), 6.74 (m, 2H, Cp), 7.01 (m, 1H, Cp); isomer **1c** (3%): 0.41 (s, 6H, Me), 3.09 (m, 2H, Cp), 6.63 (m, 2H, Cp), overlapped with other Cp from isomer **1b**), 6.89 (m, 1H, Cp). All phenyls are overlapped. <sup>13</sup>C{<sup>1</sup>H} NMR (CDCl<sub>3</sub>)  $\delta$ : major isomer **1a**:  $-2.9$  (Me), 51.1 (Cp, CHSiMe<sub>2</sub>), 92.5 (CC–SiMe<sub>2</sub>), 105.8 (CC–Ph), 122.9 (Ph), 128.3 (Ph), 132.1 (Ph), 133.1 (Ph), 138.8 (Cp), 143.6 (Cp); isomer **1b**:  $-0.5$  (Me), 45.3 (Cp, CH<sub>2</sub>), 92.9 (CC–SiMe<sub>2</sub>), 105.9 (CC–Ph), 123.2 (Ph), 128.6 (Ph), 128.8 (Ph), 131.2 (Ph), 135.1 (Cp), 144.1 (Cp), 144.6 (Cp). <sup>29</sup>Si NMR (CDCl<sub>3</sub>)  $\delta$ :  $-18.6$  ppm (major isomer **1a**),  $-28$  ppm (isomers **1b** and **1c**). FT-IR (cm<sup>-1</sup>) (ranked intensity): 434 (12), 536 (13), 690 (2), 732 (9), 756 (3), 801 (5), 819 (10), 846 (1), 981 (7), 950 (11), 1066 (14), 1250 (6), 1488 (8), 2159 (4), 2960 (15). ESI-MS ( $m/z$ ): M<sup>+</sup> (224, 26%), M<sup>+</sup> – Me (209, 10%), M<sup>+</sup> – Cp (159, 100%).

#### Synthesis of LiC<sub>5</sub>H<sub>4</sub>SiMe<sub>2</sub>C<sub>2</sub>Ph (2)

*n*BuLi (10.5 mL of a 1.6 mol/L solution in *n*-hexane) was



**Table 3.** Crystal data for compounds **3**, **4Cl<sub>2</sub>**, **6**, and **[8][OTf]**.

	<b>3</b>	<b>4Cl<sub>2</sub></b>	<b>6</b>	<b>[8][OTf]</b>
Empirical formula	C <sub>19</sub> H <sub>23</sub> KOSi	C <sub>30</sub> H <sub>30</sub> Cl <sub>2</sub> Si <sub>2</sub> Ti	C <sub>30</sub> H <sub>30</sub> CoSi <sub>2</sub>	C <sub>37</sub> H <sub>37</sub> Cl <sub>2</sub> Co <sub>2</sub> F <sub>3</sub> O <sub>3</sub> SSi <sub>2</sub>
Formula weight	334.56	565.52	505.65	863.67
Colour, form	Colourless, block	Red, plate	Red, plate	Red, plate
Crystal size (mm)	0.15×0.1×0.1	0.25×0.2×0.04	0.58×0.25×0.18	0.33×0.18×0.12
Crystal system	Monoclinic	Monoclinic	Monoclinic	Monoclinic
Space group	<i>P</i> 2(1)/ <i>c</i>	<i>P</i> 2(1)/ <i>c</i>	<i>P</i> 2(1)/ <i>n</i>	<i>P</i> 2(1)/ <i>c</i>
<i>a</i> (Å)	8.921(2)	6.532(1)	9.870(2)	18.210(4)
<i>b</i> (Å)	21.330(4)	35.024(7)	5.875(1)	10.181(2)
<i>c</i> (Å)	10.523(2)	12.645(3)	22.102(4)	20.404(4)
$\beta$ (°)	107.55(3)	95.00(3)	93.38(3)	96.53(3)
<i>V</i> (Å <sup>3</sup> )	1909.1(7)	2881.9(1)	1279.4(4)	3758.2(1)
<i>Z</i>	4	4	2	4
<i>D<sub>c</sub></i> (Mg m <sup>-3</sup> )	1.164	1.303	1.313	1.526
$\mu$ (mm <sup>-1</sup> )	0.341	0.583	0.781	1.195
Absorption correction	Semi-empirical from equivalents			
<i>F</i> (000)	712	1176	530	1768
$\theta$ range (°)	2.04–27.48	2.04–27.48	1–27.48	1–27.48
Observed reflections	7802	12061	4854	15206
Independent reflections	4360	6618	2885	8557
Data–restraints–parameters	4360–193–238	6618–0–320	2885–0–151	8557–2–418
Temp (K)	150(2)	150(2)	150(2)	150(2)
<i>R</i> indices ( <i>I</i> > 2σ( <i>I</i> )) <sup>a,b</sup>	0.058, <i>wR</i> <sub>2</sub> = 0.132	0.059, <i>wR</i> <sub>2</sub> = 0.150	0.043, <i>wR</i> <sub>2</sub> = 0.097	0.077, <i>wR</i> <sub>2</sub> = 0.208
<i>R</i> indices (all data) <sup>a,b</sup>	0.122, <i>wR</i> <sub>2</sub> = 0.161	0.096, <i>wR</i> <sub>2</sub> = 0.173	0.071, <i>wR</i> <sub>2</sub> = 0.108	0.132, <i>wR</i> <sub>2</sub> = 0.250
Goodness-of-fit ( <i>S</i> ) <sup>a</sup>	1.059	1.071	1.088	1.061
Largest diff. peak and hole (e Å <sup>-3</sup> )	0.29 and –0.42	0.53 and –0.73	0.52 and –0.43	1.20 and –1.21

<sup>a</sup>*R* =  $\sum ||F_o| - |F_c|| / \sum |F_o|$ ; *wR*(*F*<sup>2</sup>) =  $[\sum w(F_o^2 - F_c^2)^2]^{1/2}$ ; *S* =  $[\sum w(F_o^2 - F_c^2)^2 / (n - p)]^{1/2}$  (*n* = No. of data; *p* = No. of parameters varied).

<sup>b</sup>*w* =  $1/[\sigma^2(F_o^2) + (aP^2) + bP]$ , where *P* =  $(F_o^2 + 2F_c^2)/3$  and *a* and *b* are constants suggested by the refinement program.

added to purified **1** (3.72 g, 16.60 mmol; 100 mL *n*-hexane) at –30 °C. The reaction mixture was allowed to slowly warm over a period of 8 h over which time a white solid precipitated. The suspension was filtered under nitrogen, and the solids were collected, washed twice with *n*-hexane or *n*-pentane (30 mL), and dried under vacuum. Yield: 3.44 g, 90%; dp 55 °C. Note: Without the extended stirring, the yield will be low (2.29 g, 60%, 4 h. <sup>1</sup>H NMR (C<sub>5</sub>ND<sub>5</sub>)  $\delta$ : 0.79 (s, 6H, Me), 6.64 (b, 2H, Cp), 6.79 (b, 2H, Cp), 7.34 (b, 3H, Ph), 7.62 (b, 2H, Ph). <sup>13</sup>C{<sup>1</sup>H} NMR (C<sub>5</sub>ND<sub>5</sub>)  $\delta$ : 1.6 (Me), 98.8 (Cp), 104.3 (CC), 106.1 (CC), 108.5 (Cp), 113.2 (Cp), 124.6 (Ph), 128.3 (Ph), 128.6 (Ph), 132.0 (Ph). <sup>29</sup>Si NMR (C<sub>5</sub>ND<sub>5</sub>)  $\delta$ : –29.9 ppm. FT-IR (cm<sup>-1</sup>) (ranked intensity): 434 (10), 536 (12), 689 (4), 768 (2), 805 (6), 847 (1), 980 (13), 1039 (8), 1177 (9), 1220 (14), 1248 (3), 1440 (15), 1489 (7), 2159 (5), 2959 (11). ESI-MS (*m/z*): M<sup>+</sup> – Li (224, 19%), M<sup>+</sup> – (Me + Li) (209, 11%), M<sup>+</sup> – (Cp + Li) (159, 100%).

### Synthesis of KC<sub>5</sub>H<sub>4</sub>SiMe<sub>2</sub>C<sub>2</sub>Ph (**3**)

Potassium bis(trimethylsilyl)amide (0.089 g, 0.446 mmol; 5 mL Et<sub>2</sub>O) was added to **1** (0.1 g, 0.446 mmol; 20 mL *n*-hexane) at –30 °C. The reaction mixture was stirred for 3.5 h after which a white precipitate was filtered, washed twice with *n*-pentane (8 mL), and then dried in vacuo. Yield: 0.11 g, 93%. X-ray quality crystals were obtained by a slow diffusion of *n*-pentane into a THF solution of **3** at RT; dp 60 °C. <sup>1</sup>H NMR (C<sub>5</sub>ND<sub>5</sub>)  $\delta$ : 0.73 (s, 6H, Me), 6.67 (b, 2H, Cp), 6.82 (b, 2H, Cp), 7.21 (overlapped with Py-*d*<sub>5</sub>,

3H, Ph), 7.50 (d, 2H, Ph). <sup>13</sup>C{<sup>1</sup>H} NMR (C<sub>5</sub>ND<sub>5</sub>)  $\delta$ : 2.0 (Me), 110.3 (Cp), 114.5 (Cp), 128.7 (Ph), 129.0 (Ph), 132.5 (Ph) (quaternary carbons not observed owing to low solubility and stability of the compound in C<sub>5</sub>ND<sub>5</sub>). <sup>29</sup>Si NMR (C<sub>5</sub>ND<sub>5</sub>)  $\delta$ : –30.5 ppm. FT-IR (cm<sup>-1</sup>) (ranked intensity): 443 (7), 656 (13), 674 (5), 690 (8), 740 (1), 778 (4), 826 (2), 1038 (3), 1185 (6), 1246 (9), 1346 (15), 1438 (11), 1487 (12), 2147 (10), 3052 (14).

### Synthesis of (C<sub>5</sub>H<sub>4</sub>SiMe<sub>2</sub>C<sub>2</sub>Ph)<sub>2</sub>TiCl<sub>2</sub> (**4Cl<sub>2</sub>**)

A slurry of LiC<sub>5</sub>H<sub>4</sub>SiMe<sub>2</sub>C<sub>2</sub>Ph (0.91 g, 3.30 mmol; 50 mL *n*-hexane) was cooled to –35 °C and TiCl<sub>4</sub> (0.15 mL, 1.37 mmol; 2 mL *n*-hexane) was added to the slurry when the colour of the reaction mixture turned from white to yellow and finally to red. The cold bath was removed when the temperature reached –5 °C and the reaction mixture was allowed to warm up to room temperature over 4 h, at which time stirring was stopped and the solids settled, the reaction mixture was filtered, and the filtrate was cooled to –30 °C, filtered a second time, concentrated, and then left in a –30 °C freezer overnight. Red crystals were formed that were collected and dried. Yield: 0.54 g, 70%; mp 107 °C. <sup>1</sup>H NMR (C<sub>6</sub>D<sub>6</sub>)  $\delta$ : 0.65 (s, 6H, Me), 6.20 (pt, 4H, Cp), 6.79 (pt, 4H, Cp), 6.90–6.92 (m, 6H, Ph), 7.45–7.47 (m, 4H, Ph). <sup>13</sup>C{<sup>1</sup>H} NMR (C<sub>6</sub>D<sub>6</sub>)  $\delta$ : 0.7 (Me), 93.5 (SiCC), 108.0 (CCPh), 120.3 (Cp), 123.7 (Ph), 127.2 (Cp<sub>ipso</sub>), 128.9 (Ph), 129.3 (Ph), 131.3 (Cp), 132.6 (Ph). <sup>29</sup>Si NMR (C<sub>6</sub>D<sub>6</sub>)  $\delta$ : –25 ppm. FT-IR (cm<sup>-1</sup>) (ranked intensity): 537 (9), 690 (5), 756 (3), 805 (2), 847 (1), 898 (10), 1026 (12), 1043 (8),



1069 (11), 1220 (14), 1251 (7), 1442 (15), 1488 (6), 2158 (4), 2960 (13). ESI-MS ( $m/z$ ):  $M^+ - Cl$  (529). Elemental anal. calcd: C, 63.72; H, 5.35; Found: C, 64.10; H, 5.49.

### Synthesis of $(C_5H_4SiMe_2C_2Ph)_2TiMe_2$ (**4Me<sub>2</sub>**)

$(C_5H_4SiMe_2C_2Ph)_2TiCl_2$  (**4Cl<sub>2</sub>**) (0.20 g, 0.35 mmol; 40 mL  $Et_2O/n$ -hexane (1:1.5)) was treated with 3 stoichiometric equiv of  $MeMgCl$  (0.35 mL, 1.05 mmol; 3 mol/L solution in THF) at  $-15^\circ C$ . The reaction mixture was stirred for 4 h during which time it warmed to room temperature and the colour changed from red to yellow-orange. The  $LiCl$  was filtered off and the yellow-orange solution was concentrated to give orange oil. Yield: 0.15 g, 80%.  $^1H$  NMR ( $C_6D_6$ )  $\delta$ : 0.40 (s, 6H, Me), 0.42 (s, 12H, Me), 6.38 (pt, 4H, Cp), 6.47 (pt, 4H, Cp), 6.90–6.91 (m, 6H, Ph), 7.47–7.49 (m, 4H, Ph).  $^{13}C\{^1H\}$  NMR ( $C_6D_6$ )  $\delta$ : 0.9 (Me), 48.3 (Me), 93.3 (SiCC), 107.57 (CCPh), 116.8 ( $Cp_{ipso}$ ), 118.7 (Cp), 121.9 (Cp), 123.7 (Ph), 128.9 (Ph), 129.3 (Ph), 132.5 (Ph).  $^{29}Si$  NMR ( $C_6D_6$ )  $\delta$ :  $-25.8$  ppm. FT-IR ( $cm^{-1}$ ) (ranked intensity): 442 (13), 537 (11), 689 (4), 756 (3), 823 (1), 905 (10), 1027 (14), 1047 (7), 1070 (15), 1186 (9), 1251 (5), 1488 (8), 2159 (2), 2888 (12), 2958 (6). ESI-MS ( $m/z$ ):  $M^+ - Me$  (507). Elemental anal. calcd: C, 73.26; H 6.92. Found: C, 72.54; H, 6.23.

### Synthesis of $(C_5H_4SiMe_2C_2Ph)_2Fe$ (**5**)

A solution of  $LiC_5H_4SiMe_2C_2Ph$  (**2**) (0.36 g, 1.58 mmol; 3 mL THF) was added to a solution of anhydrous  $FeCl_2$  (0.1 g, 0.79 mmol; 5 mL THF) at room temperature. The reaction mixture was stirred for 4 h, during which time the colour turned dark yellow. The volatiles were then removed, the residue redissolved in  $n$ -pentane, and filtered to remove  $LiCl$ . The filtrate was then concentrated to give an orange solid. Yield: 0.317 g, 80%; mp  $75^\circ C$ . The orange solid was then sublimed at  $140^\circ C$  onto a cold finger at  $-18^\circ C$ .  $^1H$  NMR ( $C_6D_6$ )  $\delta$ : 0.52 (s, 12H, Me), 4.35 (pt, 4H, Cp), 4.51 (pt, 4H, Cp), 6.91–6.95 (m, 6H, Ph), 7.49–7.53 (m, 4H, Ph).  $^{13}C\{^1H\}$  NMR ( $C_6D_6$ )  $\delta$ : 0.6 (Me), 69.4 (Cp), 73.1 (Cp), 74.5 (Cp), 94.2 (SiCC), 106.8 (CCPh), 124.1 (Ph), 128.9 (Ph), 129.1 (Ph), 132.6 (Ph).  $^{29}Si$  NMR ( $C_6D_6$ )  $\delta$ :  $-21.5$  ppm. FT-IR ( $cm^{-1}$ ) (ranked intensity): 690 (7), 776 (2), 802 (4), 846 (1), 897 (14), 1036 (8), 1166 (3), 1220 (11), 1249 (6), 1383 (15), 1421 (13), 1442 (12), 1488 (9), 2158 (5), 2960 (10). ESI-MS ( $m/z$ ):  $M^+$  (502.2, 100%).  $\lambda_{max} = 312$  and  $348$  nm.

### Synthesis of $(C_5H_4SiMe_2C_2Ph)_2Co$ (**6**)

$LiC_5H_4SiMe_2C_2Ph$  (**2**) (0.17 g, 0.77 mmol) was added to a solution of anhydrous  $CoCl_2$  (0.05 g, 0.38 mmol; 5 mL  $Et_2O$ ), followed by the addition of 1 mL THF at room temperature. The reaction mixture was stirred for 3–4 h, during which time the colour turned dark red. The reaction mixture was then filtered to remove the  $LiCl$  and the clear solution was pumped down to give a sticky solid mass, which was then washed twice with  $n$ -pentane and dried to yield a dark maroon solid. Yield: 0.175 g, 90%; mp  $80^\circ C$ . X-ray quality crystals were obtained from concentrated  $Et_2O$  solution at  $-30^\circ C$ .  $^1H$  NMR ( $C_6D_6$ )  $\delta$ : 3.62 (b, 12H, Me), 6.81 (t, 2H, Ph), 7.07 (t, 4H, Ph), 7.46 (d, 4H, Ph); Cp protons were not observed within the range of  $-2$  to  $14$  ppm. FT-IR ( $cm^{-1}$ ) (ranked intensity): 536 (13), 599 (14), 676 (8), 688 (7), 756 (2), 774 (4), 802 (1), 822 (3), 840 (5), 1034 (6),

1158 (11), 1250 (9), 1346 (15), 1486 (10), 2146 (12). ESI-MS ( $m/z$ ):  $M^+ - 268$  (237.1, 100%). Elemental anal. calcd: C, 71.26; H, 5.98. Found: C, 71.49; H, 5.99.  $\lambda_{max} = 335$  and  $429$  nm.

### Synthesis of **7**

$CpCo(CO)_2$  (0.04 g, 0.23 mmol) was added to a  $C_6D_6$  solution of **5** (0.118 g, 0.335 mmol) in an NMR tube. The solution was then photolyzed with broad wavelength UV light for 40–50 h. The reaction was monitored for completion by  $^1H$  NMR spectroscopy, after which the reaction mixture was filtered, the solvent was removed in vacuo to give an orange solid, which was washed with 0.5 mL  $n$ -pentane and dried again. Yield: 0.136 g, 65%; mp  $180^\circ C$ .  $^1H$  NMR ( $C_6D_6$ )  $\delta$ : 0.40 (s, 6H, Me), 0.60 (s, 6H, Me), 4.16 (b, 2H, Cp), 4.27 (b, 4H, Cp), 4.46 (b, 2H, Cp), 4.76 (s, 5H, Cp), 7.04–7.16 (m, 6H, Ph), 7.55 (d, 4H, Ph).  $^{13}C\{^1H\}$  NMR ( $C_6D_6$ )  $\delta$ : 2.4 (Me), 4.1 (Me), 66.4 (SiC(Cb)), 69.3 ( $Cp_{ipso}$ ), 71.9 (Cp), 72.6 (Cp), 74.5 (Cp), 75.2 (Cp), 82.8 (CpCo), 88.1 (CPh(Cb)), 126.9 (Ph), 128.5 (Ph), 129.7 (Ph), 138.4 (Ph).  $^{29}Si$  NMR ( $C_6D_6$ )  $\delta$ :  $-9.3$  ppm. FT-IR ( $cm^{-1}$ ) (ranked intensity): 666 (7), 696 (2), 765 (3), 813 (1), 898 (11), 1036 (6), 1110 (12), 1165 (5), 1245 (4), 1384 (8), 1439 (9), 1599 (10). EI-MS ( $m/z$ ):  $M^+$  (625.9, 100%). HRMS (EI) for  $C_{35}H_{35}Si_2FeCo$  (calcd: 626.09; found: 626.09). Elemental anal. calcd: C, 71.69; H, 6.02. Found: C, 66.20; H, 5.50.  $\lambda_{max} = 357$  and  $423$  nm.

### Synthesis of $[(C_5H_4SiMe_2C_2Ph)_2Co(III)][OTf]$ (**6**)[OTf]

Addition of a solution of **8** (0.20 g, 0.40 mmol; 1 mL of  $CH_3CN$  or  $C_6H_6$ ) to 1 equiv of  $AgOTf$  (0.11 g, 0.40 mmol) resulted in the instantaneous formation of **6**][OTf]. The yield was quantitative by  $^1H$  NMR spectroscopy, but the product could not be obtained as a solid. Removing the solvent always resulted in a sticky mass, which was 90% pure by  $^1H$  NMR spectrum. Yield: 0.233 g, 90%.  $^1H$  NMR ( $C_6D_6$ )  $\delta$ : 0.47 (s, 12H, Me), 5.73 (b, 4H, Cp), 5.93 (b, 4H, Cp), 7.05–7.09 (m, 6H, Ph), 7.61 (d, 4H, Ph).  $^1H$  NMR ( $CD_3CN$ )  $\delta$ : 0.56 (s, 12H, Me), 5.81 (pt, 4H, Cp), 5.92 (pt, 4H, Cp), 7.42–7.45 (m, 6H, Ph), 7.58 (d, 4H, Ph).  $^{13}C\{^1H\}$  NMR ( $CD_3CN$ )  $\delta$ :  $-0.5$  (Me), 89.2 (Cp), 90.6 (Cp), 91.0 (Cp), 92.7 (SiCC), 109.3 (CCPh), 122.9 (Ph), 130.0 (Ph), 130.9 (Ph), 133.2 (Ph).  $^{19}F$  NMR ( $CD_3CN$ )  $\delta$ :  $-78.9$  ppm.  $^{29}Si$  NMR ( $C_6D_6$ )  $\delta$ :  $-22.5$  ppm. FT-IR ( $cm^{-1}$ ) (ranked intensity): 691 (9), 737 (14), 759 (7), 805 (6), 825 (8), 851 (2), 1043 (3), 1117 (12), 1164 (4), 1230 (10), 1255 (1), 1385 (15), 1489 (11), 2159 (5), 2973 (13). ESI-MS ( $m/z$ ):  $M^+ - OTf$  (505.1, 100%),  $M^+ + [M - OTf]^+$  (1159.3).

### Synthesis of **8**

$CpCo(CO)_2$  (0.03 g, 0.18 mmol) was added to a  $C_6D_6$  solution of **6** (0.09 g, 0.18 mmol) in an NMR tube. The solution was then photolyzed with broad wavelength UV light for 40–50 h. The reaction was monitored for completion by  $^1H$  NMR spectroscopy, after which the solution was filtered, the solvent was removed in vacuo to give a brown solid, which was washed with 0.5 mL of  $n$ -pentane four times and dried again. Yield: 0.086 g, 75%.  $^1H$  NMR ( $C_6D_6$ )  $\delta$ : 3.77 (b, 12H, Me), 4.91 (b, 5H, Cp), 7.05 (b, 2H, Ph), 7.11 (b, 4H, Ph), 7.69 (b, 4H, Ph); other Cp protons were not observed within the range of  $-2$  to  $14$  ppm. FT-IR ( $cm^{-1}$ )

(ranked intensity): 664 (13), 696 (4), 770 (2), 805 (1), 1008 (8), 1035 (7), 1156 (9), 1247 (3), 1441 (11), 1488 (14), 1070 (15), 1597 (10), 1955 (6), 2017 (5), 2955 (12). HRMS (EI) for  $C_{35}H_{35}Si_2Co_2$  calcd: 629.094; found: 629.096.

### Synthesis of [8][OTf]

Method I: Addition of a solution of **8** (0.40 g, 0.64 mmol; 2 mL of  $CH_3CN$  or  $C_6H_6$ ) to 1 equiv of AgOTf (0.16 g, 0.64 mmol) resulted in the instantaneous formation of [8][OTf]. The reaction mixture was then filtered to remove Ag, washed with *n*-pentane and  $Et_2O$ , and the solvent was removed in vacuo to give an orange solid. Yield: 0.32 g, 65%. Method II:  $CpCo(CO)_2$  (0.03 g, 0.18 mmol) was added to a  $C_6D_6$  or  $CD_3CN$  solution of [6][OTf] (0.12 g, 0.18 mmol) in an NMR tube. The solution was then photolyzed with broad wavelength UV light for 20–25 h. The reaction was monitored for completion by  $^1H$  NMR spectroscopy, after which the solution was filtered, the solvent was removed in vacuo to give an orange solid, which was washed with 0.5 mL *n*-pentane and 0.5 mL  $Et_2O$  and dried again. Yield: 0.09 g, 65%; mp 200 °C. X-ray quality crystals were obtained by the slow diffusion of *n*-pentane into a DCM solution of the compound at RT.  $^1H$  NMR ( $C_6D_6$ )  $\delta$ : 0.08 (s, 6H, Me), 0.41 (s, 6H, Me), 4.61 (s, 5H, Cp), 4.96 (b, 2H, Cp), 5.78 (b, 2H, Cp), 6.09 (b, 2H, Cp), 6.48 (b, 2H, Cp), 7.03–7.06 (m, 6H, Ph), 7.32–7.35 (m, 4H, Ph).  $^{13}C\{^1H\}$  NMR ( $C_6D_6$ )  $\delta$ : 1.0 (Me), 2.7 (Me), 61.3 (Cb), 82.7 (Cp), 88.8 (Cb), 89.5 (Cp), 89.7 (Cp), 90.0 (Cp), 90.4 (Cp), 91.2 (Cp), 127.5 (Ph), 128.9 (Ph), 129.5 (Ph), 137.0 (Ph); triflate was not observed.  $^{19}F$  NMR ( $C_6D_6$ )  $\delta$ : –78.9 ppm.  $^{29}Si$  NMR ( $C_6D_6$ )  $\delta$ : –9.8 ppm. FT-IR ( $cm^{-1}$ ) (ranked intensity): 444 (10), 516 (13), 636 (3), 671 (11), 700 (7), 775 (6), 820 (4), 894 (15), 1009 (9), 1030 (2), 1136 (5), 1223 (8), 1266 (1), 1386 (14), 1441 (12). ESI-MS ( $m/z$ ):  $M^+ - OTf$  (629, 100%),  $M^+ + 629$  (1407.2),  $[(RC_3H_4)_2Co]^+$  (505, 25%). HRMS (EI) for  $C_{35}H_{35}Si_2Co_2$  calcd: 629.094; found: 629.091.  $\lambda_{max}$  = 316 and 427 nm.

### Supplementary data

Supplementary data for this article are available on the journal Web site (canjchem.nrc.ca). CCDC 768012–768015 contain the X-ray data in CIF format for this manuscript. These data can be obtained, free of charge, via [www.ccdc.cam.ac.uk/conts/retrieving.html](http://www.ccdc.cam.ac.uk/conts/retrieving.html) (or from the Cambridge Crystallographic Data Centre, 12 Union Road, Cambridge CB2 1EZ, UK; fax +44 1223 336033; or [deposit@ccdc.cam.ac.uk](mailto:deposit@ccdc.cam.ac.uk)). Proton NMR spectra for the samples have been provided.

### Acknowledgements

We would like to thank Dr. W.E. Piers for valuable discussions at the beginning of this project. We also thank the Natural Sciences and Engineering Research Council of Canada (NSERC), the Canada Foundation for Innovation (CFI), the Ontario Ministry of Research and Innovation Early Researcher Award (OMRI-ERA), and The University of Western Ontario for generous financial support.

### References

- (1) (a) Karsch, H. H.; Graf, V. W.; Reisky, M. *Chem. Commun.*

- (*Camb.*) **1999**, (17): 1695. doi:10.1039/a904248b.; (b) Butenschön, H.; Kettenbach, R. T.; Krüger, C. *Angew. Chem. Int. Ed. Engl.* **1992**, 31 (8), 1066. doi:10.1002/anie.199210661.
- (2) Li, L.; Han, S.; Li, Q.; Chen, Z.; Pang, Z. *Eur. J. Inorg. Chem.* **2007**, 2007 (32), 5127. doi:10.1002/ejic.200700447.
- (3) (a) Gansäuer, A.; Franke, D.; Lauterbach, T.; Nieger, M. *J. Am. Chem. Soc.* **2005**, 127 (33), 11622. doi:10.1021/ja054185r. PMID:16104737.; (b) Gansäuer, A.; Winkler, I.; Worgull, D.; Franke, D.; Lauterbach, T.; Okkel, A.; Nieger, M. *Organometallics* **2008**, 27 (21), 5699. doi:10.1021/om800700c.
- (4) (a) Lancaster, S.; Hughes, D. L. *Dalton Trans.* **2003**, (9): 1779. doi:10.1039/b300552f.; (b) Sujith, S.; Lee, B. Y.; Han, J. W. *Bull. Korean Chem. Soc.* **2007**, 28 (8), 1299. doi:10.5012/bkcs.2007.28.8.1299.
- (5) Whittell, G. R.; Partridge, B. M.; Presly, O. C.; Adams, C. J.; Manners, I. *Angew. Chem. Int. Ed. Engl.* **2008**, 47 (23), 4354. doi:10.1002/anie.200705672. PMID:18442143.
- (6) Hill, M.; Erker, G.; Kehr, G.; Fröhlich, R.; Kataeva, O. *J. Am. Chem. Soc.* **2004**, 126 (35), 11046. doi:10.1021/ja048447l. PMID:15339191.
- (7) (a) Ogasawara, M.; Nagano, T.; Hayashi, T. *J. Am. Chem. Soc.* **2002**, 124 (31), 9068. doi:10.1021/ja026401r. PMID:12149008.; (b) Ruwwe, J.; Martín-Alvarez, J. M.; Horn, C. R.; Bauer, E. B.; Szafert, S.; Lis, T.; Hampel, F.; Cagle, P. C.; Gladysz, J. A. *Chem. Eur. J.* **2001**, 7 (18), 3931. doi:10.1002/1521-3765(20010917)7:18<3931::AID-CHEM3931>3.0.CO;2-Y.
- (8) (a) Nie, W.-L.; Erker, G.; Kehr, G.; Fröhlich, R. *Angew. Chem. Int. Ed.* **2004**, 43 (3), 310. doi:10.1002/anie.200351886.; (b) Paradies, J.; Greger, I.; Kehr, G.; Erker, G.; Bergander, K.; Fröhlich, R. *Angew. Chem. Int. Ed.* **2006**, 45 (45), 7630. doi:10.1002/anie.200601592.
- (9) Bai, S.-D.; Wei, X.-H.; Guo, J.-P.; Liu, D.-S.; Zhou, Z.-Y. *Angew. Chem. Int. Ed.* **1999**, 38 (13-14), 1926. doi:10.1002/(SICI)1521-3773(19990712)38:13/14<1926::AID-ANIE1926>3.0.CO;2-D.
- (10) (a) Pudelski, J. K.; Callstrom, M. R. *Organometallics* **1992**, 11 (8), 2757. doi:10.1021/om00044a009.; (b) Doisneau, G.; Balavoine, G.; Fillebeen-Khan, T. *J. Organomet. Chem.* **1992**, 425 (1-2), 113. doi:10.1016/0022-328X(92)80026-T.; (c) Pudelski, J. K.; Callstrom, M. R. *Organometallics* **1994**, 13 (8), 3095. doi:10.1021/om00020a026.
- (11) (a) Grimmond, B. J.; Corey, J. Y. *Organometallics* **1999**, 18 (22), 4646. doi:10.1021/om990504+.; (b) Jutzi, P. *Pure Appl. Chem.* **2003**, 75 (4), 483. doi:10.1351/pac200375040483.
- (12) 37–40° at 7–4.5 mm Hg. Schaaf, R. L.; Kan, P. T.; Lenk, C. T.; Deck, E. P. *J. Org. Chem.* **1960**, 25 (11), 1986. doi:10.1021/jo01081a042.
- (13) The ligand has been independently reported recently by another group. Hoffmann, F.; Wagler, J.; Roewer, G. *Eur. J. Inorg. Chem.* **2010**, 2010 (7), 1133. doi:10.1002/ejic.200900769.
- (14) Welfel, S.; Mézailles, N.; Maigrot, N.; Ricard, L.; Mathey, F.; Le Floch, P. *New J. Chem.* **2001**, 25 (10), 1264. doi:10.1039/b103779j.
- (15) Chadha, P.; Dutton, J. L.; Sgro, M. J.; Ragogna, P. J. *Organometallics* **2007**, 26 (25), 6063. doi:10.1021/om700900e.
- (16) Fromm, K. M. *Coord. Chem. Rev.* **2008**, 252 (8-9), 856. doi:10.1016/j.ccr.2007.10.032.
- (17) Evans, W. J.; Brady, J. C.; Fujimoto, C. H.; Giarikos, D. G.; Ziller, J. W. *J. Organomet. Chem.* **2002**, 649 (2), 252. doi:10.1016/S0022-328X(02)01138-5.

- (18) Sweeney, N. J.; Mendoza, O.; Müller-Bunz, H.; Pampillón, C.; Rehmann, F.-J. K.; Strohfeldt, K.; Tacke, M. *J. Organomet. Chem.* **2005**, *690* (21-22), 4537. doi:10.1016/j.jorganchem.2005.06.039.
- (19) (a) Staeb, T. H.; Chávez, J.; Gleiter, R.; Nuber, B. *Eur. J. Inorg. Chem.* **2005**, *2005* (20), 4090. doi:10.1002/ejic.200500394.; (b) Harcourt, E. M.; Yonis, S. R.; Lynch, D. E.; Hamilton, D. G. *Organometallics* **2008**, *27* (7), 1653. doi:10.1021/om7011634.
- (20) Schaefer, C.; Scholz, G.; Gleiter, R.; Oeser, T.; Rominger, F. *Eur. J. Inorg. Chem.* **2005**, *2005* (7), 1274. doi:10.1002/ejic.200400851.
- (21) (a) Garbuzava, I. A.; Garkusha, O. G.; Lokshin, B. V. *J. Organomet. Chem.* **1985**, *279* (3), 327. doi:10.1016/0022-328X(85)87031-5.; (b) Jackman, L. M.; Scarmoutzos, L. M.; DeBrosse, C. W. *J. Am. Chem. Soc.* **1987**, *109* (18), 5355. doi:10.1021/ja00252a009.

# Towards the development of new subtype-specific muscarinic receptor radiopharmaceuticals — Radiosynthesis and ex vivo biodistribution of [<sup>18</sup>F]3-(4-(2-(2-(2-fluoroethoxy)ethoxy)ethylthio)-1,2,5-thiadiazol-3-yl)-1-methyl-1,2,5,6-tetrahydropyridine

Erik M. van Oosten, Alan A. Wilson, David C. Mamo, Bruce G. Pollock, Benoit H. Mulsant, Sylvain Houle, and Neil Vasdev

**Abstract:** Muscarinic receptors have been implicated in neurological disorders including Alzheimer's disease, Parkinson's disease, and schizophrenia. Nineteen derivatives of thiadiazolyltetrahydropyridine (TZTP), a core that has previously shown high affinities towards muscarinic receptor subtypes, were synthesized and evaluated via in vitro binding assays. The title compound, a fluoro-polyethyleneglycol analog of TZTP (**4c**), was subsequently labelled with fluorine-18. Fluorine-18-labelled **4c** was produced, via an automated synthesis, in an average radiochemical yield of 36% (uncorrected for decay), with high radiochemical purity (>99%) and high specific activity (326 GBq/μmol; end-of-bombardment), within 40 min (*n* = 3). Ex vivo biodistribution studies following tail-vein injection of [<sup>18</sup>F]**4c** in conscious rats displayed sufficient brain uptake (0.4%–0.7% injected dose / gram of wet tissue in all brain regions at 5 min post injection); however, there were substantial polar metabolites present in the brain, thereby precluding future use of [<sup>18</sup>F]**4c** for imaging in the central nervous system.

**Key words:** fluorine-18, muscarinic receptor, thiadiazolyltetrahydropyridine (TZTP), positron emission tomography (PET).

**Résumé :** Les récepteurs muscariniques ont été impliqués dans des désordres neurologiques, dont la maladie d'Alzheimer, la maladie de Parkinson et la schizophrénie. On a réalisé la synthèse de dix-neuf dérivés de la thiadiazolyltétrahydropyridine (TZTP), un produit fondamental pour lequel des études antérieures ont permis de montrer de grandes affinités vis-à-vis des sous-types de récepteurs muscariniques, et on a évalué leurs propriétés par des essais de fixation in vitro. On a subéquemment marqué au fluor-18 le composé mentionné dans le titre (**4c**), un analogue fluoropolyéthylèneglycol de la TZTP. Le composé **4c** marqué au fluor-18 a été obtenu, par le biais d'une synthèse automatisée, avec un rendement radiochimique de 36 % (non corrigé pour la décroissance), avec une pureté radiochimique élevée (>99 %) et une activité spécifique élevée (326 GBq/μmol; fin du bombardement), en moins de 40 minutes (*n* = 3). Des études de biodistribution ex vivo à la suite d'injections dans la veine de la queue du [<sup>18</sup>F]**4c** dans des rats conscients ont démontré qu'il y se produit une absorption suffisante par le cerveau (0,4 à 0,7 % de la dose injectée / gramme de tissu mouillé dans toutes les régions du cerveau cinq minutes après l'injection) ; toutefois, plusieurs métabolites polaires sont présents dans le cerveau et cette situation élimine l'usage dans le futur du [<sup>18</sup>F]**4c** pour faire de l'imagerie du système nerveux central.

**Mots-clés :** fluor-18, récepteur muscarinique, thiadiazolyltétrahydropyridine (TZTP), tomographie à émission de positon (TEP).

[Traduit par la Rédaction]

Received 12 August 2010. Accepted 6 October 2010. Published on the NRC Research Press Web site at canjchem.nrc.ca on 24 November 2010.

**E.M. van Oosten.** PET Centre, Centre for Addiction and Mental Health, Toronto, ON M5T 1R8, Canada; Department of Chemistry, University of Toronto, Toronto, ON M5S 3H6, Canada.

**A.A. Wilson, S. Houle, and N. Vasdev.**<sup>1</sup> PET Centre, Centre for Addiction and Mental Health, Toronto, ON M5T 1R8, Canada; Department of Psychiatry, University of Toronto, Toronto, ON M5T 1R8, Canada.

**D.C. Mamo.** PET Centre, Centre for Addiction and Mental Health, Toronto, ON M5T 1R8, Canada; Department of Psychiatry, University of Toronto, Toronto, ON M5T 1R8, Canada; Geriatric Mental Health Program, Centre for Addiction and Mental Health, Toronto, ON M6J 1H4, Canada.

**B.G. Pollock and B.H. Mulsant.** Department of Psychiatry, University of Toronto, Toronto, ON M5T 1R8, Canada; Geriatric Mental Health Program, Centre for Addiction and Mental Health, Toronto, ON M6J 1H4, Canada.

<sup>1</sup>Corresponding author (e-mail: neil.vasdev@camhpet.ca).



## Introduction

Muscarinic acetylcholine receptors (mAChRs) are present in both the peripheral and central nervous system (CNS) and are responsible for mediating the metabotropic effects of acetylcholine.<sup>1</sup> There are 5 distinct subtypes of the muscarinic acetylcholine receptor, M<sub>1</sub>, M<sub>2</sub>, M<sub>3</sub>, M<sub>4</sub>, and M<sub>5</sub>, each having distinct functions and unique distributions in the CNS.<sup>2</sup> The M<sub>1</sub> and M<sub>2</sub> receptors are abundant in the CNS and have postulated roles in Alzheimer's disease and schizophrenia, as well as a range of cognitive disorders.<sup>3,4</sup> The M<sub>3</sub> and M<sub>5</sub> receptors are present in relatively lower concentrations in the CNS.<sup>3</sup> M<sub>3</sub> receptors have no known correlations with neuropsychiatric disorders, whereas M<sub>5</sub> receptors have been linked to schizophrenia and addictions.<sup>3,4</sup> The M<sub>4</sub> receptor is present in the CNS, particularly in the cortex, striatum, and hippocampus,<sup>2,3</sup> and is associated with Parkinson's disease and schizophrenia.<sup>1,4</sup> The synthesis of subtype-selective drugs that target mAChRs is an ongoing goal in drug development. To date, the only clinically approved drugs that target mAChRs are nonselective antagonists that are used for treating patients suffering from Parkinson's disease.

Applying imaging modalities such as single photon emission computed tomography (SPECT) and positron emission tomography (PET)<sup>5,6</sup> to elucidate the mechanism of action of new pharmaceuticals targeting muscarinic receptors *in vivo* has been of long-standing interest.<sup>7</sup> Derivatization of the thiadiazolyltetrahydropyridine (TZTP) core<sup>8</sup> has led to the development of muscarinic subtype-selective PET radiotracers.<sup>9–12</sup> The M<sub>2</sub>-specific agonist radiotracer, fluorine-18 (<sup>18</sup>F; *t*<sub>1/2</sub> = 109.7 min) labelled fluoropropylthio-TZTP ([<sup>18</sup>F]FP-TZTP),<sup>11,13,14</sup> was proven to be selective through knockout mice studies<sup>15,16</sup> and is currently the only M<sub>2</sub>-specific radiotracer established for human PET imaging.<sup>17,18</sup> Fluorine-18-labelled FP-TZTP has been used to study risk factors of ageing<sup>19–21</sup> and mood disorders.<sup>22,23</sup>

Driven largely by the theory that M<sub>1</sub> receptor density is altered in the brain of patients with Alzheimer's disease in response to the degeneration of the cholinergic pathway, another TZTP derivative, 3-(4-(hexyloxy)-1,2,5-thiadiazol-3-yl)-1-methyl-1,2,5,6-tetrahydropyridine (xanomeline), was found to exhibit M<sub>1</sub>/M<sub>4</sub> selectivity.<sup>24</sup> While it was found that xanomeline increased cognitive function of patients with Alzheimer's disease, several side effects precluded its therapeutic use. Carbon-11 (<sup>11</sup>C; *t*<sub>1/2</sub> = 20.4 min) labelled xanomeline was evaluated in human subjects<sup>9,25</sup> and a <sup>18</sup>F-labelled xanomeline derivative was evaluated in rodents<sup>25</sup> but neither radiopharmaceutical was further pursued because of inadequate receptor selectivity.

The present study sought to systematically prepare new muscarinic receptor subtype-specific TZTP analogs for development as PET radiopharmaceuticals. We report the synthesis of hydroxy- and fluoro-alkyl as well as hydroxy- and fluoro-polyethyleneglycol (PEG) ether and thioether analogs of TZTP, and the determination of their *in vitro* binding affinities (*K*<sub>i</sub>) towards the five muscarinic subtypes, as well as  $\sigma_1$  and  $\sigma_2$  receptors. All analogs synthesized in this work are amenable to labelling with either <sup>18</sup>F or <sup>11</sup>C. A promising fluoro-PEG derivative of TZTP (**4c**), identified from initial *in vitro* screening, was radiolabelled with <sup>18</sup>F and evaluated

for its potential to image muscarinic receptors in the rodent brain.

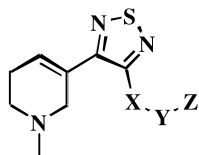
## Results and discussion

### Chemistry

The syntheses of 19 derivatives of TZTP (Table 1) are reported, including previously known compounds (**2a**,<sup>13</sup> **4a**,<sup>11,12</sup> **8a**,<sup>26</sup> **8b**,<sup>26</sup> **9c**,<sup>25</sup> and **10**<sup>8</sup>). Syntheses of the TZTP analogs were carried out by literature procedures with modifications. Thioether-PEG analogs of TZTP, with both fluoro (**4**) and hydroxyl (**2**) groups at the terminal position, were synthesized as shown in Scheme 1. To conserve the TZTP core (3-(4-chloro-1,2,5-thiadiazol-3-yl)-1-methyl-1,2,5,6-tetrahydropyridine; **1**),<sup>8</sup> fluoroalkyl and fluoro-PEG chains were synthesized from the respective diols (**5**, Scheme 2) for subsequent reactions with **1**. The diols were disubstituted with benzyl-protecting and tosyloxy-leaving groups (**6**). Nucleophilic displacement of the tosyloxy group of **6** with fluoride resulted in *O*-benzyl protected fluoroalkyl and fluoro-PEG chains (**7**). The hydroxyl analogs (**8**) were synthesized by reaction of the appropriate diol (**5**) with **1** (Scheme 3). Scheme 3 shows the synthesis of the desired fluoro-alkyl and fluoro-PEG ether-TZTP analogs (**9**), prepared by catalytic hydrogenation of **7** and *in situ* reaction with **1** in the presence of sodium hydride (NaH). Several TZTP derivatives with incorporated PEG groups have been synthesized in attempts to achieve subtype selectivity and improve water solubility, binding affinity, and agonist potency toward mAChRs.<sup>27,28</sup> The present work further explores the use of PEG groups as a means of expanding the series of TZTP derivatives, by replacing alkyl groups with PEG chains; [<sup>18</sup>F]fluoro-PEG groups have demonstrated similar pharmacological advantages when incorporated into PET radiopharmaceuticals.<sup>29</sup> In preparation for *in vitro* binding assay studies, all 19 TZTP analogs synthesized in the present work (Table 1) were characterized by <sup>1</sup>H and <sup>19</sup>F (when applicable) NMR spectroscopy, high resolution mass spectrometry, and elemental analysis (all compounds were >97% pure by elemental analysis).

### *In vitro* binding assays

The thioether-TZTP derivatives (compounds **2** and **4**) as well as the ether derivatives (compounds **8–10**) were evaluated by the National Institute of Mental Health's Psychoactive Drug Screening Program to determine their binding affinities towards each of the five muscarinic subtypes, as well as towards  $\sigma_1$  and  $\sigma_2$  receptors; the  $\sigma$  receptors are known competition sites for ligands targeting mAChRs.<sup>30</sup> In the initial assay, all six thioether-TZTP derivatives (**2a–2c** and **4a–4c**) were measured for affinity towards the aforementioned receptors (Table S1 in the Supplementary data; values in parentheses), and a fluoro-PEG derivative of TZTP with moderate affinity towards the M<sub>4</sub> receptor (**4c**; *K*<sub>i</sub> = 48 nM) was identified. Based on our initial binding assay, we advanced to radiolabelling this compound with fluorine-18, as it represents the first attempt to develop a PET radiotracer for imaging the M<sub>4</sub> receptor and is a novel fluorinated-PEG derivative of TZTP. As such, our goal was

**Table 1.** General structure and TZTP derivatives synthesized.

Structure	TZTP derivatives		
	X	Y	Z
<b>2a</b>	S	CH <sub>2</sub> CH <sub>2</sub> CH <sub>2</sub>	OH
<b>2b</b>	S	CH <sub>2</sub> CH <sub>2</sub> OCH <sub>2</sub> CH <sub>2</sub>	OH
<b>2c</b>	S	CH <sub>2</sub> CH <sub>2</sub> OCH <sub>2</sub> CH <sub>2</sub> OCH <sub>2</sub> CH <sub>2</sub>	OH
<b>4a</b>	S	CH <sub>2</sub> CH <sub>2</sub> CH <sub>2</sub>	F
<b>4b</b>	S	CH <sub>2</sub> CH <sub>2</sub> OCH <sub>2</sub> CH <sub>2</sub>	F
<b>4c</b>	S	CH <sub>2</sub> CH <sub>2</sub> OCH <sub>2</sub> CH <sub>2</sub> OCH <sub>2</sub> CH <sub>2</sub>	F
<b>8a</b>	O	CH <sub>2</sub> CH <sub>2</sub> CH <sub>2</sub>	OH
<b>8b</b>	O	CH <sub>2</sub> CH <sub>2</sub> CH <sub>2</sub> CH <sub>2</sub>	OH
<b>8c</b>	O	CH <sub>2</sub> CH <sub>2</sub> CH <sub>2</sub> CH <sub>2</sub> CH <sub>2</sub>	OH
<b>8d</b>	O	CH <sub>2</sub> CH <sub>2</sub> CH <sub>2</sub> CH <sub>2</sub> CH <sub>2</sub> CH <sub>2</sub>	OH
<b>8e</b>	O	CH <sub>2</sub> CH <sub>2</sub> OCH <sub>2</sub> CH <sub>2</sub>	OH
<b>8f</b>	O	CH <sub>2</sub> CH <sub>2</sub> OCH <sub>2</sub> CH <sub>2</sub> OCH <sub>2</sub> CH <sub>2</sub>	OH
<b>9a</b>	O	CH <sub>2</sub> CH <sub>2</sub> CH <sub>2</sub>	F
<b>9b</b>	O	CH <sub>2</sub> CH <sub>2</sub> CH <sub>2</sub> CH <sub>2</sub> CH <sub>2</sub>	F
<b>9c</b>	O	CH <sub>2</sub> CH <sub>2</sub> CH <sub>2</sub> CH <sub>2</sub> CH <sub>2</sub> CH <sub>2</sub>	F
<b>9d</b>	O	CH <sub>2</sub> CH <sub>2</sub> CH <sub>2</sub> CH <sub>2</sub> CH <sub>2</sub> CH <sub>2</sub> CH <sub>2</sub>	F
<b>9e</b>	O	CH <sub>2</sub> CH <sub>2</sub> OCH <sub>2</sub> CH <sub>2</sub>	F
<b>9f</b>	O	CH <sub>2</sub> CH <sub>2</sub> OCH <sub>2</sub> CH <sub>2</sub> OCH <sub>2</sub> CH <sub>2</sub>	F
<b>10</b>	O	CH <sub>2</sub> CH <sub>2</sub> CH <sub>2</sub> CH <sub>2</sub> CH <sub>2</sub> CH <sub>2</sub>	H

to radiolabel the title compound, **4c**, with <sup>18</sup>F and evaluate its potential for imaging the CNS via a preliminary ex vivo biodistribution study.

### Radiochemistry

The radiosynthetic approach for [<sup>18</sup>F]**4c** was similar to our previously reported synthesis for [<sup>18</sup>F]FP-TZTP,<sup>14</sup> where the appropriate tosyloxy-containing radiolabelling precursor (**3c**) was subjected to reaction with fluorine-18-labelled potassium cryptand fluoride (K[<sup>18</sup>F]/K<sub>222</sub>) in CH<sub>3</sub>CN at 90 °C for 10 min (Scheme 4) followed by HPLC purification (Fig. 1). The formulated product was >99% radiochemically pure (Fig. 2) and the log *D* was experimentally determined to be 1.73 ± 0.01 (pH = 7.4), using a previously reported method.<sup>31</sup> The automated synthesis of [<sup>18</sup>F]**4c** resulted in a radiochemical yield of 35.6% ± 15.3% based on [<sup>18</sup>F]fluoride and uncorrected for decay in a synthesis time of 37 min (*n* = 3). The specific activity of [<sup>18</sup>F]**4c** was 326 ± 198 GBq/μmol (corrected to end-of-bombardment). Fluorine-18-labelled **4c** is the first reported <sup>18</sup>F-labelled PEG derivative of TZTP. While the hydroxyl derivatives of TZTP (series **2** and **8**) are not amenable to labelling with <sup>18</sup>F, similar compounds have been readily labelled by reaction of the respective desmethyl precursors with [<sup>11</sup>C]CH<sub>3</sub>I.<sup>9,12</sup>

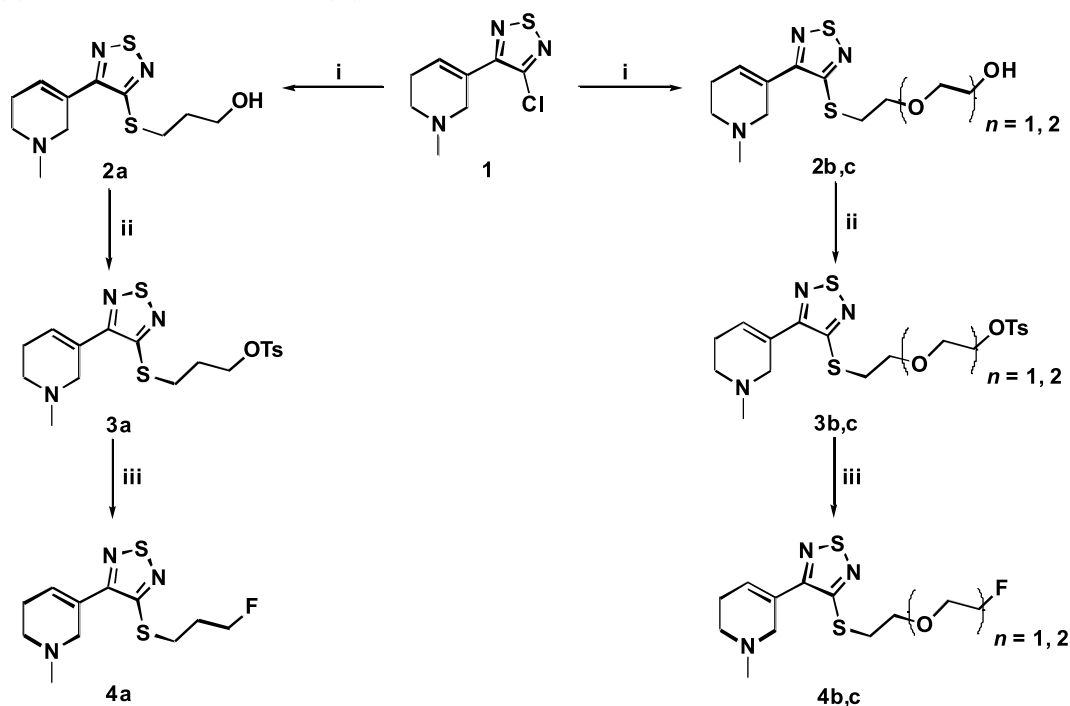
### Ex vivo biodistribution in rodents

Preliminary ex vivo biodistribution studies using [<sup>18</sup>F]**4c** were subsequently carried out in conscious male Sprague–Dawley rats.<sup>32,33</sup> Fluorine-18-labelled **4c** demonstrated fast and efficient uptake in the rodent brain (0.4%–0.7% injected dose / gram of wet tissue in all brain regions at 5 min post injection) following tail-vein injection (Fig. S1 in the Supplementary data). This uptake was followed by a fast wash-out, with most of the radioactivity cleared from the brain by 15 min. Radio-HPLC analysis of plasma identified a rapid degradation of the parent compound to both hydrophilic and lipophilic metabolites. At 15 min after injection of [<sup>18</sup>F]**4c** only 4.5% of the parent compound was unmetabolized. Analysis of brain homogenates 60 min after injection (Fig. 3) found that while the parent compound was present in the brain, there was a significant accumulation of radioactive polar metabolites (24%). Owing to the presence of radioactive metabolites in the brain, further studies were not justified because [<sup>18</sup>F]**4c** does not present suitable properties for imaging the CNS.

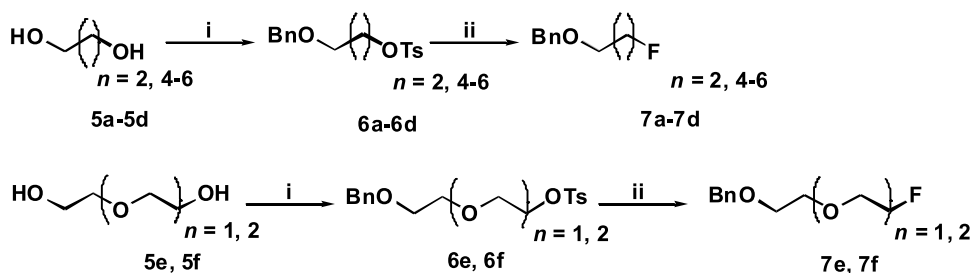
### Conclusion

We report the synthesis of 13 new TZTP derivatives that are amenable for radiolabelling with <sup>11</sup>C and (or) <sup>18</sup>F. Com-

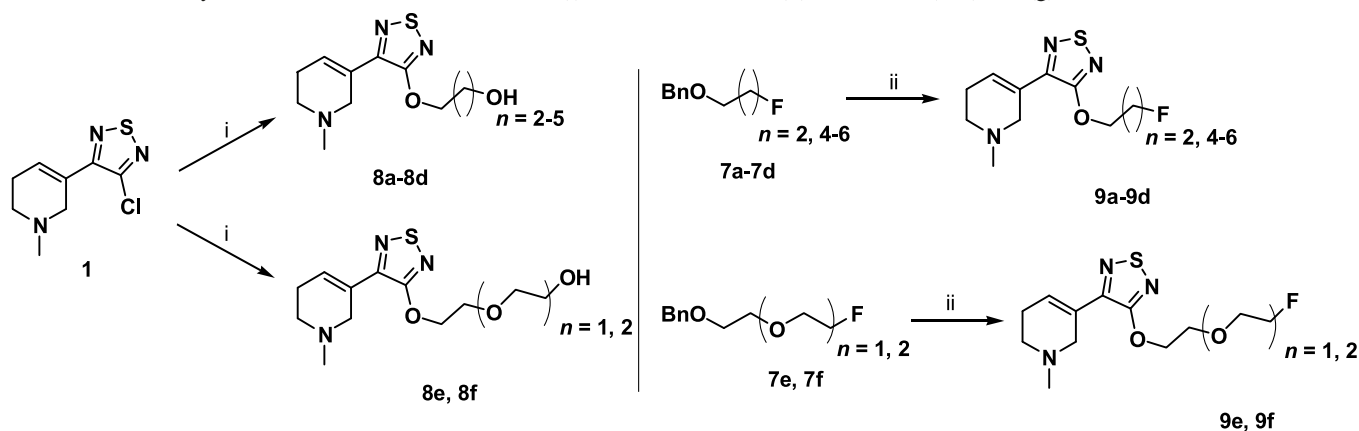
**Scheme 1.** General syntheses of thioether-TZTP derivatives and radiolabelling precursors. (i) 1, Li<sub>2</sub>S, DMF; 2, bromo- or chloro-alcohol, K<sub>2</sub>CO<sub>3</sub>, DMF. (ii) TsCl, Et<sub>3</sub>N, DMAP, CH<sub>2</sub>Cl<sub>2</sub>. (iii) TBAF, THF.



**Scheme 2.** General syntheses of benzyl-protected fluoro-alcohols. (i) 1, BnBr, KOH, neat; 2, Et<sub>3</sub>N, DMAP, TsCl, CH<sub>2</sub>Cl<sub>2</sub>. (ii) TBAF, THF, microwave heating.

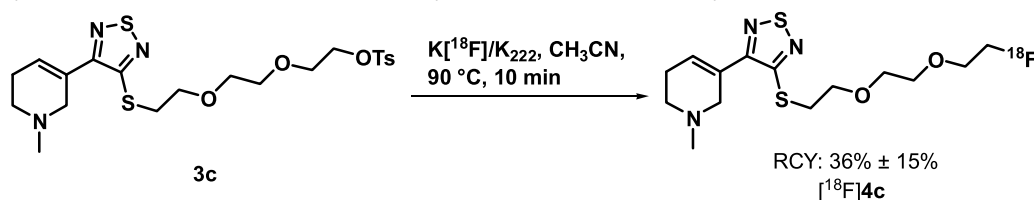
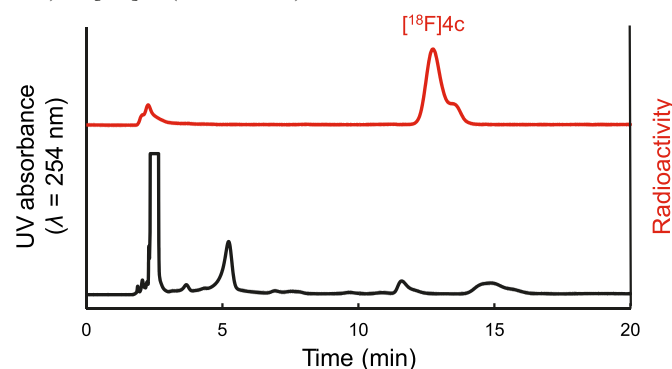
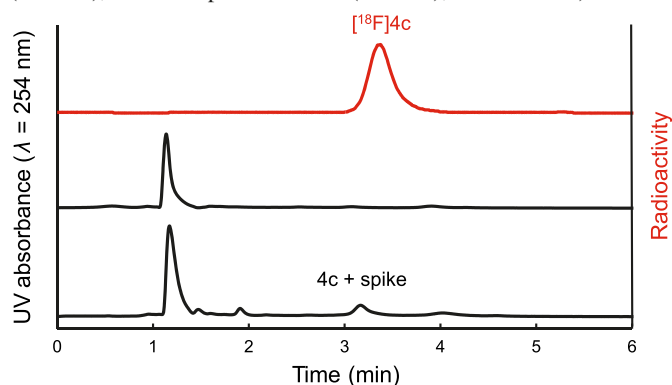


**Scheme 3.** General syntheses of ether-TZTP derivatives. (i) 5a–5f, NaH, THF. (ii) 1, Pd/C, Pd(OH)<sub>2</sub>, H<sub>2</sub>(g), THF; 2, NaH, 1, THF.



pound **4c** was chosen as a lead compound for radiolabelling based on in vitro binding assays and represents the first fluoro-PEG derivative of TZTP. Automated radiosynthesis of [<sup>18</sup>F]**4c** was achieved with good radiochemical yields, high specific activity, and excellent radiochemical purity within

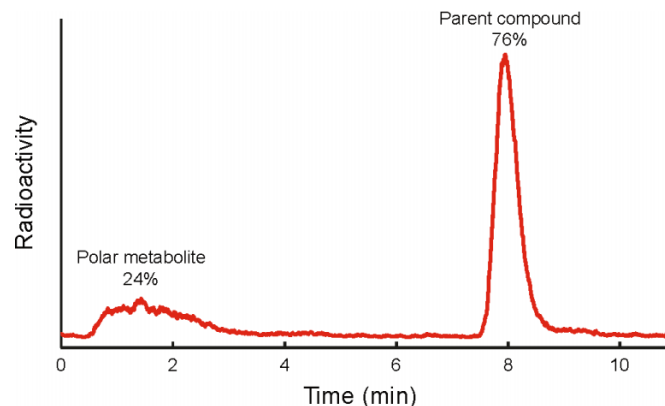
40 min. Ex vivo biodistribution studies in rodent models showed appreciable amounts of polar radioactive metabolites in the brain, suggesting that [<sup>18</sup>F]**4c** is not suitable for further development as a radiopharmaceutical for imaging the CNS.

**Scheme 4.** Radiosynthesis of [ $^{18}\text{F}$ ]**4c**. RCY = radiochemical yield, not corrected for decay.**Fig. 1.** Semipreparative HPLC purification (20:80  $\text{CH}_3\text{CN}:\text{H}_2\text{O}$  + 0.1 N ammonium formate + 1% formic acid (pH 4), Semi-Prep LUNA C18(2) (250 mm  $\times$  10 mm, 10  $\mu\text{m}$ ,  $\lambda$  = 254 nm) at 6 mL/min) of [ $^{18}\text{F}$ ]**4c** ( $t_R$  = 13 min).**Fig. 2.** Analytical HPLC (Phenomenex Prodigy C18 (ODS prep), 30:70  $\text{CH}_3\text{CN}:\text{H}_2\text{O}$  + 0.1 N ammonium formate;  $\lambda$  = 254 nm; 3.0 mL/min) of purified [ $^{18}\text{F}$ ]**4c** (from top to bottom: gamma, UV (254 nm), and UV spiked with **4c** (254 nm);  $t_R$  = 3.2 min).

## Experimental section

### General methods

3-Chloro-(pyridine-3-yl)-1,2,5-thiadiazole was purchased from commercial suppliers and was used as received without further purification unless otherwise specified. Compound **1**, 3-(3-chloro-1,2,5-thiadiazol-4-yl)-1,2,5,6-tetrahydro-1-methylpyridine,<sup>8</sup> and compound **3a**, 3-(4-(1-methyl-1,2,5,6-tetrahydropyridin-3-yl)-1,2,5-thiadiazol-3-ylthio)propyl-4-methylbenzenesulfonate,<sup>14</sup> were prepared by literature procedures. All water used was distilled and deionized and all mobile phases were made with HPLC-grade solvents. Flash column

**Fig. 3.** HPLC analysis (see the Metabolism studies section for HPLC conditions) of rat brain homogenates at 60 min post injection of [ $^{18}\text{F}$ ]**4c**.

chromatography purification was accomplished using silica gel 60 (63–200  $\mu\text{m}$ , Caledon). Preparative thin-layer chromatography (PTLC) was accomplished using silica gel GF plates (20 cm  $\times$  20 cm, 2000  $\mu\text{m}$ ) from Analtech. All new compounds were obtained as oils following purification.

High resolution mass spectrometry (HR-MS) was conducted by the Advanced Instrumentation for Molecular Structure Laboratory or by the Centre for Biological Timing and Cognition at the University of Toronto. Elemental analysis (EA) was performed by the Analytical Laboratory for Environmental Science Research and Training, University of Toronto. Proton and carbon-13 NMR spectra were recorded at 25  $^\circ\text{C}$  in  $\text{CDCl}_3$  on a Varian Mercury 300 MHz or 400 MHz spectrometer with an autoswitchable H/F/C/P 5 mm probe with gradients. Proton NMR chemical shifts were reported using either tetramethylsilane (TMS, 0.00 ppm) as an internal standard or referencing to the residual proton in  $\text{CDCl}_3$  (7.26 ppm). The proton resonances of primary alcohols were often not observed owing to exchange. For  $^{13}\text{C}$  NMR, shifts were referenced to  $\text{CDCl}_3$  (77.0 ppm). Fluorine-19 NMR shifts were referenced to external  $\text{CFCl}_3$  (0.00 ppm). Tetrabutylammonium fluoride (TBAF) was prepared by evaporation of tetrahydrofuran (THF) from a 1.0 M solution under reduced pressure, and then drying under reduced pressure overnight, as modified from a previously reported literature procedure.<sup>34</sup> THF was freshly distilled over lithium aluminum hydride ( $\text{LiAlH}_4$ ).

All animal experiments were carried out under humane conditions, with approval from the Animal Care Committee at the Centre for Addiction and Mental Health and in accordance with the guidelines set forth by the Canadian Council on Animal Care.



## Chemical synthesis

### 3-(4-(1-Methyl-1,2,5,6-tetrahydropyridin-3-yl)-1,2,5-thiadiazol-3-ylthio)propan-1-ol (**2a**)

Compound **2a** was prepared by minor modifications to a literature procedure.<sup>13</sup> Briefly, 250 mg of **1** (1.16 mmol) was dissolved in 3 mL of anhydrous DMF in an oven-dried round-bottomed flask under nitrogen. Li<sub>2</sub>S (2.9 mmol) was added to the mixture with stirring at 60 °C in an oil bath for 5 h. Upon consumption of the starting material, the reaction was cooled to room temperature (RT) and 3-bromopropanol (2.9 mmol) was added, followed by addition of K<sub>2</sub>CO<sub>3</sub> (2.9 mmol). The reaction mixture was stirred at RT for 35 min. Upon completion, the reaction was diluted with ether (50 mL), washed with H<sub>2</sub>O (3 × 50 mL) and brine (50 mL), dried over NaSO<sub>4</sub>, and concentrated. PTLC purification was performed (20:80 EtOAc:Hex) to yield 217 mg of **2a** (69%). <sup>1</sup>H NMR (CDCl<sub>3</sub>, 300 MHz) δ: 6.77–6.71 (m, 1H), 3.71 (t, <sup>3</sup>J<sub>HH</sub> = 5.9 Hz, 2H), 3.45–3.42 (m, 2H), 3.37 (t, <sup>3</sup>J<sub>HH</sub> = 6.9 Hz, 2H), 3.22 (br, 1H), 2.63–2.57 (m, 2H), 2.51–2.43 (m, 2H), 2.47 (s, 3H), 2.04–1.91 (m, 2H). HR-MS calcd. for C<sub>11</sub>H<sub>18</sub>N<sub>3</sub>OS<sub>2</sub> [M + 1]: 272.0897; found: 272.0885. EA calcd.: C 48.68, H 6.33, N 15.49; found: C 48.39, H 6.46, N 14.90.

### 2-(2-(4-(1-Methyl-1,2,5,6-tetrahydropyridin-3-yl)-1,2,5-thiadiazol-3-ylthio)ethoxy)ethanol (**2b**)

The general procedure for the synthesis of **2a** was followed using **1** (1.16 mmol) in DMF with 2.5 equiv. of Li<sub>2</sub>S, 2.5 equiv. of 2-(2-chloroethoxy)ethanol, and 2.5 equiv. of K<sub>2</sub>CO<sub>3</sub> to give 304 mg of **2b** (87%) after PTLC purification. <sup>1</sup>H NMR (CDCl<sub>3</sub>, 300 MHz) δ: 6.77–6.72 (m, 1H), 3.84 (t, <sup>3</sup>J<sub>HH</sub> = 6.3 Hz, 2H), 3.76–3.72 (m, 2H), 3.64–3.59 (m, 2H), 3.51 (t, <sup>3</sup>J<sub>HH</sub> = 6.3 Hz, 2H), 3.45–3.42 (m, 2H), 2.63–2.57 (m, 2H), 2.52–2.44 (m, 2H), 2.46 (s, 3H). HR-MS calcd. for C<sub>12</sub>H<sub>20</sub>N<sub>3</sub>O<sub>2</sub>S<sub>2</sub> [M + 1]: 302.0991; found: 302.0990. EA calcd.: C 47.81, H 6.37, N 13.94; found: C 47.92, H 6.32, N 13.60.

### 2-(2-(2-(4-(1-Methyl-1,2,5,6-tetrahydropyridin-3-yl)-1,2,5-thiadiazol-3-ylthio)ethoxy)ethoxy)ethanol (**2c**)

The general procedure for the synthesis of **2a** was followed using **1** (1.16 mmol) in DMF with 2.5 equiv. of Li<sub>2</sub>S, 2.5 equiv. of 2-(2-(2-chloroethoxy)ethoxy)ethanol, and 2.5 equiv. of K<sub>2</sub>CO<sub>3</sub>. After PTLC purification, **2c** was obtained in a 95% yield (542 mg). <sup>1</sup>H NMR (CDCl<sub>3</sub>, 300 MHz) δ: 6.77–6.71 (m, 1H), 3.83 (m, 2H), 3.75–3.71 (m, 2H), 3.69–3.66 (m, 4H), 3.63–3.59 (m, 2H), 3.51 (t, <sup>3</sup>J<sub>HH</sub> = 6.5 Hz, 2H), 3.45–3.42 (m, 2H), 2.63–2.59 (m, 2H), 2.52–2.45 (m, 2H), 2.46 (s, 3H). HR-MS calcd. for C<sub>14</sub>H<sub>24</sub>N<sub>3</sub>O<sub>3</sub>S<sub>2</sub> [M + 1]: 346.1253; found: 346.1266. EA calcd.: C 48.67, H 6.72, N 12.17; found: C 47.64, H 6.88, N 11.83.

### 2-(2-(4-(1-Methyl-1,2,5,6-tetrahydropyridin-3-yl)-1,2,5-thiadiazol-3-ylthio)ethoxy)ethyl 4-methylbenzenesulfonate (**3b**)

Compound **3b** was made by an analogous procedure to that of compound **3a**.<sup>14</sup> Briefly, 267 mg (0.89 mmol) of **2b** was dissolved in 8 mL of CH<sub>2</sub>Cl<sub>2</sub> followed by the addition of 1.5 equiv. of *p*-toluenesulfonyl chloride (TsCl), 3 equiv. of triethylamine (TEA), and a catalytic amount of dimethyl-

laminopyridine (DMAP; 1 mol%). Compound **3b** was obtained in an 86% yield (348 mg). <sup>1</sup>H NMR (CDCl<sub>3</sub>, 300 MHz) δ: 7.82–7.76 (m, 2H), 7.35–7.29 (m, 2H), 6.75–6.70 (m, 1H), 4.19–4.14 (m, 2H), 3.74 (t, <sup>3</sup>J<sub>HH</sub> = 6.3 Hz, 2H), 3.71–3.66 (m, 2H), 3.44–3.36 (m, 4H), 2.62–2.56 (m, 2H), 2.51–2.42 (m, 8H).

### 2-(2-(2-(4-(1-Methyl-1,2,5,6-tetrahydropyridin-3-yl)-1,2,5-thiadiazol-3-ylthio)ethoxy)ethoxy)ethyl 4-methylbenzenesulfonate (**3c**)

Compound **3c** was made by an analogous procedure to that of compound **3a**.<sup>14</sup> Briefly, 350 mg (1.01 mmol) of **2c** was dissolved in 8 mL of CH<sub>2</sub>Cl<sub>2</sub> followed by the addition of 1.5 equiv. of TsCl, 3 equiv. of TEA, and catalytic DMAP (1 mol%). Compound **3c** was obtained in a 72% yield (352 mg). <sup>1</sup>H NMR (CDCl<sub>3</sub>, 400 MHz) δ: 7.82–7.78 (m, 2H), 7.65–7.31 (m, 2H), 6.77–6.73 (m, 1H), 4.18–4.15 (m, 2H), 3.79 (t, <sup>2</sup>J<sub>HF</sub> = 6.4 Hz, 2H), 3.71–3.68 (m, 2H), 3.61–3.59 (m, 4H), 3.48 (t, <sup>3</sup>J<sub>HH</sub> = 6.6 Hz, 2H), 3.44–3.42 (m, 2H), 2.62–2.58 (m, 2H), 2.49–2.43 (m, 8H).

### 3-(4-(3-Fluoropropylthio)-1,2,5-thiadiazol-3-yl)-1-methyl-1,2,5,6-tetrahydropyridine (**4a**)

Compound **4a** was prepared by modifications to the literature procedures.<sup>11,13</sup> To an oven-dried round-bottomed flask containing 4.9 mmol TBAF (dried under reduced pressure overnight) was added 10 mL of freshly distilled THF, followed by 0.33 mmol of **3a**. The reaction was refluxed for 3 h and then diluted with 50 mL H<sub>2</sub>O and washed with 50 mL of EtOAc (×2). The combined organic layer was washed with 50 mL of brine, dried over Na<sub>2</sub>SO<sub>4</sub>, and concentrated. The product was purified using PTLC (7:93 MeOH:CH<sub>2</sub>Cl<sub>2</sub>) to yield 37 mg of **4a** (36%). <sup>1</sup>H NMR (CDCl<sub>3</sub>, 300 MHz) δ: 6.70–6.65 (m, 1H), 4.52 (dt, <sup>2</sup>J<sub>HF</sub> = 47.1 Hz, <sup>3</sup>J<sub>HH</sub> = 5.6 Hz, 2H), 3.39–3.35 (m, 2H), 3.33 (t, <sup>3</sup>J<sub>HH</sub> = 7.22 Hz, 2H), 2.56–2.49 (m, 2H), 2.44–2.37 (m, 2H), 2.39 (s, 3H), 2.12 (dm, <sup>3</sup>J<sub>HF</sub> = 26.5 Hz, 2H). <sup>19</sup>F NMR (CDCl<sub>3</sub>, 282 MHz) δ: –221.51 (tt, <sup>2</sup>J<sub>HF</sub> = 47.2 Hz, <sup>3</sup>J<sub>HF</sub> = 26.5 Hz). HR-MS calcd. for C<sub>11</sub>H<sub>16</sub>FN<sub>3</sub>S<sub>2</sub> [M]: 273.0770; found: 273.0772. EA calcd.: C 48.32, H 5.91, N 15.37; found: C 48.23, H 6.03, N 15.12.

### 3-(2-(2-Fluoroethoxy)ethylthio)-4-(1-methyl-1,2,5,6-tetrahydropyridin-3-yl)-1,2,5-thiadiazole (**4b**)

Compound **4b** was prepared in an analogous manner to that of **4a**. Briefly, 0.3 mmol of **3b** in THF was reacted with 5 equiv. of TBAF. **4b** was obtained in a 33% yield (36 mg). <sup>1</sup>H NMR (CDCl<sub>3</sub>, 300 MHz) δ: 6.79–6.75 (m, 1H), 4.57 (dm, <sup>2</sup>J<sub>HF</sub> = 47.6 Hz, 2H), 3.86 (t, <sup>3</sup>J<sub>HH</sub> = 6.43 Hz, 2H), 3.76 (dm, <sup>3</sup>J<sub>HF</sub> = 29.5 Hz, 2H), 3.52 (t, <sup>3</sup>J<sub>HH</sub> = 6.6 Hz, 2H), 3.49–3.45 (m, 2H), 2.66–2.61 (m, 2H), 2.53–2.47 (m, 2H), 2.48 (s, 3H). <sup>19</sup>F NMR (CDCl<sub>3</sub>, 282 MHz) δ: –223.36 (tt, <sup>2</sup>J<sub>HF</sub> = 47.6 Hz, <sup>3</sup>J<sub>HF</sub> = 29.5 Hz). HR-MS calcd. for C<sub>12</sub>H<sub>19</sub>FN<sub>3</sub>OS<sub>2</sub> [M + 1]: 304.0948; found: 304.0950. EA calcd.: C 47.50, H 5.99, N 13.85; found: C 47.67, H 6.11, N 13.35.

### 3-(2-(2-(2-Fluoroethoxy)ethoxy)ethylthio)-4-(1-methyl-1,2,5,6-tetrahydropyridin-3-yl)-1,2,5-thiadiazole (**4c**)

Compound **4c** was prepared in an analogous manner to that of **4a**. Briefly, 150 mg (0.3 mmol) of **3c** was used in THF (0.1 M) with 5 equiv. of TBAF. **4c** was obtained in a

29% yield (31 mg).  $^1\text{H}$  NMR ( $\text{CDCl}_3$ , 300 MHz)  $\delta$ : 6.80–6.75 (m, 1H), 4.56 (dm,  $^2J_{\text{HF}} = 47.8$  Hz, 2H), 3.87–3.79 (m, 3H), 3.73–3.68 (m, 5H), 3.54–3.46 (m, 4H), 2.68–2.62 (m, 2H), 2.54–2.47 (m, 2H), 2.49 (s, 3H).  $^{19}\text{F}$  NMR ( $\text{CDCl}_3$ , 282 MHz)  $\delta$ : –223.31 (tt,  $^2J_{\text{HF}} = 47.9$  Hz,  $^3J_{\text{HF}} = 29.6$  Hz). HR-MS calcd. for  $\text{C}_{14}\text{H}_{23}\text{FN}_3\text{O}_2\text{S}_2$  [ $\text{M} + 1$ ]: 348.1210; found: 348.1212. EA calcd.: C 48.39, H 6.39, N 12.10; found: C 49.07, H 6.74, N 11.66.

### 3-(Benzyloxy)propyl-4-methylbenzenesulfonate (6a)

To an oven-dried round-bottomed flask under an atmosphere of  $\text{N}_2$  was added propane-1,3-diol (**5a**, 0.11 mol), 1.4 mL (0.01 mol) of benzyl bromide, and KOH (0.02 mol, neat). The reaction proceeded at RT. Upon consumption of benzyl bromide (monitored by TLC, 40:60 EtOAc:Hex), the reaction mixture was diluted with 50 mL of  $\text{H}_2\text{O}$  and washed with  $\text{CH}_2\text{Cl}_2$  (50 mL  $\times$  2). The combined organic layers were washed with 50 mL of brine, dried over  $\text{Na}_2\text{SO}_4$ , and concentrated.  $\text{CH}_2\text{Cl}_2$  (50 mL) was added and the mixture was cooled on ice. Triethylamine (0.05 mol) and DMAP (1 mol%) were added. After 10 min of stirring, 0.03 mol of TsCl was added and the reaction proceeded until completion, as monitored by TLC (40:60 EtOAc:Hex). The mixture was then cooled on ice, diluted with 100 mL  $\text{H}_2\text{O}$ , and washed with dichloromethane (100 mL  $\times$  2). The combined organic layers were washed with 100 mL of brine, dried over  $\text{Na}_2\text{SO}_4$ , and concentrated. The final product was purified by flash chromatography (40:60 EtOAc:Hex) to yield 2.40 g of **6a** (75%).  $^1\text{H}$  NMR ( $\text{CDCl}_3$ , 300 MHz)  $\delta$ : 7.81–7.76 (m, 2H), 7.35–7.22 (m, 7H), 4.40 (s, 2H), 4.17 (t,  $^3J_{\text{HH}} = 6.3$  Hz, 2H), 3.50 (t,  $^3J_{\text{HH}} = 5.8$ , 2H), 2.42 (s, 3H), 1.98–1.90 (q,  $^3J_{\text{HH}} = 6.0$  Hz, 2H).

### 5-(Benzyloxy)pentyl-4-methylbenzenesulfonate (6b)

Compound **6b** was prepared in an analogous manner to that of **6a**. Briefly, 0.07 mol of pentane-1,5-diol (**5b**), 0.02 mol of benzyl bromide, and 0.055 mol of KOH were used. Following the workup of the reaction mixture, 10 mL of dichloromethane, 0.07 mol of triethylamine, catalytic DMAP (1 mol%), and 0.035 mol of TsCl were reacted and purified (vide supra). Compound **6b** was obtained in a 65% yield (4.54 g).  $^1\text{H}$  NMR ( $\text{CDCl}_3$ , 300 MHz)  $\delta$ : 7.81–7.76 (m, 2H), 7.36–7.26 (m, 7H), 4.47 (s, 2H), 4.02 (t,  $^3J_{\text{HH}} = 6.3$  Hz, 2H), 3.42 (t,  $^3J_{\text{HH}} = 6.6$  Hz, 2H), 2.44 (s, 3H), 1.71–1.61 (m, 2H), 1.60–1.51 (m, 2H), 1.46–1.36 (m, 2H).

### 6-(Benzyloxy)hexyl-4-methylbenzenesulfonate (6c)

Compound **6c** was prepared in an analogous manner to that of **6a**. Briefly, 0.06 mol of hexane-1,6-diol (**5c**), 0.02 mol of benzyl bromide, and 0.055 mol of KOH were used. Following the workup, 10 mL of dichloromethane, 0.07 mol of triethylamine, DMAP (1 mol%), and 0.04 mol of TsCl were reacted and purified (vide supra). Compound **6c** was obtained in a 61% yield (4.40 g).  $^1\text{H}$  NMR ( $\text{CDCl}_3$ , 300 MHz)  $\delta$ : 7.81–7.76 (m, 2H), 7.36–7.28 (m, 7H), 4.48 (s, 2H), 4.01 (t,  $^3J_{\text{HH}} = 6.6$  Hz, 2H), 3.43 (t,  $^3J_{\text{HH}} = 6.6$  Hz, 2H), 2.44 (s, 3H), 1.67–1.51 (m, 4H), 1.35–1.28 (m, 4H).

### 7-(Benzyloxy)heptyl-4-methylbenzenesulfonate (6d)

Compound **6d** was prepared in an analogous manner to that of **6a**. Briefly, 0.02 mol of hexane-1,6-diol (**5d**), 0.008 mol of benzyl bromide, and 0.015 mol of KOH were

used. After workup, 8 mL of  $\text{CH}_2\text{Cl}_2$ , 0.025 mol of triethylamine, DMAP (1 mol%), and 0.02 mol of TsCl were reacted and purified (vide supra). **6d** was obtained in a 69% yield (2.06 g).  $^1\text{H}$  NMR ( $\text{CDCl}_3$ , 300 MHz)  $\delta$ : 7.81–7.76 (m, 2H), 7.36–7.25 (m, 7H), 4.49 (s, 2H), 4.01 (t,  $^3J_{\text{HH}} = 6.4$  Hz, 2H), 3.44 (t,  $^3J_{\text{HH}} = 6.7$  Hz, 2H), 2.44 (s, 3H), 1.66–1.51 (m, 4H), 1.36–1.20 (m, 6H).

### 2-(2-(Benzyloxy)ethoxy)ethyl-4-methylbenzenesulfonate (6e)

Compound **6e** was prepared in an analogous manner to that of **6a**. Diethyleneglycol (**5e**; 0.03 mol), 0.008 mol of benzyl bromide, and 0.03 mol of KOH were used. After workup, 20 mL of dichloromethane, 0.02 mol of triethylamine, DMAP (1 mol%), and 0.07 mol of TsCl were reacted and purified (vide supra). Compound **6e** was obtained in a 43% yield (1.24 g).  $^1\text{H}$  NMR ( $\text{CDCl}_3$ , 300 MHz)  $\delta$ : 7.81–7.76 (m, 2H), 7.35–7.26 (m, 7H), 4.53 (s, 2H), 4.19–4.14 (m, 2H), 3.72–3.67 (m, 2H), 3.63–3.59 (m, 2H), 3.58–3.54 (m, 2H), 2.42 (s, 3H).

### 2-(2-(2-(Benzyloxy)ethoxy)ethoxy)ethyl-4-methylbenzenesulfonate (6f)

Compound **6f** was prepared in an analogous manner to that of **6a**. Briefly, 0.04 mol of diethyleneglycol (**5f**), 0.01 mol of benzyl bromide, and 0.04 mol of KOH were used. Following the workup, 20 mL of dichloromethane, 0.02 mol of triethylamine, DMAP (1 mol%), and 0.06 mol of TsCl were reacted and purified (vide supra). Compound **6f** was obtained in a 35% yield (1.40 g).  $^1\text{H}$  NMR ( $\text{CDCl}_3$ , 300 MHz)  $\delta$ : 7.81–7.76 (m, 2H), 7.35–7.26 (m, 7H), 4.55 (s, 2H), 4.17–4.12 (m, 2H), 3.70–3.66 (m, 2H), 3.65–3.60 (m, 4H), 3.59 (s, 4H), 3.04 (s, 3H).

### ((3-Fluoropropoxy)methyl)benzene (7a)

To a glass vial (Biotage) under an atmosphere of  $\text{N}_2$  containing 0.02 mol of TBAF (dried under reduced pressure overnight) was added 20 mL of freshly distilled THF followed by 500 mg (1.6 mmol) of **6a**. The reaction was sealed and microwave heated for 1 h at 160  $^\circ\text{C}$ . THF was removed under reduced pressure and the resulting product was dissolved in 50 mL of EtOAc and washed with 50 mL of  $\text{H}_2\text{O}$ . The aqueous layer was washed a second time with 50 mL of EtOAc and the combined organic layers were washed with 50 mL of brine, dried over  $\text{Na}_2\text{SO}_4$ , and concentrated. The product was purified by flash chromatography (30:70 EtOAc:Hex (v/v)) to yield 179 mg of **7a** (68%).  $^1\text{H}$  NMR ( $\text{CDCl}_3$ , 400 MHz)  $\delta$ : 7.37–7.25 (m, 5H), 4.56 (dt,  $^2J_{\text{HF}} = 47.1$  Hz,  $^3J_{\text{HH}} = 6.0$  Hz, 2H), 4.51 (s, 2H), 3.60 (t,  $^3J_{\text{HH}} = 6.2$  Hz, 2H), 1.99 (dm,  $^3J_{\text{HF}} = 25.8$  Hz, 2H).  $^{19}\text{F}$  NMR ( $\text{CDCl}_3$ , 376 MHz)  $\delta$ : –222.05 (tt,  $^2J_{\text{HF}} = 47.0$  Hz,  $^3J_{\text{HF}} = 25.7$  Hz).

### ((5-Fluoropentyl)oxy)methyl)benzene (7b)

Compound **7b** was prepared in an analogous manner to that of **7a**, where 0.02 mol of TBAF and 1.4 mmol of **6b** were used in 20 mL of THF. Compound **7b** was obtained in a 70% yield (198 mg).  $^1\text{H}$  NMR ( $\text{CDCl}_3$ , 400 MHz)  $\delta$ : 7.35–7.25 (m, 5H), 4.50 (s, 2H), 4.43 (dt,  $^2J_{\text{HF}} = 47.4$  Hz,  $^3J_{\text{HH}} = 6.1$  Hz, 2H), 3.48 (t,  $^3J_{\text{HH}} = 6.5$  Hz, 2H), 1.78–1.62 (m, 4H), 1.54–1.45 (m, 2H).  $^{19}\text{F}$  NMR ( $\text{CDCl}_3$ , 376 MHz)  $\delta$ : –218.66 (tt,  $^2J_{\text{HF}} = 47.4$  Hz,  $^3J_{\text{HF}} = 24.8$  Hz).

**((6-Fluorohexyloxy)methyl)benzene (7c)**

Compound **7c** was prepared in an analogous manner to that of **7a**, where 0.02 mol of TBAF and 1.4 mmol of **6c** were used in 20 mL of THF. Compound **7c** was obtained in a 72% yield (209 mg).  $^1\text{H}$  NMR ( $\text{CDCl}_3$ , 400 MHz)  $\delta$ : 7.35–7.24 (m, 5H), 4.50 (s, 2H), 4.42 (dt,  $^2J_{\text{HF}} = 47.4$  Hz,  $^3J_{\text{HH}} = 6.2$  Hz, 2H), 3.47 (t,  $^3J_{\text{HH}} = 6.6$  Hz, 2H), 1.76–1.59 (m, 4H), 1.45–1.39 (m, 4H).  $^{19}\text{F}$  NMR ( $\text{CDCl}_3$ , 376 MHz)  $\delta$ : –218.55 (tt,  $^2J_{\text{HF}} = 47.3$  Hz,  $^3J_{\text{HF}} = 24.9$  Hz).

**((7-Fluoroheptyloxy)methyl)benzene (7d)**

Compound **7d** was prepared in an analogous manner to that of **7a**, where 0.02 mol of TBAF and 1.3 mmol of **6d** were used in 20 mL of THF. Compound **7d** was obtained in an 85% yield (251 mg).  $^1\text{H}$  NMR ( $\text{CDCl}_3$ , 400 MHz)  $\delta$ : 7.35–7.24 (m, 5H), 4.50 (s, 2H), 4.42 (dt,  $^2J_{\text{HF}} = 47.5$  Hz,  $^3J_{\text{HH}} = 6.1$  Hz, 2H), 3.46 (t,  $^3J_{\text{HH}} = 6.6$  Hz, 2H), 1.75–1.58 (m, 4H), 1.45–1.30 (m, 6H).  $^{19}\text{F}$  NMR ( $\text{CDCl}_3$ , 376 MHz)  $\delta$ : –218.46 (tt,  $^2J_{\text{HF}} = 47.5$  Hz,  $^3J_{\text{HF}} = 24.9$  Hz).

**((2-(2-Fluoroethoxy)ethoxy)methyl)benzene (7e)**

Compound **7e** was prepared in an analogous manner to that of **7a**, where 0.02 mol of TBAF and 1.4 mmol of **6e** were used in 20 mL of THF. Compound **7e** was obtained in a 91% yield (252 mg).  $^1\text{H}$  NMR ( $\text{CDCl}_3$ , 400 MHz)  $\delta$ : 7.36–7.25 (m, 5H), 4.58 (s, 2H), 4.56 (dm,  $^2J_{\text{HF}} = 47.7$  Hz, 2H), 3.80–3.78 (m, 1H), 3.73–3.69 (m, 3H), 3.67–3.63 (m, 2H).  $^{19}\text{F}$  NMR ( $\text{CDCl}_3$ , 376 MHz)  $\delta$ : –223.27 (tt,  $^2J_{\text{HF}} = 47.7$  Hz,  $^3J_{\text{HF}} = 29.4$  Hz).

**((2-(2-(2-Fluoroethoxy)ethoxy)ethoxy)methyl)benzene (7f)**

Compound **7f** was prepared in an analogous manner to that of **7a**, where 0.02 mol of TBAF and 1.3 mmol of **6f** were used in 20 mL of THF. Compound **7f** was obtained in a 90% yield (273 mg).  $^1\text{H}$  NMR ( $\text{CDCl}_3$ , 400 MHz)  $\delta$ : 7.36–7.26 (m, 5H), 4.57 (s, 2H), 4.55 (dm,  $^2J_{\text{HF}} = 47.6$  Hz, 2H), 3.80–3.77 (m, 1H), 3.72–3.67 (m, 7H), 3.66–3.62 (m, 2H).  $^{19}\text{F}$  NMR ( $\text{CDCl}_3$ , 376 MHz)  $\delta$ : –223.34 (tt,  $^2J_{\text{HF}} = 47.7$  Hz,  $^3J_{\text{HF}} = 29.8$  Hz).

**3-(4-(1-Methyl-1,2,5,6-tetrahydropyridin-3-yl)-1,2,5-thiadiazol-3-yloxy)propan-1-ol (8a)**

To an oven-dried round-bottomed flask under an atmosphere of  $\text{N}_2$ , 1.16 mmol of propane-1,3-diol (**5a**) was added to 2.5 mL of freshly distilled THF. To the reaction mixture was added 0.92 mmol of 60% NaH, and the mixture was stirred at RT for 30 min. Compound **1** (0.23 mmol) was added and the reaction was refluxed overnight. The reaction mixture was diluted with 30 mL of  $\text{H}_2\text{O}$  and washed with 30 mL of  $\text{CH}_2\text{Cl}_2$  ( $\times 2$ ). The combined organic layers were then washed with 40 mL of brine, dried over  $\text{Na}_2\text{SO}_4$ , and concentrated. The product was purified by PTLC (30:70 EtOAc:Hex (v/v)) and **8a** was obtained in a yield of 25.2 mg (43%).  $^1\text{H}$  NMR ( $\text{CDCl}_3$ , 400 MHz)  $\delta$ : 7.04–7.00 (m, 1H), 4.59 (t,  $J = 6.1$  Hz, 2H), 3.78 (t,  $J = 6.1$  Hz, 2H), 3.46–3.44 (m, 2H), 2.60–2.56 (m, 2H), 2.47–2.42 (m, 2H), 2.46 (s, 3H), 2.11–2.04 (m, 2H). HR-MS calcd. for  $\text{C}_{11}\text{H}_{18}\text{N}_3\text{O}_2\text{S}$  [ $M + 1$ ]: 256.1114; found: 256.1112. EA calcd.: C 51.74, H 6.71, N 16.46; found: C 51.72, H 6.73, N 16.06.

**4-(4-(1-Methyl-1,2,5,6-tetrahydropyridin-3-yl)-1,2,5-thiadiazol-3-yloxy)butan-1-ol (8b)**

Compound **8b** was prepared in an analogous manner to that of **8a**, where 1.15 mmol of butane-1,4-diol (**5b**), 0.92 mmol of 60% NaH, and 0.23 mmol of **1** in 2.5 mL of freshly distilled THF were used. Compound **8b** was obtained in a 48% yield (30 mg).  $^1\text{H}$  NMR ( $\text{CDCl}_3$ , 300 MHz)  $\delta$ : 7.07–7.02 (m, 1H), 4.48 (t,  $^3J_{\text{HH}} = 4.46$  Hz, 2H), 3.71 (t,  $^3J_{\text{HH}} = 6.44$  Hz, 2H), 3.47–3.42 (m, 2H), 2.61–2.55 (m, 2H), 2.48–2.41 (m, 2H), 2.46 (s, 3H), 2.00–1.89 (m, 2H), 1.78–1.67 (m, 2H). HR-MS calcd. for  $\text{C}_{12}\text{H}_{20}\text{N}_3\text{O}_2\text{S}$  [ $M + 1$ ]: 270.1271; found: 270.1269. EA calcd.: C 53.51, H 7.11, N 15.60; found: C 52.56, H 6.85, N 15.49.

**5-(4-(1-Methyl-1,2,5,6-tetrahydropyridin-3-yl)-1,2,5-thiadiazol-3-yloxy)pentan-1-ol (8c)**

Compound **8c** was prepared in an analogous manner to that of **8a**, where 1.15 mmol of pentane-1,5-diol (**5c**), 0.92 mmol of 60% NaH, and 0.23 mmol of **1** in 2.5 mL of freshly distilled THF were used. Compound **8c** was obtained in a 34% yield (22 mg).  $^1\text{H}$  NMR ( $\text{CDCl}_3$ , 300 MHz)  $\delta$ : 7.07–7.02 (m, 1H), 4.47 (t,  $^3J_{\text{HH}} = 6.54$  Hz, 2H), 3.69 (t,  $^3J_{\text{HH}} = 6.42$  Hz, 2H), 3.48–3.43 (m, 2H), 2.61–2.55 (m, 2H), 2.49–2.42 (m, 2H), 2.47 (s, 3H), 1.95–1.83 (m, 2H), 1.70–1.51 (m, 4H). HR-MS calcd. for  $\text{C}_{13}\text{H}_{22}\text{N}_3\text{O}_2\text{S}$  [ $M + 1$ ]: 284.1427; found: 284.1425. EA calcd.: C 55.10, H 7.47, N 14.83; found: C 58.85, H 7.07, N 14.82.

**6-(4-(1-Methyl-1,2,5,6-tetrahydropyridin-3-yl)-1,2,5-thiadiazol-3-yloxy)hexan-1-ol (8d)**

Compound **8d** was prepared in an analogous manner to that of **8a**, where 1.15 mmol of hexane-1,6-diol (**5d**), 0.92 mmol of NaH (60% in mineral oil), and 0.23 mmol of **1** in 2.5 mL of freshly distilled THF were used. Compound **8d** was obtained in a 25% yield (17 mg).  $^1\text{H}$  NMR ( $\text{CDCl}_3$ , 300 MHz)  $\delta$ : 7.07–7.01 (m, 1H), 4.49–4.41 (m, 2H), 3.67–3.60 (m, 2H), 3.48–3.40 (m, 2H), 2.62–2.55 (m, 2H), 2.51–2.42 (m, 2H), 2.47 (s, 3H), 2.14 (br, 1H), 1.91–1.80 (m, 2H), 1.65–1.54 (m, 2H), 1.53–1.39 (m, 4H). HR-MS calcd. for  $\text{C}_{14}\text{H}_{24}\text{N}_3\text{O}_2\text{S}$  [ $M + 1$ ]: 298.1584; found: 298.1582. EA calcd.: C 56.54, H 7.79, N 13.75; found: C 55.02, H 7.42, N 13.75.

**2-(2-(4-(1-Methyl-1,2,5,6-tetrahydropyridin-3-yl)-1,2,5-thiadiazol-3-yloxy)ethoxy)ethanol (8e)**

Compound **8e** was prepared in an analogous manner to that of **8a**, where 0.084 mmol of diethyleneglycol (**5e**), 0.42 mmol of 60% NaH, and 0.46 mmol of **1** in 3 mL of freshly distilled THF were used. Compound **8e** was obtained in a 74% yield (89 mg).  $^1\text{H}$  NMR ( $\text{CDCl}_3$ , 400 MHz)  $\delta$ : 7.08–7.04 (m, 1H), 4.64–4.60 (m, 2H), 3.92–3.89 (m, 2H), 3.76–3.73 (m, 2H), 3.67–3.63 (m, 2H), 3.46–3.43 (m, 2H), 2.59–2.55 (m, 2H), 2.47–2.42 (m, 2H), 2.45 (s, 3H). HR-MS calcd. for  $\text{C}_{12}\text{H}_{20}\text{N}_3\text{O}_3\text{S}$  [ $M + 1$ ]: 286.1220; found: 286.1218. EA calcd.: C 50.50, H 6.72, N 14.73; found: C 49.91, H 6.70, N 14.37.

**2-(2-(2-(4-(1-Methyl-1,2,5,6-tetrahydropyridin-3-yl)-1,2,5-thiadiazol-3-yloxy)ethoxy)ethoxy)ethanol (8f)**

Compound **8f** was prepared in an analogous manner to that of **8a**, where 0.084 mmol of diethyleneglycol (**5f**), 0.42 mmol of 60% NaH, and 0.46 mmol of **1** in 3.0 mL of



freshly distilled THF were used. **8f** was obtained in a 65% yield (81 mg).  $^1\text{H}$  NMR ( $\text{CDCl}_3$ , 400 MHz)  $\delta$ : 6.77–6.73 (m, 1H), 3.85–3.80 (m, 2H), 3.75–3.71 (m, 2H), 3.69–3.66 (m, 4H), 3.63–3.59 (m, 2H), 3.53–3.49 (m, 2H), 3.45–3.42 (m, 2H), 2.63–2.58 (m, 2H), 2.51–2.45 (m, 2H), 2.42 (s, 3H). HR-MS: calcd. for  $\text{C}_{14}\text{H}_{24}\text{N}_3\text{O}_4\text{S}$  [ $M + 1$ ]: 330.1482; found: 330.1476. EA calcd.: C 51.04, H 7.04, N 12.76; found: C 50.07, H 6.89, N 12.52.

**3-(3-Fluoropropoxy)-4-(1-methyl-1,2,5,6-tetrahydropyridin-3-yl)-1,2,5-thiadiazole (9a)**

To an oven-dried round-bottomed flask under an atmosphere of  $\text{N}_2$  containing 3 mL of freshly distilled THF was added 0.5 mmol of **7a** followed by 10 mg each of Pd/C and  $\text{Pd}(\text{OH})_2$ . The reaction vessel was purged with  $\text{H}_2(\text{g})$  and maintained under an atmosphere of  $\text{H}_2(\text{g})$  for 2 h while stirring vigorously. Upon consumption of the starting material as monitored by TLC (60:40 EtOAc:Hex ( $v/v$ )), the reaction mixture was purged with  $\text{N}_2$  and cooled in an ice bath, and 1.0 mmol of NaH (60% in mineral oil) was added. The mixture was stirred for 30 min at RT followed by the addition of 0.2 mmol of **1**. The reaction mixture was subsequently refluxed overnight. Upon consumption of the starting material, the reaction was filtered through celite and the THF was removed under reduced pressure. The product was dissolved in 30 mL of  $\text{CH}_2\text{Cl}_2$  and washed with 30 mL of  $\text{H}_2\text{O}$ , and the aqueous layer was further extracted with 30 mL of  $\text{CH}_2\text{Cl}_2$ . The combined organic layers were washed with 30 mL of brine, dried over  $\text{Na}_2\text{SO}_4$ , and concentrated. The product was purified by PTLC (60:40 EtOAc:Hex ( $v/v$ )) to yield 21 mg **9a** (41%).  $^1\text{H}$  NMR ( $\text{CDCl}_3$ , 400 MHz)  $\delta$ : 7.04–6.99 (m, 1H), 4.63 (dm,  $^2J_{\text{HF}} = 47.0$  Hz, 2H), 4.61 (t,  $^3J_{\text{HH}} = 6.2$  Hz, 2H), 3.47–3.43 (m, 2H), 2.60–2.55 (m, 2H), 2.48–2.42 (m, 2H), 2.46 (s, 3H), 2.25 (dm,  $^3J_{\text{HF}} = 25.6$  Hz, 2H).  $^{19}\text{F}$  NMR ( $\text{CDCl}_3$ , 376 MHz)  $\delta$ : –222.38 (tt,  $^2J_{\text{HF}} = 47.0$  Hz,  $^3J_{\text{HF}} = 25.8$  Hz). HR-MS calcd. for  $\text{C}_{11}\text{H}_{17}\text{FN}_3\text{OS}$  [ $M + 1$ ]: 258.1071; found: 258.1068. EA calcd.: C 51.34, H 6.27, N 16.33; found: C 51.64, H 6.27, N 15.84.

**3-(5-Fluoropentyloxy)-4-(1-methyl-1,2,5,6-tetrahydropyridin-3-yl)-1,2,5-thiadiazole (9b)**

Compound **9b** was prepared in an analogous manner to that of **9a**, where 0.4 mmol of **7b** was used followed by 1.4 mmol of 60% NaH and 0.23 mmol of **1**. Compound **9b** was obtained in a 29% yield (19 mg).  $^1\text{H}$  NMR ( $\text{CDCl}_3$ , 400 MHz)  $\delta$ : 7.07–7.03 (m, 1H), 4.48 (dt,  $^2J_{\text{HF}} = 46.9$  Hz,  $^3J_{\text{HH}} = 6.1$  Hz, 2H), 4.47 (t,  $^3J_{\text{HH}} = 6.5$  Hz, 2H), 3.50–3.47 (m, 2H), 2.64–2.59 (m, 2H), 2.50–2.44 (m, 2H), 2.49 (s, 3H), 1.94–1.86 (m, 2H), 1.85–1.72 (m, 2H), 1.64–1.56 (m, 2H).  $^{19}\text{F}$  NMR ( $\text{CDCl}_3$ , 376 MHz)  $\delta$ : –219.18 (tt,  $^2J_{\text{HF}} = 47.1$  Hz,  $^3J_{\text{HF}} = 25.4$  Hz). HR-MS calcd. for  $\text{C}_{13}\text{H}_{21}\text{FN}_3\text{OS}$  [ $M + 1$ ]: 286.1384; found: 286.1380. EA calcd.: C 54.71, H 7.06, N 14.72; found: C 54.90, H 6.87, N 14.79.

**3-(6-Fluorohexyloxy)-4-(1-methyl-1,2,5,6-tetrahydropyridin-3-yl)-1,2,5-thiadiazole (9c)**

Compound **9c** was prepared in an analogous manner to that of **9a**, where 0.4 mmol of **7c** was used followed by 1.4 mmol of 60% NaH and 0.23 mmol of **1**. Compound **9c** was obtained in a 39% yield (27 mg).  $^1\text{H}$  NMR ( $\text{CDCl}_3$ , 400 MHz)  $\delta$ : 7.07–7.03 (m, 1H), 4.46 (t,  $^3J_{\text{HH}} = 6.9$  Hz,

2H), 4.46 (dt,  $^2J_{\text{HF}} = 47.2$  Hz,  $^3J_{\text{HH}} = 6.0$  Hz, 2H), 3.48–3.45 (m, 2H), 2.61–2.56 (m, 2H), 2.48–2.43 (m, 2H), 2.47 (s, 3H), 1.90–1.83 (m, 2H), 1.79–1.68 (m, 2H), 1.53–1.48 (m, 4H).  $^{19}\text{F}$  NMR ( $\text{CDCl}_3$ , 376 MHz)  $\delta$ : –218.79 (tt,  $^2J_{\text{HF}} = 47.2$  Hz,  $^3J_{\text{HF}} = 25.3$  Hz). HR-MS calcd. for  $\text{C}_{14}\text{H}_{23}\text{FN}_3\text{OS}$  [ $M + 1$ ]: 300.1540; found: 300.1536. EA calcd.: C 56.16, H 7.41, N 14.03; found: C 56.58, H 7.39, N 13.77.

**3-(7-Fluoroheptyloxy)-4-(1-methyl-1,2,5,6-tetrahydropyridin-3-yl)-1,2,5-thiadiazole (9d)**

Compound **9d** was prepared in an analogous manner to that of **9a**, where 0.4 mmol of **7d** was used followed by 1.4 mmol of 60% NaH and 0.23 mmol of **1**. Compound **9d** was obtained in a 35% yield (25 mg).  $^1\text{H}$  NMR ( $\text{CDCl}_3$ , 400 MHz)  $\delta$ : 7.08–7.04 (m, 2H), 4.45 (t,  $^3J_{\text{HH}} = 6.6$  Hz, 2H), 4.45 (dt,  $^2J_{\text{HF}} = 47.6$  Hz,  $^3J_{\text{HH}} = 6.2$  Hz, 2H), 3.47–3.44 (m, 2H), 2.61–2.56 (m, 2H), 2.48–2.43 (m, 2H), 2.47 (s, 3H), 1.89–1.81 (m, 2H), 1.76–1.62 (m, 2H), 1.51–1.40 (m, 5H).  $^{19}\text{F}$  NMR ( $\text{CDCl}_3$ , 376 MHz)  $\delta$ : –218.62 (tt,  $^2J_{\text{HF}} = 47.5$  Hz,  $^3J_{\text{HF}} = 25.2$  Hz). HR-MS calcd. for  $\text{C}_{15}\text{H}_{25}\text{FN}_3\text{OS}$  [ $M + 1$ ]: 314.1697; found: 314.1693. EA calcd.: C 57.48, H 7.72, N 13.41; found: C 57.69, H 7.65, N 13.17.

**3-(2-(2-Fluoroethoxy)ethoxy)-4-(1-methyl-1,2,5,6-tetrahydropyridin-3-yl)-1,2,5-thiadiazole (9e)**

Compound **9e** was prepared in an analogous manner to that of **9a**, where 0.4 mmol of **7e** was used followed by 1.4 mmol of 60% NaH and 0.23 mmol of **1**. Compound **9e** was obtained in a 45% yield (30 mg).  $^1\text{H}$  NMR ( $\text{CDCl}_3$ , 400 MHz)  $\delta$ : 7.12–7.07 (m, 1H), 4.64–4.61 (m, 2H), 4.58 (dm,  $^2J_{\text{HF}} = 47.6$  Hz, 2H), 3.96–3.92 (m, 2H), 3.79 (dm,  $^3J_{\text{HF}} = 29.4$  Hz, 2H), 3.47–3.44 (m, 2H), 2.60–2.55 (m, 2H), 2.49–2.43 (m, 2H), 2.46 (s, 3H).  $^{19}\text{F}$  NMR ( $\text{CDCl}_3$ , 376 MHz)  $\delta$ : –223.51 (tt,  $^2J_{\text{HF}} = 47.7$  Hz,  $^3J_{\text{HF}} = 28.9$  Hz). HR-MS calcd. for  $\text{C}_{12}\text{H}_{19}\text{FN}_3\text{O}_2\text{S}$  [ $M + 1$ ]: 288.1177; found: 288.1173. EA calcd.: C 50.16, H 6.361, N 14.62; found: C 50.25, H 6.44, N 14.40.

**3-(2-(2-(2-Fluoroethoxy)ethoxy)ethoxy)-4-(1-methyl-1,2,5,6-tetrahydropyridin-3-yl)-1,2,5-thiadiazole (9f)**

Compound **9f** was prepared in an analogous manner to that of **9a**, where 0.4 mmol of **7f** was used followed by 1.4 mmol of 60% NaH and 0.23 mmol of **1**. Compound **9f** was obtained in a 62% yield (46 mg).  $^1\text{H}$  NMR ( $\text{CDCl}_3$ , 400 MHz)  $\delta$ : 7.11–7.07 (m, 1H), 4.63–4.60 (m, 3H), 4.51–4.48 (m, 1H), 3.93–3.90 (m, 2H), 3.79–3.77 (m, 1H), 3.74–3.68 (m, 5H), 3.47–3.45 (m, 2H), 3.60–3.56 (m, 2H), 2.47–2.43 (m, 2H), 2.46 (s, 3H).  $^{19}\text{F}$  NMR ( $\text{CDCl}_3$ , 376 MHz)  $\delta$ : –223.30 (tt,  $^2J_{\text{HF}} = 47.7$  Hz,  $^3J_{\text{HF}} = 29.5$  Hz). HR-MS calcd. for  $\text{C}_{14}\text{H}_{23}\text{FN}_3\text{O}_3\text{S}$  [ $M + 1$ ]: 332.1439; found: 332.1434. EA calcd.: C 50.74, H 6.69, N 12.68; found: C 50.87, H 6.75, N 12.86.

**3-(Hexyloxy)-4-(1-methyl-1,2,5,6-tetrahydropyridin-3-yl)-1,2,5-thiadiazole (10)**

To an oven-dried round-bottomed flask, 71 mg (0.7 mmol) of 1-hexanol was added to 3 mL of freshly distilled THF. To the reaction mixture was added 34 mg (1.4 mmol) of 95% NaH, and the mixture was allowed to stir at RT for 30 min. Compound **1** (0.35 mmol) was subsequently added and the reaction was refluxed overnight. The reaction was diluted with 30 mL of  $\text{H}_2\text{O}$  and washed with



30 mL of  $\text{CH}_2\text{Cl}_2$  ( $\times 2$ ). The combined organic layers were then washed with 40 mL of brine, dried over  $\text{Na}_2\text{SO}_4$ , and concentrated. The product was purified by PTLC (30:70 EtOAc:Hex (v/v)) and **9** was obtained in a yield of 58 mg (60%).  $^1\text{H}$  NMR ( $\text{CDCl}_3$ , 300 MHz)  $\delta$ : 7.09–7.04 (m, 1H), 4.47–4.41 (m, 2H), 3.48–3.43 (m, 2H), 2.61–2.55 (m, 2H), 2.49–2.42 (m, 5H), 1.89–1.78 (m, 2H), 1.52–1.39 (m, 2H), 1.38–1.31 (m, 4H), 0.94–0.87 (m, 3H). HR-MS calcd. for  $\text{C}_{14}\text{H}_{24}\text{N}_3\text{OS}$  [ $M + 1$ ]: 282.1635; found: 282.1633. EA calcd.: C 59.75, H 8.24, N 14.93; found: C 59.68, H 8.14, N 14.67.

### In vitro binding assays

All  $K_i$  determinations were conducted by the National Institute of Mental Health's Psychoactive Drug Screening Program (NIMH PDSP), contract No. NO1MH32004. The NIMH PDSP is directed by Bryan L. Roth, M.D., Ph.D., at the University of North Carolina at Chapel Hill and Project Officer Jamie Driscoll at NIMH, Bethesda, Maryland, USA (<http://pdsp.med.unc.edu/>).

### Radiochemical synthesis

#### Synthesis of [ $^{18}\text{F}$ ]-3-(2-(2-fluoroethoxy)ethoxy)ethylthio)-4-(1-methyl-1,2,5,6-tetrahydropyridin-3-yl)-1,2,5-thiadiazole ([ $^{18}\text{F}$ ]**4c**)

A Scanditronix MC 17 cyclotron was used for [ $^{18}\text{F}$ ]fluoride production and the radiosynthesis was carried out via general automated methods using a GE FX<sub>FN</sub> radiofluorination module as previously reported in detail by our laboratory for the synthesis of [ $^{18}\text{F}$ ]**4a**,<sup>14</sup> with only minor modifications.

Briefly, to a reaction vessel containing reactive [ $^{18}\text{F}$ ]fluoride was added 3 mg of **3c** dissolved in 500  $\mu\text{L}$  of  $\text{CH}_3\text{CN}$ . The reaction mixture was heated to 90  $^\circ\text{C}$  for 10 min, and the reaction was quenched with 500  $\mu\text{L}$  of  $\text{H}_2\text{O}$ . The reaction mixture was then purified via semipreparative HPLC (20:80  $\text{CH}_3\text{CN}:\text{H}_2\text{O}$  + 0.1 N ammonium formate + 1% formic acid (pH 4), Semi-Prep LUNA C18(2) (250 mm  $\times$  10 mm, 10  $\mu\text{m}$ ,  $\lambda = 254$  nm)) at 6 mL/min. The major radiochemical peak ( $t_R = 13$  min) was collected and formulated as previously described.<sup>14</sup> The formulated product was analyzed by HPLC (30:70  $\text{CH}_3\text{CN}:\text{H}_2\text{O}$  + 0.1 N ammonium formate, Prodigy C18 ODS Prep column (250 mm  $\times$  4.6 mm, 10  $\mu\text{m}$ ,  $\lambda = 254$  nm)) at a flow of 3 mL/min. HPLC analysis of formulated [ $^{18}\text{F}$ ]**4c** revealed high radiochemical (>99%) purities. Coinjection of the radioactive product with an authentic standard of **4c** under several different HPLC conditions (solvents, pH, wavelength; see Table S2 in the Supplementary data) with different analytical columns further established the identity of the radiotracer. Specific activity was calculated at the end of synthesis from the formulated product and was determined by integration of the UV peak of an analytical HPLC chromatogram in comparison with standard solutions containing known concentrations of **4c**.

### Ex vivo biodistribution

Ex vivo biodistribution studies in conscious male Sprague–Dawley rats were conducted as previously described by our group.<sup>32,33</sup> All rats received  $\sim 2.6$  MBq of

[ $^{18}\text{F}$ ]**4c** in 0.3 mL of buffered saline via the tail vein and were sacrificed by decapitation at either 5, 15, 30, or 60 min after injection ( $n = 1$  per time point). The brains were removed and regions of interest (striatum, thalamus, hypothalamus, hippocampus, frontal cortex, rest of cortex, cerebellum, rest of brain, as well as whole blood from the trunk, bone, and heart) were excised, blotted, weighed, and then counted for radioactivity (Fig. 3).

### Metabolism studies

Following tail-vein injection of [ $^{18}\text{F}$ ]**4c** as described above, whole blood was collected at various time points from the trunk in a heparinized tube and centrifuged, and the plasma was separated for metabolite analysis by HPLC via the method of Hilton et al.,<sup>35</sup> with minor modifications. Briefly, rat plasma from each time point was directly loaded onto a 5 mL HPLC injector loop and injected onto a capture column (4.6 mm  $\times$  20 mm) that was packed in-house with OASIS HLB 30  $\mu\text{m}$  (Waters, New Jersey). The capture column was eluted with 1% aqueous  $\text{CH}_3\text{CN}$  (2 mL/min) for 3 min and then back-flushed (19:81  $\text{CH}_3\text{CN}:\text{H}_2\text{O}$  + 0.1 N ammonium formate, 2.0 mL/min) onto a Phenomenex 10  $\mu\text{m}$  Luna C18 column (250 mm  $\times$  4.6 mm). The column effluents from both columns were monitored through a flow detector (Bioscan Flow-Count) operated in coincidence mode. Whole brain removed from a control rat and treated with  $\sim 1$  MBq of [ $^{18}\text{F}$ ]**4c** and whole brain removed from a rat sacrificed at 60 min after injection of [ $^{18}\text{F}$ ]**4c** in the tail vein were individually homogenized with ice-cold 80% ethanol and centrifuged as previously described by our laboratory,<sup>36</sup> prior to radio-HPLC analysis of the supernatant using the aforementioned method.

### Supplementary data

Supplementary data for this article are available on the journal Web site ([canjchem.nrc.ca](http://canjchem.nrc.ca)).

### Acknowledgements

The authors gratefully acknowledge the assistance of Armando Garcia, Alvina Ng, Jun Parkes, Winston Stableford, and Min Wong for radioisotope production or biological evaluations, and acknowledge Dr. Matthew Moran and Dr. Karin Stephenson for helpful discussions. We also acknowledge Dr. Bryan Roth at the University of North Carolina at Chapel Hill and the National Institute of Mental Health's Psychoactive Drug Screening Program, contract No. NO1MH32004, for conducting  $K_i$  determinations and for helpful discussions. Funding for this work was provided by the Centre for Addiction and Mental Health (CAMH) as well as the Ontario Ministry of Research and Innovation (Early Researcher Award to N.V.).

### References

- (1) Caulfield, M. P. *Pharmacol. Ther.* **1993**, *58* (3), 319. doi:10.1016/0163-7258(93)90027-B.
- (2) Eglén, R. M. *Prog. Med. Chem.* **2005**, *43*, 105. doi:10.1016/S0079-6468(05)43004-0.
- (3) Abrams, P.; Andersson, K.-E.; Buccafusco, J. J.; Chapple, C.; Chet de Groat, W.; Fryer, A. D.; Kay, G.; Laties, A.;

- Nathanson, N. M.; Pasricha, P. J.; Wein, A. J. *Br. J. Pharmacol.* **2006**, *148* (5), 565. doi:10.1038/sj.bjp.0706780.
- (4) Langmead, C. J.; Watson, J.; Reavill, C. *Pharmacol. Ther.* **2008**, *117* (2), 232. doi:10.1016/j.pharmthera.2007.09.009.
  - (5) Ametamey, S. M.; Honer, M.; Schubiger, P. A. *Chem. Rev.* **2008**, *108* (5), 1501. doi:10.1021/cr0782426.
  - (6) Miller, P. W.; Long, N. J.; Vilar, R.; Gee, A. D. *Angew. Chem. Int. Ed.* **2008**, *47* (47), 8998. doi:10.1002/anie.200800222.
  - (7) Eckelman, W. C. *Curr. Pharm. Des.* **2006**, *12* (30), 3901. doi:10.2174/138161206778559678.
  - (8) Sauerberg, P.; Olesen, P. H.; Nielsen, S.; Treppendahl, S.; Sheardown, M. J.; Honore, T.; Mitch, C. H.; Ward, J. S.; Pike, A. J.; Bymaster, F. P.; Sawyer, B. D.; Shannon, H. E. *J. Med. Chem.* **1992**, *35* (12), 2274. doi:10.1021/jm00090a019.
  - (9) Farde, L.; Suhara, T.; Halldin, C.; Nyback, H.; Nakashima, Y.; Swahn, C. G.; Karlsson, P.; Ginovart, N.; Bymaster, F. P.; Shannon, H. E.; Foged, C.; Suzdak, P. D.; Sauerberg, P. *Dementia* **1996**, *7* (4), 187.
  - (10) Kiesewetter, D. O.; Carson, R. E.; Jagoda, E. M.; Herscovitch, P.; Eckelman, W. C. *Life Sci.* **1999**, *64* (6-7), 511. doi:10.1016/S0024-3205(98)00595-5.
  - (11) Kiesewetter, D. O.; Lee, J. T.; Lang, L.; Park, S. G.; Paik, C. H.; Eckelman, W. C. *J. Med. Chem.* **1995**, *38* (1), 5. doi:10.1021/jm00001a002.
  - (12) Reid, A. E.; Ding, Y.-S.; Eckelman, W. C.; Logan, J.; Alexoff, D.; Shea, C.; Xu, Y.; Fowler, J. S. *Nucl. Med. Biol.* **2008**, *35* (3), 287. doi:10.1016/j.nucmedbio.2008.01.001.
  - (13) Kiesewetter, D. O.; Vuong, B.-k.; Channing, M. A. *Nucl. Med. Biol.* **2003**, *30* (1), 73. doi:10.1016/S0969-8051(02)00354-2.
  - (14) van Oosten, E. M.; Wilson, A. A.; Stephenson, K. A.; Mamo, D. C.; Pollock, B. G.; Mulsant, B. H.; Yudin, A. K.; Houle, S.; Vasdev, N. *Appl. Radiat. Isot.* **2009**, *67* (4), 611. doi:10.1016/j.apradiso.2008.12.015.
  - (15) Eckelman, W. C. *Nucl. Med. Biol.* **2003**, *30* (8), 851. doi:10.1016/S0969-8051(03)00123-9.
  - (16) Jagoda, E. M.; Kiesewetter, D. O.; Shimoji, K.; Ravasi, L.; Yamada, M.; Gomez, J.; Wess, J.; Eckelman, W. C. *Neuropharmacology* **2003**, *44* (5), 653. doi:10.1016/S0028-3908(03)00050-9.
  - (17) Carson, R. E.; Kiesewetter, D. O.; Jagoda, E.; Der, M. G.; Herscovitch, P.; Eckelman, W. C. *J. Cereb. Blood Flow Metab.* **1998**, *18* (10), 1130. doi:10.1097/00004647-199810000-00010.
  - (18) Ichise, M.; Cohen, R. M.; Carson, R. E. *J. Cereb. Blood Flow Metab.* **2007**, *28* (2), 420. doi:10.1038/sj.jcbfm.9600530.
  - (19) Cohen, R. M.; Carson, R. E.; Filbey, F.; Szczepanik, J.; Sunderland, T. *Synapse* **2006**, *60* (1), 86. doi:10.1002/syn.20276.
  - (20) Cohen, R. M.; Podruchny, T. A.; Bokde, A. L. W.; Carson, R. E.; Herscovitch, P.; Kiesewetter, D. O.; Eckelman, W. C.; Sunderland, T. *Synapse* **2003**, *49* (3), 150. doi:10.1002/syn.10225.
  - (21) Podruchny, T. A.; Connolly, C.; Bokde, A.; Herscovitch, P.; Eckelman, W. C.; Kiesewetter, D. O.; Sunderland, T.; Carson, R. E.; Cohen, R. M. *Synapse* **2003**, *48* (1), 39. doi:10.1002/syn.10165.
  - (22) Benson, B. E.; Carson, R. E.; Kiesewetter, D. O.; Herscovitch, P.; Eckelman, W. C.; Post, R. M.; Ketter, T. A. *Neuropsychopharmacology* **2004**, *29* (7), 1239. doi:10.1038/sj.npp.1300404.
  - (23) Cannon, D. M.; Carson, R. E.; Nugent, A. C.; Eckelman, W. C.; Kiesewetter, D. O.; Williams, J.; Rollis, D.; Drevets, M.; Gandhi, S.; Solorio, G.; Drevets, W. C. *Arch. Gen. Psychiatry* **2006**, *63* (7), 741. doi:10.1001/archpsyc.63.7.741.
  - (24) Ferrari-DiLeo, G.; Mash, D. C.; Flynn, D. D. *Mol. Chem. Neuropathol.* **1995**, *24* (1), 69. doi:10.1007/BF03160113.
  - (25) Kiesewetter, D. O.; Jagoda, E. M.; Shimoji, K.; Ma, Y.; Eckelman, W. C. *Nucl. Med. Biol.* **2007**, *34* (2), 141. doi:10.1016/j.nucmedbio.2006.11.002.
  - (26) Kane, B. E.; Grant, M. K.; El-Fakahany, E. E.; Ferguson, D. M. *Bioorg. Med. Chem.* **2008**, *16* (3), 1376. doi:10.1016/j.bmc.2007.10.058.
  - (27) Rajeswaran, W. G.; Cao, Y.; Huang, X.-P.; Wroblewski, M. E.; Colclough, T.; Lee, S.; Liu, H.; Nagy, P. I.; Ellis, J.; Levine, B. A.; Nock, K. H.; Messer, W. S., Jr. *J. Med. Chem.* **2001**, *44* (26), 4563. doi:10.1021/jm0102405.
  - (28) Tejada, F. R.; Nagy, P. I.; Xu, M.; Wu, C.; Katz, T.; Dorsey, J.; Rieman, M.; Lawlor, E.; Warrier, M.; Messer, W. S., Jr. *J. Med. Chem.* **2006**, *49* (25), 7518. doi:10.1021/jm0606995.
  - (29) Zhang, W.; Oya, S.; Kung, M.-P.; Hou, C.; Maier, D. L.; Kung, H. F. *Nucl. Med. Biol.* **2005**, *32* (8), 799. doi:10.1016/j.nucmedbio.2005.06.001.
  - (30) Hudkins, R. L.; DeHaven-Hudkins, D. L. *Life Sci.* **1991**, *49* (17), 1229. doi:10.1016/0024-3205(91)90135-X.
  - (31) Wilson, A. A.; Jin, L.; Garcia, A.; DaSilva, J. N.; Houle, S. *Appl. Radiat. Isot.* **2001**, *54* (2), 203. doi:10.1016/S0969-8043(00)00269-4.
  - (32) Vasdev, N.; Natesan, S.; Galineau, L.; Garcia, A.; Stableford, W. T.; McCormick, P.; Seeman, P.; Houle, S.; Wilson, A. A. *Synapse* **2006**, *60* (4), 314. doi:10.1002/syn.20304.
  - (33) Wilson, A. A.; DaSilva, J. N.; Houle, S. *Nucl. Med. Biol.* **1996**, *23* (2), 141. doi:10.1016/0969-8051(95)02044-6.
  - (34) Cox, D. P.; Terpins, J.; Lawrynowicz, W. *J. Org. Chem.* **1984**, *49* (17), 3216. doi:10.1021/jo00191a035.
  - (35) Hilton, J.; Yokoi, F.; Dannals, R. F.; Ravert, H. T.; Szabo, Z.; Wong, D. F. *Nucl. Med. Biol.* **2000**, *27* (6), 627. doi:10.1016/S0969-8051(00)00125-6.
  - (36) Wilson, A. A.; Garcia, A.; Parkes, J.; McCormick, P.; Stephenson, K. A.; Houle, S.; Vasdev, N. *Nucl. Med. Biol.* **2008**, *35* (3), 305. doi:10.1016/j.nucmedbio.2007.12.009.

# Microwave-assisted Diels–Alder reaction of 1,3,3-trimethyl-2-vinyl-1-cyclohexene with chromones — An expeditious approach to analogues of the puupehenone group of marine diterpenoids and kampanols

Rajesh M. Kamble and M.M.V. Ramana

**Abstract:** A rapid assembly of the tetracyclic core of marine diterpenoids related to puupehenone and kampanols by a Diels–Alder reaction of 1,3,3-trimethyl-2-vinyl-1-cyclohexene with chromones under microwave irradiation with or without  $\text{TiCl}_4$  is described.

**Key words:** Diels–Alder, chromones, regioselectivity, stereoselectivity,  $\text{TiCl}_4$ , microwave synthesis.

**Résumé :** On décrit une méthode rapide pour rassembler le dérivé tétracyclique fondamental de diterpénoïdes marins apparentés à la puupéhénone et aux kampanols ; elle implique une réaction de Diels–Alder entre le 1,3,3-triméthyl-2-vinylcyclohex-1-ène avec des chromones, sous irradiation de microondes, avec ou sans  $\text{TiCl}_4$ .

**Mots-clés :** Diels–Alder, chromones, régiosélectivité, stéréosélectivité,  $\text{TiCl}_4$ , synthèse sous l'influence de microondes.

[Traduit par la Rédaction]

## Introduction

The Diels–Alder reaction has been extensively applied for the synthesis of a wide variety of natural products. The Diels–Alder reaction<sup>1</sup> constitutes one of the most frequently employed synthetic methods for pericyclic six-electron processes resulting in highly regio-, diastereo-, and enantioselective construction of polycyclic ring systems of fundamental interest in organic chemistry. In view of the outstanding importance of the method for the preparation of natural products, and hence also of physiologically active molecules, increasing interest has been placed in recent years on the development of [4 + 2] cycloadditions.

The Diels–Alder reaction of 1,3,3-trimethyl-2-vinyl-1-cyclohexene with dienophiles like dimethyl acetylenedicarboxylate,<sup>2,4</sup> unsymmetrical *p*-benzoquinones,<sup>5</sup> 2-carbomethoxy-4,4-dimethyl-2-cyclohexenone,<sup>6</sup> 1,4-benzoquinone,<sup>7</sup> substituted 1,4-benzoquinones,<sup>8</sup> 3-((*E*)-3-(methoxycarbonyl)propenyl)-1,3-oxazolidin-2-one,<sup>9</sup> acetylenedicarbaldehyde,<sup>10</sup> (*S*)-3-hydroxy-2-isopropyl-5-*tert*-butylsulfinyl-*p*-benzoquinone,<sup>11</sup> and conjugated ketones<sup>12</sup> has been reported. There have been very few reports of [4 + 2] cycloaddition reactions using chromones as dienophiles and in all these cases an activating functionality such as  $-\text{CHO}$ ,  $-\text{COR}$ ,  $-\text{COOR}$ ,  $-\text{CN}$ ,  $-\text{Ar}$ , etc. at C(3) has been utilized.<sup>13–15</sup> Only one Diels–Alder reaction of 1,3,3-trimethyl-2-vinyl-1-cyclohexene with 6-

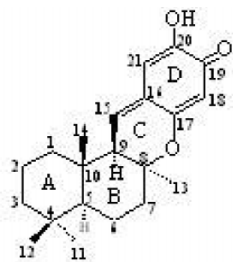
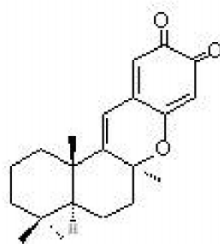
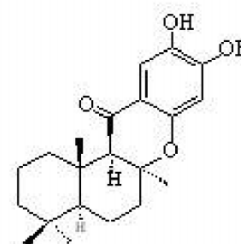
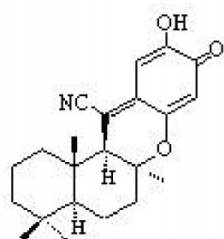
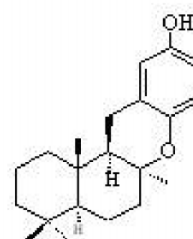
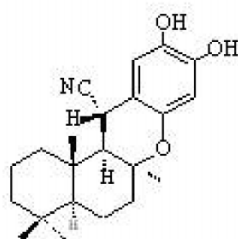
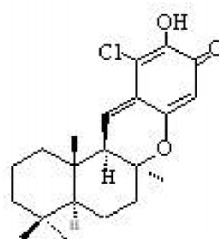
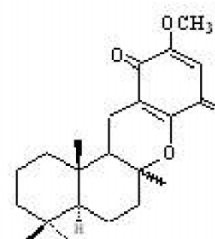
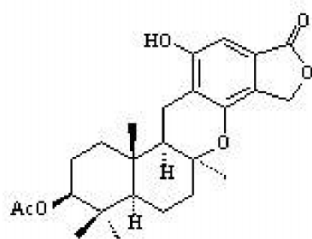
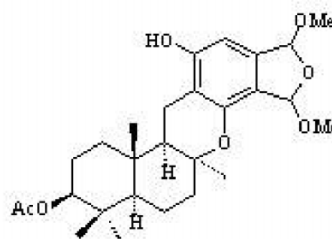
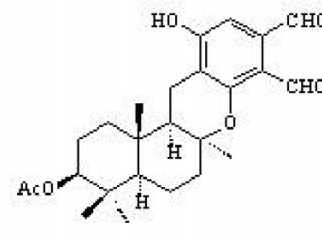
bromo-3-cyanochromone<sup>13</sup> having an activating group at C(3) has been reported in the literature. Also, Lewis acids are known to catalyze Diels–Alder reactions.<sup>1,12,13</sup> Lewis acid-catalyzed cycloadditions not only proceed more rapidly than their thermal counterparts but are also generally more regio- and stereoselective. For this reason, such reactions are of additional interest from a theoretical point of view, since they appear to represent an exception to the reactivity–selectivity principle. Theoretical interpretations of the apparently anomalous course of these Lewis acid-catalyzed reactions have been proposed by Epiotis and Shaik<sup>16</sup> and by Branchadell et al.,<sup>17</sup> while the frontier molecular orbital theory was successfully applied to explain the role of the Lewis acid catalyst.<sup>18</sup> Donor–acceptor interactions between the dienophile and the catalyst thus lower the energy of the highest occupied molecular orbital and the lowest unoccupied molecular orbital of the dienophile. For the case of a [4 + 2] cycloaddition with normal electron demand, this means that the separation between the molecular orbitals will decrease and the stabilization of the transition state will increase. The literature on the acceleration of Diels–Alder reactions by common Lewis acids such as  $\text{TiCl}_4$ ,  $\text{SnCl}_2$ ,  $\text{ZnCl}_2$ ,  $\text{ZnBr}_2$ ,  $\text{BF}_3$ ,  $\text{SnCl}_4$ , etc. is extensively reported.

In the present study, we employed microwave energy because the potential application of microwave technology in organic synthesis<sup>19</sup> is increasing rapidly owing to its reac-

Received 6 July 2010. Accepted 16 September 2010. Published on the NRC Research Press Web site at canjchem.nrc.ca on 23 November 2010.

**R.M. Kamble and M. Ramana.**<sup>1</sup> Department of Chemistry, University of Mumbai, Vidyanagari, Santacruz (East), Mumbai 400 098, India.

<sup>1</sup>Corresponding author (e-mail: mmvramana@yahoo.co.in).

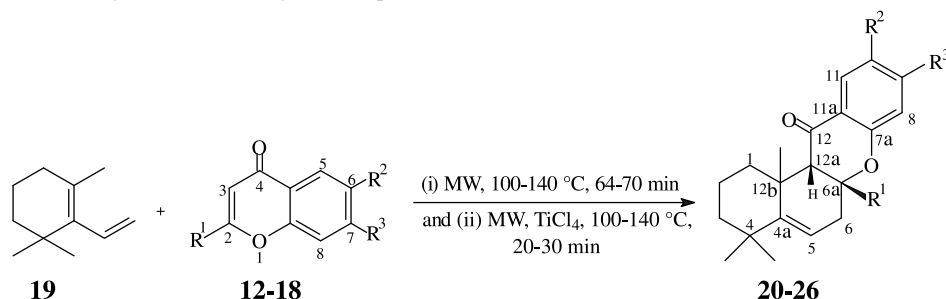
**Chart 1.** Puupehenone group of marine diterpenoids **1–8** and kampanols **9–11**.**(+)-Puupehenone 1****(+)-Puupehedione 2****(-)-15-Oxopuupehenol 3****(+)-15-Cyanopuupehenone 4****(-)-8-Epichromazonarol 5****(-)-15-Cyanopuupehenol 6****Chloropuupehenone 7****Cyclosporgiaquinone-1 8****Kampanol A 9****Kampanol B 10****Kampanol C 11**

tion simplicity, reduced pollution, and minimum reaction time providing a rapid access to large libraries of diverse small molecules.<sup>20–22</sup>

(+)-Puupehenone (**1**),<sup>23–28</sup> (+)-puupehedione (**2**),<sup>26</sup> (-)-15-

oxopuupehenol (**3**),<sup>27</sup> (+)-15-cyanopuupehenone (**4**),<sup>26,27</sup> (-)-8-epichromazonarol (**5**),<sup>29</sup> (-)-15-cyanopuupehenol (**6**),<sup>27,30</sup> chloropuupehenone (**7**),<sup>23</sup> and cyclosporgiaquinone-1 (**8**)<sup>31</sup> (Chart 1) are an important group of biologically active ma-



**Scheme 1.** Microwave-assisted synthesis of tetracyclic compounds **20–26**.**Table 1.** Reaction of 1,3,3-trimethyl-2-vinyl-1-cyclohexene (**19**) with chromones **12–18** under microwave irradiation with or without  $\text{TiCl}_4$ .

Entry	Chromone	$\text{R}^1$	$\text{R}^2$	$\text{R}^3$	Product	Temp. ( $^{\circ}\text{C}$ )		Time (min)		Isolated yield (%)	
						– $\text{TiCl}_4$	+ $\text{TiCl}_4$	– $\text{TiCl}_4$	+ $\text{TiCl}_4$	– $\text{TiCl}_4$	+ $\text{TiCl}_4$
1	<b>12</b>	Me	OMe	OMe	<b>20</b>	140	100	65	30	42	67
2	<b>13</b>	Me	OMe	H	<b>21</b>	140	140	70	20	44	63
3	<b>14</b>	Me	– $\text{OCH}_2\text{O}$ –	H	<b>22</b>	140	100	64	25	47	73
4	<b>15</b>	Me	$\text{NO}_2$	H	<b>23</b>	140	100	65	25	45	71
5	<b>16</b>	Me	H	H	<b>24</b>	100	100	65	20	42	68
6	<b>17</b>	Ph	H	H	<b>25</b>	100	100	70	30	41	68
7	<b>18</b>	H	H	H	<b>26</b>	100	100	65	20	45	67

rine terpenoids.<sup>32</sup> These are based on a mixed biogenetic origin involving a sesquiterpene unit with a quinol or quinone and consist of a multiplicity of prenyl units uncommon in terrestrial organisms. These compounds were isolated from sponges and possess a wide range of potent biological activities, including cytotoxic,<sup>26,27</sup> antiviral,<sup>26,27</sup> antimicrobial,<sup>23</sup> antifungal,<sup>26</sup> immunomodulatory,<sup>26,27</sup> antitumor,<sup>25,33</sup> antimalarial,<sup>27</sup> antibiotic,<sup>34</sup> antituberculosis,<sup>35</sup> antioxidant,<sup>36</sup> and insecticidal activities.<sup>37</sup> The characteristic structural features such as a tetracyclic framework, four quaternary methyl groups, a benzopyran ring, a trimethyl cyclohexane moiety, four stereogenic centers at AB and BC ring junctions having trans and cis relationship, respectively, and an additional chiral center at C(15) of ring C of these tetracyclic diterpenes, as well as the biological activity observed within this series, attracted chemists to develop new methods for their synthesis. Other related compounds are kampenols A–C (**9–11**, respectively) (Chart 1), which are polycyclic natural products isolated from the fungal culture broth of *Stachybotrys kampalensis*, which are novel and specific inhibitors of farnesyl protein transferase.<sup>38</sup>

Our interest in the synthesis of natural products<sup>39</sup> and the absence of reports of the Diels–Alder reaction of 1,3,3-trimethyl-2-vinyl-1-cyclohexene with chromones not having an activating group on the enone double bond led us to explore the synthetic potential of chromones such as 6,7-dimethoxy-2-methyl chromone (**12**),<sup>40</sup> 6-methoxy-2-methyl chromone (**13**),<sup>41</sup> 6,7-methylenedioxy-2-methyl chromone (**14**),<sup>42</sup> 6-nitro-2-methyl chromone (**15**),<sup>43</sup> 2-methyl chromone (**16**),<sup>44</sup> flavone (**17**),<sup>45</sup> and chromone (**18**)<sup>46</sup> as dienophiles in [4 + 2] cycloaddition reactions. We envisaged that if diene 1,3,3-trimethyl-2-vinyl-1-cyclohexene (**19**)<sup>3</sup> could be used, then such a cycloaddition would lead to a convergent approach for construction of the tetracyclic core of puerphenone and kampenol analogues.

## Results and discussion

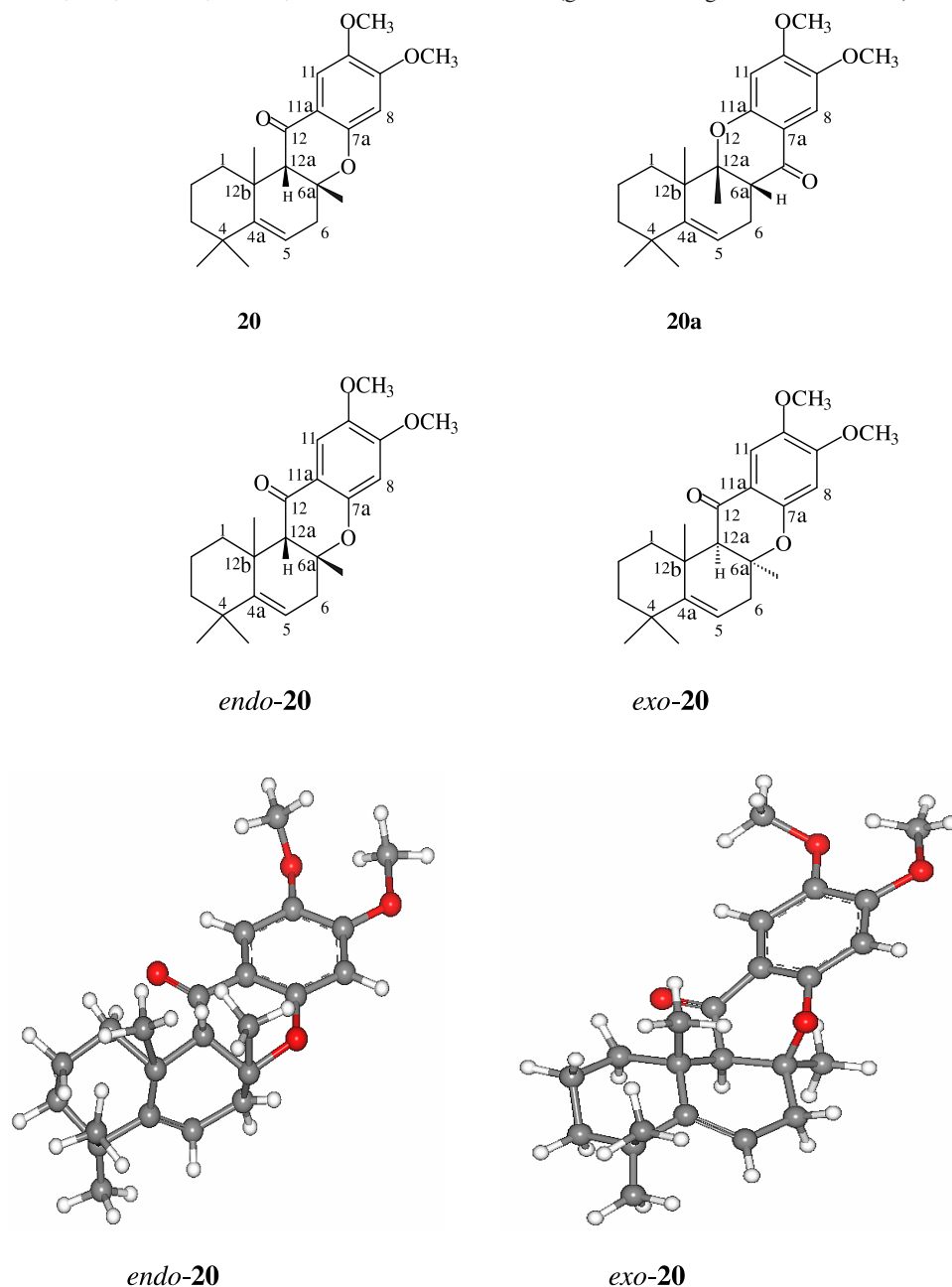
We now report for the first time a successful Diels–Alder reaction of 1,3,3-trimethyl-2-vinyl-1-cyclohexene (**19**) with chromones **12–18** not having an activating group at C(3) under microwave irradiation with or without  $\text{TiCl}_4$  catalyst (Scheme 1).

The reaction of **12** with the electron-rich diene **19** was performed in a microwave reactor at 140  $^{\circ}\text{C}$  for 65 min to give cycloadduct **20** in a moderate yield (42%). However, the use of  $\text{TiCl}_4$  and microwave radiation led to a significant enhancement in the yield of the cycloadduct (67%) and time reduction (30 min) (Table 1). The reaction was found to be regioselective as indicated by  $^1\text{H}$  NMR data, which exhibited a singlet at  $\delta$  2.71 ppm for the C(12a) proton while the C(6a) proton signal was absent; C(1) protons appeared at  $\delta$  2.18–1.65 ppm. Thus, this indicates the formation of the regioisomer **20** instead of **20a** (Fig. 1).

This reaction was also stereoselective as indicated by  $^1\text{H}$  NMR, which showed a singlet for C(6a) methyl protons at  $\delta$  1.39 ppm and C(12b) methyl protons at  $\delta$  1.21 ppm.  $^{13}\text{C}$  NMR signal for C(6a) methyl carbon exhibited a signal at 34.2 ppm and that for C(12b) methyl carbon exhibited a signal at 23.8 ppm.

These high  $\delta$  values suggest the formation of the *endo*-**20** product (Fig. 1). Recently, Wallace and co-workers<sup>48</sup> reported the synthesis of the ( $\pm$ )-*exo*-**20**, which had lower  $\delta$  values for the C(12a) proton and the C(6a) methyl and C(12b) methyl protons. Furthermore, this compound has a mp of 165  $^{\circ}\text{C}$ , whereas our compound has a mp of 102  $^{\circ}\text{C}$ . Also, the ( $\pm$ )-*exo*-**24** is an oil<sup>48</sup> and our compound **24** is a solid with a mp of 60  $^{\circ}\text{C}$ . Further, compound **24** also has higher  $\delta$  values for the C(12a) proton and C(6a) methyl and C(12b) methyl protons. All this evidence suggests the formation of the *endo*-**20** product. This represents the first ex-

**Figure 1.** Regioisomers **20**, **20a**, *endo*-**20**, *exo*-**20**, and ball-and-stick models (generated using Materials Studio<sup>47</sup>) of *endo*-**20** and *exo*-**20**.



ample of a highly stereoselective [4 + 2] cycloaddition reaction involving easily available chromone dienophiles.

Similar results were obtained with other chromones, **13**–**18** (Table 1). In all these cases, the reaction led to the generation of the tetracyclic core present in puerphenone **1** and related marine terpenoids and kampanols. Further, the catalytic hydrogenation of the C(4a)–(C5) double bond could lead to a trans-fused AB ring,<sup>7,8</sup> which is present in these natural products.

It is significant that in the above noncatalyzed microwave reactions, we could not isolate even traces of the *exo* isomer. This probably suggests that the *endo* effect controls the [4 + 2] addition in the noncatalyzed microwave reactions. In all these reactions, unreacted starting materials were recovered during column chromatographic purification.

The results in Table 1 also suggest that when the reactions were carried out at the same temperature (Table 1, entries 2, 5–7), reaction time was reduced and the percentage yields of the product were higher. This suggests that the Lewis acid used, that is TiCl<sub>4</sub>, reduces the reaction times and enhances the yield of the adduct without affecting the distereoselectivity (*endo*).

## Conclusion

In conclusion, we have accomplished the first highly stereoselective [4 + 2] cycloaddition reaction under microwave irradiation with and without TiCl<sub>4</sub> using chromones as dienophiles and have demonstrated the potential of this reaction in constructing the tetracyclic core of the marine diterpe-

noids related to puerphenone analogues **1–8** and kampanols **9–11** in a convergent manner.

## Experimental

Melting points are uncorrected. UV spectra were recorded on a Shimadzu UV–visible spectrophotometer UV-2401PC using methanol as a solvent;  $\lambda_{\text{max}}$  is given in nm ( $\epsilon$ ). IR spectra were recorded on a PerkinElmer Spectrum One FTIR spectrophotometer in KBr discs. Elemental analyses were performed on a Euro-Vector EA3000 elemental analyzer.  $^1\text{H}$  and  $^{13}\text{C}$  NMR spectra were recorded on a Bruker Avance ( $^1\text{H}$ , 300 MHz;  $^{13}\text{C}$ , 75 MHz) spectrometer using  $\text{CDCl}_3$  as solvent and TMS as an internal standard;  $\delta$  are in ppm and coupling constants ( $J$ ) in Hz. Electron impact mass spectra were obtained using a 3200 Q TRAP LC-MS/MS System MDS SCI EX Shimadzu Prominence LC and Varian 500-MS (Model 210) LC-MS IT mass spectrometer. The boiling point of petroleum ether used was in the range of 60–80 °C. Silica gel (60–120 mesh) (S.D. Fine Chemicals Ltd.) was used in column chromatography. Microwave-assisted reactions were performed using a Startsynth Microwave Synthesis Labstation model microwave reactor. All reactions were performed in the appropriate volume vessel. Temperature was measured with an IR sensor and reaction times are given as hold times.

## General procedures for microwave-assisted syntheses of cycloadducts **20–26**

### (i) General procedure for the cycloaddition without $\text{TiCl}_4$

A mixture of **19** (900 mg, 6 mmol) and **12–18** (0.6 mmol) was taken in a sealed glass vial and heated in a microwave reactor (Table 1). The reaction mixture was taken out of the microwave reactor and allowed to cool. The colorless semi-solid thus obtained was purified by silica gel column chromatography. Elution with petroleum ether/ $\text{CHCl}_3$  afforded the corresponding cycloadducts **20–26**.

### (ii) General procedure for the cycloaddition with $\text{TiCl}_4$

A mixture of **19** (900 mg, 6 mmol) and **12–18** (0.6 mmol) was taken in a 50 mL capacity round-bottom flask. Then, 0.5 mL of  $\text{TiCl}_4$  was added to the same reaction mixture. The flask was irradiated in a microwave reactor (Table 1). Then the reaction mixture was taken out of the microwave reactor and allowed to cool. The dark brown solid thus obtained was purified by silica gel column chromatography. Elution with petroleum ether/ $\text{CHCl}_3$  afforded the corresponding cycloadducts **20–26**.

### Endo-( $\pm$ )-1,2,3,4,6,6a,12a,12b-octahydro-9,10-dimethoxy-4,4,6a,12b-tetramethyl-benzo[a]xanthen-12-one (endo-20)

Colorless solid, mp 102 °C (7:3, petroleum ether/chloroform). UV–vis  $\lambda_{\text{max}}$  ( $\epsilon$ ): 339 (2822), 275 (4235), 236 (5757), 211 (5486). FTIR ( $\text{cm}^{-1}$ ): 2924, 1678 ( $\text{C}=\text{O}$ ), 1474, 1266, 1063.  $^1\text{H}$  NMR (300 MHz, ppm)  $\delta$ : 7.14 (s, 1H,  $\text{H}_{11}$ ), 7.01 (s, 1H,  $\text{H}_8$ ), 5.58 (t,  $J = 3.9$  Hz, 1H,  $\text{H}_5$ ), 3.90 (s, 3H,  $\text{OCH}_3$ ), 3.86 (s, 3H,  $\text{OCH}_3$ ), 2.71 (s, 1H,  $\text{H}_{12a}$ ), 2.61 (dd,  $J = 9.0$  and 18.0 Hz, 1H,  $\text{H}_6$ ), 2.18, 1.65 (m, 2H,  $\text{H}_1$ ), 1.72, 1.61 (m, 2H,  $\text{H}_2$ ), 1.43, 1.18 (m, 2H,  $\text{H}_3$ ), 1.39 (s, 3H,  $\text{CH}_{3-6a}$ ), 1.21 (s, 3H,  $\text{CH}_{3-12b}$ ), 1.13 (s, 3H,  $\text{CH}_{3\text{eq-4}}$ ), 1.11 (s, 3H,  $\text{CH}_{3\text{ax-4}}$ ).

$^{13}\text{C}$  NMR (75 MHz, ppm)  $\delta$ : 199.5 ( $\text{C}=\text{O}$ ), 155.2 (C-9), 154.4 (C-7a), 154.2 (C-10), 140.8 (C-4a), 137.3 (C-11a), 132.1 (C-11), 130.5 (C-8), 121.2 (C-5), 78.6 (C-6a), 64.2 (C-12a), 56.6 ( $\text{OCH}_3$ ), 56.2 ( $\text{OCH}_3$ ), 37.5 (C-1), 37.1 (C-12b), 34.2 ( $\text{CH}_3-6a$ ), 33.5 ( $\text{CH}_{3\text{eq-4}}$ ), 32.6 (C-4), 32.0 (C-6), 23.8 ( $\text{CH}_3-12b$ ), 22.7 ( $\text{CH}_{3\text{ax-4}}$ ), 20.6 (C-3), 17.5 (C-2). LC-MS (70 eV): 370 [ $\text{M}^+$ , 11]. Anal. calcd. for  $\text{C}_{23}\text{H}_{30}\text{O}_4$ : C 74.59, H 8.10; found: C 74.83, H 8.03.

### Endo-( $\pm$ )-1,2,3,4,6,6a,12a,12b-octahydro-10-methoxy-4,4,6a,12b-tetramethyl-benzo[a]xanthen-12-one (endo-21)

Colorless solid, mp 111 °C (7:3, petroleum ether/chloroform). UV–vis  $\lambda_{\text{max}}$  ( $\epsilon$ ): 321 (3856), 229 (11487). FTIR ( $\text{cm}^{-1}$ ): 3061, 2924, 1676 ( $\text{C}=\text{O}$ ), 1483, 1239, 1028.  $^1\text{H}$  NMR (300 MHz, ppm)  $\delta$ : 7.19 (s, 1H,  $\text{H}_{11}$ ), 7.09 (d,  $J = 8.9$  Hz, 1H,  $\text{H}_9$ ), 6.99 (d,  $J = 8.9$  Hz, 1H,  $\text{H}_8$ ), 5.59 (t,  $J = 3.8$  Hz, 1H,  $\text{H}_5$ ), 3.88 (s, 3H,  $\text{OCH}_3$ ), 2.80 (s, 1H,  $\text{H}_{12a}$ ), 2.59 (dd,  $J = 9.0$  and 18.1 Hz, 1H,  $\text{H}_6$ ), 2.51 (dd,  $J = 9.0$  and 18.1 Hz, 1H,  $\text{H}_6$ ), 2.16, 1.64 (m, 2H,  $\text{H}_1$ ), 1.71, 1.60 (m, 2H,  $\text{H}_2$ ), 1.42, 1.19 (m, 2H,  $\text{H}_3$ ), 1.38 (s, 3H,  $\text{CH}_{3-6a}$ ), 1.22 (s, 3H,  $\text{CH}_{3-12b}$ ), 1.14 (s, 3H,  $\text{CH}_{3\text{eq-4}}$ ), 1.12 (s, 3H,  $\text{CH}_{3\text{ax-4}}$ ).  $^{13}\text{C}$  NMR (75 MHz, ppm)  $\delta$ : 199.1 ( $\text{C}=\text{O}$ ), 154.1 (C-7a), 153.2 (C-10), 141.2 (C-4a), 137.5 (C-11a), 131.7 (C-11), 130.9 (C-9), 126.2 (C-8), 121.0 (C-5), 78.3 (C-6a), 64.1 (C-12a), 55.9 ( $\text{OCH}_3$ ), 37.2 (C-12b), 36.9 (C-1), 33.9 ( $\text{CH}_3-6a$ ), 32.8 ( $\text{CH}_{3\text{eq-4}}$ ), 32.2 (C-4), 31.8 (C-6), 23.2 ( $\text{CH}_3-12b$ ), 22.4 ( $\text{CH}_{3\text{ax-4}}$ ), 20.4 (C-3), 18.0 (C-2). LC-MS (70 eV): 340 [ $\text{M}^+$ , 5], 191 (100), 149 (17), 135 (18). Anal. calcd. for  $\text{C}_{22}\text{H}_{28}\text{O}_3$ : C 77.64, H 8.23; found: C 77.43, H 8.33.

### 2-Methyl-6,7-methylenedioxy-4H-1-benzopyran-4-one (14)

This compound was prepared utilizing the general procedure reported for the synthesis of chromone.<sup>42</sup> Faint yellow crystals, mp 101–102 °C (8:2, petroleum ether/chloroform). UV–vis  $\lambda_{\text{max}}$  ( $\epsilon$ ): 347 (3881), 276 (3303), 238 (6472), 212 (5653). FTIR ( $\text{cm}^{-1}$ ): 2922, 1632 ( $\text{C}=\text{O}$ ), 1484, 1035, 922.  $^1\text{H}$  NMR (300 MHz, ppm)  $\delta$ : 7.27 (s, 1H), 7.05 (s, 1H), 6.44 (s, 2H), 5.98 (s, 1H), 2.52 (s, 3H).  $^{13}\text{C}$  NMR (75 MHz, ppm)  $\delta$ : 201.9 ( $\text{C}=\text{O}$ ), 155.2, 154.9, 154.4, 140.4, 138.1, 132.3, 129.8, 128.4, 101.7, 26.4. LC-MS (70 eV): 204 [ $\text{M}^+$ , 21], 148 (54), 118 (83), 116 (100). Anal. calcd. for  $\text{C}_{11}\text{H}_8\text{O}_4$ : C 64.70, H 3.92; found: C 64.50, H 3.99.

### Endo-( $\pm$ )-1,2,3,4,6,6a,12a,12b-octahydro-4,4,6a,12b-tetramethyl-9,10-methylenedioxy-benzo[a]xanthen-12-one (endo-22)

Colorless solid, mp 98 °C (7:3, petroleum ether/chloroform). UV–vis  $\lambda_{\text{max}}$  ( $\epsilon$ ): 347 (3945), 276 (3386), 239 (7085), 210 (6929). FTIR ( $\text{cm}^{-1}$ ): 2924, 1680 ( $\text{C}=\text{O}$ ), 1484, 1035, 923.  $^1\text{H}$  NMR (300 MHz, ppm)  $\delta$ : 7.10 (s, 1H,  $\text{H}_{11}$ ), 7.03 (s, 1H,  $\text{H}_8$ ), 5.97 (s, 2H,  $\text{OCH}_2\text{O}$ ), 5.60 (t,  $J = 3.9$  Hz, 1H,  $\text{H}_5$ ), 2.69 (s, 1H,  $\text{H}_{12a}$ ), 2.64 (dd,  $J = 9.2$  and 18.2 Hz, 1H,  $\text{H}_6$ ), 2.55 (dd,  $J = 9.2$  and 18.2 Hz, 1H,  $\text{H}_6$ ), 2.19, 1.67 (m, 2H,  $\text{H}_1$ ), 1.69, 1.62 (m, 2H,  $\text{H}_2$ ), 1.42, 1.18 (m, 2H,  $\text{H}_3$ ), 1.39 (s, 3H,  $\text{CH}_{3-6a}$ ), 1.20 (s, 3H,  $\text{CH}_{3-12b}$ ), 1.15 (s, 3H,  $\text{CH}_{3\text{eq-4}}$ ), 1.13 (s, 3H,  $\text{CH}_{3\text{ax-4}}$ ).  $^{13}\text{C}$  NMR (75 MHz, ppm)  $\delta$ : 199.4 ( $\text{C}=\text{O}$ ), 154.8 (C-9), 154.5 (C-7a), 154.1 (C-10), 140.5 (C-4a), 137.5 (C-11a), 132.5 (C-11), 130.2 (C-8), 121.4 (C-5), 101.1 ( $\text{OCH}_2\text{O}$ ), 78.7 (C-6a), 63.8 (C-12a), 37.5 (C-12b), 37.2 (C-1), 34.1 ( $\text{CH}_3-6a$ ), 32.9 ( $\text{CH}_{3\text{eq-4}}$ ),

32.5 (C-4), 32.2 (C-6), 23.5 (CH<sub>3</sub>-12b), 22.8 (CH<sub>3ax</sub>-4), 20.5 (C-3), 17.8 (C-2). LC-MS (70 eV): 354 [M<sup>+</sup>, 4], 352 (100), 236 (10), 220 (40), 205 (21). Anal. calcd. for C<sub>22</sub>H<sub>26</sub>O<sub>4</sub>: C 74.57, H 7.34; found: C 74.83, H 7.46.

**Endo-(±)-1,2,3,4,6,6a,12a,12b-octahydro-4,4,6a,12b-tetramethyl-benzo[a]xanthen-12-one-10-nitro (endo-23)**

Colorless solid, mp 171 °C (4:6, petroleum ether/chloroform). UV-vis λ<sub>max</sub> (ε): 296 (4131), 239 (10304). FTIR (cm<sup>-1</sup>): 3063, 2925, 1679 (C=O), 1531, 1467. <sup>1</sup>H NMR (300 MHz, ppm) δ: 9.03 (s, 1H, H<sub>11</sub>), 8.46 (d, *J* = 9.2 Hz, 1H, H<sub>9</sub>), 7.54 (d, *J* = 9.2 Hz, 1H, H<sub>8</sub>), 5.55 (t, *J* = 3.9 Hz, 1H, H<sub>5</sub>), 2.78 (s, 1H, H<sub>12a</sub>), 2.62 (dd, *J* = 8.9 and 18.0 Hz, 1H, H<sub>6</sub>), 2.54 (dd, *J* = 8.9 and 18.0 Hz, 1H, H<sub>6</sub>), 2.20, 1.68 (m, 2H, H<sub>1</sub>), 1.71, 1.64 (m, 2H, H<sub>2</sub>), 1.42, 1.19 (m, 2H, H<sub>3</sub>), 1.39 (s, 3H, CH<sub>3-6a</sub>), 1.24 (s, 3H, CH<sub>3-12b</sub>), 1.16 (s, 3H, CH<sub>3eq-4</sub>), 1.13 (s, 3H, CH<sub>3ax-4</sub>). <sup>13</sup>C NMR (75 MHz, ppm) δ: 199.8 (C=O), 159.2 (C-10), 154.8 (C-7a), 148.5 (C-11), 144.6 (C-9), 140.4 (C-4a), 138.1 (C-11a), 127.8 (C-8), 120.5 (C-5), 78.5 (C-6a), 64.1 (C-12a), 37.5 (C-12b), 37.1 (C-1), 34.3 (CH<sub>3-6a</sub>), 33.7 (CH<sub>3eq-4</sub>), 32.7 (C-4), 31.7 (C-6), 23.1 (CH<sub>3-12b</sub>), 22.3 (CH<sub>3ax-4</sub>), 20.8 (C-3), 17.7 (C-2). LC-MS (70 eV): 355 [M<sup>+</sup>, 8], 327 (23), 206 (100), 160 (31), 143 (10). Anal. calcd. for C<sub>21</sub>H<sub>25</sub>NO<sub>4</sub>: C 70.98, H 7.04, N 3.94; found: C 70.72, H 6.92, N 4.06.

**Endo-(±)-1,2,3,4,6,6a,12a,12b-octahydro-4,4,6a,12b-tetramethyl-benzo[a]xanthen-12-one (endo-24)**

Colorless solid, mp 60 °C (8:2, petroleum ether/chloroform). UV-vis λ<sub>max</sub> (ε): 295 (2551), 222 (7003). FTIR (cm<sup>-1</sup>): 1676 (C=O), 1478. <sup>1</sup>H NMR (300 MHz, ppm) δ: 7.04 (d, *J* = 8.5 Hz, 1H, H<sub>11</sub>), 6.97 (d, *J* = 8.5 Hz, 1H, H<sub>8</sub>), 6.93 (t, *J* = 8.6 Hz, 1H, H<sub>9</sub>), 6.90 (t, *J* = 8.5 Hz, 1H, H<sub>10</sub>), 5.58 (t, *J* = 3.7 Hz, 1H, H<sub>5</sub>), 2.75 (s, 1H, H<sub>12a</sub>), 2.60 (dd, *J* = 9.1 and 18.1 Hz, 1H, H<sub>6</sub>), 2.52 (dd, *J* = 9.1 and 18.1 Hz, 1H, H<sub>6</sub>), 2.19, 1.66 (m, 2H, H<sub>1</sub>), 1.69, 1.60 (m, 2H, H<sub>2</sub>), 1.44, 1.17 (m, 2H, H<sub>3</sub>), 1.39 (s, 3H, CH<sub>3-6a</sub>), 1.23 (s, 3H, CH<sub>3-12b</sub>), 1.13 (s, 3H, CH<sub>3eq-4</sub>), 1.10 (s, 3H, CH<sub>3ax-4</sub>). <sup>13</sup>C NMR (75 MHz, ppm) δ: 199.2 (C=O), 155.1 (C-7a), 140.1 (C-4a), 137.7 (C-11a), 128.2 (C-11), 126.5 (C-8), 121.4 (C-9), 121.2 (C-10), 120.8 (C-5), 78.2 (C-6a), 64.5 (C-12a), 37.2 (C-12b), 37.4 (C-1), 34.0 (CH<sub>3-6a</sub>), 33.4 (CH<sub>3eq-4</sub>), 32.4 (C-6), 32.2 (C-4), 23.5 (CH<sub>3-12b</sub>), 21.9 (CH<sub>3ax-4</sub>), 21.0 (C-3), 17.4 (C-2). LC-MS (70 eV): 310 [M<sup>+</sup>, 4], 191 (100), 161 (96). Anal. calcd. for C<sub>21</sub>H<sub>26</sub>O<sub>2</sub>: C 81.29, H 8.38; found: C 81.03, H 8.50.

**Endo-(±)-1,2,3,4,6,6a,12a,12b-octahydro-4,4,12b-trimethyl-6a-phenyl-benzo[a]xanthen-12-one (endo-25)**

Colorless solid, mp 105–106 °C (8:2, petroleum ether/chloroform). UV-vis λ<sub>max</sub> (ε): 294 (4845), 250 (4076), 205 (4965). FTIR (cm<sup>-1</sup>): 3070, 2924, 1678 (C=O), 1495. <sup>1</sup>H NMR (300 MHz, ppm) δ: 6.83–7.10 (m, 9H), 5.73 (t, *J* = 3.8 Hz, 1H, H<sub>5</sub>), 2.91 (s, 1H, H<sub>12a</sub>), 2.63 (dd, *J* = 9.0 and 18.1 Hz, 1H, H<sub>6</sub>), 2.56 (dd, *J* = 9.0 and 18.1 Hz, 1H, H<sub>6</sub>), 2.20, 1.66 (m, 2H, H<sub>1</sub>), 1.69, 1.60 (m, 2H, H<sub>2</sub>), 1.40, 1.19 (m, 2H, H<sub>3</sub>), 1.24 (s, 3H, CH<sub>3-12b</sub>), 1.16 (s, 3H, CH<sub>3eq-4</sub>), 1.14 (s, 3H, CH<sub>3ax-4</sub>). <sup>13</sup>C NMR (75 MHz, ppm) δ: 199.1 (C=O), 155.5 (C-7a), 140.9 (C-4a), 137.3 (C-11a), 128.5 (C-11), 126.4 (C-8), 127.3, 122.8, 122.8, 121.7 (C-5), 121.1 (C-9), 120.8 (C-10), 119.8, 119.8, 115.5, 80.4 (C-6a), 66.5

(C-12a), 37.5 (C-12b), 37.2 (C-1), 33.2 (CH<sub>3eq-4</sub>), 32.1 (C-4), 31.2 (C-6), 24.0 (CH<sub>3-12b</sub>), 22.4 (CH<sub>3ax-4</sub>), 20.9 (C-3), 17.5 (C-2). LC-MS (70 eV): 372 [M<sup>+</sup>, 8], 344 (48), 223 (100), 121 (58), 77 (11). Anal. calcd. for C<sub>26</sub>H<sub>28</sub>O<sub>2</sub>: C 83.87, H 7.52; found: C 84.13, H 7.64.

**Endo-(±)-1,2,3,4,6,6a,12a,12b-octahydro-4,4,12b-trimethyl-benzo[a]xanthen-12-one (endo-26)**

Colorless solid, mp 55 °C (8:2, petroleum ether/chloroform). UV-vis λ<sub>max</sub> (ε): 296 (3267), 238 (4609), 219 (7800). FTIR (cm<sup>-1</sup>): 3085, 2925, 1677 (C=O), 1474. <sup>1</sup>H NMR (300 MHz, ppm) δ: 7.03 (d, *J* = 5.0 Hz, 1H, H<sub>11</sub>), 6.99 (d, *J* = 5.0 Hz, 1H, H<sub>8</sub>), 6.92 (t, *J* = 5.2 Hz, 1H, H<sub>9</sub>), 6.89 (t, *J* = 5.1 Hz, 1H, H<sub>10</sub>), 5.56 (t, *J* = 3.9 Hz, 1H, H<sub>5</sub>), 3.43 (ddd, *J* = 5.2 and 8.9 Hz, 1H, H<sub>6a</sub>), 2.79 (d, *J* = 4.8 Hz, 1H, H<sub>12a</sub>), 2.41 (ddd, *J* = 5.2 and 8.9 Hz, 1H, H<sub>6</sub>), 2.20 (ddd, *J* = 5.2 and 8.9 Hz, 1H, H<sub>6</sub>), 2.16, 1.68 (m, 2H, H<sub>1</sub>), 1.71, 1.63 (m, 2H, H<sub>2</sub>), 1.42, 1.18 (m, 2H, H<sub>3</sub>), 1.22 (s, 3H, CH<sub>3-12b</sub>), 1.15 (s, 3H, CH<sub>3eq-4</sub>), 1.12 (s, 3H, CH<sub>3ax-4</sub>). <sup>13</sup>C NMR (75 MHz, ppm) δ: 199.4 (C=O), 155.2 (C-7a), 140.2 (C-4a), 137.2 (C-11a), 128.3 (C-11), 126.2 (C-8), 121.5 (C-5), 121.2 (C-9), 120.9 (C-10), 79.2 (C-6a), 63.8 (C-12a), 37.2 (C-12b), 36.8 (C-1), 33.8 (CH<sub>3eq-4</sub>), 32.7 (C-4), 31.5 (C-6), 23.9 (CH<sub>3-12b</sub>), 22.1 (CH<sub>3ax-4</sub>), 21.1 (C-3), 17.2 (C-2). LC-MS (70 eV): 296 [M<sup>+</sup>, 12], 147 (100), 105 (12), 91 (58), 77 (72). Anal. calcd. for C<sub>20</sub>H<sub>24</sub>O<sub>2</sub>: C 81.08, H 8.10; found: C 81.34, H 8.22.

## References

- (1) Pindur, U.; Lutz, G.; Otto, C. *Chem. Rev.* **1993**, 93 (2), 741. doi:10.1021/cr00018a006.
- (2) Loperfido, J. C. *J. Org. Chem.* **1973**, 38 (2), 399. doi:10.1021/jo00942a044.
- (3) Brieger, G. *Tetrahedron Lett.* **1965**, 6 (49), 4429. doi:10.1016/S0040-4039(00)71682-0.
- (4) Hollinshead, D. M.; Howell, S. C.; Ley, S. V.; Mahon, M.; Ratcliffe, N. M.; Worthington, P. A. *J. Chem. Soc., Perkin Trans. 1* **1983**, 7, 1579. doi:10.1039/p19830001579.
- (5) Engler, T. A.; Naganathan, S.; Takusagawa, F.; Yohannes, D. *Tetrahedron Lett.* **1987**, 28 (44), 5267. doi:10.1016/S0040-4039(00)96704-2.
- (6) Engler, T. A.; Sampath, U.; Vander Velde, D.; Takusagawa, F. *Tetrahedron* **1992**, 48 (43), 9399. doi:10.1016/S0040-4020(01)88309-5.
- (7) Engler, T. A.; Naganathan, S. *Tetrahedron Lett.* **1986**, 27 (9), 1015. doi:10.1016/S0040-4039(86)80036-3.
- (8) Engler, T. A.; Sampath, U.; Naganathan, S.; Vander Velde, D.; Takusagawa, F.; Yohannes, D. *J. Org. Chem.* **1989**, 54 (24), 5712. doi:10.1021/jo00285a018.
- (9) Knol, J.; Meetsma, A.; Feringa, B. L. *Tetrahedron Asymmetry* **1995**, 6 (5), 1069. doi:10.1016/0957-4166(95)00127-B.
- (10) Gorgues, A.; Stephan, D.; Khanous, A. B. A.; Co, A. L. *Tetrahedron* **1990**, 46 (8), 2817. doi:10.1016/S0040-4020(01)88374-5.
- (11) Carreño, M. C.; García Ruano, J. L.; Toledo, M. A. *Chem. Eur. J.* **2000**, 6 (2), 288. doi:10.1002/(SICI)1521-3765(20000117)6:2<288::AID-CHEM288>3.0.CO;2-2.
- (12) Mayelvaganan, T.; Hadimani, S.; Bhat, S. V. *Tetrahedron* **1997**, 53 (6), 2185. doi:10.1016/S0040-4020(96)01120-9.
- (13) Hsung, R. P. *J. Org. Chem.* **1997**, 62 (23), 7904. doi:10.1021/jo9711479p.
- (14) Ghosh, C. K.; Bhattacharyya, A.; Bandyopadhyay, C. J.



- Chem. Soc. Chem. Commun.* **1984**, 1319. doi:10.1039/c39840001319.
- (15) Cremins, P. J.; Saengchantara, T.; Wallace, T. W. *Tetrahedron* **1987**, *43* (13), 3075. doi:10.1016/S0040-4020(01)86849-6.
- (16) Epiotis, N. D.; Shaik, S. J. *Am. Chem. Soc.* **1978**, *100* (1), 1. doi:10.1021/ja00469a001.
- (17) Branchadell, V.; Oliva, A.; Bertran, J. J. *Mol. Struct. Theochem* **1986**, *138* (1–2), 117. doi:10.1016/0166-1280(86)87014-2.
- (18) Fleming, I. *Frontier Orbitals and Organic Chemical Reactions*; Wiley: New York, 1976.
- (19) Kappe, C. O. *Angew. Chem.* **2004**, *43* (46), 6250. doi:10.1002/anie.200400655.
- (20) Gedye, R.; Rank, W.; Westaway, K. *Can. J. Chem.* **1991**, *69* (4), 706. doi:10.1139/v91-106.
- (21) Avalos, M.; Babiano, R.; Cintas, P.; Clemente, F. R.; Jimenez, J. L.; Palacios, J. C.; Sanchez, J. B. *J. Org. Chem.* **1999**, *64* (17), 6297. doi:10.1021/jo990442x.
- (22) Kaval, N.; Van der Eycken, J.; Caroen, J.; Dehaen, W.; Strohmeier, G. A.; Kappe, C. O.; Van der Eycken, E. J. *Comb. Chem.* **2003**, *5* (5), 560. doi:10.1021/cc0300098.
- (23) Ravi, B. N.; Perzanowski, H. P.; Ross, R. A.; Erdman, T. R.; Scheuer, P. J.; Finer, J.; Clardy, J. *Pure Appl. Chem.* **1979**, *51* (9), 1893. doi:10.1351/pac197951091893.
- (24) Amade, P.; Chevelot, L.; Perzanowski, H. P.; Scheuer, P. J. *Helv. Chim. Acta* **1983**, *66* (6), 1672. doi:10.1002/hlca.19830660606.
- (25) Kohmoto, S.; McConnell, O. J.; Wright, A.; Koehn, F.; Thompson, W.; Lui, M.; Snader, K. M. *J. Nat. Prod.* **1987**, *50* (2), 336. doi:10.1021/np50050a064.
- (26) Hamann, M. T.; Scheuer, P. J.; Kelly-Borges, M. *J. Org. Chem.* **1993**, *58* (24), 6565. doi:10.1021/jo00076a012.
- (27) Nasu, S. S.; Yeung, B. K. S.; Hamann, M. T.; Scheuer, P. J.; Kelly-Borges, M.; Goins, K. *J. Org. Chem.* **1995**, *60* (22), 7290. doi:10.1021/jo00127a039.
- (28) Urban, S.; Capon, R. J. *J. Nat. Prod.* **1996**, *59* (9), 900. doi:10.1021/np9603838.
- (29) Djura, P.; Stierle, D. B.; Sullivan, B.; Faulkner, D. J.; Arnold, E.; Clardy, J. *J. Org. Chem.* **1980**, *45* (8), 1435. doi:10.1021/jo01296a019.
- (30) Hamann, M. T.; Scheuer, P. J. *Tetrahedron Lett.* **1991**, *32* (41), 5671. doi:10.1016/S0040-4039(00)93525-1.
- (31) Kazlauskas, R.; Murphy, P. T.; Warren, R. G.; Wells, R. J.; Blount, J. F. *Aust. J. Chem.* **1978**, *31* (12), 2685. doi:10.1071/CH9782685.
- (32) Capon, R. J. *Studies in Natural Product Chemistry*; Atta-ur-Rahman, Ed.; Elsevier Science: New York, 1995; Vol. 15.
- (33) Barrero, A. F.; Alvarez-Manzaneda, E. J.; Chahboun, R.; Cortes, M.; Armstrong, V. *Tetrahedron* **1999**, *55* (52), 15181. doi:10.1016/S0040-4020(99)00992-8.
- (34) Bourguet-Kondracki, M. L.; Lacombe, F.; Guyot, M. *J. Nat. Prod.* **1999**, *62* (9), 1304. doi:10.1021/np9900829.
- (35) El Sayed, K. A.; Bartyzel, P.; Shen, X.; Perry, T. L.; Zjawiony, J. K.; Hamann, M. T. *Tetrahedron* **2000**, *56* (7), 949. doi:10.1016/S0040-4020(99)01093-5.
- (36) Takamatsu, S.; Hodges, T. W.; Rajbhandari, I.; Gerwick, W. H.; Hamann, M. T.; Nagle, D. G. *J. Nat. Prod.* **2003**, *66* (5), 605. doi:10.1021/np0204038.
- (37) El Sayed, K. A.; Dunbar, D. C.; Perry, T. L.; Wilkins, S. P.; Hamann, T.; Greenplate, J. T.; Wideman, M. A. *J. Agric. Food Chem.* **1997**, *45* (7), 2735. doi:10.1021/jf960746+.
- (38) Singh, S. B.; Zink, D. L.; Williams, M.; Polishook, J. D.; Sanchez, M.; Silverman, K. C.; Lingham, R. B. *Bioorg. Med. Chem. Lett.* **1998**, *8* (16), 2071. doi:10.1016/S0960-894X(98)00371-0.
- (39) Bhar, S. S.; Ramana, M. M. V. *J. Org. Chem.* **2004**, *69* (25), 8935. doi:10.1021/jo049616n.
- (40) Jones, G. H.; Mackenzie, J. B. D.; Robertson, A.; Whalley, W. B. *J. Chem. Soc.* **1949**, 562. doi:10.1039/jr9490000562.
- (41) Wiley, P. F. US Patent 2,621,189, December 9, 1952; *Chem. Abstr.* **1953**, 47, 10011h.
- (42) Chiji, H.; Aiba, T.; Izawa, M. *Agric. Biol. Chem.* **1978**, *42* (1), 159.
- (43) Da Re, P. *Farmaco (Pavia). Ed. Sci.* **1956**, *11*, 662; *Chem. Abstr.* **1959**, 53, 122101.
- (44) Badcock, G. G.; Dean, F. M.; Robertson, A.; Whalley, W. B. *J. Chem. Soc.* **1950**, 903. doi:10.1039/jr9500000903.
- (45) Furniss, B. S.; Hannaford, A. J.; Smith, P. W. G.; Tatchell, A. R. *Vogel's Textbook of Practical Organic Chemistry*; Longman: Essex, England, 1994.
- (46) Schonberg, A.; Sina, A. *J. Am. Chem. Soc.* **1950**, *72* (8), 3396. doi:10.1021/ja01164a022.
- (47) *Materials Studio*, v4.4.0.0030, Accelrys Software Inc.: San Diego, 2008.
- (48) Pritchard, R. G.; Sheldrake, H. M.; Taylor, I. Z.; Wallace, T. W. *Tetrahedron Lett.* **2008**, *49* (26), 4156. doi:10.1016/j.tetlet.2008.04.114.

# Theoretical analysis of *trans*-[PtCl<sub>2</sub>(NH<sub>3</sub>)(thiazole)] and *trans*-[PtCl<sub>2</sub>(thiazole)<sub>2</sub>] binding to biological targets — Factors influence binding kinetics and adduct stability

Dongdong Zhang, Xiuli Ren, and Lixin Zhou

**Abstract:** Full reaction energy profiles for *trans*-[PtCl<sub>2</sub>(NH<sub>3</sub>)(thiazole)] and *trans*-[PtCl<sub>2</sub>(thiazole)<sub>2</sub>] binding to sulfur- and nitrogen-containing biorelevant ligands were constructed by the density functional theory (DFT) method. Calculated results demonstrate that *trans*-platinum complexes can interact with biological targets, affording cis and trans products via very similar transition states. For different substituents, sulfur-containing ligands constitute kinetically preferred targets for platinumation, whereas the platinumation of nitrogen-containing ligands is more favorable thermodynamically. This is consistent with previous experimental studies. Calculated results also suggest that the trans effect, the influence of the ligand, the size of the ligand, and hydrogen bonding play important roles in binding kinetics and stabilizing adducts.

**Key words:** density functional theory, platinum antitumor drugs, DNA, amino acid residue.

**Résumé :** Faisant appel à la méthode de la théorie de la fonctionnelle de la densité (TFD), on a construit des profils complets pour les énergies de réaction de fixation du *trans*-[PtCl<sub>2</sub>(NH<sub>3</sub>)(thiazole)] et du *trans*-[PtCl<sub>2</sub>(thiazole)<sub>2</sub>] sur des ligands bio-pertinents contenant du soufre et de l'azote. Les résultats calculés démontrent que les complexes de platine *trans* peuvent interagir avec des cibles biologiques par le biais d'états de transitions très semblables pour conduire à la formation de produits cis et trans. Pour différents substituants, les ligands contenant du soufre constituent les cibles privilégiées d'un point de vue cinétique pour la platination alors que la platination des ligands contenant de l'azote est plus favorisée d'un point de vue thermodynamique. Ces résultats sont en accord avec les résultats expérimentaux. Les résultats calculés suggèrent aussi que l'effet trans combiné à l'influence du ligand, à la taille du ligand et à la formation de liaison hydrogène jouent des rôles importants dans la cinétique de fixation et de stabilisation des adduits.

**Mots-clés :** théorie de la fonctionnelle de la densité, médicaments antitumoraux dérivés du platine, ADN, résidu d'acide aminé.

[Traduit par la Rédaction]

## Introduction

Cisplatin<sup>1</sup> has been applied extensively in cancer chemotherapy, but toxicity and resistance limit its clinical usage. To overcome these limitations, considerable efforts have been made to find new platinum antitumor drugs with lower toxicity and better activity.<sup>2–7</sup> Even though it was previously believed that the cis configuration was required to generate active complexes, some mononuclear platinum(II) complexes with a trans configuration have exhibited significant cytotoxic activity in tumor cell lines. These complexes mainly fall into four structural types,<sup>7</sup> namely, *trans*-Pt(II) complexes containing iminoether ligands, planar amine ligands, nonplanar heterocyclic ligands, and aliphatic amine ligands.

The antitumor platinum complexes have been the focus of experimental<sup>7–14</sup> and theoretical<sup>15–21</sup> investigations since the discovery of the anticancer activity of cisplatin. Although

the precise mechanism of action of cisplatin remains unknown, it is generally accepted that its ultimate target is the N7 atom of purine bases.<sup>1</sup> Prior to the attack on DNA, the neutral platinum compound needs to be activated to the monoaqua or diaqua species.<sup>22–28</sup> The first binding to this site generates monofunctional adducts, with guanine being preferred over adenine, and further binding affords intra- and inter-strand adducts. Specifically, the 1,2-d(GpG) intra-strand adduct is essential for the antitumor effect.<sup>1</sup> The hydrated cisplatin binding to DNA was intensively studied with a variety of theoretical methods.<sup>29–35</sup> The preference for guanine over adenine as a target for platinumation was explained in terms of kinetics and thermodynamics, and the role of hydrogen bonds in stabilizing the transition states and products of cisplatin with purine bases was also analyzed in detail.<sup>36,37</sup>

The mode of action of *trans*-platinum antitumor complexes seems to be different from that of cisplatin, as it has

Received 24 March 2010. Accepted 13 September 2010. Published on the NRC Research Press Web site at canjchem.nrc.ca on 23 November 2010.

**D. Zhang, X. Ren, and L. Zhou.**<sup>1</sup> Department of Chemistry, Jinan University, Guangzhou, Guangdong 510632, P.R. China.

<sup>1</sup>Corresponding author (e-mail: tlzhou@jnu.edu.cn).

been suggested that different compounds appear to have different binding kinetics, and also the structural details of the resulting DNA adducts appear to differ to some degree.<sup>2,38</sup> Our previous computational studies of antitumor *trans*-platinum complexes containing aliphatic amine ligands<sup>39</sup> and picoline<sup>40</sup> binding to purine bases suggested that *trans*-platinum complexes could interact with DNA, affording *cis*- and *trans*-monofunctional adducts, and the *cis* product may further react with purine bases, forming bifunctional adducts such as cisplatin.

In addition to binding to DNA bases, platinum drugs did interact with sulfur- and nitrogen-containing peptides and proteins.<sup>12,41–47</sup> According to the hard and soft acids and bases principle, a strong affinity to the sulfur ligands could be expected for platinum.<sup>12</sup> However, Deubel<sup>48,49</sup> investigated the competition of sulfur- and nitrogen-containing ligands in the first substitution of hydrated cisplatin by biological targets with density functional theory (DFT) and continuum dielectric calculations, demonstrating an intrinsic preference for nitrogen over sulfur ligands for platinum. In that study,<sup>48</sup> activation free energies were estimated as the energy difference between transition states and separated reactants, and the reactant complexes were not taken into account. The neglecting of reactant complexes may result in underestimating the activation barrier for substitution reactions.

In the current study, full reaction energy profiles for the binding of two activated *trans*-platinum complexes with planar amine ligands, *trans*-[PtCl<sub>2</sub>(NH<sub>3</sub>)(thiazole)] (*trans*-PtTz) and *trans*-[PtCl<sub>2</sub>(thiazole)<sub>2</sub>] (*trans*-PtTz2),<sup>5,6,8,50</sup> to nitrogen- and sulfur-containing biological targets (Fig. 1) were constructed. We also estimated bond dissociation energies of Pt–L2 in all separated products. The objective of the present study is to reveal the competition of nitrogen and sulfur ligands in the substitutions of *trans*-PtTz and *trans*-PtTz2 by biorelevant ligands (L2), as well as the factors influencing the binding kinetics and adduct stability. The current work may contribute to a better understanding of the mechanism of action for platinum complexes and be of benefit for future drug design.

## Computational details

The geometries of separate reactants (R), reactant complexes (RC), transition states, product complexes, and separate products (P) were optimized at the DFT/B3LYP<sup>51,52</sup> level. The LanL2DZ<sup>53–55</sup> effective core potential basis set was used for the platinum atom and the 6-31G(d, p) Pople basis set was applied for all other atoms. Vibrational frequency calculations were based on analytical second derivatives on the same level of theory to confirm that the stationary point found was the local minimum for reactants and products and the first-order saddle point for transition states and to derive the zero-point vibrational energy and vibrational entropy correction at 298.15 K and 1 atm (1 atm = 101.325 kPa). The transition states were further confirmed by intrinsic reaction coordinate calculations.<sup>56,57</sup>

To obtain more accurate energies, energies were reevaluated by additional single-point calculations at the B3LYP/(LanL2DZ+6-311++G (2d, 2p)) level of theory. Solvent effects were accounted for by means of single-point calculations

on all stationary structures with the isoelectric focusing polarized continuum model.<sup>58–60</sup> The dielectric constant of water ( $\epsilon_{\text{water}} = 78.39$ ) was used to approximate the bulk effects of solvation.

The complexation energies ( $\Delta E_{\text{CE}}$ ) for reactant complexes and bond dissociation energies (BDEs) for Pt–L2 in separated products were computed at the B3LYP/(LanL2DZ+6-311++G (2d, 2p)) level with the inclusion of the basis set superposition error (BSSE).<sup>61,62</sup> The complexation energies were computed in both gas phase and aqueous solution according to the formulas

$$\Delta E_{\text{CE(g)}} = E_{\text{RC(g)}} - E_{\text{Pt(g)}} - E_{\text{L2(g)}} + \Delta E_{\text{BSSE(g)}}$$

$$\Delta G_{\text{CE(aq)}} = G_{\text{RC(aq)}} - G_{\text{Pt(aq)}} - G_{\text{L2(aq)}} + \Delta E_{\text{BSSE(g)}}$$

The BDEs for Pt–L2 were predicted according to the following formula:

$$E_{\text{BDE}} = E_{\text{fragment1(g)}} - E_{\text{fragment2(g)}} - E_{\text{product(g)}} + \Delta E_{\text{BSSE(g)}}$$

All computations were done by Gaussian 03.<sup>63</sup>

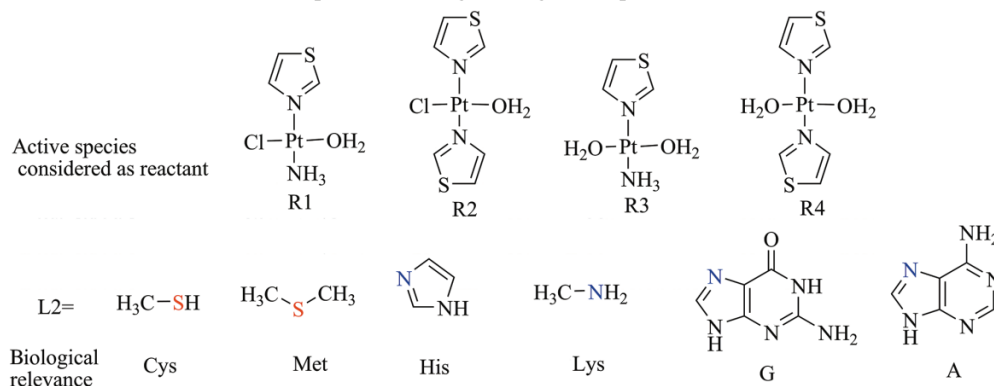
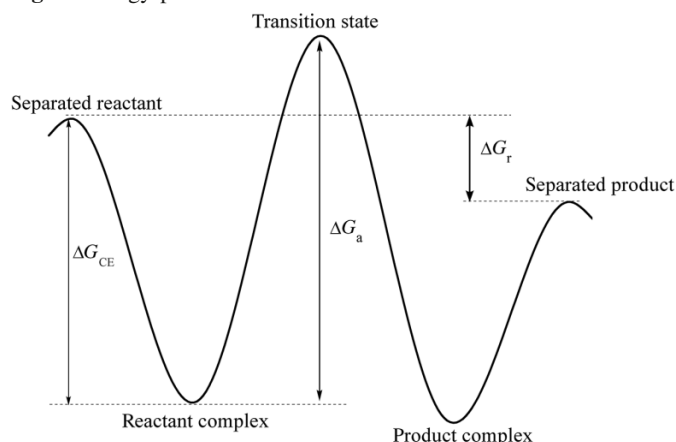
Many efforts were devoted to exploring different structural motifs, and the ones that generated the lowest energy structures were adopted for further discussion. All located structures are given in the Supplementary data. The reaction mechanism suggests the formation of reactant complexes in the first stage. Then the reaction proceeds via a transition state forming product complexes. It is well documented that the ligand substitution reactions display double-well potential energy surface as shown in Fig. 2. The activation energy was calculated as the energy difference between the transition states and reactant complexes. This approach was used with success in a number of studies.<sup>36,39,64</sup> The reaction free energy was estimated as the energy difference between the separated products and separated reactants.

## Results and discussion

For *trans*-PtTz binding to L2, there are three possible reaction paths, as shown in Fig. 3. In path 1, *trans*-PtTz reacts with L2 and forms *trans* products, and this path is denoted as TT. In paths 2 and 3, *trans*-PtTz binding to L2 affords two possible *cis* products. In *cis* product 1 (P1), L2 is *trans* to the ammine ligand, while L2 is adjacent to the ammine ligand in *cis* product 2 (P2).

There are two possible reaction paths in the case of *trans*-PtTz2 binding to L2 (Fig. 3). One path is *trans*-PtTz2 reacting with L2 and affording the *trans* product, and this path is denoted as TT; the other path is *trans*-PtTz2 binding to L2 and affording the *cis* product, which is named TC.

To predict the stability of reactant complexes, complexation free energies for activated platinum complexes with different substituents were calculated. Overall, for every activated reactant, the reactant complexes with nitrogen-containing ligands are more stable than those with sulfur-containing ligands, as shown in Fig. 4 and Fig. S1 in the Supplementary data. Notably, the major difference between Lys and Cys is the heteroatom. R1...Lys, R2...Lys, R3...Lys, and R4...Lys are preferred by 11.5, 8.2, 13.1, and 12.5 kcal/mol in complexation free energies over R1...Cys, R2...Cys,

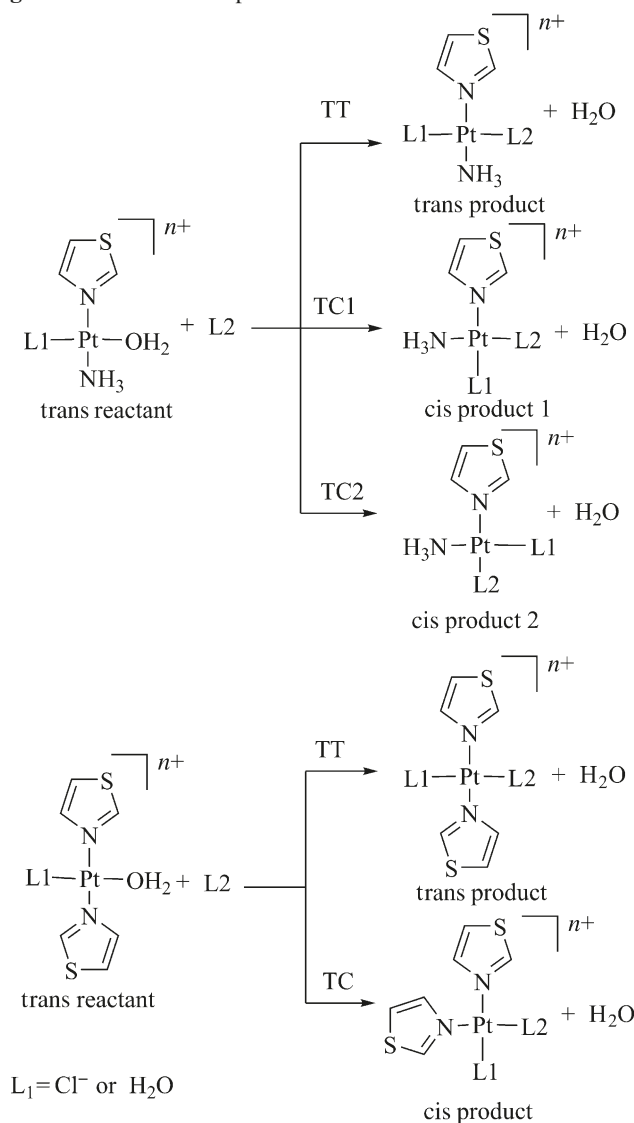
**Fig. 1.** Active species considered as reactants and potential biological targets for platination.**Fig. 2.** Energy profile of substitution reactions.

R3...Cys, and R4...Cys, respectively (Fig. 4). This reveals complexation free energies in favor of the formation of reactant complexes with nitrogen-containing ligands. However, reactant complex stabilization will increase the activation energies for reactions with nitrogen-containing ligands.

Transition states for activated reactants binding to L2 were located. Our calculations reveal that trans-reactant complexes can afford trans- and cis-product complexes via identical or very similar transition states. This is consistent with the result obtained before.<sup>39,40</sup>

The solution-phase activation free energies for platination of L2 are summarized in Table 1 and the gas-phase activation energies are given in Table S1 in the Supplementary data. Calculated results predict that the platination of sulfur-containing ligands is preferred over the platination of nitrogen-containing ligands in terms of kinetics. Remarkably, the main difference between Cys and Lys is the heteroatom. The kinetic preferences for binding to Cys over Lys are about 9.9, 10.1, 12.1, and 14.1 kcal/mol for R1, R2, R3, and R4, respectively. Although the integration of nitrogen into aromatic heterocycles lowers the activation free energy moderately (Table 1 and Table S1 in the Supplementary data), the kinetic preference of platinum for sulfur-containing over nitrogen-containing biorelevant ligands is maintained. The kinetic preference of platinum for sulfur-containing ligands is in good agreement with experimental studies of Pt complexes.<sup>12,45,47</sup>

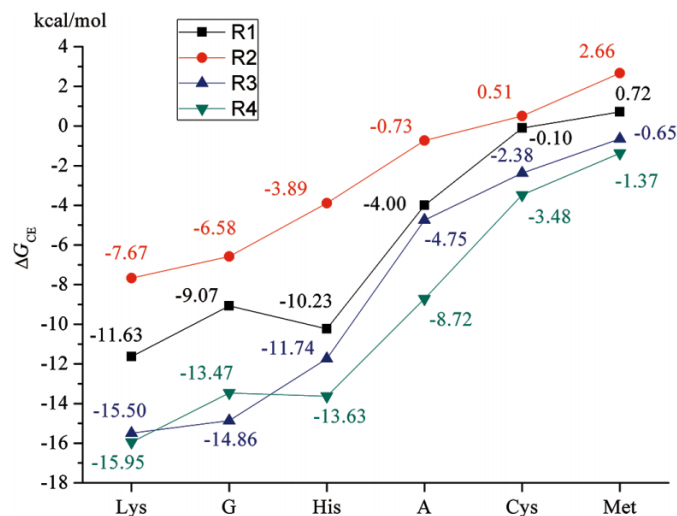
Many efforts were made to locate the lowest energy tran-

**Fig. 3.** Possible reaction paths for the substitution reactions.

sition states for activated reactants binding to purine bases. Calculated results revealed that the energy of the transition state is largely influenced by hydrogen bonding. The influence of hydrogen bonding on platinum complexes binding to purine bases was analyzed in previous works.<sup>36,37,39</sup> Our



**Fig. 4.** Complexation free energies for activated reactants with different substituents.



result is largely in agreement with the previous works. Therefore, in this research we will not discuss it further. The activation energies for R1 and R2 binding to purine bases are lower than those of mono-aquated cisplatin, which are at 24.59 and 30.15 kcal/mol<sup>37</sup> for platination of guanine and adenine, respectively. However, R3 and R4 show higher activation free energies than diaquated cisplatin binding to guanine and adenine, which are at 19.5 and 24.0 kcal/mol,<sup>36</sup> respectively. This is consistent with trans-effect theory, since in R1 and R2 the ligand trans to leaving water is chloride, while it is ammine in cisplatin and water in R3 and R4, and chloride displays a stronger trans effect than ammine, which has a stronger trans effect than water.<sup>64,65</sup>

The solution-phase reaction free energies of activated reactants binding to L2 and affording cis and trans products are compiled in Table 2 and gas-phase reaction energies are summarized in Table S2 in the Supplementary data. Overall, the platination of nitrogen-containing ligands is preferred thermodynamically over the platination of sulfur-containing ligands. In particular, the platination of Lys is thermodynamically preferred over the platination of Cys by 11.1, 7.0, 6.3, and 7.5 kcal/mol for R1, R2, R3, and R4, respectively. The thermodynamic preference of platinum for nitrogen-containing ligands is in good agreement with previous theoretical<sup>48</sup> and experimental<sup>12,45,47,66</sup> studies.

R1 reacting with L2 forms one series of trans products and two series of cis products, and R2 binding to L2 forms one series of cis products and one series of trans products, as shown in Fig. 3. In general, the solution-phase reaction free energies are very similar for R1 and R2 with a ligand affording cis and trans products (Table 2). Except for reactions of R1 with guanine, cis P2 and trans P are about 4.5 kcal/mol more favorable than cis P1 in free energy. This is due to cis P2 and trans P benefiting from the hydrogen bond between the C=O of the guanine and ammine ligand, whereas cis P1 is unable to form this hydrogen bond.

R3 reacts with L2, affording three series of products: one series of trans products and two series of cis products, cis P1 and cis P2 (Fig. 3). In general, the reaction free energy differences for R3 binding to a ligand forming trans P, cis P1,

and cis P2 are insignificant (Table 2). Except in the case of binding to guanine, cis P1 and cis P2 are preferred by about 6.0 kcal/mol over trans P in solution-phase free energy. This is due to strong hydrogen bonds formed between the water ligand and C=O of guanine in cis P1 and cis P2, while C=O of guanine forms a hydrogen bond with the ammine ligand in trans P. The C=O...H<sub>2</sub>O hydrogen bond is stronger than the C=O...H<sub>3</sub>N hydrogen bond; consequently, cis P1 and cis P2 are more stable than trans P.

In the case of R4 binding to L2, two series of products, trans and cis products, are obtained. Similarly, the reaction free energies for R4 binding to a target affording trans P and cis P are similar. However, for products with guanine, cis P is significantly stabilized by the strong hydrogen bond between the C=O of guanine and the water ligand, and as a result, cis P is 8.69 kcal/mol lower in solution-phase free energy than trans P.

When comparing reaction free energies of activated *trans*-PtTz and *trans*-PtTz2 binding to the same target, *trans*-PtTz is more thermodynamically favorable than *trans*-PtTz2 (Table 2). This can be attributed to the smaller size of the ammine group and its ability to act as a hydrogen bond donor. For example, if the reactions of R1 and R2 with Lys affording trans P are compared, R1 is 4.4 kcal/mol more thermodynamically favorable than R2. Moreover, the reaction of R1 with guanine is about 5.5 kcal/mol more favorable in reaction free energy than that of R2. This is because a strong hydrogen bond is formed between the C=O of guanine and the ammine ligand in products of R1 with guanine, cis P2, and trans P. However, this hydrogen bond is absent in products of R2 with guanine. The smaller size of the ammine group and its ability to act as a hydrogen bond donor may also be responsible for *trans*-PtTz exhibiting better antitumor activity than *trans*-PtTz2.<sup>6,67</sup> This conclusion is also consistent with previous studies of cisplatin.<sup>48,68</sup>

The predicted trend of BDEs for Pt–L2 in all separated products is depicted in Fig. 5 and the detailed BDEs for Pt–L2 energies are summarized in Tables S3–S6 in the Supplementary data. Overall, BDEs for Pt–N bonds are higher than those of Pt–S in each series of products as shown in Fig. 5. For example, in the products of R2 with L2, the BDE for Pt–Lys is 8.91 kcal/mol higher than that of Pt–Cys in cis P. The calculated BDEs reveal that the Pt–N bond is intrinsically stronger than the Pt–S bond. The stronger Pt–N bond and thermodynamic preference for the formation of Pt–N adducts provide the possibility of Pt–S products evolving into Pt–N adducts.<sup>45,47,66</sup>

Calculated results also suggest that BDEs of Pt–L2 are higher in cis products than in the trans isomers for both products of R1 and R2 with L2 (Fig. 5a). For example, comparing the BDEs of Pt–Cys in cis and trans products of R2 with Cys, the BDE for Pt–Cys in the cis isomer is 8.90 kcal/mol higher than that in its trans counterpart. This is caused by L2 being trans to Cl<sup>–</sup> in trans products while it is trans to ammine or thiazole in cis isomers, and Cl<sup>–</sup> has a stronger trans influence than ammine and thiazole.<sup>64,65</sup>

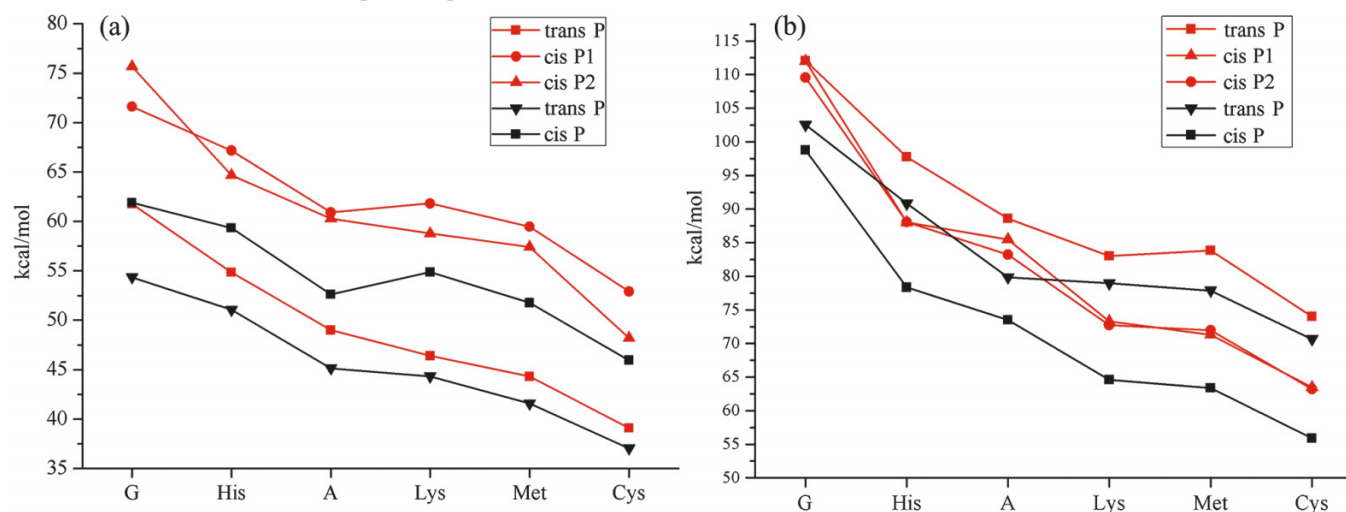
However, for the products of R3 and R4 with L2, in general, the BDEs for Pt–L2 are higher in the trans products than in their cis counterparts (Fig. 5b). For example, in the cis and trans P of R4 with Cys, the BDE for Pt–S in trans P is predicted to be 14.75 kcal/mol higher than that in cis P.

**Table 1.** Activation free energies (kcal/mol) for activated reactants binding to biological targets.

Biological targets	Reactants	Reaction paths			Reactants	Reaction paths	
		TT	TC1	TC2		TT	TC
Lys	R1	22.67	23.33	22.72	R2	24.54	24.54
	R3	28.93	28.92	28.92	R4	30.60	30.60
His	R1	22.33	22.33	22.33	R2	22.15	22.15
	R3	26.51	26.49	26.51	R4	28.52	28.52
A	R1	19.23	19.23	19.23	R2	18.94	18.97
	R3	23.39	24.77	24.85	R4	25.40	25.40
G	R1	16.56	16.56	16.56	R2	17.57	17.57
	R3	22.07	22.07	22.07	R4	21.27	21.27
Cys	R1	12.77	12.77	12.77	R2	14.39	14.40
	R3	16.82	16.82	16.83	R4	16.47	16.47
Met	R1	10.74	10.74	10.74	R2	10.93	10.93
	R3	16.04	16.05	16.04	R4	16.25	16.26

**Table 2.** Reaction free energies (kcal/mol) for activated reactants binding to biological targets.

Biological targets	Reactants	Reaction paths			Reactants	Reaction paths	
		TT	TC1	TC2		TT	TC
Lys	R1	-18.06	-20.77	-19.00	R2	-13.65	-15.57
	R3	-19.61	-19.80	-19.76	R4	-19.58	-19.11
His	R1	-18.46	-18.75	-18.06	R2	-15.47	-15.42
	R3	-20.36	-20.42	-19.37	R4	-20.60	-19.94
A	R1	-11.73	-9.87	-10.38	R2	-9.65	-8.70
	R3	-13.78	-13.86	-14.58	R4	-12.31	-13.90
G	R1	-17.96	-13.53	-17.77	R2	-12.46	-12.09
	R3	-22.16	-28.70	-28.18	R4	-18.16	-12.09
Cys	R1	-9.66	-9.63	-7.74	R2	-6.89	-8.60
	R3	-12.57	-13.09	-13.47	R4	-13.73	-13.23
Met	R1	-10.27	-10.90	-10.28	R2	-9.68	-9.66
	R3	-15.50	-13.12	-14.03	R4	-12.13	-11.09

**Fig. 5.** Calculated BDEs for Pt-L2 in products of (a) R1 and R2 with L2 and (b) R3 and R4 with L2. The red line represents products of R1 and R3 with L2 and the black line represents products R2 and R4 with L2.

The trans influence of the ligand is responsible for this, because in trans products, L2 is located in the trans position to the water ligand while L2 is trans to ammine or thiazole in cis products, and water has a weaker trans influence than ammine and thiazole. Even though in cis products of R3 and R4 with purine bases, cis isomers benefit from the hydrogen bond between the C=O of guanine or C–NH<sub>2</sub> of adenine and water ligand, the BDE for Pt–N in the trans isomer is still higher than that in the cis counterpart (Fig. 5b).

## Conclusion

We have examined the kinetic and thermodynamic behavior of *trans*-PtTz and *trans*-PtTz2 binding to biorelevant ligands. Calculated results demonstrate that *trans*-platinum complexes can interact with biological targets and afford cis and trans products via identical or very similar transition states. The factors that influence the binding kinetics and product stability are summarized as follows. (i) The substituents: Our calculations suggest that sulfur-containing biorelevant ligands constitute kinetically preferred targets for platination, while the platination of nitrogen-containing ligands is preferred thermodynamically. This result is in good agreement with experimental studies. In previous studies by Deubel,<sup>48,49</sup> the intrinsic kinetic preference for nitrogen over sulfur ligands for platinum was suggested. Nonetheless, reactant complexes were not taken into account in that study. We find that the complexation free energies favor the formation of reactant complexes with nitrogen-containing ligands. This results in reactions with nitrogen-containing ligands unfavorable in kinetics in comparison with those with sulfur-containing ligands. (ii) The trans effect of the ligand: We also find that the trans effect plays an important role in ligand substitution reactions in combination with hydrogen bonding. When chloroaqua complexes are considered as reactants, the activation free energies for two platinum complexes binding to purine bases are lower than those of cisplatin; however, if diaqua complexes are employed as reactants, activation free energies for two complexes binding to purine bases are higher than those of cisplatin. This is because in chloroaqua complexes the ligand trans to leaving water is chloride, while it is ammine in cisplatin and water in diaqua complexes, and chloride displays a stronger trans effect than ammine, which has a stronger trans effect than water. (iii) The trans influence of the ligand: In products of R1 and R2 with L2, the BDEs for Pt–L2 are higher in cis products than in the trans counterpart, while BDEs for Pt–L2 are lower in cis products than in the trans counterpart in products of R3 and R4 with L2. This is caused by the different trans influence of different ligands positioned trans to Pt–L2. In chloroaqua complexes, the ligand trans to Pt–L2 is chloride in trans products while it is ammine or thiazole in cis products, and chloride has a stronger trans influence than ammine and thiazole. In products of diaqua complexes with L2, water is located trans to the Pt–L2 in trans products whereas ammine or thiazole is positioned trans to Pt–L2 in cis products, and water shows a weaker trans influence than ammine or thiazole. (iv) The size of the ligand: When comparing *trans*-PtTz with *trans*-PtTz2, *trans*-PtTz is more thermodynamically favorable than *trans*-PtTz2. The smaller size of the ammine ligand and its ability to act as a hydrogen bond donor are responsible for this.

## Supplementary data

Supplementary data for this article are available on the journal Web site (canjchem.nrc.ca).

## Acknowledgement

This work was supported by the National Natural Science Foundation of China (grant No. 20971056).

## References

- (1) Jung, Y.; Lippard, S. J. *Chem. Rev.* **2007**, *107* (5), 1387. doi:10.1021/cr068207j.
- (2) Reedijk, J. *Eur. J. Inorg. Chem.* **2009**, *2009* (10), 1303. doi:10.1002/ejic.200900054.
- (3) Aris, S. M.; Farrell, N. P. *Eur. J. Inorg. Chem.* **2009**, *2009* (10), 1293. doi:10.1002/ejic.200801118.
- (4) Fojo, T.; Farrell, N.; Ortuzar, W.; Tanimura, H.; Weinstein, J.; Myers, T. G. *Crit. Rev. Oncol. Hematol.* **2005**, *53* (1), 25. doi:10.1016/j.critrevonc.2004.09.008.
- (5) Farrell, N.; Kelland, L. R.; Roberts, J. D.; Van Beusichem, M. *Cancer Res.* **1992**, *52* (18), 5065.
- (6) Van Beusichem, M.; Farrell, N. *Inorg. Chem.* **1992**, *31* (4), 634. doi:10.1021/ic00030a021.
- (7) Kalinowska-Lis, U.; Ochocki, J.; Matlawska-Wasowska, K. *Coord. Chem. Rev.* **2008**, *252* (12–14), 1328. doi:10.1016/j.ccr.2007.07.015.
- (8) Aris, S. M.; Knott, K. M.; Yang, X.; Gewirtz, D. A.; Farrell, N. P. *Inorg. Chim. Acta* **2009**, *362* (3), 929. doi:10.1016/j.ica.2008.01.025.
- (9) Bulluss, G. H.; Knott, K. M.; Ma, E. S. F.; Aris, S. M.; Alvarado, E.; Farrell, N. *Inorg. Chem.* **2006**, *45* (15), 5733. doi:10.1021/ic060741m.
- (10) Najajreh, Y.; Perez, J. M.; Navarro-Ranninger, C.; Gibson, D. *J. Med. Chem.* **2002**, *45* (24), 5189. doi:10.1021/jm0201969.
- (11) Liu, Y.; Pacifico, C.; Natile, G.; Sletten, E. *Angew. Chem. Int. Ed.* **2001**, *40* (7), 1226. doi:10.1002/1521-3773(20010401)40:7<1226::AID-ANIE1226>3.0.CO;2-U.
- (12) Reedijk, J. *Chem. Rev.* **1999**, *99* (9), 2499. doi:10.1021/cr980422f.
- (13) Farrell, N. *Met. Ions Biol. Syst.* **1996**, *32*, 603.
- (14) Li, C.; Li, Z. Y.; Sletten, E.; Arnesano, F.; Losacco, M.; Natile, G.; Liu, Y. Z. *Angew. Chem. Int. Ed.* **2009**, *48* (45), 8497. doi:10.1002/anie.200902948.
- (15) Moussatova, A.; Vazquez, M. V.; Martinez, A.; Dolgounitcheva, O.; Zakrzewski, V. G.; Ortiz, J. V.; Pedersen, D. B.; Simard, B. *J. Phys. Chem. A* **2003**, *107* (44), 9415. doi:10.1021/jp030651s.
- (16) Burda, J. V.; Zeizinger, M.; Sponer, J.; Leszczynski, J. *J. Chem. Phys.* **2000**, *113* (6), 2224. doi:10.1063/1.482036.
- (17) Pavelka, M.; Lucas, M.; Russo, N. *Chem. Eur. J.* **2007**, *13* (36), 10108. doi:10.1002/chem.200700887.
- (18) Alberto, M. E.; Lucas, M. F.; Pavelka, M.; Russo, N. *J. Phys. Chem. B* **2008**, *112* (35), 10765. doi:10.1021/jp800476b.
- (19) Lucas, M. F. A.; Pavelka, M.; Alberto, M. E.; Russo, N. *J. Phys. Chem. B* **2009**, *113* (3), 831. doi:10.1021/jp8086539.
- (20) Alberto, M. E.; Lucas, M. F. A.; Pavelka, M.; Russo, N. *J. Phys. Chem. B* **2009**, *113* (43), 14473. doi:10.1021/jp9056835.
- (21) Spiegel, K.; Rothlisberger, U.; Carloni, P. *J. Phys. Chem. B* **2004**, *108* (8), 2699. doi:10.1021/jp036230s.



- (22) Chval, Z.; Sip, M. *J. Mol. Struct. THEOCHEM* **2000**, 532 (1–3), 59. doi:10.1016/S0166-1280(00)00502-9.
- (23) Zhang, Y.; Guo, Z. J.; You, X. Z. *J. Am. Chem. Soc.* **2001**, 123 (38), 9378. doi:10.1021/ja0023938.
- (24) Costa, L. A. S.; Rocha, W. R.; De Almeida, W. B.; Dos Santos, H. F. *Chem. Phys. Lett.* **2004**, 387 (1–3), 182. doi:10.1016/j.cplett.2004.02.001.
- (25) Zhu, C.; Raber, J.; Eriksson, L. A. *J. Phys. Chem. B* **2005**, 109 (24), 12195. doi:10.1021/jp0518916.
- (26) Yuan, Q.; Zhou, L. *Chin. J. Chem.* **2007**, 25 (11), 1604. doi:10.1002/cjoc.200790297.
- (27) Lau, J. K. C.; Deubel, D. V. *J. Chem. Theory Comput.* **2006**, 2 (1), 103. doi:10.1021/ct050229a.
- (28) Deubel, D. V. *J. Am. Chem. Soc.* **2006**, 128 (5), 1654. doi:10.1021/ja055741k.
- (29) Robertazzi, A.; Platts, J. A. *Inorg. Chem.* **2005**, 44 (2), 267. doi:10.1021/ic0489544.
- (30) Chval, Z.; Sip, M. *Collect. Czech. Chem. Commun.* **2003**, 68 (6), 1105. doi:10.1135/cccc20031105.
- (31) Burda, J. V.; Leszczynski, J. *Inorg. Chem.* **2003**, 42 (22), 7162. doi:10.1021/ic034296w.
- (32) Mantri, Y.; Lippard, S. J.; Baik, M. H. *J. Am. Chem. Soc.* **2007**, 129 (16), 5023. doi:10.1021/ja067631z.
- (33) Burda, J. V.; Šponer, J.; Leszczynski, J. *J. Biol. Inorg. Chem.* **2000**, 5 (2), 178. doi:10.1007/s007750050362.
- (34) Baik, M. H.; Friesner, R. A.; Lippard, S. J. *J. Am. Chem. Soc.* **2002**, 124 (16), 4495. doi:10.1021/ja017588+.
- (35) Zeizinger, M.; Burda, J. V.; Leszczynski, J. *Phys. Chem. Chem. Phys.* **2004**, 6 (13), 3585. doi:10.1039/b317052g.
- (36) Raber, J.; Zhu, C.; Eriksson, L. A. *J. Phys. Chem. B* **2005**, 109 (21), 11006. doi:10.1021/jp050057d.
- (37) Baik, M. H.; Friesner, R. A.; Lippard, S. J. *J. Am. Chem. Soc.* **2003**, 125 (46), 14082. doi:10.1021/ja036960d.
- (38) Hartwig, J. F.; Lippard, S. J. *J. Am. Chem. Soc.* **1992**, 114 (14), 5646. doi:10.1021/ja00040a026.
- (39) Zhou, L. *J. Phys. Chem. B* **2009**, 113 (7), 2110. doi:10.1021/jp806661g.
- (40) Gao, Y.; Zhou, L. *Theor. Chem. Acc.* **2009**, 123 (5–6), 455. doi:10.1007/s00214-009-0557-5.
- (41) Zimmermann, T.; Chval, Z.; Burda, J. V. *J. Phys. Chem. B* **2009**, 113 (10), 3139. doi:10.1021/jp807645x.
- (42) Zimmermann, T.; Burda, J. V. *J. Chem. Phys.* **2009**, 131 (13), 135101. doi:10.1063/1.3236842.
- (43) Algueró, B.; Pedroso, E.; Marchán, V.; Grandas, A. *J. Biol. Inorg. Chem.* **2007**, 12 (6), 901. doi:10.1007/s00775-007-0243-9.
- (44) Summa, N.; Schiessl, W.; Puchta, R.; van Eikema Hommes, N.; van Eldik, R. *Inorg. Chem.* **2006**, 45 (7), 2948. doi:10.1021/ic051955r.
- (45) Algueró, B.; López de la Osa, J.; González, C.; Pedroso, E.; Marchán, V.; Grandas, A. *Angew. Chem. Int. Ed.* **2006**, 45 (48), 8194. doi:10.1002/anie.200603128.
- (46) Zimmermann, T.; Zeizinger, M.; Burda, J. V. *J. Inorg. Biochem.* **2005**, 99 (11), 2184. doi:10.1016/j.jinorgbio.2005.07.021.
- (47) Marchán, V.; Pedroso, E.; Grandas, A. *Chem. Eur. J.* **2004**, 10 (21), 5369. doi:10.1002/chem.200400470.
- (48) Deubel, D. V. *J. Am. Chem. Soc.* **2004**, 126 (19), 5999. doi:10.1021/ja0499602.
- (49) Deubel, D. V. *J. Am. Chem. Soc.* **2002**, 124 (20), 5834. doi:10.1021/ja012221q.
- (50) Kasparkova, J.; Novakova, O.; Farrell, N.; Brabec, V. *Biochemistry* **2003**, 42 (3), 792. doi:10.1021/bi026614t.
- (51) Becke, A. D. *J. Chem. Phys.* **1993**, 98 (7), 5648. doi:10.1063/1.464913.
- (52) Lee, C.; Yang, W.; Parr, R. G. *Phys. Rev. B* **1988**, 37 (2), 785. doi:10.1103/PhysRevB.37.785.
- (53) Wadt, W. R.; Hay, P. J. *J. Chem. Phys.* **1985**, 82 (1), 284. doi:10.1063/1.448800.
- (54) Hay, P. J.; Wadt, W. R. *J. Chem. Phys.* **1985**, 82 (1), 299. doi:10.1063/1.448975.
- (55) Hay, P. J.; Wadt, W. R. *J. Chem. Phys.* **1985**, 82 (1), 270. doi:10.1063/1.448799.
- (56) Gonzalez, C.; Schlegel, H. B. *J. Phys. Chem.* **1990**, 94 (14), 5523. doi:10.1021/j100377a021.
- (57) Gonzalez, C.; Schlegel, H. B. *J. Chem. Phys.* **1989**, 90 (4), 2154. doi:10.1063/1.456010.
- (58) Tomasi, J.; Mennucci, B.; Cancès, E. *J. Mol. Struct. THEOCHEM* **1999**, 464 (1–3), 211. doi:10.1016/S0166-1280(98)00553-3.
- (59) Mennucci, B.; Tomasi, J. *J. Chem. Phys.* **1997**, 106 (12), 5151. doi:10.1063/1.473558.
- (60) Mennucci, B.; Cancès, E.; Tomasi, J. *J. Phys. Chem. B* **1997**, 101 (49), 10506. doi:10.1021/jp971959k.
- (61) Simon, S.; Duran, M.; Dannenberg, J. J. *J. Chem. Phys.* **1996**, 105 (24), 11024. doi:10.1063/1.472902.
- (62) Boys, S. F.; Bernardi, F. *Mol. Phys.* **1970**, 19 (4), 553. doi:10.1080/00268977000101561.
- (63) Frisch, M. J.; Trucks, G. W.; Schlegel, H. B.; Scuseria, G. E.; Robb, M. A.; Cheeseman, J. R.; Montgomery, J. J. A.; Vreven, T.; Kudin, K. N.; Burant, J. C.; Millam, J. M.; Iyengar, S. S.; Tomasi, J.; Barone, V.; Mennucci, B.; Cossi, M.; Scalmani, G.; Rega, N.; Petersson, G. A.; Nakatsuji, H.; Hada, M.; Ehara, M.; Toyota, K.; Fukuda, R.; Hasegawa, J.; Ishida, M.; Nakajima, T.; Honda, Y.; Kitao, O.; Nakai, H.; Klene, M.; Li, X.; Knox, J. E.; Hratchian, H. P.; Cross, J. B.; Bakken, V.; Adamo, C.; Jaramillo, J.; Gomperts, R.; Stratmann, R. E.; Yazyev, O.; Austin, A. J.; Cammi, R. P. C.; Ochterski, J. W.; Ayala, P. Y.; Morokuma, K.; Voth, G. A.; Salvador, P.; Dannenberg, J. J.; Zakrzewski, V. G.; Dapprich, S.; Daniels, A. D.; Strain, M. C.; Farkas, O.; Malick, D. K.; Rabuck, A. D.; Raghavachari, K.; Foresman, J. B.; Ortiz, J. V.; Cui, Q.; Baboul, A. G.; Clifford, S.; Cioslowski, J.; Stefanov, B. B.; Liu, G.; Liashenko, A.; Piskorz, P.; Komaromi, I.; Martin, R. L.; Fox, D. J.; Keith, T.; Al-Laham, M. A.; Peng, C. Y.; Nanayakkara, A.; Challacombe, M.; Gill, P. M. W.; Johnson, B.; Chen, W.; Wong, M. W.; Gonzalez, C.; Pople, J. A. *Gaussian 03*, revision D.01; Gaussian, Inc.: Wallingford, CT, 2004.
- (64) Chval, Z.; Sip, M.; Burda, J. V. *J. Comput. Chem.* **2008**, 29 (14), 2370. doi:10.1002/jcc.20980.
- (65) Lin, Z.; Hall, M. B. *Inorg. Chem.* **1991**, 30 (4), 646. doi:10.1021/ic00004a011.
- (66) van Boom, S. S. G. E.; Chen, B. W.; Teuben, J. M.; Reedijk, J. *Inorg. Chem.* **1999**, 38 (7), 1450. doi:10.1021/ic981086o.
- (67) Farrell, N.; Povirk, L. F.; Dange, Y.; DeMasters, G.; Gupta, M. S.; Kohlhaagen, G.; Khan, Q. A.; Pommier, Y.; Gewirtz, D. A. *Biochem. Pharmacol.* **2004**, 68 (5), 857. doi:10.1016/j.bcp.2004.05.023.
- (68) Sullivan, S. T.; Ciccarese, A.; Fanizzi, F. P.; Marzilli, L. G. *J. Am. Chem. Soc.* **2001**, 123 (38), 9345. doi:10.1021/ja010483m.



# Organosulfur oxoacids. Part 2. A novel dimethylthiourea metabolite — Synthesis and characterization of the surprisingly stable and inert dimethylaminoiminomethane sulfonic acid

Jeffrey L. Petersen, Adenike A. Otoikhian, Moshood K. Morakinyo, and Reuben H. Simoyi

**Abstract:** A new metabolite of the biologically active thiocarbamide dimethylthiourea (DMTU) has been synthesized and characterized. DMTU's metabolic activation in the physiological environment is expected to be dominated by S-oxygenation, which produces, successively, the sulfinic, sulfinic, and sulfonic acids before forming sulfate and dimethylurea. Only the sulfinic and sulfonic acids are stable enough to be isolated. This manuscript reports on the first synthesis, isolation, and characterization of the sulfonic acid: dimethylaminoiminomethanesulfonic acid (DMAIMSOA). It crystallizes in the orthorhombic *Pbca* space group and exists as a zwitterion in its solid crystal form. The negative charge is delocalized over the sulfonic acid oxygens and the positive charge is concentrated over the planar N–C–N framework rather than strictly on the  $sp^2$ -hybridized cationic carbon center. As opposed to its sulfinic acid analogue, DMAIMSOA is extremely inert in acidic environments and can maintain its titer for weeks at pH 6 and below. It is, however, reasonably reactive at physiological pH conditions and can be oxidized to dimethylurea and sulfate by mild oxidants such as aqueous iodine.

**Key words:** thiourea, metabolites, bioactivation.

**Résumé :** On a effectué la synthèse d'un nouveau métabolite du thiocarbamide de la diméthylthiourée (DMTU), un produit biologiquement actif. On s'attend à ce que l'activation métabolique du DMTU dans un environnement physiologique devrait être dominée par une S-oxygénation qui conduit à la formation successive d'acides sulfénique, sulfinique et sulfonique avant de donner un sulfate et de la diméthylurée. Seuls les acides sulfinique et sulfonique sont suffisamment stables pour être isolés. Dans ce travail, on rapporte la première synthèse, l'isolation et la caractérisation de l'acide sulfonique, l'acide diméthylaminoiminométhanesulfonique (ADMAIMSO). Il cristallise dans le système orthorhombique, groupe d'espace *Pbca* et dans sa forme cristalline solide il existe sous la forme de zwitterion. La charge négative est délocalisée sur les oxygènes de l'acide sulfonique et la charge positive est concentrée sur le squelette planaire N–C–N plutôt que strictement sur le centre carboné cationique d'hybridation  $sp^2$ . Par opposition à son analogue l'acide sulfinique, le ADMAIMSO est extrêmement inerte dans des environnements acides et il peut maintenir son titre pour plusieurs semaines à des pH de 6 ou moins. Il est toutefois assez réactif dans des conditions de pH physiologique et il peut être oxydé en diméthylurée et en sulfate par des oxydants doux, tel une solution aqueuse d'iode.

**Mots-clés :** thiourée, métabolites, bioactivation.

[Traduit par la Rédaction]

## Introduction

*N,N'*-Dimethylthiourea (DMTU) is a well-known sulfur-based radical scavenger.<sup>1–4</sup> It is a small, highly diffusible molecule that efficiently scavenges toxic oxygen metabolites and reduces oxidative injury in many biologic systems. There have been very few studies undertaken on the fate and nature of the metabolites formed after such antioxidants have mediated oxidative injury.

Our bodies have evolved several very efficient methods of

handling a large numbers of xenobiotics.<sup>5</sup> Our bodies, however, do not have a consistent answer to sulfur-based xenobiotics. Nearly all relevant sulfur chemistry in the human body is of organic origin. The range of physiological effects associated with organic sulfur chemistry spans from therapeutic to toxic.<sup>6</sup> There is no other group of compounds that displays such a wide range of biological activity. While the action and effects of organosulfur compounds on human health is well-documented, the mechanisms by which these effects are expressed are not known. Drug design and the

Received 28 May 2010. Accepted 26 July 2010. Published on the NRC Research Press Web site at [canjchem.nrc.ca](http://canjchem.nrc.ca) on 25 November 2010.

J.L. Petersen. C. Eugene Bennett Department of Chemistry, West Virginia University, Morgantown, WV 26506-6045, USA.

A.A. Otoikhian, M.K. Morakinyo, and R.H. Simoyi.<sup>1</sup> Department of Chemistry, Portland State University, Portland, OR 97207-0751, USA.

<sup>1</sup>Corresponding author (e-mail: [rsimoyi@pdx.edu](mailto:rsimoyi@pdx.edu)).

ability to predict physiological effects is dependent upon our ability to understand the mechanism of metabolic activation of the relevant drug.

Sulfur compounds, such as DMTU, undergo a variety of metabolic reactions in the physiological environment such as oxidations, reductions, hydrolysis, and conjugations.<sup>7</sup> Sulfur, in most organic configurations, however, is nucleophilic, and nucleophilic atoms are usually susceptible to metabolic oxidations.<sup>8</sup> Thus, the oxidation of sulfur-containing compounds represents a very important aspect of sulfur metabolism. Oxidations of sulfur compounds appear to be involved in many cellular functions, including the reductive degradation of polypeptide hormones and proteins, regulation of protein synthesis, maintenance of intracellular redox potential, and protection of the cell from oxidative damage.<sup>9</sup> The aerobic physiological environment encourages S-oxygenation as the major metabolic activation pathway for most organo-sulfur compounds where the sulfur center is successively oxygenated, sometimes all the way to the sulfate, culminating in the cleavage of the attendant C–S bond.<sup>10,11</sup>

The molecular basis for S-oxygenation is not well-understood, although S-oxygenation of xenobiotics by microsomes supplemented with NADPH and oxygen has been known for years. In general, metabolism of chemically stable compounds depends on enzyme catalysis, and both the microsomal cytochrome P-450 system and the flavin-containing monooxygenases have been implicated in S-oxygenations catalyzed by microsomes.<sup>8,12,13</sup>

DMTU, although in most situations is effective in decreasing oxidant-mediated injury, has, however, inexplicably failed, on occasions, to reduce injury in some biological systems where oxygen metabolites were ostensibly causing damage.<sup>14,15</sup> It has also been experimentally shown that increasing the DMTU dose in rats did not increase protection and may, in fact, be associated with more injury. DMTU should exercise its physiological effects after metabolic activation and it is generally accepted that these physiological effects are derived from its metabolites.

In a previous publication from this laboratory,<sup>16</sup> we synthesized the first stable metabolite of DMTU, dimethylaminoiminomethanesulfonic acid (DMAIMSA). This metabolite was surprisingly very reactive and its aerobic decomposition in slightly basic to basic environments produced dithionite and a cascade of reactive oxygen species that were genotoxic, and could explain some of the inadvertent toxicity associated with DMTU. The general progress of the oxidation of a sulfur center initially proceeds through the sulfenic acid (unstable except in sterically hindered sulfenic acids),<sup>17–19</sup> then to the sulfinic acid (e.g., DMAIMSA), and then the sulfonic acid before cleavage of the C–S bond to form sulfate and an organic residue.<sup>20</sup> The existence of DMAIMSA had always been conjectured, but no one had managed to prepare and characterize this metabolite until the work of Otokhian and co-workers.<sup>16,21,22</sup>

Since the sulfonic acid (dimethylaminoiminomethanesulfonic acid, DMAIMSOA) is expected to be the next metabolite after formation of DMAIMSA, we undertook to synthesize and characterize this metabolite, and hopefully, from its reactivity, be able to rationalize some of the observed conflicting physiological effects of DMTU. We report in this manuscript on this oxidation metabolite of

**Table 1.** Crystal data and structure refinement for DMAIMSOA.

Empirical formula	C <sub>3</sub> H <sub>8</sub> N <sub>2</sub> O <sub>3</sub> S·H <sub>2</sub> O
Formula weight	170.19
Temperature (K)	295(2)
Wavelength (Å)	0.71073
Crystal system	Orthorhombic
Space group	<i>Pbca</i>
Unit cell dimensions	
<i>a</i> (Å)	12.533(1)
<i>b</i> (Å)	9.624(1)
<i>c</i> (Å)	12.918(1)
$\alpha$ (°)	90
$\beta$ (°)	90
$\gamma$ (°)	90
Volume (Å <sup>3</sup> )	1558.1(2)
<i>Z</i>	8
Density (calculated; g/cm <sup>3</sup> )	1.451
Absorption coefficient (cm <sup>-1</sup> )	3.81
<i>F</i> (000)	720
Crystal size (mm <sup>3</sup> )	0.20 × 0.40 × 0.44
$\theta$ range for data collection (°)	3.10–25.00
Limiting indices	0 ≤ <i>h</i> ≤ 14 0 ≤ <i>k</i> ≤ 11 –15 ≤ <i>l</i> ≤ 0
Reflections collected	1356
Independent reflections	1356
Refinement method	Full-matrix least-squares on <i>F</i> <sup>2</sup>
Data/restraints/parameters	1356/0/102
Goodness-of-fit on <i>F</i> <sup>2</sup>	1.022
Final <i>R</i> indices [ <i>I</i> > 2σ( <i>I</i> )]	<i>R</i> <sub>1</sub> = 0.0462, <i>wR</i> <sub>2</sub> = 0.1032
<i>R</i> indices (all data)	<i>R</i> <sub>1</sub> = 0.0838, <i>wR</i> <sub>2</sub> = 0.1205
Largest diff. peak and hole (e Å <sup>-3</sup> )	0.241 and –0.307

**Table 2.** Atomic coordinates (×10<sup>4</sup>) and equivalent isotropic displacement parameters (Å<sup>2</sup> × 10<sup>3</sup>) for SO<sub>3</sub>C(NHMe)<sub>2</sub>·H<sub>2</sub>O. *U*(eq) is defined as one third of the trace of the orthogonalized *U*<sub>ij</sub> tensor.

	<i>x</i>	<i>y</i>	<i>z</i>	<i>U</i> (eq)
S	3569(1)	278(1)	6551(1)	37(1)
O(1)	3597(2)	–1207(3)	6619(2)	60(1)
O(2)	3329(2)	811(3)	5538(2)	50(1)
O(3)	4444(2)	985(3)	7046(2)	58(1)
O(4)	4487(3)	2529(4)	4164(3)	66(1)
N(1)	2636(2)	1527(3)	8142(2)	39(1)
N(2)	1469(2)	372(3)	7079(2)	41(1)
C(1)	2427(3)	783(3)	7335(3)	32(1)
C(2)	1825(3)	2042(4)	8854(3)	49(1)
C(3)	1158(3)	–468(4)	6185(3)	57(1)

DMTU. Despite its similarity to DMAIMSA, DMAIMSOA proved to be very different from DMAIMSA in terms of structure and reactivity.

## Experimental

### Materials

DMTU, hydrogen peroxide, and acetonitrile (Sigma-Aldrich) were purchased and used without any further purification.

Some batches of DMTU were damp and oily and could not form DMAIMSOA upon applying the synthetic procedure outlined below. Instead, the product formed slowly turned yellow upon exposure to the atmosphere and at ambient temperatures. The consistency of the DMTU batches was extremely important for the generation of high and consistent yields of DMAIMSOA. Aqueous iodine solutions were prepared by dissolving iodine crystals (Sigma-Aldrich) in distilled water followed by filtration and storage in the dark. Standard solutions of sodium hydroxide were purchased from Fisher Scientific.

### Synthesis of DMAIMSOA

*N,N*-Dimethylaminoiminomethanesulfonic acid (DMAIMSOA) was prepared according to a modified form of a synthetic procedure given in the literature for the synthesis of dimethylaminoiminomethanesulfonic acid (DMAIMSA).<sup>16</sup> *N,N'*-Dimethylthiourea (DMTU; 10.42 g, 0.10 mol) were dissolved in 80 mL of a 50% acetonitrile–water solution, which was chilled in an acetone–CO<sub>2</sub> ice bath at –50 °C. To this ice-cold solution, 3 equiv (0.30 mol) of hydrogen peroxide, which was measured as a 30.61 mL aliquot of a 30% concentrated solution, were added dropwise with the rate of addition maintained such that the temperature of the reaction mixture did not exceed –30 °C. The 3:1 ratio of hydrogen peroxide to DMTU had to be strictly maintained to avoid the production of mixtures of oxoacids. The frozen mixture was allowed to sit until it melted and it was then stirred at room temperature for 2 h. The resulting long, colorless, needle-like crystals were filtered and washed twice with a 50% acetonitrile–water solution and deionized water and then dried in a desiccator. Typical yields before recrystallization were approximately 90%. Further recrystallization and purification was performed using the same strength of acetonitrile solution. Most of the product was lost during the washing and recrystallization of DMAIMSOA, thus giving a lower overall yield since it is highly soluble in water.

### Methods

UV–vis spectra were taken on a PerkinElmer Lambda 2S spectrophotometer equipped with a thermostatable compartment. Most experiments were performed at 25 ± 0.5 °C. Distilled and deionized water were utilized to prepare all standard solutions used in these experiments. The reaction between DMAIMSOA and HOCl was monitored by following the absorbance of DMAIMSOA at 215 nm where an absorptivity coefficient of 9025 (mol/L)<sup>–1</sup> cm<sup>–1</sup> had been deduced. The reaction between DMAIMSOA and iodine (as well as iodate) was followed by the use of the iodine–triiodide isosbestic point, which had been experimentally determined as 465 nm in this work and other previous studies from our laboratory using the same spectrophotometer.<sup>21</sup> Only freshly prepared iodine solutions were utilized. A Hi-Tech Scientific SF-DX2 stopped-flow spectrophotometer was used to follow the kinetics of DMAIMSOA oxidations and hydrolysis. KinetAsyst 2.1 software (High-Tech Scientific) was used for data acquisition and analysis. Temperature control was maintained with a NesLab RTE-101 thermostat bath. Some reaction solutions were degassed with argon and tightly capped to reduce the effects of dissolved oxygen.

### Description of the X-ray structural analysis of C<sub>3</sub>H<sub>8</sub>N<sub>2</sub>O<sub>3</sub>S·H<sub>2</sub>O

A colorless crystal of C<sub>3</sub>H<sub>8</sub>N<sub>2</sub>O<sub>3</sub>S·H<sub>2</sub>O was wedged in a glass capillary and then optically aligned on the four-circle of a Siemens P4 automated X-ray diffractometer. The reflections that were used for the unit cell determination were located and indexed by the automatic peak search routine provided by XSCANS.<sup>23</sup> C<sub>3</sub>H<sub>8</sub>N<sub>2</sub>O<sub>3</sub>S·H<sub>2</sub>O crystallizes in the centrosymmetric space group *Pbca* (*D*<sub>2h</sub><sup>15</sup>, No. 61). The final lattice parameters and orientation matrix were calculated from a nonlinear least-squares fit of the orientation angles of at least 35 reflections at 22 °C. The lattice parameters and other pertinent crystallographic information are summarized in Table 1 for C<sub>3</sub>H<sub>8</sub>N<sub>2</sub>O<sub>3</sub>S·H<sub>2</sub>O.

Intensity data were measured with graphite-monochromated Mo K $\alpha$  radiation ( $\lambda$  = 0.71073 Å) and variable  $\omega$  scans. Background counts were measured at the beginning and at the end of each scan with the crystal and counter kept stationary. The intensities of three standard reflections were measured after every 100 reflections and did not show any evidence of crystal decay. The raw data were corrected for Lorentz-polarization effects.

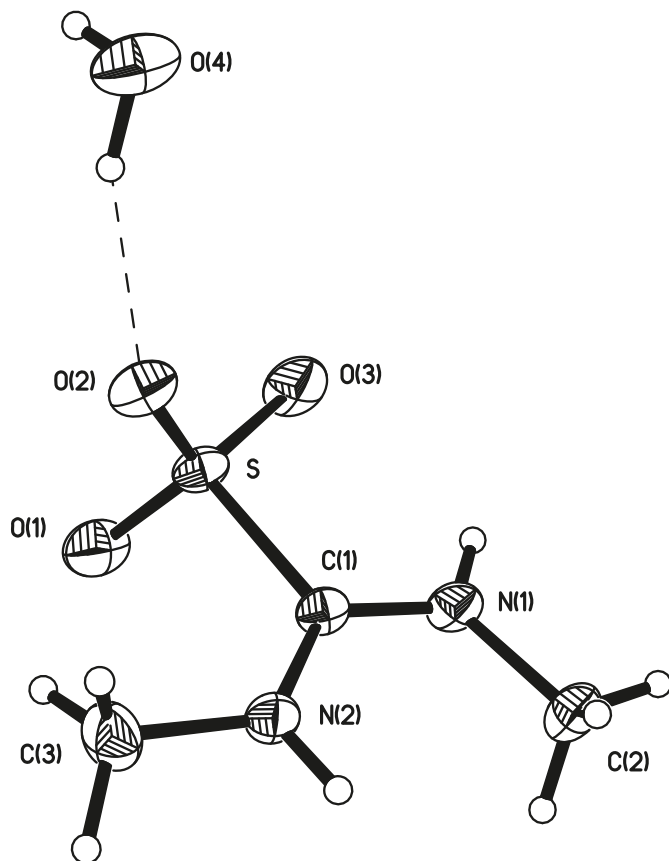
Initial coordinates for the nonhydrogen atoms were determined by a combination of direct methods and difference Fourier calculations with the use of SHELXTL 6.1.<sup>24</sup> The crystallographic asymmetric unit contains a molecule of water that is located in a general position and is hydrogen bonded to the O(2) atom. The hydrogen atoms of the water molecule were located and their positions and isotropic temperature parameters were refined. Idealized positions for the remaining hydrogen atoms were included as fixed contributions using a riding model with isotropic temperature factors set at 1.2 times that of the adjacent nonhydrogen atom. The positions of the methyl hydrogen atoms were optimized by a rigid rotating group refinement with idealized angles. Full-matrix least-squares refinement, based upon the minimization of  $\sum w_i |F_o^2 - F_c^2|^2$  with weighting  $w_i^{-1} = [\sigma^2(F_o^2) + (0.0528P)^2 + 0.880P]$  where  $P = (\max(F_o^2, 0) + 2F_c^2)/3$ , converged to give the final discrepancy indices<sup>25</sup> provided in Table 1. A correction for secondary extinction was applied. The maximum and minimum residual electron density peaks in the final difference Fourier map were 0.241 and –0.307 e Å<sup>–3</sup>, respectively (Table 2). The linear absorption coefficient, atomic scattering factors, and anomalous dispersion corrections were calculated from values found in the *International Tables of X-ray Crystallography*.<sup>26</sup>

## Results and discussion

### Description of the molecular structure of DMAIMSOA (SO<sub>3</sub>C(NHMe)<sub>2</sub>)

The molecular structure of DMAIMSOA was determined by X-ray crystallography. The perspective view is shown in Fig. 1. Like its sulfonic acid analogue,<sup>16</sup> it exists in its zwitterionic form in solid crystal form. The positive charge is delocalized over the N(2)–C(1)–N(1) framework with the sp<sup>2</sup> hybridization at the central carbon atom. Bond angles around this carbon atom add up to 360°. The C(1)–N bond distances of 1.291(4) and 1.306(4) Å are significantly shorter than a C–N bond distance of 1.47 Å, indicating considerable double bond character in both of them. The whole

**Fig. 1.** Perspective view of the molecular structure of DMAIMSOA with the atom labeling scheme. Thermal ellipsoids are scaled to enclose 30% probability.

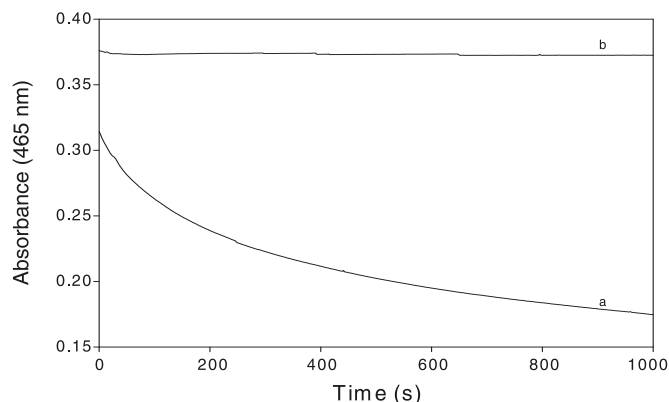


**Table 3.** Interatomic distances (Å) and bond angles (°) for DMAIMSOA.

Interatomic distances (Å)	
S—O(1)	1.433(3)
S—O(2)	1.437(3)
S—O(3)	1.440(3)
S—C(1)	1.820(3)
N(1)—C(1)	1.291(4)
N(1)—C(2)	1.458(4)
N(2)—C(1)	1.306(4)
N(2)—C(3)	1.463(5)
Bond angles (°)	
O(1)—S—O(2)	114.7(2)
O(1)—S—O(3)	115.2(2)
O(2)—S—O(3)	113.3(2)
O(1)—S—C(1)	104.6(2)
O(2)—S—C(1)	104.2(1)
O(3)—S—C(1)	103.1(2)
N(1)—C(1)—N(2)	123.9(3)
N(1)—C(1)—S	115.9(2)
C(1)—N(2)—C(3)	127.7(3)
C(1)—N(1)—C(2)	123.8(3)
N(2)—C(1)—S	120.1(3)

three-bond network, after the s-bond framework, then comprises four electrons, both derived from the nitrogen p-orbitals, which interact with the vacant p<sub>π</sub>-orbitals of the

**Fig. 2.** Comparison traces of iodine oxidation of DMAIMSA and DMAIMSOA showing the relative inertness of DMAIMSOA to oxidation. Iodine solutions with DMAIMSOA held their titer for hours with no measurable consumption of iodine observed. [I<sub>2</sub>]<sub>0</sub> = 5.24 × 10<sup>−4</sup> mol/L, (a) [DMAIMSA]<sub>0</sub> = 2.0 × 10<sup>−4</sup> mol/L, and (b) [DMAIMSOA]<sub>0</sub> = 2.0 × 10<sup>−4</sup> mol/L.



formally cationic carbon center, imparting partial double bond character to both bonds, and hence their deviation from the expected value for a single bond. The negative charge is delocalized on the three oxygen atoms on the sulfonic acid group. The S—O bonds are also nearly equivalent, ranging between 1.433(3) and 1.440(3) Å. These are shorter than a normal S—O bond owing to the delocalization of the negative charge over the three oxygen atoms. These three S—O bonds are approximately 0.04 Å shorter than the two S—O bonds in DMAIMSA, which are at approximately 1.48 Å. The three oxygens form a nearly symmetric triangular base around the sulfur center except for the oxygen atom in close proximity to the methyl group, which is slightly displaced from this pyramidal shape by about 2° (Table 3).

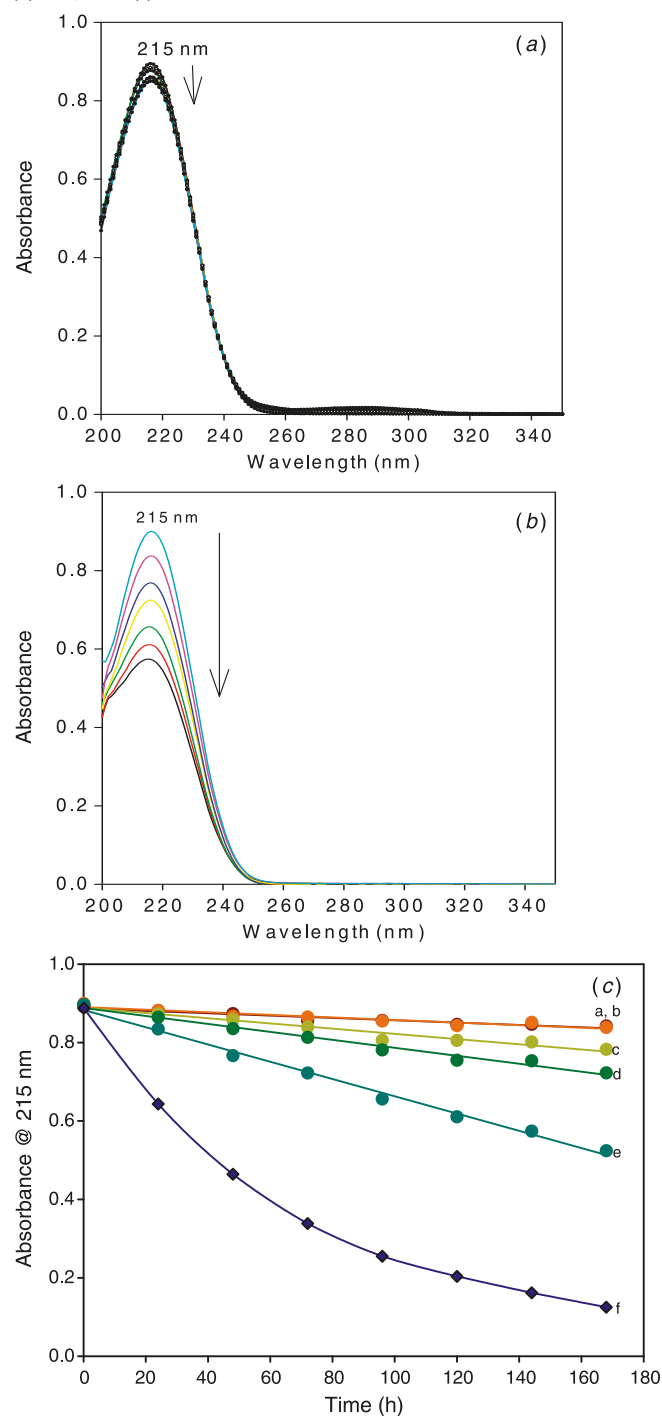
The C—S bond, at 1.820(3) Å, is 0.03 Å longer than a typical C—S bond of 1.79 Å, but is noticeably shorter than the C—S bonds of 1.880 Å in DMAIMSA and 1.867 Å in unsubstituted aminoiminomethanesulfonic acid (AIMSA, thiourea dioxide). Both sulfonic acids are highly reactive with easy cleavage of the C—S bond to release highly reducing sulfur-based leaving groups.<sup>27</sup> DMAIMSOA is not densely packed, and has a density of 1.451 g cm<sup>−3</sup>, which is comparable to that exhibited by DMAIMSA of 1.496 g cm<sup>−3</sup>. Although DMAIMSOA shows hydrogen bonding through O(2) to the single water of crystallization in the unit cell, it is incapable of supporting strong and extensive hydrogen bonding, which would have been expected to increase its density as was observed with aminoiminomethanesulfonic acid (AIMSOA, thiourea trioxide) with a density of 1.948 g cm<sup>−3</sup>.<sup>28</sup>

### Reactivity of DMAIMSOA

DMAIMSA is known to be highly reactive, and its aerobic decomposition in mildly acidic and basic environments quickly and rapidly produces dithionite.<sup>16</sup> Its oxidation to dimethylurea and sulfate is facile. Figure 2 shows a simple experiment carried out to evaluate the rates of oxidation of DMAIMSA and DMAIMSOA in slightly acidic media (pH 5.0) by the weak biological oxidant iodine. While DMAIMSA is oxidized at a reasonable rate with bimolecular kinetics with a rate constant of 20.5 (mol/L)<sup>−1</sup> s<sup>−1</sup>,



**Fig. 3.** (a) UV spectral of incubated DMAIMSOA in water at a slightly acidic pH of 6 showing its inertness. The spectra scan was taken at 24 h intervals for 7 days. There is very little change in the absorbance of DMAIMSOA. [DMAIMSOA] =  $1.0 \times 10^{-4}$  mol/L. (b) UV spectra scan of the same DMAIMSOA solution as in Fig. 3a at a physiological pH of 7.4 phosphate buffer. At this slightly basic pH there is a noticeable decomposition of DMAIMSOA. (c) The effect of pH on the rate of decomposition of DMAIMSOA in 0.05 mol/L phosphate buffer. Substantial decomposition starts at pH conditions greater than 7. [DMAIMSOA] =  $1.0 \times 10^{-4}$  mol/L; pH (a) 6.2 (unbuffered), (b) 6.2, (c) 6.6, (d) 7.0, (e) 7.4, and (f) 8.2.

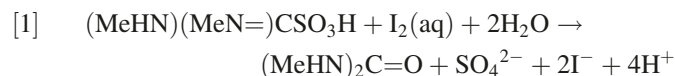


DMAIMSOA remains inert to oxidation at this pH. This was a noticeable difference in the reactivities of these aminosulfur oxoacids. This discrepancy in their reactivities has brought about a new school of thought that suggests, strongly, that in acidic media, the sulfonic oxoacid is unlikely to be an intermediate in the oxidation of the thiouredo group to sulfate and an organic residue.<sup>29</sup>

Figure 3 also displays the inertness of DMAIMSOA. In Fig. 3a, DMAIMSOA solutions are dissolved in water at a slightly acidic pH of 6 and allowed to sit, capped, and in the dark for a week. Other aminosulfur oxoacids show extensive decomposition in aqueous solutions.<sup>16</sup> Figure 3a shows that, even after 7 days, there is very little change in the absorbance of DMAIMSOA monitored at 215 nm. Figure 3b, on the other hand, shows the same DMAIMSOA solution, this time in a pH 7.4 buffer, which is slightly basic and is the physiological pH. At these conditions, there is noticeable decomposition of DMAIMSOA. The slight change in pH from Figs. 3a to 3b can impart a remarkable change in reactivity. Figure 3c shows, much more vividly, the rates of decomposition of DMAIMSOA at various pH conditions. In all traces, the pH was maintained by phosphate-type buffer solutions. The phosphate anions in this buffer mixture are not innocent, and are known to increase the rate of decomposition of aminosulfur oxoacids owing to their nucleophilic nature. Figure 3c shows that substantial decomposition commences at pH conditions greater than 7. While there is no decomposition observed around pH 6 (Fig. 3c, trace a), at pH 8.2 (Fig. 3c, trace f), however, complete decomposition of DMAIMSOA is attained within 3 min.

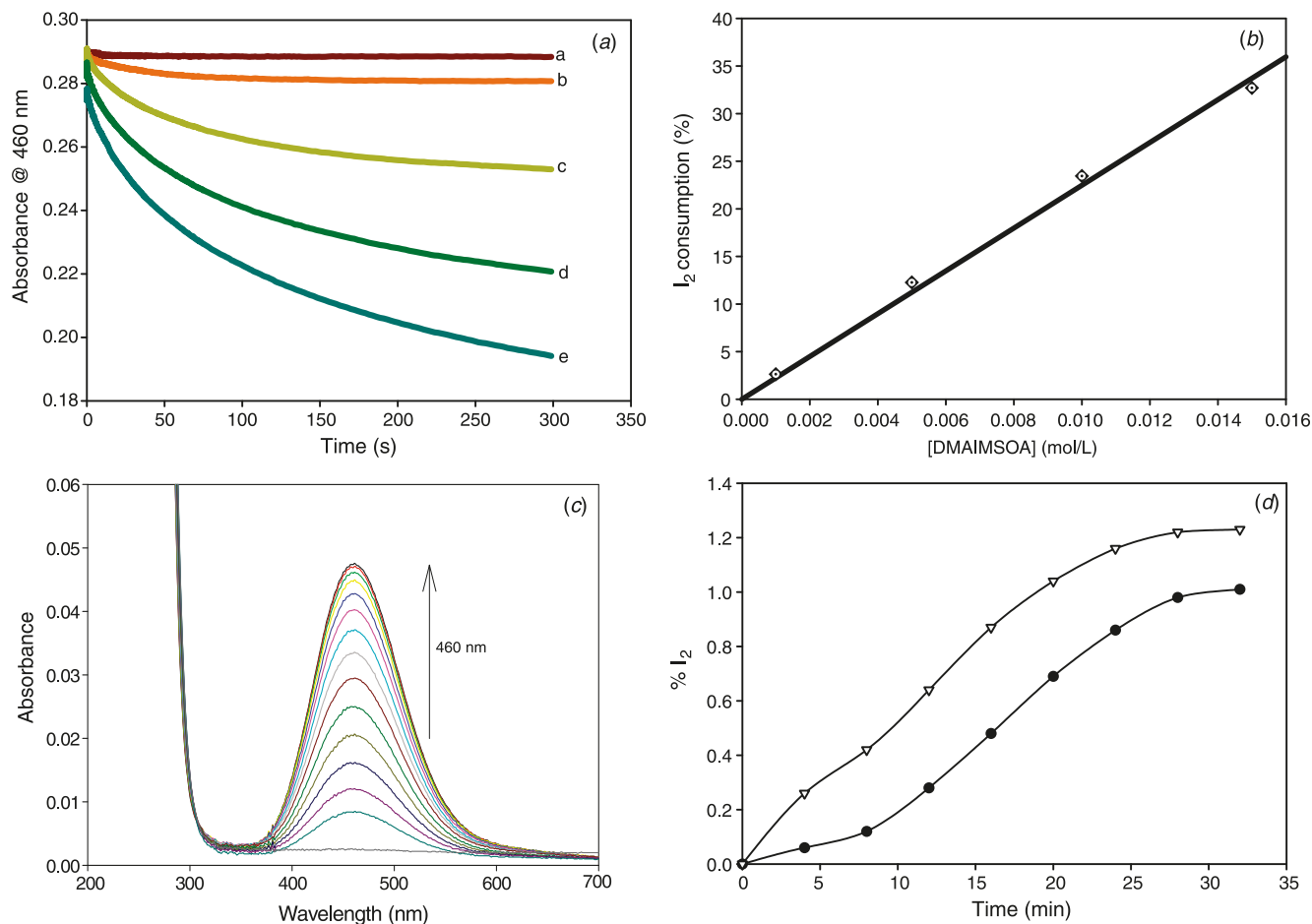
### Reactions with iodine and acidic iodate

It is not possible to spectrophotometrically observe  $I_2$ -DMAIMSOA reactions at high pH conditions because most of the aqueous iodine is converted into hypoiodous acid, which has no absorption in the visible range in neutral and acidic environments. Iodine, however, exists mostly in the aqueous molecular form and its consumption can be followed at 460 nm (see Fig. 4a). Figure 4a shows an initially reasonably fast rate of iodine consumption, which quickly slows down and shuts itself down about 300 s into the reaction. Figure 4a has an expanded scale, and shows that very little aqueous iodine is actually consumed. These  $I_2$ -DMAIMSOA solutions can be left overnight and the absorbance values reread after 24 h. After 24 h, the ratio of iodine consumed is shown in Fig. 4b. The linearity shows that the only reaction occurring is the consumption of iodine by DMAIMSOA. The expected stoichiometry for the oxidation of DMAIMSOA by iodine is 1:1

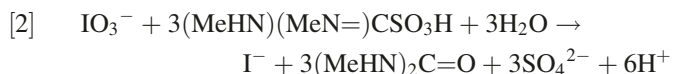


The percent consumption of iodine should allow for the calculation of the fraction of DMAIMSOA that is “oxidizable” because these fractions in Fig. 4b remain basically invariant on further incubation of the reaction solutions. This percentage iodine consumption is calculated on the basis of the stoichiometry in eq. [1] in which a 1:1 mol ratio of DMAIMSOA- $I_2$  is considered to be 100%. Using the plot in Fig. 4b and reaction stoichiometry in eq. [1], a simple calcu-

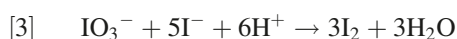
**Fig. 4.** (a) Absorbance traces showing the consumption of aqueous iodine by DMAIMSOA in unbuffered solutions. Despite the initial reasonably fast rate of consumption, very little aqueous iodine is consumed.  $[I_2(aq)] = 3.82 \times 10^{-4}$  mol/L,  $[DMAIMSOA] =$  (a) 0.0, (b) 0.001, (c) 0.005, (d) 0.010, and (e) 0.015 mol/L. (b) A linear plot showing the percent consumption of iodine in Fig. 4a after 24 h of  $I_2$ –DMAIMSOA incubation. (c) Multiple spectral scan measurements of the reaction of DMAIMSOA and acidic iodate taken every 2 min showing the formation of iodine at 460 nm. A very small amount of iodine is formed indicating that at these conditions only a negligible fraction of DMAIMSOA is oxidizable.  $[DMAIMSOA] = 0.025$  mol/L,  $[IO_3^-] = 0.025$  mol/L, and  $[H^+] = 0.05$  mol/L. (d) Comparison traces of the percent formation of iodine in the reactions of freshly prepared (closed circles) and 3-day-old (open triangles) DMAIMSOA solutions with acidic iodate.  $[DMAIMSOA] = 0.025$  mol/L,  $[IO_3^-] = 0.025$  mol/L, and  $[H^+] = 0.05$  mol/L.



lation shows that 0.77% of DMAIMSOA is oxidized after 24 h of reaction time. This shows that, at these conditions, only a very small fraction of DMAIMSOA is oxidized or oxidizable. In the acidic environment, iodate can also be used to evaluate the response of DMAIMSOA to oxidation. By using excess iodate concentrations, the amount of iodine produced can be utilized to calculate the amount of DMAIMSOA oxidized (see Fig. 4c). Initially, iodate oxidizes DMAIMSOA to produce iodide (reaction stoichiometry in eq. [2]), which is subsequently oxidized by the excess iodate to give iodine (reaction in eq. [3]) as the final reduction product of iodate.

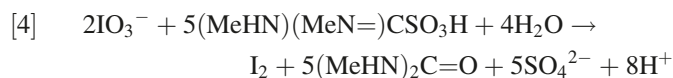


Followed by the Dushman reaction:<sup>30</sup>

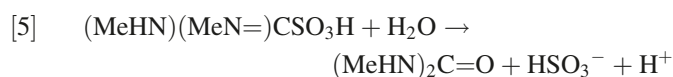


The addition of 5(eq. [2]) and eq. [3] eliminates iodide to

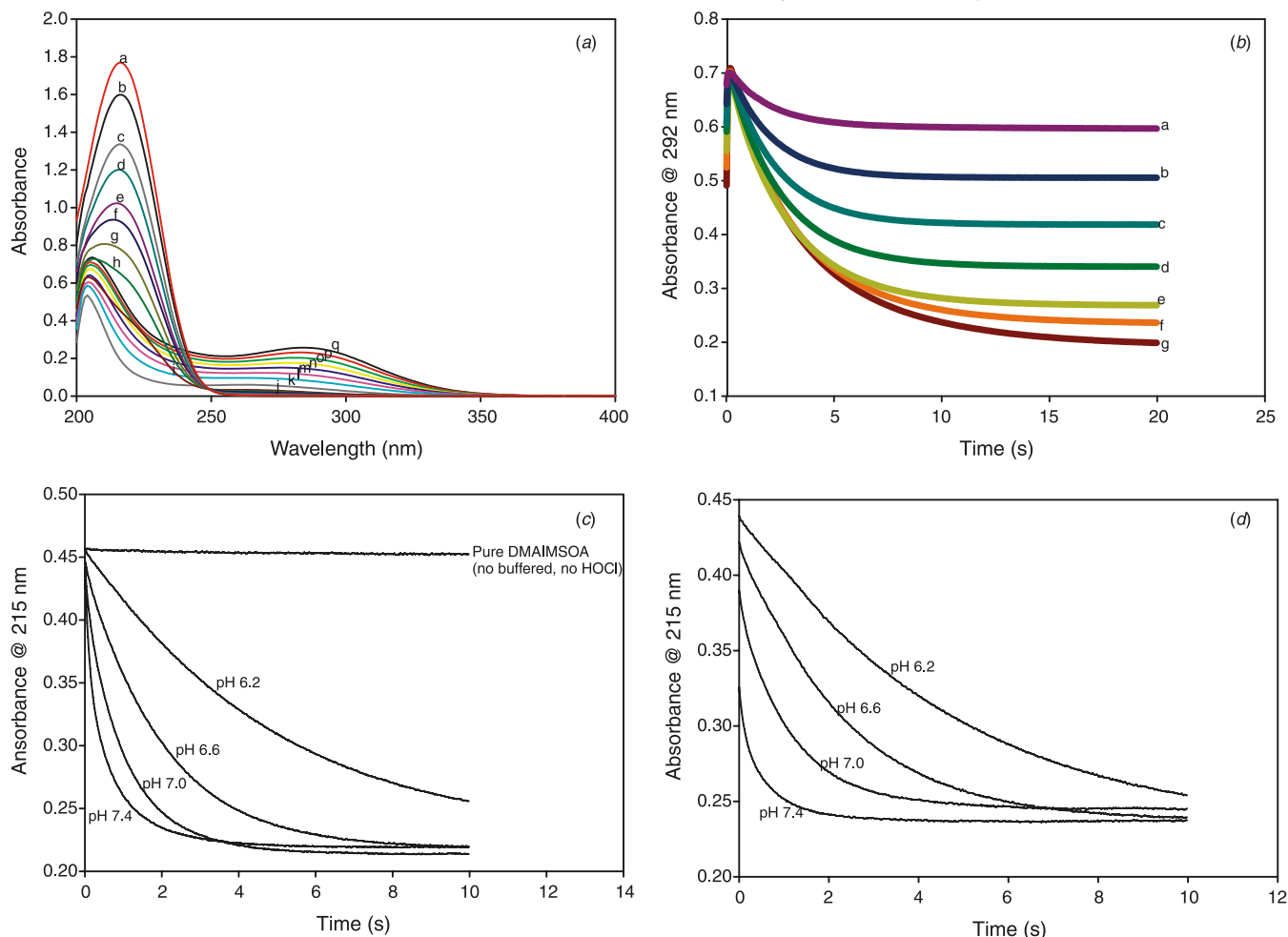
give the overall stoichiometry that gives iodine as the final product:



One can thus correlate the amount of iodine formed to the amount of DMAIMSOA consumed through the 5:1 ratio. Figure 4c shows that very little iodine is formed, also confirming that very little DMAIMSOA is oxidized under these conditions.  $IO_3^-$  is inert in basic environments, and thus this type of correlation can only be effected in this acidic environment. Previous work in our laboratory<sup>27,31</sup> and by others<sup>32</sup> had always conjectured that such aminosulfur oxoacids initially undergo an irreversible, entropy-driven hydrolysis to give a reducing sulfur species, which in DMAIMSOA's case is bisulfite:



**Fig. 5.** (a) UV spectral scans of the HOCl–DMAIMSOA reaction after 48 h of reaction time at pH 7.4 in 0.05 mol/L phosphate buffer. [DMAIMSOA] =  $2.0 \times 10^{-4}$  mol/L, [HOCl] = (a) 0 (not buffered), (b) 0 (buffered), (c)  $5.00 \times 10^{-5}$ , (d)  $7.50 \times 10^{-5}$ , (e)  $1.00 \times 10^{-4}$ , (f)  $1.25 \times 10^{-4}$ , (g)  $1.50 \times 10^{-4}$ , (h)  $1.75 \times 10^{-4}$ , (i)  $2.00 \times 10^{-4}$ , (j)  $3.00 \times 10^{-4}$ , (k)  $4.00 \times 10^{-4}$ , (l)  $5.00 \times 10^{-4}$ , (m)  $6.00 \times 10^{-4}$ , (n)  $7.00 \times 10^{-4}$ , (o)  $8.00 \times 10^{-4}$ , (p)  $9.00 \times 10^{-4}$ , and (q)  $1.00 \times 10^{-3}$  mol/L. (b) Absorbance traces at 292 nm showing variation of DMAIMSOA with HOCl at a pH of 7.4 in 0.05 mol/L phosphate buffer. [HOCl] =  $2.0 \times 10^{-3}$  mol/L, [DMAIMSOA] = (a)  $2.0 \times 10^{-4}$ , (b)  $4.0 \times 10^{-4}$ , (c)  $6.0 \times 10^{-4}$ , (d)  $8.0 \times 10^{-4}$ , (e)  $1.0 \times 10^{-3}$ , (f)  $1.2 \times 10^{-3}$ , and (g)  $1.4 \times 10^{-3}$  mol/L. (c) Absorbance traces at 215 nm showing the effect of pH on the HOCl–DMAIMSOA reaction in 0.05 mol/L phosphate buffer for a freshly prepared DMAIMSOA. [HOCl] =  $3.0 \times 10^{-3}$  mol/L and [DMAIMSOA] =  $5.0 \times 10^{-5}$  mol/L. (d) Absorbance traces of the same reaction in Fig. 5c but with a 7-day-old incubated DMAIMSOA.

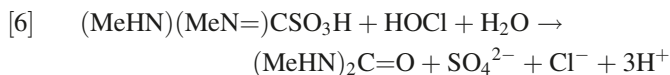


The oxidations observed in Figs. 4a–4c are effectively the oxidation of bisulfite released in the reaction in eq. [5]. The extent of the reaction in eq. [5] (a sort of pseudoequilibrium constant since eq. [5] is assumed to be irreversible) is strongly dependent on pH, and any value derived for this reaction has to be associated with a specific pH value. Further studies are needed to evaluate the general base catalysis that can be evoked by the anions that make up the various buffers that might be used to maintain the pH. It is anticipated that the type and concentrations of the buffers themselves would influence the observed extent of the reaction in eq. [5]. The reaction in eq. [5] is an extremely slow process, which proceeds at a faster rate in basic conditions. Figure 4d shows that the reaction in eq. [5] is a prerequisite for the observed oxidations in Figs. 4a and 4c. Some DMAIMSOA reaction solutions were used immediately after preparation (Fig. 4d, dark circles), while other solutions were incubated for 3 days before being used in the DMAIMSOA–IO<sub>3</sub><sup>−</sup> reac-

tions (Fig. 4d, open triangles). It is evident that after 30 min more of the DMAIMSOA is observed to have been oxidized with the incubated solutions (1.23%) over those that were not incubated (1.03%).

### Reactions in basic environments

For these experiments, hypochlorous acid was used as the oxidant. <sup>−</sup>OCl has an absorption peak at 292 nm, and does not interfere with the DMAIMSOA peak at 215 nm as HOI does. Thus, the reaction between HOCl and DMAIMSOA can be followed at both 215 and 292 nm. Figure 5a shows a series of spectral scans of the HOCl–DMAIMSOA reaction after 48 h of reaction time at pH 7.4 in a phosphate buffer. Activity is observed at both wavelengths, showing a very viable and facile reaction. The stoichiometry of this reaction was derived to be 1:1 using barium sulfate precipitation.



Absorbance traces in Fig. 5b were monitored at 292 nm, and show that the reaction essentially goes to completion and is over within 20 s. Any rate constant derived from these data is only relevant for this pH condition and for this buffer strength and concentration. The final observed rate of reaction is derived from a complex interaction of the buffer anions with DMAIMSOA and their effect in facilitating the reaction in eq. [5]. The positively charged carbon center is susceptible to nucleophilic attack with the result that the C–S bond is weakened, facilitating its cleavage. Figures 5c and 5d show that the incubation of solutions is not an important factor for reactions run in basic environments. Freshly prepared solutions gave nearly the same reaction times as those incubated for a week. Examination of the initial absorbance readings for the incubated solutions, however, show that the initial DMAIMSOA absorbances are depressed from the values recorded for unincubated solutions. The data, taken at 215 nm in Figs. 5c and 5d, are more difficult to explain if indeed the reaction in eq. [5] is irreversible. Thus, in basic environments, some equilibrium is attained, although some irreversible entropically favored decomposition also still proceeds. The reaction of HOCl with  $\text{HSO}_3^-$  is essentially diffusion controlled, and would not show the type of kinetics observed in Figs. 5b–5d.

## Conclusions

Owing to the inertness of aminoiminomethanesulfonic acid (AIMSOA) and DMAIMSOA, previous assertions from our research work had suggested that in these types of compounds that contain the thiouredo group, oxidation can proceed directly from the sulfinic acid to sulfate, bypassing the sulfonic acid.<sup>10,31,33</sup> Evidence for this involves the direct observation of an untrapped sulfoxyl anion radical in aerobic decompositions of aminosulfinic acids.<sup>34</sup> The inordinately long C–S bond in aminoiminomethanesulfonic acid (AIMSA) and DMAIMSA is easily cleaved by thermal activation or by the presence of nucleophiles. In fact, high yield guanidine formation is effected by the reaction of aminosulfinic acids with amines.<sup>35–37</sup> The nucleophilic amine center attacks the positive carbon center, culminating in the cleavage of the C–S bond and the formation of a C=N double bond.

The present synthesis and characterization, however, does not preclude the formation of the sulfonic acid as one of the stable intermediates in the oxidation of a thiouredo group in the basic environment and in the presence of basic anions or nucleophiles. Thus, in the physiological environment, metabolic activation of thiocarbamides, where S-oxygenation occurs at pH 7.4, the sulfonic acid is a viable intermediate, which can later be oxidized further to give sulfate and urea-type organic residue.

## Supplementary data

Supplementary data for this article are available on the journal Web site (canjchem.nrc.ca). CCDC 778932 contains the X-ray data in CIF format for this manuscript. These data can be obtained, free of charge, via <http://www.ccdc.cam.ac.uk/conts/retrieving.html> (or from the Cambridge Crystallographic Data Centre, 12 Union Road, Cambridge CB2 1EZ, UK; fax +44 1223 336033; or [deposit@ccdc.cam.ac.uk](mailto:deposit@ccdc.cam.ac.uk)).

uk/conts/retrieving.html (or from the Cambridge Crystallographic Data Centre, 12 Union Road, Cambridge CB2 1EZ, UK; fax +44 1223 336033; or [deposit@ccdc.cam.ac.uk](mailto:deposit@ccdc.cam.ac.uk)).

## Acknowledgements

This work was supported by Research Grant No. CHE 0614924 from the National Science Foundation.

## References

- (1) Fox, R. B. *J. Clin. Invest.* **1984**, 74 (4), 1456. doi:10.1172/JCI111558. PMID:6090504.
- (2) Curtis, W. E.; Muldrow, M. E.; Parker, N. B.; Barkley, R.; Linas, S. L.; Repine, J. E. *Proc. Natl. Acad. Sci. U.S.A.* **1988**, 85 (10), 3422. doi:10.1073/pnas.85.10.3422. PMID:3130627.
- (3) Parker, N. B.; Berger, E. M.; Curtis, W. E.; Muldrow, M. E.; Linas, S. L.; Repine, J. E. *J. Free Radic. Biol. Med.* **1985**, 1 (5–6), 415. doi:10.1016/0748-5514(85)90155-2. PMID:3018065.
- (4) Bruck, R.; Aeed, H.; Shirin, H.; Matas, Z.; Zaidel, L.; Avni, Y.; Halpern, Z. *J. Hepatol.* **1999**, 31 (1), 27. doi:10.1016/S0168-8278(99)80160-3. PMID:10424280.
- (5) Huxtable, R. J.; Lafranconi, M. W., Eds. *Sulfur and the Metabolism of Xenobiotics*. In *Biochemistry of Sulfur*; Plenum Publishing: New York, 1986.
- (6) Sausen, P. J.; Elfarrar, A. A.; Cooley, A. J. *J. Pharmacol. Exp. Ther.* **1992**, 260 (1), 393. PMID:1731048.
- (7) Park, S. B.; Howald, W. N.; Cashman, J. R. *Chem. Res. Toxicol.* **1994**, 7 (2), 191. doi:10.1021/tx00038a012. PMID:8199308.
- (8) Del Corso, A.; Cappiello, M.; Mura, U. *Int. J. Biochem.* **1994**, 26 (6), 745. doi:10.1016/0020-711X(94)90103-1. PMID:8063003.
- (9) Organisciak, D. T.; Darrow, R. M.; Jiang, Y. I.; Marak, G. E.; Blanks, J. C. *Invest. Ophthalmol. Vis. Sci.* **1992**, 33 (5), 1599. PMID:1559759.
- (10) Chigwada, T. R.; Chikwana, E.; Ruwona, T.; Olagunju, O.; Simoyi, R. H. *J. Phys. Chem. A* **2007**, 111 (45), 11552. doi:10.1021/jp074897z. PMID:17944446.
- (11) Chigwada, T. R.; Chikwana, E.; Simoyi, R. H. *J. Phys. Chem. A* **2005**, 109 (6), 1081. doi:10.1021/jp0458654. PMID:16833417.
- (12) Ziegler, D. M. *Annu. Rev. Pharmacol. Toxicol.* **1993**, 33 (1), 179. doi:10.1146/annurev.pa.33.040193.001143. PMID:8494339.
- (13) Decker, C. J.; Doerge, D. R.; Cashman, J. R. *Chem. Res. Toxicol.* **1992**, 5 (5), 726. doi:10.1021/tx00029a021. PMID:1446015.
- (14) Beehler, C. J.; Ely, M. E.; Rutledge, K. S.; Simchuk, M. L.; Reiss, O. K.; Shanley, P. F.; Repine, J. E. *J. Lab. Clin. Med.* **1994**, 123 (1), 73. PMID:8288964.
- (15) Bishop, M. J.; Chi, E. Y.; Su, M.; Cheney, F. W. *J. Appl. Physiol.* **1988**, 65 (5), 2051. PMID:2850292.
- (16) Ojo, J. F.; Petersen, J. L.; Otoikhian, A.; Simoyi, R. H. *Can. J. Chem.* **2006**, 84 (5), 825. doi:10.1139/V06-023.
- (17) Bruice, T. C.; Sayigh, A. B. *J. Am. Chem. Soc.* **1959**, 81 (13), 3416. doi:10.1021/ja01522a066.
- (18) Bruice, T. C.; Markiw, R. T. *J. Am. Chem. Soc.* **1957**, 79 (12), 3150. doi:10.1021/ja01569a043.
- (19) Ishii, A.; Komiya, K.; Nakayama, J. *J. Am. Chem. Soc.* **1996**, 118 (50), 12836. doi:10.1021/ja962995k.
- (20) Chinake, C. R.; Simoyi, R. H. *J. Phys. Chem.* **1993**, 97 (44), 11569. doi:10.1021/j100146a035.



- (21) Otoikhian, A.; Simoyi, R. H.; Petersen, J. L. *Chem. Res. Toxicol.* **2005**, *18* (7), 1167. doi:10.1021/tx050089s. PMID: 16022510.
- (22) Otoikhian, A. A.; Simoyi, R. H. *J. Phys. Chem. A* **2008**, *112* (37), 8569. doi:10.1021/jp8025013. PMID: 18714963.
- (23) XSCANS, version 2.0; a diffractometer control system; Siemens Analytical X-ray Instruments: Madison, WI, 2010.
- (24) Sheldrick, G. M. *SHELXTL6.1*; crystallographic software package; Bruker AXS, Inc.: Madison, WI, 2000.
- (25)  $R_1 = \Sigma(|F_o| - |F_c|)/\Sigma|F_o|$ ,  $wR_2 = [\Sigma[w(F_o^2 - F_c^2)^2]/\Sigma[w(F_o^2)^2]]^{1/2}$ , and  $GOF = [\Sigma[w(F_o^2 - F_c^2)^2]/(n - p)]^{1/2}$ , where  $n$  is the number of reflections and  $p$  is the total number of parameters that were varied during the last refinement cycle.
- (26) *International Tables for X-ray Crystallography*; Kynoch Press: Birmingham, 1974 (present distributor: D. Riedel, Dordrecht).
- (27) Svarovsky, S. A.; Simoyi, R. H.; Makarov, S. V. *J. Chem. Soc., Dalton Trans.* **2000**, 511. doi:10.1039/a907816i.
- (28) Makarov, S. V.; Mundoma, C.; Penn, J. H.; Petersen, J. L.; Svarovsky, S. A.; Simoyi, R. H. *Inorg. Chim. Acta* **1999**, *286* (2), 149. doi:10.1016/S0020-1693(98)00392-2.
- (29) Makarov, S. V.; Mundoma, C.; Penn, J. H.; Svarovsky, S. A.; Simoyi, R. H. *J. Phys. Chem. A* **1998**, *102* (34), 6786. doi:10.1021/jp981713v.
- (30) Liebafsky, H. A.; Roe, G. M. *Int. J. Chem. Kinet.* **1979**, *11* (7), 693. doi:10.1002/kin.550110703.
- (31) Svarovsky, S. A.; Simoyi, R. H.; Makarov, S. V. *J. Phys. Chem. B* **2001**, *105* (50), 12634. doi:10.1021/jp0122474.
- (32) Deister, U.; Neeb, R.; Helas, G.; Warneck, P. *J. Phys. Chem.* **1986**, *90* (14), 3213. doi:10.1021/j100405a033.
- (33) Olagunju, O.; Siegel, P. D.; Olojo, R.; Simoyi, R. H. *J. Phys. Chem. A* **2006**, *110* (7), 2396. doi:10.1021/jp055805d. PMID: 16480299.
- (34) Makarov, S. V.; Mundoma, C.; Svarovsky, S. A.; Shi, X.; Gannett, P. M.; Simoyi, R. H. *Arch. Biochem. Biophys.* **1999**, *367* (2), 289. doi:10.1006/abbi.1999.1264. PMID: 10395746.
- (35) Kim, K.; Lin, Y.-T.; Mosher, H. S. *Tetrahedron Lett.* **1988**, *29* (26), 3183. doi:10.1016/0040-4039(88)85116-5.
- (36) Maryanoff, C. A.; Stanzione, R. C.; Plampin, J. N.; Mills, J. E. *J. Org. Chem.* **1986**, *51* (10), 1882. doi:10.1021/jo00360a040.
- (37) Yong, Y. F.; Kowalski, J. A.; Lipton, M. A. *J. Org. Chem.* **1997**, *62* (5), 1540. doi:10.1021/jo962196k.

# Fabrication of boron carbonitride (BCN) nanotubes and giant fullerene cages

Guifang Sun, Faming Gao, and Li Hou

**Abstract:** Boron carbonitride (BCN) nanotubes have been successfully prepared using  $\text{NH}_4\text{Cl}$ ,  $\text{KBH}_4$ , and  $\text{ZnBr}_2$  as the reactants at  $480^\circ\text{C}$  for 12 h by a new benzene-thermal approach in a  $\text{N}_2$  atmosphere. As its by-product, a new form of carbon regular hexagonal nanocages are observed. The samples are characterized by X-ray diffraction (XRD), Fourier transform infrared (FTIR) spectroscopy, transmission electron microscopy (TEM), transmission electron diffraction (TED), electron energy loss spectroscopy (EELS), and high-resolution transmission electron microscopy (HRTEM). The prepared nanotubes have uniform outer diameters in the range of 150 to 500 nm and a length of up to several micrometers. The novel carbon hexagonal nanocages have a typical size ranging from 100 nm to  $1.5\ \mu\text{m}$ , which could be the giant fullerene cages of  $\text{C}_{60N^2}$  ( $N = 17 \sim 148$ ). So, high fullerenes are observed for the first time. The influences of reaction temperature and  $\text{ZnBr}_2$  on products and the formation mechanism of BCN nanotubes are discussed.

**Key words:** boron carbonitride (BCN) nanotube, benzene thermal, giant fullerene.

**Résumé :** On a préparé avec succès des nanotubes BCN par réaction de  $\text{NH}_4\text{Cl}$ , de  $\text{KBH}_4$  et de  $\text{ZnBr}_2$ , à  $480^\circ\text{C}$  pendant 12 h, en faisant appel à une nouvelle approche de benzène-thermal dans une atmosphère d'azote. On a aussi observé la formation comme sous-produit d'une nouvelle forme de nanocages hexagonales régulières à base de carbone. Les échantillons ont été caractérisés par diffraction des rayons-X (DRX), par spectroscopie infrarouge à transformation de Fourier (IR-TF), par microscopie électronique de transmission (MET), par diffraction électronique de transmission (DET), par spectroscopie de la perte d'énergie électronique (SPEE) et par microscopie électronique de transmission à haute résolution (METHR). Les nanotubes préparés possèdent des diamètres extérieurs uniformes allant de 150 à 500 nm et des longueurs allant jusqu'à plusieurs microns. La tailles typiques des nouvelles nanocages hexagonales à base de carbone vont de 100 nm à  $1,5\ \mu\text{m}$  qui s'apparentent aux cages de fullerènes géants de  $\text{C}_{60N^2}$  ( $N = 17 \sim 148$ ). On a donc observé des fullerènes géants pour la première fois. On discute aussi de l'influence de la température réactionnelle et du  $\text{ZnBr}_2$  sur les produits et sur le mécanisme de formation des nanotubes BCN.

**Mots-clés :** nanotube BCN, benzène-thermal, fullerène géant.

[Traduit par la Rédaction]

## Introduction

It is well-known that the boron carbonitride (BCN) compounds are promising superhard materials.<sup>1,2</sup> Theoretical calculations have revealed that the ternary BCN compounds, depending on the structure and composition, may manifest tunable properties between the extremes for elemental carbon and boron nitride.<sup>3</sup> Thus, BCN compounds are also candidates for potential electronic and photonic devices with a large variety of electronic properties. Much effort has been devoted to the preparation of BCN compounds, and the  $\text{BC}_x\text{N}$  compounds with an  $x$  of 0.9, 2, 2.5, 4, and 7 have been reported.<sup>4</sup> Since the discovery of carbon nanotubes (NT)<sup>5</sup> and BNNTs,<sup>6</sup> much interest has been attracted to the synthesis and characterizations of nanotubes in the  $\text{sp}^2$  bonding state. In particular, it is noteworthy that both theoretical and experimental studies of BCN have also been extended from the layered  $\text{BC}_x\text{N}$  compounds to nanotube structures.<sup>7</sup> Previously, BCN nanotubes have been fabricated by various methods.<sup>8–12</sup> However, all of the growth of the BCN

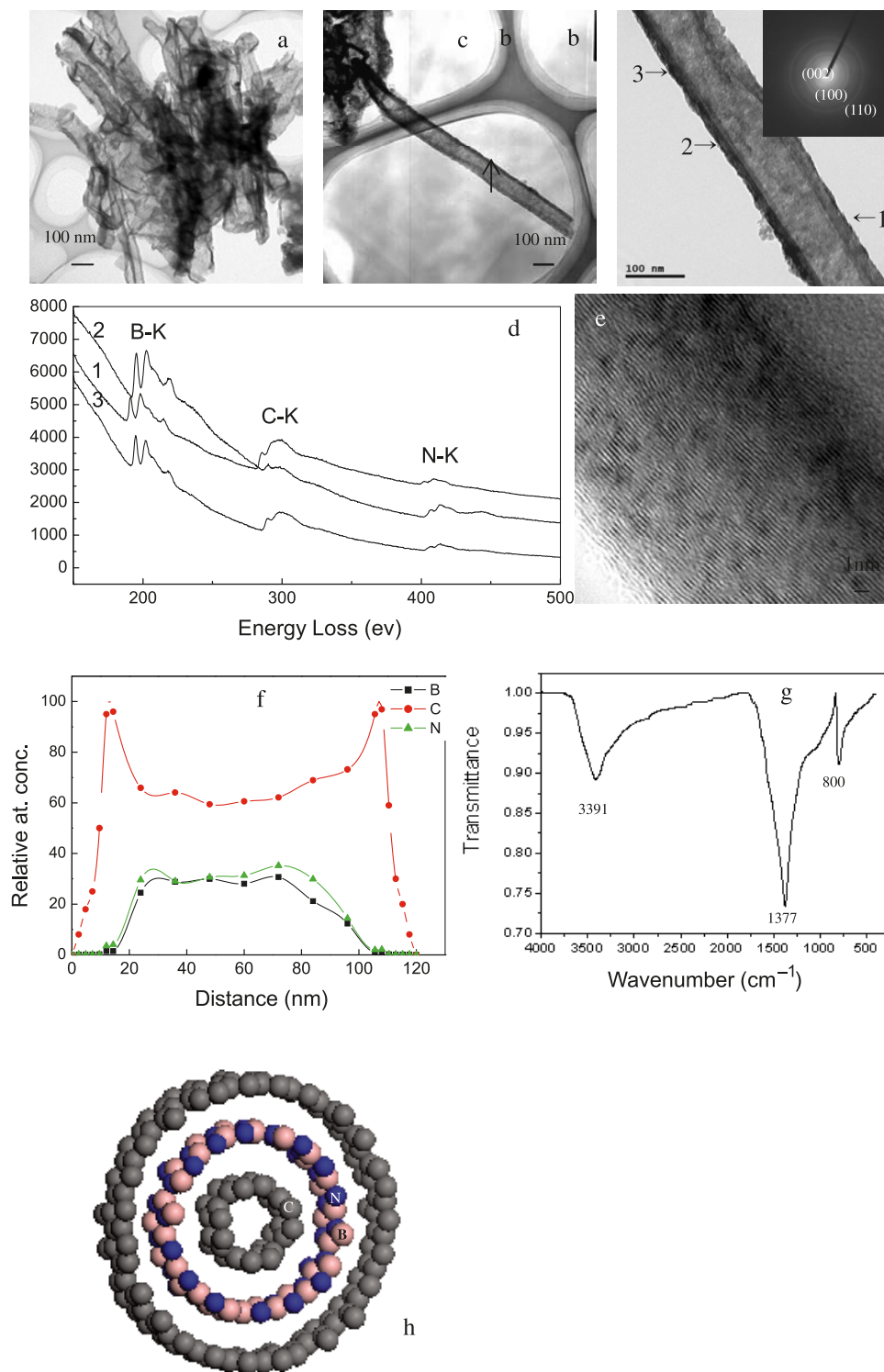
nanotubes were only carried out at higher temperatures ( $>1000^\circ\text{C}$ ). A low-temperature growth of nanotubes is highly desired. Since Liu et. al.<sup>13</sup> and Xu et. al.<sup>14</sup> successfully synthesized carbon nanotubes and BN nanotubes at very mild temperatures using the solvothermal-reduction route, it is reasonable and feasible to look for a route for low-temperature solvothermal synthesis of BCN nanotubes. In addition, the discoveries of buckminsterfullerene and carbon nanotubes have stimulated a great deal of research on different carbon morphologies owing to their promising applications in fields such as electrochemical devices, hydrogen storage, field emission devices, and nanotweezers.<sup>15</sup> Because of the flexible carbon structure, various morphologies of carbon nanostructures, including nanotubes,<sup>5</sup> nanocapsules,<sup>16</sup> onions,<sup>17</sup> nanopolyhedra,<sup>18</sup> cones,<sup>19</sup> nanorods,<sup>20</sup> nanohorns,<sup>21</sup> spheres,<sup>22</sup> and cubic nanocages,<sup>23</sup> have been discovered by scientists. These carbon nanostructures show different physical properties, and have a potential of studying materials of low dimensionality within an iso-

Received 5 February 2010. Accepted 1 October 2010. Published on the NRC Research Press Web site at canjchem.nrc.ca on 26 November 2010.

G. Sun, F. Gao,<sup>1</sup> and L. Hou. Key Laboratory of Applied Chemistry, Yanshan University, Qinhuangdao 066004, China.

<sup>1</sup>Corresponding author (e-mail: fmgao@ysu.edu.cn).

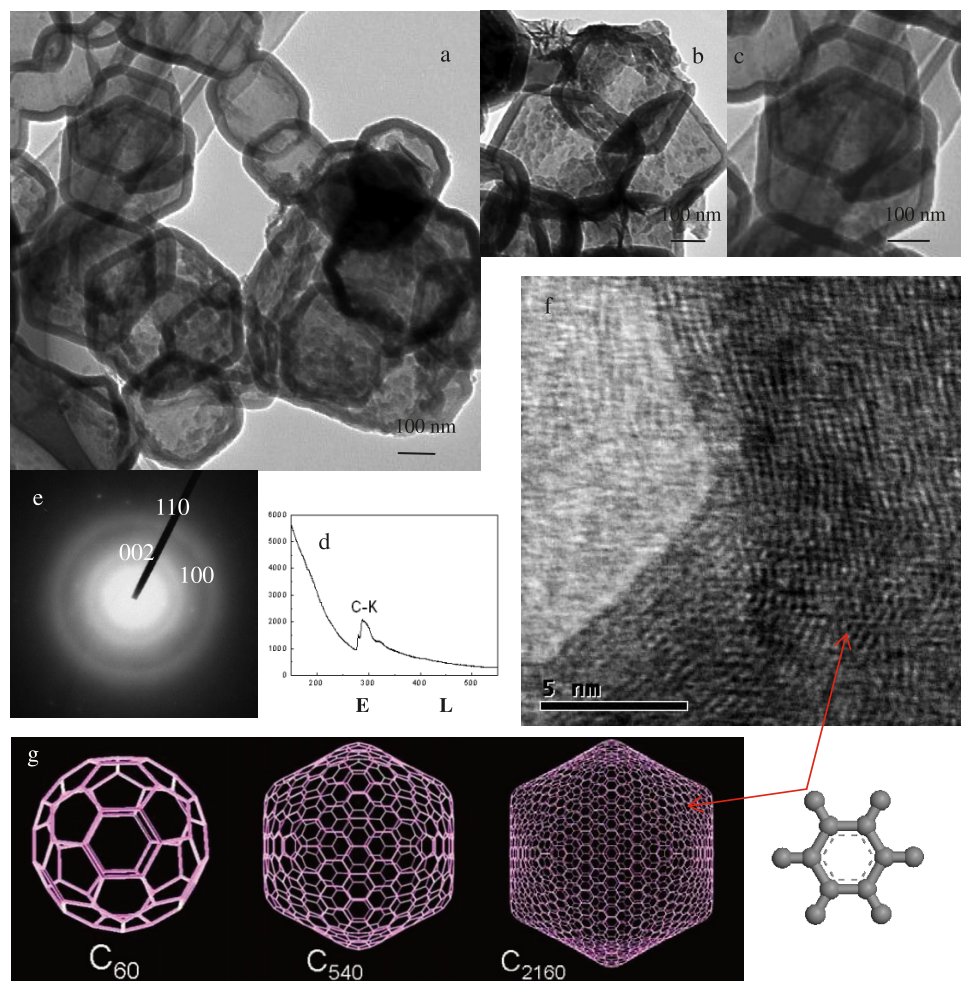
**Fig. 1.** (a) Low-magnification transmission electron microscopy (TEM) image of a number of BCN nanotubes. (b) TEM image of a representative  $\text{BC}_x\text{N}$  nanotube. (c) High-magnification TEM image of the nanotube in Fig. 1b, the inset is the transmission electron diffraction (TED) pattern of the nanotube. (d) Electron energy loss spectroscopy (EELS) at locations 1, 2, and 3. (e) High-resolution transmission electron microscopy (HRTEM) of the tube wall. (f) Elemental line scan across the BCN nanotube in Fig. 1b by TEM with an energy dispersive spectrometer (EDS). (g) FTIR spectrum of the products. (h) Scheme of the BCN nanotube.



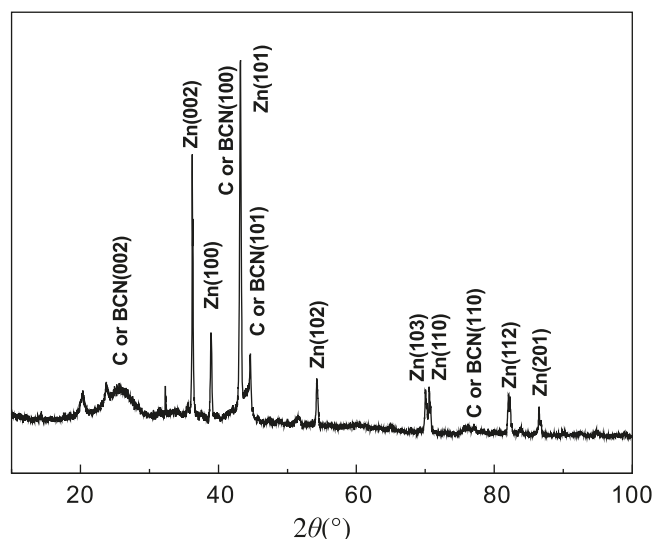
lated environment. In this paper, hollow  $\text{BC}_x\text{N}$  nanotubes and novel carbon hexagonal nanocages have been successfully prepared at 480 °C for 12 h by a new benzene-thermal

approach in a  $\text{N}_2$  atmosphere. We discovered a new form of carbon regular hexagonal nanocages that have never been reported before. We also studied the influence of reaction

**Fig. 2.** Transmission electron microscopy (TEM) images of the carbon nanocages. (a) Low-magnification TEM image of carbon hexagonal nanocages. (b) and (c) High-magnification TEM images of carbon hexagonal-shaped nanocages. (d) Electron energy loss spectroscopy (EELS) from the nanocage in Fig. 2c. (e) Transmission electron diffraction (TED) image of the nanocages in Fig. 2c. (f) High-resolution transmission electron microscopy (HRTEM) of the carbon hexagonal nanocage in Fig. 2c. (g) Atomic structure of three representative full-erene cages.



**Fig. 3.** X-ray diffraction pattern of the sample.



temperature and  $\text{ZnBr}_2$  on the reaction and morphology of the product, and discussed the formation mechanism of BCN nanotubes and carbon nanocages.

## Experimental

### Synthesis of carbon material

In a typical procedure, 9.708 g of  $\text{KBH}_4$ , 1.605 g of  $\text{NH}_4\text{Cl}$ , 0.78 g of  $\text{ZnBr}_2$ , and 30 mL of benzene were added into a 50 mL stainless steel autoclave. The autoclave was sealed and maintained at 480 °C for 12 h in a crucible furnace, and then it was allowed to cool to room temperature naturally and was carefully opened. After being filtered and washed with absolute ethyl alcohol and distilled water several times, the product was dried in a vacuum at 100 °C for 2 h. The final product was grey-black and was collected for characterization. The manipulation process was carried out in a glovebox full of  $\text{N}_2$ .

### Characterization techniques

The morphologies of the sample were characterized by



**Table 1.** Different morphologies obtained by various experiments.

Group number	Reactants	Reaction temperature (°C)	Dominated morphology of product
1	KBH <sub>4</sub> , NH <sub>4</sub> Cl, C <sub>6</sub> H <sub>6</sub>	480	h-BN nanorods
2	KBH <sub>4</sub> , NH <sub>4</sub> Cl, ZnBr <sub>2</sub> , C <sub>6</sub> H <sub>6</sub>	480	Carbon nanocages, BCN nanospheres, and nanotubes
3	KBH <sub>4</sub> , NH <sub>4</sub> Cl, ZnBr <sub>2</sub> , C <sub>6</sub> H <sub>6</sub>	<400	Nothing
4	KBH <sub>4</sub> , NH <sub>4</sub> Cl, ZnBr <sub>2</sub> , C <sub>6</sub> H <sub>6</sub>	400	BCN nanotubes
5	KBH <sub>4</sub> , NH <sub>4</sub> Cl, ZnBr <sub>2</sub> , C <sub>6</sub> H <sub>6</sub>	550	Carbon nanocages
6	KBH <sub>4</sub> , NH <sub>4</sub> Cl, ZnBr <sub>2</sub> , C <sub>6</sub> H <sub>6</sub>	800 and 900	Shorter and more curved BCN nanotubes

transmission electron microscopy (TEM) using a JEM-2010 transmission electron microscope. Transmission electron diffraction (TED) and high-resolution transmission electron microscopy (HRTEM) were used to investigate the microstructure of the powder. In addition, electron energy loss spectroscopy (EELS) and TEM was used to analyze the composition and distribution of B, C, and N. A sample of 0.1 g of the as-prepared powder with 10 mL of ethanol in a 50 mL beaker was prepared for the electron microscope by ultrasonic dispersion for 10 min. Then, the suspension was dropped on a carbon-coated copper microgrid and dried in air before performance.

## Results and discussion

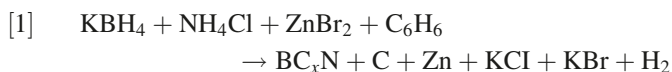
Figures 1a and 1b show transmission electron micrographs of BCN nanotubes. There were no metal particles at the tube tip ends, which were typically open as in Fig. 1b. The produced BCN nanotube in Fig. 1b appears good in shape and straighter than other BCN nanotubes presented in refs. 8–12. The prepared nanotubes have uniform outer diameters in the range of 150 to 500 nm and lengths from scores of nanometers up to several micrometers. The inner diameters of the nanotubes are ~100–400 nm. Figure 1c is the high-magnification TEM image of the nanotube in Fig. 1b and the inset in Fig. 1c is the TED pattern of the nanotube. EELS analysis of the nanotube shown in Fig. 1d revealed that it was composed of B, C, and N with distinct ionization adsorption edges at 188, 284, and 401 eV, respectively, which shows the characteristic K-shell ionization edges of B, C, and N, respectively. The  $\pi$ -type  $sp^2$  peaks of boron and carbon in the EELS spectrum are obvious for the BCN nanotubes, which can be characterizations of nanotubes in the  $sp^2$  bonding state. Taking into consideration the experimental error of ~10% in EELS measurements, the atomic ratios of B:N for most BCN nanotubes are always close to 1.0. However, the C atomic percentages change markedly. Figure 1d shows EELS results collected from locations 1, 2, and 3 in the same nanotube as indicated in Fig. 1c, respectively. The quantification results of B, C, and N at locations 1, 2, and 3 are approximately 1:2.50:1, 1:0.33:1, and 1:1.33:1, respectively. Thus, in the  $BC_xN$ , the average value of  $x$  is ~1.4. To study the composition within the tube, we show the EELS line scan (Fig. 1f) across the nanotube shown in Fig. 1b, in which the relative concentrations of B, C, and N are displayed. The anticorrelation of the elemental profiles indicates the tube exhibits segregation of BN and C layers, and it also indicates an alternating C–BN–C geometry similar to the structures in refs. 24 and 25. Two strong peaks around 1377 and 800  $cm^{-1}$  in Fig. 1g could be assigned to the B–N stretching vibrations

and B–N–B bending vibrations, respectively,<sup>26</sup> and the broad absorbed absorption peak at 3391  $cm^{-1}$  is due to water absorbed on the sample. There are no peaks corresponding to C–N and B–C vibrations, which also suggests the BCN nanotubes consist of segregated domains of BN and C, and the scheme of the BCN nanotube is shown in Fig. 1h. The typical TED pattern (inset in Fig. 1c) is taken from the individual nanotube. From the patterns, the reflections of (002), (100), and (110) of hexagonal BCN crystallites (h-BCN, JCPDS No. 35-1292) can be observed, which indicates that the product is crystallized. The high-resolution TEM image (Fig. 1e) of the typical nanotube shows the (002) basal planes aligned along the tube axis with certain crystallinity, and the interlayer spacings are measured to be ~0.335 nm, which is close to the value of (002) spacing of graphite or h-BN. From HRTEM pictures of multiwall carbon nanotubes, the slightly disordered multiwall structure of the nanotube can be observed, and the crystallinity of the BCN nanotube appears to be not as high as the nanotubes prepared by the technique of chemical vapour deposition (CVD).<sup>27,28</sup>

It is very intriguing to find a lot of hollow carbon regular hexagonal nanocages in as-synthesized nanomaterials, as shown in Fig. 2. In Fig. 2a, a TEM overview image shows several carbon hexagonal nanocages, which have typical sizes ranging from 100 nm to 1.5  $\mu m$ . Figures 2b and 2c show high-magnification TEM images of typical hexagonal-shaped carbon nanocages, which have perfect regular hexagonal nanostructures and nearly the same wall thickness of 14.3 nm. Figure 2d shows the EELS result of the nanocage in Fig. 2c, which demonstrates it is a pure carbon nanocage. From the carbon K-edge spectra, the weak initial peak, which is due to  $1s \rightarrow 2\pi^*$  transitions, shows it is a not highly crystalline material.<sup>29</sup> The typical TED pattern (Fig. 2e) is taken from the nanocage in Fig. 2c. From the pattern, the reflections of (002), (100), and (110) of graphite carbons (JCPDS No. 25-0284) can be observed, which indicates that the structure of the product is similar in structure to graphite, like fullerenes, which is composed of a sheet of linked hexagonal rings, but they contain pentagonal (or sometimes heptagonal) rings that prevent the sheet from being planar. The nature of the hexagonal nanocages is clearly demonstrated in the HRTEM image. At the hexagonal nanocage's corner, sharp folding can be observed, while the angle at the corner is strictly 120°, which demonstrates the appearance of carbon hexagonal nanocages probably arising from folding graphitic sheets into a hexagonal form, a process catalyzed by Zn in an attempt to minimize the highly energetic dangling bonds present at the edge of the growing structure. A further analysis by HRTEM (Fig. 2f)

reveals that the hollow cages could be the giant fullerene cages of  $C_{60N^2}$  ( $N = 17 \sim 148$ ). Smaller fullerenes look like asteroids. Giant fullerenes take on a hexagonal shape, as shown in Fig. 2g. The HRTEM picture of the cage in Fig. 2g shows that it is composed of many carbon rings, which correspond to the hexagonal or pentagonal rings of fullerenes, as shown by the red arrows in Figs. 2f and 2g.

A possible mechanism for the reactions is as follows.  $KBH_4$ ,  $NH_4Cl$ , and benzene are selected as the boron, nitrogen, and carbon source of BCN, respectively. Benzene can be carbonized if the temperature exceeds  $380^\circ C$ .<sup>30</sup> When the temperature reaches  $340^\circ C$ ,  $NH_4Cl$  and  $KBH_4$  begin to decompose into  $NH_3$  and  $HCl$ , and  $KH$  and  $BH_3$ , respectively, then  $NH_3$  and  $BH_3$  will react further and produce  $NH_3 \cdot BH_3$ .<sup>31</sup> When the temperature is up to  $480^\circ C$ , intermediate  $NH_3 \cdot BH_3$  and carbon will produce  $BC_xN$  nanomaterials and  $H_2$  under high pressure, which comes from  $H_2$  and the decomposed  $NH_3$ ,  $BH_3$ , and  $HCl$  gases. The as-prepared BCN nanomaterials in which the atomic ratio of B:N is 1.0 may crystallize disorderly. According to the XRD result of the unwashed product, we know  $KCl$ ,  $KBr$ ,  $Zn$ ,  $BCN$ , and carbon nanomaterials are present in the product, so the following chemical reaction is certainly responsible for the low-temperature growth of the BCN nanomaterials:



During the reaction,  $ZnBr_2$  is reduced to  $Zn$  catalyst particles, and then  $BC_xN$  nanomaterials deposit and diffuse on the surface of the fused zinc particles acting as active centers to form BCN nanotubes at the  $Zn$  particles. Combined with the production of h-BN nanorods without the addition of  $ZnBr_2$ , the open-tip morphology (Fig. 1b) of the product confirms this proposal, which indicates that the BCN nanotubes grew in a base-growth model.<sup>32</sup> In TEM examinations, the tips of BCN nanotubes were free of zinc particles existing in the sample (Fig. 3) according to X-ray diffraction, which may be due to the large diameters of the nanotubes, and come off them. Combining the results of EELS, the X-ray diffractogram indicates the presence of zinc metal crystals as catalyst, and carbon is consistent throughout the carbon nanocages.

To investigate the influence of  $ZnBr_2$  and reaction temperature on the morphologies of the product, a series of experiments were carried out (as shown in Table 1) with the procedure similar to that mentioned in the Experimental section. To identify if  $Zn$  plays a catalytic role, only  $KBH_4$ ,  $NH_4Cl$ , and benzene were directly put into an autoclave in a  $N_2$  atmosphere, and were immediately heated at a temperature of  $480^\circ C$  for 12 h without any catalyst. As a result, no BCN nanotubes or carbon nanocages were observed, indicating that  $Zn$  plays a crucial role in the growth process of BCN nanotubes and carbon nanocages as mentioned previously. To maximize BCN nanotubes or carbon nanocages in the product, a series of experiments at different temperatures were carried out. When the temperature was  $<400^\circ C$ , no product could be obtained. The product prepared at  $400^\circ C$  mostly consisted of BCN nanotubes, which were similar to those prepared at  $480^\circ C$ . When the reaction temperature was at  $550^\circ C$ , carbon nanocages prevailed in the sample, but BCN nanotubes almost disappeared. Raising the reaction

temperature to  $800$  and  $900^\circ C$ , we could find shorter and more curved BCN nanotubes produced and an improvement on the crystallinity of the BCN nanotubes, and the carbon nanocages disappeared. So thermal annealing at  $800$  and  $900^\circ C$  can promote crystallization and production of BCN nanotubes, but was not favorable to the production of longer, more aligned nanotubes and nanocages. So we can control the morphologies of the product to obtain BCN nanotubes or carbon nanocages separately by altering the reaction temperature.

## Conclusions

In conclusion, BCN nanotubes and a new form of carbon regular hexagonal nanocages have been successfully prepared using  $NH_4Cl$ ,  $KBH_4$ , and  $ZnBr_2$  as the reactants at  $480^\circ C$  for 12 h by a new benzene-thermal approach in a  $N_2$  atmosphere. Transmission electron microscopy investigations indicated that the carbon hexagonal nanocages could be giant fullerene cages.

## Acknowledgments

Financial support was from the National Natural Science Foundation of China (grant No. 21071122), the Research Fund for the Doctoral Program of Higher Education of China (grant No. 20091333110009), and the Natural Science Foundation of Hebei (grant Nos. 09965116D, E2010001169).

## References

- (1) Badzian, A. R. *Mater. Res. Bull.* **1981**, 16 (11), 1385. doi:10.1016/0025-5408(81)90057-X.
- (2) Gao, F.; He, J.; Wu, E.; Liu, S.; Yu, D.; Li, D.; Zhang, S.; Tian, Y. *Phys. Rev. Lett.* **2003**, 91 (1), 015502. doi:10.1103/PhysRevLett.91.015502.
- (3) Liu, A. Y.; Wentzcovitch, R. M.; Cohen, M. L. *Phys. Rev. B* **1989**, 39 (3), 1760. doi:10.1103/PhysRevB.39.1760.
- (4) Watanabe, M. O.; Itoh, S.; Sasaki, T.; Mizushima, K. *Phys. Rev. Lett.* **1996**, 77 (1), 187. doi:10.1103/PhysRevLett.77.187.
- (5) Iijima, S. *Nature* **1991**, 354 (6348), 56. doi:10.1038/354056a0.
- (6) Chopra, N. G.; Luyken, R. J.; Cherrey, K.; Crespi, V. H.; Cohen, M. L.; Louie, S. G.; Zettl, A. *Science* **1995**, 269 (5226), 966. doi:10.1126/science.269.5226.966.
- (7) Miyamoto, Y.; Rubio, A.; Cohen, M. L.; Louie, S. G. *Phys. Rev. B* **1994**, 50 (7), 4976. doi:10.1103/PhysRevB.50.4976.
- (8) Weng-Sieh, Z.; Cherrey, K.; Chopra, N. G.; Blase, S.; Miyamoto, Y.; Rubio, A.; Cohen, M. L.; Louie, S. G.; Zettl, A.; Gronsky, R. *Phys. Rev. B* **1995**, 51 (16), 11229. doi:10.1103/PhysRevB.51.11229.
- (9) Terrones, M.; Golberg, D.; Grobert, N.; Seeger, T.; Reyes-Reyes, M.; Mayne, M.; Kamalakaran, R.; Dorozhkin, P.; Dong, Z.-C.; Terrones, H.; Rühle, M.; Bando, Y. *Adv. Mater.* **2003**, 15 (22), 1899. doi:10.1002/adma.200305473.
- (10) Bai, X. D.; Wang, E. G.; Yu, J.; Yang, H. *Appl. Phys. Lett.* **2000**, 77 (1), 67. doi:10.1063/1.126879.
- (11) Golberg, D.; Dorozhkin, P.; Bando, Y.; Hasegawa, M.; Dong, Z. C. *Chem. Phys. Lett.* **2002**, 359 (3–4), 220. doi:10.1016/S0009-2614(02)00536-5.
- (12) Yin, L. W.; Bando, Y.; Golberg, D.; Gloter, A.; Li, M. S.; Yuan, X. L.; Sekiguchi, T. *J. Am. Chem. Soc.* **2005**, 127 (47), 16354. doi:10.1021/ja054887g.

- (13) Liu, J. W.; Shao, M. W.; Chen, X. Y.; Yu, W. C.; Liu, X. M.; Qian, Y. T. *J. Am. Chem. Soc.* **2003**, *125* (27), 8088. doi:10.1021/ja035763b.
- (14) Xu, L. Q.; Peng, Y. Y.; Meng, Z. Y.; Yu, W. C.; Zhang, S. Y.; Liu, X. M.; Qian, Y. T. *Chem. Mater.* **2003**, *15* (13), 2675. doi:10.1021/cm020853l.
- (15) Liu, J.; Xu, L.; Zhang, W.; Lin, W. J.; Chen, X.; Wang, Z.; Qian, Y. *J. Phys. Chem. B* **2004**, *108* (52), 20090. doi:10.1021/jp046702i.
- (16) Saito, Y.; Nishikubo, K.; Kawabata, K.; Matsumoto, T. *J. Appl. Phys.* **1996**, *80* (5), 3062. doi:10.1063/1.363166.
- (17) Ugarte, D. *Nature* **1992**, *359* (6397), 707. doi:10.1038/359707a0.
- (18) Ruoff, R. S.; Lorents, D. C.; Chan, B.; Malhotra, R.; Subramoney, S. *Science* **1993**, *259* (5093), 346. doi:10.1126/science.259.5093.346.
- (19) Sattler, K. *Carbon* **1995**, *33* (7), 915. doi:10.1016/0008-6223(95)00020-E.
- (20) Gogotsi, Y.; Libera, J.; Kalashnikov, N.; Yoshimura, M. *Science* **2000**, *290* (5490), 317. doi:10.1126/science.290.5490.317.
- (21) Iijima, S.; Yudasaka, M.; Yamada, R.; Bandow, S.; Suenaga, K.; Kokai, F.; Takahashi, K. *Chem. Phys. Lett.* **1999**, *309* (3–4), 165. doi:10.1016/S0009-2614(99)00642-9.
- (22) Ugarte, D. *Nature* **1992**, *359* (6397), 707. doi:10.1038/359707a0.
- (23) Saito, Y.; Matsumoto, T. *Nature* **1998**, *392* (6673), 237. doi:10.1038/32555.
- (24) Kohler-Redlich, Ph.; Terrones, M.; Manteca-Diego, C.; Hsu, W. K.; Terrones, H.; Rühle, M.; Kroto, H. W.; Walton, D. R. M. *Chem. Phys. Lett.* **1999**, *310* (5–6), 459. doi:10.1016/S0009-2614(99)00845-3.
- (25) Suenaga, K.; Colliex, C.; Demoncey, N.; Loiseau, A.; Pascard, H.; Willaime, F. *Science* **1997**, *278* (5338), 653. doi:10.1126/science.278.5338.653.
- (26) Xu, L.; Peng, Y.; Meng, Z.; Yu, W.; Zhang, S.; Liu, X.; Qian, Y. *Chem. Mater.* **2003**, *15*, 2675. doi:10.1021/cm020853l.
- (27) Yoon, H.; Lee, J. Y.; Choi, S. K.; Lee, C. J. *J. Vac. Sci. Technol. B* **2005**, *23* (2), 458. doi:10.1116/1.1865118.
- (28) Yang, Y.; Hu, Z.; Tian, Y. J.; Lu, Y. N.; Wang, X. Z.; Chen, Y. *Nanotechnology* **2003**, *14*, 733. doi:10.1088/0957-4484/14/7/307.
- (29) Guha, S.; Keller, R. C.; Yang, V.; Shahedipour, F.; Wessels, B. W. *Appl. Phys. Lett.* **2001**, *78* (1), 58. doi:10.1063/1.1337645.
- (30) Chen, L. Y.; Gu, Y. L.; Li, Z. F.; Qian, Y. T.; Yang, Z. H.; Ma, J. H. *J. Cryst. Growth* **2005**, *273* (3–4), 646. doi:10.1016/j.jcrysgro.2004.09.062.
- (31) Hu, J. Q.; Lu, Q. Y.; Tang, K. B.; Yu, S. H.; Qian, Y. T.; Zhou, G. E.; Liu, X. M.; Wu, J. X. *J. Solid State Chem.* **1999**, *148* (2), 325. doi:10.1006/jssc.1999.8454.
- (32) Amelinckx, S.; Zhang, X. B.; Bernaerts, D.; Zhang, X. F.; Ivanov, V.; Nagy, J. B. *Science* **1994**, *265* (5172), 635. doi:10.1126/science.265.5172.635.

# Interactions between gemini and nonionic pharmaceutical surfactants

Javed R. Akbar, Rubena Deubry, D. Gerrard Marangoni, and Shawn D. Wettig

**Abstract:** The nature and strength of the interactions between the 1,3-bis(dimethylhexadecyl)propanediammonium dibromide (16-3-16) gemini surfactant and a homologous series of nonionic polyoxyethylene (20) sorbitan ester surfactants having laurate (Tween 20), stearate (Tween 60), or oleate (Tween 80) alkyl tails has been investigated. The critical micelle concentration (cmc) values of the mixed gemini–tween systems were determined using the du Noüy ring surface tension method, and the results have been analyzed using Clint's, Rubingh's, Motomura's, and Maeda's theories for mixed micellar systems. The results demonstrate a synergistic mixing behaviour between the Tween surfactants and the 16-3-16 gemini surfactant, where the strength of interaction is dependent upon the chain length and saturation of the Tween alkyl tail.

**Key words:** gemini surfactants, Tween surfactants, mixed micelles, surface tension.

**Résumé :** On a étudié la nature et la force des interactions entre l'agent de surface jumeau dibromure de 1,3-bis(diméthylhexadécyl)propanediammonium (16-3-16) et une série d'agents de surface non ioniques à base d'ester de polyoxyéthylène (20) sorbitane comportant des chaînes alkyles du laurate (Tween 20), du stéarate (Tween 60) ou oléate (Tween 80). On a déterminé les valeurs de concentration micellaire critique (cmc) des systèmes mixtes jumeau–Tween en faisant appel à la méthode de la tension superficielle des anneaux de Noüy et on a analysé les résultats à l'aide des théories de Clint, de Rubingh, de Motomura et de Maeda pour les systèmes micellaires mixtes. Les résultats mettent en évidence un comportement de mélange synergistique entre les agents de surface de la famille Tween et l'agent de surface jumeau 16-3-16 et la force de l'interaction dépend de la longueur et de la saturation de la chaîne alkyle du Tween.

**Mots-clés :** agents de surface jumeaux, agents de surface Tween, micelles mixtes, tension superficielle.

[Traduit par la Rédaction]

## Introduction

Gemini surfactants represent an intriguing class of surfactants that have been extensively studied by various research groups since the late 1980s. Their unique structure, which consists of two typical surfactant monomers that are covalently linked by either a rigid or flexible spacer group, results in a number of interesting observations regarding their aggregation behavior in solution.<sup>1</sup> In comparison with their corresponding monomer counterparts, gemini surfactants are more efficient at reducing surface tension, have better wetting properties, and typically have critical micelle concentration (cmc) values that are one to two orders of magnitude lower.<sup>1–3</sup> Furthermore, gemini surfactants have been shown to form a rich array of aggregate morphologies in solution, through alteration of their chemical structure.<sup>4,5</sup> The combination of the unique properties of these surfactants along with the increasing demand for high-performance surfactants is currently driving research into their potential applications.

The prospective applications of gemini surfactants are multifold. These include their potential use in cleaning agents and detergents, cosmetics and personal care products,

preparative chemistry, pharmaceutical and biological applications, enhanced oil recovery, etc.<sup>6</sup> One particular application that is heavily being investigated is their use in drug delivery. Our group is currently interested in their use as transfection agents for DNA delivery. Thus far, we have experimentally demonstrated the effectiveness of utilizing gemini surfactants as building blocks for the construction of liposome-based DNA delivery systems for nonviral gene therapy.<sup>7–10</sup>

To effectively assess the potential applications of gemini surfactants towards drug delivery, one must realize that pharmaceutical preparations normally contain mixtures of surface-active compounds to provide the overall performance required for a particular application. In such instances, it is important to take notice that there are substantial differences in the micellization tendencies of mixtures of surfactants as compared with the single pure species. Thus, it is of great importance to evaluate and understand the interactions of gemini surfactants with common surfactants typically found in pharmaceutical applications.

Mixtures of surface-active agents form mixed micellar aggregates that can exhibit ideal or nonideal mixing behaviour

Received 23 July 2010. Accepted 16 September 2010. Published on the NRC Research Press Web site at canjchem.nrc.ca on 1 December 2010.

**J.R. Akbar, R. Deubry, and S.D. Wettig,<sup>1</sup>** School of Pharmacy, University of Waterloo, 200 University Ave. W, Waterloo, ON N2L 3G1, Canada.

**D.G. Marangoni,** Department of Chemistry, St. Francis Xavier University, P.O. Box. 5000, Antigonish, NS B2G 2W5, Canada.

<sup>1</sup>Corresponding author (e-mail: wettig@uwaterloo.ca).



in solution. Ideally, mixed surfactant systems obey Clint's model, where the cmc of the mixture can be determined from the overall composition of the combined components and the cmcs of the individual surfactants.<sup>11</sup> Clint's ideal solution theory is an effective method for explaining the mixing behaviour of surfactants with chemically similar structures.<sup>12</sup> However, deviations in ideal mixing can occur in mixtures containing chemically distinct structures as a result of a net interaction between the amphiphiles.<sup>12–17</sup> The nature and strength of this net interaction can be determined from the interaction parameter ( $\beta$ ), which can be calculated using Rubingh's model for mixed micelle formation.<sup>12</sup> Negative values of  $\beta$  indicate a synergistic interaction, where the cmc of the mixture is lower than the cmc values of the individual surfactants.<sup>12</sup> In contrast, positive values of  $\beta$  represent an antagonistic interaction between the surfactants, resulting in a positive deviation of the cmc values from ideal mixing.<sup>12</sup> Typically, synergistic effects seem to be negligible for mixtures of nonionic surfactants. However, they are moderately present in mixtures of ionic and nonionic surfactants and strongest in mixtures of anionic and cationic surfactants.

The aim of this investigation is to examine the nature and strength of the interactions between the cationic 1,3-bis(dimethylhexadecyl)propanediammonium dibromide gemini surfactant (represented as 16-3-16, where 16 is the length of the *n*-alkyl tails and 3 is the length of the polymethylene spacer) and a homologous series of nonionic polyoxyethylene (20) sorbitan esters known as the Tween surfactants that are commonly found in pharmaceutical formulations. Whereas the synergistic interactions between anionic and nonionic and anionic and zwitterionic surfactants have been extensively studied in the literature, synergism between non-ionic and cationic surfactants has received little attention.<sup>18,19</sup> The results from this study were analyzed using Clint's, Rubingh's, Motomura's, and Maeda's theories for mixed micellar systems.

## Experimental

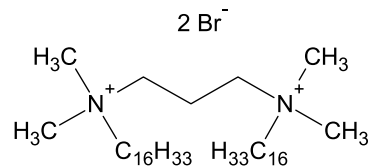
### Materials

The polyoxyethylene (20) sorbitan monolaurate (Tween 20), polyoxyethylene (20) sorbitan monostearate (Tween 60), and polyoxyethylene (20) sorbitan monooleate (Tween 80) surfactants were obtained from PCCA (Houston, Texas) and were used without any further purification. Water for all solutions was obtained from a Millipore Synergy purification system.

### Synthesis of 16-3-16

The 1,3-bis(dimethylhexadecyl)propanediammonium dibromide gemini surfactant (Scheme 1) used in this study was synthesized according to procedures previously reported in the literature.<sup>20,21</sup> Briefly, the synthesis was carried out by reflux of 2 equiv of *N,N*-dimethylhexadecylamine (plus 10% excess) and 1 equiv of 1,3 dibromopropane in HPLC grade acetonitrile for 48 h. The resulting product was purified by recrystallization from acetonitrile. The purity was confirmed by the absence of a minimum in the post micelle region of the surface tension vs log concentration plot. The structure

**Scheme 1.** Structure of the 16-3-16 gemini surfactant.



was confirmed using <sup>1</sup>H NMR spectroscopy (Bruker 300 MHz).

### Methods

Surface tension measurements were performed using a Lauda TE3 tensiometer, applying the du Noüy ring method. The temperature was kept constant at 25 °C using a circulating water bath. Surface tension values were corrected using the method of Harkins and Jordan. The cmc was determined from the break in the plot of surface tension vs concentration.

Mixed 16-3-16 and Tween solutions were prepared in the molar ratios of 0, 0.2, 0.4, 0.6, 0.8, and 1 (to a final concentration of 1 mmol/L), and separately titrated into water. Surface tension was measured as a function of concentration of the single or binary amphiphile system.

## Results and discussion

### cmc evaluation of the single and binary gemini–Tween systems

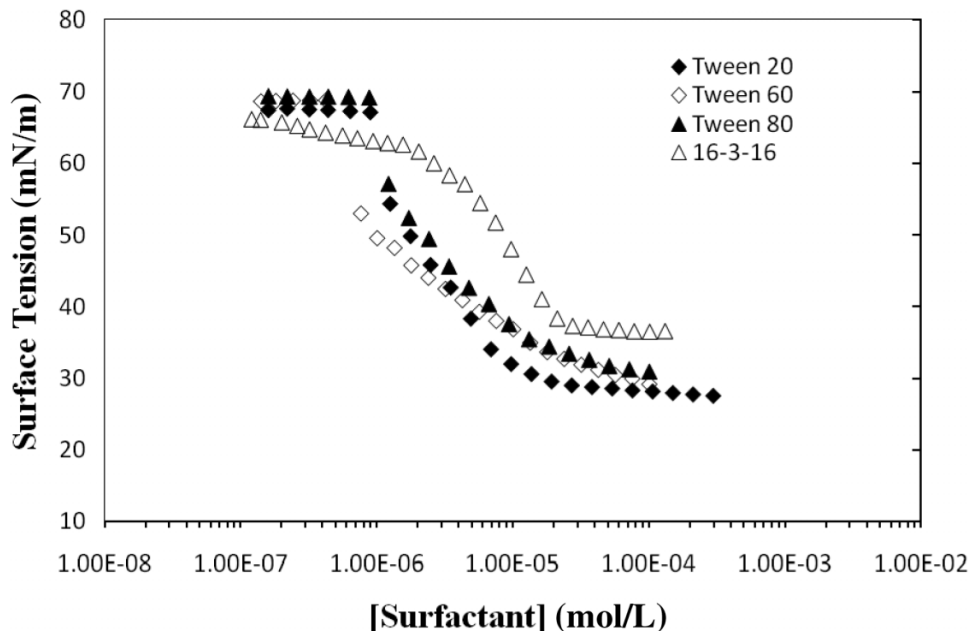
The cmcs for the pure and mixed 16-3-16 and Tween systems were determined from the breakpoint of the surface tension plots, through linear fitting of the pre-micellar and post-micellar regions. The surface tension plots for the pure 16-3-16 and Tween surfactants are shown in Fig. 1.

The experimental cmc values (Table 1) for the mixed gemini–tween systems were evaluated and compared with those values calculated using Clint's model for ideal mixed micellar systems. Clint's equation is represented by

$$[1] \quad \frac{1}{\text{cmc}_{\text{mix}}} = \sum_{i=1}^2 \frac{\alpha_i}{\text{cmc}_i}$$

where the ideal cmc of the mixture,  $\text{cmc}_{\text{mix}}$ , can be determined by the mole fraction of component *i* in solution,  $\alpha_i$ , and the cmc value of pure component *i*,  $\text{cmc}_i$ .<sup>11</sup>

In Fig. 2, the relationship between the cmc values of the mixtures and the molecular composition in solution ( $\alpha_{\text{Tween}}$ ) is shown. The solid lines in the figures are the ideal cmcs calculated using Clint's equation, whereas the broken lines represent the experimental values. As shown, the variations of the cmc values with composition appear to be quite different depending on the Tween surfactant in the mixture. Particularly, we found that the experimental cmc values for the Tween 20/16-3-16 system were initially larger than the ideal values. For both the Tween 60– and Tween 80–gemini systems, the experimental cmc values are lower than those calculated ideally, with this trend being sharper in the case of Tween 60–16-3-16. Interestingly in all cases, the difference between the ideal and experimental cmc values is less pronounced at high mole fractions of the nonionic Tween surfactant.

**Fig. 1.** Surface tension plots of the pure 16-3-16 and Tween surfactants in water at 25 °C.

The deviations of the experimental cmc values from the ideal cmc values (Table 1 and Fig. 2) is indicative of a non-ideal mixing behaviour between the gemini and Tween surfactants. In the case of the Tween 20–16-3-16 system, there appears to be a mild antagonistic interaction followed by a synergistic interaction as the mole fraction of Tween 20 is increased. In the case of the Tween 60– and Tween 80–16-3-16 systems, there appears to be a synergistic interaction between the surfactants over all compositions of the Tween surfactant. In these mixed cationic and nonionic systems, a synergistic interaction is expected because of the structural dissimilarities between the surfactants. During micellization, the nonionic Tween surfactants are expected to orient themselves between the cationic gemini surfactants, thus minimizing head group repulsion and consequently favouring micelle formation. As shown in Fig. 2, this synergistic interaction appears to be most pronounced in the mixed Tween 60 system, although all three surfactants share the same head group. This observation indicates that the length and saturation of the alkyl tail on the Tween surfactant is a determining factor in the strength of the synergistic interaction with the 16-3-16 gemini surfactant. These interaction differences were further investigated and quantified using Rubingh's approach.<sup>12</sup>

#### Evaluation of the interaction between 16-3-16 and the Tween surfactants

The nonideal behaviour of the mixed 16-3-16 and Tween systems was further analyzed and rationalized using Rubingh's model.<sup>12</sup> Through use of the regular solution approximation, Rubingh's approach allows the following equation to be derived

$$[2] \quad \frac{X_1^2 \ln(\text{cmc}_{\text{mix}} \alpha_1 / \text{cmc}_1 X_1)}{(1 - X_1)^2 \ln[\text{cmc}_{\text{mix}}(1 - \alpha_1) / \text{cmc}_2(1 - X_2)]} = 1$$

which can be used to calculate the composition of the mixed

micellar phase, where  $X_1$  is the mole fraction of surfactant 1 in the mixed micelle,  $\text{cmc}_{\text{mix}}$  is the experimental cmc value of the mixed micelle,  $\text{cmc}_1$  and  $\text{cmc}_2$  are the cmc values of surfactant 1 and 2, respectively, and  $\alpha_1$  is the mole fraction of surfactant 1.<sup>12</sup>

Through use of eq. [2],  $X_1$  can be calculated through an iterative process, which subsequently allows for the determination of the interaction parameter using the equation

$$[3] \quad \beta = \frac{\ln(\text{cmc}_{\text{mix}} \alpha_i / \text{cmc}_i X_i)}{(1 - X_i)^2}$$

where  $\beta$  represents the interaction parameter.<sup>12</sup> As previously discussed, the interaction parameter is indicative of the nature and strength of the interaction between the surfactants in the mixed micelle system.

The micellar mole fractions of the Tween surfactants in the mixtures were calculated using eq. [2] and compared with the ideal values determined using Motomura's approximation<sup>23</sup> (Table 2). Motomura's theory considers mixed micelles as a macroscopic bulk phase where the energetic parameters of such systems can be evaluated in terms of excess thermodynamic quantities.<sup>23</sup> The micelle mole fraction in the ideal state,  $X_{\text{ideal}}$ , can be calculated by the equation

$$[4] \quad X_{\text{ideal}} = \{(\alpha_1 \text{cmc}_2) / [\alpha_1 \text{cmc}_2 + (1 - \alpha_1) \text{cmc}_1]\}$$

Values are reported in Table 2, and Fig. 3 illustrates the comparison of  $X_1$  and  $X_{\text{ideal}}$  as a function of  $\alpha_{\text{Tween}}$  for the mixed Tween–16-3-16 systems. It can be seen that in the case of the Tween 60– and Tween 80–16-3-16 systems,  $X_1$  was found to deviate positively from  $X_{\text{ideal}}$  until  $\alpha_{\text{Tween}}$  approached ~0.35. These initial positive deviations from  $X_{\text{ideal}}$  demonstrate that within these low  $\alpha_{\text{Tween}}$  regions, the mixed micelles are richer in the Tween surfactants and poorer in 16-3-16 than its intended ideal state. Above the  $\alpha_{\text{Tween}}$  region of ~0.35, the mixed micelles become enriched with the 16-3-16 surfactant; a similar pattern has been ob-

**Table 1.** Measured ( $\text{cmc}_{\text{Exp}}$ ) and calculated ( $\text{cmc}_{\text{Clint}}$ ) critical micelle concentration (cmc) values for the single and binary 16-3-16 gemini surfactant and Tween systems at 25 °C.

Tween 20 + 16-3-16			Tween 60 + 16-3-16			Tween 80 + 16-3-16		
$\alpha_{\text{Tween20}}$	$\text{cmc}_{\text{Exp}}$ ( $\times 10^{-6}$ mol/L)	$\text{cmc}_{\text{Clint}}$ ( $\times 10^{-6}$ mol/L)	$\alpha_{\text{Tween60}}$	$\text{cmc}_{\text{Exp}}$ ( $\times 10^{-6}$ mol/L)	$\text{cmc}_{\text{Clint}}$ ( $\times 10^{-6}$ mol/L)	$\alpha_{\text{Tween80}}$	$\text{cmc}_{\text{Exp}}$ ( $\times 10^{-6}$ mol/L)	$\text{cmc}_{\text{Clint}}$ ( $\times 10^{-6}$ mol/L)
0	22.6 (25.5) <sup>20</sup>	—	0	22.6	—	0	22.6	—
0.2	24.5	18.8	0.2	2.15	17.4	0.2	7.34	19.3
0.4	21.5	16.1	0.4	3.50	14.1	0.4	10.5	16.9
0.6	10.3	14.1	0.6	5.59	11.9	0.6	9.29	15.0
0.8	10.5	12.5	0.8	6.91	10.3	0.8	7.01	13.5
1	11.3 (11) <sup>22</sup>	—	1	9.02 (5.5) <sup>22</sup>	—	1	12.3 (18) <sup>22</sup>	—

**Note:**  $\alpha_{\text{Tween20}}$ , mole fraction of Tween 20;  $\alpha_{\text{Tween60}}$ , mole fraction of Tween 60; and  $\alpha_{\text{Tween80}}$ , mole fraction of Tween 80.

served in a mixed nonionic C<sub>13</sub>E<sub>20</sub> and cationic sterile system.<sup>24</sup> In the case of the Tween 20/–16-3-16 system, there is no apparent trend in the deviation of  $X_1$  from  $X_{\text{ideal}}$ . It can be seen that the mixed micelle is initially enriched with the gemini surfactant at low  $\alpha_{\text{Tween}}$  values and becomes enriched with the gemini surfactant again at higher  $\alpha_{\text{Tween}}$  values (as observed in the Tween 60– and Tween 80–16-3-16 systems).

The interaction parameters for the mixed Tween and 16-3-16 systems were subsequently calculated using the previously described eq. [3], and the results are illustrated graphically in Fig. 4. The computed  $\beta$  values (Table 2) were then used to determine the activity coefficients of the individual surfactants through the equations

$$[5] \quad \ln \gamma_1 = \beta(1 - X_1)^2$$

$$[6] \quad \ln \gamma_2 = \beta(X_1)^2$$

where  $\gamma_1$  and  $\gamma_2$  are the activity coefficients of surfactant 1 and 2, respectively.<sup>12</sup>

The determined activity coefficients were next used to calculate the excess free energy of mixing ( $G_{\text{ex}}^0$ ) by the equation

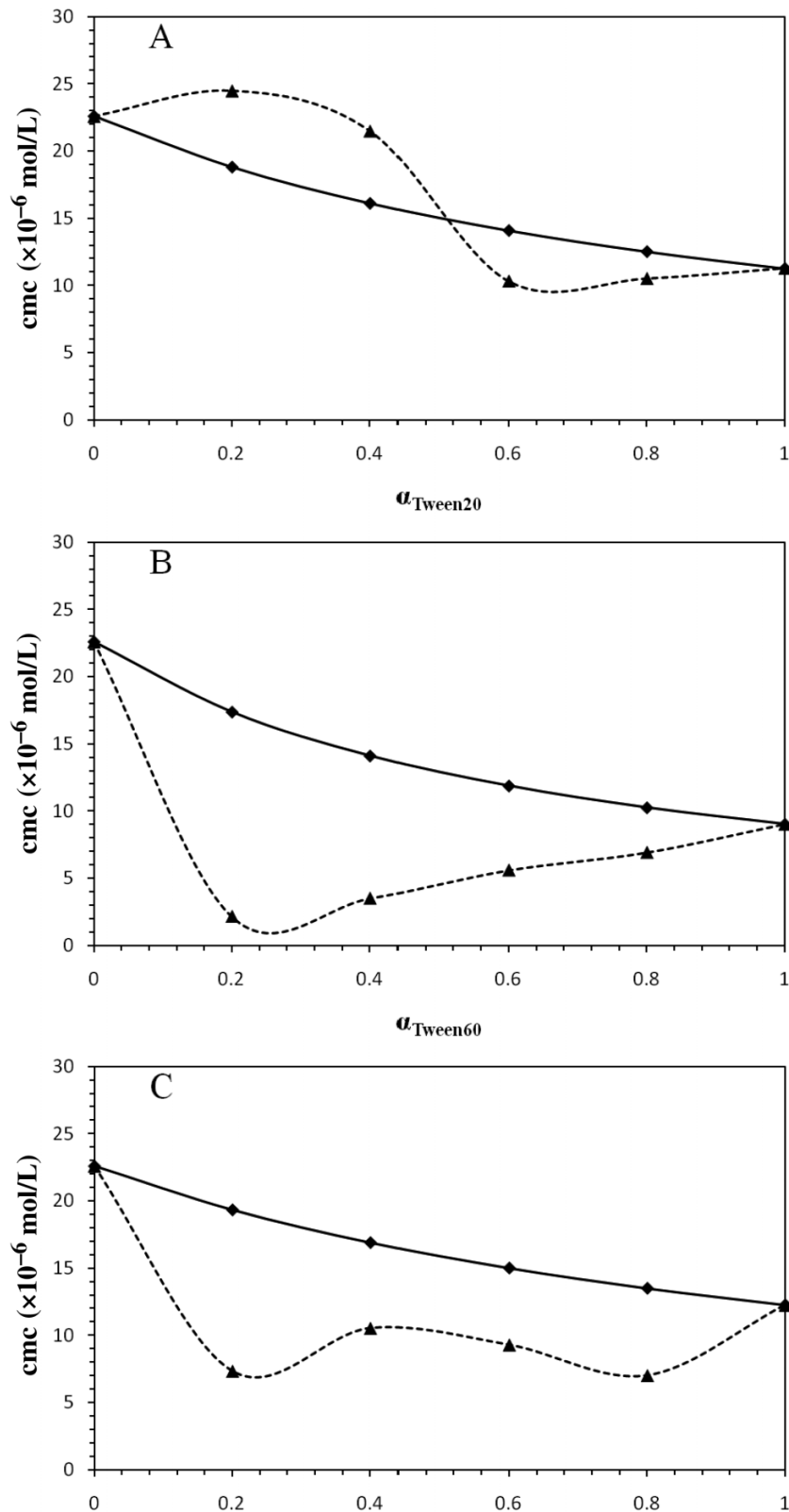
$$[7] \quad \Delta G_{\text{ex}}^0 = RT \sum_{i=1}^2 X_i \ln \gamma_i$$

where  $R$  and  $T$  represent the gas constant and absolute temperature, respectively.<sup>12</sup>

The cumulative experimental results of Rubingh's analysis for the mixed Tween–16-3-16 systems are tabulated in Table 2. Upon initial inspection, it is confirmed that a synergistic interaction is present for the Tween 60– and Tween 80–16-3-16 systems over all compositions, owing to the negative values of the interaction parameters. Furthermore, the activity coefficients were always found to be less than unity, thus confirming nonideal behaviour and an attractive interaction in the mixed systems. And finally, the negative values for the excess free energy of mixing suggest that the mixed micelles are more stable than the micelles of the individual components. For the mixed Tween 20–16-3-16 system, it is confirmed that there is an initial slight antagonistic interaction at low  $\alpha_{\text{Tween}}$  values, owing to the positive values of  $\beta$ . However, the interaction becomes synergistic at  $\alpha_{\text{Tween}}$  values of 0.6 or higher.

Upon closer examination of the experimental results, it is evident that the magnitude of the interaction parameter is dependent upon the chemical structure of the Tween surfactant in the binary system. The average values of  $\beta$  are –0.049 for the Tween 20–16-3-16 mixture, –5.1 for the Tween 60–16-3-16 mixture, and –3.0 for the Tween 80–16-3-16 mixture. Tween 60 experienced the most synergistic interaction with 16-3-16, followed by Tween 80 and then Tween 20. In all cases, the  $\beta$  values are more negative in comparison with a mixed Triton X-100 and 12-2-12 system<sup>25</sup>, and are generally in good agreement with those typically found for mixed ionic and nonionic systems.<sup>26,27</sup> The magnitudes of the interaction parameter for the mixed Tween 60– and Tween 80–16-3-16 systems suggest substantial stabilization of the mixed micelles vs the respective pure surfactant mi-

**Fig. 2.** Plots of critical micelle concentration (cmc) vs the mole fraction of Tween ( $\alpha_{\text{Tween}}$ ) for (A) Tween 20 + 16-3-16, (B) Tween 60 + 16-3-16, and (C) Tween 80 + 16-3-16 binary systems at 25 °C. Measured cmc values are represented as ( $\blacktriangle$ ) and calculated cmc values from Clint's model are represented as ( $\blacklozenge$ ).





**Table 2.** Results obtained from Rubingh's analysis of the mixed Tween and 16-3-16 systems.

System	$\alpha_{\text{Tween}}$	$X_1$	$\text{cmc}_{\text{Exp}}^{\text{a}}$ ( $\times 10^{-6}$ mol/L)	$\beta$	$\gamma_1$	$\gamma_2$	$\Delta G_{\text{ex}}^0$ (kJ/mol)
Tween 20 + 16-3-16	0	0.0	22.6	—	—	—	—
	0.2	0.17	24.5	1.4	2.6	1.0	0.47
	0.4	0.67	21.5	1.2	1.1	1.7	0.67
	0.6	0.66	10.3	-1.5	0.84	0.53	-0.83
	0.8	0.79	10.5	-1.3	0.94	0.44	-0.54
	1	1.0	11.3	—	—	—	—
Tween 60 + 16-3-16	0	0.0	22.6	—	—	—	—
	0.2	0.48	2.15	-8.5	0.10	0.15	-5.2
	0.4	0.53	3.50	-5.7	0.29	0.20	-3.5
	0.6	0.62	5.59	-3.5	0.60	0.26	-2.1
	0.8	0.74	6.91	-2.7	0.83	0.23	-1.3
	1	1.0	9.02	—	—	—	—
Tween 80 + 16-3-16	0	0.0	22.6	—	—	—	—
	0.2	0.44	7.34	-4.1	0.28	0.46	-2.5
	0.4	0.53	10.5	-1.9	0.65	0.59	-1.2
	0.6	0.62	9.29	-2.2	0.73	0.43	-1.3
	0.8	0.67	7.01	-3.7	0.68	0.19	-2.0
	1	1.0	12.3	—	—	—	—

**Note:**  $\alpha_{\text{Tween}20}$ , Tween 20 mole fraction;  $\alpha_{\text{Tween}60}$ , Tween 60 mole fraction;  $\alpha_{\text{Tween}80}$ , Tween 80 mole fraction;  $\text{cmc}_{\text{Exp}}^{\text{a}}$ , experimental critical micelle concentration;  $\beta$ , interaction parameter;  $\gamma_1$ , activity coefficient of surfactant 1;  $\gamma_2$ , activity coefficient of surfactant 2;  $\Delta G_{\text{ex}}^0$ , excess free energy of mixing; and  $X_1$ , is the mole fraction of surfactant 1 in the mixed micelle.

celles. In the case of the mixed Tween 20–16-3-16 system, the magnitude of  $\beta$  was found to deviate slightly around 0, thus suggesting a near ideal mixing behaviour for this system; such an observation has been observed in mixed cationic  $C_m\text{PB}$  and nonionic NP-9 systems.<sup>28</sup> Interestingly, when the mole fractions of the Tween surfactants are larger than 0.6, the mixed Tween–16-3-16 systems have comparable degrees of synergism.

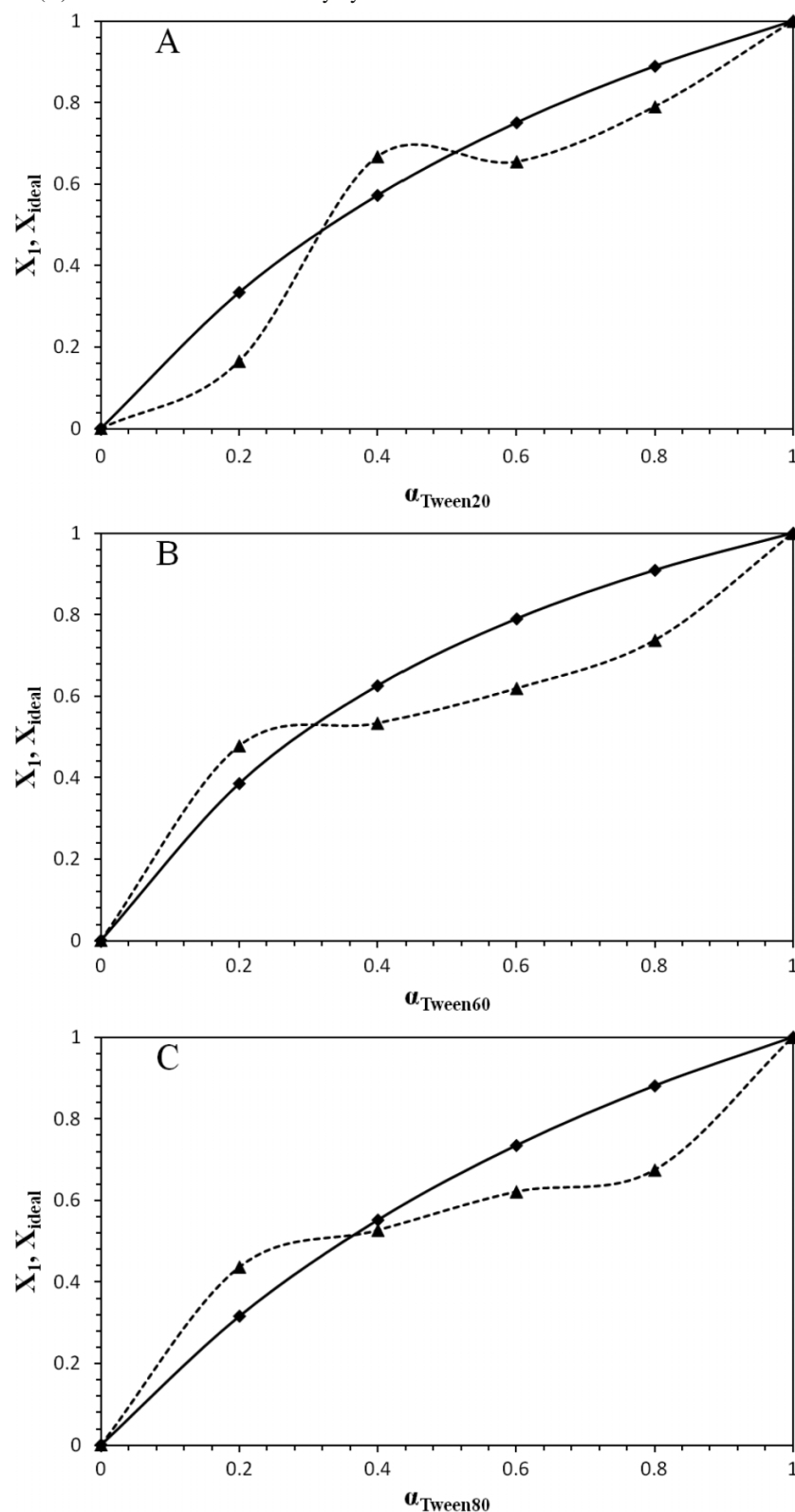
The disparities in interaction between the Tween surfactants and 16-3-16 can be rationalized using Maeda's theory<sup>29</sup> for mixed surfactant systems. According to Maeda,<sup>29</sup> the transfer process of an ionic surfactant monomer to a nonionic micelle will consist of two distinct contributions: (i) the interaction between the surfactant head groups and (ii) the interaction between the hydrocarbon chains of the respective surfactants.<sup>29</sup> In most cases, the surfactant chains that are interacting are of the same structure and of similar length; hence, this contribution is usually minor to the overall enhancement of the micellar and surface properties. If the hydrocarbon tail dissimilarity is small, differences observed in the  $\beta$  values should be interpreted in terms of a steric factor owing to differences in the head group structures. In our case, since the head groups of the nonionic species are the same in the three systems, any differences in the  $\beta$  values amongst the three Tween–gemini systems can most likely be attributed to differences in the hydrocarbon tail of the Tween surfactants.

As shown in Fig. 4, it is observed that for a fixed micellar composition, i.e., for a constant value of  $\alpha_{\text{Tween}}$ , the stability of the mixed system decreases as the alkyl chain length of the Tween surfactant becomes shorter (Tween 60 and Tween 80 vs Tween 20). Furthermore, the stability of the mixed system is shown to increase as the unsaturation is removed in the Tween alkyl tail (Tween 80 vs Tween 60). This mixed micellar stability dependence on the alkyl chain

length is consistent with the substantial contribution from the enhanced steric compatibility between the two surfactants as the alkyl chain length of the Tween surfactant is increased. As the sorbitan head groups are interspersed with the gemini surfactant head groups, the attractive interactions between the nonionic and the cationic surfactants in the micellar phase is caused by a decreased electrostatic repulsion between the positively charged gemini head groups by the nonionic surfactant. Sterically, the size of the respective head groups coupled with the decreased electrostatic repulsions leads to a change in the radius of curvature of the micelle and a change in the micelle packing parameter, resulting in a more efficient packing of the gemini surfactants in the mixed micelle vs the respective gemini and Tween micelles. It is clear that in this case, lengthening the hydrocarbon chain leads to an increase in close packing of the Tween and the gemini surfactants, which results in significant stabilization of the Tween–gemini mixed systems. Thus, Tween 60 and Tween 80 should experience a more synergistic interaction with 16-3-16, in comparison with Tween 20. With regard to the effect of alkyl tail saturation, replacement of a single bond in the middle of the chain with a double bond (in the case of the Tween 60 and Tween 80) destabilizes the micelles because of the entropy difference of the alkenyl chains of the Tween 80 vs the saturated alkyl chain of the Tween 60.

In general, the behaviours observed in Fig. 4 can be explained by taking into account the effect that the repulsive interactions of the cationic head groups has on the stability of the mixed micelles. The incorporation of the nonionic surfactants amongst the cationic surfactants in the mixed micelle reduces the destabilizing effect of these strong repulsive interactions. It is interesting to point out that some authors have indicated that the stabilization of mixed micelles composed of cationic surfactants and nonionic surfac-

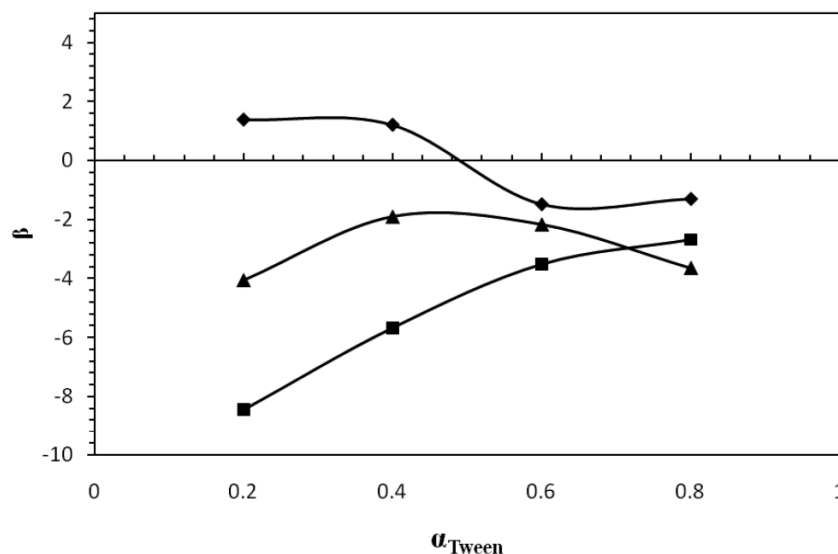
**Fig. 3.** Micellar mole fractions,  $X_1$  ( $\blacktriangle$ ) and  $X_{\text{ideal}}$  ( $\blacklozenge$ ), as a function of the mole fraction of Tween ( $\alpha_{\text{Tween}}$ ) for the (A) Tween 20 + 16-3-16, (B) Tween 60 + 16-3-16, and (C) Tween 80 + 16-3-16 binary systems.



tants consisting of polyoxyethylene (POE) groups could be explained on the basis of the ion-dipole interactions occurring between the ether oxygens and the cationic head groups.<sup>19,30</sup> Although this is a possible contribution, the sta-

bilization that occurs between the cationic gemini surfactant and the nonionic Tween surfactant in the mixed micelles is most likely consistent with electrostatic stabilization because of the progressive replacement of the gemini surfactant with

**Fig. 4.** Interaction parameter ( $\beta$ ) as a function of the mole fraction of Tween ( $\alpha_{\text{Tween}}$ ).  $\beta$  values are represented as (◆) for Tween 20, (■) for the Tween 60 systems, and (▲) for the Tween 80 binary systems with 16-3-16.



nonionic surfactants in the micelle. There may, however, also be a stabilizing interaction between the large positive charge on the head group of the gemini surfactant and the polar ethylene oxide chain and sorbitan ring of the Tweens.

It is important to note that in all cases, the magnitude of  $\beta$  was found to vary with the molar fraction of the Tween surfactant (see Fig. 4). According to Rubingh's theory, the interaction parameter should remain constant over the entire range of composition.<sup>12</sup> However, numerous studies have found  $\beta$  to vary with composition, thus showing the shortcomings of Rubingh's approach for characterizing the interaction features for all types of mixed micellar systems.<sup>31–38</sup> In particular, mixtures of ionic and nonionic surfactants have been shown to exhibit a  $\beta$  variation with composition.<sup>31,39–42</sup> Nonetheless, Rubingh's model remains as an effective approach for characterizing the nature and strength of interaction of surfactant mixtures. As illustrated in Fig. 4, there is no apparent trend in the magnitude of  $\beta$  with composition, which has been observed in the literature.<sup>25,41,42</sup>

From the data, it is possible to calculate the composition that gives the minimum cmc value. To find this optimum composition, two criteria must be fulfilled: (i) the  $\beta$  parameter must be negative and (ii)  $|\ln(\text{cmc}_2/\text{cmc}_1)| < |\beta|$ . If these criteria are fulfilled, the point where the cmc for the mixed system has its minimum can be calculated with the following equation

$$[8] \quad \alpha_{\text{Tween}} = X_1 = \frac{\left(\ln \frac{\text{cmc}_1}{\text{cmc}_2} + \beta\right)}{2\beta}$$

According to theory, the minimum occurs when the mole fraction of the surfactants in the micelle is equal to the mole fraction in the solution, and that these conditions correspond to the point of maximum synergism, i.e., when the mixture has the lowest cmc value. For the surfactants used in this study, the minimum occurs at  $\alpha_{\text{Tween}} = 0.59$  for Tween 60–16-3-16 and  $\alpha_{\text{Tween}} = 0.60$  for Tween 80–16-3-16 (note, a minimum cmc value could not be calculated for

the Tween 20–16-3-16 system as it did not satisfy criteria (ii)). These results appear to be in reasonable agreement with the literature, which suggests that the optimum composition should be close to 0.5 when the cmcs for the two surfactants are approximately the same, but the optimum is shifted toward the more hydrophobic surfactant in the case where the cmc values are quite different.<sup>43</sup> In Fig. 3, the surfactant composition in the micelle vs the surfactant composition in the solution is plotted and it can be seen that with the Tween 60 and Tween 80 systems, the composition in the micelle and the composition in the solution only coincide at a single composition. It should be noted, however, that these relations are based upon application of the regular solution theory to these systems in which several assumptions and approximations are used. Hence, these calculated values for conditions of maximum synergism should only be regarded as estimates.

## Conclusions

The nature and strength of the interactions between the 16-3-16 gemini surfactant and a homologous series of Tween surfactants was investigated. The results demonstrate a synergistic mixing behavior between the cationic gemini and the nonionic Tween surfactants, which can be explained in terms of the modified electrostatic repulsions and the change in the micellar packing parameters of the mixed systems vs the respective pure micelles, as the Tweens progressively replace the gemini surfactants in the mixed micelles. The maximum synergistic effect has been observed for the longer chain Tween 60 and Tween 80 surfactants vs the Tween 20 surfactant. Furthermore, the synergistic effect was found to decrease with the presence of an unsaturation in the alkyl tail of the Tween 80 vs Tween 60. These observations may be of interest towards the use of these surfactant mixtures in pharmaceutical applications, in particular in the design of drug delivery systems and in drug stabilization. Furthermore, the synergism observed in these systems may reduce the total amount of these surfactants required

for a particular application, which in turn reduces costs and environmental impact.

## Acknowledgements

The Lauda TE3 tensiometer was purchased with funding received from the Faculty of Science, University of Waterloo. Start-up funding (SDW) from the University of Waterloo is also gratefully acknowledged. The financial support of the Atlantic Innovation Fund, St. Francis Xavier University, and the Natural Sciences and Engineering Research Council of Canada (NSERC) is gratefully acknowledged (DGM).

## References

- (1) Menger, F. M.; Littau, C. A. *J. Am. Chem. Soc.* **1991**, *113* (4), 1451. doi:10.1021/ja00004a077.
- (2) Menger, F. M.; Keiper, J. S. *Angew. Chem. Int. Ed.* **2000**, *39* (11), 1906. doi:10.1002/1521-3773(20000602)39:11<1906::AID-ANIE1906>3.0.CO;2-Q.
- (3) Menger, F. M.; Littau, C. A. *J. Am. Chem. Soc.* **1993**, *115* (22), 10083. doi:10.1021/ja00075a025.
- (4) Alami, E.; Levy, H.; Zana, R.; Skoulios, A. *Langmuir* **1993**, *9* (4), 940. doi:10.1021/la00028a011.
- (5) Danino, D.; Talmon, Y.; Zana, R. *Langmuir* **1995**, *11* (5), 1448. doi:10.1021/la00005a008.
- (6) Xia, J.; Zana, R. Applications of gemini surfactants. In *Gemini Surfactants: Synthesis, Interfacial and Solution-Phase Behavior, and Applications*; New York: Marcel Dekker Inc., 2004; pp 296–313.
- (7) Badea, I.; Verrall, R.; Baca-Estrada, M.; Tikoo, S.; Rosenberg, A.; Kumar, P.; Foldvari, M. *J. Gene Med.* **2005**, *7* (9), 1200. doi:10.1002/jgm.763.
- (8) Foldvari, M.; Badea, I.; Wettig, S.; Verrall, R.; Bagonluri, M. *J. Expr. Nanosci.* **2006**, *1* (2), 165. doi:10.1080/17458080500411965.
- (9) Wettig, S.; Badea, I.; Donkuru, M.; Verrall, R.; Foldvari, M. *J. Gene Med.* **2007**, *9* (8), 649. doi:10.1002/jgm.1060.
- (10) Badea, I.; Wettig, S.; Verrall, R.; Foldvari, M. *Eur. J. Pharm. Biopharm.* **2007**, *65* (3), 414. doi:10.1016/j.ejpb.2007.01.002.
- (11) Clint, J. H. *J. Chem. Soc., Faraday Trans. I* **1975**, *71*, 1327. doi:10.1039/f19757101327.
- (12) Rubingh, D. N. Mixed micellar solutions. In *Solution Chemistry of Surfactants*; New York: Plenum Press, 1979; p 337.
- (13) Rosen, M.; Zhu, B. *J. Colloid Interface Sci.* **1984**, *99* (2), 427. doi:10.1016/0021-9797(84)90129-2.
- (14) Rosen, M. *Langmuir* **1991**, *7* (5), 885. doi:10.1021/la00053a012.
- (15) Holland, P.; Rubingh, D. *Mixed surfactant systems*; ACS Symposium Series 501; American Chemical Society: Washington, DC, 1992.
- (16) McLachlan, A. A.; Marangoni, D. G. *J. Colloid Interface Sci.* **2006**, *295* (1), 243. doi:10.1016/j.jcis.2005.08.008.
- (17) Singh, K.; Marangoni, D. G. *J. Colloid Interface Sci.* **2007**, *315* (2), 620. doi:10.1016/j.jcis.2007.06.062.
- (18) Alargova, R. G.; Kochijashky, I. I.; Sierra, M. L.; Kwetkat, K.; Zana, R. *J. Colloid Interface Sci.* **2001**, *235* (1), 119. doi:10.1006/jcis.2000.7311.
- (19) Soboleva, O.; Badun, G.; Summ, B. *Colloid J.* **2006**, *68* (2), 228. doi:10.1134/S1061933X06020153.
- (20) Zana, R.; Benraou, M.; Rueff, R. *Langmuir* **1991**, *7* (6), 1072. doi:10.1021/la00054a008.
- (21) Imam, T.; Devinsky, F.; Lacko, I.; Mlynarcik, D.; Krasnec, L. *Pharmazie* **1983**, *38*, 308.
- (22) Patist, A.; Bhagwat, S. S.; Penfield, K. W.; Aikens, P.; Shah, D. O. *J. Surfactants Deterg.* **2000**, *3* (1), 53. doi:10.1007/s11743-000-0113-4.
- (23) Motomura, K.; Aratono, M. In *Mixed Surfactant Systems*; New York: Dekker, 1993.
- (24) Suradkar, Y. R.; Bhagwat, S. S. *J. Chem. Eng. Data* **2006**, *51* (6), 2026. doi:10.1021/je060064a.
- (25) Bakshi, M. S.; Sachar, S.; Singh, K.; Shaheen, A. *J. Colloid Interface Sci.* **2005**, *286* (1), 369. doi:10.1016/j.jcis.2004.12.044.
- (26) Scamehorn, J. F. *Phenomena in mixed surfactant systems*; ACS Symposium Series, Vol. 311; American Chemical Society: Washington, DC, 1986.
- (27) Johnsson, B.; Lindman, B.; Holmberg, K.; Kronberg, B. *Surfactant and Polymers in Aqueous Solution*; Chichester: Wiley, 1998.
- (28) Paria, S. *Colloids Surf. A* **2006**, *281* (1–3), 113. doi:10.1016/j.colsurfa.2006.02.023.
- (29) Maeda, H. *J. Colloid Interface Sci.* **1995**, *172* (1), 98. doi:10.1006/jcis.1995.1230.
- (30) Ruiz, C. C.; Aguiar, J. *Mol. Phys.* **1999**, *97* (10), 1095. doi:10.1080/00268979909482910.
- (31) Desai, T. R.; Dixit, S. G. *J. Colloid Interface Sci.* **1996**, *177* (2), 471. doi:10.1006/jcis.1996.0060.
- (32) Basu Ray, R.; Chakraborty, I.; Ghosh, S.; Moulik, S. P. *Colloid Polym. Sci.* **2007**, *285* (4), 457. doi:10.1007/s00396-006-1589-1.
- (33) Ghosh, S.; Moulik, S. *J. Colloid Interface Sci.* **1998**, *208* (2), 357. doi:10.1006/jcis.1998.5752.
- (34) Hua, X. Y.; Rosen, M. J. *J. Colloid Interface Sci.* **1982**, *90* (1), 212. doi:10.1016/0021-9797(82)90414-3.
- (35) Rosen, M. J.; Zhu, Z. H.; Gao, T. J. *J. Colloid Interface Sci.* **1993**, *157* (1), 254. doi:10.1006/jcis.1993.1183.
- (36) Reif, I.; Somasundaran, P. *Langmuir* **1999**, *15* (10), 3411. doi:10.1021/la980103j.
- (37) Treiner, C.; Khodja, A. A.; Fromon, M. *Langmuir* **1987**, *3* (5), 729. doi:10.1021/la00077a027.
- (38) Shiloach, A.; Blankshtein, D. *Langmuir* **1998**, *14* (7), 1618. doi:10.1021/la971151r.
- (39) Khan, I. A.; Mohammad, R.; Alam, Md. S.; Kabir-ud-Din. *J. Chem. Eng. Data* **2010**, *55* (1), 370. doi:10.1021/je9003756.
- (40) Al-Wardian, A. E.; Palepu, R. M. *J. Dispersion Sci. Technol.* **2005**, *26* (2), 155. doi:10.1081/DIS-200045565.
- (41) Bakshi, M. S.; Kaur, G.; Ahmad, I. *Colloid Surf. A* **2005**, *253* (1–3), 1. doi:10.1016/j.colsurfa.2004.10.122.
- (42) Bakshi, M. S.; Singh, J.; Kaur, G. *J. Colloid Interface Sci.* **2005**, *285* (1), 403. doi:10.1016/j.jcis.2004.11.013.
- (43) Theander, K.; Pugh, R. J. *J. Colloid Interface Sci.* **2003**, *267* (1), 9. doi:10.1016/S0021-9797(03)00482-X.



# Baylis–Hillman reaction under solvent-free conditions—Remarkable rate acceleration and yield enhancement

Monmi Saikia and Jadab C. Sarma

**Abstract:** A simple and efficient method has been developed for remarkable rate acceleration and yield enhancement of the Baylis–Hillman reaction under solvent-free “neat conditions” and solvent-less isolation of products. Reaction of equimolar quantities of aldehyde and olefin in the presence of 20 mol% of DABCO under neat conditions affords the highest yield in most cases within the shortest reaction time, giving support to the mechanisms of proton transfer in protic and aprotic solvents. Solvent-free conditions are found to be especially fast, selective, and high yielding for aromatic aldehydes.

**Key words:** Baylis–Hillman reaction, solvent free, rate acceleration, catalyst.

**Résumé :** On a mis au point une méthode simple et efficace augmenter d’une façon remarquable la vitesse et le rendement de la réaction de Baylis–Hillman, dans des conditions sans solvant tant pour la réaction que pour l’extraction des produits. Dans la plupart des cas, les meilleurs rendements ont été obtenus avec les temps de réaction les plus courts par la réaction de quantités équimolaires d’aldéhyde et d’oléfine en présence de 20 mol % de DABCO dans des conditions sans solvant; ces résultats apportent un support au mécanisme de transferts de proton dans des solvants protiques et aprotiques. On a trouvé que pour les aldéhydes aromatiques, les conditions sans solvant sont particulièrement rapides, sélectives et qu’elles donnent des rendements élevés.

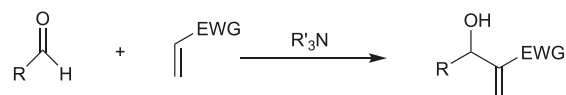
**Mots-clés :** réaction de Baylis–Hillman, sans solvant, accélération de la vitesse, catalyseur.

## Introduction

The Baylis–Hillman reaction<sup>1–4</sup> is an important reaction for carbon–carbon bond formation involving a tertiary amine (or phosphine) catalyzed coupling of an aldehyde with an  $\alpha,\beta$  unsaturated system. This reaction affords a highly functionalized product known as the Baylis–Hillman adduct, with a scope for various chemical manipulations to create frameworks for complex molecules (Scheme 1). Although the reaction was first reported in the early 1980s,<sup>5</sup> its synthetic appreciation was at a low profile in the initial stages. For the last two decades, the Baylis–Hillman reaction has attracted the curiosity of synthetic organic chemists, and the reaction has followed an exponential growth in terms of all the three essential components, i.e., activated olefin, the electrophile, and the catalyst.

Usually the Baylis–Hillman reaction is a slow reaction and requires a few days to a few weeks for completion depending upon the reactivities of both the activated alkene and the aldehyde.<sup>1</sup> Because of the synthetic potential<sup>6</sup> of the Baylis–Hillman adducts, various modifications of the experimental protocol have been proposed. Several groups of scientists had been directing their efforts to solve the problem of slow reaction rate vis-à-vis enhancement of the chemical yield. In this connection some groups of workers have

Scheme 1.



studied the variations of reaction speed and chemical yield by using different Lewis bases such as DABCO, DMAP, DBU,  $\text{Ph}_3\text{P}$ , imidazole, ionic liquid immobilized quinuclidine, tetramethyl guanidine, etc.<sup>7</sup> A few others have tried different solvents or solvent mixtures along with the effect of stoichiometry of the reactants and the catalyst.<sup>8</sup> Additives such as salt, another base as co-catalyst,<sup>9</sup> or external influences such as high pressure,<sup>10</sup> mechanical agitation,<sup>11</sup> ultrasound agitation,<sup>12</sup> etc., were applied to try to improve the rate as well as the yield of the reaction.

Coelho et al.<sup>12</sup> reported on the application of ultrasound radiation in the Baylis–Hillman reaction to obtain augmentation of the reaction rate and the chemical yield. They compared the reactivity of two catalysts viz. tri-*n*-butyl phosphine and 1,4-diazabicyclo[2.2.2]octane (DABCO) and found the later to be the catalyst of choice under ultrasound irradiation. The time for completion of the reaction was drastically reduced from 72 to 16 h for 4-nitrobenzaldehyde and from 480 to 96 h for piperonal and so on. Not only was

Received 7 December 2009. Accepted 25 August 2010. Published on the NRC Research Press Web site at canjchem.nrc.ca on 1 December 2010.

M. Saikia and J.C. Sarma.<sup>1</sup> Natural Products Chemistry Division, North-East Institute of Science and Technology, Jorhat 785006, Assam, India. (A constituent establishment of the Council of Scientific and Industrial Research, New Delhi, India).

<sup>1</sup>Corresponding author (e-mail: sarmajc04@yahoo.com).

the reaction rate enhanced, but also the chemical yield was improved substantially.

Another report of rate acceleration for the Baylis–Hillman reaction was published by Park et al.<sup>13</sup> They found remarkable rate acceleration by using octanol as an additive to the Baylis–Hillman reaction mixture.

Very recently deSouza et al.<sup>14</sup> reported rate and yield enhancement of the Baylis–Hillman reaction through utilization of an aqueous–organic solvent mixture. For the coupling of 4-nitrobenzaldehyde with acrylonitrile, *tert*-butyl alcohol–water (60:40) was reported to be the system of choice (reaction time, 20 min; yield, 99%), whereas for the same aldehyde with methyl acrylate, DMSO–water (60:40) gave better results (reaction time, 150 min; yield, 90%). In both cases, a fast reaction was observed only when the catalyst was used in a stoichiometric amount. Earlier, Yu et al.<sup>8</sup> developed a similar set of conditions using a stoichiometric amount of base catalyst DABCO and an aqueous medium to overcome the problem of long reaction time. To cite an example, the reaction of 4-nitrobenzaldehyde with methyl acrylate in the presence of DABCO (1:3:1 ratio) yielded 83% of the adduct in 3 h.

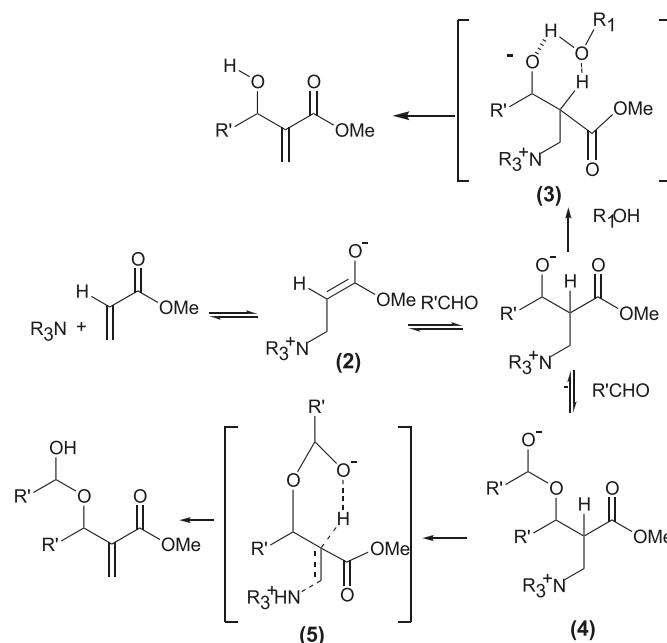
Porto et al.<sup>15</sup> and Rosa et al.<sup>16</sup> have used an ionic solvent for better yield and a faster reaction rate. Reaction time was also reduced notably and the yield of the adduct increased substantially as in the case of the reaction of 4-nitrobenzaldehyde with methyl acrylate, which afforded a 99% yield in 4 h.

## Results and discussion

The Baylis–Hillman reaction itself falls under the green chemistry transformation because of its total atom efficiency. Under green chemistry protocol, a solvent-free non-stoichiometric catalytic reaction with atom efficiency is a major criterion of greenness. Although a lot of reports have dealt with the issue of rate and yield enhancement for the Baylis–Hillman reaction, there has been no reporting from the green chemistry point of view, especially with regards to the reaction under neat conditions for synthetic utilization. However, a mechanistic study by Aggarwal et al.<sup>17</sup> used neat conditions. In other reports of the reaction under solvent-free neat conditions by Aggarwal and Mereu,<sup>18</sup> Park et al.<sup>13</sup>, and Mack and Shumba<sup>11</sup>, an additional co-catalyst or some external device is being used along with DABCO, and the thrust of the study revolves round the co-catalyst or the external device to show its importance in rate and yield enhancement. Mack and Shumba<sup>11</sup> stressed the utility of a high-speed ball milling device as a novel technique for better yield of the reaction products in as little as 0.5 h of reaction time. Whereas in the study by Park et al.<sup>13</sup> octanol was used as the additive for the acceleration of rate and enhancement of yield, Aggarwal and Mereu<sup>17</sup> demonstrated that lanthanoids were an essential co-catalyst.

In a recent report, Das et al.<sup>19</sup> demonstrated a practical method for the *aza*-Morita–Baylis–Hillman reaction using  $\alpha$ -amido sulfone as the substrate. Here, an excess of alkene was used under neat conditions with a stoichiometric amount of catalyst. Gajda and Gajda<sup>20</sup> also reported an *aza*-Morita–Baylis–Hillman reaction with *N*-carbamate protected  $\alpha$ -amidoalkyl-*p*-tolylsulfones using excess alkene. Similar in

Scheme 2.



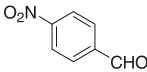
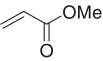
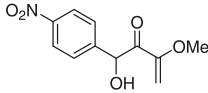

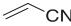
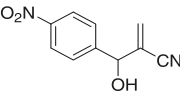
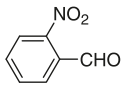
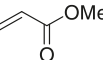
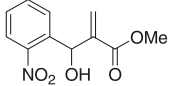
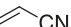
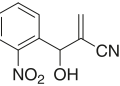
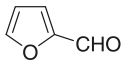
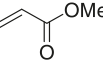
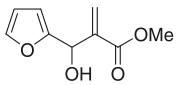

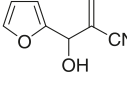
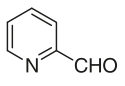
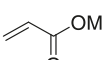
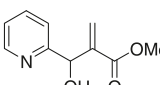
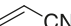
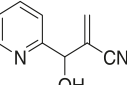
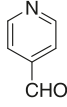
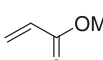
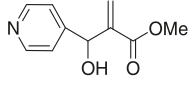
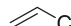
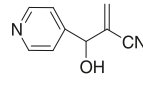
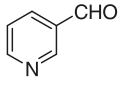
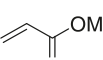
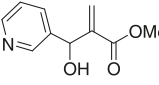
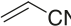
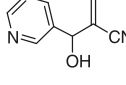
situ generation of imines in the *aza*-Morita–Baylis–Hillman reaction was also reported recently by Abermil et al.<sup>21</sup> and Cihlova et al.<sup>22</sup> They used chlorinated compounds such as  $\text{CH}_2\text{Cl}_2$  and  $\text{CHCl}_3$  as the solvent of choice.

From the scrutiny of the reactions reported by Park et al.,<sup>13</sup> a kinetic study done by McQuade and co-workers,<sup>23</sup> a re-evaluation of the mechanism done by Aggarwal and Lloyd-Jones<sup>24</sup>, and a computational study done by Aggarwal and Harvey<sup>25</sup>, it becomes apparent that proton transfer is accelerated in the presence of a protic additive such as alcohol. (Scheme 2) Aggarwal and Harvey<sup>25</sup> has again shown that in the absence of a protic additive, the reaction is autocatalytic, because the product alcohol itself can act as a hydrogen-bond donor to promote the proton transfer in the transition state (TS) (3).<sup>17</sup> In aprotic solvent or under neat conditions without sufficient quantities of alcohol at the early stage of the reaction, McQuade's<sup>23</sup> pathway involving the hemiacetal intermediate (5) must be operating. In time, as the reaction progresses (>20% conversion) the reaction becomes autocatalytic. Protonation of the enolate (2) by octanol as the solvent (not as an additive) may be the reason for the slow reaction as reported by Park et al.<sup>13</sup> Indeed this more favorable interaction would stabilize the enolate and render it less reactive and thus slow down the reaction rate.

Considering all these factors we decided to try the Baylis–Hillman reaction under solvent-free conditions, keeping the other parameters constant. To our satisfaction the reaction carried out under neat conditions gave a far better result than the ones done with additives like octanol, lanthanoids, etc. In all cases the reaction was over within a very short time, giving a higher yield than those reported in all the other methods. Our observations are compiled in Table 1. The reactions used an equimolar concentration with 20% of DABCO as the catalyst.

For direct comparison of the results obtained using the octanol additive method, we performed a few reactions of aldehydes with methyl vinyl ketone under neat conditions,

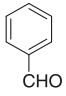
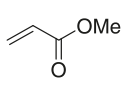
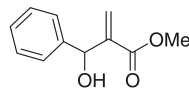
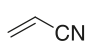
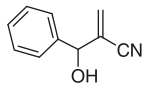
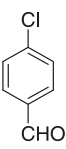
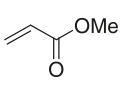
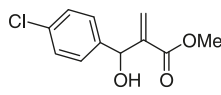
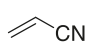
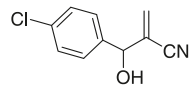
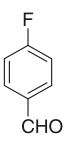
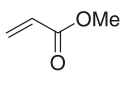
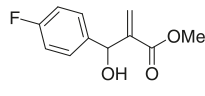
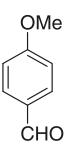
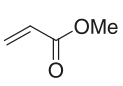
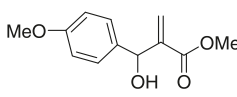
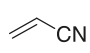
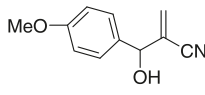
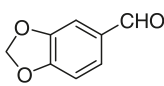
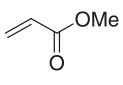
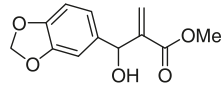
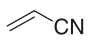
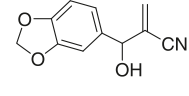
**Table 1.** Baylis–Hillman reaction of aldehyde with Michael acceptor.

Entry	Aldehyde	Alkene	Time (h)	Product <sup>a</sup>	Yield (%)	Ref.
1			0.30		99	12
2			0.20		97	7
			0.75		98	7
			0.20		99	—
3			0.75		97	12
			0.30		99	—
4			0.75		98	12
			0.20		98	12
5			0.5		100	7
			0.30		99	—
6			0.75		100	12
			0.20		99	—

keeping the other parameters fixed. The comparative results are shown in Table 2. In all the cases, except for acetaldehyde, the present method gives a better yield in a shorter time period. For aliphatic aldehydes such as propanal and its higher homologues, the reaction is very slow as usual. In fact, decanal remained unchanged for 15 days under neat conditions. For formaldehyde and acetaldehyde, there was some reaction with the formation of a BH adduct and the

dimer at a reasonable speed. As these aldehydes were used as a water solution, and considering the rate enhancement of the small aliphatic aldehydes to be due to the presence of water (a hydrogen-bond donor), we tried the reaction of propanal and decanal by adding three drops each of water in the medium, respectively. In both the cases with methyl acrylate and methyl vinyl ketone as the reactive alkenes, there was no appreciable change over 24 h, thereby indicat-

**Table 1.** (concluded).

Entry	Aldehyde	Alkene	Time (h)	Product <sup>a</sup>	Yield (%)	Ref.
7			1.5		94	12
			1.0		99	7
8			4.5		98	12
			1.2		99	7
9			3.5		100	8
10			45		75	12
			16		98	7
11			42		80	12
			15		95	12

Note: Aldehyde (1 mmol) was stirred with alkene (1mmol) in presence of DABCO (20 mol%) at room temperature.

<sup>a</sup> Products were characterized by using <sup>1</sup>H and <sup>13</sup>C NMR, FT-IR, and MS analysis.

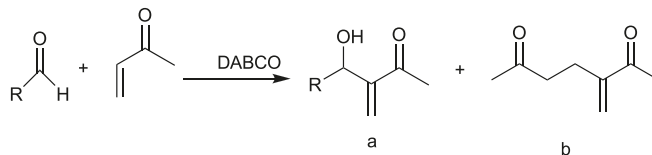
ing the present method to be selective for aromatic aldehydes.

In many earlier reactions, alkene was added in large excess with 100% catalyst loading. Later on, the stoichiometry was brought to equimolar with 50% to 15% loading of the catalyst. If participation of the aldehyde as a hemiacetal in the TS for proton transfer is important in aprotic solvents, then an excess of aldehyde should enhance the rate of the reaction. Therefore, we used a few otherwise sluggish aldehydes by adding 10% excess to that of the alkene under neat conditions with 20% of catalyst (DABCO) loading to see the difference. From the results shown in Table 3, it is clear that for the substrates of entries 1–3 the reaction time was

reduced substantially (in comparison with Table 1). For 4-methoxy benzaldehyde, the yield was enhanced, but the reaction time remained the same, and for piperonal, there was no appreciable change.

In reactions generally carried out under solvent-free conditions, the solvent is normally required to be used at a later stage (at the time of extraction of the product from the reaction mixture) and, therefore, the claim for a solvent-free green method substantially gets diluted. We, therefore, tried a representative reaction of 4-nitrobenzaldehyde with methyl acrylate in a 2 g scale and worked up by pouring the reaction mixture into ice-cold water. Precipitated product was recrystallized from ethanol to get 98% yield of the pure



**Table 2.** Comparative results of the two methods.

Entry	R	Alkene	Time (h)	Yield (%)		Methods
				a	b	
1	4-NO <sub>2</sub> C <sub>6</sub> H <sub>4</sub>	MVK	1	94	2	Present study
			12	70	0	Reference 13
2	4-ClC <sub>6</sub> H <sub>4</sub>	MVK	6	90	3.5	Present study
			12	70	0	Reference 13
3	4-MeOC <sub>6</sub> H <sub>4</sub>	MVK	50	68	10	Present study
			12	18	43	Referenec 13
4	Furfuryl	MVK	0.5	95	0	Present study
			12	26	10	Reference 13
5	CH <sub>3</sub>	MVK	3	78	10	Present study
			12	90	6	Reference 13

**Note:** MVK, methyl vinyl ketone.

**Table 3.** The effect of excess aldehyde.

Entry	R	EWG	Time (h)	Yield (%)
1	4-ClC <sub>6</sub> H <sub>4</sub>	COOMe	3.5	98
2	4-NO <sub>2</sub> C <sub>6</sub> H <sub>4</sub>	COOMe	0.25	99
3	2-NO <sub>2</sub> C <sub>6</sub> H <sub>4</sub>	COOMe	0.5	99
4	4-MeOC <sub>6</sub> H <sub>4</sub>	COOMe	45	80
5	Piperonal	COOMe	42	80

**Note:** EWG, electron-withdrawing group.

crystalline product. Thus, the method turned out to be a complete solvent-free green method.

## Conclusion

In conclusion, we report a green method with significant rate enhancement as well as yield improvement of the Baylis–Hillman reaction through solvent-free conditions. The method is bestowed with several unique green features such as a solvent-free neat reaction, a catalytic transformation, a solvent-less simple work up procedure for large-scale reaction, a higher yield than those reported so far in almost all cases, and the shortest reaction time. Hence, it significantly contributes to synthetic organic chemistry.

## Experimental

### General procedure for the Baylis–Hillman reaction

In a 50 mL round bottom flask, an equimolar quantity of aldehyde was stirred with an electron-deficient alkene with 20 mol% of DABCO as the catalyst at room temperature. The progress of the reaction was monitored by TLC. On completion, the reaction was poured into water and extracted with ethyl acetate. The extract was dried over anhydrous sodium sulfate, and the solvent was removed under reduced pressure to get a solid mass, which in most cases was recrystallized from ethanol. Otherwise, filtering through a short silica gel column yielded the pure product.

When the reaction was carried out in a 2 g scale of 4-nitrobenzaldehyde, the product was isolated by pouring the reaction mixture over ice-cold water followed by filtering and recrystallization of the product from ethanol. All the known compounds reported in Table 3 have been found to give spectral data identical to those reported. The spectral and other data of the compounds not reported earlier are reproduced here.

### 3-Hydroxy-2-methylene-3-(2-nitrophenyl) propanenitrile (entry 2, Table 3)

Gummy mater. IR (CHCl<sub>3</sub>, cm<sup>-1</sup>): 3436, 3090, 2229, 1527, 1348, 1055, 1038, 957. <sup>1</sup>H NMR (CDCl<sub>3</sub>, 300 MHz) δ: 8.06 (m, 1H), 7.85 (m, 1H), 7.75 (t, *J* = 7.7 Hz, 1H), 7.56 (t, *J* = 7.7 Hz, 1H), 6.18 (s, 1H), 6.15 (s, 1H), 5.98 (s, 1H), 3.42 (brs 1H). <sup>13</sup>C NMR: 147.90, 134.58, 134.30, 132.24, 129.80, 129.16, 125.16, 124.17, 116.62, 69.14. MS (*m/z*): 204 (M<sup>+</sup>, 2), 202.8 (16), 186.7 (100), 170.9 (6), 158.7 (22), 140.5 (64), 113.9 (8).

### 3-Hydroxy-2-methylene-3-(2-furyl) propanenitrile (entry 3, Table 3)

Gummy mater. IR (CHCl<sub>3</sub>, cm<sup>-1</sup>): 3420, 2919, 2231, 1625, 1399, 1145, 1014, 958. <sup>1</sup>H NMR (CDCl<sub>3</sub>, 300 MHz) δ: 7.44 (s, 1H), 6.41 (m, 2H), 6.20 (s, 1H), 6.15 (s, 1H), 5.36 (s, 1H), 2.43 (brs, 1H). <sup>13</sup>C NMR: 151.45, 143.42, 131.43, 123.28, 116.70, 110.75, 108.77, 67.70. MS (*m/z*): 150 (M + 1, 6), 148.9 (60), 131.8 (10), 120.9 (5), 97.2 (50), 96.7 (100), 76.9 (12), 68.9 (22).

### 3-Hydroxy-2-methylene-3-(4-pyridyl)propanenitrile (entry 5, Table 3)

mp 111–113 °C (ethanol). IR (CHCl<sub>3</sub>, cm<sup>-1</sup>): 3427, 2854, 2227, 1603, 1414, 1072, 1060, 1005. <sup>1</sup>H NMR (CDCl<sub>3</sub>, 300 MHz) δ: 8.57 (m, 2H), 7.38 (m, 2H), 6.19 (s, 1H), 6.11 (s, 1H), 5.35 (s, 1H). <sup>13</sup>C NMR: 149.55, 149.42, 130.84, 125.72, 121.65, 116.56, 72.57. MS (*m/z*): 161 (M + 1, 14), 159.9 (66), 131 (8), 107.8 (100), 105.9 (8), 79.9 (38), 77.9

(24), 52 (74). Anal. calcd. for  $C_9H_8N_2O$ : C 67.49, H 5.03, N 17.48; found: C 67.15, H 5.07, N 17.21.

### 3-Hydroxy-2-methylene-3-(3-pyridyl)propanenitrile (entry 6, Table 3)

mp 101–103 °C (ethanol). IR ( $CHCl_3$ ,  $cm^{-1}$ ): 3420, 2850, 2227, 1597, 1582, 1480, 1428, 1067, 1030, 955.  $^1H$  NMR ( $CDCl_3$ , 300 MHz)  $\delta$ : 8.43–8.45 (overlapping m, 2H), 7.81 (d,  $J = 7.8$  Hz, 1H), 7.34–7.38 (m, 1H), 6.19 (s, 1H), 6.08 (s, 1H), 5.36 (s, 1H).  $^{13}C$  NMR: 148.9, 147.4, 136.3, 135.2, 130.5, 126, 124.2, 116.8, 71.6. MS ( $m/z$ ): 161 ( $M + 1$ , 16), 160 ( $M + 50$ ), 141.9 (6), 130.8 (8), 107.9 (100), 79.9 (58), 77.9 (26), 52.9 (10). Anal. calcd. for  $C_9H_8N_2O$ : C 67.49, H 5.03, N 17.48; found: C 66.97, H 5.06, N 17.14.

### Acknowledgements

The authors are grateful to the Director, North-East Institute of Science and Technology (NEIST), Jorhat, India, for providing the facilities and to Dr. N.C. Barua for his interest and encouragement during the work. Thanks are also due to the Analytical Chemistry Division for recording the spectra. The authors would also like to thank one of the reviewers for his suggestions and specific comments, which helped in revising the manuscript.

### References

- (1) Basavaiah, D.; Rao, A. J.; Satyanarayana, T. *Chem. Rev.* **2003**, *103* (3), 811. doi:10.1021/cr010043d. PMID: 12630854.
- (2) Basavaiah, D.; Venkateswara Rao, K.; Jannapu Reddy, R. *Chem. Soc. Rev.* **2007**, *36* (10), 1581. doi:10.1039/b613741p. PMID: 17721583.
- (3) Jenn, T.; Heissler, D. *Tetrahedron* **1998**, *54* (1-2), 97. doi:10.1016/S0040-4020(97)10259-9.
- (4) Price, K. E.; Broadwater, S. J.; Walker, B. J.; McQuade, D. T. *J. Org. Chem.* **2005**, *70* (10), 3980. doi:10.1021/jo050202j. PMID: 15876086.
- (5) Ciganek, E. *Organic Reactions*; Wiley: New York, 1997; Vol. 51, pp 201–350.
- (6) Singh, V.; Batra, S. *Tetrahedron* **2008**, *64* (20), 4511. doi:10.1016/j.tet.2008.02.087.
- (7) Mi, X.; Luo, S.; Cheng, J. P. *J. Org. Chem.* **2005**, *70* (6), 2338, and references cited therein. doi:10.1021/jo048391d. PMID: 15760226.
- (8) Yu, C.; Liu, B.; Hu, L. *J. Org. Chem.* **2001**, *66* (16), 5413. doi:10.1021/jo015628m. PMID: 11485463.
- (9) Shi, M.; Jiang, J. K.; Li, C. Q. *Tetrahedron Lett.* **2002**, *43* (1), 127, and references cited therein. doi:10.1016/S0040-4039(01)02057-3.
- (10) Jenner, G. *High Press. Res.* **1999**, *16* (4), 243. doi:10.1080/08957959908200297.
- (11) Mack, J.; Shumba, M. *Green Chem.* **2007**, *9* (4), 328. doi:10.1039/b612983h.
- (12) Coelho, F.; Almeida, W. P.; Veronese, D.; Mateus, C. R.; Lopes, E. C. S.; Rossi, R. C.; Silveira, G. P. C.; Pavam, C. H. *Tetrahedron* **2002**, *58* (37), 7437. doi:10.1016/S0040-4020(02)00822-0.
- (13) Park, K. S.; Kim, J.; Choo, H.; Chong, Y. *Synlett* **2007**, 395.
- (14) de Souza, R. O. M. A.; Pereira, V. L. P.; Esteves, P. M.; Vasconcellos, M. L. A. A. *Tetrahedron Lett.* **2008**, *49* (41), 5902. doi:10.1016/j.tetlet.2008.07.140.
- (15) Porto, R. S.; Amarante, G. W.; Cavallaro, M.; Poppi, R. J.; Coelho, F. *Tetrahedron Lett.* **2009**, *50* (11), 1184. doi:10.1016/j.tetlet.2008.12.089.
- (16) Rosa, J. N.; Afonso, C. A. M.; Santos, A. G. *Tetrahedron* **2001**, *57* (19), 4189. doi:10.1016/S0040-4020(01)00316-7.
- (17) Aggarwal, V. K.; Emme, I.; Fulford, S. Y. *J. Org. Chem.* **2003**, *68* (3), 692. doi:10.1021/jo026671s. PMID: 12558387.
- (18) Aggarwal, V. K.; Mereu, A. *Chem. Commun. (Camb.)* **1999**, (22): 2311. doi:10.1039/a907754e.
- (19) Das, B.; Damodar, K.; Chowdhury, N.; Saritha, D.; Ravikanth, B.; Krishnaiah, M. *Tetrahedron* **2008**, *64* (40), 9396. doi:10.1016/j.tet.2008.07.093.
- (20) Gajda, A.; Gajda, T. *J. Org. Chem.* **2008**, *73* (21), 8643. doi:10.1021/jo801616d. PMID: 18821802.
- (21) Abermil, N.; Masson, G.; Zhu, J. *Adv. Synth. Catal.* **2010**, *352* (4), 656. doi:10.1002/adsc.200900900.
- (22) Cihalova, S.; Remes, M.; Cisarova, I.; Vesely, J. *Eur. J. Org. Chem.* **2009**, 6277.
- (23) Price, K. E.; Broadwater, S. J.; Jung, H. M.; McQuade, D. T. *Org. Lett.* **2005**, *7* (1), 147. doi:10.1021/ol047739o. PMID: 15624999.
- (24) Aggarwal, V. K.; Fulford, S. Y.; Lloyd-Jones, G. C. *Angew. Chem. Int. Ed.* **2005**, *44* (11), 1706. doi:10.1002/anie.200462462.
- (25) Robiette, R.; Aggarwal, V. K.; Harvey, J. N. *J. Am. Chem. Soc.* **2007**, *129* (50), 15513. doi:10.1021/ja0717865. PMID: 18041831.

# An improved one-pot cost-effective synthesis of N,N-disubstituted carbamoyl halides and derivatives

K. Adeppa, D.C. Rupainwar, and Krishna Misra

**Abstract:** A convenient one-pot procedure is reported for preparing N,N-disubstituted carbamoyl chlorides by using chlorocarbonylsulfenyl chloride as a carbonylating agent. It comprises the reaction of secondary amines with chlorocarbonylsulfenyl chloride in the presence of an aprotic organic solvent to produce the corresponding N,N-disubstituted carbamoyl halides. Insertion of the carbonyl group without using phosgene is the novelty of this method.

**Key words:** carbonylsulfenyl chloride, secondary amines, dichloromethane, carbamoyl halides.

**Résumé :** On a développé une méthode monotope pour préparer des chlorures de carbamoyle N,N-disubstitués qui fait appel au chlorure de chlorocarbonylsulfényle comme agent de carbonylation. Elle implique la réaction d'amines secondaires avec le chlorure de chlorocarbonylsulfényle en présence d'un solvant organique aprotique qui conduit à la formation des halogénures de carbamoyles N,N-disubstitués correspondants. La nouveauté de cette méthode correspond à l'insertion d'un groupe carbonyle sans faire appel au phosgène.

**Mots-clés :** chlorure de chlorocarbonylsulfényle, amines secondaires, dichlorométhane, halogénures de carbamoyle.

## Introduction

Carbamoyl halides<sup>1</sup> are an important class of commercially viable chemicals. These are useful intermediates in the preparation of thiolcarbamate herbicides via their reaction with thiols such as sodium alkyl mercaptides. Carbamoyl halides, particularly chlorides, are useful in the preparation of 1,4-disubstituted 5-(4*H*)-tetrazolinones;<sup>2</sup> imidazole derivatives;<sup>3</sup> Reissert analogs;<sup>4</sup> phenylcarbamates;<sup>5</sup> unsymmetrical ureas; pyrrole-*N*-carbonyl compounds;<sup>6</sup> *O*- $\alpha$ -oxoalkylcarbamates;<sup>7</sup> *O*-allylic urethanes and carbonates;<sup>8</sup> in the synthesis of carbamates;<sup>9</sup> phthalides;<sup>10</sup> in the preparation of arylisocyanates;<sup>11</sup> *N,N*-dimethyl carbamoyloxy-3-thiodiazoles-1,2,4;<sup>12</sup> and *N,N*-dialkylcarbamate esters. Carbamoyl chlorides are also used for Friedel-Crafts acylation<sup>13</sup> followed by treatment with ammonia or amines to produce aromatic amides or substituted amides, which on hydrolysis yield corresponding acids. For example, *N,N*-dimethyl carbamoyl chloride has been used in the production of herbicides<sup>14</sup> such as isoproturon, fenuron, diuron, and metoxuron, and with drugs such as neostigmine bromide, neostigmine methylsulfate,<sup>15</sup> and pyridostigmine, which is the intermediate for the antihistaminic bulk drug loratidine. *N,N*-Diethyl carbamoyl chloride has been used as an intermediate for the antifilarial bulk drug diethylcarbamazine citrate. *N*-Ethyl-*N*-methyl carbamoyl chloride is used as an intermediate for the bulk drugs rivastigmine and  $\beta$ -propiolactone.

So far, the most prevalent commercial method for producing carbamoyl chlorides is phosgenation of ammonia or

amines.<sup>16,17</sup> The main objective of the present work was to develop an efficient and economically viable procedure for preparing N,N-disubstituted carbamoyl chlorides. A further objective was to exploit the procedure for the preparation of unsymmetrical ureas<sup>18</sup> and N,N-disubstituted carbamate esters,<sup>19</sup> aromatic amides,<sup>20</sup> and thiolcarbamate herbicides. For the preparation of N,N-disubstituted carbamoyl chlorides, the commercial process involves the phosgenation of secondary amines. The use of phosgene, however, has several disadvantages. The phosgenation route is long and energy-intensive, and requires handling highly corrosive materials and highly toxic reagents and intermediates, especially phosgene and chlorine. Furthermore, the phosgenation route requires the use of process equipment that can withstand high temperatures and highly corrosive conditions, resulting in increased capital cost.

A non-phosgene process for preparing N,N-disubstituted carbamoyl chlorides, which is economical and commercially viable and that can produce N,N-disubstituted carbamoyl chlorides with good yields under extremely mild reaction conditions and short reaction times, is highly desirable. Such an attempt has been made during the present work.

## Results and discussion

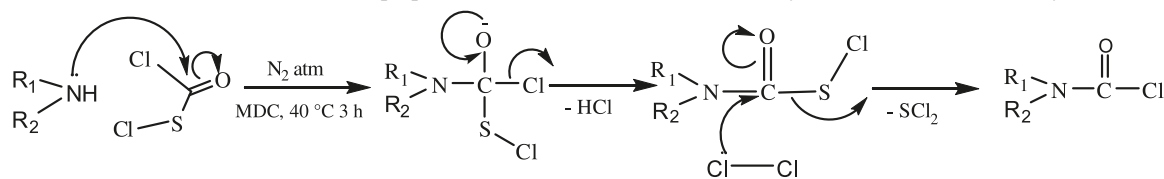
To develop a general method for the synthesis of carbamoyl chlorides and their derivatives, experiments were conducted through the carbonylation of secondary amines with chlorocarbonylsulfenyl chloride at  $\sim 40^\circ\text{C}$  for 3 h and

Received 25 March 2010. Accepted 17 August 2010. Published on the NRC Research Press Web site at canjchem.nrc.ca on 1 December 2010.

K. Adeppa and D.C. Rupainwar. U.P. Technical University, Lucknow (U.P.)-226000, India.

K. Misra.<sup>1</sup> Indian Institute of Information Technology, Allahabad (U.P.)-211002, India.

<sup>1</sup>Corresponding author (e-mail: kmisra@iiita.ac.in).

**Scheme 1.** Probable reaction mechanism for the preparation of *N,N*-disubstituted carbamoyl chlorides from secondary amines.**Table 1.** Reaction conditions and boiling points of the prepared *N,N*-disubstituted carbamoyl chlorides.

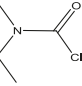
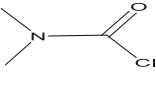
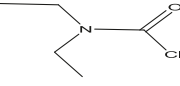
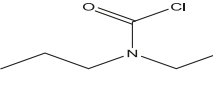
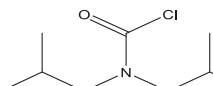
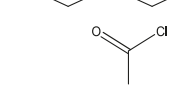
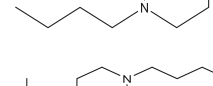
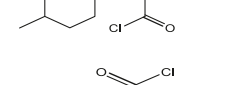
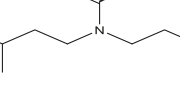
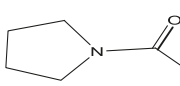
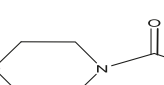
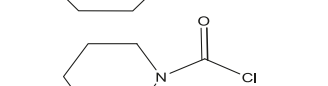
S. No	Secondary amine	<i>N,N</i> -Disubstituted carbamoyl chloride	Reaction time	Yield (%)	Boiling point (°C)
1			5h	90.00	bp <sub>40</sub> : 88-89
2			5h 20min	88.00	bp <sub>175</sub> : 167-168
3			5h 50min	88.60	bp <sub>15</sub> : 60-62
4			6h 50min	82.20	bp <sub>10</sub> : 115-116
5			6h 25min	84.00	bp <sub>15</sub> : 114-118
6			5h 20min	85.00	bp <sub>4</sub> : 99-101
7			6h 35min	88.20	bp <sub>2</sub> : 140-142
8			4h 55min	91.20	bp <sub>15</sub> : 136-140
9			6h 20min	86.40	bp <sub>20</sub> : 124-125
10			7h 10min	82.00	bp <sub>8</sub> : 101-103
11			7h 30min	85.60	bp <sub>13</sub> : 111-112
12			7h 15min	84.1	bp <sub>0.1</sub> : 150-152

chlorination at room temperature for 2 h under nitrogen using dichloromethane as a solvent. To explore the general method developed for the synthesis of carbamoyl chloride derivatives, the experiments were conducted with chlorocarbonylsulfenyl chloride and a variety of secondary alkyl amines followed by chlorination to give the corresponding *N,N*-disubstituted carbamoyl chloride derivatives in substantial yields.

We found that this one-step reaction is general and is applicable to most secondary alkyl amines. The reaction conditions for the preparation of *N,N*-disubstituted carbamoyl chlorides starting from different secondary alkyl amines are summarized in Table 1, and the GC analysis as compared with the standard samples are summarized in Table 2. A probable mechanism for the preparation of *N,N*-disubstituted carbamoyl chlorides from different secondary alkyl amines



**Table 2.** Comparative GC retention time data of prepared compounds vs standard compounds

Serial No.	<i>N,N</i> -Disubstituted carbamoyl chloride	Retention time (min)	
		Sample	Standard
1		5.62	5.62
2		4.32	4.32
3		6.56	6.56
4		6.75	6.75
5		5.95	5.95
6		5.86	5.86
7		6.43	6.43
8		7.32	7.32
9		6.52	6.52
10		7.20	7.20
11		6.32	6.32
12		6.50	6.50

**Note:** GC, THERMO Fischer model GC 1000; 8 ft glass (0.8 mm ID); 10% SE-30 on Chromosorb W (80–100 mesh); initial column temperature, 70 °C for 2 min; temperature rise rate, 25 °C/min; final column temperature, 240 °C held for 5 min; injector temperature, 240 °C; detector temperature, 250 °C. Two hundred milligrams of the sample and the standard were dissolved in 5 mL of toluene and 0.5 µL of each solution was injected.

has been suggested in Scheme 1. The present method has obvious advantages, compared with those reported in the literature, namely milder reaction conditions, use of less toxic materials, and better yields resulting in cost effectiveness of the procedure and general applicability.

## Experimental details

Dimethylamine, diethylamine, di-*n*-propylamine, diisopropyl amine, *N,N*-ethyl-methylamine, di-*n*-butylamine, piperidine, and dichloromethane were sponsored by Merck

(India), and perchloromethyl mercaptan was sponsored by India Pesticides Limited (Lucknow, India). All the products gave satisfactory boiling points. Gas chromatographic analysis was performed on a Thermo Fisher model GC-1000 gas chromatograph, and the results were consistent with the literature data.

## Chlorocarbonylsulphenyl chloride (CCSC)<sup>21</sup>

Perchloromethyl mercaptan (PCMM) (294 mL, 500 g, 2.7 mol) was taken in a 2 L reaction flask equipped with a reflux condenser, a thermometer, and a stirrer, and a mixture

of water (54 mL, 3.0 mol) in concd sulfuric acid (620 mL) was added. The heterogenous mixture was vigorously stirred for 6 h at 45–50 °C as HCl evolved, and then stirred overnight at 25 °C to ensure complete reaction of PCMM at the expense of a decreased yield of chlorocarbonylsulfenyl chloride (CCSC), which can hydrolyze. The upper phase (280 g, 80%) was separated and distilled through a column, bp 98–101 °C (lit.,<sup>21</sup> bp 98 °C) to yield 230 g (65%) of the clear light yellow liquid of CCSC (65%).

### General procedure for the preparation of *N,N*-dialkylcarbamoyl chlorides

A stirred solution of secondary amine (0.47 mol) in 800 mL dichloromethane in a 2 L reaction flask equipped with a reflux condenser and a stirrer was heated at ~40 °C under nitrogen. CCSC (65.50 g, 0.50 mol) at ~40 °C under nitrogen was added with stirring. The reaction mixture was stirred for an additional 3 h under reflux until evolution of HCl gas was completed. After cooling to room temperature (RT), the dark green liquid was chlorinated with chlorine (35.5 g, 0.50 mol) and the reaction mass was stirred for an additional 2 h under these conditions, followed by distillation at atmospheric pressure to remove solvent and sulfur dichloride. This reddish brown material was transferred into a 100 mL capacity distillation flask and distilled under reduced pressure (10 mm Hg; 1 mmHg = 133.3224 Pa). The total yield of *N,N*-disubstituted carbamoyl chloride was 80%–86%. Retention times in GLC as compared with the standard are given in Table 2.

### Conclusion

The present method describes a simple, efficient one-pot method for the synthesis of commercially important *N,N*-disubstituted carbamoyl chlorides from the corresponding secondary amines and chlorocarbonylsulfenyl chloride. The process is economically viable; the enhanced rate of reaction, negligible byproducts, and cleaner reaction profiles make it a useful and attractive process for synthesis. The generalized and simple product-isolation procedures play an important role in the development of this novel method. It is an important step toward developing a greener and more efficient commercial synthesis for a group of compounds that are used to make important intermediates for the synthesis of a large number of commercially important products. This is an improvement over the phosgenation method being used at present.

### Acknowledgements

The authors gratefully acknowledge the Centre for Biomedical Magnetic Resonance (CBMR), the Sanjay Gandhi Post Graduate Institute of Medical Sciences (SGPGI), Lucknow, India, for NMR spectra, and the Central Drug Research Institute (CDRI), Lucknow, India, for IR spectra. One of the authors (K. Adeppa) is grateful to India Pesticides Limited,

Lucknow, India, for providing all laboratory facilities and financial support, which enabled the present work to be completed successfully.

### References

- (1) Lide, D. R. Properties of dimethylcarbamoyl chloride. In *CRC Handbook of Chemistry and Physics*; 87th ed.; CRC Press: Boca Raton, FL 2006–2007; p 4002.
- (2) Yanagi, A.; Watanabe, Y.; Narabu, S.-i. Process for the Preparation of 1-4-Disubstituted-5 (4*H*)-Tetrazolinones. U.S. Patent 5,767,286, 1998.
- (3) Ngochindo, R. I. *J. Chem. Soc., Perkin Trans. 1* **1990**, 1645. doi:10.1030/P19900001645.
- (4) Badawey, E.-S. A. M.; Kappe, T. *J. Heterocycl. Chem.* **1991**, 28 (4), 995. doi:10.1002/jhet.5570280427.
- (5) Enz, A. Process for the Preparation of Phenyl Carbamate. U.S. Patent 5,602,176, 1997.
- (6) Boger, D. L.; Patel, M. *J. Org. Chem.* **1987**, 52 (11), 2319. doi:10.1021/jo00387a046.
- (7) Bruneau, C.; Dixneuf, P. H. *Tetrahedron Lett.* **1987**, 28 (18), 2005. doi:10.1016/S0040-4039(00)96031-3.
- (8) McGhee, W. D.; Riley, D. P.; Christ, M. E.; Christ, K. M. *Organometallics* **1993**, 12 (4), 1429. doi:10.1021/om00028a069.
- (9) Sang, C. S.; Jin, O. B.; Chil, H. D.; Young, Z. Y.; Tae, J. K. *Bull. Korean Chem. Soc.* **1990**, 11 (5), 467.
- (10) Paleo, M. R.; Lamas, C.; Castedo, L.; Dominguez, D. *J. Org. Chem.* **1992**, 57 (7), 2029. doi:10.1021/jo00033a024.
- (11) Bacaloglu, R.; Bunton, C. A. *Tetrahedron* **1973**, 29 (18), 2725. doi:10.1016/S0040-4020(01)93393-9.
- (12) Taliani, L.; Perronnet, J. *J. Heterocycl. Chem.* **1979**, 16 (5), 961. doi:10.1002/jhet.5570160527.
- (13) Olah, G. A.; Reddy, V. P.; Prakash, G. K. S. Friedel–Crafts Reactions. In *Kirk–Othmer Encyclopedia of Chemical Technology*; 3rd ed.; John Wiley and Sons, Inc.: New York, 1982; Vol. 11, p 286.
- (14) Plimmer, J. R.; Bradow, J. M.; Dionigi, C. P.; Johnson, R. M.; Wojkowski, S. Herbicides. In *Kirk–Othmer Encyclopedia of Chemical Technology*; 3rd ed.; John Wiley and Sons, Inc.: New York, 1982; Vol. 12, pp 324–325.
- (15) Finklea, J. F. *Correspondence — Current Intelligence Bulletin 11, Dimethylcarbamoyl chloride (DMCC)*; National Institute for Occupational Safety and Health: Cincinnati, OH, 1976; Revised.
- (16) Tilles, H. *J. Am. Chem. Soc.* **1959**, 81 (3), 714. doi:10.1021/ja01512a052.
- (17) Hoshino, O.; Saito, K.; Ishizaki, M.; Umezawa, B. *Synth. Commun.* **1987**, 17 (16), 1887. doi:10.1080/00397918708057799.
- (18) Van Gool, M.; Bartolomé, J. M.; Macdonald, G. J. *Tetrahedron Lett.* **2008**, 49 (50), 7171. doi:10.1016/j.tetlet.2008.09.171.
- (19) Rosin, M. W.; Chorev, M. T. Process for the preparation of phenyl carbamate. U.S. Patent 4,948,807, 1990.
- (20) Lemoucheux, L.; Seitz, T.; Rouden, J.; Lasne, M. C. *Org. Lett.* **2004**, 6 (21), 3703. doi:10.1021/ol0487130.
- (21) Weiss, W. German Patent 1224720, 1964.

# Canadian Journal of Chemistry

Author Index  
Volume 88, 2010

# Revue canadienne de chimie

Index des auteurs  
Volume 88, 2010

- Abderrabba, M., 613  
Abdul Rahman, N.I., 654  
Adamescu, A., 65  
Adeppa, K., 1277  
Aghapour, G., 598  
Ahmed, Z., 910  
Akbar, J.R., 1262  
Al-Abadleh, H.A., 65  
Alamdari, R.F., 563  
Ali, A.A.-S., 725  
Ali, D., 910  
Alizadeh, A., 514  
Alkorta, I., 694  
Andrei, G., 628  
Arabi, A.A., 1057  
Araújo, R.C.M.U., 338  
Asano, T., 839  
Ased, A., 1040  
Atkinson, D.B., 1017  
Ayadi, S., 613  
Baker, J., 588  
Balakrishnan, V.K., 393  
Balzarini, J., 628  
Bandrauk, A.D., 1186  
Bar, S., 605  
Barik, S., 945  
Barnes, J.A., 401  
Basilevsky, M.V., 839  
Becke, A.D., 1057  
Bedell, B.J., 969  
Beg, S., 5  
Bejan, D., 418, 928  
Benn, M.H., 831  
Beshara, C.S., 1009  
Bi, J., 1205  
Bleeker, R.S., 50  
Bohle, D.S., 969  
Bolduc, A., 236  
Bordbar, A.-K., 155  
Bosdet, M.J.D., 426  
Boudreau, J., 418  
Brash, J.L., 411  
Brisach-Wittmeyer, A., 463  
Bulut, M., 375  
Bunce, N.J., 418, 928  
Buncel, E., 910  
Burford, N., 797  
Burnell, D.J., 1118  
Burt, M.B., 1094  
Cameron, T.S., 725, 1154  
Çamur, M., 375  
Cao, L.J., 352  
Cardoso Filho, J.E.P., 996  
Carmichael, C.D., 667  
Carrington, T., Jr., 779  
Carvalho, A.B., 338  
Chadha, P., 1213  
Chan, B., 866  
Chan, J.K., 1125  
Chang, S.W., 519  
Chen, J.-R., 331  
Cheng, H., 954  
Choi, P., 260  
Chong, D.P., 577, 787  
Chu, T.S., 893  
Chua, Z., 969  
Cipot-Wechsler, J., 725  
Clements, A., 5  
Conrad, E., 797  
Cook, E., 99  
Cooper, L., 142  
Correa, J.V., 858  
Cortés, J., 383  
Crane, A.K., 1094  
Crane, S.N., 1118  
Crawford, S.M., 725  
Cristea, C., 42  
Czerniewski, A., 969  
Dai, B., 453  
Dan, Y., 185  
Dance, P., 839  
Das, S., 150  
Davis, B., 548  
De Clercq, E., 628  
Del Bene, J.E., 694  
Deng, J., 754  
De Proft, F., 858  
Deubry, R., 1262  
DiLabio, G.A., 1053  
Ding, Z., 569  
Di Vitta, C., 996  
Divsalar, A., 155  
Djukic, B., 954  
Dlugy, C., 305  
Doucet, K.G., 709  
Dufresne, S., 236  
Duhamel, J., 217  
Dutton, J.L., 1213  
Edwards, E., 839  
Eftekhar, A., 104  
Elguero, J., 694  
El-Sherif, S., 928  
El-Zoghbi, I., 1040  
Emwas, A.-H.M., 111  
Eshghi, A., 514  
Evans, A.C., 969  
Everett, W.C., 1112  
Fasano, D.M., 500  
Feng, H., 185  
Feng, R., 898  
Ferguson, M.J., 797  
Fitzwater, S.J., 500  
Ford, T.A., 716  
Foucher, D.A., 1046  
Fournier, R., 1071  
Fowe, E.P., 1186  
Frenking, G., 1079  
Friedland, S., 945  
Fryzuk, M.D., 667  
Gagliardi, G., 401  
Gaina, L., 42  
Gao, F., 1256  
Gauld, J.W., 804  
Geerlings, P., 858  
Georges, P., 104  
Gharib, F., 877  
Gholizadeh, M., 135  
Gilbert, A.T.B., 754  
Gill, P.M.W., 754  
Giri, B.R., 1136  
Glister, J.F., 709  
Goraltchouk, A., 277  
Gorelsky, S.I., 954  
Gossage, R.A., 1046  
Gosse, A.L., 1118  
Gourevich, I., 298  
Grabowski, S.J., 769  
Gray, H., 65  
Grein, F., 1125  
Grindley, T.B., 1154  
Guan, W., 434  
Guest, M.F., 142  
Gul, M., 323  
Guo, H., 622  
Gupta, P., 478  
Gupta, S., 478  
Guthrie, J.P., 79  
Guzon, D., 646  
Haghdoust, M., 135  
Hajra, A., 150  
Hamilton, I.P., 65  
Hanan, G.S., 236  
Harisha, R.S., 443  
Hassanzadeh, N., 579  
Hata, K., 1026  
Hatefipour, R., 598  
Hawe, G.I., 1104  
Heard, G.L., 1112  
Heiney, P.A., 639  
Hernandez-Marin, E., 683  
Hesp, K.D., 700  
Hof, F., 1009  
Hojati, S.F., 135  
Holland, D.M.P., 142  
Holmes, B.E., 1112

- Holý, A., 628  
 Hope-Ross, K.A., 639, 1003  
 Hor, A.-M., 247  
 Hosamani, K.M., 443  
 Hou, L., 1256  
 Hou, S., 35  
 Houle, S., 1222  
 Hsieh, Y.-H., 56  
 Huang, C.-F., 228  
 Huang, W., 804  
 Huang, Y.Y., 831  
 Hubicki, Z., 540  
 Hue, T.T., 849  
 Hunter, N., 344  
 Hurtado, M., 744  
 Ingold, K.U., 1053  
 Ingratta, M., 217  
 Iqbal, M., 434  
 Irfan, A., 434  
 Jabbari, M., 877  
 Jachulá, J., 540  
 Jacques, C., 50  
 Jäger, W., 1146  
 James, B.R., 886  
 Janeba, Z., 628  
 Janjua, M.R.S.A., 434  
 Jaque, P., 858  
 Jay-Gerin, J.-P., 646, 1026  
 Jenkins, H.A., 954  
 Jessop, P.G., 548  
 Ji, H.B., 352  
 Ji, L., 362  
 Jiang, Z., 964  
 Jiao, S.-y., 367  
 Jin, B., 485  
 Jin, Z., 411  
 Johannsen, F., 831  
 Johnson, M.J., 309  
 Jokar, M., 14  
 Joshi, P., 1034  
 Joshi, Y.C., 1034  
 Joycharat, N., 937  
 Kadla, J.F., 639, 1003  
 Kamble, R.M., 1233  
 Kang, L., 453  
 Kanjana-Opas, A., 922  
 Kannemann, F.O., 1057  
 Karalai, C., 922  
 Kate, A.S., 318  
 Katsumura, Y., 1026  
 Kavita, 1034  
 Kavitha, C.S., 443  
 Kazmaier, P.M., 910  
 Kennedy, D.C., 886  
 Kerr, R.G., 318  
 Khan, A., 1046  
 Khan, F., 247  
 Khanna, S., 247  
 Khodaei, M.M., 514  
 Khurana, J.M., 906  
 Kim, C.-K., 56  
 Kim, K.H., 519  
 Klobukowski, M., 1136  
 Kobasa, I., 659  
 Koç, İ., 375  
 Kołodzyńska, D., 540  
 Kondratyeva, I., 659  
 Kosari, M., 579  
 Krapp, A., 1079  
 Kumacheva, E., 298  
 Kundu, D., 150  
 Lamsabhi, A.M., 759  
 Lau, W., 500  
 Lavoie, S., 104  
 Lee, K.R., 519  
 Legault, J., 104  
 Lemaire, M.T., 954  
 Le Roy, R.J., 1146  
 Lewis, M., 5  
 Li, A.Y., 352  
 Li, H., 1146  
 Li, M., 981  
 Li, N., 260  
 Li, R., 401  
 Li, Y., 898  
 Liang, H., 1154  
 Liao, J., 331  
 Liko, I., 1125  
 Lin, M., 1026  
 Liu, D., 208  
 Liu, J., 208  
 Liu, L., 898  
 Liu, W., 35  
 Liu, Y., 1146  
 Liu, Z., 485, 622  
 Llano, J., 804  
 Lo, J.M.H., 1136  
 Long, Y., 569  
 Loock, H.-P., 401  
 Lukeman, M., 493  
 MacKay, M., 1154  
 MacKinnon, C.D., 309  
 MacLaren, D.C., 1063  
 Majee, A., 150  
 Maleki, B., 135  
 Mamo, D.C., 1222  
 Marangoni, D.G., 124, 1262  
 Marino, D.C., 533  
 Marriott, R.A., 1136  
 Martić, S., 524  
 Marzorati, L., 996  
 Masuda, J.D., 99  
 Mathew, M., 217  
 Matsuda, E., 556  
 Matyjaszewski, K., 228  
 Mawhinney, R.C., 309  
 Mayer, P.M., 142  
 McDonald, R., 700, 797  
 McGrath, A.J., 736  
 McLachlan, A.A., 124  
 Meesungnoen, J., 646, 1026  
 Ménard, H., 463  
 Meng, Q., 981  
 Messier, T., 493  
 Miller, D.O., 1118  
 Ming-Hua, L., 1205  
 Misra, K., 1277  
 Mó, O., 744, 759  
 Mohammadi, F., 155  
 Mohammadi, K., 155  
 Mohammadpoor-Baltork, I., 135  
 Molaei, H., 164  
 Montaut, S., 50  
 Morakinyo, M.K., 1247  
 Morshead, C.M., 277  
 Moya, H.D., 533  
 Mroué, K.H., 111  
 Mshvildadze, V., 104  
 Muchall, H.M., 1175  
 Muhammad, S., 434  
 Muir, M., 588  
 Mulsant, B.H., 1222  
 Muroya, Y., 1026  
 Mzengeza, S., 969  
 Nair, S.V., 298  
 Nakajima, A., 556  
 Nakashima, K., 208  
 Nand, B., 906  
 Nawaz, Q., 288  
 Ngaini, Z., 654  
 Nguyen, M.T., 849  
 Niknam, K., 164  
 Nkeng, P., 463  
 Nordstrom, C.M., 736  
 Nori-Shargh, D., 579  
 Nussaiba, N., 277  
 Ocal, N., 323  
 Odosiy, L., 659  
 Oguadinma, P.O., 472, 1040  
 Oh, J.K., 173  
 Oleschuk, R.D., 401  
 Oliveira, B.G., 338  
 O'Reilly, M., 831  
 Otoikhian, A.A., 1247  
 Özkaya, A.R., 375  
 Palabrica, V., 393  
 Panthong, K., 937  
 Parvez, M., 426, 831  
 Paton, A.S., 298  
 Paudel, A., 458  
 Peiris, S., 79  
 Pekcan, Ö., 267  
 Peslherbe, G.H., 1175  
 Petersen, J.L., 1247  
 Petukhova, A., 298  
 Pichette, A., 104  
 Pickup, J., 797  
 Piers, W.E., 426  
 Plodpai, P., 937  
 Pohl, R., 628  
 Poillerat, G., 463  
 Poirier, R.A., 1094  
 Pollock, B.G., 1222  
 Ponglimanont, C., 922  
 Popelier, P.L.A., 1104  
 Porcar, L., 288  
 Porumb, D., 42  
 Pottier, I.R., 1118  
 Power, W.P., 111  
 Pye, C.C., 709  
 Qian, G., 192  
 Rabieikarahrudi, P., 579  
 Radom, L., 866  
 Ragogna, P.J., 27, 1213  
 Rahman, M., 150  
 Ramana, M.M.V., 1233  
 Ramanathan, B., 318  
 Ramasami, P., 716



- Ramos, M.N., 338  
 Rauk, A., 831  
 Ravenelle, F., 202  
 Ren, X., 1240  
 Rennie, E.E., 142  
 Rharbi, Y., 288  
 Rice, N., 1094  
 Richard, K., 318  
 Robertson, C.M., 309  
 Robertson, K.N., 1154  
 Rong, H., 1205  
 Roscoe, J.M., 1136  
 Roy, P.-N., 1146  
 Ruda, H.E., 298  
 Rudolf, B., 991  
 Rupainwar, D.C., 1277  
 Rutledge, L.R., 815  
 Saberi, D., 164  
 Sabino, L.Z.L., 533  
 Saboury, A.A., 155  
 Sachar, A., 478  
 Saikia, M., 1271  
 Salae, A.-W., 922  
 Sarma, J.C., 1271  
 Scanga, V.I., 277  
 Schaper, F., 472, 1040  
 Sears, W.A., 309  
 Selim, O., 725  
 Shafieezadeh, F., 135  
 Shao-Ming, C., 1205  
 Sharghi, H., 14  
 Sharifi, S., 579  
 Sharma, N., 1034  
 Sharma, R.L., 478  
 Shaw, D.A., 142  
 Sheppard, A.C., 500  
 Sheviev, O., 305  
 Shik, A., 298  
 Shimizu, T., 458  
 Shoichet, M.S., 277  
 Shpinkova, L.G., 142  
 Silaghi-Dumitrescu, I., 42  
 Silaghi-Dumitrescu, L., 42  
 Simkin, M., 79  
 Simoyi, R.H., 1247  
 Sinnemaki, L.C., 309  
 Skene, W.G., 236, 945  
 Snoeck, R., 628  
 Song, Y.-Z., 676  
 Sorensen, T., 831  
 Sorensen, T.S., 426  
 Stewart, K.M.E., 65  
 Stoddard, R.L., 725  
 Stradiotto, M., 700  
 Su, N., 1094  
 Su, Z.-M., 434  
 Sun, C., 898  
 Sun, G., 1256  
 Sundararajan, P.R., 247  
 Tajima, K., 556  
 Takagi, N., 1079  
 Tanaka, K., 458  
 Tang, H., 1063  
 Tavor, D., 305  
 Tchirioua, E., 1040  
 Thakkar, A.J., 736  
 Thompson, A., 725  
 Tiekink, E.R.T., 996  
 Tindale, J.J., 27  
 Toro-Labbé, A., 858  
 Tountian, D., 463  
 Tran, D., 5  
 Trung, N.T., 849  
 Ueda, Y., 556  
 Ugalde, J.M., 769  
 Uğur, Ş., 267  
 Valencia, E., 383  
 van Oosten, E.M., 1222  
 Vasdev, N., 1222  
 Vaughan, K., 344  
 von Richthofen, A.A., 996  
 Voravuthikunchai, S.P., 937  
 Wächter, H., 401  
 Waggoner, K., 5  
 Wang, C.-j., 367  
 Wang, F., 981  
 Wang, L., 964  
 Wang, M., 260  
 Wang, S., 524  
 Wang, X.-G., 779  
 Wang, Y., 79, 622  
 Wang, Y.J., 202  
 Wang, Y.-x., 367  
 Wang, Z.Y., 192  
 Ward, S., 493  
 Wechsler, D., 548  
 Wedian, F., 1017  
 Wei, Y., 362  
 Weinberg, N., 839  
 Werstiuk, N.H., 1195  
 Wetmore, S.D., 815  
 Wettig, S.D., 1262  
 White, M.A., 1063  
 Wilson, A.A., 1222  
 Winter, A.J., 309  
 Wolfe, S., 1, 56  
 Wolfson, A., 305  
 Wu, D., 964  
 Wu, G., 524  
 Wu, Z., 964  
 Xia, A., 99  
 Xiao, W.-J., 331  
 Xie, J., 622  
 Xu, K.-x., 367  
 Yahyaee, H., 579  
 Yamashita, S., 1026  
 Yamato, T., 458  
 Yan, Y., 1026  
 Yan, Z., 1205  
 Yáñez, M., 744, 759  
 Yang, F., 622  
 Yang, K., 1, 56  
 Yargi, Ö., 267  
 Yingyongnarongkul, B.-e., 937  
 Yokoyama, Y., 208  
 Yoneda, A., 208  
 Yong-Cun, Y., 1205  
 Yoon, J.A., 228  
 Yousfi, M., 288  
 Yu, C., 485  
 Yu-Fei, W., 1205  
 Yuenyongsawad, S., 922  
 Yusa, S.-i., 208  
 Zekri, N., 563  
 Zhang, D., 1240  
 Zhang, H., 56  
 Zhang, L., 1175  
 Zhang, M., 569  
 Zhang, Q., 362  
 Zhang, T.Y., 893  
 Zhang, Y., 260  
 Zhao, D., 893  
 Zhao, J., 367  
 Zhao, X., 569  
 Zhao, Y., 185  
 Zhao, Z.K., 35  
 Zhong, W., 485  
 Zhou, L., 1240  
 Zhou, X., 964  
 Zhu, C., 362  
 Zhu, S., 411  
 Zhu, X.X., 202  
 Ziegler, T., 683  
 Zolfigol, M.A., 164  
 Zukerman-Schpector, J., 996

# Canadian Journal of Chemistry

Contents  
Volume 88, 2010

# Revue canadienne de chimie

Sommaire  
Volume 88, 2010

## January / Janvier

### ARTICLES / ARTICLES

- Saul Wolfe and Kiyull Yang** On the role of lysine in the active site Ser-X-X-Lys region of penicillin-recognizing enzymes 1
- Michael Lewis, Shana Beg, Aimee Clements, Dianne Tran, and Kristine Waggoner** The effect of substituent rotation on aromatic quadrupole moments 5
- Hashem Sharghi and Mahboubeh Jokar** Highly stereoselective facile synthesis of  $\beta$ -amino carbonyl compounds via a Mannich-type reaction catalyzed by  $\gamma$ - $\text{Al}_2\text{O}_3/\text{MeSO}_3\text{H}$  (alumina/methanesulfonic acid: AMA) as a recyclable, efficient, and versatile heterogeneous catalyst 14
- Jocelyn J. Tindale and Paul J. Ragogna** Ionophilic phosphonium-appended carbopalladacycle catalyst for Suzuki–Miyaura and Heck cross-coupling catalysis 27
- Wujun Liu, Shuhua Hou, and Zongbao Kent Zhao** Synthesis and electrochemical behavior of triazole-containing nicotinamide adenine dinucleotide analogs 35
- Luiza Gaina, Dan Porumb, Ioan Silaghi-Dumitrescu, Castelia Cristea, and Luminita Silaghi-Dumitrescu** On the microwave-assisted synthesis of acylphenothiazine derivatives — Experiment versus theory synergism 42
- Sabine Montaut, René S. Bleeker, and Carine Jacques** Phytochemical constituents of *Cardamine diphyllo* 50
- Kiyull Yang, Yih-Huang Hsieh, Chan-Kyung Kim, Hui Zhang, and Saul Wolfe** Hydration of acetone in the gas phase and in water solvent 56
- Adrian Adamescu, Holly Gray, Katherine M.E. Stewart, I.P. Hamilton, and Hind A. Al-Abadleh** Trends in the frequencies of  $\nu(\text{AsO}_x\text{H}_{x-1})$  [ $x = 2-4$ ] in selected As(V)-containing compounds investigated using quantum chemical calculations 65

## February / Février

### AWARD LECTURE / CONFÉRENCE D'HONNEUR

- J. Peter Guthrie, Sriyawathie Peiris, Margaret Simkin, and Yun Wang** Rate constants for decarboxylation reactions calculated using no barrier theory 79

### ARTICLES / ARTICLES

- Earl Cook, Jason D. Masuda, and Aibing Xia** Synthesis, characterization, and application of palladium complexes containing 8-quinolylphosphinite ligands 99
- André Pichette, Azadeh Eftekhari, Patricia Georges, Serge Lavoie, Vakhtang Mshvildadze, and Jean Legault** Cytotoxic phenolic compounds in leaf buds of *Populus tremuloides* 104
- Kamal H. Mroué, Abdul-Hamid M. Emwas, and William P. Power** Solid-state  $^{27}\text{Al}$  nuclear magnetic resonance investigation of three aluminum-centered dyes 111
- Aleisha A. McLachlan and D. Gerrard Marangoni** 1D and 2D NMR investigations of the interaction between oppositely charged polymers and surfactants 124
- Seyedeh Fatemeh Hojati, Iraj Mohammadpoor-Baltork, Behrooz Maleki, Mostafa Gholizadeh, Fatemeh Shafieezadeh, and Mahnaz Haghdoust** 1,3-Dibromo-5,5-dimethylhydantoin as an efficient homogeneous catalyst for the synthesis of 2-arylthiazolines and 2-arylimidazolines 135
- Paul M. Mayer, Martyn F. Guest, Emma E. Rennie, Louise Cooper, Larisa G. Shpinkova, David M.P. Holland, and David A. Shaw** Threshold ionization and dissociation of *t*-butylamine 142
- Sudarshan Das, Matiur Rahman, Dhiman Kundu, Adinath Majee, and Alakananda Hajra** Task-specific ionic-liquid-catalyzed efficient synthesis of indole derivatives under solvent-free conditions 150
- Fakhrossadat Mohammadi, Abdol-Khalegh Bordbar, Khosro Mohammadi, Adeleh Divsalar, and Ali Akbar Saboury** Circular dichroism and fluorescence spectroscopic study on the interaction of bisdemethoxycurcumin and diacetylbisdemethoxycurcumin with human serum albumin 155

- Khodabakhsh Niknam, Dariush Saberi, Hajar Molaei, and Mohammad Ali Zolfigol** Silica-bonded *S*-sulfonic acid as a recyclable catalyst for the silylation of hydroxyl groups with hexamethyldisilazane (HMDS) 164

## March / Mars

**This Special Issue is dedicated to Professor Mitchell A. Winnik to honour his outstanding contributions to research in polymer chemistry and physics. / Numéro spécial honorant le professeur Mitchell A. Winnik pour sa contribution exceptionnelle à la chimie et à la physique des polymères.**

### MINIREVIEW / MINISYNTHESE

- Jung Kwon Oh** Engineering of nanometer-sized cross-linked hydrogels for biomedical applications 173

### ARTICLES / ARTICLES

- Haiké Feng, Yi Dan, and Yue Zhao** A sensitive fluorescence method for monitoring the kinetics of microemulsion polymerization 185
- Gang Qian and Zhi Yuan Wang** Design, synthesis, and properties of benzobisthiadiazole-based donor- $\pi$ -acceptor- $\pi$ -donor type of low-band-gap chromophores and polymers 192
- Y.J. Wang, F. Ravenelle, and X.X. Zhu** NMR imaging study of cross-linked high-amylose starch tablets — The effect of drug loading 202
- Jingjing Liu, Airi Yoneda, Dian Liu, Yuuichi Yokoyama, Shin-ichi Yusa, and Kenichi Nakashima** Mixed micelles of poly(styrene-*b*-3-(methacryloylamino)propyltrimethylammonium chloride-*b*-ethylene oxide) and anionic amphiphiles in aqueous solutions 208
- Mark Ingratta, Manoj Mathew, and Jean Duhamel** How switching the substituent of a pyrene derivative from a methyl to a butyl affects the fluorescence response of polystyrene randomly labeled with pyrene 217
- Chih-Feng Huang, Jeong Ae Yoon, and Krzysztof Matyjaszewski** Synthesis of *N*-vinylcarbazole-*N*-vinylpyrrolidone amphiphilic block copolymers by xanthate-mediated controlled radical polymerization 228
- Andréanne Bolduc, Stéphane Dufresne, Garry S. Hanan, and W.G. Skene** Synthesis, photophysics, and electrochemistry of thiophene-pyridine and thiophene-pyrimidine dyad comonomers 236
- Ferdous Khan, Shalini Khanna, Ah-Mee Hor, and P.R. Sundararajan** The role of molecular volume and the shape of the hole transport molecule in the morphology of model charge transport composites 247
- Mingtao Wang, Nan Li, Phillip Choi, and Yaolin Zhang** A study of the intermolecular branch frequency dependence of tie-chain concentration in single-site linear low-density polyethylene blown films by a new FTIR method 260
- Ş. Uğur, Ö. Yargı, and Ö. Pekcan** Conductivity percolation of carbon nanotubes (CNT) in polystyrene (PS) latex film 267
- Vanessa I. Scanga, Alex Goraltchouk, Nasser Nussaiba, Molly S. Shoichet, and Cindi M. Morshead** Biomaterials for neural-tissue engineering — Chitosan supports the survival, migration, and differentiation of adult-derived neural stem and progenitor cells 277
- Y. Rharbi, M. Yousfi, Lionel Porcar, and Q. Nawaz** Methods for probing the long-range dynamic of confined polymers in nanoparticles using small-angle neutron scattering 288
- Alla Petukhova, Andrew S. Paton, Ilya Gourevich, Selvakumar V. Nair, Harry E. Ruda, Alexander Shik, and Eugenia Kumacheva** Hybrid microspheres with alternating layers of a polymer and metal nanoparticles 298

## April / Avril

### ARTICLES / ARTICLES

- Dorith Tavor, Oxana Sheviev, Christina Dlugy, and Adi Wolfson** Transfer hydrogenations of benzaldehyde using glycerol as solvent and hydrogen source 305
- Wendy A. Sears, Craig D. MacKinnon, Robert C. Mawhinney, Lauren C. Sinnemaki, Matthew J. Johnson, A. John Winter, and Craig M. Robertson** Using the nitro group to induce  $\pi$ -stacking in terthiophenes 309
- Abhijeet S. Kate, Kelly Richard, Balaji Ramanathan, and Russell G. Kerr** A halogenated pseudopterane diterpene from the Bahamian octocoral *Pseudopterogorgia acerosa* 318
- Melek Gul and Nuket Ocal** Heck-type hydroarylations and 1,3-dipolar cycloaddition reactions of new tricyclic hydrazones 323
- Jia-Rong Chen, Jie Liao, and Wen-Jing Xiao** Microwave-assisted, palladium-catalyzed carbonylative cyclization — Rapid synthesis of 2-quinolones from unprotected 2-iodoanilines and terminal alkynes 331
- Boaz G. Oliveira, Regiane C.M.U. Araújo, Antônio B. Carvalho, and Mozart N. Ramos** AGOA hydration clusters produce the solvation effect on the aziridine...hydrofluoric acid complex — A modern proposal 338

<b>Naomi Hunter and Keith Vaughan</b> Triazene derivatives of (1, <i>x</i> )-diazacycloalkanes — Part IX. Synthesis and characterization of a series of 1,4-di[2-aryl-1-diazenyl]-2,6-dimethylpiperazines	<b>344</b>
<b>An Yong Li, Li Juan Cao, and Hong Bo Ji</b> Theoretical study of H bonds of HArF and HF with isoelectronic systems N <sub>2</sub> , CO, and BF	<b>352</b>
<b>Chenjie Zhu, Lei Ji, Qian Zhang, and Yunyang Wei</b> Catalytic hypervalent iodine oxidation of alcohols to the corresponding carbonyl compounds using <i>N</i> -hydroxyphthalimide (NHPI) and <i>m</i> -chloroperbenzoic acid	<b>362</b>
<b>Kuo-xi Xu, Yu-xia Wang, Shu-yan Jiao, Jin Zhao, and Chao-jie Wang</b> Enantioselective fluorescent sensors for chiral carboxylates based on BINOL — Synthesis and chiral recognition	<b>367</b>
<b>İmran Koç, Meryem Çamur, Mustafa Bulut, and A. Riza Özkaya</b> Electrochemical and in situ spectroelectrochemical investigations into the redox and aggregation behaviours of phthalocyanines bearing octyl 4-phenyloxyacetate moieties	<b>375</b>
<b>Joaquín Cortés and Eliana Valencia</b> Mean-field study of the synergic effect of the CO–NO reaction on a heterogeneous substrate of interconnected sectors	<b>383</b>
<b>Vimal K. Balakrishnan and Virginia Palabrica</b> Determining the maximum environmental release limit of the toxic dye, CHPD	<b>393</b>

## May / Mai

### AWARD LECTURE / CONFÉRENCE D'HONNEUR

<b>Hans-Peter Looock, Jack A. Barnes, Gianluca Gagliardi, Runkai Li, Richard D. Oleschuk, and Helen Wächter</b> Absorption detection using optical waveguide cavities	<b>401</b>
-----------------------------------------------------------------------------------------------------------------------------------------------------------------------	------------

### ARTICLES / ARTICLES

<b>Zhilin Jin, John L. Brash, and Shiping Zhu</b> ATRP grafting of oligo(ethylene glycol) methacrylates from gold surface — Effect of monomer size on grafted chain and EO unit densities	<b>411</b>
<b>Jordache Boudreau, Dorin Bejan, and Nigel J. Bunce</b> Competition between electrochemical advanced oxidation and electrochemical hypochlorination of acetaminophen at boron-doped diamond and ruthenium dioxide based anodes	<b>418</b>
<b>Michael J.D. Bosdet, Warren E. Piers, Ted S. Sorensen, and Masood Parvez</b> 5b,7b-Diaza-3b,9b-diborabenz[ <i>ghi</i> ]perylene	<b>426</b>
<b>Muhammad Ramzan Saeed Ashraf Janjua, Zhong-Min Su, Wei Guan, Ahmad Irfan, Shabbir Muhammad, and Mudassir Iqbal</b> A DFT study on the electronic and redox properties of [X <sub>8</sub> V <sub>14</sub> O <sub>50</sub> ] <sup><i>n</i>-</sup> (X = Si <sup>IV</sup> , Ge <sup>IV</sup> , P <sup>V</sup> , and As <sup>V</sup> )	<b>434</b>
<b>C.S. Kavitha, K.M. Hosamani, and R.S. Harisha</b> Imino Diels–Alder reaction — An efficient synthetic protocol for 2-methyl-4-substituted tetrahydroquinolines catalyzed by copper dipyrindine dichloride	<b>443</b>
<b>Lihua Kang and Bin Dai</b> Effect of collision energy on cross sections and product alignments for the C( <sup>1</sup> D) + H <sub>2</sub> ( <i>v</i> = 0, <i>j</i> = 0) insertion reactions	<b>453</b>
<b>Tomoe Shimizu, Kan Tanaka, Arjun Paudel, and Takehiko Yamato</b> Medium-sized cyclophanes — Part 85: Benzylolation by 8-(bromomethyl)[2.2]metacyclophanes. Through-space electronic interactions of [2.2]metacyclophane benzyl cations	<b>458</b>
<b>Dihourahouni Tountian, Anne Brisach-Wittmeyer, Paul Nkeng, Gérard Poillerat, and Hugues Ménard</b> On the efficiency of phenol and cyclohexanone electrocatalytic hydrogenation — Effect of conditioning and working pH in acetic acid solution on palladium/fluorine-doped tin dioxide supported catalyst	<b>463</b>
<b>Paul O. Oguadinma and Frank Schaper</b> Synthesis and structures of isopropyl-β-diketiminato copper(I) complexes	<b>472</b>
<b>Anand Sachar, Poonam Gupta, Shallu Gupta, and R.L. Sharma</b> A novel approach towards the synthesis of tricyclic systems based on pyridine, pyran, thiopyran, azepine, oxepin, thiepin, and pyrimidine rings under different solvent conditions	<b>478</b>
<b>Chuanming Yu, Beibei Jin, Zhenyu Liu, and Weihui Zhong</b> A novel and efficient cross-coupling of tris(fluorinated phenyl)boroxins with disulfides catalyzed by CuI/1,10-phenanthroline	<b>485</b>

## June / Juin

### ARTICLES / ARTICLES

<b>Sarah Ward, Tammy Messier, and Matthew Lukeman</b> Electrophilicity of a 9-aryl-9-fluorenyl cation in water — Kinetic evidence for antiaromaticity	<b>493</b>
<b>David M. Fasano, Susan J. Fitzwater, Willie Lau, and Aurelia C. Sheppard</b> Diffusion of oligomers in latex systems — A route to low volatile organic compound (VOC) coatings	<b>500</b>
<b>Abdolhamid Alizadeh, Mohammad M. Khodaei, and Ali Eshghi</b> A solvent-free protocol for the green synthesis of arylalkylidene rhodanines in a task-specific ionic liquid	<b>514</b>
<b>Ki Hyun Kim, Sang Wook Chang, and Kang Ro Lee</b> Feruloyl sucrose derivatives from <i>Bistorta manshuriensis</i>	<b>519</b>
<b>Sanela Martić, Gang Wu, and Suning Wang</b> Interactions of cytidine with N <sup>2</sup> -functionalized guanoses and cytidine–cytidine exchange involving a GC pair — NMR and fluorescence spectroscopic study	<b>524</b>



<b>Larissa Zuppardo Lacerda Sabino, Daniele Cestari Marino, and Horacio Dorigan Moya</b> Determination of diltiazem based on the reduction of Cu(II)–BCA complexes in micellar medium	<b>533</b>
<b>Justyna Jachula, Dorota Kolodyńska, and Zbigniew Hubicki</b> Removal of Cd(II) and Pb(II) complexes with glycolic acid from aqueous solutions on different ion exchangers	<b>540</b>
<b>Dominik Wechsler, Boyd Davis, and Philip G. Jessop</b> The dehydrogenation of combined organic and inorganic hydrogen-storage carriers	<b>548</b>
<b>Akira Nakajima, Emiko Matsuda, Yuto Ueda, and Kunihiro Tajima</b> ESR analysis of the oxidation reactions of phosphorus-containing nitrene-type spin traps with gold(III) ion	<b>556</b>
<b>Negar Zekri and Reza Fareghi Alamdari</b> An efficient and selective method for the preparation of triphenylmethyl ethers of alcohols and nucleosides	<b>563</b>
<b>Xiaocui Zhao, Mengni Zhang, Yitao Long, and Zhifeng Ding</b> Redox reactions of reactive oxygen species in aqueous solutions as the probe for scanning electrochemical microscopy of single live T24 cells	<b>569</b>
<b>ADDITIONS AND CORRECTIONS / AJOUTS ET CORRECTIONS</b>	
<b>Delano P. Chong</b> Theoretical study of the electron spectra of <i>s</i> -triazine vapour	<b>577</b>

## July / Juillet

### ARTICLES / ARTICLES

<b>Davood Nori-Shargh, Neda Hassanzadeh, Meisam Kosari, Parvin Rabieikarahrudi, Hooriye Yahyaei, and Sasan Sharifi</b> Stereoelectronic interaction effects on the conformational properties of 5-methyl-5-aza-1,3-dithiacyclohexane and its analogous containing N, P, O, and Se atoms — A hybrid density functional theory (DFT), ab initio study, and natural bond orbital (NBO) analysis	<b>579</b>
<b>Jon Baker and Max Muir</b> The Meisenheimer model for predicting the principal site for nucleophilic substitution in aromatic perfluorocarbons — Generalization to include ring-nitrogen atoms and non-fluorine ring substituents	<b>588</b>
<b>Ghasem Aghapour and Razieh Hatefipour</b> Catalyst-free, direct, high regio-, and chemo-selective conversion of epoxides to 2-thiocyanatoalkyl alkanoates under neutral and solvent-free conditions	<b>598</b>
<b>Sukanta Bar</b> Organocatalysis in the stereoselective bromohydrin reaction of alkenes	<b>605</b>
<b>Sameh Ayadi and Manef Abderrabba</b> Étude DFT des réactions d'hydrogénation des cyclohexènes disubstitués en position 2 et 3	<b>613</b>
<b>Fafu Yang, Yanhua Wang, Hongyu Guo, Jianwei Xie, and Zhiqiang Liu</b> Novel lariat calix[4]-1,3-aza-crowns with two branched chains — The excellent phase transfer catalysts for nucleophilic substitution reaction	<b>622</b>
<b>Zlatko Janeba, Antonín Holý, Radek Pohl, Robert Snoeck, Graciela Andrei, Erik De Clercq, and Jan Balzarini</b> Synthesis and biological evaluation of acyclic nucleotide analogues with a furo[2,3- <i>d</i> ]pyrimidin-2(3 <i>H</i> )-one base	<b>628</b>
<b>Kyle A. Hope-Ross, Paul A. Heiney, and John F. Kadla</b> A new family of bent-core C <sub>2</sub> -symmetric liquid crystals	<b>639</b>
<b>Jintana Meesungnoen, David Guzonas, and Jean-Paul Jay-Gerin</b> Radiolysis of supercritical water at 400 °C and liquid-like densities near 0.5 g/cm <sup>3</sup> — A Monte Carlo calculation	<b>646</b>
<b>Zainab Ngaini and Norashikin I. Abdul Rahman</b> Synthesis and characterization of chalcone-substituted phosphazenes	<b>654</b>
<b>I. Kobasa, I. Kondratyeva, and L. Odosiy</b> TiO <sub>2</sub> /biscyanine and CdS/biscyanine heterostructures — Influence of the structural composition on the photocatalytic activity	<b>659</b>
<b>Christopher D. Carmichael and Michael D. Fryzuk</b> <i>Ortho</i> -phenylene-bridged aryloxy phosphine ligands and their coordination chemistry with tantalum(V)	<b>667</b>
<b>Yuan-Zhi Song</b> Electrochemical reduction of sunset yellow at a multiwalled carbon nanotube (MWCNT)-modified glassy carbon electrode and its analytical application	<b>676</b>

## August / Août

**This Special Issue is dedicated to Professor Russell J. Boyd to honour his outstanding contributions to theoretical and computational chemistry. / Numéro spécial en hommage au professeur Russell J. Boyd pour souligner sa contribution exceptionnelle au domaine de la chimie théorique et numérique.**

### ARTICLES / ARTICLES

<b>Elizabeth Hernandez-Marin and Tom Ziegler</b> A kinetic study of dimethyl sulfoxide reductase based on density functional theory	<b>683</b>
<b>Janet E. Del Bene, Ibon Alkorta, and José Elguero</b> Do corresponding coupling constants in hydrogen-bonded homo- and hetero-chiral dimers differ?	<b>694</b>

<b>Kevin D. Hesp, Robert McDonald, and Mark Stradiotto</b> Intramolecular hydroamination of unactivated alkenes with secondary alkylamines catalyzed by iridium phosphino–phenolate complexes	<b>700</b>
<b>Katherine G. Doucet, Julie F. Glistler, and Cory C. Pye</b> An ab initio study of model triazene-based anticancer agents	<b>709</b>
<b>Ponnadurai Ramasami and Thomas A. Ford</b> Ab initio studies of the vibrational spectra of some hydrogen-bonded complexes of fluoroacetylene	<b>716</b>
<b>Adeeb Al-Sheikh Ali, Judy Cipot-Wechsler, Sarah M. Crawford, Omar Selim, Rhonda L. Stoddard, T. Stanley Cameron, and Alison Thompson</b> The first series of alkali dipyrinato complexes	<b>725</b>
<b>Cara M. Nordstrom, Alaina J. McGrath, and Ajit J. Thakkar</b> Microsolvation of the formic acid dimer — $(\text{HCOOH})_2(\text{H}_2\text{O})_n$ clusters with $n = 1, \dots, 5$	<b>736</b>
<b>Marcela Hurtado, Otilia Mó, and Manuel Yáñez</b> Homoselenocysteine — An oxygen or selenium acid in the gas phase?	<b>744</b>
<b>Jia Deng, Andrew T.B. Gilbert, and Peter M.W. Gill</b> Diagnostics of molecular orbital quality	<b>754</b>
<b>Al Mokhtar Lamsabhi, Otilia Mó, and Manuel Yáñez</b> Serine– $\text{Ca}^{2+}$ versus serine– $\text{Cu}^{2+}$ complexes — A theoretical perspective	<b>759</b>
<b>Slawomir J. Grabowski and Jesus M. Ugalde</b> Ab initio calculations on $\text{C}_6\text{H}_6\cdots(\text{HF})_n$ clusters — $\text{X}-\text{H}\cdots\pi$ hydrogen bond	<b>769</b>
<b>Xiao-Gang Wang and Tucker Carrington, Jr.</b> Theoretical study of the rovibrational spectrum of $\text{He}_2\text{--OCS}$	<b>779</b>
<b>Delano P. Chong</b> Density functional theory study on the electron spectra of naphthalene and azulene vapours	<b>787</b>
<b>Eamonn Conrad, Janet Pickup, Neil Burford, Robert McDonald, and Michael J. Ferguson</b> Prototypical arsine–triell adducts ( $\text{R}_3\text{AsEX}_3$ for $\text{E} = \text{B}, \text{Al},$ and $\text{Ga}$ )	<b>797</b>
<b>WenJuan Huang, Jorge Llano, and James W. Gauld</b> A DFT study on the catalytic mechanism of UDP-glucose dehydrogenase	<b>804</b>
<b>Lesley R. Rutledge and Stacey D. Wetmore</b> The assessment of density functionals for DNA–protein stacked and T-shaped complexes	<b>815</b>
<b>Michael H. Benn, Yan Yan Huang, Frank Johannsen, Michael O'Reilly, Masood Parvez, Arvi Rauk, and Ted Sorensen</b> Concerning the conformational preferences of the 2-cyano derivatives of oxane, thiane, and selenane	<b>831</b>
<b>Paul Dance, Essex Edwards, Tsutomu Asano, Michael V. Basilevsky, and Noham Weinberg</b> Nonequilibrium solvent effects in reaction kinetics — Steady-state solutions for the Agmon–Hopfield two-dimensional stochastic model	<b>839</b>
<b>Nguyen Tien Trung, Tran Thanh Hue, and Minh Tho Nguyen</b> Theoretical analysis of the $(\text{HNO})_2$ , $(\text{HNO}\cdots\text{HNS})$ , and $(\text{HNS})_2$ dimers — A case of red and blue shifts of N–H stretching frequency	<b>849</b>
<b>Pablo Jaque, José V. Correa, Frank De Proft, Alejandro Toro-Labbé, and Paul Geerlings</b> Regaining the Woodward–Hoffmann rules for chelotropic reactions via conceptual DFT	<b>858</b>
<b>Bun Chan and Leo Radom</b> A computational study of methanol-to-hydrocarbon conversion — Towards the design of a low-barrier process	<b>866</b>

## September / Septembre

### ARTICLES / ARTICLES

<b>Morteza Jabbari and Farrokh Gharib</b> Equilibrium studies of triphenyltin(IV) complexes with glycine, glycyl-glycine, and glycyl-glycyl-glycine in different aqueous solutions of ethanol	<b>877</b>
<b>David C. Kennedy and Brian R. James</b> Syntheses of ruthenium(II)-4,4'-biimidazole complexes and their potential anti-tumour activity	<b>886</b>
<b>Dan Zhao, Tian Yu Zhang, and Tian Shu Chu</b> A quasi-classical trajectory (QCT) study of the $\text{H} + \text{OF}$ reaction stereodynamics	<b>893</b>
<b>Liyan Liu, Ying Li, Rennan Feng, and Changhao Sun</b> Direct ultrasound-assisted methylation of fatty acids in serum for free fatty acid determinations	<b>898</b>
<b>Jitender M. Khurana and Bhaskara Nand</b> Aqueous sodium hypochlorite mediated chemoselective oxidation of chalcogenides to monoxides and dioxides by microwave exposure	<b>906</b>
<b>Dildar Ali, Zaheer Ahmed, Peter M. Kazmaier, and Erwin Buncel</b> Synthesis and characterization of low-molecular-weight azo-acetoxystyrene and azo-naphthalene oligomers via stable free radical polymerization (SFRP)	<b>910</b>
<b>Abdul-Wahab Salae, Chatchanok Karalai, Chanita Ponglimanont, Akkharawit Kanjana-Opas, and Supreeya Yuenyongsawad</b> Naphthalene derivatives from <i>Diospyros wallichii</i>	<b>922</b>
<b>Shaimaa El-Sherif, Dorin Bejan, and Nigel J. Bunce</b> Electrochemical oxidation of sulfide ion in synthetic sour brines using periodic polarity reversal at Ebonex <sup>®</sup> electrodes	<b>928</b>
<b>Nantiya Joycharat, Patimaporn Plodpai, Kanda Panthong, Boon-ek Yingyongnarongkul, and Supayang Piyawan Voravuthikunchai</b> Terpenoid constituents and antifungal activity of <i>Aglaia forbesii</i> seed against phytopathogens	<b>937</b>

<b>Satyananda Barik, Sayuri Friedland, and W.G. Skene</b> Understanding the reversible anodic behaviour and fluorescence properties of fluorenylazomethines — A structure–property study	<b>945</b>
<b>Haojin Cheng, Brandon Djukic, Hilary A. Jenkins, Serge I. Gorelsky, and Martin T. Lemaire</b> Iron(II) complexes containing thiophene-substituted “bispicen” ligands — Spin-crossover, ligand rearrangements, and ferromagnetic interactions	<b>954</b>
<b>Zhaoqiong Jiang, Zhiqing Wu, Lixia Wang, Di Wu, and Xiangge Zhou</b> Preparation of aromatic amines by copper-catalyzed coupling of boronic acids with aqueous ammonia	<b>964</b>
<b>Barry J. Bedell, D. Scott Bohle, Zhijie Chua, Alexander Czerniewski, Alan C. Evans, and Shadreck Mzengeza</b> Novel $\beta$ -galactosidase-specific O <sup>2</sup> -glycosylated diazeniumdiolate probes	<b>969</b>

## October / Octobre

### ARTICLES / ARTICLES

<b>Qingxi Meng, Fen Wang, and Ming Li</b> Bisoxazoline–copper(I)-catalyzed aziridination of diazoacetate with imines — A DFT study	<b>981</b>
<b>Bogna Rudolf</b> Synthesis of metallocarbonyl substituted 1,2,3-triazole complexes via copper(I)-catalyzed azide–alkyne cycloaddition	<b>991</b>
<b>Andreas A. von Richthofen, José E. P. Cardoso Filho, Liliana Marzorati, Julio Zukerman-Schpector, Edward R.T. Tiekink, and Claudio Di Vitta</b> Reactions of toluquinone–cyclopentadiene Diels–Alder epoxide adducts with nucleophiles under heterogeneous conditions	<b>996</b>
<b>Kyle A. Hope-Ross and John F. Kadla</b> Deoxygenation of diarylmethanols with dilute mineral acid	<b>1003</b>
<b>Cory S. Beshara and Fraser Hof</b> Modular incorporation of 1-benzyltryptophan into dipeptide hosts that bind acetylcholine in pure water	<b>1009</b>
<b>Fadel Wedian and Dean B. Atkinson</b> An atmospheric pressure static reactor–ion trap mass spectrometer for studying gas-phase reactions	<b>1017</b>
<b>Y. Yan, M. Lin, Y. Katsumura, Y. Muroya, S. Yamashita, K. Hata, J. Meesungnoen, and J.-P. Jay-Gerin</b> Temperature and density effects on the absorption maximum of solvated electrons in sub- and super-critical methanol	<b>1026</b>
<b>Kavita, P. Joshi, N. Sharma, and Y.C. Joshi</b> Surface-mediated synthesis of organophosphorus-based hydrazides using basic alumina	<b>1034</b>
<b>Ibrahim El-Zoghbi, Aysha Ased, Paul O. Oguadinma, Ekou Tchirioua, and Frank Schaper</b> One-pot synthesis of $\beta$ -diketimine ligands	<b>1040</b>
<b>Aman Khan, Robert A. Gossage, and Daniel A. Foucher</b> A convenient route to distannanes, oligostannanes, and polystannanes	<b>1046</b>

## November / Novembre

**This Special Issue is dedicated to Professor Russell J. Boyd to honour his outstanding contributions to theoretical and computational chemistry. / Numéro spécial en hommage au professeur Russell J. Boyd pour souligner sa contribution exceptionnelle au domaine de la chimie théorique et numérique.**

### ARTICLES / ARTICLES

<b>K.U. Ingold and Gino A. DiLabio</b> Is the oxygen “side-on”, or “end-on” and fluctional, in peroxy radicals with magnetically equivalent oxygen atoms?	<b>1053</b>
<b>Axel D. Becke, Alya A. Arabi, and Felix O. Kannemann</b> Nonempirical density-functional theory for van der Waals interactions	<b>1057</b>
<b>Hong Tang, Douglas C. MacLaren, and Mary Anne White</b> New insights concerning the mechanism of reversible thermochromic mixtures	<b>1063</b>
<b>René Fournier</b> Density-functional and global optimization study of copper–tin core-shell clusters	<b>1071</b>
<b>Nozomi Takagi, Andreas Krapp, and Gernot Frenking</b> On the nature of homo- and hetero-dinuclear metal–metal quadruple bonds — Analysis of the bonding situation and benchmarking DFT against wave function methods	<b>1079</b>
<b>Michael B. Burt, Angela K. Crane, Ning Su, Nicole Rice, and Raymond A. Poirier</b> Ring-chain equilibria of R-but-3-enoate esters — A quantum mechanical study of direct and indirect ring-closing reactions	<b>1094</b>
<b>Glenn I. Hawe and Paul L.A. Popelier</b> A water potential based on multipole moments trained by machine learning — Reducing maximum energy errors	<b>1104</b>
<b>William C. Everett, Bert E. Holmes, and George L. Heard</b> A computational study of the threshold energies of the 1,2-FCl interchange reaction of chlorofluoroethanes	<b>1112</b>

<b>Ian R. Pottie, Sheldon N. Crane, Anna Lee Gosse, David O. Miller, and D. Jean Burnell</b>	Geminal acylation of $\alpha$ -heterosubstituted cyclohexanones and their ketals	<b>1118</b>
<b>Friedrich Grein, Justin K. Chan, and Ildir Liko</b>	On the stabilization of the carbonate dianion by sulfur dioxide	<b>1125</b>
<b>John M.H. Lo, Robert A. Marriott, Binod R. Giri, John M. Roscoe, and Mariusz Klobukowski</b>	A theoretical analysis of the kinetics of the reaction of atomic bromine with tetrahydrofuran	<b>1136</b>
<b>Hui Li, Yongdong Liu, Wolfgang Jäger, Robert J. Le Roy, and Pierre-Nicholas Roy</b>	Theoretical study of the microwave spectrum of isotopologues of OCS-(He) <sub>2</sub>	<b>1146</b>
<b>Hong Liang, Micheline MacKay, T. Bruce Grindley, Katherine N. Robertson, and T. Stanley Cameron</b>	Configurations and conformations of glycosyl sulfoxides	<b>1154</b>
<b>Lei Zhang, Gilles H. Peslherbe, and Heidi M. Muchall</b>	A general measure of conjugation in biphenyls and their radical cations	<b>1175</b>
<b>Emmanuel Penka Fowe and André Dieter Bandrauk</b>	Nonlinear time-dependent density functional theory investigation and visualization of ionizations in CO <sub>2</sub> —Effects of laser intensities and molecular orientations	<b>1186</b>
<b>Nick H. Werstiuk</b>	The 9-barbaralyl and related C <sub>9</sub> H <sub>9</sub> <sup>+</sup> carbocations — A QTAIM-DI-VISAB computational study	<b>1195</b>

## December / Décembre

### ARTICLES / ARTICLES

<b>Yang Yong-Cun, Chi Shao-Ming, Liu Ming-Hua, Huang Rong, Wang Yu-Fei, Jing Bi, and Zhao Yan</b>	Spectrophotometric study of the selective binding behavior of aliphatic oligopeptides by bridged bis( $\beta$ -cyclodextrin) linked by a 4,4'-diaminodiphenyl disulfide tether	<b>1205</b>
<b>Preeti Chadha, Jason L. Dutton, and Paul J. Ragogna</b>	Synthesis and reactivity of bis-alkynyl appended metallocenes of Ti, Fe, and Co	<b>1213</b>
<b>Erik M. van Oosten, Alan A. Wilson, David C. Mamo, Bruce G. Pollock, Benoit H. Mulsant, Sylvain Houle, and Neil Vasdev</b>	Towards the development of new subtype-specific muscarinic receptor radiopharmaceuticals — Radiosynthesis and ex vivo biodistribution of [ <sup>18</sup> F]3-(4-(2-(2-(2-fluoroethoxy)ethoxy)ethylthio)-1,2,5-thiadiazol-3-yl)-1-methyl-1,2,5,6-tetrahydropyridine	<b>1222</b>
<b>Rajesh M. Kamble and M.M.V. Ramana</b>	Microwave-assisted Diels–Alder reaction of 1,3,3-trimethyl-2-vinyl-1-cyclohexene with chromones — An expeditious approach to analogues of the puerpene group of marine diterpenoids and kampanols	<b>1233</b>
<b>Dongdong Zhang, Xiuli Ren, and Lixin Zhou</b>	Theoretical analysis of <i>trans</i> -[PtCl <sub>2</sub> (NH <sub>3</sub> )(thiazole)] and <i>trans</i> -[PtCl <sub>2</sub> (thiazole) <sub>2</sub> ] binding to biological targets — Factors influence binding kinetics and adduct stability	<b>1240</b>
<b>Jeffrey L. Petersen, Adenike A. Otoikhian, Moshood K. Morakinyo, and Reuben H. Simoyi</b>	Organosulfur oxoacids. Part 2. A novel dimethylthiourea metabolite — Synthesis and characterization of the surprisingly stable and inert dimethylaminoiminomethane sulfonic acid	<b>1247</b>
<b>Guifang Sun, Faming Gao, and Li Hou</b>	Fabrication of boron carbonitride (BCN) nanotubes and giant fullerene cages	<b>1256</b>
<b>Javed R. Akbar, Rubena Deubry, D. Gerrard Marangoni, and Shawn D. Wettig</b>	Interactions between gemini and nonionic pharmaceutical surfactants	<b>1262</b>
<b>Monmi Saikia and Jadab C. Sarma</b>	Baylis–Hillman reaction under solvent-free conditions — Remarkable rate acceleration and yield enhancement	<b>1271</b>
<b>K. Adeppa, D.C. Rupainwar, and Krishna Misra</b>	An improved one-pot cost-effective synthesis of N,N-disubstituted carbamoyl halides and derivatives	<b>1277</b>

Author Index for Volume 88 / Index des auteurs pour le volume 88

**AI-1**

Contents for Volume 88 / Sommaire pour le volume 88

**C-1**



## NOTE OF APPRECIATION / NOTE DE RECONNAISSANCE

The success of the journal is dependent upon our reviewers. The Editors gratefully acknowledge the commitment and goodwill of all the reviewers who assisted us in the publication of Volume 88. Thank you.

Le succès du journal dépend du travail acharné de nos réviseurs. Le personnel de la rédaction est reconnaissant de leur volonté et leur nombreuses contributions qui ont rendu possible la sortie du volume 88. Merci.

Agnes, G.	Brown, E.	English, A.	Ihmels, H.
Alavi, S.	Brown, S.	English, D.	Ingold, K.U.
Alder, R.	Brückner, C.	Evans, C.	Inoue, Y.
Alderete, J.B.	Bryce, D.	Falvey, D.	Jalilehvand, F.
Alessio, E.	Bunce, N.	Farrell, J.	Janda, K.
Al-Hawari, J.	Buncel, E.	Feindel, K.	Jares-Erijman, E.
Alizadeh, A.	Burford, N.	Fernandes, F.M.S.S.	Jasti, R.
Alkorta, I.	Burgess, I.	Ferretti, V.	Jenks, W.
Amic, D.	Cai, Z.	Fogg, D.	Jestin, J.
Andersen, R.	Cameron, D.	Fontaine, F.-G.	Jha, A.
Anpo, M.	Capobianco, J.	Forgione, P.	Jirak, Z.
Aquino, M.	Carrington, T.	Fyles, T.	Jockusch, R.
Arana, J.	Chahma, M.	Gabryelski, W.	Johnson, D.
Armitage, B.	Chandra, A.	Gambarotti, C.	Johnston, L.
Arndtsen, B.	Charpentier, P.	Garden, S.J.	Jonah, C.
Arnold, B.	Chen, A.	Garson, M.	Jones, N.
Arslan, T.	Chen, W.	Gauld, J.	Jones, P.
Asfour, A.-F.	Chen, Y.	Gazquez, J.L.	Joule, J.
Ata, A.	Chirakal, R.	Geffroy, P.-M.	Juaristi, E.
Aznar, M.	Choi, P.	Georges, M.	Kabalka, G.
Badgujar, D.M.	Chretien, M.	Georghiou, P.	Kantevari, S.
Bailey, W.	Chu, S.	Gesquiere, A.	Karlsson, L.
Bain, A.	Clyburne, J.	Ghosh, A.K.	Kaszynski, P.
Bakshi, M.	Corma, A.	Giacomelli, G.	Kaymakcioglu, B.
Baldacchino, G.	Corrigan, J.	Gilson, D.	Kazmaier, U.
Bally, T.	Cosa, G.	Gmehling, J.	Keay, B.
Banskota, A.	Cote, A.	Goddard, J.	Kell, A.
Barra, M.	Cozens, F.	Gorelsky, S.	Kerkines, I.S.K.
Barrett, C.	Crich, D.	Gosselin, F.	Kerman, K.
Bassindale, A.	Crimmins, M.	Grant, D.	Kierzek, R.
Baumgartner, T.	Cunningham, M.	Gray, C.	Kimmel, G.
Beaudry, C.	Dake, G.	Grein, F.	King, B.
Beland, F.	DaSilveira Neto, B.	Gribble, G.	Kinnel, R.
Belanger, D.	Davies, A.	Grindley, B.	Kirihara, M.
Bélanger, G.	Davis, M.	Guan, J.	Kita, Y.
Berezhkovskii, A.	Dawood, K.	Gudmundsdottir, A.	Klan, P.
Berger, R.	Del Bene, J.	Guerchais, V.	Klassen, N.
Berges, J.	DeRosa, M.	Gupte, S.	Klimov, V.
Biehl, E.	Desai, U.	Guthrie, P.	Klobukowski, M.
Bietti, M.	Desaulniers, J.-P.	Hadad, C.	Kobayashi,
Billiot, E.	Desimoni, G.	Hall, M.	Koci, K.
Biris, A.	Desvergne, J.-P.	Hanan, G.	Koenig, B.
Blakemore, P.	DiLabio, G.	Hastie, D.	Koodali, R.
Blotny, G.	Ding, J.	Heerklotz, H.	Kordestani, D.
Bodwell, G.	Ding, Z.	Henni, A.	Kozlowski, M.
Bohle, S.	Dolphin, D.	Hicks, R.	Kozlowski, P.
Bohne, C.	Domb, A.	Hider, R.	Kraatz, H.-B.
Boukouvalas, J.	Dudding, T.	Hitchcock, S.	Kroeker, S.
Boulon, G.	Durig, J.	Hof, F.	Kryachko, E.
Boyd, R.	Durst, T.	Hofmann, H.J.	Laszlo, P.
Brennan, A.	Dust, J.	Holdcroft, S.	LaVerne, J.
Brennan, J.	Dykstra, T.	Hosmane, N.	Lavine, B.
Brindle, I.	East, A.	Hu, Y.H.	Le, C.
Brouwer, D.	Elmes, Y.	Hudson, R.	Lee, J.S.
Brown, A.	Elguero, J.	Hunter, R.	Lemaire, M.

- Lewis, L.  
Liang, L.-C.  
Lin, H.  
Liu, J.-H.  
Liu, Q.-Z.  
Liu, S.-Y.  
Liu, Y.  
Loboda, A.  
Loeb, S.  
Loppnow, G.  
Lorquet, J.C.  
Lowary, T.  
Luk, Y.-Y.  
Lukeman, M.  
Luzzio, F.  
Macartney, D.  
Macdonald, C.  
MacGillivray, L.  
MacKinnon, C.  
Magee, D.  
Mahwinney, R.  
Maly, K.  
Manby, F.  
Mancini, P.  
Mandy, M.  
Martell, J.  
Maryanoff, B.  
Masson, G.  
Mataa, R.  
Mather, A.  
Matter, P.  
Mauzeroll, J.  
Mayer, P.  
Mayoral, J.  
McCormick, C.  
McIndoe, J.S.  
McKellar, R.  
McMillin, D.R.  
McNulty, J.  
Mebel, A.M.  
Mendenhall, D.  
Meyer, G.  
Miranda, M.  
Montaut, S.  
Mosey, N.  
Mosquera, R.  
Moss, R.  
Mostafavi, M.  
Mountford, P.  
Moutet, J.-C.  
Muchall, H.  
Mueller, J.  
Munro, A.  
Murphy, S.  
Nair, V.  
Najafi Chermahini, Al.  
Narain, R.  
Negri, F.  
Nguyen, L.  
Nguyen, T.-T.  
Ojadi, E.  
Ollevier, T.  
Ooms, K.  
Oracz, P.  
Orlova, G.  
Ostaszewski, R.  
Ouellet, S.  
Paci, I.  
Paige, M.  
Pansare, S.  
Park, S.J.  
Parlar, H.  
Pedras, M.S.  
Pelton, R.  
Peng, S.  
Penner, Gl.  
Perez-Prieto, J.  
Pettus, T.  
Phukan, P.  
Pilkington, M.  
Pizzio, Lr.  
Platz, M.  
Plettner, E.  
Poirier, M.D.  
Poirier, R.  
Popik, V.  
Prakash, G.K.S.  
Puddephatt, R.  
Quemener, G.  
Quina, F.  
Quiros, M.  
Rabilloud, F.  
Ragot, S.  
Ratcliffe, C.  
Reber, C.  
Ren, Y.  
Ridley, T.  
Robens, E.  
Robert, S.  
Rokita, S.  
Rosenberg, L.  
Rovis, T.  
Roy, C.  
Roy, P.-N.  
Ruiz-Hitzky, E.  
Russell, C.  
Russo, N.  
Sakata, S.  
Salahub, D.  
Salehi, P.  
Salpin, J.-Y.  
Sammynaiken, R.  
Sander, W.  
Sano, K.  
Sartorel, A.  
Schafer, L.  
Schaper, F.  
Scheiner, S.  
Schepp, N.  
Schirrmacher, R.  
Schlegel, H.B.  
Schmitzer, A.  
Schreckenbach, G.  
Schwan, A.  
Scott, R.  
Seidel, D.  
Sammelhack, M.  
Senior, J.  
Sereno, L.  
Shepherd, J.  
Shi, Y.  
Shimizu, L.  
Silks, L.  
Singer, R.  
Singh, K.  
Singh, V.  
Sivaguru, J.  
Skene, W.  
Sobhani, S.  
Sodupe, M.  
Song, D.  
Spivak, G.  
Stanovnik, B.  
Staroverov, V.  
Steinmetz, M.  
Stephan, D.  
Steudel, R.  
Subramanian, V.  
Sun, X.  
Suresh, S.  
Swaddle, T.  
Taber, D.  
Talanova, G.  
Tam, W.  
Tanner, M.  
Tao, Y.  
Tasinato, N.  
Tertykh, V.  
Thakkar, A.  
Thompson, A.  
Tian, W.Q.  
Tidwell, T.  
Tieleman, P.  
Tossell, J.  
Tsoukanova, V.  
Tsuzuki, S.  
Turro, C.  
Turro, N.  
Tütem, E.  
Urgaonkar, S.  
Van Alsenoy, K.  
Van Gool, M.  
Vaughan, K.  
Velkov, Z.A.  
Vereecken, L.  
Vinas, C.  
von Herk, A.  
Wade, P.  
Wagner, B.  
Wagner, M.  
Walsby, C.  
Walsh, R.  
Walton, J.  
Wan, P.  
Wang, J.Y.  
Wang, X.-C.  
Wang, Y.-G.  
Wardlaw, D.  
Wei, Y.G.  
Werstiuk, N.  
West, F.  
Westwell, A.D.  
Wetmore, S.  
Williams, V.  
Wilson, A.  
Winnik, M.  
Wisner, J.  
Withers, S.  
Wolf, M.  
Wolkenberg, S.  
Woo, T.  
Workentin, M.  
Wosnick, J.  
Wren, C.  
Wu, Z.  
Wuts, P.  
Xantheas, S.  
Xia, M.  
Xu, L.  
Xu, Y.  
Yan, H.  
Yang, X.C.  
Yet, L.  
Yeung, K.  
Yoon, M.  
Young, R.  
Yu, B.  
Yue, C.  
Yuste, F.  
Zacharie, B.  
Zechel, D.  
Zgierski, M.Z.  
Zhang, J.  
Zhang, S.  
Zhang, Xin.  
Zhao, Y.  
Zhdankin, V.  
Ziegler, T.  
Zugenmaier, P.  
Zuman, P.

## ANNOUNCEMENT / COMMUNIQUÉ

### NRC Research Press transition to Canadian Science Publishing

As of 2 September 2010, the publishing operations of the National Research Council's NRC Research Press successfully transitioned out of the National Research Council (NRC) and Federal Government and into a new not-for-profit company operating under the new name of Canadian Science Publishing (CSP). This transition is the result of an NRC decision announced in February 2009 to proceed with a Federal Government of Canada Strategic Review recommendation to transfer the publishing operations to the private sector.

The new entity will continue to provide high-quality, peer-reviewed journals and publishing services. CSP is committed to publishing and providing services in English and French and will continue to support Canadian researchers and their communities in disseminating their research worldwide through the provision of world-class, advanced scientific and technical scholarly publishing services. Journals published by CSP will continue to use the "NRC Research Press" designation.

As a leader in the scientific and technical scholarly publishing community, CSP is committed to its NRC Research Press journal subscribers and would like to thank them for their ongoing support.

### Transition des Presses scientifiques du CNRC vers les Éditions Sciences Canada

Depuis le 2 septembre 2010, les opérations d'édition des Presses scientifiques du CNRC sont passées avec succès du Conseil national de recherches du Canada (CNRC) et du gouvernement fédéral à une nouvelle société sans but lucratif nommée Éditions Sciences Canada (ESC). Cette transition est le résultat de la décision du CNRC, annoncée en février 2009, de mettre à exécution une recommandation de l'examen stratégique du gouvernement fédéral, soit le transfert de ces opérations d'édition au secteur privé.

Cette nouvelle entité continuera à fournir des revues de grande qualité évaluées par les pairs et des services d'édition. Les ESC s'engagent à fournir des services d'édition en anglais et en français et à préserver la mission de son ancienne entité, à savoir d'aider les chercheurs canadiens et leur milieu à diffuser leurs travaux de recherche à travers le monde grâce à la fourniture de services canadiens d'édition savante scientifique et technique d'avant-garde et de niveau international. Les revues publiées par les ESC continueront d'utiliser l'appellation « NRC Research Press ».

En tant que chef de file du milieu de l'édition savante scientifique et technique, les ESC sont dévouées envers les abonnés de leurs revues de NRC Research Press et les remercient de leur appui continu.